DIAGNOSTIC ULTRASOUND

5TH EDITION

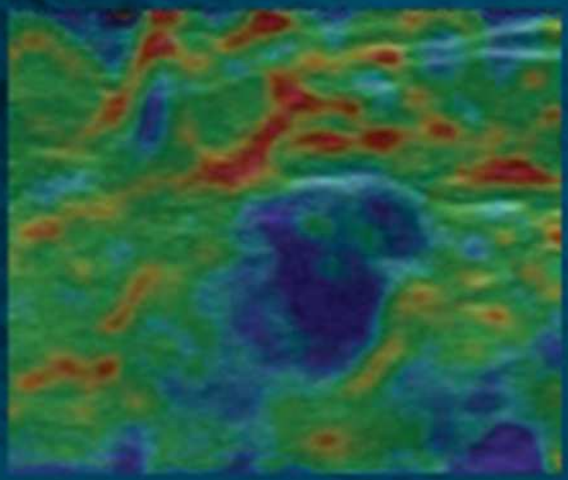
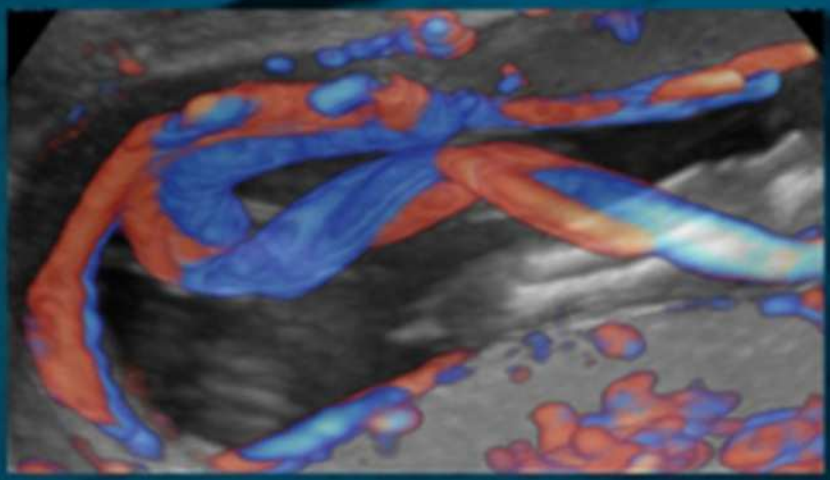

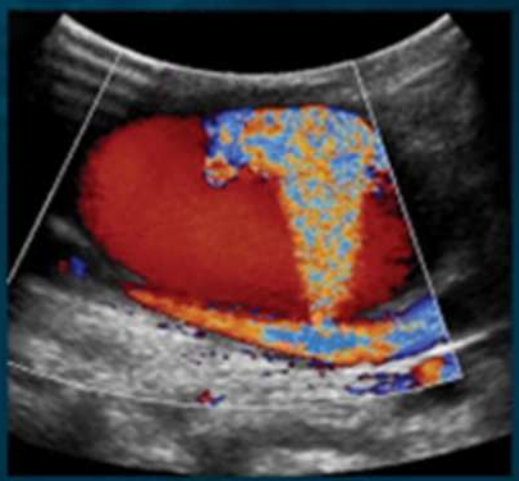

CAROL M. RUMACK

DEBORAH LEVINE

ELSEVIER

Expert CONSULT Built with inkling | E books

Any screen. Any time. Anywhere.

Activate the eBook version of this title at no additional charge.

Expert Consult eBooks give you the power to browse and find content, view enhanced images, share notes and highlights—both online and offline.

Unlock your eBook today.

1. Visit **expertconsult.inkling.com/redeem**
2. Scratch off your code
3. Type code into "Enter Code" box
4. Click "Redeem"
5. Log in or Sign up
6. Go to "My Library"

It's that easy!

Scan this QR code to redeem your eBook through your mobile device:

Place Peel Off Sticker Here

For technical assistance:
email expertconsult.help@elsevier.com
call 1-800-401-9962 (inside the US)
call +1-314-447-8200 (outside the US)

ELSEVIER

Use of the current edition of the electronic version of this book (eBook) is subject to the terms of the nontransferable, limited license granted on expertconsult.inkling.com. Access to the eBook is limited to the first individual who redeems the PIN, located on the inside cover of this book, at expertconsult.inkling.com and may not be transferred to another party by resale, lending, or other means.

2015v1.0

DIAGNOSTIC ULTRASOUND

This page intentionally left blank

DIAGNOSTIC ULTRASOUND

5TH EDITION

CAROL M. RUMACK, MD, FACR
Vice Chair of Education and Professional Development
Professor of Radiology and Pediatrics
Associate Dean for GME
University of Colorado School of Medicine
Denver, Colorado

DEBORAH LEVINE, MD, FACR
Co-Chief of Ultrasound
Director of OB/Gyn Ultrasound
Vice Chair of Academic Affairs
Department of Radiology
Beth Israel Deaconess Medical Center
Professor of Radiology
Harvard Medical School
Boston, Massachusetts

ELSEVIER

ELSEVIER

1600 John F. Kennedy Blvd.
Ste 1800
Philadelphia, PA 19103-2899

DIAGNOSTIC ULTRASOUND, FIFTH EDITION ISBN: 978-0-323-40171-5

Copyright © 2018 by Elsevier, Inc. All rights reserved.

Chapter 32: Mary C. Frates retains copyright for the original figures appearing in the chapter.
Chapter 42: Carol B. Benson and Peter M. Doubilet retain copyright for their original figures appearing in the chapter.

No part of this publication may be reproduced or transmitted in any form or by any means, electronic or mechanical, including photocopying, recording, or any information storage and retrieval system, without permission in writing from the publisher. Details on how to seek permission, further information about the Publisher's permissions policies and our arrangements with organizations such as the Copyright Clearance Center and the Copyright Licensing Agency, can be found at our website: www.elsevier.com/permissions.

This book and the individual contributions contained in it are protected under copyright by the Publisher (other than as may be noted herein).

Notices

Knowledge and best practice in this field are constantly changing. As new research and experience broaden our understanding, changes in research methods, professional practices, or medical treatment may become necessary.

Practitioners and researchers must always rely on their own experience and knowledge in evaluating and using any information, methods, compounds, or experiments described herein. In using such information or methods they should be mindful of their own safety and the safety of others, including parties for whom they have a professional responsibility.

With respect to any drug or pharmaceutical products identified, readers are advised to check the most current information provided (i) on procedures featured or (ii) by the manufacturer of each product to be administered, to verify the recommended dose or formula, the method and duration of administration, and contraindications. It is the responsibility of practitioners, relying on their own experience and knowledge of their patients, to make diagnoses, to determine dosages and the best treatment for each individual patient, and to take all appropriate safety precautions.

To the fullest extent of the law, neither the Publisher nor the authors, contributors, or editors, assume any liability for any injury and/or damage to persons or property as a matter of products liability, negligence or otherwise, or from any use or operation of any methods, products, instructions, or ideas contained in the material herein.

Previous editions copyrighted 2011, 2005, 1998, and 1993.

Library of Congress Cataloging-in-Publication Data

Names: Rumack, Carol M., editor. | Levine, Deborah, 1962- editor.
Title: Diagnostic ultrasound / [edited by] Carol M. Rumack, Deborah Levine.
Other titles: Diagnostic ultrasound (Rumack)
Description: 5th edition. | Philadelphia, PA : Elsevier, [2018] | Includes bibliographical references and index.
Identifiers: LCCN 2017019887 | ISBN 9780323401715 (hardcover : alk. paper)
Subjects: | MESH: Ultrasonography
Classification: LCC RC78.7.U4 | NLM WN 208 | DDC 616.07/543–dc23
LC record available at https://lccn.loc.gov/2017019887

Executive Content Strategist: Robin Carter
Senior Content Development: Manager: Taylor Ball
Publishing Services Manager: Catherine Jackson
Senior Project Manager: Daniel Fitzgerald
Design Manager: Amy Buxton
Illustrations Manager: Nichole Beard

Printed in China.

Last digit is the print number: 9 8 7 6 5 4 3 2 1

ELSEVIER Book Aid International Working together to grow libraries in developing countries
www.elsevier.com • www.bookaid.org

ABOUT THE EDITORS

Carol M. Rumack, MD, FACR, is Professor of Radiology and Pediatrics at the University of Colorado School of Medicine in Denver, Colorado. Her clinical practice is based at the University of Colorado Hospital. Her primary research has been in neonatal sonography of high-risk infants, particularly the brain, on which she has published and lectured widely. She is a Fellow, previous Chair of the Ultrasound Commission, past president of the American College of Radiology, and American Association for Women Radiologists, and a Fellow of both the American Institute of Ultrasound in Medicine and the Society of Radiologists in Ultrasound. She and her husband, Barry, have two children, Becky and Marc, and five grandchildren.

Deborah Levine, MD, FACR, is Professor of Radiology at Beth Israel Deaconess Medical Center, Boston, and Harvard Medical School. At Beth Israel Deaconess Medical Center she is Vice Chair of Academic Affairs of the Department of Radiology, Co-Chief of Ultrasound, and Director of Ob/Gyn Ultrasound. Her main areas of clinical and research interest are obstetric and gynecologic imaging. She is a Fellow and past Vice President of the American College of Radiology and a Fellow (and 2016-2017 President) of the Society of Radiologists in Ultrasound. She and her husband, Alex, have two children, Becky and Julie.

This page intentionally left blank

CONTRIBUTORS

Jacques S. Abramowicz, MD, FACOG, FAIUM
Professor and Director
Ultrasound Services Department of Obstetrics and Gynecology University of Chicago
Chicago, Illinois
United States

Ronald S. Adler, MD, PhD
Professor of Radiology
New York University School of Medicine
Department of Radiology
NYU Langone Medical Center
New York, New York
United States

Allison Aguado, MD
Assistant Professor
Department of Radiology
Cincinnati Children's Hospital Medical Center
Cincinnati, Ohio
United States

Rochelle Filker Andreotti, MD
Professor of Clinical Radiology
Associate Professor of Clinical Obstetrics and Gynecology
Department of Radiology and Radiological Sciences
Vanderbilt University
Nashville, Tennessee
United States

Elizabeth Asch, MD
Instructor in Radiology
Harvard Medical School
Brigham and Women's Hospital
Boston, Massachusetts
United States

Thomas D. Atwell, MD
Professor of Radiology
Department of Radiology
Mayo Clinic
Rochester, Minnesota
United States

Amanda K. Auckland, BS, RT(R), RDMS, RVT, RDCS
Diagnostic Medical Sonographer
Division of Ultrasound/Prenatal Diagnosis and Genetics
University of Colorado Hospital
Aurora, Colorado
United States

Diane S. Babcock, MD
Professor Emerita of Radiology and Pediatrics
University of Cincinnati College of Medicine
Cincinnati Children's Hospital Medical Center
Cincinnati, Ohio
United States

Beryl Benacerraf, MD
Clinical Professor of Obstetrics and Gynecology and Radiology
Brigham and Women's Hospital
Clinical Professor of Obstetrics and Gynecology
Massachusetts General Hospital
Harvard Medical School
Boston, Massachusetts
United States

Carol B. Benson, MD
Professor of Radiology
Harvard Medical School
Director of Ultrasound and Co-Director of High Risk Obstetrical Ultrasound
Department of Radiology
Brigham and Women's Hospital
Boston, Massachusetts
United States

Raymond E. Bertino, MD, FACR, FSRU
Medical Director of Vascular and General Ultrasound
OSF Saint Francis Medical Center
Clinical Professor of Radiology and Surgery
University of Illinois College of Medicine
Peoria, Illinois
United States

Edward I. Bluth, MD, FACR, FSRU
Chairman Emeritus
Ochsner Clinic Foundation
Professor
Ochsner Clinical School
University of Queensland, School of Medicine
New Orleans, Louisiana
United States

Bryann Bromley, MD
Professor of Obstetrics, Gynecology and Reproductive Biology, part time
Harvard Medical School
Department of Obstetrics and Gynecology
Massachusetts General Hospital
Brigham and Women's Hospital
Boston, Massachusetts
United States

Olga R. Brook, **MD**
Assistant Professor
Harvard Medical School
Associate Director of CT
Department of Radiology
Beth Israel Deaconess Medical Center
Boston, Massachusetts
United States

Douglas Brown, **MD**
Professor of Radiology
Department of Radiology
Mayo Clinic College of Medicine and Science
Rochester, Minnesota
United States

Dorothy Bulas, **MD**
Professor of Pediatrics and Radiology
George Washington University Medical Center
Pediatric Radiologist
Children's National Health Systems
Washington DC
United States

Peter N. Burns, **PhD**
Professor and Chairman
Department of Medical Biophysics
University of Toronto
Senior Scientist, Imaging Research
Sunnybrook Research Institute
Toronto, Ontario
Canada

Vito Cantisani, **MD, PhD**
Department of Radiologic, Oncologic and Pathologic Sciences
Policlinic Umberto I
Sapienza University
Rome
Italy

Ilse Castro-Aragon, **MD**
Assistant Professor of Radiology
Boston University School of Medicine
Section Head, Pediatric Radiology
Boston Medical Center
Boston, Massachusetts
United States

J. William Charboneau, **MD**
Emeritus Professor of Radiology
Department of Radiology
Mayo Clinic
Rochester, Minnesota
United States

Humaira Chaudhry, **MD**
Section Chief, Abdominal Imaging
Assistant Professor
Department of Radiology
Rutgers-New Jersey Medical School
Newark, NJ
United States

Tanya Punita Chawla, **MBBS, FRCR, MRCP, FRCPC**
Assistant Professor and Staff Radiologist
Joint Department of Medical Imaging
University of Toronto
Toronto, Ontario
Canada

Christina Marie Chingkoe, **MD**
Department of Radiology
Beth Israel Deaconess Medical Center
Boston, Massachusetts
United States

David Chitayat, **MD**
Professor
Department of Pediatrics, Obstetrics and Gynecology, Molecular Genetics and Laboratory Medicine and Pathobiology
Medical Director
The MSc program in Genetic Counselling, Department of Molecular Genetics
University of Toronto
Head
The Prenatal Diagnosis and Medical Genetics Program
Mount Sinai Hospital
Staff
Pediatrics, Division of Clinical and Metabolic Genetics
Hospital for Sickkids
Toronto, Ontario
Canada

Peter L. Cooperberg, **OBC, MDCM, FRCP(C), FACR**
Professor Emeritus
Department of Radiology
University of British Columbia
Vancouver, British Columbia
Canada

Lori A. Deitte, **MD, FACR**
Vice Chair of Education and Professor
Department of Radiology and Radiological Sciences
Vanderbilt University
Nashville, Tennessee
United States

Peter M. Doubilet, MD, PhD
Professor of Radiology
Harvard Medical School
Senior Vice Chair
Department of Radiology
Brigham and Women's Hospital
Boston, Massachusetts
United States

Julia A. Drose, RDMS, RDCS, RVT
Associate Professor
Department of Radiology
University of Colorado Hospital
Aurora, Colorado
United States

Alexia Egloff, MD
Diagnostic Imaging and Radiology
Children's National Health Systems
Washington DC
United States

Judy A. Estroff, MD
Instructor
Boston University School of Medicine
Department of Radiology
Boston Children's Hospital
Boston, Massachusetts
United States

Katherine W. Fong, MBBS, FRCPC
Associate Professor
Medical Imaging and Obstetrics and Gynecology
University of Toronto
Co-director, Centre of Excellence in Obstetric Ultrasound
Mount Sinai Hospital
Toronto, Ontario
Canada

J. Brian Fowlkes, PhD
Professor
Department of Radiology
University of Michigan
Ann Arbor, Michigan
United States

Mary C. Frates, MD
Associate Professor of Radiology
Department of Radiology
Harvard Medical School
Brigham and Women's Hospital
Boston, Massachusetts
United States

Hournaz Ghandehari, MD, FRCPC
Department of Medical Imaging
Abdominal Division
University of Toronto
Sunnybrook Health Sciences Centre
Toronto, Ontario
Canada

Phyllis Glanc, MDCM
Associate Professor
University of Toronto
Department Medical Imaging, Obstetric & Gynecology
Sunnybrook Health Sciences Centre
Toronto, Ontario
Canada

S. Bruce Greenberg, MD
Professor of Radiology and Pediatrics
Department of Radiology
University of Arkansas for Medical Sciences
Little Rock, Arkansas
United States

Leslie E. Grissom, MD
Clinical Professor of Radiology and Pediatrics
Department of Radiology
Sidney Kimmel Medical College at Thomas Jefferson University
Philadelphia, Pennsylvania
Attending Radiologist
Department of Medical Imaging
Nemours Alfred I. duPont Hospital for Children
Wilmington, Delaware
United States

Anthony E. Hanbidge, MB, BCh, FRCPC
Associate Professor
Department of Medical Imaging
University of Toronto
Site Director, Abdominal Imaging
Toronto Western Hospital
Joint Department of Medical Imaging
University Health Network, Mount Sinai Hospital and Women's College Hospital
Toronto, Ontario
Canada

H. Theodore Harcke, MD, FACR, FAIUM
Sidney Kimmel Medical College at Thomas Jefferson University
Chairman, Emeritus
Department of Medical Imaging
Nemours/A I duPont Hospital for Children
Wilmington, Delaware
United States

Christy K. Holland, **PhD**
Scientific Director of the Heart, Lung, and Vascular Institute
Professor
Department of Internal Medicine
Division of Cardiovascular Health and Disease
University of Cincinnati
Cincinnati, Ohio
United States

Thierry A.G.M. Huisman, **MD**
Professor of Radiology, Pediatrics, Neurology, and Neurosurgery
Director Pediatric Radiology and Pediatric Neuroradiology
Russell H. Morgan Department of Radiology and Radiological Science
The Johns Hopkins University School of Medicine
Baltimore, Maryland
United States

Bonnie J. Huppert, **MD**
Assistant Professor of Radiology
Consultant in Radiology
Department of Radiology
Mayo Clinic
Rochester, Minnesota
United States

Alexander Jesurum, PhD
Weston, Massachusetts
United States

Susan D. John, **MD**
Professor and Chair
Department of Diagnostic and Interventional Imaging
University of Texas Medical School Houston
Houston, Texas
United States

Neil Johnson, **MBBS, FRANZCR, MMed**
Professor
Department of Radiology and Pediatrics
Cincinnati Children's Hospital Medical Center
Cincinnati, Ohio
United States

Stephen I. Johnson, **MD**
Staff Radiologist
Department of Radiology
Ochsner Clinic Foundation
New Orleans, Louisiana
United States

Anne Kennedy, **MB, BCh**
Vice Chair Clinical Operations
Department of Radiology
University of Utah
Salt Lake City, Utah
United States

Julia Eva Kfouri, **BSc, MD, FRCSC-MFM**
Clinical Associate
Division of Maternal Fetal Medicine
Department of Obstetrics and Gynecology
Mount Sinai Hospital
Toronto, Ontario
Canada

Korosh Khalili, **MD, FRCPC**
Associate Professor
Department of Medical Imaging
University of Toronto
University Health Network
Princess Margaret Hospital
Toronto, Ontario
Canada

Beth M. Kline-Fath, **MD**
Professor of Radiology
Department of Radiology
Cincinnati Children's Hospital Medical Center
Cincinnati, Ohio
United States

Elizabeth Lazarus, **MD**
Associate Professor
Department of Diagnostic Imaging
Warren Alpert Medical School of Brown University
Providence, Rhode Island
United States

Deborah Levine, **MD, FACR**
Co-Chief of Ultrasound
Director of OB/Gyn Ultrasound
Vice Chair of Academic Affairs
Department of Radiology
Beth Israel Deaconess Medical Center
Professor of Radiology
Harvard Medical School
Boston, Massachusetts
United States

Mark E. Lockhart, **MD, MPH**
Professor of Radiology and Chief, Body Imaging
Department of Radiology
University of Alabama at Birmingham
Birmingham, Alabama
United States

Ana P. Lourenco, **MD**
Associate Professor of Diagnostic Imaging
Diagnostic Imaging
Alpert Medical School of Brown University
Providence, Rhode Island
United States

Martha Mappus Munden, **MD**
Associate Professor of Radiology
Department of Pediatric Radiology
Texas Children's Hospital
Houston, Texas
United States

John R. Mathieson, **MD**
Clinical Associate Professor
University of British Columbia
Vancouver, British Columbia
Medical Director and Department Head
Vancouver Island Health Authority
Victoria, British Columbia
Canada

Giovanni Mauri, **MD**
Division of Interventional Radiology
European Institute of Oncology
Milan
Italy

Colm McMahon, **MB, BAO, BCh, MRCPI, FFR(RCSI)**
Assistant Professor
Department of Radiology
Harvard Medical School
Beth Israel Deaconess Medical Center
Brookline, Massachusetts
United States

Rashmi J. Mehta, **MD, MBA**
Clinical Radiology Fellow
Department of Radiology
Beth Israel Deaconess Medical Center
Boston, Massachusetts
United States

Nir Melamed, **MD, MSc**
Associate Professor
Department of Obstetrics and Gynecology
University of Toronto
Sunnybrook Health Sciences Center
Toronto, Ontario
Canada

Christopher R.B. Merritt, **MD**
New Orleans, Louisiana
United States

Derek Muradali, **MD, FRCPC**
Associate Professor and Staff Radiologist
Department of Medical Imaging
St Michaels Hospital
University of Toronto
Toronto, Ontario
Canada

Elton Mustafaraj, **DO**
Resident, Department of Radiology
University of Illinois College of Medicine
Peoria, Illinois
United States

Lisa Napolitano, **RDMS**
Department of Radiology
Beth Israel Deaconess Medical Center
Boston, Massachusetts
United States

Sara M. O'Hara, **MD**
Professor of Radiology & Pediatrics
Department of Radiology
Cincinnati Children's Hospital
Cincinnati, Ohio
United States

Harriet J. Paltiel, **MDCM**
Associate Professor of Radiology
Harvard Medical School
Department of Radiology
Boston Children's Hospital
Boston, Massachusetts
United States

Jordana Phillips, **MD**
Department of Radiology
Beth Israel Deaconess Medical Center
Boston, Massachusetts
United States

Andrea Poretti, **MD**
Assistant Professor of Radiology
Section of Pediatric Neuroradiology
Division of Pediatric Radiology
Russell H. Morgan Department of Radiology and Radiological Science
The Johns Hopkins University School of Medicine
Baltimore, Maryland
United States

Theodora A. Potretzke, **MD**
Assistant Professor
Department of Radiology
Mayo Clinic
Rochester, Minnesota
United States

Rupa Radhakrishnan, **MBBS**
Assistant Professor
Department of Radiology
Cincinnati Children's Hospital Medical Center
Cincinnati, Ohio
United States

Carl Reading, **MD**
Professor of Radiology
Department of Radiology
Mayo Clinic
Rochester, Minnesota
United States

Michelle L. Robbin, **MD, MS**
Professor of Radiology and Biomedical Engineering
Department of Radiology
University of Alabama at Birmingham
Birmingham, Alabama
United States

Henrietta Kotlus Rosenberg, **MD**
Radiologist-in-Chief
Kravis Children's Hospital at Mount Sinai
Director of Pediatric Radiology
Department of Radiology
Mount Sinai Hospital
Professor of Radiology and Pediatrics
Icahn School of Medicine at Mount Sinai
New York, New York
United States

Carol M. Rumack, **MD, FACR**
Vice Chair of Education and Professional Development
Professor of Radiology and Pediatrics
Associate Dean for GME
University of Colorado School of Medicine
Denver, Colorado
United States

Eric Sauerbrei, **BSc, MSc, MD, FRCPC**
Professor of Radiology
Diagnostic Imaging
Queens University
Kingston, Ontario
Canada

Chetan Chandulal Shah, **MD, MBA**
Faculty, Department of Radiology
Mayo Clinic
Pediatric Radiologist
Department of Pediatric Radiology
Nemours
Wolfson Children's Hospital
Jacksonville, Florida
United States

Thomas D. Shipp, **MD**
Associate Professor of Obstetrics, Gynecology & Reproductive Biology
Harvard Medical School
Department of Obstetrics & Gynecology
Brigham & Women's Hospital
Boston, Massachusetts
United States

William L. Simpson, **Jr.**, **MD**
Associate Professor
Department of Radiology
Icahn School of Medicine at Mount Sinai
New York, New York
United States

Luigi Solbiati, **MD**
Professor of Radiology
Department of Radiology
Humanitas University and Research Hospital
Rozzano (Milan)
Italy

Daniel Sommers, **MD**
Associate Professor
Department of Radiology
University of Utah
Salt Lake City, Utah
United States

Elizabeth R. Stamm, **MD**
Associate Professor
Department of Radiology
University of Colorado Hospital
Aurora, Colorado
United States

A. Thomas Stavros, **MD, FACR**
Medical Director
Ultrasound Invision
Sally Jobe Breast Center
Englewood, Colorado
United States

Maryellen R.M. Sun, **MD**
Department of Radiology
Lowell General Hospital
Lowell, Massachusetts
United States

Wendy Thurston, MD
Assistant Professor
Department of Medical Imaging
University of Toronto
Chief, Diagnostic Imaging
Department of Diagnostic Imaging
St. Joseph's Health Centre
Courtesy Staff
Department of Medical Imaging
University Health Network
Toronto, Ontario
Canada

Ants Toi, MD, FRCPC, FAIUM
Professor of Radiology and of Obstetrics and Gynecology
University of Toronto
Radiologist
Medical Imaging
Mt. Sinai Hospital
Toronto, Ontario
Canada

Laurie Troxclair, BS, RDMS, RVT
Ochsner Clinic Foundation
New Orleans, Louisiana
United States

Mitchell Tublin, MD
Professor and Vice Chair
Department of Radiology
University of Pittsburgh School of Medicine
Pittsburgh, Pennsylvania
United States

Heidi R. Umphrey, MD, MS
Associate Professor of Radiology
Department of Radiology
University of Alabama at Birmingham
Birmingham, Alabama
United States

Sheila Unger, MD
University of Lausanne
Lausanne
Switzerland

Patrick M. Vos, MD
Clinical Assistant Professor
Department of Radiology
University of British Columbia
Vancouver, British Columbia
Canada

Therese M. Weber, MD, MS
Professor of Radiology
Department of Radiology
University of Alabama at Birmingham
Birmingham, Alabama
United States

Kirsten L. Weind Matthews, PhD, MBBS, FRCPC
Lecturer, Medical Imaging
University of Toronto
Department of Medical Imaging
Mount Sinai Hospital
Toronto, Ontario
Canada

Stephanie R. Wilson, MD
Clinical Professor
Department of Radiology
Department of Medicine, Division of Gastroenterology
University of Calgary
Calgary, Alberta
Canada

Thomas Winter, MD
Professor and Chief of Abdominal Imaging
Department of Radiology
University of Utah
Salt Lake City, Utah
United States

Cynthia E. Withers, MD
Radiologist (retired)
Sansum Clinic and Santa Barbara Cottage Hospital
Santa Barbara, California
United States

Corrie Yablon, MD
Assistant Professor
Department of Radiology
University of Michigan
Ann Arbor, Michigan
United States

Hojun Yu, MD
Radiologist
Department of Diagnostic Imaging
Queen Elizabeth II Hospital
Grande Prairie, Alberta
Canada

This page intentionally left blank

In memory of my parents, Drs. Ruth and Raymond Masters, who encouraged me to enjoy the intellectual challenge of medicine and the love of making a difference in patients' lives.
Carol M. Rumack

To Alex, Becky, and Julie—your love and support made this work possible.
Debbie Levine

This page intentionally left blank

PREFACE

The fifth edition of *Diagnostic Ultrasound* is a major revision. Previous editions have been very well accepted as reference textbooks and have been the most commonly used reference in ultrasound education and practices worldwide. The text and references have all been updated and are now all available online. We are pleased to provide over 2500 new/revised images (with over 5800 images total) and over 380 new videos (with 480 total videos). The display of real-time ultrasound has helped to capture those abnormalities that require a sweep through the pathology to truly appreciate the lesion as well. Daily we find that cine or video clips show important areas between still images that help to make certain a diagnosis or relationships between lesions. Now we rarely need to go back to reevaluate a lesion with another scan, making patient imaging more efficient. Another new offering in this textbook is a completely online "virtual" chapter on artifacts. PowerPoint videos explain many of the artifacts that are linked to images and videos in the text.

The fifth edition was a major change for our editorial team, as we said a fond farewell to Stephanie Wilson and Bill Charboneau. Their expertise is still felt in this edition, as they have contributed chapters on gastrointestinal ultrasound (liver, biliary tree, and gastrointestinal tract, which are all some of Stephanie's passions) and thyroid and interventional ultrasound (just some of Bill's areas of expertise).

Nearly 100 outstanding new and continuing authors have contributed to this edition, and all are recognized experts in the field of ultrasound. As in prior editions, we have emphasized the use of collages to show many examples of similar anatomy and pathology. These images reflect the spectrum of sonographic changes that may occur in a given disease, instead of the most common manifestation only.

The book's format has been redesigned with key points in addition to the outline at the beginning of each chapter. There are again colored boxes to highlight the important or critical features of sonographic diagnoses. Key terms and concepts are emphasized in boldface type. To direct the readers to other research and literature of interest, comprehensive reference lists are provided.

Diagnostic Ultrasound is again divided into two volumes. Volume I consists of Parts I to III. Part I contains chapters on physics and biologic effects of ultrasound and includes descriptions of elastography and contrast agents. Part II covers abdominal sonography and includes two completely revised chapters on pelvic sonography, along with chapters on interventional procedures (including those in the thorax) and organ transplantation. Part III presents small parts imaging, including thyroid, breast, scrotum, carotid, a completely revised chapter on imaging of the extracranial vessels, and two completely revised musculoskeletal imaging chapters, as well as an updated chapter on musculoskeletal intervention.

Volume II begins with Part IV, with obstetric ultrasound, which has important updates in first-trimester scanning and screening for aneuploidy including cell-free DNA. Part V comprehensively covers pediatric sonography, including pediatric interventional sonography. Completely revised chapters on the pediatric spinal canal and pediatric kidney are replete with new images and scanning techniques.

Diagnostic Ultrasound is for practicing physicians, residents, medical students, sonographers, and others interested in understanding the vast applications of diagnostic sonography in patient care. Our goal is for *Diagnostic Ultrasound* to continue to be the most comprehensive reference book available in the sonographic literature, with a highly readable style and superb images.

Carol M. Rumack, MD, FACR
Deborah Levine, MD, FACR

This page intentionally left blank

ACKNOWLEDGMENTS

We wish to express our deepest appreciation and sincerest gratitude:

To all of our outstanding authors, who have contributed extensive, newly updated, and authoritative text and images and videos. We cannot thank them enough for their efforts on this project.

To Alexander Jesurum, PhD, whose outstanding efforts kept the references updated for all of our authors and who helped in author contact and communication.

To Lisa Napolitano, RDMS, who spent hours finding and cropping videos to supplement our online edition.

To Robin Carter, Executive Content Strategist at Elsevier, who has worked closely with us on this project from the very beginning of the fifth edition.

To Taylor Ball and Dan Fitzgerald at Elsevier, who kept us on track for the process of updating and copyediting the entire manuscript.

It has been an intense year for everyone, and we are very proud of this superb edition of *Diagnostic Ultrasound.*

This page intentionally left blank

CONTENTS

VOLUME I

PART I Physics

1 **Physics of Ultrasound,** 1
Christopher R.B. Merritt

2 **Biologic Effects and Safety,** 34
J. Brian Fowlkes and Christy K. Holland

3 **Contrast Agents for Ultrasound,** 53
Peter N. Burns

PART II Abdominal and Pelvic Sonography

4 **The Liver,** 74
Stephanie R. Wilson and Cynthia E. Withers

5 **The Spleen,** 139
Patrick M. Vos, John R. Mathieson, and Peter L. Cooperberg

6 **The Biliary Tree and Gallbladder,** 165
Korosh Khalili and Stephanie R. Wilson

7 **The Pancreas,** 210
Thomas Winter and Maryellen R.M. Sun

8 **The Gastrointestinal Tract,** 256
Stephanie R. Wilson

9 **The Kidney and Urinary Tract,** 310
Mitchell Tublin, Deborah Levine, Wendy Thurston, and Stephanie R. Wilson

10 **The Prostate and Transrectal Ultrasound,** 381
Ants Toi

11 **The Adrenal Glands,** 416
Christina Marie Chingkoe, Olga R. Brook, and Deborah Levine

12 **The Retroperitoneum,** 432
Raymond E. Bertino and Elton Mustafaraj

13 **Dynamic Ultrasound of Hernias of the Groin and Anterior Abdominal Wall,** 470
Deborah Levine, Lisa Napolitano, and A. Thomas Stavros

14 **The Peritoneum,** 504
Anthony E. Hanbidge, Korosh Khalili, and Stephanie R. Wilson

15 **The Uterus,** 528
Douglas Brown and Deborah Levine

16 **The Adnexa,** 564
Rochelle Filker Andreotti and Lori A. Deitte

17 **Ultrasound-Guided Biopsy of Chest, Abdomen, and Pelvis,** 597
Theodora A. Potretzke, Thomas D. Atwell, J. William Charboneau, and Carl Reading

18 **Organ Transplantation,** 623
Derek Muradali and Tanya Punita Chawla

PART III Small Parts, Carotid Artery, and Peripheral Vessel Sonography

19 **The Thyroid Gland,** 691
Luigi Solbiati, J. William Charboneau, Vito Cantisani, Carl Reading, and Giovanni Mauri

20 **The Parathyroid Glands,** 732
Bonnie J. Huppert and Carl Reading

21 **The Breast,** 759
Jordana Phillips, Rashmi J. Mehta, and A. Thomas Stavros

22 **The Scrotum,** 818
Daniel Sommers and Thomas Winter

23 **Overview of Musculoskeletal Ultrasound Techniques and Applications,** 856
Colm McMahon and Corrie Yablon

24 **The Shoulder,** 877
Colm McMahon and Corrie Yablon

25 **Musculoskeletal Interventions,** 898
Ronald S. Adler

26 **The Extracranial Cerebral Vessels,** 915
Edward I. Bluth, Stephen I. Johnson, and Laurie Troxclair

27 **Peripheral Vessels,** 964
Mark E. Lockhart, Heidi R. Umphrey, Therese M. Weber, and Michelle L. Robbin

VOLUME II

PART IV Obstetric and Fetal Sonography

28 **Overview of Obstetric Imaging,** 1015
Deborah Levine

29 **Bioeffects and Safety of Ultrasound in Obstetrics,** 1034
Jacques S. Abramowicz

30 **The First Trimester,** 1048
Elizabeth Lazarus and Deborah Levine

31 **Chromosomal Abnormalities,** 1088
Bryann Bromley and Beryl Benacerraf

32 **Multifetal Pregnancy,** 1115
Mary C. Frates

33 **The Fetal Face and Neck,** 1133
Ana P. Lourenco and Judy A. Estroff

34 **The Fetal Brain,** 1166
Ants Toi and Deborah Levine

35 **The Fetal Spine,** 1216
Elizabeth Asch and Eric Sauerbrei

36 **The Fetal Chest,** 1243
Dorothy Bulas

37 **The Fetal Heart,** 1270
Elizabeth R. Stamm and Julia A. Drose

38 **The Fetal Gastrointestinal Tract and Abdominal Wall,** 1304
Nir Melamed, Anne Kennedy, and Phyllis Glanc

39 **The Fetal Urogenital Tract,** 1336
Katherine W. Fong, Julia Eva Kfouri, and Kirsten L. Weind Matthews

40 **The Fetal Musculoskeletal System,** 1376
Phyllis Glanc, David Chitayat, and Sheila Unger

41 **Fetal Hydrops,** 1412
Deborah Levine

42 **Fetal Measurements: Normal and Abnormal Fetal Growth and Assessment of Fetal Well-Being,** 1443
Carol B. Benson and Peter M. Doubilet

43 **Sonographic Evaluation of the Placenta,** 1465
Thomas D. Shipp

44 **Cervical Ultrasound and Preterm Birth,** 1495
Hournaz Ghandehari and Phyllis Glanc

PART V Pediatric Sonography

45 **Neonatal and Infant Brain Imaging,** 1511
Carol M. Rumack and Amanda K. Auckland

46 **Duplex Sonography of the Neonatal and Infant Brain,** 1573
Thierry A.G.M. Huisman and Andrea Poretti

47 **Doppler Sonography of the Brain in Children,** 1591
Dorothy Bulas and Alexia Egloff

48 **The Pediatric Head and Neck,** 1628
Rupa Radhakrishnan and Beth M. Kline-Fath

49 **The Pediatric Spinal Canal,** 1672
Ilse Castro-Aragon, Deborah Levine, and Carol M. Rumack

50 **The Pediatric Chest,** 1701
Chetan Chandulal Shah and S. Bruce Greenberg

51 **The Pediatric Liver and Spleen,** 1730
Sara M. O'Hara

52 **The Pediatric Urinary Tract and Adrenal Glands,** 1775
Harriet J. Paltiel and Diane S. Babcock

53 **The Pediatric Gastrointestinal Tract,** 1833
Susan D. John and Martha Mappus Munden

54 **Pediatric Pelvic Sonography,** 1870
William L. Simpson, Jr., Humaira Chaudhry, and Henrietta Kotlus Rosenberg

55 **The Pediatric Hip and Other Musculoskeletal Ultrasound Applications,** 1920
Leslie E. Grissom and H. Theodore Harcke

56 **Pediatric Interventional Sonography,** 1942
Neil Johnson and Allison Aguado

Appendix: Ultrasound Artifacts: A Virtual Chapter
Korosh Khalili, Hojun Yu, Alexander Jesurum, and Deborah Levine
Index, I-1

VIDEO CONTENTS

4 The Liver
Stephanie R. Wilson and Cynthia E. Withers

Video 4.1 **Normal liver, sagittal sweep**
Video 4.2 **Normal liver, subcostal sweep**
Video 4.3 **Focal fat in the liver**
Video 4.4 **Geographic fatty infiltration of the liver**
Video 4.5 **CEUS of FNH with classic enhancement features**
Video 4.6 **CEUS of the flash-filling hemangioma shown in Fig. 4.47**
Video 4.7 **CEUS of focal nodular hyperplasia**
Video 4.8 **CEUS of focal nodular hyperplasia**
Video 4.9 **CEUS of hepatic adenoma in a young woman**
Video 4.10 **CEUS of small hepatocellular carcinoma**
Video 4.11 **CEUS of hepatocellular carcinoma**
Video 4.12 **Classic colorectal metastasis**
Video 4.13 **CEUS of liver metastasis**
Video 4.14 **CEUS of liver metastasis**

5 The Spleen
Patrick M. Vos, John R. Mathieson, and Peter L. Cooperberg

Video 5.1 **Normal spleen in sagittal plane**
Video 5.2 **Normal spleen in transverse plane**
Video 5.3 **Contrast study of lymphoma manifesting as a hypoechoic solitary splenic lesion**

6 The Biliary Tree and Gallbladder
Korosh Khalili and Stephanie R. Wilson

Video 6.1 **Distal common bile duct and ampulla of Vater**
Video 6.2 **Intrahepatic bile duct stones**
Video 6.3 **Distal common bile duct stone**
Video 6.4 **Choledochoduodenal fistula**
Video 6.5 **Primary sclerosing cholangitis**
Video 6.6 **Primary sclerosing cholangitis**
Video 6.7 **Cholangiocarcinoma complicating primary sclerosing cholangitis**
Video 6.8 **Cholangiocarcinoma complicating primary sclerosing cholangitis**
Video 6.9 **Cholelithiasis**
Video 6.10 **Acute cholecystitis**
Video 6.11 **Perforated cholecystitis with liver abscess**

7 The Pancreas
Thomas Winter and Maryellen R.M. Sun

Video 7.1 **Normal pancreas**
Video 7.2 **Acute pancreatitis**
Video 7.3 **Acute pancreatitis**
Video 7.4 **Chronic pancreatitis**
Video 7.5 **Chronic pancreatitis**
Video 7.6 **Pancreatic pseudocyst**
Video 7.7 **Pancreatic carcinoma**
Video 7.8 **Pancreatic carcinoma**
Video 7.9 **Intraductal papillary mucinous neoplasm**
Video 7.10 **Mucinous cystic neoplasm**

8 The Gastrointestinal Tract
Stephanie R. Wilson

Video 8.1 **An incidentally detected neuroendocrine tumor (carcinoid) of the small bowel**
Video 8.2 **Classic features of Crohn disease on a sweep through the terminal ileum**
Video 8.3 **Loss of stratification of the bowel wall layers in severe subacute inflammation of the sigmoid colon in a patient with Crohn disease**
Video 8.4 **Stricture in Crohn disease**
Video 8.5 **Color Doppler shows hyperemia in thickened bowel wall in Crohn disease**
Video 8.6 **Contrast-enhanced longitudinal image of Crohn disease**
Video 8.7 **Contrast-enhanced cross-sectional image of Crohn disease**
Video 8.8 **Severe fixation and acute angulation of the ileum with stricture and enteroenteric fistula**
Video 8.9 **Incomplete small bowel obstruction in patient with Crohn disease**
Video 8.10 **Dysfunctional and excess peristalsis**
Video 8.11 **Localized perforation with a phlegmonous inflammatory mass**
Video 8.12 **Enteroenteric fistula**
Video 8.13 **Normal appendix**
Video 8.14 **Perforated appendix**
Video 8.15 **Acute diverticulitis in second trimester of pregnancy**
Video 8.16 **Paralytic ileus**
Video 8.17 **Incomplete bowel obstruction due to an inflammatory stricture from Crohn disease seen only on endovaginal scan**

9 The Kidney and Urinary Tract
Mitchell Tublin, Deborah Levine, Wendy Thurston, and Stephanie R. Wilson

Video 9.1 **Doppler jet**
Video 9.2 **Renal cell carcinoma**
Video 9.3 **Transitional cell carcinoma of the bladder**
Video 9.4 **Bladder diverticula**

11 The Adrenal Glands
Christina Marie Chingkoe, Olga R. Brook, and Deborah Levine

Video 11.1 **Normal adrenal gland**
Video 11.2 **Adrenal adenoma**
Video 11.3 **Adrenal adenoma**
Video 11.4 **Adrenal gland with calcification**

12 The Retroperitoneum
Raymond E. Bertino and Elton Mustafaraj

Video 12.1 **Type 2 endoleak from inferior mesenteric artery–aorta**
Video 12.2 **Type 2 endoleak on enhanced computed tomography scan**
Video 12.3 **Type 3 endoleak, transverse image**
Video 12.4 **Type 3 endoleak, longitudinal image**
Video 12.5 **Aortic pseudoaneurysm (contained rupture), longitudinal image**
Video 12.6 **Restenosis of stented accessory left renal artery**
Video 12.7 **Angiogram of restenosis of stented accessory left renal artery**

Video 12.8 **Angiogram of stented accessory left renal artery restenosis after restenting**
Video 12.9 **Normal right renal artery**
Video 12.10 **Left renal artery stenosis with color bruit and aliasing throughout cardiac cycle**
Video 12.11 **Nutcracker syndrome**
Video 12.12 **Nutcracker syndrome after stent placement**
Video 12.13 **Prominent arcuate veins**
Video 12.14 **Mildly prominent arcuate veins**
Video 12.15 **Angiogram of left ovarian vein during coil placement**

13 Dynamic Ultrasound of Hernias of the Groin and Anterior Abdominal Wall
Deborah Levine, Lisa Napolitano, and A. Thomas Stavros

Video 13.1 **Fat-containing indirect inguinal hernia**
Video 13.2 **Direct inguinal hernia with intraperitoneal and preperitoneal fat**
Video 13.3 **Note bowel peristalsis in this inguinal hernia**
Video 13.4 **Large fat-containing direct inguinal hernia**
Video 13.5 **Change in hernia contents during Valsalva maneuver**
Video 13.6 **Completely reducible large wide-necked fat-containing ventral hernia**
Video 13.7 **Partially reducible indirect inguinal hernia containing fat and bowel**
Video 13.8 **Nonreducible fat-containing epigastric linea alba hernia**
Video 13.9 **Large bowel-containing indirect inguinal hernia extending into scrotum**
Video 13.10 **Fat-containing femoral hernia**
Video 13.11 **Moderate-sized fat-containing nonreducible left spigelian hernia**
Video 13.12 **Large fat- and bowel-containing incompletely reducible spigelian hernia**
Video 13.13 **Diastasis recti abdominis**
Video 13.14 **Fat-containing ventral hernia**
Video 13.15 **Small fat-containing nonreducible epigastric linea alba hernia**
Video 13.16 **Two adjacent moderate-sized fat-containing incompletely reducible epigastric linea alba hernias**
Video 13.17 **Mesh with strong shadow makes evaluation for recurrent hernia difficult**
Video 13.18 **Two adjacent moderate-sized fat-containing incisional hernias in patient after transverse rectus abdominis myocutaneous (TRAM) flap breast reconstruction**
Video 13.19 **Fat-containing incisional hernia**
Video 13.20 **Moderate-sized fat-containing reducible incisional hernia**
Video 13.21 **Moderate-sized fat-containing reducible recurrent inguinal hernia at the edge of mesh**
Video 13.22 **Pantaloon hernias**
Video 13.23 **Strangulated right femoral hernia**
Video 13.24 **Round ligament and inguinal canal (canal of Nuck) in a female with hydrocele**

14 The Peritoneum
Anthony E. Hanbidge, Korosh Khalili, and Stephanie R. Wilson

Video 14.1 **Tumor infiltration of the omentum**
Video 14.2 **Tumor implant in the pouch of Douglas**
Video 14.3 **Tumor implant in the pouch of Douglas**
Video 14.4 **Peritoneal carcinomatosis—parietal peritoneum**
Video 14.5 **Peritoneal carcinomatosis—visceral peritoneum**
Video 14.6 **Peritoneal carcinomatosis—visceral peritoneum**
Video 14.7 **Peritoneal mesothelioma**
Video 14.8 **Endometrioma in the pouch of Douglas**
Video 14.9 **Endometriotic plaque**
Video 14.10 **Endometriotic plaque**

15 The Uterus
Douglas Brown and Deborah Levine

Video 15.1 **Unicornuate uterus**
Video 15.2 **Bicornuate uterus**
Video 15.3 **Fibroid with cystic necrotic change**
Video 15.4 **Adenomyosis**
Video 15.5 **Prolapsing polyp**
Video 15.6 **Endometrial polyp**
Video 15.7 **Endometrial polyp**
Video 15.8 **Endometrial carcinoma**
Video 15.9 **Endometrial carcinoma with hematometra**
Video 15.10 **Synechia**
Video 15.11 **Low position of intrauterine device (IUD)**
Video 15.12 **Vascularized retained products of conception**
Video 15.13 **Bladder flap hematoma and sutures after cesarean section**

16 The Adnexa
Rochelle Filker Andreotti and Lori A. Deitte

Video 16.1 **Bowel peristalsis**
Video 16.2 **Hemorrhagic cyst**
Video 16.3 **Endometrioma**
Video 16.4 **Atypical endometrioma**
Video 16.5 **Deep infiltrating endometriosis**
Video 16.6 **Ovarian torsion**
Video 16.7 **Clear cell carcinoma in endometrioma**
Video 16.8 **Yolk sac tumor**
Video 16.9 **Hydrosalpinx in 70-year-old woman with adnexal cyst**
Video 16.10 **Hydrosalpinx in 35-year-old with complex left adnexal cyst**
Video 16.11 **Pelvic inflammatory disease caused by *Neisseria Gonorrhoeae***

17 Ultrasound-Guided Biopsy of Chest, Abdomen, and Pelvis
Theodora A. Potretzke, Thomas D. Atwell, J. William Charboneau, and Carl Reading

Video 17.1 **Ultrasound-guided omental core biopsy**
Video 17.2 **Ultrasound-guided liver core biopsy**
Video 17.3 **Ultrasound-guided liver mass biopsy using "freehand" technique**
Video 17.4 **Ultrasound-guided liver mass biopsy using "freehand" technique**
Video 17.5 **Power Doppler imaging improving drain conspicuity**
Video 17.6 **Transvaginal adnexal cyst local anesthesia**
Video 17.7 **Transvaginal adnexal cyst aspiration**

18 Organ Transplantation
Derek Muradali and Tanya Punita Chawla

Video 18.1 **Normal renal transplant, sagittal**
Video 18.2 **Normal renal transplant, transverse**
Video 18.3 **Arteriovenous malformation renal transplant**
Video 18.4 **Partially thrombosed pseudoaneurysm in hilum of renal transplant**
Video 18.5 **Normal pancreas transplant, sagittal**
Video 18.6 **Normal pancreas transplant, transverse**

19 The Thyroid Gland
Luigi Solbiati, J. William Charboneau, Vito Cantisani, Carl Reading, and Giovanni Mauri

Video 19.1 **Colloid cysts**
Video 19.2 **Honeycomb pattern of benign nodule**
Video 19.3 **Adenoma**
Video 19.4 **Papillary carcinoma: fine calcifications**
Video 19.5 **Papillary carcinoma: coarse and fine calcifications**
Video 19.6 **Fine-needle aspiration (FNA)**
Video 19.7 **Hashimoto thyroiditis**

20 The Parathyroid Glands
Bonnie J. Huppert and Carl Reading

Video 20.1 **Cystic and solid parathyroid adenoma**
Video 20.2 **Small parathyroid adenoma**
Video 20.3 **Multiple gland parathyroid hyperplasia**
Video 20.4 **Multiple gland parathyroid hyperplasia**
Video 20.5 **Superior parathyroid adenoma**
Video 20.6 **Superior parathyroid adenoma**
Video 20.7 **Inferior parathyroid adenoma**
Video 20.8 **Inferior parathyroid adenoma**
Video 20.9 **Ectopic superior parathyroid adenoma**
Video 20.10 **Intrathyroid parathyroid adenoma**
Video 20.11 **Intrathyroid parathyroid adenoma**
Video 20.12 **Ectopic parathyroid adenoma**
Video 20.13 **Parathyromatosis in the postoperative neck**
Video 20.14 **Parathyroid adenoma**
Video 20.15 **Small inferior parathyroid adenoma and multinodular goiter**
Video 20.16 **Small inferior parathyroid adenoma and multinodular thyroid**
Video 20.17 **Ectopic intrathyroid parathyroid adenoma biopsy**
Video 20.18 **Ectopic parathyroid adenoma biopsy**
Video 20.19 **Ethanol ablation of recurrent graft-dependent hyperparathyroidism**

21 The Breast
Jordana Phillips, Rashmi J. Mehta, and A. Thomas Stavros

Video 21.1 **Importance of light pressure for color Doppler examination**
Video 21.2 **Importance of light pressure for color Doppler examination**
Video 21.3 **Normal cyst**
Video 21.4 **Intraductal papilloma**
Video 21.5 **Percutaneous biopsy using spring-loaded biopsy device**

22 The Scrotum
Daniel Sommers and Thomas Winter

Video 22.1 **Atrophic testis with seminoma**
Video 22.2 **Epidermoid cyst**
Video 22.3 **Varicocele in patient performing a Valsalva maneuver, with gray-scale and color Doppler sonography**
Video 22.4 **Postvasectomy appearance of epididymis and vas deferens**
Video 22.5 **"Dancing sperm" postvasectomy image of scrotum**
Video 22.6 **Acute orchitis**
Video 22.7 **Inferior traumatic tunica albuginea rupture, hematoma in testis, and extrusion of seminiferous tubules**

23 Overview of Musculoskeletal Ultrasound Techniques and Applications
Colm McMahon and Corrie Yablon

Video 23.1 **Normal biceps muscle and distal tendon**
Video 23.2 **Normal Achilles tendon**
Video 23.3 **Normal finger flexor tendons—dynamic imaging**
Video 23.4 **Dynamic ulnar nerve subluxation**
Video 23.5 **Short-axis imaging of a Baker cyst**

24 The Shoulder
Colm McMahon and Corrie Yablon

Video 24.1 **Dynamic assessment for subcoracoid impingement**
Video 24.2 **Illustration of imaging the supraspinatus in long axis and the transition to infraspinatus posteriorly**
Video 24.3 **Dynamic assessment for subacromial impingement**
Video 24.4 **Dynamic imaging showing increased prominence of glenohumeral effusion on external rotation**
Video 24.5 **Short-axis imaging of the supraspinatus tendon**

25 Musculoskeletal Interventions
Ronald S. Adler

Video 25.1 **Intraarticular injection of a hip under ultrasound guidance**
Video 25.2 **Biceps tendon sheath injection using a rotator interval approach**
Video 25.3 **Aspiration of a spinoglenoid notch cyst**
Video 25.4 **Injection of calcific tendinosis**
Video 25.5 **Autologous blood injection of 50-year-old woman with lateral epicondylitis**
Video 25.6 **Depiction of Tenex procedure**
Video 25.7 **Posthydrodissection of sural nerve in a 59-year-old female patient**

26 The Extracranial Cerebral Vessels
Edward I. Bluth, Stephen I. Johnson, and Laurie Troxclair

Video 26.1 **Minimal homogeneous plaque at carotid bulb (gray-scale)**
Video 26.2 **Considerable homogenous plaque at ICA (gray-scale)**
Video 26.3 **Type 3 homogeneous plaque with less than 50% sonolucency (gray-scale)**
Video 26.4 **Type 3 homogeneous plaque with low-grade stenosis of the ICA (gray-scale)**
Video 26.5 **Calcified plaque in the CCA (gray-scale)**
Video 26.6 **Heterogeneous plaque in the left ICA (type 1) (gray-scale)**
Video 26.7 **Heterogeneous plaque (type 1) with greater than 50% sonolucency within the plaque of the left ICA (gray-scale)**
Video 26.8 **Heterogeneous plaque (type 2) in the ICA (gray-scale)**
Video 26.9 **High-grade stenosis in the proximal right ICA (color Doppler)**
Video 26.10 **Heterogeneous plaque in the ICA (color Doppler)**
Video 26.11 **Heterogeneous plaque in the left ICA (power Doppler)**
Video 26.12 **High-grade stenosis in the ICA (power Doppler)**
Video 26.13 **High-grade stenosis of the ICA (power Doppler)**
Video 26.14 **Low-grade stenosis in the ICA (color Doppler)**
Video 26.15 **Normal spectral waveform of the proximal ICA**
Video 26.16 **Normal spectral waveform of the mid ICA**
Video 26.17 **Normal spectral waveform of the distal ICA**
Video 26.18 **Normal spectral waveform of the right distal CCA**
Video 26.19 **High-grade stenosis in the ICA (power Doppler)**

Video 26.20 **High-grade stenosis in the ICA (color Doppler)**
Video 26.21 **High-grade stenosis with spectral broadening (color and spectral Doppler)**
Video 26.22 **Color and spectral Doppler of low-grade stenosis in the ICA**

27 Peripheral Vessels
Mark E. Lockhart, Heidi R. Umphrey, Therese M. Weber, and Michelle L. Robbin

Video 27.1 **Acute thrombus in the superficial femoral artery**
Video 27.2 **Occlusion of the superficial femoral artery with a large collateral exiting proximal to the occlusion**
Video 27.3 **Severe calcification of the superficial femoral artery limits ability to see within the artery lumen with gray-scale imaging**
Video 27.4 **Common femoral artery pseudoaneurysm**
Video 27.5 **Common femoral artery to common femoral vein arteriovenous fistula (AVF)**
Video 27.6 **Arterial bypass graft stenosis on grayscale and color Doppler**
Video 27.7 **Large radial artery pseudoaneurysm with rent in arterial wall**
Video 27.8 **Large radial artery pseudoaneurysm**
Video 27.9 **Subclavian steal**
Video 27.10 **Normal femoral vein compression during study to assess for deep venous thrombosis**
Video 27.11 **Acute common femoral vein (CFV) thrombus**
Video 27.12 **Nonocclusive slightly mobile thrombus within the great saphenous vein (GSV) with extension into the common femoral vein (CFV)**
Video 27.13 **Acute deep venous thrombosis in right lower extremity**
Video 27.14 **Chronic vein occlusion with collaterals**
Video 27.15 **Chronic common femoral vein (CFV) occlusion with normal antegrade flow in the femoral vein, and flow reversal in the profunda femoral vein**
Video 27.16 **Slow flow in patent, compressible vein without deep venous thrombosis, longitudinal cine clip**
Video 27.17 **Slow flow in patent, compressible vein without deep venous thrombosis, transverse cine clip**
Video 27.18 **Thrombus in one of paired femoral veins**
Video 27.19 **Normal femoral vein valve**
Video 27.20 **Normal internal jugular vein (IJV) on gray scale compression cine clip**
Video 27.21 **Acute internal jugular thrombus**
Video 27.22 **Nonocclusive thrombus in one brachial vein in the paired brachial veins**
Video 27.23 **Acute thrombus around peripherally inserted central catheter (PICC) line in the basilic vein**
Video 27.24 **Acute thrombus around peripherally inserted central catheter (PICC) line in the basilic vein**
Video 27.25 **Thick-walled cephalic vein with chronic thrombus**
Video 27.26 **Large hematoma adjacent to arteriovenous fistula (AVF)**
Video 27.27 **Small AVF basilic vein pseudoaneurysm**
Video 27.28 **Graft wall irregularity and degeneration from repeated punctures**
Video 27.29 **Graft venous anastomosis stenosis with peak systolic velocity measuring 6.1 m/sec in highest velocity portion of jet**

28 Overview of Obstetric Imaging
Deborah Levine

Video 28.1 **Normal 6-week embryo with cardiac activity**
Video 28.2 **Normal first-trimester embryo with rhombencephalon appearing as a fluid collection in the region of the head**
Video 28.3 **Sagittal view of uterus with 17-week gestational age fetus in cephalic presentation and anterior placenta**
Video 28.4 **Normal intracranial anatomy at 19 weeks' gestation**
Video 28.5 **Four-chamber view of beating fetal heart**
Video 28.6 **Scan through the heart**
Video 28.7 **Normal kidneys and lumbosacral spine**
Video 28.8 **Transverse fetal spine**
Video 28.9 **Bladder and umbilical arteries**

30 The First Trimester
Elizabeth Lazarus and Deborah Levine

Video 30.1 **Early embryonic cardiac activity**
Video 30.2 **Early pregnancy failure at 7 weeks**
Video 30.3 **Expanded amnion in nonviable pregnancy**
Video 30.4 **Ten-week demise with calcified yolk sac**
Video 30.5 **Small subchorionic hemorrhage**
Video 30.6 **Right ectopic pregnancy with adnexal mass separating from the ovary with manual pressure**
Video 30.7 **Ruptured ectopic pregnancy**
Video 30.8 **Cesarean section implantation in retroflexed uterus**
Video 30.9 **Normal rhombencephalon**
Video 30.10 **Persistent trophoblastic neoplasia**
Video 30.11 **Choriocarcinoma**

31 Chromosomal Abnormalities
Bryann Bromley and Beryl Benacerraf

Video 31.1 **Nuchal translucency**
Video 31.2 **Cystic hygroma**
Video 31.3 **Nasal bone in first trimester**
Video 31.4 **Echogenic bowel**
Video 31.5 **Amniocentesis needle being withdrawn from amniotic fluid cavity**

32 Multifetal Pregnancy
Mary C. Frates

Video 32.1 **Quintuplets, 9 weeks' gestational age**
Video 32.2 **Conjoined embryos, 7 weeks' gestational age**
Video 32.3 **Monochorionic monoamniotic twins, 26 weeks' gestational age**
Video 32.4 **Three separate placentas in a trichorionic triplet pregnancy at 13 weeks' gestational age**
Video 32.5 **Velamentous cord insertion in a twin, 34 weeks' gestational age**
Video 32.6 **Growth and fluid discrepancies in dichorionic twins, 24 weeks' gestational age**
Video 32.7 **Twin-twin transfusion syndrome, 22 weeks' gestational age**
Video 32.8 **Twin reversed arterial perfusion sequence, 16 weeks' gestational age**
Video 32.9 **Monochorionic monoamniotic twins, 12 weeks' gestational age**
Video 32.10 **Monochorionic monoamniotic twins, 28 weeks' gestational age**
Video 32.11 **Monochorionic monoamniotic conjoined twins, 35 weeks' gestational age**

33 The Fetal Face and Neck
Ana P. Lourenco and Judy A. Estroff

Video 33.1 **Left 2 complete cleft lip, cleft alveolus, and cleft palate in sagittal plane in 20-week gestational age fetus**
Video 33.2 **Left unilateral complete cleft lip, cleft alveolus, and cleft palate in axial plane in 20-week gestational age fetus**
Video 33.3 **Left unilateral complete cleft lip, cleft alveolus, and cleft palate in coronal plane in 20-week gestational age fetus**
Video 33.4 **Micrognathia at gestational age 20 weeks**

34 The Fetal Brain
Ants Toi and Deborah Levine

Video 34.1 **Normal brain, axial**
Video 34.2 **Normal brain, coronal**
Video 34.3 **Normal brain, sagittal**
Video 34.4 **Choroid plexus cysts**
Video 34.5 **Bilateral ventriculomegaly**
Video 34.6 **Chiari malformation in fetus with spinal neural tube defect**
Video 34.7 **Holoprosencephaly**
Video 34.8 **Second trimester agenesis of corpus callosum**
Video 34.9 **Agenesis of corpus callosum in coronal plane**
Video 34.10 **Agenesis of corpus callosum in sagittal plane**
Video 34.11 **Agenesis of corpus callosum in axial plane with midline cyst**
Video 34.12 **Absence of septal leaflets**

35 The Fetal Spine
Elizabeth Asch and Eric Sauerbrei

Video 35.1 **Normal transaxial spine**
Video 35.2 **Normal longitudinal spine**
Video 35.3 **Myelomeningocele**
Video 35.4 **Closed neural tube defect: transaxial**
Video 35.5 **Closed neural tube defect: longitudinal**
Video 35.6 **Sacrococcygeal teratoma**

36 The Fetal Chest
Dorothy Bulas

Video 36.1 **Congenital pulmonary adenomatoid malformation**
Video 36.2 **Small pleural effusion at 16 weeks' gestational age**
Video 36.3 **Left-sided congenital diaphragmatic hernia at 32 weeks' gestational age (transverse view)**
Video 36.4 **Left-sided congenital diaphragmatic hernia at 32 weeks' gestational age (sagittal view)**
Video 36.5 **Large left-sided congenital diaphragmatic hernia with large amount of liver in chest**
Video 36.6 **Right-sided congenital diaphragmatic hernia**

37 The Fetal Heart
Elizabeth R. Stamm and Julia A. Drose

Video 37.1 **Normal apical four-chamber view**
Video 37.2 **Normal sub-costal four-chamber view**
Video 37.3 **Normal appearance of the aorta and pulmonary artery**
Video 37.4 **Color Doppler of the aorta and pulmonary artery**
Video 37.5 **Short-axis view of the color Doppler of the ventricles and great arteries**
Video 37.6 **Three-vessel and trachea view**
Video 37.7 **Aortic arch**
Video 37.8 **Aortic arch**
Video 37.9 **Atrioventricular septal defect**
Video 37.10 **Hypoplastic left heart syndrome**
Video 37.11 **Hypoplastic right heart**
Video 37.12 **Ebstein anomaly**
Video 37.13 **Tetralogy of Fallot**

38 The Fetal Gastrointestinal Tract and Abdominal Wall
Nir Melamed, Anne Kennedy, and Phyllis Glanc

Video 38.1 **Esophageal atresia**
Video 38.2 **Gastric debris**
Video 38.3 **Gastric debris**
Video 38.4 **Duodenal atresia**
Video 38.5 **Jejunal atresia**
Video 38.6 **Duplication cyst**
Video 38.7 **Meconium peritonitis**
Video 38.8 **Echogenic bowel**
Video 38.9 **Normal gallbladder**
Video 38.10 **Annular pancreas**
Video 38.11 **Splenic cyst**
Video 38.12 **Gastroschisis**
Video 38.13 **Omphalocele**
Video 38.14 **Bladder exstrophy**
Video 38.15 **Cloacal exstrophy**

39 The Fetal Urogenital Tract
Katherine W. Fong, Julia Eva Kfouri, and Kirsten L. Weind Matthews

Video 39.1 **"Lying down" adrenal sign due to unilateral renal agenesis**
Video 39.2 **Bilateral renal agenesis**
Video 39.3 **Pelvic kidney**
Video 39.4 **Cross-fused renal ectopia**
Video 39.5 **Horseshoe kidney**
Video 39.6 **Autosomal recessive polycystic kidney disease**
Video 39.7 **Perinephric urinoma**
Video 39.8 **Primary megaureter**
Video 39.9 **Megalourethra**
Video 39.10 **Cloacal dysgenesis**
Video 39.11 **Ovarian cyst**

40 The Fetal Musculoskeletal System
Phyllis Glanc, David Chitayat, and Sheila Unger

Video 40.1 **Thanatophoric dysplasia**
Video 40.2 **Clubfeet at 21 weeks**

41 Fetal Hydrops
Deborah Levine

Video 41.1 **Fetal abdomen at 30 weeks gestational age in fetus with a small amount of ascites and polyhydramnios**
Video 41.2 **Bilateral pleural effusions, left greater than right**
Video 41.3 **Large unilateral pleural effusion inverts the hemidiaphragm and is associated with ascites**
Video 41.4 **Small pericardial effusion in fetus with poorly contractile and echogenic heart**
Video 41.5 **Anasarca in fetus with congenital pulmonary airway malformation**
Video 41.6 **Middle cerebral artery Doppler**
Video 41.7 **Poorly contractile heart abnormal appearing heart, bilateral pleural effusions, and marked anasarca**

42 Fetal Measurements: Normal and Abnormal Fetal Growth and Assessment of Fetal Well-Being
Carol B. Benson and Peter M. Doubilet

Video 42.1 **Early embryonic heartbeat**
Video 42.2 **Fetal movement**
Video 42.3 **Fetal breathing movements**

43 Sonographic Evaluation of the Placenta
Thomas D. Shipp

Video 43.1 **Placental lake**
Video 43.2 **Thick placenta**
Video 43.3 **Placenta accreta**
Video 43.4 **Placenta increta**
Video 43.5 **Placenta percreta**
Video 43.6 **Abruption**
Video 43.7 **Abruption**
Video 43.8 **Preplacental hematoma**
Video 43.9 **Preplacental hematoma**
Video 43.10 **Placental infarction**
Video 43.11 **Placental infarction**
Video 43.12 **Circumvallate placenta**
Video 43.13 **Circumvallate placenta**
Video 43.14 **Bilobed placenta**
Video 43.15 **Velamentous cord insertion and two-vessel cord**
Video 43.16 **Umbilical cord insertion into placenta**
Video 43.17 **Vasa previa**

44 Cervical Ultrasound and Preterm Birth
Hournaz Ghandehari and Phyllis Glanc

Video 44.1 **Open cervix with large funnel and bulging membranes**
Video 44.2 **Closed cervix with mobile debris at the internal os**
Video 44.3 **Open cervix with mobile debris in the dilated cervical canal and adjacent to the external os**

45 Neonatal and Infant Brain Imaging
Carol M. Rumack and Amanda K. Auckland

Video 45.1 **Normal coronal sweep**
Video 45.2 **Normal sagittal sweep**
Video 45.3 **Normal mastoid sweep**
Video 45.4 **Chiari II malformation**
Video 45.5 **Ventriculomegaly in association with Chiari II malformation (seen in Video 45.4)**
Video 45.6 **Chiari II malformation, pointed frontal and large occipital horn; partial absence of corpus callosum (same neonate as in Videos 45.4 and 45.5)**
Video 45.7 **Tethered cord in patient with Chiari II malformation, sagittal scan**
Video 45.8 **Absence of cavum septi pellucidi, coronal scan**
Video 45.9 **Right subacute subependymal, intraventricular, and right frontal intraparenchymal hemorrhages, coronal scan**
Video 45.10 **Right subependymal, caudothalamic groove, and hemorrhage and intraventricular hemorrhage, sagittal scan**
Video 45.11 **Cisterna magna clot**
Video 45.12 **Acute intraventricular echogenic blood**
Video 45.13 **Bilateral intraventricular hemorrhage and intraparenchymal hemorrhage**
Video 45.14 **Acute highly echogenic hemorrhage**
Video 45.15 **Intraventricular hemorrhage**
Video 45.16 **Cystic periventricular leukomalacia**
Video 45.17 **Cytomegalovirus with punctate calcifications**
Video 45.18 **Multiple focal calcifications**
Video 45.19 **Ventricular septation**

47 Doppler Sonography of the Brain in Children
Dorothy Bulas and Alexia Egloff

Video 47.1 **Normal color Doppler of circle of Willis in 6-year-old**
Video 47.2 **Spectral wave form of the right middle cerebral artery**
Video 47.3 **Normal spectral Doppler of right bifurcation**
Video 47.4 **Four-year-old pending brain death after fall from second story**
Video 47.5 **Eight-year-old pending brain death after motor vehicle accident postcraniectomy for hematoma**

48 The Pediatric Head and Neck
Rupa Radhakrishnan and Beth M. Kline-Fath

Video 48.1 **Wharton duct stone**
Video 48.2 **Multinodular goiter**
Video 48.3 **Infantile hemangioma**
Video 48.4 **Lymphatic malformation**

49 The Pediatric Spinal Canal
Ilse Castro-Aragon, Deborah Levine, and Carol M. Rumack

Video 49.1 **Normal cauda equina**
Video 49.2 **Normal filum terminale**
Video 49.3 **Skin dimple and hypoechoic tract in subcutaneous tissues extending to normal coccyx**
Video 49.4 **Lipomyelocele in sagittal view**
Video 49.5 **Sagittal lipomyelocele**
Video 49.6 **Lipomyelocele in transverse view**
Video 49.7 **Lipomyelomeningocele**
Video 49.8 **Segmental spinal dysgenesis in sagittal view**
Video 49.9 **Segmental spinal dysgenesis patient with fatty filum**

50 The Pediatric Chest
Chetan Chandulal Shah and S. Bruce Greenberg

Video 50.1 **Moving septations within pleural fluid**
Video 50.2 **Hemidiaphragmatic motion in an infant**
Video 50.3 **Hemidiaphragmatic movement in healthy 31-month-old child**
Video 50.4 **Hemidiaphragmatic paralysis in an infant after cardiac surgery**

51 The Pediatric Liver and Spleen
Sara M. O'Hara

Video 51.1 **Normal porta hepatis showing portal vein, hepatic artery, and common bile duct**
Video 51.2 **Neonatal hepatitis**
Video 51.3 **Steatosis from obesity**
Video 51.4 **Multiple cutaneous hemangiomas in a 1-month-old infant**
Video 51.5 **Multiple cutaneous hemangiomas in a 1-month-old infant**
Video 51.6 **Hepatic abscess**
Video 51.7 **Normal flow in the main portal vein**
Video 51.8 **Normal branching vessels in the liver**
Video 51.9 **Normal third- and fourth-order branches in the liver**
Video 51.10 **Cavernous transformation of the portal vein**
Video 51.11 **Pneumobilia, an expected finding following portoenterostomy**

52 The Pediatric Urinary Tract and Adrenal Glands
Harriet J. Paltiel and Diane S. Babcock

Video 52.1 **Crossed renal ectopia**
Video 52.2 **Contrast-enhanced urosonography depicts a normal bladder**
Video 52.3 **Contrast-enhanced urosonography demonstrates vesicoureteral reflux**
Video 52.4 **Contrast-enhanced urosonography shows a normal male urethra**
Video 52.5 **Inflammatory pseudotumor**
Video 52.6 **Laceration of the mid-lateral aspect of the left kidney and perirenal hematoma**
Video 52.7 **Multicystic dysplastic kidney**
Video 52.8 **Burkitt lymphoma involving kidney**
Video 52.9 **Neuroblastoma**

54 Pediatric Pelvic Sonography
William L. Simpson, Jr., Humaira Chaudhry, and Henrietta Kotlus Rosenberg

Video 54.1 **Water vaginogram**
Video 54.2 **Normal postpubertal ovary**
Video 54.3 **Polycystic ovarian morphology**
Video 54.4 **Normal postpubertal testis**
Video 54.5 **Testicular microlithiasis**

55 The Pediatric Hip and Other Musculoskeletal Ultrasound Applications
Leslie E. Grissom and H. Theodore Harcke

Video 55.1 **Normal coronal/flexion view, midacetabulum**
Video 55.2 **Normal coronal/flexion view, posterior lip**
Video 55.3 **Subluxation, coronal/flexion view, midacetabulum**
Video 55.4 **Dislocatable hip, coronal/flexion view, midacetabulum**
Video 55.5 **Dislocatable hip, coronal/flexion view, posterior lip**
Video 55.6 **Normal transverse/flexion view**
Video 55.7 **Subluxation, transverse/flexion view**
Video 55.8 **Dislocation, transverse/flexion view**

56 Pediatric Interventional Sonography
Neil Johnson and Allison Aguado

Video 56.1 **Peripherally inserted central catheter (PICC) line placement**
Video 56.2 **Video loops showing debris attached to and obstructing the drainage catheter during diagnostic and therapeutic aspiration of heavily bloodstained abdominal fluid with floating debris**
Video 56.3 **Video loops showing debris attached to and obstructing the drainage catheter during diagnostic and therapeutic aspiration of heavily bloodstained abdominal fluid with floating debris**
Video 56.4 **Appendiceal abscess with catheter touching fecalith**
Video 56.5 **Gaucher disease patient rib biopsy**
Video 56.6 **Gaucher rib osteomyelitis drain catheter being advanced**
Video 56.7 **Gaucher rib prebiopsy showing pus and displaceable rib**
Video 56.8 **Juvenile rheumatoid arthritis tendon sheath steroid injection**

Appendix: Ultrasound Artifacts: A Virtual Chapter
Korosh Khalili, Hojun Yu, Alexander Jesurum, and Deborah Levine

Video A.1 **Propagation velocity artifact**
Video A.2 **Attenuation-related artifacts**
Video A.3 **Shadowing**
Video A.4 **Showing in region of cauda equina**
Video A.5 **Increased through transmission**
Video A.6 **Path of sound assumption**
Video A.7 **Mirror image artifact**
Video A.8 **Comet-tail artifact**
Video A.9 **Comet-tail artifact in adenomyomatosis**
Video A.10 **Refraction from the anterior abdominal wall**
Video A.11 **Anisotropy**
Video A.12 **Anisotropy at supraspinatus tendon insertion**
Video A.13 **Reverberation artifact from free intraperitoneal gas**
Video A.14 **Ring-down artifact**
Video A.15 **Ring-down artifact from air in bile ducts**
Video A.16 **Dirty shadowing**
Video A.17 **Side lobe artifact**
Video A.18 **Partial volume averaging explanation**
Video A.19 **Tissue vibration artifact**
Video A.20 **Tissue vibration artifact from left renal artery stenosis with color bruit and aliasing**
Video A.21 **Aliasing seen in common femoral artery to common femoral vein arteriovenous fistula**
Video A.22 **Twinkle explanation**
Video A.23 **Twinkle**

This page intentionally left blank

DIAGNOSTIC ULTRASOUND

This page intentionally left blank

CHAPTER 1

Physics of Ultrasound

Christopher R.B. Merritt

SUMMARY OF KEY POINTS

- Quality imaging requires an understanding of basic acoustic principles.
- Image interpretation requires recognition and understanding of common artifacts.
- Special modes of operation, including harmonic imaging, compounding, elastography, and Doppler, expand the capabilities of conventional gray-scale imaging.
- Knowledge of mechanical and thermal bioeffects of ultrasound is necessary for prudent use.
- High-intensity focused ultrasound has potential therapeutic applications.

CHAPTER OUTLINE

BASIC ACOUSTICS
Wavelength and Frequency
Propagation of Sound
Distance Measurement
Acoustic Impedance
Reflection
Refraction
Attenuation
INSTRUMENTATION
Transmitter
Transducer
Receiver
Image Display
Mechanical Sector Scanners
Arrays
Linear Arrays
Curved Arrays
Phased Arrays
Two-Dimensional Arrays
Transducer Selection
IMAGE DISPLAY AND STORAGE
SPECIAL IMAGING MODES
Tissue Harmonic Imaging
Spatial Compounding
Three-Dimensional Ultrasound
Ultrasound Elastography
Strain Elastography
Shear Wave Elastography
IMAGE QUALITY
Spatial Resolution
IMAGING PITFALLS
Shadowing and Enhancement
DOPPLER SONOGRAPHY
Doppler Signal Processing and Display
Doppler Instrumentation
Power Doppler
Interpretation of the Doppler Spectrum
Interpretation of Color Doppler
Other Technical Considerations
Doppler Frequency
Wall Filters
Spectral Broadening
Aliasing
Doppler Angle
Sample Volume Size
Doppler Gain
OPERATING MODES: CLINICAL IMPLICATIONS
Bioeffects and User Concerns
THERAPEUTIC APPLICATIONS: HIGH-INTENSITY FOCUSED ULTRASOUND

All diagnostic ultrasound applications are based on the detection and display of acoustic energy reflected from interfaces within the body. These interactions provide the information needed to generate high-resolution, gray-scale images of the body, as well as display information related to blood flow. Its unique imaging attributes have made ultrasound an important and versatile medical imaging tool. However, expensive state-of-the-art instrumentation does not guarantee the production of high-quality studies of diagnostic value. Gaining maximum benefit from this complex technology requires a combination of skills, including knowledge of the physical principles that empower ultrasound with its unique diagnostic capabilities. The user must understand the fundamentals of the interactions of acoustic energy with tissue and the methods and instruments used to produce and optimize the ultrasound display. With this knowledge the user can collect the maximum information from each examination, avoiding pitfalls and errors in diagnosis that may result from the omission of information or the misinterpretation of artifacts.[1]

Ultrasound imaging and Doppler ultrasound are based on the scattering of sound energy by interfaces of materials with different properties through interactions governed by acoustic

physics. The amplitude of reflected energy is used to generate ultrasound images, and frequency shifts in the backscattered ultrasound provide information relating to moving targets such as blood. To produce, detect, and process ultrasound data, users must manage numerous variables, many under their direct control. To do this, operators must understand the methods used to generate ultrasound data and the theory and operation of the instruments that detect, display, and store the acoustic information generated in clinical examinations.

This chapter provides an overview of the fundamentals of acoustics, the physics of ultrasound imaging and flow detection, and ultrasound instrumentation with emphasis on points most relevant to clinical practice. A discussion of the therapeutic application of high-intensity focused ultrasound concludes the chapter.

BASIC ACOUSTICS

Wavelength and Frequency

Sound is the result of mechanical energy traveling through matter as a wave producing alternating **compression** and **rarefaction.** Pressure waves are propagated by limited physical displacement of the material through which the sound is being transmitted. A plot of these changes in pressure is a sinusoidal waveform (Fig. 1.1), in which the Y axis indicates the pressure at a given point and the X axis indicates time. Changes in pressure with time define the basic units of measurement for sound. The distance between corresponding points on the time-pressure curve is defined as the **wavelength** (λ), and the time (T) to complete a single cycle is called the **period.** The number of complete cycles in a unit of time is the **frequency** *(f)* of the sound. Frequency and period are inversely related. If the period (T) is expressed in seconds, $f = 1/T$, or $f = T \times sec^{-1}$. The unit of **acoustic frequency** is the **hertz** (Hz); 1 Hz = 1 cycle per second. High frequencies are expressed in kilohertz (kHz; 1 kHz = 1000 Hz) or **megahertz** (MHz; 1 MHz = 1,000,000 Hz).

In nature, acoustic frequencies span a range from less than 1 Hz to more than 100,000 Hz (100 kHz). Human hearing is limited to the lower part of this range, extending from 20 to 20,000 Hz. Ultrasound differs from audible sound only in its frequency, and it is 500 to 1000 times higher than the sound we normally hear. Sound frequencies used for diagnostic applications typically range from 2 to 15 MHz, although frequencies as high as 50 to 60 MHz are under investigation for certain specialized imaging applications. In general, the frequencies used for ultrasound imaging are higher than those used for Doppler. Regardless of the frequency, the same basic principles of acoustics apply.

Propagation of Sound

In most clinical applications of ultrasound, brief bursts or pulses of energy are transmitted into the body and propagated through tissue. Acoustic pressure waves can travel in a direction perpendicular to the direction of the particles being displaced (**transverse** waves), but in tissue and fluids, sound propagation is primarily along the direction of particle movement (**longitudinal** waves). Longitudinal waves are important in conventional ultrasound imaging and Doppler, while transverse waves are measured in shear wave elastography. The speed at which pressure waves move through tissue varies greatly and is affected by the physical properties of the tissue. **Propagation velocity** is largely determined by the **resistance** of the medium to compression, which in turn is influenced by the **density** of the medium and its **stiffness** or elasticity. Propagation velocity is increased by increasing stiffness and reduced by decreasing density. In the body, propagation velocity of longitudinal waves may be regarded as constant for a given tissue and is not affected by the frequency or wavelength of the sound. This is in contrast to transverse (shear) waves for

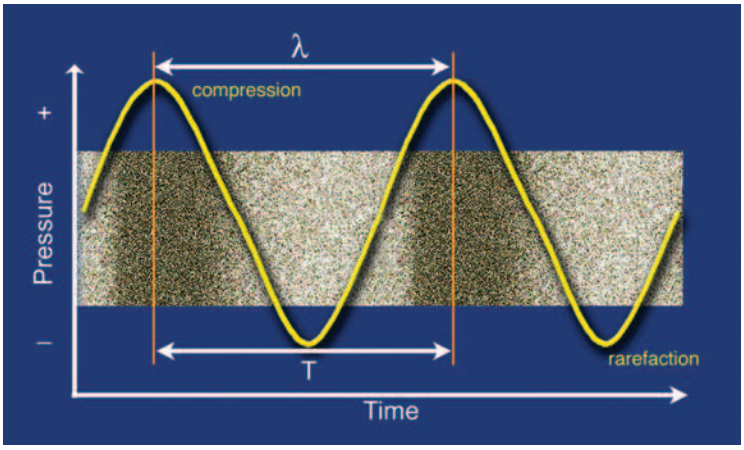

FIG. 1.1 Sound Waves. Sound is transmitted mechanically at the molecular level. In the resting state the pressure is uniform throughout the medium. Sound is propagated as a series of alternating pressure waves producing compression and rarefaction of the conducting medium. The time for a pressure wave to pass a given point is the period, *T*. The frequency of the wave is 1/T. The wavelength, λ, is the distance between corresponding points on the time-pressure curve.

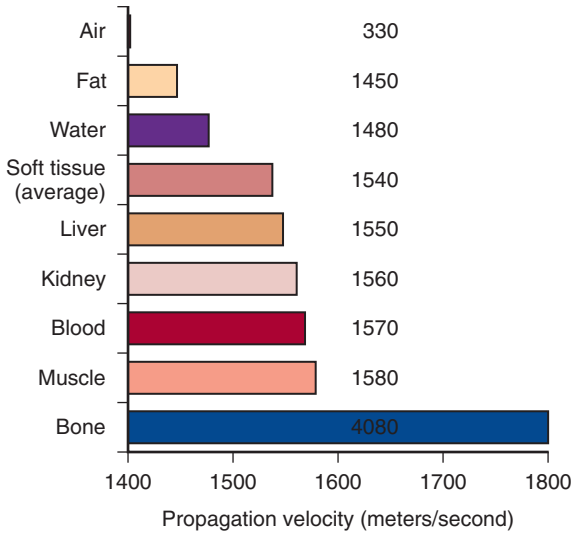

FIG. 1.2 Propagation Velocity. In the body, propagation velocity of sound is determined by the physical properties of tissue. As shown, this varies considerably. Medical ultrasound devices base their measurements on an assumed average propagation velocity of soft tissue of 1540 m/sec.

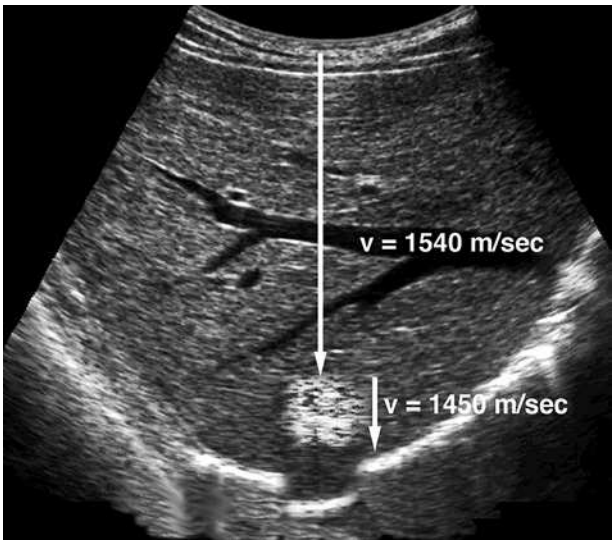

FIG. 1.3 Propagation Velocity Artifact. When sound passes through a lesion containing fat, echo return is delayed because fat has a propagation velocity of 1450 m/sec, which is less than the liver. Because the ultrasound scanner assumes that sound is being propagated at the average velocity of 1540 m/sec, the delay in echo return is interpreted as indicating a deeper target. Therefore the final image shows a **misregistration artifact** in which the diaphragm and other structures deep to the fatty lesion are shown in a deeper position than expected (simulated image).

which the velocity is determined by Young modulus, a measure of tissue stiffness or **elasticity.**

Fig. 1.2 shows typical longitudinal propagation velocities for a variety of materials. In the body the propagation velocity of sound is assumed to be 1540 meters per second (m/sec). This value is the average of measurements obtained from normal soft tissue.[2,3] Although this value represents most soft tissues, such tissues as aerated lung and fat have propagation velocities significantly less than 1540 m/sec, whereas tissues such as bone have greater velocities. Because a few normal tissues have propagation values significantly different from the average value assumed by the ultrasound scanner, the display of such tissues may be subject to measurement errors or **artifacts** (Fig. 1.3). The propagation velocity of sound (c) is related to frequency and wavelength by the following simple equation:

$$c = f\lambda$$

Thus a frequency of 5 MHz can be shown to have a wavelength of 0.308 mm in tissue: $\lambda = c/f = 1540$ m/sec $\times$ 5,000,000 $\text{sec}^{-1} =$ 0.000308 m = 0.308 mm. Wavelength is an important determinant of spatial resolution in ultrasound imaging, and selection of transducer frequency for a given application is a key user decision.

Distance Measurement

Propagation velocity is a particularly important value in clinical ultrasound and is critical in determining the distance of a reflecting interface from the transducer. Much of the information used to generate an ultrasound scan is based on the precise measurement of time and employs the principles of **echo-ranging** (Fig. 1.4). If an ultrasound pulse is transmitted into the body and the time until an echo returns is measured, it is simple to calculate the depth of the interface that generated the echo, provided the propagation velocity of sound for the tissue is known. For example, if the time from the transmission of a pulse until the return of an echo is 0.000145 seconds and the velocity of sound is 1540 m/sec, the distance that the sound has traveled must be 22.33 cm (1540 m/sec $\times$ 100 cm/m $\times$ 0.000145 sec = 22.33 cm). Because the time measured includes the time for sound to travel to the interface and then return along the same path to the transducer, the distance from the transducer to the reflecting interface is 22.33 cm/2 = 11.165 cm. By rapidly repeating this process, a two-dimensional (2-D) map of reflecting interfaces is created to form the ultrasound image. The accuracy of this measurement is therefore highly influenced by how closely the presumed velocity of sound corresponds to the true velocity in the tissue being observed (see Figs. 1.2 and 1.3), as well as by the important assumption that the sound pulse travels in a straight path to and from the reflecting interface.

Acoustic Impedance

Current diagnostic ultrasound scanners rely on the detection and display of **reflected sound** or **echoes.** Imaging based on transmission of ultrasound is also possible, but this is not used clinically at present. To produce an echo, a reflecting interface must be present. Sound passing through a totally homogeneous medium encounters no interfaces to reflect sound, and the medium appears **anechoic** or **cystic.** The junction of tissues or materials with different physical properties produces an acoustic interface. These interfaces are responsible for the reflection of variable amounts of the incident sound energy. Thus when ultrasound passes from one tissue to another or encounters a vessel wall or circulating blood cells, some of the incident sound

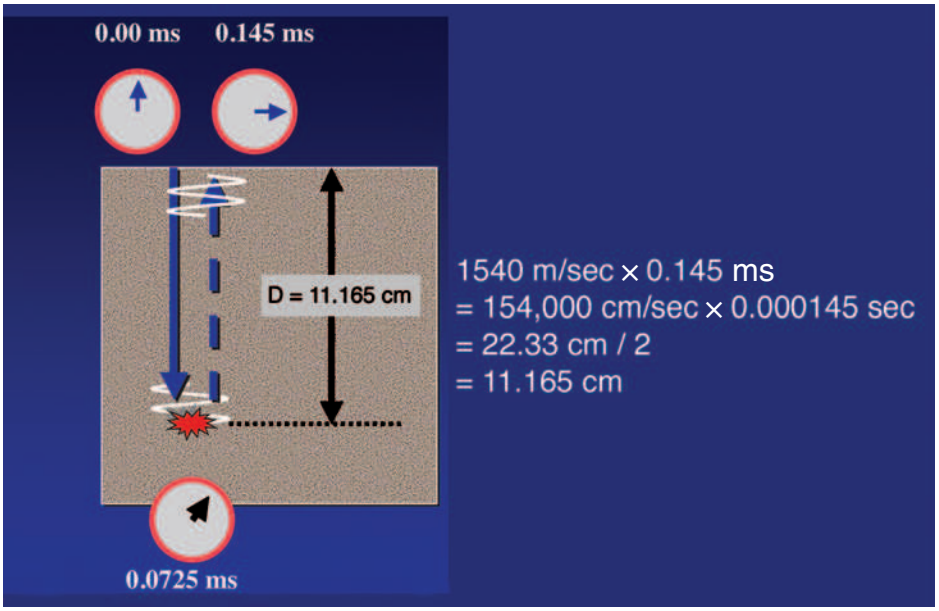

FIG. 1.4 Ultrasound Ranging. The information used to position an echo for display is based on the precise measurement of time. Here the time for an echo to travel from the transducer to the target and return to the transducer is 0.145 ms (0.000145 seconds). Multiplying the velocity of sound in tissue (1540 m/sec) by the time shows that the sound returning from the target has traveled 22.33 cm. Therefore the target lies half this distance, or 11.165 cm, from the transducer. By rapidly repeating this process, a two-dimensional map of reflecting interfaces is created to form the ultrasound image.

energy is reflected. The amount of reflection or **backscatter** is determined by the difference in the acoustic impedances of the materials forming the interface.

Acoustic impedance (Z) is determined by product of the density (ρ) of the medium propagating the sound and the propagation velocity (c) of sound in that medium ($Z = \rho c$). Interfaces with large acoustic impedance differences, such as interfaces of tissue with air or bone, reflect almost all the incident energy. Interfaces composed of substances with smaller differences in acoustic impedance, such as a muscle and fat interface, reflect only part of the incident energy, permitting the remainder to continue onward. As with propagation velocity, acoustic impedance is determined by the properties of the tissues involved and is independent of frequency.

Reflection

The way ultrasound is reflected when it strikes an acoustic interface is determined by the size and surface features of the interface (Fig. 1.5). If large and relatively smooth, the interface reflects sound much as a mirror reflects light. Such interfaces are called **specular reflectors** because they behave as "mirrors for sound." The amount of energy reflected by an acoustic interface can be expressed as a fraction of the incident energy; this is termed the **reflection coefficient** (R). If a specular reflector is perpendicular to the incident sound beam, the amount of energy reflected is determined by the following relationship:

$$R = (Z_2 - Z_1)^2 / (Z_2 + Z_1)^2$$

where Z_1 and Z_2 are the acoustic impedances of the media forming the interface.

Because ultrasound scanners only detect reflections that return to the transducer, display of specular interfaces is highly dependent on the **angle of insonation** (exposure to ultrasound waves). Specular reflectors will return echoes to the transducer only if the sound beam is perpendicular to the interface. If the interface is not at a near 90-degree angle to the sound beam, it will be reflected away from the transducer, and the echo will not be detected (see Fig. 1.5A).

Examples of Specular Reflectors

Diaphragm
Vessel wall
Wall of urine-filled bladder
Endometrial stripe

Most echoes in the body do not arise from specular reflectors but rather from much smaller interfaces within solid organs. In this case the acoustic interfaces involve structures with individual dimensions much smaller than the wavelength of the incident sound. The echoes from these interfaces are scattered in all directions. Such reflectors are called **diffuse reflectors** and account for the echoes that form the characteristic echo patterns seen in solid organs and tissues (see Fig. 1.5B). The constructive and destructive interference of sound scattered by diffuse reflectors results in the production of **ultrasound speckle,** a feature of tissue texture of sonograms of solid organs (Fig. 1.6). For some diagnostic applications, the nature of the reflecting structures creates important conflicts. For example, most vessel walls behave as specular reflectors that require insonation at a 90-degree angle for best imaging, whereas Doppler imaging requires an angle of less than 90 degrees between the sound beam and the vessel.

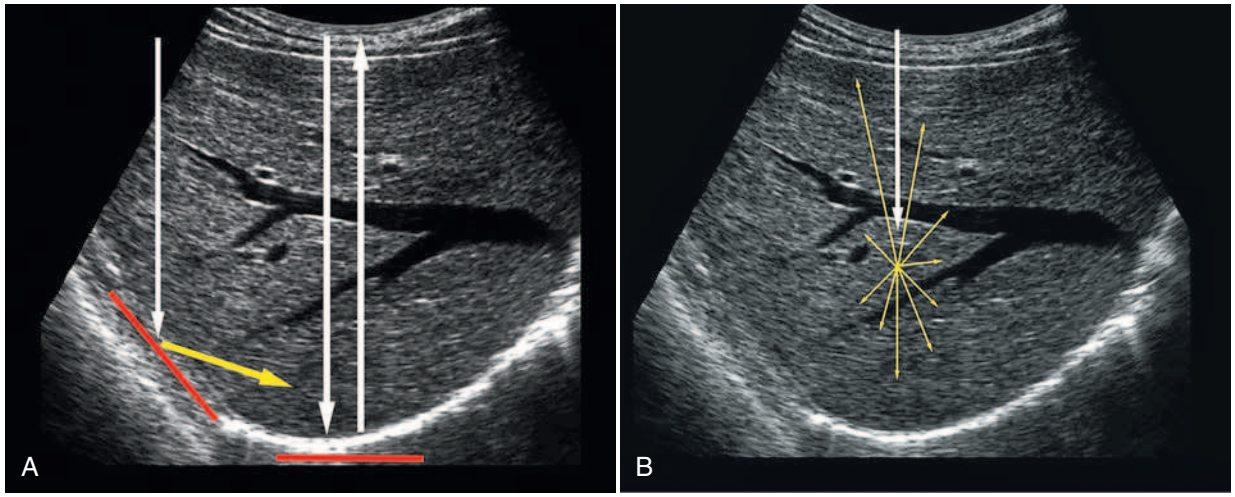

FIG. 1.5 Specular and Diffuse Reflectors. (A) Specular reflector. The diaphragm is a large and relatively smooth surface that reflects sound like a mirror reflects light. Thus sound striking the diaphragm at nearly a 90-degree angle is reflected directly back to the transducer, resulting in a strong echo. Sound striking the diaphragm obliquely is reflected away from the transducer, and an echo is not displayed *(yellow arrow).* **(B) Diffuse reflector.** In contrast to the diaphragm, the liver parenchyma consists of acoustic interfaces that are small compared to the wavelength of sound used for imaging. These interfaces scatter sound in all directions, and only a portion of the energy returns to the transducer to produce the image.

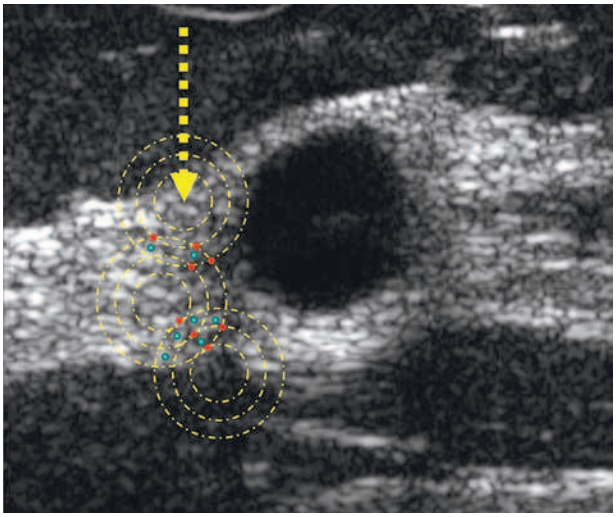

FIG. 1.6 Ultrasound Speckle. Close inspection of an ultrasound image of the breast containing a small cyst reveals it to be composed of numerous areas of varying intensity (speckle). Speckle results from the constructive *(red)* and destructive *(green)* interaction of the acoustic fields *(yellow rings)* generated by the scattering of ultrasound from small tissue reflectors. This interference pattern gives ultrasound images their characteristic grainy appearance and may reduce contrast. Ultrasound speckle is the basis of the texture displayed in ultrasound images of solid tissues.

Refraction

When sound passes from a tissue with one acoustic propagation velocity to a tissue with a higher or lower sound velocity, there is a change in the direction of the sound wave. This change in direction of propagation is called refraction and is governed by Snell law:

$$\sin\theta_1/\sin\theta_2 = c_1/c_2$$

where θ_1 is the **angle of incidence** of the sound approaching the interface, θ_2 is the **angle of refraction,** and c_1 and c_2 are the propagation velocities of sound in the media forming the interface (Fig. 1.7). Refraction is important because it is one cause of **misregistration** of a structure in an ultrasound image (Fig. 1.8). When an ultrasound scanner detects an echo, it assumes that the source of the echo is along a fixed line of sight from the transducer. If the sound has been refracted, the echo detected may be coming from a different depth or location than the image shown in the display. If this is suspected, increasing the scan angle so that it is perpendicular to the interface minimizes the artifact.

Attenuation

As the **acoustic energy** moves through a uniform medium, work is performed and energy is ultimately transferred to the transmitting medium as heat. The capacity to perform work is determined by the quantity of acoustic energy produced. **Acoustic power,** expressed in watts (W) or milliwatts (mW), describes the amount of acoustic energy produced in a unit of time. Although measurement of power provides an indication of the energy as it relates to time, it does not take into account the spatial distribution of the energy. **Intensity** (I) is used to describe the spatial distribution of power and is calculated by dividing the power by the area over which the power is distributed, as follows:

$$I\,(W/cm^2) = \text{Power}\,(W)/\text{Area}\,(cm^2)$$

The **attenuation** of sound energy as it passes through tissue is of great clinical importance because it influences the *depth* in tissue from which useful information can be obtained. This in turn affects transducer selection and a number of operator-controlled instrument settings, including time (or depth) gain compensation, power output attenuation, and system gain levels. Attenuation is measured in relative rather than absolute units. The **decibel** (dB) notation is generally used to compare different levels of ultrasound power or intensity. This value is 10 times the $\log_{10}$ of the ratio of the power or intensity values being

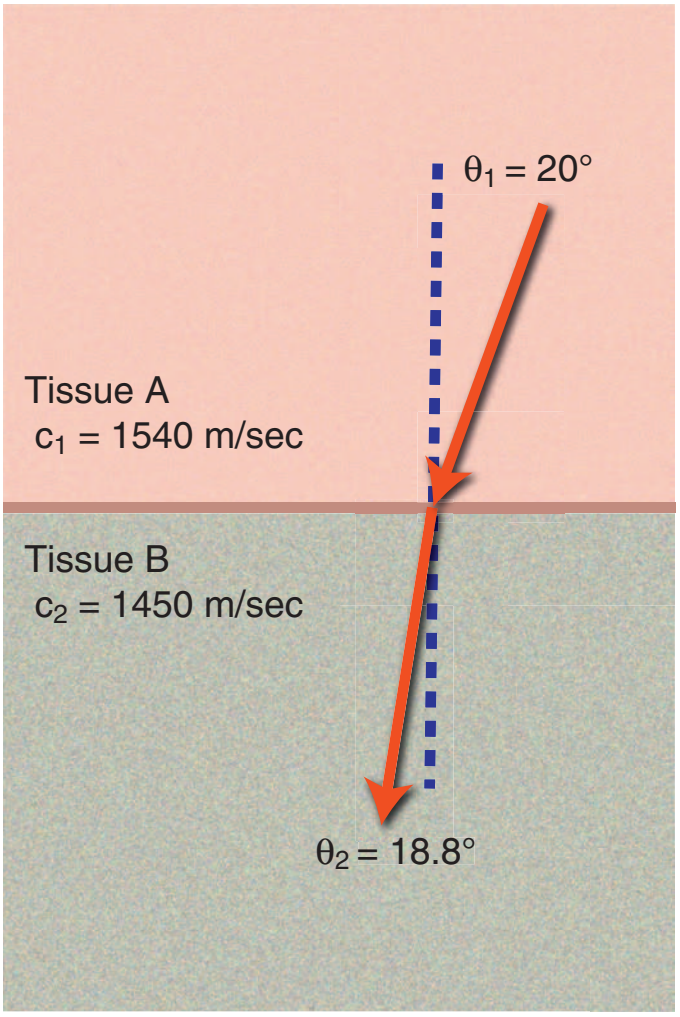

FIG. 1.7 Refraction. When sound passes from tissue A with propagation velocity (c_1) to tissue B with a different propagation velocity (c_2), there is a change in the direction of the sound wave because of refraction. The degree of change is related to the ratio of the propagating velocities of the media forming the interface ($\sin\theta_1/\sin\theta_2 = c_1/c_2$).

compared. For example, if the intensity measured at one point in tissues is 10 mW/cm^2 and at a deeper point is 0.01 mW/cm^2, the difference in intensity is as follows:

$$(10)(\log_{10} 0.01/10) = (10)(\log_{10} 0.001) = (10)(-\log_{10} 1000)$$
$$= (10)(-3) = -30 \text{ dB}$$

As it passes through tissue, sound loses energy, and the pressure waves decrease in amplitude as they travel farther from their source. Contributing to the attenuation of sound are the transfer of energy to tissue, resulting in heating (absorption), and the removal of energy by reflection and scattering. Attenuation is therefore the result of the combined effects of **absorption, scattering,** and **reflection.** Attenuation depends on the insonating frequency as well as the nature of the attenuating medium. High frequencies are attenuated more rapidly than lower frequencies, and transducer frequency is a major determinant of the useful depth from which information can be obtained with ultrasound. Attenuation determines the efficiency with which ultrasound

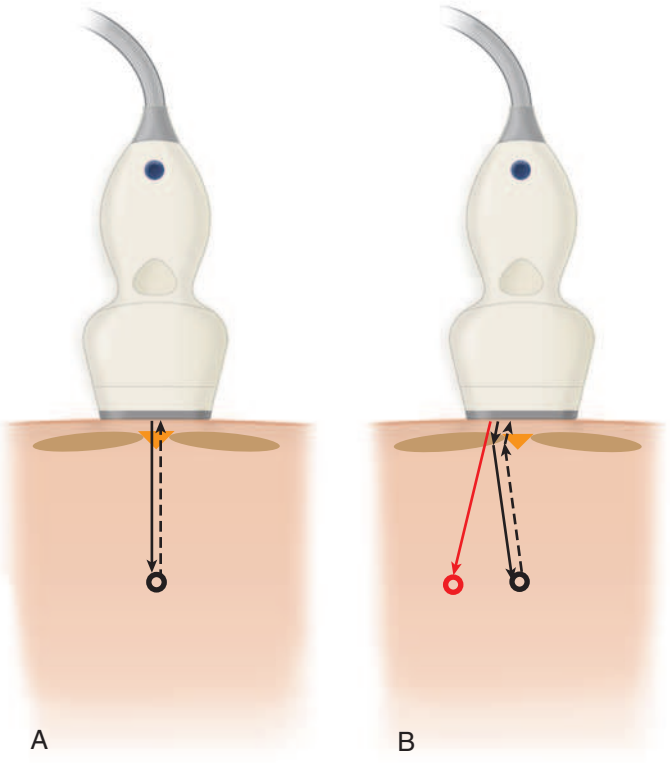

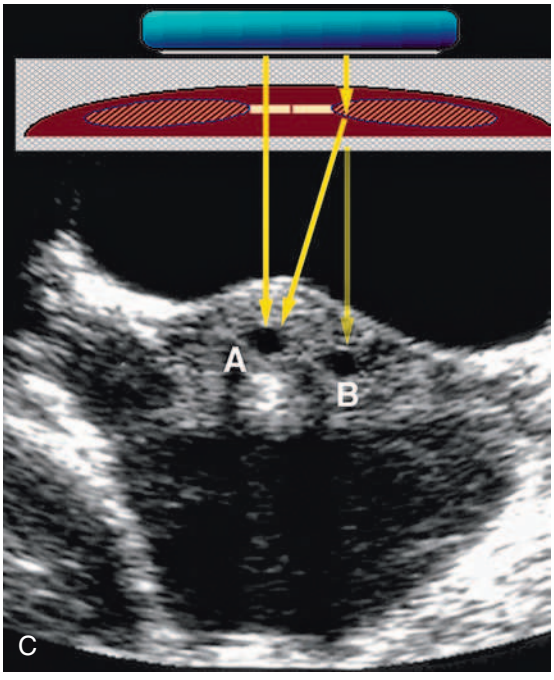

FIG. 1.8 Refraction Artifact. (A) and **(B)** Production of an artifact by refraction of sound in a transverse scan of the mid abdomen. The direct sound path properly depicts the location of the object. **(B)** A "ghost image" *(red)* produced by refraction at the edge of the rectus abdominis muscle. The transmitted and reflected sound travels along the path of the *black arrows*. The scanner assumes the returning signal is from a straight line *(red arrow)* and displays the structure at the incorrect location. **(C)** Axial transabdominal image of the uterus showing a small gestational sac *(A)* and what appears to be a second sac *(B)* due to refraction artifact.

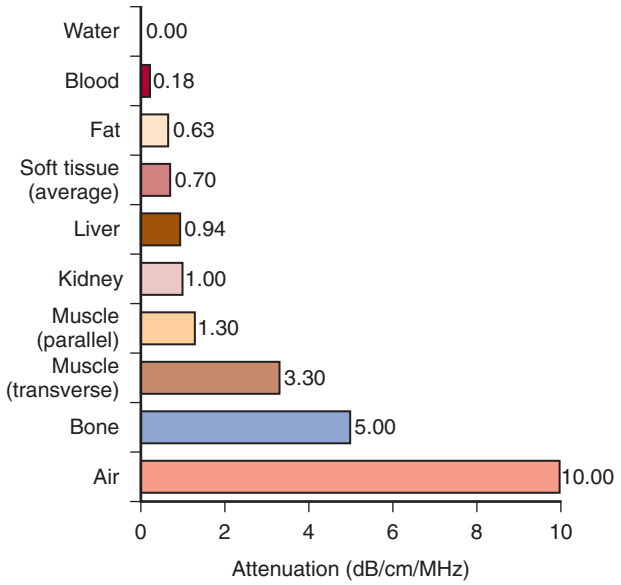

FIG. 1.9 Attenuation. As sound passes through tissue, it loses energy through the transfer of energy to tissue by heating, reflection, and scattering. Attenuation is determined by the insonating frequency and the nature of the attenuating medium. Attenuation values for normal tissues show considerable variation. Attenuation also increases in proportion to insonating frequency, resulting in less penetration at higher frequencies.

penetrates a specific tissue and varies considerably in normal tissues (Fig. 1.9).

INSTRUMENTATION

Ultrasound scanners are complex and sophisticated imaging devices, but all consist of the following basic components to perform key functions:

- Transmitter or pulser to energize the transducer
- Ultrasound transducer
- Receiver and processor to detect and amplify the backscattered energy and manipulate the reflected signals for display
- Display that presents the ultrasound image or data in a form suitable for analysis and interpretation
- Method to record or store the ultrasound image

Transmitter

Most clinical applications use pulsed ultrasound, in which brief bursts of acoustic energy are transmitted into the body. The source of these pulses, the ultrasound transducer, is energized by application of precisely timed, high-amplitude **voltage.** The maximum voltage that may be applied to the transducer is limited by federal regulations that restrict the acoustic output of diagnostic scanners. Most scanners provide a control that permits attenuation of the output voltage. Because the use of maximum output results in higher exposure of the patient to ultrasound **energy, prudent use** dictates use of the output attenuation controls to reduce power levels to the lowest levels consistent with the diagnostic problem.[4]

The transmitter also controls the rate of pulses emitted by the transducer, or the **pulse repetition frequency** (PRF). The PRF determines the time interval between ultrasound pulses and is important in determining the depth from which unambiguous data can be obtained both in imaging and Doppler modes. The ultrasound pulses must be spaced with enough time between the pulses to permit the sound to travel to the depth of interest and return before the next pulse is sent. For imaging, PRFs from 1 to 10 kHz are used, resulting in an interval of 0.1 to 1 ms between pulses. Thus a PRF of 5 kHz permits an echo to travel and return from a depth of 15.4 cm before the next pulse is sent.

Transducer

A transducer is any device that converts one form of energy to another. In ultrasound the transducer converts electric energy to mechanical energy, and vice versa. In diagnostic ultrasound systems the transducer serves two functions: (1) converting the electric energy provided by the transmitter to the acoustic pulses directed into the patient and (2) serving as the receiver of reflected echoes, converting weak pressure changes into electric signals for processing.

Ultrasound transducers use **piezoelectricity,** a principle discovered by Pierre and Jacques Curie in 1880.[5] Piezoelectric materials have the unique ability to respond to the action of an electric field by changing shape. They also have the property of generating electric potentials when compressed. Changing the polarity of a voltage applied to the transducer changes the thickness of the transducer, which expands and contracts as the polarity changes. This results in the generation of mechanical pressure waves that can be transmitted into the body. The piezoelectric effect also results in the generation of small potentials across the transducer when the transducer is struck by returning echoes. Positive pressures cause a small polarity to develop across the transducer; negative pressure during the rarefaction portion of the acoustic wave produces the opposite polarity across the transducer. These tiny polarity changes and the associated voltages are the source of all the information processed to generate an ultrasound image or Doppler display.

When stimulated by the application of a voltage difference across its thickness, the transducer vibrates. The frequency of vibration is determined by the transducer material. When the transducer is electrically stimulated, a range or **band of frequencies** results. The preferential frequency produced by a transducer is determined by the **propagation speed** of the transducer material and its thickness. In the **pulsed wave** operating modes used for most clinical ultrasound applications, the ultrasound pulses contain additional frequencies that are both higher and lower than the preferential frequency. The range of frequencies produced by a given transducer is termed its **bandwidth.** Generally, the shorter the pulse of ultrasound produced by the transducer, the greater is the bandwidth.

Most modern digital ultrasound systems employ broadbandwidth technology. **Ultrasound bandwidth** refers to the range of frequencies produced and detected by the ultrasound system. This is important because each tissue in the body has a characteristic response to ultrasound of a given frequency, and different tissues respond differently to different frequencies. The range of frequencies arising from a tissue exposed to ultrasound is referred to as the **frequency spectrum bandwidth** of the tissue, or tissue

signature. **Broad-bandwidth** technology provides a means to capture the frequency spectrum of insonated tissues, preserving acoustic information and tissue signature. Broad-bandwidth beam formers reduce speckle artifact by a process of **frequency compounding.** This is possible because speckle patterns at different frequencies are independent of one another, and combining data from multiple frequency bands (i.e., compounding) results in a reduction of speckle in the final image, leading to improved contrast resolution.

The length of an ultrasound pulse is determined by the number of alternating voltage changes applied to the transducer. For **continuous wave** (CW) ultrasound devices, a constant **alternating current** is applied to the transducer, and the alternating polarity produces a continuous ultrasound wave. For imaging, a single, brief voltage change is applied to the transducer, causing it to vibrate at its preferential frequency. Because the transducer continues to vibrate or "ring" for a short time after it is stimulated by the voltage change, the ultrasound pulse will be several cycles long. The number of cycles of sound in each pulse determines the **pulse length.** For imaging, short pulse lengths are desirable because longer pulses result in poorer axial resolution. To reduce the pulse length, **damping** materials are used in the construction of the transducer. In clinical imaging applications, very short pulses are applied to the transducer, and the transducers have highly efficient damping. This results in very short pulses of ultrasound, generally consisting of only two or three cycles of sound.

The ultrasound pulse generated by a transducer must be propagated in tissue to provide clinical information. Special transducer coatings and ultrasound coupling gels are necessary to allow efficient transfer of energy from the transducer to the body. Once in the body, the ultrasound pulses are propagated, reflected, refracted, and absorbed, in accordance with the basic acoustic principles summarized earlier.

The ultrasound pulses produced by the transducer result in a series of wavefronts that form a three-dimensional (3-D) beam of ultrasound. The features of this beam are influenced by constructive and destructive interference of the pressure waves, the curvature of the transducer, and acoustic lenses used to shape the beam. Interference of pressure waves results in an area near the transducer where the pressure amplitude varies greatly. This region is termed the **near field,** or **Fresnel zone.** Farther from the transducer, at a distance determined by the radius of the transducer and the frequency, the sound field begins to diverge, and the pressure amplitude decreases at a steady rate with increasing distance from the transducer. This region is called the **far field,** or **Fraunhofer zone.** In modern multielement transducer arrays, precise timing of the firing of elements allows correction of this divergence of the ultrasound beam and focusing at selected depths. Only reflections of pulses that return to the transducer are capable of stimulating the transducer with small pressure changes, which are converted into the voltage changes that are detected, amplified, and processed to build an image based on the echo information.

Receiver

When returning echoes strike the transducer face, minute voltages are produced across the piezoelectric elements. The receiver detects and amplifies these weak signals. The receiver also provides a means for compensating for the differences in echo strength, which result from attenuation by different tissue thickness by control of **time gain compensation** (TGC) or **depth gain compensation** (DGC).

Sound is attenuated as it passes into the body, and additional energy is removed as echoes return through tissue to the transducer. The attenuation of sound is proportional to the frequency and is constant for specific tissues. Because echoes returning from deeper tissues are weaker than those returning from more superficial structures, they must be amplified more by the receiver to produce a uniform tissue echo appearance (Fig. 1.10). This adjustment is accomplished by TGC controls that permit the user to selectively amplify the signals from deeper structures or to suppress the signals from superficial tissues, compensating for tissue attenuation. Although many newer machines provide

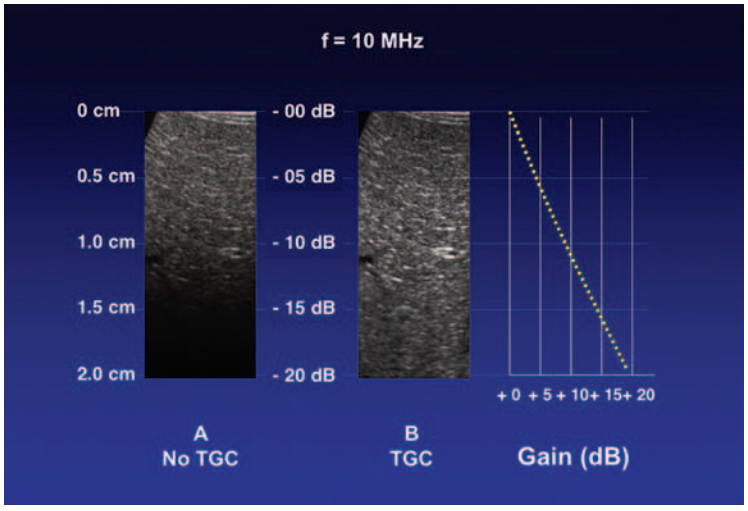

FIG. 1.10 Time Gain Compensation (TGC). Without TGC, tissue attenuation causes gradual loss of display of deeper tissues *(A)*. In this example, tissue attenuation of 1 dB/cm/MHz is simulated for a transducer of 10 MHz. At a depth of 2 cm, the intensity is –20 dB (1% of initial value). By applying increasing amplification or gain to the backscattered signal to compensate for this attenuation, a uniform intensity is restored to the tissue at all depths *(B)*.

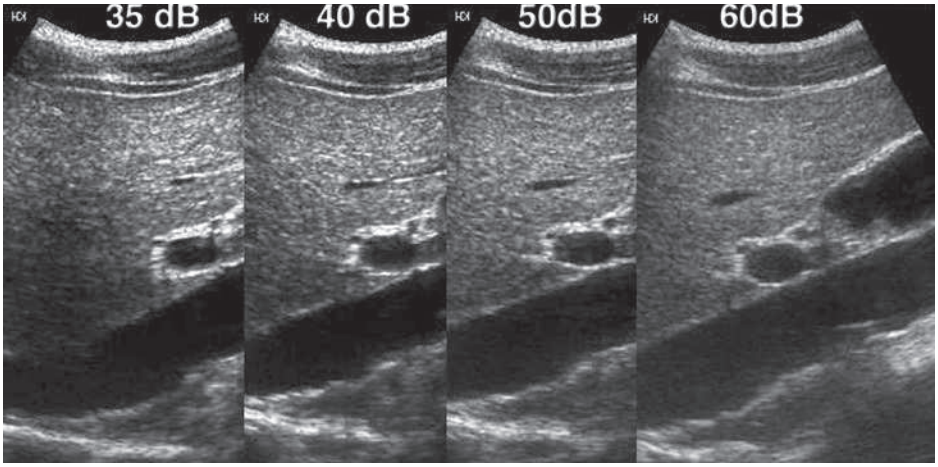

FIG. 1.11 Dynamic Range. The ultrasound receiver must compress the wide range of amplitudes returning to the transducer into a range that can be displayed to the user. Here, compression and remapping of the data to display dynamic ranges of 35, 40, 50, and 60 dB are shown. The widest dynamic range shown (60 dB) permits the best differentiation of subtle differences in echo intensity and is preferred for most imaging applications. The narrower ranges increase conspicuity of larger echo differences.

for some means of automatic TGC, the manual adjustment of this control is one of the most important user controls and may have a profound effect on the quality of the ultrasound image provided for interpretation.

Another important function of the receiver is the compression of the wide range of amplitudes returning to the transducer into a range that can be displayed to the user. The ratio of the highest to the lowest amplitudes that can be displayed may be expressed in decibels and is referred to as the **dynamic range.** In a typical clinical application, the range of reflected signals may vary by a factor of as much as $1:10^{12}$, resulting in a dynamic range of up to 120 dB. Although the amplifiers used in ultrasound machines are capable of handling this range of voltages, gray-scale displays are limited to display a signal intensity range of only 35 to 40 dB. **Compression** and **remapping** of the data are required to adapt the dynamic range of the backscattered signal intensity to the dynamic range of the display (Fig. 1.11). Compression is performed in the receiver by selective amplification of weaker signals. Additional manual postprocessing controls permit the user to map selectively the returning signal to the display. These controls affect the brightness of different echo levels in the image and therefore determine the image contrast.

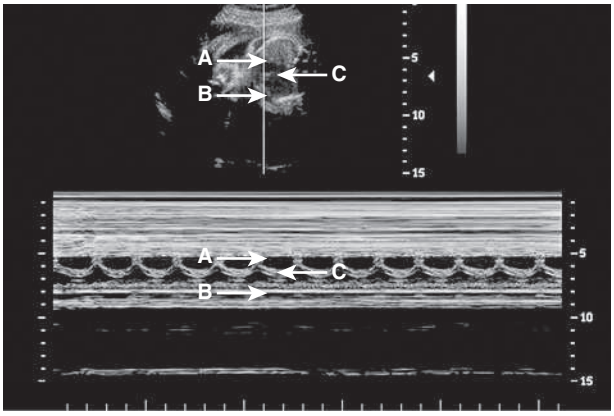

FIG. 1.12 M-Mode Display. M-mode ultrasound displays changes of echo amplitude and position with time. Display of changes in echo position is useful in the evaluation of rapidly moving structures such as cardiac valves and chamber walls. Here, the three major moving structures in the upper gray-scale image of the fetus are recorded in the corresponding M-mode image and include the near ventricular wall *(A)*, the interventricular septum *(B)*, and the far ventricular wall *(C)*. The baseline is a time scale that permits the calculation of heart rate from the M-mode data.

Image Display

Ultrasound signals may be displayed in several ways. Over the years, imaging has evolved from simple **A-mode (amplitude-mode)** and bistable display to high-resolution, real-time, gray-scale imaging. The earliest A-mode devices displayed the voltage produced across the transducer by the backscattered echo as a vertical deflection on the face of an oscilloscope. The horizontal time sweep of the oscilloscope was calibrated to indicate the distance from the transducer to the reflecting surface. In this form of display, the strength or amplitude of the reflected sound is indicated by the height of the vertical deflection displayed on the oscilloscope. With **A-mode ultrasound,** only the position and strength of a reflecting structure are recorded.

Another simple form of imaging, **M-mode (motion-mode) ultrasound,** displays echo amplitude and shows the position of moving reflectors (Fig. 1.12). M-mode imaging uses the brightness of the display to indicate the intensity of the reflected signal. The time base of the display can be adjusted to allow for varying degrees of temporal resolution, as dictated by clinical application. M-mode ultrasound is interpreted by assessing motion patterns of specific reflectors and determining anatomic relationships from characteristic patterns of motion. Currently, the major application of M-mode display is evaluation of embryonic and fetal heart rates, as well as in echocardiography, the rapid motion of cardiac valves and of cardiac chamber and vessel walls. M-mode imaging may play a future role in measurement of subtle changes in vessel wall elasticity accompanying atherogenesis.

The mainstay of imaging with ultrasound is provided by **real-time, gray-scale, B-mode display,** in which variations in display intensity or brightness are used to indicate reflected signals

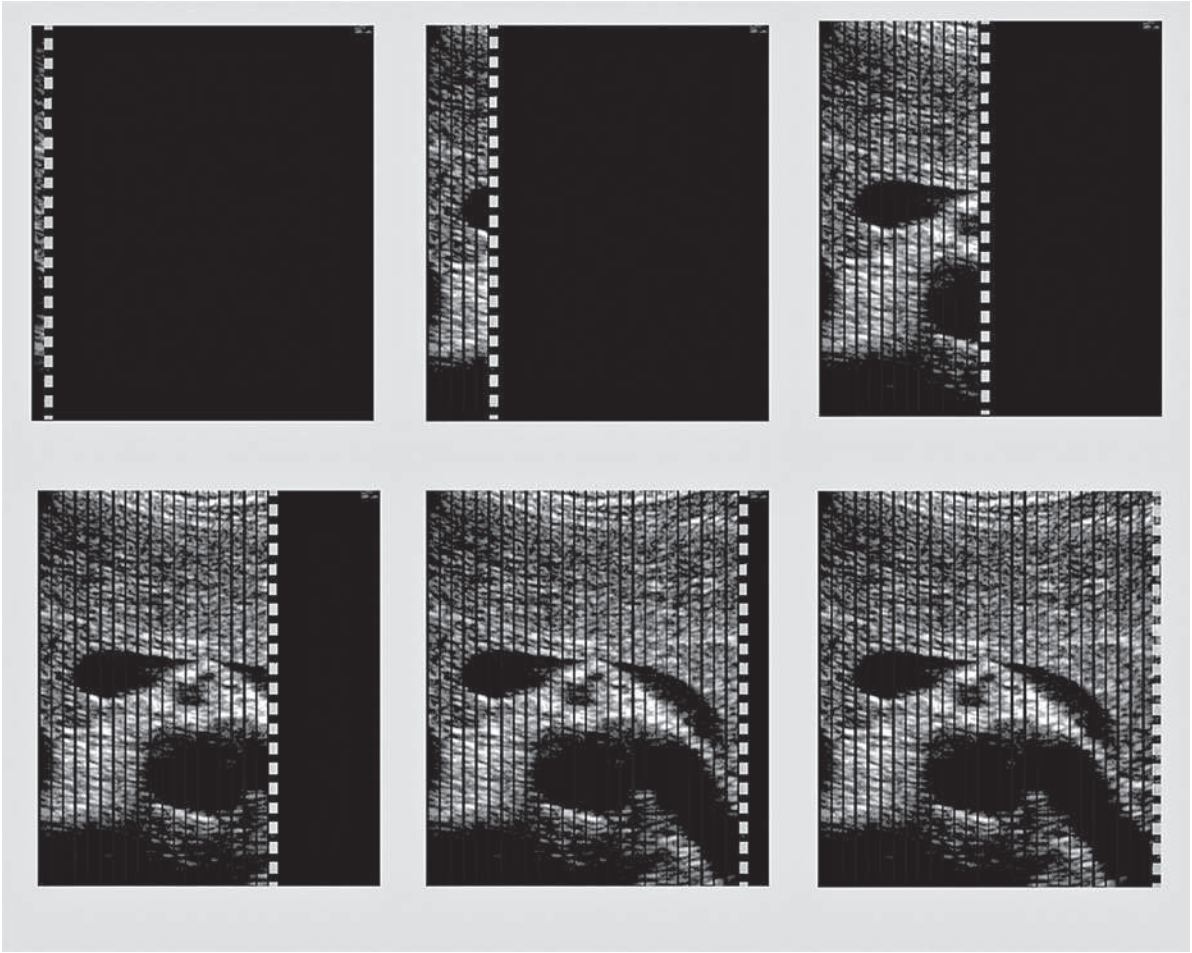

FIG. 1.13 B-Mode Imaging. A two-dimensional (2-D), real-time image is built by ultrasound pulses sent down a series of successive scan lines. Each scan line adds to the image, building a 2-D representation of echoes from the object being scanned. In real-time imaging, an entire image is created 15 to 60 times per second.

of differing amplitude. To generate a 2-D image, multiple ultrasound pulses are sent down a series of successive scan lines (Fig. 1.13), building a 2-D representation of echoes arising from the object being scanned. When an ultrasound image is displayed on a black background, signals of greatest intensity appear as white; absence of signal is shown as black; and signals of intermediate intensity appear as shades of gray. If the ultrasound beam is moved with respect to the object being examined and the position of the reflected signal is stored, the brightest portions of the resulting 2-D image indicate structures reflecting more of the transmitted sound energy back to the transducer.

In most modern instruments, digital memory is used to store values that correspond to the echo intensities originating from corresponding positions in the patient. At least 2^8, or 256, shades of gray are possible for each pixel, in accord with the amplitude of the echo being represented. The image stored in memory in this manner can then be sent to a monitor for display.

Because B-mode display relates the strength of a backscattered signal to a brightness level on the display device, it is important that the operator understand how the amplitude information in the ultrasound signal is translated into a brightness scale in the image display. Each ultrasound manufacturer offers several options for the way the dynamic range of the target is compressed for display, as well as the transfer function that assigns a given signal amplitude to a shade of gray. Although these technical details vary among machines, the way the operator uses them may greatly affect the clinical value of the final image. In general, it is desirable to display as *wide* a dynamic range as possible, to identify subtle differences in tissue echogenicity (see Fig. 1.11).

Real-time ultrasound produces the impression of motion by generating a series of individual 2-D images at rates of 15 to 60 frames per second. Real-time, 2-D, B-mode ultrasound is the major method for ultrasound imaging throughout the body and is the most common form of B-mode display. Real-time ultrasound permits assessment of both anatomy and motion. When images are acquired and displayed at rates of several times per second, the effect is dynamic, and because the image reflects the state and motion of the organ at the time it is examined, the information is regarded as being shown in real time. In cardiac applications the terms *2-D echocardiography* and *2-D echo* are used to describe real-time, B-mode imaging; in most other applications the term *real-time ultrasound* is used.

Transducers used for real-time imaging may be classified by the method used to steer the beam in rapidly generating each

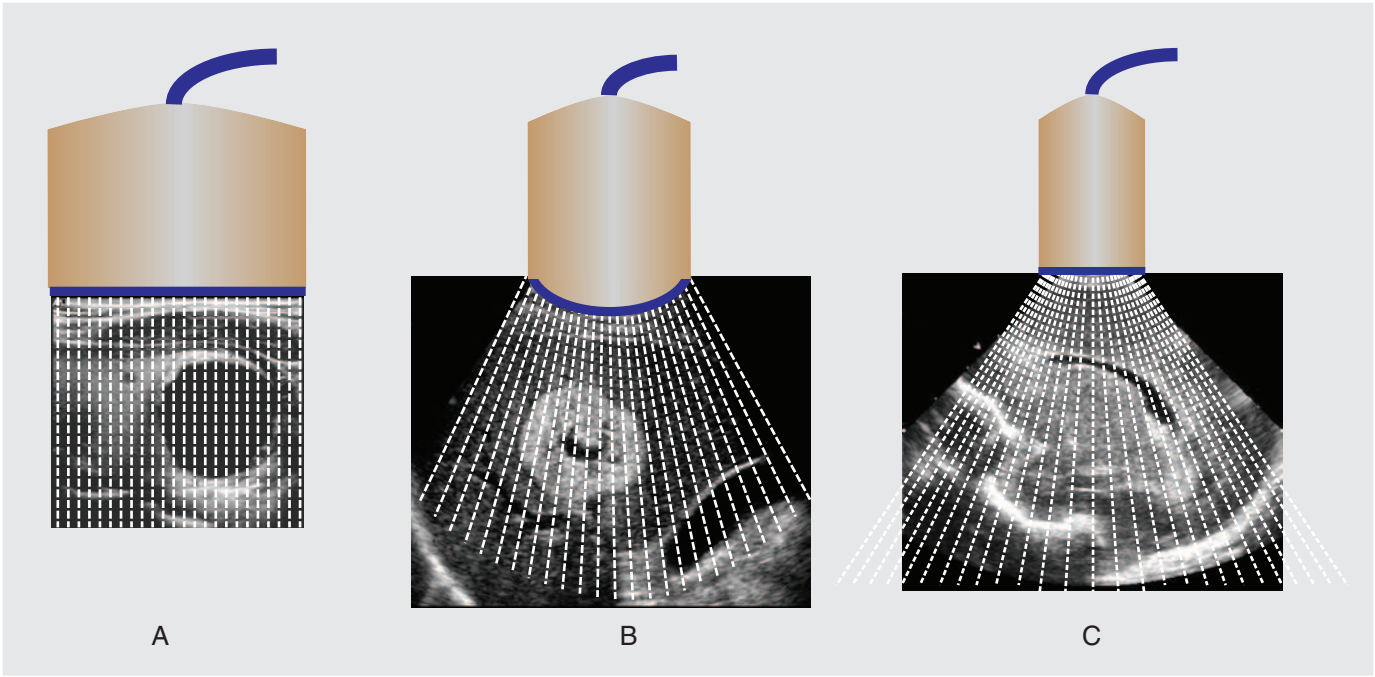

FIG. 1.14 Beam Steering. (A) Linear array. In a linear array transducer, individual elements or groups of elements are fired in sequence. This generates a series of parallel ultrasound beams, each perpendicular to the transducer face. As these beams move across the transducer face, they generate the lines of sight that combine to form the final image. Depending on the number of transducer elements and the sequence in which they are fired, focusing at selected depths from the surface can be achieved Small high-frequency linear arrays are well-suited for small parts scanning. **(B) Curved array.** A variant of the linear array, the curved array uses tranducer elements arranged in an arc, producing a pie-shaped image. These transducers are well-suited for abdominal, pelvic, and fetal examinations. **(C) Phased array.** A phased array transducer produces a sector field of view by firing multiple transducer elements in precise sequence to generate interference of acoustic wavefronts that steer the beam. The ultrasound beam that results generates a series of lines of sight at varying angles from one side of the transducer to the other, producing a sector image format. These transducers require a small contact area compared to most linear and curved arrays and are useful for scanning in areas where access is limited.

individual image, keeping in mind that as many as 30 to 60 complete images must be generated per second for real-time applications. **Beam steering** may be done through mechanical rotation or oscillation of the transducer or by electronic means (Fig. 1.14). **Electronic beam steering** is used in linear array and phased array transducers and permits a variety of image display formats. Most electronically steered transducers currently in use also provide electronic focusing that is adjustable for depth. **Mechanical beam steering** may use single-element transducers with a fixed focus or may use annular arrays of elements with electronically controlled focusing. For real-time imaging, transducers using mechanical or electronic beam steering generate displays in a rectangular or pie-shaped format. For obstetric, small parts, and peripheral vascular examinations, linear array transducers with a rectangular image format are often used. The rectangular image display has the advantage of a larger field of view near the surface but requires a large surface area for transducer contact. Sector scanners with either mechanical or electronic steering require only a small surface area for contact and are better suited for examinations in which access is limited.

Mechanical Sector Scanners

Early ultrasound scanners used transducers consisting of a single piezoelectric element. To generate real-time images with these transducers, mechanical devices were required to move the transducer in a linear or circular motion. Mechanical sector scanners using one or more single-element transducers do not allow variable focusing. This problem is overcome by using annular array transducers. Although important in the early days of real-time imaging, mechanical sector scanners with fixed-focus, single-element transducers are not presently in common use.

Arrays

Current technology uses a transducer composed of multiple elements, usually produced by precise slicing of a piece of piezoelectric material into numerous small units, each with its own electrodes. Such transducer arrays may be formed in a variety of configurations. Typically, these are linear, curved, phased, or annular arrays. High-density 2-D arrays have also been developed. By precise timing of the firing of combinations of elements in these arrays, interference of the wavefronts generated by the individual elements can be exploited to change the direction of the ultrasound beam, and this can be used to provide a steerable beam for the generation of real-time images in a linear or sector format.

Linear Arrays

Linear array transducers are used for small parts, vascular, and obstetric applications because the rectangular image format produced by these transducers is well suited for these applications.

In these transducers, individual elements are arranged in a linear fashion. By firing the transducer elements in sequence, either individually or in groups, a series of parallel pulses is generated, each forming a line of sight perpendicular to the transducer face. These individual lines of sight combine to form the image field of view (see Fig. 1.14A). Depending on the number of transducer elements and the sequence in which they are fired, focusing at selected depths from the surface can be achieved.

Curved Arrays

Linear arrays that have been shaped into convex curves produce an image that combines a relatively large surface field of view with a sector display format (see Fig. 1.14B). Curved array transducers are used for a variety of applications, the larger versions serving for general abdominal, obstetric, and transabdominal pelvic scanning. Small, high-frequency, curved array scanners are often used in transvaginal and transrectal probes and for pediatric imaging.

Phased Arrays

In contrast to mechanical sector scanners, phased array scanners have no moving parts. A sector field of view is produced by multiple transducer elements fired in precise sequence under electronic control. By controlling the time and sequence at which the individual transducer elements are fired, the resulting ultrasound wave can be steered in different directions as well as focused at different depths (see Fig. 1.14C). By rapidly steering the beam to generate a series of lines of sight at varying angles from one side of the transducer to the other, a sector image format is produced. This allows the fabrication of transducers of relatively small size but with large fields of view at depth. These transducers are particularly useful for neonatal head ultrasound, as well as for intercostal scanning, to evaluate the heart, liver, or spleen, and for examinations in other areas where access is limited.

Two-Dimensional Arrays

Transducer arrays can be formed either by slicing a rectangular piece of transducer material perpendicular to its long axis to produce a number of small rectangular elements or by creating a series of concentric elements nested within one another in a circular piece of piezoelectric material to produce an annular array. The use of multiple elements permits precise focusing. A particular advantage of 2-D array construction is that the beam can be focused in both the elevation plane and the lateral plane, and a uniform and highly focused beam can be produced (Fig. 1.15). These arrays improve spatial resolution and contrast, reduce clutter, and are well suited for the collection of data from volumes of tissue for use in 3-D processing and display. Unlike linear 2-D arrays, in which delays in the firing of the individual elements may be used to steer the beam, annular arrays do not permit beam steering and, to be used for real-time imaging, must be steered mechanically.

Transducer Selection

Practical considerations in the selection of the optimal transducer for a given application include not only the requirements for spatial resolution, but also the distance of the target object from the transducer because penetration of ultrasound diminishes as frequency increases. In general, the *highest ultrasound frequency permitting penetration to the depth of interest should be selected.* For superficial vessels and organs, such as the thyroid, breast, or testicle, lying within 1 to 3 cm of the surface, imaging frequencies of 7.5 to 15 MHz are typically used. These high frequencies are also ideal for intraoperative applications. If the region to be scanned is very superficial, such that the probe does not allow for focusing at the area of interest, a standoff pad can be utilized. For evaluation of deeper structures in the abdomen or pelvis more than 12 to 15 cm from the surface, frequencies as low as 2.25 to 3.5 MHz may be required. When maximal resolution is needed, a high-frequency transducer with excellent lateral and elevation resolution at the depth of interest is required.

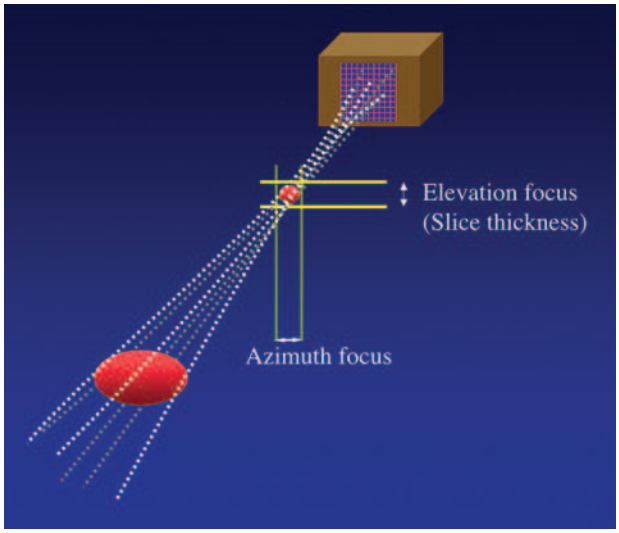

FIG. 1.15 Two-Dimensional Array. High-density, two-dimensional (2-D) arrays consist of a 2-D matrix of transducer elements, permitting acquisition of data from a volume rather than a single plane of tissue. Precise electronic control of individual elements permits adjustable focusing on both **azimuth** and elevation planes.

IMAGE DISPLAY AND STORAGE

With real-time ultrasound, user feedback is immediate and is provided by video display. The brightness and contrast of the image on this display are determined by the ambient lighting in the examination room, the brightness and contrast settings of the video monitor, the system gain setting, and the TGC adjustment. The factor most affecting image quality in many ultrasound departments is probably improper adjustment of the video display, with a lack of appreciation of the relationship between the video display settings and the appearance of hard copy or images viewed on a workstation. Because of the importance of the real-time video display in providing feedback to the user, it is essential that the display and the lighting conditions under which it is viewed are standardized and matched to the display used for interpretation. Interpretation of images and archival storage of images may be in the form of transparencies printed on film by optical or laser cameras and printers, videotape, or digital **picture**

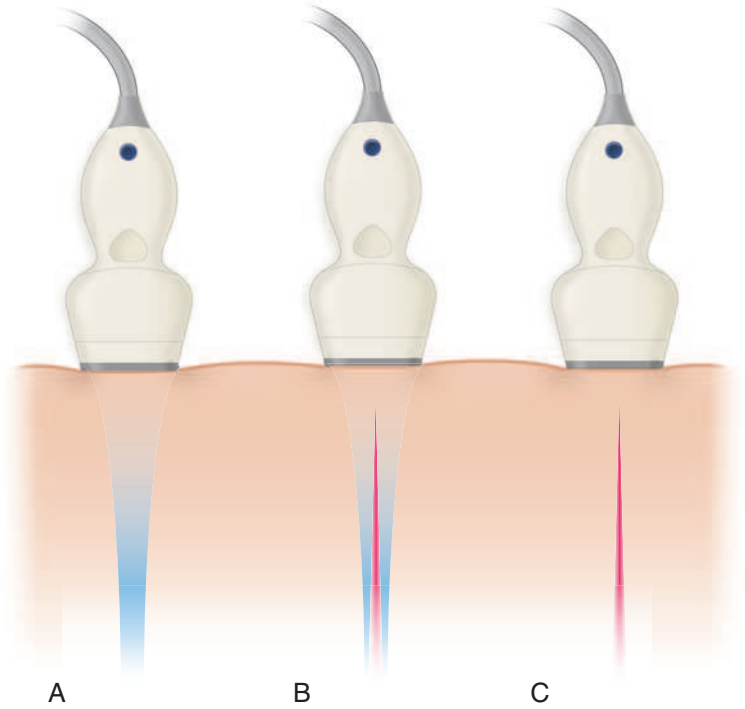

FIG. 1.16 Tissue Harmonics. As sound is propagated through tissue, the high-pressure component of the wave travels more rapidly than the rarefactional component, producing distortion of the wave and generating higher-frequency components (harmonics). **(A)** The acoustic field of the primary frequency is represented in blue. **(B)** The second harmonic (twice the primary frequency) is represented in red. **(C)** Using a broad-bandwidth transducer, the receiver can be tuned to generate an image from the harmonic frequency rather than the primary frequency. As a result, near field clutter is reduced since the harmonic only develops at depth in the tissue and the beam profile is improved, leading to better spatial resolution.

archiving and communications system (PACS). Increasingly, digital storage is being used for archiving of ultrasound images.

SPECIAL IMAGING MODES

Tissue Harmonic Imaging

Variation of the propagation velocity of sound in fat and other tissues near the transducer results in a **phase aberration** that distorts the ultrasound field, producing noise and clutter in the ultrasound image. Tissue harmonic imaging provides an approach for reducing the effects of phase aberrations.[6] Nonlinear propagation of ultrasound through tissue is associated with the more rapid propagation of the high-pressure component of the ultrasound pressure wave than its negative (rarefactional) component. This results in increasing distortion of the acoustic pulse as it travels within the tissue and causes the generation of multiples, or **harmonics,** of the transmitted frequency (Fig. 1.16).

Tissue harmonic imaging takes advantage of the generation, at depth, of these harmonics. Because the generation of harmonics requires interaction of the transmitted field with the propagating tissue, harmonic generation is not present near the transducer/skin interface, and it only becomes important some distance from the transducer. In most cases the near and far fields of the image are affected less by harmonics than by intermediate locations. Using broad-bandwidth transducers and signal filtration or coded pulses, the harmonic signals reflected from tissue interfaces can be selectively displayed. Because most imaging artifacts are caused by the interaction of the ultrasound beam with superficial structures or by aberrations at the edges of the beam profile, these artifacts are eliminated using harmonic imaging because the artifact-producing signals do not consist of sufficient energy to generate harmonic frequencies and therefore are filtered out during image formation. Images generated using tissue harmonics often exhibit reduced noise and clutter (Fig. 1.17). Because harmonic beams are narrower than the originally transmitted beams, spatial resolution is improved and side lobes are reduced.

Spatial Compounding

An important source of image degradation and loss of contrast is ultrasound **speckle.** Speckle results from the constructive and destructive interaction of the acoustic fields generated by the scattering of ultrasound from small tissue reflectors. This interference pattern gives ultrasound images their characteristic grainy appearance (see Fig. 1.6), reducing contrast (Fig. 1.18) and making the identification of subtle features more difficult. By summing images from different scanning angles through **spatial compounding** (Fig. 1.19), significant improvement in the **contrast-to-noise ratio** can be achieved (Fig. 1.20). This is because speckle is random, and the generation of an image by compounding will reduce speckle noise because only the signal is reinforced. In addition, spatial compounding may reduce artifacts that result when an ultrasound beam strikes a specular reflector at an angle

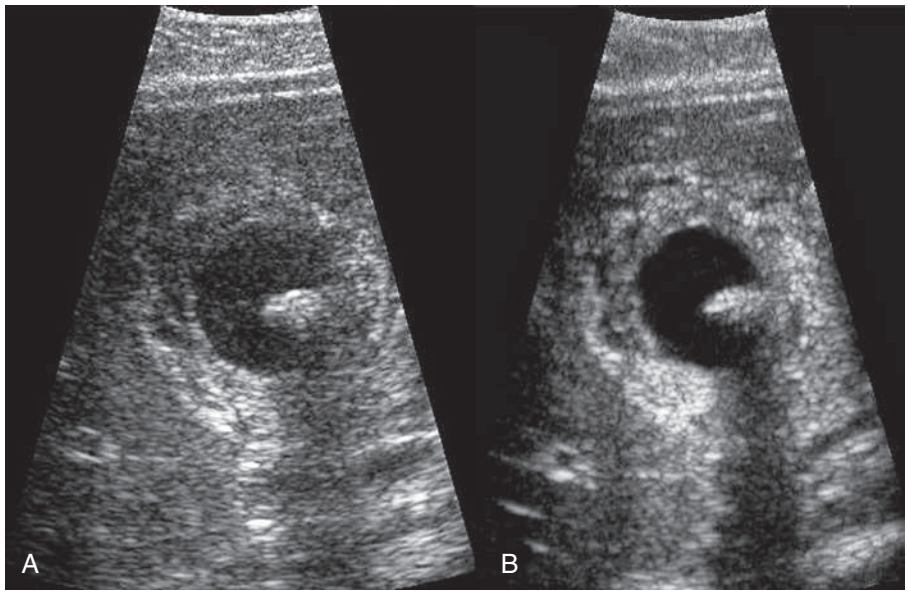

FIG. 1.17 Tissue Harmonic Imaging. (A) Conventional image and **(B) tissue harmonic image** of gallbladder of patient with acute cholecystitis. Note the reduction of noise and clutter in the tissue harmonic image. Because harmonic beams do not interact with superficial structures and are narrower than the originally transmitted beam, spatial resolution is improved and clutter and side lobes are reduced. (With permission from Merritt CR. Technology update. Radiol Clin North Am. 2001;39:385-397.[7])

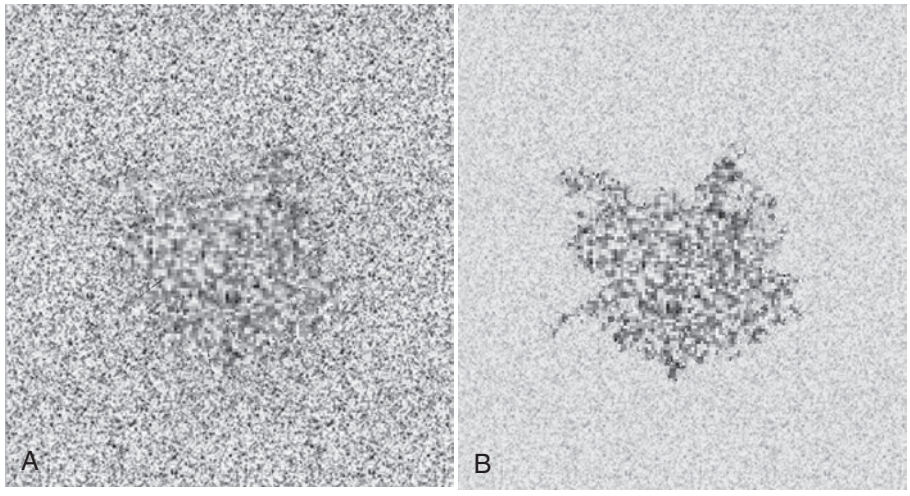

FIG. 1.18 Effect of Speckle on Contrast. (A) Speckle noise partially obscures the simulated lesion. **(B)** The speckle has been reduced, increasing contrast resolution between the lesion and the background. (With permission from Merritt CR. Technology update. Radiol Clin North Am. 2001;39:385-397.[7])

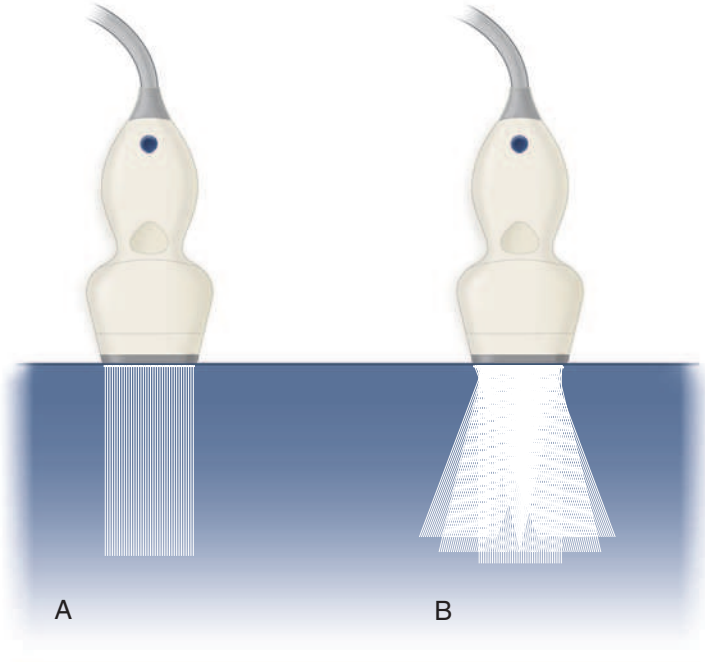

FIG. 1.19 Spatial Compounding. (A) Conventional imaging is limited to a fixed angle of incidence of ultrasound scan lines to tissue interfaces, resulting in poor definition of specular reflectors that are not perpendicular to the beam. **(B) Spatial compounding** combines images obtained by insonating the target from multiple angles. In addition to improving detection of interfaces, compounding reduces speckle noise because only the signal is reinforced; speckle is random and not reinforced. This improves contrast.

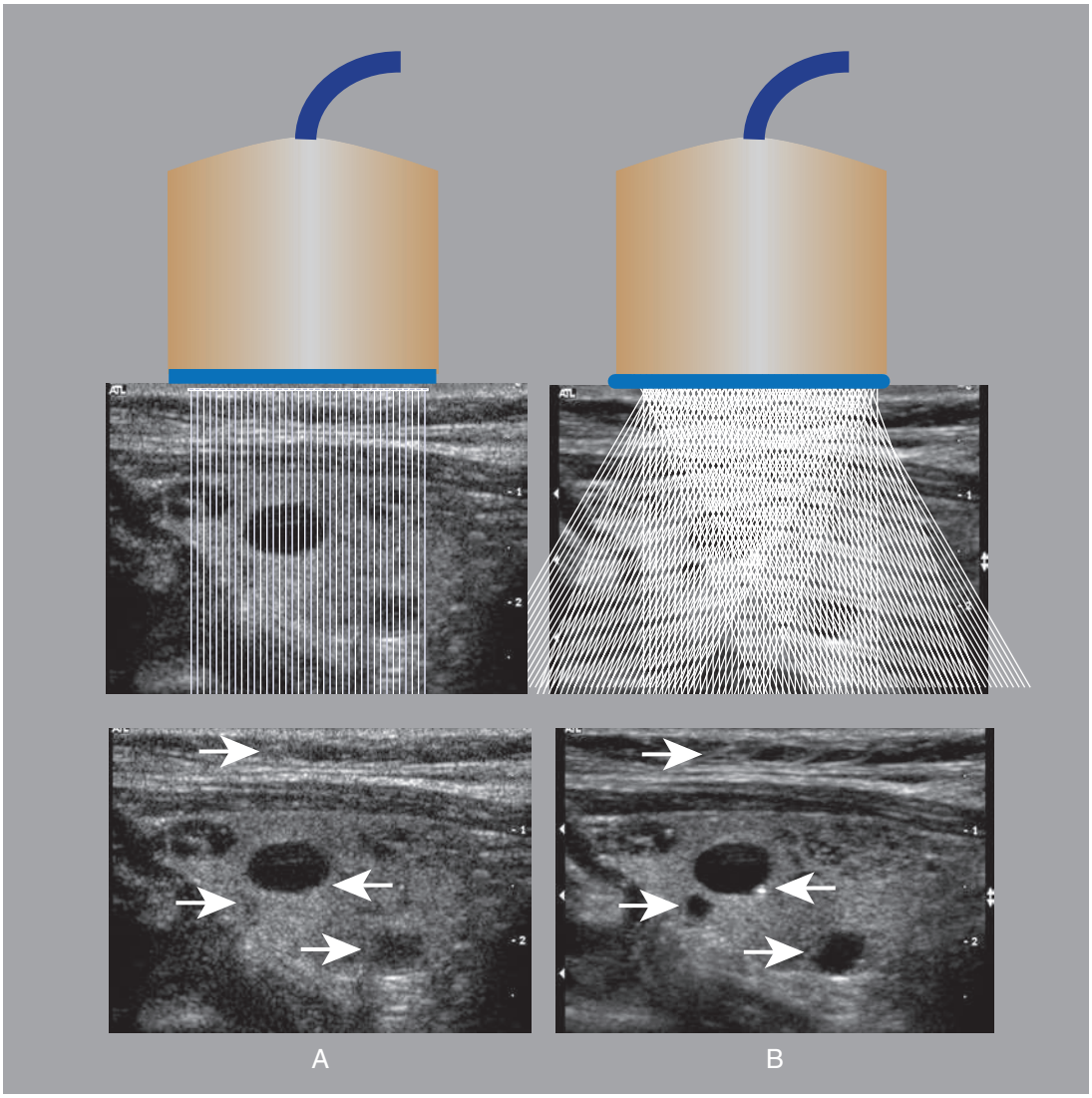

FIG. 1.20 Spatial Compounding. (A) Conventional image and **(B) compound image** of the thyroid. Note the reduced speckle as well as better definition of regions *(arrows)* such as superficial tissue as well as small cysts and calcifications.

greater or less than 90 degrees. In conventional real-time imaging, each scan line used to generate the image strikes the target at a constant, fixed angle. As a result, strong reflectors that are not perpendicular to the ultrasound beam scatter sound in directions that prevent their clear detection and display. This in turn results in poor margin definition and less distinct boundaries for cysts and other masses. Compounding has been found to reduce these artifacts. Limitations of compounding are diminished visibility of shadowing and enhancement; however, these are offset by the ability to evaluate lesions, both with and without compounding, preserving shadowing and enhancement when these features are important to diagnosis.[7]

Three-Dimensional Ultrasound

Dedicated 3-D scanners used for fetal (Fig. 1.21), gynecologic, and cardiac scanning may employ hardware-based image registration, high-density 2-D arrays, or software registration of scan planes as a tissue volume is acquired. 3-D imaging permits volume data to be viewed in multiple imaging planes and allows accurate measurement of lesion volume.

Ultrasound Elastography

Palpation is an effective method for detection of tissue abnormality based on detection of changes in tissue stiffness or elasticity and may provide the earliest indication of disease, even when conventional imaging studies are normal. Ultrasound elastography provides a noninvasive method for evaluation of tissue stiffness.[8]

Tissue contrast in conventional ultrasound imaging is based on the **bulk modulus** determined by the molecular composition of tissue, whereas elastography reflects shear properties that are determined by a higher level of tissue organization, the **strain modulus.** This higher level of tissue organization is most likely to be altered by disease. The dynamic range of the strain modulus is several orders of magnitude greater than the bulk modulus, permitting contrast resolution far exceeding conventional ultrasound imaging.[9] Elastography therefore offers the potential for a

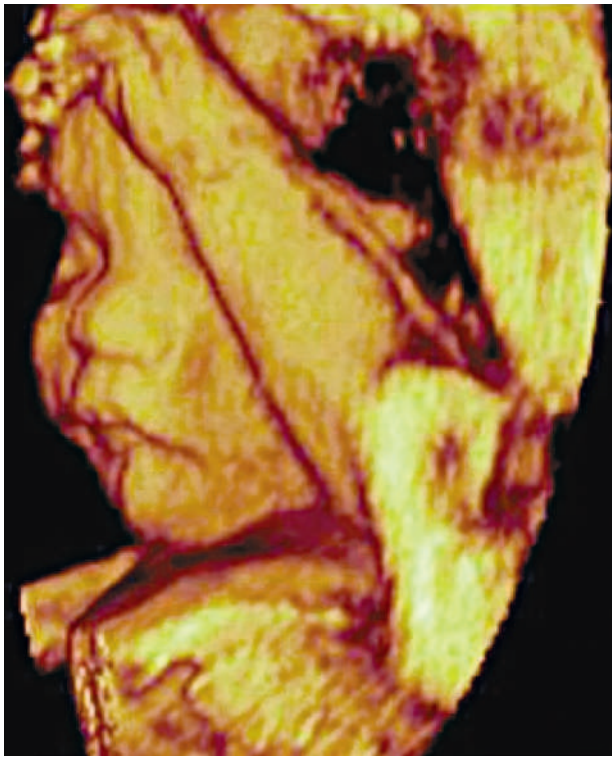

FIG. 1.21 Three-Dimensional Ultrasound Image, 24-Week Fetus. Three-dimensional ultrasound permits collection and review of data obtained from a volume of tissue in multiple imaging planes, as well as a rendering of surface features.

high degree of both sensitivity and specificity in differentiating normal and abnormal tissues.[8,10,11]

Tissue stiffness or elasticity is expressed by **Young modulus**—the ratio of compression pressure (stress) and the resulting deformation (strain)

$$E = \sigma/\varepsilon$$

where E is Young modulus expressed in Pa **(pascals),** σ is the stress, expressed in Newtons, and ε is displacement expressed in m^2.

Ultrasound-based elastography permits study of the elastic behavior of tissue through two general approaches (Fig. 1.22): strain elastography and shear wave elastography.

Strain Elastography

Strain elastography involves measurement of longitudinal tissue displacement before and after compression, usually by manual manipulation of the ultrasound transducer (see Fig. 1.22A). Speckle tracking using radiofrequency backscatter or Doppler is then used to evaluate tissue motion. Strain elastography cannot determine the Young modulus because the compression pressure (stress) cannot be measured directly. Instead, strain ratios are estimated by comparing lesion strain to surrounding normal tissues and displayed in the image in different shades of gray or through color maps (Fig. 1.23). Strain elastography provides an indication of relative stiffness of an area of interest compared to its surroundings.

Key Points of Ultrasound Elastography

- Ultrasound imaging is based on tissue bulk modulus, reflecting interactions at the molecular level.
- Changes in tissue stiffness based on the tissue shear modulus are important indications of disease.
- Ultrasound elastography provides relatative and quantitative assessment of tissue stiffness.
- Ultrasound elastography is based on tissue organization (strain modulus).
- Strain elastography provides an indication of relative tissue stiffness.
- Shear wave elastography provides a quantitative estimate of the tissue stiffness (strain modulus).

Shear Wave Elastography

Longitudinal tissue compression results in the generation of transverse shear waves[12,13] (see Fig. 1.22B). In shear wave elastography, shear waves are generated by repetitive compression produced by high-intensity pulses from the ultrasound transducer (see Fig. 1.22B). In contrast to longitudinal compressional waves that propagate very quickly in the human body (≈1540 m/sec), shear waves propagate slowly (≈1-50 m/sec). Shear waves are tracked with high frame rate images to determine their velocity. The **propagation velocity of shear waves** is directly proportional to Young modulus and provides a quantitative estimate of tissue stiffness[14,15] (Fig. 1.24).

IMAGE QUALITY

The key determinants of the quality of an ultrasound image are its spatial, contrast, and temporal resolution, as well as freedom from certain artifacts.

Spatial Resolution

The ability to differentiate two closely situated objects as distinct structures is determined by the spatial resolution of the ultrasound device. Spatial resolution must be considered in three planes, with different determinants of resolution for each. Simplest is the resolution along the axis of the ultrasound beam, or **axial resolution.** With pulsed wave ultrasound, the transducer introduces a series of brief bursts of sound into the body. Each ultrasound pulse typically consists of two or three cycles of sound. The pulse length is the product of the wavelength and the number of cycles in the pulse. Axial resolution, the maximum resolution along the beam axis, is determined by the pulse length (Fig. 1.25). Because ultrasound frequency and wavelength are inversely related, the pulse length decreases as the imaging frequency increases. Because the pulse length determines the maximum resolution along the axis of the ultrasound beam, *higher transducer frequencies provide higher image resolution.* For example, a transducer operating at 5 MHz produces sound with a wavelength of 0.308 mm. If each pulse consists of three cycles of sound, the pulse length is slightly less than 1 mm, and this becomes the maximum resolution along the beam

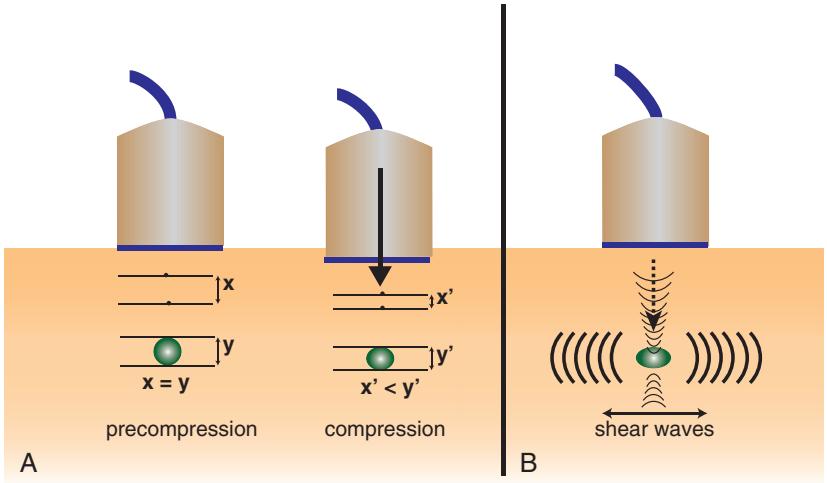

FIG. 1.22 Elastography. (A) Strain elastography (SE), and **(B) shear wave elastography (SWE).** Strain elastograms are images of tissue stiffness generated by analysis of speckle displacements before and after mechanical compression of tissue. The precompression frame is compared to a frame obtained after compression. In this example, the lesion is compressed much less than the surrounding tissue, indicating relative stiffness. SE is not quantitative and indicates only the relative hardness or softness of lesions compared to their surroundings. In SWE **(B)** high-intensity compression pulses from the transducer are focused on an area of interest, resulting in the generation of low-frequency shear waves. Speckle displacement resulting from shear (transverse) waves is tracked with multiple imaging frames in order to estimate shear wave velocity. Shear wave velocity is directly related to Young modulus, permitting a quantitative estimate of tissue stiffness.

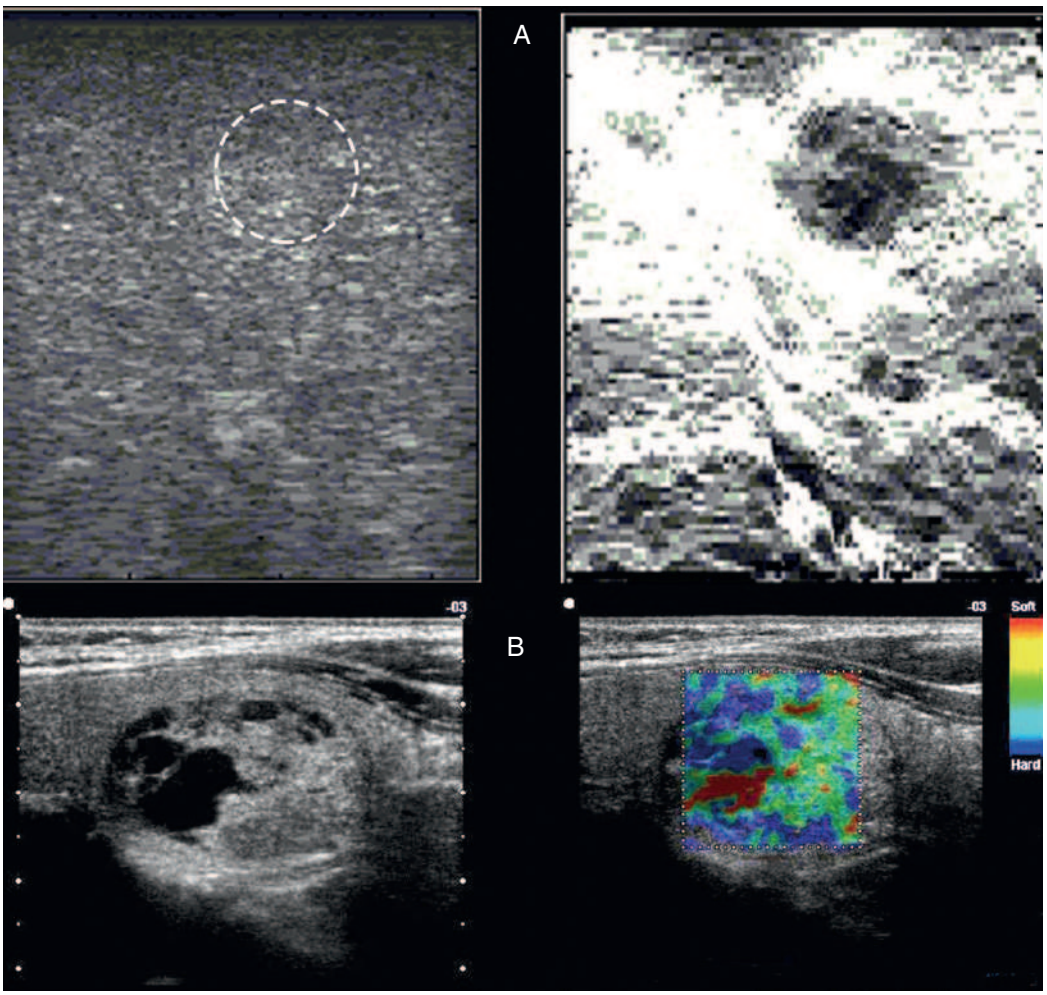

FIG. 1.23 Strain Elastograms. The upper frames **(A)** show *in vivo* images of swine liver containing a lesion produced by the injection of a small volume of absolute ethanol. In the precompression image *(left)* the lesion located within the circle is invisible. The elastogram *(right)* clearly delineates the lesion as an area of increased stiffness compared to the surrounding tissue. The lower frames **(B)** show a gray-scale image *(left)* and strain elastogram *(right)* of a mixed solid and cystic thyroid nodule. In the elastogram the color map displays relative stiffness with softer areas appearing as shades of red, orange, and yellow, and stiffer areas as dark blue. The nodule is heterogeneous with the relatively noncompressible cystic portions differentiated from more compressible surrounding tissue. (Courtesy of P. O'Kane, Thomas Jefferson University.)

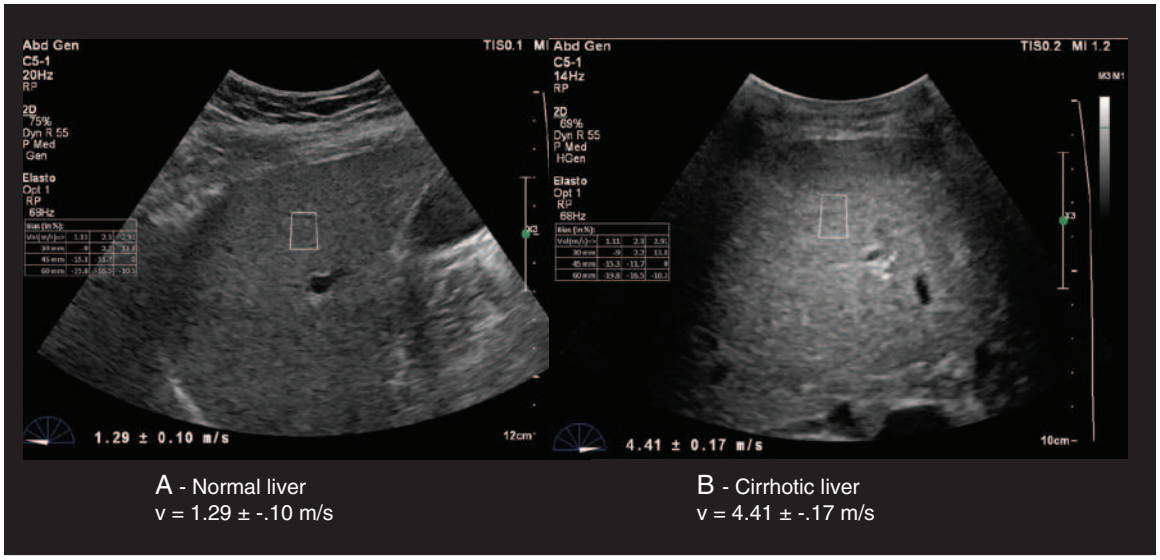

FIG. 1.24 Shear Wave Elastograms of (A) Normal and (B) Cirrhotic Liver. Shear wave velocities measured in liver tissue samples by shear wave elastography indicates a velocity of 1.29 ± 0.10 m/sec in the normal liver compared to a velocity of 4.41 ± 0.17 m/sec in the cirrhotic liver. Increased shear wave velocity is associated with increased tissue stiffness due to hepatic fibrosis. (Courtesy of P. O'Kane, Thomas Jefferson University.)

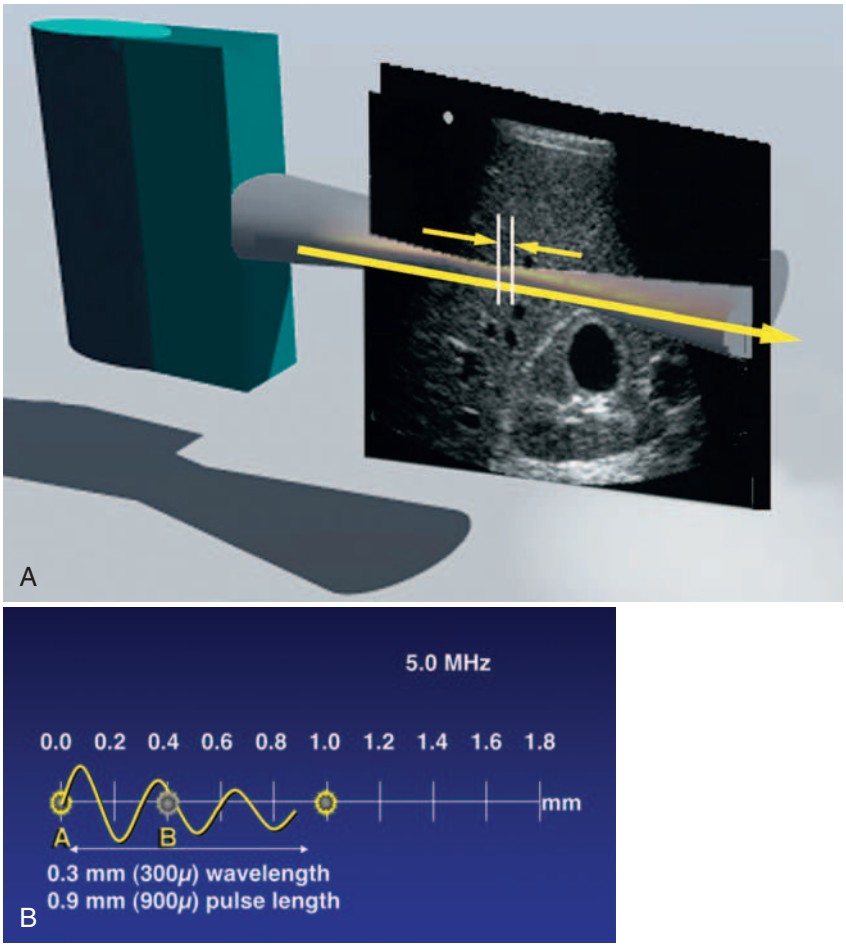

FIG. 1.25 Axial Resolution. Axial resolution is the resolution along **(A)** the beam axis and is determined by **(B)** the pulse length. The pulse length is the product of the wavelength (which decreases with increasing frequency) and the number of waves (usually two to three). Because the pulse length determines axial resolution, higher transducer frequencies provide higher image resolution. In **(B)** for example, a transducer operating at 5 MHz produces sound with a wavelength of 0.31 mm. If each pulse consists of three cycles of sound, the pulse length is slightly less than 1 mm, and objects *A* and *B,* which are 0.5 mm apart, cannot be resolved as separate structures. If the transducer frequency is increased to 15 MHz, the pulse length is less than 0.3 mm, permitting *A* and *B* to be identified as separate structures.

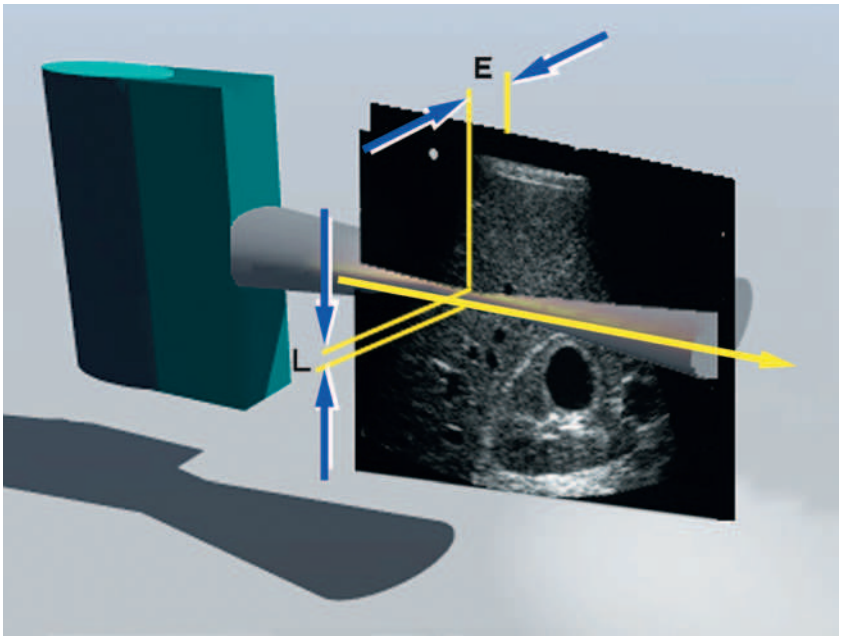

FIG. 1.26 Lateral and Elevation Resolution. Resolution in the planes perpendicular to the beam axis is an important determinant of image quality. **Lateral resolution** *(L)* is resolution in the plane perpendicular to the beam and parallel to the transducer and is determined by the width of the ultrasound beam. Lateral resolution is controlled by focusing the beam, usually by electronic phasing to alter the beam width at a selected depth of interest. Azimuth or **elevation resolution** *(E)* is determined by the slice thickness in the plane perpendicular to the beam and the transducer. Elevation resolution is controlled by the construction of the transducer. Both lateral resolution and elevation resolution are less than the axial resolution.

axis. If the transducer frequency is increased to 15 MHz, the pulse length is less than 0.4 mm, permitting resolution of smaller details.

In addition to axial resolution, resolution in the planes perpendicular to the beam axis must also be considered. **Lateral resolution** refers to resolution in the plane perpendicular to the beam and parallel to the transducer and is determined by the **width** of the ultrasound beam. Azimuth resolution, or **elevation resolution,** refers to the slice **thickness** in the plane perpendicular to the beam and to the transducer (Fig. 1.26). The width and thickness of the ultrasound beam are important determinants of image quality. Excessive beam width and thickness limit the ability to delineate small features and may obscure shadowing and enhancement from small structures, such as breast microcalcifications and small thyroid cysts. The width and thickness of the ultrasound beam determine lateral resolution and elevation resolution, respectively. Lateral and elevation resolutions are significantly poorer than the axial resolution of the beam. Lateral resolution is controlled by focusing the beam, usually by electronic phasing, to alter the beam width at a selected depth of interest. Elevation resolution is determined by the construction of the transducer and generally cannot be controlled by the user.

IMAGING PITFALLS

In ultrasound, perhaps more than in any other imaging method, the quality of the information obtained is determined by the user's ability to recognize and avoid artifacts and pitfalls. Many imaging artifacts are induced by errors in scanning technique or improper use of the instrument and therefore are preventable. Artifacts may cause misdiagnosis or may obscure important findings. Understanding artifacts is essential for correct interpretation of ultrasound examinations.

Many artifacts suggest the presence of structures not actually present. These include reverberation, refraction, and side lobes. **Reverberation artifacts** arise when the ultrasound signal reflects repeatedly between highly reflective interfaces that are usually, but not always, near the transducer (Fig. 1.27). Reverberations may also give the false impression of solid structures in areas where only fluid is present. Certain types of reverberation may be helpful because they allow the identification of a specific type of reflector, such as a surgical clip. Reverberation artifacts can usually be reduced or eliminated by changing the scanning angle or transducer placement to avoid the parallel interfaces that contribute to the artifact.

Refraction causes bending of the sound beam so that targets not along the axis of the transducer are insonated. Their reflections are then detected and displayed in the image. This may cause structures to appear in the image that actually lie outside the volume the investigator assumes is being examined (see Fig. 1.7). Similarly, side lobes may produce confusing echoes that arise from sound beams that lie outside the main ultrasound beam (Fig. 1.28). These **side lobe artifacts** are of clinical importance because they may create the impression of structures or debris in fluid-filled structures (Fig. 1.29). Side lobes may also result in errors of measurement by reducing lateral resolution. As with most other artifacts, repositioning the transducer and its focal zone or using a different transducer will usually allow the differentiation of artifactual from true echoes.

Artifacts may also remove real echoes from the display or obscure information, and important pathologic features may be missed. **Shadowing** results when there is a marked reduction in the intensity of ultrasound deep to a strong reflector or attenuator. Shadowing causes partial or complete loss of information due to attenuation of the sound by superficial structures. Another common cause of loss of image information is improper adjustment of system gain and **TGC settings.** Many low-level echoes

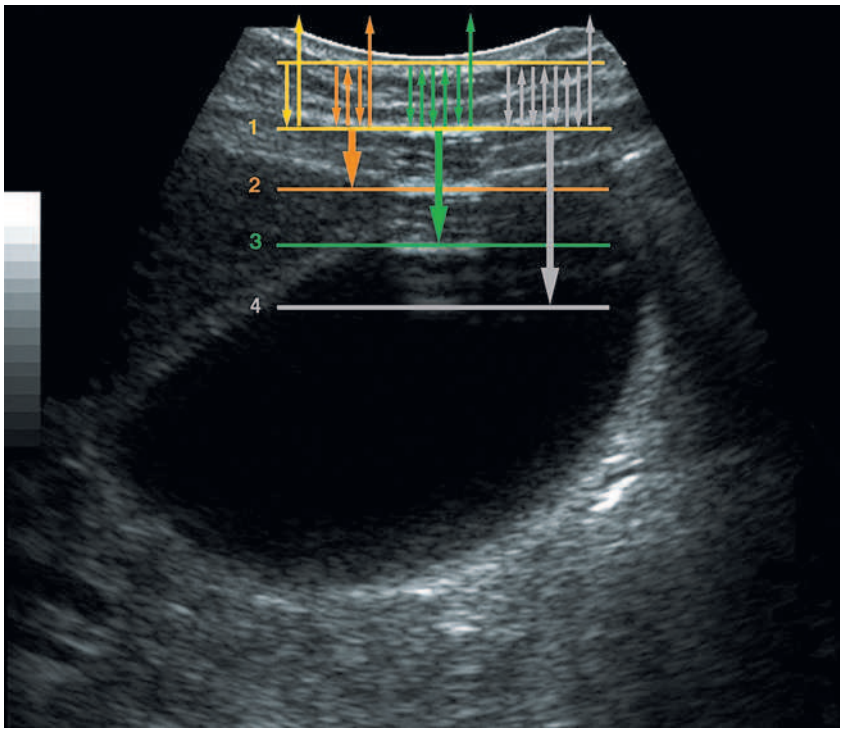

FIG. 1.27 Reverberation Artifact. Reverberation artifacts arise when the ultrasound signal reflects repeatedly between highly reflective interfaces near the transducer, resulting in delayed echo return to the transducer. This appears in the image as a series of regularly spaced echoes at increasing depth. The echo at depth *1* is produced by simple reflection from a strong interface. Echoes at levels *2, 3,* and *4* are produced by multiple reflections between this interface and the surface (simulated image).

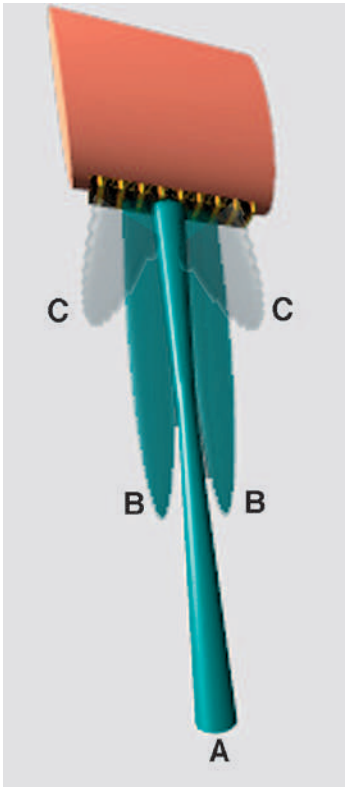

FIG. 1.28 Side Lobes. Although most of the energy generated by a transducer is emitted in a beam along the central axis of the transducer *(A),* some energy is also emitted at the periphery of the primary beam (*B* and *C*). These are called side lobes and are lower in intensity than the primary beam. Side lobes may interact with strong reflectors that lie outside of the scan plane and produce artifacts that are displayed in the ultrasound image (see also Fig. 1.29).

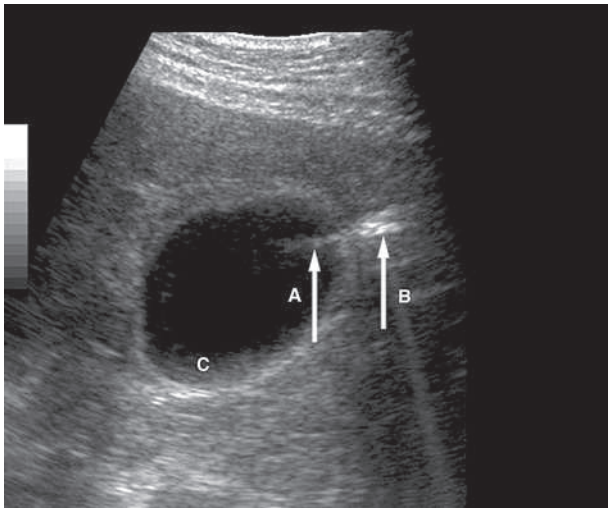

FIG. 1.29 Side Lobe Artifact. Transverse image of the gallbladder reveals a bright internal echo *(A)* that suggests a band or septum within the gallbladder. This is a side lobe artifact related to the presence of a strong out-of-plane reflector *(B)* medial to the gallbladder. The low-level echoes in the dependent portion of the gallbladder *(C)* are also artifactual and are caused by the same phenomenon. Side lobe and slice thickness artifacts are of clinical importance because they may create the impression of debris in fluid-filled structures.

are near the noise levels of the equipment, and considerable skill and experience are needed to adjust instrument settings to display the maximum information with the minimum noise. Poor scanning angles, inadequate penetration, and poor resolution may also result in loss of information. Careless selection of transducer frequency and lack of attention to the focal characteristics of

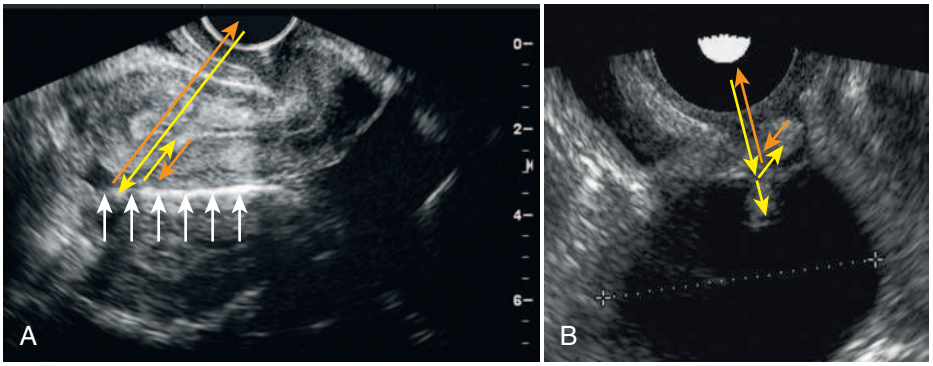

FIG. 1.30 Multipath Artifact. (A) Mirror image of the uterus is created by reflection of sound from an interface produced by gas in the rectum. **(B)** Echoes reflected from the wall of an ovarian cyst create complex echo paths that delay return of echoes to the transducer. In both examples, the longer path of the reflected sound results in the display of echoes at a greater depth than they should normally appear. In **(A)** this results in an artifactual image of the uterus appearing in the location of the rectum. In **(B)** the effect is more subtle and more likely to cause misdiagnosis because the artifact suggests a mural nodule in what is actually a simple ovarian cyst.

the beam will cause loss of clinically important information from deep, low-amplitude reflectors and small targets. Ultrasound artifacts may alter the size, shape, and position of structures. For example, a **multipath artifact** is created when the path of the returning echo is not the one expected, resulting in display of the echo at an improper location in the image (Fig. 1.30).

Shadowing and Enhancement

Although most artifacts degrade the ultrasound image and impede interpretation, two artifacts of clinical value are shadowing and enhancement. Again, shadowing results when an object (e.g., calculus) attenuates sound more rapidly than surrounding tissues. **Enhancement** occurs when an object (e.g., cyst) attenuates less than surrounding tissues. Failure of TGC applied to normal tissue to compensate properly for the attenuation of more highly attenuating (shadowing) or poorly attenuating (enhancing) structures produces the artifact (Fig. 1.31). Because attenuation increases with frequency, the effects of shadowing and enhancement are greater at higher than at lower frequencies. The conspicuity of shadowing and enhancement is reduced by excessive beam width, improper focal zone placement, and use of spatial compounding.

DOPPLER SONOGRAPHY

Conventional B-mode ultrasound imaging uses pulse-echo transmission, detection, and display techniques. Brief pulses of ultrasound energy emitted by the transducer are reflected from acoustic interfaces within the body. Precise timing allows determination of the depth from which the echo originates. When pulsed wave ultrasound is reflected from an interface, the backscattered (reflected) signal contains amplitude, phase, and frequency information (Fig. 1.32). This information permits inference of the position, nature, and motion of the interface reflecting the pulse. B-mode ultrasound imaging uses only the amplitude information in the backscattered signal to generate the image, with differences in the strength of reflectors displayed in the image in varying shades of gray. Rapidly moving targets, such as red cells in the bloodstream, produce echoes of low amplitude that are not usually displayed, resulting in a relatively anechoic pattern within the lumens of large vessels.

Although gray-scale display relies on the amplitude of the backscattered ultrasound signal, additional information is present in the returning echoes that can be used to evaluate the motion of moving targets.[16] When high-frequency sound impinges on a stationary interface, the reflected ultrasound has essentially the same frequency or wavelength as the transmitted sound. If the reflecting interface is moving with respect to the sound beam emitted from the transducer, however, there is a change in the frequency of the sound scattered by the moving object (Fig. 1.33). This change in frequency is directly proportional to the velocity of the reflecting interface relative to the transducer and is a result of the **Doppler effect.** The relationship of the returning ultrasound frequency to the velocity of the reflector is described by the Doppler equation, as follows:

$$\Delta F = (F_R - F_T) = 2 \cdot F_T \cdot v/c$$

The **Doppler frequency shift** is ΔF; F_R is the frequency of sound reflected from the moving target; F_T is the frequency of sound emitted from the transducer; v is the velocity of the target toward the transducer; and c is the velocity of sound in the medium. The Doppler frequency shift (ΔF) applies only if the target is moving directly toward or away from the transducer (Fig. 1.34A). In most clinical settings the direction of the ultrasound beam is seldom directly toward or away from the direction of flow, and the ultrasound beam usually approaches the moving target at an angle designated as the **Doppler angle** (Fig. 1.34B). In this case, ΔF is reduced in proportion to the cosine of this angle, as follows:

$$\Delta F = (F_R - F_T) = 2 \cdot F_T \cdot v \cdot \cos\theta/c$$

where θ is the angle between the axis of flow and the incident ultrasound beam. If the Doppler angle can be measured, estimation of flow velocity is possible. Accurate estimation of target velocity requires precise measurement of both the Doppler frequency shift and the angle of insonation to the direction of

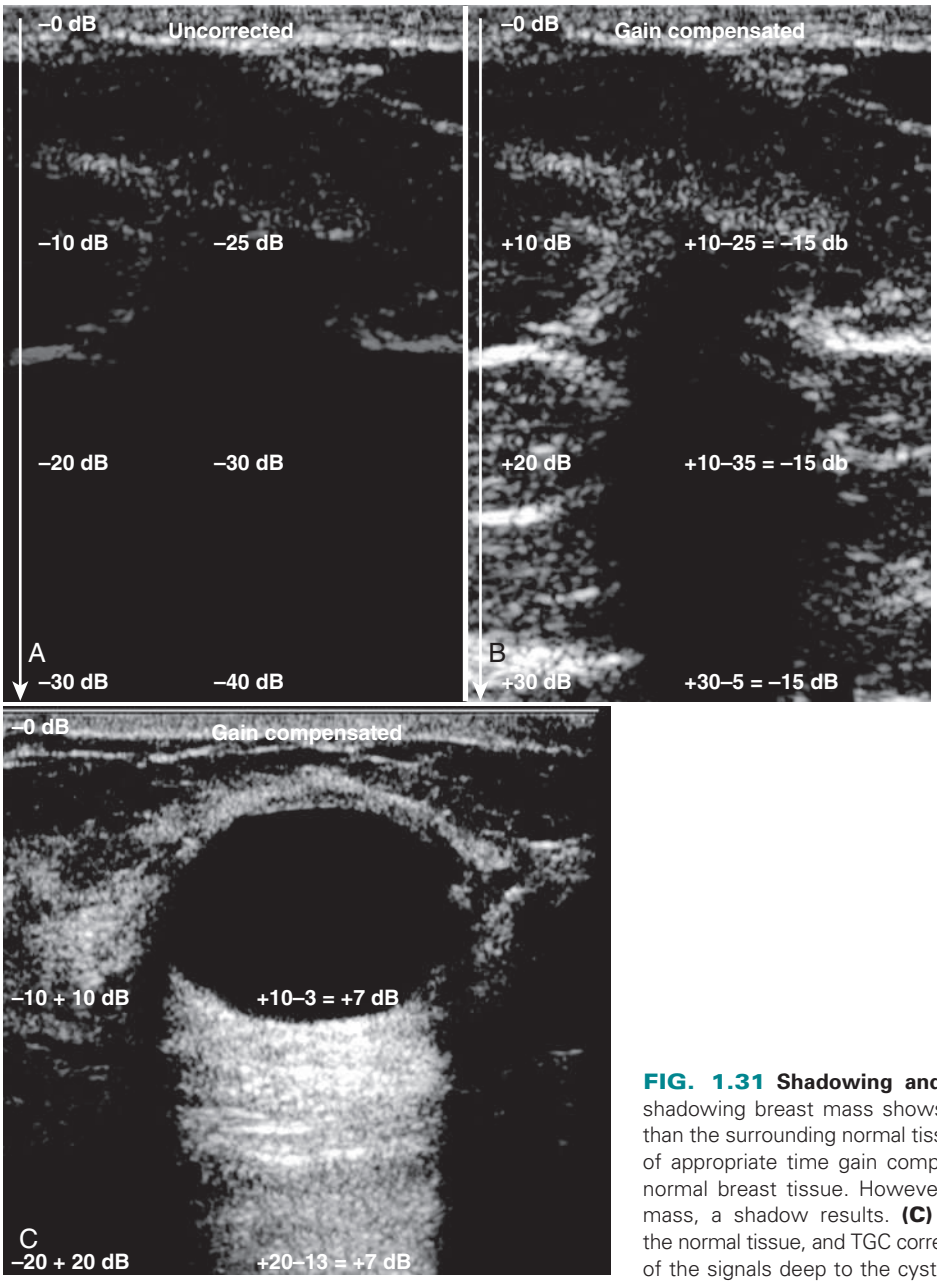

FIG. 1.31 Shadowing and Enhancement. (A) Uncorrected image of a shadowing breast mass shows that the mass attenuates 25 dB, 15 dB more than the surrounding normal tissue, which attenuates only 10 dB. **(B)** Application of appropriate time gain compensation (TGC) results in proper display of the normal breast tissue. However, because of the increased attenuation of the mass, a shadow results. **(C)** Similarly, the cyst attenuates 7 dB less than the normal tissue, and TGC correction for normal tissue results in overamplification of the signals deep to the cyst, producing enhancement of these tissues.

target movement. As the Doppler angle (θ) approaches 90 degrees, the cosine of θ approaches 0. At an **angle of 90 degrees,** there is no relative movement of the target toward or away from the transducer, and **no Doppler frequency shift** is detected (Fig. 1.35). Because the cosine of the Doppler angle changes rapidly for angles more than 60 degrees, accurate angle correction requires that Doppler measurements be made at angles of less than 60 degrees. Above 60 degrees, relatively small changes in the Doppler angle are associated with large changes in cosθ, and therefore a small error in estimation of the Doppler angle may result in a large error in the estimation of velocity. These considerations are important in using both duplex and color Doppler instruments. Optimal imaging of the vessel wall is obtained when the axis of the transducer is perpendicular to the wall, whereas maximal Doppler frequency differences are obtained when the transducer axis and the direction of flow are at a relatively small angle.

In peripheral vascular applications, it is highly desirable that measured *Doppler frequencies be corrected for the Doppler angle to provide velocity measurement.* This allows comparison of data from systems using different Doppler frequencies and eliminates error in interpretation of frequency data obtained at different Doppler angles. For abdominal applications, angle-corrected velocity measurements are encouraged, although qualitative assessments of flow are often made using only the Doppler frequency shift data.

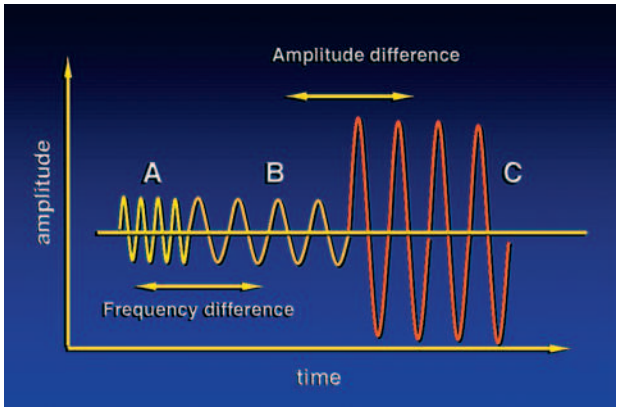

FIG. 1.32 Backscattered Information. The backscattered ultrasound signal contains amplitude, phase, and frequency information. Signals *B* and *C* differ in amplitude but have the same frequency. Amplitude differences are used to generate B-mode images. Signals *A* and *B* differ in frequency but have similar amplitudes. Such frequency differences are the basis of Doppler ultrasound.

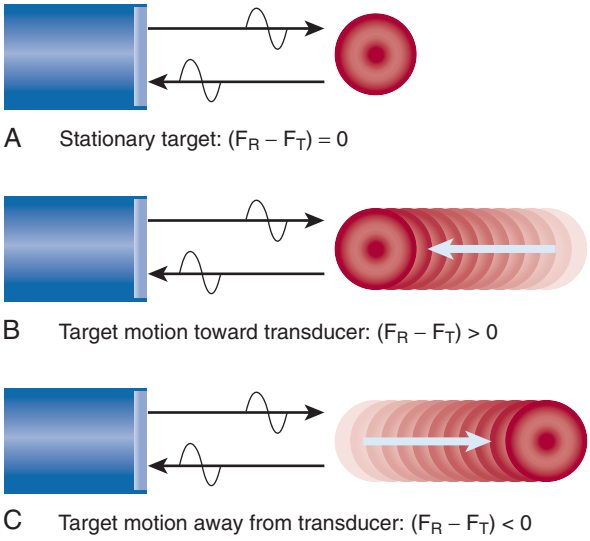

FIG. 1.33 Doppler Effect. (A) Stationary target. If the reflecting interface is stationary, the backscattered ultrasound has the same frequency or wavelength as the transmitted sound, and there is no difference in the transmitted frequency *(F_T)* and the reflected frequency *(F_R)*. **(B)** and **(C) Moving targets.** If the reflecting interface is moving with respect to the sound beam emitted from the transducer, there is a change in the frequency of the sound scattered by the moving object. When the interface moves toward the transducer **(B),** the difference in reflected and transmitted frequencies is greater than zero. When the target is moving away from the transducer **(C),** this difference is less than zero. The Doppler equation is used to relate this change in frequency to the velocity of the moving object.

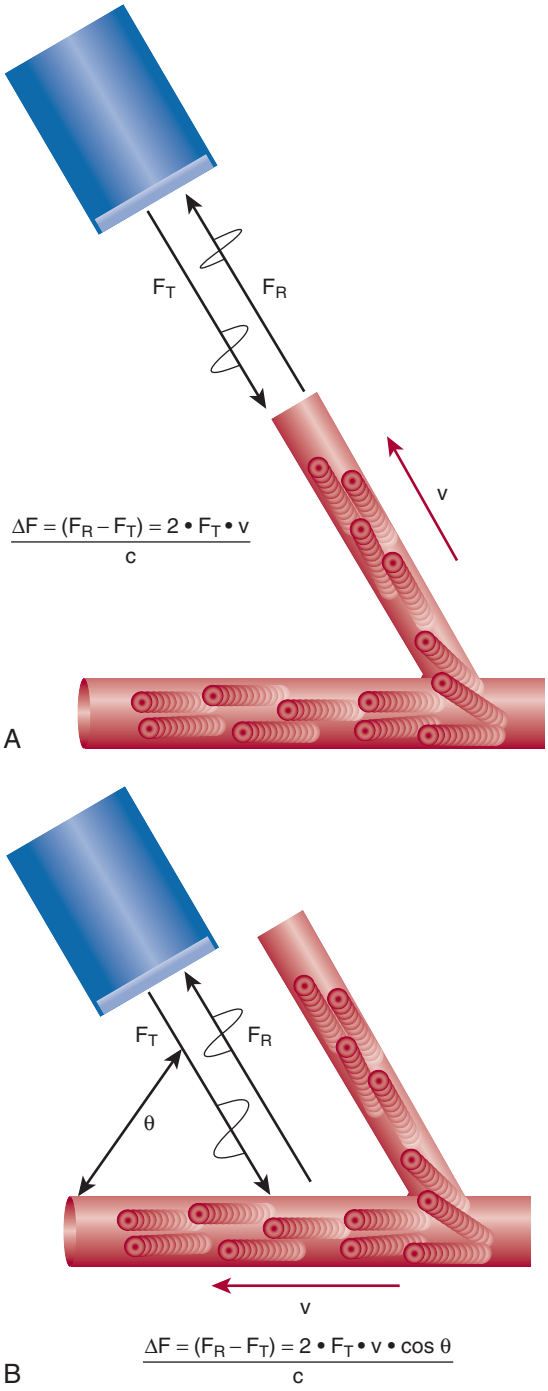

FIG. 1.34 Doppler Equations. The Doppler equation describes the relationship of the Doppler frequency shift to target velocity. **(A)** In its simplest form, it is assumed that the direction of the ultrasound beam is parallel to the direction of movement of the target. This situation is unusual in clinical practice. More often, the ultrasound impinges on the vessel at angle θ. **(B)** In this case the Doppler frequency shift detected is reduced in proportion to the cosine of θ. *ΔF,* Frequency shift; F_R, reflected frequency; F_T, transmitted frequency; *v,* velocity.

Doppler Signal Processing and Display

Several options exist for the processing of ΔF, the Doppler frequency shift, to provide useful information regarding the direction and velocity of blood. Doppler frequency shifts encountered clinically are in the audible range. This audible signal may be analyzed by ear and, with training, the operator can identify many flow characteristics. More often, the Doppler shift data are displayed in graphic form as a time-varying plot of the frequency spectrum of the returning signal. A fast Fourier transformation is used to perform the frequency analysis. The resulting Doppler frequency spectrum displays the following (Fig. 1.36):

- Variation with time of the Doppler frequencies present in the volume sampled

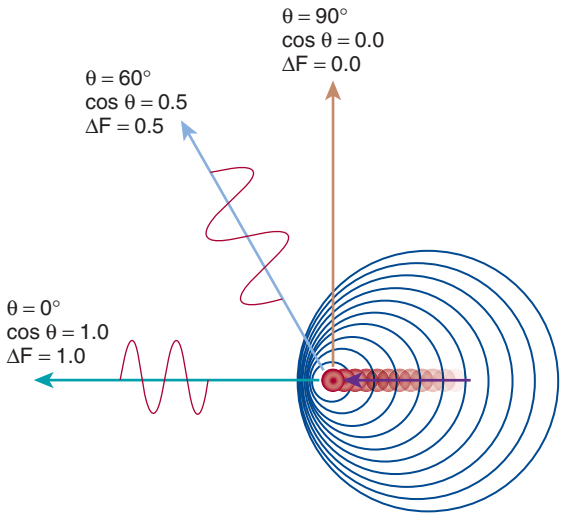

FIG. 1.35 Effect of Doppler Angle on Frequency Shift. At an angle of 60 degrees, the detected frequency shift *(ΔF)* detected by the transducer is only 50% of the shift detected at an angle of 0 degrees. At 90 degrees, there is no relative movement of the target toward or away from the transducer, and no frequency shift is detected. The detected Doppler frequency shift is reduced in proportion to the cosine of the Doppler angle. Because the cosine of the angle changes rapidly at angles above 60 degrees, the use of Doppler angles of less than 60 degrees is recommended in making velocity estimates.

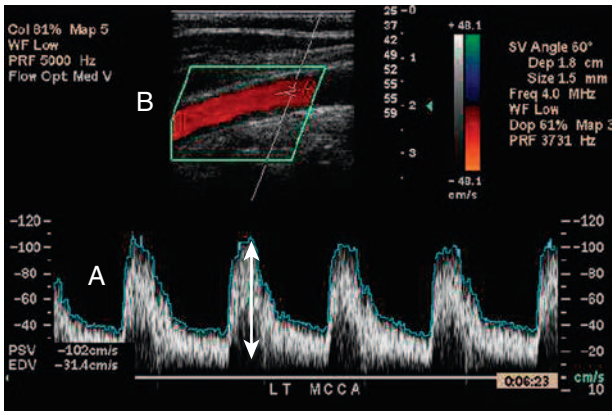

FIG. 1.36 Doppler Display. (A) Doppler frequency spectrum waveform shows changes in flow velocity and direction by vertical deflections of the waveform above and below the baseline. The width of the spectral waveform (spectral broadening) is determined by the range of frequencies present at any instant in time *(arrow)*. A brightness (gray) scale is used to indicate the amplitude of each frequency component. **(B) Color Doppler imaging.** Amplitude data from stationary targets provide the basis for the B-mode image. Signal phase provides information about the presence and direction of motion, and changes in frequency relate to the velocity of the target. Backscattered signals from red blood cells are displayed in color as a function of their motion toward or away from the transducer, and the degree of the saturation of the color is used to indicate the frequency shift from moving red cells.

- The **envelope of the spectrum,** representing the maximum frequencies present at any given point in time
- The **width of the spectrum** at any point, indicating the range of frequencies present

The amplitude of the Doppler signal is related to the number of targets moving at a given velocity. In many instruments the amplitude of each frequency component is displayed in gray scale as part of the spectrum. The presence of a large number of different frequencies at a given point in the cardiac cycle results in **spectral broadening.**

In color Doppler imaging systems, a representation of the Doppler frequency shift is displayed as a feature of the image itself (see Fig. 1.36). In addition to the detection of Doppler frequency shift data from each pixel in the image, these systems may also provide range-gated pulsed wave Doppler with spectral analysis for display of Doppler data.

Doppler Instrumentation

In contrast to A-mode, M-mode, and B-mode gray-scale ultrasonography, which display the information from tissue interfaces, Doppler ultrasound instruments are optimized to display **flow** information. The simplest Doppler devices use **continuous wave** (CW) **Doppler** rather than pulsed wave ultrasound, using two transducers that transmit and receive ultrasound continuously. The transmit and receive beams overlap in a sensitive volume at some distance from the transducer face (Fig. 1.37A). Although direction of flow can be determined with CW Doppler, these devices do not allow discrimination of motion coming from various depths, and the source of the signal being detected is difficult, if not impossible, to ascertain with certainty. Inexpensive and portable, CW Doppler instruments are used primarily at the bedside or intraoperatively to confirm the presence of flow in superficial vessels.

Because of the limitations of CW systems, most applications use range-gated, pulsed wave Doppler. Rather than a continuous wave of ultrasound emission, pulsed wave Doppler devices emit brief pulses of ultrasound energy (see Fig. 1.37B). Using pulses of sound permits use of the time interval between the transmission of a pulse and the return of the echo as a means of determining the depth from which the Doppler shift arises. The principles are similar to the echo-ranging principles used for imaging (see Fig. 1.4). In a pulsed wave Doppler system the sensitive volume from which flow data are sampled can be controlled in terms of shape, depth, and position. When pulsed wave Doppler is combined with a 2-D, real-time, B-mode imager in the form of a **duplex scanner,** the position of the Doppler sample can be precisely controlled and monitored.

In color Doppler imaging (Fig. 1.38A), frequency shift information determined from Doppler measurements is displayed as a feature of the image itself.[17] Stationary or slowly moving targets provide the basis for the B-mode image. **Signal phase** provides information about the presence and direction of motion, and changes in echo signal frequency relate to the velocity of the target. Backscattered signals from red blood cells are displayed in color as a function of their motion toward or away from the transducer, and the degree of the saturation of the color is used to indicate the relative frequency shift produced by the moving red cells.

Color Doppler flow imaging (CDFI) expands conventional duplex sonography by providing additional capabilities. The use of color saturation to display variations in Doppler shift frequency allows an estimation of relative velocity from the image alone, provided that variations in the Doppler angle are noted. The

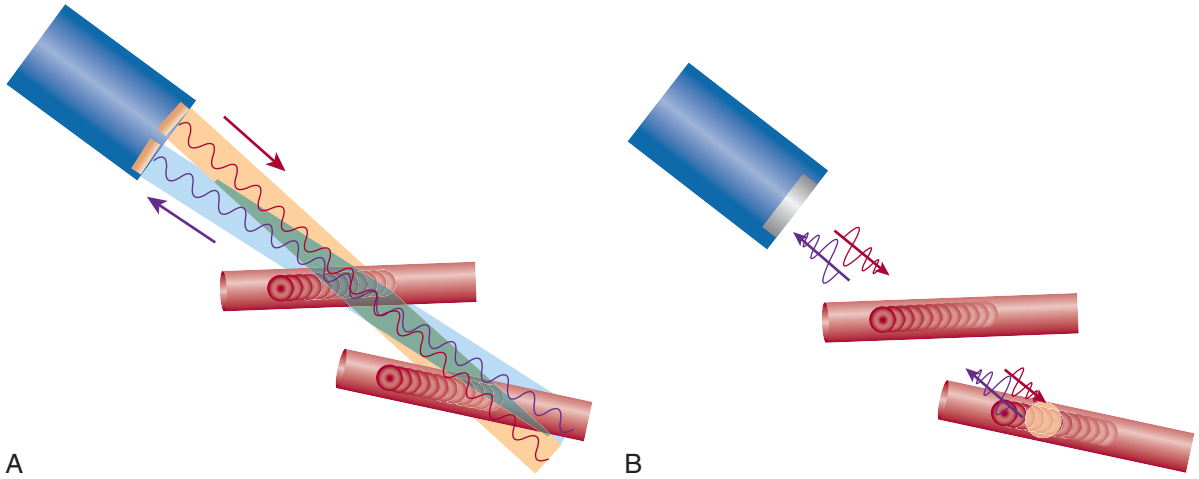

FIG. 1.37 Continuous Wave and Pulsed Wave Doppler. (A) Continuous wave (CW) Doppler uses separate transmit and receive crystals that continuously transmit and receive ultrasound. Although able to detect the presence and direction of flow, CW devices are unable to distinguish signals arising from vessels at different depths *(green-shaded area).* **(B)** Using the principle of ultrasound ranging (see Fig. 1.4), **pulsed wave Doppler** permits the sampling of flow data from selected depths by processing only the signals that return to the transducer after precisely timed intervals. The operator is able to control the position of the sample volume and, in duplex systems, to view the location from which the Doppler data are obtained.

Limitations of Color Doppler Flow Imaging
Angle dependence
Aliasing
Inability to display entire Doppler spectrum in the image
Artifacts caused by noise

Advantages of Power Doppler
No aliasing
Much less angle dependence
Noise: a homogeneous background color
Increased sensitivity for flow detection

display of flow throughout the image field allows the position and orientation of the vessel of interest to be observed at all times. The display of spatial information with respect to velocity is ideal for display of small, localized areas of turbulence within a vessel, which provide clues to stenosis or irregularity of the vessel wall caused by atheroma, trauma, or other disease. Flow within the vessel is observed at all points, and stenotic jets and focal areas of turbulence are displayed that might be overlooked with duplex instrumentation. The contrast of flow within the vessel lumen permits visualization of small vessels that are not visible when using conventional imagers and enhances the visibility of wall irregularity. CDFI aids in determination of the direction of flow and measurement of the Doppler angle.

Power Doppler

An alternative to the display of frequency information with color Doppler imaging is to use a color map that displays the integrated power of the Doppler signal instead of its mean frequency shift[18] (see Fig. 1.38B). Because frequency shift data are not displayed, there is no aliasing. The image does not provide information related to flow direction or velocity, and power Doppler imaging is much less angle dependent than frequency-based color Doppler display. In contrast to color Doppler, where noise may appear in the image as any color, power Doppler permits noise to be assigned to a homogeneous background color that does not greatly interfere with the image. This results in a significant increase in the usable dynamic range of the scanner, permitting higher effective gain settings and increased sensitivity for flow detection (Fig. 1.39).

Interpretation of the Doppler Spectrum

Doppler data components that must be evaluated both in spectral display and in color Doppler imaging include the Doppler shift frequency and amplitude, the Doppler angle, the spatial distribution of frequencies across the vessel, and the temporal variation of the signal. Because the Doppler signal itself has no anatomic significance, the examiner must interpret the Doppler signal and then determine its relevance in the context of the image.

The detection of a Doppler frequency shift indicates movement of the target, which in most applications is related to the presence of flow. The sign of the frequency shift (positive or negative) indicates the direction of flow relative to the transducer. **Vessel stenosis** is typically associated with large Doppler frequency shifts in both systole and diastole at the site of greatest narrowing, with turbulent flow in poststenotic regions. In peripheral vessels, analysis of the Doppler changes allows accurate prediction of the degree of vessel narrowing. Information related to the resistance to flow in the distal vascular tree can be obtained by analysis of changes of blood velocity with time, as shown in the **Doppler spectral display.** Doppler imaging can provide information about blood flow in both large and small vessels. Small vessel impedance is reflected in the Doppler spectral waveform of afferent vessels.

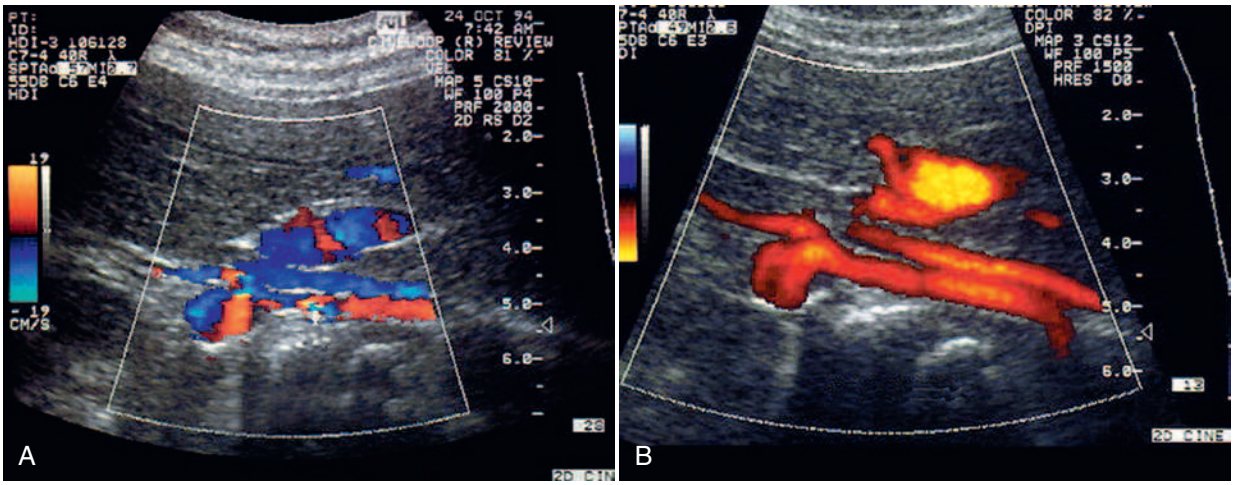

FIG. 1.38 Color Flow and Power Doppler. (A) Color flow Doppler imaging uses a color map to display information based on the detection of frequency shifts from moving targets. Noise in this form of display appears across the entire frequency spectrum and limits sensitivity. **(B) Power Doppler** uses a color map to show the distribution of the power or amplitude of the Doppler signal. Flow direction and velocity information are not provided, but noise is reduced, allowing higher gain settings and improved sensitivity for flow detection.

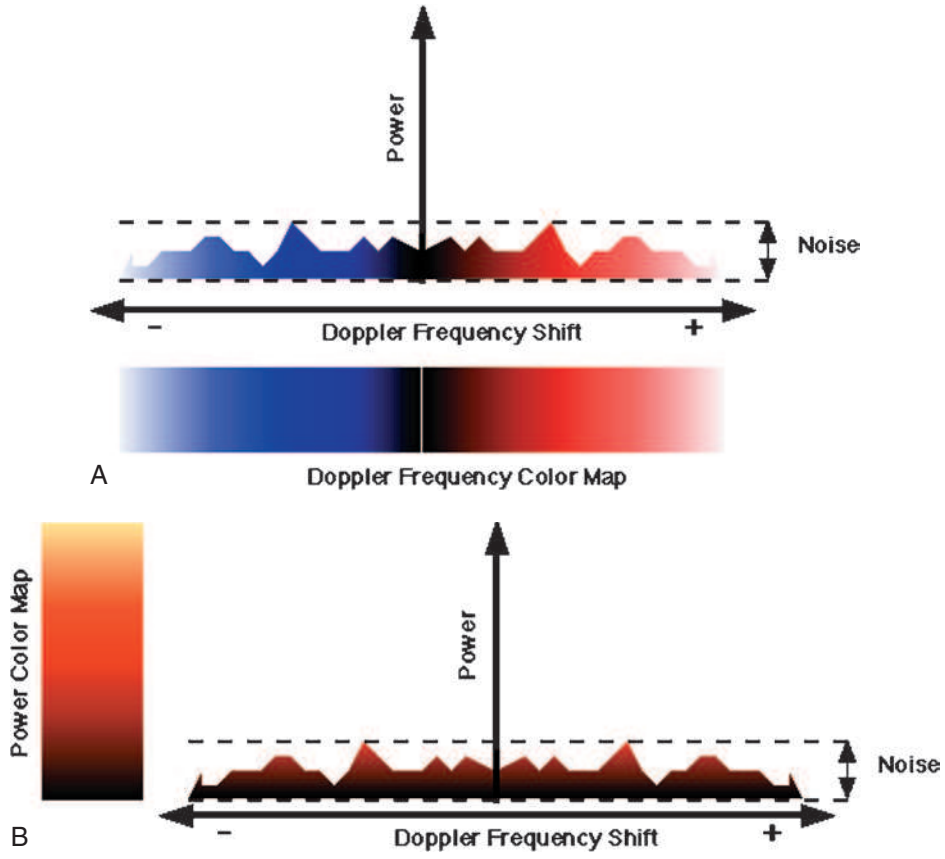

FIG. 1.39 Frequency and Power Mode Color Mapping. (A) Conventional color Doppler uses the color map to show differences in flow direction and Doppler frequency shift. Because noise appears over the entire frequency spectrum, gain levels are limited to those that do not introduce excessive noise. **(B) Power Doppler** color map, in contrast, indicates the amplitude of the Doppler signal. Because most noise is of low amplitude, it is possible to map this to colors near the background. This permits the use of high gain settings that offer significant improvements over conventional color Doppler in flow detection.

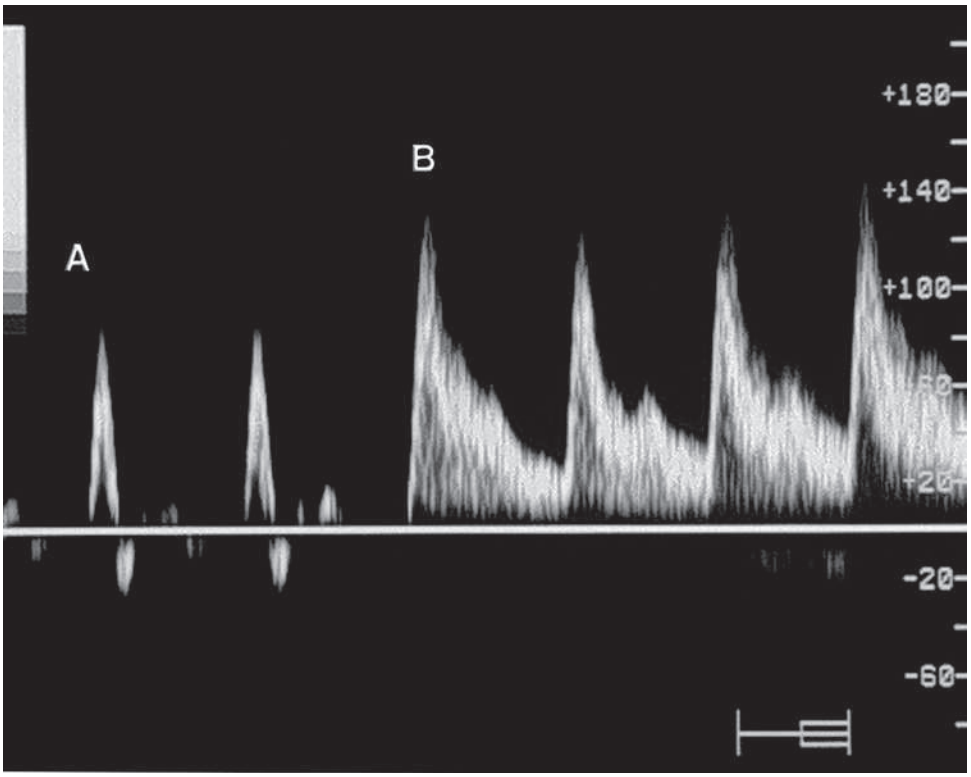

FIG. 1.40 Impedance. High-resistance waveform in brachial artery *(A),* produced by inflating forearm blood pressure cuff to a pressure above the systolic blood pressure. As a result of high peripheral resistance, there is low systolic amplitude and reversed diastolic flow. **Low-resistance waveform in peripheral vascular bed** *(B),* caused by vasodilation stimulated by the prior ischemia. Immediately after release of 3 minutes of occluding pressure, the Doppler waveform showed increased amplitude and rapid antegrade flow throughout diastole.

Fig. 1.40 provides a graphic example of the changes in the Doppler spectral waveform resulting from physiologic changes in the resistance of the vascular bed supplied by a normal brachial artery. A blood pressure cuff has been inflated to above systolic pressure to occlude the distal branches supplied by the brachial artery. This **occlusion** causes reduced systolic amplitude and cessation of diastolic flow, resulting in a waveform different than that found in the normal resting state. During the period of ischemia induced by pressure cuff occlusion of the forearm vessels, **vasodilation** has occurred. Immediately after release of the occluding pressure the Doppler waveform reflects a low-resistance peripheral vascular bed with increased systolic amplitude and rapid flow throughout diastole, typical for vasodilation.

Doppler indices include the **systolic-to-diastolic ratio** (S/D ratio), **resistive index** (RI), and **pulsatility index** (PI) (Fig. 1.41). These compare blood flow in systole and diastole, show resistance to flow in the peripheral vascular bed, and help evaluate the perfusion of tumors, renal transplants, the placenta, and other organs. With Doppler ultrasound, it is therefore possible to identify vessels, determine the direction of blood flow, evaluate narrowing or occlusion, and characterize blood flow to organs and tumors. Analysis of the Doppler shift frequency with time can be used to infer both proximal stenosis and changes in distal vascular impedance. Most work using pulsed wave Doppler imaging has emphasized the detection of stenosis, thrombosis, and flow disturbances in major peripheral arteries and veins. In these applications, measurement of peak systolic and end diastolic

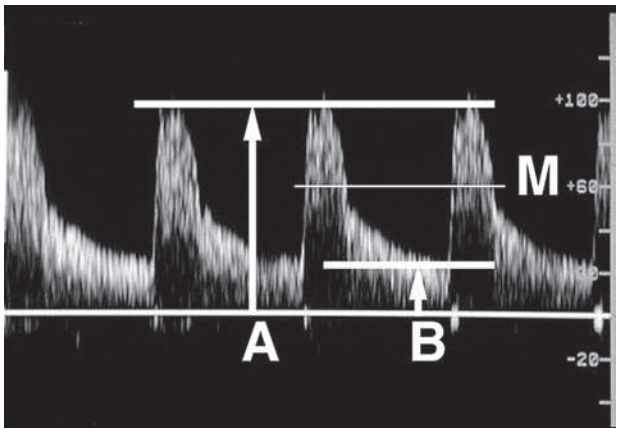

FIG. 1.41 Doppler Indices. Doppler flow indices used to characterize peripheral resistance are based on the **peak systolic frequency** or **velocity** *(A),* the **minimum** or **end diastolic frequency** or **velocity** *(B),* and the **mean frequency** or **velocity** *(M).* The most frequently used indices are the **systolic-to-diastolic ratio** (A/B); **resistive index** [(A-B)/A]; and **pulsatility index** [(A-B)/M]. In calculation of the pulsatility index, the minimum diastolic velocity or frequency is used; calculation of the systolic-to-diastolic ratio and resistive index use the end diastolic value.

frequency or velocity, analysis of the Doppler spectrum, and calculation of certain frequency or velocity ratios have been the basis of analysis. Changes in the spectral waveform measured by indices comparing flow in systole and diastole indicate the resistance of the vascular bed supplied by the vessel and the changes resulting from a variety of pathologic conditions.

Changes in Doppler indices from normal may help in the early identification of rejection of transplanted organs, parenchymal dysfunction, and malignancy. Although useful, these measurements are influenced not only by the resistance to flow in peripheral vessels, but also by heart rate, blood pressure, vessel wall length and elasticity, extrinsic organ compression, and other factors.

Interpretation of Color Doppler

Although the graphic presentation of color Doppler imaging suggests that interpretation is made easier, the complexity of the color Doppler image actually makes this a more demanding image to evaluate than the simple Doppler spectrum. Nevertheless, color Doppler imaging has important advantages over pulsed wave duplex Doppler imaging, in which flow data are obtained only from a small portion of the area being imaged. To be confident that a conventional Doppler study has achieved reasonable sensitivity and specificity in detection of flow disturbances, a methodical search and sampling of multiple sites within the field of interest must be performed. In contrast, CDFI devices permit simultaneous sampling of multiple sites and are less susceptible to this error.

Although color Doppler can indicate the presence of blood flow, misinterpretation of color Doppler images may result in important errors. Each color pixel displays a representation of the Doppler frequency shift detected at that point. The frequency shift displayed is not the peak frequency present at sampling but rather a **weighted mean frequency** that attempts to account for the range of frequencies and their relative amplitudes at sampling. Manufacturers use different methods to derive the weighted mean frequency displayed in their systems. In addition, the pulse repetition frequency (PRF) and the color map selected to display the detected range of frequencies affect the color displayed. The color assigned to each Doppler pixel is determined by the Doppler frequency shift (which in turn is determined by target velocity and Doppler angle), the PRF, and the color map selected for display; therefore the interpretation of a color Doppler image must consider each of these variables. Although most manufacturers provide on-screen indications suggesting a relationship between the color displayed and flow velocity, this is misleading because color Doppler does not show velocity and only indicates the weighted mean frequency shift measured in the vessel; without correction for the effect of the Doppler angle, velocity cannot be estimated (Fig. 1.42). Because the frequency shift at a given point is a function of velocity and the Doppler angle, depending on the frequency shift present in a given pixel and the PRF, *any* velocity may be represented by *any* color, and under certain circumstances, low-velocity flow may not be shown at all. As with spectral Doppler, **aliasing** is determined by PRF. With color Doppler, aliasing causes frequencies greater than twice the PRF to "wrap around" and to be displayed in the opposite colors of the color map. Inexperienced users tend to associate color Doppler aliasing with elevated velocity, but even low velocities may show marked aliasing if PRF is sufficiently low. As PRF is increased, aliasing of high Doppler frequency shifts is reduced; however, low-frequency shifts may be eliminated from the display, resulting in diagnostic error (Fig. 1.43).

Other Technical Considerations

Although many problems and artifacts associated with B-mode imaging (e.g., shadowing) are encountered with Doppler sonography, the detection and display of frequency information related to moving targets present additional technical considerations. It is important to understand the source of these artifacts and

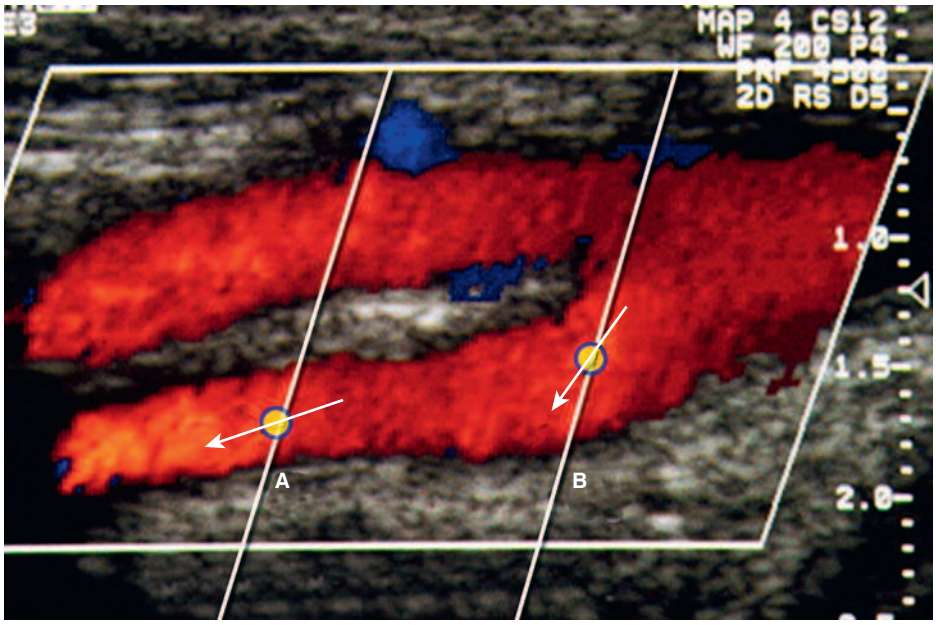

FIG. 1.42 Color Doppler. Each color pixel in a color Doppler image represents the Doppler frequency shift at that point, and it cannot be used to estimate velocity. Even though the points *A* and *B* have similar color values and therefore similar Doppler frequencies, the velocity at *A* is much higher than at *B* because of the large Doppler angle at *A* compared to *B*. The velocity represented by a given Doppler frequency increases in proportion to the Doppler angle.

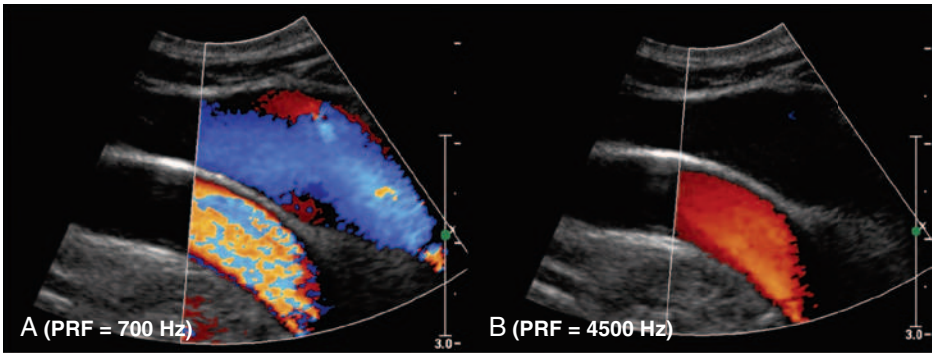

FIG. 1.43 Pulse Repetition Frequency (PRF). Depending on the color map selected, velocity of the target, Doppler angle, and PRF, a given velocity may appear as any color with color Doppler. **(A)** and **(B)** are sonograms of identical vessels. **(A)** PRF is 700 Hz, which results in aliasing of the higher Doppler frequency shifts in the carotid artery but permits the identification of relatively slow flow in the jugular vein. **(B)** PRF is 4500 Hz, eliminating aliasing in the artery but also suppressing the display of the low Doppler frequencies in the internal jugular vein.

their influence on the interpretation of the flow measurements obtained in clinical practice.

Doppler Frequency

A primary objective of the Doppler examination is the accurate measurement of characteristics of flow within a vascular structure. The moving red blood cells that serve as the primary source of the Doppler signal act as **point scatterers** of ultrasound rather than specular reflectors. This interaction results in the intensity of the scattered sound varying in proportion to the fourth power of the frequency, which is important in selecting the Doppler frequency for a given examination. As the transducer frequency increases, Doppler **sensitivity** improves, but attenuation by tissue also increases, resulting in diminished **penetration.** Careful balancing of the requirements for sensitivity and penetration is an important responsibility of the operator during a Doppler examination. Because many abdominal vessels lie several centimeters beneath the surface, Doppler frequencies in the range of 3 to 3.5 MHz are usually required to permit adequate penetration.

Wall Filters

Doppler instruments detect motion not only from blood flow but also from adjacent structures. To eliminate these low-frequency signals from the display, most instruments use **high pass filters,** or "wall" filters, which remove signals that fall below a given frequency limit. Although effective in eliminating low-frequency noise, these filters may also remove signals from low-velocity blood flow (Fig. 1.44). In certain clinical situations the measurement of these slower flow velocities is of clinical importance, and the improper selection of the wall filter may result in serious errors of interpretation. For example, low-velocity venous flow may not be detected if an improper filter is used, and low-velocity diastolic flow in certain arteries may also be eliminated from the display, resulting in errors in the calculation of Doppler indices, such as the systolic-to-diastolic ratio or resistive index. In general, the filter should be kept at the lowest practical level, usually 50 to 100 Hz.

Spectral Broadening

Spectral broadening refers to the presence of a large range of flow velocities at a given point in the pulse cycle and, by indicating turbulence, is an important criterion of high-grade vessel narrowing. Excessive system gain or changes in the dynamic range of the gray-scale display of the Doppler spectrum may suggest spectral broadening; opposite settings may mask broadening of the Doppler spectrum, causing diagnostic inaccuracy. Spectral broadening may also be produced by the selection of an excessively large sample volume or by the placement of the sample volume too near the vessel wall, where slower velocities are present (Fig. 1.45).

Aliasing

Aliasing is an artifact arising from ambiguity in the measurement of high Doppler frequency shifts. To ensure that samples originate from only a selected depth when using a pulsed wave Doppler system, it is necessary to wait for the echo from the area of interest before transmitting the next pulse. This limits the rate with which pulses can be generated, a lower PRF being required for greater depth. The PRF also determines the maximum depth from which unambiguous data can be obtained. If PRF is less than twice the maximum frequency shift produced by movement

Major Sources of Doppler Imaging Artifacts

DOPPLER FREQUENCY
Higher frequencies lead to more tissue attenuation
Wall filters remove signals from low-velocity blood flow

INCREASE IN SPECTRAL BROADENING
Excessive system gain or changes in dynamic range of the gray-scale display
Excessively large sample volume
Sample volume too near the vessel wall

INCREASE IN ALIASING
Decrease in pulse repetition frequency (PRF)
Decrease in Doppler angle
Higher Doppler frequency transducer

DOPPLER ANGLE
Relatively inaccurate above 60 degrees

SAMPLE VOLUME SIZE
Large sample volumes increase vessel wall noise

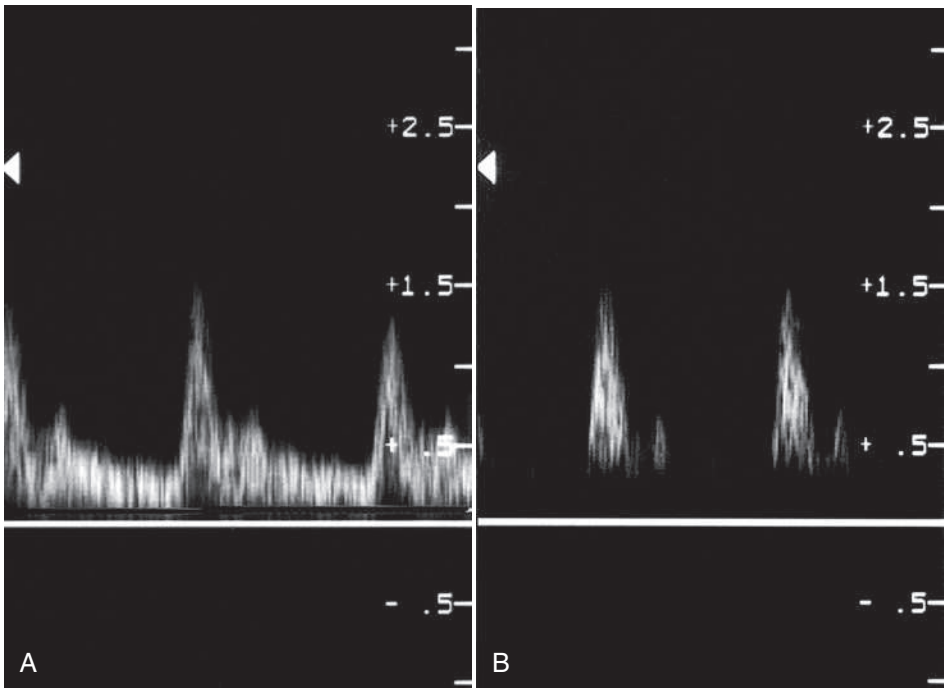

FIG. 1.44 Wall Filters. Wall filters are used to eliminate low-frequency noise from the Doppler display, but high wall filter settings may result in interpretation errors. Here the effect on the display of low-velocity flow is shown with wall filter settings of **(A)** 100 Hz and **(B)** 400 Hz. In general, wall filters should be kept at the lowest practical level, usually in the range of 50 to 100 Hz.

of the target **(Nyquist limit),** aliasing results (Fig. 1.46). When PRF is less than twice the frequency shift being detected, lower frequency shifts than are actually present are displayed. Because of the need for lower PRFs to reach deep vessels, signals from deep abdominal arteries are prone to aliasing if high velocities are present. In practice, aliasing is usually readily recognized. Aliasing can be reduced by increasing the PRF, by increasing the Doppler angle (thereby decreasing the frequency shift), or by using a lower-frequency Doppler transducer.

Doppler Angle

When making Doppler measurement of velocity, it is necessary to correct for the Doppler angle. The accuracy of a velocity estimate obtained with Doppler is only as great as the accuracy of the measurement of the Doppler angle. This is particularly true as the Doppler angle exceeds 60 degrees. In general, the **Doppler angle is best kept at 60 degrees or less** because small changes in the Doppler angle above 60 degrees result in substantial changes in the calculated velocity. Therefore measurement inaccuracies result in much greater errors in velocity estimates than do similar errors at lower Doppler angles. Angle correction is not required for the measurement of Doppler indices such as the resistive index, because these measurements are based only on the relationship of the systolic and diastolic amplitudes.

Sample Volume Size

With pulsed wave Doppler systems, the length of the Doppler sample volume can be controlled by the operator, and the width is determined by the beam profile. Analysis of Doppler signals requires that the sample volume be adjusted to exclude as much of the unwanted clutter as possible from near the vessel walls.

Doppler Gain

As with imaging, proper gain settings are essential to achieving accurate and reproducible Doppler measurements. *Excessive* Doppler gain results in noise appearing at all frequencies and may result in overestimation of velocity. Conversely, *insufficient* gain may result in underestimation of peak velocity (Fig. 1.47). A consistent approach to setting Doppler gain should be used. After placing the sample volume in the vessel, the Doppler gain should be increased to a level where noise is visible in the image, then gradually reduced to the point at which the noise first disappears completely.

OPERATING MODES: CLINICAL IMPLICATIONS

Ultrasound devices may operate in several modes, including real-time, color Doppler, spectral Doppler, and M-mode imaging. Imaging is produced in a *scanned* mode of operation. In scanned modes, pulses of ultrasound from the transducer are directed down lines of sight that are moved or steered in sequence to generate an image. This means that the number of ultrasound pulses arriving at a given point in the patient over a given interval is relatively small, and relatively little energy is deposited at any given location. In contrast, spectral Doppler imaging is an *unscanned* mode of operation in which multiple ultrasound pulses are sent in repetition along a line to collect the Doppler data. In this mode the beam is stationary, resulting in considerably greater potential for heating than in imaging modes. For imaging, PRFs are usually a few thousand hertz with very short pulses. Longer pulse durations are used with Doppler than with other imaging

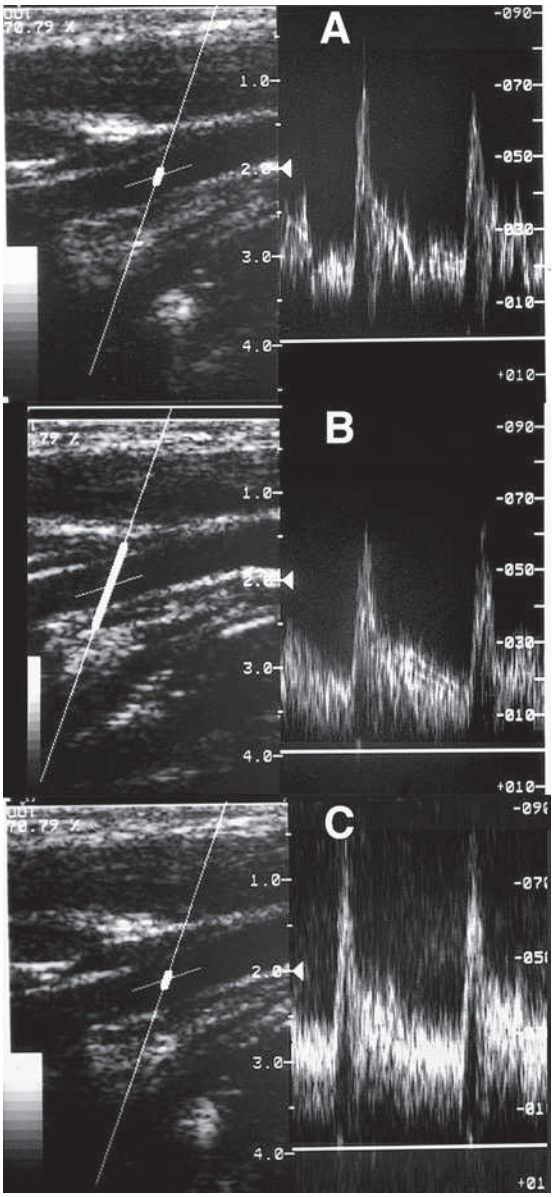

FIG. 1.45 Spectral Broadening. The range of velocities detected at a given time in the pulse cycle is reflected in the Doppler spectrum as spectral broadening. **(A) Normal spectrum.** Spectral broadening may arise from turbulent flow in association with vessel stenosis. **(B)** and **(C) Artifactual spectral broadening.** This may be produced by improper positioning of the sample volume near the vessel wall, use of **(B)** an excessively large sample volume, or **(C)** an excessive system gain.

modes. In addition, to avoid aliasing and other artifacts with Doppler imaging, it is often necessary to use higher PRFs than with other imaging applications. Longer pulse duration and higher PRF result in higher **duty factors** for Doppler modes of operation and increase the amount of energy introduced in scanning. Color Doppler, although a scanned mode, produces exposure conditions between those of real-time and Doppler imaging because color Doppler devices tend to send more pulses down each scan line and may use longer pulse durations than imaging devices. Clearly, every user needs to be aware that switching from an imaging to a Doppler mode changes the exposure conditions and the potential for biologic effects **(bioeffects).**

With current devices operating in imaging modes, concerns about bioeffects are minimal because intensities sufficient to produce measurable heating are seldom used. *With Doppler ultrasound, the potential for* ***thermal effects*** *is greater.* Preliminary measurements on commercially available instruments suggest that at least some of these instruments are capable of producing temperature rises of greater than 1°C at soft tissue/bone interfaces, if the focal zone of the transducer is held stationary. Care is therefore warranted when Doppler measurements are obtained at or near soft tissue/bone interfaces, as in the second and third trimester of pregnancy. These applications require thoughtful application of the principle of **ALARA (as low as reasonably achievable).** Under ALARA the user should use the lowest possible acoustic exposure to obtain the necessary diagnostic information.

Bioeffects and User Concerns

Although users of ultrasound need to be aware of bioeffects concerns, another key factor to consider in the safe use of ultrasound is the user. The knowledge and skill of the user are major determinants of the risk-to-benefit implications of the use of ultrasound in a specific clinical situation. For example, an unrealistic emphasis on risks may discourage an appropriate use of ultrasound, resulting in harm to the patient by preventing the acquisition of useful information or by subjecting the patient to another, more hazardous examination. The skill and experience of the individual performing and interpreting the examination are likely to have a major impact on the overall benefit of the examination. In view of the rapid growth of ultrasound and its proliferation into the hands of minimally trained clinicians, many more patients are likely to be harmed by misdiagnosis resulting from improper indications, poor examination technique, and errors in interpretation than from bioeffects. Misdiagnosis (e.g., of ectopic pregnancy) and failure to diagnose a clinically important anomaly are real dangers, and poorly trained users may be the greatest current hazard of diagnostic ultrasound.

Understanding bioeffects is essential for the prudent use of diagnostic ultrasound and is important in ensuring that the excellent risk-to-benefit performance of diagnostic ultrasound is preserved. All users of ultrasound should be prudent, understanding as fully as possible the potential risks and obvious benefits of ultrasound examinations, as well as those of alternate diagnostic methods. With this information, operators can monitor exposure conditions and implement the principle of ALARA to keep patient (and in obstetric imaging, the fetal) exposure as low as possible while fulfilling diagnostic objectives.

THERAPEUTIC APPLICATIONS: HIGH-INTENSITY FOCUSED ULTRASOUND

Although the primary medical application of ultrasound has been for diagnosis, therapeutic applications are developing rapidly, particularly the use of **high-intensity focused ultrasound** (HIFU). HIFU is based on three important capabilities of ultrasound: (1) focusing the ultrasound beam to produce highly localized energy deposition, (2) controlling the location and size of the focal zone, and (3) using intensities sufficient to destroy tissue at the focal

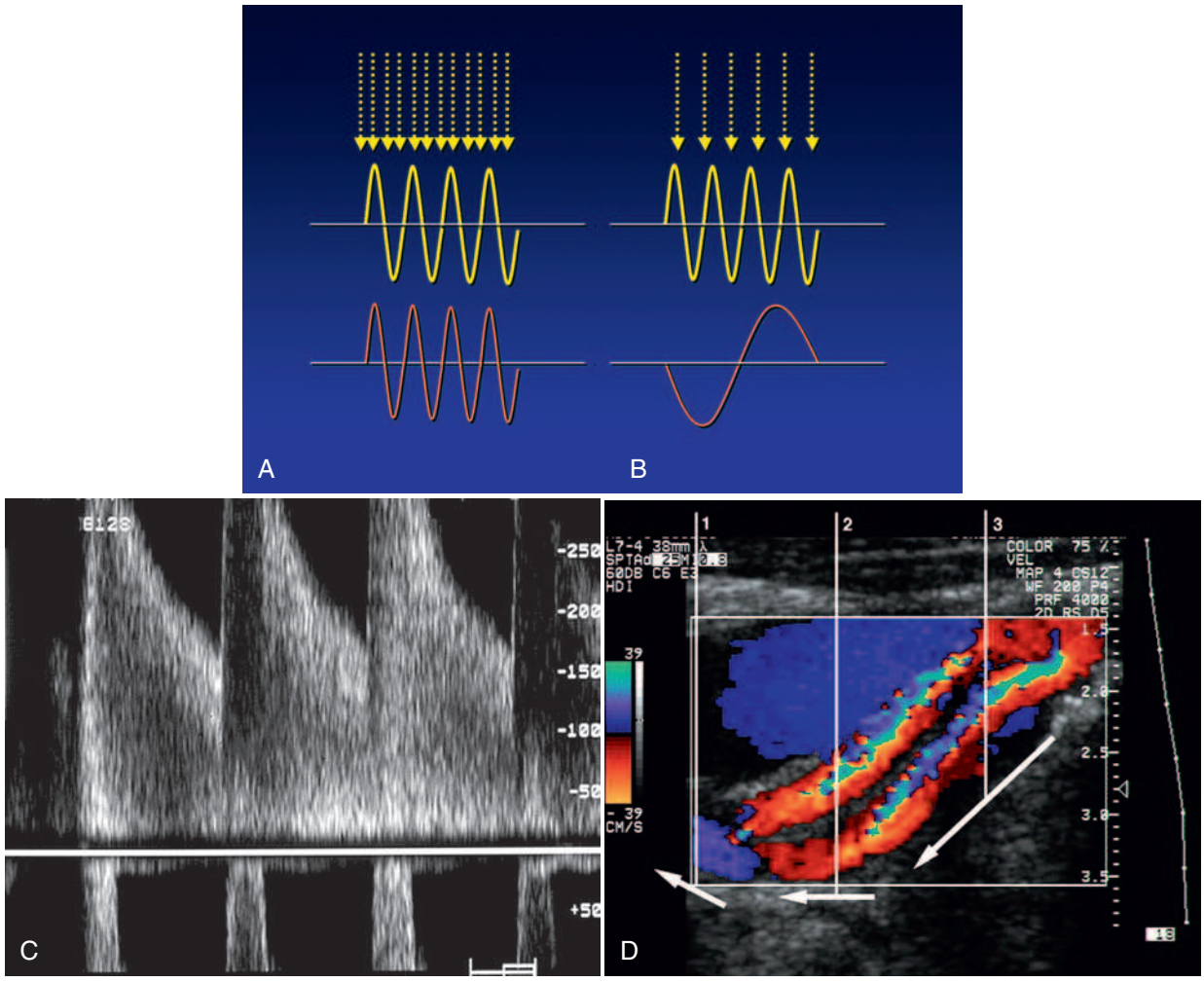

FIG. 1.46 Aliasing. Pulse repetition frequency (PRF) determines the sampling rate of a given Doppler frequency. **(A)** If PRF *(arrows)* is sufficient, the sampled waveform *(orange curve)* will accurately estimate the frequency being sampled *(yellow curve)*. **(B)** If PRF is less than half the frequency being measured, **undersampling** will result in a lower frequency shift being displayed *(orange curve)*. **(C)** In a clinical setting, **aliasing** appears in the spectral display as a "wraparound" of the higher frequencies to display below the baseline. **(D)** In color Doppler display, aliasing results in a wraparound of the frequency color map from one flow direction to the opposite direction, passing through a transition of unsaturated color. The velocity throughout the vessel is constant, but aliasing appears only in portions of the vessel because of the effect of the Doppler angle on the Doppler frequency shift. As the angle increases, the Doppler frequency shift decreases, and aliasing is no longer seen.

zone. This has led to an interest in HIFU as a means of destroying noninvasive tumor and controlling bleeding and cardiac conduction anomalies.

HIFU exploits **thermal** (heating of tissues) and **mechanical (cavitation)** bioeffect mechanisms. As ultrasound passes through tissue, attenuation occurs through scattering and absorption. Scattering of ultrasound results in the return of some of the transmitted energy to the transducer, where it is detected and used to produce an image, or Doppler display. The remaining energy is transmitted to the molecules in the acoustic field and produces heating. At the **spatial peak temporal average** (SPTA), intensities of 50 to 500 mW/cm^2 used for imaging and Doppler, heating is minimal, and no observable bioeffects related to tissue heating in humans have yet been documented with clinical devices. With higher intensities, however, tissue heating sufficient to destroy tissue may be achieved. Using HIFU at 1 to 3 MHz, focal peak intensities of 5000 to 20,000 W/cm^2 may be achieved. This energy can be delivered to a small point several millimeters in size, producing rapid temperature elevation and resulting in tissue coagulation, with little damage to adjacent tissues (Fig. 1.48). The destruction of tissue is a function of the temperature reached and the duration of the temperature elevation. In general, elevation of tissue to a temperature of 60°C for 1 second is sufficient to produce **coagulation necrosis.**

Because of its ability to produce highly localized tissue destruction, HIFU has been investigated as a tool for noninvasive or minimally invasive treatment of bleeding sites, uterine fibroids, and tumors in the prostate, liver, and breast.[19,20] As with diagnostic ultrasound, HIFU is limited by the presence of gas or bone interposed between the transducer and the target tissue. The reflection of high-energy ultrasound from strong interfaces produced by bowel gas, aerated lung, or bone may result in tissue heating along the reflected path of the sound, producing unintended tissue damage.

Major challenges with HIFU include image guidance and accurate monitoring of therapy as it is being delivered. Magnetic

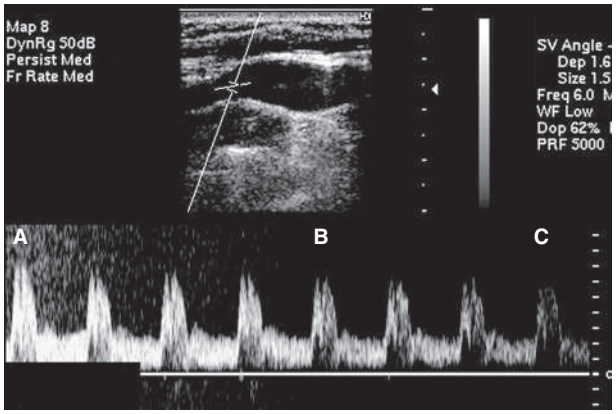

FIG. 1.47 Doppler Gain. Accurate estimation of velocity requires proper Doppler gain adjustment. **Excessive gain** will cause an overestimation of peak velocity *(A),* and **insufficient gain** will result in underestimation of velocity *(C).* To adjust gain properly, the sample volume and Doppler angle are first set at the sample site. The gain is turned up until noise appears in the background *(A),* then is gradually reduced just to the point where the background noise disappears from the image *(B). PSV,* Peak systolic velocity.

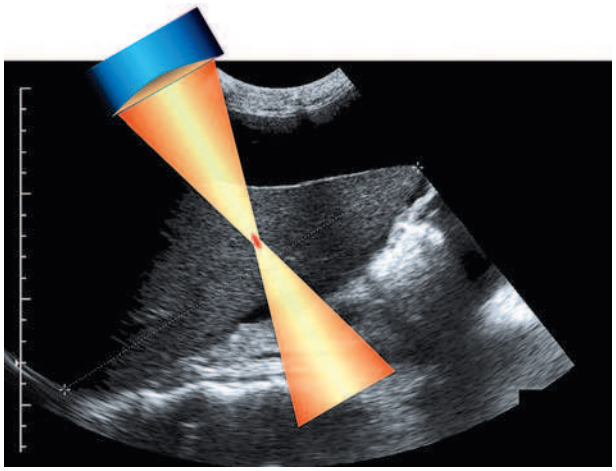

FIG. 1.48 High-Intensity Focused Ultrasound (HIFU). Local tissue destruction by heating may be achieved using HIFU delivered with focal peak intensities of several thousand W/cm^2. Tissue destruction can be confined to a small area a few millimeters in size without injury to adjacent tissues. HIFU is a promising tool for minimally invasive treatment of bleeding sites, uterine fibroids, and tumors in the prostate, liver, and breast.

resonance imaging (MRI) provides a means of monitoring temperature elevation during treatment, which is not possible with ultrasound. Guidance of therapy may be done with ultrasound or MRI, with ultrasound guidance having the advantage of verification of the acoustic window and sound path for the delivery of HIFU.

REFERENCES

1. Medical diagnostic ultrasound instrumentation and clinical interpretation. Report of the Ultrasonography Task Force. Council on Scientific Affairs. JAMA. 1991;265(9):1155-1159.
2. Chivers RC, Parry RJ. Ultrasonic velocity and attenuation in mammalian tissues. J Acoust Soc Am. 1978;63(3):940-953.
3. Goss SA, Johnston RL, Dunn F. Comprehensive compilation of empirical ultrasonic properties of mammalian tissues. J Acoust Soc Am. 1978;64(2):423-457.
4. Merritt CR, Kremkau FW, Hobbins JC. Diagnostic ultrasound: bioeffects and safety. Ultrasound Obstet Gynecol. 1992;2(5):366-374.
5. Curie J, Curie P. Développement par compression de l'électricité polaire dans les cristaux hémièdres à faces inclinées (Development, via compression, of electric polarization in hemihedral crystals with inclined faces). Bull Soc Minerol Fr. 1880;3:90-93.
6. Krishan S, Li PC, O'Donnell M. Adaptive compensation of phase and magnitude aberrations. IEEE Trans Ultrasonics Fer Freq Control. 1996;43.
7. Merritt CR. Technology update. Radiol Clin North Am. 2001;39(3):385-397.
8. Wells PN, Liang HD. Medical ultrasound: imaging of soft tissue strain and elasticity. J R Soc Interface. 2011;8(64):1521-1549.
9. Krouskop TA, Wheeler TM, Kallel F, et al. Elastic moduli of breast and prostate tissues under compression. Ultrason Imaging. 1998;20(4):260-274.
10. Ophir J, Cespedes I, Ponnekanti H, et al. Elastography: a quantitative method for imaging the elasticity of biological tissues. Ultrason Imaging. 1991; 13(2):111-134.
11. Shiina T, Nightingale KR, Palmeri ML, et al. WFUMB guidelines and recommendations for clinical use of ultrasound elastography: Part 1: basic principles and terminology. Ultrasound Med Biol. 2015;41(5):1126-1147.
12. Madsen EL, Sathoff HJ, Zagzebski JA. Ultrasonic shear wave properties of soft tissues and tissuelike materials. J Acoust Soc Am. 1983;74(5):1346-1355.
13. Sarvazyan AP, Rudenko OV, Swanson SD, et al. Shear wave elasticity imaging: a new ultrasonic technology of medical diagnostics. Ultrasound Med Biol. 1998;24(9):1419-1435.
14. Ferraioli G, Parekh P, Levitov AB, Filice C. Shear wave elastography for evaluation of liver fibrosis. J Ultrasound Med. 2014;33(2):197-203.
15. Yoneda M, Suzuki K, Kato S, et al. Nonalcoholic fatty liver disease: US-based acoustic radiation force impulse elastography. Radiology. 2010;256(2):640-647.
16. Merritt CR. Doppler US: the basics. Radiographics. 1991;11(1):109-119.
17. Merritt CR. Doppler color flow imaging. J Clin Ultrasound. 1987;15(9):591-597.
18. Rubin JM, Bude RO, Carson PL, et al. Power Doppler US: a potentially useful alternative to mean frequency-based color Doppler US. Radiology. 1994; 190(3):853-856.
19. Dubinsky TJ, Cuevas C, Dighe MK, et al. High-intensity focused ultrasound: current potential and oncologic applications. AJR Am J Roentgenol. 2008; 190(1):191-199.
20. Kennedy JE, Ter Haar GR, Cranston D. High intensity focused ultrasound: surgery of the future? Br J Radiol. 2003;76(909):590-599.

CHAPTER 2

Biologic Effects and Safety

J. Brian Fowlkes and Christy K. Holland

SUMMARY OF KEY POINTS

- Clinical ultrasound has been found to be an effective imaging modality with an excellent safety profile when used appropriately.
- Ultrasound can produce physical effects, which should be understood as part of the benefit-versus-risk assessment as with any medical procedure.
- The thermal index (TI) and mechanical index (MI) provide feedback to the user and should be minimized while obtaining the requisite medical benefit from the ultrasound examination.
- Ultrasound exposures during clinical, research, and educational examinations should be as low as reasonably achievable (ALARA).
- Users of ultrasound should be appropriately trained and familiar with the equipment operation and controls that affect ultrasound exposure.

CHAPTER OUTLINE

REGULATION OF ULTRASOUND OUTPUT
PHYSICAL EFFECTS OF SOUND
THERMAL EFFECTS
Ultrasound Produces Heat
Factors Controlling Tissue Heating
Spatial Focusing
Temporal Considerations
Tissue Type
Bone Heating
Soft Tissue Heating
Hyperthermia and Ultrasound Safety
Thermal Index
Homogeneous Tissue Model (Soft Tissue)
Tissue Model With Bone at the Focus (Fetal Applications)
Tissue Model With Bone at the Surface (Transcranial Applications)
Estimate of Thermal Effects
Summary Statement on Thermal Effects
EFFECTS OF ACOUSTIC CAVITATION
Potential Sources for Bioeffects
Sonochemistry
Evidence of Cavitation From Lithotripters
Bioeffects in Lung and Intestine
Ultrasound Contrast Agents
Considerations for Increasing Acoustic Output
Mechanical Index
Summary Statement on Gas Body Bioeffects
OUTPUT DISPLAY STANDARD
GENERAL AIUM SAFETY STATEMENTS
EPIDEMIOLOGY
CONTROLLING ULTRASOUND OUTPUT
ULTRASOUND ENTERTAINMENT VIDEOS

Ultrasound has provided a wealth of knowledge in diagnostic medicine and has greatly affected medical practice, particularly in obstetrics. Millions of sonographic examinations are performed each year, and ultrasound remains one of the fastest growing imaging modalities because of its low cost, real-time interactions, portability, and apparent lack of biologic effects (bioeffects). No casual relationship has been established between clinical applications of diagnostic ultrasound and bioeffects on the patient or operator.

REGULATION OF ULTRASOUND OUTPUT

The U.S. Food and Drug Administration (FDA) regulates the maximum output of ultrasound devices to an established level. The marketing approval process requires devices to be equivalent in efficacy and output to those produced before 1976. This historic regulation of sonography has provided a safety margin for ultrasound while allowing clinically useful performance. The mechanism has restricted ultrasound exposure to levels that apparently produce few, if any, obvious bioeffects based on the epidemiologic evidence, although animal studies have shown some evidence for biologic effects.

In an effort to increase the efficacy of diagnostic ultrasound, the maximum acoustic output for some applications has increased through an additional FDA market approval process termed "510K Track 3." The vast majority of ultrasound systems currently in use were approved through this process. The Track 3 process provides the potential for better imaging performance and, as discussed later, requires that additional information be reported

to the operator regarding the relative potential for bioeffects. Therefore informed decision making is important concerning the possible adverse effects of ultrasound in relation to the desired diagnostic information. Current FDA regulations that limit the maximum output are still in place, but in the future, systems might allow sonographers and physicians the discretion to increase acoustic output beyond a level that might induce a biologic response.

Although the choices made during sonographic examinations may not be equivalent to the risk-versus-benefit decisions associated with imaging modalities using ionizing radiation, the operator will be increasingly responsible for determining the diagnostically required amount of ultrasound exposure. Thus the operator should know the potential bioeffects associated with ultrasound exposure. Patients also need to be reassured about the safety of a diagnostic ultrasound scan. The scientific community has identified some potential bioeffects from sonography, and although no causal relation has been established, it does not mean that no effects exist. Therefore it is important to understand the interaction of ultrasound with biologic systems.

PHYSICAL EFFECTS OF SOUND

The physical effects of sound can be divided into two principal groups: **thermal** and **nonthermal.** Most medical professionals recognize the thermal effects of elevated temperature on tissue, and the effects caused by ultrasound are similar to those of any localized heat source. With ultrasound, the heating mainly results from the absorption of the sound field as it propagates through tissue. However, "nonthermal" sources can generate heat as well.

Many nonthermal mechanisms for bioeffects exist. Acoustic fields can apply **radiation forces** (not ionizing radiation) on the structures within the body at both the macroscopic and the microscopic levels, resulting in exerted pressure and torque. The temporal average pressure in an acoustic field is different from the hydrostatic pressure of the fluid, and any object in the field is subject to this change in pressure. The effect is typically considered smaller than other effects because it relies on less significant factors in the formulation of the acoustic field. Acoustic fields can also cause motion of fluids. Such acoustically induced flow is called **streaming.**

Acoustic cavitation is the action of acoustic fields within a fluid to generate bubbles and cause volume pulsation or even collapse in response to the acoustic field. The result can be heat generation and associated free radical formation, microstreaming of fluid around the bubble, radiation forces generated by the scattered acoustic field from the bubble, and mechanical actions from bubble collapse. The interaction of acoustic fields with bubbles or "gas bodies" (as they are generally called) has been a significant area of bioeffects research for many years.

THERMAL EFFECTS

Ultrasound Produces Heat

As ultrasound propagates through the body, energy is lost through **attenuation.** Attenuation causes loss of penetration and the inability to image deeper tissues. Attenuation is the result of two processes, scattering and absorption. **Scattering** of the ultrasound results from the redirection of the acoustic energy by tissue encountered during propagation. With diagnostic ultrasound, some of the acoustic energy transmitted into the tissue is scattered back in the direction of the transducer, termed **backscatter,** which allows a signal to be detected and images to be made. Energy also is lost along the propagation path of the ultrasound by **absorption.** Absorption loss occurs substantially through the conversion of the ultrasound energy into heat. This heating provides a mechanism for ultrasound-induced bioeffects.

Factors Controlling Tissue Heating

The rate of temperature increase in tissues exposed to ultrasound depends on several factors, including spatial focusing, ultrasound frequency, exposure duration, and tissue type.

Spatial Focusing

Ultrasound systems use multiple techniques to concentrate or focus ultrasound energy and improve the quality of measured signals. The analogy for light is that of a magnifying glass. The glass collects all the light striking its surface and concentrates it into a small region. In sonography and acoustics in general, the term **intensity** is used to describe the spatial distribution of ultrasonic **power** (energy per unit time), where **intensity = power/area** and the **area** refers to the cross-sectional area of the ultrasound beam. Another common beam dimension is the **beam width** at a specified location of the field. If the same ultrasonic power is concentrated into a smaller area, the intensity will increase. Focusing occurs on both transmission of the ultrasound and when receiving the backscattered signals used to form the image. The transmit focusing is of importance in terms of potential biologic effects because this phenomenon controls the applied energy to the tissue. There are ultrasound imaging systems that use plane wave transmission or limited transmit focusing, which may reduce the local intensity, but all ultrasound systems must still operate under the FDA limits.

Focusing in an ultrasound system can be used to improve the spatial resolution of the images. The side effect is an increased potential for bioeffects caused by heating and cavitation. In general, the greatest heating potential is between the scanhead and the focus, but the exact position depends on the focal distance, tissue properties, and heat generated within the scanhead itself.

Returning to the magnifying glass analogy, most children learn that the secret to incineration is a steady hand. Movement distributes the power of the light beam over a larger area, thereby reducing its intensity. The same is true in ultrasound imaging. Thus imaging systems that scan a beam through tissue reduce the spatial average intensity. **Spectral Doppler** and **M-mode** ultrasound imaging maintain the ultrasound beam in a stationary position (both considered **unscanned modes**) and therefore provide no opportunity to distribute the ultrasonic power spatially, whereas **color flow Doppler, power mode Doppler,** and **B-mode** (also called **gray-scale**) ultrasound imaging require that the beam be moved to new locations **(scanned modes)** at a rate sufficient to produce the real-time nature of these imaging modes.

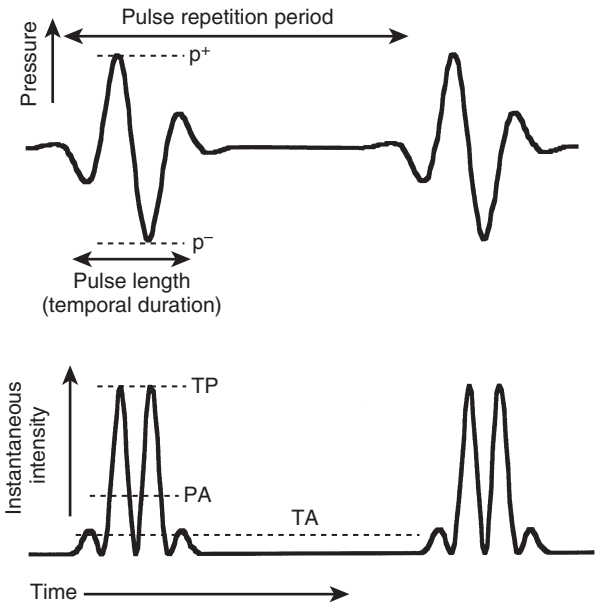

FIG. 2.1 Pressure and Intensity Parameters Measured in Medical Ultrasound. The variables are defined as follows: p^+, peak positive pressure in waveform; p^-, peak rarefactional pressure in waveform; *PA,* pulse average; *TA,* temporal average; *TP,* temporal peak.

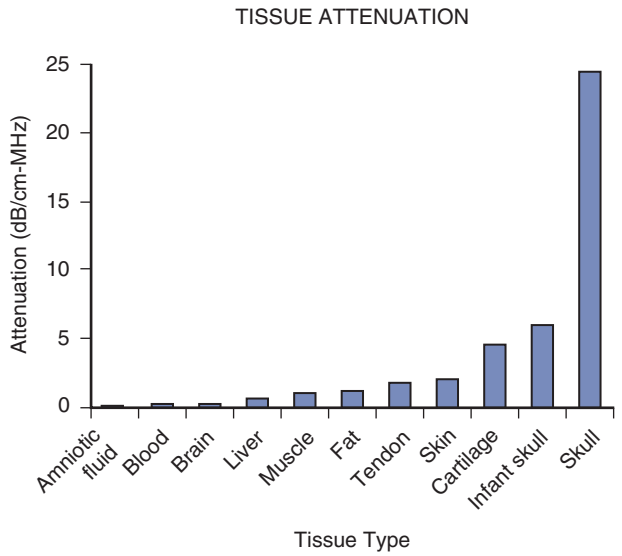

FIG. 2.2 Tissue Attenuation. Values for types of human tissue at body temperature. (Data from Duck FA, Starritt HC, Anderson SP. A survey of the acoustic output of ultrasonic Doppler equipment. Clin Phys Physiol Meas. 1987;8[1]:39-49.[47])

Temporal Considerations

The ultrasound power is the temporal rate at which ultrasound energy is produced. Therefore controlling how ultrasound is produced in time seems a reasonable method for limiting its effects.

Ultrasound can be produced in bursts rather than continuously. Ultrasound imaging systems operate on the principle of **pulse-echo,** in which a burst of ultrasound is emitted, followed by a quiescent period listening for echoes to return. This **pulsed wave** ultrasound may be swept through the image plane numerous times during an imaging sequence. On the other hand, ultrasound may be transmitted in a **continuous wave** (CW) mode, in which the ultrasound transmission is not interrupted. The **temporal peak intensity** refers to the largest intensity at any time during ultrasound exposure (Fig. 2.1). The **pulse average intensity** is the average value over the duration of the ultrasound pulse. The **temporal average intensity** is the average over the entire pulse repetition period (elapsed time between onset of ultrasound bursts). The **duty factor** is defined as the fraction of time the ultrasound field is "on." With significant time "off" between pulses (small duty factor), the temporal average value will be significantly smaller. For example, a duty factor of 10% will reduce the temporal average intensity by a factor of 10 compared with the pulse average. The time-averaged quantities are the variables most related to the potential for thermal bioeffects. Combining temporal and spatial information results in common terms such as the **spatial peak, temporal average intensity** (I_{SPTA}) and **spatial average, temporal average intensity** (I_{SATA}).

The overall duration, or **dwell time,** of the ultrasound exposure to a particular tissue is important because longer exposure of the tissue may increase the risk of bioeffects. The motion of the scanhead during an examination reduces the dwell time within a particular region of the body and can minimize the potential for bioeffects of ultrasound. Therefore performing an efficient scan, spending only the time required for diagnosis, is a simple way to reduce exposure.

Tissue Type

Numerous physical and biologic parameters control heating of tissues. Absorption is normally the dominant contributor to attenuation in soft tissue. The **attenuation coefficient** is the attenuation per unit length of sound travel and is usually given in decibels per centimeters-megahertz (dB/cm-MHz). The attenuation typically increases with increasing ultrasound frequency. The attenuation ranges from a negligible amount for fluids (e.g., amniotic fluid, blood, urine) to the highest value for bone, with some variation among different soft tissue types (Fig. 2.2).

Another important factor is the body's ability to cool tissue through blood perfusion. Well-perfused tissue will more effectively regulate its temperature by carrying away the excess heat produced by ultrasound. The exception is when heat is deposited too rapidly, as in therapeutic thermal ablation.[1]

Bone and soft tissue are two specific areas of interest based on the differences in heating phenomena. **Bone** has high attenuation of incident acoustic energy. In examinations during pregnancy, calcified bone is typically subjected to ultrasound, as in measurement of the biparietal diameter (BPD) of the skull. Fetal bone contains increasing degrees of mineralization as gestation progresses, thereby increasing risk of localized heating. Special heating situations relevant to obstetric ultrasound examinations may also occur in **soft tissue,** where overlying structures provide little attenuation of the field, such as the fluid-filled amniotic sac.

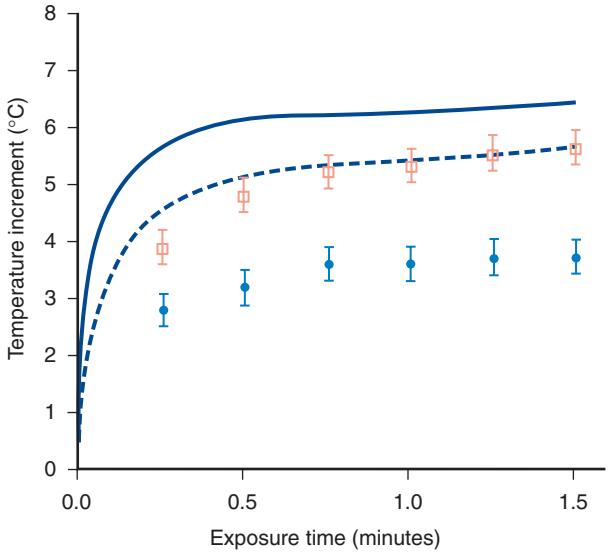

FIG. 2.3 Heating of Mouse Skull in a Focused Sound Field. For these experiments, frequency was 3.6 MHz, and temporal average focal intensity was 1.5 W/cm^2. *Solid circles,* Young (<17 wk) mice (n = 7); *open squares,* old (>6 mo) mice (n = 4); *vertical bars,* two standard errors in height; *top curves,* theoretical estimation of the temperature increases by Nyborg.[3] (With permission from Carstensen EL, Child SZ, Norton S, Nyborg W. Ultrasonic heating of the skull. J Acoust Soc Am. 1990;87[3]: 1310-1317.[2])

Bone Heating

The absorption of ultrasound at the bone surface allows for rapid deposition of energy from the field into a limited volume of tissue. The result can be a significant temperature rise. For example, Carstensen and colleagues[2] combined an analytic approach and experimental measurements of the temperature rise in mouse skull exposed to CW ultrasound to estimate the temperature increments in bone exposures. Because bone has a large absorption coefficient, the incident ultrasonic energy is assumed to be absorbed in a thin planar sheet at the bone surface. The temperature rise of mouse skull has been studied in a 3.6-MHz focused beam with a beam width of 2.75 mm (Fig. 2.3). The temporal average intensity in the focal region was 1.5 W/cm.[2] One of two models (upper curve in Fig. 2.3) in common use[3] predicts values for the temperature rise about 20% greater than that actually measured in this experiment.[2] Thus the theoretical model is conservative in nature.

Similarly for the fetal femur, Drewniak and colleagues[4] indicated that the size and calcification state of the bone contributed to the *ex vivo* heating of bone (Table 2.1). To put this in perspective and to illustrate the operator's role in controlling potential heating, consider the following scenario. By reducing the output power of an ultrasound scanner by 10 dB, the predicted temperature rise would be reduced by a factor of 10, making the increase of 3°C seen by these researchers (see Table 2.1) virtually nonexistent. **This strongly suggests the use of maximum receive gain and reduction in output power during ultrasound examinations** (see section on considerations for controlling ultrasound output). In fetal examinations an attempt should be made to maximize receive gain because this comes at no cost to the patient in terms of exposure. Distinctions are often made between bone positioned deep to the skin at the focal plane of the transducer and bone near the skin surface, as when considering transcranial applications. This distinction is discussed later with regard to the thermal index (TI).

TABLE 2.1 Fetal Femur Temperature Increments[a] at 1 W/cm^2

Gestational Age (days)	Diameter (mm)	Temperature Increments (°C)
59	0.5	0.10
78	1.2	0.69
108	3.3	2.92

[a]Temperature increments in human fetal femur exposed for 20 seconds were found to be approximately proportional to incident intensity.

With permission from Drewniak JL, Carnes KI, Dunn F. In vitro ultrasonic heating of fetal bone. J Acoust Soc Am. 1989;86(4):1254-1258.[4]

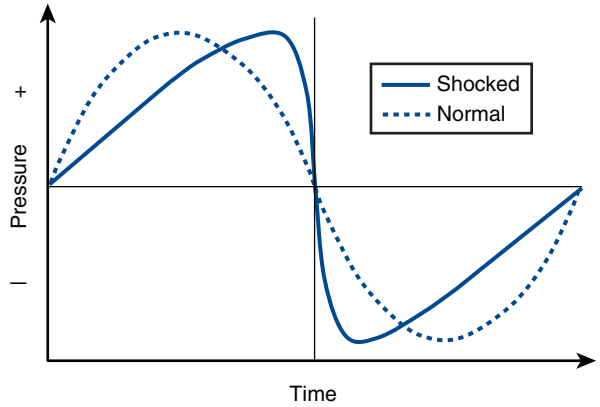

FIG. 2.4 Effect of Finite Amplitude Distortion on a Propagating Ultrasound Pulse. Note the increasing steepness in the pulse, which contains higher frequency components.

Soft Tissue Heating

Two clinical situations for ultrasound exposure in soft tissue are particularly relevant to obstetric and gynecologic applications. First, a common scenario involves **scanning through a full bladder.** The urine is a fluid with a relatively low ultrasound attenuation coefficient. The reduced attenuation allows larger acoustic amplitudes to be applied deeper within the body. Second, the propagating wave may experience **finite amplitude distortion,** resulting in energy being shifted by a nonlinear process from lower to higher frequencies. The result is a **shockwave**—a gradual wave steepening results in a waveform composed of higher frequency components (Fig. 2.4). Attenuation increases with increasing frequency; therefore the absorption of a large portion of the energy in such a wave occurs over a much shorter distance, concentrating the energy deposition in the first tissue encountered, which may include the fetus.

Ultrasound imaging systems include specific modalities that rely on nonlinear effects. In **tissue harmonic imaging,** or native harmonic imaging, the image is created using the backscatter of harmonic components induced by nonlinear propagation of the ultrasound field. This has distinct advantages in terms of reducing image artifacts and improving lateral resolution in particular. In these nonlinear imaging modes the acoustic output must be sufficiently high to produce the effect. The acoustic power currently used is still within the FDA limits, but improvements in image quality using such modes may create the need to modify or relax the regulatory restrictions. Similarly, in elasticity or shear wave imaging, the acoustic pressure may need to be increased to provide sufficient acoustic radiation force for imaging tissue stiffness. This detail will be discussed in the section on considerations for increasing acoustic output.

Transvaginal ultrasound is important to note because of the proximity of the transducer to sensitive tissues such as the ovaries. As discussed later, temperature increases near the transducer may provide a heat source at sites other than the focus of the transducer. In addition, the transducer face itself may be a significant heat source because of inefficiencies in its conversion of electric to acoustic energy. Such factors must be considered in the estimation of potential thermal effects in transvaginal ultrasound and other endocavitary applications.

Hyperthermia and Ultrasound Safety

Knowledge of the bioeffects of ultrasound heating is in part based on the experience available from other, more common forms of hyperthermia, which serve as a basis for safety criteria. Extensive data exist on the effects of short-term and extended temperature increases, or hyperthermia. Teratogenic effects from hyperthermia have been demonstrated in birds, all the common laboratory animals, farm animals, and nonhuman primates.[5] The wide range of observed bioeffects, from subcellular chemical alterations to gross congenital abnormalities and fetal death, is an indication of the effectiveness or universality of hyperthermic conditions for perturbing living systems.[6]

The National Council on Radiation Protection and Measurements (NCRP) Scientific Committee on Biological Effects of Ultrasound compiled a comprehensive list of the lowest reported thermal exposures producing teratogenic effects.[7,8] Examination of these data indicated a lower boundary for observed thermally induced bioeffects. Questions remain, however, about the relevance of this analysis of hyperthermia to the application of diagnostic ultrasound.[9] After a careful literature review, O'Brien and colleagues[10] suggested a more detailed consideration of thermal effects with regard to short-duration exposures. Fig. 2.5 shows the recommended approach to addressing the combination of temperature and duration of exposure. Note that the tolerance of shorter durations and higher temperatures suggests a substantial safety margin for diagnostic ultrasound. Regardless, it is beneficial to provide feedback to the ultrasound operator as to the relative potential for a temperature rise in a given acoustic field under conditions associated with a particular examination. This will allow an informed decision as to the exposure needed to obtain diagnostically relevant information.

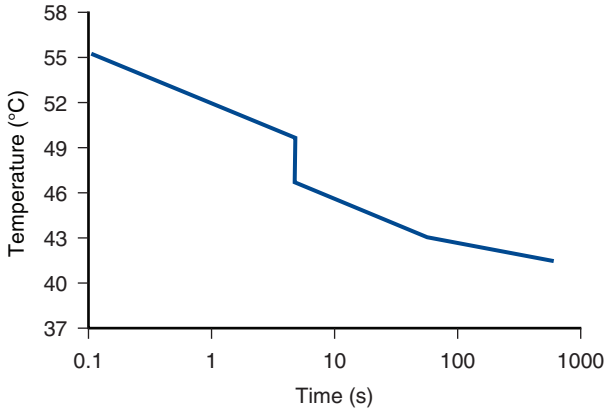

FIG. 2.5 Conservative Boundary Curve for Nonfetal Bioeffects Caused by a Thermal Mechanism. Note the increase in temperature tolerance associated with shorter durations of exposures, a modification to the earlier American Institute of Ultrasound in Medicine (AIUM) Conclusions Regarding Heat statement (March 26, 1997). The AIUM approved a revised thermal statement on April 6, 2009. For a complete description of the origins of this curve, see O'Brien and colleagues.[10] (With permission from O'Brien Jr WD, Deng CX, Harris GR, et al. The risk of exposure to diagnostic ultrasound in postnatal subjects: thermal effects. J Ultrasound Med. 2008;27[4]:517-535.[10])

Thermal Index

Based on analysis of hyperthermia data, the NCRP proposed a general statement concerning the safety of ultrasound examinations in which no temperature rise greater than 1°C is expected. In an afebrile patient within this limit, the NCRP concluded that there was no basis for expecting an adverse effect. In cases where the temperature rise might be greater, the operator should weigh the benefit against the potential risk. To assist in this decision, given the range of different imaging conditions seen in practice, a **thermal index** (TI) was approved as part of the Standard for Real-Time Display of Thermal and Mechanical Acoustical Output Indices on Diagnostic Ultrasound Equipment of the American Institute of Ultrasound in Medicine (AIUM).[11] This standard provides the operator with an indication of the relative potential risk of heating tissue, with calculations based on the imaging conditions and an on-screen display showing the TI. This standard was subsequently adopted as an international standard through the International Electrotechnical Commission (IEC).[12]

The Thermal Index

To more easily inform the physician of the operating conditions that could, in some cases, lead to a temperature elevation of 1°C, a thermal index is defined as

$$TI = \frac{W_0}{W_{deg}}$$

where W_{deg} is the ultrasonic source power (in watts) calculated as capable of producing a 1°C temperature elevation under specific conditions. W_0 is the ultrasonic source power (in watts) being used during the current exam.

Reproduced with permission of American Institute of Ultrasound in Medicine (AIUM).

The NCRP ultrasound committee introduced the TI concept.[8] The purpose of the TI is to provide an indication of the *relative* potential for increasing tissue temperature, but it is not meant to provide the *actual* temperature rise. The NCRP recommended two tissue models to aid in the calculation of the ultrasound power that could raise the temperature in tissue by 1°C: (1) a homogeneous model in which the attenuation coefficient is uniform throughout the region of interest, and (2) a fixed-attenuation model in which the minimum attenuation along the path from transducer to a distant anatomic structure is independent of the distance because of a low-attenuation fluid path (e.g., amniotic fluid).[8,13,14] Because of concern for the patient, it was recommended that "reasonable worst case" assumptions be made with respect to estimation of temperature elevations *in vivo*. The FDA, AIUM, and National Electrical Manufacturers Association (NEMA) adopted the TI as part of the output display standard. They advocate estimating the effect of attenuation in the body by reducing the acoustic power/output of the scanner (W_0) by a derating factor equal to 0.3 dB/cm-MHz for the soft tissue model.[11]

The AIUM Thermal Index Working Group considered three tissue models: (1) the homogeneous tissue or soft tissue model, (2) a tissue model with bone at the focus, and (3) a tissue model with bone at the surface, or transcranial model.[11] The TI takes on three different forms for these tissue models.

Homogeneous Tissue Model (Soft Tissue)

The assumption of homogeneity helps simplify the determination of the effects of acoustic propagation and attenuation, as well as the heat transfer characteristics of the tissue. Providing one of the most common applications for ultrasound imaging, this model applies to situations where bone is not present and can generally be used for fetal examinations during the first trimester (low calcification in bone). In the estimation of potential heating, many assumptions and compromises had to be made to calculate a single quantity that would guide the operator. Calculations of the temperature rise along the axis of a focused beam for a simple, spherically curved, single-element transducer result in two thermal peaks. The first is in the near field (between the transducer and the focus), and the second appears close to the focal region.[15,16] The **first thermal peak** occurs in a region with low ultrasound intensity and wide beam width. When the beam width is large, cooling will occur mainly because of perfusion. In the near field the magnitude of the local intensity is the chief determinant of the degree of heating. The **second thermal peak** occurs at the location of high intensity and narrow beam width at or near the focal plane. Here the cooling is dominated by conduction, and the total acoustic power is the chief determinant of the degree of heating.

Given the thermal "twin peaks" dilemma, the AIUM Thermal Index Working Group compromised in creating a TI that included contributions from both heating domains.[11] Their rationale was based on the need to minimize the acoustic measurement load for manufacturers of ultrasound systems. In addition, adjustments had to be made to compensate for effects of the large range of potential apertures. The result is a complicated series of calculations and measurements that must be performed, and to the credit of the many manufacturers, there has been considerable effort in implementing a display standard to provide user feedback. Different approaches to these calculations were considered,[10] but changes will require that the currently accepted implementation be reexamined and approved for use by the FDA and considered by the IEC.

Tissue Model With Bone at the Focus (Fetal Applications)

Applications of ultrasound in which the acoustic beam travels through soft tissue for a fixed distance and impinges on bone occur most often in obstetric scanning during the second and third trimesters. Carson and colleagues[13] recorded sonographic measurements of the maternal abdominal wall thickness in various stages of pregnancy. Based on their results, the NCRP recommended that the attenuation coefficients for the first, second, and third trimesters be 1.0, 0.75, and 0.5 dB/MHz, respectively.[7] These values represent "worst case" estimates. In addition, Siddiqi and colleagues[17] determined the average tissue attenuation coefficient for transabdominal insonification (exposure to ultrasound waves) in a patient population of nonpregnant, healthy volunteers was 2.98 dB/MHz. This value represents an average measured value and is much different from the worst-case estimates previously listed. This leads to considerable debate on how such parameters should be included in an index.

In addition, bone is a complex, hard connective tissue with a calcified collagenous intercellular structure. Its absorption coefficient for longitudinal waves is a factor of 10 greater than that for most soft tissues (see Fig. 2.2). **Shear waves** are also created in bone as sound waves strike bone at oblique incidence. The absorption coefficients for shear waves are even greater than those for longitudinal waves.[18-20]

Based on the data of Carstensen and colleagues[2] described earlier, the NCRP proposed a thermal model for bone heating. Using this model, the **Bone Thermal Index** (TIB) is estimated for conditions in which the focus of the beam is at or near bone. Again, assumptions and compromises had to be made to develop a functional TI for the case of bone exposure, as follows:

- For **unscanned mode** transducers (operating in a fixed position) with bone in the focal region, the location of the maximum temperature increase is at the surface of the bone. Therefore the TIB is calculated at the distance along the beam from the transducer where it is maximized, a worst-case assumption.
- For **scanned modes**, the **Soft Tissue Thermal Index** (TIS) is used because the temperature increase at the surface is either greater than or approximately equal to the temperature increase with bone in the focus.

Tissue Model With Bone at the Surface (Transcranial Applications)

For adult cranial applications, the same model as that with bone at the focus is used to estimate the temperature distribution in situ. However, because the bone is located at the surface, immediately after the acoustic beam enters the body, attenuation of the acoustic power output is not included.[11] In this situation the equivalent beam diameter at the surface is used to calculate the

acoustic power and derive the **Cranial Bone Thermal Index** (TIC).

Estimate of Thermal Effects

Ultrasound users should keep in mind several points when referring to the TI as a means of estimating the potential for thermal effects. First, the TI is not synonymous with temperature rise. A TI equal to 1 does not mean the temperature will rise 1°C. An increased potential for thermal effects can be expected as TI increases. Second, a high TI does not mean that bioeffects are occurring, but only that the potential exists. The thermal models employed for TI calculation may not consider factors that may reduce the actual temperature rise. However, TI should be monitored during examinations and minimized when possible. Finally, there is no consideration in the TI for the duration of the scan, so minimizing the overall examination time will reduce the potential for effects. There have been proposals suggesting the inclusion of such a dwell time effect,[21] but these have not been adopted.

Summary Statement on Thermal Effects

The AIUM statement concerning thermal effects of ultrasound includes several conclusions that can be summarized as follows[22]:

- Adult examinations resulting in a temperature rise of up to 2°C are not expected to cause bioeffects. (Many ultrasound examinations fall within these parameters.)
- A significant number of factors control heat production by diagnostic ultrasound.
- Ossified bone is a particularly important concern for ultrasound exposure.
- A labeling standard now provides information concerning potential heating in soft tissue and bone.
- Even though an FDA limit exists for fetal exposures, predicted temperature rises can exceed 2°C.
- Thermal indices are expected to track temperature increases better than any single ultrasonic field parameter.

EFFECTS OF ACOUSTIC CAVITATION

Potential Sources for Bioeffects

Knowledge concerning the interaction of ultrasound with **gas bodies** (which many term "cavitation") has significantly increased over time, although it is not as extensive as that for ultrasound thermal effects and other sources of hyperthermia. **Acoustic cavitation inception** is demarcated by a specific threshold value: the minimum acoustic pressure necessary to initiate the growth of a cavity in a fluid during the rarefaction phase of the cycle. Several parameters affect this threshold, including **initial bubble** or **cavitation nucleus size,** acoustic pulse characteristics (e.g., center frequency, pulse repetition frequency [PRF], pulse duration), ambient hydrostatic pressure, and host fluid parameters (e.g., density, viscosity, compressibility, heat conductivity, surface tension). **Inertial cavitation** refers to bubbles that undergo large variations from their equilibrium sizes in a few acoustic cycles. Specifically during contraction, the surrounding fluid inertia controls the bubble motion.[23] Large acoustic pressures are necessary to generate inertial cavitation, and the collapse of these cavities is often violent.

The AIUM Statement on Mammalian Biological Effects of Heat

APPROVED MARCH 25, 2015

1. An excessive temperature increase can result in toxic effects in mammalian systems. The biological effects observed depend on many factors, such as the exposure duration, the type of tissue exposed, its cellular proliferation rate, and its potential for regeneration. Age and stage of development are important factors when considering fetal and neonatal safety. Temperature increases of several degrees Celsius above the normal core range can occur naturally. The probability of an adverse biological effect increases with both the duration and the magnitude of the temperature rise.
2. In general, adult tissues are more tolerant of temperature increases than fetal and neonatal tissues. Therefore, higher temperatures and/or longer exposure durations would be required for thermal damage. The considerable data available on the thermal sensitivity of adult tissues support the following inferences[10]:
   a. For exposure durations up to 50 hours, there have been no significant adverse biological effects observed due to temperature increases less than or equal to 1.5°C above normal.[25]
   b. For temperature increases between 1.5°C and 6°C above normal, there have been no significant adverse biological effects observed due to temperature increases less than or equal to $6 - [\log_{10}(t/60)]/0.6$ where t is the exposure duration in seconds. For example, for temperature increases of 4°C and 6°C, the corresponding limits for the exposure durations t are 16 minutes and 1 minute, respectively.
   c. For temperature increases greater than 6°C above normal, there have been no significant adverse biological effects observed due to temperature increases less than or equal to $6 - [\log_{10}(t/60)]/0.3$ where t is the exposure duration in seconds. For example, for temperature increases of 9.6°C and 6.0°C, the corresponding limits for the exposure durations t are 5 and 60 seconds, respectively.
   d. For exposure durations less than 5 seconds, there have been no significant, adverse biological effects observed due to temperature increases less than or equal to $9 - [\log_{10}(t/60)]/0.3$ where t is the exposure duration in seconds. For example, for temperature increases of 18.3°C, 14.9°C, and 12.6°C, the corresponding limits for the exposure durations t are 0.1, 1, and 5 seconds, respectively.
3. Acoustic output from diagnostic ultrasound devices is sufficient to cause temperature elevations in fetal tissue. Although fewer data are available for fetal tissues, the following conclusions are justified[10,26]:
   a. In general, temperature elevations become progressively greater from B-mode to color Doppler to spectral Doppler applications.

The AIUM Statement on Mammalian Biological Effects of Heat[24]—cont'd

b. For identical exposure conditions, the potential for thermal bioeffects increases with the dwell time during examination.
c. For identical exposure conditions, the temperature rise near bone is significantly greater than in soft tissues, and it increases with ossification development throughout gestation. For this reason, conditions in which an acoustic beam impinges on ossifying fetal bone deserve special attention due to its close proximity to other developing tissues.
d. The current U.S. Food and Drug Administration regulatory limit for the derated spatial-peak temporal-average intensity ($I_{SPTA.3}$) is 720 mW/cm^2. For this exposure, the theoretical estimate of the maximum temperature increase in the conceptus may exceed 1.5°C.
e. Although an adverse fetal outcome is possible at any time during gestation, most severe and detectable effects of thermal exposure in animals have been observed during the period of organogenesis. For this reason, exposures during the first trimester should be restricted to the lowest outputs consistent with obtaining the necessary diagnostic information.
f. Ultrasound exposures that elevate fetal temperature by 4°C above normal for 5 minutes or more have the potential to induce severe developmental defects. Thermally induced congenital anomalies have been observed in a large variety of animal species. In current clinical practice, using commercially available equipment, it is unlikely that such thermal exposure would occur at a specific fetal anatomic site provided that the thermal index (TI) is less than 2.0 and the dwell time on that site does not exceed 4 minutes.
g. Transducer self-heating is a significant component of the temperature rise of tissues close to the transducer. This may be of significance in transvaginal scanning, but no data for the fetal temperature rise are available.

4. The temperature increase during exposure of tissues to diagnostic ultrasound fields is dependent on: (1) output characteristics of the acoustic source, such as frequency, source dimensions, scan rate, output power, pulse repetition frequency, pulse duration, transducer self-heating, exposure time, and wave shape; and (2) tissue properties, such as attenuation, absorption, speed of sound, acoustic impedance, perfusion, thermal conductivity, thermal diffusivity, anatomic structure, and the nonlinearity parameter.
5. Calculations of the maximum temperature increase resulting from ultrasound exposure are not exact because of the uncertainties and approximations associated with the thermal, acoustic, and structural characteristics of the tissues involved. However, experimental evidence shows that calculations are generally capable of predicting measured values within a factor of 2. Thus, such calculations are used to obtain safety guidelines for clinical exposures in which direct temperature measurements are not feasible. These guidelines, called thermal indices,[a] provide a real-time display of the relative probability that a diagnostic system could induce thermal injury in the exposed subject. Under most clinically relevant conditions, the soft tissue thermal index (TIS) and the bone thermal index (TIB) either overestimate or closely approximate the best available estimate of the maximum temperature increase (ΔT_{max}). For example, if TIS = 2, then $\Delta T_{max} \leq 2$°C; actual temperature increases are also dependent on dwell time.

   However, in some applications, such as fetal examinations in which the ultrasound beam passes through a layer of relatively unattenuating liquid, such as urine or amniotic fluid, the TI can underestimate ΔT_{max} by up to a factor of 2.[27,28]

[a]The thermal indices are the nondimensional ratios of attenuated acoustic power at a specific point to the attenuated acoustic power required to raise the temperature at that point in a specific tissue model by 1°C.[29]
AIUM, American Institute of Ultrasound in Medicine.
Reproduced with permission from American Institute of Ultrasound in Medicine (AIUM). Statement on mammalian biological effects of heat. Laurel, MD: AIUM; 2015. Available from: http://www.aium.org/officialStatements/17. Updated March 25, 2015. Cited October 7, 2016.[24]

The effect of **preexisting cavitation nuclei** may be one of the principal controlling factors in mechanical effects that result in biologic effects. The body is such an excellent filter that these nucleation sites may be found only in small numbers and at selected sites. For example, if water is filtered down to 2 µm, the cavitation threshold doubles.[30] Theoretically, the tensile strength of water that is devoid of cavitation nuclei is about 100 megapascals (MPa).[31] Various models have been suggested to explain bubble formation in animals,[32,33] and these models have been used extensively in cavitation threshold determination. One model is used in the prediction of SCUBA diving tables and may also have applicability to patients.[34] It remains to be seen how well such models will predict the nucleation of bubbles from diagnostic ultrasound in the body.

Fig. 2.6 shows a 1-MHz therapeutic ultrasound unit generating bubbles in gas-saturated water. The particular medium and ultrasound parameters were chosen to optimize the conditions for cavitation. Using CW ultrasound and many preexisting gas pockets in the water set the stage for the production of cavitation. Even though these acoustic pulses are longer than those typically used in diagnostic ultrasound, cavitation effects have also been observed with diagnostic pulses in fluids.[35] **Ultrasound contrast agents** composed

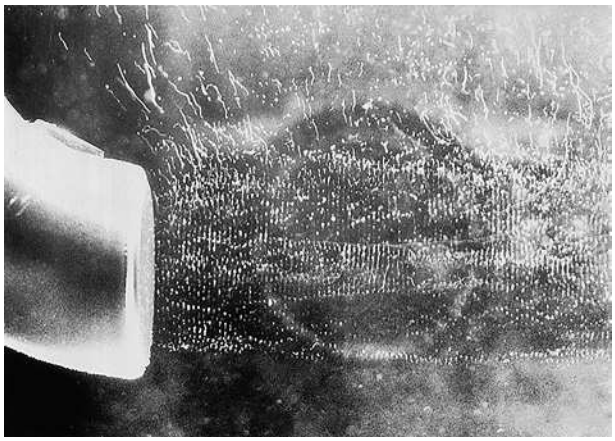

FIG. 2.6 Acoustic Cavitation Bubbles. This cavitation activity is being generated in water using a common therapeutic ultrasound device. (Courtesy of National Center for Physical Acoustics, University of Mississippi.)

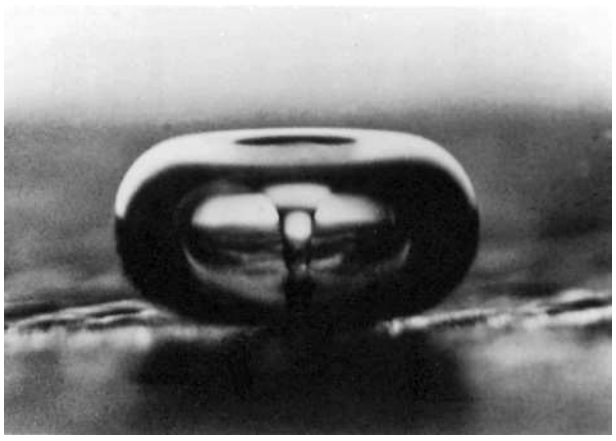

FIG. 2.8 Collapsing Bubble Near a Boundary. When cavitation is produced near boundaries, a liquid jet may form through the center of a bubble and strike the boundary surface. (Courtesy of Lawrence A. Crum.)

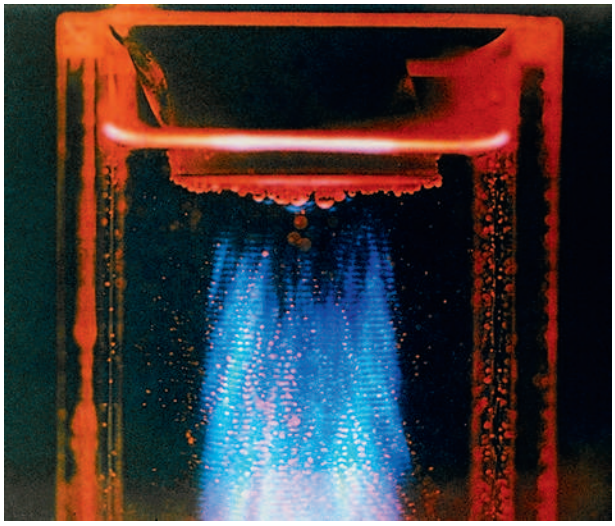

FIG. 2.7 Chemical Reaction Induced by Cavitation Producing Visible Light. The reaction is the result of free radical production. (Courtesy of National Center for Physical Acoustics, University of Mississippi.)

of stabilized gas bubbles should provide a source of cavitation nuclei, as discussed later in the section on ultrasound contrast agents.

Sonochemistry

Free radical generation and detection provide a means to observe cavitation and to gauge its strength and potential for damage. The sonochemistry of free radicals is the result of very high temperatures and pressures within the rapidly collapsing bubble. These conditions can even generate light, or **sonoluminescence.**[36] With the addition of the correct compounds, chemical luminescence can also be used for free radical detection and can be generated with short pulses similar to those used in diagnostic ultrasound.[37] Fig. 2.7 shows **chemiluminescence** generated by a therapeutic ultrasound device; the setup is backlighted (in red) to show the bubbles and experimental apparatus. The chemiluminescence emissions are the blue bands seen through the middle of the liquid sample holder. The light emitted is sufficient to be seen by simply adapting one's eyes to darkness. Electron spin resonance can also be used with molecules that trap free radicals to detect cavitation activity capable of free radical production.[38] A number of other chemical detection schemes are presently employed to detect cavitation from diagnostic devices *in vitro*.

Evidence of Cavitation From Lithotripters

It is possible to generate bubbles *in vivo* using short pulses with high amplitudes of extracorporeal shockwave lithotripsy (ESWL). The peak positive pressure for lithotripsy pulses can be as high as 50 MPa, with a rarefactional pressure of about 20 MPa. **Finite amplitude distortion** causes high frequencies to appear in high-amplitude ultrasound fields. Although ESWL pulses have significant energy at high frequencies because of finite amplitude distortion, a large portion of the energy is actually in the 100-kHz range, much lower than frequencies in diagnostic scanners. The lower frequency makes cavitation more likely. Aymé and Carstensen[39] showed that the higher frequency components in nonlinearly distorted pulses contributed little to the killing of *Drosophila* larvae.

Interestingly, evidence indicates that collapsing bubbles play a role in stone disruption.[40-42] A bubble collapsing near a surface may form a liquid jet through its center, which strikes the surface (Fig. 2.8). Placing a sheet of aluminum foil at the focus of a lithotripter generates small pinholes.[40] The impact is even sufficient to pit solid brass and aluminum plates.

At very high acoustic amplitudes, tissue can be disrupted and even emulsified using ultrasound in a process termed "histotripsy."[43-45] Peak rarefactional pressures used in this form of therapeutic ultrasound can be as high as 25 to

30 MPa, at which point gas bubbles form spontaneously in a very consistent controlled fashion that allows for therapeutic applications.

Clearly, lithotripsy and histotripsy differ greatly from diagnostic ultrasound in the acoustic power generated and are not comparable in the bioeffects produced. However, some diagnostic devices produce peak rarefactional pressures greater than 3 MPa, which is in the lower range of lithotripter outputs.[46-48] Lung damage and surface petechiae have been noted as side effects of ESWL in clinical cases.[49] Inertial cavitation was suspected as the cause, prompting several researchers to study the effects of diagnostic ultrasound exposure on the lung parenchyma.[50,51]

Bioeffects in Lung and Intestine

Lung tissue and intestinal tissue are key locations for examining for bioeffects of diagnostic ultrasound.[50] The presence of air in the alveolar spaces constitutes a significant source of gas bodies. Child and colleagues[51] measured threshold pressures for hemorrhage in mouse lung exposed to 1- to 4-MHz short-pulse diagnostic ultrasound (i.e., 10- and 1-μm pulse durations). The threshold of damage in murine lung at these frequencies was 1.4 MPa. Pathologic features of this damage included extravasation of blood cells into the alveolar spaces.[52] The authors hypothesized that cavitation, originating from gas-filled alveoli, was responsible for the damage. Their data provided the first direct evidence that clinically relevant, pulsed ultrasound exposures produce deleterious effects in mammalian tissue in the absence of significant heating. Hemorrhagic foci induced by 4-MHz pulsed Doppler ultrasound have also been reported in the monkey.[53] Damage in the monkey lung was of a significantly lesser degree than that in the mouse. In these studies it was impossible to show categorically that bubbles induced these effects because the cavitation-induced bubbles were not observed. Thresholds for petechial hemorrhage in the lung caused by ultrasound have been measured in mouse, rat, rabbit and pig.[54-56] Direct mechanical stresses associated with propagation of ultrasound in the lung were believed to contribute to the damage observed.[50,57] Thresholds for hemorrhage in the murine intestine exposed to pulsed ultrasound have also been determined.[58]

Kramer and colleagues[59] assessed cardiopulmonary function in rats exposed to pulsed ultrasound well above the acoustic output threshold of damage, at a mechanical index (MI) of 9.7. Measurements of cardiopulmonary function included arterial blood pressure, heart rate, respiratory rate, and arterial blood gases (Pco_2 and Po_2). If only one side of the rat lung was exposed, the cardiopulmonary measurements did not change significantly between baseline and postexposure values because of the functional respiratory reserve in the unexposed lobes. However, when both sides of the lung had significant ultrasound-induced lesions, the rats were unable to maintain systemic arterial pressure or resting levels of arterial Po_2.

Further studies are required to determine the relevance of these findings to humans. In general, tissues containing air (or stabilized gas) are more susceptible to damage than are tissues without gas. Also, no confirmed reports of petechial hemorrhage below an MI of 0.4 have been noted in animal studies. As recently as 2012, this threshold in lungs was confirmed in a small animal model.[60] However, it should be noted that the mechanism for pulmonary effects might not follow the functional frequency dependence embedded in the MI.[61]

Ultrasound Contrast Agents

The apparent absence of cavitation in many locations in the body can result from the lack of available cavitation nuclei. Based on evidence in the lung and intestine in mammalian models described earlier, the presence of gas bodies clearly reduces the requisite acoustic field for producing bioeffects. Many ultrasound contrast agents are composed of stabilized gas bubbles, so they could provide readily available nuclei for potential cavitation activity. This makes the investigation of bioeffects in the presence of ultrasound contrast agents an important area of research.[62-64] Studies have also shown that ultrasound exposure in the presence of contrast agents produces small vascular petechiae and endothelial damage in mammalian systems.[65-70] Acoustic emissions from activated microbubbles correlate with the degree of vascular damage.[67,68]

As a result, the AIUM has a safety statement on the bioeffects of diagnostic ultrasound with gas body contrast agents. This bioeffect may occur, but the issue remains whether it constitutes a significant physiologic risk. The safety statement is designed to make sonographers and physicians aware of the potential for bioeffects in the presence of gas contrast agents and allow them to make an informed decision based on a risk-versus-benefit assessment.

Some research also indicates the production of premature ventricular contractions (PVCs) during cardiac scanning in the presence of ultrasound contrast agents. At least one human study indicated an increase in PVCs only when ultrasound imaging was performed with a contrast agent, and not with ultrasound imaging alone or during injection of the agent without imaging.[71] Another study[72] revealed that oscillating microbubbles affect stretch activation channels[73,74] in cardiac cells, which generates membrane depolarization and triggers action potentials and thus PVCs. The importance of this bioeffect is also being debated because there is a naturally occurring rate of PVCs, and a small increase may not be considered clinically important, particularly if the patient benefits from using the agent. Additional consideration might be given to patients with specific conditions in whom additional PVCs should be avoided.

The consequences of the ultrasound contrast agent bioeffects reported thus far require more study. Although the potential exists for a bioeffect, its scale and influence on human physiology remain unclear. Contrast agents have demonstrated efficacy for specific indications, facilitating patient management.[75] In addition, clinical trials and marketing follow-up of many patients receiving ultrasound and contrast agents have reported few effects. Several publications provide evidence confirming the safety of ultrasound contrast agent use.[76-79]

The AIUM Statement on Mammalian Biological Effects in Tissues With Gas Body Contrast Agents

APPROVED MARCH 25, 2015

Presently available ultrasound contrast agents consist of suspensions of gas bodies (stabilized gaseous microbubbles). The gas bodies have the correct size for strong echogenicity with diagnostic ultrasound and also for passage through the microcirculation. Commercial agents undergo rigorous clinical testing for safety and efficacy before Food and Drug Administration approval is granted, and they have been in clinical use in the United States since 1994. Detailed information on the composition and use of these agents is included in the package inserts. In the United States, contrast agents have been approved for opacification of the left ventricular chamber and delineation of the left ventricular endocardial border. Outside the United States, additional approved indications include imaging lesions of the breast and liver, portal vein, and extracranial carotid and peripheral arteries. Many other diagnostic applications are under development or clinical testing.

Contrast agents carry some potential for nonthermal bioeffects when ultrasound interacts with the gas bodies. The mechanism for such effects is related to the physical phenomenon of acoustic cavitation. Several published reports describe adverse bioeffects in mammalian tissue *in vivo* resulting from exposure to diagnostic ultrasound with gas body contrast agents in the circulation. Induction of premature ventricular contractions by triggered contrast echocardiography in humans has been reported for a noncommercial agent and in laboratory animals for commercial agents. Microvascular leakage, killing of cardiomyocytes, and glomerular capillary hemorrhage, among other bioeffects, have been reported in animal studies. Two medical ultrasound societies have examined this potential risk of bioeffects in diagnostic ultrasound with contrast agents and provide extensive reviews of the topic: the World Federation for Ultrasound in Medicine and Biology Contrast Agent Safety Symposium[81] and the American Institute of Ultrasound in Medicine 2005 Bioeffects Consensus Conference.[62] More recently, the British Medical Ultrasound Society issued a detailed assessment of methods for the safe use of diagnostic ultrasound, including use of contrast agents.[82] Based on a review of these reports and recent literature, the Bioeffects Committee has issued the following statement.

STATEMENT ON MAMMALIAN BIOLOGICAL EFFECTS OF DIAGNOSTIC ULTRASOUND WITH GAS BODY CONTRAST AGENTS

Induction of premature ventricular contractions, microvascular leakage with petechiae, glomerular capillary hemorrhage, local cell killing, and other effects in mammalian tissue *in vivo* have been reported and independently confirmed for diagnostic ultrasound exposure with a mechanical index (MI) above about 0.4 and a gas body contrast agent present in the circulation.

Although the medical significance of such microscale bioeffects is uncertain, minimizing the potential for such effects represents prudent use of diagnostic ultrasound. In general, for imaging with contrast agents at an MI above 0.4, practitioners should use the minimal agent dose, MI, and examination time consistent with efficacious acquisition of diagnostic information. In addition, the echocardiogram should be monitored during high-MI contrast cardiac-gated perfusion echocardiography, particularly in patients with a history of myocardial infarction or unstable cardiovascular disease. Furthermore, physicians and sonographers should follow all guidance provided in the package inserts of these drugs, including precautions, warnings, and contraindications.

AIUM, American Institute of Ultrasound in Medicine.

Reproduced with permission from American Institute of Ultrasound in Medicine (AIUM). Statement on mammalian biological effects in tissues with gas body contrast agents. Laurel, MD: AIUM; 2015. Available from: http://www.aium.org/officialStatements/25. Approved March 25, 2015. Cited October 7, 2016.[80]

Considerations for Increasing Acoustic Output

Situations arise where increasing acoustic output in ultrasound imaging could provide improved performance, particularly at significant depths. The desire to increase acoustic output was the original impetus for the development of the FDA 510K Track 3 mechanism in situations in which imaging was challenging for deep tissue structures, particularly in obstetrics. Modes such as tissue harmonic imaging and elasticity and shear wave imaging may also benefit from similar considerations.

A working group of the Output Standards Subcommittee of the AIUM Technical Standards Committee examined on the potential benefits and risks of conditionally increased acoustic pressure. The resulting white paper[83] provides a rationale for a three-tiered approach for conditionally increased acoustic output that follows the model employed for elevated output in magnetic resonance imaging, and concludes with summary recommendations to facilitate clinical studies monitored by an institutional review board to investigate the benefits of an increased acoustic output in specific tissues. One of the fundamental assumptions in the MI calculation is the presence of a preexisting gas body. Based on theoretical predictions and experimentally reported cavitation thresholds for tissues that do not contain preexisting gas bodies, the working group found this assumption to be overly conservative and concluded that exceeding the recommended maximum MI given in the FDA guidance could be warranted without concern for increased risk of cavitation in these tissues. In the future, the ultrasound research community will need examine how much improvement in diagnostic ultrasound imaging might be achieved with increased acoustic output.

Mechanical Index

Calculations for cavitation prediction have yielded a trade-off between peak rarefactional pressure and frequency.[84] This

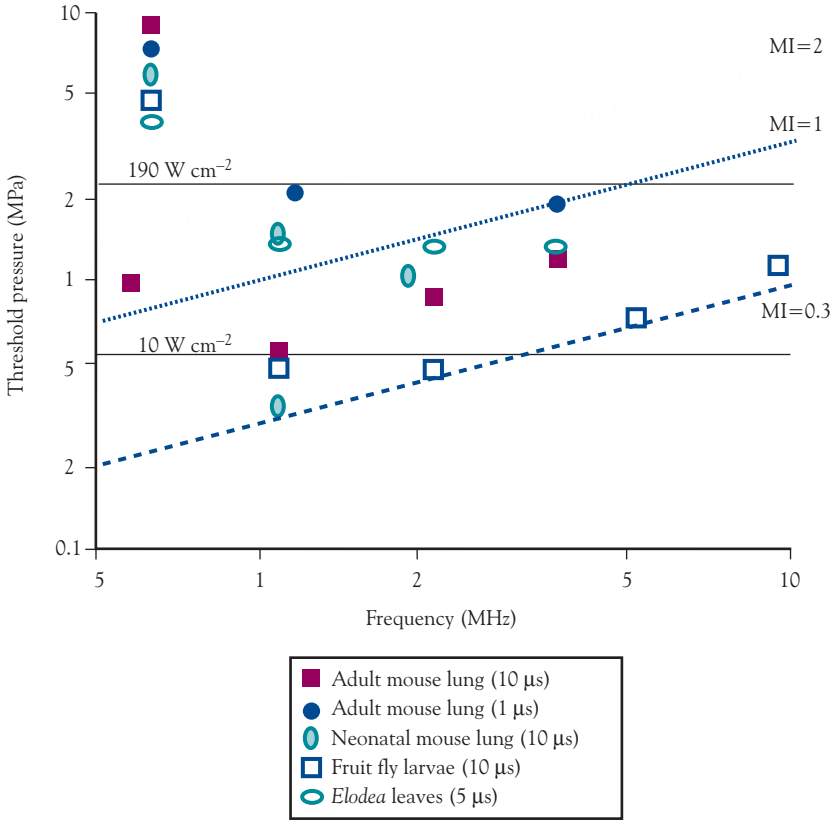

FIG. 2.9 Threshold for Bioeffects From Pulsed Ultrasound Scan Using Low Temporal Average Intensity. Data shown are the threshold for effects measured in peak rarefactional pressures (p^- in Fig. 2.1) as a function of ultrasound frequency used in the exposure. Pulse durations are shown in parentheses in the key below the graph. Also shown for reference purposes are the values for the mechanical index *(MI)* and the local spatial peak, pulse average intensity (I_{SPPA}). (With permission from American Institute of Ultrasound in Medicine. Consensus Report on Potential Bioeffects of Diagnostic Ultrasound. J Ultrasound Med. 2008;27:503-515.[22])

predicted trade-off assumes short-pulse (a few acoustic cycles) and low–duty cycle ultrasound (<1%). This relatively simple result can be used to gauge the potential for the onset of cavitation from diagnostic ultrasound. The MI was adopted by the FDA, AIUM, and NEMA as a real-time output display to estimate the potential for bubble formation *in vivo*, in analogy to the TI. As previously stated, the collapse temperature for inertial cavitation is very high. For MI, a collapse temperature of 5000 kelvins (K) was chosen based on the potential for free radical generation, and the frequency dependence of the pressure required to generate this thermal threshold takes a relatively simple form. The MI is a type of "mechanical energy index" because the square of the MI is about proportional to mechanical work that can be performed on a bubble in the acoustic rarefaction phase.

Results from several investigators have specified the MI value above which bioeffects associated with cavitation are observed in animals and insects.[22] In Fig. 2.9 the dotted lines are calculations for several MI values; all the effects appear to occur at an MI value of 0.3 or greater. In many of these cases, however, stable pockets of gas (gas bodies) are known to exist in the exposed tissues. Also, other body areas containing gas bodies might be particularly susceptible to ultrasound damage, including the intestinal lining.[85]

In response to this potential, the AIUM issued a safety statement related to the potential for bioeffects related to the interaction of ultrasound with naturally occurring nuclei.[86] Experimentation continues, and it remains to be seen if such damage occurs in human tissue.

Inherent in the formulation of the MI are the conditions only for the onset of inertial cavitation. The degree to which the threshold is exceeded, however, relates to the degree of potential bubble activity, which may correlate with the probability of a bioeffect. Note that, given present knowledge, exceeding the cavitation threshold does not mean there will be a bioeffect. Below an MI of about 0.4, the physical conditions do not favor bubble growth, even in the presence of a broad bubble nuclei distribution in the body, which is in reasonable agreement with the results of Fig. 2.9. Moreover, whereas the TI is a time-averaged measure of the interaction of ultrasound with tissue, the MI is a peak measure of this interaction. Thus there is a desirable parallel between these two measures, one thermal and one mechanical, for informing the user of the extent to which the diagnostic tool can produce undesirable changes in the body.

Summary Statement on Gas Body Bioeffects

The AIUM statements concerning bioeffects in body areas with gas bodies include several conclusions, summarized as follows[86]:

1. Current ultrasound systems can produce cavitation *in vitro* and *in vivo* and can cause blood extravasation in animal tissues.
2. The MI can gauge the likelihood for cavitation and apparently works better than other field parameters in predicting cavitation.
3. Several interesting results have been observed concerning animal models for lung damage, which indicate a potential very low threshold for damage, but the implications for human exposure have not yet been determined.
4. In the absence of gas bodies, the threshold for damage is much higher. (This is significant because ultrasound examinations may be performed predominantly in tissues with no identifiable gas bodies.)

The AIUM Statement on Mammalian Biological Effects in Tissues With Naturally Occurring Gas Bodies

APPROVED MARCH 25, 2015

Biologically significant adverse nonthermal effects have been identified in tissues containing stable bodies of gas for diagnostically relevant exposure conditions. Gas bodies occur naturally in postnatal lungs and in the folds of the intestinal mucosa. This statement concerns naturally occurring gas bodies encountered in pulmonary and abdominal ultrasound, whereas a separate statement deals with the use of gas body contrast agents.

1. The outputs of some currently available diagnostic ultrasound devices can generate levels that produce capillary hemorrhage in the lungs[60] and intestines[50] of laboratory animals.
2. Thresholds for adverse nonthermal effects associated with naturally occurring gas bodies depend on tissue characteristics and the physiologic status, including anesthesia,[87] and on physical ultrasound parameters, including attenuation by intervening tissue, exposure duration, ultrasonic output, frequency, pulse duration, and pulse repetition frequency.[50]
3. A mechanical index (MI)[a] has been formulated to assist users in evaluating the likelihood of mechanical (nonthermal) adverse biological effects for diagnostically relevant exposures, and its value is displayed on screen in accordance with output display specifications.
4. The minimum threshold value of the experimental MI (the in situ value of the peak rarefactional pressure amplitude divided by the square root of the frequency) for pulmonary capillary hemorrhage in laboratory mammals is approximately 0.4. The corresponding threshold for the intestine is MI = 1.4.
5. The implications of these observations for human exposure during thoracic or abdominal ultrasound examinations are yet to be determined.

[a]The MI is equal to the derated peak rarefactional pressure (in megapascals) at the point of the maximum derated pulse intensity integral divided by the square root of the ultrasonic center frequency (in megahertz).[12]

AIUM, American Institute of Ultrasound in Medicine.

Reproduced with permission from American Institute of Ultrasound in Medicine. AIUM Statement on Mammalian Biological Effects of Heat: AIUM; 2015. Available from: http://www.aium.org/officialStatements/6.[86]

OUTPUT DISPLAY STANDARD

Several groups, including the FDA, AIUM, and NEMA, have developed the Standard for Real-Time Display of Thermal and Mechanical Acoustical Output Indices on Diagnostic Ultrasound Equipment, which introduces a method to provide the user with information concerning the thermal and mechanical indices. Real-time display of the MI and TI will allow a more informed decision on the potential for bioeffects during ultrasound examinations (Fig. 2.10). The standard requires dynamic updates of the indices as instrument output is modified and allows the operator to learn how controls will affect these indices. Important points to remember about this display standard include the following:

- The MI should be clearly visible on the screen (or the operator should be alerted by some other means) and should begin to appear when the instrument exceeds a value of 0.4. An exception is made for instruments incapable of exceeding index values of 1; these are not required to display the bioeffects indices such as MI.
- When the indices are required to be displayed, both indices are to be displayed at all times.
- The standard also requires that appropriate default output settings be in effect at power-up, at new patient entry, or when changing to a fetal examination. After that time the operator can adjust the instrument output as necessary to acquire clinically useful information while attempting to minimize the index values.
- As indicated previously, the bioeffects indices do not include any factors associated with the time taken to perform the scan. Efficient scanning is still an important component in limiting potential bioeffects.

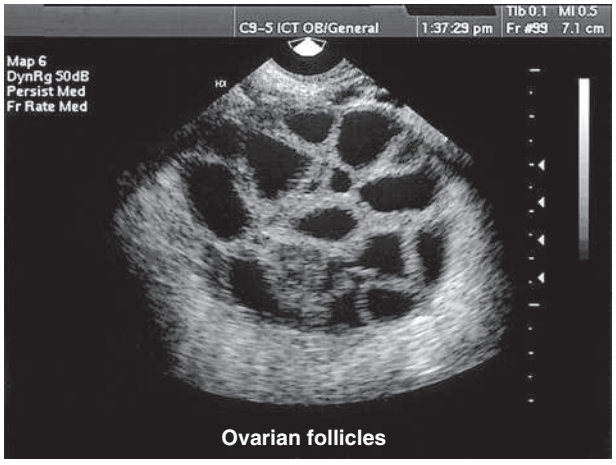

FIG. 2.10 Display of Bioeffects Indices. Typical appearance of an ultrasound scanner display showing *(right upper corner)* the thermal index in the Bone Thermal Index *(TIB)* and mechanical index *(MI)* for an endocavitary transducer.

The AIUM Safety Statements on Diagnostic Ultrasound

THE AIUM PRUDENT USE AND CLINICAL SAFETY STATEMENT[89]

Approved April 1, 2012

Diagnostic ultrasound has been in use since the late 1950s. Given its known benefits and recognized efficacy for medical diagnosis, including use during human pregnancy, the AIUM herein addresses the clinical safety of such use: No independently confirmed adverse effects caused by exposure from present diagnostic ultrasound instruments have been reported in human patients in the absence of contrast agents. Biological effects (such as localized pulmonary bleeding) have been reported in mammalian systems at diagnostically relevant exposures but the clinical significance of such effects is not yet known. Ultrasound should be used by qualified health professionals to provide medical benefit to the patient. Ultrasound exposures during examinations should be as low as reasonably achievable (ALARA).

THE AIUM PRUDENT USE IN PREGNANCY STATEMENT[90]

Approved April 1, 2012

The AIUM advocates the responsible use of diagnostic ultrasound and strongly discourages the nonmedical use of ultrasound for entertainment purposes. The use of ultrasound without a medical indication to view the fetus, obtain images of the fetus, or determine the fetal gender is inappropriate and contrary to responsible medical practice. Ultrasound should be used by qualified health professionals to provide medical benefit to the patient.

THE AIUM SAFETY IN TRAINING AND RESEARCH STATEMENT[91]

Approved April 1, 2012

Diagnostic ultrasound has been in use since the late 1950s. There are no confirmed adverse biological effects on patients resulting from this usage. Although no hazard has been identified that would preclude the prudent and conservative use of diagnostic ultrasound in education and research, experience from normal diagnostic practice may or may not be relevant to extended exposure times and altered exposure conditions. It is therefore considered appropriate to make the following recommendation: When examinations are carried out for purposes of training or research, ultrasound exposures should be as low as reasonably achievable (ALARA) within the goals of the study/training. In addition, the subject should be informed of the anticipated exposure conditions and how these compare with normal diagnostic practice. Repetitive and prolonged exposures on a single subject should be justified and consistent with prudent and conservative use.

AIUM, American Institute of Ultrasound in Medicine.

Reproduced with permission from American Institute of Ultrasound in Medicine (AIUM). Prudent use and clinical safety. Laurel, MD: AIUM; 2012. Available from: http://www.aium.org/officialStatements/34. Approved April 1, 2012. Cited October 7, 2016[89]; American Institute of Ultrasound in Medicine (AIUM). Prudent use in pregnancy. Laurel, MD: AIUM; 2012. Available from: http://www.aium.org/officialStatements/33. Approved April 1, 2012. Cited October 7, 2016[90]; and American Institute of Ultrasound in Medicine (AIUM). Safety in training and research. Laurel, MD: AIUM; 2012. Available from: http://www.aium.org/officialStatements/36. Approved April 1, 2012. Cited October 7, 2016.[91]

In the document Medical Ultrasound Safety,[88] the AIUM suggests that the operator ask the following four questions to use the output display effectively:

1. Which index should be used for the examination being performed?
2. Are there factors present that might cause the reading to be too high or low?
3. Can the index value be reduced further even when it is already low?
4. How can the ultrasound exposure be minimized without compromising the scan's diagnostic quality?

Sonographers and physicians are being presented with real-time data on acoustic output of diagnostic scanners and are being asked not only to understand the manner in which ultrasound propagates through and interacts with tissue, but also to gauge the potential for adverse bioeffects. The output display is a tool that can be used to guide an ultrasound examination and control for potential adverse effects. The thermal and mechanical indices provide the user with more information and more responsibility in limiting output.

GENERAL AIUM SAFETY STATEMENTS

It is important to consider some official positions concerning the status of bioeffects resulting from ultrasound. Most important is the high level of confidence in the safety of ultrasound in official statements. For example, in 2012 the AIUM reiterated its earlier statement concerning the clinical use of diagnostic ultrasound, which indicated that no independently confirmed adverse effects are caused by exposure from current diagnostic equipment, and the patient benefits from prudent use outweigh the risks, if any. The AIUM also strongly discourages the nonmedical use of ultrasound during pregnancy for entertainment purposes. In commenting on the use of diagnostic ultrasound in research, the AIUM recommends that in the case of ultrasound exposure for other than direct medical benefit, the person should be informed concerning the exposure conditions and how these relate to normal exposures. For the most part, even examinations for research purposes are comparable to normal diagnostic examinations and pose no additional risk. Many research examinations can be performed in conjunction with routine examinations.

The effects based on *in vivo* animal models can be summarized by the AIUM statements on mammalian biological effects of heat,[24] in tissues with gas body contrast agents,[80] and in tissues with naturally occurring gas bodies.[86] No independently confirmed experimental evidence indicates damage in animal models below certain prescribed levels (temperature rises <2°C; MI < 0.4). The value for the MI is strict because tissues containing gas bodies exhibit damage at much lower levels than tissues devoid of gas bodies. Biologic effects have not been detected even at an MI of 4.0 in the absence of gas bodies.

EPIDEMIOLOGY

With all the potential causes for bioeffects, we must now examine the epidemiologic evidence that has been used in part to justify the apparent safety of ultrasound. In 1988 Ziskin and Petitti[92] reviewed the epidemiologic studies conducted until then and concluded, "Epidemiologic studies and surveys in widespread clinical usage over 25 years have yielded no evidence of any adverse effect from diagnostic ultrasound." However, a 2008 review[93] of the epidemiology literature conducted by an AIUM subcommittee resulted in a revised AIUM statement regarding the epidemiology of diagnostic ultrasound safety in obstetrics.[94] The earlier statements indicated that no confirmed effects associated with ultrasound exposure existed at that time. However, the distinction being made in the current AIUM statement is that although some effects may have been detected now, one cannot justify a conclusion of a causal relationship based on this evidence.

Epidemiologic studies are difficult to conduct, and data analysis and interpretation of results can be even more difficult. Several epidemiologic studies of fetal exposure to ultrasound have claimed to detect certain bioeffects and have also been criticized. Only one indication of an unspecified effect was reported in a general survey involving an estimated 1.2 million examinations in Canada.[95] However, this is an extremely low incidence, with no follow-up to determine the nature of the effect. In addition, an earlier study that included 121,000 fetal examinations reported no effect.[96] Moore and colleagues[97] reported an increased incidence of low birth weight, whereas Stark and colleagues[98] examined the same data using a different statistical treatment and found no significant increase. Scheidt and colleagues[99] noted abnormal grasp and tonic neck reflexes. These results are difficult to interpret, however, given the statistical treatment of the data. Stark and colleagues[98] detected an increased incidence of dyslexia, but the same children exhibited below-average birth weights. General problems also plague the epidemiologic studies, including the lack of clearly stated exposure conditions and gestational age, problems in statistical sampling (with both positive and negative results), and use of older scanning systems, particularly with fetal Doppler ultrasound. Dyslexia was examined as part of two randomized trials, including specific long-term follow-up that showed no statistical difference between ultrasound-exposed and control subjects.[100,101]

Ziskin and Petitti[92] also summarized the factors in evaluating epidemiologic evidence. It is important to recognize that epidemiologic evidence can be used to identify an association between exposures and biologic effects, but that this does not prove the exposure caused the bioeffect. The strength of the association is established by the statistical significance of the relationship. Hill[102] and Abramowicz and colleagues[93] have developed the following seven criteria for judging **causality:**

1. Strength of the association
2. Consistency in reproducibility and with previous, related research
3. Specificity to a particular bioeffect or exposure site
4. Classic time relationship of cause followed by effect
5. Existence of a dose response
6. Plausibility of the effect
7. Supporting evidence from laboratory studies

When considering these factors, no clear causal relationship seems to exist between an adverse biologic response and ultrasound exposure of a diagnostic nature.

Newnham and colleagues[103] reported higher intrauterine growth restriction during a study designed to determine the efficacy of ultrasound in reducing the number of neonatal days and prematurity rate. Therefore the study was not designed to detect an adverse bioeffect, but a statistically significant effect was observed as a result of subsequent data analysis. Several other deficiencies in methodology are evident in the selection and exposure of the experimental groups, but in general, some association might be inferred from the results of this well-conducted, randomized clinical trial. In a case-control study, Campbell and colleagues[104] reported a statistically significant higher rate of delayed speech in children who were insonified in utero. Evidence of association is not as strong in case-control studies as in prospective studies, and measures of delayed speech are difficult. Subsequently, Salvesen and colleagues[105] found no significant differences in delayed speech, limited vocabulary, or stuttering in a study of 1107 children exposed in utero and 1033 controls.

CONTROLLING ULTRASOUND OUTPUT

The most important issue regarding potential bioeffects involves actions the physician or sonographer can take to minimize these effects. It is essential that operators understand the risks involved in the process, but without some ability to control the output of the ultrasound system, this knowledge has limited use. Some specific methods can be used to limit ultrasound exposure while maintaining diagnostically relevant images.

Controls for the ultrasound system can be divided into direct controls and indirect controls (Table 2.2). The **direct controls** are the application types and output intensity. **Application types** are those broad system controls that allow convenient selection of a particular examination type. These often come in the form of icons that are selected by the user. These default settings help minimize the time required to optimize the imaging parameters for the myriad applications for diagnostic ultrasound. These settings should be used only as indicated (e.g., do not use the cardiac settings for a fetal examination). **Output intensity** (also called "power," "output," or "transmit") controls the overall ultrasonic power emitted by the transducer. This control will generally affect the intensity at all points in the image to varying degrees, depending on the focusing. The lowest output intensity that produces a good image should be used, to minimize the exposure intensity. Focusing of the system is controlled by the operator and can be used to improve image quality while limiting required acoustic intensity. Focusing at the correct depth can improve the image without requiring increased intensity.

The many **indirect controls** greatly affect the ultrasound exposure by dictating how the ultrasonic energy is distributed temporally and spatially. By choosing the mode of ultrasound used (e.g., B-mode, pulsed Doppler, color Doppler), the operator

TABLE 2.2 Optimum Ultrasound Output: Lowest Power Output That Creates Good Images

DIRECT CONTROLS	
Application type	Examples: fetal, cardiac
Output intensity	Power, output, transmit
Focusing	Allows increasing output intensity only at the focal zone
INDIRECT CONTROLS	
Ultrasound mode	
Unscanned modes (deposits heat in one area)	Continuous wave Doppler, spectral or pulsed Doppler, M-mode
Scanned modes	B-mode or gray-scale, color flow Doppler, power mode Doppler
Pulse repetition frequency	Increases bursts of energy per time Usually controlled by changing the maximum imaging depth in B-mode or the velocity range in Doppler modes
Pulse length	Increasing sample volume in Doppler studies
Appropriate transducer	High frequency: requires more output for depth Lower frequency: less output needed at depth
Gain controls	Time gain compensation (TGC) can improve image without more output Receiver gain increases echo amplitudes without more output

The AIUM Statement on Keepsake Fetal Imaging[107]

APPROVED APRIL 1, 2012

The AIUM advocates the responsible use of diagnostic ultrasound for all fetal imaging. The AIUM understands the growing pressures from patients for the performance of ultrasound examinations for bonding and reassurance purposes, largely driven by the improving image quality of 3-D sonography and by more widely available information about these advances. Although there is only preliminary scientific evidence that 3-D sonography has a positive impact on parental-fetal bonding, the AIUM recognizes that many parents may pursue scanning for this purpose.

Such "keepsake imaging" currently occurs in a variety of settings, including the following:

1. Images or video clips given to parents during the course of a medically indicated ultrasound examination.
2. Freestanding commercial fetal imaging sites, usually without any physician review of acquired images and with no regulation of the training of the individuals obtaining the images; these images are sometimes called "entertainment videos."
3. As added-cost visits to a medical facility (office or hospital) outside the coverage of contractual arrangements between the provider and the patient's insurance carrier.

The AIUM recommends that appropriately trained and credentialed medical professionals (licensed physicians, registered sonographers, or sonography registry candidates) who have received specialized training in fetal imaging perform all fetal ultrasound scans. These individuals have been trained to recognize medically important conditions, such as congenital anomalies, artifacts associated with ultrasound scanning that may mimic pathology, and techniques to avoid ultrasound exposure beyond what is considered safe for the fetus. Any other use of "limited medical ultrasound" may constitute practice of medicine without a license. The AIUM reemphasizes that all imaging requires proper documentation and a final report for the patient medical record signed by a physician.

Although the general use of ultrasound for medical diagnosis is considered safe, ultrasound energy has the potential to produce biological effects. Ultrasound bioeffects may result from scanning for a prolonged period, inappropriate use of color or pulsed Doppler ultrasound without a medical indication, or excessive thermal or mechanical index settings. The AIUM encourages patients to make sure that practitioners using ultrasound have received specific training in fetal imaging to ensure the best possible results.

The AIUM also believes that added cost arrangements other than those of providing patients images or copies of their medical records at cost may violate the principles of medical ethics of the American Medical Association[108-110] and the American College of Obstetricians and Gynecologists.[111] The AIUM therefore reaffirms the Prudent Use in Pregnancy Statement[90] and recommends that only scenario 1 above is consistent with the ethical principles of our professional organizations.

The market for keepsake images is driven in part by past medical approaches that have used medicolegal concerns as a reason not to provide images to patients. Sharing images with patients is unlikely to have a detrimental medicolegal impact. Although these concerns need further analysis and evaluation, we encourage sharing images with patients as appropriate when indicated obstetric ultrasound examinations are performed.[90]

AIUM, American Institute of Ultrasound in Medicine.

Reproduced with permission from American Institute of Ultrasound in Medicine (AIUM). Keepsake fetal imaging. Laurel, MD: AIUM; 2012. Available from: http://www.aium.org/officialStatements/31. Approved April 1, 2012. Cited October 7, 2016.[107]

controls whether the beam is scanned. Unscanned modes deposit energy along a single path and increase the potential for heating. The **pulse repetition frequency** (PRF) indicates how often the transducer is excited. Increasing the number of ultrasound bursts per second will increase the temporal average intensity. PRF is usually controlled by changing the maximum image depth in B-mode or the velocity range in Doppler modes. **Burst length** (also called "pulse length" or "pulse duration") controls the duration of on-time for each ultrasonic burst transmitted. Increasing the burst length while maintaining the same PRF will increase the temporal average intensity. The control of burst length may not be obvious. For example, in spectral Doppler ultrasound, increasing the Doppler sample volume length will increase the burst length.

The selection of the **appropriate transducer** will also limit the need for high acoustic power. Even though higher frequencies provide better spatial resolution, the attenuation of tissue increases with increasing ultrasound frequency, so penetration may be lost. Perhaps most important are the **receiver gain controls.** The receiver gain control has no effect on the amplitude of the acoustic output. Therefore before turning up the acoustic output intensity, try increasing receiver gain first. It should be noted that some system controls actually interact with the acoustic output intensity without direct control. Check to see whether the manufacturer provides separate controls for receiver gain, **time gain compensation** (TGC), and acoustic output intensity. The TGC can improve image quality without increasing the output.

There is really no substitute for a well-instructed operator. The indices and requirements of output display standards will help only those willing to use and understand them. Real-time display of the mechanical and thermal indices on diagnostic scanners will help clinicians evaluate and minimize potential risks in the use of such instrumentation. Physicians and sonographers are encouraged to learn more about how to minimize potential bioeffects.

ULTRASOUND ENTERTAINMENT VIDEOS

Of concern is the growing use of diagnostic ultrasound for the nonmedical scanning of pregnant women to provide a fetal "keepsake" video. Unfortunately, entertainment ultrasound is promoted most vigorously in the second and third trimesters, when bone calcification can increase thermal effects. Also, women with the economic means to schedule multiple ultrasound imaging sessions may be exposing both themselves and their fetuses to even greater risk if ultrasound bioeffects are shown to be additive, or just by increasing the chances for a bioeffect. If there is no clinical benefit in such entertainment ultrasound, the benefit-to-risk ratio is clearly zero. In addition, because often the ultrasound equipment used is identical to diagnostic equipment used by clinicians, the consumer may be unaware that no medical information is being generated, interpreted, or referred to her obstetrician. (It is recognized that release forms are signed to the contrary.) The FDA[106] views this as an unapproved use of a medical device and refers users to the AIUM statement regarding keepsake videos.

REFERENCES

1. Hynynen K. Ultrasound therapy. In: Goldman LE, Fowlkes JB, editors. Medical CT and ultrasound: current technology and applications. Madison, WI: Advanced Medical Publishing; 1995. p. 249-265.
2. Carstensen EL, Child SZ, Norton S, Nyborg W. Ultrasonic heating of the skull. J Acoust Soc Am. 1990;87(3):1310-1317.
3. Nyborg WL. Solutions of the bio-heat transfer equation. Phys Med Biol. 1988;33(7):785-792.
4. Drewniak JL, Carnes KI, Dunn F. In vitro ultrasonic heating of fetal bone. J Acoust Soc Am. 1989;86(4):1254-1258.
5. Edwards MJ. Hyperthermia as a teratogen: a review of experimental studies and their clinical significance. Teratog Carcinog Mutagen. 1986;6(6): 563-582.
6. Miller MW, Ziskin MC. Biological consequences of hyperthermia. Ultrasound Med Biol. 1989;15(8):707-722.
7. National Council on Radiation Protection and Measurements (NCRP). Scientific Committee on Biological Effects of Ultrasound. Exposure criteria for medical diagnostic ultrasound. I. Criteria based on thermal mechanisms. Bethesda, MD: NCRP; 1992.
8. National Council on Radiation Protection and Measurements (NCRP). Scientific Committee on Biological Effects of Ultrasound. Exposure criteria for medical diagnostic ultrasound. II. Criteria based on all known mechanisms. Bethesda, MD: NCRP; 2002.
9. Miller MW, Nyborg WL, Dewey WC, et al. Hyperthermic teratogenicity, thermal dose and diagnostic ultrasound during pregnancy: implications of new standards on tissue heating. Int J Hyperthermia. 2002;18(5): 361-384.
10. O'Brien Jr WD, Deng CX, Harris GR, et al. The risk of exposure to diagnostic ultrasound in postnatal subjects: thermal effects. J Ultrasound Med. 2008;27(4):517-535.
11. American Institute of Ultrasound in Medicine (AIUM). Standard for real-time display of thermal and mechanical acoustical output indices on diagnostic ultrasound equipment. Rockville, MD: AIUM and National Electrical Manufacturers Association; 1992.
12. International Electrotechnical Commission. IEC 60601-2-37:2007+AMD1:2015 CSV Consolidated version medical electrical equipment—Part 2-37: Particular requirements for the basic safety and essential performance of ultrasonic medical diagnostic and monitoring equipment. Geneva, Switzerland: 2015.
13. Carson PL, Rubin JM, Chiang EH. Fetal depth and ultrasound path lengths through overlying tissues. Ultrasound Med Biol. 1989;15(7): 629-639.
14. Carson PL. Medical ultrasound fields and exposure measurements. Nonionizing electromagnetic radiations and ultrasound. NCRP Proc. Bethesda, MD: National Council on Radiation Protection and Measurements; 1988. p. 287-307.
15. Thomenius KE. Scientific rationale for the TIS index model. Presented at the National Electrical Manufacturers Association Output Display Standard Seminar; Rockville, MD; 1993.
16. Thomenius KE. Estimation of the potential for bioeffects. In: Ziskin MC, Lewin PA, editors. Ultrasonic exposimetry. Boca Raton, FL: CRC Press; 1993.
17. Siddiqi TA, O'Brien Jr WD, Meyer RA, et al. In situ exposimetry: the ovarian ultrasound examination. Ultrasound Med Biol. 1991;17(3):257-263.
18. Chan AK, Sigelmann RA, Guy AW, Lehmann JF. Calculation by the method of finite differences of the temperature distribution in layered tissues. IEEE Trans Biomed Eng. 1973;20(2):86-90.
19. Chan AK, Sigelmann RA, Guy AW. Calculations of therapeutic heat generated by ultrasound in fat-muscle-bone layers. IEEE Trans Biomed Eng. 1974;21(4):280-284.
20. Frizzell LA. Ultrasonic heating of tissues (dissertation). Rochester, NY: University of Rochester; 1975.
21. Ziskin MC. The thermal dose index. J Ultrasound Med. 2010;29(10): 1475-1479.
22. American Institute of Ultrasound in Medicine. Consensus report on potential bioeffects of diagnostic ultrasound. J Ultrasound Med. 2008;27:503-515.
23. Flynn HG. Cavitation dynamics. I. A mathematical formulation. J Acoust Soc Am. 1975;57:1379-1396.

24. American Institute of Ultrasound in Medicine (AIUM). Statement on mammalian biological effects of heat. Laurel, MD: AIUM; 2015. Available from: http://www.aium.org/officialStatements/17. Updated March 25, 2015. Cited October 7, 2016.
25. Kimmel CA, Cuff JM, Kimmel GL, et al. Skeletal development following heat exposure in the rat. Teratology. 1993;47(3):229-242.
26. Church C, Barnett S. Ultrasound-induced heating and its biological consequences. In: ter Haar G, editor. The safe use of ultrasound in medical diagnosis. London, England: British Institute of Radiology; 2012. p. 46-68.
27. Jago JR, Henderson J, Whittingham TA, Mitchell G. A comparison of AIUM/NEMA thermal indices with calculated temperature rises for a simple third-trimester pregnancy tissue model. Ultrasound Med Biol. 1999;25(4):623-628.
28. Shaw A, Pay N, Preston R. Assessment of the likely thermal index values for pulsed Doppler ultrasonic equipment—stages II and III: experimental assessment of scanner/transducer combinations. National Physical Laboratory Reports, Teddington, Middlesex, United Kingdom: 1998.
29. International Electrotechnical Commission. IEC 60601-2-37. Medical electrical equipment, Part 2-37: Particular requirements for the basic safety and essential performance of ultrasonic medical diagnostic and monitoring equipment. 2nd ed. Geneva, Switzerland: IEC; 2007.
30. Roy RA, Atchley AA, Crum LA, et al. A precise technique for the measurement of acoustic cavitation thresholds and some preliminary results. J Acoust Soc Am. 1985;78(5):1799-1805.
31. Kwak HY, Panton RL. Tensile strength of simple liquids predicted by a model of molecular interactions. J Phys D. 1985;18.
32. Harvey EN, Barnes DK, McElroy WD, et al. Bubble formation in animals. I. Physical factors. J Cell Compar Phys. 1944;24:1-22.
33. Harvey EN, Barnes DK, McElroy WD, et al. Bubble formation in animals. II. Gas nuclei and their distribution in blood and tissues. J Cell Compar Phys. 1944;24:23-34.
34. Yount DE. Skins of varying permeability: a stabilization mechanism for gas cavitation nuclei. J Acoust Soc Am. 1978;65:1429-1439.
35. Holland CK, Roy RA, Apfel RE, Crum LA. In vitro detection of cavitation induced by a diagnostic ultrasound system. IEEE Trans Ultrason Ferroelectr Freq Control. 1992;39(1):95-101.
36. Walton AJ, Reynolds GT. Sonoluminescence. Adv Physics. 1984;33:595-660.
37. Crum LA, Fowlkes JB. Acoustic cavitation generated by microsecond pulses of ultrasound. Nature. 1986;319:52-54.
38. Carmichael AJ, Mossoba MM, Riesz P, Christman CL. Free radical production in aqueous solutions exposed to simulated ultrasonic diagnostic conditions. IEEE Trans Ultrason Ferroelectr Freq Control. 1986;33(2):148-155.
39. Aymé EJ, Carstensen EL. Occurrence of transient cavitation in pulsed sawtooth ultrasonic fields. J Acoust Soc Am. 1988;84(5):1598-1605.
40. Coleman AJ, Saunders JE, Crum LA, et al. Acoustic cavitation generated by an extracorporeal shockwave lithotripter. Ultrasound Med Biol. 1987;13(2):69-76.
41. Delius M, Brendel W, Heine G. A mechanism of gallstone destruction by extracorporeal shock waves. Naturwissenschaften. 1988;75(4):200-201.
42. Williams AR, Delius M, Miller DL, Schwarze W. Investigation of cavitation in flowing media by lithotripter shock waves both in vitro and in vivo. Ultrasound Med Biol. 1989;15(1):53-60.
43. Parsons JE, Cain CA, Fowlkes JB. Spatial variability in acoustic backscatter as an indicator of tissue homogenate production in pulsed cavitational ultrasound therapy. IEEE Trans Ultrason Ferroelectr Freq Control. 2007;54(3):576-590.
44. Xu Z, Hall TL, Fowlkes JB, Cain CA. Effects of acoustic parameters on bubble cloud dynamics in ultrasound tissue erosion (histotripsy). J Acoust Soc Am. 2007;122(1):229-236.
45. Khokhlova VA, Fowlkes JB, Roberts WW, et al. Histotripsy methods in mechanical disintegration of tissue: towards clinical applications. Int J Hyperthermia. 2015;31(2):145-162.
46. Duck FA, Starritt HC, Aindow JD, et al. The output of pulse-echo ultrasound equipment: a survey of powers, pressures and intensities. Br J Radiol. 1985;58(694):989-1001.
47. Duck FA, Starritt HC, Anderson SP. A survey of the acoustic output of ultrasonic Doppler equipment. Clin Phys Physiol Meas. 1987;8(1):39-49.
48. Patton CA, Harris GR, Phillips RA. Output levels and bioeffects indices from diagnostic ultrasound exposure data reported to the FDA. IEEE Trans Ultrason Ferroelectr Freq Control. 1994;41:353-359.
49. Chaussy C, Schmiedt E, Jocham D, et al. Extracorporeal shock wave lithotripsy. Basel: Karger; 1986.
50. Church CC, Carstensen EL, Nyborg WL, et al. The risk of exposure to diagnostic ultrasound in postnatal subjects: nonthermal mechanisms. J Ultrasound Med. 2008;27(4):565-592.
51. Child SZ, Hartman CL, Schery LA, Carstensen EL. Lung damage from exposure to pulsed ultrasound. Ultrasound Med Biol. 1990;16(8):817-825.
52. Penney DP, Schenk EA, Maltby K, et al. Morphological effects of pulsed ultrasound in the lung. Ultrasound Med Biol. 1993;19(2):127-135.
53. Tarantal AF, Canfield DR. Ultrasound-induced lung hemorrhage in the monkey. Ultrasound Med Biol. 1994;20(1):65-72.
54. O'Brien Jr WD, Yang Y, Simpson DG, et al. Threshold estimation of ultrasound-induced lung hemorrhage in adult rabbits and comparison of thresholds in mice, rats, rabbits and pigs. Ultrasound Med Biol. 2006;32(11):1793-1804.
55. Baggs R, Penney DP, Cox C, et al. Thresholds for ultrasonically induced lung hemorrhage in neonatal swine. Ultrasound Med Biol. 1996;22(1):119-128.
56. Dalecki D, Child SZ, Raeman CH, et al. Ultrasonically induced lung hemorrhage in young swine. Ultrasound Med Biol. 1997;23(5):777-781.
57. O'Brien Jr WD, Frizzell LA, Weigel RM, Zachary JF. Ultrasound-induced lung hemorrhage is not caused by inertial cavitation. J Acoust Soc Am. 2000;108(3 Pt 1):1290-1297.
58. Dalecki D, Raeman CH, Child SZ, Carstensen EL. Intestinal hemorrhage from exposure to pulsed ultrasound. Ultrasound Med Biol. 1995;21(8):1067-1072.
59. Kramer JM, Waldrop TG, Frizzell LA, et al. Cardiopulmonary function in rats with lung hemorrhage induced by pulsed ultrasound exposure. J Ultrasound Med. 2001;20(11):1197-1206.
60. Miller DL. Induction of pulmonary hemorrhage in rats during diagnostic ultrasound. Ultrasound Med Biol. 2012;38(8):1476-1482.
61. Church CC, O'Brien Jr WD. Evaluation of the threshold for lung hemorrhage by diagnostic ultrasound and a proposed new safety index. Ultrasound Med Biol. 2007;33(5):810-818.
62. Miller DL, Averkiou MA, Brayman AA, et al. Bioeffects considerations for diagnostic ultrasound contrast agents. J Ultrasound Med. 2008;27(4):611-632.
63. ter Haar G. Safety and bio-effects of ultrasound contrast agents. Med Biol Eng Comput. 2009;47(8):893-900.
64. Dalecki D. WFUMB Safety Symposium on Echo-Contrast Agents: bioeffects of ultrasound contrast agents in vivo. Ultrasound Med Biol. 2007;33(2):205-213.
65. Skyba DM, Price RJ, Linka AZ, et al. Direct in vivo visualization of intravascular destruction of microbubbles by ultrasound and its local effects on tissue. Circulation. 1998;98(4):290-293.
66. Miller DL, Quddus J. Diagnostic ultrasound activation of contrast agent gas bodies induces capillary rupture in mice. Proc Natl Acad Sci USA. 2000;97(18):10179-10184.
67. Hwang JH, Brayman AA, Reidy MA, et al. Vascular effects induced by combined 1-MHz ultrasound and microbubble contrast agent treatments in vivo. Ultrasound Med Biol. 2005;31(4):553-564.
68. Samuel S, Cooper MA, Bull JL, et al. An ex vivo study of the correlation between acoustic emission and microvascular damage. Ultrasound Med Biol. 2009;35(9):1574-1586.
69. Miller DL, Dou C, Wiggins RC, et al. An in vivo rat model simulating imaging of human kidney by diagnostic ultrasound with gas-body contrast agent. Ultrasound Med Biol. 2007;33(1):129-135.

70. Hwang JH, Tu J, Brayman AA, et al. Correlation between inertial cavitation dose and endothelial cell damage in vivo. Ultrasound Med Biol. 2006;32(10):1611-1619.
71. van Der Wouw PA, Brauns AC, Bailey SE, et al. Premature ventricular contractions during triggered imaging with ultrasound contrast. J Am Soc Echocardiogr. 2000;13(4):288-294.
72. Tran TA, Le Guennec JY, Babuty D, et al. On the mechanisms of ultrasound contrast agents-induced arrhythmias. Ultrasound Med Biol. 2009;35(6):1050-1056.
73. Tran TA, Le Guennec JY, Bougnoux P, et al. Characterization of cell membrane response to ultrasound activated microbubbles. IEEE Trans Ultrason Ferroelectr Freq Control. 2008;55(1):43-49.
74. Tran TA, Roger S, Le Guennec JY, et al. Effect of ultrasound-activated microbubbles on the cell electrophysiological properties. Ultrasound Med Biol. 2007;33(1):158-163.
75. Kurt M, Shaikh KA, Peterson L, et al. Impact of contrast echocardiography on evaluation of ventricular function and clinical management in a large prospective cohort. J Am Coll Cardiol. 2009;53(9):802-810.
76. Abdelmoneim SS, Bernier M, Scott CG, et al. Safety of contrast agent use during stress echocardiography: a 4-year experience from a single-center cohort study of 26,774 patients. JACC Cardiovasc Imaging. 2009;2(9):1048-1056.
77. Grayburn PA. Product safety compromises patient safety (an unjustified black box warning on ultrasound contrast agents by the Food and Drug Administration). Am J Cardiol. 2008;101(6):892-893.
78. Kusnetzky LL, Khalid A, Khumri TM, et al. Acute mortality in hospitalized patients undergoing echocardiography with and without an ultrasound contrast agent: results in 18,671 consecutive studies. J Am Coll Cardiol. 2008;51(17):1704-1706.
79. Main ML, Ryan AC, Davis TE, et al. Acute mortality in hospitalized patients undergoing echocardiography with and without an ultrasound contrast agent (multicenter registry results in 4,300,966 consecutive patients). Am J Cardiol. 2008;102(12):1742-1746.
80. American Institute of Ultrasound in Medicine (AIUM). Statement on mammalian biological effects in tissues with gas body contrast agents. Laurel, MD: AIUM; 2015. Available from: http://www.aium.org/officialStatements/25. Approved March 25, 2015. Cited October 7, 2016.
81. Barnett SB. Safe use of ultrasound contrast agents. Ultrasound Med Biol. 2007;33(2):171-172.
82. Miller D. The safe use of contrast-enhanced diagnostic ultrasound. In: ter Haar G, editor. The safe use of ultrasound in medical diagnosis. London, England: British Institute of Radiology; 2012. p. 105-124.
83. Nightingale KR, Church CC, Harris G, et al. Conditionally increased acoustic pressures in nonfetal diagnostic ultrasound examinations without contrast agents: a preliminary assessment. J Ultrasound Med. 2015;34(7):1-41.
84. Apfel RE, Holland CK. Gauging the likelihood of cavitation from short-pulse, low-duty cycle diagnostic ultrasound. Ultrasound Med Biol. 1991;17(2):179-185.
85. Dalecki D, Raeman CH, Child SZ, Carstensen EL. A test for cavitation as a mechanism for intestinal hemorrhage in mice exposed to a piezoelectric lithotripter. Ultrasound Med Biol. 1996;22(4):493-496.
86. American Institute of Ultrasound in Medicine (AIUM). Statement on mammalian biological effects in tissues with naturally occurring gas bodies. Laurel, MD: AIUM; 2015. Available from: http://www.aium.org/officialStatements/6. Approved March 25, 2015. Cited October 7, 2016.
87. Miller DL, Dou C, Raghavendran K. Anesthetic techniques influence the induction of pulmonary capillary hemorrhage during diagnostic ultrasound scanning in rats. J Ultrasound Med. 2015;34(2):289-297.
88. American Institute of Ultrasound in Medicine (AIUM). Medical ultrasound safety. 3rd ed. Rockville, MD: AIUM; 2014.
89. American Institute of Ultrasound in Medicine (AIUM). Prudent use and clinical safety. Laurel, MD: AIUM; 2012. Available from: http://www.aium.org/officialStatements/34. Approved April 1, 2012. Cited October 7, 2016.
90. American Institute of Ultrasound in Medicine (AIUM). Prudent use in pregnancy. Laurel, MD: AIUM; 2012. Available from: http://www.aium.org/officialStatements/33. Approved April 1, 2012. Cited October 7, 2016.
91. American Institute of Ultrasound in Medicine (AIUM). Safety in training and research. Laurel, MD: AIUM; 2012. Available from: http://www.aium.org/officialStatements/36. Approved April 1, 2012. Cited October 7, 2016.
92. Ziskin MC, Petitti DB. Epidemiology of human exposure to ultrasound: a critical review. Ultrasound Med Biol. 1988;14(2):91-96.
93. Abramowicz JS, Fowlkes JB, Skelly AC, et al. Conclusions regarding epidemiology for obstetric ultrasound. J Ultrasound Med. 2008;27(4):637-644.
94. American Institute of Ultrasound in Medicine (AIUM). Conclusions regarding epidemiology for obstetric ultrasound. Laurel, MD: AIUM; 2010. Available from: http://www.aium.org/officialStatements/16. Approved 27 March 2010. Cited 7 October 2016.
95. Environment Health Directorate (EHD). Canada-wide survey of nonionizing radiation emitting medical devices. II. Ultrasound devices. Department of National Health and Welfare, Environmental Health Directorate, Report 80-EHD-53. Ottawa, Canada: 1980.
96. Ziskin MC. Survey of patient exposure to diagnostic ultrasound. In: Reid JM, Sikov MR, editors. Interaction of ultrasound and biological tissues. Washington, DC: U.S. Department of Health, Education and Welfare; 1972. p. 203.
97. Moore Jr R, Barrick M, Hamilton P. Effects of sonic radiation on growth and development. Am J Epidemiol. 1982;116.
98. Stark CR, Orleans M, Haverkamp AD, Murphy J. Short- and long-term risks after exposure to diagnostic ultrasound in utero. Obstet Gynecol. 1984;63(2):194-200.
99. Scheidt PC, Stanley F, Bryla DA. One-year follow-up of infants exposed to ultrasound in utero. Am J Obstet Gynecol. 1978;131(7):743-748.
100. Bakketeig LS, Eik-Nes SH, Jacobsen G, et al. Randomised controlled trial of ultrasonographic screening in pregnancy. Lancet. 1984;2(8396):207-211.
101. Eik-Nes SH, Okland O, Aure JC, Ulstein M. Ultrasound screening in pregnancy: a randomised controlled trial. Lancet. 1984;1(8390):1347.
102. Hill AB. The environment and disease: association or causation? Proc R Soc Med. 1965;58:295-300.
103. Newnham JP, Evans SF, Michael CA, et al. Effects of frequent ultrasound during pregnancy: a randomised controlled trial. Lancet. 1993;342(8876):887-891.
104. Campbell JD, Elford RW, Brant RF. Case-control study of prenatal ultrasonography exposure in children with delayed speech. CMAJ. 1993;149(10):1435-1440.
105. Salvesen KA, Vatten LJ, Bakketeig LS, Eik-Nes SH. Routine ultrasonography in utero and speech development. Ultrasound Obstet Gynecol. 1994;4(2):101-103.
106. U.S. Food and Drug Administration (FDA). FDA statement on fetal keepsake videos. 2015. Available from: http://www.fda.gov/MedicalDevices/Safety/AlertsandNotices/PatientAlerts/ucm064756.htm. Updated May 12, 2015. Cited October 7, 2016.
107. American Institute of Ultrasound in Medicine (AIUM). Keepsake fetal imaging. 2012. Available from: http://www.aium.org/officialStatements/31. Approved April 1, 2012. Cited October 7, 2016.
108. American Medical Association (AMA). E-8.062: Sale of non-health-related goods from physician's offices. Chicago, IL: AMA; 1998.
109. American Medical Association (AMA). E-8.063: Sale of health-related products from physician's offices. Chicago, IL: AMA; 1999.
110. American Medical Association (AMA). Addendum III: Council on Ethical and Judicial Affairs clarification on sale of products from physicians' offices (E-8062 and E-8.063). Chicago, IL: AMA; 2000.
111. ACOG Committee on Ethics. Commercial enterprises in medical practice. ACOG Committee Opinion No. 359. Obstet Gynecol. 2007;109:243-245.

CHAPTER 3

Contrast Agents for Ultrasound

Peter N. Burns

SUMMARY OF KEY POINTS

- After more than 20 years of development and a somewhat hesitant start, microbubbles have finally come of age as a contrast agent for ultrasound.
- The principal requirements for an ultrasound contrast agent are that it should be easily introducible into the vascular system, be stable for the duration of the diagnostic examination, have low toxicity, and modify one or more acoustic properties of tissues that can be detected by ultrasound imaging.
- Microbubble contrast agents for ultrasound are safe, effective, and well tolerated by patients.
- Contrast-specific modes with microbubbles show real-time perfusion in organ and tumor parenchyma. The mechanical index (MI) of the transmitted pulse is the major determinant of the response of contrast bubbles to ultrasound; continuous perfusion imaging is possible only with use of low MI, which does not disrupt the bubbles.
- Future developments offer the intriguing prospects of molecular and cellular imaging, potentiated therapy, and drug and gene delivery, all with ultrasound and microbubbles.

CHAPTER OUTLINE

REQUIREMENTS AND TYPES
Blood Pool Agents
Free Gas Bubbles
Encapsulated Air Bubbles
Second-Generation Agents
Selective Uptake Agents
THE NEED FOR BUBBLE-SPECIFIC IMAGING
Bubble Behavior and Incident Pressure
The Mechanical Index
NONLINEAR ECHOES AND HARMONIC IMAGING
Harmonic B-Mode Imaging
Harmonic Spectral and Power Doppler Imaging
Tissue Harmonic Imaging
Pulse Inversion Imaging
Pulse Inversion Doppler Imaging
Plane-Wave Contrast Imaging
Amplitude and Phase Modulation Imaging
Temporal Maximum Intensity Projection Imaging
DISRUPTING BUBBLES: INTERMITTENT IMAGING
Triggered Imaging
Intermittent Harmonic Power Doppler
Disruption-Replenishment Imaging
SAFETY CONSIDERATIONS AND REGULATORY STATUS
THE FUTURE
CONCLUSION

After more than 20 years of development and a somewhat hesitant start, microbubbles have finally come of age as a contrast agent for ultrasound. In 2016 the United States was finally added to the more than 50 countries worldwide that have approved them for radiologic indications, with the Food and Drug Administration (FDA) announcing approval for their use for liver diagnosis in adults and children. Their exploitation has already opened many new areas for diagnostic ultrasound imaging and is becoming a central area for technologic advances of the modality. The bubbles themselves comprise small spheres of a gas with low solubility in blood—such as a perfluorocarbon—stabilized by a thin shell layer of a flexible, biocompatible material which is typically a lipid, although proteins and polymers are also used. The diameter of the resulting encapsulated bubble is about 3 to 5 μm, slightly smaller than a red blood cell (Fig. 3.1). Because of this size, bubbles provide a pure intravascular contrast agent (Fig. 3.2). A suspension of bubbles in water is injected into a peripheral vein in the arm or hand; a typical whole-body human dose ranges from 0.2 to 2 mL in volume and contains on the order of 10 million bubbles, roughly comparable to the number of red blood cells in a single milliliter of blood. The effect of a bolus injection is to increase the echo from blood by a factor of 500 to 1000. After about 5 minutes the gas from the bubbles has diffused into the blood and the very small mass of shell material is metabolized. By infusing the bubbles through a saline drip, a steady enhancement lasting up to 20 minutes can also be obtained.[1] Microbubble contrast agents make possible for the first time ultrasound imaging of organ and lesion perfusion

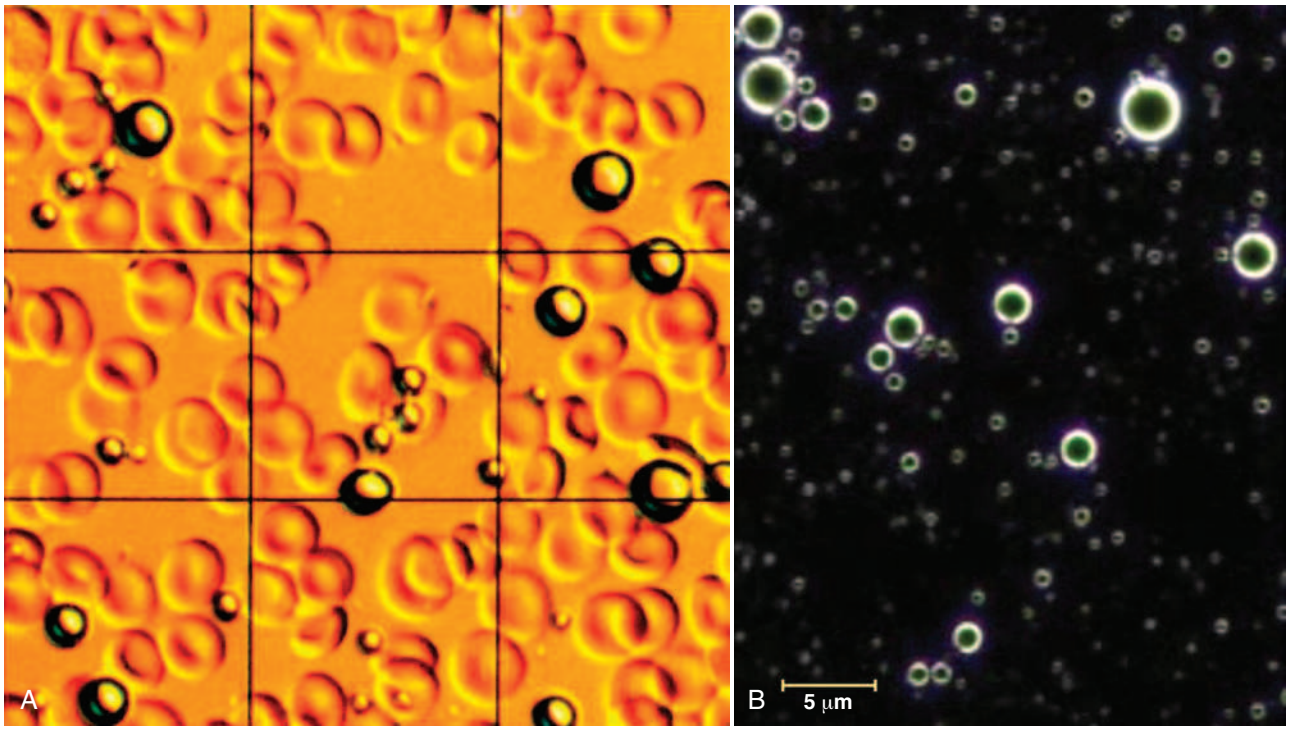

FIG. 3.1 Contrast Agents for Ultrasound. (A) Perfluoropropane bubbles with a protein shell (Optison, GE Healthcare, Milwaukee, WI), shown here against a background of red blood cells. **(B)** Lipid-coated microbubbles of perfluoropropane gas (Definity, Lantheus Medical Imaging, North Billerica, MA) are shown under a dark-field microscope.

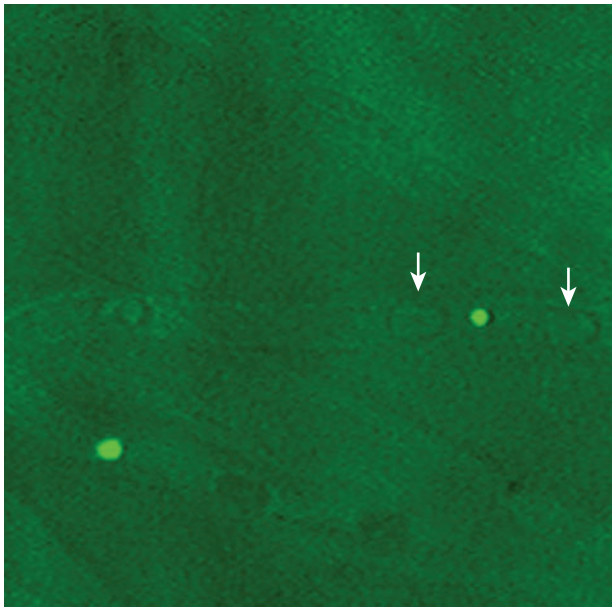

FIG. 3.2 Bubbles Are Relatively Large as Contrast Agents and Remain Within the Blood Pool. Intravital microscopy of fluorescently labelled perfluoropropane bubbles (Definity, Lantheus Medical Imaging, North Billerica, MA) shows them in capillaries, being transported much as red blood cells nearby *(arrows)*. (Courtesy of J. Lindner, Oregon Health Sciences Center.)

in real time. This chapter aims to provide both a tutorial and a reference for the practical use of contrast agents for these indications.

REQUIREMENTS AND TYPES

The principal requirements for an ultrasound contrast agent are that it should be easily introducible into the vascular system, be stable for the duration of the diagnostic examination, have low toxicity, and modify one or more acoustic properties of tissues that can be detected by ultrasound imaging. Although it is conceivable that applications will be found for ultrasound contrast agents that will justify their injection into arteries, the clinical context for contrast ultrasonography requires that these agents be capable of intravenous administration and intact passage through the heart and lungs. These are demanding specifications that have been met only in the past decade. The technology universally adopted is that of encapsulated bubbles of gas that are smaller than red blood cells and therefore capable of circulating freely in the pulmonary and systemic vasculature.

Contrast agents act by their presence in the vascular system, from where they are ultimately metabolized ("blood pool" agents), or by their selective uptake in tissue after a vascular phase. Of the properties of tissue that influence the ultrasound image, the most important are linear and nonlinear backscatter coefficient, attenuation, and acoustic propagation velocity.[2] Most agents enhance the echo by increasing as much as possible the backscatter of the tissue that bears them, while increasing the attenuation

in the tissue as little as possible, thus enhancing the echo from blood. More important, they change the nature of the echo from blood in a way that allows them to be imaged selectively in real time.

Blood Pool Agents

Free Gas Bubbles

Gramiak and Shah first used bubbles to enhance the blood echo in 1968.[3] They injected agitated saline into the left ventricle during an echocardiographic examination and saw strong echoes within the lumen of the aorta. It was subsequently shown that these echoes originated from free bubbles of air that came out of solution either during agitation or at the catheter tip during injection.[4] Agitated solutions of compounds such as indocyanine green and Renografin—already approved for intraarterial injection—were also used. The application of free gas as a contrast agent was confined to the heart, including evaluation of valvular insufficiency,[5] intracardiac shunts,[6] and cavity dimensions.[7] The fundamental limitation of bubbles produced in this way is that they are large, so they are effectively filtered by the lungs, and unstable, so they go back into solution on the order of a second. Apart from occasional use in the echocardiography laboratory to identify shunts, free bubbles are rarely used as a contrast agent today.

Encapsulated Air Bubbles

To overcome the natural instability of free gas bubbles, various shell coatings were developed to create a more stable particle (Table 3.1). In 1980 Carroll and colleagues[8] encapsulated nitrogen bubbles in gelatin and injected them into the femoral artery of rabbits with VX2 tumors in the thigh. Although echo enhancement of the tumor rim was identified, the large diameter of the coated bubbles (80 μm) precluded administration by an intravenous route. The challenge to produce a stable encapsulated microbubble of a comparable size to that of a red blood cell and that could survive passage through the heart and the pulmonary capillary network was first met by Feinstein and colleagues in 1984,[9] who produced microbubbles by sonication of a solution of human serum albumin and showed that it could be detected in the left side of the heart after a peripheral venous injection. This agent was subsequently developed commercially as Albunex (Mallinckrodt Medical, Inc., St. Louis, MO).

Another approach to stabilizing an air bubble is to add a lipid shell upon dissolution of a dry powder. Levovist (Schering AG, Berlin, Germany), is a dry mixture comprising 99.9% microcrystalline galactose microparticles and 0.1% palmitic acid. On dissolving in sterile water, the galactose disaggregates into microparticles, which provide an irregular surface for the adherence of microbubbles 3 to 4 μm in size. Stabilization of the microbubbles takes place as they become coated with palmitic acid, which separates the gas/liquid interface and slows their dissolution.[18] The resulting microbubbles have a median bubble diameter of about 3 μm with the 97th percentile at approximately 6 μm and are sufficiently stable for transit through the pulmonary circuit. The agent is chemically related to its predecessor Echovist (Schering), a galactose agent that forms larger bubbles and that has been used principally for visualization of nonvascular ductal structures such as the fallopian tubes.[19,20] Numerous early

TABLE 3.1 Regulatory and Marketing Status of Some Current Ultrasound Contrast Agents as of 2016

Name	Company/ Developer	Composition (Shell/Gas)	REGULATORY/MARKETING STATUS	
			Cardiology Indications	Radiology Indications
Definity	Lantheus Medical Imaging[10]	Lipid/perfluoropropane	Approved in United States, Canada	Approved in Canada, China, Australasia, Americas
SonoVue Lumason	Bracco[11]	Phospholipid/sulfur hexafluoride	Approved in European Union, Canada	Approved in 40 countries, including European Union, Canada, China, United States
Optison	GE Healthcare[12]	Sonicated albumin/ octafluoropropane	Approved in European Union, United States, Canada	Suspended development
Sonazoid	GE Healthcare and Daiichi Sankyo[13]	Lipid perfluorobutane	Clinical development	Approved in Japan, Korea, Norway Clinical development in European Union, United States
biSphere	Point Biomedical[14]	Polymer bilayer/air	Suspended development	Suspended development
Imagify	Acusphere[15]	Polymer/perfluorobutane	Clinical development	Suspended development
PESDA	Porter[16]	Sonicated albumin/ perfluorocarbon	Not commercially developed	Not commercially developed
BR55	Bracco[17]	Lipopeptide VEGFR-2–targeted/perfluorocarbon		Clinical development

VEGFR, Vascular endothelial growth factor receptor.

studies with Levovist[21,22] demonstrated its capacity to traverse the pulmonary bed in sufficient concentrations to enhance both color and spectral Doppler signals, as well as gray-scale examinations using nonlinear imaging modes such as pulse inversion imaging. Levovist remains approved for use in the European Union, Canada, Japan, and numerous other countries, although not the United States. Many clinical applications of intravenous contrast were pioneered using Levovist, which has now given way to the so-called "second-generation" agents and is no longer marketed.

Second-Generation Agents

Second-generation agents were designed both to increase backscatter enhancement and to last longer in the bloodstream by taking advantage of low-solubility gases such as perfluorocarbons. These heavier gases diffuse more slowly through the bubble shell and have much lower solubility in blood. Optison (GE Healthcare, Milwaukee, WI) (see Fig. 3.1A) is a perfluoropropane-filled albumin shell with a size distribution similar to that of its predecessor, Albunex. It is currently approved for cardiology indications in the European Union, the United States, and Canada. SonoVue (Bracco, Milan, Italy) uses sulfur hexafluoride in a phospholipid shell and is available for cardiology and radiology indications in the European Union, China, and a number of other countries; it is approved in the United States under the name Lumason. Definity (Lantheus Medical Imaging, North Billerica, MA) (see Fig. 3.1B) comprises a perfluoropropane microbubble coated with a flexible bilipid shell, which also showed improved stability and high enhancement at low doses.[23] It is currently approved for cardiology and radiology indications in Canada, Australasia, and a number of Central and South American countries, and for cardiology indications in the United States. Finally, Sonazoid (Daiichi Sankyo, Tokyo, Japan and GE Healthcare, Milwaukee, WI) consists of a perfluorobutane bubble in a lipid shell[24] and is currently approved for radiology indications in countries such as Japan and Korea. It should be noted that although these bubbles are very small, they are large when compared with the molecules and particles used as contrast agents for computed tomography (CT) and magnetic resonance imaging (MRI), which diffuse through the fenestrated endothelium of blood vessels into the interstitium. Thus x-ray and magnetic resonance contrast-enhanced images frequently show an "interstitial" or "parenchymal" phase of enhancement, which may be used to identify hyperpermeable vascular structures, such as those involved with tumor angiogenesis.[25] Microbubbles, on the other hand, are of a size comparable to that of a red blood cell, so they go where a red blood cell goes (see Fig. 3.2) and, more important, do not go where a red blood cell does not go. They are clinical radiology's first pure blood pool contrast agent.

Selective Uptake Agents

An ideal blood pool agent displays the same flow dynamics as blood itself, and is ultimately metabolized from the blood pool. Agents such as Definity, SonoVue, and Optison are generally not detected outside the vascular system, and therefore come close to this ideal. Contrast preparations can be made, however, that are capable of providing ultrasound enhancement during their metabolism as well as while in the blood pool. Colloidal suspensions of liquids droplets such as perfluoroctylbromide[26] and microbubble agents with certain shell properties[24,27,28] are taken up by the reticuloendothelial system, from where they ultimately are excreted. There they may provide contrast from within the liver parenchyma, demarking the distribution of Kupffer cells.[29] Agents such as Levovist and Sonazoid provide "late-phase" enhancement in the parenchyma of the liver and spleen after having cleared from the vascular system,[30] allowing detection of Kupffer cell–poor lesions such as cancers.[31,32]

A typical dose of an ultrasound contrast agent is on the order of 10s of microliters of bubble suspension per kilogram of body weight, so a whole-body dose might be on the order of 0.1 to 1 mL. Fig. 3.3 shows the enhancement of the echo from systemic arterial blood after a peripheral venous injection of a second-generation agent. A first-pass peak occurs, followed by recirculation and washout as the agent is eliminated over the next few minutes. By infusing the bubbles through a saline drip or pump, a steady enhancement lasting up to 20 minutes can be obtained.[1] The small amount of perfluorocarbon gas goes into solution in the blood and is ultimately excreted by the lungs and liver. The trace amount of shell material is reduced to biocompatible elements that, in the case of the commonly used agents, are already present in the blood.[33]

THE NEED FOR BUBBLE-SPECIFIC IMAGING

One of the major diagnostic objectives in using an ultrasound contrast agent in a solid organ is to detect flow at the perfusion—that is, the arteriolar and capillary—level. The peak enhancement in Fig. 3.3 is more than 30 dB, corresponding to a 1000-fold increase in the power of the ultrasound echo from blood. Although this may seem impressive, it does not necessarily help ultrasound to image perfusion. The echoes from blood associated with such flow, in the hepatic sinusoids for example, exist in the midst of echoes from the surrounding solid structures of the liver parenchyma, echoes that are almost always stronger than even the contrast-enhanced blood echo. When they can be seen, blood vessels in a nonenhanced image have a low echo level, so an echo-enhancing agent actually *lowers* the contrast between blood and the surrounding tissue, making the lumen of the blood vessel less visible. Thus in order to be able to image flow in small vessels of the liver, a contrast agent is required that either enhances the blood echo to a level that is substantially higher than that of the surrounding tissue or can be used with a method for suppressing the echo from noncontrast-bearing structures. Bubble-specific imaging methods provide this capability.

Bubble Behavior and Incident Pressure

The key to understanding contrast-specific imaging modes—and the key to their successful clinical use—lies in the unique interaction between a microbubble contrast agent and the process that images it. Controlling and exploiting this interaction is central to all contrast-specific methods. Unlike tissue, microbubbles

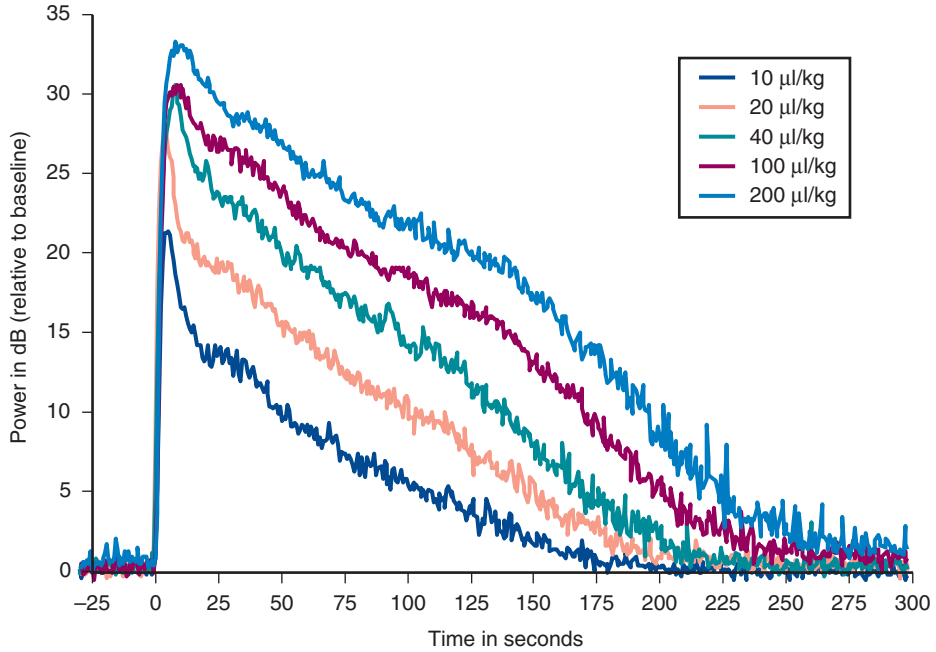

FIG. 3.3 Arterial Blood Echo Enhancement Following an Intravenous Bolus of Optison at Increasing Doses. The peak enhancement is 30 dB, corresponding to a 1000-fold increase of echo power. Note that increasing the dose by a factor of 10 does not have the same effect on the peak enhancement. Instead, it is the wash-out time that is increased.

TABLE 3.2 Three Types of Acoustic Behavior of a Typical Perfluorocarbon, Lipid-Shelled Agent in an Ultrasound Field

Peak Pressure (Approximate)	Mechanical Index (MI) at 2 MHz	Bubble Behavior	Acoustic Behavior	Application
<100 kPa	<0.07	Linear oscillation	Linear backscatter enhancement	Doppler signal enhancement
0.1-0.3 MPa	0.07-0.2	Nonlinear oscillation	Nonlinear backscatter	Real-time (low-MI) perfusion imaging
>0.5 MPa	>0.4	Disruption	Transient nonlinear echoes	Triggered perfusion or disruption-replenishment flow measurement

scatter ultrasound in a manner dependent on the amplitude of the sound to which the imaging process exposes them. The results are three broad types of bubble behavior, with three broad types of resulting echoes (Table 3.2). The types of bubble behavior depend primarily on the intensity (more precisely, the peak negative pressure and frequency) of the incident sound field produced by the scanner. At low incident pressures (corresponding to low transmit power of the scanner), the agents produce linear backscatter enhancement, resulting in an augmentation of the echo from blood. This is the behavior originally envisaged by contrast agent manufacturers. As the transmit intensity control of the scanner is increased and the negative pressure incident on a bubble goes beyond about 50 to 100 kPa, which is still below the level used in most diagnostic scans, the contrast agent backscatter begins to show nonlinear characteristics, such as the emission of harmonics. It is the detection of these that forms the basis of contrast-specific imaging modes such as harmonic and pulse inversion imaging. Finally, as the peak pressure passes about 300 kPa (or 0.3 MPa) and approaches the level emitted by a typical ultrasound imaging system in conventional B-mode imaging, bubbles produce a strong but brief echo as they are disrupted by the ultrasound beam. This behavior forms the basis of the most common way of quantifying perfusion. It should be noted that in practice, because of the different sizes present in a realistic population of bubbles[34] and the additional effect of frequency, the borders between these behaviors are not sharp. Nor will they be the same for different bubble types, the acoustic behavior of which is strongly dependent on the gas and shell properties.[35]

To reiterate, three types of behavior of bubbles in an acoustic field have been identified and depend on the amplitude and frequency of the transmitted ultrasound beam. In practice, this exposure is best monitored by means of the mechanical index (MI) displayed by the scanner. At very low MI, the bubbles act as simple but powerful echo enhancers. This is most useful for spectral Doppler enhancement but is rarely used in the

abdominal organs. At slightly higher intensities (the bottom of the range of those used diagnostically), the bubbles emit harmonics as they undergo nonlinear oscillation. These nonlinear echoes can be detected by contrast-specific imaging modes, which generally rely on trains of low-MI pulses modulated in phase and/or amplitude. Pulse inversion imaging is an example of such a method. Finally, at the higher intensity settings, comparable to those used in conventional scanning, the bubbles can be disrupted deliberately, creating a strong, transient echo. Detecting this echo with harmonic power Doppler is one of the most sensitive means available to image bubbles in very low concentrations, but it comes at the price of destroying the bubble. Because of the long replenishment periods of tissue flow, intermittent imaging using an "interval delay" in which the high-MI imaging is arrested becomes necessary. Disrupting bubbles offers a unique method for quantifying perfusion at the tissue level.

The Mechanical Index

For reasons unrelated to contrast imaging, ultrasound scanners marketed in the United States are required by the FDA to carry an on-screen label of the estimated normalized peak negative pressure to which tissue is exposed. Of course, this pressure changes according to the tissue through which the sound travels as well as the amplitude and geometry of the ultrasound beam: the higher the attenuation, the less the peak pressure in tissue will be. A scanner cannot "know" what tissue it is being used on, so the arrived-at definition of an index reflects the approximate exposure to ultrasound pressure at the focus of the beam in an average tissue. The **mechanical index** (MI) is defined as the peak rarefactional (i.e., negative) pressure divided by the square root of the ultrasound frequency. This quantity is related to the amount of mechanical work that can be performed on a bubble during a single negative half-cycle of sound[36] and is thought to give an indication of the propensity of the sound to cause cavitation in the medium. In clinical ultrasound systems, this index usually lies somewhere between 0.05 and 2.0. Although a single value is displayed for each image, in practice the actual MI varies throughout the image. In the absence of attenuation, the MI is maximal at the focus of the beam. Attenuation shifts this maximum toward the transducer. Furthermore, because it is a somewhat complex procedure to calculate the index, which is itself only an estimate of the actual quantity within the body, the indices displayed by different machines are not precisely comparable. Thus, for example, more bubble disruption might be observed at a displayed MI of 0.2 on one machine but at 0.3 with the same patient on another machine. For this reason, recommendations of machine settings for a specific examination are not transferable between manufacturers' instruments. Nonetheless, the MI is the operator's most important indication of the behavior of the contrast agent bubbles to be expected. For this reason, it is usually incorporated into the preset initial settings for a contrast imaging mode on the scanner and the **output power** adjustment brought to the operator's front line of controls. A typical initial setting of output power in a contrast mode is as low as 1% to 2% of that used in conventional imaging.

The Mechanical Index (MI)

The mechanical index (MI):

- Is defined as

$$\mathrm{MI} = \frac{P_{\mathrm{neg}}}{\sqrt{f}}$$

  where P_{neg} is the peak negative ultrasound pressure in MPa and f is the ultrasound frequency in MHz
- Reflects the normalized negative pressure to which a target (such as a bubble) is exposed in an ultrasound field
- Is defined for the focus of the ultrasound beam
- Varies with depth in the image (lessens with increasing depth)
- Varies with lateral location in the image (lessens at the sector edges)
- Is estimated differently in systems from different manufacturers

NONLINEAR ECHOES AND HARMONIC IMAGING

Two important pieces of evidence are presented by the behavior of bubbles in an acoustic field. First, the size of the echo enhancement shown in Fig. 3.3 is much larger than would be expected from such sparse scatterers of this size in blood. Second, investigations of the acoustic characteristics of early agents[37] demonstrated peaks in the spectra of attenuation and scattering that are dependent on both ultrasound frequency and the size of the microbubbles. These important observations suggest that the bubbles **resonate** in an ultrasound field. As the ultrasound wave—which consists of alternating compressions and rarefactions—propagates over the bubbles, they experience a periodic change in their radius in sympathy with the oscillations of the incident sound. Like vibrations of a string of a musical instrument, these oscillations have a natural, or resonant, frequency of oscillation at which they will both absorb and scatter ultrasound with a peculiarly high efficiency. Considering the linear oscillation of a free bubble of air in water, we can use a simple theory[2] to predict the resonant frequency of radial oscillation of a bubble 3 μm in diameter, the median diameter of a typical transpulmonary microbubble agent. As Fig. 3.4 shows, it is about 3 MHz, approximately the center frequency of ultrasound used in a typical abdominal scan. This extraordinary, and fortunate, coincidence explains why ultrasound contrast agents are so efficient and can be administered in such small quantities. It also predicts that bubbles undergoing resonant oscillation in an ultrasound field can be induced to nonlinear motion, the basis of harmonic imaging.

It has long been recognized[38] that if bubbles are "driven" by an ultrasound field at sufficiently high acoustic pressures, the oscillatory excursions of the bubble reach a point at which the alternate expansions and contractions of the bubble's size are not equal. Lord Rayleigh, the originator of the theoretical

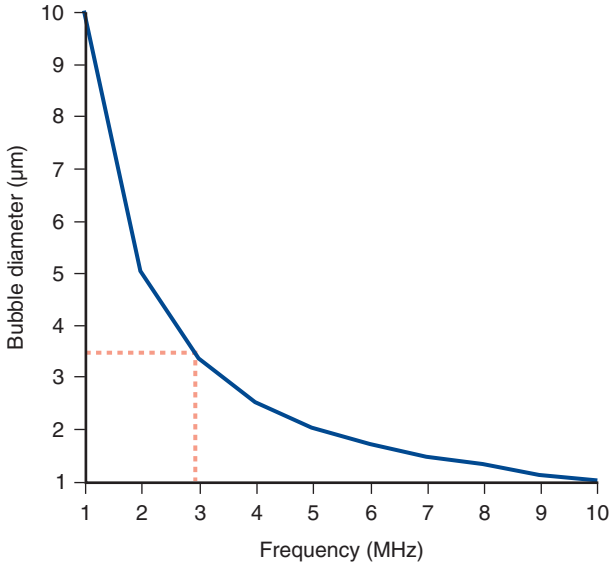

FIG. 3.4 Microbubbles Resonate in a Diagnostic Ultrasound Field. This graph shows that the resonant—or natural—frequency of oscillation of a bubble of air in an ultrasound field depends on its size. For a 3.5-μm diameter, the size needed for an intravenously injectable contrast agent, the resonant frequency is about 3 MHz.

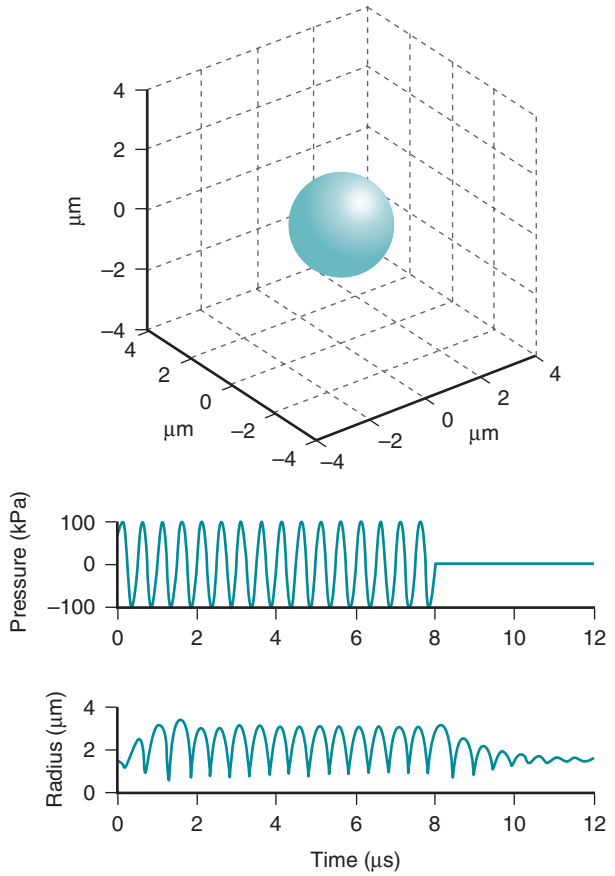

FIG. 3.5 A Microbubble in an Acoustic Field. Bubbles respond asymmetrically to diagnostic sound waves *(top graph),* stiffening when compressed by sound, yielding only small changes in radius *(bottom graph).* During the low-pressure portion of the sound wave, the bubble stiffness decreases and radius changes can be large. This asymmetric response leads to the production of harmonics in the scattered wave.

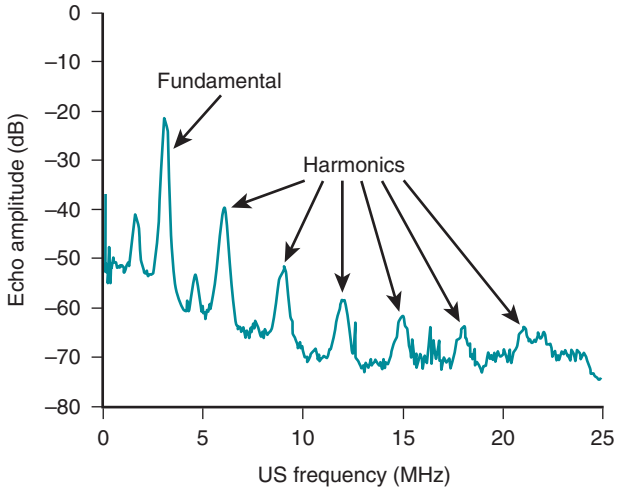

FIG. 3.6 Harmonic Emission From Optison. A sample of a contrast agent is insonated at 3 MHz and the echo analyzed for its frequency content. The largest peak of the energy in the echo is at the 3-MHz fundamental, but there are clear secondary peaks in the spectrum at 6, 9, 12, 15, and 18 MHz, as well as peaks between these harmonics (known as "ultraharmonics") and below the fundamental (known as the "subharmonic"). The second harmonic echo is about 18 dB less than that of the main, or fundamental, echo. Harmonic imaging and Doppler aim to separate and process this signal alone. (With permission from Becher H, Burns P. Handbook of contrast echocardiography: left ventricle function and myocardial perfusion. New York: Springer; 2000.[63])

understanding of sound on which ultrasound imaging is based, was first led in 1917 to investigate this by his curiosity over the creaking noises that his teakettle made as the water came to a boil.[39] The consequence of such **nonlinear** motion is that the sound emitted by the bubble, and detected by the transducer, contains harmonics, just as the resonant strings of a musical instrument, depending on how they are bowed or plucked, will produce a timbre comprising overtones (the musical term for harmonics), exact octaves above the pitch of the fundamental note. The origin of this phenomenon is the asymmetry that begins to affect bubble oscillation as the amplitude becomes large. As a bubble is compressed by the ultrasound pressure wave, it becomes stiffer and hence resists further reduction in its radius. Conversely, in the rarefaction phase of the ultrasound pulse, the bubble becomes less stiff, and therefore enlarges much more (Fig. 3.5). Fig. 3.6 shows the frequency spectrum of an echo produced by a microbubble contrast agent after exposure to a 3-MHz burst of sound. The particular agent is Optison, though most microbubble agents behave in a similar way. Ultrasound frequency is on the horizontal axis, with the relative amplitude on the vertical axis. In addition to the **fundamental echo** at 3 MHz, a series of echoes occur at whole multiples of the transmitted frequency, known as **higher harmonics.** Here, then, is one simple method to distinguish bubbles from tissue: excite them so as to produce harmonics, and detect these in preference to the fundamental echo from tissue. Key factors in the harmonic response of an agent are the incident pressure of the ultrasound field, the frequency, the size distribution of the bubbles, and the mechanical properties of the bubble capsule (a stiff capsule, for example, will dampen the oscillations and attenuate its nonlinear response).

Harmonic B-Mode Imaging

An imaging and Doppler method based on the phenomenon of harmonic emission, called "harmonic imaging,"[40] is widely available on modern ultrasound scanners. In harmonic mode, the system transmits normally at one frequency but is tuned to receive echoes preferentially at double that frequency, where the echoes from the bubbles lie. Typically, the transmit frequency lies between 1.5 and 3 MHz and the receive frequency is selected by means of a detection strategy (originally simply a radiofrequency bandpass filter whose center frequency is at the second harmonic), between 3 and 6 MHz. Harmonic imaging uses the same array transducers as conventional imaging and for most of today's ultrasound systems involves only software changes. Echoes from solid tissue, as well as red blood cells themselves, are suppressed. Real-time harmonic spectral Doppler and color Doppler modes have also been implemented in a number of commercially available systems. Clearly, an exceptional transducer bandwidth is needed to operate over such a large range of frequencies. Fortunately, much effort has been directed in recent years toward increasing the bandwidth of transducer arrays because of its important bearing on conventional imaging performance, so harmonic imaging modes do not require the additional expense of dedicated transducers.

Harmonic Spectral and Power Doppler Imaging

In harmonic images, the echo from tissue-mimicking material is reduced, but not eliminated, reversing the contrast between the agent and its surrounding environment (Fig. 3.7). The value of this effect is to increase the conspicuity of the agent when it is in blood vessels normally hidden by the strong echoes from tissue. In spectral Doppler, one would expect the suppression of the tissue echo to reduce the tissue motion or "thump" artifact that is familiar to all Doppler sonographers and limits the detection of flow in moving vessels. *In vivo* measurements from spectral Doppler show that the signal-to-noise ratio is improved by a combination of harmonic imaging and the contrast agent by as much as 35 dB.[41] Applications of this method include detection of blood flow in small vessels surrounded by tissue that is moving, such as the branches of the coronary arteries[42]; it remains a somewhat specialized technique.

In conventional color Doppler studies using a contrast agent, the increased echo signal does nothing to suppress the clutter "flash" from moving tissue, but instead adds to it a "blooming" artifact of flow signals as the receiver is overloaded with the enhanced echo from blood (Fig. 3.8). Harmonic power Doppler mode effectively overcomes this clutter problem by suppressing the signal from tissue, revealing better detail of small vessels. Combining the harmonic method with power Doppler produces an especially effective tool for the detection of flow in the small vessels of the organs of the abdomen, which may be moving with cardiac pulsation or respiration (Fig. 3.9). In a study in which flow imaged on contrast-enhanced power harmonic images was compared with histologically sized arterioles in the corresponding regions of the renal cortex,[43] it was concluded that the method is capable of demonstrating flow in vessels of less than 40-µm diameter—about 10 times smaller than the corresponding imaging resolution limit, even as the organ is moving with normal

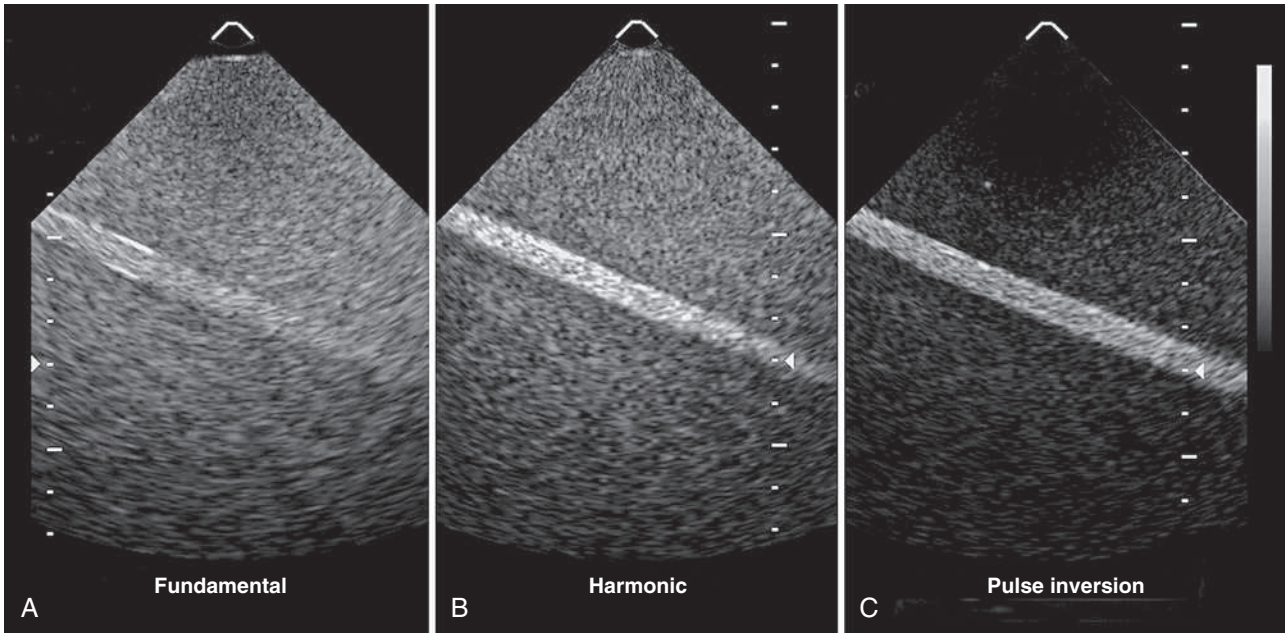

FIG. 3.7 Demonstration of Pulse Inversion Imaging. *In vitro* images of a vessel phantom containing stationary perfluorocarbon contrast agent surrounded by tissue equivalent material (Biogel and graphite). **(A)** Conventional image, mechanical index (MI) = 0.2. **(B)** Harmonic imaging, MI = 0.2, provides improved contrast between agent and tissue. **(C)** Pulse inversion imaging, MI = 0.2. By suppressing linear echoes from stationary tissue, pulse inversion imaging provides better contrast between agent and tissue than both conventional and harmonic imaging. (With permission from Becher H, Burns P. Handbook of contrast echocardiography: left ventricle function and myocardial perfusion. New York: Springer; 2000.[63])

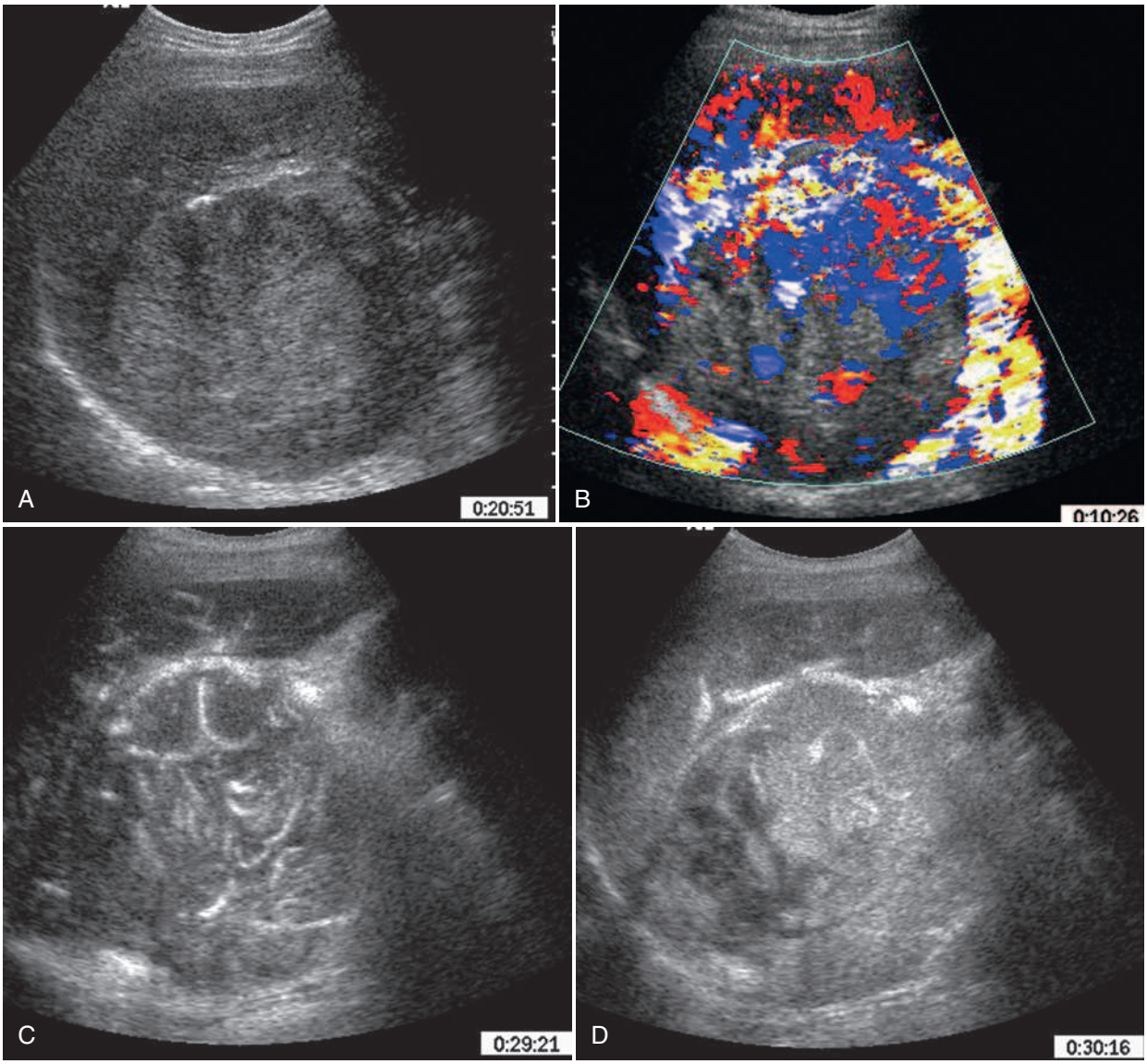

FIG. 3.8 The Need for Contrast-Specific Imaging. (A) Conventional image of liver shows a large solid mass. **(B)** Administration of contrast increases the echogenicity of blood but creates Doppler artifacts owing to blooming and tissue motion. **(C)** Contrast-specific imaging shows blood vessels not seen with Doppler. **(D)** Initiating high–mechanical index imaging after a pause reveals perfusion of the mass and a necrotic area. The lesion is a hepatocellular carcinoma. (Adapted from Burns PN, Wilson SR, Simpson DH. Pulse inversion imaging of liver blood flow: improved method for characterizing focal masses with microbubble contrast. Invest Radiol. 2000;35[1]:58-71.[53])

respiration. Using this power mode method in the heart, perfusion can be imaged in the myocardium.[44,45]

Tissue Harmonic Imaging

In second harmonic imaging, an ultrasound scanner transmits at one frequency and receives at double this frequency. The resulting improved detection of the microbubble echo is due to the peculiar behavior of a gas bubble in an ultrasound field. However, any source of a received signal at the harmonic frequency that does not come from the bubble will clearly reduce the efficacy of this method. Such unwanted signals can come from nonlinearities in the transducer or its associated electronics, and these must be tackled effectively in a good harmonic imaging system. However, tissue itself can produce harmonics that will be received by the transducer. They are developed as a wave *propagates* through tissue. Again, this is due to an asymmetry: this time, the fact that sound travels slightly faster through tissue during the compressional part of the cycle (when it is denser and hence stiffer) than during the rarefactional part. Although the effect is very small, it is sufficient to produce substantial harmonic components in the transmitted wave by the time it reaches deep tissue, so that when it is scattered by a linear target such as the myocardium, there is a harmonic component in the echo, which is detected by the scanner along with the harmonic echo from the bubble.[46] This is the reason that solid tissue is not completely dark in a typical harmonic image. The effect is to

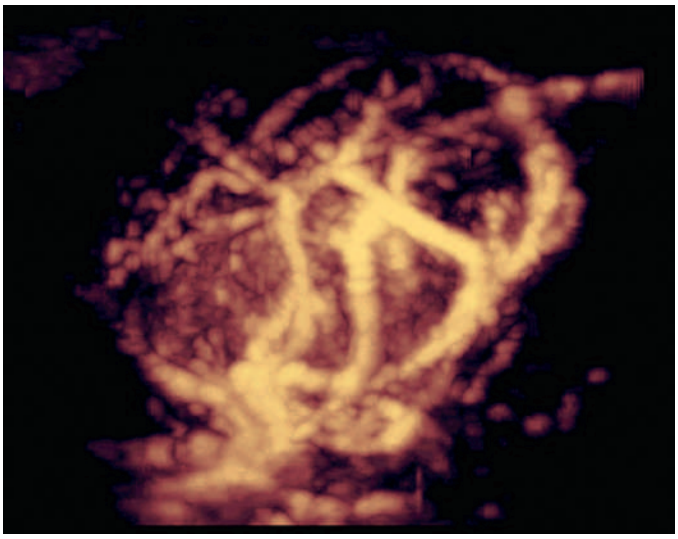

FIG. 3.9 Contrast-Specific Harmonic Imaging. Harmonic Power Doppler of a 1-cm-diameter experimental tumor (VX2 carcinoma) shows clear separation of the enhanced blood signal.

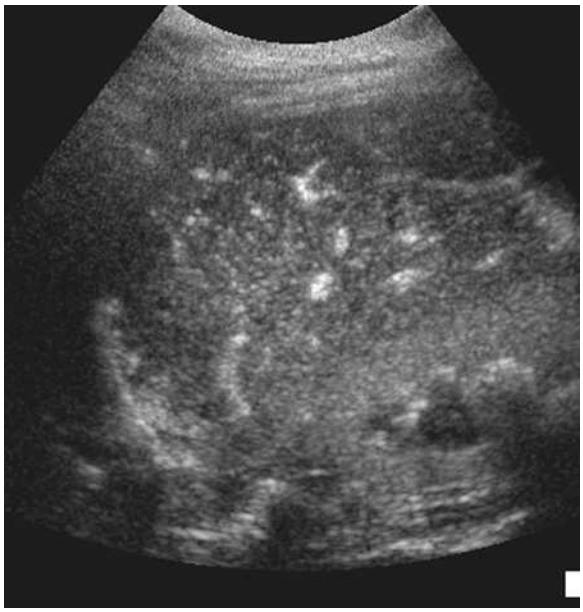

FIG. 3.10 Blood Vessel Appearance Using Harmonic B-Mode Imaging in a Patient With an Incidental Hemangioma. Note that large vessels have a punctate appearance as the high–mechanical index ultrasound disrupts the bubbles as they enter the scan plane. (With permission from Becher H, Burns P. Handbook of contrast echocardiography: left ventricle function and myocardial perfusion. New York: Springer; 2000.[63])

reduce the contrast between the bubble and tissue, rendering the problem of detecting perfusion in tissue more difficult.

Tissue harmonics, although a foe to contrast imaging, are not necessarily a bad thing. In fact, an image formed from tissue harmonics without the presence of contrast agents has so many properties that commend it over conventional imaging that it is used as the routine "default" mode in many scanner presets. Its advantages stem from the fact that tissue harmonics are developed as the beam penetrates tissue, in contrast to the conventional beam, which is generated at the transducer surface.[47,48] Artifacts that accrue from the first few centimeters of tissue, such as reverberations, are reduced by using tissue harmonic imaging. Sidelobe and other low-level interference is also suppressed, making tissue harmonic imaging the routine modality of choice in many situations, especially when visualizing fluid-filled structures.[49] Nonetheless, for contrast studies, the tissue harmonic limits the visibility of bubbles within tissue and therefore can be considered an artifact. In considering how to reduce it, it is instructive to bear in mind differences between harmonic produced by tissue propagation and by bubble echoes. First, tissue harmonics require a high peak pressure, so are only evident at high MI. Use of low-MI contrast imaging, as is most often the case, leaves only the bubble harmonics. Second, harmonics from tissue at high MI are continuous and sustained, whereas those from bubbles at high MI are transient in nature as the bubble disrupts.

Pulse Inversion Imaging

There were problems with early harmonic imaging. First, the splitting of the bandwidth of the transducer had the effect of decreasing image resolution. Second, when the received echo is weak (which from bubbles is typically the case), the overlapping region between the transmit and receive frequencies becomes a larger portion of the entire received signal, so that contrast in the harmonic image is dependent on how strong the echo is from the bubbles. In practice, this forces use of a high MI in harmonic mode, which reduces contrast more because of the tissue harmonic.[50] It also results in the transient and irreversible disruption of the bubbles.[51] As the bubbles enter the scan plane of a real-time ultrasound image, they provide an echo but then disappear. Thus vessels that lie within the scan plane are not visualized as having continuous walls in such a harmonic image, but instead have a punctate appearance (Fig. 3.10).

Pulse inversion imaging overcomes the conflict between the requirements of contrast and resolution in harmonic imaging and provides greater sensitivity, thus allowing low incident power, nondestructive, continuous imaging of microbubbles in an organ such as the liver. The method also relies on the asymmetric oscillation of an ultrasound bubble in an acoustic field, but detects "even" nonlinear components of the echo over the entire bandwidth of the transducer. In pulse inversion (also known as "phase inversion") imaging, two pulses are sent in rapid succession into the tissue. The second pulse is a mirror image of the first (Fig. 3.11): that is, it has undergone a 180-degree phase change. The scanner detects the echo from these two successive pulses and forms their sum. For ordinary tissue, which behaves in a linear manner, the sum of two inverted pulses is simply zero. For an echo with nonlinear components, such as that from a bubble, the echoes produced from these two pulses will not be simple mirror images of each other, because of the asymmetric behavior of the bubble radius with time. The result is that the sum of these two echoes is not zero. Thus a signal is detected from a bubble but not from tissue. It can be shown mathematically that this summed echo contains the nonlinear "even" harmonic components of the signal, including the second harmonic.[52] One

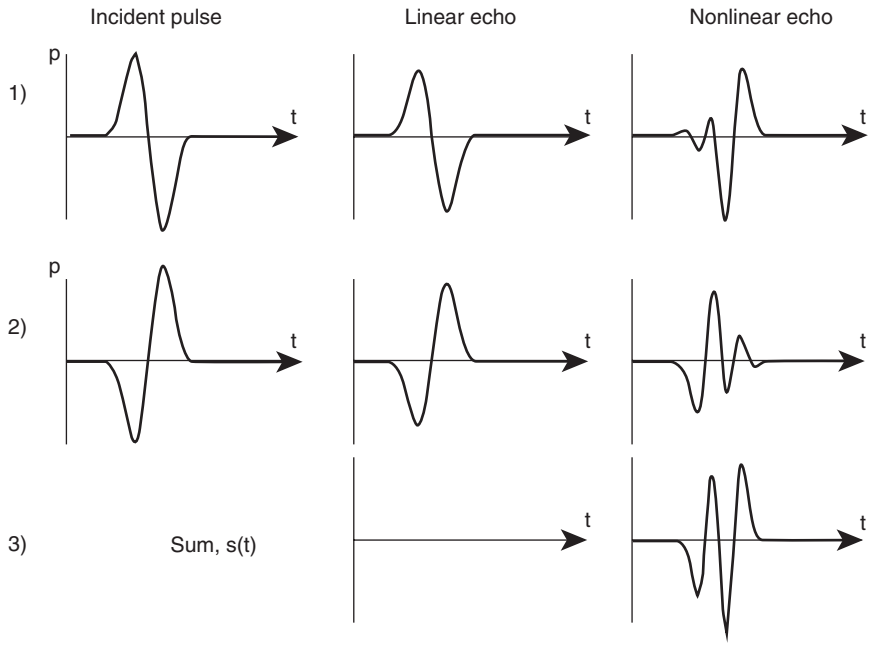

FIG. 3.11 Basic Principle of Pulse Inversion Imaging. A pulse of sound is transmitted into the body, and echoes are received from agent and tissue. A second pulse, which is an inverted copy of the first, is then transmitted in the same direction and the two resulting echoes are summed. Linear echoes from tissue are inverted copies of each other and cancel to zero. The microbubble echoes are distorted copies of each other, so the even nonlinear components of these echoes will reinforce each other when summed, producing a strong harmonic signal.

FIG. 3.12 Pulse Inversion Image of a Hypervascular Liver Mass in the Arterial Phase, Made in Real Time at Low Mechanical Index. Note that the spatial resolution of this image is comparable to that of conventional imaging, reflecting the advantage of a broad-bandwidth contrast-specific image.

advantage of pulse inversion over the filter approach to detect harmonics from bubbles is that it no longer suffers from the restriction of bandwidth. The full frequency range of sound emitted from the transducer can be detected in this way, providing a full bandwidth—that is, a high-resolution image of the echoes from bubbles.[53] Fig. 3.12 illustrates how pulse inversion imaging provides better suppression of linear echoes than harmonic imaging and is effective over the full bandwidth of the transducer, showing improvement of image resolution over harmonic mode. Because this detection method is a more efficient means of isolating the bubble echo, weaker echoes from bubbles insonated at low, nondestructive intensities can be detected. It should be noted, however, that as the MI increases, tissue harmonic renders the tissue brighter. Indeed, pulse inversion is now the preferred method used by many systems for tissue harmonic imaging. Optimal pulse inversion contrast imaging is often, then, performed at low MI. The principle of pulse inversion is the basis of many commercially named imaging modes, such as **coherent contrast imaging, ensemble harmonic imaging,** and **phase inversion imaging.**

Pulse Inversion Doppler Imaging

In spite of the improvements offered by pulse inversion over harmonic imaging for suppressing stationary tissue, the method is somewhat sensitive to echoes from moving tissue. This is because tissue motion causes linear echoes to change slightly between pulses, so that they do not cancel perfectly. Furthermore, at high MI, nonlinear propagation also causes harmonic echoes to appear in pulse inversion images, even from linear scattering structures such as the liver parenchyma. Although tissue motion artifacts can be minimized by using a short pulse repetition interval, nonlinear tissue echoes can mask the echoes from bubbles, reducing the efficacy of microbubble contrast, especially when a high MI is used. Pulse inversion Doppler seeks to address these problems by means of a generalization of the pulse inversion method.[52] This technique combines the nonlinear detection performance of pulse inversion imaging with the motion discrimination capabilities of power Doppler. Multiple transmit pulses of alternating polarity are used and Doppler signal processing techniques are applied to distinguish between bubble echoes and echoes from moving tissue and/or tissue harmonics, as desired by the operator. This method offers potential improvements in the agent-to-tissue contrast and signal-to-noise performance, although at the cost of a somewhat reduced frame rate. The most

dramatic manifestation of this method's ability to detect very weak harmonic echoes has been its demonstration of real-time perfusion imaging of the myocardium.[54] By lowering the MI to 0.1 or less, bubbles undergo stable, nonlinear oscillation, emitting continuous harmonic signals. Because of the low MI, very few bubbles are disrupted, so that imaging can take place at real-time rates. Because sustained, stable nonlinear oscillation is required for this method, perfluorocarbon gas bubbles work best.

Plane-Wave Contrast Imaging

In practice, the low frame rate that line-by-line imaging forces on pulse inversion Doppler has precluded its inclusion as a clinical scanning mode in most systems. However, line-by-line beamforming is not the only way to form an ultrasound image. It is possible to form an ultrasound image as is conventionally done by sweeping a focused beam in 100 consecutive directions, with a single, unfocused plan wave, which insonates the entire field of view with a single pulse. The echoes from each volume element of tissue are then received simultaneously on all transducer elements and processed to extract the echoes at each location in the field of view. The result is a single image, albeit of somewhat compromised quality, for a single ultrasound pulse. Thus imaging frame rates equal to the pulse repetition frequency of 5 kHz or more are possible. Although computationally demanding, the advantage of such "software beam-forming" methods are legion. One is that they provide an opportunity to send long ensembles of pulse for Doppler methods without affecting frame rate. Pulse inversion Doppler has been implemented in such systems with dramatic results, providing simultaneous perfusion, imaging, and color Doppler from a contrast injection at frame rates of 100 Hz or more.[55]

Amplitude and Phase Modulation Imaging

On receiving the echoes from a pulse inversion sequence, the receiver combines them in a way that ensures that the mirrorlike echoes from tissues combine to zero. What is left is then some combination of the nonlinear components of the bubble echo. Changing (or modulating) the pulse from one transmission to the next by flipping its phase is only one of a large number of strategies that can be employed. For example, by changing the amplitude of the pulse in consecutive transmissions and amplifying the echoes to compensate for this, linear echoes can also be cancelled out. What is left are all components of the nonlinear echoes from bubbles.[56] Precisely what nonlinear components are produced by a particular sequence of pulses can be determined mathematically and the contrast-specific imaging mode optimized for specific applications.[57] Almost all diagnostic systems now use some form of multipulse modulation processing in their contrast-specific imaging modes, variously known by such names as **power modulation pulse inversion** (PMPI) or **contrast pulse sequence** (CPS). As long as the peak negative pressure is kept low (less than about 100 kPa) so that the bubble is not disrupted by the pulses, real-time imaging of perfusion can be achieved in many organs, including the myocardium, liver, kidney, skin, prostate, and breast, even in the presence of tissue motion. Because one performance criterion that improves detection of perfusion is complete suppression of background tissue, many contrast-specific images are quite black before the contrast agent is injected, making it very hard to scan the patient. Thus side-by-side imaging, in which a simultaneous, low-MI, fundamental image is seen alongside (or superimposed on) the contrast image, has become a preferred method for hunting small lesions or guiding interventional devices such as needles or ablation probes, the echoes of which are visible in the fundamental image but suppressed in the contrast image (Fig. 3.13). Although the technology for low-MI, real-time, bubble-specific imaging in commercial ultrasound systems has stabilized over the past few years, clinical applications are still experiencing expansion, especially in tumor imaging, which in turn presents new challenges for imaging methodology.

Temporal Maximum Intensity Projection Imaging

One clinically striking elaboration of contrast-specific imaging exploits the fact that it is sufficiently sensitive to detect and display echoes from individual bubbles in real time. By creating the equivalent of an open-shutter photograph, in which bright objects create tracks of their own motion, the bubbles can be made to trace the morphology of the microvessels that contain them. The result, known as **temporal maximum intensity projection** (or temporal MIP) imaging can produce a detailed picture of vascular morphology lasting a few seconds or the duration of a breath hold. Usually the maximum intensity projection process is initiated after a flash, which disrupts the bubbles within the scan plane (Fig. 3.14). As new bubbles wash into the plane, their tracks are traced in an image, which is integrated over a chosen period between 100 ms to a few seconds.[58] These images can also provide dynamic information—for example, revealing whether the pattern of arterial enhancement of a liver lesion is centripetal or centrifugal.[59]

DISRUPTING BUBBLES: INTERMITTENT IMAGING

As the incident pressure to which a resonating bubble is exposed increases, so its oscillation becomes more wild, with radius increasing in some bubbles by a factor of 5 or more during the rarefaction phase of the incident sound. Just as a good soprano can shatter a wine glass by singing at its resonant frequency, so a microbubble, if driven by higher amplitude ultrasound, will sustain irreversible disruption of its shell. A physical picture of precisely what happens to a disrupted bubble is only now emerging from high-speed video studies using cameras with frame rates up to 25 million pictures per second[60,61] (Fig. 3.15). It seems certain, however, that the bubble shell disappears (not instantly, but over a period of time determined by the bubble composition) and releases free gas, which forms a highly effective acoustic scatterer, giving strong, nonlinear echoes for a brief period of time. This process was once incorrectly thought to constitute a release of energy, like a balloon bursting, and was wrongly termed "stimulated acoustic emission." Its use is twofold. First, intermittent imaging represents a very sensitive way to detect a bubble.[62]

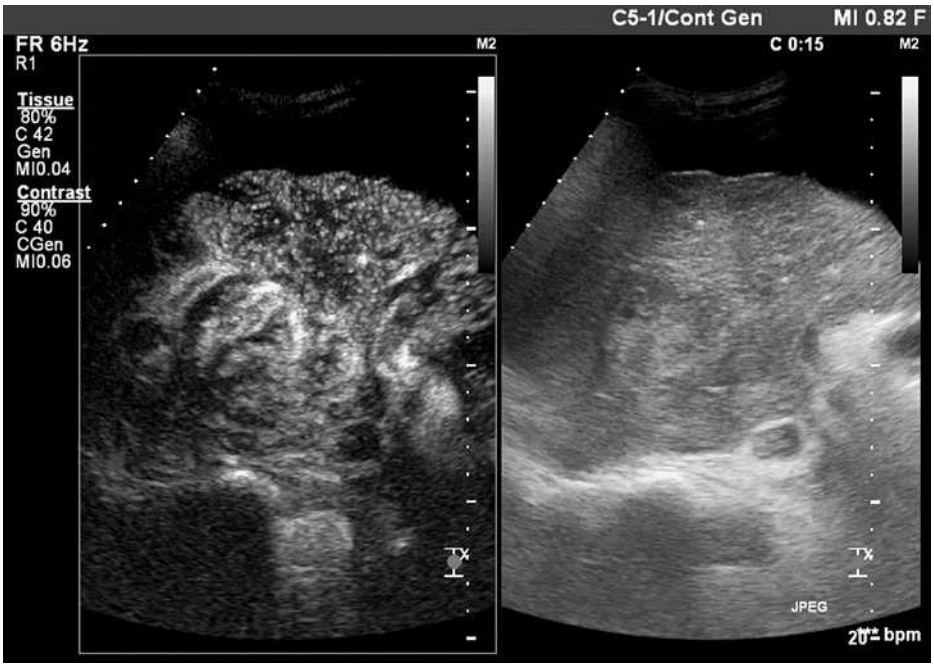

FIG. 3.13 Side-by-Side Imaging Shows a Low–Mechanical Index (MI) Real-Time Conventional Image *(Right)* at the Same Time as the Low-MI Contrast-Specific Image *(Left).* This is particularly useful for characterizing small lesions and for guiding interventional devices. The contrast mode here combines phase and amplitude modulation.

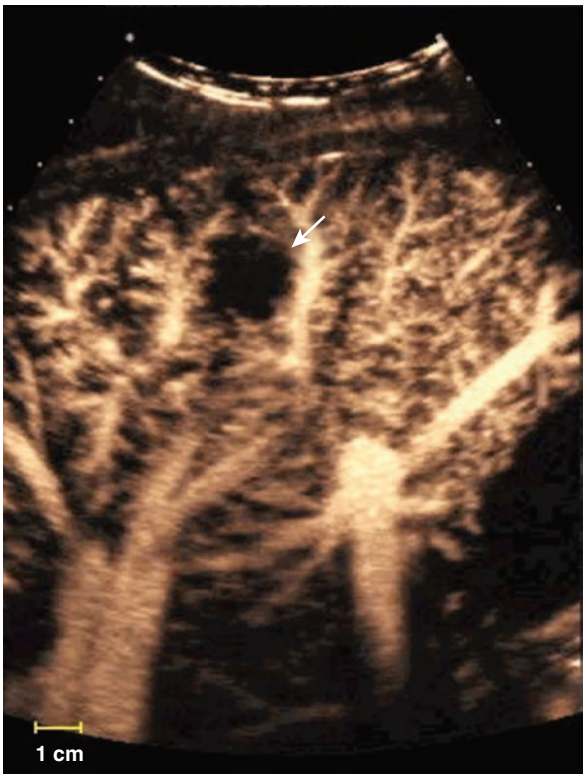

FIG. 3.14 Temporal Maximum Intensity Projection Image of Normal Liver Vasculature Shows Accumulated Enhancement in 11 Seconds After Contrast Material Arrives in Liver. Note depiction of vessel structure to fifth-order branching. Focal unenhanced region *(arrow)* is a slowly perfusing hemangioma. (Reproduced with permission from Wilson SR, Jang HJ, Kim TK, et al. Real-time temporal maximum-intensity-projection imaging of hepatic lesions with contrast-enhanced sonography. AJR Am J Roentgenol. 2008;190[3]:691-695.[58])

However, because it results in its disruption, this process cannot be performed continuously. In fact, replenishment of bubbles in a typical microvascular bed takes about 5 to 10 seconds. The technique of imaging with high MI every few seconds to display perfusion is called "triggered" or "interval delay" imaging.[63] Second, intermittent imaging by a fixed time interval can track the degree to which a region is replenished by bubbles between insonations. By demonstrating the flow rate of blood into the scan plane, intermittent imaging provides a unique method to measure tissue perfusion.

Triggered Imaging

It was discovered during the early days of harmonic imaging that by pressing the "freeze" button on a scanner for a few moments, and hence interrupting the acquisition of ultrasound images during a contrast study, it is possible to increase the effectiveness of a contrast agent. So dramatic is this effect that it was responsible for the first ultrasound images of myocardial perfusion using harmonic imaging.[64] This is a consequence of the ability of the ultrasound field, if its peak pressure is sufficiently high, to disrupt a bubble's shell and hence destroy it.[51] As the bubble is disrupted, it releases energy, thus creating a strong, transient echo that is rich in harmonics. This process is sometimes incorrectly referred to as "stimulated acoustic emission." The fact that this echo is transient in nature can be exploited for its detection. One simple method is to subtract from a disruption image a baseline image obtained either before or (more usefully) immediately after insonation. Such a method requires offline processing of stored ultrasound images, together with software that can align the ultrasound images before subtraction, and is useful only in rare circumstances.[63]

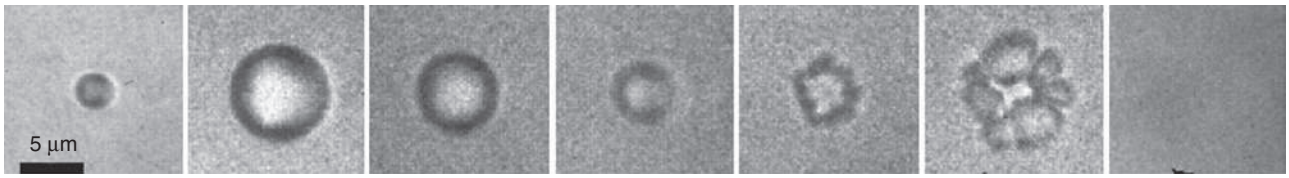

FIG. 3.15 Fragmentation of Contrast Agent Observed With a High-Speed Camera by Researchers at the University of California, Davis. The frame images are captured over 50 nanoseconds. The bubble is insonated with 2.4-MHz ultrasound with a peak negative pressure of 1.1 MPa (mechanical index [MI] ~0.7). The bubble is initially 3 µm in diameter and fragments during compression after the first expansion. Resulting bubble fragments are not seen after insonation, because they are either fully dissolved or below the optical resolution. (Courtesy of James Chomas, Paul Dayton, Kathy Ferrara, University of California, Davis CA.)

Intermittent Harmonic Power Doppler

Power Doppler imaging was developed as a way to detect the movement of targets such as red blood cells in a vessel. It works by a simple, pulse-to-pulse subtraction method,[65] in which two or more pulses are sent successively along each scan line of the image. Pairs of received echo trains are compared for each line: if they are identical, nothing is displayed, but if there is a change (owing to motion of the tissue between pulses), a color is displayed, the saturation of which is related to the amplitude of the echo that has changed. This method, although not designed for the detection of bubble disruption, is ideally suited for high-MI "disruption" imaging. The first pulse receives an echo from the bubble, and the second receives none, so the comparison yields a strong signal. In a sense, power Doppler may be thought of as a line-by-line subtraction procedure on the radiofrequency echo detected by the transducer. Interestingly, pulse inversion imaging—the most commonly used method at low MI—becomes equivalent to power Doppler if the MI is high and the bubble disrupted. Looking again at Fig. 3.11, one can easily see that if the echo from the second pulse is absent (because the bubble is gone), the sum of the two bubble echoes is the same as their difference, which is what is measured by power Doppler. The fact that the second transmitted pulse is inverted is immaterial for the bubble that has disappeared! Thus at high MI, power or pulse inversion Doppler becomes a sensitive way to detect bubbles, whether they are moving or not.

This method has been incorporated into modes specifically adapted to detect the distribution of bubbles taken up in the Kupffer cells in the postvascular phase of agents such as Levovist and Sonazoid. The transducer is slowly swept through the liver some minutes after the agent has left the vascular system; as it does so, the high-MI pulses disrupt the in situ bubbles and are detected in the image. Fig. 3.16 shows such an image, in which the defect in uptake represents the Kupffer-poor region of a cholangiocarcinoma. The preferred modes for this method are pulse inversion—which carries the attraction of high-resolution imaging but the disadvantage of a strong tissue harmonic background—or power Doppler modes known by such names as **harmonic power angio** or **agent detection imaging** (ADI). Many systems offer a low-MI "monitor" mode that can be used to give a contrast-specific or fundamental image of the liver during the scan sweep, which, when blended with the high-MI contrast mode, can be helpful to keep the scan plane aligned in the region of interest.

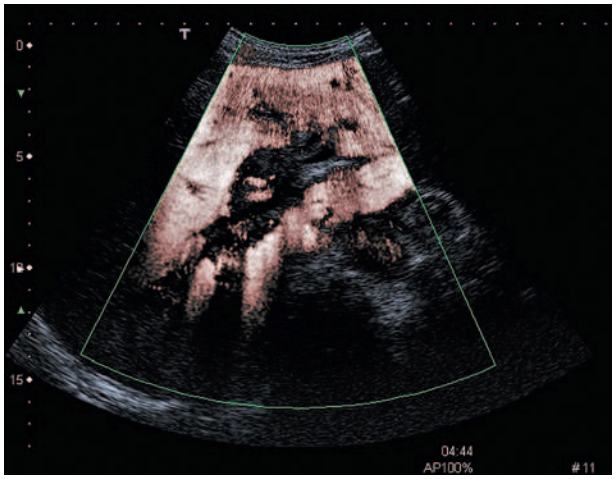

FIG. 3.16 High–Mechanical Index Power Doppler Used to Detect Levovist Bubbles by Disruption During Their Postvascular Phase in the Liver. The bubbles are detected within the Kupffer cells. The signal defect around the porta hepatis depicts a cholangiocarcinoma that was not detected in the precontrast image.

Disruption-Replenishment Imaging

By disrupting bubbles and monitoring replenishment to a region of tissue, contrast ultrasound offers a unique, noninvasive, and validated[66] method for the measurement of microvascular perfusion. In the disruption-replenishment method,[67] microbubbles are infused at a steady rate until a steady enhancement is achieved throughout the vascular system. The bubbles are then disrupted by a high-MI flash, which clears them from the scan plane (Fig. 3.17). Immediately, new bubbles begin to wash in. The rate at which they do so is related to the local flow velocity and flow rate, which can be extracted from a physical model of the process.[68] An important application for such measurement is in assessing the response of tumors and other organs to therapies that target the vasculature. In cancer therapy, a large number of new treatment strategies have been proposed that target the proliferating vasculature of a developing tumor, including drugs specifically designed to inhibit the angiogenic transformation itself.[69] Such antiangiogenic or vascular-disrupting drugs have the effect of shutting down the tumor circulation and inhibiting further growth. They do not in themselves kill cancer cells, so the tumor often responds without shrinking in size—hence the need for a functional test to determine drug response.

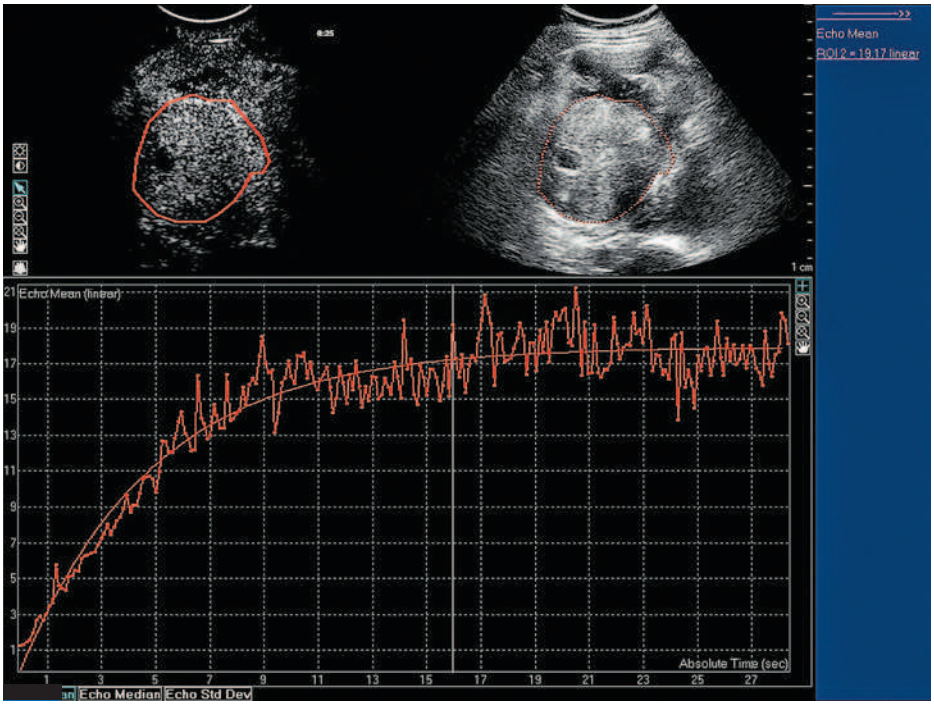

FIG. 3.17 Disruption-Replenishment Imaging Used to Quantify Flow in a Renal Cell Carcinoma in a Patient Undergoing Antiangiogenic Treatment. A side-by-side contrast image (conventional on right, simultaneous contrast-enhanced ultrasound [CEUS] on left) of a large renal cell carcinoma is made during a steady intravenous infusion of the agent Definity. Analysis software (QLAB, Philips Ultrasound, Bothell WA) measures wash-in of a region of interest from the cineloop record. The steeper the initial slope, the greater the flow rate; the higher the asymptote, the greater the vascular volume. Disruption-replenishment imaging thus allows quantitation of changes in tumor flow and relative vascular volume.

Considerable experience accumulated to date suggests that **dynamic contrast-enhanced ultrasound,** with its advantage of high sensitivity, portability, and a pure intravascular tracer, is a strong candidate for this role[70-75]; it has been incorporated into the current European guidelines for the clinical use of contrast agents.[76]

SAFETY CONSIDERATIONS AND REGULATORY STATUS

Contrast ultrasound examinations expose patients to ultrasound in a way that is identical to that of a normal ultrasound examination. Yet the use of ultrasound pulses to disrupt bubbles that sit in microscopic vessels, and the knowledge that ultrasound and bubbles can be used deliberately to penetrate cell membranes for the purpose of drug delivery and other therapies,[77] raise questions about the potential for hazard. When a bubble produces the brief echo that is associated with its disruption, it releases energy it has stored during its exposure to the ultrasound field. Can this energy damage the surrounding tissue? At higher exposure levels, ultrasound is known to produce bioeffects in tissue, the thresholds for which have been studied extensively.[78] Do these thresholds change when bubbles are present in the vasculature? Whereas the safety of ultrasound contrast agents as drugs has been established to the satisfaction of the most stringent requirements of the regulating authorities in a number of countries, it is probably fair to say that there is much to be learned about the interaction between ultrasound and tissue when bubbles are present.

The most extreme of these interactions is known as **inertial cavitation,** which refers to the rapid formation, growth, and collapse of a gas cavity in fluid as a result of ultrasound exposure. It was studied extensively before the development of microbubble contrast agents.[79] In fact, most of the mathematical models used to describe contrast microbubbles were originally developed to describe cavitation.[80] When sound waves of sufficient intensity travel through a fluid, the rarefactional half-cycle of the sound wave can actually tear the fluid apart, creating spherical cavities within the fluid. The subsequent rapid collapse of these cavities during the compressional half-cycle of the sound wave can focus large amounts of energy into a very small volume, raising the temperature at the center of the collapse to thousands of degrees Kelvin, forming free radicals and even emitting electromagnetic radiation.[81] The concern over potential cavitation-induced bioeffects in diagnostic ultrasound has led to many experimental studies, many of them assessing whether the presence of contrast microbubbles can act as cavitation seeds, potentiating bioeffects.[82-87] This work has been reviewed by ter Haar[88] and by the World Federation for Ultrasound in Medicine and Biology.[89,90] Although it has been shown that adding contrast agents to blood decreases the threshold for cavitation and related bioeffects (e.g., hemolysis,

platelet lysis), no significant effects have been reported in conditions that are comparable to the bubble concentrations and ultrasound exposure of a low-MI diagnostic clinical examination. It nonetheless remains prudent to practice an extension of the ALARA (as low as reasonably achievable) exposure principle to contrast ultrasound. The contrast ultrasound examination should expose the patient to the lowest MI, the shortest total acoustic exposure time, the lowest contrast agent dose, and the highest ultrasound frequency consistent with obtaining adequate diagnostic information.

In the meantime, at least 8 million injections of microbubble contrast for clinical diagnosis have been performed worldwide; they are very well tolerated and have an excellent safety record. In fact, postmarketing surveillance has suggested that the predominant cause of severe adverse events is anaphylactic reaction, with an estimated rate of 1 per 7000 for both the perflutren microspheres approved for cardiac indications in the United States[91] and the sulfur hexafluoride microspheres approved in Europe.[92] This rate is comparable to that of most injectable analgesics and antibiotics and lower than that for other imaging contrast agents, such as those used in CT imaging.[93] A 2006 study of more than 23,000 injections of a microbubble contrast agent for abdominal diagnosis in Europe showed no deaths and two serious adverse events, giving a serious adverse event rate of less than 1 : 10,000.[92] Although FDA approval for radiologic indications has only just occurred in the United States, there is extensive experience with ultrasound contrast in echocardiography laboratories. In 2008 Kusnetzky and colleagues reviewed more than 18,671 hospitalized patients undergoing echocardiography in an acute setting in a single center and reported no effect on mortality from the use of contrast in this group.[94] In 2008 Main and colleagues[95] analyzed registry data from 4,300,966 patients who underwent transthoracic echocardiography at rest during hospitalization, of whom 58,254 were given the contrast agent Definity. Acute crude mortality was no different between groups, but multivariate analysis revealed that in patients undergoing echocardiography, those receiving the contrast agent were 24% less likely to die within 1 day than patients not receiving contrast. The FDA has since dropped its notice of caution when using microbubble agents in patients with severe cardiopulmonary compromise.[96-98] From the accumulated knowledge of the considerable benefits of using microbubble contrast, combined with the very low incidence of adverse events associated with its administration, it is fair to conclude this technique is ready to play a major role in the practice of ultrasound diagnosis.[99] We might speculate that in offering the 2016 approval for the use of microbubble contrast in the pediatric population (children were not part of the pivotal studies included in the submission dossier), the FDA is tacitly pointing to the additional benefit that may accrue from reducing the exposure of these patients to x-rays, as well as to CT and MRI contrast agents.

THE FUTURE

Development of microbubble technology is proceeding in two complementary areas: the instruments and the bubbles. In the first, the development of three-dimensional (3-D) and fast imaging for other applications will have a substantial impact on contrast studies. Ultrafast imaging using plane waves offers the opportunity to gain quantitative flow information from large vessels, using bubble-specific vector Doppler methods, at the same time as imaging perfusion. The separation of large vessel flow from tissue perfusion is a challenge to all contrast-enhanced modalities and is likely to be solved first by ultrasound. Although 3-D contrast images have been made using mechanically swept transducers, the slow acquisition rates mean that the dynamics of enhancement—a crucial diagnostic feature—are lost. Two-dimensional matrix arrays transducers, on the other hand, offer real-time volumetric contrast imaging. In one emerging application, they allow the response of a tumor. Considering the heterogeneity of tumor perfusion, the sampling of a single plane has been shown to be unreliable; real-time 3-D imaging solves this problem, allowing very large tumors to be evaluated rapidly[75] (Fig. 3.18).

In contrast imaging, the potential for functional information yielded by the bubbles can be increased by active targeting to a specific cellular or molecular process. Thus a bubble attaches itself to the cells lining blood vessels (endothelial cells) that are involved in a disease process such as inflammation (in atherosclerosis)[100] or proliferation (in cancer).[101] This is achieved by attaching ligands to the surface of the lipid shell, such as a peptide and an antibody.[102] Antibodies to factors such as vascular cell adhesion molecule (VCAM), a marker of inflammation, and vascular endothelial growth factor (VEGF) receptor 2, a marker of vascular proliferation, have already been shown to effectively make bubbles "stick" selectively to the endothelial surface[103] (Fig. 3.19). This form of molecular imaging has potential applications in identifying the target and assessing the effectiveness of new therapies,[104] with new agents under active clinical development.[105,106] In addition, the bubbles are used as a potentiator of the therapy itself. Bubbles can concentrate and lower the threshold for thermal tissue damage in high-intensity focused ultrasound (HIFU) treatments. They can also have the effect of opening or penetrating the endothelial layer, even the blood-brain barrier,[77] allowing drugs to pass through into a region of tissue selected by the ultrasound beam. The drugs can be circulating in the bloodstream, or incorporated into the bubbles themselves. In the latter case, plasmid DNA, which cannot survive in the blood, can be carried in the bubble shell and released by acoustic disruption.[107] Oscillation of the free gas near the cell membrane allows the DNA to enter the cell. Both endothelial cells and myocytes have been successfully transfected in this potentially new form of gene therapy.[108] Finally, the barrier of the endothelium itself can be overcome by injecting liquid nanodroplets—precursors of the gas contrast agents—allowing them to diffuse into the interstitium, and then using external acoustic energy to activate them into gas bodies, which are both targeted and detectable[109] and can be used to enhance therapy.[110]

The use of bubbles as molecular and cellular probes, their targeting as a means for detection as well as drug and gene delivery, and their application as focal potentiators for minimally invasive therapies are all applications in their infancy. The coming years are likely to see an unprecedented union of ultrasound

imaging with a unique series of injectable constructs that will propel an already versatile imaging modality to the forefront of the interface between diagnosis and therapy.

CONCLUSION

Microbubble contrast agents for ultrasound are safe, effective, and well tolerated by patients. They offer a clinically approved blood pool agent unique to radiological modalities. Unlike contrast agents for other modalities, microbubbles are physically modified by the process used to image them. Understanding the behavior of bubbles while exposed to an ultrasound imaging beam is the key to performing an effective contrast ultrasound examination. The appropriate choice of a contrast-specific imaging method is based on the behavior of the agent and the requirements of the examination. The MI is the major determinant of the response of contrast bubbles to ultrasound. Low-MI harmonic and multipulse imaging offer real-time, contrast-specific methods for perfusion imaging using perfluorocarbon agents. Future developments offer the intriguing prospect of molecular and cellular imaging, potentiated therapy, and drug and gene delivery, all with ultrasound and microbubbles.

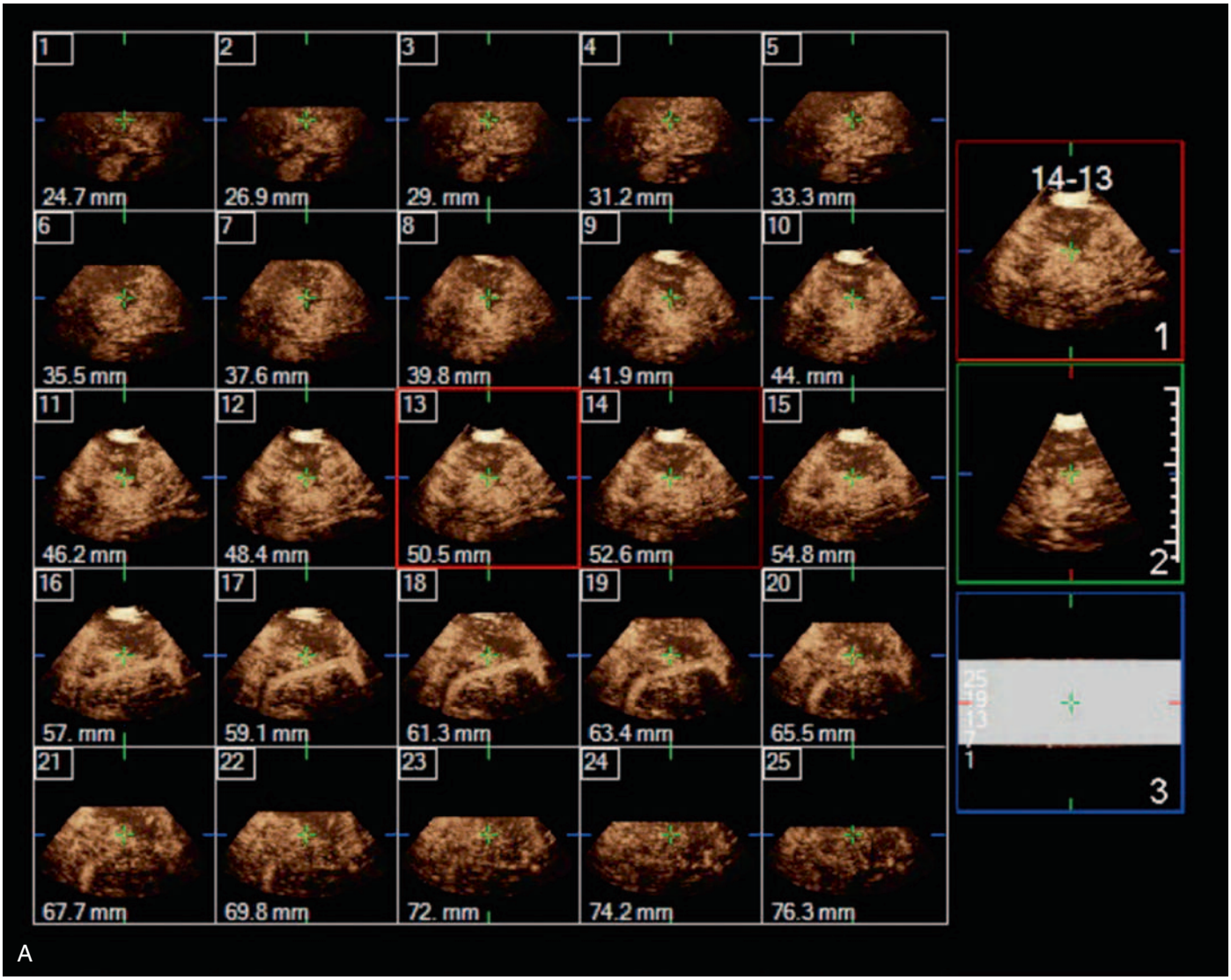

FIG. 3.18 Real-Time, Four-Dimensional Tumor Contrast Imaging Performed With a 9000-Element Ultrasound Array Transducer at a Harmonic Range of 2 to 4 MHz. Twenty-five pseudo-parallel 2.1-mm-spaced planes in a patient with renal cell carcinoma (about 5 × 5 × 8 cm) are imaged simultaneously with low–mechanical index contrast-specific imaging. **(A)** A single volume acquisition taken from a 10-Hz, 60-volume series after acoustic disruption of the microbubble agent during an intravenous infusion.

Continued

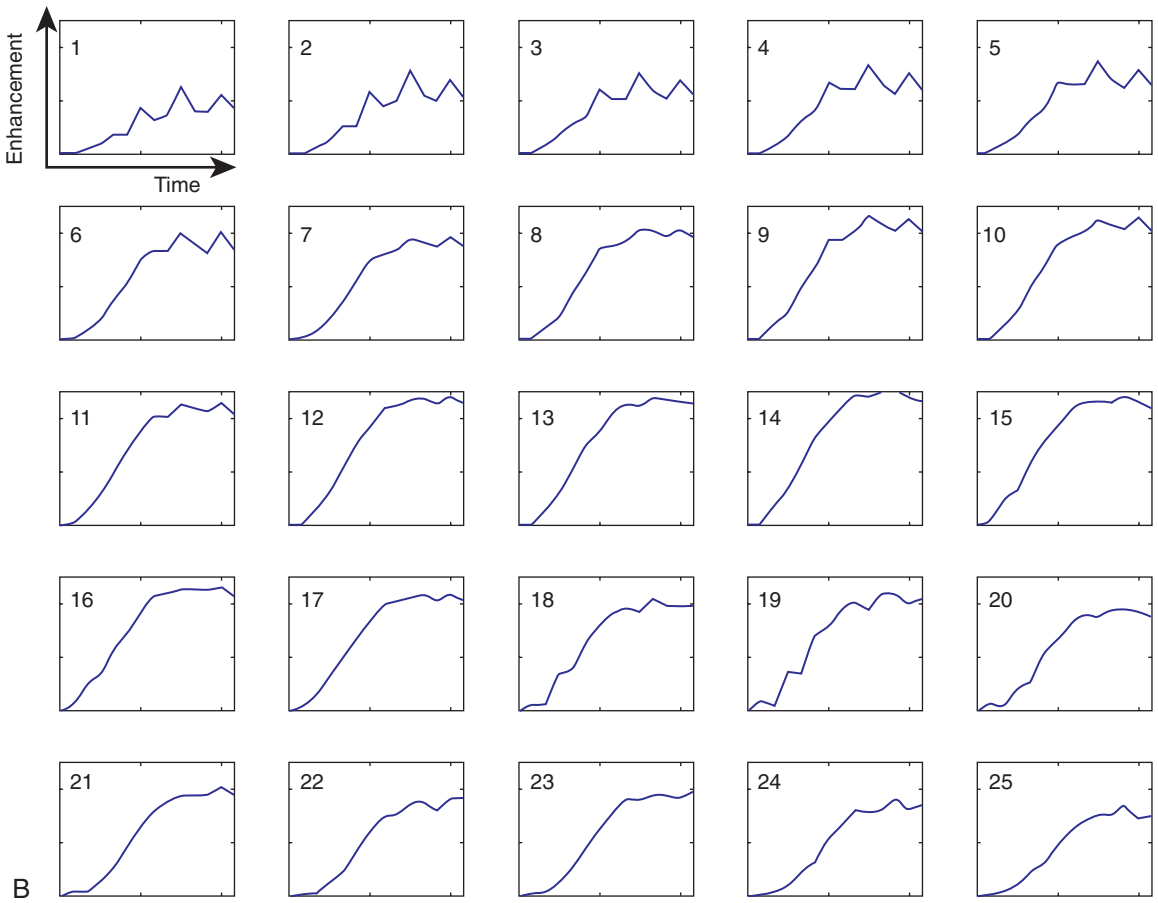

FIG. 3.18, cont'd **(B)** Time-intensity replenishment curves for each of the 25 slices, measured simultaneously. The total acquisition time is about 15 seconds; the contrast agent is Definity.

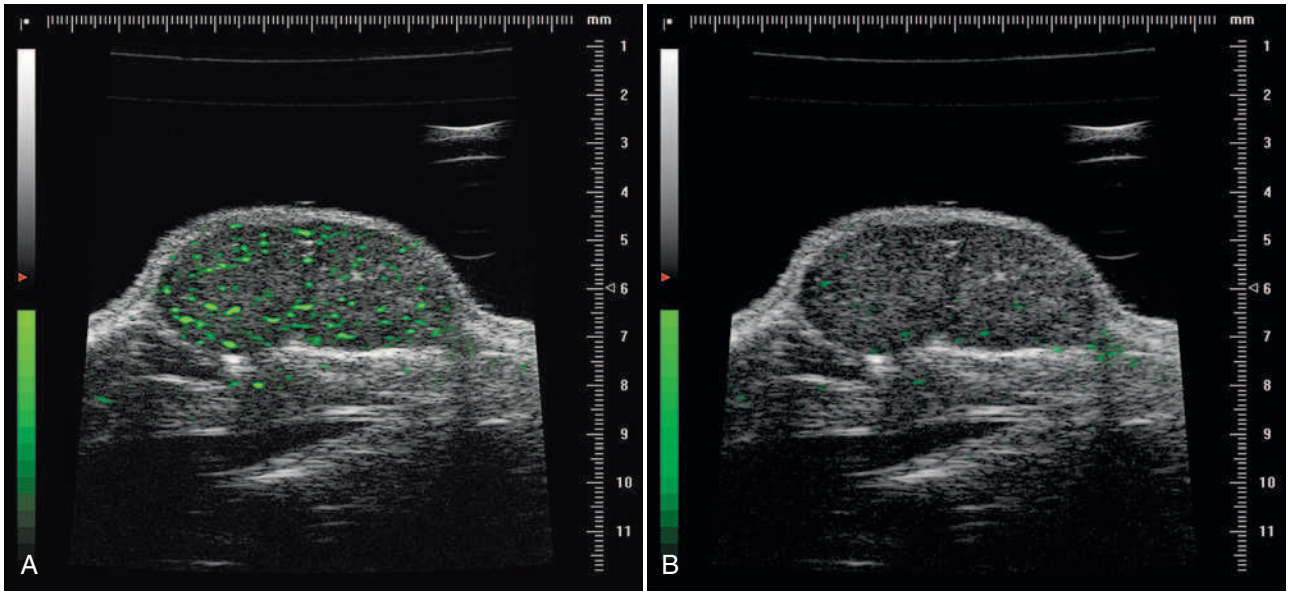

FIG. 3.19 Molecular Ultrasound Imaging of Vascular Endothelial Growth Factor Receptor 2 (VEGFR-2) With Targeted Microbubbles. Figure shows 40-MHz images of a MeWo subdermal tumor derived from human melanoma cells in a mouse after injection of VEGFR-2–targeted microbubbles. **(A)** Circulating bubbles have left the vascular system; those imaged are adhering to the receptor target. Microbubble-specific signal is shown as a green overlay. **(B)** After disruption flash, the bubble echoes disappear. The difference in bubble signal between these two images quantifies adhesion of the tracer to the target receptor. Scale units are millimeters. (Reproduced with permission from Rychak JJ, Graba J, Cheung AM, et al. Microultrasound molecular imaging of vascular endothelial growth factor receptor 2 in a mouse model of tumor angiogenesis. Mol Imaging. 2007;6[5]:289-296.[103])

REFERENCES

1. Correas JM, Burns PN, Lai X, Qi X. Infusion versus bolus of an ultrasound contrast agent: in vivo dose-response measurements of BR1. Invest Radiol. 2000;35(1):72-79.
2. Ophir J, Parker KJ. Contrast agents in diagnostic ultrasound. Ultrasound Med Biol. 1989;15(4):319-333.
3. Gramiak R, Shah PM. Echocardiography of the aortic root. Invest Radiol. 1968;3(5):356-366.
4. Kremkau FW, Gramiak R, Carstensen EL, et al. Ultrasonic detection of cavitation at catheter tips. Am J Roentgenol Radium Ther Nucl Med. 1970;110(1):177-183.
5. Kerber RE, Kioschos JM, Lauer RM. Use of an ultrasonic contrast method in the diagnosis of valvular regurgitation and intracardiac shunts. Am J Cardiol. 1974;34(6):722-727.
6. Valdes-Cruz LM, Sahn DJ. Ultrasonic contrast studies for the detection of cardiac shunts. J Am Coll Cardiol. 1984;3(4):978-985.
7. Roelandt J. Contrast echocardiography. Ultrasound Med Biol. 1982;8(5):471-492.
8. Carroll BA, Turner RJ, Tickner EG, et al. Gelatin encapsulated nitrogen microbubbles as ultrasonic contrast agents. Invest Radiol. 1980;15(3): 260-266.
9. Feinstein SB, Shah PM, Bing RJ, et al. Microbubble dynamics visualized in the intact capillary circulation. J Am Coll Cardiol. 1984;4(3):595-600.
10. Kitzman DW, Goldman ME, Gillam LD, et al. Efficacy and safety of the novel ultrasound contrast agent perflutren (definity) in patients with suboptimal baseline left ventricular echocardiographic images. Am J Cardiol. 2000;86(6):669-674.
11. Schneider M. Characteristics of SonoVue. Echocardiography. 1999;16 (7 Pt 2):743-746.
12. Skyba DM, Camarano G, Goodman NC, et al. Hemodynamic characteristics, myocardial kinetics and microvascular rheology of FS-069, a second-generation echocardiographic contrast agent capable of producing myocardial opacification from a venous injection. J Am Coll Cardiol. 1996;28(5): 1292-1300.
13. Binder T, Assayag P, Baer F, et al. NC100100, a new echo contrast agent for the assessment of myocardial perfusion—safety and comparison with technetium-99m sestamibi single-photon emission computed tomography in a randomized multicenter study. Clin Cardiol. 1999;22(4): 273-282.
14. Wei K, Crouse L, Weiss J, et al. Comparison of usefulness of dipyridamole stress myocardial contrast echocardiography to technetium-99m sestamibi single-photon emission computed tomography for detection of coronary artery disease (PB127 Multicenter Phase 2 Trial results). Am J Cardiol. 2003;91(11):1293-1298.
15. Senior R, Monaghan M, Main ML, et al. Detection of coronary artery disease with perfusion stress echocardiography using a novel ultrasound imaging agent: two phase 3 international trials in comparison with radionuclide perfusion imaging. Eur J Echocardiogr. 2009;10:26-35.
16. Porter TR, Xie F, Kricsfeld A, Kilzer K. Noninvasive identification of acute myocardial ischemia and reperfusion with contrast ultrasound using intravenous perfluoropropane-exposed sonicated dextrose albumin. J Am Coll Cardiol. 1995;26:33-40.
17. Hackl C, Schacherer D, Anders M, et al. Improved detection of preclinical colorectal liver metastases by high resolution ultrasound including molecular ultrasound imaging using the targeted contrast agent BR55. Ultraschall Med. 2016;37(3):290-296.
18. Schurmann R, Schlief R. Saccharide-based contrast agents. Characteristics and diagnostic potential. Radiol Med. 1994;87(5 Suppl. 1):15-23.
19. Fritzsch T, Schartl M, Siegert J. Preclinical and clinical results with an ultrasonic contrast agent. Invest Radiol. 1988;23(Suppl. 1):S302-S305.
20. Deichert U, Schleif R, van de Sandt M, Juhnke I. Transvaginal hysterosalpingo-contrast-sonography (Hy-Co-Sy) compared with conventional tubal diagnostics. Hum Reprod. 1989;4(4):418-424.
21. Goldberg BB, Liu JB, Burns PN, et al. Galactose-based intravenous sonographic contrast agent: experimental studies. J Ultrasound Med. 1993;12(8): 463-470.
22. Fobbe F, Ohnesorge I, Reichel M, et al. [Color-coded duplex sonography and ultrasound contrast medium in the study of peripheral arteries—initial clinical experiences]. Ultraschall Med. 1992;13(4):193-198.
23. Unger E, Shen D, Fritz T, et al. Gas-filled lipid bilayers as ultrasound contrast agents. Invest Radiol. 1994;29(Suppl. 2):S134-S136.
24. Sontum PC. Physicochemical characteristics of Sonazoid, a new contrast agent for ultrasound imaging. Ultrasound Med Biol. 2008;34(5):824-833.
25. Folkman J, Beckner K. Angiogenesis imaging. Acad Radiol. 2000;7(10): 783-785.
26. Mattrey RF, Scheible FW, Gosink BB, et al. Perfluoroctylbromide: a liver/spleen-specific and tumor-imaging ultrasound contrast material. Radiology. 1982;145(3):759-762.
27. Fritzsch T, Hauff P, Heldmann F, et al. Preliminary results with a new liver specific ultrasound contrast agent. Ultrasound Med Biol. 1994;20:137.
28. Yanagisawa K, Moriyasu F, Miyahara T, et al. Phagocytosis of ultrasound contrast agent microbubbles by Kupffer cells. Ultrasound Med Biol. 2007;33(2):318-325.
29. Leen EL, Albrecht T, Harvey CJ, et al. Multi-centre study of Sonazoid-enhanced pulse inversion harmonic imaging in the characterisation of focal hepatic lesions: preliminary results. Radiology. 2000;217:458.
30. Iijima H, Moriyasu F, Miyahara T, et al. Ultrasound contrast agent, Levovist microbubbles are phagocytosed by Kupffer cells—in vitro and in vivo studies. Hepatol Res. 2006;35(4):235-237.
31. Albrecht T, Blomley MJ, Burns PN, et al. Improved detection of hepatic metastases with pulse-inversion US during the liver-specific phase of SHU 508A: multicenter study. Radiology. 2003;227(2):361-370.
32. Moriyasu F, Itoh K. Efficacy of perflubutane microbubble-enhanced ultrasound in the characterization and detection of focal liver lesions: phase 3 multicenter clinical trial. AJR Am J Roentgenol. 2009;193(1):86-95.
33. Schlief R. Ultrasound contrast agents. Curr Opin Radiol. 1991;3(2): 198-207.
34. Chin CT, Burns PN. Predicting the acoustic response of a microbubble population for contrast imaging in medical ultrasound. Ultrasound Med Biol. 2000;26(8):1293-12300.
35. de Jong N. Physics of microbubble scattering. In: Nanda NC, Schlief R, Goldberg BB, editors. Advances in echo imaging using contrast enhancement. 2nd ed. Dubai, Saudi Arabia: Kluwer Academic Publishers; 1997. p. 39-64.
36. Apfel RE, Holland CK. Gauging the likelihood of cavitation from short-pulse, low-duty cycle diagnostic ultrasound. Ultrasound Med Biol. 1991;17(2): 179-185.
37. Bleeker HJ, Schung KK, Barnhart JL. Ultrasonic characterization of Albunex, a new contrast agent. J Acoust Soc Am. 1990;87:1792-1797.
38. Neppiras EA, Nyborg WL, Miller PL. Nonlinear behavior and stability of trapped micron-sized cylindrical gas bubbles in an ultrasound field. Ultrasonics. 1983;21:109-115.
39. Rayleigh L. On the pressure developed in a liquid during the collapse of a spherical cavity. Philos Mag Ser. 1917;6:94-98.
40. Burns PN, Powers JE, Fritzsch T. Harmonic imaging: a new imaging and Doppler method for contrast-enhanced ultrasound. Radiology. 1992;185:142 (abstract).
41. Burns PN, Powers JE, Hope Simpson D, et al. Harmonic contrast-enhanced Doppler as a method for the elimination of clutter: in vivo duplex and color studies. Radiology. 1993;189.
42. Mulvagh SL, Foley DA, Aeschbacher BC, et al. Second harmonic imaging of an intravenously administered echocardiographic contrast agent: visualization of coronary arteries and measurement of coronary blood flow. J Am Coll Cardiol. 1996;27(6):1519-1525.
43. Burns PN, Powers JE, Hope Simpson D, et al., editors. Harmonic power mode Doppler using microbubble contrast agents: an improved method for small vessel flow imaging. Proc IEEE Ultrasonics Symposium; 1994:1547-1550.
44. Burns PN, Wilson SR, Muradali D, et al. Intermittent US harmonic contrast-enhanced imaging and Doppler improves sensitivity and longevity of small vessel detection. Radiology. 1996;201:159.
45. Becher H, editor. Second harmonic imaging with Levovist: initial clinical experience. Second European Symposium on Ultrasound Contrast Imaging Book of Abstracts. Rotterdam: Erasmus Univ; 1997.

46. Hamilton MF, Blackstock DT, editors. Nonlinear acoustics. San Diego: Academic Press; 1998.
47. Averkiou MA, Roundhill DN, Powers JE. A new imaging technique based on the nonlinear properties of tissues. Proc IEEE Ultrasonics Symposium; 1997;(2):1561-1566.
48. Burns PN, Hope Simpson D, Averkiou MA. Nonlinear imaging. Ultrasound Med Biol. 2000;26(Suppl. 1):S19-S22.
49. Ortega D, Burns PN, Hope Simpson D, Wilson SR. Tissue harmonic imaging: is it a benefit for bile duct sonography? AJR Am J Roentgenol. 2001;176(3): 653-659.
50. Averkiou MA, Powers JE, Burns PN, et al. Ultrasonic tissue harmonic imaging. US Patent 6,251,074. 2001.
51. Burns PN, Wilson SR, Muradali D, et al. Microbubble destruction is the origin of harmonic signals from FS069. Radiology. 1996;201:158.
52. Hope Simpson D, Chin C, Burns P. Pulse inversion Doppler: a new method for detecting nonlinear echoes from microbubble contrast agents. IEEE Trans Ultrason Ferroelectr Freq Control. 1999;46(2):372-382.
53. Burns PN, Wilson SR, Simpson DH. Pulse inversion imaging of liver blood flow: improved method for characterizing focal masses with microbubble contrast. Invest Radiol. 2000;35(1):58-71.
54. Tiemann K, Lohmeier S, Kuntz S, et al. Real-Time contrast echo assessment of myocardial perfusion at low emission power: first experimental and clinical results using power pulse inversion imaging. Echocardiography. 1999;16(8):799-809.
55. Tremblay-Darveau C, Williams R, Milot L, et al. Combined perfusion and Doppler imaging using plane-wave nonlinear detection and microbubble contrast agents. IEEE Trans Ultrason Ferroelectr Freq Control. 2014;61(12): 1988-2000.
56. Thomas DH, Butler MB, Anderson T, et al. Single microbubble response using pulse sequences: initial results. Ultrasound Med Biol. 2009;35(1): 112-119.
57. Eckersley RJ, Chin CT, Burns PN. Optimising phase and amplitude modulation schemes for imaging microbubble contrast agents at low acoustic power. Ultrasound Med Biol. 2005;31(2):213-219.
58. Wilson SR, Jang HJ, Kim TK, et al. Real-time temporal maximum-intensity-projection imaging of hepatic lesions with contrast-enhanced sonography. AJR Am J Roentgenol. 2008;190(3):691-695.
59. Kim TK, Jang HJ, Burns PN, et al. Focal nodular hyperplasia and hepatic adenoma: differentiation with low-mechanical-index contrast-enhanced sonography. AJR Am J Roentgenol. 2008;190(1):58-66.
60. Dayton PA, Morgan KE, Klibanov AL, et al. Optical and acoustical observations of the effects of ultrasound on contrast agents. IEEE Trans Ultrason Ferroelectr Freq Control. 1999;46(1):220-232.
61. de Jong N, Frinking PJ, Bouakaz A, et al. Optical imaging of contrast agent microbubbles in an ultrasound field with a 100-MHz camera. Ultrasound Med Biol. 2000;26(3):487-492.
62. Uhlendorf V, Scholle FD. Imaging of spatial distribution and flow of microbubbles using nonlinear acoustic properties. Acoust Imaging. 1996;22:233-238.
63. Becher H, Burns P. Handbook of contrast echocardiography: left ventricle function and myocardial perfusion. New York: Springer; 2000.
64. Porter TR, Xie F. Transient myocardial contrast after initial exposure to diagnostic ultrasound pressures with minute doses of intravenously injected microbubbles. Demonstration and potential mechanisms. Circulation. 1995;92(9):2391-2395.
65. Burns PN. Interpretation of Doppler ultrasound signals. In: Burns PN, Taylor KJ, Wells PNT, editors. Clinical applications of Doppler ultrasound. 2nd ed. New York: Raven Press; 1996.
66. Masugata H, Peters B, Lafitte S, et al. Quantitative assessment of myocardial perfusion during graded coronary stenosis by real-time myocardial contrast echo refilling curves. J Am Coll Cardiol. 2001;37(1):262-269.
67. Wei K, Jayaweera AR, Firoozan S, et al. Quantification of myocardial blood flow with ultrasound-induced destruction of microbubbles administered as a constant venous infusion. Circulation. 1998;97(5):473-483.
68. Hudson JM, Karshafian R, Burns PN. Quantification of flow using ultrasound and microbubbles: a disruption replenishment model based on physical principles. Ultrasound Med Biol. 2009;35(12):2007-2020.
69. Kerbel R, Folkman J. Clinical translation of angiogenesis inhibitors. Nat Rev Cancer. 2002;2(10):727-739.
70. Goertz DE, Yu JL, Kerbel RS, et al. High-frequency Doppler ultrasound monitors the effects of antivascular therapy on tumor blood flow. Cancer Res. 2002;62(22):6371-6375.
71. Lassau N, Lamuraglia M, Vanel D, et al. Doppler US with perfusion software and contrast medium injection in the early evaluation of isolated limb perfusion of limb sarcomas: prospective study of 49 cases. Ann Oncol. 2005;16(7):1054-1060.
72. Lassau N, Lamuraglia M, Chami L, et al. Gastrointestinal stromal tumors treated with imatinib: monitoring response with contrast-enhanced sonography. AJR Am J Roentgenol. 2006;187(5):1267-1273.
73. Eggermont AM. Evolving imaging technology: contrast-enhanced Doppler ultrasound is early and rapid predictor of tumour response. Ann Oncol. 2005;16(7):995-996.
74. Weskott HP. Emerging roles for contrast-enhanced ultrasound. Clin Hemorheol Microcirc. 2008;40(1):51-71.
75. Hudson JM, Williams R, Tremblay-Darveau C, et al. Dynamic contrast enhanced ultrasound for therapy monitoring. Eur J Radiol. 2015;84(9): 1650-1657.
76. Claudon M, Dietrich CF, Choi BI, et al. Guidelines and good clinical practice recommendations for contrast enhanced ultrasound (CEUS) in the liver—update 2012: a WFUMB-EFSUMB initiative in cooperation with representatives of AFSUMB, AIUM, ASUM, FLAUS and ICUS. Ultrasound Med Biol. 2013;39(2):187-210.
77. Hynynen K, McDannold N, Vykhodtseva N, et al. Focal disruption of the blood-brain barrier due to 260-kHz ultrasound bursts: a method for molecular imaging and targeted drug delivery. J Neurosurg. 2006;105(3):445-454.
78. American Institute of Ultrasound in Medicine (AIUM). Mechanical bioeffects from diagnostic ultrasound: AIUM consensus statements. J Ultrasound Med. 2000;19:120-142.
79. Brennen C. Cavitation and bubble dynamics. New York: Oxford University Press; 1995.
80. Plesset MS. The dynamics of cavitation bubbles. J Appl Mech. 1949;16:272-282.
81. Poritsky H, editor. The collapse or growth of a spherical bubble or cavity in a viscous fluid. First US National Congress on Applied Mechanics; 1951.
82. Williams AR, Kubowicz G, Cramer E, Schlief R. The effects of the microbubble suspension SH U 454 (Echovist) on ultrasound-induced cell lysis in a rotating tube exposure system. Echocardiography. 1991;8(4):423-433.
83. Miller DL, Thomas RM. Ultrasound contrast agents nucleate inertial cavitation in vitro. Ultrasound Med Biol. 1995;21(8):1059-1065.
84. Miller MW, Miller DL, Brayman AA. A review of in vitro bioeffects of inertial ultrasonic cavitation from a mechanistic perspective. Ultrasound Med Biol. 1996;22(9):1131-1154.
85. Miller DL, Gies RA, Chrisler WB. Ultrasonically induced hemolysis at high cell and gas body concentrations in a thin-disc exposure chamber. Ultrasound Med Biol. 1997;23(4):625-633.
86. Holland CK, Roy RA, Apfel RE, Crum LA. In vitro detection of cavitation induced by a diagnostic ultrasound system. IEEE Trans Ultrason Ferroelectr Freq Control. 1992;39(1):95-101.
87. Everbach EC, Makin IR, Francis CW, Meltzer RS. Effect of acoustic cavitation on platelets in the presence of an echo-contrast agent. Ultrasound Med Biol. 1998;24(1):129-136.
88. ter Haar GR. Ultrasonic contrast agents: safety considerations reviewed. Eur J Radiol. 2002;41(3):217-221.
89. Barnett SB, Ter Haar GR, Ziskin MC, et al. International recommendations and guidelines for the safe use of diagnostic ultrasound in medicine. Ultrasound Med Biol. 2000;26(3):355-366.
90. Bouakaz A, de Jong N. WFUMB safety symposium on echo-contrast agents: nature and types of ultrasound contrast agents. Ultrasound Med Biol. 2007;33(2):187-196.
91. Kitzman DW, Goldman ME, Gillam LD, et al. Efficacy and safety of the novel ultrasound contrast agent perflutren (Definity) in patients with suboptimal baseline left ventricular echocardiographic images. Am J Cardiol. 2000;86(6):669-674.
92. Piscaglia F, Bolondi L, Italian Society for Ultrasound in Medicine and Biology (SIUMB) Study Group on Ultrasound Contrast Agents. The safety of SonoVue

in abdominal applications: retrospective analysis of 23188 investigations. Ultrasound Med Biol. 2006;32(9):1369-1375.
93. Kaufman DW. Risk of anaphylaxis in a hospital population in relation to the use of various drugs: an international study. Pharmacoepidemiol Drug Saf. 2003;12(3):195-202.
94. Kusnetzky LL, Khalid A, Khumri TM, et al. Acute mortality in hospitalized patients undergoing echocardiography with and without an ultrasound contrast agent: results in 18,671 consecutive studies. J Am Coll Cardiol. 2008;51:1704-1706.
95. Main ML, Ryan AC, Davis TE, et al. Acute mortality in hospitalized patients undergoing echocardiography with and without an ultrasound contrast agent (multicenter registry results in 4,300,966 consecutive patients). Am J Cardiol. 2008;102(12):1742-1746.
96. Main M. Ultrasound contrast agent safety: from anecdote to evidence. JACC Cardiovasc Imaging. 2009;2(9):1057-1059.
97. US Food and Drug Administration (FDA). Micro-bubble Contrast Agents (marketed as Definity (Perflutren Lipid Microsphere) Injectable Suspension and Optison (Perflutren Protein-Type Microspheres for Injection). 2008. Available from: http://www.fda.gov/Safety/MedWatch/SafetyInformation/SafetyAlertsforHumanMedicalProducts/ucm092270.htm.
98. Health_Canada. Updated safety information on DEFINITY (Perflutren Injectable Suspension). Available from: http://www.hc-sc.gc.ca/dhp-mps/medeff/advisories-avis/prof/_2008/definity_hpc-cps_2-eng.php.
99. Wilson SR, Burns PN. Microbubble-enhanced US in body imaging: what role? Radiology. 2010;257(1):24-39.
100. Rychak JJ, Lindner JR, Ley K, Klibanov AL. Deformable gas-filled microbubbles targeted to P-selectin. J Control Release. 2006;114(3):288-299.
101. Christiansen JP, Lindner JR. Molecular and cellular imaging with targeted contrast ultrasound. Proc IEEE. 2005;93:809-818.
102. Klibanov AL, Rychak JJ, Yang WC, et al. Targeted ultrasound contrast agent for molecular imaging of inflammation in high-shear flow. Contrast Media Mol Imaging. 2006;1(6):259-266.
103. Rychak JJ, Graba J, Cheung AM, et al. Microultrasound molecular imaging of vascular endothelial growth factor receptor 2 in a mouse model of tumor angiogenesis. Mol Imaging. 2007;6(5):289-296.
104. Behm CZ, Lindner JR. Cellular and molecular imaging with targeted contrast ultrasound. Ultrasound Q. 2006;22(1):67-72.
105. Pochon S, Tardy I, Bussat P, et al. BR55: a lipopeptide-based VEGFR2-targeted ultrasound contrast agent for molecular imaging of angiogenesis. Invest Radiol. 2010;45(2):89-95.
106. Brooks JD, Gambhir SS, Lutz A, Wilmann JK. A pilot clinical trial using BR55 ultrasound contrast agent in the assessment of prostate cancer by molecular imaging of VEGFR2. Stanford University. 2016. Available from: http://med.stanford.edu/clinicaltrials/trials/NCT02142608.
107. Liu Y, Miyoshi H, Nakamura M. Encapsulated ultrasound microbubbles: therapeutic application in drug/gene delivery. J Control Release. 2006;114(1):89-99.
108. Leong-Poi H, Kuliszewski MA, Lekas M, et al. Therapeutic arteriogenesis by ultrasound-mediated VEGF165 plasmid gene delivery to chronically ischemic skeletal muscle. Circ Res. 2007;101(3):295-303.
109. Williams R, Wright C, Cherin E, et al. Characterization of submicron phase-change perfluorocarbon droplets for extravascular ultrasound imaging of cancer. Ultrasound Med Biol. 2013;39(3):475-489.
110. Giesecke T, Hynynen K. Ultrasound-mediated cavitation thresholds of liquid perfluorocarbon droplets in vitro. Ultrasound Med Biol. 2003;29(9):1359-1365.

CHAPTER 4

The Liver

Stephanie R. Wilson and Cynthia E. Withers

SUMMARY OF KEY POINTS

- The liver is an ideal organ for sonographic evaluation based on its large size, homogeneous parenchyma, and location high in the abdomen with access provided from both a subcostal and an intercostal approach.
- Standard ultrasound with real-time gray-scale morphologic assessment and Doppler evaluation of the liver vasculature is augmented by newer techniques of contrast-enhanced ultrasound and elastography.
- Fatty liver is considered an epidemic in North America, and ultrasound is often the first test to suggest its presence and severity.
- Ultrasound performed at 6-month intervals is the recommended surveillance method for detection of nodules in the liver of those at risk for the development of hepatocellular carcinoma.
- Ultrasound is the method of choice for the guidance of interventional procedures performed on the liver, including ablation techniques in those with malignant tumors, biopsy of liver masses, and the insertion of therapeutic devices such as drainage tubes and transjugular intrahepatic portosystemic shunts.
- Intraoperative ultrasound of the liver allows for detection of previously unidentified tumors.

CHAPTER OUTLINE

SONOGRAPHIC TECHNIQUE
NORMAL ANATOMY
Couinaud Anatomy
Ligaments
Hepatic Circulation
Portal Veins
Arterial Circulation
Hepatic Venous System
Normal Liver Size and Echogenicity
DEVELOPMENTAL ANOMALIES
Agenesis
Anomalies of Position
Accessory Fissures
Vascular Anomalies
CONGENITAL ABNORMALITIES
Liver Cyst
Peribiliary Cysts
Autosomal Dominant Polycystic Disease
Biliary Hamartomas (von Meyenburg Complexes)
INFECTIOUS DISEASES
Viral Hepatitis
Clinical Manifestations
Bacterial Diseases
Fungal Diseases: Candidiasis
Parasitic Diseases
Amebiasis
Hydatid Disease
Schistosomiasis
Pneumocystis carinii
DISORDERS OF METABOLISM
Fatty Liver
Glycogen Storage Disease (Glycogenosis)
Cirrhosis
Doppler Ultrasound Characteristics
Elastography
VASCULAR ABNORMALITIES
Portal Hypertension
Portal Vein Thrombosis
Budd-Chiari Syndrome
Portal Vein Aneurysm
Intrahepatic Portosystemic Venous Shunts
Aneurysm, Pseudoaneurysm, and Dissection
Hereditary Hemorrhagic Telangiectasia
Peliosis Hepatis
HEPATIC MASSES
Liver Mass Characterization
Role of Microbubble Contrast Agents
Liver Mass Detection
HEPATIC NEOPLASMS
Benign Hepatic Neoplasms
Cavernous Hemangioma
Focal Nodular Hyperplasia
Hepatic Adenoma
Fatty Tumors: Hepatic Lipomas and Angiomyolipomas
Malignant Hepatic Neoplasms
Hepatocellular Carcinoma
Hemangiosarcoma (Angiosarcoma)
Hepatic Epithelioid Hemangioendothelioma
Metastatic Liver Disease
HEPATIC TRAUMA
Portosystemic Shunts
Transjugular Intrahepatic Portosystemic Shunts
PERCUTANEOUS LIVER BIOPSY
INTRAOPERATIVE ULTRASOUND
Acknowledgment

The liver is the largest organ in the human body, weighing approximately 1500 g in the adult. Because it is frequently involved in systemic and local disease, sonographic examination is often requested to assess hepatic abnormality.

SONOGRAPHIC TECHNIQUE

The liver is best examined with real-time sonography. Both supine and right anterior oblique positions should be used. Sagittal, transverse, coronal, and subcostal oblique views are suggested using both a standard abdominal transducer and a higher-frequency transducer. In many patients, the liver is tucked beneath the lower right ribs, so a transducer with a small scanning face, allowing an intercostal approach, is invaluable. Further, **volumetric imaging** contributes greatly to the evaluation of the liver as a single, appropriately selected acquisition may show virtually the entire liver, allowing for a rapid portrayal of liver anatomy, size, texture, and surface characteristics.[1] Therefore differentiation of the diffuse changes of cirrhosis and fatty liver from normal are enhanced by review of the videos (Videos 4.1 and 4.2) of the acquisitions as well as the multiplanar reconstructions (Fig. 4.1). Ultrasound also best demonstrates the relationship of focal liver masses to the vital vascular structures if surgical resection is contemplated.

NORMAL ANATOMY

The liver lies in the right upper quadrant of the abdomen. Functionally, it can be divided into three lobes: right, left, and caudate. The **right lobe** of the liver is separated from the left by the **main lobar fissure,** which passes through the gallbladder fossa to the **inferior vena cava** (IVC) (Fig. 4.2). The right lobe of the liver can be further divided into anterior and posterior segments by the **right intersegmental fissure.** The **left intersegmental fissure** divides the **left lobe** into medial and lateral segments. The **caudate lobe** is situated on the posterior aspect of the liver, with the IVC as its posterior border and the fissure for the ligamentum venosum as its anterior border (Fig. 4.3). The **papillary process** is the anteromedial extension of the caudate

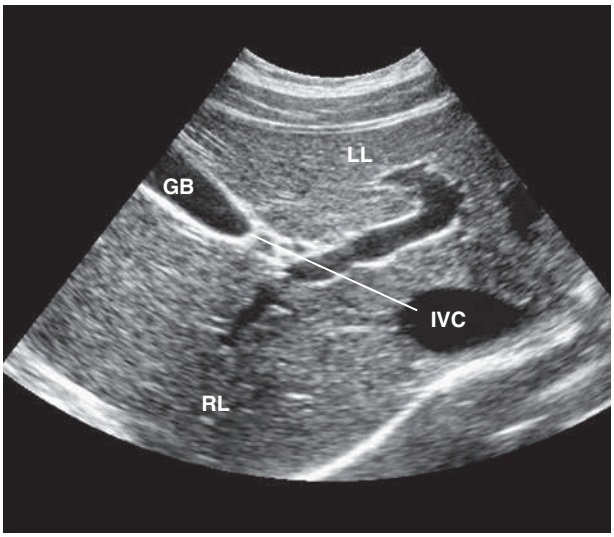

FIG. 4.2 Normal Lobar Anatomy. Right lobe of the liver *(RL)* can be separated from left lobe of the liver *(LL)* by the main lobar fissure that passes through the gallbladder fossa *(GB)* and inferior vena cava *(IVC)*.

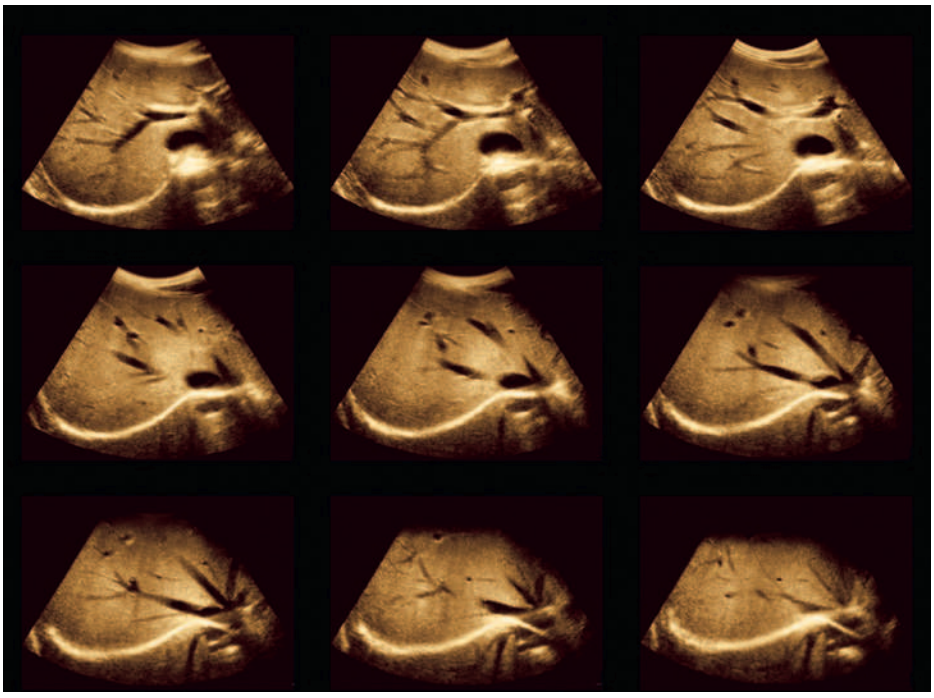

FIG. 4.1 Normal Liver. Liver shown in a nine-on-one format from a volumetric acquisition acquired in the axial plane, with the center point on the long axis of the portal veins at the porta hepatis.

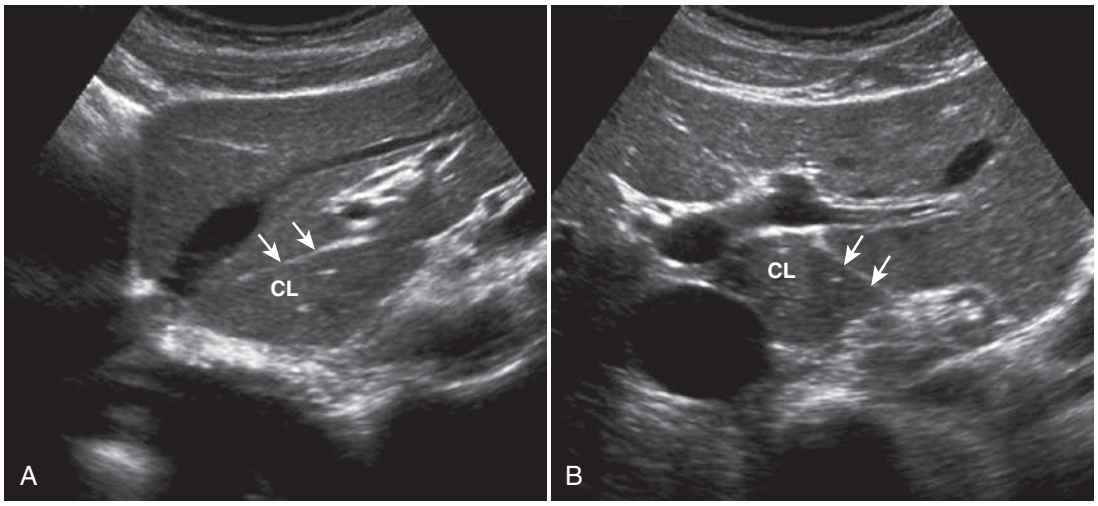

FIG. 4.3 Caudate Lobe. (A) Sagittal view and **(B)** transverse view show the caudate lobe *(CL)* separated from the left lobe by the fissure for the ligamentum venosum *(arrows)* anteriorly. Posterior is the inferior vena cava.

FIG. 4.4 Hepatic Venous Anatomy. The three hepatic veins—right *(RHV)*, middle *(MHV)*, and left *(LHV)*—are interlobar and intersegmental, separating the lobes and segments. At the level of the hepatic venous confluence with the inferior vena cava, the right hepatic vein separates the right posterior segment (segment 7) from the right anterior segment (segment 8). The left hepatic vein separates the left medial segment from the left lateral segment. The middle hepatic vein separates the right and left lobes. As shown here, the hepatic veins are best seen on a subcostal oblique view.

lobe, which may appear separate from the liver and mimic lymphadenopathy.

Understanding the vascular anatomy of the liver is essential to an appreciation of the relative positions of the hepatic segments. The major **hepatic veins** course between the lobes and segments (interlobar and intersegmental). They are ideal segmental boundaries but are visualized only when scanning the superior liver (Fig. 4.4). The **middle hepatic vein** courses within the main lobar fissure and separates the anterior segment of the right lobe from the medial segment of the left. The **right hepatic vein** runs within the right intersegmental fissure and divides the right lobe into anterior and posterior segments. In more caudal sections of the liver, the right hepatic vein is no longer identified; therefore the segmental boundary becomes a poorly defined division between the anterior and posterior branches of the right portal vein. The major branches of the right and left **portal veins** run centrally within the segments **(intrasegmental),** with the exception of the ascending portion of the left portal vein, which runs in the left intersegmental fissure. The left intersegmental fissure, which separates the medial segment of the left lobe from the lateral segment, can be divided into cranial, middle, and caudal sections. The **left hepatic vein** forms the boundary of the cranial third, the ascending branch of the left portal vein represents the middle third, and the fissure for the ligamentum teres acts as the most caudal division of the left lobe (Table 4.1).[2]

Couinaud Anatomy

Because sonography allows evaluation of liver anatomy in multiple planes, lesions can be localized to specific segments. This can aid surgical planning and follow-up of lesions over time. **Couinaud anatomy** is now the universal nomenclature for hepatic lesion localization (Table 4.2).[3] This description is based on **portal segments** and is of both **functional** and **pathologic** importance. Each segment has its own blood supply (arterial, portal venous, and hepatic venous), lymphatics, and biliary drainage. Thus the surgeon may resect a segment of a hepatic lobe, providing the vascular supply to the remaining lobe is left intact. Each segment has a branch or branches of the portal vein at its center, bounded by a hepatic vein. There are **eight segments.** The right, middle, and left hepatic veins divide the liver longitudinally into four sections. Each of these sections is further divided transversely by an imaginary plane through the right main and left main portal pedicles. **Segment I** is the caudate lobe, **segments II and III** are the left superior and inferior lateral segments, respectively, and **segment IV,** which is further divided into IVa and IVb, is

TABLE 4.1 Structures Useful for Identifying Hepatic Segments

Structure	Location	Usefulness
Right hepatic vein	Right intersegmental fissure	Divides cephalic aspect of anterior and posterior segments of right lobe
Middle hepatic vein	Main lobar fissure	Separates right and left lobes
Left hepatic vein	Left intersegmental fissure	Divides cephalic aspect of medial and lateral segments of left lobe
Right portal vein (RPV) (anterior branch)	Intrasegmental in anterior segment of right lobe	Courses centrally in anterior segment of right lobe
RPV (posterior branch)	Intrasegmental in posterior segment of right lobe	Courses centrally in posterior segment of right lobe
Left portal vein (LPV) (horizontal segment)	Anterior to caudate lobe	Separates caudate lobe posteriorly from medial segment of left lobe anteriorly
LPV (ascending segment)	Left intersegmental fissure	Divides medial from lateral segment of left lobe
Gallbladder fossa	Main lobar fissure	Separates right and left lobes
Fissure for ligamentum teres	Left intersegmental fissure	Divides caudal aspect of left lobe into medial and lateral segments
Fissure for ligamentum venosum	Left anterior margin of caudate lobe	Separates caudate lobe posteriorly from left lobe anteriorly

Modified from Marks W, Filly R, Callen P. Ultrasonic anatomy of the liver: a review with new applications. J Clin Ultrasound. 1979;7(2):137-146.[2]

TABLE 4.2 Couinaud Segments and Traditional Hepatic Anatomy

Couinaud	Traditional
Segment I	Caudate lobe
Segment II	Lateral segment left lobe (superior)
Segment III	Lateral segment left lobe (inferior)
Segment IV	Medial segment left lobe
Segment V	Anterior segment right lobe (inferior)
Segment VI	Posterior segment right lobe (inferior)
Segment VII	Posterior segment right lobe (superior)
Segment VIII	Anterior segment right lobe (superior)

the medial segment of the left lobe. The right lobe consists of **segments V and VI,** located caudal to the transverse plane, and **segments VII and VIII,** which are cephalad[4,5] (Fig. 4.5). The caudate lobe (segment I) may receive branches of both the right and the left portal vein. In contrast to the other segments, segment I has one or several hepatic veins that drain directly into the IVC.

The portal venous supply for the left lobe can be visualized using an oblique, cranially angled subxiphoid view. A "recumbent H" is formed by the main left portal vein, the ascending branch of the left portal vein, and the branches to segments II, III, and IV[6] (Fig. 4.6). Segments II and III are separated from segment IV by the left hepatic vein, as well as by the ascending branch of the left portal vein and the falciform ligament. Segment IV is separated from segments V and VIII by the middle hepatic vein and the main hepatic fissure.

The portal venous supply to the right lobe of the liver can also be seen as a recumbent H. The main right portal vein gives rise to branches that supply segments V and VI (inferiorly) and VII and VIII (superiorly). They are seen best in a sagittal or oblique sagittal plane.[6]

The oblique subxiphoid view shows the right portal vein in cross section and enables identification of the more superiorly located segment VIII (closer to confluence of hepatic veins) from segment V. Segments V and VIII are separated from segments VI and VII by the right hepatic vein.[6]

Ligaments

The liver is covered by a thin connective tissue layer called **Glisson capsule.** The capsule surrounds the entire liver and is thickest around the IVC and the porta hepatis. At the porta hepatis, the main portal vein, the proper hepatic artery, and the common bile duct are contained within investing peritoneal folds known as the **hepatoduodenal ligament** (Fig. 4.7). The **falciform ligament** conducts the umbilical vein to the liver during fetal development (Fig. 4.8). After birth, the umbilical vein atrophies, forming the **ligamentum teres** (Fig. 4.9). As the falciform ligament reaches the liver, its leaves separate. The right layer forms the upper layer of the coronary ligament; the left layer forms the upper layer of the left triangular ligament. The most lateral portion of the coronary ligament is known as the right triangular ligament (Fig. 4.10). The peritoneal layers that form the coronary ligament are widely separated, leaving an area of the liver not covered by peritoneum. This posterosuperior region is known as the **bare area** of the liver. The **ligamentum venosum** carries the obliterated ductus venosus, which until birth shunts blood from the umbilical vein to the IVC.

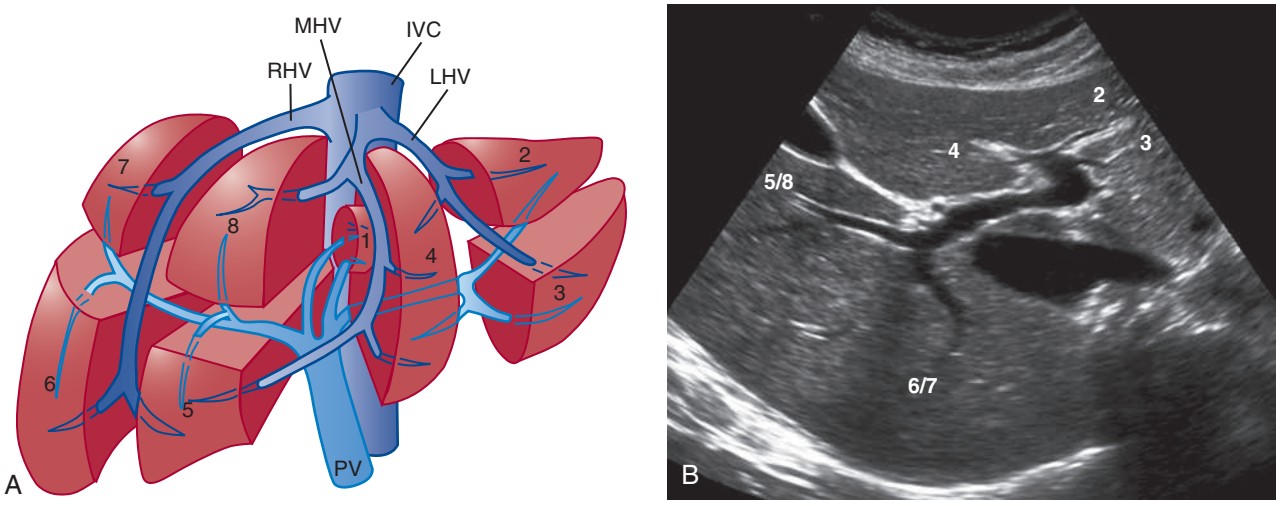

FIG. 4.5 Couinaud Functional Segmental Anatomy. (A) The liver is divided into nine segments. Blue longitudinal boundaries (right, middle, and left scissurae) are three hepatic veins. Transverse plane is defined by right main and left main portal pedicles. Segment I, caudate lobe, is situated posteriorly. **(B)** Corresponding sonogram shows the main portal vein with its right and left branches. The plane through the right and left branches is the transverse separation of the liver segments. Cephalad to this level lie segments II, IVa, VII, and VIII. Caudally located are segments III, IVb, V, and VI. *GB,* Gallbladder; *LHV,* left hepatic vein; *LPV,* left portal vein; *MHV,* middle hepatic vein; *RHV,* right hepatic vein; *RPV,* right portal vein. (With permission from Sugarbaker PH: Toward a standard of nomenclature for surgical anatomy of the liver. Neth J Surg. 1988;PO:100.[5])

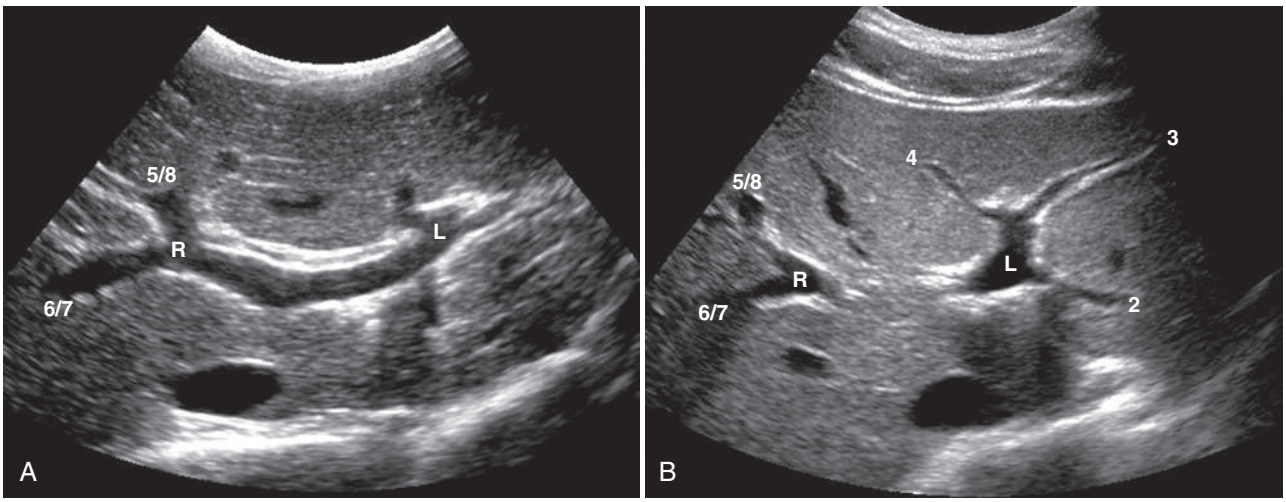

FIG. 4.6 Portal Venous Anatomy in Two Patients. (A) Best seen with a subcostal oblique view, the main portal vein is formed by the union of the right and left portal venous branches at the porta hepatis. **(B)** Segmental branches of the right and left portal veins are marked. Well seen is the recumbent-H shape of the left portal venous bifurcation, made from the ascending and horizontal left portal vein and the segmental branches to 2, 3, and 4.

Hepatic Circulation

Portal Veins

The liver receives a **dual blood supply** from both the portal vein and the hepatic artery. Although the portal vein carries incompletely oxygenated (80%) venous blood from the intestines and spleen, it supplies up to half the oxygen requirements of the hepatocytes because of its greater flow. This dual blood supply explains the low incidence of hepatic infarction.

The **portal triad** contains a branch of the portal vein, hepatic artery, and bile duct. These are contained within a connective tissue sheath that gives the portal vein an echogenic wall on sonography and that distinguishes it from the hepatic veins, which have an almost imperceptible wall. The **main portal vein** divides into right and left branches. The **right portal vein** has an anterior branch that lies centrally within the anterior segment of the right lobe and a posterior branch that lies centrally within the posterior segment of the right lobe. The **left portal vein** initially courses anterior to the caudate lobe. The ascending branch of the left portal vein then travels anteriorly in the left intersegmental fissure to divide the medial and lateral segments of the left lobe.

Arterial Circulation

The branches of the **hepatic artery** accompany the portal veins. The terminal branches of the portal vein and their accompanying hepatic arterioles and bile ducts are known as the **acinus.**

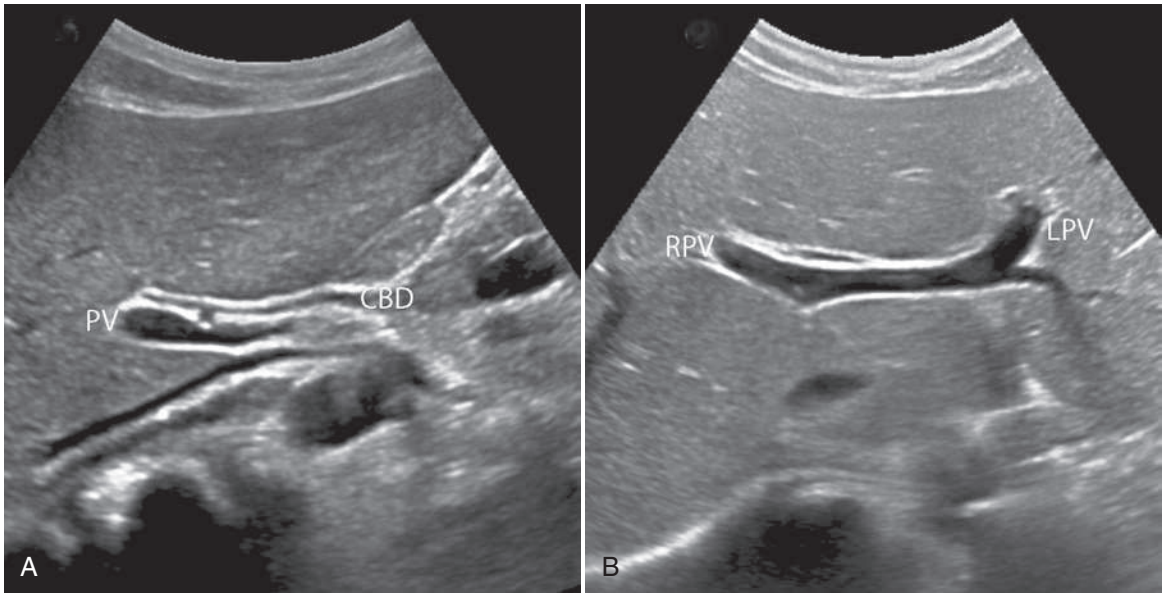

FIG. 4.7 Porta Hepatis. (A) Sagittal image of the porta hepatis shows the common bile duct *(CBD)* and main portal vein *(PV)*, which are enclosed within the hepatoduodenal ligament. **(B)** Transverse image of the porta hepatis shows the right *(RPV)* and left portal vein *(LPV)* branches.

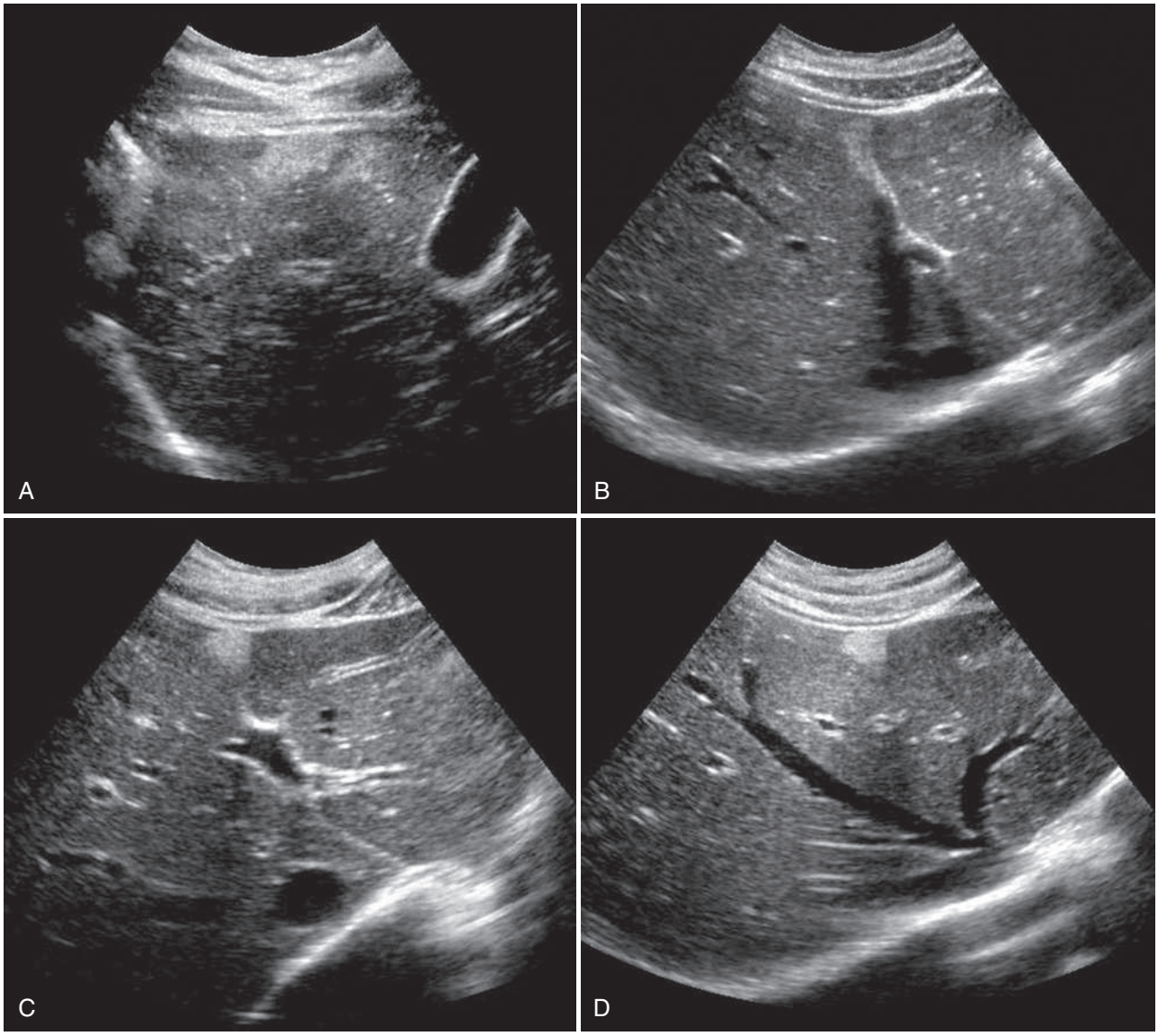

FIG. 4.8 Falciform Ligament. Contained fat helps in its localization. **(A)** Sagittal image through falciform ligament. **(B)** Subcostal oblique view of falciform ligament. **(C)** Location of the fat just anterior to the ascending branch of the left ascending portal vein branch. **(D)** Cephalad extent of the fat in the location of the ligament between the middle and the left hepatic veins.

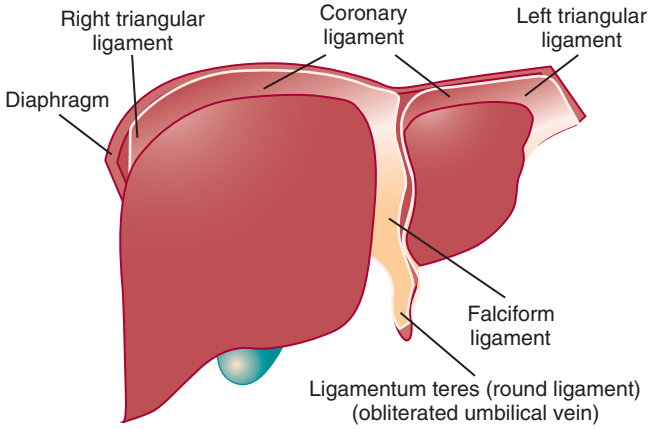

FIG. 4.9 Hepatic Ligaments. Diagram of anterior surface of the liver.

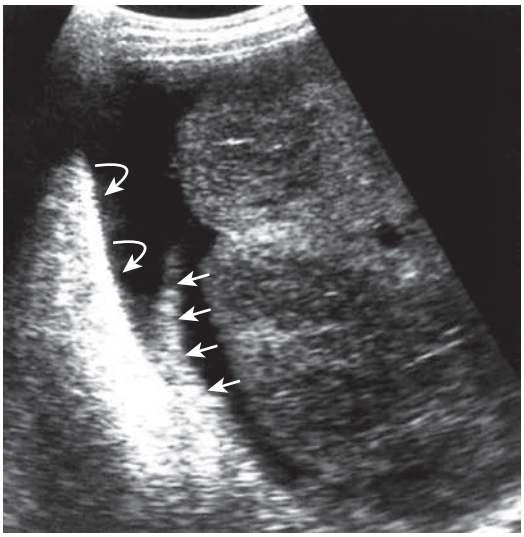

FIG. 4.10 Right Triangular Ligament. Subcostal oblique scan near dome of right hemidiaphragm *(curved arrows)*. Note lobulated contour and inhomogeneity of liver in this patient with cirrhosis. Right triangular ligament *(straight arrows)* is visualized because of ascites.

Hepatic Venous System

Blood perfuses the liver parenchyma through the sinusoids and then enters the terminal hepatic venules. These terminal branches unite to form sequentially larger veins. The hepatic veins vary in number and position. However, in the general population, there are three major veins: the right, middle, and left hepatic veins (see Fig. 4.4). All drain into the IVC and, as with the portal veins, are without valves. As discussed earlier, the right hepatic vein is usually single and runs in the right intersegmental fissure, separating the anterior and posterior segments of the right lobe. The middle hepatic vein, which courses in the main lobar fissure, forms a common trunk with the left hepatic vein in most cases. The left hepatic vein forms the most cephalad boundary between the medial and lateral segments of the left lobe.

Normal Liver Size and Echogenicity

The upper border of the liver lies approximately at the level of the fifth intercostal space at the midclavicular line. The lower border extends to or slightly below the costal margin. An accurate assessment of **liver size** is difficult with real-time ultrasound equipment because of the limited field of view. Gosink and Leymaster[7] proposed measuring the liver length in the midhepatic line. In 75% of patients with a liver length of greater than 15.5 cm, hepatomegaly is present. Niederau et al.[8] measured the liver in a longitudinal and anteroposterior diameter in both the midclavicular line and the midline and correlated these findings with gender, age, height, weight, and body surface area. They found that organ size increases with height and body surface area and decreases with age. The **mean longitudinal diameter** of the liver in the midclavicular line in this study was 10.5 cm, with standard deviation (SD) of 1.5 cm, and the mean midclavicular anteroposterior diameter was 8.1 cm (SD 1.9 cm). In most patients, measurement of the liver length suffices to measure liver size. **Riedel lobe** is a tonguelike extension of the inferior tip of the right lobe of the liver, frequently found in asthenic women.

The normal liver is homogeneous, contains fine-level echoes, and is either minimally hyperechoic or isoechoic compared to the normal renal cortex (Fig. 4.11A). The liver is hypoechoic compared to the spleen. This relationship is evident when the lateral segment of the left lobe is elongated and wraps around the spleen (Fig. 4.11B).

DEVELOPMENTAL ANOMALIES

Agenesis

Agenesis of the liver is incompatible with life. Agenesis of either right or left lobes has been reported.[9,10] In three of five reported cases of agenesis of the right lobe, the caudate lobe was also absent.[9] Compensatory hypertrophy of the remaining lobes normally occurs, and results of liver function tests (LFTs) are normal.

Anomalies of Position

In **situs inversus totalis (viscerum),** the liver is found in the left hypochondrium. In congenital **diaphragmatic hernia** or **omphalocele,** varying amounts of liver may herniate into the thorax or outside the abdominal cavity.

Accessory Fissures

Although invaginations of the dome of the diaphragm have been called "accessory fissures," these are not true fissures but rather **diaphragmatic slips.** They are a cause of pseudomasses on sonography if the liver is not carefully examined in both sagittal and transverse planes (Fig. 4.12). *True* accessory fissures are uncommon and are caused by an infolding of peritoneum. The inferior accessory hepatic fissure is a true accessory fissure that stretches inferiorly from the right portal vein to the inferior surface of the right lobe of the liver.[11]

Vascular Anomalies

The **common hepatic artery** arises from the celiac axis and divides into right and left branches at the porta hepatis. This classic textbook description of the hepatic arterial anatomy occurs

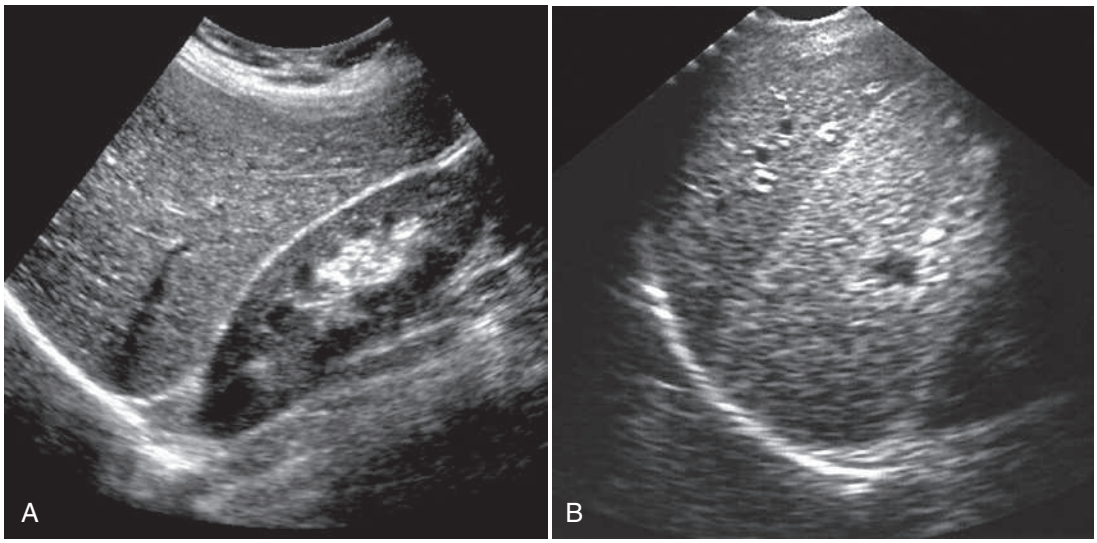

FIG. 4.11 Normal Liver Echogenicity. (A) The liver is more echogenic than the renal cortex. **(B)** The liver is less echogenic than the spleen, as seen in many thin women, whose left lobe of the liver wraps around the spleen.

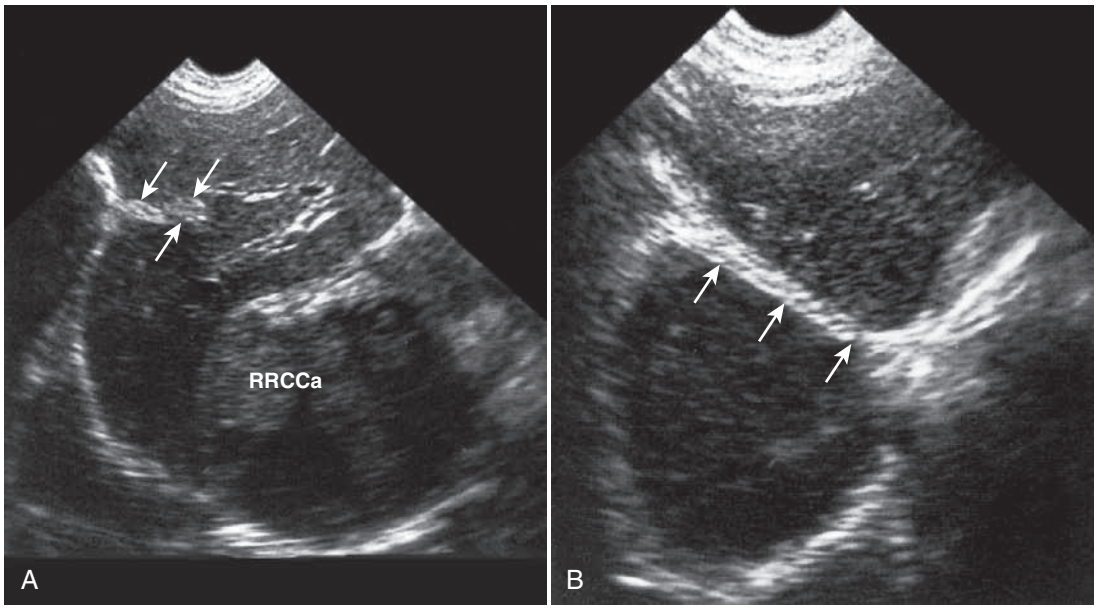

FIG. 4.12 Diaphragmatic Slip. (A) Sagittal sonogram shows echogenic mass *(arrows)* adjacent to right hemidiaphragm in this patient with right **renal cell carcinoma** *(RRCCa)*. **(B)** Subcostal oblique image reveals mass is diaphragmatic slip *(arrows)*.

in only 55% of the population. The remaining 45% have some variation of this anatomy, the main patterns of which are (1) replaced left hepatic artery originating from the left gastric artery (10%), (2) replaced right hepatic artery originating from the superior mesenteric artery (11%), and (3) replaced common hepatic artery originating from the superior mesenteric artery (2.5%).

Congenital portal vein anomalies include atresias, strictures, and obstructing valves, all of which are uncommon. Other variations of anatomy include absence of the right portal vein, with anomalies of branching from the main and left portal veins, and absence of the horizontal segment of the left portal vein.[12]

In contrast, variations in the branching of the hepatic veins and accessory hepatic veins are relatively common. The most common accessory vein drains the superoanterior segment of the right lobe (segment VIII) and is seen in approximately one-third of the population. It usually empties into the middle hepatic vein, although occasionally it joins the right hepatic vein.[13] An inferior right hepatic vein, which drains the inferoposterior portion of the liver (segment VI), is observed in 10% of individuals. This inferior right hepatic vein drains directly into the IVC and may be as large as the right hepatic vein or larger.[14] Left and right marginal veins, which drain into the left and right hepatic veins, occur in about 12% and 3% of individuals, respectively.

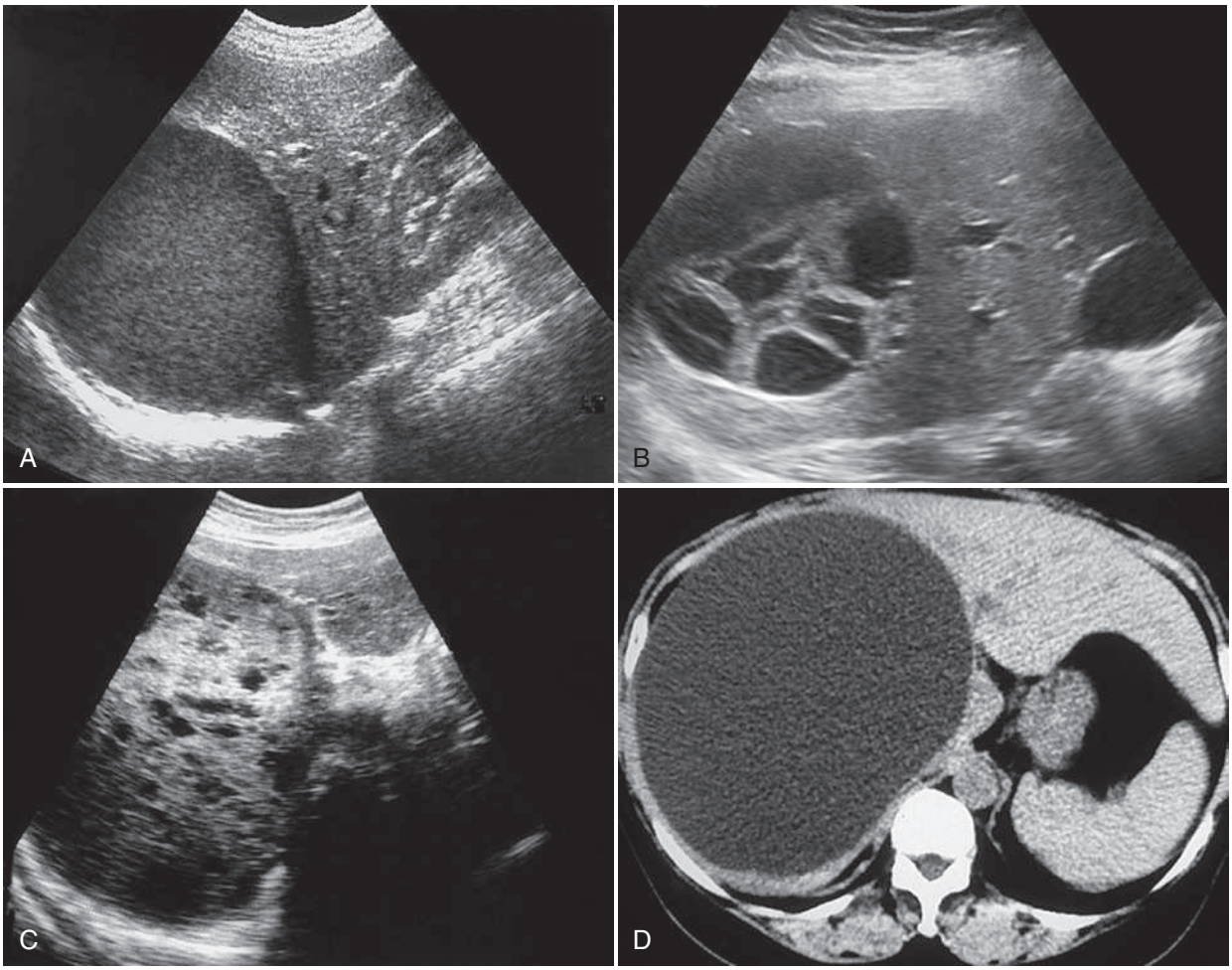

FIG. 4.13 Liver Cysts Complicated by Hemorrhage in Three Patients. **(A)** Patient presented with acute right upper quadrant pain. Ultrasound shows a thin-walled liver cyst filled with uniform low-level echogenicity consistent with blood products within the cyst. **(B)** This liver cyst shows thick internal septations (which were not vascular), consistent with organized thrombus. **(C)** and **(D)** Patient on ultrasound and on computed tomography (CT) scan. The cyst appears virtually solid on ultrasound because of organized clot, but there is enhanced through transmission. On CT, the cyst appears more homogenous.

Absence of the main hepatic veins is relatively less common, occurring in about 8% of people.[14] Awareness of the normal variations of the hepatic venous system is helpful in accurately defining the location of focal liver lesions and aids the surgeon in segmental liver resection.

CONGENITAL ABNORMALITIES

Liver Cyst

A liver cyst is defined as a fluid-filled space with an epithelial lining. Abscesses, parasitic cysts, and posttraumatic cysts therefore are not *true* cysts. The frequent presence of columnar epithelium within simple hepatic cysts suggests they have a ductal origin, although their precise cause is unclear. Their presentation at middle age is also unclear. Sonographically visualized liver cysts occur in 2.5% of the general population, increasing to 7% in the population older than 80 years.[15]

On sonographic examination, **benign hepatic cysts** are anechoic with a thin, well-demarcated wall and posterior acoustic enhancement. Occasionally, the patient may develop pain and fever secondary to cyst hemorrhage or infection. In these patients the cyst may contain internal echoes and septations (Fig. 4.13A and B), may have a thickened wall, or may appear solid (see Fig. 4.13C). Active intervention is recommended only in symptomatic patients. Although aspiration will yield fluid for evaluation, the cyst with an epithelial lining will recur. Cyst ablation with alcohol can be performed using ultrasound guidance.[16] If thick septae or nodules are seen within liver cysts, computed tomography (CT) or contrast-enhanced ultrasound is recommended because **biliary cystadenomas** and **cystic metastases** must be considered in the differential diagnosis of complex-appearing liver cysts (Fig. 4.14).

Peribiliary Cysts

Peribiliary cysts have been described in patients with severe liver disease.[17] These cysts are small, 0.2 to 2.5 cm, and are usually located centrally within the porta hepatis or at the junction of the main right and left hepatic ducts. They generally are asymptomatic but in rare cases can cause biliary obstruction.[17]

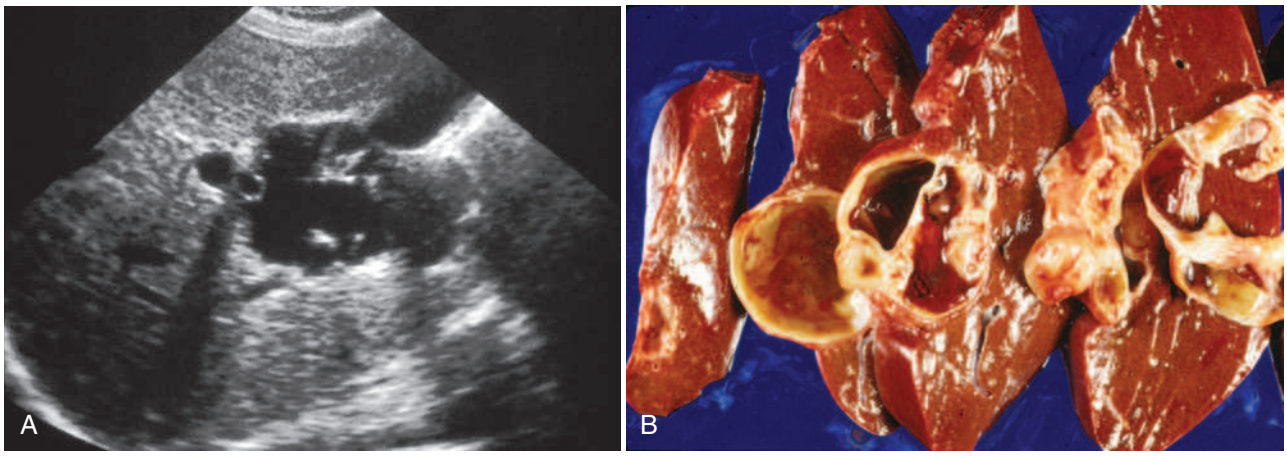

FIG. 4.14 Biliary Cystadenoma. (A) Sagittal sonogram shows irregular liver cyst with thick septa and mural nodules. **(B)** Surgical specimen.

Pathologically, peribiliary cysts are believed to represent small, obstructed periductal glands. Sonographically, they may be seen as discrete, clustered cysts or as tubular-appearing structures with thin septae, paralleling the bile ducts and portal veins.

Autosomal Dominant Polycystic Disease

Autosomal dominant polycystic kidney disease has liver cysts in 57% to 74% of patients.[18] No correlation exists between the severity of the renal disease and the extent of liver involvement. Results of LFTs are usually normal and, unlike the autosomal recessive form of polycystic kidney disease, there is no association with hepatic fibrosis or portal hypertension. Indeed, if LFT results are abnormal, complications of polycystic liver disease, such as tumor, cyst infection, and biliary obstruction, should be excluded.[18]

Biliary Hamartomas (von Meyenburg Complexes)

Bile duct hamartomas, first described by von Meyenburg in 1918, are small, focal developmental lesions of the liver composed of groups of dilated intrahepatic bile ducts set within a dense collagenous stroma.[19] These benign liver malformations are detected incidentally in 0.6% to 5.6% of autopsy series.[20]

Imaging features of von Meyenburg complexes (VMCs)[21] include single, multiple, or, most often, innumerable well-defined solid nodules usually less than 1 cm in diameter (Fig. 4.15). Nodules are usually uniformly hypoechoic[21] and less frequently hyperechoic on sonography[22,23] and hypodense on contrast-enhanced computed tomography (CECT) scan. Because of their multiplicity they can be confused with metastatic cancer. Bright echogenic foci in the liver with distal comet tail artifact without obvious mass effect are key sonographic findings (Fig. 4.16). We believe that these echogenic foci could be related to the presence of tiny cysts beyond the resolution of the ultrasound equipment. VMCs are usually isolated, insignificant observations and may occur with other congenital disorders, such as congenital hepatic fibrosis and polycystic kidney or liver disease.[20] Association of VMCs with cholangiocarcinoma has been suggested.[24]

FIG. 4.15 Von Meyenburg Complex in Cancer Patient. Sonogram shows a single, small, hypoechoic liver mass. With no other evidence of metastatic disease, a biopsy was performed and proved the benign, insignificant nature of this lesion.

INFECTIOUS DISEASES

Viral Hepatitis

Viral hepatitis is a common disease that occurs worldwide. It is responsible for millions of deaths secondary to acute hepatic necrosis or chronic hepatitis, which in turn may lead to portal hypertension, cirrhosis, and hepatocellular carcinoma (HCC). There are five distinct hepatitis viruses: hepatitis A through E. Other viruses cause hepatitis, but these are the classically characterized ones.

Hepatitis A occurs throughout the world and can be diagnosed using serosurveys with the antibody to hepatitis A virus (anti-HAV) as the marker. The primary mode of spread is the fecal-oral route. In developing countries the disease is endemic and infection occurs early in life. Hepatitis A is an acute infection leading to complete recovery or death from acute liver failure.

Hepatitis B is transmitted parenterally (e.g., blood transfusions, needle punctures) as well as by nonpercutaneous exposure through

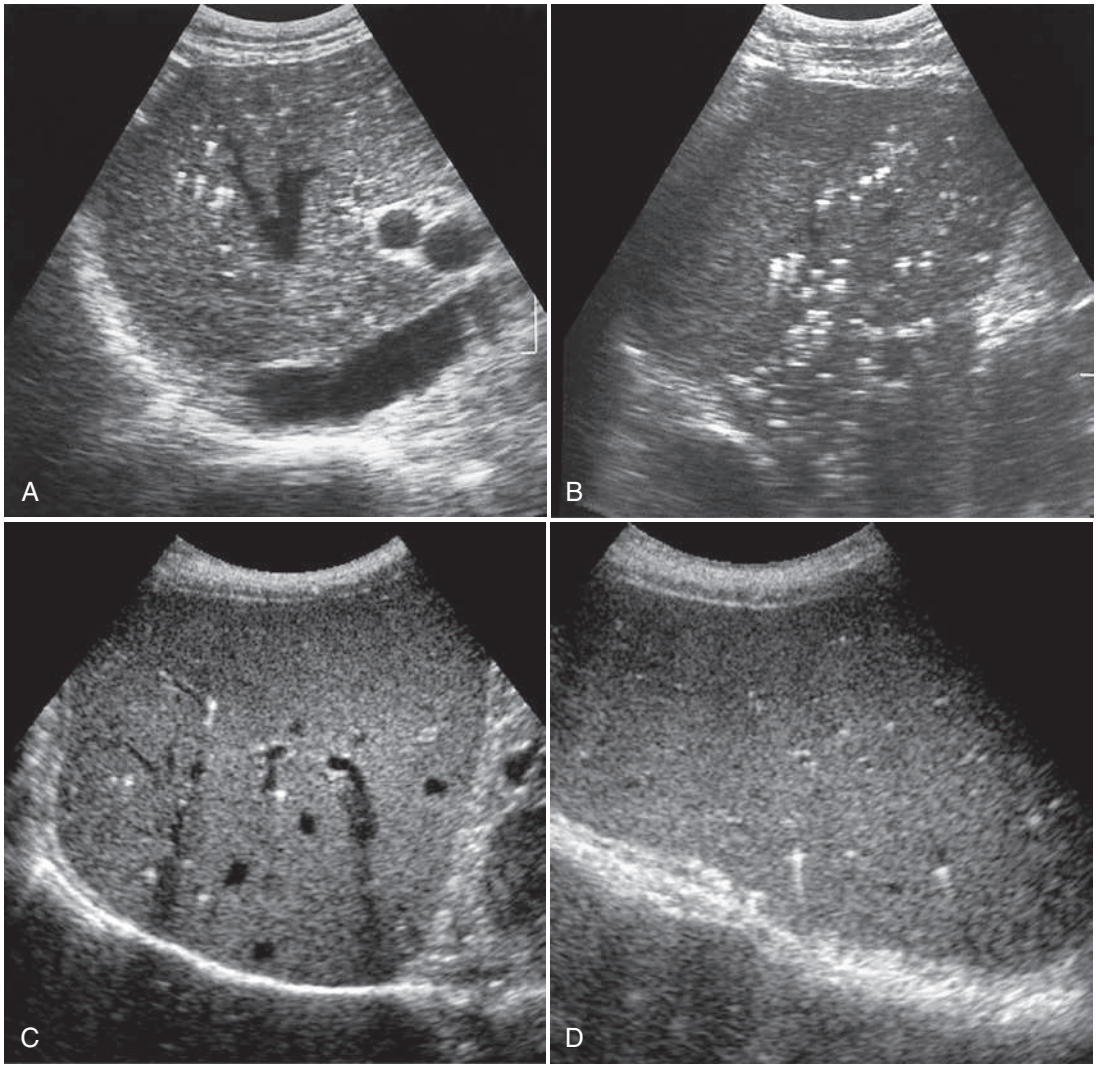

FIG. 4.16 Von Meyenburg Complex (VMC) Comet Tail Artifacts in Two Patients. **(A)** Sagittal and **(B)** transverse images of the left lobe of the liver show multiple bright echogenic foci with comet tail artifact. Biopsy showed VMC. **(C)** Sagittal and **(D)** transverse images of the right lobe in an asymptomatic patient show echogenic foci with distal comet tail artifact.

sexual contact and at birth. Hepatitis B virus (HBV), unlike HAV, has a carrier state, which is estimated worldwide at 300 million. The regions of highest carrier rates (5%-20%) are Southeast Asia, China, sub-Saharan Africa, and Greenland. The two most useful markers for acute infection are hepatitis B surface antigen (HBsAg) and antibody to hepatitis B core antigen (anti-HBc).

Hepatitis C is associated with posttransfusion hepatitis and is commonly identified in those who share needles or other equipment to inject drugs. Acutely infected patients have a much greater risk of chronic infection, with up to 85% progressing to chronic liver disease. Chronic hepatitis C virus (HCV) infection is diagnosed by the presence of antibody to HCV (anti-HCV) in the blood. Hepatitis C is a major health problem and accounts for many patients on liver transplant lists. Today, antiviral medications are changing the face of this disease with many patients having successful eradication of their virus. Unfortunately, in many of these patients the chronic liver disease has already developed and risk of developing HCC remains.

Hepatitis D, or delta hepatitis, is entirely dependent on HBV for its infectivity, requiring the HBsAg to provide an envelope coat for the hepatitis D virus (HDV). Its geographic distribution is therefore similar to that of hepatitis B. HDV is an uncommon infection in North America, occurring primarily in intravenous drug users.

Hepatitis E is similar to hepatitis A in that it is transmitted by the fecal-oral route. It is typically a self-limited disease but may persist and cause chronic hepatitis in immunocompromised patients.[25]

Clinical Manifestations

Uncomplicated **acute hepatitis** implies clinical recovery within 4 months. It is the outcome of 99% of cases of hepatitis A.

Subfulminant and fulminant **hepatic failure** follows the onset of jaundice and includes worsening jaundice, coagulopathy, and hepatic encephalopathy. Most cases of hepatic failure are caused by hepatitis B or drug toxicity and are characterized by hepatic

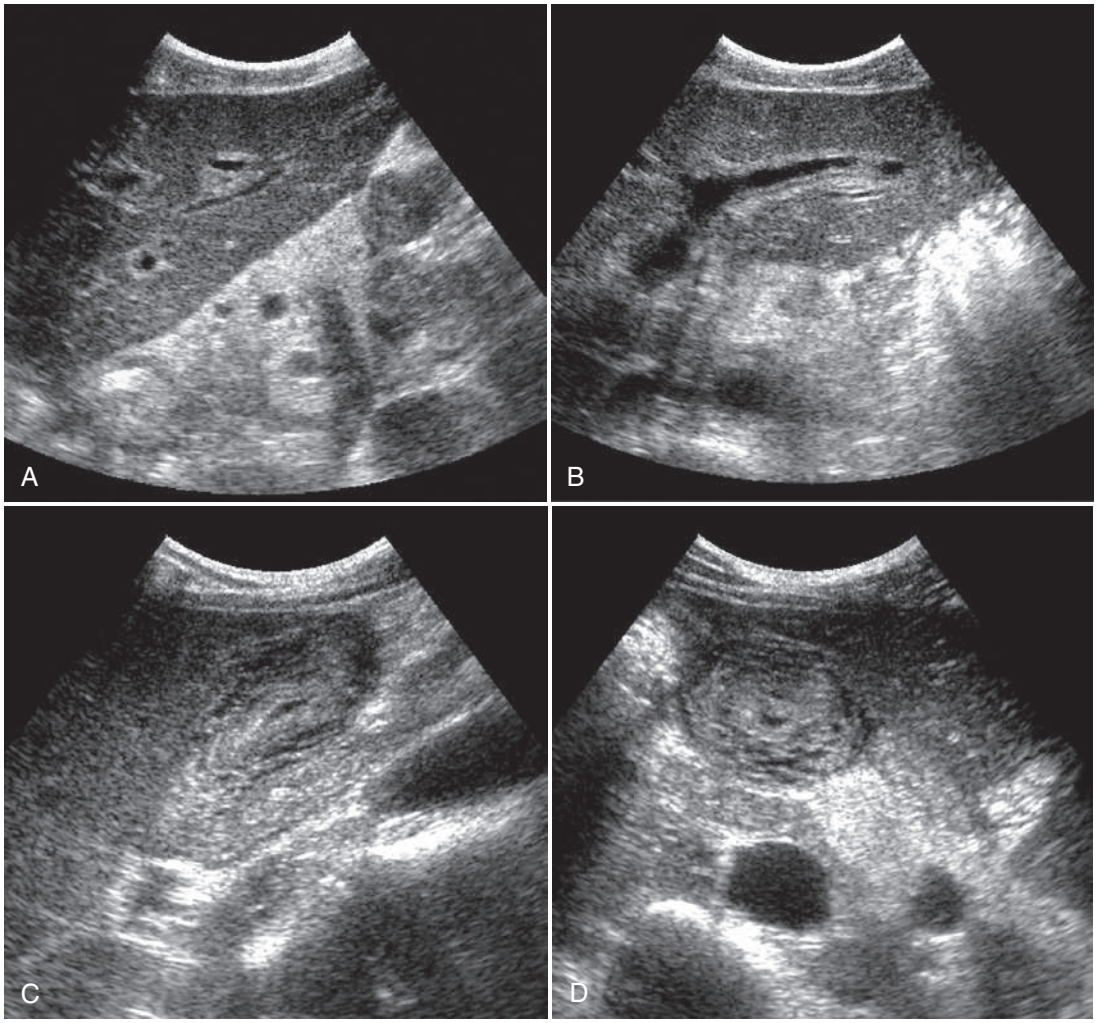

FIG. 4.17 Acute Hepatitis. (A) Sagittal and **(B)** transverse images of the left lobe of the liver show marked increased thickness and echogenicity of the soft tissue surrounding the portal vein branch, called **periportal cuffing. (C)** Sagittal and **(D)** transverse views of the gallbladder with marked mural thickening, such that the lumen is virtually obliterated. The gallbladder wall shows a multilayered appearance with extensive hypoechoic pockets of edema fluid. (With permission from Wilson SR. The liver. In Gastrointestinal disease. 6th series. Test and syllabus. Reston, VA: American College of Radiology; 2004.[26])

necrosis. Death occurs if the loss of hepatic parenchyma is greater than 40%.

Chronic hepatitis is defined as the persistence of biochemical abnormalities beyond 6 months. It has many causes other than viral, including metabolic (e.g., **Wilson disease, alpha-1 antitrypsin deficiency, hemochromatosis), autoimmune,** and **drug induced.** The prognosis and treatment of chronic hepatitis depend on the specific cause.

In acute hepatitis, there is diffuse swelling of the hepatocytes, proliferation of Kupffer cells lining the sinusoids, and infiltration of the portal areas by lymphocytes and monocytes. The sonographic features parallel the histologic findings. The liver parenchyma may have a diffusely decreased echogenicity, with accentuated brightness of the portal triads or **periportal cuffing** (Figs. 4.17 and 4.18A and B). Hepatomegaly and thickening of the gallbladder wall are associated findings (Figs. 4.17 and 4.18C and D). In most patients the liver appears normal.[26] Most cases of chronic hepatitis are also sonographically normal. When cirrhosis develops, sonography may demonstrate a coarsened echotexture and other morphologic changes of cirrhosis.

Bacterial Diseases

Pyogenic bacteria reach the liver by several routes, the most common being direct extension from the biliary tract in patients with suppurative cholangitis and cholecystitis. Other routes are through the portal venous system in patients with diverticulitis or appendicitis and through the hepatic artery in patients with osteomyelitis and subacute bacterial endocarditis. Pyogenic bacteria may also be present in the liver as a result of blunt or penetrating trauma. No cause can be found in approximately 50% of **hepatic abscesses;** the rest are mainly caused by anaerobic infection. Diagnosis of bacterial liver infection is often delayed. The most common presenting features of pyogenic liver abscess are fever, malaise, anorexia, and right upper quadrant pain. Jaundice may be present in approximately 25% of these patients.

Sonography has proved to be extremely helpful in the detection of liver abscesses. The ultrasound features of pyogenic abscesses

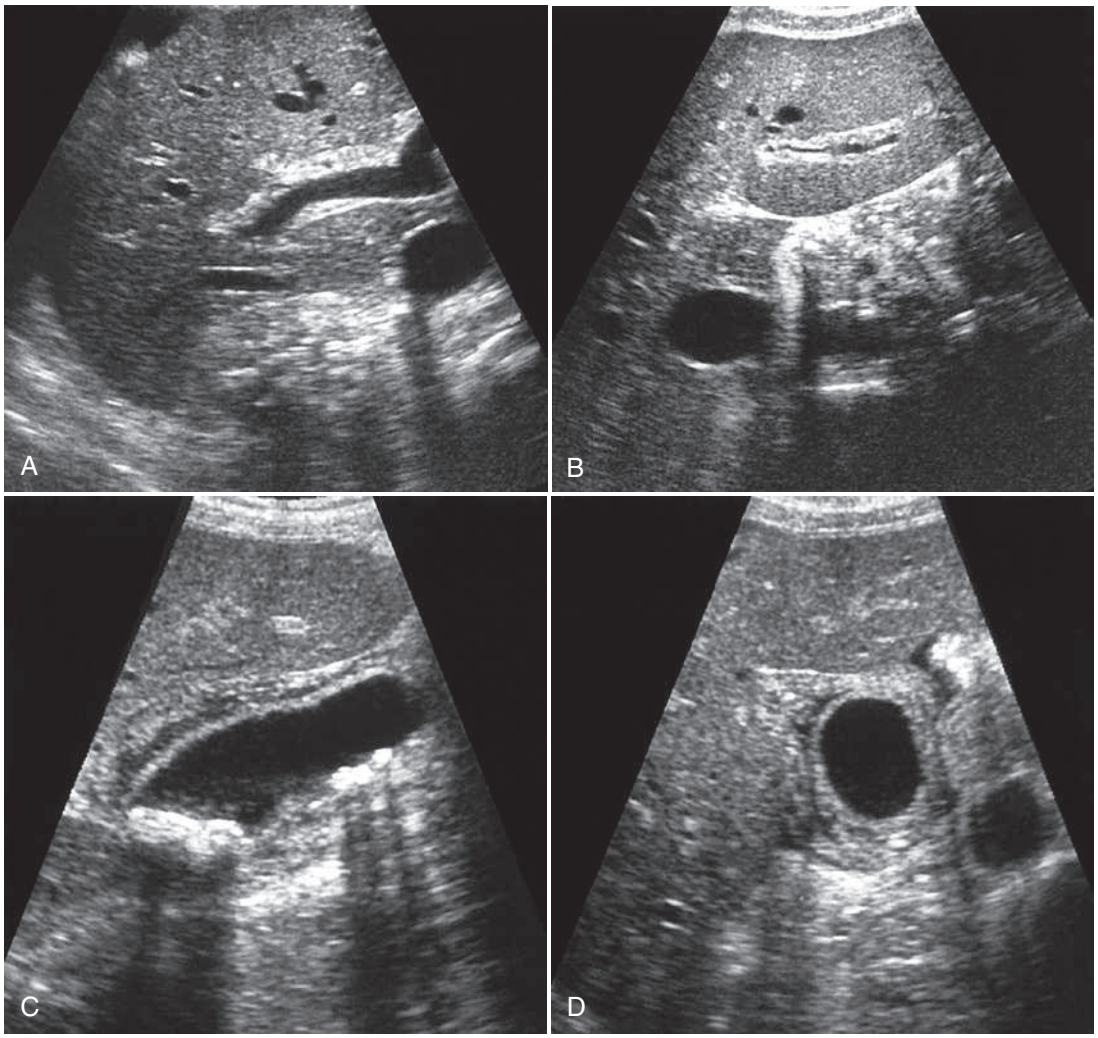

FIG. 4.18 Acute Hepatitis. Acute hepatitis in patient with fever, abnormal liver function tests, and incidental **gallstones. (A)** Transverse view of porta hepatis and **(B)** transverse view of left lobe of liver show thick, prominent echogenic bands surrounding the portal veins in the portal triads, called **periportal cuffing. (C)** Sagittal and **(D)** transverse views of the gallbladder show moderate **edema and thickening of the gallbladder wall.** The gallbladder is not large or tense, and the patient does not have acute cholecystitis. As this case illustrates, incidental cholelithiasis may be confusing.

are varied (Fig. 4.19A-F). Frankly purulent abscesses appear cystic, with the fluid ranging from echo free to highly echogenic. Regions of early suppuration may appear solid with altered echogenicity, usually hypoechoic, related to the presence of necrotic hepatocytes.[27] Occasionally, gas-producing organisms give rise to echogenic foci with a **posterior reverberation artifact** (Fig. 4.19G-I). Fluid-fluid interfaces, internal septations, and debris have all been observed. The abscess wall can vary from well defined to irregular and thick.

The differential diagnosis of pyogenic liver abscess includes amebic or echinococcal infection, simple cyst with hemorrhage, hematoma, and necrotic or cystic neoplasm. Ultrasound-guided liver aspiration is an expeditious means to confirm the diagnosis. Specimens should be sent for both aerobic and anaerobic culture. In the past, 50% of abscesses were considered sterile, probably caused by failure to transport the specimen in an oxygen-free container; thus anaerobic organisms were not identified.[28] Once the diagnosis of liver abscess is made by the identification of pus or a positive Gram stain and culture, the collection can be drained percutaneously using ultrasound or CT guidance.

Fungal Diseases: Candidiasis

The liver is frequently involved secondary to hematogenous spread of mycotic infections in other organs, most often the lungs. Patients are generally **immunocompromised,** although systemic candidiasis may occur in pregnancy or after hyperalimentation. The clinical characteristics include persistent fever in a neutropenic patient whose leukocyte count is returning to normal.[29]

The ultrasound features of **hepatic candidiasis** include the following[30]:

- "Wheel within a wheel": peripheral hypoechoic zone with inner echogenic wheel and central hypoechoic nidus. The central nidus represents focal necrosis in which fungal elements are found. This is seen early in the disease.
- Bull's-eye: 1- to 4-cm lesion with hyperechoic center and hypoechoic rim. It is present when neutrophil counts return

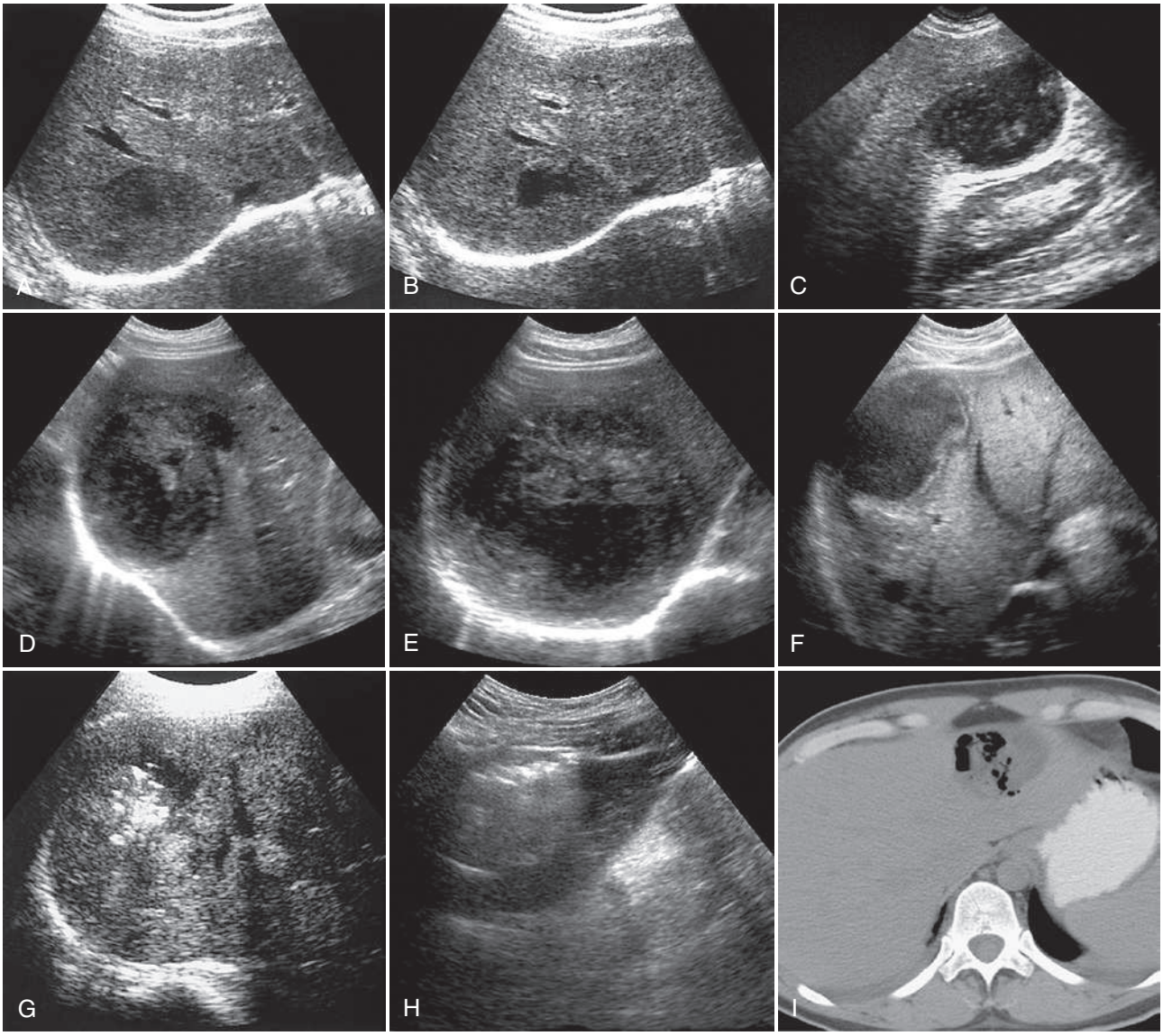

FIG. 4.19 Pyogenic Abscesses: Spectrum of Appearances. *Top row,* **Early lesions. (A)** and **(B)** Rapid evolution from phlegmon to liquefaction. **(A)** Poorly defined mass or **phlegmon** in segment 7 of the liver. **(B)** Twenty-four hours later, there is a central area of liquefaction. **(C)** Early abscess is poorly marginated and bulges the liver capsule. It is difficult to characterize this mass as solid or cystic. There was no vascularity within this or other masses. *Middle row,* **Mature abscess cavities in three patients. (D)** to **(F)** Classic mature abscess as a well-defined mass with liquefaction and internal debris. *Bottom row,* **Abscesses related to gas-forming organisms. (G)** Multiple gas bubbles are seen as innumerable bright echogenic foci within a poorly defined hypoechoic liver mass. **(H)** Sagittal image of the left lobe of the liver and **(I)** confirmatory computed tomography scan show a liver mass with extensive gas content.

to normal. The echogenic center contains inflammatory cells (Fig. 4.20).

- Uniformly hypoechoic: most common, corresponding to progressive fibrosis (Fig. 4.21A).
- Echogenic: variable calcification, representing scar formation (Fig. 4.21B).

Although percutaneous liver aspiration is helpful in obtaining the organism in pyogenic liver abscesses, it frequently yields false-negative results for the presence of *Candida* organisms.[30] This may be caused by failure to sample the central necrotic portion of the lesion, where the pseudohyphae are found.[30]

Parasitic Diseases

Amebiasis

Hepatic infection by the parasite *Entamoeba histolytica* is the most common extraintestinal manifestation of amebiasis. Transmission is by the fecal-oral route. The protozoan reaches the liver by penetrating through the colon, invading the mesenteric venules, and entering the portal vein. However, in more than one-half of patients with amebic abscesses of the liver, the colon appears normal and stool culture results are negative, thus delaying diagnosis. The most common presenting symptom is pain, which occurs in 99% of patients with amebic abscess. Approximately 15% of patients have diarrhea at diagnosis.

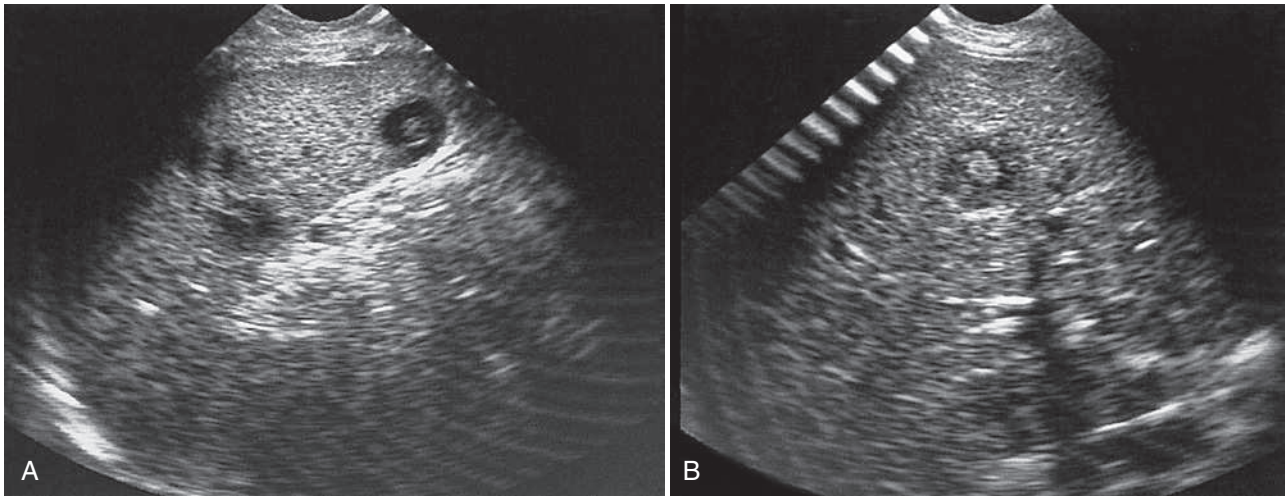

FIG. 4.20 Fungal Infection. "Bull's-eye" fungal morphology in 24-year-old man with **acute lymphoblastic leukemia** and fever. **(A)** Sagittal sonogram through the spleen shows focal hypoechoic target lesions. **(B)** The liver showed multiple masses. This magnified view shows a thick, echogenic rim and a thin, hypoechoic inner rim with a dense echogenic nidus. Biopsy revealed pseudohyphae.

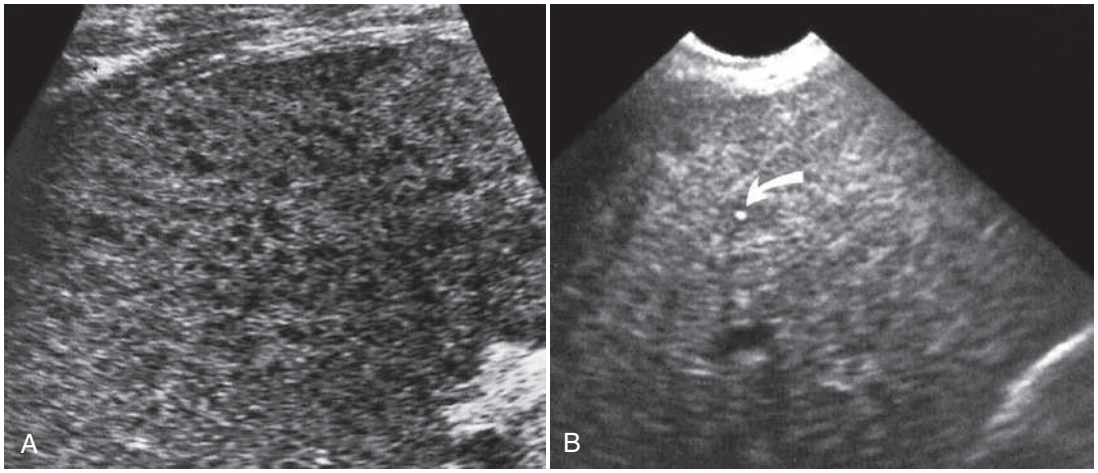

FIG. 4.21 Candidiasis. (A) Uniformly hypoechoic pattern. Multiple hypoechoic hepatic lesions are present in this young patient with acute myelogenous leukemia. **(B)** Echogenic pattern after medical therapy. Small calcified lesion *(arrow)* is visualized in another immunocompromised patient.

Sonographic features include a round or oval-shaped lesion, absence of a prominent abscess wall, hypoechogenicity compared to normal liver, fine low-level internal echoes, distal sonic enhancement, and contiguity with the diaphragm[31,32] (Fig. 4.22). All of these features, however, can be found in pyogenic abscess.

In a review of 112 amebic lesions, Ralls et al.[33] reported that two sonographic patterns were significantly more prevalent in amebic abscesses: (1) round or oval shapes in 82% versus 60% of pyogenic abscesses, and (2) hypoechoic appearance with fine internal echoes at high gain in 58% versus 36% of pyogenic abscesses. Most amebic abscesses occur in the right lobe of the liver. Diagnosis is made using a combination of the clinical features, ultrasound findings, and serologic results. The indirect hemagglutination test result is positive in more than 94% of patients.

Amebicidal drugs are effective therapy. Symptoms improve in 24 to 48 hours, and most patients are afebrile in 4 days. Those who exhibit clinical deterioration may also benefit from catheter drainage, although this is unusual. The majority of hepatic amebic abscesses disappear with adequate medical therapy.[34] The time from termination of therapy to resolution varies from 1.5 to 23 months (median, 7 months).[35] A minority of patients have residual hepatic cysts and focal regions of increased or decreased echogenicity.

Hydatid Disease

The most common cause of hydatid disease in humans is infestation by the parasite *Echinococcus granulosus,* which has a worldwide distribution. It is most prevalent in sheep- and cattle-raising countries, notably in the Middle East, Australia, and the Mediterranean. Endemic regions in the United States include the central valley in California, the lower Mississippi River Valley, Utah, and Arizona. Northern Canada is also endemic. *E. granulosus* is a tapeworm 3 to 6 mm in length that lives in the intestine

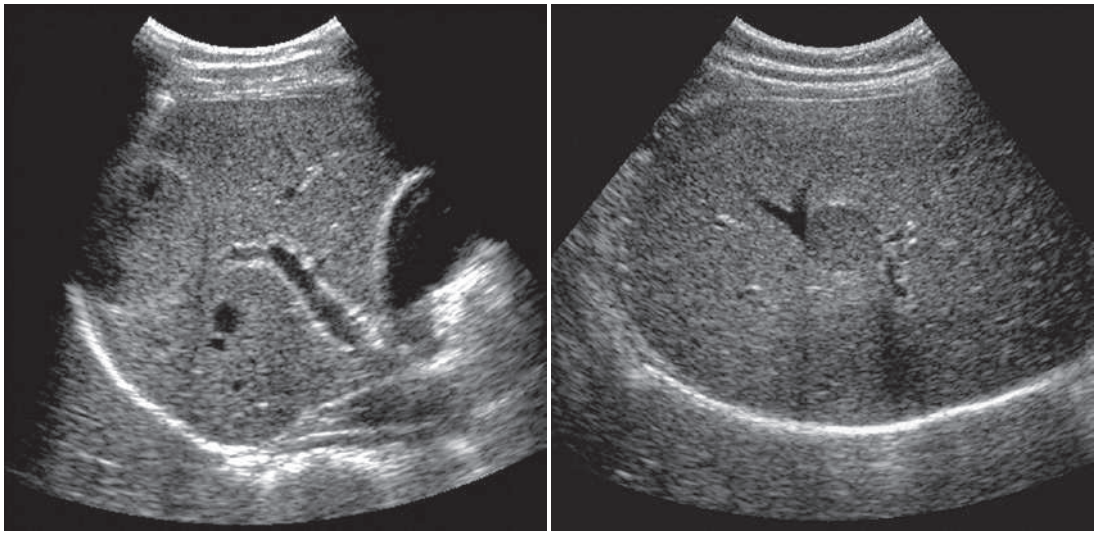

FIG. 4.22 Amebic Liver Abscess: Classic Morphology. Transverse sonograms show a well-defined oval subdiaphragmatic mass with increased through transmission. There are uniform low-level internal echoes and absence of a well-defined abscess wall.

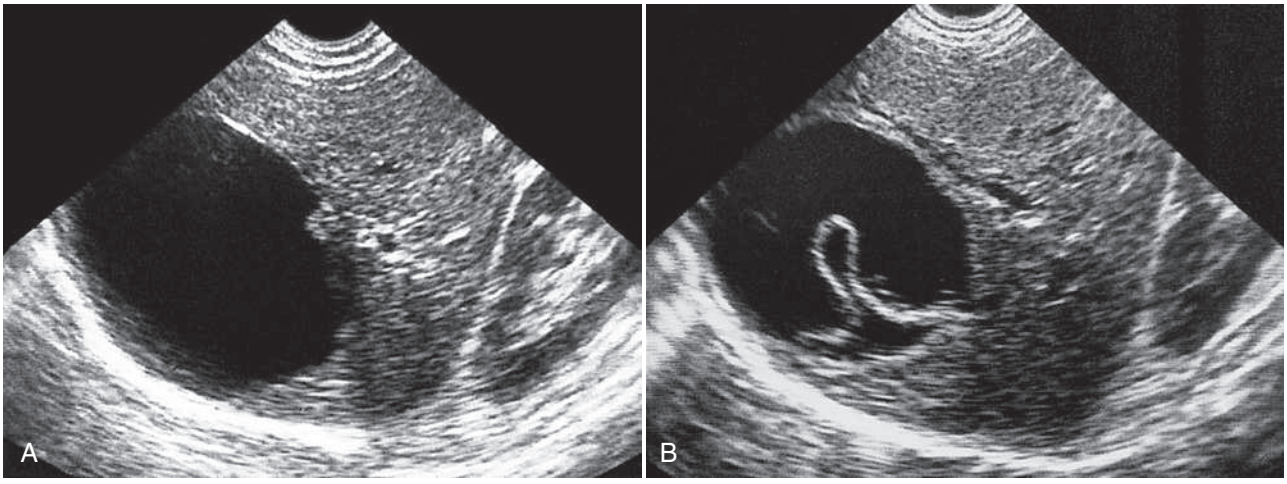

FIG. 4.23 Hydatid Cyst. (A) Baseline sonogram shows a predominately walled cyst in the right lobe with a small mural nodule and a fleck of peripheral calcium anteriorly. **(B)** Three weeks later the patient presented with right upper quadrant pain and eosinophilia. The detached endocyst is floating within the lesion.

of the definitive host, usually the dog. Its eggs are excreted in the dog's feces and swallowed by the intermediate hosts—sheep, cattle, goats, or humans. The embryos are freed in the duodenum and pass through the mucosa to reach the liver through the portal venous system. Most of the embryos remain trapped in the liver, although the lungs, kidneys, spleen, central nervous system, and bone may become secondarily involved. In the liver the right lobe is more frequently involved. The surviving embryos form slow-growing cysts. The cyst wall consists of an external membrane that is approximately 1 mm thick, which may calcify (ectocyst). The host forms a dense connective tissue capsule around the cyst (pericystia). The inner germinal layer (endocyst) gives rise to brood capsules that enlarge to form protoscolices. The brood capsules may separate from the wall and form a fine sediment called **hydatid sand.** When hydatid cysts within the organs of an herbivore are eaten, the scolices attach to the intestine and grow to adult tapeworms, thus completing the life cycle.

Several reports describe the sonographic features of hepatic hydatid disease[36-38] (Figs. 4.23 and 4.24). Lewall and McCorkell[36] proposed the following four groups for hydatid cysts:

- Simple cysts containing no internal architecture except sand
- Cysts with detached endocyst secondary to rupture (see Fig. 4.23B)
- Cysts with daughter cyst matrix (echogenic material between daughter cysts)
- Densely calcified masses

Surgery is the conventional treatment in echinococcal disease, although reports describe success with percutaneous drainage.[39-41] Although reported, anaphylaxis from hydatid cyst rupture is

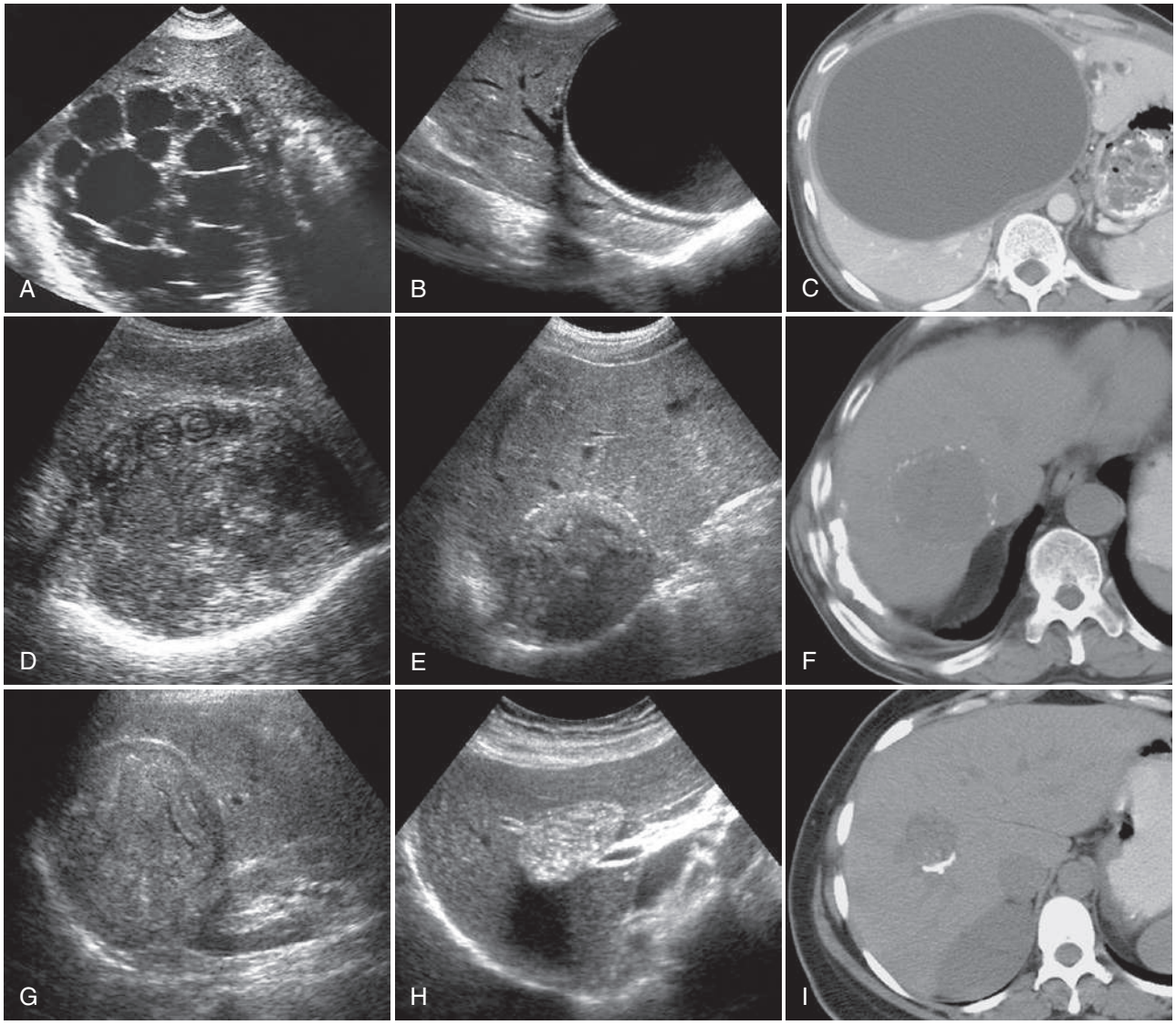

FIG. 4.24 Hydatid Liver Disease: Spectrum of Appearances. (A) Classic appearance showing a cyst containing multiple daughter cysts. **(B)** Sonogram and **(C)** confirmatory CT scan show a unilocular and simple cyst, a fairly uncommon morphology for hydatid disease. **(D)** Sonogram shows a complex mass. Anteriorly, multiple ringlike structures suggest hydatid disease. At surgery, cystic mass showed thick debris and innumerable scolices. **(E)** Sonogram and **(F)** confirmatory CT scan show an indeterminate mass with a thin rim of calcification. **(G)** Complex mass similar to that seen in **D**. There are fingerlike projections within, again suggestive of hydatid disease. **(H)** Sonogram and **(I)** confirmatory CT scan show a central liver mass with rim and internal punctate calcification.

rare. Ultrasound has been used to monitor the course of medical therapy in patients with abdominal hydatid disease.[42] A reappearance or persistence of fluid within the cavity may signify inadequate therapy and viability of the parasites.[43]

Hepatic alveolar echinococcus is a rare parasitic infestation by the larvae of *E. multilocularis.* The fox is the main host. The sonographic features include echogenic lesions, which may be single or multiple; necrotic, irregular lesions without a well-defined wall; clusters of calcification within lesions; and dilated bile ducts.[44]

Schistosomiasis

Schistosomiasis is one of the most common parasitic infections in humans, estimated to affect 200 million people worldwide. Hepatic schistosomiasis is caused by *Schistosoma mansoni, S. japonicum, S. mekongi,* and *S. intercalatum.* Hepatic involvement by *S. mansoni* is particularly severe. *S. mansoni* is prevalent in Africa, including Egypt, and South America, particularly in Venezuela and Brazil. The ova reach the liver through the portal vein and incite a chronic granulomatous reaction, first described by Symmers in 1904 as "clay-pipestem fibrosis."[45] The terminal portal vein branches become occluded, leading to presinusoidal portal hypertension, splenomegaly, varices, and ascites.

The sonographic features of schistosomiasis are widened echogenic portal tracts, sometimes reaching a thickness of 2 cm.[46,47] The porta hepatis is the region most often affected. Initially the liver size is enlarged. As the periportal fibrosis progresses, however, the liver becomes contracted, and the features of portal hypertension prevail.

FIG. 4.25 ***Pneumocystis carinii.*** Disseminated *P. carinii* infection in patient with AIDS who previously used pentamidine inhaler. Sonogram shows innumerable tiny, bright echogenic foci without shadowing throughout the liver parenchyma.

Pneumocystis carinii

Pneumocystis carinii is the most common organism causing **opportunistic infection** in patients with acquired immunodeficiency syndrome (AIDS). *Pneumocystis* pneumonia is the most common cause of life-threatening infection in patients with human immunodeficiency virus (HIV). *P. carinii* also affects patients undergoing bone marrow and organ transplantation, as well as those receiving corticosteroids or chemotherapy.[48] Extrapulmonary *P. carinii* infection was being reported with frequency in the early 1990s.[49-52] It was postulated that the use of maintenance aerosolized pentamidine achieved lower systemic levels than the intravenous form, allowing subclinical pulmonary infections and systemic dissemination of the protozoa. This treatment is now infrequently used by AIDS patients, so disseminated infection is rarely seen. Extrapulmonary *P. carinii* infection has been documented in the liver, spleen, renal cortex, thyroid gland, pancreas, and lymph nodes.

The sonographic findings of *P. carinii* involvement of the liver range from tiny, diffuse, nonshadowing echogenic foci to extensive replacement of the normal hepatic parenchyma by echogenic clumps representing dense calcification (Fig. 4.25). A similar sonographic pattern has been identified with hepatic infection by ***Mycobacterium avium-intracellulare*** and **cytomegalovirus.**[53]

DISORDERS OF METABOLISM

Fatty Liver

Fatty liver is an acquired, reversible disorder of metabolism, resulting in an accumulation of triglycerides within the hepatocytes. The most common cause likely is **obesity.** Fatty liver is recognized as a significant component of the **metabolic syndrome,** the importance of which is being increasingly recognized. Excessive alcohol intake produces a fatty liver by stimulating lipolysis, as does starvation. Other causes of fatty infiltration include poorly controlled hyperlipidemia, diabetes, excess exogenous or endogenous corticosteroids, pregnancy, total parenteral hyperalimentation, severe hepatitis, glycogen storage disease, jejunoileal bypass procedures for obesity, cystic fibrosis, congenital generalized lipodystrophy, several chemotherapeutic agents (including methotrexate), and toxins such as carbon tetrachloride and yellow phosphorus. Correction of the primary abnormality will usually reverse the process, although it is now recognized that fatty infiltration of the liver is the precursor for significant chronic disease and HCC in some patients. Fatty liver is attributed with the increasing incidence of HCC now seen in Western countries.

Sonography of fatty infiltration varies depending on the amount of fat and whether deposits are diffuse or focal[54] (Fig. 4.26). **Diffuse steatosis** may appear as follows:

- **Mild**—Minimal diffuse increase in hepatic echogenicity with normal visualization of diaphragm and intrahepatic vessel borders
- **Moderate**—Moderate diffuse increase in hepatic echogenicity with slightly impaired visualization of intrahepatic vessels and diaphragm
- **Severe**—Marked increase in echogenicity with poor penetration of posterior segment of right lobe of liver and poor or no visualization of hepatic vessels and diaphragm

Focal fatty infiltration and focal fatty sparing may mimic neoplastic involvement.[55] In **focal fatty infiltration,** regions of increased echogenicity are present within a background of normal liver parenchyma (Video 4.3). Conversely, islands of normal liver parenchyma may appear as hypoechoic masses within a dense, fatty infiltrated liver (Video 4.4). Features of **focal fatty change** include the following (Fig. 4.27):

- Focal fatty sparing and focal fatty liver most often involve the periportal region of the medial segment of the left lobe (segment IV).[56,57]
- Sparing also frequently occurs by the gallbladder fossa and along the liver margins.
- Focal subcapsular fat may occur in diabetic patients receiving insulin in peritoneal dialysate[58] (Fig. 4.27H and I).
- Lack of mass effect; hepatic vessels generally are not displaced, although traversing vessels in metastases have been reported.[59]
- Geometric margins are present, although focal fat may appear round, nodular, or interdigitated with normal tissue.[60]
- Rapid change with time; fatty infiltration may resolve as early as 6 days.

Contrast-enhanced ultrasound (CEUS) is valuable in the differentiation of fatty change from neoplasia, because all of the fatty or spared regions will appear isovascular in both the arterial and the portal venous phase of enhancement. CT and magnetic resonance imaging (MRI) can be used in distinguishing diffuse from focal fatty infiltration and in assessing for focal lesions. Radionuclide liver and spleen scintigraphic examination will yield normal results, indicating adequate numbers of Kupffer cells within the fatty regions.[54] Some postulate that these focal spared areas are caused by a regional decrease in portal blood flow, as demonstrated by CT scans during arterial portographic examinations.[61] Knowledge of typical patterns and use of CT,

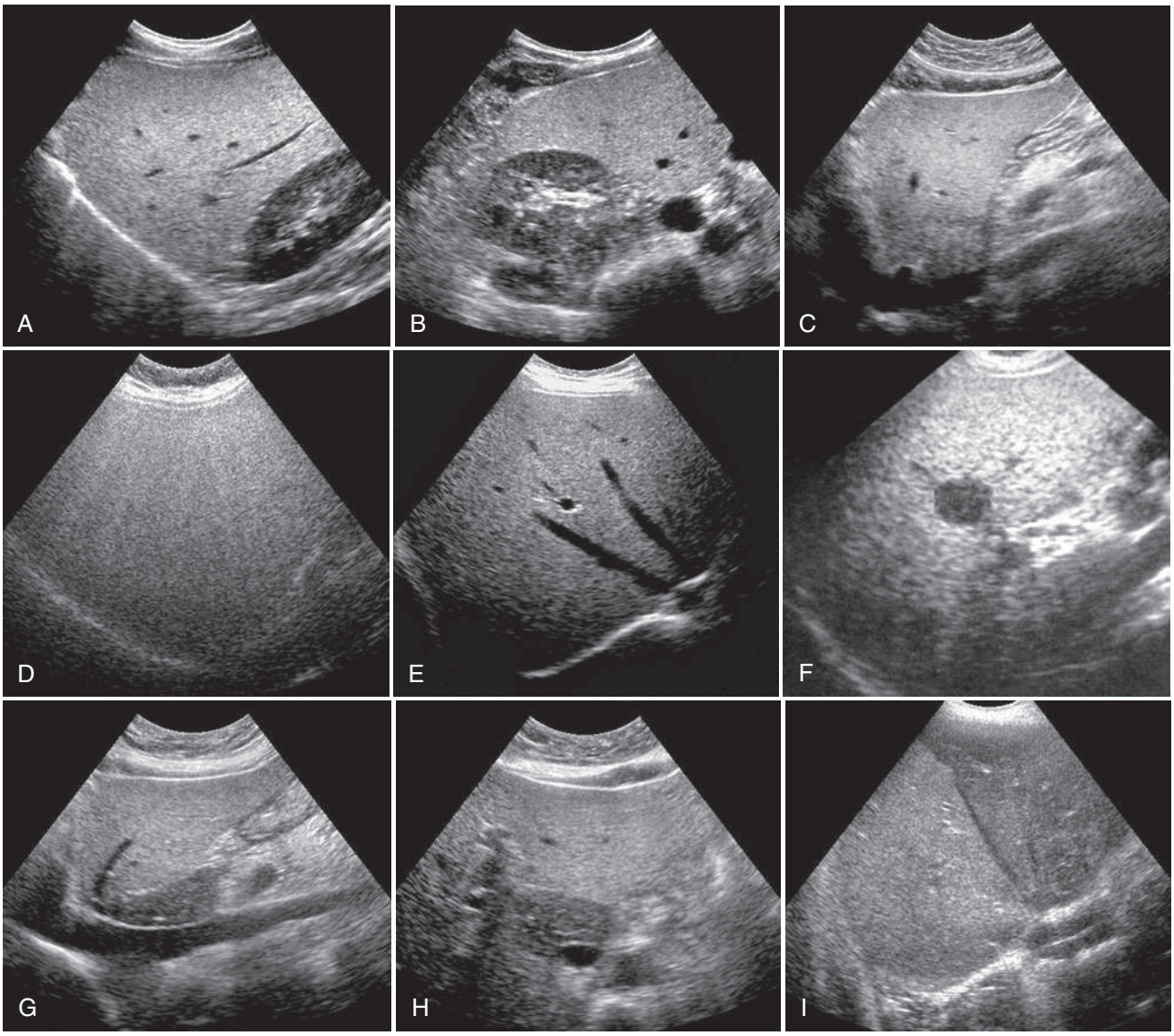

FIG. 4.26 Diffuse Fat: Spectrum of Appearances. Mild fatty infiltration: (A) sagittal right lobe, **(B)** transverse right lobe, **(C)** sagittal left lobe. The liver is diffusely bright and echogenic; sound penetration remains good. **Marked fatty infiltration: (D)** sagittal right lobe, **(E)** subcostal oblique view. The liver is enlarged and attenuating, sound penetration is poor, and the walls of the hepatic veins are not defined. **Focal fatty sparing: (F)** mimicking a hypoechoic mass; normal liver on biopsy and follow-up. **(G)** Sagittal and **(H)** transverse images show focal fatty sparing of the caudate lobe. **(I)** Geographic fatty sparing of the entire left lobe marginated by the middle hepatic vein.

CEUS, MRI, or nuclear medicine scintigraphy will avoid the necessity for biopsy in most patients with focal fatty alteration.

Glycogen Storage Disease (Glycogenosis)

Von Gierke first recognized glycogen storage disease (GSD) affecting the kidneys and liver in 1929.[62] Type 1 GSD (von Gierke disease, glucose 6-phosphatase deficiency) is manifested in the neonatal period by hepatomegaly, nephromegaly, and hypoglycemic convulsions. Because of the enzyme deficiency, large quantities of glycogen are deposited in the hepatocytes and proximal convoluted tubules of the kidney. With dietary management and supportive therapy, more patients currently survive to childhood and young adulthood. As a result, several patients have developed benign adenomas or, less often, HCC.[63]

Sonographically, type 1 GSD appears indistinguishable from other causes of diffuse fatty infiltration. Secondary hepatic adenomas are well-demarcated, solid masses of variable echogenicity. Malignant transformation can be recognized by rapid growth of the lesions, which may become more poorly defined.[63]

Cirrhosis

The World Health Organization (WHO) defines cirrhosis as a diffuse process characterized by fibrosis and the conversion of normal liver architecture into structurally abnormal nodules.[64] Three major pathologic mechanisms combine to create cirrhosis: **cell death, fibrosis,** and **regeneration.** Cirrhosis has been classified as **micronodular,** in which nodules are 0.1 to 1 cm in diameter, and **macronodular,** characterized by nodules of varying size, up to 5 cm in diameter. Alcohol consumption is the most

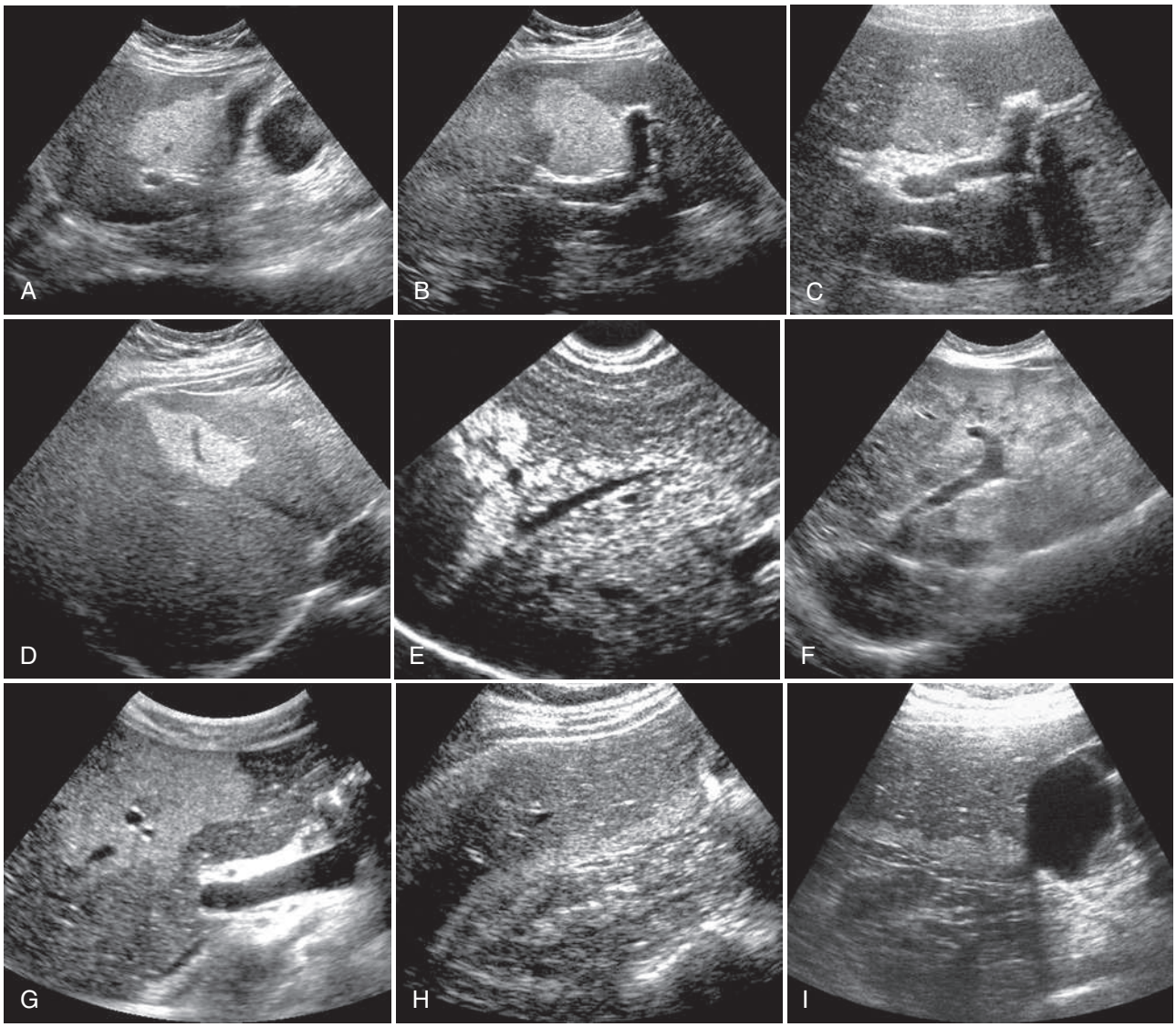

FIG. 4.27 Focal Fat: Spectrum of Appearances. (A) Sagittal and **(B)** subcostal oblique images show the most common location for **classic focal fat,** in segment 4, anterior to the portal venous bifurcation at the porta hepatis, where it is large and masslike. **(C)** Another patient showing a more common, milder form of the same fat deposition. **(D)** to **(G) Tumoral fat.** Fat deposits in all images suggest a focal liver mass. The liver vasculature is unaltered in its course at the location of the fatty masses. **(E)** Focal fat of pregnancy. **(H)** and **(I) Hepatic steatonecrosis** shown in views of the right lobe of the liver is a rare observation in diabetic patients who receive insulin in their peritoneal dialysate.

common cause of micronodular cirrhosis, and chronic viral hepatitis is the most frequent cause of the macronodular form. Patients who continue to drink may go on to end-stage liver disease, which is indistinguishable from cirrhosis of other causes. Other causes are **biliary cirrhosis** (primary and secondary), **Wilson disease, primary sclerosing cholangitis,** and **hemochromatosis.** The classic clinical presentation of cirrhosis is hepatomegaly, jaundice, and ascites. However, serious liver injury may be present without any clinical clues. In fact, only 60% of patients with cirrhosis have signs and symptoms of liver disease.

Cirrhosis has serious prognostic implications and patients may succumb to progressive liver failure and the sequelae of portal hypertension. They also have a greatly increased risk for the development of HCC. Appropriate at-risk populations, therefore, undergo surveillance ultrasound, performed at 6-month intervals in search of liver nodules above threshold size, which are then characterized as benign, indeterminate, or malignant nodules with the use of contrast-enhanced imaging techniques and enter a well-defined pathway for further evaluation and management.

Because liver biopsy is invasive, the ability to detect cirrhosis by noninvasive means, such as sonography, holds great clinical interest. The morphologic patterns associated with cirrhosis include the following (Fig. 4.28):

- **Volume redistribution.** In the early stages of cirrhosis the liver may be enlarged, whereas in advanced stages the liver is often small, with relative enlargement of the caudate lobe, left lobe, or both, compared with the right lobe. Several studies have evaluated the ratio of the caudate lobe width to the right lobe width (C/RL) as an indicator of cirrhosis. A C/RL value

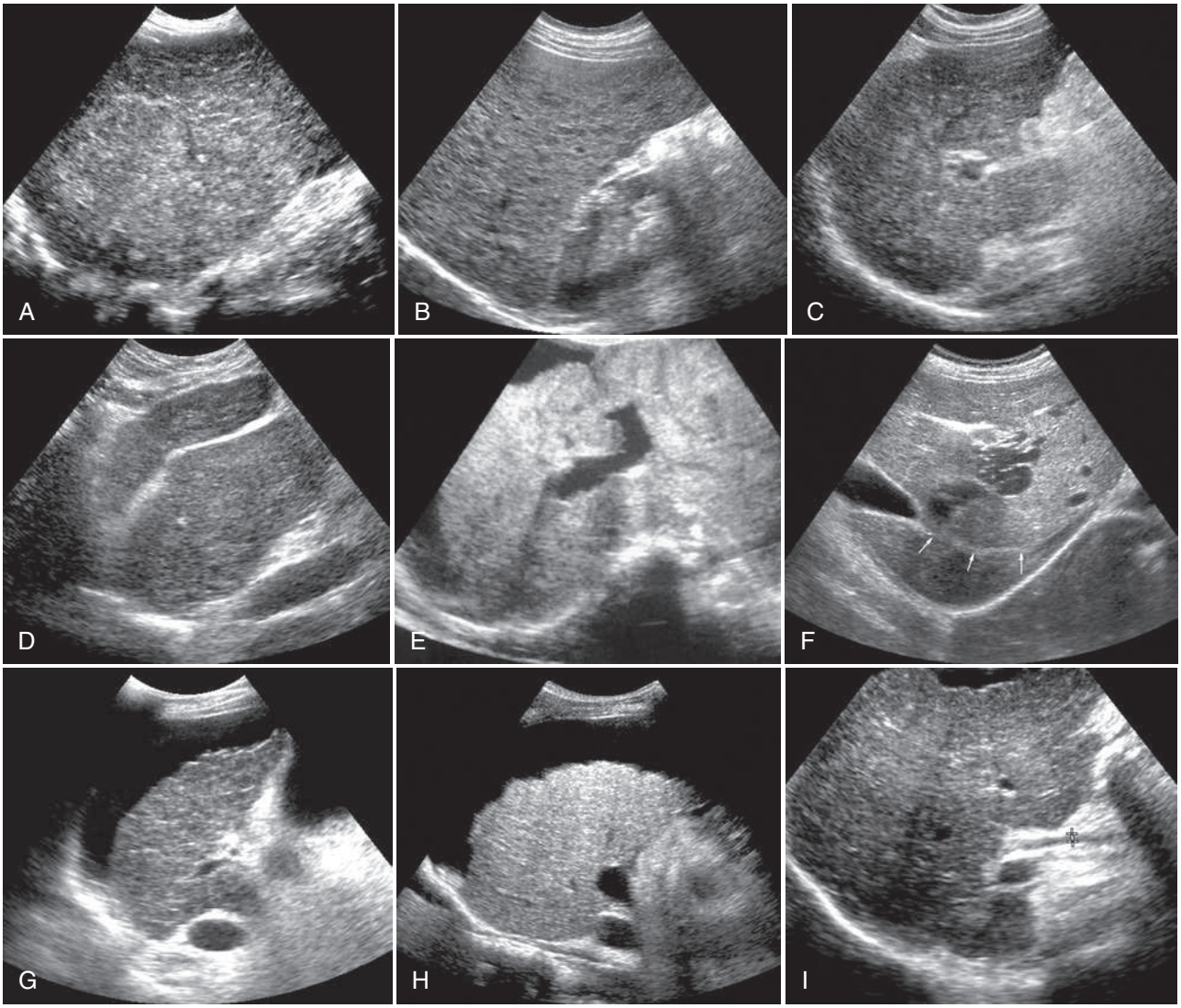

FIG. 4.28 Cirrhosis: Spectrum of Appearances. *Top row,* **Parenchymal changes. (A)** Coarse parenchyma and innumerable tiny, hyperechoic nodules. **(B)** Coarse parenchyma and innumerable tiny, hypoechoic nodules. **(C)** Coarse parenchyma and surface nodularity. *Middle row,* **Lobar redistribution. (D)** Sagittal image showing an enormous caudate lobe. **(E)** Transverse sonogram shows the right lobe is small, with enlargement of the left lateral segment. **(F)** Subcostal oblique view showing a tiny right lobe of the liver, which is separated from the large left lobe by the main lobar fissure *(arrows). Bottom row,* **Contour abnormality. (G)** and **(H)** Small, end-stage livers with surface nodularity, best appreciated in patients with ascites, as shown here. **(I)** Liver contour varies greatly, as shown here, where a large nodule protrudes from the deep liver border.

of 0.65 is considered indicative of cirrhosis. The specificity is high (100%), but the sensitivity is low (43%-84%), indicating that the C/RL ratio is a useful measurement if it is abnormal.[65] However, no patients in these studies had Budd-Chiari syndrome, which may also cause caudate lobe enlargement.

- **Coarse echotexture.** Increased echogenicity and coarse echotexture are frequent observations in diffuse liver disease. These are subjective findings, however, and may be confounded by inappropriate time gain compensation (TGC) settings and overall gain. Liver attenuation is correlated with the presence of fat, not fibrosis.[66] Cirrhotic livers without fatty infiltration had attenuation values similar to those of controls. This accounts for the relatively low accuracy in distinguishing diffuse liver disease[67] and the conflicting reports regarding attenuation values in cirrhosis.
- **Nodular surface.** Irregularity of the liver surface during routine scanning has been appreciated as a sign of cirrhosis when the appearance is gross or when ascites is present.[68] The nodularity corresponds to the presence of regenerating nodules and fibrosis.
- **Regenerating nodules.** These regenerating hepatocytes are surrounded by fibrotic septae. Because regenerating nodules have a similar architecture to the normal liver, ultrasound and CT have limited ability to detect them. Regenerating nodules tend to be isoechoic or hypoechoic with a thin, echogenic border that corresponds to fibrofatty connective tissue.[68] MRI has a greater sensitivity than both CT and ultrasound in regenerating nodule detection. Because some regenerating nodules contain iron, gradient echo sequences demonstrate these nodules as hypointense.[69]

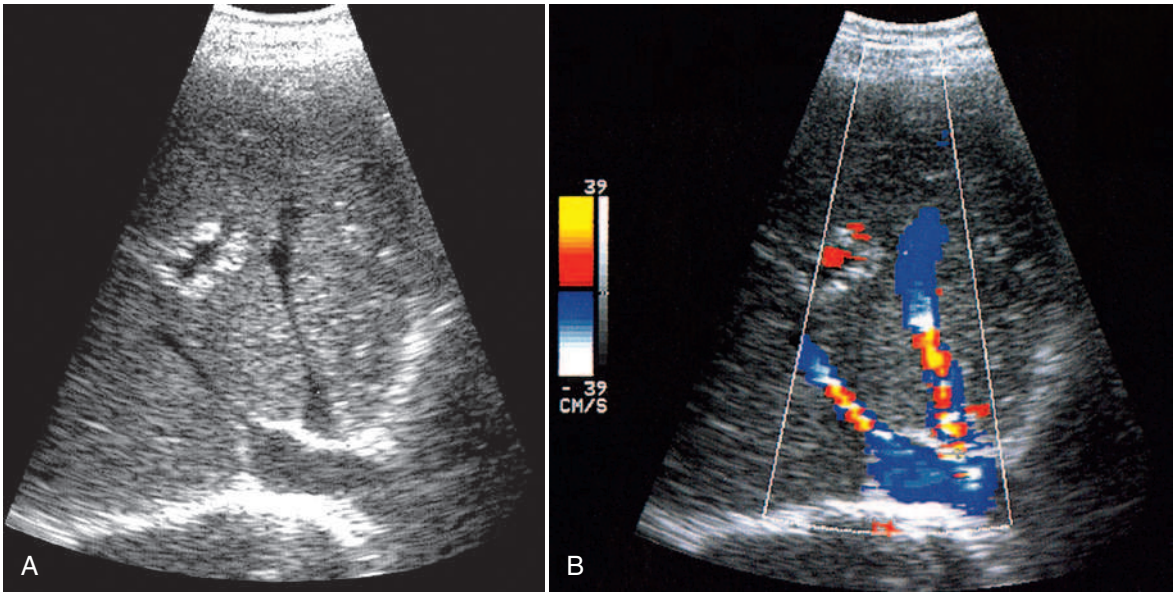

FIG. 4.29 Hepatic Vein Strictures: Cirrhosis. (A) Gray-scale image of hepatic veins shows a tapered luminal narrowing. **(B)** Color Doppler image shows appropriately directed blood flow toward the inferior vena cava. There is color aliasing from the rapid-velocity flow through the points of narrowing.

Cirrhosis: Sonographic Features

Volume redistribution
Coarse echotexture
Nodular surface
Nodules: regenerative and dysplastic
Portal hypertension: ascites, splenomegaly, and varices

- **Dysplastic nodules.** Dysplastic nodules or adenomatous hyperplastic nodules are larger than regenerating nodules (diameter of 10 mm) and are considered premalignant.[70] They contain well-differentiated hepatocytes, a portal venous blood supply, and atypical or frankly malignant cells. The portal venous blood supply can be detected with color Doppler flow imaging and distinguished from the hepatic artery–supplied HCC.[71] In a patient with cirrhosis and a liver mass, percutaneous biopsy is often performed to exclude or diagnose HCC.

Doppler Ultrasound Characteristics

The normal Doppler waveform of the hepatic veins reflects the hemodynamics of the right atrium. The waveform is triphasic: two large antegrade diastolic and systolic waves and a small retrograde wave corresponding to the atrial "kick." Because the walls of the hepatic veins are thin, disease of the hepatic parenchyma may alter their compliance. In many patients with compensated cirrhosis (no portal hypertension), the Doppler waveform is abnormal. **Two abnormal patterns** have been described: decreased amplitude of phasic oscillations with loss of reversed flow and a flattened waveform.[72,73] These abnormal patterns have also been found in patients with fatty infiltration of the liver.[72]

As cirrhosis progresses, luminal narrowing of the hepatic veins may be associated with flow alterations visible on color and spectral Doppler ultrasound. High-velocity signals through an area of narrowing produce color aliasing and turbulence (Fig. 4.29).

The hepatic artery waveform also shows altered flow dynamics in cirrhosis and chronic liver disease. Lafortune et al.[74] found an increase in the resistive index of the hepatic artery after a meal in patients with a normal liver. The vasoconstriction of the hepatic artery occurs as a normal response to the increased portal venous flow stimulated by eating (20% change). In patients with cirrhosis and chronic liver disease, the normal increase in postprandial resistive index is blunted.[75]

Elastography

Sonographic evaluation of liver morphology for the prediction of the presence and status of cirrhosis is invaluable but subjective. Furthermore, it may uncommonly be normal even with quite advanced disease. Historically, therefore, diagnosis and staging of liver cirrhosis have been performed based on invasive liver biopsy. At histology, liver fibrosis is graded from METAVIR stage F0, indicating a normal liver, through to METAVIR stage F4, indicating cirrhosis. Patients with METAVIR stage F2 are felt to have clinically important fibrosis necessitating special attention and referral to hepatology service as these patients are at risk for portal hypertension, liver failure, and development of HCC. Today, the addition of elastography provides objective, noninvasive, and repeatable evaluation of the status of liver fibrosis.[76-78] Elastography is performed with several different techniques and two of them, point shear wave elastography (SWE) and two-dimensional SWE, are integral components of high-end ultrasound systems sold today, thereby allowing for evaluation of fibrosis at the time of a routine dedicated liver ultrasound.

SWE is performed of segments VII and VIII on a supine patient under direct ultrasound visualization by obtaining multiple

samples from the generation of shear waves in the liver within a small region of interest with utilization of acoustic radiation force impulse (ARFI) imaging. Results are expressed in either kPa or meters per second, and in North America, seemingly the latter are preferred. There are published data giving the range of values for each technique and equipment used.[79] The introduction of these techniques is invaluable to reduce the requirement for liver biopsy, to allow for follow-up of patients undergoing new antiviral therapy with chronic liver disease, and to allow for preoperative assessment of those with liver cancer for optimal selection of therapy options. The current status of this technique was recently published in a special report by the Society of Radiologists in Ultrasound.[80]

VASCULAR ABNORMALITIES

Portal Hypertension

Normal portal vein pressure is 5 to 10 mm Hg (14 cm H_2O). Portal hypertension is defined by (1) wedge hepatic vein pressure or direct portal vein pressure more than 5 mm Hg greater than IVC pressure, (2) splenic vein pressure greater than 15 mm Hg, or (3) portal vein pressure (measured surgically) greater than 30 cm H_2O. Pathophysiologically, portal hypertension can be divided into presinusoidal and intrahepatic groups, depending on whether the hepatic vein wedge pressure is normal (presinusoidal) or elevated (intrahepatic).

Presinusoidal portal hypertension can be subdivided into extrahepatic and intrahepatic forms. The causes of extrahepatic presinusoidal portal hypertension include **thrombosis of the portal or splenic veins.** This should be suspected in any patient who presents with clinical signs of portal hypertension (ascites, splenomegaly, and varices) and a normal liver biopsy. Thrombosis of the portal venous system occurs in children secondary to umbilical vein catheterization, omphalitis, and neonatal sepsis. In adults the causes of portal vein thrombosis include **trauma, sepsis, HCC, pancreatic carcinoma, pancreatitis, portacaval shunts, splenectomy,** and **hypercoagulable states.** The **intrahepatic presinusoidal** causes of portal hypertension are the result of diseases affecting the portal zones of the liver, notably **schistosomiasis, primary biliary cirrhosis, congenital hepatic fibrosis,** and toxic substances, such as **polyvinyl chloride** and **methotrexate.**

Cirrhosis is the most common cause of **intrahepatic portal hypertension** and accounts for greater than 90% of all cases of portal hypertension in the West. In cirrhosis the distorted vascular channels increase resistance to portal venous blood flow and obstruct hepatic venous outflow. Diffuse metastatic liver disease also produces portal hypertension by the same mechanism. Over time, thrombotic diseases of the IVC and hepatic veins, as well as constrictive pericarditis and other causes of severe right-sided heart failure, will lead to centrilobular fibrosis, hepatic regeneration, cirrhosis, and finally portal hypertension.

Sonographic findings of portal hypertension include the **secondary signs** of splenomegaly, ascites, and portosystemic venous collaterals (Figs. 4.30 and 4.31). When the resistance to blood flow in the portal vessels exceeds the resistance to flow in the small communicating channels between the portal and systemic circulations, portosystemic collaterals form. Thus although the caliber of the portal vein initially may be increased

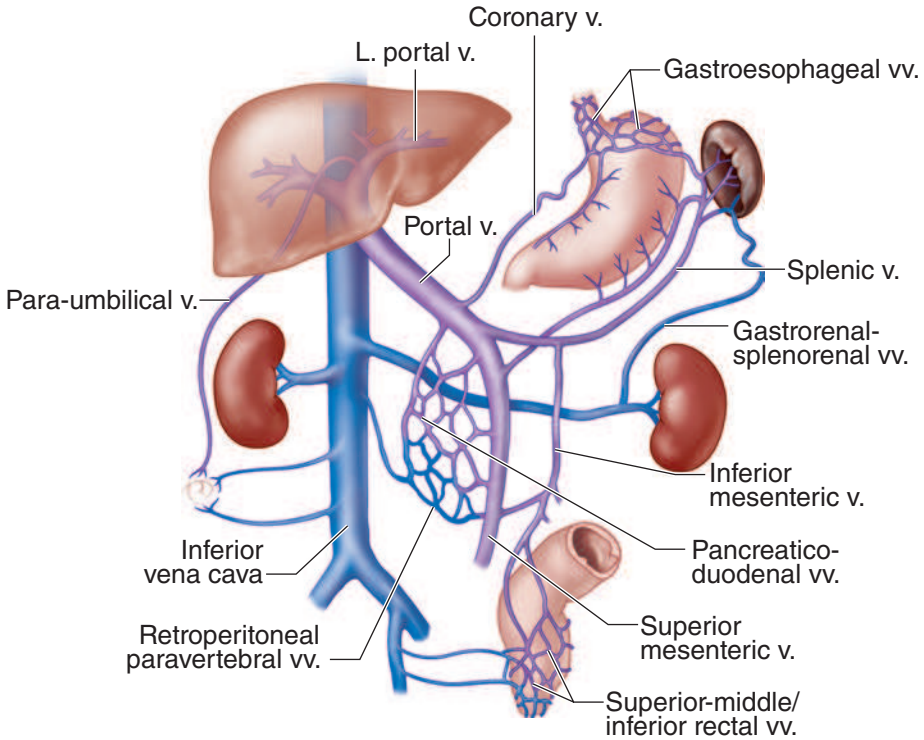

FIG. 4.30 Portal Hypertension. Major sites of portosystemic venous collaterals.

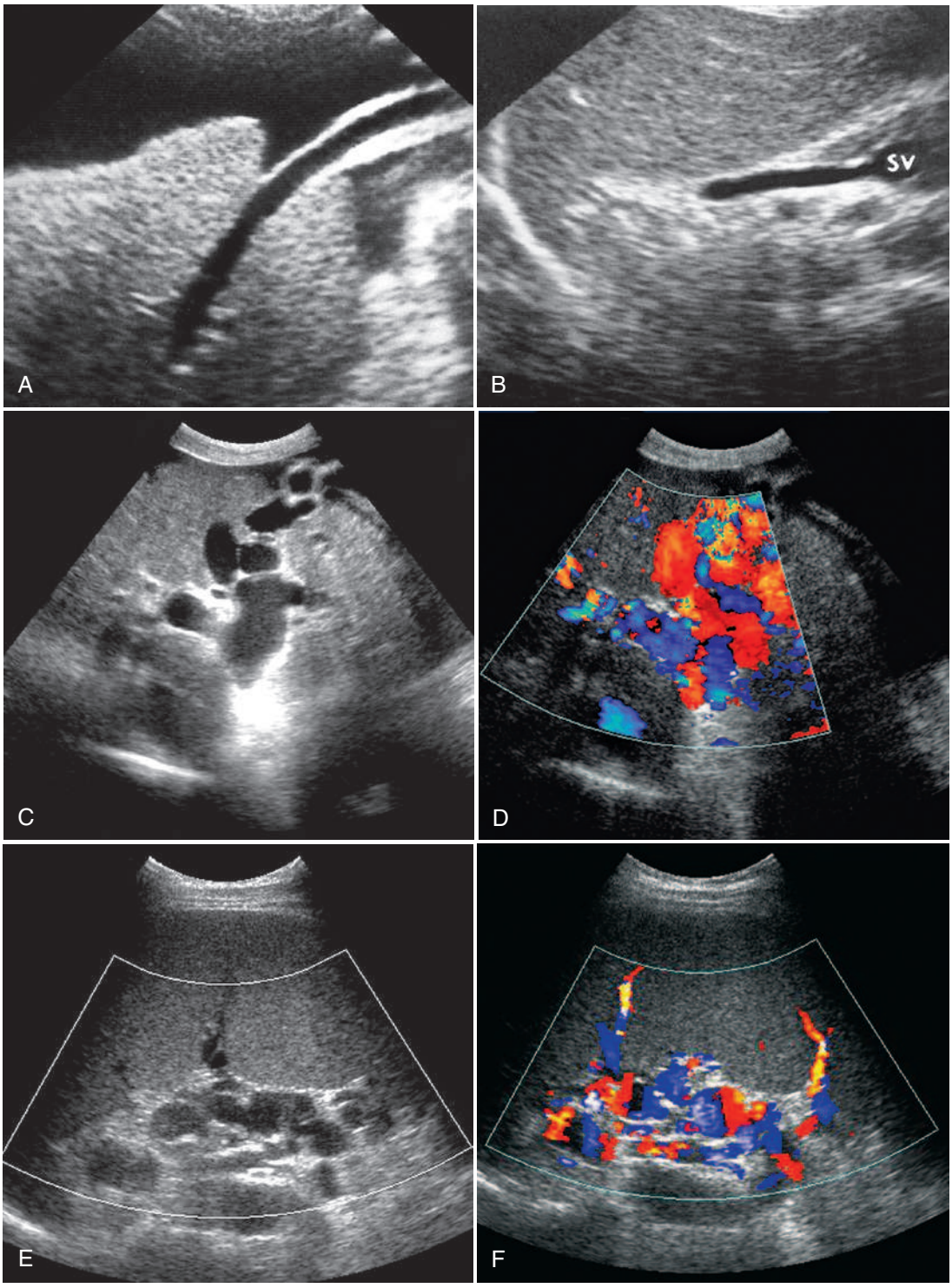

FIG. 4.31 Portal Hypertension. (A) Sagittal image of recanalized paraumbilical vein in patient with gross ascites. **(B)** Sagittal image shows enlarged coronary vein running cephalad from the splenic vein *(SV)*. **(C)** Gray-scale image and **(D)** color Doppler image show extensive varices in the distribution of the coronary vein. **(E)** Gray-scale image and **(F)** color Doppler image show splenic hilar varices.

(>1.3 cm) in portal hypertension,[81] with the development of portosystemic shunts, the portal vein caliber will decrease.[82] Five **major sites of portosystemic venous collaterals** are visualized by ultrasound[83-85] (see Fig. 4.30).

- **Gastroesophageal junction:** Between the coronary and short gastric veins and the systemic esophageal veins. These varices are of particular importance because they may lead to life-threatening or fatal hemorrhage. Dilation of the coronary vein (>0.7 cm) is associated with severe portal hypertension (portohepatic gradient >10 mm Hg)[82] (Fig. 4.31C and D).
- **Paraumbilical vein:** Runs in the falciform ligament and connects the left portal vein to the systemic epigastric veins

near the umbilicus **(Cruveilhier-Baumgarten syndrome)**[86] (Fig. 4.31A). Some studies suggest that, if the hepatofugal flow in the patent paraumbilical vein exceeds the hepatopetal flow in the portal vein, patients may be protected from developing esophageal varices.[87,88]

- **Splenorenal and gastrorenal:** Tortuous veins may be seen in the region of the splenic and left renal hilus (Fig. 4.31E and F), which represent collaterals between the splenic, coronary, and short gastric veins and the left adrenal or renal veins.
- **Intestinal:** Regions in which the gastrointestinal tract becomes retroperitoneal so that the veins of the ascending and descending colon, duodenum, pancreas, and liver may anastomose with the renal, phrenic, and lumbar veins (systemic tributaries).
- **Hemorrhoidal:** The perianal region where the superior rectal veins, which extend from the inferior mesenteric vein, anastomose with the systemic middle and inferior rectal veins.

Duplex Doppler sonography provides additional information regarding direction of portal flow. False results may occur, however, when sampling is obtained from periportal collaterals in patients with portal vein thrombosis or hepatofugal portal flow.[89] Normal portal venous flow rates vary in the same individual, increasing postprandially and during inspiration[75,90] and decreasing after exercise or in the upright position.[91] An increase of less than 20% in the diameter of the portal vein with deep inspiration indicates portal hypertension with 81% sensitivity and 100% specificity.[92]

The **normal portal vein** demonstrates an undulating **hepatopetal** (toward the liver) flow. Mean portal venous flow velocity is 15 to 18 cm/sec and varies with respiration and cardiac pulsation. As portal hypertension develops, the flow in the portal vein loses its undulatory pattern and becomes monophasic. As the severity of portal hypertension increases, flow becomes biphasic and finally **hepatofugal** (away from the liver). Intrahepatic arterial-portal venous shunting may also be seen.

Chronic liver disease is also associated with increased splanchnic blood flow. Evidence suggests that portal hypertension is partly caused by the hyperdynamic flow state of cirrhosis. Zwiebel et al.[93] found that blood flow was increased in the superior mesenteric arteries and splenic arteries of patients with cirrhosis and splenomegaly, compared with normal controls. Of interest, in patients with cirrhosis and normal-sized livers, splanchnic blood flow was not increased. Patients with isolated splenomegaly and normal livers were not included in this study.

The limitations of Doppler sonography in the evaluation of portal hypertension include the inability to determine vascular pressures and flow rates accurately. Patients with portal hypertension are often ill, with contracted livers, abundant ascites, and floating bowel, all of which create a technical challenge. In a comparison of duplex Doppler sonography with magnetic resonance angiography, MRI imaging was superior in the assessment of patency of the portal vein and surgical shunts, as well as in detection of varices.[94] However, when technically adequate, the Doppler study was accurate in the assessment of normal portal anatomy and flow direction. Duplex Doppler sonography has the added advantages of decreased cost and portability of the equipment and therefore should be used as the initial screening method for portal hypertension.

Portal Vein Thrombosis

Portal vein thrombosis has been associated with malignancy, including HCC, metastatic liver disease, carcinoma of the pancreas, and primary leiomyosarcoma of the portal vein,[95] as well as with chronic pancreatitis, hepatitis, septicemia, trauma, splenectomy, portacaval shunts, hypercoagulable states such as pregnancy and in neonates, omphalitis, umbilical vein catheterization, and acute dehydration.[96]

Sonographic findings of portal vein thrombosis include echogenic thrombus within the lumen of the vein, portal vein collaterals, expansion of the caliber of the vein, and cavernous transformation[96] (Figs. 4.32 and 4.33). **Cavernous transformation of the portal vein** refers to numerous wormlike vessels at the porta hepatis, which represent periportal collateral circulation.[97] This pattern is observed in long-standing thrombosis, requiring up to 12 months to occur, and thus is more likely to develop with benign disease.[98] **Acute thrombus** may appear relatively anechoic and thus may be overlooked unless Doppler ultrasound interrogation is performed. **Malignant thrombosis** of the portal vein has a high association with HCC and is often expansive, as is malignant occlusion from other primary or secondary disease (Fig. 4.32A and B and Fig. 4.34).

Doppler sonography is useful in distinguishing between benign and malignant portal vein thrombi in patients with cirrhosis. Both bland and malignant thrombi may demonstrate venous blood flow. Pulsatile (arterial) flow, however, has been found to be 95% specific for the diagnosis of malignant portal vein thrombosis (see Fig. 4.32). The sensitivity was only 62% because many malignant thrombi are hypovascular.[99]

Budd-Chiari Syndrome

The Budd-Chiari syndrome is a relatively rare disorder characterized by occlusion of the lumens of the hepatic veins with or without occlusion of the IVC lumen. The degree of occlusion and presence of collateral circulation predict the clinical course. Some patients die in the acute phase of liver failure. Causes of Budd-Chiari syndrome include coagulation abnormalities such as **polycythemia rubra vera, chronic leukemia, and paroxysmal nocturnal hemoglobinuria; trauma;** tumor extension from **primary HCC, renal carcinoma,** and **adrenocortical carcinoma; pregnancy; congenital abnormalities;** and **obstructing membranes.** The classic patient in North America is a young adult woman taking oral contraceptives who presents with an acute onset of ascites, right upper quadrant pain, hepatomegaly, and, to a lesser extent, splenomegaly. In some cases, no causal factor is found. The syndrome is more common in other geographic areas, including India, South Africa, and Asia.

Sonographic evaluation of the patient with Budd-Chiari syndrome includes gray-scale and Doppler features.[100-111] Ascites is invariably seen. The liver is typically large and bulbous in the acute phase (Fig. 4.35A). Hemorrhagic infarction may produce significant altered regional echogenicity. As infarcted areas become more fibrotic, echogenicity increases.[109] The caudate lobe is often

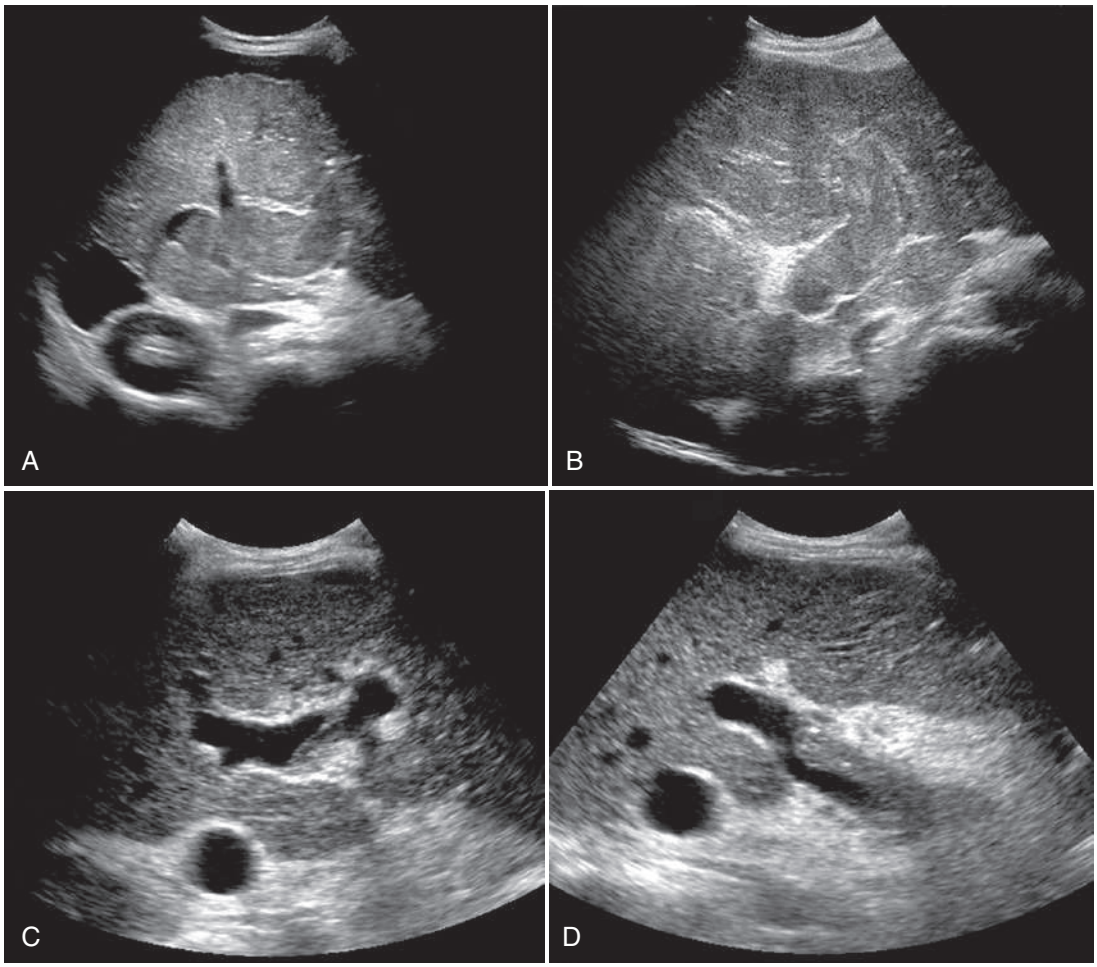

FIG. 4.32 Portal Vein Thrombosis: Benign and Malignant. Malignant thrombus: transverse views of **(A)** the vein at the porta hepatis and **(B)** left ascending left portal vein. Both are distended with occlusive thrombus. **Benign thrombus: (C)** transverse and **(D)** sagittal images of simple, bland nonocclusive thrombus in the left portal vein at the porta hepatis.

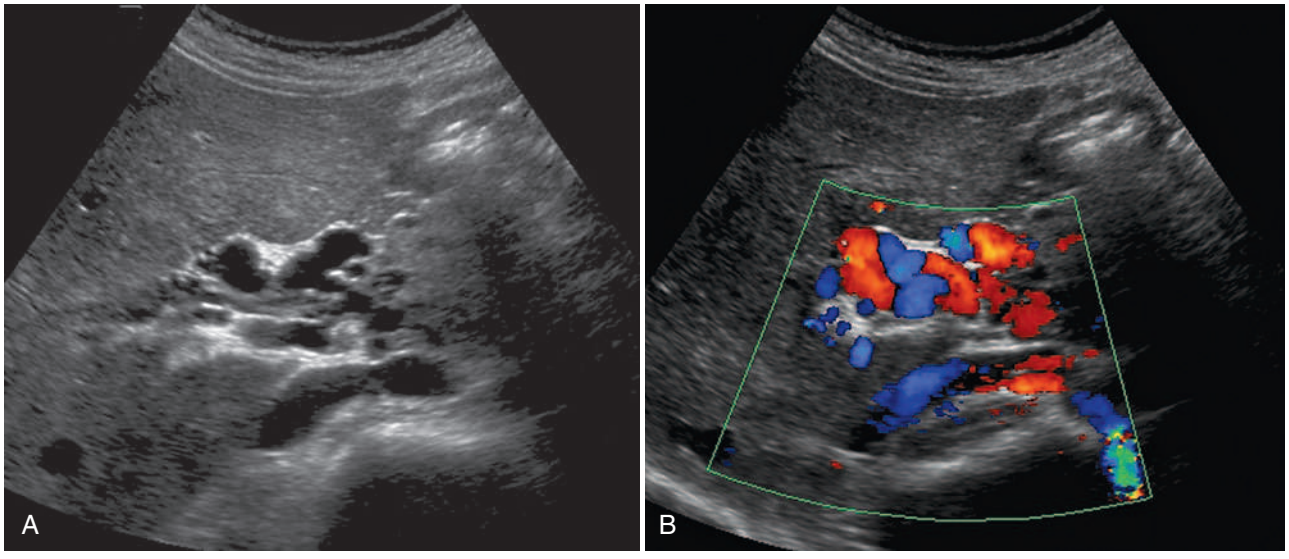

FIG. 4.33 Cavernous Transformation of Portal Vein. (A) Gray-scale image. **(B)** Color Doppler image. Numerous periportal collateral vessels are present.

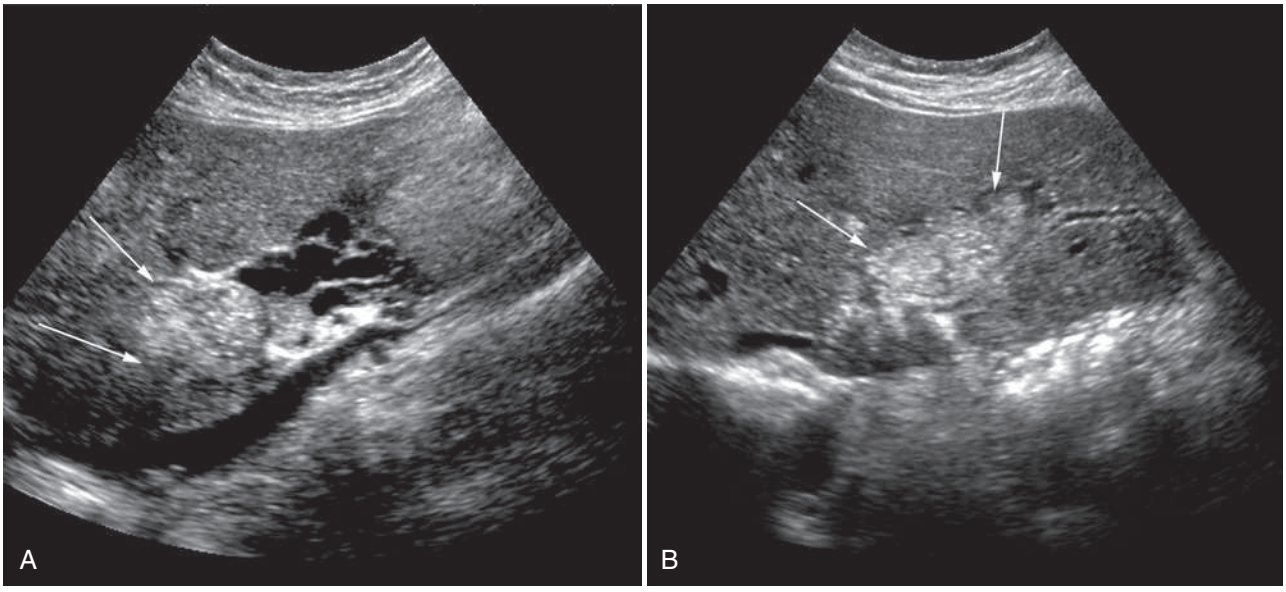

FIG. 4.34 Metastasis to the Portal Vein From Colon Cancer. (A) Sagittal view of the main portal vein at the porta hepatis and **(B)** subcostal oblique sonogram of the left ascending branch of the portal vein show the portal vein is distended and highly echogenic *(arrows)*. There is also evidence of cavernous transformation, an uncommon accompaniment of malignant portal vein occlusion.

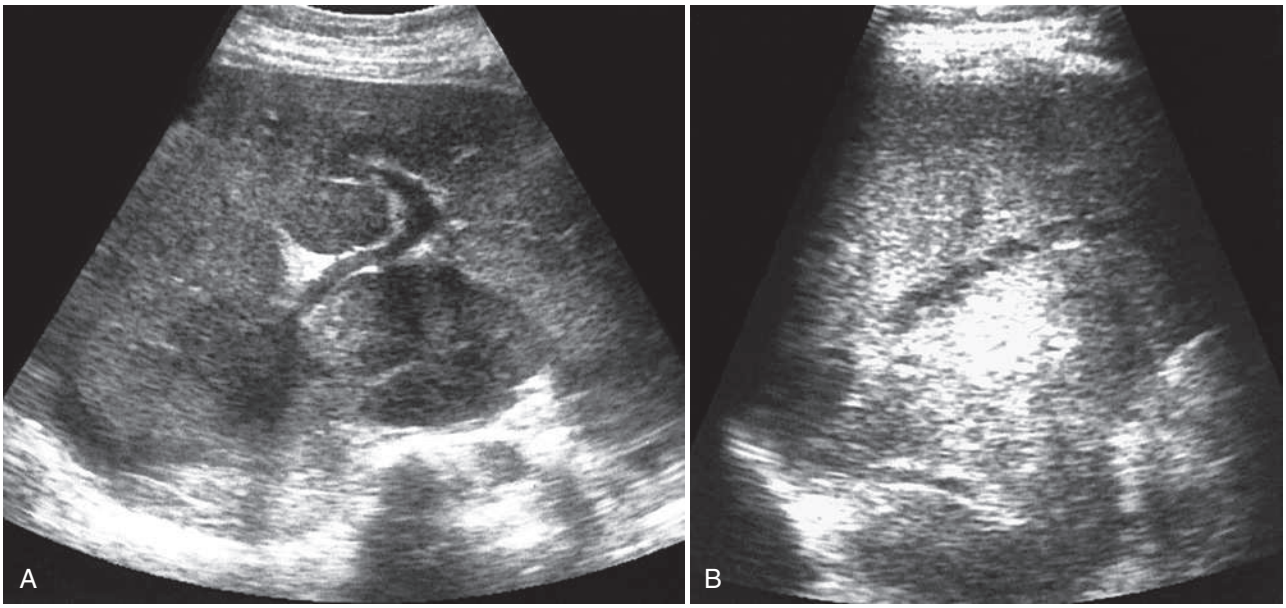

FIG. 4.35 Acute Budd-Chiari Syndrome. (A) Transverse view of liver shows a large, bulbous caudate lobe. **(B)** Sagittal view of right hepatic vein shows echoes within the vein lumen consistent with thrombosis, with absence of the vessel toward the inferior vena cava. Doppler ultrasound showed no flow in this vessel.

spared in Budd-Chiari syndrome because the emissary veins drain directly into the IVC at a lower level than the involved main hepatic veins. Increased blood flow through the caudate lobe leads to relative caudate enlargement.

Real-time scanning allows the radiologist to evaluate the IVC and hepatic veins noninvasively. Sonographic features include evidence of the **hepatic vein occlusion** (Fig. 4.35B and Fig. 4.36) and the development of **abnormal intrahepatic collaterals** (Fig. 4.37). The extent of hepatic venous involvement in Budd-Chiari syndrome includes partial or complete inability to see the hepatic veins, stenosis with proximal dilation, intraluminal echogenicity, thickened walls, thrombosis (Figs. 4.38 and 4.39), and extensive intrahepatic collaterals[107,108] (see Fig. 4.37). Membranous "webs" may be identified as echogenic or focal obliterations of the lumen.[107] Real-time ultrasonography, however, underestimates the presence of thrombosis and webs and may be inconclusive in a cirrhotic patient with hepatic veins that are difficult to image.[108] Intrahepatic collaterals, on gray-scale images, show as

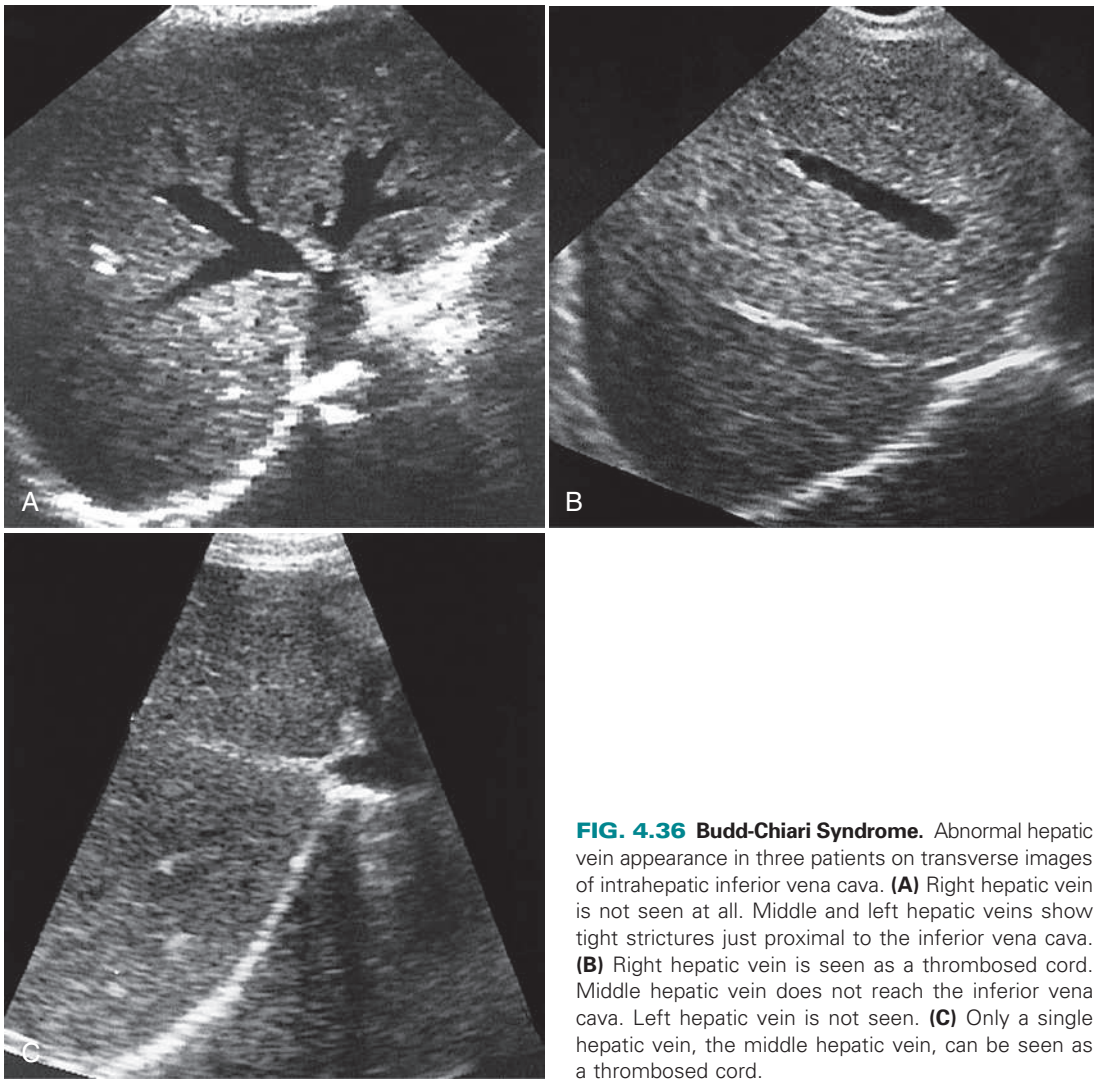

FIG. 4.36 Budd-Chiari Syndrome. Abnormal hepatic vein appearance in three patients on transverse images of intrahepatic inferior vena cava. **(A)** Right hepatic vein is not seen at all. Middle and left hepatic veins show tight strictures just proximal to the inferior vena cava. **(B)** Right hepatic vein is seen as a thrombosed cord. Middle hepatic vein does not reach the inferior vena cava. Left hepatic vein is not seen. **(C)** Only a single hepatic vein, the middle hepatic vein, can be seen as a thrombosed cord.

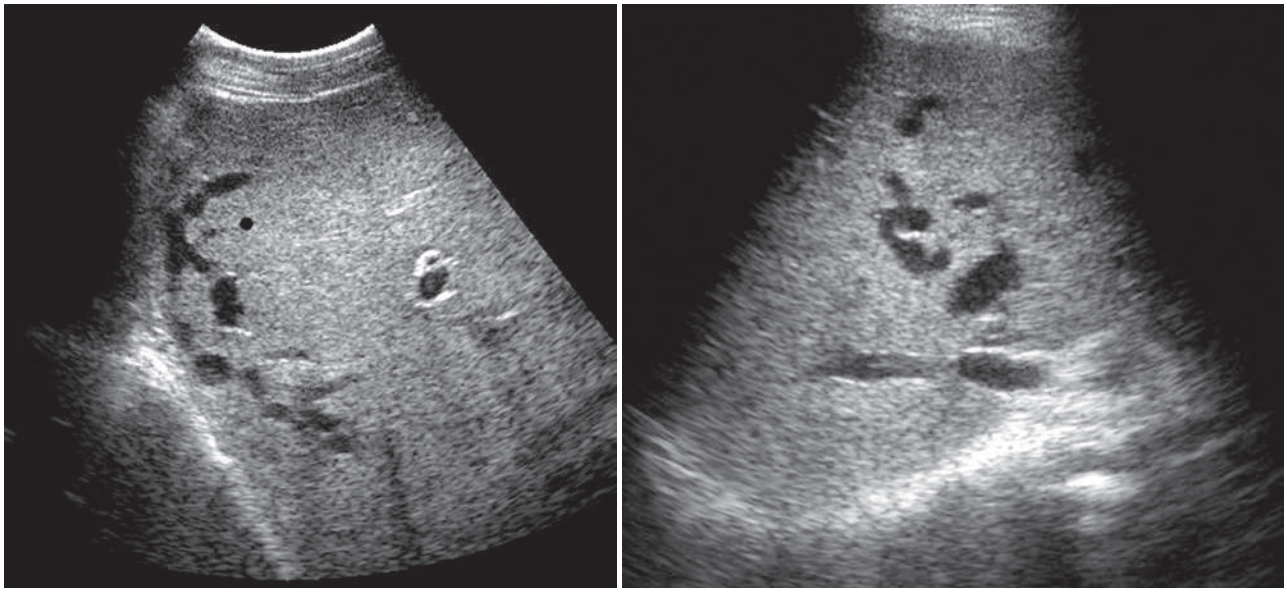

FIG. 4.37 Budd-Chiari Syndrome. Abnormal intrahepatic collaterals on gray-scale sonograms in two patients. Both images show vessels with abnormal locations and increased tortuosity compared with the normal intrahepatic vasculature.

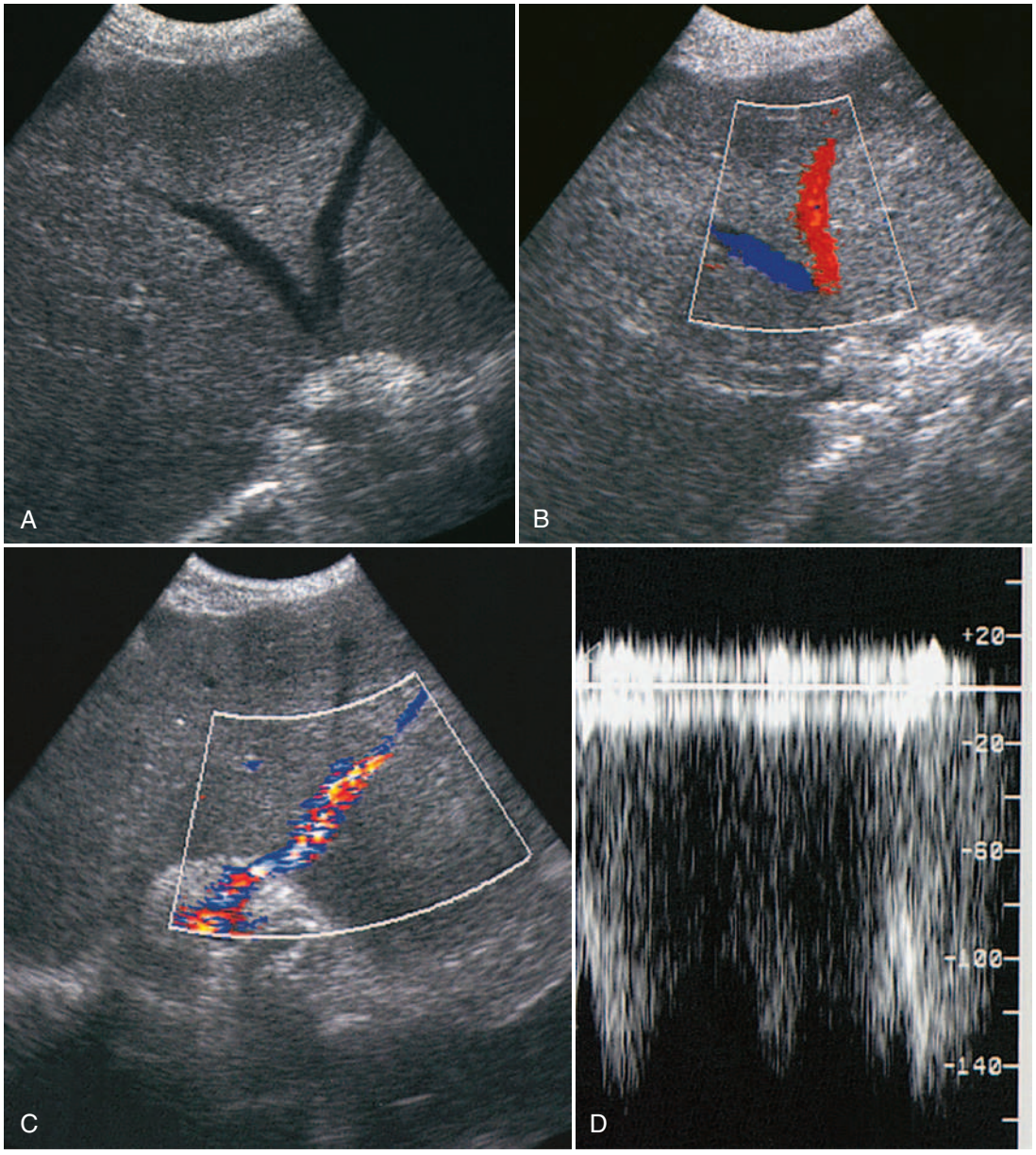

FIG. 4.38 Budd-Chiari Syndrome. (A) Gray-scale transverse image of hepatic venous confluence shows complete absence of the right hepatic vein with obliteration of the lumen of a common trunk for the middle and left hepatic veins. **(B)** Color Doppler image shows that blood flow in the middle hepatic vein *(blue)* is normally directed toward the inferior vena cava. As the trunk is obliterated, all the blood is flowing out of the left hepatic vein *(red),* which is abnormal. Other images showed anastomoses of the left hepatic vein with surface collaterals. **(C)** Color Doppler image shows an anomalous left hepatic vein with flow to the inferior vena cava (normal direction) and aliasing from a long stricture. **(D)** Spectral Doppler waveform of the anomalous left hepatic vein shows a very high abnormal velocity of approximately 140 cm/sec, confirming the tight stricture.

tubular vascular structures in an abnormal location and typically are seen extending from a hepatic vein to the liver surface, where they anastomose with systemic capsular vessels.

Duplex Doppler ultrasound and **color Doppler flow imaging** (CDFI) can help determine both the presence and the direction of hepatic venous flow in the evaluation of patients with suspected Budd-Chiari syndrome. The middle and left hepatic veins are best scanned in the transverse plane at the level of the xiphoid process. The right hepatic vein is best evaluated from a right intercostal approach.[105] The intricate pathways of blood flow out of the liver in the patient with Budd-Chiari syndrome can be mapped with documentation of hepatic venous occlusions, hepatic-systemic collaterals, hepatic venous–portal venous collaterals, and increased caliber of anomalous or accessory hepatic veins.

The normal blood flow in the IVC and hepatic veins is **phasic** in response to both the cardiac and respiratory cycles.[100] In Budd-Chiari syndrome, flow in the IVC, hepatic veins, or both, changes from phasic to **absent, reversed, turbulent,** or **continuous.**[104,112] Continuous flow has been called the **pseudoportal Doppler signal** and appears to reflect either partial IVC obstruction or extrinsic IVC compression.[103] The portal blood flow also may be affected and is characteristically either slowed or reversed.[104]

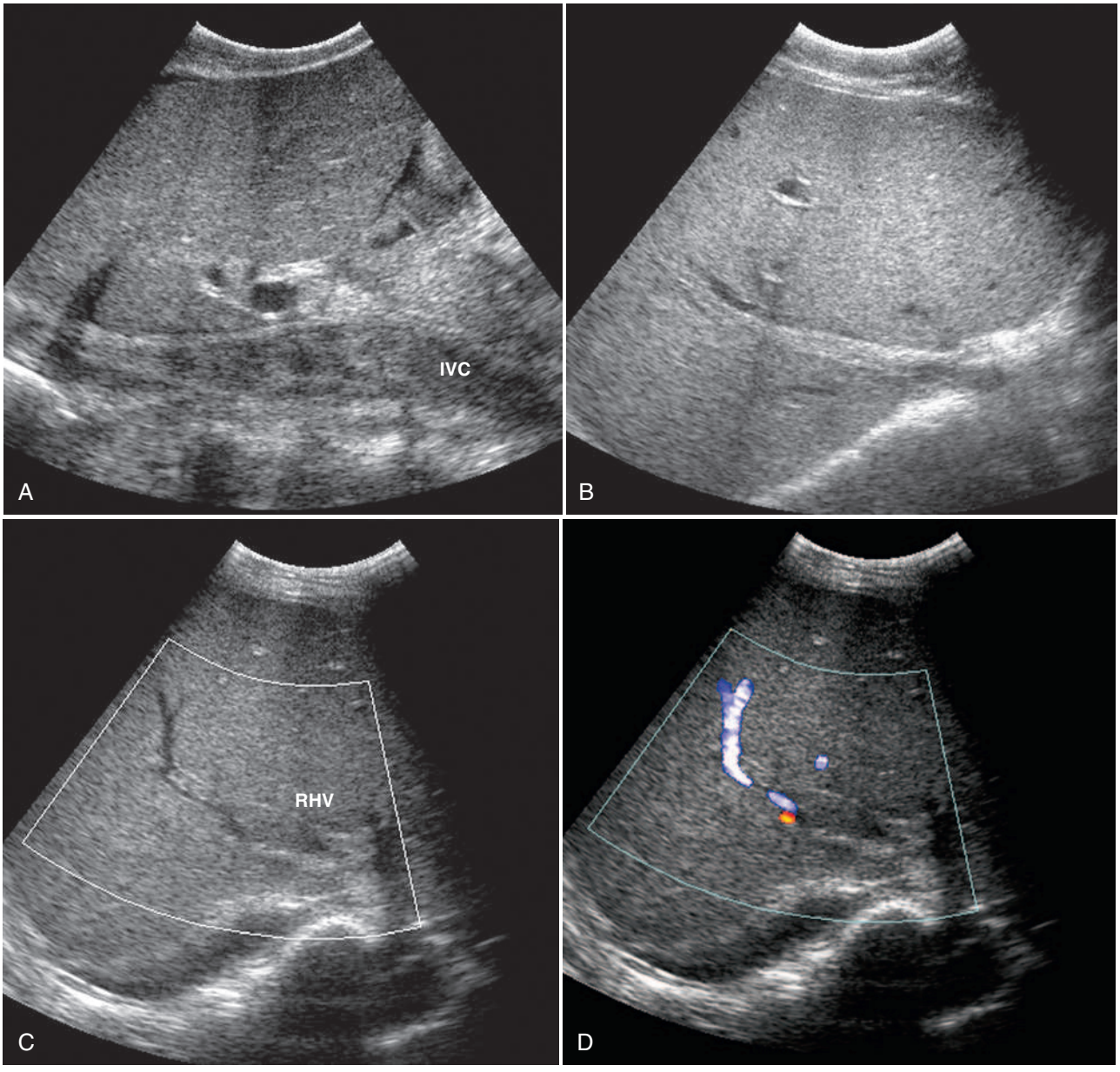

FIG. 4.39 Budd-Chiari Syndrome With Extensive Inferior Vena Cava Thrombosis. (A) Sagittal image of the inferior vena cava *(IVC)* shows that it is distended with echogenic thrombus. **(B)** Middle hepatic vein as a thrombosed cord. **(C)** Gray-scale image of right hepatic vein *(RHV)* and **(D)** color Doppler image show that anomalous right hepatic vein is distended with thrombus. There is flow in the vein proximal to the thrombus.

The use of Doppler in the patient with suspected Budd-Chiari syndrome lends strong supportive evidence to the gray-scale impression of missing, compressed, or otherwise abnormal hepatic veins and IVC.[102,112] Associated reversal of flow in the portal vein and epigastric collaterals is also optimally assessed with this technique.[112]

Hepatic veno-occlusive disease causes progressive occlusion of the small hepatic venules. The disease is endemic in Jamaica, secondary to **alkaloid toxicity** from bush tea. In North America, most cases are iatrogenic, secondary to hepatic irradiation and chemotherapy used in bone marrow transplantation.[101] Patients with hepatic veno-occlusive disease are clinically indistinguishable from those with Budd-Chiari syndrome. Duplex Doppler sonography demonstrates normal caliber, patency, and phasic forward (toward the heart) flow of the main hepatic veins and IVC.[101] Flow in the portal vein, however, may be abnormal, showing either reversed or "to and fro" flow.[101,113] In addition, the diagnosis of hepatic veno-occlusive disease may be suggested in a patient with decreased portal blood flow (compared with baseline measurement before ablative therapy).[101]

Portal Vein Aneurysm

Aneurysms of the portal vein are rare. Their origin is either congenital or acquired secondary to portal hypertension. Portal vein aneurysms have been described proximally at the junction of the superior mesenteric and splenic veins and distally involving

the portal venous radicles. The sonographic appearance is that of a vascular mass connected to the portal system with turbulent flow.

Intrahepatic Portosystemic Venous Shunts

Intrahepatic arterial-portal fistulas are well-recognized complications of large-gauge percutaneous liver biopsy and trauma. Conversely, intrahepatic portohepatic venous shunts are rare. Their cause is controversial and believed to be either congenital or related to portal hypertension.[114,115] Patients typically are middle aged and present with hepatic encephalopathy. Anatomically, portohepatic venous shunts are more common in the right lobe. Sonography demonstrates a tortuous tubular vessel or complex vascular channels, which connect a branch of the portal vein to a hepatic vein or the IVC.[114-116] The diagnosis is confirmed angiographically.

Aneurysm, Pseudoaneurysm, and Dissection

The hepatic artery is the fourth most common site of an intra-abdominal aneurysm, following the infrarenal aorta, iliac, and splenic arteries. Eighty percent of patients with a hepatic artery aneurysm experience **catastrophic rupture** into the peritoneum, biliary tree, gastrointestinal tract, or portal vein.[117] **Hepatic artery pseudoaneurysm** secondary to **chronic pancreatitis** has been described. The duplex Doppler sonographic examination revealed turbulent arterial flow within a sonolucent mass.[117] Primary dissection of the hepatic artery is rare and in most cases leads to death before diagnosis.[118] Sonography may show the intimal flap with the true and false channels.

Hereditary Hemorrhagic Telangiectasia

Hereditary hemorrhagic telangiectasia, or **Osler-Weber-Rendu,** is an autosomal dominant disorder that causes arteriovenous (AV) malformations in the liver, hepatic fibrosis, and cirrhosis. Patients present with multiple telangiectasias and recurrent episodes of bleeding. Sonographic findings include a large feeding common hepatic artery up to 10 mm, multiple dilated tubular structures representing AV malformations, and large draining hepatic veins secondary to AV shunting.[119]

Peliosis Hepatis

Peliosis hepatis is a rare liver disorder characterized by blood-filled cavities ranging from less than a millimeter to many centimeters in diameter. It can be distinguished from hemangioma by the presence of portal tracts within the fibrous stroma of the blood spaces. The pathogenesis of peliosis hepatis involves rupture of the reticulin fibers that support the sinusoidal walls, secondary to cell injury or nonspecific hepatocellular necrosis. The diagnosis of peliosis can be made with certainty only by histologic examination. Most cases of peliosis affect the liver, although other solid internal organs and lymph nodes may be involved in the process as well.

Although early reports described incidental detection of peliosis hepatis at autopsy in patients with chronic wasting disorders, it has now been seen following renal and liver transplantation, in association with a multitude of drugs, especially anabolic steroids, and with an increased incidence in patients with HIV.[119] The HIV association may occur alone or as part of bacillary angiomatosis in the spectrum of opportunistic infections of AIDS.[120] Peliosis hepatis has the potential to be aggressive and lethal.

The imaging features of peliosis hepatis have been described in single case reports,[121-123] although often without adequate histologic confirmation. Angiographically, the peliotic lesions have been described as accumulations of contrast detected late in the arterial phase and becoming more distinct in the parenchymal phase.[124] On sonography, described lesions are nonspecific and have shown single or multiple masses of heterogeneous echogenicity.[119,120,125] Calcifications have been reported[125] (Fig. 4.40). Peliosis hepatis is difficult to diagnose both clinically and radiologically and must be suspected in a susceptible individual with a liver mass.

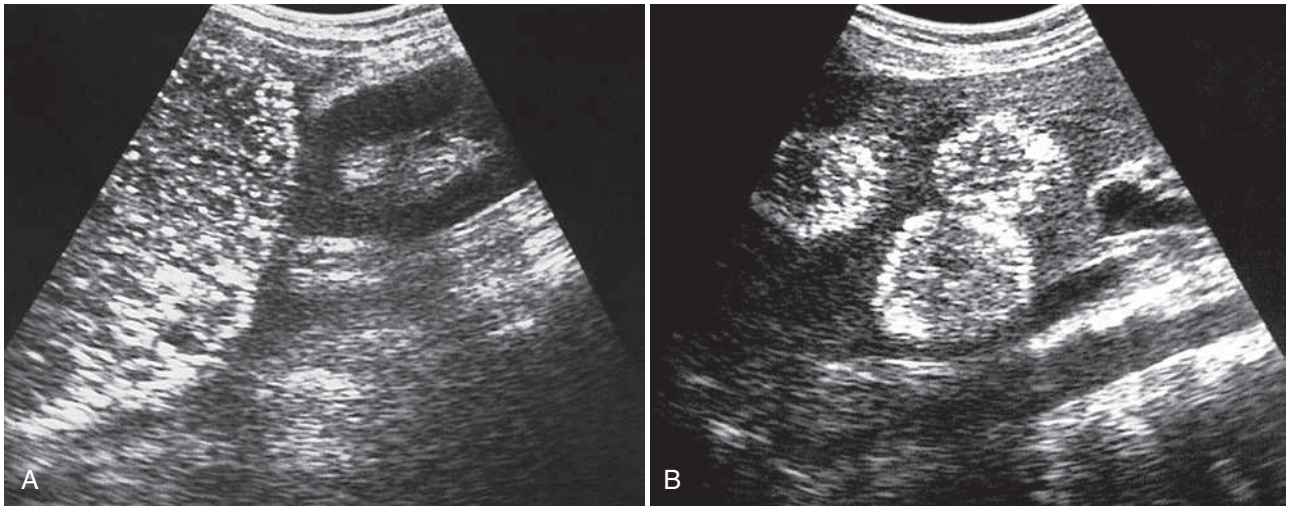

FIG. 4.40 Peliosis Hepatis. Peliosis hepatis in 34-year-old woman with deteriorating liver function necessitating transplantation. **(A)** Sagittal right lobe and **(B)** sagittal left lobe scans show multiple large liver masses with innumerable tiny punctate calcifications. (With permission from Muradali D, Wilson SR, Wanless IR, et al. Peliosis hepatis with intrahepatic calcifications. J Ultrasound Med. 1996;15[3]:257-260.[125])

HEPATIC MASSES

Focal liver masses include a variety of malignant and benign neoplasms, as well as masses with developmental, inflammatory, and traumatic causes. In cross-sectional imaging, two basic issues relate to a focal liver lesion: **characterization** of a known liver lesion (what is it?) and **detection** (is it there?). The answer to either question requires a focused examination, often adjusted according to the clinical situation.

Liver Mass Characterization

Characterization of a liver mass on conventional sonography is based on the **appearance** of the mass on gray-scale imaging and **vascular information** derived from spectral, color, and power Doppler sonography. With excellent spatial and contrast resolution, the gray-scale morphology of a mass allows for the differentiation of cystic and solid masses, and characteristic appearances may suggest the correct diagnosis without further evaluation. Often, however, definitive diagnosis is not based on gray-scale information alone, but on vascular information obtained on conventional Doppler ultrasound examination. However, conventional Doppler often fails in the evaluation of a focal liver mass, particularly in a large patient or on a small or deep liver lesion, or on a mass with inherent weak Doppler signals. Motion artifact is also highly problematic for abdominal Doppler ultrasound studies, and a left lobe liver mass close to the pulsation of the cardiac apex, for example, can limit assessment by conventional Doppler. For these reasons, conventional ultrasound is not regarded highly for characterization of focal liver masses, and a mass detected on ultrasound is historically evaluated further with CECT or MRI for definitive characterization.

Role of Microbubble Contrast Agents

Worldwide, noninvasive diagnosis of focal liver masses is achieved with CECT and MRI based on recognized enhancement patterns in the arterial and portal venous phases. These noninvasive methods of characterization have become so accurate that excisional and percutaneous biopsy for diagnosis of liver masses is now rarely performed. In recent years, however, CEUS has joined the ranks of CT and MRI in providing similar diagnostic information as well as information unique to CEUS.[126] Injection of a microbubble contrast agent to enhance the Doppler signal from blood and imaging with a specialized imaging technique such as pulse inversion sonography allow for preferential detection of the signal from the contrast agent while suppressing the signal from background tissue.

Ultrasound contrast agents currently in use are second-generation agents comprising tiny bubbles of a perfluorocarbon gas contained within a stabilizing shell. Microbubble contrast agents are blood pool agents that do not diffuse through the vascular endothelium. This is of potential importance when imaging the liver because comparable contrast agents for CT and MRI may diffuse into the interstitium of a tumor. Our personal experience with perfluorocarbon microbubble agents is largely based on the use of Definity (Lantheus Medical Imaging, Billerica, MA) and brief exposure to Optison (GE Healthcare, Milwaukee, WI).[127,128] We routinely perform CEUS for characterization of incidentally detected liver masses, those found on surveillance scans of patients at risk for HCC, and any focal mass referred by our clinicians found on outside imaging or indeterminate on CT and MRI.[129]

Microbubble contrast agents for ultrasound are unique in that they interact with the imaging process.[127] The major determinant of this interaction is the peak negative pressure of the transmitted ultrasound pulse, reflected by the **mechanical index** (MI). The bubbles show stable, nonlinear oscillation when exposed to an ultrasound field with a low MI, with the production of harmonics of the transmitted frequency, including the frequency double that of the sound emitted by the transducer, the **second harmonic.** When the MI is raised sufficiently, the bubbles undergo irreversible disruption, with the production of a brief but bright, high-intensity ultrasound signal (see Chapter 3).

Liver lesion characterization with microbubble contrast agents is based on lesional vascularity and lesional enhancement in the arterial phase (10-40 sec), portal venous phase (40-90 sec), and late phase (up to 5 minutes). **Lesional vascularity** assessment depends on continuous imaging of the agents while they are within the vascular pool. We document the presence, number, distribution, and morphology of any lesional vessels. A low MI is essential because it will preserve the contrast agent population without destruction of the bubbles in the imaging field, allowing for prolonged periods of real-time observation. The morphology of the lesional vessels is discriminatory and facilitates the diagnosis of liver lesions (Fig. 4.41).

Lesional enhancement is best determined by comparing the echogenicity of the lesion to the echogenicity of the liver at a similar depth on the same frame and requires knowledge of liver blood flow. The liver has a dual blood supply from the hepatic artery and portal vein. The liver derives a larger proportion of its blood from the portal vein, whereas most liver tumors derive their blood supply from the hepatic artery. At the initiation of the injection, the low-MI technique will cause the entire field of view (FOV) to appear virtually black, regardless of the baseline appearance of the liver and the lesion in question. In fact, a known mass may be invisible at this point. As the microbubbles arrive in the FOV, the discrete vessels in the liver and then those within a liver lesion will be visualized, followed by increasing generalized enhancement as the microvascular volume of liver and lesion fills with the contrast agent. The liver parenchyma will appear more echogenic in the arterial phase than at baseline, and even more enhanced in the portal venous phase, as a reflection of its blood flow. Vascularity and enhancement patterns of a liver lesion, by comparison, will therefore reflect the actual blood flow and hemodynamics of the lesion in question, such that a hyperarterialized mass will appear more enhanced against a less enhanced liver on an arterial phase sequence. Conversely, a hypoperfused lesion will appear as a dark or hypoechoic region within the enhanced liver on an arterial phase sequence.

Currently, evaluation of lesional enhancement is usually performed with the low-MI technique just described. However, details of vessel morphology and lesional enhancement are even more sensitively assessed using a bubble-tracking technique called **maximum-intensity projection** (MIP) imaging.[130] In this

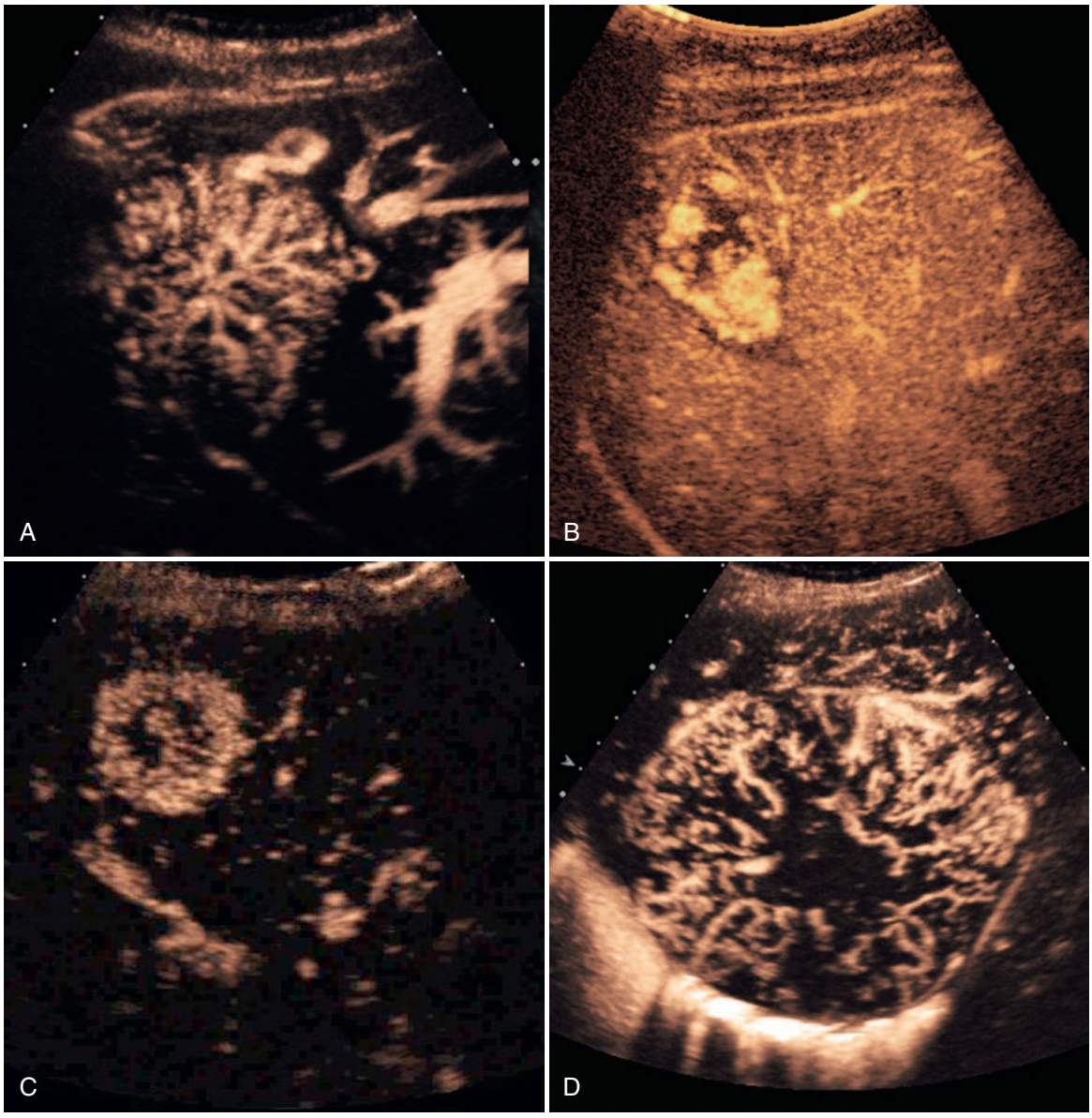

FIG. 4.41 Early Arterial Phase Vascular Morphology. Shown on real-time dynamic ultrasound, this is contributory to diagnosis of focal liver masses. **(A)** Stellate vessels are highly suggestive of **focal nodular hyperplasia. (B)** Peripheral discontinuous nodular enhancement without linear vascularity suggests **hemangioma. (C)** Rim enhancement has a high association with malignant disease, especially **metastases** and **cholangiocarcinoma. (D)** Dysmorphic tortuous vessels are suggestive of malignant tumors, in this case a **hepatocellular carcinoma.** The filling from the periphery, as here, is common for this diagnosis.

technique, performed either at wash-in of contrast or at the peak of arterial phase enhancement, a **brief high-MI exposure will destroy all the bubbles** within the FOV. Sequential frames, as the lesion and liver are reperfused, will track the bubble course providing exquisite resolution (Fig. 4.42, Videos 4.5 and 4.6).

There are established **algorithms** for the diagnosis of focal liver masses with CEUS, with similarities to CT and MRI algorithms but also important differences[131-133] (Table 4.3). Diagnosis of **benign liver masses, hemangioma,** and **focal nodular hyperplasia** (FNH) is extremely accurate showing characteristic features of enhancement in the arterial phase and **sustained enhancement** in the portal venous phase (Fig. 4.43), such that their enhancement equals or exceeds the enhancement of the adjacent liver. **Malignant tumors,** by comparison, tend to show **washout,** such that the tumor appears unenhanced in the portal venous phase of enhancement (Fig. 4.44). Exceptions to this general rule include frequent washout of benign **hepatic adenoma** and delayed or no washout of HCC. Discrimination of benign and malignant liver masses has similar high accuracy.[134]

Liver Mass Detection

Excellent spatial resolution allows small lesions to be well seen on sonography. Therefore it is not size but **echogenicity** that

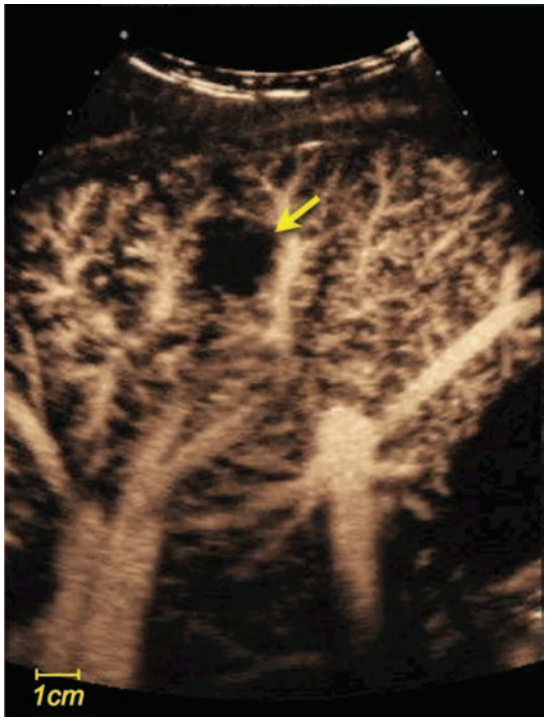

FIG. 4.42 Normal Liver Vasculature. Temporal maximum-intensity projection image shows accumulated enhancement in 11 seconds after contrast material arrives in liver. Depiction of vessel structure to fifth-order branching is evident. Focal unenhanced region *(arrow)* is slowly perfusing **hemangioma.** (With permission from Wilson S, Jang H, Kim T, et al. Real-time temporal maximum-intensity-projection imaging of hepatic lesions with contrast-enhanced sonography. AJR Am J Roentgenol. 2008;190[3]:691-695.[130])

determines lesion conspicuity on a sonogram. That is, a tiny mass of only a few millimeters will be easily seen if it is increased or decreased in echogenicity compared with the adjacent liver parenchyma. Because many metastases are either hypoechoic or hyperechoic relative to the liver, a careful examination should allow for their detection. Nonetheless, many metastatic lesions are of similar echogenicity to the background liver, making their detection difficult or impossible, even if they are of a substantial size. This occurs when the backscatter from the lesion is virtually identical to the backscatter from the liver parenchyma.

To combat this inherent problem of lack of contrast between many metastatic liver lesions and the background liver on conventional sonography, contrast-enhanced liver ultrasound is helpful (Fig. 4.45). CEUS increases the backscatter from the liver compared with the liver lesions, thereby improving their detection. This occurs rapidly following the arterial phase of enhancement and generally lasts for several minutes beginning in the portal venous and persisting for the late phase.

Of historic interest is the use of the first-generation contrast agent Levovist (Schering AG, Berlin). After clearance of the contrast agent from the vascular pool, the microbubble persisted in the liver, probably within the Kupffer cells on the basis of phagocytosis. A high-MI sweep through the liver produced bright enhancement in the distribution of the bubbles. Therefore all normal liver enhances. Liver metastases, lacking Kupffer cells, do not enhance and therefore show as black or hypoechoic holes within the enhanced parenchyma[135] (Fig. 4.45A and B). In a multicenter study conducted in Europe and Canada, more and smaller lesions were seen than on baseline scan.[136] Overall, lesion detection was equivalent to that of CT and MRI. The decibel difference between the lesions and the liver parenchyma is increased many fold because of increased backscatter from contrast agent within the normal liver tissue. Although many results were compelling, these first-generation contrast agents are no longer marketed.

Today, current requirements for improved lesion detection use a similar technique of CEUS with a **perfluorocarbon contrast agent** and low-MI scanning in both the arterial and the portal venous phase. The use of a low-MI imaging technique for lesion detection has advantages in terms of scanning because the microbubble population is preserved and timing is not so critical. Virtually all metastases will be unenhanced relative to the liver in the portal and the late phase and the liver parenchyma will remain optimally enhanced. Therefore malignant lesions tend to appear hypoechoic in the portal phase, allowing for improved lesion detection (Fig. 4.45C and D). This observation, that malignant lesions tend to be hypoechoic in the portal venous phase of perfluorocarbon liver enhancement, is helpful for both lesion detection and lesion characterization. Enhancement of benign lesions, FNH, and hemangioma generally equals or exceeds liver enhancement in the portal venous phase.

Detection of hypervascular liver masses (e.g., HCC, metastases) is also improved by scanning with perfluorocarbon agents in the arterial phase. These lesions will generally show as hyperechoic masses relative to the liver parenchyma in the arterial phase because they are predominantly supplied by hepatic arterial flow.

HEPATIC NEOPLASMS

Sonographic visualization of a focal liver mass may occur in a variety of clinical scenarios, ranging from incidental detection to identification in a symptomatic patient or as part of a focused search in a patient at risk for hepatic neoplasm. **Hemangiomas, FNH,** and **adenomas** are the benign neoplasms typically encountered in the liver, whereas **HCC** and **metastases** account for the majority of malignant tumors.

The role of imaging in the evaluation of an identified focal liver mass is to determine which masses are potentially clinically important, requiring confirmations of their diagnoses, and which masses are likely to be insignificant and benign, not requiring further evaluation to confirm their nature. On a sonographic study, there is considerable overlap in the appearances of focal liver masses. Once a liver mass is seen, however, the excellent contrast and spatial resolution of state-of-the-art ultrasound equipment have provided guidelines for the initial management of patients, which include recognition of the following features:

- A **hypoechoic halo** identified around an echogenic or isoechoic liver mass is an ominous sonographic sign necessitating definitive diagnosis.
- A **hypoechoic and solid liver mass** is highly likely to be significant and also requires definitive diagnosis.

TABLE 4.3 Schematic of Algorithm for Liver Mass Diagnosis on Contrast-Enhanced Ultrasound

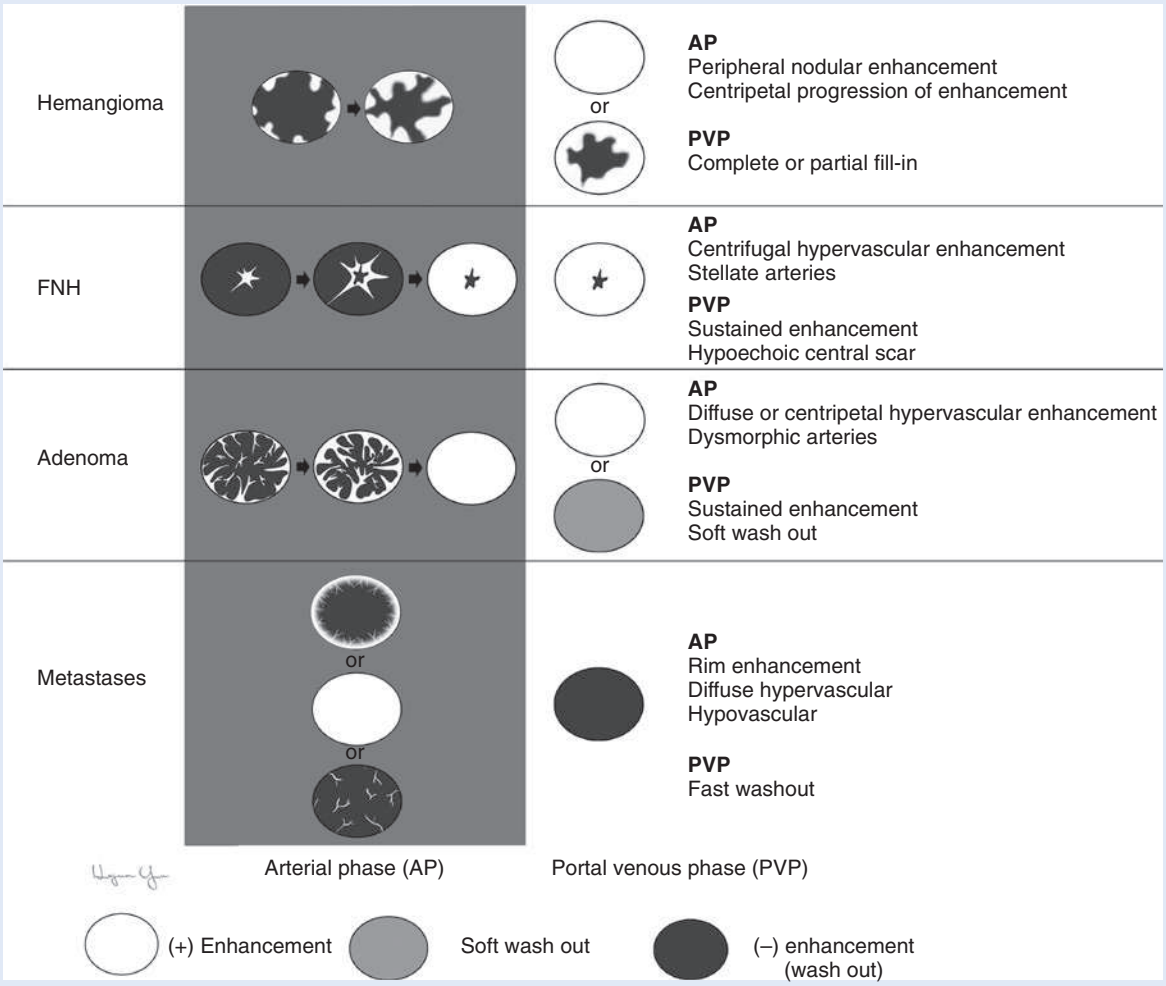

AP, Arterial phase; *FNH,* focal nodular hyperplasia; *PVP,* portal venous phase.
With permission from Wilson SR, Burns PN. Microbubble-enhanced US in body imaging: what role? Radiology. 2010;257(1):24-39.[148]

- **Multiple solid liver masses** may be significant and suggest possible metastatic or multifocal malignant liver disease. However, hemangiomas are also frequently multiple.
- **Clinical history** of malignancy, chronic liver disease or hepatitis, and symptoms referable to the liver are requisite information for interpretation of a focal liver lesion.

Benign Hepatic Neoplasms

Cavernous Hemangioma

Cavernous hemangiomas are the most common benign tumors of the liver, occurring in approximately 4% of the population. They occur in all age groups but are more common in adults, particularly women, with a female-to-male ratio of approximately 5:1. Histologically, hemangiomas consist of multiple vascular channels that are lined by a single layer of endothelium and separated and supported by fibrous septa. The vascular spaces may contain thrombi.

The vast majority of hemangiomas are small, asymptomatic, and discovered incidentally. Large lesions may, in rare cases, produce symptoms of acute abdominal pain, caused by hemorrhage or thrombosis within the tumor. Thrombocytopenia, caused by sequestration and destruction of platelets within a large cavernous hemangioma **(Kasabach-Merritt syndrome),** occasionally occurs in infants and is rare in adults.

Traditional teaching suggests that once identified in the adult, hemangiomas usually have reached a stable size, rarely changing in appearance or size.[137,138] In our practice, however, we have documented substantial growth of some lesions over many years of follow-up. Hemangiomas may enlarge during pregnancy or with the administration of estrogens, suggesting the tumor is hormone dependent.

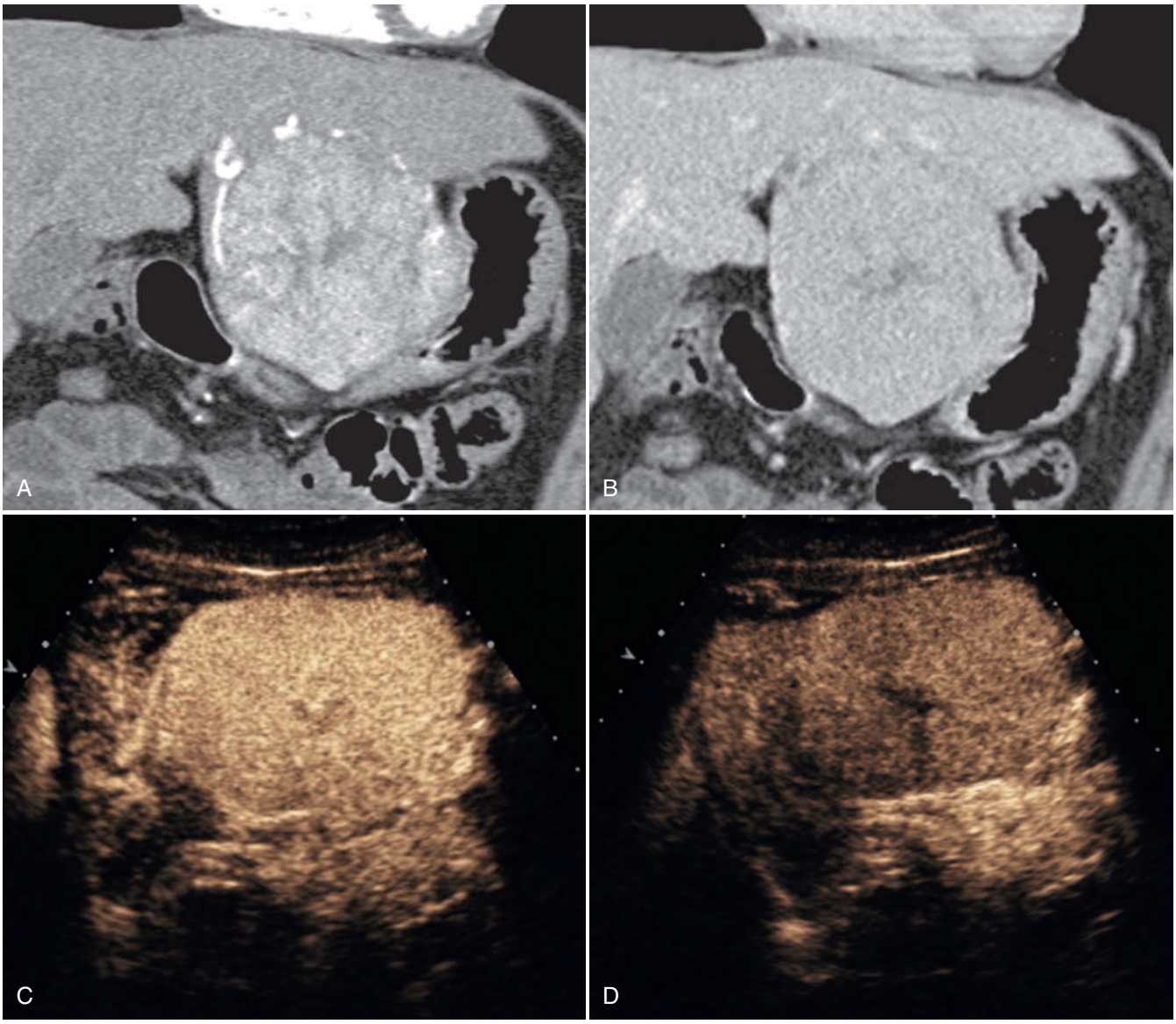

FIG. 4.43 Sustained enhancement in the portal venous phase, on contrast-enhanced ultrasound (CEUS) and contrast-enhanced computed tomography (CECT) scan, suggestive of a benign mass. **(A)** and **(C)** are arterial phase images on CT and CEUS, respectively, both showing arterial phase hyperenhancement. **(B)** and **(D)** are portal venous phase images on CT and CEUS, respectively, both showing sustained enhancement and a nonenhanced scar. This sustained enhancement is concordant on the two scans and suggests a benign tumor. This is a confirmed FNH. See also Video 4.5. (With permission from Wilson S, Greenbaum L, Goldberg B. Contrast-enhanced ultrasound: what is the evidence and what are the obstacles? AJR Am J Roentgenol. 2009;193[1]:55-60.[129])

The sonographic appearance of cavernous hemangioma varies. Typically the lesion is small (<3 cm in diameter), well defined, homogeneous, and hyperechoic[139] (Fig. 4.46A). The increased echogenicity has been related to the numerous interfaces between the walls of the cavernous sinuses and the blood within.[140] Inconsistently seen and nonspecific, posterior acoustic enhancement has been correlated with hypervascularity on angiography[141] (Fig. 4.46H). Approximately 67% to 79% of hemangiomas are hyperechoic,[142,143] of which 58% to 73% are homogeneous.[135,141] Other features include a nonhomogeneous central area containing hypoechoic portions, which may appear uniformly granular (Fig. 4.46D-F) or lacelike in character (Fig. 4.46D); an echogenic border, either a thin rim or a thick rind (Fig. 4.46E-G); and a tendency toward scalloping of the margin (Fig. 4.46B).[144] Larger lesions tend to be heterogeneous, with central hypoechoic foci corresponding to fibrous collagen scars (Fig. 4.46C), large vascular spaces, or both. A hemangioma may appear hypoechoic within the background of a fatty infiltrated liver.[145] Calcification is rare (Fig. 4.46I).

Hemangiomas are characterized by extremely slow blood flow that will not routinely be detected by either color or duplex Doppler sonography. Occasional lesions may show a low to midrange kilohertz (kHz) shift from both peripheral and central blood vessels. The ability of power Doppler ultrasound, which

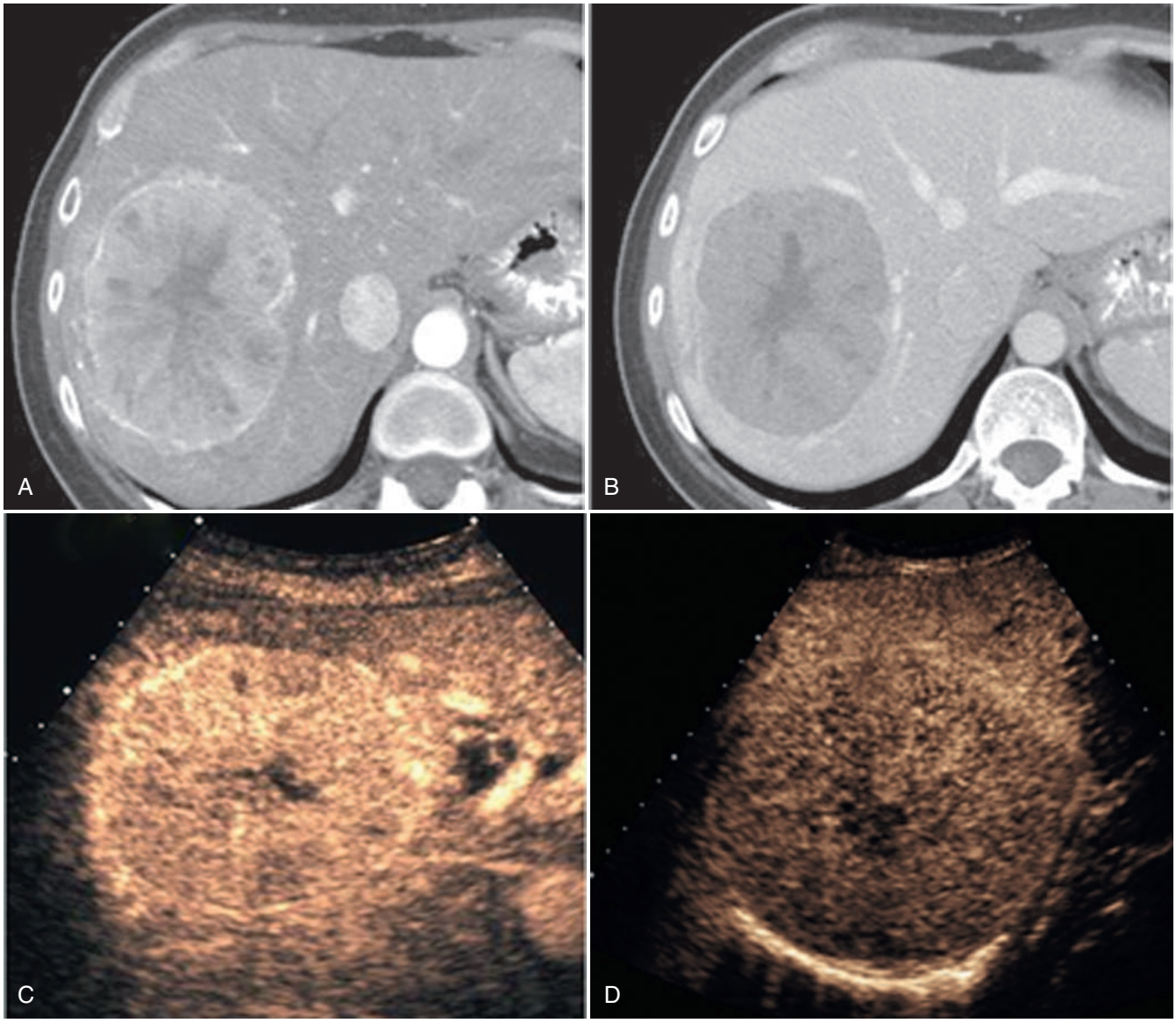

FIG. 4.44 Washout in the portal venous phase, on computed tomography (CT) and contrast-enhanced ultrasound (CEUS) is suggestive of a malignant mass in this patient with hepatocellular carcinoma. Contrast-enhanced CT scan in the **(A)** arterial phase and **(B)** portal venous phase. **(C)** and **(D)** Same mass at the same time intervals on CEUS. On each scan, there is hyperenhancement in the arterial phase and washout in the portal venous phase highly correlated with a malignant mass.

is more sensitive to slow flow, to detect signals within a hemangioma is controversial.[146]

Cavernous hemangiomas are often observed on abdominal sonograms performed for any reason, and confirmation of all visualized lesions has proved to be costly and unnecessary. Therefore it is considered acceptable practice to manage some patients conservatively without confirmation of the diagnosis. When a hyperechoic lesion typical of a cavernous hemangioma is incidentally discovered, no further examination is usually necessary, or at most, a repeat ultrasound is performed in 3 to 6 months to document lack of change.

Conversely, potentially significant lesions may mimic the morphology of a hemangioma on ultrasound and produce a single mass or multiple masses of uniform increased echogenicity. These include metastases from a colon primary or a vascular primary tumor, such as a neuroendocrine tumor and small HCCs in particular. In a prospective evaluation of 1982 patients with newly diagnosed cirrhosis, Caturelli et al.[147] found that 50% of echogenic liver lesions with morphology suggestive of hemangioma had that diagnosis, although 50% of these proved to be HCC. The authors also showed that in 1648 patients with known cirrhosis and new appearance of an echogenic hemangioma-like mass, all were HCC. These results emphasize the necessity to prove the diagnosis of all masses with this morphology in high-risk patients. Therefore in a patient with a known malignancy, an increased risk for hepatoma, abnormal results of LFTs, clinical symptoms referable to the liver, or an atypical sonographic pattern, one of the following additional imaging techniques is generally

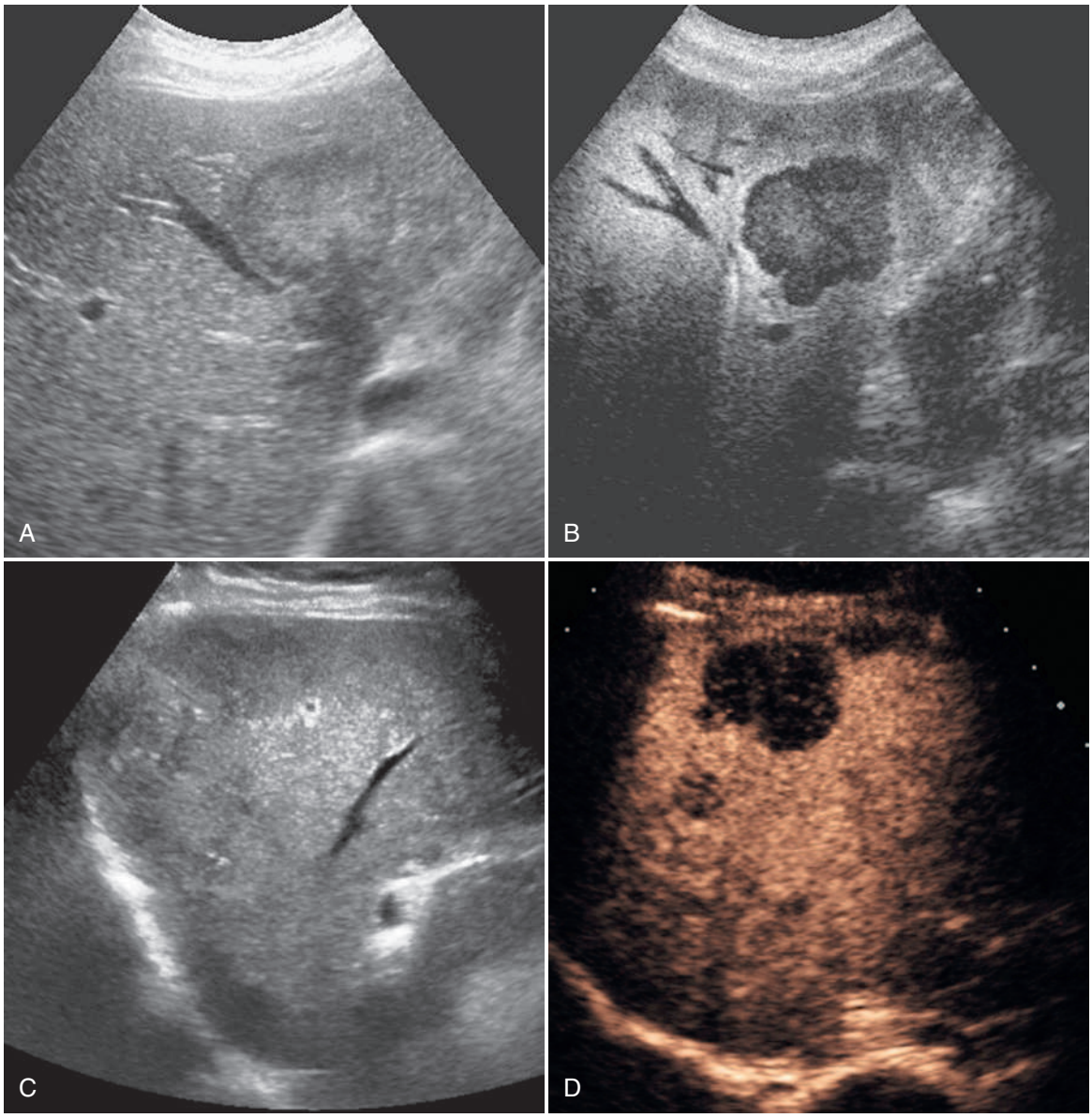

FIG. 4.45 Contrast-Enhanced Ultrasound (CEUS) Images of Increased Conspicuity of Metastases in Two Patients. (A) and **(B)** are of historic significance. **(A)** Subtle isoechoic mass in the liver. **(B)** Postvascular image with contrast agent Levovist showing increased echogenicity of the liver. The mass now appears black with increased conspicuity. **(C)** Baseline image showing a hypoechoic region in the liver without good margination raising the possibility it could be fat sparing. **(D)** CEUS performed with a perfluorocarbon contrast agent shows punched-out washout of a large metastasis, again increasing the conspicuity. Two additional small masses are shown. More and smaller metastases are detected with CEUS than on baseline.

recommended to confirm the suspicion of hemangioma: CEUS, CT, or MRI.

In the arterial phase on CEUS, hemangiomas show peripheral puddles and pools that are brighter than the adjacent enhanced liver parenchyma. There are no linear vessels. Over time, centripetal progression of the enhancement leads to complete globular fill-in, with sustained enhancement equal to or better than the liver in the portal venous phase, which may last for several minutes[148] (Fig. 4.47). This enhancement may occur rapidly or slowly and may be incomplete, even in the late portal venous phase (Video 4.6). We have diagnosed almost 100% of hemangiomas with CEUS, including those of small size, removing the necessity for confirmation with other imaging modalities.

In a small minority of patients, imaging will not allow definitive diagnosis of hemangioma. Percutaneous biopsy of hepatic hemangiomas has been safely performed.[149,150] Cronan et al.[149] performed biopsies on 15 patients (12 of whom were outpatients) using a 20-gauge needle. In all patients the histologic sample was diagnostic and was characterized by large spaces with an endothelial lining. It is recommended when sampling lesions that normal liver be interposed between the abdominal wall and the hemangioma to allow hepatic tamponade of any potential bleeding.

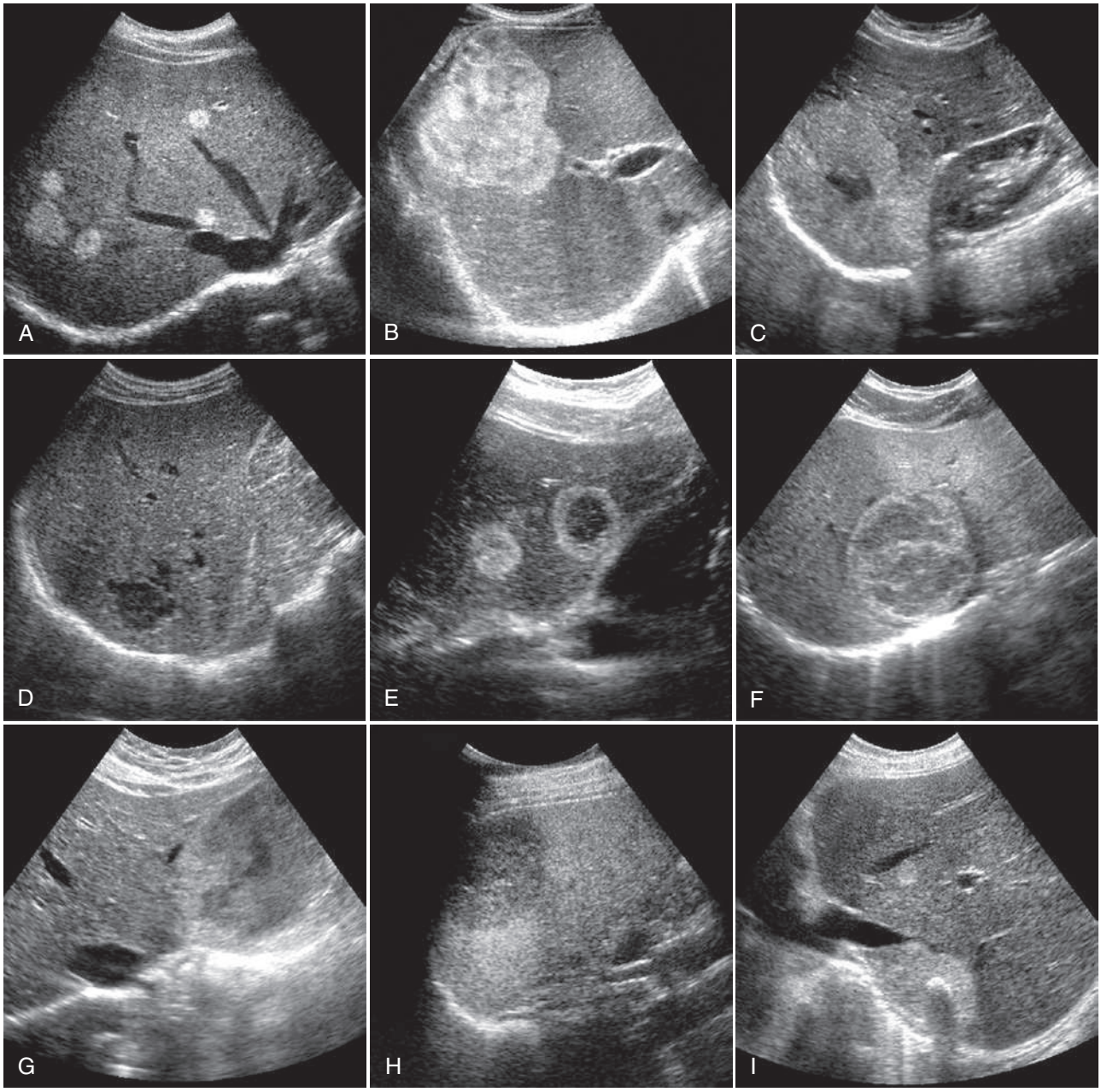

FIG. 4.46 Hemangiomas: Spectrum of Appearances. *Top row,* **Classic morphology. (A)** Multiple small echogenic masses. **(B)** Single large, lobulated echogenic mass. **(C)** Echogenic lobulated mass with a hypoechoic area centrally, probably related to central thrombosis or scarring. *Middle row,* **Atypical morphology. (D)** Atypical hemangioma. It is hypoechoic and has a thin echogenic border. **(E) Classic and atypical morphologies.** The atypical hemangioma has a thick, uniform echogenic border. **(F)** Atypical hemangioma is partially hypoechoic centrally with an irregular echogenic rim. *Bottom row,* **Infrequent observations. (G)** Exophytic hemangioma bulging from the left lateral lobe of the liver. **(H)** Hypoechoic mass with increased through transmission, a suggestive but infrequently encountered sign of hemangioma. **(I)** Central calcification in a hemangioma with distal acoustic shadowing. This is a rare ending in hemangiomas.

Sclerosis of hemangioma creates diagnostic difficulty. In our experience, these sclerotic hemangiomas mimic a malignant mass on all modalities showing frequent portal venous phase washout and lacking the classic peripheral discontinuous peripheral globules or puddles that are virtually diagnostic of hemangioma on contrast-enhanced studies. Biopsy is, therefore, frequently necessary to confirm sclerotic hemangioma.

Focal Nodular Hyperplasia

FNH is the second most common benign liver mass after hemangioma. These masses are believed to be developmental hyperplastic lesions related to an area of congenital vascular malformation, probably a preexisting arterial spider-like malformation.[151] Hormonal influences may be a factor because FNH is much more common in women than men, particularly in the

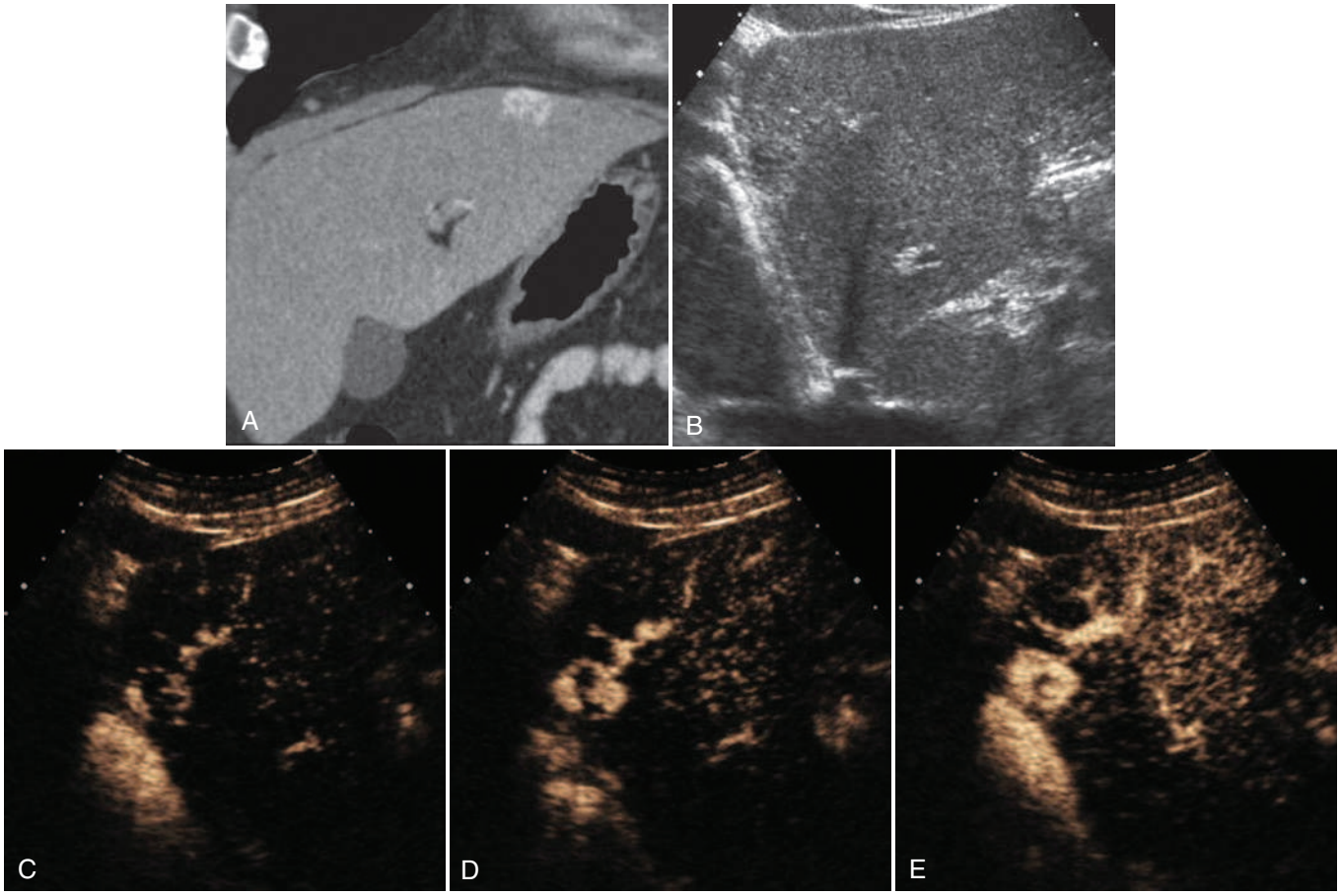

FIG. 4.47 Characterization of Hemangioma With Definity Enhancement. Resolution of an indeterminate mass on computed tomography (CT) scan is shown in a 65-year-old man with carcinoma of the esophagus. **(A)** CT scan of the thorax shows an indeterminate incidental enhanced mass in the left lobe of the liver. **(B)** Sagittal sonogram shows the mass is hypoechoic. **(C)-(E)** Frames taken between 10 and 14 seconds after the injection of contrast agent showing peripheral nodular enhancement and centripetal progression of enhancement in spite of the rapidity of lesion filling. This is a classic flash-filling hemangioma. The lesion remained enhanced to 5 minutes *(not shown)*. See also Video 4.6. (With permission from Wilson S, Burns P. Microbubble-enhanced US in body imaging: what role? Radiology. 2010;257[1]:24-39.[148])

childbearing years.[152,153] As with hemangioma, FNH is invariably an incidentally detected liver mass in an asymptomatic patient.

FNH is typically a solitary well-circumscribed mass with a central scar. Most lesions are less than 5 cm in diameter. Although usually single, multiple FNH masses have been reported. Microscopically, lesions include normal hepatocytes, Kupffer cells, biliary ducts, and the components of portal triads, although no normal portal venous structures are found. As a hyperplastic lesion, there is proliferation of normal, nonneoplastic hepatocytes that are abnormally arranged. Bile ducts and thick-walled arterial vessels are prominent, particularly in the central fibrous scar. The excellent blood supply makes hemorrhage, necrosis, and calcification rare. These lesions often produce a contour abnormality to the surface of the liver or may displace the normal blood vessels within the parenchyma.

On **sonography,** FNH is often a subtle liver mass that is difficult to differentiate in echogenicity from the adjacent liver parenchyma. Considering the histologic similarities to normal liver, this is not a surprising fact and has led to descriptions of FNH on all imaging as a "stealth lesion" that may be extremely subtle or completely hidden.[154] Subtle contour abnormalities (Fig. 4.48) and displacement of vascular structures should raise the possibility of FNH. The central scar may be seen on gray-scale sonograms as a hypoechoic, linear or stellate area within the central portion of the mass[155] (Fig. 4.48A). On occasion, the scar may appear hyperechoic. FNH may also display a range of gray-scale appearances, from hypoechoic to rarely hyperechoic.

Doppler ultrasound features of FNH are highly suggestive, in that well-developed peripheral and central blood vessels are seen. Pathologic studies in FNH describe an anomalous arterial blood vessel larger than expected for the location in the liver.[151] Our experience suggests that this feeding vessel is usually quite obvious on color Doppler imaging, although other vascular masses may appear to have unusually large feeding vessels as well.[156] The blood vessels can be seen to course within the central scar with either a linear or a stellate configuration. Spectral interrogation usually shows predominantly arterial signals centrally, with a midrange (2-4 kHz) shift.

Similar to hemangioma, FNH is consistently diagnosed with **CEUS.**[157-160] In the arterial phase, lesions are hypervascular, and highly suggestive morphologies include the presence of stellate lesional vessels, a tortuous feeding artery, and a centrifugal filling

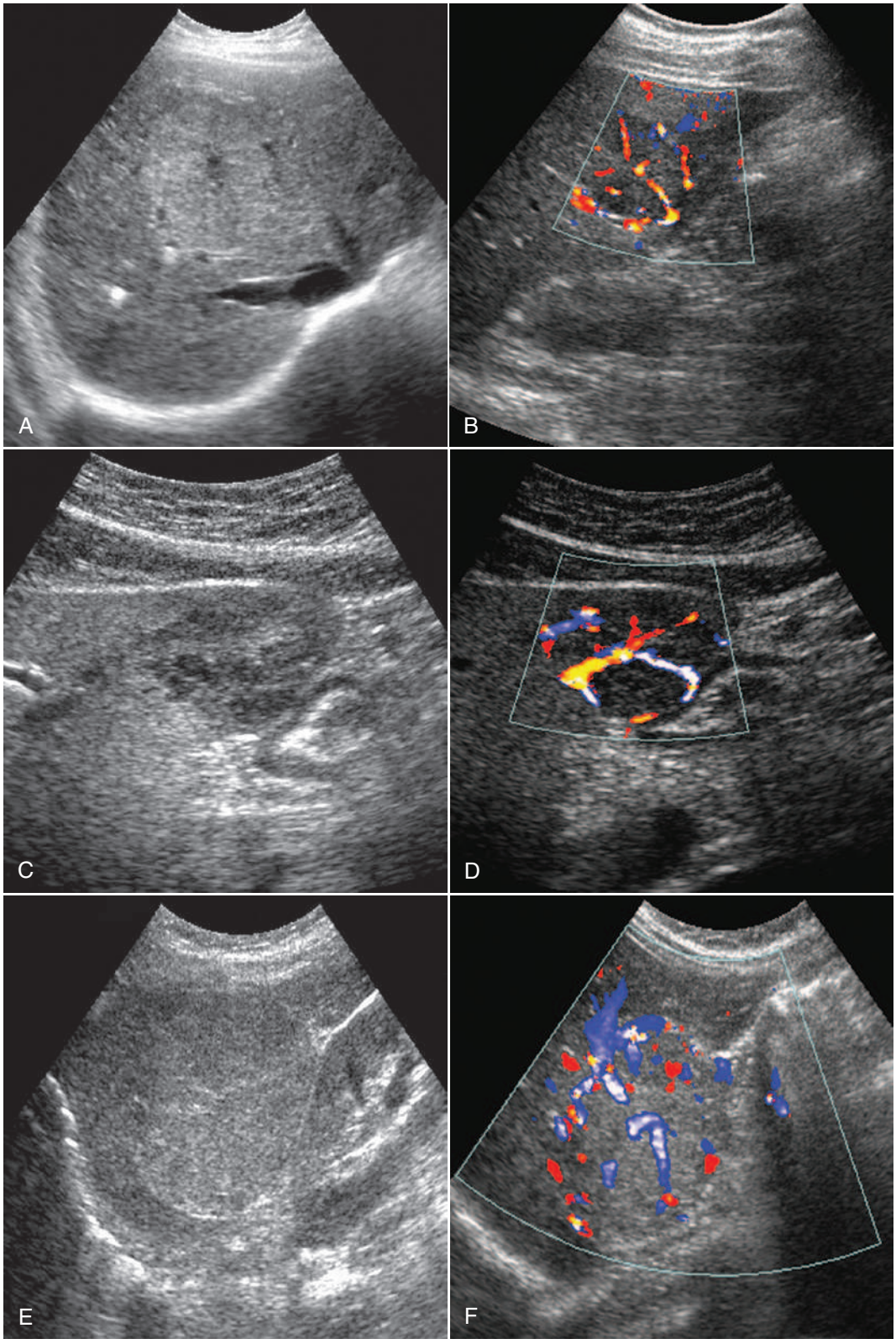

FIG. 4.48 Focal Nodular Hyperplasia (FNH) in Three Patients. Gray-scale equivalents (**A, C,** and **E**) of color Doppler images (**B, D,** and **F**). **(A)** Virtually normal image only suggests an isoechoic and subtle mass. **(B)** Doppler image shows a stellate arterial pattern and confirms the authenticity of the observation. **(C)** Fatty liver and focal hypoechoic region in the tip of segment 3. Fatty sparing was considered. **(D)** Doppler features show a hypervascular mass with a stellate appearance, the classic finding in FNH. **(E)** Contour-altering mass in the right lobe of the liver. **(F)** Doppler image again shows the central stellate vascularity suggesting FNH. This hypervascularity with stellate vasculature is usually readily observed with conventional sonography in FNH.

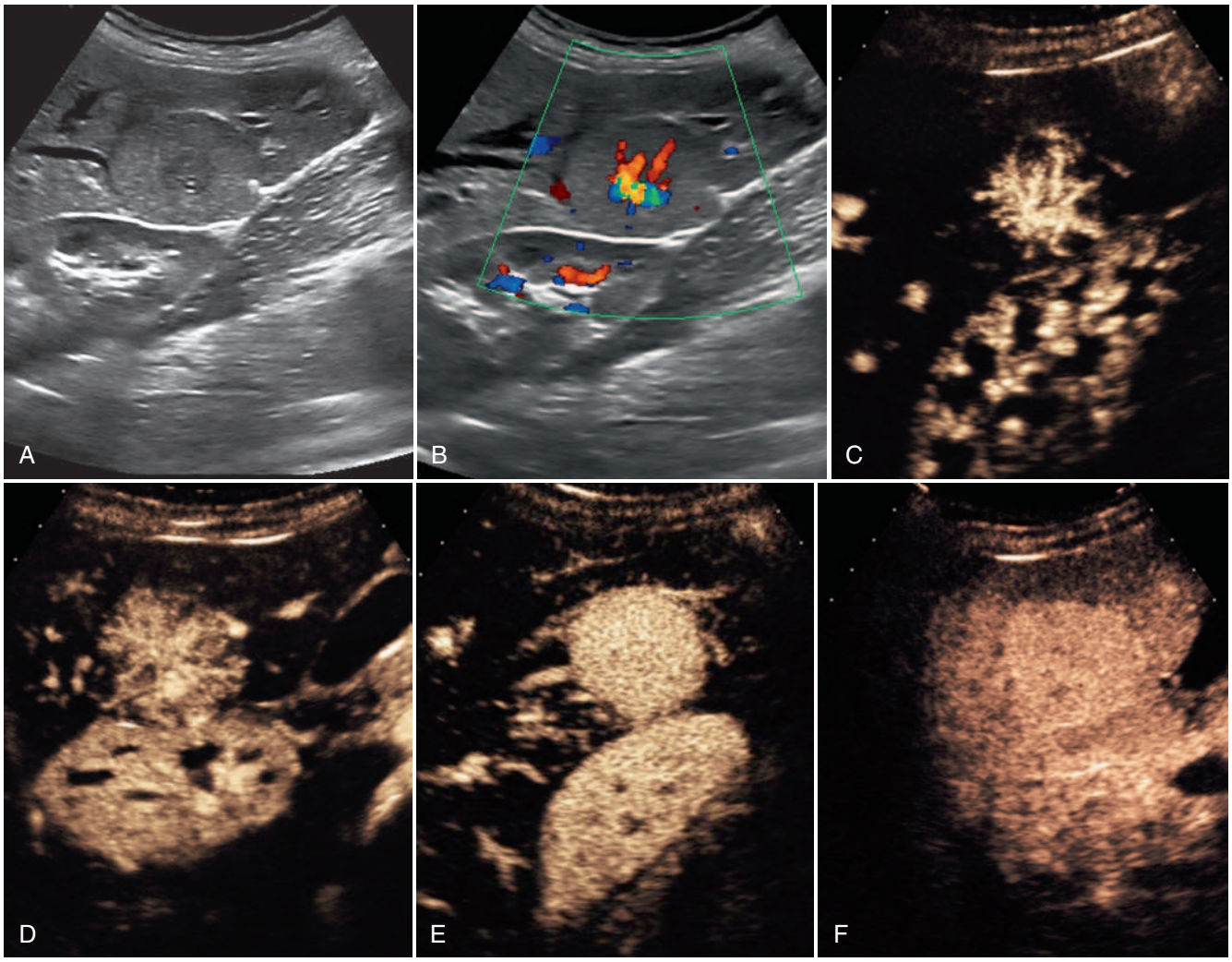

FIG. 4.49 Classic Focal Nodular Hyperplasia (FNH) on Contrast-Enhanced Ultrasound (CEUS). **(A)** Sagittal image of the liver in an asymptomatic woman shows a slightly exophytic very round isoechoic mass in the liver. **(B)** Addition of color Doppler shows strong central signal. **(C)-(E)** Sequential frames in the arterial phase show a stellate vessel morphology and centrifugal filing, from the center of the mass to its periphery. **(F)** Hypervascular mass has sustained enhancement, appearing brighter than the liver at 4 minutes, confirming the benign nature of this mass. See also Videos 4.7 and 4.8.

direction (Fig. 4.49 and Videos 4.7 and 4.8). Arterial phase enhancement is homogeneous and in excess of the adjacent liver. Portal venous enhancement is sustained such that lesion enhancement equals or exceeds that of adjacent liver with a nonenhancing scar (Video 4.5). Infrequently, FNH may show washout, which is often weak and delayed. An unenhanced scar may be seen in both arterial and portal phases. Ultrasound alone should be able to suggest the presence of these insignificant lesions without referral for further imaging.

Sulfur colloid scanning is invaluable in patients with suspect FNH because 50% of lesions will take up sulfur colloid similar to the adjacent normal liver, and another 10% will be "hot." Therefore only 40% of patients with FNH will lack confirmation of their diagnosis after performing a sulfur colloid scan.[160,161] In these patients, CECT or MRI may be performed for diagnosis.

Biopsy may be required in a minority of patients with FNH who do not have a hot or a warm lesion on sulfur colloid scanning, especially if CT or MRI features are not specific. Cytology is not confirmatory because normal hepatocytes may be found in normal liver, adenoma, and FNH. Core liver biopsy is required to show the disorganized pattern characteristic of this pathology. Because FNH rarely leads to clinical problems and does not undergo malignant transformation, conservative management is recommended.[162]

Hepatic Adenoma

Hepatic adenoma is the most important benign tumor of the liver because of its frequency and potential for complications that are life threatening, including bleeding and malignant transformation. Hepatic adenomas are much less common than FNH. However, a dramatic rise in their incidence since the 1970s clearly established a link to oral contraceptive use. As expected, therefore, hepatic adenomas are more common in women. The tumor may be asymptomatic, but often the patient or the physician feels a mass in the right upper quadrant. Pain may occur as a result of bleeding or infarction within the lesion. The most alarming manifestation is shock caused by tumor rupture and hemoperitoneum. Hepatic adenomas have also been reported

in association with GSD. In particular, the frequency of adenoma for type 1 GSD (von Gierke disease) is 40%.[163] Because of its propensity to hemorrhage and risk of malignant degeneration,[162] surgical resection is recommended. The genotyping/phenotyping of hepatic adenomas reveals three major subtypes, with the ability to predict also those with malignant potential on the basis of the tumor phenotype, with β-catenin–activated adenomas at higher risk of HCC.[164]

Pathologically, a hepatic adenoma is usually solitary, 8 to 15 cm, and well encapsulated. Microscopically, the tumor consists of normal or slightly atypical hepatocytes. Bile ducts and Kupffer cells are few or absent. Hepatic adenomas may show either calcification or fat (Figs. 4.50 and 4.51), both of which appear echogenic on sonography, making their gray-scale appearance suggestive in some cases.

Differentiation of hepatic adenomas from FNH is often not possible by their gray-scale or Doppler characteristics. Further, both have a similar demographic, occurring in young women in their childbearing years, often with a history of oral contraceptive use. Most adenomas are cold on technetium-99m sulfur colloid imaging as a result of absent or greatly decreased numbers of Kupffer cells. Isolated cases of radiocolloid uptake by the adenoma have been reported.[165] Today, MRI is a frequently used modality for the characterization of adenomas.[166]

In the typical clinical scenario, differentiation of FNH from adenoma poses a regular problem. Both masses are frequently incidentally detected in asymptomatic women, their baseline appearance at sonography is variable, and both produce a hypervascular mass in the arterial phase on contrast CT or MRI.[167] Their management are totally different. However, differentiation

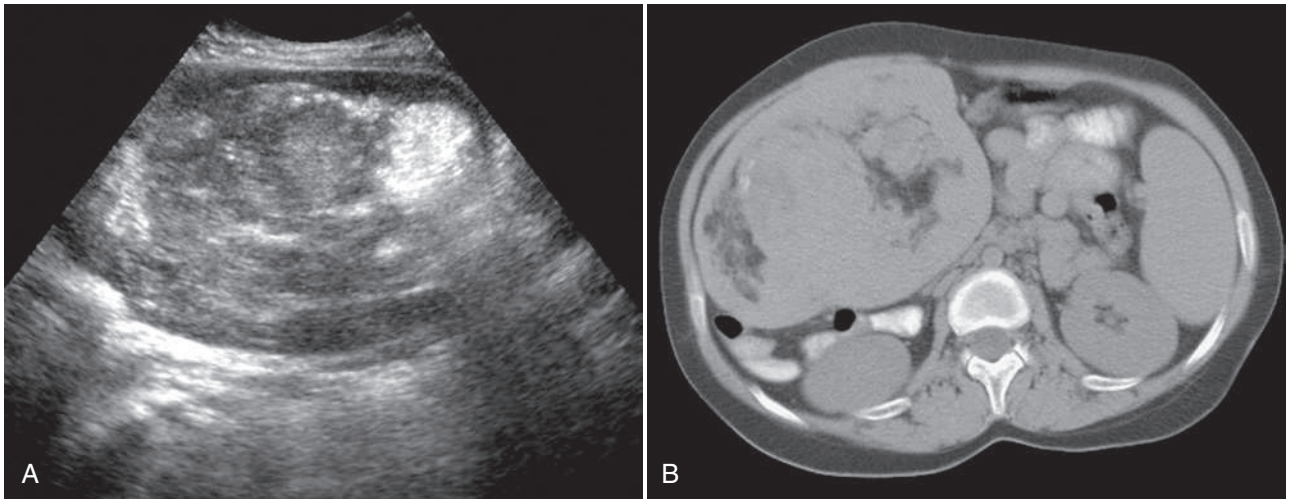

FIG. 4.50 Hepatic Adenoma. (A) Sonogram, and **(B)** confirmatory computed tomography (CT) scan, show a large exophytic liver mass in an asymptomatic young woman. The mass shows highly echogenic foci, which correspond to areas of fat and calcification on the CT scan.

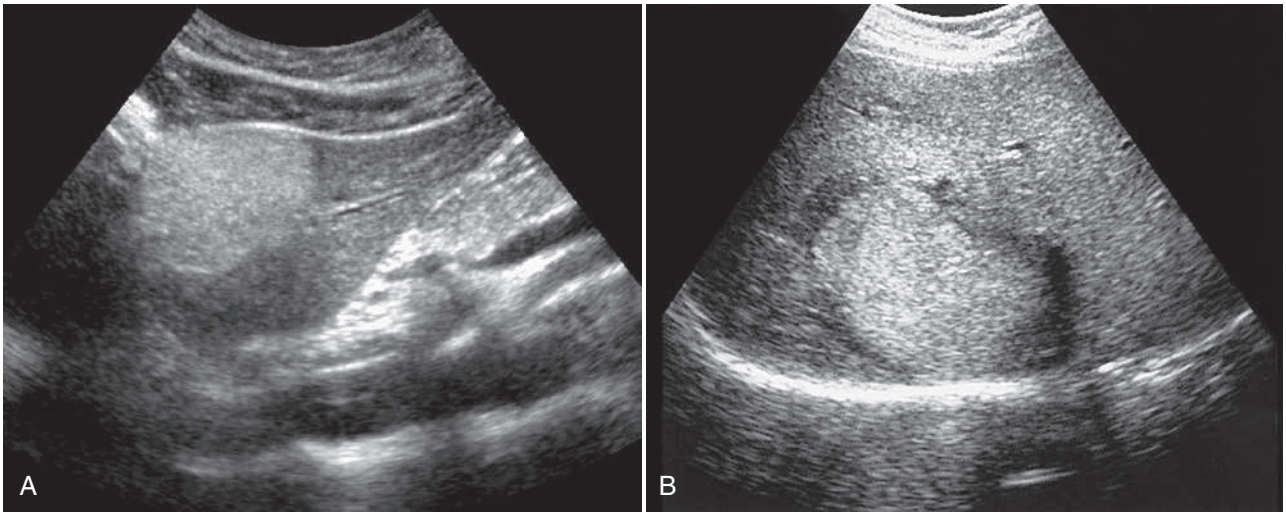

FIG. 4.51 Hepatic Adenoma: Gray-Scale Appearances in Two Patients. (A) Sagittal sonogram of the left lobe of the liver of an asymptomatic 35-year-old man shows a highly echogenic mass. It is unusual to see an adenoma in an otherwise normal man. **(B)** Oblique sonogram of a 26-year-old Chinese woman shows a highly echogenic mass with a hypoechoic halo. The hypoechoic halo was related to a surrounding zone of liver atrophy on biopsy. These highly echogenic masses show diffuse steatosis and are, therefore, HNF1a-inactivated adenomas.

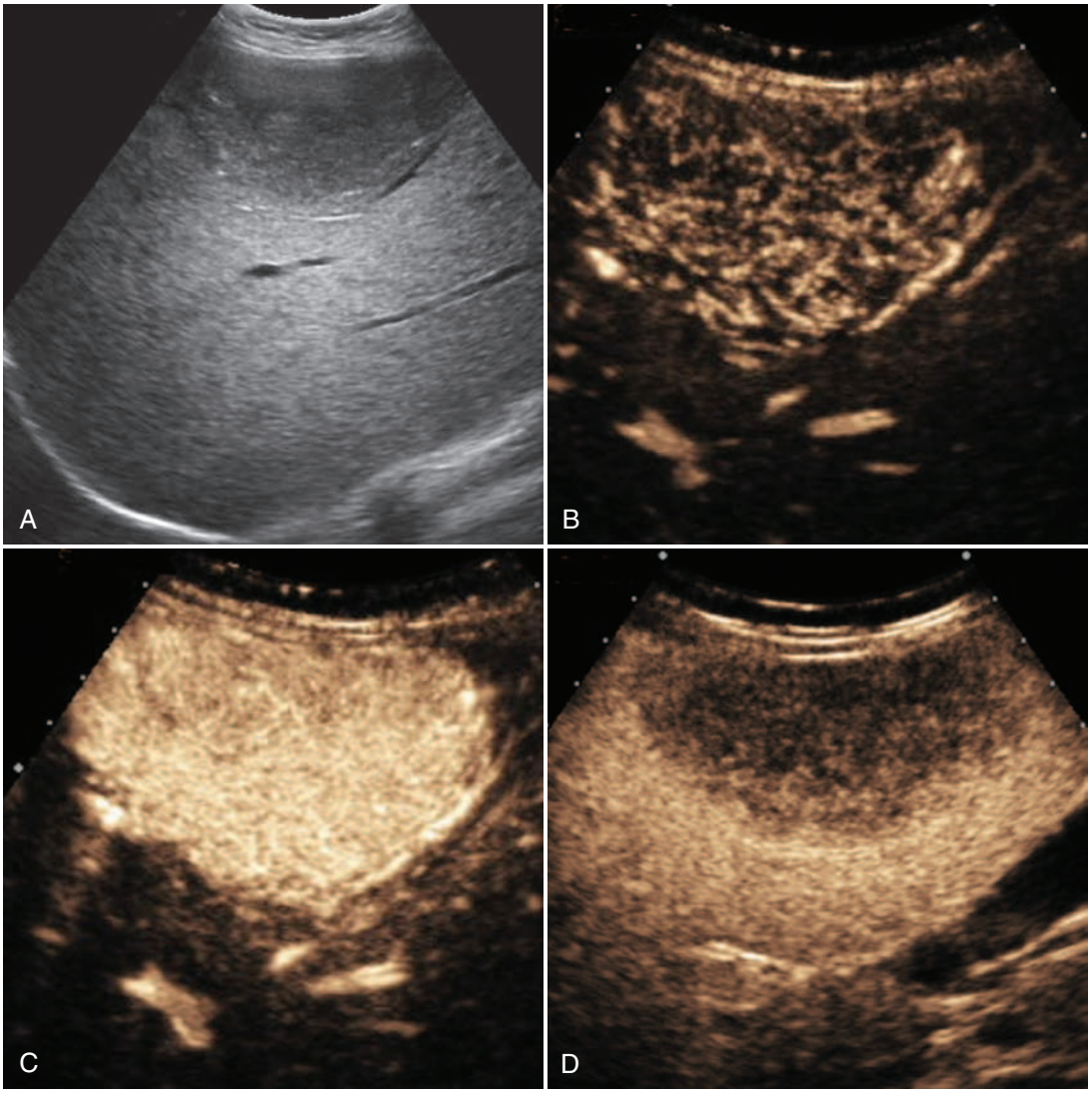

FIG. 4.52 Hepatic Adenoma: Maximum-Intensity Projection (MIP) Imaging on Contrast-Enhanced Ultrasound (CEUS). **(A)** Baseline scan on an asymptomatic 29-year-old woman with abnormal liver function tests shows a fatty liver and superficial hypoechoic focal mass. **(B)** Early arterial phase MIP image shows diffuse vascularity. **(C)** At the peak of arterial phase enhancement, the mass is hypervascular and homogeneous. **(D)** In the portal venous phase the mass shows washout, necessitating confirmation of diagnosis with biopsy. See also Video 4.9. (With permission from Wilson S, Burns P. Microbubble-enhanced US in body imaging: what role? Radiology. 2010;257[1]:24-39.[148])

is generally possible on ultrasound with CEUS (Fig. 4.52). HNF1a-inactivated adenomas are often echogenic at baseline, due to diffuse steatosis, and hypervascular in the arterial phase with no washout in the portal venous phase, consistent with a benign mass. Inflammatory adenomas are more variable on baseline imaging, from hyperechoic to isoechoic or hypoechoic, and most often show arterial phase hyperenhancement with centripetal filling and late weak washout, which are frequently described CEUS findings for this diagnosis (Video 4.9). However, the other adenomas do not show these specific features, frequently making their diagnosis a challenge.[166] Our impression also is that hepatic adenoma, although hypervascular, does not show the profuse vascularity typical of FNH (see Fig. 4.52).

In a patient with right upper quadrant pain and possible hemorrhage, a fluid component may be evident within or around the mass on ultrasound (Fig. 4.53), and free intraperitoneal blood may be seen. The sonographic changes with bleeding are variable, depending on the duration and amount of hemorrhage. In appropriate cases, it is important to perform an unenhanced CT scan of the liver before contrast injection. The hemorrhage will appear as high-density regions within the mass (Fig. 4.53C). The lesion often demonstrates rapid, transient enhancement during the arterial phase.[168]

Fatty Tumors: Hepatic Lipomas and Angiomyolipomas

Hepatic lipomas are extremely rare, and only isolated cases have been reported in the imaging literature.[169,170] There is an association between hepatic lipomas and renal angiomyolipomas and tuberous sclerosis. The lesions are asymptomatic. Ultrasound demonstrates a well-defined echogenic mass indistinguishable from a hemangioma, echogenic metastasis, or focal fat, unless the mass is large

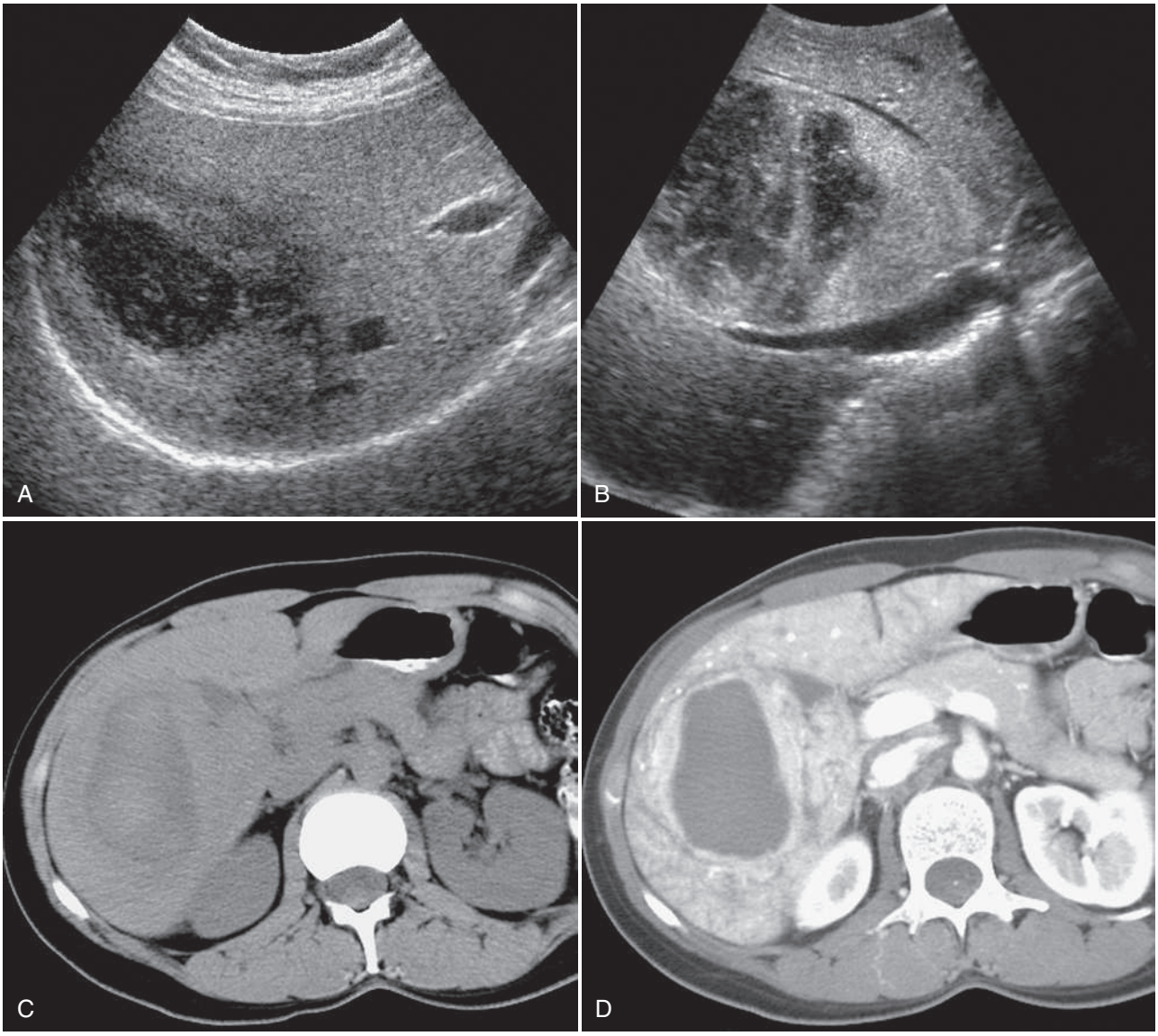

FIG. 4.53 Bleeding Hepatic Adenomas. (A) and **(B)** Sonograms of two young women presenting with acute abdominal pain from hemorrhage into hepatic adenomas. The masses are highly complex, and their appearance in a patient with pain suggests hemorrhage into a preexisting lesion. **(C)** Unenhanced and **(D)** enhanced computed tomography scans of the patient in B show the value of the unenhanced scan, which confirms the high-attenuation blood within the adenoma.

and near the diaphragm, in which case differential sound transmission through the fatty mass will produce a **discontinuous or broken diaphragm echo**[170] (Fig. 4.54A). CT or MRI can be used to confirm the fatty nature of a mass (Fig. 4.54B). Angiomyolipomas, by comparison, may also appear echogenic on sonography (Fig. 4.54C), although they may have insufficient fat to appear consistently with fatty attenuation on CT, making diagnostic confirmation more difficult without biopsy.

Malignant Hepatic Neoplasms

Hepatocellular Carcinoma

HCC is one of the most common malignant tumors, particularly in Southeast Asia, sub-Saharan Africa, Japan, Greece, and Italy. HCC occurs predominantly in men, with a male-to-female ratio of approximately 5:1. Causal factors depend on the geographic distribution. Although alcoholic cirrhosis remains a common predisposing cause for hepatoma in the West, both hepatitis C and hepatitis B are now of worldwide importance. These viral infections also account for the high incidence of HCC in sub-Saharan Africa, Southeast Asia, China, Japan, and in the Mediterranean. Of growing importance in the Western world, fatty liver with the development of steatohepatitis is increasingly important as an antecedent to the development of cirrhosis and HCC. HCC is one of the only solid tumors in North America with an increasing incidence credited almost solely to the increasing significance of nonalcoholic fatty liver disease. Aflatoxins, toxic metabolites produced by fungi in certain foods, have also been implicated in the pathogenesis of hepatomas in developing countries.

The clinical presentation of HCC is often delayed until the tumor reaches an advanced stage. Symptoms include right upper quadrant pain, weight loss, and abdominal swelling when ascites

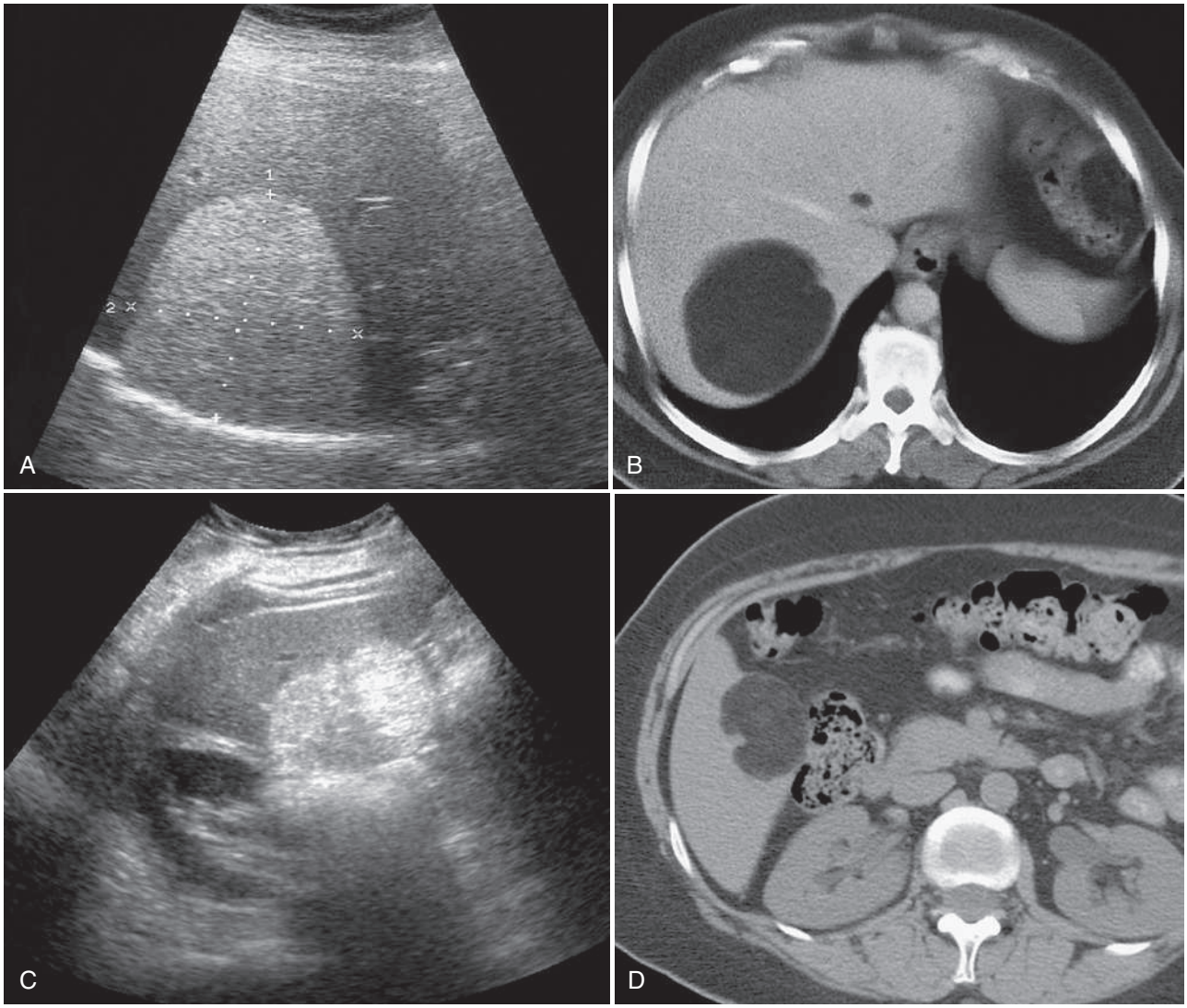

FIG. 4.54 Fatty Tumors of Liver: Lipoma and Angiomyolipoma. (A) Sonogram shows a highly echogenic, solid focal liver mass, which initially suggests a hemangioma. The **discontinuity of the diaphragm echo** caused by the altered rate of sound transmission is a clue to the correct diagnosis. **(B)** Confirmatory computed tomography scan shows the fat density of the mass, a confirmed hepatic lipoma. **(C)** and **(D)** Another highly echogenic and slightly exophytic mass in the liver, initially suggesting a hemangioma. (**A** and **B** with permission from Garant M, Reinhold C. Residents' corner. Answer to case of the month #36. Hepatic lipoma. Can Assoc Radiol J. 1996;47[2]:140-142.[242] **C** and **D** with permission from Wilson SR. The liver. In Gastrointestinal disease. 6th series. Test and syllabus. Reston Virginia: American College of Radiology; 2004.[26])

is present. Serum alpha feto-protein levels are frequently elevated. Treatments and earlier diagnosis have improved over time. Among HCC cases diagnosed from 1998 to 2007, transplant recipients experienced 84% 5-year survival. Cases with tumors less than 3 cm in size that received radiofrequency ablation had a 5-year survival rate of 53%, while cases undergoing liver resection had a 5-year survival rate of 47%. Overall the HCC survival rate from 1998 to 2007 was 18%, whereas the survival rate was 7% among cases without reported invasive surgery or local tumor destruction.[171]

Pathologically, HCC occurs in the following three forms:

- Solitary tumor
- Multiple nodules
- Diffuse infiltration

There is a propensity toward venous invasion. The portal vein is involved in 30% to 60% of cases and more often than the hepatic venous system.[172-174]

The **sonographic appearance** of HCC is variable. The masses may be hypoechoic, complex, or echogenic. Most small (<5 cm) HCCs are hypoechoic (Fig. 4.55A), corresponding histologically to a solid tumor without necrosis.[175,176] A thin, peripheral hypoechoic halo, which corresponds to a fibrous capsule, is seen most often in small HCCs.[177] With time and increasing size, the masses tend to become more complex and inhomogeneous as a result of necrosis and fibrosis (Fig. 4.55E). Calcification is uncommon.[178] Small tumors may appear diffusely hyperechoic, secondary to fatty metamorphosis or sinusoidal dilation (Fig. 4.55C), making them indistinguishable from focal fatty infiltration,

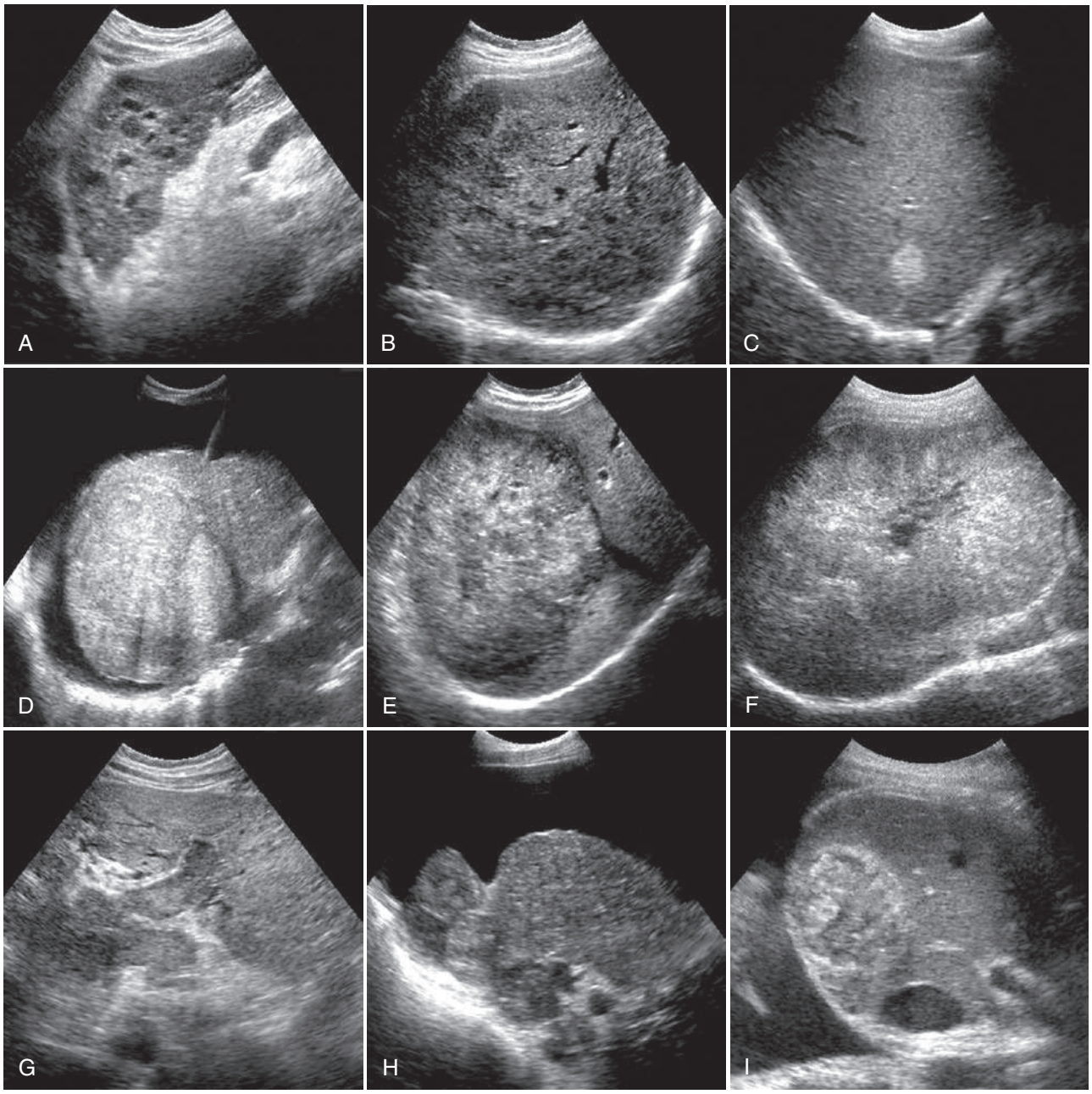

FIG. 4.55 Hepatocellular Carcinoma: Spectrum of Appearances. (A) Small, focal hypoechoic nodules. **(B)** Multifocal hypoechoic nodules, which may be difficult to differentiate from the background cirrhotic nodules. **(C)** Focal echogenic nodule mimicking hemangioma. **(D)** Large echogenic nodule in a cirrhotic liver. **(E)** Large mixed-echogenic mass. Hypoechoic regions corresponded at pathology to areas of necrosis. **(F)** Large lobulated mass with central hypoechoic region suggesting a scar. **(G)** Expansive tumor filling the portal vein is the only observation on the sonogram. **(H)** Small cirrhotic liver showing exophytic tumors. **(I)** Superficial mass of mixed echogenicity in a young patient with hepatitis B presenting with spontaneous liver rupture.

cavernous hemangiomas, and lipomas.[175,176,179] Intratumoral fat also occurs in larger masses; because it tends to be focal, it is unlikely to cause confusion in diagnosis. Patients with rare surface lesions may present with spontaneous rupture and hemoperitoneum (Fig. 4.55I).

Studies evaluating focal liver lesions with duplex Doppler and CDFI suggest HCC has characteristic high-velocity signals.[180-182] Doppler sonography is excellent for detecting neovascularity within tumor thrombi within the portal veins, diagnostic of HCC even without demonstration of the parenchymal lesion (Fig. 4.56).

CEUS is much more sensitive for the detection of lesional vascularity than is color Doppler (Table 4.4). Lesions are hypervascular (Videos 4.10 and 4.11), often showing dysmorphic vessels (Fig. 4.57) and frequently showing unenhanced regions representing either necrosis or scarring.[183,184] In the portal venous phase, lesions show washout, such that they are less enhanced than the adjacent liver (see Fig. 4.44). This washout is characteristically

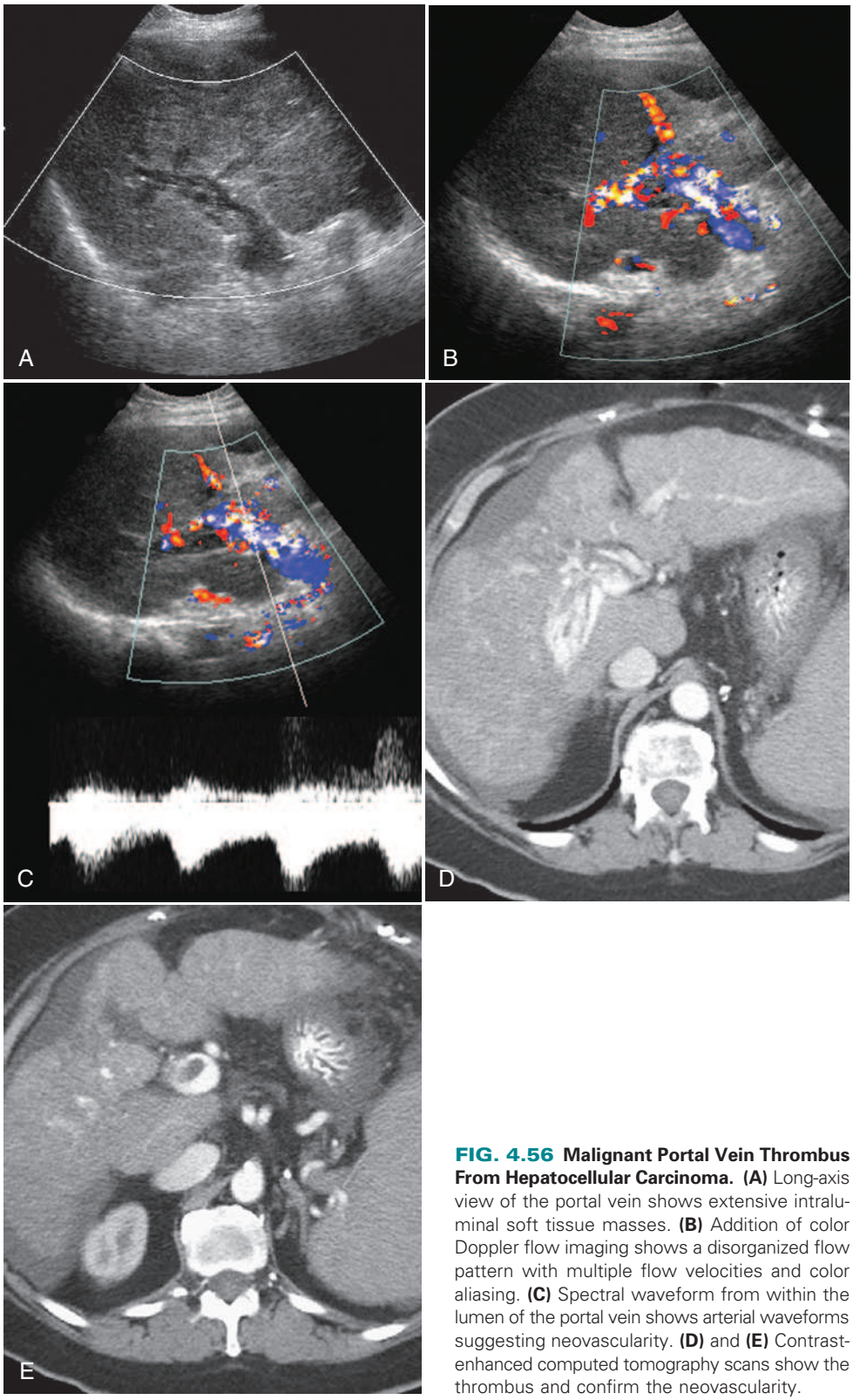

FIG. 4.56 Malignant Portal Vein Thrombus From Hepatocellular Carcinoma. (A) Long-axis view of the portal vein shows extensive intraluminal soft tissue masses. **(B)** Addition of color Doppler flow imaging shows a disorganized flow pattern with multiple flow velocities and color aliasing. **(C)** Spectral waveform from within the lumen of the portal vein shows arterial waveforms suggesting neovascularity. **(D)** and **(E)** Contrast-enhanced computed tomography scans show the thrombus and confirm the neovascularity.

TABLE 4.4 Schematic of Algorithm for Diagnosis of Nodules in Cirrhotic Liver on Computer-Enhanced Ultrasound

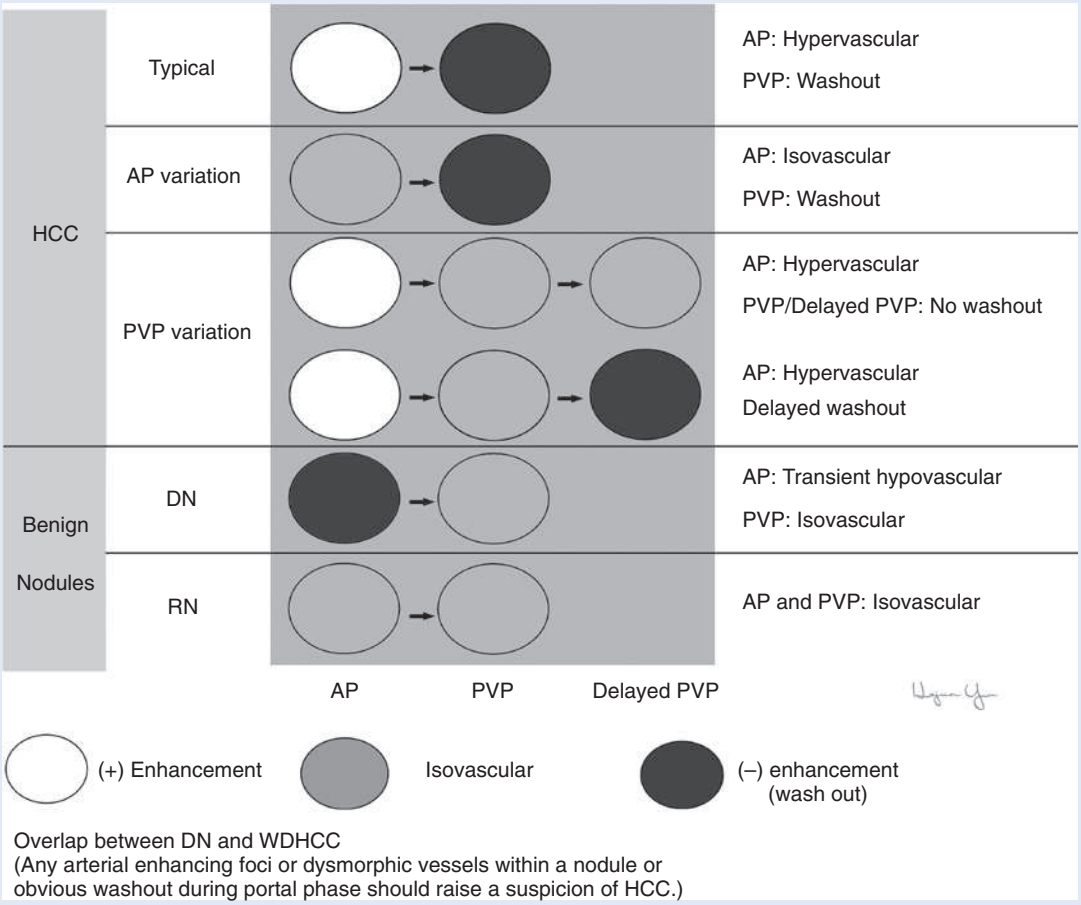

AP, Arterial phase; *HCC,* hepatocellular carcinoma; *PVP,* portal venous phase; *WDHCC,* well-differentiated hepatocellular carcinoma.
With permission from Wilson SR, Burns PN. Microbubble-enhanced US in body imaging: what role? Radiology. 2010;257(1):24-39.[148]

slow and weak. Variations to this classic pattern are well described[184] and include arterial phase hypovascularity and delayed or no washout in the portal venous phase (Fig. 4.58). Regenerative **nodules,** by comparison, show similar arterial phase and portal venous phase vascularity and enhancement to the remainder of the cirrhotic liver. **Dysplastic nodules** may show transient arterial phase hypovascularity followed by isovascularity. Identification of this feature prompts biopsy in our institution.

Microbubble-enhanced sonography may contribute also to the detection of HCC. Sweeps of the liver in the arterial phase may detect hypervascular foci potentially representing HCC. Sweeps in the portal venous and late phases, by comparison, show HCC as hypoechoic or washout regions, again allowing for the detection of unsuspected lesions. The arterialized liver of cirrhosis, however, is problematic for several reasons. First, it shows dysmorphology of all liver vessels, in general, and the appreciation of focal increased vascularity in a small nodule is more difficult. Portal venous phase imaging is also weakened when the liver receives a greater proportion of its blood supply from the hepatic artery. Therefore washout of a specific nodule may not be as evident as in a normal liver. CT and MRI are frequently performed to screen for and evaluate HCC. The importance of CEUS for the management of small nodules detected in the surveillance for HCC is controversial and CEUS is included in some international guidelines but not others.[185] CEUS may play a pivotal role on the basis of its real-time demonstration of continuous hemodynamic changes of liver tumors, a purely intravascular contrast material, availability in patients with renal failure, excellent patient compliance, and repeatability in short intervals. CEUS is integrated into our approach for management and diagnosis of nodules in patients at high risk for HCC.

Fibrolamellar carcinoma is a histologic subtype of HCC found in younger patients (adolescents and young adults) without coexisting liver disease. The serum alpha-fetoprotein levels are usually normal. The tumors are usually solitary, 6 to 22 cm, well differentiated, and often encapsulated by fibrous tissue.[186-188] With

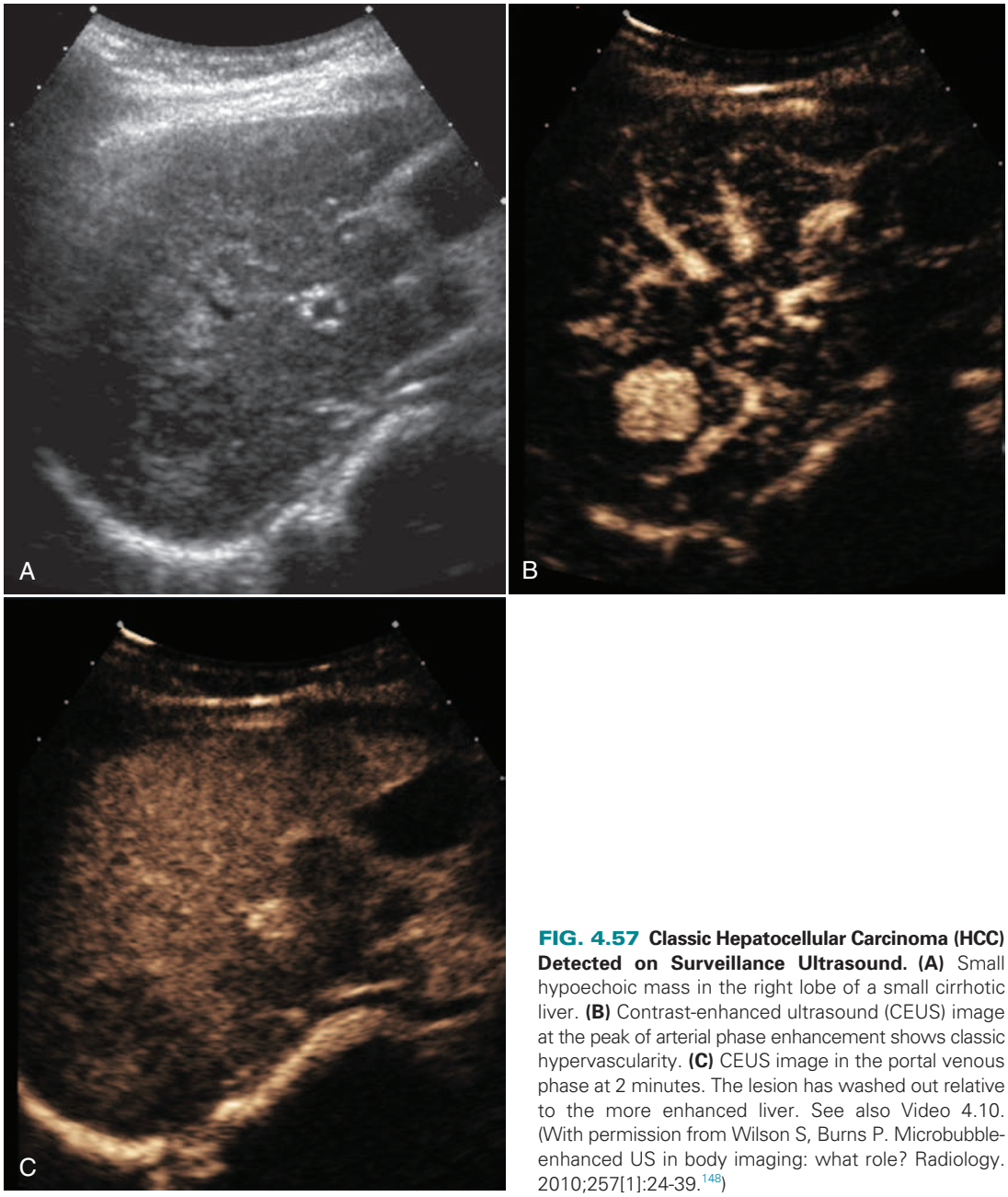

FIG. 4.57 Classic Hepatocellular Carcinoma (HCC) Detected on Surveillance Ultrasound. (A) Small hypoechoic mass in the right lobe of a small cirrhotic liver. **(B)** Contrast-enhanced ultrasound (CEUS) image at the peak of arterial phase enhancement shows classic hypervascularity. **(C)** CEUS image in the portal venous phase at 2 minutes. The lesion has washed out relative to the more enhanced liver. See also Video 4.10. (With permission from Wilson S, Burns P. Microbubble-enhanced US in body imaging: what role? Radiology. 2010;257[1]:24-39.[148])

5-year survival rates of 25% to 30%, the prognosis is generally better for fibrolamellar carcinoma than HCC.[189,190] Most patients, however, demonstrate advanced disease at diagnosis. Aggressive surgical resection of tumor is recommended at presentation as well as for recurrent disease.[187] The echogenicity of fibrolamellar carcinoma is variable. Punctate calcification and a central echogenic scar (features that are distinctly unusual in hepatomas) are more common in the fibrolamellar subtype.

Hemangiosarcoma (Angiosarcoma)

Hepatic hemangiosarcoma is an extremely rare malignant tumor. It occurs almost exclusively in adults, reaching its peak incidence in the sixth and seventh decades of life. Hemangiosarcoma is of particular interest because of its association with specific carcinogens: **thorotrast, arsenic,** and **polyvinyl chloride.** Only a few cases of hepatic hemangiosarcoma have been reported in the radiologic literature. The sonographic appearance is a large mass of mixed echogenicity.[191,192]

Hepatic Epithelioid Hemangioendothelioma

Epithelioid hemangioendothelioma (EHE) is a rare malignant tumor of vascular origin that occurs in adults. Soft tissues, lung, and liver are affected. The prognosis is variable; many patients survive longer than 5 years with or without treatment.[193] Hepatic

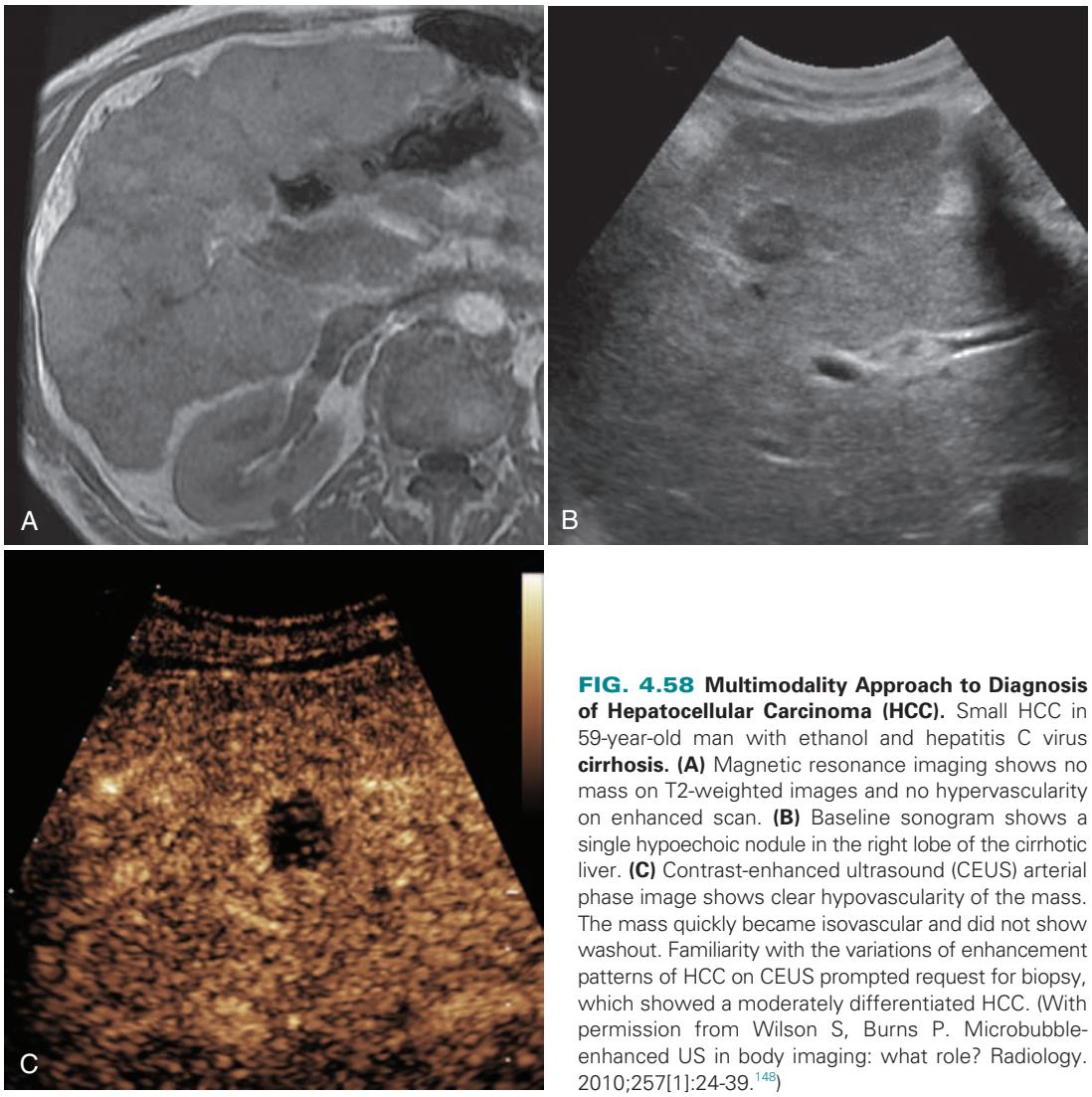

FIG. 4.58 Multimodality Approach to Diagnosis of Hepatocellular Carcinoma (HCC). Small HCC in 59-year-old man with ethanol and hepatitis C virus **cirrhosis. (A)** Magnetic resonance imaging shows no mass on T2-weighted images and no hypervascularity on enhanced scan. **(B)** Baseline sonogram shows a single hypoechoic nodule in the right lobe of the cirrhotic liver. **(C)** Contrast-enhanced ultrasound (CEUS) arterial phase image shows clear hypovascularity of the mass. The mass quickly became isovascular and did not show washout. Familiarity with the variations of enhancement patterns of HCC on CEUS prompted request for biopsy, which showed a moderately differentiated HCC. (With permission from Wilson S, Burns P. Microbubble-enhanced US in body imaging: what role? Radiology. 2010;257[1]:24-39.[148])

EHE begins as multiple hypoechoic nodules, which grow and coalesce over time, forming larger, confluent masses that tend to involve the periphery of the liver. Foci of calcification may be present.[193,194] The hepatic capsule overlying the lesions of EHE may be retracted inward, secondary to fibrosis incited by the tumor; this unusual feature is highly suggestive of the diagnosis. Importantly, peripheral postchemotherapy metastases and tumors causing biliary obstruction and segmental atrophy may have a similar appearance. The diagnosis of hepatic EHE is made by percutaneous liver biopsy and immunohistochemical staining.

Metastatic Liver Disease

In the United States, metastatic liver disease is 18 to 20 times more common than HCC. Detection of metastasis greatly alters the patient's prognosis and often the management. The incidence of hepatic metastases depends on the type of primary tumor and its stage at initial detection. At autopsy, 25% to 50% of patients dying from cancer have liver metastases. Patients with short-term survival (<1 year) after initial detection of liver metastases are those with HCC and carcinomas of the pancreas, stomach, and esophagus. Patients with longer-term survival are those with head and neck carcinomas and carcinoma of the colon. Most patients with melanoma have an extremely low incidence of hepatic metastases at diagnosis. Liver involvement at autopsy, however, may be as high as 70%.

The most common **primary tumors** resulting in liver metastases, in decreasing order of frequency, are gallbladder, colon, stomach, pancreas, breast, and lung. Most metastases to the liver are blood-borne through the hepatic artery or portal vein, but lymphatic spread of tumors from stomach, pancreas, ovary, or uterus may also occur. The portal vein provides direct access to the liver for tumor cells originating from the gastrointestinal tract and probably accounts for the high frequency of liver metastases from organs that drain into the portal circulation.

Advantages of ultrasound as a screening test for metastatic liver disease include its relative accuracy, speed, lack of ionizing radiation, and availability. Further, the multiplanar capability of ultrasound allows for excellent segmental localization of masses, with the ability to detect proximity to or involvement of the vital vascular structures. Although isolated reports describe detection of metastases on sonography in skilled hands as competitive with CT and MRI, sonography is not uniformly used as the first-line investigative technique to search for metastatic disease worldwide; CT has filled that role. Experience suggests that ultrasound without microbubble contrast agents does not compete with triphasic CT for metastasis detection.[136] Although greatly improved with the addition of contrast agents, as described earlier, we doubt CEUS will ever be widely used in routine clinical practice for the large numbers of patients who have scans for metastatic disease. Nonetheless, on a case-by-case basis, and as a problem-solving modality, CEUS may play a contributory role in the evaluation of the patient with metastatic liver disease.

On **conventional gray-scale sonography,** patients with metastatic liver disease may present with a single liver lesion (Fig. 4.59A), although more often they present with multiple focal liver masses. All metastatic lesions in a given liver may have identical sonographic morphology; however, biopsy-confirmed lesions of differing appearances may have the same underlying histologic structure. Of importance, metastases may also be present in a liver that already has an underlying diffuse or focal abnormality, most often hemangioma. Metastatic involvement of the liver may take on different forms, showing diffuse liver involvement and, in rare cases, geographic infiltration (Fig. 4.59C-F).

Knowledge of a prior or concomitant malignancy and features of disseminated malignancy at sonography are helpful in correct interpretation of sonographically detected liver masses. Although no confirmatory features of metastatic disease are seen on sonography, suggestive features include **multiple solid lesions** of varying size and a **hypoechoic halo** surrounding a liver mass. A halo around the periphery of a liver mass on sonography is an ominous sign strongly associated with malignancy, particularly metastatic disease but also HCC.

In our investigation of 214 consecutive patients with focal liver lesions, 66 had lesions that showed a hypoechoic halo; 13 had HCCs (Fig. 4.60A and B); 43 had metastases (Fig. 4.60C-F); four had FNH; and two had adenomas (see Fig. 4.51). Four lesions were unconfirmed. In 1992, Wernecke et al.[195] described the importance of the hypoechoic halo in the differentiation of malignant from benign focal hepatic lesions. Its identification has a positive and negative predictive value of 86% and 88%, respectively. Therefore we conclude that although not absolutely indicative of malignancy, a halo is seen with lesions that require further investigation and confirmation of their nature, regardless of the patient's presentation or status. Radiologic-histologic correlation of a hypoechoic halo surrounding a liver mass has revealed that, in the majority of cases, the hypoechoic rim corresponds to normal liver parenchyma, which is compressed by the rapidly expanding tumor. Less frequently, the hypoechoic rim represents proliferating malignant cells, tumor fibrosis or vascularization, or a fibrotic rim.[196-198]

The sonographic appearance of metastatic liver disease has been described as echogenic, hypoechoic, target, calcified, cystic, and diffuse. Although the ultrasound appearance is not specific for determining the origin of the metastasis, certain generalities apply (Fig. 4.61).

Echogenic metastases tend to arise from a gastrointestinal origin or from HCC (Fig. 4.61I). The more vascular the tumor is, the more likely it is that the lesion is echogenic.[180,199] Therefore metastases from **renal cell carcinoma, neuroendocrine tumors, carcinoid, choriocarcinoma,** and **islet cell carcinoma** also tend to be hyperechoic. It is this particular group of tumors that may mimic a hemangioma on sonography.

Hypoechoic metastases are generally hypovascular and may be monocellular or hypercellular without interstitial stroma. Hypoechoic lesions represent the typical pattern seen in untreated metastatic breast or lung cancer (Figs. 4.60 and 4.61), as well as **gastric, pancreatic,** and **esophageal tumors.** Lymphomatous involvement of the liver may also manifest as hypoechoic masses (Fig. 4.62). The uniform cellularity of **lymphoma** without significant background stroma is thought to be related to its hypoechoic appearance on sonography. Although at autopsy the liver is often a secondary site of involvement by Hodgkin and non-Hodgkin lymphoma, the disease tends to be diffusely infiltrative and undetected by sonography and CT.[200] The pattern of multiple hypoechoic hepatic masses is more typical of primary **non-Hodgkin lymphoma** of the liver or **lymphoma associated with AIDS.**[200,201] The lymphomatous masses may appear anechoic and septated, mimicking hepatic abscesses.

The **bull's-eye or target pattern** is characterized by a peripheral hypoechoic zone (see Fig. 4.60). The appearance is nonspecific and common, although it is frequently identified in metastases from **bronchogenic carcinoma.**[202]

Calcified metastases are distinctive by virtue of their marked echogenicity and distal acoustic shadowing (Fig. 4.61B). **Mucinous adenocarcinoma** of the colon is most frequently associated with calcified metastases. Calcium may appear as large, echogenic, and shadowing foci or, more often, shows innumerable tiny punctate echogenicities without clear shadowing. Other primary malignancies that give rise to calcified metastases are **endocrine pancreatic tumors, leiomyosarcoma, adenocarcinoma of the stomach, neuroblastoma, osteogenic sarcoma, chondrosarcoma,** and **ovarian cystadenocarcinoma and teratocarcinoma.**[203]

Cystic metastases are uncommon and generally exhibit features that distinguish them from the ubiquitous benign hepatic cyst, including mural nodules, thick walls, fluid-fluid levels, and internal septations.[204,205] Primary neoplasms with a cystic component, such as **cystadenocarcinoma of the ovary** and pancreas and **mucinous carcinoma of the colon,** may produce cystic secondary lesions, although infrequently. More often, cystic neoplasms result from extensive necrosis, seen most often in metastatic **sarcomas,** which typically have low-level echoes and a thickened, shaggy wall (Fig. 4.61H). Metastatic **neuroendocrine** and **carcinoid** tumors are typically highly echogenic and often show secondary cystic change (Fig. 4.61I). Large colorectal metastases may also rarely be necrotic, producing a predominantly cystic liver mass.

Diffuse disorganization of the hepatic parenchyma reflects **infiltrative metastatic disease** and is the most difficult to

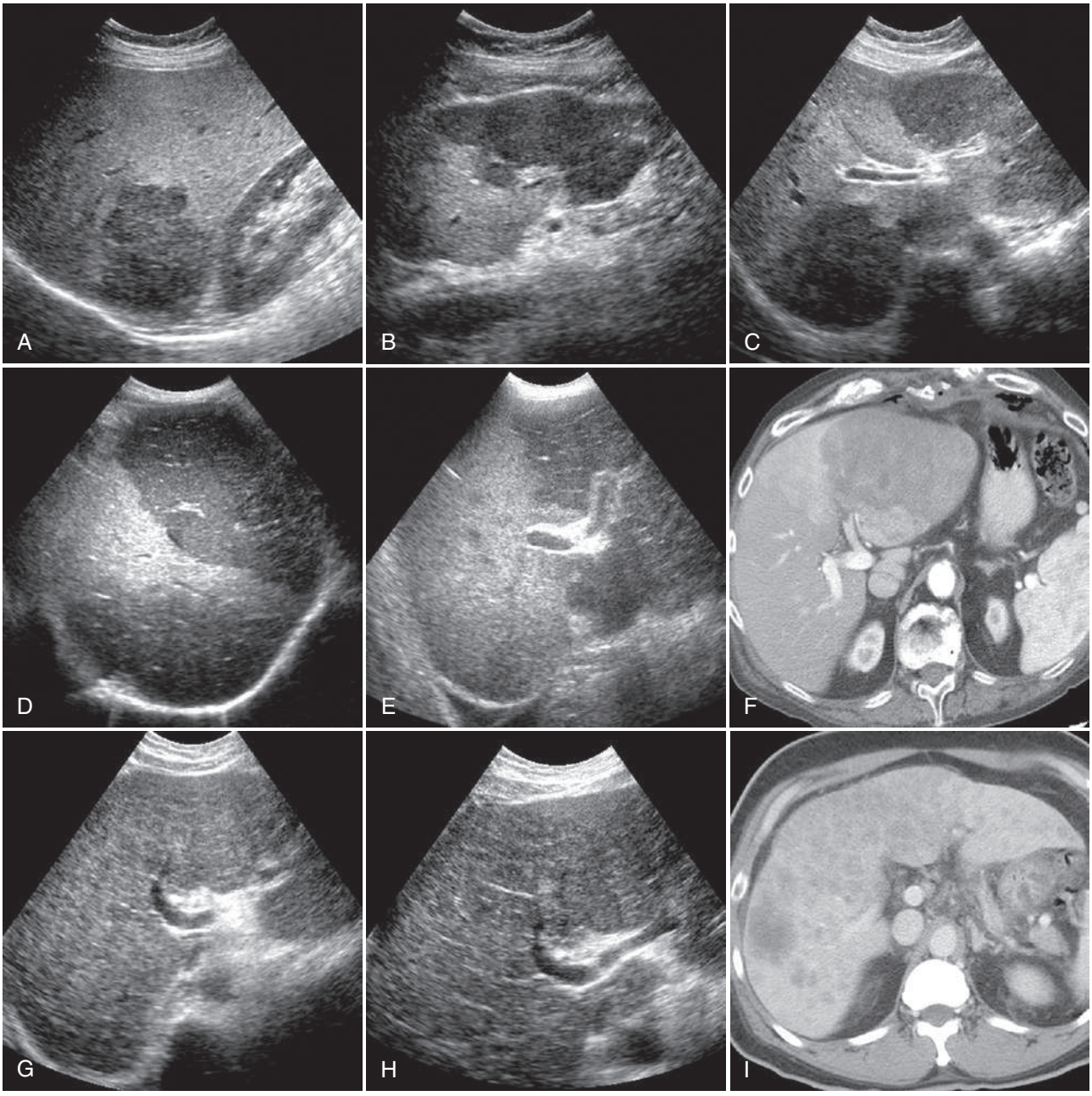

FIG. 4.59 Liver Metastases in Three Patients. *Top row,* **Focal liver masses:** most common variety and easiest to appreciate. **(A)** Sagittal image of the right lobe shows a well-defined and lobulated hypoechoic mass. **(B)** Sagittal image of the left lobe shows confluent masses in segment 3. **(C)** Transverse image shows the two focal hypoechoic masses separated by normal liver. *Middle row,* **Rare geographic pattern of metastases. (D)** and **(E)** Subcostal views show the right and left lobes of the liver. A sharp geographic or maplike border separates the normal echogenic liver from the hypoechoic tumor. The distribution and echogenicity variation suggest possible fatty change or perfusion abnormality. **(F)** Confirmatory computed tomography (CT) scan. *Bottom row,* **Diffuse tumor involvement:** often the most difficult to appreciate on ultrasound, as shown here. **(G)** Transverse sonogram; **(H)** similar view with greater magnification. Both images show a coarse liver parenchyma that is more suggestive of cirrhosis than the extensive tumor shown on **(I)** CT scan.

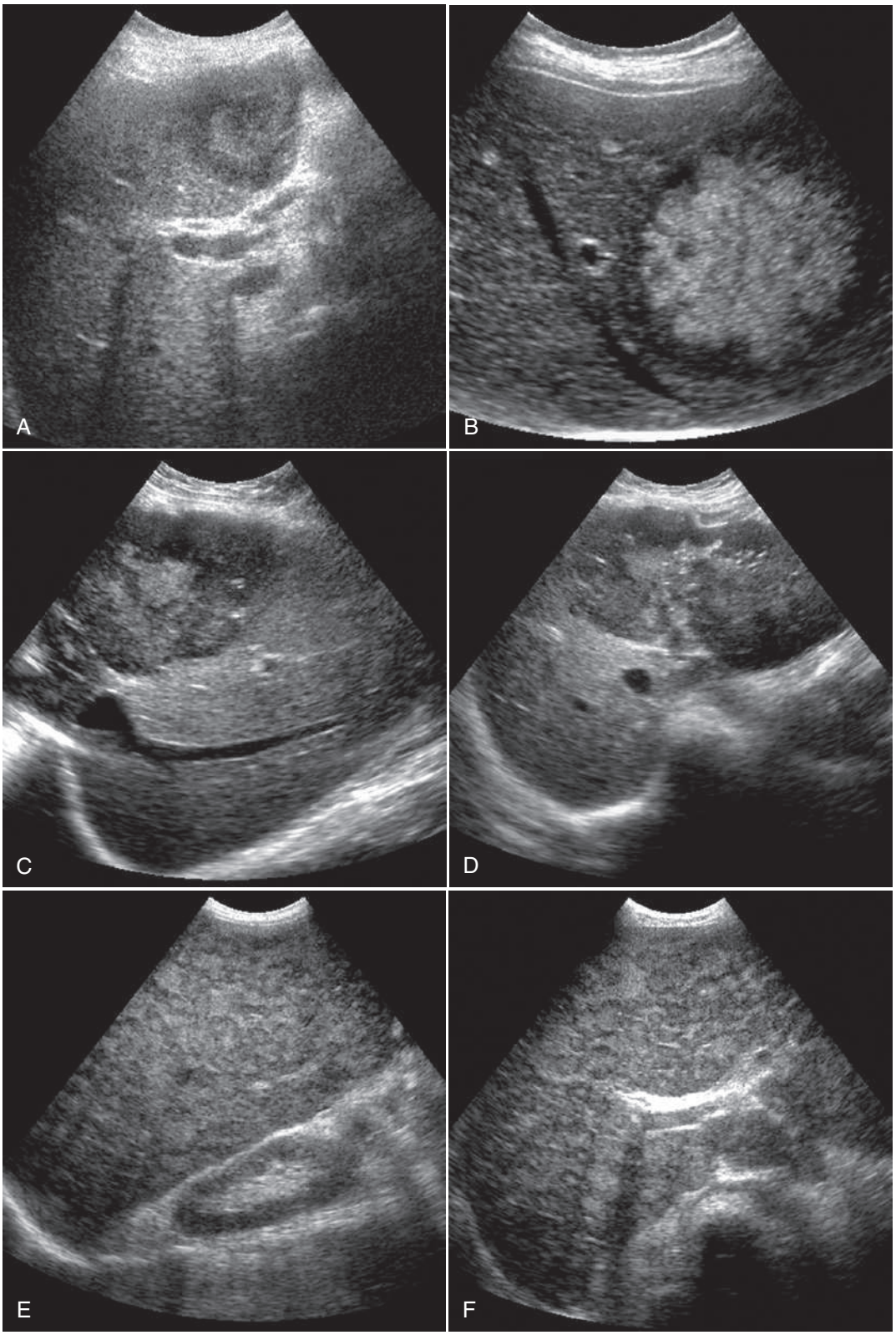

FIG. 4.60 Hypoechoic Halo in Malignant Disease. (A) and **(B) Hepatocellular carcinoma** showing as echogenic masses with a surrounding halo. **(C)** and **(D)** Sagittal and transverse images of a large solitary **breast metastasis. (E)** and **(F)** Large liver full of small masses with hypoechoic halos from **small cell carcinoma of the lung.**

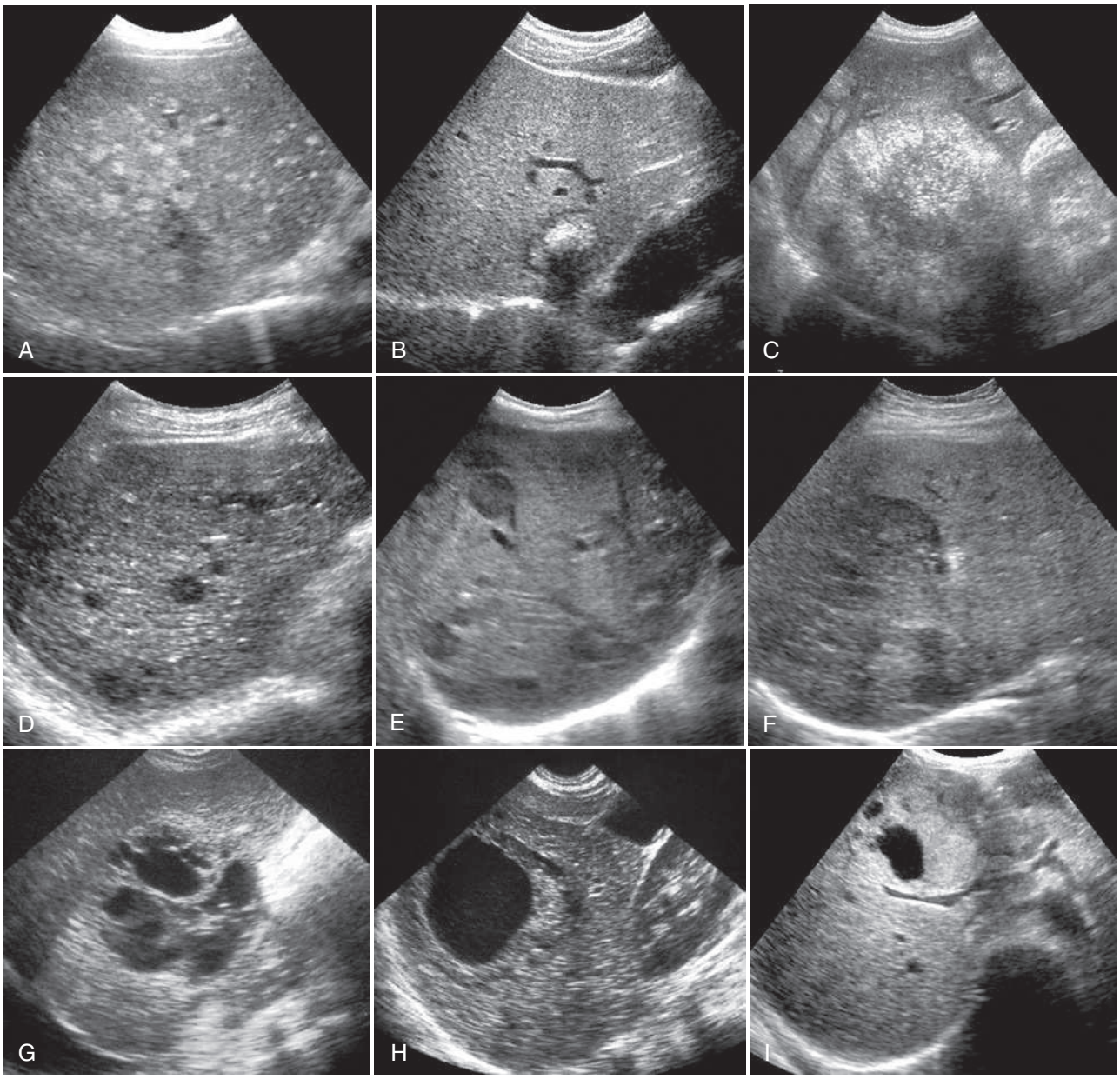

FIG. 4.61 Patterns of Metastatic Liver Disease. *Top row,* **Echogenic lesions. (A)** Multiple tiny echogenic metastases from choriocarcinoma. **(B)** Colon metastasis with clump of calcium and distal acoustic shadowing. **(C)** Large, poorly differentiated metastatic adenocarcinoma, with tiny punctate echogenicities suggesting microcalcification. *Middle row,* **Hypoechoic lesions of increasing size** from **(D)** pancreas; **(E)** lung; and **(F)** adenocarcinoma, from unknown primaries. *Bottom row,* **Cystic metastases. (G)** Rare metastatic liposarcoma from the thigh. Metastasis has a cystic growth pattern. **(H)** Metastatic sarcoma from the small bowel with necrosis, and **(I)** highly echogenic metastasis with a well-defined cystic component, highly suggestive of metastatic carcinoid or neuroendocrine tumor.

appreciate on sonography, probably because of the loss of the reference normal liver for comparison (Fig. 4.59G-I). In our experience, **breast and lung carcinomas,** as well as **malignant melanomas,** are the most common primary tumors to present this pattern. The diagnosis can be even more difficult if the patient has a fatty liver from chemotherapy. In these patients, CEUS, CT, or MRI may be helpful. Segmental and lobar tumor infiltration by secondary tumor may also be difficult to detect because it may mimic other benign conditions, such as **fatty infiltration** (Fig. 4.59D-F) or **cirrhosis** (Fig. 4.63).

CEUS plays a major role in the diagnosis and detection of metastases.[136,206] Arterial phase enhancement is variable, although most metastases, regardless of their expected enhancement, show transient hypervascularity in the arterial phase, followed by rapid washout. In the portal venous phase, metastases show washout, which tends to be complete and also rapid, beginning within

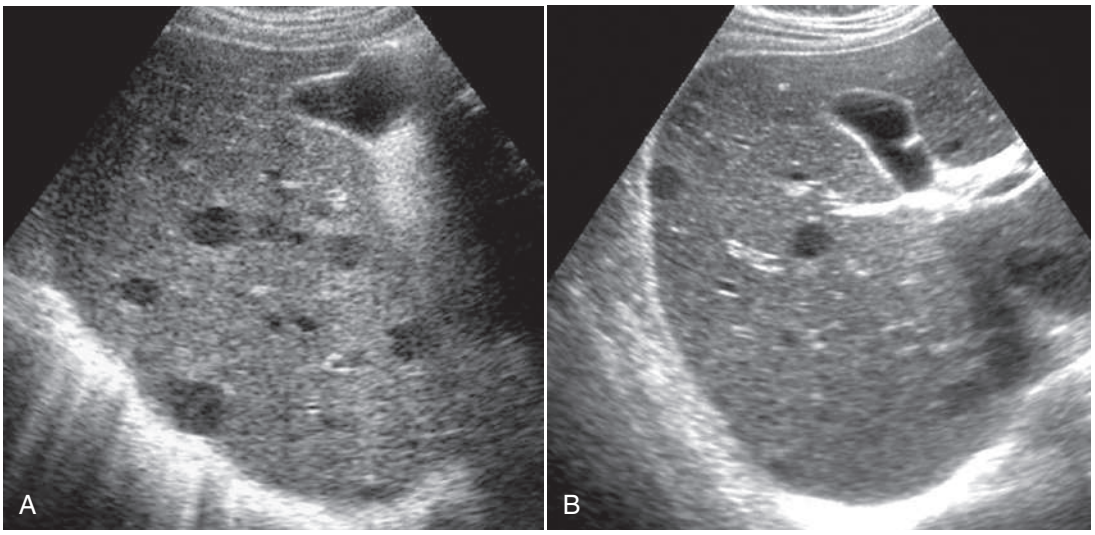

FIG. 4.62 Lymphoma of the Liver. (A) Sagittal and **(B)** transverse sonograms show small, focal hypoechoic nodules throughout the liver. Lymphoma may also involve the liver diffusely without producing a focal sonographic abnormality.

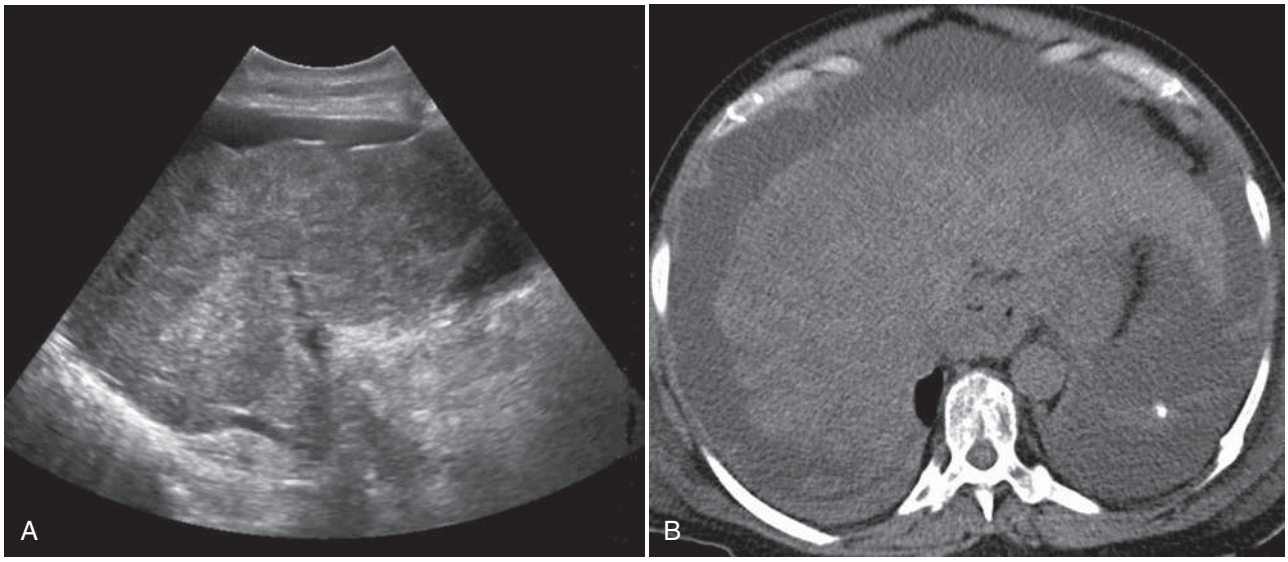

FIG. 4.63 Pseudocirrhosis in Woman With Metastatic Breast Cancer. Older woman presented to emergency department with increased abdominal girth. **(A)** Intercostal sonogram of the liver shows heterogeneous nodular parenchyma, surface nodularity, and ascites; all suggest cirrhosis. **(B)** Unenhanced computer tomography image of the liver confirms the findings, including ascites, surface nodularity, and heterogeneous parenchyma. Contrast enhancement did not suggest focal metastatic disease. At autopsy, diffuse breast metastases were found.

the arterial phase (Fig. 4.64 and Videos 4.12, 4.13, and 4.14). Therefore metastases will appear as black punched-out areas within the enhanced parenchyma. Hypovascularity and rim enhancement can also be shown.

Peripheral cholangiocarcinoma is an infrequent tumor presenting with a solitary liver mass similar to a metastasis, both on gray-scale images and CEUS. Capsular retraction may be appreciated.

Hepatic involvement by **Kaposi sarcoma,** although frequent in patients with AIDS at autopsy, is rarely diagnosed by imaging studies.[207] Sonography has demonstrated periportal infiltration and multiple small, peripheral hyperechoic nodules.[208,209]

Because of the nonspecific appearance of metastatic liver disease, **ultrasound-guided biopsy** is widely used to establish a primary tissue diagnosis. In addition, ultrasound is an excellent means to monitor the response to chemotherapy in oncology patients.

HEPATIC TRAUMA

The approach to the management of blunt hepatic injury is becoming increasingly more conservative. Surgical exploration is indicated for patients who are in shock or hemodynamically unstable. In the hemodynamically stable patient, many institutions

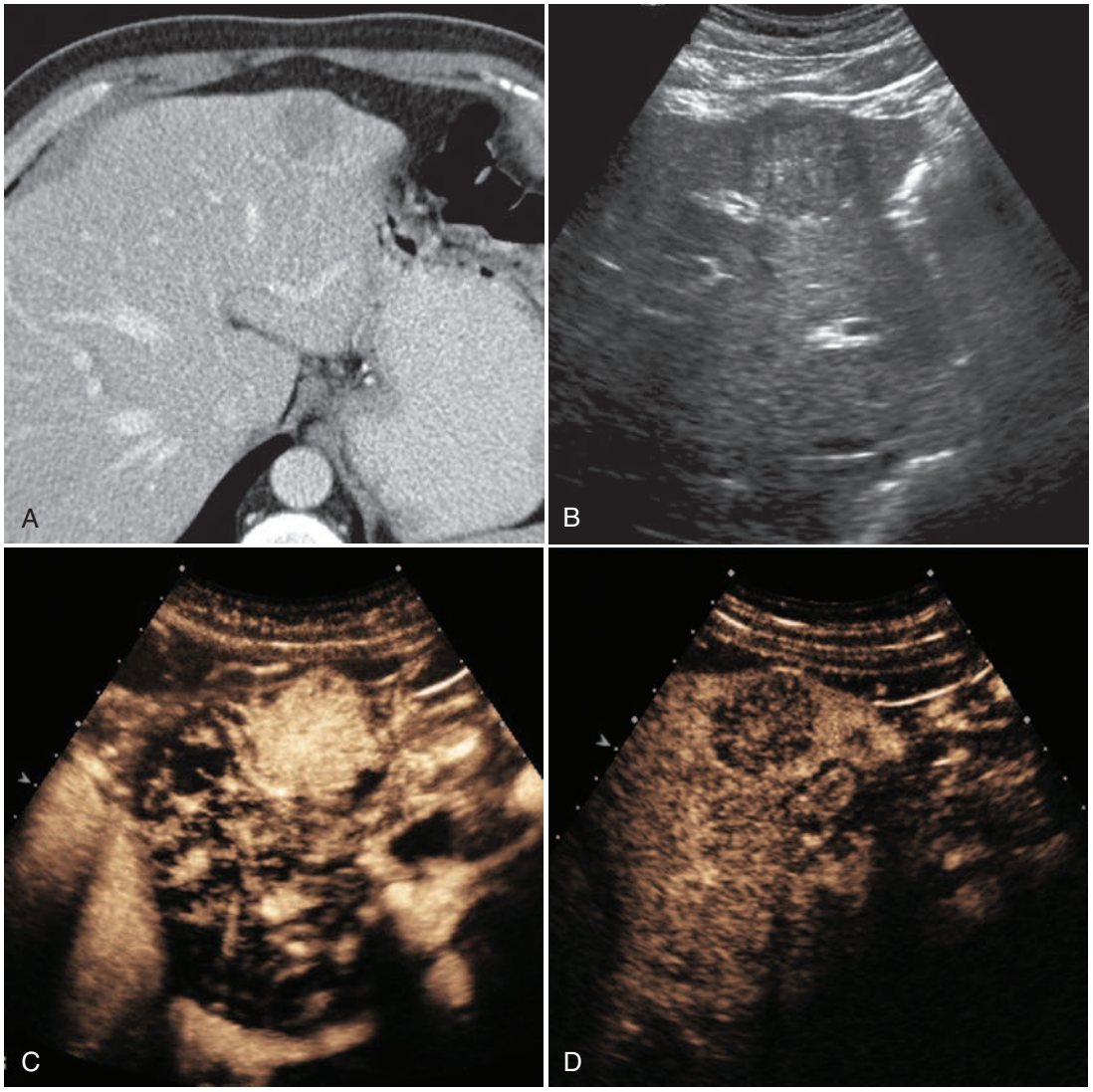

FIG. 4.64 Timing of Washout. This 49-year-old man had proven metastasis from colon cancer. **(A)** Axial computer tomography image shows a low-attenuation mass in the lateral segment of the left lobe. **(B)** Baseline sonogram shows that the mass is slightly exophytic and of mixed echogenicity. **(C)** Contrast-enhanced ultrasound arterial phase image at the peak of enhancement shows hypervascularity. **(D)** Image at 45 seconds shows clear washout of the lesion, which had begun at 28 seconds. See also Videos 4.12, 4.13, and 4.14. (With permission from Wilson S, Burns P. Microbubble-enhanced US in body imaging: what role? Radiology. 2010;257[1]:24-39.[148])

initially perform abdominal CT to assess the extent of liver trauma. Ultrasound may be used for serial monitoring of the healing pattern. In certain circumstances ultrasound can be used as a screening tool in blunt abdominal trauma (focused assessment with sonography in trauma [FAST]) by assessing for free fluid that would indicate solid organ injury.[210-214]

The predominant site of hepatic injury in blunt trauma is the right lobe, in particular the posterior segment.[215] Foley et al.[216] found that the most common type of injury was a perivascular laceration paralleling branches of the right and middle hepatic veins and the anterior and posterior branches of the right portal vein. Other findings were subcapsular, pericapsular, and isolated hematomas; liver fracture, defined as a laceration extending between two visceral surfaces; lacerations involving the left lobe; and hemoperitoneum[216] (Fig. 4.65). Hepatic infarcts are rarely identified after blunt abdominal trauma because of the dual blood supply of the liver.

VanSonnenberg et al.[217] evaluated the sonographic findings of acute trauma to the liver (<24 hours after injury or transhepatic cholangiogram) and determined that fresh hemorrhage was echogenic. Within the first week, the hepatic laceration becomes more hypoechoic and distinct as a result of resorption of devitalized tissue and ingress of interstitial fluid. After 2 to 3 weeks, the laceration becomes increasingly indistinct because of fluid resorption and filling of the spaces with granulation tissue.

Portosystemic Shunts

Surgical portosystemic shunts are performed to decompress the portal system in patients with portal hypertension. The most

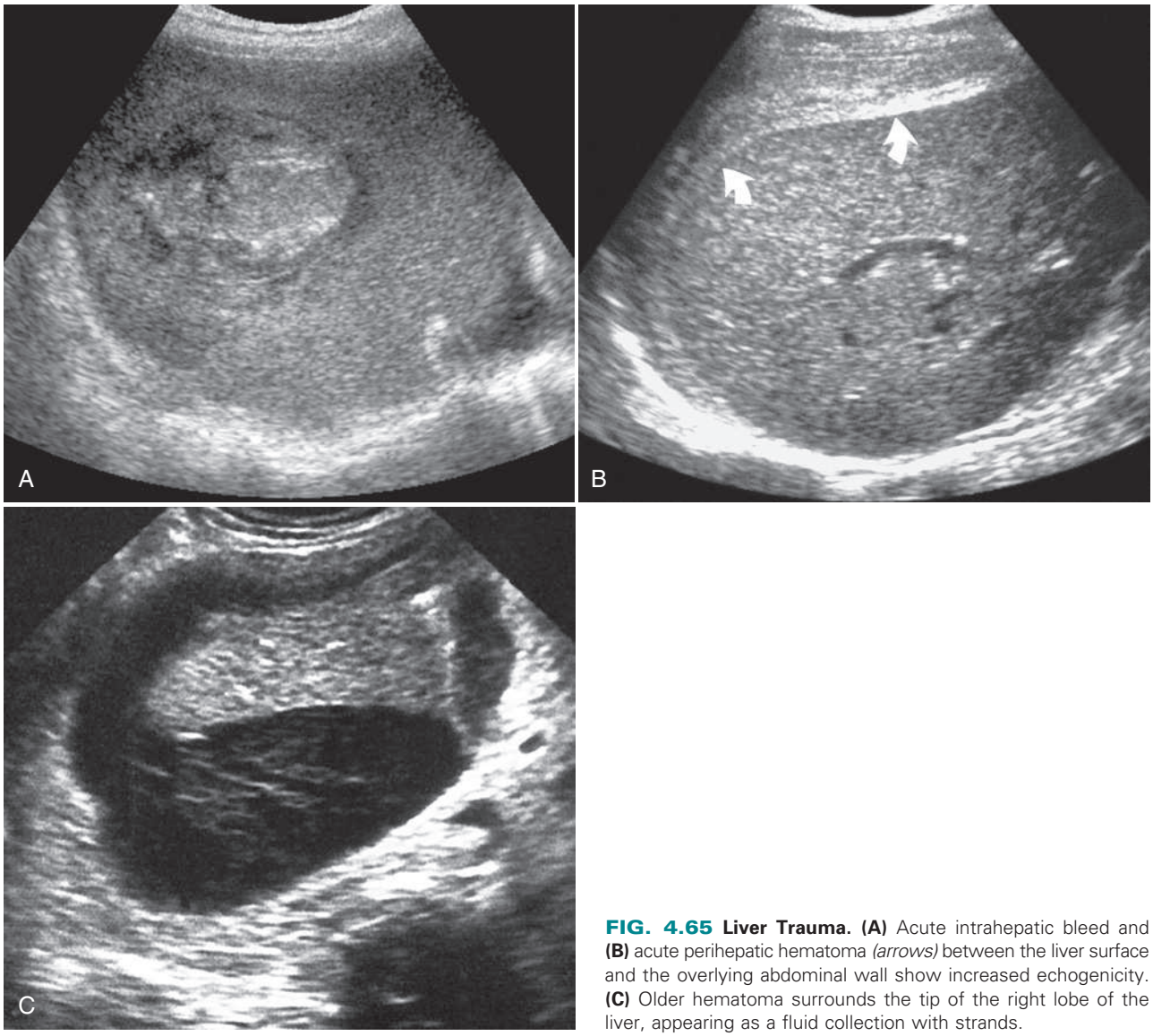

FIG. 4.65 Liver Trauma. (A) Acute intrahepatic bleed and **(B)** acute perihepatic hematoma *(arrows)* between the liver surface and the overlying abdominal wall show increased echogenicity. **(C)** Older hematoma surrounds the tip of the right lobe of the liver, appearing as a fluid collection with strands.

common surgical shunts include mesocaval, distal splenorenal (Warren shunts), mesoatrial, and portacaval. Duplex Doppler sonography and color Doppler flow imaging (CDFI) are reliable noninvasive methods of assessing shunt patency or thrombosis.[218-221] Both modalities are effective in assessing portacaval, mesoatrial, and mesocaval shunts.[218] Shunt patency is confirmed by demonstrating flow at the anastomotic site. If the anastomosis cannot be visualized, hepatofugal portal flow is an indirect sign of patency.[219,220]

Distal splenorenal communications are particularly difficult to examine with duplex Doppler sonography because overlying bowel gas and fat hinder accurate placement of the Doppler cursor.[218,222] CDFI more readily locates the splenic and renal limbs of Warren shunts. The splenic limb is best imaged from a left subcostal approach, whereas the left renal vein is optimally scanned through the left flank. Grant et al.[218] reported that color Doppler sonography correctly inferred patency or thrombosis in all 14 splenorenal communications by evaluating the flow in both limbs of the shunt.

Transjugular Intrahepatic Portosystemic Shunts

Transjugular intrahepatic portosystemic shunts **(TIPS)** are the most popular technique for relief of symptomatic portal hypertension, specifically varices with gastrointestinal bleeding, and less often, refractory ascites. Performed percutaneously with insertion of an expandable metal stent, TIPS have less morbidity and mortality than surgical shunt procedures.[223]

The technique of performing TIPS requires transjugular access to the infrahepatic IVC, with selection of the optimal hepatic vein on the basis of its angle and diameter, most often the right hepatic vein. After targeting the portal vein with either fluoroscopy or Doppler sonography, a transjugular puncture needle is passed from the hepatic vein to the intrahepatic portal vein and a shunt created. The tract is dilated to an approximate diameter of 10 mm,

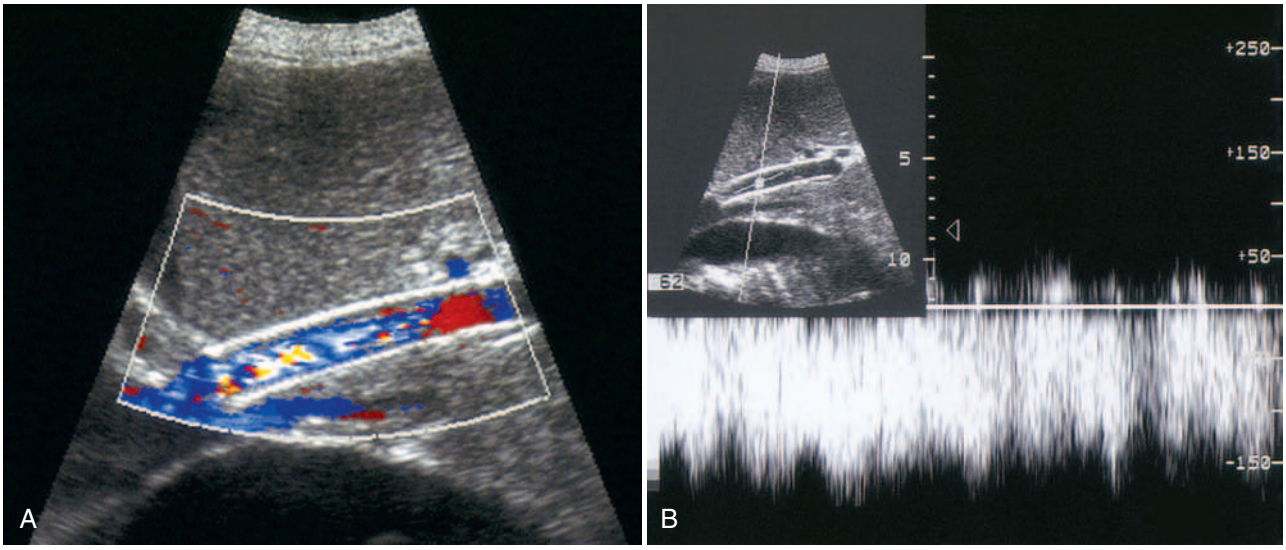

FIG. 4.66 Transjugular Intrahepatic Portosystemic Shunt (TIPS). (A) Color Doppler image of TIPS shows flow throughout the shunt appropriately directed toward the heart, with a turbulent pattern. **(B)** Angle-corrected midshunt velocity is normal at 150 cm/sec.

with monitoring of the portal pressure gradient and filling of varices on portal venography. A bridging stent is left in place.[224]

In addition to acute problems directly attributed to the procedure itself, TIPS may be complicated by stenosis or occlusion of the stent caused by hyperplasia of the pseudointimal lining. At 1 year, primary patency rates vary from 25% to 66%, with a primary assisted patency of about 83%.[225,226] Doppler sonography provides a noninvasive method for monitoring of TIPS patients because malfunction of the graft may be silent in its early phase. Scans should be performed immediately after the procedure, at 3-month intervals, and as indicated clinically.

Normal postprocedural Doppler findings include high-velocity, turbulent blood flow (mean peak systolic velocity, 135-200 cm/sec)[227] throughout the stent and hepatofugal flow in the intrahepatic portal venous branches, as the liver parenchyma drains through the shunt into the systemic circulation. Increased hepatic artery peak systolic velocity is also a normal observation, as is increased velocity in the main portal vein, because the stent serves as a low-resistance conduit, bypassing the high-resistance hepatic circulation. The reported mean main portal vein velocity in patients with patent shunts ranges from 37 to 47 cm/sec.[228-230] Hepatic artery velocities increase from 79 cm/sec preshunt to 131 cm/sec after the procedure.[227]

Sonographic evaluation should include measurement of angle-corrected stent velocities at three points along the stent and in the main portal vein, as well as evaluation of the direction of flow in the intrahepatic portal vein and in the involved hepatic vein (Figs. 4.66 and 4.67).

Sonographically detected complications include the following:

- Stent occlusion
- Stent stenosis
- Hepatic venous stenosis

Malfunction of Transjugular Intrahepatic Portosystemic Shunts: Sonographic Signs

DIRECT SIGNS

No flow, consistent with shunt thrombosis or occlusion
Peak shunt velocity: <90 or >190 cm/sec
Change in peak shunt velocity: decrease of >40 cm/sec or increase of >60 cm/sec
Main portal vein velocity <30 cm/sec
Reversal of flow in hepatic vein away from inferior vena cava, suggesting hepatic vein stenosis
Hepatopetal intrahepatic portal venous flow

SECONDARY SIGNS

Reaccumulation of ascites
Reappearance of varices
Reappearance of recanalized paraumbilical vein

Detection of these complications is related to identification of both direct abnormalities and secondary signs.[231-234] **Direct signs** include no flow, abnormal peak shunt velocity, a change in the peak shunt velocity, a low velocity in the main portal vein, reversal of hepatic vein flow, and hepatopetal intrahepatic portal venous flow. **Secondary signs** include reaccumulation of ascites and reappearance of varices and of recanalized paraumbilical vein.

PERCUTANEOUS LIVER BIOPSY

Percutaneous biopsy of malignant disease involving the liver has a sensitivity greater than 90% in most study series.[235,236]

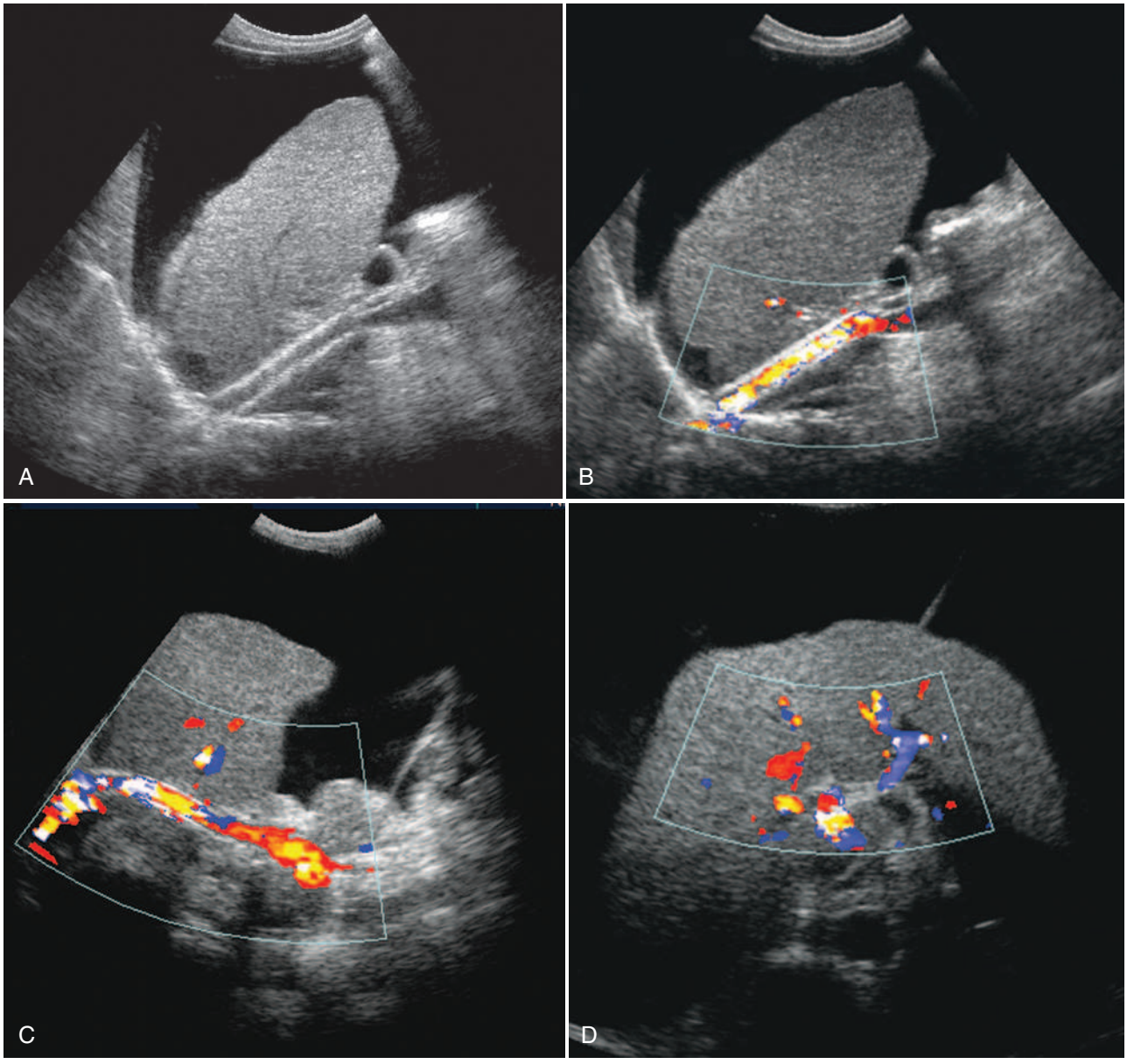

FIG. 4.67 Secondary Signs of Functional Shunt. All images show gross ascites, which suggests a dysfunctional shunt. **(A)** Gray-scale and **(B)** color Doppler images show a patent transjugular intrahepatic portosystemic shunt. Velocities throughout the shunt were about 130 cm/sec, which is normal. **(C)** Sagittal image shows that flow in the main portal vein is appropriately directed toward the shunt, appearing red. **(D)** Transverse image of the porta hepatis shows the ascending left portal venous branch is blue, flowing toward the shunt; this is also the correct direction. Therefore despite the ascites, the ultrasound evaluation does not show a dysfunctional shunt.

Relative contraindications to percutaneous biopsy are an uncorrectable bleeding diathesis, an unsafe access route, and an uncooperative patient. Ultrasound guidance allows real-time observation of the needle tip as it is advanced into the lesion. Several biopsy attachments allow continuous observation of the needle as it follows a predetermined path. Alternatively, many experienced radiologists prefer a "freehand" technique. Even small masses (2.5 cm) can undergo successful biopsy using sonographic guidance.[237] Ultrasound guidance may also be used in percutaneous aspiration and drainage of complicated fluid collections in the liver. Ultrasound-guided percutaneous ethanol injection has been used in the treatment of HCC and hepatic metastases.[238]

INTRAOPERATIVE ULTRASOUND

Intraoperative ultrasound is now an established application of ultrasound technology. The exposed liver is scanned with a sterile, 7.5-MHz transducer or one covered by a sterile sheath. Intraoperative ultrasound has been found to change the operative strategy in 31% to 49% of patients undergoing hepatic resection, either by allowing more precise resection or by indicating inoperability because of unsuspected masses or venous invasion.[239,240] Studies emphasize further improvement of surgical outcome with the addition of CEUS to intraoperative procedures.[241] Improved detection of metastases on CEUS undoubtedly accounts for this improvement.

Acknowledgment

Dr. Hojun Yu for his wonderful schematics and artwork.

REFERENCES

1. Wilson S, Gupta C, Eliasziw M, Andrew A. Volume imaging in the abdomen with ultrasound: how we do it. AJR Am J Roentgenol. 2009;193(1):79-85.
2. Marks W, Filly R, Callen P. Ultrasonic anatomy of the liver: a review with new applications. J Clin Ultrasound. 1979;7(2):137-146.
3. Couinaud C. Le foie études anatomiques et chirurgicales. Paris: Masson & Cie; 1957.
4. Soyer P, Bluemke DA, Bliss DF, et al. Surgical segmental anatomy of the liver: demonstration with spiral CT during arterial portography and multiplanar reconstruction. AJR Am J Roentgenol. 1994;163(1):99-103.
5. Sugarbaker PH. Toward a standard of nomenclature for surgical anatomy of the liver. Neth J Surg. 1988;PO:100.
6. Lafortune M, Madore F, Patriquin H, Breton G. Segmental anatomy of the liver: a sonographic approach to the Couinaud nomenclature. Radiology. 1991;181(2):443-448.
7. Gosink B, Leymaster C. Ultrasonic determination of hepatomegaly. J Clin Ultrasound. 1981;9(1):37-41.
8. Niederau C, Sonnenberg A, Müller JE, et al. Sonographic measurements of the normal liver, spleen, pancreas, and portal vein. Radiology. 1983;149(2):537-540.
9. Radin DR, Colletti PM, Ralls PW, et al. Agenesis of the right lobe of the liver. Radiology. 1987;164(3):639-642.
10. Belton RL, VanZandt TF. Congenital absence of the left lobe of the liver: a radiologic diagnosis. Radiology. 1983;147(1):184.
11. Lim JH, Ko YT, Han MC, et al. The inferior accessory hepatic fissure: sonographic appearance. AJR Am J Roentgenol. 1987;149(3):495-497.
12. Fraser-Hill MA, Atri M, Bret PM, et al. Intrahepatic portal venous system: variations demonstrated with duplex and color Doppler US. Radiology. 1990;177(2):523-526.
13. Cosgrove D, Arger P, Coleman B. Ultrasonic anatomy of hepatic veins. J Clin Ultrasound. 1987;15(4):231-235.
14. Makuuchi M, Hasegawa H, Yamazaki S, et al. The inferior right hepatic vein: ultrasonic demonstration. Radiology. 1983;148(1):213-217.
15. Gaines PA, Sampson MA. The prevalence and characterization of simple hepatic cysts by ultrasound examination. Br J Radiol. 1989;62(736):335-337.
16. Bean WJ, Rodan BA. Hepatic cysts: treatment with alcohol. AJR Am J Roentgenol. 1985;144(2):237-241.
17. Baron RL, Campbell WL, Dodd GD. Peribiliary cysts associated with severe liver disease: imaging-pathologic correlation. AJR Am J Roentgenol. 1994;162(3):631-636.
18. Levine E, Cook LT, Grantham JJ. Liver cysts in autosomal-dominant polycystic kidney disease: clinical and computed tomographic study. AJR Am J Roentgenol. 1985;145(2):229-233.
19. Chung EB. Multiple bile-duct hamartomas. Cancer. 1970;26(2):287-296.
20. Redston MS, Wanless IR. The hepatic von Meyenburg complex: prevalence and association with hepatic and renal cysts among 2843 autopsies [corrected]. Mod Pathol. 1996;9(3):233-237.
21. Lev-Toaff AS, Bach AM, Wechsler RJ, et al. The radiologic and pathologic spectrum of biliary hamartomas. AJR Am J Roentgenol. 1995;165(2):309-313.
22. Tan A, Shen J, Hecht A. Sonogram of multiple bile duct hamartomas. J Clin Ultrasound. 1989;17(9):667-669.
23. Salo J, Bru C, Vilella A, et al. Bile-duct hamartomas presenting as multiple focal lesions on hepatic ultrasonography. Am J Gastroenterol. 1992;87(2):221-223.
24. Burns CD, Kuhns JG, Wieman TJ. Cholangiocarcinoma in association with multiple biliary microhamartomas. Arch Pathol Lab Med. 1990;114(12):1287-1289.
25. Debing Y, Moradpour D, Neyts J, Gouttenoire J. Update on hepatitis E virology: implications for clinical practice. J Hepatol. 2016;65(1):200-212.
26. Wilson SR. The liver. In: Gastrointestinal disease. 6th series. Test and syllabus. Reson, VA: American College of Radiology; 2004.
27. Wilson SR, Arenson AM. Sonographic evaluation of hepatic abscesses. J Can Assoc Radiol. 1984;35(2):174-177.
28. Sabbaj J. Anaerobic pyogenic liver abscess. Ann Intern Med. 1972;77(4):629.
29. Lawrence PH, Holt SC, Levi CS, Gough JC. Ultrasound case of the day. Hepatosplenic candidiasis. Radiographics. 1994;14(5):1147-1149.
30. Pastakia B, Shawker TH, Thaler M, et al. Hepatosplenic candidiasis: wheels within wheels. Radiology. 1988;166(2):417-421.
31. Berry M, Bazaz R, Bhargava S. Amebic liver abscess: sonographic diagnosis and management. J Clin Ultrasound. 1986;14(4):239-242.
32. Ralls PW, Colletti PM, Quinn MF, Halls J. Sonographic findings in hepatic amebic abscess. Radiology. 1982;145(1):123-126.
33. Ralls PW, Barnes PF, Radin DR, et al. Sonographic features of amebic and pyogenic liver abscesses: a blinded comparison. AJR Am J Roentgenol. 1987;149(3):499-501.
34. Ralls PW, Barnes PF, Johnson MB, et al. Medical treatment of hepatic amebic abscess: rare need for percutaneous drainage. Radiology. 1987;165(3):805-807.
35. Ralls PW, Quinn MF, Boswell WD, et al. Patterns of resolution in successfully treated hepatic amebic abscess: sonographic evaluation. Radiology. 1983;149(2):541-543.
36. Lewall DB, McCorkell SJ. Hepatic echinococcal cysts: sonographic appearance and classification. Radiology. 1985;155(3):773-775.
37. Gharbi HA, Hassine W, Brauner MW, Dupuch K. Ultrasound examination of the hydatic liver. Radiology. 1981;139(2):459-463.
38. Beggs I. The radiology of hydatid disease. AJR Am J Roentgenol. 1985;145(3):639-648.
39. Bret PM, Fond A, Bretagnolle M, et al. Percutaneous aspiration and drainage of hydatid cysts in the liver. Radiology. 1988;168(3):617-620.
40. Mueller PR, Dawson SL, Ferrucci JT, Nardi GL. Hepatic echinococcal cyst: successful percutaneous drainage. Radiology. 1985;155(3):627-628.
41. Akhan O, Ozmen MN, Dinçer A, et al. Liver hydatid disease: long-term results of percutaneous treatment. Radiology. 1996;198(1):259-264.
42. Bezzi M, Teggi A, De Rosa F, et al. Abdominal hydatid disease: US findings during medical treatment. Radiology. 1987;162(1):91-95.
43. Jha R, Lyons EA, Levi CS. US case of the day. Hydatid cyst (Echinococcus granulosus) in the right lobe of the liver. Radiographics. 1994;14(2):455-458.
44. Didier D, Weiler S, Rohmer P, et al. Hepatic alveolar echinococcosis: correlative US and CT study. Radiology. 1985;154(1):179-186.
45. Symmers WSC. Note on a new form of liver cirrhosis due to the presence of the ova of Bilharzia hæmatobia. J Pathol. 1904;9(2):237-239.
46. Fataar S, Bassiony H, Satyanath S, et al. Characteristic sonographic features of schistosomal periportal fibrosis. AJR Am J Roentgenol. 1984;143(1):69-71.
47. Cerri GG, Alves VA, Magalhães A. Hepatosplenic schistosomiasis mansoni: ultrasound manifestations. Radiology. 1984;153(3):777-780.
48. Kuhlman JE. Pneumocystic infections: the radiologist's perspective. Radiology. 1996;198(3):623-635.
49. Lubat E, Megibow AJ, Balthazar EJ, et al. Extrapulmonary Pneumocystis carinii infection in AIDS: CT findings. Radiology. 1990;174(1):157-160.
50. Spouge AR, Wilson SR, Gopinath N, et al. Extrapulmonary Pneumocystis carinii in a patient with AIDS: sonographic findings. AJR Am J Roentgenol. 1990;155(1):76-78.
51. Radin DR, Baker EL, Klatt EC, et al. Visceral and nodal calcification in patients with AIDS-related Pneumocystis carinii infection. AJR Am J Roentgenol. 1990;154(1):27-31.
52. Telzak EE, Cote RJ, Gold JWM, et al. Extrapulmonary Pneumocystis carinii infections. Rev Infect Dis. 1990;12(3):380-386.
53. Towers MJ, Withers CE, Hamilton PA, et al. Visceral calcification in patients with AIDS may not always be due to Pneumocystis carinii. AJR Am J Roentgenol. 1991;156(4):745-747.
54. Wilson SR, Rosen IE, Chin-Sang HB, Arenson AM. Fatty infiltration of the liver–an imaging challenge. J Can Assoc Radiol. 1982;33(4):227-232.
55. Yates CK, Streight RA. Focal fatty infiltration of the liver simulating metastatic disease. Radiology. 1986;159(1):83-84.
56. White EM, Simeone JF, Mueller PR, et al. Focal periportal sparing in hepatic fatty infiltration: a cause of hepatic pseudomass on US. Radiology. 1987;162(1):57-59.

57. Sauerbrei EE, Lopez M. Pseudotumor of the quadrate lobe in hepatic sonography: a sign of generalized fatty infiltration. AJR Am J Roentgenol. 1986;147(5):923-927.
58. Wanless IR, Bargman JM, Oreopoulos DG, Vas SI. Subcapsular steatonecrosis in response to peritoneal insulin delivery: a clue to the pathogenesis of steatonecrosis in obesity. Mod Pathol. 1989;2(2):69-74.
59. Apicella PL, Mirowitz SA, Weinreb JC. Extension of vessels through hepatic neoplasms: MR and CT findings. Radiology. 1994;191(1):135-136.
60. Quinn SF, Gosink BB. Characteristic sonographic signs of hepatic fatty infiltration. AJR Am J Roentgenol. 1985;145(4):753-755.
61. Arai K, Matsui O, Takashima T, et al. Focal spared areas in fatty liver caused by regional decreased portal flow. AJR Am J Roentgenol. 1988;151(2): 300-302.
62. Von Gierke E. Hepato-nephromegalia glykogenica (Glykogenspeicherkrankheit der Leber und Nieren). Beitr Pathol Anat (Jena). 1929;82: 497-513.
63. Grossman H, Ram PC, Coleman RA, et al. Hepatic ultrasonography in type I glycogen storage disease (von Gierke disease). Detection of hepatic adenoma and carcinoma. Radiology. 1981;141(3):753-756.
64. Anthony PP, Ishak KG, Nayak NC, et al. The morphology of cirrhosis. Recommendations on definition, nomenclature, and classification by a working group sponsored by the World Health Organization. J Clin Pathol. 1978;31(5):395-414.
65. Giorgio A, Amoroso P, Lettieri G, et al. Cirrhosis: value of caudate to right lobe ratio in diagnosis with US. Radiology. 1986;161(2):443-445.
66. Taylor KJ, Riely CA, Hammers L, et al. Quantitative US attenuation in normal liver and in patients with diffuse liver disease: importance of fat. Radiology. 1986;160(1):65-71.
67. Sanford NL, Walsh P, Matis C, et al. Is ultrasonography useful in the assessment of diffuse parenchymal liver disease? Gastroenterology. 1985; 89(1):186-191.
68. Freeman MP, Vick CW, Taylor KJ, et al. Regenerating nodules in cirrhosis: sonographic appearance with anatomic correlation. AJR Am J Roentgenol. 1986;146(3):533-536.
69. Murakami T, Kuroda C, Marukawa T, et al. Regenerating nodules in hepatic cirrhosis: MR findings with pathologic correlation. AJR Am J Roentgenol. 1990;155(6):1227-1231.
70. Theise N. Macroregenerative (dysplastic) nodules and hepatocarcinogenesis: theoretical and clinical considerations. Semin Liver Dis. 1995; 15(04):360-371.
71. Tanaka S, Kitamra T, Fujita M, et al. Small hepatocellular carcinoma: differentiation from adenomatous hyperplastic nodule with color Doppler flow imaging. Radiology. 1992;182(1):161-165.
72. Colli A, Cocciolo M, Riva C, et al. Abnormalities of Doppler waveform of the hepatic veins in patients with chronic liver disease: correlation with histologic findings. AJR Am J Roentgenol. 1994;162(4):833-837.
73. Bolondi L, Li Bassi S, Gaiani S, et al. Liver cirrhosis: changes of Doppler waveform of hepatic veins. Radiology. 1991;178(2):513-516.
74. Lafortune M, Dauzat M, Pomier-Layrargues G, et al. Hepatic artery: effect of a meal in healthy persons and transplant recipients. Radiology. 1993;187(2):391-394.
75. Joynt LK, Platt JF, Rubin JM, et al. Hepatic artery resistance before and after standard meal in subjects with diseased and healthy livers. Radiology. 1995;196(2):489-492.
76. Friedrich-Rust M, Romen D, Vermehren J, et al. Acoustic radiation force impulse-imaging and transient elastography for non-invasive assessment of liver fibrosis and steatosis in NAFLD. Eur J Radiol. 2012;81(3): e325-e331.
77. Garra BS. Elastography: current status, future prospects, and making it work for you. Ultrasound Q. 2011;27(3):177-186.
78. Bamber J, Cosgrove D, Dietrich C, et al. EFSUMB guidelines and recommendations on the clinical use of ultrasound elastography. Part 1: Basic principles and technology. Ultraschall Med. 2013;34(2): 169-184.
79. Ferraioli G, Tinelli C, Lissandrin R, et al. Ultrasound point shear wave elastography assessment of liver and spleen stiffness: effect of training on repeatability of measurements. Eur Radiol. 2014;24(6):1283-1289.
80. Barr R, Ferraioli G, Palmeri M, et al. Elastography assessment of liver fibrosis: Society of Radiologists in Ultrasound consensus conference statement. Radiology. 2015;276(3):845-861.
81. Bolondi L, Gandolfi L, Arienti V, et al. Ultrasonography in the diagnosis of portal hypertension: diminished response of portal vessels to respiration. Radiology. 1982;142(1):167-172.
82. Lafortune M, Marleau D, Breton G, et al. Portal venous system measurements in portal hypertension. Radiology. 1984;151(1):27-30.
83. Subramanyam BR, Balthazar EJ, Madamba MR, et al. Sonography of portosystemic venous collaterals in portal hypertension. Radiology. 1983;146(1):161-166.
84. Jüttner HU, Jenney JM, Ralls PW, et al. Ultrasound demonstration of portosystemic collaterals in cirrhosis and portal hypertension. Radiology. 1982;142(2):459-463.
85. Patriquin H, Lafortune M, Burns PN, Dauzat M. Duplex Doppler examination in portal hypertension: technique and anatomy. AJR Am J Roentgenol. 1987;149(1):71-76.
86. Lafortune M, Constantin A, Breton G, et al. The recanalized umbilical vein in portal hypertension: a myth. AJR Am J Roentgenol. 1985;144(3): 549-553.
87. Mostbeck GH, Wittich GR, Herold C, et al. Hemodynamic significance of the paraumbilical vein in portal hypertension: assessment with duplex US. Radiology. 1989;170(2):339-342.
88. Di Candio G, Campatelli A, Mosca F, et al. Ultrasound detection of unusual spontaneous portosystemic shunts associated with uncomplicated portal hypertension. J Ultrasound Med. 1985;4(6):297-305.
89. Nelson RC, Lovett KE, Chezmar JL, et al. Comparison of pulsed Doppler sonography and angiography in patients with portal hypertension. AJR Am J Roentgenol. 1987;149(1):77-81.
90. Bellamy EA, Bossi MC, Cosgrove DO. Ultrasound demonstration of changes in the normal portal venous system following a meal. Br J Radiol. 1984;57(674):147-149.
91. Ohnishi K, Saito M, Nakayama T, et al. Portal venous hemodynamics in chronic liver disease: effects of posture change and exercise. Radiology. 1985;155(3):757-761.
92. Bolondi L, Mazziotti A, Arienti V, et al. Ultrasonographic study of portal venous system in portal hypertension and after portosystemic shunt operations. Surgery. 1984;95(3):261-269.
93. Zwiebel WJ, Mountford RA, Halliwell MJ, Wells PN. Splanchnic blood flow in patients with cirrhosis and portal hypertension: investigation with duplex Doppler US. Radiology. 1995;194(3):807-812.
94. Finn JP, Kane RA, Edelman RR, et al. Imaging of the portal venous system in patients with cirrhosis: MR angiography vs duplex Doppler sonography. AJR Am J Roentgenol. 1993;161(5):989-994.
95. Wilson SR, Hine AL. Leiomyosarcoma of the portal vein. AJR Am J Roentgenol. 1987;149(1):183-184.
96. Van Gansbeke D, Avni EF, Delcour C, et al. Sonographic features of portal vein thrombosis. AJR Am J Roentgenol. 1985;144(4):749-752.
97. Kauzlaric D, Petrovic M, Barmeir E. Sonography of cavernous transformation of the portal vein. AJR Am J Roentgenol. 1984;142(2): 383-384.
98. Aldrete JS, Slaughter RL, Han SY. Portal vein thrombosis resulting in portal hypertension in adults. Am J Gastroenterol. 1976;65(3):236-243.
99. Dodd GD, Memel DS, Baron RL, et al. Portal vein thrombosis in patients with cirrhosis: does sonographic detection of intrathrombus flow allow differentiation of benign and malignant thrombus? AJR Am J Roentgenol. 1995;165(3):573-577.
100. Taylor KJ, Burns PN, Woodcock JP, Wells PN. Blood flow in deep abdominal and pelvic vessels: ultrasonic pulsed-Doppler analysis. Radiology. 1985;154(2):487-493.
101. Brown BP, Abu-Yousef M, Farner R, et al. Doppler sonography: a noninvasive method for evaluation of hepatic venocclusive disease. AJR Am J Roentgenol. 1990;154(4):721-724.
102. Ralls PW, Johnson MB, Radin DR, et al. Budd-Chiari syndrome: detection with color Doppler sonography. AJR Am J Roentgenol. 1992;159(1): 113-116.
103. Keller MS, Taylor KJ, Riely CA. Pseudoportal Doppler signal in the partially obstructed inferior vena cava. Radiology. 1989;170(2):475-477.

104. Hosoki T, Kuroda C, Tokunaga K, et al. Hepatic venous outflow obstruction: evaluation with pulsed duplex sonography. Radiology. 1989;170(3): 733-737.
105. Grant EG, Perrella R, Tessler FN, et al. Budd-Chiari syndrome: the results of duplex and color Doppler imaging. AJR Am J Roentgenol. 1989; 152(2):377-381.
106. Murphy FB, Steinberg HV, Shires GT, et al. The Budd-Chiari syndrome: a review. AJR Am J Roentgenol. 1986;147(1):9-15.
107. Park JH, Lee JB, Han MC, et al. Sonographic evaluation of inferior vena caval obstruction: correlative study with vena cavography. AJR Am J Roentgenol. 1985;145(4):757-762.
108. Menu Y, Alison D, Lorphelin JM, et al. Budd-Chiari syndrome: US evaluation. Radiology. 1985;157(3):761-764.
109. Becker C, Scheidegger J, Marincek B. Hepatic vein occlusion: morphologic features on computed tomography and ultrasonography. Gastrointest Radiol. 1986;11(1):305-311.
110. Stanley P. Budd-Chiari syndrome. Radiology. 1989;170(3):625-627.
111. Makuuchi M, Hasegawa H, Yamazaki S, et al. Primary Budd-Chiari syndrome: ultrasonic demonstration. Radiology. 1984;152(3):775-779.
112. Millener P, Grant EG, Rose S, et al. Color Doppler imaging findings in patients with Budd-Chiari syndrome: correlation with venographic findings. AJR Am J Roentgenol. 1993;161(2):307-312.
113. Kriegshauser JS, Charboneau JW, Letendre L. Hepatic venocclusive disease after bone-marrow transplantation: diagnosis with duplex sonography. AJR Am J Roentgenol. 1988;150(2):289-290.
114. Mori H, Hayashi K, Fukuda T, et al. Intrahepatic portosystemic venous shunt: occurrence in patients with and without liver cirrhosis. AJR Am J Roentgenol. 1987;149(4):711-714.
115. Chagnon SF, Vallee CA, Barge J, et al. Aneurysmal portahepatic venous fistula: report of two cases. Radiology. 1986;159(3):693-695.
116. Park JH, Cha SH, Han JK, Han MC. Intrahepatic portosystemic venous shunt. AJR Am J Roentgenol. 1990;155(3):527-528.
117. Falkoff GE, Taylor KJ, Morse S. Hepatic artery pseudoaneurysm: diagnosis with real-time and pulsed Doppler US. Radiology. 1986;158(1): 55-56.
118. Garcia P, Garcia-Giannoli H, Meyran S, et al. Primary dissecting aneurysm of the hepatic artery: sonographic, CT, and angiographic findings. AJR Am J Roentgenol. 1996;166(6):1316-1318.
119. Cloogman HM, DiCapo RD. Hereditary hemorrhagic telangiectasia: sonographic findings in the liver. Radiology. 1984;150(2):521-522.
120. Leong SS, Cazen RA, Yu GS, et al. Abdominal visceral peliosis associated with bacillary angiomatosis. Ultrastructural evidence of endothelial destruction by bacilli. Arch Pathol Lab Med. 1992;116(8):866-871.
121. Jamadar DA, D'Souza SP, Thomas EA, Giles TE. Radiological appearances in peliosis hepatis. Br J Radiol. 1994;67(793):102-104.
122. Toyoda S, Takeda K, Nakagawa T, Matsuda A. Magnetic resonance imaging of peliosis hepatis: a case report. Eur J Radiol. 1993;16(3):207-208.
123. Lloyd RL, Lyons EA, Levi CS, et al. The sonographic appearance of peliosis hepatis. J Ultrasound Med. 1982;1(7):293-294.
124. Tsukamoto Y, Nakata H, Kimoto T, et al. CT and angiography of peliosis hepatis. AJR Am J Roentgenol. 1984;142(3):539-540.
125. Muradali D, Wilson SR, Wanless IR, et al. Peliosis hepatis with intrahepatic calcifications. J Ultrasound Med. 1996;15(3):257-260.
126. Burns P, Wilson S. Focal liver masses: enhancement patterns on contrast-enhanced images—concordance of US scans with CT scans and MR images. Radiology. 2007;242(1):162-174.
127. Burns P, Wilson S, Simpson D. Pulse inversion imaging of liver blood flow. Invest Radiol. 2000;35(1):58.
128. Wilson S, Burns P, Muradali D, et al. Harmonic hepatic US with microbubble contrast agent: initial experience showing improved characterization of hemangioma, hepatocellular carcinoma, and metastasis. Radiology. 2000;215(1):153-161.
129. Wilson S, Greenbaum L, Goldberg B. Contrast-enhanced ultrasound: what is the evidence and what are the obstacles? AJR Am J Roentgenol. 2009;193(1):55-60.
130. Wilson S, Jang H, Kim T, et al. Real-time temporal maximum-intensity-projection imaging of hepatic lesions with contrast-enhanced sonography. AJR Am J Roentgenol. 2008;190(3):691-695.
131. Wilson S, Burns P. An algorithm for the diagnosis of focal liver masses using microbubble contrast-enhanced pulse-inversion sonography. AJR Am J Roentgenol. 2006;186(5):1401-1412.
132. Brannigan M, Burns P, Wilson S. Blood flow patterns in focal liver lesions at microbubble-enhanced US. Radiographics. 2004;24(4):921-935.
133. Quaia E, Degobbis F, Tona G, et al. Differential patterns of contrast enhancement in different focal liver lesions after injection of the microbubble US contrast agent SonoVue]. Radiol Med. 2004;107(3):155-165.
134. von Herbay A, Vogt C, Willers R, Haussinger D. Real-time imaging with the sonographic contrast agent SonoVue: differentiation between benign and malignant hepatic lesions. J Ultrasound Med. 2004;23(12): 1557-1568.
135. Blomley MJ, Albrecht T, Cosgrove DO, et al. Improved imaging of liver metastases with stimulated acoustic emission in the late phase of enhancement with the US contrast agent SH U 508A: early experience. Radiology. 1999;210(2):409-416.
136. Albrecht T, Blomley M, Burns P, et al. Improved detection of hepatic metastases with pulse-inversion US during the liver-specific phase of SHU 508A: multicenter study. Radiology. 2003;227(2):361-370.
137. Mungovan JA, Cronan JJ, Vacarro J. Hepatic cavernous hemangiomas: lack of enlargement over time. Radiology. 1994;191(1):111-113.
138. Gibney RG, Hendin AP, Cooperberg PL. Sonographically detected hepatic hemangiomas: absence of change over time. AJR Am J Roentgenol. 1987;149(5):953-957.
139. Bree RL, Schwab RE, Neiman HL. Solitary echogenic spot in the liver: is it diagnostic of a hemangioma? AJR Am J Roentgenol. 1983;140(1): 41-45.
140. McArdle C. Ultrasonic appearances of a hepatic hemangioma. J Clin Ultrasound. 1978;6(2):124.
141. Taboury J, Porcel A, Tubiana JM, Monnier JP. Cavernous hemangiomas of the liver studied by ultrasound. Enhancement posterior to a hyperechoic mass as a sign of hypervascularity. Radiology. 1983;149(3):781-785.
142. Itai Y, Furui S, Araki T, et al. Computed tomography of cavernous hemangioma of the liver. Radiology. 1980;137(1):149-155.
143. Itai Y, Ohnishi S, Ohtomo K, et al. Hepatic cavernous hemangioma in patients at high risk for liver cancer. Acta Radiol. 1987;28(6): 697-701.
144. Moody AR, Wilson SR. Atypical hepatic hemangioma: a suggestive sonographic morphology. Radiology. 1993;188(2):413-417.
145. Marsh J, Gibney R, Li D. Hepatic hemangioma in the presence of fatty infiltration: an atypical sonographic appearance. Gastrointest Radiol. 1989;14(1):262-264.
146. Choi BI, Kim TK, Han JK, et al. Power versus conventional color Doppler sonography: comparison in the depiction of vasculature in liver tumors. Radiology. 1996;200(1):55-58.
147. Caturelli E, Pompili M, Bartolucci F, et al. Hemangioma-like lesions in chronic liver disease: diagnostic evaluation in patients. Radiology. 2001;220(2):337-342.
148. Wilson S, Burns P. Microbubble-enhanced US in body imaging: what role? Radiology. 2010;257(1):24-39.
149. Cronan JJ, Esparza AR, Dorfman GS, et al. Cavernous hemangioma of the liver: role of percutaneous biopsy. Radiology. 1988;166(1):135-138.
150. Solbiati L, Livraghi T, De Pra L, et al. Fine-needle biopsy of hepatic hemangioma with sonographic guidance. AJR Am J Roentgenol. 1985;144(3):471-474.
151. Wanless I, Mawdsley C, Adams R. On the pathogenesis of focal nodular hyperplasia of the liver. Hepatology. 1985;5(6):1194-1200.
152. Ross D. Regression of focal nodular hyperplasia after discontinuation of oral contraceptives. Ann Intern Med. 1976;85(2):203.
153. Knowles D, Casarella W, Johnson P, Wolff M. The clinical, radiologic, and pathologic characterization of benign hepatic neoplasms. Medicine (Baltimore). 1978;57(3):223-238.
154. Buetow PC, Pantongrag-Brown L, Buck JL, et al. Focal nodular hyperplasia of the liver: radiologic-pathologic correlation. Radiographics. 1996;16(2): 369-388.
155. Scatarige JC, Fishman EK, Sanders RC. The sonographic "scar sign" in focal nodular hyperplasia of the liver. J Ultrasound Med. 1982;1(7): 275-278.

156. Golli M, Van Nhieu JT, Mathieu D, et al. Hepatocellular adenoma: color Doppler US and pathologic correlations. Radiology. 1994;190(3): 741-744.
157. Dietrich CF, Schuessler G, Trojan J, et al. Differentiation of focal nodular hyperplasia and hepatocellular adenoma by contrast-enhanced ultrasound. Br J Radiol. 2005;78(932):704-707.
158. Ungermann L, Eliáš P, Žižka J, et al. Focal nodular hyperplasia: spoke-wheel arterial pattern and other signs on dynamic contrast-enhanced ultrasonography. Eur J Radiol. 2007;63(2):290-294.
159. Yen Y-H, Wang J-H, Lu S-N, et al. Contrast-enhanced ultrasonographic spoke-wheel sign in hepatic focal nodular hyperplasia. Eur J Radiol. 2006;60(3):439-444.
160. Drane W, Krasicky G, Johnson D. Radionuclide imaging of primary tumors and tumor-like conditions of the liver. Clin Nucl Med. 1987; 12(7):569-582.
161. Welch TJ, Sheedy PF, Johnson CM, et al. Focal nodular hyperplasia and hepatic adenoma: comparison of angiography, CT, US, and scintigraphy. Radiology. 1985;156(3):593-595.
162. Kerlin P, Davis GL, McGill DB, et al. Hepatic adenoma and focal nodular hyperplasia: clinical, pathologic, and radiologic features. Gastroenterology. 1983;84(5 Pt 1):994-1002.
163. Brunelle F, Tammam S, Odievre M, Chaumont P. Liver adenomas in glycogen storage disease in children. Pediatr Radiol. 1984;14(2):94-101.
164. Bioulac-Sage P, Laumonier H, Couchy G, et al. Hepatocellular adenoma management and phenotypic classification: the Bordeaux experience. Hepatology. 2009;50(2):481-489.
165. Lubbers PR, Ros PR, Goodman ZD, Ishak KG. Accumulation of technetium-99m sulfur colloid by hepatocellular adenoma: scintigraphic-pathologic correlation. AJR Am J Roentgenol. 1987;148(6):1105-1108.
166. Laumonier H, Cailliez H, Balabaud C, et al. Role of contrast-enhanced sonography in differentiation of subtypes of hepatocellular adenoma: correlation with MRI findings. AJR Am J Roentgenol. 2012; 199(2):341-348.
167. Kim T, Jang H-J, Burns P, et al. Focal nodular hyperplasia and hepatic adenoma: differentiation with low-mechanical-index contrast-enhanced sonography. AJR Am J Roentgenol. 2008;190(1):58-66.
168. Ito K, Honjo K, Fujita T, et al. Liver neoplasms: diagnostic pitfalls in cross-sectional imaging. Radiographics. 1996;16(2):273-293.
169. Roberts JL, Fishman EK, Hartman DS, et al. Lipomatous tumors of the liver: evaluation with CT and US. Radiology. 1986;158(3):613-617.
170. Martí-Bonmatí L, Menor F, Vizcaino I, Vilar J. Lipoma of the liver: US, CT, and MRI appearance. Gastrointest Radiol. 1989;14(1):155-157.
171. Altekruse S, McGlynn KA, Dickie LA, Kleiner DE. Hepatocellular carcinoma confirmation, treatment, and survival in Surveillance, Epidemiology and End Results registries, 1992-2008. Hepatology. 2012;55(2): 476-482.
172. Subramanyam BR, Balthazar EJ, Hilton S, et al. Hepatocellular carcinoma with venous invasion. Sonographic-angiographic correlation. Radiology. 1984;150(3):793-796.
173. Jackson VP, Martin-Simmerman P, Becker GJ, Holden RW. Real-time ultrasonographic demonstration of vascular invasion by hepatocellular carcinoma. J Ultrasound Med. 1983;2(6):277-280.
174. LaBerge JM, Laing FC, Federle MP, et al. Hepatocellular carcinoma: assessment of resectability by computed tomography and ultrasound. Radiology. 1984;152(2):485-490.
175. Tanaka S, Kitamura T, Imaoka S, et al. Hepatocellular carcinoma: sonographic and histologic correlation. AJR Am J Roentgenol. 1983;140(4):701-707.
176. Sheu JC, Chen DS, Sung JL, et al. Hepatocellular carcinoma: US evolution in the early stage. Radiology. 1985;155(2):463-467.
177. Choi BI, Takayasu K, Han MC. Small hepatocellular carcinomas and associated nodular lesions of the liver: pathology, pathogenesis, and imaging findings. AJR Am J Roentgenol. 1993;160(6):1177-1187.
178. Teefey SA, Stephens DH, Weiland LH. Calcification in hepatocellular carcinoma: not always an indication of fibrolamellar histology. AJR Am J Roentgenol. 1987;149(6):1173-1174.
179. Yoshikawa J, Matsui O, Takashima T, et al. Fatty metamorphosis in hepatocellular carcinoma: radiologic features in 10 cases. AJR Am J Roentgenol. 1988;151(4):717-720.
180. Tanaka S, Kitamura T, Fujita M, et al. Color Doppler flow imaging of liver tumors. AJR Am J Roentgenol. 1990;154(3):509-514.
181. Taylor KJ, Ramos I, Morse SS, et al. Focal liver masses: differential diagnosis with pulsed Doppler US. Radiology. 1987;164(3):643-647.
182. Reinhold C, Hammers L, Taylor CR, et al. Characterization of focal hepatic lesions with duplex sonography: findings in 198 patients. AJR Am J Roentgenol. 1995;164(5):1131-1135.
183. Nicolau C, Catala V, Vilana R, et al. Evaluation of hepatocellular carcinoma using SonoVue, a second generation ultrasound contrast agent: correlation with cellular differentiation. Eur Radiol. 2004;14(6):1092-1099.
184. Jang H, Kim T, Burns P, Wilson S. Enhancement patterns of hepatocellular carcinoma at contrast-enhanced US: comparison with histologic differentiation. Radiology. 2007;244(3):898-906.
185. Bruix J, Sherman M. Management of hepatocellular carcinoma: an update. Hepatology. 2011;53(3):1020-1022.
186. Friedman AC, Lichtenstein JE, Goodman Z, et al. Fibrolamellar hepatocellular carcinoma. Radiology. 1985;157(3):583-587.
187. Stevens WR, Johnson CD, Stephens DH, Nagorney DM. Fibrolamellar hepatocellular carcinoma: stage at presentation and results of aggressive surgical management. AJR Am J Roentgenol. 1995;164(5):1153-1158.
188. Brandt DJ, Johnson CD, Stephens DH, Weiland LH. Imaging of fibrolamellar hepatocellular carcinoma. AJR Am J Roentgenol. 1988;151(2): 295-299.
189. Okuda K, Musha H, Nakajima Y, et al. Clinicopathologic features of encapsulated hepatocellular carcinoma. A study of 26 cases. Cancer. 1977;40(3):1240-1245.
190. Kanai T, Hirohashi S, Upton M, et al. Pathology of small hepatocellular carcinoma. A proposal for a new gross classification. Cancer. 1987;60(4): 810-819.
191. Fitzgerald EJ, Griffiths TM. Computed tomography of vinyl-chloride-induced angiosarcoma of liver. Br J Radiol. 1987;60(714):593-595.
192. Mahony B, Jeffrey RB, Federle MP. Spontaneous rupture of hepatic and splenic angiosarcoma demonstrated by CT. AJR Am J Roentgenol. 1982;138(5):965-966.
193. Furui S, Itai Y, Ohtomo K, et al. Hepatic epithelioid hemangioendothelioma: report of five cases. Radiology. 1989;171(1):63-68.
194. Radin DR, Craig JR, Colletti PM, et al. Hepatic epithelioid hemangioendothelioma. Radiology. 1988;169(1):145-148.
195. Wernecke K, Vassallo P, Bick U, et al. The distinction between benign and malignant liver tumors on sonography: value of a hypoechoic halo. AJR Am J Roentgenol. 1992;159(5):1005-1009.
196. Marchal GJ, Pylyser K, Tshibwabwa-Tumba EA, et al. Anechoic halo in solid liver tumors: sonographic, microangiographic, and histologic correlation. Radiology. 1985;156(2):479-483.
197. Wernecke K, Henke L, Vassallo P, et al. Pathologic explanation for hypoechoic halo seen on sonograms of malignant liver tumors: an in vitro correlative study. AJR Am J Roentgenol. 1992;159(5):1011-1016.
198. Kruskal J, Thomas P, Nasser I, et al. Hepatic colon cancer metastases in mice: dynamic in vivo correlation with hypoechoic rims visible at US. Radiology. 2000;215(3):852-857.
199. Rubaltelli L, Maschio AD, Candiani F, Miotto D. The role of vascularization in the formation of echographic patterns of hepatic metastases: microangiographic and echographic study. Br J Radiol. 1980;53(636):1166-1168.
200. Sanders LM, Botet JF, Straus DJ, et al. CT of primary lymphoma of the liver. AJR Am J Roentgenol. 1989;152(5):973-976.
201. Townsend RR, Laing FC, Jeffrey RB, Bottles K. Abdominal lymphoma in AIDS: evaluation with US. Radiology. 1989;171(3):719-724.
202. Yoshida T, Matsue H, Okazaki N, Yoshino M. Ultrasonographic differentiation of hepatocellular carcinoma from metastatic liver cancer. J Clin Ultrasound. 1987;15(7):431-437.
203. Bruneton J, Ladrée D, Caramella E, et al. Ultrasonographic study of calcified hepatic metastases: a report of 13 cases. Gastrointest Radiol. 1982;7(1): 61-63.
204. Wooten W, Green B, Goldstein H. Ultrasonography of necrotic hepatic metastases. Radiology. 1978;128(2):447-450.
205. Federle MP, Filly RA, Moss AA. Cystic hepatic neoplasms: complementary roles of CT and sonography. AJR Am J Roentgenol. 1981;136(2): 345-348.

206. Murphy-Lavallee J, Jang HJ, Kim TK, et al. Are metastases really hypovascular in the arterial phase? The perspective based on contrast-enhanced ultrasonography. J Ultrasound Med. 2007;26(11):1545-1556.
207. Nyberg D, Federle M. AIDS-related Kaposi sarcoma and lymphomas. Semin Roentgenol. 1987;22(1):54-65.
208. Luburich P, Bru C, Ayuso MC, et al. Hepatic Kaposi sarcoma in AIDS: US and CT findings. Radiology. 1990;175(1):172-174.
209. Towers MJ, Withers CE, Rachlis AR, et al. Ultrasound diagnosis of hepatic Kaposi sarcoma. J Ultrasound Med. 1991;10(12):701-703.
210. Chiu WC, Cushing BM, Rodriguez A, et al. Abdominal injuries without hemoperitoneum: a potential limitation of focused abdominal sonography for trauma (FAST). J Trauma. 1997;42(4):617-623.
211. Rozycki GS, Ochsner MG, Schmidt JA, et al. A prospective study of surgeon-performed ultrasound as the primary adjuvant modality for injured patient assessment. J Trauma. 1995;39(3):492-498.
212. Sirlin CB, Casola G, Brown MA, et al. Patterns of fluid accumulation on screening ultrasonography for blunt abdominal trauma: comparison with site of injury. J Ultrasound Med. 2001;20(4):351-357.
213. Wherrett LJ, Boulanger BR, McLellan BA, et al. Hypotension after blunt abdominal trauma: the role of emergent abdominal sonography in surgical triage. J Trauma. 1996;41(5):815-820.
214. Kimura A, Otsuka T. Emergency center ultrasonography in the evaluation of hemoperitoneum: a prospective study. J Trauma. 1991;31(1):20-23.
215. Moon KL, Federle MP. Computed tomography in hepatic trauma. AJR Am J Roentgenol. 1983;141(2):309-314.
216. Foley WD, Cates JD, Kellman GM, et al. Treatment of blunt hepatic injuries: role of CT. Radiology. 1987;164(3):635-638.
217. vanSonnenberg E, Simeone JF, Mueller PR, et al. Sonographic appearance of hematoma in liver, spleen, and kidney: a clinical, pathologic, and animal study. Radiology. 1983;147(2):507-510.
218. Grant EG, Tessler FN, Gomes AS, et al. Color Doppler imaging of portosystemic shunts. AJR Am J Roentgenol. 1990;154(2):393-397.
219. Lafortune M, Patriquin H, Pomier G, et al. Hemodynamic changes in portal circulation after portosystemic shunts: use of duplex sonography in 43 patients. AJR Am J Roentgenol. 1987;149(4):701-706.
220. Chezmar JL, Bernardino ME. Mesoatrial shunt for the treatment of Budd-Chiari syndrome: radiologic evaluation in eight patients. AJR Am J Roentgenol. 1987;149(4):707-710.
221. Ralls P, Lee K, Mayekawa D, et al. Color Doppler sonography of portocaval shunts. J Clin Ultrasound. 1990;18(5):379-381.
222. Foley W, Gleysteen J, Lawson T, et al. Dynamic computed tomography and pulsed Doppler ultrasonography in the evaluation of splenorenal shunt patency. J Comput Assist Tomogr. 1983;7(1):106-112.
223. Freedman AM, Sanyal AJ, Tisnado J, et al. Complications of transjugular intrahepatic portosystemic shunt: a comprehensive review. Radiographics. 1993;13(6):1185-1210.
224. Kerlan RK, LaBerge JM, Gordon RL, Ring EJ. Transjugular intrahepatic portosystemic shunts: current status. AJR Am J Roentgenol. 1995;164(5):1059-1066.
225. LaBerge JM, Ring EJ, Gordon RL, et al. Creation of transjugular intrahepatic portosystemic shunts with the wallstent endoprosthesis: results in 100 patients. Radiology. 1993;187(2):413-420.
226. Haskal ZJ, Pentecost MJ, Soulen MC, et al. Transjugular intrahepatic portosystemic shunt stenosis and revision: early and midterm results. AJR Am J Roentgenol. 1994;163(2):439-444.
227. Foshager MC, Ferral H, Nazarian GK, et al. Duplex sonography after transjugular intrahepatic portosystemic shunts (TIPS): normal hemodynamic findings and efficacy in predicting shunt patency and stenosis. AJR Am J Roentgenol. 1995;165(1):1-7.
228. Haskal Z, Carroll J, Jacobs J, et al. Sonography of transjugular intrahepatic portosystemic shunts: detection of elevated portosystemic gradients and loss of shunt function. J Vasc Interv Radiol. 1997;8(4):549-556.
229. Murphy T, Beecham R, Kim H, et al. Long-term follow-up after TIPS: use of Doppler velocity criteria for detecting elevation of the portosystemic gradient. J Vasc Interv Radiol. 1998;9(2):275-281.
230. Surratt RS, Middleton WD, Darcy MD, et al. Morphologic and hemodynamic findings at sonography before and after creation of a transjugular intrahepatic portosystemic shunt. AJR Am J Roentgenol. 1993;160(3):627-630.
231. Chong WK, Malisch TA, Mazer MJ, et al. Transjugular intrahepatic portosystemic shunt: US assessment with maximum flow velocity. Radiology. 1993;189(3):789-793.
232. Dodd GD, Zajko AB, Orons PD, et al. Detection of transjugular intrahepatic portosystemic shunt dysfunction: value of duplex Doppler sonography. AJR Am J Roentgenol. 1995;164(5):1119-1124.
233. Feldstein VA, LaBerge JM. Hepatic vein flow reversal at duplex sonography: a sign of transjugular intrahepatic portosystemic shunt dysfunction. AJR Am J Roentgenol. 1994;162(4):839-841.
234. Kanterman RY, Darcy MD, Middleton WD, et al. Doppler sonography findings associated with transjugular intrahepatic portosystemic shunt malfunction. AJR Am J Roentgenol. 1997;168(2):467-472.
235. Charboneau JW, Reading CC, Welch TJ. CT and sonographically guided needle biopsy: current techniques and new innovations. AJR Am J Roentgenol. 1990;154(1):1-10.
236. Downey DB, Wilson SR. Ultrasonographically guided biopsy of small intra-abdominal masses. Can Assoc Radiol J. 1993;44(5):350-353.
237. Livraghi T, Festi D, Monti F, et al. US-guided percutaneous alcohol injection of small hepatic and abdominal tumors. Radiology. 1986;161(2):309-312.
238. Shiina S, Yasuda H, Muto H, et al. Percutaneous ethanol injection in the treatment of liver neoplasms. AJR Am J Roentgenol. 1987;149(5):949-952.
239. Rifkin MD, Rosato FE, Branch HM, et al. Intraoperative ultrasound of the liver. An important adjunctive tool for decision making in the operating room. Ann Surg. 1987;205(5):466-472.
240. Parker G, Lawrence W, Horsley J, et al. Intraoperative ultrasound of the liver affects operative decision making. Ann Surg. 1989;209(5):569-577.
241. Leen E, Ceccotti P, Moug S, et al. Potential value of contrast-enhanced intraoperative ultrasonography during partial hepatectomy for metastases. Ann Surg. 2006;243(2):236-240.
242. Garant M, Reinhold C. Residents' corner. Answer to case of the month #36. Hepatic lipoma. Can Assoc Radiol J. 1996;47(2):140-142.

CHAPTER 5

The Spleen

Patrick M. Vos, John R. Mathieson, and Peter L. Cooperberg

SUMMARY OF KEY POINTS

- Ultrasound can be used to diagnose or exclude splenic abnormalities, but computed tomography and/or magnetic resonance imaging may be needed in indeterminate cases.
- There is no single upper limit of normal for spleen size, since size varies with patient sex, weight, and height. Use of a strict 12-cm upper limit of normal for the spleen will lead to overdiagnosis of splenomegaly.
- The differential diagnosis of splenomegaly is long. Associated clinical and radiologic features can be helpful in assessing the cause.
- Focal splenic lesions may be benign or malignant and thus should be carefully assessed.
- Common causes of multiple splenic nodules include infection (e.g., mycobacteria, histoplasmosis), sarcoidosis, and malignancy (e.g., lymphoma, metastases).

CHAPTER OUTLINE

EMBRYOLOGY AND ANATOMY
SONOGRAPHIC TECHNIQUE
SONOGRAPHIC APPEARANCE
PATHOLOGIC CONDITIONS
Splenomegaly
Focal Abnormalities
Splenic Cysts
Nodular Splenic Lesions
Focal Solid Splenic Lesions
Other Abnormalities
Sickle Cell Disease
Gaucher Disease
Gamna-Gandy Bodies
Splenic Trauma
CONGENITAL ANOMALIES
INTERVENTIONAL PROCEDURES
PITFALLS IN INTERPRETATION

Computed tomography (CT) and/or magnetic resonance imaging (MRI) are currently the techniques of choice for the imaging evaluation of the spleen. However, ultrasound can also be very useful to diagnose or exclude splenic abnormalities and is particularly helpful in the follow-up of patients with known splenic abnormalities. Splenic lesions may be encountered in a variety of clinical settings, and the radiologist should be aware of the spectrum of processes that may involve the spleen as well as the clinical context in which they occur.[1]

The spleen and left upper quadrant (LUQ) should be routinely evaluated on all abdominal investigations, especially in patients with suspected splenomegaly, LUQ pain, or trauma. In general, the spleen can be examined by ultrasound without difficulty. Because the normal spleen is uniform in echogenicity, focal abnormalities stand out clearly. Similarly, perisplenic abnormalities and fluid collections are usually easily identified. Inadequate assessment of the spleen and surrounding structures is therefore relatively rare. Occasionally, because the spleen is located high in the LUQ, difficulties can be encountered. Shadowing from ribs, overlying bowel gas, and overlying lung can obscure visualization of the deeper structures. Expertise and persistence may be required to overcome these obstacles.

EMBRYOLOGY AND ANATOMY

The spleen arises from a mass of mesenchymal cells located between the layers of the **dorsal mesentery,** which connects the stomach to the posterior peritoneal surface over the aorta (Fig. 5.1A). These mesenchymal cells differentiate to form the **splenic pulp,** the supporting connective tissue structures, and the **splenic capsule.** The **splenic artery** penetrates the primitive spleen, and arterioles branch through the connective tissue into the splenic sinusoids.

As the embryonic stomach rotates 90 degrees on its longitudinal axis, the spleen and dorsal mesentery are carried to the left along with the greater curvature of the stomach (Fig. 5.1B). The base of the dorsal mesentery fuses with the posterior peritoneum over the left kidney, giving rise to the **splenorenal ligament.** This explains why, although the spleen is intraperitoneal, the splenic artery enters from the retroperitoneum through the splenorenal ligament (Fig. 5.1C). In most adults, a portion of the splenic capsule is firmly attached to the fused dorsal mesentery anterior to the upper left kidney, giving rise to the **bare area** of the spleen.[2] The size of the splenic bare area varies but usually involves less than half the posterior splenic surface (Fig. 5.2). This anatomic

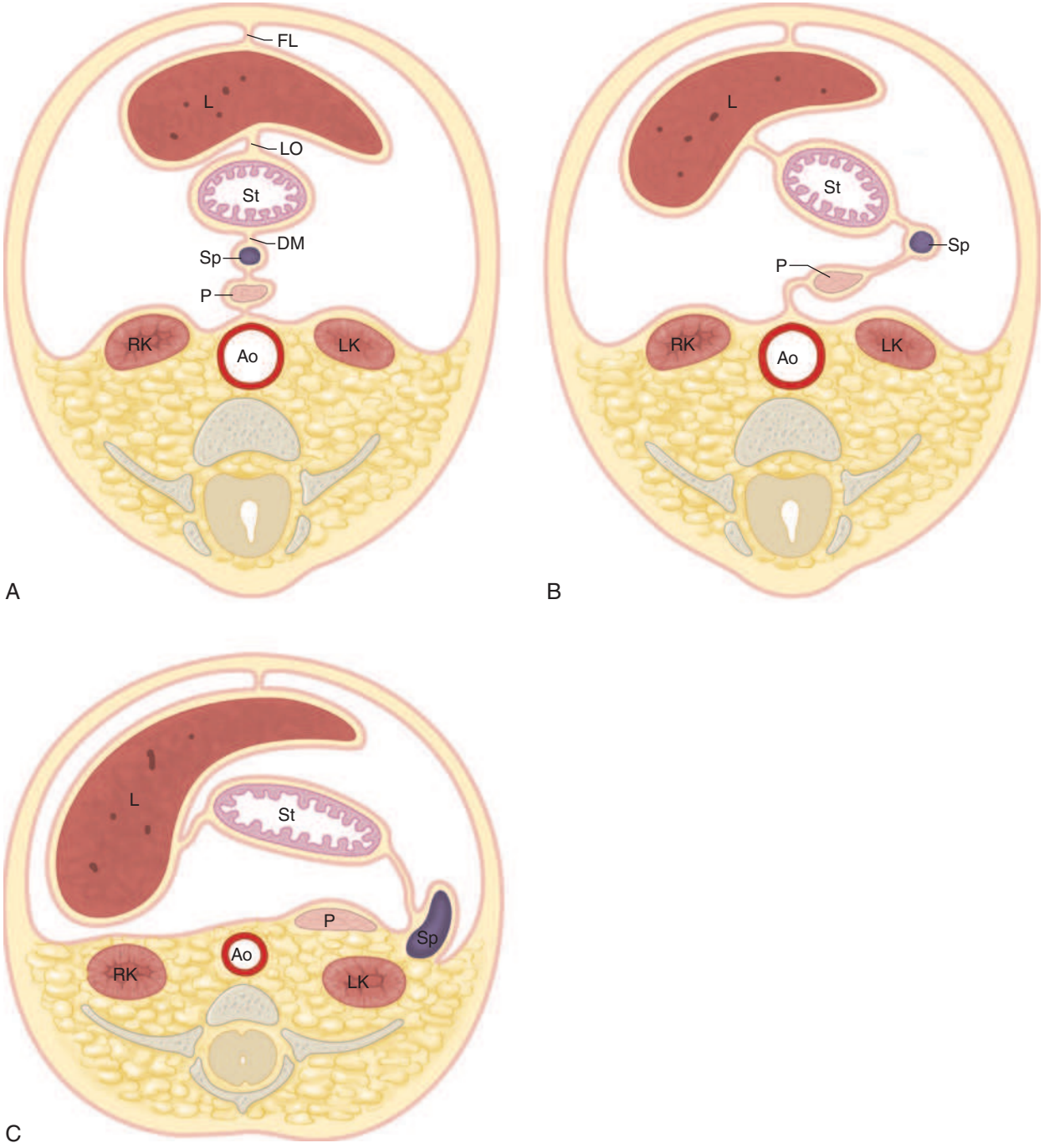

FIG. 5.1 Embryologic Development of the Spleen. Schematic axial drawings of the upper abdomen. **(A) Embryo: 4 to 5 weeks.** The mesentery anterior to the stomach *(St)* is the ventral mesentery. The ventral mesentery is divided into two portions by the liver *(L)* into the **falciform ligament** *(FL)* anteriorly and the **gastrohepatic ligament** or **lesser omentum** *(LO)* posteriorly. Posterior to the stomach is the **dorsal mesentery** *(DM)*, which contains the developing spleen *(Sp)* and pancreas *(P)*. The dorsal mesentery is divided into two portions by the spleen: the **splenogastric ligament** anteriorly and the **splenorenal ligament** posteriorly. The pancreas *(P)* has not yet become retroperitoneal and remains within the dorsal mesentery. **(B) Embryo: 8 weeks.** The stomach rotates counterclockwise, displacing the liver to the right and the spleen to the left. The portion of the dorsal mesentery containing the pancreas, splenic vessels, and spleen begins to fuse to the anterior retroperitoneal surface, giving rise to the splenogastric ligament and the "bare area" of the spleen. If fusion is incomplete, the spleen will be attached to the retroperitoneum only by a long mesentery, giving rise to a mobile or "wandering" spleen. **(C) Newborn.** Fusion of the dorsal mesentery is now complete. The pancreas is now completely retroperitoneal, and a portion of the spleen has fused with the retroperitoneum. Note the close relation of the pancreatic tail to the splenic hilum. *Ao,* Aorta; *LK,* left kidney; *RK,* right kidney.

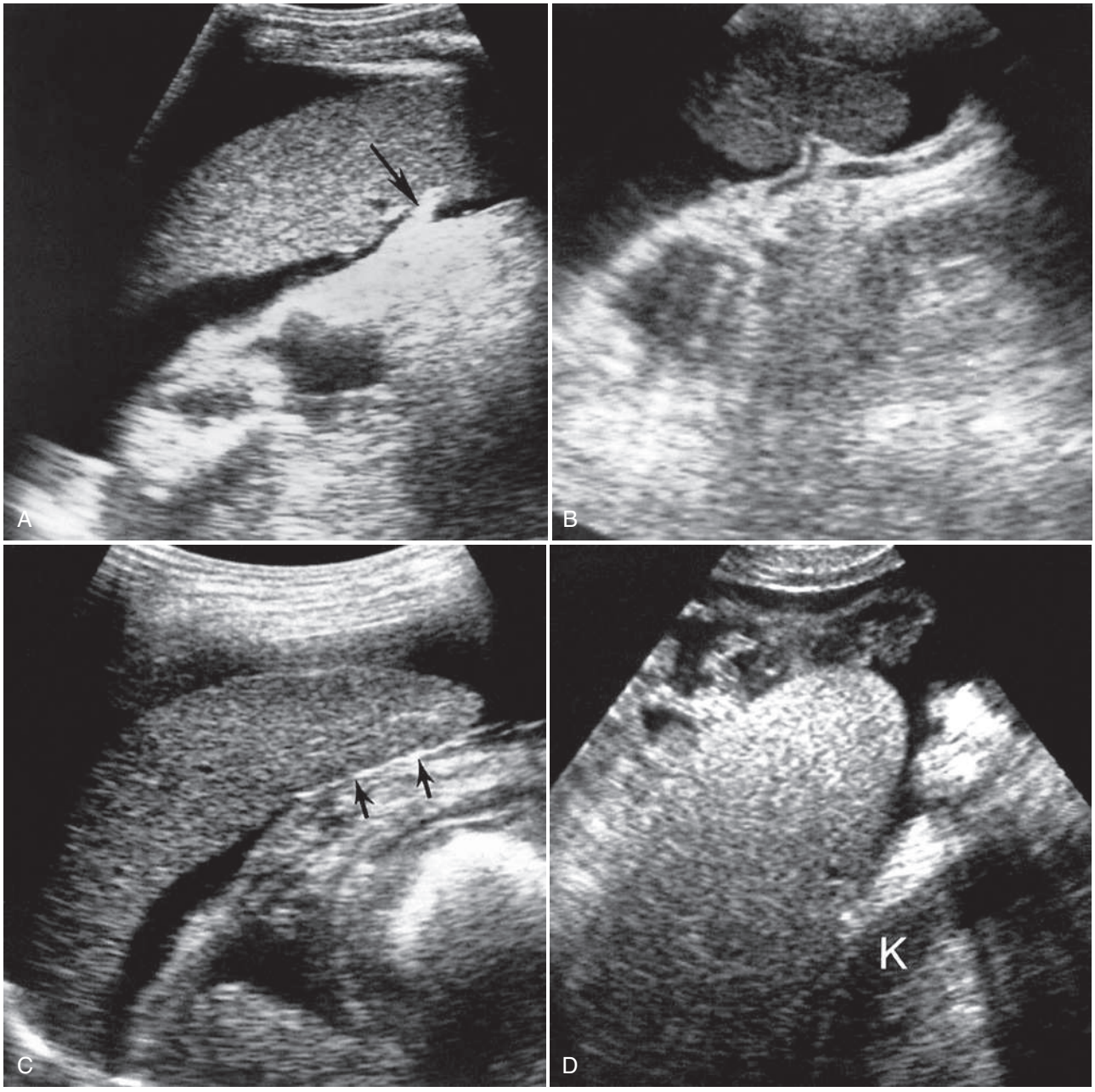

FIG. 5.2 Bare Area of the Spleen. Variability in the relationship of the spleen to the anterior retroperitoneal surface is demonstrated in patients with ascites. **(A)** This spleen has **no bare area.** The splenorenal ligament *(arrow)* is outlined on both sides by ascitic fluid. **(B)** Part of the lower pole of the spleen is fused posteriorly. **(C)** Lower pole is fused to the retroperitoneum *(arrows).* **(D)** Large proportion of this patient's spleen is fused posteriorly. Note the close relation of the spleen to the left kidney *(K).*

feature is analogous to the bare area of the liver and can be helpful in distinguishing intraperitoneal from pleural fluid collections.

The normal adult spleen is convex superolaterally, is concave inferomedially, and has a homogeneous echo pattern (Videos 5.1 and 5.2). The spleen lies between the **fundus of the stomach** and the **diaphragm,** with its long axis in the line of the left 10th rib. The diaphragmatic surface is convex and is usually situated between the 9th and 11th ribs. The visceral or inferomedial surface has gentle indentations where it comes into contact with the stomach, left kidney, pancreas, and splenic flexure. The spleen is suspended by the splenorenal ligament, which is in contact with the **posterior peritoneal wall,** the **phrenicocolic ligament,** and the **gastrosplenic ligament.** The gastrosplenic ligament is composed of the two layers of the dorsal mesentery that separate the lesser sac posteriorly from the greater sac anteriorly.

Its weight is related to the patient's age and gender; the spleen usually weighs less than 150 g on autopsy (range, 80-300 g).[3] In adults, the spleen decreases in size and weight with advancing age and is smaller in women. It also increases slightly during digestion and can vary in size according to the nutritional status of the body.

Splenic functions include phagocytosis, fetal hematopoiesis, adult lymphopoiesis, immune response, and erythrocyte storage.

The spleen may be congenitally absent. Under a variety of conditions, including surgical misadventure, the spleen also may be removed. Currently, the surgical trend is toward preservation of the spleen when possible.[4] A person can live fully without a spleen. However, particularly in childhood, the immune response may be impaired, especially to encapsulated bacteria. Overwhelming postsplenectomy **sepsis** is a long-term risk in asplenic patients, and appropriate preventive measures should be taken to minimize this risk.[5,6]

SONOGRAPHIC TECHNIQUE

All routine abdominal sonographic examinations, regardless of the indications, should include at least one **coronal view** of the spleen and the upper pole of the left kidney. The most common and easy approach to visualize the spleen (Video 5.1) is to maintain the patient in the supine position and place the transducer in the coronal plane of section posteriorly in one of the lower left intercostal spaces. The patient can then be examined in various degrees of inspiration to maximize the window to the spleen. Deep inspiration introduces air into the lung in the lateral costophrenic angle and may obscure visualization. A modest inspiration depresses the central portion of the left hemidiaphragm and spleen inferiorly so that they can be visualized. The plane of section should then be swept posteriorly and anteriorly to view the entire volume of the spleen. We generally find that a thorough examination in the **coronal plane** of section is highly accurate for excluding any lesion within or around the spleen and for documenting the spleen's approximate size.

If an abnormality is discovered within or around the spleen, other planes of section should be used. An **oblique plane** of section along the intercostal space can avoid rib shadowing (Fig. 5.3). In some patients with narrow intercostal spaces, however, intercostal scanning can be difficult. A **transverse plane** from a lateral, usually intercostal, approach may help to localize a lesion within the spleen anteriorly or posteriorly.

If the spleen is not enlarged and is not surrounded by a large mass, scanning from an anterior position—as one would for imaging the liver—is not helpful because of the interposition of gas within the stomach and the splenic flexure of the colon. However, if the patient has a relatively large liver, or spleen, the spleen may be visualized from an anterior approach (Fig. 5.4). If there is free intraperitoneal fluid around the spleen or a left pleural effusion, the spleen may be better visualized from an anterolateral approach. Often, it is beneficial to have the patient roll onto the right side as much as 45 degrees, or even 90 degrees, so that a more posterior approach can be used to visualize the spleen. The spleen may also rotate to the right, making it easier to visualize.

Generally, the same curvilinear transducers and technical settings are used for examination of the spleen as for the other abdominal organs. A high-frequency linear array transducer can be used for more detail. Techniques such as harmonic and compound imaging are used to improve image quality and detect subtle lesions. Color Doppler may also be useful for solitary lesions (Fig. 5.5).[7]

The use of contrast-enhanced ultrasound (CEUS) is increasing in both research and clinical settings. Multiple reports have recently described CEUS of the spleen (Video 5.3) and its characterization of splenic lesions.[8,9] However, its role in general practice has not yet been confirmed.

SONOGRAPHIC APPEARANCE

The shape of the normal spleen is variable. The spleen consists of **two components** joined at the hilum: a **superomedial** component and an **inferolateral** component. More superiorly, on transverse scanning, the spleen has a typical fat, "inverted comma"

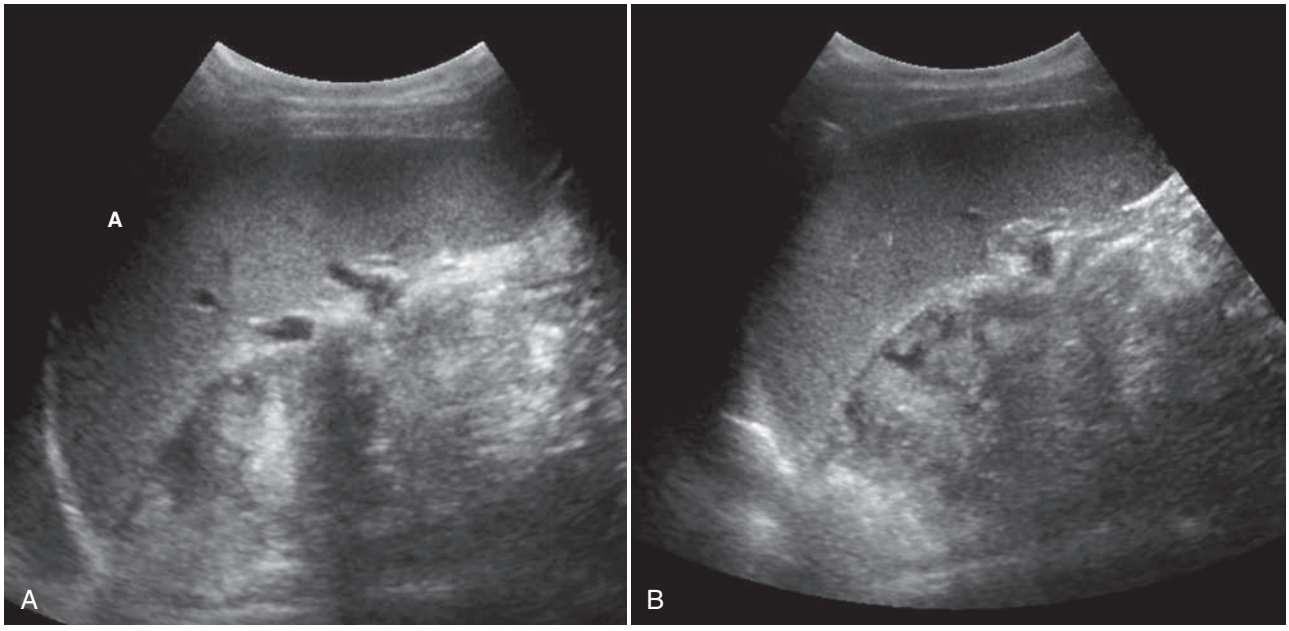

FIG. 5.3 Importance of Scan Plane. (A) Coronal ultrasound scan shows part of the spleen obscured by air in the lung. **(B)** Improved visualization of the spleen on coronal oblique scan aligned with the 10th interspace between the ribs.

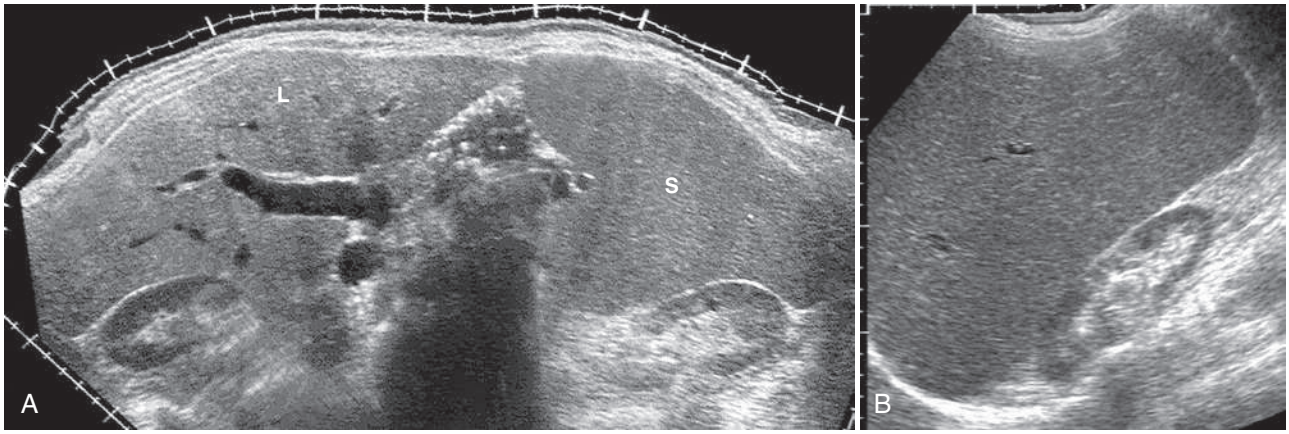

FIG. 5.4 Splenomegaly. (A) Transverse and **(B)** coronal extended–field of view images demonstrate marked splenic *(S)* enlargement. *L,* Liver.

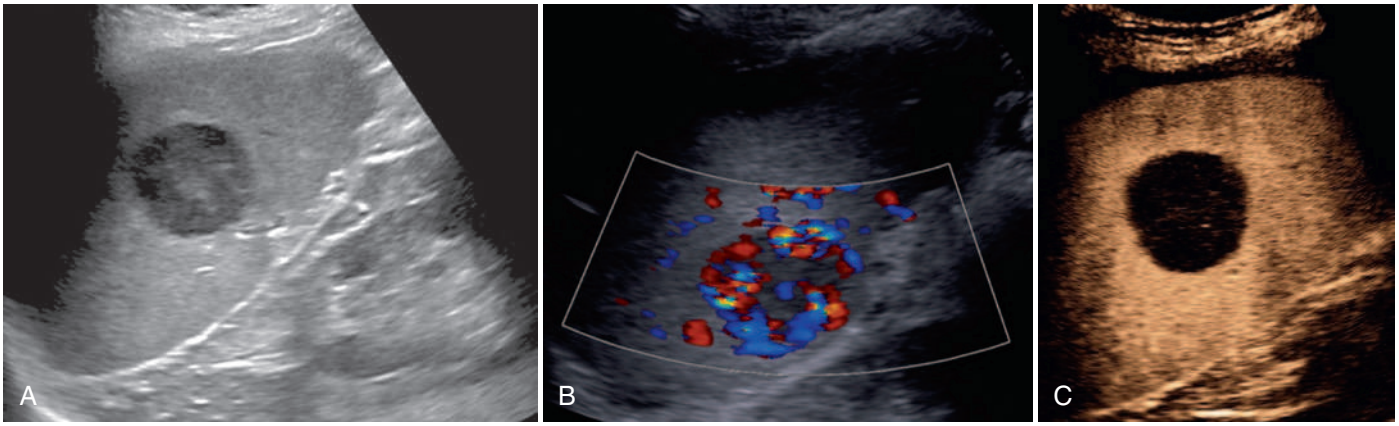

FIG. 5.5 Lymphoma Manifesting as a Hypoechoic Solitary Splenic Lesion. (A) Sagittal image shows a well-defined hypoechoic lesion. **(B)** Color Doppler shows peripheral flow within the lesion. **(C)** Delayed image from contrast-enhanced sonogram shows filling from the periphery. (Courtesy of Stephanie Wilson, MD.) See also Video 5.3.

shape, with a thin component extending anteriorly and another component extending medially, either superior to or adjacent to the upper pole of the kidney. This component (superomedial) can be seen to indent the gastric fundus on plain films of the abdomen or cross sectional imaging. As the scan plane moves inferiorly, only the inferior component of the spleen is seen. This component (inferolateral) can be outlined by a thin rim of fat above the splenic flexure. It may extend inferiorly to the costal margin and present clinically as a palpable spleen. However, either the superomedial or the inferolateral component can enlarge independently, without enlargement of the other component.

It is important to recognize the **normal structures** that are related to the spleen. The diaphragm cradles the spleen posteriorly, superiorly, and laterally. The left liver lobe may extend into the LUQ superior and lateral to the spleen (Fig. 5.6). The fundus of the stomach and lesser sac are medial and anterior to the splenic hilum. The gastric fundus may contain gas or fluid, which should not be confused with a fluid collection. The tail of the pancreas lies posterior to the stomach and lesser sac. It approaches the hilum of the spleen, closely related to the splenic artery and vein. Consequently, the spleen can be used as a "window" to evaluate the pancreatic tail area. The left kidney generally lies inferior and medial to the spleen. A useful landmark in identifying the spleen and splenic hilum is the **splenic vein,** which generally can be demonstrated without difficulty.

The normal splenic **parenchyma** is homogeneous. The liver is generally considered to be more echogenic than the spleen, but in fact the echogenicity of the parenchyma is higher in the spleen than in the liver. Using a dual-image setting, the operator may compare the echogenicity of these two organs. The impression that the liver has greater echogenicity results from its large number of reflective vessels.

As in measuring other body structures, it is helpful to have measurements that establish the **upper limits of normal.** The size of a normal spleen depends on gender, age, and body height. The range of the "normal sized" adult spleen, combined with its complex three-dimensional shape, makes it difficult to establish a normal range of sonographic measurements. Ideally, the clinician would assess splenic **volume** or **weight.** Techniques have been developed to measure serial sections of the spleen by planimetry and then compute the volume of the spleen by adding the values for each section.[10] However, these techniques are cumbersome and not popular. The most frequently used method is "eyeballing" the size (Fig. 5.7; see also Fig. 5.4). Unfortunately, this method

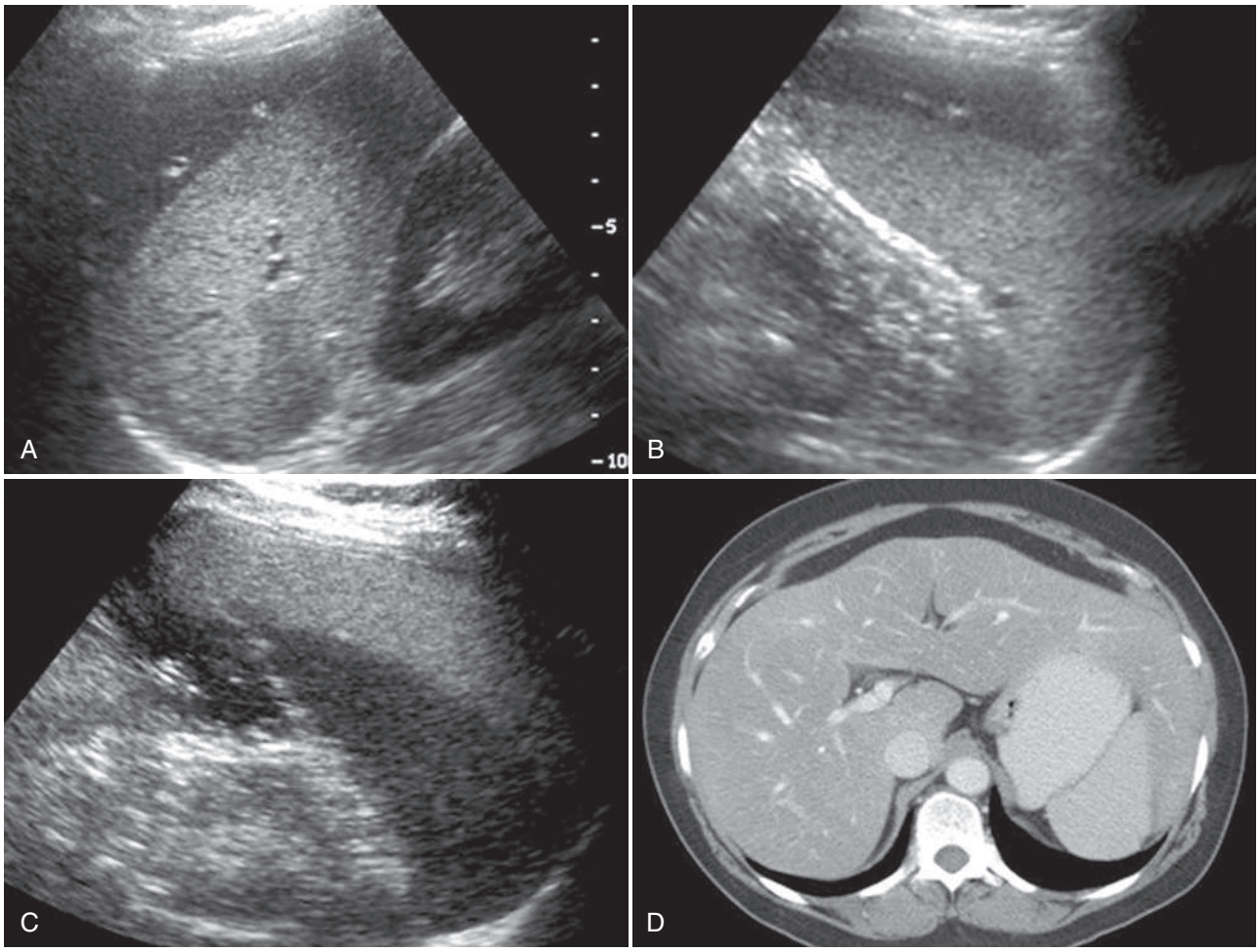

FIG. 5.6 Relationship of Spleen With Surrounding Structures. Left liver lobe extends into the left upper quadrant superior to the spleen. **(A)** Coronal and **(B)** transverse sonograms demonstrate the left liver lobe superior to the spleen. The liver is hypoechoic compared with the spleen. **(C)** and **(D)** Liver extends over spleen in a different patient with a fatty liver. **(C)** Transverse sonogram shows an echogenic liver and a relatively hypoechoic spleen. **(D)** Axial computed tomography image shows the left liver lobe draping around the spleen.

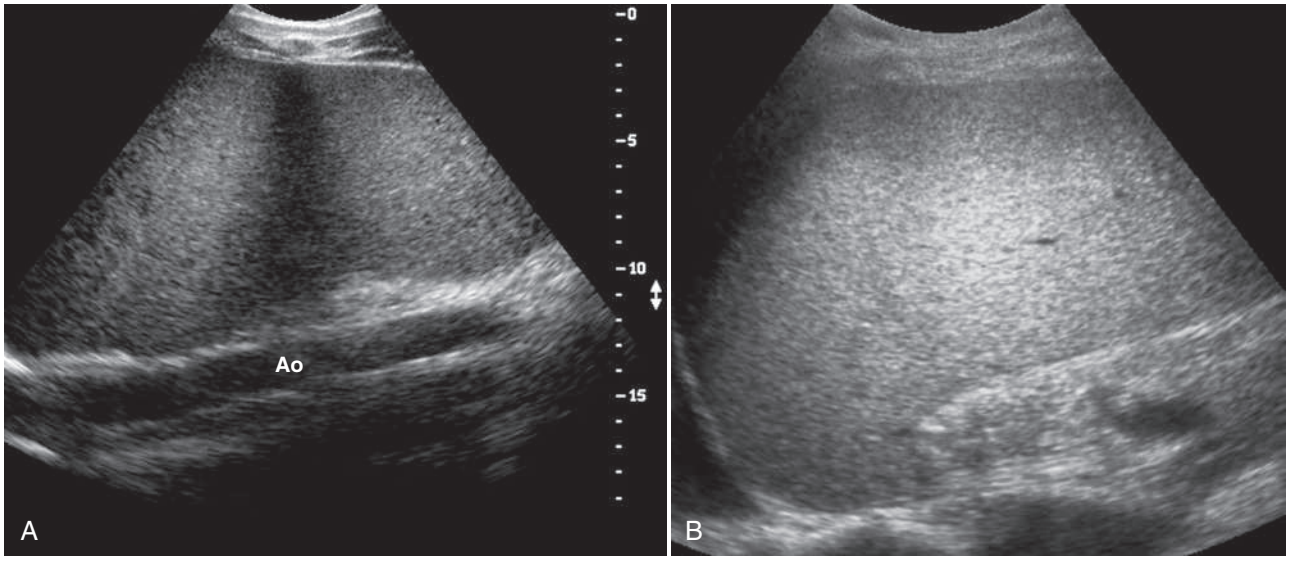

FIG. 5.7 Splenomegaly in Two Patients. (A) Coronal ultrasound scan shows an enlarged spleen with margins beyond the sector format. Midportion is partially obscured by a rib shadow. **(B)** Increased echogenicity of a large spleen. *Ao,* Aorta.

of assessment requires considerably more experience than is necessary for other imaging techniques and is relatively inaccurate. Various clinicians have used different methods to measure splenic size. The length of the spleen measured on a coronal or coronal oblique view that includes the hilum is the most common technique[11,12] (Fig. 5.8). This view can be obtained during deep inspiration or quiet breathing. Importantly, this method correlates well with the splenic volume, particularly when performed with the patient in the **right lateral decubitus** position.[12]

Multiple studies have tried to establish nomograms of spleen size. In a study of 703 normal adults, the **length** of the spleen was less than 11 cm, the **width** (breadth) less than 7 cm, and the **thickness** less than 5 cm in 95% of patients.[13] Rosenberg et al.[11] established an upper limit of normal splenic length of 12 cm for girls and 13 cm for boys (≥15 years). Hosey et al.[14] demonstrated a mean splenic length of 10.65 cm. In this study, men also had larger spleens than women. Spielmann et al.[15] showed that the length of the spleen correlates with height and established nomograms for tall, healthy athletes. In women taller than 5 feet (ft), 6 inches (168 cm), the mean splenic length of 10 cm increased by 0.1 cm for each 1-inch incremental increase in height. In men taller than 6 ft (180 cm), the mean splenic length of 11 cm increased by 0.2 cm for each 1-inch incremental increase in height. Upper limits of normal in splenic length were 14 cm in women 6 ft, 6 inches (198 cm) tall and 16.3 cm in men 7 ft (213 cm) tall. Chow et al. assessed 1230 healthy volunteers and found that spleen length and volume were significantly and independently associated with sex, body height, and weight, with men and taller and heavier individuals having longer and larger spleens. The spleen length of 20 of 324 women (6%) and 234 of 906 men (26%) exceeded a strict upper limit of normal of 12 cm.[16]

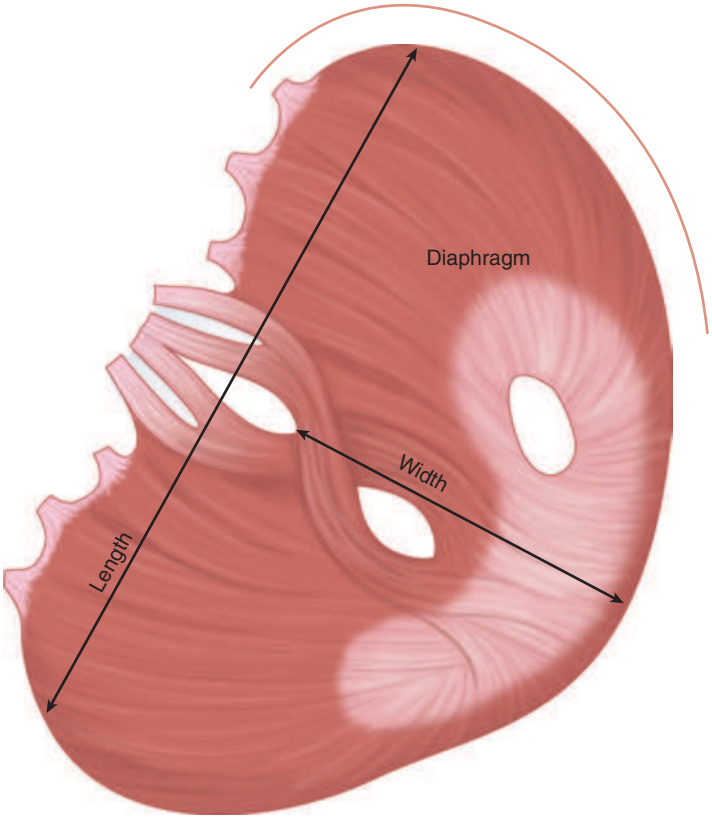

FIG. 5.8 Splenic Measurement. Diagram shows sonographic approach to measuring splenic length and width. Splenic size is best measured by obtaining a coronal view that includes the hilum.

PATHOLOGIC CONDITIONS

Splenomegaly

The differential diagnosis of splenomegaly is exceedingly long. It includes infection (e.g., mononucleosis, tuberculosis, malaria), hematologic disorders (myelofibrosis, lymphoma, leukemia),[17] congestion (portal hypertension, portal/splenic vein thrombosis, congestive heart failure), inflammation (sarcoidosis), neoplasia (hemangioma, metastases), and infiltration (e.g., Gaucher disease)[18] (Table 5.1).

Frequency and causes of splenomegaly vary between developing and developed countries and even between hospitals in the same region.[19] Sonography is very helpful in determining the degree of enlargement. In "borderline" splenomegaly, however, diagnosis can be difficult.

The spleen is capable of growing to an enormous size. It can extend inferiorly into the left iliac fossa, and it can cross the midline and appear as a mass inferior to the left lobe of the liver on longitudinal section. The degree of splenomegaly is generally not a reliable tool in providing a more concise differential diagnosis. The differential diagnosis of **massive splenomegaly,** defined as a spleen size greater than 18 cm, is less extensive and includes hematologic disorders and infections[18] (see Table 5.1). Sonographic assessment of the splenic architecture is used to differentiate between focal lesions (single or multiple) causing splenomegaly and diffuse splenomegaly.

The most common finding is diffuse enlargement; in these patients, imaging is typically not helpful in providing a specific diagnosis. When the spleen enlarges, it can become more echogenic, but the clinician cannot differentiate between the different types of splenomegaly on the basis of its echogenicity (see Fig. 5.7B). In experimental studies researchers have tried to quantify the degree of fibrosis in liver and spleen using the echotexture characteristics, but no clinical applications have yet been established.[20] More promising is the use of splenic elastography in patients with portal hypertension. Studies have shown that use of elastography in patients at risk for cirrhosis can lead to improved triage of patients with respect to degree of liver fibrosis[21,22] as well as esophageal varices and bleeding.[23]

Associated clinical and radiologic features can be helpful in establishing a differential diagnosis. Liver disease and evidence of portal venous collaterals can establish **portal hypertension** as the cause of splenomegaly (Fig. 5.9). Focal lesions, multiorgan involvement, and lymphadenopathy may indicate **lymphoma.**

However, in many patients, extensive radiologic and laboratory investigations will fail to yield a diagnosis. In these cases of "isolated" splenomegaly, the risks of serious underlying disease must be balanced against the risks of further invasive

TABLE 5.1 Causes of Splenomegaly

Splenomegaly (<18 cm)	Massive Splenomegaly (>18 cm)
HEMATOLOGIC	
Red blood cell membrane defects	
Hemoglobinopathies	
Autoimmune hemolytic anemias	Thalassemia major
RHEUMATOLOGIC	
Rheumatoid arthritis	
Systemic lupus erythematosus	
Sarcoidosis	
INFECTIOUS	
Viruses	Visceral leishmaniasis
Bacteria	Hyperreactive malarial splenomegaly syndrome
Mycobacteria	*Mycobacterium avium-intracellulare* complex
Fungi	
Parasites	
CONGESTIVE	
Hepatic cirrhosis	
Venous thromboses (hepatic, portal, splenic)	
Congestive heart failure	
INFILTRATIVE	
Lymphomas	Lymphomas
Myeloproliferative neoplasms	Myeloproliferative neoplasms
Metastatic cancer	
Amyloidosis	
Gaucher disease	Gaucher disease
Niemann-Pick disease	
Glycogen storage disease	
Hemophagocytic syndrome	
Langerhans cell histiocytosis	

Data from Abramson JS, Chatterji M, Rahemtullah A. Case records of the Massachusetts General Hospital. Case 39-2008. A 51-year-old woman with splenomegaly and anemia. N Engl J Med. 2008;359(25):2707-2718[17]; Pozo AL, Godfrey EM, Bowles KM. Splenomegaly: investigation, diagnosis and management. Blood Rev. 2009;23(3):105-111.[18]

investigations, such as diagnostic splenic biopsy or splenectomy.[17] In selected cases, ultrasound-guided splenic biopsy of focal abnormalities can be helpful in establishing a diagnosis, with an acceptable complication rate and high accuracy.[24,25]

Complications of splenomegaly include **hypersplenism** and **spontaneous splenic rupture.** Spontaneous splenic rupture typically occurs in patients with an enlarged spleen after minimal trauma or insignificant events such as coughing.[26,27]

Focal Abnormalities

Ultrasound can be helpful in finding and characterizing focal splenic lesions. However, because of the overlap in the appearance of splenic lesions, it is often not possible to make a specific diagnosis based on the sonographic findings alone. Splenic lesions can be solitary or multiple, diffuse, and infiltrative. Focal lesions can be cystic, complex cystic, or solid. Further, lesions can be categorized according to size as **micronodular** (<1 cm), **nodular** (1-3 cm), or **focal** (>3 cm) masses.[28] Knowledge of past medical history, clinical presentation, and sonographic findings is required to provide an appropriate differential diagnosis and guide further management.[29] Ultimately, percutaneous biopsy or splenectomy may be required to obtain a definitive diagnosis.

Types of Splenic Cysts

- Congenital cysts
- Pseudocysts
- Hydatid (echinococcal) cysts
- Pancreatic pseudocysts
- Endothelial-lined cysts
  - Lymphangiomas
  - Cystic hemangiomas
- Peliosis
- Cystic metastasis[a]
- Abscess[a]
- Hematoma[a]

[a]Not true cysts.

Splenic Cysts

Splenic cysts, as with cysts elsewhere in the body, appear as anechoic lesions with posterior acoustic enhancement. Simple cysts are round to ovoid in shape and have a thin, sharply defined wall. **Complex cysts** do not meet these criteria and may demonstrate septations, thick walls, calcifications, solid components, or internal echoes. Occasionally, cysts can grow to a very large size, becoming predominantly **exophytic.** It may then be difficult to appreciate their splenic origin (Fig. 5.10).

The most common splenic cystic lesions are primary congenital cysts, pseudocysts, and hydatid cysts. Uncommon splenic cystic lesions include pancreatic pseudocysts, lymphangiomas, hemangiomas, peliosis, hamartomas, angiosarcomas, and cystic metastases.[30] Other lesions that can mimic cysts on ultrasound are **abscesses, lymphoma, necrotic metastases,** and **hematomas.**[31]

In the developed world, most splenic cysts are asymptomatic incidental findings discovered during routine imaging and generally represent congenital cysts or pseudocysts. These cysts may cause symptoms when large or when present with complications such as internal hemorrhage, infection, or rupture. **Primary congenital cysts,** also called **epidermoid cysts** or **true cysts,** are characterized by the presence of an epithelial lining on pathologic examination.[32] Thought to arise from embryonic rests of primitive mesothelial cells within the spleen, typical epidermoid cysts present as well-defined, thin-walled anechoic lesions that do not change over time (Fig. 5.11A). **Pseudocysts,** also known as **false cysts,** have no cellular lining and are presumably secondary to trauma, infarct, or infection.[33] These cysts are more often

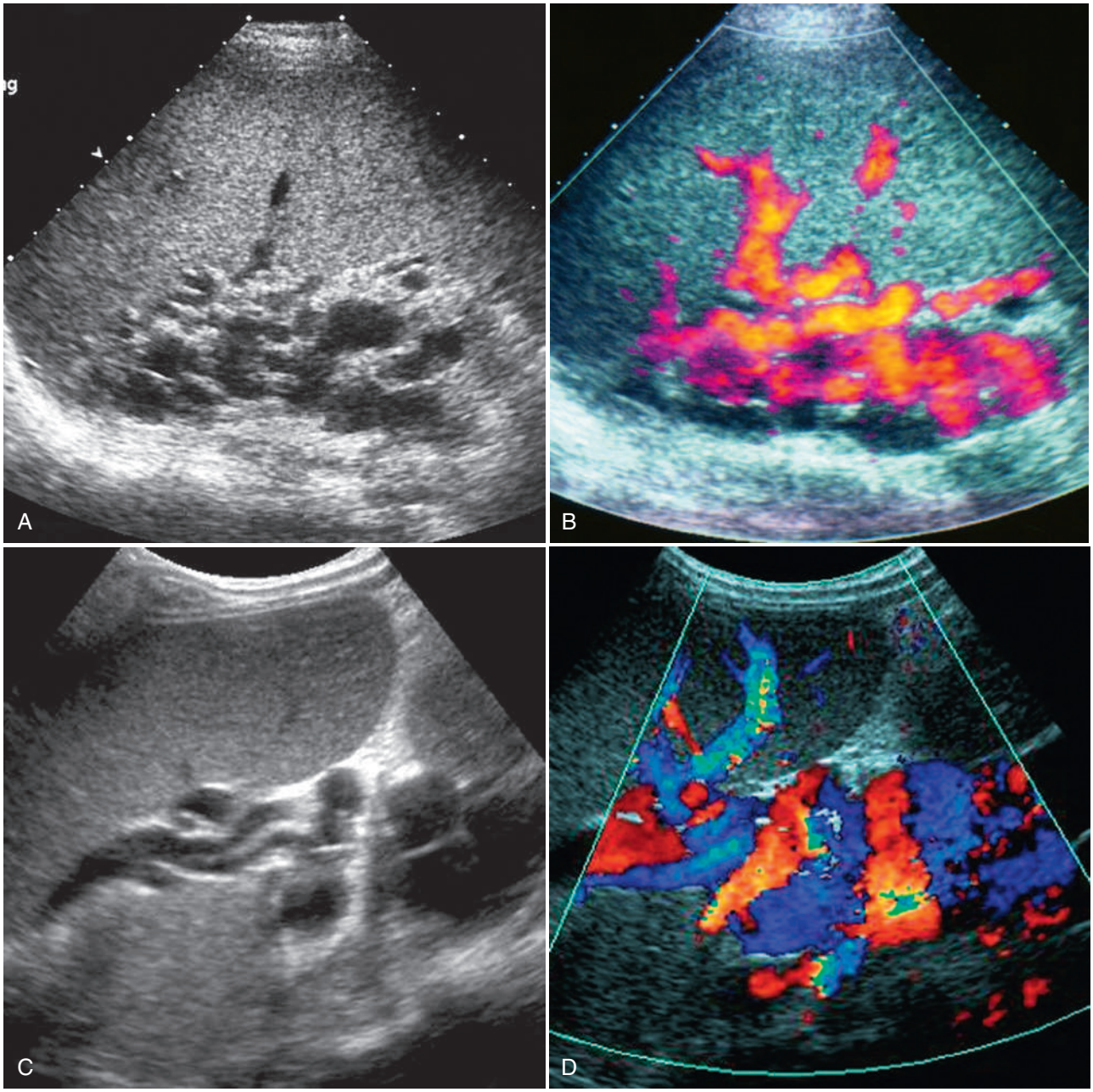

FIG. 5.9 Varices in Patients With Portal Hypertension. (A) Coronal gray-scale and **(B)** power Doppler images show splenomegaly and tortuous varices medial to the spleen. **(C)** and **(D)** Varices medial and inferior to the spleen representing a splenorenal shunt.

complex, with wall calcifications and internal echoes (Fig. 5.11B). However, differentiation between both types of cysts is usually not possible because there is considerable overlap both on imaging and on pathologic examination[34] (Fig. 5.11C). Furthermore, a history of significant trauma or infection is rarely established in patients with a pseudocyst. Both types of cysts can be complex, with wall calcifications or increased echogenicity of the fluid caused by cholesterol crystals, inflammatory debris, or hemorrhage[35] (Fig. 5.12; see also Fig. 5.10).

Hydatid (or **echinococcal**) **disease** is the most common cause of splenic cysts in endemic areas. Isolated splenic involvement without liver and peritoneal disease is rare.[36] The appearance of a hydatid cyst depends on the stage of the disease and varies from simple to complex, with or without daughter cysts (Fig. 5.13). The diagnosis is made by combining the appropriate history, geographic background, serologic testing, and imaging appearances.[37,38] Percutaneous fine-needle aspiration can be diagnostic, provided the pathologist has been alerted to search for the scolices.

Pseudocysts related to **pancreatitis** in or adjacent to the spleen are usually diagnosed by the associated features of pancreatitis.[39] Splenic **peliosis** is very rare and characterized by multiple blood-filled cystic spaces, sometimes involving the entire spleen.[40] On ultrasound, these lesions appear as multiple indistinct hypoechoic lesions. The lesions may be hyperechoic if thrombosis is present.

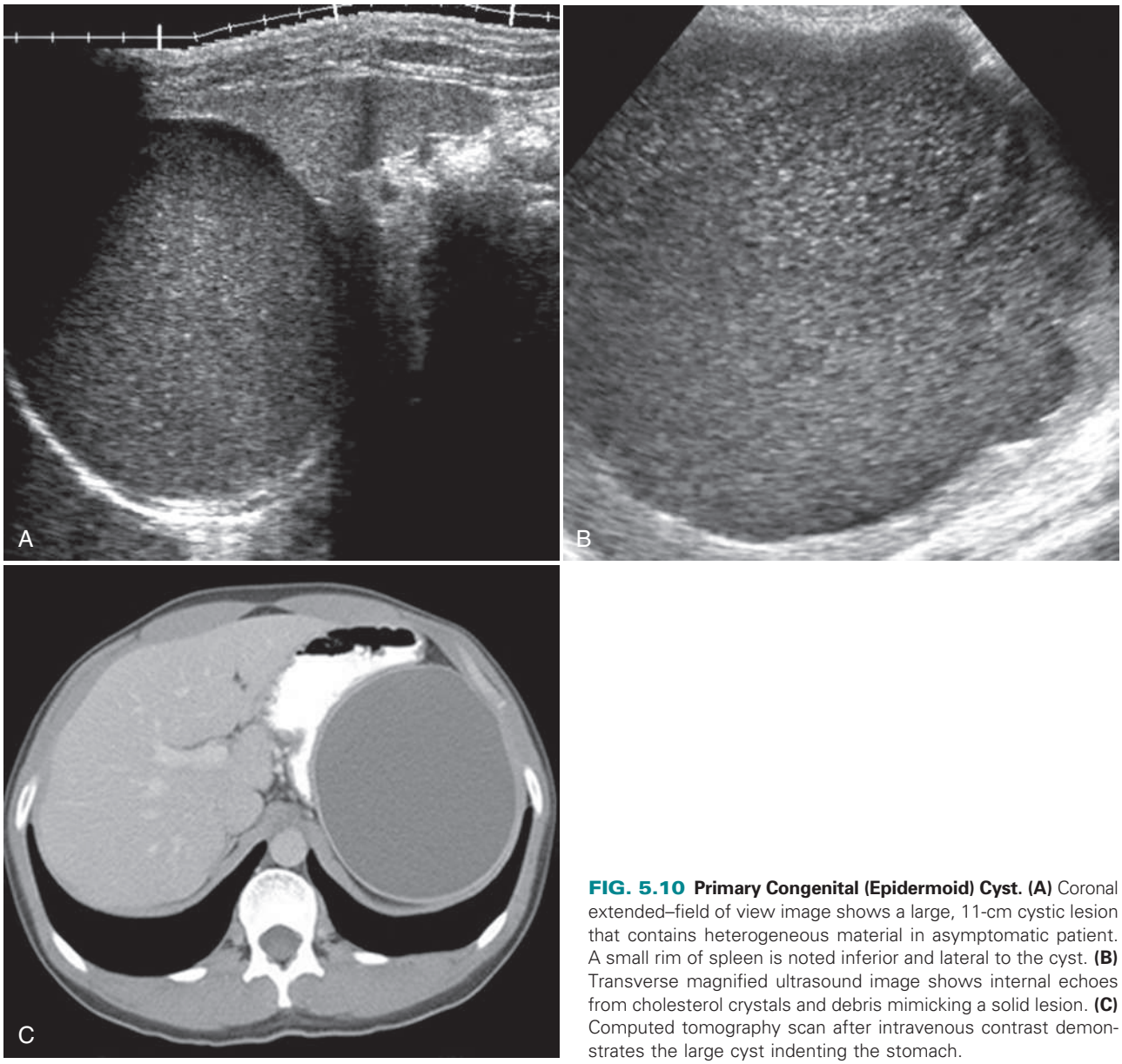

FIG. 5.10 Primary Congenital (Epidermoid) Cyst. (A) Coronal extended–field of view image shows a large, 11-cm cystic lesion that contains heterogeneous material in asymptomatic patient. A small rim of spleen is noted inferior and lateral to the cyst. **(B)** Transverse magnified ultrasound image shows internal echoes from cholesterol crystals and debris mimicking a solid lesion. **(C)** Computed tomography scan after intravenous contrast demonstrates the large cyst indenting the stomach.

Endothelial-lined cysts include lymphangiomas and cystic hemangiomas.[41,42] **Lymphangiomas** have been described as multiple cysts of varying size, ranging from a few millimeters to several centimeters, divided by thin septa.[43] **Hemangiomas** with cystic spaces of variable size have been reported.

Cystic metastases to the spleen are typically seen in patients with widespread metastatic disease, such as ovarian or colon carcinoma. Occasionally, necrotic metastases mimic a cystic lesion.

The most common causes of **splenic abscess** are endocarditis, septicemia, and trauma.[44] Splenic pyogenic abscesses may have an appearance similar to that of simple cysts, but the diagnosis is typically made in conjunction with the clinical findings. The presence of gas indicates an infectious cause. Gas may cause a confusing picture if only a small, curvilinear or punctate hyperechoic focus is seen. The presence of a reverberation artifact (dirty shadowing) indicates the presence of gas (Fig. 5.14). However, the sonographic findings of a pyogenic abscess are variable, and in indeterminate cases, aspiration is useful for diagnosis.[45] Percutaneous catheter drainage can be used as a safe and successful treatment option.[46]

Nodular Splenic Lesions

Nodular lesions are often multiple and can be subdivided into micronodular (<1 cm) and nodular (1-3 cm). If splenic nodules are present in a patient with a known diagnosis such as lymphoma, tuberculosis, or sarcoidosis, these nodules likely represent the same disease. However, if no diagnosis has been established and the splenic nodules are an isolated finding, the diagnosis is rarely made on the imaging features alone. The most common causes of splenic nodules include infection (e.g., **mycobacteria, histoplasmosis**), **sarcoidosis,** and malignancy (e.g., **lymphoma,** metastases). Other, less common causes of splenic nodular lesions with similar imaging findings include **Gamna-Gandy bodies,**

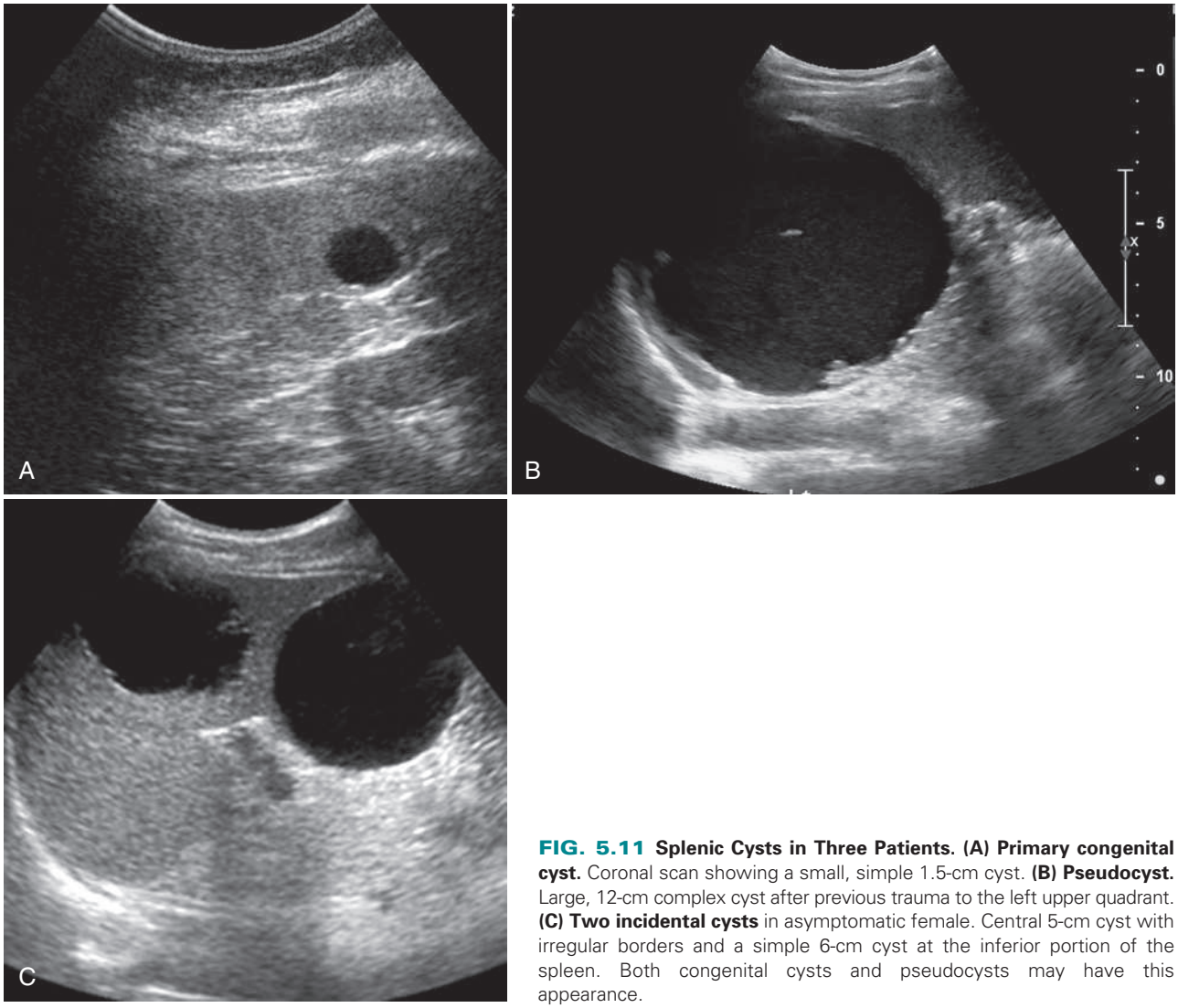

FIG. 5.11 Splenic Cysts in Three Patients. (A) Primary congenital cyst. Coronal scan showing a small, simple 1.5-cm cyst. **(B) Pseudocyst.** Large, 12-cm complex cyst after previous trauma to the left upper quadrant. **(C) Two incidental cysts** in asymptomatic female. Central 5-cm cyst with irregular borders and a simple 6-cm cyst at the inferior portion of the spleen. Both congenital cysts and pseudocysts may have this appearance.

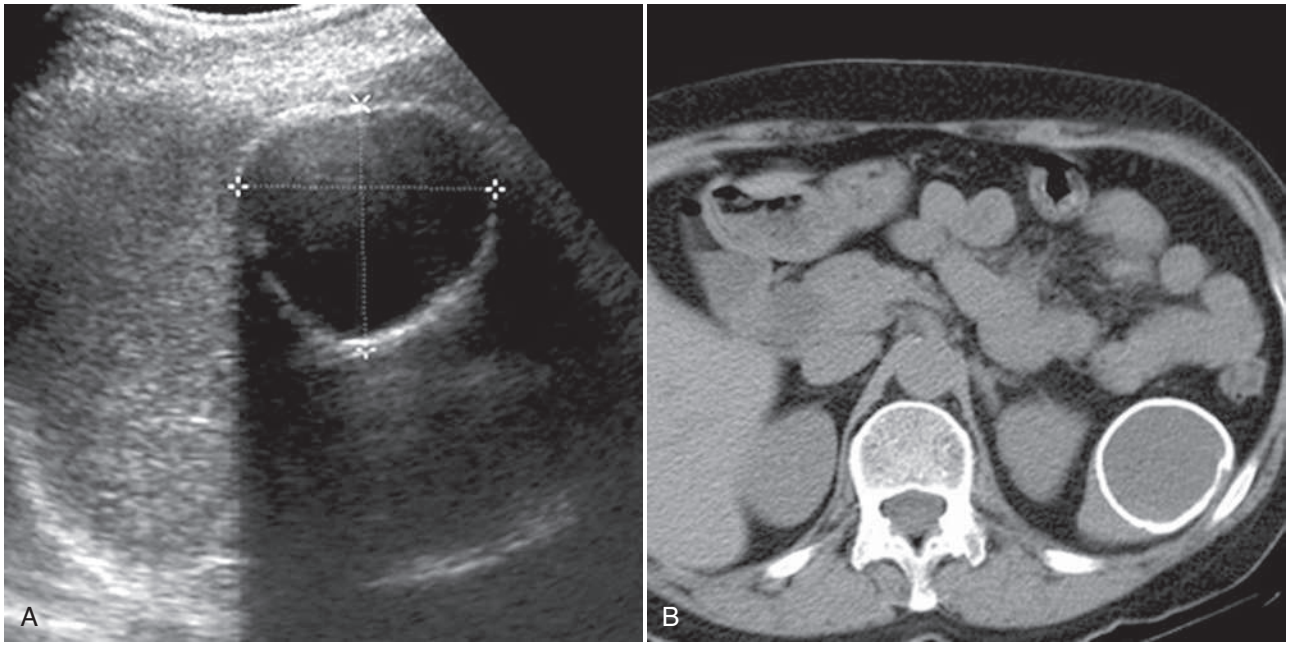

FIG. 5.12 Calcified Splenic Cyst. (A) Coronal image shows the cyst with calcified wall (calipers). Note the shadowing from the near wall. **(B)** Noncontrast-enhanced computed tomography image demonstrates the wall calcification. Congenital cysts, pseudocysts, and "burned out" hydatid cysts may have similar appearance.

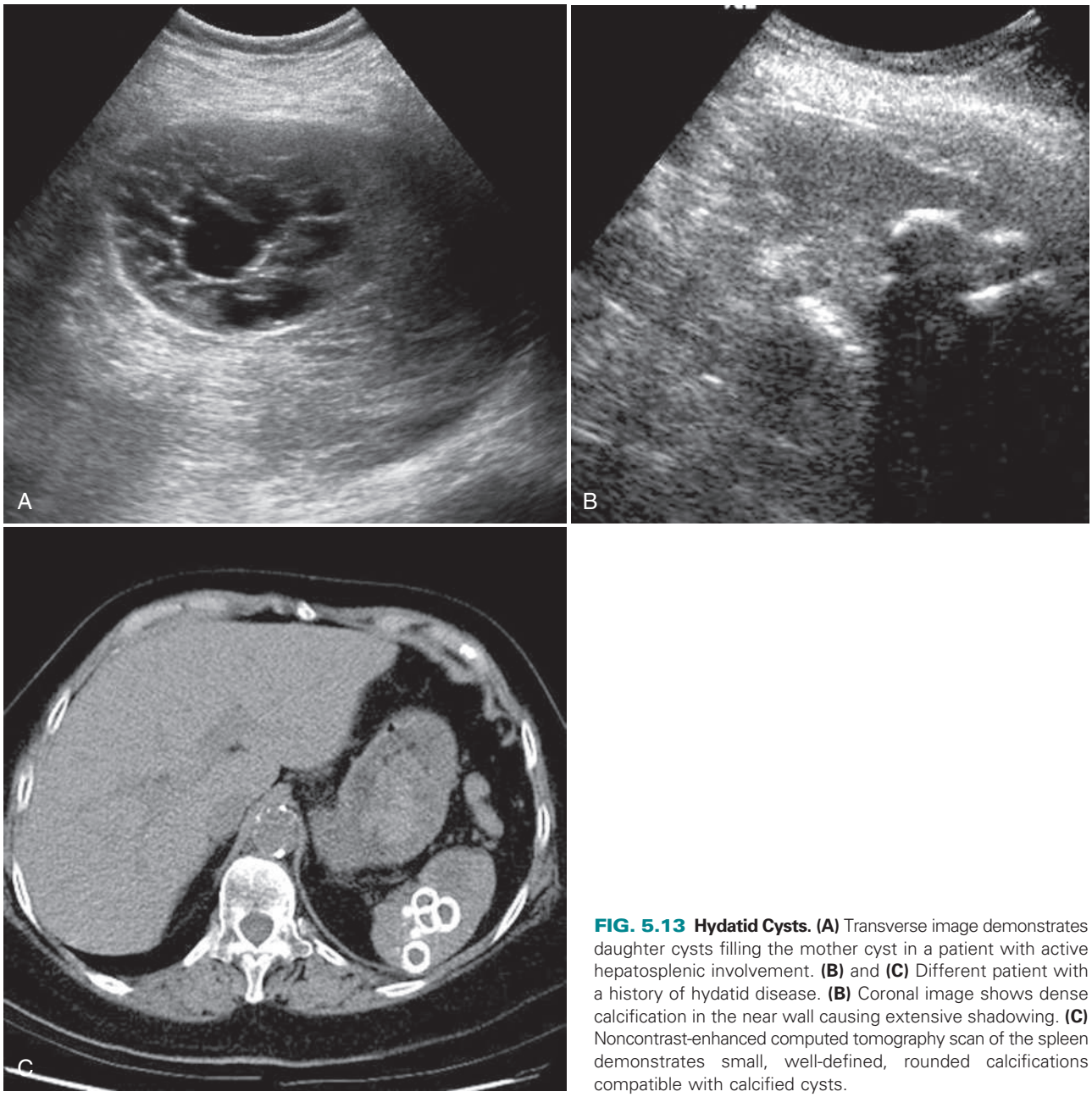

FIG. 5.13 Hydatid Cysts. (A) Transverse image demonstrates daughter cysts filling the mother cyst in a patient with active hepatosplenic involvement. **(B)** and **(C)** Different patient with a history of hydatid disease. **(B)** Coronal image shows dense calcification in the near wall causing extensive shadowing. **(C)** Noncontrast-enhanced computed tomography scan of the spleen demonstrates small, well-defined, rounded calcifications compatible with calcified cysts.

Pneumocystis jiroveci (formerly known as *P. carinii* pneumonia) and **cat-scratch disease.**[47-49]

Active **tuberculosis** involving the spleen is typically seen in miliary dissemination and can occur with both tuberculosis and atypical mycobacterial infections. The typical sonographic findings are multiple hypoechoic nodules 0.2 to 1 cm in size (Fig. 5.15). Sometimes the nodules are hyperechoic or present as larger, echo-poor or cystic lesions representing tuberculous abscesses (Figs. 5.16 and 5.17).

When the nodules or granulomas heal, they can be become calcified and appear as small, scattered, discrete, bright echogenic lesions with posterior shadowing in an otherwise normal spleen (Fig. 5.18). These probably are the most frequently encountered nodular splenic lesions. Splenic artery calcifications are also common and should not be confused with a granuloma (Fig. 5.19).

Microabscesses are typically seen in immunocompromised patients with generalized infections. They often coexist in the liver and spleen and are similar in appearance. Microabscesses usually present as multiple hypoechoic nodules (Fig. 5.20A). In **hepatosplenic candidiasis** the two most common sonographic patterns are hypoechoic nodules and hyperechoic foci 2 to 5 mm in size, occasionally containing central calcification. Two other sonographic patterns have also been described. In the **wheels-within-wheels** appearance the outer hypoechoic "wheel" is thought to represent a ring of fibrosis surrounding the inner echogenic "wheel" of inflammatory cells and a central hypoechoic, necrotic area.[50] The **bull's-eye** appearance consists of echogenic

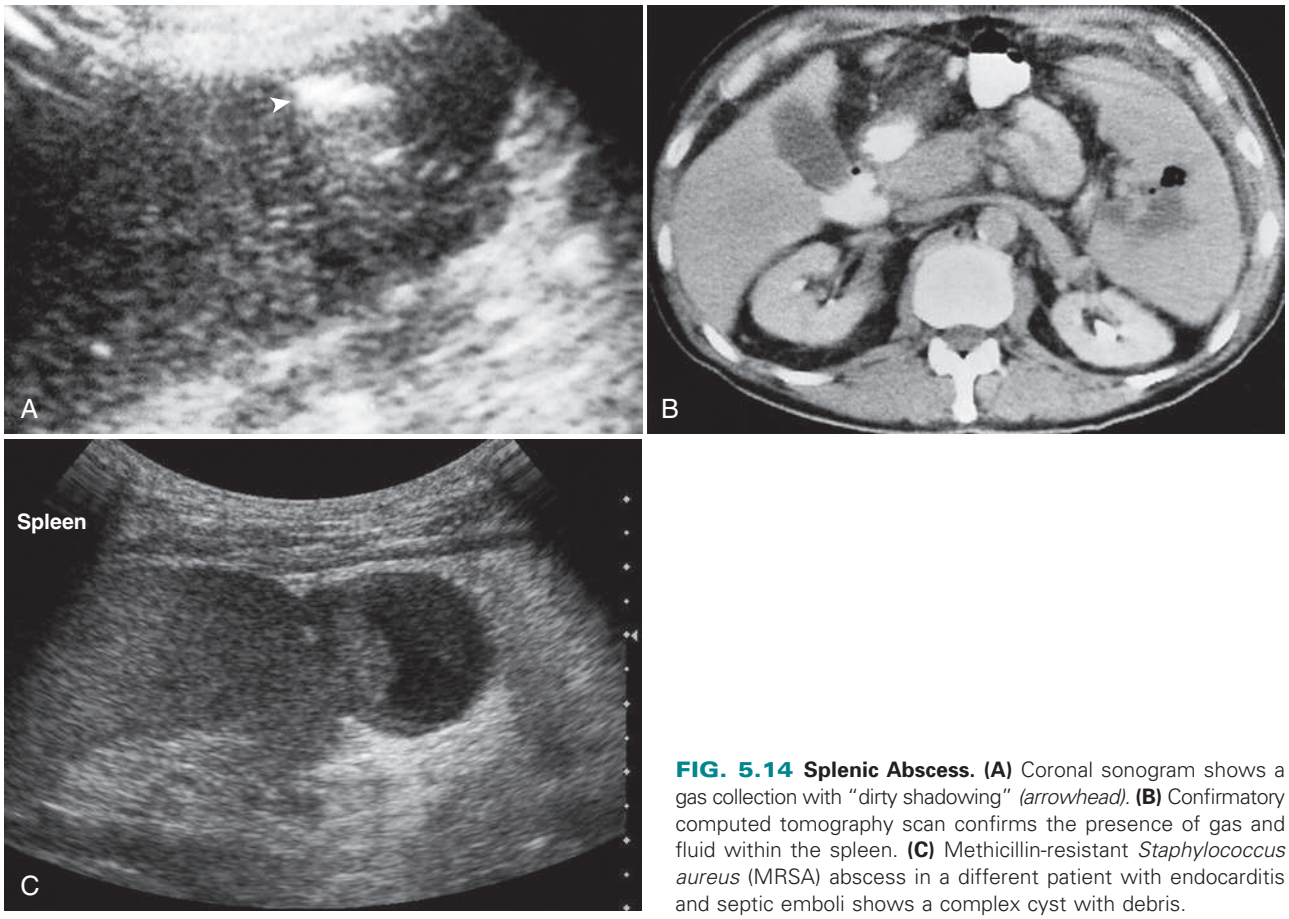

FIG. 5.14 Splenic Abscess. (A) Coronal sonogram shows a gas collection with "dirty shadowing" *(arrowhead).* **(B)** Confirmatory computed tomography scan confirms the presence of gas and fluid within the spleen. **(C)** Methicillin-resistant *Staphylococcus aureus* (MRSA) abscess in a different patient with endocarditis and septic emboli shows a complex cyst with debris.

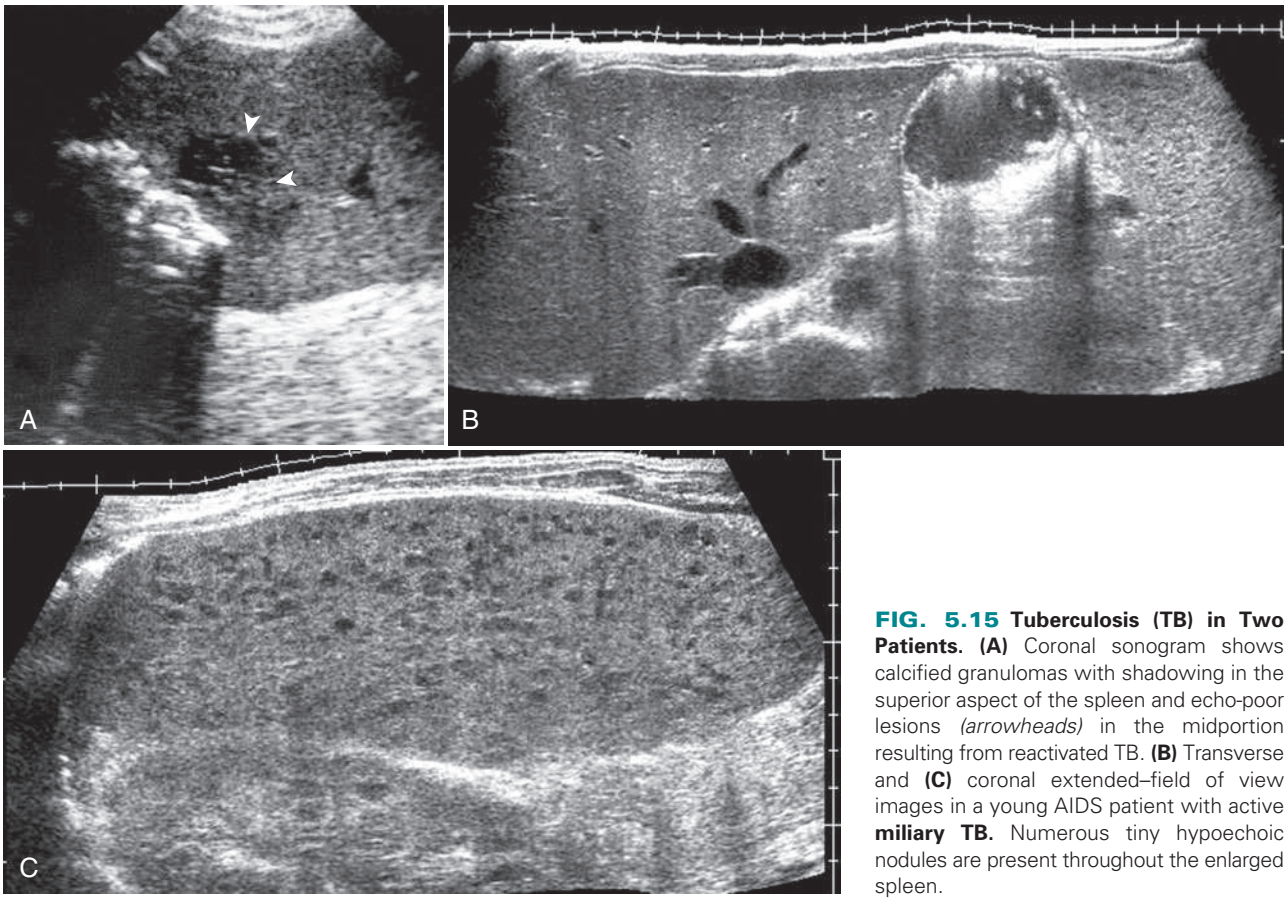

FIG. 5.15 Tuberculosis (TB) in Two Patients. (A) Coronal sonogram shows calcified granulomas with shadowing in the superior aspect of the spleen and echo-poor lesions *(arrowheads)* in the midportion resulting from reactivated TB. **(B)** Transverse and **(C)** coronal extended–field of view images in a young AIDS patient with active **miliary TB.** Numerous tiny hypoechoic nodules are present throughout the enlarged spleen.

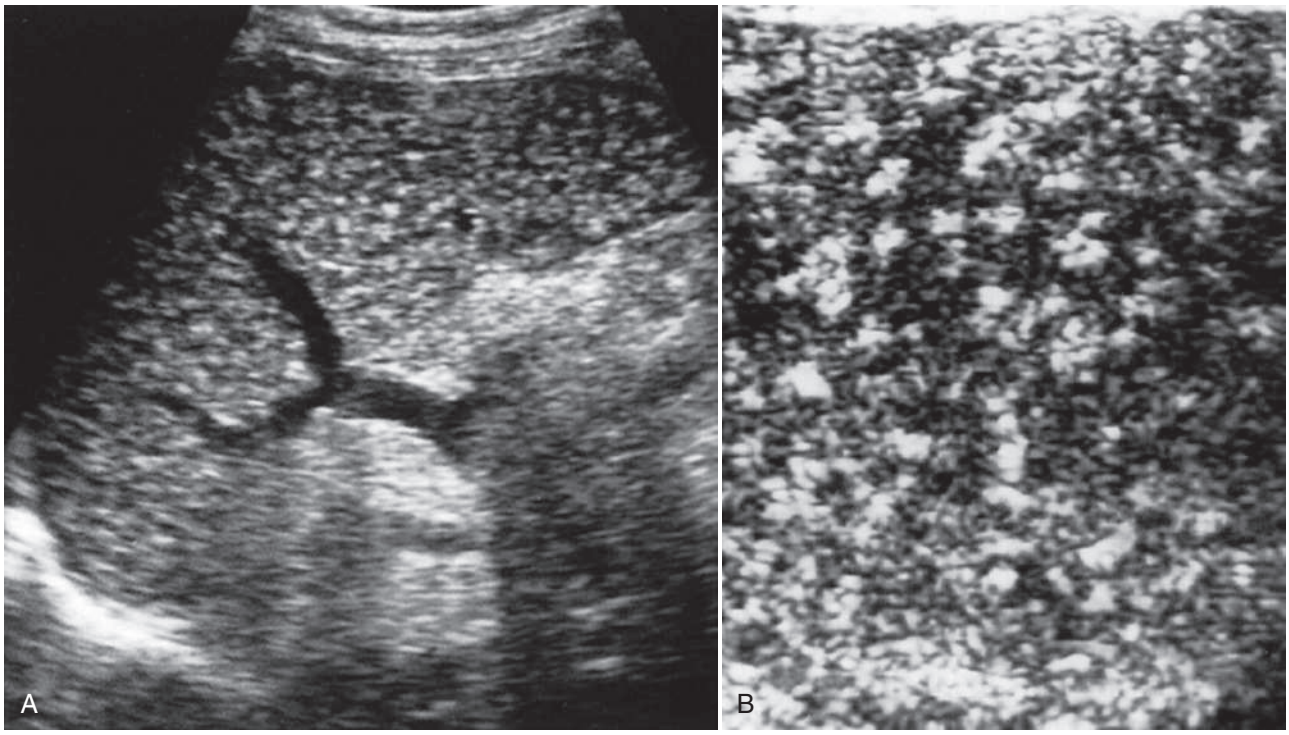

FIG. 5.16 Miliary Tuberculosis of the Spleen. (A) Coronal and **(B)** high-resolution linear array ultrasound images show multiple tiny echogenic foci of tuberculous granulomata in this patient with active tuberculosis.

FIG. 5.17 Atypical Tuberculosis of the Spleen in AIDS Patient. Tiny echogenic foci throughout the spleen. Isolated foci were also identified in the liver and kidneys. Several core biopsies through the liver confirmed these to be *Mycobacterium avium-intracellulare* granulomas. Disseminated *Pneumocystis jiroveci,* formerly *P. carinii* pneumonia (PCP), can also appear in this way.

inflammatory cells in the center surrounded by a hypoechoic fibrotic outer rim[51] (Fig. 5.20B).

Lymphoma and **metastatic disease** can also present with a small, diffuse nodular pattern, especially Hodgkin disease and low-grade non-Hodgkin lymphoma[52] (Fig. 5.21A).

Causes of Splenic Nodules

INFECTIOUS
Tuberculosis/*Mycobacterium avium-intracellulare* complex
Pyogenic abscesses
Histoplasmosis
Candida abscesses
Cat-scratch disease
Pneumocystis jiroveci (formerly *P. carinii* pneumonia)

INFLAMMATORY
Sarcoidosis

MALIGNANT
Lymphoma
Metastases

OTHER
Gamna-Gandy bodies (fibrosiderotic nodules)
Gaucher disease

Focal Solid Splenic Lesions

Malignancies. The spleen is frequently involved in patients with **lymphoma.** Patients with lymphomatous involvement of the spleen often present with associated abdominal lymphadenopathy and constitutional symptoms. In **Hodgkin disease,** splenic enlargement occurs in 30% to 40% of patients, but in one-third of these patients there is no lymphomatous involvement of the spleen at histopathology. Conversely, one-third of patients with Hodgkin disease and splenic involvement have a normal-sized spleen. In **non-Hodgkin lymphoma** the spleen is involved in 40% of patients during the course of their disease. **Four**

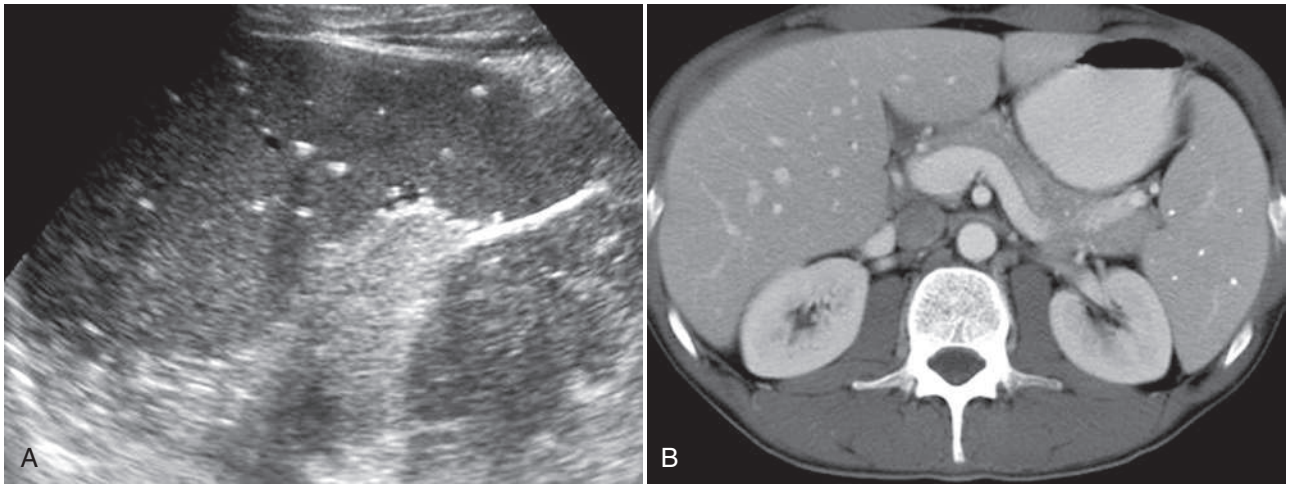

FIG. 5.18 Calcified Granulomas in a Patient With Sarcoidosis. (A) Multiple tiny bright foci throughout the spleen, some demonstrating posterior shadowing. **(B)** Computed tomography scan after intravenous contrast shows multiple small parenchymal calcifications throughout the spleen.

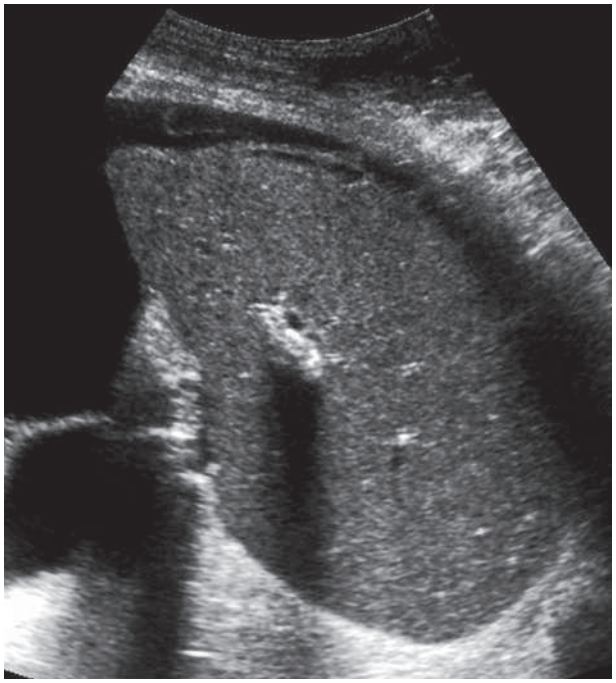

FIG. 5.19 Splenic Artery Calcifications. Central splenic artery calcifications in a patient on peritoneal dialysis.

sonographic patterns of lymphomatous involvement of the spleen have been described,[53] corresponding with the pathologic findings: (1) diffuse involvement, typically an enlarged spleen with a normal echotexture or patchy inhomogeneity; (2) focal small (<3 cm) hypoechoic nodular lesions; (3) focal large (>3 cm) nodular lesions; and (4) bulky solid mass lesions (Fig. 5.21). Focal lesions in lymphoma are typically hypoechoic and hypovascular.[31] Occasionally, after central necrosis with subsequent liquefaction, lesions may present as anechoic cysts or mimic an abscess.[54] Hyperechoic lesions are uncommon.

Primary splenic malignancies include primary lymphoma, angiosarcoma, and hemangiopericytoma. **Isolated (primary) lymphoma** of the spleen is rare and is encountered in less than 1% of all patients with lymphoma. It typically represents Hodgkin disease.[52] **Angiosarcoma** is a rare primary malignant vascular neoplasm of the spleen with a very poor prognosis. Sonographic findings include a heterogeneous echotexture, complex mass or masses, and splenomegaly (Fig. 5.22). Increased Doppler flow may be seen in the solid components of the tumor.[55,56] **Hemangiopericytoma** is a very rare tumor that may arise in the spleen with variable malignant potential. On ultrasound, it may appear as a hypoechoic vascular mass distinct from the surrounding splenic parenchyma.[40]

Metastases to the spleen are relatively rare and generally occur as a late phenomenon. They are typically seen in patients with widespread metastatic disease rather than as a presenting feature.[57] Isolated metastases to the spleen are very uncommon. Splenic metastases are relatively frequent in **malignant melanoma** but can be encountered in any metastatic disease, including carcinoma of the lung, breast, ovary, stomach, or colon and in Kaposi sarcoma.[58] Metastases are usually hypoechoic but may be echogenic, heterogeneous, or even cystic[1] (Fig. 5.23).

Benign Lesions. **Hemangioma** is the most common primary benign neoplasm of the spleen; incidence ranges from 0.3% to 14% in autopsy series.[59] Hemangiomas are usually isolated phenomena but can be part of a generalized condition, such as hemangiomatosis or Klippel-Trenaunay-Weber syndrome.[60,61] The lesions often have a well-defined echogenic appearance similar to the typical appearance of hemangiomas in the liver, but this appearance is seen much less frequently in the spleen than in the liver (Fig. 5.24). Lesions of mixed echogenicity, with cystic spaces of variable sizes and foci of calcification, have also been reported.[41,59]

Other benign tumors of the spleen are rare and include hamartomas, littoral cell angioma, sclerosing angiomatoid nodular transformation (SANT), and inflammatory pseudotumor. **Hamartomas** are typically well-defined, homogeneous, isoechoic to mildly hypoechoic or hyperechoic lesions[62] (Fig. 5.25). Hamartomas may contain cystic areas or coarse calcifications, and

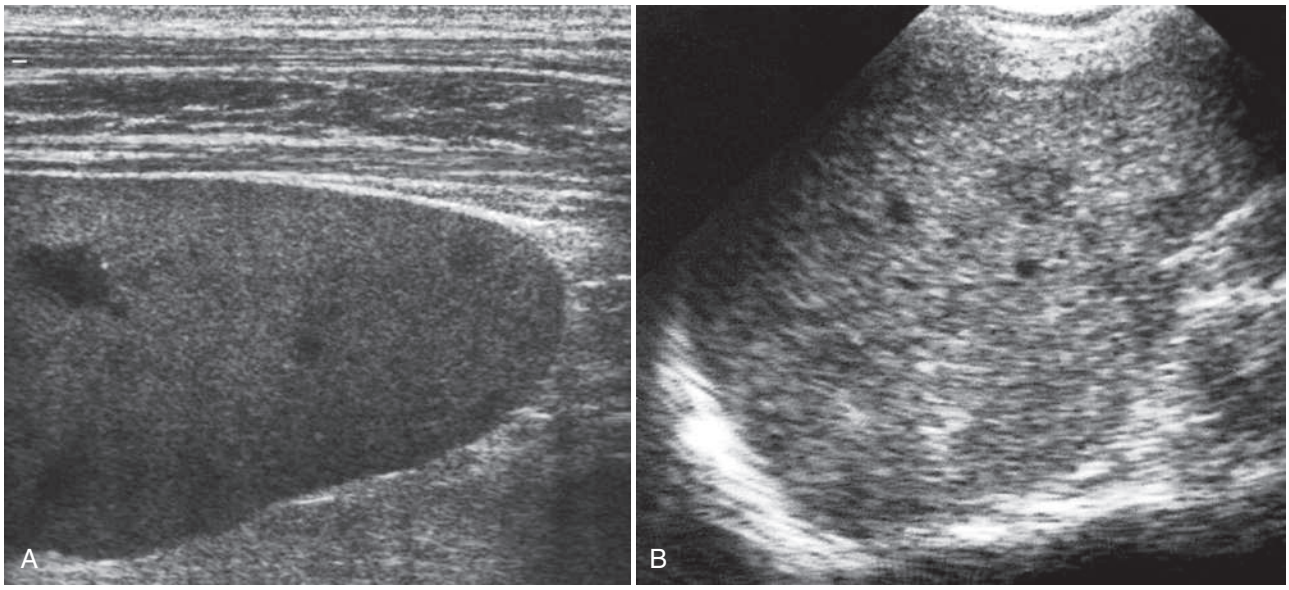

FIG. 5.20 Microabscesses in Two Patients. (A) High-frequency linear array ultrasound image shows multiple poorly defined microabscesses in a patient with *Klebsiella* septicemia. **(B)** *Candida* abscesses of the spleen in a patient with AIDS. Note that lesion in the middle has an echogenic center, characteristic of *Candida*.

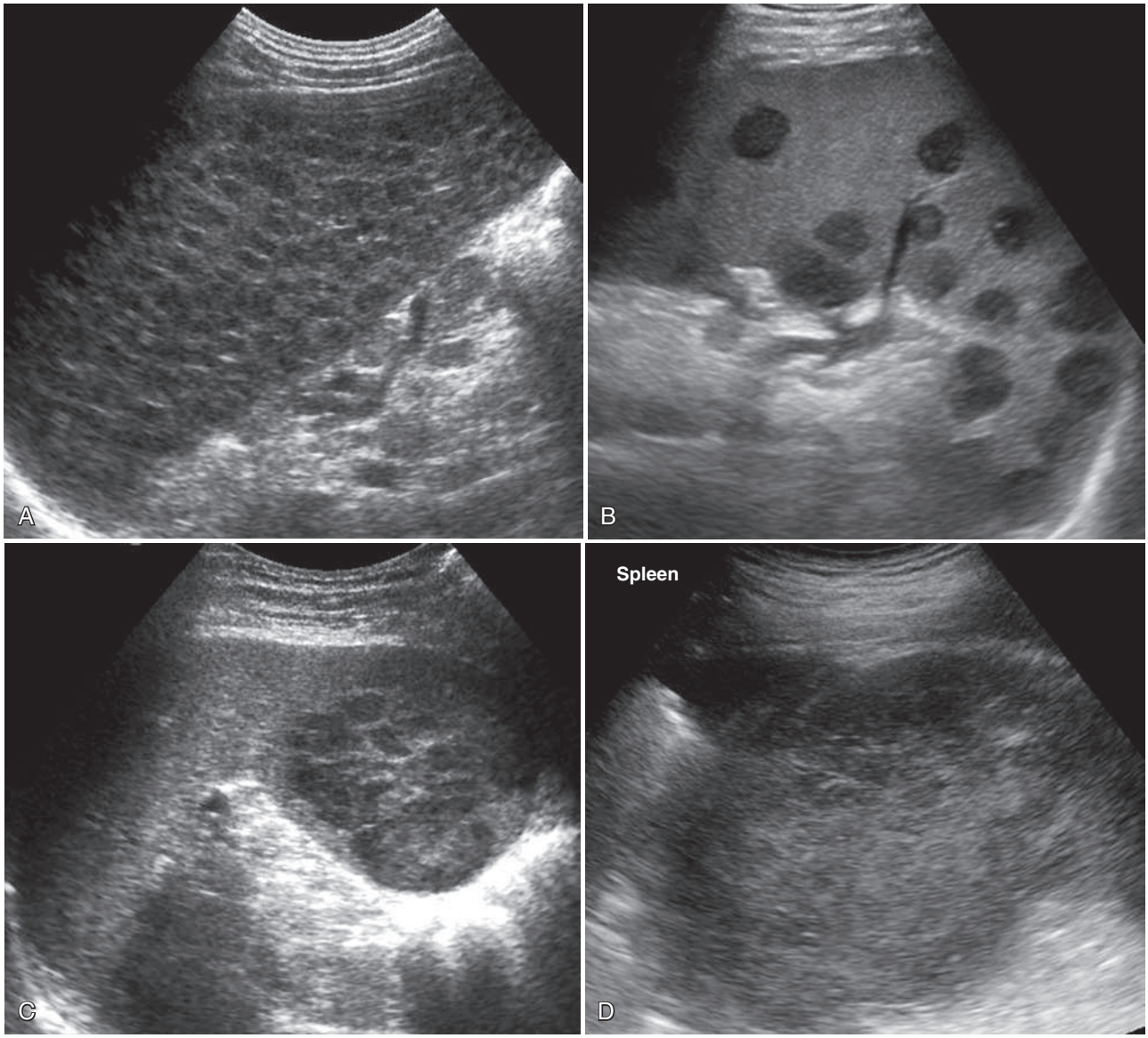

FIG. 5.21 Patterns of Lymphoma in Different Patients. (A) Numerous small nodules resulting from T-cell lymphoma in an enlarged spleen. **(B)** Multiple solid nodules in a patient with follicular lymphoma. **(C)** Bulky solid mass in a patient with non-Hodgkin lymphoma. **(D)** Large, poorly defined mass caused by B-cell lymphoma replacing the spleen and extending beyond the normal contour. Lymphoma may also involve the spleen diffusely without focal abnormalities.

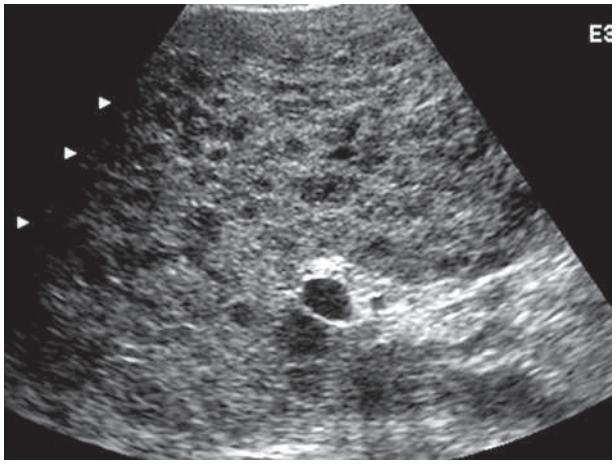

FIG. 5.22 Primary Splenic Malignancy: Angiosarcoma. Transverse image shows multiple poorly defined hypoechoic lesions. Other sonographic findings include a heterogeneous echotexture, complex masses, and splenomegaly.

Focal Solid Splenic Masses

BENIGN
Hemangioma
Hamartoma
Littoral cell angioma
Lymphangioma
Sclerosing angiomatoid nodular transformation
Inflammatory pseudotumor

MALIGNANT
Lymphoma
Metastases
Angiosarcoma
Hemangiopericytoma

OTHER
Infarct

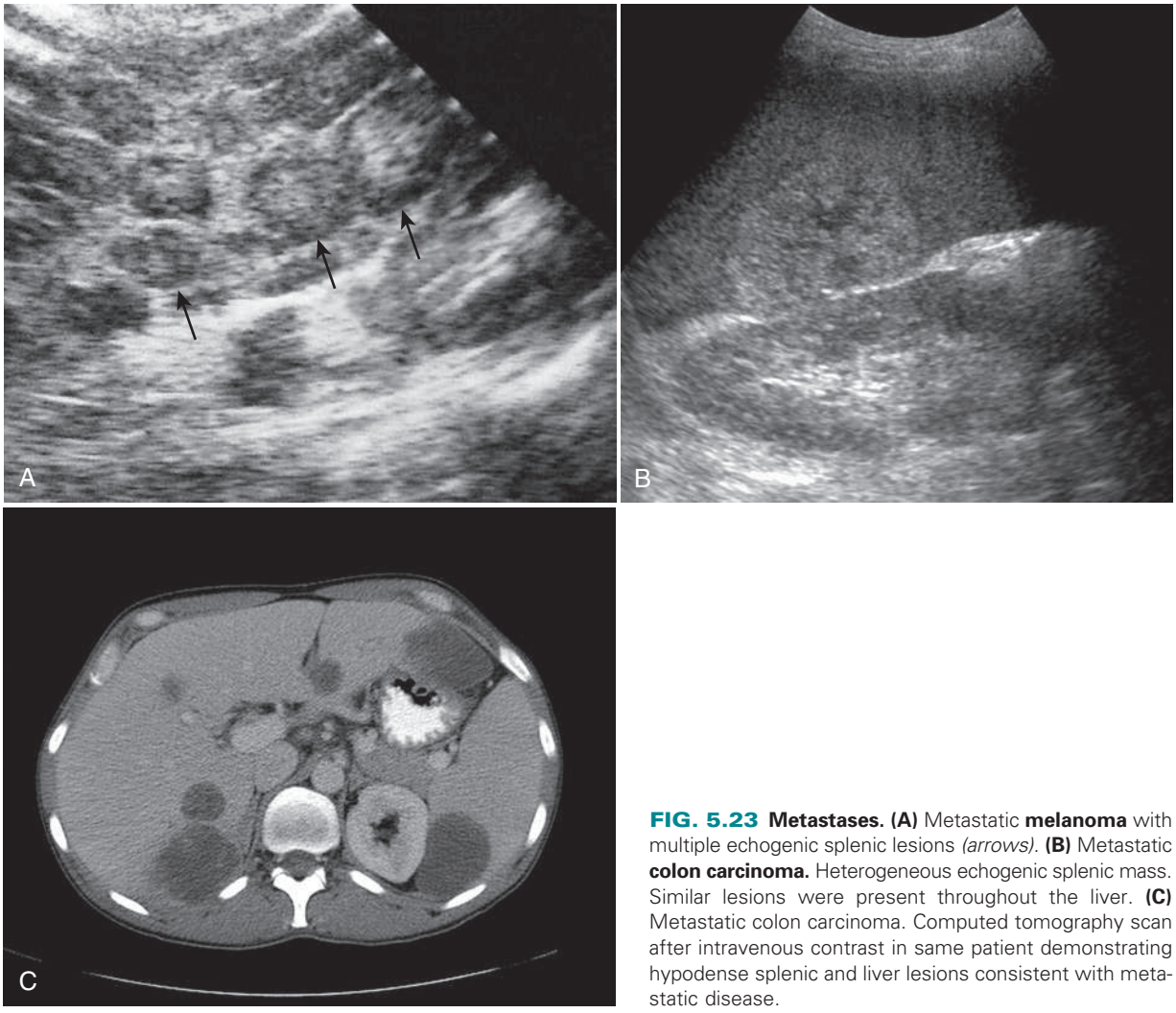

FIG. 5.23 Metastases. (A) Metastatic **melanoma** with multiple echogenic splenic lesions *(arrows)*. **(B)** Metastatic **colon carcinoma.** Heterogeneous echogenic splenic mass. Similar lesions were present throughout the liver. **(C)** Metastatic colon carcinoma. Computed tomography scan after intravenous contrast in same patient demonstrating hypodense splenic and liver lesions consistent with metastatic disease.

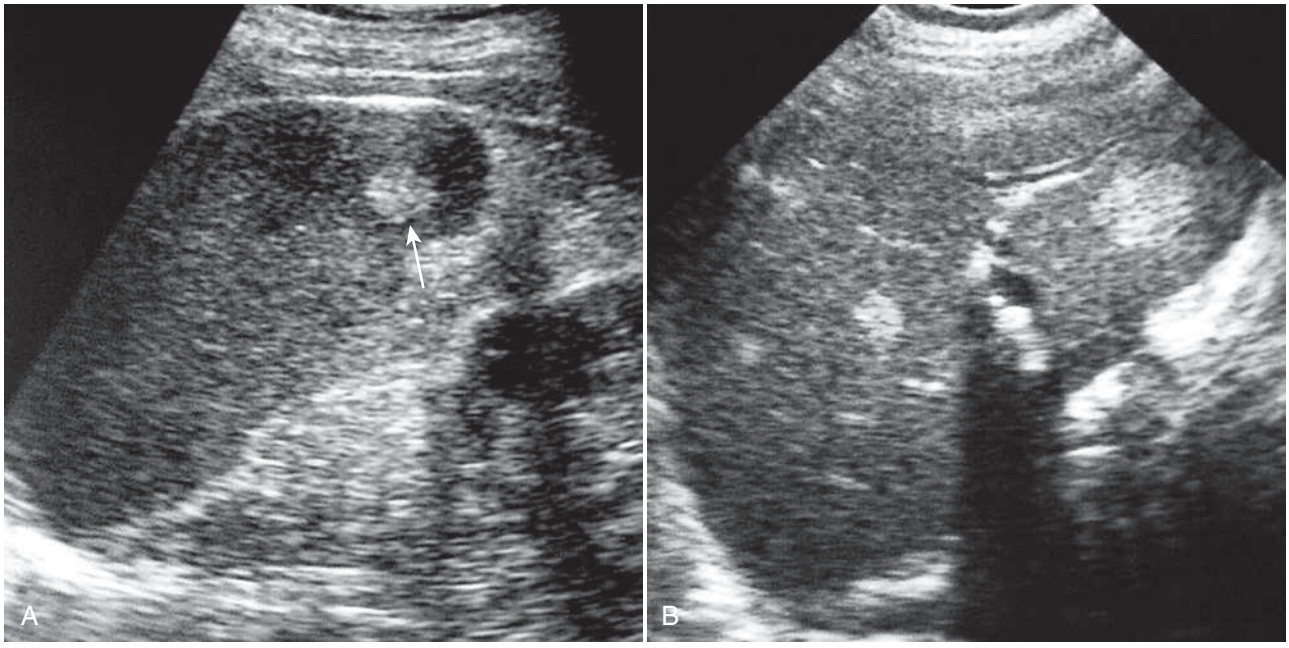

FIG. 5.24 Hemangioma in Two Patients. (A) Small (1.4-cm), well-defined, rounded, echogenic lesion *(arrow)* is similar to the typical liver hemangiomas. **(B)** Coronal ultrasound scan shows multiple echogenic splenic hemangiomas of different sizes in the spleen. Note the calcified splenic artery adjacent to the vein.

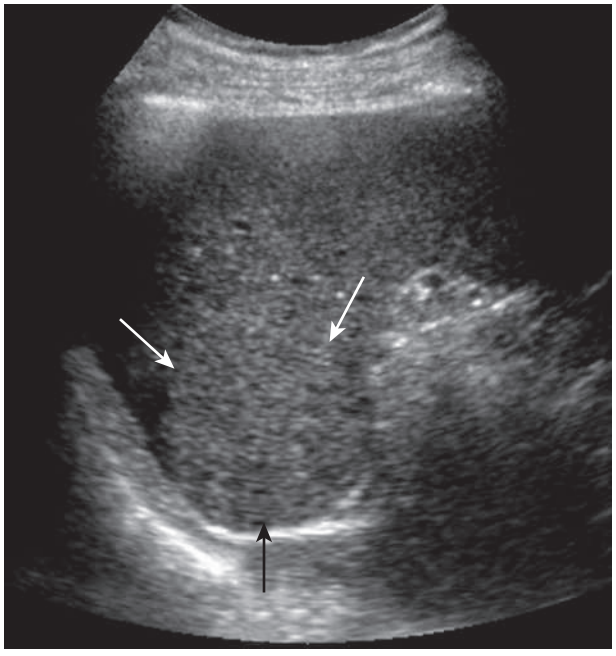

FIG. 5.25 Hamartoma. Round, 5-cm, slightly hyperechoic lesion *(arrows)* arising from the medial margins of the spleen.

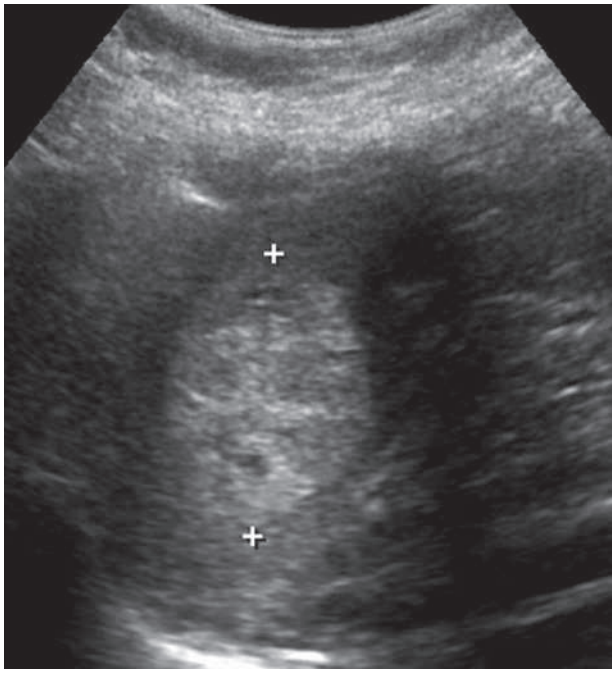

FIG. 5.26 Littoral Cell Angioma. Oval, well-defined, 5-cm echogenic lesion. Splenectomy was performed when this lesion demonstrated growth during follow-up.

some demonstrate increased vascularity on color Doppler imaging.[63] The sonographic appearance of **littoral cell angioma** is variable and includes reports of hypoechoic and hyperechoic focal lesions as well as a diffuse mottled pattern without discrete lesions[40,64] (Fig. 5.26). Sclerosing angiomatoid nodular transformation is a rare benign vascular lesion of the spleen. Appearance on ultrasound has been described as heterogeneous hypoechoic.[65] These may grow, and thus be difficult to distinguish from more concerning lesions, and thus may need biopsy for diagnosis. **Inflammatory pseudotumors** usually present as a well-defined hypoechoic mass.[66]

Splenic infarction is one of the more common causes of focal splenic lesions and may mimic a mass on ultrasound. If a typical peripheral, wedge-shaped, hypoechoic lesion is noted, splenic

infarction should be the first diagnostic consideration[67,68] (Figs. 5.27 and 5.28). However, the sonographic appearance of splenic infarcts varies and includes multinodular or masslike changes with irregular margins.[69] The temporal evolution of the ultrasound appearance of splenic infarctions has shown that the echogenicity of the lesion is related to the age of the infarction. Infarctions are hypoechoic in early stages and progress to hyperechoic lesions when fibrosis develops over time.[70,71]

Other Abnormalities

Sickle Cell Disease

Sickle cell disease almost always affects the spleen. The most common splenic complications are autosplenectomy, acute sequestration, hypersplenism, massive infarction, and abscess. In homozygous **sickle cell disease**, multiple infarcts generally result in a small, fibrotic spleen and complete loss of function **(autosplenectomy).** Although promising new therapies are being developed, many homozygous sickle cell patients become **asplenic** in late childhood or early adulthood. This results in a small spleen, often difficult to visualize, with a diffuse echogenic appearance. Patients with heterozygous sickle cell disease often present with **splenomegaly** and may demonstrate the sequelae of **infarction.**[72,73] In some patients, areas of preserved splenic tissue are present in an otherwise small and fibrotic spleen, and these should not be mistaken for an abscess or mass.

Acute splenic sequestration is a life-threatening complication of sickle cell disease and typically occurs in infants and children with homozygous sickle cell disease. It represents sudden trapping of blood in the spleen, resulting in splenic enlargement. On ultrasound, the spleen is larger than expected and heterogeneous with multiple hypoechoic areas.[72] It is important to recognize that in homozygous sickle cell patients, an apparently normal-sized spleen may actually indicate splenomegaly.

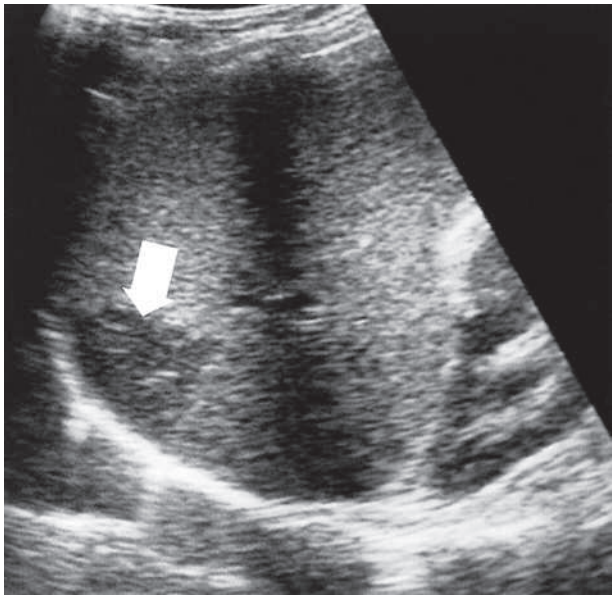

FIG. 5.27 Splenic Infarct. Triangular hypoechoic infarct *(arrow)* in the superior aspect of the spleen extends to the splenic capsule.

Gaucher Disease

In Gaucher disease, splenomegaly occurs almost universally, and approximately one-third of patients have multiple splenic nodules. These nodules frequently are well-defined hypoechoic lesions, but they may also be irregular, hyperechoic, or of mixed echogenicity[74,75] (Fig. 5.29). Pathologically, these nodules represent focal areas of Gaucher cells associated with fibrosis and infarction. In rare cases, the entire spleen may be involved, with ultrasound showing a diffuse heterogeneous spleen.

Gamna-Gandy Bodies

Gamna-Gandy bodies (Gamna nodules) are fibrosiderotic nodules that result from organized focal hemorrhagic infarcts, typically seen in congestive splenomegaly and sickle cell disease. Gamna-Gandy bodies appear as multiple punctate hyperechoic foci on ultrasound but are usually better seen on MRI.[76]

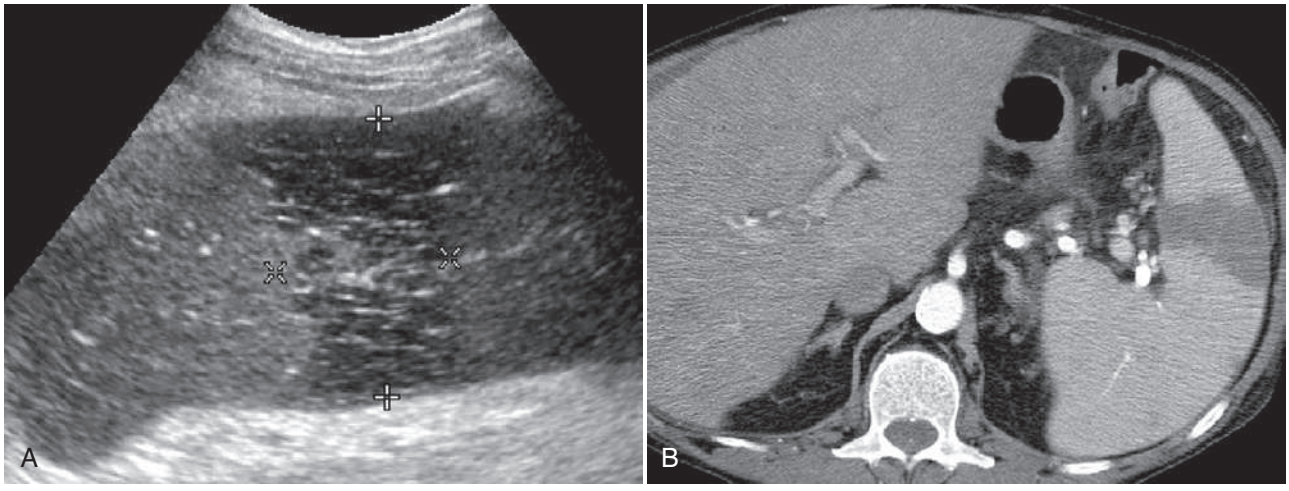

FIG. 5.28 Splenic Infarct. (A) Coronal image shows a well-defined hypoechoic central area reaching the splenic capsule medial and lateral in a patient with splenomegaly receiving peritoneal dialysis. **(B)** Corresponding computed tomography scan after intravenous contrast demonstrates the wedge-shaped nonenhancing area in keeping with an infarct.

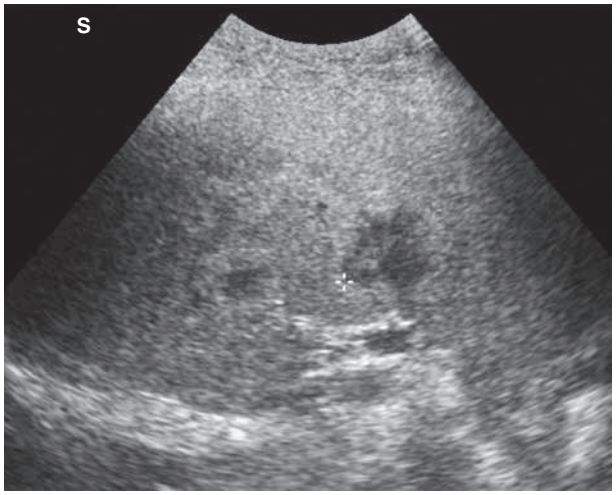

FIG. 5.29 Gaucher Disease. Enlarged spleen containing a 2-cm heterogeneous nodule. (Courtesy of M. Maas, MD, Amsterdam.)

Splenic Trauma

The spleen is the most frequently injured visceral organ in patients with blunt abdominal trauma. The spectrum of splenic injuries ranges from contusion to a completely shattered spleen. The severity of the splenic injury can be scored using the American Association for the Surgery of Trauma **Organ Injury Scoring Scale.**[77] Treatment options depend on hemodynamic and clinical criteria and include conservative management with or without embolization and surgery.[4]

Ultrasound can be very helpful and highly accurate in the diagnosis of splenic injury. However, CT has proved particularly useful in this area because the severity of splenic injury is better assessed and other abdominal injuries can be identified in one examination.[78] In addition, traumatic splenic vascular injuries (e.g., active bleeding, pseudoaneurysms, arteriovenous fistulas) are difficult to detect with ultrasound.[79] However, splenic injury is not always clinically apparent and **spontaneous splenic rupture** or **pathologic splenic rupture** can occur after negligible trauma or insignificant events such as coughing.[26] This is typically seen in patients with a pathologically enlarged spleen caused by the altered consistency and splenic extension below the rib cage.

Advantages of ultrasound are that it is fast, portable, and easily integrated into the resuscitation of patients with trauma without delaying therapeutic measures.[80] In addition, if the patient is hemodynamically unstable, obtaining a CT scan may not be feasible.[81] Therefore ultrasound examinations performed in the emergency department after blunt abdominal trauma should not only focus on free intraabdominal fluid but also evaluate the solid organs. Further, now that nonsurgical management is preferred, ultrasound is helpful for numerous follow-up examinations. CEUS may also be used to increase the sensitivity of ultrasound for parenchymal injury.[82]

When the spleen is involved in blunt abdominal trauma, two outcomes are possible. If the capsule remains intact, the result may be an **intraparenchymal** or **subcapsular hematoma** (Fig. 5.30). If the capsule ruptures, a focal or free intraperitoneal hematoma may result. With capsular rupture, it might be possible to demonstrate fluid surrounding the spleen in the LUQ. Although blood often spreads within the peritoneal cavity and can be found in the pelvis or in the Morison pouch, on some occasions it becomes walled off in the LUQ (Fig. 5.31).

It is important to consider the timing of the sonographic examination relative to the trauma. Immediately after the traumatic incident, the hematoma is liquid and can easily be differentiated from splenic parenchyma. After the blood clots, and for the subsequent 24 to 48 hours, the echogenicity of the perisplenic hematoma may closely resemble the echogenicity of normal splenic parenchyma and may mimic splenomegaly. Subsequently, the blood re-liquefies and the diagnosis becomes easy again. In splenic injuries, there are often focal areas of inhomogeneity within the spleen, but these can be subtle (Fig. 5.32).

There is no clear consensus as to whether imaging follow-up is clinically useful.[83] If follow-up is performed, the clinician may see the subcapsular hematoma differentiated from the pericapsular, organized hematoma by the capsule itself (see Fig. 5.30B). The splenic capsule is very thin and frequently not visualized separately from adjacent fluid. In these cases the shape of the fluid collection can provide an important clue to the location of the hematoma. If the collection is crescentic and conforms to the contour of the spleen, the hematoma is likely subcapsular. Irregularly shaped collections are seen more with perisplenic hematomas.

Perisplenic fluid may persist for weeks or even months after splenic injury. Although there may actually be a condition of delayed rupture of the spleen, it is possible that all ruptures of the spleen occurred at the time of injury and were walled off initially.[84] Delayed rupture may be only the extension of blood into the peritoneal cavity after liquefaction of a perisplenic hematoma.

Aside from splenic capsule rupture, there may be internal damage to the spleen with an intact splenic capsule. This can result in intraparenchymal or subcapsular hematoma of the spleen, which initially appears only as an inhomogeneous area in the otherwise uniform splenic parenchyma. Subsequently, the hematoma may resolve, and repeat scans may show cystic change at the site of the original injury.

Sonographically, a perisplenic hematoma can closely mimic a perisplenic abscess. A hematoma can also become infected and transform into a left subphrenic abscess.[44] If the distinction cannot be made clinically, fine-needle aspiration can differentiate between a hematoma and an abscess.

CONGENITAL ANOMALIES

Accessory spleens, also known as **splenunculi,** are common normal variants found in up to 30% of autopsies. They are typically located near the splenic hilum and have similar echogenicity as the normal spleen. Splenunculi may be confused with enlarged lymph nodes around the spleen or with masses in the tail of the pancreas. When the spleen enlarges, the accessory spleens may also enlarge. **Ectopic accessory spleens** described in various locations, including the pancreas and scrotum, are typically confused with abnormal masses or, in rare cases, can undergo torsion and cause acute abdominal pain.[85,86] The vast majority

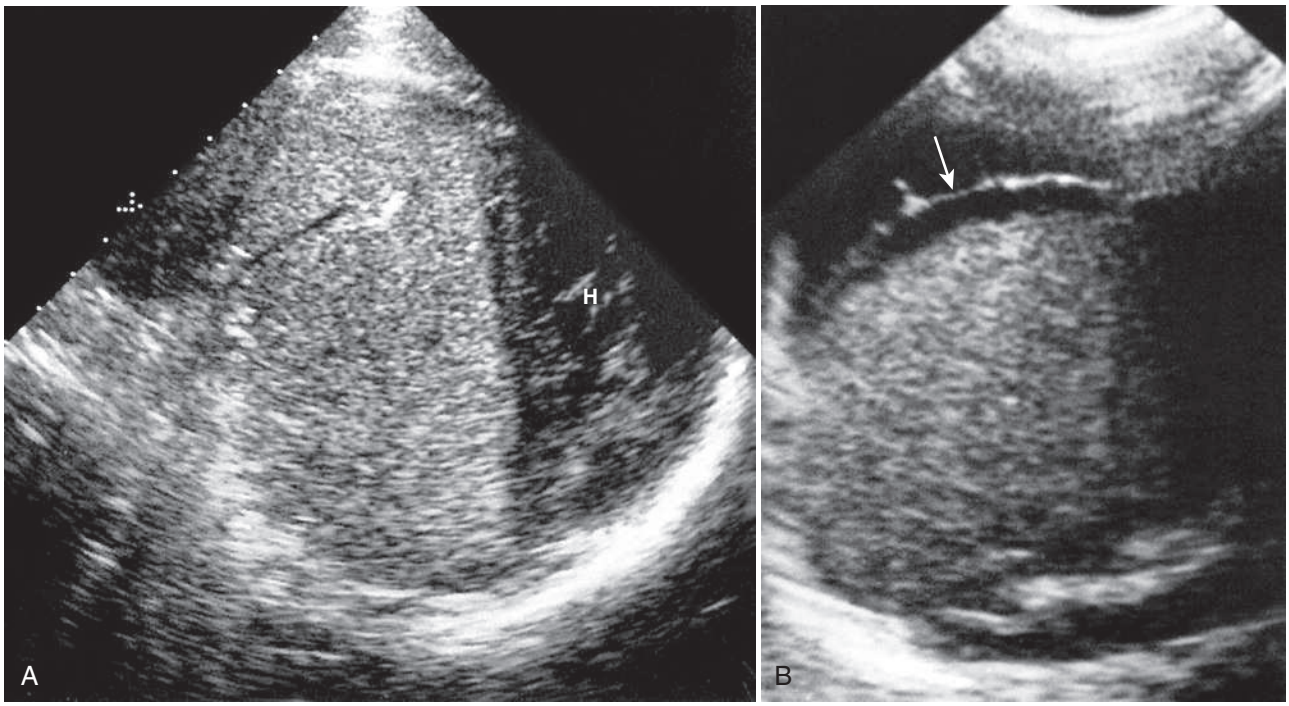

FIG. 5.30 Subcapsular Hematoma. (A) Transverse scan shows a fluid- and debris-filled crescentic hematoma *(H)* in the lateral aspect of the spleen. **(B)** Thin, brightly echogenic crescentic line *(arrow)* represents the splenic capsule.

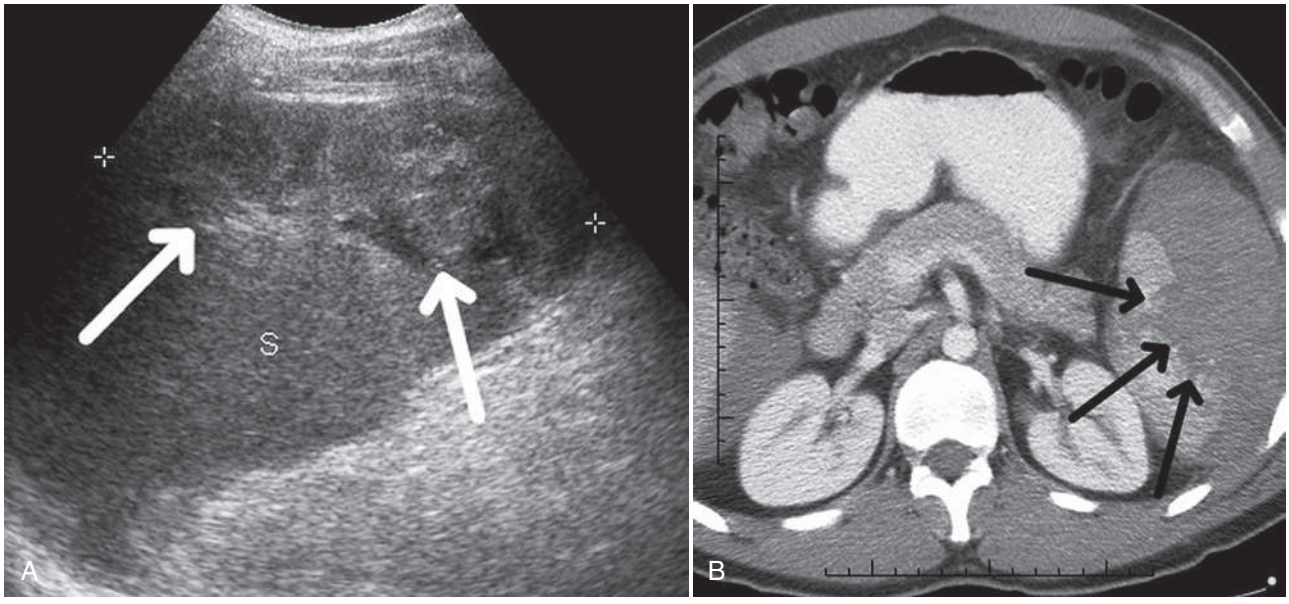

FIG. 5.31 Perisplenic Hematoma. (A) Coronal scan shows a hematoma *(arrows)* lateral to the spleen *(S)*. **(B)** Corresponding contrast-enhanced computed tomography image shows the splenic laceration *(arrows)* and large, perisplenic hematoma. Free fluid is also seen in the right upper abdomen.

of accessory spleens, however, are easy to recognize sonographically as small, rounded masses, usually less than 5 cm in diameter, with the same echogenicity as the spleen (Fig. 5.33). CT, MRI, or, in challenging cases, scintigraphy with technetium-labeled heat-damaged red blood cells, can confirm the diagnosis.[87]

A "**wandering spleen**" (or **mobile** spleen) can be found in unusual locations and may be mistaken for a mass (Fig. 5.34). It is caused by absence or extreme laxity of the supporting ligaments and a long, mobile mesentery (see Fig. 5.1B). The mobile spleen may undergo torsion, resulting in acute or chronic abdominal pain.[88,89] If the diagnosis of a wandering spleen is made in a patient with acute abdominal pain, the diagnosis of torsion is supported by color flow Doppler imaging showing absence of blood flow.[90]

The other two major congenital splenic anomalies are the asplenia and polysplenia syndromes. These conditions are best understood if viewed as part of the spectrum of **visceral heterotaxy.** A normal arrangement of asymmetrical body parts is

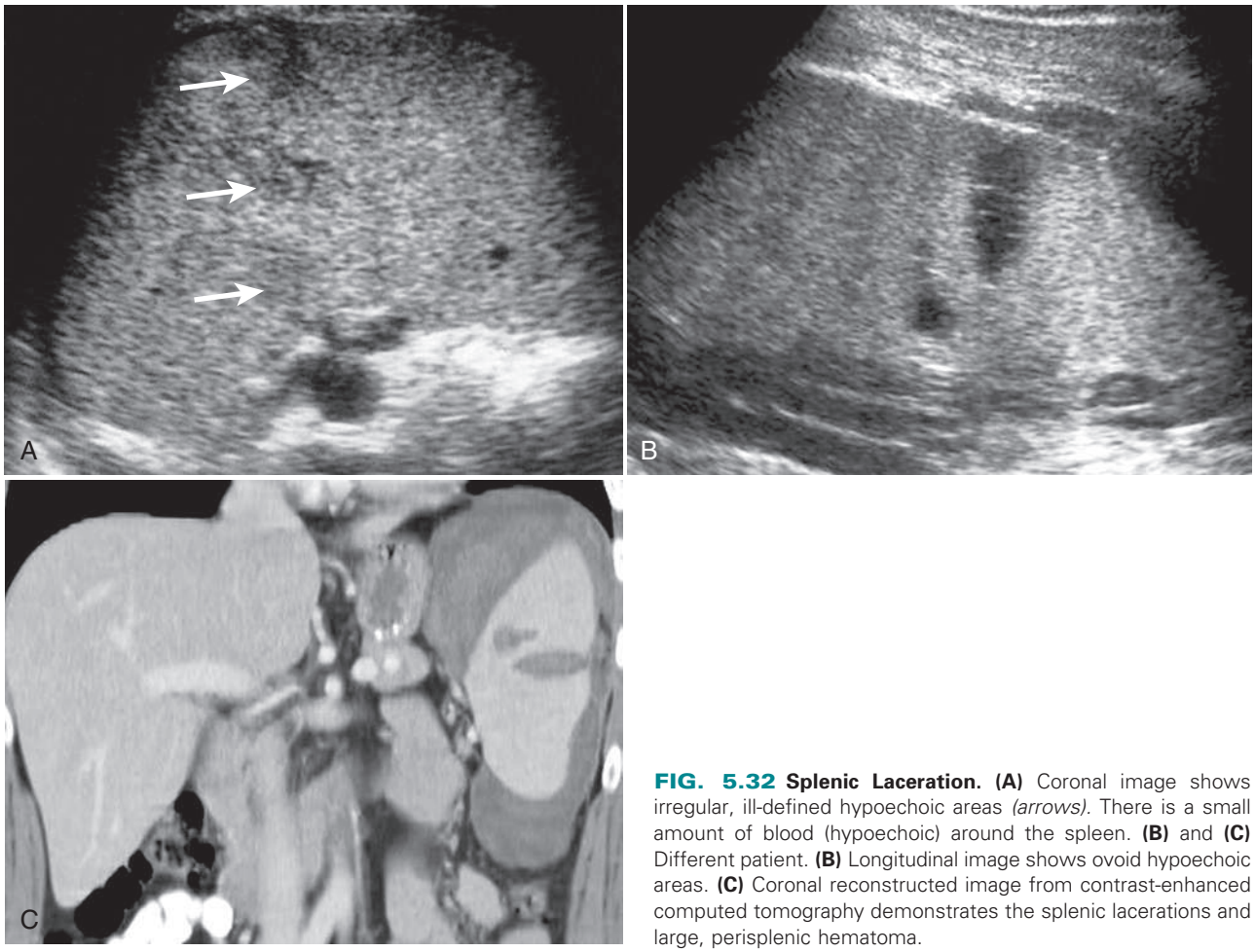

FIG. 5.32 Splenic Laceration. (A) Coronal image shows irregular, ill-defined hypoechoic areas *(arrows)*. There is a small amount of blood (hypoechoic) around the spleen. **(B)** and **(C)** Different patient. **(B)** Longitudinal image shows ovoid hypoechoic areas. **(C)** Coronal reconstructed image from contrast-enhanced computed tomography demonstrates the splenic lacerations and large, perisplenic hematoma.

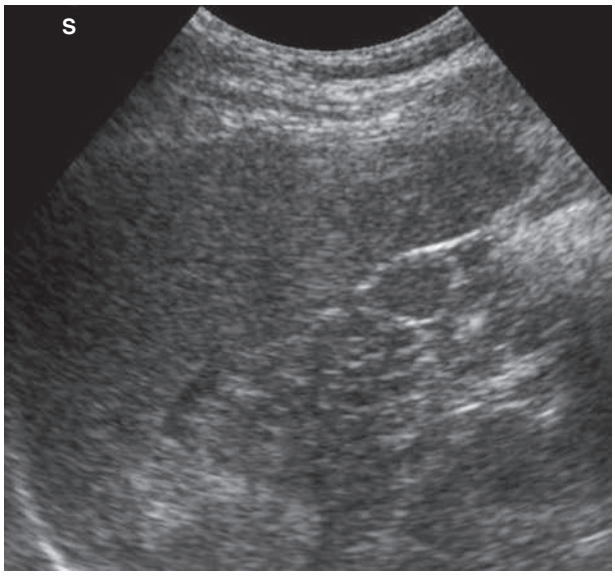

FIG. 5.33 Accessory Spleen. Coronal sonogram shows an accessory spleen adjacent to the inferior medial portion of the spleen.

known as situs solitus. The mirror image condition is called situs inversus. Between these two extremes is a wide spectrum of abnormalities called situs ambiguus. Splenic abnormalities in patients with visceral heterotaxy consist of polysplenia and asplenia. Interestingly, patients with **polysplenia** have **bilateral left-sidedness,** or a dominance of left-sided over right-sided body structures. They may have two morphologically left lungs, left-sided azygous continuation of an interrupted inferior vena cava, biliary atresia, absence of the gallbladder, gastrointestinal malrotation, and frequently cardiovascular abnormalities. Conversely, patients with **asplenia** may have **bilateral right-sidedness.** They may have two morphologically right lungs, midline location of the liver, reversed position of the abdominal aorta and inferior vena cava, anomalous pulmonary venous return, and **horseshoe kidneys.** The wide range of possible anomalies accounts for the variety of presenting symptoms, but absence of the spleen itself causes impairment of the immune response, and such patients can present with serious infections, such as sepsis and bacterial meningitis.[6]

Polysplenia must be differentiated from **posttraumatic splenosis.**[91] Splenosis is an acquired condition defined as autotransplantation of viable splenic tissue throughout different anatomic compartments of the body. It occurs after traumatic or iatrogenic rupture of the spleen.[92] Nuclear medicine imaging,

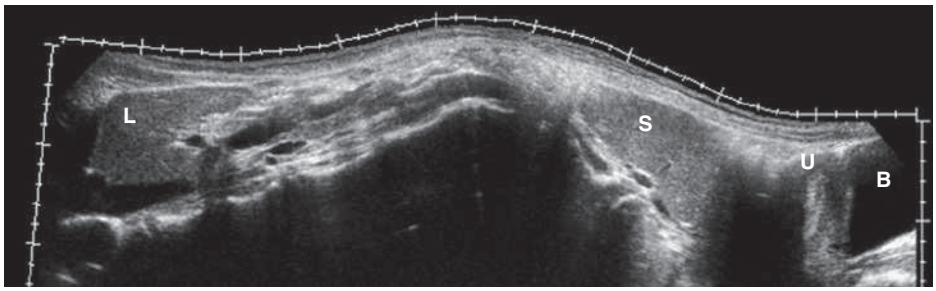

FIG. 5.34 Wandering Spleen. Sagittal extended–field of view image of midline abdomen in asymptomatic young woman. *B,* Bladder; *L,* liver, *S,* spleen; *U,* uterus.

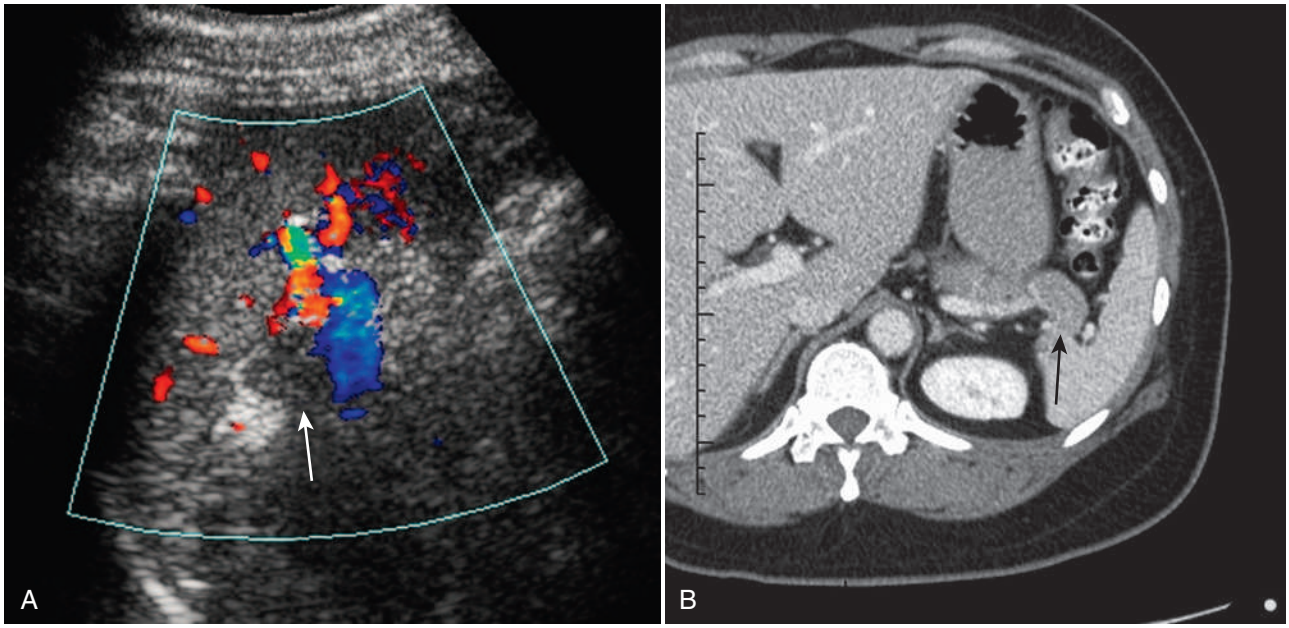

FIG. 5.35 Pancreatic Tail Simulating Mass. (A) Sonogram shows 2-cm lesion adjacent to the splenic hilum *(arrow).* **(B)** Computed tomography scan shows that "lesion" is the normal pancreatic tail *(arrow).*

with technetium-labeled heat-damaged red blood cells, is the most sensitive study for both posttraumatic splenosis and congenital polysplenia. Accessory spleens as small as 1 cm can be demonstrated by this method.[87]

INTERVENTIONAL PROCEDURES

Multiple reports and case series have described percutaneous splenic interventions.[93,94] Although typically described in smaller series, safety and success rates are similar to those performed elsewhere in the abdomen.[95]

Ultrasound-guided splenic biopsy can help establish a diagnosis with a low rate of complication rates and a high diagnostic yield.[24] Fine-needle and core-needle biopsies have been performed successfully to diagnose focal abnormalities, including abscesses, sarcoidosis, primary splenic malignancies, metastases, and lymphoma.[96,97]

In patients with abscesses, cysts, hematomas, and infected necrotic tumors, percutaneous catheter drainage is often successful.[46] Even radiofrequency ablation (RFA) procedures involving the spleen have been reported.[98]

Despite these reports, however, many interventional radiologists remain reluctant to perform splenic interventions. The main concern has been fear of **bleeding** caused by the highly vascular nature of the organ. However, clinicians should take into consideration that a successful image-guided percutaneous procedure could prevent the need for splenectomy.[95]

PITFALLS IN INTERPRETATION

Sonographers must be wary of several ultrasound pitfalls when scanning the LUQ and spleen. The first is the crescentic, echo-poor area superior to the spleen, which can be caused by the left lobe of the liver in thin individuals[99-102] (see Fig. 5.6). The left liver lobe can mimic the appearance of a subcapsular hematoma or a subphrenic abscess. Observing the liver sliding over the more echogenic spleen during quiet respiration can lead to the correct diagnosis. Hepatic and portal veins may help to identify this structure as the liver.

The tail of the pancreas may simulate a mass adjacent to the hilum of the spleen (Fig. 5.35). This is particularly true if the plane of section is aimed along the long axis of the pancreatic

tail. Identifying the splenic artery and vein may be helpful in confirming the normal tail of the pancreas.

Similarly, the fundus of the stomach may nestle in the hilum of the spleen. An oblique plane during scanning may pass through the spleen and include the hilum, with an echogenic portion of the stomach simulating an intrasplenic lesion. In some patients, this is just the fat around the stomach. Occasionally, fluid in the fundus of the stomach can simulate a perisplenic fluid collection. This can usually be resolved by scanning transversely or by letting the patient drink some water during the scan.

An occasional anatomic variant can occur if the inferior portion of the spleen is located posterolateral to the upper pole of the left kidney. This variant has been called the **retrorenal spleen.** Awareness of its existence can prevent the misdiagnosis of an abnormal mass. If visualized sonographically, it should be avoided in any interventional procedure performed on the left kidney.[103]

It can be very difficult to determine the site of origin of large, LUQ masses arising from the spleen, left adrenal gland, left kidney, tail of the pancreas, stomach, or retroperitoneum. Differential motion observed during shallow respiration may be helpful. Additionally, the identification of the splenic vein entering the splenic hilum can be definitive. CT or MRI should be used to clarify challenging cases.

REFERENCES

1. Kamaya A, Weinstein S, Desser TS. Multiple lesions of the spleen: differential diagnosis of cystic and solid lesions. Semin Ultrasound CT MR. 2006;27(5):389-403.
2. Zhao Z, Liu S, Li Z, et al. Sectional anatomy of the peritoneal reflections of the upper abdomen in the coronal plane. J Comput Assist Tomogr. 2005;29(4):430-437.
3. DeLand FH. Normal spleen size. Radiology. 1970;97(3):589-592.
4. Gauer JM, Gerber-Paulet S, Seiler C, Schweizer WP. Twenty years of splenic preservation in trauma: lower early infection rate than in splenectomy. World J Surg. 2008;32(12):2730-2735.
5. Cadili A, de Gara C. Complications of splenectomy. Am J Med. 2008;121(5):371-375.
6. Spelman D, Buttery J, Daley A, et al. Guidelines for the prevention of sepsis in asplenic and hyposplenic patients. Intern Med J. 2008;38(5):349-356.
7. Gorg C, Gorg K, Bert T, Barth P. Colour Doppler ultrasound patterns and clinical follow-up of incidentally found hypoechoic, vascular tumours of the spleen: evidence for a benign tumour. Br J Radiol. 2006;79(940):319-325.
8. Catalano O, Sandomenico F, Vallone P, et al. Contrast-enhanced sonography of the spleen. Semin Ultrasound CT MR. 2006;27(5):426-433.
9. Gorg C. The forgotten organ: contrast enhanced sonography of the spleen. Eur J Radiol. 2007;64(2):189-201.
10. Yetter EM, Acosta KB, Olson MC, Blundell K. Estimating splenic volume: sonographic measurements correlated with helical CT determination. AJR Am J Roentgenol. 2003;181(6):1615-1620.
11. Rosenberg HK, Markowitz RI, Kolberg H, et al. Normal splenic size in infants and children: sonographic measurements. AJR Am J Roentgenol. 1991;157(1):119-121.
12. Lamb PM, Lund A, Kanagasabay RR, et al. Spleen size: how well do linear ultrasound measurements correlate with three-dimensional CT volume assessments? Br J Radiol. 2002;75(895):573-577.
13. Frank K, Linhart P, Kortsik C, Wohlenberg H. Sonographic determination of spleen size: normal dimensions in adults with a healthy spleen]. Ultraschall Med. 1986;7(3):134-137.
14. Hosey RG, Mattacola CG, Kriss V, et al. Ultrasound assessment of spleen size in collegiate athletes. Br J Sports Med. 2006;40(3):251-254.
15. Spielmann AL, DeLong DM, Kliewer MA. Sonographic evaluation of spleen size in tall healthy athletes. AJR Am J Roentgenol. 2005;184(1):45-49.
16. Chow KU, Luxembourg B, Seifried E, Bonig H. Spleen size is significantly influenced by body height and sex: establishment of normal values for spleen size at US with a cohort of 1200 healthy individuals. Radiology. 2016;279(1):306-313.
17. Abramson JS, Chatterji M, Rahemtullah A. Case records of the Massachusetts General Hospital. Case 39-2008. A 51-year-old woman with splenomegaly and anemia. N Engl J Med. 2008;359(25):2707-2718.
18. Pozo AL, Godfrey EM, Bowles KM. Splenomegaly: investigation, diagnosis and management. Blood Rev. 2009;23(3):105-111.
19. Swaroop J, O'Reilly RA. Splenomegaly at a university hospital compared to a nearby county hospital in 317 patients. Acta Haematol. 1999;102(2):83-88.
20. Jeong JW, Lee S, Lee JW, et al. The echotextural characteristics for the diagnosis of the liver cirrhosis using the sonographic images. Conf Proc IEEE Eng Med Biol Soc. 2007;2007:1343-1345.
21. Pfeifer L, Zopf S, Siebler J, et al. Prospective evaluation of acoustic radiation force impulse (ARFI) elastography and high-frequency B-mode ultrasound in compensated patients for the diagnosis of liver fibrosis/cirrhosis in comparison to mini-laparoscopic biopsy. Ultraschall Med. 2015;36(6):581-589.
22. Grgurevic I, Puljiz Z, Brnic D, et al. Liver and spleen stiffness and their ratio assessed by real-time two dimensional-shear wave elastography in patients with liver fibrosis and cirrhosis due to chronic viral hepatitis. Eur Radiol. 2015;25(11):3214-3221.
23. Shibata S, Umemura T, Yamazaki T, et al. Liver stiffness-spleen size-to-platelet ratio risk score identifies esophageal varices in Japanese patients with chronic hepatitis C. Hepatol Res. 2016;46(9):884-889.
24. Tam A, Krishnamurthy S, Pillsbury EP, et al. Percutaneous image-guided splenic biopsy in the oncology patient: an audit of 156 consecutive cases. J Vasc Interv Radiol. 2008;19(1):80-87.
25. Sammon J, Twomey M, Crush L, et al. Image-guided percutaneous splenic biopsy and drainage. Semin Intervent Radiol. 2012;29(4):301-310.
26. Wehbe E, Raffi S, Osborne D. Spontaneous splenic rupture precipitated by cough: a case report and a review of the literature. Scand J Gastroenterol. 2008;43(5):634-637.
27. Gorg C, Colle J, Gorg K, et al. Spontaneous rupture of the spleen: ultrasound patterns, diagnosis and follow-up. Br J Radiol. 2003;76(910):704-711.
28. Paterson A, Frush DP, Donnelly LF, et al. A pattern-oriented approach to splenic imaging in infants and children. Radiographics. 1999;19(6):1465-1485.
29. Warshauer DM, Hall HL. Solitary splenic lesions. Semin Ultrasound CT MR. 2006;27(5):370-388.
30. Lashbrook DJ, James RW, Phillips AJ, et al. Splenic peliosis with spontaneous splenic rupture: report of two cases. BMC Surg. 2006;6:9.
31. Ishida H, Konno K, Ishida J, et al. Splenic lymphoma: differentiation from splenic cyst with ultrasonography. Abdom Imaging. 2001;26(5):529-532.
32. Urrutia M, Mergo PJ, Ros LH, et al. Cystic masses of the spleen: radiologic-pathologic correlation. Radiographics. 1996;16(1):107-129.
33. Williams RJ, Glazer G. Splenic cysts: changes in diagnosis, treatment and aetiological concepts. Ann R Coll Surg Engl. 1993;75(2):87-89.
34. Morgenstern L. Nonparasitic splenic cysts: pathogenesis, classification, and treatment. J Am Coll Surg. 2002;194(3):306-314.
35. Dachman AH, Ros PR, Murari PJ, et al. Nonparasitic splenic cysts: a report of 52 cases with radiologic-pathologic correlation. AJR Am J Roentgenol. 1986;147(3):537-542.
36. Durgun V, Kapan S, Kapan M, et al. Primary splenic hydatidosis. Dig Surg. 2003;20(1):38-41.
37. Akhan O, Koroglu M. Hydatid disease of the spleen. Semin Ultrasound CT MR. 2007;28(1):28-34.
38. Celebi S, Basaranoglu M, Karaaslan H, Demir A. A splenic hydatid cyst case presented with lumbar pain. Intern Med. 2006;45(17):1023-1024.
39. Heider R, Behrns KE. Pancreatic pseudocysts complicated by splenic parenchymal involvement: results of operative and percutaneous management. Pancreas. 2001;23(1):20-25.

40. Abbott RM, Levy AD, Aguilera NS, et al. From the archives of the AFIP: primary vascular neoplasms of the spleen: radiologic-pathologic correlation. Radiographics. 2004;24(4):1137-1163.
41. Willcox TM, Speer RW, Schlinkert RT, Sarr MG. Hemangioma of the spleen: presentation, diagnosis, and management. J Gastrointest Surg. 2000;4(6): 611-613.
42. Wunderbaldinger P, Paya K, Partik B, et al. CT and MR imaging of generalized cystic lymphangiomatosis in pediatric patients. AJR Am J Roentgenol. 2000;174(3):827-832.
43. Bezzi M, Spinelli A, Pierleoni M, Andreoli G. Cystic lymphangioma of the spleen: US-CT-MRI correlation. Eur Radiol. 2001;11(7):1187-1190.
44. Fotiadis C, Lavranos G, Patapis P, Karatzas G. Abscesses of the spleen: report of three cases. World J Gastroenterol. 2008;14(19):3088-3091.
45. Changchien CS, Tsai TL, Hu TH, et al. Sonographic patterns of splenic abscess: an analysis of 34 proven cases. Abdom Imaging.2002;27(6):739-745.
46. Ferraioli G, Brunetti E, Gulizia R, et al. Management of splenic abscess: report on 16 cases from a single center. Int J Infect Dis. 2009;13(4): 524-530.
47. Koh DM, Burn PR, Mathews G, et al. Abdominal computed tomographic findings of Mycobacterium tuberculosis and Mycobacterium avium intracellulare infection in HIV seropositive patients. Can Assoc Radiol J. 2003;54(1):45-50.
48. Thanos L, Zormpala A, Brountzos E, et al. Nodular hepatic and splenic sarcoidosis in a patient with normal chest radiograph. Eur J Radiol. 2002;41(1):10-11.
49. O'Neal CB, Ball SC. Splenic pneumocystosis: an atypical presentation of extrapulmonary Pneumocystis infection. AIDS Read. 2008;18(10): 503-508.
50. Pastakia B, Shawker TH, Thaler M, et al. Hepatosplenic candidiasis: wheels within wheels. Radiology. 1988;166(2):417-421.
51. Rudolph J, Rodenwaldt J, Ruhnke M, et al. Unusual enhancement pattern of liver lesions in hepatosplenic candidiasis. Acta Radiol. 2004;45(5): 499-503.
52. Matone J, Lopes Filho GD, Scalabrin M, et al. Primary splenic lymphoma in patient with hepatitis C virus infection: case report and review of the literature. Int Surg. 2000;85(3):248-251.
53. Gorg C, Weide R, Schwerk WB. Malignant splenic lymphoma: sonographic patterns, diagnosis and follow-up. Clin Radiol. 1997;52(7):535-540.
54. Takabe K, Al-Refaie W, Chin B, et al. Can large B-cell lymphoma mimic cystic lesions of the spleen? Int J Gastrointest Cancer. 2005;35(1):83-88.
55. Neuhauser TS, Derringer GA, Thompson LD, et al. Splenic angiosarcoma: a clinicopathologic and immunophenotypic study of 28 cases. Mod Pathol. 2000;13(9):978-987.
56. Thompson WM, Levy AD, Aguilera NS, et al. Angiosarcoma of the spleen: imaging characteristics in 12 patients. Radiology. 2005;235(1): 106-115.
57. Berge T. Splenic metastases. Frequencies and patterns. Acta Pathol Microbiol Scand [A]. 1974;82(4):499-506.
58. Lam KY, Tang V. Metastatic tumors to the spleen: a 25-year clinicopathologic study. Arch Pathol Lab Med. 2000;124(4):526-530.
59. Ros PR, Moser Jr RP, Dachman AH, et al. Hemangioma of the spleen: radiologic-pathologic correlation in ten cases. Radiology. 1987;162(1 Pt 1):73-77.
60. Jindal R, Sullivan R, Rodda B, et al. Splenic malformation in a patient with Klippel-Trenaunay syndrome: a case report. J Vasc Surg. 2006;43(4): 848-850.
61. Dufau JP, le Tourneau A, Audouin J, et al. Isolated diffuse hemangiomatosis of the spleen with Kasabach-Merritt-like syndrome. Histopathology. 1999;35(4):337-344.
62. Tang S, Shimizu T, Kikuchi Y, et al. Color Doppler sonographic findings in splenic hamartoma. J Clin Ultrasound. 2000;28(5):249-253.
63. Yu RS, Zhang SZ, Hua JM. Imaging findings of splenic hamartoma. World J Gastroenterol. 2004;10(17):2613-2615.
64. Tee M, Vos P, Zetler P, Wiseman SM. Incidental littoral cell angioma of the spleen. World J Surg Oncol. 2008;6:87.
65. Kim HJ, Kim KW, Yu ES, et al. Sclerosing angiomatoid nodular transformation of the spleen: clinical and radiologic characteristics. Acta Radiol. 2012; 53(7):701-706.
66. Yan J, Peng C, Yang W, et al. Inflammatory pseudotumour of the spleen: report of 2 cases and literature review. Can J Surg. 2008;51(1): 75-76.
67. Romano S, Scaglione M, Gatta G, et al. Association of splenic and renal infarctions in acute abdominal emergencies. Eur J Radiol. 2004; 50(1):48-58.
68. Miller LA, Mirvis SE, Shanmuganathan K, Ohson AS. CT diagnosis of splenic infarction in blunt trauma: imaging features, clinical significance and complications. Clin Radiol. 2004;59(4):342-348.
69. Gorg C, Zugmaier G. Chronic recurring infarction of the spleen: sonographic patterns and complications. Ultraschall Med. 2003;24(4):245-249.
70. Balcar I, Seltzer SE, Davis S, Geller S. CT patterns of splenic infarction: a clinical and experimental study. Radiology. 1984;151(3):723-729.
71. Goerg C, Schwerk WB. Splenic infarction: sonographic patterns, diagnosis, follow-up, and complications. Radiology. 1990;174(3 Pt 1): 803-807.
72. Lonergan GJ, Cline DB, Abbondanzo SL. Sickle cell anemia. Radiographics. 2001;21(4):971-994.
73. Madani G, Papadopoulou AM, Holloway B, et al. The radiological manifestations of sickle cell disease. Clin Radiol. 2007;62(6):528-538.
74. Chippington S, McHugh K, Vellodi A. Splenic nodules in paediatric Gaucher disease treated by enzyme replacement therapy. Pediatr Radiol. 2008;38(6):657-660.
75. Patlas M, Hadas-Halpern I, Abrahamov A, et al. Spectrum of abdominal sonographic findings in 103 pediatric patients with Gaucher disease. Eur Radiol. 2002;12(2):397-400.
76. Chan YL, Yang WT, Sung JJ, et al. Diagnostic accuracy of abdominal ultrasonography compared to magnetic resonance imaging in siderosis of the spleen. J Ultrasound Med. 2000;19(8):543-547.
77. Moore EE, Shackford SR, Pachter HL, et al. Organ injury scaling: spleen, liver and kidney. J Trauma. 1989;29:1664-1666.
78. Weninger P, Mauritz W, Fridrich P, et al. Emergency room management of patients with blunt major trauma: evaluation of the multislice computed tomography protocol exemplified by an urban trauma center. J Trauma. 2007;62(3):584-591.
79. Hamilton JD, Kumaravel M, Censullo ML, et al. Multidetector CT evaluation of active extravasation in blunt abdominal and pelvic trauma patients. Radiographics. 2008;28(6):1603-1616.
80. Brown MA, Casola G, Sirlin CB, et al. Blunt abdominal trauma: screening us in 2,693 patients. Radiology. 2001;218(2):352-358.
81. Farahmand N, Sirlin CB, Brown MA, et al. Hypotensive patients with blunt abdominal trauma: performance of screening US. Radiology. 2005; 235(2):436-443.
82. Miele V, Piccolo CL, Galluzzo M, et al. Contrast-enhanced ultrasound (CEUS) in blunt abdominal trauma. Br J Radiol. 2016;20150823.
83. McCray VW, Davis JW, Lemaster D, Parks SN. Observation for nonoperative management of the spleen: how long is long enough? J Trauma. 2008; 65(6):1354-1358.
84. Gamblin TC, Wall Jr CE, Royer GM, et al. Delayed splenic rupture: case reports and review of the literature. J Trauma. 2005;59(5):1231-1234.
85. Meyer-Rochow GY, Gifford AJ, Samra JS, Sywak MS. Intrapancreatic splenunculus. Am J Surg. 2007;194(1):75-76.
86. Netto JM, Pérez LM, Kelly DR, et al. Splenogonadal fusion diagnosed by Doppler ultrasonography. Scientific World Journal. 2004;4(Suppl. 1): 253-257.
87. MacDonald A, Burrell S. Infrequently performed studies in nuclear medicine: Part 1. J Nucl Med Technol. 2008;36(3):132-143.
88. Soleimani M, Mehrabi A, Kashfi A, et al. Surgical treatment of patients with wandering spleen: report of six cases with a review of the literature. Surg Today. 2007;37(3):261-269.
89. Misawa T, Yoshida K, Shiba H, et al. Wandering spleen with chronic torsion. Am J Surg. 2008;195(4):504-505.
90. Danaci M, Belet U, Yalin T, et al. Power Doppler sonographic diagnosis of torsion in a wandering spleen. J Clin Ultrasound. 2000;28(5):246-248.
91. Gayer G, Hertz M, Strauss S, Zissin R. Congenital anomalies of the spleen. Semin Ultrasound CT MR. 2006;27(5):358-369.
92. Fremont RD, Rice TW. Splenosis: a review. South Med J. 2007;100(6): 589-593.

93. Lucey BC, Boland GW, Maher MM, et al. Percutaneous nonvascular splenic intervention: a 10-year review. AJR Am J Roentgenol. 2002;179(6): 1591-1596.
94. Kang M, Kalra N, Gulati M, et al. Image guided percutaneous splenic interventions. Eur J Radiol. 2007;64(1):140-146.
95. Lieberman S, Libson E, Sella T, et al. Percutaneous image-guided splenic procedures: update on indications, technique, complications, and outcomes. Semin Ultrasound CT MR. 2007;28(1):57-63.
96. López JI, Del Cura JL, De Larrinoa AF, et al. Role of ultrasound-guided core biopsy in the evaluation of spleen pathology. APMIS. 2006; 114(7-8):492-499.
97. Liang P, Gao Y, Wang Y, et al. US-guided percutaneous needle biopsy of the spleen using 18-gauge versus 21-gauge needles. J Clin Ultrasound. 2007;35(9):477-482.
98. Liu Q, Ma K, Song Y, et al. Two-year follow-up of splenic radiofrequency ablation in patients with cirrhotic hypersplenism: does increased hepatic arterial flow induce liver regeneration? Surgery. 2008;143(4):509-518.
99. Rao MG. Enlarged left lobe of the liver mistaken for a mass in the splenic region. Clin Nucl Med. 1989;14(2):134.
100. Li DK, Cooperberg PL, Graham MF, Callen P. Pseudo perisplenic "fluid collections": a clue to normal liver and spleen echogenic texture. J Ultrasound Med. 1986;5(7):397-400.
101. Crivello MS, Peterson IM, Austin RM. Left lobe of the liver mimicking perisplenic collections. J Clin Ultrasound. 1986;14(9):697-701.
102. Arenson AM, McKee JD. Left upper quadrant pseudolesion secondary to normal variants in liver and spleen. J Clin Ultrasound. 1986;14(7): 558-561.
103. Dodds WJ, Darweesh RM, Lawson TL, et al. The retroperitoneal spaces revisited. AJR Am J Roentgenol. 1986;147(6):1155-1161.

CHAPTER 6

The Biliary Tree and Gallbladder

Korosh Khalili and Stephanie R. Wilson

SUMMARY OF KEY POINTS

- Ultrasound should be the first imaging modality used in the evaluation of the patients with potential disease of the biliary tree.
- Awareness of various scanning techniques and use of harmonic and compound imaging improve visualization of various diseases affecting the biliary tree.
- Stones in the intrahepatic and extrahepatic biliary tree can be easily overlooked; familiarity with their appearance and a high index of suspicious improve their detection.
- Cholecystitis is a common disease with variable degrees of severity. A high index of suspicion and sensitivity, particularly to distention and hyperemia of the gallbladder, allows for improved detection.
- The clinical presentation of the patient, particularly pain and signs of inflammation, helps in differentiating the common inflammatory conditions of the biliary tree and gallbladder from the rarer malignancies which they may mimic.

CHAPTER OUTLINE

THE BILIARY TREE
Anatomy and Normal Variants
Sonographic Technique
Choledochal Cysts
Caroli Disease
Overview of Biliary Tree Obstruction
Choledocholithiasis
Intrahepatic Stones
Common Bile Duct Stones
Mirizzi Syndrome
Hemobilia
Pneumobilia
Biliary Tree Infection
Acute (Bacterial, Ascending) Cholangitis
Liver Flukes
Recurrent Pyogenic Cholangitis
Ascariasis
HIV Cholangiopathy
Immune-Related Diseases of the Biliary Tree
Primary Biliary Cirrhosis and Autoimmune Cholangitis
Primary Sclerosing Cholangitis
IgG4-Related Cholangitis
Cholangiocarcinoma
Intrahepatic Cholangiocarcinoma
Hilar Cholangiocarcinoma
Distal Cholangiocarcinoma
Metastases to Biliary Tree
THE GALLBLADDER
Anatomy and Normal Variants
Sonographic Technique
Gallstone Disease
Biliary Sludge
Acute Cholecystitis
Gangrenous Cholecystitis
Perforated Gallbladder
Emphysematous Cholecystitis
Acalculous Cholecystitis
Torsion (Volvulus) of Gallbladder
Chronic Cholecystitis
Porcelain Gallbladder
Adenomyomatosis (Adenomatous Hyperplasia)
Polypoid Masses of Gallbladder
Cholesterol Polyps
Adenomas, Adenomyomas, and Inflammatory Polyps
Malignancies
Gallbladder Carcinoma
Patterns of Tumor Spread
Sonographic Appearance

Sonographic evaluation of the biliary tract is one of the most appropriate and efficacious uses of the ultrasound examination. The cystic nature of both the gallbladder and the bile ducts, particularly when dilated, provides an inherently high-contrast resolution in comparison to the adjacent tissues. The excellent spatial resolution of sonography, and the acoustic window provided by the liver allow for a high-quality examination in most patients. Currently, sonography remains the imaging modality of choice for the detection of gallstones, assessment of acute right upper quadrant (RUQ) pain, and initial evaluation of the patient with jaundice or elevated liver function tests. In conjunction with magnetic resonance imaging (MRI), magnetic resonance cholangiopanreatography (MRCP), and contrast-enhanced computed tomography (CT), sonography also plays a key role in the multimodality evaluation of more complex biliary problems, such as the diagnosis and staging of hilar cholangiocarcinoma. The recent development of contrast-enhanced sonography for detection of hepatic masses further broadens this role. From the smallest ultrasound departments operating in remote geographic areas to the largest tertiary institutions, no other anatomic location in the body is better studied with sonography than the biliary tract.

THE BILIARY TREE

Anatomy and Normal Variants

An understanding of the normal location of the bile ducts and common anatomic variations is important in staging malignancies and directing intervention. In biliary terminology, *proximal* denotes the portion of the biliary tree that is in relative proximity to the liver and hepatocytes, whereas *distal* refers to the caudal end closer to the bowel. The term *branching order* applies to the level of division of the bile ducts starting from the **common hepatic duct** (CHD); first-order branches are the right and left hepatic ducts, second-order branches are their respective divisions (also known as secondary biliary *radicles*), and so on. *Central* specifies proximity to the porta hepatis, whereas *peripheral* refers to the higher-order branches of the intrahepatic biliary tree extending well into the hepatic parenchyma. Knowledge of **Couinaud functional anatomy** of the liver is also vital in description of the intrahepatic biliary abnormalities (see Chapter 4).

The *intrahepatic ducts* are not in a fixed relation to the portal veins within the portal triads and can be anterior or posterior to the vein or even tortuous about the vein.[1] The right and left hepatic ducts, that is, the first-order branches of the CHD, are routinely seen on sonography, and normal second-order branches may be visualized[2] (Fig. 6.1). Spectral and color Doppler ultrasound are often needed to distinguish hepatic arteries from ducts, though ducts tend to be straight whereas arteries are tortuous. In our experience, visualization of third-order or higher-order branches is often an abnormal finding and requires a search for the cause of dilation. Most of the right and left hepatic ducts are

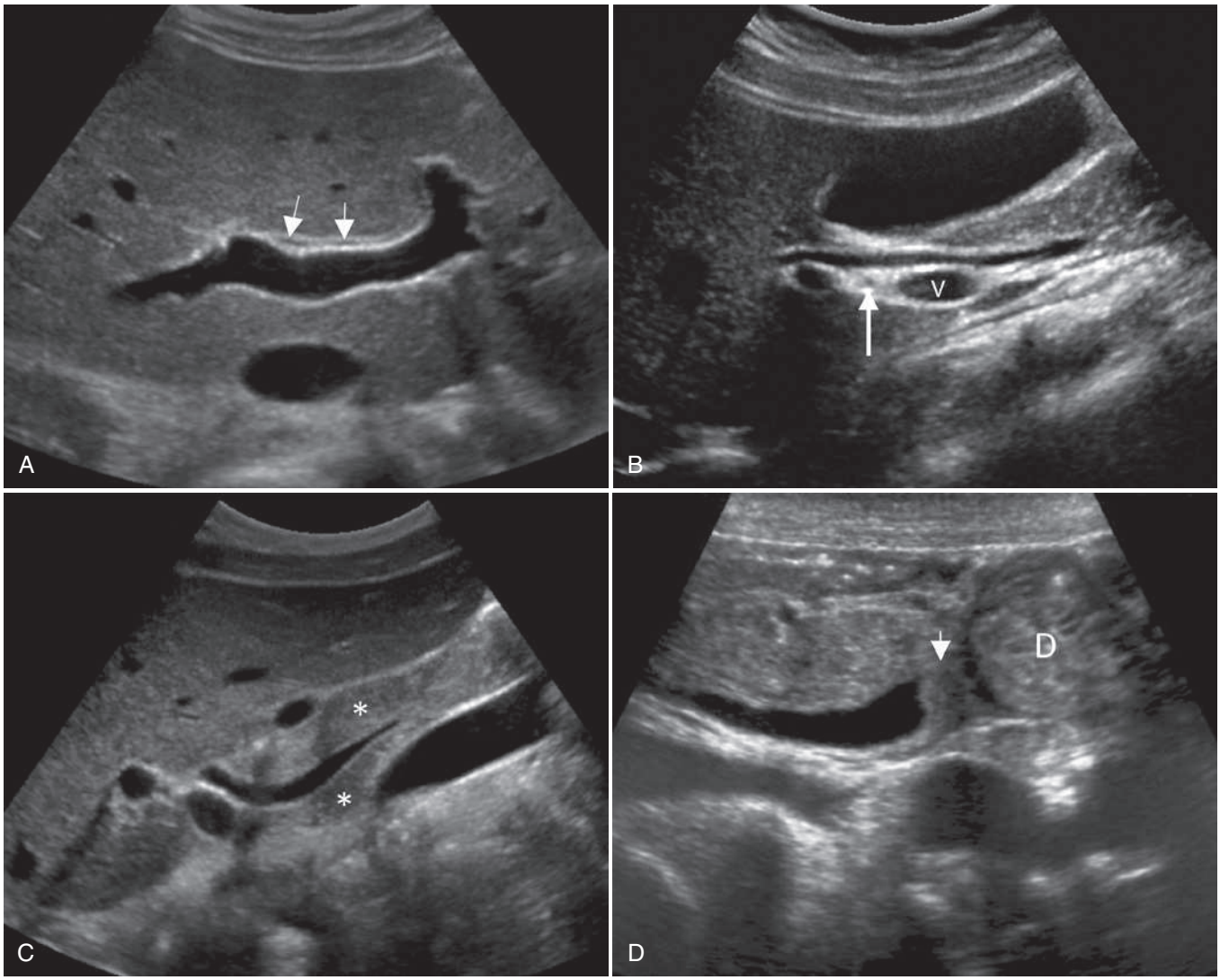

FIG. 6.1 Normal Bile Ducts. (A) Right and left hepatic ducts *(short arrows)* are normally seen lying anterior to the portal veins. **(B)** Common hepatic/common bile ducts of normal caliber in sagittal view lying in the typical position anterior to the portal vein *(V)* and hepatic artery *(arrow)*. **(C)** Mid and distal common bile duct in longitudinal view. Note the pancreas (*), the cranial margin of which demarcates the transition between the suprapancreatic and intrapancreatic segments. **(D)** Distal common bile duct and the ampulla of Vater *(short arrow)* are shown running posterior to the pancreatic head and inserting into the duodenum *(D)*. See also Video 6.1.

extrahepatic and, along with the CHD, form the hilar or central portion of the biliary tree at the porta hepatis. This is the most common location for cholangiocarcinoma. The normal diameter of the first-order and higher-order branches of the CHD has been suggested to be 2 mm or less, and no more than 40% of the diameter of the adjacent portal vein.[2]

The most common **biliary branching pattern** occurs in 56% to 58% of the population[3,4] (Figs. 6.2 and 6.3). On the right side, the right hepatic duct forms from the right anterior and right posterior branches, draining the anterior (segments 5 and 8) and posterior (segments 6 and 7) segments of the right lobe, respectively. On the left side, segment 2 and 3 branches join to the left of the falciform ligament to form the left hepatic duct. This duct becomes extrahepatic in location as it extends to the right of the falciform ligament, where it is joined by ducts of segments 4 and 1.

The key to understanding the common normal variants of biliary branching lies in the variability of the site of insertion of the **right posterior duct** (RPD) (segments 6 and 7). The RPD often extends centrally toward the porta hepatis in a cranial direction. It passes superior and posterior to the **right anterior duct** (RAD) and then turns caudally, joining the RAD to form the short right hepatic duct (see Fig. 6.2). Three other common sites of insertion of the RPD account for the majority of the **biliary anatomic variations.** If the RPD extends more to the left than usual, it can join the junction of the right and left hepatic ducts ("trifurcation pattern"; ≈8% of normal variants) or the left hepatic duct (≈13%) (Fig. 6.4). If the RPD extends in a caudal-medial direction instead, it can join the CHD or common bile duct (CBD) directly (≈5%). Anomalous drainage of various segmental hepatic ducts directly into the CHDs is less common.

The **normal caliber** of the CHD/CBD in patients without history of biliary disease is up to 6 mm in most studies[5] (see Fig. 6.1). Controversy surrounds whether there is a normal widening of the duct with increasing age.[6] Similarly, studies on an association between cholecystectomy and a large-caliber CBD are inconclusive. Although diameters of up to 10 mm have been recorded in an asymptomatic normal population, the great majority of the diameters are under 7 mm. Therefore a ductal diameter of 7 mm or greater should prompt further investigations, such as correlation with serum levels of cholestatic liver enzymes.

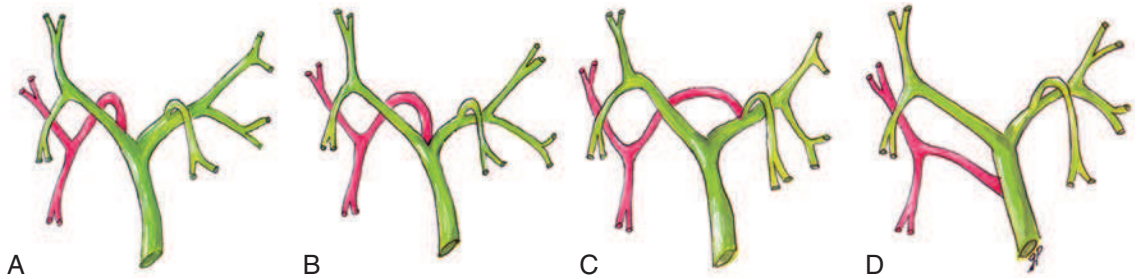

FIG. 6.2 Common Variants of Bile Duct Branching. Right posterior duct (RPD) is in red. **(A)** RPD joins the right anterior duct in 56% to 58% of the population. **(B)** Trifurcation pattern, 8%. **(C)** RPD joins the left hepatic duct, 13%. **(D)** RPD joins the common hepatic or common bile duct directly, 5%.

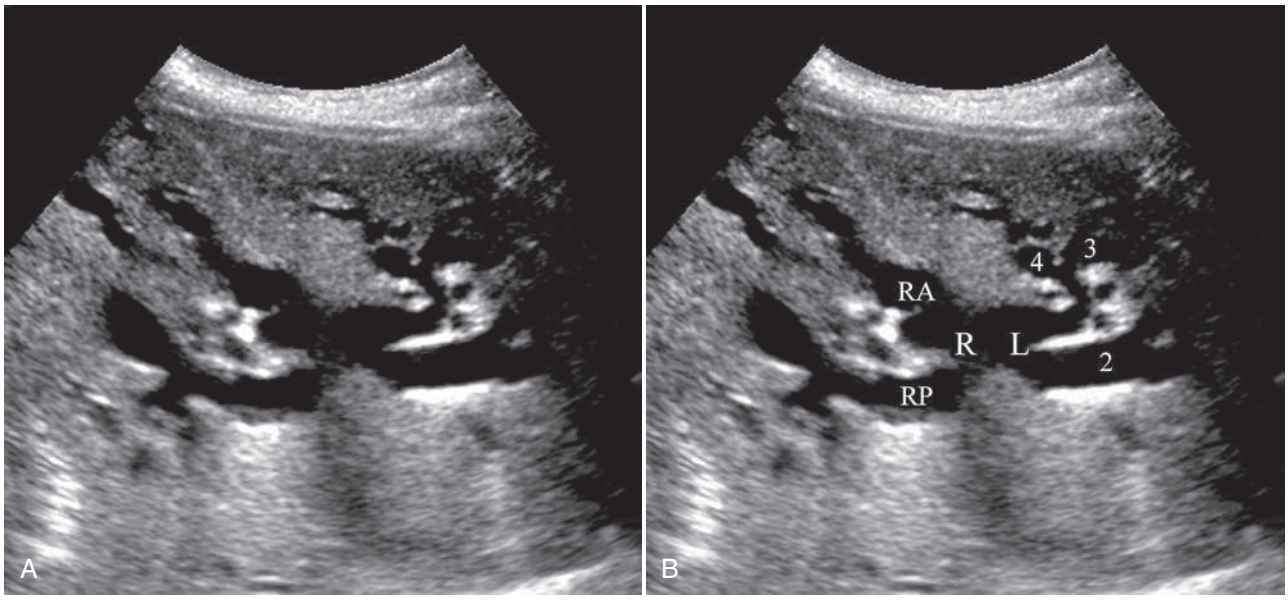

FIG. 6.3 Typical Ductal Branching Order. Intrahepatic biliary tree is dilated because of an obstructed common bile duct (not shown). **(A)** and **(B)** Subcostal oblique views foreshorten the right *(R)* and left *(L)* hepatic ducts. *RA,* Right anterior duct; *RP,* right posterior duct; *2,* segment 2 duct; *3,* segment 3 duct; *4,* segment 4 duct.

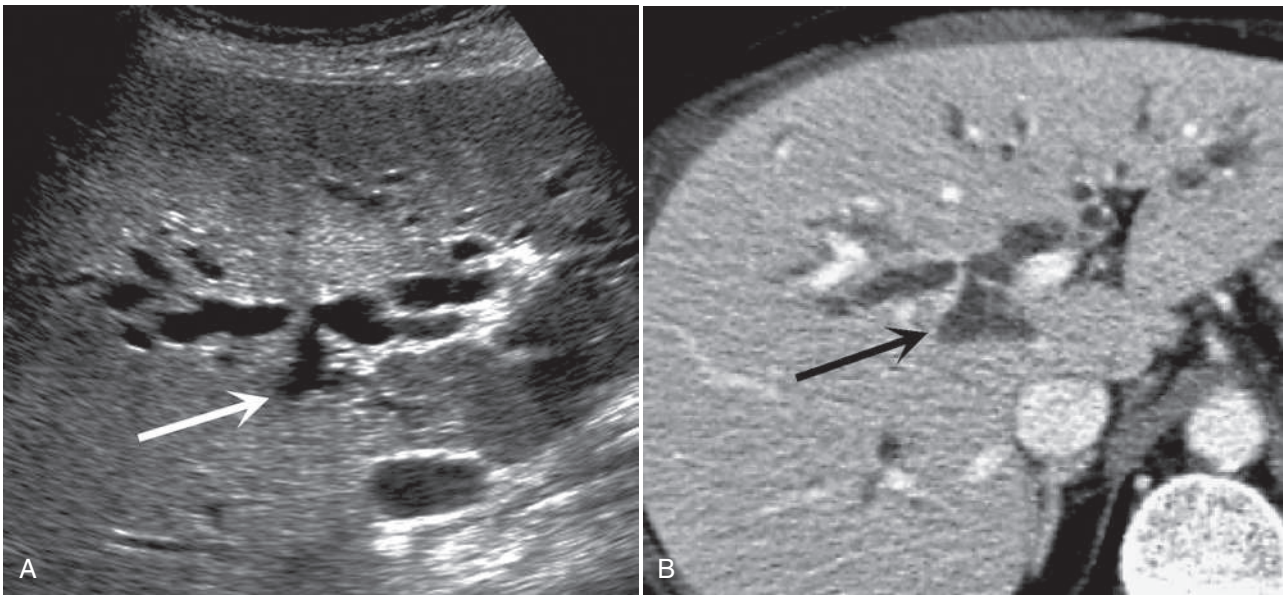

FIG. 6.4 Aberrant Right Posterior Duct. (A) Transverse image obtained cranial to the porta hepatis depicts the aberrant right posterior duct *(arrow)* inserting into the left hepatic duct. This is the most common anomaly of the biliary tree. **(B)** Corresponding enhanced computed tomography image shows the same anomaly.

The site of insertion of the **cystic duct** into the bile duct is quite variable. The cystic duct may join the bile duct along its lateral, posterior, or medial border. It may also run a parallel course to the duct and insert into the lower one-third of the duct, close to the ampulla of Vater.[7] The **common bile duct** is commonly divided into three segments: the suprapancreatic, retropancreatic, and interstitial/ampullary components. It extends caudally within the hepatoduodenal ligament, lying anterior to the portal vein and to the right of the hepatic artery. It then passes posterior to the first portion of the duodenum and the head of the pancreas, sometimes embedded in the latter. The superior margin of the pancreatic head demarcates the transition between the suprapancreatic and retropancreatic segments of the CBD. It ends in the ampulla of Vater, which is occasionally identified on transabdominal ultrasound with the use of high-frequency linear transducers (see Fig. 6.1D, Video 6.1).

Sonographic Technique

Our technique for assessment of the intrahepatic ducts includes a routine scan, as would be performed for liver evaluation, including both sagittal and transverse scans. In addition, we perform a *focused scan* to assess the porta hepatis, recognizing that its orientation requires an oblique plane to show the length of the right and left hepatic ducts in a single image. For this we utilize a subcostal oblique view with the left edge of the transducer more cephalad than the right edge. The face of the transducer is directed toward the right shoulder. With a full suspended inspiration, a sweep of the transducer from the shoulder to the umbilical region will show the middle hepatic vein, then the long axis of the right and left hepatic ducts at the porta hepatis, followed by the common duct in cross section. By rotating the transducer 90 degrees to this plane, a second suspended inspiration will allow for a long-axis view of the CHD and CBD at the porta hepatis. The visualization of the distal CBD can be a challenge because of overlying duodenal or transverse colonic gas. If the gallbladder is distended, it is often an excellent window through which the distal CBD and pancreatic head can be visualized. With the patient in supine or left lateral decubitus position, the probe may be placed on the gallbladder and angled slightly to the left toward the pancreatic head. Protrusion of the abdomen or examination of the patient in standing upright position also allows the intervening colon to migrate caudally and improves visibility of the pancreatic head.

Harmonic imaging and spatial compound imaging allow for improved contrast between the ducts and adjacent tissues, leading to improved visualization of the duct, its luminal contents, and wall[8] (Fig. 6.5). Furthermore, the conspicuity of stones and their posterior acoustic shadowing is increased. Spatial compounding, while diminishing posterior shadowing, also results in improved contrast to speckle ratio and better depicts intraductal and periductal structures. We advocate routine use of harmonic and compound imaging in the assessment of the biliary tree. Specific scanning techniques for assessment of choledocholithiasis and cholangiocarcinoma are discussed in the appropriate sections.

Choledochal Cysts

Choledochal cysts represent a heterogeneous group of congenital diseases that may manifest as focal or diffuse cystic dilation of the biliary tree. These cysts occur most often in East Asian populations; the incidence in Japan is 1 in 13,000 versus 1 in 100,000 in Western populations.[9,10] The female-to-male ratio is 3:1 to 4:1.

Although most patients present early in life, about 20% of choledochal cysts are encountered in adulthood, when sonography is performed for symptoms of gallstone disease.[11] The most widely used classification system divides choledochal cysts into **five types**[12] (Figs. 6.6 and 6.7). **Type I** choledochal cysts, a fusiform dilation of the CBD, are the most common (80%) and, along

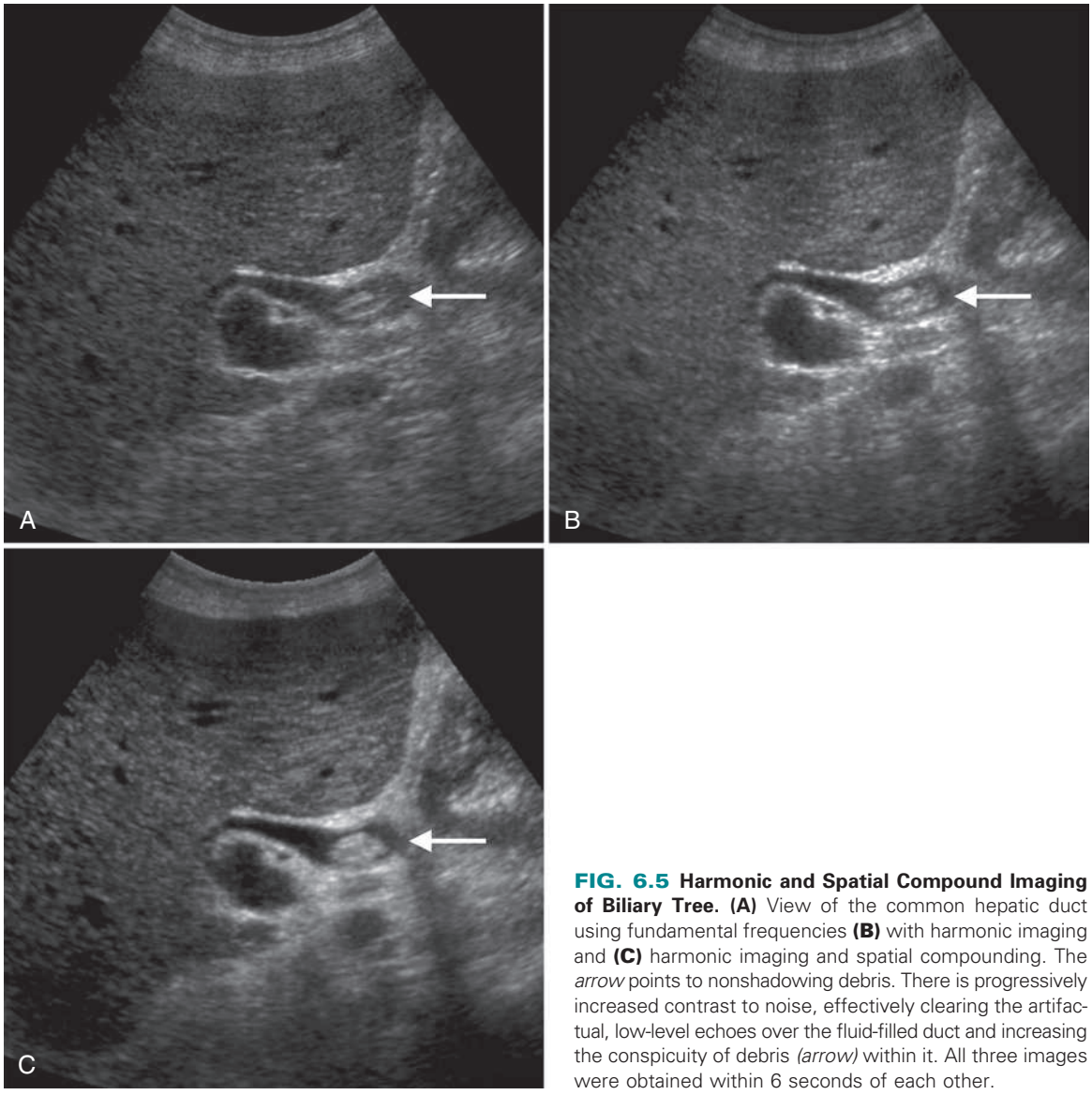

FIG. 6.5 Harmonic and Spatial Compound Imaging of Biliary Tree. (A) View of the common hepatic duct using fundamental frequencies **(B)** with harmonic imaging and **(C)** harmonic imaging and spatial compounding. The *arrow* points to nonshadowing debris. There is progressively increased contrast to noise, effectively clearing the artifactual, low-level echoes over the fluid-filled duct and increasing the conspicuity of debris *(arrow)* within it. All three images were obtained within 6 seconds of each other.

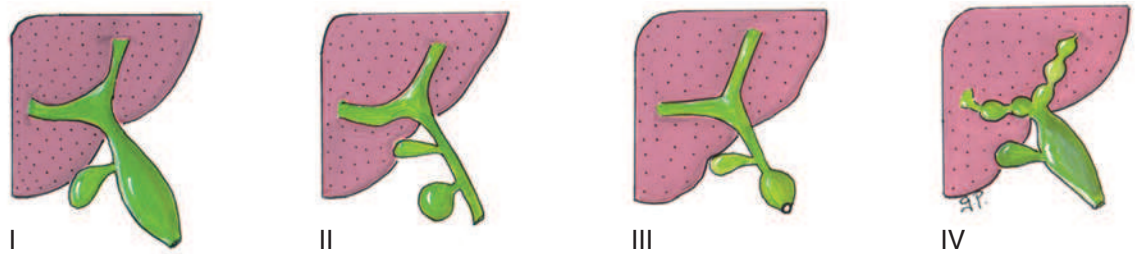

FIG. 6.6 Todani Classification System for Choledochal Cysts. Type I cyst: diffuse dilation of the extrahepatic bile duct; this is the most common type (80%). **Type II cyst:** true diverticulum of the bile duct; very rare. **Type III cyst:** also called choledochocele; diffuse dilation of the very distal (intraduodenal) common bile duct. **Type IV cyst:** multifocal dilations of the intrahepatic and extrahepatic bile ducts. **Type V cyst,** Caroli disease, is omitted because it is not a true choledochal cyst. (With permission from Todani T, Watanabe Y, Narusue M, et al. Congenital bile duct cysts: classification, operative procedures, and review of thirty-seven cases including cancer arising from choledochal cyst. Am J Surg. 1977;134:263-269.[12])

with type IVa, are associated with an abnormally long common channel (>20 mm) between the distal bile duct and the pancreatic duct. This long common channel could allow for reflux of pancreatic juices into the CBD, causing dilation, but this remains controversial.[9,13] **Type II** cysts are true diverticula of the bile ducts and are very rare. **Type III** cysts, the "choledochoceles," are confined to the intraduodenal portion of the CBD. **Type IVa** cysts are multiple intrahepatic and extrahepatic biliary dilations, whereas **type IVb** cysts are confined to the extrahepatic biliary tree. Caroli disease has been classified as a **type V** cyst, but it

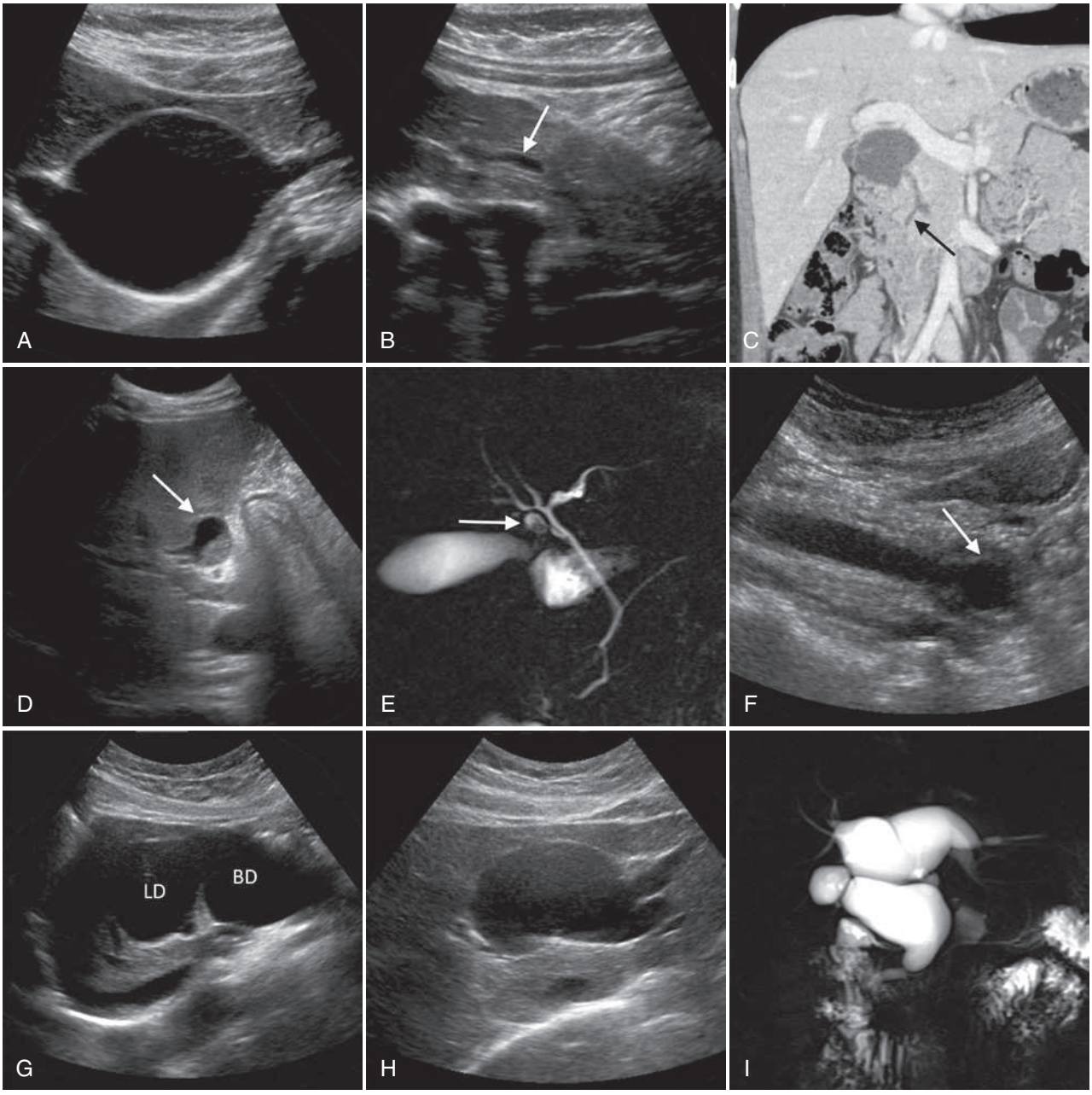

FIG. 6.7 Choledochal Cysts. (A)-(C) Type I. Fusiform dilation of the common bile duct (CBD) is seen, but no obstructive lesion is noted. This is the most common type of choledochal cyst. **(B)** Careful examination of the distal CBD using high-frequency linear transducer reveals a long common channel *(arrow)* between the CBD and pancreatic duct. **(C)** Coronal computed tomography image confirms the presence of long common channel *(arrow)*. **(D)** and **(E) Type II.** A large diverticulum *(arrow)* is shown in **(D)** arising from the common hepatic duct at the portal hepatis and containing mobile debris. **(E)** Thick-slab magnetic resonance cholangiopanreatography (MRCP) confirms the same. **(F) Type III.** Fusiform dilation of the distal CBD *(arrow)* is demonstrated protruding into the duodenum. **(G)-(I)**. **Type IV. (G)** Sagittal view of the liver shows a markedly dilated bile duct (BD) and left hepatic duct (LD). **(H)** Transverse view of the left lobe of the liver depicts marked enlargement of the left hepatic duct with dilated branches. **(I)** Thick-slab MRCP shows both intrahepatic and extrahepatic involvement.

has a different embryonic origin and is not a true choledochal cyst.[10]

On sonography, a cystic structure is identified that may contain internal sludge, stones, or even solid neoplasm. In some cases the cyst is large enough that its connection to the bile duct is not immediately recognized. Use of various scanning windows and angles allows for demonstration of the relationship of the lesion to the biliary tract, differentiating it from pancreatic pseudocysts or enteric duplication cysts. Biliary scintigraphy, MRCP, and endoscopic retrograde cholangiopancreatography (ERCP) have been used to delineate further the structure of choledochal cysts. ERCP is necessary to ensure that the dilation is not a result of distal neoplasm, especially in the case of type I choledochal cysts (see Fig. 6.7). Because there is a risk of cholangiocarcinoma with all choledochal cysts, surgical resection is advocated.

Caroli Disease

Caroli disease is a rare congenital disease of the intrahepatic biliary tree that results from malformation of the **ductal plates,** the primordial cells that give rise to the intrahepatic bile ducts. There are two types of Caroli disease: the simple, classic form and the second, more common form, which occurs with **congenital hepatic fibrosis.**[14] The second form has also been called **Caroli syndrome.** Caroli disease has been associated with cystic renal disease, most often renal tubular ectasia **(medullary sponge kidneys).** However, both forms may also be seen in patients with autosomal recessive polycystic kidney disease. Caroli disease affects men and women equally, and more than 80% of patients present before the age of 30 years.[15]

Caroli disease leads to *saccular dilation* or, less often, *fusiform dilation* of the intrahepatic biliary tree, resulting in biliary stasis, stone formation, and bouts of cholangitis and sepsis (Fig. 6.8). The disease most often affects the intrahepatic biliary tree diffusely, but it may be focal. The dilated ducts contain stones and sludge. Unlike recurrent pyogenic cholangitis, the ductal contents do not form a cast of the dilated system and thus are more easily identified as ductal contents.[16] Also, small portal vein branches surrounded by dilated bile ducts and *bridging echogenic septa* traversing the dilated ducts have been described on ultrasound. These correspond to persistent embryonic ductal structures.[17] If associated with congenital hepatic fibrosis, findings of altered hepatic architecture and portal hypertension are also present. **Cholangiocarcinoma** develops in 7% of patients with Caroli disease.[15]

Overview of Biliary Tree Obstruction

Elevation of cholestatic liver parameters, which may appear clinically as jaundice, is a frequent indication for sonographic examination of the abdomen. The major objective in performing these scans is to determine if the patient has obstruction of the bile ducts, as opposed to a hepatocellular or biliary ductular disease. Sonography is highly sensitive in the detection of dilation of the biliary tree and is therefore an excellent modality for

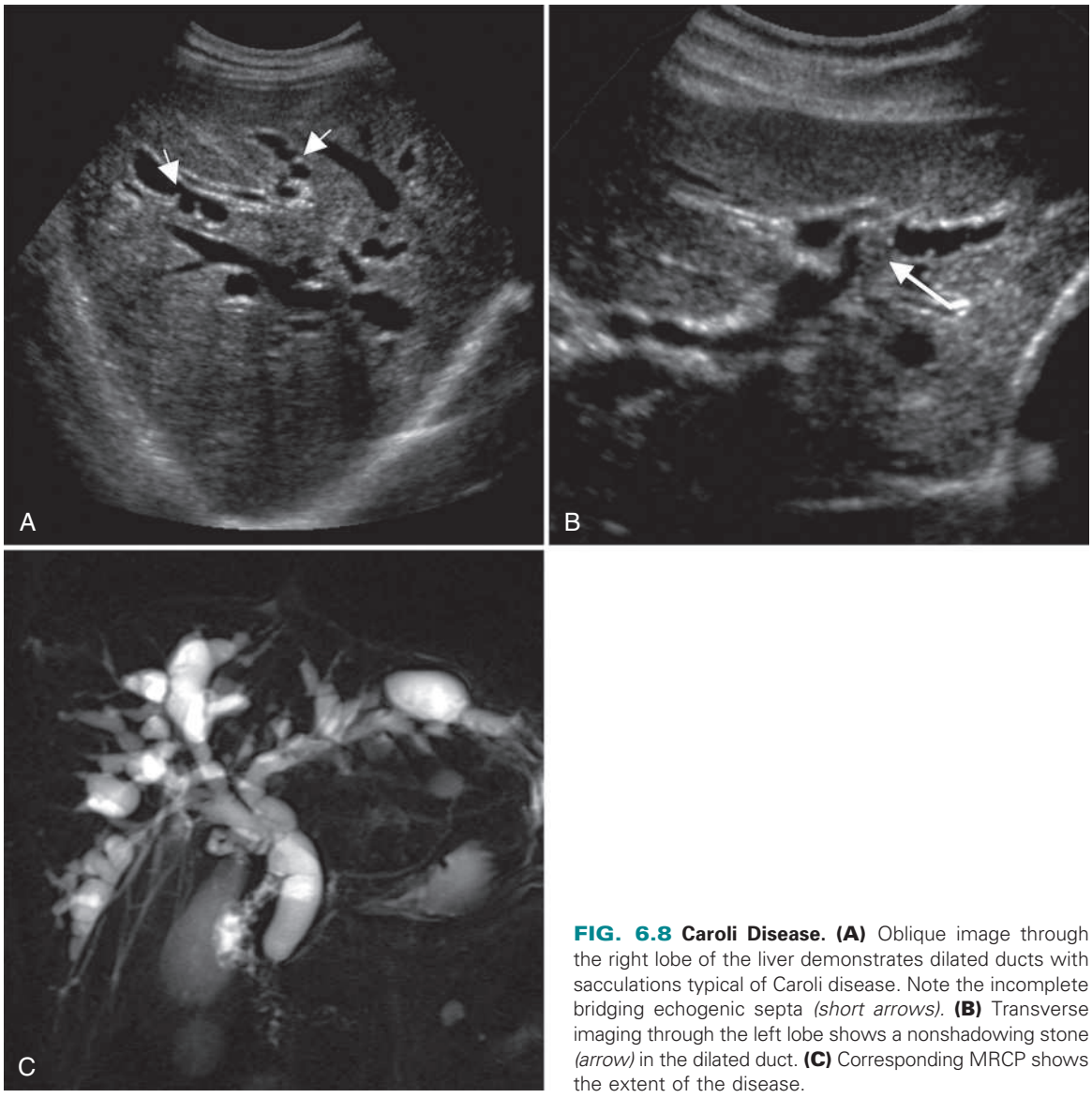

FIG. 6.8 Caroli Disease. (A) Oblique image through the right lobe of the liver demonstrates dilated ducts with sacculations typical of Caroli disease. Note the incomplete bridging echogenic septa *(short arrows).* **(B)** Transverse imaging through the left lobe shows a nonshadowing stone *(arrow)* in the dilated duct. **(C)** Corresponding MRCP shows the extent of the disease.

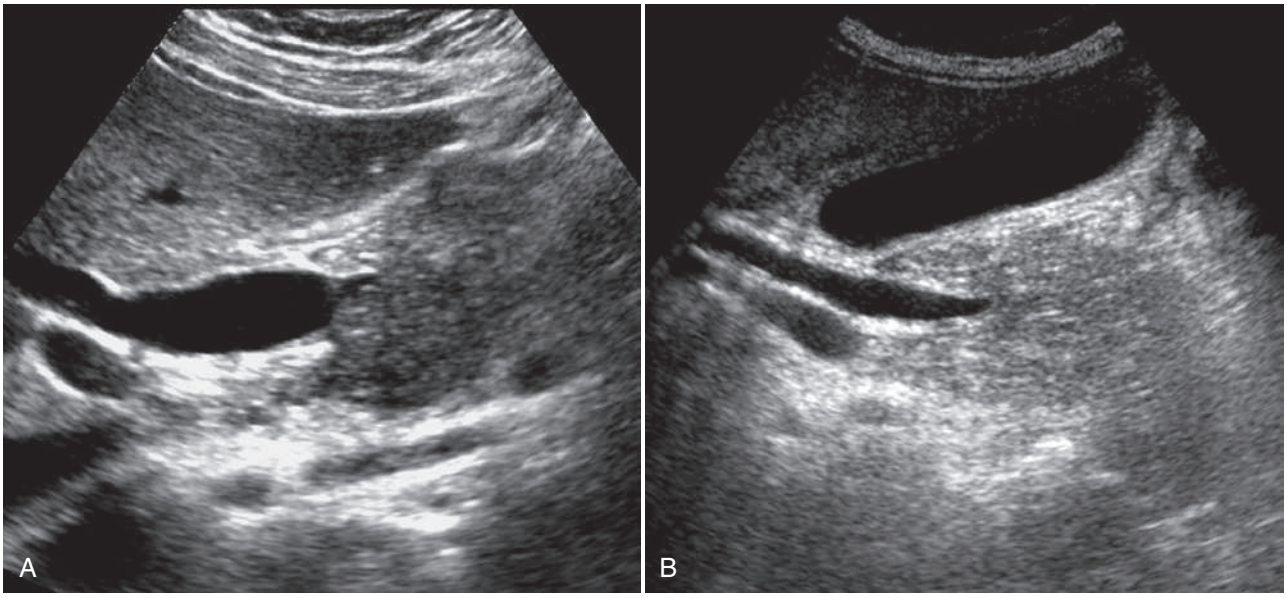

FIG. 6.9 Common Bile Duct Obstruction Caused by Extrinsic Factors. (A) Pancreatic adenocarcinoma. Short transition zone with shouldering, large duct caliber, along with an obstructive mass are typical findings in malignant obstruction. **(B) Pancreatitis.** Elongated tapering of the duct suggests a benign cause. Note mild sympathetic **gallbladder wall thickening** caused by adjacent inflammation.

Causes of Biliary Obstruction

BENIGN MISCELLANEOUS
Choledocholithiasis[a]
Hemobilia[a]
Congenital biliary diseases
  Caroli disease[a]
  Choledochal cysts
Cholangitis
  Infectious
Acute pyogenic cholangitis[a]
Biliary parasites[a]
Recurrent pyogenic cholangitis[a]
HIV cholangiopathy
  Sclerosing cholangitis

NEOPLASMS
Cholangiocarcinoma
Gallbladder carcinoma
Locally invasive tumors (esp. pancreatic adenocarcinoma)
Ampullary tumors
Metastases

EXTRINSIC COMPRESSION
Mirizzi syndrome[a]
Pancreatitis
Adenopathy

[a]Denotes causes of painful jaundice.

initiation of the imaging investigation (Fig. 6.9). These scans should be performed with knowledge of the patient's clinical condition, especially whether the patient has painless jaundice or has painful jaundice, as seen with acute obstruction or infection affecting the biliary tree.

Acute biliary obstruction in the absence of infection may present with RUQ pain and a predominant transaminitis suggesting **acute hepatitis** rather than cholestasis.[18,19] Early on, the bile ducts may only be minimally dilated, with imaging findings of a nonspecific hepatitis manifest by edema in the portal triads (echogenic periportal thickening) and fluid accumulation in the gallbladder wall. Therefore in patients with unexplained acute hepatitis, the distal biliary tree should always be examined carefully for choledocholithiasis even if the bile ducts do not appear significantly dilated.

The ultrasound examination should focus on answering the following three questions:

1. Are the bile ducts or gallbladder dilated?
2. If dilated, to what level?
3. What is the cause of the obstruction?

Choledocholithiasis

Choledocholithiasis is classified into primary and secondary forms. **Primary choledocholithiasis** denotes de novo formation of stones, often made of calcium bilirubinate **(pigment stones)** within the ducts. The etiologic factors are often related to diseases causing strictures or dilation of the bile ducts, leading to stasis, as follows:

- Sclerosing cholangitis
- Caroli disease
- Parasitic infections of the liver (e.g., *Clonorchis, Fasciola, Ascaris*)[20]
- Chronic hemolytic diseases, such as sickle cell disease
- Prior biliary surgery, such as biliary-enteric anastomoses

Migration of stones from the gallbladder into the CBD constitutes **secondary choledocholithiasis.** Whereas primary choledocholithiasis is relatively rare outside endemic regions (East Asia), secondary choledocholithiasis is quite common, representing the worldwide distribution of gallstone disease. Bile duct stones are found in 8% to 18% of patients with symptomatic gallstones.[21]

Intrahepatic Stones

Harmonic and compound imaging have improved the ability to find small stones within the intrahepatic bile ducts, especially with dilated ducts. Visualization of small intrahepatic stones is quite difficult on MRCP and other biliary imaging modalities; because of the intrinsic high contrast of stones on ultrasound, it is often the first modality to detect intrahepatic stones.

The appearance of stones depends on their size and texture (Fig. 6.10, Video 6.2). Most stones are highly echogenic with posterior acoustic shadowing, although small (<5 mm) or soft pigment stones (especially in the patient with recurrent pyogenic cholangitis) may not show shadowing. When the affected ducts are filled with stones, the individual stones may not be appreciated; instead, a bright, echogenic linear structure with posterior shadowing is seen. Stones should always be suspected if discrete or linear echogenicities with or without shadowing are seen in the region of the portal triads, paralleling the course of the portal veins within the liver. Harmonic imaging improves both the contrast resolution and the detection of the acoustic shadow and is therefore recommended for routine assessment of the biliary tree.[22]

Common Bile Duct Stones

The majority of stones in the CBD are in the distal duct close to or at the ampulla of Vater. Therefore sonographic evaluation should include assessment of the entire duct, focusing on the periampullary region. Unfortunately, this region is often the most

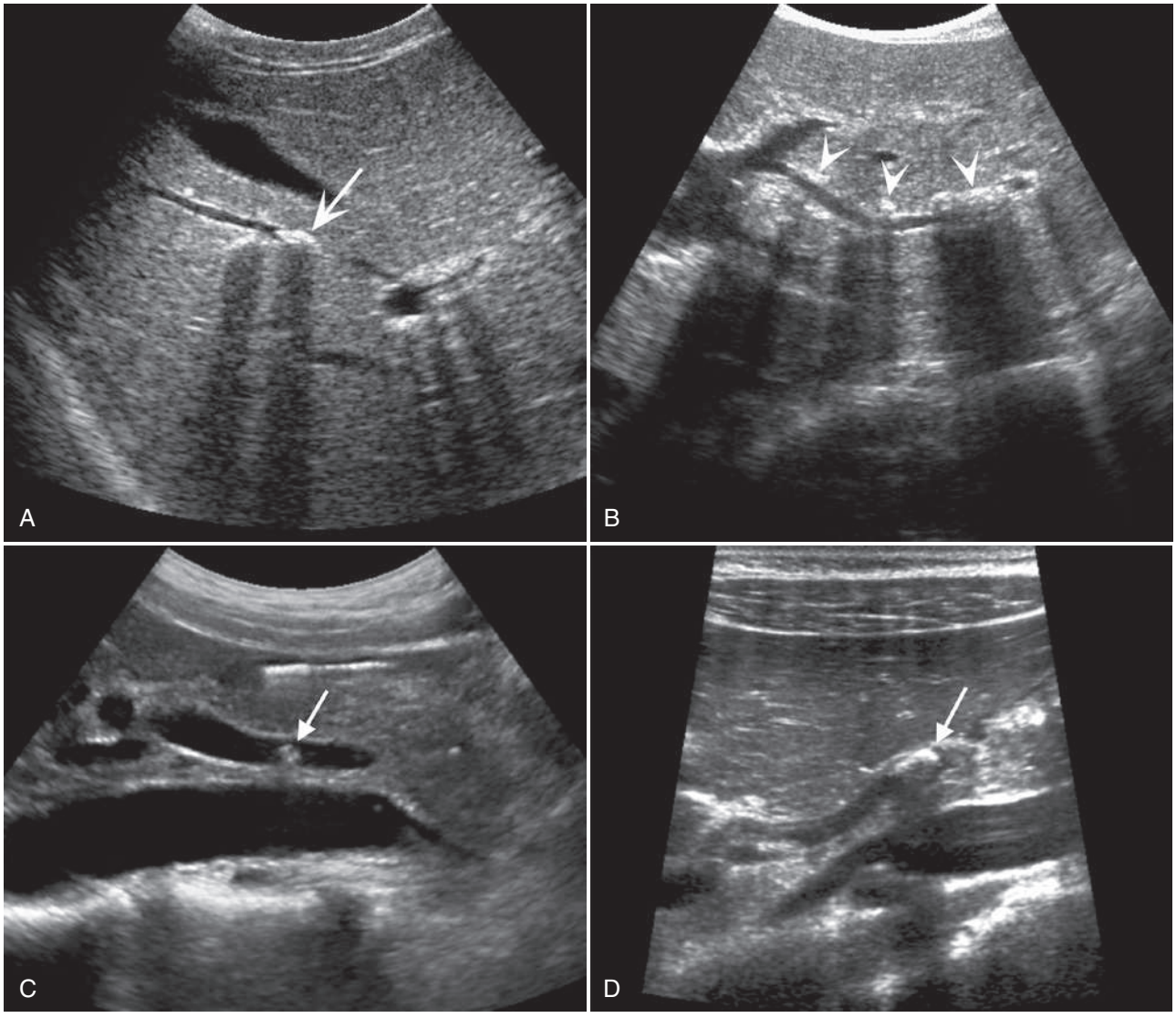

FIG. 6.10 Choledocholithiasis. (A) Intrahepatic stones. Small stones *(arrow)* are seen in the right lobe causing acoustic shadowing. Note the dilated duct proximal to the larger stone. **(B) Multiple stone clusters** *(arrowheads)* in the left lobe appearing as echogenic linear structures with shadowing. Both patients (in **A** and **B**) had **cystic fibrosis. (C)** and **(D) Common bile duct (CBD) stones. (C)** Small stone *(arrow)* may not show shadowing. **(D)** Distal stone *(arrow)* with posterior acoustic shadowing. See also Videos 6.2 and 6.3.

difficult area to visualize because it may be hidden by bowel gas, making detection of distal CBD stones difficult. Maneuvers to improve assessment include the following:

- **Changes in patient position.** The CBD may be examined in supine, left lateral decubitus, and standing positions. The change in the relative position of adjacent organs and bowel gas may allow improved visualization of the distal duct.
- **Choice of sonographic window.** The subcostal view is most useful for the assessment of the porta hepatis and proximal CBD. An epigastric view is best for the distal CBD.
- **Use of compression sonography.** Physically compressing the epigastrium may collapse the superficial bowel and displace the bowel gas that is blocking the view.
- **Detailed assessment of the distal CBD.** The distal intrapancreatic CBD is often best visualized with the probe focused on the pancreatic head in the **transverse** plane. Once the dilated CBD is identified, a slight rocking of the transducer to just "peek" at the point of caliber change will often allow a glimpse of a stone impacted in the distal duct, which is otherwise hidden from sonographic view. Similarly, a **sagittal** view focused on the pancreatic head should show the dilated CBD on the dorsal aspect of the head. Again, slight manipulation of the transducer, focusing on the point of caliber change, is best to see a solitary stone impacted in the distal duct. If the gallbladder is distended, it may be used as an acoustic window through which the distal CBD and ampulla may be visible.

The classic appearance of CBD stones is a rounded echogenic lesion with **posterior acoustic shadowing** (see Fig. 6.10, Video 6.3). Importantly, no fluid rim will be seen around an impacted distal CBD stone because it is compressed against the duct wall. The lateral margins of the stone are therefore not seen, decreasing the conspicuity of the stone, versus a stone seen in the gallbladder or proximal duct, where it is likely to be surrounded by bile. Small stones may lack good acoustic shadows and appear only as a reproducible bright, linear echogenicity, either straight or curved. Awareness of this subtle appearance of CBD stones definitely improves their detection.

Pitfalls in the diagnosis of choledocholithiasis include blood clot **(hemobilia), papillary tumors,** and occasionally **biliary sludge;** none of these will shadow. **Surgical clips** in the porta hepatis, mostly from previous cholecystectomy, appear as linear echogenic foci with shadowing.[23] The short length, the relatively high degree of echogenicity, the lack of ductal dilation, and the absence of the gallbladder should allow differentiation of surgical clips from stones.

Mirizzi Syndrome

Mirizzi syndrome is a clinical syndrome of jaundice with pain and fever resulting from obstruction of the CHD caused by a stone impacted in the cystic duct. It occurs most often when the cystic duct and CHD run a parallel course. The stone is often impacted in the distal cystic duct, and the accompanying inflammation and edema result in the obstruction of the adjacent CHD. The obstruction of the cystic duct causes recurrent bouts of cholecystitis, and the impacted stone may erode into the CHD, resulting in a **cholecystocholedochal fistula** and biliary obstruction.[24] Identification of the fistula complication (called **Mirizzi type II**) is important because the treatment requires surgical repair of the fistula. **Acute cholecystitis, cholangitis,** and even **pancreatitis** may occur.[25]

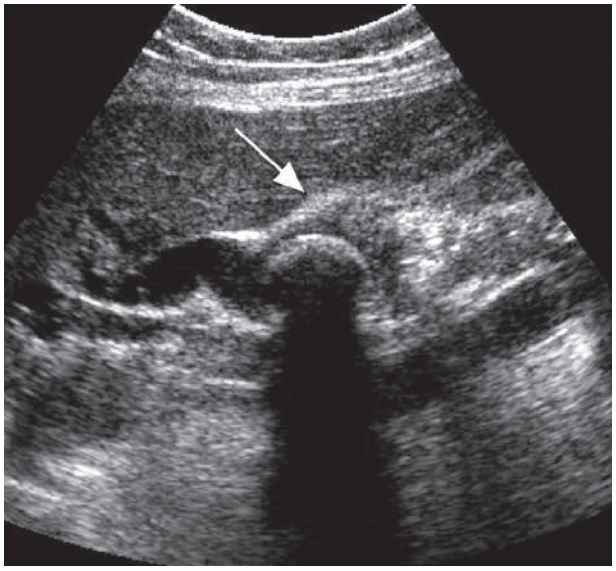

FIG. 6.11 Mirizzi Syndrome. Mirizzi syndrome in a patient with abdominal pain and jaundice. Sagittal sonogram shows a dilated common bile duct obstructed by a large stone impacted in the distal cystic duct. This appearance may be mistaken for a common bile duct stone. There is thickening of the wall of the cystic duct *(arrow)*.

Mirizzi syndrome should be considered on sonography when biliary obstruction with dilation of the biliary ducts to the CHD level is seen with acute or chronic cholecystitis. Thus the gallbladder has features of acute cholecystitis but may or may not be distended.[2] A stone impacted in the cystic duct with surrounding edema at the level of the obstruction is confirmatory (Fig. 6.11).

Hemobilia

Iatrogenic biliary trauma, mostly caused by percutaneous biliary procedures or liver biopsies, accounts for approximately 65% of all causes of hemobilia. Other causes include **cholangitis** or **cholecystitis** (10%), vascular malformations or aneurysms (7%), abdominal **trauma** (6%), and malignancies, especially **hepatocellular carcinoma** and **cholangiocarcinoma** (7%).[26] Pain, gastrointestinal bleeding, and biochemical jaundice are the usual complaints at presentation. Apart from the blood loss, which occasionally is severe, complications are rare and include cholecystitis, cholangitis, and **pancreatitis.**

The appearance of blood within the biliary tree is similar to blood clots encountered elsewhere (Fig. 6.12). Most often, the clot is echogenic or of mixed echogenicity, and retractile, conforming to the shape of the duct. Occasionally, hemobilia may appear tubular with a central hypoechoic area. Acute hemorrhage will appear as fluid with low-level internal echoes. Blood clots may be mobile. Extension into the gallbladder is common. The clinical history is often essential to the diagnosis.

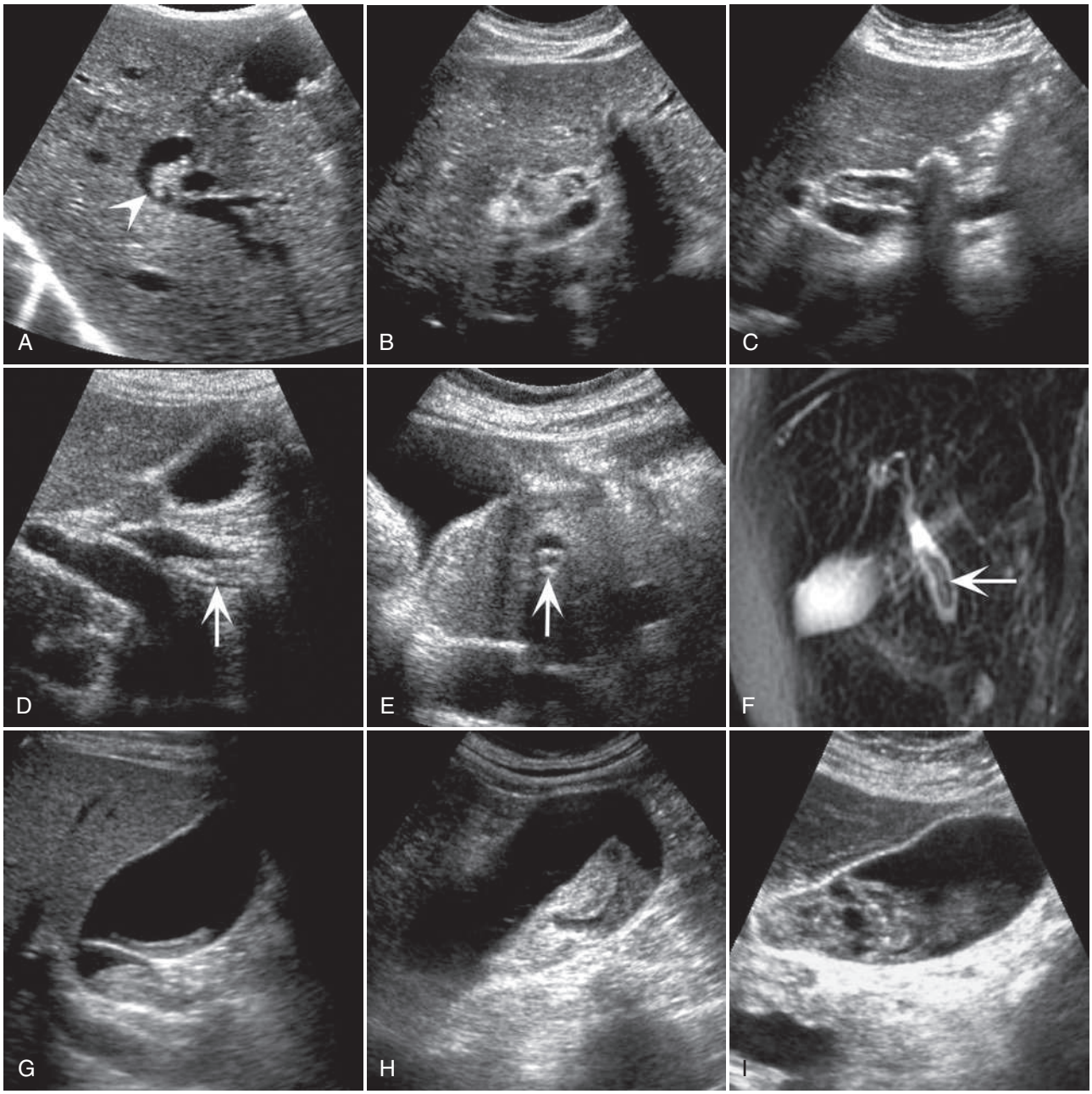

FIG. 6.12 Hemobilia: Spectrum on Sonography. (A) Echogenic blood clot *(arrowhead)* within a dilated duct, after insertion of biliary drainage catheter. Biliary obstruction was caused by pancreatic tumor. **(B)** and **(C)** Echogenic clot in the common hepatic duct in two patients after liver biopsy. **(D)** and **(E)** Spontaneous hemobilia in patient receiving anticoagulation therapy. Note the tubular appearance of the clot *(arrow)* with central hypoechoic lumen. **(F)** Corresponding MRCP image depicts the same. **(G)-(I)** Blood in gallbladder in three different patients. All patients developed pain after liver biopsy. **(H)** Note the angled edge typical of blood clot.

Pneumobilia

Air within the biliary tree usually results from previous biliary intervention, biliary-enteric anastomoses, or CBD stents. In the acute abdomen, pneumobilia may be caused primarily by three entities. **Emphysematous cholecystitis** may lead to pneumobilia; its risk factors and findings are discussed under "Acute Cholecystitis." Inflammation caused by an impacted stone in the CBD may cause erosion of the duct wall, leading to **choledochoduodenal fistula.** The third entity, prolonged acute cholecystitis, may lead to erosion into an adjacent loop of bowel, most frequently the duodenum or transverse colon, called **cholecystenteric fistula.** Stones may then pass from the gallbladder into the bowel and can cause a gastric outlet or small bowel obstruction called **gallstone ileus.**

Air in the bile ducts has a characteristic appearance. Bright, echogenic linear structures following the portal triads are seen, more often in a nondependent position (Fig. 6.13). Posterior **"dirty" shadowing, reverberation,** and **ring-down artifacts** are seen with large quantities of air. Movement of the air bubbles, best seen just after changing the patient's position, is diagnostic.

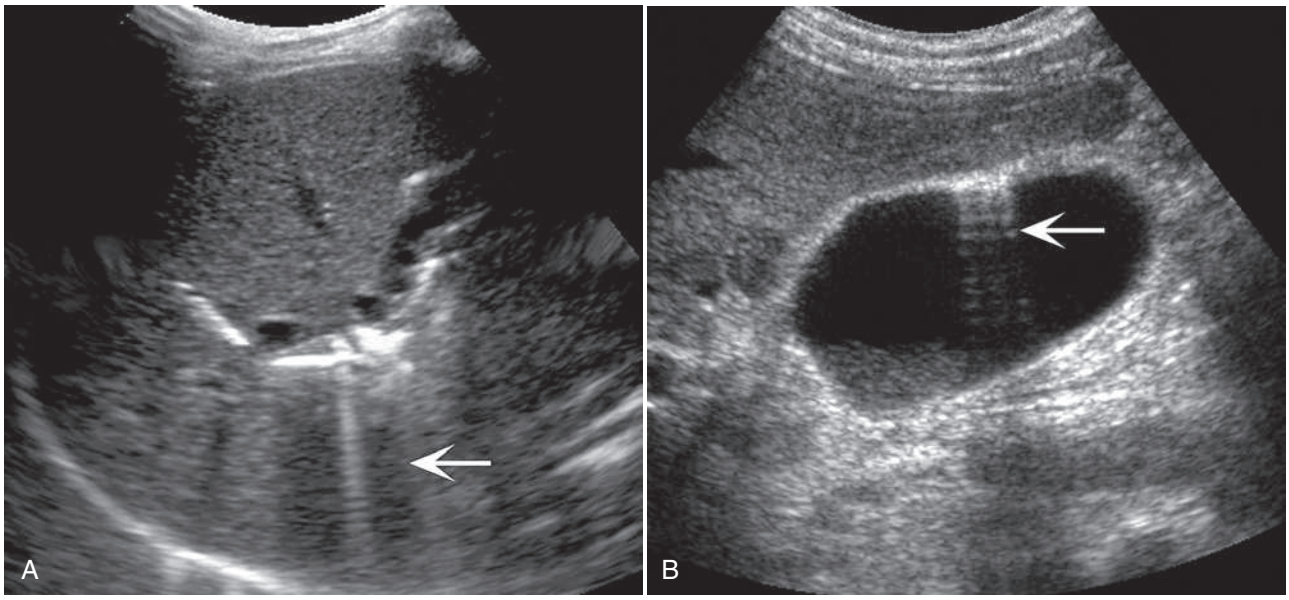

FIG. 6.13 Pneumobilia. (A) Extensive air within the central ducts manifests as linear echogenic structures paralleling the portal veins. Note the dirty shadowing *(arrow)* and ring-down artifact. **(B)** Air in the gallbladder. Pneumobilia often extends into the gallbladder. Note the ring-down artifact *(arrow).*

Extensive arterial calcifications, seen especially in diabetic patients, can mimic pneumobilia.

Biliary Tree Infection

Acute (Bacterial, Ascending) Cholangitis

Antecedent **biliary obstruction** is an essential component of bacterial cholangitis, associated in 85% of cases with CBD stones.[27] Other causes of obstruction include biliary stricture as a result of trauma or surgery, congenital abnormalities such as choledochal cysts, and partially obstructive tumors. Intrinsic or extrinsic neoplasms causing complete biliary obstruction rarely cause pyogenic cholangitis before biliary intervention.[19] The clinical presentation is usually that of (1) fever (≈90%), (2) RUQ pain (≈70%), and (3) jaundice (≈60%), the classical **Charcot triad.** There is leukocytosis, or at least a left shift, and elevated levels of serum alkaline phosphatase and bilirubin in the great majority of patients. Often, mild serum hepatic transaminitis is present, but occasionally, levels above 1000 are seen early in the disease because of a sudden increase in intrabiliary pressures.[19] The bile is most often infected by gram-negative enteric bacteria, which are often retrieved in blood cultures.

Acute cholangitis is a medical emergency. Sonography is advocated as the first imaging modality to determine the cause and level of obstruction and to exclude other diseases, such as cholecystitis, acute hepatitis, and Mirizzi syndrome. Sonography is more accurate than CT and more practical than MRI, endoscopic ultrasound, and ERCP in the initial assessment of patients with potential acute biliary disease.[28]

The **sonographic findings** of bacterial cholangitis include the following (Fig. 6.14):

- Dilation of the biliary tree
- Choledocholithiasis and possibly sludge
- Bile duct wall thickening
- Hepatic abscesses

Dilation of the biliary tree, when present, can be diagnosed by sonography. A CBD diameter greater than 6 mm is considered abnormal in most patients. *Subtle dilation* of the intrahepatic biliary tree is a frequently overlooked finding that should be specifically sought. This includes use of subcostal oblique scanning of the porta hepatis to assess the caliber of the right and left hepatic ducts, as well as evaluation of the CBD, which may measure normal but still show a somewhat "tense" or distended morphology. Dilation of the biliary tree is seen in 75% of patients. The obstructive stone is usually lodged in the distal CBD but may be mobile, causing intermittent obstruction. Air is rarely seen within the ducts; thus its presence suggests a **choledochoenteric fistula** in the absence of previous biliary manipulation (Fig. 6.15, Video 6.4). Circumferential thickening of the bile duct wall, similar to other causes of cholangitis, may be present and may extend to the gallbladder. Multiple small hepatic abscesses—sometimes grouped in a lobe or segment of the liver—may be seen but tend to become visible on sonography when they have undergone liquefaction and are a late finding.

Liver Flukes

Fascioliasis. *Fasciola hepatica* infection is unevenly endemic in many regions of the world, including Asia, Europe, Northern Africa, and South America (mainly Peru and Bolivia).[29] Infection is caused by consumption of water or raw vegetables contaminated with the larvae (metacercariae) of the *F. hepatica* fluke. The infection has two stages: the acute phase, lasting 3 to 5 months, and the chronic phase, which may last several years to over a decade. The acute phase corresponds to the migration of the

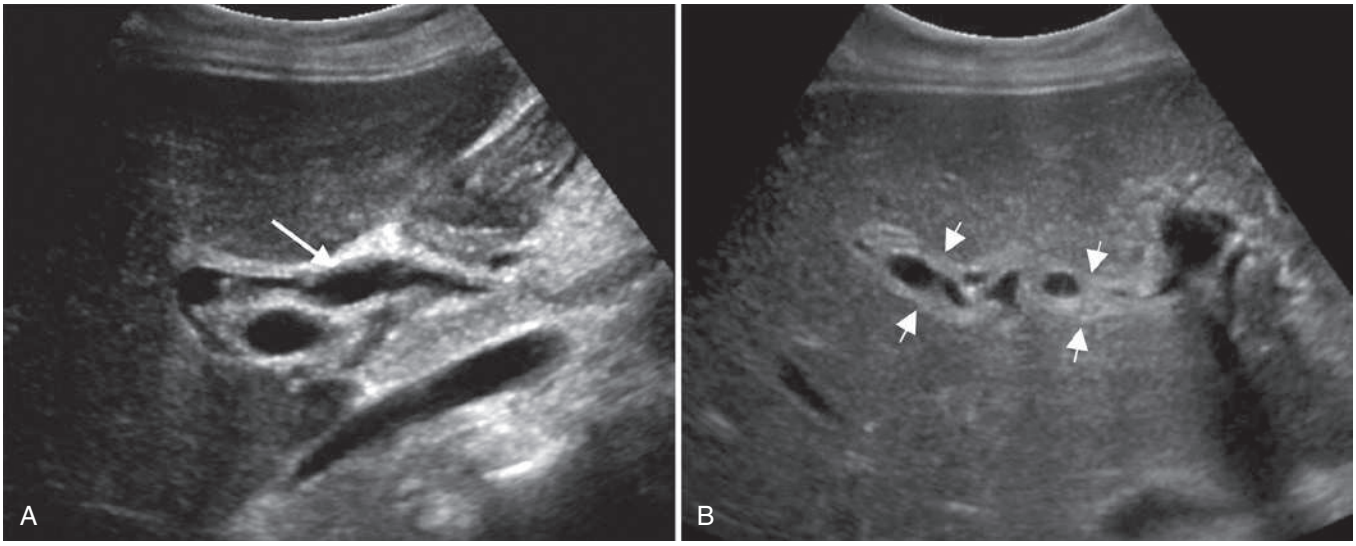

FIG. 6.14 Acute Bacterial Cholangitis. (A) Bile duct wall thickening *(arrow)* in a dilated duct. **(B)** Extensive periportal edema manifest by echogenic thickening of periportal tissues *(short arrows)*.

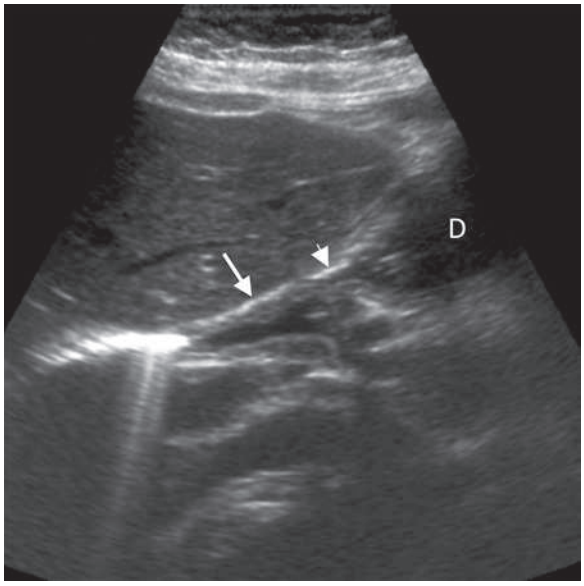

FIG. 6.15 Choledochoduodenal Fistula. Gas within the common bile duct *(arrow)* and marked mucosal thickening caused by inflammation. The fistulous tract *(short arrow)* extends from the duodenal bulb *(D)*. See also Video 6.4.

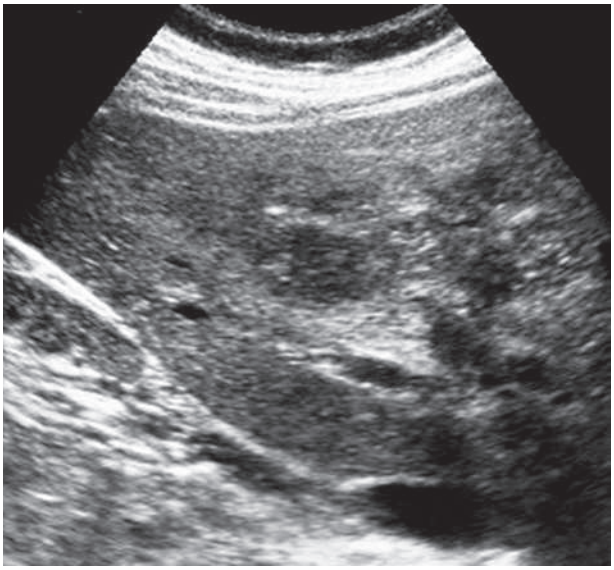

FIG. 6.16 *Fasciola Hepatica* Infection, Acute (Parenchymal) Phase. Oblique image through the right lobe shows poorly defined hypoechoic lesions in the liver parenchyma. Patients often present with fever and pain. (Courtesy of Dr. Adnan Kabaalioglu, Akdeniz University Hospital, Antalya, Turkey.)

immature larvae through the bowel wall, peritoneal cavity, and liver capsule, into the liver parenchyma. Patients may present with acute RUQ pain, hepatomegaly, and prolonged fevers. The final destination of the larvae is the biliary tree, where the parasite matures and produces eggs, indicating the chronic phase of infection. The mature *Fasciola* is the largest of the liver flukes (20-40 mm in length), is flat in shape (1 mm thin), and can be directly seen within the bile ducts. Symptoms then relate to biliary obstruction with intermittent jaundice, fevers, and intrahepatic abscesses. One-half of the patients are asymptomatic in the chronic phase.[29]

The **imaging appearance** of fascioliasis depends on the phase of infection. In the acute phase, sonography demonstrates nonspecific findings of hepatomegaly, hilar adenopathy, and hypoechoic or mixed echogenicity lesions[30,31] (Fig. 6.16). The hepatic lesions are often multiple, confluent, subcapsular, and ill-defined and are present in approximately 90% of patients.[31] The specific finding of the migratory tract of the larvae, manifest by small cystlike clusters in serpiginous tracts in the periphery of the liver are better imaged with CT or MRI.[32] Serial examination may show slowly evolving disease with progressive central migration of lesions and periportal tracking representing lymphangiectasia in the portal triads.[33] Sonography is more specific in the **chronic ductal phase** of the disease, depicting ductal dilation and the flukes in the ducts and gallbladder as flat, sometimes moving, material (Fig. 6.17). However, the most

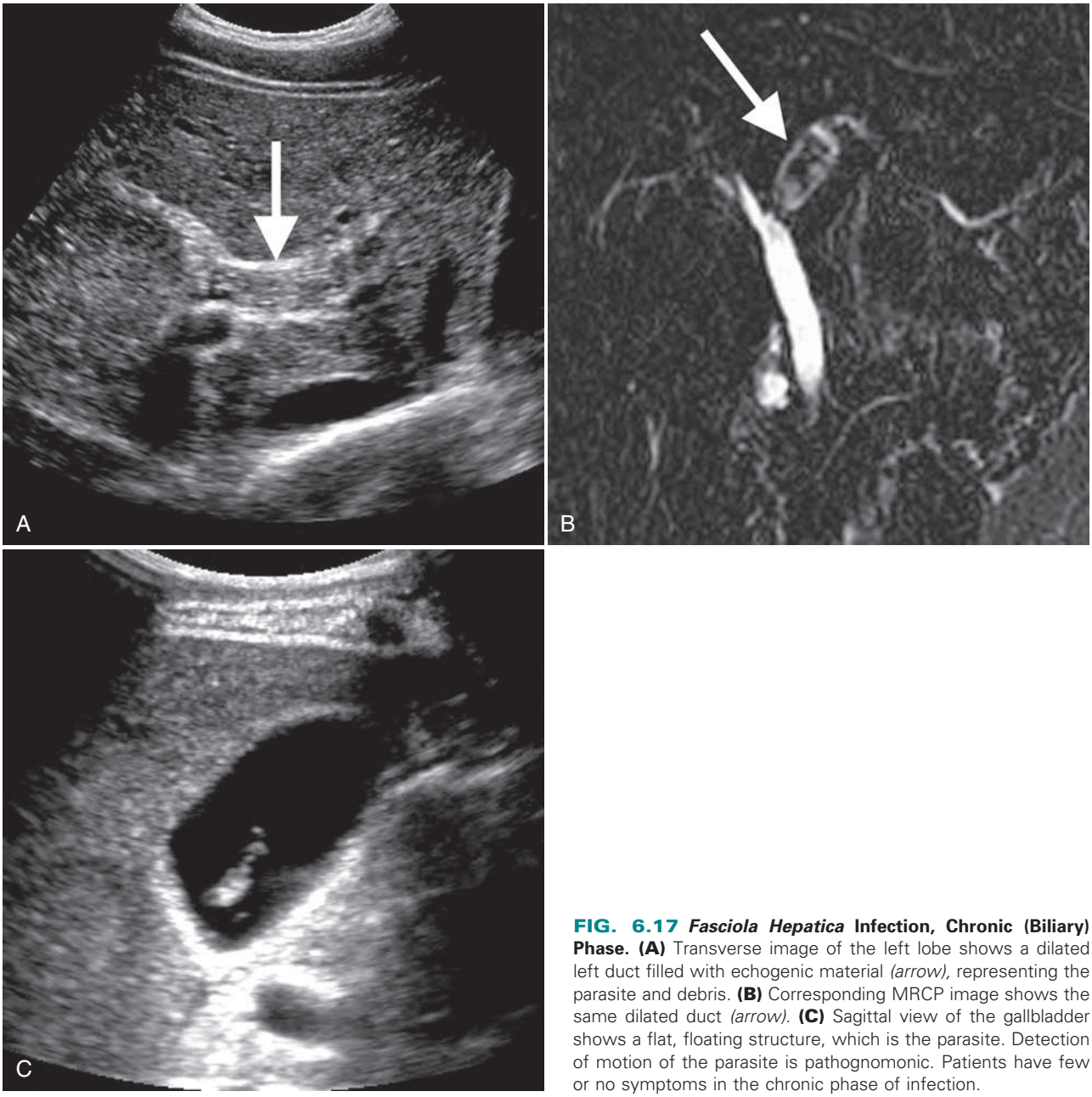

FIG. 6.17 *Fasciola Hepatica* Infection, Chronic (Biliary) Phase. (A) Transverse image of the left lobe shows a dilated left duct filled with echogenic material *(arrow),* representing the parasite and debris. **(B)** Corresponding MRCP image shows the same dilated duct *(arrow).* **(C)** Sagittal view of the gallbladder shows a flat, floating structure, which is the parasite. Detection of motion of the parasite is pathognomonic. Patients have few or no symptoms in the chronic phase of infection.

common findings are gallbladder and bile duct wall thickening.[34] The living flukes within the gallbladder were present in 37% of patients in a series of 87 patients.[31]

Clonorchiasis and Opisthorchiasis. *Clonorchis sinensis* (endemic in East and Southeast Asia), *Opisthorchis viverrini* (endemic in Cambodia, Laos, Thailand, and Vietnam) and *Opisthorchis felineus* (endemic in Central Asia, Russia, and Ukraine) are similar in morphology and life cycle but vary in their geographic distribution.[29] The infection is acquired by ingestion of raw fish (carp) contaminated by the larvae (metacercariae), which migrate through the ampulla of Vater, up the bile duct, then mature and live within the small and medium-sized intrahepatic bile ducts. The mature flukes are smaller than *F. hepatica,* measuring 8 to 15 mm. The acute phase of infection tends to be asymptomatic for *C. sinensis* and *O. viverrini.* The infestation may last for many years or decades.[29]

Ultrasound imaging of *C. sinensis* and *O. viverrini* infestation shows similar findings, which are present in moderate and severe infestation.[35] The principal abnormality is the diffuse dilation of the peripheral intrahepatic bile ducts, often with normal or minimally dilated central and extrahepatic ducts (Fig. 6.18). The peripheral dilation results from the predilection of the fluke for these ducts. Active infection is suggested by increased periportal echoes (likely representing edema) and floating echogenic foci in the gallbladder, representing the flukes or debris.[35] The biliary dilation may persist even after treatment. Chronic infection by these flukes has been directly linked to **cholangiocarcinoma** and is postulated as a cause of recurrent pyogenic cholangitis.

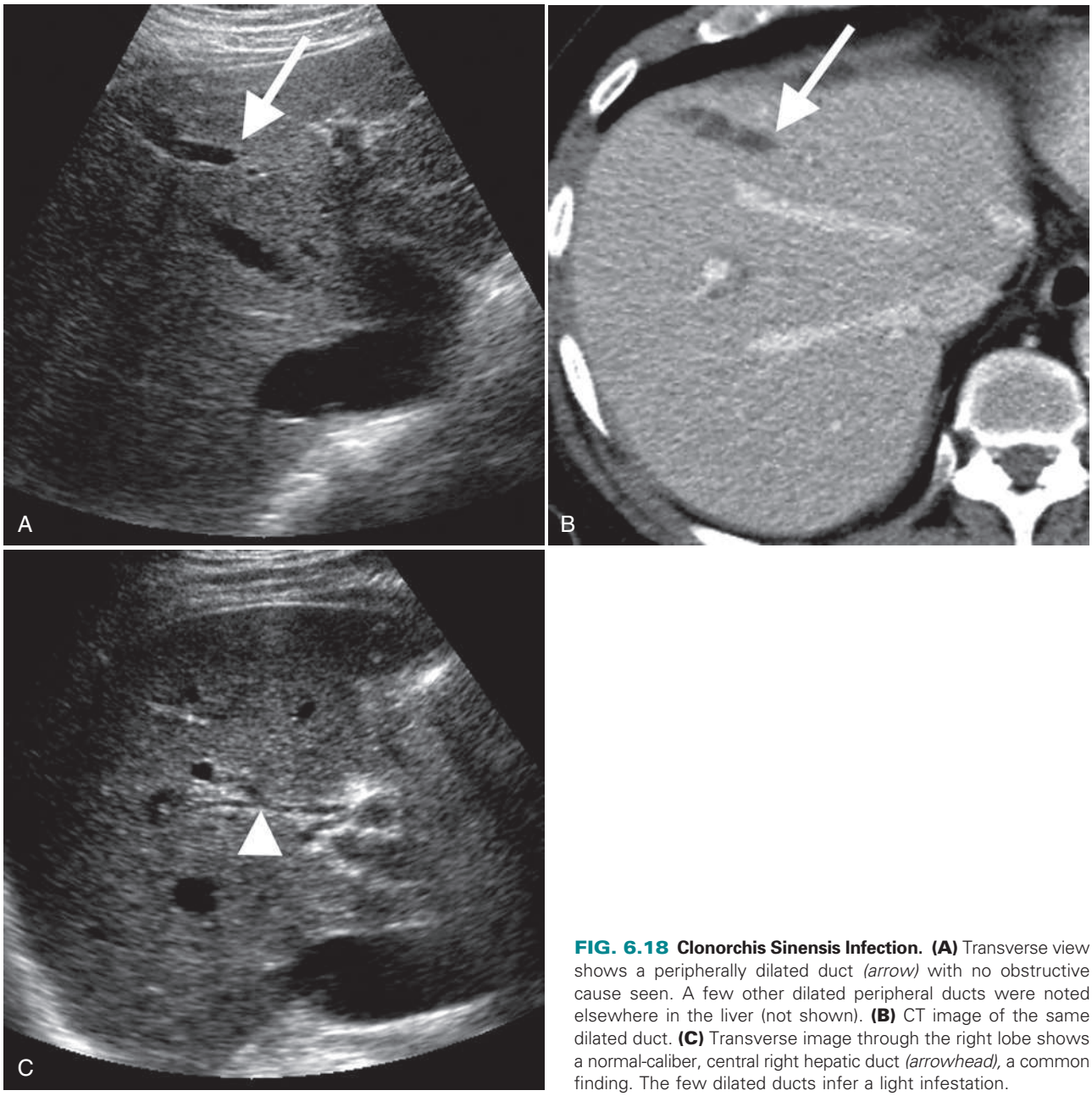

FIG. 6.18 Clonorchis Sinensis Infection. (A) Transverse view shows a peripherally dilated duct *(arrow)* with no obstructive cause seen. A few other dilated peripheral ducts were noted elsewhere in the liver (not shown). **(B)** CT image of the same dilated duct. **(C)** Transverse image through the right lobe shows a normal-caliber, central right hepatic duct *(arrowhead),* a common finding. The few dilated ducts infer a light infestation.

The imaging of *O. felineus* infestation has not been systematically described.

Recurrent Pyogenic Cholangitis

Recurrent pyogenic cholangitis has been known by other names, including **hepatolithiasis** and (now obsolete) **Oriental cholangiohepatitis.** It is a disease characterized by chronic biliary obstruction, stasis, and stone formation, leading to recurrent episodes of acute pyogenic cholangitis. Its incidence is highest in Southeast and East Asia. It is rare and sporadic in other populations. Although liver fluke infections (especially *C. sinensis*), malnutrition, and portal bacteremia have all been implicated, the cause of recurrent pyogenic cholangitis remains unknown.[36] Any segment of the liver may be affected, but the lateral segment of the left lobe is most often involved. Acute complications of the disease, most importantly sepsis, may be fatal and may need urgent percutaneous biliary decompression or surgery. The chronic stasis and inflammation eventually lead to severe atrophy of the affected segment. Biliary cirrhosis and cholangiocarcinoma are long-term complications. The treatment of hepatolithiasis lies in repeated biliary dilation and stone removal.[37]

Ultrasound is often used for both screening and monitoring of recurrent pyogenic cholangitis.[19] The typical **appearance on sonography** is dilated ducts filled with sludge and stones, confined to one or more segments of the liver (Figs. 6.19 and 6.20). Patients may also have multiple echogenic masses in the liver, and recognizing that these, in fact, lie within extremely dilated ducts requires care. When dilated ducts are identified, their

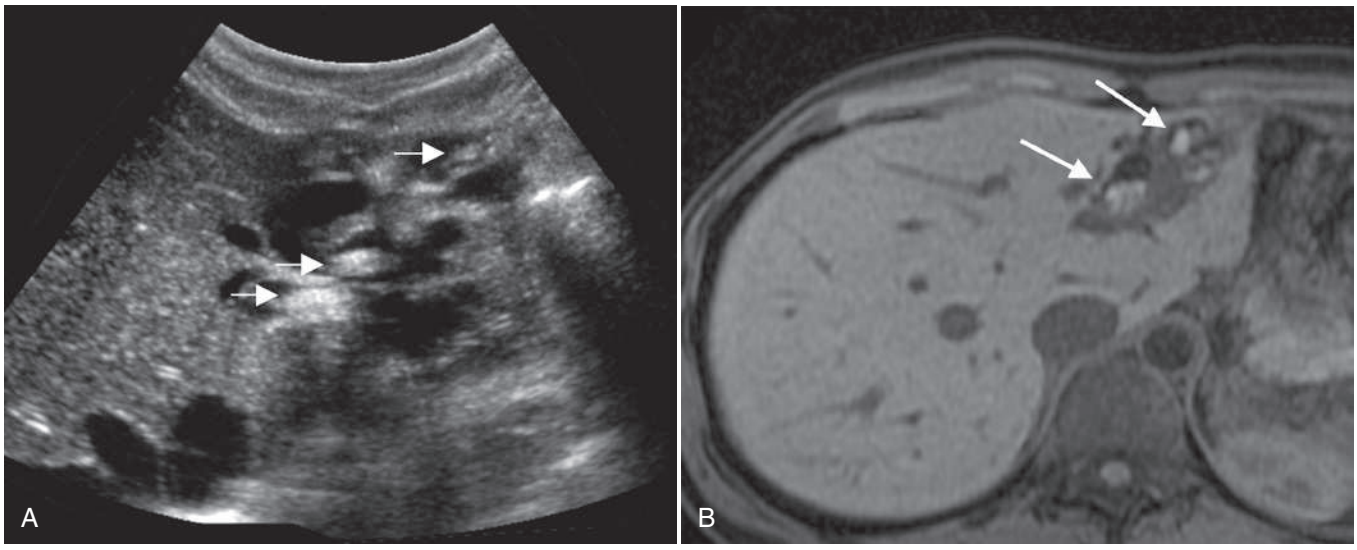

FIG. 6.19 Segmental Recurrent Pyogenic Cholangitis. (A) Transverse sonogram and **(B)** T1-weighted MRI scan depict severe atrophy of segment 3 around dilated, stone-filled ducts *(arrows).*

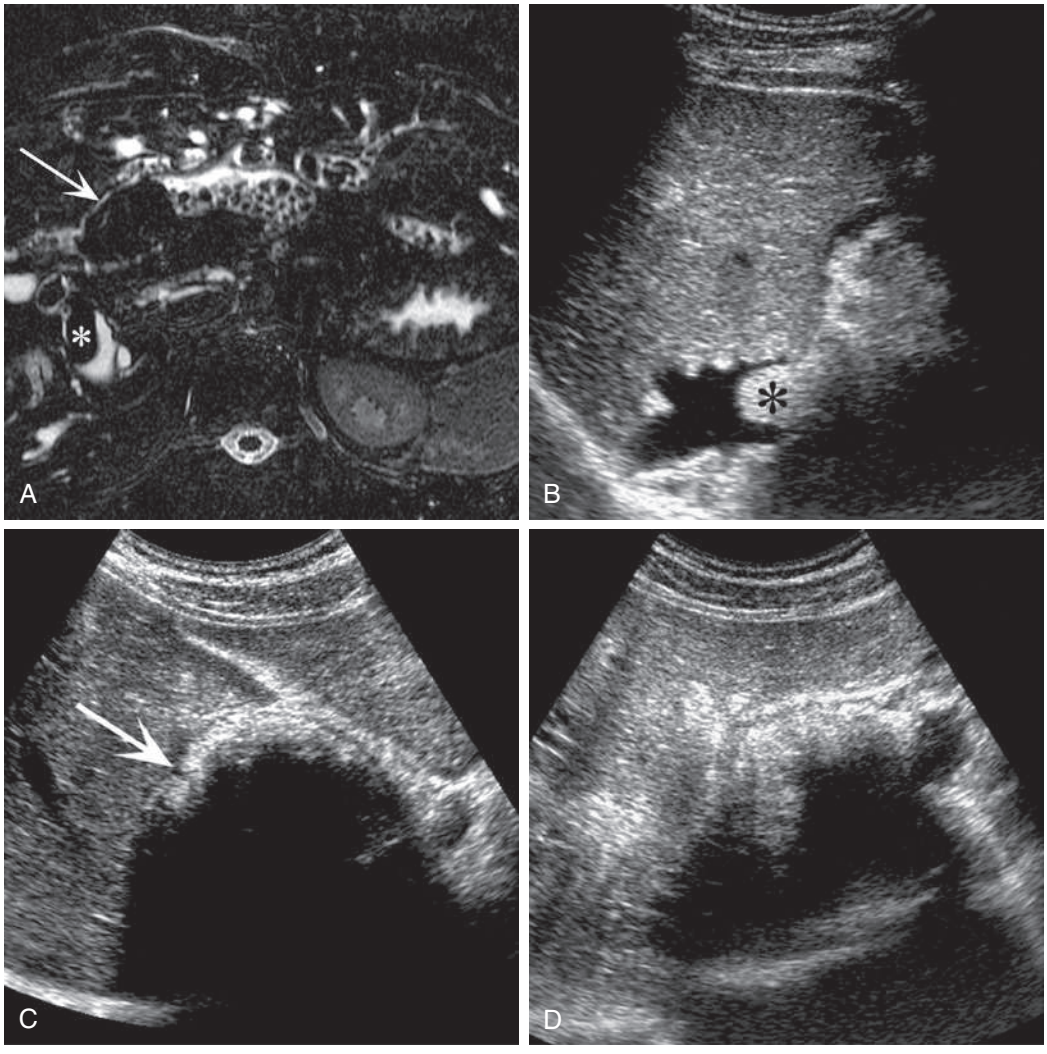

FIG. 6.20 Recurrent Pyogenic Cholangitis. (A) Transverse MRCP view through the liver demonstrates greatly dilated biliary tree filled with stones. **(B)** Transverse ultrasound image of the right lobe shows a large stone (*) in the dilated right posterior duct, corresponding to abnormality on MRCP view. **(C)** Huge stone in the central duct *(arrow)* with marked posterior acoustic shadowing. **(D)** Multiple small stones in the left lobe, which appear as a masslike, echogenic conglomerate on the sonogram. This is the most common appearance of recurrent pyogenic cholangitis, especially when accompanied by atrophy of the hepatic parenchyma.

contents may be hypoechoic or echogenic, and the stones may not show shadowing. With severe atrophy of the affected segment, minimal liver parenchyma may be present, and the crowded, stone-filled ducts may appear as a single, heterogeneous mass.

Ascariasis

Ascaris lumbricoides is a parasitic roundworm estimated to infect up to one-quarter of the world's population. It uses a **fecal-oral route** of transmission and is most common in children, presumably because of their lower hygiene.[38] The worm is generally 20 to 30 cm long and up to 6 mm in diameter. It is active within the small bowel and may enter the biliary tree retrogradely through the ampulla of Vater, causing acute biliary obstruction. Generally, infected patients are asymptomatic but may present with biliary colic, cholangitis, acalculous cholecystitis, or pancreatitis.

The **appearance** of biliary ascariasis on sonography depends on the number of worms within the bile ducts at the time of the study. Most often, a single worm is identified that appears as a tube or as parallel echogenic lines within the bile ducts. The appearance is similar to a biliary stent, which should be excluded on clinical history. On the transverse view, the rounded worm surrounded by the duct wall gives a target appearance. The worm may be folded on itself or may occupy any portion of the ductal system, including far into the liver parenchyma, close to the capsule, or within the gallbladder. Movement of the worm during the scan facilitates the diagnosis. When infestation is heavy, multiple worms may lie adjacent to each other within a distended duct, resembling spaghetti. Occasionally, the worms may appear as an amorphous, echogenic filling defect, making the diagnosis more difficult.[38]

HIV Cholangiopathy

Also known as acquired immunodeficiency syndrome **(AIDS) cholangitis,** human immunodeficiency virus (HIV) cholangiopathy is an inflammatory process affecting the biliary tree in the advanced stages of HIV infection. It is most often caused by an opportunistic infection and therefore occurs in patients with CD4 counts of less than 100. Patients present with severe RUQ pain or epigastric pain, a nonicteric cholestatic picture, and greatly elevated serum alkaline phosphatase with a normal bilirubin level. In most patients a pathogen is recovered, usually ***Cryptosporidium*** or, less often, **cytomegalovirus.**[39]

Sonography has been advocated as the first imaging test for assessment of HIV cholangiopathy (Fig. 6.21). A negative scan

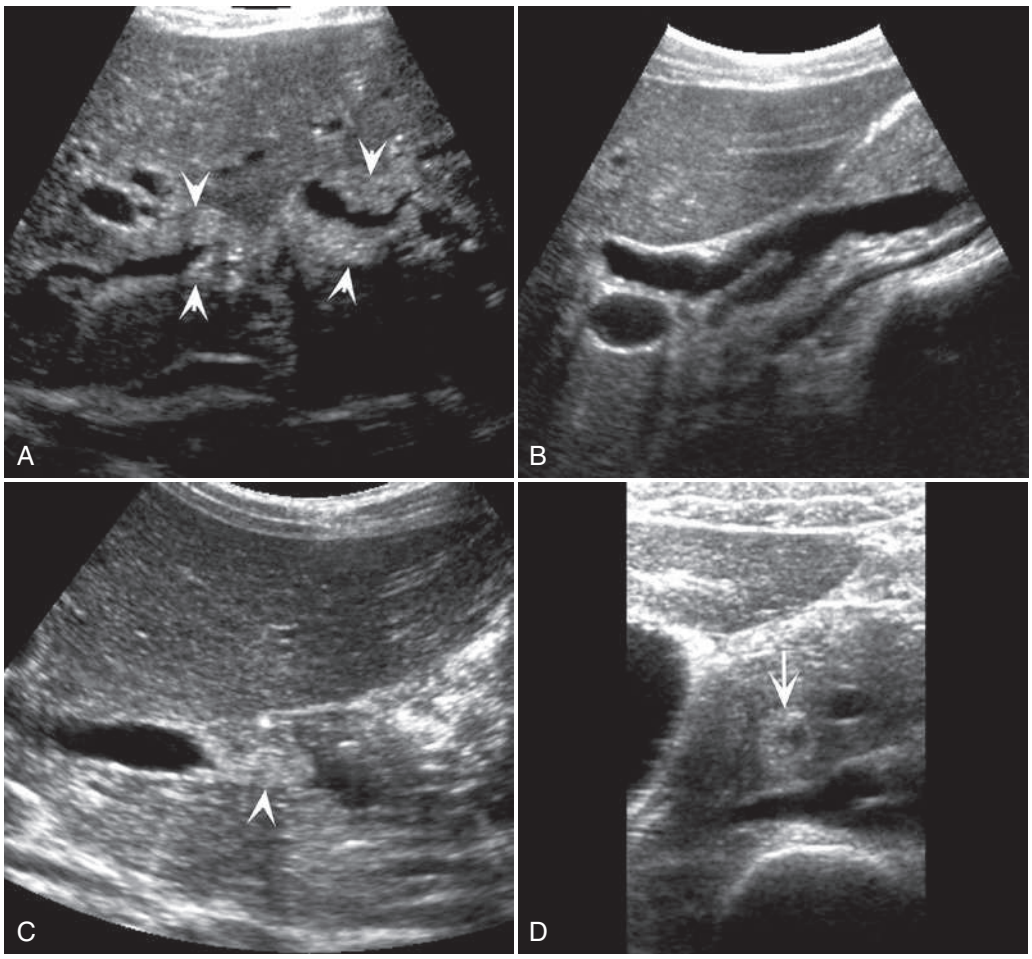

FIG. 6.21 HIV Cholangiopathy. (A) Intrahepatic biliary tree. Note the thick rind of echogenic tissue *(arrowheads)* surrounding the central portal triads and causing irregular narrowing of the bile ducts. **(B)** Common bile duct (CBD) is dilated, and its wall is minimally irregular. **(C)** Papillary stenosis. The dilated CBD abruptly tapers in an echogenic, inflamed ampulla *(arrowhead).* **(D)** Transverse view of ampulla *(arrow),* which is enlarged and echogenic, viewed in the caudal aspect of pancreatic head.

effectively rules out the disease. The findings include the following:

- Bile duct wall thickening of the intrahepatic and extrahepatic biliary tree.
- Focal strictures and dilations identical to those of primary sclerosing cholangitis.
- Dilation of the CBD caused by an inflamed and stenosed papilla of Vater (papillary stenosis). The inflamed papilla itself may be seen as an echogenic nodule protruding into the distal duct.[40]
- Diffuse gallbladder wall thickening.[41]

Immune-Related Diseases of the Biliary Tree

Primary Biliary Cirrhosis and Autoimmune Cholangitis

Primary biliary cirrhosis and autoimmune cholangitis (also called **autoimmune cholangiopathy**) affect biliary ductules that are too small to resolve by imaging. Only gross changes in the liver architecture resulting from biliary cirrhosis are detected. **Biliary cirrhosis,** resulting from any cause of chronic diffuse biliary obstruction, appears as diffusely enlarged liver unless the liver disease is end-stage.

Primary Sclerosing Cholangitis

Sclerosing cholangitis is a chronic inflammatory disease process affecting the biliary tree. If the cause of the disease is unknown, the term *primary sclerosing cholangitis* is used.

Primary sclerosing cholangitis is a chronic disease affecting the entire biliary tree. The process involves a fibrosing inflammation of the small and large bile ducts, leading to biliary strictures and cholestasis and eventually biliary cirrhosis, portal hypertension, and hepatic failure.[42,43] It occurs more frequently in men, with median age of 39 years at diagnosis.[38] About 80% of the patients have concomitant **inflammatory bowel disease,** typically **ulcerative colitis,** but this association occurs less often in a non-Western population. It may also occur with other autoimmune disorders.[36]

Most patients diagnosed with primary sclerosing cholangitis are asymptomatic. Ultrasound is a key component of the multimodality assessment of patients with this disease. The high spatial resolution of ultrasound allows for detection of minute early changes that can be missed with MRCP. Sonographic findings include irregular, circumferential bile duct wall thickening of varying degree, encroaching on and narrowing the lumen (Fig. 6.22, Videos 6.5 and 6.6). Focal strictures and dilations of the bile ducts ensue. The extrahepatic disease is more easily visible. A high degree of suspicion and careful examination of the portal triads in all hepatic segments is required to detect intrahepatic ductal involvement. **Irregularity of the thickened bile duct mucosa** is a key feature that should be sought. An earlier study suggested false normal appearance of the intrahepatic bile ducts in 25% of patients.[39] The gallbladder and cystic duct are involved in 15% to 20% of patients.[40] **Choledocholithiasis,** once thought to exclude the disease, is now recognized as a complication and is more frequently seen in symptomatic patients.[41] They are most often nonshadowing (Fig. 6.22D). The stones are easily overlooked and should be specifically sought especially with patients with deteriorating cholestatic liver enzymes. Patients with primary sclerosing cholangitis also have hepatic findings of biliary cirrhosis, namely hepatomegaly, and enlarged periportal lymph nodes. In advanced cases, findings of cirrhosis are present, often with diffuse atrophy of the liver but occasionally manifest as peripheral atrophy with central hypertrophy of the liver.[44]

Cholangiocarcinoma develops in 7% to 30% of patients with primary sclerosing cholangitis and is particularly a difficult diagnosis to make in this setting.[43] Rapid progression of the disease or development of a visible mass is a clue to this complication (Fig. 6.23, Videos 6.7 and 6.8). Hepatic transplantation is required in the latter stages of the disease. Unfortunately, the disease may recur in the transplanted organ in 1% to 20% of patients.[45]

IgG4-Related Cholangitis

Immunoglobulin G subtype 4 (IgG4)–related cholangitis is the biliary manifestation of **IgG4-related disease** or **multifocal systemic fibrosclerosis.** The exact cause of the disease is unknown but is associated with elevation of serum immunoglobulin G and specifically IgG subtype 4 levels in a majority of patients. In the abdomen, the most commonly affected organ is the pancreas, resulting in **autoimmune pancreatitis,** followed by the biliary tree and gallbladder, the kidneys **(interstitial nephritis),** and the retroperitoneum **(retroperitoneal fibrosis).**[46] A history of salivary or lacrimal gland disease is also common. The disease predominates in older patients and is more common in males. Unlike primary sclerosing cholangitis, the disease tends to be **steroid responsive.** IgG4-related cholangitis affects both large and small ducts. There is a lymphoplasmacytic infiltrate about the ducts with associated fibrosis causing strictures; if untreated it can lead to cirrhosis. Given the similarity in imaging appearance to primary sclerosing cholangitis, until recently it has been mistaken for this disease.

Several features help the differentiation or at least direct the referring clinicians to further investigations. In IgG4-related disease, the patient is usually older and the disease may spontaneously resolve or improve. Bile duct wall thickening can be much

Causes of Secondary Sclerosing Cholangitis

IgG4-related sclerosing cholangitis
AIDS cholangiopathy
Bile duct neoplasm[a]
Biliary tract surgery, trauma
Choledocholithiasis
Congenital abnormalities of biliary tract
Ischemic stricturing of bile ducts
Toxic strictures related to intraarterial infusion of floxuridine
Posttreatment for hydatid cyst

[a]Primary sclerosing cholangitis not previously established.
Modified from Narayanan Menon KV, Wiesner RH. Etiology and natural history of primary sclerosing cholangitis. *J Hepatobiliary Pancreat Surg.* 1999;6(4):343-351.[43]

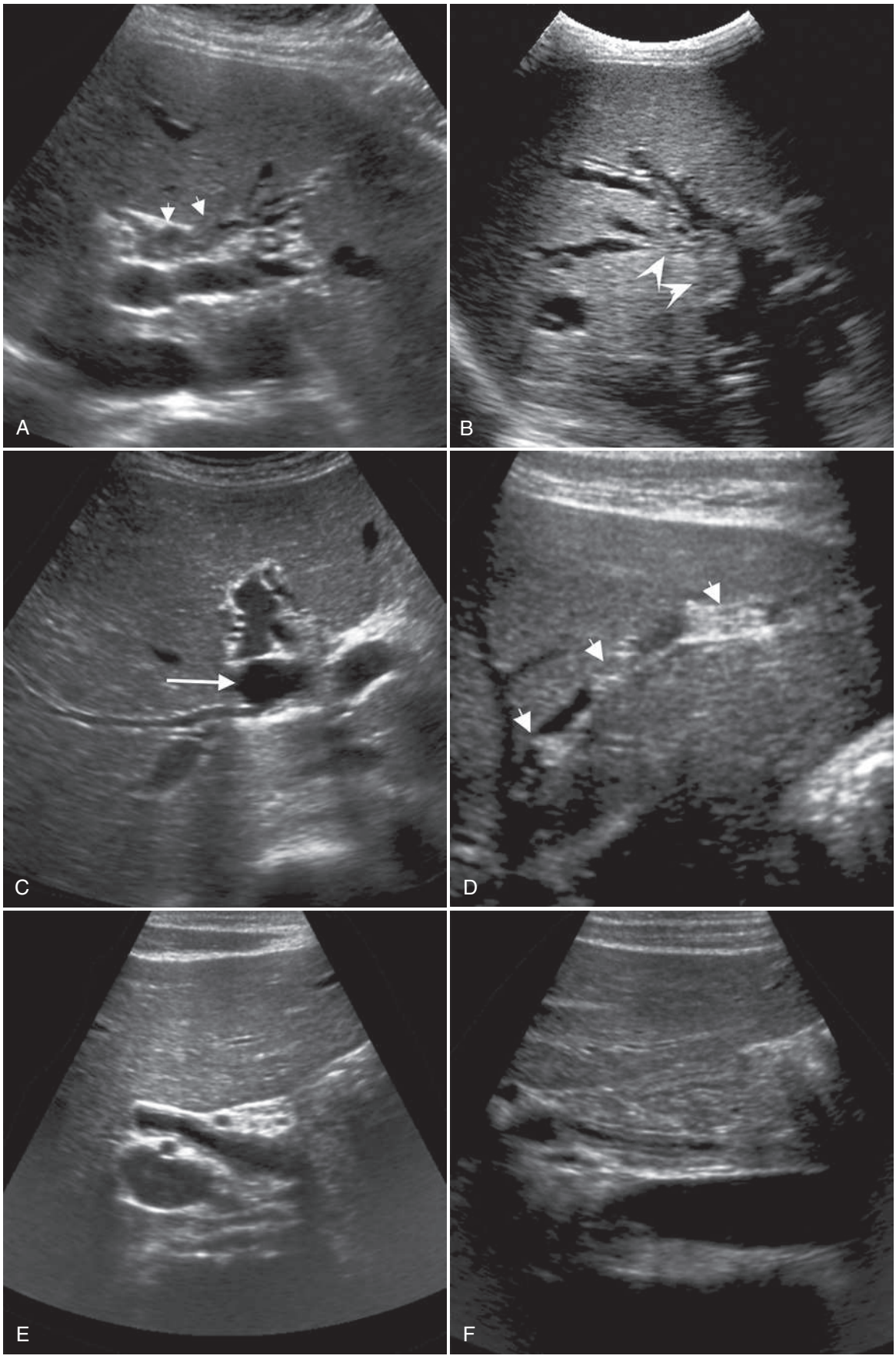

FIG. 6.22 Primary Sclerosing Cholangitis. (A) Isoechoic inflammatory tissue causing obliteration of right and left hepatic ducts *(short arrows)* with proximal dilation. **(B)** Dilated intrahepatic ducts "rat-tail" as they extend centrally toward the hepatic hilum. Note the hypoechoic ductal/periductal tissue obstructing the central ducts *(arrowheads).* **(C)** Saccular diverticula *(arrow)* of the duct are occasionally seen presumably due to distal obstruction. **(D)** Intraductal stones *(short arrows)* are seen, which often do not shadow. **(E)** and **(F)** Common bile duct wall thickening of moderate and severe degrees, respectively. Note the extremely narrowed, anechoic central lumen with a finely serrated appearance. See also Videos 6.5 and 6.6.

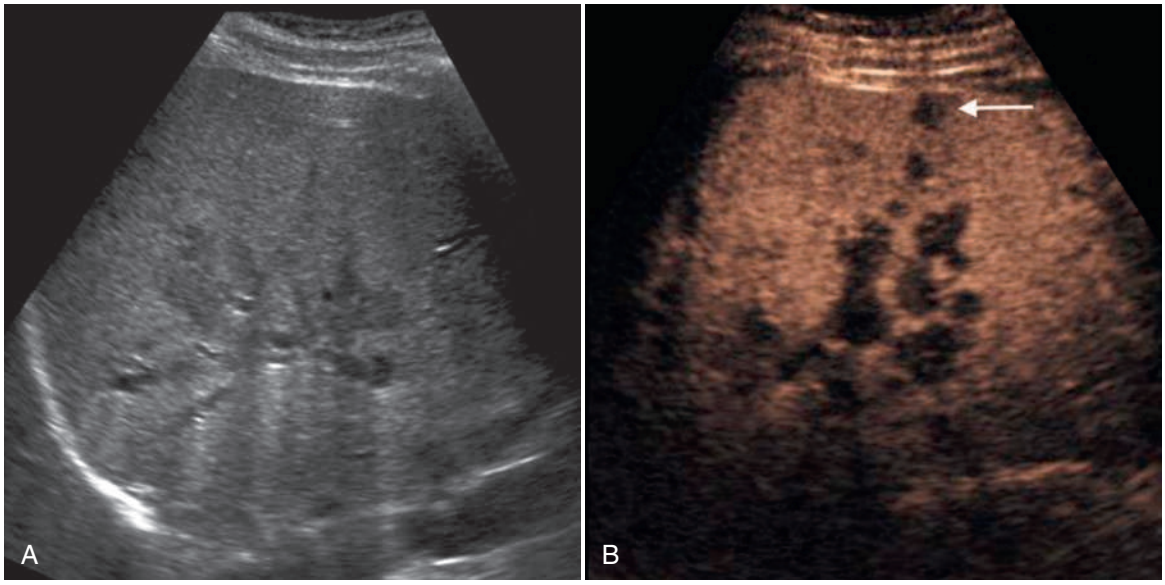

FIG. 6.23 Cholangiocarcinoma in Primary Sclerosing Cholangitis. (A) An infiltrative mass is seen centered on dilated ducts. **(B)** Contrast-enhanced ultrasound in the venous phase improves the visualization of the tumor margins and extent, including a satellite subcapsular focus not visible on the gray-scale scan. See also Videos 6.7 and 6.8.

more pronounced than in primary sclerosing cholangitis (single wall thickness > 3 mm) and can appear masslike (Fig. 6.24).[47] Strictures are longer and continuous as opposed to skip disease in primary sclerosing cholangitis, but mucosal irregularity, which is an important feature of primary sclerosing cholangitis, is difficult to appreciate. Many patients with IgG4-related cholangitis have involvement of other organs, which can be searched for during the scan; pancreatic involvement virtually makes the diagnosis. Many of the changes improve within weeks of commencement of steroid therapy.

Cholangiocarcinoma

Cholangiocarcinoma is an uncommon neoplasm that may arise from any portion of the biliary tree. Its incidence varies geographically and is highest in populations with known risk factors. Overall incidence ranges from 1 or 2 per 100,000 population in the United States, 2 to 6 in other Western countries, 5.5 in Japan, and up to 130 per 100,000 in northeastern Thailand, where the liver fluke *Opisthorchis viverrini* is endemic.[48,49] The frequency of cholangiocarcinoma increases with age, with the peak incidence in the eighth decade. Most cholangiocarcinomas are sporadic, but several risk factors exist, usually related to chronic biliary stasis and inflammation. **Primary sclerosing cholangitis** is the most common risk factor for cholangiocarcinoma in the Western world; the lifetime risk of developing a clinically detectable cholangiocarcinoma in these patients is about 10%.[50] The most common risk factors in other populations are **recurrent biliary infections** and **stone disease.**

Cholangiocarcinomas are classified based on the anatomic location: **intrahepatic,** also called peripheral (≈10%); **hilar,** also called **Klatskin** (≈60%); and **distal** (≈30%).[51] Approximately 90% of cholangiocarcinomas are **adenocarcinomas,** with squamous carcinomas the next most common subtype.[52] Macroscopically, cholangiocarcinomas are divided into three subtypes: sclerosing, nodular, and papillary; the first two subtypes frequently occur together. **Nodular-sclerosing tumors,** the most common subtype, appear as a firm mass surrounding and narrowing the affected duct, with a nodular intraductal component. Most hilar cholangiocarcinomas are of the nodular-sclerosing variety. These tumors incite a prominent desmoplastic reaction and demonstrate a periductal, perineural, and lymphatic pattern of spread along the ducts, as well as subendothelial spread within the ducts. **Papillary cholangiocarcinomas** represent approximately 10% of these tumors and are most common in the distal CBD. Patients present with an intraductal polypoid mass that expands, rather than constricts, the duct.[51,53,54]

The overall prognosis for cholangiocarcinoma is poor. In a large, single-center series, the 5-year survival rate for patients with intrahepatic, hilar, and distal cholangiocarcinoma was 23%, 6%, and 24%, respectively, and improved to only 44%, 11%, and 28% in patients who underwent resection.[55]

Intrahepatic Cholangiocarcinoma

Intrahepatic cholangiocarcinoma, also called **peripheral cholangiocarcinoma,** are the least common location for cholangiocarcinomas, but they represent the second most common primary malignancy of the liver. They arise from the second-order or higher-order branches of the biliary tree within the liver parenchyma, and their histologic origin is different than that of extrahepatic ducts. The incidence of intrahepatic cholangiocarcinomas has been increasing in part because of the increase in numbers of patients with liver cirrhosis and long-term hepatitis C infection.[56] Hepatitis B also has recently been identified as a risk factor.[57] These tumors are associated with a poor prognosis because the mass is often unresectable.[58,59]

The most common manifestation of intrahepatic cholangiocarcinoma is a large hepatic mass. The sonographic appearance is often that of a hypovascular solid mass with heterogeneous

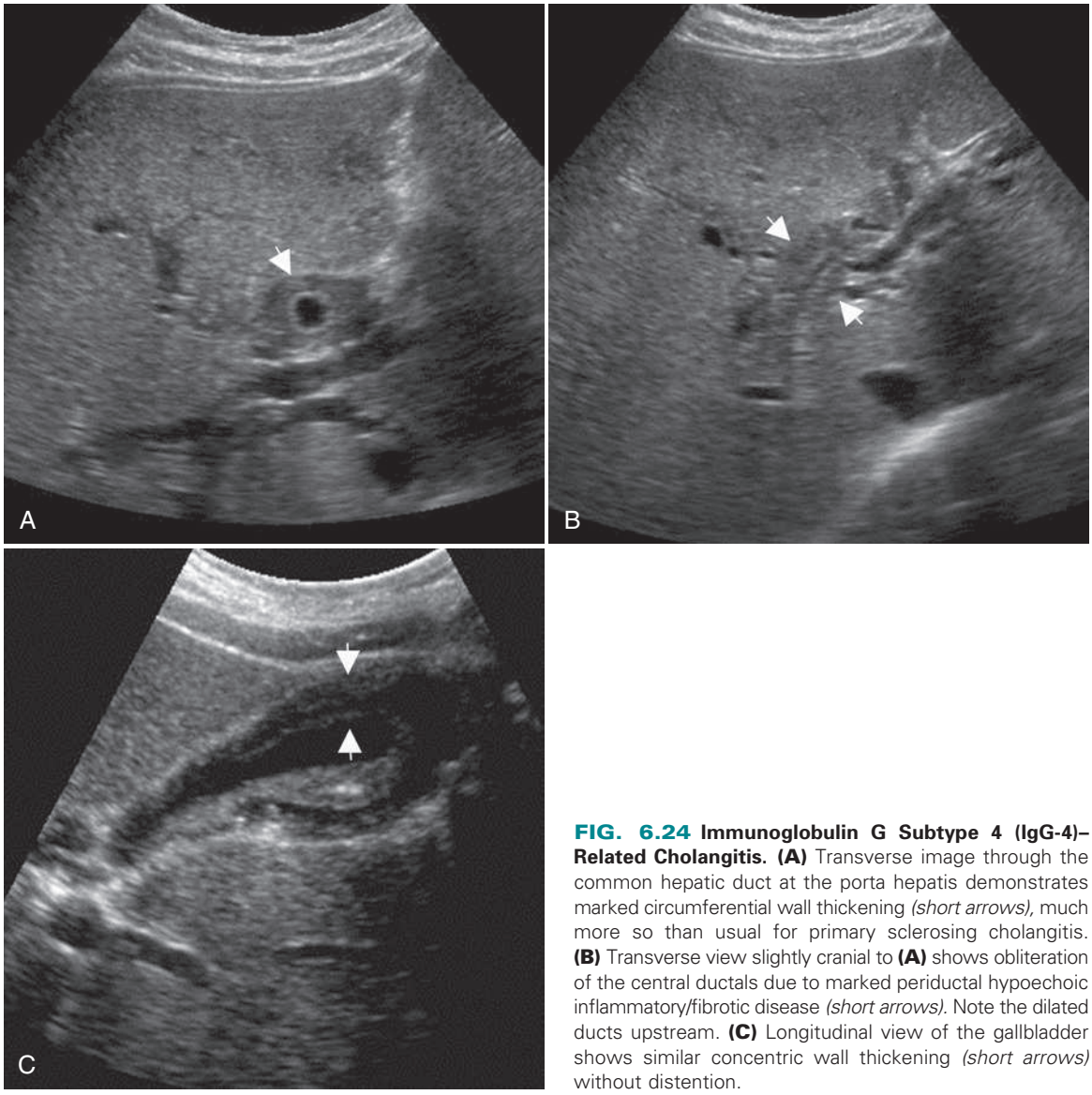

FIG. 6.24 Immunoglobulin G Subtype 4 (IgG-4)–Related Cholangitis. (A) Transverse image through the common hepatic duct at the porta hepatis demonstrates marked circumferential wall thickening *(short arrows),* much more so than usual for primary sclerosing cholangitis. **(B)** Transverse view slightly cranial to **(A)** shows obliteration of the central ductals due to marked periductal hypoechoic inflammatory/fibrotic disease *(short arrows).* Note the dilated ducts upstream. **(C)** Longitudinal view of the gallbladder shows similar concentric wall thickening *(short arrows)* without distention.

echotexture, and it may appear hypoechoic, isoechoic, or hyperechoic (Fig. 6.25). A clue to the differentiation from **hepatocellular carcinoma** is a much higher incidence of **ductal obstruction,** reportedly occurring in 31% of patients with intrahepatic cholangiocarcinoma and only 2% of those with hepatocellular carcinoma.[60,61] Contrast-enhanced ultrasound also provides differentiating features (see Chapter 4 for further discussion). However, a solitary metastasis to the liver may cause intrahepatic ductal obstruction and therefore may be difficult to distinguish.[62]

A more unusual manifestation of intrahepatic cholangiocarcinoma is a purely intraductal mass, called **intraductal intrahepatic cholangiocarcinoma.** These polypoid masses distend the affected ducts, often third-order or fourth-order branches, spreading within the duct and filling it with **mucin.** These tumors have a much better prognosis and are thought to be histologically separate from other intrahepatic cholangiocarcinomas, resembling papillary tumors of the extrahepatic bile ducts.[59,63] The most common appearance of the intraductal intrahepatic cholangiocarcinoma is one or more polypoid masses confined to the bile ducts. Abundant mucin production, manifest sonographically with a subtle layered appearance, can greatly distend the affected lobar and distal ducts (Fig. 6.26). Occasionally a focal mass is not evident as the disease diffusely affects the bile ducts, as a result of **biliary papillomatosis,** a rare condition in which there is diffuse papillary adenoma formation throughout the biliary tree.[64] A less common form may present as a solid mass within a cystic structure, representing tumor within an extremely distended duct that does not communicate with the biliary tree (Fig. 6.27).

Hilar Cholangiocarcinoma

The correct identification and staging of hilar cholangiocarcinoma are challenging with all imaging modalities because of the tumor's **desmoplastic** nature (causing fibrous tissue formation), its peribiliary and subendothelial patterns of growth, and the

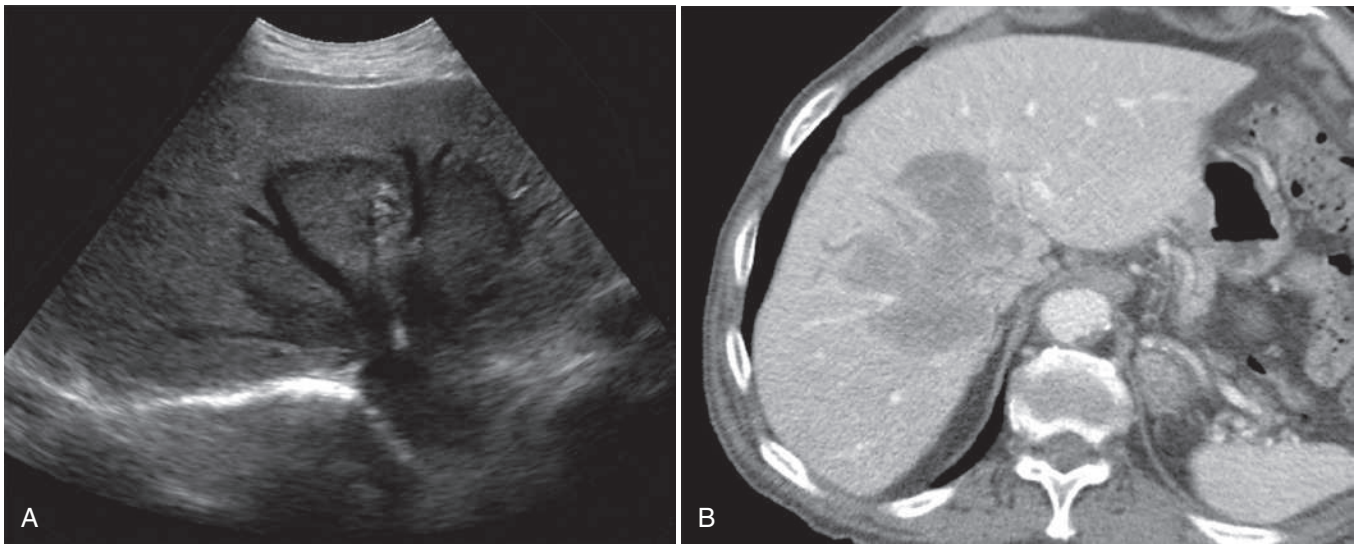

FIG. 6.25 Peripheral Cholangiocarcinoma. (A) Ultrasound and **(B)** CT images depict a solid mass encasing but not obliterating the right and middle hepatic veins, a finding suggestive of peripheral cholangiocarcinoma.

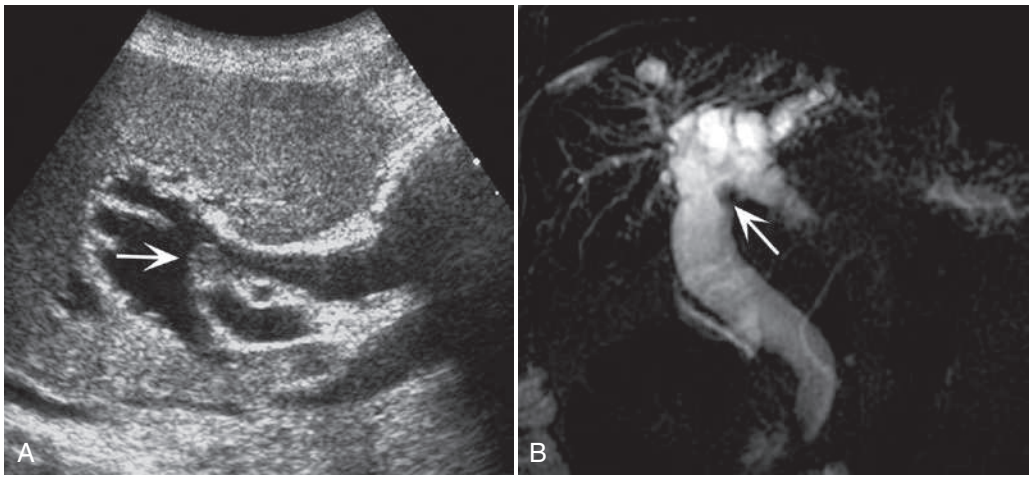

FIG. 6.26 Intraductal Papillary, Mucin-Producing Tumor of Bile Ducts. (A) Ultrasound and **(B)** MRCP images show papillary tumor arising from the common hepatic duct *(arrow)* and causing diffuse ductal dilation due to excessive mucin production.

complex anatomy of the porta hepatis, with structures lying just outside the liver and surrounded by connective tissue. Ultrasound plays an important role in both detection and staging of hilar cholangiocarcinomas because it is often the first modality used in assessment of these tumors. Furthermore, ultrasound is often performed before any biliary manipulation and stent placement. Because biliary intervention often obscures the intraductal disease and causes secondary bile duct thickening, sonography may be the only cross-sectional modality to assess the unmanipulated ducts. Most patients with hilar cholangiocarcinoma present for a sonographic evaluation with jaundice, pruritus, and elevated cholestatic liver parameters, or with vague symptoms and elevated serum alkaline phosphatase or γ-glutamyl transpeptidase levels.

Patterns of Tumor Growth. Hilar cholangiocarcinomas often begin in either the right or the left bile duct and extend both proximally into higher-order branches and distally into the CHD and contralateral bile ducts. The spread of tumor may be subendothelial, or within the peribiliary connective tissue, leading to obstruction or irregular ductal narrowing. The tumors also extend outside the ducts to involve adjacent portal vein and arteries. Chronic obstruction, especially if accompanied with portal vein involvement, leads to atrophy of the involved lobe. Nodal disease often begins in the porta hepatis and within the hepatoduodenal ligaments (local nodes) and extends to celiac, superior mesenteric, peripancreatic, and posterior pancreatoduodenal stations (distant nodes).[65] Metastases are usually to the liver and peritoneal surfaces.

Treatment and Staging. Curative treatment of cholangiocarcinoma requires surgical resection; the vast majority of patients with unresectable disease die within 12 months of diagnosis.[51] The current surgical approach to patients with hilar cholangiocarcinoma is resection of the involved lobe with extensive hilar dissection to remove tumor extending to the contralateral lobe (extended lobectomy). A biliary-enteric anastomosis is created to allow bile drainage. Currently, no widely used staging systems

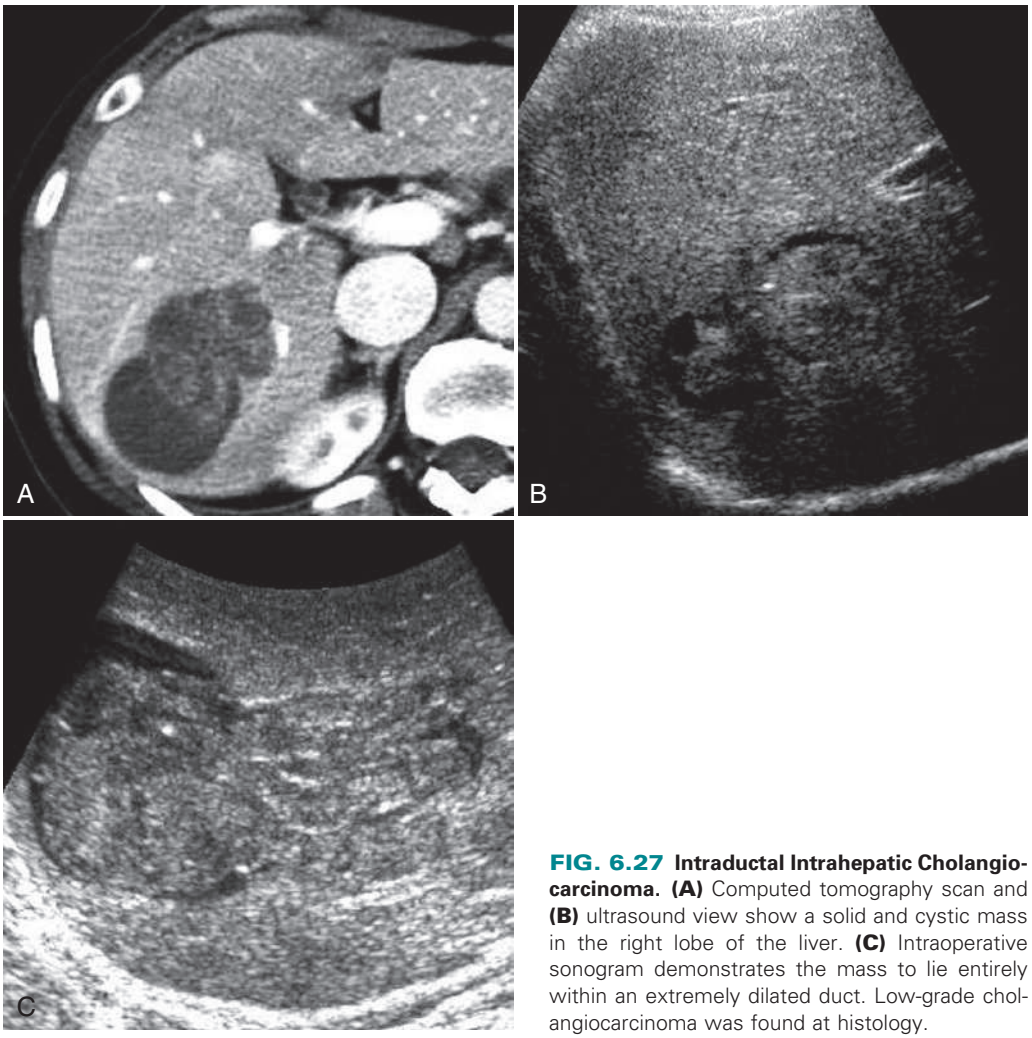

FIG. 6.27 Intraductal Intrahepatic Cholangiocarcinoma. (A) Computed tomography scan and **(B)** ultrasound view show a solid and cystic mass in the right lobe of the liver. **(C)** Intraoperative sonogram demonstrates the mass to lie entirely within an extremely dilated duct. Low-grade cholangiocarcinoma was found at histology.

accurately stratify patients based on surgical resectability. However, Jarnagin et al.[65] proposed a system that allows for preoperative staging of hilar cholangiocarcinoma. Because a lobectomy is performed, the remaining liver parenchyma, its portal vein, hepatic artery, and at least some proximal length of its lobar bile duct (first-order branch of CHD) should ideally be free of disease. The main portal vein and proper hepatic artery should also ideally be disease free. The remaining liver should not have undergone significant atrophy because it may not be able to maintain hepatic function. Although regional nodes may be removed en bloc with the tumor, distant nodal disease precludes resection. Advancements in surgical techniques now allow biliary-enteric anastomoses using second-order ducts and vessel resection with reconstruction; therefore criteria for resectability vary according to the age of the patient and local surgical preference.[66]

Assessment by Conventional and Doppler Sonography. An accurate assessment of hilar cholangiocarcinoma requires diligent, hands-on involvement by the responsible physician. The use of various views and patient positions as well as familiarity with biliary anatomy and common variants significantly improves sonographic performance. Once dilated intrahepatic ducts have been detected, the following parameters should be assessed:

- Level of the obstruction
- Presence of a mass
- Lobar atrophy

Criteria for Unresectable Hilar Cholangiocarcinoma

Hepatic duct involvement up to secondary biliary radicles bilaterally
Encasement or occlusion of the main portal vein proximal to its bifurcation
Atrophy of one hepatic lobe with encasement of contralateral portal vein branch
Atrophy of one hepatic lobe with contralateral involvement of secondary biliary radicles
Distant metastases (peritoneum, liver, and lung)

With permission from Jarnagin WR. Cholangiocarcinoma of the extrahepatic bile ducts. *Semin Surg Oncol.* 2000;19(2):156-176.[51]

- Patency of main, right, and left portal veins
- Encasement of hepatic artery
- Local and distant adenopathy
- Presence of metastases

Dilation of the higher-order intrahepatic bile ducts with nonunion of the right and left ducts is the classic appearance of hilar cholangiocarcinomas[62] (Figs. 6.28 and 6.29). When encountered, dilated ducts should be followed centrally toward the hepatic hilum to determine which order of branching (segmental ducts and higher or right/left hepatic ducts) is involved with tumor. Tumor extension into segmental ducts bilaterally precludes resection.

The obstructing tumor is not always visualized by sonography. Rates of sonographic detection of masses range from 21% to 87%, with more recent studies showing higher rates.[67-69] When a mass is not directly visualized, its presence can be inferred based on the level of obstruction, although this often underestimates the tumor extent.[70] **Lobar atrophy** leads to crowding of the dilated bile ducts and, if long-standing, a shift in the axis of the liver caused by hypertrophy of the contralateral side. The atrophy of the lobe is often accompanied by obliteration of its portal vein and precludes its resection. **Differences in lobar echogenicity,** caused by the varying degree of ductal and vascular obstruction between the two lobes, is an uncommon finding (Fig. 6.30).

The main, right, and left **portal veins** should all be examined with both gray-scale and color Doppler sonography. Narrowing of the right or left portal veins leads to compensatory increased flow in the accompanying hepatic artery; when prominent arterial signal is noted on color Doppler, the portal venous flow should be carefully examined (see Fig. 6.30). Tumor encasing, narrowing, or obliterating the main portal vein or the proper hepatic artery renders the tumor unresectable, unless en bloc resection of the vessels is contemplated. Detection of the extrahepatic tumor infiltration and early peritoneal metastases is difficult with sonography, and CT or MRI is recommended as an adjunct for preoperative assessment.

Assessment by Contrast-Enhanced Sonography. The role of contrast is in the assessment of the liver-invasive component of cholangiocarcinoma, and the differentiation of intraductal enhancing tumor from sludge and debris within the duct. Both the liver-specific phase of enhancement in agents that are retained by the reticuloendothelial system and the venous/delayed phase in agents that remain purely within the intravascular space are useful in this regard. Depending on the agent, the delayed or liver-specific phase of enhancement significantly increases the contrast difference between the liver parenchyma and invasive tumors that show washout or lack uptake. Therefore the invasive component of cholangiocarcinoma—not seen in a significant minority of patients—becomes visible in most, if not all, cases[70] (see Fig. 6.23; Fig. 6.31, Videos 6.7 and 6.8). This improved visibility allows for improved performance of sonography in the staging of hilar cholangiocarcinomas.[70]

Distal Cholangiocarcinoma

Distal cholangiocarcinomas are clinically indistinguishable from the hilar forms, with progressive jaundice seen in 75% to 90% of patients.[51] Although the nodular-sclerosing subtype still predominates, polypoid masses are seen more frequently. Surgical resection is the most effective therapy, so a careful search for spread that would preclude resection is vital. The tumor may locally extend cranially within the ducts, even involving the cystic and right and left hepatic ducts; therefore the superior extent of the tumor must be clearly defined. The tumor may also extend beyond the duct walls. Patients may present with a distal obstructive mass with identical appearance to pancreatic adenocarcinoma. The status of the adjacent vascular structures must be determined, including portal and superior mesenteric veins and common hepatic artery. Spread to **lymph nodes** adjacent to the tumor is common. Spread to more distant nodes, such as celiac, superior mesenteric, and periportal regions may preclude resection.[51] Surgical approach to a distal cholangiocarcinoma is a pancreaticoduodenectomy.

On sonography the distal cholangiocarcinoma has a variable appearance. A **polypoid tumor** appears as a duct-expanding, well-defined intraductal mass, often with no internal vascularity (Fig. 6.32). The **nodular-sclerosing tumor** causes focal irregular ductal constriction and duct wall thickening. In more advanced disease the tumor appears as a hypoechoic, hypovascular mass with poorly defined margins invading adjacent structures.

Metastases to Biliary Tree

Metastases to the biliary tree mimic the varied appearance of cholangiocarcinoma, affecting both the intrahepatic and extrahepatic ducts (Fig. 6.33). The history of past or concurrent malignancy along with multiple lesions should suggest metastases. In our experience the breast, colon, and skin (melanoma) constitute the primary sites of malignancy.

THE GALLBLADDER

Anatomy and Normal Variants

The gallbladder is a pear-shaped organ lying in the inferior margin of the liver, between the right and left lobes (Fig. 6.34). The middle hepatic vein lies in the same anatomic plane and may be used to help find the **gallbladder fossa.** The **interlobar fissure,** the third structure separating the two hepatic lobes, extends from the origin of the right portal vein to the gallbladder fossa. This fissure has been seen in up to 70% of hepatic ultrasound studies[71] and may also be used as a landmark for the gallbladder fossa. The gallbladder is divided into the fundus, body, and neck; the fundus is the most anterior, and often inferior, segment. In the region of the gallbladder neck, there may be an infundibulum, called the **Hartmann pouch,** which is a common location for impaction of gallstones.[11]

The gallbladder derives as an outpouching from the embryonic biliary tree. The proximal portion of the pouch forms the cystic duct, and the distal portion forms the gallbladder. Within the cystic duct (and sometimes the gallbladder neck) are small mucosal folds called the **spiral valves of Heister;** these are occasionally identified on sonography. During its initial development, the gallbladder lies in an intrahepatic position, but as it

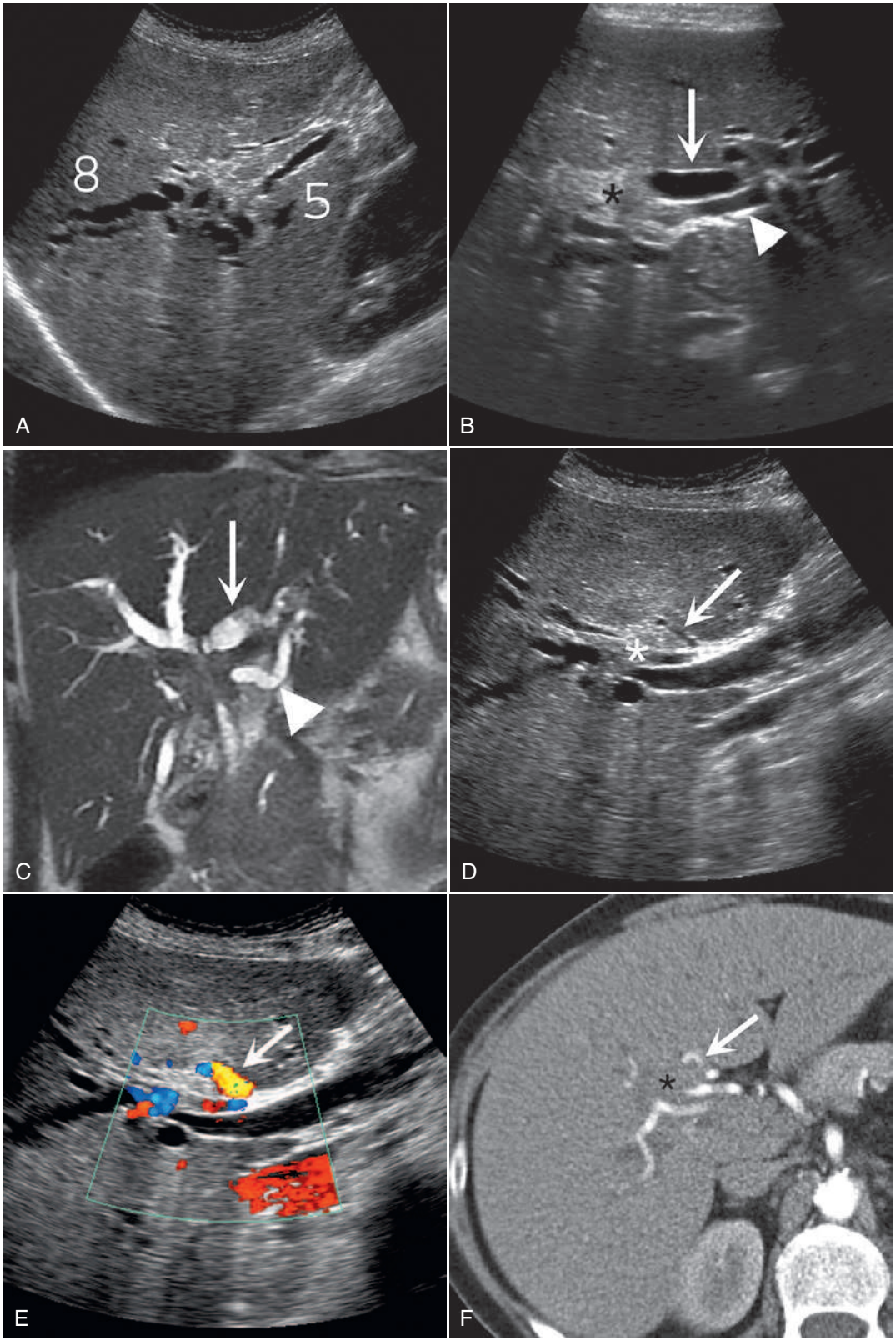

FIG. 6.28 Resectable Hilar Cholangiocarcinoma. (A) Sagittal image of the right lobe shows an invasive central echogenic tumor with segmental dilation of the ducts of segments 8 and 5, indicating second-order branch involvement. **(B)** Transverse view of the central left lobe shows the tumor (*) obstructing the distal left hepatic duct *(arrow)* and an aberrant segment 4 duct *(arrowhead)*. **(C)** Coronal T2-weighted MRI confirms the ultrasound findings of the central tumor obstructing the left hepatic *(arrow)* and aberrant segment 4 ducts *(arrowhead)*. **(D)** Transverse image of the porta hepatis depicts the tumor (*) narrowing the right portal vein and displacing branches of the right hepatic artery *(arrow)*. **(E)** Doppler image (same plane as **D**) confirms the right hepatic artery involvement. **(F)** Corresponding CT image in the arterial phase also shows intimate contact of tumor (*) with right hepatic artery branches *(arrow)*. The tumor did not extend deep into the left lobe, and the main and left hepatic arteries and portal vein were not involved; therefore the patient underwent an extended right-sided hepatectomy.

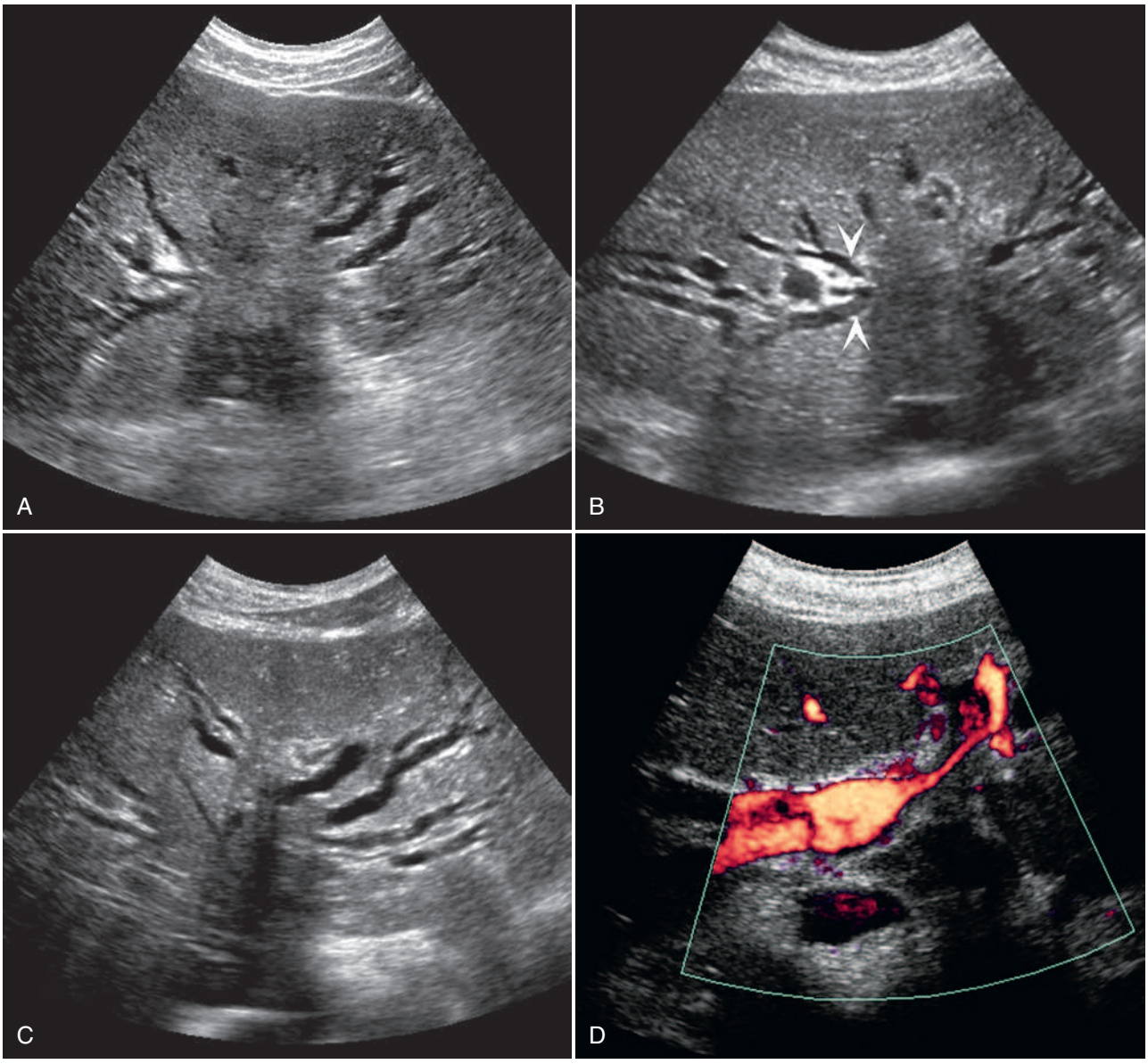

FIG. 6.29 Unresectable Hilar Cholangiocarcinoma. (A) Dilated right-sided and left-sided intrahepatic ducts with nonunion centrally, as seen here, are hallmarks of hilar cholangiocarcinoma. Determination of the level of obstruction is key in assessing resectability. **(B)** In right lobe view, the right anterior and posterior ducts *(arrowheads)* approach each other but never join to form the right hepatic duct. **(C)** In left lobe view, second-order and third-order branches end abruptly, blocked by tumor. Because the tumor completely involves the first-order branches (right and left hepatic ducts) bilaterally, it is unresectable. **(D)** Tumor also encases and narrows the left portal vein.

migrates to the surface of the liver, it acquires a peritoneal covering (part of liver capsule) typically covering 50% to 70% of its surface.[11] The remainder of the gallbladder surface is covered with adventitial tissue that merges with connective tissue in contiguity with the liver. In generalized edematous processes or local inflammation, this potential space between the gallbladder and liver is a common area for edema. Failure to migrate may lead to an **intrahepatic gallbladder** (or partially intrahepatic), a rare but important finding that may preclude laparoscopic surgery[72] (Fig. 6.35). Conversely, the gallbladder may become fully enveloped in visceral peritoneum, hanging from a mesentery that extends from the liver. This leads to increased mobility of the gallbladder and appears to be a risk factor in the rare development of **torsion (volvulus) of the gallbladder.**[73]

Failure to identify the gallbladder on sonographic examination most often results from a previous cholecystectomy. Occasionally, chronic cholecystitis leading to a collapsed and fibrosed gallbladder makes its detection difficult. At times a collapsed gallbladder filled with stones (wall-echo-shadow, see Fig. 6.36B) will be mistaken for bowel gas. **Agenesis of the gallbladder** is rare, occurring in up to 0.09% of the population.[74] Although most often incidental, dilation of the bile duct and choledocholithiasis may occur with gallbladder agenesis, leading to attempted cholecystectomy in some patients. In most cases the cystic duct

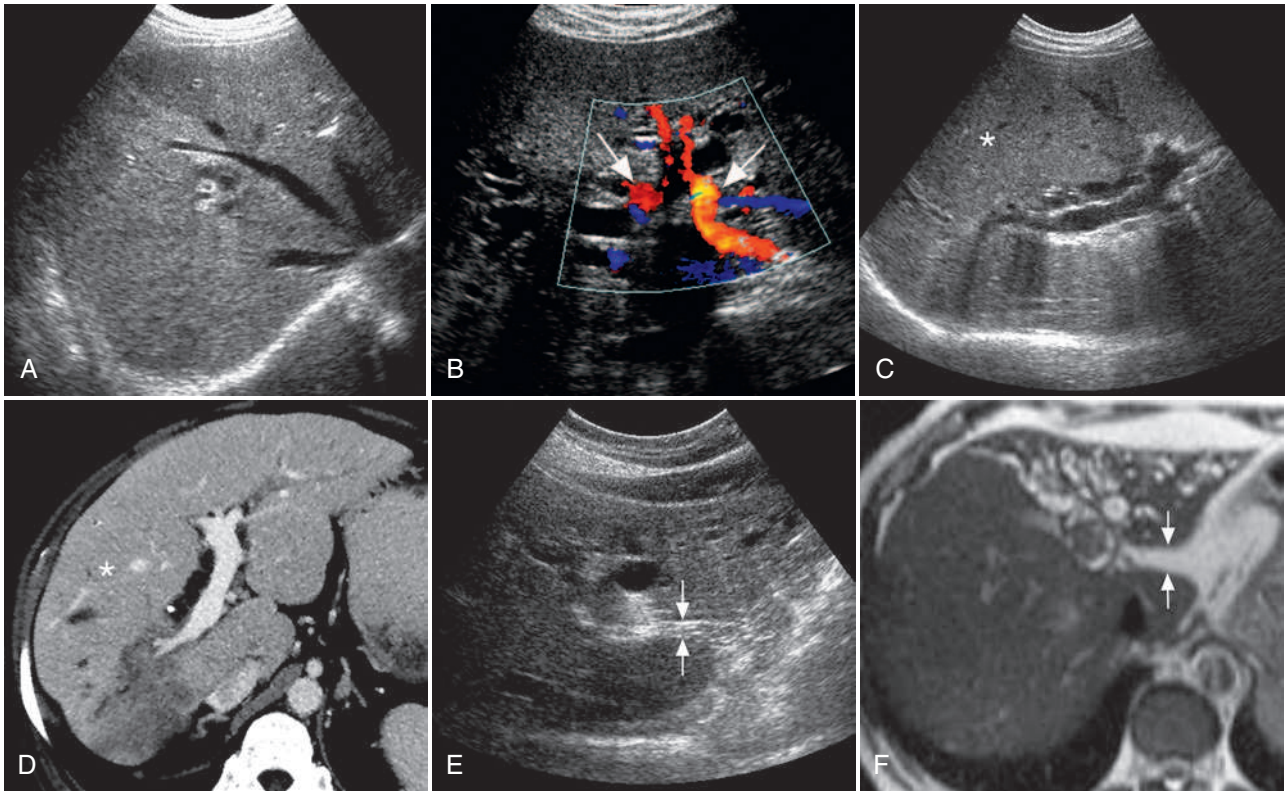

FIG. 6.30 Secondary Findings in Hilar Cholangiocarcinoma. (A) Difference in lobar echogenicity. The right lobe of the liver is demarcated from the left by its increased echogenicity. The right biliary system was obstructed by tumor centrally. **(B) Compensatory increased flow in hepatic arteries.** Enlarged hepatic arterial branches *(arrows)* on either side of the ascending branch of the left portal vein are clearly seen, whereas no flow is noted in the portal vein. This finding suggests severe stenosis or obstruction of the portal vein. **(C)** and **(D) Lobar atrophy.** Marked atrophy of the right lobe with compensatory hypertrophy of the left lobe (*). Enlarged medial segment of the left lobe. **(E)** and **(F) Lobar atrophy.** Marked atrophy of the left lobe of the liver. Besides the small size, widening of the fissure for ligamentum venosum *(arrows)* and concave liver margins are secondary clues. **(F)** Axial SSFSE T2-weighted MRI shows the same.

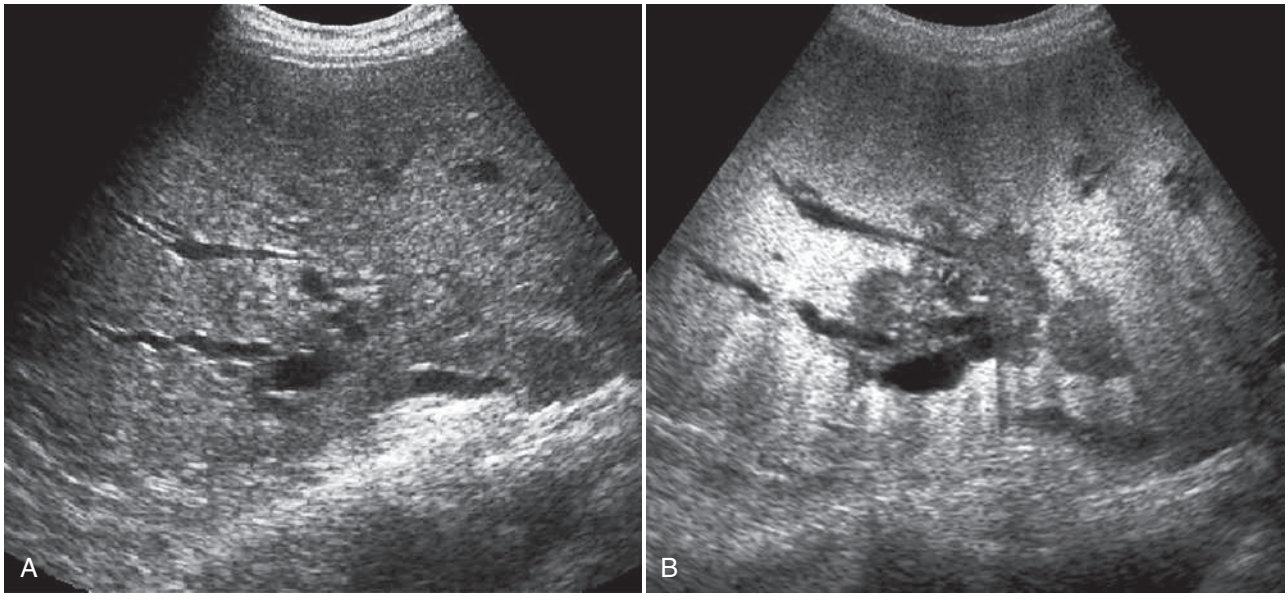

FIG. 6.31 Cholangiocarcinoma: Conventional Versus Contrast Evaluation. (A) Routine gray-scale image demonstrates dilated ducts terminating abruptly. The tumor is not visible. **(B)** Contrast-enhanced image obtained in the postvascular phase clearly depicts the margins of the unenhancing tumor.

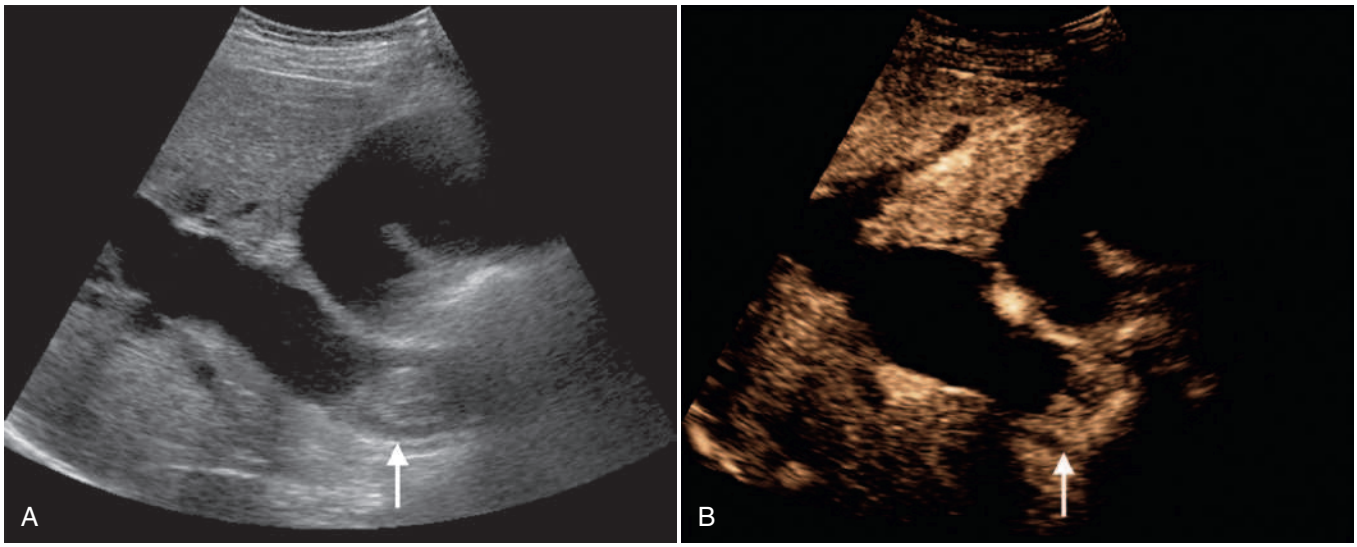

FIG. 6.32 Distal Cholangiocarcinoma. (A) Polypoid solid intraductal mass *(arrow)* within the distal common bile duct, causing ductal obstruction. **(B)** Corresponding contrast-enhanced image demonstrates internal enhancement *(arrow),* proving a vascularized tumor.

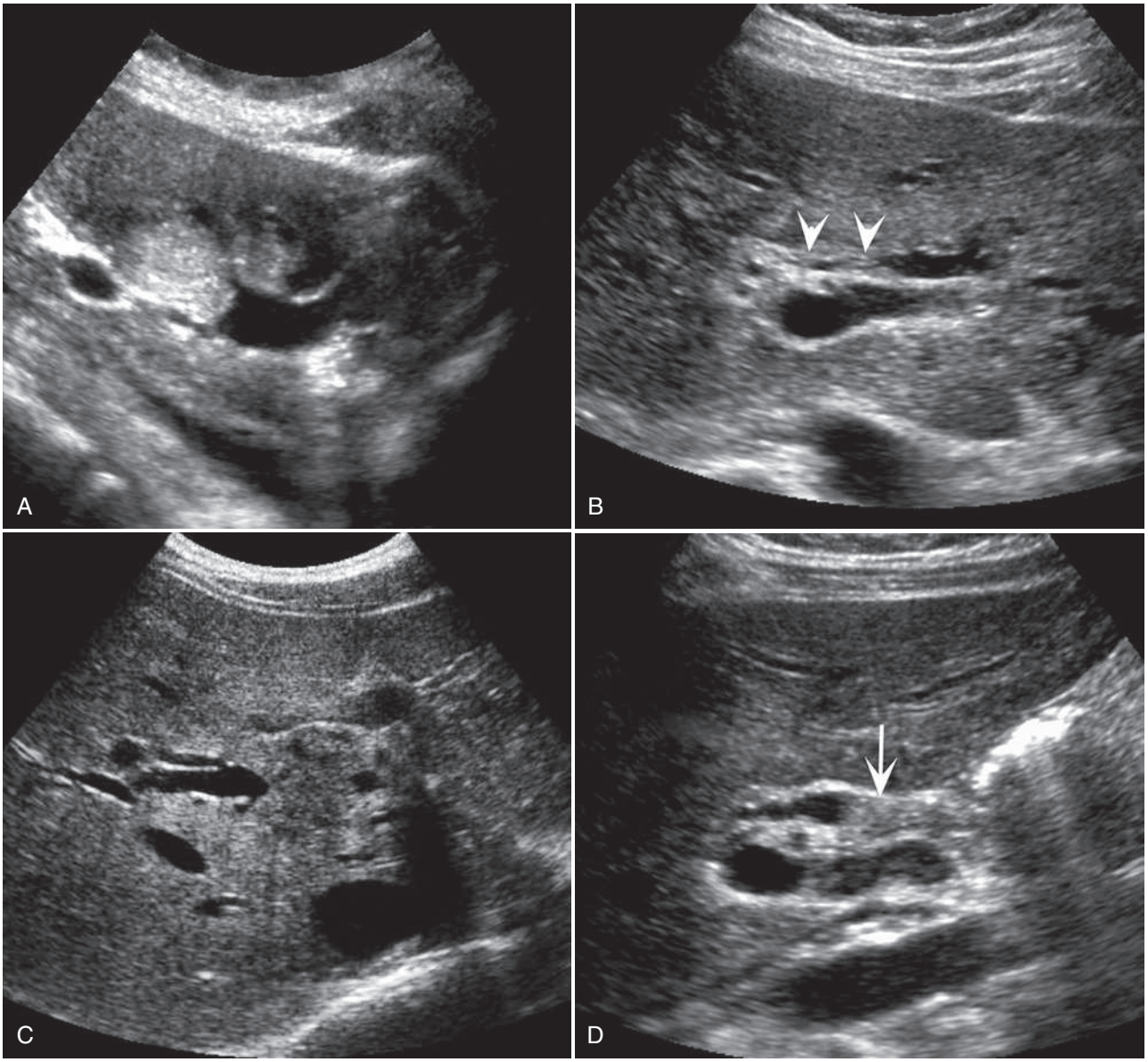

FIG. 6.33 Metastases to the Biliary Tree: Spectrum of Appearances. (A) Entirely intraductal echogenic mass obstructing left lobe of liver. **(B)** Periductal/duct wall infiltration *(arrowheads)* with obliteration of the left hepatic duct. **(C)** Poorly defined hilar tumor with ductal obstruction. **(D)** Echogenic intraductal tumor *(arrow)* within the extrahepatic ducts. In all cases, tumor mimics cholangiocarcinoma. The diagnosis in all four images was metastatic breast carcinoma.

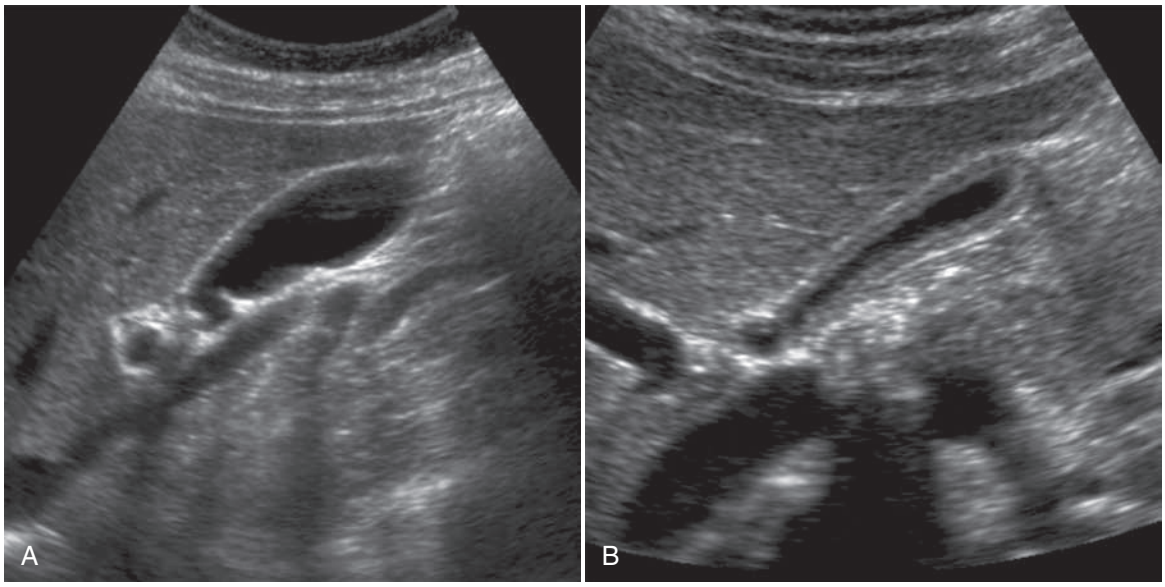

FIG. 6.34 Normal Gallbladder. (A) Distended (fasting). **(B)** Contracted (postprandial).

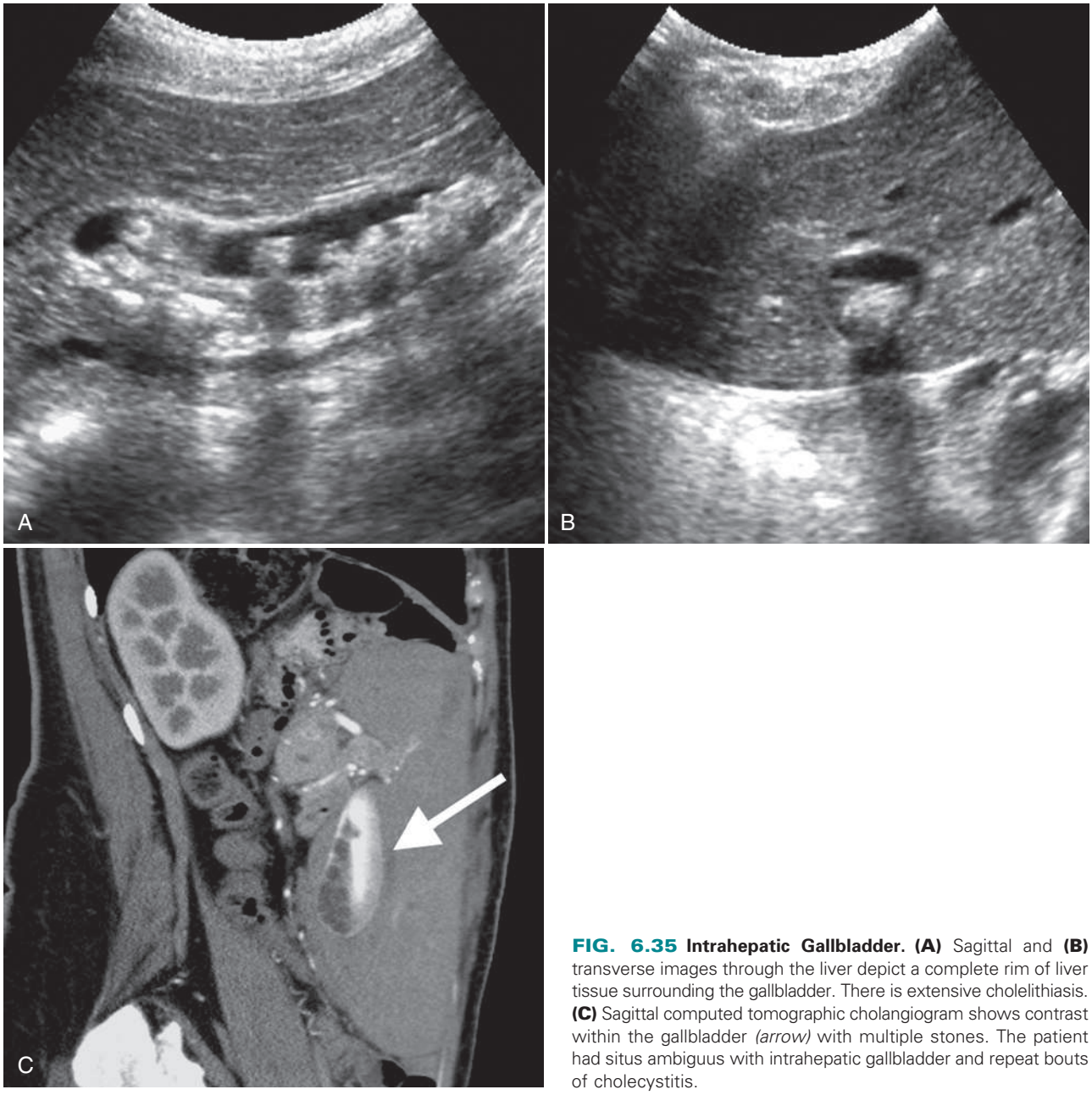

FIG. 6.35 Intrahepatic Gallbladder. (A) Sagittal and **(B)** transverse images through the liver depict a complete rim of liver tissue surrounding the gallbladder. There is extensive cholelithiasis. **(C)** Sagittal computed tomographic cholangiogram shows contrast within the gallbladder *(arrow)* with multiple stones. The patient had situs ambiguus with intrahepatic gallbladder and repeat bouts of cholecystitis.

Causes of Sonographic Nonvisualization of Gallbladder

Previous cholecystectomy
Physiologic contraction
Fibrosed gallbladder duct—chronic cholecystitis
Air-filled gallbladder or emphysematous cholecystitis
Tumefactive sludge
Agenesis of gallbladder
Ectopic location

is also absent. The lack of visualization of the gallbladder on sonography in symptomatic patients warrants CT or MRCP to avoid an unnecessary surgical procedure. The gallbladder may also lie in **ectopic** positions, including suprahepatic, suprarenal, within the anterior abdominal wall, or in the falciform ligament.[11]

The gallbladder may fold unto itself, the body onto the neck, or the fundus onto the body. The latter is called a **phrygian cap** and has no clinical importance. A **septate gallbladder** is composed of two or more intercommunicating compartments divided by thin septa.[11] This is distinguished from the hourglass gallbladder (see "Adenomyomatosis"), which has thick septa separating the components. **Duplication of the gallbladder** often occurs with duplication of the cystic duct and may be diagnosed prenatally. Variations of the cystic duct are discussed in the section on anatomy of the biliary tree.

The gallbladder derives its blood supply from the **cystic artery,** which arises from the right hepatic artery, or less often from the gastroduodenal artery. In acute cholecystitis an enlarged, prominent cystic artery may be identified on sonography.

Sonographic Technique

Evaluation of the gallbladder is usually performed with routine sagittal and transverse sonograms. If the gallbladder is not visualized, however, maneuvers to evaluate the gallbladder fossa are essential to avoid missing gallbladder disease. This is done primarily with subcostal oblique sonograms, performed with the left edge of the transducer more cephalad than the right edge. The face of the transducer is directed toward the right shoulder. A sweep from cephalad to caudad shows the middle hepatic vein superiorly and the gallbladder fossa inferiorly in a single plane. They form the anatomic boundary separating the right and left liver lobes. The fossa runs from the anterior surface of the right portal vein obliquely to the surface of the liver. It may have a variable appearance, mainly influenced by the state of the gallbladder, and after gallbladder removal the fossa appears as an echogenic line as a result of the remaining connective tissues.

Ingestion of food, particularly fatty food, stimulates the gallbladder to contract. The contracted gallbladder appears thick walled and may obscure luminal or wall abnormalities. Therefore the examination of the gallbladder should be performed after a minimum of 4 hours of fasting.

Gallstone Disease

Gallstone disease is common worldwide. The prevalence of gallstones is highest in the European and North American populations (≈10%) and lowest in the East Asian (≈4%) and sub-Saharan African (2%-5%) populations.[75] Common risk factors are age, female gender (but not in Asian populations), fecundity, obesity, diabetes, and pregnancy. Although most patients are asymptomatic, about one in five develops a complication, often biliary colic. The risk of acute cholecystitis or other serious complications of gallstones in patients with a history of biliary colic is about 1% to 2% per year.[76]

Sonography is highly sensitive in the **detection of stones** within the gallbladder. The varying size and number of stones within the gallbladder lead to a variable appearance on sonography (Fig. 6.36, Video 6.9). The large difference in the acoustic impedance of stones and adjacent bile makes them highly reflective, which results in an echogenic appearance with strong posterior acoustic shadowing. Small stones (<5 mm) may not show shadowing but will still appear echogenic. **Mobility** is a key feature of stones, allowing differentiation from polyps or other entities. Various maneuvers may be used to demonstrate mobility of a stone; scanning with the patient in the right or left lateral decubitus or upright standing position may allow the stone to roll within the gallbladder.

Multiple stones may appear as one large stone, producing uniform acoustic shadowing. When the gallbladder is filled with small stones or a single giant stone, the gallbladder fossa will appear as an echogenic line with posterior shadowing. This can be differentiated from air or calcification in the gallbladder wall by analysis of the echoes. With stones the gallbladder *wall* is first visualized in the near field, followed by the bright *echo* of the stone, followed by the acoustic *shadowing,* called the **wall-echo-shadow complex** (Fig. 6.36B). When air or calcification is present, the normal gallbladder wall is not seen, and only the bright echo and the posterior dirty shadowing are seen.

Milk of calcium bile, also known as **limey bile,** is a rare condition in which the gallbladder becomes filled with a pasty, semisolid substance of mainly calcium carbonate.[77] It is often associated with gallbladder stasis and in rare cases may cause acute cholecystitis or migrate into the bile ducts. The appearance on sonography is highly echogenic material with posterior acoustic shadowing, forming a bile calcium level on various patient positions (Fig. 6.37).

Biliary Sludge

Biliary sludge, also known as **biliary sand** or **microlithiasis,** is defined as a mixture of particulate matter and bile that occurs when solutes in bile precipitate. Its existence was first recognized with the advent of sonography. The exact prevalence of sludge is unknown in the general population because most studies have examined high-risk populations. The predisposing factors in development of sludge are pregnancy, rapid weight loss, prolonged fasting, critical illness, long-term total parenteral nutrition, ceftriaxone or prolonged octreotide therapy, and bone marrow transplantation. In one study, over a 3-year period, about 50% of cases resolved spontaneously, 20% persisted asymptomatically, 5% to 15% developed gallstones, and 10% to

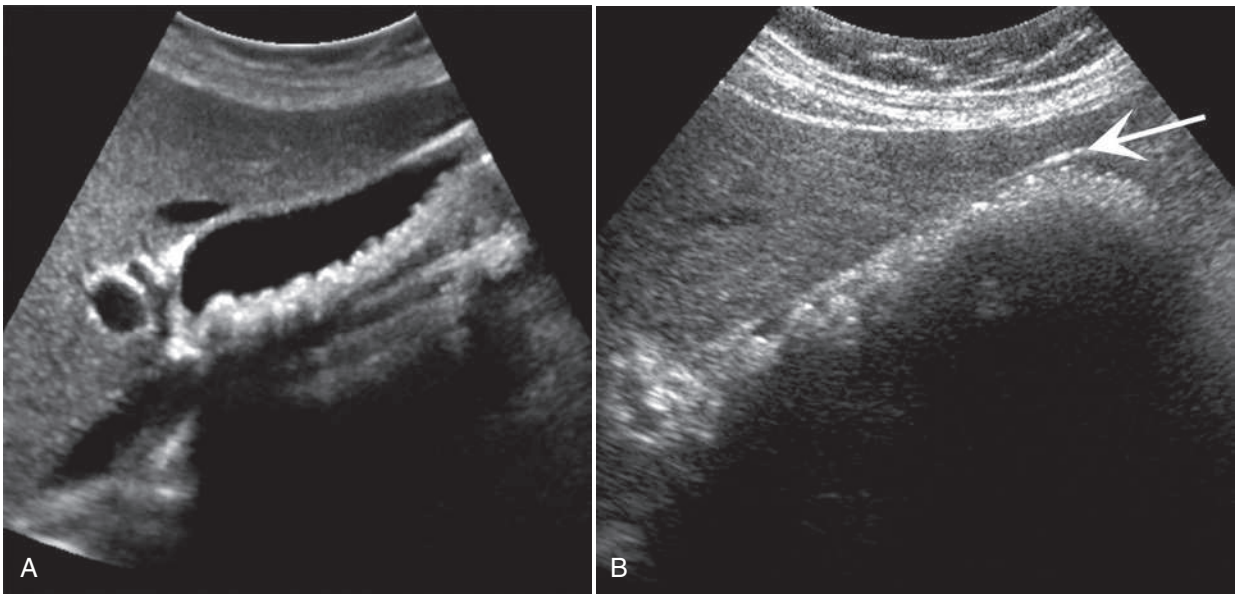

FIG. 6.36 Gallstones. (A) Sagittal image shows multiple dependent stones appearing as echogenic foci with posterior acoustic shadowing. **(B)** "Wall-echo-shadow complex" in a gallbladder filled with stones. Gallbladder wall *(arrow)* is thin. See also Video 6.9.

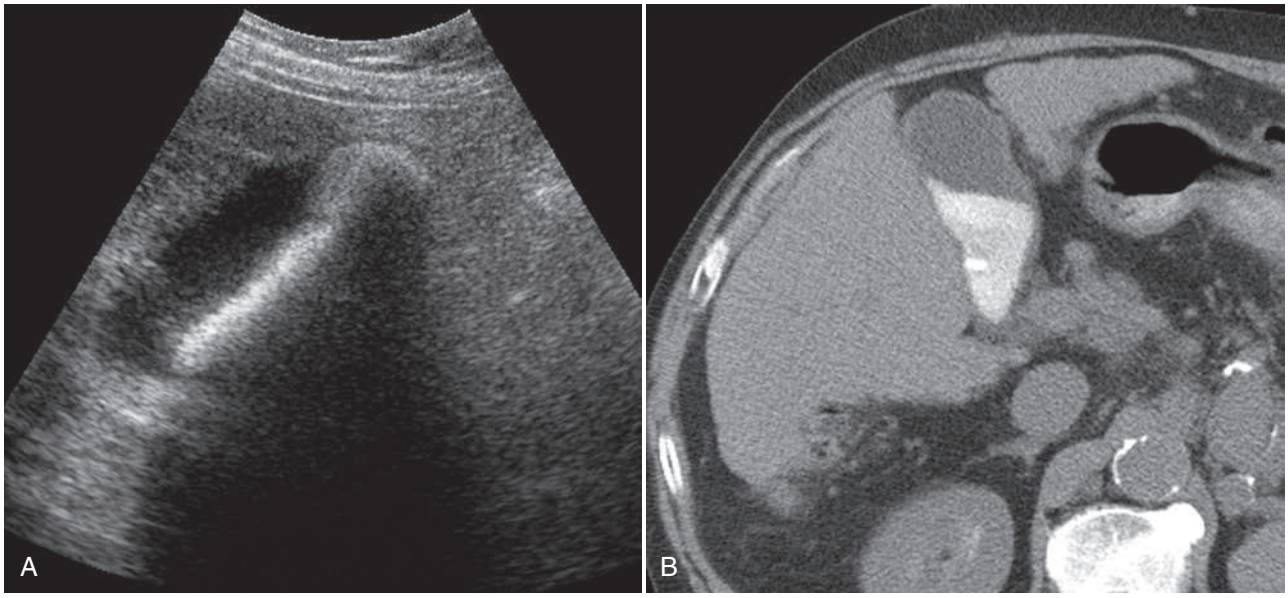

FIG. 6.37 Milk of Calcium Bile. (A) Sonogram and **(B)** corresponding CT scan show a bile calcium level.

15% became symptomatic.[78] The complications of biliary sludge are stone formation, **biliary colic, acalculous cholecystitis,** and **pancreatitis.**

The sonographic appearance of sludge is that of amorphous, low-level echoes within the gallbladder in a dependent position, with no acoustic shadowing. With a change in patient position, sludge may slowly resettle in the most dependent location. In fasting, critically ill patients, sludge may be present in large quantities and completely fill the gallbladder. Sludge that mimics polypoid tumors is called **tumefactive sludge** (Fig. 6.38). Lack of internal vascularity, potential mobility of the sludge, and a normal gallbladder wall are all clues to the presence of sludge. When doubts persist, lack of contrast enhancement on ultrasound, CT, or MRI allows conservative management. Occasionally, sludge has the same echotexture as the liver, camouflaging the gallbladder; called **hepatization** of the gallbladder, this may be easily recognized by identifying the normal gallbladder wall, and lack of Doppler flow within the sludge.

Acute Cholecystitis

Acute cholecystitis is a relatively common disease, accounting for 5% of the patients arriving to the emergency department with abdominal pain and 3% to 9% of hospital admissions.[79] It is caused by gallstones in more than 90% of patients.[80] Impaction of the stones in the cystic duct or the gallbladder neck results in obstruction, with luminal distention, ischemia, superinfection,

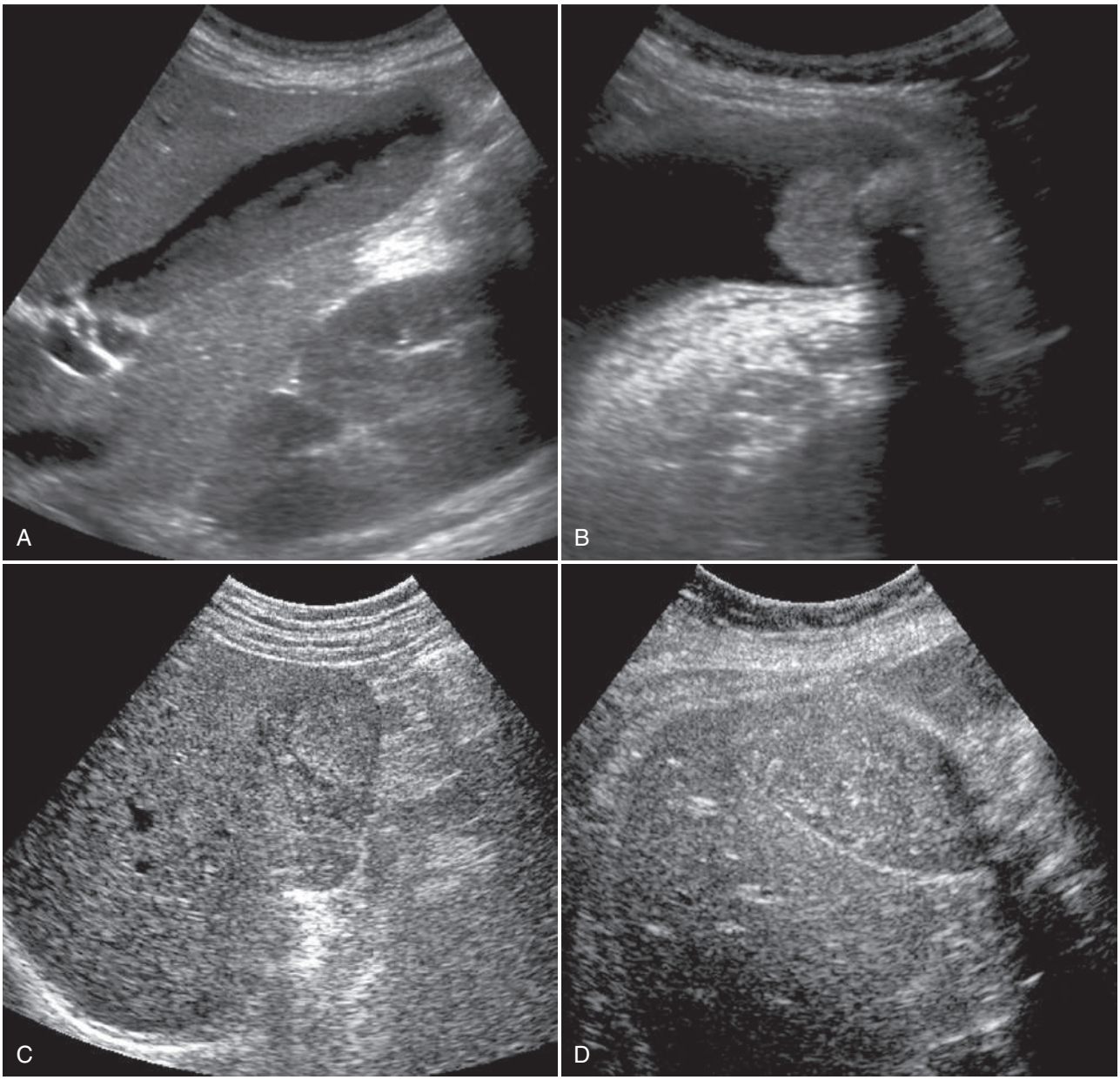

FIG. 6.38 Tumefactive Sludge in Three Patients. (A) Sagittal sonogram shows gallbladder filled with tumorlike sludge. **(B)** Transverse image shows a polypoid appearance of sludge on the dependent gallbladder wall, with an embedded stone (note shadowing). **(C)** Sagittal and **(D)** subcostal oblique sonograms of the same patient show "hepatization" of the gallbladder, with internal echoes mimicking the normal liver parenchyma. In all three patients the gallbladder wall was normal. There was no vascularity detected from the tumefactive sludge.

and eventually necrosis of the gallbladder. In the under-50 age group, women are affected three times more often than men, although incidence of acute cholecystitis is similar in older age groups.[76] However, cholecystitis tends to be more severe in men.[81] Clinically, patients experience prolonged, constant RUQ or epigastric pain associated with RUQ tenderness. Fever, leukocytosis, and increased serum alkaline phosphatase and bilirubin levels may be present.

Sonography is currently the most practical and accurate method to diagnose acute cholecystitis (Figs. 6.39 and 6.40, Video 6.10). When adjusted for verification bias, sensitivity and specificity of ultrasound are approximately 88% and 80%, respectively.[82] Cholescintigraphy uses ionizing radiation, cannot be performed at the bedside, and also has a significant false-positive rate. Although less accurate than sonography in the diagnosis of acute cholecystitis, CT may be useful for depiction of complications.[83] Sonographic findings include the following[84] (Table 6.1):

- Thickening of the gallbladder wall (>3 mm)
- Distention of the gallbladder lumen (diameter > 4 cm)
- Gallstones
- Impacted stone in cystic duct or gallbladder neck
- Pericholecystic fluid collections
- Positive sonographic Murphy sign
- Hyperemic gallbladder wall on Doppler interrogation

TABLE 6.1 Acute Calculous Cholecystitis: Pathologic-Sonographic Correlation

Pathophysiology	Sonographic Appearance
Obstruction of cystic duct or neck of gallbladder	Stones in gallbladder, possibly in neck or cystic duct
Continued secretions	Gallbladder distention
Inflammatory cell infiltration	Thickening of gallbladder wall
and	Gallbladder wall often striated with pockets of edema fluid
Gallbladder wall edema	Positive sonographic Murphy sign (>90%)
Hypervascularity	Hyperemia of gallbladder wall
Gallbladder stasis with bacterial overgrowth by 72 hours	Biliary sludge
Empyema of gallbladder	Heterogeneous luminal contents of variable echogenicity with layering
Increased pressure in gallbladder lumen and wall	Sloughed membranes; hypovascularity
Gangrene	Loss of Murphy sign
Perforation	Loss of gourd shape; collection in or adjacent to gallbladder fossa

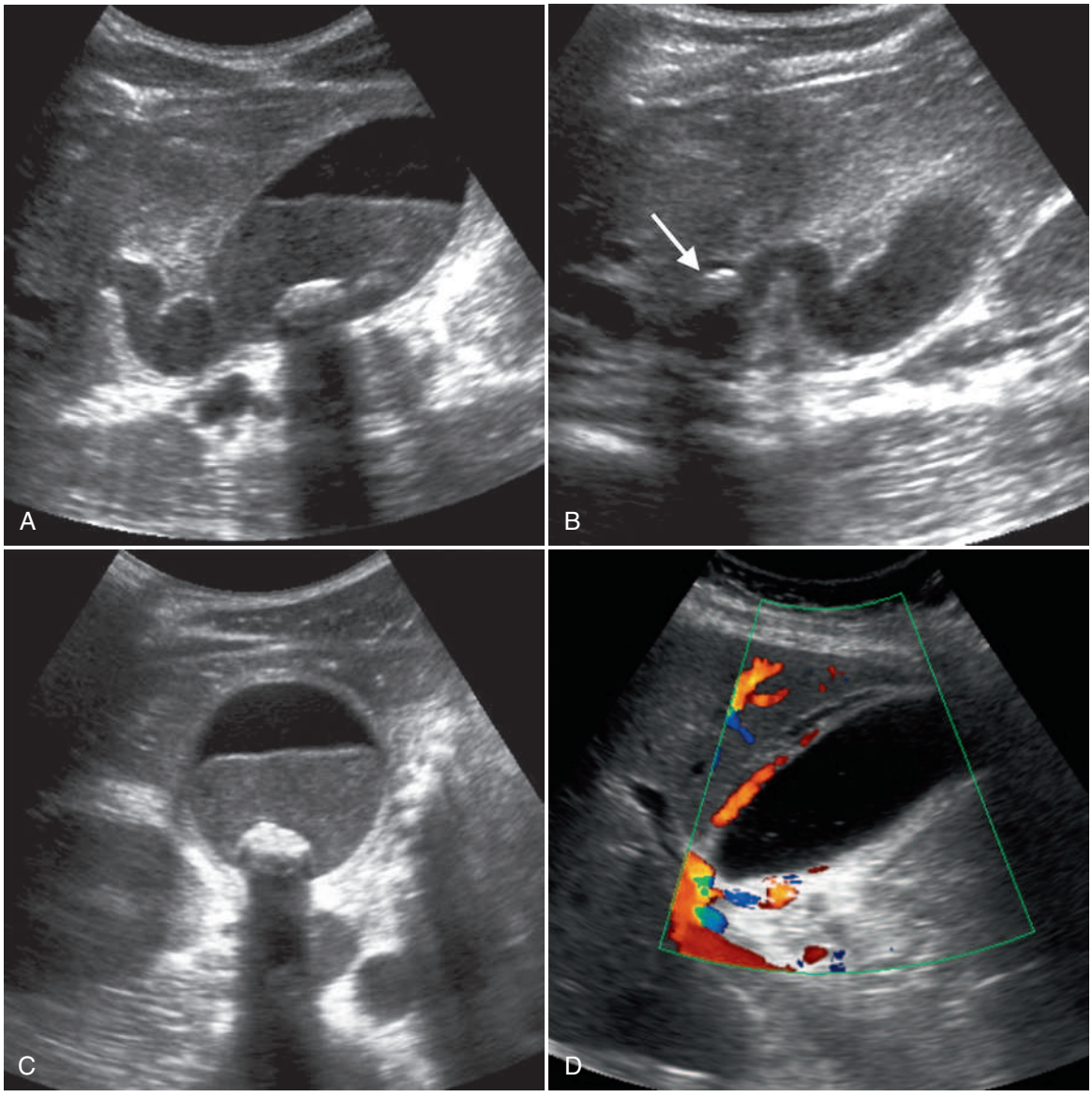

FIG. 6.39 Acute Cholecystitis. Classic acute cholecystitis in a young man. **(A)** Sagittal images show a tense distended gallbladder, wall thickening, fluid-debris level, and a nonobstructive stone with posterior acoustic shadowing. **(B)** Further scrutiny of the distended cystic duct reveals the obstructive stone *(arrow)*. **(C)** Transverse image through the gallbladder shows the gallbladder forming a near perfect circle, due to internal increased pressure. **(D)** Sagittal Doppler image shows a prominent cystic artery and hyperemia in the wall of the gallbladder as well as the adjacent liver.

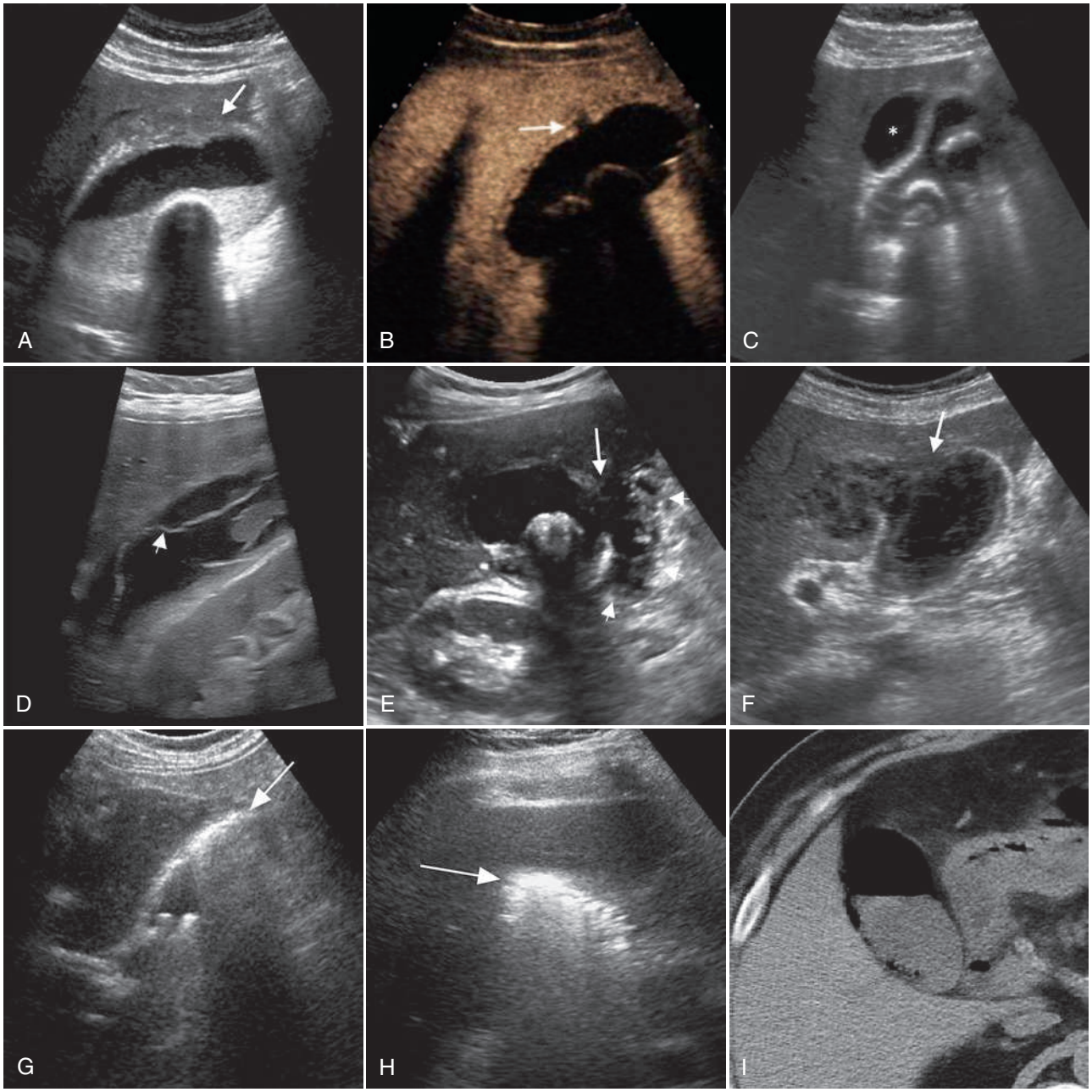

FIG. 6.40 Acute Cholecystitis: Complications. (A)-(C) Early perforation and sequelae. (A) The gallbladder is tense with thickened walls and sludge and a stone. There is poor definition of its near wall *(arrow)* with adjacent heterogeneity of the hepatic parenchyma. **(B)** Contrast-enhanced scan demonstrates a defect *(arrow)* in the gallbladder wall. The patient was treated with antibiotics. **(C)** Three-month follow-up scan in the now asymptomatic patient shows a localized fluid collection (*) between the wall of the gallbladder and liver parenchyma. **(D) Gangrenous cholecystitis.** Sloughed membranes *(short arrow)* appear as linear intraluminal echoes. **(E) Perforation,** shown as disruption of the gallbladder wall *(arrow)* with a subhepatic abscess *(short arrows)*. **(F) Perforation into the liver.** There is a large defect *(arrow)* in the wall of the gallbladder with an adjacent hepatic abscess. See also Video 6.11. **(G)-(I) Emphysematous cholecystitis. (G)** Sagittal sonogram of the gallbladder with a focus of intraluminal air appearing as a bright echogenic focus *(arrow)* with dirty shadowing. **(H)** Gallbladder that is filled with air *(arrow)*. The gallbladder is not actually visualized, and knowledge of the location of the gallbladder fossa is essential to avoid mistaking this for bowel gas. **(I)** Corresponding CT scan shows air in the gallbladder wall and lumen.

Gallbladder wall thickening has many causes. The appearance of the gallbladder wall in acute cholecystitis is nonspecific, but marked thickening of the wall with visible stratification, as seen in generalized edematous states, is usually not present (Fig. 6.41). Multiple focal, noncontiguous, hypoechoic pockets of edema fluid within the thickened wall are typically observed. The inflamed gallbladder is often significantly distended, unless its wall is perforated. Gallstones, including the obstructing stone, and sludge are usually identified. A thin rim of fluid, representing edema, is often seen around much of the organ.

A sonographic **Murphy sign** is maximal tenderness over the gallbladder when the probe is used to compress the RUQ. It is

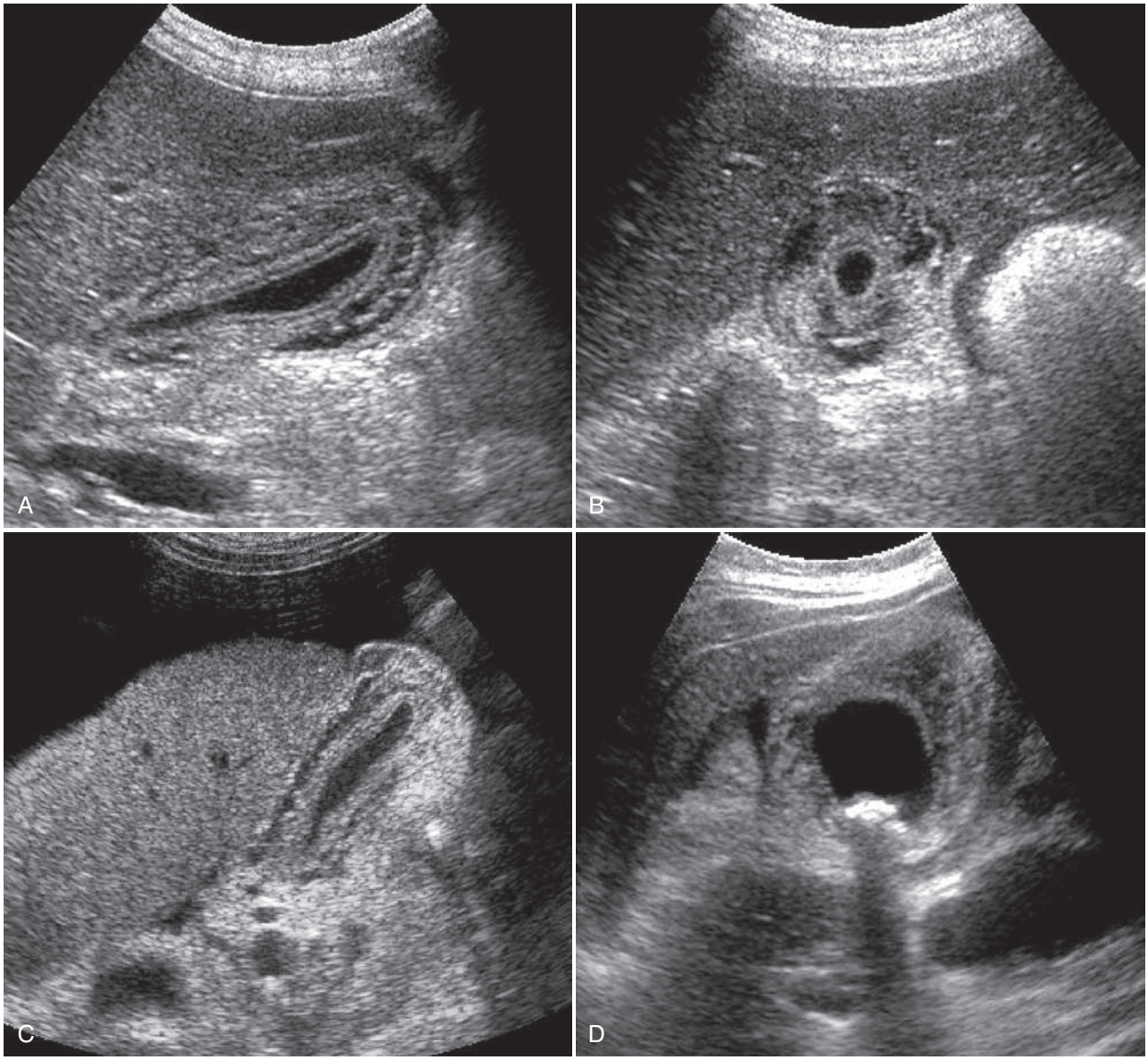

FIG. 6.41 Systemic Causes of Gallbladder Wall Edema. (A) Sagittal and **(B)** transverse images of patient with **hypoalbuminemia** show marked thickening of the gallbladder wall with a small lumen. **(C)** Sagittal image of the gallbladder in a patient with **cirrhosis** demonstrating similar changes to those in **(A)** and **(B)**. Note nodular liver ascites. **(D)** Patient with **congestive heart failure,** small amount of ascites, no pain, and negative Murphy sign has marked gallbladder wall thickening and incidental gallstones.

often better elicited with deep inspiration, which displaces the gallbladder fundus below the costal margin, allowing for direct compression. Sonographic Murphy sign may be absent in older patients, if analgesics were taken before the study, or when prolonged inflammation has led to gangrenous cholecystitis. **Hyperemia** in the gallbladder wall and the adjacent liver and a **prominent cystic artery** are relatively specific findings in acute cholecystitis (see Fig. 6.39D). Power Doppler has been shown to be superior to color Doppler in detecting such hyperemia.[85] Hyperemia is only qualitatively assessed, however, and motion artifact somewhat limits the utility of power Doppler. The latest generation of sonography equipment has highly sensitive Doppler techniques, and detection of flow in the cystic artery of a normal gallbladder is common. In our experience this limits the qualitative assessment of gallbladder wall hyperemia. We rely heavily on the morphologic changes in the gallbladder for the diagnosis of acute cholecystitis but find Doppler ultrasound quite useful in equivocal cases.

Although none of the signs just described is pathognomonic of acute cholecystitis, the combination of multiple findings should lead to the correct diagnosis. Some patients with acute cholecystitis may not show classic findings, making diagnosis challenging. This occurs in patients with mild inflammation but occurs more often in patients hospitalized for other reasons, not receiving an oral diet, and unable to communicate symptoms. A distended gallbladder in these patients should trigger a high index of suspicion, and careful RUQ scanning is recommended. **Perforated duodenal ulcer, acute hepatitis, pancreatitis, colitis**

Causes of Gallbladder Wall Thickening

GENERALIZED EDEMATOUS STATES
Congestive heart failure
Renal failure
End-stage cirrhosis
Hypoalbuminemia

INFLAMMATORY CONDITIONS
Primary
- Acute cholecystitis
- Cholangitis
- Chronic cholecystitis

Secondary
- Acute hepatitis
- Perforated duodenal ulcer
- Pancreatitis
- Diverticulitis/colitis

NEOPLASTIC CONDITIONS
Gallbladder adenocarcinoma
Metastases

MISCELLANEOUS
Adenomyomatosis
Mural varicosities

or **diverticulitis,** and even **pyelonephritis** can demonstrate a Murphy sign and **sympathetic gallbladder wall thickening** (Fig. 6.42). Absence of a distended gallbladder and gallstones is often a clue to the nonbiliary origin of the cholecystic process.

Gangrenous Cholecystitis

When acute cholecystitis is especially severe or prolonged, the gallbladder may undergo necrosis. Sonographic findings of gangrenous cholecystitis include nonlayering bands of echogenic tissue within the lumen representing sloughed membranes and blood (see Fig. 6.40D). The gallbladder wall also becomes irregular, with small collections within the wall that may represent abscesses or hemorrhage.[76] Murphy sign is absent in two-thirds of patients,[86] presumably because of necrosis of the nerve supply to the gallbladder. **Hemorrhagic cholecystitis** represents a rare gangrenous process marked by bleeding within the gallbladder wall and lumen. The clinical symptoms are indistinguishable from gangrenous cholecystitis, and only occasionally does the patient experience a gastrointestinal bleed.

Perforated Gallbladder

Perforation of the gallbladder occurs in 5% to 10% of patients with acute cholecystitis, generally in cases of prolonged inflammation.[76] The focus of perforation, seen as a small defect or rent in the wall of the gallbladder, is often visible (see Fig. 6.40, Video 6.11). Clues to perforation are the deflation of the gallbladder, with loss of its normal gourdlike shape, and a focal **pericholecystic fluid collection.** The latter is often a small fluid collection around the wall defect, unlike the thin rim of fluid around the entire organ in uncomplicated cholecystitis.[87] The collection may have internal strands typical of abscesses elsewhere (see Fig. 6.40E). Perforation of the gallbladder may extend into the adjacent liver parenchyma, forming an abscess collection. The presence of a cystic liver lesion around the gallbladder fossa should suggest a pericholecystic abscess.

Emphysematous Cholecystitis

Emphysematous cholecystitis represents less than 1% of all cases of acute cholecystitis, but it is rapidly progressive and fatal in approximately 15% of patients. Emphysematous cholecystitis differs from acute cholecystitis in several ways. It is three to seven times more common in men than women; about one-half of patients have **diabetes;** and one-third to one-half have no gallstones.[76,88] The gas is produced by gas-forming bacteria, presumably after an ischemic event affecting the gallbladder.[88] These patients have a much higher incidence of gallbladder perforation than those with typical acute cholecystitis, and urgent surgical treatment is advocated for all patients.

The appearance of emphysematous cholecystitis on sonography depends on the amount of gas present (see Fig. 6.40G-I). The gas is often within both the lumen and the wall of the gallbladder. Small amounts of gas appear as echogenic lines, with posterior dirty shadowing, reverberation, or ring-down artifact. Large amounts of gas can be more difficult to appreciate. The absence of a normal gallbladder is a clue. A bright, echogenic line with posterior dirty shadowing is seen within the entire gallbladder fossa. Movement of gas bubbles is a helpful finding and may be precipitated by compression of the gallbladder fossa. Pneumobilia may also be seen.[88]

Acalculous Cholecystitis

Acalculous cholecystitis may occur in patients with no risk factors but is more common in critically ill patients, who thus have a worse prognosis. Risk factors include major surgery, severe trauma, sepsis, total parenteral nutrition, diabetes, atherosclerotic disease, and HIV infection.[80] In nonhospitalized patients, it is more common in older male patients with atherosclerotic disease,[89] who have a much better prognosis.

The diagnosis of acalculous cholecystitis can be difficult because gallbladder distention, wall thickening, internal sludge, and pericholecystic fluid may all be present in critically ill patients without cholecystitis.[90] Patients may be obtunded or receiving analgesics, reducing the sensitivity of Murphy sign. The combination of findings suggests the diagnosis; the more signs present, the greater is the likelihood of cholecystitis.[91] Nevertheless, cholescintigraphy or percutaneous sampling of the luminal contents should be used more liberally to assist in the diagnosis.

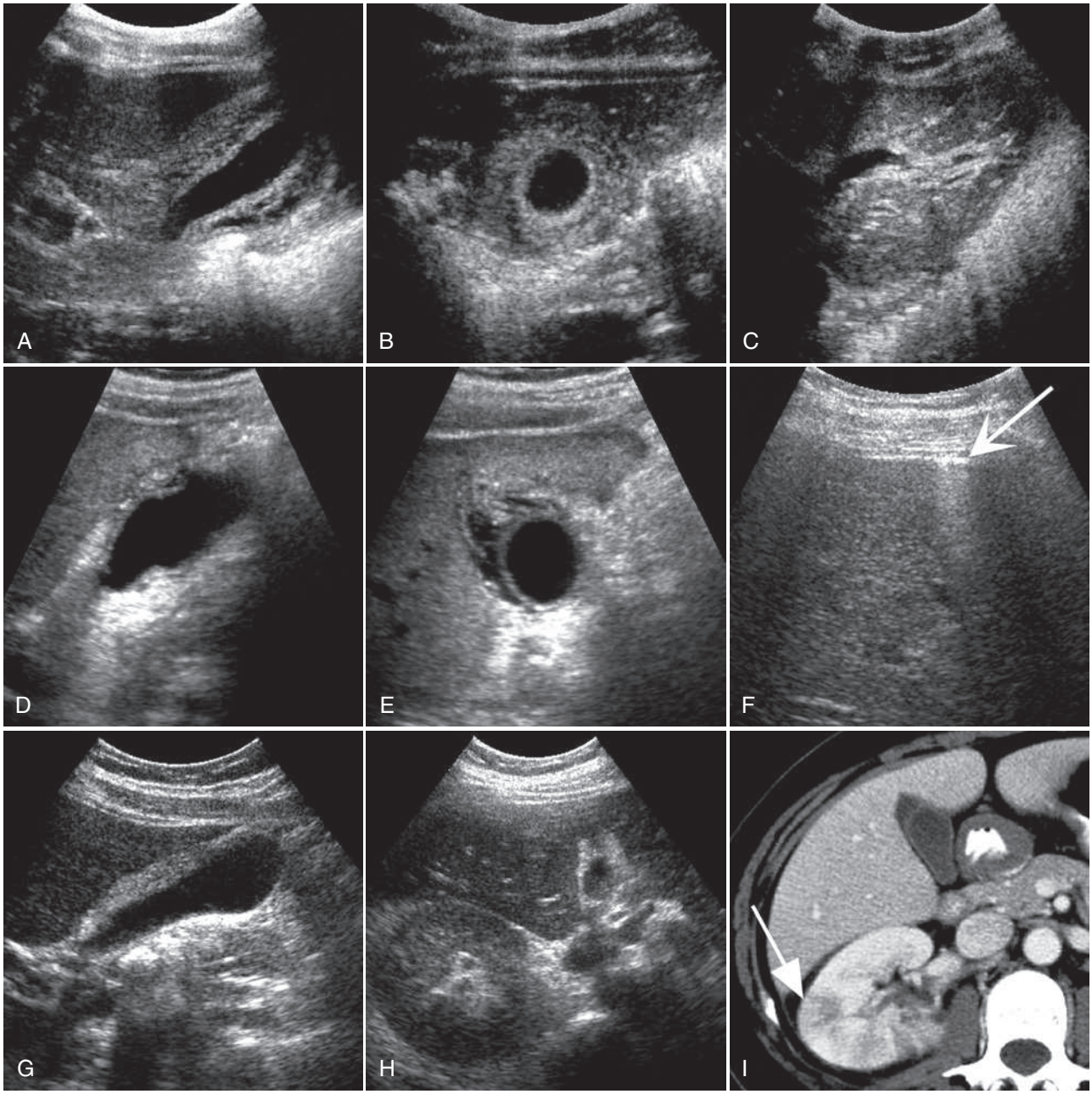

FIG. 6.42 Sympathetic Thickening of the Gallbladder Wall in Three Patients With Positive Sonographic Murphy Sign. (A)-(C) Acute hepatitis. (A) and **(B)** Views of the gallbladder show marked circumferential thickening of the gallbladder wall. The lumen is not distended. **(C)** Left lobe of the liver shows periportal cuffing. **(D)-(F) Perforation of a duodenal ulcer. (D)** and **(E)** Asymmetrical, marked thickening of the gallbladder wall. **(F) Free intraperitoneal air.** The peritoneal line in the epigastrium *(arrow)* marks a linear area of increased echogenicity with posterior dirty shadowing. **(G)-(I) Acute pyelonephritis. (G)** and **(H)** Asymmetrical thickening of the gallbladder wall. **(I)** CT scan shows striated nephrogram *(arrow)*. (**D-F** courtesy of Dr. A.E. Hanbidge, University of Toronto.)

Torsion (Volvulus) of Gallbladder

Gallbladder torsion is a rare, acute entity. Patients have symptoms of acute cholecystitis. Volvulus is often seen in older women and may be related to a mobile gallbladder with a long suspensory mesentery. The hallmarks on imaging are a massively distended and inflamed gallbladder lying in an unusual horizontal position, with its long axis oriented in a left-to-right direction. A twist of the cystic artery and cystic duct may be visible. If the torsion is greater than 180 degrees, gangrene of the gallbladder ensues; otherwise, obstruction of the cystic duct and acute cholecystitis occur. In either case, treatment is usually surgical.[92]

Chronic Cholecystitis

Chronic cholecystitis is associated with the mere presence of gallstones; therefore patients are usually asymptomatic and have mild disease. Chronic cholecystitis has the same incidence and risk factors as gallstone disease. More advanced cases involve wall thickening and fibrosis, appearing on sonographic

examination as a thick-walled gallbladder with gallstones. Differentiation from acute cholecystitis is made by the absence of other signs, namely, gallbladder distention, Murphy sign, and hyperemia in the wall.[93] Bouts of acute cholecystitis may complicate chronic cholecystitis.

Xanthogranulomatous cholecystitis is a rare form of chronic cholecystitis in which collections of lipid-laden macrophages occur within grayish yellow nodules or streaks in the gallbladder wall. In addition to gallstones, hypoechoic nodules or bands within the thickened wall, representing the lipid-laden xanthogranulomatous nodules, may suggest the diagnosis.[94]

Porcelain Gallbladder

Calcification of the gallbladder wall is termed *porcelain gallbladder.* Its cause is unknown, but it occurs in association with gallstone disease and may represent a form of chronic cholecystitis. This rare entity is seen in up to 0.8% of cholecystectomy specimens, with a female predominance and most often found in the sixth decade of life.[95] Two large studies disputed a high incidence of gallbladder carcinoma in porcelain gallbladder, suggesting the coincidental occurrence of the two entities in up to 7% of patients.[96,97] Nevertheless, prophylactic resection is advised.[94]

The degree and pattern of calcification determine the sonographic appearance (Fig. 6.43). When the entire gallbladder wall is thickly calcified, a hyperechoic semilunar line with dense posterior acoustic shadowing is noted. Mild calcification appears as an echogenic line with variable degrees of posterior acoustic shadowing. The luminal contents may be visible. Interrupted clumps of calcium appear as echogenic foci with posterior shadowing.[76] Differential diagnosis includes gallstones and emphysematous cholecystitis. Because the calcifications occur in the wall of the gallbladder, the wall-echo-shadow complex is absent (see "Gallstone Disease").

Adenomyomatosis (Adenomatous Hyperplasia)

Gallbladder adenomyomatosis is a benign condition caused by exaggeration of the normal invaginations of the luminal epithelium **(Rokitansky-Aschoff sinuses)** with associated smooth muscle proliferation (Fig. 6.44). The affected areas demonstrate thickening of the gallbladder wall with internal cystic spaces, the key to the radiologic diagnosis. The great majority of adenomyomatoses are asymptomatic.[98]

Adenomyomatosis may be **focal** or **diffuse.** The most common appearance on sonography is tiny, echogenic foci in the gallbladder wall that create **comet-tail artifacts,** presumably caused by either the cystic space itself or the internal debris (Fig. 6.45). Prominent masslike focal areas of adenomyomatosis, called **adenomyomas,** are the next most common manifestation. Careful evaluation of the adenomyoma, sometimes requiring higher frequency or linear probes, can show several features that are diagnostic of the entity and allow for differentiation from neoplasm. The most diagnostic finding, although not the most common, is the presence of cystic spaces. Echogenic foci with comet-tail or "twinkling" artifact on Doppler examination are also typical. Focal adenomyomatosis is most common in the gallbladder fundus, less often narrowing the midportion of the organ, called **hourglass gallbladder** (Fig. 6.46).

Fundal adenomyomas are often folded onto the body of the gallbladder and can occasionally be mistaken for a pericholecystic or even a hepatic mass. The entire gland wall may be involved, causing collapse of the lumen. The absence of the cystic spaces, echogenic foci, or twinkling artifact or the presence of internal vascularity should prompt further investigation to differentiate from neoplasm. MRI or MRCP allows for improved specificity, with the presence of cystic spaces within the thickened wall leading to the diagnosis.[99]

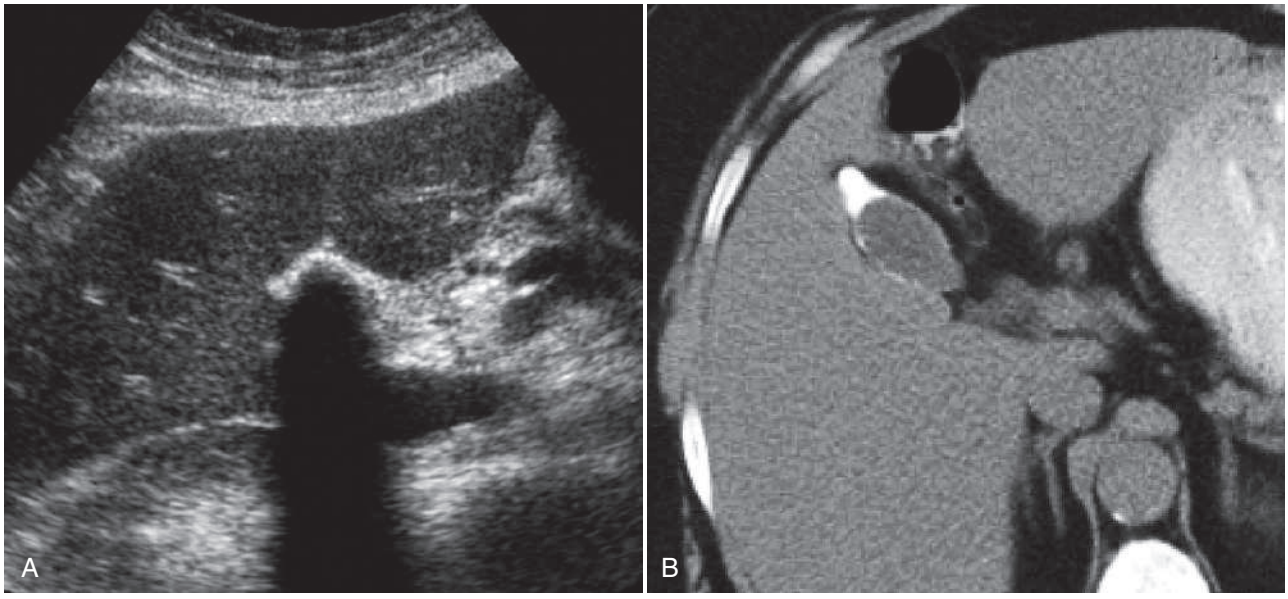

FIG. 6.43 Porcelain Gallbladder. (A) Sonogram. **(B)** Corresponding CT scan. On ultrasound, this appearance could be mistaken for a stone within the gallbladder lumen. There is, however, no gallbladder wall superficial to the echogenic focus.

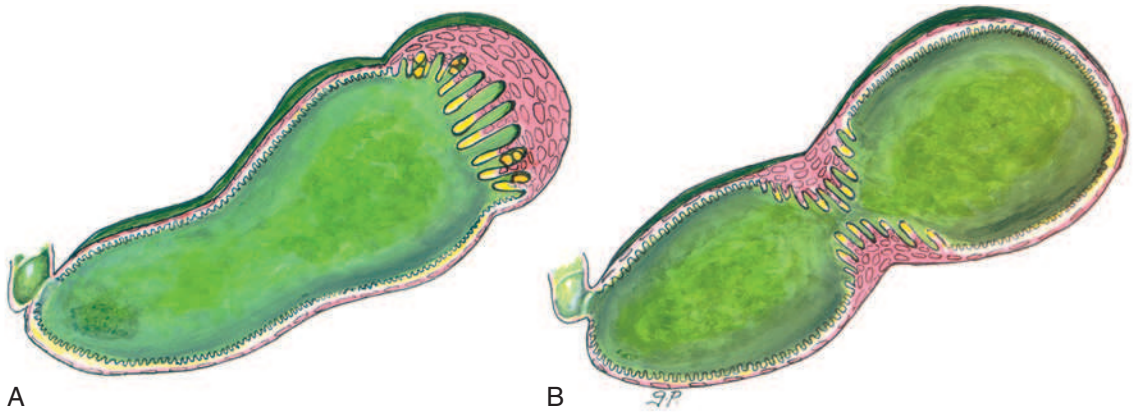

FIG. 6.44 Segmental Adenomyomatosis. (A) Fundal adenomyoma. **(B)** Hourglass adenomyomatosis. In both cases, note the constricted contour of the gallbladder and thickening of the wall with hypertrophy of the smooth muscle. On sonography, the exaggerated Rokitansky-Aschoff sinuses may appear as cystic spaces or as echogenic foci with comet-tail artifact, possibly caused by cholesterol crystals (depicted here as *yellow particles*) lodged in them.

Polypoid Masses of Gallbladder

Differentiation of benign and malignant polyps is essential because benign masses are common and malignant polyps require early intervention to improve outcome. Current evidence suggests that risk of malignancy in polyps less than 6 mm in size is negligible and they require no further follow-up.[100-102] More recent data suggest that gallbladder adenomas form a small fraction of 6- to 10-mm polyps and because they may have a risk of malignant transformation, imaging follow-up is recommended.[101,103] Whether such practice, based on retrospective surgical series, is justified through a cost-benefit analysis remains unknown, especially in a Western population where gallbladder cancer is rare.[104] Malignancy has been documented in 37% to 88% of resected polyps greater than 10 mm and therefore resection of these larger polyps is advised.[105]

Apart from size, research from both endoscopic and high-resolution ultrasound has identified additional features that help differentiate nonneoplastic from neoplastic polyps. The presence of hypoechoic foci centrally within the polyp has been shown to be a significant predictor of neoplastic polyps with sensitivity/specificity of 85%/67% on high-resolution transabdominal ultrasound and 91%/89% on endoscopic ultrasound.[106,107] Also the presence of a central vessel within the polyp (vascular core) and hypoechoic appearance are suggestive of a neoplastic polyp.

Cholesterol Polyps

Approximately one-half of all polypoid gallbladder lesions are cholesterol polyps. These represent the focal form of gallbladder **cholesterolosis,** a common nonneoplastic condition of unknown origin. Cholesterolosis results in accumulation of lipids within macrophages. The diffuse form, commonly known as **"strawberry gallbladder,"** is not visible on imaging. Cholesterolosis has the same risk factors as gallstone disease, but the two conditions rarely coexist.[98] Cholesterol polyps usually are 2 to 10 mm, although lesions up to 20 mm have been described.[105] On pathologic series, one-fifth are solitary, but the mean number of polyps is eight.[98]

Common Polypoid Masses of the Gallbladder

Cholesterol polyps[a] (50%-60%)
Inflammatory polyps[a] (5%-10%)
Adenoma[a] (<5%)
Focal adenomyomatosis
Gallbladder adenocarcinoma
Metastases (especially melanoma)

[a]Data from Bilhartz LE. Acalculous cholecystitis, cholesterolosis, adenomyomatosis, and polyps of the gallbladder. In: Feldman M, et al., editors. Sleisenger and Fordtran's gastrointestinal and liver disease. 7th ed. New York: Elsevier Science; 2002. pp. 1123-1125.[98]

The sonographic appearance of cholesterol polyps is multiple ovoid, nonshadowing lesions attached to the gallbladder wall (Fig. 6.47). Unlike small, nonshadowing stones, polyps are not mobile. Larger lesions may contain a fine pattern of echogenic foci.[108]

Adenomas, Adenomyomas, and Inflammatory Polyps

Adenomas are true benign neoplasms of the gallbladder, with a premalignant potential much lower than for colonic adenomas. Adenomas represent less than 5% of gallbladder polyps and occur as solitary lesions. They have a propensity to occur in patients with primary sclerosing cholangitis and polyposis syndromes.[109] Adenomas are usually pedunculated, and larger lesions may contain foci of malignant transformation.[98] Adenomas tend to be homogeneously hyperechoic but become more heterogeneous as they increase in size[105] (Fig. 6.48). Thickening of the gallbladder wall adjacent to an adenoma should suggest malignancy. Central hypoechoic foci, representing central vessels or microscopic cysts are quite suggestive.[107] On occasion, an **adenomyoma** may appear as a sessile, polypoid gallbladder lesion. Imaging features, especially hyperechoic foci with or without comet-tail artifact and microcysts, should allow differentiation.[106] **Inflammatory**

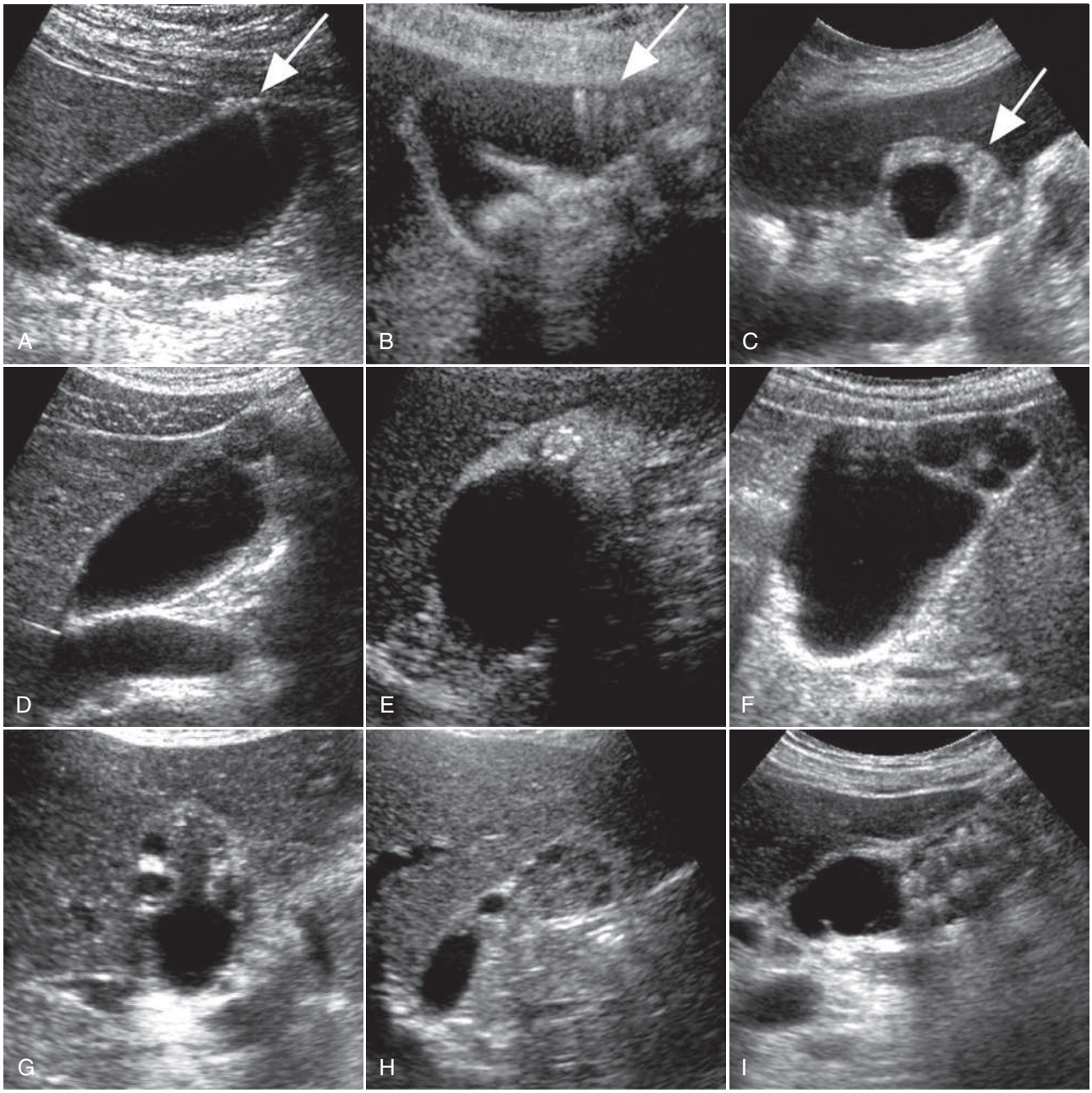

FIG. 6.45 Adenomyomatosis: Spectrum of Appearances. (A)-(C) Focal adenomyomatosis, the most common manifestation. **(A)** Small focal area of thickening of the anterior fundal wall *(arrow)* with a bright echogenic focus with a distal comet-tail artifact. **(B)** Multiple bright foci *(arrow)* with distal artifacts. **(C)** Highly echogenic focal thickening of the gallbladder wall *(arrow)*. Increased echogenicity is unusual for a malignant tumor that is more likely to appear hypoechoic. **(D)-(F) Fundal adenomyomas. (D)** Adenomyoma appears hypoechoic and masslike. **(E)** Caplike area with multiple tiny, highly echogenic foci that suggest multiple crystals in the Rokitansky-Aschoff sinuses. **(F)** Multiple cystic spaces within the adenomyoma. **(G)-(I) Segmental adenomyomatosis. (G)** and **(H)** Masslike areas obliterating the gallbladder lumen. Multiple cystic spaces suggest the correct diagnosis. **(I)** Multiple echogenic foci suggest crystals in the Rokitansky-Aschoff sinuses.

polyps of the gallbladder constitute 5% to 10% of gallbladder polyps and are multiple in one-half of the cases.[98] Inflammatory polyps tend to occur in the background of gallstone disease and chronic cholecystitis.[110] The sonographic appearance of these lesions has not been systematically studied.

Malignancies

Primary gallbladder adenocarcinomas may appear as a polypoid mass. Melanoma is reported to be the cause of 50% to 60% of metastases to the gallbladder. These appear as hyperechoic, broad-based polypoid lesions, potentially multiple and usually more than 10 mm in diameter.[111] But in our experience, the most common metastases to the gallbladder are from signet ring cell adenocarcinomas, particularly from gastric primaries. However, these are not polypoid but rather diffusely infiltrative in nature, causing contraction of the gallbladder with a hyperemic wall. In a series of 20 pathologically proven gallbladder metastases, bowel adenocarcinomas accounted for 60% of

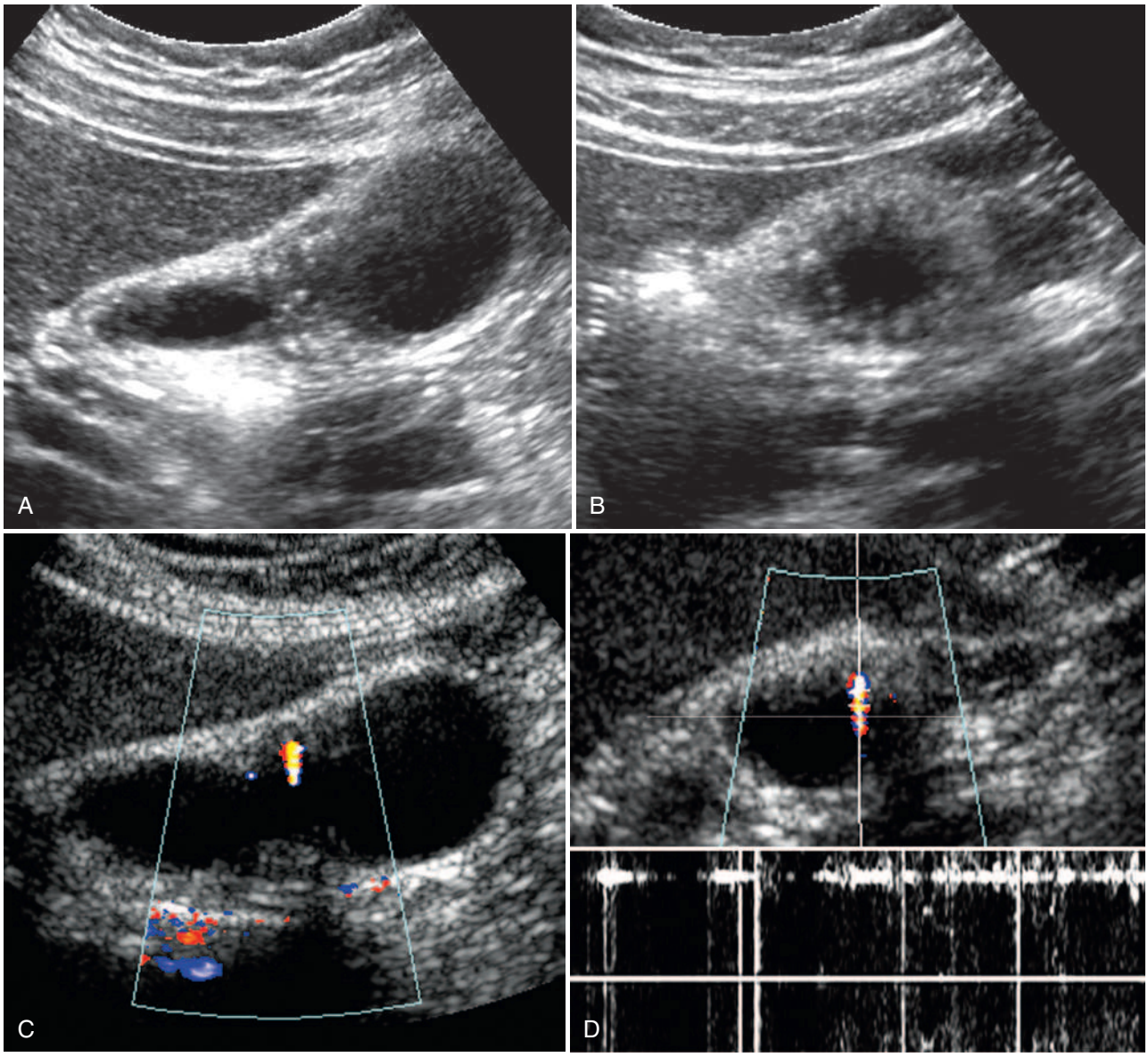

FIG. 6.46 Hourglass Adenomyoma. (A) Sagittal and **(B)** transverse sonograms show thickening of the gallbladder wall, creating an hourglass configuration. At the point of wall thickening, there are innumerable bright echogenic foci with comet-tail artifact, suggesting cholesterol crystals in Rokitansky-Aschoff sinuses. **(C)** and **(D)** Color and spectral Doppler show "twinkling" artifact without real vascularity, supportive of the correct diagnosis.

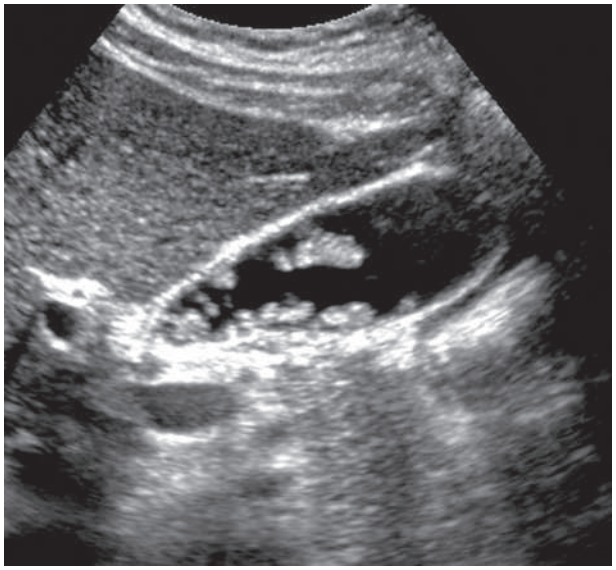

FIG. 6.47 Gallbladder Polyps. Small size (≤10 mm) and multiple tumors are features most suggestive of a benign lesion.

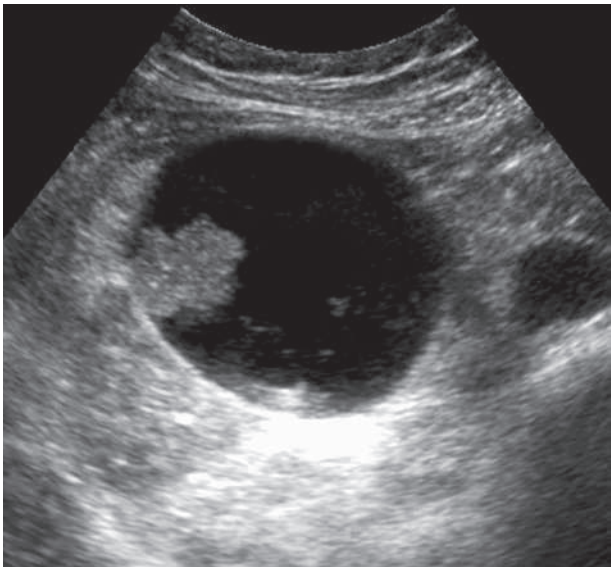

FIG. 6.48 Gallbladder Adenoma. Transverse image through the gallbladder shows a polypoid lesion found incidentally in a patient with mild acute cholecystitis. The lesion was a tubulovillous adenoma on resection.

the primary sites.[112] Advanced hepatocellular carcinoma can directly invade the gallbladder fossa and extend through the gallbladder wall to appear as a luminal mass. The large hepatic component of the mass and its hypervascular nature assist in the diagnosis.

Gallbladder Carcinoma

Gallbladder carcinoma is an uncommon malignancy occurring mainly in the older population, with a 3:1 female-to-male ratio. High incidence of gallbladder cancer is reported along the Pacific coast of South America and in East and South Asian countries.[113] In a majority of cases, carcinoma is associated with gallstones. Chronic gallstone disease and resultant dysplasia have been cited as a causative factor.[114] More recently, pancreaticobiliary maljunction (long common channel between the pancreatic and the bile duct that extends outside of the duodenal wall) and chronic ***Salmonella typhi*** carrier state have been implicated as risk factors.[113,115] About 98% of gallbladder carcinomas are

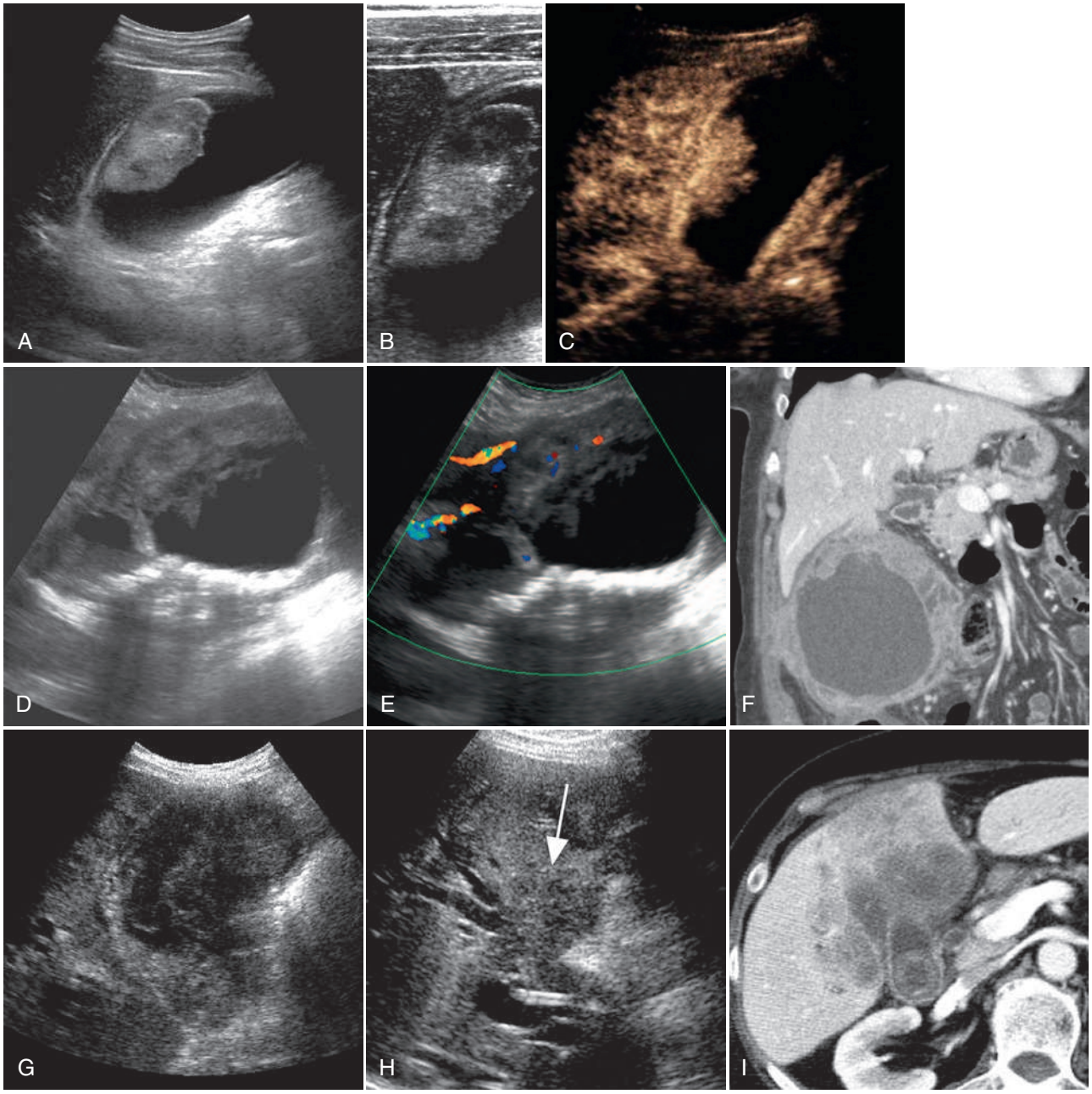

FIG. 6.49 Gallbladder Cancer: Spectrum of Appearances. (A) and **(B) Polypoid mass. (A)** A large polypoid mass. **(B)** Examination with high-frequency linear probe shows no invasion beyond the gallbladder wall. **(C)** Contrast-enhanced examination confirms the solid vascular nature of the mass and rules out hepatic extension. **(D)-(F) Wall thickening. (D)** and **(E)** Extensive asymmetrical, heterogeneous wall thickening in a markedly enlarged gallbladder with abnormal flow on Doppler assessment. **(F)** Corresponding CT scan. **(G)-(I) Invasive gallbladder cancer. (G)** and **(H)** Huge mass replacing the gallbladder fossa and invading the liver. **(H)** Biliary obstruction caused by the invasive mass *(arrow).* **(I)** Corresponding CT scan.

adenocarcinomas, with squamous cell carcinoma and metastases accounting for the rest. The following three patterns of disease have been described:

- Mass arising in the gallbladder fossa, obliterating the gallbladder and invading the adjacent liver (most common pattern)
- Focal or diffuse, irregular wall thickening
- Intraluminal polypoid mass

Patterns of Tumor Spread

Because the gallbladder wall is quite thin, without a muscularis mucosa and little connective tissue to separate it from the liver parenchyma, contiguous hepatic invasion is the most common pattern of spread. Gallbladder tumors also extend along the cystic duct into the porta hepatis, where they mimic hilar cholangiocarcinomas. Tumor extension into bile ducts or encasement of the portal vein or hepatic artery may ensue. Direct invasion into adjacent loops of bowel, especially the duodenum or colon, may also occur. A resultant **cholecystenteric fistula** and inflammation may be mistaken for a benign abscess collection. Metastases to the peritoneum are a common finding.

Lymphatic spread is also a common feature of gallbladder carcinoma and may occur in the absence of invasion of adjacent organs.[116] The first nodes to be affected are in the hilar region. Adenopathy may then extend either down the hepatoduodenal ligament, to affect peripancreatic and mesenteric nodes, or across the gastrohepatic ligament to celiac nodal stations.

Surgical resection is the only chance of cure; however, reported resection rates range from 10% to 30%.[116] If the tumor is not confined to the mucosa, an extended cholecystectomy, involving resection of 3- to 5-cm rim of liver adjacent to the gallbladder fossa, or a formal right hepatectomy is required. Regional lymph nodes of the cystic bile ducts and CBDs are also removed. Noncontiguous hepatic or peritoneal metastases, celiac or peripancreatic nodal disease, or encasement of the main portal vein or hepatic artery should be carefully sought because they render the patient unresectable.

Sonographic Appearance

The appearance on sonography varies depending on the **pattern** of carcinoma (Fig. 6.49). When masses replacing the normal gallbladder fossa are small, it may be difficult to appreciate them because they may blend into the liver. The absence of a normal-appearing gallbladder with no history of cholecystectomy should raise suspicion. A clue to the diagnosis is the common presence of an immobile stone that is engrossed by the tumor, the "trapped stone." On Doppler interrogation the mass may demonstrate internal arterial and venous flow. Diffuse, malignant thickening of the wall differs from other causes in that the wall is irregular with loss of the normal mural layers. Polypoid intraluminal masses are differentiated from nonneoplastic abnormalities by immobility of the mass, larger size (>1 cm), and prominent internal vascularity. Gallbladder carcinomas may produce large quantities of *mucin,* which distends the gallbladder.

Contrast-enhanced ultrasound has been reported to be a useful tool in differentiating benign from malignant gallbladder disease. In one study, the disruption of the wall of the gallbladder as detected by contrast-enhanced ultrasound was reported as a having a sensitivity of 85% and specificity of 100% in diagnosing gallbladder cancer.[117]

Sonography performs very well in locally staging gallbladder carcinoma. Bach et al.[118] reported 94% sensitivity and 63% accuracy for prediction of resectability compared with surgical findings. More recently, high-resolution ultrasound of gallbladder cancer using higher frequency probes (5-12 MHz) has shown excellent performance in differentiating T1 from higher tumor stages.[106] However, sonography is often difficult in patients with unresectable disease because of limited detection of noncontiguous hepatic, lymph node, and especially peritoneal metastases. A CT scan is recommended to improve detection of metastatic gallbladder disease.

REFERENCES

1. Bret PM, de Stempel JV, Atri M, et al. Intrahepatic bile duct and portal vein anatomy revisited. Radiology. 1988;169(2):405-407.
2. Bressler EL, Rubin JM, McCracken S. Sonographic parallel channel sign: a reappraisal. Radiology. 1987;164(2):343-346.
3. Puente SG, Bannura GC. Radiological anatomy of the biliary tract: variations and congenital abnormalities. World J Surg. 1983;7(2):271-276.
4. Russell E, Yrizzary JM, Montalvo BM, et al. Left hepatic duct anatomy: implications. Radiology. 1990;174(2):353-356.
5. Bowie JD. What is the upper limit of normal for the common bile duct on ultrasound: how much do you want it to be? Am J Gastroenterol. 2000;95(4):897-900.
6. Horrow MM, Horrow JC, Niakosari A, et al. Is age associated with size of adult extrahepatic bile duct: sonographic study. Radiology. 2001;221(2):411-414.
7. Lamah M, Karanjia ND, Dickson GH. Anatomical variations of the extrahepatic biliary tree: review of the world literature. Clin Anat. 2001;14(3):167-172.
8. Anvari A, Forsberg F, Samir AE. A primer on the physical principles of tissue harmonic imaging. Radiographics. 2015;35(7):1955-1964.
9. Sato M, Ishida H, Konno K, et al. Choledochal cyst due to anomalous pancreatobiliary junction in the adult: sonographic findings. Abdom Imaging. 2001;26(4):395-400.
10. de Vries JS, de Vries S, Aronson DC, et al. Choledochal cysts: age of presentation, symptoms, and late complications related to Todani's classification. J Pediatr Surg. 2002;37(11):1568-1573.
11. Adkins Jr RB, Chapman WC, Reddy VS. Embryology, anatomy, and surgical applications of the extrahepatic biliary system. Surg Clin North Am. 2000;80(1):363-379.
12. Todani T, Watanabe Y, Narusue M, et al. Congenital bile duct cysts: classification, operative procedures, and review of thirty-seven cases including cancer arising from choledochal cyst. Am J Surg. 1977;134(2):263-269.
13. Matsumoto Y, Fujii H, Itakura J, et al. Recent advances in pancreaticobiliary maljunction. J Hepatobiliary Pancreat Surg. 2002;9(1):45-54.
14. Parada LA, Hallen M, Hagerstrand I, et al. Clonal chromosomal abnormalities in congenital bile duct dilatation (Caroli's disease). Gut. 1999;45(5):780-782.
15. Suchy FJ. Anatomy, histology, embryology, developmental anomalies, and pediatric disorders of the biliary tract. In: Feldmen M, et al., editors. Sleisenger and Fordtran's gastrointestinal and liver disease. 7th ed. New York: Elsevier Science; 2002. p. 1033.
16. Fulcher AS, Turner MA, Sanyal AJ. Case 38: Caroli disease and renal tubular ectasia. Radiology. 2001;220(3):720-723.
17. Marchal GJ, Desmet VJ, Proesmans WC, et al. Caroli disease: high-frequency US and pathologic findings. Radiology. 1986;158(2):507-511.
18. Agahi A, McNair A. Choledocholithiasis presenting with very high transaminase level. BMJ Case Rep. 2012;2012.
19. Hanau LH, Steigbigel NH. Acute (ascending) cholangitis. Infect Dis Clin North Am. 2000;14(3):521-546.
20. Greenberger NJ, Paumgartner G. Diseases of the gallbladder and bile ducts. In: Braunwald E, et al., editors. Harrison's principles of internal medicine. 15th ed. New York: McGraw-Hill; 2001.

21. Ko CW, Lee SP. Epidemiology and natural history of common bile duct stones and prediction of disease. Gastrointest Endosc. 2002;56(6 Suppl.):S165-S169.
22. Ortega D, Burns PN, Hope Simpson D, Wilson SR. Tissue harmonic imaging: is it a benefit for bile duct sonography? AJR Am J Roentgenol. 2001;176(3):653-659.
23. Baron RL, Tublin ME, Peterson MS. Imaging the spectrum of biliary tract disease. Radiol Clin North Am. 2002;40(6):1325-1354.
24. Turner MA, Fulcher AS. The cystic duct: normal anatomy and disease processes. Radiographics. 2001;21(1):3-22.
25. Abou-Saif A, Al-Kawas FH. Complications of gallstone disease: Mirizzi syndrome, cholecystocholedochal fistula, and gallstone ileus. Am J Gastroenterol. 2002;97(2):249-254.
26. Green MH, Duell RM, Johnson CD, Jamieson NV. Haemobilia. Br J Surg. 2001;88(6):773-786.
27. Horton JD, Bilhartz LE. Gallstone disease and its complications: clinical manifestations of gallstone disease. In: Feldman M, et al., editors. Sleisenger and Fordtran's gastrointestinal and liver disease. 7th ed. New York: Elsevier Science; 2002. p. 1065-1087.
28. Harvey RT, Miller Jr WT. Acute biliary disease: initial CT and follow-up US versus initial US and follow-up CT. Radiology. 1999;213(3):831-836.
29. Marcos LA, Terashima A, Gotuzzo E. Update on hepatobiliary flukes: fascioliasis, opisthorchiasis and clonorchiasis. Curr Opin Infect Dis. 2008;21(5):523-530.
30. Cosme A, Ojeda E, Poch M, et al. Sonographic findings of hepatic lesions in human fascioliasis. J Clin Ultrasound. 2003;31(7):358-363.
31. Kabaalioglu A, Ceken K, Alimoglu E, et al. Hepatobiliary fascioliasis: sonographic and CT findings in 87 patients during the initial phase and long-term follow-up. AJR Am J Roentgenol. 2007;189(4):824-828.
32. Lim JH, Kim SY, Park CM. Parasitic diseases of the biliary tract. AJR Am J Roentgenol. 2007;188(6):1596-1603.
33. Han JK, Jang HJ, Choi BI, et al. Experimental hepatobiliary fascioliasis in rabbits: a radiology-pathology correlation. Invest Radiol. 1999;34(2):99-108.
34. Teke M, Onder H, Cicek M, et al. Sonographic findings of hepatobiliary fascioliasis accompanied by extrahepatic expansion and ectopic lesions. J Ultrasound Med. 2014;33(12):2105-2111.
35. Choi D, Hong ST. Imaging diagnosis of clonorchiasis. Korean J Parasitol. 2007;45(2):77-85.
36. Mahadevan U, Bass NM. Sclerosing cholangitis and recurrent pyogenic cholangitis. In: Feldman M, et al., editors. Sleisenger and Fordtran's gastrointestinal and liver disease. 7th ed. New York: Elsevier Science; 2002. p. 1131-1152.
37. Cosenza CA, Durazo F, Stain SC, et al. Current management of recurrent pyogenic cholangitis. Am Surg. 1999;65(10):939-943.
38. Olsson R, Danielsson A, Jarnerot G, et al. Prevalence of primary sclerosing cholangitis in patients with ulcerative colitis. Gastroenterology. 1991;100(5 Pt 1):1319-1323.
39. Majoie CB, Smits NJ, Phoa SS, et al. Primary sclerosing cholangitis: sonographic findings. Abdom Imaging. 1995;20(2):109-112.
40. Stockbrugger RW, Olsson R, Jaup B, Jensen J. Forty-six patients with primary sclerosing cholangitis: radiological bile duct changes in relationship to clinical course and concomitant inflammatory bowel disease. Hepatogastroenterology. 1988;35:289-294.
41. Pokorny CS, McCaughan GW, Gallagher ND, Selby WS. Sclerosing cholangitis and biliary tract calculi—primary or secondary? Gut. 1992;33(10):1376-1380.
42. MacCartney RL. Noncalculous inflammatory disorders of the biliary tract. In: Gore RM, Levine MS, Laufer I, editors. Textbook of gastrointestinal radiology. Philadelphia: Saunders; 1994. p. 1727-1745.
43. Narayanan Menon KV, Wiesner RH. Etiology and natural history of primary sclerosing cholangitis. J Hepatobiliary Pancreat Surg. 1999;6(4):343-351.
44. Kecskés Á, Khalili K, Fischer SE, et al. Peripheral atrophy/central hypertrophy complex in chronic hepatic Schistosoma mansoni infection with histological correlation. Eur J Radiol Extra. 2012;78(3):e119-e124.
45. Graziadei IW, Wiesner RH, Batts KP, et al. Recurrence of primary sclerosing cholangitis following liver transplantation. Hepatology. 1999;29(4):1050-1056.
46. Vlachou PA, Khalili K, Jang HJ, et al. IgG4-related sclerosing disease: autoimmune pancreatitis and extrapancreatic manifestations. Radiographics. 2011;31(5):1379-1402.
47. Tokala A, Khalili K, Menezes R, et al. Comparative MRI analysis of morphologic patterns of bile duct disease in IgG4-related systemic disease versus primary sclerosing cholangitis. AJR Am J Roentgenol. 2014;202(3):536-543.
48. Darwin PE, Kennedy AS, Bonheur JL. Cholangiocarcinoma. eMedicine. 2009.
49. Watanapa P, Watanapa WB. Liver fluke-associated cholangiocarcinoma. Br J Surg. 2002;89(8):962-970.
50. de Groen PC, Gores GJ, LaRusso NF, et al. Biliary tract cancers. N Engl J Med. 1999;341(18):1368-1378.
51. Jarnagin WR. Cholangiocarcinoma of the extrahepatic bile ducts. Semin Surg Oncol. 2000;19(2):156-176.
52. Sohn TA, Lillemoe KD. Tumors of the gallbladder, bile ducts, and ampulla. In: Feldman M, et al., editors. Sleisenger and Fordtran's gastrointestinal and liver disease. 7th ed. New York: Elsevier Science; 2002. p. 1153-1165.
53. Colombari R, Tsui WM. Biliary tumors of the liver. Semin Liver Dis. 1995;15(4):402-413.
54. Gihara S, Kojiro M. Pathology of cholangiocarcinoma. In: Okuda K, Ishak KG, editors. Neoplasms of the liver. Tokyo: Springer Verlag; 1987. p. 236-301.
55. Nakeeb A, Pitt HA, Sohn TA, et al. Cholangiocarcinoma. A spectrum of intrahepatic, perihilar, and distal tumors. Ann Surg. 1996;224(4):463-473.
56. Patel T. Worldwide trends in mortality from biliary tract malignancies. BMC Cancer. 2002;2:10.
57. Aishima S, Kuroda Y, Nishihara Y, et al. Proposal of progression model for intrahepatic cholangiocarcinoma: clinicopathologic differences between hilar type and peripheral type. Am J Surg Pathol. 2007;31:1059-1067.
58. Maetani Y, Itoh K, Watanabe C, et al. MR imaging of intrahepatic cholangiocarcinoma with pathologic correlation. AJR Am J Roentgenol. 2001;176(6):1499-1507.
59. Sano T, Kamiya J, Nagino M, et al. Macroscopic classification and preoperative diagnosis of intrahepatic cholangiocarcinoma in Japan. J Hepatobiliary Pancreat Surg. 1999;6(2):101-107.
60. Wibulpolprasert B, Dhiensiri T. Peripheral cholangiocarcinoma: sonographic evaluation. J Clin Ultrasound. 1992;20(5):303-314.
61. Lee NW, Wong KP, Siu KF, Wong J. Cholangiography in hepatocellular carcinoma with obstructive jaundice. Clin Radiol. 1984;35(2):119-123.
62. Bloom CM, Langer B, Wilson SR. Role of US in the detection, characterization, and staging of cholangiocarcinoma. Radiographics. 1999;19(5):1199-1218.
63. Lee JW, Han JK, Kim TK, et al. CT features of intraductal intrahepatic cholangiocarcinoma. AJR Am J Roentgenol. 2000;175(3):721-725.
64. Antila KM, Makisalo H, Arola J, Numminen K. Best cases from the AFIP: biliary papillomatosis. Radiographics. 2008;28(7):2059-2063.
65. Jarnagin WR, Fong Y, DeMatteo RP, et al. Staging, resectability, and outcome in 225 patients with hilar cholangiocarcinoma. Ann Surg. 2001;234(4):507-517.
66. Matsuo K, Rocha FG, Ito K, et al. The Blumgart preoperative staging system for hilar cholangiocarcinoma: analysis of resectability and outcomes in 380 patients. J Am Coll Surg. 2012;215(3):343-355.
67. Robledo R, Muro A, Prieto ML. Extrahepatic bile duct carcinoma: US characteristics and accuracy in demonstration of tumors. Radiology. 1996;198(3):869-873.
68. Hann LE, Greatrex KV, Bach AM, et al. Cholangiocarcinoma at the hepatic hilus: sonographic findings. AJR Am J Roentgenol. 1997;168(4):985-989.
69. Choi BI, Lee JH, Han MC, et al. Hilar cholangiocarcinoma: comparative study with sonography and CT. Radiology. 1989;172(3):689-692.
70. Khalili K, Metser U, Wilson SR. Hilar biliary obstruction: preliminary results with Levovist-enhanced sonography. AJR Am J Roentgenol. 2003;180(3):687-693.
71. Fried AM, Kreel L, Cosgrove DO. The hepatic interlobar fissure: combined in vitro and in vivo study. AJR Am J Roentgenol. 1984;143(3):561-564.
72. Martin DF, Laasch HL. The biliary tract. In: Grainger RG, Allison DJ, editors. Diagnostic radiology: a textbook of medical imaging. 4th ed. New York: Churchill Livingstone; 2001. p. 1277.
73. Stieber AC, Bauer JJ. Volvulus of the gallbladder. Am J Gastroenterol. 1983;78(2):96-98.
74. Waisberg J, Pinto Jr PE, Gusson PR, et al. Agenesis of the gallbladder and cystic duct. Sao Paulo Med J. 2002;120(6):192-194.
75. Kratzer W, Mason RA, Kachele V. Prevalence of gallstones in sonographic surveys worldwide. J Clin Ultrasound. 1999;27(1):1-7.

76. Gore RM, Yaghmai V, Newmark GM, et al. Imaging benign and malignant disease of the gallbladder. Radiol Clin North Am. 2002;40(6):1307-1323, vi.
77. Naryshkin S, Trotman BW, Raffensperger EC. Milk of calcium bile. Evidence that gallbladder stasis is a key factor. Dig Dis Sci. 1987;32(9):1051-1055.
78. Ko CW, Sekijima JH, Lee SP. Biliary sludge. Ann Intern Med. 1999;130(4 Pt 1):301-311.
79. Trowbridge RL, Rutkowski NK, Shojania KG. Does this patient have acute cholecystitis? JAMA. 2003;289(1):80-86.
80. Indar AA, Beckingham IJ. Acute cholecystitis. BMJ. 2002;325(7365):639-643.
81. Strasberg SM. Clinical practice. Acute calculous cholecystitis. N Engl J Med. 2008;358(26):2804-2811.
82. Shea JA, Berlin JA, Escarce JJ, et al. Revised estimates of diagnostic test sensitivity and specificity in suspected biliary tract disease. Arch Intern Med. 1994;154(22):2573-2581.
83. Fidler J, Paulson EK, Layfield L. CT evaluation of acute cholecystitis: findings and usefulness in diagnosis. AJR Am J Roentgenol. 1996;166(5):1085-1088.
84. Wilson SR. Gastrointestinal disease. Reston, VA: American College of Radiology; 2004.
85. Uggowitzer M, Kugler C, Schramayer G, et al. Sonography of acute cholecystitis: comparison of color and power Doppler sonography in detecting a hypervascularized gallbladder wall. AJR Am J Roentgenol. 1997;168(3):707-712.
86. Simeone JF, Brink JA, Mueller PR, et al. The sonographic diagnosis of acute gangrenous cholecystitis: importance of the Murphy sign. AJR Am J Roentgenol. 1989;152(2):289-290.
87. Sood BP, Kalra N, Gupta S, et al. Role of sonography in the diagnosis of gallbladder perforation. J Clin Ultrasound. 2002;30(5):270-274.
88. Konno K, Ishida H, Naganuma H, et al. Emphysematous cholecystitis: sonographic findings. Abdom Imaging. 2002;27(2):191-195.
89. Ryu JK, Ryu KH, Kim KH. Clinical features of acute acalculous cholecystitis. J Clin Gastroenterol. 2003;36(2):166-169.
90. Boland GW, Slater G, Lu DS, et al. Prevalence and significance of gallbladder abnormalities seen on sonography in intensive care unit patients. AJR Am J Roentgenol. 2000;174(4):973-977.
91. Helbich TH, Mallek R, Madl C, et al. Sonomorphology of the gallbladder in critically ill patients. Value of a scoring system and follow-up examinations. Acta Radiol. 1997;38(1):129-134.
92. Ikematsu Y, Yamanouchi K, Nishiwaki Y, et al. Gallbladder volvulus: experience of six consecutive cases at an institute. J Hepatobiliary Pancreat Surg. 2000;7(6):606-609.
93. Schiller VL, Turner RR, Sarti DA. Color Doppler imaging of the gallbladder wall in acute cholecystitis: sonographic-pathologic correlation. Abdom Imaging. 1996;21(3):233-237.
94. Parra JA, Acinas O, Bueno J, et al. Xanthogranulomatous cholecystitis: clinical, sonographic, and CT findings in 26 patients. AJR Am J Roentgenol. 2000;174(4):979-983.
95. Opatrny L. Porcelain gallbladder. CMAJ. 2002;166(7):933.
96. Towfigh S, McFadden DW, Cortina GR, et al. Porcelain gallbladder is not associated with gallbladder carcinoma. Am Surg. 2001;67(1):7-10.
97. Stephen AE, Berger DL. Carcinoma in the porcelain gallbladder: a relationship revisited. Surgery. 2001;129(6):699-703.
98. Bilhartz LE. Acalculous cholecystitis, cholesterolosis, adenomyomatosis, and polyps of the gallbladder. In: Feldman M, et al., editors. Sleisenger and Fordtran's gastrointestinal and liver disease. 7th ed. New York: Elsevier Science; 2002. p. 1123-1125.
99. Yoshimitsu K, Honda H, Aibe H, et al. Radiologic diagnosis of adenomyomatosis of the gallbladder: comparative study among MRI, helical CT, and transabdominal US. J Comput Assist Tomogr. 2001;25(6):843-850.
100. Csendes A, Burgos AM, Csendes P, et al. Late follow-up of polypoid lesions of the gallbladder smaller than 10 mm. Ann Surg. 2001;234(5):657-660.
101. Ito H, Hann LE, D'Angelica M, et al. Polypoid lesions of the gallbladder: diagnosis and followup. J Am Coll Surg. 2009;208(4):570-575.
102. Corwin MT, Siewert B, Sheiman RG, Kane RA. Incidentally detected gallbladder polyps: is follow-up necessary?—Long-term clinical and US analysis of 346 patients. Radiology. 2010;258(1):277-282.
103. Park JY, Hong SP, Kim YJ, et al. Long-term follow up of gallbladder polyps. J Gastroenterol Hepatol. 2009;24(2):219-222.
104. Gurusamy KS, Abu-Amara M, Farouk M, Davidson BR. Cholecystectomy for gallbladder polyp. Cochrane Database Syst Rev. 2009;(1):CD007052.
105. Levy AD, Murakata LA, Abbott RM, Rohrmann Jr CA. From the archives of the AFIP. Benign tumors and tumorlike lesions of the gallbladder and extrahepatic bile ducts: radiologic-pathologic correlation. Armed Forces Institute of Pathology. Radiographics. 2002;22(2):387-413.
106. Kim JH, Lee JY, Baek JH, et al. High-resolution sonography for distinguishing neoplastic gallbladder polyps and staging gallbladder cancer. AJR Am J Roentgenol. 2015;204(2):W150-W159.
107. Cho JH, Park JY, Kim YJ, et al. Hypoechoic foci on EUS are simple and strong predictive factors for neoplastic gallbladder polyps. Gastrointest Endosc. 2009;69(7):1244-1250.
108. Sugiyama M, Atomi Y, Kuroda A, et al. Large cholesterol polyps of the gallbladder: diagnosis by means of US and endoscopic US. Radiology. 1995;196(2):493-497.
109. Mellnick VM, Menias CO, Sandrasegaran K, et al. Polypoid lesions of the gallbladder: disease spectrum with pathologic correlation-erratum. Radiographics. 2015;35(3):973.
110. Maeyama R, Yamaguchi K, Noshiro H, et al. A large inflammatory polyp of the gallbladder masquerading as gallbladder carcinoma. J Gastroenterol. 1998;33(5):770-774.
111. Holloway BJ, King DM. Ultrasound diagnosis of metastatic melanoma of the gallbladder. Br J Radiol. 1997;70(839):1122-1125.
112. Yoon WJ, Yoon YB, Kim YJ, et al. Metastasis to the gallbladder: a single-center experience of 20 cases in South Korea. World J Gastroenterol. 2009;15(38):4806-4809.
113. Nagaraja V, Eslick GD. Systematic review with meta-analysis: the relationship between chronic Salmonella typhi carrier status and gall-bladder cancer. Aliment Pharmacol Ther. 2014;39(8):745-750.
114. Levy AD, Murakata LA, Rohrmann Jr CA. Gallbladder carcinoma: radiologic-pathologic correlation. Radiographics. 2001;21(2):295-314.
115. Kamisawa T, Kuruma S, Tabata T, et al. Pancreaticobiliary maljunction and biliary cancer. J Gastroenterol. 2014;50(3):273-279.
116. Curley SA. The gallbladder. In: Abeloff MD, editor. Clinical oncology. 2nd ed. New York: Churchill Livingstone; 2000. p. 1415-1420.
117. Xie XH, Xu HX, Xie XY, et al. Differential diagnosis between benign and malignant gallbladder diseases with real-time contrast-enhanced ultrasound. Eur Radiol. 2009;20(1):239-248.
118. Bach AM, Loring LA, Hann LE, et al. Gallbladder cancer: can ultrasonography evaluate extent of disease? J Ultrasound Med. 1998;17(5):303-309.

CHAPTER 7

The Pancreas

Thomas Winter and Maryellen R.M. Sun

SUMMARY OF KEY POINTS

- Knowledge of a few key scanning techniques will optimize imaging of the entire pancreas.
- Understanding of the embryologic development, normal anatomy, and anatomic variants of the pancreas aids in detection and characterization of disease.
- Ultrasound plays an important role in assessment of acute and chronic pancreatitis, allowing for detection of gallstones, bile duct dilation, and guiding aspiration and drainage when needed.
- Computed tomography is the imaging modality of choice for staging pancreatic cancer, but ultrasound can be used to detect, characterize, and stage solid pancreatic neoplasms.
- Cystic pancreatic lesions are common, and it is important to understand the benign and malignant features of these lesions.

CHAPTER OUTLINE

ANATOMY AND SONOGRAPHIC TECHNIQUE
Pancreatic Body
Pancreatic Head
Pancreatic Tail
Pancreatic Parenchyma
Fatty Pancreas
Embryology and Pancreatic Duct
Imaging Anatomic Variants
Peripancreatic Structures
ACUTE PANCREATITIS
Approach to Imaging
Ultrasound Findings
Complications
Acute Fluid Collections
Pseudocysts
Necrosis and Abscess
Treatment
Vascular Complications
CHRONIC PANCREATITIS
Approach to Imaging
Ultrasound Findings
Pseudocysts
Portal and Splenic Vein Thrombosis
Masses Associated With Chronic Pancreatitis
PANCREATIC NEOPLASMS
Periampullary Neoplasm
Pancreatic Carcinoma
Detection of Pancreatic Cancer
Ultrasound Findings
Resectability Imaging
Color Doppler Ultrasound
CYSTIC PANCREATIC LESIONS
Simple Pancreatic Cysts
Cystic Neoplasms
Serous Cystic Neoplasm
Intraductal Papillary Mucinous Neoplasm
Mucinous Cystic Neoplasm
Solid-Pseudopapillary Tumor
Rare Cystic Tumors
OTHER PANCREATIC MASSES
Endocrine Tumors
Unusual and Rare Neoplasms
Lipoma
Metastatic Tumors
CONTRAST-ENHANCED ULTRASOUND
Acknowledgment

Pancreatic sonography can be an efficient and valuable tool in many common diseases, such as pancreatitis and pancreatic neoplasm. Sonography is often the first test used in patients with jaundice or abdominal pain. However, sonography is "technically dependent" and necessitates understanding techniques to optimize pancreatic sonography. Knowledge of sonographic findings in common (and less common) pancreatic diseases is crucial to obtaining good imaging and clinical outcomes in these patients.

ANATOMY AND SONOGRAPHIC TECHNIQUE

Patient preparation is important in pancreatic sonography. An 8-hour fast before the study (usually overnight) is recommended, but we allow our patients to drink water and take medicines orally.

The three key regions of the pancreas are the head, body, and tail. The visualization of each requires knowledge of pancreatic anatomy, appropriate patient positioning, and often the use of multiple transducers. The pancreas lies obliquely in the anterior pararenal space of the **retroperitoneum,** with the head caudal to the body and tail. The pancreas is draped over the **spine and aorta;** thus the neck and body are more superficial than the head and tail. The more caudal position of the head often leads to the technical error of not visualizing the entire head on "transverse" scans. This can be avoided by understanding the anatomy and by visualizing the normal uncinate process behind the gastrocolic trunk on images of the pancreatic head (Fig. 7.1). Knowledge of a few key scanning techniques will optimize imaging of the entire pancreas.

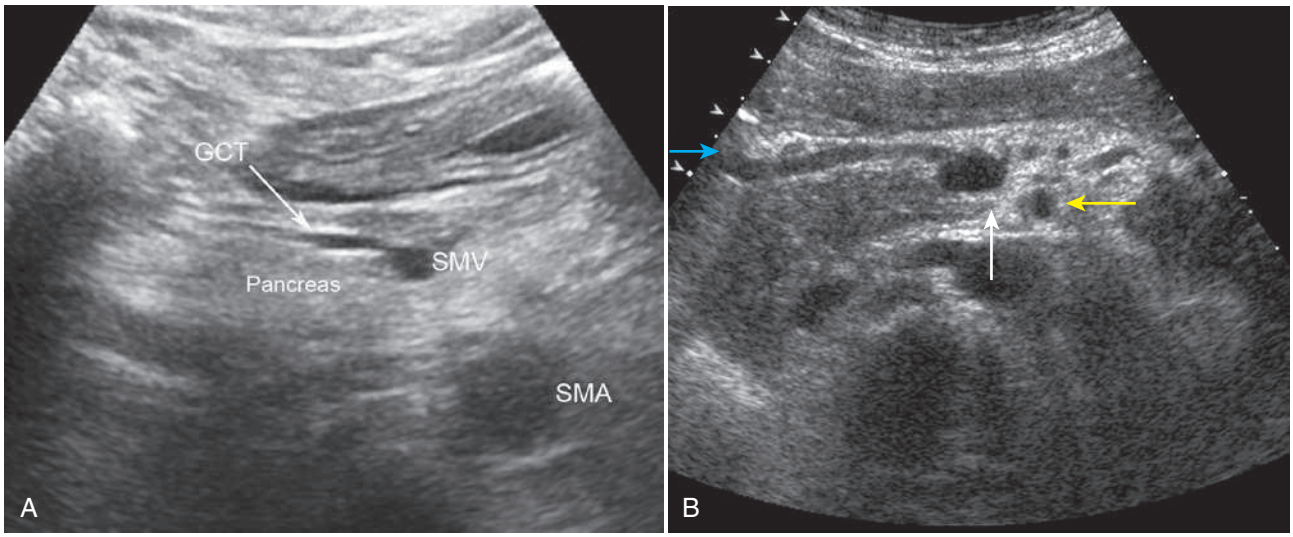

FIG. 7.1 Normal Pancreatic Head and Gastrocolic Trunk. (A) Transverse image of the pancreatic head and its ventral landmark, the gastrocolic venous trunk *(GCT).* The caudal uncinate *(Pancreas)* is dorsal to the GCT. **(B)** In another patient, note the triangular point of the uncinate that points medially *(white arrow)* behind the SMV and nearly reaches the SMA *(yellow arrow).* GCT *(blue arrow)* enters the SMV. *SMA,* Superior mesenteric artery; *SMV,* superior mesenteric vein.

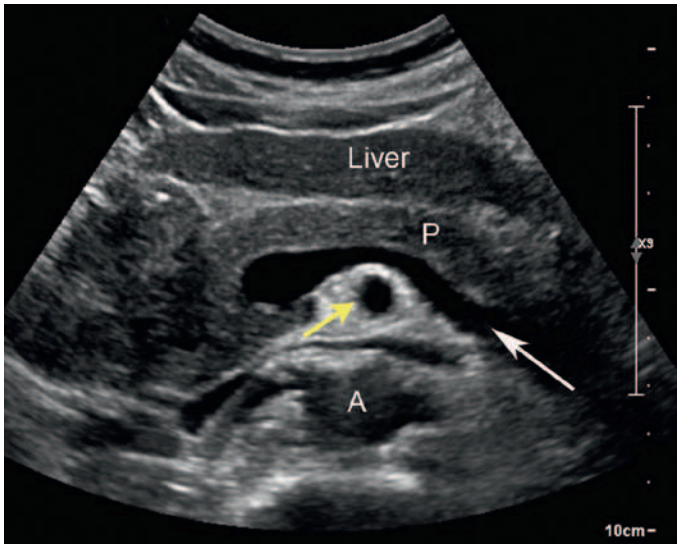

FIG. 7.2 Normal Pancreatic Body and Landmarks. Transverse image of the pancreatic body and its dorsal landmark, the splenic vein *(white arrow)* and portosplenic confluence. Note the normal parenchymal echogenicity, similar to that of the liver echogenicity. The superior mesenteric artery *(yellow arrow)* is surrounded by a collar of fat. *A,* Aorta; *P,* pancreas. See also Video 7.1.

Pancreatic Body

Compression scanning with a "large footprint," curved linear transducer is the key technique in visualizing the body of the pancreas. Compression displaces gas and fluid from the overlying stomach and duodenum and places the transducer closer to the pancreas itself. The key vascular landmarks for the body of the pancreas are the **splenic vein,** its confluence with the **superior mesenteric vein** (SMV), and the **superior mesenteric artery** (SMA) (Fig. 7.2, Video 7.1). Some call the region between the body and head of the pancreas the "neck," generally referring to the part of the pancreatic body ventral to the SMA-SMV and portosplenic confluence (Fig. 7.3).

Start scanning with the patient supine. Initially, scan the patient in quiet respiration. Breath holding may cause the patient to contract the abdominal muscles, preventing good compression. Images obtained in various degrees of held inspiration or, less often, expiration may facilitate pancreatic visualization. In inspiration the liver may be a useful sonographic window. In some patients a high-riding transverse colon may prevent good visualization of the pancreatic body. Unlike the stomach and duodenum, the contents of which are generally compressible, the colon often contains stool, which contains suspended gas. Stool cannot be compressed and is therefore an impediment to pancreatic sonography. In these patients, scanning caudal to the transverse colon and angling cephalic behind the colon may be useful. The left lateral decubitus position may also be useful, especially to see the left part of the body and more central tail. Position the transducer to the right of the midline and angle "down the barrel" (longitudinal axis) of the pancreatic body and tail (Fig. 7.4).

Other potentially useful techniques include scanning during a Valsalva maneuver and scanning after oral water or contrast administration,[1-3] sometimes combined with scanning while the patient is standing or sitting, using the fluid-filled stomach as a window.

Pancreatic Head

The head is the key pancreatic structure; common bile duct stones, periampullary neoplasms, and pancreatic/extrahepatic duct obstructions occur here. Failure to adequately visualize the pancreatic head is a common but usually avoidable technical failure. Supine compression imaging is useful but rarely allows demonstration of the periampullary region. Vascular landmarks for the pancreatic head are the **inferior vena cava** (IVC) dorsally, the SMA and SMV medially, and the **gastroduodenal artery**

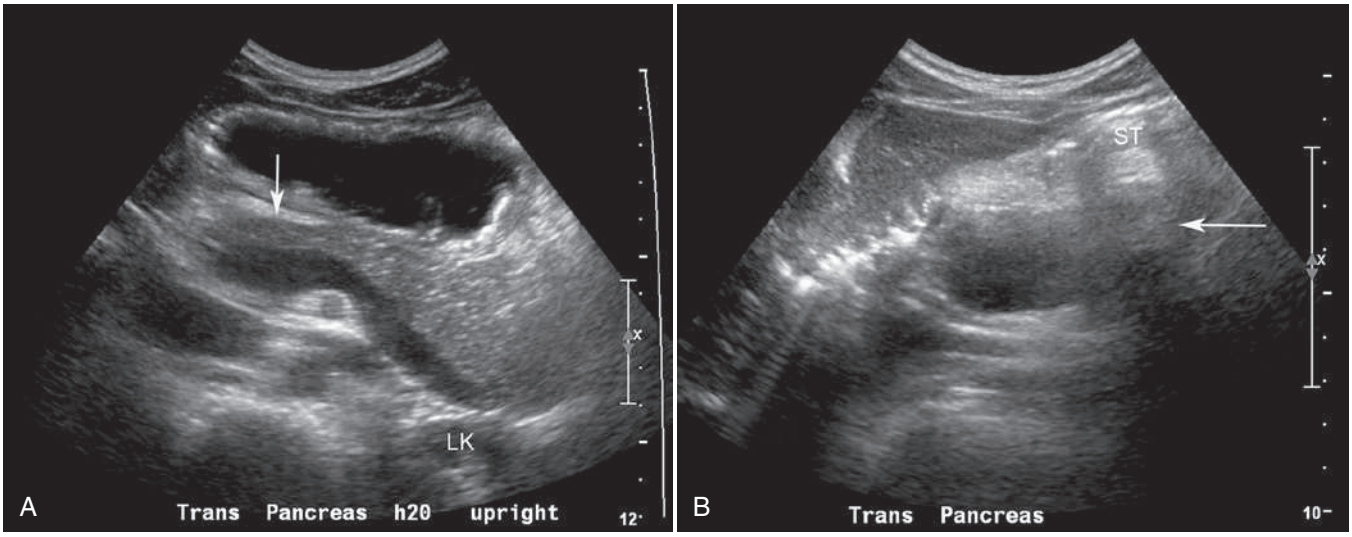

FIG. 7.3 Normal Pancreatic Neck and Body. (A) Transverse image of pancreatic body. The "neck" of the pancreas *(arrow)* is that part of the body ventral to the superior mesenteric artery and portosplenic confluence. **(B)** Role of technique in sonographic visualization of the pancreas. Transverse image of region of pancreas shows poor visualization of the gland *(arrow);* water was administered orally and patient placed in the upright position to achieve the image shown in **(A)**. *LK,* Left kidney*; ST,* stomach.

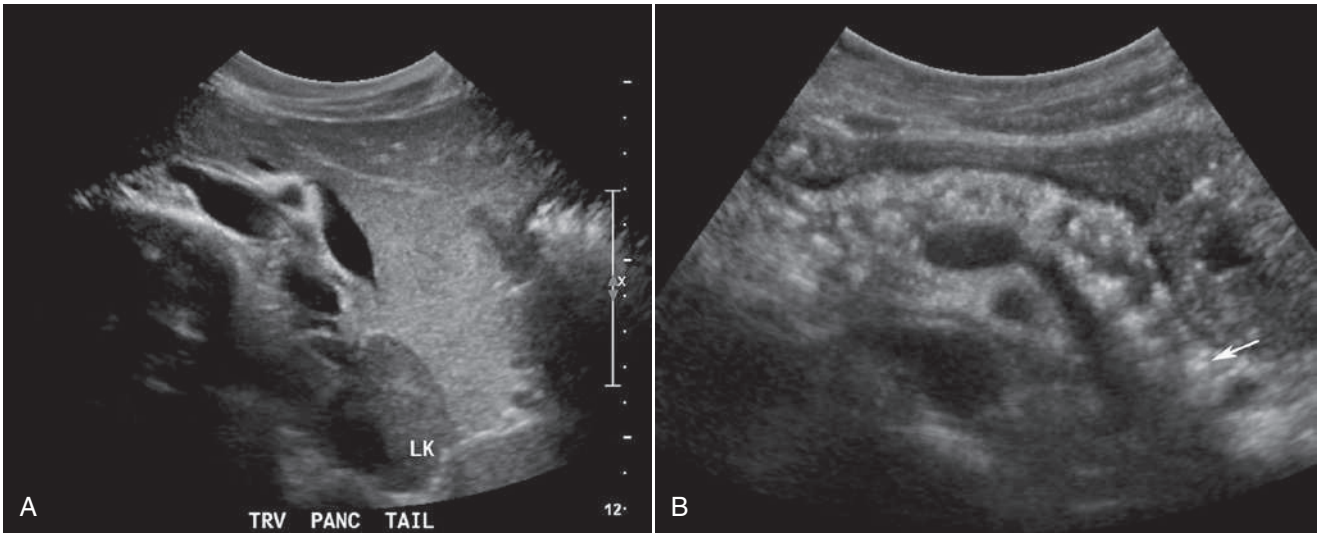

FIG. 7.4 Pancreatic Body and Tail. (A) Transverse image of the pancreatic body and tail obtained by positioning the transducer to the right of the midline and angling back toward the left. **(B)** In another patient with **chronic pancreatitis,** the transverse view shows the dilated pancreatic duct with scattered calcifications extending to the end of the duct in the pancreatic tail *(arrow). LK,* Left kidney.

(GDA) and the **pancreaticoduodenal arcade** anterolaterally (Fig. 7.5). The pancreatic head is usually directly ventral to the IVC. Cephalic to the pancreas, the IVC is adjacent to the portal vein; this location is the entrance into the lesser peritoneal sac, the **epiploic foramen (foramen of Winslow).**

The **uncinate process** (or uncinate) is a portion of the caudal pancreatic head that wraps around behind the SMA and SMV, ending in a point oriented medially. The uncinate process is medial and dorsal to the SMA and SMV (Fig. 7.6; see also Fig. 7.1B). The GDA is a landmark for the ventrolateral pancreatic head; the GDA courses between the pancreas and the second portion of the duodenum (Fig. 7.7).

Another useful vascular landmark for the pancreatic head and uncinate process is the **gastrocolic trunk** (GCT). Several splanchnic veins variably join to form the GCT. These often include the right or middle colic vein, right gastroepiploic vein, and pancreaticoduodenal veins. The GCT enters the right side of the SMV just anterior to the pancreatic head, thus serving as a ventral landmark for the uncinate process[4] (see Fig. 7.1).

The left lateral decubitus position is best to see the pancreas adjacent to the duodenum. In the left lateral decubitus position, scan in inspiration, and use the gallbladder or liver to either side of the gallbladder to view the rightmost portion of the pancreas

and the ampullary portion of the pancreatic and bile ducts (Fig. 7.8). It is best to be explicit when describing locations within the pancreas (e.g., mass within the tail of the pancreas) rather than using the terms *proximal* and *distal* because these terms are ambiguous when applied to the pancreas and may mean different things to different people.[5]

Pancreatic Tail

It is rarely necessary or helpful for the patient to drink water before the head or body of the pancreas is scanned. The **water-filled stomach,** however, may provide an excellent window for visualizing the pancreatic tail, the most difficult portion of the pancreas to visualize sonographically. To see the tail, place the patient in a right anterior oblique position and scan through the water-filled stomach (Fig. 7.9). Another helpful way to see the region of the pancreatic tail is coronal imaging through the spleen and left kidney, with the patient in a right lateral decubitus position (Fig. 7.10). Color Doppler sonography can reveal the splenic artery and vein, facilitating identification of the tail. Scanning through the spleen and left kidney, although not always revealing the normal pancreatic tail itself, may show abnormalities in the region of the tail (e.g., pseudocysts, masses) that are not visible on other views. The view through the left kidney and spleen should be routine in all pancreatic sonograms.

Pancreatic Parenchyma

The sonographic appearance of the normal pancreas varies widely in parenchymal echogenicity and texture, shape, and size. The

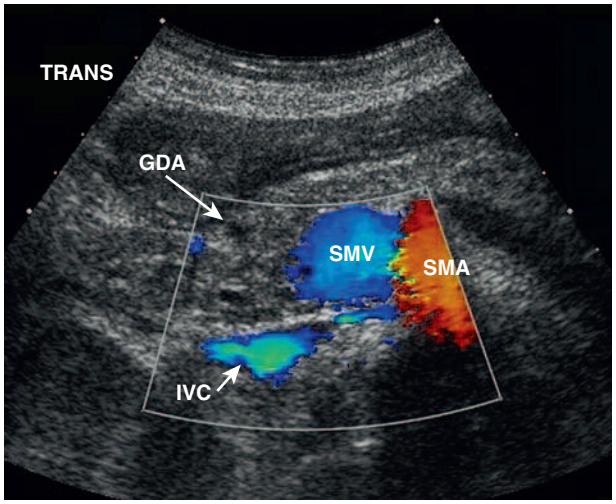

FIG. 7.5 Normal Pancreatic Head and Vascular Landmarks. Transverse sonogram shows vascular landmarks for the pancreatic head: inferior vena cava *(IVC)* dorsally, superior mesenteric artery *(SMA)* and superior mesenteric vein *(SMV)* medially, and gastroduodenal artery *(GDA)*.

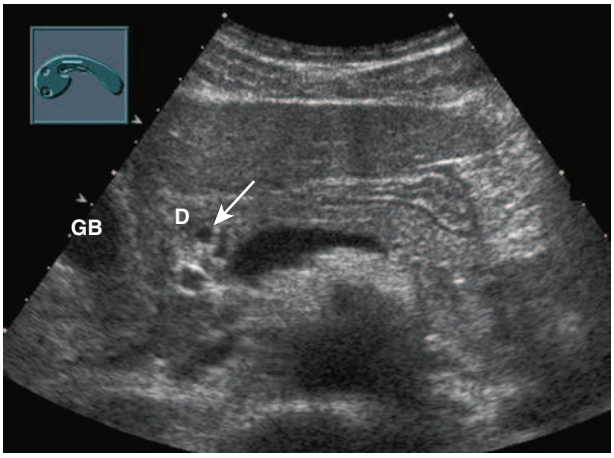

FIG. 7.7 Normal Gallbladder, Duodenum, and Pancreatic Head. Transverse sonogram shows the gastroduodenal artery (GDA) *(arrow)* as a landmark for the ventrolateral pancreatic head. The GDA courses between the pancreas and the second portion of the duodenum *(D)*. The gallbladder *(GB)* is lateral to the duodenum. The image shows the cephalic portion of the pancreatic head.

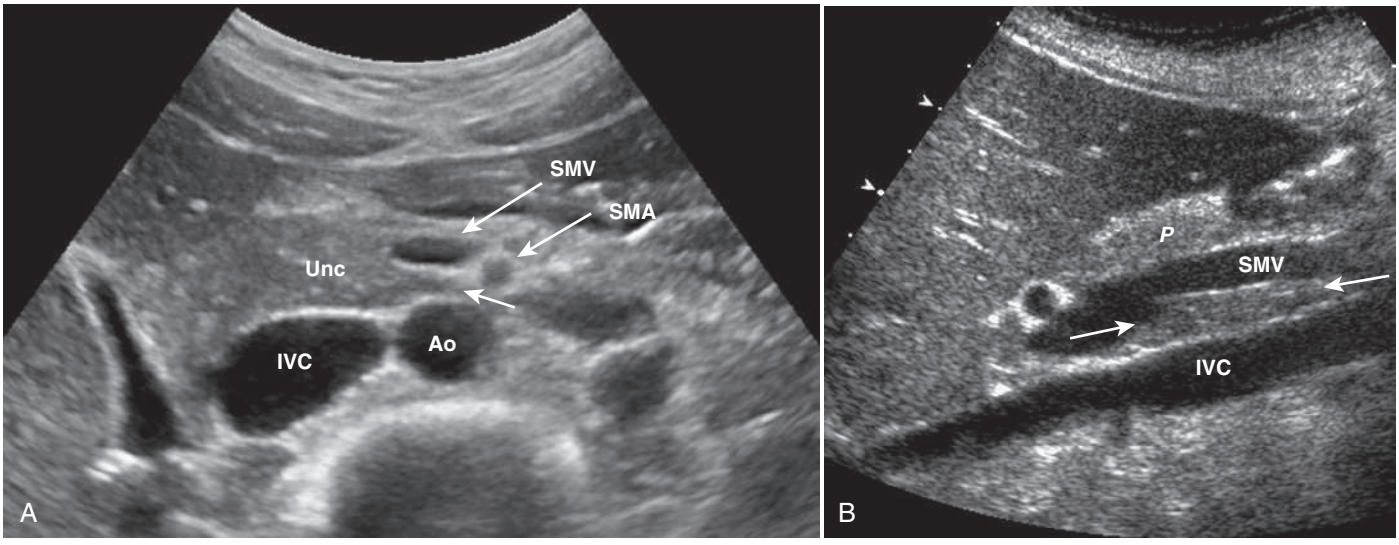

FIG. 7.6 Normal Uncinate Process. (A) Transverse sonogram showing the uncinate process *(Unc)*, the part of the pancreatic head dorsal to the superior mesenteric vein *(SMV)* and superior mesenteric artery *(SMA)*. Note the pointed medial tip of the uncinate *(small arrow)* (see also Fig. 7.1B). **(B)** Longitudinal sonogram in another patient shows the uncinate process *(arrows)* dorsal to the SMV and ventral to the inferior vena cava *(IVC)*. The neck/body of the pancreas *(P)* is ventral to the SMV. *Ao,* Aorta; *IVC,* inferior vena cava.

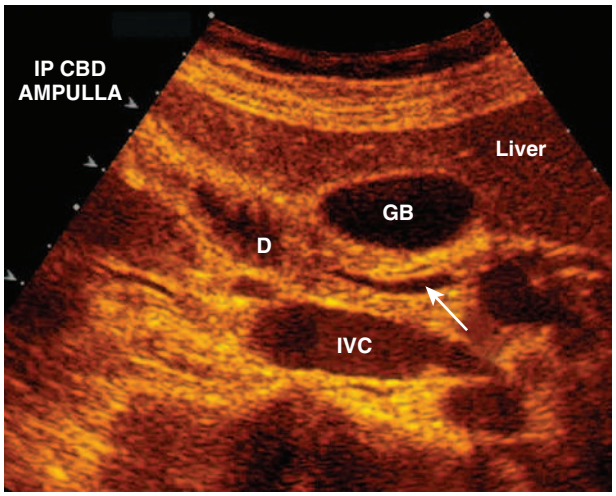

FIG. 7.8 Normal Ampullary Area and Bile Duct. Sonographic scan through the gallbladder *(GB)* and liver, with the patient in the left lateral decubitus position, to visualize the ampullary region shows the normal distal bile duct *(arrow)* as it passes through the pancreatic head and enters the duodenum through the major papilla. *D,* Duodenum; *IP CBD,* intrapancreatic common bile duct.

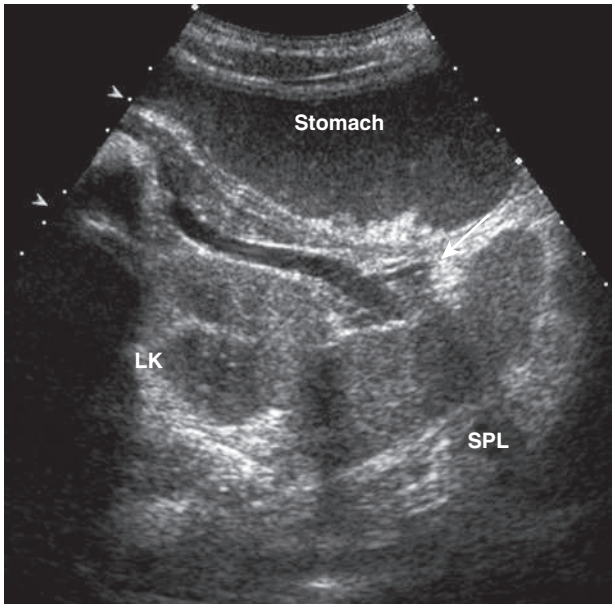

FIG. 7.9 Normal Pancreatic Body and Tail. Transverse image of the pancreatic body and tail, surrounding the splenic vein, seen through the fluid-filled stomach, with patient in a right anterior oblique position. *LK,* Left kidney; *SPL,* spleen.

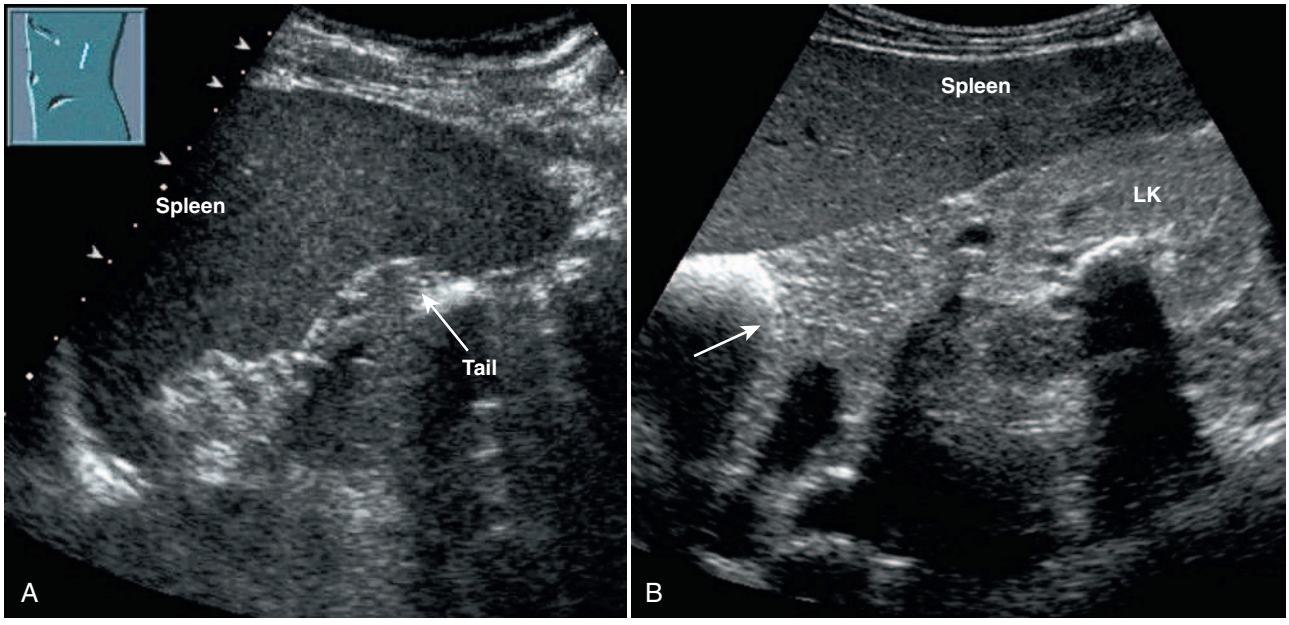

FIG. 7.10 Normal Pancreatic Tail. Pancreatic tail seen through the spleen, with patient in right lateral decubitus position. **(A)** Longitudinal coronal image shows the normal pancreatic tail *(arrow)* through the spleen. **(B)** Transverse image of the normal pancreatic tail *(arrow)*. Note large stone in the left kidney *(LK)* with a conspicuous acoustic shadow.

pancreatic parenchyma is usually isoechoic or hyperechoic compared with the hepatic parenchyma (Fig. 7.11; see also Figs. 7.2 and 7.3). Evidence indicates that pancreatic echogenicity increases with age.[6]

The parenchymal **texture** varies widely from homogeneous to a lobular internal architecture (Fig. 7.12). Pancreatic **size** varies considerably from individual to individual. Guerra et al.[7] found that the size of the head of the pancreas ranged from 6 to 28 mm (17.7 ± 4.2 mm), body size from 4 to 23 mm (10.1 ± 3.8 mm), and tail size from 5 to 28 mm (16.4 ± 4.2 mm). Men and women had comparable pancreatic size. The size of the pancreas diminishes with age.[7,8]

The **shape** of the pancreas can also vary considerably.[9] Variations in the shape of the pancreatic head are the most troublesome

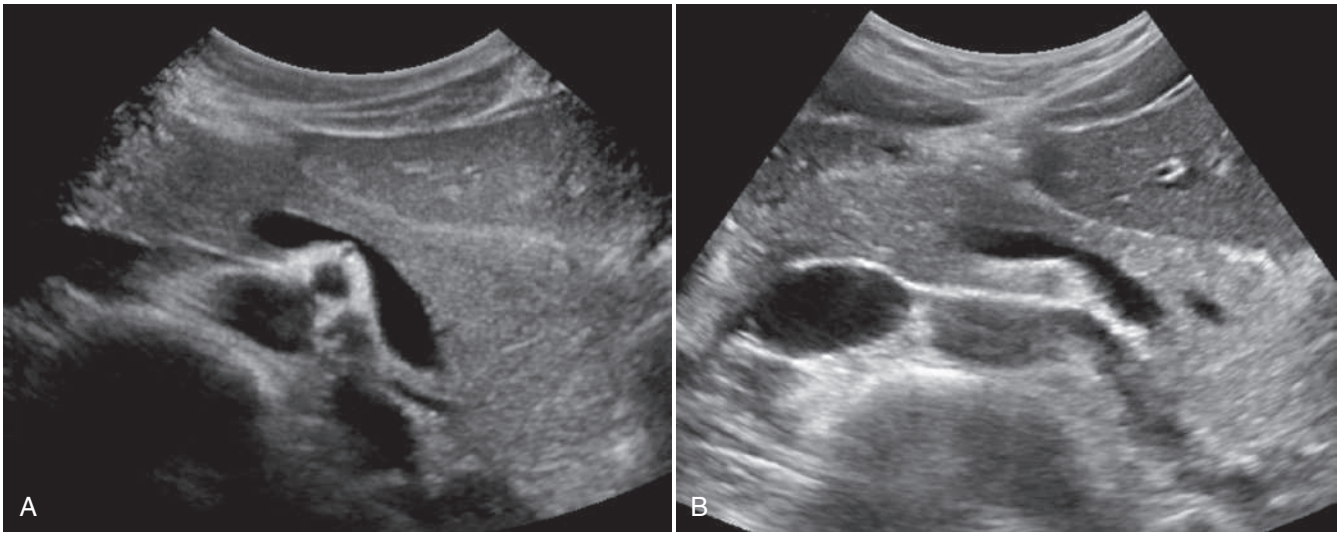

FIG. 7.11 Normal Pancreatic Parenchymal Echogenicity. (A) Transverse sonogram showing pancreas has echogenicity similar to that of the liver. **(B)** Transverse sonographic image of another patient, showing pancreas with a much more echogenic appearance.

because they can simulate a pancreatic head mass, a **pseudomass.** Typically, these bulges extend to the right of the GDA and superior pancreaticoduodenal artery (Fig. 7.13). Another common pseudomass is a bulge on the anterior body, often seen where the left lobe of the liver touches the pancreas. Pseudomasses have texture and echogenicity identical to normal pancreas, allowing differentiation from true pancreatic mass lesions. When high-quality images of the pancreas cannot be obtained because of technical difficulties, however, it may be difficult to differentiate a pseudomass from a true neoplasm of the pancreas. In these cases, comparison to appearance on prior exam or correlation with computed tomography (CT) or magnetic resonance imaging (MRI) may be needed for further assessment.

Fatty Pancreas

Because the pancreatic parenchyma can be very echogenic normally, it may be difficult or impossible to diagnose fatty infiltration with sonography. Although the fatty pancreas has been described as being more echogenic than the normal pancreas,[10] this is difficult to judge (see Fig. 7.12). The pancreas can appear sonographically normal with complete fatty replacement[11] (Fig. 7.14). CT is sensitive in diagnosing fatty replacement, whereas ultrasound is unreliable. Severe fatty replacement of the pancreatic parenchyma can occur with **cystic fibrosis, diabetes, obesity,** and occasionally, old age and **Shwachman-Diamond syndrome.** Shwachman-Diamond syndrome is a rare congenital genetic disorder characterized by pancreatic insufficiency, bone marrow dysfunction, and skeletal abnormalities.[12]

An interesting pseudomass can be caused by a relatively hypoechoic pancreatic head or uncinate process (ventral pancreas) compared with the dorsal pancreas (Fig. 7.15). Some evidence suggests that this phenomenon is related to relative fatty sparing in that part of the gland.[13-15] Based on a large prospective study, Coulier[16] found that "hypoechoic ventral embryologic cephalic pancreas" is never found before age 25 and is most common in middle-aged women with a "moderately echoic pancreas."

Embryology and Pancreatic Duct

The embryologic precursors of the adult pancreas develop as two outpouchings ("buds"), called the **dorsal (cranial) pancreatic anlage** and **ventral (caudal) pancreatic anlage.** These embryonic buds arise from opposite sides of the junction of the primitive foregut and midgut (Fig. 7.16). The two pancreatic anlagen (primordia) rotate to be in proximity, typically fusing at 6 to 8 weeks of gestation.[17] The dorsal (cranial) pancreatic bud becomes the body and tail of the pancreas. The ventral (caudal) bud becomes the pancreatic head and uncinate process, ending up in a position caudal to the body and tail. The ventral bud is also the embryologic origin of the gallbladder, bile duct, and liver. The bile duct and pancreatic head sharing a common origin explains the usual fusion (60%-80%) of the pancreatic and bile duct in the ampulla and their common entry into the duodenum through the major papilla.

The pancreatic duct is crucial to the **exocrine function** of the pancreas, conveying the pancreatic digestive secretions to the duodenum. Most adults have a single, **main pancreatic duct** that originates when portions of the two ducts from each pancreatic anlage fuse. The main pancreatic duct empties into the duodenum via the major papilla, usually after merging with the common bile duct in the ampulla. In 20% to 40% of individuals the ducts do not join—only the bile duct enters the duodenum through the major papilla.[18] The pancreatic duct enters separately, usually near the bile duct.

The duct in the body and tail (from the dorsal pancreatic anlage) fuses with the duct in the head (from the ventral pancreatic anlage) to form the main pancreatic duct. A portion of the duct from the body and tail, the **accessory duct** (Fig. 7.17), often persists (≈50% in autopsy series) and enters the duodenum

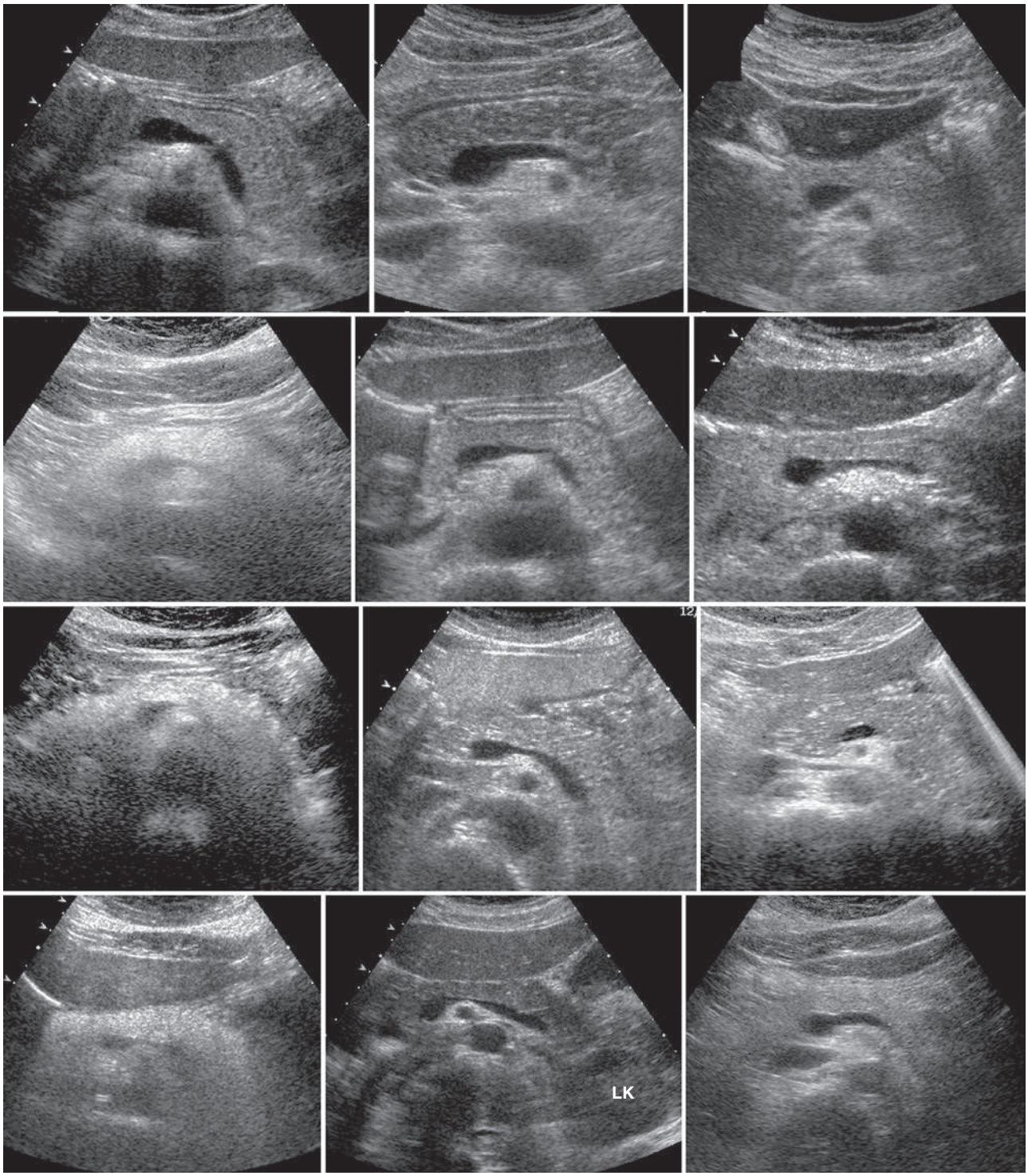

FIG. 7.12 Normal Pancreatic Parenchymal Echogenicity. Transverse sonograms in 12 normal patients demonstrate the various patterns of normal pancreatic parenchyma. Echogenicity, texture, and size vary considerably. *LK,* Left kidney.

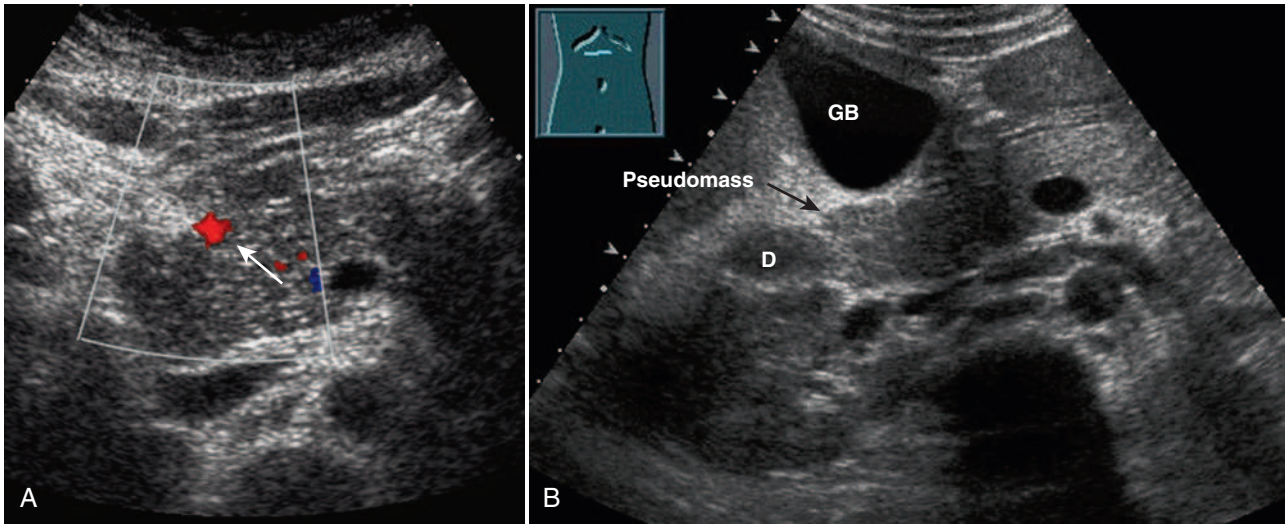

FIG. 7.13 Normal Anatomic Variations: Pancreatic Head Pseudomass. Variations in shape of the pancreatic head include bulges to the right of gastroduodenal artery. **(A)** Transverse image of a pseudomass that extends to the right of the gastroduodenal artery *(arrow)*. **(B)** Transverse image of another pseudomass. *D,* Duodenum.

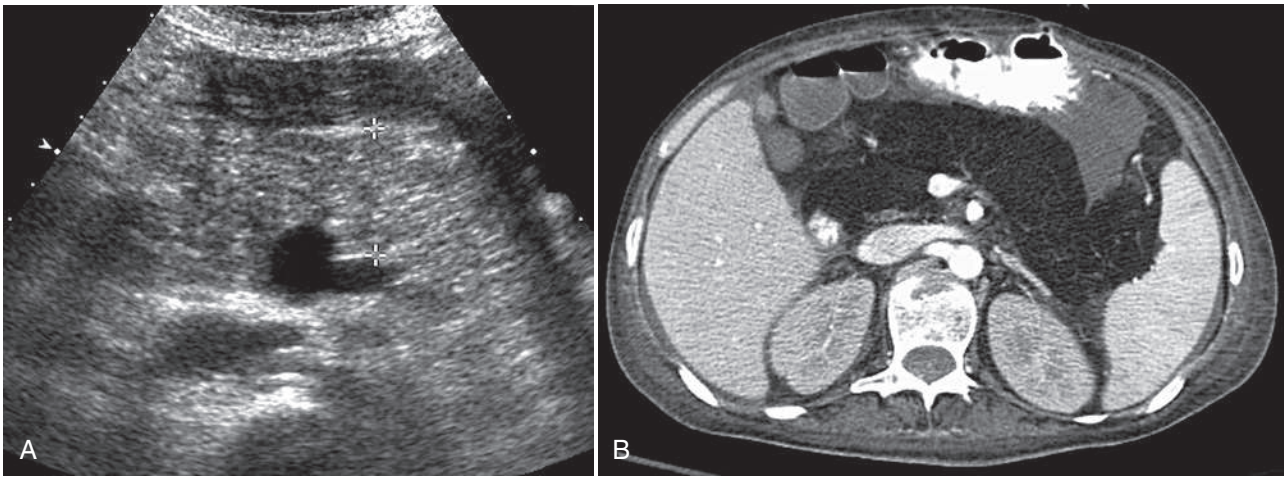

FIG. 7.14 Fatty Infiltration of Pancreas. (A) In this transverse image, the appearance and echogenicity of the pancreas (calipers) do not differ substantially from many normal glands. **(B)** Computed tomography scan shows diffuse fatty infiltration. (Courtesy of Drs. Vinay Duddlewar and Jabi Shiriki.)

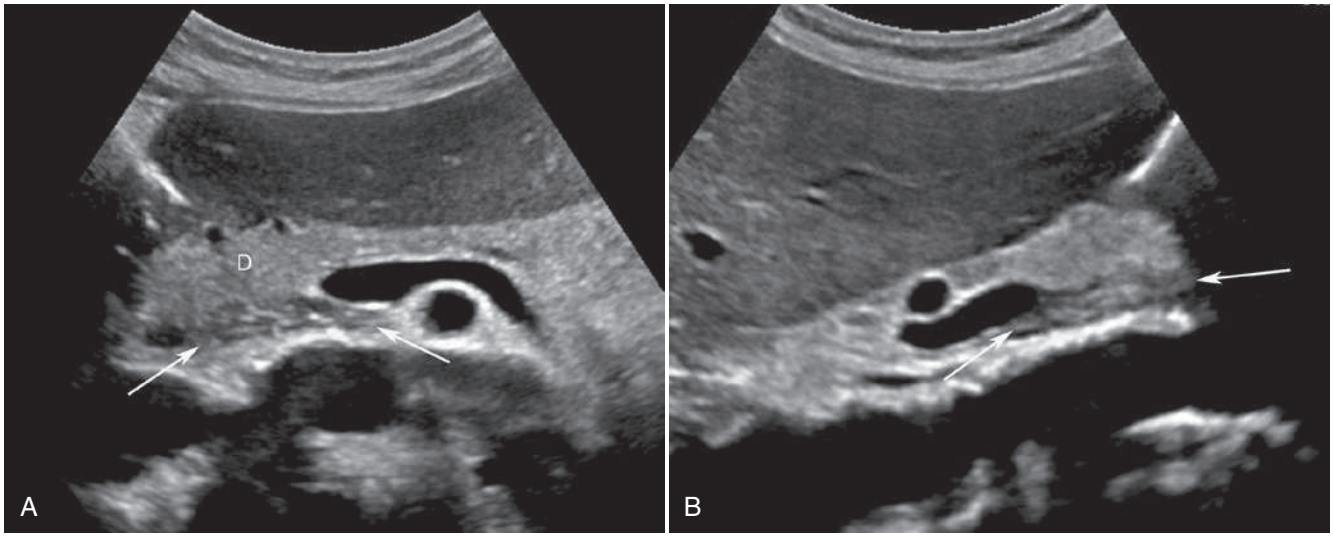

FIG. 7.15 Hypoechoic Ventral Pancreas. (A) Transverse sonogram of pancreatic head. Note the hypoechoic uncinate *(arrows),* likely related to less fatty change than present in the dorsal component *(D)*. **(B)** Longitudinal sonogram of pancreas. The more posterior uncinate *(arrows)* is lower in echogenicity than the remainder of the pancreas.

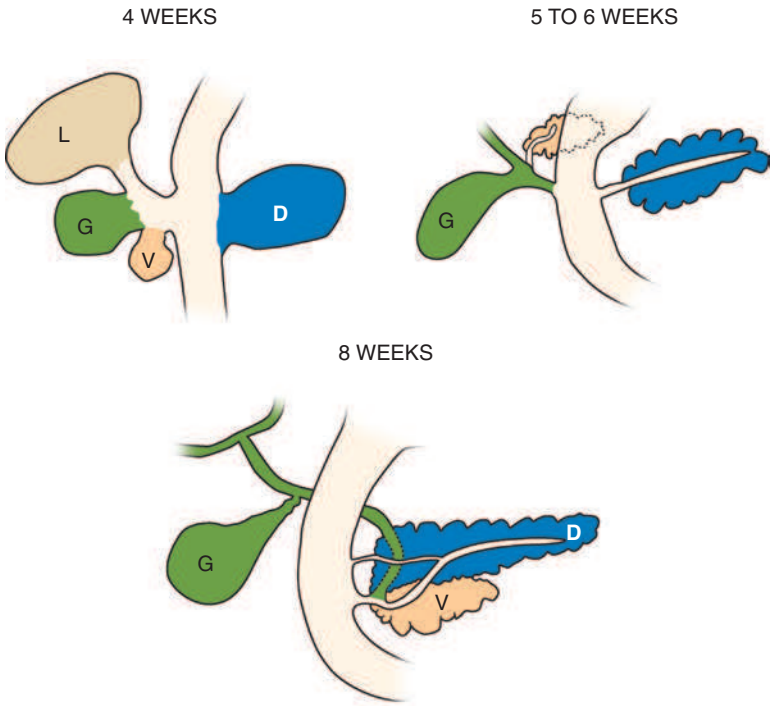

FIG. 7.16 Embryologic Development of Pancreas. At 4 weeks the embryologic precursors of the adult pancreas develop as two outpouchings ("buds"), called the dorsal *(D, blue)* and ventral *(V, brown)* pancreatic **anlage.** The ventral bud is also the embryologic origin of the gallbladder *(G)*, bile duct, and liver *(L)*. The embryonic pancreatic buds arise from opposite sides of the junction of the primitive foregut and midgut. **At 5 to 6 weeks** the two pancreatic anlagen rotate into proximity. **At 6 to 8 weeks** the anlagen typically fuse. The dorsal pancreatic bud becomes the body and tail of the pancreas.

through the minor papilla.[19] The minor duodenal papilla is several centimeters proximal to the major papilla.

Usually, only an insignificant amount of the pancreatic secretions drain through the accessory duct. An exception occurs when the accessory duct is the only duct entering the duodenum; the duct from the pancreatic head empties into the dorsal duct, not the duodenum (Fig. 7.18A). This anatomic variant is found in 10% of individuals who have an accessory duct. Another exception is **pancreatic divisum,** in which the ventral and dorsal pancreatic ducts do not fuse (Fig. 7.18B). This results in most of the pancreatic secretions (those secreted by dorsal pancreas) entering the duodenum through the accessory duct via the minor papilla.

The descriptive terminology of the pancreatic ducts is confusing. It is most clear to use the functional description shown in Fig. 7.17B, that is, the main pancreatic duct and accessory duct. Most authors use the terms *accessory duct* and the **duct of Santorini** synonymously. Some define the duct of Santorini as the entire dorsal duct, including the accessory duct. The main pancreatic duct is sometimes called the **duct of Wirsung,** whereas others reserve that name for the ventral duct only.

In normal individuals the pancreatic duct diameter is usually 3 mm or less. Hadidi[20] found that the mean duct diameter was 3 mm in the head, 2.1 mm in the body, and 1.6 mm in the tail. The diameter of the duct can vary significantly. In fasting individuals, the duct is often seen as a linear structure in the pancreatic body (Fig. 7.19). The diameter increases with age, although 3 mm is still an appropriate upper limit of normal in older patients.[6] Using a 2.5-mm upper limit of normal, Wachsberg[21] showed that inspiration could increase duct size to exceed that limit in 12% of patients without pancreatic disease. **Secretin injection** increases duct size, presumably because of increased pancreatic secretion,[22] which likely explains the observation that pancreatic duct size may increase postprandially in some normal individuals.[8]

Imaging Anatomic Variants

Transabdominal ultrasound plays little role in the diagnosis of anatomic variants of the pancreas, which are generally discovered and evaluated with CT, endoscopic retrograde cholangiopancreatography (ERCP), and magnetic resonance cholangiopancreatography (MRCP).[17,23] Endoscopic ultrasound has been found to be useful in diagnosing pancreas divisum, especially in patients with unexplained pancreatitis.[24] Congenital variants of the pancreas are common, occurring in about 10% of the population. Variants include **pancreas divisum, annular pancreas,** and **partial agenesis.** Most pancreatic variants are of no clinical significance and are found incidentally with imaging, at surgery, or on autopsy. Pancreas divisum, the most common variant, may predispose to **pancreatitis,** although the literature is unclear about this association.[25] The vast majority of patients (95%) with divisum do not develop pancreatitis.[26]

Peripancreatic Structures

The **intraperitoneal stomach** is generally located immediately ventral to the retroperitoneal pancreatic body, with the collapsed potential space of the lesser peritoneal sac between the two organs

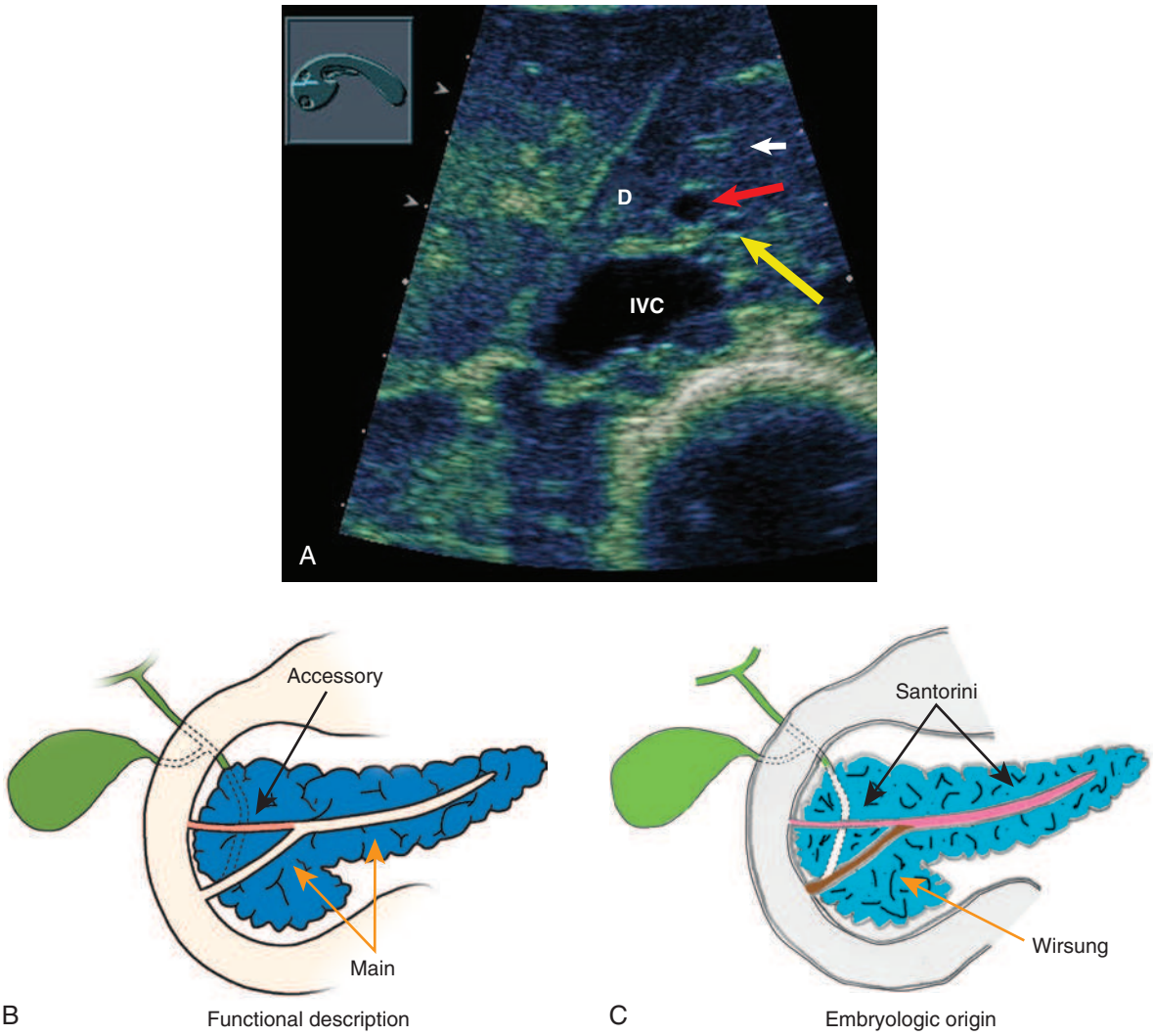

FIG. 7.17 Pancreatic Ductal Anatomy. (A) Pancreatic head. Transverse sonogram shows the accessory pancreatic duct *(white arrow).* The main pancreatic duct *(yellow arrow)* is seen dorsal and medial to the common bile duct *(red arrow). D,* Duodenum; *IVC,* inferior vena cava. **(B) Pancreatic ductal system, functional description.** Accessory duct is shown in tan *(black arrow)* and the main duct in white *(orange arrows).* The accessory duct persists in only a minority of individuals. **(C) Pancreatic ductal system, embryologic origin.** Dorsal component of main adult duct and the accessory duct (*black arrows,* duct of Santorini, *pink*) both originate from the dorsal anlage. Ventral component of main duct (*orange arrow,* duct of Wirsung, *brown*) in pancreatic head arises from the ventral anlage and usually fuses with main duct from pancreatic body (dorsal anlage).

(Fig. 7.20). This explains why fluid in the stomach can sometimes be helpful in sonographic visualization of the pancreas. The **lesser peritoneal sac** is situated between the lesser omentum, greater omentum, and the stomach anteriorly and the parietal peritoneum and transverse mesocolon posteriorly (Fig. 7.21).

The **antrum** and **duodenal bulb** are intraperitoneal structures, whereas the **duodenal sweep** (second and third parts of duodenum) is retroperitoneal and hugs the pancreatic head. The third portion of the duodenum is a useful landmark, defining the caudal aspect of the pancreatic head. The transverse colon and hepatic flexure often overlie the pancreas, sometimes obscuring direct visualization.

The **transverse mesocolon** arises from the anterior pancreas and duodenum, formed by the parietal peritoneum that invests the pancreas and duodenum. The transverse mesocolon invests the transverse colon and forms part of the posterior limits of the lesser peritoneal sac.

The tail of the pancreas lies within the splenorenal ligament and contacts the left kidney, left colic (splenic) flexure, and the hilum of the spleen posteriorly. Thus a portion of the pancreatic tail is intraperitoneal and somewhat mobile.

ACUTE PANCREATITIS

Acute pancreatitis is defined by the International Symposium on Acute Pancreatitis (Atlanta, 1992) as "an acute inflammatory process of the pancreas with variable involvement of other regional tissues or remote organ systems associated with raised pancreatic enzyme levels in blood and/or urine."[27] More than 300,000 patients are admitted to US hospitals annually with acute pancreatitis.[28] It is difficult to determine the prevalence of acute pancreatitis because mild pancreatitis is often missed. The annual incidence of acute pancreatitis has been reported as 5 to 35 per 100,000 population.[29]

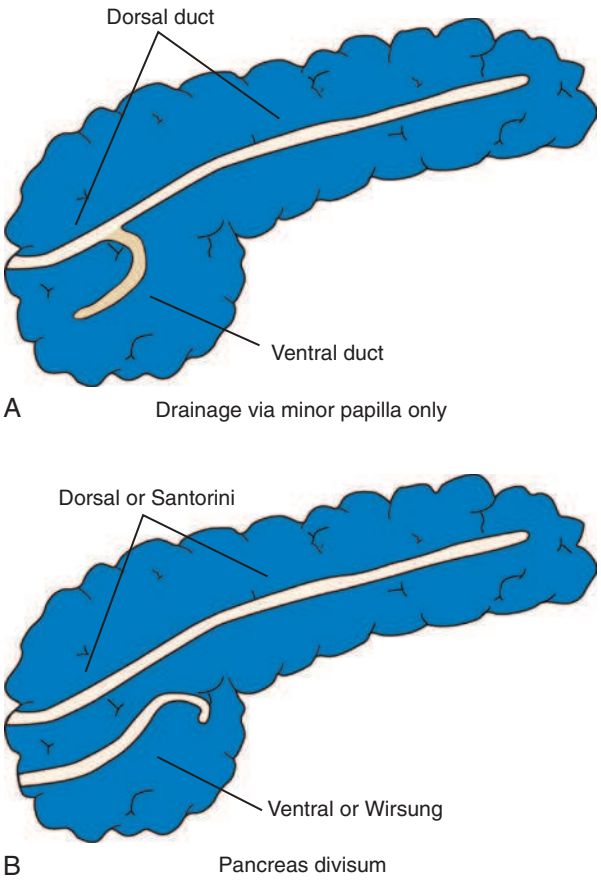

FIG. 7.18 Pancreatic Ductal Variants With Secretions Entering Duodenum via Minor Papilla. (A) Minor papilla only. Ventral duct from pancreatic head empties into the dorsal duct instead of the duodenum. **(B) Pancreas divisum** lacks formation of the main adult duct because the ducts from each pancreatic anlage did not fuse. The duct from the dorsal anlage remains separate from the main duct in the head. This anatomic variant is present in 5% to 10% of the population.

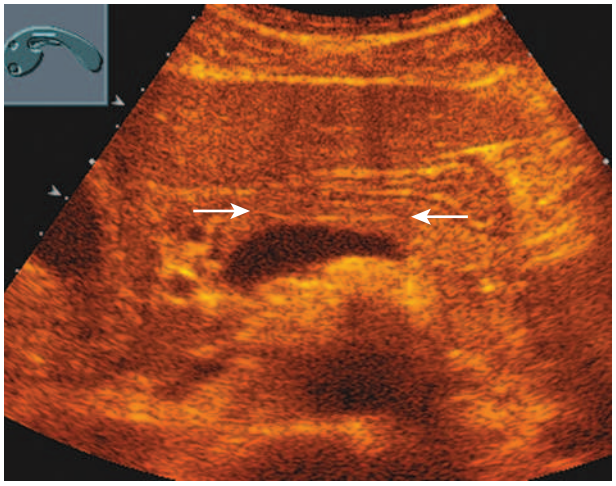

FIG. 7.19 Normal Pancreatic Duct. Transverse image of the pancreas shows the appearance of the pancreatic duct as a linear, collapsed structure in the body *(arrows)*.

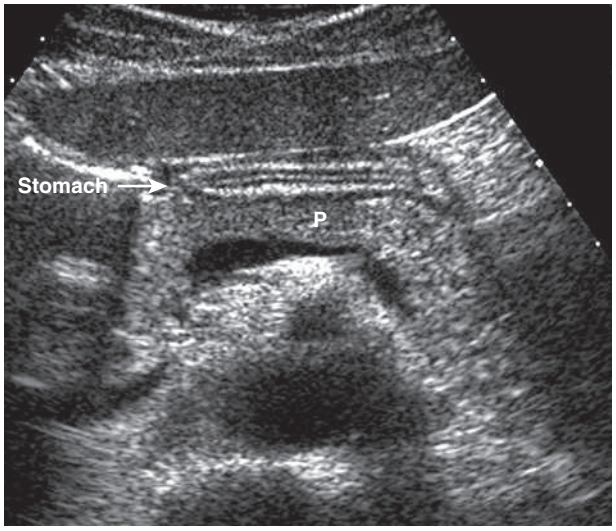

FIG. 7.20 Potential Space of Lesser Peritoneal Sac. Transverse image demonstrates the potential space of the lesser peritoneal sac between the stomach *(arrow)* and pancreas *(P)*.

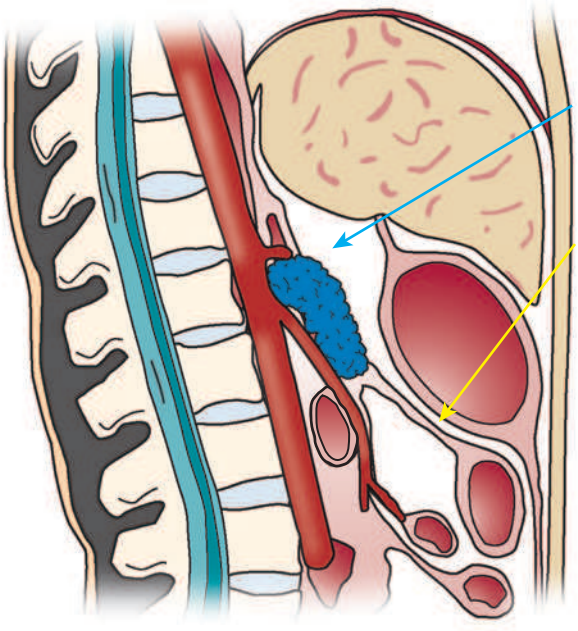

FIG. 7.21 Peritoneal Reflections and Transverse Mesocolon. Transverse mesocolon *(yellow arrow)* arises from the anterior pancreas and duodenum, formed by the parietal peritoneum that invests the pancreas and duodenum. The transverse mesocolon invests the transverse colon and forms part of the posterior limits of the lesser peritoneal sac *(blue arrow)*.

The clinical spectrum of acute pancreatitis ranges from a benign, self-limited disorder (75% of patients) to severe pancreatitis that may be fulminant and quickly cause death from multiorgan failure.[30] Mild acute pancreatitis generally resolves spontaneously with supportive management. Acute interstitial/edematous pancreatitis results in an enlarged and congested gland without appreciable necrosis or hemorrhage.[31] Banks and Freeman[32] found that the overall mortality of pancreatitis is approximately 5%. Mortality in the first 2 weeks usually results from organ failure, and after that, from infection. Mortality was

3% in patients with nonnecrotic (interstitial) pancreatitis and 17% for those with necrotizing pancreatitis. The same review noted 30% mortality with infected necrosis versus 12% for uninfected necrosis. Organ failure is even more skewed; there was no mortality with no organ failure, 3% with single-organ failure, and 47% mortality with multiorgan failure.[32]

The causes of acute pancreatitis are numerous and diverse. One problem in evaluating and treating acute pancreatitis has been the lack of a universally accepted classification system. The International Symposium on Acute Pancreatitis (Atlanta, 1992) attempted to address these problems by proposing a classification system that is clinically oriented.[33] With better understanding of the disease, improved imaging options, and myriad new treatments, the Atlanta classification of acute pancreatitis was updated and revised.[28,34,35] The predominant causes of acute pancreatitis are gallstones and alcohol abuse, accounting for about 80% of all cases[36] (Table 7.1).

All patients, including known alcoholics, who present with their first episode of acute pancreatitis should have sonography to evaluate the biliary tree for **gallstones.**[37] Evaluation of the biliary tree is crucial in patients with acute pancreatitis because cholecystectomy with removal of common duct stones prevents recurrence of acute pancreatitis,[38] which can be fatal. Gallstones affect about 15% of the US population,[39] but prevalence varies widely by ethnicity. After a careful search of the gallbladder for stones, the bile duct should be evaluated for choledocholithiasis and obstruction. Reports vary, but the prevalence of **common duct stones** in patients with symptomatic gallstones is likely 10% to 20%. If the ducts are not dilated sonographically, however, the prevalence of common duct stones is probably about 5%.[40] With careful technique, ultrasound can identify common duct stones with a sensitivity of approximately 75% in expert hands.[41,42]

When biliary dilation or choledocholithiasis is present sonographically, a stone may be impacted in the distal common duct. It seems reasonable to assume that urgent intervention to relieve the obstruction is necessary in these patients. There is conflicting evidence, however, whether patients benefit from intervention in the acute setting.[43-47] Acosta et al.[48] reported results from a prospective randomized clinical trial of patients with biliary pancreatitis that showed better outcomes with decompression of the duct within 48 hours from the onset of symptoms. It made no difference if the decompression was spontaneous or from surgical treatment or ERCP.

How gallstones cause acute pancreatitis is unknown, although it is somehow related to passage of stones into and through the common duct. Gallstones cause 30% to 50% of acute pancreatitis attacks, whereas only 3% to 7% of patients with gallstones develop pancreatitis.[38] Another important cause of acute pancreatitis is **biliary sludge (microlithiasis).** These cases comprise most of what was previously characterized as **"idiopathic" pancreatitis.**[49] The myriad other causes of acute pancreatitis include neoplasm,[50,51] infection, pancreas divisum, toxins, drugs, and genetic, traumatic, and iatrogenic (endoscopy, postoperative) factors.[36] From 5% to 7% of patients with pancreaticobiliary tumors, benign or malignant, present with acute pancreatitis.[47]

TABLE 7.1 Causes of Acute Pancreatitis

Cause	Acute Pancreatitis Cases
Gallstones	40%
Alcoholism	40%
Idiopathic	10%
Other	10%

Approach to Imaging

Abdominal sonography and contrast-enhanced computed tomography (CECT) are the two most useful imaging modalities in patients with acute pancreatitis. Other useful, but usually secondary diagnostic and therapeutic studies include MRI, MRCP, ERCP, and endoscopic ultrasound. The choice of modality depends on the clinical situation. Ultrasound should be performed to detect gallstones and bile duct obstruction in all patients in whom biliary acute pancreatitis is possible. CECT is indicated early in the clinical course of patients with severe pancreatitis, mainly to diagnose pancreatic necrosis.[52] Pancreatic necrosis is considered significant when more than 30% of the gland is affected or an area larger than 3 cm is present. Patients with pancreatic necrosis must be observed closely for clinical deterioration and treated with prophylactic antibiotics.[53-55] Sharma and Howden[56] found that antibiotic prophylaxis significantly reduced sepsis by 21% and mortality by 12% compared with no prophylaxis. CT is also the most accurate examination when seeking delayed complications of acute pancreatitis.

MRCP is an accurate means of detecting stones in the gallbladder and bile ducts of patients with acute pancreatitis.[36,57] Abdominal MRI can provide information similar to CECT, including the diagnosis of pancreatic necrosis.[58,59] Because of expense, MRCP and MRI are often reserved for patients in whom CT or ultrasound does not provide adequate information to

Imaging in Acute Pancreatitis

ROLE OF ULTRASOUND

Detect gallstones as a cause of acute pancreatitis
Detect bile duct dilation and obstruction
Diagnose unsuspected acute pancreatitis or confirm diagnosis of acute pancreatitis
Guide aspiration and drainage

ROLE OF COMPUTED TOMOGRAPHY

Detect pancreatic necrosis (patients with suspected severe pancreatitis)
Detect complications of acute pancreatitis
Diagnose unsuspected acute pancreatitis or confirm diagnosis of acute pancreatitis
Diagnose conditions mimicking acute pancreatitis, including gastrointestinal ischemia, ulceration, or perforation and ruptured abdominal aortic aneurysm
Guide aspiration and drainage

guide management and for those who have a contraindication to CECT.

Endoscopic ultrasound is more sensitive than abdominal ultrasound for the detection of common bile duct stones and can be useful in suspected gallstone pancreatitis.[60] Endoscopic ultrasound is also valuable in diagnosing microlithiasis and pancreas divisum.[61]

Because of its complications (including pancreatitis) and expense, ERCP, formerly both a diagnostic and a therapeutic modality, is now usually reserved for therapy.[62] Sometimes coupled with endoscopic sphincterotomy and stone removal, ERCP is a valuable therapeutic modality in choledocholithiasis with jaundice, dilated common bile duct, acute pancreatitis, or cholangitis.[63]

Ultrasound Findings

Evaluation of the gallbladder and bile ducts is the focus of most sonographic examinations performed in patients with acute pancreatitis. Nevertheless, understanding pancreatic and extrapancreatic abnormalities associated with acute pancreatitis is important. The combined use of serum amylase and serum lipase yields sensitivity and specificity of 90% to 95% in diagnosing acute pancreatitis,[64] but mild cases may be missed. In mild acute pancreatitis the patient may present for diagnosis after transient elevated amylase and lipase levels have resolved; thus no serologic indicators of pancreatitis may be present.[65] In these patients the diagnosis of mild acute pancreatitis is clinical. On the other hand, the diagnosis may be missed in patients with severe pancreatitis because pain is absent or masked by other, more severe symptoms. Analyzing fatal pancreatitis between 1980 and 1985, Lankisch et al.[66] reported that 30% of cases were not diagnosed until autopsy.

After a careful search of the gallbladder and bile duct for **stones,** the entire pancreas should be scanned. After scanning the pancreas, peripancreatic pathology should be sought in the lesser sac, anterior pararenal spaces, and transverse mesocolon.

The reported prevalence of sonographic abnormality in acute pancreatitis varies from 33% to 92%. In a retrospective evaluation of patients with acute pancreatitis, using a defined scanning protocol to look for pancreatitis-associated findings, Finstad et al.[37] found that sonography revealed abnormalities in 45 of 48 patients (92%) (Table 7.2).

TABLE 7.2 Sonographic Abnormalities in Patients With Acute Pancreatitis

Abnormality	No. of Patients (48 Total)	Prevalence
Peripancreatic inflammation	29	60%
Heterogeneous parenchyma	27	56%
Decreased gland echogenicity	21	44%
Indistinct ventral margin	16	33%
Pancreas enlarged[a]	13	27%
Focal intrapancreatic echo change	11	23%
Peripancreatic fluid collections	10	21%
Focal mass	8[b]	17%
Perivascular inflammation	5	10%
Pancreatic duct dilation	2	4%
Venous thrombosis	2	4%

[a]Anteroposterior dimension was ≥23 mm at superior mesenteric artery.
[b]Five of eight were hypoechoic.
Modified from Finstad TA, Tchelepi H, Ralls PW. Sonography of acute pancreatitis: prevalence of findings and pictorial essay. Ultrasound Q. 2005;21(2):95-104.[37]

Pancreatic echogenicity typically decreases in patients who have acute pancreatitis because of interstitial edema. In some patients, echogenicity is normal. In rare cases, echogenicity may increase, possibly because of hemorrhage, necrosis, or fat saponification. Cotton et al.[67] noted that, compared with the liver, the pancreatic echogenicity was increased in 16% of normal individuals and 32% of patients with acute pancreatitis. Finstad et al.[37] found no acute pancreatitis patients with globally increased echogenicity, although focal areas of increased echogenicity and inhomogeneity did occur.

Enlargement of the pancreas is almost universal in acute pancreatitis. Unfortunately, enlargement may be difficult to judge, because pancreatic size before the onset of pancreatitis is usually unknown and varies widely. In 1995 Guerra et al.[7] found that the thickness of the body of the normal pancreas in 261 adults was 10.1 mm (±3.8 mm; range, 4-23 mm). In 2005, Finstad et al.[37] in his series of patients with acute pancreatitis found that the mean anteroposterior measurement of the pancreatic body at the SMA level was 21.1 mm (±6.4 mm; range, 12-45 mm), almost twice the average found in normal individuals by Guerra et al. It seems reasonable, therefore, to use **22 mm** (mean plus 3 standard deviations) as the upper limit of normal pancreatic thickness, understanding that this is likely to be an insensitive parameter for diagnosing acute pancreatitis (Fig. 7.22).

The classic finding of **decreased gland echogenicity** is present in only 44% of patients. In addition, when there is fatty infiltration of the liver, the normal pancreas may appear hypoechoic, a pattern called **"pseudopancreatitis"** (Fig. 7.23). Pancreatic heterogeneity is a subjective but common finding, present in more than 50% of patients (Fig. 7.24). Focal hypoechoic regions are noted in some patients (Fig. 7.25).

The least subjective, most common, and thus most useful finding is **pancreatitis-associated inflammation** (Fig. 7.26; see also Figs. 7.22 and 7.24). Extrapancreatic inflammatory changes may be detected even when the pancreatic contour is normal and the pancreas is not obviously enlarged. Pancreatic inflammation is typically hypoechoic or anechoic (Fig. 7.27) and conforms to a known retroperitoneal or peritoneal space (Video 7.2). It may be difficult or impossible to distinguish inflammation from fluid (Fig. 7.28). In contrast to inflammation, fluid collections

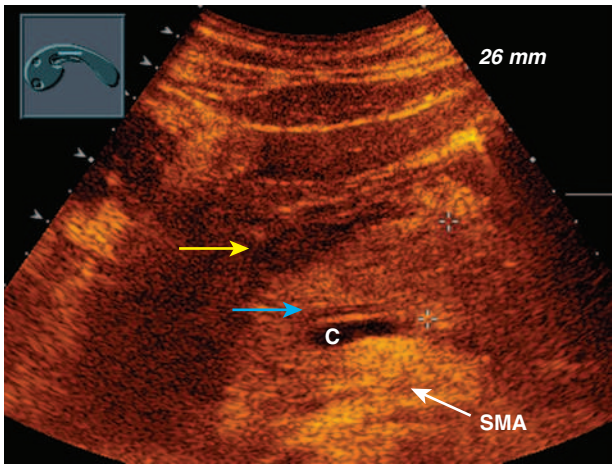

FIG. 7.22 Enlarged Pancreas, Acute Pancreatitis With Inflammation. Transverse image of the pancreas shows 26-mm anteroposterior dimension (calipers) at the level of the superior mesenteric artery *(SMA)*. Note the acute inflammation ventral to the pancreas *(yellow arrow)* and ventral to *(blue arrow)* the splenic vein–superior mesenteric vein confluence *(C)*.

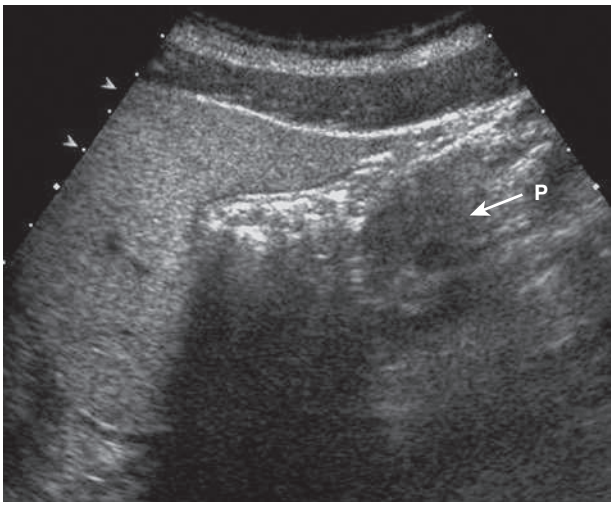

FIG. 7.23 Pseudopancreatitis. Longitudinal image of pancreas *(P)* and liver shows that the fatty liver is more echogenic than the normal pancreas, simulating a hypoechoic pancreas.

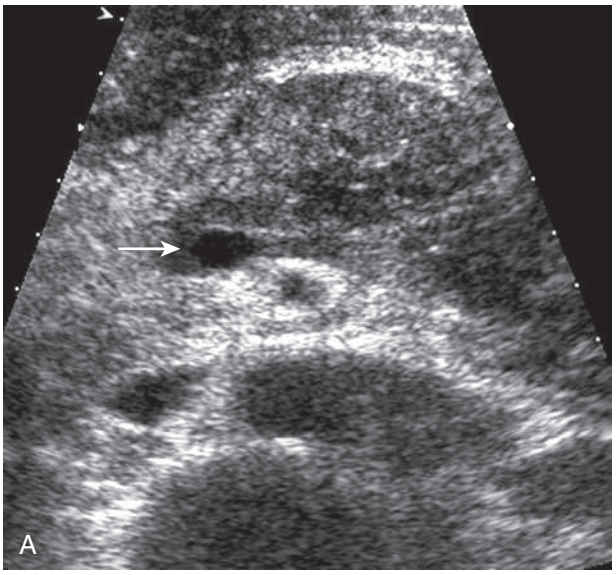

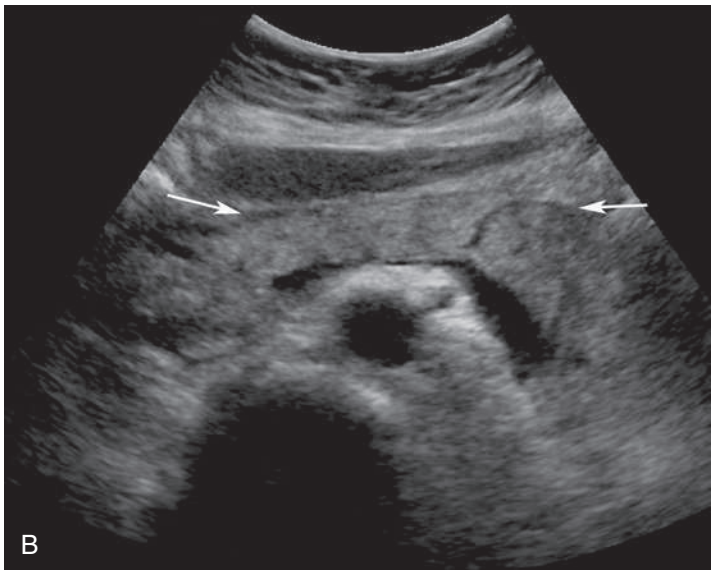

FIG. 7.24 Heterogeneous Pancreas, Acute Pancreatitis. (A) Transverse image shows that heterogeneity can be a subtle, subjective finding. Arrow indicates the perivascular inflammation and splenic vein–superior mesenteric vein clot. **(B)** Transverse sonogram in a different patient shows heterogeneous pancreatic echotexture with trace areas of peripancreatic fluid about the gland and interspersed between parenchymal lobules *(arrows)*. **(C)** Transverse contrast-enhanced computed tomography (CT) image of the same patient in **(B)** shows corresponding CT appearance of heterogeneous gland with peripancreatic fluid.

often have convex margins, are thicker and more localized, may cause a mass effect, and sometimes have through transmission of sound (Fig. 7.29, Video 7.3).

Inflammation is most often seen ventral and adjacent to the pancreas in the **prepancreatic retroperitoneum** (see Figs. 7.22, 7.26, and 7.28), the right and left anterior pararenal spaces, the perirenal spaces, and the transverse mesocolon. The **anterior pararenal spaces** are best seen through a coronal flank approach (Fig. 7.30). The patient is scanned while in a decubitus position with the transducer angled to achieve a sagittal scan plane through the flank. Areas of inflammation within the anterior pararenal space are often seen immediately adjacent to the echogenic fat within the **perirenal space.** Acute pancreatic inflammation within the anterior pararenal space occasionally outlines **Gerota fascia.** An inflammatory mass (formerly called a **phlegmon,** although this term has been abandoned in the newest Atlanta classification[28]) may be present (Fig. 7.31; see also Fig. 7.28). The **transverse mesocolon** region can be seen well in most patients on longitudinal scans. Inflammation can extend caudal to the pancreas and behind the stomach (Fig. 7.32; see also Fig. 7.21) and may reach the transverse colon. The transverse colon itself may be difficult to identify; in the transverse plane it lays directly ventral

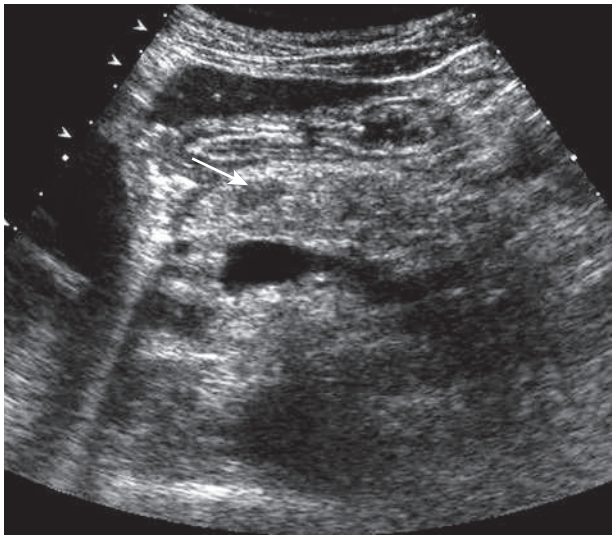

FIG. 7.25 Focal Hypoechoic Area, Acute Pancreatitis. Transverse image shows heterogeneous pancreas with focal hypoechoic area *(arrow).*

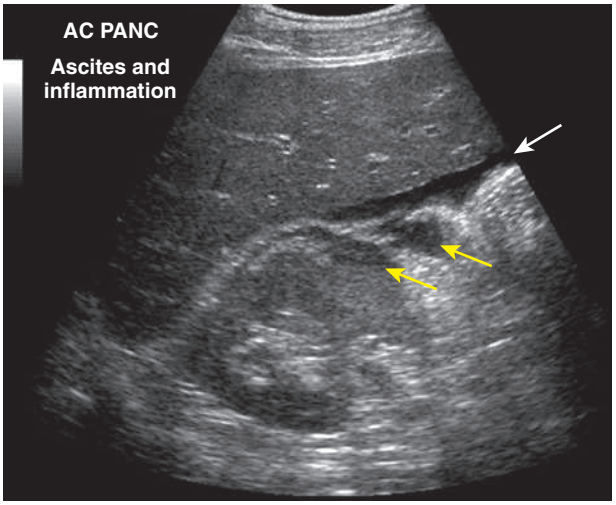

FIG. 7.27 Inflammation and Ascitic Fluid, Acute Pancreatitis. Transverse image of right upper quadrant shows acute inflammation in the anterior pararenal (retroperitoneal) space and the perirenal space *(yellow arrows).* Ascites is present in the adjacent subhepatic space *(white arrow).* See also Video 7.2.

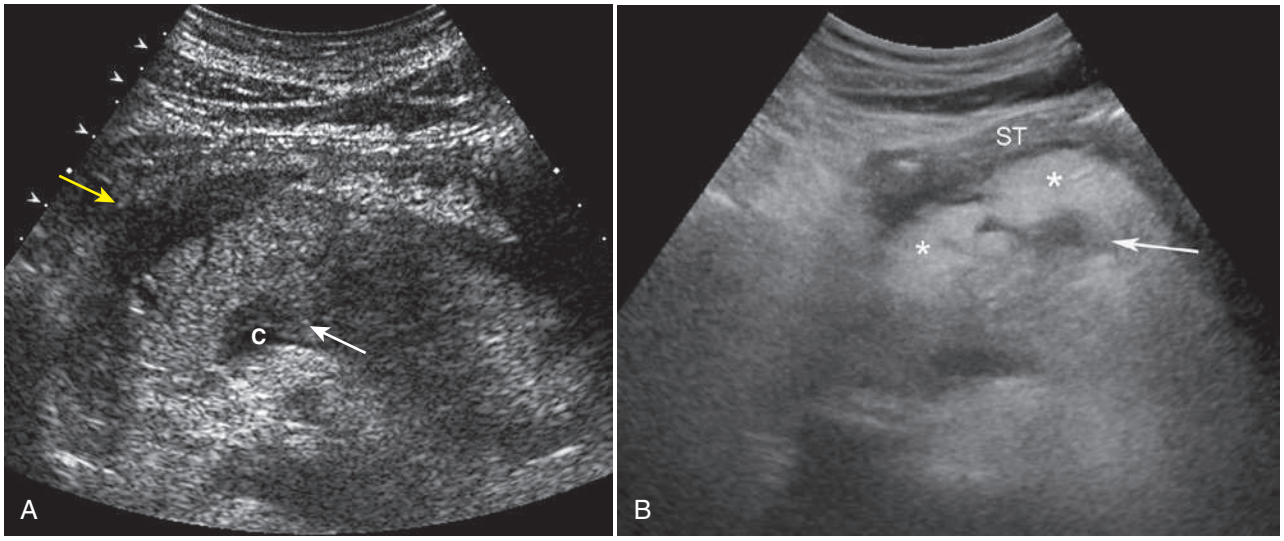

FIG. 7.26 Inflammation From Acute Pancreatitis. (A) Transverse image shows acute inflammation ventral to the pancreas *(yellow arrow)* and ventral to *(white arrow)* the splenic vein–superior mesenteric vein confluence *(C).* The pancreas is enlarged and heterogeneous. **(B)** Transverse image shows acute inflammation ventral to the pancreas, displacing the stomach *(ST)* anteriorly. There is an echogenic appearance of the peripancreatic fat (*) and interspersed small fluid collection *(arrow).*

(anterior) to the head and uncinate process of the pancreas. Spread of inflammation along perivascular spaces, especially the splenic vein and splenoportal confluence, is characteristic of acute pancreatitis (Figs. 7.33, 7.34, and 7.35; see also Figs. 7.22, 7.24, and 7.26). This perivascular inflammation may explain why some patients develop thrombosis of the portal veins (Figs. 7.36 and 7.37; see also Fig. 7.34). Occasionally, retroperitoneal findings similar to those seen in acute pancreatitis can be seen in patients with ascites, perhaps because of a "leaky" peritoneum.

Complications

Complications of acute pancreatitis can be classified as systemic complications (those related to organ failure) and local complications.[34,68]

Local Complications of Acute Pancreatitis

Acute fluid collections
Pseudocysts
Pancreatic abscess
Necrosis
Infected necrosis
Hemorrhage
Venous thrombosis
Pseudoaneurysms

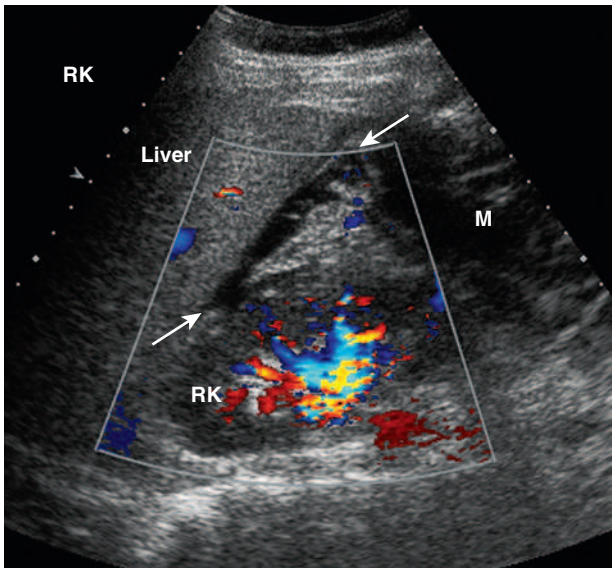

FIG. 7.28 Inflammation Simulates Free Fluid. Longitudinal image of right upper quadrant shows that the acute inflammation *(arrows)* in the anterior pararenal (retroperitoneal) space simulates free fluid and might be mistaken for ascites. Note the retroperitoneal inflammatory mass *(M)*. *RK,* Right kidney.

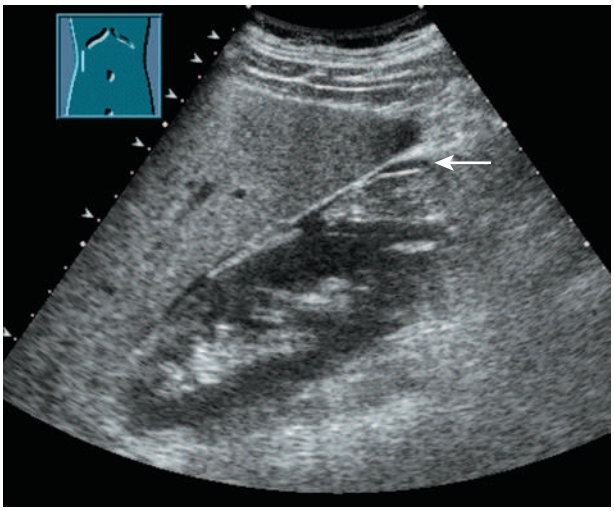

FIG. 7.30 Inflammation in Right Anterior Pararenal and Perirenal Spaces. Longitudinal coronal image of right upper quadrant, with decubitus position facilitating visualization of the pararenal and perirenal spaces. The inflammation partially outlines the perirenal space *(arrow),* which is contained by **Gerota fascia.**

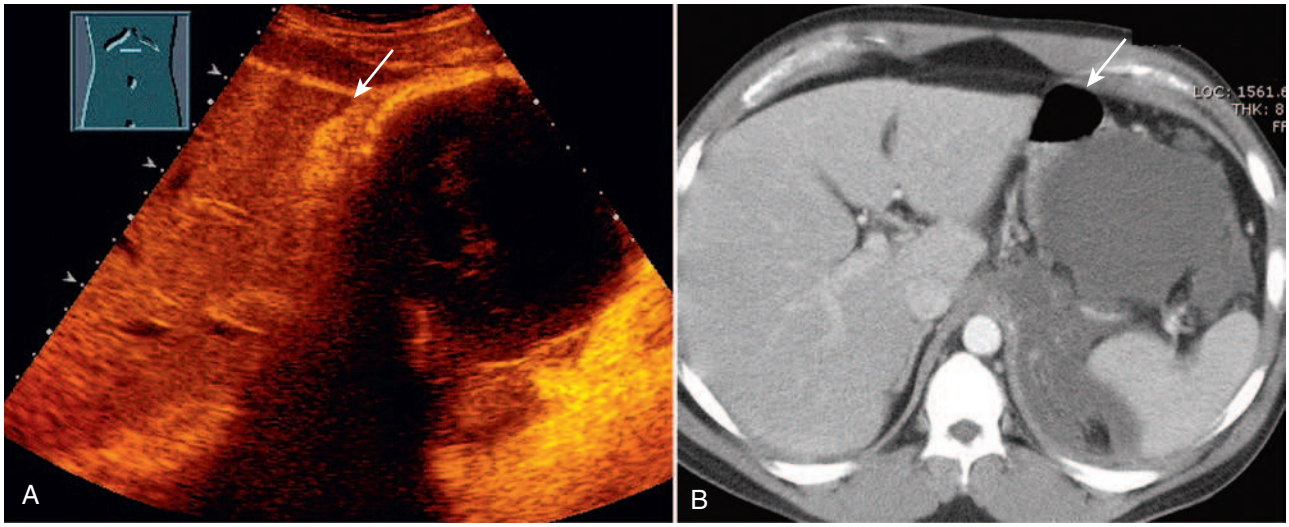

FIG. 7.29 Pancreatitis-Associated Fluid Collection. (A) Transverse sonogram and **(B)** computed tomography image of a "lesser sac" fluid collection. Such collections are actually in the prepancreatic retroperitoneum. Note the displaced stomach *(arrows)*. See also Video 7.3.

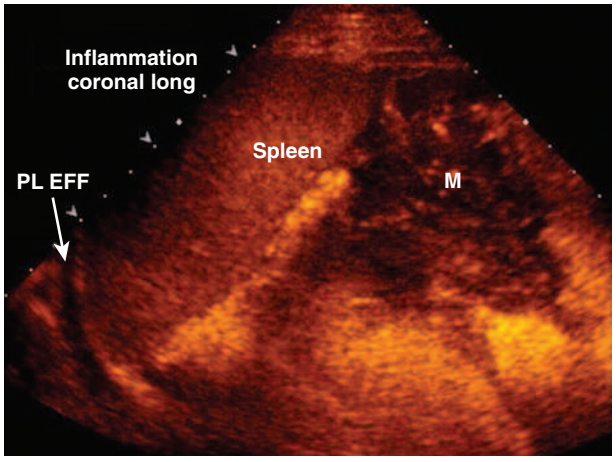

FIG. 7.31 Inflammatory Mass in Left Anterior Pararenal Space. Longitudinal coronal image of left upper quadrant shows retroperitoneal inflammatory mass *(M)*. Such masses were formerly called "phlegmons" before this term was proscribed by the 1992 International Symposium on Acute Pancreatitis (Atlanta). *PL EFF,* Left pleural effusion.

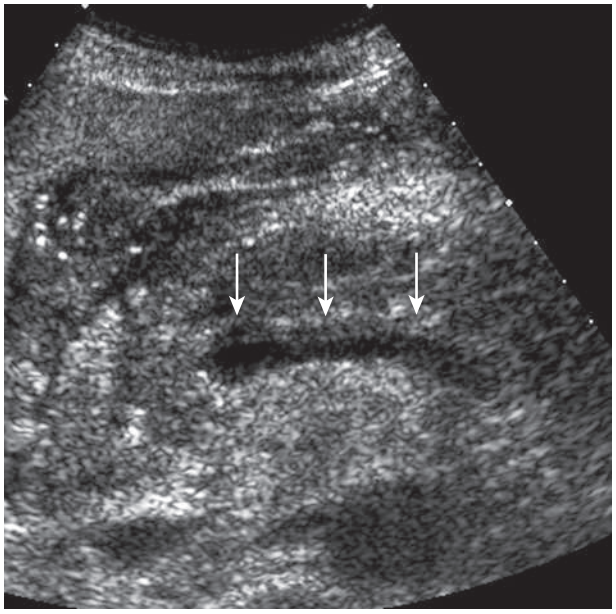

FIG. 7.33 Perivascular Inflammation. Transverse image of the pancreatic body shows hypoechoic inflammation *(arrows)* around the splenic vein.

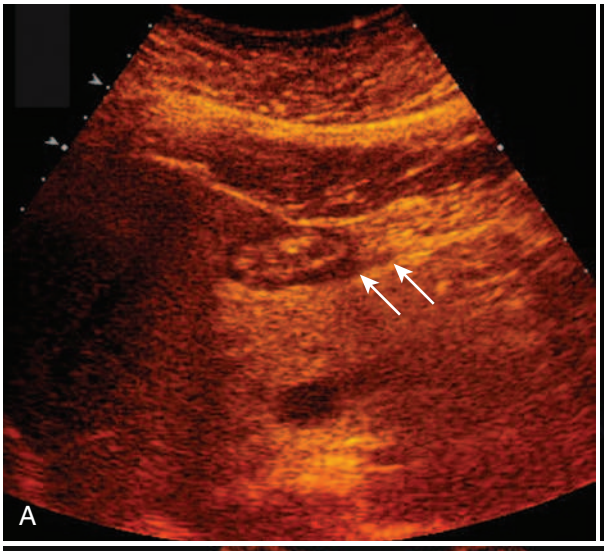

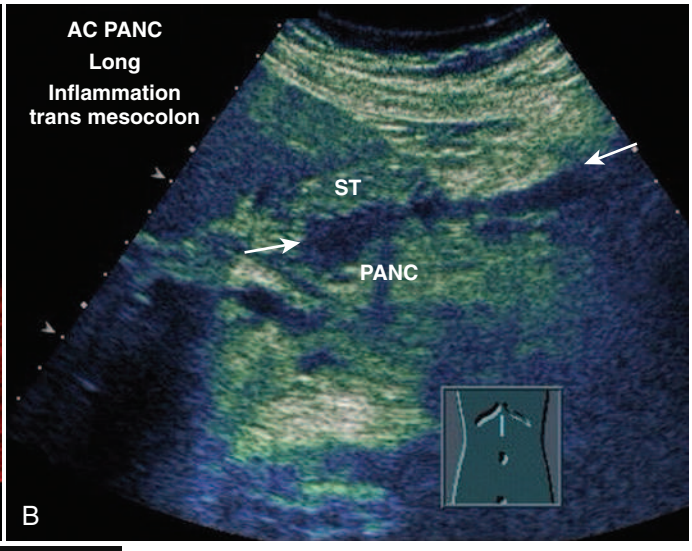

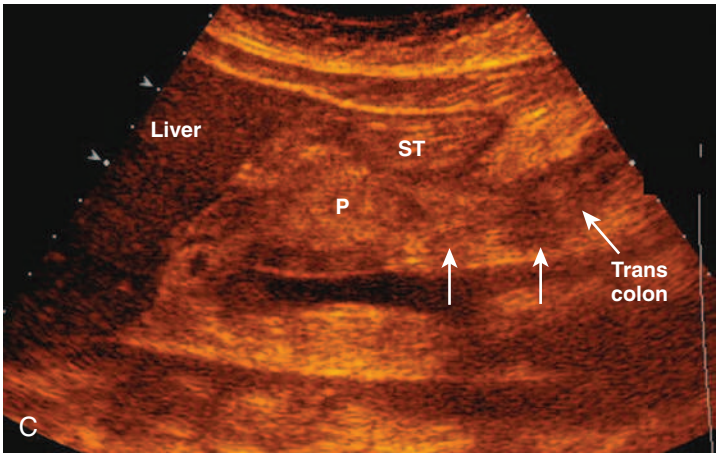

FIG. 7.32 Inflammation in Transverse Mesocolon. Longitudinal images. **(A)** Subtle, relatively minor inflammation *(arrows)*. **(B)** More significant inflammation *(arrows)*. **(C)** Transverse colon, which may be difficult to visualize; mesocolon inflammation is more diffuse *(arrows)*. *P,* Pancreas; *PANC,* pancreas; *ST,* stomach.

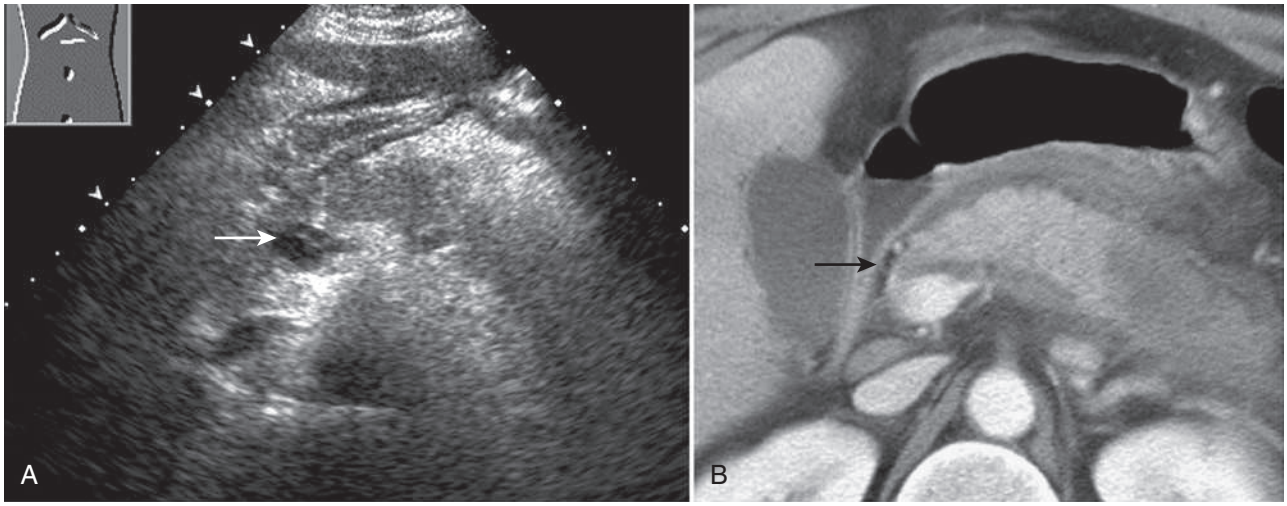

FIG. 7.34 Pancreatitis Causes Perivascular Inflammation. (A) Transverse sonogram and **(B)** computed tomography (CT) image of the pancreas show obvious evidence of perivascular inflammation *(arrows),* hypoechoic on sonogram and low density on CT.

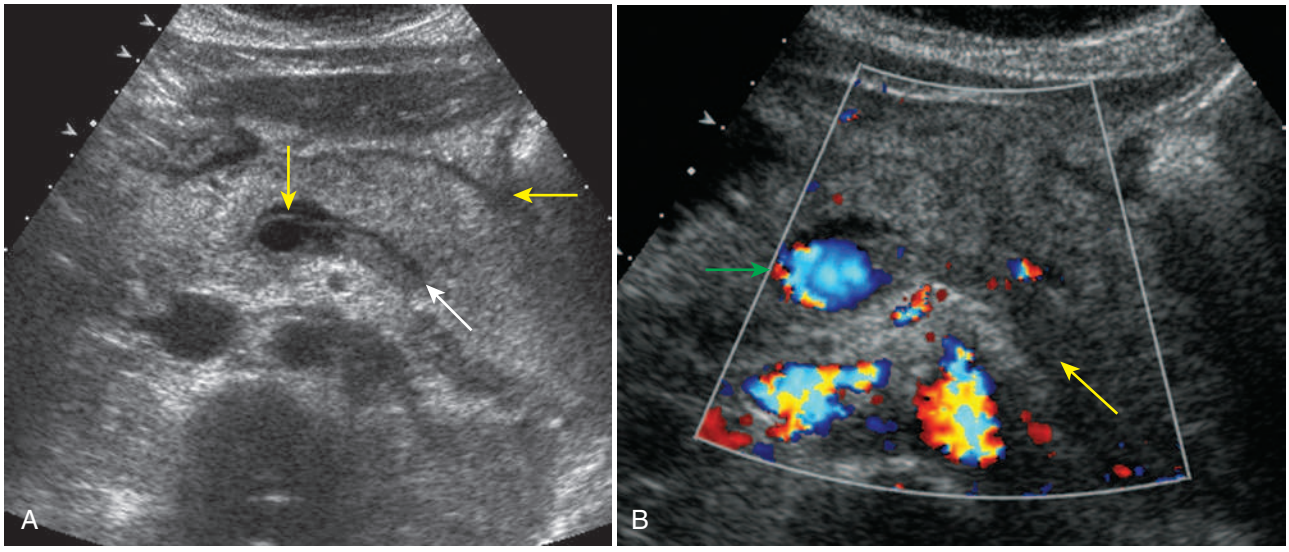

FIG. 7.35 Perivascular Inflammation and Clot Caused by Pancreatitis. (A) Transverse sonogram of pancreas shows the confluence free of thrombus, but clot in the splenic vein *(white arrow).* Note the obvious signs of perivascular and peripancreatic inflammation *(yellow arrows).* **(B)** Transverse color Doppler sonogram confirms splenic vein clot *(yellow arrow)* and the open confluence *(green arrow).*

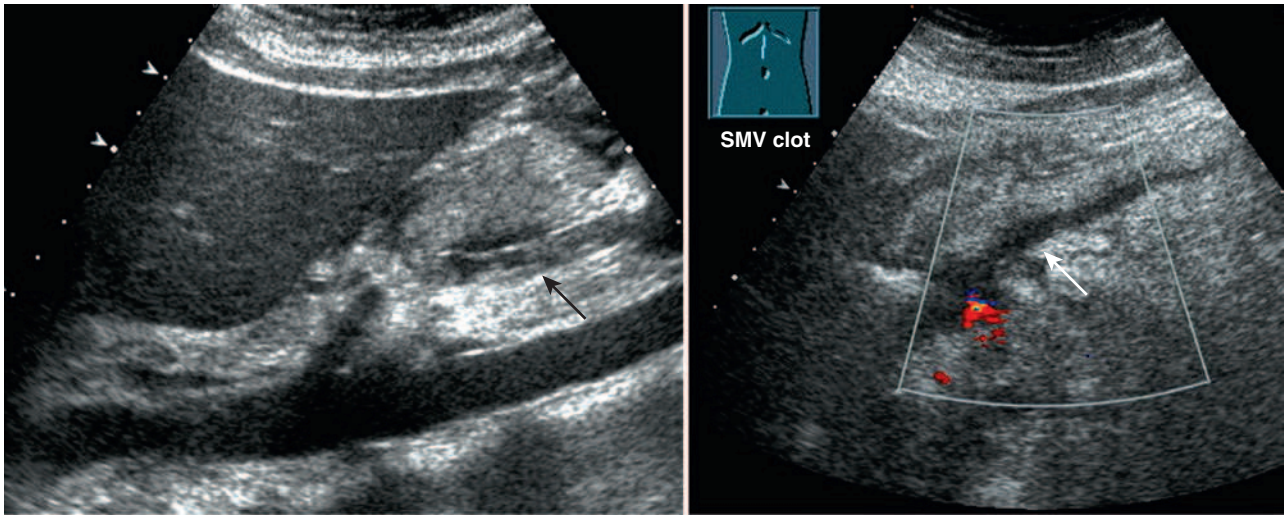

FIG. 7.36 Superior Mesenteric Vein Clot. Longitudinal sonograms show clot in the superior mesenteric vein (SMV) *(arrows)* in two patients with acute pancreatitis.

Acute Fluid Collections

Pancreatitis-associated fluid collections represent a spectrum of disease and thus can be problematic to classify (Figs. 7.38 and 7.39; see also Fig. 7.29). Fluid collections, when they contain debris or necrosis or may be infected, cannot always be categorized. Approximately 40% of patients with acute pancreatitis develop acute fluid collections.[69,70] About half of these appear to resolve spontaneously,[69] with almost 70% resolving in patients with nonnecrotizing pancreatitis.[70] Thus drainage or other intervention in acute collections is inappropriate, unless a rare superinfection occurs. The Atlanta Classification suggests that the differentiation between acute fluid collection and **pseudocyst** should be made after 4 weeks from the onset of disease.[27,34] Others suggest that a fluid collection that persists for 6 weeks can be considered a pseudocyst. The 6-week definition is based on classic surgical management; the pseudocyst wall requires 6 weeks to "mature" to the point where it can be drained surgically.[71]

Pseudocysts

Pancreatic pseudocysts are a well-known complication of acute and chronic pancreatitis. Pseudocysts comprise 75%[72] to 90%[73] of all cystic lesions of the pancreas. The "wall" of pancreatic pseudocysts consists of fibrous and granulation tissue. Thus unlike true cysts or cystic neoplasms, pseudocysts do not have an epithelial lining. Pseudocysts are more common in patients with chronic than acute pancreatitis. Pseudocyst prevalence ranges from 5% to 16% in patients with acute pancreatitis. In chronic pancreatitis, prevalence varies from 20% to 40%, with the highest rates in alcohol-related chronic pancreatitis.[74] On occasion, pseudocysts can be caused by trauma (Fig. 7.40).

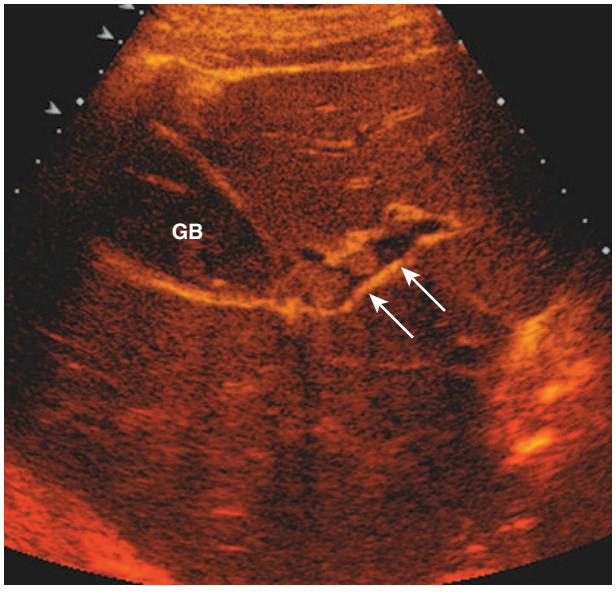

FIG. 7.37 Left Portal Vein Clot. Transverse sonogram shows clot in the left portal vein *(arrows)* caused by pancreatitis. *GB,* Gallbladder.

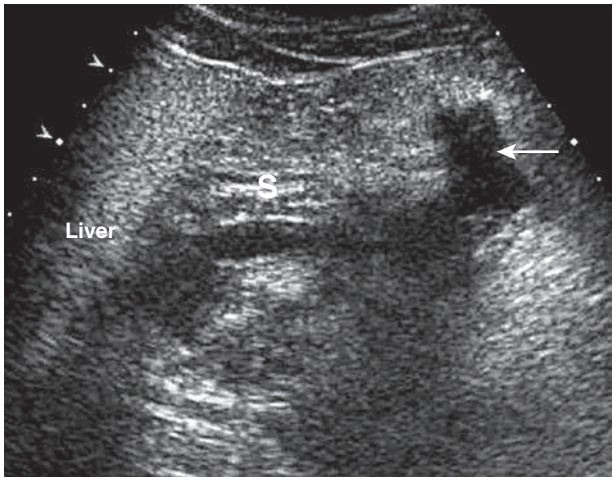

FIG. 7.38 Acute Fluid Collection. Longitudinal image shows inflammation and an acute fluid collection *(arrow)* in the transverse mesocolon. *S,* Stomach.

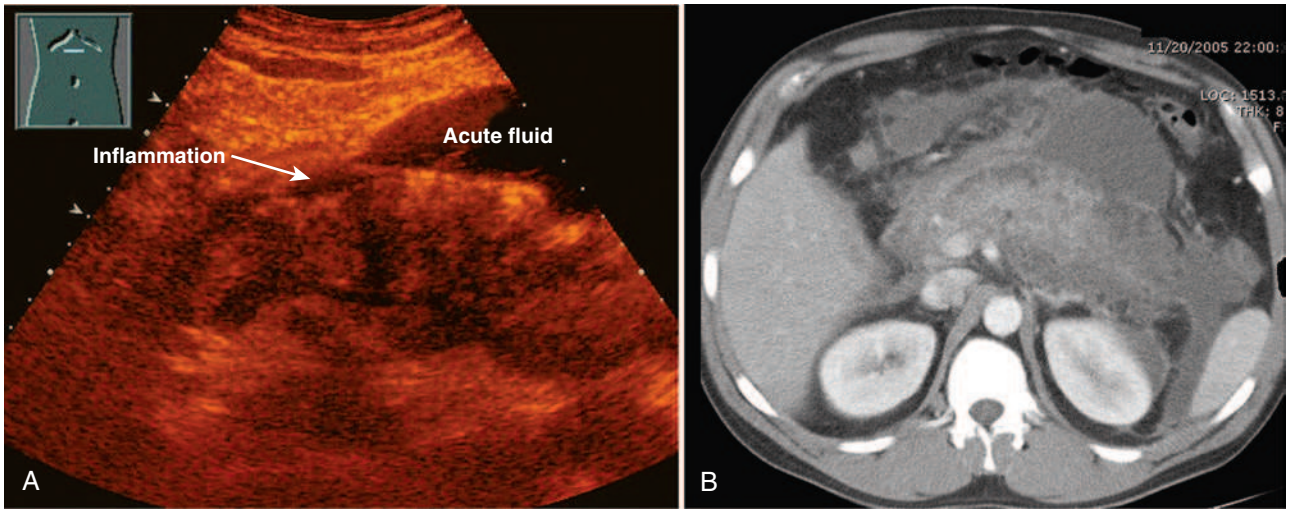

FIG. 7.39 Pancreatitis-Associated Fluid Collection. (A) Transverse sonogram and **(B)** CT image show enlarged and heterogeneous pancreas, with prominent peripancreatic inflammation *(arrow)* and an acute fluid collection that later resolved spontaneously.

The most important issue in diagnosing pseudocysts on images is avoiding confusion with cystic neoplasm, a mistake that can lead to adverse clinical outcomes.[75] Unfortunately, this distinction may be difficult. The major criterion for diagnosing a pseudocyst is a clinical history or imaging evidence of acute or chronic pancreatitis. Failing this, differentiating a pseudocyst from cystic pancreatic lesions becomes problematic. The sonographic findings in pseudocysts are variable. Pseudocysts can range in appearance from almost purely cystic to collections with considerable mural irregularity, septations, and internal echogenicity because of debris (Fig. 7.41) from necrosis, hemorrhage (see Fig. 7.40), or infection. Successful differentiation of cystic neoplasm from pseudocyst thus depends on a high degree of suspicion for possible cystic neoplasm and understanding findings strongly suggestive of "the usual suspects": **serous cystic neoplasm (microcystic adenoma), mucinous cystic neoplasm, solid-pseudopapillary tumor,** and **intraductal papillary mucinous neoplasm.**[76] Characterization of cystic neoplasms by CT or MRI is unreliable, even when the reviewers' diagnostic certainty was 90% or more.[77]

Conservative management of pseudocysts is appropriate unless complications occur. As noted, many pseudocysts resolve spontaneously. Persistent uncomplicated pseudocysts require no intervention and can be safely observed.[78,79] Indications for drainage of a pseudocyst include abdominal pain, usually related to growth of (or hemorrhage into) the pseudocyst, biliary obstruction (Fig. 7.41), and gastrointestinal (usually duodenal) obstruction.[80] Internal or external fistula formation can result in pancreatic ascites or pleural effusion.[81] Inflammation from pancreatitis can digest and dissect through tissue plane boundaries. For example, pseudocysts and inflammatory masses can present in the neck[81,82] or the groin[83] (Fig. 7.42).

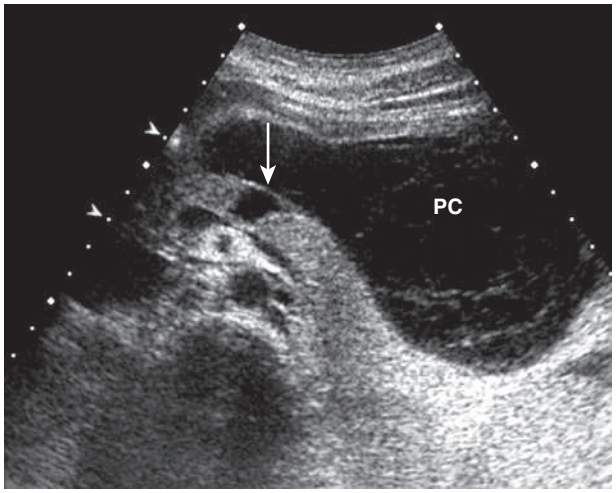

FIG. 7.40 Pancreatic Fracture and Associated Pseudocyst. Transverse sonogram shows the fracture/laceration *(arrow)* of the pancreatic body. A pseudocyst *(PC)* has developed ventral to the pancreas. Trauma is an uncommon cause of pancreatic pseudocysts. (Courtesy of Stephanie Wilson, MD.)

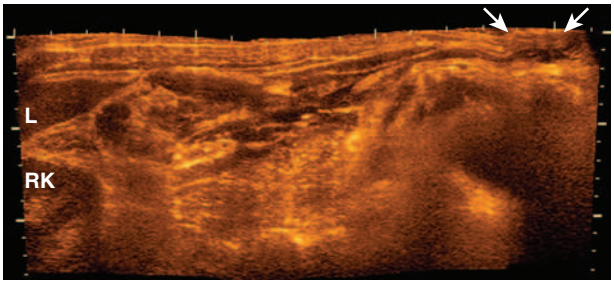

FIG. 7.42 Inflammation From Pancreatitis Causing Groin Mass. Longitudinal extended field of view sonogram from right upper quadrant to right groin. An inflammatory mass *(arrows)* is caudal to the inguinal ligament. Extensive spread of acute inflammation is common in acute pancreatitis. *L,* Liver; *RK,* right kidney.

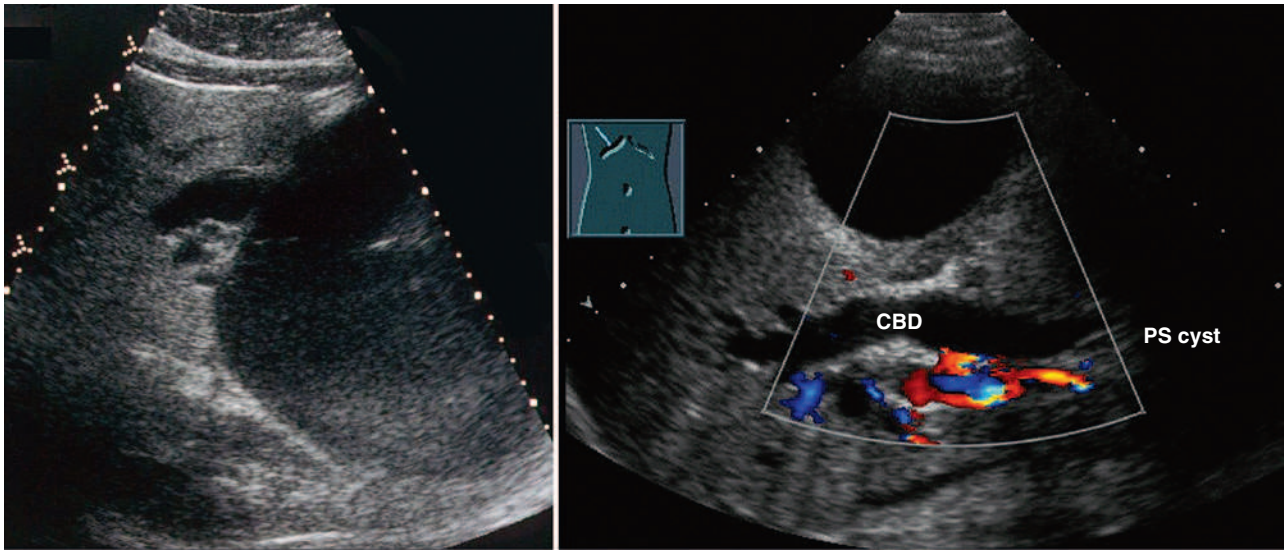

FIG. 7.41 Pseudocysts Causing Biliary Obstruction. Longitudinal oblique sonograms in two different patients demonstrate common bile duct *(CBD)* dilation from obstruction. Biliary obstruction is an indication for pseudocyst *(PS cyst)* drainage.

Necrosis and Abscess

Significant pancreatic necrosis has been defined by the Atlanta Classification system as nonenhanced pancreatic parenchyma greater than 3 cm or involving more than 30% of the area of the pancreas on CECT.[27,28] These patients are at greater risk than patients without necrosis and are treated with prophylactic antibiotics and observed closely. Necrosis cannot be definitively diagnosed by ultrasound, although ultrasound contrast agents may change that situation.

The original Atlanta Classification terminology describing significant infection associated with pancreatitis was somewhat confusing. *Pancreatic abscess* was reserved for infected fluid collections, essentially pseudocysts that become infected. **Infected pancreatic necrosis,** a much more serious condition, can also result in pus-filled collections, which might also be called *abscesses* in other clinical settings. Thus it is best to think of **two distinct types of acute pancreatitis–associated abscess,** as follows:

1. The original Atlanta Classification pancreatic abscess, an infected fluid collection/pseudocyst, which has minimal necrosis. The revised Atlanta classification has dropped the term *pancreatic abscess* because of confusion over its meaning.[34]
2. Infected necrosis with a fluid collection, which arises from infection of necrotic pancreatic tissue.

Treatment

The major approaches to the treatment of pseudocysts include surgery, percutaneous image-guided drainage and endoscopic-guided drainage. Andrén-Sandberg et al.[71] state:

> *There are no randomized studies for the management protocols for pancreatic pseudocysts. … First of all, it is important to differentiate acute from chronic pseudocysts for management, but at the same time not miss cystic neoplasias. Conservative treatment should always be considered the first option (pseudocysts should not be treated just because they are there).*

It is difficult to determine the best method to treat pseudocysts. The cause of pancreatitis, communication of the pancreatic duct with the pseudocyst, and local technical expertise must be considered when choosing a treatment method. Although the data are unclear, **percutaneous drainage** of pseudocysts likely is overall less successful than surgical or endoscopic drainage.[84] Nevertheless, percutaneous drainage can be used as a first option with other techniques reserved for percutaneous drainage failures. In the large subset of patients with normal duct anatomy and no communication of the pseudocyst with the pancreatic duct, percutaneous drainage is successful in more than 80%. On the other hand, percutaneous drainage failed in 77% to 91% of patients who had duct obstruction or strictures.[80] Therefore ERCP,[85] and in some cases MRCP,[58,74] may be useful in the selection of treatment technique.

Infected fluid collections without significant necrosis may often be best treated by percutaneous drainage.[85] Percutaneous drainage can also be used in **infected necrosis,** for which it is curative in some patients[86] and is a useful temporizing technique in others.[84] Although management of infection in pancreatitis is evolving,[27] therapy for infected pancreatic necrosis remains surgical debridement.

Vascular Complications

Vascular complications occur in both acute and chronic pancreatitis. **Pseudoaneurysms** and **venous thrombosis** are the most important vascular complications. Most cases of clinically insignificant hemorrhagic pancreatitis are related to venous and small vessel disease, whereas potentially fatal hemorrhage is usually related to enzymatic digestion or pseudoaneurysm of major vessels, including the splenic, gastroduodenal (Fig. 7.43), and superior pancreaticoduodenal arteries. The prevalence of hemorrhage in patients with a pseudocyst is 5%, but with an up to 40% rate of mortality.[87] Vascular erosion can produce a sudden, painful expansion of the cyst or gastrointestinal bleeding caused by bleeding into the pancreatic duct ("hemosuccus pancreaticus").[88] Thrombosis of the portal venous system may occur in both acute and chronic pancreatitis[68]; **splenic vein thrombosis** is most common (Fig. 7.44). Agarwal et al.[89] reported a 22% prevalence of splenic vein thrombosis in patients with chronic pancreatitis. Bernades et al.[90] reported the prevalence of **portal vein thrombosis** as 5.6% (15/266). Splenic vein thrombosis may result in upper gastrointestinal bleeding from gastric varices; this condition is called **"sinistral" (left-sided) portal hypertension.**

CHRONIC PANCREATITIS

The prevalence of chronic pancreatitis ranges from 3.5 to 10 per 100,000 in the population. Chronic pancreatitis is characterized by intermittent pancreatic inflammation with progressive, irreversible damage to the gland. The key histologic features are fibrosis,

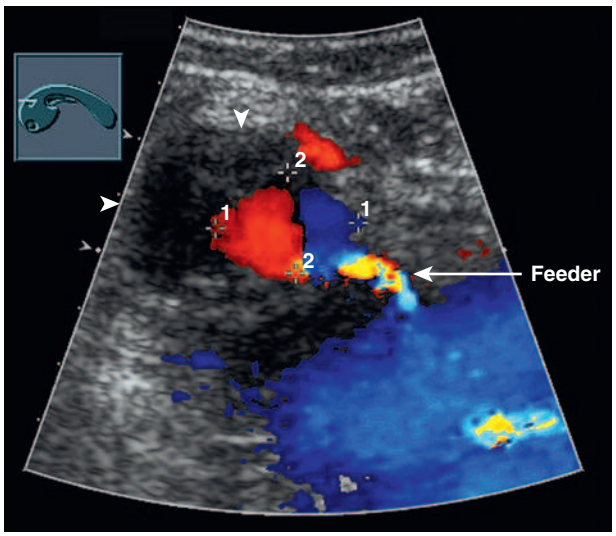

FIG. 7.43 Pancreatic Pseudoaneurysm. Transverse color Doppler sonogram shows acute pancreatitis–associated pseudoaneurysm arising from the gastroduodenal artery. The clotted portion of the pseudoaneurysm *(arrowheads)* is noted. Calipers denote the patent portion of the pseudoaneurysm. Pseudoaneurysm is a rare complication of pancreatitis, much less common than venous thrombosis. Notice the "yin and yang" *(red/blue)* color Doppler appearance representing the blood swirling in the lesion.

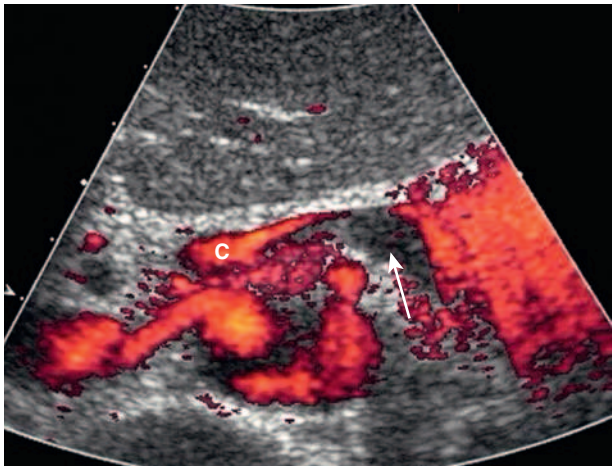

FIG. 7.44 Splenic Vein Clot. Transverse power Doppler image shows partial splenic vein clot *(arrow)* caused by chronic pancreatitis. *C,* Confluence of splenic and superior mesenteric veins.

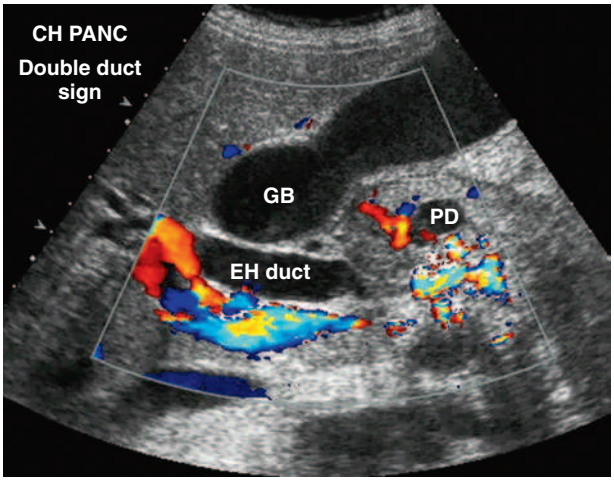

FIG. 7.45 "Double-Duct" Sign. Longitudinal oblique image shows dilation from obstruction of the pancreatic duct *(PD)* and extrahepatic bile duct *(EH).* Chronic pancreatitis often causes the double-duct sign. *GB,* Gallbladder.

acinar atrophy, chronic inflammation, and distorted and blocked ducts.[91] Chronic pancreatitis ultimately leads to permanent structural change and deficient endocrine and exocrine function. Some lasting morphologic changes include alterations in parenchymal texture, glandular atrophy, glandular enlargement, focal masses, dilation and beading of the pancreatic duct (often with intraductal calcifications), and pseudocysts.

Alcoholism is the predominant cause of chronic pancreatitis (70%-90% in Western countries).[92] Other causes include pancreatic duct obstruction caused by strictures, hypertriglyceridemia, hypercalcemia, autoimmune pancreatitis, tropical pancreatitis, and other genetic mutations.[93]

Chronic pancreatitis is characterized clinically by pain, malabsorption, and diabetes. Treatment of uncomplicated chronic pancreatitis is usually conservative, with the major aim to improve the patient's quality of life by alleviating pain and mitigating malabsorption and diabetes. Surgical and endoscopic interventions are reserved for complications such as pseudocysts, abscesses, and malignancy.[91] Obstruction and thrombosis of the portal veins may occur (see Fig. 7.37). Chronic pancreatitis may also lead to obstruction of the pancreatic and bile ducts, sometimes resulting in the "double-duct" sign (Fig. 7.45). In settings with a high prevalence of alcoholism, the double-duct sign is caused by chronic pancreatitis more often than by periampullary neoplasm.[94] The frequency of common bile duct obstruction in patients hospitalized for chronic pancreatitis ranges from 3% to 23% (mean, 6%). The frequency of duodenal obstruction is about 1.2% in hospitalized patients.[95] All of these findings occur in various combinations and with differing frequency.[8]

Approach to Imaging

The imaging diagnosis of chronic pancreatitis depends on detecting the structural changes associated with advanced disease. Unfortunately, these changes are rarely present in early disease, decreasing imaging sensitivity. Consequently, imaging is not very useful in patients with early chronic pancreatitis. Furthermore, morphologic changes do not correlate well with endocrine or exocrine function.[96]

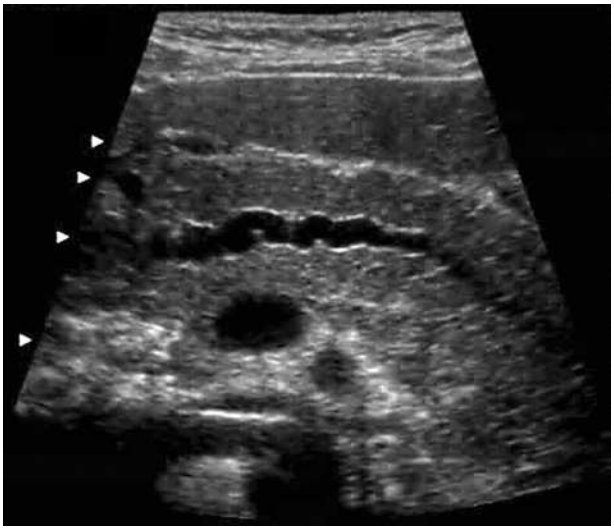

FIG. 7.46 Dilation of Pancreatic Duct. Transverse sonogram of the pancreatic body shows a beaded, dilated pancreatic duct, resulting from chronic pancreatitis.

Despite the common belief that it is diagnostically inferior overall to CECT, MRCP, and endoscopic ultrasound,[97-99] ultrasound is often recommended as the first diagnostic test.[91] Bolondi et al.[8] stated that ultrasound diagnosis of chronic pancreatitis remains difficult because of "the polymorphism of anatomic changes and the relatively high incidence of false-negative results in early stages of the disease."

Ultrasound Findings

Sonography can be effective in diagnosing chronic pancreatitis, but other tests are generally required if intervention is contemplated. The hallmark of chronic pancreatitis is **ductal dilation** (Fig. 7.46) and **calcifications,** which can be in the branch ducts (Fig. 7.47), main duct (Fig. 7.48), or both (Video 7.4). When these findings are present in a patient with pain and a history of alcoholism, the diagnosis of chronic pancreatitis is secure.

FIG. 7.47 Dilated Pancreatic Duct and Branch Duct Calcifications. Ductal calcification is a hallmark of chronic pancreatitis. Transverse sonogram shows many branch duct stones.

CT is superior to sonography in detecting calcifications and ductal dilation. Calcifications are often made much more conspicuous on ultrasound images by looking for the **color comet-tail artifact,** also known as the "twinkling artifact"[99,100] (Fig. 7.49; see also Fig. 7.48B and Video 7.5).

Areas of increased and decreased echogenicity are related to the effects of patchy fibrosis. These focal areas of altered echogenicity are often subjective and difficult to appreciate.

Pseudocysts

Pseudocysts are more common in patients with chronic (20%-40%) than with acute (5%-16%) pancreatitis (Figs. 7.50 and 7.51, Video 7.6).[74] Pseudocysts may present with various shapes, contain necrotic debris (Fig. 7.52), hemorrhage (≈5%)[72] (Fig. 7.53), or even have a completely solid pattern.[8]

Portal and Splenic Vein Thrombosis

Thrombosis of the portal venous system can occur in chronic pancreatitis because of (1) intimal injury from recurrent acute

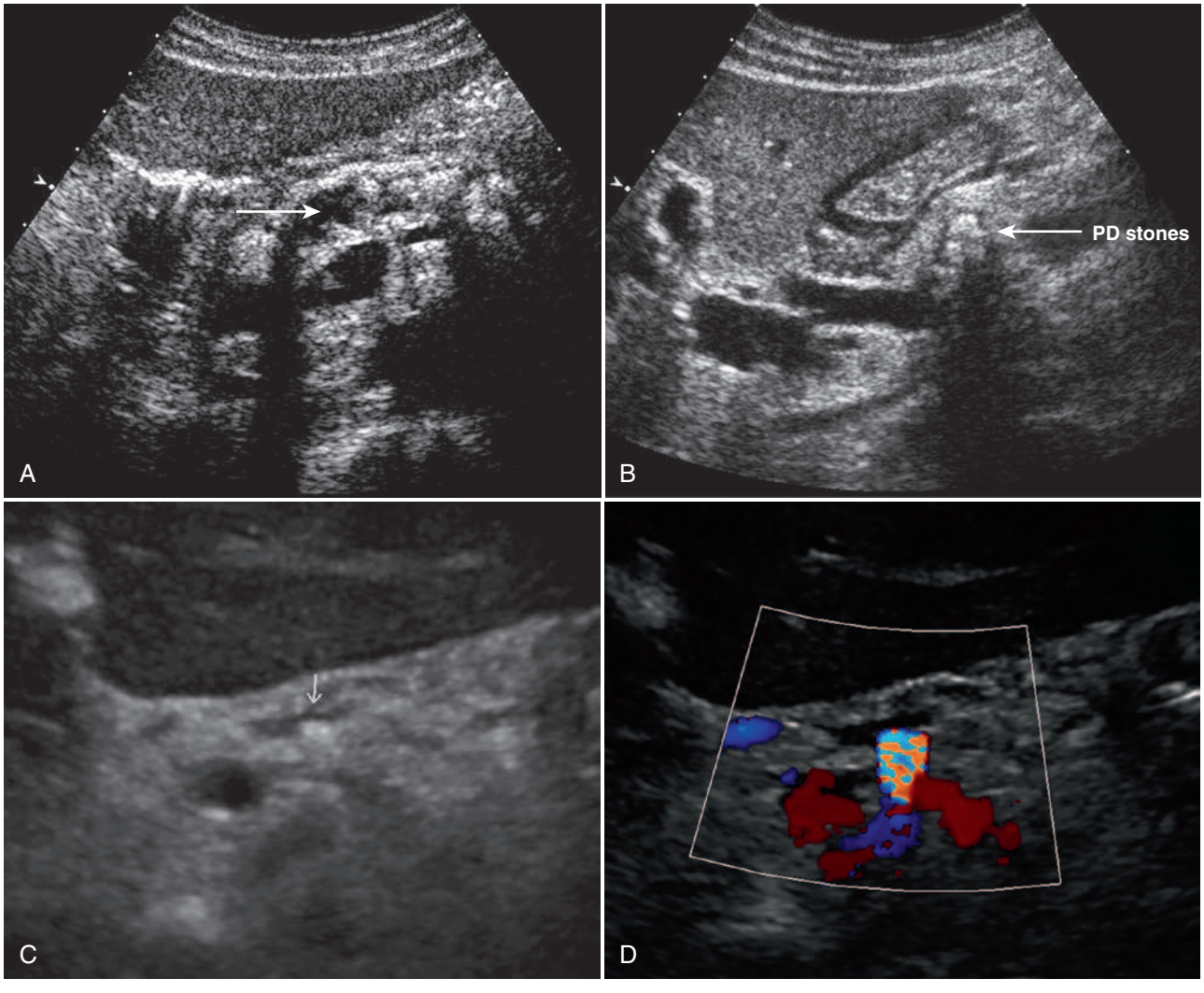

FIG. 7.48 Dilated Pancreatic Duct and Intraductal Stone. (A) Transverse and **(B)** longitudinal sonograms show chronic pancreatitis with dilation of the pancreatic duct *(PD)* and multiple stones in the main duct *(arrow)*. Branch duct stones are manifest as almost confluent, echogenic parenchymal foci. **(C)** Transverse gray-scale and **(D)** color Doppler sonograms show chronic pancreatitis with dilation of the pancreatic duct and stone in the main duct *(arrow)*. **(D)** Color comet-tail (aka "twinkle") artifact at color Doppler imaging can increase stone conspicuity. See also Video 7.4.

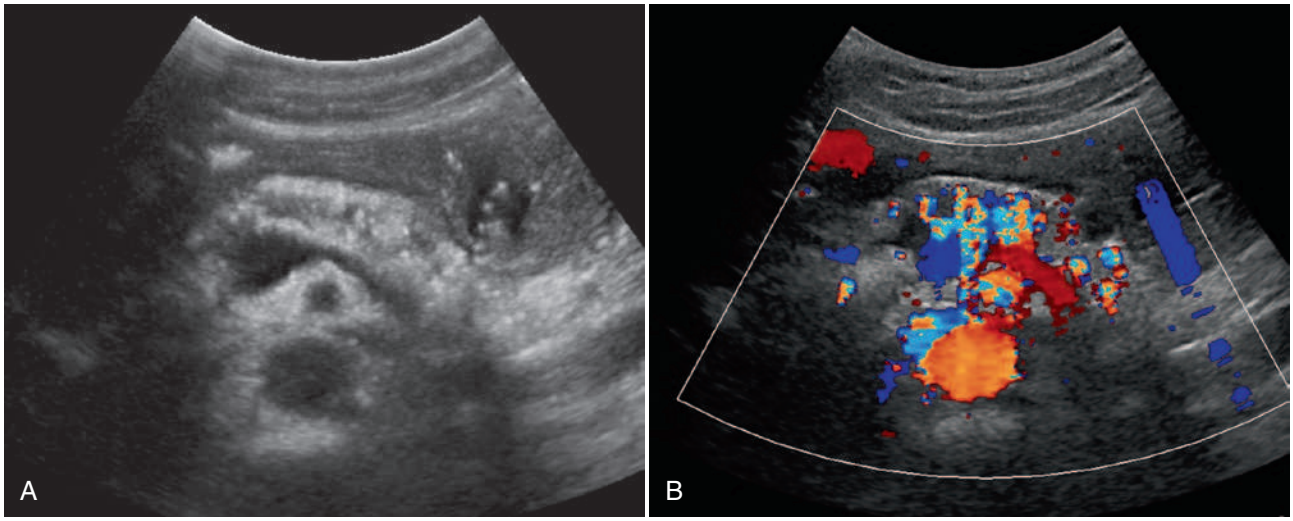

FIG. 7.49 Calcifications in Chronic Pancreatitis Highlighted by Color Comet-Tail Artifact. (A) Transverse gray-scale and **(B)** color Doppler sonograms show that color comet-tail artifact makes the extensive pancreatic calcification much more conspicuous. See also Video 7.5.

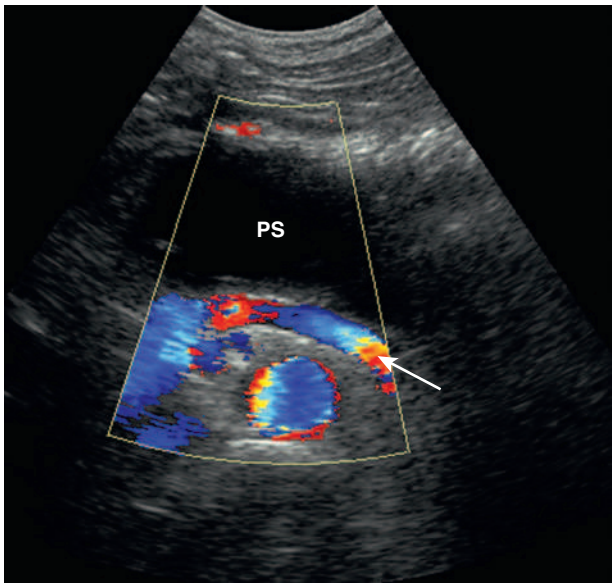

FIG. 7.50 Pseudocyst in Pancreatic Body in Patient With Chronic Pancreatitis. This pseudocyst *(PS)* is almost free of internal debris. The flow reversal in the splenic vein *(arrow)* is related to cirrhotic portal hypertension. See also Video 7.6.

inflammation, (2) chronic fibrosis and inflammation, or (3) compression by either a pseudocyst or an enlarged pancreas.[101] **Splenic vein thrombosis** is relatively common in patients with chronic pancreatitis (5%[102]–40%[101]) (see Fig. 7.44). **Portal vein thrombosis** occurs less frequently. Bernades et al.[90] reported the prevalence of splenoportal vein obstruction as 13%, with the splenic vein obstructed in 8%, portal vein in 4%, and SMV in 1%.

Pancreatitis-associated thrombus in the splenic or portal vein often results in collaterals different from those in portal hypertension from liver disease. Rather than conveying blood away from the diseased liver, these collaterals conduct blood *toward* the liver, bypassing the clot. Splenic vein thrombosis will often result in **left-sided** ("sinistral") **portal hypertension** (Fig. 7.54). This can result in isolated gastric varices, which can cause life-threatening gastrointestinal bleeding. The hepatopetal pathway to bypass the splenic vein clot (Fig. 7.55) includes short gastric collaterals that lead to the **gastric mural varices** (Fig. 7.56), then flow toward the liver in the coronary vein. It may be difficult or impossible to detect splenic vein clot or even the splenic vein itself. Therefore the diagnosis of splenic vein clot may depend on detection of collaterals, such as short gastric varices or an enlarged coronary vein.[103] When the main portal vein is clotted, blood flows to the liver around the clot. If the portal vein clot persists, these hepatopetal collaterals may enlarge, resulting in cavernous transformation of the portal vein. **Gallbladder wall varices** were present in 30% of patients with portal vein thrombosis in one study[104] (Fig. 7.57). These can be successfully diagnosed with color Doppler[105] or gray-scale[106] imaging.

Masses Associated With Chronic Pancreatitis

Focal pancreatic masses occur in approximately 30% of patients who have chronic pancreatitis. Carcinoma- and pancreatitis-related masses are usually easy to differentiate clinically and by imaging (Fig. 7.58). In some patients, however, the distinction may be difficult[107] (Fig. 7.59). Pancreatitis-associated masses are found in a surprisingly large percentage of patients having surgery for suspected pancreatic malignancy (5%-18.4%).[108] In one series, 10.6% (47 patients) of 442 patients undergoing **pancreaticoduodenectomy (Whipple resection)** had benign disease.[109] Of these 47 patients, 40 (85%) were resected because of a suspected malignancy.

The presence of calcification within a mass makes the diagnosis of chronic pancreatitis likely (Fig. 7.60). Only 4% to 6% of ductal adenocarcinomas have calcifications.[110,111] The pattern of calcification in patients with ductal adenocarcinoma is different from

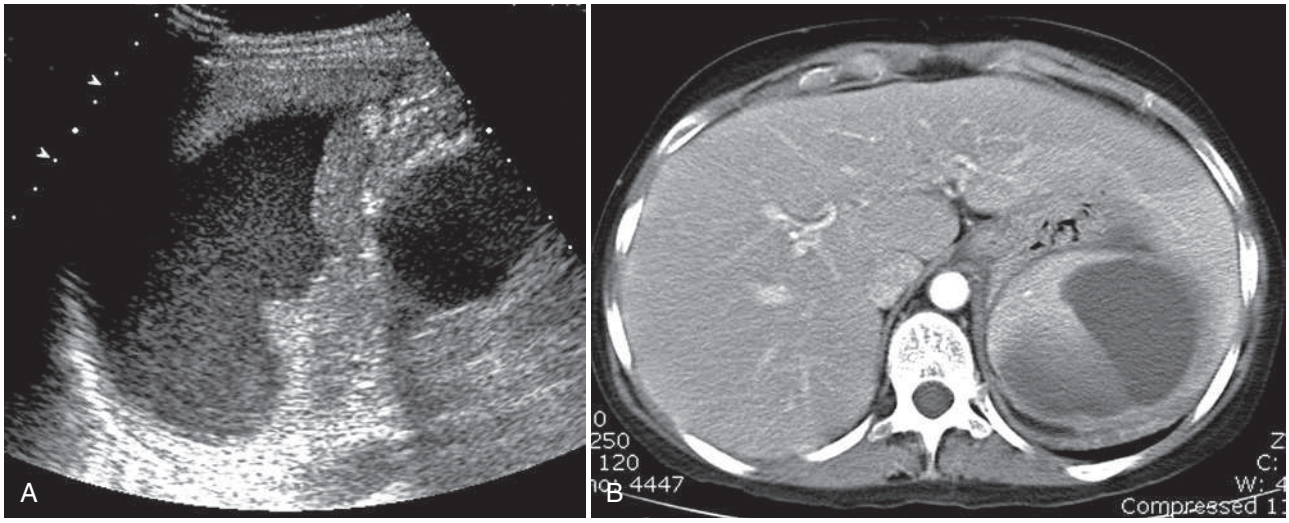

FIG. 7.51 Hemorrhagic Pseudocyst in Pancreatic Tail. (A) Complex, debris-filled pseudocyst seen through pancreatic tail in patient with chronic pancreatitis. **(B)** Computed tomography scan shows debris in the pseudocyst.

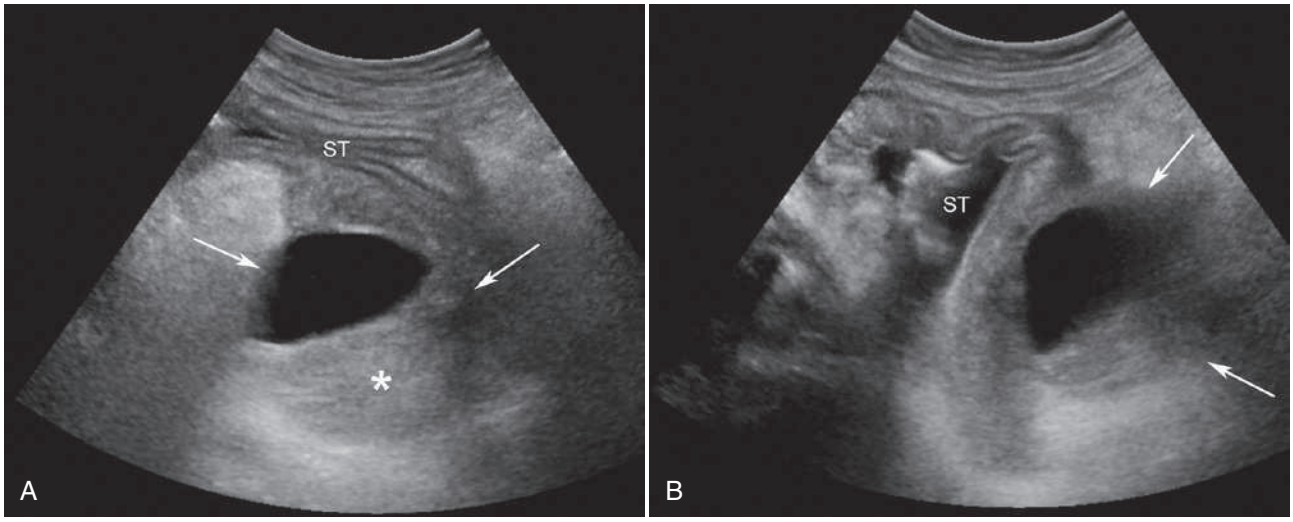

FIG. 7.52 Debris-Containing Pseudocyst. (A) Transverse sonogram shows a well-organized collection *(arrows)* abutting the stomach *(ST)* with internal debris (*) and a fluid-debris level. **(B)** Sagittal sonogram demonstrates the debris-containing pseudocyst *(arrows)* abutting the greater curvature of the stomach. The gastric wall is thickened as a result of reactive inflammatory changes.

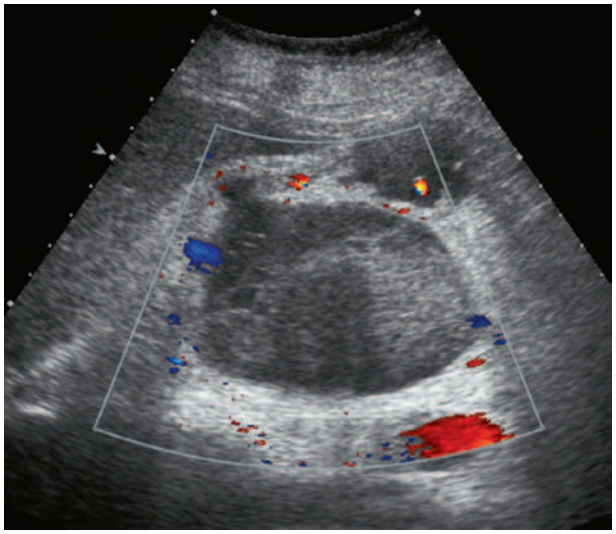

FIG. 7.53 Hemorrhagic Pseudocyst in Pancreatic Body. Chronic pancreatitis–associated debris-filled pseudocyst; it may be difficult or impossible to distinguish a hemorrhagic pseudocyst from a debris-filled nonhemorrhagic pseudocyst.

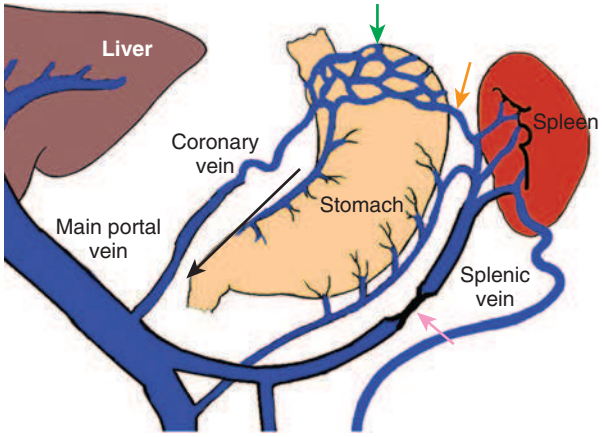

FIG. 7.54 Splenic Vein Clot With Left-Sided ("Sinistral") Portal Hypertension. This can result in isolated gastric varices *(green arrow),* which can cause life-threatening gastrointestinal bleeding. The hepatopetal pathway to bypass the splenic vein clot *(purple arrow)* includes short gastric collaterals *(orange arrow). Long black arrow* indicates direction of blood flow.

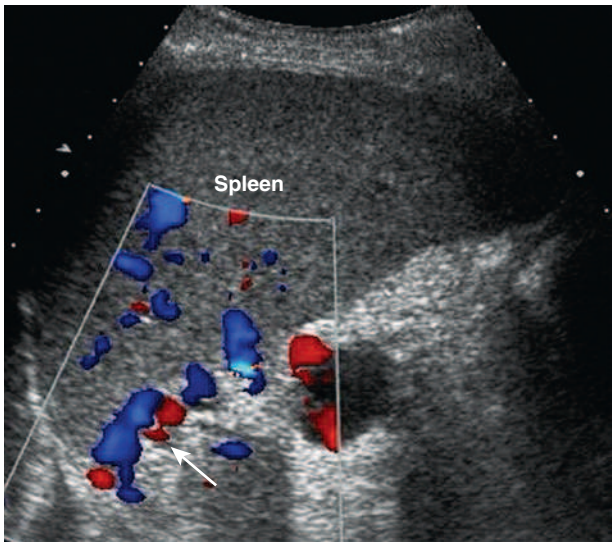

FIG. 7.55 Short Gastric Collaterals From Splenic Vein Clot. Longitudinal coronal color Doppler sonogram in a patient with left-sided (sinistral) portal hypertension shows blood in the short gastric venous collaterals *(arrow)* flowing away from the splenic hilum.

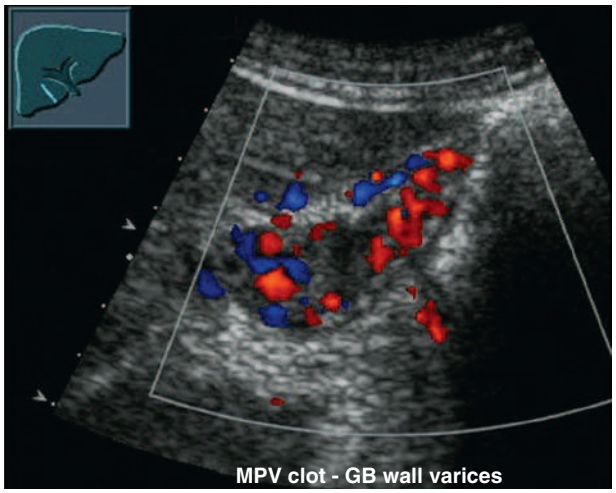

FIG. 7.57 Gallbladder Wall Varices and Clot. Oblique color Doppler sonogram shows main portal vein (MPV) clot engenders hepatopetal collaterals, including cavernous transformation of the portal vein and, in some patients, gallbladder (GB) wall varices.

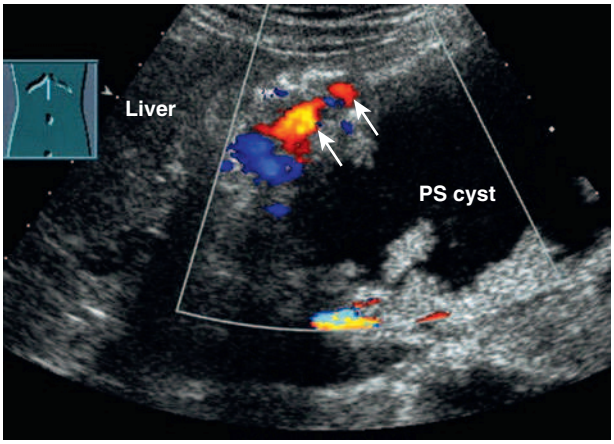

FIG. 7.56 Gastric Mural Varices. Longitudinal color Doppler sonogram in a patient with left-sided portal hypertension. The actual gastric mural varices *(arrows)* are visualized, unusual in these patients. The pseudocyst *(PS cyst)* that caused the splenic vein clot is compressing the stomach.

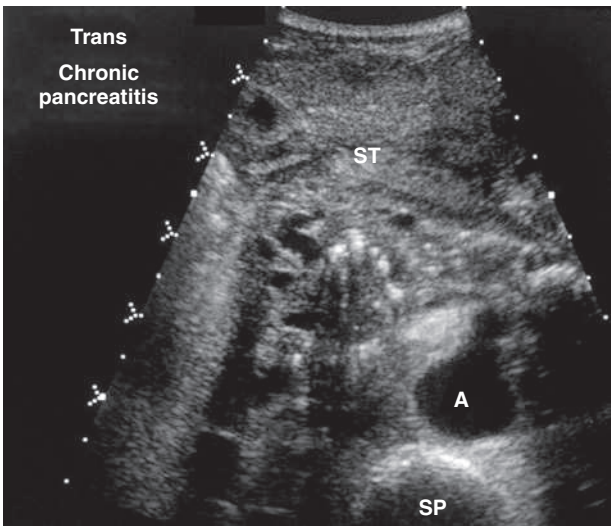

FIG. 7.58 Chronic Pancreatitis–Associated Mass, With Calcification and Dilated Ducts. Transverse sonogram of pancreatic head. When classic findings such as ductal dilation and multiple calcifications are present, the diagnosis of chronic pancreatitis is clear. *A,* Aorta; *SP,* spine; *ST,* stomach.

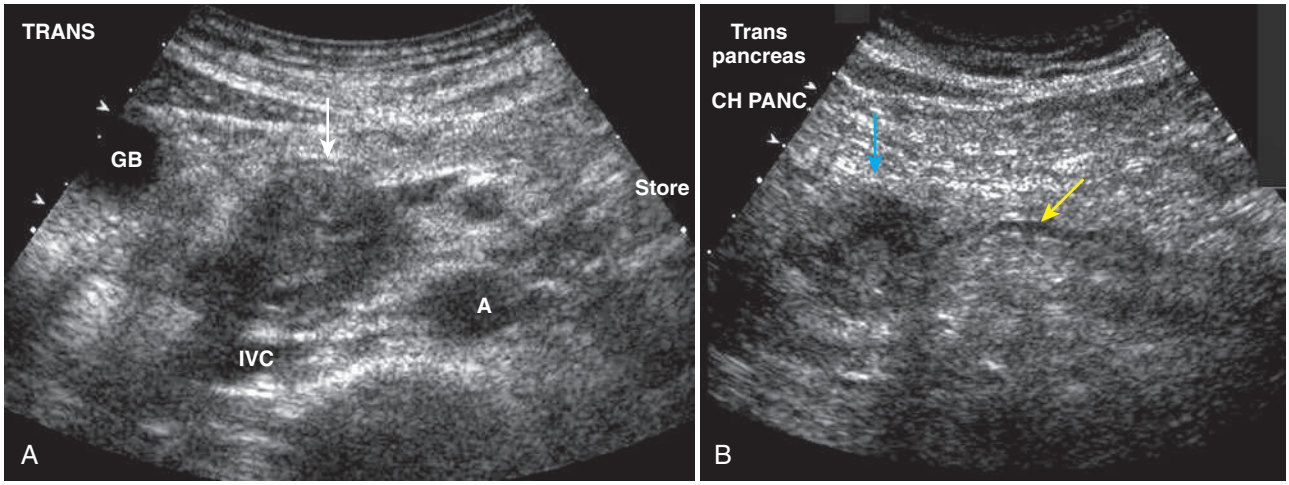

FIG. 7.59 Chronic Pancreatitis–Associated Masses in Pancreatic Head Simulating Carcinoma. Two different patients. **(A)** Transverse sonogram reveals a mass *(arrow)* that lacks calcification and other features of chronic pancreatitis, simulating a malignant mass. **(B)** Transverse sonogram reveals a mass *(blue arrow)* that simulates a malignancy; *yellow arrow,* pancreatic duct. *A,* Aorta; *GB,* gallbladder; *IVC,* inferior vena cava.

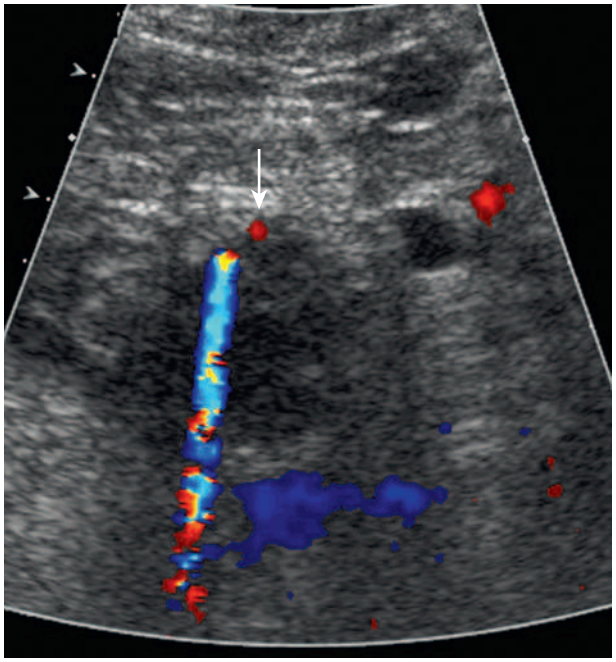

FIG. 7.60 Mass With Color Comet-Tail Artifact From Calcification. Transverse sonogram reveals a mass *(arrow)*. Calcification, revealed by a prominent color comet-tail artifact, indicates a likely diagnosis of chronic pancreatitis.

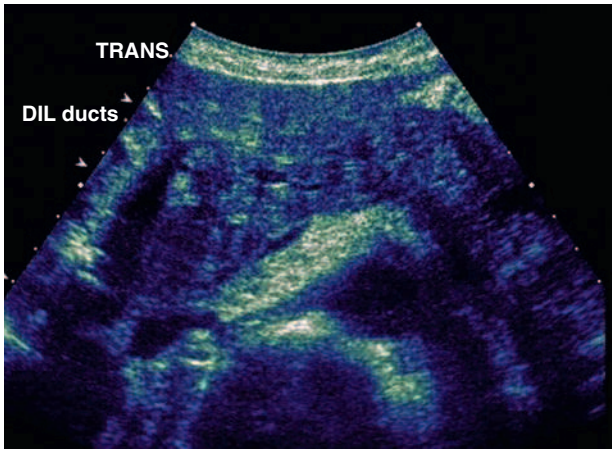

FIG. 7.61 Many Small, Dilated Ducts. Transverse sonogram shows multiple dilated branch ducts in the pancreatic head, more typical of chronic pancreatitis and rarely found in pancreatic cancer.

that of patients with the usual chronic pancreatitis. In chronic pancreatitis calcifications are multiple and ductal. In carcinoma there are generally only one or a few coarse calcifications, usually unrelated to dilated ducts. Hyperechoic masses, even without discrete calcifications, are usually (but not always) related to chronic pancreatitis. An uncalcified isoechoic or hypoechoic mass occurring in a patient without clinical or imaging evidence of chronic pancreatitis is nonspecific. In this case, other imaging or biopsy is indicated to differentiate carcinoma from chronic pancreatitis. As noted, the double-duct sign is nonspecific, occurring in both pancreatitis and pancreatic carcinoma. Finding multiple dilated branch ducts in the pancreatic head is more typical of chronic pancreatitis and is rarely found in pancreatic cancer (Fig. 7.61). Pseudocysts are common in chronic pancreatitis (20%-40%)[74] and rare in carcinoma,[112] but they occur in both conditions. So-called obstructive pseudocysts that occur with carcinoma usually are peripheral to body or tail lesions. Pancreatitis-associated pseudocysts occur anywhere in the gland, usually arising in areas of necrosis.

Autoimmune pancreatitis is a masslike imitator of pancreatic carcinoma[113] (Figs. 7.62 and 7.63). Autoimmune pancreatitis accounts for many cases previously classified as "idiopathic pancreatitis," comprising perhaps 4% to 6% of all patients diagnosed with chronic pancreatitis. The autoimmune pancreatitis terminology is confusing; synonyms include **chronic sclerosing pancreatitis, lymphoplasmacytic sclerosing pancreatitis,** and **tumefactive chronic pancreatitis.**[114] About 2% of pancreatic masses resected for suspected malignancy are found instead to be autoimmune pancreatitis.[115] Although benign masses from the usual causes of chronic pancreatitis are more common, autoimmune pancreatitis masses are much more likely to be confused for carcinoma.[116] In one series, 13 of 19 (68%) masses caused by the usual types of chronic pancreatitis were resected for a clinical suspicion of malignancy, whereas all 11 (100%) of autoimmune pancreatitis–related masses were thought to be malignant preoperatively.[109]

Anecdotal experience suggests that when a definite pancreatic mass is seen sonographically but not imaged on CT, chronic pancreatitis is the likely cause of the mass. Another slightly confounding fact is that patients with chronic pancreatitis have an increased lifetime risk of developing pancreatic carcinoma (4%)[117] compared with the general population (1%-2%).[118]

PANCREATIC NEOPLASMS

Periampullary Neoplasm

Periampullary neoplasms are difficult to differentiate from one another and are generally managed identically—by **pancreaticoduodenectomy (Whipple resection). Jaundice** is the most common presenting feature of these tumors (85%).[119] Tumors in this group include **pancreatic ductal adenocarcinoma** (about two-thirds of periampullary neoplasms), **ampullary carcinoma** (15%-25%), **duodenal carcinoma** (10%), and distal **cholangiocarcinoma** (10%).[119] Survival rates are best for patients with duodenal and ampullary carcinoma, but only in comparison to the poor survival rates for those with cholangiocarcinoma and especially pancreatic cancer.

Image evaluation of these tumors is basically the same as that described later for pancreatic ductal adenocarcinoma. The approach varies depending on the clinical presentation and local expertise. Most agree, however, with Ross and Bismar,[119] that "the relative availability, economy, and usefulness of the results make transabdominal ultrasound a common initial imaging study for patients with suspected obstructive jaundice."

Pancreatic Carcinoma

Pancreatic ductal adenocarcinoma is the most common primary pancreatic neoplasm, accounting for 85% to 95% of all pancreatic

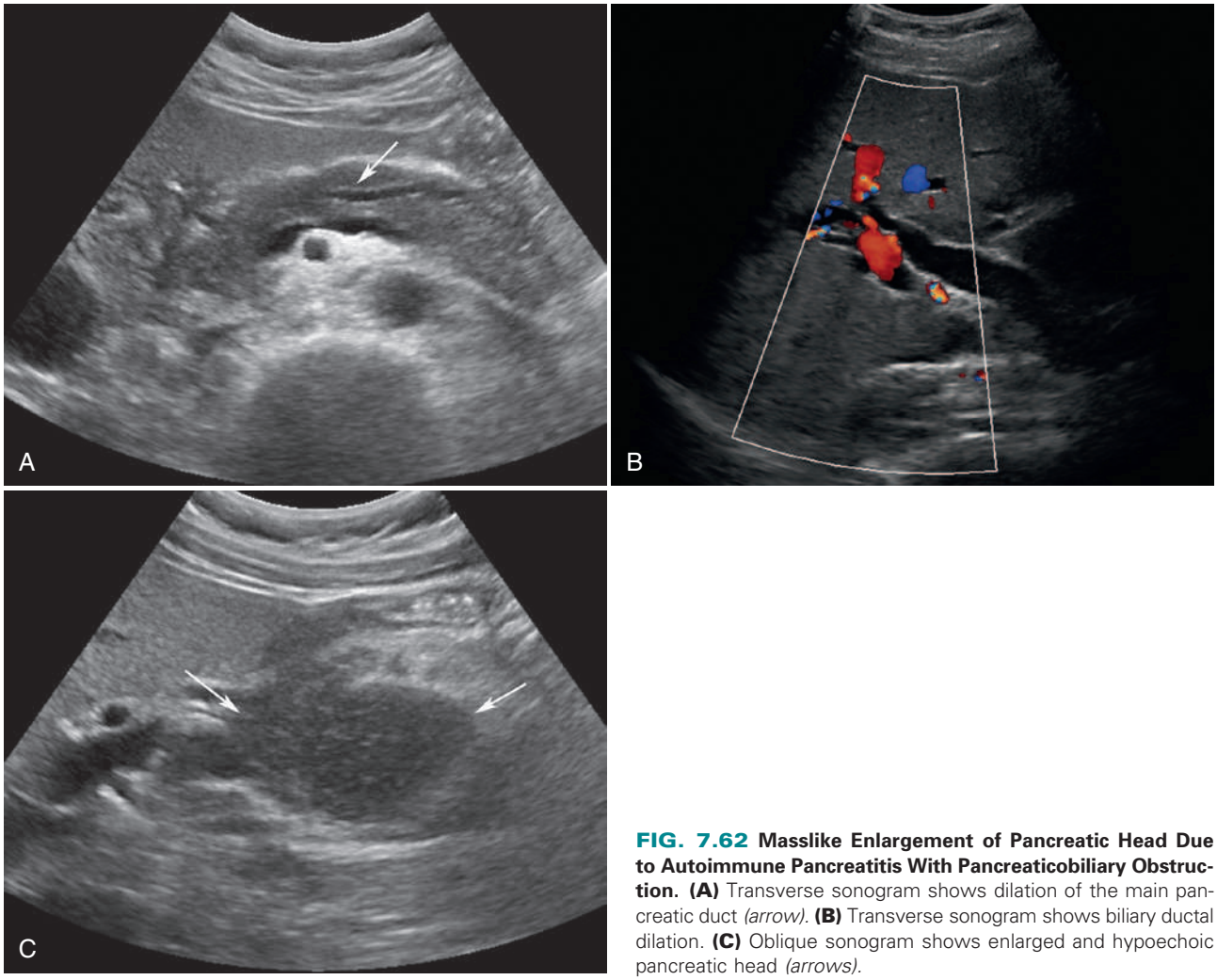

FIG. 7.62 Masslike Enlargement of Pancreatic Head Due to Autoimmune Pancreatitis With Pancreaticobiliary Obstruction. (A) Transverse sonogram shows dilation of the main pancreatic duct *(arrow)*. **(B)** Transverse sonogram shows biliary ductal dilation. **(C)** Oblique sonogram shows enlarged and hypoechoic pancreatic head *(arrows)*.

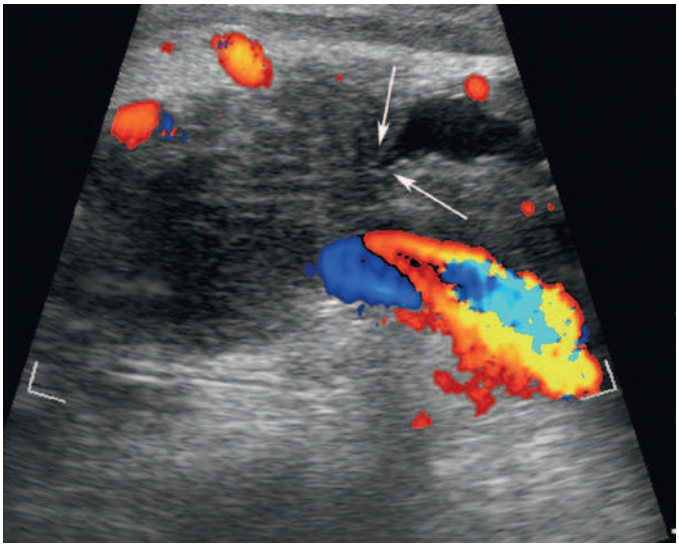

FIG. 7.63 Mass in Pancreatic Head Due to Autoimmune Pancreatitis. Transverse **intraoperative ultrasound** image shows marked dilation of the main pancreatic duct with obstruction *(arrows)* due to involvement of the pancreatic head and neck by autoimmune pancreatitis.

malignancies.[120,121] Ductal adenocarcinoma has a slight male predominance, most frequently affecting patients 60 to 80 years of age. The prevalence of pancreatic carcinoma tripled during the mid-20th century. The mortality rate for patients with pancreatic cancer has continued to decline since 1975 in men and has leveled off in women after increasing from 1975 to 1984.[122] Pancreatic cancer represents only 2% of all cancers but is the fourth most common cause of cancer death in the United States. Overall 5-year survival is poor: 2% to 5%. Risk factors include tobacco smoking (twice the risk as for nonsmokers), obesity, chronic pancreatitis, diabetes, cirrhosis, and use of smokeless tobacco. A family history of pancreatic cancer also increases risk.[123] Rare syndromes associated with increased risk include Peutz-Jeghers syndrome.[124]

The selection of imaging techniques in patients with pancreatic cancer requires a rational approach based on grim realities about the disease. Although sophisticated imaging of candidates for resection consumes much time and effort, it is crucial to remember that only a few patients have potentially resectable disease at initial diagnosis. These are the patients who can potentially benefit from sophisticated "resectability" studies. Further, even for that small minority who can be resected with a hope for cure, the

Pancreatic Cancer Imaging: Three Key Concepts

1. The vast majority of patients with pancreatic cancer can be classified as "unresectable for cure," based on the initial ultrasound or CT.
2. Only 10% to 20% of patients require sophisticated "resectability" studies, whether done with CT, MRI, or ultrasound (transabdominal or endoscopic).
3. The survival statistics for patients with pancreatic cancer have been exaggerated in the literature. The usefulness of surgery is questionable in this malignancy.

prognosis is poor. Most patients with newly diagnosed pancreatic carcinoma have advanced unresectable disease at initial diagnosis. In most studies from major oncology centers, only 10% to 20% of the patients are eligible for curative surgery at diagnosis.[125,126] The initial routine imaging study, whether ultrasound or CT, can usually detect advanced disease.[127]

Although the diagnosis of periampullary tumors and safety of the Whipple procedure have improved over the decades, prognosis for patients with pancreatic cancer remains poor. In a meta-analysis of virtually the entire surgical literature on resection of pancreatic cancer, Gudjonsson[128] found significant errors and exaggerations in the reporting of survival figures, and that the overall survival rate actually was less than 0.4%. The best overall survival rate in detailed surgical studies is only 3.6%, and for a nonsurgical study, 1.7%. In another report, Gudjonsson[129] stated,

> *Resections for pancreatic cancer have been performed for 65 years, with approximately 20,000 reported. A number of authors claim a 5-year survival rate of 30% to 58%. Review of the literature reveals only about 1,200 5-year survivors; however, 10 times as many individual resected survivors have been reported (in various countries), and nonresected survivors are overlooked. This high survival percentage is obtained by reducing the subset on which calculations are based and by using methods such as the Kaplan-Meier method, which produces higher figures as increasing numbers of patients are lost to follow-up. After adjustments, hardly more than 350 resected survivors could be found. Revision of statistical methods is urgently needed.*

Conlon et al.[126] reported that 5-year survival does not equal cure. In their series of 118 resected patients, median survival was 14.3 months. Twelve patients survived 5 years after surgery (10.2% of resected patients), but 5 of these 12 patients died of pancreatic cancer in the sixth postoperative year. At the time of the report, 6 patients were alive and without evidence of disease at a median follow-up of 101 months (range, 82-133 months). In periampullary tumors other than ductal adenocarcinoma, 5-year survival rate is higher, for example, 9% versus 36% in the study by Wade et al.[130] Despite these grim facts, most surgeons favor an aggressive approach, as expressed by Farnell et al.[131]:

> *Significant progress has been made in diagnosis, preoperative staging, and safety of surgery; however, long-term survival after resection is unusual, and cure is rare. That said, the authors maintain their aggressive posture regarding this disease, recognizing that resection offers the only potential for cure.*

Because of prevailing surgical opinion, radiologists will continue to be asked to do studies to assess the potential resectability of pancreatic cancer in the 10% to 20% of patients in whom the initial study does not show advanced disease.

Detection of Pancreatic Cancer

Sonography and CT are the primary tools used to detect focal pancreatic disease, especially pancreatic carcinoma and periampullary neoplasms. Sonography often detects pancreatic carcinoma because it is the method of choice to screen patients with jaundice[132] and is frequently used to assess patients with pain. There are few recent US studies of ultrasound in pancreatic carcinoma. Nonetheless, sonography clearly is effective in detecting pancreatic carcinoma,[127,133,134] with a sensitivity of 72% to 98%.[68] **Multidetector computed tomography** (MDCT) has a reported sensitivity of 86% to 97% for all pancreatic tumors.[132] CT is less operator dependent than ultrasound, which, along with CT's higher reimbursement, likely accounts for most radiologists' preference for CT in tumor detection. Sonography may be useful to characterize abnormalities noted on CT, such as determining whether a lesion is cystic or solid. MRI, MRCP, ERCP, and endoscopic ultrasound are all comparably sensitive to CT, but reserved for problem solving or special circumstances.[120]

Ultrasound Findings

From 60% to 70% of pancreatic cancers originate from the pancreatic head, 25% to 35% are in the body and tail, and 3% to 5% are diffuse[110,121] (Fig. 7.64). This distribution explains in part the good detection rates of cancer, because the head and body are more easily seen sonographically than the tail. The hallmark of periampullary pancreatic cancer is the double-duct sign, with both bile duct dilation (Fig. 7.65) and pancreatic duct dilation (Fig. 7.66). Pancreatic ductal adenocarcinoma may cause considerable desmoplastic reaction, so even a mass that appears eccentric can cause ductal obstruction (Fig. 7.67). If a mass in the pancreatic head region is found and there is no ductal dilation, lesions other than pancreatic ductal adenocarcinoma should be sought.

Reviewing findings in 62 patients with pancreatic carcinoma, Yassa et al.[110] found that tumors were ovoid or spherical in 37 patients (60%) and irregular in 25 (40%). Forty tumors (65%) deformed the shape of the gland, whereas six lesions (10%) caused no glandular contour abnormality and were visualized only because tumor echogenicity differed from that of the normal pancreas. Thirty-four tumors (55%) were homogeneously hypoechoic compared with the normal pancreas, 25 (40%) had heterogeneous echotexture (Fig. 7.68), 2 (3%) were homogeneously hyperechoic, and 1 (2%) was isoechoic. Many of the heterogeneous tumors were predominantly hypoechoic with areas of varied echogenicity. **Calcifications** were noted in 4 patients (6%) and **small, intratumoral cystic areas** in 9 patients (15%) (Fig. 7.69, Video 7.7). **Postobstructive pseudocysts** were found in 4 patients (6%) (Fig. 7.70). Such pseudocysts may be caused by obstructive

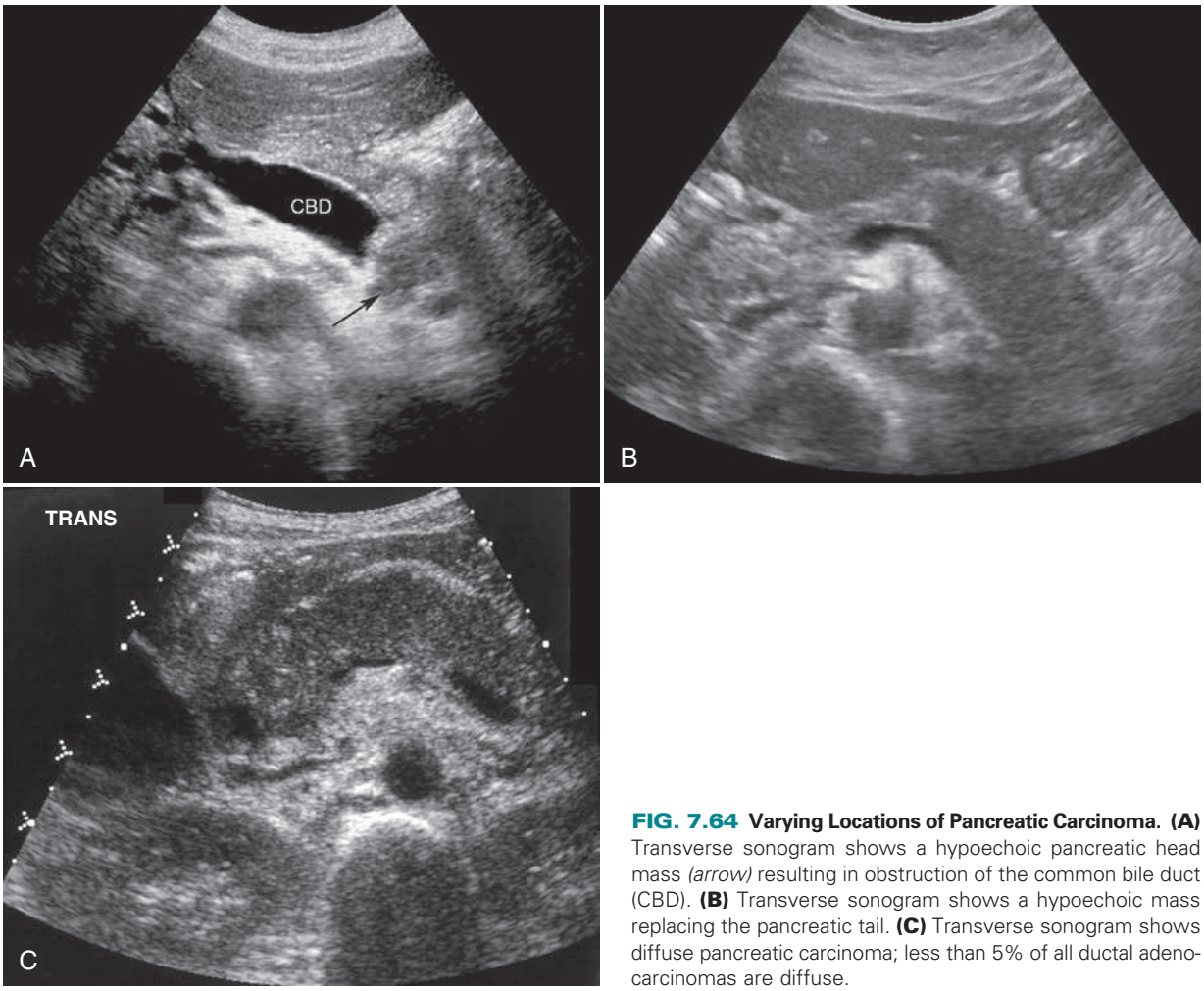

FIG. 7.64 Varying Locations of Pancreatic Carcinoma. (A) Transverse sonogram shows a hypoechoic pancreatic head mass *(arrow)* resulting in obstruction of the common bile duct (CBD). **(B)** Transverse sonogram shows a hypoechoic mass replacing the pancreatic tail. **(C)** Transverse sonogram shows diffuse pancreatic carcinoma; less than 5% of all ductal adenocarcinomas are diffuse.

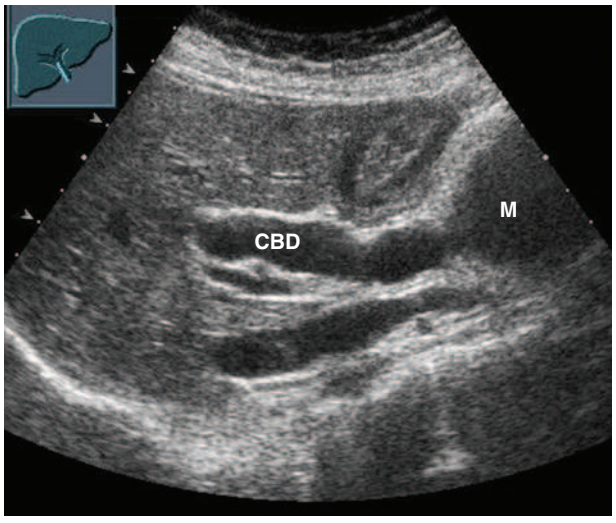

FIG. 7.65 Large Pancreatic Carcinoma. Longitudinal oblique sonogram shows large, hypoechoic mass *(M)* obstructing the extrahepatic common bile duct *(CBD)*.

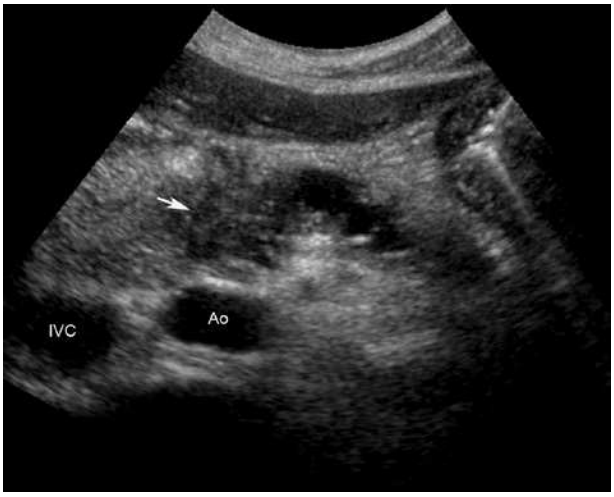

FIG. 7.66 Pancreatic Carcinoma. Transverse sonogram shows hypoechoic mass *(arrow)* obstructing the pancreatic duct. Note the "beaded" pattern of the dilated, obstructed duct. *Ao,* Aorta; *IVC,* inferior vena cava.

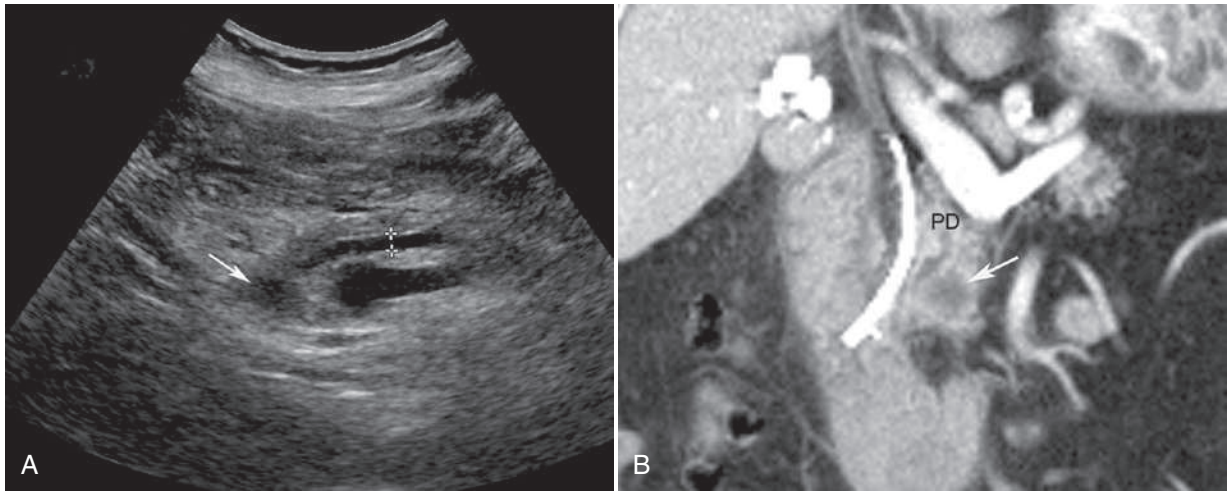

FIG. 7.67 Eccentric Pancreatic Ductal Adenocarcinoma. (A) Transverse sonogram shows that pancreatic carcinoma may cause considerable fibrosis (desmoplastic reaction) and obstruct adjacent ducts. Thus even this uncinate process mass *(arrow),* which appears somewhat distant from the dilated pancreatic duct (calipers) and common bile duct (CBD), can cause ductal obstruction. **(B)** Coronal contrast-enhanced computed tomography confirms that the uncinate process mass *(arrow)* is eccentric to the obstructed pancreatic duct *(PD)*. CBD obstruction has been relieved by stenting.

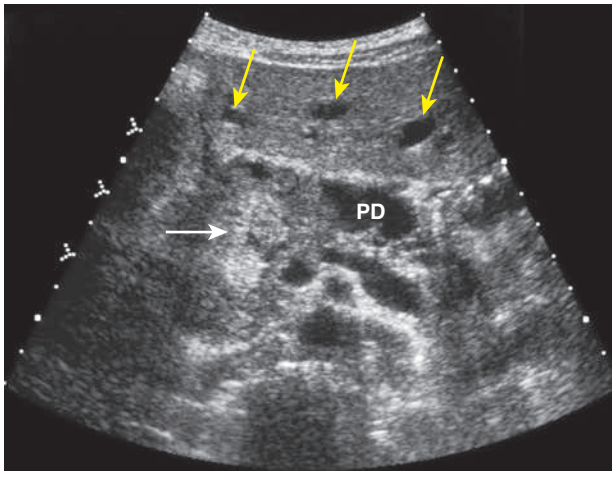

FIG. 7.68 Heterogeneous, Mainly Echogenic Pancreatic Carcinoma. Transverse sonogram shows tumor obstructing the extrahepatic bile duct. Increased echogenicity *(white arrow)* is unusual in pancreatic ductal adenocarcinoma. This heterogeneous cancer causes a double-duct sign with pancreatic duct dilation *(PD)*. The intrahepatic duct dilation is manifest as dilated minor ducts *(yellow arrows)*.

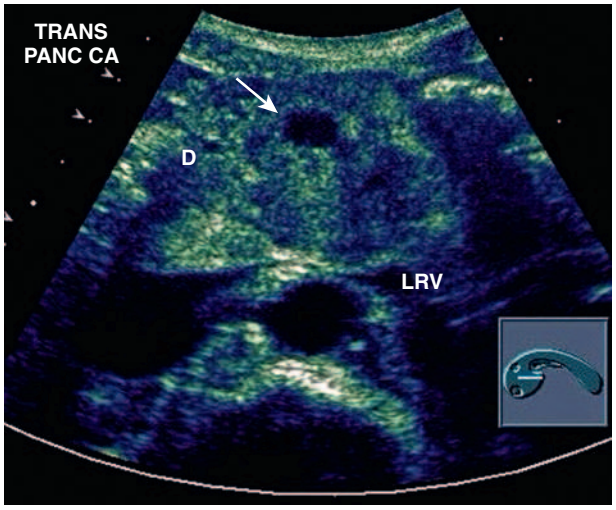

FIG. 7.69 Cystic Area in Pancreatic Ductal Adenocarcinoma. Transverse sonogram shows a complex mass in the pancreatic head. Small, intratumoral cystic areas *(arrow)* are present in about 10% to 15% of pancreatic cancers. These cysts can be seen in chronic pancreatitis as well, rendering this feature unhelpful in differentiating the two conditions. *D,* Duodenum; *LRV,* left renal vein. See also Video 7.7.

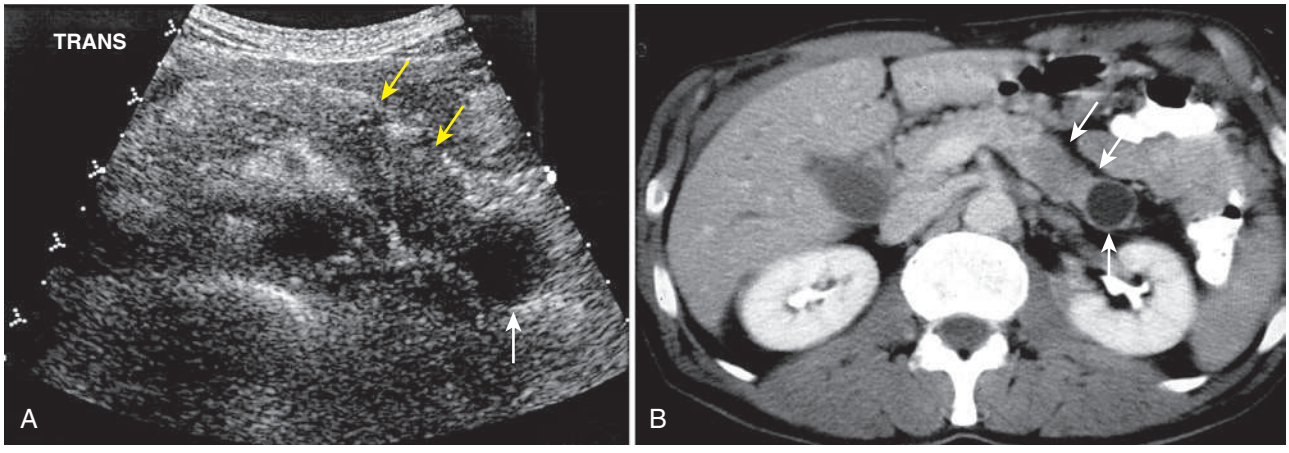

FIG. 7.70 Pancreatic Ductal Adenocarcinoma Causing "Obstructive Pseudocyst." (A) Transverse sonogram reveals a subtle cancer in the body of the pancreas *(yellow arrows)* with a pseudocyst peripheral to the mass *(white arrow)*. **(B)** Computed tomography image at a similar level shows identical findings.

pancreatitis.[135] **Glandular atrophy** may occur from obstruction caused by a tumor. This atrophy is more easily appreciated with CT than ultrasound. It is important to remember that masses caused by chronic pancreatitis can closely simulate periampullary cancers. Very few carcinomas have internal flow that can be imaged on color Doppler.

Resectability Imaging

As the safety of pancreaticoduodenectomy (Whipple procedure) improves, some surgeons have become more aggressive. Also, with advances in surgery, many pancreatic cancers are technically resectable. Unfortunately, the technical ability to resect does not equate to improved outcome (compared to no resection).

Findings that suggest unresectability for cure include tumor larger than 2 cm, extracapsular extension, **vascular invasion** (arterial or venous, although some literature suggests that portal vein resection with jump grafts may have a survival benefit), lymphadenopathy, and metastatic disease. Image findings of unresectability are reliable. Only rarely can such a tumor be resected for cure at surgery. Conversely, many tumors believed resectable because of their imaging appearance are discovered to be unresectable at surgery. Unfortunately, even "resectable" patients with local disease have a 5-year survival rate of only 10%[126] to 20%.[122]

As noted, only a small percentage of patients who have no evidence of advanced disease on initial imaging studies (10%-20%) require sophisticated resectability studies, whether done with transabdominal ultrasound, CT, MRI, positron emission tomography, or endoscopic ultrasound.[136-139] The usefulness of three-dimensional–reconstructed thin-section MDCT evaluation of pancreatic tumors,[140,141] is unmistakable. MDCT has clear advantages over ultrasound for duodenal and retroperitoneal invasion, as well as for detection of malignant lymph nodes. It is unclear, however, how many resectability CT scans would be needed if resectability sonograms were done first. Sonography, especially with color Doppler, can be effective in detecting patients who are unresectable for cure.[134,142-145] Data from Ralls et al. shows a predictive value of 100% for unresectability.[143] In the prediction of resectability, however, 40% of patients thought to be potentially resectable based on color Doppler ultrasound interpretation were found unresectable at surgery. Given these facts, it seems best to use less invasive ultrasound to screen the subgroup of patients needing resectability studies, reserving MDCT for those with no sonographic signs of advanced disease.[146]

Color Doppler Ultrasound

Ralls et al. have developed a technique to assess the resectability of pancreatic tumors using color Doppler sonography.[143] Images are obtained with a large-footprint, curved linear array transducer, using compression technique and color Doppler sonography to evaluate the relationship of the tumor mass to critical vessels, including the main portal vein, SMV (Fig. 7.71), splenic vein, left renal vein, and IVC. Arteries evaluated include the aorta, celiac axis (Fig. 7.72), splenic and common hepatic arteries, and SMA (Fig. 7.73, Video 7.8). Vessels that are touched or occluded by tumor are categorized according to a **pancreatic color Doppler score** (Table 7.3). Other factors affecting resectability (metastasis, enlarged nodes) are recorded.

Color Doppler flow sonography can correctly predict unresectability in 80% or more of pancreatic carcinoma patients. Most of these patients would then require less CT and subsequent imaging evaluation, thus decreasing expense and the need to use more invasive tests. A Polish study found that the diagnostic accuracy of routine, color, and power Doppler and 3-D ultrasound was comparable to that of helical CT in detecting and staging pancreatic carcinoma.[127] The use of ultrasound contrast agents shows some promise to improve the sonographic evaluation of pancreatic tumors,[147] but this is currently an investigational technique.

Pancreatic Cancer Imaging: Suggested Approach

Color Doppler ultrasound should be used to screen patients for resectability of pancreatic cancer.
MDCT or other examinations may then be used in patients with no sonographic evidence of advanced disease.

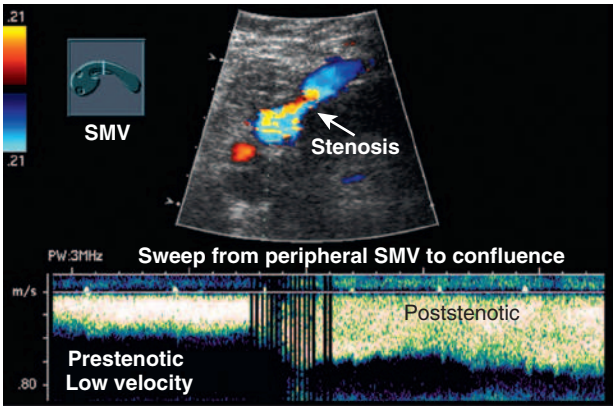

FIG. 7.71 Pancreatic Ductal Adenocarcinoma Narrowing Superior Mesenteric Vein (SMV). Longitudinal oblique spectral Doppler sample volume was swept from the prestenotic lower-velocity region to the poststenotic area (high velocity). Color Doppler image reveals the area of stenosis *(arrow)*.

TABLE 7.3 Pancreatic Color Doppler Score

Score	Description
0	Tumor *does not touch* a vessel.
1	Tumor touches, 1%-24% around the vessel circumference.
2	Tumor touches, 25%-49% around the vessel circumference.
3	Tumor touches, 50%-99% around the vessel circumference.
4	Tumor encased, 100% around the vessel circumference.
5	Vessel invaded or occluded.

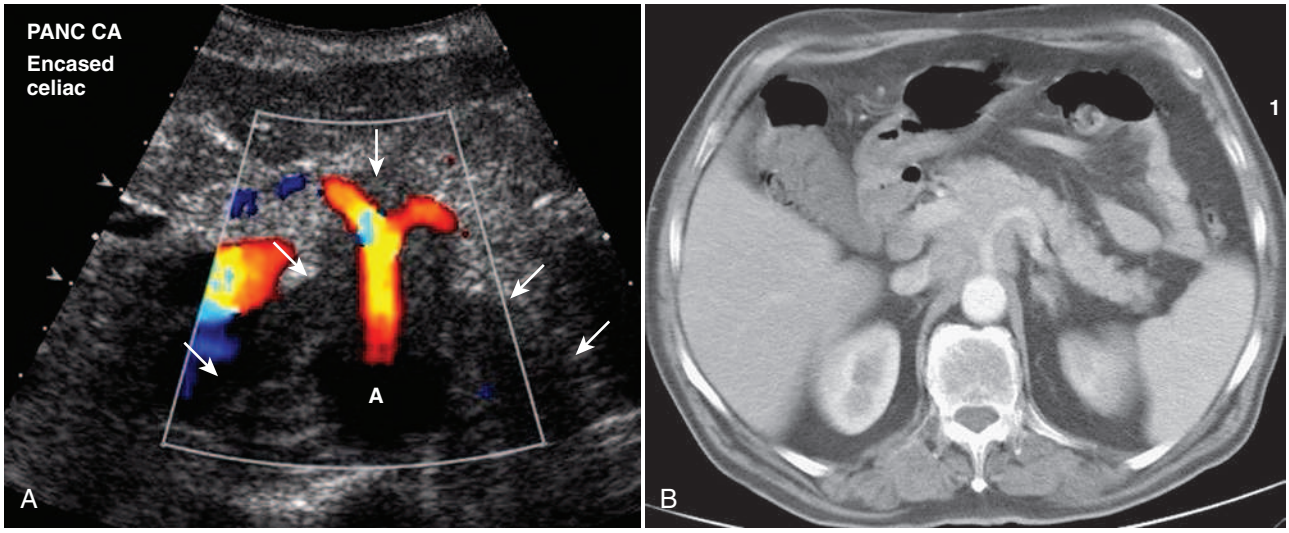

FIG. 7.72 Pancreatic Ductal Adenocarcinoma Encasing Celiac Axis and Aorta. (A) Transverse color Doppler sonogram shows a hypoechoic mass *(arrows)* that encases the aorta *(A)* and celiac axis. **(B)** Computed tomography image at a similar level shows the same findings. This lesion is clearly unresectable for cure.

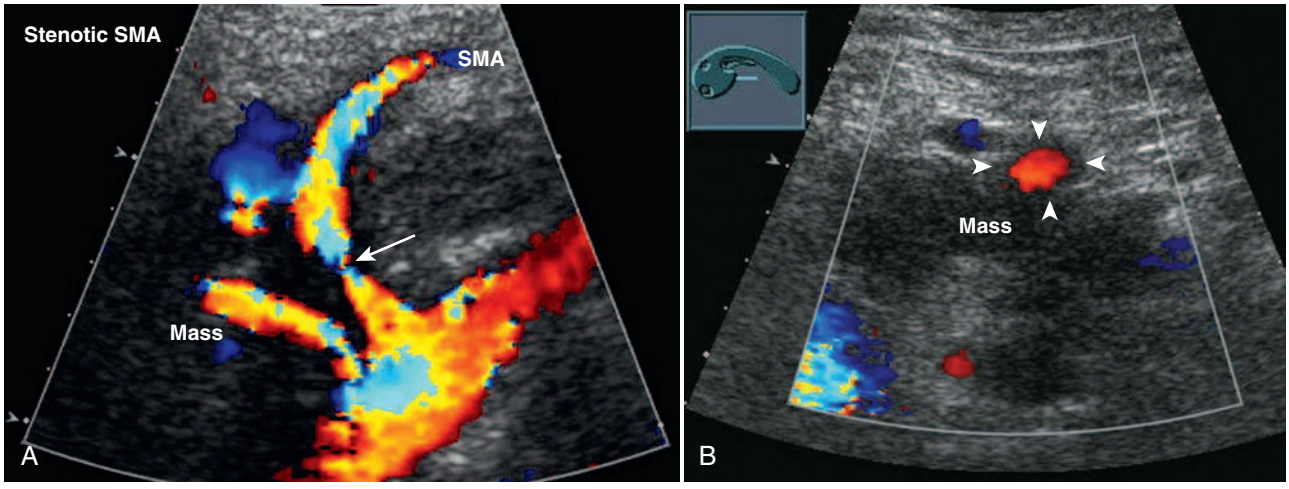

FIG. 7.73 Pancreatic Ductal Adenocarcinoma Encasing Superior Mesenteric Artery (SMA). (A) Longitudinal color Doppler sonogram shows that hypoechoic mass, which also encases the celiac axis, narrows the SMA *(arrow)*. **(B)** Transverse color Doppler sonogram in a different patient demonstrates much more subtle encasement *(arrowheads)*. Ductal adenocarcinoma narrows and occludes veins much more frequently than arteries. This narrowing is equivalent to classic angiographic encasement. See also Video 7.8.

CYSTIC PANCREATIC LESIONS

Understanding cystic pancreatic lesions is increasingly important because improved imaging techniques result in the detection of progressively more of these lesions, often as incidental findings.[72,148,149] New concepts and pathologic definitions of cystic neoplasms, especially mucinous and intraductal papillary forms, have altered the approach to diagnosis and management of these lesions.

Although the number of cystic lesions of the pancreas detected is increasing because of improved imaging techniques,[148,149] pancreatic pseudocyst remains the most common, accounting for 75% or more of all cystic lesions.[72] A careful history must be obtained to rule out previous acute or chronic pancreatitis, so as to minimize the chance of confusing a pseudocyst with other cystic masses. Nonpseudocyst lesions include simple cysts and cystic neoplasms. Although certain image features may be helpful, the differential diagnosis of cystic lesions, especially when small, is unreliable by CT or MRI. Visser et al.[77] found that, even when their diagnostic certainty was 90% or greater, characterization was unreliable.

Fortunately, it appears reasonably safe to follow unilocular pancreatic cystic lesions with a diameter 3 cm or less[72] (Fig. 7.74). Sahani et al.[150] reported that 35 of 36 unilocular pancreatic cystic lesions 3 cm or less were benign. Internal septations were associated with borderline or in situ malignancy in 10 of 50 cases (20%). Other surgeons believe that resection of these lesions is a better approach.[73,151] The usefulness of tumor markers and cyst fluid cytology is debated.[73,152-154] Most agree that high-risk patients and features should be managed more aggressively,

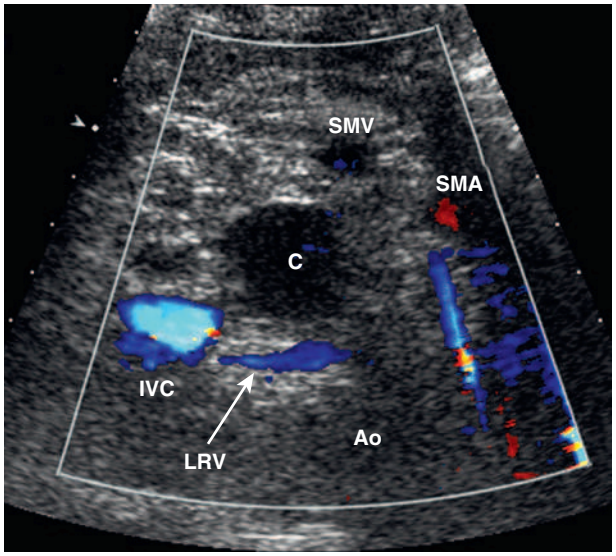

FIG. 7.74 Benign Pancreatic Cyst (Presumed). Transverse color Doppler sonogram shows 2-cm cyst discovered incidentally on abdominal sonogram and followed for 4 years without a change in size. It is generally safe to follow small completely simple pancreatic cysts (please see text). *Ao,* Aorta; *C,* cyst; *IVC,* inferior vena cava; *LRV,* left renal vein; *SMA,* superior mesenteric artery; *SMV,* superior mesenteric vein.

High-Risk Features of Cystic Pancreatic Lesions

Symptomatic patients
Growth on serial examinations
Diameter > 3 cm
Internal soft tissue
Mural or septal thickening

including symptomatic patients, growth of the cyst on serial studies, tumor greater than 3 cm in diameter, internal soft tissue, and mural or septal thickening. Multiple societies have proposed algorithms to follow incidentally detected pancreatic cysts,[155] but there is a great deal of uncertainty in this process,[156,157] and future assessment may rely on novel tumor markers and molecular analysis rather than cross-sectional imaging morphology.[158] Data from 2015 suggest that pancreatic cysts found incidentally by using CT or MRI may be associated with increased mortality for patients younger than 65 years and an overall increased risk of pancreatic adenocarcinoma.[159]

Simple Pancreatic Cysts

Simple pancreatic cysts are rare in the general population, with a prevalence of 0.2%[160] to 1.2%.[151] These low percentages may underestimate true prevalence because imaging[161] and autopsy[162] studies have recorded a substantially higher prevalence, about 20% and 24.3%, respectively. Our experience suggests that the lower prevalence rates are closer to the actual experience in clinical imaging. Detecting a simple pancreatic cyst should raise suspicion of an inherited disease that has a high prevalence of cysts, such as **autosomal dominant polycystic kidney disease** (ADPKD)[163] or **von Hippel–Lindau** (VHL) **disease.**[164] Multiple pancreatic cysts can also occur in individuals with **cystic fibrosis.**[165]

Multiple pancreatic cysts are more common in VHL disease than in ADPKD. Prevalence of pancreatic cysts in patients with VHL ranges from 50% to 90%, making pancreatic cysts the most common type of lesion in VHL disease.[164] Thus multiple simple pancreatic cysts should suggest the diagnosis of VHL (Fig. 7.75). In addition to simple cysts, other pancreatic lesions associated with VHL include serous cystic neoplasm and pancreatic endocrine tumors, with a slightly increased risk of ductal adenocarcinoma.[164]

TABLE 7.4 Estimated Prevalence of Cystic Pancreatic Lesions[a]

Rank	Neoplasm
1	Intraductal papillary mucinous neoplasm
2	Serous cystic neoplasm (microcystic adenoma)
3	Mucinous cystic neoplasm
4	Solid-pseudopapillary tumor
5	Other cystic tumors

[a]Subjective estimate based on the authors' experience.

Cystic Neoplasms

Cystic tumors of the pancreas account for about 10% of cystic pancreatic lesions. Although most solid tumors are ductal adenocarcinomas with a poor prognosis, cystic tumors are usually either benign lesions or low-grade malignancies. Malignant cystic tumors account for about 1% of all pancreatic malignancies.[73] Mucinous tumors such as intraductal papillary mucinous neoplasm and mucinous cystic neoplasm are often malignant. The risk of malignancy is greater in older individuals. Reliable prevalence data are difficult to find[166] but are estimated in Table 7.4.

Serous Cystic Neoplasm

Serous cystic neoplasm, previously known as **microcystic adenoma,** is typically a benign tumor, although a few invasive, malignant examples have been reported.[73,166] Serous cystic neoplasm occurs more frequently in women and is most often found in the pancreatic head.[154] These lesions are composed of myriad tiny cysts, generally too small to be individually resolved sonographically (Fig. 7.76). The multiple reflective interfaces caused by the walls of the tiny cysts leads to an echogenic appearance, analogous to that of autosomal recessive polycystic kidney disease. Through transmission is usual. Larger cysts (1-3 cm in diameter) often are present at the periphery of the lesion. A radially oriented, fibrous pattern occurs in a minority of patients,[149] and a central calcification is often present (30%-50%) (Fig. 7.77). Small lesions (<2 cm) may appear identical to simple cysts. This pattern is common in the **serous oligocystic adenoma** variant.[154]

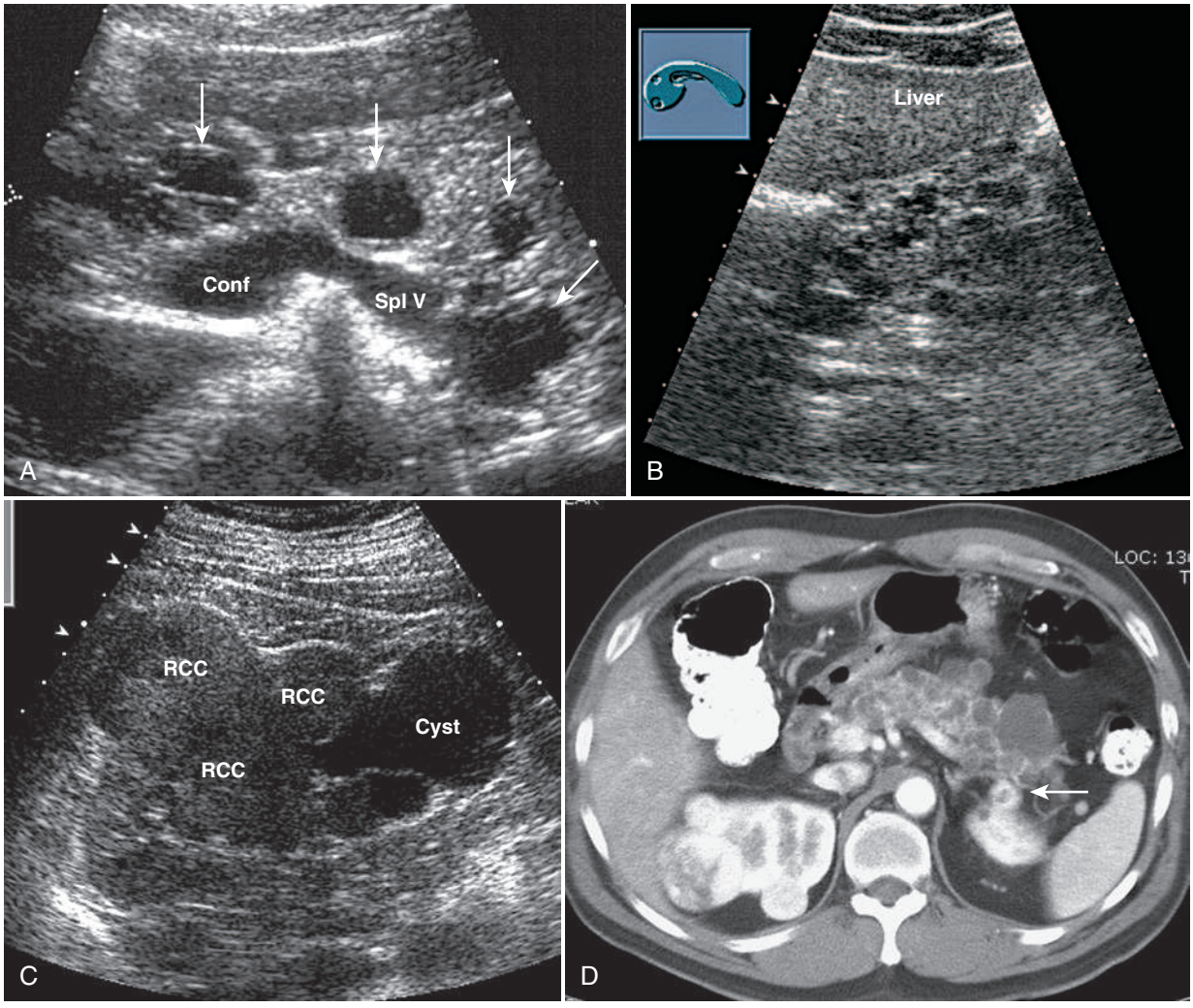

FIG. 7.75 Von Hippel–Lindau (VHL) Disease With Multiple Pancreatic Cysts. (A) Transverse sonogram shows multiple simple pancreatic cysts *(arrows).* **(B)-(D)** Another patient. **(B)** Transverse sonogram of pancreas shows multiple pancreatic cysts, suggesting the diagnosis of von Hippel–Lindau disease. **(C)** Longitudinal sonogram of the right kidney shows associated VHL lesions: multiple renal cell carcinomas *(RCC)* and a large renal cyst. **(D)** Computed tomography image at a similar level shows myriad pancreatic cysts and some of the right-sided RCCs. A small, left-sided RCC is noted *(arrow). Conf,* Confluence; *Spl V,* splenic vein.

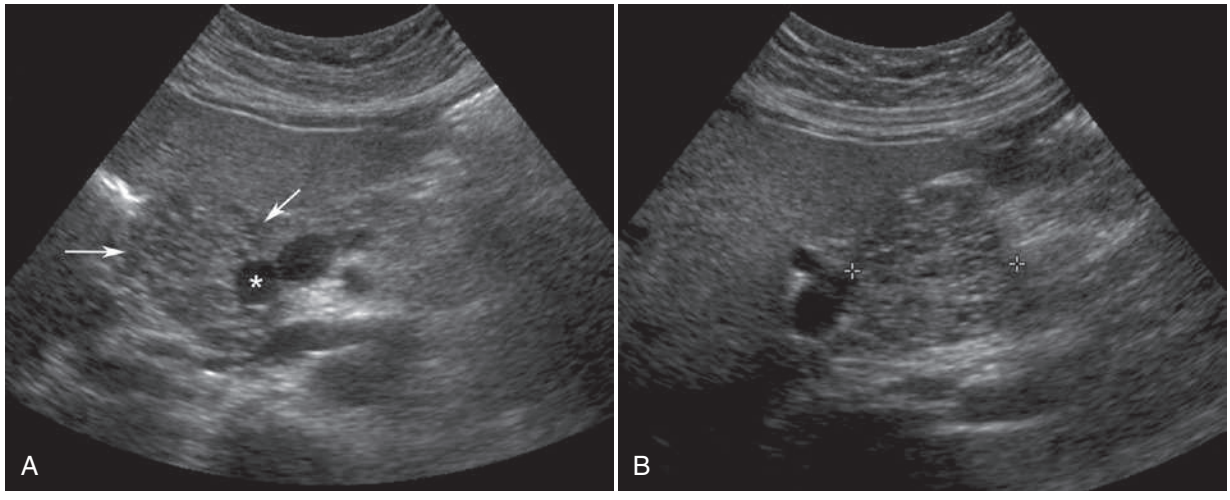

FIG. 7.76 Serous Cystic Neoplasm. (A) Transverse sonogram shows classic serous cystic neoplasm findings, with many tiny cysts resulting in an echogenic and nearly solid appearance *(arrows);* a larger cystic component is seen at the periphery of the lesion (*). Note lack of pancreatic duct dilation. **(B)** Sagittal sonogram shows classic serous cystic neoplasm findings, including many tiny cysts. No normal pancreas is shown.

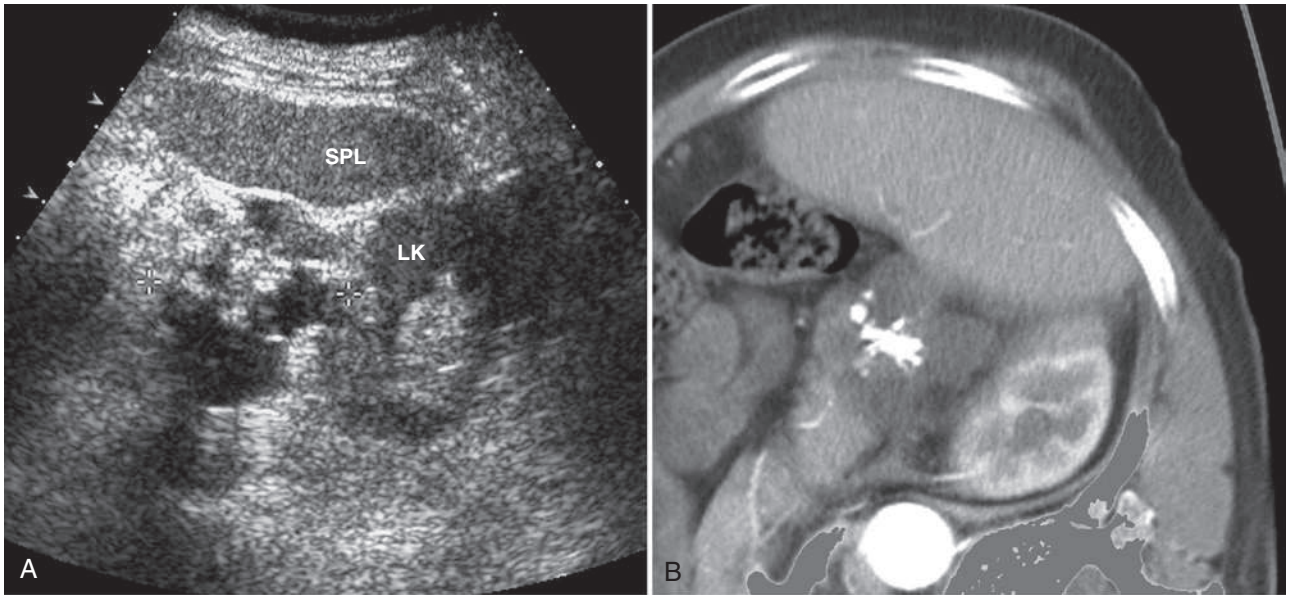

FIG. 7.77 Serous Cystic Neoplasm. (A) Transverse sonogram shows lesion through the spleen *(SPL)* and left kidney *(LK)*. Calcifications and some larger peripheral cysts are noted. **(B)** Computed tomography image, rotated and cropped to match the ultrasound image, shows the dense calcifications.

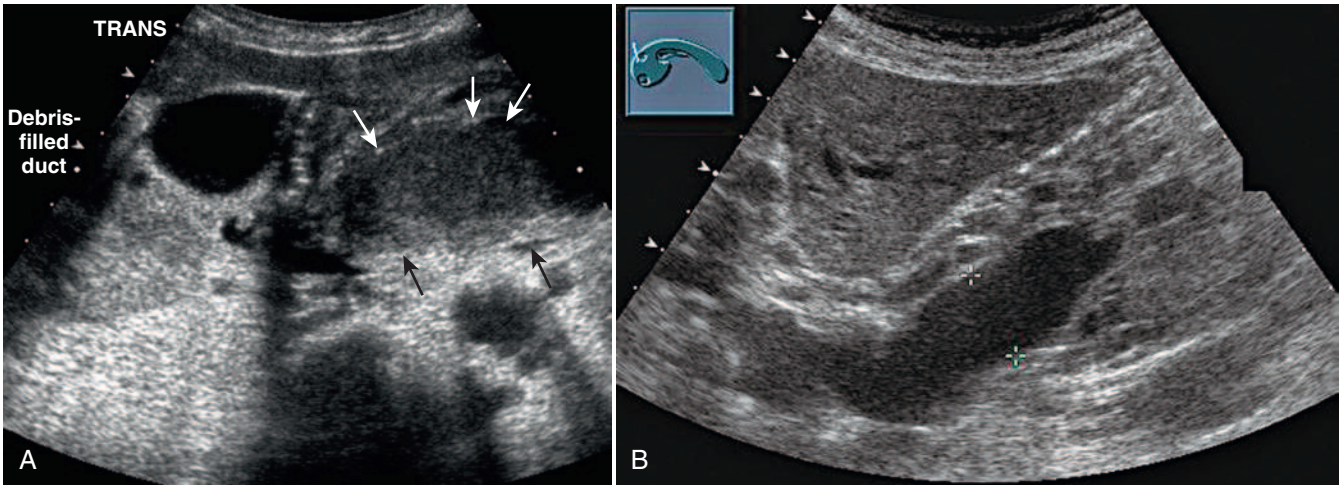

FIG. 7.78 Intraductal Papillary Mucinous Neoplasm (IPMN). (A) Transverse sonogram shows massively dilated main pancreatic duct *(white and black arrows)* filled with mucin, characteristic of main duct IPMN. **(B)** Another patient in whom a longitudinal oblique sonogram shows IPMN causing massive bile duct obstruction. Both benign and malignant IPMNs can cause bile duct obstruction. See also Video 7.9.

Intraductal Papillary Mucinous Neoplasm

Intraductal papillary mucinous neoplasm (IPMN) was unreported before 1982[167]; other names include **intraductal papillary mucinous tumor, intraductal mucin-hypersecreting neoplasm,** and **ductectatic mucinous neoplasm.**[154] Unlike mucinous cystic neoplasm, IMPN arises from the pancreatic ducts, usually in the head of the pancreas. IMPN occurs in an older population than mucinous cystic neoplasm and affects men and women equally.

Mucin is secreted into the ducts, causing prominent dilation (Fig. 7.78, Video 7.9) and sometimes mucin extrusion from the ampulla of Vater.[166] IPMN often presents as acute pancreatitis. Both benign and malignant lesions can cause bile duct obstruction[168] (Fig. 7.79). IPMN ranges from a benign to an overtly malignant lesion. Invasive adenocarcinoma is seen in approximately 30% of resected cases. Invasive or in situ carcinomas are likely present in about 70% of patients.[149] The overall 5-year survival rate for patients with a resected IPMN is higher than 70%.[166] Controversy surrounds the evolving management of these patients. Some believe that asymptomatic patients or those with lesions of branch duct origin can be observed or treated with segmental pancreatectomy.[169]

The hallmark of IPMN on ultrasound is **ductal dilation** (Fig. 7.80; see also Fig. 7.78). Findings include lobulated multicystic dilation of the branch ducts, diffuse dilation of the main pancreatic duct, and intraductal papillary tumors.[170] Because mucin has a

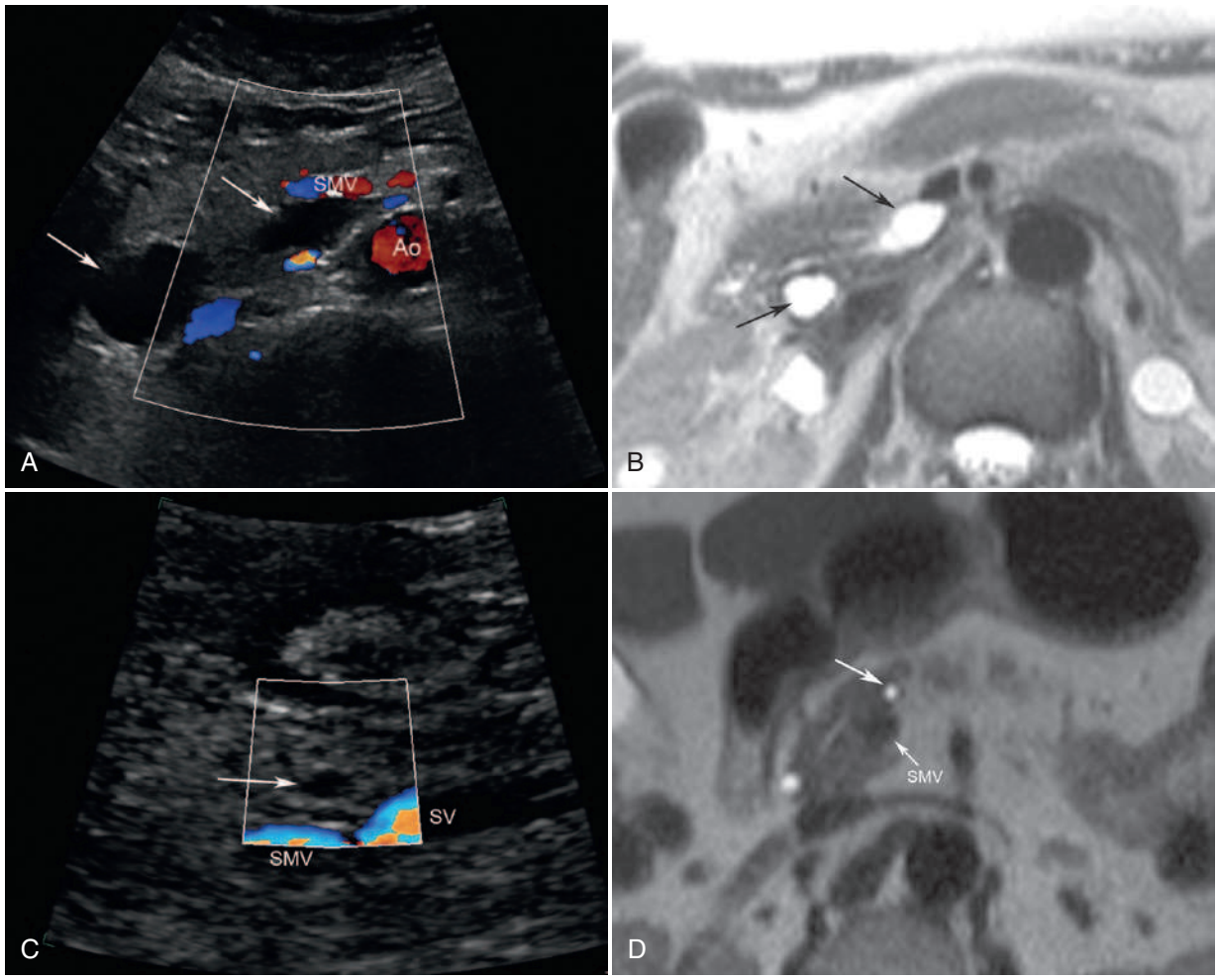

FIG. 7.79 Side Branch Intraductal Papillary Mucinous Neoplasm (IPMN). (A) Transverse image of pancreatic head and neck shows two cystic lesions *(arrows)* corresponding to side branch IPMN. **(B)** Transverse T2-weighted single-shot fast spin echo (SSFSE) magnetic resonance (MR) image of side branch IPMN lesions *(arrows)* shown in **(A)**. **(C)** In another patient, transverse sonographic image depicts a smaller side branch IPMN *(arrow)* in pancreatic body. **(D)** Corresponding axial T2-weighted SSFSE MR image shows same IPMN *(arrow). Ao,* Aorta; *SMV,* superior mesenteric vein; *SV,* splenic vein.

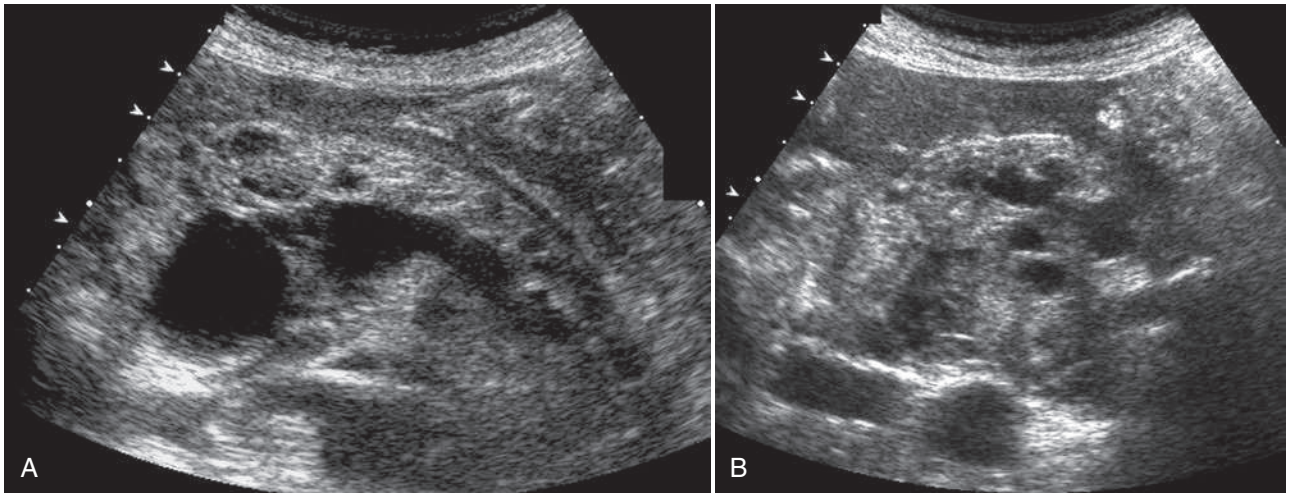

FIG. 7.80 Intraductal Papillary Mucinous Neoplasm (IPMN). IPMN with main and branch duct involvement. **(A)** Transverse sonogram shows lobulated dilation of the branch ducts and diffuse dilation of the main pancreatic duct. **(B)** Transverse sonogram of pancreatic head and proximal body shows dilation of branch ducts in the enlarged head.

sonographic appearance that may be similar to debris or sludge, the degree and extent of ductal dilation may be more difficult to appreciate on ultrasound than on CT or MRI. Calcification is rare.

Mucinous Cystic Neoplasm

Mucinous cystic neoplasms arise as de novo cystic tumors, unlike IPMNs, which arise from the pancreatic ducts. Mucinous cystic neoplasms occur most often in the pancreatic body or tail but may occur anywhere in the gland.[169] They may be unilocular and simulate a simple cyst but generally have up to six internal loculations. Internal septations may be thin or thick, and may be papillary; internal debris is common (Fig. 7.81, Video 7.10). Calcifications, usually linear and peripheral, occur in about 15% to 20% of lesions. Mucinous cystic neoplasm is found in perimenopausal women as thick-walled multilocular cystic masses, usually in the tail of the pancreas.[166]

Mucinous cystic neoplasm is the lesion most likely to be confused with pseudocyst because of their similar appearance in some cases. Mucinous cystic neoplasm shares histologic and prognostic similarities with mucinous ovarian cystic tumors. Because of the newer pathologic definition that requires the

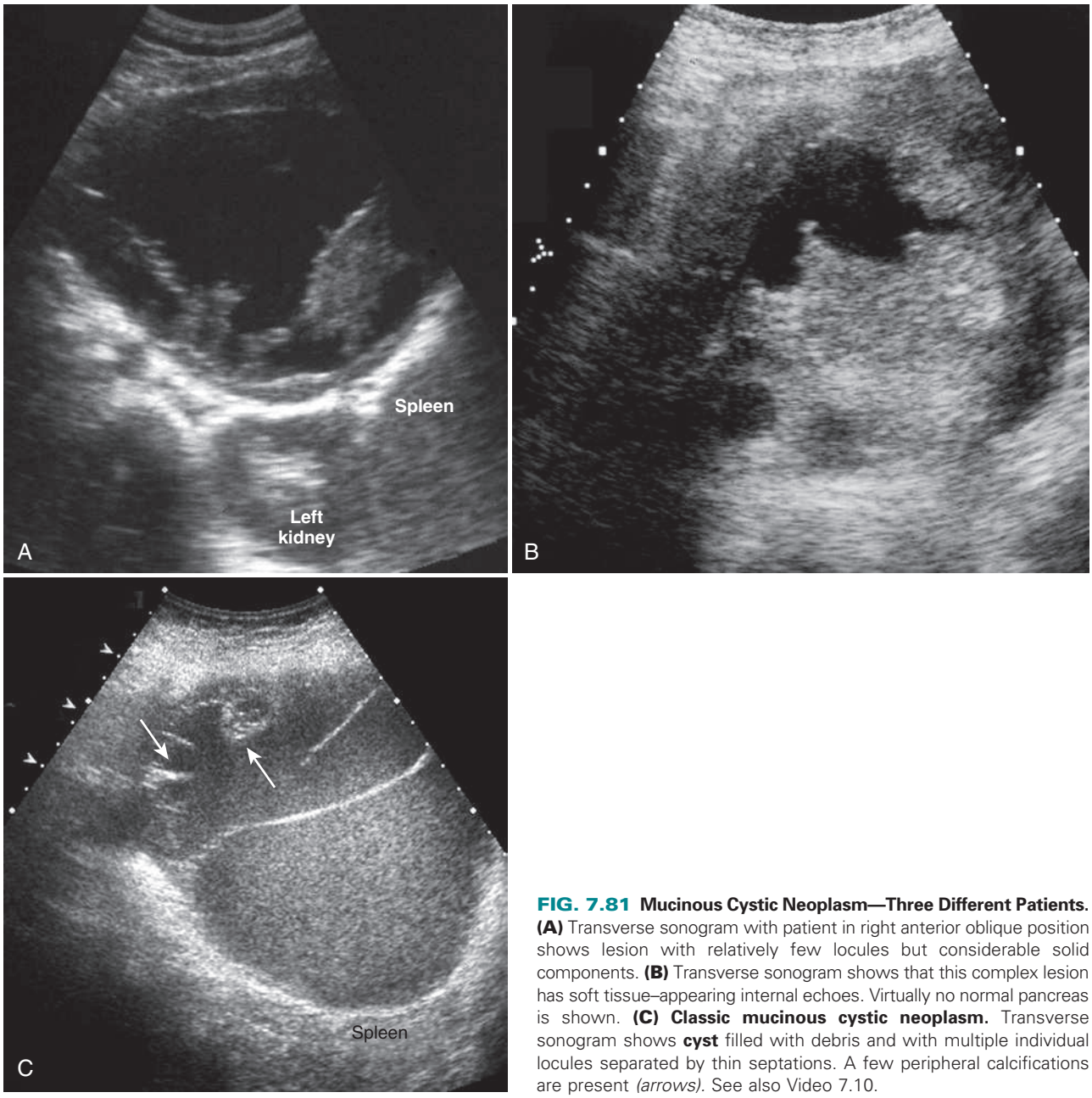

FIG. 7.81 Mucinous Cystic Neoplasm—Three Different Patients. **(A)** Transverse sonogram with patient in right anterior oblique position shows lesion with relatively few locules but considerable solid components. **(B)** Transverse sonogram shows that this complex lesion has soft tissue–appearing internal echoes. Virtually no normal pancreas is shown. **(C) Classic mucinous cystic neoplasm.** Transverse sonogram shows **cyst** filled with debris and with multiple individual locules separated by thin septations. A few peripheral calcifications are present *(arrows)*. See also Video 7.10.

presence of ovarian stroma in mucinous cystic neoplasm, these tumors are now rarely diagnosed in men.[166,171] Mucinous tumors, previously classified as mucinous cystic neoplasms in men, would likely now be considered IPMNs. Mucinous cystic neoplasms may be benign, may have "low malignant potential," or may be overtly malignant. Thus these tumors are generally managed as malignant lesions.

Solid-Pseudopapillary Tumor

Solid-pseudopapillary tumor is the most recent name advocated by the World Health Organization[172,173] and is found most frequently in young female patients. Previous names include **solid and cystic tumor, solid and papillary epithelial neoplasm, papillary-cystic neoplasm, papillary cystic epithelial neoplasm, papillary cystic tumor,** and **Frantz tumor.** About 15% of solid-pseudopapillary tumors are malignant. The likelihood of malignancy increases with patient age.[154] Resection is generally curative.

Solid-pseudopapillary tumors occur most often in the tail of the pancreas. They are usually round, encapsulated masses[174] with variable amounts of necrotic, cystic-appearing areas and soft tissue foci (Fig. 7.82). The cavities in solid-pseudopapillary tumors are not "true" cysts but rather necrotic regions containing blood and debris.[166] Central and rim calcifications have been reported in 29% of patients.[154] Buetow et al.[175] described 31 cases studied with ultrasound, CT, and MRI and noted variable echotexture; anechoic and hypoechoic areas were seen centrally. Through transmission was seen in all cases in which internal cystic areas were grossly depicted, regardless of the echotexture.

FIG. 7.82 Large Solid-Pseudopapillary Tumor. Transverse sonogram shows a large lesion in the pancreatic tail, the most common location for these tumors.

Rare Cystic Pancreatic Tumors

Acinar cell cystadenocarcinoma
Cystic choriocarcinoma
Cystic lymphangioma
Cystic teratoma
Cystic pancreatic endocrine tumor
Metastases

Rare Cystic Tumors

Virtually any imaginable histology has been reported as a "necrotic" or "cystic" lesion of the pancreas.[165,176-178] In general, there is no characteristic ultrasound appearance for these rare tumors.

OTHER PANCREATIC MASSES

Endocrine Tumors

Pancreatic endocrine tumors are a small but important group of pancreatic neoplasms, previously called **islet cell tumors** or **neuroendocrine tumors;** the current suggested terminology is **gastroenteropancreatic neuroendocrine tumors (GEP-NETs).**[179] Formerly thought to arise from pancreatic islets, these tumors are now believed to originate from neuroendocrine stem cells in the duct epithelium.[180] These tumors are rare, with an annual incidence of approximately 5 cases per million.[181] Pancreatic endocrine tumors constitute 1% to 5% of pancreatic neoplasms.[182] The two different presentations depend on whether there is endocrine hyperfunction.[183] **Hyperfunctioning** lesions, about 90% of pancreatic endocrine tumors tend to present clinically when the tumor is small. The endocrine manifestations cause clinical symptoms before the tumor grows enough to cause problems because of its size, invasion, or metastasis.

Insulinomas and **gastrinomas** are the most common hyperfunctioning pancreatic endocrine tumors (about 80% of all pancreatic endocrine tumors); others are rare (Table 7.5).

Hyperfunctioning pancreatic endocrine tumors tend to be small, 1- to 3-cm (see Fig. 7.83), round or oval, hypoechoic masses with smooth margins and, with the exception of insulinoma, malignant. When a hyperfunctioning pancreatic endocrine tumor is suspected, preoperative localization is appropriate. Choice of modality depends on institutional preference and includes transabdominal ultrasound, CT, or endoscopic ultrasound.[184] MDCT is superior to sonography in detecting small endocrine tumors,[185] but sometimes ultrasound shows lesions that are occult on CT. It is difficult to image pancreatic endocrine tumors with conventional transabdominal sonography; they are usually small when the patient presents with hormonal abnormalities. Sensitivity of detection with ultrasound varies. Detection rates for insulinomas range from 9%[186] to 65%.[184] The sensitivity of ultrasound in the detection of gastrinoma is only 20% to 30%.[187] Sonographically, most **hyperfunctioning** pancreatic endocrine tumors are small. Serotonin-secreting pancreatic endocrine tumors may be associated with marked dilation of the pancreatic duct.[188,189] Intraoperative sonography is the most sensitive and accurate means of evaluating these neoplasms[184] (Fig. 7.83).

Nonhyperfunctioning tumors cause no endocrine-related symptoms. Therefore these tumors must be larger to present

TABLE 7.5 Pancreatic Endocrine Tumors (PETs)

Tumor Type	Located in Pancreas	Size	All PETs
	Hyperfunctioning		
Insulinoma	90%-100%	2-3 cm	45%
Gastrinoma	40%-60%	1-2 cm	35%
Others			10%
VIPoma	90%		
Glucagonoma	100%		
Somatostatinoma	50%-60%		
Carcinoid PET	100%		
	Nonhyperfunctioning		
All tumors		>5 cm	10%

VIP, Vasoactive intestinal polypeptide.

FIG. 7.83 Insulinoma on Intraoperative Ultrasound. This 10-mm lesion was discovered because of hyperinsulinism. (Courtesy of Dr. Hisham Tchelepi.)

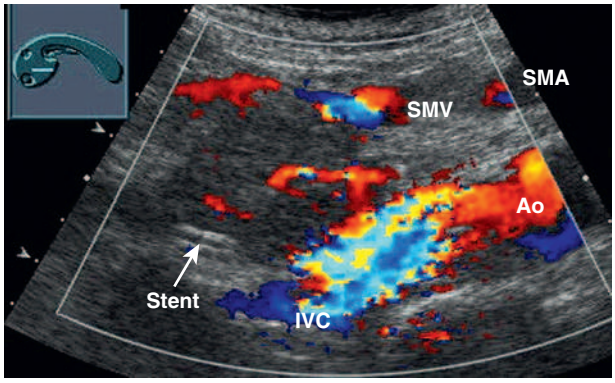

FIG. 7.84 Pancreatic Endocrine Tumor, Nonhyperfunctioning. Longitudinal oblique color Doppler sonogram shows 5-cm, hypoechoic malignant tumor large enough to cause bile duct obstruction, requiring stenting. Internal color flow is typical with pancreatic endocrine tumors. *Ao,* Aorta; *IVC,* interior vena cava; *SMA,* superior mesenteric artery; *SMV,* superior mesenteric vein.

clinically—because of pain,[185] mass effect, or, if malignant, invasion and metastasis[119] (Fig. 7.84). Incidental detection of smaller, nonhyperfunctioning tumors is becoming more frequent (Fig. 7.85). These tumors are usually well defined and round or oval. They generally appear hypoechoic compared to the normal parenchyma. These tumors may have cystic changes and calcification.[187] The larger, nonhyperfunctioning pancreatic endocrine tumors may be difficult to differentiate from the more common pancreatic ductal adenocarcinoma. Sonographic findings that suggest the diagnosis are (1) prominent internal color flow (rare in carcinoma), (2) lack of biliary or pancreatic ductal dilation in a pancreatic head lesion, and (3) lack of progression or metastasis on serial imaging.

Unusual and Rare Neoplasms

On ultrasound, many histologic variants of pancreatic ductal adenocarcinoma are indistinguishable from tumors with the usual histologic features. These include **adenosquamous cell carcinoma, anaplastic carcinoma,** and **pleomorphic giant cell carcinoma. Acinar cell carcinoma** and pleomorphic giant cell carcinoma, although often indistinguishable from ductal adenocarcinoma, may be larger and may exhibit central necrosis. Primary **pancreatic lymphoma** is prohibitively rare, although adenopathy or diffuse involvement from more generalized disease occurs with some frequency.[120] Other rare pancreatic tumors include connective tissue–origin tumors (sarcomas), **pancreaticoblastomas, dysontogenetic cysts,** and metastases.[190,191]

Lipoma

In contrast to the usual echogenic appearance of fat and fatty lesions, pancreatic lipomas are usually **hypoechoic**[192,193] (Fig. 7.86). Other lipomas may have a mixed appearance, with a variable amount of internal echoes, or they may appear hyperechoic. The cause of hypoechoic fat is not known but may involve the number

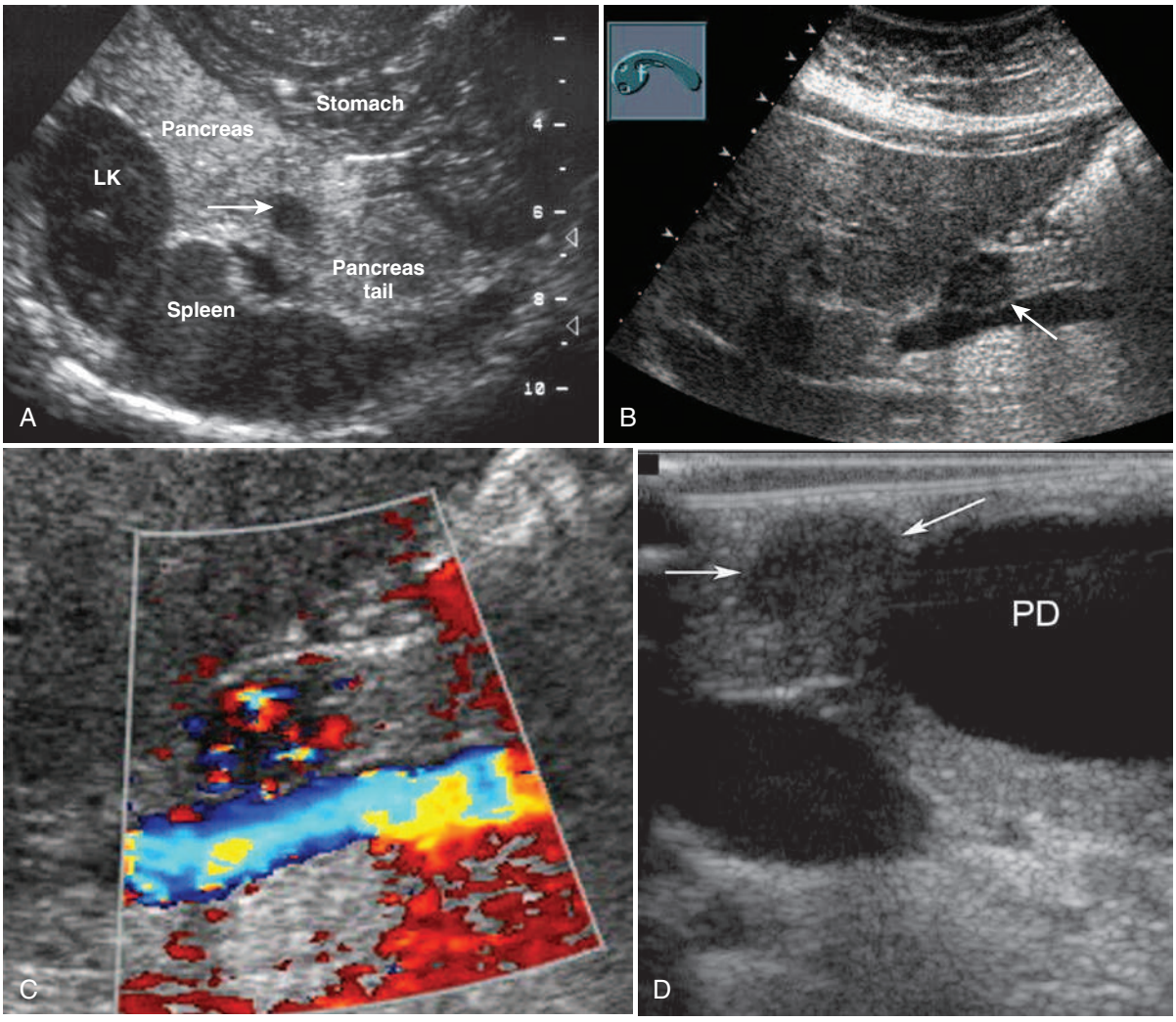

FIG. 7.85 Small, Nonhyperfunctioning Pancreatic Endocrine Tumors. (A) Transverse sonogram shows 9-mm hypoechoic nonhyperfunctioning pancreatic endocrine tumor *(arrow)* discovered incidentally during an abdominal ultrasound. The pancreatic tail was removed. **(B)** and **(C)** In another patient, gray-scale **(B)** and color Doppler **(C)** sonograms show 2-cm hypervascular pancreatic endocrine tumor indenting the superior mesenteric artery *(arrow).* **(D)** In another patient, **intraoperative ultrasound shows a** 9-mm lesion *(arrows)* that was discovered incidentally. Marked dilation of the pancreatic duct is noted and can be a hallmark of serotonin-secreting pancreatic endocrine tumors. Intraoperative ultrasound is considered essential in many institutions for the surgical management of pancreatic endocrine tumors. *PD,* Pancreatic duct.

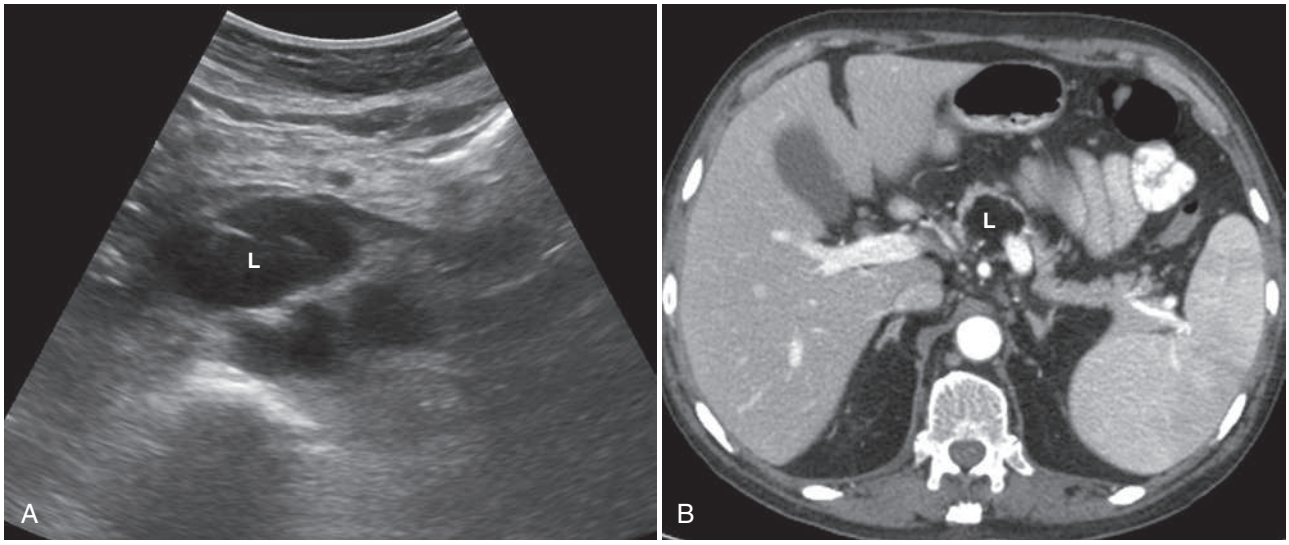

FIG. 7.86 Pancreatic Lipoma. (A) Transverse sonogram of almost anechoic pancreatic lipoma *(L).* In contrast to the usual echogenic appearance of fat and fatty lesions, pancreatic lipomas are usually hypoechoic. **(B)** Computed tomography image confirms the fatty nature of the lesion. (Courtesy of Dr. Vinay Duddlewar.)

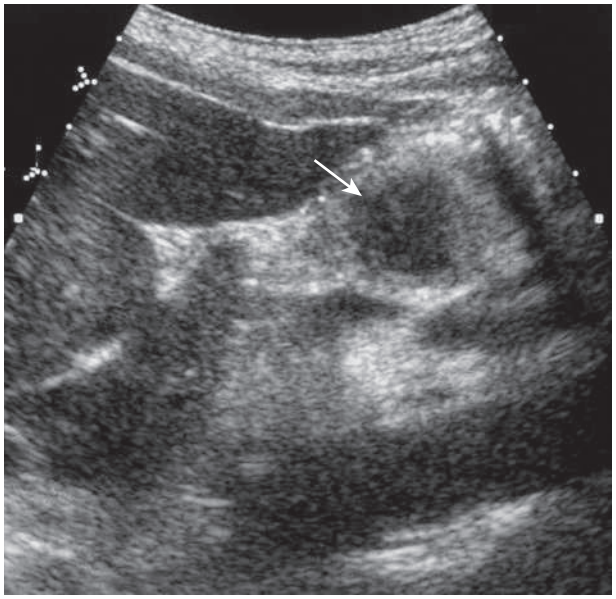

FIG. 7.87 Lung Carcinoma Metastasis to Pancreas. Longitudinal sonogram shows typical hypoechoic metastasis *(arrow)*. Pancreatic metastases are the most common pancreatic neoplasm in autopsy series but are rarely found clinically because they generally occur late with widespread metastatic disease.

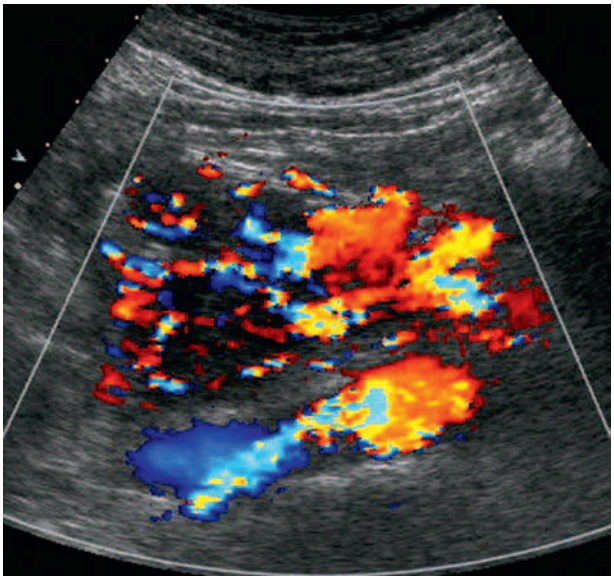

FIG. 7.88 Renal Cell Carcinoma Metastasis to Pancreas. Longitudinal color Doppler sonogram shows hypervascular metastasis. Differentiation from a hypervascular pancreatic endocrine tumor may be difficult in these cases.

of blood vessels, amount and thickness of connective tissue stroma, number of fibrous septae that separate fat lobules, and amount of water content in the fat.[192,194]

Metastatic Tumors

In autopsy series, metastasis is the most common pancreatic neoplasm, found about four times as often as pancreatic cancer.[191] Clinical discovery of metastasis was rare until the advent of modern imaging.[195] Pancreatic metastases are rarely clinically significant because they generally occur late in patients with widespread metastatic disease. Primary tumors that most often metastasize to the pancreas include **renal cell carcinoma, breast carcinoma, lung carcinoma** (Fig. 7.87), **melanoma, colon carcinoma,** and **stomach carcinoma.**[120,191,195]

With metastasis to the pancreas, there may be a long interval between initial diagnosis of the primary lesion and discovery of the metastasis. This is especially true of renal cell carcinoma and, to a lesser degree, melanoma. Klein et al.[195] found that the mean delay between discovery of the primary renal cell carcinoma and metastasis was 10 years; the longest interval was more than 24 years. A classic scenario is the discovery of a hypervascular mass (or masses) in the pancreas of a patient who had a remote, presumably cured renal cell carcinoma (Fig. 7.88). Differential diagnosis from a hypervascular pancreatic endocrine tumor may be difficult in such cases.

CONTRAST-ENHANCED ULTRASOUND

Contrast-enhanced ultrasound (CEUS) shows promise as a technique that will be beneficial in both endoscopic ultrasound and transabdominal ultrasound of the pancreas. Historically, CEUS was best considered an experimental technique.[98,196] However, more recent data suggest that CEUS may become much more routine.[197-199] Fan states, "CEUS has obvious superiority over conventional US in the general diagnostic accuracy of solid pancreatic lesions and in the diagnostic consistency among doctors. The performances of CEUS are similar to that of CECT in the diagnosis of pancreatic carcinoma and focal pancreatitis."[200] CEUS might be helpful in diagnosing pancreatic necrosis in patients with severe acute pancreatitis.[147]

Acknowledgment

The authors would like to acknowledge Dr. Philip Ralls, the prior author of this chapter. His supreme dedication and passion for quality ultrasound practice and education in all areas was exemplary, and his images and text form the backbone of this updated version.

REFERENCES

1. Harisinghani MG, Saini S, Schima W, et al. Simethicone coated cellulose as an oral contrast agent for ultrasound of the upper abdomen. Clin Radiol. 1997;52(3):224-226.
2. Lev-Toaff AS, Langer JE, Rubin DL, et al. Safety and efficacy of a new oral contrast agent for sonography: a phase II trial. AJR Am J Roentgenol. 1999;173(2):431-436.
3. Abu-Yousef MM, El-Zein Y. Improved US visualization of the pancreatic tail with simethicone, water, and patient rotation. Radiology. 2000;217(3):780-785.
4. Mori H, McGrath FP, Malone DE, Stevenson GW. The gastrocolic trunk and its tributaries: CT evaluation. Radiology. 1992;182(3):871-877.
5. Winter 3rd TC. "Proximal" versus "distal" in the pancreas. Radiographics. 2013;33(2):622-623.
6. Glaser J, Stienecker K. Pancreas and aging: a study using ultrasonography. Gerontology. 2000;46(2):93-96.
7. Guerra M, Gutiérrez L, Carrasco R, Arroyo A. Size and echogenicity of the pancreas in Chilean adults: echotomography study in 261 patients]. Rev Med Chil. 1995;123(6):720-726.

8. Bolondi L, Li Bassi S, Gaiani S, Barbara L. Sonography of chronic pancreatitis. Radiol Clin North Am. 1989;27(4):815-833.
9. Mortele KJ, Rocha TC, Streeter JL, Taylor AJ. Multimodality imaging of pancreatic and biliary congenital anomalies. Radiographics. 2006;26(3):715-731.
10. Daneman A, Gaskin K, Martin DJ, Cutz E. Pancreatic changes in cystic fibrosis: CT and sonographic appearances. AJR Am J Roentgenol. 1983;141(4):653-655.
11. So CB, Cooperberg PL, Gibney RG, Bogoch A. Sonographic findings in pancreatic lipomatosis. AJR Am J Roentgenol. 1987;149(1):67-68.
12. Coccia P, Ruggerio A, Attinà G, et al. Shwachman-Diamond syndrome: an emergency challenge. Signa Vitae. 2007;2:10-13.
13. Marchal G, Verbeken E, Van Steenbergen W, et al. Uneven lipomatosis: a pitfall in pancreatic sonography. Gastrointest Radiol. 1989;14(3):233-237.
14. Donald JJ, Shorvon PJ, Lees WR. A hypoechoic area within the head of the pancreas—a normal variant. Clin Radiol. 1990;41(5):337-338.
15. Atri M, Nazarnia S, Mehio A, et al. Hypoechogenic embryologic ventral aspect of the head and uncinate process of the pancreas: in vitro correlation of US with histopathologic findings. Radiology. 1994;190(2):441-444.
16. Coulier B. Hypoechogenic aspects of the ventral embryonic cephalic pancreas: a large prospective clinical study]. J Belge Radiol. 1996;79(3): 120-124.
17. Yu J, Turner MA, Fulcher AS, Halvorsen RA. Congenital anomalies and normal variants of the pancreaticobiliary tract and the pancreas in adults: part 2, Pancreatic duct and pancreas. AJR Am J Roentgenol. 2006;187(6):1544-1553.
18. Misra SP, Dwivedi M. Pancreaticobiliary ductal union. Gut. 1990;31(10):1144-1149.
19. Dawson W, Langman J. An anatomical-radiological study on the pancreatic duct pattern in man. Anat Rec. 1961;139:59-68.
20. Hadidi A. Pancreatic duct diameter: sonographic measurement in normal subjects. J Clin Ultrasound. 1983;11(1):17-22.
21. Wachsberg RH. Respiratory variation of the diameter of the pancreatic duct on sonography. AJR Am J Roentgenol. 2000;175(5):1459-1461.
22. Glaser J, Hogemann B, Krummenerl T, et al. Sonographic imaging of the pancreatic duct. New diagnostic possibilities using secretin stimulation. Dig Dis Sci. 1987;32(10):1075-1081.
23. Borghei P, Sokhandon F, Shirkhoda A, Morgan DE. Anomalies, anatomic variants, and sources of diagnostic pitfalls in pancreatic imaging. Radiology. 2013;266(1):28-36.
24. Petrone MC, Arcidiacono PG, Testoni PA. Endoscopic ultrasonography for evaluating patients with recurrent pancreatitis. World J Gastroenterol. 2008;14(7):1016-1022.
25. Delhay M, Matos C, Deviere J. Acute relapsing pancreatitis. Congenital variants: diagnosis, treatment, outcome. JOP. 2001;2(6):373-381.
26. Klein SD, Affronti JP. Pancreas divisum, an evidence-based review: part I, pathophysiology. Gastrointest Endosc. 2004;60(3):419-425.
27. Bollen TL, van Santvoort HC, Besselink MG, et al. The Atlanta Classification of acute pancreatitis revisited. Br J Surg. 2008;95(1):6-21.
28. Zaheer A, Singh VK, Qureshi RO, Fishman EK. The revised Atlanta classification for acute pancreatitis: updates in imaging terminology and guidelines. Abdom Imaging. 2013;38(1):125-136.
29. Vege SS, Yadav D, Chari ST. Pancreatitis. In: Talley NJ, Locke GR, Saito YA, editors. Gastrointestinal epidemiology. Malden, Mass: Blackwell; 2007.
30. Tenner S, Sica G, Hughes M, et al. Relationship of necrosis to organ failure in severe acute pancreatitis. Gastroenterology. 1997;113(3):899-903.
31. Swaroop VS, Chari ST, Clain JE. Severe acute pancreatitis. JAMA. 2004;291(23):2865-2868.
32. Banks PA, Freeman ML. Practice guidelines in acute pancreatitis. Am J Gastroenterol. 2006;101(10):2379-2400.
33. Bradley 3rd EL. A clinically based classification system for acute pancreatitis. Summary of the International Symposium on Acute Pancreatitis, Atlanta, Ga, September 11 through 13, 1992. Arch Surg. 1993;128(5):586-590.
34. Banks PA, Bollen TL, Dervenis C, et al. Classification of acute pancreatitis—2012: revision of the Atlanta classification and definitions by international consensus. Gut. 2013;62(1):102-111.
35. Thoeni RF. The revised Atlanta classification of acute pancreatitis: its importance for the radiologist and its effect on treatment. Radiology. 2012;262(3):751-764.
36. Topazian M, Gorelick FS. Acute pancreatitis. In: Yamada T, Alpers DH, Kaplowitz N, et al., editors. Textbook of gastroenterology. Philadelphia: Lippincott-Williams & Wilkins; 2003. p. 2026.
37. Finstad TA, Tchelepi H, Ralls PW. Sonography of acute pancreatitis: prevalence of findings and pictorial essay. Ultrasound Q. 2005;21(2):95-104.
38. Riela A, Zinsmeister AR, Melton LJ, DiMagno EP. Etiology, incidence and survival of acute pancreatitis in Olmsted County, Minnesota. Gastroenterology. 1991;100.
39. Everhart JE, Khare M, Hill M, Maurer KR. Prevalence and ethnic differences in gallbladder disease in the United States. Gastroenterology. 1999;117(3):632-639.
40. Collins C, Maguire D, Ireland A, et al. A prospective study of common bile duct calculi in patients undergoing laparoscopic cholecystectomy: natural history of choledocholithiasis revisited. Ann Surg. 2004;239(1):28-33.
41. Dong B, Chen M. Improved sonographic visualization of choledocholithiasis. J Clin Ultrasound. 1987;15(3):185-190.
42. Laing FC, Jeffrey RB, Wing VW. Improved visualization of choledocholithiasis by sonography. AJR Am J Roentgenol. 1984;143(5):949-952.
43. Kelly TR, Wagner DS. Gallstone pancreatitis: a prospective randomized trial of the timing of surgery. Surgery. 1988;104(4):600-605.
44. Neoptolemos JP, Carr-Locke DL, London NJ, et al. Controlled trial of urgent endoscopic retrograde cholangiopancreatography and endoscopic sphincterotomy versus conservative treatment for acute pancreatitis due to gallstones. Lancet. 1988;2:979-983.
45. Fan ST, Lai EC, Mok FP, et al. Early treatment of acute biliary pancreatitis by endoscopic papillotomy. N Engl J Med. 1993;328(4):228-232.
46. Nowak A, Nowakowska-Dulawa E, Marek TA, et al. Final results of the prospective, randomized controlled study on endoscopic sphincterotomy versus conventional management in acute biliary pancreatitis. Gastroenterology. 1995;105:380.
47. Folsch UR, Nitsche R, Ludtke R, et al. Early ERCP and papillotomy compared with conservative treatment for acute biliary pancreatitis. The German Study Group on Acute Biliary Pancreatitis. N Engl J Med. 1997;336(4):237-242.
48. Acosta JM, Katkhouda N, Debian KA, et al. Early ductal decompression versus conservative management for gallstone pancreatitis with ampullary obstruction: a prospective randomized clinical trial. Ann Surg. 2006;243(1):33-40.
49. Lee SP, Nicholls JF, Park HZ. Biliary sludge as a cause of acute pancreatitis. N Engl J Med. 1992;326(9):589-593.
50. Kinney TP, Freeman ML. Approach to acute, recurrent, and chronic pancreatitis. Minn Med. 2008;91(6):29-33.
51. Lin A, Feller ER. Pancreatic carcinoma as a cause of unexplained pancreatitis: report of ten cases. Ann Intern Med. 1990;113(2):166-167.
52. Johnson CD, Stephens DH, Sarr MG. CT of acute pancreatitis: correlation between lack of contrast enhancement and pancreatic necrosis. AJR Am J Roentgenol. 1991;156(1):93-95.
53. Pederzoli P, Bassi C, Vesentini S, Campedelli A. A randomized multicenter clinical trial of antibiotic prophylaxis of septic complications in acute necrotizing pancreatitis with imipenem. Surg Gynecol Obstet. 1993;176(5): 480-483.
54. Banks PA. Acute pancreatitis: medical and surgical management. Am J Gastroenterol. 1994;89(8 Suppl.):S78-S85.
55. Dambrauskas Z, Gulbinas A, Pundzius J, Barauskas G. Meta-analysis of prophylactic parenteral antibiotic use in acute necrotizing pancreatitis. Medicina (Kaunas). 2007;43(4):291-300.
56. Sharma VK, Howden CW. Prophylactic antibiotic administration reduces sepsis and mortality in acute necrotizing pancreatitis: a meta-analysis. Pancreas. 2001;22(1):28-31.
57. Verma D, Kapadia A, Eisen GM, Adler DG. EUS vs MRCP for detection of choledocholithiasis. Gastrointest Endosc. 2006;64(2):248-254.
58. Miller FH, Keppke AL, Dalal K, et al. MRI of pancreatitis and its complications: part 1, acute pancreatitis. AJR Am J Roentgenol. 2004;183(6): 1637-1644.
59. Arvanitakis M, Delhaye M, De Maertelaere V, et al. Computed tomography and magnetic resonance imaging in the assessment of acute pancreatitis. Gastroenterology. 2004;126(3):715-723.
60. Chak A, Hawes RH, Cooper GS, et al. Prospective assessment of the utility of EUS in the evaluation of gallstone pancreatitis. Gastrointest Endosc. 1999;49(5):599-604.

61. Kimmey MB, Vilmann P. Endoscopic ultrasonography. In: Yamada T, Alpers DH, Kaplowitz N, et al., editors. Textbook of gastroenterology. 4th ed. Philadelphia: Lippincott-Williams & Wilkins; 2003.
62. Baillie J. Endoscopic therapy in acute recurrent pancreatitis. World J Gastroenterol. 2008;14(7):1034-1037.
63. NIH Consensus. NIH state-of-the-science statement on endoscopic retrograde cholangiopancreatography (ERCP) for diagnosis and therapy. NIH Consens State Sci Statements. 2002;19(1):1-26.
64. Nam JH, Murthy S. Acute pancreatitis—the current status in management. Expert Opin Pharmacother. 2003;4(2):235-241.
65. Clavien PA, Robert J, Meyer P, et al. Acute pancreatitis and normoamylasemia. Not an uncommon combination. Ann Surg. 1989;210(5):614-620.
66. Lankisch PG, Schirren CA, Kunze E. Undetected fatal acute pancreatitis: why is the disease so frequently overlooked? Am J Gastroenterol. 1991;86(3):322-326.
67. Cotton PB, Lees WR, Vallon AG, et al. Gray-scale ultrasonography and endoscopic pancreatography in pancreatic diagnosis. Radiology. 1980;134(2):453-459.
68. Martínez-Noguera A, D'Onofrio M. Ultrasonography of the pancreas. 1. Conventional imaging. Abdom Imaging. 2007;32(2):136-149.
69. Kourtesis G, Wilson SE, Williams RA. The clinical significance of fluid collections in acute pancreatitis. Am Surg. 1990;56(12):796-799.
70. Lenhart DK, Balthazar EJ. MDCT of acute mild (nonnecrotizing) pancreatitis: abdominal complications and fate of fluid collections. AJR Am J Roentgenol. 2008;190(3):643-649.
71. Andrén-Sandberg A, Ansorge C, Eiriksson K, et al. Treatment of pancreatic pseudocysts. Scand J Surg. 2005;94(2):165-175.
72. Garcea G, Ong SL, Rajesh A, et al. Cystic lesions of the pancreas. A diagnostic and management dilemma. Pancreatology. 2008;8(3):236-251.
73. Gasslander T, Arnelo U, Albiin N, Permert J. Cystic tumors of the pancreas. Dig Dis. 2001;19(1):57-62.
74. Aghdassi A, Mayerle J, Kraft M, et al. Diagnosis and treatment of pancreatic pseudocysts in chronic pancreatitis. Pancreas. 2008;36(2):105-112.
75. Singhal D, Kakodkar R, Sud R, Chaudhary A. Issues in management of pancreatic pseudocysts. JOP. 2006;7(5):502-507.
76. Kim YH, Saini S, Sahani D, et al. Imaging diagnosis of cystic pancreatic lesions: pseudocyst versus nonpseudocyst. Radiographics. 2005;25(3):671-685.
77. Visser BC, Yeh BM, Qayyum A, et al. Characterization of cystic pancreatic masses: relative accuracy of CT and MRI. AJR Am J Roentgenol. 2007;189(3):648-656.
78. Yeo CJ, Bastidas JA, Lynch-Nyhan A, et al. The natural history of pancreatic pseudocysts documented by computed tomography. Surg Gynecol Obstet. 1990;170(5):411-417.
79. Cheruvu CV, Clarke MG, Prentice M, Eyre-Brook IA. Conservative treatment as an option in the management of pancreatic pseudocyst. Ann R Coll Surg Engl. 2003;85(5):313-316.
80. Bergman S, Melvin WS. Operative and nonoperative management of pancreatic pseudocysts. Surg Clin North Am. 2007;87(6):1447-1460, ix.
81. Gupta R, Munoz JC, Garg P, et al. Mediastinal pancreatic pseudocyst—a case report and review of the literature. Medgenmed. 2007;9(2):8.
82. Wechalekar M, Falodia S, Gamanagatti S, Makharia GK. An extension of pancreatic pseudocysts in the neck. Pancreas. 2007;34(1):171-173.
83. Erzurum VZ, Obermeyer R, Chung D. Pancreatic pseudocyst masquerading as an incarcerated inguinal hernia. South Med J. 2000;93(2):221-222.
84. Lang EK, Paolini RM, Pottmeyer A. The efficacy of palliative and definitive percutaneous versus surgical drainage of pancreatic abscesses and pseudocysts: a prospective study of 85 patients. South Med J. 1991;84(1):55-64.
85. Nealon WH, Walser E. Main pancreatic ductal anatomy can direct choice of modality for treating pancreatic pseudocysts (surgery versus percutaneous drainage). Ann Surg. 2002;235(6):751-758.
86. Baril NB, Ralls PW, Wren SM, et al. Does an infected peripancreatic fluid collection or abscess mandate operation? Ann Surg. 2000;231(3):361-367.
87. Flati G, Salvatori F, Porowska B, et al. Severe hemorrhagic complications in pancreatitis. Ann Ital Chir. 1995;66(2):233-237.
88. Risti B, Marincek B, Jost R, et al. Hemosuccus pancreaticus as a source of obscure upper gastrointestinal bleeding: three cases and literature review. Am J Gastroenterol. 1995;90(10):1878-1880.
89. Agarwal AK, Raj Kumar K, Agarwal S, Singh S. Significance of splenic vein thrombosis in chronic pancreatitis. Am J Surg. 2008;196(2):149-154.
90. Bernades P, Baetz A, Levy P, et al. Splenic and portal venous obstruction in chronic pancreatitis. A prospective longitudinal study of a medical-surgical series of 266 patients. Dig Dis Sci. 1992;37(3):340-346.
91. Witt H, Apte MV, Keim V, Wilson JS. Chronic pancreatitis: challenges and advances in pathogenesis, genetics, diagnosis, and therapy. Gastroenterology. 2007;132(4):1557-1573.
92. Behrman SW, Fowler ES. Pathophysiology of chronic pancreatitis. Surg Clin North Am. 2007;87(6):1309-1324, vii.
93. Etemad B, Whitcomb DC. Chronic pancreatitis: diagnosis, classification, and new genetic developments. Gastroenterology. 2001;120(3):682-707.
94. Ralls PW, Halls J, Renner I, Juttner H. Endoscopic retrograde cholangiopancreatography (ERCP) in pancreatic disease: a reassessment of the specificity of ductal abnormalities indifferentiating benign from malignant disease. Radiology. 1980;134(2):347-352.
95. Vijungco JD, Prinz RA. Management of biliary and duodenal complications of chronic pancreatitis. World J Surg. 2003;27(11):1258-1270.
96. Kim DH, Pickhardt PJ. Radiologic assessment of acute and chronic pancreatitis. Surg Clin North Am. 2007;87(6):1341-1358, viii.
97. Del Frate C, Zanardi R, Mortele K, Ros PR. Advances in imaging for pancreatic disease. Curr Gastroenterol Rep. 2002;4(2):140-148.
98. Kinney TP, Freeman ML. Recent advances and novel methods in pancreatic imaging. Minerva Gastroenterol Dietol. 2008;54(1):85-95.
99. Rizk MK, Gerke H. Utility of endoscopic ultrasound in pancreatitis: a review. World J Gastroenterol. 2007;13(47):6321-6326.
100. Rahmouni A, Bargoin R, Herment A, et al. Color Doppler twinkling artifact in hyperechoic regions. Radiology. 1996;199(1):269-271.
101. Sakorafas GH, Tsiotou AG. Splenic-vein thrombosis complicating chronic pancreatitis. Scand J Gastroenterol. 1999;34(12):1171-1177.
102. Rosch W, Lux G, Riemann JF, Hoh L. Chronic pancreatitis and the neighboring organs]. Fortschr Med. 1981;99(29):1118-1121.
103. Miller FH, Keppke AL, Wadhwa A, et al. MRI of pancreatitis and its complications: part 2, chronic pancreatitis. AJR Am J Roentgenol. 2004;183(6):1645-1652.
104. Chawla Y, Dilawari JB, Katariya S. Gallbladder varices in portal vein thrombosis. AJR Am J Roentgenol. 1994;162(3):643-645.
105. Ralls PW, Mayekawa DS, Lee KP, et al. Gallbladder wall varices: diagnosis with color flow Doppler sonography. J Clin Ultrasound. 1988;16(8):595-598.
106. Rosen IE, Wilson SR. Varices of the gallbladder. J Can Assoc Radiol. 1980;31(1):73-74.
107. DelMaschio A, Vanzulli A, Sironi S, et al. Pancreatic cancer versus chronic pancreatitis: diagnosis with CA 19-9 assessment, US, CT, and CT-guided fine-needle biopsy. Radiology. 1991;178(1):95-99.
108. Yadav D, Notahara K, Smyrk TC, et al. Idiopathic tumefactive chronic pancreatitis: clinical profile, histology, and natural history after resection. Clin Gastroenterol Hepatol. 2003;1(2):129-135.
109. Abraham SC, Wilentz RE, Yeo CJ, et al. Pancreaticoduodenectomy (Whipple resections) in patients without malignancy: are they all 'chronic pancreatitis'? Am J Surg Pathol. 2003;27(1):110-120.
110. Yassa NA, Yang J, Stein S, et al. Gray-scale and color flow sonography of pancreatic ductal adenocarcinoma. J Clin Ultrasound. 1997;25(9):473-480.
111. Shawker TH, Garra BS, Hill MC, et al. The spectrum of sonographic findings in pancreatic carcinoma. J Ultrasound Med. 1986;5(3):169-177.
112. Kimura W, Sata N, Nakayama H, et al. Pancreatic carcinoma accompanied by pseudocyst: report of two cases. J Gastroenterol. 1994;29(6):786-791.
113. Weber SM, Cubukcu-Dimopulo O, Palesty JA, et al. Lymphoplasmacytic sclerosing pancreatitis: inflammatory mimic of pancreatic carcinoma. J Gastrointest Surg. 2003;7(1):129-137.
114. Zandieh I, Byrne MF. Autoimmune pancreatitis: a review. World J Gastroenterol. 2007;13(47):6327-6332.
115. Toomey DP, Swan N, Torreggiani W, Conlon KC. Autoimmune pancreatitis. Br J Surg. 2007;94(9):1067-1074.
116. Gardner TB, Levy MJ, Takahashi N, et al. Misdiagnosis of autoimmune pancreatitis: a caution to clinicians. Am J Gastroenterol. 2009;104(7):1620-1623.

117. Lowenfels AB, Maisonneuve P, Cavallini G, et al. Pancreatitis and the risk of pancreatic cancer. International Pancreatitis Study Group. N Engl J Med. 1993;328(20):1433-1437.
118. Lowenfels AB, Maisonneuve P. Risk factors for pancreatic cancer. J Cell Biochem. 2005;95(4):649-656.
119. Ross WA, Bismar MM. Evaluation and management of periampullary tumors. Curr Gastroenterol Rep. 2004;6(5):362-370.
120. Faria SC, Tamm EP, Loyer EM, et al. Diagnosis and staging of pancreatic tumors. Semin Roentgenol. 2004;39(3):397-411.
121. Elsayes KM, Narra VR, Abou El Abbass HA, et al. Pancreatic tumors: diagnostic patterns by 3D gradient-echo post contrast magnetic resonance imaging with pathologic correlation. Curr Probl Diagn Radiol. 2006;35(4):125-139.
122. American Cancer Society. Cancer facts & figures. Atlanta: ACS; 2008.
123. Canto MI, Goggins M, Hruban RH, et al. Screening for early pancreatic neoplasia in high-risk individuals: a prospective controlled study. Clin Gastroenterol Hepatol. 2006;4(6):766-781.
124. Klein AP, Hruban RH, Brune KA, et al. Familial pancreatic cancer. Cancer J. 2001;7(4):266-273.
125. Wilkowski R, Thoma M, Bruns C, et al. Chemoradiotherapy with gemcitabine and continuous 5-FU in patients with primary inoperable pancreatic cancer. JOP. 2006;7(4):349-360.
126. Conlon KC, Klimstra DS, Brennan MF. Long-term survival after curative resection for pancreatic ductal adenocarcinoma. Clinicopathologic analysis of 5-year survivors. Ann Surg. 1996;223(3):273-279.
127. Klek S, Kulig J, Popiela T, et al. The value of modern ultrasonographic techniques and computed tomography in detecting and staging of pancreatic carcinoma. Acta Chir Belg. 2004;104(6):659-667.
128. Gudjonsson B. Carcinoma of the pancreas: critical analysis of costs, results of resections, and the need for standardized reporting. J Am Coll Surg. 1995;181:483-503.
129. Gudjonsson B. Survival statistics gone awry: pancreatic cancer, a case in point. J Clin Gastroenterol. 2002;35(2):180-184.
130. Wade TP, el-Ghazzawy AG, Virgo KS, Johnson FE. The Whipple resection for cancer in U.S. Department of Veterans Affairs Hospitals. Ann Surg. 1995;221(3):241-248.
131. Farnell MB, Nagorney DM, Sarr MG. The Mayo clinic approach to the surgical treatment of adenocarcinoma of the pancreas. Surg Clin North Am. 2001;81(3):611-623.
132. Tamm EP, Bhosale PR, Lee JH. Pancreatic ductal adenocarcinoma: ultrasound, computed tomography, and magnetic resonance imaging features. Semin Ultrasound CT MR. 2007;28(5):330-338.
133. Karlson BM, Ekbom A, Lindgren PG, et al. Abdominal US for diagnosis of pancreatic tumor: prospective cohort analysis. Radiology. 1999;213(1):107-111.
134. Campbell JP, Wilson SR. Pancreatic neoplasms: how useful is evaluation with US? Radiology. 1988;167(2):341-344.
135. Kosmahl M, Pauser U, Anlauf M, Kloppel G. Pancreatic ductal adenocarcinomas with cystic features: neither rare nor uniform. Mod Pathol. 2005;18(9):1157-1164.
136. Pappas S, Federle MP, Lokshin AE, Zeh 3rd HJ. Early detection and staging of adenocarcinoma of the pancreas. Gastroenterol Clin North Am. 2007;36(2):413-429, x.
137. Gress FG, Hawes RH, Savides TJ, et al. Role of EUS in the preoperative staging of pancreatic cancer: a large single-center experience. Gastrointest Endosc. 1999;50(6):786-791.
138. Boujaoude J. Role of endoscopic ultrasound in diagnosis and therapy of pancreatic adenocarcinoma. World J Gastroenterol. 2007;13(27):3662-3666.
139. Kalra MK, Maher MM, Mueller PR, Saini S. State-of-the-art imaging of pancreatic neoplasms. Br J Radiol. 2003;76(912):857-865.
140. Nino-Murcia M, Tamm EP, Charnsangavej C, Jeffrey Jr RB. Multidetector-row helical CT and advanced postprocessing techniques for the evaluation of pancreatic neoplasms. Abdom Imaging. 2003;28(3):366-377.
141. Vargas R, Nino-Murcia M, Trueblood W, Jeffrey Jr RB. MDCT in pancreatic adenocarcinoma: prediction of vascular invasion and resectability using a multiphasic technique with curved planar reformations. AJR Am J Roentgenol. 2004;182(2):419-425.
142. Angeli E, Venturini M, Vanzulli A, et al. Color Doppler imaging in the assessment of vascular involvement by pancreatic carcinoma. AJR Am J Roentgenol. 1997;168(1):193-197.
143. Ralls PW, Wren SM, Radin R, et al. Color flow sonography in evaluating the resectability of periampullary and pancreatic tumors. J Ultrasound Med. 1997;16(2):131-140.
144. Tomiyama T, Ueno N, Tano S, et al. Assessment of arterial invasion in pancreatic cancer using color Doppler ultrasonography. Am J Gastroenterol. 1996;91(7):1410-1416.
145. Wren SM, Ralls PW, Stain SC, et al. Assessment of resectability of pancreatic head and periampullary tumors by color flow Doppler sonography. Arch Surg. 1996;131(8):812-817.
146. Ishida H, Konno K, Hamashima Y, et al. Assessment of resectability of pancreatic carcinoma by color Doppler sonography. Abdom Imaging. 1999;24(3):295-298.
147. Rickes S, Malfertheiner P. Echo-enhanced sonography—an increasingly used procedure for the differentiation of pancreatic tumors. Dig Dis. 2004;22(1):32-38.
148. Fernández-del Castillo C, Targarona J, Thayer SP, et al. Incidental pancreatic cysts: clinicopathologic characteristics and comparison with symptomatic patients. Arch Surg. 2003;138(4):427-434.
149. Edirimanne S, Connor SJ. Incidental pancreatic cystic lesions. World J Surg. 2008;32(9):2028-2037.
150. Sahani DV, Saokar A, Hahn PF, et al. Pancreatic cysts 3 cm or smaller: how aggressive should treatment be? Radiology. 2006;238(3):912-919.
151. Spinelli KS, Fromwiller TE, Daniel RA, et al. Cystic pancreatic neoplasms: observe or operate. Ann Surg. 2004;239(5):651-657.
152. Maker AV, Lee LS, Raut CP, et al. Cytology from pancreatic cysts has marginal utility in surgical decision-making. Ann Surg Oncol. 2008;15(11):3187-3192.
153. Belsley NA, Pitman MB, Lauwers GY, et al. Serous cystadenoma of the pancreas: limitations and pitfalls of endoscopic ultrasound-guided fine-needle aspiration biopsy. Cancer. 2008;114(2):102-110.
154. Megibow AJ. Update in imaging of cystic pancreatic masses for gastroenterologists. Clin Gastroenterol Hepatol. 2008;6(11):1194-1197.
155. Berland LL, Silverman SG, Gore RM, et al. Managing incidental findings on abdominal CT: white paper of the ACR incidental findings committee. J Am Coll Radiol. 2010;7(10):754-773.
156. Johnson PT, Horton KM, Megibow AJ, et al. Common incidental findings on MDCT: survey of radiologist recommendations for patient management. J Am Coll Radiol. 2011;8(11):762-767.
157. Brook OR, Beddy P, Pahade J, et al. Delayed growth in incidental pancreatic cysts: are the Current American College of Radiology recommendations for follow-up appropriate? Radiology. 2015;140972.
158. Freeny PC, Saunders MD. Moving beyond morphology: new insights into the characterization and management of cystic pancreatic lesions. Radiology. 2014;272(2):345-363.
159. Chernyak V, Flusberg M, Haramati LB, et al. Incidental pancreatic cystic lesions: is there a relationship with the development of pancreatic adenocarcinoma and all-cause mortality? Radiology. 2015;274(1):161-169.
160. Ikeda M, Sato T, Morozumi A, et al. Morphologic changes in the pancreas detected by screening ultrasonography in a mass survey, with special reference to main duct dilatation, cyst formation, and calcification. Pancreas. 1994;9(4):508-512.
161. Zhang XM, Mitchell DG, Dohke M, et al. Pancreatic cysts: depiction on single-shot fast spin-echo MR images. Radiology. 2002;223(2):547-553.
162. Kimura W, Nagai H, Kuroda A, et al. Analysis of small cystic lesions of the pancreas. Int J Pancreatol. 1995;18(3):197-206.
163. Chang MY, Ong AC. Autosomal dominant polycystic kidney disease: recent advances in pathogenesis and treatment. Nephron Physiol. 2008;108(1):p1-p7.
164. Leung RS, Biswas SV, Duncan M, Rankin S. Imaging features of von Hippel-Lindau disease. Radiographics. 2008;28(1):65-79.
165. Cahill ME, Parmentier JM, Van Ruyssevelt C, Pauls CH. Pancreatic cystosis in cystic fibrosis. Abdom Imaging. 1997;22(3):313-314.
166. Adsay NV. Cystic neoplasia of the pancreas: pathology and biology. J Gastrointest Surg. 2008;12(3):401-404.
167. Ohashi KM, Maruyama Y. Four cases of mucin-producing cancer of the pancreas: specific findings in the ampulla of Vater [Japanese]. Prog Dig Endosc. 1982;20:348-351.
168. Zamora C, Sahel J, Cantu DG, et al. Intraductal papillary or mucinous tumors (IPMT) of the pancreas: report of a case series and review of the literature. Am J Gastroenterol. 2001;96(5):1441-1447.

169. Sarr MG, Kendrick ML, Nagorney DM, et al. Cystic neoplasms of the pancreas: benign to malignant epithelial neoplasms. Surg Clin North Am. 2001;81(3):497-509.
170. Lim JH, Lee G, Oh YL. Radiologic spectrum of intraductal papillary mucinous tumor of the pancreas. Radiographics. 2001;21(2):323-337.
171. Suzuki M, Fujita N, Onodera H, et al. Mucinous cystic neoplasm in a young male patient. J Gastroenterol. 2005;40(11):1070-1074.
172. Klimstra DS, Wenig BM, Heffess CS. Solid-pseudopapillary tumor of the pancreas: a typically cystic carcinoma of low malignant potential. Semin Diagn Pathol. 2000;17(1):66-80.
173. Shuja A, Alkimawi KA. Solid pseudopapillary tumor: a rare neoplasm of the pancreas. Gastroenterol Rep (Oxf). 2014;2(2):145-149.
174. Sidden CR, Mortele KJ. Cystic tumors of the pancreas: ultrasound, computed tomography, and magnetic resonance imaging features. Semin Ultrasound CT MR. 2007;28(5):339-356.
175. Buetow PC, Buck JL, Pantongrag-Brown L, et al. Solid and papillary epithelial neoplasm of the pancreas: imaging-pathologic correlation on 56 cases. Radiology. 1996;199(3):707-711.
176. Tucci G, Muzi MG, Nigro C, et al. Dermoid cyst of the pancreas: presentation and management. World J Surg Oncol. 2007;5:85.
177. Demos TC, Posniak HV, Harmath C, et al. Cystic lesions of the pancreas. AJR Am J Roentgenol. 2002;179(6):1375-1388.
178. Koenig TR, Loyer EM, Whitman GJ, et al. Cystic lymphangioma of the pancreas. AJR Am J Roentgenol. 2001;177(5):1090.
179. Cives M, Strosberg J. An update on gastroenteropancreatic neuroendocrine tumors. Oncology (Williston Park). 2014;28(9):749-756, 758.
180. Kloppel G, Heitz PU. Pancreatic endocrine tumors. Pathol Res Pract. 1988;183(2):155-168.
181. Phan GQ, Yeo CJ, Hruban RH, et al. Surgical experience with pancreatic and peripancreatic neuroendocrine tumors: Review of 125 patients. J Gastrointest Surg. 1998;2(5):473-482.
182. Shah S, Mortele KJ. Uncommon solid pancreatic neoplasms: ultrasound, computed tomography, and magnetic resonance imaging features. Semin Ultrasound CT MR. 2007;28(5):357-370.
183. O'Grady HL, Conlon KC. Pancreatic neuroendocrine tumours. Eur J Surg Oncol. 2008;34(3):324-332.
184. Grant CS. Insulinoma. Best Pract Res Clin Gastroenterol. 2005;19(5): 783-798.
185. Horton KM, Hruban RH, Yeo C, Fishman EK. Multi-detector row CT of pancreatic islet cell tumors. Radiographics. 2006;26(2):453-464.
186. Doppman JL, Chang R, Fraker DL, et al. Localization of insulinomas to regions of the pancreas by intra-arterial stimulation with calcium. Ann Intern Med. 1995;123(4):269-273.
187. Buetow PC, Miller DL, Parrino TV, Buck JL. Islet cell tumors of the pancreas: clinical, radiologic, and pathologic correlation in diagnosis and localization. Radiographics. 1997;17(2):453-472.
188. Kawamoto S, Shi C, Hruban RH, et al. Small serotonin-producing neuroendocrine tumor of the pancreas associated with pancreatic duct obstruction. AJR Am J Roentgenol. 2011;197(3):W482-W488.
189. Shi C, Siegelman SS, Kawamoto S, et al. Pancreatic duct stenosis secondary to small endocrine neoplasms: a manifestation of serotonin production? Radiology. 2010;257(1):107-114.
190. Degen L, Wiesner W, Beglinger C. Cystic and solid lesions of the pancreas. Best Pract Res Clin Gastroenterol. 2008;22(1):91-103.
191. Cubilla AL, Fitzgerald PJ. Cancer of the exocrine pancreas: the pathologic aspects. CA Cancer J Clin. 1985;35(1):2-18.
192. Ryan MF, Hamilton PA, Smith AJ, Khalifa M. Radiologic features of pancreatic lipoma. Can Assoc Radiol J. 2003;54(1):41-44.
193. Barutcu O, Cihangiroglu M, Yildirim T, et al. Fat containing unusual tumor of the pancreas. Eur Radiol. 2002;12(4):770-773.
194. Spencer GM, Rubens DJ, Roach DJ. Hypoechoic fat: a sonographic pitfall. AJR Am J Roentgenol. 1995;164(5):1277-1280.
195. Klein KA, Stephens DH, Welch TJ. CT characteristics of metastatic disease of the pancreas. Radiographics. 1998;18(2):369-378.
196. D'Onofrio M, Zamboni G, Faccioli N, et al. Ultrasonography of the pancreas. 4. Contrast-enhanced imaging. Abdom Imaging. 2007;32(2):171-181.
197. Ardelean M, Sirli R, Sporea I, et al. Contrast enhanced ultrasound in the pathology of the pancreas—a monocentric experience. Med Ultrason. 2014;16(4):325-331.
198. Grossjohann HS. Contrast-enhanced ultrasound for diagnosing, staging and assessment of operability of pancreatic cancer. Dan Med J. 2012;59(12):B4536.
199. D'Onofrio M, Gallotti A, Principe F, Mucelli RP. Contrast-enhanced ultrasound of the pancreas. World J Radiol. 2010;2(3):97-102.
200. Fan Z, Li Y, Yan K, et al. Application of contrast-enhanced ultrasound in the diagnosis of solid pancreatic lesions—a comparison of conventional ultrasound and contrast-enhanced CT. Eur J Radiol. 2013;82(9):1385-1390.

CHAPTER 8

The Gastrointestinal Tract

Stephanie R. Wilson

SUMMARY OF KEY POINTS

- High-resolution ultrasound allows for excellent depiction of the bowel, including the normal multilayered appearance of the bowel wall and many pathologic features.
- Ultrasound is a safe, objective, and accurate method for measuring the severity of inflammatory activity in inflammatory bowel disease, an essential requirement considering the young population most often affected by this chronic and often debilitating disease.
- Contrast-enhanced ultrasound is an objective biomarker that may accurately evaluate disease activity in those with bowel wall inflammation.
- Elastography measures bowel wall stiffness, increasing in those with chronic disease, helping to differentiate patients amenable to medical therapy from those requiring surgical intervention.
- Transrectal ultrasound (TRUS) is an excellent noninvasive and well-tolerated procedure for staging of rectal tumors.
- Transvaginal ultrasound increases accuracy of bowel ultrasound in many women as pathologic features located deep in the pelvis may only be visible with this technique.
- Transperineal scan allows for accurate depiction of perianal inflammatory masses without necessity of performing often painful scans with endoanal or endorectal placement of the transducer.

CHAPTER OUTLINE

ANATOMY AND SONOGRAPHIC TECHNIQUE
The Gut Signature
Gut Wall Pathology
Imaging Technique
Doppler Evaluation of Gut Wall
Contrast-Enhanced Ultrasound and Elastography of the Bowel
GASTROINTESTINAL TRACT NEOPLASMS
Adenocarcinoma
Gastrointestinal Stromal Tumors
Lymphoma
Metastases
INFLAMMATORY BOWEL DISEASE: CROHN DISEASE
Classic Features
Gut Wall Thickening
Inflammatory Fat
Lymphadenopathy
Hyperemia
Mucosal Abnormalities
Conglomerate Masses
COMPLICATIONS
Strictures
Incomplete Mechanical Bowel Obstruction
Localized Perforation
Inflammatory Masses
Fistula Formation
Perianal Inflammatory Disease
ACUTE ABDOMEN
Right Lower Quadrant Pain
Acute Appendicitis
Crohn Appendicitis
Right-Sided Diverticulitis
Acute Typhlitis
Mesenteric Adenitis With Terminal Ileitis
Right-Sided Segmental Omental Infarction
Left Lower Quadrant Pain
Acute Diverticulitis
OTHER ABNORMALITIES
Mechanical Bowel Obstruction
Paralytic Ileus
Gut Edema
Gastrointestinal Tract Infections
AIDS Patients
Pseudomembranous Colitis
Congenital Cysts
Ischemic Bowel Disease
Pneumatosis Intestinalis
Mucocele of Appendix
Gastrointestinal Tract Hematoma
Peptic Ulcer
Bezoars
Intraluminal Foreign Bodies
Celiac Disease
Cystic Fibrosis
ENDOSONOGRAPHY
Upper Gastrointestinal Tract
Rectum: Tumor Staging of Rectal Carcinoma
Anal Canal
Fecal Incontinence
Perianal Inflammatory Disease
Acknowledgment

Gastrointestinal (GI) tract sonography is frequently frustrating and always challenging. Gas content within the gut lumen can make visibility difficult or even impossible; intraluminal fluid may mimic cystic masses; and fecal material can create a variety of artifacts and pseudotumors. Nevertheless, normal gut has a reproducible pattern, or gut signature, and a variety of gut diseases create recognizable sonographic abnormalities. Therefore ultrasound may play a valuable role in the evaluation of patients in a variety of clinical situations, including suspicion of acute conditions of the GI tract, especially appendicitis and diverticulitis.

Recent years have shown growing interest in the use of ultrasound for surveillance of patients with inflammatory bowel disease. Further, endosonography, performed with high-frequency transducers in the gut lumen, is an increasingly popular technique for assessing the esophagus, stomach, and rectum.

ANATOMY AND SONOGRAPHIC TECHNIQUE

The Gut Signature

The gut is a continuous hollow tube with **four concentric layers** (Fig. 8.1). From the lumen outward, these layers are (1) mucosa, which consists of an epithelial lining, loose connective tissue (or lamina propria), and muscularis mucosa; (2) submucosa; (3) muscularis propria, with inner circular and outer longitudinal fibers; and (4) serosa or adventitia. These histologic layers correspond with the sonographic appearance[1-3] (Table 8.1) and are referred to as the **gut signature,** where up to **five layers** may be visualized (Fig. 8.2).

The sonographic layers appear alternately echogenic and hypoechoic; the first, third, and fifth layers are echogenic, and the second and fourth layers are hypoechoic. This relationship of the histologic layering with the sonographic layering is best remembered by recognition that the muscular components of the gut wall—the muscularis mucosa and the muscularis propria—constitute the hypoechoic layers on sonography.

On routine sonograms, the gut signature may vary from a "bull's-eye" in cross section, with an echogenic central area and a hypoechoic rim, to full depiction of the five sonographic layers. The quality of the scan and the resolution of the transducer determine the degree of layer differentiation. Ultrasound is superior to both computed tomography (CT) and magnetic resonance imaging (MRI) for resolution of the gut wall layers. The normal gut wall is uniform and compliant, with an average thickness of 3 mm if distended and 5 mm if not. Other morphologic features that allow recognition of specific portions of the gut include the gastric rugae (in the stomach), valvulae conniventes (plicae circulares in the small intestines), and haustra (in the colon) (Fig. 8.3).

Real-time sonography allows assessment of the content and diameter of the GI lumen and the motility of the gut. Hypersecretion, mechanical obstruction, and ileus are implicated when gut fluid is excessive. **Peristalsis** is normally seen in the small bowel and stomach. Activity may be increased with mechanical obstruction and inflammatory enteritides. Decreased activity is seen with paralytic ileus and in the end stages of mechanical bowel obstruction.

TABLE 8.1 Gut Signature: Histologic-Sonographic Correlation

Histology	Sonography
Superficial mucosa/interface (epithelium and lamina propria)	Echogenic
Muscularis mucosa	Hypoechoic
Submucosa	Echogenic
Muscularis propria (inner circular and outer longitudinal fibers)	Hypoechoic
Serosa/interface	Echogenic

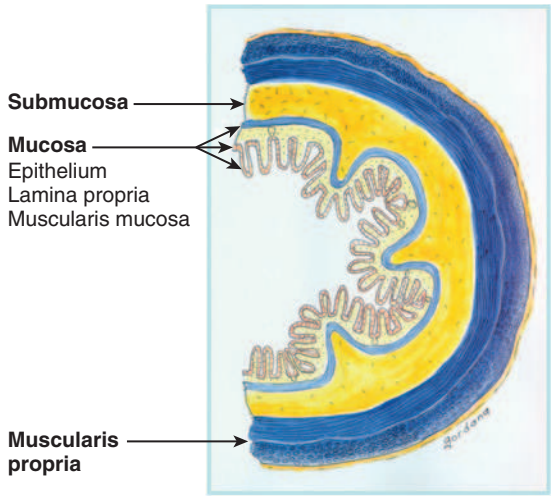

FIG. 8.1 Schematic Depiction of the Histologic Layers of the Gut Wall.

Gut Wall Pathology

Evaluation of thickened gut on sonography is far superior to the evaluation of normal gut for two important reasons. Thick gut, particularly if associated with abnormality of the perienteric soft tissues, creates a mass effect, which is easily seen on sonography. In addition, thickened gut is frequently relatively gasless, improving its sonographic evaluation. Gut wall pathology creates characteristic sonographic patterns (Fig. 8.4). The most familiar, the **target pattern,** was first described by Lutz and Petzoldt[4] in 1976 and later by Bluth et al.,[5] who referred to the pattern as a "**pseudokidney,**" noting that a pathologically significant lesion was found in more than 90% of patients with this pattern. In both descriptions the hypoechoic external rim corresponds to thickened gut wall, whereas the echogenic center relates to residual gut lumen or mucosal ulceration.

Identification of thickened gut on sonographic examination may be related to a variety of diseases. Diagnostic possibilities are predicted by determining the (1) extent and location of disease, (2) preservation or destruction of wall layering, and (3) concentricity or eccentricity of wall involvement. Benignancy is favored by long segment involvement with concentric thickening and wall layer preservation. The classic benign pathology showing gut wall thickening is **Crohn disease.** Malignancy is favored by short segment involvement with eccentric disease and wall layer destruction. The classic malignant pathology showing gut wall thickening is **adenocarcinoma of the stomach or colon.** These are guidelines rather than rules, because chronically thickened gut in Crohn disease may show layer destruction related to fibrotic and subacute inflammatory change, and infiltrative adenocarcinoma may show some wall layer preservation. Lymphadenopathy and hyperemia of the thickened gut wall

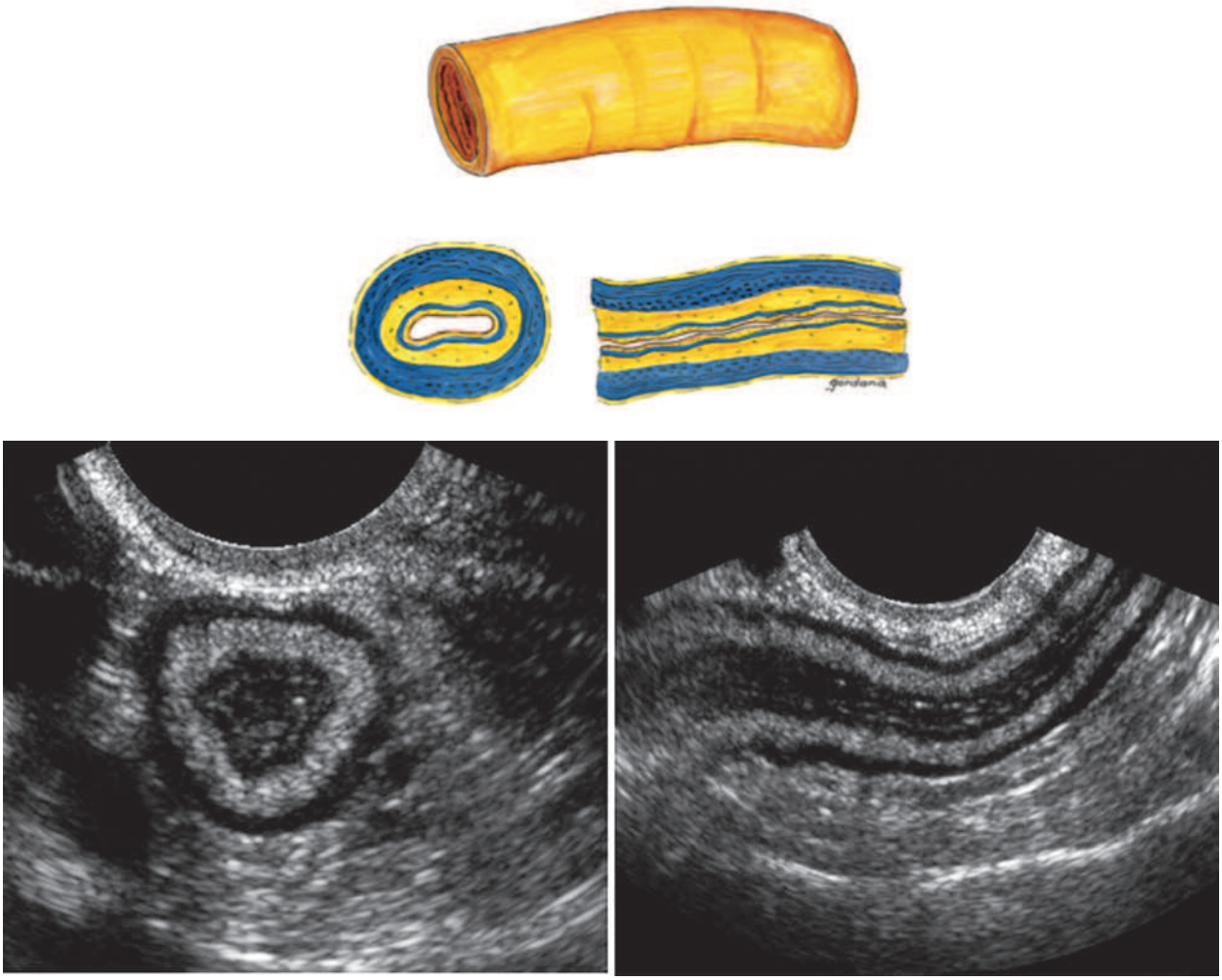

FIG. 8.2 Gut Signature in a Patient With Mild Gut Thickening Caused by Crohn Disease. The muscle layers are hypoechoic. The submucosa and superficial mucosa layers are hyperechoic. There is a small amount of fluid and air in the gut lumen.

may be seen in association with both malignant and benign gut wall thickening.

Gut wall masses, as distinguished from thickened gut wall, may be intraluminal, mural, or exophytic, all with or without ulceration. Intraluminal gut masses and mucosal masses have a variable appearance on sonography but are frequently hidden by gas or luminal content. In contrast, gut pathology creating an exophytic mass (without or with mucosal involvement or ulceration) may form masses that are more readily visualized. These may be difficult to assign to a GI tract origin if typical gut signatures, targets, or pseudokidneys are not seen on sonographic examination. Consequently, intraperitoneal masses of varying morphology, which do not clearly arise from the solid abdominal viscera or the lymph nodes, should be considered to have a potential gut origin.

Imaging Technique

Routine sonograms are best performed when the patient has fasted. A real-time survey of the entire abdomen is performed with a 3.5- to 5-MHz transducer, and any obvious masses or gut signatures are observed. The pelvis is scanned before and after the bladder is emptied because the full bladder facilitates visualization of pathologic conditions in some patients and displaces abdominal bowel loops in others. A routine gut evaluation should include assessment of all of the small bowel and the colon. In women, **transvaginal sonography** is invaluable for evaluation of the portions of the gut within the true pelvis, particularly the rectum, sigmoid colon, and, in some patients, the ileum. Further, oral fluid and a Fleet enema may improve localization and diagnosis of intraluminal or intramural gastric masses and rectal masses, respectively. Still images in long-axis and cross-sectional views as well as cine sweeps to show pathologic features allow for optimal review.

Areas of interest then receive detailed analysis, including **compression sonography**[6] (Fig. 8.5). Although this technique was initially described using high-frequency linear probes, 5- to 9-MHz convex probes and some sector probes work extremely well. The critical factor is a transducer with a short focal zone,

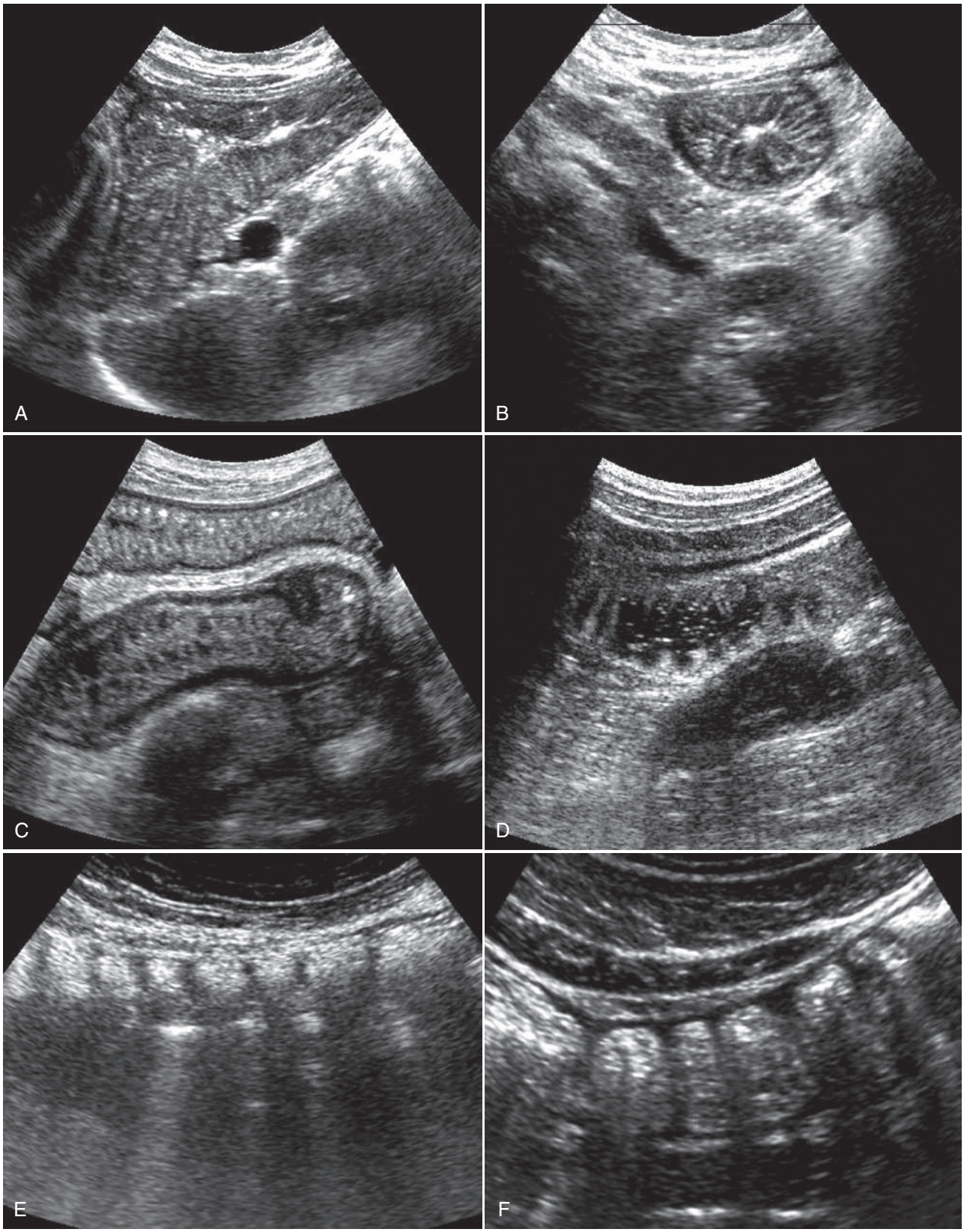

FIG. 8.3 Gut Recognition. **(A)** Sagittal and **(B)** cross-sectional views of the stomach show normal gastric rugae. The collapsed stomach shows variable wall thickness. **(C)** and **(D)** Valvulae conniventes (plicae circulares) of the small bowel. These are more easily seen when **(C)** there is fluid in the lumen of the bowel or **(D)** the valvulae are edematous. **(E)** and **(F)** Variations in the appearance of the colonic haustrations in two normal persons.

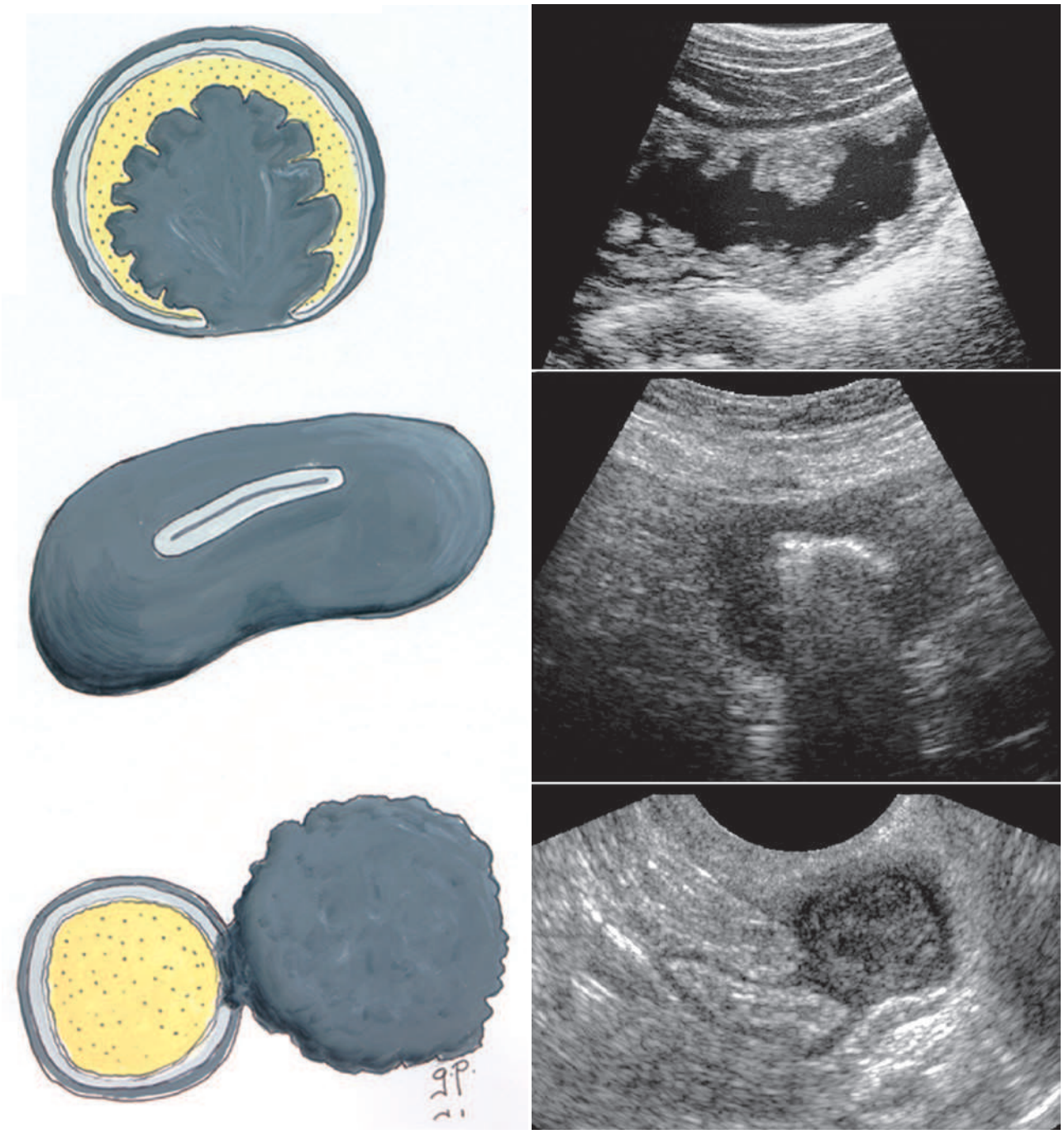

FIG. 8.4 Gut Wall Pathology. Schematic of sonographic appearances with sonographic equivalents. *Top,* **Intraluminal mass.** Inflammatory pseudopolyp on sonogram. *Middle,* **Pseudokidney sign,** with symmetrical wall thickening and wall layer destruction. Carcinoma of the colon on sonogram. *Bottom,* **Exophytic mass.** Serosal seed on visceral peritoneum of the gut on sonogram. (With permission from Wilson SR. The bowel wall looks thickened: what does that mean? In: Cooperberg PL, editor. RSNA categorical course syllabus. Chicago: RSNA; 2002. pp. 219-228.[1])

allowing optimal resolution of structures close to the skin. Slow, graded pressure is applied. Normal gut will be compressed and gas pockets displaced away from the region of interest. In contrast, thickened abnormal loops of bowel and obstructed noncompressible loops will remain unchanged. Patients with peritoneal irritation or local tenderness will usually tolerate the slow, gentle increase in pressure of compression sonography, whereas they show a marked painful response if rapid, uneven scanning is performed.

Doppler Evaluation of Gut Wall

Normal gut shows little signal on conventional color Doppler because interrogation is difficult in a normal and mobile bowel loop. Both **neoplasia** and **inflammatory disease** show increased vascularity compared with the normal gut wall (Fig. 8.6), whereas ischemic and edematous gut tends to be relatively hypovascular. The addition of color and spectral Doppler ultrasound evaluation to the study of the gut wall provides supportive evidence that gut wall thickening is caused by either ischemic or inflammatory

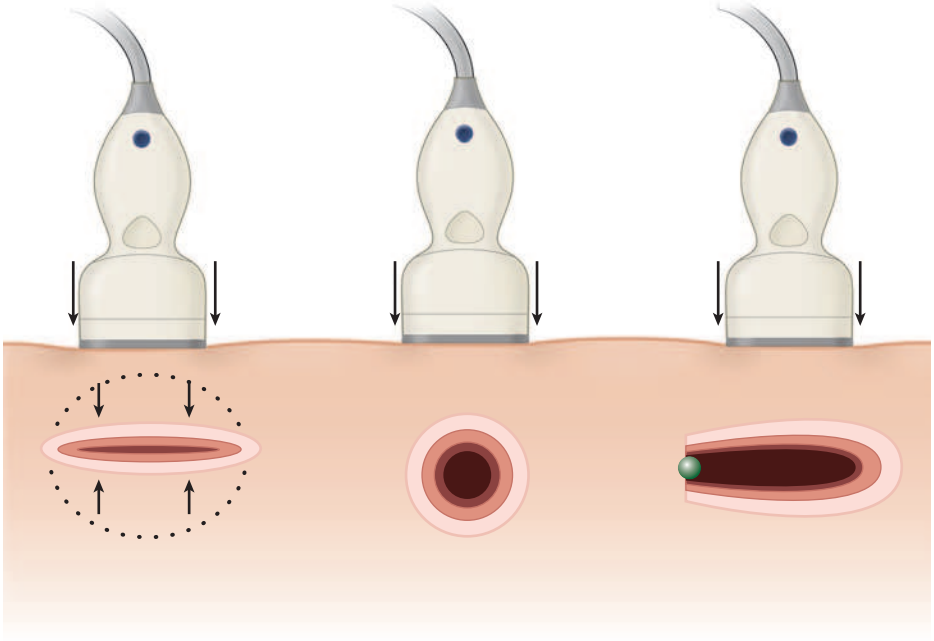

FIG. 8.5 Schematic of Compression Sonography. *Left,* Normal gut is compressed. *Middle,* Abnormally thickened gut, or *right,* an obstructed loop, such as that seen in acute appendicitis, will be noncompressible.

change in the patient with acute abdominal pain. Teefey et al.[7] examined 35 patients and found absent or barely visible blood flow on color Doppler and absence of arterial signal to be suggestive of ischemia. In contrast, readily detected color Doppler flow was consistent with inflammation.

Contrast-Enhanced Ultrasound and Elastography of the Bowel

Two exciting new applications of ultrasound of the bowel include contrast-enhanced ultrasound (CEUS) and elastography. The former provides objective repeatable measures of mural blood flow, which may change in response to inflammation and neoplasia, and the latter measures bowel wall stiffness.[9] Although these investigations are still in their infancy, their additional benefit over routine gray-scale ultrasound with Doppler is evident. Their great contribution to the evaluation of those with inflammatory bowel disease will be discussed in that section. CEUS is also useful in the assessment of mass lesions to determine the presence of vascularity analogous to the role of contrast enhancement on CT or MRI scan.

GASTROINTESTINAL TRACT NEOPLASMS

The role of sonography in the evaluation of GI tract neoplasms is similar to that of CT. Visualization is limited in cases of early mucosal lesions or with small intramural nodules, whereas tumors growing to produce an exophytic mass, a thickened segment of gut, or a sizable intraluminal mass are more easily detected (Fig. 8.7, Video 8.1). Sonograms are frequently performed early in the diagnostic workup of patients with GI tract tumors, often before their initial identification. Vague abdominal symptomatology, abdominal pain, a palpable abdominal mass, and anemia are common indications for these scans. Appreciation of the typical morphologies associated with GI tract neoplasia may lead to accurate recognition, localization, and even staging of disease, with the opportunity for directing appropriate further investigation, including sonography-guided aspiration biopsy.

Adenocarcinoma

Adenocarcinoma is the most common malignant tumor of the GI tract. Grossly, it has variable growth patterns (see Fig. 8.7), including infiltrative, polypoid, fungating, and ulcerated tumors. Most GI tract mucosal cancers are not visualized on sonography. However, large masses, either intraluminal or exophytic, and annular tumors create sonographic abnormalities.[10,11] Tumors of variable length may thicken the gut wall in either a concentric symmetrical or an asymmetrical pattern. A target or pseudokidney morphology may be created (see Fig. 8.4). Air in mucosal ulcerations typically produces linear echogenic foci, often with ring-down artifact, within the bulk of the mass. Tumors are usually, but not invariably, hypoechoic. Annular lesions may produce gut obstruction with dilation, hyperperistalsis, and increased luminal fluid of the gut proximal to the tumor site.[11] Evidence of direct invasion, regional lymph node enlargement, and liver metastases should be sought.

Adenocarcinoma accounts for 80% of all malignant gastric neoplasms, where infiltration may be superficial or transmural, the latter creating a linitis plastica, or "leather bottle," stomach. Adenocarcinoma occurs much less frequently in the small bowel than in the stomach or large bowel. It accounts for approximately

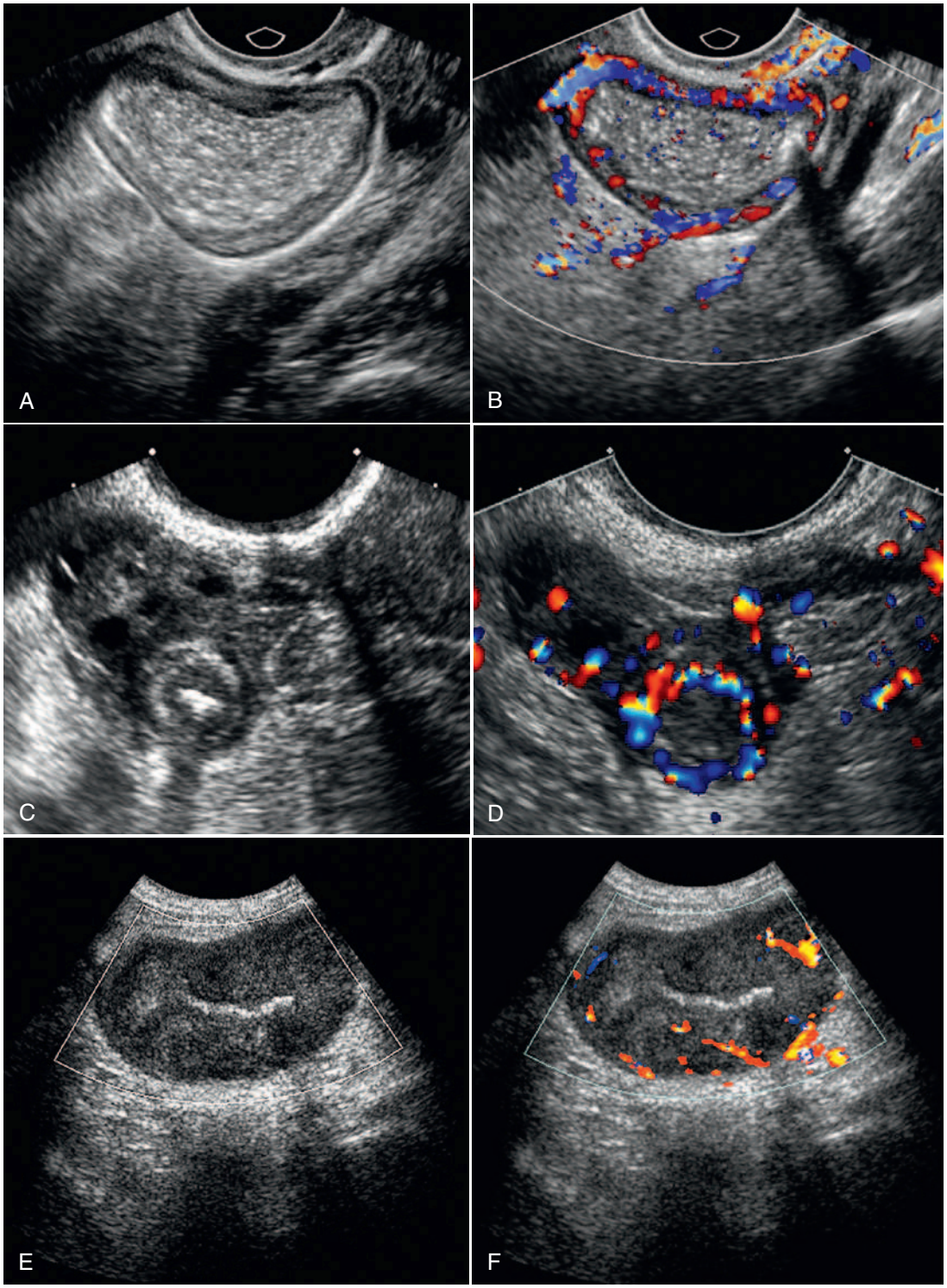

FIG. 8.6 Contribution of Doppler to Gut Assessment in Three Patients. (A) and **(B)** Cross-sectional images of the ileum proximal to an inflammatory stricture in **Crohn disease.** The lumen is distended with fluid. The wall is slightly thick. **(B)** Color Doppler image shows marked hyperemia of the gut wall as a reflection of its inflammation. **(C)** and **(D)** Transvaginal views in a young woman with right lower quadrant pain show the appendix as a round, tubular structure adjacent to the ovary. **(D)** Color Doppler image shows that appendix is hyperemic, consistent with inflammation. **(E)** and **(F)** Transverse images of the ascending colon show wall thickening with total layer destruction related to **invasive colon carcinoma.** Neoplastic tumors of the gut invariably show vascularity as here.

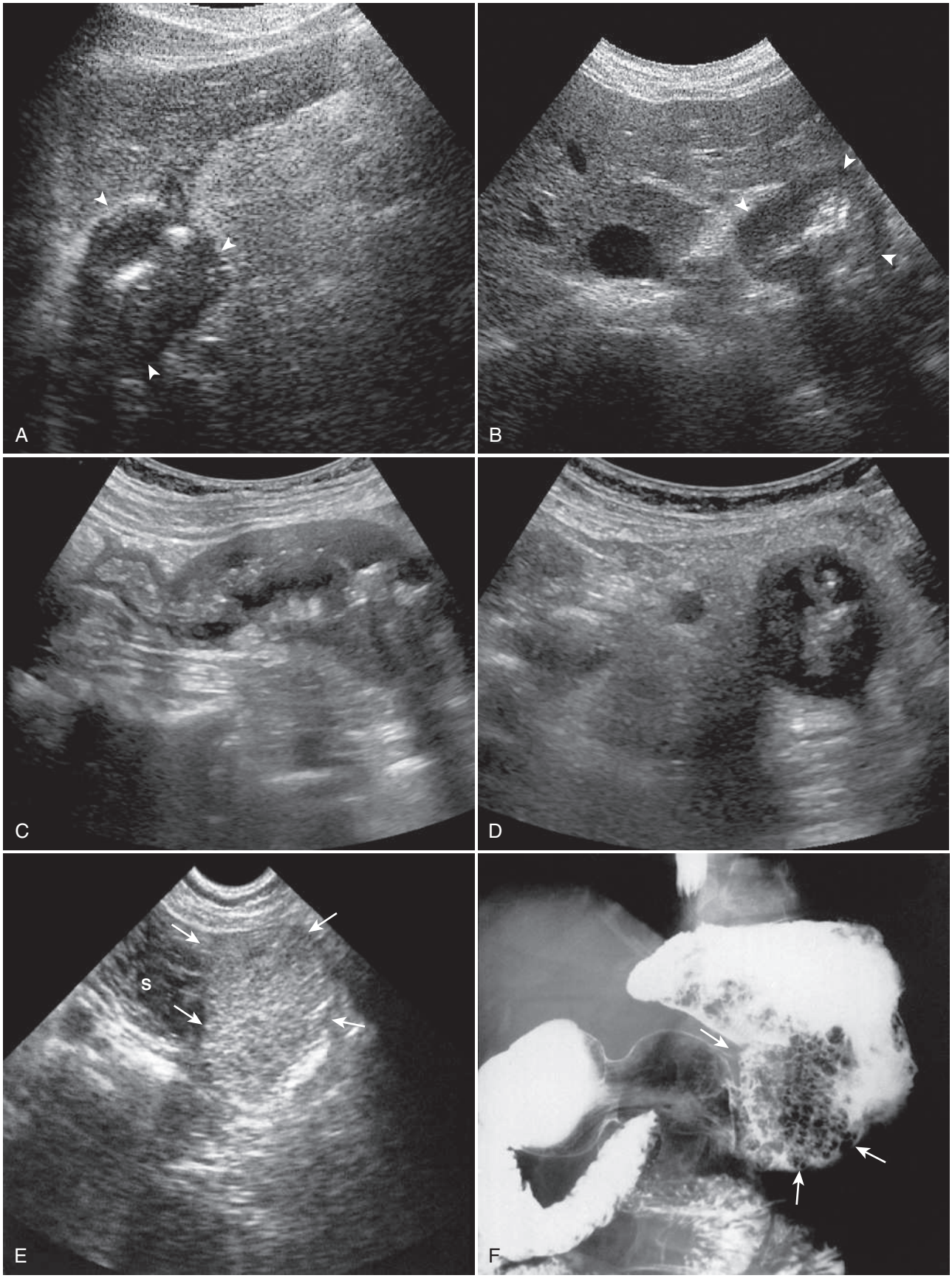

FIG. 8.7 Adenocarcinoma of the Gut in Three Patients. (A) and **(B) Cancer at gastroesophageal junction. (A)** Sagittal and **(B)** transverse sonograms of the upper abdomen show a pseudokidney *(arrowheads)* adjacent to the left lobe of the liver. **(C)** and **(D) Carcinoma of descending colon. (C)** Long-axis image of the colon shows an abrupt transition from normal to thickened bowel. **(D)** An axial image shows a hypoechoic, circumferential mass with an "apple core" appearance. There is echogenic infiltrated fat and an enlarged hypoechoic lymph node adjacent to the tumor. **(E)** and **(F) Intraluminal villous adenocarcinoma of stomach. (E)** Transverse sonogram after fluid ingestion shows a relatively well-defined, inhomogeneous, echogenic mass *(arrows)* within body of stomach. Fluid is in the stomach lumen *(S)*. **(F)** Confirmatory barium swallow shows the villous tumor *(arrows)*. See also Video 8.1.

50% of the small bowel tumors found, 90% of them arising in either the proximal jejunum (Fig. 8.8A and B) or the duodenum. Crohn disease is associated with a significantly increased incidence of adenocarcinoma that usually develops in the ileum. Small bowel adenocarcinomas are generally annular in gross morphology, frequently with ulceration. **Colon carcinoma** is very common and accounts for virtually all malignant colorectal neoplasms. Colorectal adenocarcinoma grows with two major gross morphologic patterns: **polypoid intraluminal tumors,** which are most prevalent in the cecum and ascending colon, and **annular constricting lesions** (see Fig. 8.7C and D), which are most common in the descending and sigmoid colon. In rare cases, infiltrative tumors similar to those seen in the stomach may occur in the colon (Fig. 8.8C and D).

Gastrointestinal Stromal Tumors

Of the mesenchymal tumors affecting the gut, those of smooth muscle origin are the most common and account for about 1% of all GI tract neoplasms. These gastrointestinal stromal tumors (GISTs) are found most often in the stomach and the small bowel. Colonic tumors are the least common and occur most often in the rectum. Although GISTs may be found as an incidental observation at surgery, sonography, or autopsy, these vascular tumors frequently become very large and may undergo ulceration, degeneration, necrosis, and hemorrhage.[12]

On sonography, smooth muscle (stromal) tumors typically produce round mass lesions of varying size and echogenicity, often with central cystic areas[13] related to hemorrhage or necrosis (Fig. 8.9). Their gut origin is not always easily determined, but if ulceration is present, pockets of gas in an ulcer crater may suggest their origin. Smooth muscle tumors of gut origin should be considered in the differential diagnosis of incidentally noted, indeterminate abdominal masses in asymptomatic patients, particularly if they show central cystic or necrotic change (Fig. 8.9E and F). These tumors are very amenable to sonographic-guided aspiration biopsy.

Lymphoma

The gut may be involved with lymphoma in two basic forms: as widespread dissemination in stage III or IV lymphoma of any

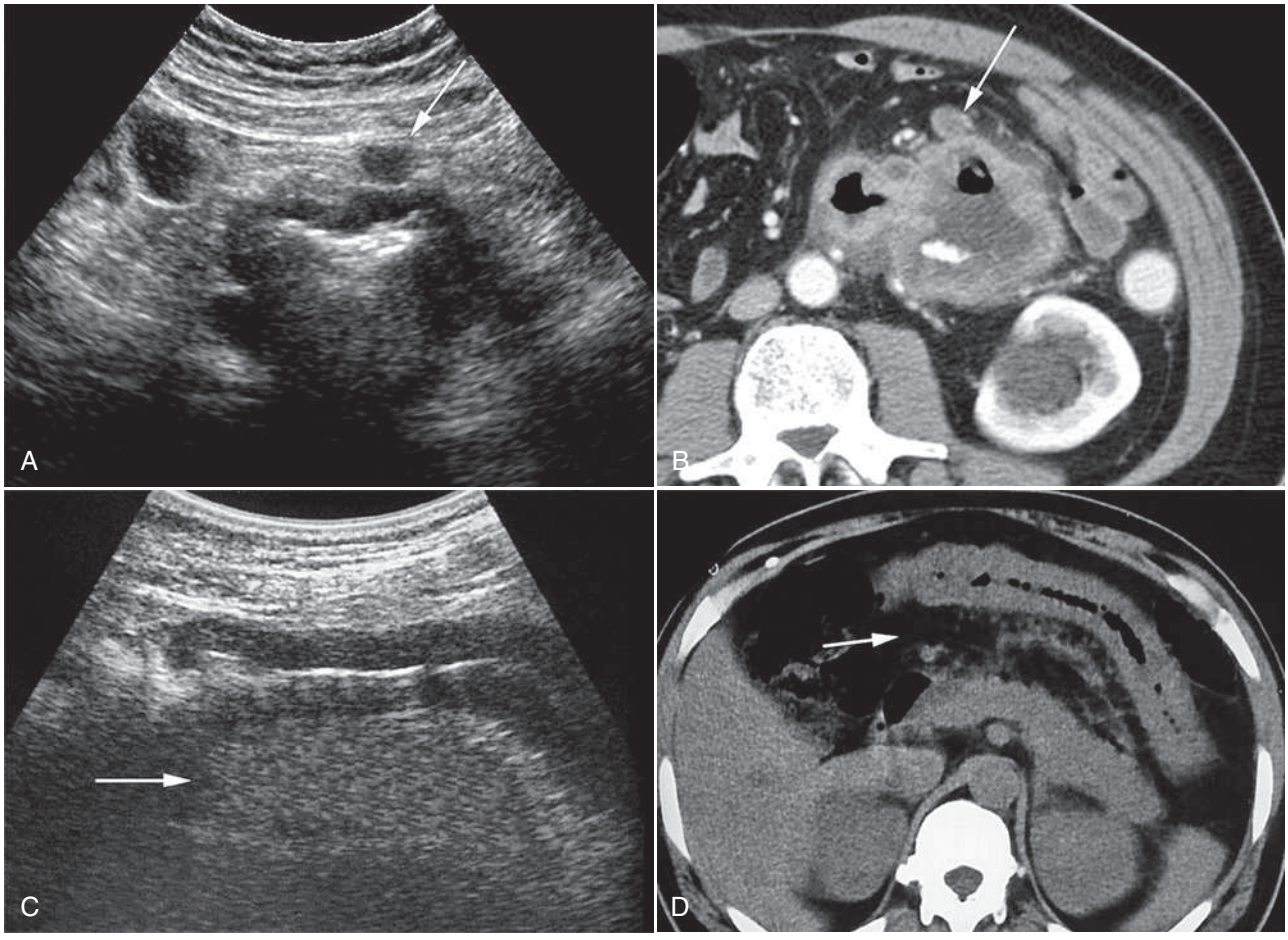

FIG. 8.8 Adenocarcinoma of Bowel: Sonographic-CT Correlation. (A) Sonogram and **(B)** CT scan show large, necrotic, left upper quadrant mass at the ligament of Treitz with enlargement of the perienteric lymph nodes *(arrow)* in a 60-year-old man who presented with abdominal discomfort and blood loss. **(C)** and **(D)** Infiltrative carcinoma of transverse colon in a 42-year-old man who presented to the emergency department with acute abdominal pain. **(C)** Transverse sonogram of the epigastrium shows a featureless segment of thick gut with total loss of wall layering in the location of the transverse colon. Deep to the gut is a diffuse echogenic mass effect *(arrow)* suggesting infiltrated or inflamed fat. **(D)** Confirmatory CT scan. The infiltrated fat is black and streaky on the CT image. Neoplasia was not suspected on the basis of either imaging test or at surgery.

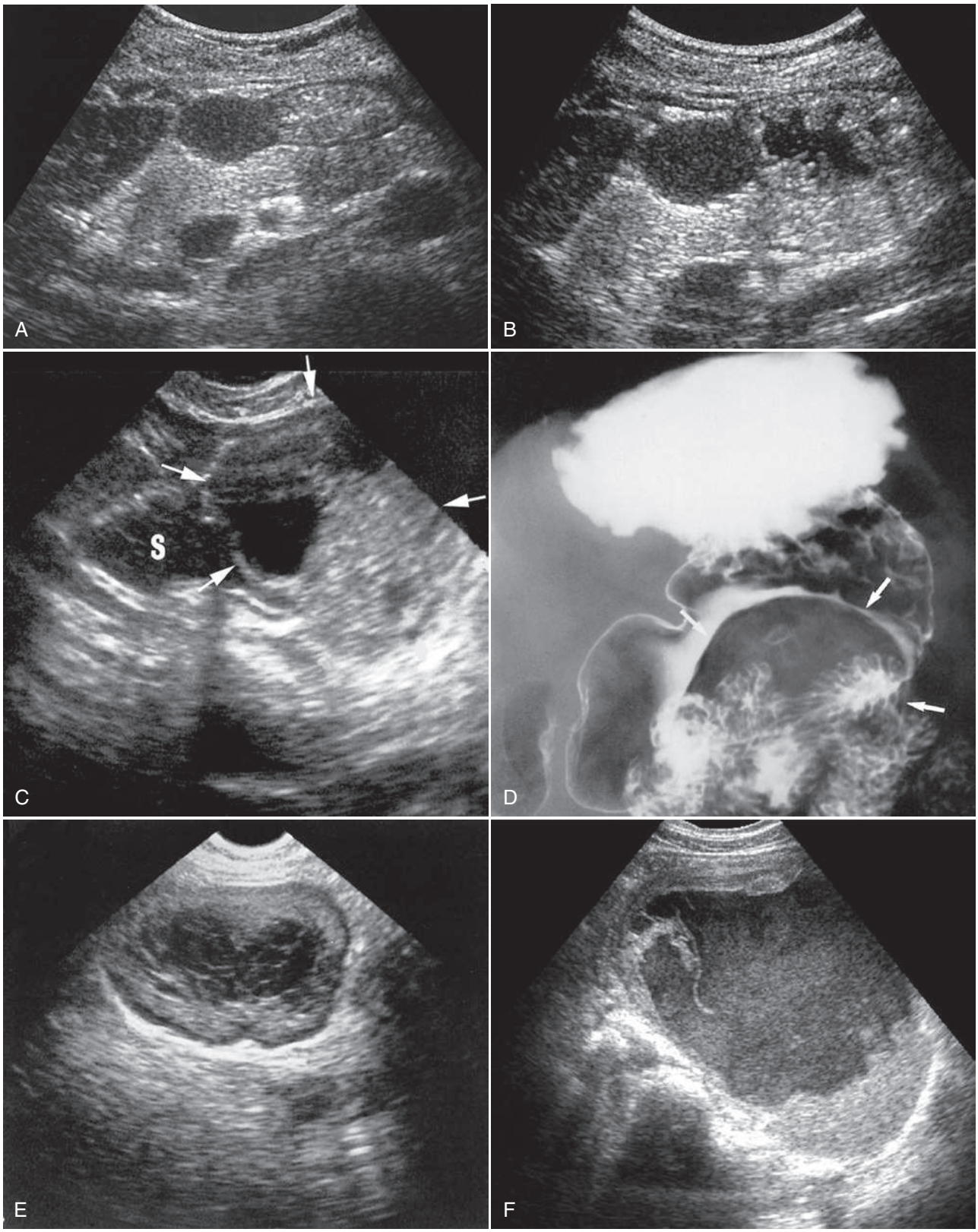

FIG. 8.9 Gastrointestinal Stromal Tumors (GISTs) in Four Patients. (A) and **(B)** Exophytic gut mass, a **gastric leiomyoma. (A)** Transverse sonogram of epigastrium shows the normal gastric gut signature and the focal exophytic mass. **(B)** After water ingestion, the lumen contains fluid that appears hypoechoic. The solid mass is clearly seen. **(C)** and **(D) Gastric leiomyosarcoma. (C)** Transverse sonogram after fluid ingestion shows a complex, smooth intramural mass *(arrows)* projecting into the fluid-filled stomach lumen *(S)*. **(D)** Confirmatory barium swallow shows the intramural tumor *(arrows)*. **(E)** and **(F)** Two patients with a large, upper abdominal, complex, and necrotic-appearing mass on sonography. Although the gut origin of the masses is not evident on the images, the correct diagnosis of GIST was suggested based on the appearance. The jejunum is the origin of the tumor in **(E)** and the stomach in **(F)**.

cell type or, more often, as primary lymphoma of the GI tract, which is virtually always a **non-Hodgkin lymphoma.** Primary tumors constitute only 2% to 4% of all GI tract malignant tumors[12] but account for 20% of those found in the small bowel. Three predominant growth patterns are observed: nodular or polypoid, carcinoma-like ulcerations, and infiltrating tumor masses that frequently invade the adjacent mesentery and lymph nodes.

Small, submucosal nodules may be easily overlooked on sonography. However, many patients have large, easily visible, very hypoechoic, ulcerated masses in the stomach or small bowel[14,15] (Fig. 8.10). Long, linear, high-amplitude echoes with **ring-down artifacts,** indicating gas in the residual lumen or ulcerations, and aneurysmal dilation of the bowel lumen are common observations. This particular pathologic state has been recognized as one of the more frequent presentations of patients with acquired immunodeficiency syndrome **(AIDS)–related lymphoma.** Regional lymph node enlargement may be visualized, although generalized lymph node abnormality is uncommon.

Metastases

Malignant melanoma and primary tumors of the lung and breast are the tumors most likely to have secondary involvement of the GI tract[16] (Fig. 8.11). In order of frequency, the stomach, small bowel, and colon are involved. On sonography, small submucosal nodules that tend to ulcerate are rarely seen, whereas large, diffusely infiltrative tumors with large ulcerations are common, particularly in the small bowel where they create hypoechoic, well-defined masses that often have bright, specular echoes with ring-down artifacts in areas of ulceration.

Secondary neoplasm affecting the omentum and peritoneum may cause **ascites** (which may be particulate ascites), tiny or confluent superficial secondary nodules on the gut surface, or extensive **omental cakes** that virtually engulf the involved gut loops[17] (Fig. 8.12). Metastases to the peritoneum most often arise from primary tumors in the ovary or the gut. A **drop metastasis** in the pelvic pouch of Douglas shows as a small, solid, peritoneal nodule without obvious origin from the pelvic viscera.

INFLAMMATORY BOWEL DISEASE: CROHN DISEASE

Inflammatory bowel disease (IBD) comprises Crohn disease and ulcerative colitis. **Ulcerative colitis** is a mucosal inflammation of the colon and often shows little in the way of gross morphologic

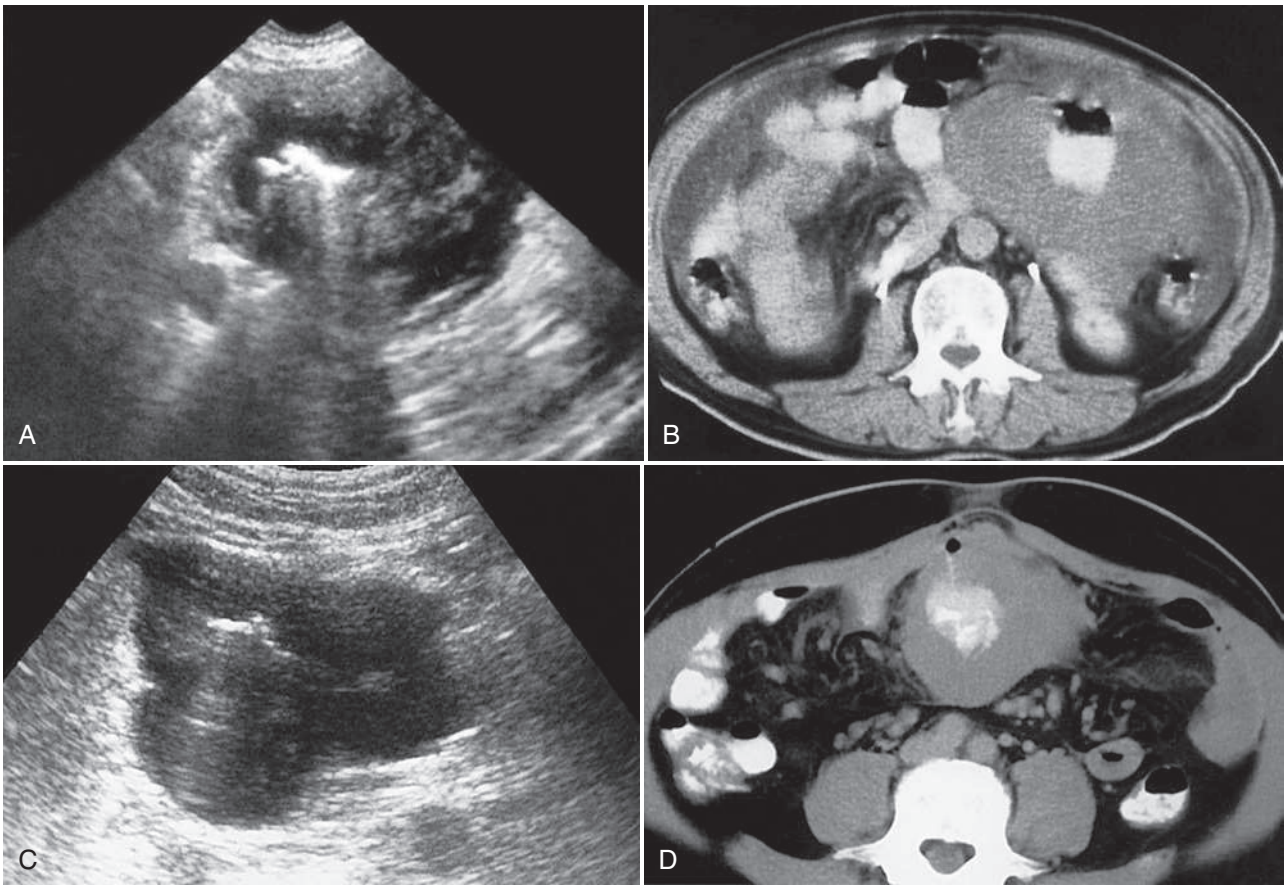

FIG. 8.10 Small Bowel Lymphoma in Two Patients. (A) Transverse left sonogram shows a hypoechoic round mass lesion. Central echogenicity with ring-down gas artifact suggests its gut origin. **(B)** Correlative CT scan shows large, soft tissue mass with corresponding residual gut lumen. **(C)** Sonogram in AIDs patient shows a focal midabdominal, hypoechoic mass with no wall layer definition, which is classic for gut lymphoma. The luminal gas appears as central bright echogenicity with dirty shadowing. **(D)** Correlative CT scan.

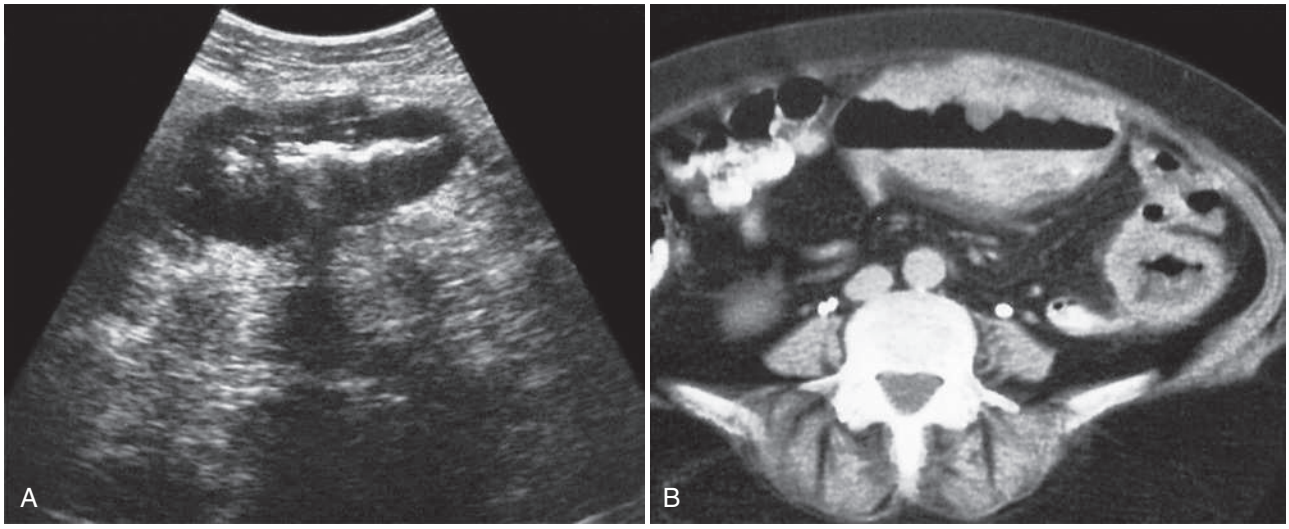

FIG. 8.11 Metastatic Malignant Melanoma to Small Bowel. (A) Transverse paraumbilical sonogram shows well-defined, hypoechoic mass with central irregular echogenicity with gas artifact suggesting gut origin. **(B)** Confirmatory CT scan.

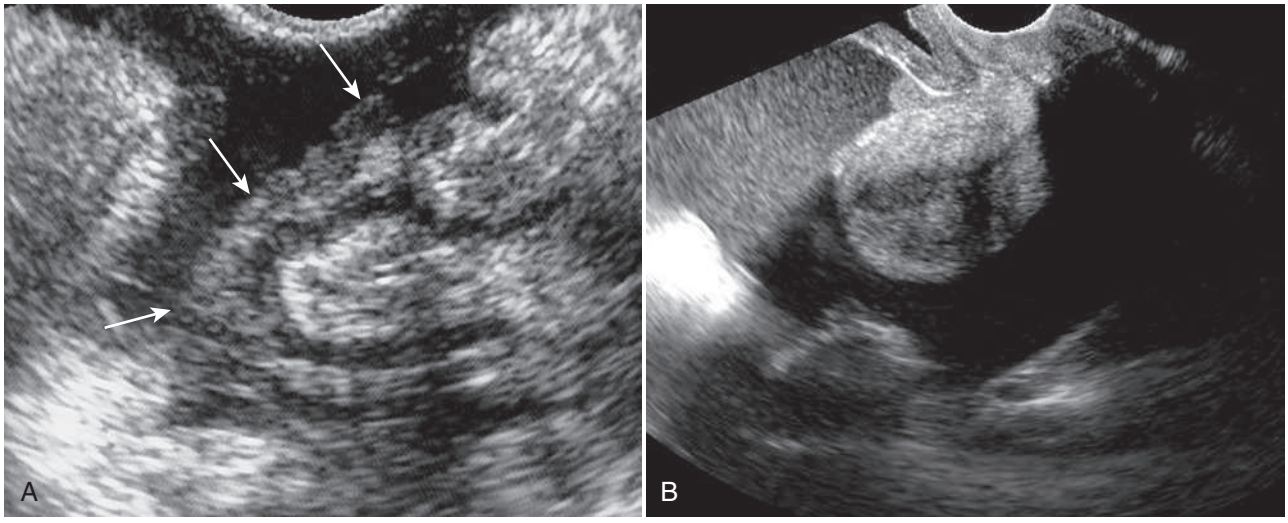

FIG. 8.12 Peritoneal Metastases in Two Patients. (A) Transvaginal image shows ascites and visceral peritoneal plaque on the surface of the small bowel loop *(arrows)* from metastatic ovarian cancer. **(B)** Transvaginal scan of peritoneal drop metastasis from stomach primary shows grossly particulate ascites. There is a small peritoneal implant in the vesicouterine angle.

change except with acute disease. Further, the involved colon is readily evaluated with colonoscopy and also with all cross-sectional imaging, making its assessment relatively straightforward. **Crohn disease,** by comparison, is a chronic transmural. The peak age of onset is early in life, between the ages of 15 and 40 years, thus affecting patients during their most productive years. The natural course of the disease includes alternating periods of active inflammation and remission with a strong tendency to complicate over time, with the development of penetrating and/or fibrostenotic lesions. As a result, surgical intervention rates have been high. Historically, Crohn disease was managed according to patient symptomatology. It is recognized, however, that neither inflammatory markers nor symptoms are an accurate reflection of the state of the disease. Today, therefore, there is a dramatic shift in approach with an effort to treat to the target of mucosal healing on endoscopy, including the use of aggressive biologic therapy and the increasing popularity of early introduction of anti–tumor necrosis factor-α (anti-TNFα). These management changes necessitate frequent monitoring of all patients because repeated endoscopic performance is poorly tolerated, expensive, and not without risk. Therefore safe, objective, noninvasive, and accurate methods for measuring the severity of inflammatory activity are vital.

Imaging plays a major role in the diagnosis of disease,[18] in the detection of recurrence, and in the recognition of complications, which may be associated with a silent clinical course. Surveillance imaging and monitoring response to therapy (which may be both expensive and toxic) is of prime importance. In a meta-analysis comparing different modalities for diagnosis of IBD, mean sensitivity estimates for the diagnosis on a per-patient

basis were high and not significantly different for ultrasound (89.7%), MRI (93.0%), and CT (84.3%).[19] Therefore in this era of cost and radiation awareness, ultrasound is rising in importance for imaging of IBD.[20] Sonography is our routine evaluation technique for initial disease diagnosis, the detection of recurrence,[21] the determination of the extent, complications[22] and activity of disease, and in the assessment of response to treatment.

Although any portion of the gut may be involved, Crohn disease most commonly affects the terminal ileum and the colon. This transmural, granulomatous inflammatory process affects all layers of the gut wall and also the perienteric soft tissues. Grossly, the gut wall may become very thick and rigid with secondary luminal narrowing. Discrete or continuous ulcers and deep fissures are characteristic, frequently leading to fistula formation. Mesenteric lymph node enlargement and matting of involved loops are common. The mesentery may be markedly thickened and fatty, creeping over the edges of the gut to the antimesenteric border. The classic features of Crohn disease—wall thickening, inflammatory fat, lymphadenopathy, and hyperemia—reflect these gross morphologic changes. Complications of Crohn disease include **stricture, incomplete bowel obstruction, perforation, fistulas, and inflammatory masses.**[21]

The immediate objectives of a sonogram on a patient with known or suspected IBD, therefore, include documentation of the distribution and the extent of the disease, as well as the disease activity. A global assessment is made on ultrasound grading all of the classic features from 0, not present; through 1, mild; 2, moderate; and 3, showing severe change[23] (Table 8.2). Utilization of such a scoring system allows for consistency of performance and reproducibility of results. It also facilitates comparisons for monitoring response to therapy.

Crohn Disease on Sonography

CLASSIC FEATURES
Gut wall thickening
Inflammatory fat
Mesenteric lymphadenopathy
Hyperemia

COMPLICATIONS
Strictures
Mechanical bowel obstruction
Perforation
Inflammatory masses
Fistulas
Appendicitis

TABLE 8.2 Ultrasound Global Assessment Showing Crohn Disease Activity Scores on Gray-Scale Ultrasound and Color Doppler Imaging

Gray-Scale Ultrasound Features of Activity	Classification			
	INACTIVE	MILD	MODERATE	SEVERE
Wall thickness (mm)	<4.0	4.0-6.0	6.1-8.0	>8.1
Inflammatory fat	• Absent • Perienteric region resembles normal mesenteric fat	• Masslike • Slightly echogenic • Of less area than the bowel on axial view	• Masslike • More echogenic • Equal area to the bowel on axial view	• Masslike • Significantly echogenic • Of greater area than the bowel on axial view
Color Doppler imaging (CDI) Mural blood flow	• Absent	• Small regions of color without the vessel	• Medium-length segments of color vessels in the bowel wall	• Circumferential or continuous depiction of vessels in the bowel wall with or without mesenteric vessels
Ultrasound global assessment	• No signs of active disease	• Mild wall thickness • Minimal inflammatory fat • Present but not minimal signal on CDI • Wall layer preservation	• Moderate wall thickness • Moderate inflammatory fat • Moderate signal on CDI • ± Wall layer preservation[a]	• Moderate to severely thickened bowel wall • Abundant inflammatory fat • Long continuous mural blood vessels on CDI • ± Wall layer preservation[a] • Spiculation of serosal border[a]

[a]Loss of wall layering and serosal spiculation both suggest increasing disease severity.
Reproduced with permission from Medellin-Kowalewski A, Wilkens R, Wilson A, et al. Quantitative contrast-enhanced ultrasound parameters in Crohn disease: their role in disease activity determination with ultrasound. AJR Am J Roentgenol. 2016;206(1):64-73.[23]

Classic Features

Gut Wall Thickening

Gut wall thickening is the most frequently observed abnormality in patients with Crohn disease and varies in proportion to disease severity. Its identification comprises the basis for initial disease detection, for detection of recurrence,[24] and for determining the extent of disease. In a meta-analysis on the accuracy of sonography in detecting Crohn disease, Fraquelli et al.[25] showed sensitivity and specificity of 88% and 93%, respectively, when a bowel wall thickness threshold greater than 3 mm was used, and 75% and 97% with a threshold greater than 4 mm.

Gut wall thickening in Crohn disease is most frequently concentric and may be marked.[26,27] Wall echogenicity varies depending on the degree of inflammatory infiltration and fibrosis. Stratification with retention of the gut layers is typical (Fig. 8.13A and B; also see Fig. 8.2, Videos 8.2 and 8.3). A target or pseudokidney appearance is possible in acute disease or long-standing fibrotic or subacute inflammatory disease as the gut wall layering is progressively lost (Fig. 8.13C and D). Long-standing and often burnt-out disease may also show wall thickening with fat deposition in the submucosa, which appears as increased echogenicity of this layer (Fig. 8.13E and F). Actively involved gut typically appears rigid and fixed, with decreased or absent peristalsis (Video 8.4). Involvement of the serosal border of the bowel may result in **spiculation** of the border of the bowel (Fig. 8.14). Skip areas are frequent. Involved segments vary in length from a few millimeters to many centimeters. Bowel wall thickening may be caused by acute inflammatory change or related to chronic fibrosis and smooth muscle hypertrophy.

Inflammatory Fat

Mesenteric edema and inflammation of the mesenteric fat are also characteristic of Crohn disease, producing a mass in the mesentery adjacent to the diseased gut that may creep over the border of the abnormal gut or completely engulf it, the so-called **creeping fat.** Fat creeping onto the margins of the involved gut creates a uniform echogenic halo around the mesenteric border of the gut, with a thyroidlike appearance in cross section (Fig. 8.15). It may become more heterogeneous and even hypoechoic in long-standing disease. Creeping fat is the most common cause of gut loop separation seen on GI contrast studies.[21] It is also the most striking and detectable abnormality on sonography of patients with perienteric inflammatory processes. Therefore detection of creeping fat should lead to a detailed evaluation of the regional gut.

Lymphadenopathy

Tender and enlarged mesenteric and perienteric nodes are common features of the active phase of inflammation with Crohn disease (Fig. 8.16). Lymphadenopathy may persist in the inactive phase. The nodes appear as focal hypoechoic masses circumferentially surrounding the gut and in the expected location of the mesenteric attachment. Nodes are frequently quite round, are of moderate size, and typically lose the normal linear echogenic streak from the nodal hilum. Similar to the gut, the lymph nodes show hyperemia as a reflection of their inflammation.

Hyperemia

Mesenteric vascularization and neoangiogenesis are recognized components of the inflammatory process, and evaluation of blood flow is a useful tool for monitoring inflammatory activity and response to therapy. Disease activity correlates with hyperemia, as seen on **color Doppler evaluation**[28] (Fig. 8.17, Video 8.5). Although subjective, this addition of color Doppler to gray-scale sonography can provide valuable supportive evidence of inflammatory change in the gut and adjacent inflamed fat[21] (see Fig. 8.6B, D, and F). However, color Doppler shows blood flow in major blood vessels with relatively fast-moving blood and does not show blood flow at the perfusion level. To overcome this limitation of activity assessment, there has been increasing interest over recent years in the use of CEUS of the bowel, performed with the injection of microbubble contrast agents. Using ultrasound quantitative techniques, CEUS allows for objective measurement of blood flow at the perfusion level as a reflection of activity. On observation, we look for transmural enhancement of the bowel wall and also a "comb sign," reflective of blood flow within the mesenteric vasculature (Fig. 8.18, Videos 8.6 and 8.7). Generation of time intensity curves allows for measurement of the peak enhancement and the area under the curve. Studies have shown a direct correlation between the level of bowel wall enhancement and active inflammatory disease, as assessed on colonoscopy.[29,30] Further, Ripollés et al.[29] show that CEUS measurements perform better than wall thickness in prediction of disease severity at colonoscopy. In our own laboratory, we have integrated the objective measurements of blood flow on CEUS with the baseline gray-scale assessments of wall thickness and inflammatory fat to improve the objectivity of activity assessments on ultrasound.[23]

Mucosal Abnormalities

Although endoscopy remains the major tool for evaluating mucosal and luminal abnormality, ultrasound may on occasion show luminal polypoid masses, such as inflammatory polyps, and deep ulcerations with pockets of echogenic air projecting within the gut wall. Ultrasound may also show intramural sinus tracts with air dissecting within the layers of the bowel wall (Fig. 8.19), as a complication of both Crohn disease and diverticulitis.

Conglomerate Masses

Conglomerate masses may be related to clumps of matted bowel, inflamed edematous mesentery, increased fat deposition in the mesentery, or, infrequently, mesenteric lymphadenopathy. Involved loops may demonstrate angulation and fixation resulting from retraction of the thickened fibrotic mesentery.

COMPLICATIONS

Strictures

Strictures are the most common complication of Crohn disease requiring surgical intervention. These are due to rigid narrowing of the gut lumen, contributed to by mural inflammation, fibrosis, and smooth muscle hypertrophy. The luminal surfaces of involved

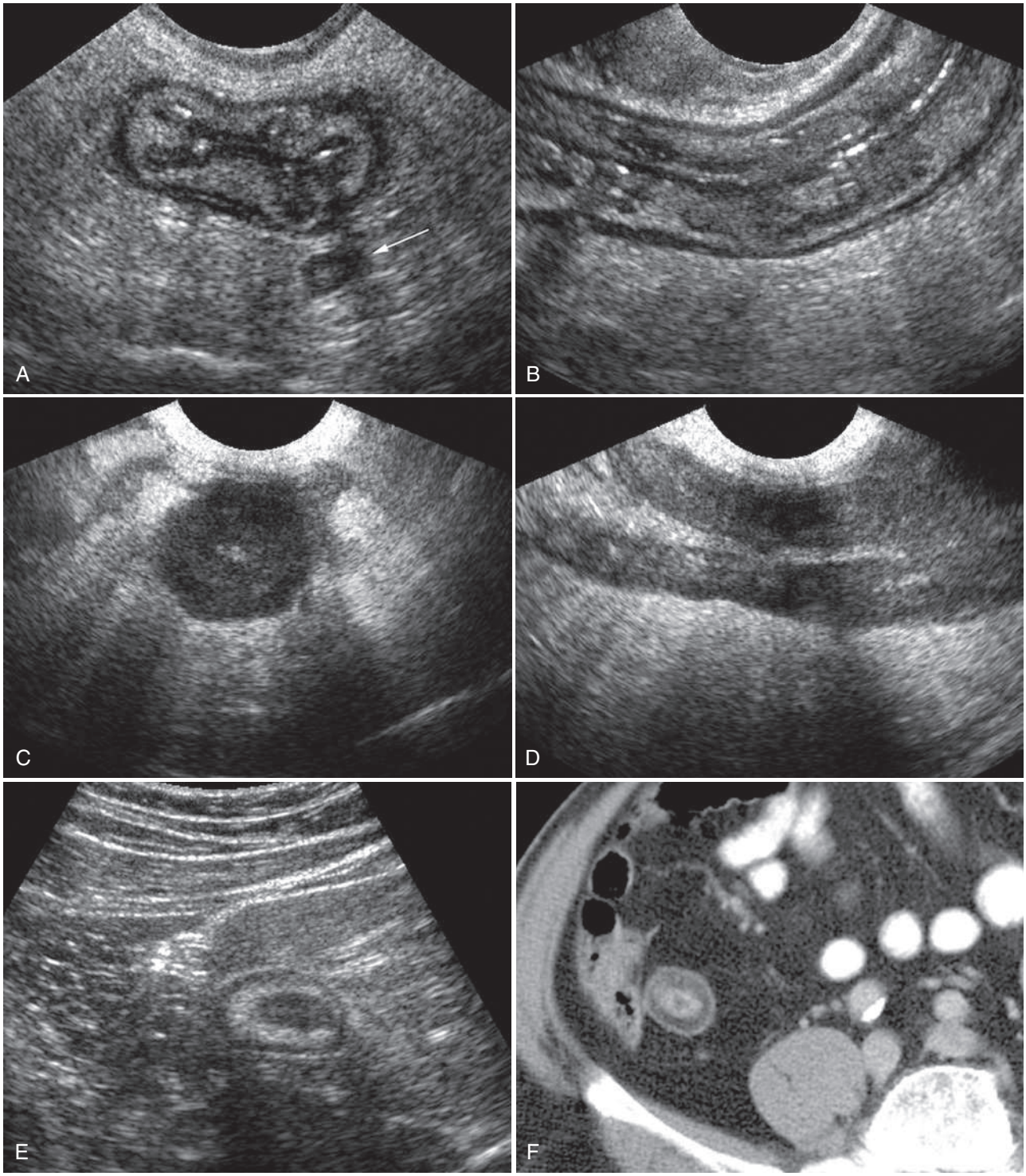

FIG. 8.13 Gut Wall Thickening in Three Patients With Crohn Disease. (A) Cross-sectional and **(B)** sagittal views showing the typical thickening in active disease with wall layer retention; *arrow,* lymph node. **(C)** Cross-sectional and **(D)** sagittal views show complete loss of wall layering, as seen with active disease. **(E)** Sonogram and **(F)** corresponding CT image of the terminal ileum in a patient with burnt-out disease and fatty deposition in the submucosa, which appears echogenic on the sonogram. See also Videos 8.2 and 8.3. (**C** and **D** with permission from Wilson SR. The bowel wall looks thickened: what does that mean? In: Cooperberg PL, editor. RSNA categorical course syllabus. Chicago: RSNA; 2002. pp. 219-228.[1])

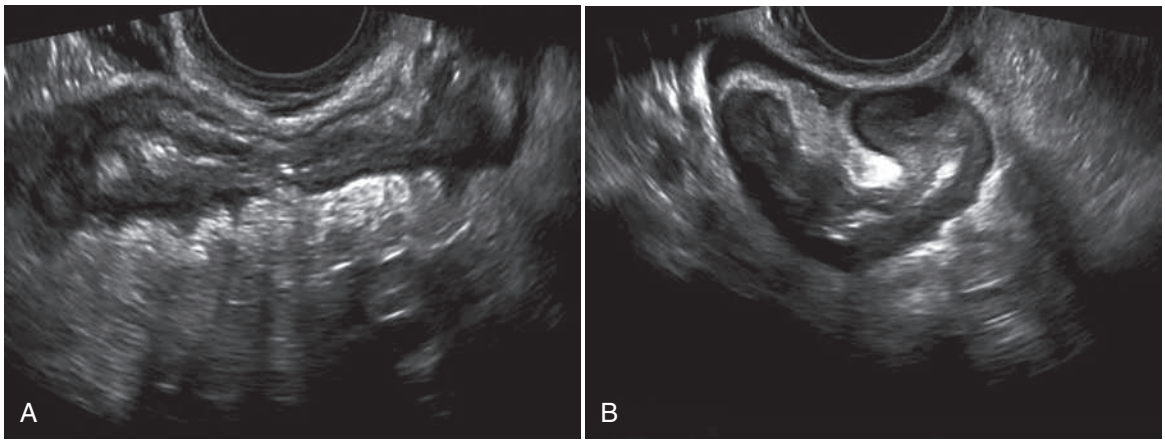

FIG. 8.14 Concerning Features for Severe Disease and Complication on Bowel Ultrasound in Two Patients. (A) A long-axis view of the terminal ileum shows bowel wall thickening and abundant surrounding echogenic inflammatory fat. The serosal margin of the bowel shows spiculation. **(B)** A long-axis view of the terminal ileum shows a hypoechoic bowel with loss of wall layering. There is a fixed acute angulation as well as spiculation of the serosal margin. Both the spiculation and fixed angulation have an association with stricture and perforation.

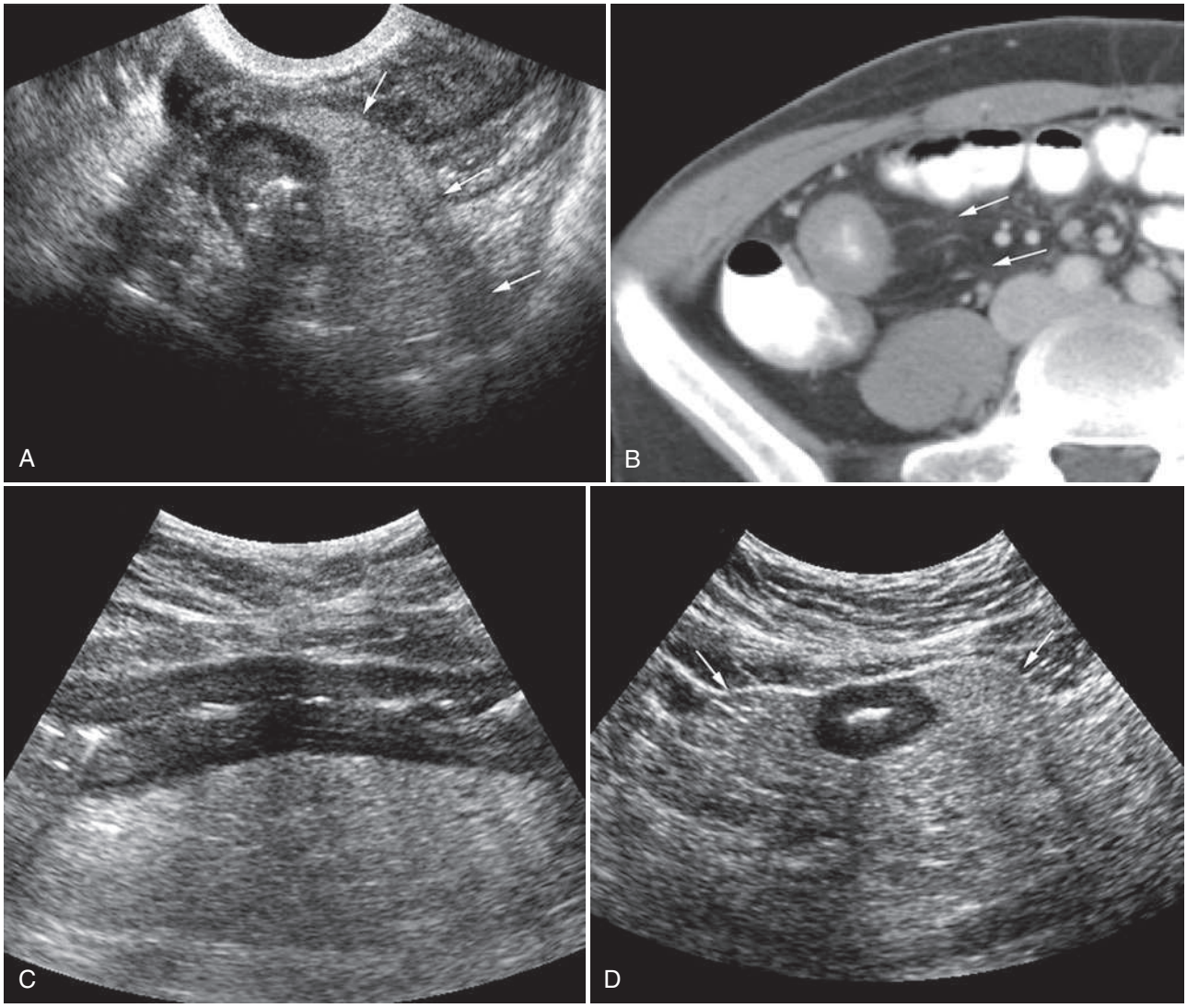

FIG. 8.15 Creeping Fat in Two Patients With Crohn Disease. (A) Cross-sectional view of terminal ileum shows a hyperechoic mass effect *(arrows)* along the medial border of the gut representing creeping fat. **(B)** Confirmatory CT scan shows both the thick wall of the terminal ileum and the streaky fat *(arrows)*. In another patient, **(C)** long-axis and **(D)** cross-sectional images of the sigmoid colon show gut wall thickening and surrounding echogenic inflammatory fat *(arrows)*.

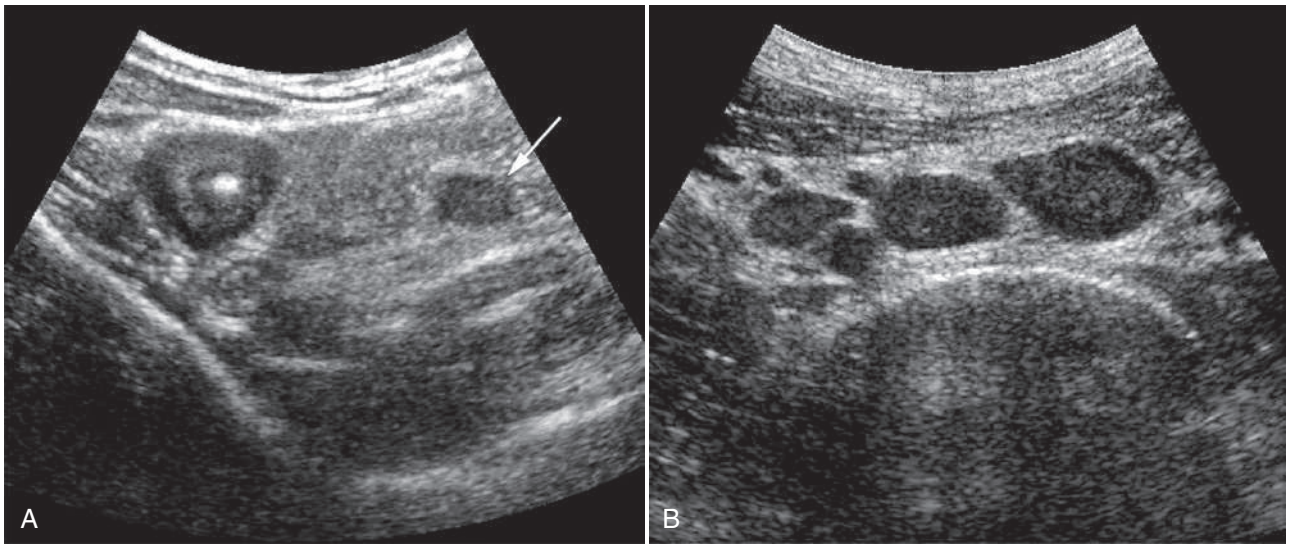

FIG. 8.16 Lymphadenopathy in Two Patients With Crohn Disease. (A) Transverse image in the right lower quadrant shows a thick terminal ileum in cross section. There is inflamed fat in the location of the mesentery. A mesenteric node *(arrow)* shows as a small, solid, hypoechoic mass within the fat. **(B)** Multiple mesenteric nodes of varying size show as hypoechoic soft tissue masses within the mesentery, optimally shown in an oblique plane between the region of the ileocecal valve and the aortic bifurcation.

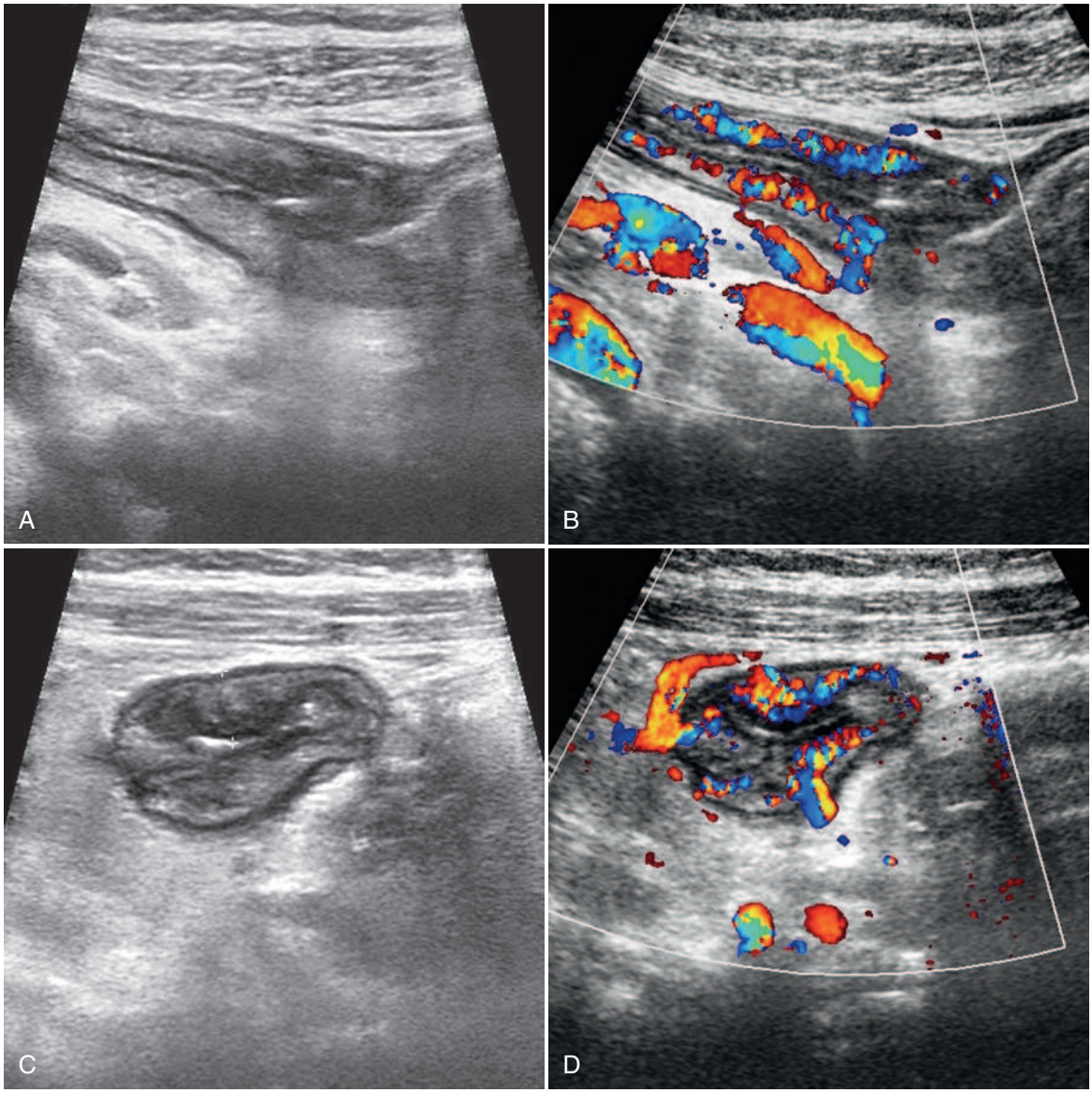

FIG. 8.17 Classic Features of Active Crohn Disease. Gray-scale **(A, C)** and color Doppler **(B, D)** images of the terminal ileum show moderate wall thickening (7 mm), moderate inflammatory fat, and moderate hyperemia on color Doppler imaging. See also Videos 8.4 and 8.5.

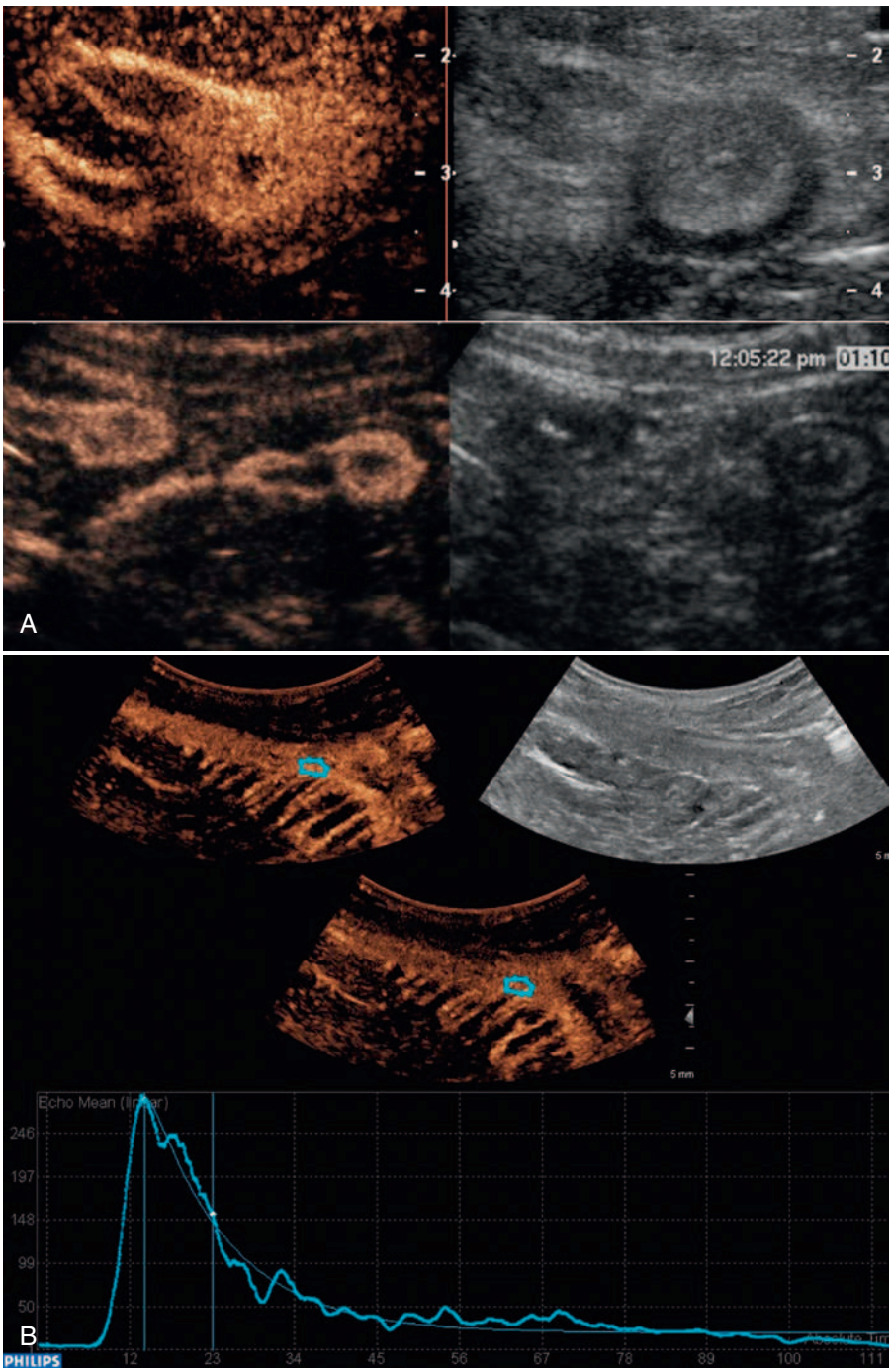

FIG. 8.18 Contrast-Enhanced Ultrasound of the Bowel in Crohn Disease, Subjective and Objective. **(A)** Two images of contrast-enhanced bowel, axial view, show the comblike vessels from vascularization of the mesentery and the transmural enhancement of the bowel wall. The adjacent images on the right are low mean intensity poor detail gray-scale, used for reference. **(B)** Images are in long axis. A region of interest in the bowel wall and a subsequent objective time intensity curve allow measurement of the peak enhancement and area under the curve. At the bottom is the time intensity curve that allows for quantification of the enhancement parameters. See also Videos 8.6 and 8.7. (**A** with permission from Wilson S. Evaluation of the small intestine by ultrasonography. In: Gourtsoyiannis N, editor. Radiologic imaging of the small intestine. Heidelberg: Springer-Verlag; 2002. pp. 73-86.[18])

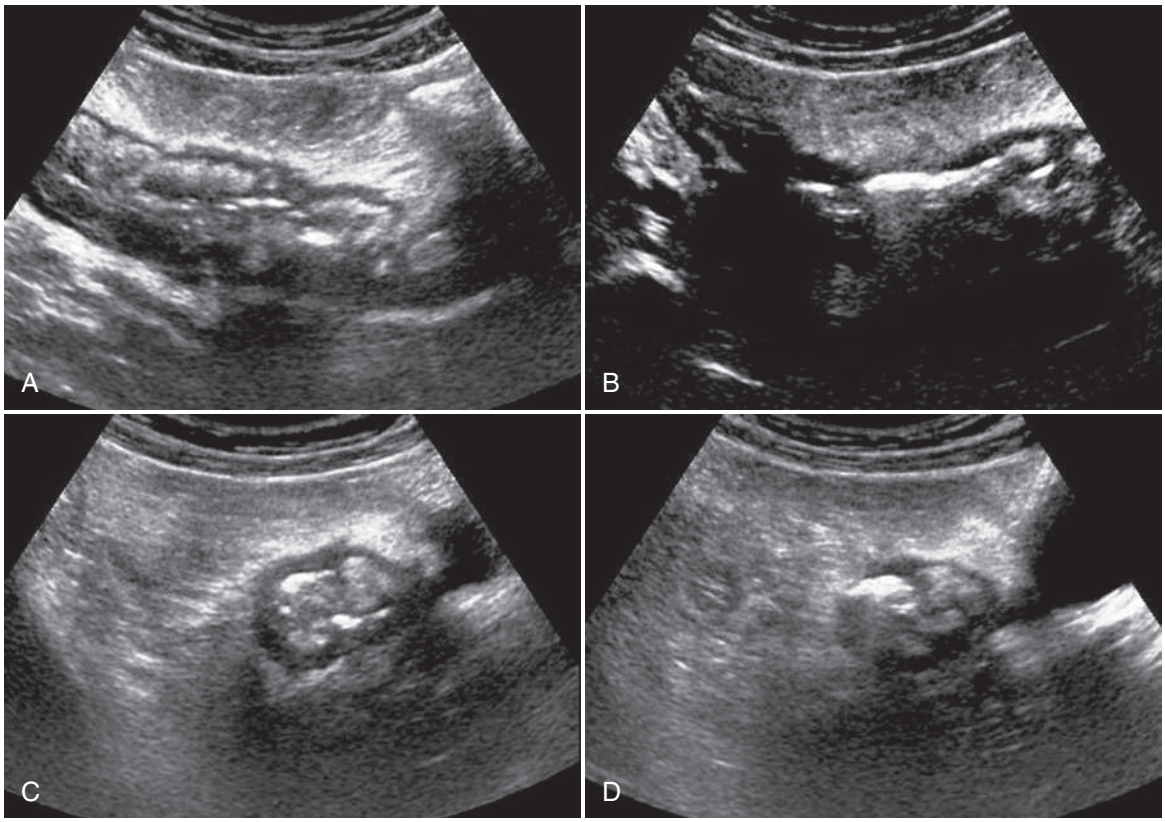

FIG. 8.19 Intramural Sinus Tract in Active Crohn Disease of the Neoterminal Ileum. (A) and **(B)** Long-axis views of the terminal ileum show wall thickening and surrounding abundant inflammatory fat. The luminal surfaces are in apposition and are central within the thickened loop. **(B)** Bright echogenic line running parallel to the serosa, an intramural sinus tract filled with air. **(C)** and **(D)** Axial images show two bright echogenic linear streaks suggesting air dissected within the layers of the bowel, deep to the echogenic submucosal layer.

segments of gut most often appear to be in fixed constant apposition, with the lumen appearing as a linear echogenic central area within a thickened gut loop (Fig. 8.20). This is in contrast to thickened sections, where the luminal diameter may be maintained (Fig. 8.21). Fixed acute angulations are frequent associations with advanced strictures (Video 8.8). Incomplete mechanical obstruction may be inferred if dilated, hyperperistaltic segments are seen proximal to a stricture (Fig. 8.21C and D, Videos 8.9 and 8.10). Peristaltic waves from the obstructed gut, proximal to a narrowed segment, may produce visible movement through the strictured segment. Less often, involved segments of gut show luminal dilation with sacculation, as well as narrowing, and the retained lumen is of variable caliber. Concretions and bezoars may develop in gut between strictured segments.

Parente et al.[31] showed that bowel ultrasound is an accurate technique for detecting small bowel strictures, especially in patients with severe disease who are candidates for surgery.

Management of strictures in Crohn disease is challenging. Differentiating between patients who have a predominantly inflammatory versus a mainly fibrotic component of their stricture is imperative to improve selection between medical therapy and surgery. Investigations using only gray-scale ultrasound features are frequently inconclusive.

However, bowel ultrasound has been shown to detect fibrosis using a variety of elastographic techniques. Shear wave elastography uses acoustic radiation force impulse technology to assess elastic properties of tissue through an acoustic ultrasound force that propagates a shear wave through tissue. Measurements of the velocity in meters per second (m/sec) of this shear wave traversing through the tissue are made. Shear wave elastography provides an objective and reproducible quantitative measurement of tissue stiffness.[32] Early investigations assessing fibrosis in animal models with elastography show some promising results.[33] Our recent experience combines both CEUS and point shear wave elastography. Our results suggest CEUS parameters reflect inflammation and elastography values reflect the chronic features of fibrosis and smooth muscle hypertrophy, improving greatly our contributions to patient management.[34]

Incomplete Mechanical Bowel Obstruction

Obstructive symptoms of bloating abdominal pain and abdominal distention are frequently associated with stricture in IBD. On sonography, distended prestenotic loops of bowel are fluid distended and show dysfunctional and excess peristalsis (see Fig. 8.21C and D, Videos 8.9 and 8.10).

Localized Perforation

Although free perforation of the bowel is rare in Crohn disease, localized perforation with phlegmonous masses contained within the surrounding perienteric inflammatory fat is common

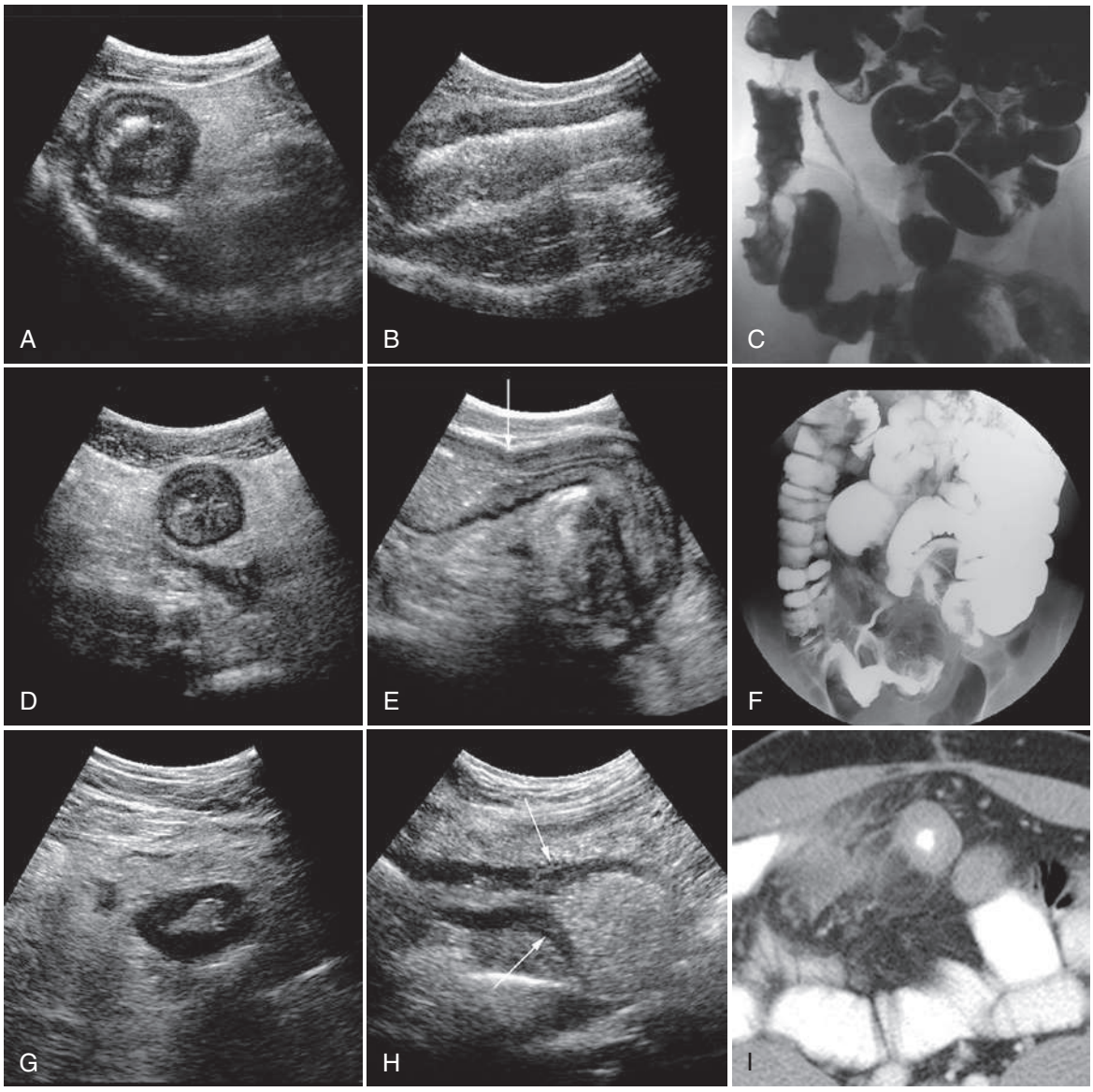

FIG. 8.20 Strictures in Three Patients With Crohn Disease. **(A)** An axial view of the terminal ileum shows wall thickening and surrounding inflammatory fat. **(B)** The long-axis image shows long segment thickening with luminal apposition. **(C)** Confirmatory fluoroscopic image from a small bowel enema shows the long, tight stricture in the ileum. **(D)** and **(E)** Sonograms of the terminal ileum show an abrupt transition in the caliber of the gut *(arrow).* The gut proximal to the arrow is dilated and fluid filled. The distal gut has a stricture, confirmed on **(F)**, the small bowel enema. **(G)** Short-axis image through the stricture shows the thickened wall and surrounding inflamed fat. **(H)** Long-axis image of the neoterminal ileum shows a thickened, featureless wall with a caliber alteration *(arrows).* **(I)** Confirmatory CT scan.

(Fig. 8.22, Video 8.11). Spiking of the border of acutely inflamed gut is characteristic (see Fig. 8.14). On occasion, an air-containing tract may be identified, traversing the bowel wall into the perienteric fat. Phlegmonous masses should alert the sonographer to possible underlying localized perforation.

Inflammatory Masses

Inflammatory masses involving the fibrofatty mesentery are the most common complication of Crohn disease, although the development of abscesses with drainable pus occurs infrequently. Before the stage of liquefaction, phlegmonous change may be noted as poorly defined, hypoechoic areas without fluid content interdigitating into the surrounding inflamed fat (Figs. 8.23A and B and 8.24A). Abscess formation results in a complex or fluid-filled mass (Figs. 8.23G-I and 8.24B). Gas content within an abscess is helpful in suggesting an abscess, but this gas content is also a potential source of sonographic error, particularly if large quantities are present. Abscesses may be intraperitoneal or extraperitoneal or may be in remote locations such as the liver, abdominal wall (Fig. 8.23H and I), and psoas muscles. An excellent application of CEUS is in the characterization of inflammatory masses related to the bowel in a variety of clinical situations. The differentiation of phlegmonous inflammatory masses, without drainable pus, from those with liquid content

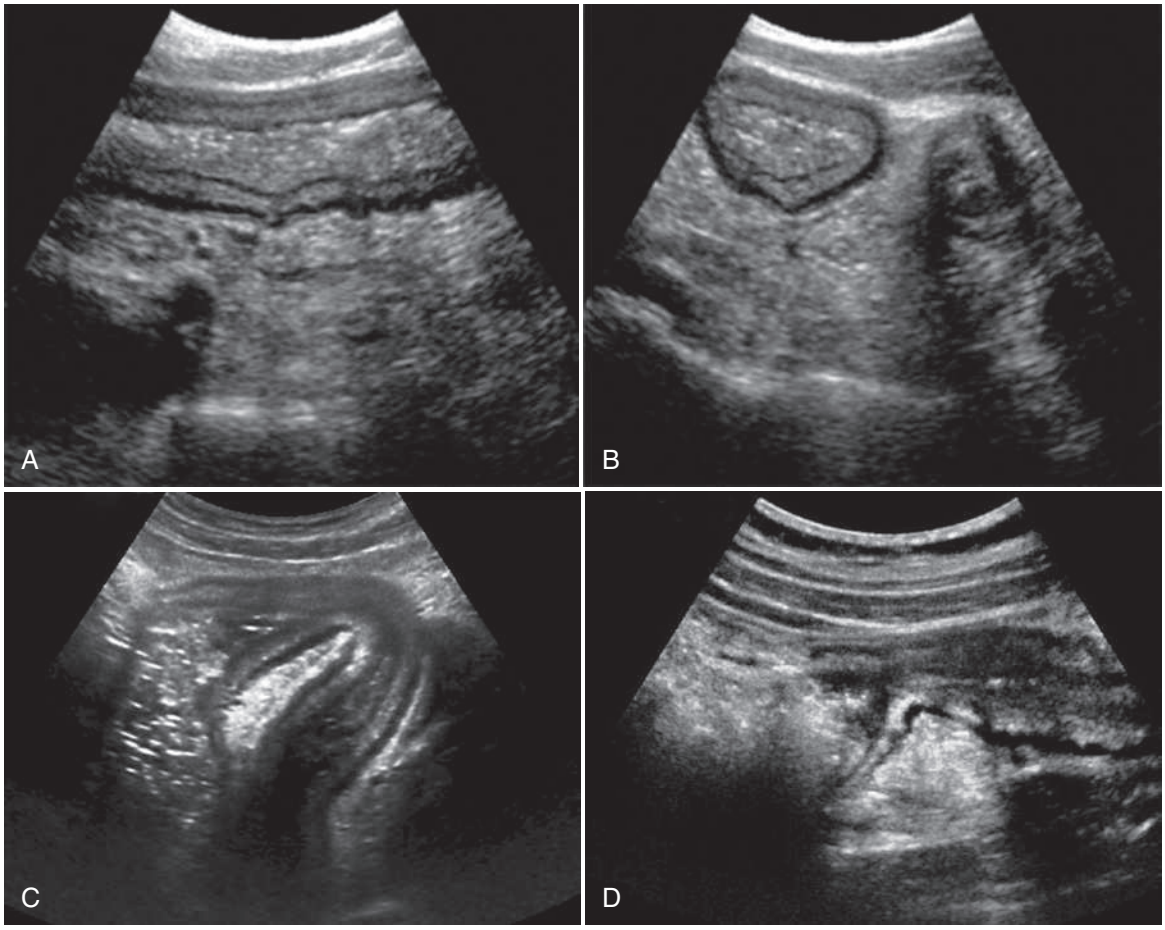

FIG. 8.21 Bowel Proximal to a Stricture in Three Patients. (A) and **(B)** Images of the small bowel slightly proximal to a stricture show a fluid-distended lumen and moderate mural wall thickening. **(C)** and **(D)** Two patients with prestenotic fluid-distended bowel and a stricture distal with an obvious transition point. See also Videos 4.9 and and 4.10.

is frequently a challenge.[35] The addition of CEUS will quickly and effectively differentiate these masses as phlegmons are invariably hypervascular, whereas all fluid-containing abscesses are completely avascular on CEUS (Fig. 8.25)

Fistula Formation

This characteristic penetrating complication of Crohn disease occurs most often at the proximal end of a thickened, strictured segment of bowel. Although mucosal ulcerations are not well assessed on sonography, deep fissures in the gut wall or intramural sinus tracts appear as echogenic linear areas penetrating deeply into the wall beyond the margin of the gut lumen (see Fig. 8.22, Video 8.11). With fistula formation, linear bands of varying echogenicity can be seen extending from segments of abnormal gut to the skin (Fig. 8.26C), bladder (Figs. 8.26B and 8.27D), vagina, or other abnormal loops (Video 8.12). If there is gas or movement in the fistula during the sonographic study, the fistula will usually appear bright or echogenic, with or without ring-down artifact related to air in the tract. Conversely, if the tract is empty or partially closed, the fistula may appear as a hypoechoic or hypoechoic tract. Palpation of the abdomen during the examination may produce movement of fluid or air through the fistula, assisting in its identification.

Perianal Inflammatory Disease

Perianal inflammation is a frequent and debilitating complication of Crohn disease and its presence at initial diagnosis is a poor prognostic indicator. Highly complex, transsphincteric tracts may extend to involve the deep tissues of the buttocks (Fig. 8.28), perineum, scrotum (men), and labia and vagina (women). Unlike commonly encountered perianal fistulas based on the cryptoglandular theory, fistulas in Crohn disease have no predilection for the location of the internal openings and are highly complex. In patients of either gender, we have found **transperineal scanning** to be the most comfortable and often most informative technique, performed alone or in combination with transrectal ultrasound.[36] Further, in women, transvaginal scan contributes greatly to our assessment of rectal and perirectal disease. It is also ideal for showing enterovesical, enterovaginal, and rectovaginal fistulas.[37] Rectal involvement in Crohn disease is characterized by (1) thickening of the rectal wall with wall layer preservation, (2) inflammation of the perirectal fat, and (3) enlargement of the perirectal lymph nodes.

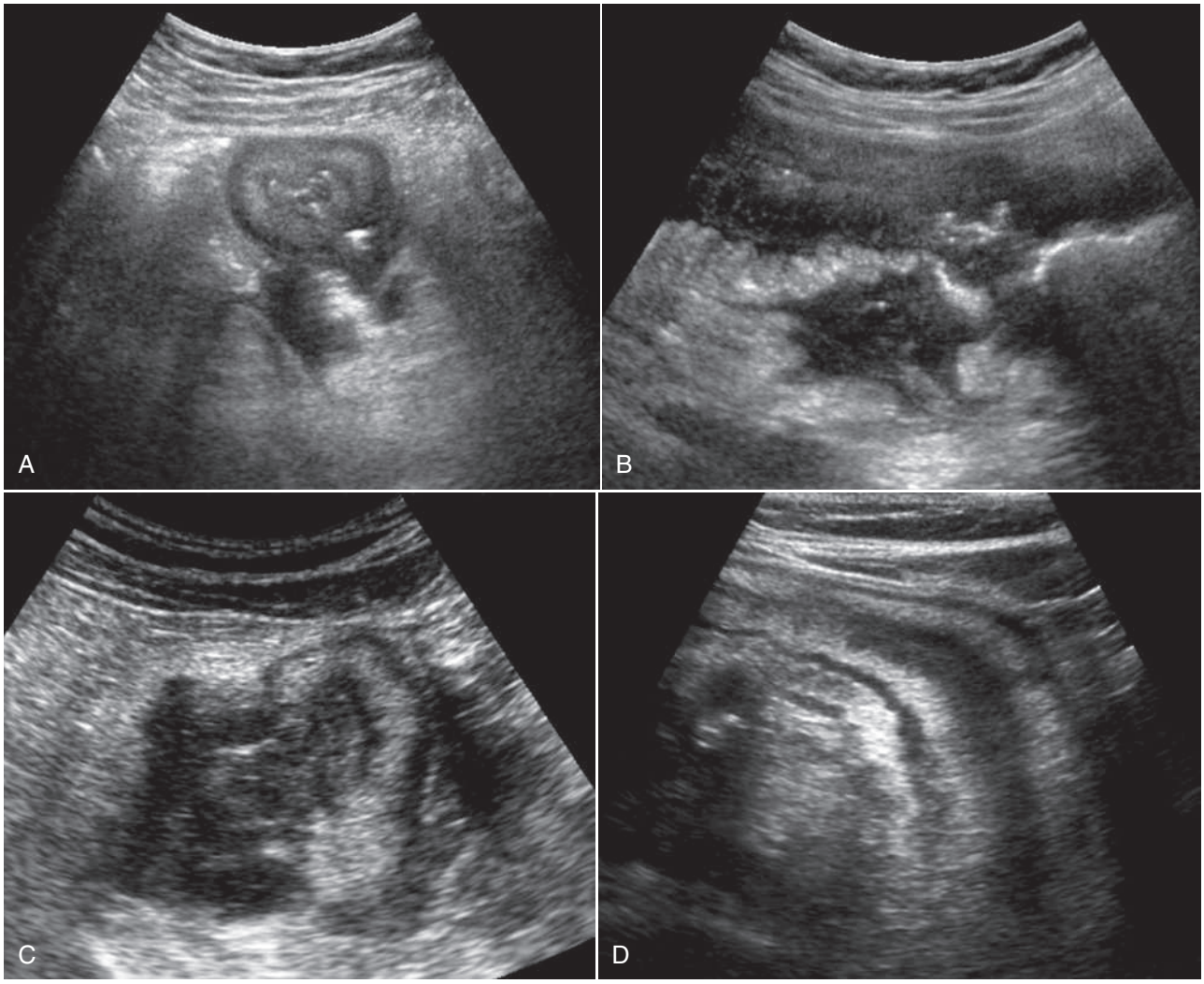

FIG. 8.22 Localized Perforation With Phlegmon. Two young women with acute flare of Crohn disease symptoms. **(A)** and **(B)** First patient. **(A)** Cross-sectional and **(B)** long-axis images of the bowel show wall thickening and a deep hypoechoic mass with fingerlike projections into the surrounding perienteric fat, suggesting phlegmon. Also, on **(A)**, air appears as a bright focus extending beyond the lumen of the bowel into the bowel wall, suggesting localized perforation. **(C)** and **(D)** Second patient. **(C)** Cross-sectional image of the ileum shows a large area of disruption of the bowel wall, an adjacent hypoechoic phlegmon, and an air tract from localized perforation. **(D)** Long-axis image of loop of ileum shows that the wall is uniformly thickened with layer preservation. The phlegmon is on the margin of the bowel and not shown in the longitudinal view. See also Video 8.11.

ACUTE ABDOMEN

Sonography is a valuable imaging tool in patients with specific suspected acute GI abnormalities such as acute appendicitis or acute diverticulitis.[38] However, its contribution to the assessment of patients with possible GI tract disease is less certain. Seibert et al.[39] emphasized the value of ultrasound in assessing the patient with a distended and gasless abdomen and detecting ascites, unsuspected masses, and abnormally dilated, fluid-filled loops of small bowel. In my experience, sonography has been helpful not only in the gasless abdomen but also in a variety of other situations. The real-time aspect of sonographic study allows for direct patient–sonographer/physician interaction, with confirmation of palpable masses and focal points of tenderness. The doctrine "scan where it hurts" is invaluable and has led sonographers to describe the value of the sonographic equivalent to clinical examination with such descriptors as a sonographic Murphy sign or sonographic McBurney sign. Similar to the radiographic approach to plain film interpretation, a systematic approach is essential in the sonographic assessment of the abdomen in a patient with an acute abdomen of uncertain origin.

The abdominal ultrasound evaluation should include visible gas and fluid (to determine their luminal or extraluminal location), the perienteric soft tissues, and the GI tract itself. Identification of gas in a location where it is not usually found is a clue to many important diagnoses. The gas itself may appear as a bright, echogenic focus, but the identification of the artifacts associated with the gas pockets usually leads to their detection. These include both ring-down artifact and "dirty" shadowing. Extraluminal gas may be intraperitoneal (**Free intraperitoneal**

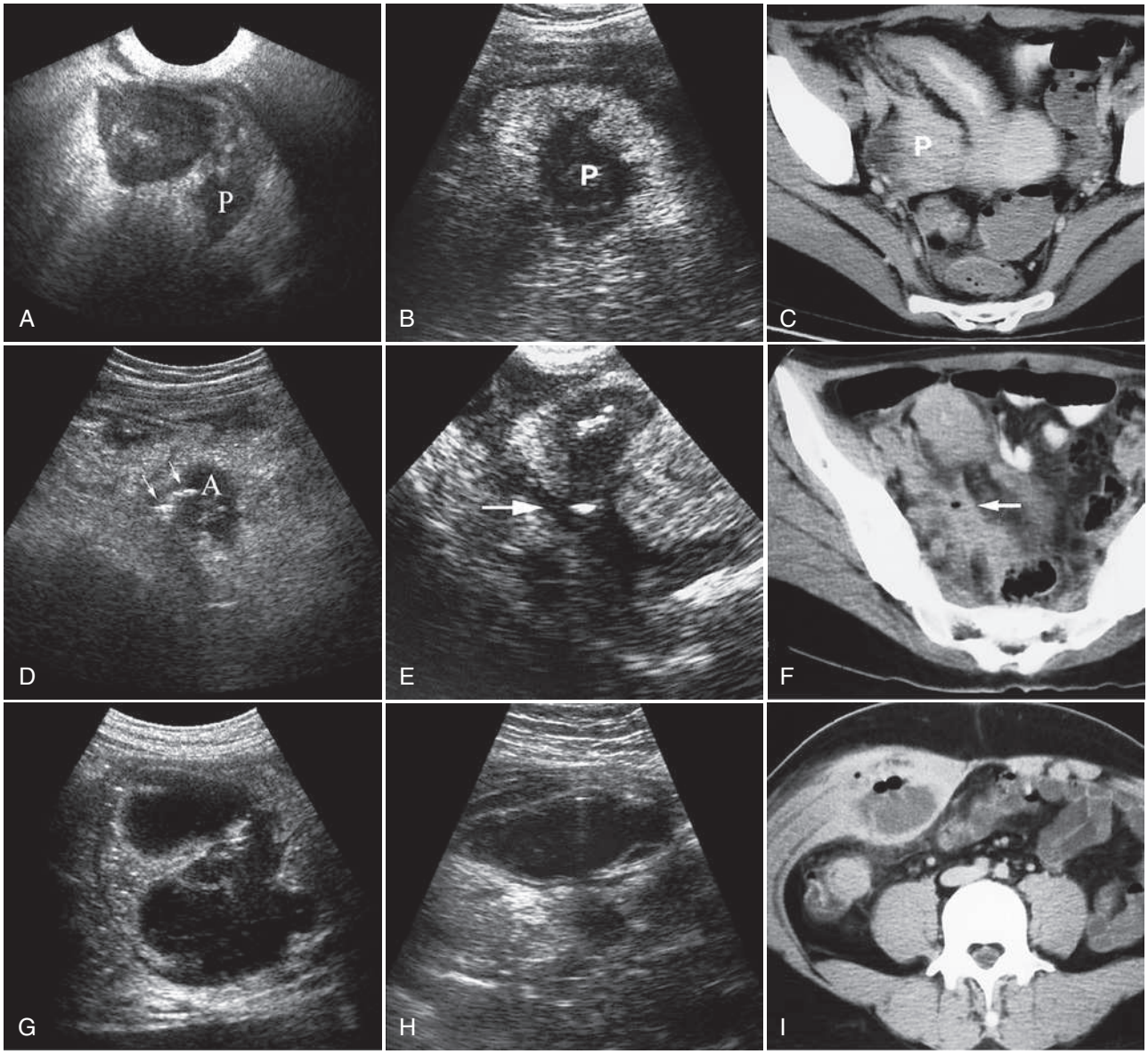

FIG. 8.23 Inflammatory Masses in Crohn Disease. *Top row,* **Phlegmons** *(P).* **(A)** Loop of thick sigmoid colon is seen in cross section. Adjacent to the margin is a poorly defined, hypoechoic zone within extensive inflamed fat. **(B)** Transverse sonogram in the right lower quadrant shows a thick terminal ileum superficially. Within the extensive inflamed fat is a poorly defined, hypoechoic zone representing the phlegmon. **(C)** Confirmatory CT scan. *Middle row,* **Inflammatory masses,** with air but no drainable pus. **(D)** Transverse image of the right lower quadrant shows abundant inflamed fat. Centrally, there is a small fluid collection or abscess *(A)* with small, echogenic shadowing foci *(arrows)* caused by air bubbles. **(E)** Cross-sectional sonogram through the terminal ileum shows gut thickening, echogenic inflamed fat, and a poorly defined, focal hypoechoic area deep to the gut. Bubbles of gas outside the gut are seen as bright, echogenic foci *(arrow)* on sonography. **(F)** Confirmatory CT scan. *Bottom row,* **Drainable abscesses. (G)** Large, interloop fluid collection. **(H)** Sonogram and **(I)** confirmatory CT scan show a superficial fluid collection with small gas bubbles in the anterior abdominal wall. (**B, E, F, H,** and **I** with permission from Sarrazin J, Wilson SR. Manifestations of Crohn disease at US. Radiographics. 1996;16[3]:499-520.[21])

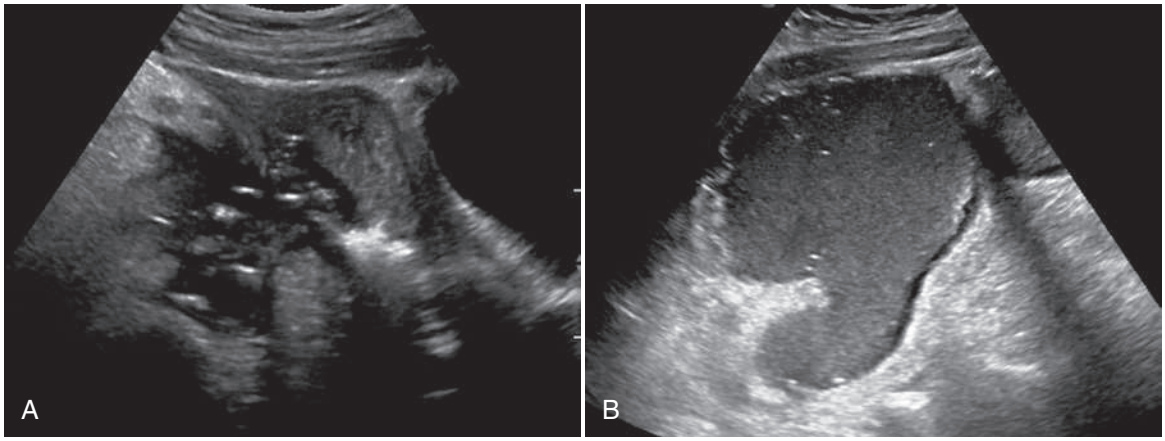

FIG. 8.24 Inflammatory Masses on Sonography. (A) Classic phlegmon with no drainable pus. The mass is hypoechoic and interdigtitates with the surrounding inflammatory fat. There are bright foci of extraluminal air within. **(B)** Classic abscess—a well-defined mass with uniform low-level echoes within related to the presence of pus.

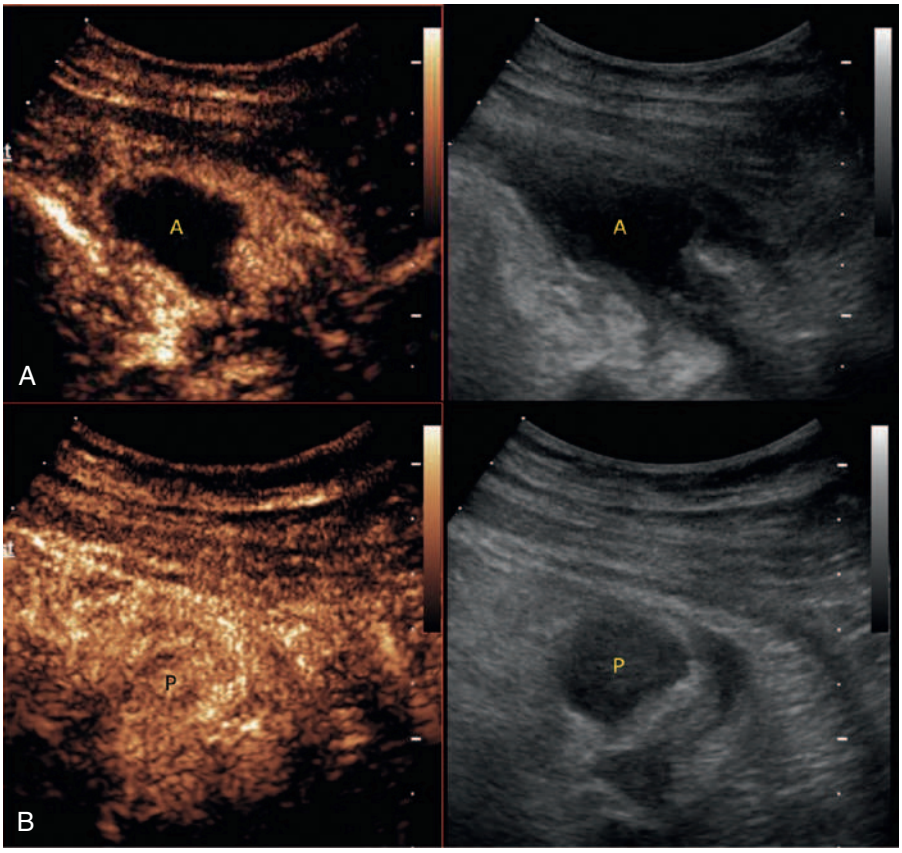

FIG. 8.25 Use of Contrast-Enhanced Ultrasound (CEUS) to Distinguish Between Abscess and Phlegmon; Exams in Two Patients. Both examinations include a contrast-enhanced image *(left)* and low-resolution gray-scale image *(right)*. **(A)** Hypoechoic mass on baseline is completely avascular on CEUS diagnostic for a fluid-containing abscess *(A)*. **(B)** Hypoechoic mass is uniformly vascular on CEUS, diagnostic for a hypervascular inflammatory mass, a phlegmon. (With permission from Wilson S. Evaluation of the small intestine by ultrasonography. In: Gourtsoyiannis N, editor. Radiologic imaging of the small intestine. Heidelberg: Springer-Verlag; 2002. pp. 73-86.[18])

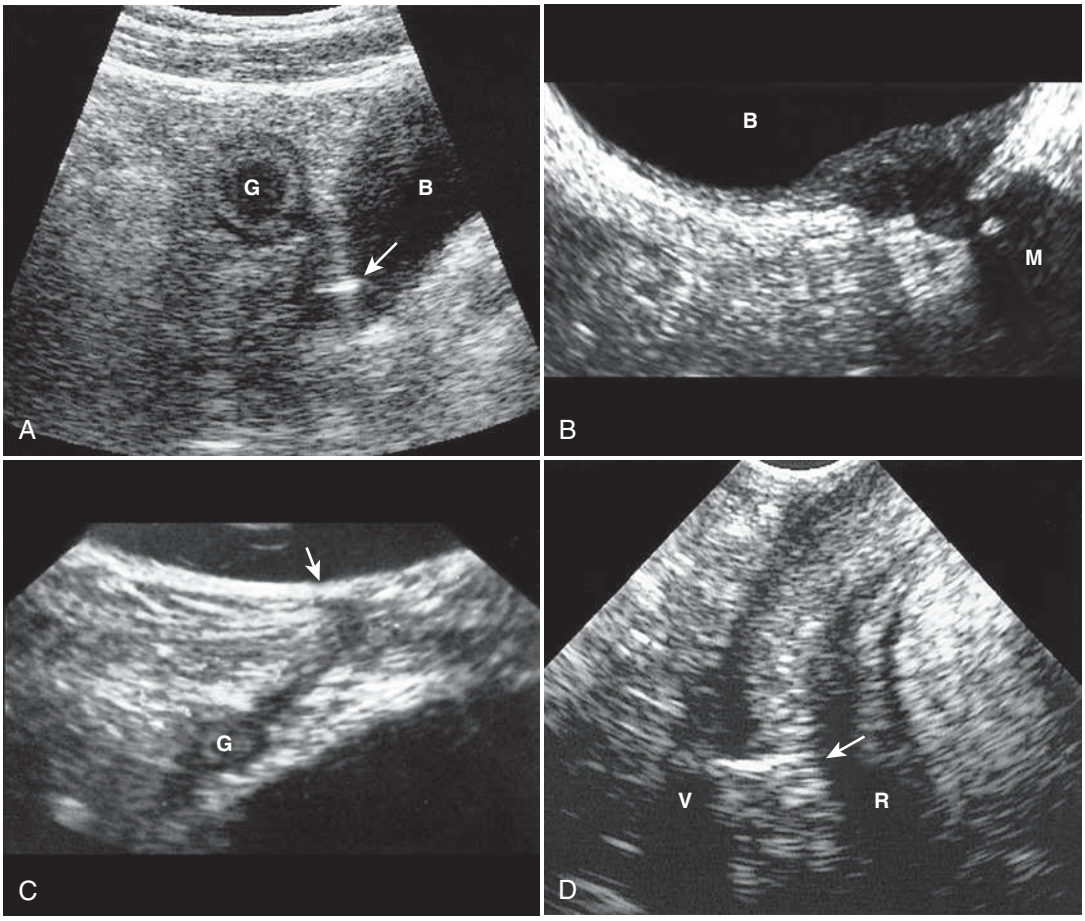

FIG. 8.26 Fistulas in Patients With Crohn Disease. (A) and **(B) Enterovesical fistulas. (A)** Tract between the abnormal gut *(G)* and the bladder *(B)*. An air bubble within shows as a bright, echogenic focus *(arrow)*. **(B)** Hypoechoic tract connects an inflammatory mass *(M)* to the bladder *(B)*. **(C) Enterocutaneous fistula.** Hypoechoic tract runs from a loop of abnormal gut *(G)* to the skin surface *(arrow)*. **(D) Rectovaginal fistula** on transvaginal sonogram appears as a bright, air-containing tract *(arrow)* coursing from the rectum *(R)* to the vagina *(V)*. See also Video 8.12 for **enteroenteric fistula.**

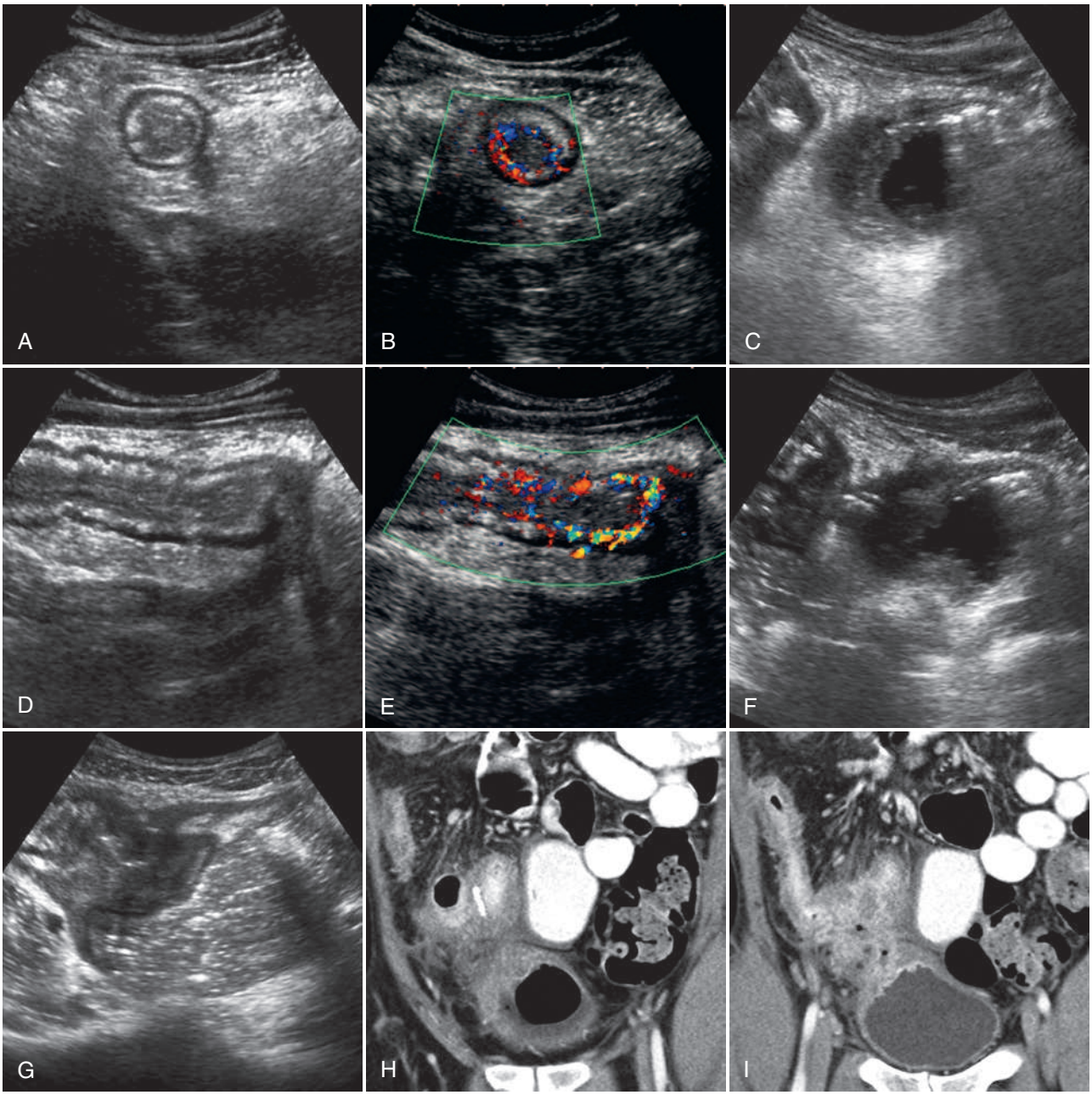

FIG. 8.27 Enterovesical Fistula in Crohn Disease. (A) and **(B)** Cross-sectional images of the terminal ileum show wall thickening and hyperemia. **(C)** Air in the bladder appears as nondependent bright echoes with dirty shadowing. **(D)** and **(E)** Long-axis views of the ileum show the hyperemia and the constant luminal apposition, consistent with stricture. **(F)** Bladder with the luminal air and an air-containing tract from the bladder to the adjacent bowel. **(G)** Dilated, fluid-filled bowel proximal to the thickening, suggesting incomplete mechanical bowel obstruction. **(H)** and **(I)** Coronal CT images confirm the bladder air and an inflammatory mass related to the bladder dome.

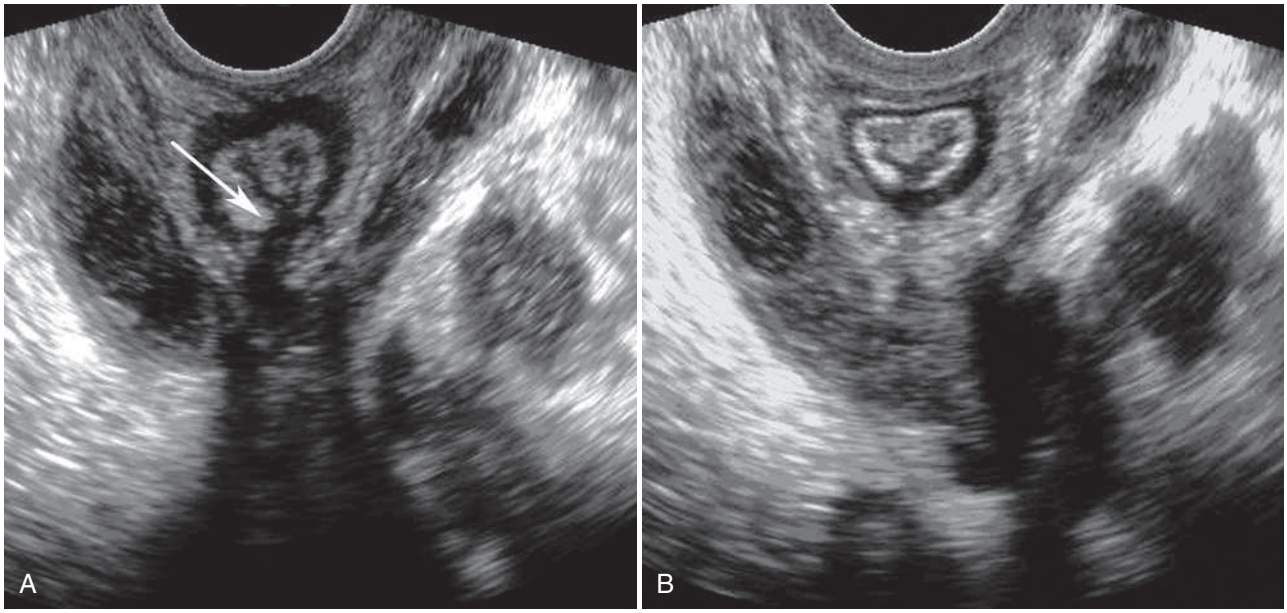

FIG. 8.28 Perianal Inflammatory Crohn Disease. (A) Axial image of the anal canal shows an internal opening *(arrow)* posteriorly at 6 o'clock. A transsphincteric fistula runs to a large, horseshoe-shaped posterior abscess more optimally shown in **(B)**, which also shows deeper collections in the left buttock.

air) or retroperitoneal, and its presence should suggest either hollow viscus perforation or infection with gas-forming organisms[40] (Fig. 8.29). Nonluminal gas may be easily overlooked, particularly if the collection is large. Gas in the wall of the GI tract, **pneumatosis intestinalis,** with or without gas in the portal veins, raises the possibility of ischemic gut.

The likelihood of gas artifacts between the abdominal wall and the underlying liver to be related to free intraperitoneal gas was well described by Lee et al.[40] In my group's work, we have found that the peritoneal stripe appears as a bright, continuous, echogenic line, and that air adjacent to the peritoneal stripe produces enhancement of this layer, because the gas has a higher acoustic impedance to sound waves than does the peritoneum itself. Careful peritoneal assessment is best done with a 5-MHz probe or even a 7.5-MHz probe, with the focal zone set at the expected level of the peritoneum. In a clinical situation, enhancement of the peritoneal stripe is a highly specific but insensitive sign to detect pneumoperitoneum.[41]

Loculated **fluid collections** can mimic portions of the GI tract. Left upper quadrant and pelvic collections suggestive of the stomach and rectum may be clarified by adding fluid orally and rectally. Assessing peristaltic activity and wall morphology also helps in distinguishing luminal from extraluminal collections. Interloop and flank collections are aperistaltic and tend to correspond in contour to the adjacent abdominal wall or intestinal loops, frequently forming acute angles, which are rarely seen with intraluminal fluid.

The appearance of the **perienteric soft tissues** is frequently the first and most obvious clue to abdominal pathology on abdominal sonograms. Inflammation of the perienteric fat shows as a hyperechoic mass effect (see Fig. 8.15), often without the usual appearance of normal gut and its contained small pockets of gas. Neoplastic infiltration of the perienteric fat is often

Acute Abdomen: Sonographic Approach

GAS
Intraluminal
Extraluminal
- Intraperitoneal
- Retroperitoneal
- Gut wall
- Gallbladder/biliary ducts
- Portal veins

FLUID
Intraluminal
- Normal caliber gut
- Dilated gut

Extraluminal
- Free
- Loculated

MASSES
Neoplastic
Inflammatory

Perienteric Soft Tissues
Inflamed fat
Lymph nodes

Gut
Wall
Caliber
Peristalsis

Clinical Interaction
Palpable mass
Maximal tenderness
Sonographic Murphy sign
Sonographic McBurney sign

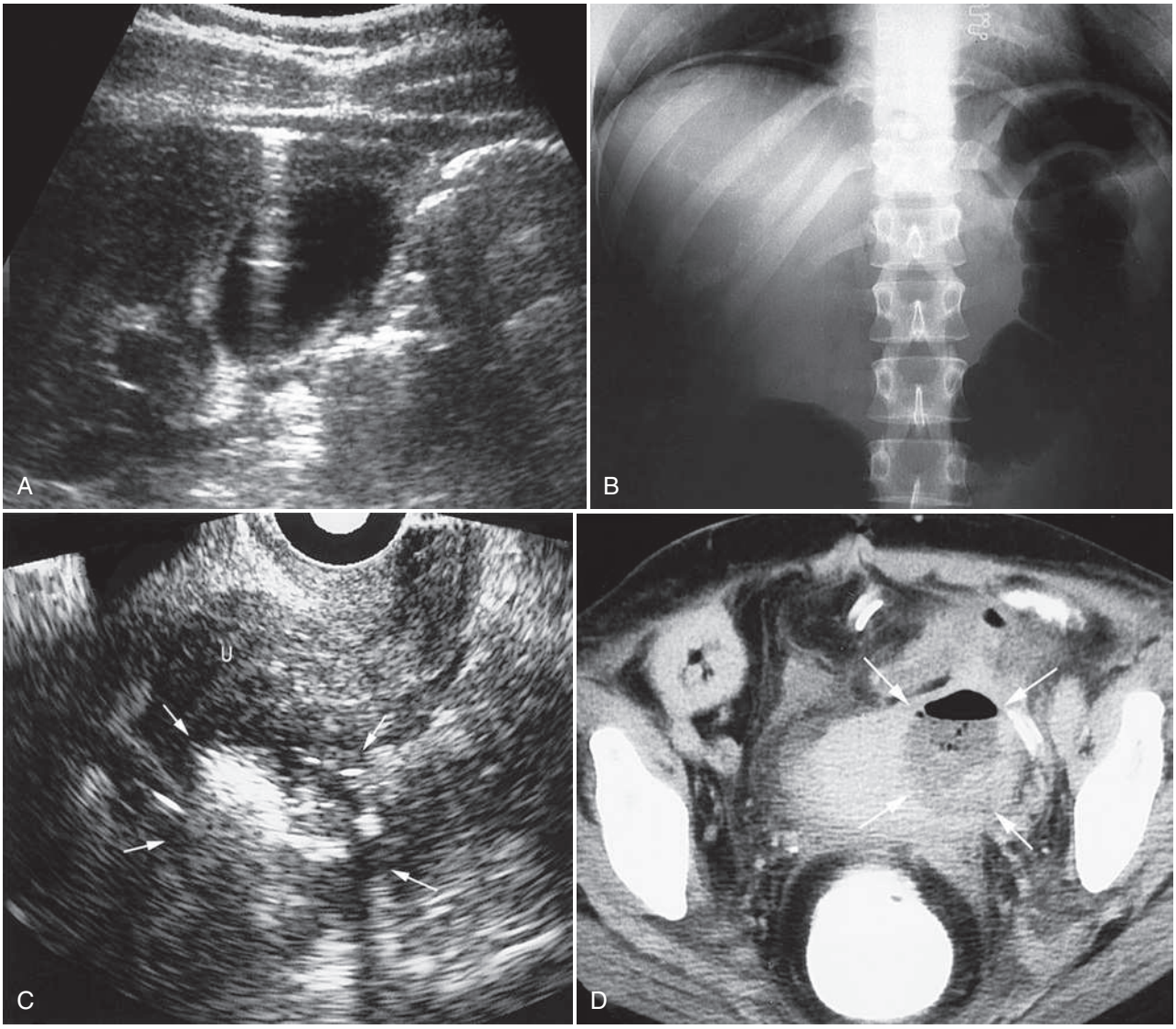

FIG. 8.29 Value of Gas for Sonographic Diagnosis in Two Patients. (A) Pneumoperitoneum. Sonogram shows a bright, echogenic focus representing free air between the abdominal wall and liver. Also shown is enhancement of the peritoneal stripe. **(B)** Confirmatory plain film. **(C)** Transvaginal image shows a large, gas-containing **abscess** *(arrows)* posterior to the uterus *(U)*, secondary to acute **diverticulitis** in a renal transplant recipient. **(D)** Confirmatory CT scan shows the air containing deep abscess *(arrows)*.

indistinguishable from inflammatory infiltration on ultrasound (see Fig. 8.8C and D).

Mesenteric adenopathy is another manifestation of both inflammatory and neoplastic processes of the gut that should be specifically sought when performing abdominal sonography. As elsewhere, lymph nodes tend to change in size and shape when replaced by abnormal tissue. A normal, oval or flattened lymph node with a normal linear hilar echo becomes increasingly round and hypoechoic with either inflammatory or neoplastic replacement. In contrast to the sonographic appearance of loops of gut, mesenteric lymph nodes typically appear as focal, discrete hypoechoic masses of varying size (see Fig. 8.16). Their identification on sonography suggests enlargement because they are not usually seen on routine examinations. In the presence of mesenteric adenopathy, abnormal masses related to or causing a GI tract abnormality should also be sought; these most often are neoplastic or inflammatory in origin.

Right Lower Quadrant Pain

Acute Appendicitis

Acute appendicitis is the most common explanation for the "acute abdomen presentation" to an emergency department. Patients typically have right lower quadrant (RLQ) pain, tenderness, and leukocytosis. A mass may also be palpable. The patient with a classic presentation may have an appendectomy without preoperative imaging. This approach often becomes complicated when a normal appendix is removed in a patient with symptoms caused by other factors. On the other hand, surgery may be delayed in some patients with acute appendicitis if the presentation is atypical. This approach may lead to perforation before the surgery, making it a complicated and difficult procedure, often followed by abscess formation. In older clinical literature before routine cross-sectional imaging was available, laparotomy resulted in removal of normal, noninflamed appendices in 16% to 47% of cases (mean, 26%).[42,43] Also, perforation occurred in up to 35%

of patients.[44] It is a balance between this negative laparotomy rate and the perforation rate at surgery that motivates cross-sectional imaging before initiating treatment for the patient with acute RLQ pain. For a patient with suspected appendicitis, the sonographic objectives are to identify the patient with acute appendicitis, to identify the patient without acute appendicitis, and, in this latter population, to identify an alternate explanation for the RLQ pain.

Symptoms of appendicitis, RLQ pain, and elevated white blood cell count overlap with a variety of other GI conditions, including **typhlitis, mesenteric adenitis, Crohn disease,** right-sided **diverticulitis, segmental infarction of the omentum,** and, in women, acute gynecologic conditions such as **ruptured or torsion of an adnexal cyst** or **pelvic inflammatory disease.**[45] Urologic disease, especially stone-related and right-sided segmental omental infarction, may also mimic acute appendicitis. Addressing the value of sonography in establishing an alternative diagnosis in patients with suspected acute appendicitis, Gaensler et al.[46] found that 70% of patients with another diagnosis had abnormalities visualized on the sonogram. From a retrospective review of 462 patients with suspected appendicitis who underwent appendectomy, Bendeck et al.[47] found that women in particular benefit most from preoperative imaging, with a statistically significant, lower negative appendectomy rate than women with no preoperative imaging.

Both CT and ultrasound provide sensitive and accurate diagnosis of appendicitis. The choice of imaging modality is determined somewhat by local expertise.[48] Some institutions also screen patients on the basis of their weight, sending thin patients for ultrasound and reserving CT for larger patients. These considerations aside, we recommend **sonographic evaluation of all women (and children)**—with the addition of transvaginal scan for all patients whose pain is still not explained after completion of a traditional suprapubic pelvic sonogram.

The pathophysiology of acute appendicitis likely involves obstruction of the appendiceal lumen, with 35% of cases demonstrating a fecalith.[49] Mucosal secretions continue, increasing the intraluminal pressure and compromising venous return. The mucosa becomes hypoxic and ulcerates. Bacterial infection ensues, eventually with gangrene and perforation. A walled-off abscess is more common than free peritoneal contamination.

Acute appendicitis begins with transient, visceral, or referred crampy pain in the periumbilical area associated with nausea and vomiting. Coincident with inflammation of the serosa of the appendix, the pain shifts to the RLQ and may be associated with physical signs of peritoneal irritation. Both clinical and experimental data support the belief that some patients have repeated attacks of appendicitis.[50,51]

In 1986 Puylaert[6] described the value of **graded compression sonography** in the evaluation of 60 consecutive patients suspected of having acute appendicitis. Puylaert's initial reports of success in diagnosing acute appendicitis depended solely on visualization of the abnormal appendix, a blind-ended, noncompressible, aperistaltic tube arising from the tip of the cecum with a gut signature (Fig. 8.30). However, other investigators reported seeing normal appendices on a sonogram.[52,53] The normal appendix is compressible, with a wall thickness of 3 mm or less[54] (Fig. 8.31, Video 8.13). Jeffrey et al.[55] concluded that size can differentiate the normal from the acutely inflamed appendix. Threshold levels for the diameter of the appendix, above which acute appendicitis is highly likely, have been set at either 6 mm or 7 mm, with a resultant change in sensitivity and specificity. Sonographic visualization of an appendix with an **appendicolith,** regardless of appendiceal diameter, should also be regarded as a positive test. Rettenbacher et al.[56] added assessment of appendiceal **morphology** in confirming suspicion of appendicitis. A round or partly round appendix had a high correlation with acute appendicitis, whereas an ovoid appendix did not. Color Doppler is also contributory, showing hyperemia in the appendiceal wall in the acutely inflamed appendix.

Lee et al.[57] described visualization of the appendix in 485 of 570 patients (85%) using graded compression sonography alone. Use of a posterior manual compression technique allowed for identification of the appendix in an additional 57 of the remaining 85 patients, increasing the percentage of identified appendices to 95%.

The appendix positioned in the true pelvis may show subtle evidence of inflammation on a suprapubic scan because the pathology may be deep in the pelvic cavity. In our experience, this occurs most often in women, possibly related to a more capacious pelvis, and the clinical presentation is frequently that of pelvic inflammatory disease. This particular disease is optimally studied with transvaginal placement of the ultrasound probe because the appendix is often intimately related to either the uterus or the ovaries. The origin of such an appendix from the base of the cecum may be impossible to determine on transvaginal sonography, and compression with the ultrasound probe is often not feasible. Nonetheless, the identification of the blind-ended tip of the appendix with an increased diameter, luminal distention, and inflammation of the surrounding fat is obvious (Fig. 8.32). If rupture of a pelvic appendix has occurred before the sonogram, the identification of a **pelvic abscess** without identification of the appendix itself may produce an equivocal result as to the source of the pelvic inflammatory problem.

Although the sensitivity of sonography for the diagnosis of appendicitis decreases with **perforation,** features associated with

Acute Appendicitis: Sonographic Diagnosis

IDENTIFY APPENDIX

Blind ended
Noncompressible
Aperistaltic tube
Gut signature
Arising from base of cecum (typically appendix is caudal to the base of the cecum but it may also be retrocecal and retroileal)
Diameter greater than 6 mm (some use 7 mm for greater specificity)

SUPPORTIVE FEATURES

Inflamed perienteric fat
Pericecal collections
Appendicolith

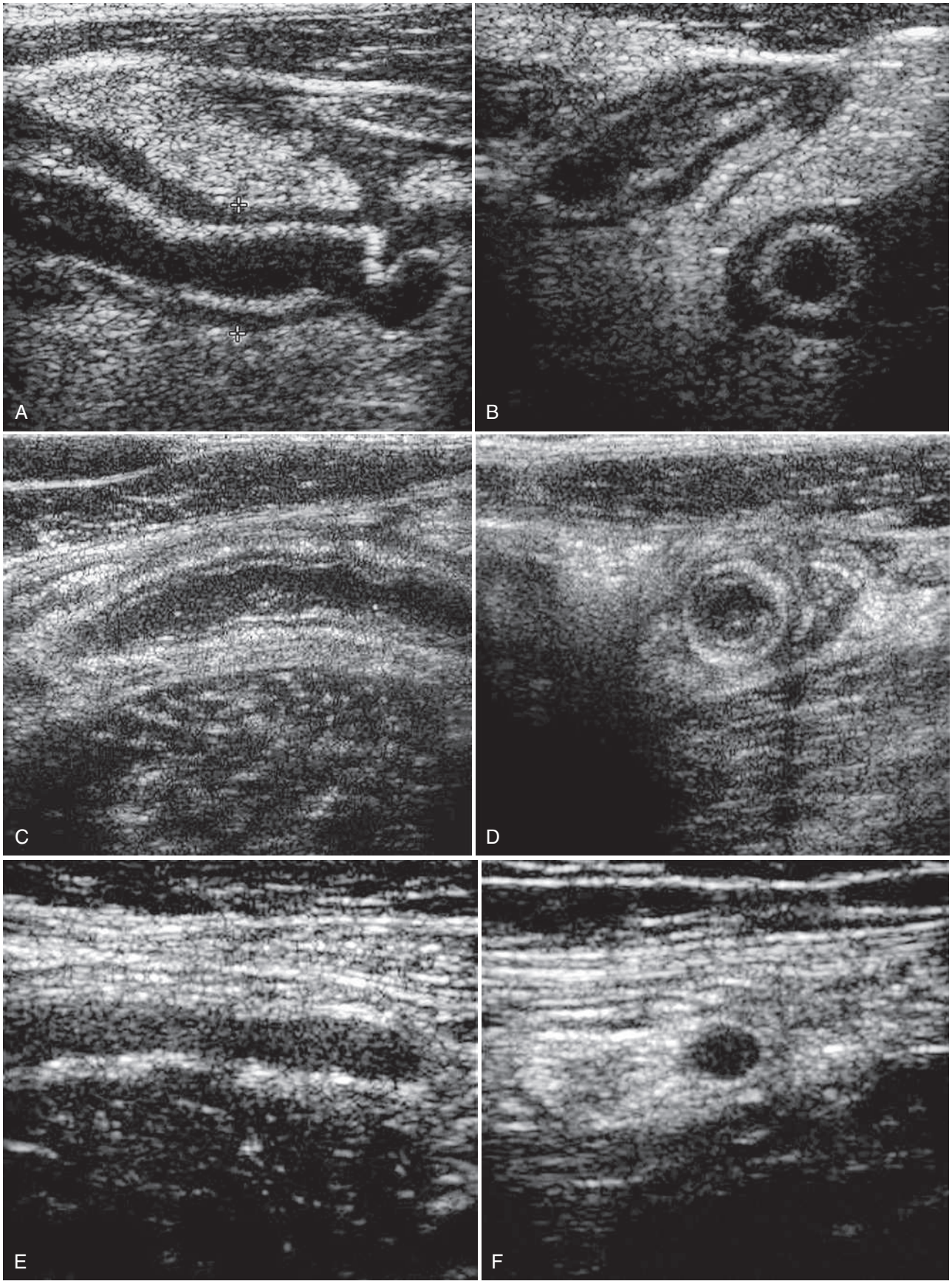

FIG. 8.30 Acute Appendicitis in Three Patients. (A), (C), and **(E)** Long-axis views show the blind-ended tip of the appendix. **(C)** Tip is directed to the left of the image as the appendix ascends cephalad from its origin from the cecum. **(B), (D),** and **(F)** Corresponding cross-sectional views. The appendix looks round in short axis on all cases, and the lumen is distended with fluid. The appendix is surrounded with inflamed fat. The gut signature is preserved in the top two cases **(A-D)**. The bottom case (**E** and **F**) shows loss of definition of the wall layers, suggesting gangrenous change.

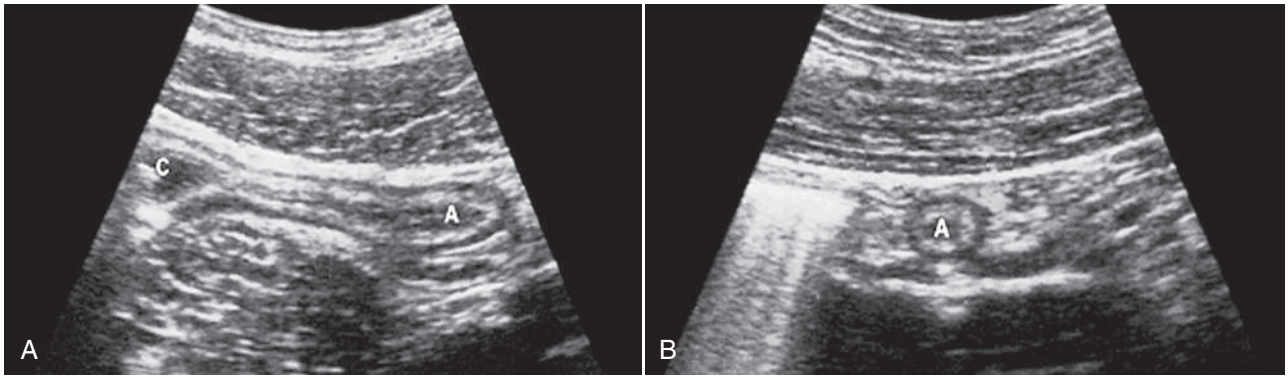

FIG. 8.31 Normal Appendix. (A) Long-axis image and **(B)** cross-sectional image show the normal appendix *(A)* arising from the base of the cecum *(C)*. The appendix shows a gut signature, a blind end, and measures 6 mm or less in diameter. See also Video 8.13.

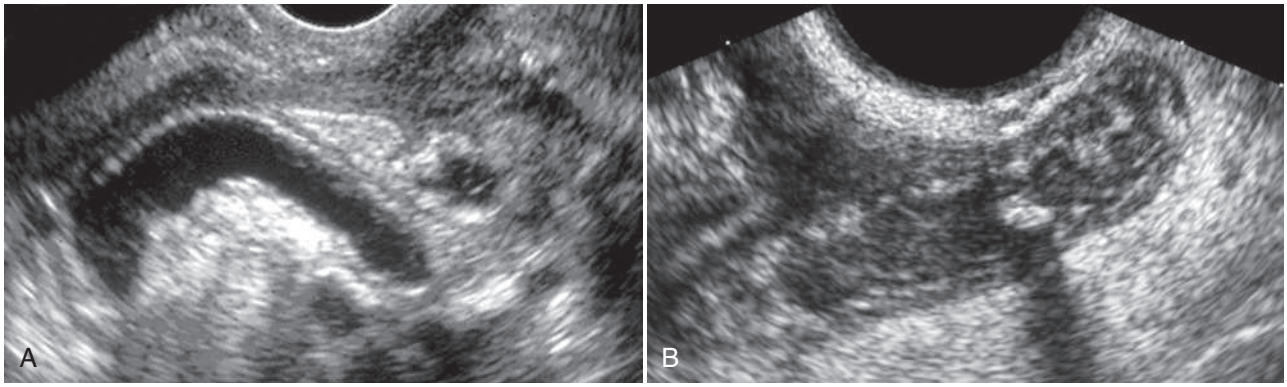

FIG. 8.32 Value of Transvaginal Sonography for Diagnosis of Acute Appendicitis. (A) Long-axis view of the appendix on transvaginal sonography was the only view to show the blind-ended tip of the fluid-distended appendix. **(B)** Appendix is a large, fluid-filled, thick-walled structure and shows a shadowing appendicolith.

Sonography of Appendiceal Perforation

Loculated pericecal fluid
- Phlegmon
- Abscess

Prominent pericecal fat
Circumferential loss of submucosal layer of the appendix

its occurrence include loculated pericecal fluid, phlegmon or abscess, prominent pericecal or periappendiceal fat, and circumferential loss of the submucosal layer of the appendix[58] (Fig. 8.33, Video 8.14). False-positive diagnosis for acute appendicitis may occur if a normal appendix or a thickened terminal ileum is mistaken for an inflamed appendix.

Crohn Appendicitis

Patients with Crohn disease may have acute appendicitis caused by IBD involvement of the appendix, in contrast to acute suppurative appendicitis. The wall of the appendix typically is extremely thickened and hyperemic with wall layer preservation, and the luminal surfaces are often in apposition[59] (Fig. 8.34). This appearance contrasts with that in suppurative appendicitis, where luminal distention is the expectation and wall thickening is moderate at best.

Crohn appendicitis is a self-limited process,[60,61] and treatment may be conservative if the appropriate diagnosis can be established with noninvasive techniques. In a small number of the patients for whom we have suggested this diagnosis, follow-up sonograms have shown resolution of the sonographic findings with no disease progression. Patients with Crohn disease who present with Crohn appendicitis account for about 10% of total presentations. This patient population typically has a more benign course. If the appendix is removed surgically in the mistaken belief that the patient has acute suppurative appendicitis, recurrence or progression of Crohn disease is rare.

Right-Sided Diverticulitis

Acute inflammation of a right-sided diverticulum is distinct from the more common diverticulitis that is encountered in the left hemicolon. These diverticula occur more often in women than in men and have a predilection for Asian populations. Most patients are young adults. Right-sided diverticula are usually solitary and are congenital in origin. They are **true** diverticula and therefore have all layers of the gut wall. Their inflammation is associated with RLQ pain, tenderness, and leukocytosis, with a mistaken diagnosis of appendicitis in virtually all cases.

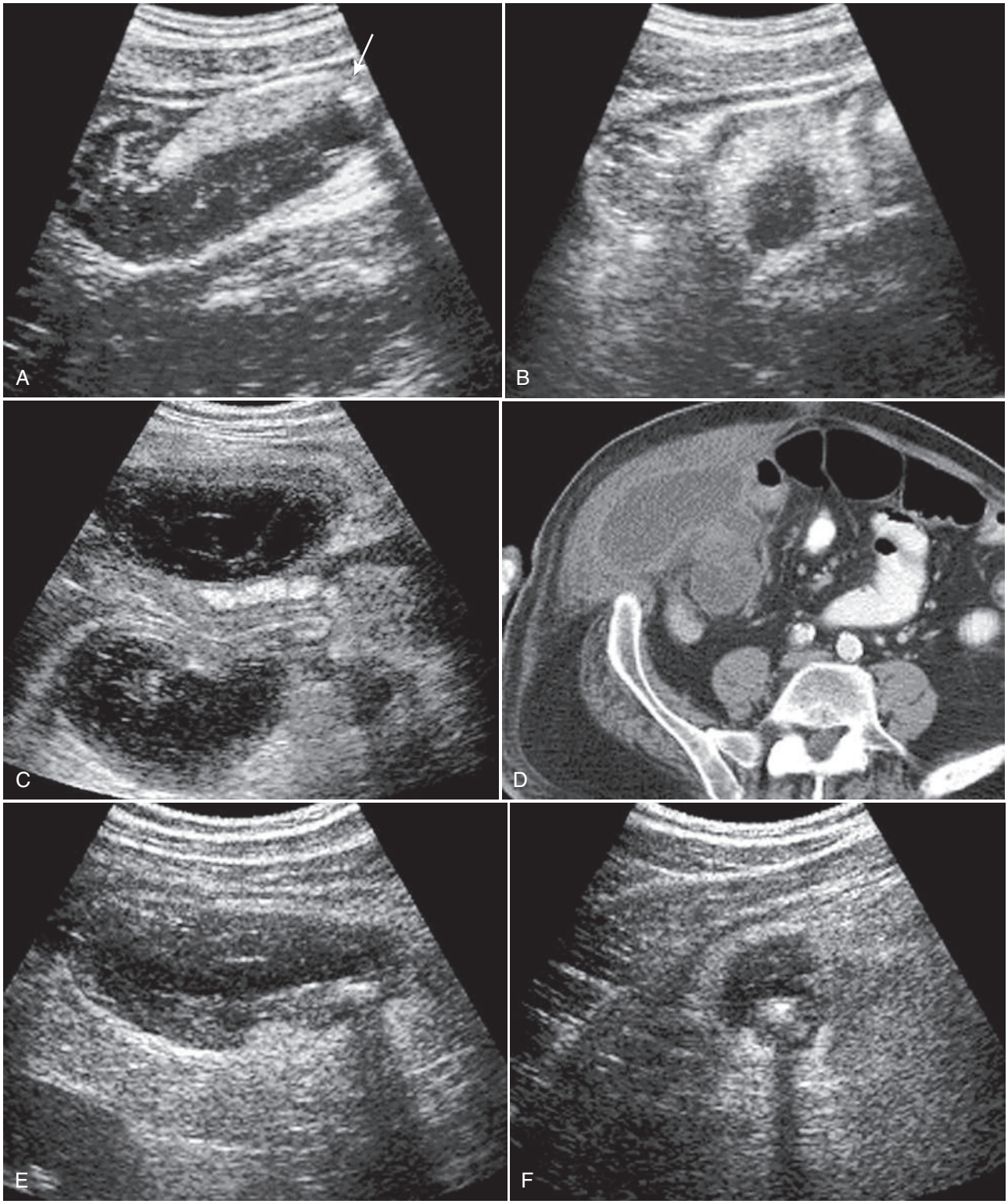

FIG. 8.33 Perforation of Appendix in Three Patients. (A) Long-axis image and **(B)** cross-sectional image show the blind-ended appendix. There is loss of definition of the wall layers, and the appendix is surrounded by an echogenic mass effect representing inflamed fat in the mesoappendix. **(A)** Arrow points to a bubble of extraluminal gas at the tip of the appendix; tip perforation was confirmed at surgery. **(C)** Sonogram and **(D)** CT scan show a **periappendiceal abscess.** The decompressed appendix is seen centrally on the sonogram. **(E)** Long-axis and **(F)** transverse images in the right lower quadrant show an abscess with an escaped **appendicolith** with acoustic shadowing. The appendix is no longer visible. See also Video 8.14. (**C** with permission from Birnbaum B, Wilson S. Appendicitis at the millennium. Radiology. 2000;215[2]:337-348.[48])

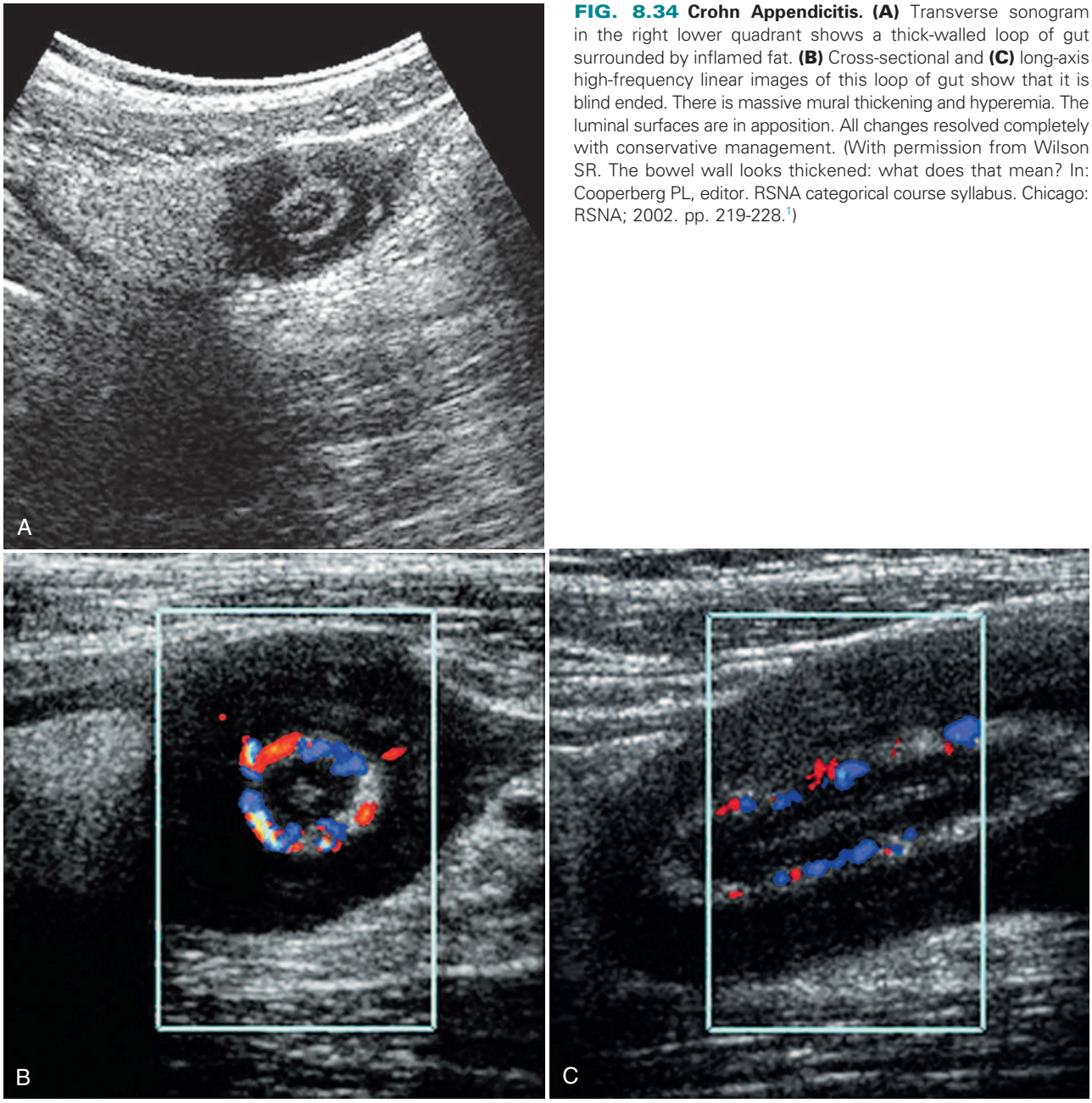

FIG. 8.34 Crohn Appendicitis. (A) Transverse sonogram in the right lower quadrant shows a thick-walled loop of gut surrounded by inflamed fat. **(B)** Cross-sectional and **(C)** long-axis high-frequency linear images of this loop of gut show that it is blind ended. There is massive mural thickening and hyperemia. The luminal surfaces are in apposition. All changes resolved completely with conservative management. (With permission from Wilson SR. The bowel wall looks thickened: what does that mean? In: Cooperberg PL, editor. RSNA categorical course syllabus. Chicago: RSNA; 2002. pp. 219-228.[1])

On sonography, acute diverticulitis is associated with inflammation of the pericolonic fat. The diverticula may be located in the cecum or the adjacent ascending colon. When inflamed, they may have one of two appearances.[62] Most often, the diverticulum may show as a pouch or saclike structure arising from the colonic wall[63] (Fig. 8.35). Wall layers are continued into the wall of the congenital diverticulum. Hyperemia of the diverticulum and the inflamed fat is typical. If a fecalith is present within the diverticulum, it may show as a bright, echogenic focus located within or beyond a segment of thickened colonic wall. Occasionally, the culprit diverticulum is not evident and the only observations are those of inflamed fat and focal thickening of the colonic wall. In the appropriate clinical milieu, this is highly suspicious for acute diverticulitis. Treatment of acute diverticulitis is conservative and not surgical, emphasizing the importance of preoperative imaging in patients with RLQ pain attributed to this condition.

Acute Typhlitis

Immunocompromised patients are most often affected with acute typhlitis. Although infrequent today in North America, AIDS patients previously accounted for the overwhelming majority of cases of acute typhlitis seen since 1990. **Cytomegalovirus** (CMV) and ***Cryptosporidium*** are the pathogens isolated most often in

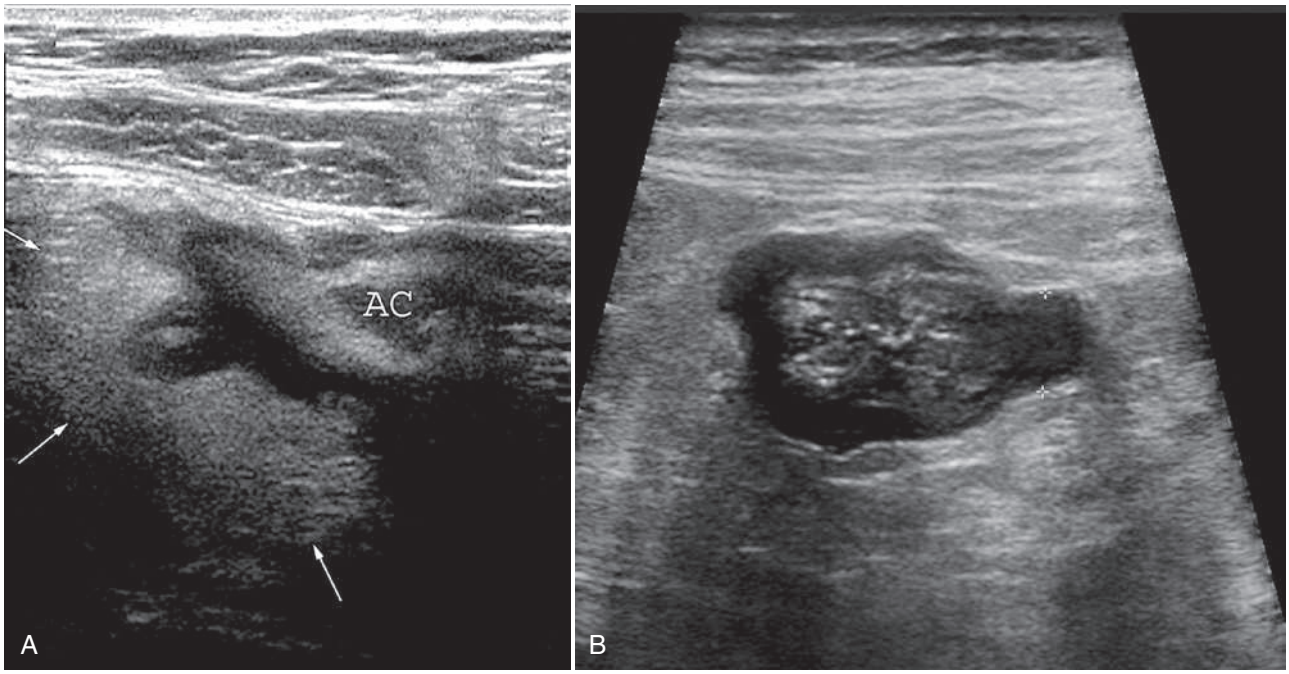

FIG. 8.35 Right-Sided Diverticulitis in Two Patients. Transverse sonograms through the ascending colon *(AC)* show a hypoechoic pouchlike projection, representing the inflamed diverticulum, which arises from **(A)** the lateral wall of the gut and **(B)** the medial border of the gut. Both are surrounded by inflamed fat *(arrows)*.

patients with typhlitis and **colitis,** although other organisms have been implicated. Sonographic study most often shows striking concentric, uniform thickening of the colon wall, usually localized to the cecum and the adjacent ascending colon[64] (Fig. 8.36). The colon wall may be several times the normal thickness, reflecting inflammatory infiltration throughout the gut wall.[65,66] Acute abdominal catastrophe in patients with AIDS is usually a complication of CMV colitis with deep ulceration and may result in hemorrhage, perforation, and peritonitis.[67] **Tuberculous colitis** may similarly affect the right colon and is frequently associated with **lymphadenopathy** (particularly involving the mesenteric and omental nodes), **splenomegaly,** intrasplenic masses, ascites, and peritoneal masses, all of which may be assessed using sonography.

Mesenteric Adenitis With Terminal Ileitis

Mesenteric adenitis, in association with acute terminal ileitis, is the most frequent GI cause of misdiagnosis of acute appendicitis. Patients typically have RLQ pain and tenderness. On the sonographic examination, enlarged mesenteric lymph nodes and mural thickening of the terminal ileum are noted. *Yersinia enterocolitica* and *Campylobacter jejuni* are the most common causative agents.[68,69]

Right-Sided Segmental Omental Infarction

Right-sided segmental infarction of the omentum is a rare condition invariably mistaken clinically for acute appendicitis.[70] Of unknown origin, it is postulated to occur with an anomalous and fragile blood supply to the right lower omentum, making it susceptible to painful infarction. Patients experience RLQ pain and tenderness and are diagnosed clinically with acute appendicitis. On sonography, a plaque or cakelike area of increased echogenicity, suggesting inflamed or infiltrated fat, is seen superficially in the right flank with adherence to the peritoneum[70] (Fig. 8.37). No underlying gut abnormality is shown. Because segmental infarction is a self-limited process, its correct diagnosis will prevent unnecessary surgery. CT scan is confirmatory, showing streaky fat in a masslike configuration in the right side of the omentum.

Left Lower Quadrant Pain

The sonographic evaluation of the patient with left lower quadrant (LLQ) pain is less problematic than that of the patient with pain on the right side as acute diverticulitis is the explanation for the overwhelming majority of cases for which a valid explanation for the pain is found. The diagnostic features of **acute diverticulitis** are also less variable than those for acute appendicitis, making a suspicion of diverticulitis a good indication for the use of sonographic examination.

Acute Diverticulitis

Diverticula of the colon are usually acquired deformities and are found most frequently in Western urban populations.[71] The incidence of diverticula increases with age,[72] affecting approximately half the population by the ninth decade. Muscular dysfunction and hypertrophy are constant associated features. Diverticula are usually multiple, and their most common location is the sigmoid and left colon. Both acute diverticulitis and **spastic diverticulosis** may be associated with a classic triad of presentation: LLQ pain, fever, and leukocytosis. Diverticula may also be

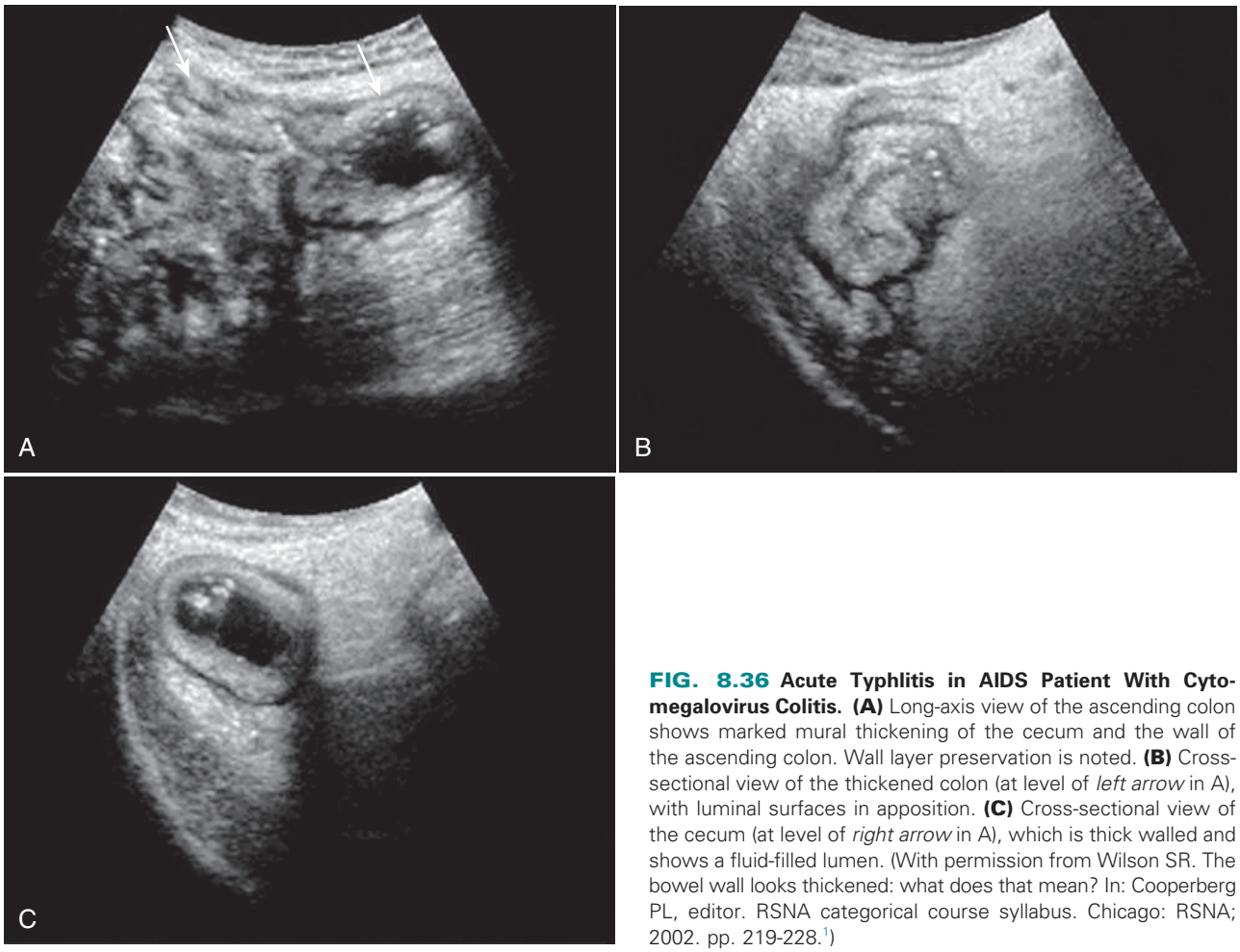

FIG. 8.36 Acute Typhlitis in AIDS Patient With Cytomegalovirus Colitis. (A) Long-axis view of the ascending colon shows marked mural thickening of the cecum and the wall of the ascending colon. Wall layer preservation is noted. **(B)** Cross-sectional view of the thickened colon (at level of *left arrow* in A), with luminal surfaces in apposition. **(C)** Cross-sectional view of the cecum (at level of *right arrow* in A), which is thick walled and shows a fluid-filled lumen. (With permission from Wilson SR. The bowel wall looks thickened: what does that mean? In: Cooperberg PL, editor. RSNA categorical course syllabus. Chicago: RSNA; 2002. pp. 219-228.[1])

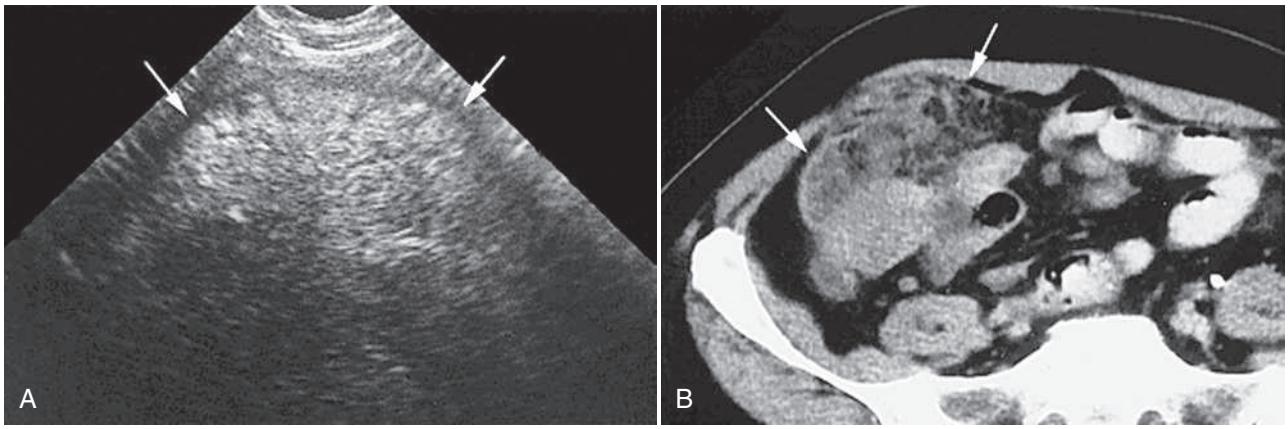

FIG. 8.37 Acute Omental Infarction. (A) Sonogram shows a large, tender mass in the right lower quadrant (RLQ; *arrows*) in older man with acute RLQ pain. The mass is uniformly echogenic and attenuating, with an ultrasound appearance suggesting inflamed fat. **(B)** Confirmatory CT scan shows the heterogeneous superficial fatty mass.

found singly and in the right colon, where no association with muscular hypertrophy or dysfunction has been established.

Inspissated fecal material is believed to incite the initial inflammation in the apex of the diverticulum leading to acute diverticulitis.[73] Spread to the peridiverticular tissues and microperforation or macroperforation may follow. Localized abscess formation occurs more often than peritonitis. Fistula formation, with communication to the bladder, vagina, skin, or other bowel loops, is present in a minority of cases. Surgical specimens demonstrate shortening and thickening of the involved segment of colon, associated with muscular hypertrophy. The peridiverticular inflammatory response may be minimal or extensive.

Sonography appears to be of value in early assessment of patients thought to have acute diverticulitis.[74,75] Classic features include segmental thickened gut and inflamed diverticula and inflamed perienteric fat. A negative scan combined with a low clinical suspicion is usually a good indication to stop investigation. However, a negative scan in a patient with a highly suggestive clinical picture justifies a CT scan. Similarly, demonstration of extensive pericolonic inflammatory changes on the sonogram may be appropriately followed by CT scan to define better the nature and extent of the pericolonic disease before surgery or other intervention.

Because diverticula and smooth muscle hypertrophy of the colon are so prevalent, it seems likely that they would be frequently seen on routine sonography, but this is not the usual experience. However, with the development of acute diverticulitis, both the inflamed diverticulum and the thickened colon become evident. Presumably, the impacted fecalith, with or without microabscess formation, accentuates the diverticulum, whereas smooth muscle spasm, inflammation, and edema accentuate the gut wall thickening. Identification of diverticula on the sonogram strongly indicates diverticulitis.[76]

Diverticula are arranged in parallel rows along the margins of the teniae coli, so careful technique is required to make their identification. After demonstration of a thickened loop of gut, the long axis of the loop should be determined (Fig. 8.38). Slight tilting of the transducer to the margins of the loop will increase visualization of the diverticula, because they may be on the lateral and medial edges of the loop rather than directly anterior or posterior (Fig. 8.39). Cross-sectional views are then obtained along the entire length of the thickened gut. Abnormalities must be confirmed on both views. Errors related to overlapping gut loops, in particular, can be virtually eliminated with this careful technique. Identification of diverticula on sonography is correlated highly with inflammation, because it is unusual to show the diverticula in the absence of inflammation (Fig. 8.40).

Failure to identify gas-containing abscesses or interloop abscesses is the major source of error when using sonography to evaluate patients with suspected diverticulitis. The meticulous technique of following involved thickened segments of colon in long-axis and transverse section will help detect even small amounts of extraluminal gas.

Sonographic features of diverticulitis include segmental concentric thickening of the gut wall that is frequently strikingly hypoechoic, reflecting the predominant thickening in the muscle layer; inflamed diverticula, seen as bright, echogenic foci with acoustic shadowing or ring-down artifact within or beyond the thickened gut wall; acute inflammatory changes in the pericolonic fat, seen as poorly defined hyperechoic zones without obvious gas or fluid content (Fig. 8.41, Video 8.15); and abscess formation, seen as loculated fluid collections in an intramural, pericolonic, or remote location. With the development of extraluminal inflammatory masses, the diverticulum may no longer be identified on sonography, presumably being incorporated into the inflammatory process. Therefore demonstration of a thickened segment of colon with an adjacent inflammatory mass may be consistent with diverticulitis, but also with neoplastic or other inflammatory disease. Intramural sinus tracts appear as high-amplitude, linear echoes, often with ring-down artifact, within the gut wall. Typically, the tracts are deep, between the muscularis propria and the serosa. Fistulas appear as linear tracts that extend from the involved segment of gut to the bladder, vagina, or adjacent loops. Their echogenicity depends on their content, usually gas or fluid. Thickening of the mesentery and inflamed mesenteric fat may also be seen (Fig. 8.41).

The sonographic and clinical features of diverticulitis are more specific than those of acute appendicitis, and errors of diagnosis occur less often. However, **torsion of appendices epiploicae** (omentales) may produce a sonographic appearance so closely resembling acute diverticulitis that differentiation may be difficult.[76] The inflamed or infarcted fat of the appendix shows as shadowing of increased echogenicity related to the margin of the colon, mimicking an inflamed diverticulum. However, regional perienteric inflammatory change is usually minimal, with fewer systemic symptoms. The noninflamed colonic appendices epiploicae are not visible, except with ascites, where they are seen as uniformly spaced, echogenic foci along the margins of the colon.

Sonography of Diverticulitis

GUT
Segmental concentric thickening of wall
- Hypoechoic reflecting muscular hypertrophy

INFLAMED DIVERTICULA
Echogenic foci within or beyond gut wall
Intramural sinus tracts
- High-amplitude linear echoes within gut wall
- Acoustic shadowing or ring-down artifact

PERIENTERIC SOFT TISSUE
Inflammation of pericolonic fat
- Hyperechoic mass effect

Thickening of the mesentery
Abscess formation
- Loculated fluid collection
- Often with gas component

Fistulas
- Linear tracts from gut to bladder, vagina, or adjacent loops
- Hypoechoic or hyperechoic

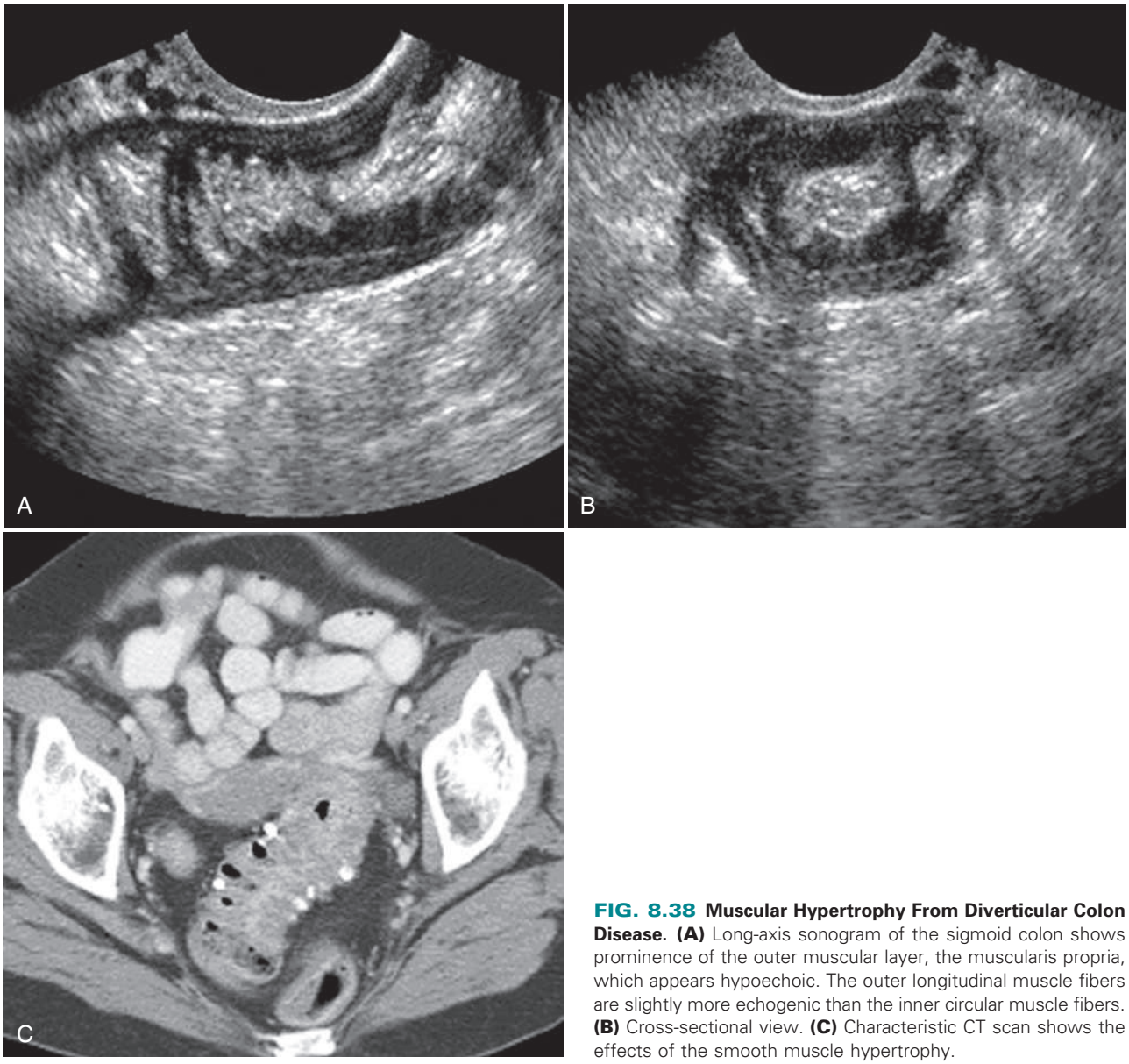

FIG. 8.38 Muscular Hypertrophy From Diverticular Colon Disease. (A) Long-axis sonogram of the sigmoid colon shows prominence of the outer muscular layer, the muscularis propria, which appears hypoechoic. The outer longitudinal muscle fibers are slightly more echogenic than the inner circular muscle fibers. **(B)** Cross-sectional view. **(C)** Characteristic CT scan shows the effects of the smooth muscle hypertrophy.

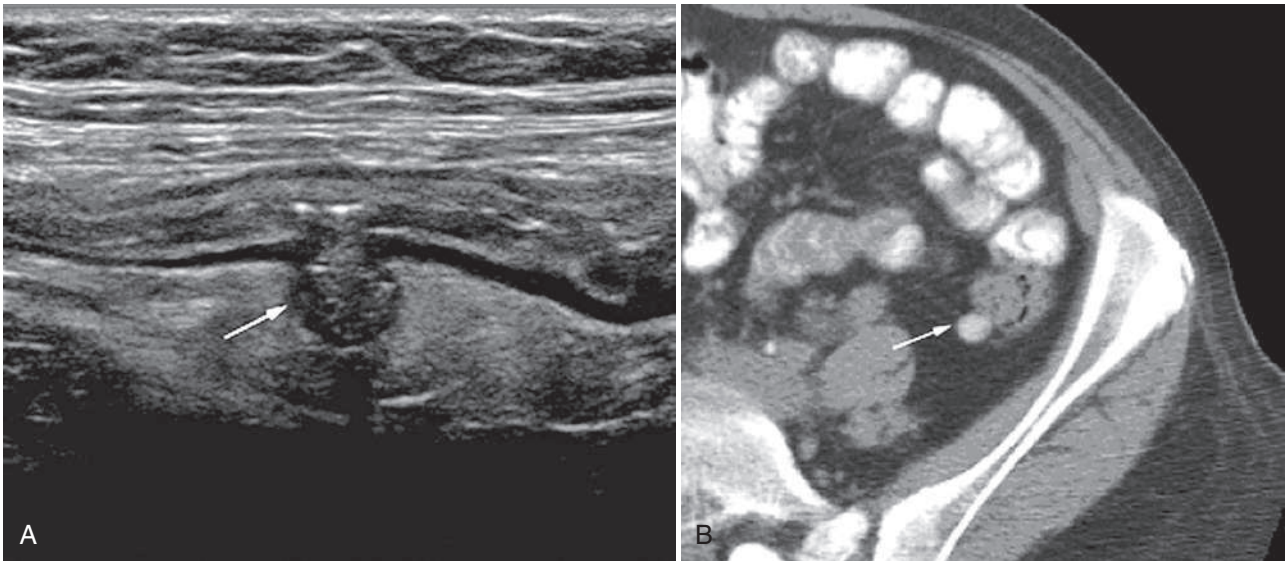

FIG. 8.39 Diverticulum of Colon. (A) Long-axis sonogram and **(B)** correlative CT scan show a small pouch *(arrows)* arising from the wall of the descending colon. There is mild inflammatory change in the perienteric fat.

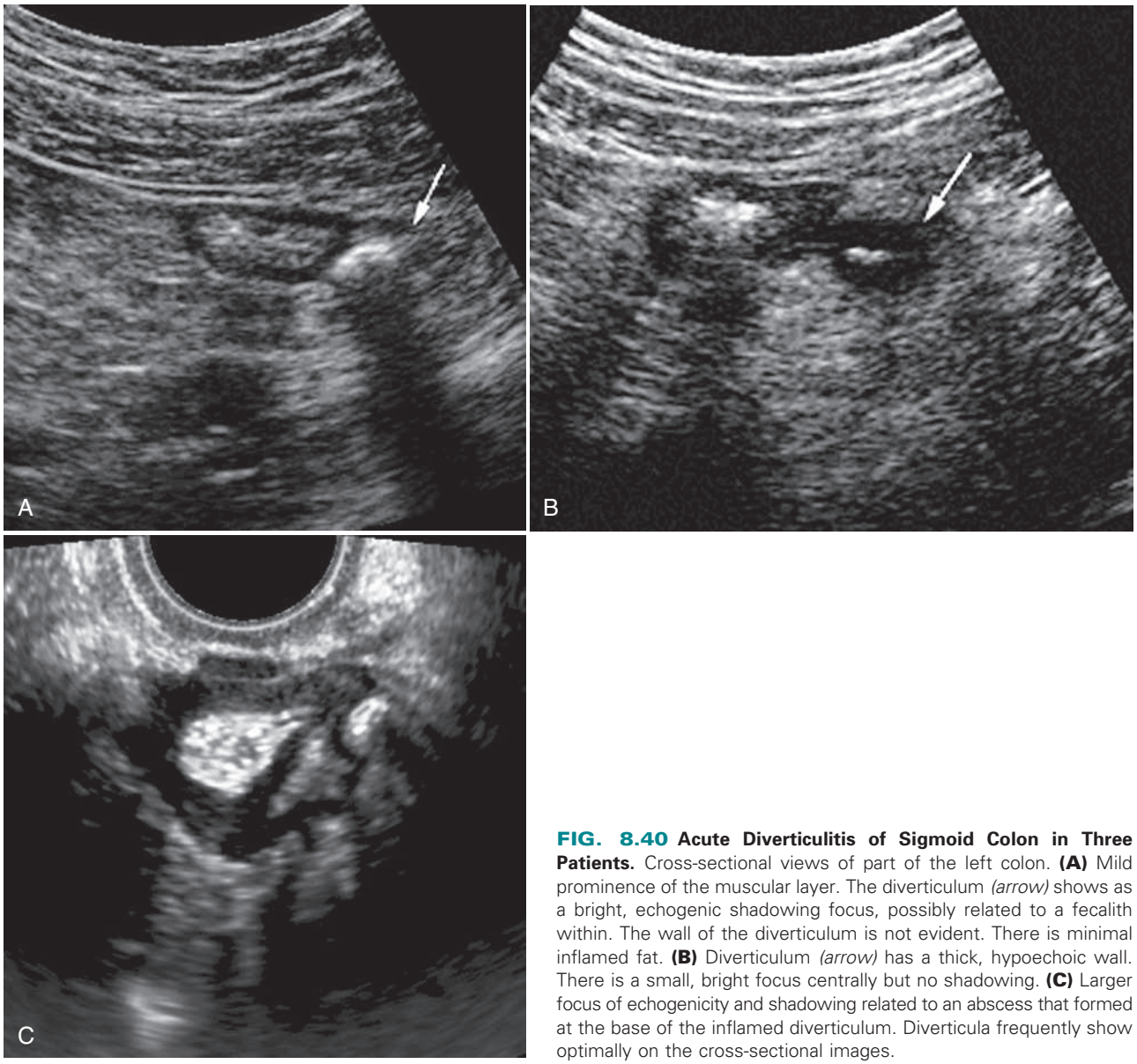

FIG. 8.40 Acute Diverticulitis of Sigmoid Colon in Three Patients. Cross-sectional views of part of the left colon. **(A)** Mild prominence of the muscular layer. The diverticulum *(arrow)* shows as a bright, echogenic shadowing focus, possibly related to a fecalith within. The wall of the diverticulum is not evident. There is minimal inflamed fat. **(B)** Diverticulum *(arrow)* has a thick, hypoechoic wall. There is a small, bright focus centrally but no shadowing. **(C)** Larger focus of echogenicity and shadowing related to an abscess that formed at the base of the inflamed diverticulum. Diverticula frequently show optimally on the cross-sectional images.

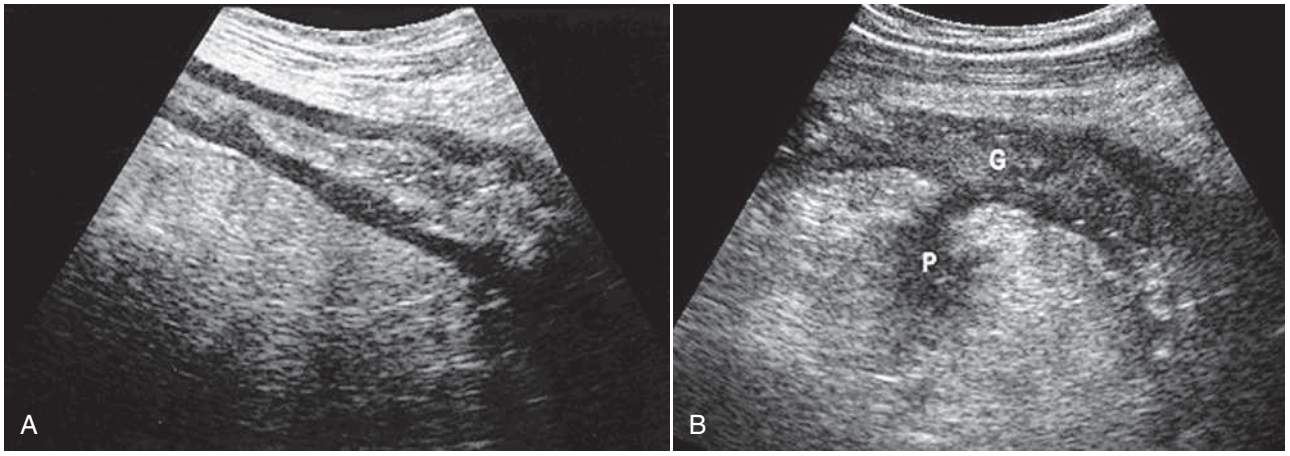

FIG. 8.41 Pericolonic Changes With Diverticulitis in Two Patients. (A) Long-axis view of descending colon shows a long segment of thickened gut with prominent muscularis propria. Edema of the perienteric fat is striking and shows as a homogeneous echogenic mass effect deep to the gut. **(B)** Similarly inflamed fat; phlegmonous change *(P)* shows as a hypoechoic zone centrally within the fat. *G,* Gut. See also Video 8.15.

OTHER ABNORMALITIES

Occlusion of the GI tract lumen producing obstruction may be either **mechanical,** where an actual physical impediment to the progression of the luminal content exists, or **functional,** where paralysis of the intestinal musculature impedes progression (paralytic ileus).

Mechanical Bowel Obstruction

Mechanical bowel obstruction (MBO) is characterized by (1) dilation of the GI tract proximal to the site of luminal occlusion, (2) accumulation of large quantities of fluid and gas, and (3) hyperperistalsis as the gut attempts to pass the luminal content beyond the obstruction. If the process is prolonged, exhaustion and overdistention of the bowel loops may occur, with a secondary decrease in peristaltic activity. There are three broad categories of mechanical obstruction: **obturation obstruction,** related to blockage of the lumen by material in the lumen; **intrinsic abnormalities of the gut wall,** associated with luminal narrowing; and **extrinsic bowel lesions,** including adhesions. **Strangulation** obstruction develops when the circulation of the obstructed intestinal loop becomes impaired.

Sonography in patients with suspected MBO is frequently unhelpful as **adhesions,** the most common cause of intestinal obstruction, are not visible on the sonogram. Also, the presence of abundant **gas** in the intestinal tract, characteristic of most patients with obstruction, frequently produces sonograms of nondiagnostic quality. However, in the minority of patients with MBO who do not have significant gaseous distention, sonography may be helpful. In a prospective study of 48 patients, Meiser and Meissner[77] found that ultrasound was positive in 25% of patients with a "normal" plain film. Ultrasound alone allowed complete diagnosis of the cause of obstruction in 6 patients in a retrospective study of sonography on 26 patients with known colonic obstruction; it also correctly predicted the location of colonic obstruction in 22 cases (85%) and the cause of the obstruction in 21 cases (81%).[11] Of 13 patients ultimately confirmed to have adenocarcinoma, 5 had a mass on sonography, 5 had segmental thickening, and 11 others showed a target sign of intussusception.

Sonographic study of potential MBO should include assessment of the following:

- GI tract **caliber** from the stomach to the rectum, noting any point at which the caliber alters (Fig. 8.42).
- **Content** of any dilated loops, with special attention to their fluid and gaseous nature (Fig. 8.43; see also Videos 8.9, 8.10, and 8.16).
- **Peristaltic activity** within the dilated loops, which is typically greatly exaggerated and abnormal, frequently producing a to-and-fro motion of the luminal content. With strangulation, peristalsis may decrease or cease.
- **Site of obstruction** for *luminal* (large gallstones, bezoars,[78] foreign bodies, intussusception, occasional polypoid tumors), *intrinsic* (segmental gut wall thickening and stricture formation from Crohn disease, annular carcinomas), and *extrinsic* (abscesses, endometriomas) abnormality as a cause of the obstruction (Video 8.16).
- **Location of gut loops,** noting any abnormal position. Obstruction associated with external hernias is ideal for sonographic detection in that dilated loops of gut may be traced to a portion of the gut with normal caliber but abnormal location (Fig. 8.44). Spigelian and inguinal hernias are the types most frequently seen on sonograms.

Unique sonographic features are seen in the following:

Closed-loop obstruction occurs if the bowel lumen is occluded at two points along its length, a serious condition that facilitates strangulation and necrosis. As the obstructed loop is closed off from the more proximal portion of the GI tract, little or no gas is present within the obstructed segments, which may become dilated and fluid filled. Consequently, the abdominal radiograph may be unremarkable (Fig. 8.45A), and sonography may be most helpful by showing the dilated involved segments (Fig. 8.45B) and often the normal-caliber bowel distal to the point of obstruction. The features of closed-loop obstruction are well described on ultrasound and include dilated small bowel, a C- or U-shaped bowel loop (Fig. 8.45C), a whirl sign, and two adjacent collapsed loops.[79,80] This last important observation is difficult to observe on ultrasound, in contrast to CT scan. However, we have correctly suspected closed-loop obstruction in many patients on the basis of virtually normal plain films, small bowel dilation, and a U- or C-shaped bowel loop, especially if there is gut wall thickening or pneumatosis intestinalis suggesting gut infarction.

Afferent loop obstruction is an uncommon complication of subtotal gastrectomy, with Billroth II gastrojejunostomy, that may occur by twisting at the anastomosis, internal hernias, or anastomotic stricture. Again, a gasless, dilated loop may be readily recognized on sonography in a location consistent with the enteroenteric anastomosis coursing from the right upper quadrant across the midline. Its detection, location, and shape should allow for correct sonographic diagnosis of afferent loop obstruction.[81]

Intussusception, invagination of a bowel segment (the intussusceptum) into the next distal segment (the intussuscipiens), is seen on sonography of the abdomen most often as a transient and infrequent occurrence. However, it is a relatively infrequent cause of MBO in the adult, usually associated with a tumor as a lead point. In our experience, this is often a lipoma that appears as a highly echogenic, intraluminal mass related to its fat content. A sonographic appearance of multiple concentric rings, related to the invaginating layers of the telescoped bowel and seen in cross section, is virtually pathognomonic[82] (Fig. 8.46A). Occasionally, only a target appearance may be seen.[83,84] The longitudinal appearance suggesting a "hay fork"[84] is not as reliably detected. In both projections, the mesenteric fat invaginating with the intussusceptum will show as an eccentric area of increased echogenicity. A lipoma, as a lead point, similarly shows as a focus of increased echogenicity (Fig. 8.46B and C).

Midgut malrotation predisposes to MBO and infarction. It is infrequently encountered in adults. A sonographic abnormality related to the superior mesenteric vessels suggests malrotation.[85] On transverse sonograms, the superior mesenteric vein is seen on the left ventral aspect of the superior mesenteric artery, a reversal of the normal relationship.

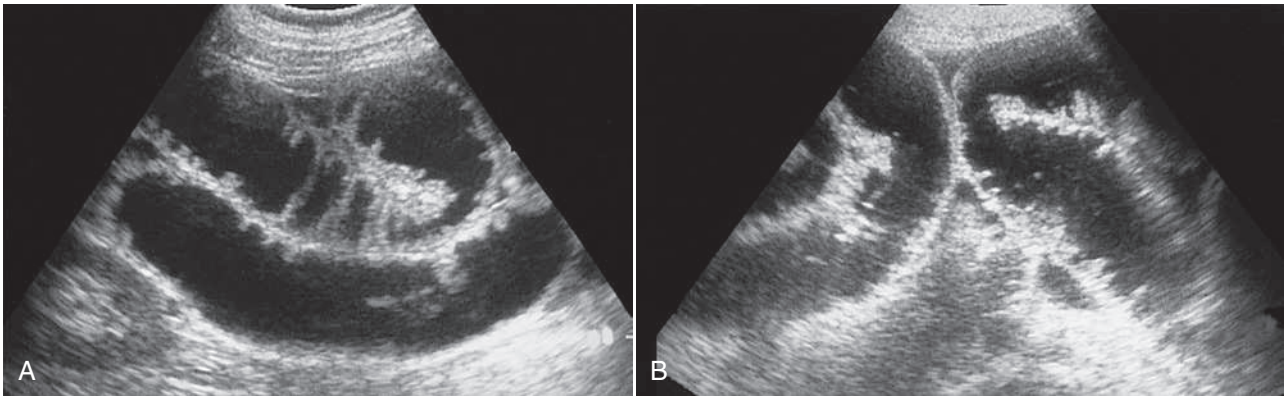

FIG. 8.42 Mechanical Small Bowel Obstruction. (A) Sagittal image of right flank shows multiple, adjacent, long loops of dilated, fluid-filled small bowel with the classic morphology for a distal mechanical small bowel obstruction. **(B)** Transverse image in the left lower quadrant confirms the multiplicity of dilated loops involved in the process. A small amount of ascites is seen between the dilated loops.

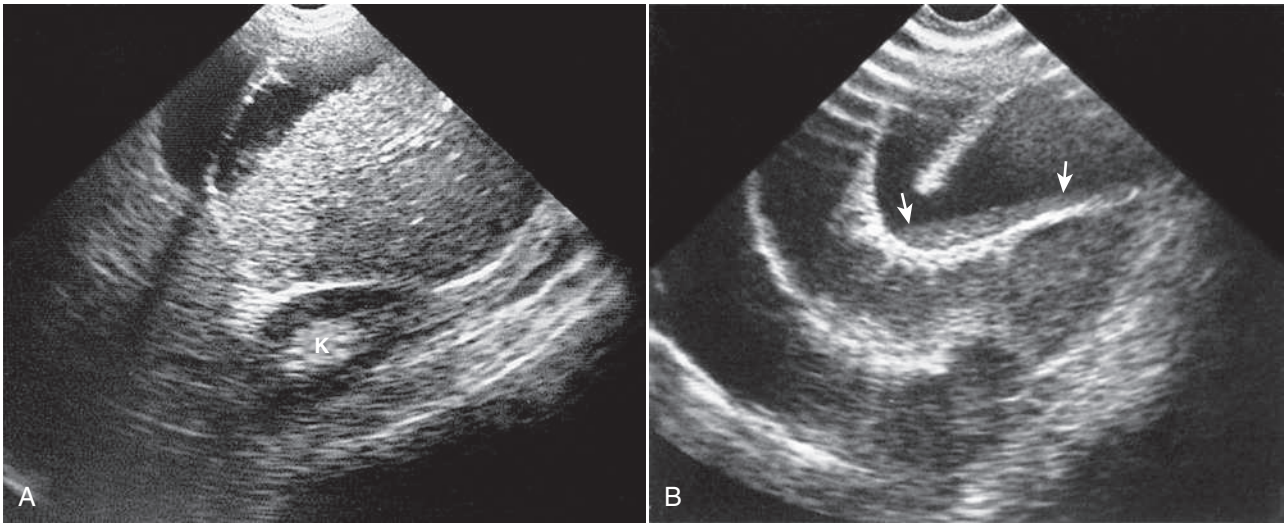

FIG. 8.43 Dilated Hypoperistaltic Segments. (A) Sagittal sonogram in the right flank of a patient with a Crohn stricture shows gross dilation of the ascending colon. A long, fluid-sediment level is seen as a reflection of the hypoperistalsis of this segment of obstructed gut. **(B)** Sagittal sonogram in a patient with paralytic ileus shows extensive small bowel dilation. Loops are fluid filled and quiet with fluid-fluid level *(arrowheads)*. See also Video 8.16. *K,* Kidney. (**A** with permission from Sarrazin J, Wilson SR. Manifestations of Crohn disease at US. Radiographics. 1996;16[3]:499-520.[21])

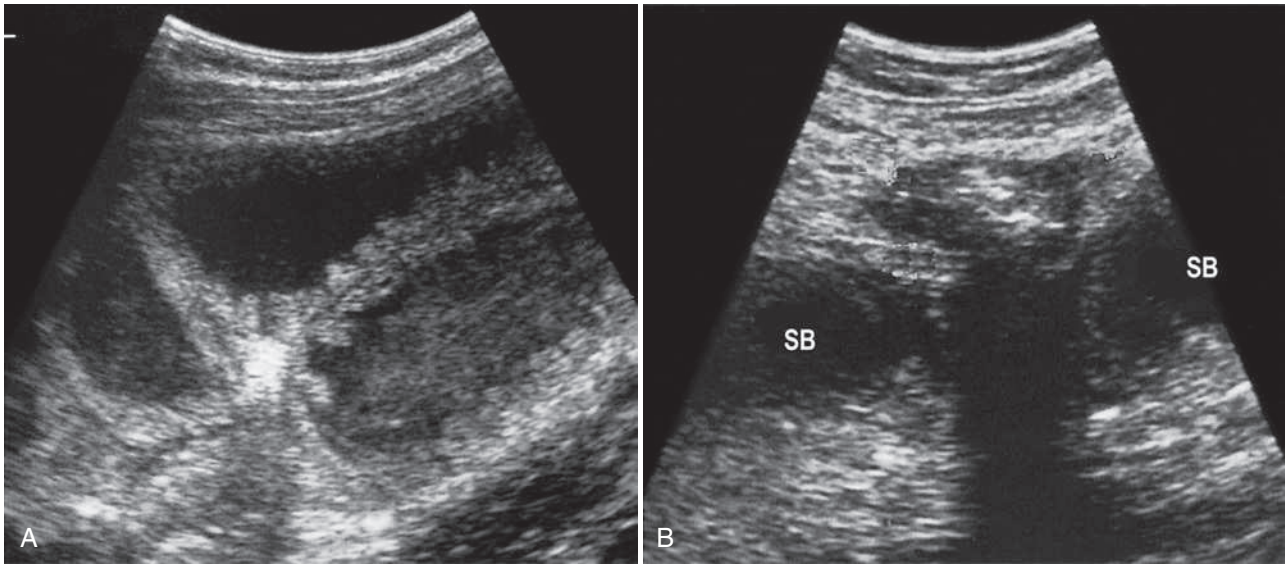

FIG. 8.44 Mechanical Small Bowel Obstruction: Ventral Hernia. (A) Sonogram shows dilated fluid-filled loops of small bowel with edematous valvulae conniventes. **(B)** Transverse paraumbilical sonogram shows normal-caliber gut lying in abnormal superficial location between two dilated loops of small bowel *(SB)*.

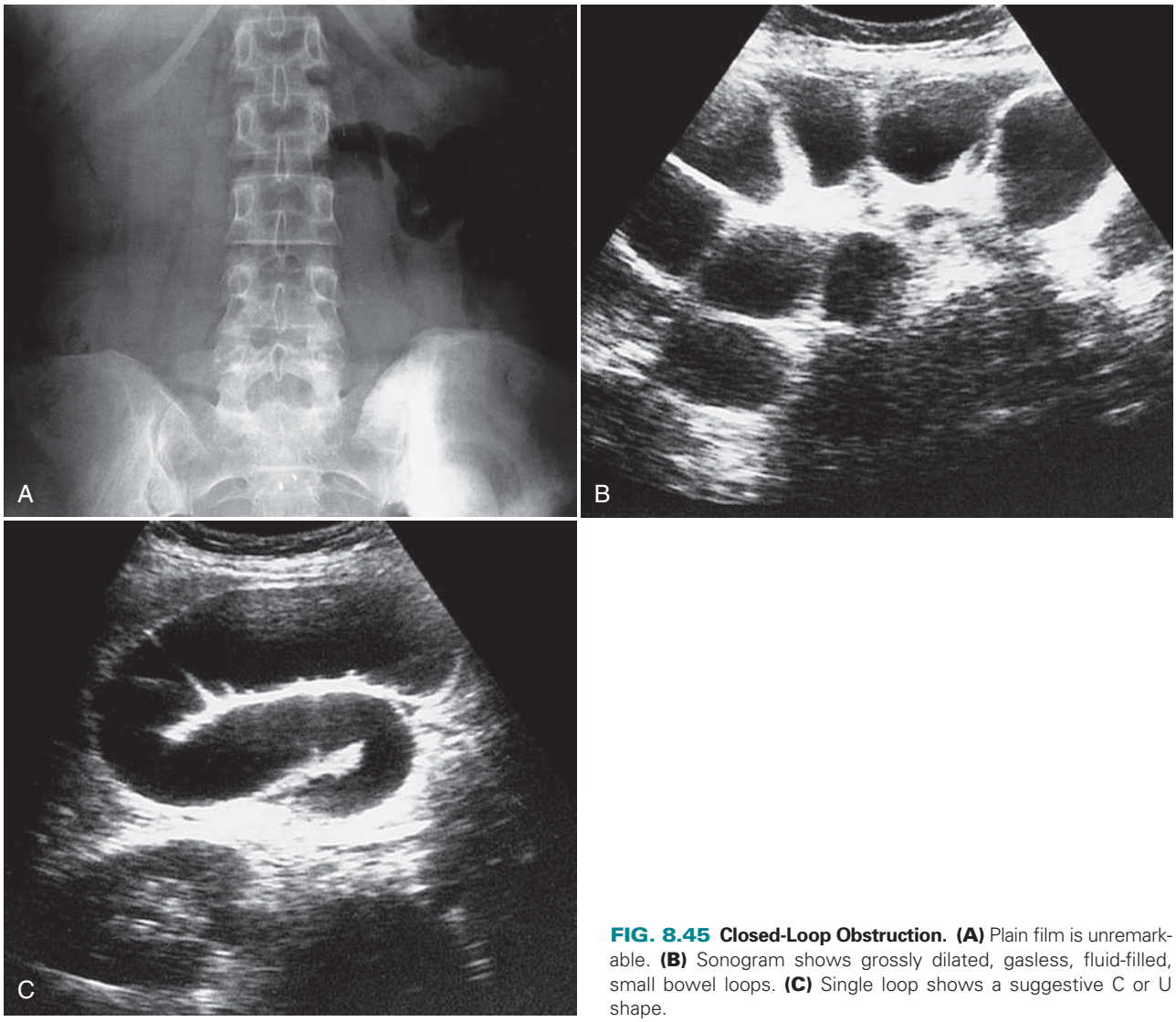

FIG. 8.45 Closed-Loop Obstruction. (A) Plain film is unremarkable. **(B)** Sonogram shows grossly dilated, gasless, fluid-filled, small bowel loops. **(C)** Single loop shows a suggestive C or U shape.

Paralytic Ileus

Paralytic ileus is a type of bowel obstruction related to adynamic function of the bowel wall. Paralysis of the intestinal musculature, in response to general or local insult, may impede the progression of luminal contents. Although the lumen remains patent, no progression occurs. Sonography is usually of little value because these patients characteristically have poor-quality sonograms resulting from large quantities of gas in the intestinal tract. However, on rare occasions, the sonogram may demonstrate dilated, fluid-filled, very quiet, or aperistaltic loops of intestine. A fluid-fluid level in a dilated loop is characteristic of paralytic ileus, reflecting lack of movement of the intestinal contents (see Fig. 8.43).

Gut Edema

Patients with **acute vasculitis** of various causes may present with acute abdominal pain and ascites, with massive edema of the small bowel wall seen as the major abnormality on imaging. Hypoalbuminemia, congestive heart failure, and spontaneous venous thrombosis may also show diffuse edema of the gut wall. Prominent, thickened, hypoechoic valvulae conniventes (Fig. 8.47) and gastric rugae are relatively easy to recognize on the sonographic study, which should also include Doppler evaluation of the mesenteric and portal veins.

Gastrointestinal Tract Infections

Although fluid-filled, actively peristaltic gut may be seen with infectious viral or bacterial gastroenteritis, most affected patients do not demonstrate a sonographic abnormality. However, some pathogens, notably *Yersinia enterocolitica, Mycobacterium tuberculosis,* and *Campylobacter jejuni,* produce highly suggestive sonographic abnormalities in the ileocecal area, as described earlier. Certain high-risk populations, such as those with AIDS and neutropenia,[64] appear to be susceptible to **acute typhlitis** and **colitis,** which also have a highly suggestive sonographic appearance.

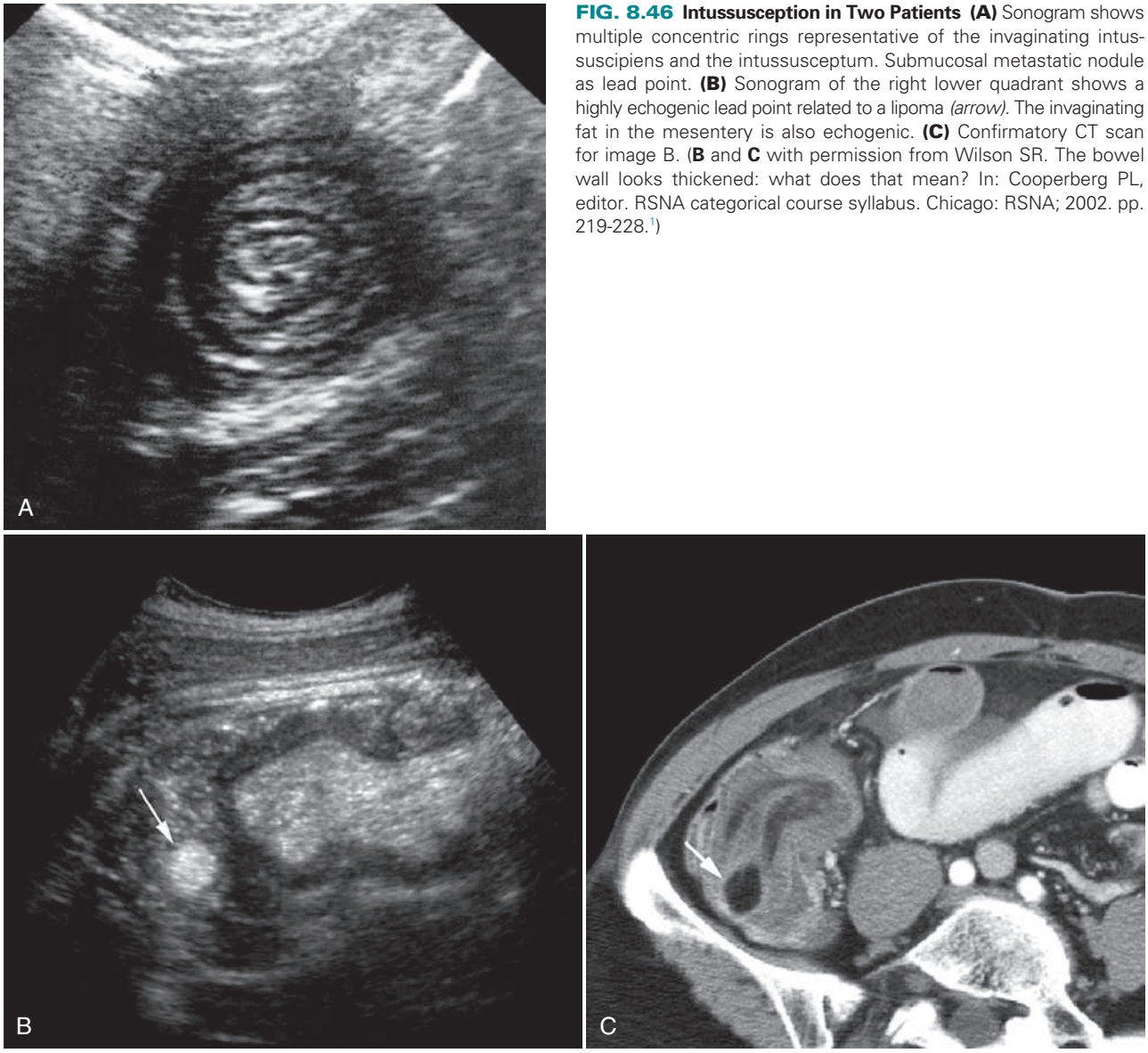

FIG. 8.46 Intussusception in Two Patients (A) Sonogram shows multiple concentric rings representative of the invaginating intussuscipiens and the intussusceptum. Submucosal metastatic nodule as lead point. **(B)** Sonogram of the right lower quadrant shows a highly echogenic lead point related to a lipoma *(arrow).* The invaginating fat in the mesentery is also echogenic. **(C)** Confirmatory CT scan for image B. (**B** and **C** with permission from Wilson SR. The bowel wall looks thickened: what does that mean? In: Cooperberg PL, editor. RSNA categorical course syllabus. Chicago: RSNA; 2002. pp. 219-228.[1])

AIDS Patients

Today, effective antiviral medications for HIV infection have drastically changed the outlook for those living with AIDS in the Western world. Nonetheless, patients with AIDS are at increased risk for development of both GI tract neoplasia, especially lymphoma (see Fig. 8.10C and D), and unusual opportunistic infections, most often *Candida* esophagitis and CMV colitis[65,66] (see Fig. 8.36).

Pseudomembranous Colitis

Pseudomembranous colitis is a necrotizing inflammatory bowel condition that may occur as a response to a heterogeneous group of insults. At present, antibiotic therapy with effects from the toxin of *Clostridium difficile,* a normal inhabitant of the GI tract, is most often implicated. Watery diarrhea is the most common symptom and usually occurs during antibiotic therapy but may be quite remotely associated, occurring up to 6 weeks later. Endoscopic demonstration of pseudomembranous exudative plaques on the mucosal surface of the gut and culture of the enterotoxin of *C. difficile* are diagnostic. Superficial ulceration of the mucosa is associated with inflammatory infiltration of the lamina propria and the submucosa, which may be thickened to many times the normal size.[86]

Sonography is frequently performed before pseudomembranous colitis is diagnosed, often based on a history of fever, abdominal pain, and watery diarrhea. Sonographic features have only rarely been described[87,88] but are suggestive of pseudomembranous colitis. Usually the entire colon is involved in a process that may produce striking thickening of the colon wall. Exaggerated haustral markings and a nonhomogeneous thickened submucosa, with virtual apposition of the mucosal surfaces of the thickened walls, are characteristic[63] (Fig. 8.48).

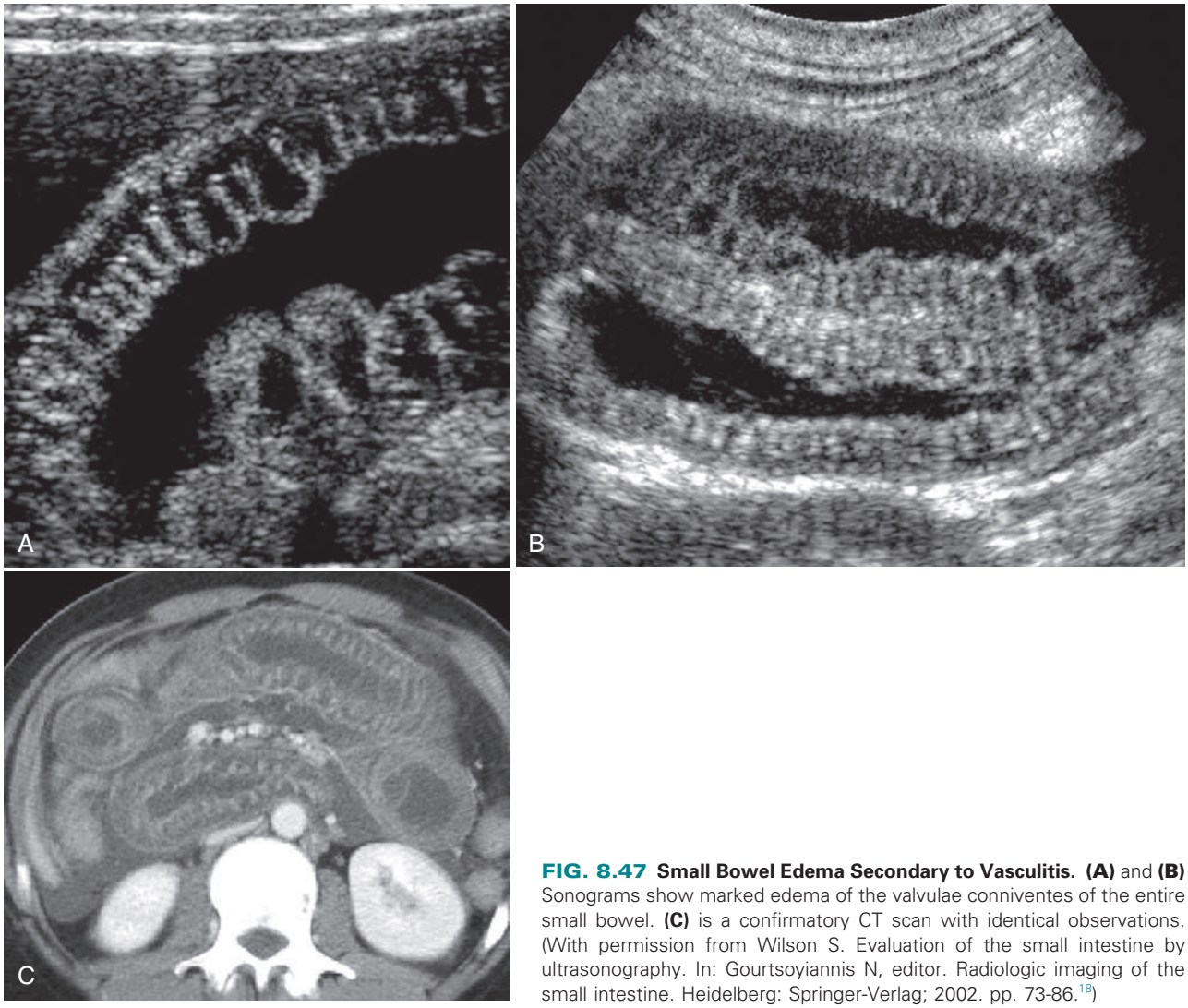

FIG. 8.47 Small Bowel Edema Secondary to Vasculitis. (A) and **(B)** Sonograms show marked edema of the valvulae conniventes of the entire small bowel. **(C)** is a confirmatory CT scan with identical observations. (With permission from Wilson S. Evaluation of the small intestine by ultrasonography. In: Gourtsoyiannis N, editor. Radiologic imaging of the small intestine. Heidelberg: Springer-Verlag; 2002. pp. 73-86.[18])

Pseudomembranous colitis should be suspected in any patient with diffuse colonic wall thickening but without a previous history of IBD. Because the history of concurrent or prior antibiotic therapy is not always given, direct questioning of the patient is frequently helpful.

Congenital Cysts

Duplication cysts, characterized by the presence of the normal layers of the gut wall, can occur in any portion of the GI tract. These cysts may be visualized on sonogram, either routine or endoscopic, and should be considered as diagnostic possibilities whenever unexplained abdominal cysts are seen. **Tailgut cysts** are variants of abdominal cysts that are seen in the presacral region and are related to the rectum (Fig. 8.49).

Ischemic Bowel Disease

Ischemic bowel disease most often affects the colon and is most prevalent in older persons with arteriosclerosis. In younger patients, it may complicate cardiac arrhythmia, vasculitis, coagulopathy, embolism, shock, or sepsis.[12] Sonographic features of ischemic bowel disease have been poorly described, although gut wall thickening may be encountered. Pneumatosis intestinalis may complicate gut ischemia with a characteristic sonographic appearance.

Pneumatosis Intestinalis

Pneumatosis intestinalis is a relatively rare condition in which intramural pockets of gas are found throughout the GI tract. It has been associated with a wide variety of underlying conditions, including chronic obstructive pulmonary disease, collagen vascular disease, IBD, traumatic endoscopy, and post–jejunoileal bypass. In many situations, affected patients are asymptomatic and the observation is incidental. However, its demonstration is of great clinical significance when necrotizing enterocolitis or ischemic bowel disease is present. Both conditions are associated with mucosal necrosis in which gas from the lumen passes to the gut wall.

Sonographic description of pneumatosis intestinalis is limited to isolated case reports. High-amplitude echoes may be demonstrated in the gut wall, with typical air artifact or shadowing[89,90]

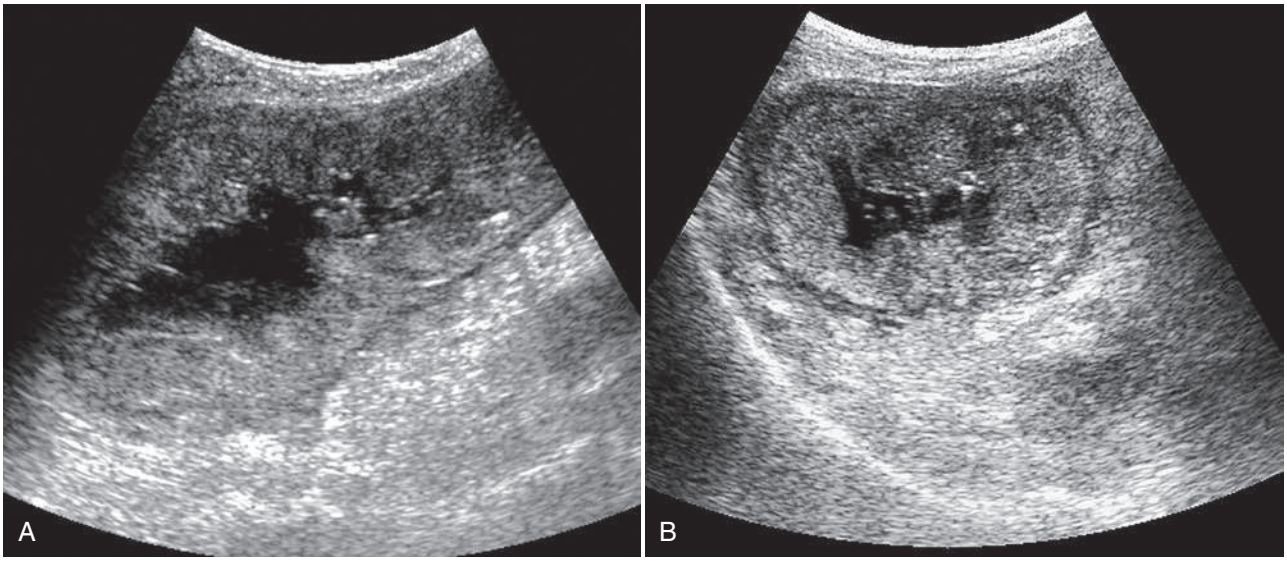

FIG. 8.48 Pseudomembranous Colitis. (A) Long-axis view and **(B)** cross-sectional view of the ascending colon show striking mural thickening of the gut wall. (With permission from O'Malley M, Wilson S. US of gastrointestinal tract abnormalities with CT correlation. Radiographics. 2003;23[1]:59-72.[63])

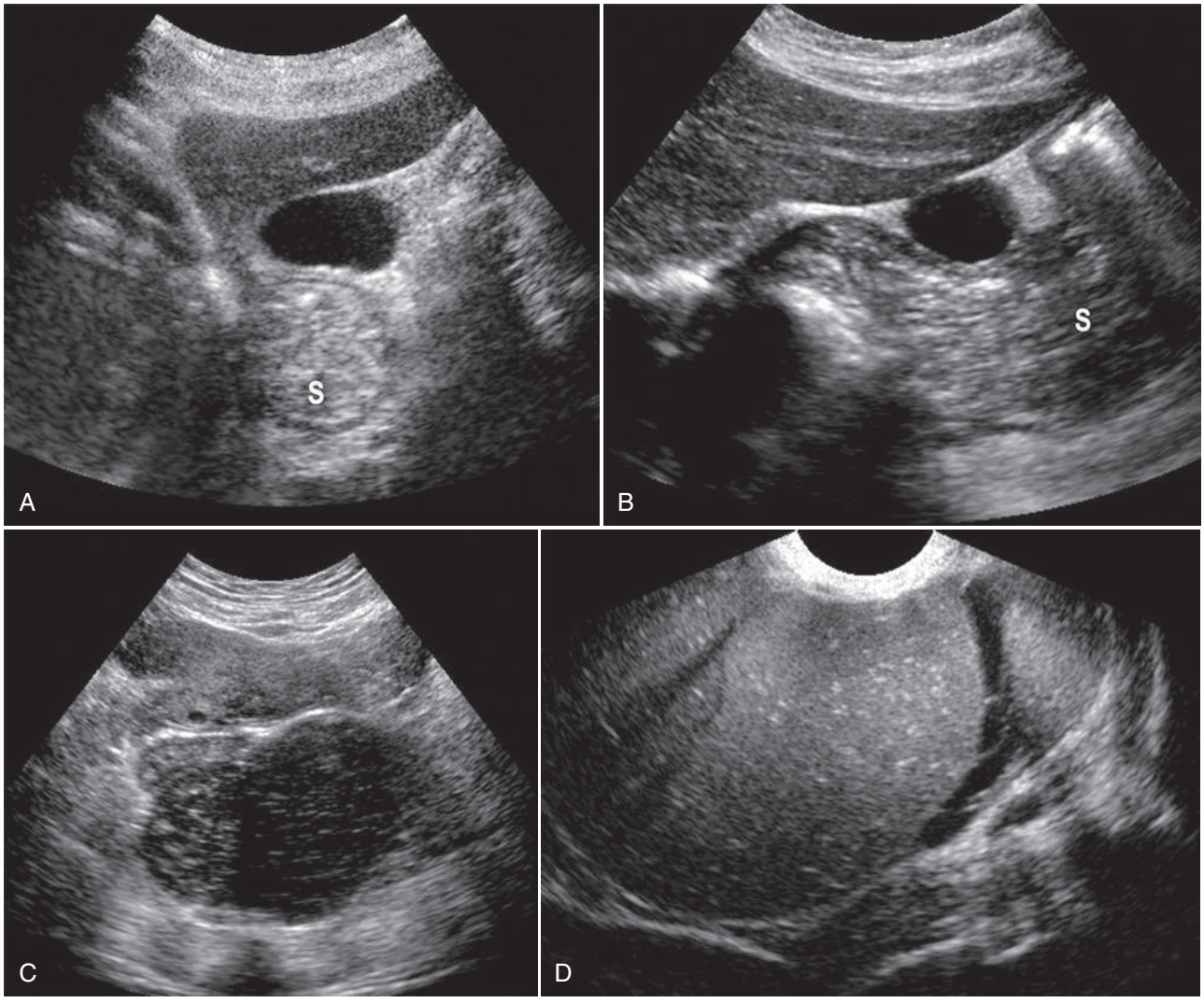

FIG. 8.49 Congenital Cysts. (A) Sagittal and **(B)** transverse sonograms in the epigastrium show an incidental gastric duplication cyst adjacent to the lesser curve of the stomach *(S)*. **(C)** Suprapubic and **(D)** transvaginal pelvic scans show a complex, presacral pelvic mass, an incidental tailgut cyst.

(Fig. 8.50). Gut wall thickening may be noted if the pneumatosis is associated with underlying IBD. If gut ischemia is suspected, careful evaluation of the liver is recommended to look for evidence of portal venous air.

Mucocele of Appendix

Mucocele of the appendix is relatively uncommon, occurring in 0.25% of 43,000 appendectomy specimens in one series. Many patients with this condition are asymptomatic. A mass may be palpated in approximately 50% of cases. **Benign** and **malignant** varieties occur in a ratio of approximately 10:1.[91] In the benign form the appendiceal lumen is obstructed by either inflammatory scarring or fecaliths. The glandular mucosa in the isolated segment continues to secrete sterile mucus. The neoplastic variety of mucocele is associated with primary mucous **cystadenoma** or **cystadenocarcinoma** of the appendix. Although the gross morphology of the appendix may be similar in the benign and malignant varieties, the malignant form is often associated with pseudomyxoma peritonei if rupture occurs.[92]

On sonography, **mucoceles** typically produce large, hypoechoic, well-defined RLQ cystic masses with variable internal echogenicity, wall thickness, and wall calcification (Fig. 8.51). The internal contents often show a laminated or whorled appearance. These masses are frequently retrocecal and may be mobile.

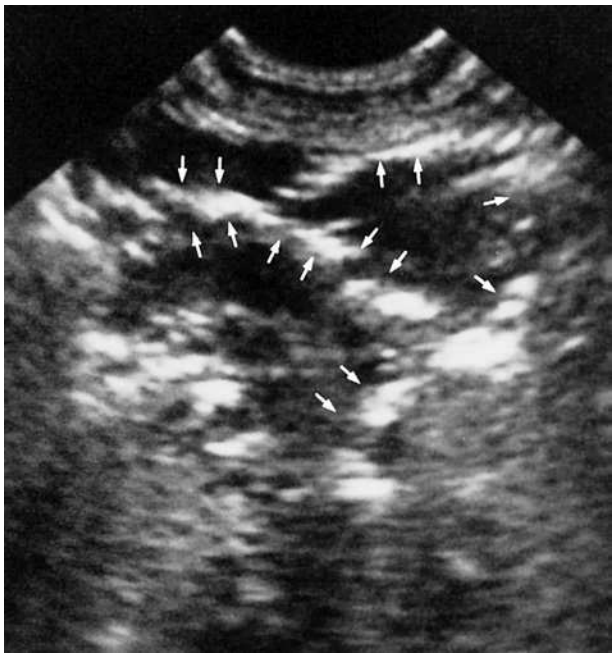

FIG. 8.50 Pneumatosis Intestinalis. Sonogram shows three loops of gut with bright, high-amplitude echoes *(arrows)* originating within the gut wall.

Gastrointestinal Tract Hematoma

Blunt abdominal trauma, complicated by duodenal hematoma and rectal trauma, either sexual or iatrogenic after rectal biopsy, are the major causes of local hematomas seen on sonography. Hematoma is usually localized to the submucosa. Larger or more diffuse hematomas may complicate anticoagulation therapy or bleeding disorders associated with leukemia. If hematomas are large, diffuse gut wall thickening may be seen on sonograms.

Peptic Ulcer

Peptic ulcer, a defect in the epithelium to the depth of the submucosa, may be seen in either **gastric** or **duodenal** locations. Although rarely visualized, peptic ulcer has a fairly characteristic sonographic appearance. A gas-filled ulcer crater is seen as a bright, echogenic focus with ring-down artifact, either in a focal area of wall thickening or beyond the wall, depending on the depth of penetration (Fig. 8.52). **Edema** in the acute phase and **fibrosis** in the chronic phase may produce localized wall thickening and deformity.

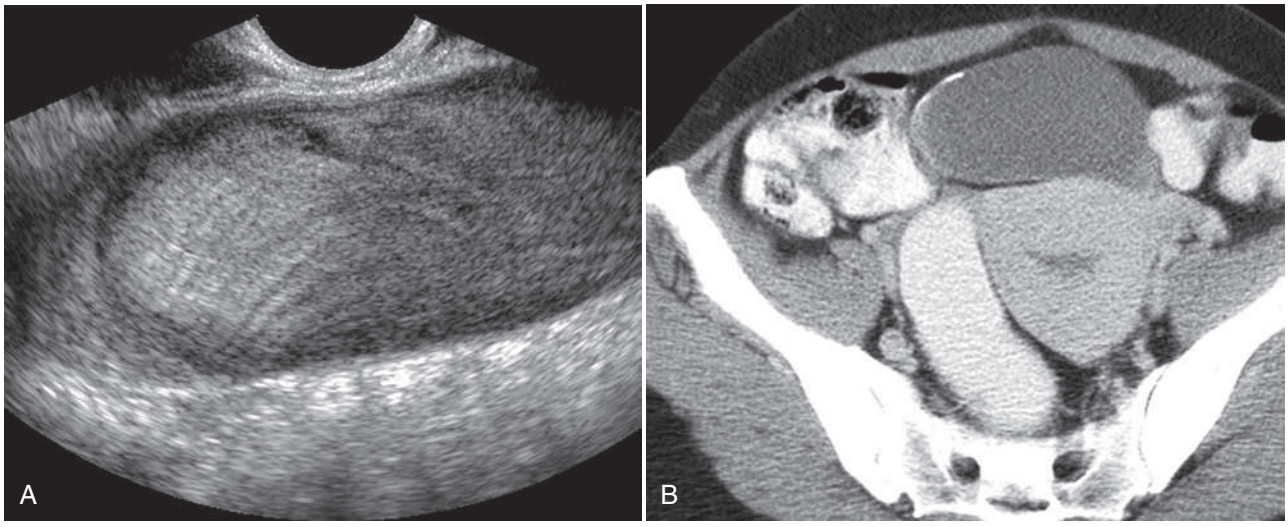

FIG. 8.51 Mucocele of the Appendix. (A) Sonogram and **(B)** CT scan show a large, mucus-filled appendix as an incidental observation. The whorled appearance on the sonogram is characteristic. There is a fleck of calcification in the wall on the CT scan.

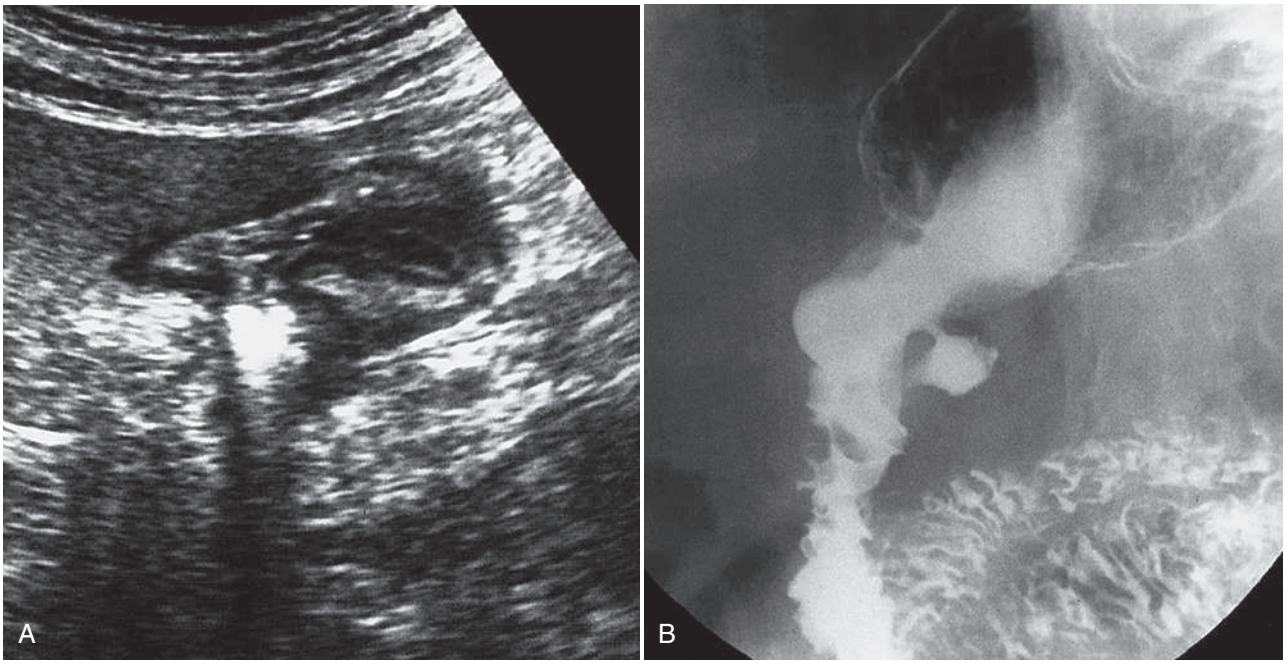

FIG. 8.52 Peptic Ulcer. (A) Cross-sectional sonogram of the stomach shows a hypoechoic eccentric mass with a bright, central echogenic focus representing air in the ulcer crater. **(B)** Confirmatory scan with barium swallow.

Bezoars

Bezoars are masses of foreign material or food, typically found in the stomach after surgery for peptic ulcer disease **(phytobezoars)** or after ingestion of indigestible organic substances such as hair **(trichobezoars).** These masses may produce shadowing intraluminal densities on the sonogram and have been documented as a rare cause of small bowel obstruction.[78] They may also form in the small bowel in association with chronic stasis.

Intraluminal Foreign Bodies

Large foreign bodies, including bottles, candles, sexual vibrators, contraband, tools, and food, may be identified in the GI tract, particularly in the rectum and sigmoid colon, where they produce fairly sharp, distinct specular echoes with sharp, acoustic shadows. Their recognition is enhanced by suspicion of their presence.

Celiac Disease

Undiagnosed adult patients with celiac disease are encountered infrequently in general ultrasound departments. Nonetheless, I have occasionally seen patients in whom sonography is the first test to suggest the correct diagnosis. Sonographic observations include abnormal fluid-filled small intestine with moderate dilation of the involved loops. Abnormal morphology is observed, which Dietrich et al.[93] describe as a reduction in Kerckring plicae circulares (valvulae conniventes) with loss of density and uniformity. Peristalsis is increased above normal. An increase in the caliber of the superior mesenteric artery and portal vein may also be seen.[94]

Cystic Fibrosis

Aggressive treatment of the pulmonary problems of cystic fibrosis (CF) increases the likelihood of encountering adult patients in a general ultrasound department that performs abdominal sonography. Thickening of the gut wall, particularly of the right hemicolon and to a lesser extent the left colon and small bowel, may be seen in association with infiltration of both the pericolonic and the mesenteric fat.[95] These may often be incidental observations without significant associated symptomatology. In advanced CF, a fibrosing colonopathy with stricture may be seen.[96,97] The culture of *C. difficile* is also documented in some patients with CF and colon wall thickening, without the accompanying symptoms of abdominal pain and diarrhea.[98] However, positive stool culture is not the rule in CF patients with detectable colon wall thickening.

ENDOSONOGRAPHY

Endoscopic sonography, performed with high-frequency transducers in the lumen of the gut, allows for detection of mucosal abnormality, delineation of the layers of the gut wall, and definition of the surrounding soft tissues to a depth of 8 to 10 cm from the transducer crystal. Thus tumors hidden below normal mucosa, tumor penetration into the layers of the gut wall, and tumor involvement of surrounding vital structures or lymph nodes may be well evaluated. Staging of previously identified mucosal tumors is one of the major applications of endosonographic technique.

Upper Gastrointestinal Tract

Rotating, high-frequency transducers, using 7.5-MHz crystals fitted into a fiberoptic endoscope, are most suitable for endosonography of the esophagus, stomach, and duodenum. Light sedation of the patient is usually required. The patient is placed in the left lateral decubitus position and the endoscope inserted to the desired location. Intraluminal gas is aspirated, and a balloon covering the transducer crystal is inflated with deaerated water. Localization is determined from the distance of insertion from

the teeth and identification of anatomic landmarks, such as the spleen, liver, pancreas, and gallbladder. Rotation and deflection of the transducer tip allow scanning of visualized lesions in different planes.[99]

Identification, localization, and characterization of benign masses are possible with endosonography. **Varices** are seen as compressible hypoechoic or cystic masses deep to the submucosa or in the outer layers of the esophagus, gastroesophageal junction, or gastric fundus.[100] Benign tumors such as **fibromas** or **leiomyomas** are well-defined, solid masses without mucosal involvement that can be localized to the layer of the wall from which they arise, usually the submucosa and the muscularis propria, respectively. Peptic ulcer typically produces marked thickening of all layers of the gastric wall, with a demonstrated ulcer crater. Ménétrier disease produces thickening of the mucosal folds.

Staging of **esophageal carcinoma** involves assessment of depth of tumor invasion and evaluation of involvement of the local lymph nodes and adjacent vital structures.[101] Constricting lesions that do not allow passage of the endoscope may produce technically unsatisfactory or incomplete examinations.

Gastric lymphoma is typically very hypoechoic; its invasion is along the gastric wall or horizontal, and involvement of extramural structures and lymph nodes is less than with gastric carcinoma. Thus, localized mucosal ulceration with extensive infiltration of the deeper layers suggests lymphoma, which may also grow with a polypoid pattern or as a diffuse infiltration without ulceration.[102] **Gastric carcinoma,** in contrast, arises from the gastric mucosa, is usually more echogenic, tends to invade vertically or through the gastric wall, and frequently involves the perigastric lymph nodes at diagnosis.

Rectum: Tumor Staging of Rectal Carcinoma

Transrectal (endorectal) sonography is an established modality for the staging of rectal carcinoma.[103-105] Its resolution of the layers of the rectum surpasses the performance of both CT and MRI. Although a variety of pathologic conditions may be assessed with endorectal sonography, the staging of previously detected rectal carcinoma is its major role. Patients are scanned in the left lateral decubitus position following a cleansing enema. Both axial and sagittal images are obtained. A variety of rigid intrarectal probes are commercially available, using a range of transducer technologies with phased array, mechanical sector, and rotating crystals.

Further, we have also been routinely evaluating women with rectal carcinoma using a transvaginal probe placed in the vagina after a Fleet enema. This technique is excellent, especially for larger tumors, because the rectovaginal septum, the tumor, and the lymph nodes in the mesorectum are more optimally seen.[106]

Tumors are staged according to the Astler-Coller modification[107] of the Dukes Classification, or more simply with the **primary tumor** component of the Union Internationale Contre le Cancer (UICC) **TNM classification,**[108] where **T** represents the primary tumor, **N** the nodal involvement, and **M** the distant metastases (Fig. 8.53).

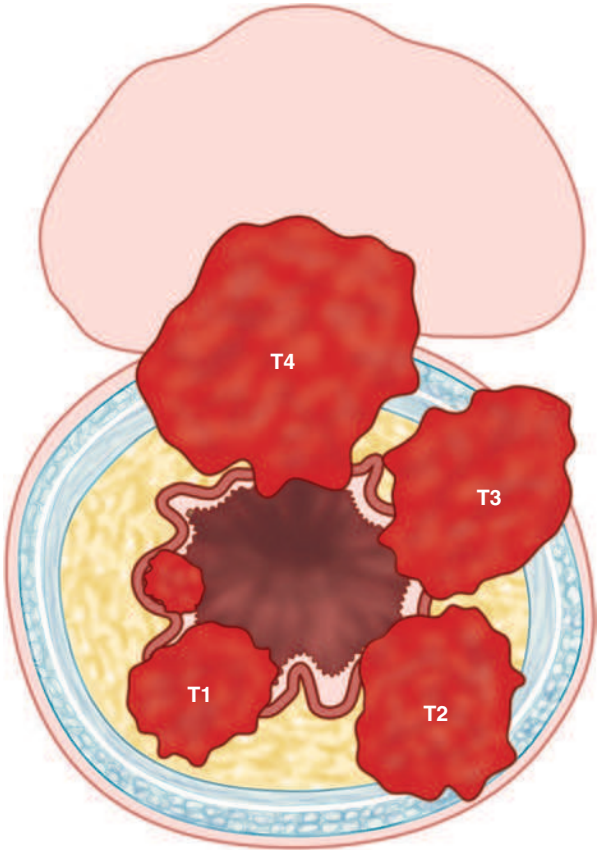

FIG. 8.53 Schematic of Tumor (T) Component of TNM Staging of Rectal Cancer on Sonography. Tumors *(red)* exhibit progressively deeper invasion beginning at 10 o'clock, where T superficial noninvasive lesion involves only superficial layers of intestinal wall. At 7 o'clock, T1 lesion invades submucosa *(yellow)*. At 5 o'clock, T2 lesion invades muscularis propria *(blue)*. At 2 o'clock, T3 lesion exhibits full-thickness invasion through layers of rectal wall, with invasion of surrounding perirectal fat. In directly anterior aspect (12 o'clock), T4 lesion exhibits invasion of prostate gland.

Rectal carcinoma arises from the mucosal surface of the gut. Tumors appear as relatively hypoechoic masses that may distort the rectal lumen. Invasion of the deeper layers, the submucosa, the muscularis propria, and the perirectal fat produces discontinuity of these layers on the sonogram (Fig. 8.54). Superficial ulceration or crevices that allow small bubbles of gas to be trapped deep to the crystal surface may demonstrate ring-down artifact and shadowing, with loss of layer definition deep to the ulceration. Lymph nodes appear as round or oval, hypoechoic masses in the perirectal fat (Fig. 8.54C). Color Doppler is an excellent addition to transrectal probes, showing the extent of tumors on the basis of their hypervascularity (Fig. 8.55) Infrequently, actual deposits may be shown within enlarged nodes. Therefore definitive staging requires pathologic assessment of both the tumor and the regional nodes.

Limitations of rectal sonography include the following: inability to identify microscopic tumor invasion, to image stenotic tumors, and to image tumors greater than 15 cm from the anal verge. It is also limited for distinguishing nodes involved with tumor from those with reactive change and to identify normal-sized nodes with microscopic tumor invasion.

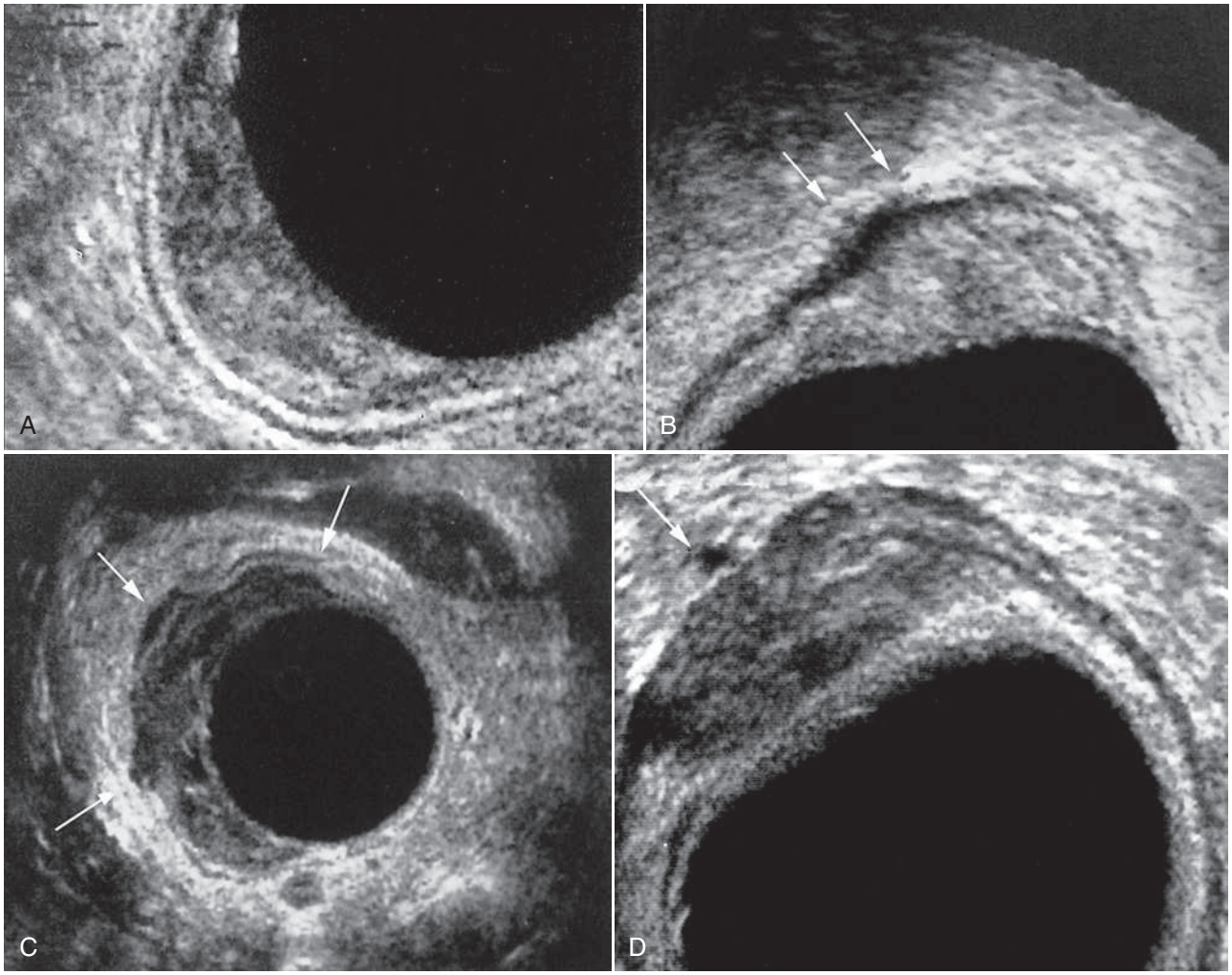

FIG. 8.54 Rectal Tumors Seen at Transrectal Sonography. (A) Rectal carcinoma: T1. Hypoechoic mass between 6 o'clock and 8 o'clock is noted. The submucosa (the echogenic line) and the muscularis propria (the external hypoechoic line) are intact. **(B) Rectal carcinoma: T2.** Tumor is seen anteriorly. The muscularis propria *(arrows)* is the hypoechoic line that is thickened and nodular, consistent with tumor involvement. **(C) Rectal carcinoma: T3.** A large tumor involves the entire right lateral wall of the rectum. Invasion of the perirectal fat *(arrows)* is noted in several locations. A large node is seen at the 6 o'clock position; smaller nodes are seen at 5 o'clock and 8 o'clock. **(D) Metastatic prostate carcinoma to rectal wall.** Hypoechoic mass is seen between 10 o'clock and 1 o'clock. It involves the deep layers of the rectal wall and not the rectal mucosa. There is a small lymph node *(arrow).* (With permission from Berton F, Gola G, Wilson S. Perspective on the role of transrectal and transvaginal sonography of tumors of the rectum and anal canal. AJR Am J Roentgenol. 2008;190[6]:1495-1504.[106])

Recurrent rectal cancer after local resection is usually extraluminal, involving the resection margin secondarily. Serial transrectal sonography may be used in conjunction with serum carcinoembryonic antigen levels to detect these recurrences. A pericolic hypoechoic mass or local thickening of the rectal wall, in either deep or superficial layers, is taken as evidence of recurrence. Previous radiation treatment may produce a diffuse thickening of the entire rectal wall, usually of moderate or high echogenicity, with an appearance that is usually easily differentiated from the focal hypoechoic appearance of recurrent cancer. Sonographic-guided biopsy of a detected abnormality facilitates histologic differentiation of recurrence from postoperative, inflammatory, or postradiation change.

Prostatic carcinoma may invade the rectum directly, or more remote tumors may involve the rectum, usually as a result of seeding to the posterior peritoneal pouch. Because these tumors initially involve the deeper layers of the rectal wall, with mucosal involvement occurring as the disease progresses, their sonographic appearance is distinct from that of primary rectal carcinoma (see Fig. 8.54D).

Benign mesenchymal tumors, especially of smooth muscle origin, are uncommon in the rectum. When seen, their sonographic features are the same as elsewhere (Fig. 8.56). **Mucous retention cysts,** resulting from obstruction of mucous glands, produce cystic masses of varying size that are located deep in the rectal wall.

Anal Canal

Cancer of the anal canal is a very rare tumor that is well shown on anal sonography (Fig. 8.57).

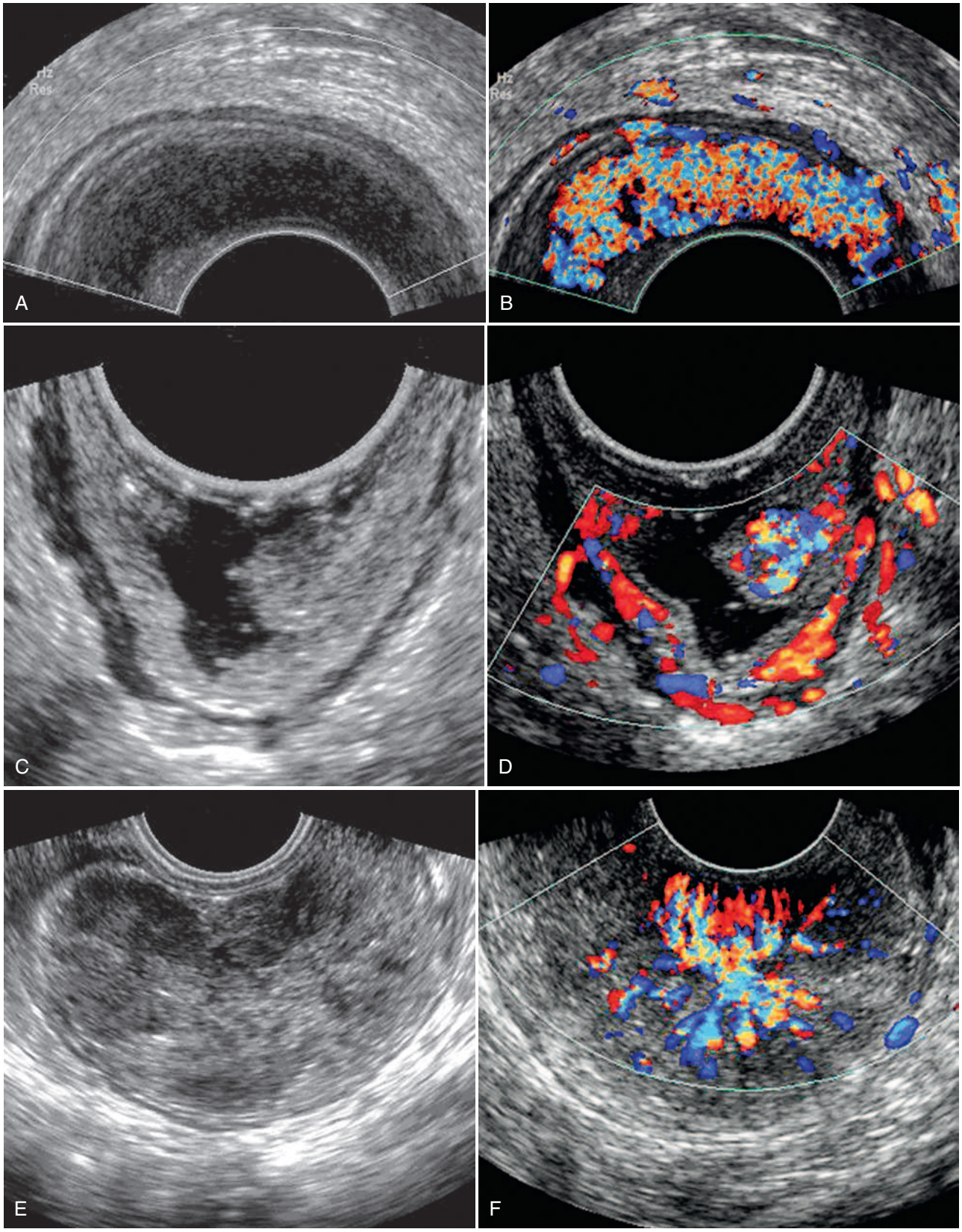

FIG. 8.55 Contribution of Color Doppler at Transrectal Sonography to Staging and Diagnosis of Rectal Cancer. (A) and **(B) T2 rectal cancer** in 58-year-old man. **(A)** Axial image shows hypoechoic tumor. Destruction of submucosa is evident with involvement of muscularis propria on right side of image. **(B)** Color Doppler shows typical hypervascularity. Color demarcates tumor from normal rectal wall on left side of image. **(C)** and **(D)** Small **rectal adenocarcinoma** originating in adenomatous polyp in 55-year-old man. **(C)** Axial image shows an isoechoic polypoid mass with a broad base surrounded by fluid within the rectal lumen. Mass involves the submucosal layer only. **(D)** Color Doppler image shows profuse vascularity and vascular stalk of the polypoid mass. **(E)** and **(F)** tubulovillous adenoma in 58-year-old woman. **(E)** Axial transvaginal image shows a mixed-echogenic mass that seems to fill the lumen of the rectum. **(F)** Color Doppler frequently shows this type of stellate, branching vascularity in tubulovillous tumors. (With permission from Berton F, Gola G, Wilson S. Perspective on the role of transrectal and transvaginal sonography of tumors of the rectum and anal canal. AJR Am J Roentgenol. 2008;190[6]:1495-1504.[106])

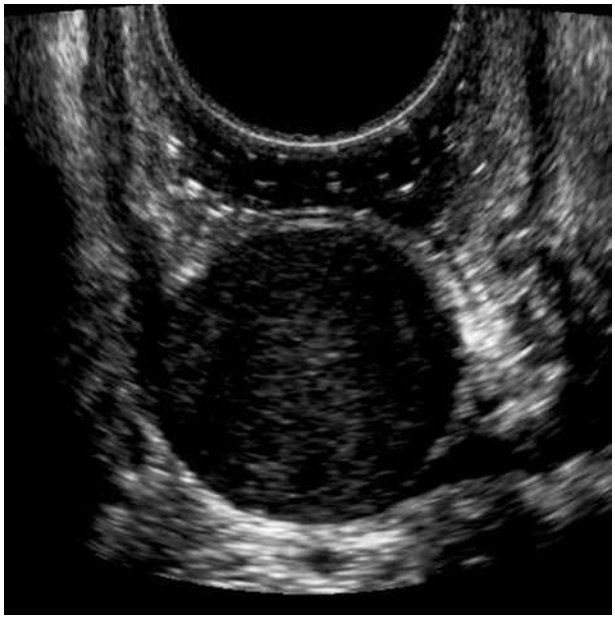

FIG. 8.56 Gastrointestinal Stromal Tumor (GIST) of Rectum. Transrectal sonographic image shows solid, well-defined, round mass arising from muscularis propria layer in 59-year-old woman with asymptomatic palpable mass found at routine physical examination. Tumor is growing with submucosal pattern, and mucosal surface bulges into fluid-filled lumen.

FIG. 8.57 Cancer of Anal Canal. (A) Long-axis image and **(B)** cross-sectional image show a hypoechoic tumor disrupting the normal planes of the anal canal. **(C)** Sonogram shows the vascularity of the tumor. (With permission from Berton F, Gola G, Wilson S. Perspective on the role of transrectal and transvaginal sonography of tumors of the rectum and anal canal. AJR Am J Roentgenol. 2008;190[6]:1495-1504.[106])

Fecal Incontinence

Anal endosonography, performed with the addition of a hard cone attachment to a radial 7.5-MHz probe, allows accurate assessment of the anal canal, including the internal and external sphincters.[109] Performed primarily for assessment of fecal incontinence, this test shows the integrity of the sphincters with documentation of the degree and size of muscle defects. We do not use this technique any longer, preferring instead assessment of the sphincter and perianal soft tissues with a combination of transvaginal and transperineal scan.[37,110-113]

Young women, following traumatic obstetric delivery, are most often afflicted with fecal incontinence. The internal anal sphincter, in continuity with the muscularis propria of the rectum above, is seen as a thick circular hypoechoic or hypoechoic ring just deep to the convoluted mucosal echoes (Fig. 8.58). The external anal sphincter, in contrast, is less well defined and more echogenic, appearing gray on the ultrasound examination, and in continuity with fibers from the puborectalis sling. Traumatic disruption of the muscle layers will show as defects in the continuity of the normal muscle texture, most often anterior (Fig. 8.59). Post-traumatic scarring may be associated with a change of shape of the anal canal from round to oval.

Perianal Inflammatory Disease

Perianal inflammatory disease is seen in two distinct patient populations: (1) those with **Crohn disease** who develop perianal inflammation as part of their disease and (2) those who develop a **perianal abscess** or **perianal fistula** as a spontaneous event. The first group is described earlier in the section on Crohn disease. In other patients, perianal infection arises in small,

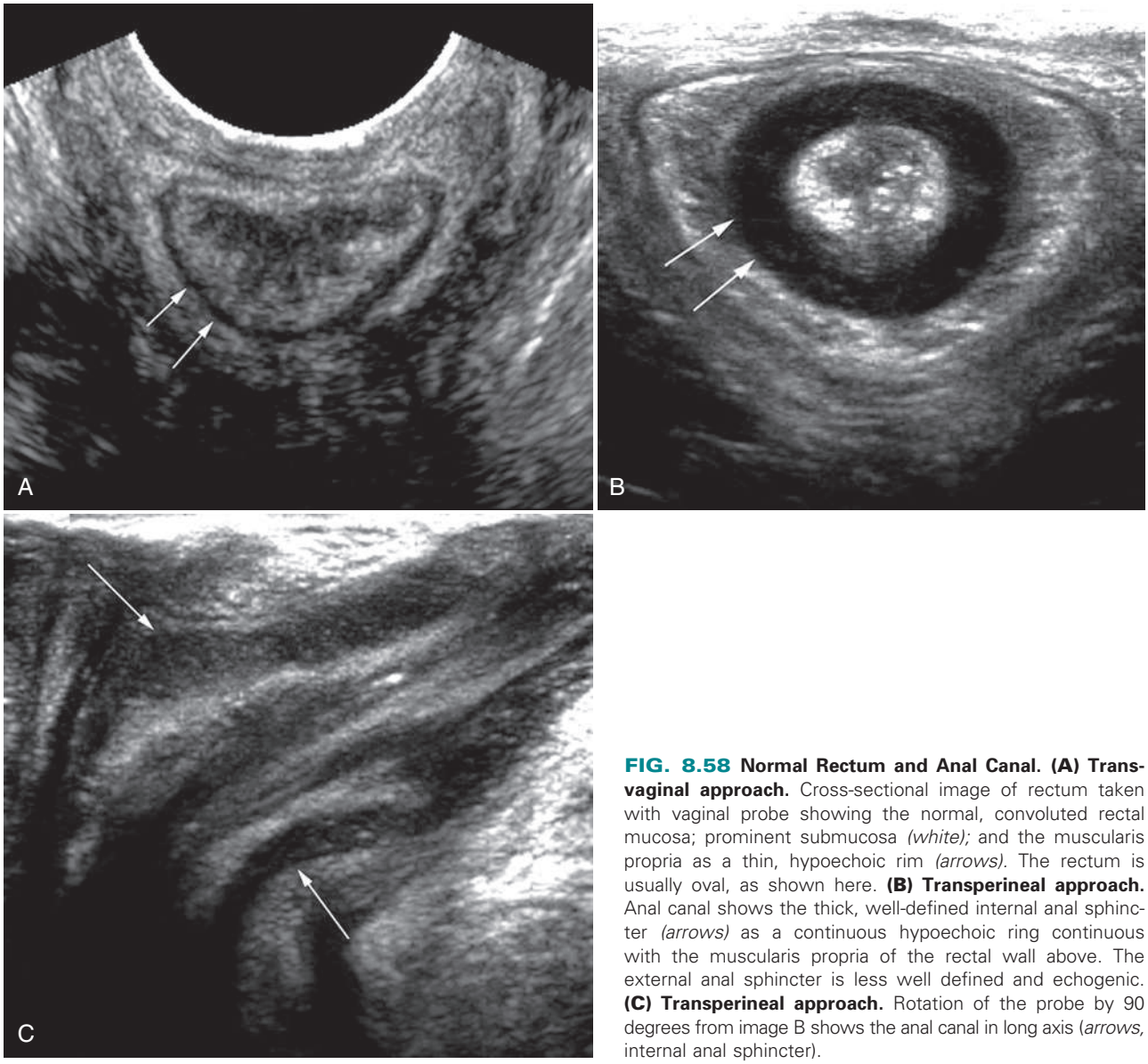

FIG. 8.58 Normal Rectum and Anal Canal. (A) Transvaginal approach. Cross-sectional image of rectum taken with vaginal probe showing the normal, convoluted rectal mucosa; prominent submucosa *(white);* and the muscularis propria as a thin, hypoechoic rim *(arrows).* The rectum is usually oval, as shown here. **(B) Transperineal approach.** Anal canal shows the thick, well-defined internal anal sphincter *(arrows)* as a continuous hypoechoic ring continuous with the muscularis propria of the rectal wall above. The external anal sphincter is less well defined and echogenic. **(C) Transperineal approach.** Rotation of the probe by 90 degrees from image B shows the anal canal in long axis (*arrows,* internal anal sphincter).

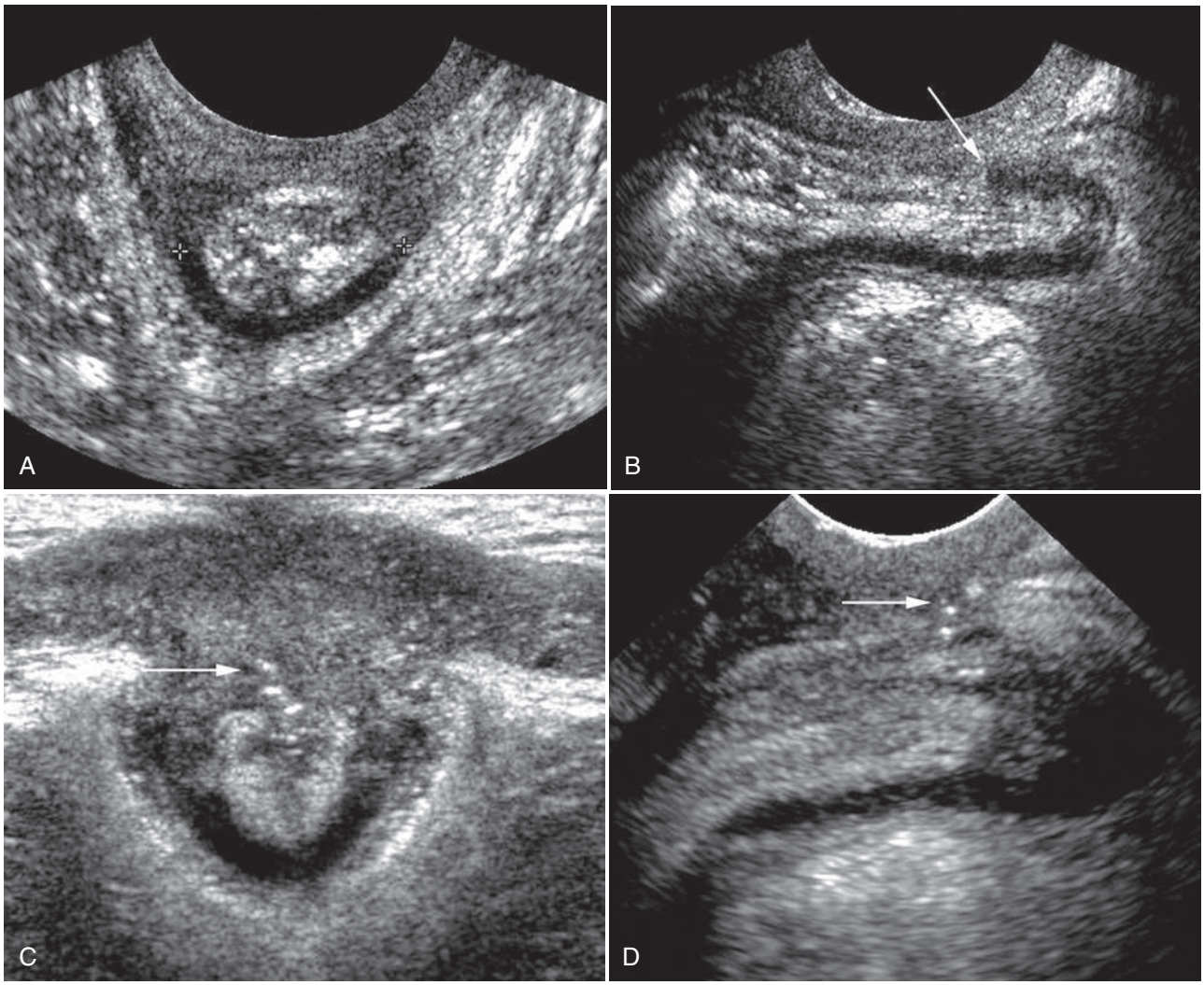

FIG. 8.59 Traumatic Disruption of Anal Sphincter in Two Patients. (A) Cross-sectional and **(B)** long-axis views of the anal canal from a transvaginal approach show disruption of the sphincter anteriorly from 9 to 3 o'clock. The arrow on the sagittal image shows the cephalad extent of the internal anal sphincter. **(C)** Cross-sectional and **(D)** long-axis views of the anal canal show full-thickness disruption of the anterior anal canal between 11 and 1 o'clock. The arrow in each image shows air bubbles within an anovaginal fistula.

intersphincteric anal glands predominantly located at the dentate line. This occurs most frequently in young adult men. Documentation of fluid collections and the relationship of inflammatory tracts to the sphincter mechanism are important for surgical treatment. We prefer transvaginal sonography (Video 8.17) in conjunction with transperineal sonography in women and transperineal sonography in men for evaluation of this problem.

Scans are performed with curved and high-frequency linear probes placed firmly on the skin of the perineum between the introitus and the anal canal in women and between the scrotum and the anal canal in men.[111] Firm pressure on the transducer is required to afford good visualization of the anal canal. We begin the procedure with the transducer in the transverse plane relative to the body. The transducer should be directed cephalad and anterior to the plane of the anal canal, then angled slowly through the plane of the anal canal, which will show it in cross section from the anorectal junction to the external anal opening. Rotation of the transducer by 90 degrees will allow for imaging in the longitudinal plane. Tracts and collections in the perineum, buttocks, scrotum, and labia can also be assessed and followed in a retrograde direction to their connection with the anal canal.

Sonography of Perianal Inflammatory Disease

Internal opening in the anal canal or rectum
Tracts and their relationship to anal sphincter
External openings
Fluid collections

Perianal inflammatory tracts and masses are classified according to Parks et al.[114] Their classification provides an anatomic description of fistulous tracts, which acts as a guide to operative

treatment. The four main subtypes are **intersphincteric** (between internal and external sphincter), **transsphincteric** (crossing both internal and external anal sphincter into ischiorectal or ischioanal fossa), **suprasphincteric,** and **extrasphincteric.** In each patient, we also document the internal opening and the external openings, as possible. Tracts show on the ultrasound scan as hypoechoic linear areas or fluid-containing tubular areas, depending on their size and activity (Fig. 8.60). As with fistulas elsewhere, air bubbles within the tract show as bright, echogenic foci that may move during the scan, helping with their identification. In our initial experience with 54 patients with perianal inflammatory masses, sonographic findings were confirmed in 22 of 26 patients (85%) who underwent surgical treatment for their disease.

Acknowledgment

The author would like to acknowledge Gordana Popovich for her artwork.

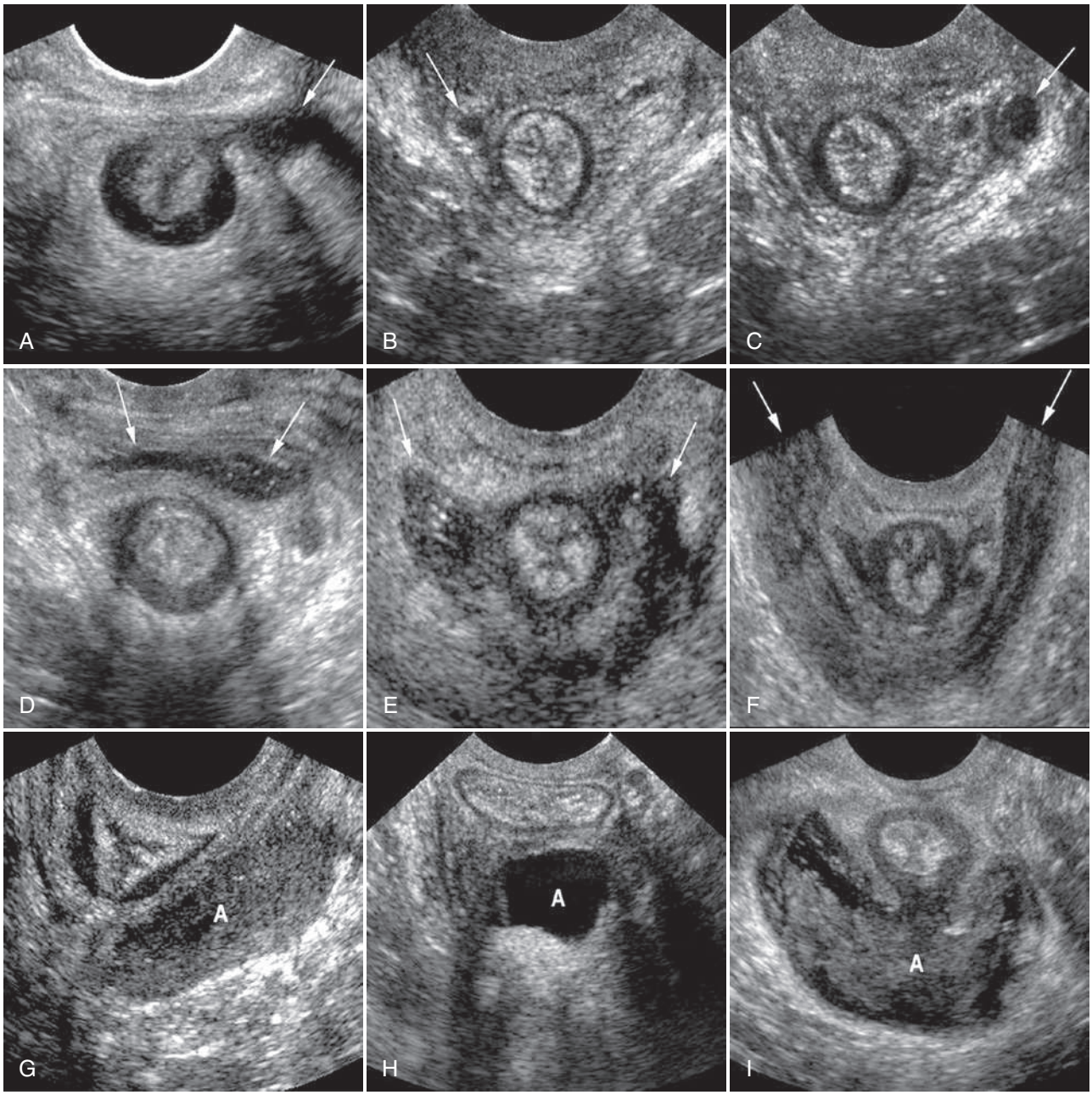

FIG. 8.60 Perianal Inflammatory Disease in Nine Patients. *Top row,* **Simple inflammatory openings and tracts** *(arrows).* Cross-sectional images of the anal canal show internal opening at 1 o'clock with **(A)** transsphincteric tract running to a small collection; **(B)** intersphincteric tract; **(C)** larger extrasphincteric tract. *Middle row,* **More complex tracts** *(arrows).* **(D)** Anterior extrasphincteric tract shows fluid within. **(E)** Bilateral, complex, intersphincteric tracts and collections show bright, echogenic foci representing extraluminal air. **(F)** Boomerang, or horseshoe, tract surrounds the anal canal posteriorly and laterally. There are internal openings at 2, 4, and 9 o'clock. *Bottom row,* **Perianal abscesses** *(A).* **(G)** Abscess on left posterolateral aspect of the anal canal is particle filled. **(H)** Large, posterior abscess is complex, with a dependent debris level. **(I)** Large, posterior abscess shows a large internal opening posteriorly at 6 o'clock.

REFERENCES

1. Wilson SR. The bowel wall looks thickened: what does that mean? In: Cooperberg PL, editor. RSNA categorical course syllabus. Chicago: RSNA; 2002. pp. 219-228.
2. Heyder N, Kaarmann H, Giedl J. Experimental investigations into the possibility of differentiating early from invasive carcinoma of the stomach by means of ultrasound. Endoscopy. 1987;19(6):228-232.
3. Kimmey MB, Martin RW, Haggitt RC, et al. Histologic correlates of gastrointestinal ultrasound images. Gastroenterology. 1989;96(2 Pt 1): 433-441.
4. Lutz HT, Petzoldt R. Ultrasonic patterns of space occupying lesions of the stomach and the intestine. Ultrasound Med Biol. 1976;2(2):129-132.
5. Bluth E, Merritt C, Sullivan M. Ultrasonic evaluation of the stomach, small bowel, and colon. Radiology. 1979;133(3 Pt 1):677-680.
6. Puylaert JB. Acute appendicitis: US evaluation using graded compression. Radiology. 1986;158(2):355-360.
7. Teefey SA, Roarke MC, Brink JA, et al. Bowel wall thickening: differentiation of inflammation from ischemia with color Doppler and duplex US. Radiology. 1996;198(2):547-551.
8. Romanini L, Passamonti M, Navarria M, et al. Quantitative analysis of contrast-enhanced ultrasonography of the bowel wall can predict disease activity in inflammatory bowel disease. Eur J Radiol. 2014;83(8):1317-1323.
9. Dillman JR, Stidham RW, Higgins PDR, et al. Ultrasound shear wave elastography helps discriminate low-grade from high-grade bowel wall fibrosis in ex vivo human intestinal specimens. J Ultrasound Med. 2014;33(12):2115-2123.
10. Lim JH. Colorectal cancer: sonographic findings. AJR Am J Roentgenol. 1996;167(1):45-47.
11. Lim JH, Ko YT, Lee DH, et al. Determining the site and causes of colonic obstruction with sonography. AJR Am J Roentgenol. 1994;163(5):1113-1117.
12. Shorter RG. Gastrointestinal pathology: an atlas and text. Mayo Clin Proc. 1989;64(12):1567-1568.
13. Kaftori J, Aharon M, Kleinhaus U. Sonographic features of gastrointestinal leiomyosarcoma. J Clin Ultrasound. 1981;9(1):11-15.
14. Derchi LE, Banderali A, Bossi C, et al. The sonographic appearances of gastric lymphoma. J Ultrasound Med. 1984;3(6):251-256.
15. Salem S, Hiltz C. Ultrasonographic appearance of gastric lymphosarcoma. J Clin Ultrasound. 1978;6(6):429-430.
16. Telerman A, Gerard B, Van den Heule B, Bleiberg H. Gastrointestinal metastases from extra-abdominal tumors. Endoscopy. 1985;17(3):99-101.
17. Yeh H. Ultrasonography of peritoneal tumors. Radiology. 1979;133(2):419-424.
18. Wilson S. Evaluation of the small intestine by ultrasonography. In: Gourtsoyiannis N, editor. Radiologic imaging of the small intestine. Heidelberg: Springer-Verlag; 2002. pp. 73-86.
19. Horsthuis K, Bipat S, Bennink R, Stoker J. Inflammatory bowel disease diagnosed with US, MR, scintigraphy, and CT: meta-analysis of prospective studies. Radiology. 2008;247(1):64-79.
20. Panés J, Bouzas R, Chaparro M, et al. Systematic review: the use of ultrasonography, computed tomography and magnetic resonance imaging for the diagnosis, assessment of activity and abdominal complications of Crohn's disease. Aliment Pharmacol Ther. 2011;34(2):125-145.
21. Sarrazin J, Wilson SR. Manifestations of Crohn disease at US. Radiographics. 1996;16(3):499-520.
22. Gasche C, Moser G, Turetschek K, et al. Transabdominal bowel sonography for the detection of intestinal complications in Crohn's disease. Gut. 1999;44(1):112-117.
23. Medellin-Kowalewski A, Wilkens R, Wilson A, et al. Quantitative contrast-enhanced ultrasound parameters in Crohn disease: their role in disease activity determination with ultrasound. AJR Am J Roentgenol. 2016;206(1):64-73.
24. DiCandio G, Mosca F, Campatelli A, et al. Sonographic detection of postsurgical recurrence of Crohn disease. AJR Am J Roentgenol. 1986;146(3):523-526.
25. Fraquelli M, Colli A, Casazza G, et al. Role of US in detection of Crohn disease: meta-analysis 1. Radiology. 2005;236(1):95-101.
26. Dubbins PA. Ultrasound demonstration of bowel wall thickness in inflammatory bowel disease. Clin Radiol. 1984;35(3):227-231.
27. Worlicek H, Lutz H, Heyder N, Matek W. Ultrasound findings in Crohn's disease and ulcerative colitis: a prospective study. J Clin Ultrasound. 1987;15(3):153-163.
28. Spalinger J, Patriquin H, Miron M, et al. Doppler US in patients with Crohn disease: vessel density in the diseased bowel reflects disease activity. Radiology. 2000;217(3):787-791.
29. Ripollés T, Martínez M, Paredes J, et al. Crohn disease: correlation of findings at contrast-enhanced US with severity at endoscopy. Radiology. 2009;253(1):241-248.
30. Ripollés T, Rausell N, Paredes J, et al. Effectiveness of contrast-enhanced ultrasound for characterisation of intestinal inflammation in Crohn's disease: a comparison with surgical histopathology analysis. J Crohns Colitis. 2013;7(2):120-128.
31. Parente F, Maconi G, Bollani S, et al. Bowel ultrasound in assessment of Crohn's disease and detection of related small bowel strictures: a prospective comparative study versus x ray and intraoperative findings. Gut. 2002;50(4):490-495.
32. Ferraioli G, Tinelli C, Lissandrin R, et al. Point shear wave elastography method for assessing liver stiffness. World J Gastroenterol. 2014;20(16):4787-4796.
33. Dillman J, Stidham R, Higgins P, et al. US elastography–derived shear wave velocity helps distinguish acutely inflamed from fibrotic bowel in a Crohn Disease animal model. Radiology. 2013;267(3):757-766.
34. Lu C, Gui X, Chen W, et al. Ultrasound shear wave elastography identifies muscle wall hypertrophy and is a novel surrogate for inflammation in Crohn's disease. United European Gastroenterol J. 2015;3:P0333.
35. Ripollés T, Martínez-Pérez M, Blanc E, et al. Contrast-enhanced ultrasound (CEUS) in Crohn's disease: technique, image interpretation and clinical applications. Insights Imaging. 2011;2(6):639-652.
36. Stewart LK, McGee J, Wilson SR. Transperineal and transvaginal sonography of perianal inflammatory disease. AJR Am J Roentgenol. 2001;177(3):627-632.
37. Damani N, Wilson S. Nongynecologic applications of transvaginal US. Radiographics. 1999;19(Spec No):S179-S200.
38. Puylaert J. Ultrasound of acute GI tract conditions. Eur Radiol. 2001;11(10):1867-1877.
39. Seibert JJ, Williamson SL, Golladay ES, et al. The distended gasless abdomen: a fertile field for ultrasound. J Ultrasound Med. 1986;5(6):301-308.
40. Lee DH, Lim JH, Ko YT, Yoon Y. Sonographic detection of pneumoperitoneum in patients with acute abdomen. AJR Am J Roentgenol. 1990;154(1):107-109.
41. Muradali D, Wilson S, Burns PN, et al. A specific sign of pneumoperitoneum on sonography: enhancement of the peritoneal stripe. AJR Am J Roentgenol. 1999;173(5):1257-1262.
42. Pieper R, Forsell P, Kager L. Perforating appendicitis. A nine-year survey of treatment and results. Acta Chir Scand Suppl. 1986;530:51-57.
43. Kazarian K, Roeder W, Mersheimer W. Decreasing mortality and increasing morbidity from acute appendicitis. Am J Surg. 1970;119(6):681-685.
44. Van Way 3rd CW, Murphy JR, Dunn EL, Elerding SC. A feasibility study of computer aided diagnosis in appendicitis. Surg Gynecol Obstet. 1982;155(5):685-688.
45. Berry J, Malt R. Appendicitis near Its centenary. Ann Surg. 1984;200(5): 567-575.
46. Gaensler EH, Jeffrey RB, Laing FC, Townsend RR. Sonography in patients with suspected acute appendicitis: value in establishing alternative diagnoses. AJR Am J Roentgenol. 1989;152(1):49-51.
47. Bendeck S, Nino-Murcia M, Berry G, Jeffrey R. Imaging for suspected appendicitis: negative appendectomy and perforation rates. Radiology. 2002;225(1):131-136.
48. Birnbaum B, Wilson S. Appendicitis at the millennium. Radiology. 2000;215(2):337-348.
49. Shaw R. Appendix calculi and acute appendicitis. Br J Surg. 1965;52(6):451-459.
50. Savrin R, Clausen K, Martin E, Cooperman M. Chronic and recurrent appendicitis. Am J Surg. 1979;137(3):355-357.
51. Dachman AH, Nichols JB, Patrick DH, Lichtenstein JE. Natural history of the obstructed rabbit appendix: observations with radiography, sonography, and CT. AJR Am J Roentgenol. 1987;148(2):281-284.
52. Jeffrey RB, Laing FC, Townsend RR. Acute appendicitis: sonographic criteria based on 250 cases. Radiology. 1988;167(2):327-329.
53. Abu-Yousef MM, Bleicher JJ, Maher JW, et al. High-resolution sonography of acute appendicitis. AJR Am J Roentgenol. 1987;149(1):53-58.
54. Rioux M. Sonographic detection of the normal and abnormal appendix. AJR Am J Roentgenol. 1992;158(4):773-778.
55. Jeffrey RB, Laing FC, Lewis FR. Acute appendicitis: high-resolution real-time US findings. Radiology. 1987;163(1):11-14.

56. Rettenbacher T, Hollerweger A, Macheiner P, et al. Ovoid shape of the vermiform appendix: a criterion to exclude acute appendicitis—evaluation with US. Radiology. 2003;226(1):95-100.
57. Lee J, Jeong Y, Hwang J, et al. Graded compression sonography with adjuvant use of a posterior manual compression technique in the sonographic diagnosis of acute appendicitis. AJR Am J Roentgenol. 2002;178(4):863-868.
58. Borushok KF, Jeffrey Jr RB, Laing FC, Townsend RR. Sonographic diagnosis of perforation in patients with acute appendicitis. AJR Am J Roentgenol. 1990;154(2):275-278.
59. Agha FP, Ghahremani GG, Panella JS, Kaufman MW. Appendicitis as the initial manifestation of Crohn's disease: radiologic features and prognosis. AJR Am J Roentgenol. 1987;149(3):515-518.
60. Roth T, Zimmer G, Tschantz P. Maladie de Crohn appendiculaire. Ann Chir. 2000;125(7):665-667.
61. Higgins MJ, Walsh M, Kennedy SM, et al. Granulomatous appendicitis revisited: report of a case. Dig Surg. 2001;18(3):245-248.
62. Chou Y, Chiou H, Tiu C, et al. Sonography of acute right side colonic diverticulitis. Am J Surg. 2001;181(2):122-127.
63. O'Malley M, Wilson S. US of gastrointestinal tract abnormalities with CT correlation. Radiographics. 2003;23(1):59-72.
64. Teefey SA, Montana MA, Goldfogel GA, Shuman WP. Sonographic diagnosis of neutropenic typhlitis. AJR Am J Roentgenol. 1987;149(4):731-733.
65. Frager DH, Frager JD, Brandt LJ, et al. Gastrointestinal complications of AIDS: radiologic features. Radiology. 1986;158(3):597-603.
66. Balthazar EJ, Megibow AJ, Fazzini E, et al. Cytomegalovirus colitis in AIDS: radiographic findings in 11 patients. Radiology. 1985;155(3):585-589.
67. Teixidor HS, Honig CL, Norsoph E, et al. Cytomegalovirus infection of the alimentary canal: radiologic findings with pathologic correlation. Radiology. 1987;163(2):317-323.
68. Puylaert JB. Mesenteric adenitis and acute terminal ileitis: US evaluation using graded compression. Radiology. 1986;161(3):691-695.
69. Puylaert JB, Lalisang RI, van der Werf SD, Doornbos L. Campylobacter ileocolitis mimicking acute appendicitis: differentiation with graded-compression US. Radiology. 1988;166(3):737-740.
70. Puylaert JB. Right-sided segmental infarction of the omentum: clinical, US, and CT findings. Radiology. 1992;185(1):169-172.
71. Painter NS, Burkitt DP. Diverticular disease of the colon, a 20th century problem. Clin Gastroenterol. 1975;4(1):3-21.
72. Parks TG. Natural history of diverticular disease of the colon. A review of 521 cases. Br Med J. 1969;4(5684):639-642.
73. Fleischner F, Ming S. Revised concepts on diverticular disease of the colon. Radiology. 1965;84(4):599-609.
74. Wilson SR, Toi A. The value of sonography in the diagnosis of acute diverticulitis of the colon. AJR Am J Roentgenol. 1990;154(6): 1199-1202.
75. Parulekar SG. Sonography of colonic diverticulitis. J Ultrasound Med. 1985;4(12):659-666.
76. Derchi LE, Reggiani L, Rebaudi F, Bruschetta M. Appendices epiploicae of the large bowel. Sonographic appearance and differentiation from peritoneal seeding. J Ultrasound Med. 1988;7(1):11-14.
77. Meiser G, Meissner K. [Sonographic differential diagnosis of intestinal obstruction—results of a prospective study of 48 patients]. Ultraschall Med. 1985;6(1):39-45.
78. Tennenhouse JE, Wilson SR. Sonographic detection of a small-bowel bezoar. J Ultrasound Med. 1990;9(10):603-605.
79. Siewert B, Raptopoulos V. CT of the acute abdomen: findings and impact on diagnosis and treatment. AJR Am J Roentgenol. 1994;163(6):1317-1324.
80. Balthazar EJ. George W. Holmes Lecture. CT of small-bowel obstruction. AJR Am J Roentgenol. 1994;162(2):255-261.
81. Lee DH, Lim JH, Ko YT. Afferent loop syndrome: sonographic findings in seven cases. AJR Am J Roentgenol. 1991;157(1):41-43.
82. Parienty RA, Lepreux JF, Gruson B. Sonographic and CT features of ileocolic intussusception. AJR Am J Roentgenol. 1981;136(3):608-610.
83. Weissberg D, Scheible W, Leopold G. Ultrasonographic appearance of adult intussusception. Radiology. 1977;124(3):791-792.
84. Alessi V, Salerno G. The "Hay-fork" sign in the ultrasonographic diagnosis of intussusception. Gastrointest Radiol. 1985;10(1):177-179.
85. Gaines PA, Saunders AJS, Drake D. Midgut malrotation diagnosed by ultrasound. Clin Radiol. 1987;38(1):51-53.
86. Totten MA, Gregg JA, Fremont-Smith P, Legg M. Clinical and pathological spectrum of antibiotic-associated colitis. Am J Gastroenterol. 1978;69(3 Pt 1):311-319.
87. Downey DB, Wilson SR. Pseudomembranous colitis: sonographic features. Radiology. 1991;180(1):61-64.
88. Bolondi L, Ferrentino M, Trevisani F, et al. Sonographic appearance of pseudomembranous colitis. J Ultrasound Med. 1985;4(9):489-492.
89. Vernacchia FS, Jeffrey RB, Laing FC, Wing VW. Sonographic recognition of pneumatosis intestinalis. AJR Am J Roentgenol. 1985;145(1):51-52.
90. Sigel B, Machi J, Ramos JR, et al. Ultrasonic features of pneumatosis intestinalis. J Clin Ultrasound. 1985;13(9):675-678.
91. Cotrin RS, Kumar V, Collins T, editors. Robbins pathologic basis of disease. 6th ed. Philadelphia: Saunders; 1999. pp. 1583-1584.
92. Young R, Gilks C, Scully R. Mucinous tumors of the appendix associated with mucinous tumors of the ovary and pseudomyxoma peritonei. Am J Surg Pathol. 1991;15(5):415-429.
93. Dietrich CF, Brunner V, Seifert H, et al. [Intestinal B-mode sonography in patients with endemic sprue. Intestinal sonography in endemic sprue]. Ultraschall Med. 1999;20(6):242-247.
94. Rettenbacher T, Hollerweger A, Macheiner P, et al. Adult celiac disease: US signs. Radiology. 1999;211(2):389-394.
95. Pickhardt PJ, Yagan N, Siegel MJ, et al. Cystic fibrosis: CT findings of colonic disease. Radiology. 1998;206(3):725-730.
96. Haber HP, Benda N, Fitzke G, et al. Colonic wall thickness measured by ultrasound: striking differences in patients with cystic fibrosis versus healthy controls. Gut. 1997;40(3):406-411.
97. Connett G, Lucas J, Atchley J, et al. Colonic wall thickening is related to age and not dose of high strength pancreatin microspheres in children with cystic fibrosis. Eur J Gastroenterol Hepatol. 1999;11(2):181-184.
98. Welkon CJ, Long SS, Thompson Jr CM, Gilligan PH. Clostridium difficile in patients with cystic fibrosis. Am J Dis Child. 1985;139(8):805-808.
99. Shorvon PJ, Lees WR, Frost RA, Cotton PB. Upper gastrointestinal endoscopic ultrasonography in gastroenterology. Br J Radiol. 1987;60(713):429-438.
100. Strohm WD, Classen M. Benign lesions of the upper GI tract by means of endoscopic ultrasonography. Scand J Gastroenterol Suppl. 1986;21(123): 41-46.
101. Takemoto T, Ito T, Aibe T, Okita K. Endoscopic ultrasonography in the diagnosis of esophageal carcinoma, with particular regard to staging it for operability. Endoscopy. 1986;18(Suppl. 3):22-25.
102. Bolondi L, Casanova P, Caletti GC, et al. Primary gastric lymphoma versus gastric carcinoma: endoscopic US evaluation. Radiology. 1987;165(3):821-826.
103. Hildebrandt U, Feifel G. Preoperative staging of rectal cancer by intrarectal ultrasound. Dis Colon Rectum. 1985;28(1):42-46.
104. Wang KY, Kimmey MB, Nyberg DA, et al. Colorectal neoplasms: accuracy of US in demonstrating the depth of invasion. Radiology. 1987;165(3): 827-829.
105. Yamashita Y, Machi J, Shirouzu K, et al. Evaluation of endorectal ultrasound for the assessment of wall invasion of rectal cancer. Dis Colon Rectum. 1988;31(8):617-623.
106. Berton F, Gola G, Wilson S. Perspective on the role of transrectal and transvaginal sonography of tumors of the rectum and anal canal. AJR Am J Roentgenol. 2008;190(6):1495-1504.
107. Astler V, Coller F. The prognostic significance of direct extension of carcinoma of the colon and rectum. Ann Surg. 1954;139(6):846-852.
108. Spiessl B, Beahrs OH, Hermanek P, et al., editors. TNM atlas: illustrated guide to the TNM/pTNM-classification of malignant tumours. 3rd ed. Berlin: Springer Verlag; 2003.
109. Law P, Bartram C. Anal endosonography: technique and normal anatomy. Gastrointest Radiol. 1989;14(1):349-353.
110. Rifkin MD, Ehrlich SM, Marks G. Staging of rectal carcinoma: prospective comparison of endorectal US and CT. Radiology. 1989;170(2):319-322.
111. Berton F, Gola G, Wilson S. Sonography of benign conditions of the anal canal: an update. AJR Am J Roentgenol. 2007;189(4):765-773.
112. Stewart LK, Wilson SR. Transvaginal sonography of the anal sphincter: reliable, or not? AJR Am J Roentgenol. 1999;173(1):179-185.
113. Sudakoff G, Quiroz F, Foley W. Sonography of anorectal, rectal, and perirectal abnormalities. AJR Am J Roentgenol. 2002;179(1):131-136.
114. Parks AG, Gordon PH, Hardcastle JD. A classification of fistula-in-ano. Br J Surg. 1976;63(1):1-12.

CHAPTER 9

The Kidney and Urinary Tract

Mitchell Tublin, Deborah Levine, Wendy Thurston, and Stephanie R. Wilson

SUMMARY OF KEY POINTS

- Renal ultrasound is the screening modality of choice for the initial evaluation of renal insufficiency. Relevant imaging markers include parenchymal echogenicity, renal length, and collecting system dilatation.
- The primary role for ultrasound in the evaluation of renal masses is to differentiate between cystic and solid lesions, although an appropriate differential diagnosis may be given based on clinical history and cyst complexity.
- Echogenic renal masses are problematic, and although several discriminatory features have been proposed, renal computed tomography or magnetic resonance imaging is typically employed for larger lesions to differentiate between renal cell carcinoma and angiomyolipoma.
- The role of ultrasound in the evaluation of hematuria continues to evolve. Ultrasound is an effective screening modality for typical "urologic" causes of hematuria (namely, renal calculi) in younger patients.
- Focal and diffuse bladder wall thickening at ultrasound is nonspecific and may be caused by a variety of infectious, inflammatory reactions or neoplastic processes. Urine analysis, clinical history, and potentially cystoscopy are typically performed after thickening is identified at sonography.

CHAPTER OUTLINE

EMBRYOLOGY
Development of the Kidneys and Ureter
Development of the Bladder
Development of the Urethra
ANATOMY
Kidney
Ureter
Bladder
SONOGRAPHIC TECHNIQUE
Kidney
Ureter
Bladder and Urethra
HYDRONEPHROSIS
PITFALLS IN ASSESSMENT OF OBSTRUCTION
CONGENITAL ANOMALIES
Anomalies Related to Renal Growth
Hypoplasia
Fetal Lobation
Compensatory Hypertrophy
Anomalies Related to Ascent of Kidney
Ectopia
Crossed Renal Ectopia
Horseshoe Kidney
Anomalies Related to Ureteral Bud
Renal Agenesis
Supernumerary Kidney
Duplex Collecting System and Ureterocele
Ureteropelvic Junction Obstruction
Congenital Megacalices
Congenital Megaureter
Anomalies Related to Vascular Development
Aberrant Vessels
Retrocaval Ureter
Anomalies Related to Bladder Development
Bladder Agenesis
Bladder Duplication
Bladder Exstrophy
Urachal Anomalies
Anomalies Related to Urethral Development: Diverticula
GENITOURINARY INFECTIONS
Pyelonephritis
Acute Pyelonephritis
Renal and Perinephric Abscess
Pyonephrosis
Emphysematous Pyelonephritis
Emphysematous Pyelitis
Chronic Pyelonephritis
Xanthogranulomatous Pyelonephritis
Papillary Necrosis
Tuberculosis
Fungal Infections
Candida Albicans
Parasitic Infections
Schistosomiasis
Echinococcal (Hydatid) Disease
Acquired Immunodeficiency Syndrome
Cystitis
Infectious Cystitis
Malacoplakia
Emphysematous Cystitis
Chronic Cystitis
FISTULAS, STONES (CALCULI), AND CALCIFICATION
Bladder Fistulas
Renal Calculi
Ureteral Calculi
Bladder Calculi
Nephrocalcinosis
GENITOURINARY TUMORS
Renal Cell Carcinoma
Imaging and Treatment Approaches
Sonographic Appearance
Biopsy and Prognosis
Pitfalls in Interpretation
Transitional Cell Carcinoma
Renal Tumors
Ureteral Tumors
Bladder Tumors
Squamous Cell Carcinoma
Adenocarcinoma
Oncocytoma
Angiomyolipoma
Lymphoma
Kidney
Ureter

Bladder
Leukemia
Metastases
Kidney
Ureter
Bladder
Urachal Adenocarcinoma
Rare Neoplasms
Kidney
Bladder
RENAL CYSTIC DISEASE
Cortical Cysts
Parapelvic Cysts
Medullary Cysts
Medullary Sponge Kidney
Medullary Cystic Disease
Polycystic Kidney Disease
Multicystic Dysplastic Kidney
Lithium Nephropathy
Multilocular Cystic Nephroma
Localized Cystic Disease
Neoplasm-Associated Renal Cystic Disease
Acquired Cystic Kidney Disease
Von Hippel–Lindau Disease
Tuberous Sclerosis
TRAUMA
Renal Injuries
Ureteral Injuries
Bladder Injuries
VASCULAR ABNORMALITIES
Renal Vascular Doppler Sonography
Renal Artery Occlusion and Infarction
Arteriovenous Fistula and Malformation
Renal Artery Stenosis
Renal Artery Aneurysm
Renal Vein Thrombosis
Ovarian Vein Thrombosis
MEDICAL GENITOURINARY DISEASES
Acute Tubular Necrosis
Acute Cortical Necrosis
Glomerulonephritis
Acute Interstitial Nephritis
Diabetes Mellitus
Amyloidosis
Endometriosis
Interstitial Cystitis
NEUROGENIC BLADDER
BLADDER DIVERTICULA
POSTSURGICAL EVALUATION
Nephrectomy
Urinary Diversion
CONCLUSION
Acknowledgment

The prime function of the kidney is excretion of metabolic waste products. The kidneys do this by converting more than 1700 liters of blood per day into 1 liter of highly concentrated urine.[1] The kidney is an endocrine organ that secretes many hormones, including erythropoietin, renin, and prostaglandins. The kidneys also function to maintain homeostasis by regulating water-salt and acid-base balance. The renal collecting system, ureters, and urethra function as conduits, and the bladder serves as a reservoir for urinary excretion.

EMBRYOLOGY

Development of the Kidneys and Ureter

Three sets of kidneys develop in human embryos: the pronephros, mesonephros, and metanephros (definitive or permanent kidney).[2] The **pronephroi** appear early in the fourth embryologic week and are rudimentary and nonfunctioning. The **mesonephroi** form late in the fourth week and function as interim kidneys until the developing metanephroi begin to function (ninth week). The **metanephroi** (permanent kidneys) develop from two sources: the **ureteric bud** and **metanephrogenic blastema.**[2] The ureteric bud forms the ureter, renal pelvis, calices, and collecting ducts, interacting with and penetrating the metanephrogenic blastema. This interaction is necessary to initiate ureteric bud branching and differentiation of nephrons within the blastema (Fig. 9.1). Initially, the permanent kidneys are found in the pelvis. With fetal growth, the kidneys come to lie in the upper retroperitoneum. With ascent, the kidneys rotate medially 90 degrees so that the renal pelvis is directed anteromedially. The kidneys are in their adult location and position by the ninth gestational week. As the kidneys ascend, they derive their blood supply from nearby vessels; adult blood supply is from the abdominal aorta.

Development of the Bladder

In the seventh gestational week the urorectal septum fuses with the cloacal membrane, dividing it into a ventral **urogenital sinus** and a **dorsal rectum.** The bladder develops from the urogenital sinus. Initially, the bladder is continuous with the allantois, which eventually becomes a fibrous cord called the **urachus,** the adult median umbilical ligament. As the bladder enlarges, the distal portion of the mesonephric ducts is incorporated as connective tissue into the bladder trigone. At the same time, the ureters come to open separately into the bladder.[2] In infants and children the bladder is an abdominal organ; it is not until after puberty that it becomes a true pelvic structure[2] (Fig. 9.2).

Development of the Urethra

The epithelium of most of the male urethra and the entire female urethra is derived from the endoderm of the urogenital sinus. The urethral connective tissue and smooth muscle form from adjacent splanchnic mesenchyme.[2]

ANATOMY

Kidney

In the adult, each kidney measures approximately 11 cm long, 2.5 cm thick, and 5 cm wide and weighs 120 to 170 grams.[3] Emamian et al.[4] demonstrated that the parenchymal volume of the right kidney is smaller than that of the left kidney, possibly because of a relatively larger potential space for left renal growth (growth of right kidney inhibited by liver) or relatively increased left renal blood flow (left renal artery typically shorter than right renal artery). Renal length correlates best with body height, and renal size decreases with advancing age because of parenchymal reduction.

The left kidney usually lies 1 to 2 cm higher than the right kidney.[3] The kidneys are mobile and will move depending on body position. In the supine position, the superior pole of the left kidney is at the level of the 12th thoracic vertebra, and the inferior pole is at the level of the third lumbar vertebra.

The **normal adult kidney** is bean shaped with a smooth, convex contour anteriorly, posteriorly, and laterally. Medially,

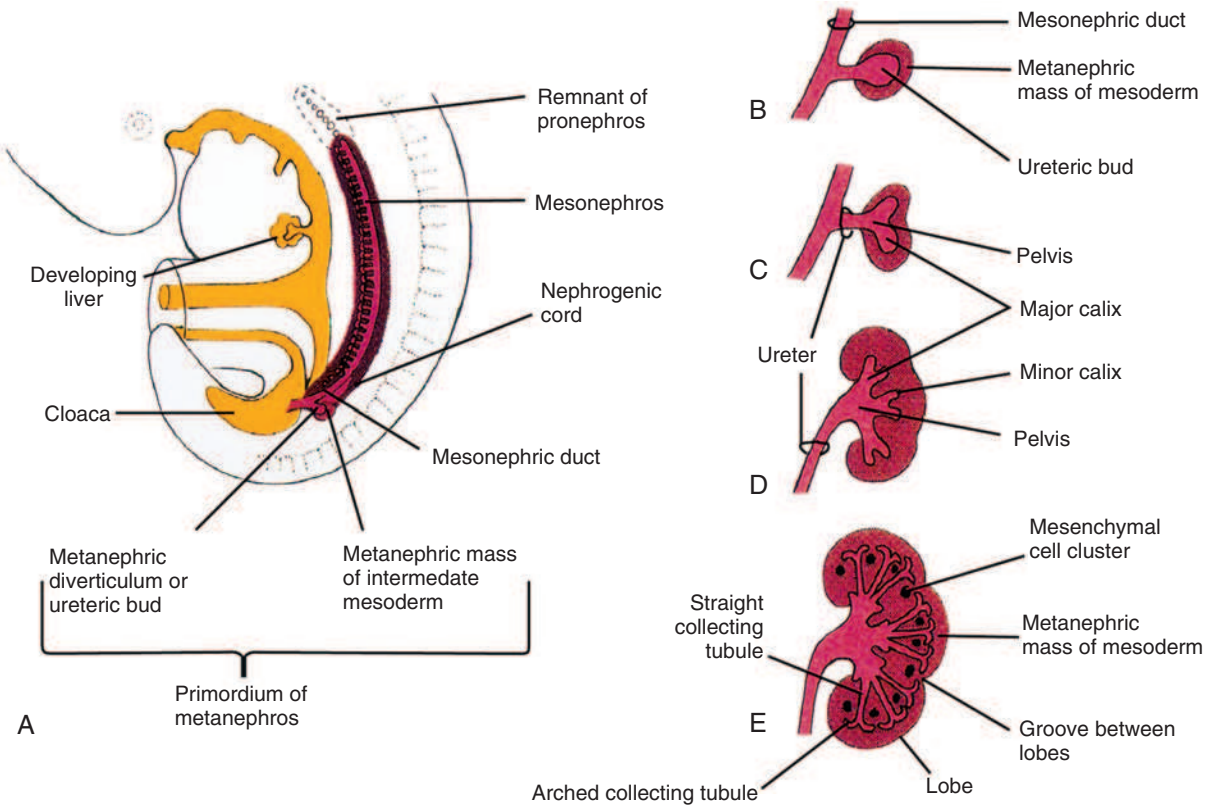

FIG. 9.1 Embryology of the Kidney and Ureter. (A) Lateral view of a 5-week embryo shows the three embryologic kidneys. **(B)-(E)** Successive stages of development of the ureteric bud (fifth to eighth week) into the ureter, pelvis, calices, and collecting tubules. (With permission from The urogenital system. In: Moore KL, Persaud TVN, editors. The developing human: clinically oriented embryology. 5th ed. Philadelphia: Saunders; 1993. pp. 265-303.[2])

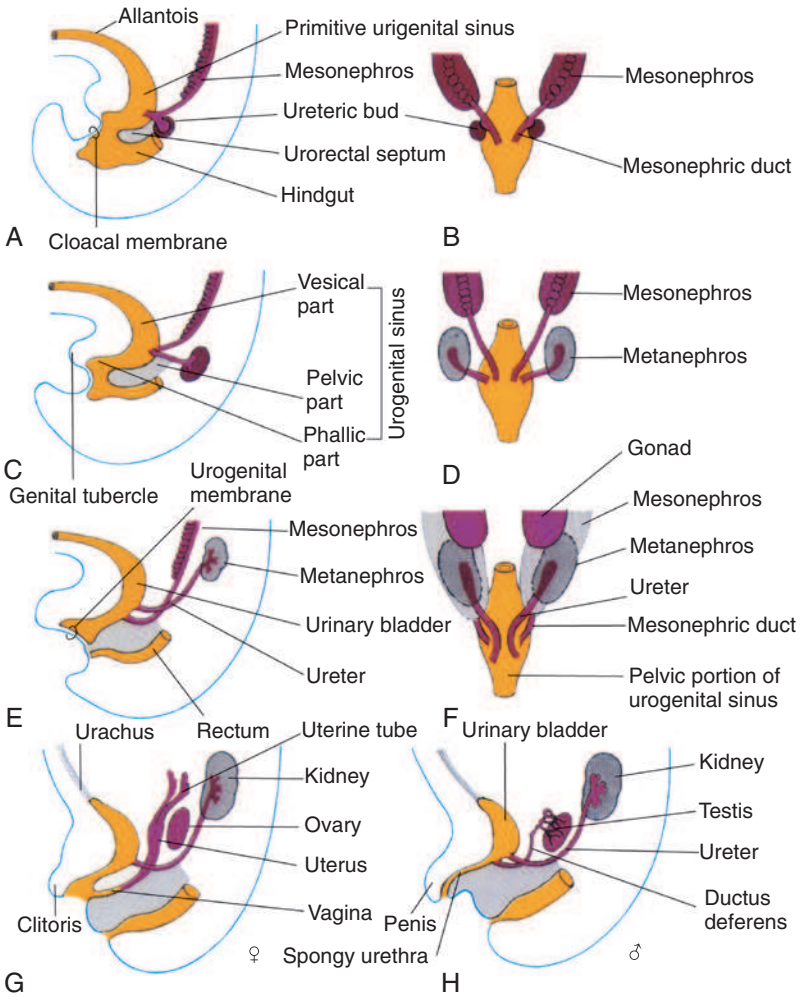

FIG. 9.2 Embryology of the Bladder and Urethra. Diagrams show division of the cloaca into the urogenital sinus and rectum; absorption of the mesonephric ducts; development of the urinary bladder, urethra, and urachus; and change in location of the ureters. **(A)** and **(B)** Five-week embryo. **(C)-(H)** Seven- to 12-week embryo. (**A, C, E,** and **G,** female; **B, D, F,** and **H,** male.) (With permission from The urogenital system. In: Moore KL, Persaud TVN, editors. The developing human: clinically oriented embryology. 5th ed. Philadelphia: Saunders; 1993. pp. 265-303.[2])

the surface is concave; the medial surface is known as the **renal hilum.** The renal hilum is continuous with a central cavity called the **renal sinus.** Within the renal sinus are the major branches of the renal artery, major tributaries of the renal vein, and the collecting system.[3] The remainder of the renal sinus is packed with fat. The collecting system (renal pelvis) lies posterior to the renal vessels in the renal hilum (Fig. 9.3).

Renal parenchyma is composed of cortex and medullary pyramids. The **renal medullary pyramids** are hypoechoic relative to the renal cortex and can be identified in most normal adults (Fig. 9.4). Normal **renal cortex** is typically less echogenic than adjacent liver and spleen. Platt et al.[5] found that 72% of 153 patients with renal cortical echogenicity equal to that of the liver had normal renal function. Greater renal echogenicity than liver echogenicity showed a specificity and a positive predictive value for abnormal renal function of 96% and 67%, respectively. However, the sensitivity of this ultrasound criterion was poor (20%).

During normal development, two parenchymal masses called **ranunculi** partially fuse. **Parenchymal junctional defects** occur at the site of fusion and must not be confused with pathologic processes (e.g., renal scar, angiomyolipoma). The junctional parenchymal defect is most often located anteriorly and superiorly, typically at the junction of the upper and middle thirds of the kidney, and can be traced medially and inferiorly into the renal sinus. Usually, it is oriented more horizontally than vertically and therefore it is best appreciated on sagittal scans[6] (Fig. 9.5). Junctional cortical defects are more often shown within the right kidney, although left junctional cortical defects may be detected with favorable acoustic windows.

A **hypertrophied column of Bertin** (HCB) is a normal variant; it represents unresorbed polar parenchyma from one or both of the two subkidneys that fuse to form the normal kidney.[7] Sonographic features that may aid in the demarcation of HCB include indentation of the renal sinus laterally and a border formed by the junctional parenchymal defect. Hypertrophied columns are usually located at the junction of the upper and middle thirds of the kidney and contain renal cortex that is continuous with the adjacent renal cortex of the same subkidney.

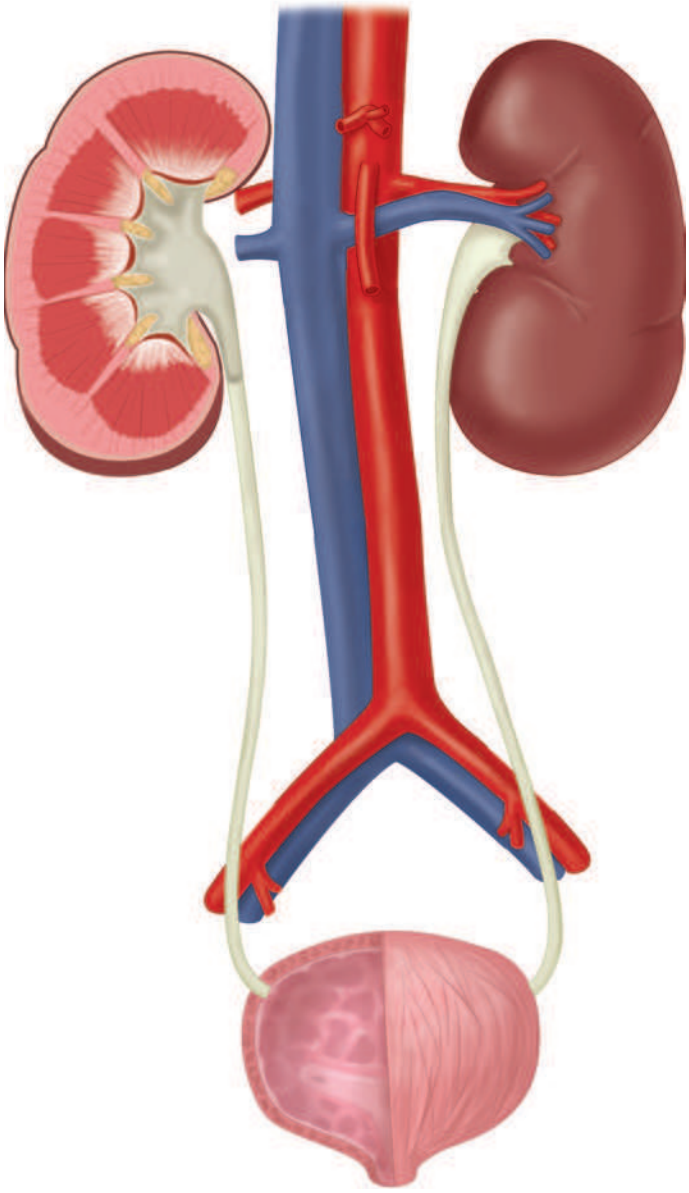

FIG. 9.3 Anatomy of the Kidney, Ureter, and Bladder.

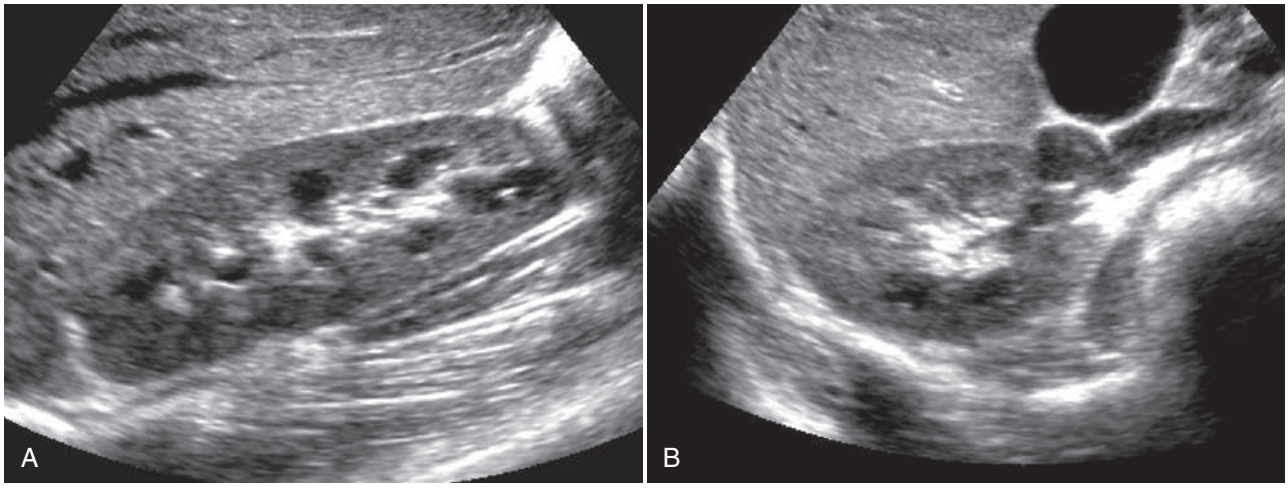

FIG. 9.4 Normal Kidney. (A) Sagittal and **(B)** transverse sonograms of normal anatomy with corticomedullary differentiation show relatively hypoechoic medullary pyramids, with cortex slightly less echogenic than the liver and spleen.

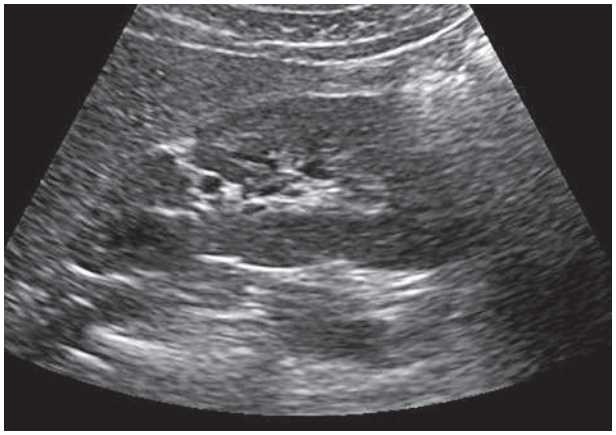

FIG. 9.5 Anterior Junction Line. Sagittal sonogram demonstrates an echogenic line that extends from the renal sinus to perinephric fat. The defect is typically located at the junction of the upper and middle thirds of the kidney, as in this example.

Sonographic Criteria for Hypertrophied Column of Bertin

Indentation of renal sinus laterally
Bordered by junctional parenchymal defect
Location at junction of upper and middle thirds
Continuous with adjacent renal cortex
Similar color flow to surrounding parenchyma
Contains renal pyramids
Less than 3 cm in size

Columns contain renal pyramids and usually measure less than 3 cm[7,8] (Fig. 9.6). The echogenicity of HCB and adjacent renal cortex depend on the scan plane. Alterations in tissue orientation produce different acoustic reflectivity.[7] The echoes of the HCB are brighter than those of adjacent renal cortex when seen en face[7] (Fig. 9.6). It may be difficult to differentiate a small, hypovascular tumor from an HCB; however, demonstration of arcuate arteries by color Doppler ultrasound indicates an HCB rather than a tumor. Occasionally, contrast-enhanced computed tomography (CT) may be necessary to differentiate between an HCB and a non–border-deforming renal lesion.

The kidney has a thin, fibrous **capsule.** The capsule is surrounded by perirenal fat. Perirenal fat is encased anteriorly by **Gerota fascia** and posteriorly by **Zuckerkandl fascia.**[9] The right perirenal space opens superiorly at the bare area of the liver, and both perirenal spaces communicate with the pelvic peritoneal space.[10] Right and left perirenal spaces communicate with each other across the midline at the level of the third to fifth lumbar vertebrae.[10]

Ureter

The ureter is a long (30-34 cm), mucosal-lined conduit that delivers urine from the renal pelvis to the bladder. Each ureter varies in diameter from 2 to 8 mm.[3] As it enters the pelvis, the ureter passes anterior to the common/external iliac artery. The ureter has an oblique course through the bladder wall (see Fig. 9.3).

Bladder

The bladder is positioned in the pelvis, inferior and anterior to the peritoneal cavity and posterior to the pubic bones.[3] Superiorly, the peritoneum is reflected over the anterior aspect of the bladder. Within the bladder, the ureteric and urethral orifices demarcate an area known as the **trigone;** the urethral orifice also marks the **bladder neck.** The bladder neck and trigone remain constant in shape and position; however, the remainder of the bladder will change shape and position depending on the volume of urine within it. Deep to the peritoneum covering the bladder is a loose, connective tissue layer of subserosa that forms the adventitial layer of the bladder wall. Adjacent to the adventitia are three muscle layers: the outer (longitudinal), middle (circular), and internal longitudinal layers. Adjacent to the muscle, the innermost layer of the bladder is composed of mucosa. The bladder wall should be smooth and of uniform thickness. The wall thickness depends on the degree of bladder distention.

SONOGRAPHIC TECHNIQUE

The ability to visualize organs of the genitourinary tract by ultrasound depends on the patient's body habitus, operator experience, and scanner platform. High-frequency probes should be used for patients with a favorable body habitus. Harmonic imaging is often useful for difficult-to-scan patients (e.g., obese patients). Compound imaging and speckle reduction may increase lesion conspicuity and decrease artifacts.

Kidney

The kidneys should be assessed in the transverse and coronal plane. Optimal patient positioning varies; supine and lateral decubitus positions often suffice, although oblique and occasionally prone positioning may be necessary (e.g., obese patients). Usually, a combination of subcostal and intercostal approaches is required to evaluate the kidneys fully; the upper pole of the left kidney may be particularly difficult to image without a combination of approaches. When the collecting system is dilated, additional images should be taken to assess for the level of obstruction, any obstructing lesion, and appearance of the kidneys after voiding (see "Hydronephrosis").

Ureter

The proximal ureter is best visualized using a coronal oblique view with the kidney as an acoustic window. The ureter is followed to the bladder, maintaining the same approach. A nondilated ureter may be impossible to visualize because of overlying bowel gas. Transverse scanning of the retroperitoneum often demonstrates a dilated ureter, which can then be followed caudally with both transverse and sagittal imaging. In women, a dilated distal ureter is well seen with transvaginal scanning.

Bladder and Urethra

The **bladder** is best evaluated when it is moderately filled; an overfilled bladder causes patient discomfort. The bladder should be scanned in the transverse and sagittal planes. To better visualize the bladder wall in women, transvaginal scanning may be helpful. If the nature of a large, fluid-filled mass in the pelvis is uncertain,

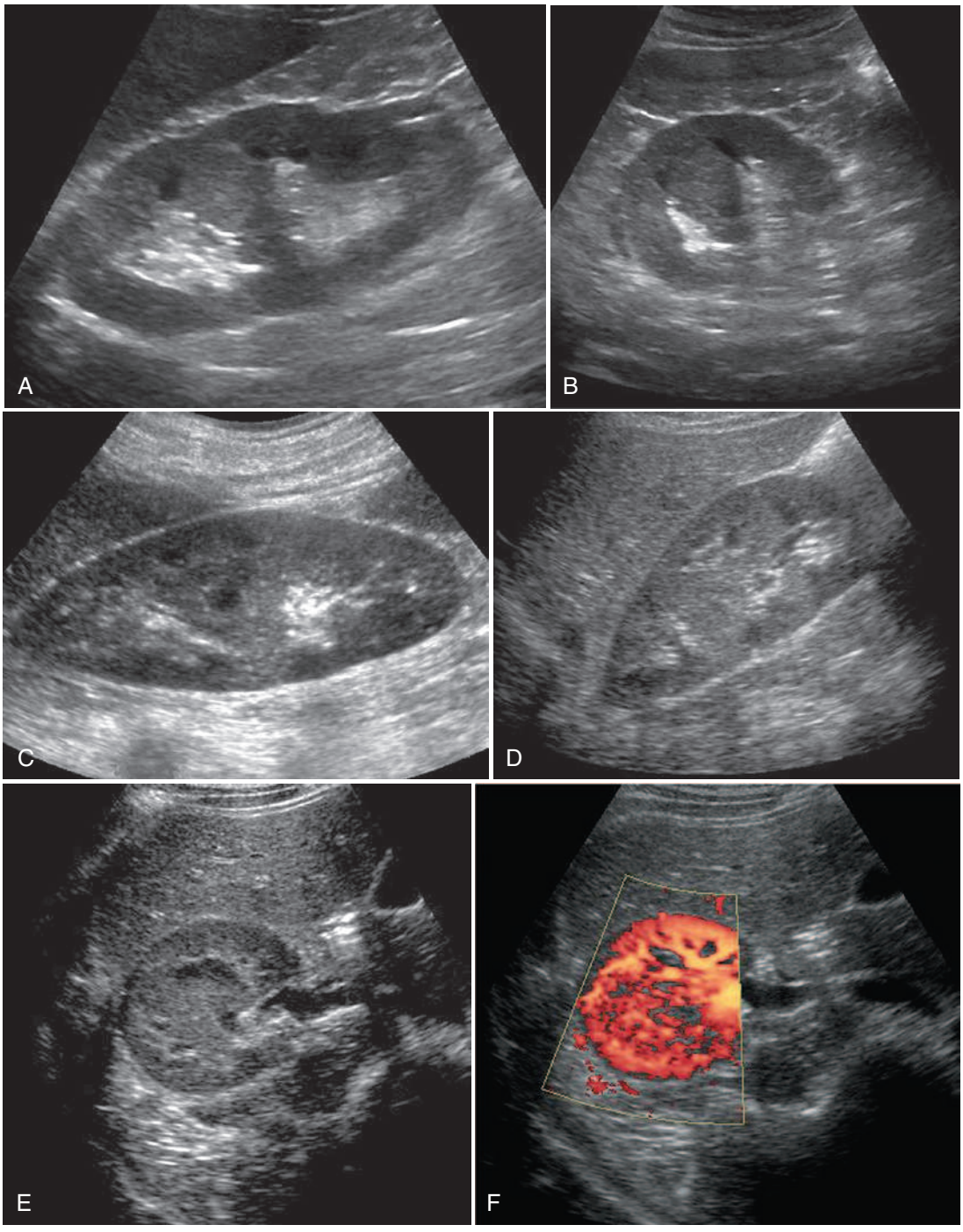

FIG. 9.6 Hypertrophied Column of Bertin. (A) Sagittal and **(B)** transverse sonograms show classic appearance of the column of Bertin. **(C)** Medullary pyramids can be seen within the hypertrophied column of Bertin. **(D)** Echogenicity of the column may vary based on orientation. **(E)** Transverse sonogram and **(F)** corresponding power Doppler image confirm a hypertrophied column.

voiding or insertion of a Foley catheter will clarify the location and appearance of the bladder relative to the fluid-filled mass.

Incomplete bladder emptying can be due to prostate enlargement, neurogenic bladder, or pelvic floor weakness. Bladder stones and infection are important complications. Initial assessment includes assessment of the kidneys and ureter for dilatation, as well as calculation of both a prevoid and postvoid residual. We typically calculate bladder volume by taking the three orthogonal measurements and multiplying by .6 (this is different from most organs, which multiply by .52). This slightly larger value is because the shape of the bladder is more of a cuboidal shape than a prolate ellipse.

The **urethra** in a woman can be scanned with transvaginal, transperineal, or translabial sonography[11] (Fig. 9.7). The posterior or the prostatic urethra in men is best visualized with transrectal probes (Fig. 9.8).

HYDRONEPHROSIS

The term *hydronephrosis* refers to dilatation of the collecting system. Obstruction is often present, but this is not always the case. There are many causes of a dilated renal collecting system, and ultrasound is the initial imaging modality of choice for the majority of these assessments (except as discussed in the previous section where noncontrast-enhanced CT may be used in the initial assessment of acute renal colic). Initial sonographic evaluation should include an assessment of the degree of dilatation, appearance of surrounding renal parenchyma, assessment for level of obstruction and any obstructing lesion. Numerous grading systems for the assessment of the degree of hydronephrosis have been proposed following Ellenbogen and colleagues' original article on the topic.[12] None has been readily adopted, however, and most radiologists continue to use descriptive terminology such as *mild, moderate,* and *severe.*[13]

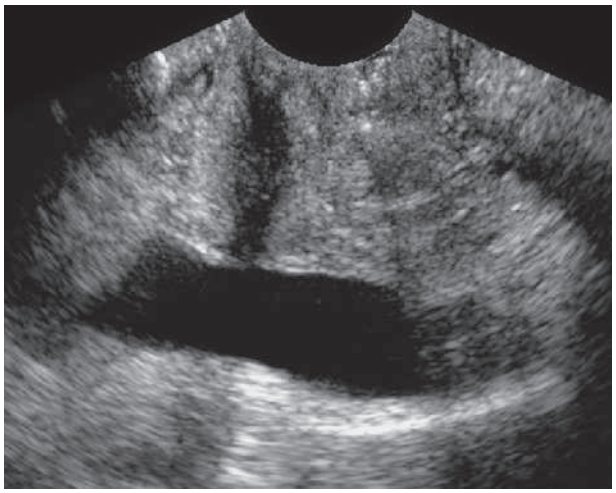

FIG. 9.7 Translabial Ultrasound of Female Urethra. Sagittal sonogram shows the tubular hypoechoic urethra extending from the bladder to the skin surface.

A practical pearl for the ultrasound evaluation of hydronephrosis is to assess the degree of dilatation before and after bladder voiding. Hydronephrosis that persists after voiding suggests an anatomic obstruction. If collecting system dilatation diminishes postvoiding, then one might consider nonobstructive pelvicaliectasis (i.e., vesicoureteral reflux). Most obstructing lesions are located within the pelvis (fibroids, prostatic hypertrophy, ovarian tumor, bladder tumor) and thus are obvious on sonographic evaluation. When the pelvis is normal, the length of the ureter should be assessed for dilatation and/or obstructing lesion. In pregnancy, it is helpful to have the patient lie in the decubitus position with the symptomatic side up to allow for the weight of the uterus to move off of the ureter.

Over time the obstructed kidney will initially become enlarged. Later, renal damage may occur with parenchymal atrophy and blunting of calices.

In pregnancy, the urinary tract frequently is dilated. Smooth muscle relaxation occurs as a result of elevated hormone levels. Mass effect on the ureter may be caused by the enlarged uterus. Because of the location of the ureters, the right ureter is frequently more dilated than the left ureter. Physiologic dilatation of the urinary tract in pregnancy is suggested when the distal ureters taper at the sacral promontory. Pregnant patients are also at increased risk for urinary tract infections (UTIs), which can complicate the assessment. In addition, stone disease can occur and this needs to be distinguished from the physiologic dilatation associated with pregnancy.

In acute hydronephrosis of pregnancy, patients may present with severe flank or lower abdominal pain radiating to the groin due to ureteric obstruction. The obstruction usually occurs at the level of the pelvic brim. Symptoms may improve with change in posture with the patient in the lateral decubitus position, symptomatic side up. In extreme cases, ureteral stunting may be required. When severe overdistention syndrome occurs, rupture of the urinary tract may occur, which can be identified as fluid collection around the periphery of the kidney by ultrasound.

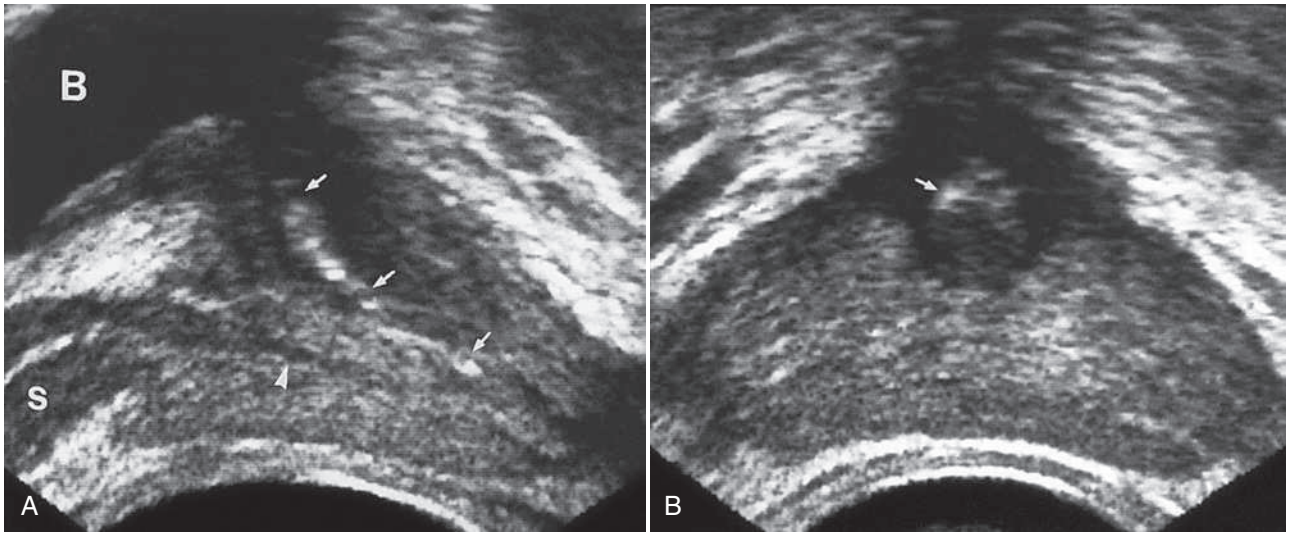

FIG. 9.8 Transrectal Ultrasound of Male Urethra. (A) Sagittal and **(B)** transverse sonograms show the urethra with calcifications in the urethral glands *(arrows)* surrounded by the echo-poor muscle of the internal urethral sphincter. *B,* Bladder; *arrowhead,* ejaculatory duct; *S,* seminal vesicles. (Courtesy of Ants Toi, MD, Toronto Hospital.)

Causes of Hydronephrosis

Genitourinary Obstruction	Comments
Renal/ureteral stone	Look for stone in common sites of obstruction: ureterovesical junction and ureteropelvic junction
Transitional cell carcinoma	Hematuria
Sloughed papilla	
Blood clot	Hematuria
Posterior urethral valves	Bilateral, pediatric diagnosis
Ureterocele	May be orthotopic or heterotopic If heterotopic, look for renal duplication abnormality
Ureteropelvic junction obstruction	Extrarenal pelvis may be dilated out of proportion to calices
Ureteral stricture (prior infection, surgery, radiation)	History aids in diagnosis
Neurogenic bladder	Check for postvoid residual
Extrinsic Obstruction	
Retrocaval ureter	May need CT for diagnosis
Prostatic hypertrophy	Enlarged prostate impinges on bladder
Tumor (fibroid, ovarian carcinoma, lymphoma)	Abnormal mass seen in pelvis
Lymphadenopathy	Abnormal mass seen in pelvis
Retroperitoneal fibrosis	Mass encasing the aorta CT may be needed for diagnosis
Aneurysm	Should be obvious on Doppler assessment of vessels
Endometriosis	Mass typically seen in pelvis
Pregnancy	Ureter dilated to pelvic brim
Nonobstructive	
Vesicoureteral reflux	Cortical scarring, typically in upper poles
Congenital megacalices	May be unilateral or bilateral If associated with congenital megaureter, both dilated ureter and calices will be present May need contrast-enhanced CT for diagnosis
Prior obstruction	Prior severe dilatation may not return to normal
Infection	Signs and symptoms of infection
High flow states (diabetes insipidus, psychogenic polydipsia)	Typically mild dilatation
Distended bladder	Returns to normal after bladder emptying

PITFALLS IN ASSESSMENT OF OBSTRUCTION

Although obstruction typically causes dilatation, early in the process the renal collecting system may not dilate. In cases of renal failure, a poorly functioning kidney may not make sufficient urine to demonstrate dilatation. In addition, in cases of severe obstruction, pelvocaliceal rupture may lead to decompression of the collecting system with a perinephric hematoma/urinoma. Hydronephrosis (a condition in which dilated calices communicate with central collecting system) should be distinguished from multiple parapelvic cysts (which do not communicate).

CONGENITAL ANOMALIES

Anomalies Related to Renal Growth

Hypoplasia

Renal hypoplasia is a renal parenchymal anomaly in which there are too few nephrons. Renal function depends on the mass of the kidney. True hypoplasia is a rare anomaly. Many patients with **unilateral** hypoplasia are asymptomatic; the condition is typically an incidental finding. Patients with **bilateral** hypoplasia often have renal insufficiency. Hypoplasia is believed to result from the ureteral bud making contact with the most caudal portion of the metanephrogenic blastema. This can occur with delayed development of the ureteric bud or from delayed contact of the bud with the cranially migrating blastema. Hypoplasia is established when fewer but otherwise histologically normal renal lobules are identified.[14] At ultrasound, the kidney is small but otherwise appears normal.

Fetal Lobation

Fetal lobation is usually present until 4 or 5 years of age; however, persistent lobation is seen in 51% of adult kidneys.[15] There is infolding of the cortex without loss of cortical parenchyma. At ultrasound, sharp clefts are shown overlying the columns of Bertin.[16]

Compensatory Hypertrophy

Compensatory hypertrophy may be diffuse or focal. It occurs when existing healthy nephrons enlarge to allow healthy renal parenchyma to perform more work. The diffuse form is seen

with contralateral nephrectomy, **renal agenesis, renal hypoplasia, renal atrophy,** and **renal dysplasia.** Diffuse compensatory hypertrophy is suggested at ultrasound when an enlarged but otherwise normal-appearing kidney is identified. The focal form is seen when residual islands of normal tissue enlarge in an otherwise diseased kidney; focal compensatory hypertrophy may be particularly prominent in the setting of **reflux nephropathy.** Large areas of nodular but normal renal tissue identified between scars may mimic a solid renal mass.[5]

Anomalies Related to Ascent of Kidney

Ectopia

Failure of the kidney to ascend during embryologic development results in a **pelvic kidney;** prevalence is 1 in 724 pediatric autopsies.[16] These kidneys are often small and abnormally rotated. Fifty percent of pelvic kidneys have decreased function.[16] The ureters are often short; poor drainage and collecting system dilatation predispose pelvic kidneys to infection and stone formation. The blood supply is often complex; multiple arteries may be derived from regional arteries (typically, internal iliac or common iliac). If the kidney ascends too high, it may pass through the foramen of Bochdalek and become a true **thoracic kidney;** this is usually of no clinical significance. A search for a pelvic kidney should be performed if the kidney is not identified within renal fossae (Fig. 9.9). If the kidney has ascended too high, ultrasound is helpful to determine if the diaphragm is intact.

Crossed Renal Ectopia

In crossed renal ectopia, both kidneys are found on the same side. In 85% to 90% of cases, the ectopic kidney will be fused to the other kidney **(crossed-fused ectopia).** The upper pole of the ectopic kidney is usually fused to the lower pole of the other kidney, although fusion may occur anywhere. The incidence is 1 in 1000 to 1 in 1500 at autopsy.[15] Fusion of metanephrogenic blastema does not allow proper rotation or ascent; thus both kidneys are more caudally located, although the ureterovesical junctions (UVJs) are located normally. At sonography, both kidneys are on the same side and are typically fused (Fig. 9.10). In patients with renal colic, knowing that the UVJs are in the normal location is particularly important, since bilateral ureters need to be assessed.

Horseshoe Kidney

The incidence of horseshoe kidneys in the general population is 0.01% to 0.25%. Horseshoe kidneys occur when metanephrogenic blastema fuse prior to ascent; fusion is usually at the lower poles (95%). Typically, the isthmus is composed of functioning renal tissue, although rarely it is made up of fibrous tissue. The horseshoe kidney sits anterior to the abdominal great vessels and derives its blood supply from the aorta and other regional vessels, such as inferior mesenteric, common iliac, internal iliac, and external iliac arteries. Abnormal rotation of renal pelves often results in **ureteropelvic junction (UPJ) obstruction;** the horseshoe kidney is thus predisposed to infection and stone formation. Additional associated anomalies include **vesicoureteral reflux, collecting system duplication, renal dysplasia, retrocaval ureter, supernumerary kidney, anorectal malformation, esophageal atresia, rectovaginal fistula, omphalocele,** and cardiovascular and skeletal abnormalities.

At sonography, horseshoe kidneys are usually lower than normal and the lower poles project medially. Transverse imaging of the retroperitoneum will demonstrate the renal isthmus crossing the midline anterior to abdominal great vessels (Fig. 9.11). Hydronephrosis (pyelocaliectasis) and collecting system calculi may be evident.

Anomalies Related to Ureteral Bud

Renal Agenesis

Renal agenesis may be unilateral or bilateral. **Bilateral** renal agenesis is a rare anomaly that is incompatible with life. The prevalence rate of bilateral agenesis at autopsies is 0.04%. The condition has a 3:1 male predominance.[15] **Unilateral** renal

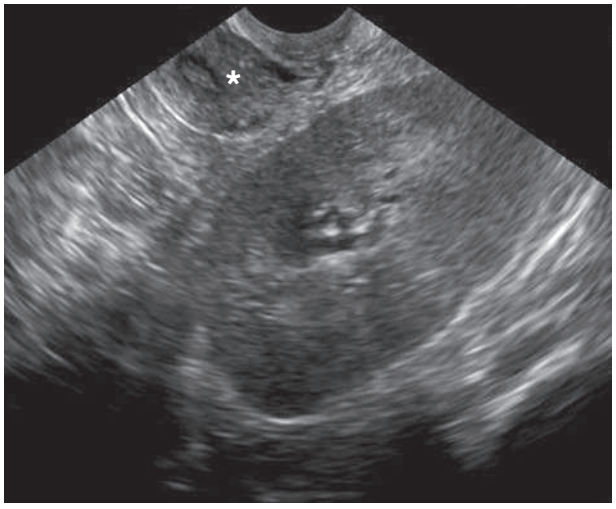

FIG. 9.9 Pelvic Kidney. Transverse sonogram demonstrates a left pelvic kidney posterior to the uterus (*).

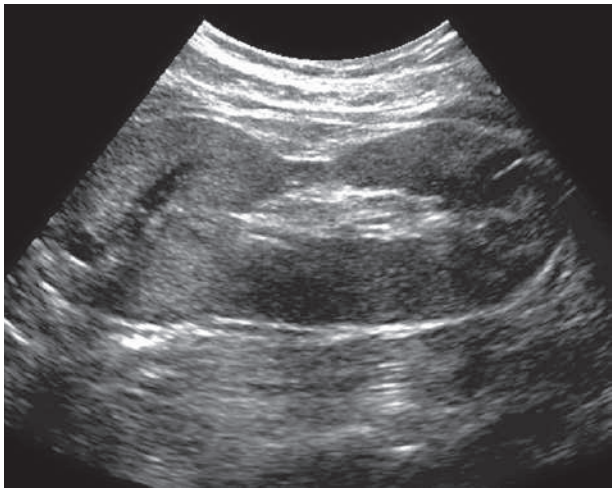

FIG. 9.10 Cross-Fused Ectopia. Sagittal sonogram demonstrates two kidneys fused to each other.

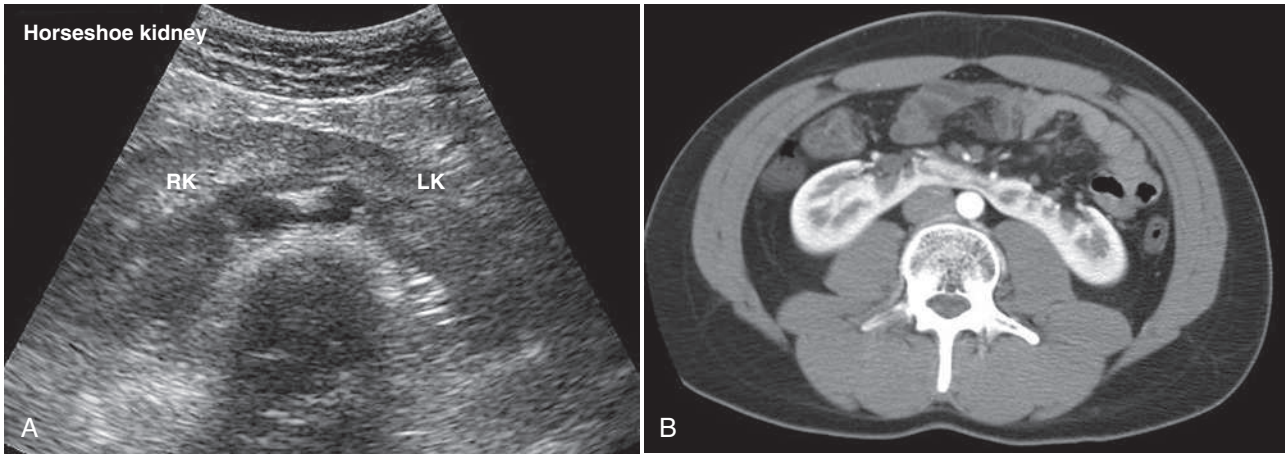

FIG. 9.11 Horseshoe Kidney. (A) Transverse sonogram shows the isthmus crossing anterior to the retroperitoneal great vessels, with the renal parenchyma of each limb of the horseshoe draping over the spine. **(B)** Confirmatory contrast-enhanced CT examination. *LK,* Left kidney; *RK,* right kidney.

agenesis is usually an incidental finding; the contralateral kidney of these patients may be quite large secondary to compensatory hypertrophy. Renal agenesis occurs when there is (1) absence of the metanephrogenic blastema, (2) absence of ureteral bud development, or (3) absence of interaction and penetration of the ureteral bud with the metanephrogenic blastema. Renal agenesis is associated with genital tract anomalies, which are often cystic pelvic masses in both men and women. Other associated anomalies include skeletal abnormalities, **anorectal malformations,** and **cryptorchidism.**

At ultrasound, although the kidney is absent, a normal adrenal gland is usually found. The adrenal gland will be absent in 8% to 17% of patients with renal agenesis.[16] It may be difficult to differentiate between renal agenesis and a small, hypoplastic or dysplastic kidney. With all these conditions, the contralateral kidney will be enlarged as a result of compensatory hypertrophy. Usually, the colon falls into the empty renal bed. Care should be taken not to confuse a loop of gut with a normal kidney.

Supernumerary Kidney

Supernumerary kidney is an exceedingly rare anomaly. The supernumerary kidney is usually smaller than normal and can be found above, below, in front of, or behind the normal kidney. The supernumerary kidney often has only a few calices and a single infundibulum. The formation of a supernumerary kidney is likely caused by the same mechanism that gives rise to a duplex collecting system.[15] Two ureteric buds reach the metanephrogenic blastema, which then divides, or alternatively, there are initially two blastema. On sonography, an extra kidney will be found.

Duplex Collecting System and Ureterocele

Duplex collecting system is the most common congenital anomaly of the urinary tract, with an incidence of 0.5% to 10% of live births.[15] The degree of duplication is variable. Duplication is complete when there are two separate collecting systems and two separate ureters, each with their own ureteral orifice. Duplication is incomplete when the ureters join and enter the bladder through a single ureteral orifice. Ureteropelvic duplication arises when two ureteral buds form and join with the metanephrogenic blastema or when there is division of a single ureteral bud early in embryogenesis. Normally during embryologic development, the ureteral orifice migrates superiorly and laterally to become part of the bladder trigone. With complete duplication, the ureter from the lower pole of the kidney migrates to assume its normal location, whereas the ureter draining the superior pole of the kidney migrates abnormally to a more medial and inferior ureteral orifice. Patients have an increased incidence of UPJ obstruction and uterus didelphys.[16]

In complete duplication, the ureter draining the lower pole has a more perpendicular course through the bladder wall, making it more prone to reflux. The ectopic ureter from the upper pole is prone to obstruction, reflux, or both (Fig. 9.12). Obstruction can result in cystic dilatation of the intramural portion of the ureter, giving rise to a ureterocele. **Ureteroceles** may be unilateral or bilateral and may occur in normal, duplicated, or ectopic ureters. Ureteroceles may result in ureteral obstruction and give rise to recurrent or persistent UTIs. If large, they may block the contralateral ureteral orifice and the urethral orifice at the bladder neck. Treatment of these symptomatic ureteroceles is surgical. However, most ureteroceles are transient, incidental, and clinically insignificant.

At ultrasound, a duplex collecting system is seen as two central echogenic renal sinuses with intervening, bridging renal parenchyma. Unfortunately, this sign is insensitive and is only seen in 17% of duplex kidneys.[17] Hydronephrosis of the upper-pole moiety and visualization of two distinct collecting systems and ureters are diagnostic. The bladder should always be carefully evaluated for the presence of a ureterocele. A ureterocele will appear as a round, cystlike structure within the bladder (Fig. 9.13). Occasionally, it may be large enough to occupy the entire bladder and will cause obstruction of the bladder neck. In female patients, transvaginal sonography can be helpful to identify small ureteroceles[18] (Fig. 9.14). These ureteroceles may be transient. Madeb et al.[19] demonstrated that transvaginal sonography with color Doppler and spectral analysis can provide additional information about flow dynamics, eliminating the need for invasive procedures.

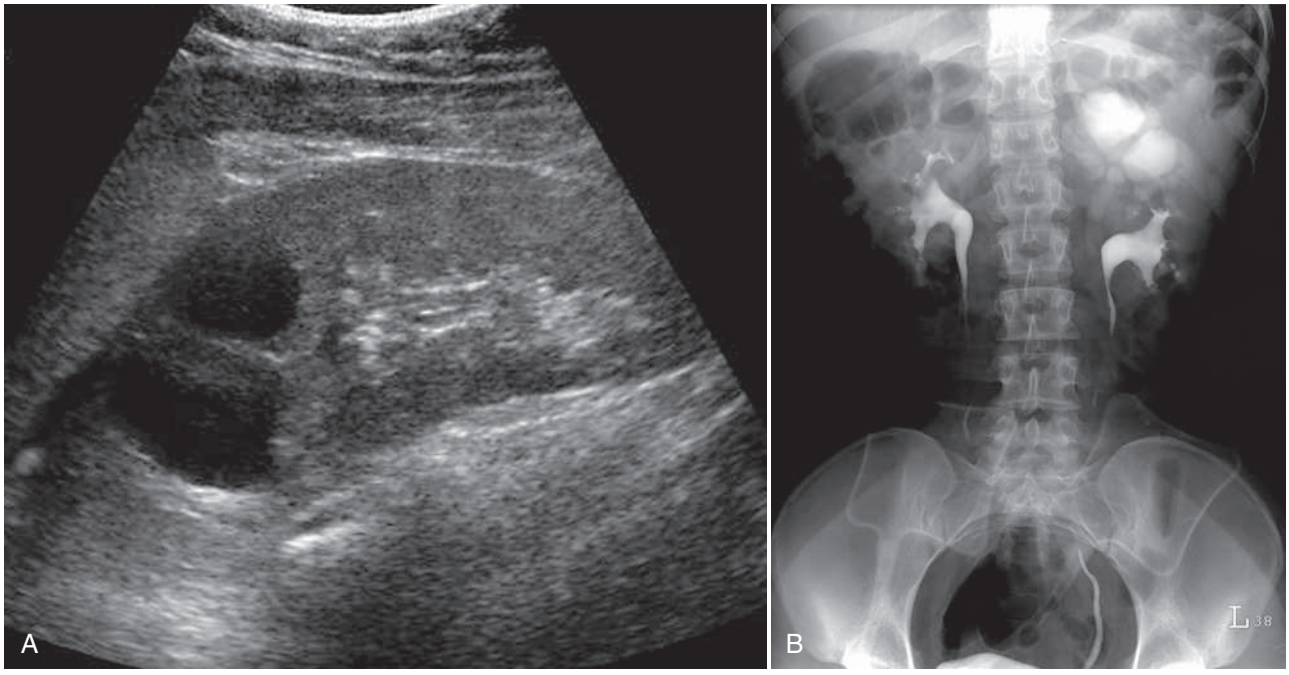

FIG. 9.12 Duplex Collecting System. (A) Sagittal sonogram shows an upper-pole cystic mass. Note collecting system dilatation and cortical thinning. **(B)** Delayed intravenous urogram shows duplicated left collecting system and dilated upper-pole moiety.

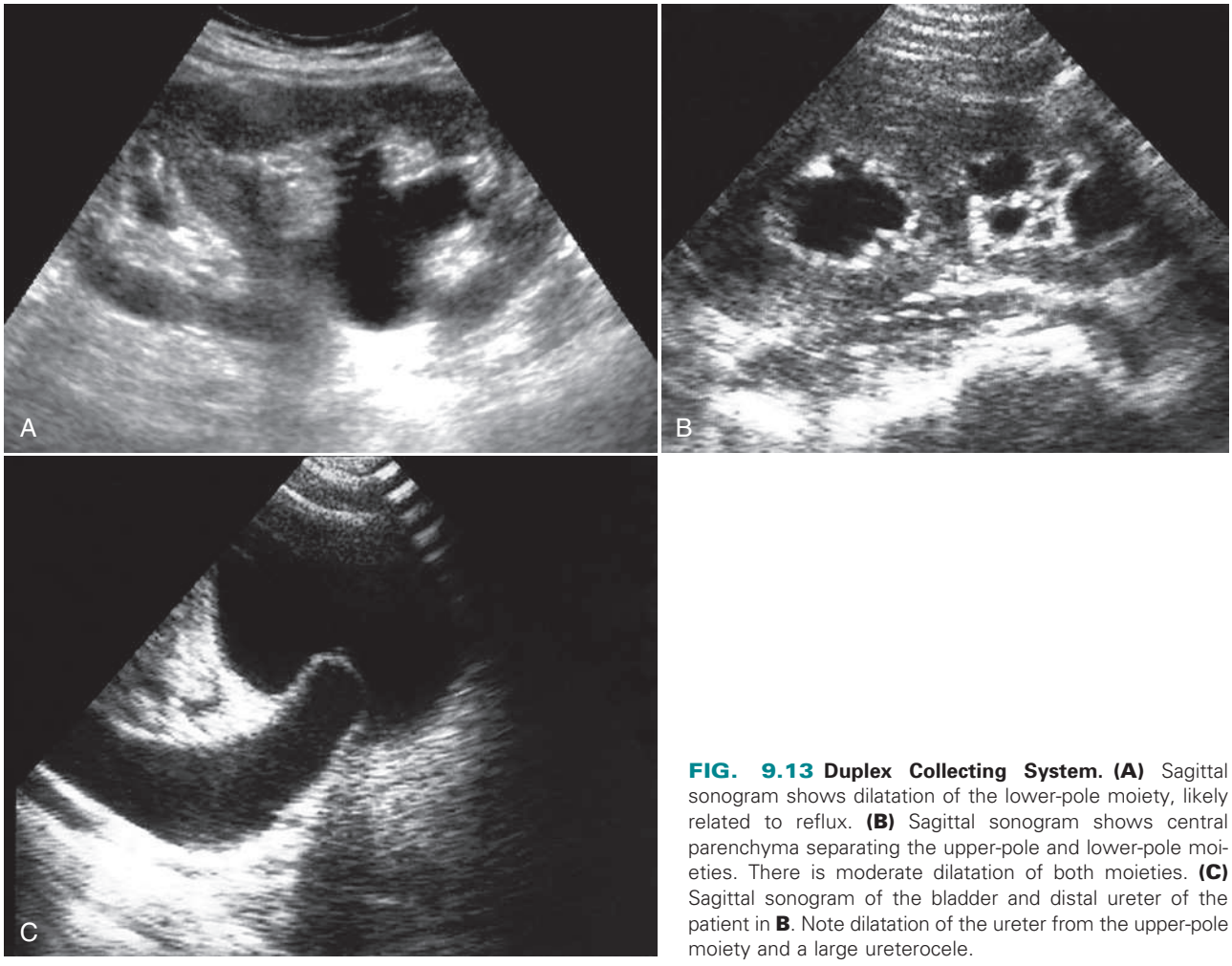

FIG. 9.13 Duplex Collecting System. (A) Sagittal sonogram shows dilatation of the lower-pole moiety, likely related to reflux. **(B)** Sagittal sonogram shows central parenchyma separating the upper-pole and lower-pole moieties. There is moderate dilatation of both moieties. **(C)** Sagittal sonogram of the bladder and distal ureter of the patient in **B**. Note dilatation of the ureter from the upper-pole moiety and a large ureterocele.

Ureteropelvic Junction Obstruction

UPJ obstruction is a common anomaly with a 2:1 male predominance. The left kidney is affected twice as frequently as the right kidney. UPJ obstruction is bilateral in 10% to 30% of cases.[20] Most adult patients present with chronic, vague, back or flank pain. Symptomatic patients and those with complications, including superimposed infection, stones, or impaired renal function, should be treated. Patients have an increased incidence of contralateral multicystic dysplastic kidney and renal agenesis. Most idiopathic UPJ obstructions are thought to be functional rather than anatomic.[20] Histologic evaluation of affected specimens has demonstrated excessive collagen between muscle bundles, deficient or absent muscle, and excessive longitudinal muscle.[20] Occasionally, intrinsic valves, true luminal stenosis, and aberrant arteries are the cause of obstruction. At ultrasound, hydronephrosis is present to the level of the UPJ (Fig. 9.15). Marked ballooning of the renal pelvis is often shown, and if long-standing, there will be associated renal parenchymal atrophy. The caliber of the ureter, on the other hand, is normal. Careful evaluation of the contralateral kidney should be performed to exclude associated anomalies.

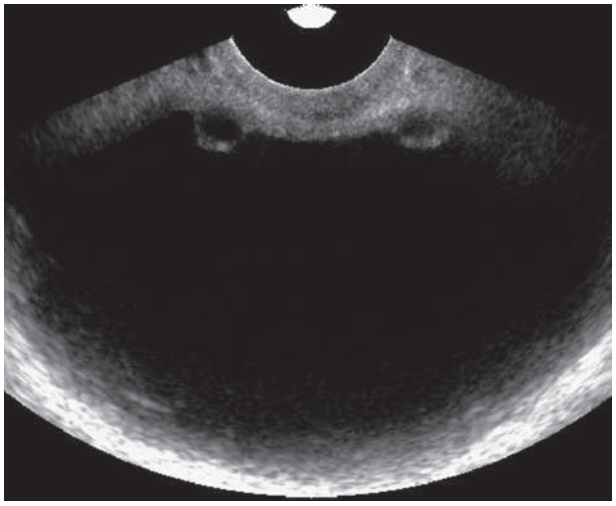

FIG. 9.14 Small Bilateral Ureteroceles. Transverse transvaginal sonogram demonstrates two small cystic structures related to the bladder wall. With the probe in the vagina, the bladder trigone and the ureteric orifices are shown in the near field of the transducer.

Congenital Megacalices

Congenital megacalices refer to typically unilateral, nonobstructive enlargement of the calices. It is nonprogressive; overlying parenchyma and renal function are maintained. Infection and stone formation are increased because of caliceal enlargement. The exact pathogenesis is speculative; the most common association is with primary megaureter.[21] At ultrasound, numerous enlarged clubbed calices are shown. Papillary impressions are absent, and cortical thickness is maintained.

Congenital Megaureter

Megaureter (congenital megaureter, megaloureter) results in functional ureteric obstruction. The most distal segment of ureter is aperistaltic: focal ureteral lack of peristalsis results in a wide spectrum of findings, from insignificant distal ureterectasis to progressive hydronephrosis/hydroureter. As with UPJ obstructions, men are affected more often, and the left ureter is typically involved.[20] Bilateral involvement has been demonstrated in 8% to 50% of patients. The classic finding at ultrasound is **fusiform dilatation** of the distal third of the ureter (Fig. 9.16). Depending on the severity, associated pyelocaliectasis may or may not be present. Calculi may form just proximal to the adynamic segment.

Anomalies Related to Vascular Development

Aberrant Vessels

As it ascends during embryologic development, the kidney derives its blood supply from successively higher levels of the aorta.

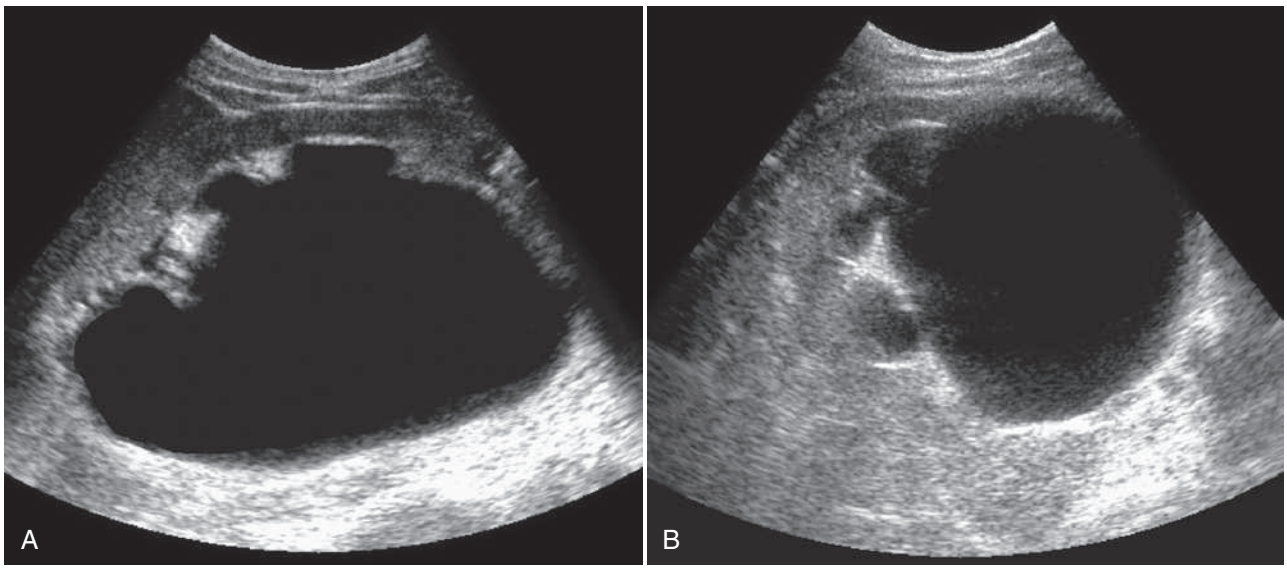

FIG. 9.15 Ureteropelvic Junction Obstruction. (A) Sagittal and **(B)** transverse sonograms demonstrate marked ballooning of the renal pelvis with associated proximal caliectasis.

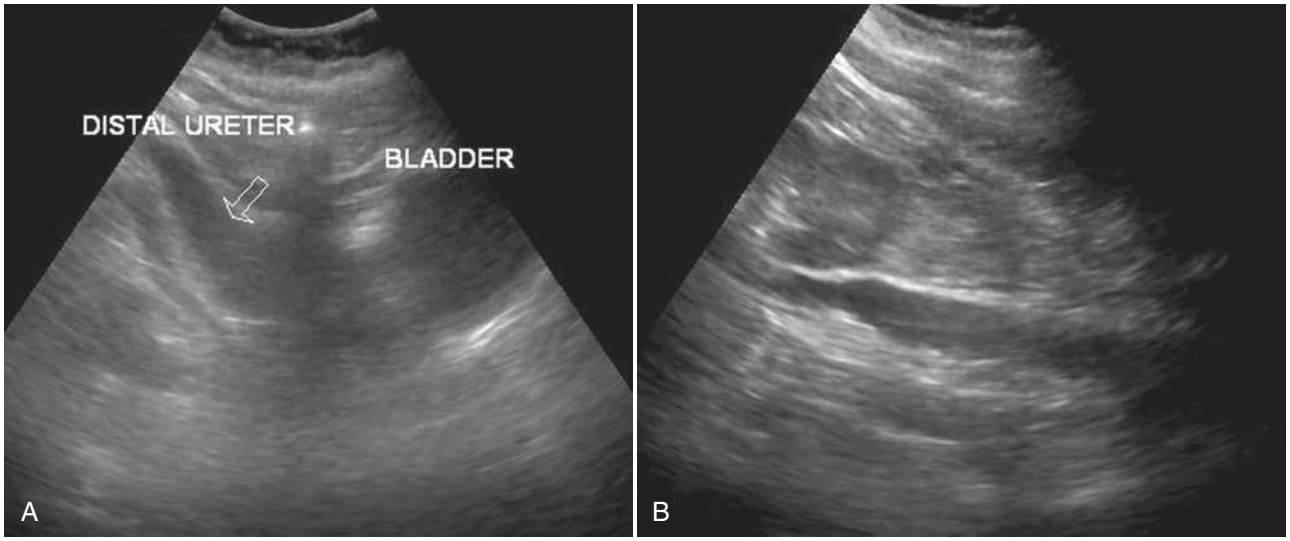

FIG. 9.16 Congenital Megaureter. (A) Sagittal sonogram shows marked dilatation of the distal ureter up to the ureterovesical junction. **(B)** Sagittal sonogram shows moderate midregion ureterectasis.

Aberrant renal arteries will be present if the vascular supply from the lower levels of the aorta persists. Aberrant vessels can compress the ureter anywhere along its course. Color Doppler ultrasound may be useful to identify obstructing vessels crossing at the UPJ.

Retrocaval Ureter

Retrocaval ureter is a rare but well-recognized congenital anomaly with a 3:1 male predominance. Most patients present with pain in the second to fourth decade of life. Normally, the infrarenal inferior vena cava (IVC) develops from the **supracardinal vein;** if it develops from the **subcardinal vein,** the ureter will pass posterior to the IVC. The ureter then passes medially and anteriorly between the aorta and IVC to cross the right iliac vessels. It then enters the pelvis and bladder in a normal manner. Sonography shows collecting system and proximal ureteral dilatation. In easy-to-scan patients the compressed retrocaval ureter may be identified.

Anomalies Related to Bladder Development

Bladder Agenesis

Bladder agenesis is a rare anomaly. Most infants with bladder agenesis are stillborn; virtually all surviving infants are female.[22] Many associated anomalies are often present. At ultrasound, the bladder is absent.

Bladder Duplication

Bladder duplication is divided into three types, as follows[16]:

Type 1: A complete or incomplete peritoneal fold separates the two bladders.

Type 2: An internal septum divides the bladder. The septum may be complete or incomplete and may be oriented in a sagittal or coronal plane. There may be multiple septa.

Type 3: A transverse band of muscle divides the bladder into two unequal cavities.

Bladder Exstrophy

Bladder exstrophy occurs in 1 in 30,000 live births, with a 2:1 male predominance.[16] Failure in development of the mesoderm below the umbilicus leads to absence of the lower abdominal and anterior bladder wall. There is a high incidence of associated musculoskeletal, gastrointestinal, and genital tract anomalies. These patients have an increased (200-fold) incidence of bladder carcinoma (adenocarcinoma in 90%).[16]

Urachal Anomalies

Normally, the urachus closes in the last half of fetal life.[16] The four types of congenital urachal anomalies, in order of frequency, are as follows[16,23,24] (Fig. 9.17):

1. Patent urachus (50%)
2. Urachal cyst (30%)
3. Urachal sinus (15%)
4. Urachal diverticulum (5%)

Urachal anomalies have a 2:1 predominance in males. A **patent urachus** is usually associated with urethral obstruction and serves as a protective mechanism to allow normal fetal development. A **urachal cyst** forms if the urachus closes at the umbilical and bladder ends but remains patent in between. The cyst is usually situated in the lower third of the urachus. There is an increased incidence of adenocarcinoma. At ultrasound, a midline cyst with or without internal echoes is seen superior to the bladder. A **urachal sinus** forms when the urachus closes at the bladder end but remains patent at the umbilicus. A **urachal diverticulum** forms if the urachus closes at the umbilical end but remains patent at the bladder. Urachal diverticula are usually incidentally found. There is an increased incidence of carcinoma and stone formation.

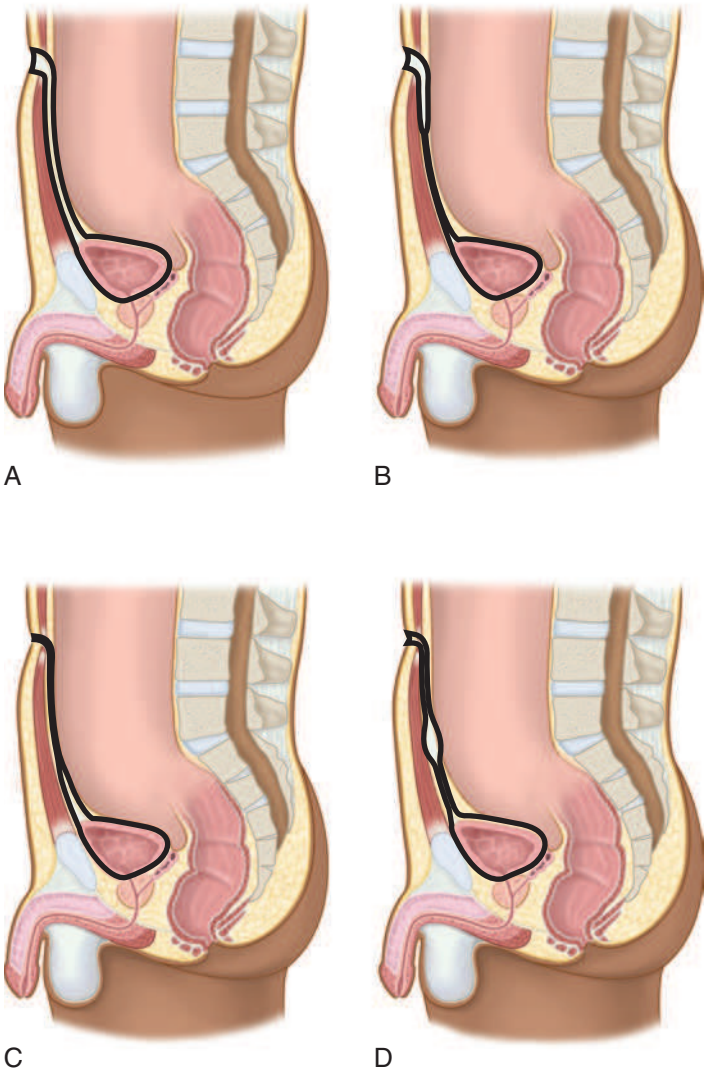

FIG. 9.17 Congenital Urachal Anomalies. (A) Patent urachus extends from the bladder to the umbilicus. **(B)** Urachal sinus. **(C)** Urachal diverticulum. **(D)** Urachal cyst.

Anomalies Related to Urethral Development: Diverticula

The majority of urethral diverticula are acquired secondary to injury or infection, although congenital diverticula occur rarely. Most urethral diverticula in women form as a result of infection of the periurethral glands; some may be related to childbirth. Most diverticula are found in the midurethra and are bilateral. Often, a fluctuant anterior vaginal mass is felt. Stones may develop because of urinary stasis. Transvaginal or translabial scanning may demonstrate a simple or complex cystic structure communicating with the urethra through a thin neck (Fig. 9.18).

GENITOURINARY INFECTIONS

Pyelonephritis

Acute Pyelonephritis

Acute pyelonephritis is a tubulointerstitial inflammation of the kidney. Two routes may lead to inflammation: ascending infection (85%; e.g., *Escherichia coli*) and hematogenous seeding (15%; e.g., *Staphylococcus aureus*). Women age 15 to 35 years are most often affected[25]; 2% of pregnant women will develop acute pyelonephritis.[26] Most adults present with flank pain and fever and can be diagnosed clinically with the aid of laboratory studies (bacteriuria, pyuria, and leukocytosis). With appropriate antibiotics, both clinical and laboratory findings show rapid improvement. Imaging is necessary only when symptoms and laboratory abnormalities persist: imaging is useful to identify potential causes of insufficiently treated infection, including renal and perirenal abscesses, calculi, and urinary obstruction. The Society of Uroradiology proposed using acute **pyelonephritis** to describe acutely infected kidneys, eliminating the need for terms such as bacterial nephritis, lobar nephronia, renal cellulitis, lobar nephritis, renal phlegmon, and renal carbuncle.[27]

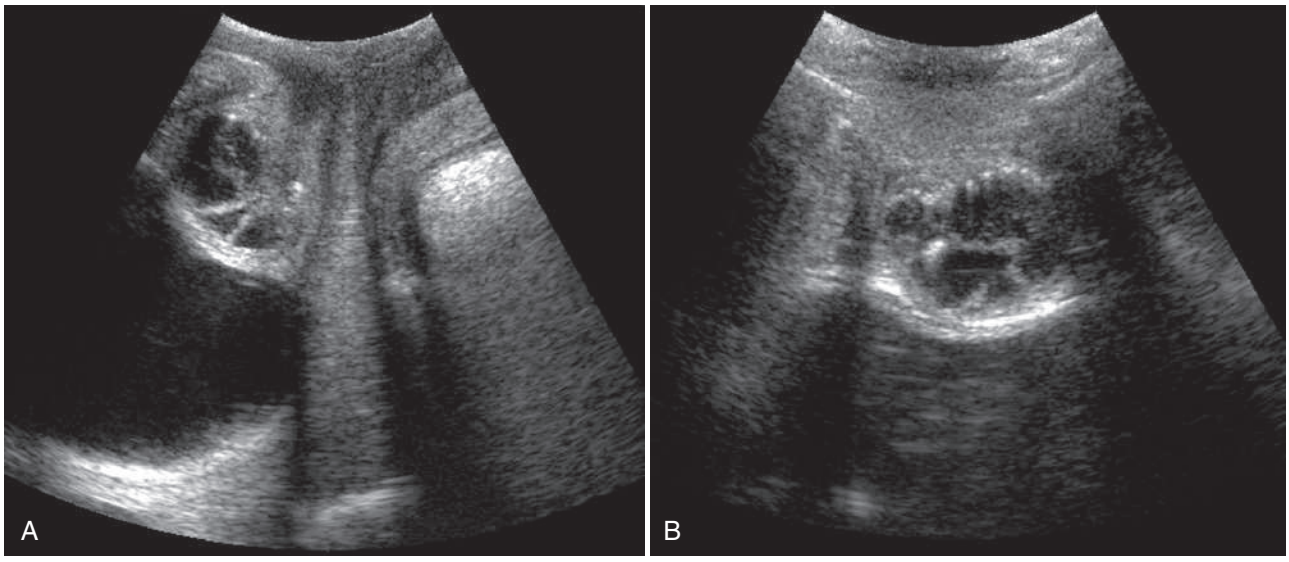

FIG. 9.18 Urethral Diverticulum in Young Woman With Palpable Vaginal Mass. (A) Sagittal and **(B)** transverse translabial sonograms show a complex cystic mass adjacent to the anterior urethra.

At **ultrasound,** the majority of kidneys with acute pyelonephritis appear normal. However, ultrasound findings of pyelonephritis include (Fig. 9.19) renal enlargement, compression of the renal sinus, decreased echogenicity (secondary to edema) or increased echogenicity (potentially from hemorrhage), loss of corticomedullary differentiation, poorly marginated mass(es), gas within the renal parenchyma,[26,27] and focal or diffuse absence of color Doppler perfusion corresponding to the swollen inflamed areas.

If the pyelonephritis is **focal,** the poorly marginated masses may be echogenic, hypoechoic, or of mixed echogenicity. **Echogenic masses** may be the most common appearance of focal pyelonephritis.[28]

Sonography, including power Doppler, is less sensitive than CT, magnetic resonance imaging (MRI), or technetium-99m single-photon emission computed tomography (^{99m}Tc-DMSA SPECT) renal cortical scintigraphy for demonstrating changes of acute pyelonephritis. However, ultrasound is more accessible and less expensive and thus an excellent screening modality for monitoring and follow-up of complications,[29] as well as in the assessment of pregnant patients with acute pyelonephritis because of its lack of ionizing radiation.[26,27]

A unique renal infection known as **alkaline-encrusted pyelitis** has been described in **renal transplants** and native kidneys of

Acute Pyelonephritis on Sonography

Renal enlargement
Compression of renal sinus
Abnormal echotexture (either increased or decreased)
Loss of corticomedullary differentiation
Poorly marginated mass(es)
Gas within renal parenchyma
Focal or diffuse absence of color Doppler perfusion corresponding to the swollen inflamed areas

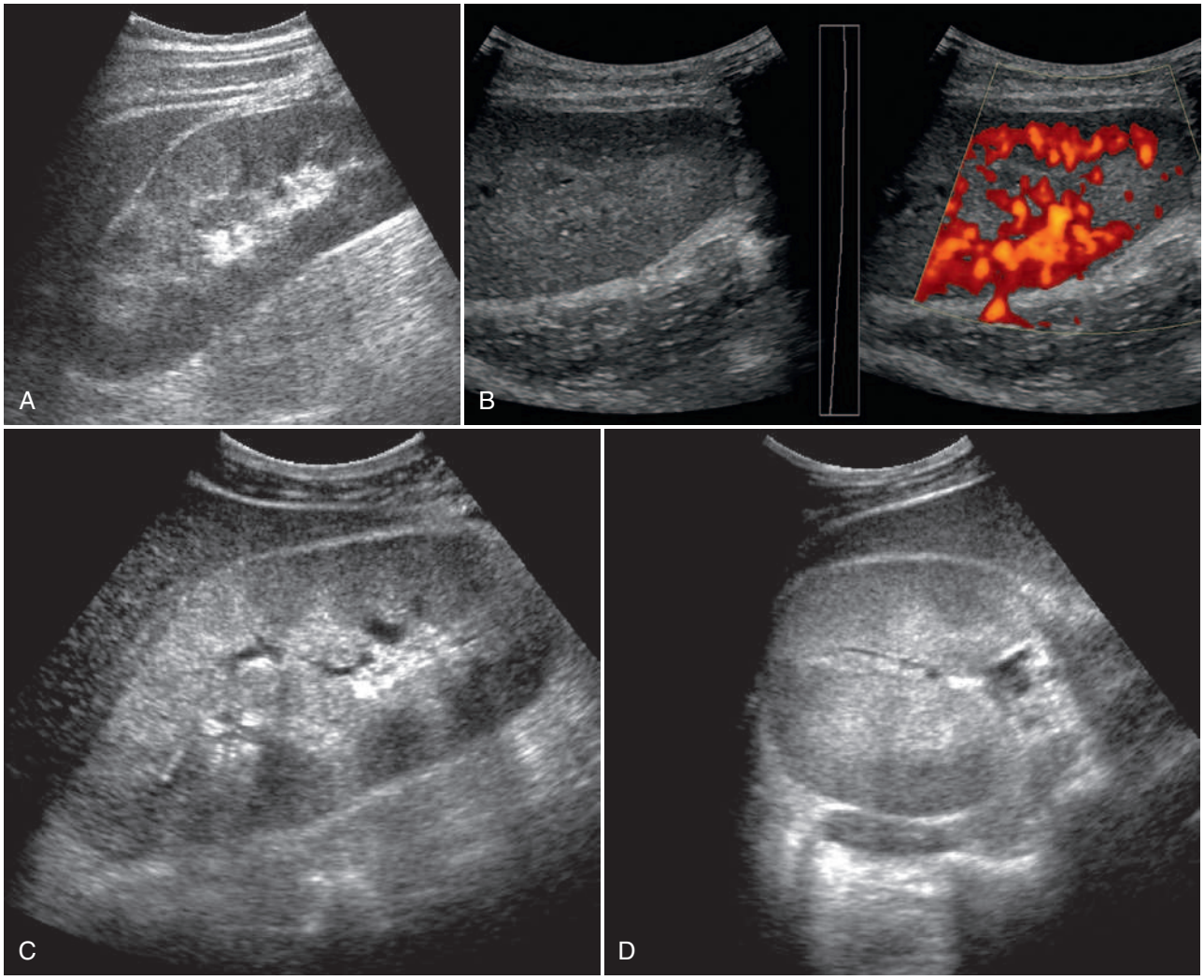

FIG. 9.19 Acute Pyelonephritis in Three Patients. (A) Subtle focal increased echogenic areas are seen in the anterior cortex of the right kidney. **(B)** Power Doppler perfusion defect in lower pole of kidney of patient with documented *E. coli* pyelonephritis. Note normal corresponding gray-scale image. **(C)** Sagittal and **(D)** transverse sonograms in a third patient show a swollen and edematous kidney with focal altered echogenicity and loss of corticomedullary differentiation. The renal sinus fat is attenuated by swollen parenchyma.

debilitated and immunocompromised patients.[30] This entity is most frequently caused by *Corynebacterium urealyticum,* a urea-splitting microorganism. Urothelial stone encrustation develops in the kidney and bladder. If the kidney is affected, the patient may present with hematuria, stone passage, or an ammonium odor to the urine. Dysuria and suprapubic pain are the most common clinical signs if the bladder is involved. Treatment is with antibiotics and local acidification of the urine. On sonography, alkaline-encrusted pyelitis is suggested if thickened, calcified urothelium is identified.[30] The calcification can be thin and smooth or thick and irregular. Care should be taken to distinguish urothelial calcification from layering of collecting system calculi.[30]

Renal and Perinephric Abscess

Untreated or inadequately treated acute pyelonephritis may lead to parenchymal necrosis and abscess formation. Patients at increased risk for **renal abscesses** include those with diabetes, compromised immunity, chronic debilitating diseases, urinary tract obstruction, infected renal calculi, and intravenous drug abuse.[26,31] Renal abscesses tend to be solitary and may spontaneously decompress into the collecting system or perinephric space. **Perinephric abscesses,** also a complication of **pyonephrosis,** may result from direct extension of peritoneal or retroperitoneal infection or interventions.[24] Small abscesses are treated conservatively with antibiotics, whereas larger abscesses often require percutaneous drainage and, if drainage is unsuccessful, surgery.

At ultrasound, renal abscesses appear as round, thick-walled, hypoechoic complex masses with through transmission (Fig. 9.20). Internal mobile debris and septations may be seen. Occasionally, "dirty shadowing" may be noted posterior to gas within the abscess. The differential diagnosis includes (1) hemorrhagic or infected cysts, (2) parasitic cysts, (3) multiloculated cysts, and (4) cystic neoplasms. Although not as accurate as CT in determining the presence and extent of perinephric abscess extension,[26] sonography is an excellent modality for following conservatively treated patients with abscesses to document resolution.

Pyonephrosis

Pyonephrosis implies purulent material in an obstructed collecting system. Depending on the level of obstruction, any portion of the collecting system, including the ureter, can be affected. Early diagnosis and treatment are crucial to prevent development of bacteremia and life-threatening septic shock. The mortality rates of bacteremia and septic shock are 25% and 50%, respectively[32]; 15% of patients are asymptomatic at presentation.[33] In the young adult, UPJ obstruction and calculi are the most frequent cause of pyonephrosis, whereas malignant ureteral obstruction is typically the predisposing factor in older patients.[26] Pyonephrosis is suggested when ultrasound shows mobile collecting system debris (with or without a fluid-debris level), collecting system gas, and stones (Fig. 9.21).

Emphysematous Pyelonephritis

Emphysematous pyelonephritis (EPN) is an uncommon, life-threatening infection of the renal parenchyma characterized by gas formation.[34] Most patients are women (2:1) and diabetic (90%), with a mean age of 55 years. In diabetic patients, EPN tends to occur in nonobstructed collecting systems; the reverse is true in nondiabetic patients. Bilateral disease occurs in 5% to 10% of EPN patients. *Escherichia coli* is the offending organism in 62% to 70% of cases; *Klebsiella* (9%), *Pseudomonas* (2%) *Proteus, Aerobacter,* and *Candida* are additional causative organisms.[26,31] At presentation, most patients are extremely ill with fever, flank pain, hyperglycemia, acidosis, dehydration, and electrolyte imbalance[35]; 18% present only with fever of unknown origin.[36]

Wan et al.[37] retrospectively studied 38 patients with EPN and identified two types of disease: **EPN1,** characterized by parenchymal destruction and streaky or mottled gas, and **EPN2,**

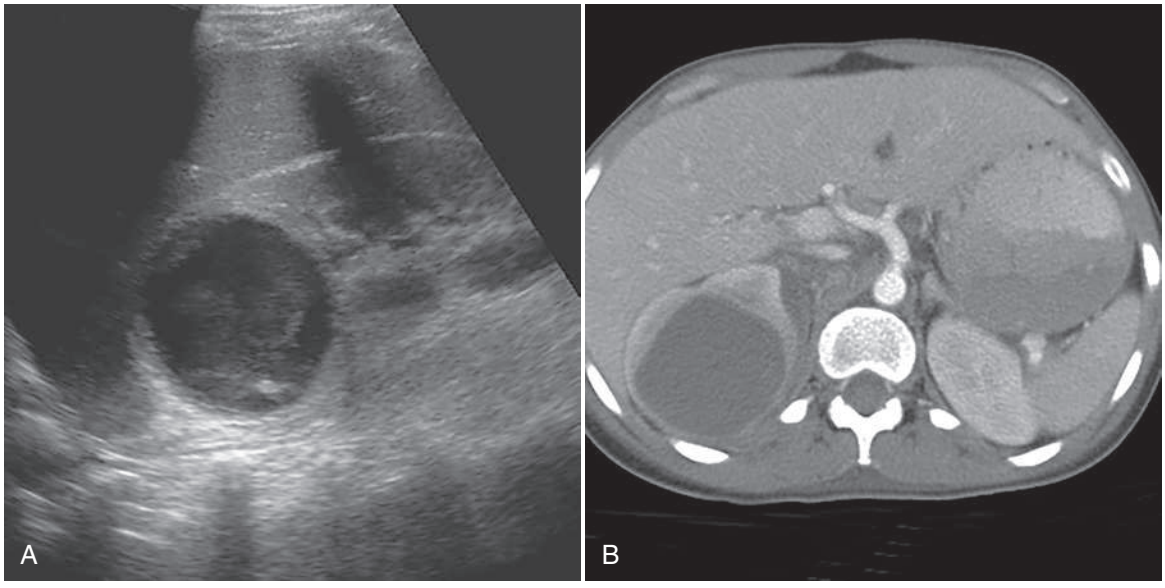

FIG. 9.20 Renal Abscess. (A) Sagittal ultrasound shows a complex cystic upper-pole lesion containing layering low level echoes. **(B)** Corresponding contrast-enhanced CT exam shows a large right upper-pole cystic lesion with a thick rind. The patient was successfully treated with ultrasound guided drain placement and antibiotics.

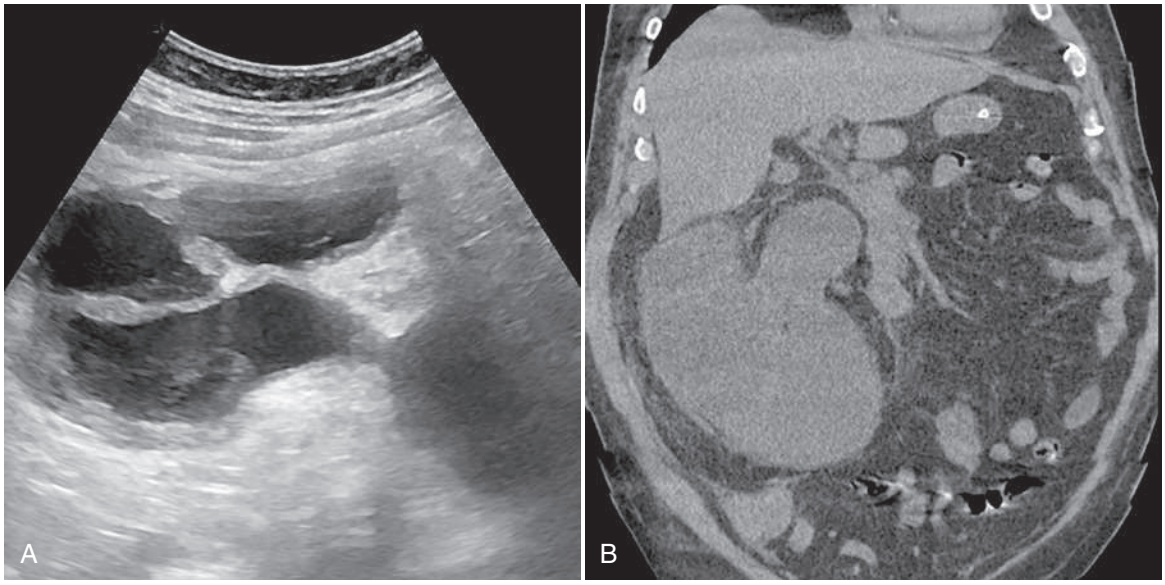

FIG. 9.21 Pyonephrosis. (A) Sagittal ultrasound of an older male with *Proteus mirabilis* sepsis shows a deformed, chronically hydronephrotic kidney, with layering collecting system echoes. **(B)** Corresponding noncontrast-enhanced CT shows a large right hydronephrotic sac and perinephric infiltration. Clinical history and imaging findings prompted successful, emergent drainage.

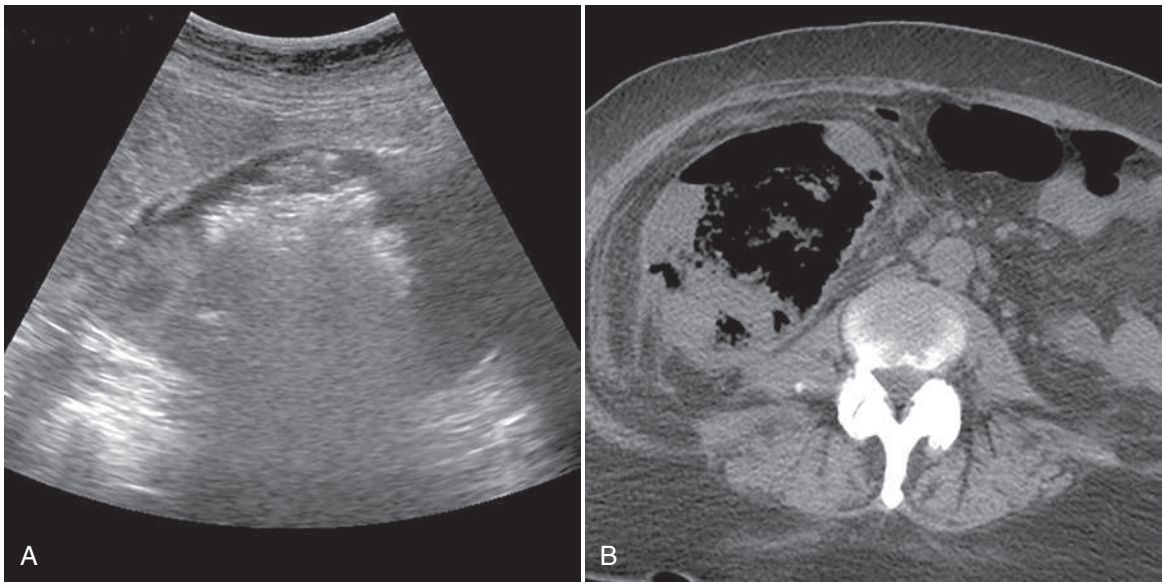

FIG. 9.22 Emphysematous Pyelonephritis Type 1 (EPN1). (A) Sagittal sonogram of right renal fossa shows extensive shadowing gas occupying most of the right kidney. **(B)** Corresponding noncontrast-enhanced CT demonstrates diffuse parenchymal destruction of the right kidney with extensive mottled gas. Nephrectomy was eventually performed in this septic, diabetic patient. Caution must be exercised to avoid missing EPN1 altogether on ultrasound. Failure to see a kidney in a septic patient should prompt alternative cross-sectional imaging.

characterized as renal or perirenal fluid collections, with bubbly or loculated gas or with gas in the collecting system. Mortality rates for EPN1 and EPN2 were 69% and 18%, respectively. The authors postulated that the different clinical outcomes of EPN1 and EPN2 result from the patient's immune status and the vascular supply of the affected kidney. Emergency nephrectomy is the treatment of choice for EPN1, whereas percutaneous drainage is recommended for EPN2. CT is the preferred method to image patients with EPN, to determine the location and extent of renal and perirenal gas. Sonographic evaluation of EPN1 or EPN2 may be difficult because dirty shadowing from parenchymal gas will obscure deeper structures; shadowing might also prompt an erroneous interpretation of renal calculi or bowel gas[38] (Fig. 9.22).

Emphysematous Pyelitis

Emphysematous pyelitis refers to gas localized within the urinary collecting system.[34] This disease entity is seen most often in women with diabetes or obstructing stone disease; a mortality rate of 20% has been reported. It is important to exclude iatrogenic causes of gas within the collecting system. At ultrasound, nondependent linear echogenic lines with dirty distal posterior

acoustic shadowing, indicative of gas are seen within the collecting system (Fig. 9.23). As with EPN, CT is often required to identify emphysematous pyelitis because dirty acoustic shadowing from gas at ultrasound may obscure the exact extent of renal and perirenal disease.

Chronic Pyelonephritis

Chronic pyelonephritis is an interstitial nephritis often associated with vesicoureteric reflux. **Reflux nephropathy** is believed to cause 10% to 30% of all cases of **end-stage renal disease** (ESRD)[39] (Fig. 9.24). Chronic pyelonephritis usually begins in childhood and is more common in women. The renal changes may be unilateral or bilateral but usually are asymmetric. Reflux into the collecting tubules occurs when the papillary duct orifices are incompetent. This reflux occurs more often in compound papillae, which are typically found at the poles of the kidneys. Cortical scarring therefore tends to occur over polar calices. There is associated papillary retraction with caliceal clubbing. At ultrasound, a dilated blunt calix is seen, associated with overlying **cortical scar** or **cortical atrophy**[40] (Fig. 9.25). These changes may be multicentric and bilateral. If the disease is unilateral, there may be compensatory hypertrophy of the contralateral kidney. If the disease is multicentric, compensatory hypertrophy of normal intervening parenchyma may create an island of normal tissue simulating a tumor.

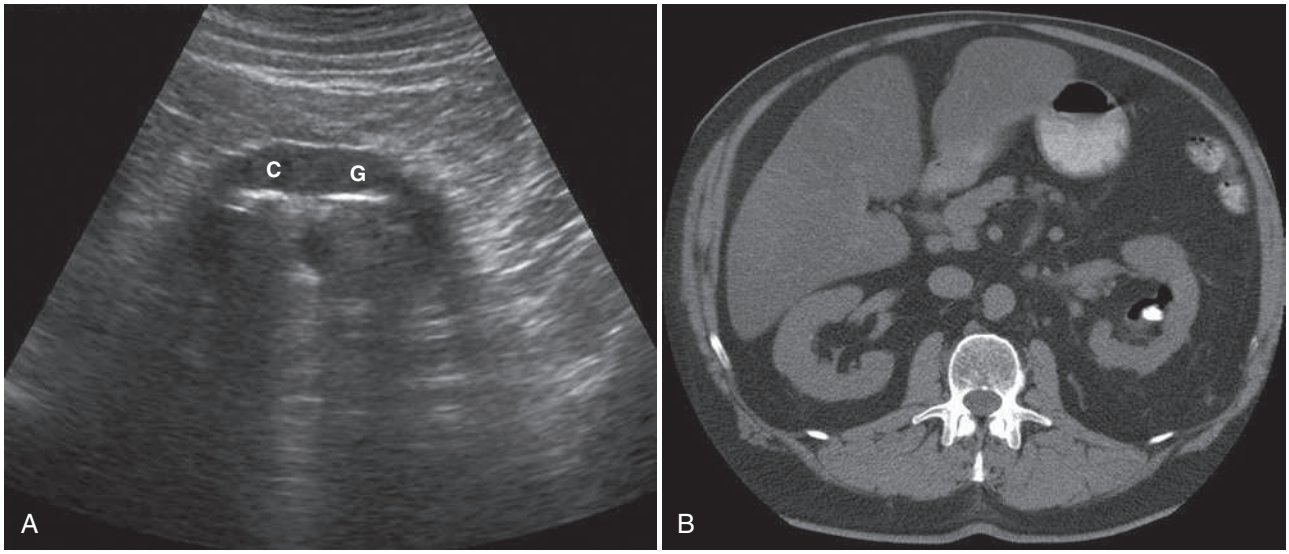

FIG. 9.23 Emphysematous Pyelitis. (A) Transverse sonogram of left kidney shows "clean" shadowing posterior to a renal calculus *(C)* and "dirty" shadowing posterior to nondependent collecting system gas *(G)*. **(B)** Confirmatory unenhanced CT image shows both a calculus and gas within the left collecting system.

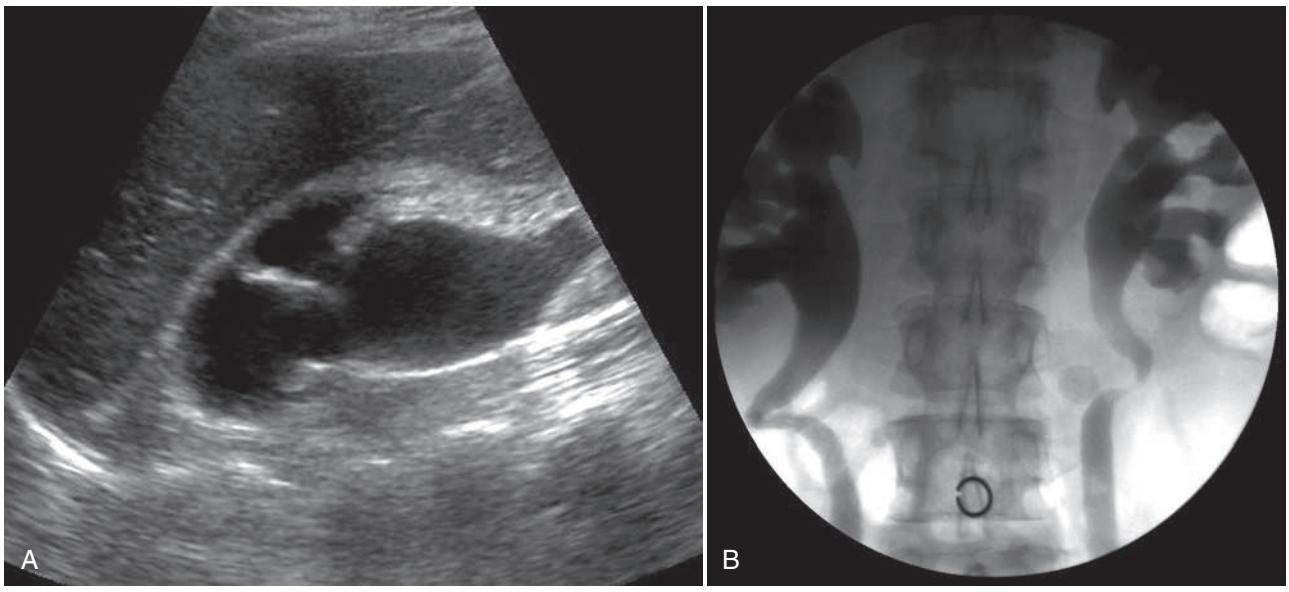

FIG. 9.24 Reflux Nephropathy: Renal Transplantation Evaluation. (A) Sagittal sonogram shows marked right hydronephrosis and absence of overlying cortex. **(B)** Cystogram confirms massive bilateral ureteral reflux.

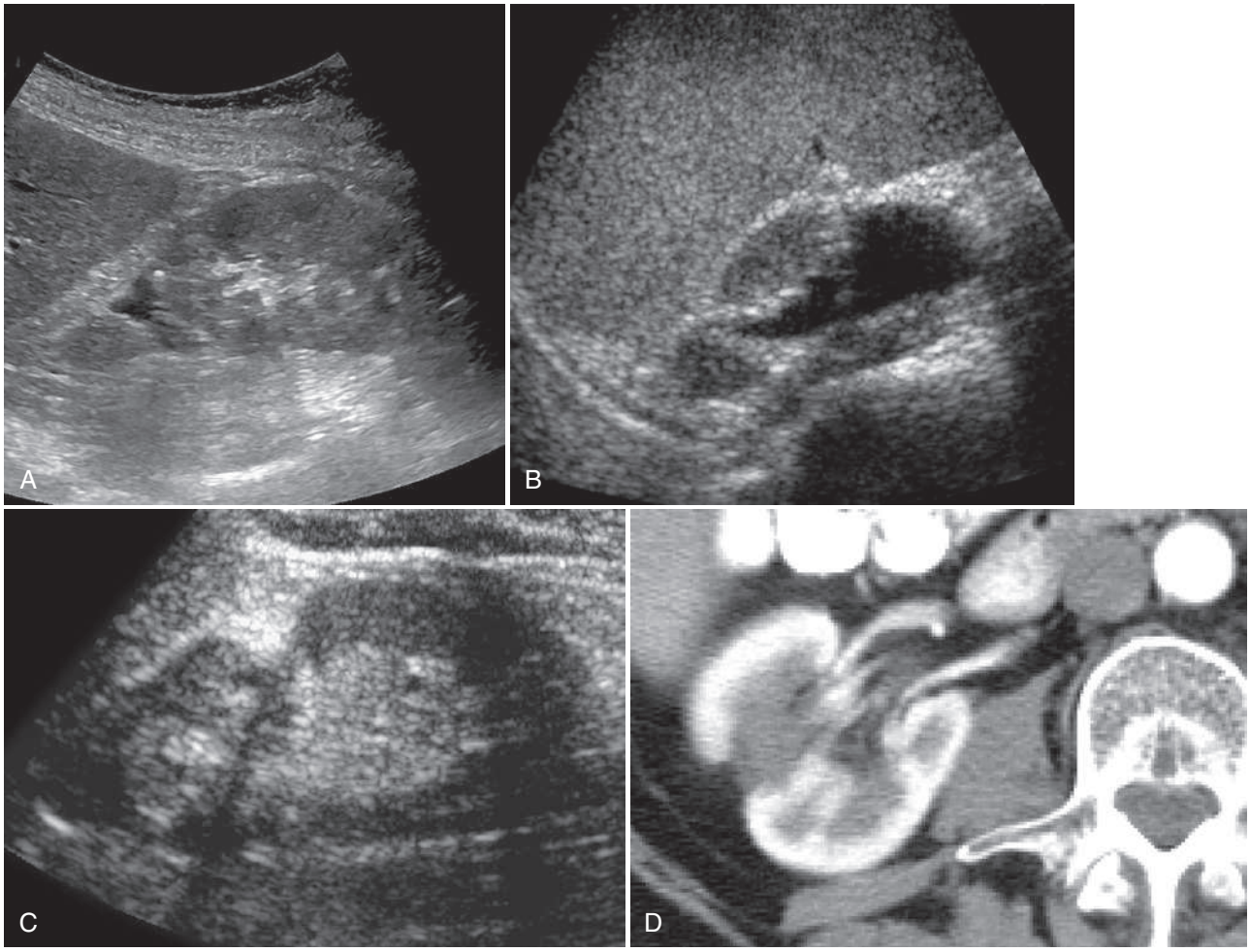

FIG. 9.25 Chronic Pyelonephritis. (A) Sagittal sonogram of a patient with a history of vesicoureteral reflux shows upper-pole atrophy and severe cortical loss overlying a deformed, dilated calyx. **(B)** Sagittal sonogram shows an atrophic kidney with scarring and dilatation of the collecting system caused by reflux. **(C)** Sagittal sonogram shows an echogenic wedge-shaped scar in the midpole of the kidney. **(D)** Confirmatory CT scan.

Xanthogranulomatous Pyelonephritis

Xanthogranulomatous pyelonephritis (XGP) is a chronic, suppurative renal infection in which destroyed renal parenchyma is replaced with lipid-laden macrophages. XGP is typically unilateral and may be diffuse, segmental, or focal. XGP is typically associated with nephrolithiasis (70%) and obstructive nephropathy.[41-43] The disease most commonly occurs in middle-aged women and diabetic patients.[43] Presenting signs are nonspecific: pain, mass, weight loss, and UTI (*Proteus* or *E. coli*).[41] The diffusely involved kidney is usually nonfunctional. Ultrasound findings of diffuse XGP include renal enlargement, maintenance of a reniform shape, and lack of corticomedullary differentiation. Multiple hypoechoic areas correspond to dilated calices or inflammatory parenchymal masses.[41] Through transmission is variable and depends on the degree of liquefaction of the parenchymal masses. Occasionally, the large, complex cystic masses may mimic pyonephrosis. A **staghorn calculus** will result in extensive shadowing from the central renal sinus (Fig. 9.26). Perinephric extension may occur, but this is often best appreciated with CT. **Diffuse** XGP has no specific sonographic features but is suggested when parenchymal thinning, hydronephrosis, stones, debris in a dilated collecting system, and perinephric fluid collections are present.[44] **Segmental** XGP will be seen as one or more hypoechoic masses, often associated with a single calyx.[41,45] An obstructing calculus may be seen near the papilla. **Focal** XGP arises in the renal cortex and does not communicate with the renal pelvis. It cannot be distinguished sonographically from tumor or abscess.[41]

Papillary Necrosis

Causative factors implicated in the ischemia that leads to papillary necrosis include analgesic abuse, diabetes, UTI, renal vein thrombosis, prolonged hypotension, urinary tract obstruction, dehydration, sickle cell anemia, and hemophilia.[46] Initially, the papilla swells (Fig. 9.27); then a communication with the caliceal system occurs. The central aspect of the papilla cavitates and may slough. With papillary cavitation, ultrasound shows cystic collections within the medullary pyramids. If the papilla sloughs, the affected adjacent calyx will be clubbed. The sloughed papilla can be seen in the collecting system as an echogenic nonshadowing structure. If the sloughed papilla calcifies, distal acoustic shadowing simulating medullary nephrocalcinosis will be seen.[47]

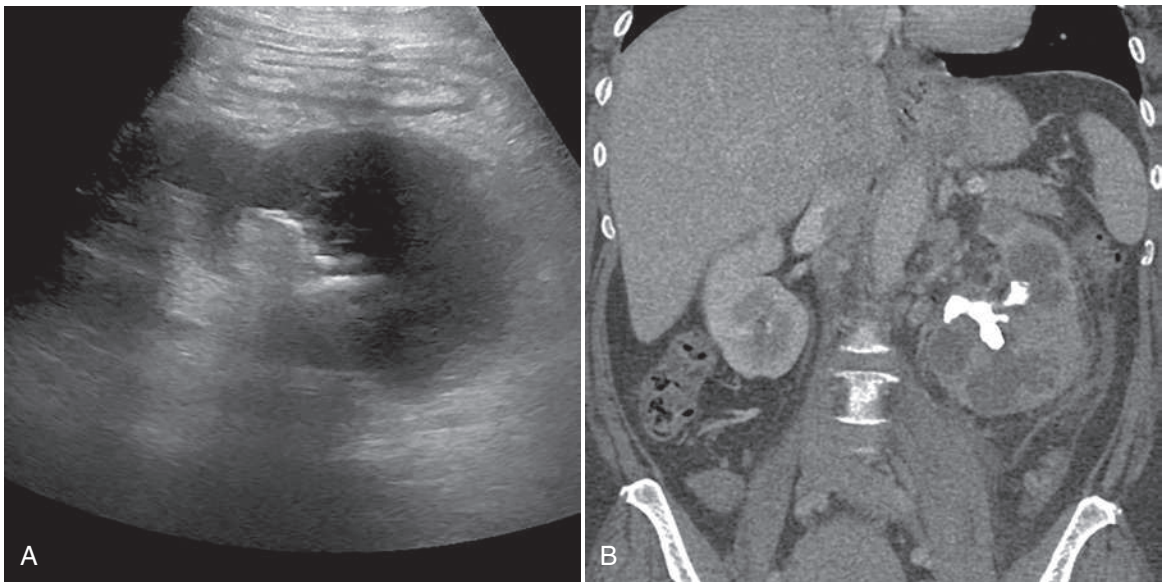

FIG. 9.26 Xanthogranulomatous Pyelonephritis. (A) Sagittal sonogram shows an enlarged hypoechoic kidney and a large showing staghorn calculus. **(B)** Corresponding contrast-enhanced CT demonstrates a diffusely enlarged left kidney, multiple intrarenal abscesses, and a large, central obstructing calculus.

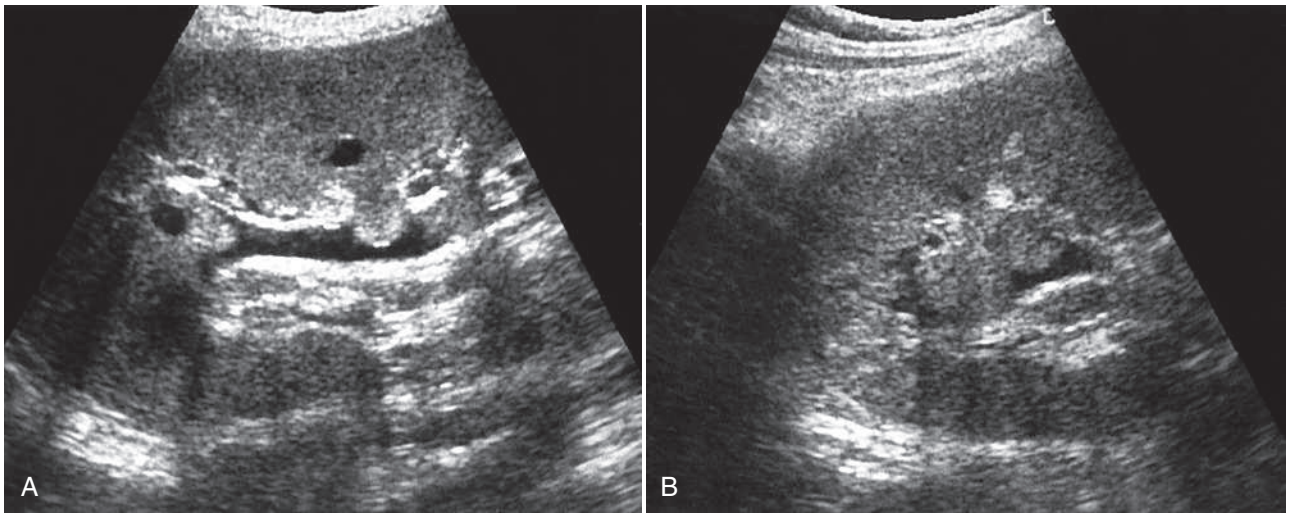

FIG. 9.27 Papillary Necrosis. (A) Sagittal and **(B)** transverse sonograms show swollen bulbous papillae.

Sonographic Findings of Papillary Necrosis

Swollen pyramids
Papillary cavitation
Adjacent clubbed calix
Sloughed papilla in collecting system that can calcify and simulate a stone
Sloughed papilla may cause obstruction

Hydronephrosis may develop if the sloughed papilla obstructs the ureter.

Tuberculosis

Urinary tract tuberculosis (TB) occurs with hematogenous seeding of the kidney by *Mycobacterium tuberculosis* from an extraurinary source (typically lung). Urinary tract TB usually manifests 5 to 10 years after the initial pulmonary infection. Chest radiographs may be normal (35%-50% of patients) or may show active TB (10%) or inactive healed TB (40%-55%). Most patients present with lower urinary tract signs and symptoms that include frequency, dysuria, nocturia, urgency, and gross or microscopic hematuria, whereas 10% to 20% of patients are asymptomatic.[48] Urinalysis findings include sterile pyuria, microscopic hematuria, and acidic pH. TB is definitively diagnosed with acid-fast bacilli urine cultures; however, this usually requires 6 to 8 weeks for growth.

Although both kidneys are seeded initially, clinical manifestations of urinary tract TB are typically unilateral. The early or acute changes include development of multiple small bilateral tuberculomas. Das et al.[49] found that the most frequently encountered sonographic abnormality was **focal renal lesions**

(Fig. 9.28). Small focal lesions (5-15 mm) were echogenic or were hypoechoic with an echogenic rim. Larger, mixed-echogenicity focal lesions (>15 mm) were poorly defined. Bilateral disease was noted in 30% of patients. Most tuberculomas will heal spontaneously or after antituberculous therapy. At some later date (perhaps years later), one or more of the tubercles may enlarge. With enlargement, cavitation and communication with the collecting system will occur. The resultant pathologic changes resemble papillary necrosis; papillary involvement is noted when a sonolucent linear tract is shown extending from the involved calix into the papilla. Soft tissue caliceal masses representing sloughed papilla may be seen. After rupture into the collecting system, *M. tuberculosis* bacilluria develops and allows the spread of the renal infection to other parts of the urinary tract. Spasm or edema in the region of the UVJ may occur, giving rise to hydronephrosis and hydroureter. Ureteric linear ulcers may also occur, typically within the distal ureter. Bladder involvement is seen in 33% of patients with genitourinary tract TB.[49] Early bladder manifestations include mucosal edema and ulceration. Early clinical symptoms (dysuria and frequency) are also nonspecific. If edema occurs at the bladder trigone, ureteric obstruction may occur. At ultrasound, early bladder involvement will appear as focal or diffuse wall thickening; the thickening can be quite extensive (Fig. 9.29).

The later or more chronic changes of genitourinary tract TB include fibrotic strictures, extensive cavitation, calcification, mass lesions, perinephric abscesses, and fistulas.[48] The chronic changes, in particular those related to fibrotic strictures, result in functional renal damage. Strictures may occur anywhere in the intrarenal collecting system and ureter. The obstruction then results in proximal collecting system dilatation and pressure atrophy of the renal parenchyma. With time, calcification in the areas of caseation or sloughed papilla may occur. If renal infection ruptures into the perinephric space, an abscess may develop. Perinephric abscesses may ultimately result in fistulas to adjacent viscera. The hallmark of chronic, upper tract renal TB is a small, nonfunctional, calcified kidney, the **"putty" kidney.** In the bladder, chronic infection and fibrosis result in a thickened, small-capacity bladder.[48] Speckled or curvilinear calcification of the bladder wall may rarely occur.[50]

Most cases of genitourinary tract TB can be diagnosed with a combination of intravenous/retrograde urography, ultrasound, CT, and CT urography.[51] Premkumar et al.[52] demonstrated in 14 patients with advanced urinary tract TB that detailed morphologic information and functional renal status are best assessed with CT and urography. Das et al.[53] reported that ultrasound-guided, fine-needle aspiration (1) may be diagnostic in patients with negative urine cultures and (2) may confirm a diagnosis of upper genitourinary tract TB in those patients with suspicious lesions and positive cultures.

Fungal Infections

Patients with a history of diabetes mellitus, chronic indwelling catheters, malignancy, hematopoietic disorders, chronic antibiotic or steroid therapy, transplantation, and intravenous drug abuse are at risk for developing fungal infections of the urinary tract.[54]

Candida Albicans

Candida albicans is the most common fungal agent that affects the urinary tract. Renal parenchymal involvement, typically manifested by small parenchymal abscesses, occurs in the context of diffuse systemic involvement. The abscesses may calcify over

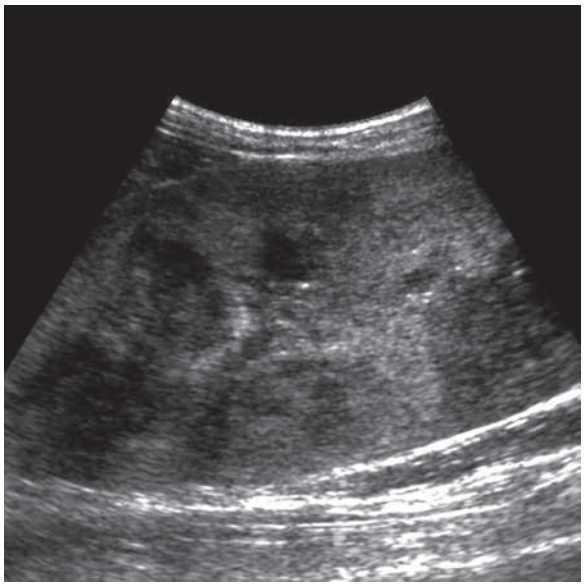

FIG. 9.28 Progressive Renal Tuberculosis. Sagittal sonogram shows small, irregular hypoechoic medullary lesions. Areas of cavitation ultimately connect to the collecting system. (With permission from Wasnik AP. Tuberculosis, urinary tract. In: Kamaya A, Wong-You-Cheong J, editors. Diagnostic ultrasound: abdomen and pelvis. Philadelphia: Elsevier; 2016. pp. 490-493.[51])

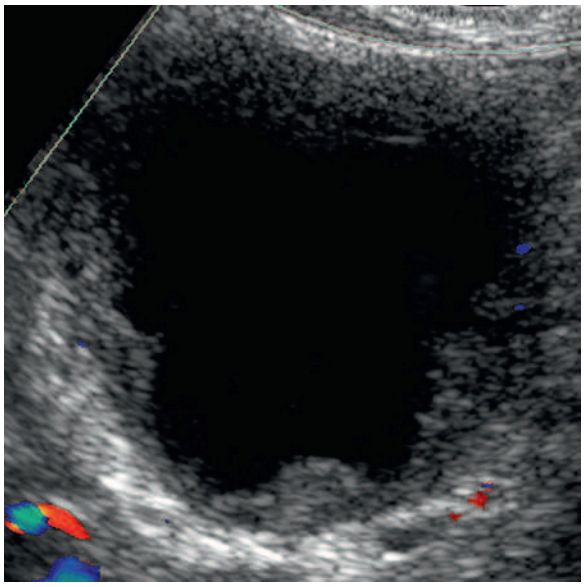

FIG. 9.29 Urinary Bladder Tuberculosis. Transverse sonogram shows irregular mucosal thickening, particularly at the ureteric orifice—a characteristic feature of early bladder tuberculosis. (With permission from Wasnik AP. Tuberculosis, urinary tract. In: Kamaya A, Wong-You-Cheong J, editors. Diagnostic ultrasound: abdomen and pelvis. Philadelphia: Elsevier; 2016. pp. 490-493.[51])

time.[55] Extension into the perinephric space is also possible. Invasion of the collecting system ultimately results in fungus balls. Collecting system **mycetomas** may be differentiated from blood clots, radiolucent stones, transitional cell tumors, sloughed papillae, fibroepithelial polyps, cholesteatomas, and leukoplakia based on clinical history and urine cultures.[56-58] On sonography, **candidal microabscesses** are typically small, hypoechoic cortical lesions; the appearance is similar to other bacterial abscesses. **Fungus balls** appear as echogenic, nonshadowing soft tissue masses within the collecting system[59] (Fig. 9.30). Fungus balls are mobile and may cause obstruction and hydronephrosis.

Parasitic Infections

A wide variety of parasitic infections are common in developing countries. Sonographers should be particularly familiar with schistosomiasis and echinococcal (hydatid) disease.

Schistosomiasis

Schistosoma haematobium is the most common agent to affect the urinary tract. The worms enter the human host by penetrating the skin. They are then carried via the portal venous system to the liver, where they mature into their adult form. *S. haematobium* likely enters the perivesical venous plexus from the hemorrhoidal plexus.[60] The female worm then deposits eggs into the venules of the bladder wall and ureter. Granuloma formation and obliterative endarteritis occur. Serologic tests demonstrating ova allow diagnosis. Hematuria is the most frequent complaint.[60]

At sonography, the kidneys are normal until late in the disease. Pseudotubercles develop in the ureter and bladder, and the urothelium becomes thickened (Fig. 9.31).[61] Over time the pseudotubercles calcify; the calcification may be fine, granular and linear, or thick and irregular. If repeated infections occur, the bladder will become small and fibrotic. Bladder stasis results in an increased incidence of ureteral and bladder calculi.[60] Patients with chronic disease also have an increased incidence of squamous cell carcinoma.[60]

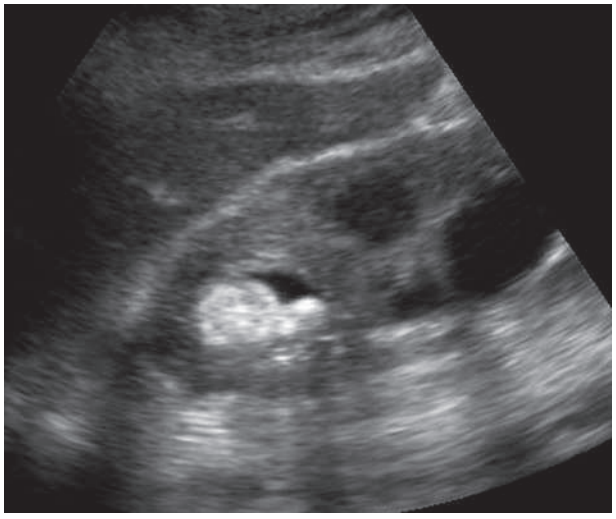

FIG. 9.30 Fungus Ball. Sagittal sonogram shows an echogenic soft tissue mass within a dilated upper-pole cortex.

Echinococcal (Hydatid) Disease

The two major types of hydatid disease that affect the urinary tract are caused by *Echinococcus multilocularis* and the more common *Echinococcus granulosus.* Renal hydatid disease is found in 2% to 5% of patients with hydatid disease,[60] is usually solitary, and typically involves the renal poles.[62] Hydatid cysts may occur along the ureter or within the bladder. Each hydatid cyst consists of three layers: the pericyst, ectocyst, and endocyst. Echinococcal disease is often silent until the cyst grows large enough to rupture or compress adjacent structures.

The ultrasound manifestation of early hydatid disease is an **anechoic cyst.** Mural nodularity suggests scolices. When **daughter cysts** are present, a multiloculated cystic mass will be seen (Fig. 9.32). The membranes from the endocyst may detach and precipitate to the bottom of the hydatid fluid to become "hydatid sand."[63] Varying patterns of calcification occur, ranging from eggshell to dense reticular calcification. Ring-shaped calcifications inside a larger, calcified lesion suggest calcified daughter cysts.[60,63] A specific ultrasound diagnosis is difficult without an appropriate clinical history. However, several features may suggest hydatid disease, including floating membranes, daughter cysts, and thick, double-contour cyst walls.[64]

Acquired Immunodeficiency Syndrome

The disease course and imaging manifestations of human immunodeficiency virus (HIV) infection, acquired immunodeficiency syndrome (AIDS), and HIV-associated nephropathy have rapidly evolved largely because of advances in the care of HIV-positive patients. Highly active antiretroviral therapy (HAART) has resulted in a decreased incidence of opportunistic infections and improved survival.

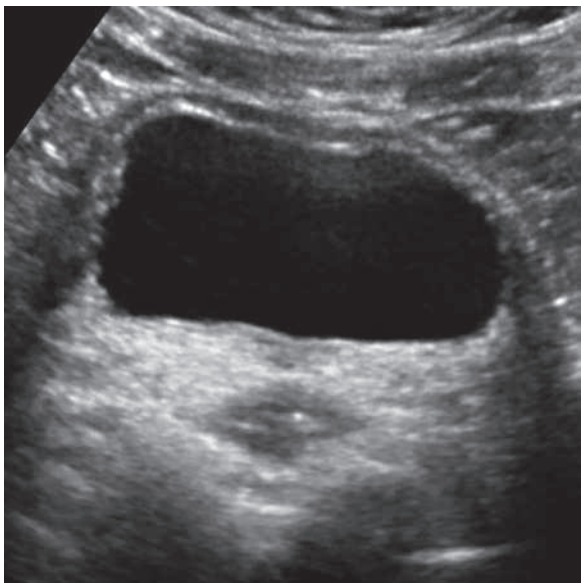

FIG. 9.31 Bladder Schistosomiasis. Transverse sonogram shows mild bladder wall thickening and linear anterior wall echogenicity due to early calcification. (With permission from Wasnik AP. Schistosomiasis, bladder. In: Kamaya A, Wong-You-Cheong J, editors. Diagnostic ultrasound: abdomen and pelvis. Philadelphia: Elsevier; 2016. pp. 548-549.[61])

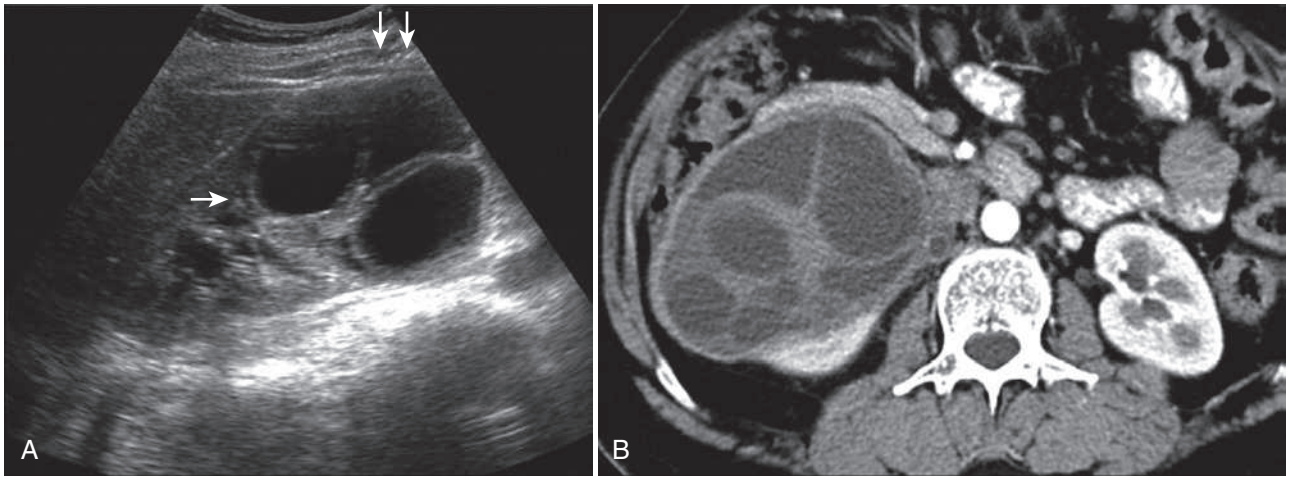

FIG. 9.32 Renal Hydatid Cyst. (A) Sagittal sonogram shows a complex multiloculated lower-pole cystic mass *(arrows).* **(B)** Contrast-enhanced CT shows multiple confluent daughter cysts. (Courtesy of Drs. Vikram Dogra and Suleman Merchant.)

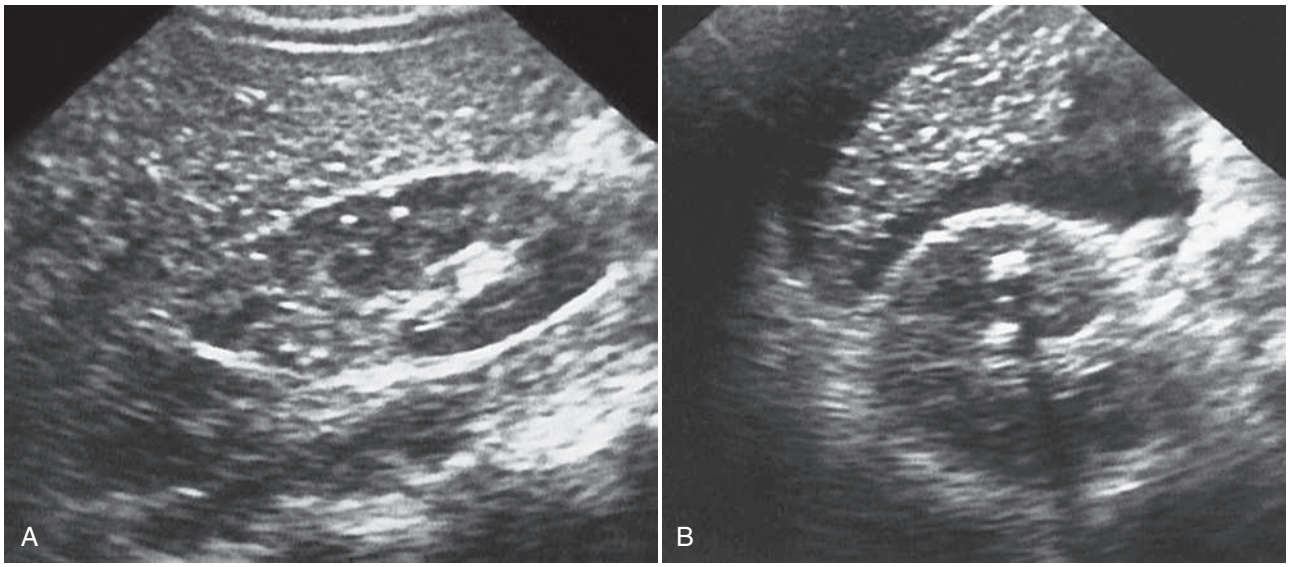

FIG. 9.33 Proven *Pneumocystis* Nephropathy in a Patient With AIDS. (A) Sagittal and **(B)** transverse sonograms show multiple scattered echogenic foci within the renal parenchyma. Some foci demonstrate the distal acoustic shadowing of calcification. Similar findings are seen in the liver. (With permission from Spouge AR, Wilson S, Gopinath N, et al. Extrapulmonary Pneumocystis carinii in a patient with AIDS: sonographic findings. AJR Am J Roentgenol. 1990;155:76-78.[66])

Early literature noted the increased incidence of opportunistic genitourinary infections (cytomegalovirus [CMV], *Candida albicans, Cryptococcus, Pneumocystis jiroveci* [formerly *P. carinii*], *Mycobacterium avium-intracellulare, Mucormycosis*) and tumors (lymphoma, Kaposi sarcoma) in these immunocompromised patients.[65] The appearance of these infections is often nonspecific (and now rare), but diffuse visceral/renal calcifications suggest disseminated *P. jiroveci*, CMV, or *M. avium-intracellulare* infections[66-68] (Fig. 9.33). The genitourinary infections that now occur in these patients, including pyelonephritis, renal abscesses, and cystitis, are similar to those seen in non–HIV-infected individuals.

Use of HAART has also changed the spectrum of chronic renal diseases seen in HIV-positive patients. The incidence of ESRD in HIV patients decreased initially after the institution of HAART; however, the increased prevalence of HIV in the US population has resulted in an increased number of patients with **HIV-associated nephropathy** (HIVAN).[69] In HIV-positive patients, HIVAN is the most common cause of chronic kidney disease; black patients are at particular risk. The histologic hallmark of HIVAN is focal segmental glomerulosclerosis. Nephropathy in HIV-positive patients may also be caused by HIV immune complex disease and HIV thrombotic microangiopathy. Adverse renal effects of various drugs also complicate the diagnosis of chronic renal failure.[70] However, other disease processes not directly associated with HIV infection (e.g., hypertension, diabetic nephropathy, interstitial nephritis) may result in ESRD in patients successfully treated with HAART.[71] Definitive diagnosis of HIVAN is usually made after renal biopsy. Renal sonography is useful in these patients to exclude obstruction

and determine renal size. Early reports also suggested that **greatly increased renal echogenicity** is a fairly specific finding of HIVAN (and **heroin nephropathy**)[65,72,73] (Fig. 9.34). Other features in HIV-positive patients with renal insufficiency include globular-appearing kidneys, decreased corticomedullary differentiation, decreased renal sinus fat, and parenchymal heterogeneity.[74]

Cystitis

Infectious Cystitis

Women are at increased risk for cystitis because of colonization of the short female urethra by rectal flora. Bladder outlet obstruction or prostatitis results in cystitis in men. The most common pathogen is *E. coli*.[75] Mucosal edema and decreased bladder capacity are common. Findings may be more prominent at the trigone and bladder neck. Patients will present with bladder irritability and hematuria. The most common finding at sonography is diffuse bladder wall thickening. If cystitis is focal, **pseudopolyps** may form, which are impossible to differentiate from tumor[76] (Fig. 9.35A).

Malacoplakia

Malacoplakia is a rare granulomatous infection with a predilection for the urinary bladder. The disease is seen more often in women (4:1), with a peak incidence in the sixth decade.[77] The pathogenesis of malacoplakia is not known; however, an association with **diabetes mellitus, alcoholic liver disease, mycobacterial infections, sarcoidosis,** and **transplantation** suggests an altered immune response.[78] Patients may present with hematuria and symptoms of bladder irritability. At sonography, single or multiple mucosal-based masses ranging from 0.5 to 3.0 cm are seen, typically at the bladder base. Malacoplakia may be locally invasive[77] (Fig. 9.35B).

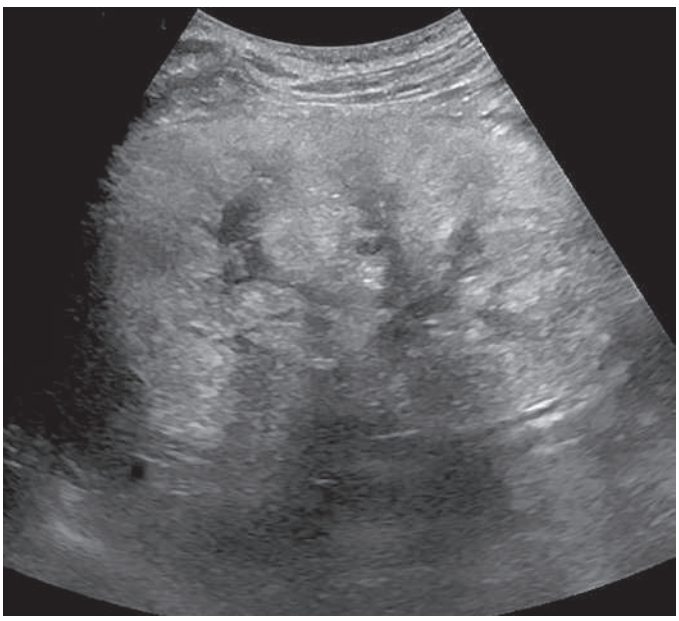

FIG. 9.34 HIV-Associated Nephropathy (HIVAN). Sagittal sonogram shows an enlarged, markedly echogenic kidney. Biopsy confirmed focal segmental glomerulosclerosis.

Emphysematous Cystitis

Emphysematous cystitis occurs most often in female patients and those with diabetes. Patients present with symptoms of cystitis and occasionally have pneumaturia.[75] The most common offending organism is *E. coli*. Both intraluminal and intramural gas are present. In these severely ill patients, the urothelium is ulcerated and necrotic and may slough completely. Emphysematous cystitis is suggested at sonography when echogenic foci within the bladder wall are associated with ring-down artifact or dirty shadowing[79] (Fig. 9.36A and B). Gas may be seen in the bladder lumen as well. The bladder wall is usually thickened and echogenic.[34] A lack of bladder wall thickening may be a helpful sonographic feature to distinguish the gas of emphysematous cystitis from gas introduced by catheterization (Fig. 9.36C).

Chronic Cystitis

Chronic inflammation of the bladder may be caused by various agents. Although the histology may also vary, the imaging manifestations, including a small, thickened bladder, are nonspecific. Chronic cystitis may result in invagination of solid "nests" of urothelium into the lamina propria **(Brunn epithelial nests),** which may result in morphologic changes that mimic neoplasia.[80] If the central portion of a Brunn nest degenerates, a cyst results **(cystitis cystica).** If chronic irritation persists, the Brunn nests may develop into glandular structures **(cystitis glandularis).** These may be precursors of adenocarcinoma.[75] Cystitis cystica and cystitis glandularis may be manifested at ultrasound as bladder wall cysts or solid papillary masses (see Fig. 9.35C). Because the appearance of these conditions on imaging can be mistaken for malignancy, cystoscopy with biopsy is necessary for diagnostic confirmation.

Causes of Bladder Wall Thickening

FOCAL

Neoplasm
Transitional cell carcinoma
Squamous cell carcinoma
Adenocarcinoma
Lymphoma
Metastases

Infectious/Inflammatory
Tuberculosis (acute)
Schistosomiasis (acute)
Cystitis
Malacoplakia
Cystitis cystica
Cystitis glandularis
Fistula

Medical Diseases
Endometriosis
Amyloidosis

Trauma
Hematoma

DIFFUSE

Neoplasm
Transitional cell carcinoma
Squamous cell carcinoma
Adenocarcinoma

Infectious/Inflammatory
Cystitis
Tuberculosis (chronic)
Schistosomiasis (chronic)

Medical Diseases
Interstitial cystitis
Amyloidosis

Neurogenic Bladder
Detrusor hyperreflexia

Bladder Outlet Obstruction
With muscular hypertrophy

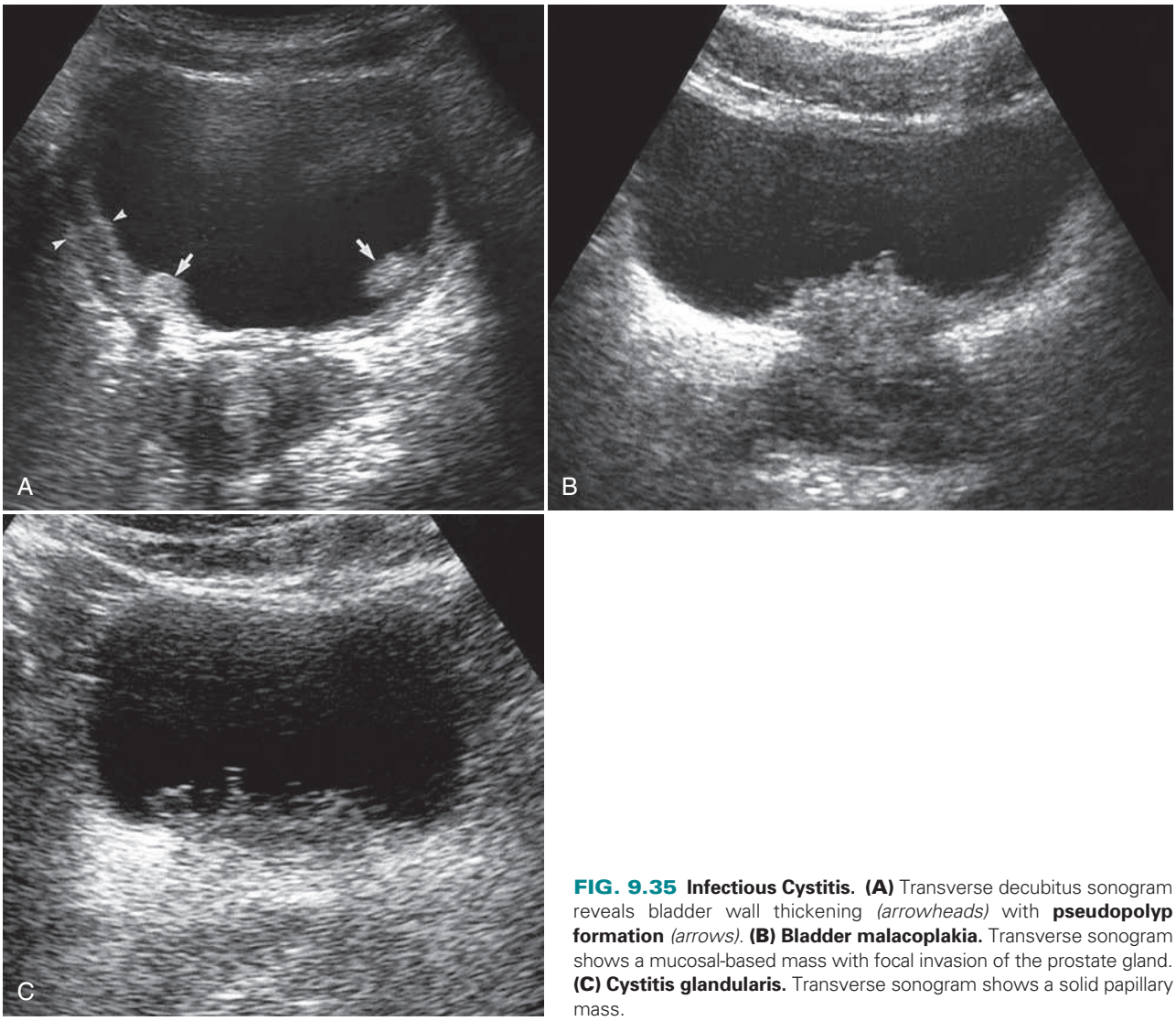

FIG. 9.35 Infectious Cystitis. (A) Transverse decubitus sonogram reveals bladder wall thickening *(arrowheads)* with **pseudopolyp formation** *(arrows).* **(B) Bladder malacoplakia.** Transverse sonogram shows a mucosal-based mass with focal invasion of the prostate gland. **(C) Cystitis glandularis.** Transverse sonogram shows a solid papillary mass.

FISTULAS, STONES (CALCULI), AND CALCIFICATION

Bladder Fistulas

Bladder fistulas can be congenital or acquired. Causes of acquired fistulas include trauma, inflammation, radiation, and neoplasm. Fistula from the bladder to the vagina, gut, skin, uterus, and the ureter may occur. **Vesicovaginal fistulas** are most often related to gynecologic or urologic surgery, bladder carcinoma, and carcinoma of the cervix. **Vesicoenteric** fistulas typically occur as a complication of **diverticulitis** or **Crohn disease. Vesicocutaneous** fistulas result from surgery or trauma. **Vesicouterine** fistulas are a rare complication of cesarean section. **Vesicoureteral** fistulas are also rare and usually occur after hysterectomy.[81]

All these fistulas are difficult to identify directly by sonography because the tracts are often thin and short. Occasionally, linear bands of varying echogenicity may be seen.[82,83] If the bladder communicates with gut, vagina, or skin, an abnormal collection of gas may be seen in the bladder lumen. At ultrasound, this appears as a nondependent linear echogenic focus with distal dirty shadowing. Palpation of the abdomen during scanning may cause gas to percolate through the fistula, enhancing its detection[83] (Fig. 9.36D). For depicting often short vesicovaginal fistulas, color Doppler sonographic flow jets may be shown with diluted microbubble contrast agents in the bladder.[84]

Renal Calculi

Renal stones are common, with a reported prevalence of 12% in the general population.[85] Stone disease increases with advancing age, and white men are most often affected. From 60% to 80% of calculi are composed of calcium.[86] Multiple predisposing conditions, including **dehydration, urinary stasis, hyperuricemia, hyperparathyroidism,** and **hypercalciuria,** may result in renal calculi, but no cause is identified in most patients. **Caliceal**

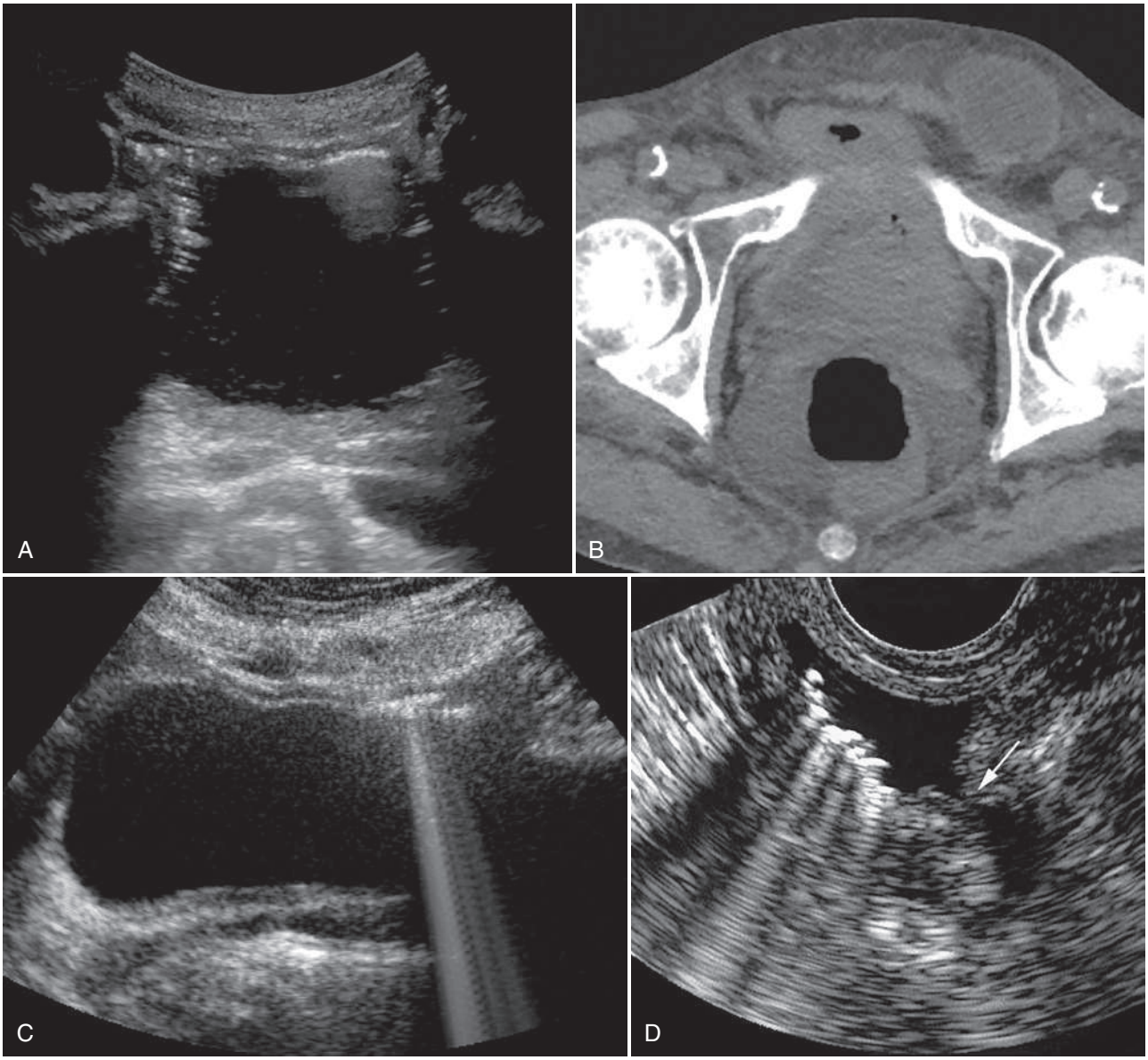

FIG. 9.36 Gas Within the Bladder; Emphysematous Cystitis. (A) Transverse sonogram shows intraluminal gas along left anterior bladder wall. Note "dirty" posterior shadowing. **(B)** Corresponding CT in this patient with confirmed emphysematous cystitis shows mild bladder wall thickening and adjacent gas. (Courtesy of Shweta Bhatt, MD.) **(C)** Iatrogenic air introduced at cystoscopy appears as a nondependent bright echogenic focus with multiple reflection artifacts. **(D)** Enterovesical fistula *(arrow)* showing gas in the bladder as multiple bright echogenic foci on a transvaginal sonogram.

calculi that are nonobstructing are usually asymptomatic. Patients with small caliceal calculi may have gross or microscopic hematuria and may have colic symptoms despite the lack of imaging findings suggestive of obstruction.[87] A calculus that migrates and causes infundibular or UPJ obstruction often results in clinical signs and symptoms of flank pain. If a stone passes into the ureter, the calculus may lodge in three areas of ureteric narrowing: just past the UPJ; where the ureter crosses the iliac vessels; and at the UVJ. The very small diameter of the UVJ (1-5 mm) accounts for the large percentage of calculi that lodge within the distal ureter.[86] Approximately 80% of stones smaller than 5 mm will pass spontaneously.

Renal calculi can be detected using many different imaging modalities, including plain films, tomography, intravenous urography, ultrasound, and unenhanced CT. Sensitivities of 12% to 96% for the ultrasound detection of calculi have been reported. This wide discrepancy is a result of differing definitions (renal or ureteral), composition, and sizes of calculi.[88] Stones greater than 5 mm were detected with 100% sensitivity by ultrasound. Ultrasound with or without plain radiography competes favorably with unenhanced CT in select patients with ureteral colic.[89-91] The sensitivity of ultrasound detection of urinary calculi in patients with acute flank pain is 77% to 93%.[92-94] The 2016 European Association of Urology guidelines for diagnosis and

treatment of urolithiasis list ultrasound as the primary diagnostic imaging tool.[95]

However, noncontrast-enhanced low-dose CT has higher sensitivity (95%) and specificity (97%) for urolithiasis than does ultrasound.[96] Thus many centers use low-dose CT, particularly in patients in whom ureteral stones are suspected or patients whose initial screening ultrasound examination is negative or equivocal but clinical suspicion remains elevated.

Operator technique clearly impacts the ability of ultrasound to depict renal calculi. On sonography, renal calculi are seen as echogenic foci with sharp, distal acoustic shadowing (Fig. 9.37). Even in favorable locations, however, small urinary tract calculi may be difficult to detect if they have a weak posterior acoustic shadow. The trade-off between tissue penetration and resolution should be considered when selecting probe frequency, with appropriate focal zones applied to maximize signature shadowing. Harmonic imaging should also be routinely used, particularly in obese patients. The application of color Doppler may also improve the detection of small, minimally shadowing calculi.[97] Lee et al.[98] demonstrated that most urinary tract stones (83%) show color and power Doppler sonographic **twinkling artifacts,** although the artifact at least partially depends on stone composition[99] (Fig. 9.38). The relevance of this adjunct technique in the screening of patients with potential urinary colic has been questioned, however. In a recent retrospective study, Dillman et al. demonstrated a high (51%) false positive rate for the twinkle artifact when using noncontrast-enhanced CT as a reference standard.[100]

Several features that mimic renal calculi at ultrasound can result in false positive examination results, including **intrarenal gas** (see Fig. 9.23), **renal artery** *calcification* (Fig. 9.39), calcified **sloughed papilla,** calcified **transitional cell tumor, alkaline-encrusted pyelitis, and encrusted ureteral stents.** Although the ultrasound evaluation of the secondary manifestation of an obstructing ureteral calculus—collecting system dilatation—is usually straightforward, pitfalls include (1) evaluation before hydronephrosis develops, leading to a false negative result, and (2) mistaking parapelvic cysts and nonobstructive pyelocaliectasis as hydronephrosis.[101]

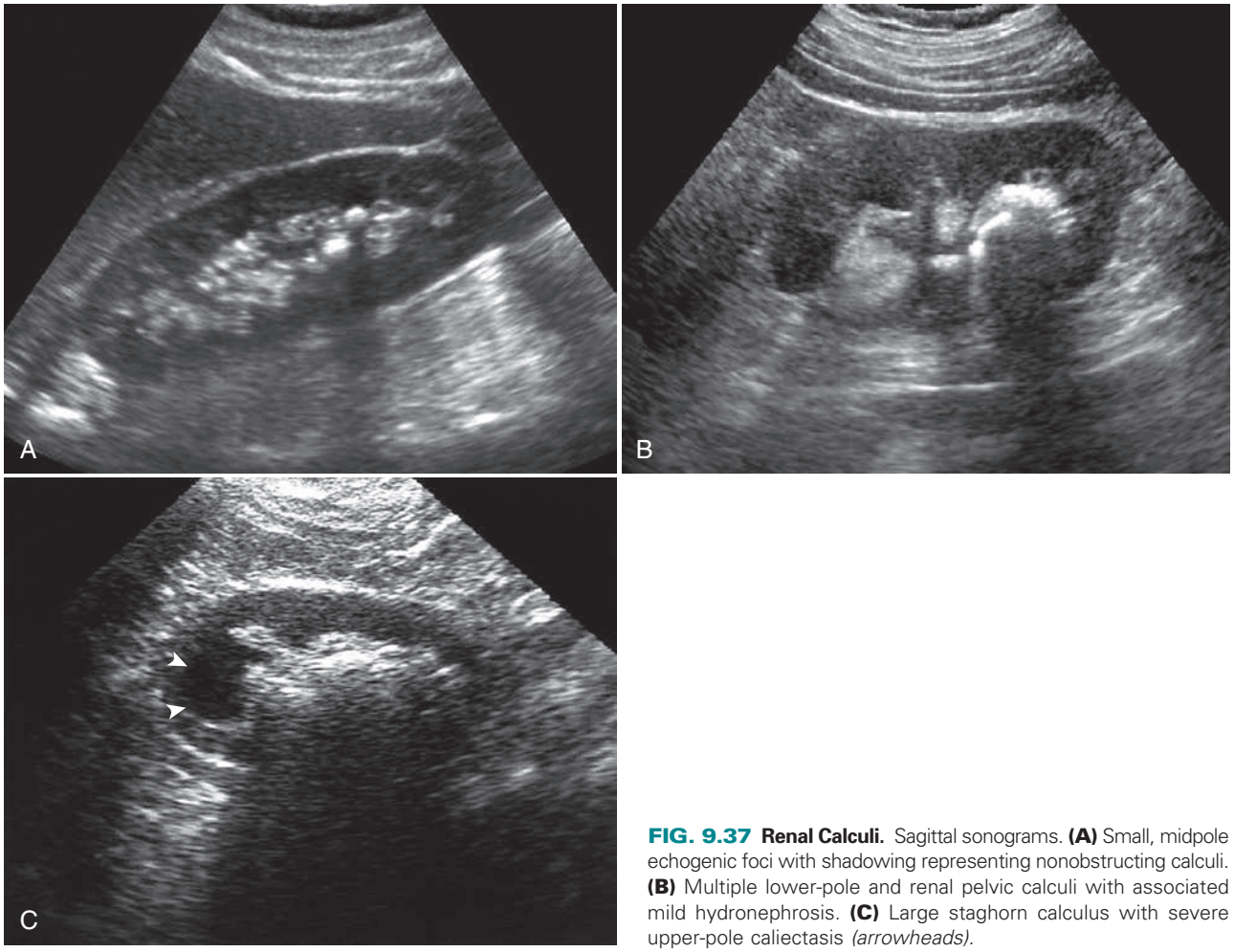

FIG. 9.37 Renal Calculi. Sagittal sonograms. **(A)** Small, midpole echogenic foci with shadowing representing nonobstructing calculi. **(B)** Multiple lower-pole and renal pelvic calculi with associated mild hydronephrosis. **(C)** Large staghorn calculus with severe upper-pole caliectasis *(arrowheads).*

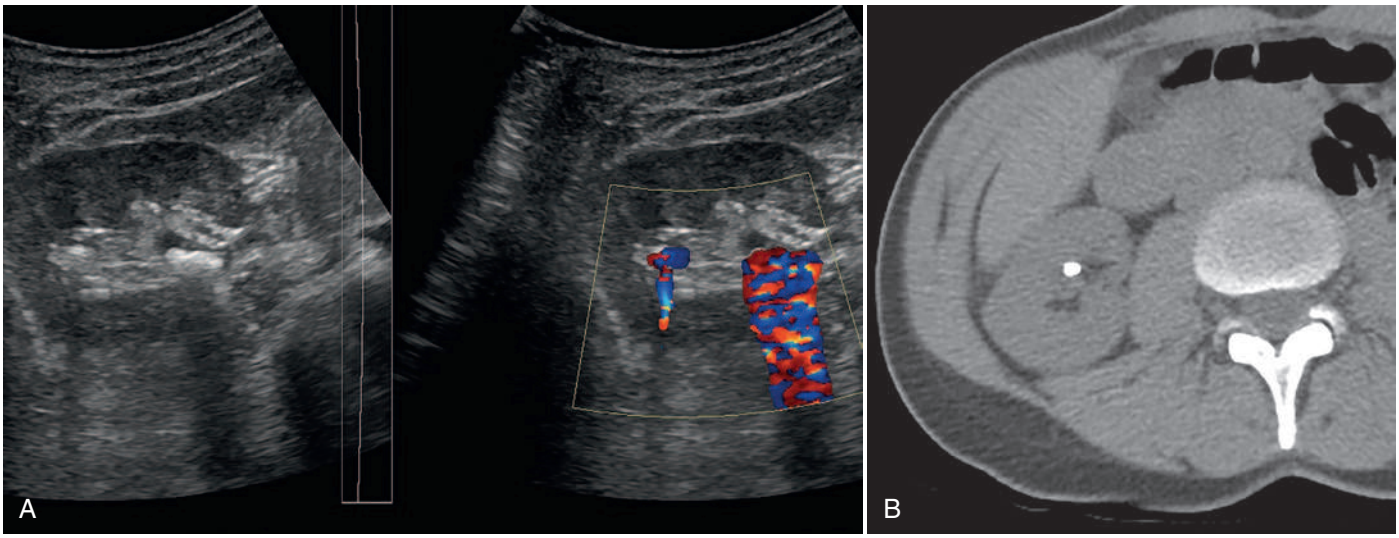

FIG. 9.38 Twinkle Artifacts Indicating Renal Calculi. (A) Transverse sonogram and simultaneous Doppler image show shadowing calculi, posterior shadowing, and color Doppler twinkle artifact. **(B)** A follow-up CT shows the larger calculus. The color Doppler twinkle artifact may sometimes aid in detection of small calculi, although often no corresponding calculi are shown on noncontrast-enhanced CT. The reason for this discrepancy is not clear, although it may be due to relatively large (5-mm) collimation typically used for the CT evaluation of calculi.

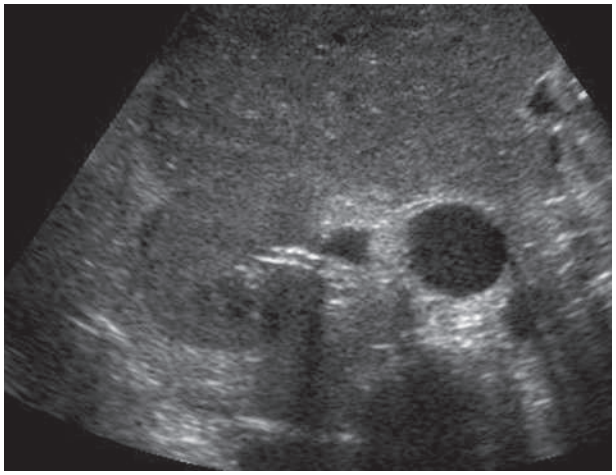

FIG. 9.39 Sonographic Feature Mimicking Renal Calculus. Transverse sonogram shows a linear distal renal artery calcification.

Entities That Mimic Renal Calculi

Intrarenal gas
Renal artery calcification
Calcified sloughed papilla
Calcified transitional cell tumor
Alkaline-encrusted pyelitis
Encrusted calcification of ureteric stent

Ureteral Calculi

The search for ureteral calculi may be particularly difficult at sonography because of overlying bowel gas and the deep retroperitoneal location of the ureter (Fig. 9.40). However, **transvaginal** or **transperineal** scanning aid in detection of distal ureteral calculi that are not seen with a transabdominal suprapubic approach.[83,102,103]

When the ureter is dilated, the distal 3 cm will be seen as a tubular hypoechoic structure entering the bladder obliquely. A stone will be identified as an echogenic focus with sharp, distal acoustic shadowing within the ureteric lumen (Fig. 9.41). There may be associated mucosal edema at the bladder trigone. Transabdominal evaluation of the ureteral orifices for jets is helpful to assess for obstruction (Video 9.1).[104] At gray-scale ultrasound, a stream of low-level echoes can be seen entering the bladder from the ureteral orifice. The jet is likely shown at ultrasound because of both motion and a density difference between the jet and urine in the bladder.[105] Good hydration before the study maximizes the density difference between ureteral and bladder urine and aids in jet visualization.[106]

In addition to gray-scale evaluation, Doppler ultrasound improves detection of ureteric jets. **Color Doppler** allows for simultaneous visualization of both ureteral orifices[104] (Fig. 9.42). Depending on the state of hydration, jet frequency may vary from less than one per minute to continuous flow; however, jets should be symmetric in a healthy individual. Patients with high-grade ureteral obstruction will have either a completely absent jet or a continuous, low-level jet on the symptomatic side. Patients with low-grade obstruction may or may not have **asymmetric jets.**[104] Semiqualitative assessment of relative jet frequency from the affected side[107] may improve diagnostic accuracy, but this technique has not been widely adopted. Thus centers that evaluate ureteral jets with color Doppler use the technique as an adjunct for assessing ureteric obstruction and the possibility of spontaneous ureteral stone passage.

Initial studies suggested that the addition of renal **duplex Doppler** to the gray-scale ultrasound examination would allow diagnosis of both acute and chronic urinary tract obstruction.[108] Several studies indicated that the complex hemodynamics that occur with unrelieved obstruction can be semiquantitatively assessed by measuring intrarenal arterial resistive indices (RI =

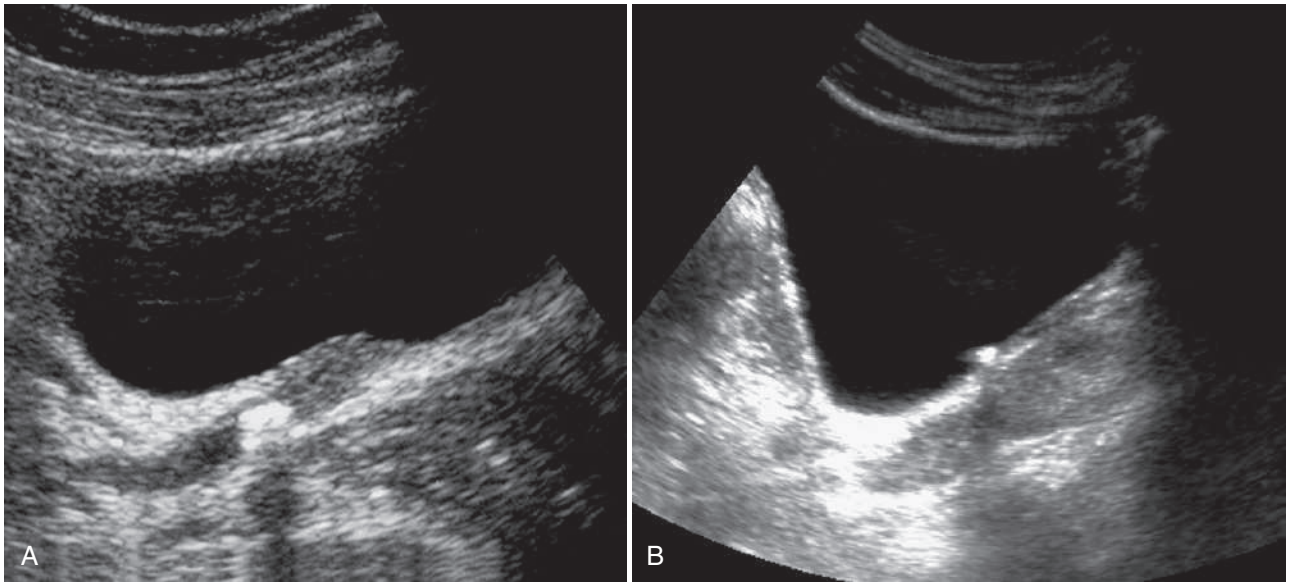

FIG. 9.40 Distal Ureteral Calculi. Sagittal sonograms of the distal ureters in two patients. **(A)** Calculus is 1 cm from the ureterovesical junction (UVJ), with extensive edema of the distal ureteric mucosa. **(B)** Tiny calculus at UVJ with no obvious edema. Note posterior acoustic shadowing.

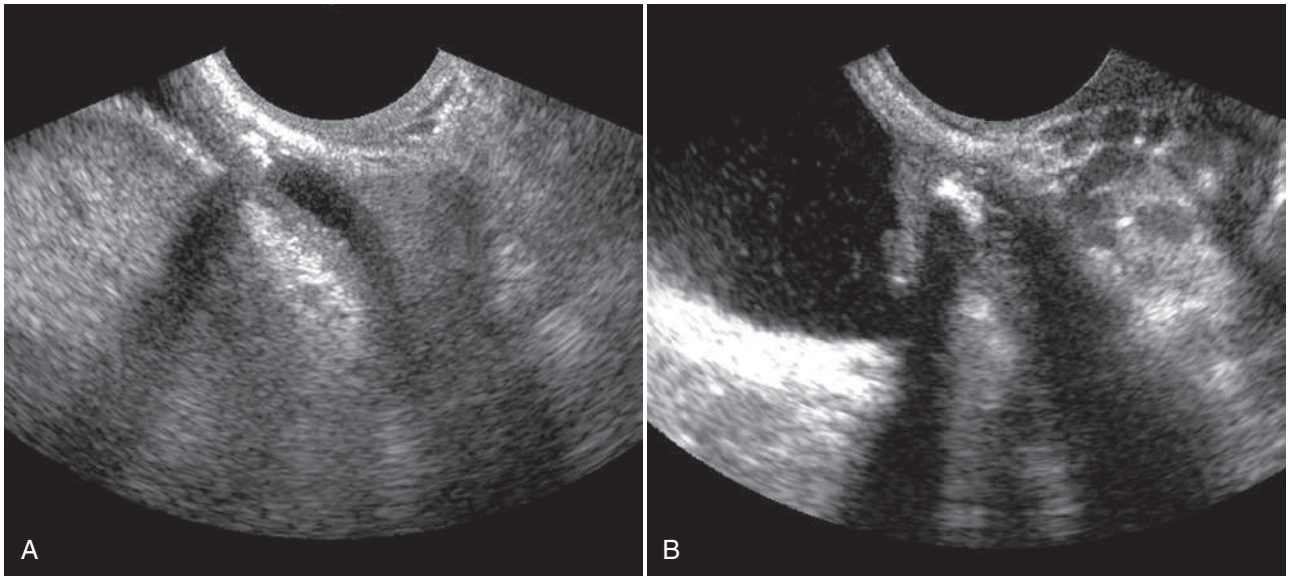

FIG. 9.41 Ureterovesical Calculus. Transvaginal sonograms in two patients show the value of this technique. **(A)** Small calculus obstructs a mildly dilated ureter at UVJ. **(B)** Larger calculus with extensive surrounding ureteric edema.

peak systolic velocity–end diastolic velocity/peak systolic velocity). It is believed that with obstruction, renal pelvic wall tension increases, initially resulting in a short period of prostaglandin-mediated vasodilation.[109] With prolonged obstruction, many hormones, including **renin-angiotensin, kallikrein-kinin,** and **prostaglandin-thromboxane,** reduce vasodilation and produce diffuse vasoconstriction. Geavlete et al.[110] found that if there was an intravesical ureteric jet on the renal colic side associated with arcuate or intralobar RI values of 0.7 or less and difference between renal RI values of 0.06 or less, spontaneous passage of the stone occurred in 71% of cases. Platt et al.[108] used a threshold RI greater than 0.70 to indicate obstruction, noting a difference in RI of 0.08 to 0.1 when comparing the patients' obstructed and non-obstructed kidneys. Initial reports advocating the Doppler assessment of renal obstructive physiology were tempered by a series of less promising studies.[101,109] The RI is largely dependent on tissue/vascular compliance (diminished compliance results in elevated RI, and vice versa) and driving pulse pressures, and thus is not uniformly affected by obstruction.[111-114]

Bladder Calculi

Bladder calculi most often result from either stone migration from the kidney or bladder stasis. Urinary stasis is usually related to a **bladder outlet obstruction, cystocele, neurogenic bladder,**

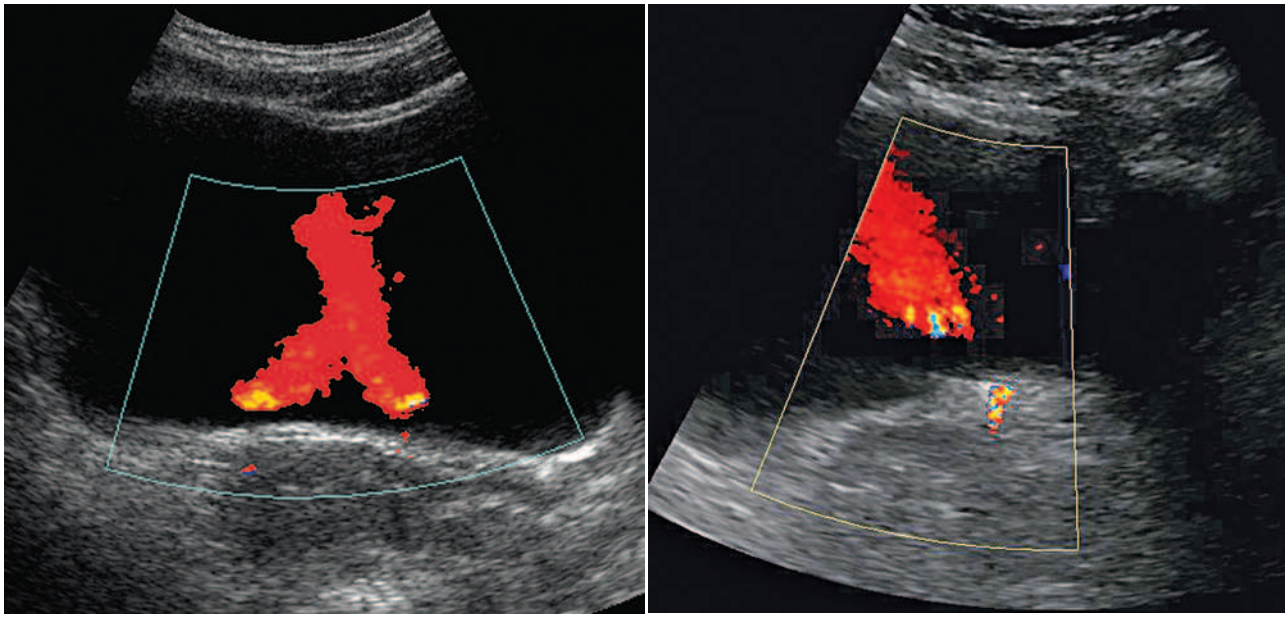

FIG. 9.42 Color Doppler Evaluation of Ureteral Colic. Transverse images of the bladder in two patients. **(A)** Normal symmetrical bilateral ureteral jets. **(B)** Persistent left ureteral jet distal to a partially obstructing left UVJ calculus. Note twinkle artifact posterior to ureteral calculus.

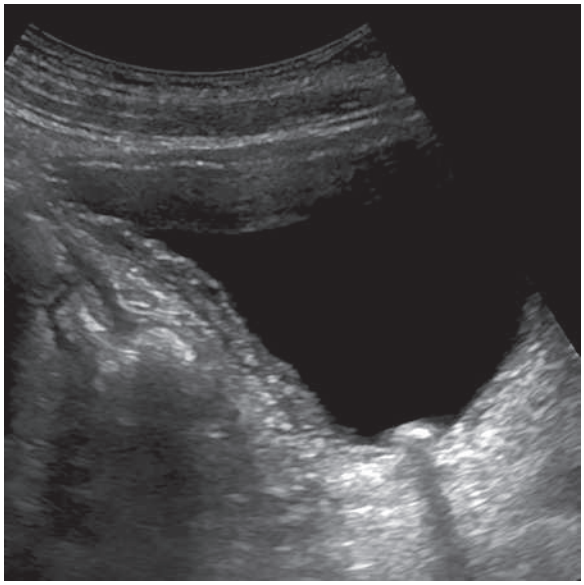

FIG. 9.43 Bladder Calculus. Sagittal sonogram shows a small dependent echogenic focus with posterior sharp acoustic shadowing. Note bladder wall trabeculation.

or a **foreign body in the bladder.** Bladder calculi may be asymptomatic. If symptomatic, patients will complain of bladder pain or foul-smelling urine with or without hematuria. At sonography, a mobile, echogenic mass with distal acoustic shadowing will be seen (Fig. 9.43). If the stone is large, edema of the ureteral orifices and thickening of the bladder wall may be visualized. Occasionally, stones can adhere to the bladder wall because of adjacent inflammation; these calculi are known as **"hanging" bladder stones.**

Nephrocalcinosis

Nephrocalcinosis refers to renal parenchymal calcification. The calcification may be dystrophic or metastatic. With **dystrophic calcification,** there is deposition of calcium in devitalized (ischemic or necrotic) tissue.[115] This type of parenchymal calcification occurs in tumors, abscesses, and hematomas. **Metastatic nephrocalcinosis** occurs most often with hypercalcemic states caused by **hyperparathyroidism, renal tubular acidosis,** and **renal failure.** Metastatic nephrocalcinosis can be further categorized by the location of calcium deposition as cortical or medullary. Causes of **cortical nephrocalcinosis** include **acute cortical necrosis, chronic glomerulonephritis, chronic hypercalcemic states, ethylene glycol poisoning, sickle cell disease,** and **renal transplant rejection.** Causes of **medullary nephrocalcinosis** include **hyperparathyroidism (40%), renal tubular acidosis (20%), medullary sponge kidney, bone metastases, chronic pyelonephritis, Cushing syndrome, hyperthyroidism, malignancy, renal papillary necrosis, sarcoidosis, sickle cell disease, vitamin D excess,** and **Wilson disease.**[115]

The Anderson-Carr-Randall theory of stone progression postulates that the concentration of calcium is high in the fluid around the renal tubules. The calcium is removed by lymphatics, and if the amount exceeds lymphatic capacity, deposits of calcium in the fornical tips and margins of the medulla will result. The ultrasound manifestation of early medullary calcification are nonshadowing echogenic rims surrounding medullary pyramids.[116] However, increased medullary echogenicity can also be caused by medullary sponge kidney[117] (Fig. 9.44); it can be a normal transient finding in neonates.[118] Further calcium deposition results in acoustic shadowing (Fig. 9.45). The calcifications may perforate the calix and form a nidus for further stone growth.[119]

Although the physiology of cortical nephrocalcinosis differs from that of medullary nephrocalcinosis, its ultrasound

manifestations are similar; early cortical calcification may be suggested by increased cortical echogenicity. With progressive calcification, a continuous, shadowing calcified rim develops.

GENITOURINARY TUMORS

Renal Cell Carcinoma

Renal cell carcinoma (RCC) accounts for approximately 3% of all adult malignancies and 86% of all primary malignant renal parenchymal tumors.[120] There is a 2:1 male predominance, and peak age is 50 to 70 years. The cause is unknown, although weak associations with smoking,[121] chemical exposure, asbestosis, obesity, and hypertension have been shown. The vast majority of RCCs are sporadic, but an estimated 4% occur in the context of inherited syndromes.[122,123] These "inherited" RCCs occur at an earlier age, are multifocal and bilateral, and affect men and women equally.[122] **Von Hippel–Lindau (VHL) disease** is the best known inherited RCC syndrome; 24% to 45% of patients who have VHL disease will develop RCC. Most of these lesions are multicentric and bilateral and are clear cell carcinomas.[124-126] Other inherited renal cancer syndromes include **hereditary papillary renal cancer, Birt-Hogg-Dubé syndrome, hereditary leiomyoma RCC, familial renal oncocytoma, hereditary nonpolyposis colon cancer,** and **medullary RCC.** An increased incidence of RCC in patients with **tuberous sclerosis** has also been reported.[123] Another important but nonsyndromic risk factor for RCC is the **acquired cystic kidney disease** that occurs in patients receiving long-term hemodialysis or peritoneal dialysis. The RCCs in these patients are small and hypovascular and tend to be relatively less aggressive.[127,128]

Histologic subtypes of RCC include **clear cell** (70%-75%), **papillary** (15%), **chromophobe** (5%), **oncocytic** (2%-3%), and **collecting duct** or **medullary** (<1%) tumors. Patients with papillary, chromophobe, and oncocytic tumors have a much better prognosis than those with clear cell and collecting duct tumors. Attempts have been made to differentiate histologic subtypes at imaging, largely based on enhanced-CT kinetics, but overlapping patterns have precluded attempts at preoperative imaging classification. However, potentially relevant features may be shown at ultrasound; for example, lack of necrosis and the presence of calcification appear to be associated with a better prognosis (papillary and chromophobe subtypes).[129]

Before the advent of cross-sectional imaging, most patients with RCC presented with advanced metastatic disease. In a 1971 series the **classic diagnostic triad** of flank pain, gross hematuria, and palpable renal mass was seen in 4% to 9% of patients at presentation.[130] Systemic symptoms (e.g., anorexia, weight loss) are common with advanced disease. Manifestations reported secondary to hormone production include **erythrocytosis (erythropoietin), hypercalcemia (parathormone, vitamin D metabolites, prostaglandins), hypokalemia (adrenocorticotropic hormone [ACTH]), galactorrhea (prolactin), hypertension (renin), and gynecomastia (gonadotropin).** RCC metastases to virtually every organ in the body have been described.

FIG. 9.44 Medullary Sponge Kidney. Sagittal sonogram shows markedly increased renal medullary echogenicity ("medullary rings").

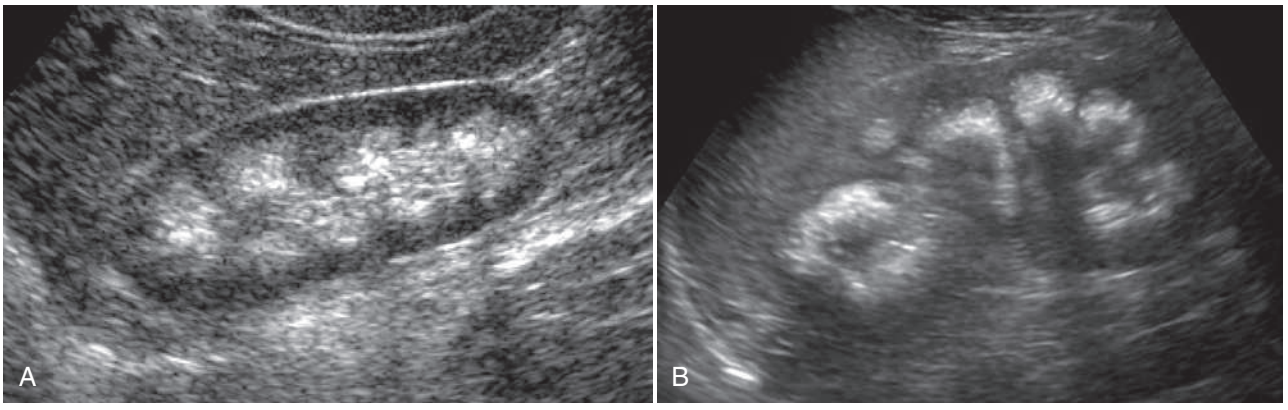

FIG. 9.45 Medullary Nephrocalcinosis in Two Patients. (A) Anderson-Carr-Randall kidney. Sagittal sonogram demonstrates increased echogenicity in a rimlike pattern around all medullary pyramids and several punctate, shadowing calculi. **(B)** Sagittal sonogram shows extensive medullary calcification in a patient with renal tubular acidosis.

Imaging and Treatment Approaches

Before the advent of CT, renal tumors less than 3 cm represented 5% of lesions, whereas now these small lesions represent 9% to 38% of all renal tumors.[131] Jamis-Dow et al.[132] found that CT was more sensitive than ultrasound for the detection of small renal masses (<1.5 cm) and that both ultrasound and CT could equally characterize a mass larger than 1 cm. They also demonstrated that a combination of ultrasound and CT allowed accurate characterization of a lesion larger than 1.0 cm in 95% of cases. With the advent of helical CT, respiratory misregistration and partial volume averaging are minimal; thus nephrographic-phase helical CT scans enable better lesion detection and characterization and typically is sufficient for diagnosis.[133-136]

A particular role of MRI is in the characterization of high-attenuation renal masses.[137] Most centers, however, still reserve renal MRI for patients with (1) an allergy to iodinated contrast, (2) CT-indeterminate renal masses, or (3) extent of vascular involvement inadequately determined by ultrasound and CT. Previously, renal MRI was also performed to assess lesional enhancement in patients with renal insufficiency. However, recognition of the central role of gadolinium in the development of nephrogenic systemic fibrosis highlighted the potential risks in these patients.[138] Thus ultrasound has again assumed a preeminent role for mass characterization in patients with renal insufficiency at risk for nephropathy after iodinated contrast exposure at CT or for nephrogenic systemic fibrosis after gadolinium exposure at MRI.

Contrast-enhanced ultrasound (CEUS) also holds promise for assessment of renal lesions. Quaia et al. compared sonography without contrast material versus CEUS and CT for the characterization of 40 complex cystic renal masses and found that the diagnostic accuracy of CEUS (80%-83%) was better than that of nonconstrast sonography (30%) and CT (63%-75%) for all readers.[139] In another European study of 143 lesions, CEUS was shown to predict malignancy with 97% sensitivity, 45% specificity, and 90% accuracy. CEUS was superior to CT in the staging and characterization of RCC, as well as in the subgroup of patients with cystic lesions.[140]

The increased detection of small, incidental lesions and better understanding of the natural history of these tumors have led to less aggressive approaches to RCCs. The traditional surgical approach, radical nephrectomy, is now usually reserved for larger, central lesions. The greater likelihood of small, benign, solid lesions in older patients[141] and the limited metastatic potential of small (<3 cm) lesions[142] have prompted a "watchful waiting" approach, particularly in older or ill patients.[143] Nephron-sparing surgery (open/laparoscopic partial nephrectomy, laparoscopic cryoablation, percutaneous radiofrequency ablation/cryoablation) may be offered to younger patients or older patients unwilling or unable to undergo imaging surveillance (Fig. 9.46). Primary/secondary efficacy and long-term survival rates with these techniques are likely comparable to those resulting from traditional nephrectomy.[144] Gervais et al.[145] found that radiofrequency ablation of exophytic RCCs up to 5 cm in size can be performed successfully. Tumors with a component in the renal sinus are more difficult to treat. Retrospective studies have suggested that cryoablation may be the preferred ablation modality in this setting[146] although a recent large meta-analysis has indicated little difference in complication rates between techniques.[147]

Sonographic Appearance

Most RCCs are solid. Tumors may be hypoechoic, isoechoic, or hyperechoic (Fig. 9.47, Video 9.2). An early ultrasound series reported that the majority of RCCs are isoechoic (86%), whereas the minority is hypoechoic (10%) or echogenic (4%).[148] Later series noted the ultrasound appearance of the smaller RCCs that are now often depicted with cross-sectional imaging. These smaller RCCs (<3 cm) are often echogenic compared with surrounding

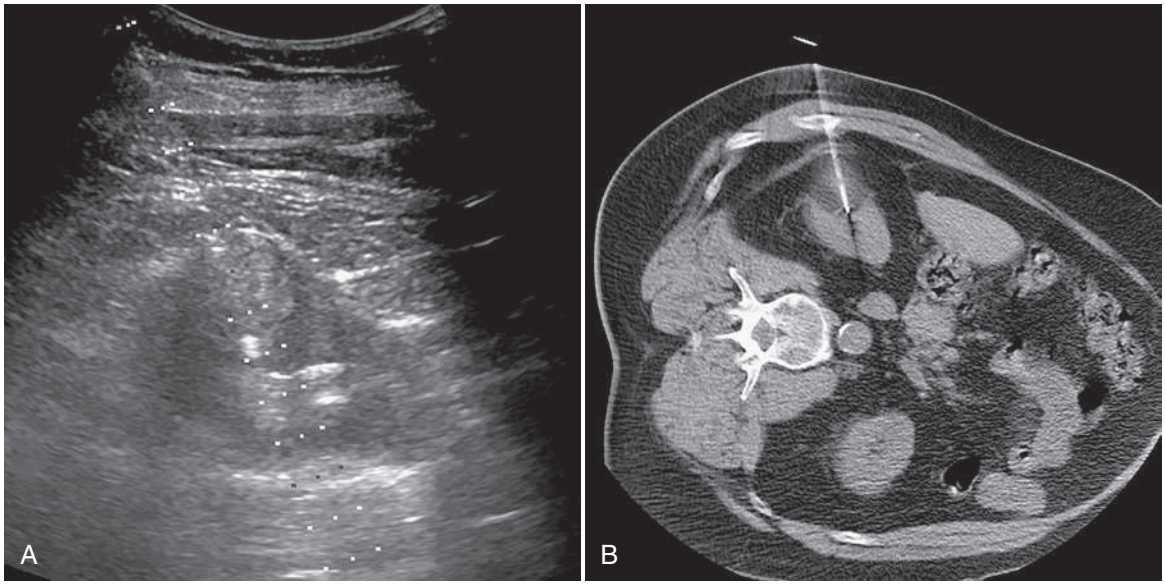

FIG. 9.46. Ultrasound-Guided Cryoablation of Renal Cell Carcinoma. (A) Transverse sonogram shows placement of a cryoablation probe within the posterior aspect of a small (<3 cm) echogenic renal cell carcinoma. A prior ultrasound-guided biopsy had confirmed clear cell carcinoma. **(B)** Corresponding noncontrast-enhanced CT shows the ablation zone as a low attenuation "ice-ball." Ultrasound may facilitate renal biopsy and probe placement, although the ablation is monitored under CT.

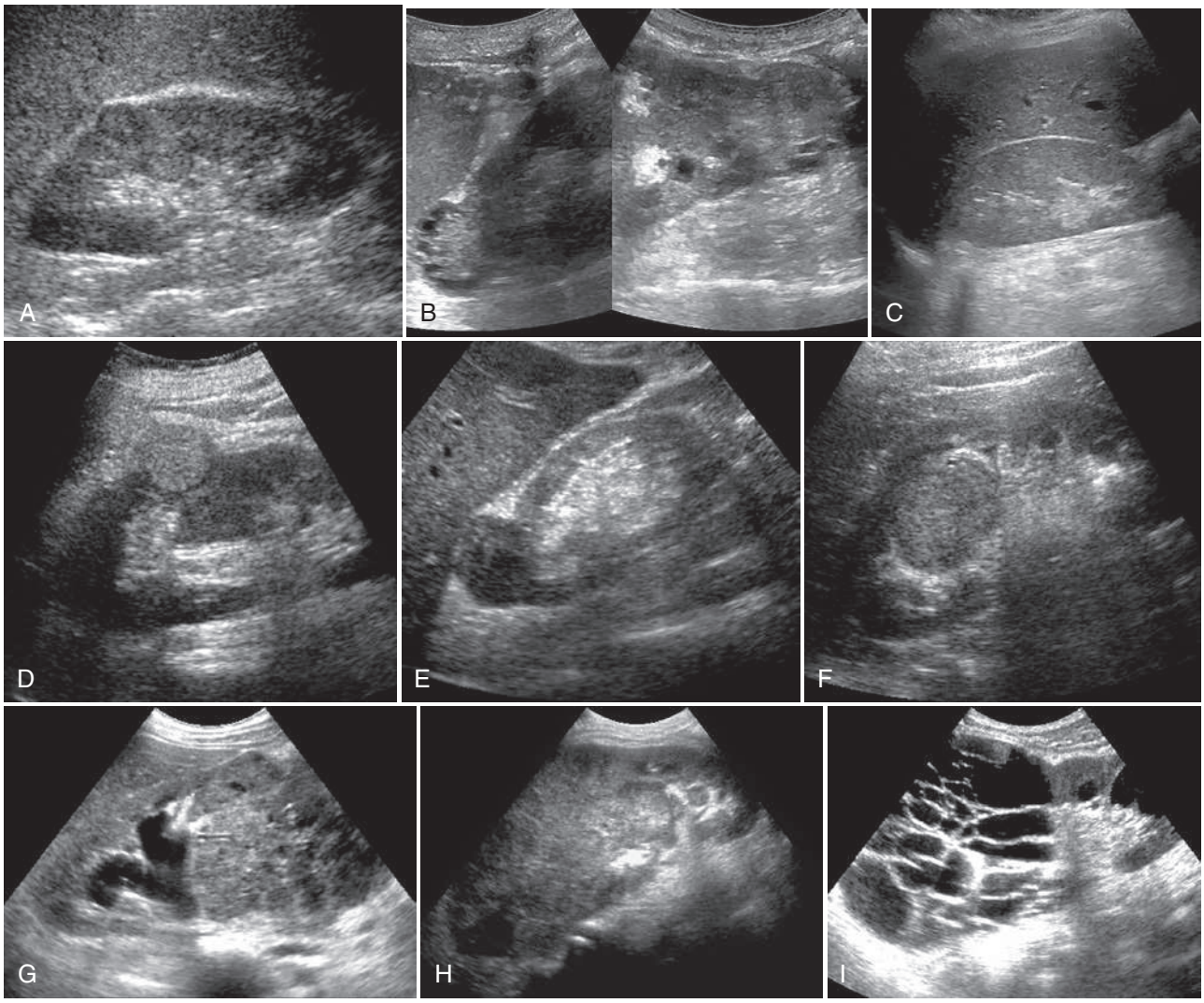

FIG. 9.47 Sonographic Appearances of Renal Cell Carcinoma on Sagittal Sonograms. (A) Tiny incidental hypoechoic tumor. **(B)** Exophytic echogenic upper-pole tumor with peripheral cystic spaces and larger uniform echogenic lower-pole tumor in same patient. **(C)** Small echogenic nodule simulating an angiomyolipoma. **(D)** Exophytic echogenic midpole renal mass. **(E)** Exophytic hypoechoic upper-pole renal mass. **(F)** Large central renal sinus mass with no associated caliectasis. **(G)** Large solid heterogeneous mass in the lower pole of the kidney compressing the renal pelvis with upper-pole caliectasis. **(H)** Large infiltrative renal mass with maintenance of reniform shape. **(I)** Large upper-pole cystic mass showing numerous thick internal septations. See also Video 9.2.

renal parenchyma; Forman et al.[149] found that 77% of smaller RCCs were echogenic, and Yamashita et al.[150,151] reported 61% as echogenic.

The small, echogenic RCC may be difficult to differentiate from a benign angiomyolipoma (AML) at ultrasound. Yamashita et al.[151] emphasized the overlap in RCC/AML imaging appearance. A thin, hypoechoic rim, thought to be a pseudocapsule at histology, was reported in 84% of RCCs and no AMLs. Weak shadowing posterior to AMLs and hypoechoic halos or cystic spaces in RCCs were also thought to be characteristic features.[152] Nonetheless, although increased echogenicity of a solid renal lesion has high sensitivity for AML (99%), it is not specific. If a lesion is of a size that would lead to a change in management, echogenic renal lesions should be further assessed with either MRI or CT.[153]

The exact pathologic basis for the hyperechoic appearance of RCC is not understood, but increased echogenicity has been reported in RCCs with papillary, tubular, or microcystic architecture and in tumors with minute calcification, necrosis, cystic degeneration, or fibrosis.[131] Macroscopic calcification are identified in 8% to 18% of RCCs. This calcification may be punctate, curvilinear, diffuse (rare), central, or peripheral.[154-158] Daniel et al.[157] showed that central calcification was associated with a malignant tumor in 87% of cases. When posterior rim shadowing or diffuse calcification make it impossible to characterize a renal lesion by ultrasound, CT is needed to identify additional features of malignancy (e.g., enhancement of associated soft tissue mass).[159]

Papillary tumors account for 15% of all RCCs.[129,160] The papillary type is characterized by slower growth, a lower stage at presentation, and a better prognosis.[161] Papillary tumors also tend to be hypoechoic or isoechoic, although no consistent sonographic pattern exists, because some may also be hyperechoic.[160]

From 5% to 7% of all RCCs are **cystic** tumors.[162] Four histologic growth patterns within cystic RCCs have been described: multilocular, unilocular, necrotic (cystic necrosis), and tumors originating in a simple cyst[163] (Figs. 9.48 and 9.49). Recognition of subtypes have clinical significance because the multilocular and unilocular subtypes are less aggressive.[162] At sonography, **multilocular** cystic RCC appears as a cystic mass with internal septations. These septations may be thick (>2 mm), nodular, and may contain calcification (see Fig. 9.47). The characteristic ultrasound appearance of a **unilocular** cystic RCC is a debris-filled mass with thick, irregular walls that may be calcified. The appearance of **necrotic** RCCs depends on the degree of tumor necrosis. Tumors originating in a **simple cyst** are rare (excluding VHL patients). At ultrasound, a mural tumor nodule will be found at the base of a simple cyst. A combined approach with helical CT and ultrasound allows accurate characterization of the internal nature of most cystic renal lesions.[164]

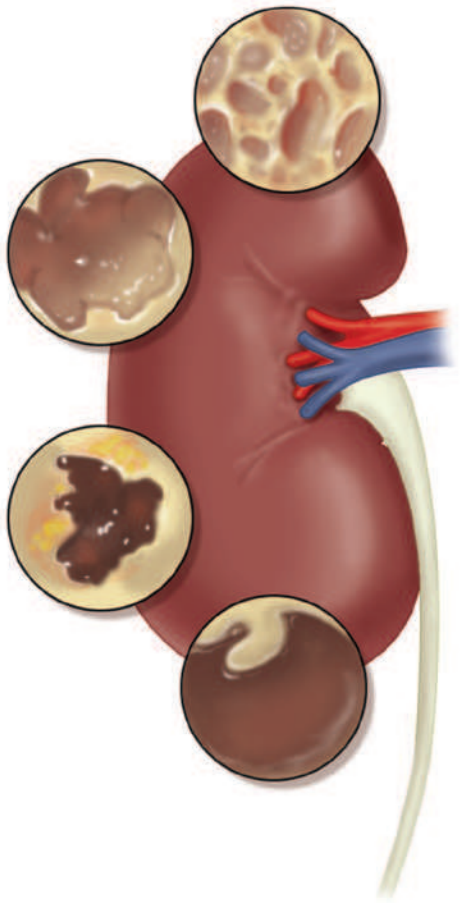

FIG. 9.48 Cystic Growth Patterns of Renal Cell Carcinoma. *Upper pole,* Multilocular; *upper lateral,* unilocular; *lower lateral,* cystic necrosis; *lower pole,* origin in the wall of a simple cyst. (With permission from Yamashita Y, Watanabe O, Miyazaki H, et al. Cystic renal cell carcinoma. Acta Radiol. 1994;35:19-24.[162])

The use of **Doppler ultrasound**[165] for detection of tumor vascularity has been reported. Most malignant renal tumors (70%-83%) have Doppler shift frequency of 2.5 kHz.[165-169] Similar changes may be noted with inflammatory masses; however, patients with renal infection should be clinically apparent. Unfortunately, the absence of high-frequency Doppler shift does not exclude malignancy.[168] Confirmation of blood flow within malignant solid and cystic renal tumors has also been performed with microbubble contrast agents and low–mechanical index pulse inversion sonography. Criteria for neovascularity used with CT or MRI for mass characterization—septal and nodular enhancement—can also be used with stable, second-generation ultrasound contrast agents[170,171] (Fig. 9.50). However, lack of US Food and Drug Administration approval, reimbursement issues, and logistics associated with technologist/radiologist-intensive, contrast-enhanced sonography protocols have hindered widespread adoption of this technique.

Biopsy and Prognosis

Recent pathologic and biopsy series of small (<3 cm), solid enhancing renal masses have shown that a surprising number of these lesions are benign (i.e., **AML, oncocytoma, metanephric adenoma**). Moreover, image-directed needle biopsy (aspiration or core) has been shown to be a relatively safe and usually conclusive procedure.[172-176] Further advances in immunohistology and greater acceptance of percutaneous ablation techniques

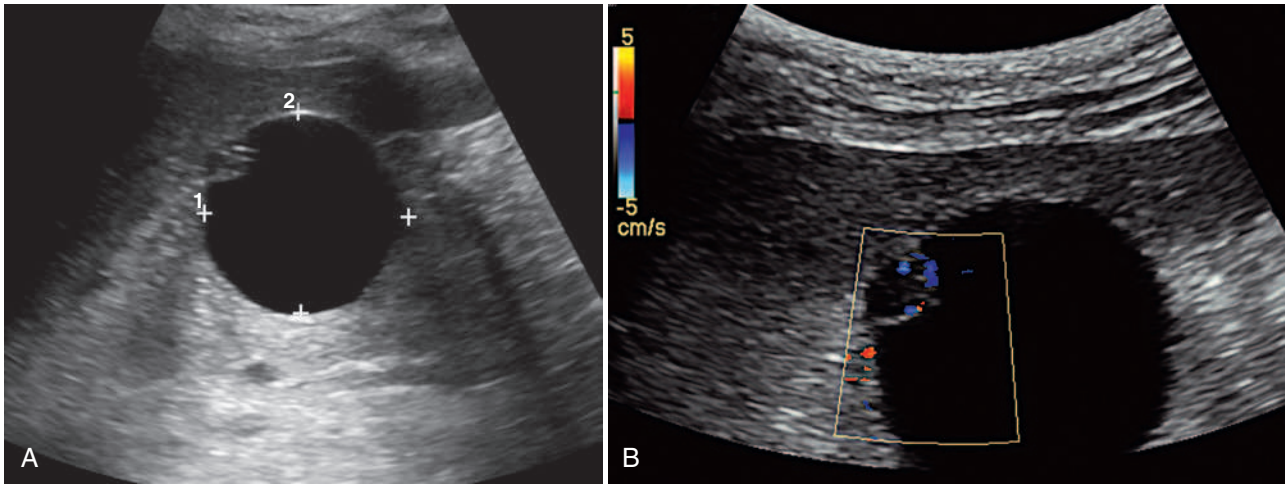

FIG. 9.49 Renal Cell Carcinoma Within Cyst. (A) Complex cyst with mural nodule. **(B)** Color Doppler shows flow within septation. (Courtesy of Vikram Dogra, MD.)

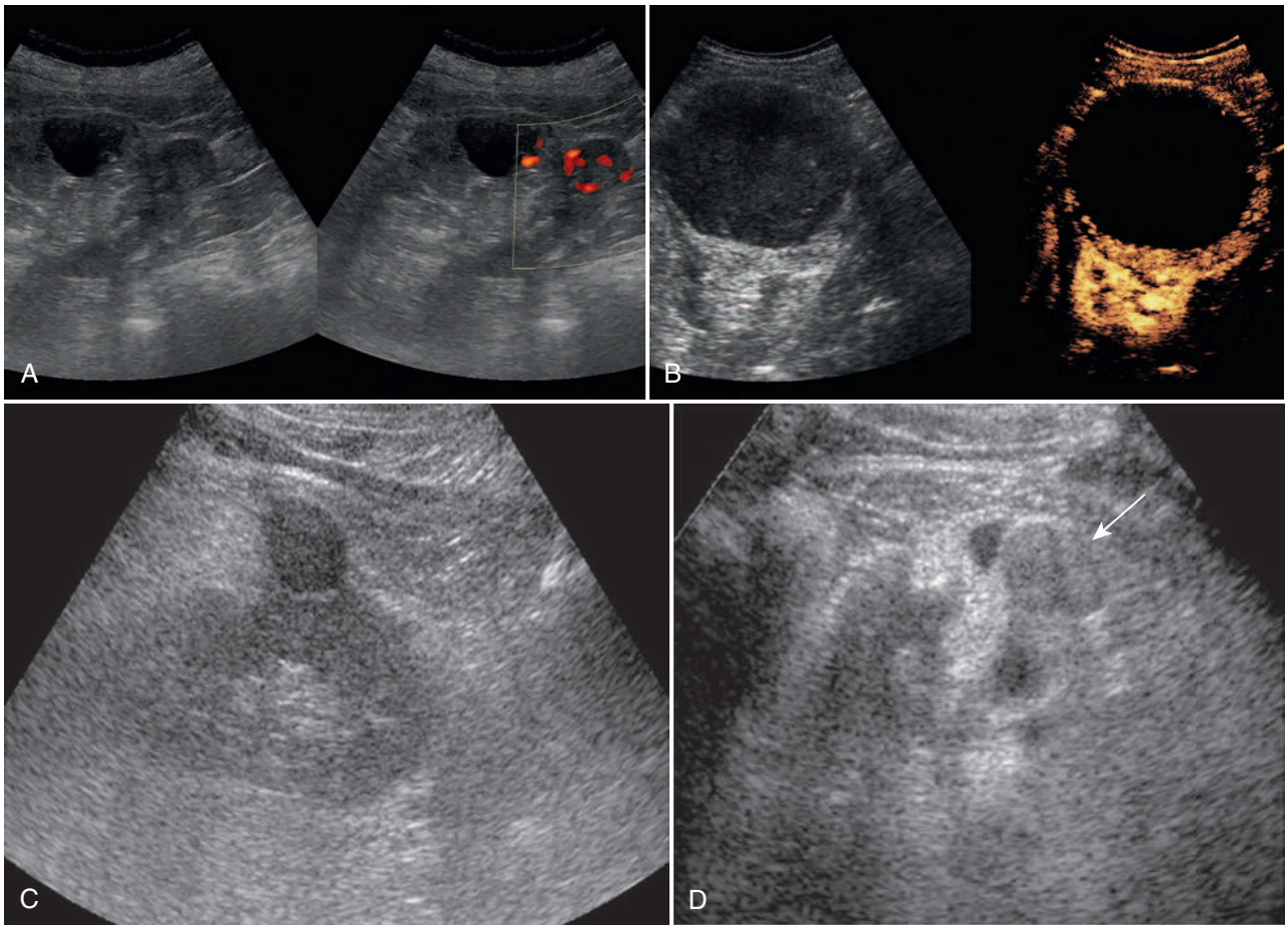

FIG. 9.50 Value of Color Doppler and Microbubble-Enhanced Sonography for Determining Vascularity of a Renal Mass. (A) Sagittal sonogram shows an isoechoic lower-pole mass and an adjacent cyst; the simultaneous power Doppler image shows flow within the mass (biopsy confirmed renal cell carcinoma). **(B)** Sonogram of a patient with renal failure shows a large complex cyst containing low-level echoes. The simultaneous microbubble enhanced image shows no enhancement of the center of the mass, but it confirms enhancement of the nodular, thick wall of a cystic renal cell carcinoma. **(C)** Baseline transverse sonogram of exophytic hypoechoic midpole renal mass. **(D)** Nephrographic phase image shows enhancement of both normal kidney and relatively hypovascular renal cell carcinoma *(arrow)*. (**C** and **D** courtesy of Ed Grant, MD.)

continue to increase the role of imaging-directed, particularly ultrasound-guided, renal mass biopsy[177] (Fig. 9.51).

For patients with imaging findings (or biopsy results) definitive for RCC, the **stage at diagnosis** directly impacts prognosis. The Robson staging classification for RCC is the following:

I: Tumor confined within renal capsule
II: Tumor invasion of perinephric fat
III: Tumor involvement of regional lymph nodes or venous structures
IV: Invasion of adjacent organs or distant metastases

Five-year survival rates for patients with Robson stages I, II, III, and IV are 67%, 51%, 33.5%, and 13.5%, respectively.[178] Patients with stage I and stage II disease are treated surgically (partial or radical nephrectomy). Patients with stage III disease, with extensive metastatic lymphadenopathy, are often treated palliatively. Patients with stage III disease and tumor thrombus are treated with radical nephrectomy and thrombectomy. Patients with stage IV disease usually receive palliative treatment only,[179] although greater understanding of the molecular biology of RCC has led to clinical trials of novel, small-molecule-targeted inhibitors and monoclonal antibodies.[180]

Pitfalls in Interpretation

Ultrasound is inferior to CT and MRI for staging RCC. Unfortunately, obesity and overlying bowel gas often make it difficult to assess for lymphadenopathy or vascular involvement. In thin patients and in those with minimal bowel gas, however, the renal veins and retroperitoneum can be well assessed with ultrasound. Sonography is excellent for assessment of the intrahepatic IVC and for determination of the cephalad extent of venous tumor thrombus with RCC (Fig. 9.52). Habboub et al.[181] found the accuracy of detecting renal vein and IVC involvement at sonography was 64% and 93%, respectively. The addition of color Doppler sonography improved accuracy for diagnosing both renal vein and IVC thrombus to 87% and 100%, respectively. It is crucial to determine the location and extent of vascular tumor thrombus to plan the surgical approach.

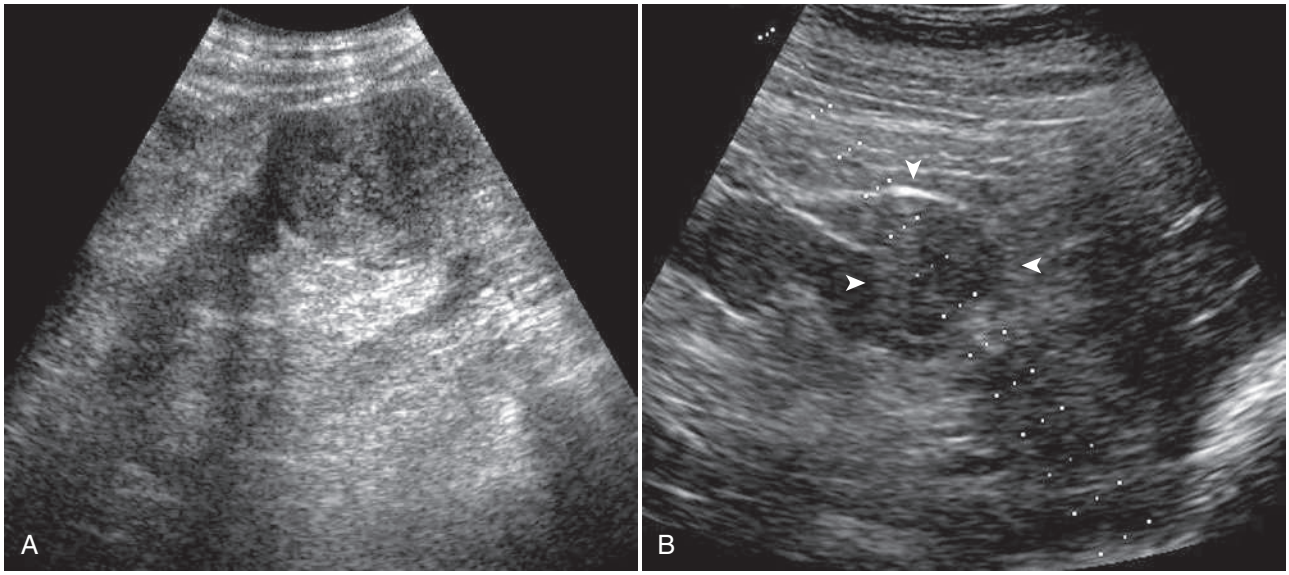

FIG. 9.51 Renal Oncocytoma. (A) Sagittal sonogram shows a large, isoechoic, partially exophytic renal mass that cannot be differentiated from renal cell carcinoma. **(B)** Ultrasound-guided biopsy of an isoechoic renal lesion *(arrowheads)* in another patient, performed before possible cryoablation, confirms an oncocytoma.

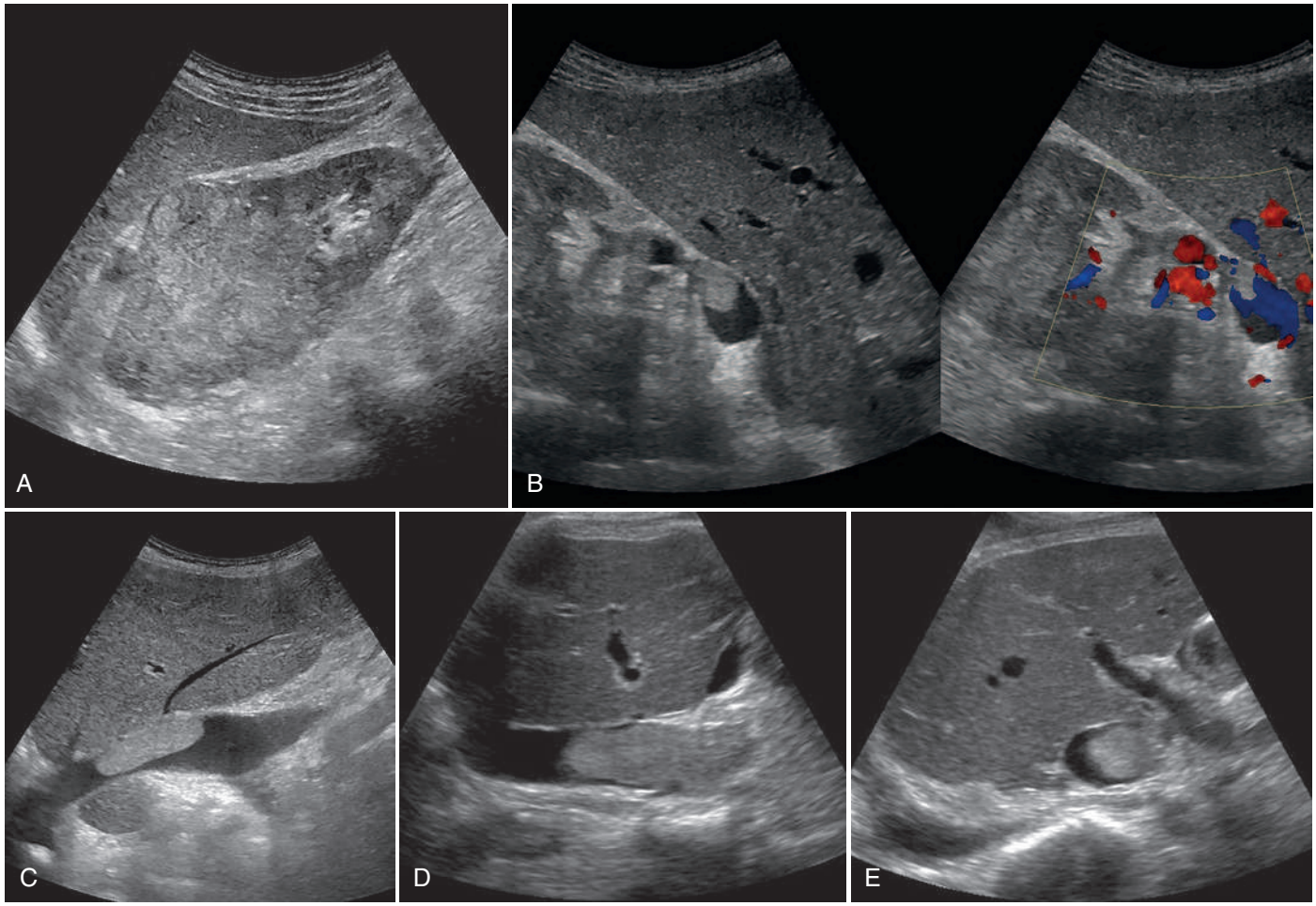

FIG. 9.52 Venous Thrombosis With Renal Cell Carcinoma. (A) Sagittal sonogram shows a huge infiltrating right upper-pole renal cell carcinoma. **(B)** Transverse ultrasound and simultaneous color Doppler image shows nonocclusive but expansile malignant thrombus within right renal vein and inferior vena cava (IVC). **(C)** Sagittal ultrasound of the same patient shows echogenic, nonocclusive thrombus within suprarenal IVC. Clot extends to 1 cm below the hepatic venous confluence. **(D)** Sagittal sonogram in another patient shows expansile, malignant thrombus within retrohepatic IVC. **(E)** Transverse sonogram in the same patient in D showing partially adherent malignant thrombus in the IVC.

Transitional Cell Carcinoma

Transitional cell carcinoma (TCC) of the renal pelvis accounts for 7% of all primary renal tumors.[182] **Renal** TCC is two to three times more common than **ureteral** neoplasms. **Bladder** TCC, because of its large surface area, is 50 times more common than renal pelvic TCC.[183] The multifocal and bilateral nature of TCC requires accurate diagnosis and staging to allow appropriate surgical planning. Yousem et al.[184] reviewed 645 cases of TCC of the bladder, ureter, and kidney and found that 3.9% of patients with bladder cancer developed an upper tract lesion (mean, within 61 months); 13% of patients with ureteral TCC and 11% of those with renal TCC developed **metachronous tumors** (mean, within 28 and 22 months, respectively). **Synchronous TCC** was present in 2% of patients with bladder TCC, 39% with ureteral TCC, and 24% with renal TCC. Upper tract disease surveillance may be performed by retrograde pyelography, urine cytology, CT urography, and/or magnetic resonance urography.[185]

TCCs may be papillary or nonpapillary. **Papillary** TCCs are exophytic polypoid lesions attached to the mucosa by a stalk. This type of tumor tends to be lower grade at presentation; polypoid TCC typically infiltrates slowly and metastasizes late in the disease. **Nonpapillary,** sessile TCCs present as nodular or flat tumors; the mucosal thickening that is a hallmark of sessile TCC may be difficult to depict even at CT. These tumors are usually high grade and infiltrating.[183]

Renal Tumors

Transitional cell tumors of the kidney are more common in men than women (4:1). Renal TCC is typically seen in older patients; the mean age at diagnosis is 65 years.[183] About 75% of patients with renal pelvic tumors present with gross or microscopic hematuria; 25% have flank pain. Renal TCC is discovered incidentally in less than 5% of patients.[183]

Unfortunately, the sonographic assessment of the **renal sinus** poses unique problems and is a challenge to evaluate for pathologic processes because of its variable appearance. Fat within the renal sinus can appear as a hypoechoic mass and can simulate a solid TCC (Fig. 9.53). In uncertain cases, confirmation with CT

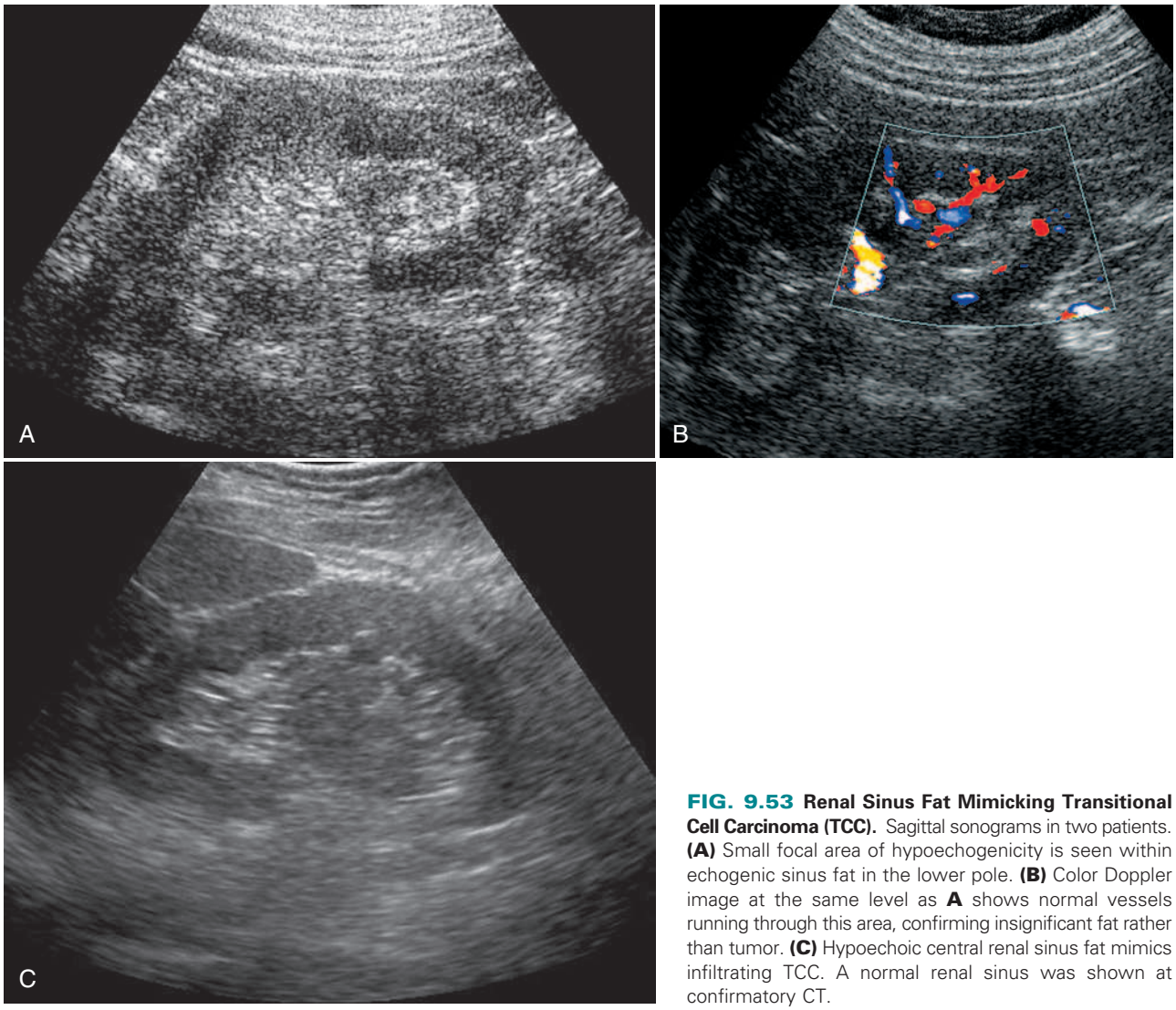

FIG. 9.53 Renal Sinus Fat Mimicking Transitional Cell Carcinoma (TCC). Sagittal sonograms in two patients. **(A)** Small focal area of hypoechogenicity is seen within echogenic sinus fat in the lower pole. **(B)** Color Doppler image at the same level as **A** shows normal vessels running through this area, confirming insignificant fat rather than tumor. **(C)** Hypoechoic central renal sinus fat mimics infiltrating TCC. A normal renal sinus was shown at confirmatory CT.

urography is recommended to exclude neoplasm, particularly in patients with hematuria (Fig. 9.54).

The sonographic appearance of renal TCC is variable and depends on the morphology of the lesion (papillary, nonpapillary, or infiltrative), location, size, and the presence or absence of hydronephrosis (Fig. 9.55). Small, nonobstructing tumors may be impossible to visualize at ultrasound. With growth, **papillary tumors** will be seen as discrete, solid, central, hypoechoic renal sinus masses with or without associated proximal caliectasis (Fig. 9.56). The differential diagnosis includes **blood clots, sloughed papillae, and fungus balls.**

Tumor infiltration within the renal pelvis or renal parenchyma may be subtle. Findings suggestive of infiltrating TCC are distortion and enlargement of the kidney and maintenance of an overall reniform shape (Fig. 9.56). Sessile lesions are particularly difficult to image directly by ultrasound, but the secondary finding of an obstructing lesion (caliectasis, pelviectasis) is usually easily depicted. A small subset of both sessile and papillary TCCs may have dystrophic calcifications, which makes it difficult to differentiate tumor from a sloughed, calcified papilla.[186] TCC rarely invades the renal vein.[187]

Ureteral Tumors

TCC of the ureter accounts for 1% to 6% of all upper urinary tract cancers.[183,188] Men are affected more often than women (3:1). As with renal TCC, ureteral lesions are usually identified in older patients; peak prevalence of ureteral TCC is between the fifth and seventh decades.[183] The majority of tumors are found in the lower third of the ureter (70%-75%).[183,188] About 60% of ureteral TCCs are papillary and 40% nonpapillary.[183] The most common symptoms are hematuria, frequency, dysuria, and pain.[188] The traditional imaging modalities of choice for evaluation of ureteral TCC have included intravenous urography or retrograde pyelography, but the advantages of multidetector CT urography (ability to detect and stage even small urothelial lesions) have been documented.[189,190] At sonography, hydronephrosis and hydroureter are seen, and occasionally a solid ureteral mass may be shown.[188]

Bladder Tumors

TCC of the bladder is a common malignant tumor. Bladder TCCs occur more often in men (3:1), with a peak incidence in

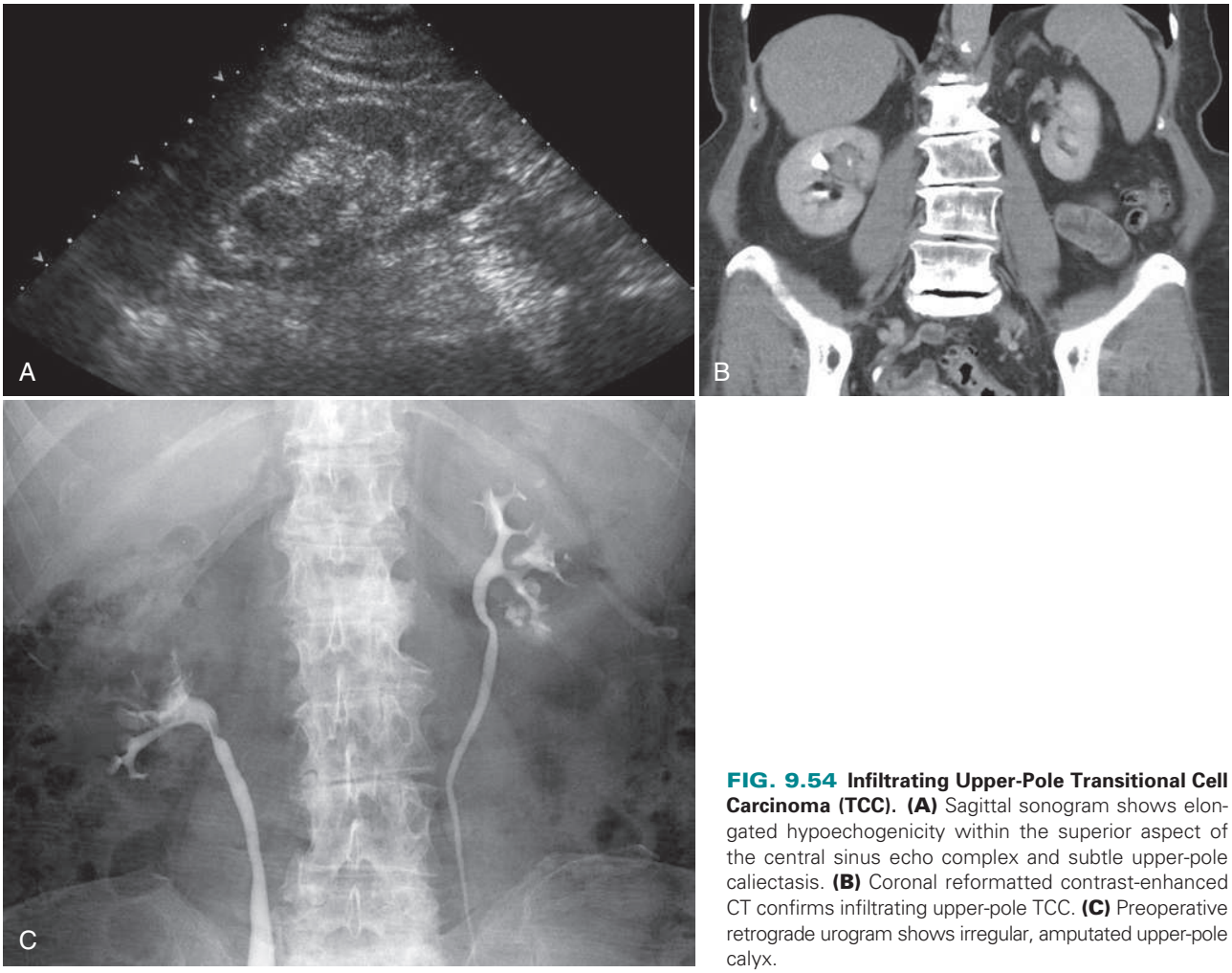

FIG. 9.54 Infiltrating Upper-Pole Transitional Cell Carcinoma (TCC). (A) Sagittal sonogram shows elongated hypoechogenicity within the superior aspect of the central sinus echo complex and subtle upper-pole caliectasis. **(B)** Coronal reformatted contrast-enhanced CT confirms infiltrating upper-pole TCC. **(C)** Preoperative retrograde urogram shows irregular, amputated upper-pole calyx.

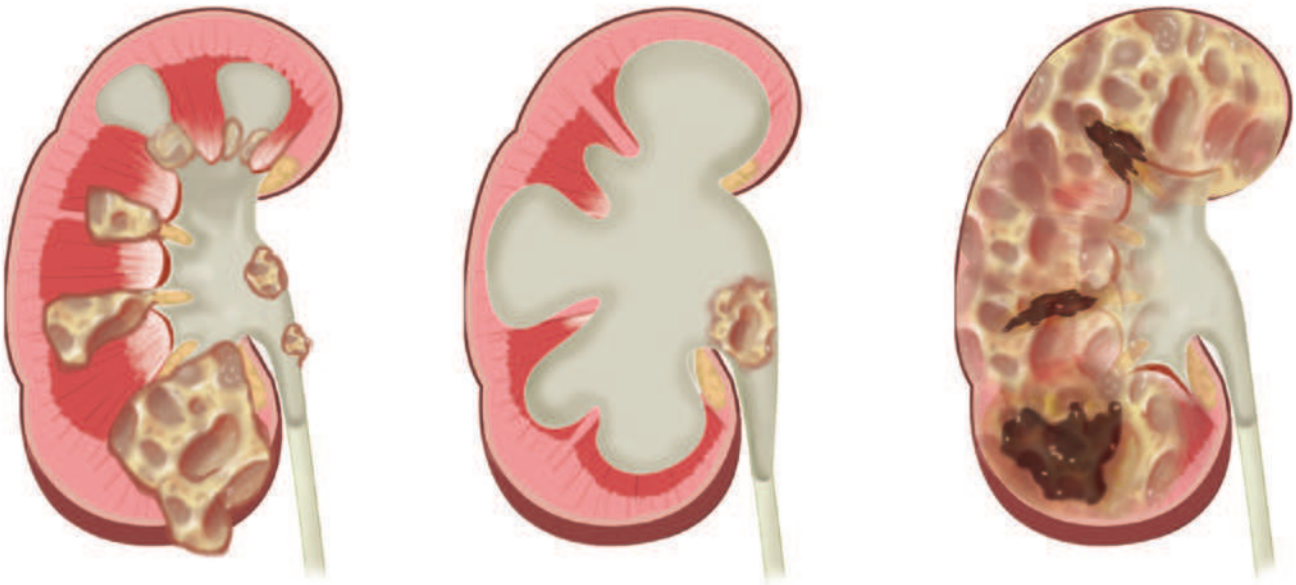

FIG. 9.55 **Morphologic Growth Patterns of Renal Transitional Cell Carcinoma.**

the sixth and seventh decades. They occur most frequently at the trigone and along the lateral and posterior walls of the bladder. Approximately 70% of bladder cancers are superficial; the remaining 30% are invasive. Patients typically present with hematuria, although they may also complain of frequency, dysuria, and suprapubic pain. Sonographic detection of **polypoid bladder tumors** is excellent (≥95%).[191] The appearance is that of a nonmobile focal mass or of urothelial thickening (Fig. 9.57, Video 9.3). Ultrasound appearances are nonspecific, however, and the differential diagnosis is extensive, including cystitis, wall thickening caused by **bladder outlet obstruction, postradiation/postoperative change,** adherent **blood clot,** invasive **prostate carcinoma, lymphoma, metastasis, endometriosis,** and **neurofibromatosis.** Some papillary bladder tumors may also calcify. Cystoscopy and biopsy are necessary for diagnosis. Both transvaginal and transrectal ultrasound may also be used to assess a bladder wall mass if suprapubic visualization is compromised.

Transitional cell (and squamous cell) carcinomas may also arise within **urinary bladder diverticula.** Many diverticula have narrow necks, making them inaccessible for cystoscopic examination, so imaging plays an important role in the detection of these tumors. The periureteric and posterolateral wall locations of most bladder diverticula allow for adequate sonographic visualization.[192] At ultrasound, diverticular tumors are moderately echogenic, nonshadowing masses. Although ultrasound is good for tumor detection, staging is still best performed clinically in combination with CT or MRI.[193]

Squamous Cell Carcinoma

Squamous cell carcinoma (SCC) is rare but is the second most common malignant urothelial tumor after TCC. SCC accounts for 6% to 15% of renal pelvic tumors and 5% to 8% of all bladder tumors.[194,195] Chronic infection, irritation, and stones lead to **squamous metaplasia** and **leukoplakia** of the urothelium. Leukoplakia is thought to be premalignant. SCC tends to be a solid, flat, infiltrating lesion with extensive ulceration. Distant metastases are usually present at diagnosis. As with other infiltrating renal lesions, renal SCC appears at sonography as a diffusely enlarged kidney that has maintained its reniform shape. Normal renal echotexture is destroyed, and often a stone (47%-58%)[194] will be present. It thus may be impossible to differentiate renal SCC from **XGP**. Often, perinephric tumor extension and metastases are present. Ureteral SCC is rare; hydronephroureterectasis proximal to the tumor mass will be apparent. Occasionally, the lesion is seen as a poorly defined, irregular, solid mass. Associated stones are often present. Bladder SCCs tend to be large, solid, and infiltrating. SCCs may also arise within bladder diverticula.[192] Ultrasound may be an effective modality for detecting pedunculated bladder SCC, but CT or MRI are more appropriate modalities for detecting perivesical invasion, regional adenopathy, and distant metastases.

Adenocarcinoma

Adenocarcinoma of the renal pelvis, ureter, and bladder is rare. Almost all patients with adenocarcinoma of the renal pelvis have a history of chronic UTI,[196] and two-thirds have a stone, typically a **staghorn calculus.** Clinicians must be careful to differentiate adenocarcinoma of the bladder from adenocarcinoma of the rectum, uterus, or prostate that has invaded the bladder. The prognosis is poor. At sonography, a renal pelvic, ureteric, or bladder mass is seen, occasionally with calcification. An associated stone is often present.

Oncocytoma

Oncocytes are large, epithelial cells. The characteristic granular eosinophilic cytoplasm in these cells results from extensive cytoplasmic mitochondria. Oncocytomas may occur in the parathyroid glands, thyroid, adrenal glands, salivary glands, and

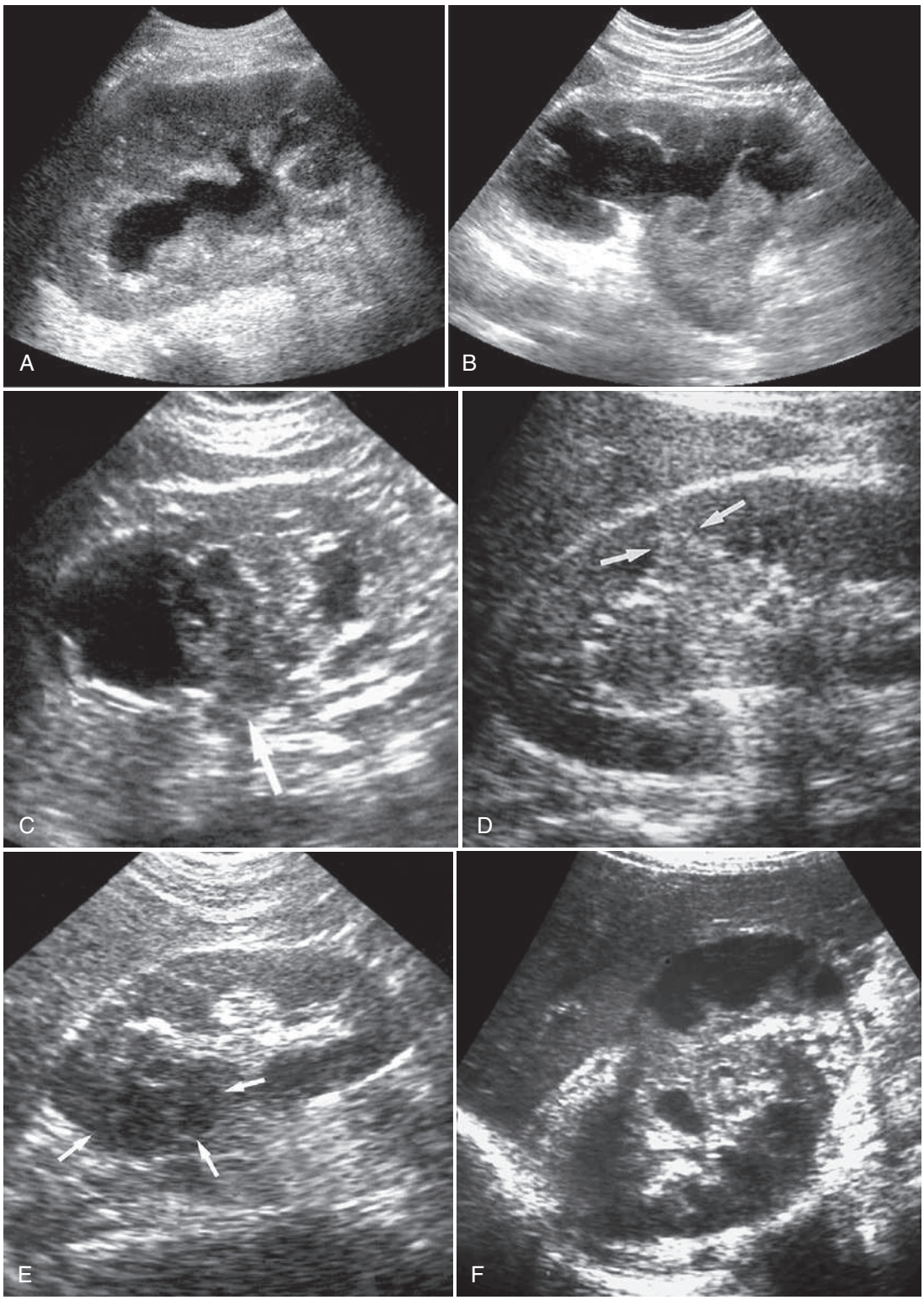

FIG. 9.56 Transitional Cell Carcinoma (TCC) of the Kidney. (A)-(C) Sagittal sonograms in three different patients showing hydronephrosis related to large, central, solid pelvic tumors (*arrow* in C). **(D)** Infiltrative TCC in the upper pole extends from the calix into the renal parenchyma *(arrows)*. **(E)** Large, lobulated, solid parenchymal infiltrative mass *(arrows)* with no associated caliectasis. **(F)** Perirenal tumor extension.

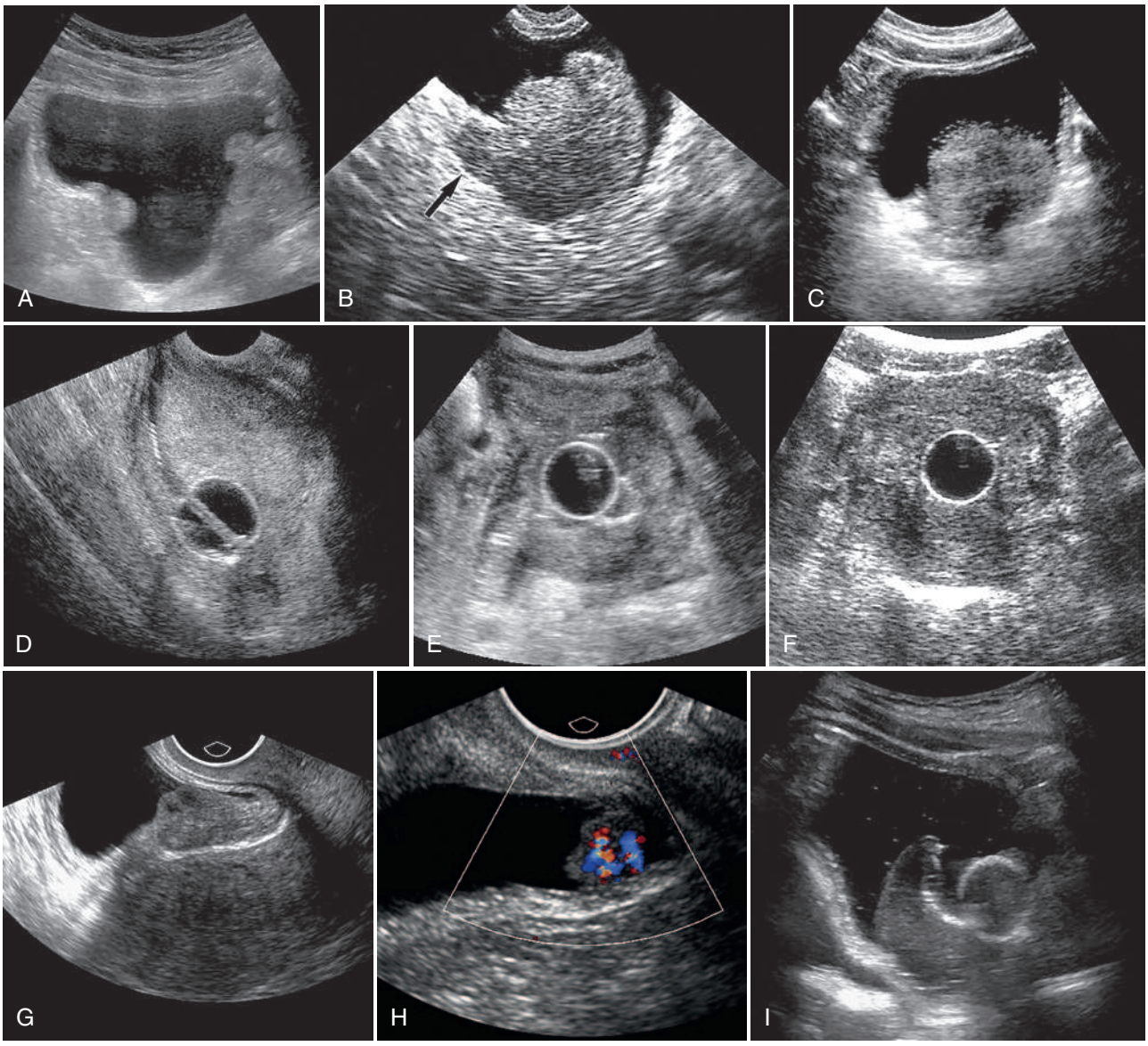

FIG. 9.57 Bladder Masses With Many Origins: Imaging Spectrum. (A) Multifocal polypoid urothelial transitional cell carcinoma (TCC). **(B)** Invasive TCC involving the perivesical fat *(arrow)*. **(C)** Benign prostatic hypertrophy simulating a large invasive bladder wall mass. **(D)** Diffuse TCC on a transvaginal sagittal image; Foley catheter is in place. **(E)** Diffuse invasive TCC on suprapubic scan. **(F)** Interstitial cystitis closely simulates diffuse tumor. **(G)** Endometrioma appearing as a solid mass within posterior bladder wall on a transvaginal sagittal image. Note uterus posterior to bladder mass. **(H)** Pheochromocytoma presenting as a vascular polypoid bladder mass at color Doppler transvaginal evaluation. **(I)** Dependent bladder clot posterior to Foley catheter balloon simulates a bladder mass. Intraluminal gas along bladder dome induces "dirty shadowing." See also Video 9.3.

kidneys. Oncocytomas account for 3% to 7% of all renal tumors.[197,198] They occur more often in men (1.7:1), with a peak incidence in the sixth and seventh decades.[199] Most patients are asymptomatic.[197] Oncocytomas vary in size and may be multicentric (5%-10%) or bilateral (3%). Bilateral tumors are seen particularly in hereditary syndromes **(Birt-Hogg-Dubé, hereditary oncocytosis).**[198,200] Hemorrhage and calcification are uncommon. These tumors histologically may have a benign or a more malignant appearance. Differentiation between oncocytomas and chromophobe RCCs may be difficult,[201] and hybrid lesions consisting of both oncocytic and chromophobe RCC elements have been reported (see Fig. 9.51).

Not surprisingly, oncocytoma and RCC cannot be differentiated by imaging. Davidson et al.[202] demonstrated that CT homogeneity and a central stellate "scar" are poor predictors in differentiating oncocytomas from RCCs. In earlier surgical series, oncocytomas represented about 5% of all tumors originally diagnosed as RCC on imaging.[203] A higher percentage of benign oncocytomas will likely be documented in future series of smaller, incidental lesions sampled before nephron-sparing procedures.

There is no distinctive ultrasound appearance of oncocytomas. These lesions may be homogeneous or heterogeneous with a distinct or poorly demarcated wall.[204] A central scar, central necrosis, or calcification may be seen, although these features

may also be identified with RCC (see Fig. 9.51). The lack of specificity of imaging features of oncocytomas typically prompts surgical resection, although as mentioned previously, recent improvements in immunohistochemistry may prompt imaging surveillance for patients with biopsy results consistent with benign oncocytomas.

Angiomyolipoma

AMLs are benign renal tumors composed of varying proportions of adipose tissue, smooth muscle cells, and blood vessels. AMLs may occur sporadically or may be found in patients with **tuberous sclerosis.** In patients without stigmata of tuberous sclerosis, AMLs are typically unilateral and discovered in middle-aged women. Up to 50% of patients with AMLs will have clinical stigmata of tuberous sclerosis (mental retardation, epilepsy, facial sebaceous adenomas), and up to 80% of patients with tuberous sclerosis will have one or more AMLs.[205] AMLs associated with tuberous sclerosis are usually small, multiple, bilateral tumors, with no gender predilection. **Sporadic** AMLs are histologically identical to those associated with tuberous sclerosis. It is unusual for small tumors (<4 cm)[206] to be symptomatic; with growth, however, these tumors may hemorrhage, with symptoms such as hematuria, flank pain, and palpable flank mass.

At sonography, the echo pattern of AMLs depends on the proportions of fat, smooth muscle, vascular elements, and hemorrhage. These tumors may be located within renal parenchyma or may be exophytic (Fig. 9.58). If muscle, hemorrhage, or vascular elements predominate, the tumor may be hypoechoic. Siegel et al.[152] showed that the multiple fat and nonfat interfaces in the more typical AMLs, along with the large acoustic impedance differences at these interfaces, causes scattering and attenuation of sound waves. This histology leads to the classic ultrasound

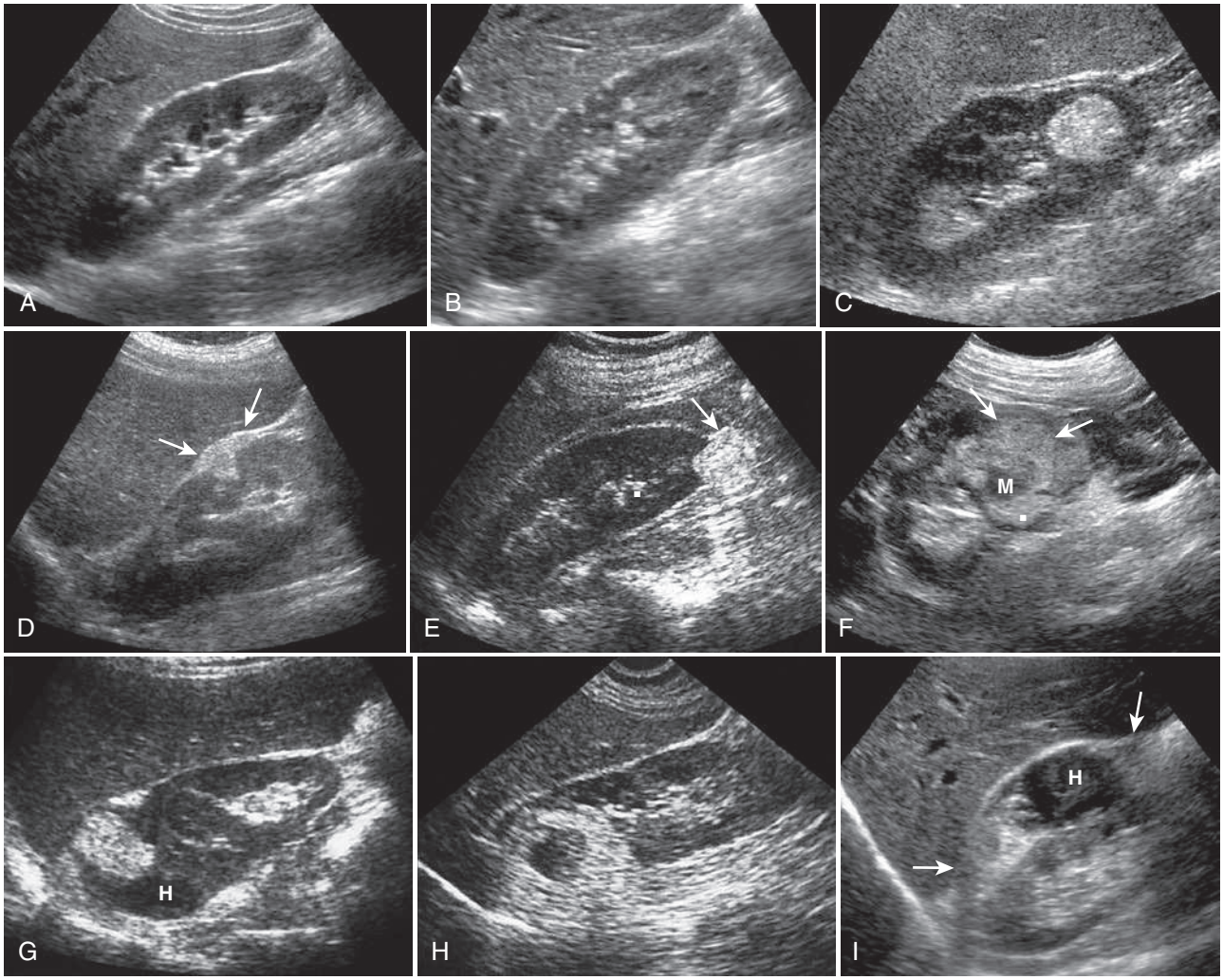

FIG. 9.58 Imaging Spectrum of Angiomyolipomas (AMLs). (A) Classic small hyperechoic intraparenchymal tumor. **(B)** Multiple small echogenic foci in the anterior cortex of the midpole. **(C)** Solitary, large, highly echogenic mass in the lower pole. **(D)** Exophytic echogenic mass involves the cortex and the perirenal space *(arrows)*. The flat appearance suggests a compliant soft tumor. **(E)** Large exophytic lower-pole echogenic mass *(arrow)*. The echogenicity of the mass may be very similar to the perirenal fat. **(F)** Large, complex intrarenal mass *(arrows)* is mildly echogenic and has a hypoechoic component representing myomatous elements *(M)*. **(G)-(I)** Hemorrhagic AMLs. **(G)** Exophytic ruptured upper-pole AML with a perirenal hematoma *(H)*. **(H)** Echogenic mass with central hypoechoic hemorrhage. **(I)** Large, predominantly exophytic AML. The kidney below the mass appears normal. The mass *(arrows)* shows increased echogenicity from the fat in the AML and a large hypoechoic hemorrhage *(H)*.

appearance of an AML: an echogenic lesion with shadowing. As mentioned earlier, although several distinguishing features have been suggested, there is significant imaging overlap between classic AMLs and small, echogenic RCCs. Involvement of regional lymph nodes and extension of AMLs into the IVC have also been described.[207] Further, it may be difficult to differentiate a large, exophytic AML from a large, retroperitoneal **liposarcoma** (Fig. 9.59). Helpful features that may allow differentiation from liposarcomas include (1) a defect in the renal parenchyma where the tumor originates and (2) the presence of enlarged vessels and other associated AMLs.[208] The blood vessels in an AML lack normal elastic tissue and are prone to aneurysm formation and hemorrhage.[209] Color flow Doppler sonography appears to be the best imaging modality to detect an intratumoral pseudoaneurysm in a hemorrhagic AML.[210]

Small, asymptomatic AMLs may be followed for growth; if large, symptomatic, or hemorrhaged, surgery is often performed.

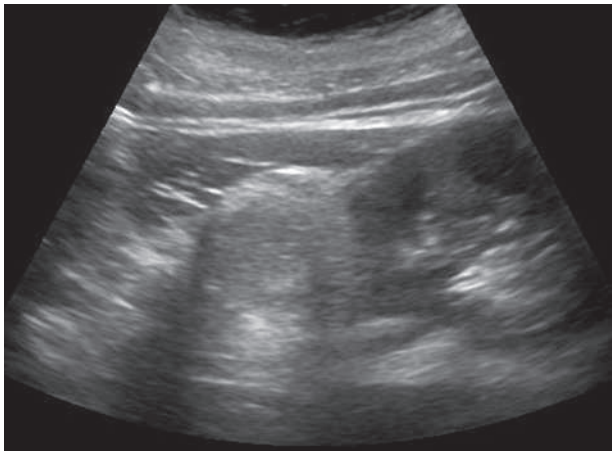

FIG. 9.59 Exophytic Angiomyolipoma. Sagittal sonogram shows a large, exophytic, echogenic angiomyolipoma.

If possible, renal-sparing surgery is preferable, because these tumors are benign or may be multiple. Embolization may also be used to treat actively bleeding AMLs.[211]

Lymphoma

Kidney

The kidney does not contain lymphoid tissue. Thus lymphomatous involvement of the kidney occurs from either hematogenous dissemination or contiguous extension of retroperitoneal disease. Renal involvement occurs more often in the setting of non-Hodgkin lymphoma than Hodgkin lymphoma. By the time renal disease is evident, disseminated disease is usually apparent. Urinary tract symptoms are uncommon. Occasionally, flank pain, a flank mass, or hematuria may occur. Nonetheless, at autopsy, renal involvement is found in one-third of lymphoma patients,[212] and bilateral renal disease is more common than unilateral disease. Isolated renal disease may be seen in patients undergoing treatment.

The sonographic appearance of **renal lymphoma** depends on the pattern of involvement. **Focal parenchymal involvement** may appear as solitary or multiple nodules. These masses appear homogeneous and hypoechoic or anechoic (Fig. 9.60). They may simulate cysts; however, increased through transmission is absent.[213,214] As with other infiltrating renal tumors, **infiltrating lymphoma** is manifested by maintenance of a reniform shape despite disruption of renal architecture. The kidney may be enlarged (Fig. 9.61). Tumor may invade the renal sinus and destroy the echogenic, central echo complex.[215] **Direct invasion** of the kidney by large retroperitoneal **lymph node masses** may occur with associated vascular and ureteral encasement. Large, retroperitoneal, hypoechoic conglomerate adenopathy may extend into the renal pelvis and cause hydronephrosis. The absence of renal venous invasion, despite extensive retroperitoneal and renal

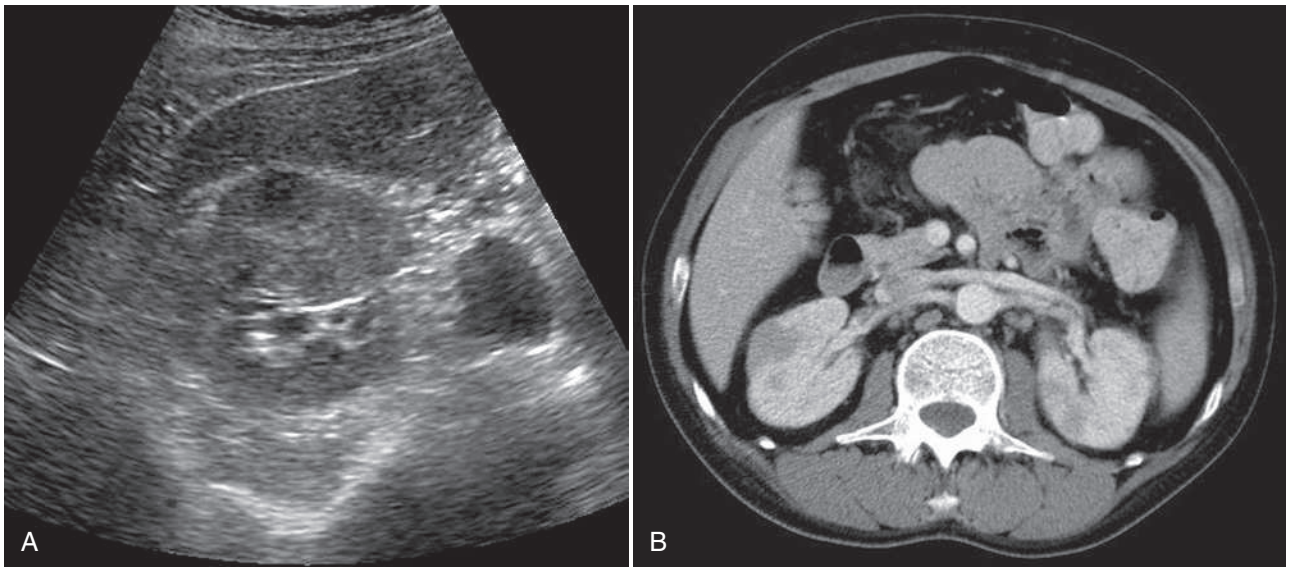

FIG. 9.60 Renal Lymphoma. (A) Transverse sonogram shows a subtle right midpole contour deformity and vague hypoechoic lesion. **(B)** Contrast-enhanced CT confirms mildly border-deforming renal lesion and shows contralateral lesions.

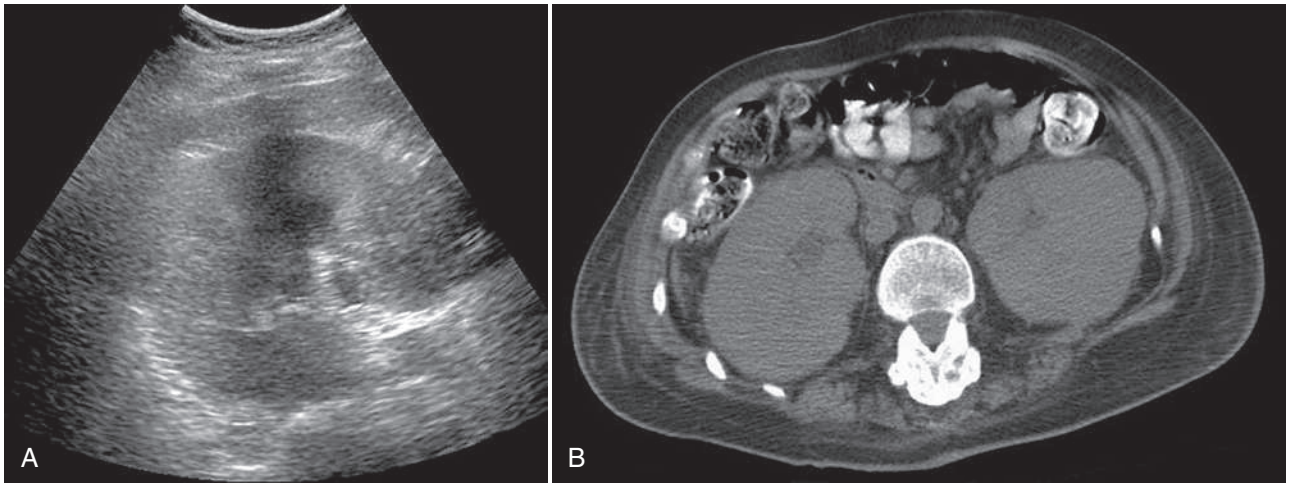

FIG. 9.61 Renal Lymphoma. (A) Transverse sonogram shows enlarged, echogenic globular kidney. **(B)** Noncontrast-enhanced CT shows marked bilateral renomegaly.

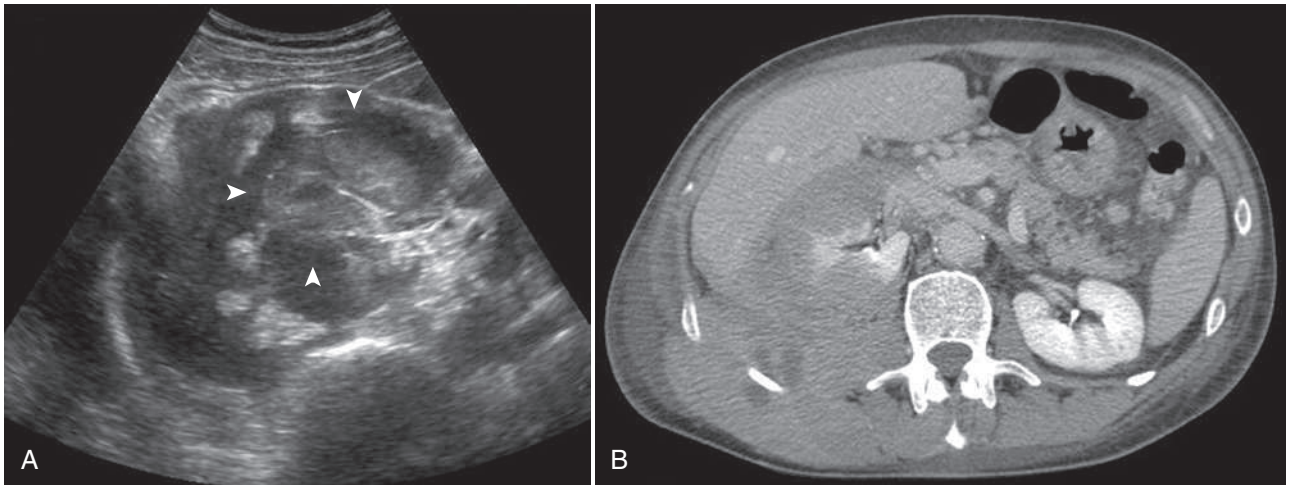

FIG. 9.62 Perirenal Burkitt Lymphoma. (A) Transverse sonogram shows extensive, poorly defined perirenal tumor. The kidney *(arrowheads)* is compressed and invaded by tumor. **(B)** Contrast-enhanced CT shows bulky perirenal tumor. Tumor involves both the kidney and the overlying flank musculature.

Sonographic Appearance of Renal Lymphoma

Focal parenchymal involvement
Diffuse infiltration
Invasion from retroperitoneal mass
Perirenal involvement

sinus tumor, may help in differentiating renal lymphoma from RCC. Rarely, **perirenal predominant tumor** may be depicted at ultrasound as a surrounding hypoechoic perirenal mass or rind. Tumor may be confused with hematoma or extramedullary hematopoiesis[216,217] (Fig. 9.62).

Ureter

The ureter may be either encased or displaced by surrounding retroperitoneal lymphoma. Ureteral displacement by periureteral tumor is more common; actual invasion of the ureteral wall occurs in only one-third of cases.[188] The result is usually dilatation of the intrarenal collecting system and ureter to the level of the retroperitoneal mass. This is usually easily appreciated on sonography.

Bladder

Primary bladder lymphoma arises from lymphoid follicles in the submucosa. Submucosal tumor usually infiltrates the other layers of the bladder wall.[218] Most patients with primary bladder lymphoma are 40 to 60 years of age, and women are affected more than men. At sonography, a bladder wall mass is seen. If the mass is large, ulceration may occur (Fig. 9.63).

Leukemia

Leukemic involvement of the kidney may be **diffuse** or **focal.** In autopsy series, renal leukemic infiltration was reported in 65% of patients.[219] Despite this, renal leukemia is difficult to identify at ultrasound. The classic appearance of **renal leukemia** at ultrasound is **bilateral renal enlargement.** However, 15% of patients with leukemia will have nonspecific renomegaly without

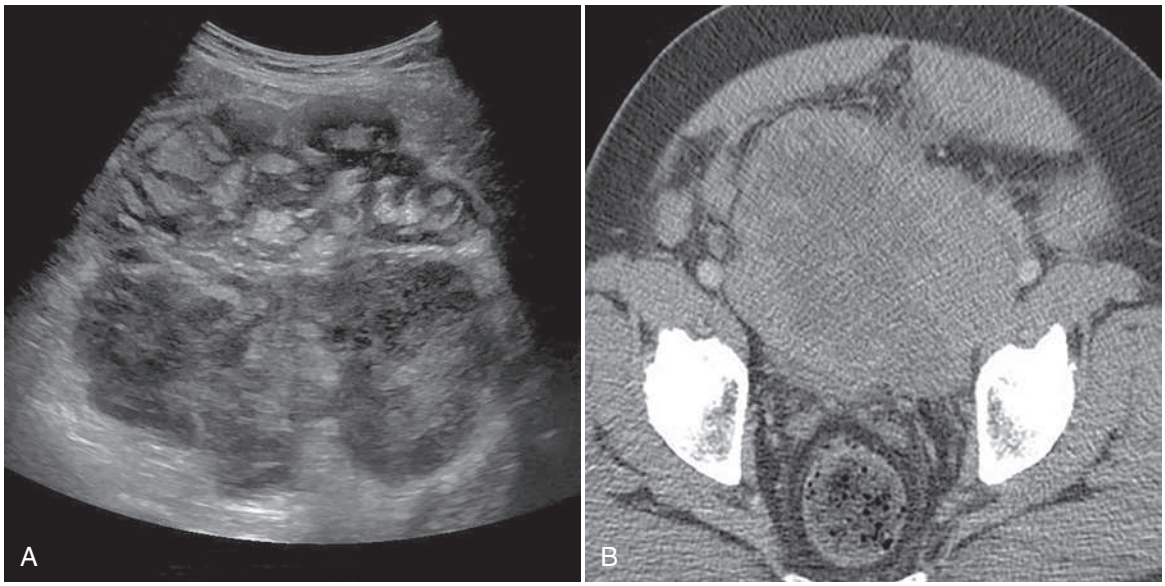

FIG. 9.63 Diffuse B-Cell Bladder Lymphoma. (A) Transverse sonogram shows a large irregular mass that replaces the bladder. **(B)** Corresponding contrast-enhanced CT shows a bulky mass that occupies the entire bladder lumen. (Courtesy of R. Brooke Jeffrey, MD.)

leukemic infiltration.[220] Renal leukemia may also be manifested as a coarsened renal echo pattern with distortion of the central sinus echo complex.[221] Alternatively, the kidneys may be diffusely echogenic. Focal masses may be single or multiple.[222] These patients are prone to renal, subcapsular, and perinephric hemorrhage.

Metastases

Kidney

Renal metastases are typically clinically occult, but autopsy series done before cross-sectional imaging documented an incidence of 2% to 20%.[223] The true prevalence of renal metastases in the era of cross-sectional imaging is unknown, but the prevalence of subclinical, imaging-apparent renal involvement is likely greater than estimated by gross autopsy.

Spread to the kidneys is by a hematogenous route. The most **common primary tumors** giving rise to renal metastases are (1) lung carcinoma, (2) breast carcinoma, and (3) RCC of the contralateral kidney.[120] Other tumors that may produce renal metastases include colon, stomach, cervix, ovary, pancreas, and prostate.[120] Renal metastatic spread may manifest as a solitary mass, multiple masses, or a diffusely infiltrating mass that enlarges the kidney. Choyke et al.[224] evaluated 27 patients with renal metastases and found that metastases are usually multifocal; however, large, solitary tumors may occur that are otherwise indistinguishable from primary RCC. Also, a new renal lesion in a patient with advanced cancer is more likely a metastatic than a primary tumor. If a single renal lesion is discovered synchronously in a patient with a known primary tumor, or with a tumor in remission with no evidence of other metastases, renal biopsy is necessary to differentiate a primary RCC from a renal metastasis.

Contrast-enhanced CT is the best radiographic technique for detecting renal metastasis, although ultrasound is almost as sensitive.[224] At sonography, the appearance depends on the **pattern of involvement.** A solitary metastasis will be seen as a solid mass indistinguishable from RCC; this often occurs with colon carcinoma.[224] Central necrosis, hemorrhage, and calcification may be evident. Multiple metastases usually appear as small, poorly marginated, hypoechoic masses. Involvement of the perinephric space is possible, particularly with malignant melanoma and lung cancer.[224] Infiltrating renal metastases are particularly subtle at ultrasound; as with other infiltrating processes, the only manifestation at sonography may be an enlarged, but still reniform, kidney (Fig. 9.64).

Ureter

Ureteral metastases are rare; evidence of diffuse metastases elsewhere is seen in 90% of cases.[225] Metastatic disease to the ureter occurs by hematogenous or lymphatic dissemination. Tumors that may secondarily involve the ureter include melanoma, bladder, colon, breast, stomach, lung, prostate, kidney, and cervical lesions. Three types of ureteral involvement occur: (1) infiltration of the periureteral soft tissues, (2) transmural involvement of the ureteral wall, and (3) submucosal nodules. With the first two types, imaging may demonstrate strictures with or without an associated mass. Intraluminal lesions may be shown with the third type.[188] At sonography, the site of tumor involvement may be seen if a mass is present. Usually, however, the only manifestation of ureteral involvement is secondary hydronephrosis.

Bladder

Although rare, metastases to the bladder may occur with malignant melanoma, lung, gastric, or breast cancer. The appearance

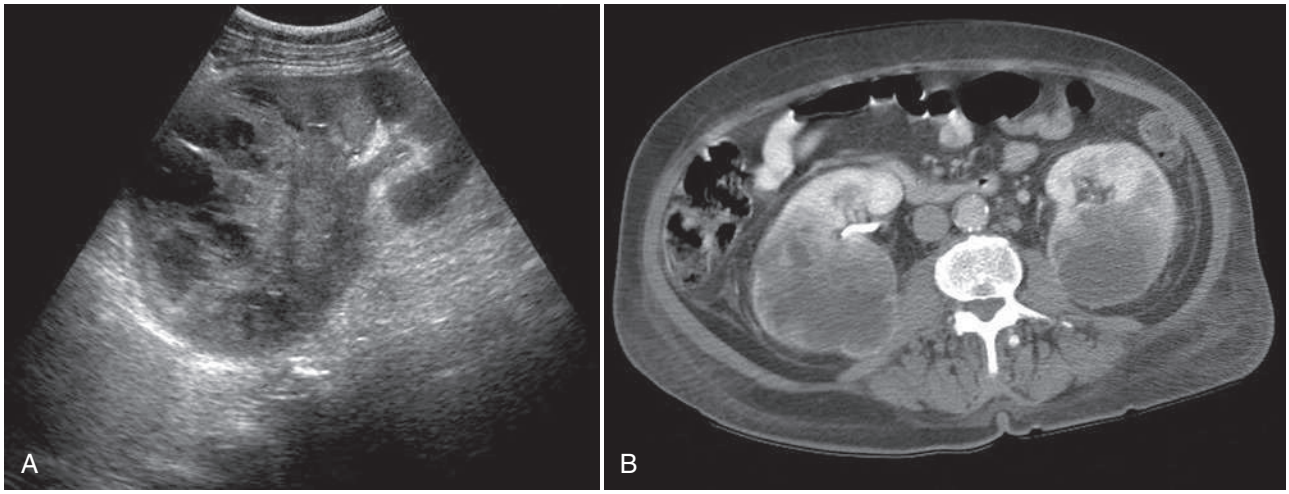

FIG. 9.64 Renal Metastases (Lung Primary). (A) Sagittal sonogram shows infiltrating, mixed-echogenicity tumor throughout the upper pole of the kidney. **(B)** Contrast-enhanced CT demonstrates bilateral infiltrating metastases.

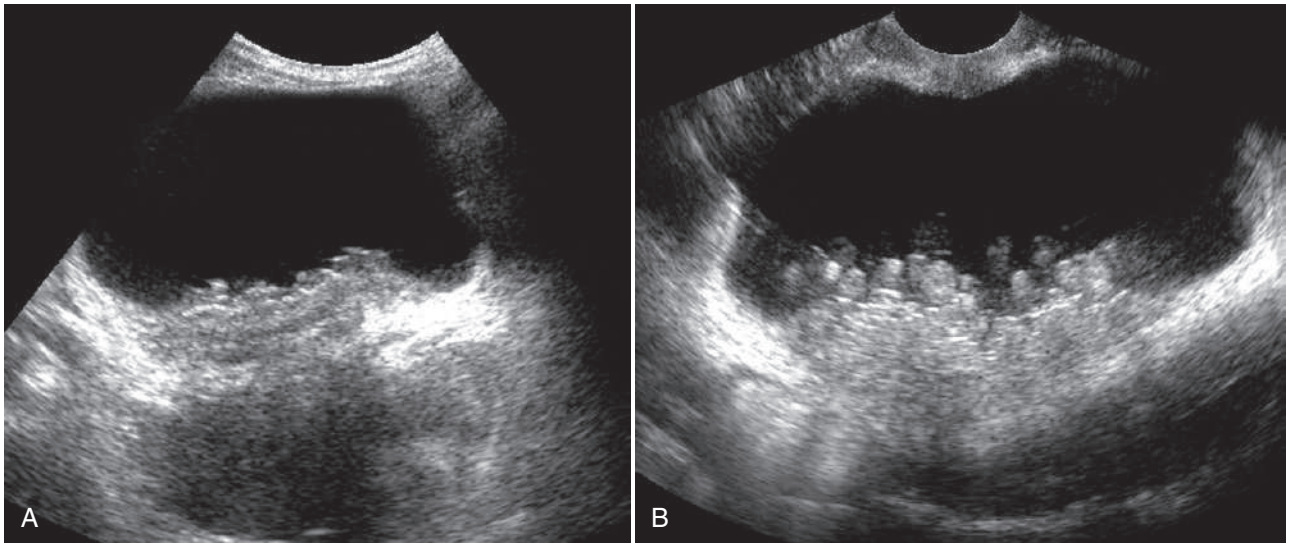

FIG. 9.65 Bladder Metastasis From Gastric Adenocarcinoma. (A) Transverse suprapubic sonogram shows a papillary solid intraluminal mass with obvious bladder wall involvement. **(B)** Confirmatory transvaginal scan shows the papillary nature of the tumor to better advantage.

at ultrasound is nonspecific; a solid mass may be seen in the bladder wall (Fig. 9.65).

Urachal Adenocarcinoma

The urachus measures 3 to 10 cm in length and represents the obliterated remnant of the allantois. It is lined by transitional epithelium. The urachal remnant is divided into supravesical, intramural, and intramucosal portions. Urachal neoplasms are rare, usually arising in the upper part of the intramural portion of the urachal remnant or in the lower part of the extravesical portion of the bladder.[226] Urachal cancers represent 0.01% of all adult cancers, 0.17% to 0.34% of all bladder cancers, and 20% to 39% of all primary bladder adenocarcinomas.[227] About 75% of urachal cancers occur in men.[228] Most tumors arise at the bladder dome at the vesicourachal junction. Urachal tumors have a poor prognosis and tend to invade the anterior abdominal wall. Most patients present with hematuria, although other common symptoms include frequency, dysuria, and mucosuria.[228] At sonography, a bladder dome mass is seen, often calcified (50%-70%). The mass may be solid, cystic, or complex cystic-solid. Tumor extension into the perivesical fat, space of Retzius, and the abdominal wall is common. Local recurrence after resection is common.

Rare Neoplasms

Kidney

Juxtaglomerular tumors are rare benign tumors that more frequently affect women. **Renin secretion** by these lesions results in **hypertension.** At sonography, they are usually small, solid, and hyperechoic.[229] Excision will alleviate the hypertension. **Leiomyomas** are benign tumors that arise from the renal capsule. They are usually discovered incidentally but may grow large enough to become clinically evident. On sonography, a solid,

well-defined peripheral mass is seen. **Carcinoid tumor** is a rare renal tumor that tends to be solid, with peripheral or central calcification.[230] Other benign tumors that have been described include **lipomas** and **hemangiomas.**

Renal sarcomas are aggressive tumors that account for approximately 1% of all malignant renal tumors. **Leiomyosarcoma** is the most common, representing 58% of all renal sarcomas. **Hemangiopericytoma** represents 20%. At sonography, these tumors cannot be distinguished from RCC. **Liposarcoma** accounts for 20% of all renal sarcomas. Depending on the amount of mature fat present, these tumors can be quite hyperechoic and indistinguishable from AMLs. Less common sarcomas include **rhabdomyosarcoma, fibrosarcoma,** and **osteogenic sarcoma. Wilms tumor** may rarely occur in adults and cannot be differentiated radiologically from RCC.

Bladder

Mesenchymal bladder tumors also are rare, accounting for about 1% of all bladder tumors. **Leiomyoma** is the most common benign bladder tumor. Most leiomyomas arise from the submucosa near the bladder trigone.[231] These tumors may show intravesical (63%), intramural (7%), or extravesical (30%) growth.[231] At sonography, a well-defined, round or oval, solid mass will be seen. Cystic degeneration may occur. **Neurofibromas** of the bladder may be seen as an isolated finding or may occur with diffuse systemic disease. These tumors are similar to leiomyomas at ultrasound. **Cavernous hemangiomas** are most often found in the dome and posterolateral bladder wall.[232] At sonography, two types have been described: (1) a round, well-defined, solid, hyperechoic, intraluminal mass that is highly vascular on color Doppler ultrasound and (2) diffuse wall thickening with multiple hypoechoic spaces and calcification.[232] Bladder **pheochromocytomas** are rare; they account for only 1% of all pheochromocytomas.[231] Patients may have symptoms that include headaches, sweating, and tachycardia related to bladder distention or voiding. Pheochromocytomas arise in the submucosa and may be found anywhere in the bladder, but usually at the dome. At ultrasound, a well-defined, solid, intramural bladder wall mass will be seen (Fig. 9.66). Malignant mesenchymal bladder tumors are rare; the most common are **leiomyosarcomas** and **rhabdomyosarcomas.** At sonography, a large, infiltrative mass is seen.

RENAL CYSTIC DISEASE

Cortical Cysts

Simple renal cysts are benign and fluid filled. Although their exact pathogenesis is unknown, they likely originate from distal convoluted or collecting ducts.[233] Incidence of simple cysts increases with advancing age, and they are found in at least

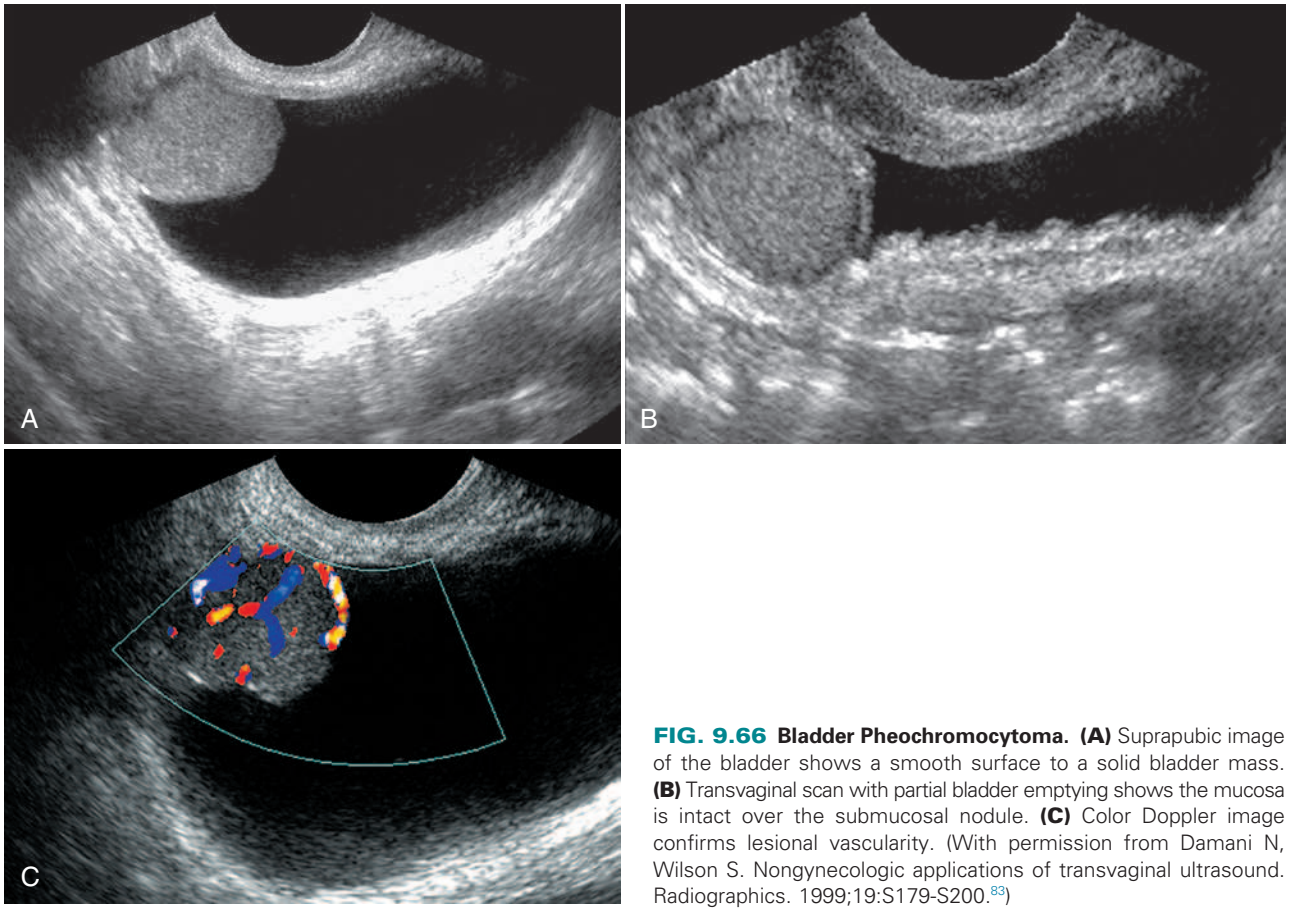

FIG. 9.66 Bladder Pheochromocytoma. (A) Suprapubic image of the bladder shows a smooth surface to a solid bladder mass. **(B)** Transvaginal scan with partial bladder emptying shows the mucosa is intact over the submucosal nodule. **(C)** Color Doppler image confirms lesional vascularity. (With permission from Damani N, Wilson S. Nongynecologic applications of transvaginal ultrasound. Radiographics. 1999;19:S179-S200.[83])

33% of persons over age 60.[234] Most cysts are asymptomatic. Patients with large cysts, however, may present with flank pain or hematuria. A cyst is confidently characterized at sonography when it (1) is anechoic; (2) has a sharply defined, imperceptible back wall; (3) is round or ovoid; and (4) enhances sound transmission.

If all these sonographic criteria are met, further evaluation or follow-up of the cyst is not required (Fig. 9.67). If a renal cyst is large and symptomatic, cyst puncture, aspiration, and sclerosis using a variety of agents may be performed. Several simple cysts may be found in both kidneys, and rarely, several simple cysts may involve only one kidney or a localized portion of one kidney.

Complex renal cysts do not meet the strict criteria of a simple renal cyst and include cysts containing internal echoes, septations, calcifications, perceptible defined walls, and mural nodularity (Fig. 9.68). Depending on the degree of abnormality, most complex renal cysts require further imaging with CT or magnetic resonance.

Internal echoes within a cyst are usually the result of hemorrhage or infection. Approximately 6% of cysts are complicated by hemorrhage.[235] Infection of a cyst may occur by hematogenous seeding, by vesicoureteric reflux, or as a complication of cyst puncture or surgical manipulation. A thickened cyst wall and a debris-fluid or gas-fluid level suggest an infected cyst. Cysts that are thought to be hemorrhagic at ultrasound (i.e., cysts that contain low-level echoes but otherwise fulfill criteria for a benign cyst) may be followed with serial ultrasound. Infected cysts require aspiration and drainage for diagnosis and treatment.

Septations may be seen within a renal cyst and are often the result of hemorrhage, infection, or percutaneous aspiration. Occasionally, two adjacent cysts may appear as a large, septated cyst. If septa are thin or barely perceptible, smooth, and attach to the cyst wall without thickened elements, a benign cyst can be diagnosed[236] (Fig. 9.68B-D). Complex cysts with irregular, thickened (>1 cm) septa, or with septa that have solid elements

Approach to Complex Renal Cyst Discovered on Sonography

INTERNAL ECHOES

Follow up with ultrasound if no other features of malignancy are present

Perform CT or MRI if associated features of malignancy are present (perceptible thickened wall, multiple or thick septations, or extensive septal calcification)

SEPTATIONS

Follow up with ultrasound if septations are few and thin (≤1 mm)

Perform CT or MRI if there is septal irregularity and nodularity, multiple complex septations, or solid elements at septal wall attachment

CALCIFICATION

Follow up with ultrasound if there is a small amount of calcium or milk of calcium without an associated soft tissue mass

Perform CT if thick, irregular, or amorphous calcification is found

Perform CT if calcification obscures adequate sonographic visualization

PERCEPTIBLE DEFINED WALL OR MURAL NODULARITY

If presumed malignant, perform CT/MRI

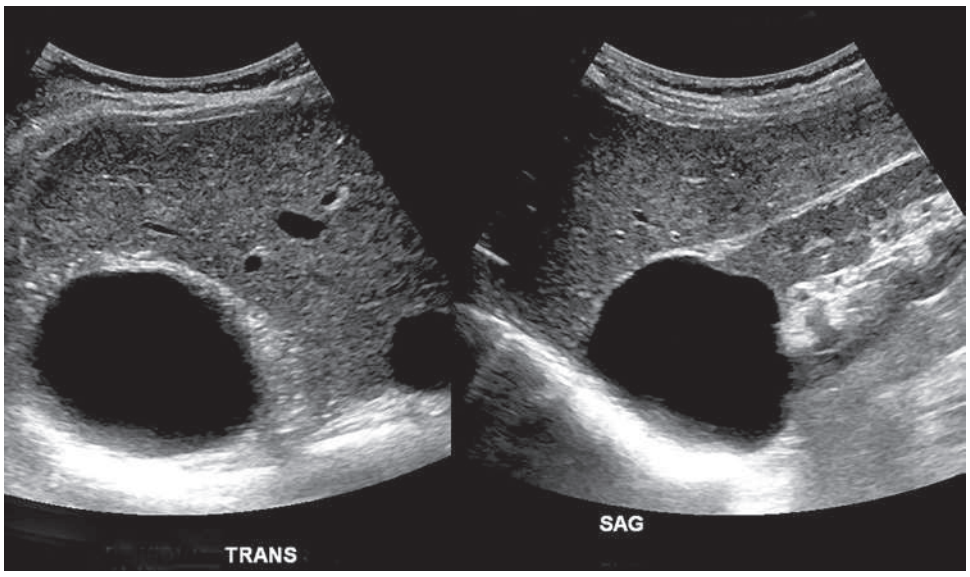

FIG. 9.67. Renal Cyst. Transverse and sagittal images show classic features of a renal cyst: a smooth, imperceptible wall, an echo-free center, and posterior acoustic enhancement caused by increased through transmission.

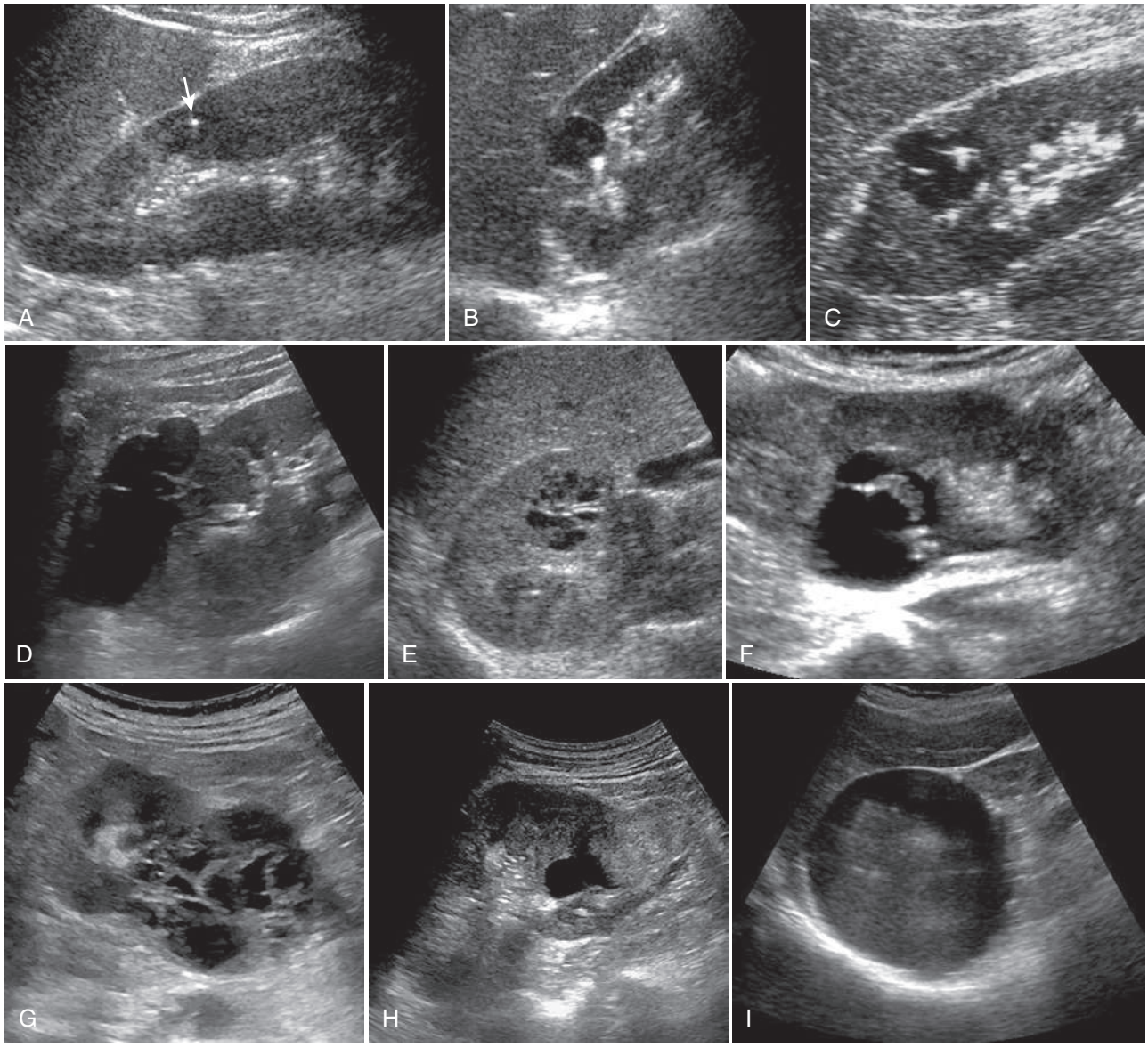

FIG. 9.68 Complex Renal Cysts. (A) Tiny renal cyst *(arrow)* in the anterior cortex is not resolved. A bright echogenic focus with ring-down artifact is the only visible abnormality. **(B)** Discernible cyst shows a bright echogenic focus with ring-down artifact. This echogenicity does not represent calcification. **(C)** Complex benign cyst with a few thin septations. Ring-down artifact originates from the septations and the cyst wall. **(D)** Complex cyst containing several thin septations. Septation was imperceptible at follow-up MRI. Septation is accentuated at ultrasound, and Bosniak classification is ultimately made based on features at MRI or CT. **(E)** Cyst shows numerous internal thick and thin septations. **(F)** Complex cyst shows thick nodular septations. **(G)** Cyst containing thick, nodular septations. Lack of enhancement of septations at CT suggested a Bosniak category 3 lesion, although a decrease in size of the mass at short follow-up imaging confirmed a hemorrhagic cyst. **(H)** Cyst with large solid component post trauma. Real-time color Doppler examination confirmed that the solid component was mobile and avascular. Intracystic clot resolved at follow-up sonography. **(I)** Large hemorrhagic cyst shows extensive internal debris within an otherwise simple-appearing cyst.

at the wall attachment, should be viewed with concern (Fig. 9.68E-G). Cyst aspiration is not indicated in these multiseptated cystic lesions.[236] Ultrasound is often better than CT in defining the internal characteristics of a cystic lesion.

Calcification of renal cysts may be fine and linear or amorphous and thick. Thin wall or septal calcification suggests a complicated cyst rather than malignancy, if all other features of a benign cyst are shown at ultrasound, with no associated soft tissue mass enhancement at CT.[237] Thick, irregular, amorphous calcification is more worrisome, however, and should prompt additional assessment with CT.[237] On the other hand, layering milk of calcium within a cyst is a benign finding. Mimicking cyst wall calcification, the bright, echogenic foci with ring-down artifact are frequently seen in septa and cyst walls at ultrasound (Fig. 9.68A-C). These foci are of no consequence, and no corresponding calcification is shown at CT. Thickened walls or mural nodularity typically excludes a diagnosis of a benign cyst (Fig. 9.68E-H) although ultimate management is based on corresponding features at CT/MRI and, in the appropriate clinical context (e.g., fever, leukocytosis or trauma), imaging follow-up.

The assessment of the **malignant potential** of renal cysts based on complexity at imaging was the basis of the classification introduced in 1991 by Bosniak.[238] Many sonographers attempt to classify cyst complexity using Bosniak terminology. It should be emphasized, however, that Bosniak criteria are primarily based on contrast-enhanced cross-sectional imaging. Malignancy risk assessment may be flawed, however, if the sonographer arbitrarily uses ultrasound features of more complex lesions to assign Bosniak grades. Minimally complex (Bosniak 2) lesions at CT can have a much more malignant appearance at ultrasound.

The **Bosniak category 1 cystic lesion** has all the benign features of a simple cyst. The **Bosniak category 2 cystic lesion** is more complicated and may have thin septa and calcification. On CT, a high-attenuation (proteinaceous or hemorrhagic, with an attenuation of less than 60 Hounsfield units [HU] that enhances less than 10 HU after contrast administration) may often appear as a simple cyst at ultrasound. High levels of protein with cyst fluid may appear at ultrasound as low-level echoes, an appearance that might erroneously suggest a solid lesion. In addition, thin septations within a Bosniak type 2 cyst at CT will often appear much more ominous at ultrasound. The risk of malignancy in a cystic lesion classified as **Bosniak 2F** (by CT) is estimated at 5%.[239]

The **Bosniak category 3 cystic lesion** is indeterminate at CT. Thick, irregular septations, calcifications, and wall nodularity increase the risk of malignancy. As indicated earlier, imaging follow-up is done in the appropriate clinical setting, as when a renal abscess is suspected in a patient with fever, leukocytosis, and pyuria, or in older patients with comorbidities. Other lesions in this category include highly complex hemorrhagic cysts, **multilocular cystic nephroma,** localized cystic disease, and cystic RCC. CT enhancement of septa, mural nodules, and solid components within highly complex cysts significantly increases the risk of malignancy in the **Bosniak category 4 cystic lesion.**

Ultrasound has played a largely adjunct role in risk stratification of more complex renal cystic lesions because it does not readily demonstrate renal tumor neovascularity. Wall or septal enhancement that is obvious at CT may be rarely depicted at ultrasound as focally increased color or power Doppler flow (see Fig. 9.49). However, microbubble contrast agents may increase the importance of ultrasound in renal mass characterization (see Fig. 9.50). Renal lesion enhancement using continuous, low–mechanical index pulse inversion imaging (or an equivalent) may mimic the enhancement shown at contrast-enhanced CT or MRI.[170,240] The ability of CEUS to show neovascularity may be particularly relevant for patients with renal insufficiency and may assist in assessing adequacy of ablation.[241]

Parapelvic Cysts

Parapelvic cysts do not communicate with the collecting system. They may originate from lymphatics or embryologic rests.[242] Most are asymptomatic, although in rare cases parapelvic cysts may cause hematuria, hypertension, or hydronephrosis; may become infected; or may bleed.[243] At sonography, parapelvic cysts appear as well-defined, anechoic, renal sinus masses (Fig. 9.69). If they have hemorrhaged, internal echoes will be seen in the cysts. It may be difficult to differentiate multiple parapelvic cysts from hydronephrosis (Fig. 9.69). Optimized technique and real-time examination usually suffice to distinguish between multiple noncommunicating, haphazard parapelvic cysts and the communicating, dilated calices and renal pelvis that are the hallmark of hydronephrosis. In rare instances where differentiation is not possible with sonography, MRI or CT can be helpful.

Medullary Cysts

Medullary Sponge Kidney

Medullary sponge kidney is described as dilated, ectatic collecting tubules. It may be focal or diffuse. The cause is unknown. The incidence of medullary sponge kidney in the general population is not known, but it is found in up to 12% of patients with renal calculi.[218,244] Associations with **hemihypertrophy, Ehlers-Danlos syndrome, congenital hypertrophic pyloric stenosis, hyperparathyroidism, Caroli disease,** and **autosomal recessive polycystic disease** have been reported.[218] Uncomplicated medullary sponge kidney is usually not associated with symptoms; with stone formation, however, renal colic, hematuria, dysuria, and flank pain may occur.[245] The onset of symptomatic medullary sponge kidney is usually in the third or fourth decade of life.[218]

Tubular ectasia may be difficult to impossible to recognize at ultrasound (see Fig. 9.44). When **nephrocalcinosis** is present, multiple echogenic shadowing foci are seen localized to the medullary pyramids (see Fig. 9.45). Erosion of a calcification into the collecting system can result in obstruction.

Medullary Cystic Disease

Familial juvenile nephronophthisis and medullary cystic disease are both characterized by small cysts at the corticomedullary junction and medulla. The kidneys are small or normal sized. **Tubulointerstitial fibrosis** is a hallmark of both entities.[246] Juvenile nephronophthisis is an autosomal recessive condition. Patients present with polyuria, salt wasting, and ultimately ESRD. **Medullary cystic disease,** on the other hand, is an autosomal dominant condition. Patients with this disease present in the third or fourth decade of life with similar renal symptoms as nephronophthisis.[247] At sonography, small echogenic kidneys with medullary cysts (0.1-1.0 cm) are seen.

Polycystic Kidney Disease

Autosomal recessive polycystic kidney disease (ARPKD) is divided into four types—perinatal, neonatal, infantile, and juvenile—depending on the patient's age at the onset of clinical manifestations. ARPKD is characterized pathologically as a spectrum of dilated renal collecting tubules, hepatic cysts, and periportal fibrosis. Younger patients present predominantly with renal insufficiency. Hepatic involvement is typically dominant in older patients with ARPKD. ARPKD occurs in 1:6000 to 1:14,000 live births. Patients with perinatal disease have massively enlarged kidneys, hypoplastic lungs, and oligohydramnios. Death usually results from pulmonary hypoplasia and renal failure. Older children will present with manifestations of portal hypertension. Renal sonographic features of ARPKD include a lack of corticomedullary differentiation and massively enlarged echogenic kidneys (Fig. 9.70). Occasionally, macroscopic cysts will be noted.

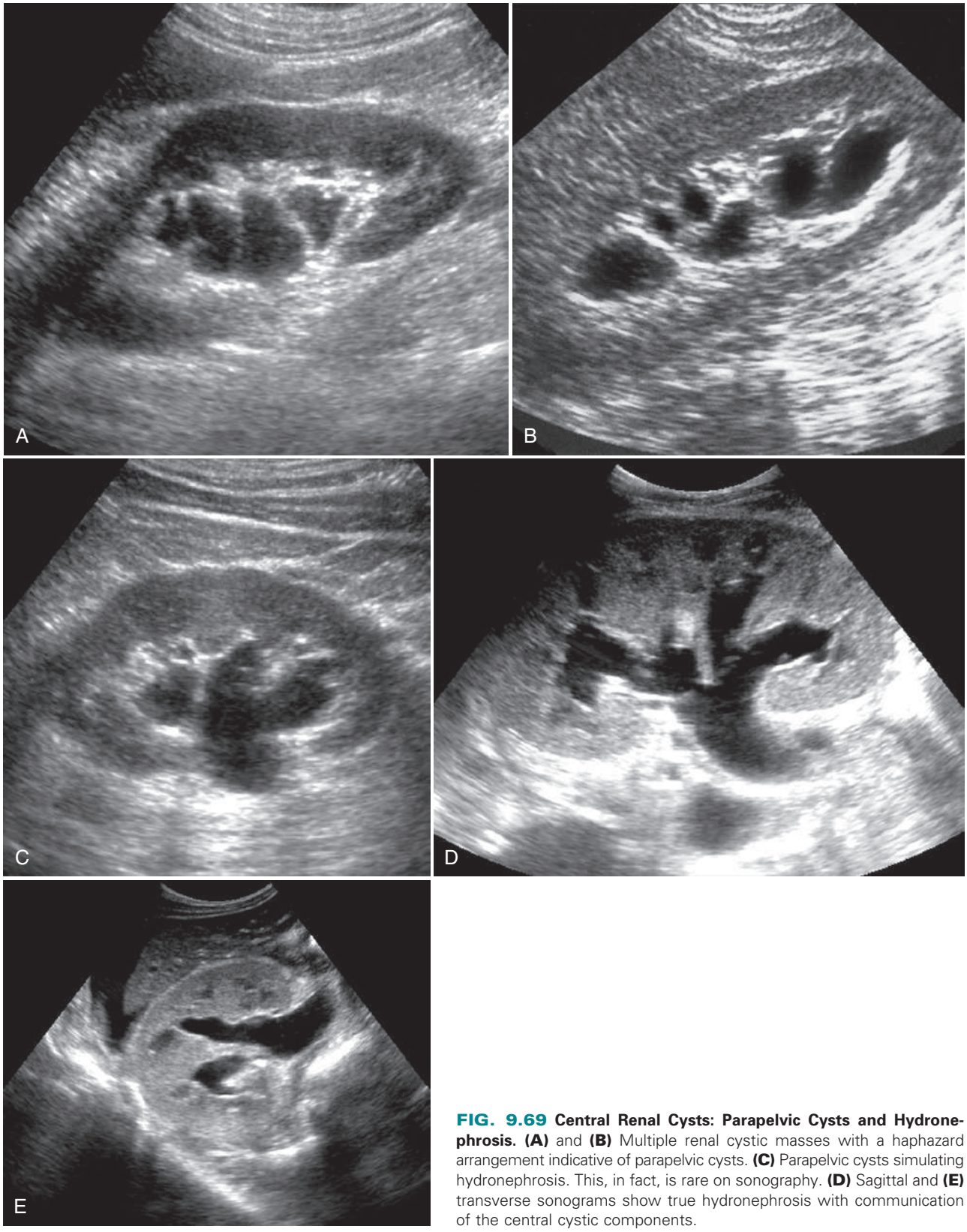

FIG. 9.69 Central Renal Cysts: Parapelvic Cysts and Hydronephrosis. (A) and **(B)** Multiple renal cystic masses with a haphazard arrangement indicative of parapelvic cysts. **(C)** Parapelvic cysts simulating hydronephrosis. This, in fact, is rare on sonography. **(D)** Sagittal and **(E)** transverse sonograms show true hydronephrosis with communication of the central cystic components.

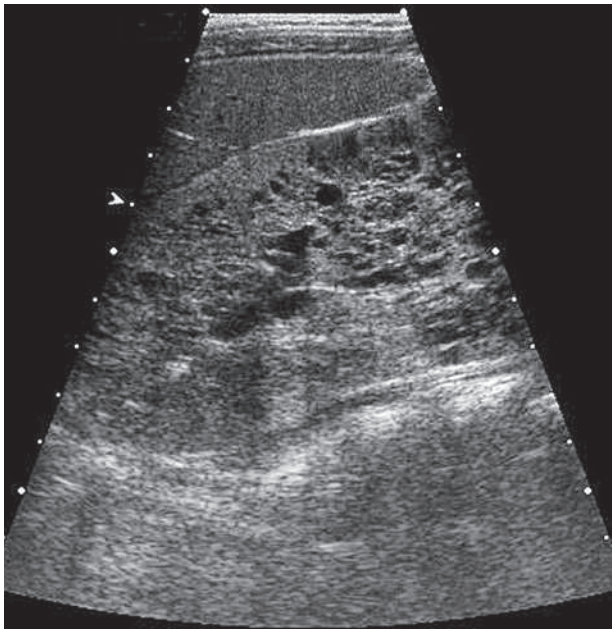

FIG. 9.70 Autosomal Recessive Polycystic Kidney Disease. Two-year-old patient with renal insufficiency. Sagittal sonogram shows marked renal enlargement and innumerable microcysts.

Autosomal dominant polycystic kidney disease (ADPKD) results in a large number of bilateral cortical and medullary renal cysts. The cysts vary in size and are often asymmetric. ADPKD is the most common hereditary renal disorder and has no gender predilection. Its incidence is 1:500 to 1:1000, and ADPKD accounts for 10% to 15% of patients receiving dialysis. Up to 50% of patients have no family history. Seemingly sporadic involvement is caused by variable expression and spontaneous mutations. Signs and symptoms of palpable masses, pain, hypertension, hematuria, and UTI usually do not develop until the fourth or fifth decade. Renal failure develops in 50% of patients and is usually present by age 60.[248] Complications of ADPKD include infection, hemorrhage, stone formation, cyst rupture, and obstruction. Stone formation tends to occur in patients with more and larger cysts.[249] Associated anomalies include liver cysts (30%-60%); pancreatic cysts (10%); splenic cysts (5%); cysts in thyroid, ovary, endometrium, seminal vesicles, lung, brain, pituitary gland, breast, and epididymis; cerebral berry aneurysms (18%-40%); abdominal aortic aneurysm; cardiac lesions; and colonic diverticula. Patients with ADPKD who are not receiving dialysis do not have an increased incidence of RCC.[248]

Ultrasound is used for screening families of patients with ADPKD, as well as for routine follow-up. At sonography, the kidneys are enlarged and replaced by multiple bilateral, asymmetric cysts of varying size (Fig. 9.71). Cysts complicated by hemorrhage or infection have thick walls, internal echoes, and/or fluid-debris levels. Dystrophic calcification within cyst walls or stones may be seen as echogenic foci with sharp, distal acoustic shadowing.

Renal cysts in patients younger than 30 years are rare. Ravine et al.[250] modified the criteria of Bear et al.[251] and reported that patients age 30 or younger with a family history of ADPKD require two renal cysts (unilateral or bilateral) to have the diagnosis of ADPKD disease. For patients age 30 to 59, two cysts in each kidney are required, and for those age 60 or older, four cysts in each kidney are needed. These criteria were modified to account for the relatively later onset of disease in patients with type 2 polycystic kidney disease, but fewer than two renal cysts in at-risk individuals older than age 40 was still sufficient to exclude the disease.[252]

Multicystic Dysplastic Kidney

Multicystic dysplastic kidney (MCDK) is a nonhereditary developmental anomaly also known as **renal dysplasia, renal dysgenesis,** and **multicystic kidney.** The kidney is small, malformed, and composed of multiple cysts with little, if any, normal renal parenchyma. The kidney functions poorly if at all. The dysplastic change is usually unilateral and involves the entire kidney, although rarely it may be bilateral, segmental, or focal. If bilateral, involving the entirety of both kidneys, it is incompatible with life. Men and women are equally affected, as are both sides. Up to 30% of patients have a contralateral UPJ obstruction. The exact pathogenesis is obscure. However, 90% of cases are associated with some form of urinary tract obstruction during embryogenesis. The severity of the malformation and the age of the patient at diagnosis account for the varying manifestations of MCKD, from a large, multicystic mass present at birth to a kidney with smaller cysts that are asymptomatic and not discovered until adulthood.

Ultrasound findings of MCKD include (1) multiple noncommunicating cysts of varying size, (2) absence of normal parenchyma and normal renal sinus, and (3) focal echogenic areas representing primitive mesenchyma or tiny cysts[253] (Fig. 9.72). In adults a small, cystic renal fossa mass is seen, and cyst wall calcification is appreciated as echogenic foci with shadowing. Calcification may be so extensive that ultrasound visualization is impossible, and CT is required to make the diagnosis. Segmental disease is usually seen in duplex kidneys, and if the cysts are tiny, the mass may appear solid and echogenic.

Lithium Nephropathy

Known complications of chronic lithium administration include nephrogenic diabetes insipidus (polyuria-polydipsia syndrome) and/or chronic renal disease. Diabetes insipidus develops in up to 40% of patients on chronic lithium therapy, and is typically reversible. On the other hand, a smaller subset of patients may develop chronic focal interstitial nephritis that is manifested by a progressive, permanent defect in urine concentrating ability and chronic renal insufficiency. The diagnosis is typically made based on clinical criteria, but biopsy findings include tubulointerstitial fibrosis, tubular dilatation, and microcysts.[254]

The histopathology of chronic lithium nephrotoxicity is manifested at ultrasound by numerous microcysts and punctate echogenic foci. These foci are thought to be microcysts rather than nonshadowing calcification[255] (Fig. 9.73).

Multilocular Cystic Nephroma

Multilocular cystic nephroma (MLCN) is an uncommon benign cystic neoplasm composed of multiple noncommunicating cysts

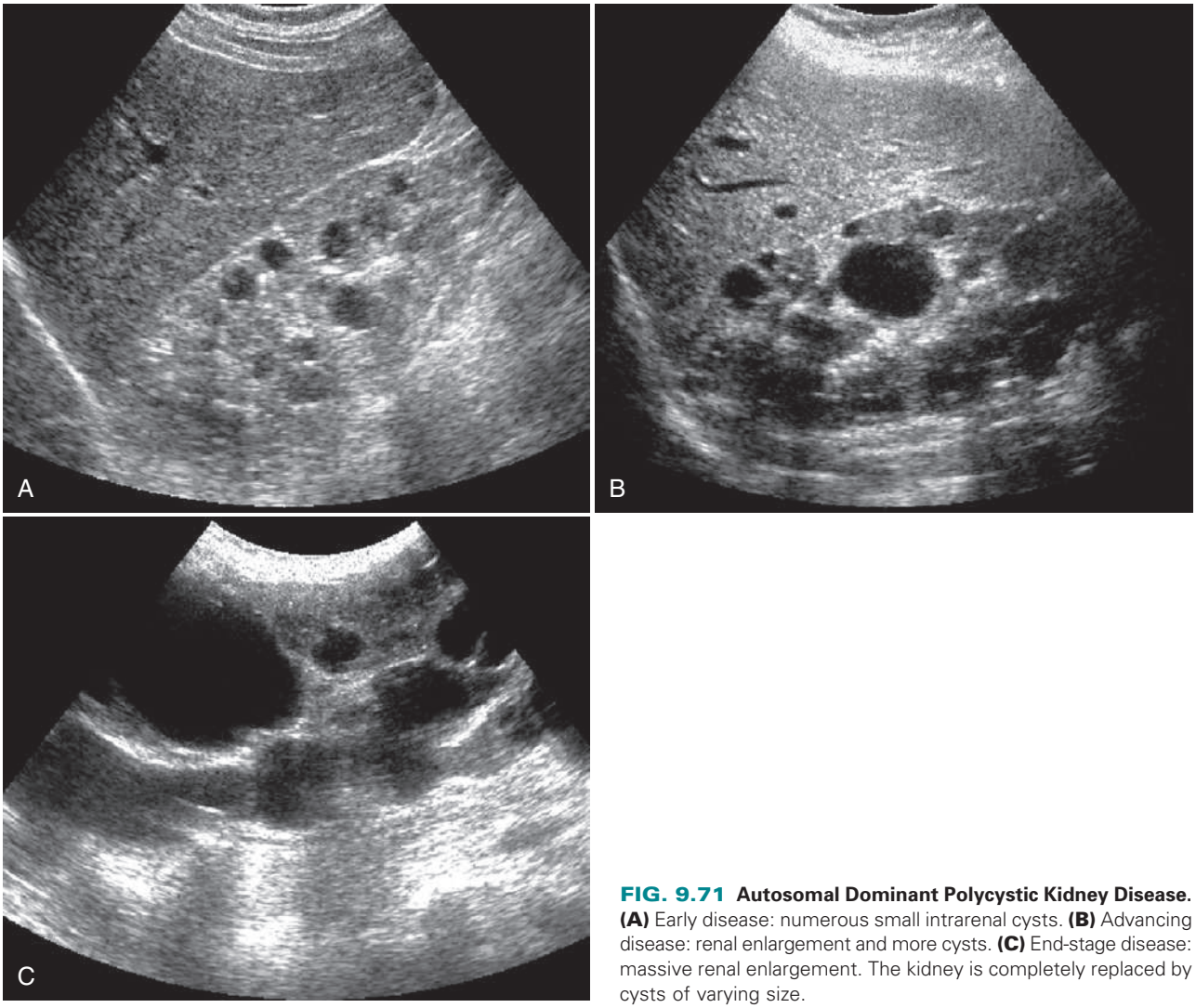

FIG. 9.71 Autosomal Dominant Polycystic Kidney Disease. **(A)** Early disease: numerous small intrarenal cysts. **(B)** Advancing disease: renal enlargement and more cysts. **(C)** End-stage disease: massive renal enlargement. The kidney is completely replaced by cysts of varying size.

FIG. 9.72 Multicystic Dysplastic Kidney. Small, malformed kidney containing multiple cysts. (Courtesy of Deborah Rubens, MD.)

contained within a well-defined capsule. Occasionally, sarcomatous stroma is present, making this a more malignant lesion. MLCN has no predilection for side, and occasionally, bilateral tumors are seen. These tumors are found in male patients less than 4 years of age and in female patients age 4 to 20 or 40 to 60 years.[256]

Most children present with an abdominal mass. Adults may be asymptomatic or may present with abdominal pain, hematuria, hypertension, or UTI.

The ultrasound appearance of MLCN is variable and depends on the number and size of the locules. With multiple large locules, noncommunicating cysts will be seen within a well-defined mass (Fig. 9.74). If the locules are tiny, a more solid-appearing nonspecific echogenic mass will be present. Calcification of the capsule and septa is uncommon. With either appearance, it is impossible with imaging to differentiate MLCN from cystic RCC.

Localized Cystic Disease

Localized cystic disease is a rare, benign, nonhereditary entity that may mimic MLCN. In localized cystic disease, multiple closely opposed cysts occupy either a portion of kidney or an entire kidney—thus the previous description of "unilateral polycystic disease."[257] At ultrasound, localized cystic disease appears a conglomerate mass of multiple cysts of varying size separated by normal or atrophic renal parenchyma (Fig. 9.75). The lack of cysts within other organs (or the contralateral kidney) and the absence of an appropriate family history prompt the

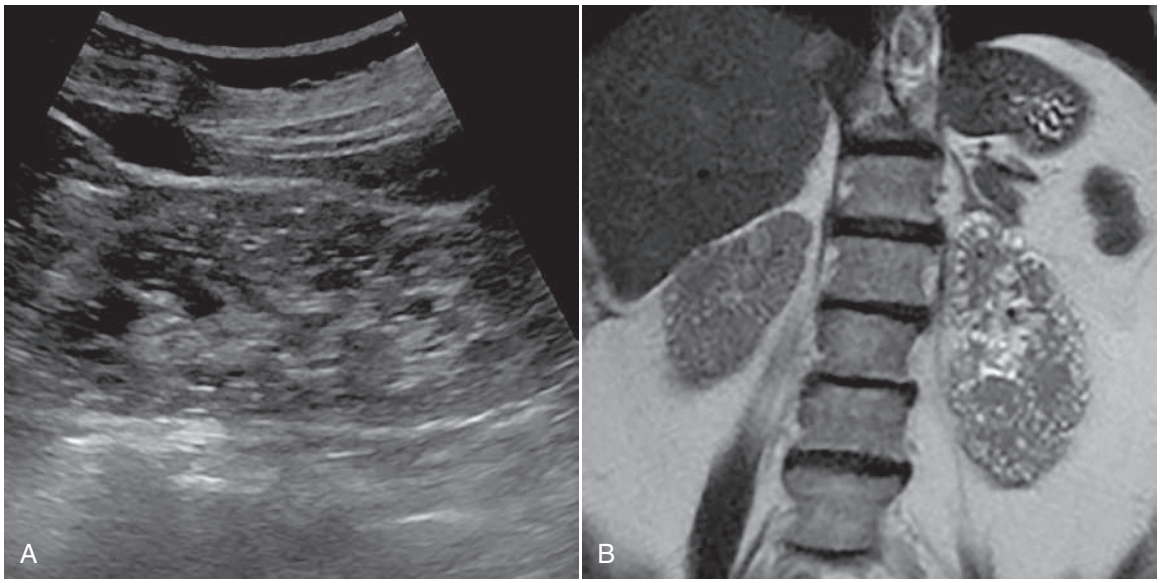

FIG. 9.73 Chronic Lithium Nephropathy. (A) Sagittal sonogram of a patient on long-term maintenance lithium therapy with a history of mild renal insufficiency and diabetes insipidus shows innumerable microcysts and punctate nonshadowing echogenic foci. **(B)** Corresponding T2-weighted MRI in the same patient confirms innumerable microcysts.

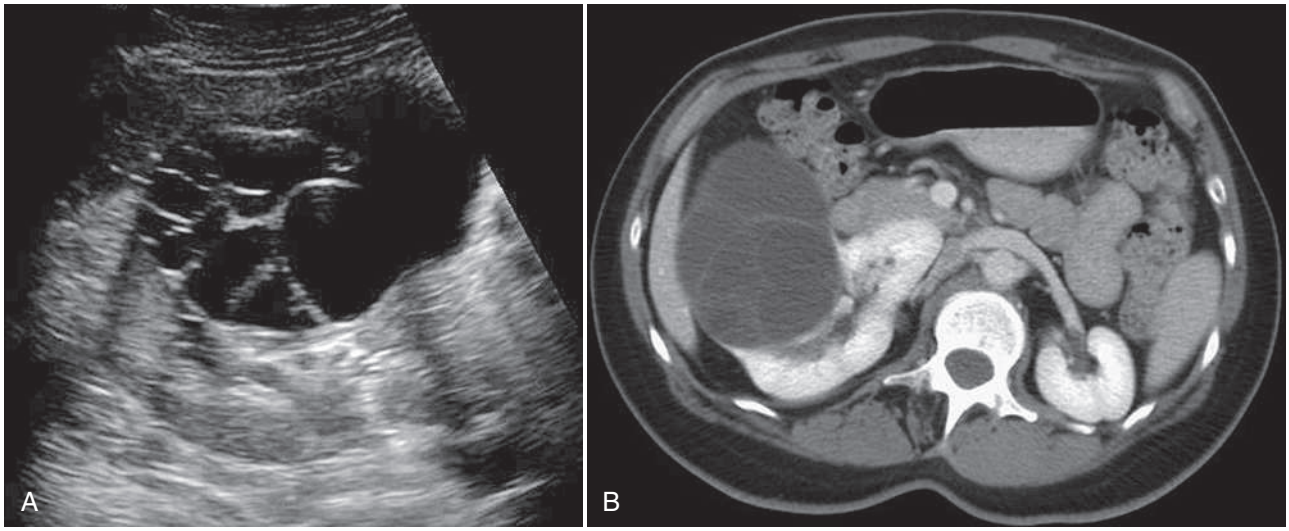

FIG. 9.74 Multilocular Cystic Nephroma. (A) Transverse sonogram demonstrates a multiseptated, exophytic, complex cystic mass with noncommunicating locules. **(B)** Confirmatory contrast-enhanced CT.

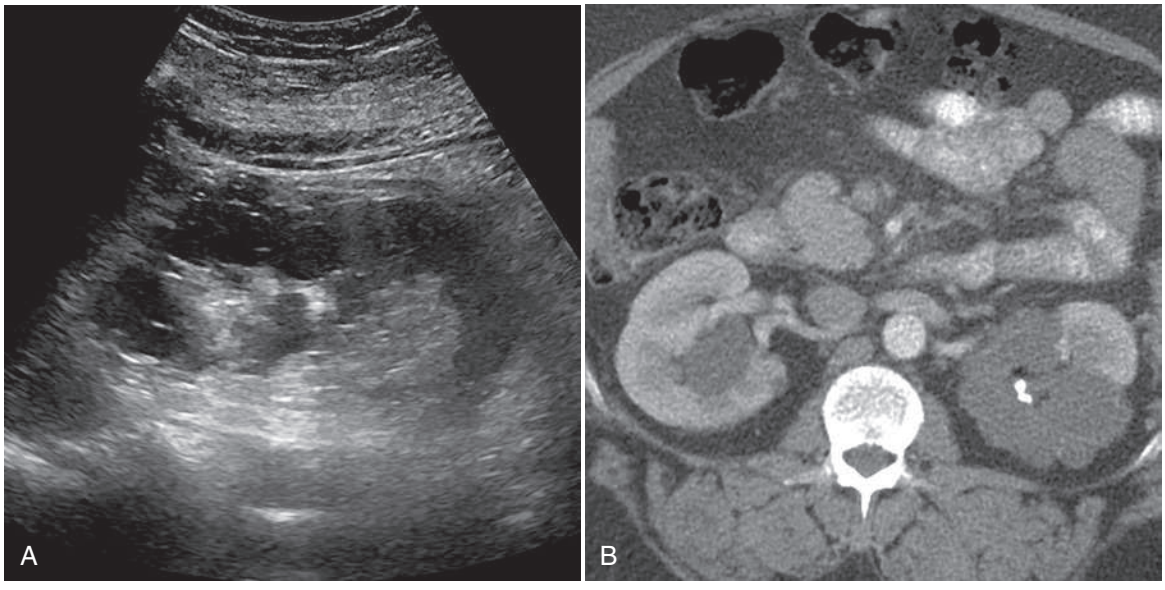

FIG. 9.75. Localized Cystic Disease. (A) Sagittal sonogram shows multiple, closely opposed cysts throughout upper pole of kidney. **(B)** Corresponding contrast-enhanced CT shows that the upper pole of the left kidney is replaced by innumerable cysts.

ultrasound diagnosis of localized cystic disease, although CT or MRI confirmation is typically needed. In addition, CT (or MRI) better shows the thick, fibrous, encapsulating capsule characteristic of MLCN.[258]

Neoplasm-Associated Renal Cystic Disease

Acquired Cystic Kidney Disease

Acquired cystic kidney disease (ACKD) occurs in the native kidneys of patients with **renal failure** undergoing either hemodialysis or peritoneal dialysis. ACKD affects 40% to 90% of these patients, depending on the duration of dialysis.[127,128,247,259] RCC occurs in 4% to 10% of patients with ACKD.[259] The pathogenesis of ACKD is speculative. Epithelial hyperplasia caused by tubular obstruction resulting from toxic substances plays some role in the development of both cysts and tumors.[259] On histology, multiple small cysts (0.5-3 cm) involving both renal cortex and medulla are found. Hemorrhage into cysts is common. Ultrasound, CT, and MRI are useful in the evaluation and follow-up of patients with ACKD and its complications.[127,128,260] ACKD and tumor development persist even after successful renal transplantation. ACKD and tumors may develop in renal allografts during dialysis therapy.[261]

At sonography, finding three to five cysts in each kidney in a patient with chronic renal failure is diagnostic.[261] The cysts are usually small, as are the kidneys, which typically are quite echogenic (Fig. 9.76). Internal echoes are seen in cysts that have hemorrhaged. Tumors are solid or cystic with mural nodules.

Von Hippel–Lindau Disease

VHL disease is transmitted as an autosomal dominant gene with variable expression and moderate penetrance. Its incidence is 1:35,000.[248] The predominant significant abnormalities include **retinal angiomatosis,** central nervous system **hemangioblastomas, pheochromocytomas,** and **renal cell carcinoma** (40%). RCC in VHL patients usually is multifocal (75%-90%) and bilateral (75%). These patients are often offered nephron-sparing surgery. In addition, renal cysts, the most common finding in VHL disease, are found in 76% of patients.[262] Cysts range from 0.5 to 3.0 cm in size and are mostly cortical based. Ultrasound may be used as an initial screening test for VHL disease. However, CT or MRI is better for detection of the small, multifocal, bilateral tumors found in VHL disease and are the preferred modalities for surveillance after nephron-sparing surgery (Fig. 9.77).

Tuberous Sclerosis

Tuberous sclerosis is an autosomal dominant syndrome characterized by mental retardation, seizures, and adenoma sebaceum. Many cases also result from spontaneous mutation. The incidence ranges from 1:9000 to 1:170,000.[263] Associated renal lesions include cysts, AML, and RCC (1%-2%).[248] The renal cysts vary in size from microscopic to 3 cm. At sonography, if only cysts are present, it may be difficult to differentiate tuberous sclerosis from ADPKD. The presence of cysts and multiple AMLs suggests

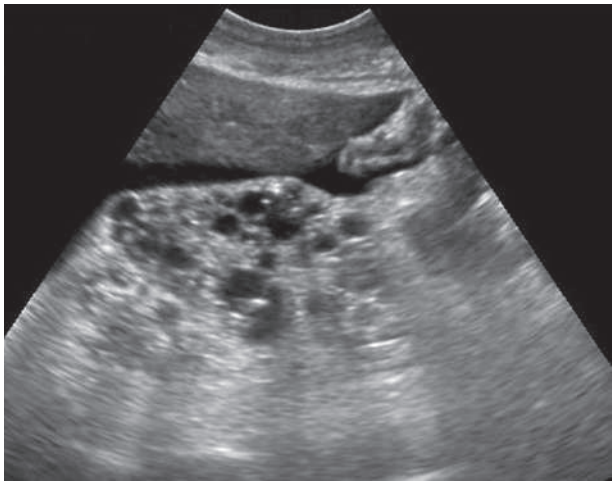

FIG. 9.76 Acquired Cystic Kidney Disease. Sagittal sonogram demonstrates an echogenic small kidney containing multiple cysts. A small amount of intraperitoneal dialysate fluid is seen.

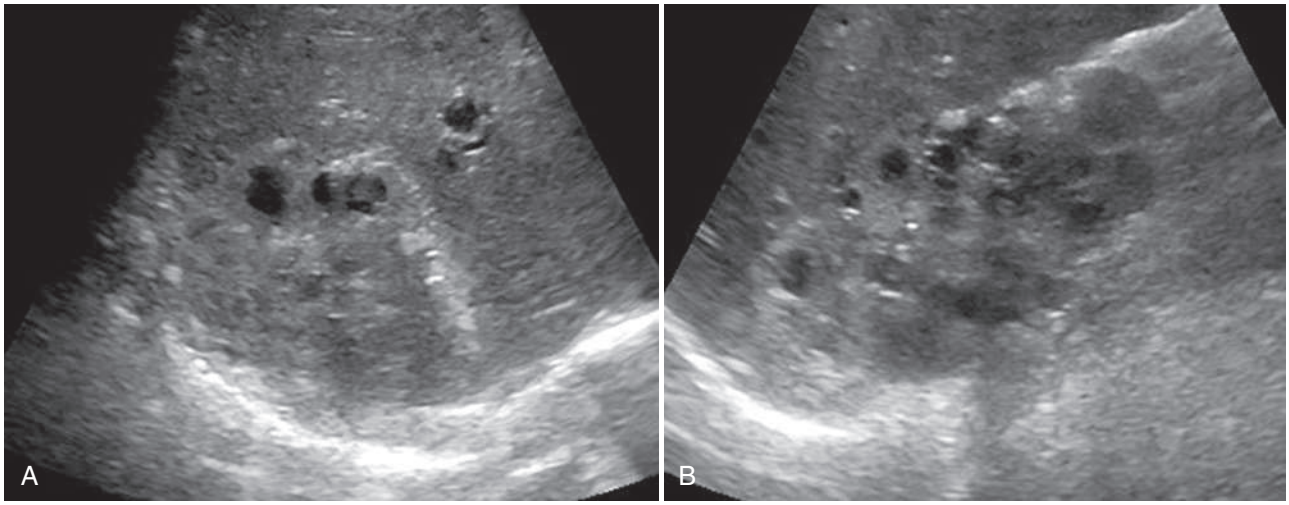

FIG. 9.77 Von Hippel–Lindau Disease. (A) Transverse and **(B)** sagittal sonograms show multiple small, complex cystic lesions.

tuberous sclerosis (Fig. 9.78). Periodic CT screening is recommended to assess for AML growth and tumor development.

TRAUMA

Renal Injuries

Traumatic injury to the kidney may be blunt or penetrating. Most forms of **blunt** trauma to the kidney are relatively minor and heal without treatment. **Penetrating** injuries are usually the result of gunshot or stab wounds. Kidneys with cysts, tumors, and hydronephrosis are more prone to injury. Renal injuries are classified into the following four categories[264]:

I: Minor injury (75%-85%): contusions, subcapsular hematoma, small cortical infarct and lacerations that do not extend into the collecting system

II: Major injury (10%): renal lacerations that extend into the collecting system and segmental renal infarct

III: Catastrophic injury (5%): vascular pedicle injury and shattered kidney

IV: Uteropelvic junction avulsion

Category I lesions are treated conservatively, whereas category III and IV lesions require urgent surgery. Category II lesions are treated conservatively or surgically depending on severity.[264,265]

CT is regarded as the premier imaging modality for the evaluation of suspected renal trauma.[264] Because renal trauma is frequently accompanied by injuries to other organs, CT has the advantage of multiorgan imaging. Theoretically, sonography has the capability of evaluating traumatized kidneys; in reality, technical limitations usually hinder an adequate examination. Sonography does not provide information regarding renal function and is probably best used in the follow-up of patients with known renal parenchymal trauma. **Renal hematomas** may be hypoechoic, hyperechoic, or heterogeneous. **Lacerations** are seen as linear defects that may extend through the kidney if a fracture is present (Fig. 9.79). Associated **perirenal collections** consisting of blood and urine will be present if the kidney is fractured. **Subcapsular hemorrhage** can be seen as a perirenal fluid collection that flattens the underlying renal contour (Fig. 9.80). A **shattered kidney** consists of multiple fragments of disorganized tissue with associated hemorrhage and urine collection in the renal bed. Color

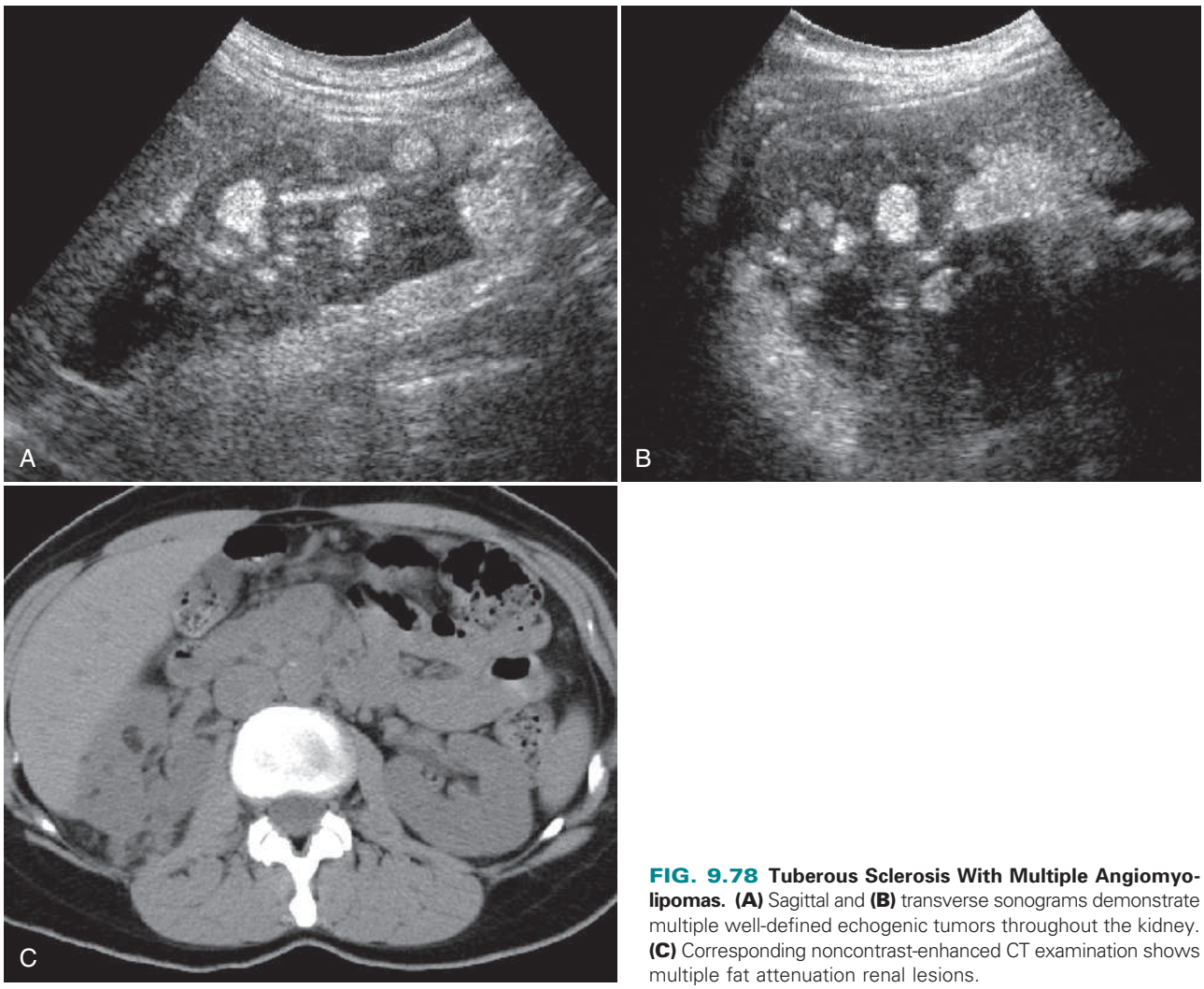

FIG. 9.78 Tuberous Sclerosis With Multiple Angiomyolipomas. (A) Sagittal and **(B)** transverse sonograms demonstrate multiple well-defined echogenic tumors throughout the kidney. **(C)** Corresponding noncontrast-enhanced CT examination shows multiple fat attenuation renal lesions.

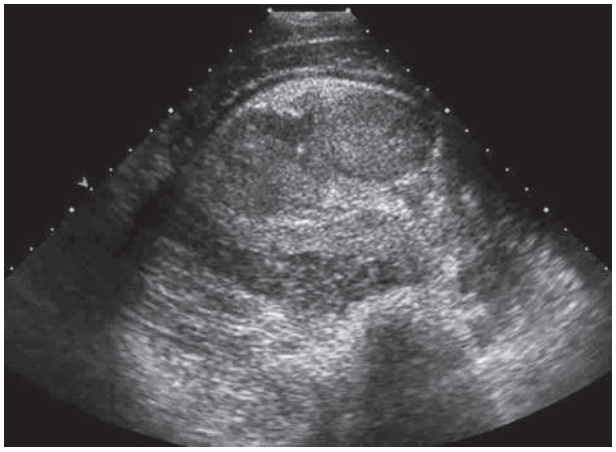

FIG. 9.79 Renal Laceration. Transverse sonogram shows capsular disruption and mixed-echogenicity perirenal hematoma. (Courtesy of John McGahan, MD.)

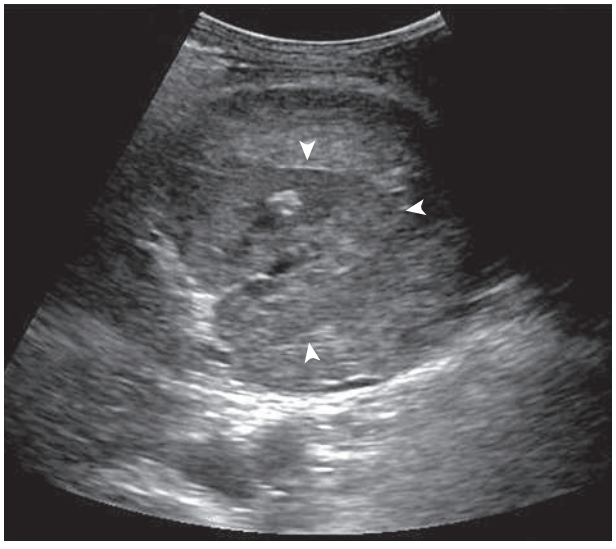

FIG. 9.80 Subcapsular Hematoma After Renal Biopsy. Note compression of kidney *(arrowheads)* by large, hyperechoic subcapsular hematoma.

Doppler sonography may be helpful in the assessment of **vascular pedicle injuries.** As use of CEUS becomes more prevalent, there may be a role for CEUS in the initial bedside assessment and follow-up of renal injuries in critically ill patients.[266,267]

Ureteral Injuries

Traumatic injury of the ureter is most often a complication of either gynecologic (70%) or urologic (30%) surgery.[268] Blunt and penetrating injuries are much less common. Sonography is not useful in the assessment of these injuries, except to detect sizable fluid collections and hydronephrosis.

Bladder Injuries

Bladder injury may be the result of blunt, penetrating, or iatrogenic trauma. Bladder injury may result in extraperitoneal or intraperitoneal rupture, or a combination. Sonography is usually not helpful in the assessment of these injuries, except to identify large fluid collections or free intraperitoneal fluid.

VASCULAR ABNORMALITIES

Renal Vascular Doppler Sonography

The number and size of arteries supplying a kidney are quite variable. Duplex and color Doppler imaging are able to demonstrate both normal and abnormal renal blood flow. Normal flow within the renal artery and its branches has a "low resistance" perfusion pattern, with continuous forward blood flow during diastole. Several Doppler parameters have been used to describe changes in Doppler arterial spectra that may accompany renal disease. The most common parameter is the RI. Keogan et al.[269] recommend averaging a number of RI measurements in a kidney before a single representative average is reported. Most sonographers consider an RI of 0.7 to be the upper threshold of normal in adults, although renal RIs greater than 0.7 may be seen in children younger than 4 years of age and in older patients, despite normal renal function.[270-272] Mostbeck et al.[273] also showed how the RI varies with heart rate and can range from 0.57 ± 0.06 (pulse, 120/min) to 0.70 ± 0.06 (pulse, 70/min).

Despite this variability, early literature indicated the potential of Doppler for improving the sonographic assessment of **renal dysfunction.** Changes in intrarenal spectra (quantified using RI) were associated with acute or chronic urinary obstruction, several intrinsic native renal diseases, renal transplant rejection, and renal vascular disease. Less favorable results in follow-up studies and discouraging clinical experience prompted most radiologists to abandon the RI. Studies show that the RI varies as a result of **driving pulse pressures,** which explains Mostbeck's observation of rate-dependent changes in RIs, as well as changes in vascular/interstitial compliance.[112-114]

Renal Artery Occlusion and Infarction

Renal artery occlusion may be caused by either emboli or in situ thrombosis. The degree of renal insult depends on the size and location of the occluded vessel. If the main renal artery is occluded, the entire kidney will be affected, whereas segmental infarction and focal infarction occur with peripherally located vascular occlusion. The acutely infarcted kidney is often normal appearing at gray-scale sonography. However, no flow within the kidney is shown at duplex and color/power Doppler examination (Fig. 9.81). Segmental or focal infarction may appear as a wedge-shaped mass indistinguishable from acute pyelonephritis. With time, an echogenic mass[274] or scar may form. With chronic occlusion, a small, scarred, end-stage kidney will be seen.

Arteriovenous Fistula and Malformation

Abnormal arteriovenous communications can be acquired (75%) or congenital (25%). **Acquired** lesions are usually iatrogenic, although spontaneous abnormal arteriovenous communications may occur with eroding tumors. Most acquired lesions consist of a single, dominant feeding artery and a single, dominant draining vein. **Congenital** malformations consist of a tangle of

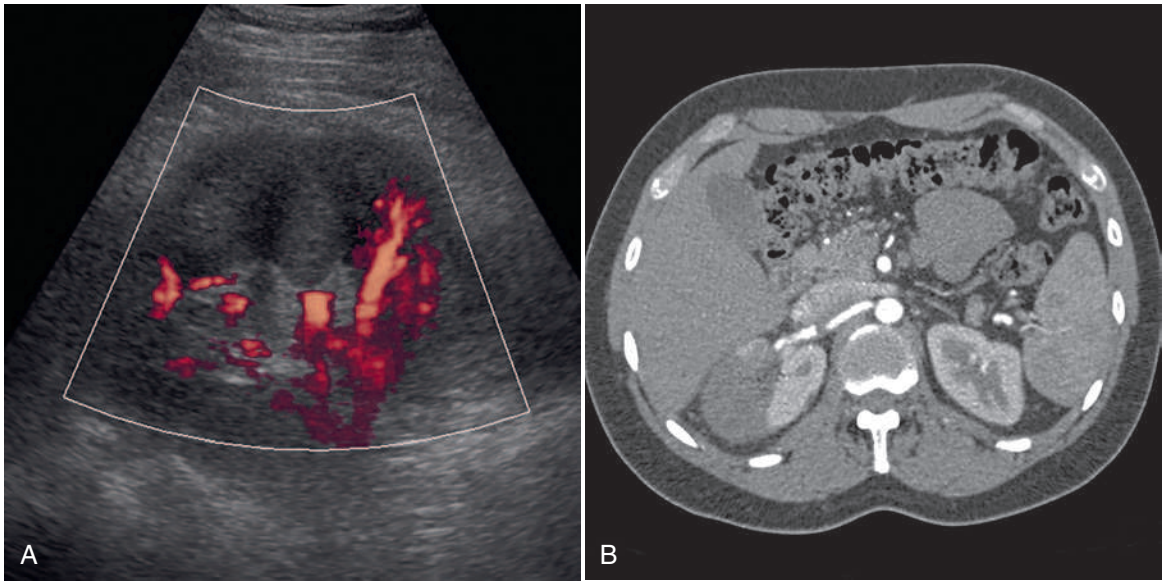

FIG. 9.81. Renal Infarct. (A) Transverse power Doppler sonogram shows an avascular slightly echogenic "lesion." **(B)** Corresponding CT angiogram shows an acute right upper-pole renal infarct and focal clot within mid right renal artery. (Courtesy of William Middleton, MD. Mallinckrodt Institute of Radiology, St. Louis Missouri.)

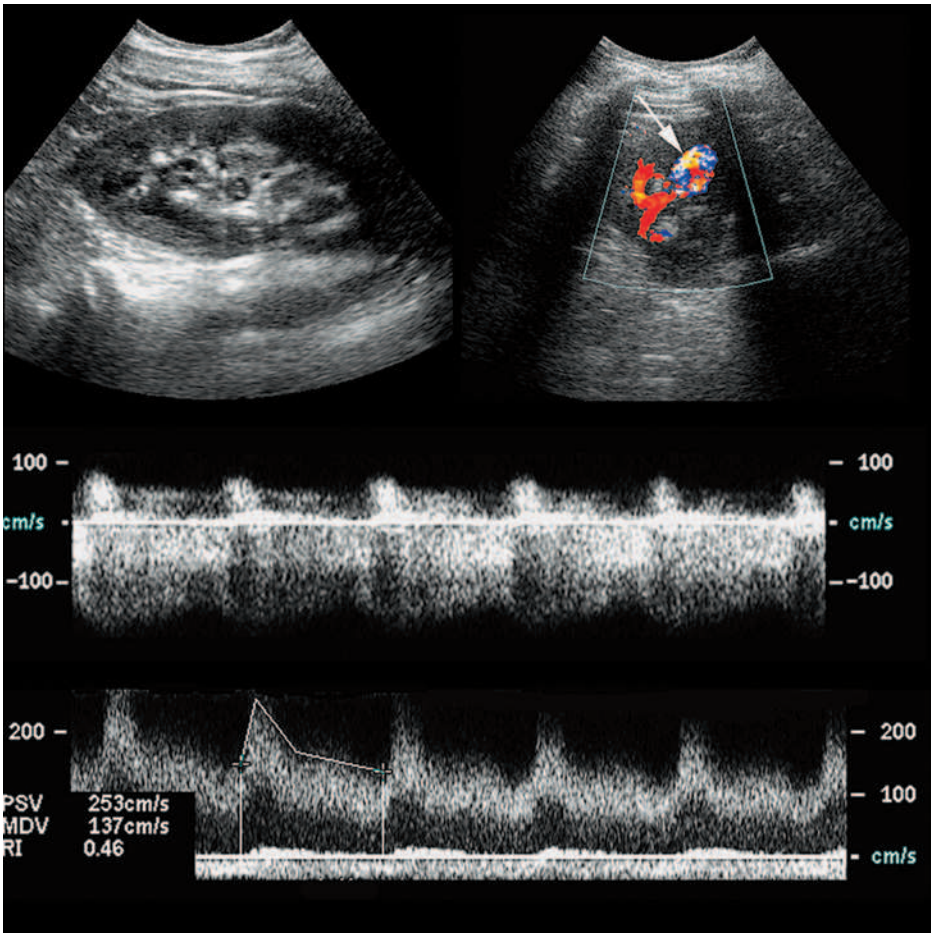

FIG. 9.82 Renal Arteriovenous Malformation (AVM). Top: *Left image,* Normal sagittal sonogram of the kidney. *Right image,* Focus of color aliasing *(arrow).* **Middle:** Spectral waveform shows a high-velocity draining vein. **Bottom:** Spectral wave form shows an arterial signal from within the AVM. Note high-velocity, low "resistance" flow (RI = 0.46).

small, abnormal vessels. Gray-scale sonography may reveal no abnormality. The addition of duplex and color Doppler imaging has been helpful in defining these lesions.[275] Duplex Doppler demonstrates increased flow velocity, a decreased RI (0.3-0.4), and turbulent diastolic flow in the arterial limb. Arterial pulsations in the draining vein are also observed. Spectral broadening is present. Color Doppler sonography may demonstrate a tangle of tortuous vessels with multiple colors, indicative of the haphazard orientation and turbulent flow within the malformation (Fig. 9.82).

Renal Artery Stenosis

Hypertension may be **primary** (95%-99%) or **secondary** (1%-5%). The vast majority of patients with secondary hypertension have renovascular disease. **Renovascular disease** is most frequently caused by **atherosclerosis** (66%), and the majority of the remaining cases largely result from **fibromuscular dysplasia.**[276] Many different imaging techniques have been used in an effort to detect patients with renovascular hypertension. These include intravenous and intraarterial digital subtraction angiography, captopril renal scintigraphy, duplex and color Doppler ultrasound, CT angiography, and magnetic resonance angiography.

Numerous studies and clinical experience in ultrasound laboratories have suggested the utility of **Doppler ultrasound** as an initial screening examination for renal vascular hypertension. The screening approach may involve (1) detection of abnormal Doppler signals at or just distal to the stenosis or (2) detection of abnormal Doppler signals in the intrarenal vasculature. Typical direct criteria for hemodynamically significant stenosis (>60%-70%) include a focal peak systolic velocity of higher than 200 cm/sec, poststenotic turbulence, and a renal artery to aortic ratio of greater than 3.5.[277]

Evaluation of the main renal arteries in their entirety is usually not possible with ultrasound. It is estimated that the main renal arteries are not seen in up to 42% of patients.[278] In addition, 14% to 24% of patients have accessory renal arteries that are usually not detected sonographically. Therefore, evaluation of the main renal arteries as a screening approach for renal artery stenosis often fails, particularly in difficult-to-scan patients. The second approach is to interrogate the intrarenal vasculature. Normally, there is a steep upstroke in systole with a second small peak in early systole. A **tardus-parvus waveform** downstream from a stenosis refers to a slowed systolic acceleration with low amplitude of the systolic peak (Fig. 9.83). To evaluate the delayed upstroke, two measurements are taken:

- **Acceleration time:** time from start of systole to peak systole
- **Acceleration index:** slope of the systolic upstroke

An acceleration time greater than 0.07 second and a slope of systolic upstroke less than 3 m/sec^2 are suggested as thresholds to assess for renal artery stenosis.[278] Simple recognition of the change in pattern may be adequate[279] (Fig. 9.84). Pharmacologic manipulation with **captopril**[280] can enhance the waveform abnormalities in patients with renal artery stenosis. The use of intravascular contrast agents increases the technical success rate for the evaluation of renal artery stenosis.[281] They may also play a role in the assessment and follow-up of patients undergoing renal artery angioplasty and stent placement.[282]

Despite abundant literature indicating the promise of either direct or indirect Doppler approaches, both techniques can be tedious in hard-to-scan patients. Widely varying reported sensitivities and specifities for both approaches for the detection of "significant" renal arterial stenosis have also called into question

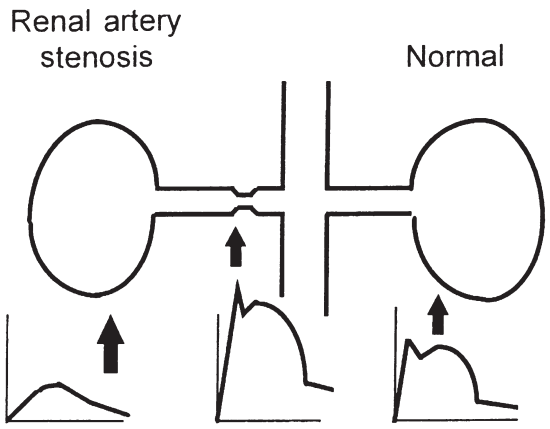

FIG. 9.83 Schematic Diagram of Renal Artery Doppler Tracings. *Right side,* Tracing from a normal renal artery. Note early systolic peak. *Middle,* Tracing shows high-velocity flow measured at the stenosis. *Left side,* Tracing shows the dampened tardus-parvus waveform downstream from the stenosis. (With permission from Mitty HA, Shapiro RS, Parsons RB, Silberzweig JE. Renovascular hypertension. Radiol Clin North Am. 1996;34:1017-1036.[278])

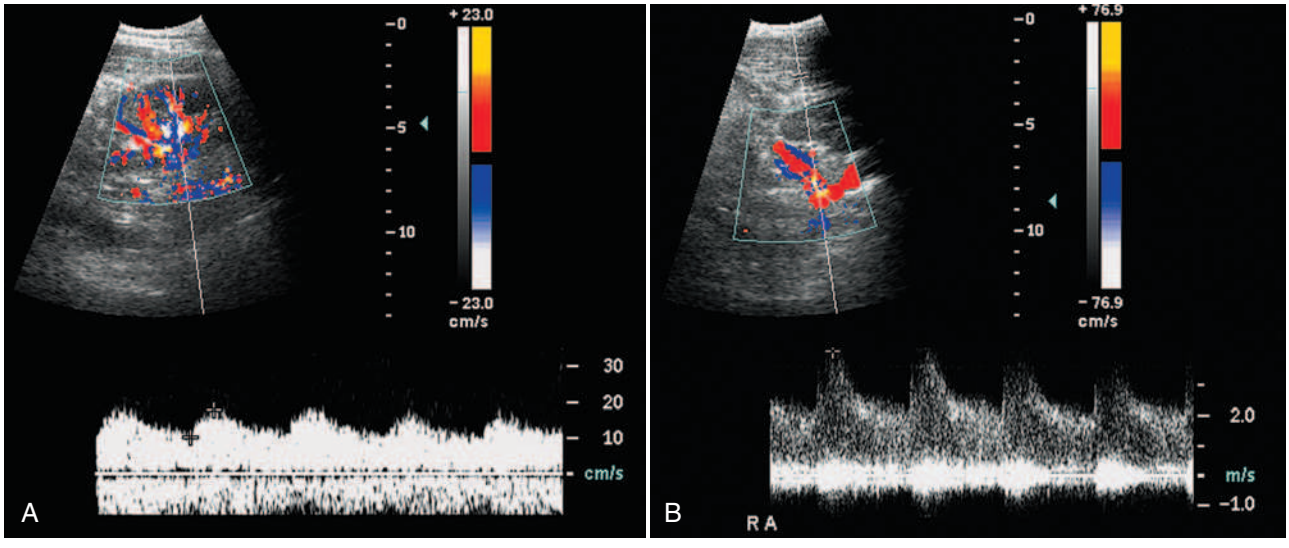

FIG. 9.84 Renal Artery Stenosis. (A) Intrarenal spectral waveform shows a tardus-parvus signal with a prolonged acceleration time and low resistive index (RI). **(B)** Waveform at the origin of the renal artery from the aorta shows a high peak velocity of 410 cm/sec with an RI of 0.43.

the potential of Doppler as a primary screening modality. Moreover, several recent trials showing no benefit of revascularization/stenting over conservative, pharmacologic antihypertensive management of renal arterial stenosis may impact screening algorithms in the future.[283,284]

Renal Artery Aneurysm

Renal artery aneurysms are saccular or fusiform dilatations of the renal artery or one of its branches. The incidence of renal artery aneurysm is 0.09% to 0.3%.[285] The cause may be congenital, inflammatory, traumatic, atherosclerotic, or related to fibromuscular disease. If the aneurysm is large (>2.5 cm), noncalcified, or associated with pregnancy, the possibility of rupture increases and treatment is recommended. At gray-scale sonography, a cystic mass may be seen. The addition of duplex and color Doppler imaging will readily demonstrate arterial flow within the cystic mass (Fig. 9.85).

Renal Vein Thrombosis

Renal vein thrombosis (RVT) usually results from an underlying abnormality of the kidney, dehydration, or hypercoagulability. Tumors of the kidney and left adrenal gland may grow into the veins, resulting in RVT. Extrinsic compression related to tumors, **retroperitoneal fibrosis, pancreatitis,** and **trauma** cause RVT by attenuating the vessel and slowing flow. In adults the most common cause of RVT is **membranous glomerulonephritis;** 50% of patients with this disease will have RVT. If thrombosis is acute, the patient may have flank pain and hematuria. Venous collaterals develop with more chronic occlusion; patients with chronic RVT thus are often asymptomatic.

The sonographic features of acute RVT are nonspecific and include an enlarged, edematous, hypoechoic kidney with loss of normal corticomedullary differentiation.[286,287] Occasionally, thrombus will be seen within the renal vein (Fig. 9.86), but acutely, it may be anechoic and difficult to visualize. The use of duplex and color Doppler ultrasound can help; however, the inability to detect flow within renal veins does not necessarily indicate RVT. Extremely slow flow often will not be detected in difficult-to-scan patients despite optimized technique. Absent or reversed end diastolic flow in the intraparenchymal native renal arteries is a secondary sign of RVT. Platt et al.[288] evaluated 20 native kidneys in 12 patients with clinical findings suggestive of acute RVT. They found that normal arterial Doppler studies should not prevent further workup if RVT is suspected (2 in 4 with normal Doppler had RVT), and that absent or reversed diastolic signals should not be considered specific for RVT (2 in 10 with absent or reversed diastolic flow had RVT). If findings are equivocal, MRI should be performed. Chronic RVT usually results in a small, end-stage, echogenic kidney.

Ovarian Vein Thrombosis

Ovarian vein thrombosis is most commonly seen in postpartum women, but it may also be seen as a result of pelvic inflammatory disease, Crohn disease, or after gynecologic surgery. The right side is affected more often than the left. Gray-scale, duplex, and color Doppler sonography may reveal a long, tubular structure filled with thrombus extending from the region of the renal vein to deep within the pelvis. Patients are usually treated with anticoagulation and antibiotics.

MEDICAL GENITOURINARY DISEASES

Patients presenting with elevated creatinine levels are often sent to the ultrasound department for an initial screening test. The purpose is to rule out an underlying mechanical obstruction. If

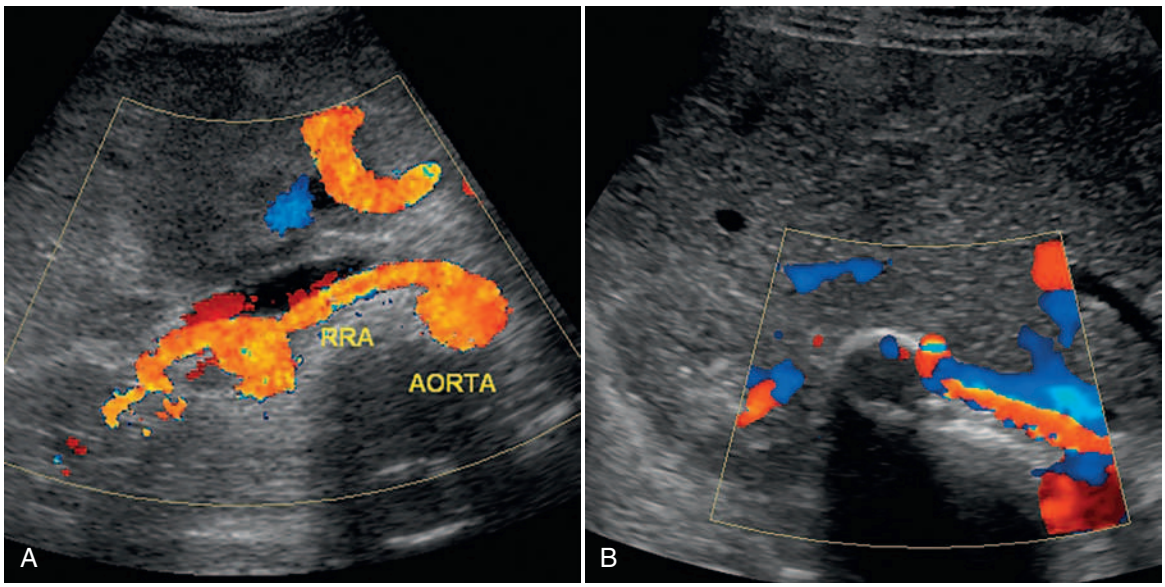

FIG. 9.85 Renal Artery Aneurysm. (A) Color Doppler ultrasound image shows a distal right renal artery aneurysm. **(B)** Color Doppler of another patient shows a peripherally calcified but thrombosed distal right renal artery (RRA) aneurysm.

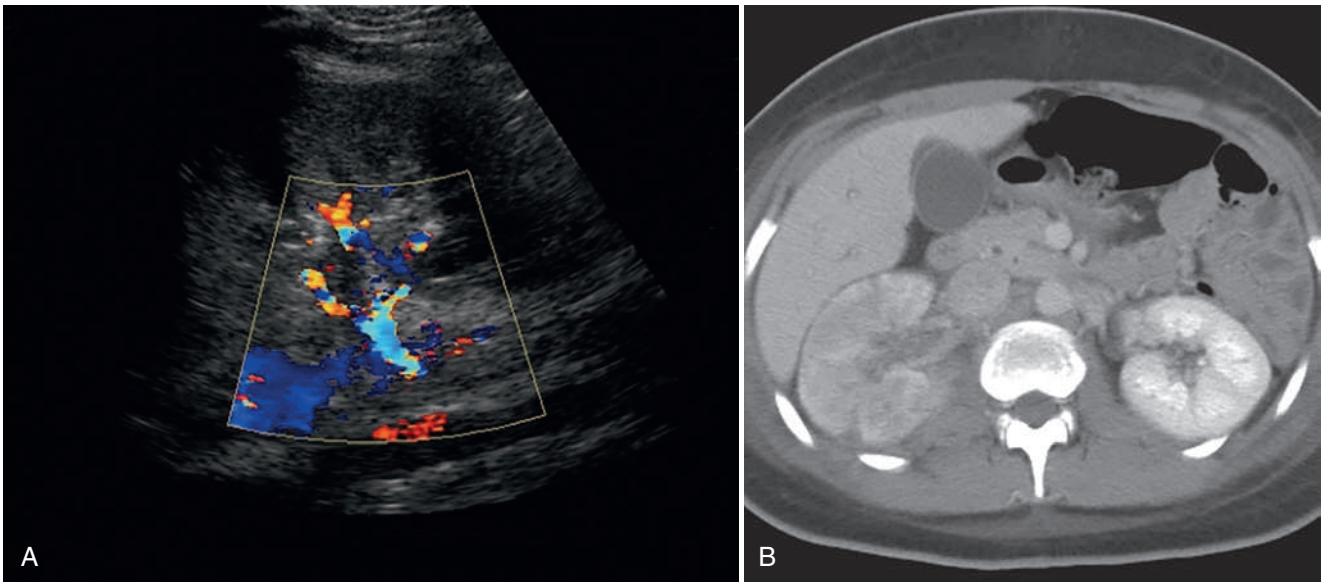

FIG. 9.86 Renal Vein Thrombosis. (A) Color Doppler image shows an echogenic right kidney and nonocclusive right renal vein thrombus extending into inferior vena cava. **(B)** Corresponding contrast-enhanced CT shows an enlarged right kidney, a delayed right nephrogram, and a right renal vein thrombus. (Courtesy of Shweta Bhatt, MD.)

obstruction is not found, this often indicates a renal parenchymal abnormality—thus the terms ***medical renal disease*** or ***renal parenchymal disease.*** The acutely injured kidney may be hyperechoic, echogenic, or normal appearing at ultrasound; a thin rim of perirenal fluid is often shown in the acute setting.[289,290] The chronically diseased kidney is small and echogenic (Fig. 9.87). Unfortunately, it is usually impossible to distinguish between the numerous causes of intrinsic renal disease based on the appearance of the kidney at ultrasound, although renal size is a clinically relevant parameter used to distinguish between acute and chronic processes. Thus percutaneous biopsy is often necessary when clinical features and history are inconclusive.

Acute Tubular Necrosis

Acute tubular necrosis (ATN) is the most common cause of acute reversible renal failure and is related to deposition of cellular debris within the renal collecting tubules. Both ischemic and toxic insults will cause tubular damage. Initiating factors include hypotension, dehydration, drugs, heavy metals, and solvent exposure. The sonographic appearance of ATN depends on the underlying cause. With ATN caused by hypotension, kidneys may appear normal, whereas drugs, metals, and solvents will cause enlarged, echogenic kidneys. Prerenal disease and ATN account for 75% of all patients presenting with acute renal failure.

Acute Cortical Necrosis

Acute cortical necrosis (ACN) is a rare cause of acute renal failure resulting from ischemic necrosis of the cortex with sparing of the medullary pyramids. The outermost aspect of cortex remains viable as a result of capsular blood supply. ACN occurs in association with sepsis, burns, severe dehydration, snakebite, and pregnancy complicated by **placental abruption** or **septic abortion.** The exact cause is uncertain, although it is likely related to a transient episode of intrarenal vasospasm, intravascular thrombosis, or glomerular capillary endothelial damage. At sonography, the renal cortex is initially hypoechoic[291] (Fig. 9.88). With time (mean, 2 months), both kidneys atrophy and the cortex may calcify.

Glomerulonephritis

Necrosis and mesangial proliferation of the glomerulus are the hallmarks of **acute glomerulonephritis.** Systemic diseases that also have acute glomerulonephritis as a feature include **polyarteritis nodosa, systemic lupus erythematosus, Wegener granulomatosis, Goodpasture syndrome, thrombocytopenic purpura,** and **hemolytic uremic syndrome.** Patients often present with hematuria, hypertension, and azotemia. At sonography, both kidneys are affected; the size of the kidneys may be normal, but renomegaly is often encountered. The echo pattern of the cortex is altered; renal cortex may be normal, echogenic, or hypoechoic, but the medulla is spared (see Fig. 9.87). With treatment, the kidneys may revert to a normal size and echogenicity. **Chronic glomerulonephritis** occurs with unabated acute disease over weeks to months following an acute episode. Profound, global, symmetrical parenchymal loss occurs. The calices and papillae are normal, and the amount of peripelvic fat increases. Small, smooth, echogenic kidneys are seen, with prominence of the central echo complex.

Acute Interstitial Nephritis

Acute interstitial nephritis is an acute hypersensitivity reaction of the kidney most often related to drugs. Penicillin, methicillin, rifampin, sulfa drugs, nonsteroidal antiinflammatory drugs, cimetidine, furosemide, and thiazides have been implicated. Usually, renal failure will resolve with cessation of drug therapy. At sonography, enlarged echogenic kidneys are noted.

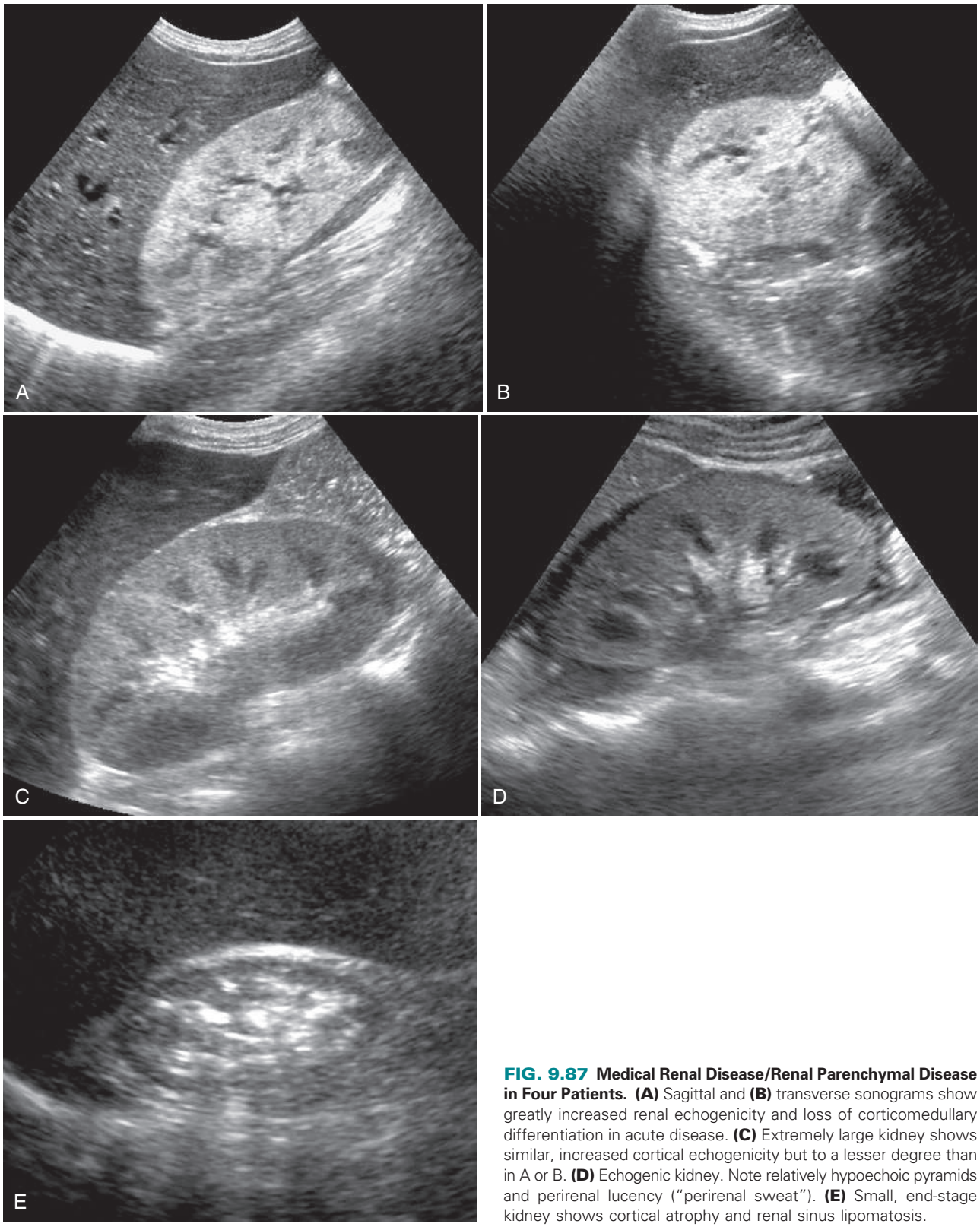

FIG. 9.87 Medical Renal Disease/Renal Parenchymal Disease in Four Patients. (A) Sagittal and **(B)** transverse sonograms show greatly increased renal echogenicity and loss of corticomedullary differentiation in acute disease. **(C)** Extremely large kidney shows similar, increased cortical echogenicity but to a lesser degree than in A or B. **(D)** Echogenic kidney. Note relatively hypoechoic pyramids and perirenal lucency ("perirenal sweat"). **(E)** Small, end-stage kidney shows cortical atrophy and renal sinus lipomatosis.

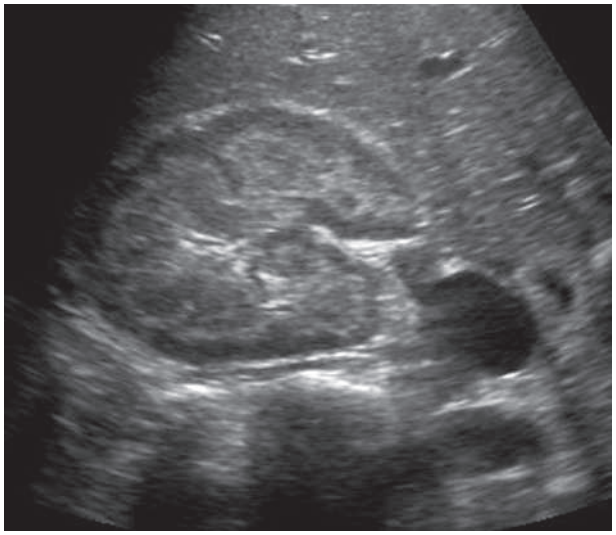

FIG. 9.88 Acute Cortical Necrosis. Transverse sonogram shows a rim of cortical hypoechogenicity.

FIG. 9.89 Bladder Endometrioma. Transvaginal scan demonstrates cystic components in a mural mass that are typical for an endometrioma. (With permission from Damani N, Wilson S. Nongynecologic applications of transvaginal ultrasound. Radiographics. 1999;19:S179-S200.[83])

Diabetes Mellitus

Diabetes mellitus is the most common cause of **chronic renal failure.** Diabetic nephropathy is believed to be related to glomerular hyperfiltration. Renal hypertrophy occurs. With time, diffuse intercapillary glomerulosclerosis develops, causing a progressive decrease in renal size. At sonography, the kidneys are initially enlarged but, with time and progressive renal insufficiency, the kidneys decrease in size and increase in cortical echogenicity, and corticomedullary junctions are preserved. With end-stage disease, the kidneys become smaller and more echogenic, and the medulla becomes as echogenic as the cortex.[292]

Amyloidosis

Amyloidosis may be primary or secondary and usually is a systemic disease; 10% to 20% of cases are localized to one organ system.[293] Patients with amyloidosis often present with renal failure. Patients with primary disease are more often men, with a mean age of 60 years. Causes of secondary amyloidosis include **multiple myeloma** (10%-15%), **rheumatoid arthritis** (20%-25%), **tuberculosis** (50%), **familial Mediterranean fever** (26%-40%), **RCC,** and **Hodgkin disease.**[293] During the acute phase, the kidneys are be symmetrically enlarged. With disease progression, the kidneys shrink; cortical atrophy and increased echogenicity are shown at ultrasound. Focal renal masses, amorphous calcification, a central renal pelvic mass that may be a hemorrhage or amyloid deposit, and perirenal soft tissue masses may be seen. Similarly, involvement of the ureter and bladder may be localized or diffuse. Wall thickening or masses with or without calcification may be demonstrated. The diagnosis is made with biopsy.

Endometriosis

Endometriosis occurs when endometrial tissue is found outside the uterus in women during the reproductive years. Patients typically present with pain, infertility, dysmenorrhea, and dyspareunia. Approximately 1% of women with pelvic endometriosis will have urinary tract involvement, most frequently in the bladder. Patients with bladder endometriosis will present with hematuria. Bladder endometriosis may be focal or diffuse. Less often the ureter and rarely the kidney are affected. At sonography, patients with bladder endometriosis may present with a mural or intraluminal cyst or a complex or solid lesion. Diagnosis is usually made cystoscopically with biopsy (Fig. 9.89).

Interstitial Cystitis

Interstitial cystitis is a chronic inflammation of the bladder wall of unknown origin. It usually affects middle-aged women and has been associated with other systemic diseases, including systemic lupus erythematosus, rheumatoid arthritis, and polyarteritis.[75] Irritative voiding symptoms predominate, and hematuria (30%) may occur.[294] At sonography, a small-capacity, thick-walled bladder is seen (Fig. 9.90). Ureteric obstruction may be present. In some cases it is impossible to differentiate interstitial cystitis from diffuse TCC of the bladder; patients should have cystoscopy with biopsy for confirmation.

NEUROGENIC BLADDER

Voiding is a well-coordinated neurologic process controlled by areas within the cerebral cortex. These areas control the detrusor muscle of the bladder as well as both the internal and the external urethral sphincter. For simplicity, lesions causing neurogenic bladder are divided into those causing either detrusor **areflexia** (a lower motor neuron lesion) or detrusor **hyperreflexia** (lesions above the sacral reflux arc).

At sonography, detrusor areflexia results in a smooth, large-capacity, thin-walled bladder. The bladder may extend high into the abdomen (Fig. 9.91A). Detrusor hyperreflexia produces a thick-walled, vertical, trabeculated bladder, often with associated upper tract dilatation (Fig. 9.91B and C). A large, postvoid residual will be seen.[295] If neurogenic bladder dysfunction is not properly

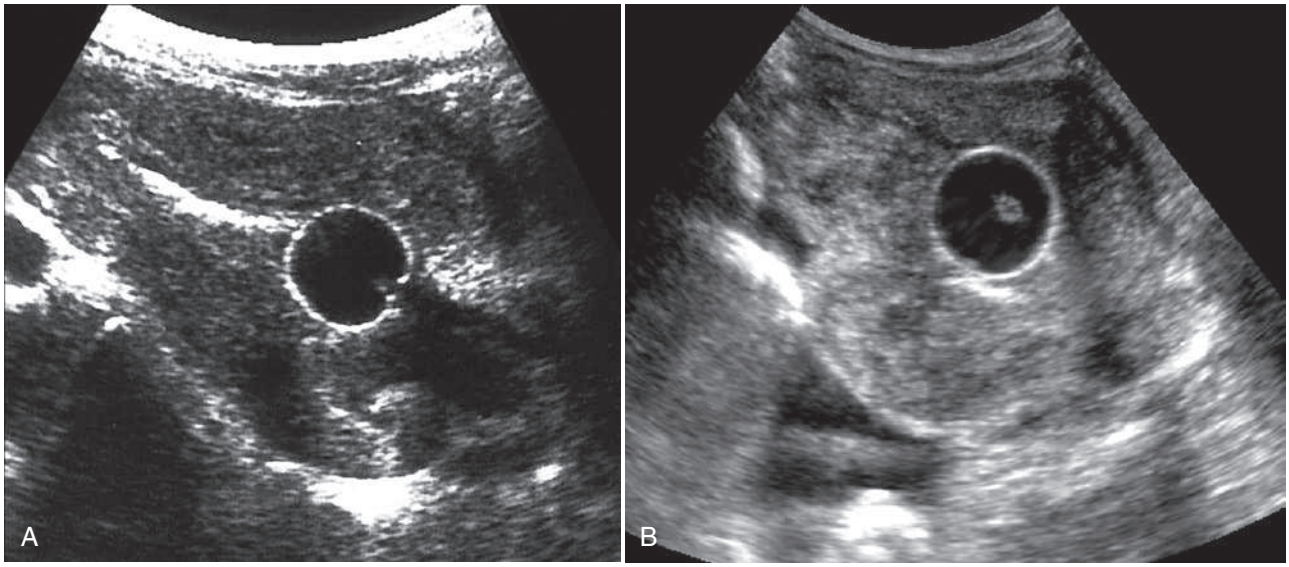

FIG. 9.90 Diffuse Bladder Wall Thickening. Two patients presenting with urinary retention. **(A)** Interstitial cystitis. **(B)** Diffuse transitional cell carcinoma in second patient. Both sonograms show marked circumferential bladder wall thickening after Foley catheterization. Cystoscopy and biopsy are required for differentiation.

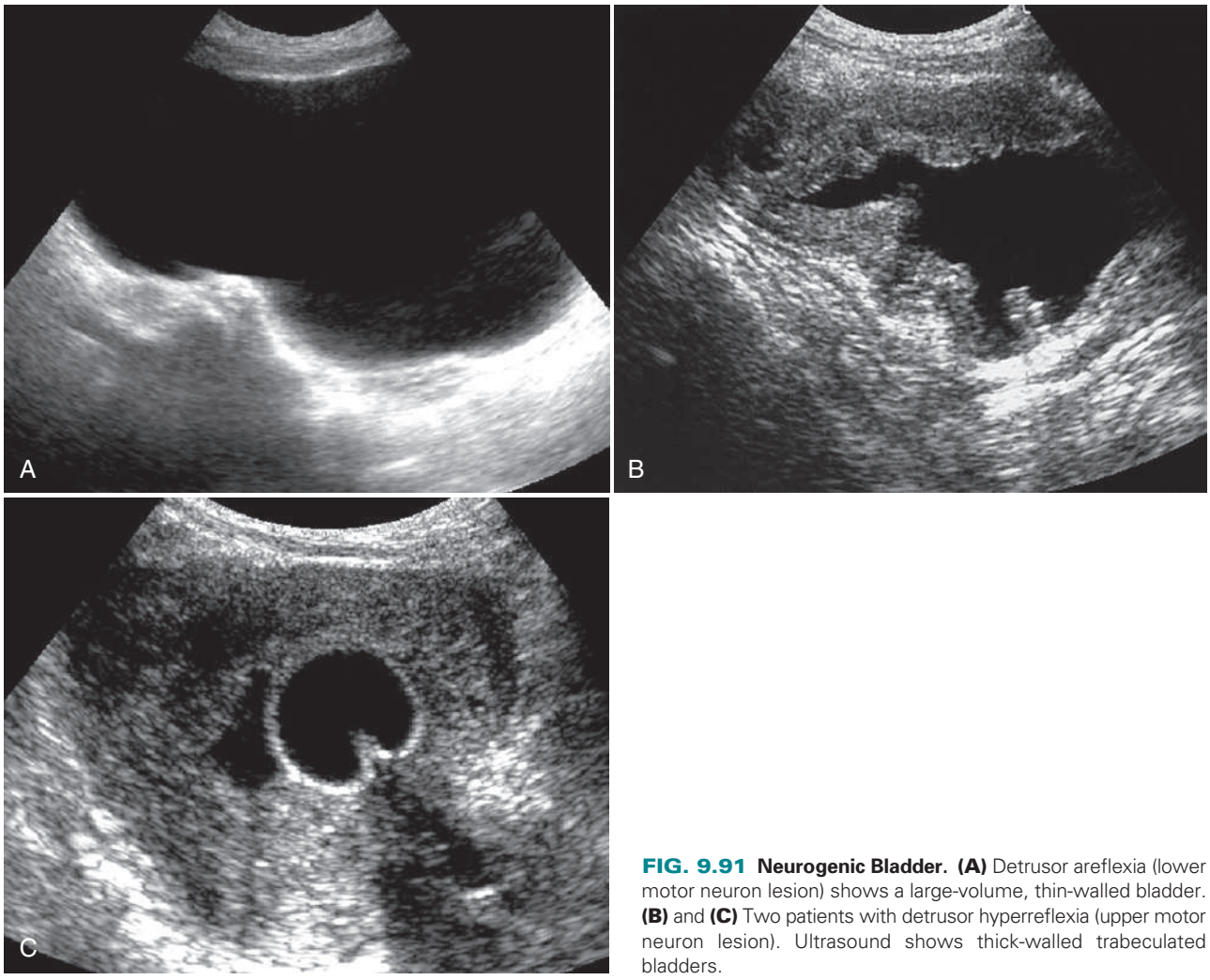

FIG. 9.91 Neurogenic Bladder. (A) Detrusor areflexia (lower motor neuron lesion) shows a large-volume, thin-walled bladder. **(B)** and **(C)** Two patients with detrusor hyperreflexia (upper motor neuron lesion). Ultrasound shows thick-walled trabeculated bladders.

diagnosed and treated, rapid deterioration of renal function may occur.

BLADDER DIVERTICULA

Bladder diverticula may be congenital or acquired. Congenital diverticula are known as **Hutch diverticula** and are located near the ureteral orifice. Most acquired diverticula result from bladder outlet obstruction. Bladder mucosa herniates through weak areas in the wall that are typically located posterolaterally near the ureteral orifices. The diverticular neck may be narrow or wide. It is the narrow-neck diverticula that lead to urinary stasis and give rise to complications, including infection, stones, tumors, and ureteral obstruction. Tumors arising in a diverticulum have a poorer prognosis than tumors arising within the bladder. Diverticula are composed only of mucosa and submucosa, without the muscularis layer present. Tumors therefore grow and invade much more quickly into the surrounding perivesical fat.

At sonography, diverticula appear as an outpouching sac from the bladder. The internal echogenicity of the diverticulum varies depending on its contents. The neck is often easily appreciated (Fig. 9.92, Video 9.4). Urine may be seen flowing into and out of the diverticulum.

POSTSURGICAL EVALUATION

Nephrectomy

Vascularized retroperitoneal fat is often placed with partial nephrectomy defects. The fat may simulate a renal mass at both CT and ultrasound. At sonography, the mass may be hyperechoic or isoechoic.[296,297] Surgical history correlation and an awareness

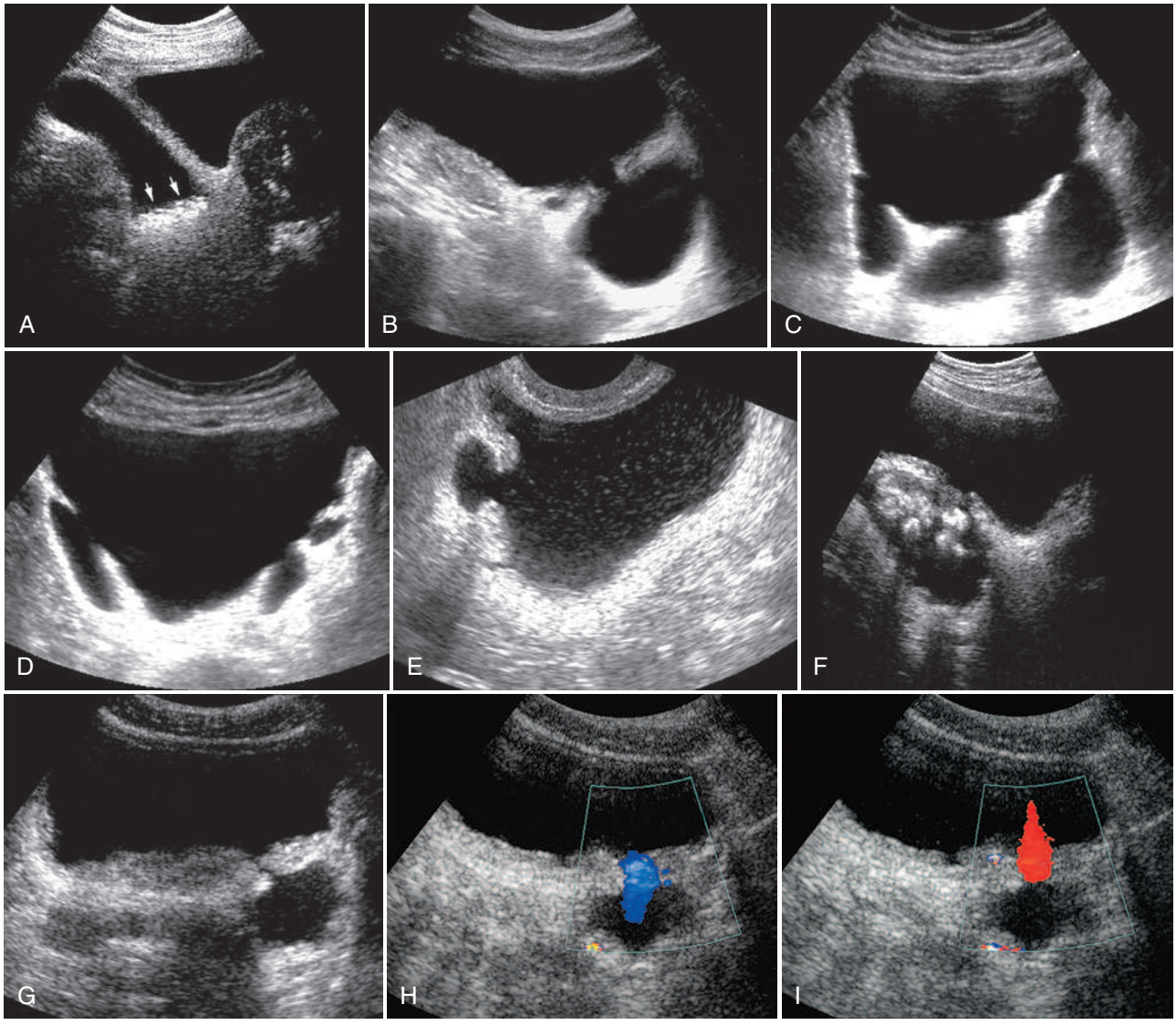

FIG. 9.92 Bladder Diverticula: Imaging Spectrum. (A) Large bladder diverticulum containing multiple calculi *(arrows)*. **(B)** Posterolateral Hutch diverticulum. **(C)** Multiple wide-neck diverticula. **(D)** Multiple diverticula of varying size. **(E)** Transvaginal sonogram shows an unusual diverticulum in a woman, with debris in the bladder lumen. **(F)** Large transitional cell carcinoma with extensive calcification fills the diverticulum. **(G)-(I)** Patient with a narrow-neck diverticulum. **(H)** and **(I)** Urine flow into and out of the diverticulum. See also Video 9.4.

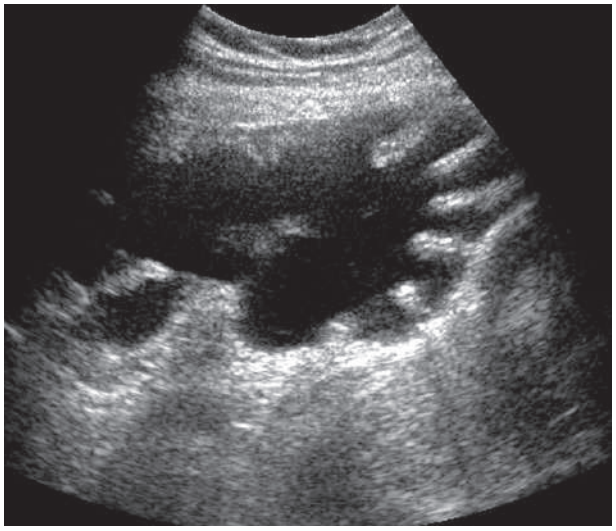

FIG. 9.93 Ileal Conduit (Urinary Diversion). Ultrasound image of the conduit may show gut wall signature and variable filling.

of this potential mimic should obviate additional, unnecessary imaging evaluation.

Urinary Diversion

Urinary diversions, or **ileal conduits,** are constructed for patients with nonfunctioning bladders or for postcystectomy patients. A portion of bowel is used to create a pouch that can mimic normal bladder function. The pouch may attach to the abdominal wall (cutaneous pouch) or urethra (orthotopic pouch). Postoperative complications are similar for both and include urine extravasation, reflux, fistula formation, abscess, urinoma, hematoma, deep vein thrombosis, ileus, and small bowel obstruction. The role of sonography is for detecting complications rather than for evaluating the pouch itself. If the pouch is urine filled, sonographic assessment is possible (Fig. 9.93). Often, thickened or irregularly shaped bowel wall, pseudomasses, intraluminal mucus collections, and intussuscepted bowel segments can be seen.[298] Stone formation in a pouch may occur.

CONCLUSION

Sonography plays a central role in the evaluation of renal, ureteral, and bladder anatomy and disease processes. The ability of ultrasound to identify and characterize genitourinary disease is an ongoing imaging success story.

Acknowledgment

The authors would like to thank Dr. Jenny Tomashpolskaya for her wonderful illustrations.

REFERENCES

1. Cotran RS, Kumar V, Robbins SL. Robbins pathologic basis of disease. 5th ed. Philadelphia: Saunders; 1994.
2. Moore KL, Persaud TVN. The developing human: clinically oriented embryology. 5th ed. Philadelphia: Saunders; 1993.
3. Netter FH. Anatomy, structure, and embryology. In: The CIBA collection of medical illustrations, vol. 6. Kidneys, ureters, and urinary bladder. CIBA Pharmaceutical; 1987. p. 2-35.
4. Emamian SA, Nielsen MB, Pedersen JF, Ytte L. Kidney dimensions at sonography: correlation with age, sex, and habitus in 665 adult volunteers. AJR Am J Roentgenol. 1993;160(1):83-86.
5. Platt JF, Rubin JM, Bowerman RA, Marn CS. The inability to detect kidney disease on the basis of echogenicity. AJR Am J Roentgenol. 1988;151(2):317-319.
6. Carter AR, Horgan JG, Jennings TA, Rosenfield AT. The junctional parenchymal defect: a sonographic variant of renal anatomy. Radiology. 1985;154(2):499-502.
7. Yeh HC, Halton KP, Shapiro RS, et al. Junctional parenchyma: revised definition of hypertrophic column of Bertin. Radiology. 1992;185(3):725-732.
8. Leekam RN, Matzinger MA, Brunelle M, et al. The sonography of renal columnar hypertrophy. J Clin Ultrasound. 1983;11(9):491-494.
9. Chesbrough RM, Burkhard TK, Martinez AJ, Burks DD. Gerota versus Zuckerkandl: the renal fascia revisited. Radiology. 1989;173(3):845-856.
10. Bechtold RE, Dyer RB, Zagoria RJ, Chen MY. The perirenal space: relationship of pathologic processes to normal retroperitoneal anatomy. Radiographics. 1996;16(4):841-854.
11. Martensson O, Duchek M. Translabial sonography in evaluating the lower female urogenital tract. AJR Am J Roentgenol. 1996;166(6):1327-1331.
12. Ellenbogen PH, Scheible FW, Talner LB, Leopold GR. Sensitivity of gray scale ultrasound in detecting urinary tract obstruction. AJR Am J Roentgenol. 1978;130(4):731-733.
13. Swenson DW, Darge K, Ziniel SI, Chow JS. Characterizing upper urinary tract dilation on ultrasound: a survey of North American pediatric radiologists' practices. Pediatr Radiol. 2015;45(5):686-694.
14. Netter FH. Congenital and hereditary disorders. In: The CIBA collection of medical illustrations, vol. 6. Kidneys, ureters, and urinary bladder. CIBA Pharmaceutical; 1987. p. 223-249.
15. Congenital anomalies of the urinary tract. In: Elkin M, editor. Radiology of the urinary system. Boston: Little, Brown; 1980.
16. Friedland GW, Devries PA, Nino-Murcia M, et al. Congenital anomalies of the urinary tract. In: Pollack HM, editor. Clinical urography: an atlas and textbook of urologic imaging. Philadelphia: Saunders; 1990. p. 559-787.
17. Horgan JG, Rosenfield NS, Weiss RM, Rosenfield AT. Is renal ultrasound a reliable indicator of a nonobstructed duplication anomaly? Pediatr Radiol. 1984;14(6):388-391.
18. Shimoya K, Shimizu T, Hashimoto K, et al. Diagnosis of ureterocele with transvaginal sonography. Gynecol Obstet Invest. 2002;54(1):58-60.
19. Madeb R, Shapiro I, Rothschild E, et al. Evaluation of ureterocele with Doppler sonography. J Clin Ultrasound. 2000;28(8):425-429.
20. Talner LB. Specific causes of obstruction. In: Pollack HM, editor. Clinical urography: an atlas and textbook of urological imaging. Philadelphia: Saunders; 1990. p. 1629-1751.
21. Vargas B, Lebowitz RL. The coexistence of congenital megacalyces and primary megaureter. AJR Am J Roentgenol. 1986;147(2):313-316.
22. Tortora Jr FL, Lucey DT, Fried FA, Mandell J. Absence of the bladder. J Urol. 1983;129(6):1235-1237.
23. Spataro RF, Davis RS, McLachlan MS, et al. Urachal abnormalities in the adult. Radiology. 1983;149(3):659-663.
24. Schnyder P, Candardjis G. Vesicourachal diverticulum: CT diagnosis in two adults. AJR Am J Roentgenol. 1981;137(5):1063-1065.
25. Piccirillo M, Rigsby CM, Rosenfield AT. Sonography of renal inflammatory disease. Urol Radiol. 1987;9(2):66-78.
26. Papanicolaou N, Pfister RC. Acute renal infections. Radiol Clin North Am. 1996;34(5):965-995.
27. Talner LB, Davidson AJ, Lebowitz RL, et al. Acute pyelonephritis: can we agree on terminology? Radiology. 1994;192(2):297-305.
28. Farmer KD, Gellett LR, Dubbins PA. The sonographic appearance of acute focal pyelonephritis 8 years experience. Clin Radiol. 2002;57(6):483-487.
29. Majd M, Nussbaum Blask AR, Markle BM, et al. Acute pyelonephritis: comparison of diagnosis with 99mTc-DMSA, SPECT, spiral CT, MR imaging, and power Doppler US in an experimental pig model. Radiology. 2001;218(1):101-108.
30. Thoumas D, Darmallaicq C, Pfister C, et al. Imaging characteristics of alkaline-encrusted cystitis and pyelitis. AJR Am J Roentgenol. 2002;178(2):389-392.
31. Lowe LH, Zagoria RJ, Baumgartner BR, Dyer RB. Role of imaging and intervention in complex infections of the urinary tract. AJR Am J Roentgenol. 1994;163(2):363-367.

32. Brun-Buisson C, Doyon F, Carlet J, et al. Incidence, risk factors, and outcome of severe sepsis and septic shock in adults. A multicenter prospective study in intensive care units. French ICU Group for Severe Sepsis. JAMA. 1995;274(12):968-974.
33. Yoder IC, Pfister RC, Lindfors KK, Newhouse JH. Pyonephrosis: imaging and intervention. AJR Am J Roentgenol. 1983;141(4):735-740.
34. Grayson DE, Abbott RM, Levy AD, Sherman PM. Emphysematous infections of the abdomen and pelvis: a pictorial review. Radiographics. 2002;22(3):543-561.
35. Patel NP, Lavengood RW, Fernandes M, et al. Gas-forming infections in genitourinary tract. Urology. 1992;39(4):341-345.
36. Michaeli J, Mogle P, Perlberg S, et al. Emphysematous pyelonephritis. J Urol. 1984;131(2):203-208.
37. Wan YL, Lee TY, Bullard MJ, Tsai CC. Acute gas-producing bacterial renal infection: correlation between imaging findings and clinical outcome. Radiology. 1996;198(2):433-438.
38. Joseph RC, Amendola MA, Artze ME, et al. Genitourinary tract gas: imaging evaluation. Radiographics. 1996;16(2):295-308.
39. Bhathena DB, Weiss JH, Holland NH, et al. Focal and segmental glomerular sclerosis in reflux nephropathy. Am J Med. 1980;68(6):886-892.
40. Kay CJ, Rosenfield AT, Taylor KJ, Rosenberg MA. Ultrasonic characteristics of chronic atrophic pyelonephritis. AJR Am J Roentgenol. 1979;132(1):47-49.
41. Hartman DS, Davis Jr CJ, Goldman SM, et al. Xanthogranulomatous pyelonephritis: sonographic—pathologic correlation of 16 cases. J Ultrasound Med. 1984;3(11):481-488.
42. Anhalt MA, Cawood CD, Scott Jr R. Xanthogranulomatous pyelonephritis: a comprehensive review with report of 4 additional cases. J Urol. 1971;105(1):10-17.
43. Gammill S, Rabinowitz JG, Peace R, et al. New thoughts concerning xanthogranulomatous pyelonephritis (X-P). Am J Roentgenol Radium Ther Nucl Med. 1975;125(1):154-163.
44. Tiu CM, Chou YH, Chiou HJ, et al. Sonographic features of xanthogranulomatous pyelonephritis. J Clin Ultrasound. 2001;29(5):279-285.
45. Cousins C, Somers J, Broderick N, et al. Xanthogranulomatous pyelonephritis in childhood: ultrasound and CT diagnosis. Pediatr Radiol. 1994;24(3):210-212.
46. Davidson AJ. Chronic parenchymal disease. In: Pollack HM, editor. Clinical urography: an atlas and textbook of urological imaging. Philadelphia: Saunders; 1990. p. 2277-2288.
47. Hoffman JC, Schnur MJ, Koenigsberg M. Demonstration of renal papillary necrosis by sonography. Radiology. 1982;145(3):785-787.
48. Elkin M. Urogenital tuberculosis. In: Pollack HM, editor. Clinical urography: an atlas and textbook of urological imaging. Philadelphia: Saunders; 1990. p. 1020-1052.
49. Das KM, Indudhara R, Vaidyanathan S. Sonographic features of genitourinary tuberculosis. AJR Am J Roentgenol. 1992;158(2):327-329.
50. Pollack HM, Banner MP, Martinez LO, Hodson CJ. Diagnostic considerations in urinary bladder wall calcification. AJR Am J Roentgenol. 1981;136(4):791-797.
51. Wasnik AP. Tuberculosis, urinary tract. In: Kamaya A, Wong-You-Cheong J, editors. Diagnostic ultrasound: abdomen and pelvis. Philadelphia: Elsevier; 2016. pp. 490-493.
52. Premkumar A, Lattimer J, Newhouse JH. CT and sonography of advanced urinary tract tuberculosis. AJR Am J Roentgenol. 1987;148(1):65-69.
53. Das KM, Vaidyanathan S, Rajwanshi A, Indudhara R. Renal tuberculosis: diagnosis with sonographically guided aspiration cytology. AJR Am J Roentgenol. 1992;158(3):571-573.
54. Spring D. Fungal diseases of the urinary tract. In: Pollack HM, editor. Clinical urography: an atlas and textbook of urological imaging. Philadelphia: Saunders; 1990. p. 987-998.
55. Shirkhoda A. CT findings in hepatosplenic and renal candidiasis. J Comput Assist Tomogr. 1987;11(5):795-798.
56. Vazquez-Tsuji O, Campos-Rivera T, Ahumada-Mendoza H, et al. Renal ultrasonography and detection of pseudomycelium in urine as means of diagnosis of renal fungus balls in neonates. Mycopathologia. 2005;159(3):331-337.
57. Mindell HJ, Pollack HM. Fungal disease of the ureter. Radiology. 1983;146(1):46.
58. Boldus RA, Brown RC, Culp DA. Fungus balls in the renal pelvis. Radiology. 1972;102(3):555-557.
59. Stuck KJ, Silver TM, Jaffe MH, Bowerman RA. Sonographic demonstration of renal fungus balls. Radiology. 1982;142(2):473-474.
60. Palmer P, Reeder MM. Parasitic disease of the urinary tract. In: Pollack HM, editor. Clinical urography: an atlas and textbook of urological imaging. Philadelphia: Saunders; 1990. p. 999-1019.
61. Wasnik AP. Schistosomiasis, urinary tract. In: Kamaya A, Wong-You-Cheong J, editors. Diagnostic ultrasound: abdomen and pelvis. Philadelphia: Elsevier; 2016. pp. 548-549.
62. Diamond HM, Lyon ES, Hui NT, De Pauw AP. Echinococcal disease of the kidney. J Urol. 1976;115(6):742-744.
63. King D. Ultrasonography of echinococcal cysts. J Clin Ultrasound. 1976;64-67.
64. Turgut AT, Odev K, Kabaalioglu A, et al. Multitechnique evaluation of renal hydatid disease. AJR Am J Roentgenol. 2009;192(2):462-467.
65. Pastor-Pons E, Martinez-Leon MI, Alvarez-Bustos G, et al. Isolated renal mucormycosis in two patients with AIDS. AJR Am J Roentgenol. 1996;166(6):1282-1284.
66. Spouge AR, Wilson SR, Gopinath N, et al. Extrapulmonary Pneumocystis carinii in a patient with AIDS: sonographic findings. AJR Am J Roentgenol. 1990;155(1):76-78.
67. Towers MJ, Withers CE, Hamilton PA, et al. Visceral calcification in patients with AIDS may not always be due to Pneumocystis carinii. AJR Am J Roentgenol. 1991;156(4):745-747.
68. Falkoff GE, Rigsby CM, Rosenfield AT. Partial, combined cortical and medullary nephrocalcinosis: US and CT patterns in AIDS-associated MAI infection. Radiology. 1987;162(2):343-344.
69. Schwartz EJ, Szczech LA, Ross MJ, et al. Highly active antiretroviral therapy and the epidemic of HIV+ end-stage renal disease. J Am Soc Nephrol. 2005;16(8):2412-2420.
70. Kumar N, Perazella MA. Differentiating HIV-associated nephropathy from antiretroviral drug-induced nephropathy: a clinical challenge. Curr HIV/AIDS Rep. 2014;11(3):202-211.
71. de Silva TI, Post FA, Griffin MD, Dockrell DH. HIV-1 infection and the kidney: an evolving challenge in HIV medicine. Mayo Clin Proc. 2007;82(9):1103-1116.
72. Hamper UM, Goldblum LE, Hutchins GM, et al. Renal involvement in AIDS: sonographic-pathologic correlation. AJR Am J Roentgenol. 1988;150(6):1321-1325.
73. Schaffer RM, Schwartz GE, Becker JA, et al. Renal ultrasound in acquired immune deficiency syndrome. Radiology. 1984;153(2):511-513.
74. Di Fiori JL, Rodrigue D, Kaptein EM, Ralls PW. Diagnostic sonography of HIV-associated nephropathy: new observations and clinical correlation. AJR Am J Roentgenol. 1998;171(3):713-716.
75. Clayman RV, Weyman PJ, Bahnson RR. Inflammation of the bladder. In: Pollack HM, editor. Clinical urography: an atlas and textbook of urological imaging. Philadelphia: Saunders; 1990. p. 902-924.
76. Stark GL, Feddersen R, Lowe BA, et al. Inflammatory pseudotumor (pseudosarcoma) of the bladder. J Urol. 1989;141(3):610-612.
77. Kenney P, Breatnach ES, Stanley RJ. Chronic inflammation. In: Pollack HM, editor. Clinical urography: an atlas and textbook of urological imaging. Philadelphia: Saunders; 1990. p. 822-843.
78. Lewin KJ, Fair WR, Steigbigel RT, et al. Clinical and laboratory studies into the pathogenesis of malacoplakia. J Clin Pathol. 1976;29(4):354-363.
79. Kauzlaric D, Barmeir E. Sonography of emphysematous cystitis. J Ultrasound Med. 1985;4(6):319-320.
80. Wiener DP, Koss LG, Sablay B, Freed SZ. The prevalence and significance of Brunn's nests, cystitis cystica and squamous metaplasia in normal bladders. J Urol. 1979;122(3):317-321.
81. Lang EK, Fritzsche P. Fistulas of the genitourinary tract. In: Pollack HM, editor. Clinical urography: an atlas and textbook of urological imaging. Philadelphia: Saunders; 1990. p. 2579-2593.
82. Wilson S. The gastrointestinal tract. In: Rumack CM, Wilson SR, Charboneau JW, editors. Diagnostic ultrasound. St Louis: Mosby–Year Book; 1991. p. 181-207.
83. Damani N, Wilson SR. Nongynecologic applications of transvaginal US. Radiographics. 1999;19:S179-S200.
84. Volkmer BG, Kuefer R, Nesslauer T, et al. Colour Doppler ultrasound in vesicovaginal fistulas. Ultrasound Med Biol. 2000;26(5):771-775.

85. Sierakowski R, Finlayson B, Landes RR, et al. The frequency of urolithiasis in hospital discharge diagnoses in the United States. Invest Urol. 1978;15(6):438-441.
86. Spirnak JP, Resnick M, Banner MP. Calculus disease of the urinary tract: general considerations. In: Pollack HM, editor. Clinical urography: an atlas and textbook of urological imaging. Philadelphia: Saunders; 1990. p. 1752-1758.
87. Furlan A, Federle MP, Yealy DM, et al. Nonobstructing renal stones on unenhanced CT: a real cause for renal colic? AJR Am J Roentgenol. 2008;190(2):W125-W127.
88. Ripolles T, Errando J, Agramunt M, Martinez MJ. Ureteral colic: US versus CT. Abdom Imaging. 2004;29(2):263-266.
89. Katz DS, Lane MJ, Sommer FG. Unenhanced helical CT of ureteral stones: incidence of associated urinary tract findings. AJR Am J Roentgenol. 1996;166(6):1319-1322.
90. Smith RC, Rosenfield AT, Choe KA, et al. Acute flank pain: comparison of non-contrast-enhanced CT and intravenous urography. Radiology. 1995;194(3):789-794.
91. Smith RC, Verga M, McCarthy S, Rosenfield AT. Diagnosis of acute flank pain: value of unenhanced helical CT. AJR Am J Roentgenol. 1996;166(1):97-101.
92. Catalano O, Nunziata A, Altei F, Siani A. Suspected ureteral colic: primary helical CT versus selective helical CT after unenhanced radiography and sonography. AJR Am J Roentgenol. 2002;178(2):379-387.
93. Patlas M, Farkas A, Fisher D, et al. Ultrasound vs CT for the detection of ureteric stones in patients with renal colic. Br J Radiol. 2001;74(886):901-904.
94. Ripolles T, Agramunt M, Errando J, et al. Suspected ureteral colic: plain film and sonography vs unenhanced helical CT. A prospective study in 66 patients. Eur Radiol. 2004;14(1):129-136.
95. Turk C, Petrik A, Sarica K, et al. EAU Guidelines on diagnosis and conservative management of urolithiasis. Eur Urol. 2016;69(3):468-474.
96. Niemann T, Kollmann T, Bongartz G. Diagnostic performance of low-dose CT for the detection of urolithiasis: a meta-analysis. AJR Am J Roentgenol. 2008;191(2):396-401.
97. Rubens DJ, Bhatt S, Nedelka S, Cullinan J. Doppler artifacts and pitfalls. Radiol Clin North Am. 2006;44(6):805-835.
98. Lee JY, Kim SH, Cho JY, Han D. Color and power Doppler twinkling artifacts from urinary stones: clinical observations and phantom studies. AJR Am J Roentgenol. 2001;176(6):1441-1445.
99. Chelfouh N, Grenier N, Higueret D, et al. Characterization of urinary calculi: in vitro study of "twinkling artifact" revealed by color-flow sonography. AJR Am J Roentgenol. 1998;171(4):1055-1060.
100. Dillman JR, Kappil M, Weadock WJ, et al. Sonographic twinkling artifact for renal calculus detection: correlation with CT. Radiology. 2011;259(3):911-916.
101. Cronan JJ, Tublin ME. Role of the resistive index in the evaluation of acute renal obstruction. AJR Am J Roentgenol. 1995;164(2):377-378.
102. Laing FC, Benson CB, DiSalvo DN, et al. Distal ureteral calculi: detection with vaginal US. Radiology. 1994;192(2):545-548.
103. Hertzberg BS, Kliewer MA, Paulson EK, Carrol BA. Distal ureteral calculi: detection with transperineal sonography. AJR Am J Roentgenol. 1994;163(5):1151-1153.
104. Burge HJ, Middleton WD, McClennan BL, Hildebolt CF. Ureteral jets in healthy subjects and in patients with unilateral ureteral calculi: comparison with color Doppler US. Radiology. 1991;180(2):437-442.
105. Price CI, Adler RS, Rubin JM. Ultrasound detection of differences in density. Explanation of the ureteric jet phenomenon and implications for new ultrasound applications. Invest Radiol. 1989;24(11):876-883.
106. Baker SM, Middleton WD. Color Doppler sonography of ureteral jets in normal volunteers: importance of the relative specific gravity of urine in the ureter and bladder. AJR Am J Roentgenol. 1992;159(4):773-775.
107. de Bessa Jr J, Denes FT, Chammas MC, et al. Diagnostic accuracy of color Doppler sonographic study of the ureteric jets in evaluation of hydronephrosis. J Pediatr Urol. 2008;4(2):113-117.
108. Platt JF, Rubin JM, Ellis JH. Acute renal obstruction: evaluation with intrarenal duplex Doppler and conventional US. Radiology. 1993;186(3):685-688.
109. Tublin ME, Dodd 3rd GD, Verdile VP. Acute renal colic: diagnosis with duplex Doppler US. Radiology. 1994;193(3):697-701.
110. Geavlete P, Georgescu D, Cauni V, Nita G. Value of duplex Doppler ultrasonography in renal colic. Eur Urol. 2002;41(1):71-78.
111. Tublin ME, Bude RO, Platt JF. Review. The resistive index in renal Doppler sonography: where do we stand? AJR Am J Roentgenol. 2003;180(4):885-892.
112. Tublin ME, Tessler FN, Murphy ME. Correlation between renal vascular resistance, pulse pressure, and the resistive index in isolated perfused rabbit kidneys. Radiology. 1999;213(1):258-264.
113. Murphy ME, Tublin ME. Understanding the Doppler RI: impact of renal arterial distensibility on the RI in a hydronephrotic ex vivo rabbit kidney model. J Ultrasound Med. 2000;19(5):303-314.
114. Bude RO, Rubin JM. Relationship between the resistive index and vascular compliance and resistance. Radiology. 1999;211(2):411-417.
115. Banner M. Nephrocalcinosis. In: Pollack HM, editor. Clinical urography: an atlas and textbook of urological imaging. Philadelphia: Saunders; 1990. p. 1768-1775.
116. al-Murrani B, Cosgrove DO, Svensson WE, Blaszczyk M. Echogenic rings—an ultrasound sign of early nephrocalcinosis. Clin Radiol. 1991;44(1):49-51.
117. Patriquin HB, O'Regan S. Medullary sponge kidney in childhood. AJR Am J Roentgenol. 1985;145(2):315-319.
118. Khoory BJ, Andreis IA, Vino L, Fanos V. Transient hyperechogenicity of the renal medullary pyramids: incidence in the healthy term newborn. Am J Perinatol. 1999;16(9):463-468.
119. Patriquin H, Robitaille P. Renal calcium deposition in children: sonographic demonstration of the Anderson-Carr progression. AJR Am J Roentgenol. 1986;146(6):1253-1256.
120. Bennington JL, Beckwith JB. Tumors of the kidney, renal pelvis, and ureter. Washington, DC: US Armed Forces Institute of Pathology; 1975.
121. Bennington JL, Laubscher FA. Epidemiologic studies on carcinoma of the kidney. I. Association of renal adenocarcinoma with smoking. Cancer. 1968;21(6):1069-1071.
122. Cohen AJ, Li FP, Berg S, et al. Hereditary renal-cell carcinoma associated with a chromosomal translocation. N Engl J Med. 1979;301(11):592-595.
123. Choyke PL, Glenn GM, Walther MM, et al. Hereditary renal cancers. Radiology. 2003;226(1):33-46.
124. Choyke PL, Glenn GM, Walther MM, et al. von Hippel-Lindau disease: genetic, clinical, and imaging features. Radiology. 1995;194(3):629-642.
125. Choyke PL, Glenn GM, Walther MM, et al. The natural history of renal lesions in von Hippel-Lindau disease: a serial CT study in 28 patients. AJR Am J Roentgenol. 1992;159(6):1229-1234.
126. Linehan WM, Vasselli J, Srinivasan R, et al. Genetic basis of cancer of the kidney: disease-specific approaches to therapy. Clin Cancer Res. 2004;10(18 Pt 2):6282s-6289s.
127. Takase K, Takahashi S, Tazawa S, et al. Renal cell carcinoma associated with chronic renal failure: evaluation with sonographic angiography. Radiology. 1994;192(3):787-792.
128. Levine E, Grantham JJ, Slusher SL, et al. CT of acquired cystic kidney disease and renal tumors in long-term dialysis patients. AJR Am J Roentgenol. 1984;142(1):125-131.
129. Kim JK, Kim TK, Ahn HJ, et al. Differentiation of subtypes of renal cell carcinoma on helical CT scans. AJR Am J Roentgenol. 2002;178(6):1499-1506.
130. Skinner DG, Colvin RB, Vermillion CD, et al. Diagnosis and management of renal cell carcinoma. A clinical and pathologic study of 309 cases. Cancer. 1971;28(5):1165-1177.
131. Curry NS. Small renal masses (lesions smaller than 3 cm): imaging evaluation and management. AJR Am J Roentgenol. 1995;164(2):355-362.
132. Jamis-Dow CA, Choyke PL, Jennings SB, et al. Small (< or = 3-cm) renal masses: detection with CT versus US and pathologic correlation. Radiology. 1996;198(3):785-788.
133. Szolar DH, Kammerhuber F, Altziebler S, et al. Multiphasic helical CT of the kidney: increased conspicuity for detection and characterization of small (< 3-cm) renal masses. Radiology. 1997;202(1):211-217.
134. Urban BA. The small renal mass: what is the role of multiphasic helical scanning? Radiology. 1997;202(1):22-23.
135. Birnbaum BA, Jacobs JE, Ramchandani P. Multiphasic renal CT: comparison of renal mass enhancement during the corticomedullary and nephrographic phases. Radiology. 1996;200(3):753-758.
136. Zeman RK, Zeiberg A, Hayes WS, et al. Helical CT of renal masses: the value of delayed scans. AJR Am J Roentgenol. 1996;167(3):771-776.

137. Silverman SG, Mortele KJ, Tuncali K, et al. Hyperattenuating renal masses: etiologies, pathogenesis, and imaging evaluation. Radiographics. 2007;27(4):1131-1143.
138. Shellock FG, Spinazzi A. MRI safety update 2008: part 1, MRI contrast agents and nephrogenic systemic fibrosis. AJR Am J Roentgenol. 2008;191(4):1129-1139.
139. Quaia E, Bertolotto M, Cioffi V, et al. Comparison of contrast-enhanced sonography with unenhanced sonography and contrast-enhanced CT in the diagnosis of malignancy in complex cystic renal masses. AJR Am J Roentgenol. 2008;191(4):1239-1249.
140. Ignee A, Straub B, Brix D, et al. The value of contrast enhanced ultrasound (CEUS) in the characterisation of patients with renal masses. Clin Hemorheol Microcirc. 2010;46(4):275-290.
141. Lane BR, Babineau D, Kattan MW, et al. A preoperative prognostic nomogram for solid enhancing renal tumors 7 cm or less amenable to partial nephrectomy. J Urol. 2007;178(2):429-434.
142. Pahernik S, Ziegler S, Roos F, et al. Small renal tumors: correlation of clinical and pathological features with tumor size. J Urol. 2007;178(2):414-417.
143. Bosniak MA, Birnbaum BA, Krinsky GA, Waisman J. Small renal parenchymal neoplasms: further observations on growth. Radiology. 1995;197(3):589-597.
144. Deane LA, Clayman RV. Review of minimally invasive renal therapies: Needle-based and extracorporeal. Urology. 2006;68(1 Suppl.):26-37.
145. Gervais DA, McGovern FJ, Arellano RS, et al. Renal cell carcinoma: clinical experience and technical success with radio-frequency ablation of 42 tumors. Radiology. 2003;226(2):417-424.
146. Rosenberg MD, Kim CY, Tsivian M, et al. Percutaneous cryoablation of renal lesions with radiographic ice ball involvement of the renal sinus: analysis of hemorrhagic and collecting system complications. AJR Am J Roentgenol. 2011;196(4):935-939.
147. El Dib R, Touma NJ, Kapoor A. Cryoablation vs radiofrequency ablation for the treatment of renal cell carcinoma: a meta-analysis of case series studies. BJU Int. 2012;110(4):510-516.
148. Charboneau JW, Hattery RR, Ernst 3rd EC, et al. Spectrum of sonographic findings in 125 renal masses other than benign simple cyst. AJR Am J Roentgenol. 1983;140(1):87-94.
149. Forman HP, Middleton WD, Melson GL, McClennan BL. Hyperechoic renal cell carcinomas: increase in detection at US. Radiology. 1993;188(2):431-434.
150. Yamashita Y, Takahashi M, Watanabe O, et al. Small renal cell carcinoma: pathologic and radiologic correlation. Radiology. 1992;184(2):493-498.
151. Yamashita Y, Ueno S, Makita O, et al. Hyperechoic renal tumors: anechoic rim and intratumoral cysts in US differentiation of renal cell carcinoma from angiomyolipoma. Radiology. 1993;188(1):179-182.
152. Siegel CL, Middleton WD, Teefey SA, McClennan BL. Angiomyolipoma and renal cell carcinoma: US differentiation. Radiology. 1996;198(3):789-793.
153. Farrelly C, Delaney H, McDermott R, Malone D. Do all non-calcified echogenic renal lesions found on ultrasound need further evaluation with CT? Abdom Imaging. 2008;33(1):44-47.
154. Sniderman KW, Krieger JN, Seligson GR, Sos TA. The radiologic and clinical aspects of calcified hypernephroma. Radiology. 1979;131(1):31-35.
155. Phillips TL, Chin FG, Palubinskas AJ. Calcification in renal masses: an eleven-year survey. Radiology. 1963;80:786-794.
156. Kikkawa K, Lasser EC. "Ring-like" or "rim-like" calcification in renal cell carcinoma. Am J Roentgenol Radium Ther Nucl Med. 1969;107(4):737-742.
157. Daniel Jr WW, Hartman GW, Witten DM, et al. Calcified renal masses. A review of ten years experience at the Mayo Clinic. Radiology. 1972; 103(3):503-508.
158. Onitsuka H, Murakami J, Naito S, et al. Diffusely calcified renal cell carcinoma: CT features. J Comput Assist Tomogr. 1992;16(4):654-656.
159. Weyman PJ, McClennan BL, Lee JK, Stanley RJ. CT of calcified renal masses. AJR Am J Roentgenol. 1982;138(6):1095-1099.
160. Press GA, McClennan BL, Melson GL, et al. Papillary renal cell carcinoma: CT and sonographic evaluation. AJR Am J Roentgenol. 1984;143(5):1005-1009.
161. Mancilla-Jimenez R, Stanley RJ, Blath RA. Papillary renal cell carcinoma: a clinical, radiologic, and pathologic study of 34 cases. Cancer. 1976;38(6):2469-2480.
162. Yamashita Y, Watanabe O, Miyazaki T, et al. Cystic renal cell carcinoma. Imaging findings with pathologic correlation. Acta Radiol. 1994;35(1):19-24.
163. Hartman DS, Davis Jr CJ, Johns T, Goldman SM. Cystic renal cell carcinoma. Urology. 1986;28(2):145-153.
164. Zagoria RJ. Imaging of small renal masses: a medical success story. AJR Am J Roentgenol. 2000;175(4):945-955.
165. Ramos IM, Taylor KJ, Kier R, et al. Tumor vascular signals in renal masses: detection with Doppler US. Radiology. 1988;168(3):633-637.
166. Taylor KJ, Ramos I, Carter D, et al. Correlation of Doppler US tumor signals with neovascular morphologic features. Radiology. 1988;166(1 Pt 1):57-62.
167. Taylor KJ, Ramos I, Morse SS, et al. Focal liver masses: differential diagnosis with pulsed Doppler US. Radiology. 1987;164(3):643-647.
168. Kier R, Taylor KJ, Feyock AL, Ramos IM. Renal masses: characterization with Doppler US. Radiology. 1990;176(3):703-707.
169. Kuijpers TJ, Obdeijn AI, Kruyt RH, Oudkerk M. Solid breast neoplasms: differential diagnosis with pulsed Doppler ultrasound. Ultrasound Med Biol. 1994;20(6):517-520.
170. Ascenti G, Mazziotti S, Zimbaro G, et al. Complex cystic renal masses: characterization with contrast-enhanced US. Radiology. 2007;243(1):158-165.
171. Quaia E, Bertolotto M, Cioffi V, et al. Comparison of contrast-enhanced sonography with unenhanced sonography and contrast-enhanced CT in the diagnosis of malignancy in complex cystic renal masses. AJR Am J Roentgenol. 2008;191(4):1239-1249.
172. Silverman SG, Gan YU, Mortele KJ, et al. Renal masses in the adult patient: the role of percutaneous biopsy. Radiology. 2006;240(1):6-22.
173. Caoili EM, Bude RO, Higgins EJ, et al. Evaluation of sonographically guided percutaneous core biopsy of renal masses. AJR Am J Roentgenol. 2002;179(2):373-378.
174. Johnson PT, Nazarian LN, Feld RI, et al. Sonographically guided renal mass biopsy: indications and efficacy. J Ultrasound Med. 2001;20(7):749-753.
175. Shannon BA, Cohen RJ, de Bruto H, Davies RJ. The value of preoperative needle core biopsy for diagnosing benign lesions among small, incidentally detected renal masses. J Urol. 2008;180(4):1257-1261.
176. Beland MD, Mayo-Smith WW, Dupuy DE, et al. Diagnostic yield of 58 consecutive imaging-guided biopsies of solid renal masses: should we biopsy all that are indeterminate? AJR Am J Roentgenol. 2007;188(3):792-797.
177. Maurice MJ, Zhu H, Kiechle JE, et al. Increasing biopsy utilization for renal cell carcinoma is closely associated with treatment. Urology. 2015;86(5):906-913.
178. McNichols DW, Segura JW, DeWeerd JH. Renal cell carcinoma: long-term survival and late recurrence. J Urol. 1981;126(1):17-23.
179. Zagoria RJ, Bechtold RE, Dyer RB. Staging of renal adenocarcinoma: role of various imaging procedures. AJR Am J Roentgenol. 1995;164(2):363-370.
180. Chowdhury S, Larkin JM, Gore ME. Recent advances in the treatment of renal cell carcinoma and the role of targeted therapies. Eur J Cancer. 2008;44(15):2152-2161.
181. Habboub HK, Abu-Yousef MM, Williams RD, et al. Accuracy of color Doppler sonography in assessing venous thrombus extension in renal cell carcinoma. AJR Am J Roentgenol. 1997;168(1):267-271.
182. Buckley JA, Urban BA, Soyer P, et al. Transitional cell carcinoma of the renal pelvis: a retrospective look at CT staging with pathologic correlation. Radiology. 1996;201(1):194-198.
183. Leder RA, Dunnick NR. Transitional cell carcinoma of the pelvicalices and ureter. AJR Am J Roentgenol. 1990;155(4):713-722.
184. Yousem DM, Gatewood OM, Goldman SM, Marshall FF. Synchronous and metachronous transitional cell carcinoma of the urinary tract: prevalence, incidence, and radiographic detection. Radiology. 1988;167(3):613-618.
185. Silverman SG, Leyendecker JR, Amis Jr ES. What is the current role of CT urography and MR urography in the evaluation of the urinary tract? Radiology. 2009;250(2):309-323.
186. Dinsmore BJ, Pollack HM, Banner MP. Calcified transitional cell carcinoma of the renal pelvis. Radiology. 1988;167(2):401-404.
187. Hartman DS, Pyatt RS, Dailey E. Transitional cell carcinoma of the kidney with invasion into the renal vein. Urol Radiol. 1983;5(2):83-87.
188. Winalski CS, Lipman JC, Tumeh SS. Ureteral neoplasms. Radiographics. 1990;10(2):271-283.
189. Caoili EM, Cohan RH, Korobkin M, et al. Urinary tract abnormalities: initial experience with multi-detector row CT urography. Radiology. 2002;222(2):353-360.
190. Caoili EM, Cohan RH, Inampudi P, et al. MDCT urography of upper tract urothelial neoplasms. AJR Am J Roentgenol. 2005;184(6):1873-1881.

191. Dershaw DD, Scher HI. Sonography in evaluation of carcinoma of bladder. Urology. 1987;29(4):454-457.
192. Dondalski M, White EM, Ghahremani GG, Patel SK. Carcinoma arising in urinary bladder diverticula: imaging findings in six patients. AJR Am J Roentgenol. 1993;161(4):817-820.
193. Barentsz JO, Ruijs SH, Strijk SP. The role of MR imaging in carcinoma of the urinary bladder. AJR Am J Roentgenol. 1993;160(5):937-947.
194. Narumi Y, Sato T, Hori S, et al. Squamous cell carcinoma of the uroepithelium: CT evaluation. Radiology. 1989;173(3):853-856.
195. Blacher EJ, Johnson DE, Abdul-Karim FW, Ayala AG. Squamous cell carcinoma of renal pelvis. Urology. 1985;25(2):124-126.
196. Mirone V, Prezioso D, Palombini S, Lotti T. Mucinous adenocarcinoma of the renal pelvis. Eur Urol. 1984;10(4):284-285.
197. Merino MJ, Livolsi VA. Oncocytomas of the kidney. Cancer. 1982;50(9):1852-1856.
198. Honda H, Bonsib S, Barloon TJ, Masuda K. Unusual renal oncocytomas: pathologic and CT correlations. Urol Radiol. 1992;14(3):148-154.
199. Hartman GW, Hattery RR. Benign neoplasms of the renal parenchyma. In: Pollack HM, editor. Clinical urography: an atlas and textbook of urological imaging. Philadelphia: Saunders; 1990. p. 1193-1215.
200. Prasad SR, Surabhi VR, Menias CO, et al. Benign renal neoplasms in adults: cross-sectional imaging findings. AJR Am J Roentgenol. 2008;190(1):158-164.
201. Kuroda N, Toi M, Hiroi M, Enzan H. Review of chromophobe renal cell carcinoma with focus on clinical and pathobiological aspects. Histol Histopathol. 2003;18(1):165-171.
202. Davidson AJ, Hayes WS, Hartman DS, et al. Renal oncocytoma and carcinoma: failure of differentiation with CT. Radiology. 1993;186(3):693-696.
203. Goiney RC, Goldenberg L, Cooperberg PL, et al. Renal oncocytoma: sonographic analysis of 14 cases. AJR Am J Roentgenol. 1984;143(5):1001-1004.
204. Tikkakoski T, Paivansalo M, Alanen A, et al. Radiologic findings in renal oncocytoma. Acta Radiol. 1991;32(5):363-367.
205. Gentry LR, Gould HR, Alter AJ, et al. Hemorrhagic angiomyolipoma: demonstration by computed tomography. J Comput Assist Tomogr. 1981;5(6):861-865.
206. Oesterling JE, Fishman EK, Goldman SM, Marshall FF. The management of renal angiomyolipoma. J Urol. 1986;135(6):1121-1124.
207. Arenson AM, Graham RT, Shaw P, et al. Angiomyolipoma of the kidney extending into the inferior vena cava: sonographic and CT findings. AJR Am J Roentgenol. 1988;151(6):1159-1161.
208. Israel GM, Bosniak MA, Slywotzky CM, Rosen RJ. CT differentiation of large exophytic renal angiomyolipomas and perirenal liposarcomas. AJR Am J Roentgenol. 2002;179(3):769-773.
209. Yamakado K, Tanaka N, Nakagawa T, et al. Renal angiomyolipoma: relationships between tumor size, aneurysm formation, and rupture. Radiology. 2002;225(1):78-82.
210. Lapeyre M, Correas JM, Ortonne N, et al. Color-flow Doppler sonography of pseudoaneurysms in patients with bleeding renal angiomyolipoma. AJR Am J Roentgenol. 2002;179(1):145-147.
211. Earthman WJ, Mazer MJ, Winfield AC. Angiomyolipomas in tuberous sclerosis: subselective embolotherapy with alcohol, with long-term follow-up study. Radiology. 1986;160(2):437-441.
212. Richmond J, Sherman RS, Diamond HD, Craver LF. Renal lesions associated with malignant lymphomas. Am J Med. 1962;32:184-207.
213. Horii SC, Bosniak MA, Megibow AJ, et al. Correlation of CT and ultrasound in the evaluation of renal lymphoma. Urol Radiol. 1983;5(2):69-76.
214. Heiken JP, Gold RP, Schnur MJ, et al. Computed tomography of renal lymphoma with ultrasound correlation. J Comput Assist Tomogr. 1983;7(2):245-250.
215. Gregory A, Behan M. Lymphoma of the kidneys: unusual ultrasound appearance due to infiltration of the renal sinus. J Clin Ultrasound. 1981;9(6):343-345.
216. Jafri SZ, Bree RL, Amendola MA, et al. CT of renal and perirenal non-Hodgkin lymphoma. AJR Am J Roentgenol. 1982;138(6):1101-1105.
217. Deuskar V, Martin LF, Leung W. Renal lymphoma: an unusual example. Can Assoc Radiol J. 1987;38(2):133-135.
218. Binkovitz LA, Hattery RR, LeRoy AJ. Primary lymphoma of the bladder. Urol Radiol. 1988;9(4):231-233.
219. Kirshbaum JD. Leukemia: a clinical and pathological study of 123 fatal cases in 14,400 necropsies. Arch Intern Med. 1943;71:777.
220. Sternby NH. Studies in enlargement of leukaemic kidneys. Acta Haematol. 1955;14(6):354-362.
221. Kumari-Subaiya S, Lee WJ, Festa R, et al. Sonographic findings in leukemic renal disease. J Clin Ultrasound. 1984;12(8):465-472.
222. Araki T. Leukemic involvement of the kidney in children: CT features. J Comput Assist Tomogr. 1982;6(4):781-784.
223. Pascal RR. Renal manifestations of extrarenal neoplasms. Hum Pathol. 1980;11(1):7-17.
224. Choyke PL, White EM, Zeman RK, et al. Renal metastases: clinicopathologic and radiologic correlation. Radiology. 1987;162(2):359-363.
225. Ambos MA, Bosniak MA, Megibow AJ, Raghavendra B. Ureteral involvement by metastatic disease. Urol Radiol. 1979;1(2):105-112.
226. Mengiardi B, Wiesner W, Stoffel F, et al. Case 44: adenocarcinoma of the urachus. Radiology. 2002;222(3):744-747.
227. Rao BK, Scanlan KA, Hinke ML. Abdominal case of the day. AJR Am J Roentgenol. 1986;146(5):1074-1079.
228. Brick SH, Friedman AC, Pollack HM, et al. Urachal carcinoma: CT findings. Radiology. 1988;169(2):377-381.
229. Dunnick NR, Hartman DS, Ford KK, et al. The radiology of juxtaglomerular tumors. Radiology. 1983;147(2):321-326.
230. McKeown DK, Nguyen GK, Rudrick B, Johnson MA. Carcinoid of the kidney: radiologic findings. AJR Am J Roentgenol. 1988;150(1):143-144.
231. Chen M, Lipson SA, Hricak H. MR imaging evaluation of benign mesenchymal tumors of the urinary bladder. AJR Am J Roentgenol. 1997;168(2):399-403.
232. Kogan MG, Koenigsberg M, Laor E, Bennett B. US case of the day. Cavernous hemangioma of the bladder. Radiographics. 1996;16(2):443-447.
233. Baert L, Steg A. Is the diverticulum of the distal and collecting tubules a preliminary stage of the simple cyst in the adult? J Urol. 1977;118(5):707-710.
234. Laucks SJ, McLauchlan MSF. Aging and simple renal cysts of the kidney. Br J Radiol. 1982;54:12-15.
235. Jackman RJ, Stevens GM. Benign hemorrhagic renal cyst. Nephrotomography, renal arteriography, and cyst puncture. Radiology. 1974;110(1):7-13.
236. Bosniak MA. The current radiological approach to renal cysts. Radiology. 1986;158(1):1-10.
237. Israel GM, Bosniak MA. Calcification in cystic renal masses: is it important in diagnosis? Radiology. 2003;226(1):47-52.
238. Bosniak MA. The small (less than or equal to 3.0 cm) renal parenchymal tumor: detection, diagnosis, and controversies. Radiology. 1991;179(2):307-317.
239. Israel GM, Bosniak MA. Follow-up CT of moderately complex cystic lesions of the kidney (Bosniak category IIF). AJR Am J Roentgenol. 2003;181(3):627-633.
240. Park BK, Kim B, Kim SH, et al. Assessment of cystic renal masses based on Bosniak classification: comparison of CT and contrast-enhanced US. Eur J Radiol. 2007;61(2):310-314.
241. Meloni MF, Bertolotto M, Alberzoni C, et al. Follow-up after percutaneous radiofrequency ablation of renal cell carcinoma: contrast-enhanced sonography versus contrast-enhanced CT or MRI. AJR Am J Roentgenol. 2008;191(4):1233-1238.
242. Hidalgo H, Dunnick NR, Rosenberg ER, et al. Parapelvic cysts: appearance on CT and sonography. AJR Am J Roentgenol. 1982;138(4):667-671.
243. Chan JC, Kodroff MB. Hypertension and hematuria secondary to parapelvic cyst. Pediatrics. 1980;65(4):821-823.
244. Ginalski JM, Portmann L, Jaeger P. Does medullary sponge kidney cause nephrolithiasis? AJR Am J Roentgenol. 1990;155(2):299-302.
245. Goldman S, Hartman DS. Medullary sponge kidney. In: Pollack HM, editor. Clinical urography: an atlas and textbook of urological imaging. Philadelphia: Saunders; 1990. p. 1167-1177.
246. Resnick JS, Hartman DS. Medullary cystic disease of the kidney. In: Pollack HM, editor. Clinical urography: an atlas and textbook of urological imaging. Philadelphia: Saunders; 1990. p. 1178-1184.
247. Bisceglia M, Galliani CA, Senger C, et al. Renal cystic diseases: a review. Adv Anat Pathol. 2006;13(1):26-56.
248. Choyke PL. Inherited cystic diseases of the kidney. Radiol Clin North Am. 1996;34(5):925-946.
249. Grampsas SA, Chandhoke PS, Fan J, et al. Anatomic and metabolic risk factors for nephrolithiasis in patients with autosomal dominant polycystic kidney disease. Am J Kidney Dis. 2000;36(1):53-57.

250. Ravine D, Gibson RN, Walker RG, et al. Evaluation of ultrasonographic diagnostic criteria for autosomal dominant polycystic kidney disease 1. Lancet. 1994;343(8901):824-827.
251. Bear JC, McManamon P, Morgan J, et al. Age at clinical onset and at ultrasonographic detection of adult polycystic kidney disease: data for genetic counselling. Am J Med Genet. 1984;18(1):45-53.
252. Pei Y, Obaji J, Dupuis A, et al. Unified criteria for ultrasonographic diagnosis of ADPKD. J Am Soc Nephrol. 2009;20(1):205-212.
253. Sanders RC, Hartman DS. The sonographic distinction between neonatal multicystic kidney and hydronephrosis. Radiology. 1984;151(3):621-625.
254. Markowitz GS, Radhakrishnan J, Kambham N, et al. Lithium nephrotoxicity: a progressive combined glomerular and tubulointerstitial nephropathy. J Am Soc Nephrol. 2000;11(8):1439-1448.
255. Di Salvo DN, Park J, Laing FC. Lithium nephropathy: unique sonographic findings. J Ultrasound Med. 2012;31(4):637-644.
256. Madewell JE, Goldman SM, Davis Jr CJ, et al. Multilocular cystic nephroma: a radiographic-pathologic correlation of 58 patients. Radiology. 1983;146(2):309-321.
257. Lee JK, McClennan BL, Kissane JM. Unilateral polycystic kidney disease. AJR Am J Roentgenol. 1978;130(6):1165-1167.
258. Slywotzky CM, Bosniak MA. Localized cystic disease of the kidney. AJR Am J Roentgenol. 2001;176(4):843-849.
259. Master U, Cruz C, Schmidt R, et al. Renal malignancy in peritoneal dialysis patients with acquired cystic kidney disease. Adv Perit Dial. 1992;8:145-149.
260. Taylor AJ, Cohen EP, Erickson SJ, et al. Renal imaging in long-term dialysis patients: a comparison of CT and sonography. AJR Am J Roentgenol. 1989;153(4):765-767.
261. Levine E. Acquired cystic kidney disease. Radiol Clin North Am. 1996;34(5):947-964.
262. Levine E, Collins DL, Horton WA, Schimke RN. CT screening of the abdomen in von Hippel-Lindau disease. AJR Am J Roentgenol. 1982;139(3):505-510.
263. Kuntz N. Population studies. In: Gomez MR, editor. Tuberous sclerosis. 2nd ed. New York: Raven Press; 1988. p. 214.
264. Kawashima A, Sandler CM, Corl FM, et al. Imaging of renal trauma: a comprehensive review. Radiographics. 2001;21(3):557-574.
265. Federle MP. Evaluation of renal trauma. In: Pollack HM, editor. Clinical urography: an atlas and textbook of urological imaging. Philadelphia: Saunders; 1990. p. 1472-1494.
266. Regine G, Atzori M, Miele V, et al. Second-generation sonographic contrast agents in the evaluation of renal trauma. Radiol Med. 2007;112(4):581-587.
267. McGahan JP, Horton S, Gerscovich EO, et al. Appearance of solid organ injury with contrast-enhanced sonography in blunt abdominal trauma: preliminary experience. AJR Am J Roentgenol. 2006;187(3):658-666.
268. Lang EK. Ureteral injuries. In: Pollack HM, editor. Clinical urography: an atlas and textbook of urological imaging. Philadelphia: Saunders; 1990. p. 1495-1504.
269. Keogan MT, Kliewer MA, Hertzberg BS, et al. Renal resistive indexes: variability in Doppler US measurement in a healthy population. Radiology. 1996;199(1):165-169.
270. Platt JF, Ellis JH, Rubin JM. Examination of native kidneys with duplex Doppler ultrasound. Semin Ultrasound CT MR. 1991;12(4):308-318.
271. Bude RO, DiPietro MA, Platt JF, et al. Age dependency of the renal resistive index in healthy children. Radiology. 1992;184(2):469-473.
272. Terry JD, Rysavy JA, Frick MP. Intrarenal Doppler: characteristics of aging kidneys. J Ultrasound Med. 1992;11(12):647-651.
273. Mostbeck GH, Gossinger HD, Mallek R, et al. Effect of heart rate on Doppler measurements of resistive index in renal arteries. Radiology. 1990;175(2):511-513.
274. Erwin BC, Carroll BA, Walter JF, Sommer FG. Renal infarction appearing as an echogenic mass. AJR Am J Roentgenol. 1982;138(4):759-761.
275. Takebayashi S, Aida N, Matsui K. Arteriovenous malformations of the kidneys: diagnosis and follow-up with color Doppler sonography in six patients. AJR Am J Roentgenol. 1991;157(5):991-995.
276. Hillman BJ. Imaging advances in the diagnosis of renovascular hypertension. AJR Am J Roentgenol. 1989;153(1):5-14.
277. Spyridopoulos TN, Kaziani K, Balanika AP, et al. Ultrasound as a first line screening tool for the detection of renal artery stenosis: a comprehensive review. Med Ultrason. 2010;12(3):228-232.
278. Mitty HA, Shapiro RS, Parsons RB, Silberzweig JE. Renovascular hypertension. Radiol Clin North Am. 1996;34(5):1017-1036.
279. Stavros AT, Parker SH, Yakes WF, et al. Segmental stenosis of the renal artery: pattern recognition of tardus and parvus abnormalities with duplex sonography. Radiology. 1992;184(2):487-492.
280. Rene PC, Oliva VL, Bui BT, et al. Renal artery stenosis: evaluation of Doppler US after inhibition of angiotensin-converting enzyme with captopril. Radiology. 1995;196(3):675-679.
281. Dowling RJ, House MK, King PM, et al. Contrast-enhanced Doppler ultrasound for renal artery stenosis. Australas Radiol. 1999;43(2):206-209.
282. Sharafuddin MJ, Raboi CA, Abu-Yousef M, et al. Renal artery stenosis: duplex US after angioplasty and stent placement. Radiology. 2001;220(1):168-173.
283. Investigators A, Wheatley K, Ives N, et al. Revascularization versus medical therapy for renal-artery stenosis. N Engl J Med. 2009;361(20):1953-1962.
284. Cooper CJ, Murphy TP, Cutlip DE, et al. Stenting and medical therapy for atherosclerotic renal-artery stenosis. N Engl J Med. 2014;370(1):13-22.
285. Fleshner NE, Johnston KW. Repair of an autotransplant renal artery aneurysm: case report and literature review. J Urol. 1992;148(2 Pt 1):389-391.
286. Rosenfield AT, Zeman RK, Cronan JJ, Taylor KJ. Ultrasound in experimental and clinical renal vein thrombosis. Radiology. 1980;137(3):735-741.
287. Braun B, Weilemann LS, Weigand W. Ultrasonic demonstration of renal vein thrombosis. Radiology. 1981;138(1):157-158.
288. Platt JF, Ellis JH, Rubin JM. Intrarenal arterial Doppler sonography in the detection of renal vein thrombosis of the native kidney. AJR Am J Roentgenol. 1994;162(6):1367-1370.
289. Haddad MC, Medawar WA, Hawary MM, et al. Perirenal fluid in renal parenchymal medical disease ("floating kidney"): clinical significance and sonographic grading. Clin Radiol. 2001;56(12):979-983.
290. Yassa NA, Peng M, Ralls PW. Perirenal lucency ("kidney sweat"): a new sign of renal failure. AJR Am J Roentgenol. 1999;173(4):1075-1077.
291. Sty JR, Starshak RJ, Hubbard AM. Acute renal cortical necrosis in hemolytic uremic syndrome. J Clin Ultrasound. 1983;11(3):175-178.
292. Rodriguez-de-Velasquez A, Yoder IC, Velasquez PA, Papanicolaou N. Imaging the effects of diabetes on the genitourinary system. Radiographics. 1995;15(5):1051-1068.
293. Urban BA, Fishman EK, Goldman SM, et al. CT evaluation of amyloidosis: spectrum of disease. Radiographics. 1993;13(6):1295-1308.
294. Gomes CM, Sanchez-Ortiz RF, Harris C, et al. Significance of hematuria in patients with interstitial cystitis: review of radiographic and endoscopic findings. Urology. 2001;57(2):262-265.
295. Amis Jr ES, Blaivas JG. Neurogenic bladder simplified. Radiol Clin North Am. 1991;29(3):571-580.
296. Papanicolaou N, Harbury OL, Pfister RC. Fat-filled postoperative renal cortical defects: sonographic and CT appearance. AJR Am J Roentgenol. 1988;151(3):503-505.
297. Millward SF, Lanctin HP, Lewandowski BJ, Lum PA. Fat-filled postoperative renal pseudotumour: variable appearance in ultrasonography images. Can Assoc Radiol J. 1992;43(2):116-119.
298. Ng C, Amis Jr ES. Radiology of continent urinary diversion. Radiol Clin North Am. 1991;29(3):557-570.

CHAPTER 10

The Prostate and Transrectal Ultrasound

Ants Toi

SUMMARY OF KEY POINTS

- Prostate cancer is a significant health problem and its management is changing rapidly.
- Currently, transrectal ultrasound (TRUS) with biopsy is the primary modality to diagnose prostate cancer.
- New modalities including multiparametric magnetic resonance imaging and biomarkers are being introduced for prostate cancer assessment.
- Understanding of prostate cancer has evolved with recognition of aggressive and indolent forms, which are managed differently.
- Screening for prostate cancer has become controversial, and population screening is being replaced by focused "smart screening."
- TRUS has applications in assessment of nonmalignant prostate conditions and assessment of nonprostate abnormalities within the field of view of the transrectal probe.

CHAPTER OUTLINE

ANATOMY
Zonal Anatomy
Vascular and Neural Structures
SONOGRAPHIC APPEARANCE
EQUIPMENT AND TECHNIQUE
BENIGN CONDITIONS
Normal Variants
Benign Prostatic Hyperplasia
Chronic Prostatitis/Chronic Pelvic Pain Syndrome
Prostate Cysts
Seminal Vesicles and Vas Deferens
INFERTILITY AND TRANSRECTAL ULTRASOUND
HEMATOSPERMIA
PROSTATE CANCER
Epidemiology
Prostate-Specific Antigen and Variants
Alternate Prostate Cancer Biomarkers
Screening
Clinical Staging and Histologic Grading
Therapy
Sonographic Appearance of Prostate Cancer
Gray-Scale Ultrasound
Color Flow and Power Doppler Imaging
Contrast-Enhanced Ultrasound
Three-Dimensional Ultrasound and Transrectal Ultrasound–Magnetic Resonance Imaging Fusion
Elastography
ULTRASOUND-GUIDED BIOPSY
Preparation for Biopsy
Antibiotic Prophylaxis
Bowel Preparation
Analgesia
Anticoagulation
Technique
Side Effects and Complications
Indications and Sampling
mpMRI-TRUS Fusion Biopsy
Transperineal Biopsy and Template Biopsy
Biopsy After Radical Prostatectomy
Biopsy in Men With Absent Anus
OTHER APPLICATIONS OF TRANSRECTAL ULTRASOUND AND BIOPSY IN MEN AND WOMEN
CONCLUSIONS

In the early 1980s **transrectal ultrasound** (TRUS) of the prostate was believed to be the pivotal imaging test of the prostate for benign conditions (e.g., benign hyperplasia, obstructive infertility) and for cancer evaluation, including screening, diagnosis, biopsy, staging, and monitoring of response to therapy. With experience and emergence of new techniques such as multiparametric magnetic resonance imaging (mpMRI), the uses, strengths, and limitations of TRUS and other newer prostate imaging modalities such as elastography, contrast-enhanced ultrasound (CEUS) including targeted microbubbles, and scintigraphy have become better defined.[1-6] Most current referrals for TRUS relate to prostate cancer evaluation, biopsy, and guidance of therapeutic procedures. TRUS was initially considered a primary screening test for prostate cancer. This role has now been replaced by prostate-specific antigen (PSA) and digital rectal examination (DRE).[7,8] Currently the understanding of prostate cancer is undergoing rapid changes in every aspect including screening, serum and urine tests, diagnosis, management, pathology, staging, and therapy. New

approaches are being proposed almost monthly. There is even discussion that the most commonly detected low-grade Gleason score 3 + 3 = 6 cancer may not behave as a significant malignancy that needs active and immediate treatment.[9,10] mpMRI is assuming an increasing role for detection of clinically significant prostate cancer, biopsy guidance, staging, and guidance of therapy. Its availability, applications, and interpretation are evolving rapidly. Additional modalities including new biomarkers, scintigraphic imaging, positron emission tomography (PET)–computed tomography (CT) and PET–magnetic resonance imaging (MRI), and labeled metabolic tracers are being introduced.[6]

Occasional patient referrals for prostate examination relate to urinary dysfunction, infertility, pelvic pain, and prostatitis. TRUS guidance has also proven useful to assess and perform biopsy on any accessible lesion in the pelvis in both men and women.[1,11]

ANATOMY

Zonal Anatomy

Original textbook anatomic descriptions of the prostate referred to **lobar anatomy,** describing anterior, posterior, lateral, and median lobes; this designation has not been useful in identification and evaluation of carcinoma of the prostate.[3,12] Detailed anatomic dissections of the prostate reveal **zonal anatomy** in which the prostate is divided into the four glandular zones surrounding the prostatic urethra (Fig. 10.1):

- Peripheral zone
- Transition zone
- Central zone
- Anterior fibromuscular zone

These zones have differing embryologic origins and disease susceptibilities. In the normal young gland, sonography can rarely identify these zones separately unless a pathologic condition is present (Figs. 10.2 and 10.3). At sonography it is helpful to consider the prostate as having a peripheral or outer gland (peripheral zone plus central zone) and inner gland (transition zone plus anterior fibromuscular stroma plus internal urethral sphincter).[3,13-15]

The prostate does not have a true anatomic capsule, but it is surrounded by an outer fibromuscular band that is visible as a clear line demarking the prostate from the surrounding fat but that becomes blurred at the posterolateral margins at sites of entry of the neurovascular bundles.[3,16]

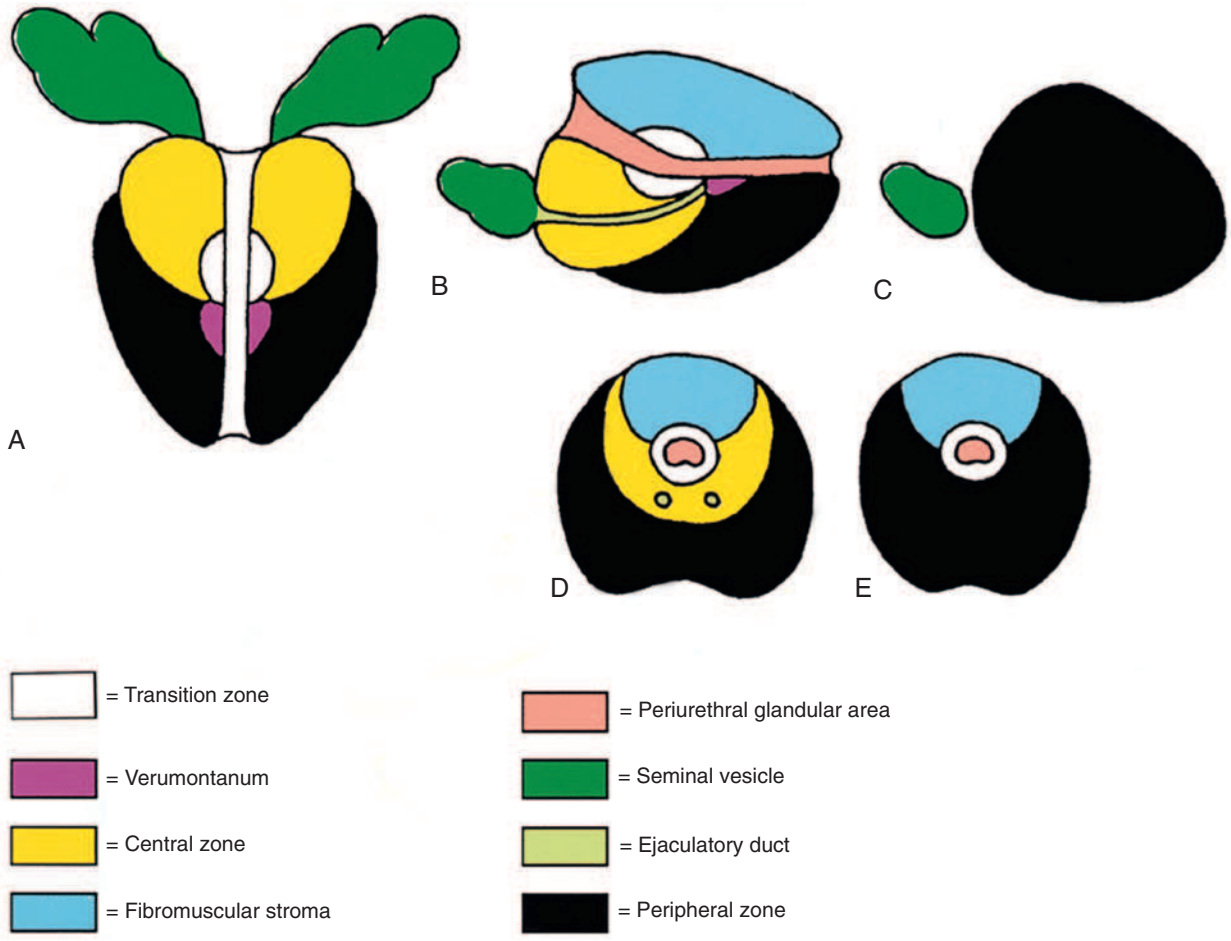

FIG. 10.1 Diagram of Prostate Zonal Anatomy. This is the anatomy in a young man because the transition zone *(white areas)* is small. The transition zone will undergo marked enlargement in older men with benign prostatic hyperplasia. **(A)** Coronal section at midprostate level. **(B)** Sagittal midline section. **(C)** Parasagittal section. **(D)** Axial section through base. **(E)** Axial section through apex.

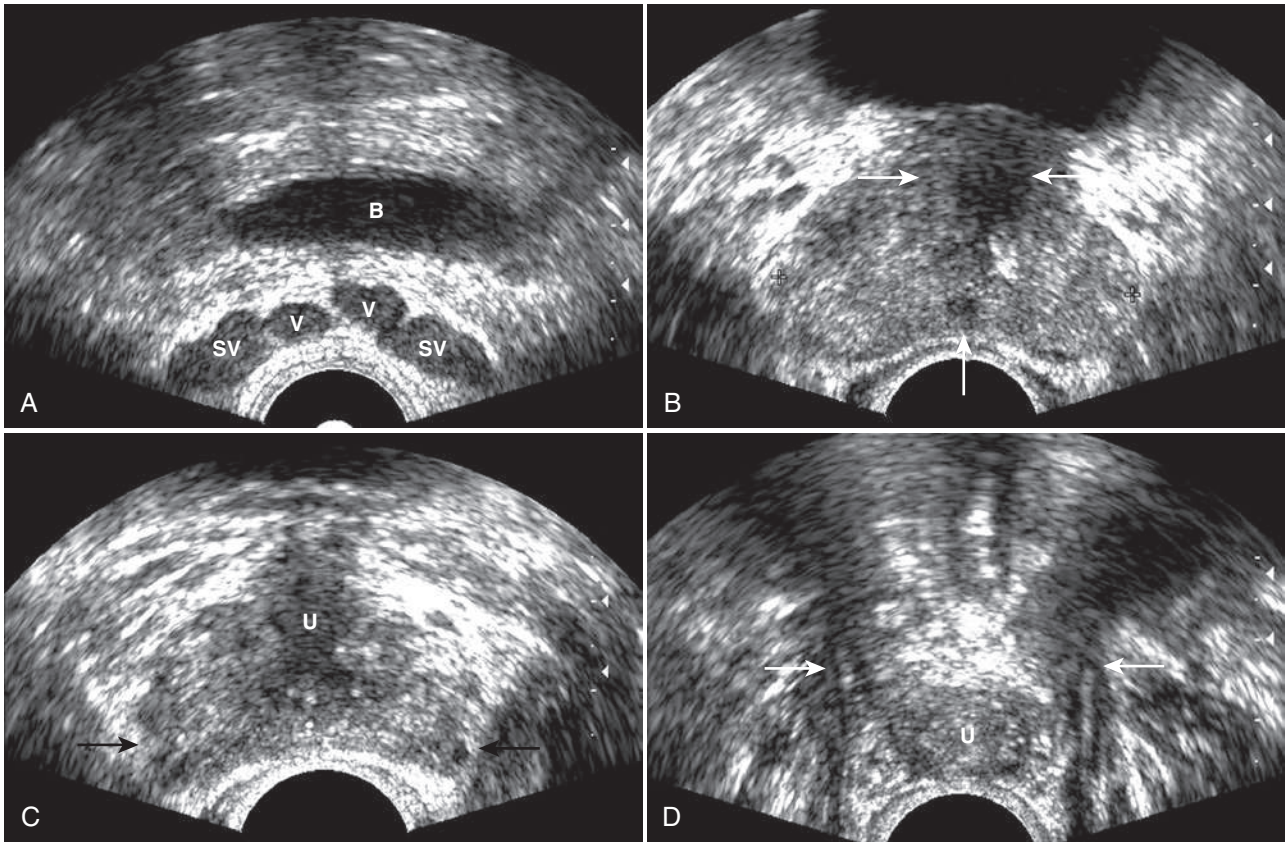

FIG. 10.2 Axial Sonograms of Prostate. (A) Transverse image above base shows the seminal vesicles *(SV)* and vas deferens *(V)*. **(B)** Axial scan at midgland level. Note the normal hypoechoic muscular internal urethral sphincter *(horizontal arrows)* and the ejaculatory ducts *(vertical arrow)*. **(C)** Axial scan at lower third of prostate shows hypoechoic urethra *(U)*. Most of the visible gland at this level is peripheral zone. Note the irregular outline at the posterolateral aspects *(arrows),* resulting from the entrance of the neurovascular bundles. **(D)** Axial scan just below apex of prostate shows cross section of distal urethra *(U)*. Pelvic sling muscles are visible *(arrows). B,* Bladder.

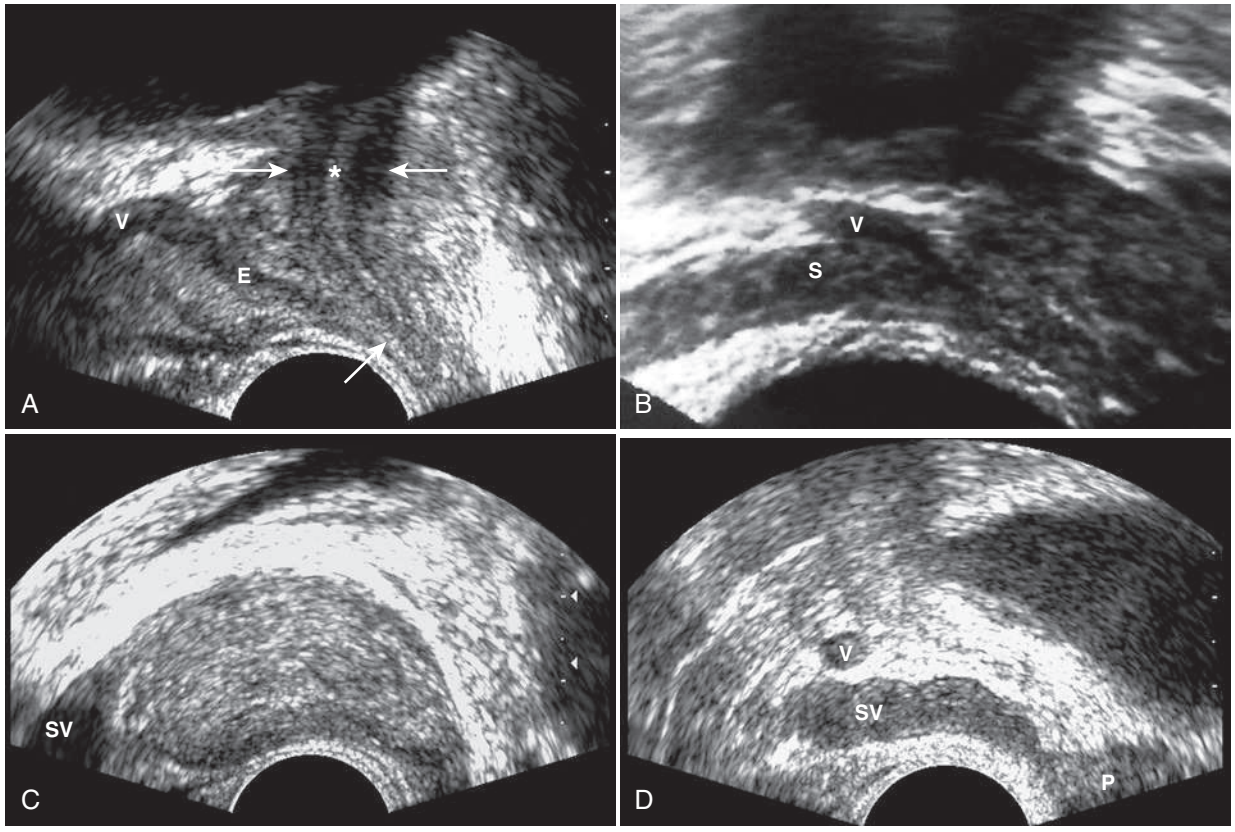

FIG. 10.3 Sagittal Views of Prostate. (A) Midsagittal view shows internal urethral sphincter *(white arrows),* which contains the echogenic collapsed urethra (*). The ejaculatory ducts *(E)* course from the vas deferens *(V)* to the verumontanum *(oblique arrow)*. **(B)** Midsagittal view at base shows the vas deferens *(V)* and adjacent seminal vesicles *(S)* as they enter the prostate. **(C)** Parasagittal view shows the lateral prostate, which is homogeneous and isoechoic and composed almost totally of peripheral zone tissue. **(D)** Parasagittal view above the prostate shows the normal seminal vesicles *(SV)* and vas deferens *(V)* in cross section above the prostate *(P). SV,* Seminal vesicle.

The **peripheral zone,** the largest of the glandular zones, arises from the urogenital sinus and in a young man before the onset of **benign prostatic hyperplasia** (BPH) contains approximately 70% of the prostatic glandular tissue and is the site for about 70% of prostate cancers.[17,18] It is separated from the **transition zone** and central zone by the **surgical capsule,** a hypoechoic line that is rendered hyperechoic by the frequent accumulation of corpora amylacea or calcifications along it. Traditionally, urologists at the time of suprapubic or transurethral prostate resection believed that they dissected to this line, which demarked hypertrophied periurethral glands from posterior lobe—hence "surgical" capsule. The peripheral zone occupies the posterior, lateral, and apical regions of the prostate, extending anteriorly around the margins, like an egg cup holding the "egg" of the central gland (Fig. 10.4A).

The young **transition zone** contains about 5% of the prostatic glandular tissue. It is visible as two small glandular areas positioned like saddlebags adjacent to the proximal urethral sphincter, which is a muscular tube up to 2 cm in diameter. It is the site of origin of most BPH and about 20% of prostate cancers.[17,19]

The **central zone** along with the seminal vesicles (SVs) arises from the wolffian ducts. It constitutes approximately 25% of the glandular tissue and is wedged at the prostate base between the peripheral and transition zones. The ducts of the vas deferens (VD) and SVs enter the base of the prostate at the central zone, where they are renamed the **ejaculatory ducts** and pass through it en route to the **verumontanum.** The central zone is relatively resistant to disease processes and is the site of only about 5% of prostate cancer.[17-19]

At the base of the prostate at the bladder neck is the thick, muscular, continence-providing, **internal urethral sphincter.** Its substantial homogeneous muscle content can make it appear hypoechoic. It contains periurethral glands that often contain calcifications.[12,13,19]

Vascular and Neural Structures

The prostate is supplied by the prostaticovesical arteries, which arise from the internal iliac arteries on each side and give rise to the prostatic artery and inferior vesical artery. The **prostatic artery** gives rise to the urethral and capsular arteries. The **inferior vesical artery** supplies the bladder base, SVs, and ureter. The urethral artery supplies about one-third of the prostate, and the capsular branches supply the remainder.[20]

On Doppler ultrasound the prostate is mildly to moderately vascular. The neurovascular bundles are visible at the posterolateral angles (Fig. 10.5). The capsular and urethral arteries are easily seen, and branches to the inner gland and peripheral zone are visible in a somewhat radial pattern with the periurethral vessels as the axle. A dense cluster of vessels is often seen capping the base of the prostate, and care must be taken not to mistake these for tumor vascularity.[20]

Nerve supply to the prostate has been clarified.[15,21,22] Parasympathetic supply is through the S2-S4 sacral roots, and sympathetic supply is through the hypogastric nerve. These combine in the pelvic plexus just above and lateral to the prostate and give rise to about 6 to 16 small branches that supply the SVs, prostate, levator ani, and corpora cavernosa. The cavernosal branches are responsible for erections. The nerves and blood vessels travel together as the neurovascular bundle in the Denonvilliers (rectoprostatic) fascia at the posterolateral aspect of the prostate, where the vessels are visible with color flow Doppler ultrasound. These nerves are vulnerable to injury during surgery, radiotherapy, and other interventions and are avoided at nerve-sparing prostatectomy to preserve potency.[15,21,22]

SONOGRAPHIC APPEARANCE

Images are oriented using the standards for abdominal sonography and other cross-sectional imaging modalities. The images are displayed as though one were standing at the feet of a supine patient and looking headward. The rectum is at the bottom of the screen; the right prostate is on the left of the screen. On sagittal views, the base (head end) is on the left side.

On axial ultrasound, above the prostatic base, the **seminal vesicles** are paired, relatively hypoechoic, multiseptated structures cephalad to the base of the prostate normally measuring about 1 cm diameter (see Fig. 10.2A). The adjacent vasa deferentia are visible as uniform muscular tubes measuring about 6 mm in diameter coursing from the internal inguinal ring to lie beside the SVs and enter the midbase of the prostate, where they become the **ejaculatory ducts,** which connect to the **verumontanum** (seminal colliculus).

In the axial plane, the urethra between the bladder neck and verumontanum and its surrounding smooth muscle, the internal sphincter, can be a quite conspicuous hypoechoic structure measuring 2 cm in diameter that can mimic the appearance of a transurethral resection defect (see Figs. 10.2B and 10.3A). Those unfamiliar with transrectal and pelvic ultrasound may mistake the sphincter for hypoechoic tumor. The muscular sphincter ends at the verumontanum, which forms a small bulge pointed anteriorly, often with a small, conspicuous calcification at its apex, giving it an Eiffel Tower appearance.

The inner transition zone is separated from the peripheral zone by the usually hypoechoic surgical capsule (see Fig. 10.4A). This line is less visible in young men but becomes conspicuous as BPH enlarges the transition zone (see Figs. 10.2B and 10.4A). The peripheral zone has a uniform, homogeneous texture and is slightly more echogenic than the transition zone. Peripheral zone echogenicity is defined as **isoechoic** and taken as the standard for prostate echogenicity and other areas of the gland are compared to its echogenicity. Laterally, the peripheral zone curves anteriorly to enclose the transition zone. This upward curved part was named the "anterior horns" by Babaian from Texas because it resembled the horns of a steer. Prominent veins of Batson venous plexus are visible in the periprostatic fat, sometimes containing calcified shadowing phleboliths.[12]

On midsagittal view the muscular internal urethral sphincter extends from the bladder to the verumontanum, sometimes surrounded by corpora amylacea in the periurethral glands (see Fig. 10.3A). The anterior fibromuscular zone is an inconspicuous area anterior to the internal sphincter. At the verumontanum the distal urethra angles slightly anteriorly and ultimately exits the apex of the prostate just before it enters the urogenital

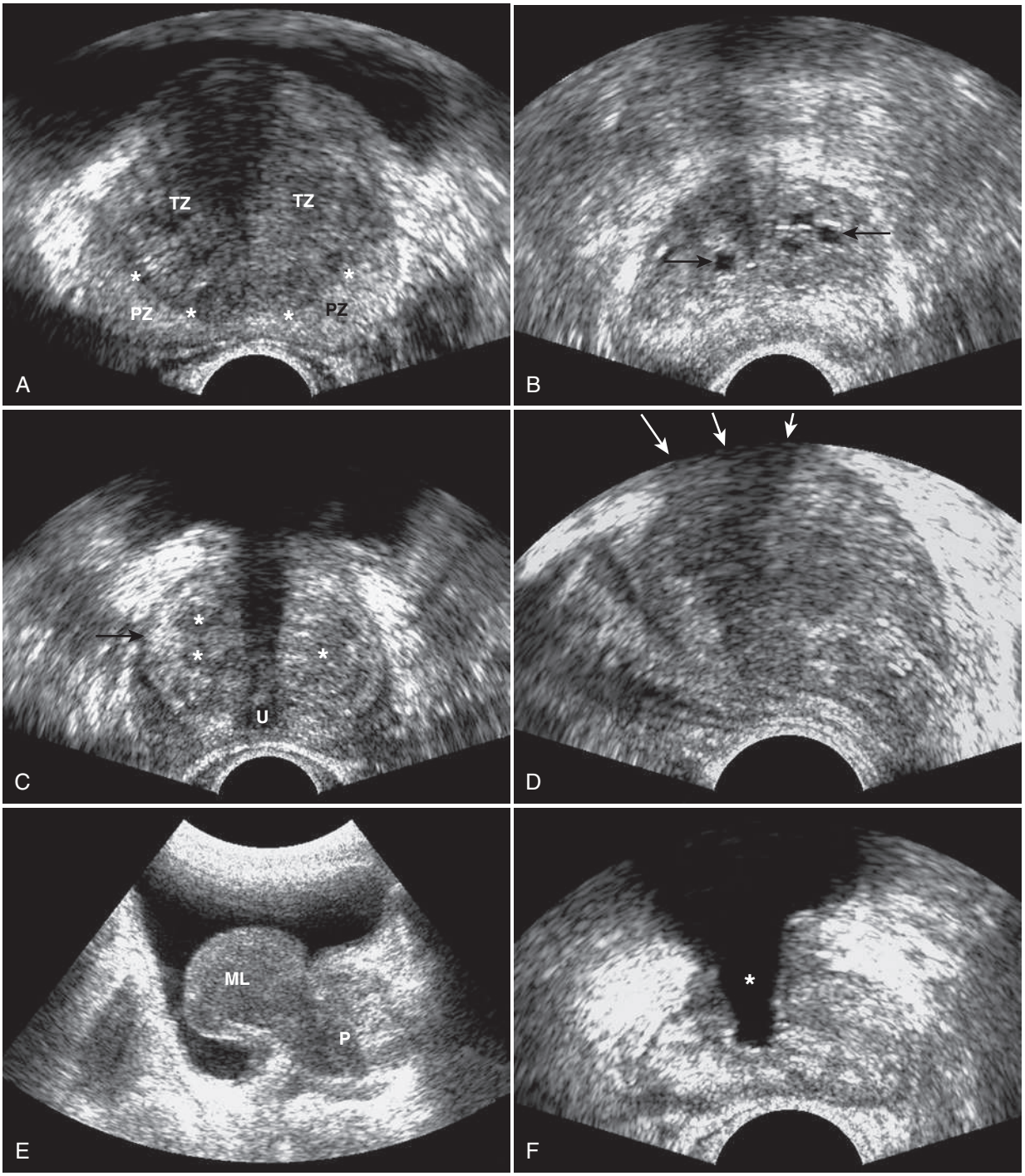

FIG. 10.4 Benign Prostatic Hyperplasia (BPH). (A) Axial view shows the greatly enlarged, slightly hypoechoic transition zone *(TZ)*, which compresses the more echogenic peripheral zone *(PZ)*. Their interface is the surgical capsule (*). The region inside the surgical capsule (transition zone) is also called the "inner gland" and the region outside the surgical capsule, the "outer gland," which is composed of peripheral zone plus central zone. (Peripheral zone is the "egg cup" holding the "egg" of the central gland.) **(B)** Benign degenerative cysts in the transition zone *(arrows)*. These have no clinical significance. The transition zone can become acoustically very heterogeneous, making cancer diagnosis difficult. **(C)** Heterogeneous nature of hyperplasia in the transition zone. Both hyperechoic *(black arrow)* and hypoechoic (*) areas are present. *U,* Urethra. **(D)** Sagittal view shows pitfall in transrectal ultrasound (TRUS) of BPH. If the field of view is not deep enough *(arrows),* prominent median lobe enlargement may be cut off and may escape detection. **(E)** Transvesical midsagittal scan shows obvious massive enlargement of the median lobe *(ML)* protruding into the bladder. Evaluation for symptoms of prostatism is better done transvesically than transrectally with TRUS. *P,* Prostate. **(F)** Axial view of typical transurethral resection of prostate (TURP) surgical defect (*).

diaphragm, which is the external urethral sphincter. In the midplane the ejaculatory ducts (see Fig. 10.3A) are visible as hypoechoic tracts extending from the VD at the base to the centrally located verumontanum.

Parasagittally with hyperplasia, the anterior hyperplastic transition zone can be seen separated from the posteriorly situated peripheral zone by the surgical capsule. The VD and SVs are visible above the base. Still more laterally, the transition zone ends, leaving only the part of the peripheral zone curving anteriorly at the sides of the gland (anterior horns).[12]

Histologically, the prostate does not have a true membranous capsule but is surrounded by condensed connective tissue through which the vessels and nerves course. On transverse and sagittal imaging, the border appears sharply defined except at the posterolateral margins where the neurovascular bundle enters the prostate and makes the margin look ragged. This can hinder determination of extracapsular extension by tumors[3,16] (see Fig. 10.2C).

EQUIPMENT AND TECHNIQUE

Most modern ultrasound machines can be equipped with **transrectal probes** and biopsy guides suitable for examination of the prostate and rectum. It is advantageous to use the thinnest probe to negotiate "tight" anal sphincters. End-fire probes (Fig. 10.6) are suitable for most biopsy applications and allow for multiplanar imaging in transverse and axial projections. They are well suited for biopsy guidance, allowing easy access to all prostate regions including the apex and anterior gland. The current

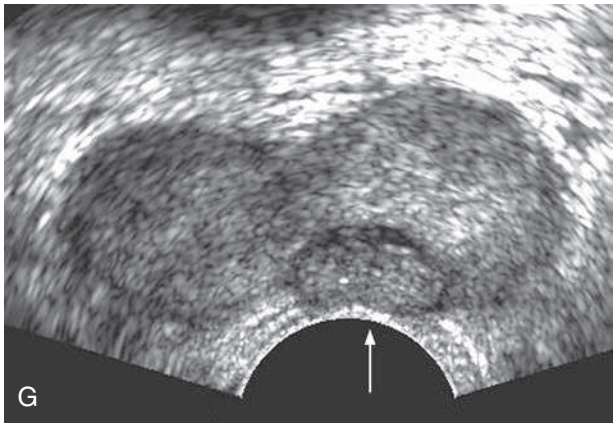

FIG. 10.4 cont'd (G) Benign peripheral zone hyperplastic nodule. Transverse image shows prominent isoechoic posterior nodule that bulges the capsule and has a well-defined hypoechoic rim *(arrow)*. It resembles BPH nodules, which are normally seen in the transition zone, but it is located in the peripheral zone. At palpation these feel hard and can be mistaken for cancer. Biopsy is needed for reassurance to confirm their benign nature. *P,* Prostate; *U,* urethra.

FIG. 10.6 Typical End-Fire Ultrasound Probe for Transrectal and Intracavitary Work. Active element is at tip of probe, and needle in guide fires parallel to probe (end-fire). In clinical use the probe and guide would be covered by protective sheaths.

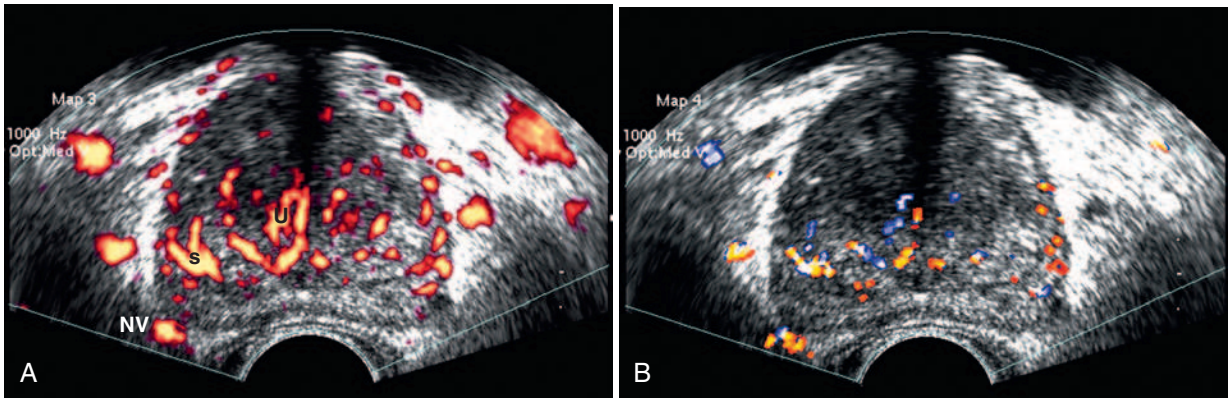

FIG. 10.5 Normal Doppler Ultrasound Anatomy in Patient With Moderate Benign Prostatic Hyperplasia (BPH). (A) Axial view with power Doppler ultrasound shows the urethral vessels *(U)*, some vessels along the surgical capsule *(S)*, and the neurovascular bundle *(NV)* on one side. This is an average degree of vascularity. Note the large vessels, mostly veins, outside the prostate. Care must be taken when biopsy is performed outside the prostate to avoid injury to these vessels. **(B)** Color Doppler flow imaging is more difficult to interpret owing to different colors related to flow direction.

trends emphasize high central frequency (8-10 MHz) and broad bandwidth. This increases spatial resolution but may decrease lesion conspicuity. Probes with a center frequency of about 5 MHz appear to provide a good balance between resolution and tissue/cancer contrast.[23]

Probes should be covered with sheaths or condoms during the examination and sterilized between patients, following manufacturers' recommendations. Linear probes help with transperineal techniques.[24]

In general, **rectal cleansing** is done before the scan. A self-administered rectal enema is preferred, but laxatives can be used. Some believe enemas decrease infectious complications of biopsy.[25,26] A **digital rectal examination** before probe insertion is performed to ensure that there are no rectal abnormalities to interfere with safe probe insertion and to correlate images with palpable abnormalities. The patient usually lies in a **left lateral decubitus** position for the scan. Some examiners prefer a lithotomy position, particularly if the examination is done in conjunction with other urologic procedures or transperineal interventions. With use of adequate lubrication, the probe is gently inserted into the rectum. To decrease discomfort, viscous lidocaine (Xylocaine) gel can be used as the lubricant in patients with tight sphincters or anal pathology such as fissures or inflamed hemorrhoids.

A **systematic approach** works best for examination and helps ensure that the whole gland is assessed. Typically the prostate is scanned and appropriate images are taken, first in gray scale starting in the transverse plane, from the SVs and proceeding to the apex, and then in the sagittal plane, from right to left lobe. Subsequently the scan is repeated with Doppler flow ultrasound imaging in the transverse plane to evaluate vascularity and vascular symmetry.

Measurements are taken as follows: maximal transverse width (W; right to left), anteroposterior plane (AP; anterior midline to rectal surface), length (L; maximal head to foot). **Prostate volume** is usually calculated with the "oblate spheroid" formula: volume = $0.5236 \times (W \times AP \times L)$. Volume measurement is only moderately repeatable to within 10%. Prostate volume can be converted to **prostate weight** because the specific gravity of prostate tissue is about 1; thus 1 cc (mL) is equivalent to 1 g.

Color or power Doppler ultrasound is used routinely when searching for cancer. Vessel density is more easily evaluated with **power Doppler,** which portrays color more evenly and is three to five times more sensitive than the color Doppler. Cancer detection is increased by about 5% to 10% with use of power Doppler, and vascular lesions have a slightly higher Gleason score (5.9% vs. 6.9%).[27,28] Overall it is still felt that although vascular density as shown by Doppler increases cancer detection, its absence is not sensitive enough to avoid systematic biopsy. Increased vascularity is not specific and can be seen with hypertrophy or inflammation, as well as cancer.[27,28] Spectral Doppler indices (such as resistive index [RI], pulsatility index [PI], and peak systolic velocity) vary with patient age and cannot differentiate between cancer and benign prostate conditions.[29] A pitfall of Doppler ultrasound is the normal, high vascular density seen capping the base of the left and right lobes, which should not be mistaken for enhanced vascularity seen with tumors.

BENIGN CONDITIONS

Normal Variants

Benign ductal ectasia is seen in older men who develop atrophy and dilation of peripheral prostatic ducts and has no clinical significance. The ducts appear as single or grouped, 1- to 2-mm-diameter tubular structures in the peripheral zone radiating from the capsule toward the urethra. Clusters of these can form hypoechoic areas that could be mistaken as prostate cancer (Fig. 10.7).

Prostatic calcifications and **corpora amylacea** are normal findings visible as bright echogenic foci or clumps consisting of proteinaceous debris in dilated prostatic ducts, most often in periurethral glands and along the surgical capsule. When densely clustered they can attenuate sound and block anterior visibility, and on Doppler they create a prominent "twinkle" artifact (see Fig. 10.7D). Subclinical infections, inflammation, and atrophy may contribute to their formation. Corpora amylacea have no clinical significance and are not usually palpable even if dense or clumped. Peripheral zone calcifications should not be accepted as a cause for palpable firmness or nodules. Patients with palpable abnormality need further evaluation, frequently with biopsy.

Benign Prostatic Hyperplasia

Prostate enlargement with **benign prostatic hypertrophy** (BPH) is a common cause of **lower urinary tract symptoms** (LUTS) in older men and affects about 50% of men older than 60 years and over 90% older than 70. The cause of BPH is unclear but is probably related to hormonal changes with aging and results in hypertrophy and hyperplasia of the fibrous, muscular, and glandular elements, primarily affecting the transition and periurethral zones.[1,19]

Lower urinary tract symptoms, also called **prostatism** and **bladder outlet obstruction,** can relate to increases in prostate size and muscular tone, both causing urethral constriction. Symptoms include frequency, nocturia, weak stream, hesitancy, intermittence, incomplete emptying, and urgency and are quantified using the American Urological Association (AUA) symptom index.[19,30] Many men have a misguided concern about prostate size. The issue is *urinary obstruction,* not prostate size. Prostate size correlates poorly with urinary obstruction. Urinary dysfunction is multifactorial and can also arise from abnormalities of the central nervous system, spine, bladder, prostate, and urethra. Patients with urinary dysfunction need evaluation of all these systems, not just the prostate. Ultrasound investigation of the patient with symptoms of prostatism is best done transvesically to assess prostate size, identify median lobe enlargement, and evaluate bladder volume and postvoid residual, bladder wall character, trabeculation, diverticula, tumors, and calculi, and the kidneys and ureters should be evaluated for hydronephrosis and masses. TRUS plays only a small role but helps if there is a clinical concern for prostate cancer (BPH is one cause for PSA

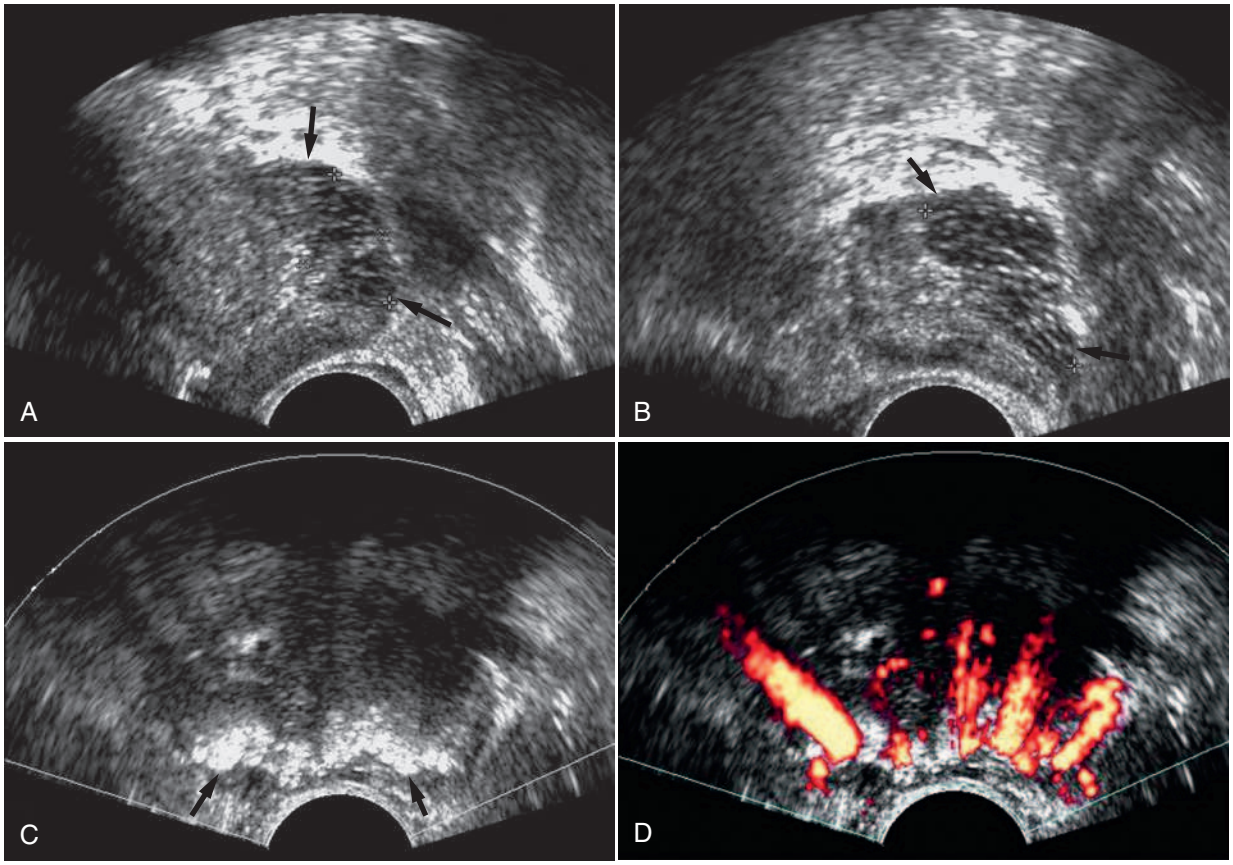

FIG. 10.7 Normal Anatomic Variants. (A) Axial view with benign glandular ectasia *(arrows)* visible as a peripheral hypoechoic area containing multiple radially oriented tubes. This hypoechoic appearance should not be mistaken for cancer. **(B)** Parasagittal view of benign ectatic glands *(arrows)*. **(C)** Axial view shows extensive echogenic material, both calcifications and corpora amylacea *(arrows),* along the surgical capsule and peripheral zone. This has no clinical significance and usually is not palpable. It hinders ultrasonic visibility. **(D)** Doppler examination of same patient shows the extensive Doppler noise artifact caused by the calcifications. Virtually all the visible color is artifactual.

elevation) or there is need for precise gland volume determination to plan surgical or medical treatment.[19]

The appearance of BPH is heterogeneous and depends on underlying histopathologic changes. This heterogeneity hinders cancer detection for both TRUS and mpMRI. Typically there is enlargement of the inner gland **(transition zone)** with hypoechoic, isoechoic, or hyperechoic nodules.[31] The specific echo pattern depends on the admixture of glandular, stromal, and muscular elements and nodules, which may be fibroblastic, fibromuscular, muscular, adenomatous, or fibroadenomatous. Hyperplasia of the periurethral glandular elements results in "median lobe" enlargement manifesting as a bulge into the urinary bladder (see Fig. 10.4E). Calcifications and **degenerative or retention cysts** are common.[31] Benign BPH nodules tend to have distinct margins, whereas transition zone cancer usually manifests as a diffuse, poorly marginated, usually hypoechoic nodule that may cause an asymmetrical bulge of the adjacent anterior contour similar to findings on mpMRI.[32]

Because of the distortion of the gland in patients with BPH, some hyperplastic nodules may bulge into the peripheral zone when they actually originate in the transition zone. Hypoechoic, well-circumscribed transition zone nodules are virtually always benign.[33] Although BPH nodules are generally confined to the transition zone, on occasion they can form entirely within the **peripheral zone,** appearing as an isoechoic nodule with a well-circumscribed halo and often containing a small degenerative cyst and frequently create a prominent bulge at the capsule. They are similar in appearance to BPH nodules seen in the transition zone on TRUS and mpMRI (see Fig. 10.4G). Because these benign, peripheral zone nodules are palpable as a firm or hard, cancer-like nodule, they should undergo biopsy to confirm their benign nature and obviate continuing concern.[34,35]

After exclusion of other systemic causes of the symptoms, such as neurologic disease, diabetes, and local urinary conditions, treatment focuses on the prostate. **Transurethral resection of the prostate** (TURP) is considered the standard of care for many patients, but other treatments can include watchful waiting, medical therapy, minimally invasive therapies, open surgery, and laser therapy.[19,36]

TURP initially leaves a large basal surgical defect that rapidly contracts as the gland collapses into the defect, often surprising unwary urologists who may think they have removed considerably more tissue than the visible defect suggests (see Fig. 10.4F).

Chronic Prostatitis/Chronic Pelvic Pain Syndrome

Understanding of the condition called "prostatitis" has changed over the years. It is not merely "infection in the prostate." Rather, prostatitis refers to a **chronic pain syndrome** in which, surprisingly, infection, inflammation, and even involvement of the prostate are not always present. It is commonly termed **chronic prostatitis/chronic pelvic pain syndrome** (CP/CPPS).[37,38] Prostatitis and pelvic pain complaints encompass many clinical syndromes and can severely affect the quality of life of many men who have chronic pain, sexual dysfunction, and LUTS. Patients and physicians are often frustrated because diagnosis and treatments can be time-consuming and ineffective. The impact of prostatitis on quality of life has been likened to the morbidity of myocardial infarction, angina, or Crohn disease. Interestingly, men with CP/CPPS also have an increased incidence of cardiovascular disease, neurologic disease, sinusitis, anxiety or depression, and sexual dysfunction. Prostatitis can elevate PSA and on mpMRI can mimic cancer, leading to potential unneeded cancer investigations.[32] An estimated 9% to 13% of all men in the 40- to 50-year-old age group are affected. About 25% of visits to urologists are related to prostatitis symptoms. In men younger than 50 years, CP/CPPS is the leading cause of visits to a urologist, and in men older than 50, it is the third most common cause, after BPH and cancer. The lack of public awareness of this condition likely relates to men's general reluctance to discuss "personal" concerns.[37,39]

A consensus group at the National Institutes of Health produced a Chronic Prostatitis Symptom Index (NIH-CPSI) and diagnostic flowcharts to help in diagnosis and characterization of symptom severity.[38,39]

I. Acute bacterial prostatitis
II. Chronic bacterial prostatitis
III. CP/CPPS
    A. Inflammatory
    B. Noninflammatory
IV. Asymptomatic inflammatory prostatitis

Acute bacterial prostatitis is the least common form of prostatitis, seen in about 2 of 10,000 office visits, and 5% to 10% of cases become chronic. Patients have symptoms of acute urinary or systemic infection usually caused by infection with gram-negative organisms such as *Escherichia coli*. TRUS is generally of little use in acute prostatitis and can be very painful. About half of these men have findings including edema, prostate enlargement, increased blood flow, venous engorgement, hypoechoic peripheral halo, and altered patchy echo changes that can be decreased, increased, or both. TRUS and mpMRI findings can mimic neoplasia[40] (Fig. 10.8). The diagnosis is mainly clinical. Symptoms should subside promptly with antibiotic therapy, but treatment is continued for 4 to 6 weeks. If symptoms do not subside quickly, abscess formation should be considered. **Abscesses** occur in 0.5% to 2.5% of patients with acute bacterial prostatitis and are more common in those with underlying diabetes mellitus or immunosuppression (including human immunodeficiency virus [HIV] infection) and after catheterization or instrumentation (see Fig. 10.8E). In such patients, TRUS should be promptly performed for diagnosis. Small abscesses may not need drainage, but larger abscesses over about 1.5 cm in diameter can be easily drained transrectally or transperineally using TRUS guidance, or they can be unroofed at cystoscopy. Experience has shown that simple transrectal aspiration can be effective without need for a drainage catheter. Abscesses have resolved even after a single drainage, but repeat aspiration is easily performed if needed.[40]

Chronic bacterial prostatitis is also uncommon. Patients are typically afebrile but have recurrent episodes of bacterial urinary infection–like symptoms. Most have no ultrasound findings, but during acute episodes this condition may appear similar to acute prostatitis on TRUS and mpMRI. In general, urine cultures are negative but some have gram-negative organisms, most often *E. coli*. Empirically, about half of patients with chronic bacterial prostatitis respond to 6- to 12-week courses of antimicrobial therapy.[40]

Chronic prostatitis/chronic pelvic pain syndrome (CP/CPPS) is the most common form of prostatic inflammation. These men have lower genitourinary pain with variable voiding and sexual dysfunction but no evidence of bacterial infection or other cause of pain. CP/CPPS accounts for about 90% of cases and affects about 2 per 100 men. It is the most difficult to understand and treat. CP/CPPS is classified into two types: **inflammatory type** (diagnosed by seeing leukocytes in prostate secretions, urine, or semen) and **noninflammatory type** (no evidence of inflammation; also called **prostatodynia**). The cause is unknown, and the CP/CPPS name takes into account that the prostate may not be the sole source of discomfort. The symptoms, however, are identical to those of true prostate infection. Neurologic factors, psychological factors, stress, and genetic predisposition have been implicated, as well as association with other conditions such as fibromyalgia, irritable bowel syndrome, and chronic fatigue syndrome. No cause is identified in the majority of men with CP/CPPS. Patients may respond to antibiotics, alpha blockers, nonsteroidal antiinflammatory drugs (NSAIDs), and analgesics, which are often used in multimodal fashion.[38,41] In most cases the prostate appears normal on ultrasound. Some sonograms show nonspecific findings such as peripheral hypoechoic areas, calcifications, venous congestion, increased arterial flow, bladder neck thickening, hypoechoic prostatic rim, and periurethral hypogenicity, and on TRUS and mpMRI the findings can mimic neoplasia.[32,38]

Asymptomatic inflammatory prostatitis is diagnosed in men who have no history of genitourinary pain complaints but who are shown to have inflammatory changes at histology. Often biopsy is done because of PSA elevations that are common with prostate inflammation, even with asymptomatic inflammation.[40]

Diagnostic protocols have attempted to differentiate among the various types of prostatitis using history, physical examination, and urine or other cultures.[38,39] An issue for TRUS and biopsy is that many of these men have chronically elevated but often fluctuating PSA levels, even in excess of 10 ng/mL, and the often-multiple inflammatory areas can mimic cancer on ultrasound and mpMRI, leading to biopsy to exclude cancer[32] (see Fig. 10.8).

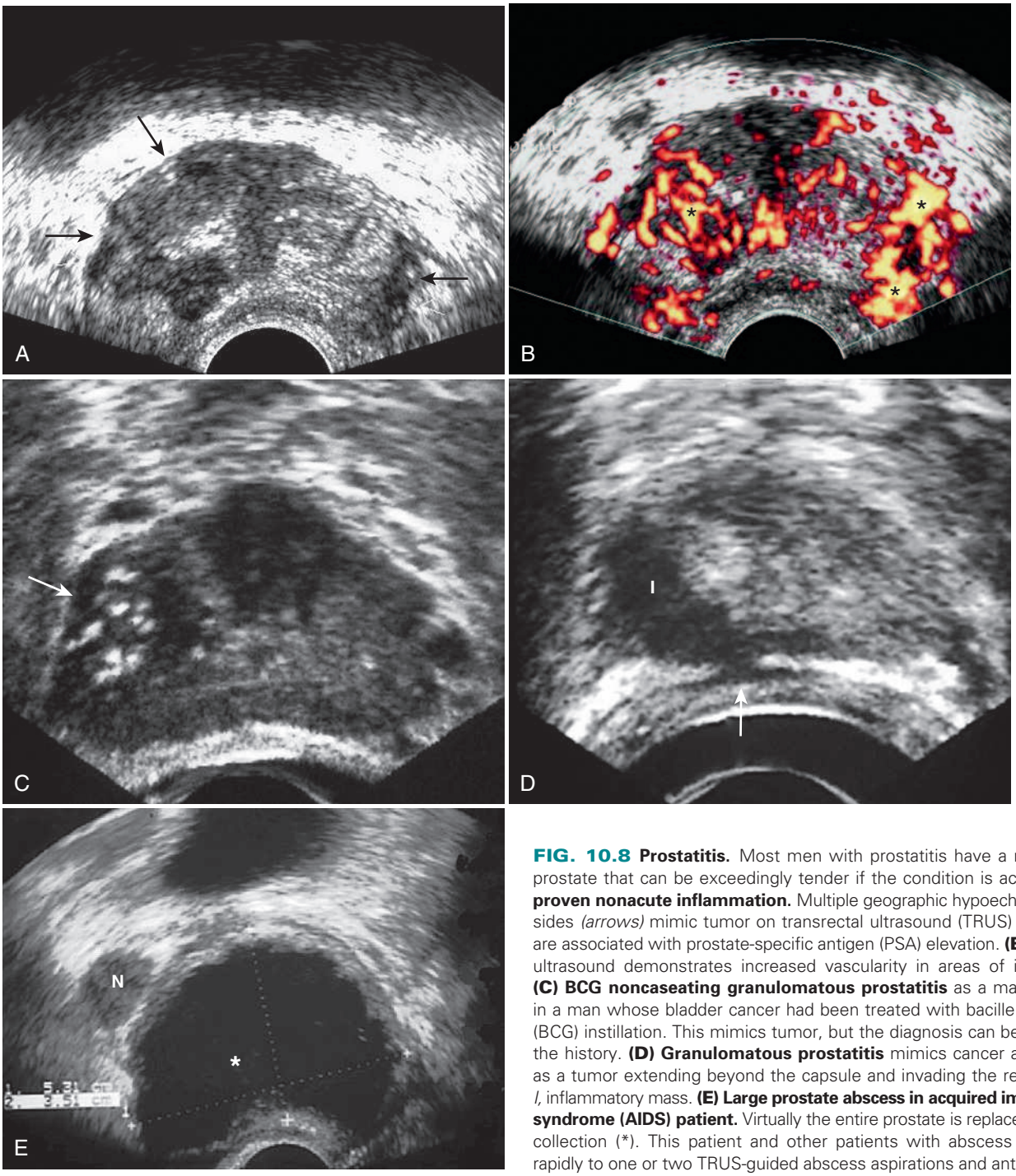

FIG. 10.8 Prostatitis. Most men with prostatitis have a normal-appearing prostate that can be exceedingly tender if the condition is acute. **(A) Biopsy-proven nonacute inflammation.** Multiple geographic hypoechoic areas on both sides *(arrows)* mimic tumor on transrectal ultrasound (TRUS) and Doppler and are associated with prostate-specific antigen (PSA) elevation. **(B)** Power Doppler ultrasound demonstrates increased vascularity in areas of inflammation (*). **(C) BCG noncaseating granulomatous prostatitis** as a mass lesion *(arrow)* in a man whose bladder cancer had been treated with bacille Calmette-Guérin (BCG) instillation. This mimics tumor, but the diagnosis can be suspected from the history. **(D) Granulomatous prostatitis** mimics cancer and here appears as a tumor extending beyond the capsule and invading the rectal wall *(arrow); I,* inflammatory mass. **(E) Large prostate abscess in acquired immunodeficiency syndrome (AIDS) patient.** Virtually the entire prostate is replaced by the abscess collection (*). This patient and other patients with abscess have responded rapidly to one or two TRUS-guided abscess aspirations and antibiotics. *N,* Node.

Other infectious or inflammatory conditions affecting the prostate do not fit easily into these groups. These include conditions such as malacoplakia, eosinophilic prostatitis, cytomegalovirus (CMV) prostatitis, and granulomatous prostatitis. **Granulomatous prostatitis** is usually idiopathic but can follow prior instrumentation and may be caused by bacteria (e.g., tuberculosis, brucellosis, syphilis), fungi (e.g., coccidioidomycosis, blastomycosis, histoplasmosis, cryptococcosis), and parasites (e.g., schistosomiasis). Most cases in North America are caused by bacille Calmette-Guérin (BCG). BCG is commonly instilled into the bladder to treat transitional cell carcinoma. It leaks into the prostate, where it can cause granulomatous inflammation. Granulomatous prostatitis mimics cancer on DRE, TRUS, and mpMRI and elevates PSA level. A history of BCG instillation can be reassuring, but biopsy generally is needed to exclude cancer.[1,38]

Prostate Cysts

Prostate cysts are common and have been grouped into six categories: (1) parenchymal cysts, (2) isolated medial cysts (utricle

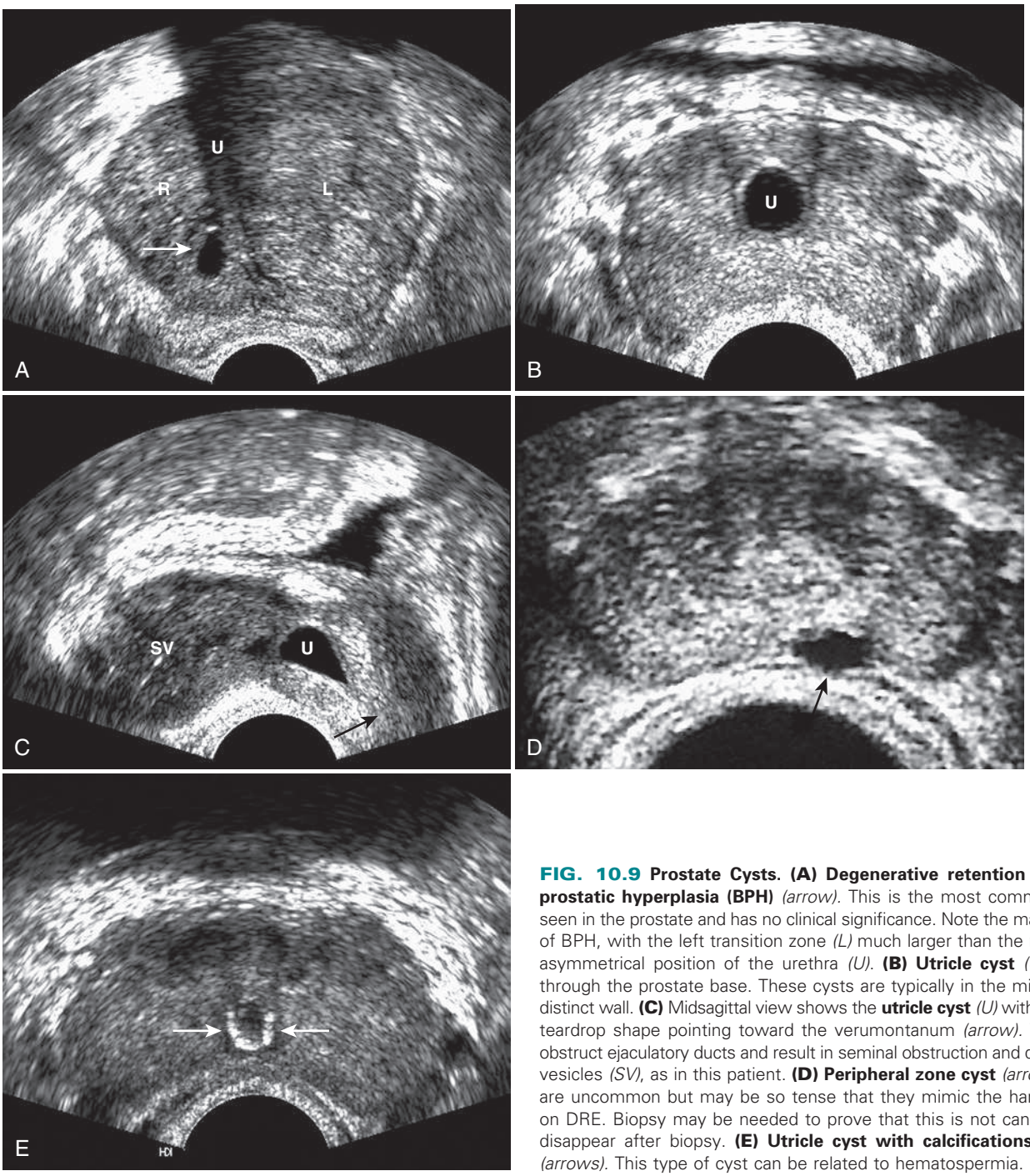

FIG. 10.9 Prostate Cysts. (A) Degenerative retention cyst of benign prostatic hyperplasia (BPH) *(arrow).* This is the most common type of cyst seen in the prostate and has no clinical significance. Note the marked asymmetry of BPH, with the left transition zone *(L)* much larger than the right *(R)*, and the asymmetrical position of the urethra *(U).* **(B) Utricle cyst** *(U)* on axial view through the prostate base. These cysts are typically in the midline and have a distinct wall. **(C)** Midsagittal view shows the **utricle cyst** *(U)* with its characteristic teardrop shape pointing toward the verumontanum *(arrow).* These cysts can obstruct ejaculatory ducts and result in seminal obstruction and dilation of seminal vesicles *(SV),* as in this patient. **(D) Peripheral zone cyst** *(arrow).* These cysts are uncommon but may be so tense that they mimic the hardness of cancer on DRE. Biopsy may be needed to prove that this is not cancer. These cysts disappear after biopsy. **(E) Utricle cyst with calcifications along its wall** *(arrows).* This type of cyst can be related to hematospermia.

and müllerian), (3) ejaculatory duct cysts, (4) abscesses, (5) cystic tumors, and (6) cysts related to parasitic disease (schistosomiasis, hydatid disease).[42,43] By far, the most common cysts are **parenchymal degenerative cysts** in hyperplastic nodules in the transition zone. These have no clinical significance but on occasion can become large enough to contribute to urinary or ejaculatory obstruction. Typically, these are seen as unilocular or thinly septated multilocular cysts in a typical BPH nodule in the transition zone (see Fig. 10.9A). Some patients develop atrophic dilation of prostate ducts, which appear as 1- to 2-mm-diameter clusters of radially oriented tubules or cysts in the peripheral zone. These have no significance (see Fig. 10.9A,B).

Retention cysts are focal cysts typically smaller than 1 cm at the surface of the prostate and result from duct obstruction. They can be very tense and become palpable as a hard prostate nodule mimicking cancer on DRE but on ultrasound appear as a typical cyst. They have no significance, but if they are palpable, aspiration helps confirm their benign nature and avoids future clinical concern when a hard "nodule" is again palpated at that site (see Fig. 10.9D).

Congenital cysts of the prostate occur in or close to the midline and are related to the wolffian (mesonephric or pronephric [archinephric]) ducts or müllerian (paramesonephric) ducts[44] (Fig. 10.9B–C). Most men with congenital cystic lesions in the prostate and SV are asymptomatic, but occasional symptoms arise if the cysts become large or infected.

Congenital abnormalities are common in and around the prostate and SVs.[42] The müllerian tubercle gives rise to the prostatic utricle, a small, midline blind pouch situated near the summit of the verumontanum. Prostatic **utricle cysts** are caused by dilation of the prostatic utricle. Utricle cysts rarely contain spermatozoa but can be associated with genitourinary anomalies including unilateral renal agenesis, hypospadias, and undescended testis. Utricle cysts are always in the midline and are usually small but occasionally can enlarge to several centimeters in diameter (see Fig. 10.9B–C). **Müllerian duct cysts** may arise from remnants of the paramesonephric duct. Müllerian duct cysts are usually small and usually midline but may extend lateral to the midline and enlarge to extend above the prostate. They have no other associations and never contain spermatozoa. As with utricle cysts, they have a teardrop shape pointing toward the verumontanum, a thick visible wall, and occasional mural or contained calcifications. In practice, utricle and müllerian cysts appear similar and their differentiation is not important. When large, both may obstruct ejaculatory ducts or develop calcifications (see Fig. 10.9E) and become painful or infected and rarely may develop tumors.[43,44]

Ejaculatory duct cysts are usually small and probably represent cystic dilation of the ejaculatory duct, possibly as a result of obstruction. Alternatively, they may be diverticula of the duct. They tend to be fusiform in shape and are typically pointed at both ends. Ejaculatory duct cysts contain spermatozoa when aspirated. They can be associated with infertility and may be seen in patients with a low sperm count. Some may cause perineal pain.[43,44]

Other disorders that mimic prostate cysts include SV cysts, ectopic ureterocele, **Cowper duct cysts** (in urogenital diaphragm below apex of prostate), and bladder diverticula.

Prostate abscesses are cystlike cavities with thick, irregular walls and debris containing fluid and resemble abscesses seen elsewhere (see Fig. 10.8E). Coliform organisms such as *E. coli* are the most common cause. Predisposing conditions include diabetes, instrumentation, and immunodeficiency. Transrectal aspiration or TURP drainage can be an effective treatment in addition to antimicrobial therapy.[42-44] Cysts caused by parasites are rare in Western countries and can result from schistosomiasis (bilharziasis) or hydatid (echinococcal) disease.[42,43]

Cystic neoplasms are rare, but cystadenoma and cystadenocarcinoma have been described.[42,43]

Seminal Vesicles and Vas Deferens

The **seminal vesicles** and **vas deferens** develop from the mesonephric duct and are associated with renal and ureteric development. Developmental anomalies of the SV/VD are often associated with renal and ureteric abnormalities. Normal SVs measure about 1 × 5 cm, and VD, about 6 mm. The SVs function to produce and secrete seminal fluid and not to store sperm. The vasa deferentia drain via the ejaculatory ducts through the prostate into the verumontanum. Primary pathology of the SV and VD is being increasingly detected with use of TRUS and MRI.[45,46]

Hypoplasia or agenesis of the SV occurs surprisingly commonly. It may be unilateral or bilateral and can be associated with agenesis or ectopia of the VD and ipsilateral kidney. Patients with **cystic fibrosis** commonly have bilateral agenesis of the SV and VD but normal kidneys.[45,46]

Seminal vesicle cysts are rare and usually solitary (Fig. 10.10C). Most are asymptomatic. The cysts can enlarge and become symptomatic and can be aspirated with TRUS guidance. They may be associated with ipsilateral renal anomalies, including renal agenesis, because the SVs are derivatives of the wolffian (mesonephric) ducts, which also give rise to the ureter and VD. Congenital SV cyst and absence of the ipsilateral kidney is known as Zinner syndrome. Other associations include adult polycystic disease, hemivertebra, and ipsilateral absence of testis. The SV is a common site of ectopic insertion of the ureter.[44,46,47]

Calcification of the SV and VD can occur with diabetes or infection. **Diabetic** calcification tends to involve the walls and resembles "tram tracks" on x-ray films, whereas **infectious or inflammatory** calcification is luminal and segmental and may be associated with SV calcifications. In endemic areas, tuberculosis and schistosomiasis should be considered.[45,46]

On occasion, a 1-cm-diameter eggshell calcification is seen in the SV. These calcifications are asymptomatic and likely related to inflammation.

Malignancy in the SV is most commonly secondary to carcinoma of the prostate, bladder, or rectum and appears as a mass involving the SV. If SV involvement is suspected at time of prostate TRUS biopsy, then additional cores can be taken from the SV and may alter treatment plans. Primary neoplasms of the SV are very rare and include benign cystadenomas, leiomyoma, fibromas, and others and malignant lesions such as adenocarcinoma. Tumor mimics such as amyloid deposits are increasingly becoming recognized.[45,47]

INFERTILITY AND TRANSRECTAL ULTRASOUND

Infertility is defined as failure to achieve pregnancy after 1 year of regular unprotected intercourse and affects about 15% of couples. Male factors are solely responsible in about 20% of couples and contributory in another 30% to 40%. When present, male infertility is usually but not always detected by abnormal semen analysis. The AUA and the European Association of Urology have defined "best practice" policies for investigating male infertility, and both partners should be evaluated simultaneously.[48,49] The **goals of male evaluation** include the following:

1. Identification of potentially correctable conditions
2. Identification of irreversible conditions for which alternative treatments (e.g., donor insemination) or adoption may be used, preventing ineffective therapies
3. Detection of health-threatening conditions underlying infertility

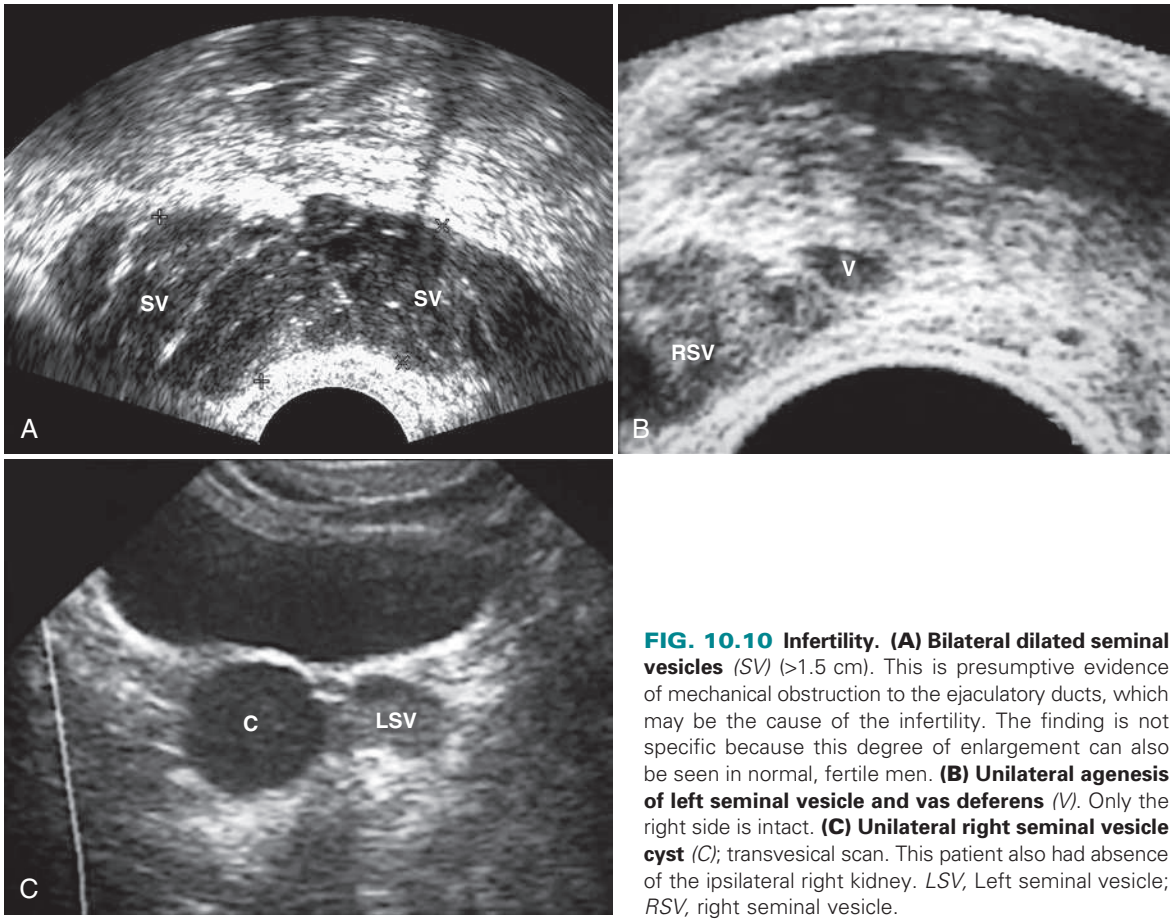

FIG. 10.10 Infertility. (A) Bilateral dilated seminal vesicles *(SV)* (>1.5 cm). This is presumptive evidence of mechanical obstruction to the ejaculatory ducts, which may be the cause of the infertility. The finding is not specific because this degree of enlargement can also be seen in normal, fertile men. **(B) Unilateral agenesis of left seminal vesicle and vas deferens** *(V)*. Only the right side is intact. **(C) Unilateral right seminal vesicle cyst** *(C)*; transvesical scan. This patient also had absence of the ipsilateral right kidney. *LSV,* Left seminal vesicle; *RSV,* right seminal vesicle.

4. Detection of genetic abnormalities (e.g., cystic fibrosis) that may affect the health of children if affected sperm are harvested or used for assisted reproductive techniques.

Male factors can be categorized as pretesticular, testicular, and posttesticular. **Pretesticular factors** include conditions such as faulty reproductive behavior and genetic abnormalities (e.g., *CFTR* gene of cystic fibrosis, Y chromosome microdeletions). **Testicular factors** include congenital and acquired intrinsic disorders of spermatogenesis (e.g., infections, trauma, and treated cryptorchidism) that, except for varicocele, are generally irreversible. Also tumors and testicular microlithiasis are more common in infertile men. **Posttesticular causes** of **azoospermia** (no sperm in ejaculate) and **oligospermia** (low numbers of sperm in ejaculate) generally relate to obstructive issues and are found in about 40% of infertile men, although only 1% to 5% have **ejaculatory duct obstructions** that are amenable to surgical therapies such as prostate cyst unroofing or **transurethral resection of ejaculatory ducts.**[50] This excludes vasectomy reversal, which is successful in 70% to 95% of patients and results in achievement of pregnancy in 30% to 70% of couples. In 100 consecutive azoospermic men, the causes of azoospermia were genetic abnormalities, 27%; diseases or external influence (orchitis, radiotherapy, infections, surgery, trauma), 22%; corrected cryptorchidism, 27%; and unexplained, 22%.[51] This illustrates the broad spectrum of disorders apart from ejaculatory duct obstructions that relate to azoospermia and that are part of the investigation of infertile men.[48,49]

Imaging investigations—ultrasound and MRI—are used to evaluate for abnormalities and focus on the scrotum and testes, prostate, and seminal ducts and occasionally the developmentally related urinary tract.[50,52,53]

The **role of TRUS** and increasingly MRI is to identify anatomically correctable ejaculatory duct obstructions and anomalies in men who are azoospermic or oligospermic and who have VD on palpation. Obstructions can result from calculi in the vas, müllerian or wolffian duct cysts, postsurgical or inflammatory scars, calculi, or atresia of the ejaculatory ducts (see Fig. 10.10). Note that the presence or absence of the VD is diagnosed clinically by palpation of the spermatic cord and not through imaging. Vasography has been used to demonstrate obstruction, but this generally has been discontinued because of the risk of injury to the VD. On occasion, TRUS can be used to inject SVs with ultrasound or x-ray contrast agents to demonstrate patency of the ejaculatory ducts or to retrieve sperm from the SVs for assisted reproduction.[50,52,53]

There are no specific symptoms associated with **ejaculatory duct obstruction.** The diagnosis is suggested in infertile males with azoospermia or oligospermia who have low ejaculate volume, normal secondary sex characteristics and testes, pain during or after ejaculation or orgasm, or history of prostatitis. The relative frequencies of TRUS findings in infertile men with low-volume azoospermia are as follows: normal appearance (25%); bilateral absence of VD (34%); bilateral occlusion of the VD, SVs, and ejaculatory ducts by calcification or fibrosis (16%); unilateral

absence of the VD (11%); obstructing cysts of the SVs, vas ejaculatory ducts, or prostate (9%); and ductal obstruction due to calculi (4%). All these symptoms and findings are also seen in normal, fertile men but are more common in men with obstructive infertility.[50]

The treatment of suspected distal ejaculatory obstruction consists of transurethral resection of the ejaculatory duct, unroofing of the ducts, or draining of obstructing cysts and results in symptom improvement in 50% to 100% and pregnancies in 20% to 30%.[50]

Absence of the vas deferens is a clinical diagnosis made by palpating the spermatic cord. Congenital bilateral absence of the vas deferens (CBAVD) is found in almost all men with cystic fibrosis gene mutations *(CFTR)* whether they are symptomatic or not. It affects about 1% of infertile men and accounts for 4% to 17% of azoospermia and is commonly associated with SV abnormalities. There is a low association with renal anomalies. However, 44% to 60% of men with autosomal dominant polycystic kidney disease also have bilateral VD agenesis. In contrast, men with unilateral absence of the vas are less likely to have cystic fibrosis but more likely to have ipsilateral abnormalities of wolffian duct derivatives including the kidneys.[45,49,53]

HEMATOSPERMIA

Hematospermia is the macroscopic presence of blood in the semen. In most cases it is a benign, self-limiting condition that typically resolves spontaneously over a few weeks. It affects about 1 in 5000 men, peaks between 30 and 40 years of age, and causes significant anxiety among men and their partners who fear cancer or sexually transmitted disease and loss of sexual function. The differential diagnosis is extensive, but most cases are **iatrogenic** (following interventions such as biopsy or cystoscopy), **infectious,** or **inflammatory** and can be effectively treated with minimal investigation and simple reassurance. Malignant tumors, mainly prostate, testis, and SV, are an uncommon cause of hematospermia and are found in only 3.5% of cases, predominantly in men over age 40 years.[54,55]

Hematospermia

COMMON CAUSES
Idiopathic (about 15%)
Sexually transmitted diseases
Trauma (including iatrogenic and self-inflicted)
Prostatic diseases (prostatitis, benign prostatic hyperplasia (BPH), calculi, tuberculosis, schistosomiasis, prostate cancer)
Testis or epididymis (infection, trauma)
Systemic diseases (bleeding disorders, liver disease, severe hypertension)

UNCOMMON CAUSES
Seminal vesicle disorders (carcinoma, calculi)
Prostate cysts (ejaculatory, müllerian, especially with calculi)
Urethra (abnormal vessels, polyps)
Testis tumor
Systemic disorders (amyloidosis)

The primary aim of investigation is to allay anxiety, because the great majority of hematospermia cases, especially in younger men and after single episodes, are highly unlikely to be associated with sinister pathology. In addition to history and physical examination, most patients initially undergo evaluation for sexually transmitted diseases, urinalysis, and urine culture. Men older than 40 should also be assessed for malignancy, especially prostate cancer, even though this is an uncommon cause.

Imaging may be helpful in unexplained or persistent cases. TRUS shows findings in 74% to 95% of men with persistent hematospermia including prostate calcifications, ejaculatory duct calculi, dilated ejaculatory ducts, BPH, dilated SVs, SV calcifications, ejaculatory duct cysts, and prostatitis (see Figs. 10.9E and 10.10A). Color Doppler ultrasound may be able to depict the rare vascular malformation. In practice, it can be difficult to establish that the TRUS finding is responsible for hematospermia because similar findings are often seen in asymptomatic men. MRI can be helpful in persistent cases because it is able to detect bleeding sites that are not apparent on ultrasound, especially bleeding into the SVs.[45,54-56]

Treatment beyond reassurance is not needed in most patients with hematospermia. Alternatively, therapy is directed to any discovered causes and can include antimicrobial therapy, cyst unroofing or aspiration, and systemic therapy for hypertension and bleeding diathesis. Urologic consultation is suggested if the bleeding is persistent and in men older than 40 years who have increased risk of cancer.[54,55]

PROSTATE CANCER

Prostate cancer is a significant health problem for men and their partners. In the United States it is the most common male cancer; in 2016 it was estimated to affect 181,000 men (21% of all male cancers), and after lung cancer, the second most common cause of cancer deaths (26,000 men or 8% of cancer deaths).[57,58] It is important for those evaluating prostate cancer with imaging studies such as TRUS and mpMRI to be aware of and follow the very rapid changes in screening, diagnosis, management, and even pathologic definitions of what constitutes significant aggressive cancer.[9,10,59] Prostate cancer is a difficult problem filled with uncertainties and dilemmas for men, their partners, and physicians. Effective treatments exist but have side effects that substantially alter quality of life, and there is risk of overdiagnosis and overtreatment.[58,60-63]

Unlike some other cancers, not every prostate cancer progresses rapidly and inevitably to metastases and death. There is a large burden of indolent disease that would not benefit from radical therapy, which must be differentiated from aggressive progressive disease. Prostate cancer mainly affects men older than 50 and thus competes with comorbidities as a cause of death.[64] At autopsy, significant grade (Gleason score of 7 or higher) cancer was found in 32% of men who died from other causes.[65] Prostate cancer has a long course, not uncommonly taking about 10 years from asymptomatic diagnosis to cause-specific death. This makes it difficult to determine if screening and treatment protocols are effective, because trials take more than 10 years during which diagnostic and therapeutic changes could make study results irrelevant.[58,63,66,67]

To complicate matters further, no consensus has emerged for the optimal treatment of **clinically localized disease,** which has become the most common presentation in the United States (91% of cases) since the advent of PSA screening in 1991.[68]

Epidemiology

Prostate adenocarcinoma is the most frequently diagnosed cancer in men, two to three times more than lung and colorectal cancer. It is a disease seen primarily in men older than 50. It is the fourth most common male malignancy worldwide. The rates are highest in Scandinavia and North America, especially in African Americans (272 per 100,000), and lowest in China (1.9 per 100,000), but rates are increasing in those countries.[19,69] Genetics and environment, including a fatty diet, play roles in prostate cancer incidence. The risk doubles with a single affected relative and is even higher with multiple affected relatives. The incidence and stage at diagnosis have been decreasing since the early 1990s, partly because of the introduction of PSA screening.[70,71] More than 95% of primary malignant tumors of the prostate are adenocarcinomas. Rarely other primary neoplasms are found, including prostate transitional cell carcinoma, sarcomas, lymphomas, and neuroendocrine tumors.[72] The prostate can be secondarily affected by tumors of regional structures, including the bladder and rectum.

It has been reported that 24-year median follow-up of clinically localized prostate cancer and showed that cause-specific mortality increases with Gleason score and age at diagnosis. With Gleason score of 6 or lower, comorbidities are a more likely cause of mortality, but with higher scores cancer-related death is likely, especially in the 50- to 64-year age group, in which cause-specific mortality approaches 80% to 90% at 15 to 20 years.[64] Of interest, most pathologists currently do not report Gleason score below 6 as cancer, and there is discussion that perhaps even Gleason 3 + 3 = 6 does not represent aggressive life-threatening cancer that needs immediate radical therapy.[9,10,59,73]

Prostate Cancer: Key Facts

Most common cancer diagnosed in men
The second leading cause of cancer deaths in men (after lung cancer)
The fourth most common male malignancy worldwide
Many and varied treatments that are personalized to patient situation
Treatments are associated with quality-of-life issues
Many men have low-grade tumors that may not need treatment or affect longevity

Prostate-Specific Antigen and Variants

PSA is the most commonly used tumor marker to detect prostate cancer and follow patients after therapy.[74,75] PSA is a normally occurring enzyme in the kallikrein family driven by androgen and secreted by the epithelial cells of prostate ducts and functions to liquefy the ejaculate. The prostate epithelium is the main source of PSA and only trace amounts are found in other tissues in men and women. Intact tissues allow only small amounts to leak into the blood where it is partly unbound (free) and partly bound to proteins such as alpha-1-antichymotrypsin. Serum PSA levels are a nonspecific indication of prostate abnormality or irritation that allows excess leakage of this normal enzyme into the blood. Free PSA is composed of three isoforms: pro-PSA, BPH-associated PSA, and intact free PSA. **Elevated total PSA levels** can occur with cancer but also are variably seen with benign conditions including BPH and inflammation and after ejaculation, prostate manipulation, biopsy, and cystoscopy. In general, DRE and TRUS without biopsy do not elevate PSA significantly, but it is prudent to draw the blood before disturbing the prostate. PSA levels can be artificially reduced by a factor of 2 with antiandrogenic medications such as finasteride (Proscar) and dutasteride (Avodart). Unpredictably reduced levels are found with herbal medications such as palmetto and PC SPEC. With cancer the proportion of bound PSA increases resulting and can decrease the ratio of free to total PSA **(percent free PSA, %fPSA).**[75]

Although PSA is accepted as a prostate cancer marker, there are issues with its use. It is organ specific but not cancer specific, and levels overlap in benign conditions and cancer. Also, not all cancer elevates PSA and cancer can be found in 6.6% of men with low PSA (<0.5 ng/mL). The discriminatory level is uncertain. Initially 4 ng/mL was considered the threshold for consideration of biopsy, but this has decreased to as low as 2.6 ng/mL. It is generally agreed that unexplained PSA over 10 ng/mL is an indication for biopsy and has a positive predictive value (PPV) of about 80%. Biopsy of men in the problematic 4- to 10-ng/mL range finds cancer in about 40%. This highlights the problem with PSA testing: PSA of 4 ng/mL has a sensitivity of about 79% but a low specificity of 59%. The low specificity means that many men without significant cancer would be subjected to the risks of biopsy and overdiagnosis and overtreatment. These issues have led to controversy in the use of PSA for screening.[58,76] However, screening aside, PSA remains the optimal tool to follow men for recurrence after curative therapy.

Several approaches have been considered to try to improve both sensitivity and especially specificity so that in the 2.6- to 10-ng/mL gray area initial and repeat biopsy are performed only in men at risk for significant aggressive cancer and can be avoided in men at low risk or at risk for just indolent cancer. Most urologists feel that their clinical acumen, which takes into consideration PSA, family history, patient clinical status and history, prior biopsy results, and discussion with the patient, remains the mainstay of determining need for both initial and repeat biopsy. Although PSA and its variants remain the dominant test, there is a rapidly increasing catalog of additional blood, urine, and tissue tests that may be taken into consideration and may provide supporting information regarding diagnosis, prognosis, and need for enhanced therapy.[74,75,77]

With cancer the proportion of bound PSA increases, resulting in a decrease in the ratio of free to total PSA **(percent free PSA, %fPSA).**[75] Using a ratio of 25%, Catalona and colleagues detected 95% of cancers and avoided 20% of biopsies.[78] There is no general agreement on cut points, which range from about 15% to 25% (or ratio 0.15-0.25). The instability of fPSA (free PSA) after phlebotomy unfortunately has limited its use for general screening.[75]

PSA density (PSAd) is the ratio of PSA to prostate volume. This test assumes prostate cancer makes more PSA than benign

tissue and tries to allow for elevated PSA in men with enlarged glands due to BPH. Cut points range from 0.12 to 0.15. This test is less often used to determine need for biopsy but commonly used as one of the risk criteria for entering men into active surveillance programs.[10,75,79,80]

PSA velocity evaluates rate of increase of PSA over time. It assumes that PSA rises faster with cancer and requires at least three PSA determinations over 18 months showing a rise over 0.75 ng/mL per year.[81] This test is less often used currently but may have a role in active surveillance.[10,82]

Role of Prostate-Specific Antigen (PSA)

PSA and digital rectal examination today are the standard of care for initial prostate cancer screening
PSA level is associated directly with the tumor burden of prostate cancer
Not all cancers produce PSA
20% to 40% of men with clinically significant cancer will have a "normal" PSA level
PSA may be elevated by nonmalignant conditions
PSA variants are used to improve screening accuracy
- PSA density
- PSA velocity
- Free/total PSA ratio

Used during active surveillance, to evaluate for progression and reclassification
Used after active therapy, to follow patients for recurrence
Can be combined with other biomarkers to improve sensitivity and specificity

Alternate Prostate Cancer Biomarkers

PSA remains the most commonly used biomarker, but numerous other biomarkers are being developed to overcome the limitations of PSA to indicate need for initial and repeat biopsy, to help distinguish between indolent and aggressive tumors, to help select appropriate therapy, and to follow patients after therapy. Biomarkers can be evaluated in blood, other body fluids, urine, or tissues. Some have been approved for use and others remain investigational. In general, their role is supportive to clinical acumen and initial PSA use. In many instances their incremental value has not yet been established. Also, multiparametric risk nomograms and mpMRI are increasingly being used.[74,75,77,83]

PCA3 score uses noncoding RNA in urine and is approved for use. PCA3 is not found in normal prostate tissue but is expressed in 95% of prostate cancers. It is recommended as a test to help determine need for repeat biopsy with elevated PSA. A cut point of 35 has been recommended, which would yield optimal balance between sensitivity (47%) and specificity (72%) while missing 21% of high-grade tumors.[74,75,77,83-85]

Prostate Health Index (PHI) is approved for men 50 years or older in the PSA 4- to 10-ng/mL range and negative DRE findings. It combines several isoforms of PSA. It is used to help support need for biopsy in the PSA 4 to 10 range.[74,75,77,84,85]

4Kscore is currently not a US Food and Drug Administration (FDA)–approved test. It uses four different PSA forms and an algorithm including age, DRE findings, and prior biopsy status to predict a risk score for finding aggressive cancer in a future biopsy.[74,75,77]

TMPRSS2:ERG is currently not an FDA-approved test. It is a urine test for pathologic fusion of *TMPRSS2* and *ERG* genes that is found in 50% of prostate cancer specimens. It has a low sensitivity but high specificity for predicting prostate cancer at biopsy.[74,75,77]

On biopsy samples, tissues near cancer show altered field or "halo" effects that can be evaluated on biopsy samples and can manifest as changes in genes **(Oncotype DX test)** or tissue methylation **(ConfirmMDx test).** A negative biopsy result in a patient with positive tissue markers suggests that a nearby cancer was missed and can help determine need for repeat biopsy.[74,75,77]

Increasingly the concept of combining these tests and other tests including mpMRI and clinical parameters in the form of "risk calculators" is proving useful. The more popular risk calculators in current use are the ERSPC-RC, PCTP-RC, and UCSF-CAPRA calculators, which can be found online or downloaded to smartphones (http://www.prostatecancer-riskcalculator.com/seven-prostate-cancer-risk-calculators; http://deb.uthscsa.edu/URORiskCalc/Pages/uroriskcalc.jsp; https://urology.ucsf.edu/research/cancer/prostate-cancer-risk-assessment-and-the-ucsf-capra-score).[86,87]

Screening

Early stage prostate cancer is curable but rarely symptomatic. The presence of symptoms suggests advanced disease with little likelihood of cure. This would suggest that screening is reasonable to detect asymptomatic disease while it is still curable. The goal of any cancer screening, including prostate, is the early identification of cancer or precancerous lesions before symptoms develop and at a point when treatment improves outcomes. The World Health Organization (WHO) has proposed criteria that should be met before population screening is offered. The condition should be an important health problem with a known natural history; have agreed-on treatment that is acceptable, available, and effective; have a recognizable latent stage to allow time for screening; and have a screening test that is acceptable and effective and has a reasonable cost.[88] Many of these conditions are met for prostate cancer, but issues remain that have introduced controversy into screening.[60]

TRUS is not used as a primary screening modality in screening for prostate cancer. TRUS has sensitivity of 30% to 67% and specificity of 52% to 61%, compared with mpMRI sensitivity of 72% to 90% and specificity of 55% to 79%.[89] It is hoped that CEUS and ultrasound elastography will improve ultrasound accuracy. There is increasing discussion of use of hybrid or multiparametric imaging to improve detection and characterization.[4,6,90-92] Most techniques are qualitative and not quantitative, and operator skills remain paramount. This results in variabilities in accuracy and performance characteristics that are apparent in the literature for cancer detection.

The current recommended screening tests are PSA and DRE followed by confirmatory diagnostic transrectal biopsy.[7] The added value of TRUS for cancer detection at screening over PSA plus DRE is about 5%.[93] Diagnosis requires tissue to be obtained by biopsy. Currently this is most efficiently and effectively done

with TRUS guidance. MRI in-bore biopsy and MRI-TRUS fusion biopsies are being introduced but currently are less practical and limited by access and costs. Cancer detection by mpMRI is imperfect, and currently systematic biopsy cannot be avoided if the MRI is negative.

Prostate cancer mortality has decreased since 1990 and there has been a 75% reduction in the proportion of advanced disease at diagnosis. This is attributed to opportunistic PSA screening rather than new and improved therapies.[94] However, there are concerns regarding generalized population screening. On one hand, prostate cancer remains an important cause of morbidity and mortality. On the other hand, prostate cancer affects older men and typically has a 10-year course. Men of this age have competing causes of mortality, so men with cancer often die with, and not from, their cancer. PSA screening has limited sensitivity and specificity. The diagnostic transrectal biopsy is not infallible and has risks. There is a large background of low-volume low-grade (Gleason 6) cancer that is not likely to need active therapy. This raises concerns regarding overdiagnosis and overtreatment because therapy (surgery, radiation, hormones) is not without risk and has significant side effects affecting quality of life.

Several studies have evaluated the role of screening and therapy for prostate cancer; some have shown benefit but others have not, possibly because of study design limitations.[95,96] The major quoted screening studies are the ERSPC (European Randomized Study of Screening for Prostate Cancer)[97] and the US study PLCO (Prostate, Lung, Colorectal and Ovarian Cancer Screening Trial).[98] The ERSPC first consented and then randomized men into a screening arm offered PSA testing every 4 years and a control arm. Biopsy was offered for PSA above 3 ng/mL. At 13 years, the screened arm showed a 29% decrease in mortality. To prevent one cancer death, the number needed to invite for screening was 781 and number needed to detect was 27. The Göteborg subset of this study used a more real-world approach that first randomized men to be invited to screening and then obtained consents. Biopsy was recommended for PSA above 2.5 ng/mL. At 14 years, the investigators reported that the relative risk for dying from cancer decreased to 0.44, with number needed to screen of 293 and number needed to treat of 12.[97,99]

The PLCO randomized men to annual PSA and DRE or usual care groups. Biopsy indication was PSA above 4 ng/mL or palpable nodule. At 13 years there was no significant difference in mortality. Subsequent analysis showed that about 90% of the control arm had undergone PSA screening either before or during the study. True comparison was not possible because both screen and control arms in effect were screened with PSA.[58,95,98]

Considering these and other studies, in 2012 the US Preventive Services Task Force (USPSTF) issued a D recommendation against prostate cancer screening (no net benefit or harms outweigh benefits).[96] Notwithstanding decreasing prostate cancer mortality since introduction of PSA screening, the USPSTF concluded that any screening benefits were outweighed by the seeming lack of overall benefit as shown especially in the PLCO study, the risks of overdiagnosis and overtreatment, the risks of biopsy and therapy, the large proportion of indolent disease that is unlikely to be symptomatic, and competing mortality in older men. This recommendation is strongly contested by many who believe that it will decrease detection of prostate cancer while still treatable and result in increasing morbidity and mortality; this appears to be happening.[58,100,101] Also, urologic groups are promoting "smart screening" that focuses screening on those most likely to benefit and only after shared decision making; to avoid harms of active therapy, they recommend active surveillance of men with seemingly indolent cancer (low-volume Gleason 6, also called IDLE [indolent lesions of epithelial origin]). In general, in men without risk factors, screening is recommended starting at about age 50 years, is repeated at 1- to 4-year intervals, and is stopped at about 70 years or with life expectancy below 10 years. A low (<1.0 ng/mL) baseline PSA between 40 and 49 years of age is associated with low cancer risk and can be used to further lengthen intervals between testing. Before biopsy, the PSA should be repeated to allow normal fluctuations from producing a false-positive result. Antibiotics should not be given to asymptomatic patients to lower PSA to test if there is an asymptomatic infection causing the PSA elevation. In high-risk groups such as those with a first-degree relative with prostate cancer or African-American men, screening should start at about age 40. The new biomarkers, mpMRI, and risk calculators could further be used to increase specificity of screening tests and need for biopsy or therapy.[58,73,88,95,102]

Clinical Staging and Histologic Grading

Staging relates to extent of disease spread; **grading** relates to histologic appearance of aggressiveness. **Clinical staging** of prostate adenocarcinoma uses pretreatment parameters to estimate extent of tumor, determine treatment options, and predict prognosis by using DRE; PSA; biopsy characteristics; imaging including TRUS, CT, isotope scan, and mpMRI; and nomograms such as the Partin tables, which combine multiple characteristics such as PSA, clinical stage, and Gleason score (Fig. 10.11, Table 10.1).[103] **Pathologic staging** requires histologic evaluation of

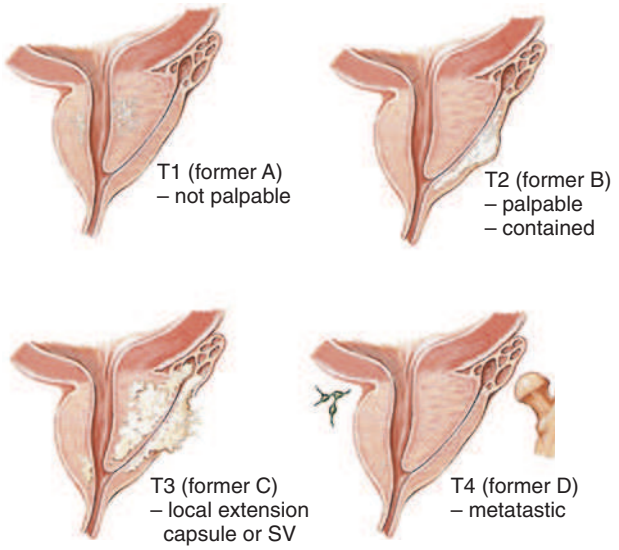

FIG. 10.11 Contemporary prostate cancer staging using the tumor-nodes-metastasis (TNM) classification. *SV,* Seminal vesicle.

TABLE 10.1 Staging of Prostate Cancer, 2010

Stage	Description	Comments
CLINICAL STAGING (cT__)		
cTX	**Primary tumor cannot be assessed**	
cT0	**No evidence of primary tumor**	Describes cancer on biopsy but no cancer is found at radical prostatectomy, possibly because of microfocal cancer that is not included in prostatectomy histologic sections. This occurs in about 0.4% of cases and in general has a good prognosis.
cT1	**Clinically inapparent tumor that is not palpable nor visible by imaging**	Describes tumors that are not palpable or visible on TRUS or mpMRI, possibly because of size, soft consistency, or anterior location. These may be found on TURP, where about 6% of men will have <5% of positive chips. Prognosis is variable and about 10%-26% may have subsequent progression especially when many chips are involved.
cT1a	Tumor incidental histologic finding in ≤5% of tissue resected	
cT1b	Tumor incidental histologic finding in >5% of tissue resected	
cT1c	Tumor identified by needle biopsy	Describes men with impalpable disease who have positive needle biopsy (e.g., after screening showed elevated PSA).
cT2	**Tumor confined within prostate**	Describes palpable organ-confined tumors. Invasion into the prostatic apex or into (but not beyond) the prostatic capsule is included in T2.
cT2a	Tumor involves ≤½ of one lobe	cT2a and cT2b tumors involve only one lobe and cT2c both lobes. However, pathologic examination suggests this distinction is arbitrary because most tumors are multifocal and present in both lobes, and prognosis also depends on tumor volume and grade and not just findings of palpation and ultrasound.
cT2b	Tumor involves >½ of one lobe but not both lobes	
cT2c	Tumor involves both lobes	
cT3	**Tumor extends through the prostate capsule**	Describes tumors with extracapsular extension, a poor prognostic factor. Pathologically it manifests as cancer in adjacent fat, neurovascular bundles, anterior muscle, or bladder neck or invading seminal vesicles. Seminal vesicle invasion may occur via extension along ejaculatory ducts, direct invasion from prostate, or rarely discontinuous metastasis.
cT3a	Extracapsular extension (unilateral or bilateral)	
T3b	Tumor invades seminal vesicle(s)	
T4	**Tumor is fixed or invades adjacent structures other than seminal vesicles such as external sphincter rectum, bladder, levator muscles, and/or pelvic wall**	
PATHOLOGIC STAGING (pT)		
pT2	**Organ confined**	
pT2a	Unilateral, one-half of one side or less	
pT2b	Unilateral, involving more than one-half of side but not both sides	
pT2c	Bilateral disease	
pT3	**Extraprostatic extension**	
pT3a	Extraprostatic extension or microscopic invasion of bladder neck	
pT3b	Seminal vesicle invasion	
pT4	**Invasion of rectum, levator muscles, and/or pelvic wall**	
Regional Lymph Nodes (N)		Based on clinical and/or pathologic assessment
NX	Regional lymph nodes were not assessed	
N0	No regional lymph node metastasis	
N1	Metastasis in regional lymph nodes(s)	
Distant Metastasis (M)		Distant nodes are deemed metastases
M0	No distant metastasis	
M1	Distant metastasis	
M1a	Nonregional lymph node(s)	
M1b	Bone(s)	
M1c	Other sites with or without bone disease	

mpMRI, Multiparametric magnetic resonance imaging; *PSA,* prostate-specific antigen; *TRUS,* transrectal ultrasound; *TURP,* transurethral resection of the prostate.

With permission from AJCC. American Joint Committee on Cancer: Prostate Cancer Staging: American Joint Committee on Cancer; 2010. Cited 21 May 2016. 7. Available from: https://cancerstaging.org/references-tools/quickreferences/Documents/ProstateSmall.pdf.[103]

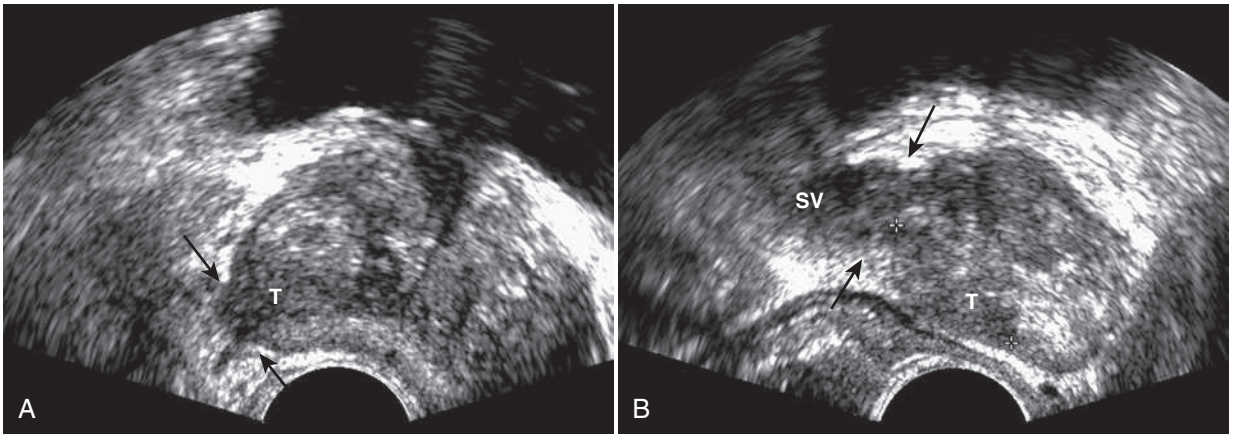

FIG. 10.12 Staging of Extensive Prostate Cancer. (A) Stage T3A cancer (T) has extended outside the prostate at the neurovascular bundle *(arrows)*. Note how difficult it is to differentiate tumor extension from the normal irregularity caused by the neurovascular bundle. **(B) Stage T3C** (parasagittal view) cancer (T) extending *(arrows)* into the seminal vesicles (SV).

prostate, SVs, and lymph nodes and is more accurate for prognosis. Clinical staging (designated as cT_) is important for deciding management but is less accurate than histologic evaluation (designated as pathologic stage pT_) of the prostate and surrounding tissues because DRE and imaging modalities have limitations in predicting extraprostatic extension and 60% to 90% of tumors are multifocal. Compared with pathologic evaluation, clinical understaging occurs in about 40% to 60% and overstaging in about 5%.

Staging with imaging is used selectively in high-risk groups using isotope bone scans, CT, and mpMRI. When the risk of extraprostatic disease is low, consideration is given to avoidance of these tests to reduce radiation exposure and costs. It is estimated that in the current PSA era over 90% of cases are localized, obviating need for routine staging by CT, MRI, or bone scan at initial diagnosis. Recommendations for staging by imaging differ among organizations. In general, bone scans are recommended for men with PSA above 10 to 20 ng/mL, Gleason score of 8 or higher, or symptoms. Soft tissue imaging with CT, MRI, or PET-CT is recommended for cT3 or cT4 cancers, nomogram risks of extensive disease exceeding 10%, and men with symptoms.[104,105]

Neither of the current imaging modalities, MRI or TRUS, is completely accurate in predicting extracapsular extent (ECE) or SV involvement, but they are superior to clinical assessment.[106] MRI appears superior to TRUS because TRUS is operator dependent. In experienced hands MRI performance characteristics are sensitivity, 65%; specificity, 73%; PPV, 88%; and negative predictive value (NPV), 38%. SV invasion gauged by altered shape and signal has sensitivity of 83% and specificity of 99%. Detection of node involvement is typically not possible with TRUS but is similar for CT and MRI, with sensitivity of 7%, specificity of 100%, PPV of 85%, and NPV of 100%. However a normal CT or MRI scan does not exclude nodal involvement.[90]

TRUS findings suggesting ECE are similar to MRI findings and include capsule bulge or distortion, asymmetry of neurovascular bundle, and obliteration of rectoprostatic angle. SV invasion is suggested by visible extension into or a mass in the SV (Fig. 10.12). In very experienced hands TRUS was shown to be as accurate as MRI for determining ECE (area under curve for TRUS of 0.81 vs. MRI, 0.71)[107] and superior to nomograms that predict stage.[108] However, experience and equipment appear to be important, and overall reported TRUS accuracy in determining ECE ranges as follows: sensitivity, 12% to 90%; specificity, 46% to 91%; PPV, 46% to 85%; NPV, 38%; and SV invasion sensitivity, 9% to 60%, and specificity, 82% to 100%.[109] Because imaging has limitations for preoperative staging, many physicians rely on their clinical acumen or use multifactorial staging nomograms (e.g., Kattan, Partin) that make use of DRE, PSA, Gleason score, and other variables.[6,106,110,111] However, experienced physicians have found meticulous TRUS to be more accurate than DRE and tables for staging[108] (see Fig. 10.12).

Remember also that although 95% of malignant prostate tumors are adenocarcinomas, the remaining 5% are unusual tumors of many cell types that do not elevate PSA. These frequently affect younger patients in whom the initial symptoms are those of metastatic disease including urinary dysfunction and skeletal pain. At imaging they mimic locally extensive and metastatic prostate cancer.[72,112]

Histologic grading describing the microscopic pathologic spectrum of prostate adenocarcinoma was devised by Dr. Donald Gleason in the 1960s and updated in 2014. It uses five progressive histologic patterns of gland disorganization to assign a **Gleason pattern** 1 through 5, which correlates with tumor aggression. Most prostate cancers are heterogeneous and display several patterns. The two most prevalent patterns are added to give a score (e.g., primary pattern 4 and secondary pattern 3 give a **Gleason score** of 4 + 3 = 7/10). Recently patterns 1 and 2 and scores of 5 or lower were eliminated, so currently scores range from 6 to 10.[59,73,113]

Recently Gleason score 3 + 3 = 6, specifically pattern 3, has come under discussion as to its malignant and aggressive potential and clinical importance. In the current PSA era Gleason 6 is the most commonly diagnosed score at biopsy and accounts for about 49% of cases. Although Gleason 3 + 3 = 6 demonstrates many visible characteristics of malignancy including local invasion and molecular and genetic markers, its clinical behavior

appears indolent. Some have suggested that Gleason 6 be renamed IDLE (indolent lesions of epithelial origin). However, finding only Gleason 6 cancer at biopsy may undergrade about 22% of men in whom sampling missed coexistent higher pattern cancer and in whom higher grades are found subsequently at radical prostatectomy. In these cases, prognosis relates to the higher initially undetected grade. It is recommended that men initially found to have Gleason 3 + 3 = 6 cancer undergo a follow-up confirmatory and more extensive biopsy before they are included in active surveillance programs to try to ensure that no higher grade cancer is present. mpMRI is proving useful for additional lesion targeting before repeat biopsy, but to date a negative mpMRI scan should not be used to avoid confirmatory biopsy or avoid systematic biopsy in addition to sampling of MRI targets.[59,73,114,115]

The high frequency of Gleason 6 cancer and the perceived "moderately severe" level of cancer that the term "grade 6/10" conveys to patients during discussion has led to difficulties in counseling patients who are not aware that 6/10 is actually very low risk and likely indolent disease. As a result, patients may request inappropriate radical therapies leading to overtreatment and its attendant risks and side effects with little benefit. A workaround has been to continue to use the Gleason scoring (6-10) but assign tumor grades from 1 to 5: 3 + 3 = grade 1; 3 + 4 = grade 2; 4 + 3 = grade 3; 4 + 4 = grade 4; 9 or 10 = grade 5. This would assign Gleason 6 the lowest grade 1 during discussions and hopefully provide sufficient psychological reassurance to patients to consider active surveillance and avoid immediate radical therapy.[9,73,115]

Therapy

Many treatment options are available depending on grade, stage, patient choices, and risk strata. There are many guidelines for determining risk levels.[116] Two commonly used ones are Epstein and D'Amico. The Epstein risk score predicts risk of clinically insignificant tumors, defined as less than 0.5 mL volume at prostatectomy. It is based on biopsy characteristics and defines low risk as Gleason 6 or lower, fewer than three positive cores, and less than 50% involvement of any core.[117] The D'Amico score predicts risk of biochemical failure after radiation therapy. It defines cancers as low risk (clinical stage T1c or T2a, PSA ≤10 ng/mL, or Gleason 6), intermediate risk (T2b, PSA 10-20 ng/mL, or Gleason 7), and high risk (T2c, PSA > 20 ng/mL, or Gleason 8-10).[118] Nomograms may further be used to help with patient decisions. The Kattan nomogram estimates survival when managed without curative intent.[110,119] The UCSF-CAPRA score estimates recurrence risk after radical prostatectomy.[120] To date, there is no consensus regarding optimal treatment for the most common, clinically localized cancer. Treatments are personalized after shared decision making with the patient and taking into consideration life expectancy, overall health, tumor characteristics, and the risks and benefits of the various therapies.[61,121,122] Treatment options include established therapies such as radical prostatectomy and radiotherapy (escalated-dose conformal external beam radiotherapy, brachytherapy with radioactive seed implants). Men with advanced disease can undergo watchful waiting or palliative therapy.[19,61,121]

Focal therapy is still an investigational treatment seeking to provide cure to focal intraprostatic lesions while avoiding the incontinence and impotence complications of treating the whole gland with surgery or radiation. It is being considered for men with an unequivocal solitary focal low-grade index lesion that is defined as the largest lesion and presumed to be the most aggressive. Small low-volume Gleason satellites do not seem to matter and are felt to need no treatment. It is an appealing approach in young patients with Gleason 6 or 7 cancer with a low proportion of grade 4 and volume greater than 1.3 mL proven by mpMRI-fusion biopsy or transperineal template biopsy. Early results have shown good "trifecta" outcomes (continent, potent, no evidence of disease) in 84%, which is higher than obtained with whole-gland active therapy. Several novel focal tissue ablating methods are used with TRUS or MRI guidance to kill tissue by heating, cooling, radiation, electroporation, and focal vascular occlusion. High-intensity focused ultrasound (HIFU) focally heats tissue. Cryotherapy freezes tissue. Electroporation uses low-energy direct current to disrupt cell membranes. Vascular-targeted photodynamic therapy (VTP) uses a novel systemically injected agent, TOOKAD, which when focally activated by laser causes local vascular occlusion and secondary tissue anoxic destruction.[10,123]

Cancer control by the established surgical and radiation therapies in low-risk patients with organ-confined disease exceeds 90% at 10 years but falls rapidly with higher grade and more extensive disease. All the treatments have varying degrees of side effects that can significantly affect quality of life, including incontinence, erectile dysfunction, and urethral strictures, in addition to the usual surgical concerns. Patients may select a specific treatment depending on local expertise and the expected complications. High cure rates and long-term survival have made quality of life and side effects important issues when considering treatment.[63,66,121]

Radical prostatectomy is the "reference standard" of therapy and has a disease-free survival advantage over expectant management.[124] Cure rates in men with low-grade cancer exceed 90% but decrease with advanced grades and stages. For example, when nodes are involved at radical prostatectomy, 10-year survival falls to about 15%. An attempt is made to avoid injury to the neurovascular bundle, if safe for cancer control, to avoid erectile and continence problems (nerve-sparing prostatectomy). In skilled hands, continence is about 90% and erectile function is preserved in 50% to 90%, depending on patient age. Alternatives to the classic open retropubic prostatectomy are laparoscopic surgery and robotic surgery, which have similar outcomes in experienced hands, although postoperative recovery is faster.[121,122]

The two general approaches for radiotherapy are external beam and implanted radioactive seeds (brachytherapy). Conformal escalated-dose **external beam radiotherapy** uses image guidance, usually CT, to confine and conform the beam tightly to the prostate. This allows an increasing or escalating target dose while minimizing collateral damage to adjacent organs. Tight field planning is aided by fiducial (reference) markers placed into the prostate under TRUS guidance to improve planning and to allow higher doses (escalated dose) that can be precisely confined

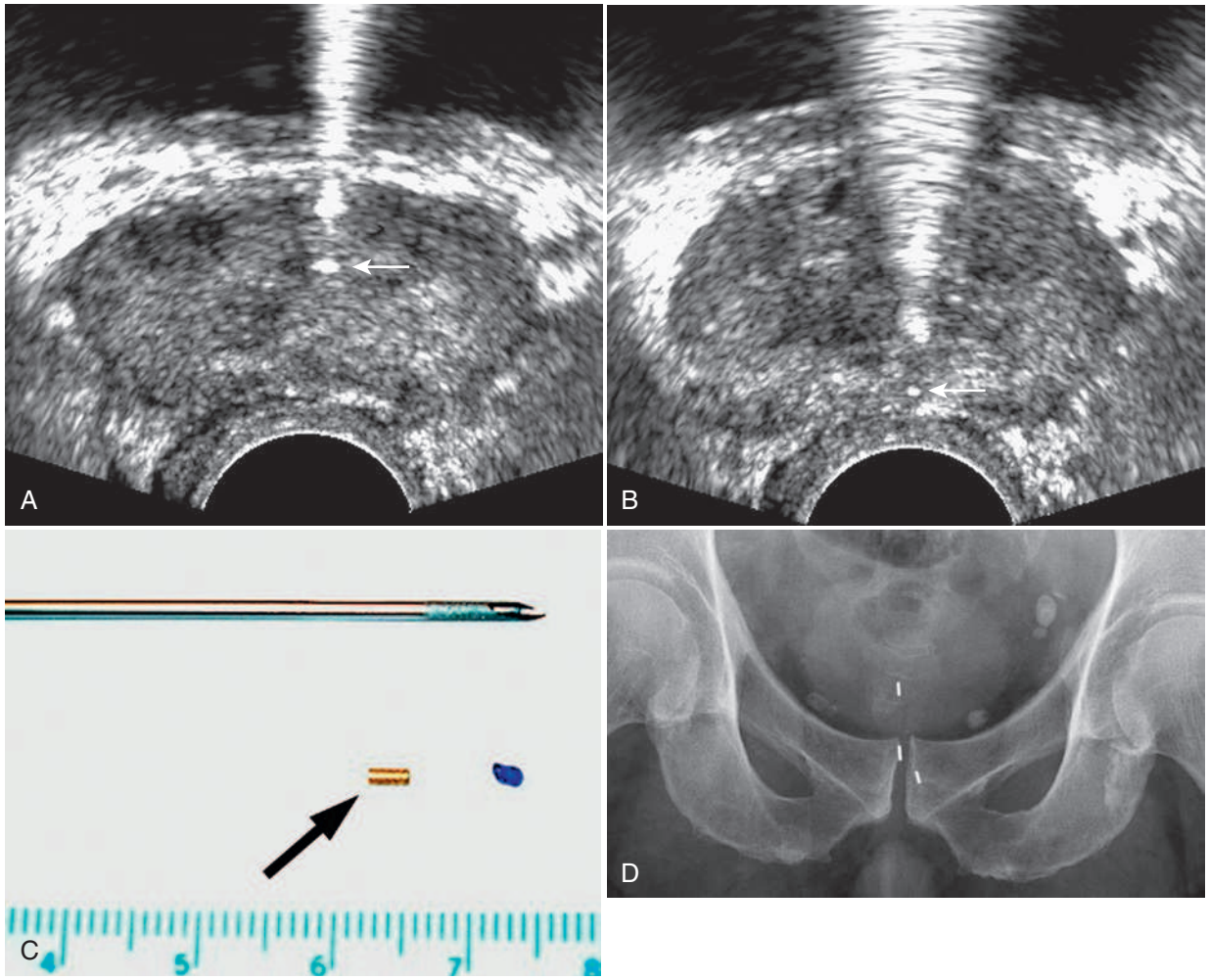

FIG. 10.13 Ultrasound-Guided Radiotherapy. Fiducial marker seeds inserted with transrectal ultrasound (TRUS) guidance and used to guide escalated-dose external beam radiotherapy. **(A)** Transverse image shows basal seed *(arrow)* with characteristic comet-tail reverberation artifact. **(B)** Rectal surface seed *(arrow)*. **(C)** Fiducial (marker or reference) gold seed, which is inserted into the prostate to precisely guide escalated-dose conformal radiotherapy *(arrow)*. The smaller seed is a bone wax plug used to keep the seed in the needle before placement. **(D)** Pelvic x-ray film shows the three marker seeds in place.

(conformed) to the prostate to lessen collateral damage to adjacent organs (Fig. 10.13). Five-year freedom from biochemical recurrence (no PSA rise) is 70% to 85%. Erectile function is preserved in about 50% and continence in 80% of patients, but long-standing rectal irritation may occur.[61,66,121]

Brachytherapy involves intraoperative placement of radioactive seeds, usually iodine-125, into the prostate using TRUS guidance and a perineal template (Fig. 10.14). Direct radioactive seed placement into the prostate allows higher local radiation doses. The technique is restricted to low-risk patients with PSA less than 10 ng/mL, Gleason score of 6 or less, and gland volume less than 50 mL. Erectile function is preserved in about 50% and continence in about 80% of patients, although urinary stricture and bowel irritation are common.[66]

Two new treatment strategies, watchful waiting and active surveillance, are being introduced to delay invasive therapy and its side effects and avoid possible overtreatment. **Watchful waiting** is used in men who have asymptomatic cancer but are unlikely to benefit from therapy because of comorbid conditions. They are monitored until they become symptomatic and then receive symptomatic palliative care, usually with hormones.

Active surveillance (active monitoring with curative intent) is an increasingly popular "PSA era phenomenon" that is almost unique to prostate cancer and seeks to avoid overtreatment. It recognizes that many men with low-risk cancer will never suffer from the cancer and are 10 times more likely to die from other causes such as cardiovascular disease. It also takes into consideration the apparent indolent behavior of Gleason grade 3 lesions (Gleason score 3 + 3 = 6), which do not appear to metastasize or cause death. There is no general consensus on optimal protocols and there are very many published guidelines for inclusion criteria, monitoring, and criteria for triggering of definitive therapy. It is suggested that pure Gleason 3 + 3 = 6 disease and tumor volumes of up to 1.3 mL (diameter about 1.4 cm) may behave in a benign manner, and patients could be offered surveillance.[115,116,123]

Strict criteria are suggested to define suitable low-risk patients, typically including PSA below 10 ng/mL, Gleason score of 6 or lower, stage T1c or T2a, less than 50% of length of any biopsy

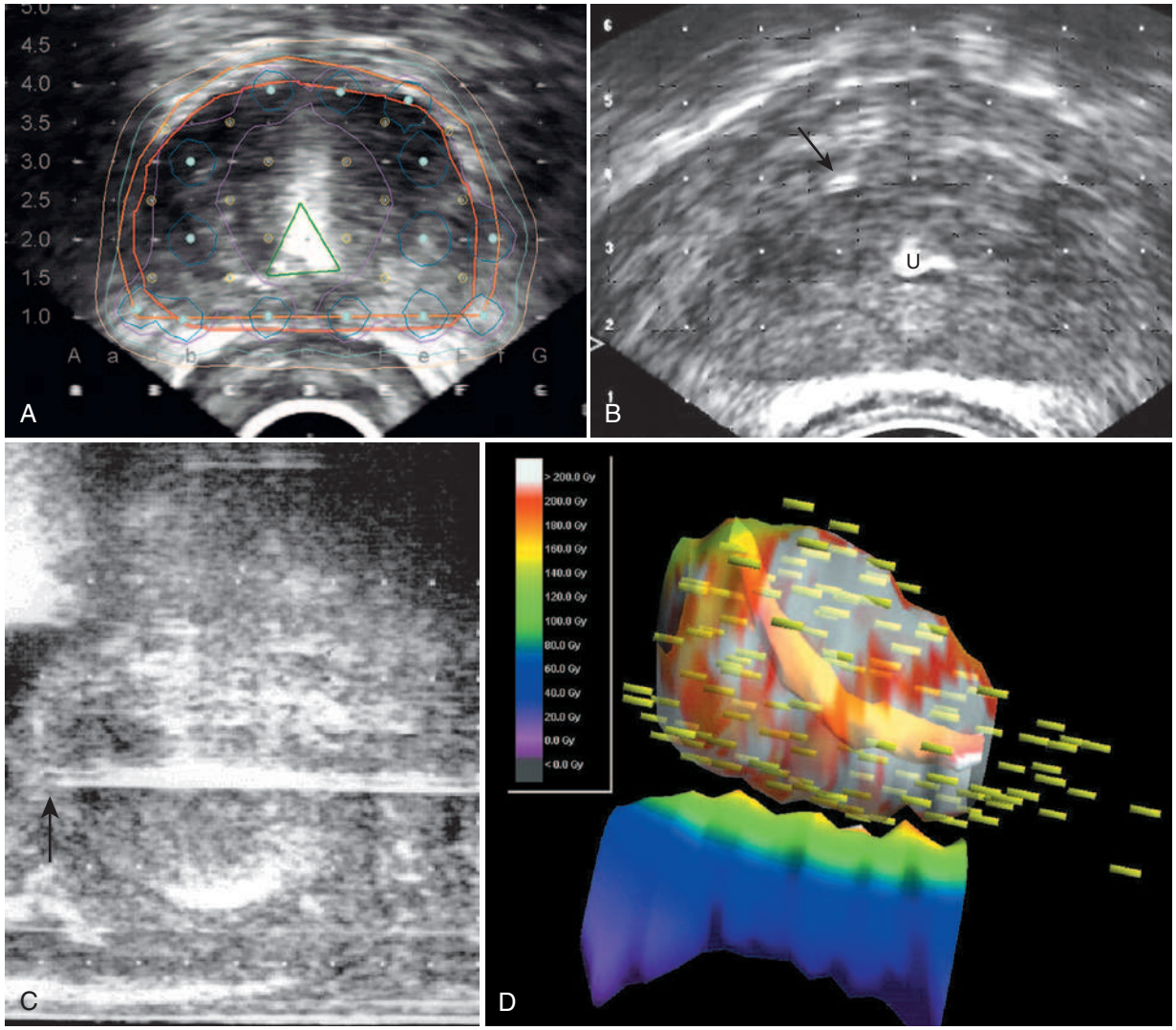

FIG. 10.14 Ultrasound-Guided Brachytherapy. Transrectal ultrasound (TRUS) used to plane and guide brachytherapy (radioactive seed implantation) using a special stepping device and perineal needle template. This same template can be used to guide transperineal saturation biopsy. **(A)** One of multiple transverse prostate images used to plan seed sites *(dots)* and determine radiation isodose dose curves *(colored lines).* Urethral dose is avoided *(white central area inside the green triangle).* Note the grid markers at the bottom *(A, a, b … G)* and on the left side *(1.0, 1.5, 2.0 … 4.5)* and the grid dots superimposed on the field. **(B)** TRUS-guided seed placement in the operating room; *U,* urethra. Transverse image shows the guiding grid dots and the tip of one inserting needle as a hamburger-like echo *(arrow).* **(C)** Sagittal image shows brachytherapy needle inserted to base of prost ate *(arrow)* to insert a row of seeds. **(D)** Postprocedural CT reconstruction shows the position of the seeds *(green)* and that the entire prostate is receiving a high *(white)* radiation dose. (Courtesy of Dr. Juanita Crook, Radiation Oncology, Princess Margaret Hospital, Toronto.)

core, fewer than three positive biopsy cores, and life expectancy of over 10 years. In general, after initial diagnosis of low-risk disease and a confirming biopsy and if patients agree, they are actively monitored with combinations of PSA, PSA kinetics, PSA density, DRE, TRUS, repeat biopsy, and the new biomarkers to detect signs of progression resulting in reclassification, which triggers therapy. Use of mpMRI to specifically allow targeting of high-risk areas at repeat biopsy is emerging, but currently the effectiveness of the mpMRI approach has not been established.[125]

Significant progression and reclassification that triggers treatment is variably defined by a rapid rise in PSA (doubling time < 2 years) and increase in tumor grade or volume. Using this approach and with 14-year follow-up, Klotz has reported that 1.5% of men showed progression and 30% of men requested active therapy; cancer-specific mortality was only 5%, and in the interval 10 times as many men died of unrelated causes and were never symptomatic and avoided prostate cancer treatment and attendant complications. Other groups have shorter follow-up but have reported similar results.[115,116,123]

Progression of known or treated disease is monitored with PSA because it provides an easier and more objective indicator of total tumor burden and neoplastic activity than TRUS or mpMRI.[2,4,89]

Sonographic Appearance of Prostate Cancer

Gray-Scale Ultrasound

About 30% to 50% of prostate cancers are visible on TRUS, but detection varies depending on operator experience and equipment. The classic appearance of cancer is that of a **hypoechoic nodule** typically located in the **peripheral zone** abutting the capsule that cannot be attributed to benign causes[3,126,127] (Figs. 10.15, 10.16, and 10.17). The corollary to this is that about half of cancers are not visible on TRUS. Normal appearances on TRUS do not imply the absence of cancer and should not delay systematic biopsy if there is clinical suspicion of cancer.

Previously the sonographic appearance of prostate cancer was extensively debated. Early investigators incorrectly thought that most prostate cancers were hyperechoic. In 1985 Lee and colleagues[126] first convincingly demonstrated the **hypoechoic** appearance of cancer. Others subsequently confirmed that a substantial portion but not all peripheral zone cancers are hypoechoic to some extent.[127,128] The pathologic basis of the hypoechogenicity is the replacement of normal loose glandular tissue by a packed homogeneous mass of tumor cells with fewer reflecting interfaces and thus fewer echoes. Tumors that grow by infiltration or have a strongly glandular structure will preserve tissue interfaces and echogenicity and thus appear isoechoic.[127]

When attempting to correlate the echogenicity of neoplasms with the amount of stromal fibrosis, it was found that hypoechoic lesions had less stromal fibrosis than did their more echogenic counterparts. Also, hypoechoic lesions tended to be more aggressive than isoechoic lesions. Tumor size plays a role in visibility. Shinohara and colleagues reported 88% detection of tumors over 20 mm, 19% of tumors 4 to 10 mm, and none under 4 mm.[129]

Hyperechoic cancer has been described but occurs infrequently. Uncommon histologic types of cancer, including the cribriform pattern and comedonecrosis with focal calcifications, can be focally **echogenic.** The calcifications associated with comedonecrosis are tiny and act as crystals that are highly echogenic, more so than dystrophic calcifications. On scanning they are conspicuous and appear to twinkle, giving a "starry sky" appearance[127] (see Fig. 10.17C).

About 30% of prostate cancers are difficult or impossible to detect with TRUS because they are **isoechoic** and do not contrast

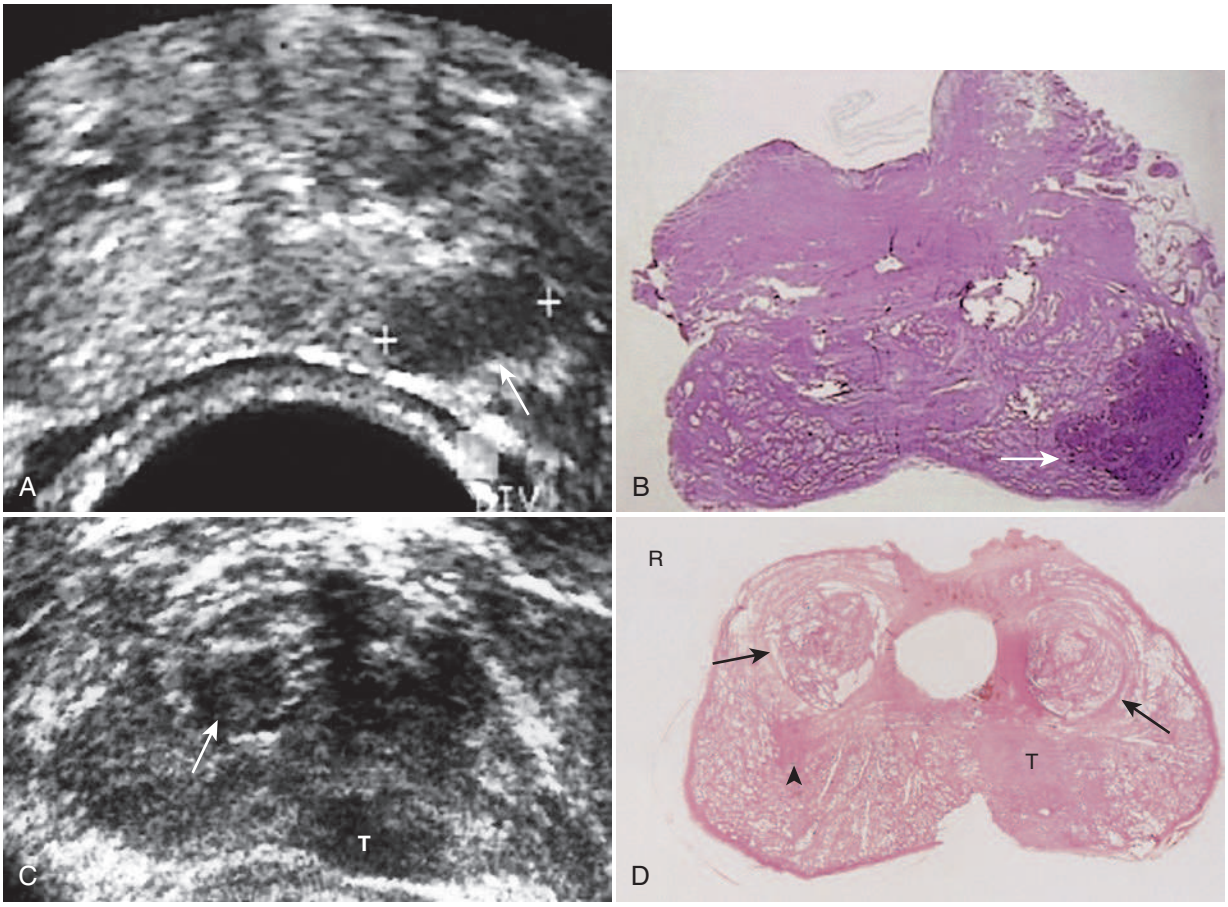

FIG. 10.15 Prostate Cancer: Typical Appearances. (A) Hypoechoic nodule in peripheral zone along the capsule that cannot be attributed to benign causes *(arrow).* **(B)** Pathology section of **A** shows the homogeneous solid cellular mass of tumor tissue *(arrow),* which reflects sound poorly compared with the adjacent prostate, which has the multiple glandular interfaces. **(C) Typical hypoechoic peripheral zone cancer nodule** *(T).* Note also the well-circumscribed hypoechoic benign prostatic hyperplasia (BPH) nodule in the right transition zone *(arrow).* **(D)** Section of (C) for correlation shows the homogeneous tumor mass *(T).* There is a second small lesion on the right side *(arrowhead).* Also note the bilateral BPH nodules *(arrows).*

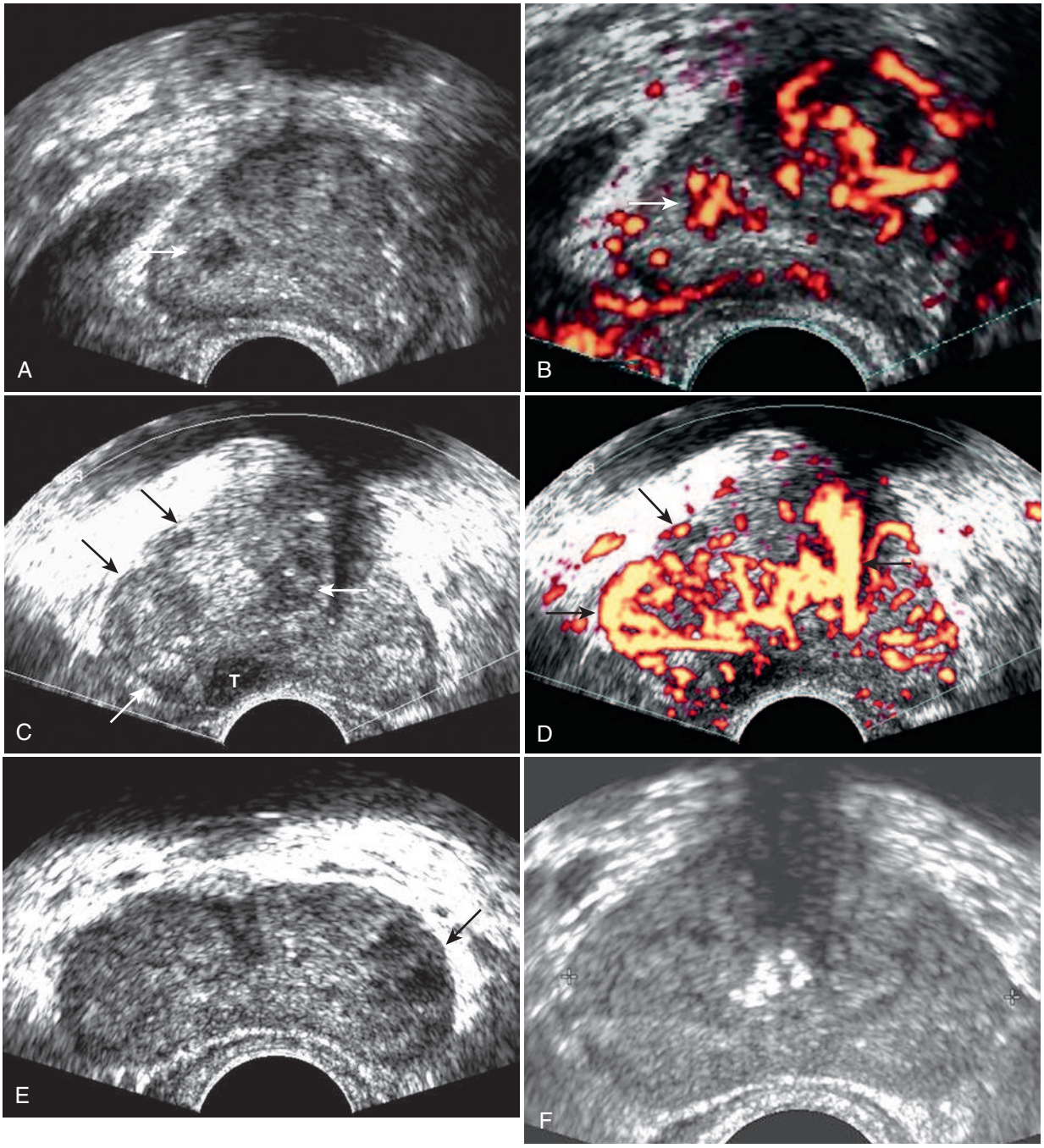

FIG. 10.16 Prostate Cancer: Less Common Appearances. (A) Small hypoechoic lesion entirely inside the peripheral zone *(arrow)* proved to be cancer. Digital rectal examination (DRE) findings were negative, but prostate-specific antigen (PSA) was slightly elevated. **(B)** Power Doppler scan of **A** shows increased vascularity *(arrow)* in region of the nodule. **(C)** Small "tip of the iceberg" lesion visible posteriorly in the right lobe *(T)*. Cancer is filling virtually the entire right lobe *(white and black arrows)*. Most of this tumor is isoechoic and thus not visible on gray-scale imaging. Remember that prostate cancer is typically multifocal and larger than the lesion seen on transrectal ultrasound (TRUS). **(D)** Power Doppler scan shows large abnormal area of hypervascularity involving not only the small peripheral hypoechoic lesion, but also most of the transition zone *(arrows);* PSA, 265 ng/mL; Gleason score, 7/10. **(E)** Multifocal cancer involving both right and left lobes: one hypoechoic, the other isoechoic. DRE findings were negative; PSA, 4.5 ng/mL with a 14% free/total ratio. In the left lobe there is a suspicious area anteriorly *(arrow)*. The right lobe appears very normal and free of lesions. At biopsy, both lobes had Gleason 6/10 cancer. **(F)** Isoechoic significant cancer not visible on ultrasound. DRE and TRUS findings were negative. PSA of 10.7 ng/mL led to biopsy, which showed bilateral Gleason 7 cancer.

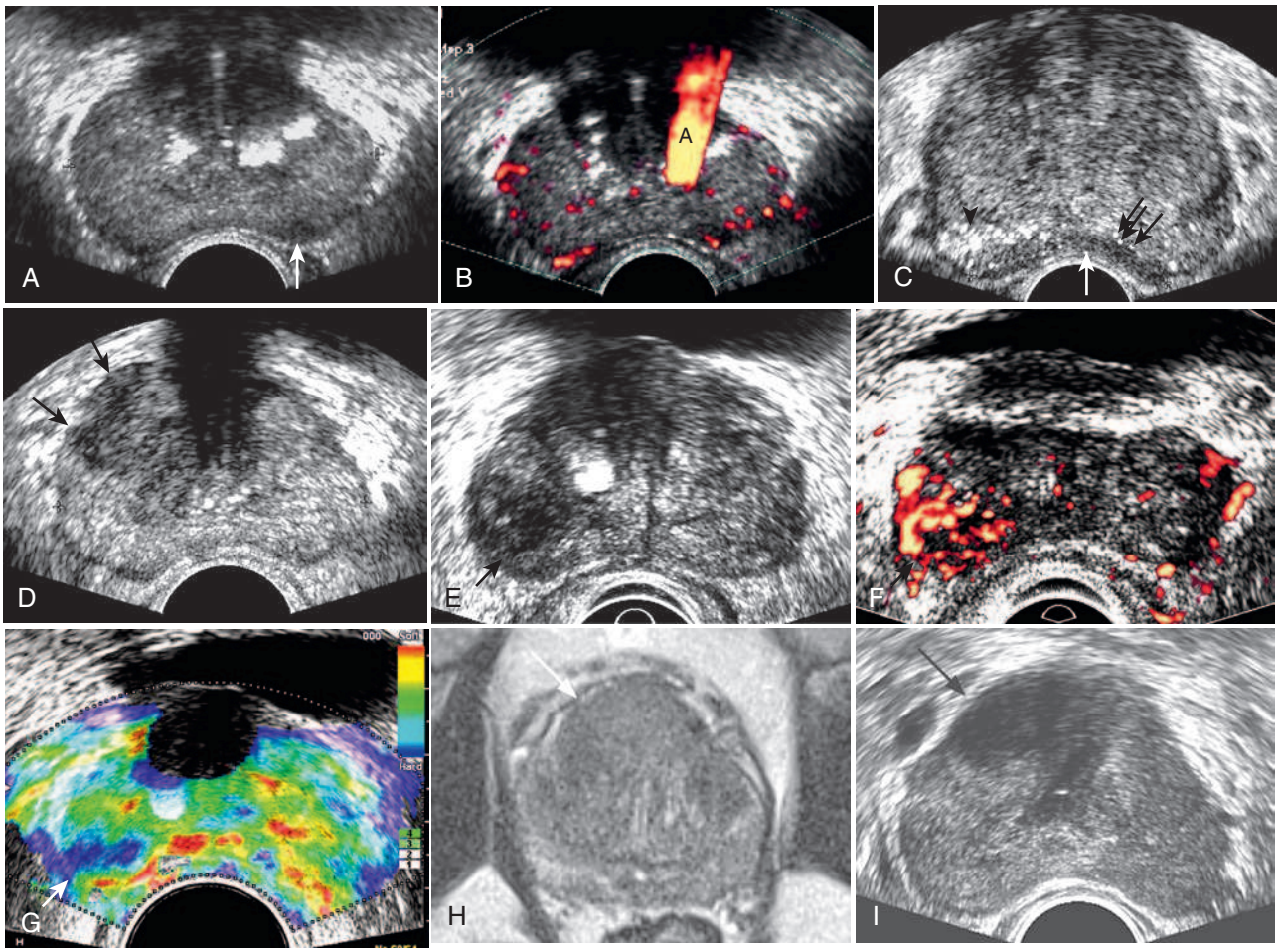

FIG. 10.17 Prostate Cancer: Other Appearances. (A) Almost isoechoic, impalpable **nonvascular cancer.** Digital rectal examination (DRE) findings were normal; prostate-specific antigen (PSA), 6.08 ng/mL with 12% free/total ratio. Transrectal ultrasound (TRUS) is only mildly suspicious for cancer at left *(arrow).* Biopsy showed isoechoic ultrasonically undetectable, Gleason 7/10 cancer in the right side involving 25% of the tissue. On the left, where there is a visible lesion *(arrow),* the biopsy was only 15% cancer. This highlights the need to do both systematic and targeted biopsy. **(B)** Power Doppler shows almost no detectable signal despite **extensive bilateral cancer.** Only about 80% of cancers demonstrate increased vascularity. The strong Doppler color signal anteriorly is all artifactual *(A),* from calcification. **(C) Extensive cancer** with "starry sky" appearance caused by comedonecrosis in the tumor. The malignant nodule extends across the entire peripheral zone *(between cursors).* On the right, the calcified clumps are normal corpora amylacea *(arrowhead).* On the left, the densities have a different character: small, more scattered, round, and very echogenic, and will "twinkle" on probe movement *(arrows).* These are highly suggestive of comedonecrosis in tumor. **(D)** Isolated **transition zone cancer** visible as an amorphous hypoechoic bulge of the right anterior transition zone *(arrows).* DRE was negative. Biopsy to investigate PSA of 12.0 ng/mL showed Gleason 6/10 cancer. **(E)** Typical hypoechoic **peripheral zone lesion.** Biopsy showed Gleason 8/10 cancer *(arrow).* **(F) Power Doppler** scan shows enhanced vascularity in lesion *(arrow).* **(G) Elastography** of same lesion *(arrow)* in **(F)** shows blue color in lesion, implying stiff tissue. **(H)** T2-weighted magnetic resonance imaging (T2W MRI) scan shows suspicious "charcoal" texture lesion bulging capsule in the right anterior fibromuscular zone *(arrow).* Prior systematic biopsy findings were not unexpectedly negative because only the posterior 2 cm of the prostate would be sampled. **(I)** Corresponding TRUS shows the same lesion. Such lesions are often missed on TRUS because attention and biopsy are confined to the posterior peripheral zone and because the procedure is performed by operators who use TRUS only to guide systematic biopsy without first evaluating the gland.

with the surrounding prostate gland (see Figs. 10.16C and 10.17A). When present, an isoechoic tumor can be detected only if secondary signs are appreciated, including glandular asymmetry, capsular bulging, and areas of attenuation. This is often true of transition zone cancer[127,130] (see Figs. 10.16E and 10.17D, H, and I).

When the tumor replaces the entire peripheral zone, it often is **less echogenic** than the inner gland, which is a reversal of the normal sonographic relation. When the entire gland is replaced with tumor on a BPH background, the gland may be diffusely inhomogeneous (see Fig. 10.17B).

Only about half of **hypoechoic** areas are cancer.[131] Other benign causes of hypoechoic areas seen in the prostate include normal internal sphincter muscle, hyperplasia, prostatitis, hematoma, vessels, benign glandular ectasia, and cysts.[2,91,127]

Fortunately, 70% of prostate cancers arise in the homogeneous **peripheral zone** where the homogeneous background makes

them easier to detect. About 20% are in the **transition zone,** where detection is hindered by the heterogeneous and variably vascular background of hyperplasia. Clues to transition zone cancer are the identification of a poorly marginated hypoechoic area that appears different from other BPH nodules and the focal loss of surgical capsule and asymmetrical bulge of the contour.[132]

Tumors in the **anterior midline** fibromuscular area anterior to the urethra are difficult to detect because this area is far from the probe and obstructed by the urethra; these tumors often become very large before being detected. These have also been called PEATs **(prostate evasive anterior tumors).** Biopsy of these tumors can be difficult. The typical systematic transition zone biopsy may miss them because of their far anterior and midline location and the desire to avoid the urethra during biopsy. Just remembering to look in this area at TRUS examination and using mpMRI are helpful in detection of these anterior tumors[133] (see Fig. 10.17H–I).

Some suggest that systematic biopsy without scanning or looking for lesions is adequate for cancer detection. We feel it remains important to search for suspicious areas at TRUS. Biopsy of suspicious lesions doubles the likelihood of cancer detection (58% vs. 31%), shows greater percent of core involvement (50% vs. 10%), and doubles the likelihood of Gleason score of 7 or higher (69% vs. 28%).[87,134,135]

New ultra-high-frequency (29 MHz) probes are under evaluation. With such high resolution, it appears that additional appearances and tissue characteristics may become helpful to discriminate between benign and cancerous tissue that are different from the hypoechoic nodule seen with lower resolution. With high frequency, benign areas tend to show ducts or a "Swiss cheese" appearance and malignant areas appear more isoechoic and may have a heterogeneous mottled appearance with microcalcifications, shadowing regions, and subtle capsular irregularity. A scoring system called PRI-MUS (prostate risk identification using micro-ultrasound) has been proposed; this can be helpful in predicting presence and grade of cancer.[136]

Transrectal Ultrasound (TRUS) Findings Suspicious for Prostate Cancer

Hypoechoic nodule not attributable to benign causes
Often in peripheral zone
Nodule with vascularity
Nodule and capsule bulge
Capsule bulge
Capsule irregularity
Focal hypervascularity
Loss of surgical capsule definition

Color Flow and Power Doppler Imaging

Doppler imaging has been evaluated for detection of neovascularity associated with cancer. This approach is especially attractive to find isoechoic cancer because pathologic examinations show cancers have increased neovascular density. Malignant neovascularity vessel diameter ranges from about 0.01 to 0.05 mm. However, Doppler ultrasound is limited to detecting flow in vessels about 10 times larger, with diameter greater than 0.1 mm. As a result, increased flow may not be apparent until lesions have grown enough to generally increase blood flow[91,137] (see Fig. 10.16B and D). Both color Doppler flow imaging and the more sensitive power Doppler can be used. I prefer power Doppler, which is more sensitive to flow detection, gives a more uniform display of vascular density, and produces images that are more stable with different equipment settings[133,137] (see Fig. 10.5). Flow inside a lesion is more specific than peripheral flow. Overall, Doppler increases cancer detection by about 5% to 17% over gray-scale imaging.[130,137,138] Suspicious hypoechoic nodules that are also vascular tend to have larger tumor volume and higher Gleason score.[139]

Doppler imaging has pitfalls. Not all cancers are vascular, and the absence of vascularity should not prevent systematic biopsy or biopsy of a suspicious nodule. Vascularity may be increased with nonmalignant conditions such as inflammation (see Fig. 10.8B). There is no increased benefit for color flow Doppler in the transition zone because BPH nodules can range from hypovascular to hypervascular.[6,139] The capsule of the prostate is very vascular, especially at the base and apex, and this can mimic neovascularity to the uninitiated operator. Prostate calcifications and corpora amylacea cause considerable Doppler twinkle artifact and may prevent diagnostic studies (see Fig. 10.7D).

Contrast-Enhanced Ultrasound

Tumor-associated neovascularity consists of small disorganized vessels of 10 to 100 μm diameter, which are below the usual Doppler resolution limit of about 100 to 1000 μm (0.1-1.0 mm). Microbubble contrast agents have been developed that act as intravascular contrast agents and allow imaging of contrast-enhanced vessels down to 50 to 100 μm. Apart from visual inspection of increased vascular intensity, several other parameters can be assessed, including bolus arrival time, time to peak intensity, wash in–wash out curves. 5α-Reductase inhibitors have been used to suppress normal vascularity and increase conspicuity of neovascularity. Additional developments are underway to attach ligands to the microbubbles that bind to specific tissue or tumor targets and can be used to enhance lesion delectability or, more important, to target delivery of therapeutic agents.[2-4,91]

Sensitivity and specificity of CEUS for cancer detection are about 70% and 74%. CEUS requires experienced operators and currently there is inadequate standardization of agents, imaging techniques, and diagnostic criteria. It can assist in detection of cancer but as yet cannot replace systematic biopsy.[2,91,140]

Three-Dimensional Ultrasound and Transrectal Ultrasound–Magnetic Resonance Imaging Fusion

Because three-dimensional (3-D) depends on two-dimensional (2-D) scanning, in general there is no improvement in cancer detection, but there may be slight improvement in cancer staging.[137] There may be a role for 3-D imaging in accurate volume determinations when precise volumes are needed to monitor changes in gland size. The Urostation (Koelis, France) MRI-TRUS fusion biopsy platform uses 3-D imaging to co-register MRI and

TRUS images and records areas where biopsy specimens have been taken.[91] Increasingly, mpMRI and MRI-TRUS fusion biopsy are proving helpful in complex cases such as in patients with multiple negative extensive biopsies but rising PSA.

Elastography

Tumors are about 5 to 28 times stiffer than normal prostate. Elastography of the prostate assumes that stiff areas such as tumors with increased cellularity allow less internal movement. The amount of movement is presented as a color-coded map from blue (stiff) to red (elastic) (see Fig. 10.17G). In strain elastography, force is applied by probe motion, a technique that is very operator dependent and does not allow quantification. In shear wave elastography, the probe is held still and strain is provided by sound waves, which allow better standardization and direct measurement of Young's modulus.

Meta-analysis of elastography reports sensitivity of 71% to 82% and specificity of 60% to 90%. Cancer detection increases with lesion size and Gleason score. However, elastography does not evaluate the gland uniformly. Performance is better in the peripheral zone, which is adjacent to the probe, especially the apex and midgland, and is less accurate at the base, anterior gland, and transition zone. The technique remains operator dependent. Although it can assist in lesion localization, it does not allow avoidance of systematic biopsy. False-positive results are seen with chronic inflammation and atrophy. Experience has shown that elastography is subjective and has a long learning curve and that images are difficult to reproduce.[4,6,91,141]

ULTRASOUND-GUIDED BIOPSY

Biopsy should be offered to men who would benefit from tissue diagnosis following informed consent and after shared decision making. Most men are initially identified by PSA over 2.5 to 4 ng/mL and/or palpable nodule. Other factors taken into consideration with regard to biopsy include comorbidities, risk calculators, results of imaging and biomarker tests, and patient preferences. But the final decision is individual, relying on the physician's acumen and patient's wishes. Indications differ between initial and subsequent biopsies.[26,142,143]

Preparation for Biopsy

Typically, TRUS biopsy is performed in an ambulatory setting. Appropriate clinical information should be available to know why the biopsy is needed and to allow for its safe performance. This includes results of DRE, PSA, and other relevant tests including imaging, prior biopsy results, relevant medications, and comorbidities. Risk factors that can alter risks of infection or bleeding should be identified so they can be appropriately managed. Informed consent should be obtained.

Antibiotic Prophylaxis

Transrectal biopsy requires antibiotic prophylaxis to minimize risk of infection and sepsis. Specific antibiotic choices can be found by consulting regional urologic association guidelines and infectious disease specialists and taking into account local and regional antibiotic resistance patterns. For low-risk patients most guidelines recommend fluoroquinolone (ciprofloxacin) or a cephalosporin. Minimal coverage should start 1 hour before the procedure and last for 24 hours; some are more comfortable with 3-day courses, although this additional coverage is debated as being unnecessary and possibly contributing to antibiotic resistance. Patients at increased risk of infection may benefit from supplemental antibiotics such as aminoglycosides or ceftriaxone. Risk factors include recent urinary infections, recent antibiotic use, recent instrumentation or catheter, international travel especially to southeast Asia, hospital exposure (both patients and workers), and immunotherapy. Endocarditis prophylaxis for patients with valvular heart disease is no longer recommended.[144] Use of rectal swab stool culture to individualize antibiotic choices has been suggested and may decrease infections. Although there are concerns about the logistics of implementing this approach for every patient, it may be helpful in high-risk patients and those with prior complications. For complex cases, infectious disease consultation may helpful. Most prostate biopsies are done transrectally (Fig. 10.18), but some suggest that transperineal biopsy should be reintroduced to decrease infection risk because of the increasing prevalence of cephalosporin-resistant *E. coli*.[145]

Postbiopsy sepsis can occur acutely after biopsy, and its seriousness may not be initially appreciated by the patient or his physician. I find it useful to emphasize to the patient the potential seriousness of infection and the need for prompt medical attention and provide patients with a letter to their physicians stating that postbiopsy sepsis should be managed promptly with blood and urine cultures and intravenous broad-spectrum antibiotics.[146-148]

Bowel Preparation

Laxatives or a cleansing enema is helpful to clean the rectum to improve visibility. Some believe that an enema decreases infection risk, but this has not been confirmed. Povidone-iodine enemas and suppositories have been suggested to decrease infections, but this has not been confirmed.[26,148]

Analgesia

Analgesia is important to decrease discomfort of the procedure. Periprostatic nerve block with 1% lidocaine is standard. In general, 5 mL is injected into the neurovascular bundle on each side (10 mL total) at the base in the fatty triangle between the prostate and SV. Some suggest additional injections at the apex and sides of the prostate, but we have not found these to provide improved analgesia. Analgesic gel may be helpful if the anus is tight or sensitive. Some have found oral medications, including acetaminophen and combinations, to be helpful. In rare cases conscious sedation may be needed.[26,149,150]

Anticoagulation

Aspirin and NSAIDs do not need to be discontinued and are associated with clinically insignificant bleeding. Antiplatelet drugs such as clopidogrel (Plavix) should be discontinued for 5 to 10 days before the biopsy. More potent anticoagulants should be discontinued, but only after consultation with the prescribing physician to ensure patient safety. Bridging anticoagulation with

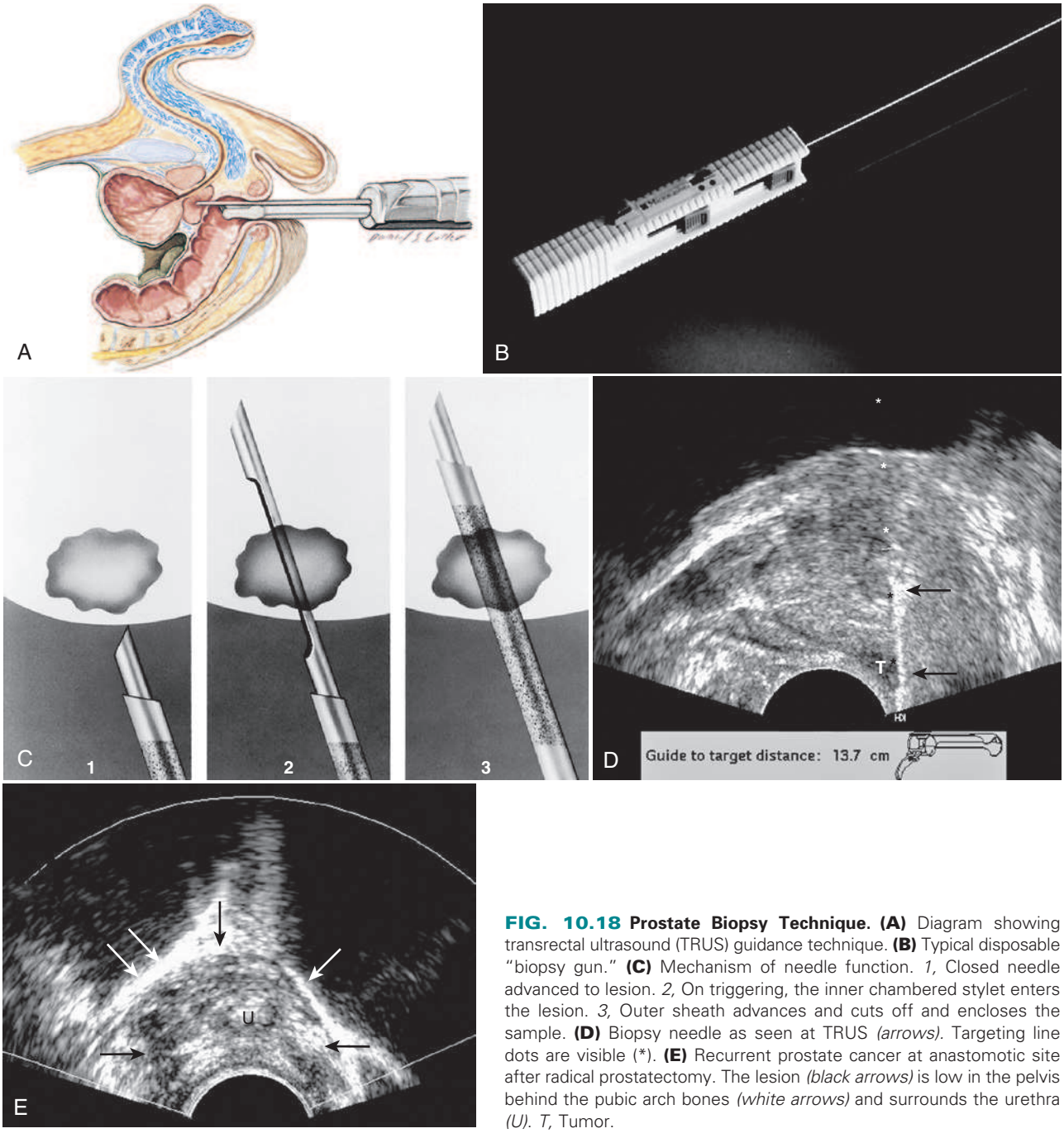

FIG. 10.18 Prostate Biopsy Technique. (A) Diagram showing transrectal ultrasound (TRUS) guidance technique. **(B)** Typical disposable "biopsy gun." **(C)** Mechanism of needle function. *1,* Closed needle advanced to lesion. *2,* On triggering, the inner chambered stylet enters the lesion. *3,* Outer sheath advances and cuts off and encloses the sample. **(D)** Biopsy needle as seen at TRUS *(arrows).* Targeting line dots are visible (*). **(E)** Recurrent prostate cancer at anastomotic site after radical prostatectomy. The lesion *(black arrows)* is low in the pelvis behind the pubic arch bones *(white arrows)* and surrounds the urethra *(U). T,* Tumor.

short-acting heparin may be needed. Warfarin should be discontinued for 5 days, and international normalized ratio (INR) should be confirmed to be 2 or lower. The newer oral anticoagulants such as dabigatran should be withheld for 3 days and coagulation testing is not needed. In general, anticoagulants can be restarted after 24 hours. Coagulation specialists should be consulted if patients have other bleeding disorders.[26,151,152]

Technique

The patient lies in the decubitus position. A DRE is performed before probe insertion to palpate the prostate, to confirm that probe insertion is safe, and to relax the sphincter. We insert the probe with needle guide attached at the outset to save time and examine the prostate with the guide in place. The decision to perform the biopsy has already been made, so only target details need to be clarified. A variety of probes and guides are available. Ching and colleagues have suggested that end-fire probes and guides provide better sampling than side-fire devices.[24] End-fire probes, unlike side-fire probes, allow easy sampling of all parts of the prostate including the apex and far anterior transition zone. Electronic guidelines direct the needle path (see Fig. 10.18D).

Local anesthetic can be injected as soon as the probe is inserted and before the gland is examined, to allow the agent to have

additional time to act. After injection, prostate measurements are made and the SVs and prostate are examined in a standardized manner. Suspicious areas are imaged and noted for targeted biopsy.

Biopsy is best done by a single operator who controls both the probe and the gun and takes samples as appropriate for the situation. The **automatic biopsy gun** with 18-gauge needles is standard and has remarkable patient acceptance and safety. With the gun cocked, the needle is "parked" in the guide, ensuring that the tip is safely inside the guide. The probe and contained needle are moved to the target using the targeting line. With end-fire probes, better samples are obtained if the prostate is compressed during the biopsy. A simple, swift motion advances the gun and needle tip to the surface of the lesion. Once in position, the device is triggered and the needle advances approximately 2 to 3 cm to cut the tissue core and trap it in the beveled chamber of the inner needle. We sample suspicious areas first in case the patient cannot tolerate the entire procedure, and finish with systematic sampling. Biopsy through the urethra, internal urethral sphincter, and ejaculatory ducts is avoided. When the biopsy is finished, the probe is removed and the site is palpated for hematomas. After the biopsy, we keep the patient for an hour to allow observation and recovery, the first 20 minutes lying down and the remainder seated. This helps in management of late onset of vasovagal complications.

Side Effects and Complications

Minor side effects that do not require treatment are common. These include bleeding in the urine (50%) and stool (30%) and hematospermia (50%). Minor bleeding in the urine and stool generally lasts only a few days but can continue for several weeks. The ejaculate may remain discolored for many months. Transient erectile dysfunction is uncommon (<1%), but it is not clear if this is psychological as a result of concerns related to biopsy or physiologic.[25,143,148]

About 1% to 5% of patients have a hypotensive vasovagal-like reaction after biopsy, which can occur up to 60 minutes after the procedure. It is characterized by pallor, sweating, nausea and vomiting, bradycardia of 50 to 60 beats/min, and hypotension. Most men recover spontaneously and rapidly after being placed in Trendelenburg head-down position. We keep patients in the clinic for an hour after the biopsy to avoid problems with these delayed vasovagal hypotensive reactions.

Significant biopsy complications requiring physician intervention or hospitalization are relatively uncommon, but incidence of hospital admissions for any reason within 30 days of biopsy is about 4.8% to 6.9% regardless of the mode of guidance, needle size, or approach and is probably not related to number of biopsy cores. These complications include minor transient fever (5%-7%), sepsis necessitating hospitalization (1%-3%), large hematoma (uncommon), transient symptoms of obstruction (6%-25%), urinary retention necessitating catheterization (0.2%-2.6%), and significant rectal bleeding (1%). Immediate visible rectal bleeding usually responds to 2 to 5 minutes of finger or probe pressure. With the use of prophylactic antibiotics, the incidence of septic complications requiring therapy is about 1% to 2%. Hospitalizations after biopsy are mainly (about 70%) due to infections with antibiotic resistant *E. coli*. These infections have been increasing owing to increased prevalence of ciprofloxacin resistance and are more common in patients at risk. Sepsis can rapidly progress to septic shock. Patients should be advised to seek help promptly if they start feeling feverish or unwell. Tumor seeding is virtually unknown.[25,143,147,148]

Biopsy should never be taken lightly. Some patients have required prolonged hospitalization, and there are rare reports of spinal infections and patients dying from biopsy-related complications.

Indications and Sampling

Biopsy is performed in patients suspected to have significant cancer in whom the results would alter clinical management. Currently for the first biopsy the AUA recommends only TRUS guidance without preceding mpMRI.[153]

The **number of samples and locations** used in prostate biopsy have been controversial. Initially it was thought that only suspicious areas should be sampled. It was quickly discovered, however, that only about 50% of hypoechoic areas contained cancer, and that significant cancer also could be present in normal-appearing areas of the prostate.[131,154] This led to "targeted plus systematic" biopsy. Currently if no lesion is seen, then obtaining 10 to 12 systematic cores is felt to be appropriate on the initial visit (Fig. 10.19). This balances the likelihood of detecting significant cancer while minimizing overdetection of insignificant disease, but also acknowledges that about 20% to 30% of significant cancer could be missed. Further increase in number of systematic cores above 12 to 14 or use of saturation biopsy is felt to be not beneficial, nor does it appear to decrease detection-positive rate at subsequent biopsies. Additional cores should be obtained from suspicious areas that lie outside the systematic pattern.

Indications for Prostate Biopsy

INITIAL BIOPSY

Whenever tissue diagnosis would alter management
Abnormal findings on digital rectal examination
Unexplained PSA elevation
Abnormal findings on transrectal ultrasound
Excessive PSA velocity
Positive chips at transurethral resection of prostate
Metastatic adenocarcinoma when primary is not evident
Approved research

REPEAT BIOPSY

Initial biopsy is negative but there is continued clinical suspicion
Initial suspicious histology (high-volume HG-PIN, ASAP, microscopic cancer)
PSA level greater than 10 ng/mL or rising
Follow-up of men under active surveillance
Evaluation for recurrence after therapy
Approved research

ASAP, Atypical small acinar proliferation; *HG-PIN,* high-grade prostate intraepithelial neoplasia; *PSA,* prostate-specific antigen.

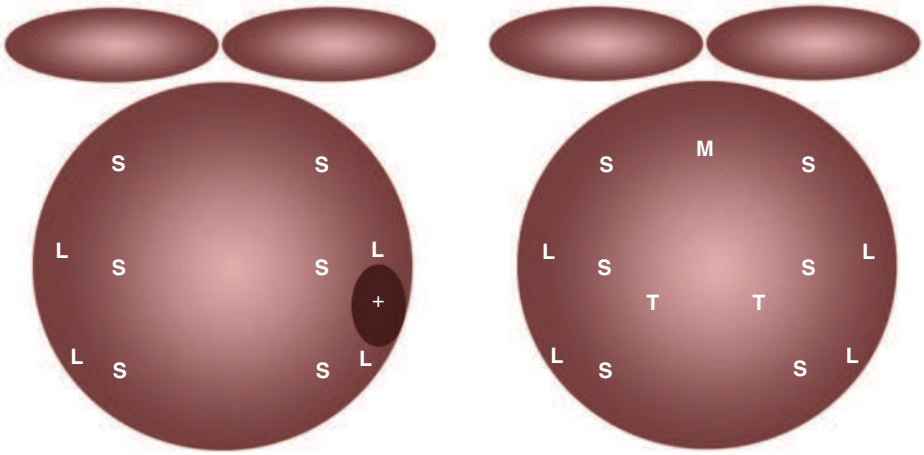

FIG. 10.19 Biopsy Sites as Viewed en Face From Posterior Aspect of Prostate. Left image shows the standard 10 prostate biopsy sites. Additional samples are taken of any lesion that is evident outside the systematic pattern (+). Right image shows a typical extended pattern of biopsies, in this case a 13-core pattern. In addition to the sextant sites *(S)*, samples are taken from the lateral peripheral zones *(L)*, deep in the anterior transition zone *(T)*, and from the peripheral zone in the midline *(M)* at the base, cephalad to the verumontanum. *L*, lateral or "anterior horn"; *S*, sextant.

Systematic samples are obtained from the peripheral zone at the base, middle, and apex of the gland both medially and laterally from each lobe.[25,26,135,142,143] Some term this patterned approach as "random biopsy" or "blind biopsy." It is neither random nor blind, but rather sampling follows a specific systematic pattern along with a search for suspicious targets. It is important that the lateral samples include the "anterior horns" (part of peripheral zone that curves anteriorly around the sides of the transition zone) and the apical peripheral zone. Others have found that both medial and lateral samples are equally important, and that it remains important to search for hypoechoic nodules.[153,155] This approach should result in an overall 30% to 60% positive biopsy rate, and about a 60% or higher yield for lesions that are suspicious at ultrasound.[135] Although TRUS biopsy is the established and currently recommended procedure for the *initial* biopsy because of its simplicity and cost-effectiveness, there is emerging enthusiasm to consider mpMRI before the first biopsy.[156,157] Optimistic reports from a highly experienced luminary center in biopsy-naïve patients showed overall cancer detection with TRUS of 57%, with 37% being low grade. In contrast, mpMRI in bore biopsy yielded 70% cancer, of which only 6% was low grade. By relying on mpMRI findings, these researchers estimated a decrease in biopsy rate of 51% and an 81% decrease in low-risk cancer detection. Nonetheless, follow-up of negative biopsy was still recommended.[158] Reviews of published reports find little difference between TRUS and MRI for initial biopsy and suggest that, currently, systematic TRUS biopsy may suffice for first biopsy and that there is still need for research and training before restricting biopsy only to mpMRI targets because systematic TRUS biopsy detects significant cancer in about 12% of men with negative mpMRI findings.[159]

About 20% to 30% of men with initial negative biopsy have cancer that was missed. The box lists indications for repeat or additional biopsy. Following negative initial biopsy, some have suggested that after four negative repeat sessions the yield is only 4%, but others find a continued cancer yield of about 15% on each repeat.

Timing of the repeat biopsy varies with clinical indications and pathologic findings at initial biopsy. In low-risk cancer patients opting for active surveillance, an initial confirmatory repeat is suggested in 3 to 18 months and then follow-up as per local protocols. Atypical small acinar proliferation (ASAP) is found in about 4% (1%-23%) of biopsies. Many pathologists believe that ASAP is a minute cancer focus and may represent either a tiny tumor or possibly a few cells from the margin of a larger adjacent tumor. Repeat biopsy is recommended in 3 to 6 months and yields cancer in about 40%. Multifocal high-grade prostate intraepithelial neoplasia (HG-PIN) is found in about 5% (0%-25%). It is a histologic abnormality found in association with cancer but not necessarily leading to cancer. With multifocal HG-PIN, repeat biopsy is suggested in 1 year and cancer yield is about 40%. Repeat biopsy is not recommended for unifocal HG-PIN unless clinical findings are worrisome.[26,142,143]

There is no generally accepted protocol for sample sites at repeat biopsy, but most recommend repeating the systematic 12-core biopsy and adding about four additional transition zone cores (see Fig. 10.19, right).

Most of the cancers will be found in the original systematic sites with only a small contribution from the added transition zone and midline.[114] It is important at repeat to especially evaluate the anterior fibromuscular area, a common site for large missed cancers[133] (see Fig. 10.17H–I). Most would not consider transperineal template biopsy with multiple cores for simple repeat but would consider it for special situations such as staging for focal therapy.[26,142,143,160]

mpMRI-TRUS Fusion Biopsy

mpMRI is emerging for lesion localization before biopsy, especially repeat biopsy. At *initial* biopsy both mpMRI targeted and systematic 12-core approaches have similar cancer detection rates. Targeted

mpMRI approaches require fewer cores to detect significant cancer and avoid detection of many clinically insignificant cancers, but still miss some significant cancer. At time of repeat biopsy following prior negative biopsy, MRI guidance increases overall cancer detection by about 1.62 times over systematic biopsy and should be considered before repeat biopsy.[159-161] mpMRI is especially helpful to search sites that are typically not sampled at systematic 12-core biopsy including the transition zone and anterior fibromuscular area (see Fig. 10.17H–I) Currently there are caveats to mpMRI use, including need for high-quality MRI or expert readers, use of standardized PI-RADS 2 reporting formats, definitions of what constitutes "significant cancer," costs, and access, but developments are occurring rapidly in all these areas.[160,162]

There are several general methods of MRI guidance: cognitive, MRI-TRUS fusion, and in-bore biopsy.[163,164] With **cognitive guidance** the operator reviews the MRI and uses this knowledge to target the same areas at TRUS biopsy. This is the easiest and likely most used approach currently. With **MRI-TRUS fusion** biopsy, the MRI images and targets are co-registered and fused to TRUS images. Biopsy is performed with one of several available tracking and co-registration devices and is slightly more sensitive in detection of significant cancer than the cognitive approach.[161,162,165] With **in-bore** biopsy, the biopsy is carried out in the MRI gantry.

Transperineal Biopsy and Template Biopsy

Transperineal biopsy is considered for two separate reasons: to decrease infections and to provide accurate cancer characterization and mapping for focal therapy and active surveillance. Both can use freehand approaches or use the same template that is used in brachyradiotherapy (see Fig. 10.14). Chang and colleagues have suggested that transperineal biopsy provides more sterile access to the prostate and avoids concerns of increasing antibiotic resistance and sepsis.[145,166]

Before considering active surveillance or focal therapy, some have expressed concern that sampling by conventional biopsy is inadequate to detect and map significant disease. In these cases **transperineal template mapping** or saturation biopsy under general anesthesia is performed, taking samples using the brachytherapy template, which allows 40 to 70 evenly distributed cores taken 5 mm apart (see Fig. 10.19). Compared with conventional TRUS biopsy, cancer detection increases to about 70% from 20% to 40%. Complications are similar to those of TRUS biopsy, but transient urinary retention is seen in up to 39%.[166]

Biopsy After Radical Prostatectomy

Radical prostatectomy should reduce PSA to virtually undetectable levels. Recurrent disease is suspected if the PSA starts rising. In this situation, many urologists just arrange for radiotherapy of the prostate bed and pelvis and do not rely on biopsy. If histologic proof is needed before therapy, TRUS with biopsy can be used to evaluate the anastomotic site and look for local lymphadenopathy and pelvic masses (see Fig. 10.18E). If requested, in such cases we obtain two samples from either side of the anastomosis and perform biopsy of any other abnormal masses and any SV remnants. mpMRI can help identify suspicious areas. Care must be taken not to mistake large pelvic vessels for masses; this can be avoided by using Doppler before biopsy (Fig. 10.20).

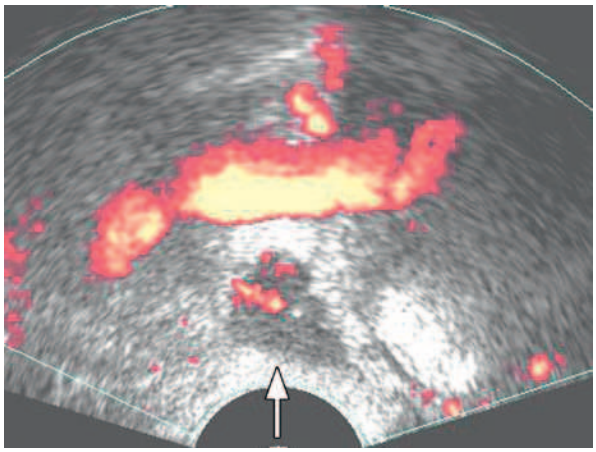

FIG. 10.20 Other Transrectal Ultrasound (TRUS) Applications: Pelvic Mass. Woman with perirectal mass *(arrow)* shown to be recurrent colon cancer by TRUS-guided biopsy. Note the large adjacent vessel. When biopsy is performed outside the prostate, Doppler helps avoid injury to vessels. The transrectal technique is useful for biopsy of any pelvic mass in men or women that can be accessed by the probe.

Biopsy in Men With Absent Anus

Men who have had their anus closed by abdominoperineal resection are difficult to manage when their PSA becomes elevated. Prostate visibility is restricted through both the transabdominal and the transperineal approach. Transperineal ultrasound–guided biopsy with local anesthesia is moderately successful in obtaining prostate tissue. It is helpful to precede the biopsy with mpMRI, which may locate suspicious areas that cannot be seen with ultrasound. Antibiotic prophylaxis and coagulation management is the same as with TRUS biopsy. We scan the patient in the decubitus position just as with regular transrectal biopsy, use the same transrectal probe because of its small size, push it firmly against the perineum, and proceed as with a transrectal biopsy using local skin cleansing. Others scan using the lithotomy position. A Foley catheter with inflated balloon and some fluid in the bladder can help to identify the prostate and to avoid urethral injury. About 20 mL of 1% lidocaine is needed for perineal anesthesia. Both lobes are systematically sampled and extra cores are taken from suspicious regions.[167] Cancer yield is about 30%; others report it as high as 40% to 82%. If ultrasound visibility is very restricted owing to perineal distortion by surgery, then an alternative approach using mpMRI for initial lesion detection followed by CT transsciatic biopsy or in-bore MRI-guided biopsy could be considered.

OTHER APPLICATIONS OF TRANSRECTAL ULTRASOUND AND BIOPSY IN MEN AND WOMEN

In both men and women the transrectal route is useful to evaluate and perform biopsy on any pelvic mass or structure that is within range of the probe and needle. TRUS also provides high-resolution pelvic access in girls and women when transvaginal ultrasound is not possible (see Fig. 10.20).

A few caveats exist. Because of the large vessels in the pelvis, it is important to use Doppler ultrasound to investigate any area where biopsy is contemplated. Remember that pelvic kidneys may mimic pathologic masses. Also, anterior meningoceles may mimic masses behind the rectum and should not be entered because of the risk of infection.

We have performed abscess drainage and biopsies of numerous masses, including ovarian masses, recurrent masses after diverse primary tumor surgery, periureteric masses, bladder masses, and pericolic masses, in both men and women. All these procedures have the same preparation and protocol as the basic prostate biopsy.[11]

In addition, the distal ureters and ureterovesical junctions are readily accessible to evaluation for distal ureteric obstructing lesions, including calculi.

CONCLUSIONS

TRUS has revolutionized prostate assessment and biopsy. TRUS-guided biopsy is currently the standard for prostate biopsy. Concepts regarding all aspects of prostate cancer are rapidly changing and there is rapid emergence of new biomarkers, therapies, and imaging modalities including mpMRI, all of which will facilitate assessment and management of men with prostate cancer.

Transrectal probes provide access to all regional structures in men and women, and TRUS can also help with their management.

REFERENCES

1. Futterer JJ, Heijmink SW, Spermon JR. Imaging the male reproductive tract: current trends and future directions. Radiol Clin North Am. 2008;46(1):133-147, vii.
2. Ghai S, Toi A. Role of transrectal ultrasonography in prostate cancer. Radiol Clin North Am. 2012;50(6):1061-1173.
3. Harvey CJ, Pilcher J, Richenberg J, et al. Applications of transrectal ultrasound in prostate cancer. Br J Radiol. 2012;85(Spec No. 1):S3-S17.
4. Hwang SI, Lee HJ. The future perspectives in transrectal prostate ultrasound guided biopsy. Prostate Int. 2014;2(4):153-160.
5. Penzkofer T, Tempany-Afdhal CM. Prostate cancer detection and diagnosis: the role of MR and its comparison with other diagnostic modalities—a radiologist's perspective. NMR Biomed. 2014;27(1):3-15.
6. Marko J, Gould CF, Bonavia GH, Wolfman DJ. State-of-the-art imaging of prostate cancer. Urol Oncol. 2016;34(3):134-146.
7. Carter HB, Albertsen PC, Barry MJ, et al. Early detection of prostate cancer: AUA guideline. J Urol. 2013;190(2):419-426.
8. Smith RA, Manassaram-Baptiste D, Brooks D, et al. Cancer screening in the United States, 2015: a review of current American Cancer Society guidelines and current issues in cancer screening. CA Cancer J Clin. 2015;65(1):30-54.
9. Berman DM, Epstein JI. When is prostate cancer really cancer? Urol Clin North Am. 2014;41(2):339-346.
10. Klotz L. Active surveillance and focal therapy for low-intermediate risk prostate cancer. Transl Androl Urol. 2015;4(3):342-354.
11. Giede C, Toi A, Chapman W, Rosen B. The use of transrectal ultrasound to biopsy pelvic masses in women. Gynecol Oncol. 2004;95(3):552-556.
12. Lee F, Torp-Pedersen ST, Siders DB, et al. Transrectal ultrasound in the diagnosis and staging of prostatic carcinoma. Radiology. 1989;170(3 Pt 1):609-615.
13. McNeal JE. The zonal anatomy of the prostate. Prostate. 1981;2(1):35-49.
14. Selman SH. The McNeal prostate: a review. Urology. 2011;78(6):1224-1228.
15. Lawrentschuk N, Lindner U, Fleshner N. Current textbooks and anatomy of the prostate—a case for an update. BJU Int. 2009;103(10):1319-1322.
16. Ayala AG, Ro JY, Babaian R, et al. The prostatic capsule: does it exist? Its importance in the staging and treatment of prostatic carcinoma. Am J Surg Pathol. 1989;13(1):21-27.
17. McNeal JE, Redwine EA, Freiha FS, Stamey TA. Zonal distribution of prostatic adenocarcinoma. Correlation with histologic pattern and direction of spread. Am J Surg Pathol. 1988;12(12):897-906.
18. Lee CH, Akin-Olugbade O, Kirschenbaum A. Overview of prostate anatomy, histology, and pathology. Endocrinol Metab Clin North Am. 2011;40(3):565-575, viii-ix.
19. Kutikov A, Guzzo TJ, Malkowicz SB. Clinical approach to the prostate: an update. Radiol Clin North Am. 2006;44(5):649-663, vii.
20. Leventis AK, Shariat SF, Utsunomiya T, Slawin KM. Characteristics of normal prostate vascular anatomy as displayed by power Doppler. Prostate. 2001;46(4):281-288.
21. Costello AJ, Brooks M, Cole OJ. Anatomical studies of the neurovascular bundle and cavernosal nerves. BJU Int. 2004;94(7):1071-1076.
22. Walsh PC. The discovery of the cavernous nerves and development of nerve sparing radical retropubic prostatectomy. J Urol. 2007;177(5):1632-1635.
23. Goldstein A. Pertinent physics of an optimal examination. Prog Clin Biol Res. 1987;237:31-48.
24. Ching CB, Moussa AS, Li J, et al. Does transrectal ultrasound probe configuration really matter? End fire versus side fire probe prostate cancer detection rates. J Urol. 2009;181(5):2077-2082.
25. Bjurlin MA, Wysock JS, Taneja SS. Optimization of prostate biopsy: review of technique and complications. Urol Clin North Am. 2014;41(2):299-313.
26. Ismail MT, Gomella LG. Transrectal prostate biopsy. Urol Clin North Am. 2013;40(4):457-472.
27. Smeenge M, de la Rosette JJ, Wijkstra H. Current status of transrectal ultrasound techniques in prostate cancer. Curr Opin Urol. 2012;22(4):297-302.
28. Zhao HX, Zhu Q, Wang ZC. Detection of prostate cancer with three-dimensional transrectal ultrasound: correlation with biopsy results. Br J Radiol. 2012;85(1014):714-719.
29. Danish Qaseem SM, Ghonge NP, Aggarwal B, Singhal S. Prospective evaluation of prostate with transrectal spectral Doppler with biopsy correlation: a clinicopathologic study. Br J Radiol. 2016;89(1060):20150830.
30. AUA Practice Guidelines Committee. AUA guideline on management of benign prostatic hyperplasia (2003). Chapter 1: Diagnosis and treatment recommendations. J Urol. 2003;170(2 Pt 1):530-547.
31. Lee F, Torp-Pedersen S, Littrup PJ, et al. Hypoechoic lesions of the prostate: clinical relevance of tumor size, digital rectal examination, and prostate-specific antigen. Radiology. 1989;170(1 Pt 1):29-32.
32. Rosenkrantz AB, Taneja SS. Radiologist, be aware: ten pitfalls that confound the interpretation of multiparametric prostate MRI. AJR Am J Roentgenol. 2014;202(1):109-120.
33. Burks DD, Drolshagen LF, Fleischer AC, et al. Transrectal sonography of benign and malignant prostatic lesions. AJR Am J Roentgenol. 1986;146(6):1187-1191.
34. Oyen RH, Van de Voorde WM, Van Poppel HP, et al. Benign hyperplastic nodules that originate in the peripheral zone of the prostate gland. Radiology. 1993;189(3):707-711.
35. Yu J, Fulcher AS, Turner MA, et al. Prostate cancer and its mimics at multiparametric prostate MRI. Br J Radiol. 2014;87(1037):20130659.
36. McVary KT, Roehrborn CG, Avins AL, et al. Update on AUA guideline on the management of benign prostatic hyperplasia. J Urol. 2011;185(5):1793-1803.
37. Pontari MA. Chronic prostatitis/chronic pelvic pain syndrome. Urol Clin North Am. 2008;35(1):81-89, vi.
38. Polackwich AS, Shoskes DA. Chronic prostatitis/chronic pelvic pain syndrome: a review of evaluation and therapy. Prostate Cancer Prostatic Dis. 2016;19(2):132-138.
39. Rothman JR, Jaffe WI. Prostatitis: updates on diagnostic evaluation. Curr Urol Rep. 2007;8(4):301-306.
40. Langer JE, Cornud F. Inflammatory disorders of the prostate and the distal genital tract. Radiol Clin North Am. 2006;44(5):665-677, vii.

41. Pontari MA. Etiologic theories of chronic prostatitis/chronic pelvic pain syndrome. Curr Urol Rep. 2007;8(4):307-312.
42. Galosi AB, Montironi R, Fabiani A, et al. Cystic lesions of the prostate gland: an ultrasound classification with pathological correlation. J Urol. 2009;181(2):647-657.
43. Nghiem HT, Kellman GM, Sandberg SA, Craig BM. Cystic lesions of the prostate. Radiographics. 1990;10(4):635-650.
44. Curran S, Akin O, Agildere AM, et al. Endorectal MRI of prostatic and periprostatic cystic lesions and their mimics. AJR Am J Roentgenol. 2007;188(5):1373-1379.
45. Kim B, Kawashima A, Ryu JA, et al. Imaging of the seminal vesicle and vas deferens. Radiographics. 2009;29(4):1105-1121.
46. Reddy MN, Verma S. Lesions of the seminal vesicles and their MRI characteristics. J Clin Imaging Sci. 2014;4:61.
47. Patel B, Gujral S, Jefferson K, et al. Seminal vesicle cysts and associated anomalies. BJU Int. 2002;90(3):265-271.
48. Jarow J, Sigman M, Kolettis PN, et al. The Optimal Evaluation of the Infertile Male: Best Practice Statement Reviewed and validity confirmed 2011. Cited 24 April 2016. Available from: https://www.auanet.org/education/guidelines/male-infertility-d.cfm.
49. Jungwirth A, Giwercman A, Tournaye H, et al. European Association of Urology guidelines on male infertility: the 2012 update. Eur Urol. 2012;62(2):324-332.
50. Smith JF, Walsh TJ, Turek PJ. Ejaculatory duct obstruction. Urol Clin North Am. 2008;35(2):221-227, viii.
51. Fedder J, Cruger D, Oestergaard B, Petersen GB. Etiology of azoospermia in 100 consecutive nonvasectomized men. Fertil Steril. 2004;82(5):1463-1465.
52. Ammar T, Sidhu PS, Wilkins CJ. Male infertility: the role of imaging in diagnosis and management. Br J Radiol. 2012;85(Spec No. 1):S59-S68.
53. Jhaveri KS, Mazrani W, Chawla TP, et al. The role of cross-sectional imaging in male infertility: a pictorial review. Can Assoc Radiol J. 2010;61(3):144-155.
54. Akhter W, Khan F, Chinegwundoh F. Should every patient with hematospermia be investigated? A critical review. Cent European J Urol. 2013;66(1):79-82.
55. Aslam MI, Cheetham P, Miller MA. A management algorithm for hematospermia. Nat Rev Urol. 2009;6(7):398-402.
56. Prando A. Endorectal magnetic resonance imaging in persistent hematospermia. Int Braz J Urol. 2008;34(2):171-179.
57. Siegel RL, Miller KD, Jemal A. Cancer statistics, 2016. CA Cancer J Clin. 2016;66(1):7-30.
58. Tabayoyong W, Abouassaly R. Prostate cancer screening and the associated controversy. Surg Clin North Am. 2015;95(5):1023-1039.
59. Pierorazio PM, Walsh PC, Partin AW, Epstein JI. Prognostic Gleason grade grouping: data based on the modified Gleason scoring system. BJU Int. 2013;111(5):753-760.
60. Carlsson S, Leapman M, Carroll P, et al. Who and when should we screen for prostate cancer? Interviews with key opinion leaders. BMC Med. 2015;13:288.
61. Cotter K, Konety B, Ordonez MA. Contemporary management of prostate cancer. F1000Res. 2016;5.
62. Agency for Healthcare Research and Quality (AHRQ). Therapies for clinically localized prostate cancer. Comparative effectiveness review summary guides for clinicians. AHRQ Comparative Effectiveness Reviews. Rockville, MD: Agency for Healthcare Research and Quality; 2016.
63. Wilt TJ, MacDonald R, Rutks I, et al. Systematic review: comparative effectiveness and harms of treatments for clinically localized prostate cancer. Ann Intern Med. 2008;148(6):435-448.
64. Albertsen PC, Hanley JA, Fine J. 20-year outcomes following conservative management of clinically localized prostate cancer. JAMA. 2005;293(17):2095-2101.
65. Zlotta AR, Egawa S, Pushkar D, et al. Prevalence of prostate cancer on autopsy: cross-sectional study on unscreened Caucasian and Asian men. J Natl Cancer Inst. 2013;105(14):1050-1058.
66. Sanda MG, Dunn RL, Michalski J, et al. Quality of life and satisfaction with outcome among prostate-cancer survivors. N Engl J Med. 2008;358(12):1250-1261.
67. Nam RK, Jewett MA, Krahn MD. Prostate cancer: 2. Natural history. CMAJ. 1998;159(6):685-691.
68. Catalona WJ, Smith DS, Ratliff TL, et al. Measurement of prostate-specific antigen in serum as a screening test for prostate cancer. N Engl J Med. 1991;324(17):1156-1161.
69. Stephenson AJ, Klein E. Epidemiology, etiology, and prevention of prostate cancer. 11th ed. Philadelphia, PA: Elsevier; 2016.
70. Bostwick DG, Burke HB, Djakiew D, et al. Human prostate cancer risk factors. Cancer. 2004;101(10 Suppl.):2371-2490.
71. Bratt O. Hereditary prostate cancer: clinical aspects. J Urol. 2002;168(3):906-913.
72. Chang JM, Lee HJ, Lee SE, et al. Pictorial review: unusual tumours involving the prostate: radiological-pathological findings. Br J Radiol. 2008;81(971):907-915.
73. Eggener SE, Badani K, Barocas DA, et al. Gleason 6 prostate cancer: translating biology into population health. J Urol. 2015;194(3):626-634.
74. Crawford ED, Ventii K, Shore ND. New biomarkers in prostate cancer. Oncology (Williston Park). 2014;28(2):135-142.
75. Saini S. PSA and beyond: alternative prostate cancer biomarkers. Cell Oncol (Dordr). 2016;39(2):97-106.
76. Morgan T, Palapattu G, Wei J. Screening for Prostate cancer—beyond total PSA, utilization of novel biomarkers. Curr Urol Rep. 2015;16(9):63.
77. Leapman MS, Nguyen HG, Cooperberg MR. Clinical utility of biomarkers in localized prostate cancer. Curr Oncol Rep. 2016;18(5):30.
78. Catalona WJ, Partin AW, Slawin KM, et al. Use of the percentage of free prostate-specific antigen to enhance differentiation of prostate cancer from benign prostatic disease: a prospective multicenter clinical trial. JAMA. 1998;279(19):1542-1547.
79. Elliott CS, Shinghal R, Presti Jr JC. The performance of prostate specific antigen, prostate specific antigen density and transition zone density in the era of extended biopsy schemes. J Urol. 2008;179(5):1756-1761.
80. Morash C. PSA density: The comeback kid? Can Urol Assoc J. 2012;6(1):51-52.
81. Carter HB, Pearson JD, Metter EJ, et al. Longitudinal evaluation of prostate-specific antigen levels in men with and without prostate disease. JAMA. 1992;267(16):2215-2220.
82. Iremashvili V, Kava BR, Manoharan M, et al. Is it time to revisit the role of prostate-specific antigen kinetics in active surveillance for prostate cancer? Urology. 2016;95:139-144.
83. Eggener S. Prostate cancer screening biomarkers: an emerging embarrassment of 'riches'? Eur Urol. 2016;70(1):54-55.
84. Stephan C, Ralla B, Jung K. Prostate-specific antigen and other serum and urine markers in prostate cancer. Biochim Biophys Acta. 2014;1846(1):99-112.
85. Filella X, Foj L. Emerging biomarkers in the detection and prognosis of prostate cancer. Clin Chem Lab Med. 2015;53(7):963-973.
86. Foley RW, Maweni RM, Gorman L, et al. The ERSPC risk calculators significantly outperform the PCPT 2.0 in the prediction of prostate cancer; a multi-institutional study. BJU Int. 2016 Feb 2. [Epub ahead of print].
87. Trottier G, Roobol MJ, Lawrentschuk N, et al. Comparison of risk calculators from the Prostate Cancer Prevention Trial and the European Randomized Study of Screening for Prostate Cancer in a contemporary Canadian cohort. BJU Int. 2011;108(8 Pt 2):E237-E244.
88. Shieh Y, Eklund M, Sawaya GF, et al. Population-based screening for cancer: hope and hype. Nat Rev Clin Oncol. 2016;13(9):550-565.
89. Heintz E, Hultcrantz M, Mejare I, et al. Limited evidence for the use of imaging to detect prostate cancer: a systematic review. Eur J Radiol. 2014;83(9):1601-1606.
90. Bjurlin MA, Rosenkrantz AB, Beltran LS, et al. Imaging and evaluation of patients with high-risk prostate cancer. Nat Rev Urol. 2015;12(11):617-628.
91. Sarkar S, Das S. A review of imaging methods for prostate cancer detection. Biomed Eng Comput Biol. 2016;7(Suppl. 1):1-15.
92. Wibmer AG, Burger IA, Sala E, et al. Molecular imaging of prostate cancer. Radiographics. 2016;36(1):142-159.
93. Babaian RJ, Mettlin C, Kane R, et al. The relationship of prostate-specific antigen to digital rectal examination and transrectal ultrasonography. Findings of the American Cancer Society National Prostate Cancer Detection Project. Cancer. 1992;69(5):1195-1200.

94. Etzioni R, Tsodikov A, Mariotto A, et al. Quantifying the role of PSA screening in the US prostate cancer mortality decline. Cancer Causes Control. 2008;19(2):175-181.
95. Alberts AR, Schoots IG, Roobol MJ. Prostate-specific antigen-based prostate cancer screening: past and future. Int J Urol. 2015;22(6):524-532.
96. Moyer VA, U.S. Preventive Services Task Force. Screening for prostate cancer: U.S. Preventive Services Task Force recommendation statement. Ann Intern Med. 2012;157(2):120-134.
97. Schroder FH, Hugosson J, Roobol MJ, et al. Screening and prostate cancer mortality: results of the European Randomised Study of Screening for Prostate Cancer (ERSPC) at 13 years of follow-up. Lancet. 2014;384(9959): 2027-2035.
98. Andriole GL, Crawford ED, Grubb 3rd RL, et al. Prostate cancer screening in the randomized Prostate, Lung, Colorectal, and Ovarian Cancer Screening Trial: mortality results after 13 years of follow-up. J Natl Cancer Inst. 2012;104(2):125-132.
99. Hugosson J, Carlsson S, Aus G, et al. Mortality results from the Göteborg randomised population-based prostate-cancer screening trial. Lancet Oncol. 2010;11(8):725-732.
100. Herget KA, Patel DP, Hanson HA, et al. Recent decline in prostate cancer incidence in the United States, by age, stage, and Gleason score. Cancer Med. 2016;5(1):136-141.
101. Barry MJ, Nelson JB. Patients present with more advanced prostate cancer since the USPSTF screening recommendations. J Urol. 2015;194(6): 1534-1536.
102. Kim EH, Andriole GL. Prostate-specific antigen-based screening: controversy and guidelines. BMC Med. 2015;13:61.
103. American Joint Committee on Cancer. Prostate cancer staging: American Joint Committee on Cancer; 2010. Cited 21 May 2016. 7. Available from: https://cancerstaging.org/references-tools/quickreferences/Documents/ProstateSmall.pdf.
104. Crawford ED, Stone NN, Yu EY, et al. Challenges and recommendations for early identification of metastatic disease in prostate cancer. Urology. 2014;83(3):664-669.
105. Wollin DA, Makarov DV. Guideline of guidelines: imaging of localized prostate cancer. BJU Int. 2015;116(4):526-530.
106. Cheng L, Montironi R, Bostwick DG, et al. Staging of prostate cancer. Histopathology. 2012;60(1):87-117.
107. Jung AJ, Coakley FV, Shinohara K, et al. Local staging of prostate cancer: comparative accuracy of T2-weighted endorectal MR imaging and transrectal ultrasound. Clin Imaging. 2012;36(5):547-552.
108. Eisenberg ML, Cowan JE, Davies BJ, et al. The importance of tumor palpability and transrectal ultrasonographic appearance in the contemporary clinical staging of prostate cancer. Urol Oncol. 2011;29(2):171-176.
109. Hsu CY, Joniau S, Oyen R, et al. Transrectal ultrasound in the staging of clinical T3a prostate cancer. Eur J Surg Oncol. 2007;33(1):79-82.
110. Kattan MW, Cuzick J, Fisher G, et al. Nomogram incorporating PSA level to predict cancer-specific survival for men with clinically localized prostate cancer managed without curative intent. Cancer. 2008;112(1): 69-74.
111. Makarov DV, Trock BJ, Humphreys EB, et al. Updated nomogram to predict pathologic stage of prostate cancer given prostate-specific antigen level, clinical stage, and biopsy Gleason score (Partin tables) based on cases from 2000 to 2005. Urology. 2007;69:1095-1101.
112. Andreou A, Whitten C, MacVicar D, et al. Imaging appearance of sarcomas of the prostate. Cancer Imaging. 2013;13:228-237.
113. Epstein JI, Egevad L, Amin MB, et al. The 2014 International Society of Urological Pathology (ISUP) Consensus Conference on Gleason Grading of Prostatic Carcinoma: definition of grading patterns and proposal for a new grading system. Am J Surg Pathol. 2016;40(2):244-252.
114. Babaian RJ, Toi A, Kamoi K, et al. A comparative analysis of sextant and an extended 11-core multisite directed biopsy strategy. J Urol. 2000;163(1):152-157.
115. Klotz L. Active surveillance for low-risk prostate cancer. Curr Urol Rep. 2015;16(4):24.
116. Bruinsma SM, Bangma CH, Carroll PR, et al. Active surveillance for prostate cancer: a narrative review of clinical guidelines. Nat Rev Urol. 2016; 13(3):151-167.
117. Epstein JI, Walsh PC, Carmichael M, Brendler CB. Pathologic and clinical findings to predict tumor extent of nonpalpable (stage T1c) prostate cancer. JAMA. 1994;271(5):368-374.
118. D'Amico AV, Whittington R, Malkowicz SB, et al. Biochemical outcome after radical prostatectomy, external beam radiation therapy, or interstitial radiation therapy for clinically localized prostate cancer. JAMA. 1998;280(11):969-974.
119. Ondracek RP, Kattan MW, Murekeyisoni C. Validation of the Kattan normogram for prostate cancer recurrence after radical prostatectomy. J Natl Compr Canc Netw. 2016;14(11):1395-1401.
120. Cooperberg MR, Freedland SJ, Pasta DJ, et al. Multiinstitutional validation of the UCSF cancer of the prostate risk assessment for prediction of recurrence after radical prostatectomy. Cancer. 2006;107(10):2384-2391.
121. Thompson I, Thrasher JB, Aus G, et al. Guideline for the management of clinically localized prostate cancer: 2007 update. J Urol. 2007;177(6): 2106-2131.
122. Sanda MG, Kaplan ID. A 64-year-old man with low-risk prostate cancer: review of prostate cancer treatment. JAMA. 2009;301(20):2141-2151.
123. van der Poel H, Klotz L, Andriole G, et al. Role of active surveillance and focal therapy in low- and intermediate-risk prostate cancers. World J Urol. 2015;33(7):907-916.
124. Bill-Axelson A, Holmberg L, Ruutu M, et al. Radical prostatectomy versus watchful waiting in early prostate cancer. N Engl J Med. 2005;352(19): 1977-1984.
125. Scarpato KR, Barocas DA. Use of mpMRI in active surveillance for localized prostate cancer. Urol Oncol. 2016;34(7):320-325.
126. Lee F, Gray JM, McLeary RD, et al. Transrectal ultrasound in the diagnosis of prostate cancer: location, echogenicity, histopathology, and staging. Prostate. 1985;7(2):117-129.
127. Shinohara K, Scardino PT, Carter SS, Wheeler TM. Pathologic basis of the sonographic appearance of the normal and malignant prostate. Urol Clin North Am. 1989;16(4):675-691.
128. Engelbrecht MR, Barentsz JO, Jager GJ, et al. Prostate cancer staging using imaging. BJU Int. 2000;86(Suppl. 1):123-134.
129. Shinohara K, Wheeler TM, Scardino PT. The appearance of prostate cancer on transrectal ultrasonography: correlation of imaging and pathological examinations. J Urol. 1989;142(1):76-82.
130. Lee HY, Lee HJ, Byun SS, et al. Classification of focal prostatic lesions on transrectal ultrasound (TRUS) and the accuracy of TRUS to diagnose prostate cancer. Korean J Radiol. 2009;10(3):244-251.
131. Dyke CH, Toi A, Sweet JM. Value of random US-guided transrectal prostate biopsy. Radiology. 1990;176(2):345-349.
132. Engelbrecht MR, Jager GJ, Laheij RJ, et al. Local staging of prostate cancer using magnetic resonance imaging: a meta-analysis. Eur Radiol. 2002;12(9): 2294-2302.
133. Lawrentschuk N, Haider MA, Daljeet N, et al. 'Prostatic evasive anterior tumours': the role of magnetic resonance imaging. BJU Int. 2010;105(9): 1231-1236.
134. Noh TI, Shin YS, Shim JS, et al. Are hypoechoic lesions on transrectal ultrasonography a marker for clinically significant prostate cancer? Korean J Urol. 2013;54(10):666-670.
135. Toi A, Neill MG, Lockwood GA, et al. The continuing importance of transrectal ultrasound identification of prostatic lesions. J Urol. 2007;177(2):516-520.
136. Ghai S, Eure G, Fradet V, et al. Assessing cancer risk in novel 29 MHz micro-ultrasound images of the prostate: creation of the protocol of prostate risk identification using micro-ultrasound. J Urol. 2016;196(2):562-569.
137. Amiel GE, Slawin KM. Newer modalities of ultrasound imaging and treatment of the prostate. Urol Clin North Am. 2006;33(3):329-337.
138. Mitterberger M, Pinggera GM, Pallwein L, et al. The value of three-dimensional transrectal ultrasonography in staging prostate cancer. BJU Int. 2007;100(1):47-50.
139. Wijkstra H, Wink MH, de la Rosette JJ. Contrast specific imaging in the detection and localization of prostate cancer. World J Urol. 2004;22(5): 346-350.
140. Li Y, Tang J, Fei X, Gao Y. Diagnostic performance of contrast enhanced ultrasound in patients with prostate cancer: a meta-analysis. Acad Radiol. 2013;20(2):156-164.

141. Salomon G, Schiffmann J. Real-time elastography for the detection of prostate cancer. Curr Urol Rep. 2014;15(3):392.
142. Scattoni V, Maccagnano C, Capitanio U, et al. Random biopsy: when, how many and where to take the cores? World J Urol. 2014;32(4):859-869.
143. Ukimura O, Coleman JA, de la Taille A, et al. Contemporary role of systematic prostate biopsies: indications, techniques, and implications for patient care. Eur Urol. 2013;63(2):214-230.
144. Nishimura RA, Carabello BA, Faxon DP, et al. ACC/AHA 2008 guideline update on valvular heart disease: focused update on infective endocarditis: a report of the American College of Cardiology/American Heart Association Task Force on Practice Guidelines endorsed by the Society of Cardiovascular Anesthesiologists, Society for Cardiovascular Angiography and Interventions, and Society of Thoracic Surgeons. J Am Coll Cardiol. 2008;52(8):676-685.
145. Chang DT, Challacombe B, Lawrentschuk N. Transperineal biopsy of the prostate—is this the future? Nat Rev Urol. 2013;10(12):690-702.
146. Averch T, Tessier T, Clemens JC, Franks M. AUA Quality Improvement Summit 2014: Conference proceedings on infectious complications of transrectal needle biopsy. AUA; 2014. Cited 4 June 2016. Available from: https://www.auanet.org/common/pdf/practices-resources/quality/white-papers/QI-Summit.pdf.
147. Cussans A, Somani BK, Basarab A, Dudderidge TJ. The role of targeted prophylactic antimicrobial therapy before transrectal ultrasonography-guided prostate biopsy in reducing infection rates: a systematic review. BJU Int. 2016;117(5):725-731.
148. Liss MA, Ehdie B, Loeb S, Meng MV. AUA White Paper: The prevention and treatment of the more common complications related to prostate biopsy update. AUA; 2016. Updated 2016; cited 4 June 2016. Available from: https://www.auanet.org/common/pdf/education/clinical-guidance/AUA-PNB-White-Paper.pdf.
149. Lee C, Woo HH. Current methods of analgesia for transrectal ultrasonography (TRUS)–guided prostate biopsy—a systematic review. BJU Int. 2014;113(Suppl. 2):48-56.
150. Nazir B. Pain during transrectal ultrasound-guided prostate biopsy and the role of periprostatic nerve block: what radiologists should know. Korean J Radiol. 2014;15(5):543-553.
151. Culkin DJ, Exaire EJ, Green D, et al. Anticoagulation and antiplatelet therapy in urological practice: ICUD/AUA review paper. J Urol. 2014;192(4):1026-1034.
152. Patel IJ, Davidson JC, Nikolic B, et al. Addendum of newer anticoagulants to the SIR consensus guideline. J Vasc Interv Radiol. 2013;24(5):641-645.
153. Taneja SS, Bjurlin MA, Carter B, Cookson MS. AUA White Paper: Optimal techniques of prostate biopsy and specimen handling. AUA; 2015. Updated 2015; cited 4 June 2016. [AUA guideline for biopsy]. Available from: www.White Paper: AUA/Optimal Techniques of Prostate Biopsy and Specimen Handling.pdf.
154. Hodge KK, McNeal JE, Terris MK, Stamey TA. Random systematic versus directed ultrasound guided transrectal core biopsies of the prostate. J Urol. 1989;142(1):71-74.
155. Neill MG, Toi A, Lockwood GA, et al. Systematic lateral prostate biopsy—are the benefits worth the costs? J Urol. 2008;179(4):1321-1326.
156. Kim CK. Magnetic resonance imaging-guided prostate biopsy: present and future. Korean J Radiol. 2015;16(1):90-98.
157. Murphy G, Haider M, Ghai S, Sreeharsha B. The expanding role of MRI in prostate cancer. AJR Am J Roentgenol. 2013;201(6):1229-1238.
158. Pokorny MR, de Rooij M, Duncan E, et al. Prospective study of diagnostic accuracy comparing prostate cancer detection by transrectal ultrasound-guided biopsy versus magnetic resonance (MR) imaging with subsequent MR-guided biopsy in men without previous prostate biopsies. Eur Urol. 2014;66(1):22-29.
159. Schoots IG, Roobol MJ, Nieboer D, et al. Magnetic resonance imaging–targeted biopsy may enhance the diagnostic accuracy of significant prostate cancer detection compared to standard transrectal ultrasound-guided biopsy: a systematic review and meta-analysis. Eur Urol. 2015;68(3):438-450.
160. Rosenkrantz AB, Taneja SS. Prostate MRI and MRI-targeted biopsy in patients with prior negative biopsy. AUA and SAR joint consensus statement: AUA, SAR; 2016. Cited 4 June 2016. Available from: https://www.auanet.org/common/pdf/education/clinical-guidance/Consensus-Statement-Prostate-MRI-and-MRI-Targeted-Biopsy.pdf.
161. Gayet M, van der Aa A, Beerlage HP, et al. The value of magnetic resonance imaging and ultrasonography (MRI/US)–fusion biopsy platforms in prostate cancer detection: a systematic review. BJU Int. 2016;117(3):392-400.
162. Valerio M, Donaldson I, Emberton M, et al. Detection of clinically significant prostate cancer using magnetic resonance imaging–ultrasound fusion targeted biopsy: a systematic review. Eur Urol. 2015;68(1):8-19.
163. Costa DN, Pedrosa I, Donato Jr F, et al. MR imaging–transrectal US fusion for targeted prostate biopsies: implications for diagnosis and clinical management. Radiographics. 2015;35(3):696-708.
164. Stephenson SK, Chang EK, Marks LS. Screening and detection advances in magnetic resonance image–guided prostate biopsy. Urol Clin North Am. 2014;41(2):315-326.
165. Logan JK, Rais-Bahrami S, Turkbey B, et al. Current status of magnetic resonance imaging (MRI) and ultrasonography fusion software platforms for guidance of prostate biopsies. BJU Int. 2014;114(5):641-652.
166. Sivaraman A, Sanchez-Salas R, Barret E, et al. Transperineal template-guided mapping biopsy of the prostate. Int J Urol. 2015;22(2):146-151.
167. Shinohara K, Gulati M, Koppie T, Terris MK. Transperineal prostate biopsy after abdominoperineal resection. J Urol. 2003;169(1):141-144.

CHAPTER 11

The Adrenal Glands

Christina Marie Chingkoe, Olga R. Brook, and Deborah Levine

SUMMARY KEY POINTS

- The adrenal glands are responsible for maintaining homeostasis and regulating hormonal production and secretion within the body.
- The adrenal cortex is comprised of the zona glomerulosa, fasciculata, and reticularis, which are responsible for aldosterone, glucocorticoid, and androgen regulation, respectively. The adrenal medulla regulates catecholamines.
- Sonographic visualization of the right adrenal gland is best through a transverse oblique and coronal view, using the liver as an acoustic window. Sonographic visualization of the left adrenal gland is best along the posterior axillary line through an oblique coronal view, using either the spleen or the left kidney as an acoustic window.
- Adrenal lesions can be localized via dynamic scanning: adrenal glands are fixed relative to the great vessels and move independently from the kidneys during deep inspiration and upright positioning.
- Benign adrenal masses include adenomas (which may be functional or nonfunctional), myelolipomas, pheochromocytomas, cysts, hemorrhage, and postinfectious calcifications.
- Malignant adrenal masses include adrenocortical carcinoma, metastases (most often from lung or breast primary), and lymphoma.
- Ultrasound guidance can be used for percutaneous or transhepatic biopsies, as well as for interventions including radiofrequency, cryotherapy, or chemical ablation.

CHAPTER OUTLINE

ANATOMY AND PHYSIOLOGY
SONOGRAPHIC IMAGING AND SCANNING TECHNIQUE
BENIGN ADRENAL MASSES
Adrenal Adenomas
Sonographic Features
Myelolipomas
Sonographic Features
Pheochromocytomas
Sonographic Features
Adrenal Cysts
Sonographic Features
Adrenal Hemorrhage
Sonographic Features
Infectious and Inflammatory Masses
Sonographic Features
MALIGNANT ADRENAL MASSES
Adrenocortical Carcinomas
Sonographic Features
Metastases
Sonographic Features
Lymphoma
Sonographic Features
RARE ADRENAL MASSES
MANAGEMENT OF ADRENAL LESIONS
INTERVENTIONS
Ultrasound-Guided Biopsy and Interventions
Endoscopic Ultrasound
Intraoperative Ultrasound
Acknowledgments

The adrenal glands are the smallest paired organs in the abdomen, measuring approximately 4 to 6 cm in length, 2 to 3 cm in width, and 0.2 to 0.6 cm in thickness, equivalent to 4 g.[1,2] In spite of their size, the adrenal glands are responsible for maintaining homeostasis and regulating hormonal production and secretion within the body. The mainstay of adrenal gland imaging is computed tomography (CT) because of its wide availability, ease of anatomic visibility, and ability for lesion characterization. However, adrenal lesions can be identified during sonographic evaluation of the abdomen, and because abdominal sonography is a common examination, these lesions are relatively frequently found on sonography. It is therefore important for the radiologist to have a thorough understanding of the role that ultrasound can play in adrenal gland imaging, including the diagnosis and management of lesions.

ANATOMY AND PHYSIOLOGY

The adrenal glands are located in the perirenal space, superior to the kidneys, at the level of the 11th or 12th thoracic rib, lateral to the first lumbar vertebra. The adrenal glands are comprised of a **superoanteromedial ridge,** an often larger and more superiorly located medial limb, as well as a smaller more inferiorly located lateral limb. Although the shape of the adrenal glands can vary, the thickness of the limbs, particularly the lateral limbs, remain relatively constant and therefore are the most useful

indicators of **gland hypertrophy.**[2] They are supplied by the suprarenal arteries comprised of the superior suprarenal artery, which arises from the inferior phrenic artery; the middle suprarenal artery, arising from the abdominal aorta; and the inferior suprarenal artery, arising from the main renal artery. They are drained by the suprarenal veins, which empty into the inferior vena cava on the right and the left renal vein or the left inferior phrenic vein on the left side (Figs. 11.1 and 11.2).

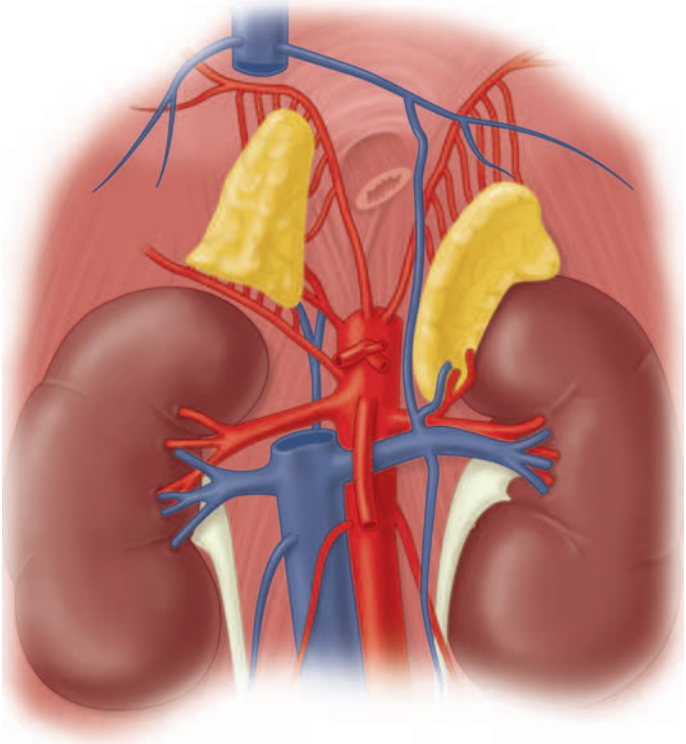

FIG. 11.1 Anatomy and Blood Supply of the Adrenal Glands.

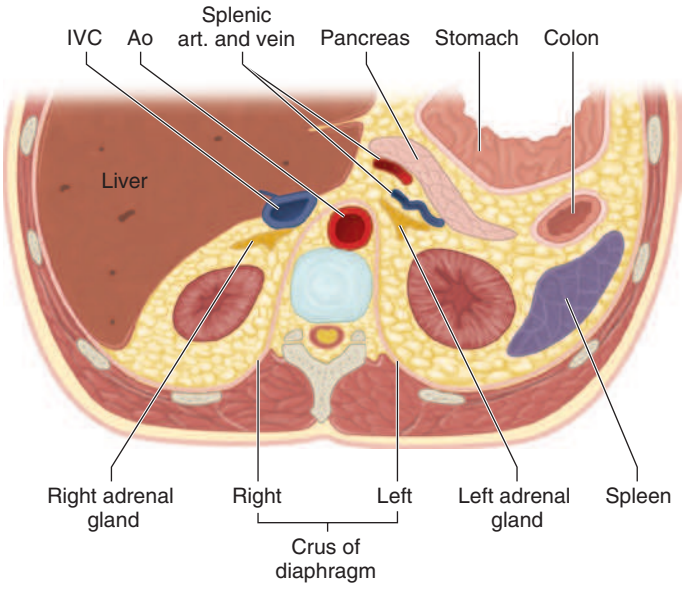

FIG. 11.2 Cross-Sectional Anatomy of the Adrenal Glands. *Ao,* Aorta; *art.,* artery; *IVC,* inferior vena cava.

The adrenal glands can be divided into the cortex and medulla, with each part derived from different embryologic origins, thereby accounting for differences in function. The **adrenal cortex** originates from mesenchymal cells of the posterior abdominal peritoneal lining. Between the sixth and eighth week of gestation, the mesenchymal cells proliferate, invaginate into the retroperitoneum, and then further proliferate, forming three distinct layers within the cortex: the zona glomerulosa, zona fasciculata, and zona reticularis from peripheral to central, respectively. The **zona glomerulosa** is responsible for aldosterone production and secretion, which subsequently influences sodium retention at the level of the renal tubules to regulate intravascular fluid volume and pressure. The **zona fasciculata** secretes glucocorticosteroids, including cortisol, to regulate stress and inflammatory responses. **The zona reticularis** is involved in androgen secretion and regulation. The adrenal cortex in a nonstressed adult secretes about 20 mg of cortisol daily and with stressful stimuli may increase secretion up to 150 to 200 mg/day. The physiologic importance of the adrenal androgens is not known. In excess, androgens may cause hirsutism or virilization in females and precocious pseudopuberty in males.[3]

The **adrenal medulla** originates from neuroectodermal cells, which become enveloped by the adrenal cortex during the seventh week of gestation, and differentiate into chromaffin cells.[4] These are responsible for the synthesis and secretion of the catecholamines epinephrine and norepinephrine, to regulate the body's sympathetic responses. These hormones play an important role in the response to actual or anticipated stress but are not essential to life.[3]

SONOGRAPHIC IMAGING AND SCANNING TECHNIQUE

Sonography remains widely used in abdominal imaging, and normal adrenal glands can be visualized with careful scanning. However, sonographic visualization of the adrenal glands can be difficult, given their location deep to the ribs and on the left side, posterior to stomach. Marchal et al. reported that the normal right and left adrenal glands were visualized by high-resolution real-time sonography in 92% and 71% of patients, respectively.[5] Cortex and medulla were differentiated in 13% of patients. However, Günther et al. studied 60 healthy subjects with high-resolution real-time sonography and identified adrenal glands in only one thin female.[6] In newborn infants, real-time high-frequency scanning identified the right and left adrenal glands in 97% and 83% of patients, respectively.[7] In a study of 882 patients and 991 adrenal masses, Fan et al. noted the sensitivity, specificity, and accuracy of ultrasound diagnoses of benign versus malignant adrenal masses to be 89%, 99%, and 93%, respectively, with a positive predictive value of 90.9% and a negative predictive value of 94.2%.[8]

With the introduction of high-resolution, real-time sector scanners, the adrenal glands have become easier to examine. Ideally, the patient should fast for 6 to 8 hours before the examination to reduce the amount of intervening bowel gas.

The key to the identification of the adrenals is to remember they lie anterior to the upper pole of the kidneys. The right

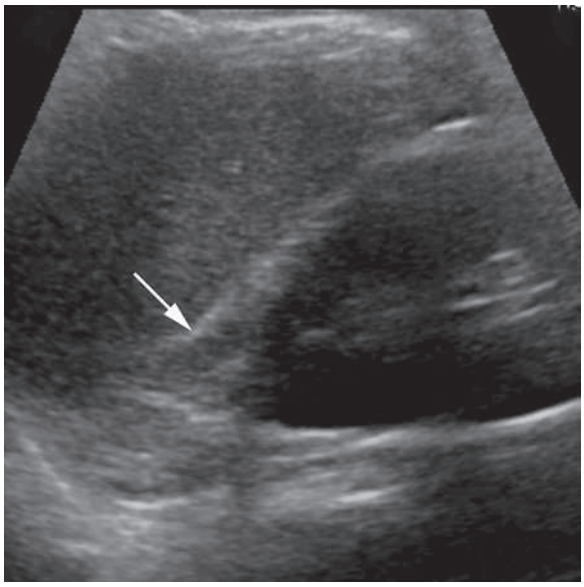

FIG. 11.3 Normal Adult Right Adrenal Gland. Sagittal sonogram shows the adrenal gland as a hypoechoic structure *(arrow)* between the liver and right kidney. See also Video 11.1.

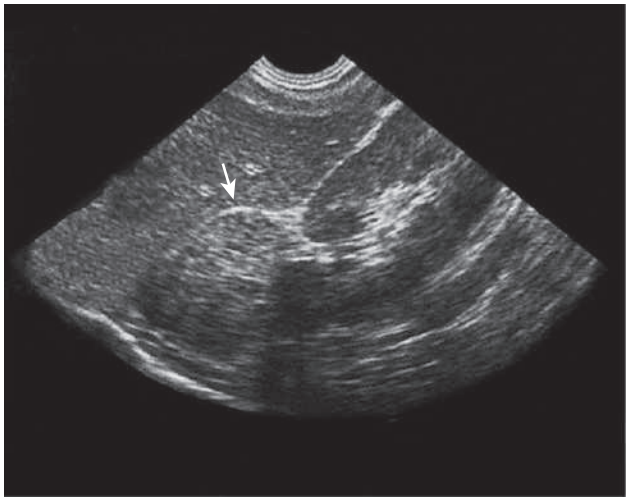

FIG. 11.4 Retroperitoneal Fat Stripe Displacement. Sagittal sonogram shows anterior displacement of the retroperitoneal fat stripe *(arrow)* by right adrenal cortical cancer.

adrenal gland is best seen through a transverse oblique and coronal view, using the liver as an acoustic window. The key to the identification of the right adrenal gland is the posterior location relative to the inferior vena cava (IVC). It is medial to the porta hepatis on scanning the right flank. The left adrenal gland is best seen along the posterior axillary line on an oblique coronal view, using either the spleen or the left kidney as an acoustic window.[9]

Normal sonographic appearance of the adrenal gland includes an inverted V or Y shape. Given its anatomic orientation, the entire gland is very difficult to visualize on a single plane. Furthermore, the adrenal gland is overall more echogenic relative to the background retroperitoneal fat, with the adrenal medulla depicted as a more distinctly linear echogenic component of the gland. The echogenic linear medulla is most prominent in the fetus and newborn. Oppenheimer et al. proposed that the increased medullary echogenicity in newborn infants is caused by increased collagen around the central vessels and haphazard orientation of its cell population, resulting in multiple reflective interfaces[7] (Fig. 11.3, Video 11.1).

The small size of the adrenal glands, in tandem with patient factors that limit visibility such as body habitus, result in several pitfalls for proper sonographic visualization. Normal anatomic structures can be mistaken for adrenal masses. On the right side these include lymph nodes, small bowel loops, and prominent native or collateral vasculature. On the left side, these include splenules, lobulated splenic margins, gastric fundus, small bowel loops, pancreatic parenchymal lobulations, and lymph nodes, as well as prominent native or collateral vasculature. Additionally, lesions arising from the liver, kidneys, or pancreas can also be mistaken for adrenal masses. Anterior displacement of the retroperitoneal fat reflection is a good indication of a primary adrenal lesion[8] (Fig. 11.4). Additionally, dynamic sonographic scanning demonstrating separation of the adrenal glands from the kidneys during deep inspiration and upright positioning is a useful troubleshooting technique as the adrenal glands are anchored with the perirenal fascia by fibrous tissue and are therefore fixed in position relative to the great vessels compared to the kidneys.

Adrenal Pseudomasses

Right Side	Left Side	Either Side
Liver mass	Splenule	Renal mass
	Pancreatic parenchymal lobulation	Lymph node
		Small bowel
	Pancreatic tail mass	Thickened diaphragmatic crus
	Gastric fundus	

BENIGN ADRENAL MASSES

Adrenal Adenomas

Adrenal adenomas are the most commonly encountered adrenal lesion, representing 60% to 80% of all adrenal masses. Autopsy studies have documented that adrenal adenomas are seen in 3% to 9% of the population.[2,10,11] Adenomas are often less than 3 cm in size and can therefore be difficult to see on sonography. Magnetic resonance imaging (MRI) and CT have improved sensitivity and specificity in diagnosing adenomas, particularly with characterization of microscopic fat content and washout characteristics, respectively. The presence of abundant intracellular lipid on imaging studies sufficiently excludes malignancy in all incidentally found adrenal lesions[12] (Fig. 11.5, Videos 11.2 and 11.3). Because adrenal lesions are so commonly present, in patients with no known malignancy these lesions are almost always benign. Even in patients with a known malignancy, an incidentally found adrenal lesion is more likely to be an adenoma than metastatic disease.[13]

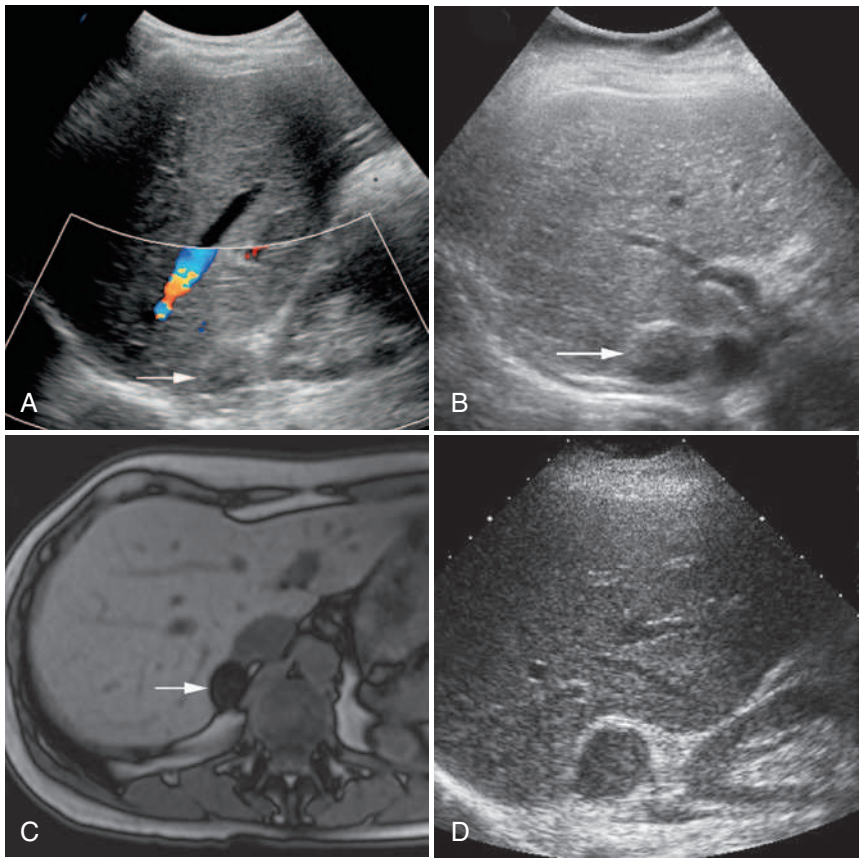

FIG. 11.5 Adrenal Adenoma. (A) Sagittal and **(B)** transverse sonograms show a hyperechoic right adrenal mass *(arrow)* between the liver and upper pole of the right kidney. **(C)** MRI demonstrates diffuse loss of signal on out-of-phase imaging confirming the presence of intravoxel fat and the diagnosis of adenoma *(arrow)*. See also Videos 11.2 and 11.3. **(D)** In another patient, sagittal sonogram shows a small solid right adrenal mass.

Nonfunctioning adenomas are more common than functioning adenomas and are often larger in size by the time of diagnosis as patients are asymptomatic. MRI evaluation to determine intracellular lipid content or contrast-enhanced CT to ascertain physiologic washout characteristics is helpful in characterizing adenomas.

Although adenomas can grow, progressive or rapid interval increase in size may suggest underlying malignancy or collision tumor, where a malignant lesion arises within an adenoma.[14] In this context, further imaging and possibly histologic evaluation is warranted. 18-Fluorodeoxyglucose positron emission tomography (^{18}FDG-PET) CT has been found to be useful in differentiating a collision tumor from an adenoma.[15]

Functioning adrenal adenomas are often diagnosed earlier, and with a smaller size, than nonfunctioning adenomas given the clinical manifestations of the tumor. For example, **Cushing syndrome** occurs with excessive glucocorticoid levels. Clinical symptoms include increased weight gain, fat redistribution with increased abdominal fat, characteristic buffalo hump and moon facies, and decreased fat deposition in the extremities. Cushing syndrome is most often encountered secondarily in the setting of chronic steroid use. Primary Cushing syndrome caused by hyperfunctioning adrenal lesions account for about 15% to 20% of cases, with adenomas, adenomas within a myelolipoma, adenomas of uncertain malignant potential, and adrenal carcinomas accounting for 92% of cases.[16] Unilateral disease is most common and 70% of cases occur as a result of adrenal hyperplasia.[17] In contradistinction, **Cushing disease** is hypercortisolism secondary to a primary adrenocorticotropic hormone (ACTH)–producing pituitary tumor. The two can be differentiated via biochemical analysis. An autonomously cortisol secreting adrenal lesion would yield low serum ACTH as well as elevated plasma cortisol unsuppressed by low dose dexamethasone test.[18]

Conn syndrome results from oversecretion of aldosterone.[19] Primary aldosteronism can result from adrenal adenoma (70%), adrenal hyperplasia (30%), and, in rare cases, adrenal carcinoma.[20] Clinical manifestations include **hypertension** and **hypokalemia.** Patients with hyperaldosteronism from an adenoma typically are female, whereas those with hyperaldosteronism from hyperplasia are usually male.[21,22] These tumors tend to be small (<2 cm). Biochemically, elevated urine and serum aldosterone levels, hypokalemia, hypernatremia, and elevated bicarbonate and low plasma pH levels are found. A suppressed renin level indicates primary hyperaldosteronism.

Adrenal vein sampling can be performed to determine whether there is hypersecretion from the adrenal gland. **Laparoscopic adrenalectomy** and **radiofrequency ablation** are the treatments for hyperfunctioning adenomas.[23,24]

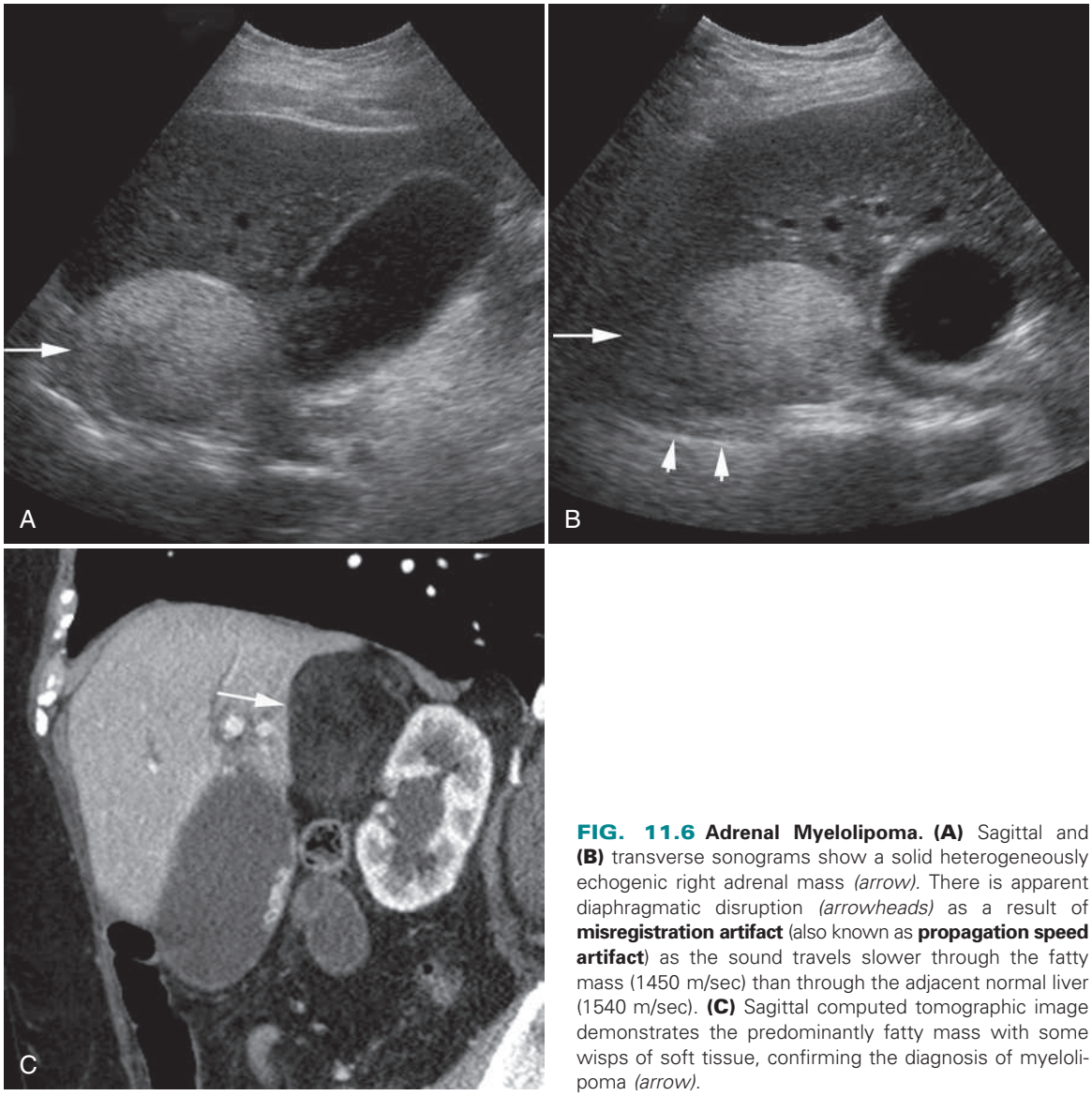

FIG. 11.6 Adrenal Myelolipoma. (A) Sagittal and **(B)** transverse sonograms show a solid heterogeneously echogenic right adrenal mass *(arrow)*. There is apparent diaphragmatic disruption *(arrowheads)* as a result of **misregistration artifact** (also known as **propagation speed artifact**) as the sound travels slower through the fatty mass (1450 m/sec) than through the adjacent normal liver (1540 m/sec). **(C)** Sagittal computed tomographic image demonstrates the predominantly fatty mass with some wisps of soft tissue, confirming the diagnosis of myelolipoma *(arrow)*.

Sonographic Features

Sonographic features for adenomas can be nonspecific but commonly appear as small homogeneously hypoechoic masses with well-defined borders and no substantial demonstrable vascularity. Nonfunctional adenomas are often larger and can have heterogeneous features such as cystic necrosis, hemorrhage, and sometimes calcification that make them difficult to distinguish from malignant lesions.

Myelolipomas

Myelolipomas are rare benign tumors classically containing mature adipose and hematopoietic tissue, with an estimated prevalence of 0.08% to 0.4%.[12] They have been histologically compared to angiomyolipomas of the kidneys and therefore exhibit similar imaging characteristics, being well-defined and diffusely echogenic. Their etiology and pathogenesis are unknown, although these lesions are thought to arise in the zona fasciculata of the adrenal cortex. Men and women are equally affected, with tumors most often occurring in the fifth or sixth decade of life. Differential considerations include other fat-containing masses within the retroperitoneum (Fig. 11.6).

Fat-Containing Suprarenal Masses

Adrenal myelolipoma
Exophytic renal angiomyolipoma
Lipoma
Retroperitoneal liposarcoma
Retroperitoneal teratoma
Pheochromocytoma (rare)

Sonographic Features

Macroscopic fat within myelolipomas can be appreciated as homogeneous, highly echogenic components with associated acoustic shadowing. When small, they may be difficult to

differentiate from the adjacent echogenic retroperitoneal fat. **Propagation speed artifact** (also called **misregistration artifact,** see Chapter 1, Fig. 1.3) results from decreased sound velocity through fatty masses. **Apparent diaphragmatic disruption,** originally described by Richman et al. with an adrenal myelolipoma, can result from this velocity change.[25] The presence of this artifact is good evidence as to the fatty nature of a mass. Musante et al. found this artifact only when tumors were larger than 4 cm.[26] Additionally, in their study of 13 patients, only 11 cases demonstrated echogenic components, of which 5 were homogeneous and 6 were heterogeneous.[26] Lesions with greater proportions of myeloid tissue can appear more heterogeneous with isoechoic or hypoechoic components. The heterogeneity may also be caused by internal hemorrhage, which is common. Focal areas of calcification may be seen. In these cases, CT or MRI can be useful in discerning the presence of macroscopic fat.

Pheochromocytomas

Pheochromocytomas are functional neuroendocrine tumors of the adrenal medulla with associated catecholamine hypersecretion. As such, clinical symptoms include refractory hypertension, palpitations, flushing, diarrhea, and weight loss. The incidence of pheochromocytoma has been described in up to 5% of incidentally found adrenal lesions and can be seen in 0.6% of patients with unexplained hypertension.[12] Of these, 10% can be bilateral.

Pheochromocytomas are associated with many **neuroectodermal disorders,** including tuberous sclerosis, neurofibromatosis, von Hippel–Lindau disease, and **multiple endocrine neoplasia** IIa (50%) and IIb (90%).[27] In such cases, bilateral involvement can be seen in up to 80% of cases.[28]

Multiple endocrine neoplasia (MEN) is a familial disease that is categorized into three types:

- **MEN I** affects pancreatic islets, the adrenal cortex, and pituitary and parathyroid glands.
- **MEN IIa** (Sipple syndrome) includes medullary thyroid carcinoma, parathyroid hyperplasia, and pheochromocytoma.
- **MEN IIb** (III) includes all features of IIa, with marfanoid facies, mucosal neuromas, and gastrointestinal ganglioneuromatosis.

Inherited as an **autosomal dominant** trait, MEN II is believed to be caused by a genetic defect in the neural crest.[29] Pheochromocytomas in MEN syndromes are typically in the adrenal gland, usually bilateral (65%), multicentric within the gland, more often malignant, and frequently asymptomatic.[30] Patients diagnosed with MEN II should be screened biochemically and with imaging on a routine basis because they will eventually develop bilateral adrenal pheochromocytomas.

As imaging findings can be variable, correlation with elevated serum or urine metanephrines and increased activity on **^{123}I-metaiodobenzulguanidine (MIBG)** studies is useful for more definitive diagnosis.[31] Although pheochromocytomas are most commonly benign, malignant degeneration has been described in approximately 9% of cases.[8,32] Metastatic involvement of lymph nodes, liver, lung, and bone has been described.

Sonographic Features

Pheochromocytomas appear as heterogeneous lesions that can vary in size but are often larger than adenomas, with a mean of 5.9 ± 3.2 cm in a study evaluating 161 cases.[8] Pheochromocytomas can be solid, mixed solid and cystic, or cystic. Many have well-defined capsules or rim and avid vascularity on Doppler interrogation. Raja et al. studied the sonographic appearance of 20 pheochromocytomas and found 9 (45%) appeared solid and heterogeneous, 7 (35%) appeared solid and homogeneous, and 4 (20%) were predominantly cystic with a peripheral rim.[33] There may also be fluid-fluid levels within the cystic components due to underlying necrosis or hemorrhage. In some cases, lipid degeneration of pheochromocytomas has also been described, and macroscopic or microscopic lipid can be identified[12] (Fig. 11.7).

Adrenal Cysts

Adrenal cysts are uncommon, accounting for approximately 6% of incidentally detected adrenal lesions.[4] Causes are variable and include pseudocysts, endothelial cysts, epithelial cysts, and parasitic cysts.[34] The origin of cystic lesions is quite variable among different studies because of variations in patient demographics. In a retrospective review of adrenal cystic lesions in New York over a 20-year period, Sebastiano et al. found 31 lesions of which 39% were pseudocysts, 6% endothelial cysts, and 55% epithelial or neuroectogenic cysts.[35] A study by Erickson et al. from Mayo Clinic evaluated 41 lesions over a 25-year period and found 78% pseudocysts, 19% endothelial cysts, and 2% epithelial cysts.[36] Generally pseudocysts are the most commonly occurring cystic lesion described in surgery, whereas endothelial cysts are more commonly encountered in autopsy series (up to 45%).[36,37]

Histologically, **pseudocysts** are characterized as having fibrous walls with no endothelial or epithelial component. They most often occur secondary to hemorrhage. **Endothelial cysts** include lymphangiomatous cysts in 42% and hemangiomatous cysts in 3% of cases.[34] **Epithelial cysts** are congenital and include glandular retention cysts, mesothelial cysts, and cystic adenomas.[38] **Parasitic cysts** have been most commonly described with echinococcal infection.[39] In these cases, the appearance can vary depending on the stage of disease and may present as simple cysts, septated cysts, cysts with daughter cysts, cysts with solid nodules, or calcification.

Cysts with complex features are indeterminate and percutaneous aspiration may be indicated for definitive characterization to exclude cystic or necrotic malignancies. Traditionally, lesions with clear aspirates were often followed while those with bloody aspirates were deemed indeterminate and underwent surgical excision. Currently, the decision for surgery depends more on the size of the lesion and overall complexity of its features.[40]

Sonographic Features

On imaging, simple adrenal cysts appear homogeneously anechoic with through transmission with thin nonenhancing walls and absent septa (Fig. 11.8). Superimposed hemorrhage can occur within the cysts resulting in echogenic contents with sedimentation or fluid-fluid level, septa, or calcification. Complex features

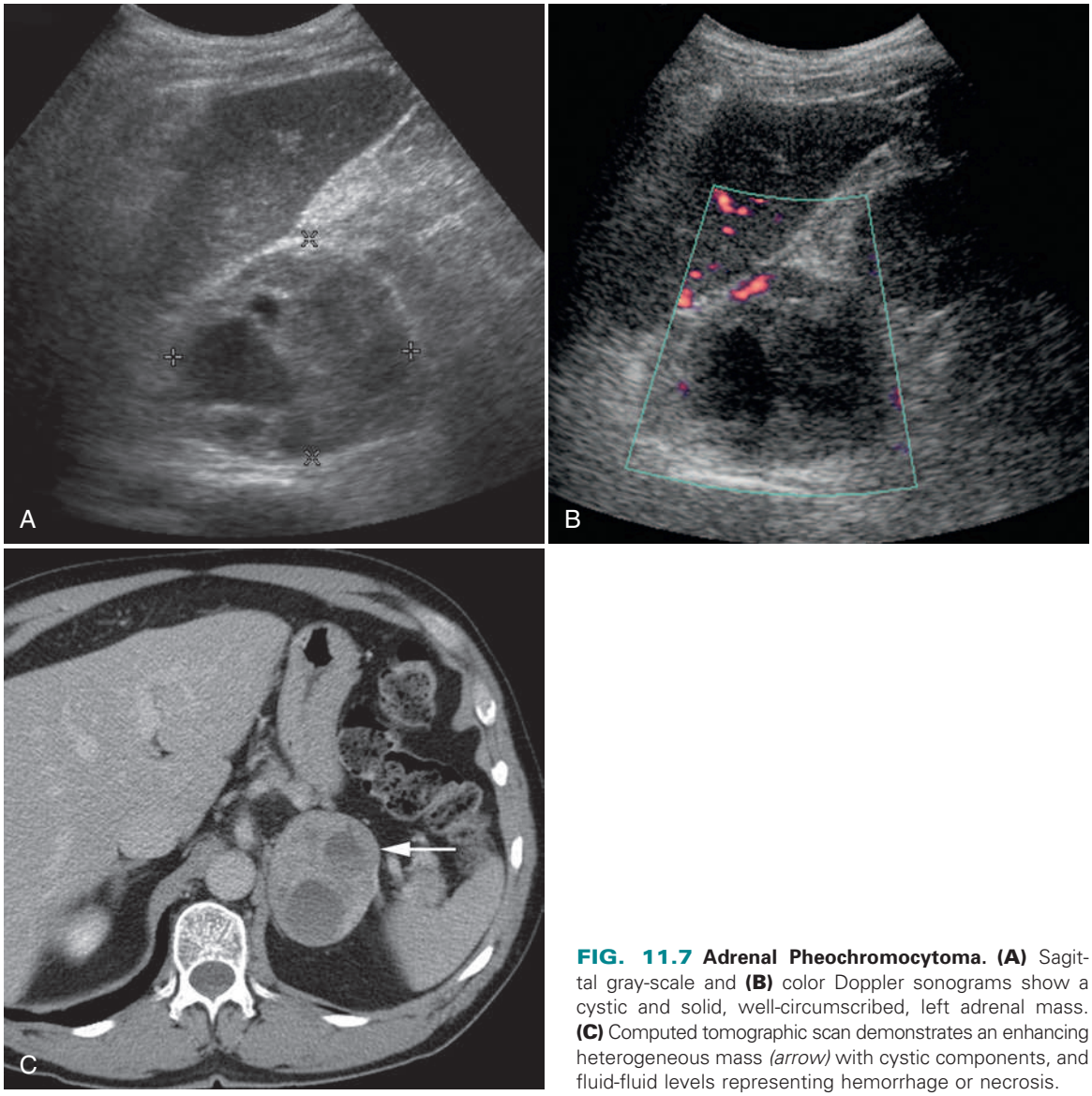

FIG. 11.7 Adrenal Pheochromocytoma. (A) Sagittal gray-scale and **(B)** color Doppler sonograms show a cystic and solid, well-circumscribed, left adrenal mass. **(C)** Computed tomographic scan demonstrates an enhancing heterogeneous mass *(arrow)* with cystic components, and fluid-fluid levels representing hemorrhage or necrosis.

of cystic lesions include thickened wall or septations, or internal vascularity.

Cystic Adrenal Lesions

Pseudocyst
Endothelial cyst
Epithelial cyst
Infection (echinococcus, abscess)
Necrotic neoplasm
Cystic pheochromocytoma
Lymphangioma
Adrenal hemorrhage

Adrenal Hemorrhage

Adrenal hemorrhage is bilateral in 20% of cases. This is most commonly associated with anticoagulation use, trauma, postoperative status from surgery, postprocedure after adrenal venography, sepsis, or burns. In rare cases, spontaneous adrenal hemorrhage has been associated with meningococcal septicemia known as **Waterhouse-Friderichsen syndrome.** In the context of trauma, adrenal hemorrhage often suggests traumatic injury to other solid abdominal organs. Bilateral adrenal hemorrhage predisposes for adrenal insufficiency.[41] Adrenal hemorrhage can sometimes be associated with an underlying lesion, which can be difficult to ascertain in the acute setting. An underlying lesion may be suspected in cases of intralesional enhancement on MRI or metabolic activity on ^{18}FDG-PET CT.[40]

Sonographic Features

In the acute setting, adrenal hemorrhage can appear solid and diffusely or heterogeneously echogenic. The hemorrhage becomes progressively heterogeneous in echogenicity with time, and chronic hematomas can have central cystic components. Calcification can also occur in the chronic setting. Adrenal hemorrhage is avascular on Doppler interrogation.[42] (Fig. 11.9).

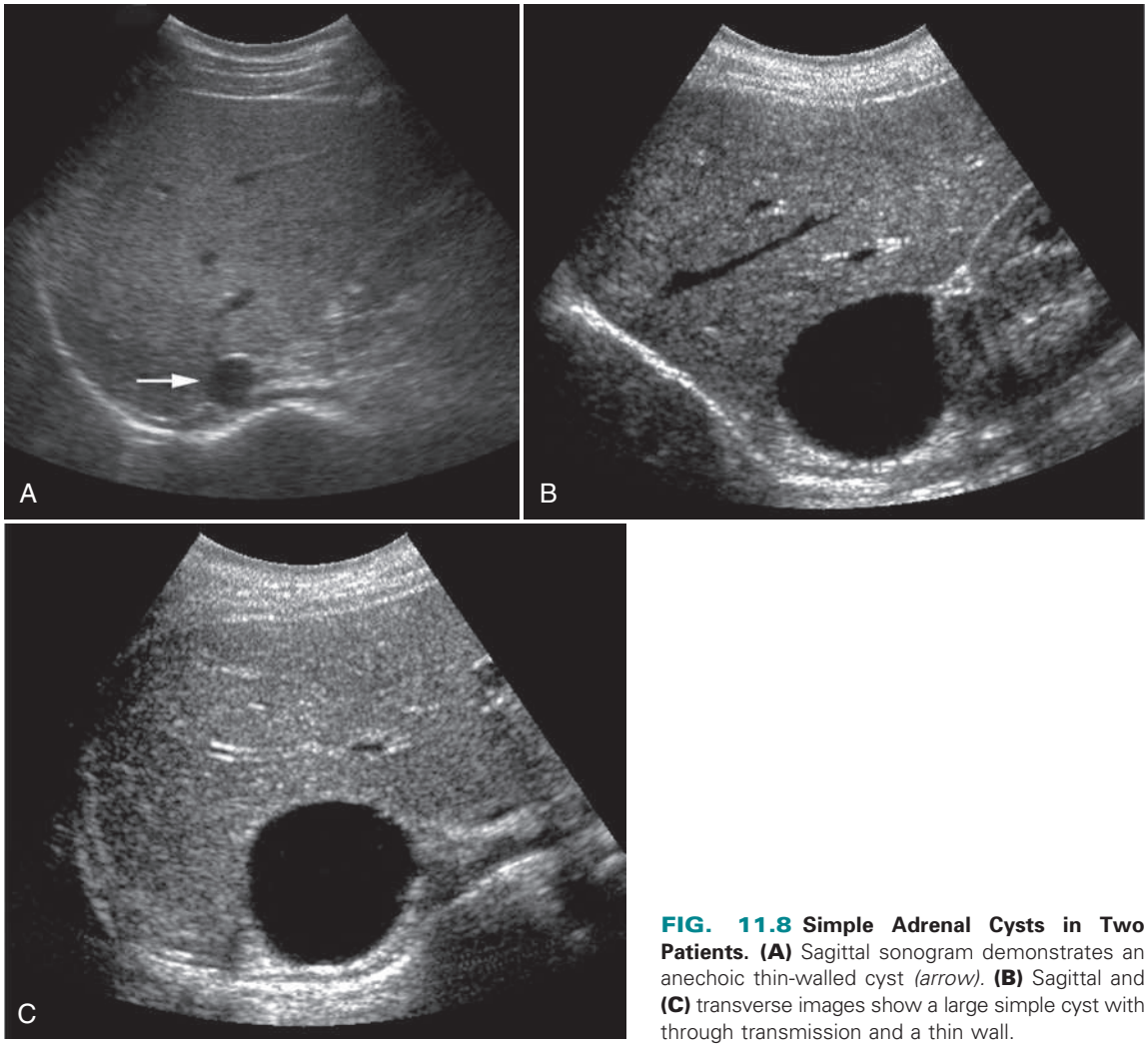

FIG. 11.8 Simple Adrenal Cysts in Two Patients. (A) Sagittal sonogram demonstrates an anechoic thin-walled cyst *(arrow)*. **(B)** Sagittal and **(C)** transverse images show a large simple cyst with through transmission and a thin wall.

Infectious and Inflammatory Masses

Tuberculosis, histoplasmosis, blastomycosis, paracoccidiomycosis, meningococcal, echinococcal, cytomegalovirus (CMV), herpesvirus, and *Pneumocystis* infections are the most common infectious diseases of the adrenal gland.[27,41,42]

Tuberculosis of the adrenal gland has been noted to be one of the most common causes of adrenal insufficiency worldwide.[43] Chest radiographs and sputum cultures may be negative even in cases of positive adrenal tuberculous infection. Tuberculosis and **histoplasmosis** are the two most common causes of adrenal calcification in the adult population.[44] In the setting of disseminated fungal infection, histoplasmosis and **paracoccidiomycosis** are most commonly seen, where up to 80% have adrenal involvement based on autopsy series.[45-47]

Echinococcal infection of the adrenal gland rarely occurs in isolation and is more often seen in the presence of widespread multiorgan echinococcal infection.[47,48]

Immunosuppression resulting from acquired immunodeficiency syndrome (AIDS), transplantation, or other causes increases these patients' risk for infectious involvement of the adrenal gland. Common organisms include fungi (histoplasmosis), mycobacteria, CMV, herpesvirus, *Pneumocystis carinii (jiroveci)*, human immunodeficiency virus (HIV), and toxoplasmosis.[41] Grizzle[42] described focal or diffuse damage of the glands by CMV in 70% of AIDS patients who died. In a study involving 74 AIDS patients, Pulakhandam et al. found that up to 50% had CMV infection at autopsy, of which 84% had adrenal involvement.[49]

Bacterial adrenal abscesses are found more frequently in neonates and are relatively uncommon in adults.[50,51] In the neonate, hematogenous seeding of normal glands or those affected by hemorrhage can result in abscess formation.[52]

Sonographic Features

Sonographic features are indistinguishable among these infections, and diagnosis is based on the patient's geographic profile, occupational exposure, and laboratory testing. Acute adrenal involvement in granulomatous infections can lead to enlargement of the gland, with nodular contours and hypervascularity. Superimposed areas of necrosis and hemorrhage can also be seen in cases of caseous necrosis. In the chronic setting, gland atrophy and calcifications can be present, which appear as coarse echogenic foci with acoustic shadowing.[19,20] (Fig. 11.10, Video 11.4).

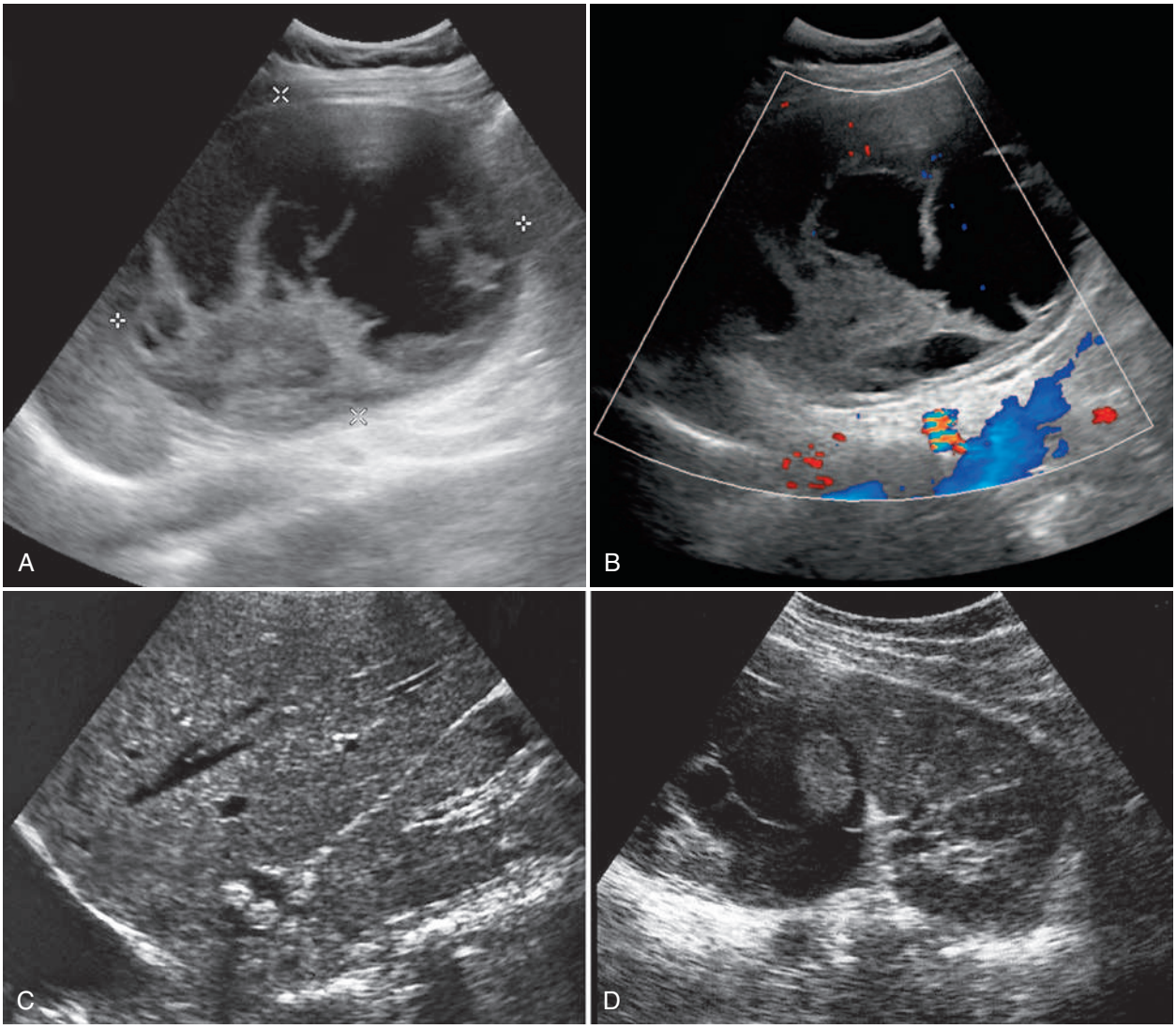

FIG. 11.9 Spontaneous Adrenal Hemorrhage. (A) Sagittal gray-scale and **(B)** color Doppler sonograms demonstrate a heterogeneous cystic left adrenal mass with irregular appearing clot and no demonstrable vascularity. On magnetic resonance imaging (not shown) this was compatible with hemorrhage without underlying lesion. **(C)** Chronic adrenal hemorrhage. Sagittal sonogram shows two echogenic foci representing clotted blood in an enlarged right adrenal gland. **(D)** Acute hemorrhage. Sagittal sonogram shows a large complex mass displacing the left kidney inferiorly and anteriorly.

Echinococcal infection of the adrenal gland manifests similarly to echinococcal disease seen elsewhere and is most often characterized by cysts with varying amounts of septation, secondary cysts, and calcification.[47,48] CMV infection of the adrenal glands appears as hypoechoic masses that may be heterogeneous and may contain gas if abscess formation occurs. Adrenal abscesses typically appear as complex, avascular cystic masses.

MALIGNANT ADRENAL MASSES

Adrenocortical Carcinomas

Adrenocortical carcinomas are rare primary malignant adrenal tumors with an estimated prevalence of 1 to 2 million worldwide. There is a bimodal age distribution with peak incidence occurring in children younger than 5 years or in adults in their fourth to

Causes of Adrenal Calcification

- Infection
  - Tuberculosis
  - Histoplasmosis
  - Echinococcus
  - Paracoccidiomycosis
- Prior hemorrhage
- Neoplasm
  - Adrenocortical carcinoma
  - Myelolipoma
  - Pheochromocytoma
  - Neuroblastoma
- Ganglioneuroma
- Hemangioma (rare)

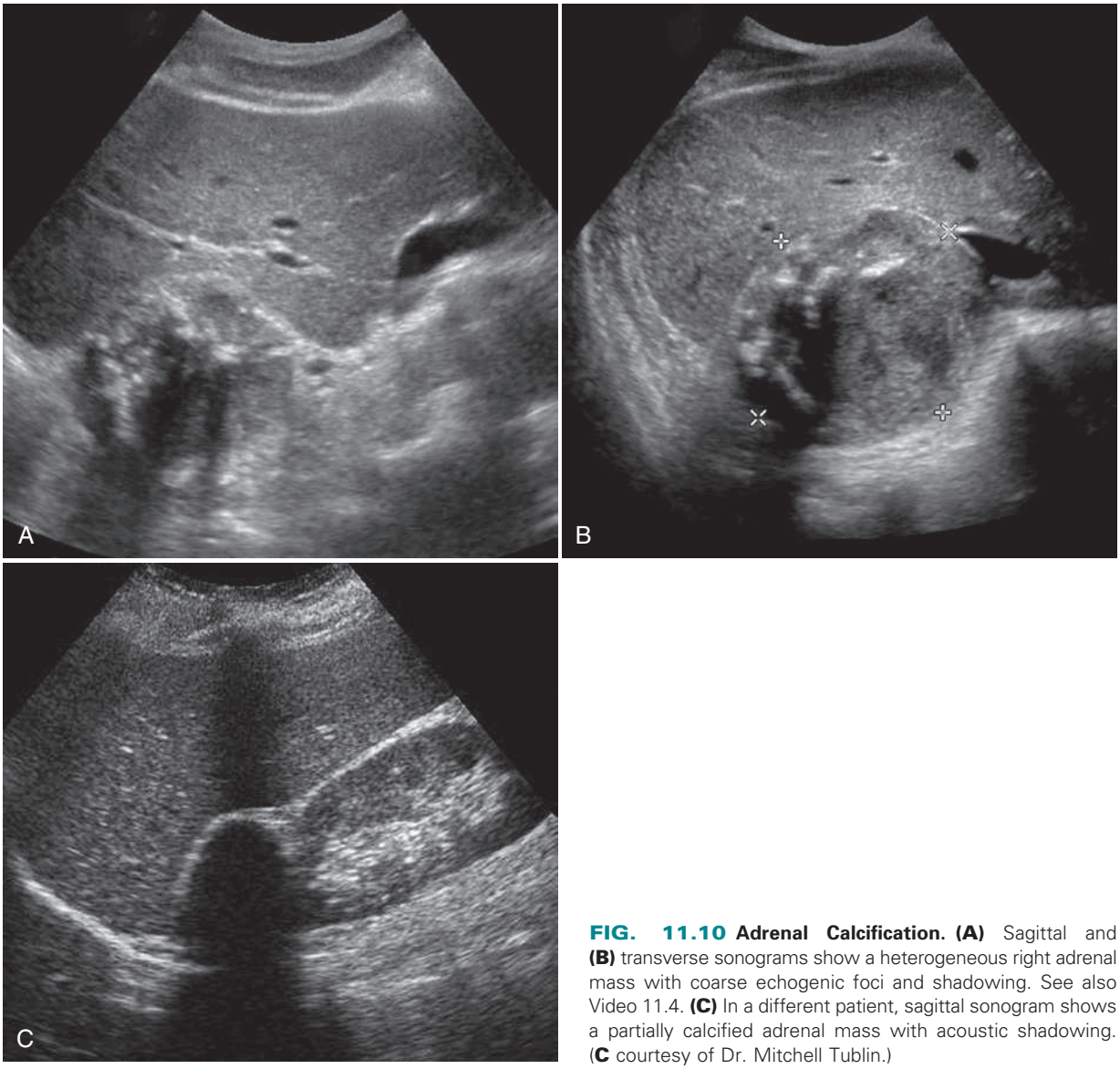

FIG. 11.10 Adrenal Calcification. (A) Sagittal and **(B)** transverse sonograms show a heterogeneous right adrenal mass with coarse echogenic foci and shadowing. See also Video 11.4. **(C)** In a different patient, sagittal sonogram shows a partially calcified adrenal mass with acoustic shadowing. (**C** courtesy of Dr. Mitchell Tublin.)

fifth decade of life.[44,51] Increased prevalence has been reported in patients with particular familial neoplastic syndromes, including **familial adenomatous polyposis, Beckwith-Wiedemann syndrome,** and **Li-Fraumeni syndrome,** Carney syndrome, MEN I, as well as mutations involving the *p53* tumor suppressor gene.[45,51] Adrenocortical carcinomas are hyperfunctioning in 55% to 78% of cases, manifesting with Cushing syndrome, virilization or precocious puberty, feminization in males, primary hyperaldosteronism, or combined hormonal excess in 33%, 35%, 10%, 2.5%, and 3% of cases, respectively.[46] Functioning adrenocortical carcinomas are often diagnosed at an earlier stage because of their clinical symptomatology and can therefore measure less than 6 cm in size. Nonfunctioning adrenocortical carcinomas are large, with 81% to 90% measuring over 6 cm at the time of diagnosis (Fig. 11.11).[47] Because of their later presentation, nonfunctional carcinomas tend to be more aggressive, and hepatic metastases and tumor thrombus within the adrenal vein or IVC may be present at the time of initial presentation. The presence of metastases and tumor thrombus confers poorer prognosis. Management of adrenocorticocarcinoma requires a thorough imaging and biochemical workup to assess for tumor resectability.[48] The mainstay of treatment is surgery; however, despite resection, prognosis is often poor with estimated 5-year survival rates of 16% to 38% and estimated recurrence rates at 85%.[47]

Sonographic Features

Adrenocortical carcinomas (Figs. 11.11 and 11.12) are often large heterogeneous masses with areas of cystic necrosis, hemorrhage, and calcification, as well as demonstrable vascularity or prominent supplying vessel. Lobulated borders are common. The adjacent veins should be examined to assess for venous tumor extension.

Metastases

Adrenal metastases are the most common malignant lesions of the adrenal gland and the second most common adrenal lesion

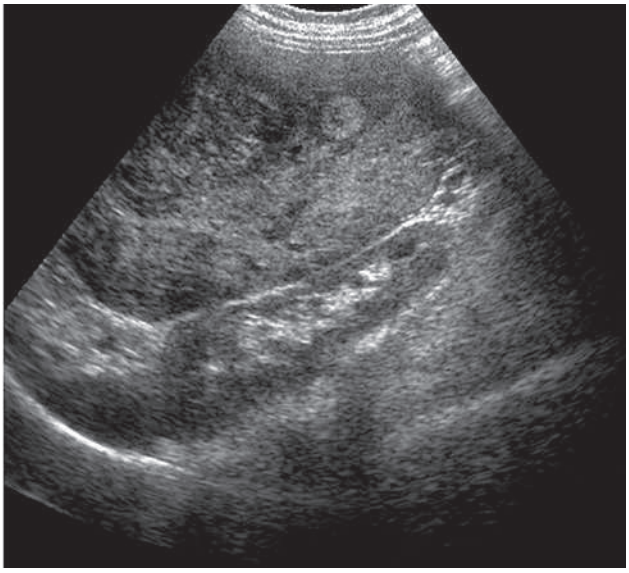

FIG. 11.11 Large Adrenocortical Carcinoma. Sagittal sonogram of the left flank shows a large heterogeneous solid mass anterior to the left kidney.

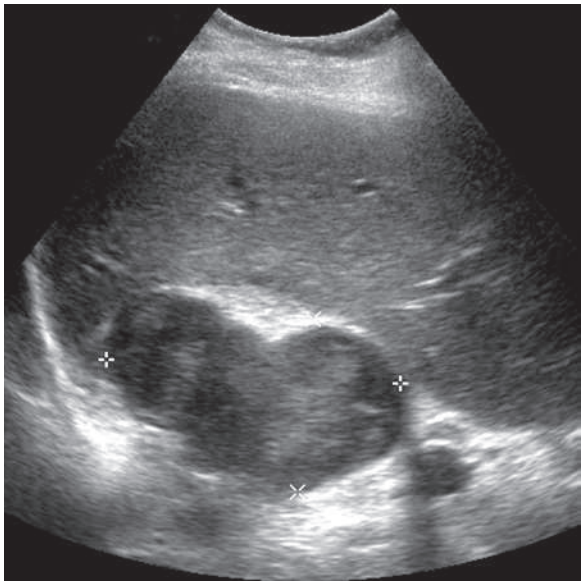

FIG. 11.12 Adrenocortical Carcinoma. Transverse sonogram shows a heterogeneous large lobulated right adrenal mass *(calipers).*

after adenomas.[53] In an autopsy series involving 464 patients with adrenal metastases over a 30-year period, Lam and Lo found that 90% of the lesions were carcinoma, of which 56% were adenocarcinomas. The most common primary tumor site was the lung at 35%.[51] Adrenal metastases can also be secondary to malignancies of breast, hepatocellular, thyroid, renal, pancreatic, gastrointestinal, or melanoma origins. Direct invasion of the adrenal gland can also be seen in some cases of renal cell and hepatocellular carcinomas. In these cases, the aggressive tumors disrupt fascial planes and invade the adrenal gland.

Sonographic Features

Metastatic lesions are variable in size, often with ill-defined borders and inhomogeneously hypoechoic features (Fig. 11.13). Bilateral lesions are seen in 40% of cases and often occur in patients with metastatic disease elsewhere. Many metastatic lesions are large, greater than 4 cm in size, with irregular shape and features of cystic necrosis. In some cases, metastases can appear small and homogeneously hypoechoic and thus be mistaken for benign adenomas on sonography. Therefore when adrenal lesions are identified in patients with known malignancy, further CT or MRI characterization should be pursued to determine if the lesion meets the criteria for an adenoma.[54] In cases of direct invasion of the adrenal gland by adjacent primary malignancy, it may be difficult to distinguish the adrenal gland from the primary tumor on ultrasound (Fig. 11.14).

Lymphoma

Adrenal involvement in lymphoma is most commonly seen as secondary involvement from lymphomatous disease elsewhere, with an estimated prevalence of 5% and up to 35% in autopsy cases.[53,55] Primary adrenal lymphoma is rare, with fewer than 200 cases reported in literature.[56,57] Primary adrenal lymphoma is most commonly seen in older men, with a mean age of 65 years.[47] Non-Hodgkin lymphoma is more common than Hodgkin lymphoma, of which the diffuse large B-cell subtype is most common.[58] The most common clinical manifestation of adrenal lymphoma is **adrenal insufficiency,** which can be seen in up to two-thirds of cases. Patients can also present with hypoglycemia, hyponatremia, or **Addisonian crisis.**[59] Some patients may also have nonspecific symptoms of pain and fever. Hepatosplenomegaly, lymphadenopathy, and bone marrow involvement are

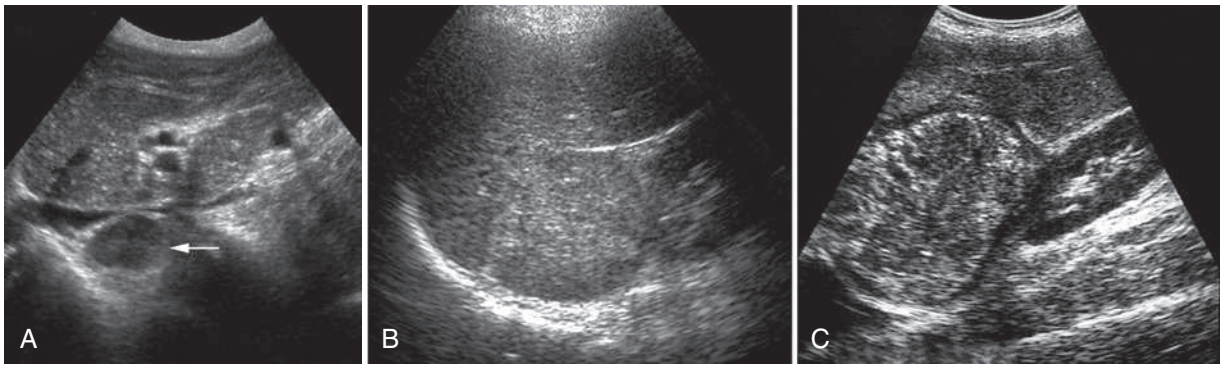

FIG. 11.13 Adrenal Metastasis in Three Different Patients. (A)-(C) Sagittal sonograms show heterogenous adrenal mass.

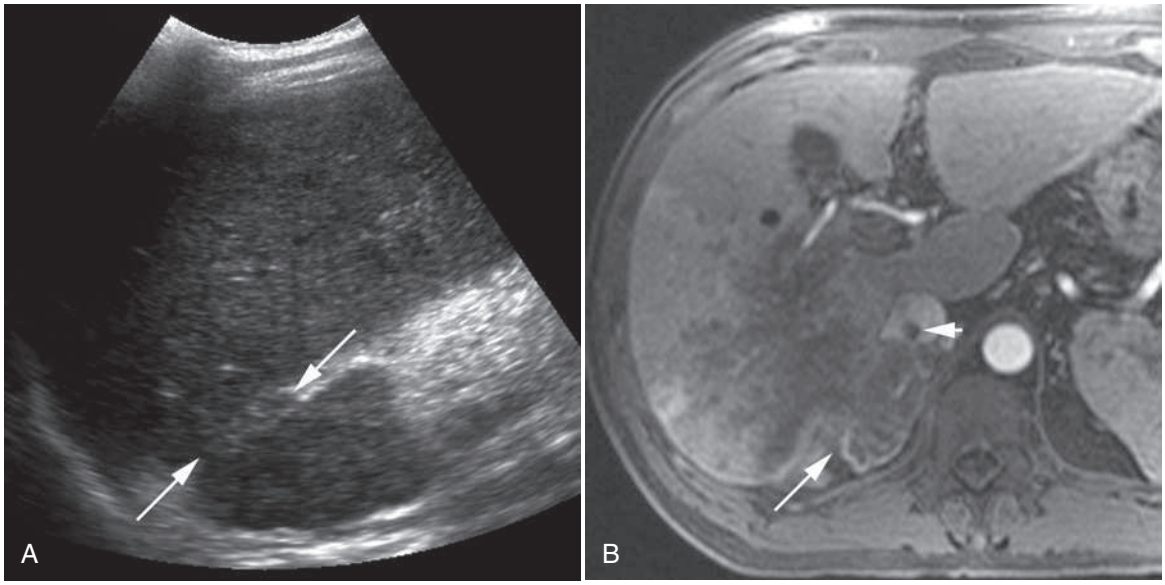

FIG. 11.14 Direct Invasion of the Right Adrenal Gland by Hepatocellular Carcinoma. (A) Sagittal sonogram demonstrates a large mass with ill-defined borders extending to the suprarenal space, resulting in loss of the normal fat plane *(arrows)*. **(B)** MRI of the same patient demonstrates invasion of the right adrenal gland by the primary hepatic tumor *(arrows)*. A small thrombus is also seen in the inferior vena cava *(arrowhead)*.

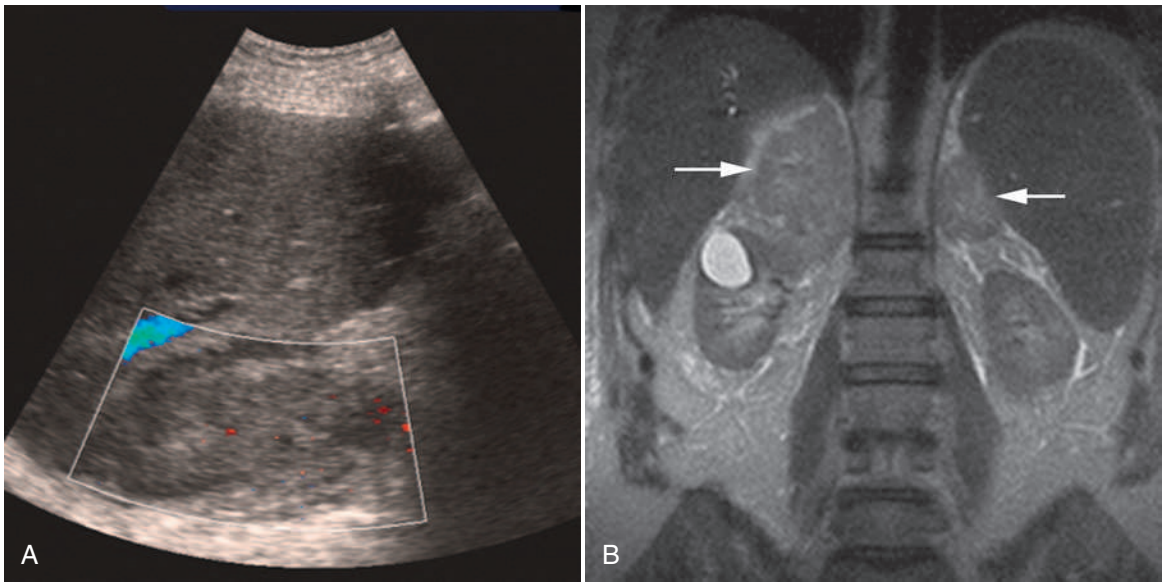

FIG. 11.15 Adrenal Lymphoma. (A) Sagittal color Doppler sonogram shows a solid, fairly homogeneous right adrenal mass with no demonstrable vascularity. **(B)** Coronal MRI of the same patient demonstrates bilateral adrenal masses *(arrows)*. Note also splenomegaly.

uncommon in primary adrenal lymphoma but are seen more often in secondary adrenal lymphoma.[56] In secondary adrenal lymphoma, concomitant lymphomatous involvement of the kidneys, retroperitoneum, and adjacent vessels can be seen. Treatment includes chemotherapy or radiation therapy, often with poor prognosis because of disease extent. In particular, rituximab-containing chemotherapeutic agents are preferred.

Sonographic Features

Lymphomatous deposits within the adrenal gland are often large and homogeneously very hypoechoic with little internal architecture. In some cases, lesions have mixed heterogeneous echogenicity or targetoid morphology and can develop cystic necrosis or hemorrhage. Bilateral lesions are seen in 50% to 70% of cases[1,8,56] (Fig. 11.15).

RARE ADRENAL MASSES

Ganglioneuromas are rare benign masses of Schwann cells, ganglion cells, and nerve fibers from the retroperitoneal sympathetic chain coursing along the adrenal glands.[60,61] These tumors are most commonly incidentally found in children and young adults and can be large in size. On ultrasound, they appear as large heterogeneous masses with variable vascularity. Calcification

can also be present in about 20% of cases. Resection confers good prognosis with low recurrence rates.

Neuroblastomas are malignant cells that arise from the sympathetic chain in the retroperitoneum or adrenal gland and are sometimes referred to as the malignant form of **ganglioneuromas.** Although they are the most common extracranial malignancy in infants and the pediatric population, they are extremely rare in the adult population and can occur in the adrenals or elsewhere in the abdomen and pelvis.[62] In the adrenal gland, they classically appear as heterogeneous masses often with calcification and hemorrhage. Adults often present with stage IV incurable disease.[62]

Other rare adrenal masses include hemangioma, lymphangioma, plasmacytoma, oncocytoma, neurilemoma, teratoma, and angiosarcoma.

MANAGEMENT OF ADRENAL LESIONS

Adrenal incidentalomas are defined as incidentally found adrenal lesions measuring over 1 cm.[63] The incidence is reported to be up to 5% in the general population and up to 7% in adults older than 70 years.[64,65] Approximately 90% of these lesions are benign in patients with no underlying malignancy. However, in the cancer population, the incidence of malignant adrenal lesions can be as high as 26% to 75%.[65,66] Both benign and malignant lesions can exhibit hormonal function; therefore it is integral to evaluate incidental lesions for underlying function and malignancy.

The initial workup for patients with an adrenal incidentaloma includes (1) 1 mg dexamethasone overnight suppression test with serum cortisol; (2) a plasma fractionated metanephrine, which is preferred over a urinary fractionated metanephrine or both; and (3) serum aldosterone, plasma renin activity, and serum potassium. These are evaluated for subclinical manifestations of Cushing syndrome, pheochromocytoma, and hyperaldosteronism, respectively.

The American College of Radiology white paper on the incidentally discovered adrenal mass outlines the recommended imaging algorithm.[13] Of note, ultrasound is not considered appropriate in definitively characterizing adrenal lesions. For patients with no history of malignancy with lesions 1 to 4 cm, initial evaluation is performed with noncontrast-enhanced CT. A mass of any size with typical features of an adenoma or myelolipoma does not require further imaging or workup. If the lesion has nondiagnostic features, then a 1-year follow-up with unenhanced CT or unenhanced MRI is recommended to reassess for size change. If the lesion is stable in size after 1 year, then it can be deemed benign with no additional imaging or workup. An enlarging lesion may warrant biopsy or resection. Masses that measure greater than 4 cm are initially evaluated with a contrast-enhanced CT or contrast-enhanced MRI. Resection should be considered if the lesion does not have typical features of an adenoma, myelolipoma, hemorrhage, or simple cyst.

In patients with known malignancy, adrenal lesions smaller than 4 cm are initially evaluated with noncontrast-enhanced CT. A mass larger than 4 cm should undergo biopsy or ^{18}FDG-PET CT to diagnose metastases.[65,67] Although pheochromocytoma is rare in cases of incidentally found lesions, it is prudent to exclude this with urinary or plasma catecholamine levels or a glucagon stimulation test before a biopsy is pursued.

Laparoscopic adrenalectomy is often recommended for smaller lesions measuring up to 1.2 cm but also in many tumors larger than 4 cm with the exception of adrenocortical carcinomas. Adrenocortical carcinomas require open adrenalectomy to obtain clear resection margins because these tumors respond poorly to adjuvant therapy.[67] Image-guided ablation is also increasingly useful in the management of small lesions and in the management of patients who are poor candidates for surgery.[24]

INTERVENTIONS

Ultrasound-Guided Biopsy and Interventions

Adrenal lesions that are easily visualized on ultrasound can be amenable for ultrasound-guided biopsy, drainage, or ablation. Adrenal biopsies and drainages are predominantly performed under CT guidance because of improved visibility, but larger lesions can also be performed guided by ultrasound. On the right side, a transhepatic approach is preferred to avoid the pleural space (Fig. 11.16). On the left side, posterior, lateral, and anterior approaches have been described. Generally, a posterior approach is preferred over an anterior approach to decrease the risk for pancreatitis. Welch et al.[68] reviewed their 10-year experience with adrenal biopsy, which included 277 percutaneous biopsies in 270 patients. Sensitivity was 81%, specificity 99%, and accuracy 90%. Positive predictive value was 99%, and negative predictive value was 80%. Complication rate was 2.8%. Potential complications of percutaneous adrenal biopsy depend on the approach and include hematoma (0.05%-2.5%), pneumothorax (most common), pancreatitis (6%), sepsis, and needle tract seeding.[69,70] Needle biopsy of a pheochromocytoma may precipitate a hypertensive crisis and should be avoided.[71]

A variety of techniques have been described for adrenal **ablation,** including radiofrequency, cryotherapy, chemical ablation with acetic acid, or ethanol via a percutaneous approach with a 19- to 22-gauge needle.[72] Alternatively, ablation can be performed via accessing the ipsilateral adrenal artery. Complications include hypertensive crisis, pain, and adrenal insufficiency, particularly if more than 90% of the adrenal tissue is destroyed.

Endoscopic Ultrasound

Endoscopic ultrasound is being used with greater frequency; an **echoendoscope** is inserted via the alimentary tract to visualize surrounding organs. The right adrenal gland tends to be difficult to visualize endoscopically because of the retrocaval location of the gland. The right adrenal gland is best visualized with the endoscopic ultrasound probe in the longitudinal position in the duodenum oriented toward the greater curvature of the stomach. It is estimated that approximately 30% of glands are identified[73] (Fig. 11.17). The left adrenal gland is more easily identified, best with a linear echoendoscope within the stomach aimed between the descending aorta and celiac trunk. The adrenal glands appear as seagull-shaped organs posterior to the pancreatic body that

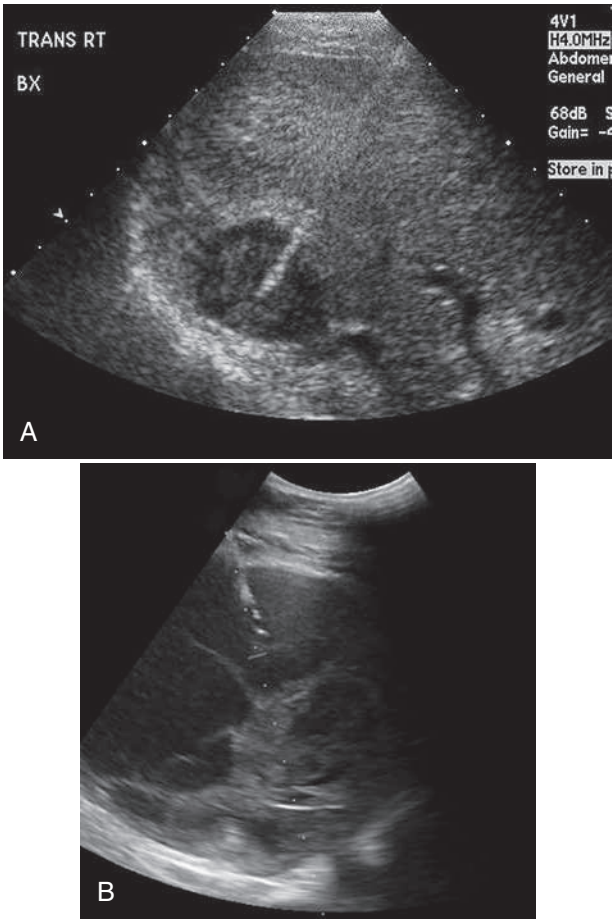

FIG. 11.16 Percutaneous Adrenal Biopsy. (A) Transverse sonogram shows transhepatic placement of a needle (echogenic line) into a small right adrenal metastasis in a patient with lung cancer. (Courtesy of Dr. J. William Charboneau.) **(B)** Sagittal sonogram in a different patient demonstrates percutaneous biopsy of an adrenal lesion.

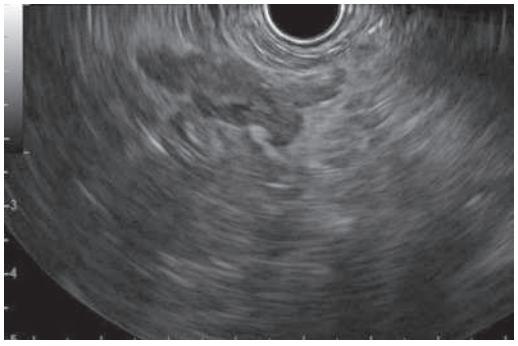

FIG. 11.17 Endoscopic Ultrasound Image of the Adrenal Glands. Endoscopic ultrasound evaluation demonstrates diffuse nodular thickening of the adrenal gland compatible with nodular adrenal hyperplasia. (Courtesy of Dr. Tyler Berzin.)

come into view with a clockwise rotation of the probe. Martinez et al. performed endoscopic fine-needle aspiration of the adrenal glands in 94 patients with sensitivity, specificity, accuracy, positive predictive value, and negative predictive value at 86%, 97%, 92%, 96%, and 89% for malignant lesions, and 97%, 86%, 92%, 89%, 96% for benign lesions, respectively.[73] In 24 patients with endoscopic ultrasound-guided fine-needle aspiration of the adrenal glands, Jhala et al. reported that adequate cellularity was obtained from all patients, with no significant complications.[74] Similarly, Puri et al. performed endoscopic ultrasound-guided fine-needle aspiration in 21 consecutive patients and found no significant adverse events in cases where conventional imaging modalities were deemed unsuccessful.[75]

Intraoperative Ultrasound

Intraoperative ultrasound can be performed in cases of partial adrenalectomy to ensure clear resection margins or for improved localization of an underlying lesion. This is especially valuable in cases of adrenal sparing surgery, where a laparoscopic ultrasound probe can be used to identify multiple lesions within the adrenal gland, as well as to decipher the plane between the lesion and the native gland.[76]

Acknowledgments

The authors thank Lisa Napolitano, Dr. Trevor Morrison, and Dr. Tyler Berzin for their assistance in image collection The authors also acknowledge authors of this chapter in the fourth edition of this text, Drs. AR Ahuja, W Thurston, and SR Wilson, since their text formed the backbone of this revised chapter.

REFERENCES

1. Wan Y-L. Ultrasonography of the adrenal gland. J Med Ultrasound. 2007;15(4):213-227.
2. Ma G, Liu SW, Zhao ZM, et al. Sectional anatomy of the adrenal gland in the coronal plane. Surg Radiol Anat. 2008;30(3):271-280.
3. Lurie S, Neelon F. Physiology of the adrenal gland. In: Pollack HM, editor. Clinical urography: an atlas and textbook of urological imaging. Philadelphia: Saunders; 1990. p. 2306-2312.
4. Lockhart ME, Smith JK, Kenney PJ. Imaging of adrenal masses. Eur J Radiol. 2002;41(2):95-112.
5. Marchal G, Verbeken E, Oyen R, et al. Ultrasound of the normal kidney: a sonographic, anatomic and histologic correlation. Ultrasound Med Biol. 1986;12(12):999-1009.
6. Günther RW, Kelbel C, Lenner V. Real-time ultrasound of normal adrenal glands and small tumors. J Clin Ultrasound. 1984;12(4):211-217.
7. Oppenheimer DA, Carroll BA, Yousem S. Sonography of the normal neonatal adrenal gland. Radiology. 1983;146(1):157-160.
8. Fan J, Tang J, Fang J, et al. Ultrasound imaging in the diagnosis of benign and suspicious adrenal lesions. Med Sci Monit. 2014;20:2132-2141.
9. Kim KW, Kim JK, Choi HJ, et al. Sonography of the adrenal glands in the adult. J Clin Ultrasound. 2012;40(6):357-363.
10. Dunnick NR, Korobkin M, Francis I. Adrenal radiology: distinguishing benign from malignant adrenal masses. AJR Am J Roentgenol. 1996;167(4):861-867.
11. Mayo-Smith WW, Boland GW, Noto RB, Lee MJ. State-of-the-art adrenal imaging. Radiographics. 2001;21(4):995-1012.
12. Herr K, Muglia VF, Koff WJ, Westphalen AC. Imaging of the adrenal gland lesions. Radiol Bras. 2014;47(4):228-239.
13. Remer EM, Casalino DD, Bishoff JT, et al. Expert panel on urologic imaging. ACR Appropriateness Criteria®: incidentally discovered adrenal mass. 2012. Available from: https://acsearch.acr.org/docs/69366/Narrative/.
14. McDermott S, O'Connor OJ, Cronin CG, Blake MA. Radiological evaluation of adrenal incidentalomas—current methods and future prospects. Best Pract Res Clin Endocrinol Metab. 2012;26(1):21-33.
15. Boland GW, Blake MA, Holalkere NS, Hahn PF. PET/CT for the characterization of adrenal masses in patients with cancer: qualitative versus quantitative accuracy in 150 consecutive patients. AJR. 2009;192:956-962.

16. Rockall AG, Babar SA, Sohaib SAA, et al. CT and MR imaging of the adrenal glands in ACTH-independent Cushing syndrome. Radiographics. 2004;24(2):435-452.
17. Korobkin M, Francis IR. Adrenal imaging. Semin Ultrasound CT MR. 1995;16(4):317-330.
18. Daitch JA, Goldfarb DA, Novick AC. Cleveland clinic experience with adrenal Cushing syndrome. J Urol. 1997;158(6):2051-2055.
19. Conn J. Evolution of primary aldosteronism as a highly specific clinical entity. JAMA. 1960;172(15):1650-1653.
20. Slee P, Schaberg A, van Brummelen P. Carcinoma of the adrenal cortex causing primary hyperaldosteronism. A case report and review of the literature. Cancer. 1983;51(12):2341-2345.
21. Conn J, Knopf R, Nesbit R. Clinical characteristics of primary aldosteronism from an analysis of 145 cases. Am J Surg. 1964;107(1):159-172.
22. Grant CS, Carpenter P, van Heerden JA, Hamberger B. Primary aldosteronism. Arch Surg. 1984;119(5):585-590.
23. Germain A, Klein M, Brunaud L. Surgical management of adrenal tumors. J Visc Surg. 2011;148(4):e250-e261.
24. Mendiratta-Lala M, Brennan DD, Brook OR, et al. Efficacy of radiofrequency ablation in the treatment of small functional adrenal neoplasms. Radiology. 2011;258(1):308-316.
25. Richman TS, Taylor KJW, Kremkau FW. Propagation speed artifact in a fatty tumor (myelolipoma): significance for tissue differential diagnosis. J Ultrasound Med. 1983;2:45-47.
26. Musante F, Derchi LE, Zappasodi F, et al. Myelolipoma of the adrenal gland: sonographic and CT features. AJR Am J Roentgenol. 1988;151(5): 961-964.
27. Shumam W, Moss A. The adrenal glands. In: Moss AA, Gamsu G, Genant H, editors. Computed tomography of the body with magnetic resonance imaging. 2nd ed. Philadelphia: Saunders; 1992. p. 1021-1057.
28. Renard J, Clerici T, Licker M, Triponez F. Pheochromocytoma and abdominal paraganglioma. J Visc Surg. 2011;148(6):e409-e416.
29. Cho KJ, Freier DT, McCormick TL, et al. Adrenal medullary disease in multiple endocrine neoplasia type II. AJR Am J Roentgenol. 1980;134(1): 23-29.
30. Brunt LM, Wells SA. The multiple endocrine neoplasia syndromes. Invest Radiol. 1985;20(9):916-927.
31. Quint LE, Glazer GM, Francis IR, et al. Pheochromocytoma and paraganglioma: comparison of MR imaging with CT and I-131 MIBG scintigraphy. Radiology. 1987;165(1):89-93.
32. Jacques AET, Sahdev A, Sandrasagara M, et al. Adrenal phaeochromocytoma: correlation of MRI appearances with histology and function. Eur Radiol. 2008;18(12):2885-2892.
33. Raja A, Leung K, Stamm M, et al. Multimodality imaging findings of pheochromocytoma with associated clinical and biochemical features in 53 patients with histologically confirmed tumors. AJR Am J Roentgenol. 2013;201(4):825-833.
34. Rozenblit A, Morehouse HT, Amis ES. Cystic adrenal lesions: CT features. Radiology. 1996;201(2):541-548.
35. Sebastiano C, Zhao X, Deng F-M, Das K. Cystic lesions of the adrenal gland: our experience over the last 20 years. Hum Pathol. 2013;44(9): 1797-1803.
36. Erickson LA, Lloyd RV, Hartman R, Thompson G. Cystic adrenal neoplasms. Cancer. 2004;101(7):1537-1544.
37. Abeshouse GA, Goldstein RB, Abeshouse BS. Adrenal cysts; review of the literature and report of three cases. J Urol. 1959;81(6):711-719.
38. Ricci Z, Chernyak V, Hsu K, et al. Adrenal cysts: natural history by long-term imaging follow-up. AJR Am J Roentgenol. 2013;201(5):1009-1016.
39. Akcay MN, Akcay G, Balik AA, Boyuk A. Hydatid cysts of the adrenal gland: review of nine patients. World J Surg. 2004;28:97-99.
40. Jordan E, Poder L, Courtier J, et al. Imaging of nontraumatic adrenal hemorrhage. AJR Am J Roentgenol. 2012;199(1):W91-W98.
41. Reznek RH, Armstrong P. The adrenal gland. Clin Endocrinol (Oxf). 1994;40(5):561-576.
42. Grizzle WE. Pathology of the adrenal gland. Semin Roentgenol. 1988; 23(4):323-331.
43. Guo Y-K, Yang Z-G, Li Y, et al. Uncommon adrenal masses: CT and MRI features with histopathologic correlation. Eur J Radiol. 2007;62(3): 359-370.
44. Fulmer BR. Diagnosis and management of adrenal cortical carcinoma. Curr Urol Rep. 2007;8(1):77-82.
45. Dunnick NR. The adrenal gland. In: Taveras JM, Ferrucci T, editors. Radiology. Philadelphia: Lippincott; 1990.
46. Lack EE. Tumors of the adrenal glands and extraadrenal paraganglia. Series 4, fascicle 8. Washington, DC: American Registry of Pathology; 2007. p. 1-297.
47. Lattin Jr GE, Sturgill ED, Tujo CA, et al. From the radiologic pathology archives: adrenal tumors and tumor-like conditions in the adult: radiologic-pathologic correlation. Radiographics. 2014;34(3):805-829.
48. Polat P, Kantarci M, Alper F, et al. Hydatid disease from head to toe. Radiographics. 2003;23(2):475-494.
49. Pulakhandam U, Dincsoy HP. Cytomegalovirus adrenalitis and adrenal insufficiency in AIDS. Am J Clin Pathol. 1990;93(5):651-656.
50. O'Brien WM, Choyke PL, Copeland J, et al. Computed tomography of adrenal abscess. J Comput Assist Tomogr. 1987;11(3):550-551.
51. Atkinson Jr GO, Kodroff MB, Gay Jr BB, Ricketts RR. Adrenal abscess in the neonate. Radiology. 1985;155(1):101-104.
52. Paling MR, Williamson BR. Adrenal involvement in non-Hodgkin lymphoma. AJR Am J Roentgenol. 1983;141(2):303-305.
53. Sancho JJ, Triponez F, Montet X, Sitges-Serra A. Surgical management of adrenal metastases. Langenbecks Arch Surg. 2011;397(2):179-194.
54. Elsayes KM, Mukundan G, Narra VR, et al. Adrenal masses: MR imaging features with pathologic correlation. Radiographics. 2004;24(Suppl. 1): S73-S86.
55. Straus DJ, Filippa DA, Lieberman PH, et al. The non-Hodgkin's lymphomas. I. A retrospective clinical and pathologic analysis of 499 cases diagnosed between 1958 and 1969. Cancer. 1983;51(1):101-109.
56. Rashidi A, Fisher SI. Primary adrenal lymphoma: a systematic review. Ann Hematol. 2013;92(12):1583-1593.
57. Martínez-Esteve A, García-Gómez FJ, Madrigal-Toscano MD, Borrego-Dorado I. Primary bilateral diffuse large B-cell lymphoma of the adrenals. Br J Haematol. 2015;170(1):3.
58. Tanpitukpongse TP, Kamalian S, Punsoni M, et al. Radiology-pathology conference: primary adrenal lymphoma. Clin Imaging. 2012;36(2): 156-159.
59. Singh D, Kumar L, Sharma A, et al. Adrenal involvement in non-Hodgkin's lymphoma: four cases and review of literature. Leuk Lymphoma. 2004;45(4):789-794.
60. Linos D, Tsirlis T, Kapralou A, et al. Adrenal ganglioneuromas: incidentalomas with misleading clinical and imaging features. Surgery. 2011;149(1): 99-105.
61. Li L, Shao J, Gu J, et al. Adrenal ganglioneuromas: experience from a retrospective study in a Chinese population. Urol J. 2014;11(2): 1485-1490.
62. Jrebi NY, Iqbal CW, Joliat G-R, et al. Review of our experience with neuroblastoma and ganglioneuroblastoma in adults. World J Surg. 2014;38(11): 2871-2874.
63. Young WF. The incidentally discovered adrenal mass. N Engl J Med. 2007;356(6):601-610.
64. Song JH, Chaudhry FS, Mayo-Smith WW. The incidental adrenal mass on CT: prevalence of adrenal disease in 1,049 consecutive adrenal masses in patients with no known malignancy. AJR Am J Roentgenol. 2008; 190(5):1163-1168.
65. Turner DJ, Miskulin J. Management of adrenal lesions. Curr Opin Oncol. 2009;21(1):34-40.
66. Blake MA, Cronin CG, Boland GW. Adrenal imaging. AJR Am J Roentgenol. 2010;194(6):1450-1460.
67. Kuruba R, Gallagher SF. Current management of adrenal tumors. Curr Opin Oncol. 2008;20(1):34-46.
68. Welch TJ, Sheedy PF, Stephens DH, et al. Percutaneous adrenal biopsy: review of a 10-year experience. Radiology. 1994;193(2):341-344.
69. Kane NM, Korobkin M, Francis IR, et al. Percutaneous biopsy of left adrenal masses: prevalence of pancreatitis after anterior approach. AJR Am J Roentgenol. 1991;157(4):777-780.

70. Zornoza J. Fine-needle biopsy of lymph nodes, adrenal glands and periureteral tissues. In: Pollack HM, editor. Clinical urography: an atlas and textbook of urologic imaging. Philadelphia: Saunders; 1990. p. 2854-2860.
71. Casola G, Nicolet V, vanSonnenberg E, et al. Unsuspected pheochromocytoma: risk of blood-pressure alterations during percutaneous adrenal biopsy. Radiology. 1986;159(3):733-735.
72. Uppot RN, Gervais DA. Imaging-guided adrenal tumor ablation. AJR Am J Roentgenol. 2013;200(6):1226-1233.
73. Martinez M, LeBlanc J, Al-Haddad M, et al. Role of endoscopic ultrasound fine-needle aspiration evaluating adrenal gland enlargement or mass. World J Nephrol. 2014;3(3):92-100.
74. Jhala NC, Jhala D, Eloubeidi MA, et al. Endoscopic ultrasound-guided fine-needle aspiration biopsy of the adrenal glands. Cancer. 2004;102(5):308-314.
75. Puri R, Thandassery RB, Choudhary NS, et al. Endoscopic ultrasound-guided fine-needle aspiration of the adrenal glands: analysis of 21 patients. Clin Endosc. 2015;48(2):165-170.
76. Asher KP, Gupta GN, Boris RS, et al. Robot-assisted laparoscopic partial adrenalectomy for pheochromocytoma: the National Cancer Institute technique. Eur Urol. 2011;60(1):118-124.

CHAPTER 12

The Retroperitoneum

Raymond E. Bertino and Elton Mustafaraj

SUMMARY OF KEY POINTS

- If an abdominal aortic aneurysm progresses to rupture, survival is very unlikely. If discovered before rupture, survival is highly likely.
- Most aneurysms are fusiform, which makes them readily diagnosable with ultrasound. Clinicians must also be aware of related entities that are more difficult to diagnose with ultrasound, including eccentric aneurysms, pseudoaneurysms, and penetrating ulcers.
- Ultrasound is *not* an appropriate method for the diagnosis of vascular emergencies in the abdomen. Particularly, it is not appropriate in the settings of possible ruptured abdominal aortic aneurysm and of acute mesenteric ischemia.
- In less acute situations, ultrasound has a strong role in the diagnosis of aortic aneurysm, renal artery stenosis, and chronic mesenteric ischemia. It also has a role in surveillance of aneurysms to assess growth and in treated aneurysms to assess for endoleaks.
- Ultrasound also has a role in the diagnosis of abdominal venous abnormalities. Clinicians should particularly be aware of the diagnoses of nutcracker syndrome and pelvic congestion syndrome, conditions that are probably underdiagnosed.

CHAPTER OUTLINE

ATHEROSCLEROSIS
ABDOMINAL AORTIC ANEURYSM
Mortality
Definition
Pathophysiology
Natural History and Medical Therapy
Screening
Recent Studies
Ultrasound Approach
Surveillance
Sonographic Technique
Computed Tomography
False-Positive/False-Negative Results
Ultrasound Versus Computed Tomography for Evaluation of Rupture
Treatment Planning
Postoperative Ultrasound Assessment
OTHER ENTITIES CAUSING ABDOMINAL AORTIC DILATION
Inflammatory Abdominal Aortic Aneurysm
Arteriomegaly and Aortic Ectasia
Penetrating Ulcer
Pseudoaneurysm
STENOTIC DISEASE OF THE ABDOMINAL AORTA
DISEASES OF ABDOMINAL AORTA BRANCHES
Renal Arteries
Anatomy
Renal Artery Stenosis and Renovascular Hypertension
Renal Artery Duplex Doppler Sonography
Renal Artery Aneurysm
Mesenteric Arteries
Anatomy
Mesenteric Ischemia
Median Arcuate Ligament Syndrome
Mesenteric Artery Duplex Doppler Sonography
Iliac Veins and Inferior Vena Cava
Anatomy
Anatomic Variants
Thrombosis
Nutcracker Syndrome
Pelvic Congestion Syndrome
Budd-Chiari Syndrome
Inferior Vena Cava Neoplasms
Other Inferior Vena Cava Findings
NONVASCULAR DISEASES OF THE RETROPERITONEUM
Solid Masses
Retroperitoneal Fibrosis
CONCLUSION

ATHEROSCLEROSIS

Atherosclerosis causes more deaths than any other disease in the Western world.[1] It is the main cause of cardiovascular diseases, including heart disease, cerebrovascular accident (stroke), hypertension, and peripheral vascular disease. It is a primary contributor to several other conditions, such as heart failure, arrhythmias (including atrial fibrillation), and cardiomyopathy. Cardiovascular disease has been the leading cause of death in the United States every year since 1900 except during the 1918 flu epidemic.[2]

There has been significant recent improvement. In 2013 cardiovascular disease was listed as the underlying cause for 800,937 deaths, a 28.8% drop from 2003.[2] In 2013 coronary heart

disease, when considered separately from other cardiovascular diseases, was still by far the single leading cause of death (370,213 deaths) in the United States.[2] Stroke, when considered separately from other cardiovascular diseases, was the underlying cause for 128,978 deaths in 2013.[2] By 2013, stroke had dropped to become the fifth leading cause of death, ranking behind heart disease, cancer, chronic lower respiratory diseases, and unintentional injuries in that order.[2]

Atherosclerosis is a complex process. Current understanding of its pathogenesis views atherosclerosis as a chronic inflammatory response triggered by injury to the endothelium. The endothelial injury results in increased permeability of the intima, allowing accumulation of low-density lipoprotein into the arterial wall. Inflammation results and plaque is produced, consisting of lipids, smooth muscle cells, fibrous tissue, macrophages, and calcium within the arterial wall.[1] Hemorrhage may also be present within the plaque. Atherosclerotic plaque can cause decreased blood flow to target organs by narrowing the arterial lumen, which can result in ischemic signs and symptoms such as claudication and erectile dysfunction (aortoiliac disease), hypertension and renal insufficiency (renal artery disease), and mesenteric ischemia (mesenteric artery disease).

Although there is controversy, many researchers believe that the processes inherent in atherosclerosis contribute to aneurysm formation.[3] Other, less common causes of aneurysms include cystic medial necrosis, trauma, and infection.[1]

ABDOMINAL AORTIC ANEURYSM

The abdominal aorta slowly tapers from the diaphragmatic hiatus to the aortic bifurcation (Fig. 12.1). Most of the tapering occurs in the proximal abdominal aorta as its largest branches (celiac, superior mesenteric, and renal arteries) arise. The normal size of the supraceliac abdominal aorta ranges from 2.5 to 2.7 cm in men and 2.1 to 2.3 cm in women. The normal diameter of the infrarenal aorta ranges from 2.0 to 2.4 cm in men and 1.7 to 2.2 cm in women.[4]

FIG. 12.1 Abdominal Aorta Anatomy. The abdominal aorta tapers from the aortic hiatus to the aortic bifurcation. The greatest tapering occurs as the aorta gives off its largest branches: the celiac, superior mesenteric, and renal arteries.

Mortality

Abdominal aortic aneurysm (AAA) is a common disease in the older population. Annually, 40,000 patients undergo elective repair in the United States.[5] AAA rupture is a catastrophic event. Many patients with ruptured aneurysms die before reaching a hospital. Of those admitted with rupture, many do not survive to go to surgery. For those with ruptured AAA that make it to surgery, the operative mortality rate is decreasing. Statistics from 2010 show an operative mortality rate of 33.4% for open procedures, a decrease of 10.1% from 2000.[5] When endovascular repair is used, the mortality rate is even lower—19.8% in 2010.[5] The overall mortality rate of a ruptured AAA is reported as being 85% to 90%,[6] largely because many patients with aortic rupture never make it to the operating room. Mortality for those undergoing elective repair in 2010 was 0.9% for endovascular repair and 4.8% for those undergoing open repair.[5] These facts suggest that the majority of deaths from AAA ruptures are preventable.

Much research has been conducted on reducing the number of deaths caused by AAAs. Ultrasound screening has proved to be a cost-effective step. Medical therapies may reduce the rate of growth of AAAs once they are detected. For large aneurysms, open or endovascular repair is much safer when done electively than emergently. With this knowledge, the AAA mortality rate can be greatly reduced.

Definition

There are many definitions of an arterial **aneurysm.**[7] A general definition is an increase in the diameter of an artery of at least 50% compared to the normal diameter of that artery.[4] For example, if a patient has an aorta that measures 2.2 cm in diameter, the aorta would be classified as aneurysmal at 3.3 cm. This definition can be difficult to apply to an abdominal aorta because it may not be clear what constitutes the normal aortic diameter in a specific patient.

The majority of AAAs are infrarenal. The most practical and common definition of infrarenal AAA specifies that an aneurysm is present when the infrarenal aorta has a diameter of 3.0 cm or greater. Aortas can also be referred to as **subaneurysmal** when they measure between 2.5 and 2.9 cm.[8] Subaneurysmal aortas have about a 50% chance of developing into a true aneurysm at 5 years.[9]

The definition that an AAA is present if the infrarenal aorta measures 3.0 cm or greater works well in most situations. However, the definition can be insufficient, particularly in small patients. It should be remembered that an aorta measuring 2.5 cm in diameter is properly called aneurysmal in a patient who has a more proximal aortic diameter measuring 1.6 cm.

Aneurysms that involve the renal arteries or the suprarenal aorta are less common and often occur with an aneurysmal thoracic aorta. AAAs that occur at or above the renal arteries are included in the Crawford classification of thoracoabdominal

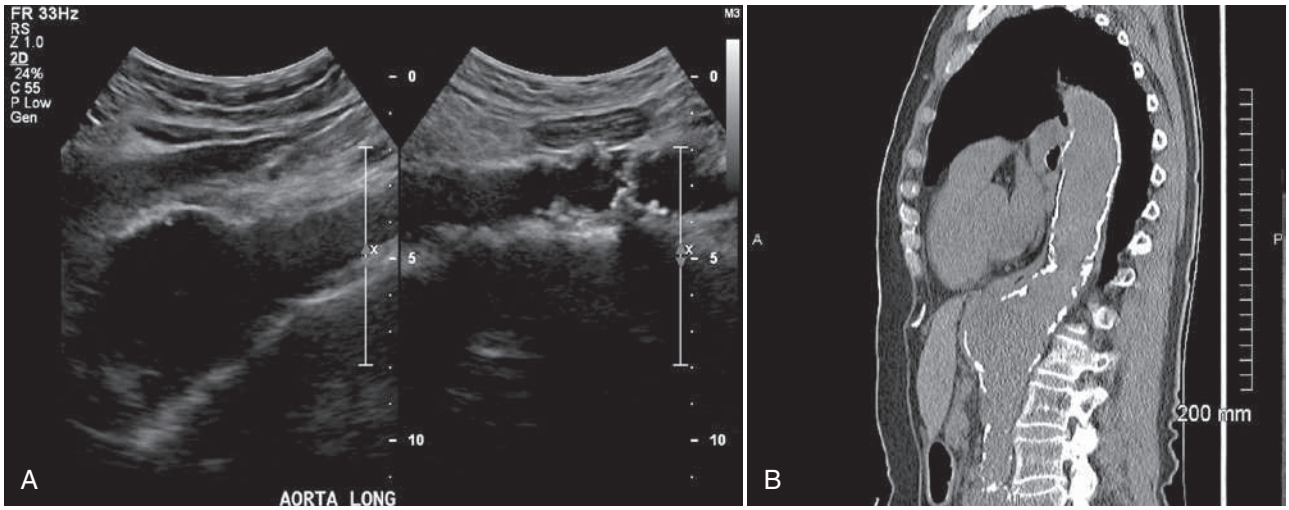

FIG. 12.2 Isolated Aneurysms of the Suprarenal Abdominal Aorta Are Rare. Most suprarenal abdominal aorta aneurysms (AAAs) also involve the thoracic aorta above the diaphragm. Isolated suprarenal AAAs are included in the Crawford classification of thoracoabdominal aneurysms. **(A)** Longitudinal ultrasound image shows isolated suprarenal AAA measuring 5.5 cm. **(B)** Sagittal reformatted CT demonstrates the isolated suprarenal AAA.

aneurysms[10] (Fig. 12.2). In the literature, unless otherwise specified, the term "abdominal aortic aneurysm" usually is used to mean "infrarenal abdominal aortic aneurysm."

Pathophysiology

Arteries have three layers: intima, media, and adventitia. The **intima,** the inner layer, is composed of the endothelium and the internal elastic lamina, along with scant intervening tissue. The intima is the main layer involved in the formation of atherosclerotic plaques. The **adventitia,** the outer layer, consists of connective tissue and carries nerves and the vasa vasorum.[1]

The **media** supplies much of the strength of the aorta and consists of elastin, collagen, smooth muscle cells, and extracellular matrix proteins. AAA formation is a disease largely involving the media and also the adventitia.[11,12] The aorta is an elastic artery and the aortic media has high elastin content.[1] With AAA, there is a significant decrease in elastin and collagen content in the media and adventitia.[11] Destruction of elastin is mediated by enzymes such as **matrix metalloproteinases** (MMPs). Medications may be able to reduce the rate of elastin destruction, either by suppression of the MMPs or inhibiting other biochemical pathways.[13] Statins and doxycycline are known inhibitors of MMP enzymes. Good evidence, however, is lacking regarding what may be the best medical therapy to help reduce the rate of AAA growth.[14]

Natural History and Medical Therapy

AAA is a disease of older persons. AAAs rarely occur before age 50 and affect men four times more often than women. The risk of developing an AAA also increases with smoking and with a family history of AAA in a first-degree relative. Other factors that increase risk are a history of peripheral vascular disease, cardiovascular disease, and hypertension.[15] AAAs typically increase in diameter at a rate of 1.7 to 2.6 mm per year. This rate of growth increases as the AAA becomes larger.[15] The rate of growth is faster in women.[16,17]

As the size of the AAA increases, the risk of rupture increases. Rupture is rare when the AAA is less than 4.0 cm in diameter, with near 0% risk per year. The rate of rupture increases to 1% when the AAA is 4 to 4.9 cm, 1.0% to 11 % for AAAs 5.0 to 5.9 cm in diameter, 10% to 22% for AAAs 6.0 to 6.9 cm, and 30% to 33% for aneurysms larger than 7 cm.[18] Although data for larger aneurysms are conflicting, when the diameter is greater than 6.0 cm, clearly the risk of rupture is significantly higher than for smaller aneurysms.[19,20] Other risk factors for rupture include current smoking and chronic obstructive pulmonary disease. In addition, the rupture rate for women is four times that of men.[21] Rupture in women occurs in smaller aneurysms, although the exact amount of increased risk is not well quantified. Because smaller AAAs in women have a risk similar to larger ones in men, elective treatment in women should occur at a smaller aneurysm size than in men.[17,18] Recommendations about how much smaller vary from 3 mm to greater than 5 mm.[22]

Current medical therapy is limited in its ability to prevent the growth of an AAA. Rate of aneurysm growth is increased in smokers and may be decreased in diabetics. Medications including statins and doxycycline have been suggested as possibly reducing the rate of aneurysm growth.[23-25] To date, none of the current strategies for reducing rate of growth through medications has been shown to be very effective.[14,26]

Screening

Recent Studies

The malady of AAA meets the 10 World Health Organization criteria for the institution of screening programs.[27] Research has been extensive, particularly in Europe, on the effectiveness and cost-effectiveness of ultrasound screening for AAA.

A meta-analysis commissioned by the US Preventive Services Task Force (USPSTF) combined analyses from four studies, including European studies. The analysts concluded that "for men age 65 to 75, an invitation to attend AAA screening reduces

AAA-related mortality." Based on these results, in 2005 the USPSTF published a recommendation for one-time screening for men aged 65 to 75 who had ever smoked.[28] In 2014 the USPSTF issued an update reiterating this recommendation.[29] The task force also recommended selective screening based on risk factors for men aged 65 to 75 who had never smoked. The risk factors they referenced were older age, positive smoking history, first-degree relative with AAA, history of other vascular aneurysm, coronary artery disease, cerebrovascular disease, atherosclerosis, hypercholesterolemia, obesity, and hypertension. The USPSTF believed the evidence to support screening for AAA in women smokers was inconclusive and consequently made no specific recommendation about such screening. The USPSTF recommended against routine screening for women who had never smoked.

The Screening Abdominal Aortic Aneurysms Very Efficiently **(SAAAVE) Act** was passed by the US Congress and signed on February 8, 2006. Since January 1, 2007, Medicare has covered a one-time, ultrasound screening to check for AAA in qualified patients. Qualified patients are men with a history of smoking (i.e., those who have smoked more than 100 cigarettes total during their lives) and men and women with a family history of AAA in a first-degree relative. To be covered, patients must undergo the AAA screening study as part of the Welcome to Medicare Physical Exam and complete the screening within the first 6 months of Medicare eligibility. Analysis of data from the first 2 years after the SAAVE Act was passed indicates that a minority (<20%) of the Medicare population that was eligible for AAA screening underwent screening. The impact of the SAAVE Act on the rate of AAA screening during those first 2 years was described as modest.[30]

Across the world, a few countries currently have nationwide screening programs although several others have begun pilot studies. National screening has been implemented in Sweden, in all member nations of the United Kingdom (England, Scotland, Wales, and Northern Ireland), and in the United States. Sweden has achieved an impressive attendance rate of 85% of those eligible for its screening program.[8]

Ultrasound Approach

Screening for AAA must have high sensitivity. It is mandatory that the entire infrarenal abdominal aorta be examined. The screening ultrasound has one of three results: positive, negative, or indeterminate.[31] The number of expected indeterminate exams should be very low, much less than 5%.

There are currently two paradigms for ultrasound in the screening of AAAs. The first is embodied in the current guidelines issued by the American College of Radiology (ACR) and involves obtaining a full set of documentation images on every patient.[31] When the screening examination is positive for AAA, the recommended images are adequate to document aneurysm size accurately. The screening examination thus also serves as the first diagnostic exam. This type of screening exam is not very different from a full "diagnostic" examination and is probably the most common type in radiology departments.

The second paradigm is used by several mobile companies offering aneurysm screening to the general population. These for-profit programs are prepaid by the individuals requesting screening; profit is based on doing a high volume of cases within a short time, keeping cost to a minimum. It is unclear whether adequate quality control mechanisms are in place for these exams, which often have only two possible results: positive and negative. Positive exams do not result in extension of the study to be diagnostic. Instead, a positive exam results in a recommendation to the patient to have a diagnostic evaluation. This allows the provider to save time and reduce cost.

The decreased cost of this type of examination offers a potential benefit. If the low cost of this type of service could be widely reproduced, and if the issue of quality control were addressed, screening that is both accurate and cost-effective could become available for a wider segment of the population.

Unfortunately, at least some of the programs make recommendations to their customers that cannot be supported by the literature such as the concept of needing to screen for AAA on a yearly basis. Screening on a yearly basis certainly will increase the number of patients using the service and increase profit but hardly seems to represent an disinterested attempt to improve health care.[32] Atherosclerotic aneurysm formation is a very slow process and there is absolutely no need for yearly screening for someone without an aneurysm. There are some who would question whether a second screening is ever needed if the first screening was performed at age 65 or later. Certainly, once a first well-performed screen is negative there is no justification for rescreening except perhaps after many years.

Surveillance

Once an AAA is discovered, the patient moves from screening to a **surveillance** program in which the aneurysm size is periodically checked. Because an AAA tends to grow more rapidly as its size increases, there is general agreement that a smaller aneurysm needs to be checked less frequently than a larger one. Otherwise, however, consensus is lacking on frequency of sonographic surveillance. Recommendations for assessing aneurysms less than 4.0 cm in diameter range from 1 to 3 years.[33] For the U.K. Small Aneurysm Trial, Brady et al.[34] concluded that surveillance could be performed at intervals of 36, 24, 12, and 3 months for aneurysms of 35, 40, 45, and 50 mm, respectively. Following this schedule, the risk of the AAA size on recheck being greater than 55 mm would be less than 1%. Achieving a 5% rate would require even less frequent surveillance. Society for Vascular Surgery practice guidelines recommend surveillance at 36, 12, and 6 months for aneurysms between 3.0 and 3.4 cm, between 3.5 and 3.9 cm, and between 4.0 and 5.4 cm, respectively. They also recommend surveillance every 5 years for aortas between 2.6 and 2.9 cm in size.[35] It has been suggested that aortic aneurysms may need even less frequent surveillance than what is cited above.[36]

Up until several years ago, we scanned most aneurysms yearly. Our aneurysm clinic now follows AAAs sonographically every 2 years when the aneurysm is less than 40 mm, every year for aneurysms 40 to 44 mm, and every 6 months once the aneurysm reaches 45 mm.

Surveillance of aneurysms lends itself well to being followed by a database. Our interventional radiology–run aneurysm clinic started a database in 2003 to follow AAAs.[37] Patients with known

AAAs of any size are entered into the database. Patients are seen once in our interventional radiology clinic so that they can meet the physicians and advanced practice nurses involved and can be informed about their disease, its treatment, and how their aneurysm is to be followed. The clinic orders all subsequent aortic ultrasounds and monitors all results. After that first visit, all communication is by phone and by mail. The database is monitored periodically to make sure patients keep their appointments. When the aneurysm reaches 5.0 cm in greatest diameter, patients again begin to be seen regularly in the clinic.

Sonographic Technique

Pertinent history should be obtained when doing surveillance on a known aneurysm. Questions of interest are whether the patient has back and/or abdominal pain or tenderness. These symptoms can be experienced by patients who have inflammatory aneurysms. In the absence of an inflammatory aneurysm, these symptoms are considered an indication for aneurysm repair.

The following principles apply both to screening examinations and studies for surveillance. Evaluation of the entire infrarenal aorta is necessary. Identifying the aortic bifurcation guarantees that one has seen far enough distally. By identifying the celiac, superior mesenteric, or renal arteries or the aortic hiatus of the diaphragm, sonographers can guarantee that the proximal examination has been carried high enough. Images should be obtained in both transverse and longitudinal planes. The goal is to find the maximum diameter of the aorta, measured from outer edge of the wall to outer edge of the opposite wall. Measurements should be taken perpendicular to the axis of the lumen of the aorta. To guarantee that the measurement is perpendicular, longitudinal images are usually best for obtaining the most accurate measurements (Fig. 12.3). The measurement includes both the front and the back walls.

Most infrarenal aneurysms are fusiform in shape with a relatively circular cross section. With a fusiform aneurysm, measurement of its size taken from any longitudinal plane through the aorta will be the same (Fig. 12.4). The walls of the aorta are generally well seen with longitudinal imaging because they are parallel to the face of the transducer, resulting in a strong echo from the walls. Transverse imaging is particularly important to identify the small proportion of aneurysms that are eccentric. If the aneurysm is eccentric, the measurement must be taken in the plane of the aneurysm's eccentricity to find the largest diameter of the aneurysm (Figs. 12.5 and 12.6).

We routinely image patients from two windows: the anterior abdominal midline (sagittal plane), which allows imaging of the maximum length of the abdominal aorta, and the left flank (near the coronal plane), with the patient in the right lateral

FIG. 12.3 Measuring Abdominal Aorta Aneurysms (AAAs). AAA measurements from longitudinal images are usually the most accurate and are taken perpendicular to the lumen. The measurement includes both the front and the back walls.

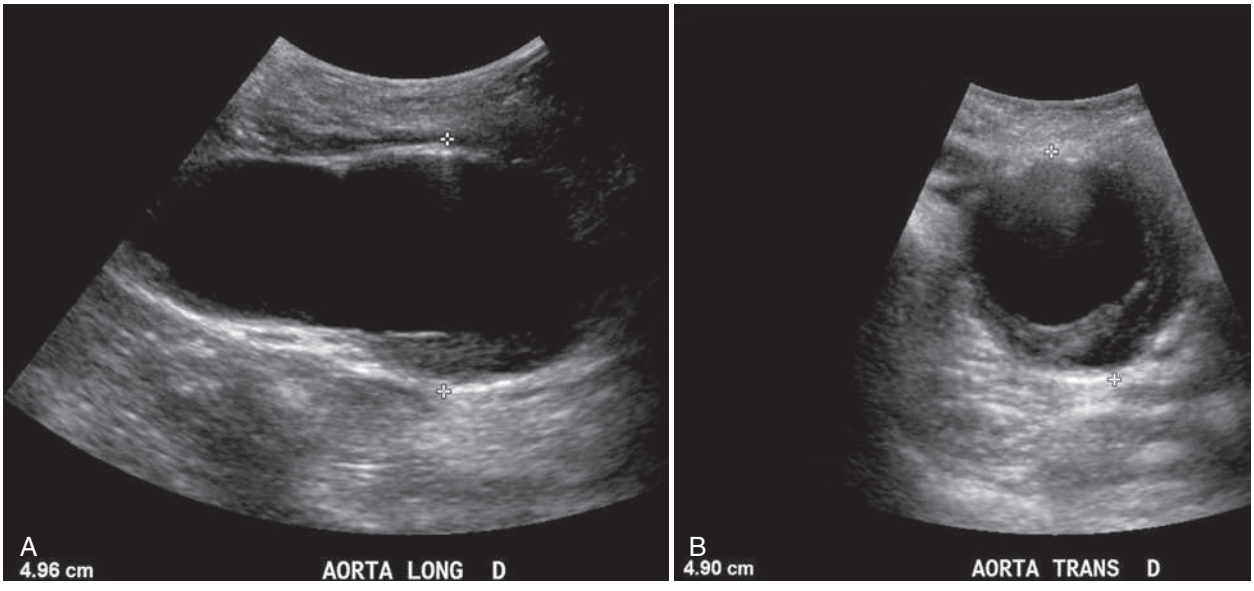

FIG. 12.4 Most Abdominal Aortic Aneurysms (AAAs) Are Fusiform. When fusiform, the AAA is circular in cross section. **(A)** Longitudinal and **(B)** transverse gray-scale sonograms show measurement of the AAA.

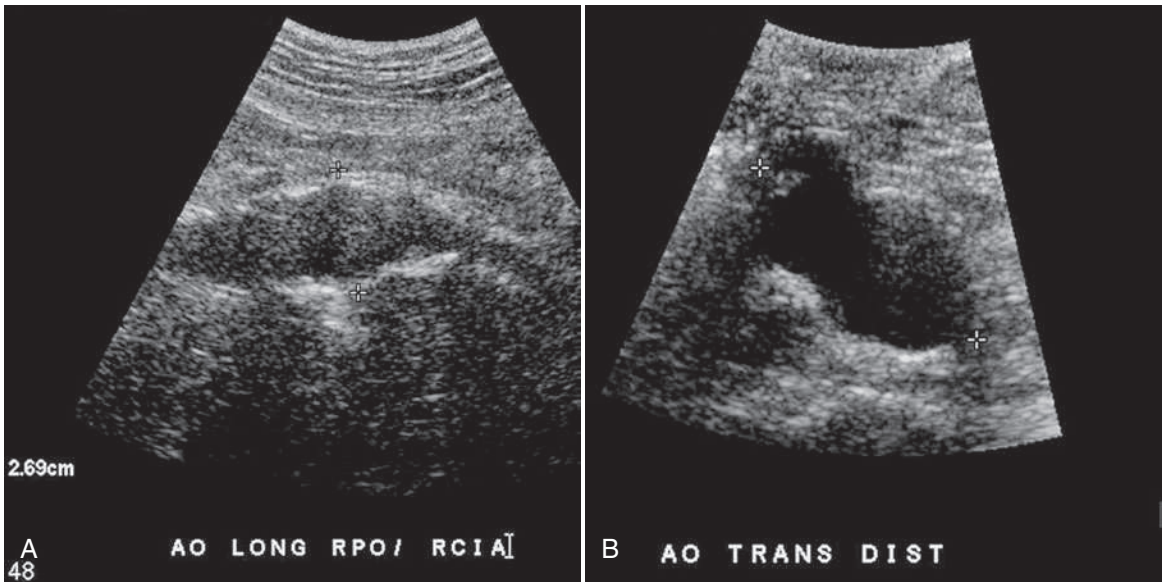

FIG. 12.5 Aorta With Saccular Aneurysm. (A) Viewed in the longitudinal plane, the aorta appears normal. **(B)** Transverse imaging of the aorta is required to reliably detect a saccular aneurysm. Unless a longitudinal image can be obtained in the plane of the greatest diameter of a saccular aneurysm, transverse imaging must be used to measure the greatest diameter.

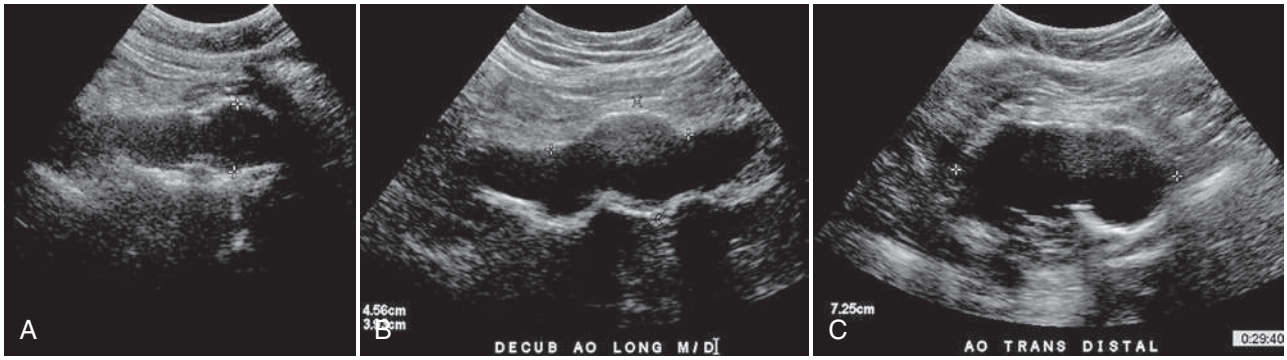

FIG. 12.6 Small Aortic Aneurysm Just Reaching 3.0 cm. (A) Longitudinal scan. Note that the abdominal aortic aneurysm was incorrectly measured from inner wall to inner wall (*calipers,* 2.9 cm) instead of the correct method, which is outer wall to outer wall. **(B)** The patient was lost to follow-up of the aneurysm. He returned 6 years later with a 6-week history of abdominal and back pain. The aneurysm was incidentally rediscovered during the course of abdominal ultrasound. On longitudinal imaging, the aneurysm had increased in size (4.6 cm). **(C)** Transverse view shows that the aortic lumen is actually larger and now is eccentric, with a largest diameter of 7.3 cm. In retrospect, the patient's 6-week history of abdominal and back pain probably had been from the contained perforation of the aneurysm.

decubitus position. The middle and distal abdominal aorta are often better seen in this position, particularly in obese patients. The proximal common iliac arteries may also be better seen in this position.

We obtain longitudinal and transverse cine loops from an anterior window and from a left lateral window. The longitudinal cine loops allow for easy remeasurement of the aorta by the reviewing physician. The transverse cine loops allow the reviewing physician to determine whether there is eccentricity of the aneurysm.

Computed Tomography

Computed tomography (CT) has a limited role in AAA screening and surveillance but should be used in any of the following situations:

1. The patient is so obese or otherwise difficult to image that whether the aneurysm may be eccentric cannot be determined with reasonable certainty on initial scanning. Once the aneurysm is shown to be fusiform, performing most of the further surveillance with ultrasound is reasonable.
2. The aneurysm is known to be eccentric, and the area of eccentricity is not optimally seen with ultrasound.
3. The patient is acutely symptomatic (including emergency room patients).
4. Portions of the iliac arteries that are known to be aneurysmal are not well seen.
5. The AAA is suspected to be an inflammatory AAA (described later) and has not yet been imaged with CT.
6. The aneurysm is suspected of having reached a size at which treatment planning is needed.

FIG. 12.7 False-Positive Abdominal Aortic Aneurysm. The deep cursor has been placed on the echo caused by the anterior edge of lumbar vertebral body, posterior to the aorta. Mistaking the anterior lumbar spine for the posterior wall of the aorta may cause a false-positive exam, particularly if visualization is poor because of obesity. Transverse imaging can usually detect the error. Longitudinal imaging in the coronal plane also helps avoid this error.

False-Positive/False-Negative Results

Screening for aortic aneurysm should be highly accurate. Nonetheless, we have encountered two sets of circumstances where it is possible to have a false-positive study. The first can happen when the aorta at the diaphragmatic hiatus measures 3.0 cm or greater and is mistakenly called "aneurysmal." The normal size of the supraceliac aorta is 2.1 to 2.7 cm.[4] Based on a definition of aneurysm that requires the diameter to be 1.5 times or more the normal diameter, a small aorta would not become aneurysmal until it reached approximately 3.2 cm in diameter, whereas the larger supraceliac aorta would not be aneurysmal even at 4.0 cm.

The second circumstance where we have seen several false-positive studies is when the spine is mistaken for the posterior wall of the aorta. This is particularly likely to occur when visualization is poor, as in a very obese patient. The true posterior wall of the aorta may then be difficult to determine. Usually, transverse imaging or imaging from the left flank will help define the true posterior wall to help determine if an aneurysm is present (Fig. 12.7).

False-negative studies may occur if visualization of the infrarenal aorta is incomplete. If the entire infrarenal aorta is well seen in longitudinal imaging, the diagnostician can exclude the presence of a fusiform aneurysm, the most common type of AAA. However, if the entire infrarenal aorta is not well seen in the transverse plane, an eccentric aneurysm is not excluded (see Figs. 12.5 and 12.6).

Ultrasound Versus Computed Tomography for Evaluation of Rupture

As previously mentioned, **rupture** of aortic aneurysms is catastrophic, usually resulting in the patient's death. Although it played a role in the rapid diagnosis of ruptured AAAs in the emergency room 30 years ago,[38] ultrasound no longer has such a place at most institutions. The near ubiquitousness of high-speed multidetector CT scanners has made CT diagnosis extremely rapid. CT has a number of other advantages in comparison to ultrasound. CT, even without intravenous contrast, is diagnostic of AAA in all cases, is highly diagnostic of retroperitoneal bleeding associated with aneurysm rupture, and is not operator dependent.

Because of these factors, obtaining a formal ultrasound in patients with an emergent need for diagnosis in most settings is unwise. If the patient has a ruptured AAA, time is of the essence, and the patient needs the most complete information that can be obtained in a reliable way. Performing ultrasound risks wasting precious minutes that may be the difference between patient survival and death (Fig. 12.8).

Treatment Planning

Treatment of large AAAs involves either open surgical repair or **endovascular aortic repair** (EVAR). Endovascular repair involved the placement of an **endoluminal graft** (also known as a **stent graft**) to create a new channel for blood flow through the aneurysm isolating the aneurysmal sac.

Computed tomography angiography (CTA) is the most appropriate imaging method for AAA treatment planning. In the setting of open repair, CTA accurately assesses the degree to which the iliac arteries may be involved with the aneurysm. In addition, evaluation of the mesenteric arteries is of value to determine whether reimplantation of the inferior mesenteric artery (IMA) is needed. For EVAR, the distance of the renal arteries from the top of the aneurysm and the presence and location of accessory renal arteries are important. Knowledge of the three-dimensional anatomy of the aneurysm and size and configuration of the iliac arteries is critical.

Postoperative Ultrasound Assessment

After open surgical repair of an aortic aneurysm, imaging surveillance generally is not performed. Imaging is used to assess **postoperative complications,** including thrombosis, infection, stenosis (graft kink, neointimal hyperplasia, atherosclerosis), and **anastomotic pseudoaneurysm.** Ultrasound may play a role in the diagnosis of any of these complications. Another complication is **aortoenteric fistula,** generally to the third portion of the duodenum, which is potentially catastrophic and presents most often with upper gastrointestinal bleeding. Ultrasound has no role to play in the diagnosis of aortoenteric fistula.

Ultrasound has a larger, potentially much larger, role to play after repair of AAAs with EVAR. Current recommendations include lifelong imaging surveillance for endoleaks and graft migration in patients who have undergone EVAR for AAA.[39] An **endoleak** is an area of the AAA that has been excluded by the stent graft that nonetheless continues to have blood flow. There are four types of endoleaks, categorized by four different sources of blood flowing into the aneurysmal sac (Fig. 12.9). Egress of blood from the sac is usually through patent aortic branches in all types of endoleak.

With a **type 1 leak,** one of the ends of the stent graft is not tightly apposed to the arterial wall, allowing blood to enter the aneurysmal sac (Fig. 12.10). A **type 2 leak** is caused by retrograde

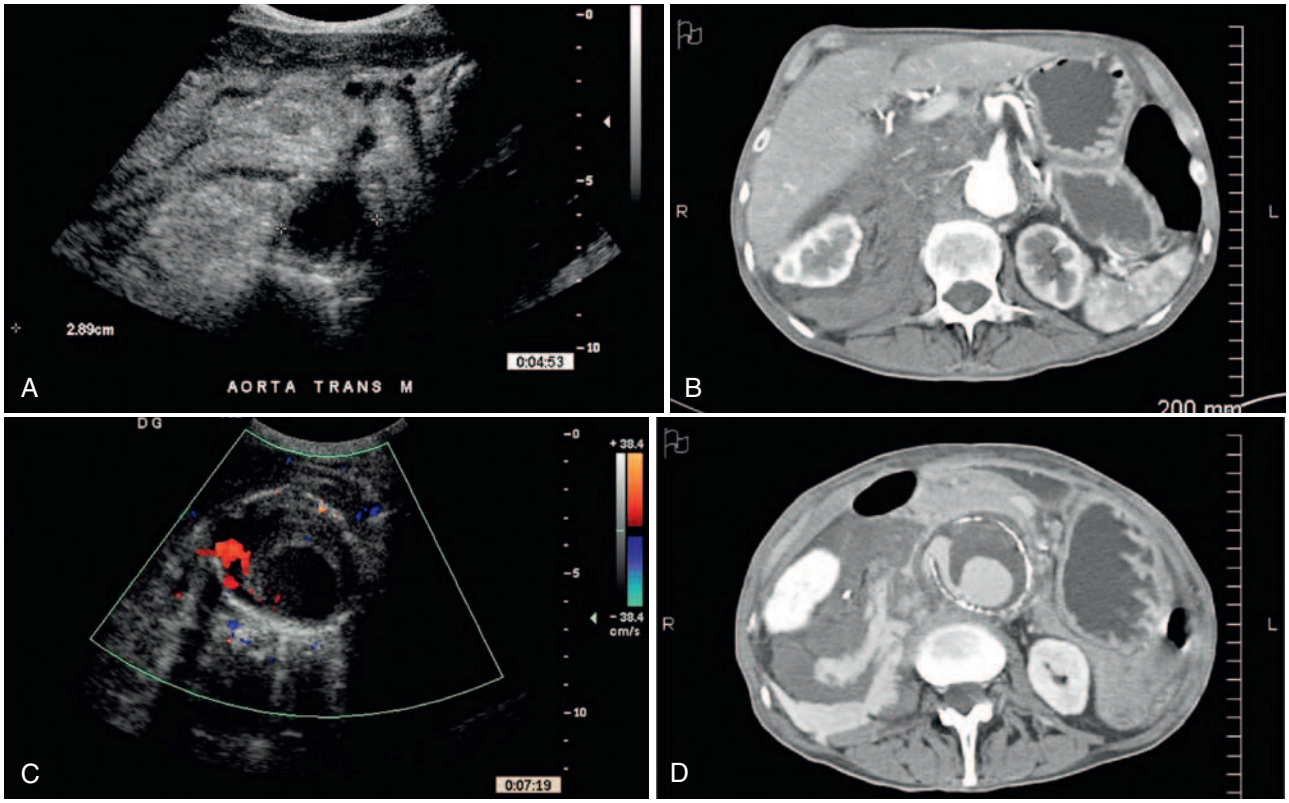

FIG. 12.8 Ruptured Abdominal Aortic Aneurysm (AAA). The use of both **(A)** ultrasound and **(B)** computed tomography (CT) in suspected rupture of AAA should be avoided because of the addition of time for the workup. (In this case 45 minutes elapsed between the ultrasound and CT.) CT is preferred in this setting because it can usually be done expeditiously and more reliably answers the pertinent questions. **(C)** Transverse ultrasound and **(D)** contrast-enhanced CT show the same AAA visualized at the site of rupture. The patient did not survive.

flow into the aneurysm sac through an aortic branch, usually the IMA or a lumbar artery (Fig. 12.11, Videos 12.1 and 12.2). In a **type 3 leak,** there is disruption of the integrity of the stent graft, caused by a fabric tear or a separation of component parts of the modular stent graft (Fig. 12.12, Videos 12.3 and 12.4). A **type 4 leak** is caused by porosity of the stent graft fabric with blood actually going through the pores in the fabric. This is seen only early after placement and is self-correcting. The term **endotension** refers to an aneurysm sac that stays pressurized in the presence of a stent graft. This is sometimes referred to as a type 5 endoleak. Its presence is inferred by continued growth in the aneurysm sac size in the absence of detecting another type of leak.[40,41]

With an endoleak, a treated aneurysm may continue to grow and eventually rupture. Endoleaks occur in approximately one-third of AAAs treated with stent grafts.[42] Types 1 and 3 endoleaks require immediate treatment when diagnosed. Type 4 endoleaks are generally seen only during placement of the stent graft and are self-limited, requiring no treatment. More judgment is involved in the care of type 2 leaks. Small leaks may be watched over time to see if they resolve and whether expansion of the aneurysm occurs.[42,43]

Because of the possibility of endoleaks, AAAs treated with stent grafts undergo routine imaging surveillance. Imaging most often includes yearly, contrast-enhanced, multiphase CT examinations. This regular imaging greatly increases cost and exposes patients to contrast and substantial radiation. Color duplex Doppler sonography alone can be used to visualize endoleaks. Several studies suggest that standard color duplex Doppler ultrasound may be the preferred method of surveillance.[44,45] Studies comparing contrast-enhanced duplex with standard color duplex have found the addition of contrast improves the quality of the study. Several studies suggest that contrast-enhanced ultrasound is at least as sensitive as CT for the detection of endoleaks.[46-48] The issue is still a topic of research,[49] although with more experience, contrast-enhanced ultrasound likely will play a significant role in AAA endoluminal graft surveillance.

As already mentioned, surveillance for graft migration is also necessary after EVAR. In those undergoing surveillance for endoleak with color duplex Doppler sonography, plain radiography can be used to assess for graft migration.

OTHER ENTITIES CAUSING ABDOMINAL AORTIC DILATION

Inflammatory Abdominal Aortic Aneurysm

Inflammatory AAAs constitute as much as 5% or more of all AAAs.[50] According to some investigators, inflammatory AAA is likely related to retroperitoneal fibrosis (see later discussion),

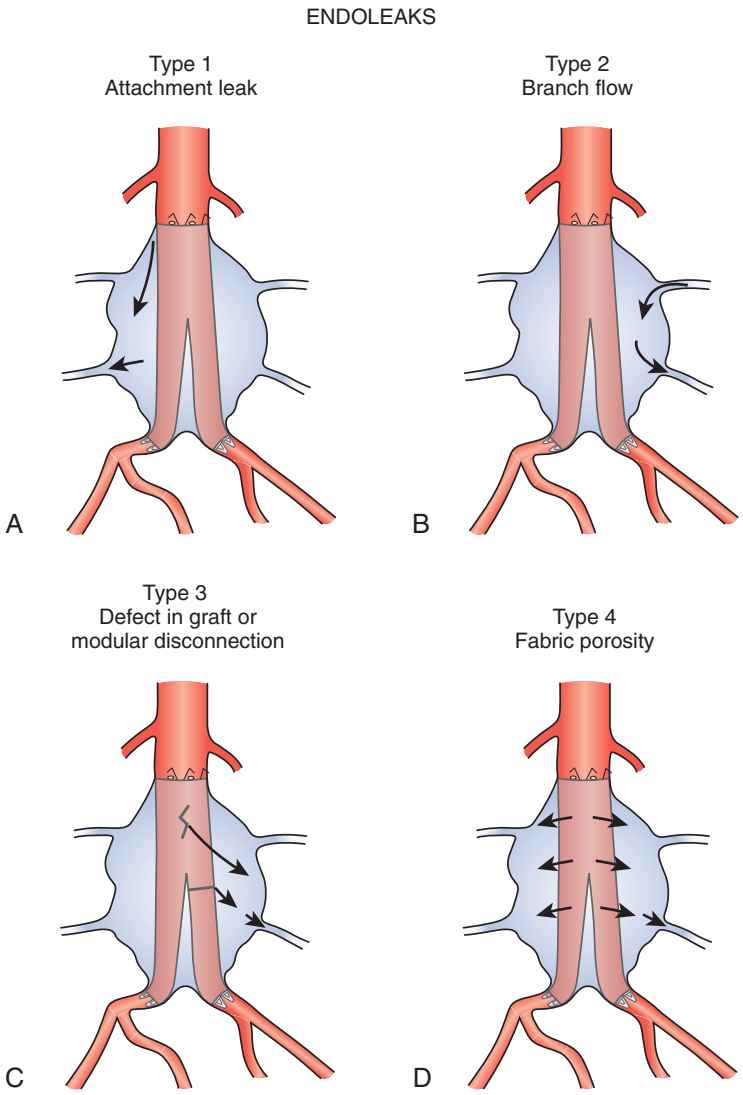

FIG. 12.9 Endoleaks of Abdominal Aortic Aneurysm After Endovascular Aneurysm Repair. (A) Type 1 leak (attachment leak). Blood continues to enter the aneurysm sac at one of the three ends of the bifurcated stent graft, the points where the stent graft should be tightly affixed to the arterial wall. Egress, as with all endoleaks, is through branches of the aorta that remain patent. Treatment of type 1 leaks is indicated. **(B) Type 2 leak (branch artery leak).** Blood enters the aneurysm sac through a patent branch artery. This type of leak can be self-limited and may be just observed. Treatment is indicated if the aneurysm enlarges. **(C) Type 3 leak (loss of integrity of stent graft).** Either the modules of the stent graft have become separated or a rent has formed in the fabric of the stent graft. Blood enters the sac from the stent graft lumen through the site of loss of stent graft integrity. Treatment is indicated. **(D) Type 4 leak (fabric porosity).** Blood enters the sac from the stent graft lumen through intact cloth of the stent graft. This is self-limited and present only at surgery. The pores of the fabric quickly become occluded by blood products.

with both included as part of a classification referred to as **chronic periaortitis.**[50-52] The newly discovered entity of **immunoglobulin G4 (IgG4)–related periaortitis** and periarteritis likely is also part of this complex.[53]

Inflammatory AAAs are recognized by extremely thickened aortic wall and surrounding fibrosis that tends to spare the posterior wall (Fig. 12.13). As in retroperitoneal fibrosis, the inflammation may involve the ureters, causing obstruction. Inflammatory AAAs are less prone to rupture than other AAAs but are more prone to producing symptoms such as back pain. Antiinflammatory drugs, including steroids and methotrexate, have been used to treat the inflammation.[50-52] With surgical or endovascular treatment, the inflammation surrounding many AAAs resolves (Fig. 12.14).[54] Sonographically, inflammatory AAAs may be recognized by a rind of tissue surrounding the aorta. Needle biopsy is usually necessary to confirm the diagnosis and to exclude the small chance that the mass instead is due to neoplasm, particularly lymphoma.

Arteriomegaly and Aortic Ectasia

Arteriomegaly is diffuse arterial dilation involving several arteries, each with an increased diameter of at least 50% compared with the normal diameter. **Ectasia** refers to diffuse or focal dilation that is less than 50% increased in diameter.[4]

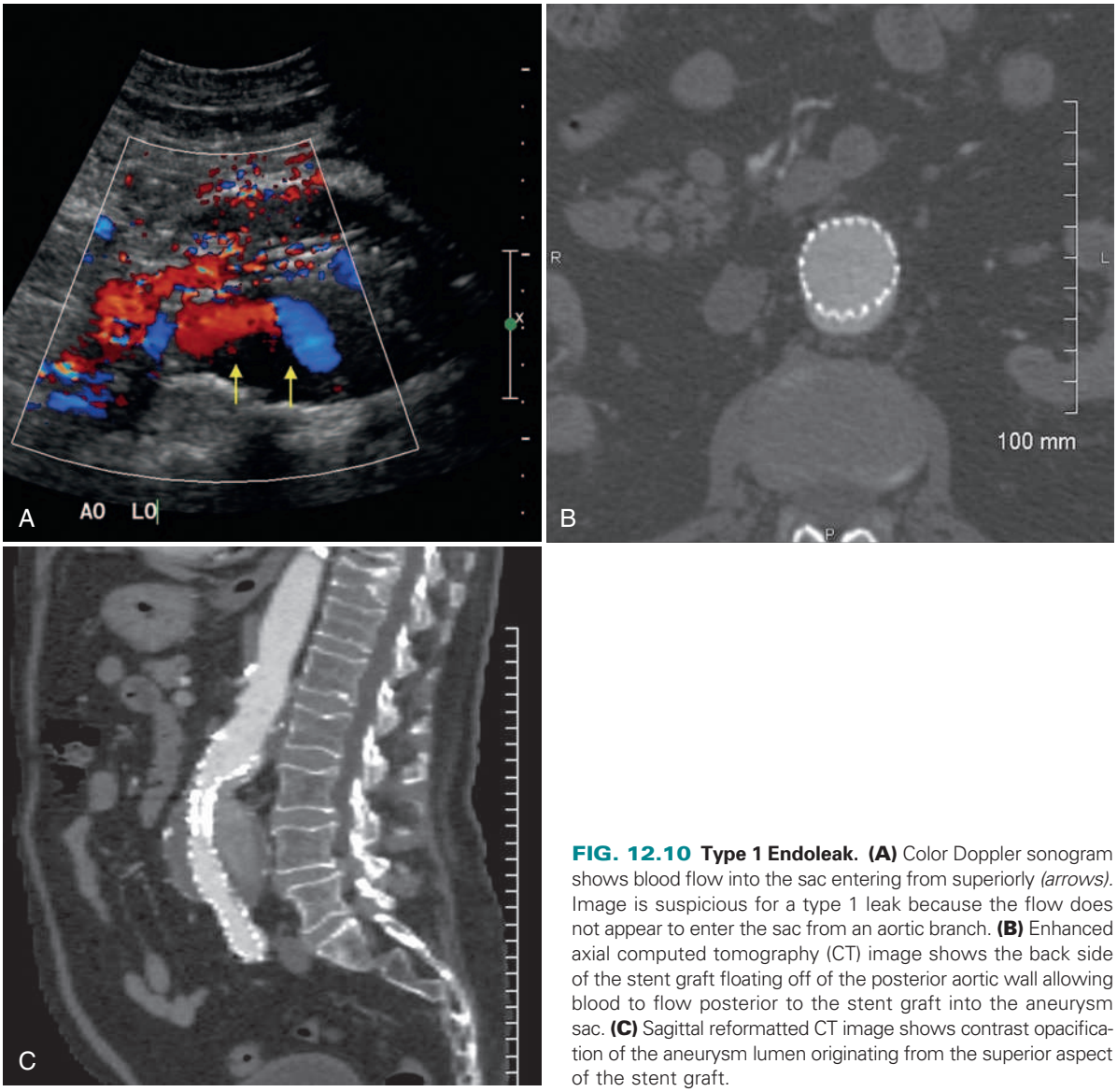

FIG. 12.10 Type 1 Endoleak. (A) Color Doppler sonogram shows blood flow into the sac entering from superiorly *(arrows)*. Image is suspicious for a type 1 leak because the flow does not appear to enter the sac from an aortic branch. **(B)** Enhanced axial computed tomography (CT) image shows the back side of the stent graft floating off of the posterior aortic wall allowing blood to flow posterior to the stent graft into the aneurysm sac. **(C)** Sagittal reformatted CT image shows contrast opacification of the aneurysm lumen originating from the superior aspect of the stent graft.

Penetrating Ulcer

Penetrating ulcer has been recognized for approximately 30 years.[55] It is believed to result when an atherosclerotic ulceration penetrates the media, allowing an intramural hematoma to form.[56] This outpouching into the media may progress, developing into a saccular aneurysm. Penetrating ulcers occur more frequently in the thoracic aorta but are also seen in the abdominal aorta[57,58] (Fig. 12.15).

Pseudoaneurysm

A true aneurysm is a dilation of an artery that is contained by all three layers of the arterial wall. In contrast, a **pseudoaneurysm** is a dilation that may be confined by only two layers, only one layer, or only adjacent soft tissue. In the abdominal aorta, a pseudoaneurysm is most likely to occur as a late surgical complication of aortic aneurysm repair or of other arterial surgery, almost always at sites of anastomosis. It can also be the result of incomplete rupture of a penetrating ulcer or aneurysm (Video 12.5). Sonographically, the appearance often is similar to a true aneurysm. With the proper findings, the diagnosis of pseudoaneurysm versus true aneurysm is made largely based on the clinical setting (e.g., previous trauma or aneurysm repair).

STENOTIC DISEASE OF THE ABDOMINAL AORTA

Stenosis or occlusion of the abdominal aorta can be congenital or caused by atherosclerosis, vasculitis (arteritis), trauma, or embolus. Dissection may also result in stenosis. **Midaortic syndrome** is a rare congenital stenosis that is also called **abdominal coarctation.**

Symptoms of aortic stenosis or occlusion include intermittent claudication and impotence. These symptoms, along with the finding of decreased femoral pulses, are called **Leriche syndrome,** although the term often is used more broadly to refer to all the

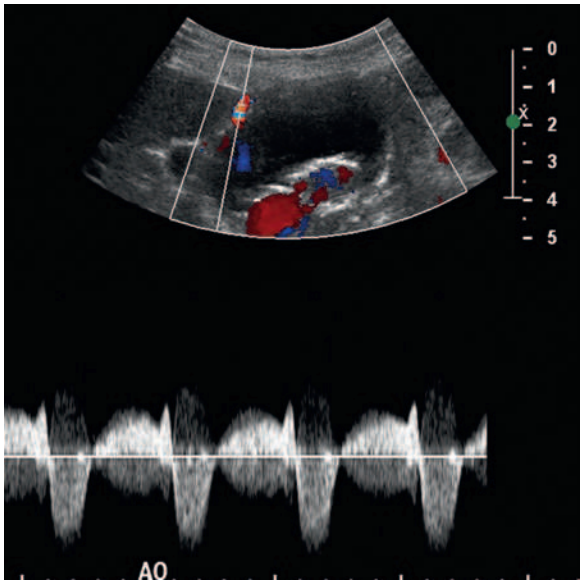

FIG. 12.11 Type 2 Endoleak. To-and-fro flow in the inferior mesenteric artery filling a small patent space in the aneurysm sac. See also Videos 12.1 and 12.2.

signs and symptoms that may result from aortic occlusive disease or even the occlusion itself. In the great majority of patients with aortic stenosis or occlusion, the disease is caused by atherosclerosis. However, certain clinical settings suggest other causes.

With embolic disease, a dramatic abrupt onset of symptoms is the best historical evidence of the nature of the event. The patient can often relate exactly what he or she was doing when the symptoms started, even if the event was weeks in the past (e.g., "I had just gotten up from cutting roses …"). The rapidity with which the patient seeks treatment depends on the severity of the reduction in blood flow. Embolus to any artery must be viewed as a very serious and signal event. The majority of emboli to the abdominal aorta come from the heart. Having an arterial embolism of any type is similar to having a pulmonary embolism; having one puts the patient at risk for having more. If the origin of the embolus is cardiac, the next one that forms may go to some less favorable place, such as the cerebral circulation, resulting in stroke, or to the mesenteric circulation, resulting in intestinal infarction. The workup of any patient identified as having an embolus should be expeditious, and anticoagulation

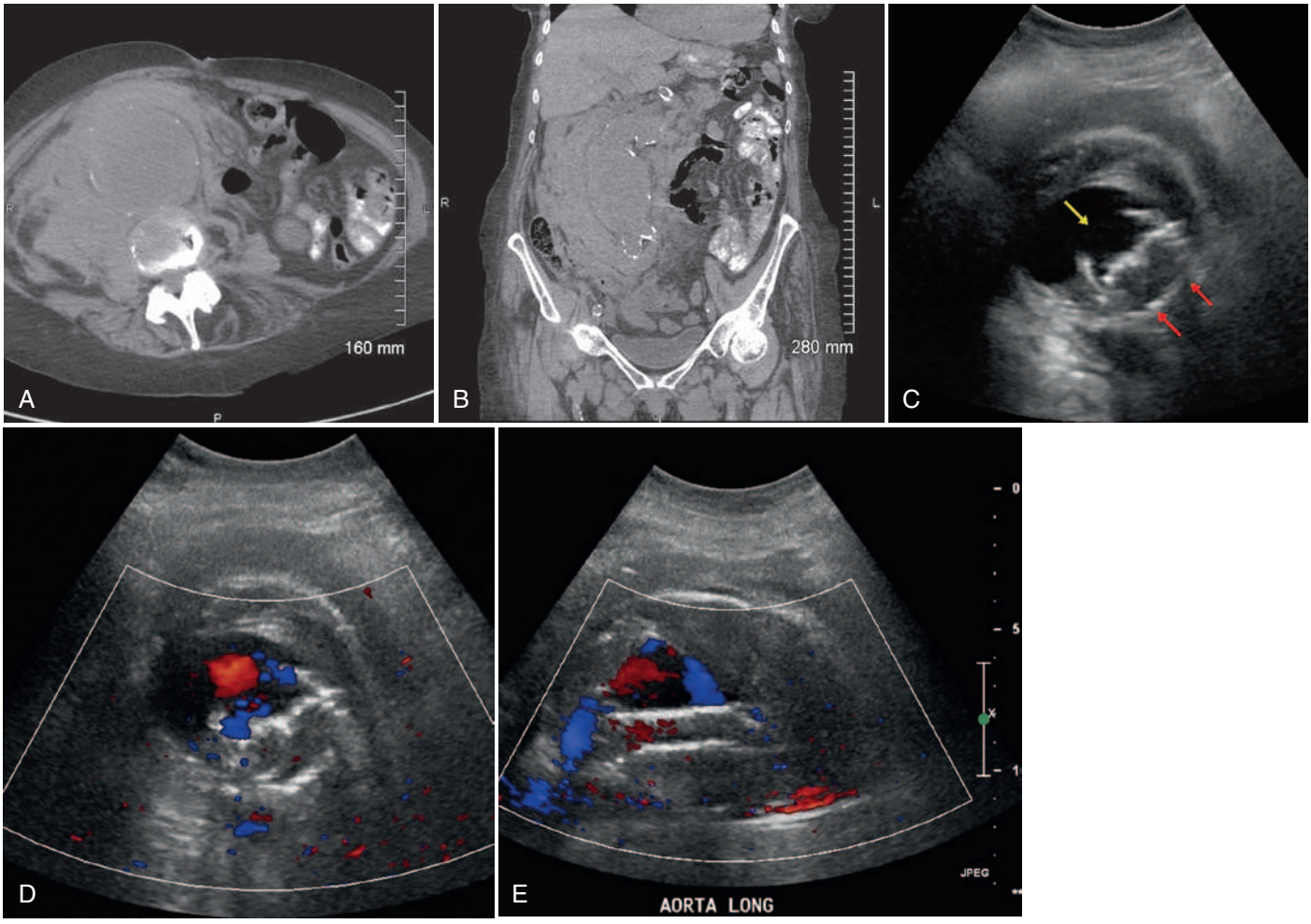

FIG. 12.12 Type 3 Endoleak. (A) Axial and **(B)** coronal computed tomography images show a ruptured abdominal aortic aneurysm. The patient had emergent endovascular aortic repair (EVAR) using disparate components in an attempt to fashion a workable endograft. **(C)** Axial gray-scale and **(D)** color Doppler images one day post EVAR show a gap *(yellow arrow)* between the tubular portion of the stent graft and the bifurcated portion *(red arrows)*. Blood flow visible throughout the gap. **(E)** Longitudinal image shows flow into the sac that appears to arise from the graft and not from an aortic branch artery. See also Videos 12.3 and 12.4.

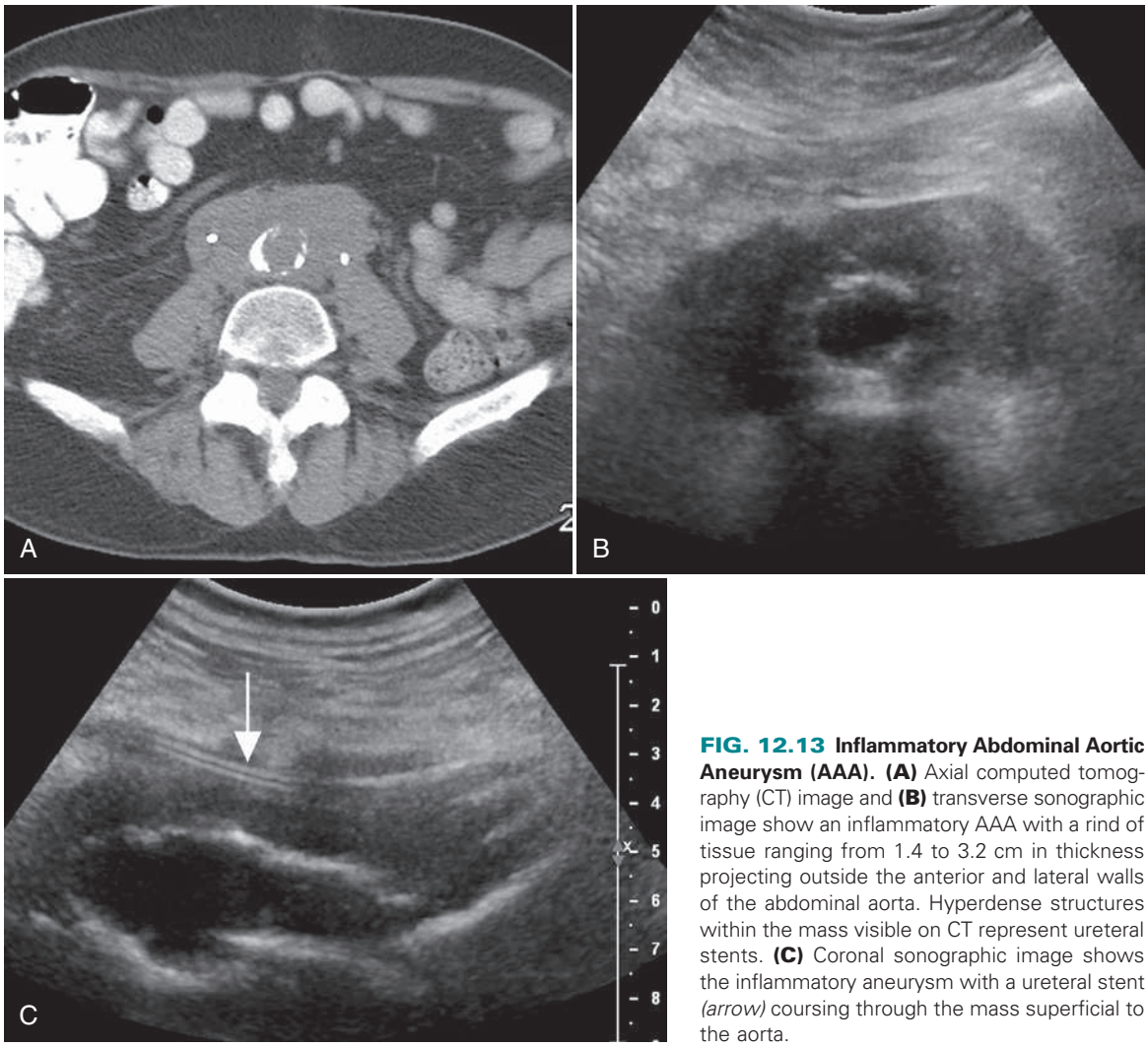

FIG. 12.13 Inflammatory Abdominal Aortic Aneurysm (AAA). (A) Axial computed tomography (CT) image and **(B)** transverse sonographic image show an inflammatory AAA with a rind of tissue ranging from 1.4 to 3.2 cm in thickness projecting outside the anterior and lateral walls of the abdominal aorta. Hyperdense structures within the mass visible on CT represent ureteral stents. **(C)** Coronal sonographic image shows the inflammatory aneurysm with a ureteral stent *(arrow)* coursing through the mass superficial to the aorta.

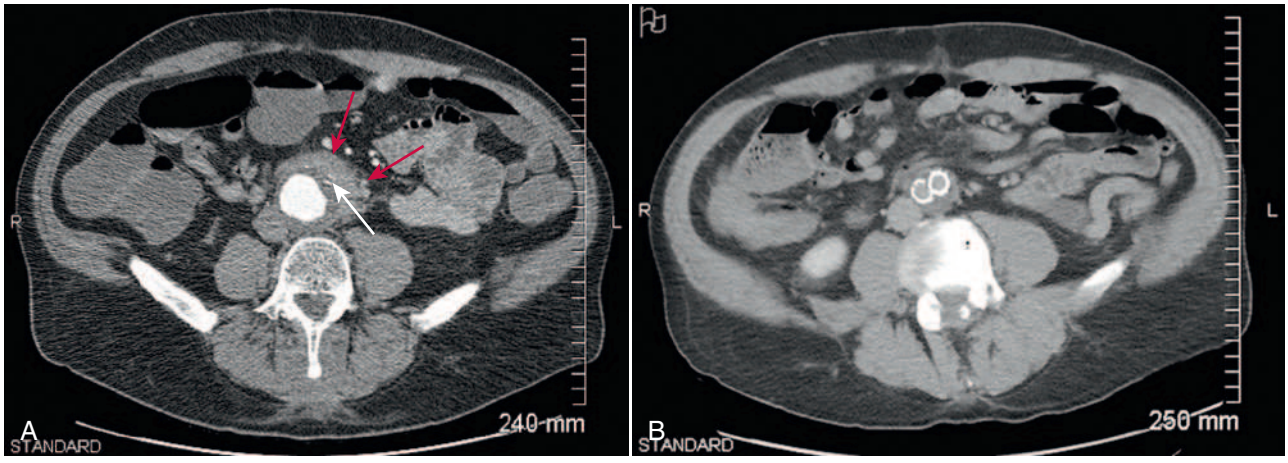

FIG. 12.14 Inflammatory Abdominal Aortic Aneurysm (AAA) Before and After Treatment. (A) Computed tomography (CT) scan of inflammatory AAA, which has maximal diameter of 4.9 cm. Note calcification *(white arrow)* indicating the aortic wall. Inflammatory tissue is present outside the aorta *(red arrows)*. Patient was symptomatic and was treated with an endoluminal graft shortly after this scan. **(B)** CT scan 2 years later shows that aortic size is smaller. Inflammatory mass has disappeared.

FIG. 12.15 Penetrating Ulcer. (A) Longitudinal image shows an outpouching of the aorta with an otherwise relatively normal abdominal aorta. **(B)** Computed tomography image at level of outpouching. The rest of the aorta was not dilated and had no more than minimal atherosclerosis. **(C)** and **(D)** Angiography images before and after placement of a stent graft.

is usually in order, certainly until the source is determined and addressed.

Takayasu arteritis is a cause of aortic stenosis and is of particular note because it may occur in younger patients. It can affect the abdominal aorta or its branches.[59] Takayasu arteritis can present with symptoms resulting from aortic stenosis or branch vessel stenosis.

Posttraumatic aortic stenosis can occur in patients of any age, including younger patients. The initial aortic injury results from a forceful, nonpenetrating injury to the abdomen.[60] The resulting intimal injury can cause subintimal fibrosis, which can result in stenosis. Trauma can also result in more acute aortic injuries, including intimal tears, pseudoaneurysm formation, and aortic rupture.[61]

Isolated dissection of the abdominal aorta is rare. Involvement of the abdominal aorta more frequently results from extension of thoracic dissection, which can result in obstruction of the abdominal aorta or branch arteries.

In most cases of suspected aortic stenosis, we prefer to evaluate the aorta with CTA instead of sonography. Peripheral vascular disease is first confirmed in the patient by obtaining ankle brachial indices before and after exercise with or without arterial duplex sonography of the lower extremities. The next step in the workup is to obtain a map of the arteries supplying blood flow to the lower extremities to direct treatment. Maps of the arterial tree are more easily and reliably obtained either by CTA or by conventional catheter angiography than with sonography.

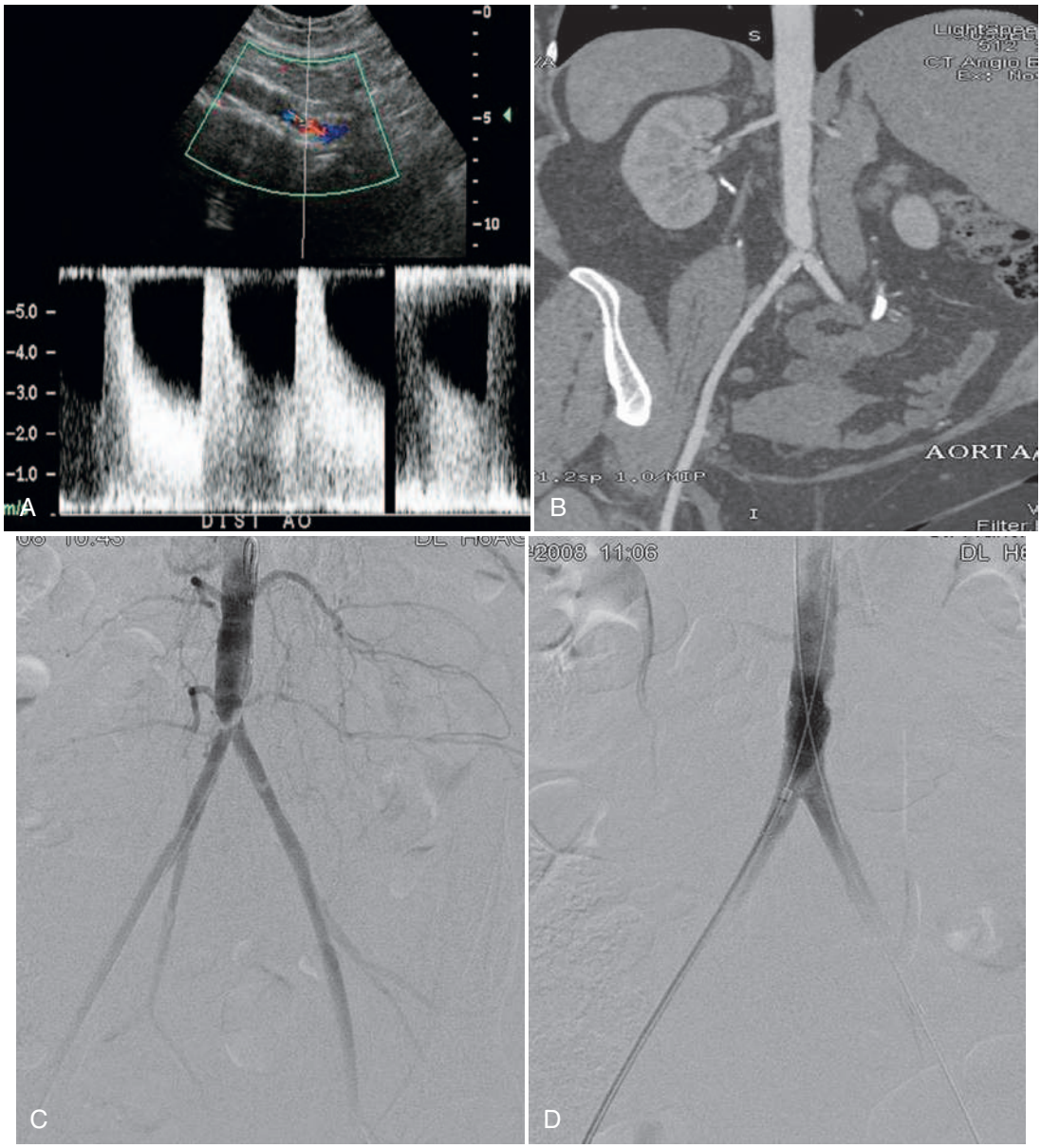

FIG. 12.16 Stenotic Aortic Bifurcation. (A) Duplex Doppler sonogram shows velocity of greater than 500 cm/sec at stenosis at the aortic bifurcation. Proximal to the stenosis, the aortic velocity varied from 35 to 50 cm/sec. Note the stenosis has an extremely high diastolic velocity of about 250 cm/sec. **(B)** Computed tomographic angiography shows very focal stenosis of the abdominal aorta at its bifurcation. **(C)** Angiography shows severe stenosis. **(D)** Stenosis treated with "kissing" stents with good result.

However, situations still arise in which aortic or iliac duplex Doppler sonography is indicated to assess for stenotic disease (Fig. 12.16). Several windows are necessary to complete an entire examination of the aorta and iliac arteries. Maintaining a proper Doppler angle of 60 degrees or less can be difficult.

DISEASES OF ABDOMINAL AORTA BRANCHES

Renal Arteries

Anatomy

The renal arteries usually arise distal to the **superior mesenteric artery** but can originate as far distally as the common iliac arteries. The main renal arteries are the only large lateral branches of the abdominal aorta.

When seen in cross section, viewing the aorta as if it were the face of a clock, the right renal artery arises from the aorta between the 9 and 11 o'clock positions. It then courses posterior to the inferior vena cava. The left renal artery most commonly arises between the 3 and 4 o'clock locations. The left renal artery typically arises directly posterior to the left renal vein.[62]

In most cases, a single renal artery supplies each kidney. In 30% of kidneys, however, one or both kidneys are supplied by two or more arteries.[63] When there are two renal arteries, the smaller artery is an **accessory artery.** Accessory arteries most often arise within 1 to 2 cm of the main renal artery. However, they may arise anywhere from the SMA to, in rare cases, as far distal as the common iliac arteries. Some accessory arteries do

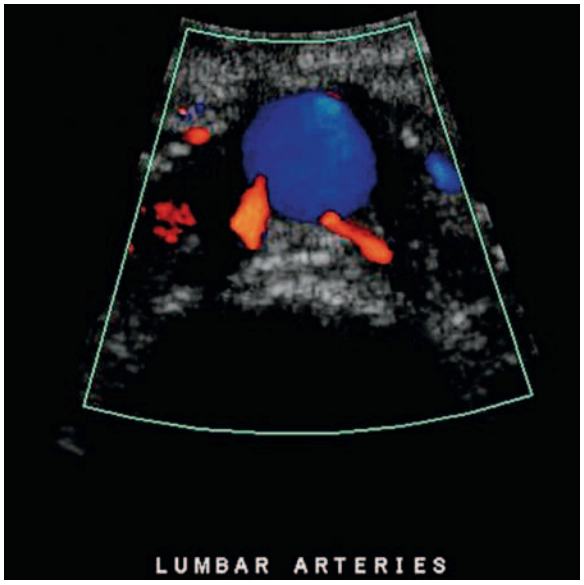

FIG. 12.17 Lumbar Arteries. Color Doppler sonogram of one set of the paired lumbar arteries shows their typical posterior origins.

not enter the kidney at the hilum and instead enter the kidney at one of the poles. These accessory arteries are referred to as **polar arteries.**

Other arteries that can occasionally be confused for an accessory renal artery are the lumbar arteries. Occasionally seen near the abdominal aorta, lumbar arteries are small and arise more posteriorly than accessory renal arteries (Fig. 12.17). Lumbar arteries can be properly identified by their very-high-resistance waveform, similar to that of an extremity artery of a person at rest. Lumbar arteries can sometimes be identified by their course as they hug the vertebral body, coursing sharply posteriorly along the lateral vertebral bodies.

In renal anomalies such as crossed-fused ectopia or horseshoe kidney (see Chapter 9), the arterial supply is highly variable, making thorough duplex evaluation of the arteries challenging.[64,65]

Renal Artery Stenosis and Renovascular Hypertension

Recent data from the US Department of Health and Human Services indicates that 32.6% of the population age 20 and older either have hypertension or are being treated for hypertension.[2] More than 90% of cases do not have a clear cause.[66] A minority of cases are caused by decreased arterial blood supply to the kidneys, activating the renin-angiotensin system that, through a complex series of events, results in elevated blood pressure. This mechanism causes only 1% to 5% of hypertension, but with the high prevalence of hypertension, the number of patients with renovascular hypertension is high.[67] Screening for renovascular hypertension is most appropriate in the presence of certain clinical features.

Treatment recommendations for renovascular hypertension caused by renal artery stenosis are in flux. Until recently, endovascular stenting constituted the standard of care. Recent studies, however, have failed to show a benefit to renal artery stent placement when compared with optimal medical management.[68] There has been reasoned criticism of these studies.[69] Nevertheless, as a result of these studies, the volume of renal artery stenting at our institution and others has substantially decreased. Which patients should receive endovascular treatment remains a topic of discussion. One proposed paradigm is that patients with known renal artery stenosis who have good blood pressure control and stable renal function achieved with medical management no longer should be treated with renal artery stenting. Endovascular treatment is reserved for those who fail medical management or whose cases have certain high-risk clinical features.[70-72]

Many radiologic tests are available to assess for renal artery stenosis, including conventional angiography, CTA, magnetic resonance angiography (MRA), captopril scintigraphy, and renal artery duplex Doppler sonography. Opinions differ regarding the most advantageous strategy for using these tests.[67,73] The advantages of renal artery duplex Doppler sonography include low cost and the ability to achieve diagnostic information in most patients, regardless of the degree of renal function. Many articles support the use of renal artery duplex Doppler in the diagnostic evaluation of renovascular hypertension.[74-76]

To be a good first-line test, renal artery duplex Doppler sonography must have high sensitivity and accuracy. Utility is greatest when there is proper clinical screening of patients for the test so that the pretest probability is higher than that of the hypertensive population as a whole. Performing the test must also be practical for ultrasound laboratories. There is a learning curve and while technologists are on the learning curve, the exam may suffer from inaccuracy or be unusually prolonged. The exam is probably best done in facilities where it is practical to periodically monitor results versus the results of conventional angiography, CTA, or MRA. Such monitoring is valuable for advancing on the learning curve and in raising the confidence in the examination. Once technologists are proficient in the examination, it can be performed fairly rapidly.

Clinical Findings in Patients With Hypertension That Increase Probability of Renovascular Cause (Renal Artery Stenosis)

- History of peripheral vascular disease, cerebrovascular disease, or coronary artery disease
- Recent onset of hypertension
- Refractory hypertension (not responsive with at least three medications)
- Malignant hypertension (with papilledema) or accelerated (without papilledema but usually with fundus changes)
- Abdominal or flank bruit
- Elevated creatinine and/or cholesterol levels (even higher suspicion if creatinine levels increase after treatment with angiotensin-converting enzyme inhibitor)
- Unexplained congestive heart failure or acute pulmonary edema

Data from Safian RD, Textor SC. Renal-artery stenosis. N Engl J Med. 2001;344(6):431-442[77]; Krijnen P, van Jaarsveld BC, Steyerberg EW, et al. A clinical prediction rule for renal artery stenosis. Ann Intern Med. 1998;129(9):705-711.[78]

Feasibility of the examination in obese patients is also a concern. A few years after starting our duplex Doppler sonography program, we studied a total of 100 consecutive main renal arteries (50 patients), recording the body mass index (BMI) of each patient (unpublished data, 2002, Saint Francis Medical Center, Peoria, Ill). Of the 100 arteries, 20 were in obese patients (BMI ≥ 30) and 4 in extremely obese patients (BMI ≥ 40), 30 arteries were in overweight patients (BMI ≥ 25), and 46 were in patients of normal weight. We were able to complete a technically adequate examination in 96 of the 100 arteries. Of the 4 arteries with failed studies, 3 were in overweight patients, and 1 was in a patient of normal weight. All 24 arteries of the obese or morbidly obese patients were successfully studied.

Our technologists routinely score the quality of the duplex sonography of each renal artery on a 5-point scale. All examinations graded 2 or higher are considered diagnostically adequate; the entire extrarenal portion of the artery has been successfully interrogated. Our mean Duplex quality score was from 4 to 4.6 in all the categories. Our experience shows that renal duplex Doppler sonography can be completed successfully in most obese patients.

Causes of Renal Artery Stenosis. The most common causes of renal artery stenosis in adults are atherosclerosis and fibromuscular dysplasia.[77] Atherosclerotic disease most often occurs in the proximal third of the artery, often at the origin of the artery.[77] Percutaneous transluminal angioplasty alone has had mixed results in the treatment of atherosclerotic disease. In lesions that are at the origin of the artery, there tends to be strong elastic recoil that allows the balloon to be inflated fully but causes the artery to revert quickly to its stenotic state on deflation of the balloon. The development of stents has changed the situation by allowing the artery to be scaffolded. After stenting, there remains a risk of restenosis secondary to neointimal hyperplasia.[74,79] **Restenosis** is seen in 10% to 20% of patients between 6 and 12 months after stenting[80,81] and is yet higher for patients followed for longer than 1 year (Videos 12.6, 12.7, and 12.8). Because of the relatively low cost, lack of iodinated contrast, and high accuracy, renal artery duplex Doppler sonography is an ideal method to use when following stented arteries.

Fibromuscular dysplasia (FMD) is the second most common cause of renovascular hypertension and typically occurs in women aged 20 to 50 years. Multiple pathologic subtypes are seen; the most common FMD in the renal arteries is medial fibroplasia.[82,83] FMD lesions most often occur in the distal two-thirds of the renal artery and often have an angiographic appearance suggestive of a thin, fibrous web. The classic appearance on angiography is the "string of pearls," caused by multiple dysplastic regions in a row with short areas of poststenotic dilation immediately distal to each stenosis (Fig. 12.18). FMD often responds well to simple percutaneous transluminal angioplasty. A single treatment often is effective in controlling blood pressure and is enduring.[84] Stent placement is rarely needed for FMD.

Another cause of impaired blood flow to the kidney that may result in renovascular hypertension is **dissection.** If the dissection extends to the renal artery, the raised intimal flap in the aorta may partially or completely occlude the renal artery orifice. Alternatively, if the dissection extends into the renal artery, the raised intima may cause stenosis or occlusion within the artery itself. Endovascular treatment is frequently successful either by stenting of the narrowed artery or by fenestration of the dissected intima[85] (Fig. 12.19).

FIG. 12.18 Fibromuscular Dysplasia: Angiography. Note the "string of beads" appearance, most often in the distal two-thirds of the renal artery.

Embolus can result in abruptly impaired blood flow to some or all of a kidney. The patient frequently complains of flank pain. Diagnosis often is delayed, resulting in irreversible damage to the kidney involved. The kidney can tolerate only a brief episode of warm ischemia.[86] Revascularization of the kidney is unlikely to result in full return of function if it is delayed more than 90 minutes.[87]

Vasculitis is an uncommon cause of renal artery stenosis in adults. The vasculitides that are most likely to cause stenosis of large vessels are **Takayasu arteritis** and **giant cell arteritis.**[88]

Renal artery stenosis can also occur in children; FMD is the most common cause. **Neurofibromatosis** and **vasculitis** can also cause renal artery stenosis in children.[89] **Midaortic syndrome,** which is a hypoplasia of the abdominal aorta, can also result in reduced renal blood flow. **Aortic coarctation** most commonly is discovered in other ways but, if not recognized, also will cause renovascular hypertension (Fig. 12.20).

Renal Artery Duplex Doppler Sonography

When performing renal artery duplex Doppler sonography, it is critical to interrogate the entire extrarenal portion of the artery. The examination is not adequate unless the entire extrarenal portion of the main renal artery is seen and interrogated by Doppler every 2 to 3 mm. Accessory arteries and large, early extrarenal branches of the main renal artery are also similarly assessed. Even then, stenoses in accessory arteries or branch renal arteries may be missed. Fortunately, nonvisualization of branch arteries or accessories is unlikely to affect patient management.[90,91]

Visualization of the renal artery is the key to successful ultrasound interrogation (Video 12.9). At our institution, patients are prepared by eating a bland, low-fiber diet the day before and taking nothing by mouth (NPO) after midnight the night before. We ask them to avoid caffeine, smoking, and dairy products. The sonographic examination is more likely to be successful with a prepped patient.

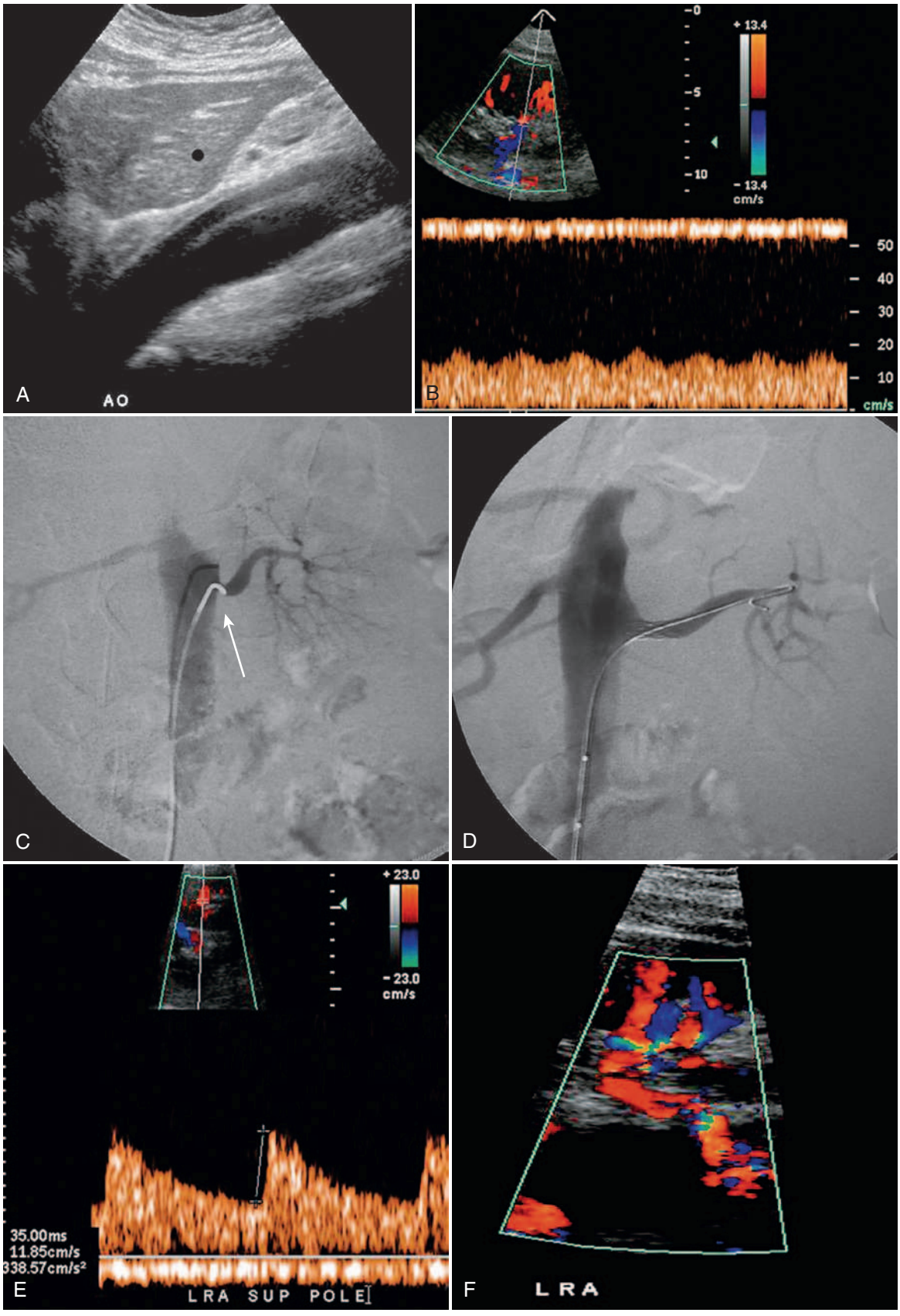

FIG. 12.19 Aortic Dissection With Raised Intima in Lumen of Aorta. (A) Ultrasound of the proximal abdominal aorta *(Ao)* in 30-year-old cocaine user. **(B)** Duplex Doppler sonogram shows highly abnormal intrarenal waveforms from left kidney. Also, it is very difficult to see the main left renal artery with color Doppler. The systolic rise time is 190 msec and acceleration is 34 cm/sec^2. **(C)** Selective injection of the left renal artery at angiography. Angiography shows moderate stenosis at origin of the left renal artery *(arrow)*. **(D)** After stenting of left renal artery, angiography shows origin is widely patent. **(E)** Greatly improved intrarenal waveforms in left renal artery after stenting. Note that systolic rise time is 35 msec and acceleration is 339 cm/sec^2. **(F)** Left renal artery is easy to see with color duplex Doppler after stenting because of increased flow.

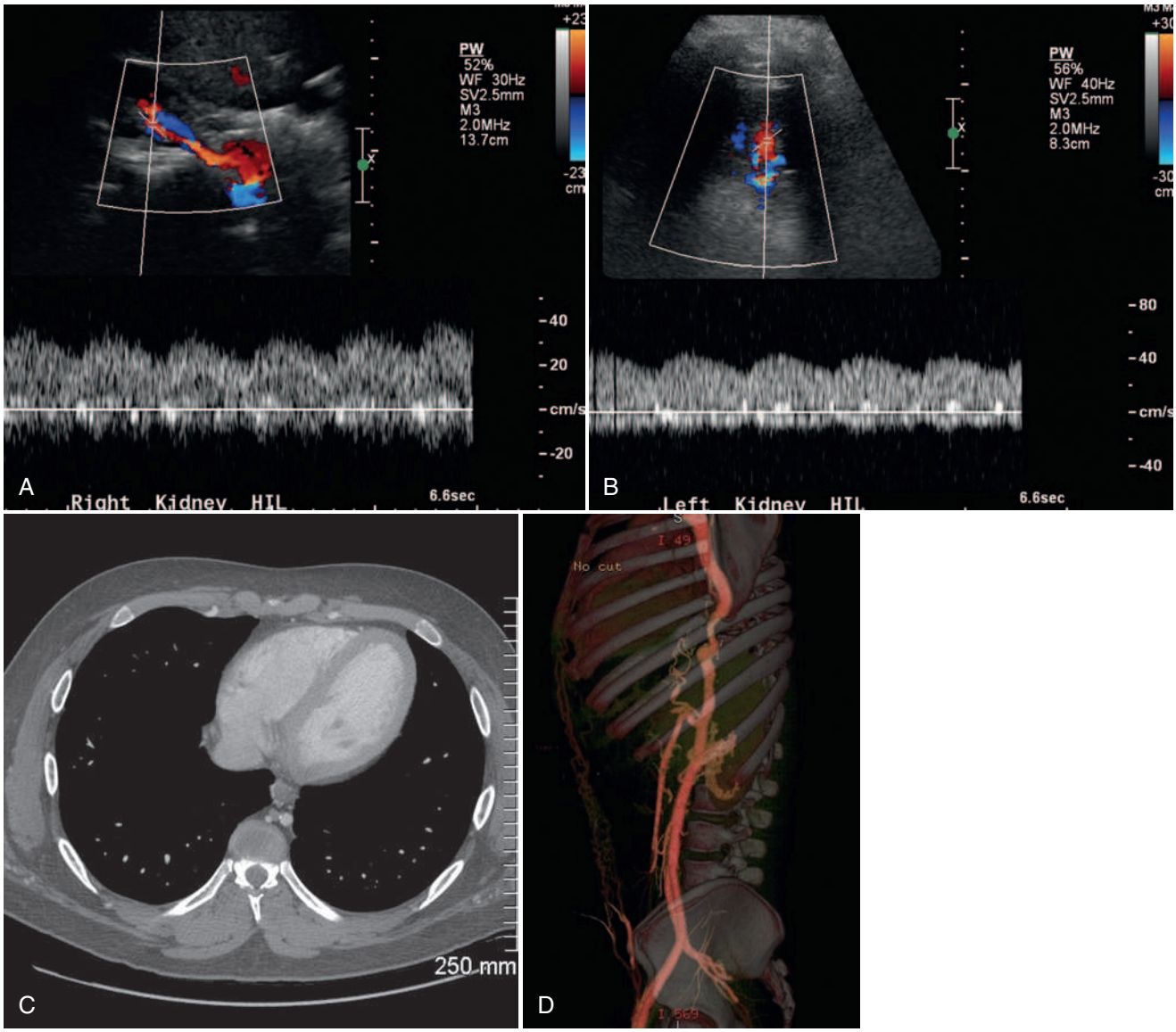

FIG. 12.20 Descending Thoracic Aortic Coarctation. (A) and **(B)** Renal duplex ultrasound of a 15-year-old football lineman presenting with hypertension. Waveforms from the right and left renal arteries. Waveforms bilaterally have low velocity, low resistance, and a rounded peak, all indications of a poststenotic waveform. No renal artery stenosis was seen. Waveforms suggested a more proximal aortic stenosis and are what might be expected with thoracic coarctation. **(C)** Axial computed tomography (CT) scan shows a severely narrowed thoracic aorta. **(D)** 3D CT reconstruction shows severe narrowing of the descending thoracic aorta.

Color Doppler sonography is usually necessary for visualization of the entire extrarenal portion of the artery. In rare cases, however, the right renal artery can be seen better without color Doppler, using the liver as a window. Color Doppler sometimes makes the site of stenosis obvious because of a color bruit or increased diastolic velocity, causing a portion of the artery to remain filled with color throughout the cardiac cycle. At our facility, we typically set the color scale relatively low to increase our ability to see the artery. The entire length of the artery often is more readily seen with this setting.

We set the wall filter to the lowest setting allowed by the manufacturer. If the renal artery is not well seen, color gain is increased. The very highest color sensitivity is achieved by increasing gain to the point where color artifact starts to fill the image and then slightly backing off the gain to remove the artifact. When necessary, power output is increased to aid visualization. We set the ensemble packet size (this setting is controlled in varying ways on different machines) to the highest size possible to increase sensitivity of flow detection. Maintaining an adequate frame rate (>10 frames/sec) is important. We keep the frame rate adequate by making the color window as narrow as reasonably possible. We also decrease the line density of the image and the sector width of the transducer. Our pictures of the renal artery often are not "pretty" because of the aliasing and the high color gain. Our goal, however, is to see the artery. With these settings, we can see the entire extrarenal portion of the artery in almost all patients, regardless of size.

We generally use a 5-1 curvilinear transducer. With thin patients, interrogation from the anterior midline is likely to be successful. At our facility, however, the flank approach is most

often used; it has a higher probability of seeing the entire renal artery in obese patients. Also, achieving an acceptable Doppler angle of less than 60 degrees is easier from the flank. Breath holding is often used, although it does not work well in many patients, either because the patient is dyspneic, or because of a slow but steady cephalad drift of the kidneys, which occurs in some patients despite breath holding. Even without breath holding, the examination often is successful.

When possible, we avoid examining patients who are in heart failure, who have acute dyspnea, who have acutely decreased mobility, or who are on ventilators. All these patients have a reduced ability to accomplish the breath holding. Renal duplex Doppler sonograms generally are not emergent. The examination will likely become much easier, more successful, and more highly accurate once the patient's condition improves.

Performance of the renal artery duplex Doppler study mainly relies on obtaining accurate velocities throughout the main renal artery. However, measurement of the resistive index (RI) is also important. Treatment of renal artery stenosis is less likely to be effective in reducing blood pressure when the segmental artery RI is high (≥0.80), probably because of irreversible damage to the small blood vessels in kidneys with a high RI.[92]

Attention to **intrarenal waveforms** is also of some importance. A highly abnormal waveform can be a valuable indicator of stenosis. A delayed systolic peak (tardus, i.e., "tardy") and velocities that are greatly decreased (parvus, i.e., "puny") can be a strong sign of a more proximal stenosis. The intrarenal waveform can be analyzed quantitatively by calculating the systolic rise time and the acceleration (Fig. 12.21). Although we calculate these parameters, a qualitative assessment of the appearance of the waveform usually serves just as well. We rely on a **tardus-parvus waveform** to make the diagnosis only when the finding is pronounced (compare Fig. 12.19B and E; see also Fig. 12.20A and B).

Finally, because of the regular occurrence of renal lesions or abnormalities that affect patient care, we believe that ultrasound of the kidneys should be considered when renal artery duplex Doppler ultrasound is performed, unless the patient has had recent (<1 or 2 years) cross-sectional imaging. Incidental findings in our ultrasound department have included xanthogranulomatous pyelonephritis, adrenal tumors, hydronephrosis, and several renal cell carcinomas.[93]

Doppler Interpretation. There are many proposed guidelines for Doppler interpretation. Proposed parameters to assess for stenosis include the **peak systolic velocity** (PSV), **renal aortic ratio** (RAR; defined as highest systolic velocity in renal artery divided by aortic systolic velocity, with aortic velocity measured at or above SMA origin),[94] **acceleration time, acceleration index, renal interlobar ratio,**[95,96] and **renal-renal ratio.**[95,97,98] An influential article suggested a combination of RAR of 3.5 or greater *or* PSV of 200 or greater as the criterion for renal artery stenosis of more than 60%.[75] We use a variation of these criteria, using the same RAR as the study but a higher PSV of 350.

False-Positive/False-Negative Results. To obtain the highest accuracy, it is important to avoid relying solely on the numerical data obtained. When a high velocity is seen or when the renal aortic ratio is high, the interpreting radiologist must also actively look for secondary signs of stenosis, such as a characteristic harsh audible signal at the site of stenosis, increased diastolic flow, color bruit, color aliasing, and poststenotic turbulence (Fig. 12.22, Video 12.10). Without ancillary findings, the interpreter must consider the possibility that the high velocity or high RAR represents a false-positive result.

False-negative findings are a risk primarily when visualization is marginal and the entire artery has not been adequately evaluated. In perhaps 5% to 10% of patients, accurate diagnosis cannot be made because of inadequate visualization of one or both arteries.

The examination is challenging to the uninitiated operator, but establishment of a renal artery duplex Doppler program can be rewarding. Because of the lower cost versus other diagnostic tests, Doppler ultrasound lowers the threshold for the diagnosis of renovascular hypertension. Hurdles mainly relate to the learning curve and the initial investment of time. Starting a program is more feasible in a large center where demand will likely be higher than in a smaller facility. Once the program is mature, the study is financially viable and can result in improved patient care.

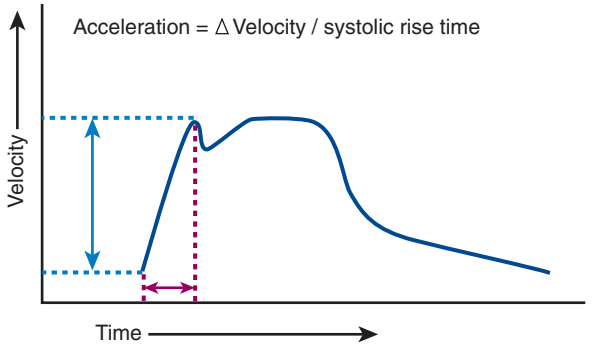

FIG. 12.21 Renal Artery Systolic Waveform. Normal waveform. In early systole there is a rapid acceleration of blood in the renal artery. The systolic rise time *(purple arrow)* is the time expended during this rapid acceleration. The acceleration is the change in velocity during the systolic rise *(blue arrow)* divided by the systolic rise time.

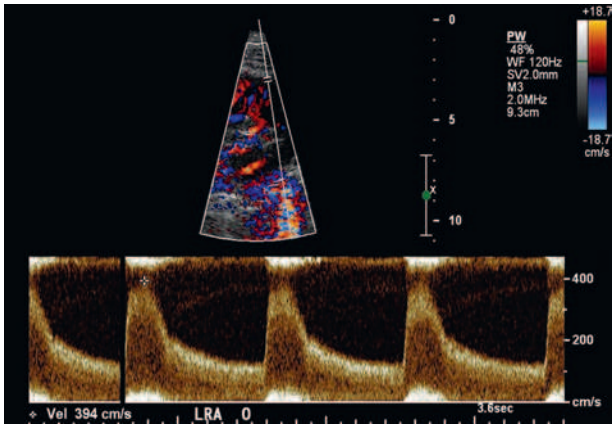

FIG. 12.22 Secondary Signs of Stenosis. Increased diastolic flow, as seen here, can help confirm the presence of renal artery stenosis. Other secondary signs include color bruit, poststenotic turbulence, and a tardus-parvus waveform. See also Video 12.10.

Renal Artery Aneurysm

Renal artery aneurysms are uncommon and may be saccular or fusiform. They can be seen with atherosclerosis or FMD. They are more reliably seen and followed with CT than with ultrasound. Most renal artery aneurysms do not result in significant morbidity or mortality.[99] They grow slowly; a recent study showed a growth rate of 0.16 mm/year.[100] Treatment should be considered if the aneurysm is greater than 2.0 cm. Treatment is indicated if the aneurysm is believed to be causing symptoms (e.g., hematuria, pain, hypertension) or if the patient is a woman of childbearing age who anticipates becoming pregnant.[100-102] The patient and family must be made aware of a renal aneurysm to be alert to symptoms so that diagnosis and treatment can be expedited. Currently, no well-accepted guidelines address how often renal artery aneurysms should be imaged.

Mesenteric Arteries

Anatomy

Three arteries constitute the main sources of arterial blood flow to the gastrointestinal tract: celiac, superior mesenteric, and inferior mesenteric. The **celiac artery** arises anteriorly from the abdominal aorta at the level of the aortic hiatus of the diaphragm. The celiac artery supplies blood to the spleen, pancreas, liver, stomach, and proximal duodenum. The standard branching pattern of the celiac artery is into the splenic and common hepatic arteries, which are easily identified. The third branch of the celiac artery is the left gastric, which is much less frequently seen with sonography. The common hepatic artery branches into the proper hepatic artery and the gastroduodenal artery; the latter is important as a conduit for collateral blood flow to the celiac circulatory territory when the celiac artery is highly stenosed or occluded.

The **superior mesenteric artery** (SMA) typically arises from the anterior aorta approximately 1 cm below the celiac artery origin. The SMA supplies blood to the pancreas, distal duodenum, jejunum, ileum, and proximal colon as far distal as the splenic flexure. In about 20% of people, the SMA supplies some of the hepatic blood flow through a replaced or accessory right hepatic artery. Other important branches of the SMA include the inferior pancreaticoduodenal artery (IPDA) and the middle colic artery. The IPDA and its branches form an arcade of blood vessels around the head of the pancreas with the gastroduodenal artery.[103,104] In celiac arterial occlusion, the IPDA-gastroduodenal arcade often becomes the primary route for blood to reach the celiac circulation (Fig. 12.23). In cases of SMA occlusion, blood often flows in the opposite direction through the arcade, supplying the occluded SMA with blood from the celiac artery.

The **inferior mesenteric artery** supplies the descending colon, sigmoid colon, and superior rectum. The IMA arises from the anterior aorta slightly to the left of midline, approximately two-thirds the distance between the renal artery origins and the aortic bifurcation. When the aorta is viewed transversely, the IMA arises at approximately the 1 o'clock position. Viewed longitudinally, the appearance is similar to that of the SMA, except the IMA is significantly smaller and always courses inferiorly to the left of the aorta. After 1 to 2 cm, the IMA bifurcates into a superior hemorrhoidal artery that runs caudally slightly to the left of midline and into a left colic artery that runs laterally to the descending colon. The left colic artery immediately divides into ascending and descending branches. The superior hemorrhoidal artery gives off sigmoid branches as it courses inferiorly to the rectum (Fig. 12.24).

Connections between the SMA and IMA occur in the region of the splenic flexure. The IMA can supply blood to the SMA when the proximal SMA is occluded. Blood then flows from the IMA through the marginal artery of Drummond or through the sometimes present and more direct arc of Riolan to the middle colic artery and then into the SMA. The middle colic artery is an anterior branch of the SMA and is generally identified sonographically only in cases of SMA occlusion when it becomes a source of collateral supply and has increased flow.

Mesenteric Ischemia

Acute Ischemia. **Acute mesenteric ischemia** occurs when there is an abrupt reduction of arterial flow to the intestines. The most common cause is cardiac embolus. Acute mesenteric ischemia also may be caused by aortic dissection. Less often, abrupt reduction of arterial flow results from SMA thrombosis, decreased cardiac output without any obstruction of the arterial tree, or thrombosis of the superior mesenteric vein.[105] Only a single artery needs to be compromised acutely to cause mesenteric ischemia, most often the SMA. Patients present with an abrupt onset of severe abdominal pain, nausea and vomiting, and diarrhea. Later in the course, they may develop "currant jelly" stools from intestinal bleeding and mucosal sloughing.

Acute mesenteric ischemia is a medical emergency. Mortality is high, at least 50%.[106] The wide differences in reported mortality likely relates to the rapidity of diagnosis. Patient survival depends on quick and accurate diagnosis and treatment. In most cases, ultrasound has no role in the diagnosis of acute mesenteric ischemia.[107] These patients can be of any size and often have a large amount of gas in the bowel that compromises sonographic diagnosis. In most cases, the clinician simply cannot risk wasting time by initiating the diagnostic workup with mesenteric duplex Doppler sonography. CTA or angiography is the test of choice.[108] ACR Appropriateness Criteria state that ultrasound "is not recommended for initial evaluation of patients with suspected acute mesenteric ischemia because timing of the diagnosis is very critical."[109]

Chronic Ischemia. Duplex Doppler sonography has a more central role in the diagnosis of **chronic mesenteric ischemia.** Chronic ischemia is usually the result of atherosclerosis slowly occluding the arteries that supply the intestines. Because the buildup of plaque is slow, collateral circulation has an opportunity to develop and supply some of the needed blood flow to the intestines. Mesenteric artery stenosis is relatively common, reported in 17.5% of the independent-living older population. Most patients with severe narrowing of one or more of the arteries supplying the intestines have no symptoms and need no treatment.[108] These patients maintain adequate blood flow to the gut through collateral circulation. The collateral blood flow usually

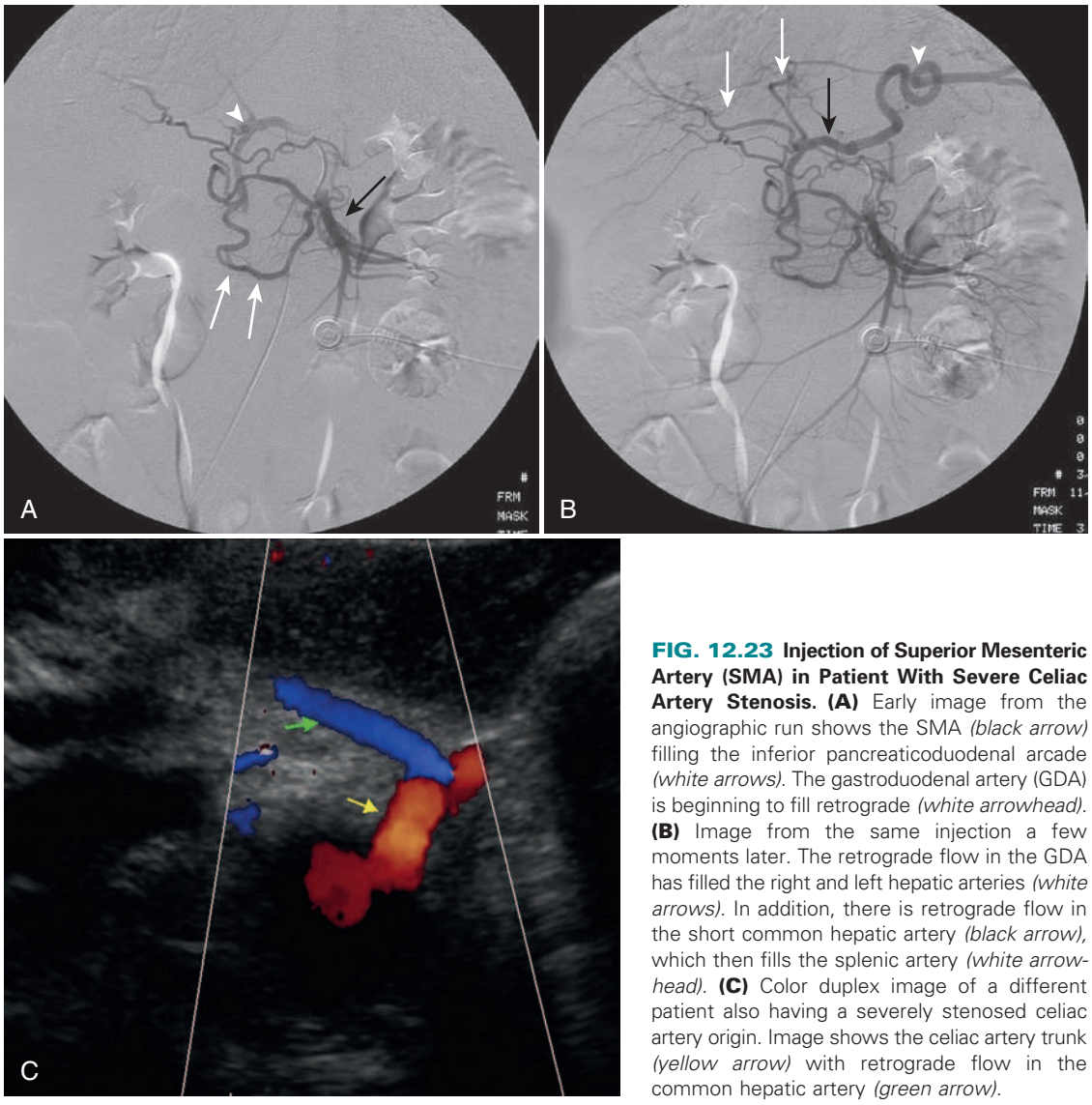

FIG. 12.23 Injection of Superior Mesenteric Artery (SMA) in Patient With Severe Celiac Artery Stenosis. (A) Early image from the angiographic run shows the SMA *(black arrow)* filling the inferior pancreaticoduodenal arcade *(white arrows)*. The gastroduodenal artery (GDA) is beginning to fill retrograde *(white arrowhead)*. **(B)** Image from the same injection a few moments later. The retrograde flow in the GDA has filled the right and left hepatic arteries *(white arrows)*. In addition, there is retrograde flow in the short common hepatic artery *(black arrow)*, which then fills the splenic artery *(white arrowhead)*. **(C)** Color duplex image of a different patient also having a severely stenosed celiac artery origin. Image shows the celiac artery trunk *(yellow arrow)* with retrograde flow in the common hepatic artery *(green arrow)*.

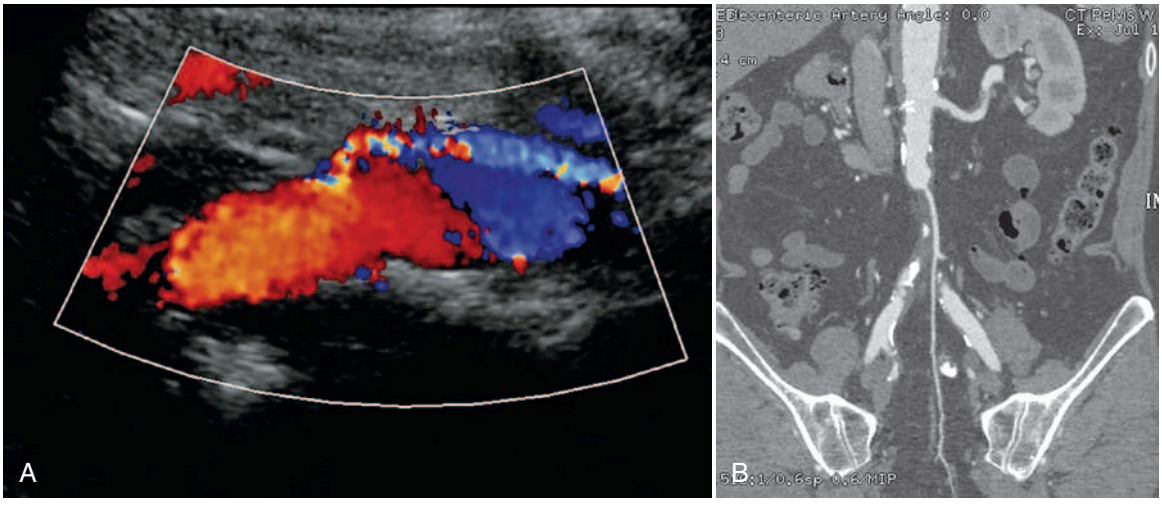

FIG. 12.24 Inferior Mesenteric Artery (IMA) Has Similar Appearance to Superior Mesenteric Artery When Scanned Longitudinally. (A) Color Doppler longitudinal sonogram. **(B)** Curved reformatted computed tomography image of the IMA.

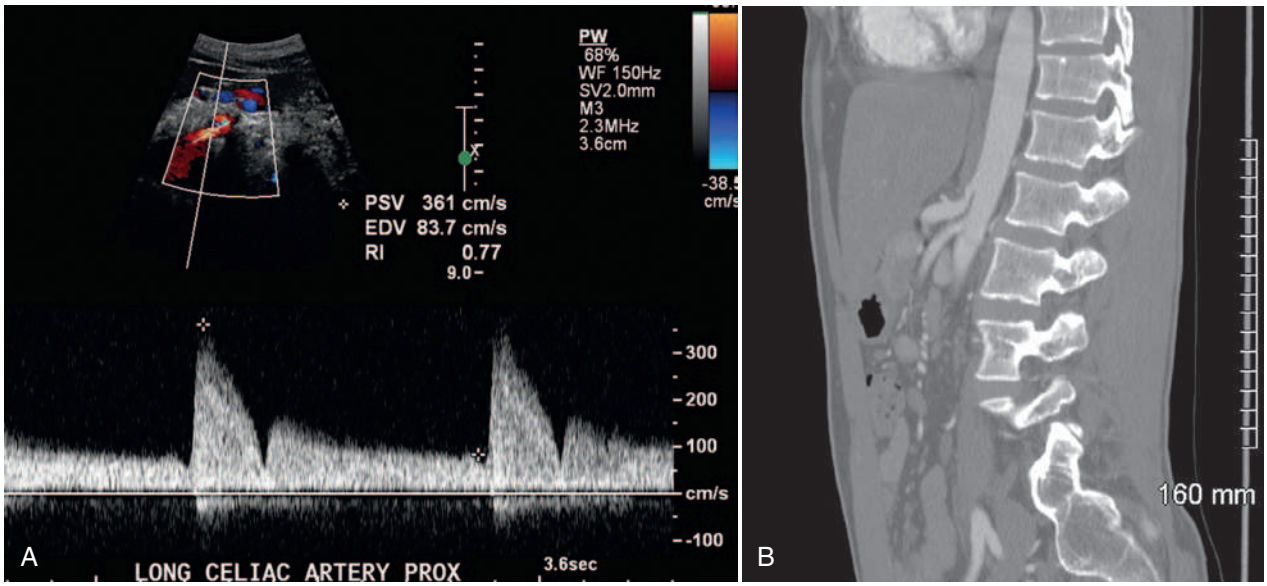

FIG. 12.25 Median Arcuate Ligament Syndrome. Male, 37 years old, with history of severe abdominal pain for more than 20 years. **(A)** Duplex exam shows elevated velocity in the celiac artery of 361 cm/sec. **(B)** Computed tomography angiography sagittal reconstruction image shows the characteristic narrowing of the celiac artery caused by the median arcuate ligament. Patient had immediate and enduring relief of symptoms after surgery to release the median arcuate ligament.

must be impaired before the patient becomes symptomatic. In most cases, two of the three arteries that supply mesenteric blood flow (celiac artery, SMA, IMA) must be severely diseased before a patient experiences chronic mesenteric ischemia, but even many patients with multiple-artery disease are not symptomatic.[108] Again, the clinician must remember that, although uncommon, significant mesenteric ischemia can result from the narrowing of one artery, particularly the SMA.[110]

The onset of chronic ischemia is insidious, with the classic patient experiencing weight loss and postprandial pain. Atypical features in the history are common and often include complaints of "indigestion." Patients with chronic ischemia frequently are very thin, which facilitates ultrasound.

Vasculitis, most often **Takayasu arteritis,** can also lead to mesenteric ischemia. Although typically the symptoms are chronic, involvement of the mesenteric arteries can be rapidly progressive and result in bowel infarction.[111]

Median Arcuate Ligament Syndrome

Most commonly, patients with symptomatic mesenteric ischemia have at least two of the mesenteric arteries narrowed or completely occluded. Patients with the median arcuate ligament syndrome have narrowing only of the celiac artery.

The **median arcuate ligament** of the diaphragm is close to the celiac artery. This ligament is a band of fibrous tissue that crosses the aorta, usually above the origin of the celiac artery, although the crossing can be below. Deformity and narrowing of the celiac artery caused by the median arcuate ligament are fairly common angiographic findings on lateral aortography. One study reported that 24% of aortograms performed for unrelated reasons showed celiac artery stenosis of at least 50% caused by the median arcuate ligament.[112]

In **median arcuate ligament syndrome,** patients with only narrowing of the celiac artery experience significant postprandial pain that results in avoidance of eating and weight loss. The syndrome is poorly understood, but the pain is believed to be possibly related to ischemia.[113,114] Other investigators support a neurogenic cause.[115] Some patients respond dramatically to surgery and become symptom free.[113-116] Surgical decision making in these patients is very important to help decide those who are likely to benefit from surgery. Surgery consists of dividing the median arcuate ligament and may include celiac artery revascularization (Fig. 12.25).

Mesenteric Artery Duplex Doppler Sonography

Mesenteric artery duplex Doppler ultrasound is most often performed with the patient fasting. Most studies assessing the addition of a postprandial study conclude that it is not of value.[117-119]

Blood flow to the intestines in the fasting state is relatively low. Normal waveforms in the SMA and IMA are high resistance. When the patient eats, blood is shunted to the intestines, and the SMA has a lower-resistance waveform. The celiac artery supplies the liver and spleen, which have a higher need for flow than the intestines when the patient is fasting. Accordingly, the celiac artery has lower resistance than the SMA or IMA when interrogated with the patient fasting.

Because chronic mesenteric ischemia can be fatal, it is critical that the examination be performed and interpreted in a way that guarantees very high sensitivity. The majority of stenoses that result in chronic mesenteric ischemia are within the first 1 to 2 cm of the origin of the celiac artery, SMA, and IMA. It is possible, although rare, to have a branch artery occlusion that results in chronic mesenteric ischemia. Ultrasound is not a reliable

technique for screening for these more distal stenoses or occlusions.

The evaluation of the celiac artery starts at its origin and proceeds to its bifurcation into the splenic and common hepatic arteries. As with all duplex Doppler studies, the sample volume is advanced slowly through the celiac artery with waveforms viewed every 2 to 3 mm and any abnormal sites documented with an image. A standard set of waveforms from the proximal, middle, and distal celiac artery is also obtained.

In patients with very severe celiac stenosis or occlusion, the celiac artery often receives its blood supply from the SMA through the pancreaticoduodenal arcade. The blood flow in the gastroduodenal artery reverses, carrying the blood from the arcade back to the common hepatic artery. Blood flow then arrives at the liver through the proper hepatic artery. To arrive at the spleen, blood flow from the gastroduodenal artery flows retrograde in the common hepatic artery to reach the splenic artery. Assessment of blood flow direction in the common hepatic artery should be part of the sonographic examination of the celiac artery to detect cases in which this collateral flow is present (see Fig. 12.23).

The evaluation of the SMA starts at the origin and is carried distally with viewing of waveforms every 2 to 3 mm, documenting waveforms in the proximal, middle, and distal artery. The examination can be performed with or without breath holding. However, without breath holding, motion of the sample volume with respect to the celiac artery and SMA often occurs. With the patient breathing, the sonographer may believe a waveform is being obtained from the SMA when in fact the celiac artery is being sampled or vice versa. Care should be exercised when not using breath holding to guarantee that the proper vessel is being evaluated. The SMA exam is also challenging because of the very sharp turn it makes proximally. The turn creates problems with accurate angle correction, and great care with the Doppler angle is important.

The IMA has only a short trunk before it branches into the left colic, sigmoidal, and superior hemorrhoidal arteries. In many, perhaps most, patients the IMA is readily found, being the only anterior branch of the abdominal aorta below the level of the renal arteries. Its identification can be impeded by patient size and bowel gas and by the fact that it not as large of an artery as the celiac artery or SMA. The IMA requires Doppler interrogation only for 2 to 3 cm.

Finally, special maneuvers must be used when celiac artery stenosis caused by the median arcuate ligament is suspected. The traditional test is to remeasure flow velocity in the artery when the patient takes a deep inspiration. We have found this test to be inconsistent. Reexamination of the artery with the patient standing may be superior in its ability to show normalization of velocities in the celiac artery in the setting of compression by the median arcuate ligament.[120] Our experience supports that remeasurement with the patient standing is greatly superior compared with deep inspiration at normalizing blood flow in a compressed celiac artery (Fig. 12.26).

Mesenteric Artery Duplex Interpretation. Probably the most widely accepted duplex criteria state that PSVs greater than 275 cm/sec in the SMA and 200 cm/sec in the celiac artery are indicative of stenosis of greater than 70% in these arteries.[121] These criteria are the ones suggested in the ACR Appropriateness Criteria.[109] A more recent article suggests higher cutoffs of 295 cm/sec in the SMA and 240 cm/sec in the celiac artery as being indicative of greater than 50% stenosis.[122] Other investigators have found diastolic velocities to be a more accurate indicator. One group found an end diastolic velocity (EDV) greater than 45 cm/sec with a PSV greater than 300 cm/sec to be an accurate indicator of SMA stenosis greater than 50%.[123] Another group found EDV greater than 70 cm/sec to be highly accurate for diagnosing SMA stenosis of more than 50%, with an EDV greater than 100 cm/sec needed to diagnose celiac artery stenosis of over 50%.[124]

In our laboratory, we have found the criteria using systolic velocities (but not diastolic) to be highly sensitive but to result in a substantial number of false-positive studies. Because of the high sensitivity, we are confident that for a high-quality examination that does not show systolic velocities higher than those stated above (200 cm/sec in the celiac artery; 275 cm/sec in the SMA), the diagnosis of chronic mesenteric ischemia is excluded. When velocities reach one of the thresholds given above, we look for secondary features that support the diagnosis of significant stenosis before we become confident that the stenosis is real. These secondary features include an increased diastolic velocity and the presence of significant poststenotic turbulence (Fig. 12.27). Color bruit is also supportive of severe stenosis. In the absence of secondary findings, the radiologist must consider the possibility of a false-positive result. In this setting, we have a low threshold to recommend either CTA or MRA to assist in the diagnosis (Fig. 12.28).

There have been no widely accepted duplex Doppler criteria for what constitutes significant stenosis of the IMA. Therefore evaluation for severe stenosis must be based on qualitative more than on quantitative data. High systolic velocity in the presence of high diastolic velocity and poststenotic turbulence is indicative of severe stenosis. A PSV greater than 200 cm/sec in the IMA may be an accurate indicator of severe stenosis.[125] Stenosis of the IMA may be an important contributor to the development of mesenteric ischemia. We have seen and treated many patients with mesenteric ischemia in whom a stenotic IMA was the sole blood supply to the gut.

Treatment of chronic mesenteric ischemia can be surgical or endoluminal. Rates of restenosis with endoluminal treatment are high, and thus, posttreatment surveillance is important. As with all arteries treated with stents, restenosis is usually caused by intimal hyperplasia, which is common within bare-metal stents but even more common at the end of the stent (Fig. 12.29). There is suggestion that covered stents may have a lower restenosis rate in the mesenteric arteries.[126]

Posttreatment duplex surveillance is confounded by Doppler velocities often remaining high in stented SMAs.[127,128] Some speculate that this velocity elevation may be caused by a change in the elastic properties of the arterial wall induced by its incorporation of the stent.

The goal of stenting often is not to restore normal flow, but only to restore enough flow to make the patient asymptomatic. Those arteries treated with stenting often supply collateral flow

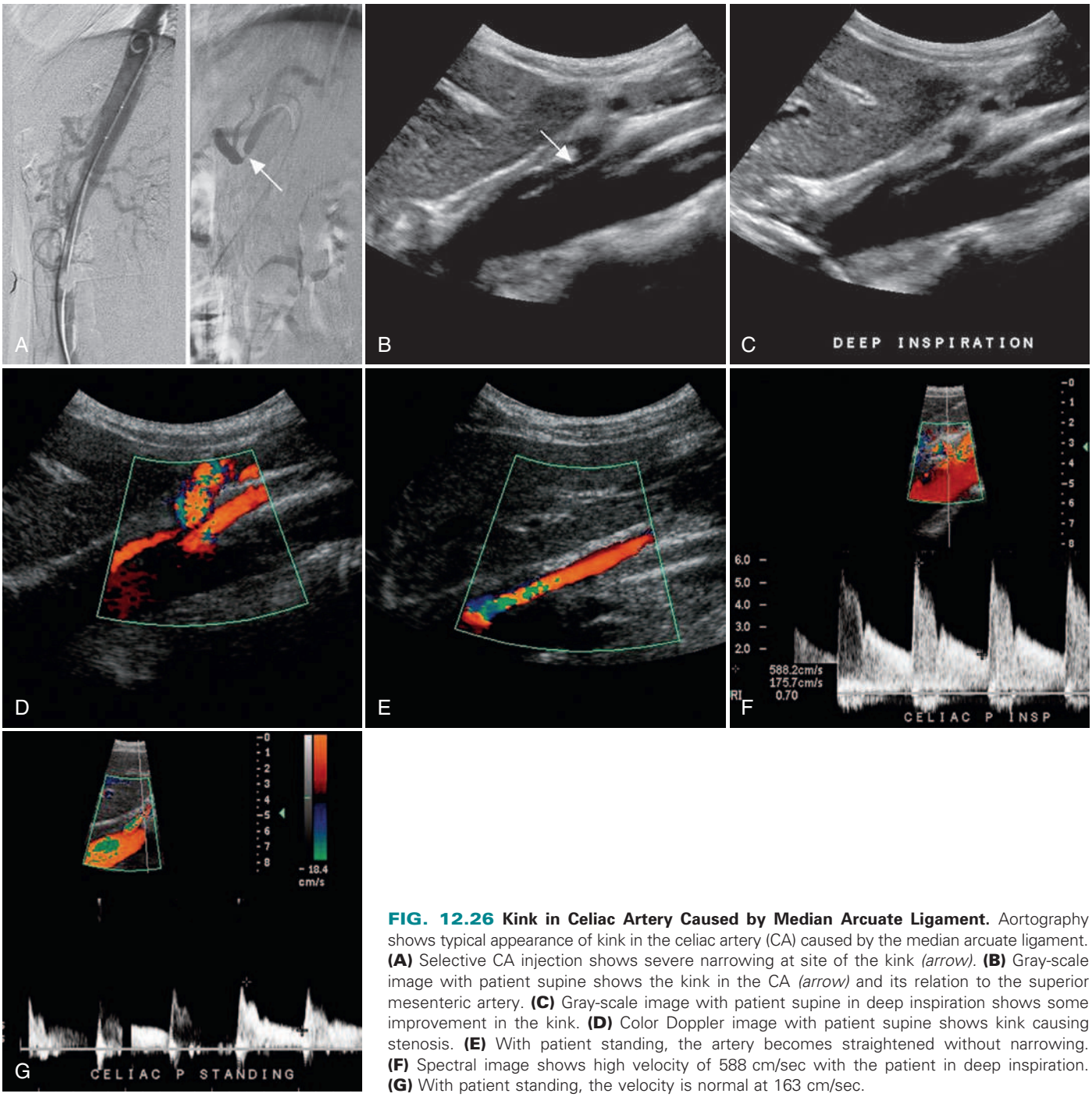

FIG. 12.26 Kink in Celiac Artery Caused by Median Arcuate Ligament. Aortography shows typical appearance of kink in the celiac artery (CA) caused by the median arcuate ligament. **(A)** Selective CA injection shows severe narrowing at site of the kink *(arrow)*. **(B)** Gray-scale image with patient supine shows the kink in the CA *(arrow)* and its relation to the superior mesenteric artery. **(C)** Gray-scale image with patient supine in deep inspiration shows some improvement in the kink. **(D)** Color Doppler image with patient supine shows kink causing stenosis. **(E)** With patient standing, the artery becomes straightened without narrowing. **(F)** Spectral image shows high velocity of 588 cm/sec with the patient in deep inspiration. **(G)** With patient standing, the velocity is normal at 163 cm/sec.

to any untreated arteries that remain stenotic or occluded (e.g., an SMA stent placed in a patient who has an occluded celiac artery). The stented arteries often have increased flow throughout their course. This results in velocities that are uniformly elevated throughout the artery. We have found this result not only in the SMA but also in the other mesenteric arteries (Fig. 12.30). Treatment decisions after stenting must be made in the context of the entire clinical picture and not on the basis of velocities alone. If the patient is entirely asymptomatic, treatment will generally not be undertaken regardless of the results of mesenteric artery duplex scanning.

Iliac Veins and Inferior Vena Cava

As with veins throughout the body, the range of pathology occurring in the iliac veins and inferior vena cava (IVC) is narrow. Thrombosis of the iliac veins and IVC is probably the most common pathology, but is much less common than lower extremity venous thrombosis.

Often, the iliac veins and the infrarenal IVC are not well evaluated directly with ultrasound. Therefore ultrasound exams are infrequently done with the intent of doing a primary evaluation of the entire IVC and iliac veins. The main exception is infants,

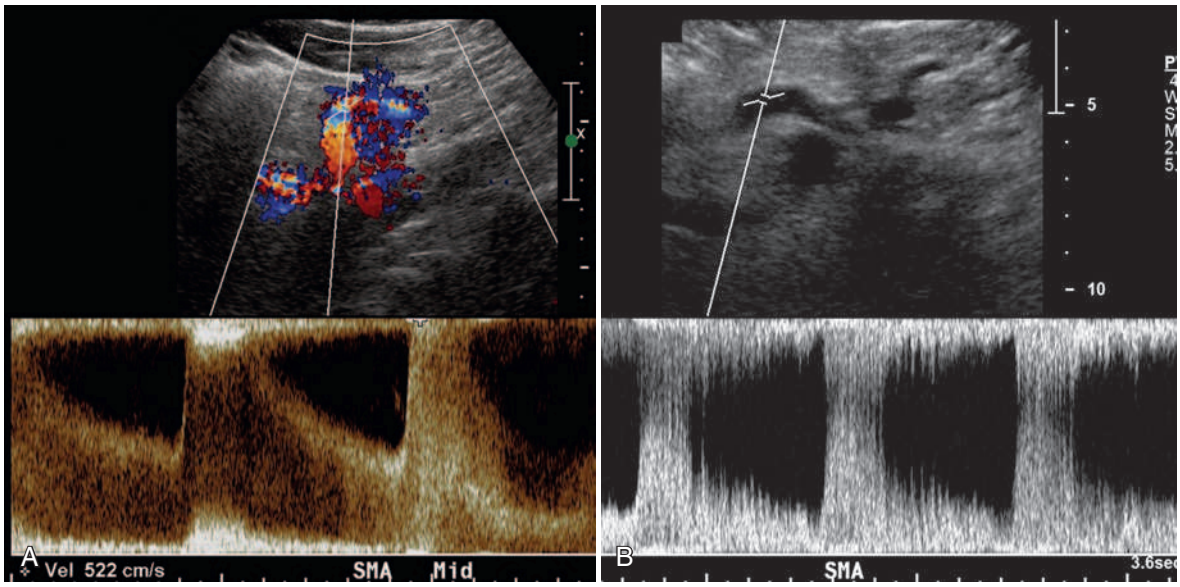

FIG. 12.27 Poststenotic Turbulence. (A) Spectral waveform at site of stenosis shows very high diastolic velocities of greater than 500 cm/sec. Color portion of the image shows color bruit consisting of color outside the vessel near the stenosis site. Color bruit is believed to be caused by tissue vibration. **(B)** Spectral waveform shows the typical "spike hairdo" waveform caused by poststenotic turbulence. There is mirror-image artifact. Because of the very high velocities, the baseline of the waveform has been placed at the bottom, causing the "flow below the baseline" to appear at the top of the tracing. Flow below the baseline is also typical of turbulence.

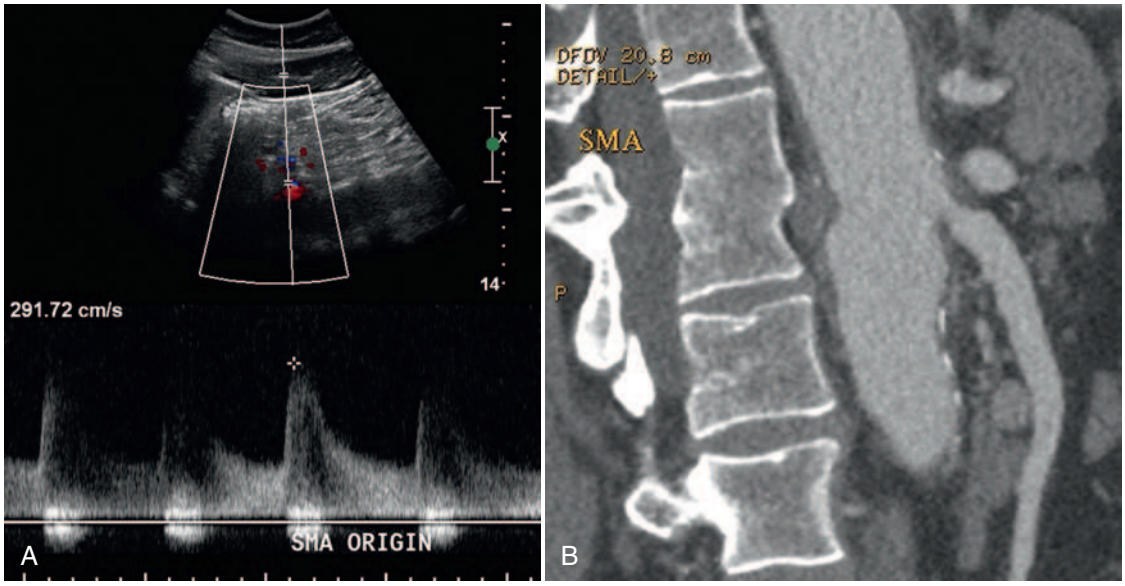

FIG. 12.28 Takayasu Arteritis. Patient, 34 years old, with blood pressure discrepancy between the right and left arms. Subsequent workup showed occlusion of the left subclavian artery and severe stenosis of the right renal artery origin. Two years later, the arteritis flared and the patient developed severe stenosis of the celiac artery and the superior mesenteric artery *(SMA)*. **(A)** Mesenteric duplex shows elevation of both systolic and diastolic velocities. **(B)** Curved reformatted computed tomography image shows moderate narrowing of the SMA origin. Note the wall thickening of the SMA at its origin caused by mural inflammation. The patient was treated medically.

in whom IVC evaluation with ultrasound has a better opportunity to provide good diagnostic information.

Anatomy

The IVC can be divided into several segments. The most proximal (i.e., central) segment is the suprahepatic (posthepatic), which is short and intrathoracic. In adults this segment is approximately 2.5 cm in length and has the hepatic veins as tributaries. The next segment is intrahepatic, with accessory hepatic and caudate veins as tributaries. The next segment is the infrahepatic/suprarenal, which has the renal veins as tributaries. The last segment is infrarenal, which is the longest segment and has the right gonadal vein as a tributary. Proceeding distally, the IVC divides into the common iliac veins. The left common iliac vein

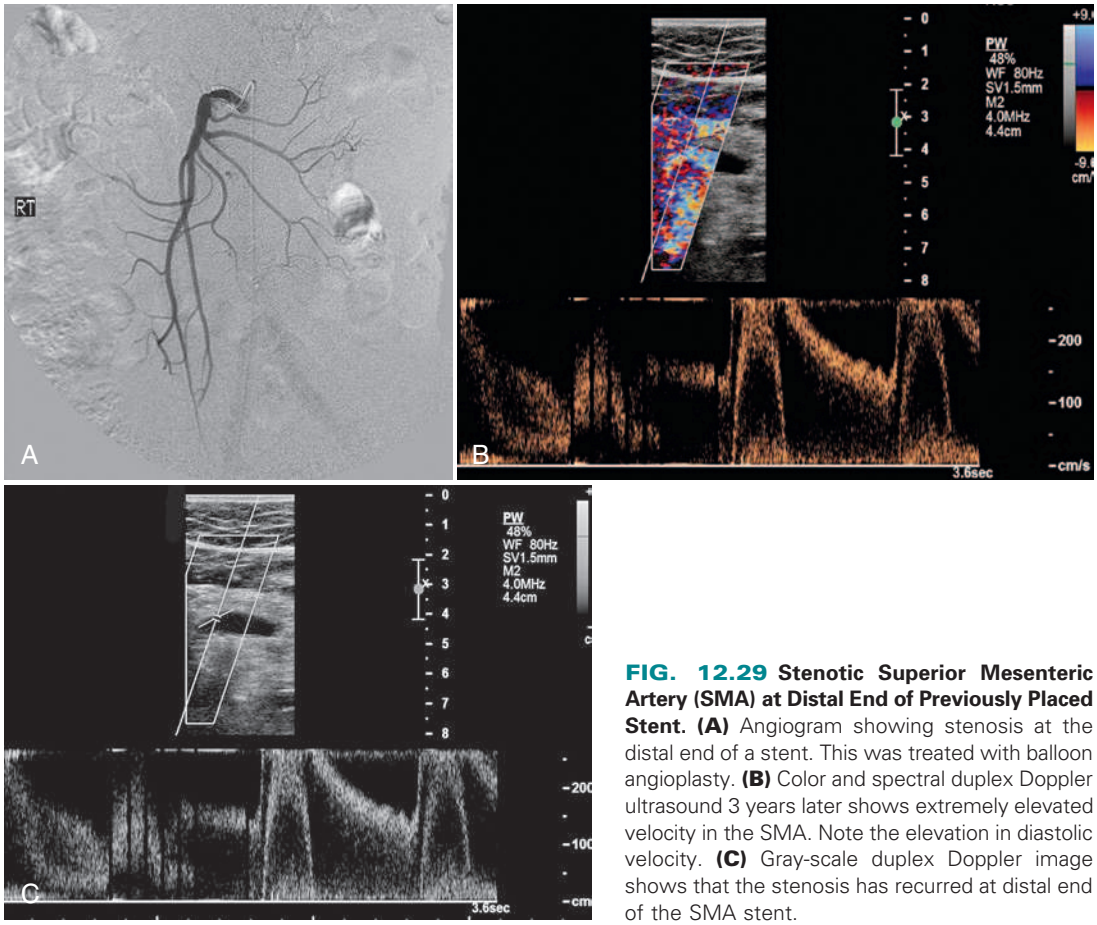

FIG. 12.29 Stenotic Superior Mesenteric Artery (SMA) at Distal End of Previously Placed Stent. (A) Angiogram showing stenosis at the distal end of a stent. This was treated with balloon angioplasty. **(B)** Color and spectral duplex Doppler ultrasound 3 years later shows extremely elevated velocity in the SMA. Note the elevation in diastolic velocity. **(C)** Gray-scale duplex Doppler image shows that the stenosis has recurred at distal end of the SMA stent.

passes between the right common iliac artery and the spine, where it can become compressed producing May-Thurner physiology (called **May-Thurner syndrome** when it results in thrombosis). The common iliac veins have major tributaries of the internal and external iliac veins.

Anatomic Variants

There are three major variations of IVC anatomy, the most common a **duplicated IVC.** The duplication is of the infrarenal portion of the IVC, with incidence of approximately 2% (Fig. 12.31A). Most often, the IVC's left channel enters the left renal vein. The suprarenal IVC has normal anatomy. The second most common anomaly is a **left IVC** (0.5%; Fig. 12.31B), which also usually drains into the left renal vein. As with a duplicated IVC, anatomy above the level of the renal veins is normal. With both these anomalies, the anomalous left-sided segment may cross the aorta below the level of the left renal vein. Also, the anomalous segment may cross either anterior or posterior to the aorta.[129]

The third major anomaly is **azygous continuation of the IVC.** The infrarenal IVC flows superiorly into the hemiazygos or azygos veins. The IVC does not course through the liver in this setting; there is no intrahepatic IVC. The hepatic veins drain normally into the short suprahepatic (posthepatic) IVC, which enters the right atrium. Incidence of azygous continuation is approximately 0.6%.[129]

Regarding IVC tributaries, there are variations in the anatomy of the hepatic veins, left renal vein, and gonadal veins. The hepatic veins have numerous variations important in preprocedural planning of liver resection or transplantation.[130] The most common variation is the presence of an **accessory right hepatic vein.**[131]

The **left renal vein** usually passes in front of the abdominal aorta to join the IVC. It also can be **circumaortic** (up to 8.7%),[129] where the left renal vein has two branches, one passing behind the aorta and the other anterior to the aorta. Less often, it is **retroaortic** (up to 2.4%), where a single left renal vein passes behind the aorta. In both cases, the portion of the left renal vein passing behind the aorta most frequently descends a short distance toward the pelvis as it passes behind the aorta.[129]

The **right gonadal vein** joins the IVC just below the level of the right renal vein or at the right renal vein in 90% of cases. In the remaining 10%, it joins the right renal vein. When IVC anatomy is standard, the **left gonadal vein** almost always drains into the left renal vein. In a duplicated or left IVC, the left gonadal vein most often drains into the left-sided IVC.[132]

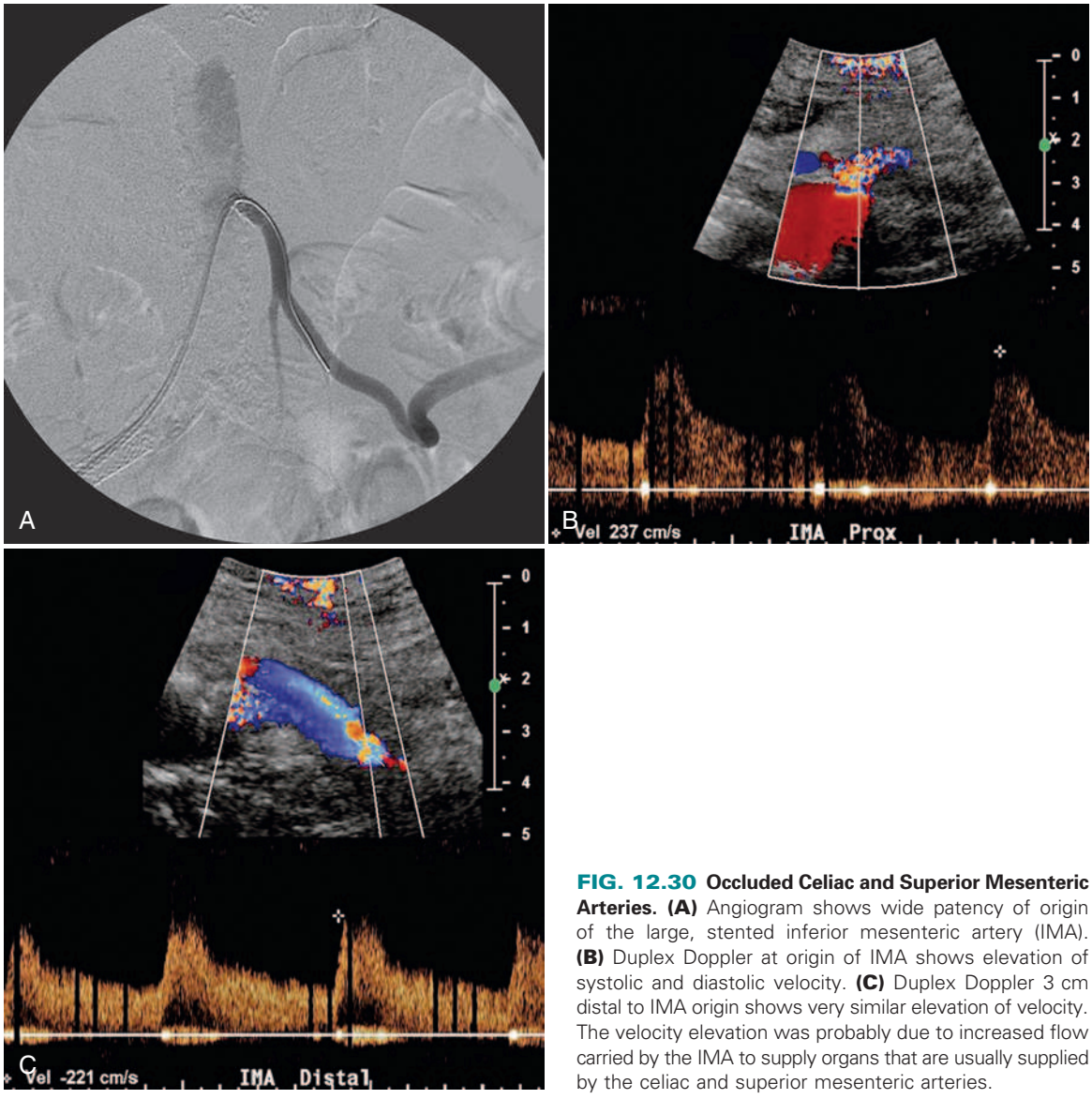

FIG. 12.30 Occluded Celiac and Superior Mesenteric Arteries. (A) Angiogram shows wide patency of origin of the large, stented inferior mesenteric artery (IMA). **(B)** Duplex Doppler at origin of IMA shows elevation of systolic and diastolic velocity. **(C)** Duplex Doppler 3 cm distal to IMA origin shows very similar elevation of velocity. The velocity elevation was probably due to increased flow carried by the IMA to supply organs that are usually supplied by the celiac and superior mesenteric arteries.

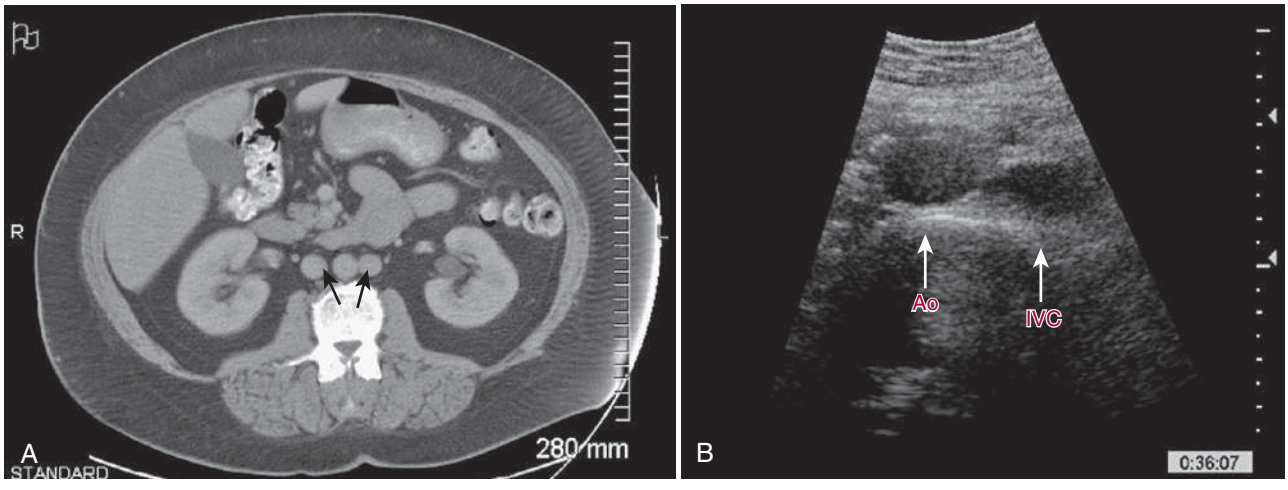

FIG. 12.31 Inferior Vena Cava (IVC) Anomalies. (A) Computed tomography image of duplicated IVC *(black arrows),* the most common anomaly of the IVC. The left IVC joined the left renal vein. The IVC above the level of the renal veins was in the normal location. **(B)** Ultrasound of another IVC anomaly, a left IVC running to the left of the aorta *(Ao)*. The left IVC joins the left renal vein.

Thrombosis

The iliac veins and IVC are large veins with high-volume flow. They are less prone to primary thrombosis than are deep veins of the extremities. Perhaps the most common scenario to result in IVC thrombosis is when clot embolizes into an IVC filter. Isolated iliac vein thrombosis is uncommon, occurring in 1.6% of cases of lower extremity deep venous thrombosis.[133]

Iliac thrombus most often results from extension of lower extremity venous thrombosis. Extrinsic compression of the IVC or iliac veins, as in May-Thurner physiology or a gravid uterus, may also result in thrombosis. Iliac vein thrombosis in adults is infrequently directly seen sonographically because of lack of an adequate window. Most often, the possibility of iliac thrombosis can only be inferred sonographically.

Sonographic clues to iliac vein thrombosis are found in the common femoral veins. When thrombus in the common femoral vein extends as far proximally as can be seen, it is easy to infer possible extension into the iliac veins. More subtle cases involve continuous, low, or absent flow in an open (nonthrombosed) common femoral vein. Common femoral vein waveforms generally show respiratory phasicity or cardiac phasicity, or both. When **phasicity** is not clearly seen, as in continuous, low, or absent flow, it suggests obstruction to flow more proximally (Fig. 12.32). Before ordering other tests to look for more proximal obstruction, it is worthwhile to perform a few maneuvers to eliminate nonpathologic causes of lack of phasicity. First, have the patient remove underwear if it is tight. Second, sonographically check the fullness of the bladder. If moderately or greatly distended, the patient should be asked to empty the bladder. Third, if the patient is in the second or third trimester of pregnancy, check the waveforms in posterior oblique or decubitus positions. If the compression is caused by the gravid uterus compressing the veins, these maneuvers will often allow the waveform to return to normal, showing that there is no fixed blockage of the veins (Fig. 12.33).

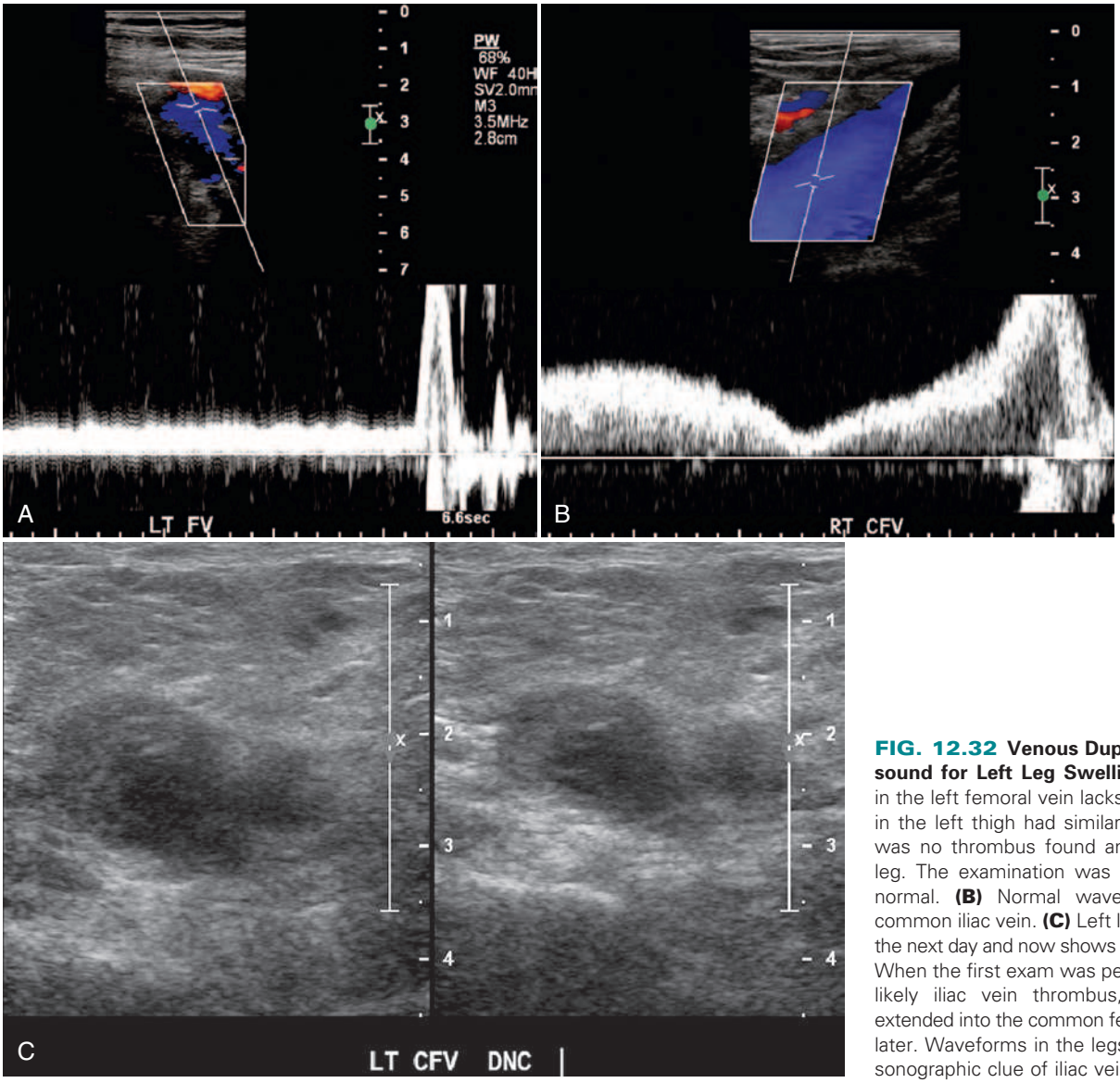

FIG. 12.32 Venous Duplex Doppler Ultrasound for Left Leg Swelling. (A) Waveform in the left femoral vein lacks phasicity. All veins in the left thigh had similar waveforms. There was no thrombus found anywhere in the left leg. The examination was mistakenly read as normal. **(B)** Normal waveform in the right common iliac vein. **(C)** Left leg was reexamined the next day and now shows extensive thrombus. When the first exam was performed, there was likely iliac vein thrombus, which then had extended into the common femoral vein 24 hours later. Waveforms in the legs are often the only sonographic clue of iliac vein thrombosis.

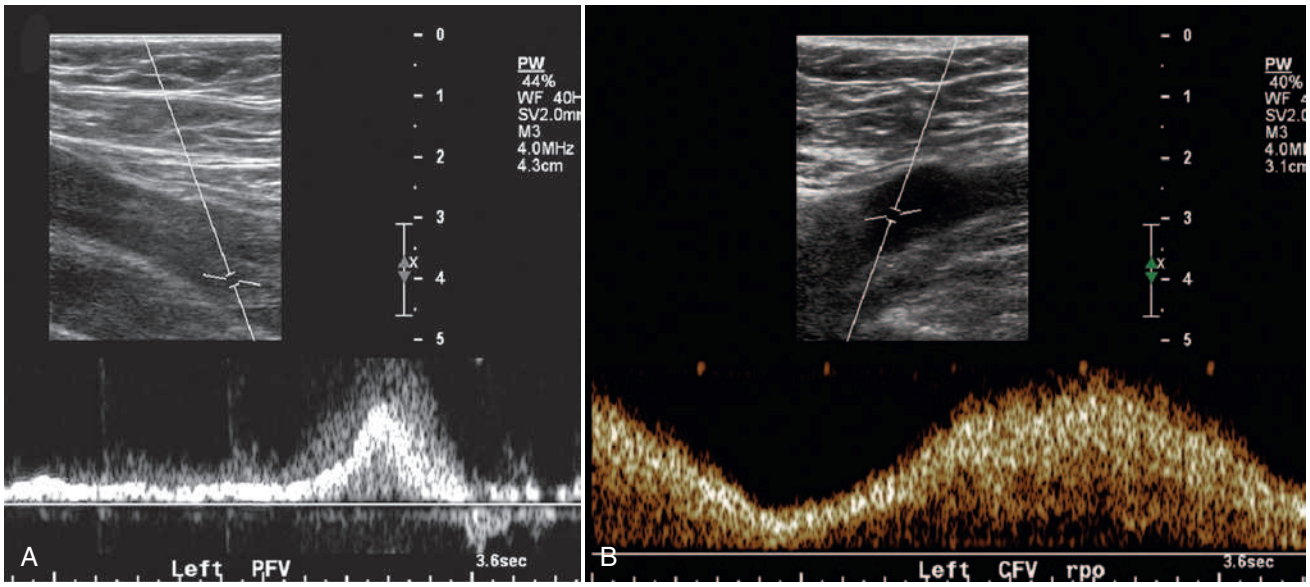

FIG. 12.33 Patient in Third Trimester of Pregnancy With Leg Swelling. (A) Waveform in the left profunda femoral vein with patient supine shows decreased phasicity. All veins in the left thigh had a similar waveform. The only variation seen in flow is when an augmentation (calf or thigh squeeze) was performed, causing a brief increase in flow. **(B)** Patient turned into right posterior oblique position. Turning has moved the gravid uterus off of the left iliac veins. Flow in the left common femoral vein shows normal respiratory phasicity.

If these maneuvers are not successful at restoring a normal waveform, there may be an obstruction proximal to the common femoral vein(s). If unilateral, there is likely to be iliac vein obstruction. If bilateral, the obstruction may be of the iliac veins bilaterally or of the IVC. In our experience the lack of common femoral vein phasicity is more likely to be a false-positive finding if it is bilateral rather than unilateral.

In the setting of absent common femoral vein phasicity, more proximal obstruction may be caused by acute or chronic thrombosis, May-Thurner physiology, or extrinsic compression of the vein by a benign or malignant mass or fluid collection. When lack of phasicity is found, other imaging studies may be performed to evaluate possible causes. This is particularly important if the patient has clinical findings suggestive of a more proximal obstruction. We typically use contrast-enhanced CT (Fig. 12.34) and, in pregnancy, MRI. Pelvic venography is another option.

In infants, particularly those with femoral venous catheters, scanning of the IVC can be valuable in assessing for thrombosis. The intrahepatic IVC is generally well seen. Thrombus can often be seen in gray scale and confirmed with color and spectral Doppler ultrasound. The infrahepatic IVC is more difficult to see but often can be adequately assessed using a far lateral approach obtaining coronal images using either kidney as a window.

Nutcracker Syndrome

Nutcracker phenomenon is described as extrinsic compression of the left renal vein resulting in mesoaortic (medial) segment narrowing and hilar (lateral) segment dilation of the vein (Videos 12.11 and 12.12).[134] **Nutcracker syndrome** refers to the associated clinical symptoms (flank pain, abdominal pain, hematuria, and/or proteinuria) when associated with the anatomic and hemodynamic findings of nutcracker phenomenon.[134] The syndrome can be divided into anterior (compression of the left renal vein between the aorta and SMA) and posterior (compression of a retroaortic left renal vein between the aorta and vertebral column) categories. Posterior nutcracker syndrome is rare, likely because the incidence of retroaortic left renal vein is only 0.5% to 3.7%.[135]

The overall prevalence of nutcracker syndrome is unknown, and diagnostic and treatment criteria are not well established. Proposed diagnostic steps in suspected cases include laboratory tests to evaluate for the cause of hematuria, ultrasound with sonography, CTA or MRA of the abdomen, and venography with renocaval pressure gradient measurements.[136] Peak velocity ratios and anterior-posterior diameter ratios greater than 5 between the mesoaortic and hilar segments of the left renal vein have been proposed as ultrasound diagnostic criteria.[137] However, the examiner needs to consider cases of long-standing nutcracker phenomenon where well-developed collateral vessels may decrease the blood flow through the narrowed portion of the left renal vein. Color Doppler should be used in these instances to evaluate for blood flow in collateral vessels.[138] CTA or MRA evaluation shows an acute angle origin of the SMA from the aorta, reported 54 degrees ± 5 degrees.[139] The distance between the SMA and anterior wall of the aorta in nutcracker phenomenon has been reported as 3 mm (normal, 5-6 mm).[139] Venography and renocaval pullback pressure gradient is an invasive evaluation but considered by most as the reference standard.[140] The pressure difference between the IVC and left renal vein normally is less than 1 mm Hg.[141] In patients with nutcracker phenomenon, the pressure gradient is 3.0 mm Hg or greater, consistent with left renal vein hypertension.[134] However, we have seen more than one patient with nutcracker syndrome who did not have a significant gradient

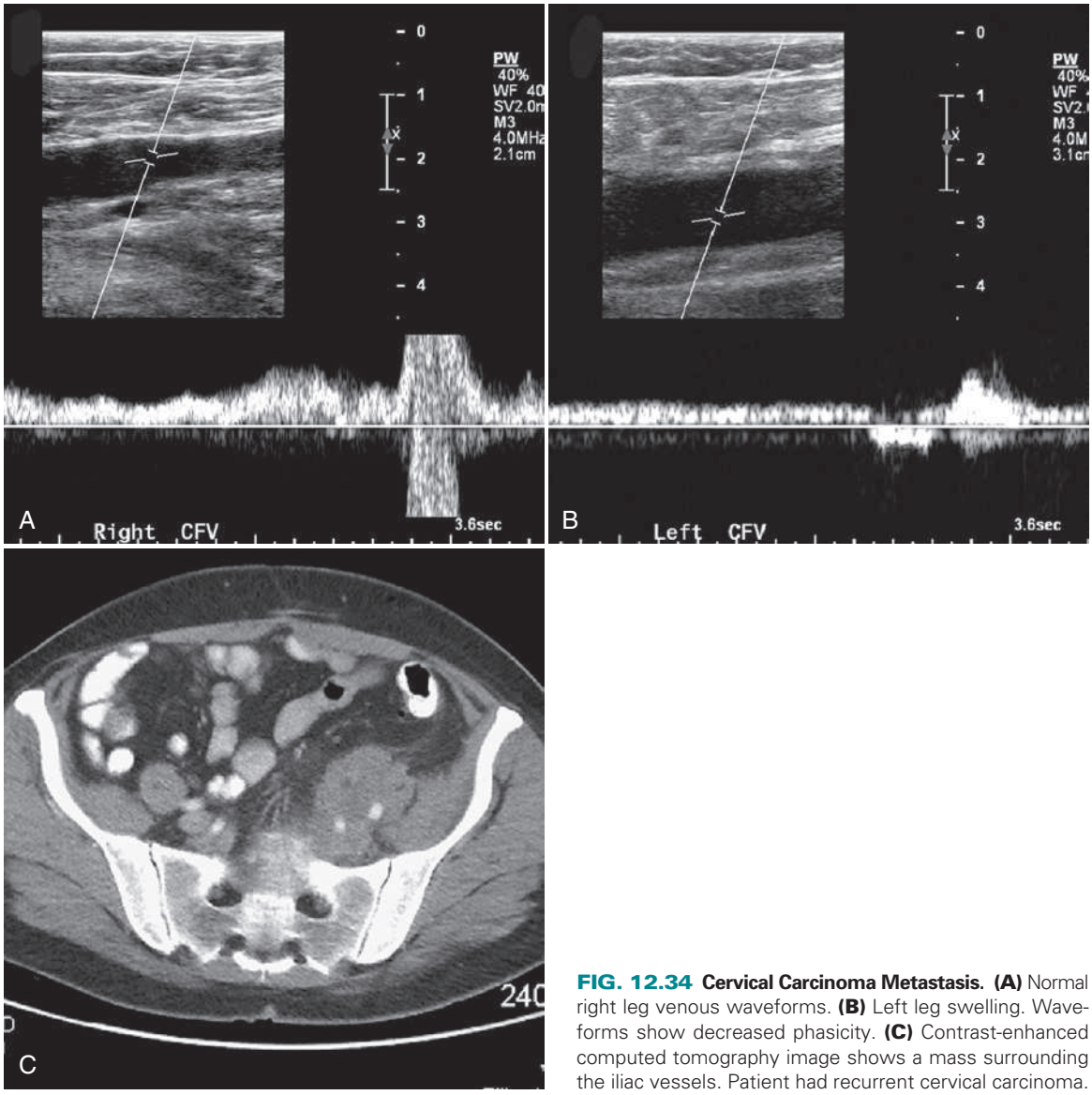

FIG. 12.34 Cervical Carcinoma Metastasis. (A) Normal right leg venous waveforms. **(B)** Left leg swelling. Waveforms show decreased phasicity. **(C)** Contrast-enhanced computed tomography image shows a mass surrounding the iliac vessels. Patient had recurrent cervical carcinoma.

on pressure measurement and yet became symptom free after a stent was placed in the left renal vein.

Just as diagnosis criteria for nutcracker syndrome are not well established and controversial, so are the treatment options. Surgical options include left renal vein transposition, renal venous bypass, auto transplantation of the kidney, and SMA transposition.[140] More recent studies, however, suggest that endovascular stenting should be considered as the primary treatment option because of its minimal invasive nature and successful outcomes (Fig. 12.35).[142]

Pelvic Congestion Syndrome

Pelvic congestion syndrome can present with vague chronic pelvic pain, usually of longer than 6 months duration.[143] The correct diagnosis is often delayed because of broad differential diagnoses for pelvic pain in women. The pain is related to pelvic and ovarian varicosities, which develop from chronic venous reflux or venous outflow obstruction of the pelvic veins.[144] Multiparity is an important risk factor. Multiple pregnancies result in increased venous distention and valve incompetence that leads to chronic venous reflux.[143,145] Nutcracker phenomenon, described earlier, also is a risk factor for development of pelvic congestion syndrome.

Ultrasound findings include dilated ovarian veins of more than 6 mm in diameter with reversed caudal flow, pelvic varicocele (>5 mm in diameter), and dilated arcuate veins (>5 mm in diameter) crossing the myometrium between pelvic varicoceles (Videos 12.13 and 12.14).[146,147] Examining the patient in the standing position should be considered because the pelvic veins may collapse when supine.[144] CT and MRI findings include four or more dilated parauterine veins (>4 mm in diameter) and ovarian vein diameter greater than 8 mm.[148] Time-resolved MRA demonstrates retrograde flow in the ovarian veins.[149] When clinical history is suggestive, venography is considered the reference

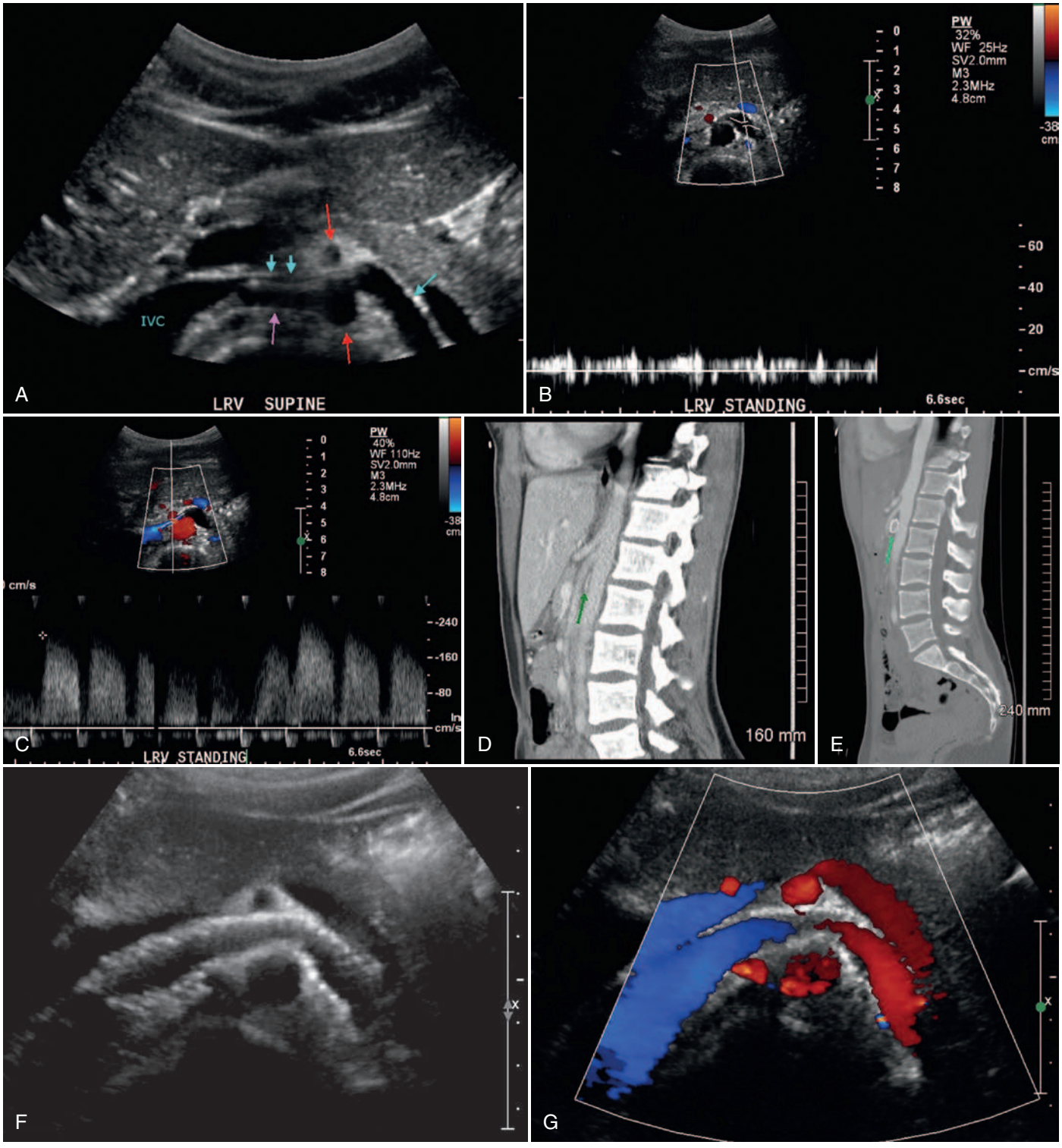

FIG. 12.35 Nutcracker Syndrome. Female, 17 years old, with left abdominal pain. **(A)** Transverse ultrasound image in the abdomen shows an enlarged left renal vein (LRV) *(blue arrow)* just before it crosses between the superior mesenteric artery (SMA) and aorta *(red arrows).* The LRV is narrowed and barely visible *(blue short arrows)* anterior to the right renal artery *(pink arrow).* **(B)** Duplex image of LRV shows slow flow in the dilated portion of the vein. **(C)** Duplex of the stenotic portion of the vein shows increased flow velocity of 210 cm/sec. **(D)** Sagittal reformatted computed tomography angiography shows that the LRV looks like a slit *(green arrow)* where it crosses between the aorta and the SMA. **(E)** Sagittal reformatted images after stent placement shows that the anterior-posterior diameter of the LRV is improved *(green arrow).* **(F)** Transverse gray-scale image shows the stent in the LRV. **(G)** Color duplex shows uniform flow in the stent. Spectral Doppler (not shown) demonstrated normal velocities throughout.

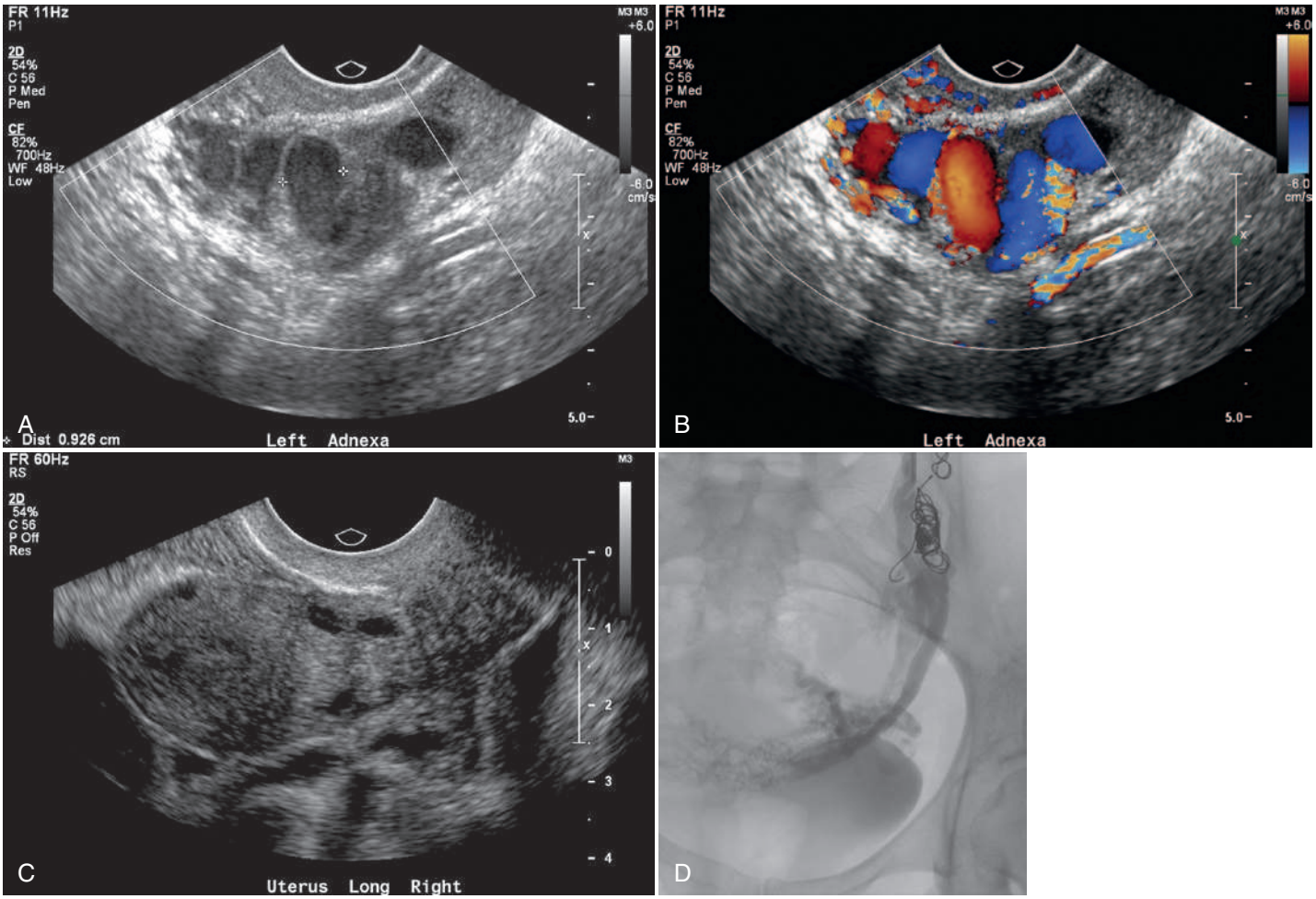

FIG. 12.36 Pelvic Congestion Syndrome. (A) Pelvic transvaginal gray-scale and **(B)** color Doppler images of dilated left ovarian veins with the largest vein measuring 9 mm in diameter. **(C)** Sagittal transvaginal image shows dilated uterine arcuate veins. These connect the left ovarian vein with the right. **(D)** Pelvic venography in a different patient performed during ovarian vein embolization. Numerous collateral veins arise from the left ovarian vein and cross the pelvis. These would be expected to connect to the right ovarian vein. See also Video 12.15.

standard.[148,150] Venographic findings include an enlarged left ovarian vein, retrograde flow of contrast into the left ovarian vein, and delayed clearance of contrast.[145,150] Medical management includes treatment with medroxyprogesterone acetate or goserelin acetate (gonadotropin-releasing hormone agonist).[151] Transcatheter embolization of the ovarian veins may be performed as a primary treatment or in patients with failed medical management. It results in clinical improvement in 60% to 100% of the patients[150] (Fig. 12.36 and Video 12.15).

Budd-Chiari Syndrome

Budd-Chiari syndrome is a rare condition caused by obstruction to outflow of the hepatic veins. In Caucasians the condition is often related to hypercoagulability. In Asians, membranous obstruction of the IVC is the most common cause.[152] When there is isolated stenosis of the IVC, percutaneous transluminal angioplasty with or without stent placement is often successful. Transjugular intrahepatic portosystemic shunt (TIPS) placement is often effective for hepatic vein obstruction.[153]

Budd-Chiari syndrome has many intrahepatic manifestations.[154,155] IVC manifestations are visible sonographically and include an IVC web just above the hepatic veins,[152] narrowing of the intrahepatic IVC caused by swelling of the liver, and IVC thrombosis.[153]

Inferior Vena Cava Neoplasms

Neoplasm of the IVC is rare and most often occurs in the setting of extension of solid organ tumors extending through their venous drainage to enter the IVC. This phenomenon is seen when renal cell carcinoma extends through the renal veins into the IVC. The same phenomenon can occur with hepatocellular and adrenocortical carcinoma extending through the hepatic and adrenal veins into the IVC.

Primary neoplasms of the IVC are even rarer. Leiomyosarcoma can occur at other sites in the systemic veins as well, but most often it arises in the IVC.

Ultrasound is not the primary method of imaging these tumors. When findings of IVC tumor involvement are seen

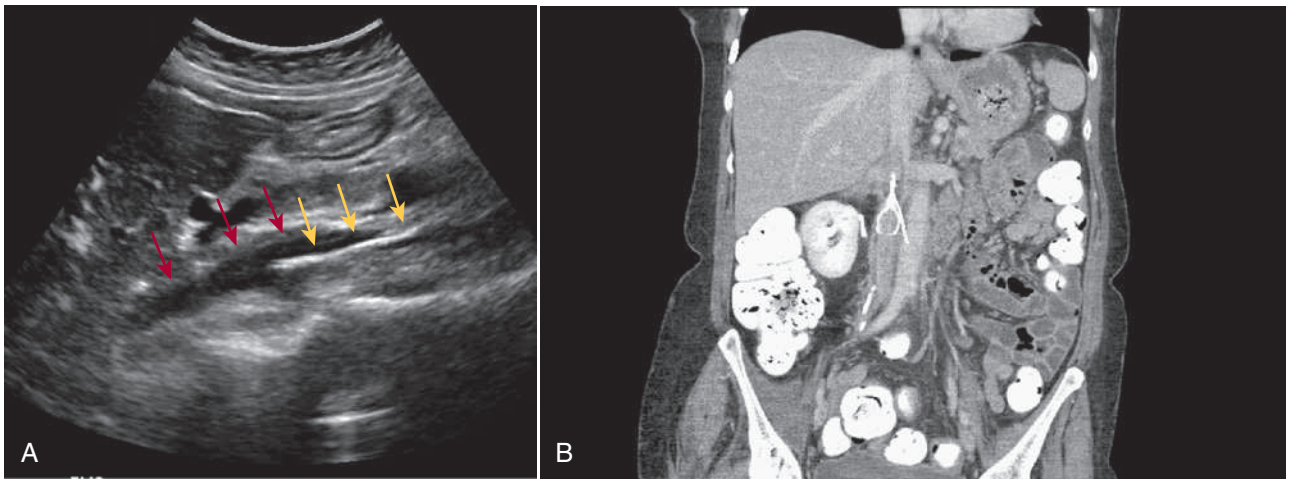

FIG. 12.37 Inferior Vena Cava (IVC) Filters. (A) IVC filters can be very difficult to see. Bright linear echoes *(yellow arrows)* indicate a tine of the filter within the IVC *(red arrows)*. This image represents an unusually good visualization of a filter. **(B)** Coronal reconstruction of computed tomography shows the location and form of the filter. (Courtesy of Anthony Hanbidge, MD.)

sonographically, cross-sectional imaging with CT or MRI should generally be recommended to determine the full extent of the abnormality.

Other Inferior Vena Cava Findings

Dilation of the IVC and hepatic vein orifices is seen in patients with congestive heart failure.[156]

Placement of **IVC filters** has become more common. In our experience, they are inconsistently seen. When seen, filters appear as an echogenic foreign body in the IVC. It is rarely possible to determine more about the filter than its presence and approximate location (Fig. 12.37). The IVC may become sclerotic in patients with long-standing filters, in whom it may be possible to see an absence of the IVC along with retroperitoneal collateral veins. The legs of the filters can also penetrate the wall of the IVC. This finding is fairly common on CT and most often is an incidental finding, although complications may result.[157] IVC penetration may be able to be observed sonographically as an echogenic foreign body extending outside of the IVC.

NONVASCULAR DISEASES OF THE RETROPERITONEUM

Excepting specific organs covered in other chapters, ultrasound is not the primary modality used in defining nonvascular problems in the retroperitoneum. When the abnormalities described next are seen sonographically, further cross-sectional imaging with CT or MRI often is needed to define the abnormality completely.

Solid Masses

Probably the most common solid mass is lymphadenopathy (enlarged lymph nodes). Causes of nodal enlargement can be benign or malignant (e.g., infection, lymphoma), but in all cases, malignancy must be excluded. Lymph nodes are most commonly hypoechoic. The identification of a structure as a probable lymph node is often by location in a paraaortic or paracaval region or in the mesentery.

Metastatic disease is another cause of solid masses in the retroperitoneum. Metastasis most frequently occurs to lymph nodes but can be seen in other sites. Often, it is impossible to tell with certainty whether the mass is nodal or is centered in some other type of tissue (Fig. 12.38).

Primary malignancies in the retroperitoneum are rare. The most common malignant retroperitoneal tumor is lymphoma.[158] The next most common are sarcomas: liposarcoma, leiomyosarcoma, and fibrous histiocytoma. These tumors generally undergo surgical resection and have a relatively high rate of recurrence.[159]

Benign masses also occur in the retroperitoneum, including **fibromas, schwannomas, neurofibromas,** and **lipomas. Extraadrenal paragangliomas** (extraadrenal **pheochromocytomas**) are usually benign but can be malignant.[160] The distinction between benign and malignant retroperitoneal masses cannot generally be made sonographically, and the finding of an unexpected mass in the retroperitoneum should generally prompt further evaluation with CT or MRI.

Fluid collections may also be seen in the retroperitoneum, including hematoma, urinoma, lymphocele, abscess, and pancreatic pseudocyst. If well seen and when indicated, sonography in conjunction with fluoroscopy is often the best way to drain these collections.

Retroperitoneal Fibrosis

As mentioned previously, retroperitoneal fibrosis is often grouped with inflammatory AAA in the disease process called **chronic periaortitis.** Retroperitoneal fibrosis can be seen as a mass usually surrounding the aorta and the common iliac arteries. It can involve adjacent structures, most often the ureters, resulting in displacement of the ureters and often in obstruction. When related to AAA, retroperitoneal fibrosis often regresses with repair of the AAA.

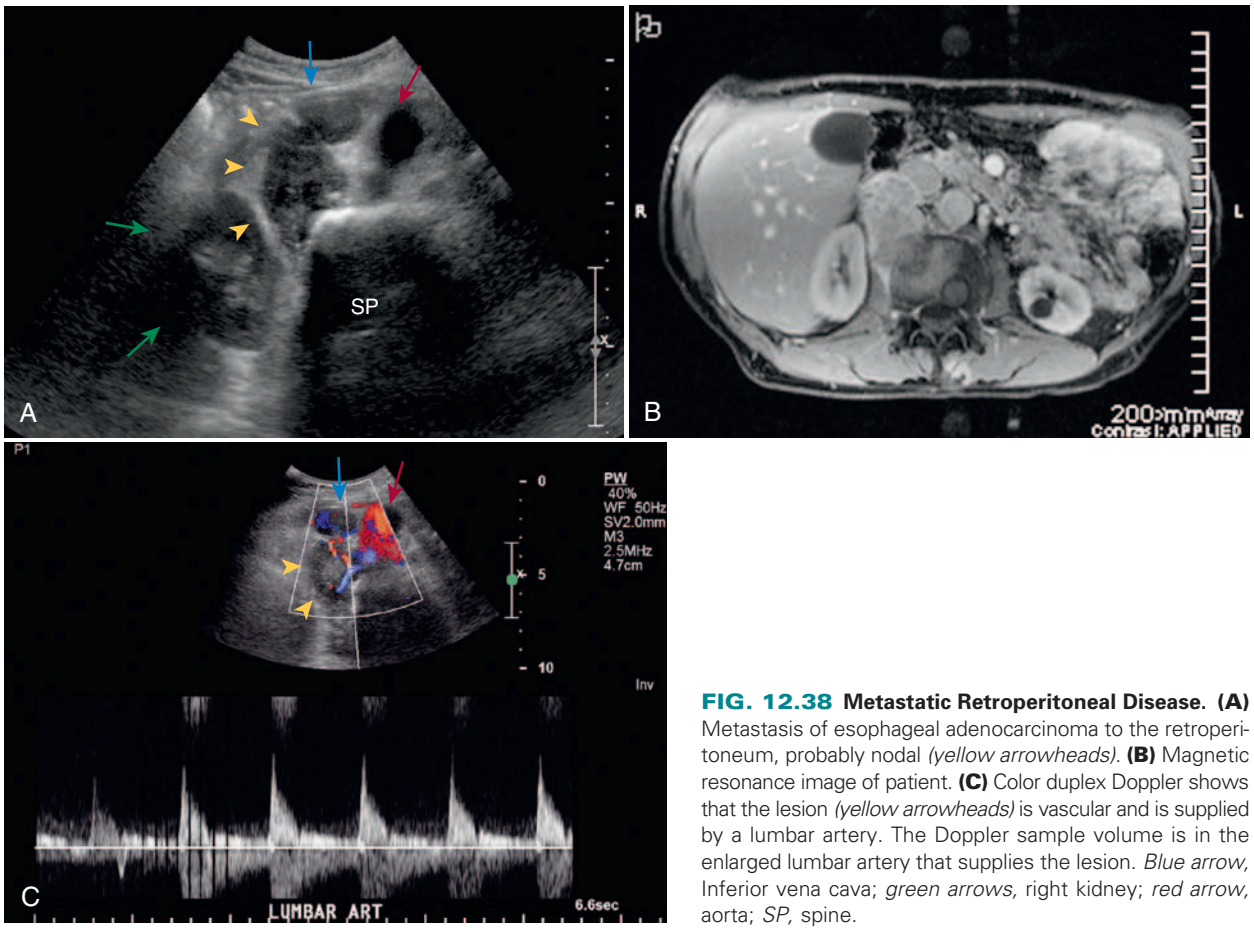

FIG. 12.38 Metastatic Retroperitoneal Disease. (A) Metastasis of esophageal adenocarcinoma to the retroperitoneum, probably nodal *(yellow arrowheads).* **(B)** Magnetic resonance image of patient. **(C)** Color duplex Doppler shows that the lesion *(yellow arrowheads)* is vascular and is supplied by a lumbar artery. The Doppler sample volume is in the enlarged lumbar artery that supplies the lesion. *Blue arrow,* Inferior vena cava; *green arrows,* right kidney; *red arrow,* aorta; *SP,* spine.

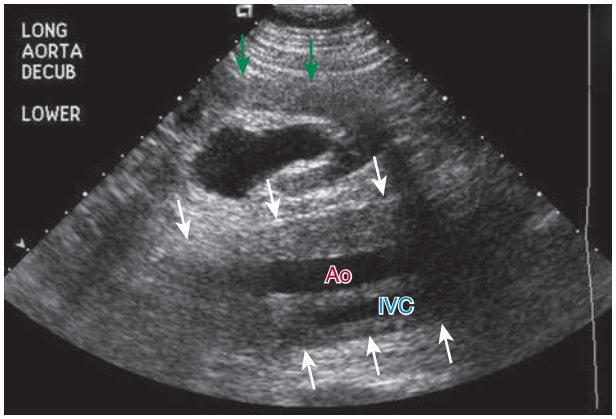

FIG. 12.39 Chronic Periaortitis. Coronal ultrasound image of chronic periaortitis with no abdominal aortic aneurysm (retroperitoneal fibrosis) *(white arrows)* surrounding the aorta *(Ao).* Inferior vena cava *(IVC)* is also faintly visible, surrounded by the mass. Left kidney *(green arrows)* is hydronephrotic because of entrapment of the left ureter by the periaortic mass. (Courtesy of Carl Reading, MD.)

In retroperitoneal fibrosis, ultrasound shows a mass encasing the abdominal aorta (Fig. 12.39). The back wall of the aorta is usually spared. A periaortic mass seen to separate the aorta from the spine suggests that the cause is instead malignant.[161] Ultrasound is not sensitive for detection of retroperitoneal fibrosis,[162] although it is sensitive for detection of AAA, which may be present. Sonography is also sensitive for the detection of ureteral obstruction and hydronephrosis, the most common complication.

CONCLUSION

Ultrasound often is used for targeted evaluation of solid organs and blood vessels in the retroperitoneum. Solid organ evaluation is covered in other chapters. For diseases of blood vessels of the retroperitoneum, ultrasound is generally an excellent diagnostic method and often the first modality used in diagnosis. For several reasons ultrasound is not a primary method for imaging the connective tissue regions of the retroperitoneum. To perform a thorough diagnostic examination when scanning the retroperitoneal organs and blood vessels, the clinician must have a clear concept of all retroperitoneal findings that may be encountered so that the best patient care can be provided.

REFERENCES

1. Mitchell RN. Blood vessels. In: Kumar V, Abbas AK, Aster JC, editors. Robbins and Cotran pathologic basis of disease. 9th ed. Philadelphia: Saunders-Elsevier; 2015. p. 483-522.
2. Mozaffarian D, Benjamin EJ, Go AS, et al. Heart disease and stroke statistics—2016 update: a report from the American Heart Association. Circulation. 2016;133(4):e38-e360.
3. Golledge J, Norman PE. Atherosclerosis and abdominal aortic aneurysm: cause, response, or common risk factors? Arterioscler Thromb Vasc Biol. 2010;30(6):1075-1077.
4. Johnston KW, Rutherford RB, Tilson MD, et al. Suggested standards for reporting on arterial aneurysms. Subcommittee on Reporting Standards for Arterial Aneurysms, Ad Hoc Committee on Reporting Standards, Society for Vascular Surgery and North American Chapter, International Society for Cardiovascular Surgery. J Vasc Surg. 1991;13(3):452-458.
5. Dua A, Kuy S, Lee CJ, et al. Epidemiology of aortic aneurysm repair in the United States from 2000 to 2010. J Vasc Surg. 2014;59(6):1512-1517.
6. Kent KC. Clinical practice. Abdominal aortic aneurysms. N Engl J Med. 2014;371(22):2101-2108.
7. Wanhainen A, Bjorck M, Boman K, et al. Influence of diagnostic criteria on the prevalence of abdominal aortic aneurysm. J Vasc Surg. 2001;34(2):229-235.
8. Stather PW, Dattani N, Bown MJ, et al. International variations in AAA screening. Eur J Vasc Endovasc Surg. 2013;45(3):231-234.
9. Svensjo S, Bjorck M, Wanhainen A. Editor's choice: five-year outcomes in men screened for abdominal aortic aneurysm at 65 years of age: a population-based cohort study. Eur J Vasc Endovasc Surg. 2014;47(1):37-44.
10. Crawford ES, Snyder DM, Cho GC, Roehm Jr JO. Progress in treatment of thoracoabdominal and abdominal aortic aneurysms involving celiac, superior mesenteric, and renal arteries. Ann Surg. 1978;188(3):404-422.
11. Johnsen SH, Forsdahl SH, Singh K, Jacobsen BK. Atherosclerosis in abdominal aortic aneurysms: a causal event or a process running in parallel? The Tromsø study. Arterioscler Thromb Vasc Biol. 2010;30(6):1263-1268.
12. Michel JB, Martin-Ventura JL, Egido J, et al. Novel aspects of the pathogenesis of aneurysms of the abdominal aorta in humans. Cardiovasc Res. 2011;90(1):18-27.
13. Golledge J, Muller J, Daugherty A, Norman P. Abdominal aortic aneurysm: pathogenesis and implications for management. Arterioscler Thromb Vasc Biol. 2006;26(12):2605-2613.
14. Dunne JA, Bailey MA, Griffin KJ, et al. Statins: the holy grail of abdominal aortic aneurysm (AAA) growth attenuation? A systematic review of the literature. Curr Vasc Pharmacol. 2014;12(1):168-172.
15. Wilmink AB, Quick CR. Epidemiology and potential for prevention of abdominal aortic aneurysm. Br J Surg. 1998;85(2):155-162.
16. Solberg S, Singh K, Wilsgaard T, Jacobsen BK. Increased growth rate of abdominal aortic aneurysms in women. The Tromsø study. Eur J Vasc Endovasc Surg. 2005;29(2):145-149.
17. Mofidi R, Goldie VJ, Kelman J, et al. Influence of sex on expansion rate of abdominal aortic aneurysms. Br J Surg. 2007;94(3):310-314.
18. Moll FL, Powell JT, Fraedrich G, et al. Management of abdominal aortic aneurysms clinical practice guidelines of the European society for vascular surgery. Eur J Vasc Endovasc Surg. 2011;41(Suppl. 1):S1-S58.
19. Brown LC, Powell JT. Risk factors for aneurysm rupture in patients kept under ultrasound surveillance. UK Small Aneurysm Trial Participants. Ann Surg. 1999;230(3):289-296.
20. Brewster DC, Cronenwett JL, Hallett Jr JW, et al. Guidelines for the treatment of abdominal aortic aneurysms. Report of a subcommittee of the Joint Council of the American Association for Vascular Surgery and Society for Vascular Surgery. J Vasc Surg. 2003;37(5):1106-1117.
21. Brown PM, Zelt DT, Sobolev B. The risk of rupture in untreated aneurysms: the impact of size, gender, and expansion rate. J Vasc Surg. 2003;37(2):280-284.
22. Norman PE, Powell JT. Abdominal aortic aneurysm: the prognosis in women is worse than in men. Circulation. 2007;115(22):2865-2869.
23. Baxter BT, Pearce WH, Waltke EA, et al. Prolonged administration of doxycycline in patients with small asymptomatic abdominal aortic aneurysms: report of a prospective (Phase II) multicenter study. J Vasc Surg. 2002;36(1):1-12.
24. Schlosser FJ, Tangelder MJ, Verhagen HJ, et al. Growth predictors and prognosis of small abdominal aortic aneurysms. J Vasc Surg. 2008;47(6):1127-1133.
25. Mosorin M, Juvonen J, Biancari F, et al. Use of doxycycline to decrease the growth rate of abdominal aortic aneurysms: a randomized, double-blind, placebo-controlled pilot study. J Vasc Surg. 2001;34(4):606-610.
26. Sweeting MJ, Thompson SG, Brown LC, Powell JT. Meta-analysis of individual patient data to examine factors affecting growth and rupture of small abdominal aortic aneurysms. Br J Surg. 2012;99(5):655-665.
27. Wilson JM, Jungner YG. Principles and practice of mass screening for disease]. Bol Oficina Sanit Panam. 1968;65(4):281-393.
28. Fleming C, Whitlock EP, Beil TL, Lederle FA. Screening for abdominal aortic aneurysm: a best-evidence systematic review for the U.S. Preventive Services Task Force. Ann Intern Med. 2005;142(3):203-211.
29. LeFevre ML, U.S. Preventive Services Task Force. Screening for abdominal aortic aneurysm: U.S. Preventive Services Task Force recommendation statement. Ann Intern Med. 2014;161(4):281-290.
30. Shreibati JB, Baker LC, Hlatky MA, Mell MW. Impact of the Screening Abdominal Aortic Aneurysms Very Efficiently (SAAAVE) Act on abdominal ultrasonography use among Medicare beneficiaries. Arch Intern Med. 2012;172(19):1456-1462.
31. Pellerito JS, Gabriel H, Katzen JB, et al. ACR–AIUM–SRU practice parameter for the performance of diagnostic and screening ultrasound of the abdominal aorta in adults: American College of Radiology; 2015. Available from: http://www.acr.org/~/media/102C4741C2A44691939F0EE3258E0BD2.pdf.
32. Life Line Screening. Abdominal aortic aneurysm screening; 2016. Available from: http://www.lifelinescreening.com/What-We-Do/What-We-Screen-For/Abdominal-Aortic-Aneurysms.
33. McCarthy RJ, Shaw E, Whyman MR, et al. Recommendations for screening intervals for small aortic aneurysms. Br J Surg. 2003;90(7):821-826.
34. Brady AR, Thompson SG, Fowkes FG, et al. Abdominal aortic aneurysm expansion: risk factors and time intervals for surveillance. Circulation. 2004;110(1):16-21.
35. Chaikof EL, Brewster DC, Dalman RL, et al. SVS practice guidelines for the care of patients with an abdominal aortic aneurysm: executive summary. J Vasc Surg. 2009;50(4):880-896.
36. RESCAN Collaborators, Bown MJ, Sweeting MJ, et al. Surveillance intervals for small abdominal aortic aneurysms: a meta-analysis. JAMA. 2013;309(8):806-813.
37. Bertino R, Pai D, Beach D, et al. Establishment of an interventional radiology clinic to follow untreated abdominal aortic aneurysms. J Am Coll Radiol. 2006;3(4):291-295.
38. Shuman WP, Hastrup Jr W, Kohler TR, et al. Suspected leaking abdominal aortic aneurysm: use of sonography in the emergency room. Radiology. 1988;168(1):117-119.
39. Dill-Macky MJ. Aortic endografts: detecting endoleaks using contrast-enhanced ultrasound. Ultrasound Q. 2006;22(1):49-52.
40. Bashir MR, Ferral H, Jacobs C, et al. Endoleaks after endovascular abdominal aortic aneurysm repair: management strategies according to CT findings. AJR Am J Roentgenol. 2009;192(4):W178-W186.
41. Mennander A, Pimenoff G, Heikkinen M, et al. Nonoperative approach to endotension. J Vasc Surg. 2005;42(2):194-199.
42. Baum RA, Stavropoulos SW, Fairman RM, Carpenter JP. Endoleaks after endovascular repair of abdominal aortic aneurysms. J Vasc Interv Radiol. 2003;14(9 Pt 1):1111-1117.
43. Avgerinos ED, Chaer RA, Makaroun MS. Type II endoleaks. J Vasc Surg. 2014;60(5):1386-1391.
44. Karthikesalingam A, Al-Jundi W, Jackson D, et al. Systematic review and meta-analysis of duplex ultrasonography, contrast-enhanced ultrasonography or computed tomography for surveillance after endovascular aneurysm repair. Br J Surg. 2012;99(11):1514-1523.
45. Gray C, Goodman P, Herron CC, et al. Use of colour duplex ultrasound as a first line surveillance tool following EVAR is associated with a reduction in cost without compromising accuracy. Eur J Vasc Endovasc Surg. 2012;44(2):145-150.

46. Dill-Macky MJ, Wilson SR, Sternbach Y, et al. Detecting endoleaks in aortic endografts using contrast-enhanced sonography. AJR Am J Roentgenol. 2007;188(3):W262-W268.
47. Giannoni MF, Palombo G, Sbarigia E, et al. Contrast-enhanced ultrasound imaging for aortic stent-graft surveillance. J Endovasc Ther. 2003;10(2): 208-217.
48. Gurtler VM, Sommer WH, Meimarakis G, et al. A comparison between contrast-enhanced ultrasound imaging and multislice computed tomography in detecting and classifying endoleaks in the follow-up after endovascular aneurysm repair. J Vasc Surg. 2013;58(2):340-345.
49. Millen A, Canavati R, Harrison G, et al. Defining a role for contrast-enhanced ultrasound in endovascular aneurysm repair surveillance. J Vasc Surg. 2013;58(1):18-23.
50. Hellmann DB, Grand DJ, Freischlag JA. Inflammatory abdominal aortic aneurysm. JAMA. 2007;297(4):395-400.
51. Vaglio A, Salvarani C, Buzio C. Retroperitoneal fibrosis. Lancet. 2006;367(9506):241-251.
52. Palmisano A, Vaglio A. Chronic periaortitis: a fibro-inflammatory disorder. Best Pract Res Clin Rheumatol. 2009;23(3):339-353.
53. Inoue D, Zen Y, Abo H, et al. Immunoglobulin G4-related periaortitis and periarteritis: CT findings in 17 patients. Radiology. 2011;261(2):625-633.
54. Paravastu SC, Ghosh J, Murray D, et al. A systematic review of open versus endovascular repair of inflammatory abdominal aortic aneurysms. Eur J Vasc Endovasc Surg. 2009;38(3):291-297.
55. Stanson AW, Kazmier FJ, Hollier LH, et al. Penetrating atherosclerotic ulcers of the thoracic aorta: natural history and clinicopathologic correlations. Ann Vasc Surg. 1986;1(1):15-23.
56. Hayashi H, Matsuoka Y, Sakamoto I, et al. Penetrating atherosclerotic ulcer of the aorta: imaging features and disease concept. Radiographics. 2000;20(4):995-1005.
57. Tsuji Y, Tanaka Y, Kitagawa A, et al. Endovascular stent-graft repair for penetrating atherosclerotic ulcer in the infrarenal abdominal aorta. J Vasc Surg. 2003;38(2):383-388.
58. Nathan DP, Boonn W, Lai E, et al. Presentation, complications, and natural history of penetrating atherosclerotic ulcer disease. J Vasc Surg. 2012; 55(1):10-15.
59. Chung JW, Kim HC, Choi YH, et al. Patterns of aortic involvement in Takayasu arteritis and its clinical implications: evaluation with spiral computed tomography angiography. J Vasc Surg. 2007;45(5):906-914.
60. Diaz JA, Campbell BT, Moursi MM, et al. Delayed manifestation of abdominal aortic stenosis in a child presenting 10 years after blunt abdominal trauma. J Vasc Surg. 2006;44(5):1104-1106.
61. Shalhub S, Starnes BW, Tran NT, et al. Blunt abdominal aortic injury. J Vasc Surg. 2012;55(5):1277-1285.
62. Verschuyl EJ, Kaatee R, Beek FJ, et al. Renal artery origins: best angiographic projection angles. Radiology. 1997;205(1):115-120.
63. Kadir S. Arterial and venous systems of the viscera: kidneys. Normal and variant angiographic anatomy. Philadelphia: Saunders; 1991.
64. Glodny B, Petersen J, Hofmann KJ, et al. Kidney fusion anomalies revisited: clinical and radiological analysis of 209 cases of crossed fused ectopia and horseshoe kidney. BJU Int. 2009;103(2):224-235.
65. Boatman DL, Cornell SH, Kolln CP. The arterial supply of horseshoe kidneys. Am J Roentgenol Radium Ther Nucl Med. 1971;113(3):447-451.
66. Oparil S, Zaman MA, Calhoun DA. Pathogenesis of hypertension. Ann Intern Med. 2003;139(9):761-776.
67. Vasbinder GB, Nelemans PJ, Kessels AG, et al. Diagnostic tests for renal artery stenosis in patients suspected of having renovascular hypertension: a meta-analysis. Ann Intern Med. 2001;135(6):401-411.
68. Cooper CJ, Murphy TP, Cutlip DE, et al. Stenting and medical therapy for atherosclerotic renal-artery stenosis. N Engl J Med. 2014;370(1):13-22.
69. Sos TA, Mann SJ. Did renal artery stent placement fail in the Cardiovascular Outcomes with Renal Atherosclerotic Lesions (CORAL) study or did the CORAL Study Fail Renal Artery Stent Placement? The CORAL roll-in experience and the CORAL trials. J Vasc Interv Radiol. 2014;25(4): 520-523.
70. Parikh SA, Shishehbor MH, Gray BH, et al. SCAI expert consensus statement for renal artery stenting appropriate use. Catheter Cardiovasc Interv. 2014;84(7):1163-1171.
71. Mohan IV, Bourke V. The management of renal artery stenosis: an alternative interpretation of ASTRAL and CORAL. Eur J Vasc Endovasc Surg. 2015;49(4):465-473.
72. Herrmann SM, Saad A, Textor SC. Management of atherosclerotic renovascular disease after Cardiovascular Outcomes in Renal Atherosclerotic Lesions (CORAL). Nephrol Dial Transplant. 2015;30(3):366-375.
73. Zucchelli PC. Hypertension and atherosclerotic renal artery stenosis: diagnostic approach. J Am Soc Nephrol. 2002;13(Suppl. 3):S184-S186.
74. White CJ. Catheter-based therapy for atherosclerotic renal artery stenosis. Circulation. 2006;113(11):1464-1473.
75. Olin JW, Piedmonte MR, Young JR, et al. The utility of duplex ultrasound scanning of the renal arteries for diagnosing significant renal artery stenosis. Ann Intern Med. 1995;122(11):833-838.
76. Labropoulos N, Ayuste B, Leon Jr LR. Renovascular disease among patients referred for renal duplex ultrasonography. J Vasc Surg. 2007;46(4): 731-737.
77. Safian RD, Textor SC. Renal-artery stenosis. N Engl J Med. 2001;344(6): 431-442.
78. Krijnen P, van Jaarsveld BC, Steyerberg EW, et al. A clinical prediction rule for renal artery stenosis. Ann Intern Med. 1998;129(9):705-711.
79. Henry M, Amor M, Henry I, et al. Stents in the treatment of renal artery stenosis: long-term follow-up. J Endovasc Surg. 1999;6(1):42-51.
80. Isles CG, Robertson S, Hill D. Management of renovascular disease: a review of renal artery stenting in ten studies. QJM. 1999;92(3):159-167.
81. Del Conde I, Galin ID, Trost B, et al. Renal artery duplex ultrasound criteria for the detection of significant in-stent restenosis. Catheter Cardiovasc Interv. 2014;83(4):612-618.
82. Plouin PF, Perdu J, La Batide-Alanore A, et al. Fibromuscular dysplasia. Orphanet J Rare Dis. 2007;2:28.
83. Slovut DP, Olin JW. Fibromuscular dysplasia. N Engl J Med. 2004;350(18): 1862-1871.
84. Sos TA, Pickering TG, Sniderman K, et al. Percutaneous transluminal renal angioplasty in renovascular hypertension due to atheroma or fibromuscular dysplasia. N Engl J Med. 1983;309(5):274-279.
85. Williams DM, Lee DY, Hamilton BH, et al. The dissected aorta: percutaneous treatment of ischemic complications—principles and results. J Vasc Interv Radiol. 1997;8(4):605-625.
86. Corriere MA. Renovascular disease—acute ischemia. In: Cronenwett JL, Johnston KW, editors. Rutherford's vascular surgery. 8th ed. Philadelphia: Saunders; 2014. p. 2335-2344.
87. Blum U, Billmann P, Krause T, et al. Effect of local low-dose thrombolysis on clinical outcome in acute embolic renal artery occlusion. Radiology. 1993;189(2):549-554.
88. Weyand CM, Goronzy JJ. Medium- and large-vessel vasculitis. N Engl J Med. 2003;349(2):160-169.
89. Courtel JV, Soto B, Niaudet P, et al. Percutaneous transluminal angioplasty of renal artery stenosis in children. Pediatr Radiol. 1998;28(1):59-63.
90. Ritz E. Accessory renal arteries—mostly, but not always, innocuous. J Am Soc Nephrol. 2006;17:3-4.
91. Bude RO, Forauer AR, Caoili EM, Nghiem HV. Is it necessary to study accessory arteries when screening the renal arteries for renovascular hypertension? Radiology. 2003;226(2):411-416.
92. Radermacher J, Chavan A, Bleck J, et al. Use of Doppler ultrasonography to predict the outcome of therapy for renal-artery stenosis. N Engl J Med. 2001;344(6):410-417.
93. Teefey SA, Coley BD, Crisci K, et al. ACR–AIUM–SPR–SRU practice parameter for the performance of native renal artery duplex sonography: American College of Radiology; 2014. Available from: http://www.acr.org/~/media/ACR/Documents/PGTS/guidelines/US_Renal_Sonography.pdf.
94. AbuRahma AF, Srivastava M, Mousa AY, et al. Critical analysis of renal duplex ultrasound parameters in detecting significant renal artery stenosis. J Vasc Surg. 2012;56(4):1052-1059.
95. Li JC, Jiang YX, Zhang SY, et al. Evaluation of renal artery stenosis with hemodynamic parameters of Doppler sonography. J Vasc Surg. 2008;48(2): 323-328.
96. Stavros AT, Parker SH, Yakes WF, et al. Segmental stenosis of the renal artery: pattern recognition of tardus and parvus abnormalities with duplex sonography. Radiology. 1992;184(2):487-492.

97. Williams GJ, Macaskill P, Chan SF, et al. Comparative accuracy of renal duplex sonographic parameters in the diagnosis of renal artery stenosis: paired and unpaired analysis. AJR Am J Roentgenol. 2007;188(3): 798-811.
98. Taylor DC, Kettler MD, Moneta GL, et al. Duplex ultrasound scanning in the diagnosis of renal artery stenosis: a prospective evaluation. J Vasc Surg. 1988;7(2):363-369.
99. Tham G, Ekelund L, Herrlin K, et al. Renal artery aneurysms. Natural history and prognosis. Ann Surg. 1983;197(3):348-352.
100. Klausner JQ, Harlander-Locke MP, Plotnik AN, et al. Current treatment of renal artery aneurysms may be too aggressive. J Vasc Surg. 2014;59(5): 1356-1361.
101. Nosher JL, Chung J, Brevetti LS, et al. Visceral and renal artery aneurysms: a pictorial essay on endovascular therapy. Radiographics. 2006;26(6): 1687-1704.
102. Bui BT, Oliva VL, Leclerc G, et al. Renal artery aneurysm: treatment with percutaneous placement of a stent-graft. Radiology. 1995;195(1): 181-182.
103. Uflacker R. Abdominal aorta and branches. In: Atlas of vascular anatomy: an angiographic approach. 2nd ed. Philadelphia: Lippincott Williams & Wilkins; 2007.
104. Kadir S, Lundell C, Saeed M. Celiac, superior and inferior mesenteric arteries. In: Atlas of normal and variant angiographic anatomy. Philadelphia: Saunders; 1991.
105. Oldenburg WA, Lau LL, Rodenberg TJ, et al. Acute mesenteric ischemia: a clinical review. Arch Intern Med. 2004;164(10):1054-1062.
106. Martin MC, Wyers MC. Mesenteric vascular disease: acute ischemia. In: Cronenwett JL, Johnston KW, editors. Rutherford's vascular surgery. 8th ed. Philadelphia: Saunders-Elsevier; 2014. p. 2398-2413.
107. Hirsch AT, Haskal ZJ, Hertzer NR, et al. ACC/AHA Guidelines for the management of patients with peripheral arterial disease (lower extremity, renal, mesenteric, and abdominal aortic): a collaborative report from the American Associations for Vascular Surgery/Society for Vascular Surgery, Society for Cardiovascular Angiography and Interventions, Society for Vascular Medicine and Biology, Society of Interventional Radiology, and the ACC/AHA Task Force on Practice Guidelines (writing committee to develop guidelines for the management of patients with peripheral arterial disease)—summary of recommendations. J Vasc Interv Radiol. 2006;17(9): 1383-1397.
108. Wilson DB, Mostafavi K, Craven TE, et al. Clinical course of mesenteric artery stenosis in elderly Americans. Arch Intern Med. 2006;166(19): 2095-2100.
109. Oliva IB, Davarpanah AH, Rybicki FJ, et al. ACR Appropriateness Criteria® imaging of mesenteric ischemia. Abdom Imaging. 2013;38(4):714-719.
110. Huber TS, Lee WA. Chronic mesenteric ischemia. In: Cronenwett JL, Johnston KW, editors. Vascular surgery. 7th ed. Philadelphia: Saunders-Elsevier; 2010. p. 2273-2288.
111. Simon S, Schittko G, Bosenberg H, et al. Fulminant course of a Takayasu's arteritis and rare mesenteric arterial maninfestion. Z Rheumatol. 2006;65(6):520, 522-526.
112. Levin DC, Baltaxe HA. High incidence of celiac axis narrowing in asymptomatic individuals. Am J Roentgenol Radium Ther Nucl Med. 1972;116(2): 426-429.
113. Delis KT, Gloviczki P, Altuwaijri M, McKusick MA. Median arcuate ligament syndrome: open celiac artery reconstruction and ligament division after endovascular failure. J Vasc Surg. 2007;46(4):799-802.
114. Mensink PB, van Petersen AS, Kolkman JJ, et al. Gastric exercise tonometry: the key investigation in patients with suspected celiac artery compression syndrome. J Vasc Surg. 2006;44(2):277-281.
115. Balaban DH, Chen J, Lin Z, et al. Median arcuate ligament syndrome: a possible cause of idiopathic gastroparesis. Am J Gastroenterol. 1997;92(3): 519-523.
116. Loffeld RJ, Overtoom HA, Rauwerda JA. The celiac axis compression syndrome. Report of 5 cases. Digestion. 1995;56(6):534-537.
117. Volteas N, Labropoulos N, Leon M, et al. Detection of superior mesenteric and coeliac artery stenosis with colour flow Duplex imaging. Eur J Vasc Surg. 1993;7(6):616-620.
118. Gentile AT, Moneta GL, Lee RW, et al. Usefulness of fasting and postprandial duplex ultrasound examinations for predicting high-grade superior mesenteric artery stenosis. Am J Surg. 1995;169(5):476-479.
119. Muller AF. Role of duplex Doppler ultrasound in the assessment of patients with postprandial abdominal pain. Gut. 1992;33(4):460-465.
120. Wolfman D, Bluth EI, Sossaman J. Median arcuate ligament syndrome. J Ultrasound Med. 2003;22(12):1377-1380.
121. Moneta GL, Lee RW, Yeager RA, et al. Mesenteric duplex scanning: a blinded prospective study. J Vasc Surg. 1993;17(1):79-84.
122. AbuRahma AF, Stone PA, Srivastava M, et al. Mesenteric/celiac duplex ultrasound interpretation criteria revisited. J Vasc Surg. 2012;55(2): 428-436.
123. Bowersox JC, Zwolak RM, Walsh DB, et al. Duplex ultrasonography in the diagnosis of celiac and mesenteric artery occlusive disease. J Vasc Surg. 1991;14(6):780-786.
124. Perko MJ, Just S, Schroeder TV. Importance of diastolic velocities in the detection of celiac and mesenteric artery disease by duplex ultrasound. J Vasc Surg. 1997;26(2):288-293.
125. Pellerito JS, Revzin MV, Tsang JC, et al. Doppler sonographic criteria for the diagnosis of inferior mesenteric artery stenosis. J Ultrasound Med. 2009;28(5):641-650.
126. Oderich GS, Erdoes LS, Lesar C, et al. Comparison of covered stents versus bare metal stents for treatment of chronic atherosclerotic mesenteric arterial disease. J Vasc Surg. 2013;58(5):1316-1323.
127. Mitchell EL, Chang EY, Landry GJ, et al. Duplex criteria for native superior mesenteric artery stenosis overestimate stenosis in stented superior mesenteric arteries. J Vasc Surg. 2009;50(2):335-340.
128. Aburahma AF, Mousa AY, Stone PA, et al. Duplex velocity criteria for native celiac/superior mesenteric artery stenosis vs in-stent stenosis. J Vasc Surg. 2012;55(3):730-738.
129. Kellman GM, Alpern MB, Sandler MA, Craig BM. Computed tomography of vena caval anomalies with embryologic correlation. Radiographics. 1988;8(3):533-556.
130. Radtke A, Schroeder T, Sotiropoulos GC, et al. Anatomical and physiological classification of hepatic vein dominance applied to liver transplantation. Eur J Med Res. 2005;10(5):187-194.
131. Xing X, Li H, Liu WG. Clinical studies on inferior right hepatic veins. Hepatobiliary Pancreat Dis Int. 2007;6(6):579-584.
132. Kadir S. Gonadal vessels. Normal and variant angiographic anatomy. Philadelphia: Saunders; 1991.
133. Ouriel K, Green RM, Greenberg RK, Clair DG. The anatomy of deep venous thrombosis of the lower extremity. J Vasc Surg. 2000;31(5):895-900.
134. Kurklinsky AK, Rooke TW. Nutcracker phenomenon and nutcracker syndrome. Mayo Clin Proc. 2010;85(6):552-559.
135. Karazincir S, Balci A, Gorur S, et al. Incidence of the retroaortic left renal vein in patients with varicocele. J Ultrasound Med. 2007;26(5):601-604.
136. Ahmed K, Sampath R, Khan MS. Current trends in the diagnosis and management of renal nutcracker syndrome: a review. Eur J Vasc Endovasc Surg. 2006;31(4):410-416.
137. Kim SH, Cho SW, Kim HD, et al. Nutcracker syndrome: diagnosis with Doppler US. Radiology. 1996;198(1):93-97.
138. Takebayashi S, Ueki T, Ikeda N, Fujikawa A. Diagnosis of the nutcracker syndrome with color Doppler sonography: correlation with flow patterns on retrograde left renal venography. AJR Am J Roentgenol. 1999;172(1): 39-43.
139. Cuéllar i Calàbria H, Quiroga Gómez S, Sebastià Cerqueda C, et al. Nutcracker or left renal vein compression phenomenon: multidetector computed tomography findings and clinical significance. Eur Radiol. 2005;15(8): 1745-1751.
140. Avgerinos ED, McEnaney R, Chaer RA. Surgical and endovascular interventions for nutcracker syndrome. Semin Vasc Surg. 2013;26(4):170-177.
141. Zhang H, Li M, Jin W, et al. The left renal entrapment syndrome: diagnosis and treatment. Ann Vasc Surg. 2007;21(2):198-203.
142. Chen S, Zhang H, Shi H, et al. Endovascular stenting for treatment of Nutcracker syndrome: report of 61 cases with long-term followup. J Urol. 2011;186(2):570-575.
143. Ignacio EA, Dua R, Sarin S, et al. Pelvic congestion syndrome: diagnosis and treatment. Semin Intervent Radiol. 2008;25(4):361-368.

144. O'Brien MT, Gillespie DL. Diagnosis and treatment of the pelvic congestion syndrome. J Vasc Surg Venous Lymphat Disord. 2015;3(1):96-106.
145. Rane N, Leyon JJ, Littlehales T, et al. Pelvic congestion syndrome. Curr Probl Diagn Radiol. 2013;42(4):135-140.
146. Durham JD, Machan L. Pelvic congestion syndrome. Semin Intervent Radiol. 2013;30(4):372-380.
147. Park SJ, Lim JW, Ko YT, et al. Diagnosis of pelvic congestion syndrome using transabdominal and transvaginal sonography. AJR Am J Roentgenol. 2004;182(3):683-688.
148. Koo S, Fan CM. Pelvic congestion syndrome and pelvic varicosities. Tech Vasc Interv Radiol. 2014;17(2):90-95.
149. Yang DM, Kim HC, Nam DH, et al. Time-resolved MR angiography for detecting and grading ovarian venous reflux: comparison with conventional venography. Br J Radiol. 2012;85(1014):e117-e122.
150. Phillips D, Deipolyi AR, Hesketh RL, et al. Pelvic congestion syndrome: etiology of pain, diagnosis, and clinical management. J Vasc Interv Radiol. 2014;25(5):725-733.
151. Soysal ME, Soysal S, Vicdan K, Ozer S. A randomized controlled trial of goserelin and medroxyprogesterone acetate in the treatment of pelvic congestion. Hum Reprod. 2001;16(5):931-939.
152. Lee BB, Villavicencio L, Kim YW, et al. Primary Budd-Chiari syndrome: outcome of endovascular management for suprahepatic venous obstruction. J Vasc Surg. 2006;43(1):101-108.
153. Cura M, Haskal Z, Lopera J. Diagnostic and interventional radiology for Budd-Chiari syndrome. Radiographics. 2009;29(3):669-681.
154. Brancatelli G, Vilgrain V, Federle MP, et al. Budd-Chiari syndrome: spectrum of imaging findings. AJR Am J Roentgenol. 2007;188(2):W168-W176.
155. Bargallo X, Gilabert R, Nicolau C, et al. Sonography of Budd-Chiari syndrome. AJR Am J Roentgenol. 2006;187(1):W33-W41.
156. Gore RM, Mathieu DG, White EM, et al. Passive hepatic congestion: cross-sectional imaging features. AJR Am J Roentgenol. 1994;162(1):71-75.
157. Kinney TB. Update on inferior vena cava filters. J Vasc Interv Radiol. 2003;14(4):425-440.
158. Sanyal R, Remer EM. Radiology of the retroperitoneum: case-based review. AJR Am J Roentgenol. 2009;192(6 Suppl.):S112-S117.
159. Gronchi A, Lo Vullo S, Fiore M, et al. Aggressive surgical policies in a retrospectively reviewed single-institution case series of retroperitoneal soft tissue sarcoma patients. J Clin Oncol. 2009;27(1):24-30.
160. Nishino M, Hayakawa K, Minami M, et al. Primary retroperitoneal neoplasms: CT and MR imaging findings with anatomic and pathologic diagnostic clues. Radiographics. 2003;23(1):45-57.
161. Cronin CG, Lohan DG, Blake MA, et al. Retroperitoneal fibrosis: a review of clinical features and imaging findings. AJR Am J Roentgenol. 2008;191(2):423-431.
162. Moussavian B, Horrow MM. Retroperitoneal fibrosis. Ultrasound Q. 2009;25(2):89-91.

CHAPTER 13

Dynamic Ultrasound of Hernias of the Groin and Anterior Abdominal Wall

Deborah Levine, Lisa Napolitano, and A. Thomas Stavros

SUMMARY OF KEY POINTS

- Dynamic ultrasound is the key examination for assessing the groin or anterior abdominal wall pain. Dynamic components of the examination include Valsalva and compression maneuvers and scanning in both supine and upright positions. Dynamic sonography enables clinicians to determine hernia type, size, contents, reducibility, and tenderness.
- Evaluation of groin pain in athletes is frequently more complex than in nonathletes because of associated tendinosis and osteitis pubis. Adding magnetic resonance imaging to dynamic ultrasound is usually necessary to identify underlying pathologic processes and to decide the best combination of surgical and nonsurgical treatments.
- Patients with one hernia frequently have multiple hernias, so in any patient in whom a hernia is sonographically demonstrable, the examination should be continued, looking for other types of ipsilateral and contralateral groin or anterior abdominal hernias. Even when no additional hernias are found, it is important to the surgeon to specifically mention in the report that a complete search of both groin areas was made and no additional hernias were found.
- Strangulation is the most dreaded complication of groin hernias. Gray-scale findings of strangulation—hyperechoic fat, isoechoic thickening of the hernia sac, fluid within the sac, and thickening of the walls of bowel loops—are all more sensitive for strangulation than is Doppler ultrasound.
- Recurrent pain after herniorrhaphy is a relatively common problem. Dynamic sonography can be helpful in assessing both acute and chronic recurrences of groin pain. Most hernia repairs now use mesh. The key to sonographic identification of recurrent hernias is to assess the edges of the mesh with dynamic maneuvers, because recurrent hernias arise from the edges of the mesh.
- Many pathologic processes, both rare and nonspecific, can simulate hernia, but cysts or hydroceles of the processus vaginalis (or canal of Nuck) and round ligament varices are relatively common and have virtually pathognomonic sonographic appearances.

CHAPTER OUTLINE

TECHNICAL REQUIREMENTS
THE REPORT FOR DYNAMIC ULTRASOUND OF GROIN HERNIAS
HERNIA CONTENTS
DYNAMIC MANEUVERS
KEY SONOGRAPHIC LANDMARKS
INGUINAL AND INGUINAL REGION HERNIAS
Indirect Inguinal Hernias
Direct Inguinal Hernias
Femoral Hernias
Spigelian Hernias
Sports Hernias
ABDOMINAL WALL OR VENTRAL HERNIAS
Linea Alba Hernias
Umbilical Hernias
Paraumbilical or Periumbilical Hernias
Incisional Hernias
Multiple Hernias
ADDITIONAL ISSUES REGARDING HERNIAS
Recurrent Groin Hernias
Hernia Complications
Entities That Simulate Groin Hernias
Entities That Simulate Anterior Abdominal Wall Hernias
SUMMARY

Patients with groin pain may have a variety of conditions including, but not limited to, hip abnormalities, tendonitis, lymphadenopathy, or hernia.[1] Groin pain is a common presenting symptom in adult patients. Herniorrhaphy is the most common surgical procedure in the United States, with more than 800,000 operations performed annually.[2] An estimated 2.3 million inpatient abdominal hernia repairs were performed from 2001 to 2010, of which an estimated 567,000 were performed emergently. A general increase in the rate of total emergent hernias was observed from 16.0 to 19.2 emergent hernia repairs per 100,000

person-years in 2001 and 2010, respectively.[3] The lifetime risk of inguinal hernia requiring repair is high, estimated at 27.2% for men and 2.6% for women.[4] Over 90% of these procedures are performed on male infants younger than 1 year,[4] and thus these numbers do not reflect the incidence in adults.

Large hernias typically cause an obvious lump or bulge and are often diagnosed clinically and infrequently require imaging[5] (except to evaluate the contralateral side preoperatively). On the other hand, patients with hernias with pain but without a lump or bulge are more often referred for diagnostic imaging. Computed tomography (CT) and magnetic resonance imaging (MRI) have been used to identify and describe hernias (Fig. 13.1). However, real-time ultrasound has advantages over other imaging modalities: the ability to scan the patient in both upright and supine positions, to use **dynamic maneuvers** such as Valsalva and compression, and to document motion in real time (Fig. 13.2). Positioning and dynamic maneuvers affect the operator's ability to diagnose a hernia, alter its size and contents, and evaluate its reducibility. Sonography also enables the user to assess tenderness and clinical importance of a hernia. Thus ultrasound is the imaging modality of choice for assessment of inguinal masses and inguinal pain.[6,7]

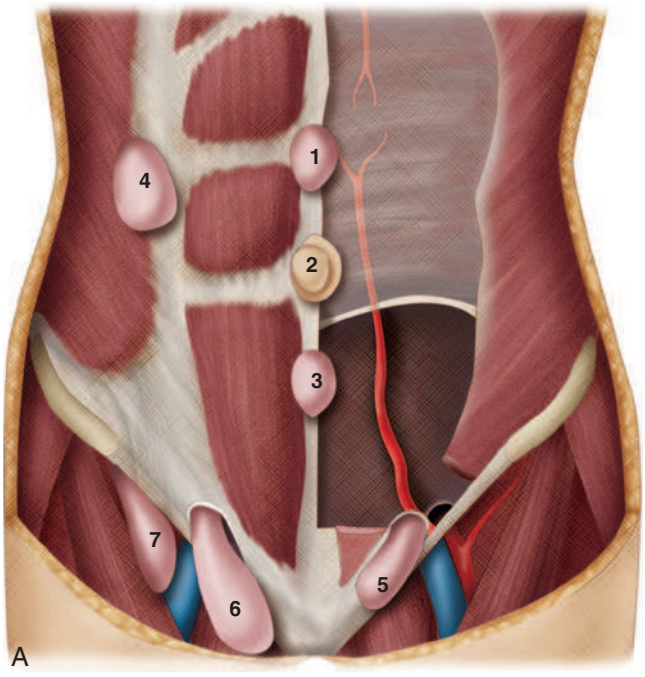

FIG. 13.1 Types of Hernias. (A) Diagram of the anterior abdominal wall, depicting site of abdominal wall hernias. *1,* **Supraumbilical hernia.** *2,* **Umbilical hernia.** *3,* **Infraumbilical hernia.** *4,* **Spigelian hernia.** *5,* **Erect inguinal hernia.** *6,* **Indirect inguinal hernia.** *7,* **Femoral hernia. (B) Indirect inguinal hernias on computed tomography (CT).** Abdominal CT scan shows bilateral fat-containing indirect inguinal hernias *(arrows).* (**A** with permission from Granja M, Rivero O, Aguirre D. Abdominal wall hernias. In: Sahani DV, Samir AE, editors. Abdominal imaging. 2nd ed. Philadelphia: Elsevier; 2017:1014-1025.[43])

The most common definition of the groin is that it is the region of the ilioinguinal crease at the junction of the abdomen and the thigh and the adjacent areas immediately above and below. In the strictest sense, the only "groin hernias" are **inguinal (direct or indirect).** However, **spigelian** and **femoral** hernias lie so close to the inguinal area that they are considered to be groin hernias as well.

Hernias occur in areas of natural weakness—in areas where vessels penetrate the abdominal wall (femoral and spigelian), where fetal migration of testis, spermatic cord, or round ligament have occurred (**indirect** inguinal), and through broad flat tendons called "aponeuroses" (**direct** inguinal). Hernias do not occur through the belly of abdominal wall muscles unless they have been surgically incised or otherwise injured.

TECHNICAL REQUIREMENTS

A high-frequency (≥12 MHz) 50-mm-long transducer is optimal in the majority of patients. In obese patients a lower-frequency transducer may be necessary, usually a 7- to 9-MHz curved array. Use of a 50-mm transducer is important because its larger field of view (FOV) allows better identification of landmarks, especially in patients who have diastasis of aponeuroses. When long-footprint linear transducers are not available, use of a trapezoidal or virtual convex display can be helpful. In some cases, extended-FOV modes can be helpful, particularly in indirect inguinal hernias that extend into the scrotum and long incisional hernias. It is important to be able to store and review video loops in order to capture dynamic events critical to diagnosis. Color and power Doppler ultrasound features show the degree of vascularity associated with inflammatory processes and solid masses and the viability of the herniated bowel loops.[8]

THE REPORT FOR DYNAMIC ULTRASOUND OF GROIN HERNIAS

It is important to use correct terminology in reporting the results of a dynamic groin ultrasound examination. In addition to the indication, the report should contain the following elements: (1) the examination name; (2) the specific dynamic components of the examination; (3) the side examined; (4) presence or absence of a hernia; (5) hernia size; (6) hernia contents; (7) reducibility of the hernia; and (8) whether the hernia is tender or nontender. Tenderness is important in determining whether a hernia is more likely to be incidental or clinically significant. This is particularly important when a hernia is found as an incidental finding in a patient who is asymptomatic.

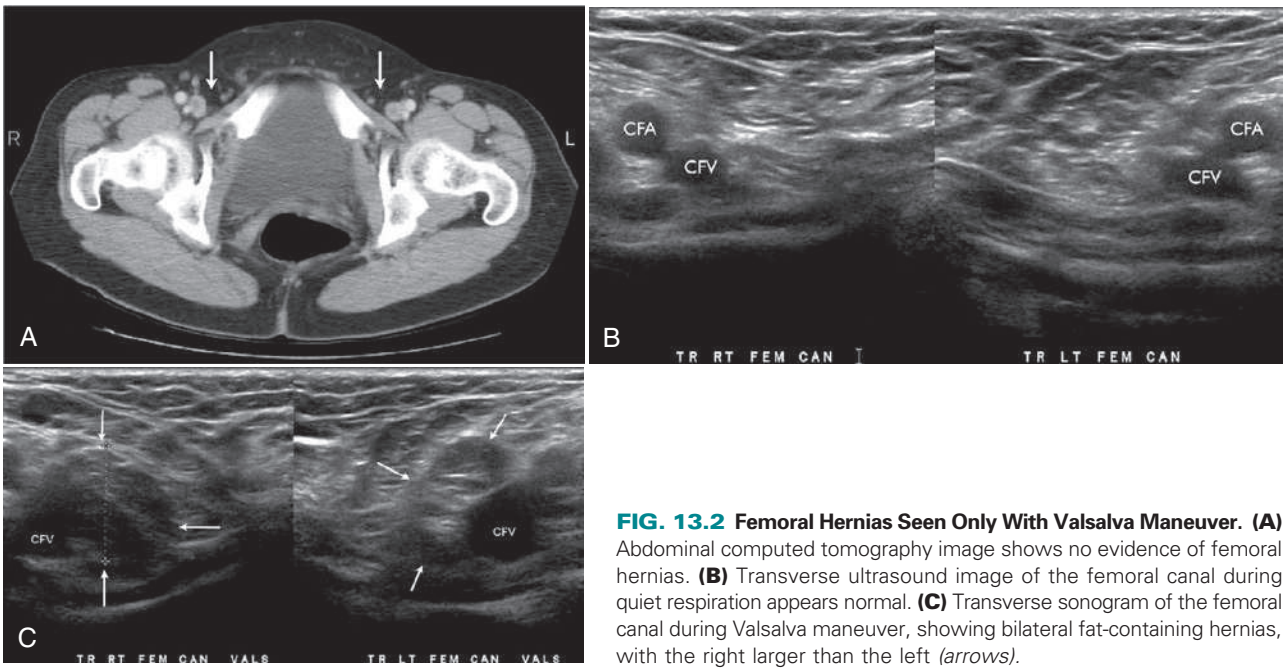

FIG. 13.2 Femoral Hernias Seen Only With Valsalva Maneuver. (A) Abdominal computed tomography image shows no evidence of femoral hernias. **(B)** Transverse ultrasound image of the femoral canal during quiet respiration appears normal. **(C)** Transverse sonogram of the femoral canal during Valsalva maneuver, showing bilateral fat-containing hernias, with the right larger than the left *(arrows).*

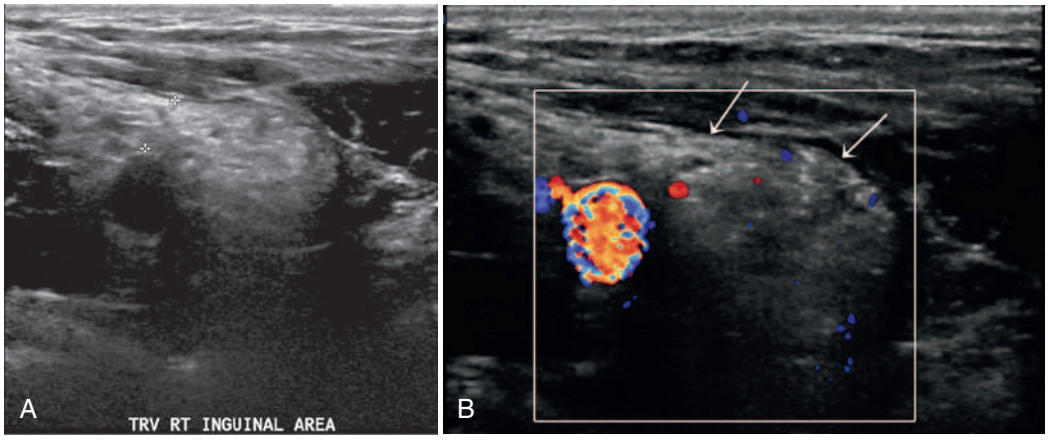

FIG. 13.3 Indirect Inguinal Hernia. A 25-year-old man with right inguinal pain and a fat-containing indirect hernia. **(A)** Transverse sonogram shows a hernia *(calipers)* in the right inguinal region. **(B)** Color Doppler image shows that the hernia *(arrows)* is lateral to the vessels. Only fat was seen in the hernia sac. See also Video 13.1.

When a hernia has been described in the report, we also report about our search for additional types of ipsilateral or contralateral groin hernias. In a patient with an inguinal hernia, presence of an ipsilateral femoral or spigelian hernia may necessitate use of a larger piece of mesh. Presence of a contralateral hernia may lead to bilateral rather than unilateral repair. Children in particular are often found to have bilateral inguinal hernias.[9]

HERNIA CONTENTS

Hernias are composed of a sac, the parts of which are described as the neck, the body and fundus, and the hernia contents. The inguinal hernia sac consists of peritoneum, which protrudes through the abdominal defect or "hernial orifice" and envelopes the hernial contents. The neck of the sac is situated at the defect. Hernias with a narrow or rigid neck are more likely to obstruct and strangulate. The body is the widest part of the hernia sac, and the fundus is the portion furthest away from the defect. Viscera most likely to enter a hernia sac are those normally situated in the region of the defect and those that are mobile—for example, the omentum and small bowel.

Most sonographically detected hernias do not contain bowel. In fact, most hernias contain only fat (Fig. 13.3, Video 13.1). The origin of the fat may be **intraperitoneal** (mesenteric or omental), **preperitoneal,** or, in rare instances, both (Video 13.2). Hernias that contain intraperitoneal fat may contain bowel later and thus may be a greater risk than those that contain only preperitoneal fat. Some hernias contain free fluid of intraperitoneal origin (Fig. 13.4). Hernias that contain bowel are considered higher risk because strangulation may lead to infarction of bowel (Fig. 13.5, Video 13.3). Large hernias that are the most likely to contain bowel are easier to detect clinically and less

FIG. 13.4 Fluid-Containing Incarcerated Direct Inguinal Hernia. Long-axis image of a fluid-containing femoral hernia that caused pain and swelling.

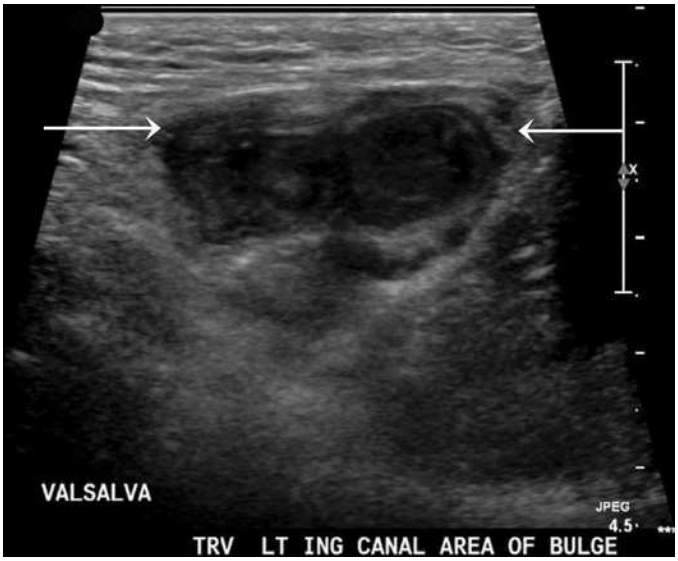

FIG. 13.5 Bowel-Containing Inguinal Hernia. Short-axis view of the inguinal canal shows an indirect inguinal hernia that contains bowel. See also Video 13.3 showing peristalsis.

often require sonographic imaging for diagnosis. Hernias can contain small bowel, colon, or appendix. The Amyand hernia is a rare inguinal hernia (about 1% of inguinal hernias, <1% of appendicitis cases) that contains the appendix[10,11] (Fig. 13.6). Other, much less common hernia contents include ovaries and/or "bladder ears."

DYNAMIC MANEUVERS

The dynamic maneuvers that are the key to ultrasound's ability to depict and evaluate hernias include watching the region during quiet breathing, the Valsalva maneuver, the compression maneuver, and upright positioning. Dynamic maneuvers are useful because many hernias spontaneously reduce when the patient is supine and breathing quietly.[8] Hernias that contain only fat are almost isoechoic with surrounding tissues and therefore relatively inconspicuous. Watching the groin region during quiet breathing allows for visualization of bowel peristalsis. Assessment with color Doppler allows for assessment of bowel perfusion (implying viability). Dynamic maneuvers can cause the fat within a hernia to move, making the hernia contents more conspicuous. The direction of movement can be helpful, because movement of surrounding tissues is almost always in the anteroposterior (AP) direction, whereas hernia contents often move horizontally or obliquely during compression maneuvers (Video 13.4). Hernia contents may change with dynamic maneuvers. Finally, reducibility and tenderness can be assessed.

The **Valsalva maneuver** is most useful when the patient is supine. It forces hernia contents anteriorly, and often horizontally in an inferomedial direction (Fig. 13.7), and at times elicits pain. Some hernias become visible only during the Valsalva maneuver (see Fig. 13.2). In other cases, hernia sacs that can be seen in quiet respiration elongate and widen during the Valsalva maneuver. Hernias that appear to contain only fat during quiet respiration may be shown to contain bowel during the Valsalva maneuver (Video 13.5). In general, hernia sacs should become larger with the Valsalva maneuver. If they stay the same size, this is worrisome for incarceration.

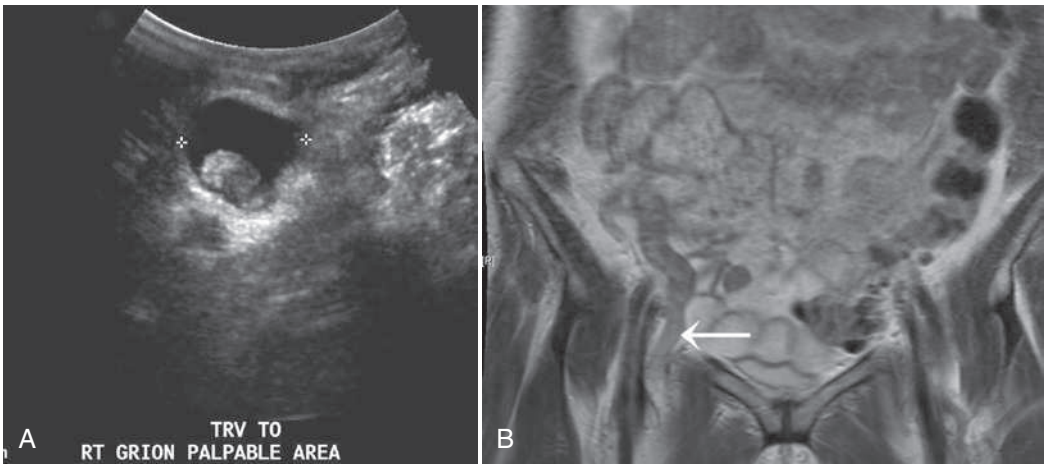

FIG. 13.6 Amyand Hernia. (A) Right lower quadrant sonogram shows a complex cyst in the region of patient's pain. **(B)** Magnetic resonance image shows the appendix *(arrow)* extending into the hernia.

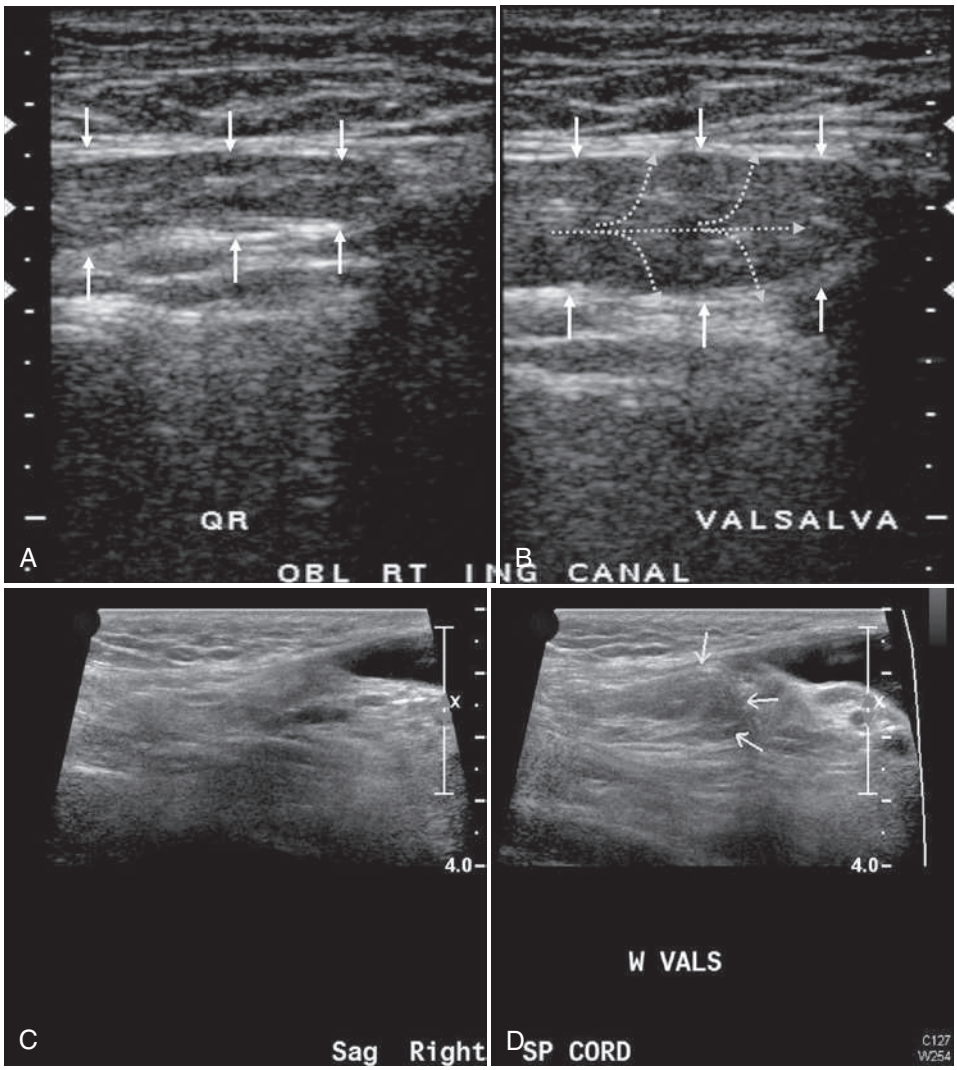

FIG. 13.7 Value of Valsalva Maneuver. Indirect Inguinal Hernias. (A) and **(B)** Split-screen long-axis views of a fat-containing indirect inguinal hernia during quiet respiration and Valsalva maneuvers. The left image shows the hernia during quiet respiration *(arrows)*. The right image, obtained during a Valsalva maneuver, shows the hernia contents being forced distally in a horizontal direction within the inguinal canal *(arrows and dotted arrows)*. **(C)** and **(D)** Split-screen views in another patient show the more obvious hernia with Valsalva maneuver.

The **compression maneuver** is essential to assess reducibility and tenderness in patients who have sonographically detectable hernias, regardless of whether the patient is upright or supine. Compression maneuvers are also useful in supine patients in whom the Valsalva maneuver is ineffective. Compression helps assess **reducibility** of a hernia. Hernias may be completely reducible (Video 13.6), partially reducible (Video 13.7), or nonreducible (Video 13.8). The shape of hernias correlates with reducibility. A hernia with a broad fundus and narrow neck is likely to be nonreducible, whereas a hernia with a broad neck compared with the fundus is more likely to be reducible (Fig. 13.8). Assessing tenderness is very important because dynamic sonography is so sensitive that it can detect many asymptomatic and clinically unimportant hernias. Furthermore, in some patients the pain is caused by other etiologies.

Upright positioning is essential in all patients being sonographically evaluated for groin hernia. Many patients are symptomatic only in the upright position, or they are more symptomatic in the upright position. Fluid is often best demonstrated with the patient in the upright position. It may take minutes for the free fluid to "puddle" in the inferior end of the hernia sac once the patient has been standing. Therefore delayed imaging in the upright position may be helpful in demonstrating **peritoneal fluid.** Other hernias contain bowel only in the upright position. Some hernias are either only visible in the upright position[6] or are much better demonstrated in the upright position (direct inguinal and femoral). The reducibility of a hernia may vary between supine and upright position, so it is important to assess reducibility in both positions. In most patients, groin hernias are more reducible in the supine than in the upright position, whereas in others the opposite is true.

KEY SONOGRAPHIC LANDMARKS

Ultrasound shows characteristic features of groin hernias that lie above the inguinal ligament. Four types of hernias occur

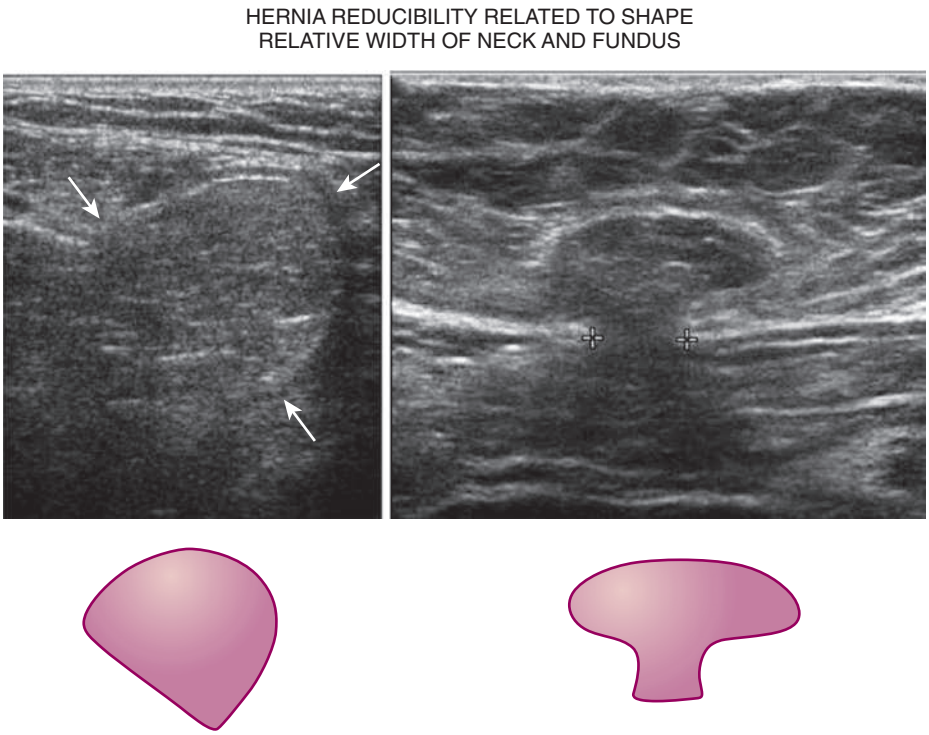

FIG. 13.8 Typical Hernia Shapes. *Left,* Direct inguinal hernia shows a wide neck in comparison to the fundus. This hernia shape correlates with complete reducibility. *Right,* Linea alba hernia shows a very narrow neck in comparison to the fundal width. This hernia shape correlates with nonreducibility and increased risk of strangulation.

within the broader definition of the groin: indirect inguinal, direct inguinal, spigelian, and femoral. The key landmark in distinguishing among the first three types is the **inferior epigastric artery** (IEA). This artery arises from the external iliac artery and then courses superomedially, crossing the spigelian fascia and the semilunar line, eventually coursing along the midposterior aspect of the rectus abdominis muscle. The IEA can be identified sonographically in all patients along the midposterior surface of the rectus abdominis muscle at a level about halfway between the umbilicus and pubic symphysis while scanning in a transverse plane (Fig. 13.9). The IEA lies anterior to the peritoneum and thus is never obscured by bowel gas. Once identified in the transverse plane, the IEA can be traced inferiorly and laterally to its origin from the external iliac artery. There are four main types of inguinal hernias (Table 13.1, Fig. 13.10).

Once the origin of the IEA is identified, the transducer should be rotated into an axis that is parallel to the inguinal ligament, which courses obliquely from superolaterally to inferomedially. The patient should be scanned in long axis parallel to the inguinal ligament and short axis perpendicular to the inguinal ligament.

INGUINAL AND INGUINAL REGION HERNIAS

Inguinal hernias can be classified as direct or indirect. The terms **direct** and **indirect** refer to how hernias appear during open surgical repairs. **Direct inguinal hernias** protrude into the surgically opened inguinal canal "directly" from posteriorly. **Indirect inguinal hernias,** on the other hand, enter the surgically opened inguinal canal "indirectly" from a superolateral direction after passing through the internal inguinal ring (deep inguinal ring). From a sonographic point of view, "direct" and "indirect" are potentially confusing. It would be less confusing to characterize them as internal inguinal ring (indirect) hernia and nonring (direct) hernia. In a retrospective review of ultrasound examinations of 172 groins in 151 patients, 119 hernias were diagnosed in 107 patients, 60% were indirect inguinal hernias, 19% were direct inguinal hernias, 18% were femoral hernias, and 3% were combined hernias (direct and indirect inguinal hernia). Ninety-two percent contained fat and 30% contained bowel.[12] The overall rates of sensitivity and specificity of ultrasound for diagnosing the presence of groin hernia were 96% and 96% (increasing to 98% and 100% after 2011), and determination of type of hernia was 96% accurate (increasing to 98% after 2011).[12] In a prospective study of 118 patient with a clinical diagnosis of groin hernia, ultrasound was found to be 100% sensitive and specific for the diagnosis of hernia, with distinction between direct and indirect inguinal hernias having sensitivities of 86% and 97%, respectively.[13] Clearly, experience and technique are important factors in achieving high accuracy.

Strength of the transversalis fascia is altered in many patients with inguinal hernias. It is felt that collagen structure and metalloproteinase activity are different in patients with hernias than in the general population, thus putting the transversalis fascia, owing to its location with high pressure with little additional support, at risk for stretching, tearing, and failure.[14-19] Thus patients

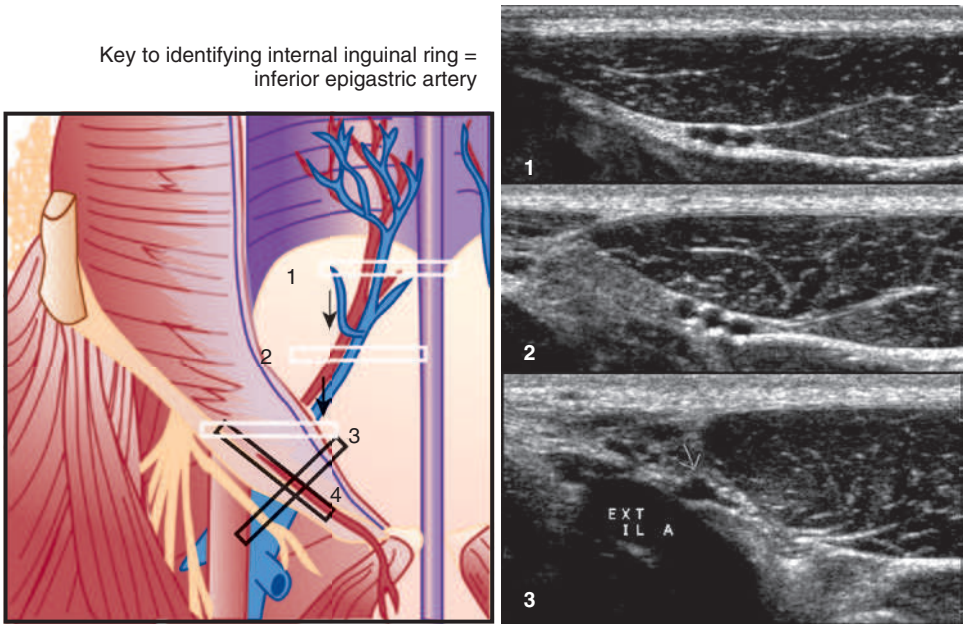

FIG. 13.9 Inferior Epigastric Vessels (IEVs) Are Main Landmarks for Evaluating Inguinal Area. Image 1 was obtained in a transverse plane about halfway between the umbilicus and the pubic symphysis. The inferior epigastric artery and its paired veins lie along the midlateral posterior surface of the rectus abdominis muscle. Image 2 was obtained several centimeters inferiorly, and the IEVs lie more laterally. Image 3 was obtained at a level where the IEVs *(arrow)* lie at the edge of the rectus muscle. This is the level at which most spigelian hernias occur. Once the origin of the inferior epigastric artery is identified, the transducer should be rotated into planes that are parallel (see line 4 on the drawing) and perpendicular (see image 3) to the inguinal canal—long-axis and short-axis views.

TABLE 13.1 Types of Inguinal Hernias

Hernia Type	Key Findings	Classic Teaching Point
Indirect inguinal	Herniated structures enter the inguinal canal lateral to the epigastric artery and superior to the inguinal ligament, and extend for a variable distance through the inguinal canal.	Most common groin hernia. Extension into scrotum or labia majora is almost always due to indirect hernia.
Direct inguinal	Arise from conjoined tendon, inferior and medial to inferior epigastric artery. Herniation at the inferior aspect of **Hesselbach triangle.**	Associated with increased abdominal pressure (ascites, obesity, pregnancy), older age, and weak musculature
Spigelian	Arise through the spigelian fascia just lateral to where it is penetrated by the internal epigastric artery. The transverse abdominis tendon is always torn. In most cases the internal oblique aponeurosis is also torn.	Sonography shows a complex mass within the anterolateral aspect of the abdominal wall, which may contain fluid- or gas-filled loops of bowel.
Femoral	Within the femoral canal, inferior to the inguinal ligament.	This type of hernia has a relatively high association with incarceration.

with known disorders of tissue strength, including Ehlers-Danlos, Marfan, and Hurler-Hunter syndromes, polycystic kidney disease, and osteogenesis imperfecta, are at increased risk for inguinal hernia.[14,19-21]

Indirect Inguinal Hernias

The characteristic finding of an indirect inguinal hernia is abnormal movement of intraabdominal contents (fat, bowel, or both) through the deep inguinal ring and through the inguinal canal. In the short axis, the indirect inguinal hernia can be seen moving into and out of the plane adjacent to the spermatic cord (in males).[1,8,22,23]

Indirect inguinal hernias are the most common type of groin hernia, being five times more common than direct hernias.[24] In boys, the indirect inguinal hernia is the result of a congenital defect of a patent processus vaginalis. In adults, an indirect hernia is acquired as a result of weakness and dilation of the internal inguinal ring.[25,26] Indirect hernias represent a persistence of a patent **process vaginalis.** In males the testis descends from the abdominal cavity into the scrotum, which can result in delayed

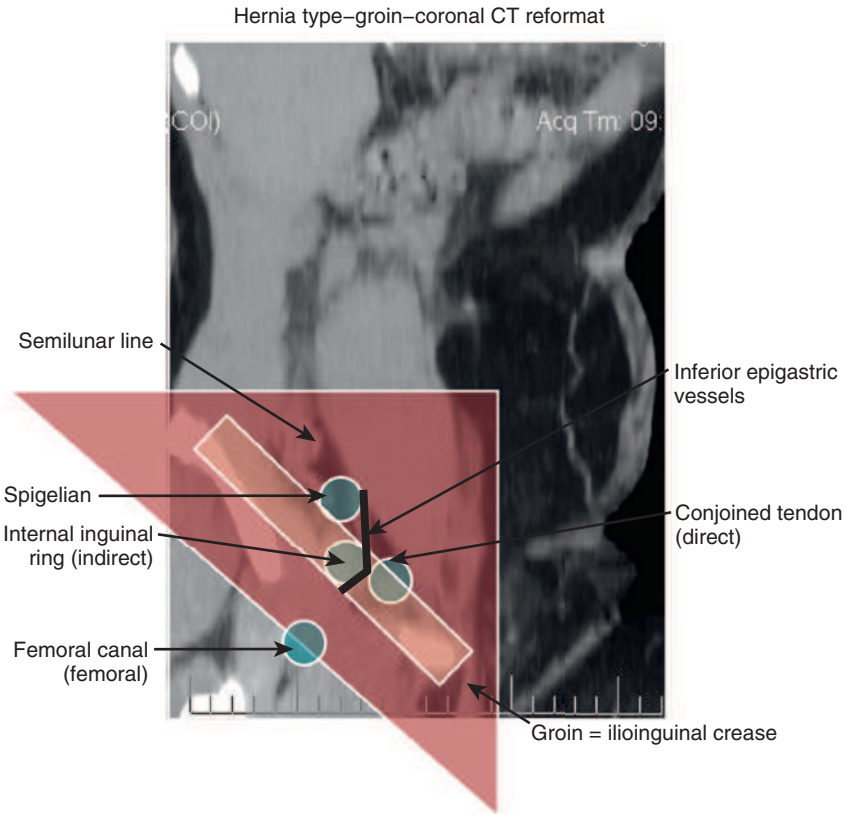

FIG. 13.10 Locations of Four Types of "Groin" Hernias. Abdominal and pelvic computed tomography *(CT)* image, reformatted in coronal plane. **Indirect inguinal hernias** arise within the internal or deep inguinal ring, which lies in the crotch between the external iliac artery and the proximal inferior epigastric artery. **Direct inguinal hernias** arise through the "conjoined tendon," which lies inferior and medial to the origin of the inferior epigastric artery. **Spigelian hernias** arise through the spigelian fascia just lateral to the inferior epigastric artery, where it reaches the lateral margin of the rectus muscle. **Femoral hernias** lie within the femoral canal, inferior to the inguinal canal and inguinal ligament.

or incomplete closure of the inguinal canal. Thus indirect inguinal hernias are more common in males. However, delayed or incomplete closure of the **canal of Nuck** can occur in females. The neck of an indirect inguinal hernia is the segment that lies within the internal inguinal ring, and the fundus lies within the inguinal canal (Fig. 13.11). The neck (internal inguinal ring) lies just superior and lateral to the IEA's origin and tends to be oriented in an AP direction, whereas the fundus (inguinal canal) is oriented horizontally and courses inferiorly and medially, passing superficial to the IEA's origin The fundus of an indirect inguinal hernia lies anterior and lateral to the **spermatic cord** in males and the **round ligament** in females (Fig. 13.12). In the short axis, the internal inguinal ring and the neck of the indirect inguinal hernia lie between the external iliac artery along its lateral side and the IEA along its medial side.

In the long axis, indirect inguinal hernias can have two appearances: sliding and nonsliding. The **sliding type** of indirect inguinal hernia has a relatively wide neck compared with the fundus, with loss of the angle between the neck and fundus. It is usually reducible and is more likely to contain bowel and other intraperitoneal contents. The **nonsliding type** has a relatively narrower neck compared with the fundus and maintains the almost 90-degree angle between the neck and fundus (Fig. 13.13). Nonsliding hernias usually contain only properitoneal fat and are nonreducible, and may be misclassified as "spermatic cord lipoma" or "inguinal canal lipoma" at surgery. True spermatic

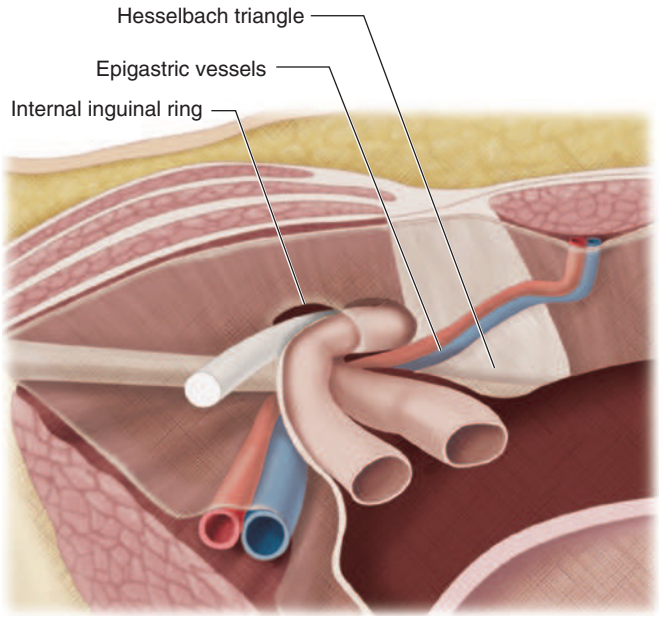

FIG. 13.11 Indirect Inguinal Hernia. Diagram of the deep aspect of the anterior abdominal wall depicting a left indirect inguinal hernia. The hernia sac protrudes through the internal inguinal ring, located lateral to the epigastric vessels. Note the Hesselbach triangle, located medial and inferior to the epigastric vessels. (Reproduced with permission from Granja M, Rivero O, Aguirre D. Abdominal wall hernias. In: Sahani DV, Samir AE, editors. Abdominal imaging. 2nd ed. Philadelphia: Elsevier; 2017:1014-1025.[43])

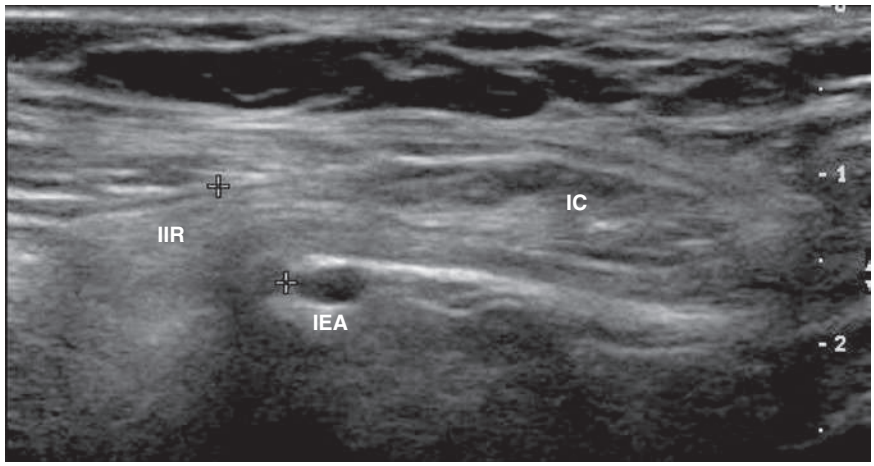

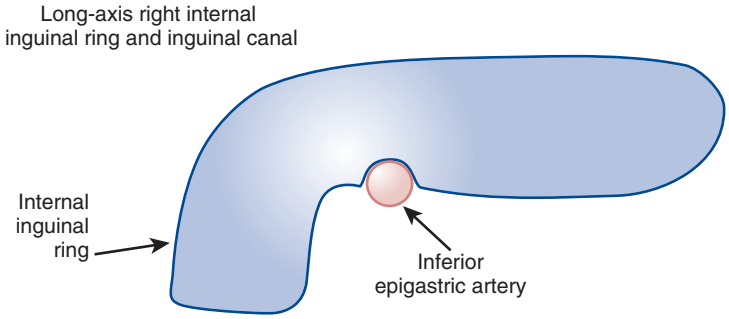

FIG. 13.12 Indirect Inguinal Hernia. Long-axis view shows that neck of the hernia lies in the internal inguinal ring *(IIR),* which lies superior and lateral to the proximal inferior epigastric artery *(IEA).* Hernia sac then courses horizontally in an inferomedial direction within the inguinal canal *(IC).* Indirect inguinal hernias always pass superficial to the IEA.

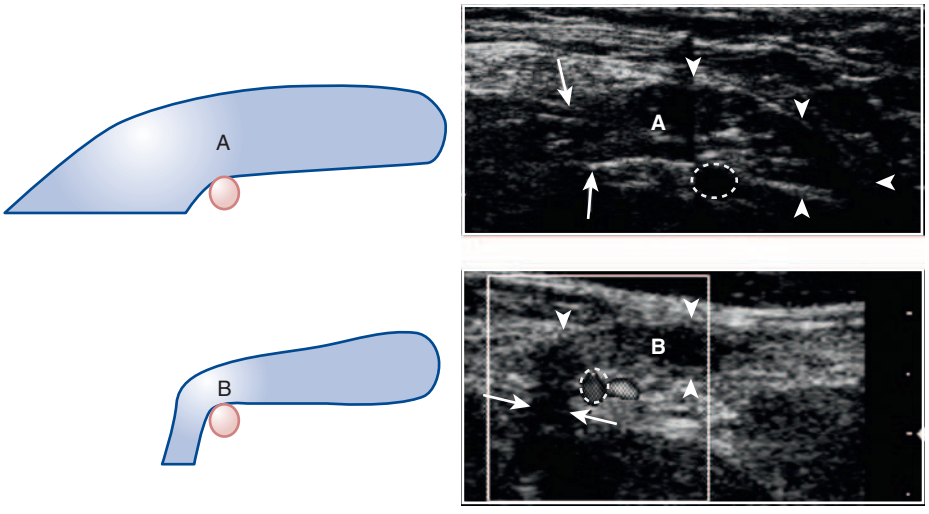

FIG. 13.13 Indirect Inguinal Hernias: Two Types. (A) Sliding type. The neck *(arrows)* is as wide as or wider than the fundus *(arrowheads),* with loss of the angle between the internal inguinal ring and inguinal canal. Sliding hernias usually contain intraperitoneal contents and are reducible. **(B) Nonsliding type.** The neck *(arrows)* is narrow in comparison to the fundus *(arrowheads),* and the nearly 90-degree angle between the internal inguinal ring and inguinal canal is preserved. Nonsliding hernias usually contain only properitoneal fat and are nonreducible. They have often been misclassified as "lipomas" of the inguinal canal or spermatic cord. *Circle,* inferior epigastric artery.

cord lipomas can occur, but are rare. Nonsliding indirect inguinal hernias are more difficult to diagnose sonographically than sliding types because (1) they tend to be smaller; (2) they contain only fat, which is almost isoechoic with surrounding tissues; and (3) their nonreducibility minimizes motion of contents during dynamic maneuvers. In the short axis, the sliding type of direct inguinal hernia can be diagnosed at either the level of the internal inguinal ring or the level of the inguinal canal. However, the nonsliding type can be diagnosed only at the level of the inguinal canal, where it is widest.

In some cases, it can be difficult to demonstrate the relationship of the hernia neck to the inferior epigastric vessels. In such cases, it is helpful to assess the relationship of the hernia sac to the spermatic cord. In males, indirect inguinal hernias tend to lie

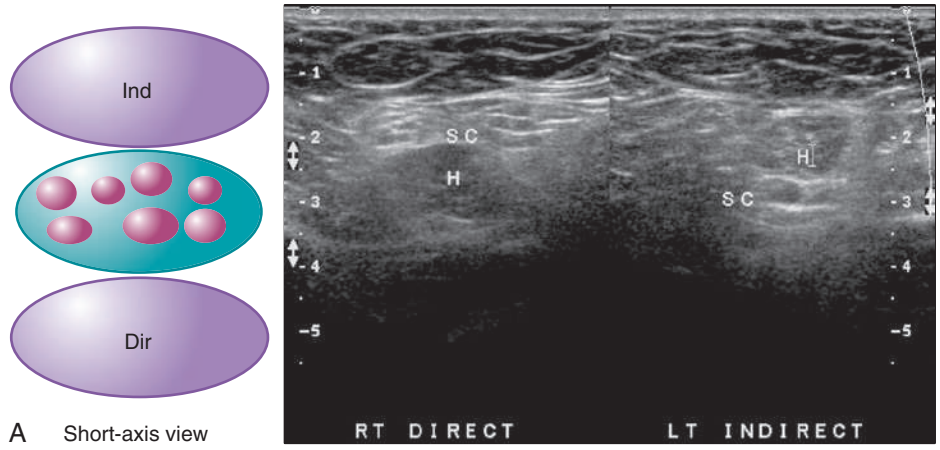

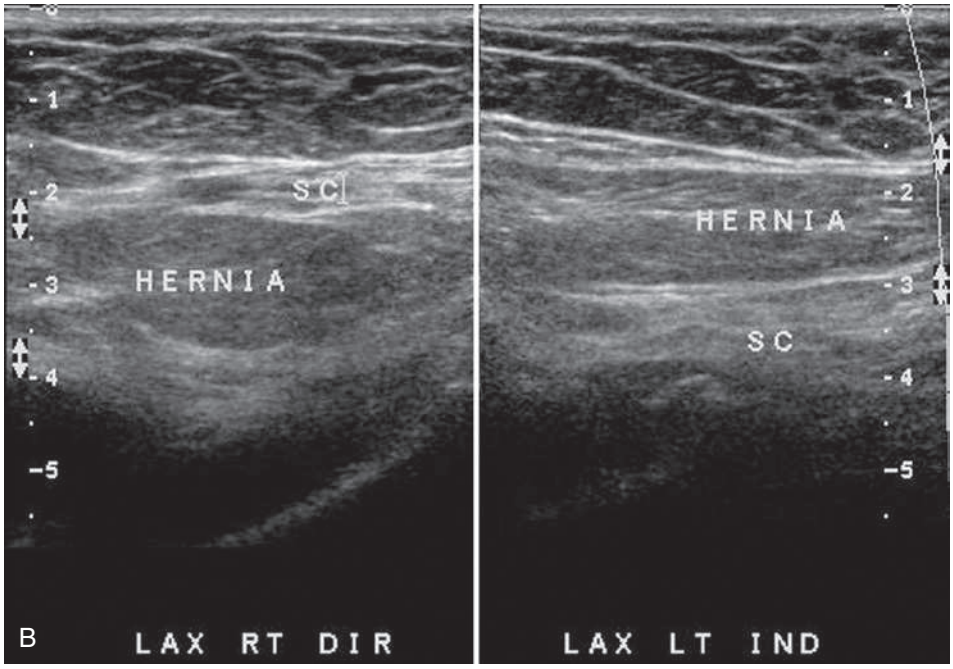

FIG. 13.14 Hernia Sacs Relative to Spermatic Cord. (A) Direct *(Dir)* and indirect *(Ind)* hernia sacs relative to the spermatic cord *(SC). Left,* Drawing shows that indirect inguinal hernia sac tends to lie anterior to spermatic cord, whereas direct inguinal hernia sac lies posterior to the cord. *Center,* Short-axis view shows fat-containing direct inguinal hernia *(H)* posterior and medial to the spermatic cord *(SC). Right,* Short-axis view shows fat-containing indirect inguinal hernia *(H)* lying anterior and lateral to the spermatic cord *(SC).* **(B)** Long-axis views of right direct and left indirect inguinal hernias in the same patient. *Left,* Image shows the right direct inguinal hernia sac lying posterior to the spermatic cord *(SC). Right,* Image shows the left indirect inguinal hernia sac lying anterior to the spermatic cord *(SC).*

along the anterolateral aspect of the spermatic cord, whereas direct inguinal hernia sacs tend to lie posteromedial to the cord (Fig. 13.14). In females, indirect inguinal hernias lie anterior to the round ligament (Fig. 13.15). Large indirect inguinal hernias can flatten and splay the spermatic cord (Figs. 13.16 and 13.17), causing pain that radiates into the scrotum. Indirect inguinal hernias are much more likely than direct inguinal hernias to extend into the scrotum or labium majus (Fig. 13.18, Video 13.9).

Direct Inguinal Hernias

The characteristic finding of a direct inguinal hernia is focal intraabdominal tissue moving anteriorly through the Hesselbach triangle.[1,8,22,23] On ultrasound, this tissue of variable echogenicity will move characteristically in a posterior-to-anterior direction.[1]

Direct inguinal hernias are the second most common type of groin hernia and are acquired. The incidence increases with age, as this type of hernia results from a weakening of the tranversalis fascia in the Hesselbach triangle.[27] The Hesselbach triangle is anatomically bounded inferiorly by the inguinal ligament, medially by the lateral margin of the rectus abdominis, and superolaterally by the IEA.

Direct hernias arise in two ways: either a passing through a defect in the "conjoined tendon" (Fig. 13.19) or by greatly stretching the tendon into the inguinal canal (Fig. 13.20). During open hernia repair, direct inguinal hernias protrude "directly" into the opened inguinal canal from a posterior direction. Indirect

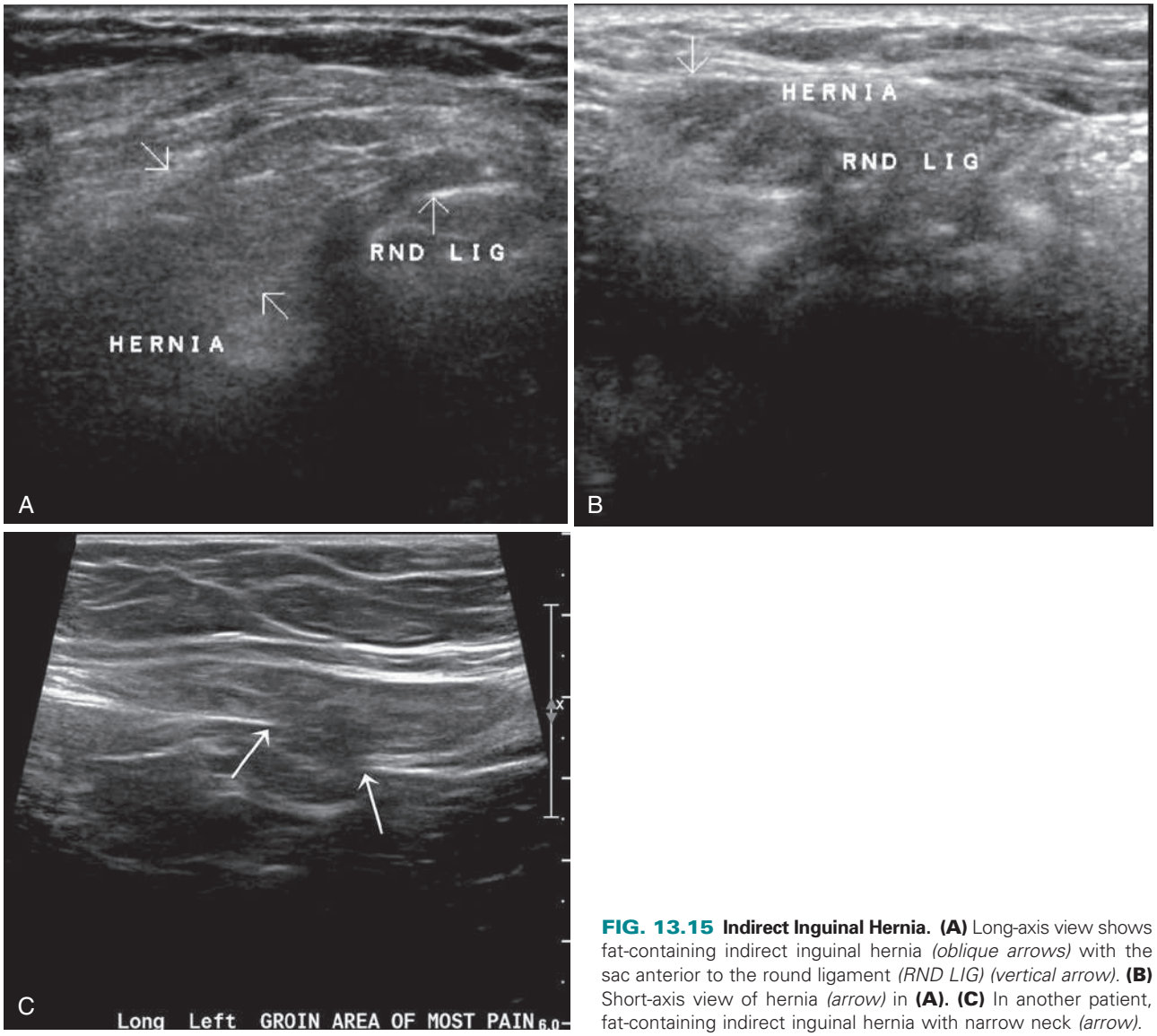

FIG. 13.15 Indirect Inguinal Hernia. (A) Long-axis view shows fat-containing indirect inguinal hernia *(oblique arrows)* with the sac anterior to the round ligament *(RND LIG) (vertical arrow)*. **(B)** Short-axis view of hernia *(arrow)* in **(A). (C)** In another patient, fat-containing indirect inguinal hernia with narrow neck *(arrow)*.

inguinal hernias, on the other hand, extend into the opened inguinal canal "indirectly" from a superior and lateral direction. The conjoined tendon area, and thus the neck of a direct inguinal hernia, arises inferior and medial to the inferior epigastric vessels (Fig. 13.21).

The neck of direct inguinal hernias is typically wider than the fundus. This makes incarceration and strangulation of direct hernias rare. Most small to medium direct inguinal hernias are completely reducible, but large direct inguinal hernias may be incompletely reducible, especially in the upright position. Most direct inguinal hernias spontaneously reduce completely in the supine position during quiet respiration, and therefore they are visible only during Valsalva maneuvers or in the upright position.

The **conjoined tendon** consists of the aponeuroses of the internal oblique and transverse abdominis muscles and the underlying transversalis (transverse) fascia. It is located inferior to the lower edge of the external oblique aponeurosis. In most patients the aponeuroses of the internal oblique and transverse abdominis muscles are not closely adherent to each other; the aponeurosis of the transverse abdominis is separated from the underlying transversalis fascia and peritoneum by a variable layer of preperitoneal fat; and the conjoined tendon is not well defined (Fig. 13.22).

Thinning and anterior bulging of the conjoined tendon **(conjoined tendon insufficiency)** is a precursor to development of direct inguinal hernias. In males the anterior bulging displaces and rotates the spermatic cord laterally. The thinning and bulging of the conjoined tendon push the aponeuroses of the internal oblique and transverse abdominis muscles closer together, making the conjoined tendon appear to be a more discrete structure than when the patient is in the supine position and in quiet respiration (Figs. 13.23 and 13.24). As the thinning and bulging progress, a **tear** can form within the tendon, leading to the formation of a direct inguinal hernia. Smaller direct inguinal hernias extend anteriorly into the floor of the inguinal canal, but larger

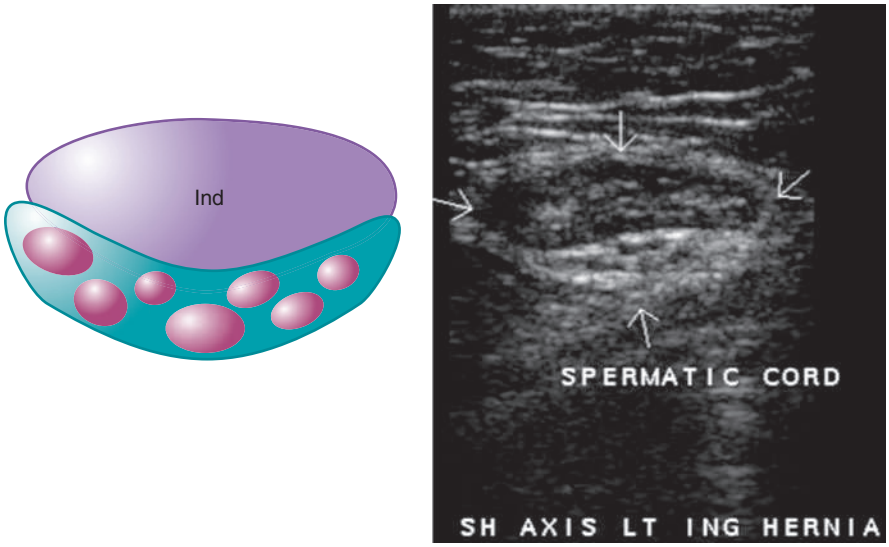

FIG. 13.16 Indirect *(Ind)* Inguinal Hernia. (A) Drawing and **(B)** sonogram. Short-axis view shows indirect inguinal hernia displacing and compressing the hyperechoic spermatic cord posteriorly.

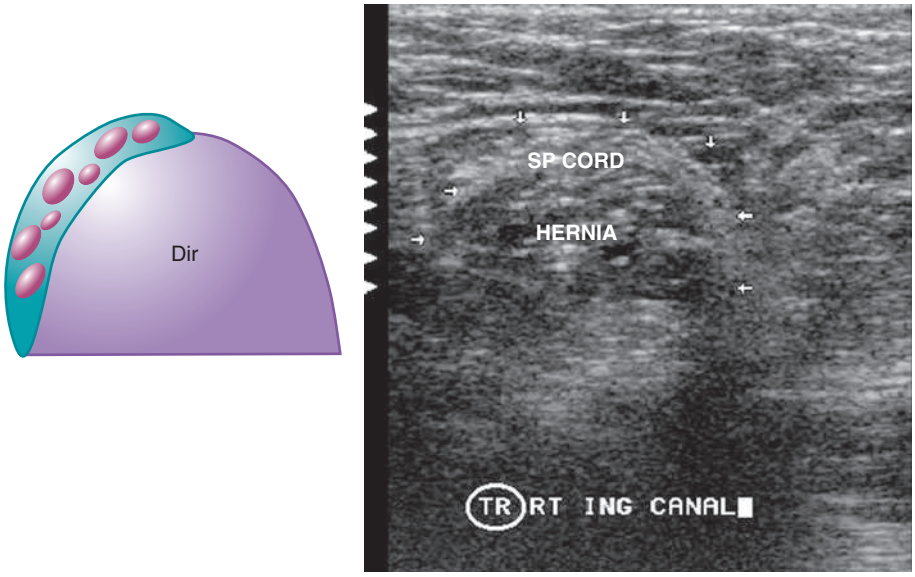

FIG. 13.17 Direct *(Dir)* Inguinal Hernia. Short-axis view shows direct inguinal hernia displacing and compressing the hyperechoic spermatic cord *(SP CORD)* anteriorly and laterally. See also Video 13.10.

hernias turn inferomedially, extending distally within the canal. Factors associated with conjoined tendon insufficiency progression to frank direct inguinal hernia include increased intraabdominal pressure (obesity, pregnancy, ascites, coughing, straining) and generalized connective tissue weakness. Because these underlying causes affect both sides, direct inguinal hernias are frequently bilateral, although often asymmetric in size and symptoms (Fig. 13.25). Direct inguinal hernia and its precursor, posterior inguinal wall insufficiency, are a common problem for athletes (see Sports Hernias).

Femoral Hernias

The characteristic finding of a femoral hernia is abnormal intraabdominal contents moving in an inferior direction through the femoral canal.[1,8] Femoral hernias have been described as having a sonographic appearance of a hypoechoic sac with speckled internal echoes. When examining during the Valsalva maneuver, a femoral hernia passes deep to the inguinal ligament, expands the femoral canal, displacing the normal canal fat, and effaces the femoral vein.[28]

Femoral hernias are less common than inguinal hernias and are difficult to diagnose clinically unless strangulated. Unlike inguinal hernias, femoral hernias are more common in women than in men.[8,24] Ultrasound has high accuracy (96.9%) for diagnosis of nonpalpable femoral hernias in patients with symptoms.[29] It is thought that the increased intrapelvic pressure that occurs during the third trimester of pregnancy, together with the hormone-induced softening of tissues, predisposes to the development of femoral hernias. They are twice as common on the right as on the left side.[30]

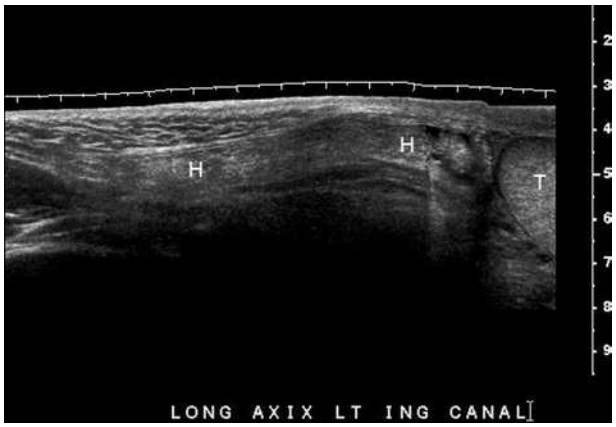

FIG. 13.18 Indirect Inguinal Hernia. Long-axis extended–field-of-view (FOV) image shows extremely large, indirect inguinal hernia *(H)* extending down the entire length of the inguinal canal into the scrotum. *T,* Testis. See also Video 13.9.

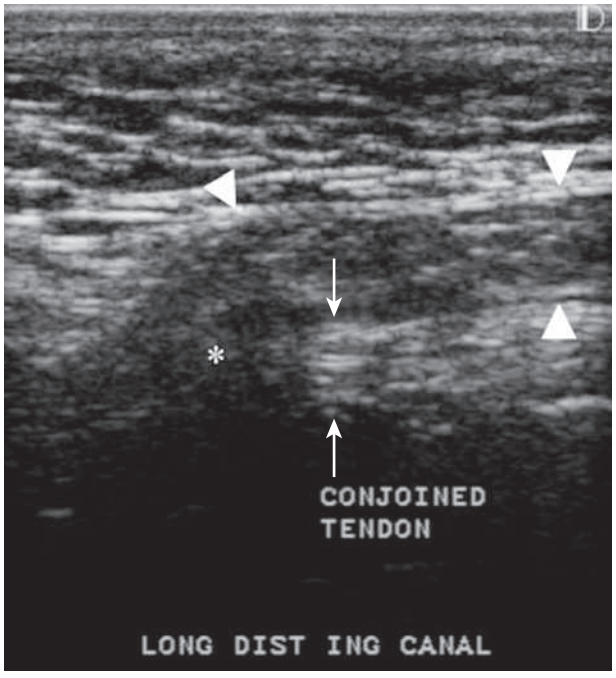

FIG. 13.19 Direct Inguinal Hernia. Long-axis view shows fat-containing direct inguinal hernia passing through an acute tear (*) in the conjoined tendon *(arrows)* and extending down the inguinal canal *(arrowheads).*

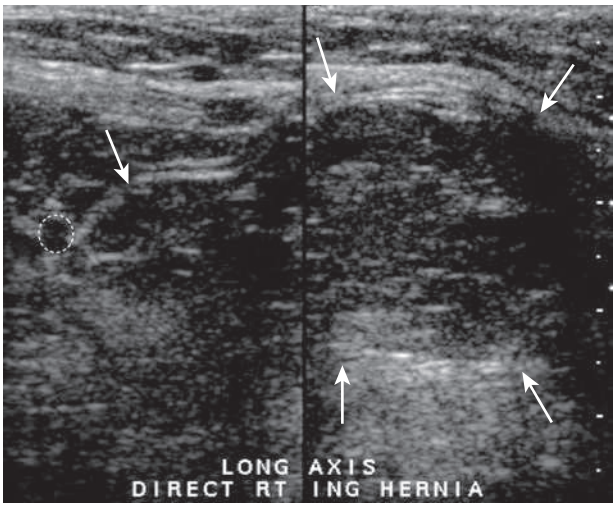

FIG. 13.20 Direct Inguinal Hernia. Long-axis view of large, direct inguinal hernia shows the thinned and stretched conjoined tendon and underlying transversalis fascia and peritoneum *(arrows)* forming the hernia sac. Note that the neck of direct inguinal hernias arises inferior and medial to the inferior epigastric artery *(circle).*

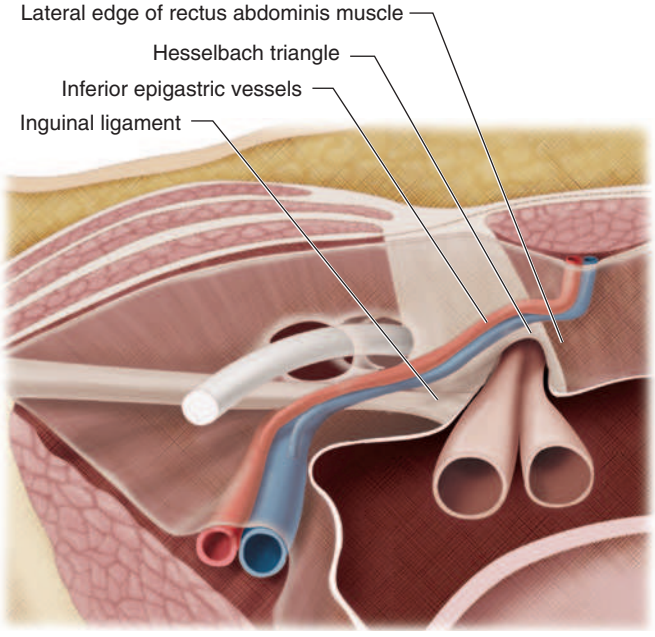

FIG. 13.21 Direct Inguinal Hernia. Diagram of the deep aspect of the anterior abdominal wall depicting a left direct inguinal hernia. The hernia sac protrudes through the Hesselbach triangle, which is bounded by the inferior epigastric vessels, lateral edge of the rectus abdominis muscle, and inguinal ligament. (With permission from Granja M, Rivero O, Aguirre D. Abdominal wall hernias. In: Sahani DV, Samir AE, editors. Abdominal imaging. 2nd ed. Philadelphia: Elsevier; 2017:1014-1025.[43])

Femoral hernias arise within the femoral canal inferior to the inguinal canal and ilioinguinal crease. The **femoral canal** lies just medial to the **common femoral vein** (CFV) and just superior to the **saphenofemoral junction** (Fig. 13.26, Video 13.10). The most common location for femoral hernias is medial to the CFV, but a few lie anterior to the common femoral vessels (Figs. 13.27 and 13.28). Most femoral hernias that lie anterior to the CFV arise medially and then extend anteriorly. It is rare for a femoral hernia to actually arise anteriorly **(Teale hernia)** (Fig. 13.29). Although femoral hernias reportedly can lie posterior or lateral to the CFV, we have never seen one in either of these locations. A femoral hernia tends to have a narrow neck in comparison to the width of its fundus, a shape that predisposes the femoral hernia to strangulation. Because of the narrowness of the femoral ring (the opening that forms the neck of a femoral hernia), it is more likely than an inguinal hernia to become incarcerated and strangulated[24,31] (Fig. 13.30). Femoral hernia contents vary, and most contain only fat. Femoral hernias that contain bowel are almost always nonreducible and frequently are strangulated.

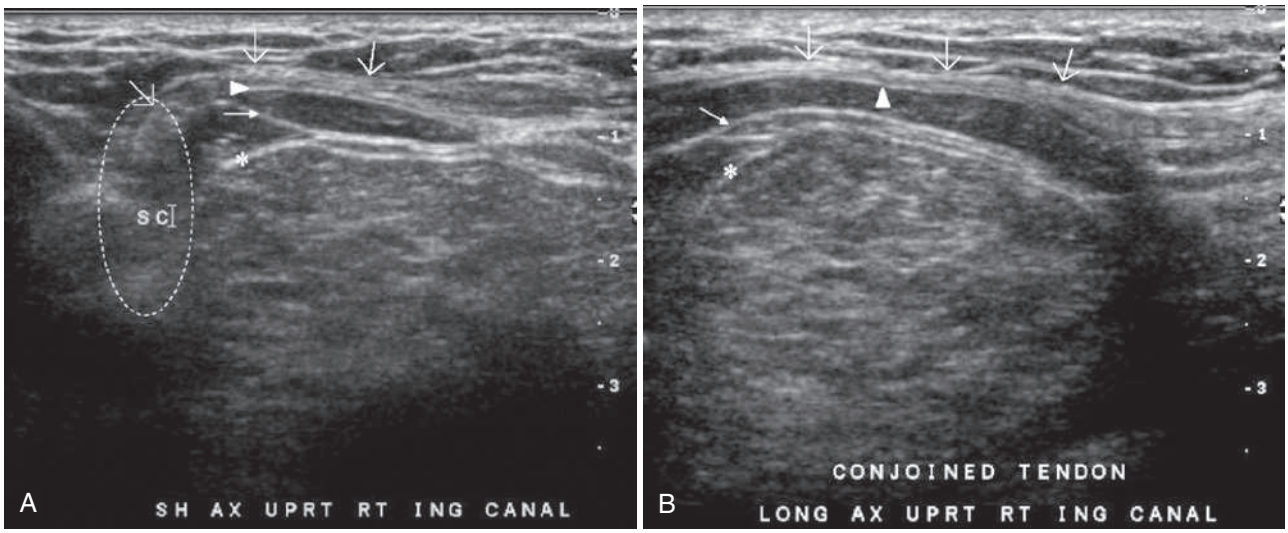

FIG. 13.22 Direct Inguinal Hernia. (A) Short-axis view of direct inguinal hernia shows a thinned and bulging conjoined tendon, consisting of the internal oblique aponeurosis *(superficial arrows)* and transverse abdominis aponeurosis *(arrowhead),* and underlying transversalis fascia *(horizontal arrow)* and peritoneum (*). *SC* and *oval dotted lines* indicate spermatic cord. **(B)** Long-axis view shows the conjoined tendon *(among three vertical arrows and arrowhead),* underlying transversalis fascia *(oblique arrow),* and peritoneum (*).

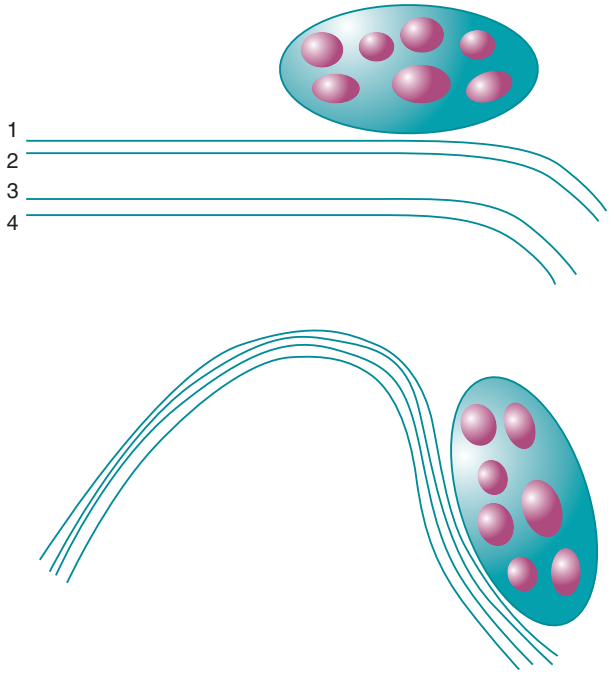

FIG. 13.23 Conjoined Tendon: Two Views. *Upper illustration,* Relationship of the conjoined tendon to the spermatic cord in quiet respiration in the supine position. The layers are separated by loose connective tissues or fat. *Lower illustration,* Bulging of the conjoined tendon during Valsalva maneuver or in the upright position. The layers tend to be pushed together and are more difficult to distinguish from one another. When the aponeuroses of the internal oblique *(1)* and transverse abdominis *(2)* muscles are pushed together, the conjoined tendon appears as a more discrete structure. *3,* Transversalis fascia; *4,* peritoneum. The anterior bulging of the conjoined tendon pushes the spermatic cord laterally and rotates it from a "wider-than-tall" orientation to a "taller-than-wider" orientation.

The femoral canal lies deeper than the inguinal canal and may be more difficult to assess with a high-frequency linear array transducer. Small and even moderate-sized femoral hernias frequently reduce completely in the supine position during quiet respiration and are most readily demonstrated during the Valsalva maneuver or in the upright position during compression maneuvers. Femoral hernias are often bilateral (see Fig. 13.2C).

Spigelian Hernias

Spigelian hernias are usually considered anterior abdominal wall hernias rather than groin hernias. They can occur anywhere along the course of the **spigelian fascia,** the complex aponeurotic tendon that lies between the oblique muscles laterally and the rectus muscles medially. However, almost all spigelian hernias occur at the inferior end of the **semicircular line,** inferior to the arcuate line, where the posterior rectus sheath is absent, and where the spigelian fascia is penetrated and weakened by the inferior epigastric vessels (Fig. 13.31). In many patients, this location is within 2 cm of the internal inguinal ring. Furthermore, when symptomatic, the pain caused by spigelian hernias can be difficult to distinguish from that caused by indirect inguinal hernias. Therefore we are including spigelian hernias in our discussion of groin hernias, because sonographic diagnosis of these patients is possible when they are referred for lower quandrant pain.[32]

Spigelian hernias are associated with conditions that increase intraabdominal pressure.[33,34] The spigelian fascia is composed of several different layers of loosely apposed aponeurotic tendons. From external to internal lie the aponeuroses of the external oblique, internal oblique, and transverse abdominis muscles. Internal to the aponeuroses lie the transversalis fascia and peritoneum. In spigelian hernias the transverse abdominis tendon

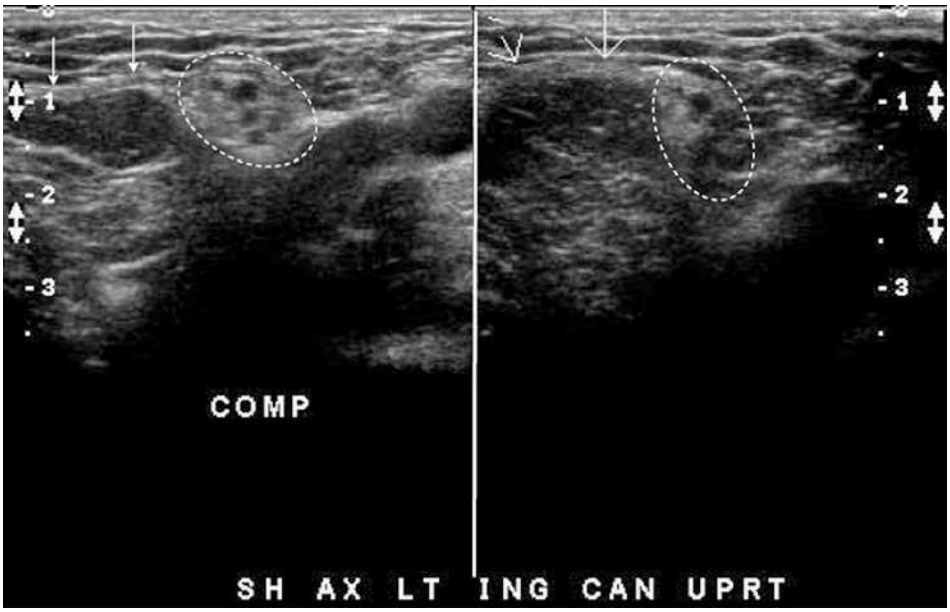

FIG. 13.24 Conjoined Tendon: Two More Views. *Left image,* Relationship of the conjoined tendon *(arrows)* to the spermatic cord *(dashed oval)* in quiet respiration in the supine position. The conjoined tendon lies posterior to the spermatic cord. *Right image,* Valsalva maneuver results in anterior bulging of the conjoined tendon, which now protrudes anterior to the spermatic cord and pushes and rotates the cord laterally.

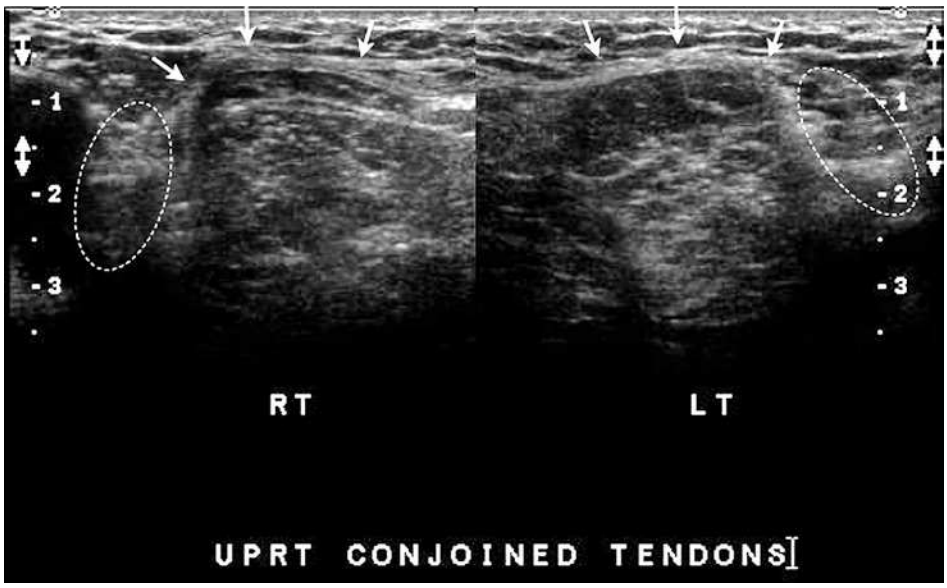

FIG. 13.25 Bilateral Inguinal Hernias. Short-axis views show bilateral fat-containing direct inguinal hernias, which are common. Markings are the same as in Fig. 13.24.

is always torn. In most cases the internal oblique aponeurosis is also torn (Fig. 13.32). The external oblique tendon is always intact and usually forces the hernia sac to extend either medially over the anterior aspect of the rectus abdominis muscle or laterally over the external oblique muscle, forcing it into the shape of an anvil or mushroom (Figs. 13.33 and 13.34). As with femoral hernias, spigelian hernias have narrow necks and broad fundi (Video 13.11 and Video 13.12), making them at least partially nonreducible and predisposing them to strangulation (Fig. 13.35). Because spigelian hernias pass through multiple layers of tendons, projections of the hernia may also extend intraparietally between the multiple layers of lateral muscles (either between the transverse abdominis and internal oblique muscles or between the internal and external oblique muscles). In some cases the spigelian fascia, like the linea alba, can become diastatic and widen. Extended-FOV modes may be helpful in demonstrating the anatomy in such cases (see Figs. 13.32 and 13.33). Sonography shows a complex mass within the anterolateral aspect of the abdominal wall, which may contain fluid or gas-filled loops of bowel.[35]

Sports Hernias

Sports hernia is a common cause of groin and pubic pain among elite and professional athletes. In a review of chronic groin pain in athletes, sports hernia was found in 50%.[36] Sports hernia, also

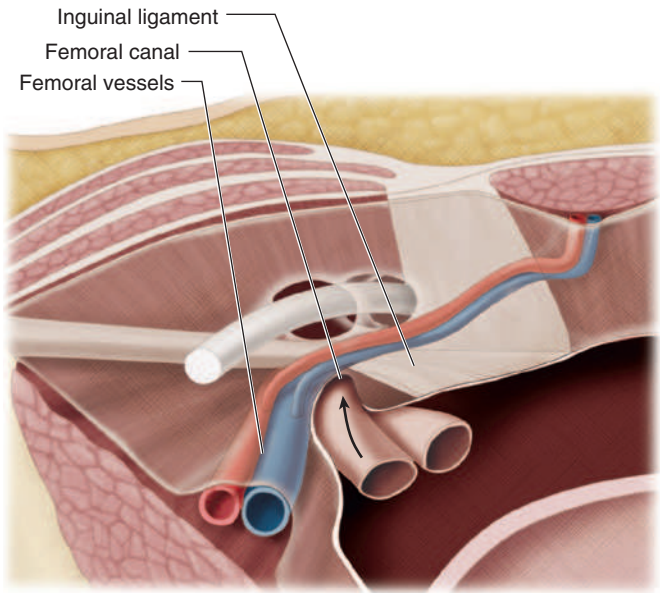

FIG. 13.26 Femoral Hernia. Diagram of the deep aspect of the anterior abdominal wall depicting a left femoral hernia. The hernia sac protrudes through the femoral canal *(arrow)* medial to the femoral vessels and inferior to the inguinal ligament.

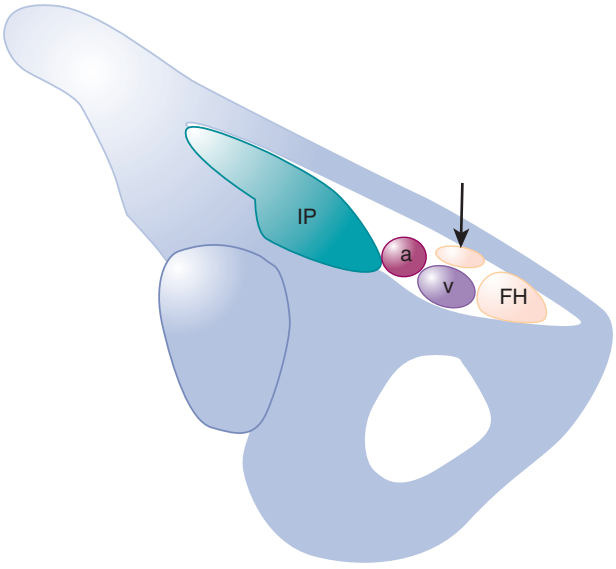

FIG. 13.27 Femoral Hernia: Relationship to Femoral Vessels. Short-axis view shows that most femoral hernias arise medial to the common femoral vein (CFV) and can extend anterior to the CFV as they enlarge. A few small femoral hernias (Teale hernias) may arise anterior to the CFV *(arrow). a,* Common femoral artery; *FH* and *arrow,* most common femoral hernia locations; *IP,* iliopsoas muscles; *v,* CFV.

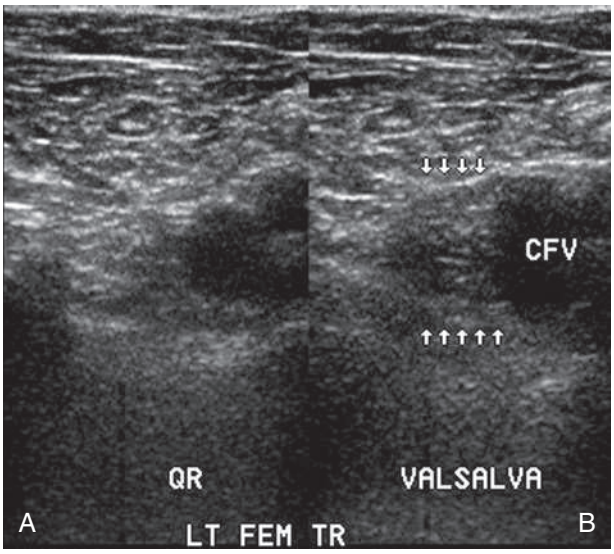

FIG. 13.28 Femoral Hernia on Valsalva Maneuver. (A) No evidence of a femoral hernia during quiet respiration. **(B)** During a Valsalva maneuver, a fat-containing femoral hernia *(arrows)* appears medial to the common femoral vein *(CFV).*

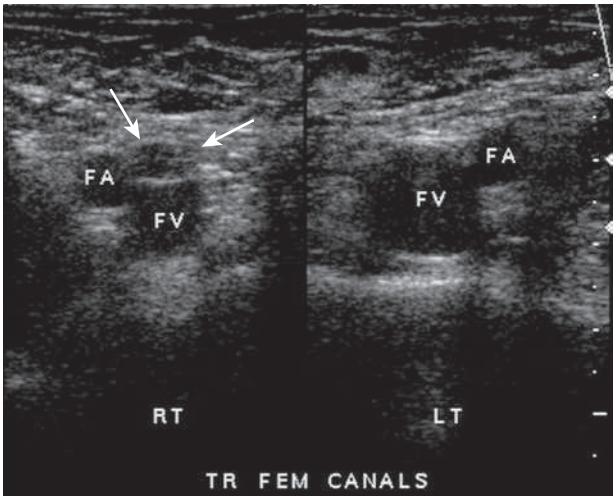

FIG. 13.29 Teale Femoral Hernia. Small, Teale type of right femoral hernia lying anterior to the common femoral vein *(FV),* but with no femoral hernia on the left. *FA,* Femoral artery.

called "sportsman's hernia" and "athletic pubalgia," is complex because it occurs in an area where many tendons come together and are difficult to separate from one another, and where weakness in one tendon may lead to failure of another or to instability of the pubic symphysis. Also, multiple abnormalities often contribute to pain. Surgery may help some of the underlying causes, but not others.

Sports hernias most often occur in elite athletes whose sport involves cutting, pivoting, kicking, and sharp turns, such as soccer, ice hockey, or football.[37] "Sports pubalgia" can be especially debilitating for elite and professional athletes, causing long periods of disability, and can be career threatening. Sports hernias are much more common in men than in women because of differences in the insertion of the rectus muscles into the pubis, but the incidence is increasing in women.

The type of hernia most often associated with groin pain in athletes is the **direct inguinal hernia** or its precursor, "posterior inguinal wall deficiency" (conjoined tendon insufficiency). In many athletes with groin pain, however, the hernia is not the only, or even the main, cause of pain. Dynamic ultrasound is the best modality for demonstrating groin hernias associated

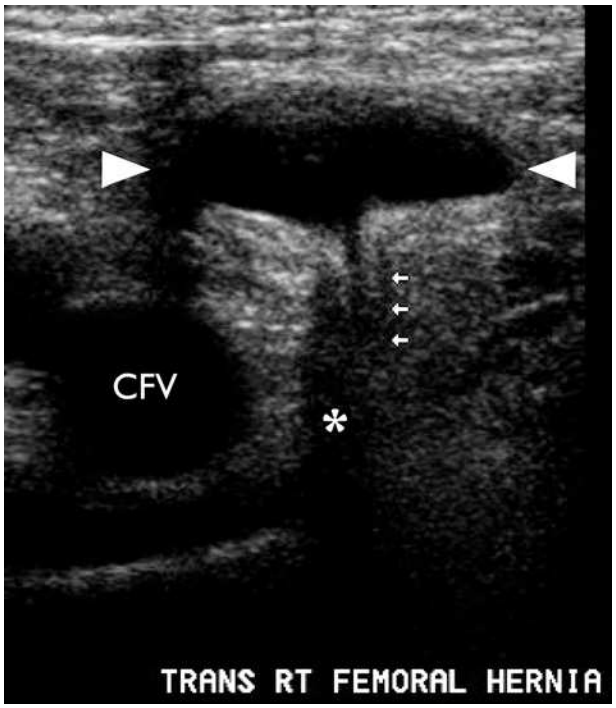

FIG. 13.30 Nonreducible Femoral Hernia. Short-axis view shows large, nonreducible femoral hernia that arises within the femoral canal (*) medial to the common femoral vein *(CFV)*. The long, narrow neck *(arrows)* extends directly anteriorly, and the large fundus *(arrowheads)* filled with peritoneal fluid causes this hernia to be at extremely high risk for strangulation.

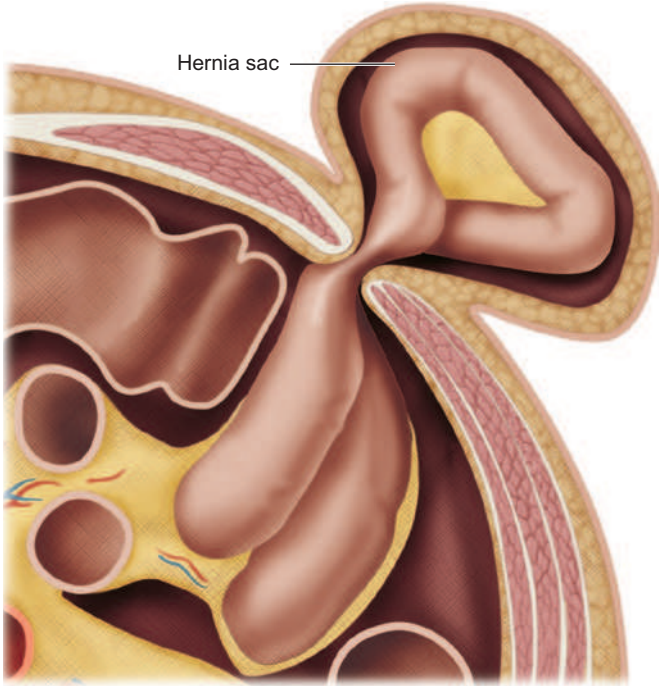

FIG. 13.31 Spigelian Hernia. Diagrammatic axial view of the abdomen at the level of the umbilicus depicting a complete Spigelian hernia. The hernia sac protrudes through the linea semilunaris. In complete spigelian hernias the hernia sac protrudes through the complete thickness of the wall musculature. (With permission from Granja M, Rivero O, Aguirre D. Abdominal wall hernias. In: Sahani DV, Samir AE, editors. Abdominal imaging. 2nd ed. Philadelphia: Elsevier; 2017:1014-1025.[43])

with sports pubalgia.[38] In a study of 1450 athletes in a sports medicine clinic who had long-standing pubalgia but no clear evidence of hernia, 580 (40%) were felt to have "sport hernia." In 573 patients, ultrasound examination detected some protrusion of the posterior wall with normal or minimally dilated inguinal rings; 498 of them coincided with areas affected by pain. Compared with findings of laparoscopy, ultrasound had a sensitivity of 95.42% and a specificity of 100%.[38]

The underlying pathology is usually **tendinosis** (degenerative change in tendons without signs of inflammation) of either the adductor longus origin or the rectus abdominis insertion. The tendons of these two muscles interdigitate, making them inseparable from each other as they insert onto the pubis. Tendinosis of one tendon usually leads to tendinosis of the other, and eventually to instability of the pubic symphysis and **osteitis pubis.** Tendinosis of the rectus abdominis muscle can also lead to microtears in which the aponeuroses of the internal oblique and transverse abdominis muscles (components of conjoined tendon) insert onto the rectus sheath, causing them to bulge anteriorly into the inguinal canal (posterior inguinal wall insufficiency or conjoined tendon insufficiency) and also leading to dilation of the external (superficial) inguinal ring. The thinned and bulged conjoined tendon pushes the spermatic cord laterally, rotates it, and compresses it. Because of the effects on the spermatic cord, the resulting pain often radiates into the scrotum.

Posterior inguinal wall insufficiency is usually bilateral, even though symptoms may be only unilateral. In the short axis, posterior inguinal wall insufficiency appears indistinguishable from direct inguinal hernia (see Figs. 13.23 and 13.24). In the long axis, however, posterior inguinal wall insufficiency and direct inguinal hernia have different shapes. The posterior wall insufficiency is semicircular, whereas the direct inguinal hernia protrudes inferiorly within the inguinal canal in a fingerlike projection (Fig. 13.36). At the level of the proximal inguinal canal, insufficiency and hernia can be distinguished only in the long axis, appearing identical in the short axis. More distally within the inguinal canal, however, the distinction can be made in the short axis. The direct inguinal hernia sac will be seen posterior to the spermatic cord (see Fig. 13.14), whereas in posterior inguinal wall insufficiency, the inguinal canal will appear normal.

Posterior inguinal wall insufficiency can progress to direct inguinal hernia in two ways: the conjoined tendon can tear completely, or the tendon can become so thinned and stretched that it is pushed inferomedially into the distal inguinal canal. Both complications arise inferior and medial to the origin of the inferior epigastric vessels. In patients with acute tendon tears, the neck is small, and the hernia sac appears thin (transversalis fascia and peritoneum) (Fig. 13.37). In severe stretching of the conjoined tendon, however, the neck is wide, and the hernia sac appears thicker (aponeuroses of internal oblique and transverse abdominis muscles as well as transversalis fascia and peritoneum) (see Figs. 13.20 and 13.36).

Because there is usually some degree of **tendinosis** or **osteitis pubis,** even when a direct inguinal hernia or posterior inguinal wall insufficiency is present, simply assessing sonographically for hernia is often insufficient for the workup of these patients.

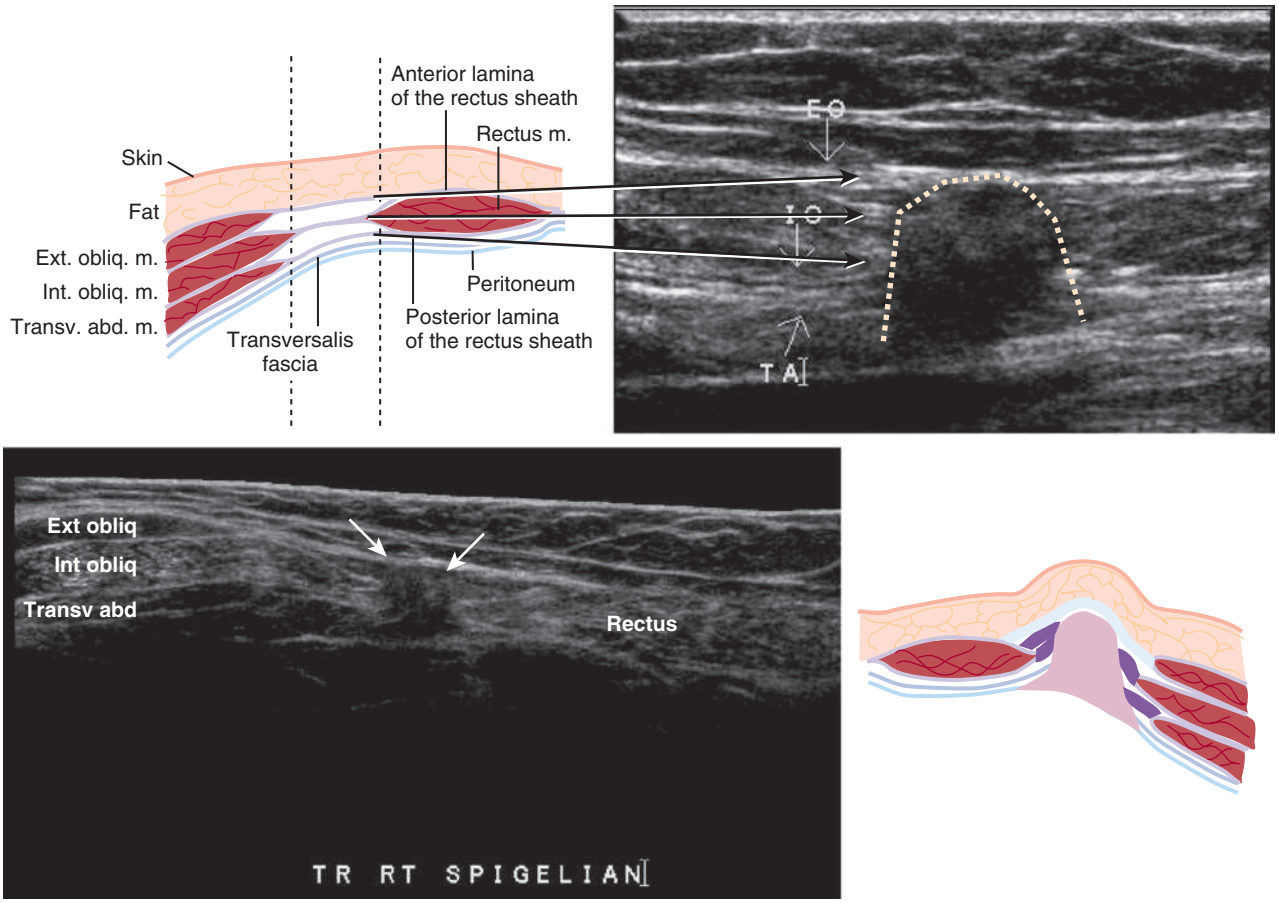

FIG. 13.32 Spigelian Hernia: Torn Aponeuroses. Small, spigelian hernia in which the aponeuroses of both the transverse abdominis *(TA)* and internal oblique *(IO)* muscles are torn, but in which the external oblique *(EO)* aponeurosis, as usual, is intact. This is the most common pattern of aponeurosis defects in spigelian hernias.

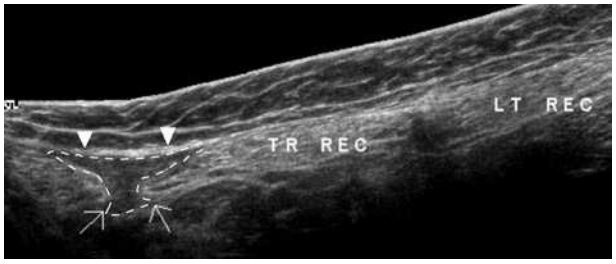

FIG. 13.33 Spigelian Hernia: "Mushroom" Shape. Transverse extended–field-of-view sonogram shows small, nonreducible, fat-containing right spigelian hernia. Because the external oblique aponeurosis is not torn, it forces the hernia sac to extend medially over the anterior surface of the right rectus muscle and laterally over the anterior aspect of the right external oblique muscle. This results in a mushroom or anvil shape, which correlates with nonreducibility and an increased risk of strangulation.

FIG. 13.34 Spigelian Hernia: Typical Shape. Nonreducible left spigelian hernia contains bowel and has a narrow neck and broad fundus, the typical shape for spigelian hernias.

Ultrasound can show tendinosis in the rectus and adductor tendons in some cases (Fig. 13.38), but not as reliably as MRI, which can also demonstrate osteitis pubis and findings such as the secondary cleft. In a patient with other pathology, only repairing an inguinal hernia or posterior wall deficiency may not cure the patient's groin pain. Thus optimal imaging workup of athletes with groin pain usually requires both dynamic ultrasound of the groin and MRI.[37,39] In patients with inguinal hernia or inguinal wall insufficiency, both surgical repair of the hernia and surgical or medical treatment of the associated tendinosis and pubic symphysis instability may be necessary.

Laparoscopic repair of sports hernia via either transabdominal preperitoneal or extraperitoneal approach has a high success

rate and earlier recovery of full sports activity compared with open surgery or conservative management.[40-42]

ABDOMINAL WALL OR VENTRAL HERNIAS

Ventral hernias are hernias through the anterior and lateral abdominal wall (excluding inguinal hernias). Midline hernias include umbilical, paraumbilical, epigastric, and hypogastric. Included in our discussion of abdominal wall hernias are incisional hernias, although these of course can occur where any incision has been made. Spigelian hernias are discussed earlier with inguinal region hernias, but when located above the groin, they are also considered in this group of ventral hernias. After adhesions, abdominal wall hernias are the second leading cause of small bowel obstruction and account for 10% to 15% of all small bowel obstructions.[43,44] However, as these authors point out, the presence of a hernia does not imply that it is the source of the obstruction. To establish the hernia as the obstructing point, one must make an effort to demonstrate the dilated loop leading into the hernia sac and a collapsed loop exiting from the point.[44] These hernias have increased in incidence over time,[45] perhaps related to our aging population and comorbidities such as obesity.

FIG. 13.35 Strangulated Spigelian Hernia. Transverse extended–field-of-view image shows strangulated left spigelian hernia containing large bowel and fat *(arrows)*. Note the hyperechoic texture of the edematous strangulated contents.

Linea Alba Hernias

Linea alba hernias are anterior abdominal wall hernias that protrude through the linea alba. Those that occur superior to the umbilicus are called **epigastric hernias,** and those that occur inferior to the umbilicus are called **hypogastric hernias.** Hypogastric hernias are much less common than epigastric hernias because the linea alba is much narrower and shorter inferior to

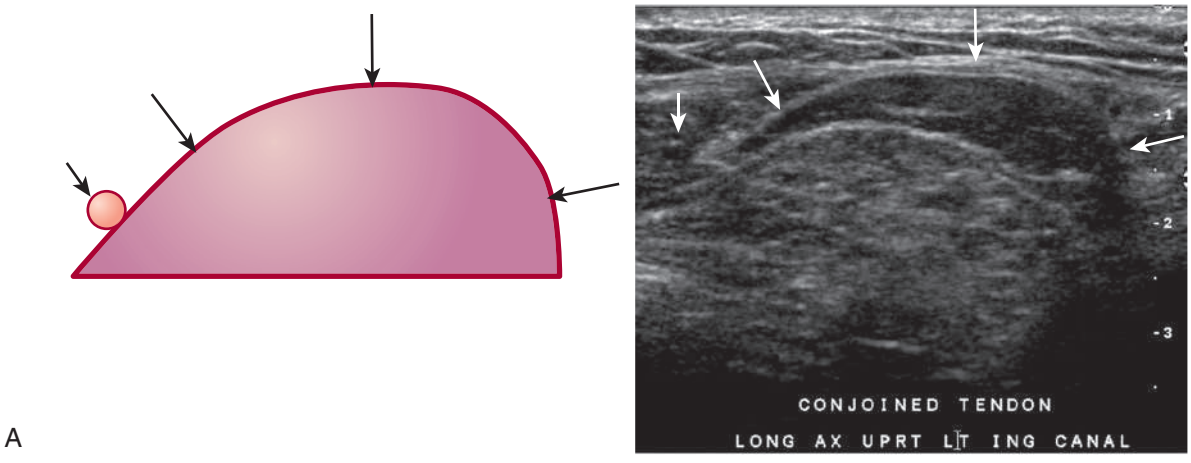

A

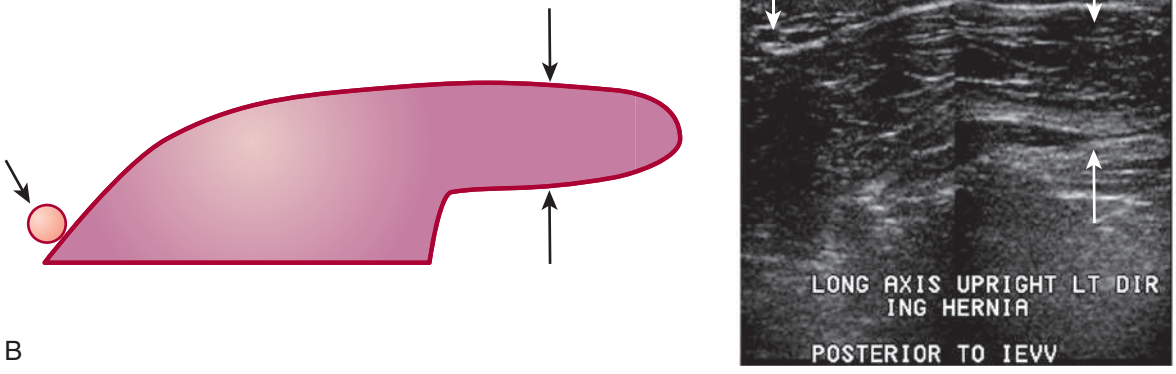

B

FIG. 13.36 Inguinal Wall Insufficiency Versus Direct Inguinal Hernia. Long-axis views show different appearance of posterior inguinal wall insufficiency and direct inguinal hernia. **(A)** Insufficiency of the posterior inguinal wall *(long arrows)*. *Short arrow* is inferior epigastric artery. **(B)** Frank direct inguinal hernia extends distally within the inguinal canal in a fingerlike projection *(long arrows)* posterior to the spermatic cord. At the level of the proximal inguinal canal, the distinction is possible only on long-axis views, because insufficiency and frank hernia appear identical on short-axis views obtained proximally. *Short arrow* is inferior epigastric artery.

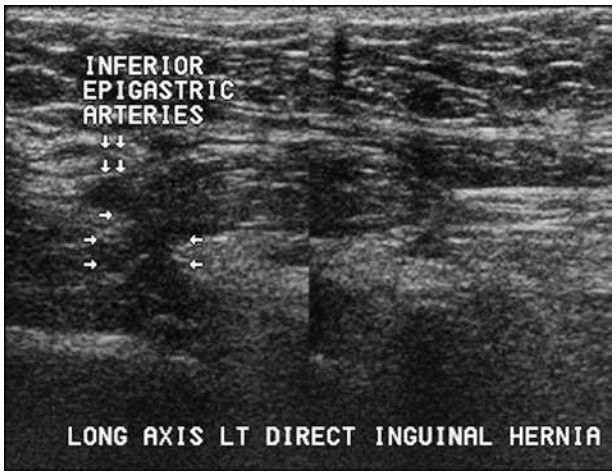

FIG. 13.37 Acute Tear of Conjoined Tendon *(Arrows).* Note that the neck is small in comparison to the fundus in this long-axis view. This is an unusual configuration for a direct inguinal hernia.

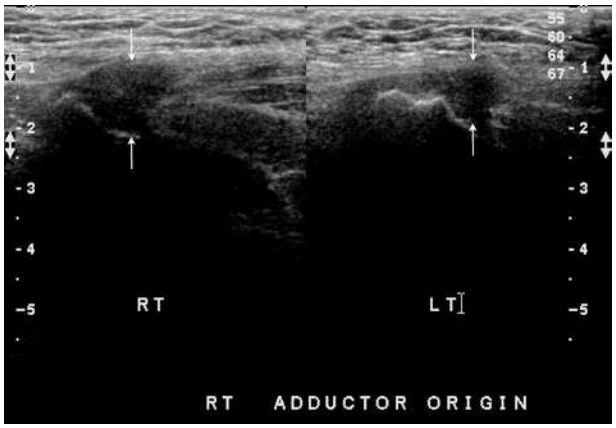

FIG. 13.38 Bilateral Tendinosis of Adductor Longus Tendons. Note that the edema and thickening of the tendon *(arrows)* is greater on the symptomatic right side than on the contralateral left side. The tendinosis in patients with athletic punbalgia is usually bilateral, but asymmetric.

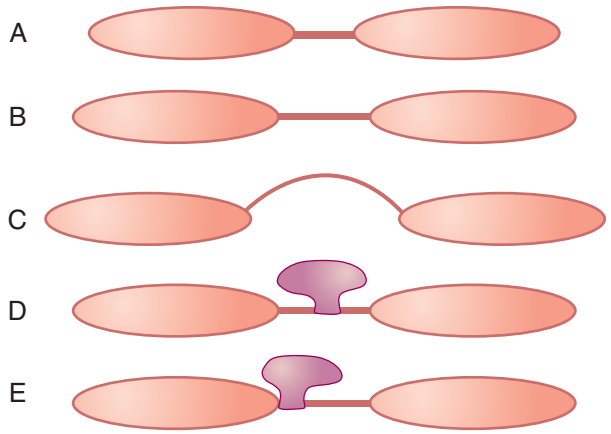

FIG. 13.39 Linea Alba Between Rectus Abdominis Muscles: Spectrum of Appearances. Transverse views. **(A)** Normal, thick linea alba. **(B)** Thinner but wider linea alba, possibly resulting from fewer decussations of rectus sheath fibers or representing diastasis recti when the patient is in the supine position in quiet respiration. **(C)** Marked thinning and bulging of the linea alba that occurs in diastasis recti during a Valsalva maneuver or in the upright position. **(D)** Typical small, epigastric linea alba hernia with its neck near the midline of the linea alba. **(E)** Small linea alba hernia with neck occurring eccentrically near the right edge of the linea alba. Note that linea alba hernias typically have narrow necks and broad fundi in the transverse view, a shape that correlates with nonreducibility and increased risk of strangulation.

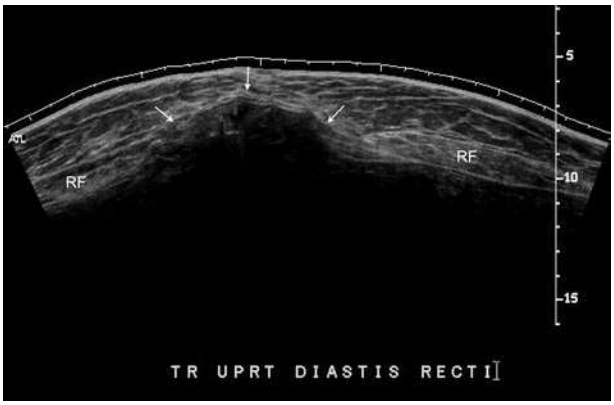

FIG. 13.40 Linea Alba–Diastasis Recti. Extended–field-of-view image obtained upright in the transverse plane shows marked widening, thinning, and bulging of the linea alba–diastasis recti abdominis.

the umbilicus than superior to the umbilicus. These are usually related to diastasis of the rectus abdominis muscles.

The **linea alba** is a thick layer of aponeurosis that separates the rectus abdominis muscles. It is formed by fusion and interlacing of fibers of the anterior and posterior sheaths of the right and left rectus muscles. Unlike the "conjoined tendon" and semilunar line, in which there are multiple thin layers of thin, loosely associated aponeuroses that do not form a discrete, well-defined structure, the linea alba is single, thick, well defined, extremely hyperechoic, and easily seen on ultrasound in most patients (Fig. 13.39A). However, the degree of decussation of fibers from the right and left sides varies. Most patients have three layers of interlaced fibers, but a minority of patients show only a single layer of interlaced fibers. In the latter group the linea alba is weaker and more predisposed to stretching (diastasis recti abdominis) and tearing (epigastric linea alba hernia).

Any cause of prolonged increased intraabdominal pressure can predispose toward weakening of the linea alba, including pregnancy, morbid obesity, and ascites. The first step is often **diastasis recti abdominis,** thinning and stretching of the linea alba that is most apparent during straining or in the upright position. The stretching of the linea alba pulls the decussated fibers apart, decreasing their interlacing, weakening the tendon, and predisposing to **epigastric herniation.**

In patients with diastasis, the linea alba is thinner and wider than normal. When the patient is supine and in quiet respiration, the associated anterior bulging of the tendon is not evident (see Fig. 13.39B). However, having the patient perform a Valsalva maneuver or raise the head off the pillow while lying supine, or having the patient stand, will make the anterior bulging visible (see Fig. 13.39C; Fig. 13.40, Video 13.13). In patients with diastasis recti abdominis, the anterior bulging extends along the entire craniocaudal length of the epigastric segment of the linea alba. In patients with epigastric hernia, any bulging will be more

localized along the craniocaudal axis. Although diastasis usually does not, epigastric hernias often do cause tenderness.

Epigastric linea alba hernias are easier to diagnose than are groin hernias as long as they are scanned with the proper transducer and the sonographer or physician is actually visually inspecting the linea alba. Epigastric hernias are usually superficial enough in location that they are best shown with 10- to 12-MHz linear array transducers. With these transducers, the defect through the linea alba is usually quite conspicuous because it is either isoechoic or hypoechoic compared with the extremely hyperechoic linea alba. The defect is usually very near the midline, but it may occur eccentrically toward the right or left side of the linea alba (see Fig. 13.39D-E; Figs. 13.41 and 13.42, Video 13.14). The most frequent reason for missing an epigastric linea alba hernia is that the examination for abdominal pain was performed with the standard 3-MHz curved linear array transducer, focused too deep in the elevation axis to identify any structures except large hernias in obese patients. The clinician must have an index of suspicion to use the appropriate transducer.

Although clinically detected epigastric hernias tend to be quite large and often contain bowel and other intraperitoneal contents, sonographically detected epigastric hernias are usually small to moderate-sized and contain only preperitoneal fat (Video 13.15). In hernias that contain only preperitoneal fat, the underlying peritoneal membrane and transversalis fascia are intact and the hernia cannot be seen or repaired laparoscopically. Epigastric hernias always have a very narrow neck in comparison to the size of the fundus and thus are usually not reducible and are at increased risk for strangulation, even when small. Some epigastric hernias that contain only preperitoneal fat are so small that it is difficult to believe that herniation is the cause of pain (Fig. 13.43). These hernias are not palpable, and patients typically have pain, which more likely results from the tear or tendinosis of the linea alba than from herniation of a tiny amount of properitoneal fat.

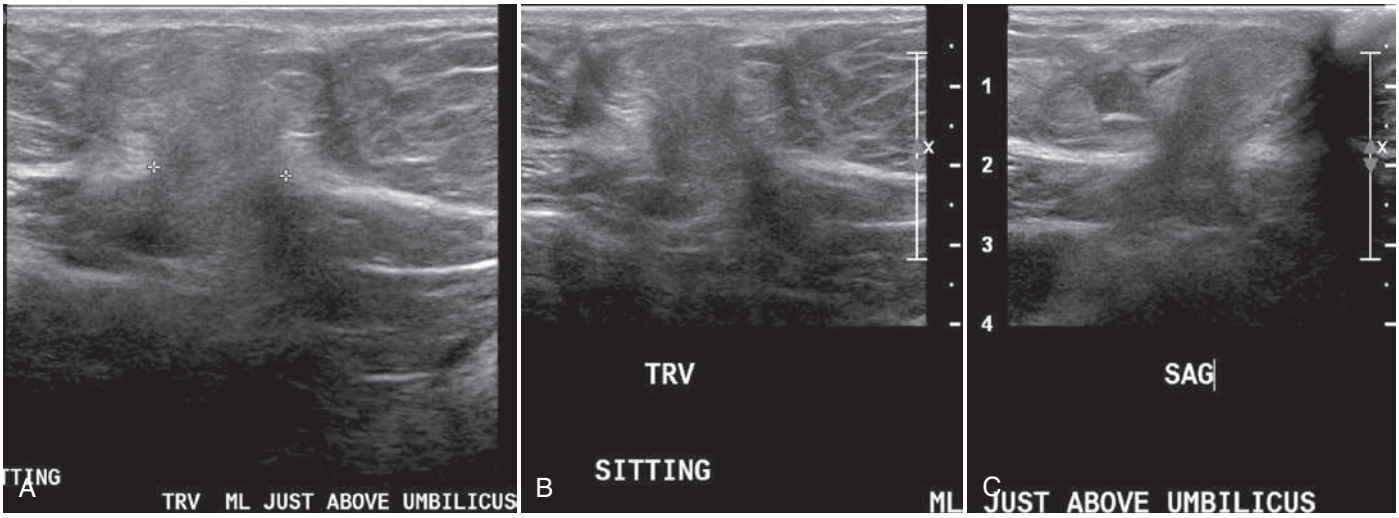

FIG. 13.41 Epigastric Linea Alba Hernia. Mesenteric fat protrudes through a 1-cm defect *(calipers)* in the linea alba at midline just above the umbilicus. Images were obtained in the transverse supine **(A),** transverse with patient sitting **(B),** and sagittal with patient sitting **(C).** Note the change in the appearance of the hernia defect with change in patient position.

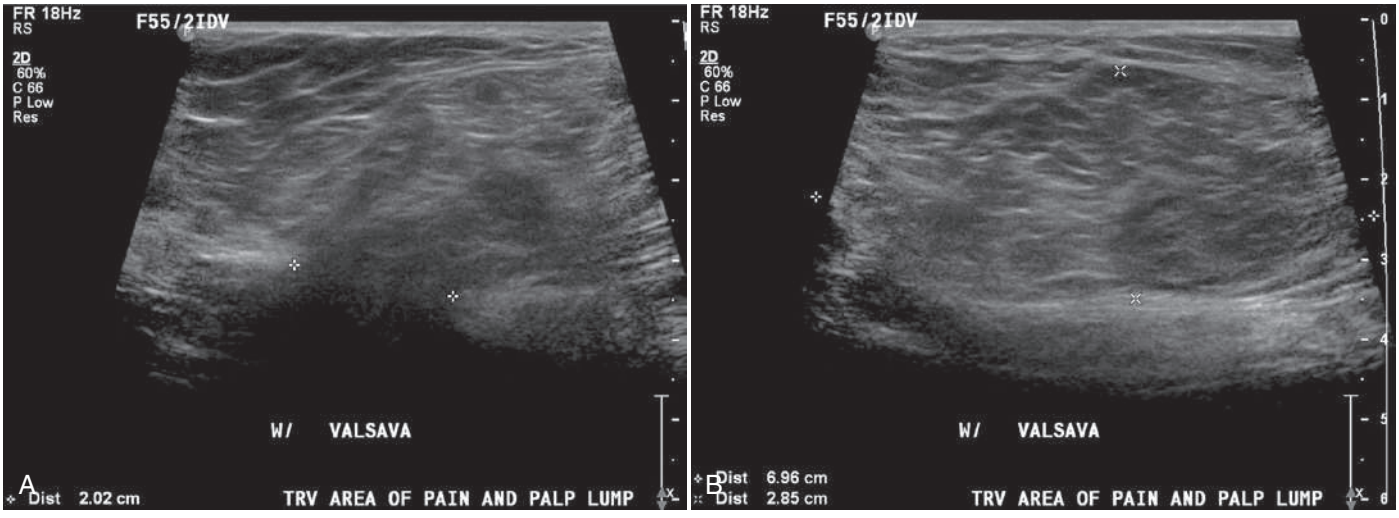

FIG. 13.42 Large Ventral Hernia. Large fat-containing hernia is visible just left of midline. **(A)** and **(B)** Transverse images show the hernia in the region of patient's pain in palpable abnormality. See also Video 13.14.

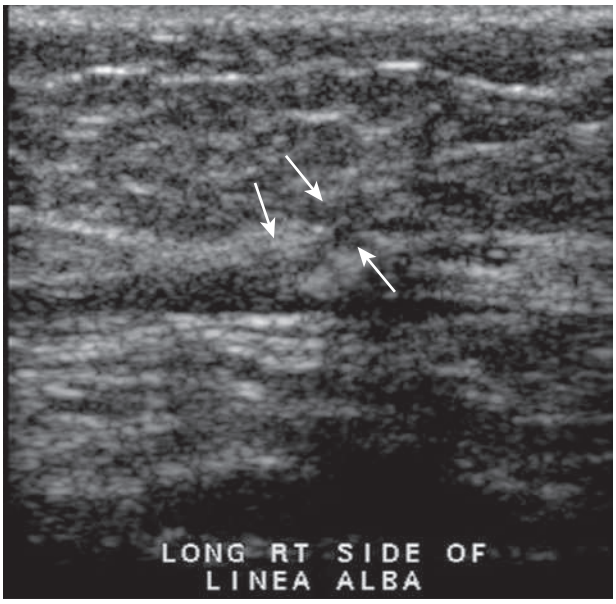

FIG. 13.43 Linea Alba Tear. Tiny tear of the linea alba *(arrows)* caused pain but was not palpable. Such tears are relatively common in patients with preexisting diastasis recti abdominis.

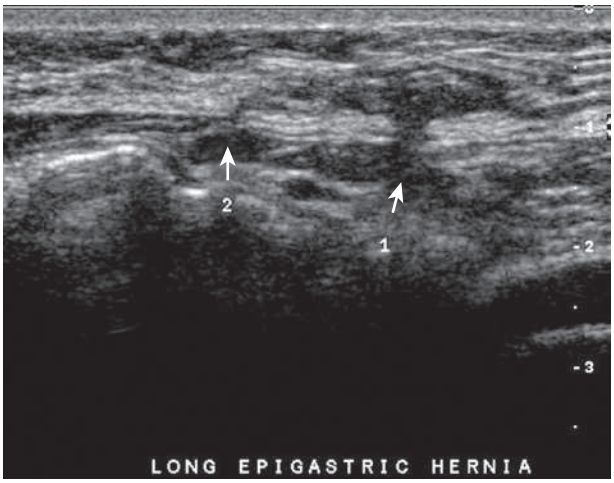

FIG. 13.44 Two Epigastric Hernias. Longitudinal view shows a small, fat-containing, nonreducible, epigastric linea alba hernia inferiorly and a tiny tear superiorly. This patient had three other small hernias more superiorly. Multiple epigastric linea alba hernias are common enough that the entire length of the linea alba should be investigated in any patient with an identified epigastric hernia. See also Video 13.16.

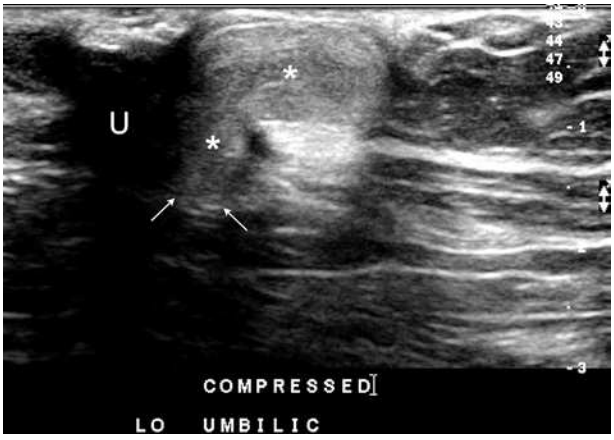

FIG. 13.45 Hypogastric Linea Alba Hernia. Longitudinal view shows a moderate-sized, fat-containing, periumbilical hypogastric linea alba hernia (*) immediately inferior to the umbilicus *(U)*. Note that neck of the hernia *(arrows)* is very narrow and that the edematous strangulated fat is hyperechoic in comparison to the surrounding subcutaneous fat.

Simply identifying diastasis in a patient with epigastric midline pain is insufficient. The linea alba in the area of pain and along its entire epigastric segment must be examined for hernias, because patients with diastasis are at increased risk for multiple epigastric hernias. It is important to assess the entire length of the linea alba in any patient in whom one epigastric linea alba hernia is found. Most hernias contain only properitoneal fat, so they cannot be seen laparoscopically and must be repaired externally. If surgeons do not know that multiple hernias are present, they may use too small a piece of mesh to repair all the hernias. It is our experience that "recurrent" epigastric hernias are more likely to be secondary hernias that were not recognized and repaired, rather than true recurrences (Fig. 13.44, Video 13.16 and Video 13.17).

The much less common **hypogastric linea alba hernia** usually lies within a few centimeters of the umbilicus. Inferior to this area, the rectus muscles are more closely apposed or even fused. As with epigastric hernias, hypogastric linea alba hernias have narrow necks, usually are small to moderate-sized, contain only preperitoneal fat, are usually not reducible, and are prone to strangulation (Fig. 13.45).

Umbilical Hernias

Umbilical hernias occur through a widened **umbilical ring.** In newborns, they result from delayed return to the abdomen of bowel loops that lie in the base of the umbilical cord in the first trimester. In many cases, umbilical hernias in newborns will regress spontaneously by 3 or 4 years of age. Those that do not regress by age 4 are usually repaired.

Umbilical hernias can, however, develop at any time during life. Any cause of chronically increased intraabdominal pressure or connective tissue weakness can lead to dilation of the umbilical ring and formation of an umbilical hernia. Umbilical hernias contain intraperitoneal contents, but smaller umbilical hernias usually contain only intraperitoneal fat (Fig. 13.46). We are asked to evaluate umbilical hernias sonographically much less frequently than we are asked to evaluate patients for groin pain, because the diagnosis of umbilical hernia is usually obvious clinically. The role of ultrasound is usually limited to evaluating for umbilical pain in patients who are so morbidly obese that an umbilical hernia cannot be detected clinically, or to assess for strangulation. In obese patients the umbilicus courses obliquely from deep superiorly to superficial inferiorly (Fig. 13.47). Thus the umbilical ring may be much more superiorly located than is suspected from the location of the umbilicus in obese patients. Untreated umbilical hernias tend to increase in size over time. They are usually reducible but may become nonreducible and can also

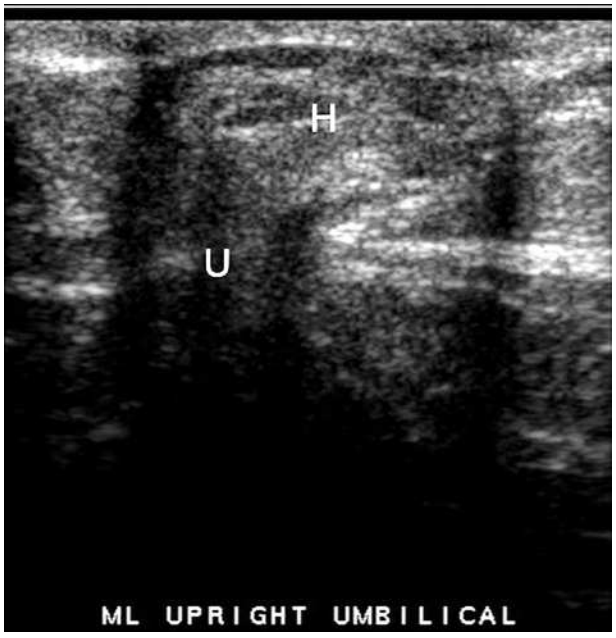

FIG. 13.46 Umbilical Hernia. Longitudinal view shows moderate-sized, fat- and bowel-containing umbilical hernia *(H)*. Umbilical hernias pass through dilated umbilical rings *(U)*.

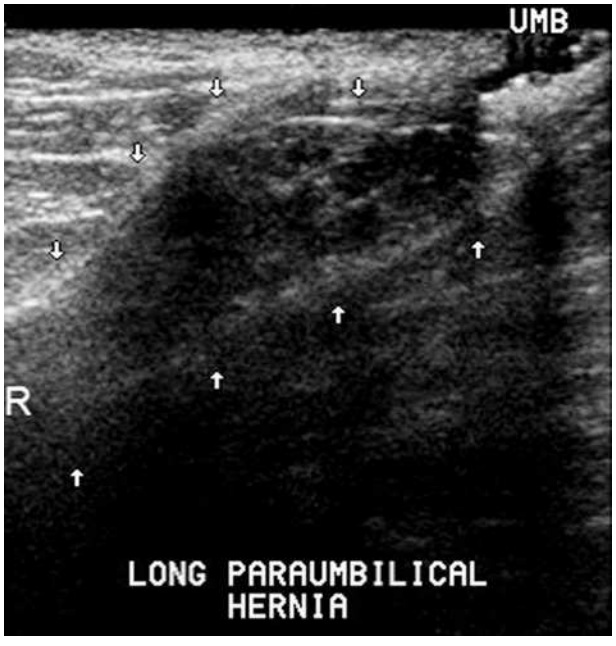

FIG. 13.47 Umbilical Hernia. Longitudinal view of moderate-sized, fat-containing umbilical hernia *(arrows)* in a morbidly obese patient with umbilical pain. The hernia was not clinically apparent. In such obese patients the umbilicus lies several centimeters inferior to the umbilical ring. Thus one must investigate superior to the umbilicus to identify small to moderate hernias.

become strangulated. Clinically, it may be difficult to distinguish between acute omphalitis and a strangulated small umbilical hernia. Both can cause pain and redness in the umbilical area. Sonography, however, can readily make the distinction (Figs. 13.48 and 13.49).

FIG. 13.48 Small, Nonreducible, Strangulated Umbilical Hernia. Note in this transverse view that the edematous strangulated fat within the hernias is hyperechoic compared with the surrounding subcutaneous fat.

The sonographic evaluation of umbilical hernias is similar to that for any hernia. Dynamic maneuvers are used, with identification of type, size, contents, reducibility, and tenderness.

Paraumbilical or Periumbilical Hernias

A "paraumbilical" hernia is not really a distinct type of hernia. It is usually either an epigastric or a hypogastric **linea alba** hernia that lies very close to the umbilicus. **Periumbilical** linea alba hernias, whether epigastric or hypogastric, are particularly likely to become strangulated (see Fig. 13.45, Fig. 13.50).

Incisional Hernias

Incisional hernias are a complication in 4% to 28% of patients undergoing open abdominal surgery, with the majority of articles quoting about 10% in patients undergoing major abdominal operations.[46-49] However, the rates of incisional hernias are associated with the type of surgery, older age, and obesity, and repair of incisional hernias has become the most common hernia repair procedure. Incisional hernias can occur in any area along the anterior abdominal wall where an incision is made, including laparoscopy ports and stomal sites. The herniation can result from thinning and stretching of the scar or from a tear in a segment of the scar. Whether the scar is stretched or torn affects the shape of the hernia, its reducibility, and its risk of strangulation. Incisional hernias resulting from **thinning and stretching** of the scar have wide necks and are reducible, whereas those resulting from **tears** in the scar are more likely to have narrow necks and to be nonreducible (Fig. 13.51, Video 13.18). Incisional hernias can occur where natural hernias cannot, through the bellies of muscles that have been incised. Incisional hernias can occur through very small scars (e.g., laparoscopy ports) (Video 13.19 and Video 13.20). Obese patients who have undergone transverse rectus abdominis myocutaneous (TRAM) flap breast reconstruction surgery are particularly likely to have one or more incisional hernias (see Video 13.18). In a study comparing

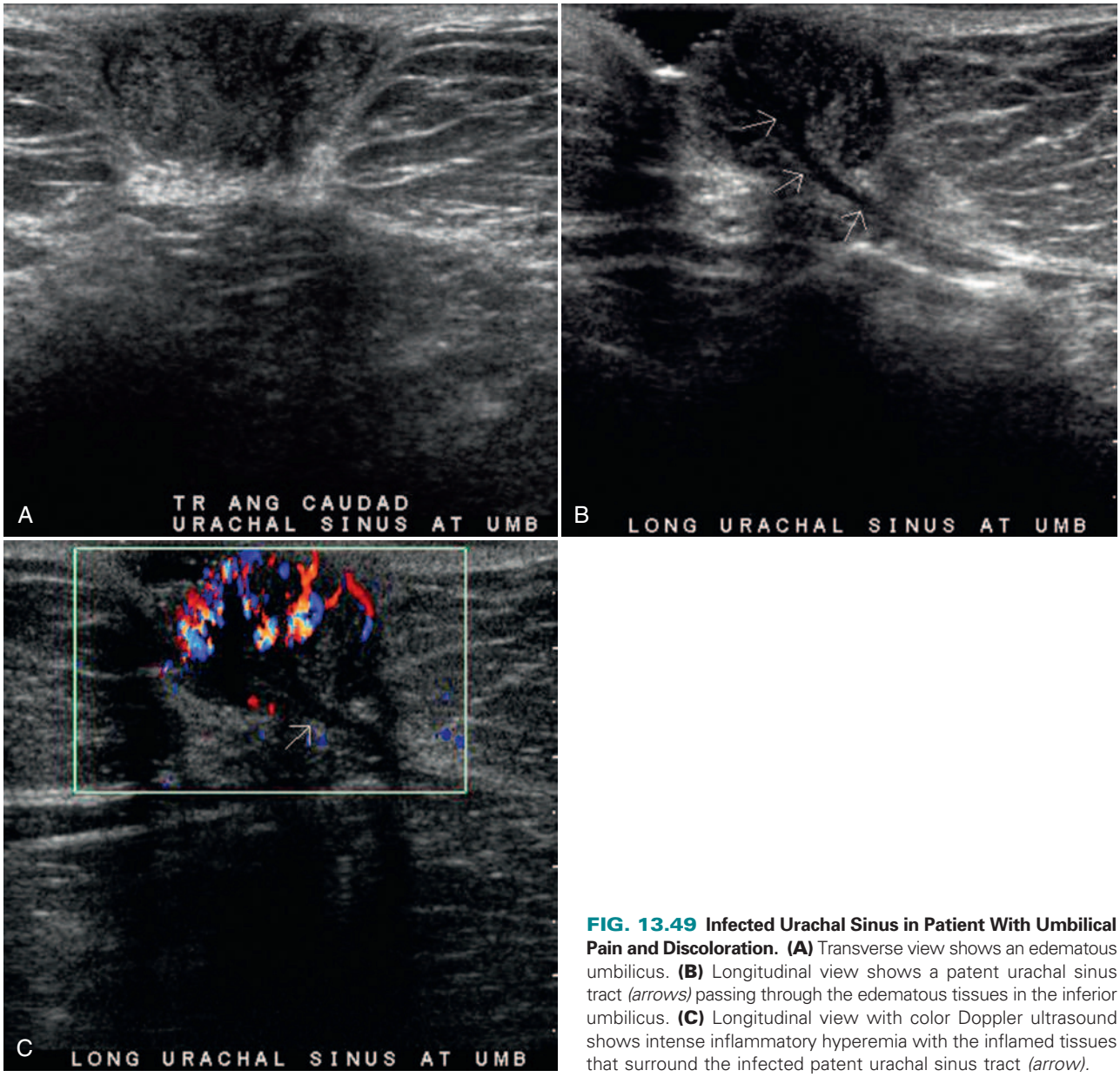

FIG. 13.49 Infected Urachal Sinus in Patient With Umbilical Pain and Discoloration. (A) Transverse view shows an edematous umbilicus. **(B)** Longitudinal view shows a patent urachal sinus tract *(arrows)* passing through the edematous tissues in the inferior umbilicus. **(C)** Longitudinal view with color Doppler ultrasound shows intense inflammatory hyperemia with the inflamed tissues that surround the infected patent urachal sinus tract *(arrow)*.

dynamic ultrasound versus CT in the assessment of suspected incisional hernias, of 109 patients, 102 and 107 had incisional hernia noted on CT and ultrasound, respectively. The measurements of the hernias were similar comparing the techniques.[50] Repair of the hernia can be by either laparoscopic or open repair.[51] In a retrospective study of ventral wall hernias, the main indication was pain in 78%, and 10% had an acute presentation with incarceration or strangulation.[52] Mesh repair is being increasingly performed because it seems to be associated with fewer recurrences.[53]

Multiple Hernias

Patients who have one type of hernia are more likely to have additional hernias. These patients are more likely to have contralateral hernias of the same type, and they are more likely to have either ipsilateral or contralateral hernias of different types. There are several reasons for this. First, **bilateralism** may be caused by timing of closure of fetal canals, and delayed closure for any reason is likely to affect both sides simultaneously. Second, underlying factors that lead to formation of hernias can affect all sites simultaneously. Factors that increase the risk of hernias include any cause of chronically increased intraabdominal pressure, as well as repetitive stress. Pregnancies, morbid obesity, and ascites can increase intraabdominal pressure long enough to lead to development of hernias. Certain professions lead to repetitive stress injuries. Sedentary lifestyle, nutritional deficiencies, and hereditary factors can result in weak connective tissues.

In a patient with unilateral groin pain but no demonstrable hernia on that side during dynamic ultrasound, the study can be stopped after examining the symptomatic side. However, in

any patient in whom one type of groin hernia is found during the dynamic ultrasound examination, the clinician must look for the other three types of ipsilateral groin hernias. Femoral and indirect inguinal hernias can occur together (Fig. 13.52). In addition, direct and indirect inguinal hernias can occur on the same side. On long-axis views, the necks of the hernias resemble pant legs straddling the inferior epigastric vessels, explaining why the combination of the two hernias has been termed a **pantaloon hernia** (Fig. 13.53, Video 13.22). The contralateral groin is evaluated as well. This is especially important in patients who will undergo laparoscopic hernia repairs, because surgeons are more likely to perform bilateral repairs using a laparoscopic approach than when performing external herniorrhaphy. Direct inguinal hernias and femoral hernias are most likely to be bilateral. Multiple linea alba and incisional hernias are also relatively common.

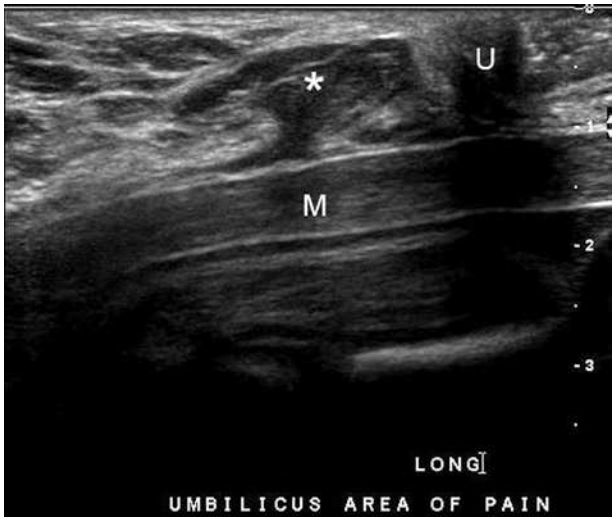

FIG. 13.50 Small Periumbilical Hernia. Patient had periumbilical pain during the third trimester of pregnancy. Longitudinal view shows a fat-containing, nonreducible epigastric linea alba hernia (*). The increased intraabdominal pressure, together with the softening of ligaments that occurs in the late third trimester, predisposes to all types of hernias. *U,* Umbilicus; *M,* myometrium of gravid uterus.

ADDITIONAL ISSUES REGARDING HERNIAS

Recurrent Groin Hernias

Hernia repair can be performed by direct anterior incision of the inguinal canal or laparoscopically. Hernia repairs performed decades ago were done without mesh. Originally, fascia was pulled up to reinforce the inguinal area, but this tended to widen the femoral canal and led to "recurrent" femoral hernias. "Tension-free" external repairs using proline mesh were developed to prevent this. Recent data suggest that results of laparoscopic repairs equal those of external repairs. Laparoscopic repairs have the advantage of allowing bilateral repair, but require general anesthesia. External repairs are generally limited to one side, but can be done with regional anesthesia. Most hernia repairs now are "tension free" and employ mesh. Mesh can be used with both external and laparoscopic repairs.

Unfortunately, recurrent or residual groin pain after herniorrhaphy is relatively common. Recurrent hernia is not the only cause of residual or recurrent groin pain after herniorrhaphy, and dynamic sonography is an integral part of the evaluation of other causes in patients with acute or chronic postherniorrhaphy pain.

In the acute phase, **residual pain** unchanged from preoperative pain is rare and usually the result of an unsuccessful hernia repair. The original hernia persists and can be demonstrated sonographically. More often, acute pain is caused by entities other than recurrent hernia, including incisional pain or pain caused by acute **hematomas** (Fig. 13.54A) or **seromas** (Fig. 13.54B), and sometimes pain radiating into the scrotum as the result of spermatic cord compression by a seroma, a hematoma,

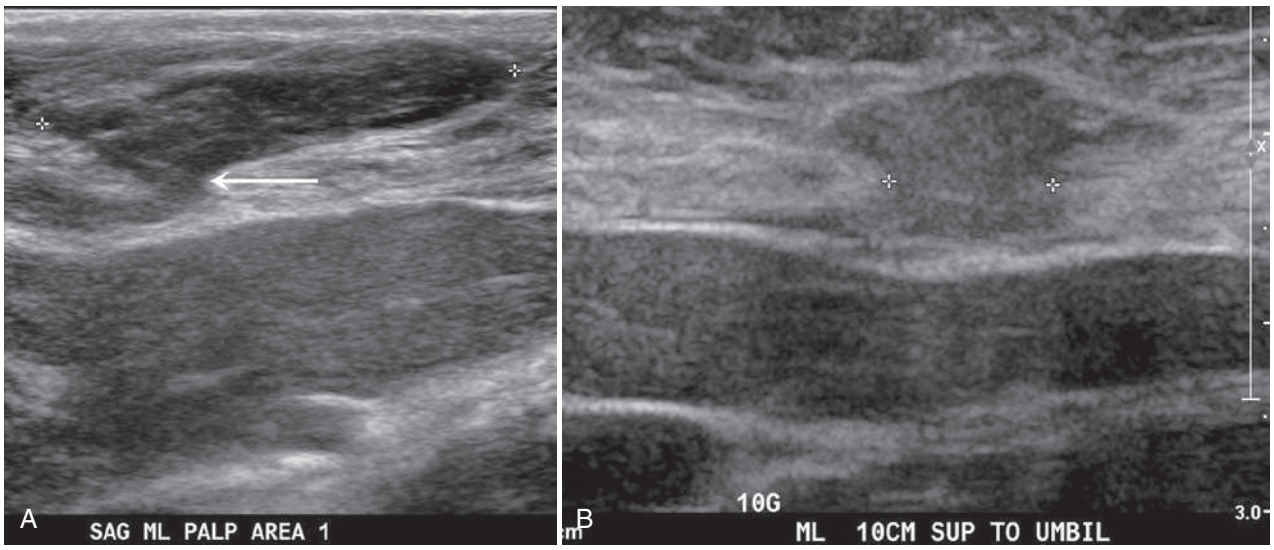

FIG. 13.51 Incisional Hernia. (A) and **(B)** Two patients with fat-containing incisional hernias. **(A)** *Arrow* shows the narrow neck of a fat containing incisional hernia, while *calipers* show the extent of the fat within the hernia. The narrow neck increases the risk of strangulation. **(B)** In another fat containing incisional hernia the neck is much wider *(calipers)*. See also Video 13.19 and Video 13.20.

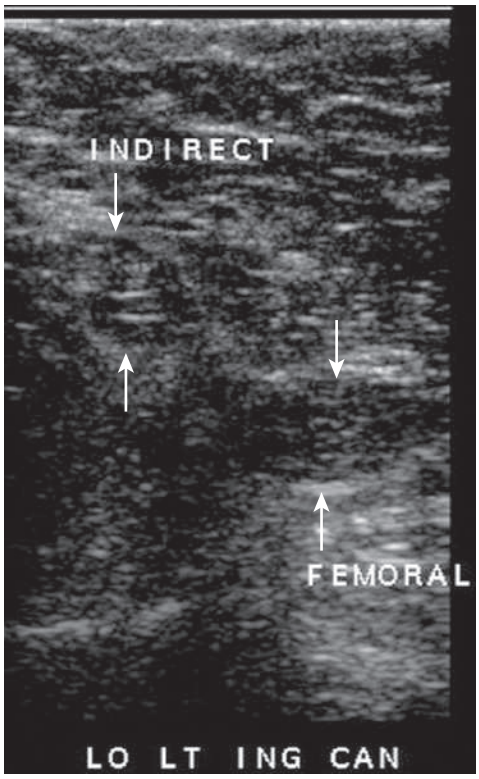

FIG. 13.52 Two Hernias. Longitudinal image of indirect inguinal and femoral hernias.

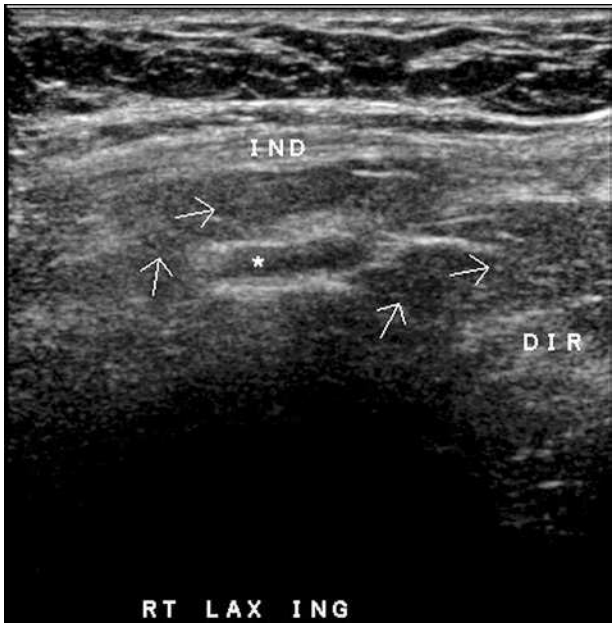

FIG. 13.53 Pantaloon Hernia. Long-axis view of right inguinal area shows both direct *(DIR)* and indirect *(IND)* inguinal hernias with the inferior epigastric vessels (*) between them, a pantaloon hernia. The necks of the direct and indirect inguinal hernia resemble pant legs straddling the inferior epigastric vessels.

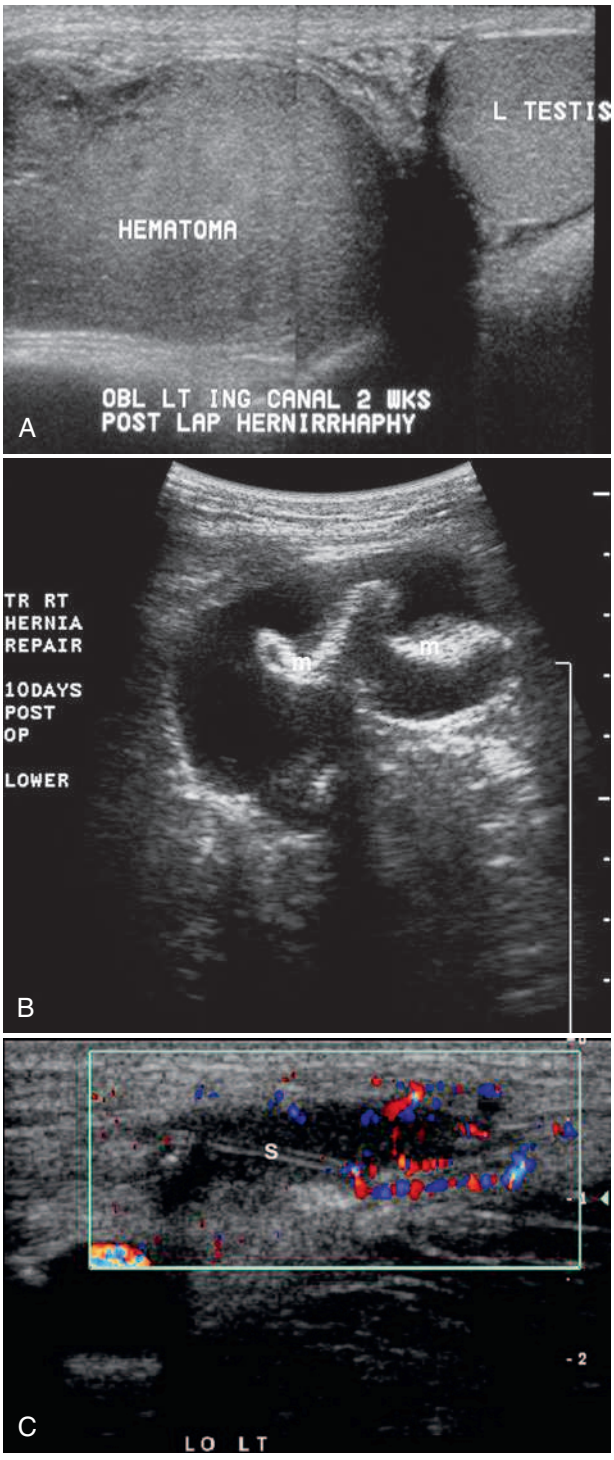

FIG. 13.54 Complications After Hernia Surgery in Patients With Pain and Swelling After Hernia Repair. (A) Hematoma. **(B)** Seroma. **(C)** Stitch abscess.

the mesh, or a repair that makes the internal inguinal ring too tight. In such cases it is important to assess the ipsilateral scrotum and testis with gray-scale imaging and Doppler ultrasound, because cord compression of any etiology can lead to **testicular infarction.** Doppler ultrasound evidence of testicular ischemia may indicate the need for emergency decompression by either evacuating an inguinal canal hematoma or seroma or

loosening the repaired internal inguinal ring. Inguinal canal hematomas or seromas that do not compress the spermatic cord or cause testicular ischemia, on the other hand, can usually be managed conservatively. Postherniorrhaphy hematomas or seromas can become secondarily infected and evolve into abscesses. **Stitch granulomas** or **stitch abscesses** can cause pain (see Fig. 13.54C).

Late recurring pain also has a variety of causes, but recurrent hernia becomes a greater concern, particularly when the pain is similar in type to that present before surgery. Late pain etiology includes recurrent hernia, seroma, hematoma, abscess, traction on the edges of the mesh, immune reaction to the mesh, spiral clips, compression of the spermatic cord, and fibrosis and scarring of the ilioinguinal nerve. Again, dynamic sonography is essential in evaluating such patients, although it is more difficult than in patients not previously repaired.

In patients who underwent herniorrhaphy without mesh, the recurrent hernia is usually of the same type as the original. However, it is not unusual, even after tension-free repairs, to find a "recurrent" femoral hernia. In such cases, especially after external repair, the femoral hernia may have been present before the repair, but subclinical and unrecognized. This is a major reason why it is important to look for *all* types of groin hernias during dynamic sonography. In our experience, "recurrent" femoral hernias are less common after tension-free repairs that employ mesh, because they usually employ a piece of mesh large enough to cover the conjoined tendon, internal inguinal ring, femoral canal, and spigelian area.

In patients whose hernias were repaired with mesh, it is not possible to determine sonographically whether a recurrent inguinal hernia is direct or indirect. It is only possible to determine that it is a *recurrent* inguinal hernia. The key to finding recurrent hernias in patients who have mesh in place is to identify the mesh and then assess for herniations along the edges of the mesh with dynamic maneuvers. In patients being evaluated for recurrent hernia, the most useful dynamic maneuver is usually the compression maneuver with the patient in the upright position.

Because many types of mesh are available, the appearance varies greatly (Fig. 13.55). In ideal cases, we can actually see the texture of the mesh. In most cases, however, the mesh can be seen only as an echogenic line of variable thickness with variable shadowing or as an area of variable shadowing. Some newer types of mesh are thin and much more difficult to identify sonographically. Normal mesh can have folds and can be rolled at the edges, and it normally bulges mildly outwardly in the upright position and during Valsalva maneuvers. Patient history is rarely helpful because patients are unaware of the type of mesh used.

However, every effort should be made to identify the mesh, because recurrent hernias do not occur through the center but rather at the *edges* of the mesh. Most recurrent hernias occur along the **inferomedial edge** of the mesh (Fig. 13.56; Video 13.21), but it is still important to identify the mesh and then assess the entire periphery of the mesh, because hernias can occur along any edge of the mesh. Herniation from the edge of the mesh likely occurs because the affected edge has "pulled loose" (Fig. 13.57).

The edges of the mesh can be anchored to surrounding connective tissues with sutures, surgical clips, or special spiral clips. The sutures and clips hold the mesh in place for about the first 6 weeks after surgery. After this, fibrosis forms and generally holds the mesh in place. It is during the first 6 postoperative weeks, before the mesh has fibrosed to the anterior abdominal wall, that mesh is most likely to pull loose from its anchors. In our experience, this is most likely to occur after laparoscopic repairs—not because the repair has been defective or because laparoscopic repair is less effective, but because the patient feels "too well, too soon" after the minimally invasive repair and resumes activities that put the repair at risk within the first 6 weeks. Some patients may complain of a tearing sensation during some movement, followed by the onset of recurrent inguinal pain, but in most patients the onset is more insidious.

A chronic hematoma or seroma can cause chronic pain, and its evacuation can relieve the pain. Therefore searching for a hematoma or seroma is a standard part of the postherniorrhaphy sonogram. Some patients can develop an allergic or hypersensitivity reaction to the mesh, with a thin seroma localized to the mesh surface.

When sonography demonstrates no hernia, hematoma, or seroma, it is important to assess the mesh for tenderness. In many cases without sonographically demonstrable pathology, the mesh is tender for a variety of reasons. First, the mesh may compress the spermatic cord; compressing the mesh will cause pain that radiates into the scrotum. Second, the mesh may be placing traction on the fibrosis that holds its edges in place; this is especially common in patients with significant weight gain since surgery. The mesh usually bulges anteriorly in such cases. In other cases, the fibrosis that holds the mesh in place has entrapped nerves, notably the **ilioinguinal nerve.**

The **spiral clips** used to anchor the mesh require special mention. Because these can become tender and a source of postherniorrhaphy pain, spiral clips are now seldom used. However, their past popularity means many patients have them. Spiral clips have a characteristic radiographic and sonographic appearance (Fig. 13.58). In some postherniorrhaphy patients with no other sonographically demonstrable pathology, the only finding is focal tenderness directly over the offending clip. Surgical removal of the clip will relieve the pain and tenderness and typically will not adversely affect the soundness of the repair, because the edge of the mesh will be held firmly in place by fibrosis, even after the clip is removed.

Hernia Complications

Hernia complications include incarceration, obstruction, and strangulation. **Incarcerated hernias** are simply hernias that are nonreducible. **Obstructed hernias** contain incarcerated bowel loops that have become mechanically obstructed. **Strangulated hernias** contain incarcerated contents with compromised vascularity. Not all strangulated hernias contain bowel loops; even preperitoneal fat can become strangulated. Most incarcerated hernias are neither obstructed nor strangulated, but all obstructed and strangulated hernias are also incarcerated. Only incarcerated hernias that are also obstructed or strangulated are surgical emergencies. Even strangulated hernias that contain only

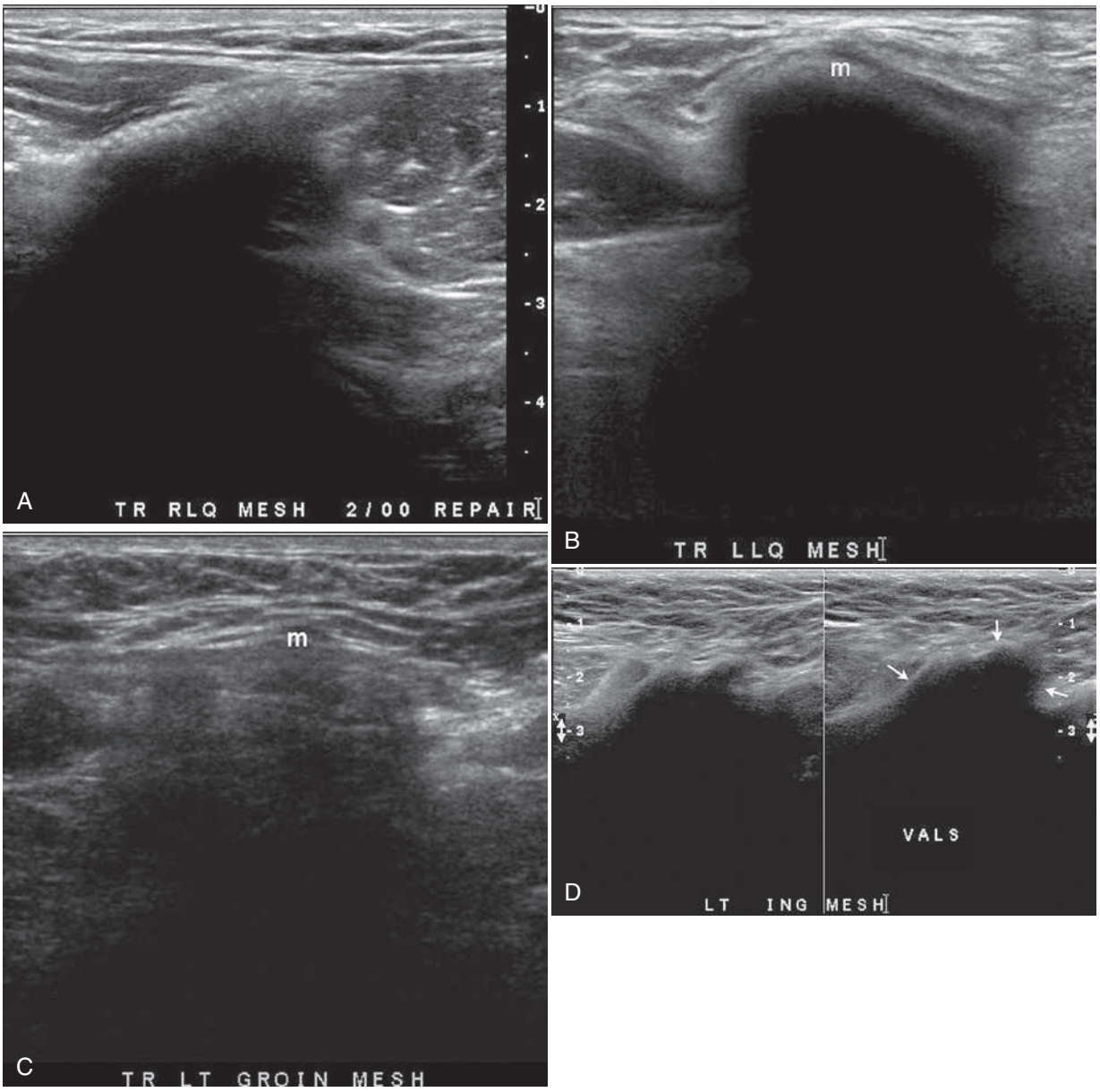

FIG. 13.55 Mesh After Hernia Repair. (A) Normal mesh. The mesh used in this hernia repair is thick and echogenic, and individual fibers within the mesh are visible. It casts a strong acoustic shadow. The mesh can be well seen in only a small percentage of cases. **(B) Herniorrhaphy mesh with strong shadow.** Mesh typically appears thick and echogenic and casts a strong acoustic shadow, but individual fibers within the mesh *(m)* are not visible sonographically. **(C) Herniorrhaphy mesh with weak shadow.** Thin, poorly defined mesh casts only a weak acoustic shadow. Such mesh can be identified only with high-frequency transducers, optimal technique, and careful search. **(D) Wrinkled herniorrhaphy mesh.** Mesh can bulge during the Valsalva maneuver or when the patient is scanned in the upright position; this may be normal. These split-screen images show wrinkled mesh in the supine position in quiet respiration *(left image)* and bulging with straightening of some of the wrinkles in the upright position *(right image)*.

preperitoneal fat may not be emergencies. It is the presence of bowel loops within strangulated hernias that makes them emergent. Instead of incarcerated, we use the term **nonreducible** because the referring clinician is less likely to confuse it with strangulation.

The **shape** of hernias affects their reducibility and their likelihood of becoming obstructed or strangulated in the future. The hernia type affects its shape. Hernias that have relatively **broad necks** in comparison to their fundi are usually completely reducible and rarely become obstructed or strangulated. Groin hernias that typically have broad necks and infrequently strangulate are direct inguinal hernias and some indirect inguinal hernias. Hernias that have relatively **narrow necks** in comparison to their fundi are more likely to be nonreducible, to become obstructed, and to strangulate. Hernia types that typically have narrow necks and are at high risk for strangulation include femoral (Video 13.23), spigelian (see Figs. 13.33 and 13.35), linea alba (see Fig. 13.45; Fig. 13.59), umbilical, and some indirect inguinal hernias.

Although **vascular compromise** is the hallmark of strangulation, Doppler ultrasound is not the most sensitive modality for

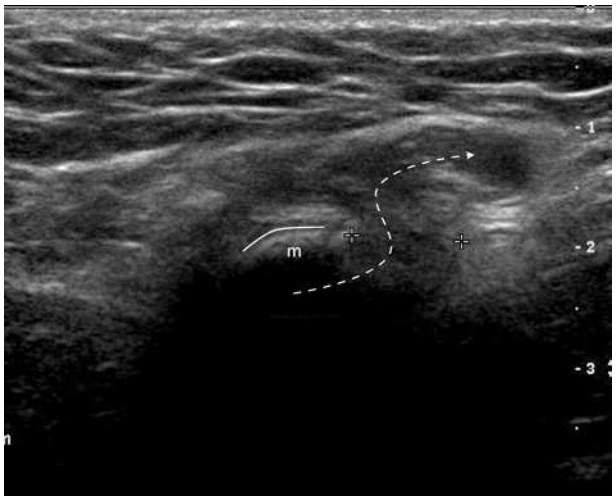

FIG. 13.56 Recurrent Inguinal Hernia. Short-axis view shows small, fat-containing, reducible *(dotted line)* hernia arising from inferomedial edge of the mesh *(m),* where recurrent inguinal hernias most often arise. See also Video 13.21.

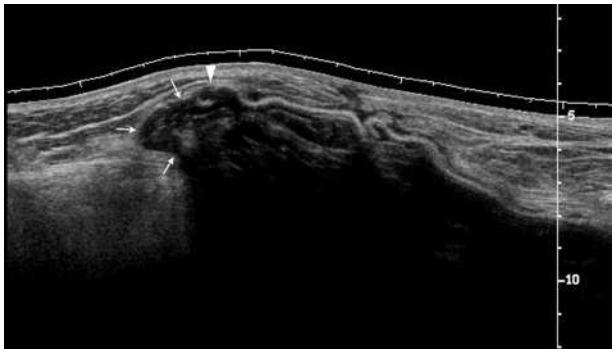

FIG. 13.57 Detached Mesh With Hernia. Transverse extended–field-of-view image shows that a large piece of mesh used to repair a large ventral hernia has become detached along its right edge *(arrowhead),* allowing a recurrent hernia to protrude from under the detached edge *(arrows).*

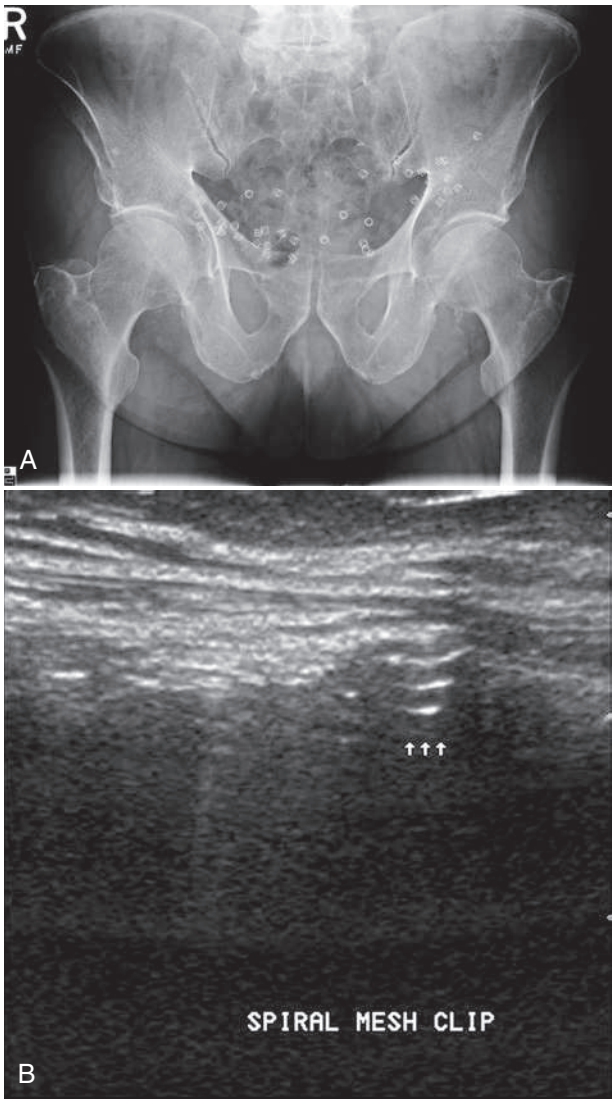

FIG. 13.58 Spiral Clips. (A) Anteroposterior radiograph of the pelvis shows spiral clips in both inguinal areas from bilateral inguinal herniorrhaphies. **(B)** Characteristic sonographic appearance of a spiral clip *(arrows).*

demonstrating signs of strangulation. Gray-scale sonography, however, is sensitive. Doppler ultrasound shows arterial flow within hernias with some success (Fig. 13.60), but often is not sensitive enough to demonstrate venous flow and cannot show lymphatic flow at all. Lymphatic and venous vessel walls are very thin and easily compressed within by the tissues surrounding the neck of the hernia. Arteries, on the other hand, are relatively thick walled and incompressible and in general are not compressed by the surrounding tissues. Thus in strangulated hernias the lymphatics and veins become obstructed long before arterial flow decreases. Blood can still supply the strangulated hernia long after venous and lymphatic outflow stops. The continued inflow in the presence of obstructed outflow (1) increases intravascular pressure, (2) causes increased transudation and exudation of fluid into the extracellular spaces, and (3) changes the gray-scale appearance of the hernia even when Doppler ultrasound can still detect arterial inflow. When both arterial and venous flow are seen in an otherwise unremarkable ventral hernia, emergency surgery may not be indicated.[54] However, in a study by Rettenbacher, the absence of blood flow in the contents of a hernia could not be taken as a sign of incarceration because most incarcerated hernias in his series (78%) had detectable blood flow on color Doppler sonography.[34]

In a retrospective study of sonographically examined hernias (predominately after indeterminate surgical physical examination) 149 abdominal wall hernias (in 131 patients) were found and underwent surgery (Table 13.2). The most sensitive findings of incarceration were free fluid in the hernia sac, bowel wall thickening in the hernia, fluid in the herniated bowel loop, and dilated bowel loops in the abdomen.[34] All 23 incarcerated abdominal wall hernias were correctly interpreted preoperatively as incarcerated by the investigating radiologists, whereas 2 of 126 nonincarcerated hernias were considered incarcerated and were therefore falsely positive for incarceration on sonography.[34]

Strangulation of the hernia, which implies compromise of blood flow, has additional findings including the following:

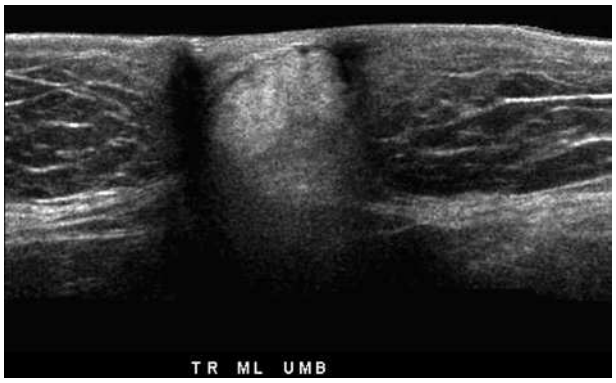

FIG. 13.59 Linea Alba Strangulated Hernia. Long-axis extended–field-of-view sonogram shows strangulated hypogastric linea alba hernia. The hallmark of strangulation is **hyperechogenicity** of the fat with the hernia.

- Hyperechoic fat (see Fig. 13.59)
- Isoechoic thickening of the normally thin and echogenic hernia sac (Fig. 13.61, see Video 13.23)
- Fluid within the sac (see Fig. 13.61, Video 13.23)
- Thickening of bowel wall in bowel-containing hernias (Fig. 13.62)

In most strangulated hernias, more than one of these gray-scale findings are present, even when Doppler ultrasound demonstrates normal flow within the hernia contents. Care should be taken in equating fluid within the hernia sac with strangulation; nonstrangulated hernias that contain intraperitoneal contents can contain peritoneal fluid, especially in female patients.

Entities That Simulate Groin Hernias

A wide spectrum of space-occupying lesions in the groin can simulate hernias of the groin (Fig. 13.63). **Cysts** or **hydroceles** of the inguinal canal can occur in both males and females. In males these localized fluid collections can occur when the segment of the processus vaginalis peritonei within the inguinal canal

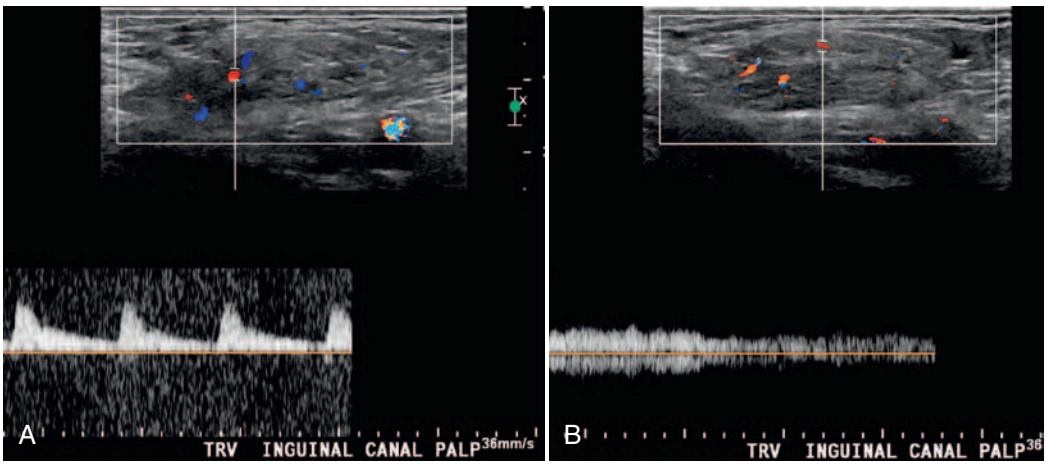

FIG. 13.60 Color and pulsed Doppler shows **(A)** arterial and **(B)** venous flow in fat-containing inguinal hernia.

TABLE 13.2 Findings of Hernia Strangulation

Sonographic Finding	Percent Incarcerated (N = 23)	Percent Not Incarcerated (N = 126)
Contents of hernia		
Fat only	n = 6	n = 54
Fat and bowel	n = 4	n = 47
Bowel only	n = 13	n = 16
Urinary bladder		n = 3
Free fluid in the hernia sac	91% (21/23)	3% (4/126)
Bowel wall thickening in the hernia (≥4 mm)	88% (15/17)	0% (0/63)
Fluid in the herniated bowel loop	82% (14/17)	3% (2/63)
Dilated loops of bowel in abdomen	65% (11/17)	0 (0/63)
Absence of blood flow in the hernia	22% (5/23)	25% (31/126)
Absence of peristalsis within hernia	76% (13/17)	38% (24/63)

Modified from Rettenbacher T, Hollerweger A, Macheiner P, et al. Abdominal wall hernias: cross-sectional imaging signs of incarceration determined with sonography. AJR Am J Roentgenol. 2001;177(5):1061-1066.[34]

FIG. 13.61 Strangulated Femoral Hernia. Short-axis view shows strangulated left femoral hernia that shows two additional gray-scale findings of strangulation: transudative or exudative fluid and isoechoic thickening of the hernia sac wall. See also Video 13.23.

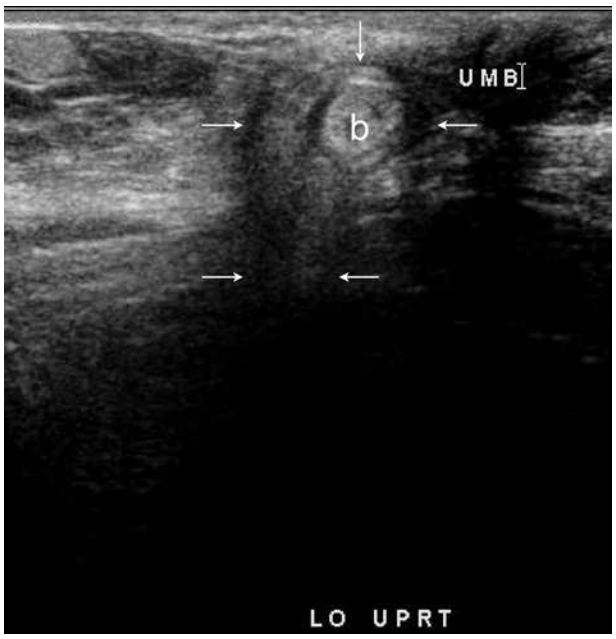

FIG. 13.62 Strangulated Periumbilical Epigastric Linea Alba Hernia. The fat is hyperechoic, the sac wall is isoechoic and thickened, and a small bowel loop *(b)* has a thickened wall and is aperistaltic. The hernia sac is outlined by *arrows*.

does not fuse while segments proximal and distal to it do fuse. This leads to accumulation of fluid within the unfused segment of processus vaginalis and forms a localized process hydrocele. In males these occur within the inguinal canal next to the spermatic cord and can compress the cord. In females the unfused processus vaginalis is called the canal of Nuck, so this localized cyst or hydrocele is termed a **cyst** or **hydrocele of the canal of Nuck** (see Fig. 13.63A; Video 13.24). Hydroceles are usually unilocular and fixed in position within the canal, but can become lobulated and septated as they enlarge.

Hematomas and inflammation may occur in the inguinal regional in proximity to the round ligament and can give rise to cysts and leiomyomas. Unlike inguinal canal hydroceles, which are fixed in position, **round ligament cysts** can be mobile and can move back and forth between the abdominal cavity and the inguinal canal. The round ligament contains smooth muscle fibers from which **leiomyomas** can arise. **Round ligament varices** develop as collateral pathways for uterine venous drainage during pregnancy. They are usually asymptomatic and incidental, but in some patients can cause a tender, palpable, inguinal or labial abnormality that can mimic a hernia[55] (see Fig. 13.63B). They usually resolve spontaneously and completely after delivery, but in a few patients can persist and cause inguinal pain and swelling months or years after the last pregnancy. They are relatively inapparent with the patient in the supine position, but become larger and have faster flow in the upright position. Occasionally, round ligament variceal **thrombosis** occurs spontaneously, most often in the postpartum period when collateral uterine flow through them regresses. **Endometriomas** can occur along the course of the round ligament within the inguinal canal (see Fig. 13.63C). They often have a history of cyclic variation in size and tenderness.

The most common benign tumor of the inguinal region is a lipoma.[6] Most so-called inguinal canal lipomas are not true lipomas, but rather **nonsliding-type indirect inguinal hernias** that contain only properitoneal fat. However, true **lipomas** can occur anywhere along the length of the inguinal canal and into the scrotum or labium majus (see Fig. 13.63D-E).

Other benign tumors of the groin include leiomyomas, dermoid cysts, epidermoid cysts, and lymphangiomas.

Other entities that can occur in the inguinal region include desmoids, sarcomas, hematomas, seromas, undescended testes, and metastatic peritoneal implants.[6]

Inguinal lymphadenopathy, common femoral or external iliac artery aneurysms and pseudoaneurysms, iliopsoas bursae, and sebaceous cysts can all occur within the groin, but *outside* the inguinal canal. In addition, pain from intraabdominal inflammatory processes can simulate groin pain; acute appendicitis and acute diverticulitis can cause pain near the groin.

Entities That Simulate Anterior Abdominal Wall Hernias

Subcutaneous or intramuscular lipomas have a sonographic appearance identical to those of the inguinal canal or labium. In patients being evaluated for incisional hernias, **exuberant scars** and **fat necrosis** resulting from previous surgeries can clinically simulate an anterior abdominal wall incisional hernia. **Hematomas** of the rectus abdominis (Fig. 13.64A) or oblique muscles can cause pain and swelling that simulate anterior abdominal wall hernia. The patient usually (but not always) has a history of significant acute trauma.

Anterior abdominal wall desmoids are usually sporadic. They arise from the fibrous elements of the anterior abdominal

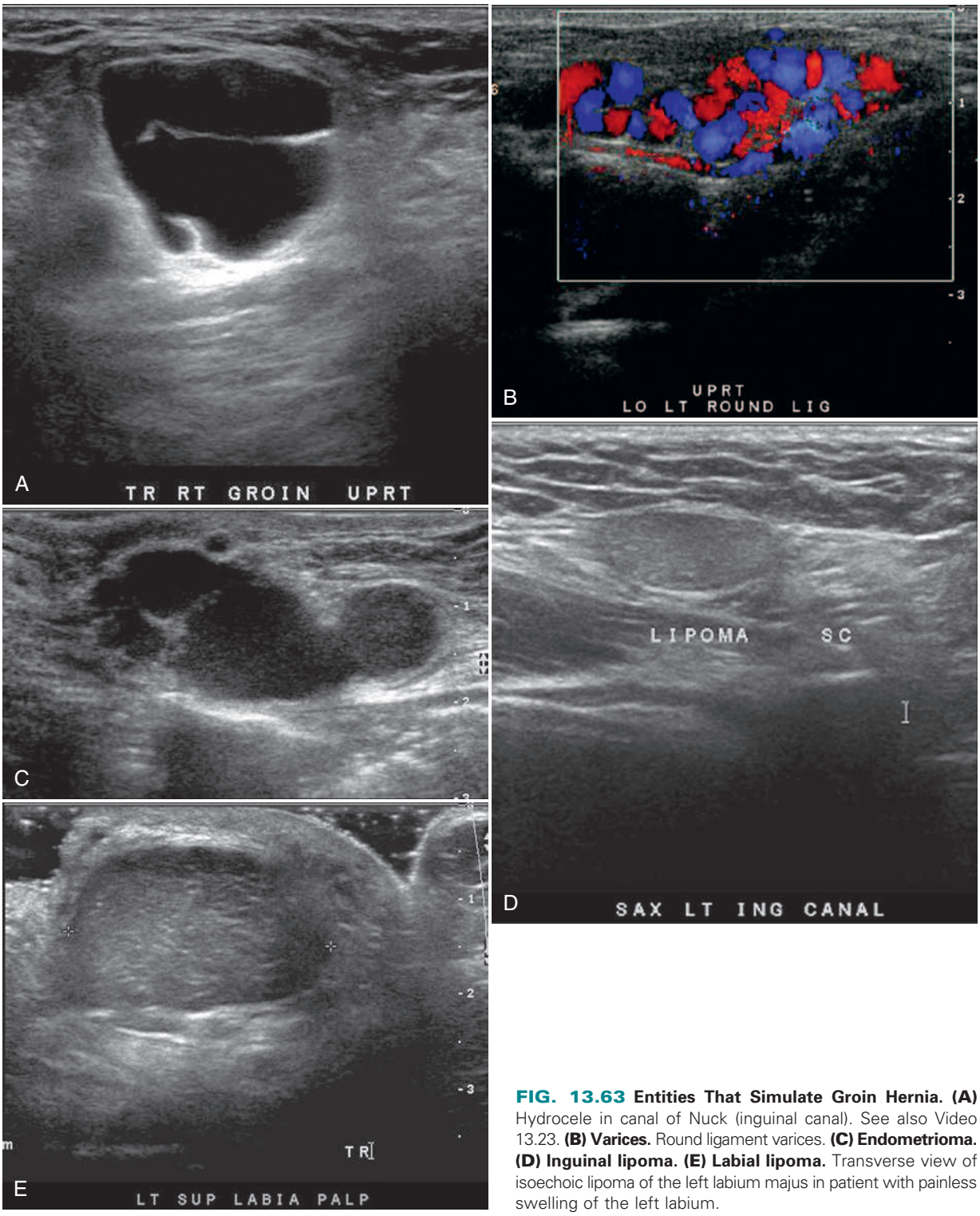

FIG. 13.63 Entities That Simulate Groin Hernia. (A) Hydrocele in canal of Nuck (inguinal canal). See also Video 13.23. **(B) Varices.** Round ligament varices. **(C) Endometrioma. (D) Inguinal lipoma. (E) Labial lipoma.** Transverse view of isoechoic lipoma of the left labium majus in patient with painless swelling of the left labium.

wall aponeuroses or muscle sheaths. Desmoids are locally invasive and tend to recur if not excised widely enough, but do not metastasize distantly. Sonographically, desmoids are solid nodules or masses that are irregular in shape and have some internal vascularity (see Figs. 13.64B). Desmoids are difficult to distinguish from sarcomas, except for slightly less blood flow on color or power Doppler ultrasound. If not excised, desmoids grow progressively. Benign and malignant connective tissue tumors of the anterior abdominal wall such as **fibromas** (see Fig. 13.64C) and **fibrosarcomas** (see Fig. 13.64D) can simulate anterior abdominal wall hernias.

SUMMARY

Dynamic ultrasound is the key examination for assessing groin or anterior abdominal wall pain. Dynamic components of the

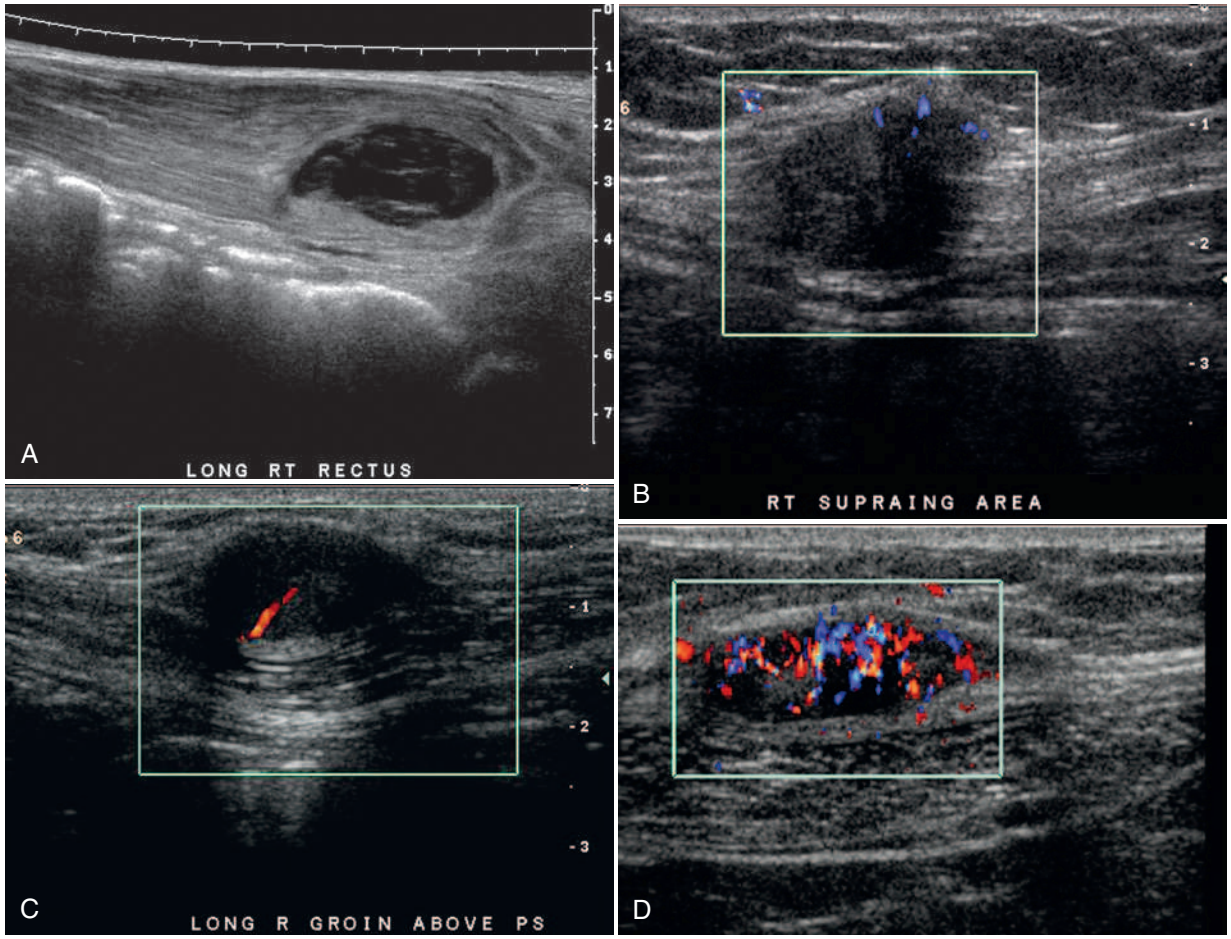

FIG. 13.64 Entities That Simulate Anterior Abdominal Wall Hernia. (A) Muscle tear with hematoma. **(B) Desmoid tumor.** Anterior abdominal wall desmoid tumor has a small amount of peripheral blood flow. **(C) Fibroma.** Long-axis view of a benign fibroma of the anterior rectus sheath of the inferior right rectus abdominis muscle that caused a nontender swelling near the right groin. Note that there is minimal internal vascularity. **(D) Fibrosarcoma.** Transverse view of a fibrosarcoma of the anterior sheath of the left rectus abdominis muscle that manifested as a painless lump. It is similar in appearance to the fibroma shown in **(C)** but is much more vascular.

examination include Valsalva and compression maneuvers and scanning in both supine and upright positions. Dynamic sonography enables clinicians to determine hernia type, size, contents, reducibility, and tenderness.

Evaluation of groin pain in athletes is frequently more complex than in nonathletes because of associated tendinosis and osteitis pubis. Adding MRI to dynamic ultrasound is usually necessary to identify underlying pathologic processes and decide the best combination of surgical and nonsurgical treatments.

Patients with one hernia frequently have multiple hernias, so in any patient in whom a hernia is sonographically demonstrable, the examination should be continued, looking for other types of ipsilateral and contralateral groin or anterior abdominal hernias. Even when no additional hernias are found, it is important to the surgeon to specifically mention in the report that a complete search of both groin areas was made and no additional hernias were found.

Strangulation is the most dreaded complication of groin hernias. Gray-scale findings of strangulation—hyperechoic fat, isoechoic thickening of the hernia sac, fluid within the sac, and thickening of the walls of bowel loops—are all more sensitive for strangulation than is Doppler ultrasound.

Recurrent pain after herniorrhaphy is a relatively common problem. Dynamic sonography can be helpful in assessing both acute and chronic recurrences of groin pain. Most hernia repairs now use mesh. The key to sonographic identification of recurrent hernias is to assess the edges of the mesh with dynamic maneuvers, because recurrent hernias arise from the edges of the mesh.

Many pathologic processes can simulate hernia, both rare and nonspecific, but cysts or hydroceles of the processus vaginalis (or canal of Nuck) and round ligament varices are relatively common and have virtually pathognomonic sonographic appearances.

REFERENCES

1. Jacobson JA, Khoury V, Brandon CJ. Ultrasound of the groin: techniques, pathology, and pitfalls. AJR Am J Roentgenol. 2015;205(3):513-523.
2. Rutkow IM. Demographic and socioeconomic aspects of hernia repair in the United States in 2003. Surg Clin North Am. 2003;83(5):1045-1051, v-vi.

3. Beadles CA, Meagher AD, Charles AG. Trends in emergent hernia repair in the United States. JAMA Surg. 2015;150(3):194-200.
4. Primatesta P, Goldacre MJ. Inguinal hernia repair: incidence of elective and emergency surgery, readmission and mortality. Int J Epidemiol. 1996; 25(4):835-839.
5. Robinson P, Hensor E, Lansdown MJ, et al. Inguinofemoral hernia: accuracy of sonography in patients with indeterminate clinical features. AJR Am J Roentgenol. 2006;187(5):1168-1178.
6. Yang DM, Kim HC, Lim JW, et al. Sonographic findings of groin masses. J Ultrasound Med. 2007;26(5):605-614.
7. Oh SN, Jung SE, Rha SE, et al. Sonography of various cystic masses of the female groin. J Ultrasound Med. 2007;26(12):1735-1742.
8. Jamadar DA, Jacobson JA, Morag Y, et al. Sonography of inguinal region hernias. AJR Am J Roentgenol. 2006;187(1):185-190.
9. Kervancioglu R, Bayram MM, Ertaskin I, Ozkur A. Ultrasonographic evaluation of bilateral groins in children with unilateral inguinal hernia. Acta Radiol. 2000;41(6):653-657.
10. Vermillion JM, Abernathy SW, Snyder SK. Laparoscopic reduction of Amyand's hernia. Hernia. 1999;3:159-160.
11. Cigsar EB, Karadag CA, Dokucu AI. Amyand's hernia: 11 years of experience. J Pediatr Surg. 2016;51(8):1327-1329.
12. Lee RK, Griffith JF, Ng WH. High accuracy of ultrasound in diagnosing the presence and type of groin hernia. J Clin Ultrasound. 2015;43(9): 538-547.
13. Bradley M, Morgan D, Pentlow B, Roe A. The groin hernia—an ultrasound diagnosis? Ann R Coll Surg Engl. 2003;85(3):178-180.
14. Matthews RD, Neumayer L. Inguinal hernia in the 21st century: an evidence-based review. Curr Probl Surg. 2008;45(4):261-312.
15. Friedman DW, Boyd CD, Norton P, et al. Increases in type III collagen gene expression and protein synthesis in patients with inguinal hernias. Ann Surg. 1993;218(6):754-760.
16. Klinge U, Binnebosel M, Mertens PR. Are collagens the culprits in the development of incisional and inguinal hernia disease? Hernia. 2006;10(6):472-477.
17. Oguzkurt P, Kayaselcuk F, Tuncer I, et al. Evaluation of extracellular matrix protein composition in sacs associated with undescended testis, hydrocele, inguinal hernia, and peritoneum. Urology. 2007;70(2):346-350.
18. Szczesny W, Cerkaska K, Tretyn A. Dabrowiecki S. Etiology of inguinal hernia: ultrastructure of rectus sheath revisited. Hernia. 2006;10(3): 266-271.
19. Bendavid R. The unified theory of hernia formation. Hernia. 2004;8(3): 171-176.
20. Abrahamson J. Etiology and pathophysiology of primary and recurrent groin hernia formation. Surg Clin North Am. 1998;78(6):953-972, vi.
21. Liem MS, van der Graaf Y, Beemer FA. van Vroonhoven TJ. Increased risk for inguinal hernia in patients with Ehlers-Danlos syndrome. Surgery. 1997;122(1):114-115.
22. Brandon CJ, Jacobson JA, Fessell D, et al. Groin pain beyond the hip: how anatomy predisposes to injury as visualized by musculoskeletal ultrasound and MRI. AJR Am J Roentgenol. 2011;197(5):1190-1197.
23. Stavros AT, Rapp C. Dynamic ultrasound of hernias of the groin and anterior abdominal wall. Ultrasound Q. 2010;26(3):135-169.
24. Burkhardt JH, Arshanskiy Y, Munson JL, Scholz FJ. Diagnosis of inguinal region hernias with axial CT: the lateral crescent sign and other key findings. Radiographics. 2011;31(2):E1-E12.
25. Bhosale PR, Patnana M, Viswanathan C, Szklaruk J. The inguinal canal: anatomy and imaging features of common and uncommon masses. Radiographics. 2008;28(3):819-835.
26. Lee GH, Cohen AJ. CT imaging of abdominal hernias. AJR Am J Roentgenol. 1993;161(6):1209-1213.
27. Park HR, Park SB, Lee ES, Park HJ. Sonographic evaluation of inguinal lesions. Clin Imaging. 2016;40(5):949-955.
28. Brandel DW, Girish G, Brandon CJ, et al. Role of sonography in clinically occult femoral hernias. J Ultrasound Med. 2016;35(1):121-128.
29. Gupta H, Subedi N, Robinson P. Effectiveness of sonography in detecting clinically occult femoral hernias. J Ultrasound Med. 2016;35(8): 1675-1679.
30. Zarvan NP, Lee Jr FT, Yandow DR, Unger JS. Abdominal hernias: CT findings. AJR Am J Roentgenol. 1995;164(6):1391-1395.
31. Shadbolt CL, Heinze SB, Dietrich RB. Imaging of groin masses: inguinal anatomy and pathologic conditions revisited. Radiographics. 2001;21 Spec No:S261-S271.
32. Mufid MM, Abu-Yousef MM, Kakish ME, et al. Spigelian hernia: diagnosis by high-resolution real-time sonography. J Ultrasound Med. 1997;16(3): 183-187.
33. Ganz E, Tazzioli G, Mosca D, et al. Ventrolateral hernias of the abdominal wall. The anatomicopathologic, clinical and therapeutic considerations]. Minerva Chir. 1997;52(12):1441-1445.
34. Rettenbacher T, Hollerweger A, Macheiner P, et al. Abdominal wall hernias: cross-sectional imaging signs of incarceration determined with sonography. AJR Am J Roentgenol. 2001;177(5):1061-1066.
35. Wechsler RJ, Kurtz AB, Needleman L, et al. Cross-sectional imaging of abdominal wall hernias. AJR Am J Roentgenol. 1989;153(3):517-521.
36. Lovell G. The diagnosis of chronic groin pain in athletes: a review of 189 cases. Aust J Sci Med Sport. 1995;27(3):76-79.
37. Caudill P, Nyland J, Smith C, et al. Sports hernias: a systematic literature review. Br J Sports Med. 2008;42(12):954-964.
38. Santilli OL, Nardelli N, Santilli HA, Tripoloni DE. Sports hernias: experience in a sports medicine center. Hernia. 2016;20(1):77-84.
39. Brittenden J, Robinson P. Imaging of pelvic injuries in athletes. Br J Radiol. 2005;78(929):457-468.
40. Munegato D, Bigoni M, Gridavilla G, et al. Sports hernia and femoroacetabular impingement in athletes: a systematic review. World J Clin Cases. 2015;3(9): 823-830.
41. Paajanen H, Montgomery A, Simon T, Sheen AJ. Systematic review: laparoscopic treatment of long-standing groin pain in athletes. Br J Sports Med. 2015;49(12):814-818.
42. Susmallian S, Ezri T, Elis M, et al. Laparoscopic repair of "sportsman's hernia" in soccer players as treatment of chronic inguinal pain. Med Sci Monit. 2004;10(2):CR52-CR54.
43. Granja M, Rivero O, Aguirre D. Abdominal wall hernias. In: Sahani DV, Samir AE, editors. Abdominal imaging. 2nd ed. Philadelphia: Elsevier; 2017. p. 1014-1025.
44. Macari M, Megibow A. Imaging of suspected acute small bowel obstruction. Semin Roentgenol. 2001;36(2):108-117.
45. Dabbas N, Adams K, Pearson K, Royle G. Frequency of abdominal wall hernias: is classical teaching out of date? JRSM Short Rep. 2011;2(1):5.
46. Pans A, Elen P, Dewe W, Desaive C. Long-term results of polyglactin mesh for the prevention of incisional hernias in obese patients. World J Surg. 1998;22(5):479-482.
47. Trimbos JB, Smit IB, Holm JP, Hermans J. A randomized clinical trial comparing two methods of fascia closure following midline laparotomy. Arch Surg. 1992;127(10):1232-1234.
48. Matory Jr WE, O'Sullivan J, Fudem G, Dunn R. Abdominal surgery in patients with severe morbid obesity. Plast Reconstr Surg. 1994;94(7):976-987.
49. Mudge M, Hughes LE. Incisional hernia: a 10 year prospective study of incidence and attitudes. Br J Surg. 1985;72(1):70-71.
50. Baucom RB, Beck WC, Phillips SE, et al. Comparative evaluation of dynamic abdominal sonography for hernia and computed tomography for characterization of incisional hernia. JAMA Surg. 2014;149(6):591-596.
51. Awaiz A, Rahman F, Hossain MB, et al. Meta-analysis and systematic review of laparoscopic versus open mesh repair for elective incisional hernia. Hernia. 2015;19(3):449-463.
52. Courtney CA, Lee AC, Wilson C, O'Dwyer PJ. Ventral hernia repair: a study of current practice. Hernia. 2003;7(1):44-46.
53. Mathes T, Walgenbach M, Siegel R. Suture versus mesh repair in primary and incisional ventral hernias: a systematic review and meta-analysis. World J Surg. 2016;40(4):826-835.
54. Liang RJ, Wang HP, Huang SP, et al. Color Doppler sonography for ventral hernias in patients with acute abdomen: preliminary findings. J Clin Ultrasound. 2001;29(8):435-440.
55. Ryu KH, Yoon JH. Ultrasonographic diagnosis of round ligament varicosities mimicking inguinal hernia: report of two cases with literature review. Ultrasonography. 2014;33(3):216-221.

CHAPTER 14

The Peritoneum

Anthony E. Hanbidge, Korosh Khalili, and Stephanie R. Wilson

SUMMARY OF KEY POINTS

- Ultrasound has a role in peritoneal imaging.
- Success is dependent on operator awareness and thorough technique.
- Inclusion of transvaginal scan in women will greatly improve accuracy.
- Ultrasound is excellent for detecting and characterizing peritoneal fluid.
- Ultrasound is very useful for detecting and characterizing neoplastic and inflammatory peritoneal disease.
- Ultrasound is often the modality of choice to guide paracentesis and biopsy of peritoneal masses.

CHAPTER OUTLINE

PERITONEUM, OMENTUM, AND MESENTERY
SONOGRAPHIC TECHNIQUE
ASCITES
PERITONEAL INCLUSION CYSTS (BENIGN ENCYSTED FLUID)
MESENTERIC CYSTS
PERITONEAL TUMORS
Peritoneal Carcinomatosis
Primary Tumors of Peritoneum
Pseudomyxoma Peritonei
INFLAMMATORY DISEASE OF PERITONEUM
Abscess
Tuberculous Peritonitis
Sclerosing Peritonitis
LOCALIZED INFLAMMATORY PROCESS OF PERITONEAL CAVITY
RIGHT-SIDED SEGMENTAL OMENTAL INFARCTION
ENDOMETRIOSIS
LEIOMYOMATOSIS PERITONEALIS DISSEMINATA
PNEUMOPERITONEUM
CONCLUSION

Ultrasound of the abdomen and pelvis has become an extension of the physical examination when evaluating patients with abdominal symptoms and signs. It is accurate, safe, readily available, portable, and relatively inexpensive. Evaluations have traditionally focused on assessing the solid viscera, the gallbladder, and bile ducts. Frequently, images of only these organs are recorded, and the peritoneal cavity is often neglected or subjected to cursory evaluation. The general belief is that ultrasound is not particularly helpful at imaging the peritoneum because of technical limitations, such as poor visibility and interference from bowel gas. There is also unfamiliarity with the common sonographic features encountered with peritoneal disease, as reflected by extensive literature on ultrasound of the liver, gallbladder, bile ducts, pancreas, spleen, kidneys, bladder, and reproductive organs but little on sonographic evaluation of the peritoneum and peritoneal cavity. As a result, teaching of optimal sonographic technique to evaluate these areas is minimal.

If peritoneal disease is a clinical concern, computed tomography (CT)[1,2] or magnetic resonance imaging (MRI)[3-5] is generally used to investigate. We believe that ultrasound can also be sensitive and specific in this regard.[6] To be successful, however, two criteria must be met: (1) the operator must be aware of the potential involvement of the peritoneum and peritoneal cavity with a disease process, and (2) these areas must receive a thorough sonographic assessment.

PERITONEUM, OMENTUM, AND MESENTERY

The **peritoneum** is a serous membrane lined with epithelial cells. It is divided into the parietal and visceral peritoneum. The **parietal peritoneum** lines the anterior and posterior walls of the abdominal cavity and is visible with ultrasound as a thin, smooth, echogenic line in the deepest layer of the anterior abdominal wall. Bowel loops can usually be seen deep to the parietal peritoneum, moving independent of it with respiration. The **visceral peritoneum,** on the other hand, covers the intraabdominal organs and is not visible with ultrasound in its normal state. The potential space between these two layers is known as the **peritoneal cavity,** which usually contains a small volume of fluid that acts as a lubricant.[7,8]

The **small bowel mesentery** is a specialized, fan-shaped, peritoneal fold extending from the second lumbar vertebra to the right iliac fossa. It connects the jejunum and ileum to the posterior abdominal wall. It is composed of a double layer of peritoneum, blood vessels, nerves, lacteals (lymphatic capillaries in villi), lymph nodes, and a variable amount of fat. Normal bowel mesentery is best assessed with ultrasound in the presence of **ascites;** it appears as freely floating, smooth leaves separated by fluid, directed toward the center of the abdomen, away from small bowel loops (Fig. 14.1). In the absence of ascites, the mesentery is more difficult to appreciate but has been described as a series of elongated, aperistaltic structures separated from each other by specular echoes, best appreciated in the left lower quadrant.[9] It is frequently difficult to localize a disease process to the mesentery, and the relationship to other anatomic landmarks may be helpful. For example, lymphoma may be correctly localized to the mesentery if a mass is seen that encases the mesenteric vessels.

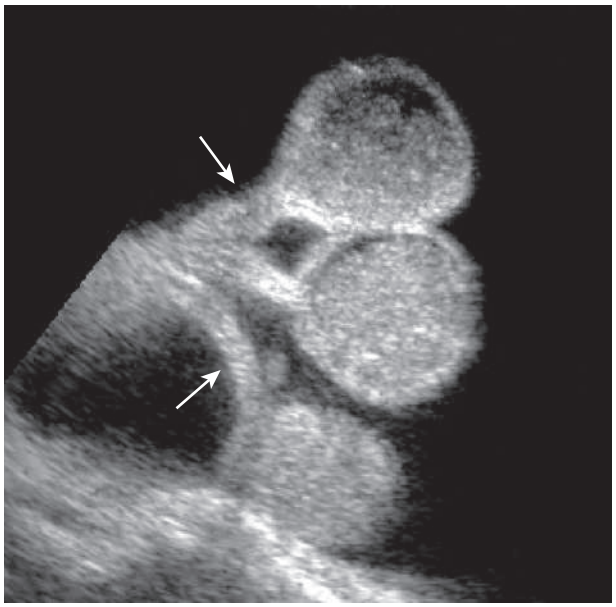

FIG. 14.1 Normal Mesentery With Gross Ascites. Oblique sagittal ultrasound image of the midabdomen shows the normal small bowel mesenteric leaves *(arrows)* outlined by fluid.

The **omenta** are also specialized peritoneal folds. They are composed of a double layer of peritoneum, blood vessels, lymphatics, and a variable amount of fat. The **lesser omentum** connects the lesser curvature of the stomach and proximal duodenum with the liver. The **greater omentum** descends from the greater curvature of the stomach, anterior to the abdominal contents, often as low as the pelvis, then reflects back on itself to form a four-layered structure that ascends and separates to enclose the transverse colon. A potential space exists between the two layers of the greater omentum, which is continuous with the lesser sac.

In the normal state, the omenta may be extremely difficult or impossible to distinguish with ultrasound. In the presence of ascites, the free inferior edge of the normal **greater omentum** may be visible floating in the fluid with variable thickness, depending on the fat content. In patients with disease the greater omentum may become infiltrated, thickened, and nodular (Fig. 14.2, Video 14.1). Its superficial location allows for careful sonographic evaluation with high-frequency transducers, and disease processes may often be correctly identified and localized to the greater omentum even in the absence of ascites.

SONOGRAPHIC TECHNIQUE

Sonographic assessment of the peritoneum requires the motivation to evaluate, as far as possible, the parietal and visceral peritoneum, mesentery, omentum, and peritoneal cavity. The initial survey of the peritoneum and peritoneal cavity is performed with a standard-frequency, 3.5-MHz or 5-MHz transducer (Fig. 14.3A).

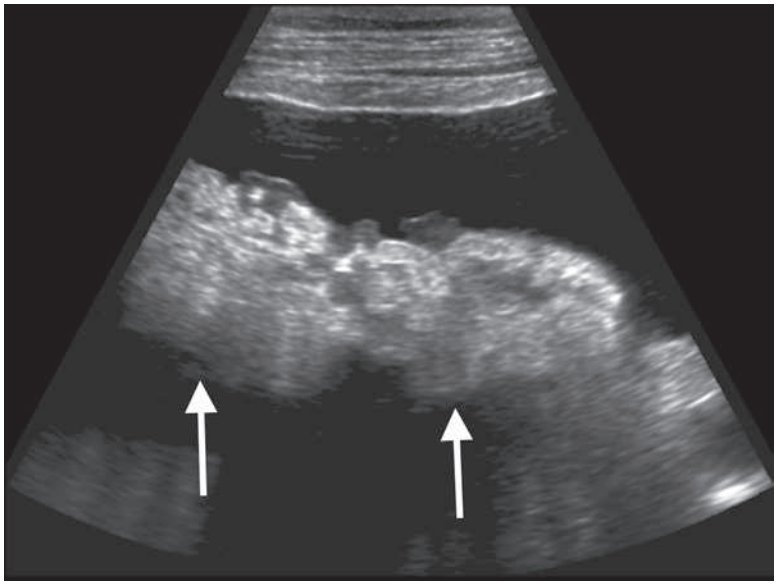

FIG. 14.2 Tumor Infiltration of the Omentum. Sagittal ultrasound image of the midabdomen shows thickening and hypoechoic nodularity of the omentum *(arrows)* immediately posterior to free fluid deep to the anterior abdominal wall. See also Video 14.1.

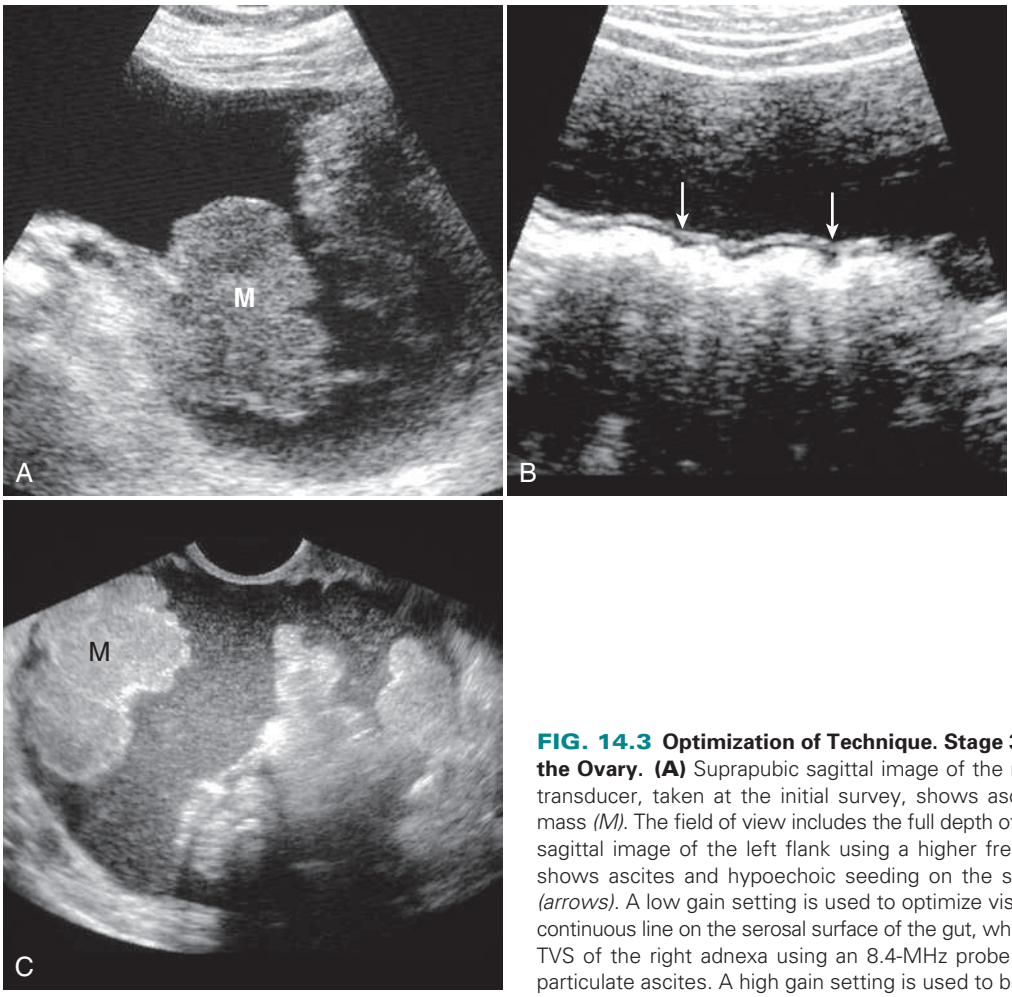

FIG. 14.3 Optimization of Technique. Stage 3 Papillary Serous Adenocarcinoma of the Ovary. (A) Suprapubic sagittal image of the right adnexa using a 5.2-MHz curvilinear transducer, taken at the initial survey, shows ascites and a solid, lobulated, hypoechoic mass *(M)*. The field of view includes the full depth of the peritoneal cavity. **(B)** Transabdominal sagittal image of the left flank using a higher frequency, 7.4-MHz, curvilinear transducer shows ascites and hypoechoic seeding on the serosal surface of the descending colon *(arrows)*. A low gain setting is used to optimize visualization of the seeding, seen as a thin, continuous line on the serosal surface of the gut, which contains shadowing air. **(C)** Transverse TVS of the right adnexa using an 8.4-MHz probe shows the right adnexal mass *(M)* and particulate ascites. A high gain setting is used to better characterize the particulate ascites.

The **field of view** (FOV) is set to include the full depth of the peritoneal cavity, but no more; this adds perspective to the image. The **focal zone** is continually adjusted to evaluate in detail different depths within the FOV. The **power** and **gain** settings are also adjusted using a high gain setting to characterize free fluid as anechoic or particulate and a low gain setting to visualize hypoechoic nodules or masses optimally. Once the initial survey is complete, higher-frequency transducers are used to more carefully evaluate and characterize abnormalities in the near field (Fig. 14.3B).

When scanning transabdominally, graded compression is used to displace bowel gas. Determination of the site of origin of a peritoneal process may be aided by several techniques. Palpation of an abnormal mass, either with the transducer or with the free hand, will determine both the compliance and the mobility of a mass. Masses arising from the parietal peritoneum are often fixed, whereas masses arising from the visceral peritoneum may be mobile. This distinction may also be demonstrated by changing the patient's position or with changes in respiration. For example, in the right upper quadrant, a lesion in the near field is likely to be located on the parietal peritoneum if the liver moves independent of it with respiration.

A **transvaginal sonography (TVS)** examination is critical for all female patients at risk for or with suspected peritoneal disease (Fig. 14.3C). The pelvic pouch of Douglas is a common site of involvement, particularly in carcinomatosis and acute conditions. This technique allows exquisite assessment of both the parietal and the visceral pelvic peritoneum.[10,11] In addition to assessing the uterus and ovaries, the probe should be directed to the pouch of Douglas, by elevating the examining hand (Fig. 14.4), and to both pelvic side-walls. A dynamic assessment is often helpful to help establish the origin of a nodule or mass (Videos 14.2 and 14.3). The TVS may also facilitate improved visualization of pelvic bowel loops and the urinary bladder.

Ultrasound is an accurate, fast, and efficient means of guiding interventions involving the peritoneum and peritoneal cavity and is frequently the modality of choice to guide diagnostic and therapeutic paracentesis and biopsy of peritoneal masses.[12]

ASCITES

One of the earliest uses of sonography in the abdomen and pelvis involved the detection of ascites.[13] Normally, 50 to 75 mL of free fluid is present in the peritoneal cavity, acting as a lubricant. Ascites occurs with excess accumulation of peritoneal fluid. Ascites can be classified as **transudate** or **exudate** depending on the protein content. In North America, cirrhosis, peritoneal carcinomatosis, congestive heart failure, and tuberculosis account

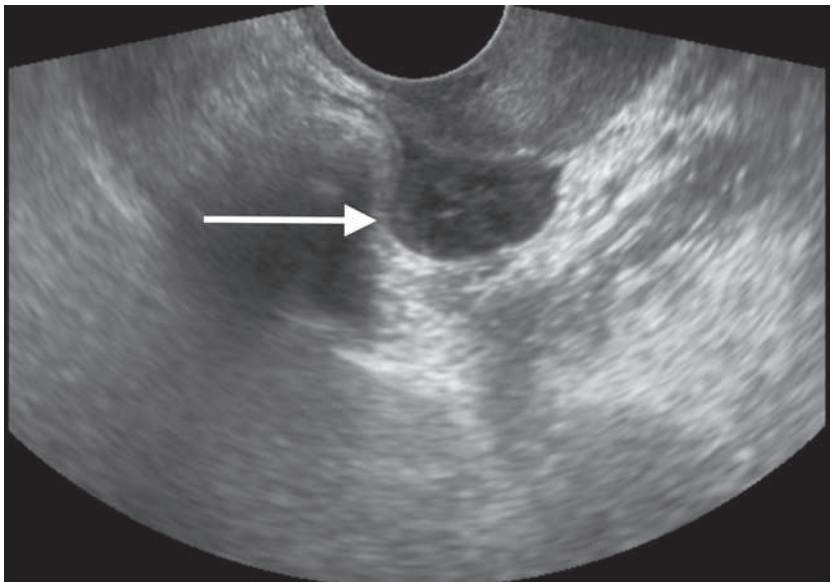

FIG. 14.4 Tumor Implant in the Pouch of Douglas. Oblique transverse TVS shows a small solid hypoechoic nodule *(arrow)* in the pouch of Douglas. See also Videos 14.2 and 14.3.

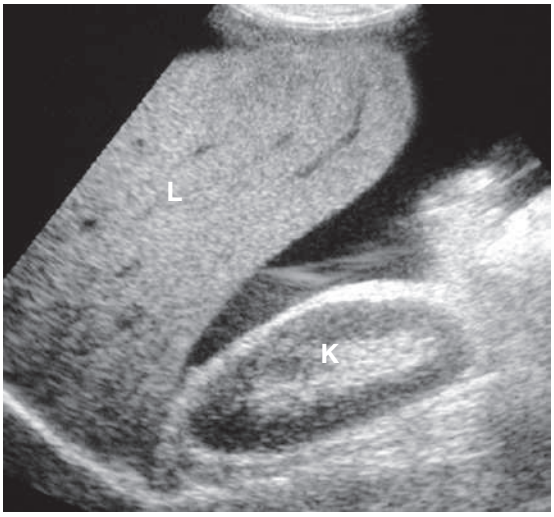

FIG. 14.5 Cirrhosis of the Liver With Portal Hypertension. Sagittal ultrasound image of the right upper quadrant readily demonstrates a large amount of ascites surrounding an enlarged, bulbous, fatty liver *(L)*. *K,* Right kidney.

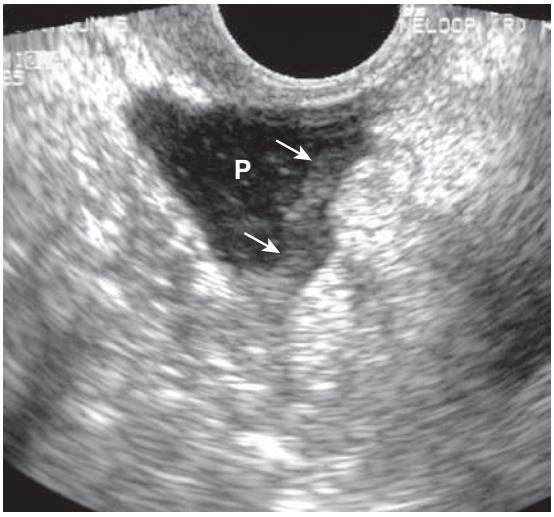

FIG. 14.6 Grade 2/3 Ovarian Mucinous Cystadenocarcinoma. Transverse TVS of the right adnexa shows a small amount of particulate free fluid *(P)* and serosal seeding *(arrows)* on loops of bowel in the pelvis. This was visible only on the TVS.

for 90% of all cases of ascites. Accumulations of blood, urine, chyle, bile, or pancreatic juice are more unusual causes.

Ascites can be detected with physical examination when the volume reaches 500 mL. Transabdominal ultrasound can readily detect large volumes of ascites (Fig. 14.5). TVS is more sensitive in this regard, and volumes of free fluid as small as 0.8 mL can be demonstrated with the transvaginal probe[14] (Fig. 14.6). With the patient lying supine, free fluid tends to accumulate in the paracolic gutters and pelvis,[15] particularly the superior end of the right paracolic gutter and Morison pouch. These areas should therefore be carefully assessed when ascites is suspected. Ultrasound is also accurate at quantifying[16] and localizing ascites and may be used to guide both diagnostic and therapeutic paracentesis.

In addition to its excellent capability to quantify ascites, ultrasound can also characterize ascites as anechoic or particulate. This may be helpful in determining the source because **particulate ascites** suggests the presence of blood, pus, or neoplastic cells in the fluid. The observation of particulate ascites should prompt a more detailed assessment of the peritoneum with ultrasound,[17,18] further imaging with CT/MRI, and diagnostic paracentesis.

Hemoperitoneum has many causes, including trauma, ruptured aneurysm, ruptured ectopic pregnancy, ruptured liver mass (e.g., adenoma, hepatoma), and postsurgical bleeding. Spontaneous hemorrhage may occur in patients receiving anticoagulants. The appearance of acute blood is varied, including anechoic or particulate free fluid (Fig. 14.7). A fluid-debris level may develop if the patient has maintained a stable position for

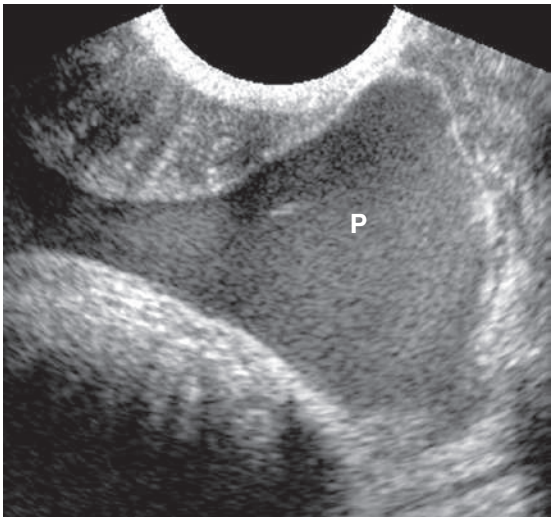

FIG. 14.7 Hemoperitoneum in Ruptured Ectopic Pregnancy. Oblique transverse TVS of the left adnexa shows particulate free fluid *(P)*.

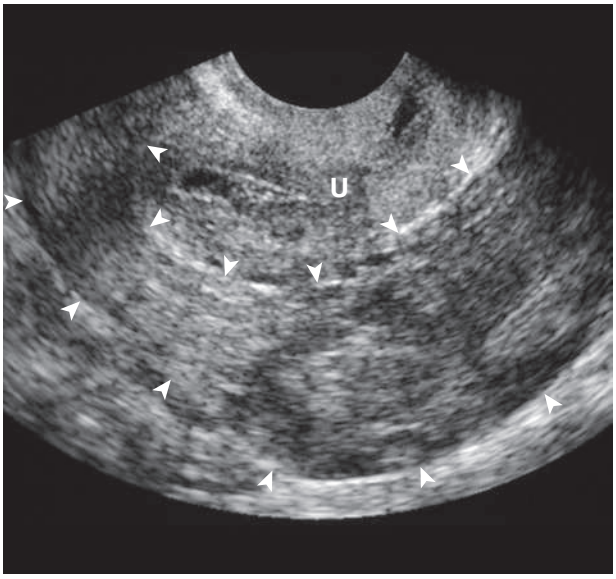

FIG. 14.9 Pelvic Hematoma 2 Days After Surgery in Female Patient Taking Anticoagulants. Sagittal TVS image shows the uterus *(U)*, with fluid in the endometrial canal, surrounded by a large, hypoechoic heterogeneous hematoma *(arrowheads)*.

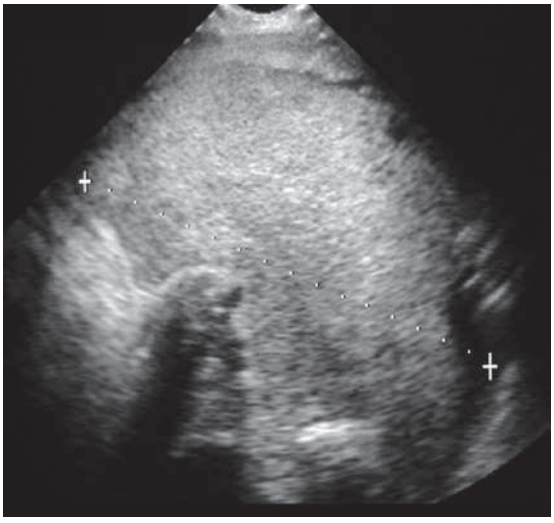

FIG. 14.8 Blood Clot. Acute blood clot secondary to rupture of a pseudoaneurysm at the hepatic artery anastomosis after liver transplantation. Sagittal ultrasound image of the left lower quadrant shows a solid, heterogeneous mass *(calipers)*.

a time. Massive hemorrhage often results in a large, echogenic mass that may become more heterogeneous as lysis occurs over time (Figs. 14.8 and 14.9).

Focused abdominal sonography for trauma (FAST) has become an accepted screening modality for intraabdominal injuries in the traumatized patient.[19-23] The primary focus of this limited study is to detect free intraperitoneal fluid with ultrasound in the trauma center. Fluid detected in this setting strongly suggests significant intraabdominal injury requiring urgent laparotomy. FAST has replaced peritoneal lavage in many centers.

Chylous ascites is an unusual condition in which lymph accumulates within the peritoneal cavity. The causes are varied, including **trauma, surgery, lymphangioma, lymphoma, intestinal lymphangiectasia,** and **cystic hygroma.** Sonography may show particulate ascites or a fluid-fluid level because of layering of the lymphatic fluid.[24,25]

It is sometimes difficult to decide if fluid visualized in the peritoneal cavity is free or loculated. Altering the patient's position may be helpful to establish if the fluid moves under the force of gravity. For example, free fluid in the right paracolic gutter with the patient lying supine may move from this location if the patient lies in a left lateral decubitus position. The morphology of the fluid collection may also be helpful. **Free fluid** tends to conform to the surrounding organs and will frequently exhibit acute angles when in contact with surrounding structures such as bowel loops. **Loculated fluid,** on the other hand, tends to have rounded margins and show mass effect, frequently displacing surrounding structures from their usual location. Loculated fluid collections can occur anywhere in the abdomen and pelvis. Characterization of fluid and the demonstration of complexity of localized or generalized peritoneal fluid collections are strengths of ultrasound, and ultrasound is superior to CT scan in this regard (Fig. 14.10).

PERITONEAL INCLUSION CYSTS (BENIGN ENCYSTED FLUID)

The fluid produced by active ovaries in premenopausal patients is usually absorbed by the peritoneum. This balance can be upset by disease processes involving the pelvis, such as previous surgery, trauma, **pelvic inflammatory disease, inflammatory bowel disease,** or **endometriosis.** In these patients the fluid produced by the ovaries may not be absorbed but may become trapped by adhesions. Over time, an inclusion cyst forms that frequently encases the ovary and may cause pelvic pain and pressure. Inclusion cysts vary in size and complexity and may be relatively simple or may contain internal echoes and septations.[26-28] They often cause confusion when imaging is performed and may be

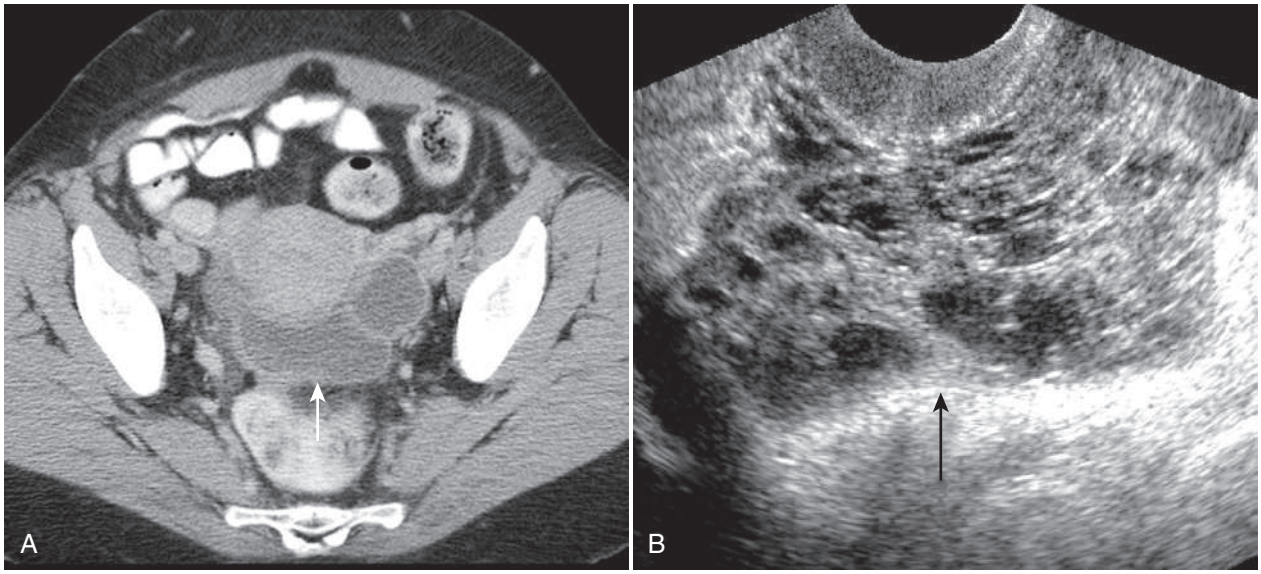

FIG. 14.10 Fibrinous Peritonitis. (A) Axial, contrast-enhanced pelvic CT scan shows loculated fluid in the pouch of Douglas and left adnexa with an enhancing rim *(arrow)*. **(B)** Transverse TVS shows the high degree of complexity of this fluid *(arrow)* to much better advantage.

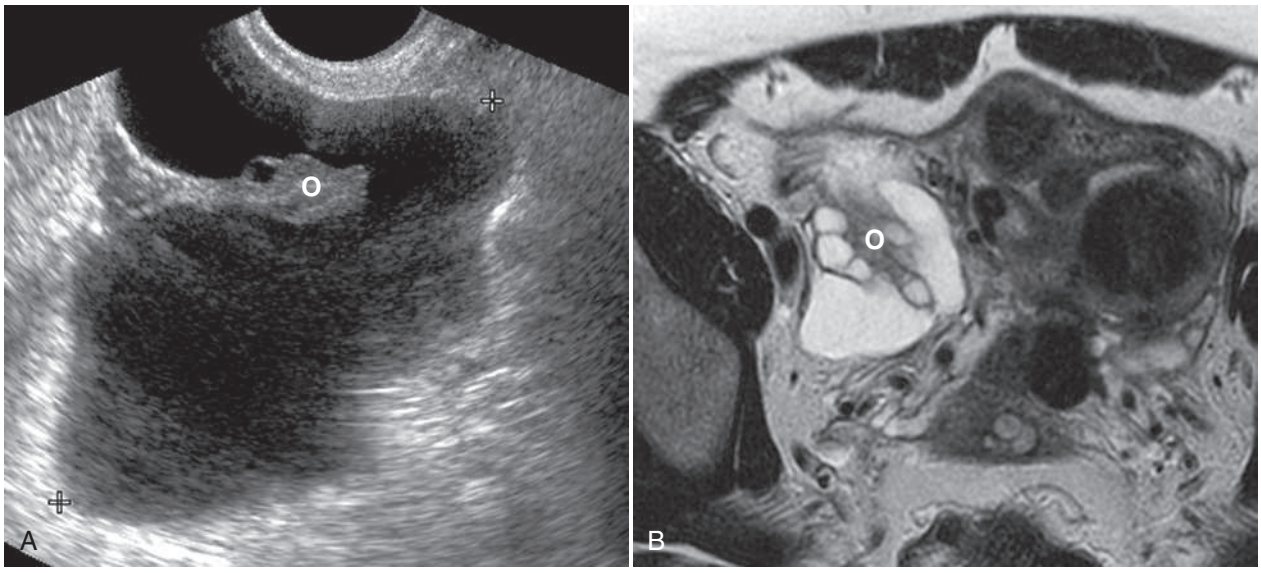

FIG. 14.11 Peritoneal Inclusion Cyst. (A) Transverse TVS of the right adnexa. **(B)** Axial T2-weighted MRI through the midpelvis. Both images show the normal right ovary *(O)* surrounded by encysted fluid, conforming to the contours of the peritoneal cavity. (Reproduced from Wilson SR. Pseudomyxoma peritonei. In: Cohen HL, editor. Gastrointestinal disease, test and syllabus. Reston, VA: American College of Radiology; 2004. pp. 73-84.[28])

misinterpreted as representing ovarian cysts, parovarian cysts, hydrosalpinges, or even ovarian cancer. The key to the correct diagnosis is to suspect this condition based on the patient's profile, then demonstrate a normal ovary, either within or on the margin of the inclusion cyst, most often with TVS (Fig. 14.11). Complex peritoneal inclusion cysts are also known as multicystic **mesotheliomas.**[29]

MESENTERIC CYSTS

Mesenteric cysts are rare intraabdominal masses often discovered incidentally at imaging. However, they may present clinically with abdominal distention because of their size, or acutely with pain because of a complication such as hemorrhage, rupture, or torsion. Mesenteric cysts are most often of lymphatic **(lymphangioma)** or mesothelial origin but may also be of enteric **(enteric duplication cyst)** or urogenital origin. **Dermoid cysts** and **pseudocysts** (infectious, inflammatory, or traumatic) are seen as well.[30,31] Mesenteric cysts vary in size from less than 1 cm to greater than 25 cm, filling the entire peritoneal cavity. They may be entirely simple to highly complex with extensive internal septations, as sometimes seen with lymphangiomas[32,33] (Fig. 14.12). Smaller mesenteric cysts are frequently mobile, changing location with palpation or with changes in the patient's position.

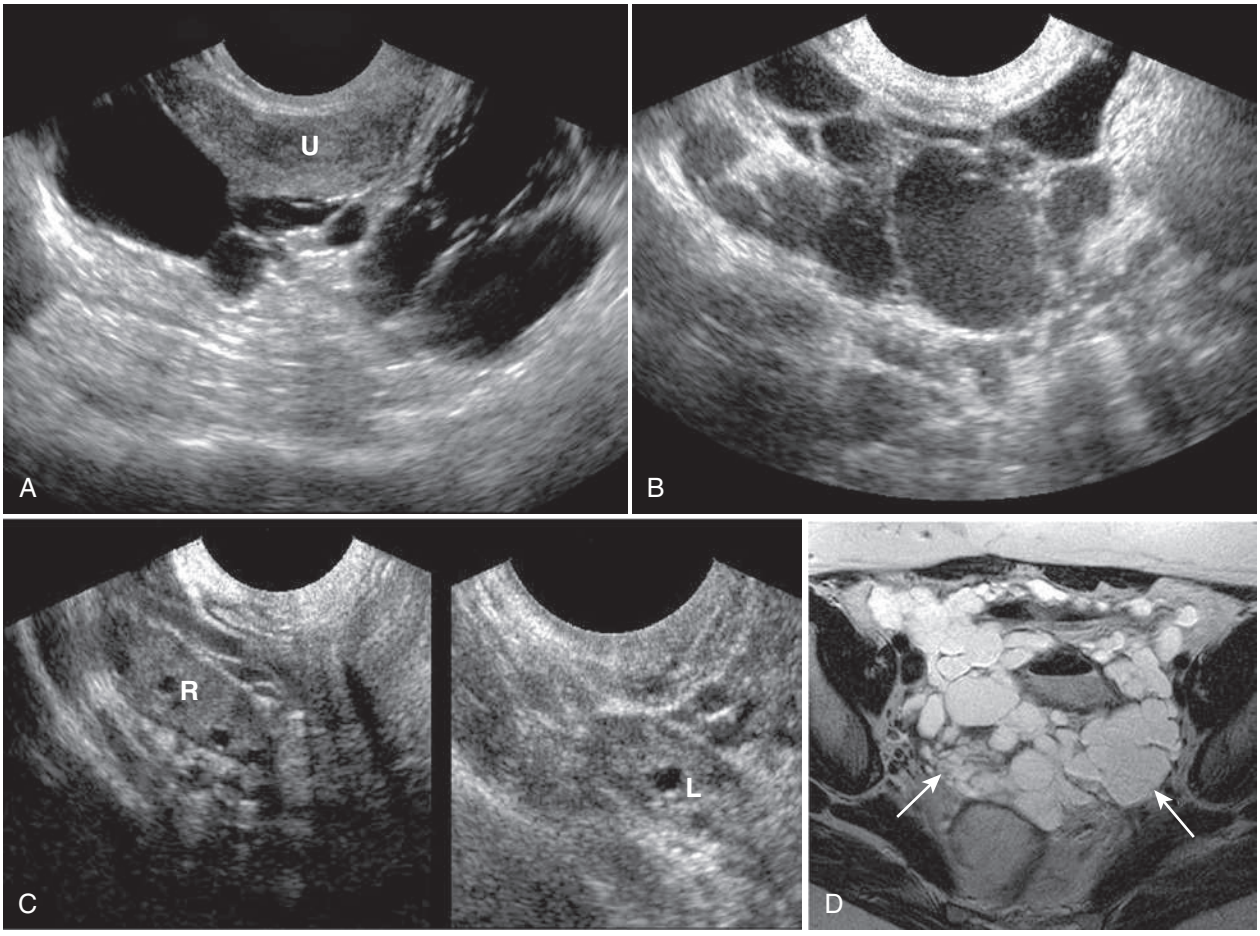

FIG. 14.12 Pelvic Lymphangioma in Asymptomatic Woman. (A) Transverse TVS shows the normal uterus *(U)* in cross section, surrounded by innumerable cysts with thin septations. There is no nodularity. Real-time examination suggested that these cysts were soft and compliant. **(B)** TVS lateral to the uterus shows that the cystic changes are extensive. Their distribution and extent do not suggest an ovarian origin. **(C)** Two TVS images show a normal right *(R)* and a normal left *(L)* ovary. This excludes the ovaries as a source of the pathology. **(D)** Axial T2-weighted MRI confirms the extensive intraperitoneal thin-walled cystic masses *(arrows)*. (Reproduced from Wilson SR. Pseudomyxoma peritonei. In: Cohen HL, editor. Gastrointestinal disease, test and syllabus. Reston, VA: American College of Radiology; 2004. pp. 73-84.[28])

Asymptomatic cysts are frequently managed conservatively, particularly if simple or with the typical appearance of a lymphangioma. Surgery is usually reserved to alleviate pressure symptoms or to address acute complications.

PERITONEAL TUMORS

Tumors involving the peritoneum are often encountered with ultrasound and are generally malignant. **Metastatic tumors** are much more common than **primary peritoneal tumors.** The ovary is the primary site of disease in the vast majority of female patients. Other sites of primary disease with a propensity to spread to the peritoneum include the **stomach, colon, breast, pancreas, kidney, bladder, uterus,** and **skin (melanoma).**

Peritoneal Carcinomatosis

Peritoneal carcinomatosis is the term used to describe diffuse involvement of the peritoneum with metastatic disease. Carcinomatous seeding involving the parietal peritoneum (Fig. 14.13, Fig. 14.14A, Video 14.4) or visceral peritoneum (Figs. 14.14B and 14.15, Videos 14.5 and 14.6) may produce discrete hypoechoic nodules, irregular masses, or hypoechoic rind-like thickening

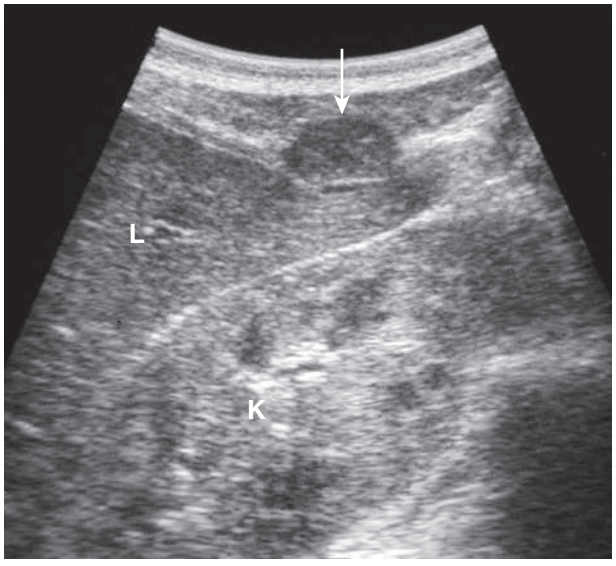

FIG. 14.13 Parietal Peritoneal Metastasis From Squamous Cell Carcinoma of the Lung. Sagittal image of the right upper quadrant shows a hypoechoic nodule *(arrow)* anterior to the liver *(L)*. With respiration, the liver moved freely and independent of the nodule, which stayed stationary, correctly suggesting its location on the parietal peritoneum. *K,* Kidney. See also Video 14.4.

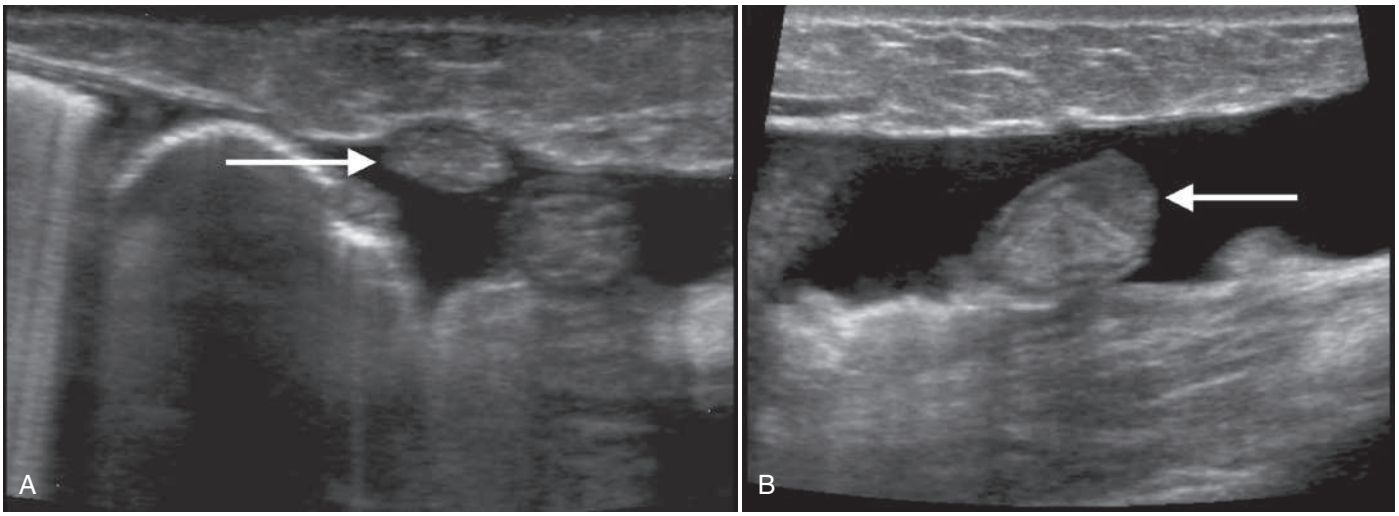

FIG. 14.14 Peritoneal Carcinomatosis. (A) Oblique sagittal ultrasound image of the midabdomen shows free fluid in the peritoneal cavity and a mildly hypoechoic nodular tumor implant involving the parietal peritoneum *(arrow)* immediately deep to the anterior abdominal wall. **(B)** Oblique sagittal ultrasound image of the midabdomen shows free fluid in the peritoneal cavity and a hypoechoic nodular tumor implant involving the visceral peritoneum *(arrow)* on the serosal surface of a small bowel loop. See also Videos 14.5 and 14.6.

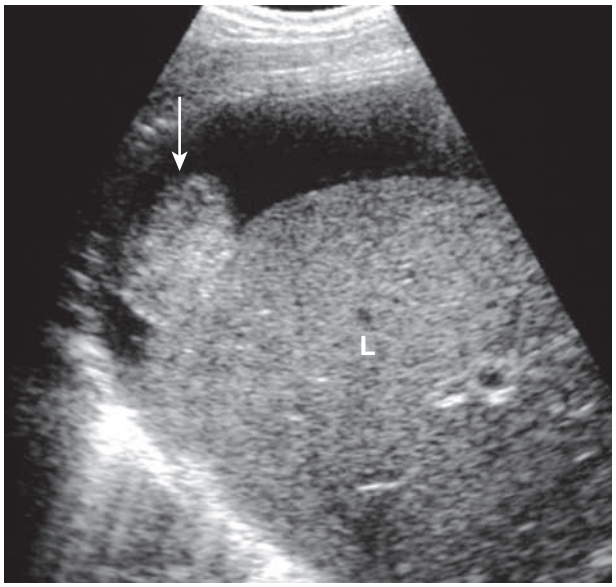

FIG. 14.15 Visceral Peritoneal Metastasis From Adenocarcinoma of the Colon. Oblique sagittal image of the right upper quadrant shows an echogenic nodule *(arrow)* on the surface of the liver *(L)*, surrounded by ascites. With respiration, the nodule moved in concert with the liver, correctly suggesting its location on the visceral peritoneum.

of the peritoneum.[18] Ascites is common and may be the only finding. The **pouch of Douglas, greater omentum, Morison pouch,** and the right subphrenic space are common sites,[34] and therefore any sonographic evaluation of the peritoneum for metastatic disease should include careful and detailed assessment of these areas (Fig. 14.16). The **parietal peritoneal line** is often preserved on sonography with small seeds but is often lost as the lesion increases in size. Growth of a lesion is usually inward, toward the peritoneal cavity, but growth outward with invasion of the abdominal wall can occur (Fig. 14.17). If **psammomatous calcification** occurs within a peritoneal nodule, it appears echogenic with ultrasound, and if the calcification is dense, it may demonstrate posterior acoustic shadowing (Fig. 14.18).

Peritoneal carcinomatosis can be detected with ultrasound in the absence of ascites (Figs. 14.19 and 14.20), but its presence greatly enhances the detection of peritoneal lesions. Nodules as small as 2 to 3 mm may be seen on the parietal and visceral peritoneum with the transvaginal probe (Fig. 14.21). The detection of omental involvement is also enhanced by ascites. Infiltration of the omentum leads to an "omental cake,"[35] which may float freely in the ascitic fluid (Fig. 14.22). Alternatively, the omentum may be adherent to the parietal peritoneum in the near field (Fig. 14.23), or it may be deeper in the peritoneal cavity, adherent to the visceral peritoneum and surrounding small bowel loops (Fig. 14.24). **Thickening of the mesentery, mesenteric nodules,** and **lymphadenopathy** are other possible features of carcinomatosis.

After the full extent of peritoneal involvement has been documented with ultrasound, a careful search should be made for the primary lesion within the abdomen and pelvis, if not already identified. This search should not be limited to the solid organs, gallbladder, and bile ducts and should include the stomach and bowel.

Primary Tumors of Peritoneum

Primary tumors of the peritoneum are rare and include **primary peritoneal serous papillary carcinoma, malignant mesothelioma,** and **lymphoma.** Primary peritoneal serous papillary carcinoma is a multicentric peritoneal tumor that is morphologically identical to **ovarian serous papillary carcinoma** of equivalent grade but that can spare or minimally invade the ovaries.[36] Women with primary peritoneal serous papillary carcinoma are more likely to present with ascites than women with ovarian serous papillary carcinoma and have a worse 3-year survival rate.[37]

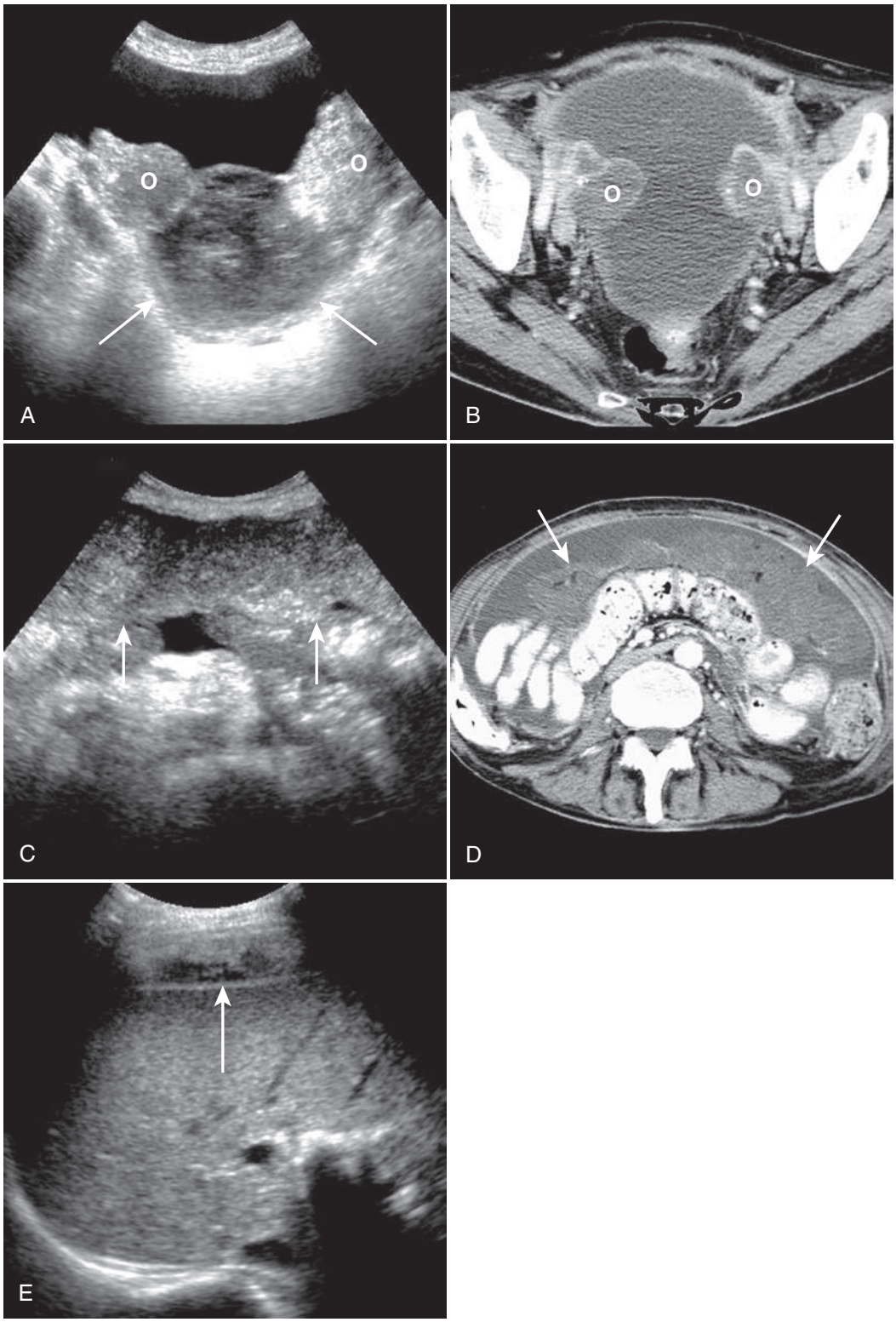

FIG. 14.16 Peritoneal Carcinomatosis From Mucinous Adenocarcinoma, Presumably of Gastrointestinal Origin. (A) Transverse transabdominal pelvic sonogram and **(B)** CT scan at the same level show ascites and bilateral ovarian solid masses *(O)* suggestive of Krukenberg tumors. The marked complexity of the fluid with particles and septations is better appreciated on the ultrasound scan (*arrows* in A). **(C)** Transverse midabdominal ultrasound image and **(D)** corresponding CT scan show a thick "omental cake" *(arrows)* displacing bowel loops posteriorly in the peritoneal cavity. Free fluid is also visualized. **(E)** Oblique ultrasound image in the right upper quadrant shows a rim of complex, mixed-echogenic material overlying and indenting the convexity of the liver *(arrow)*. There is echogenic nodularity on the parietal peritoneum of the diaphragm. This did not move with the liver on respiration, confirming its origin from the parietal peritoneum. (Reproduced from Wilson SR. Pseudomyxoma peritonei. In: Cohen HL, editor. Gastrointestinal disease, test and syllabus. Reston, VA: American College of Radiology 2004. pp. 73-84.[28])

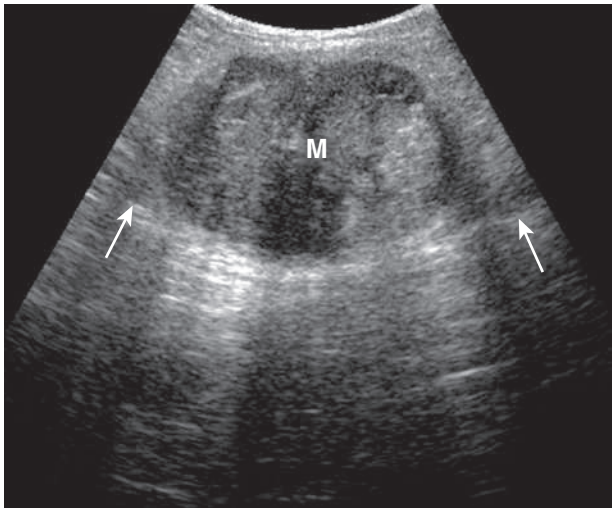

FIG. 14.17 Abdominal Wall Seed in Patient With Known Peritoneal Carcinomatosis. Transverse ultrasound image of the midabdomen shows a hypoechoic solid mass *(M)* in the anterior abdominal wall, superficial to the parietal peritoneum *(arrows)*.

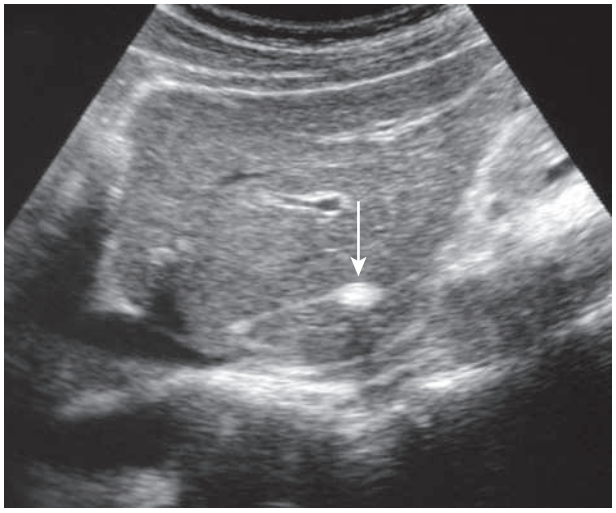

FIG. 14.18 Well-Differentiated Stage 3 Papillary Serous Ovarian Cancer. Sagittal ultrasound image through the liver shows a calcified implant *(arrow)* in the ligamentum venosum, with posterior acoustic shadowing.

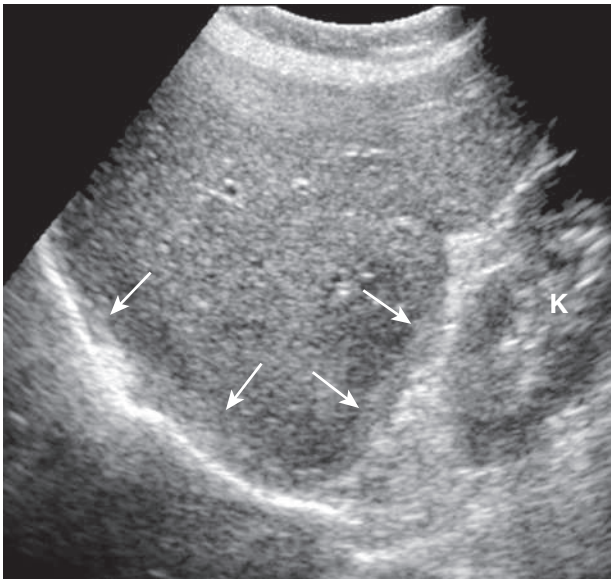

FIG. 14.19 Stage 3 Papillary Serous Ovarian Cancer Without Ascites. Sagittal ultrasound image in the right upper quadrant shows a subtle, thin, echogenic "rind" of seeding *(arrows)* on the surface of the liver, extending into the Morison pouch. *K,* Kidney.

Imaging may demonstrate the typical features of peritoneal carcinomatosis, but no obvious primary site[38-42] (Fig. 14.25). The ovaries are generally normal in size but may be enlarged by surface involvement.

Primary peritoneal mesothelioma accounts for 10% to 30% of all cases of malignant mesothelioma[1,2,29,43] and is most common in middle-aged men. The tumor proves invariably fatal, and as with mesothelioma of the pleura, there is an association with asbestos exposure. Up to 65% of chest radiographs show evidence of asbestos exposure at diagnosis. In this condition the parietal and visceral peritoneums are diffusely thickened or are extensively involved by tumor plaques or nodules (Fig. 14.26, Video 14.7). These plaques and nodules may aggregate to form discrete masses. The viscera may be encased or invaded by tumor. Ascites is a common finding and is seen in up to 90% of cases.[44] As with peritoneal carcinomatosis, the nodules and plaques are often hypoechoic in peritoneal mesothelioma (Fig. 14.27). Pleural effusions and pleural plaques may also be appreciated with ultrasound. The solid organs should be evaluated for direct invasion or metastases. Ultrasound-guided biopsy can be performed to confirm the diagnosis.[45] Generally, core biopsies from a number of locations are required because of difficulty sometimes encountered in establishing the diagnosis of peritoneal mesothelioma.

Primary lymphoma of the peritoneum is extremely rare and is the non-Hodgkin variety.[2,46] There is an increased incidence in patients with acquired immunodeficiency syndrome (AIDS).[47] Again, features include diffuse peritoneal seeding, often with more focal masses. Lymphomatous masses may be extremely hypoechoic and can be mistaken for fluid collections with cursory assessment (Fig. 14.28).

Pseudomyxoma Peritonei

Pseudomyxoma peritonei is a rare, often fatal intraabdominal disease characterized by dissecting gelatinous ascites and multifocal peritoneal implants of columnar epithelium that secrete copious globules of extracellular mucin.[48] Controversy surrounds the origin of pseudomyxoma peritonei. Some studies suggest synchronous ovarian and appendiceal tumors in 90% of patients,[49] whereas most now believe that the condition almost always originates from a perforated appendiceal epithelial tumor.[50] The disease process tends to remain localized to the peritoneal cavity, and extraperitoneal spread is rare. Pseudomyxoma peritonei encompasses benign, borderline, and malignant mucinous neoplasms, resulting in a variable and poorly predictable prognosis. The overall 5-year survival is 40% to 50%, depending on cell type.[51]

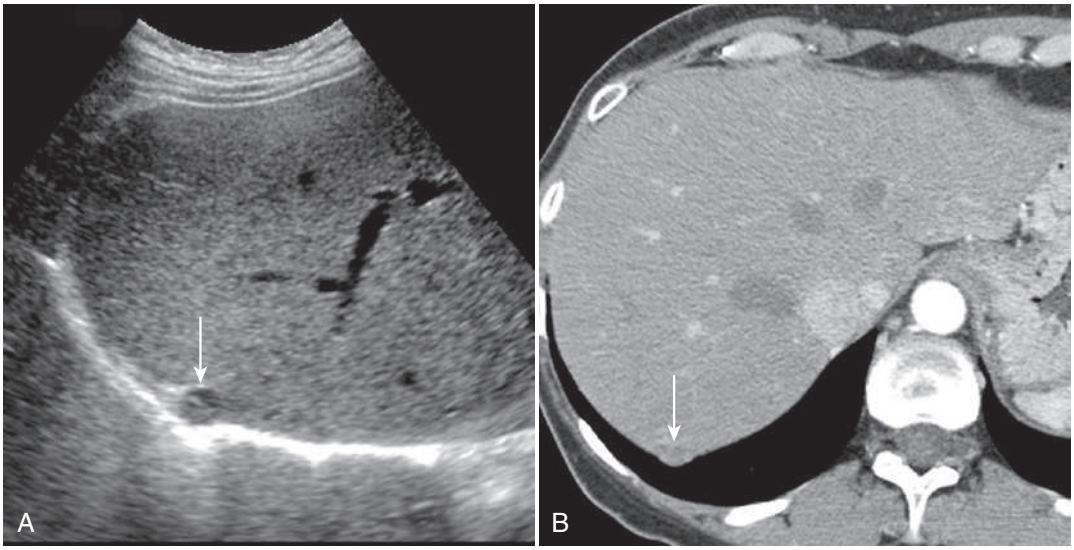

FIG. 14.20 Peritoneal Implant Without Ascites. (A) Transverse ultrasound image and **(B)** axial CT image of the right upper quadrant show a small peritoneal implant *(arrow)* overlying segment 7 of the liver. Note that the implant is better appreciated on the ultrasound image.

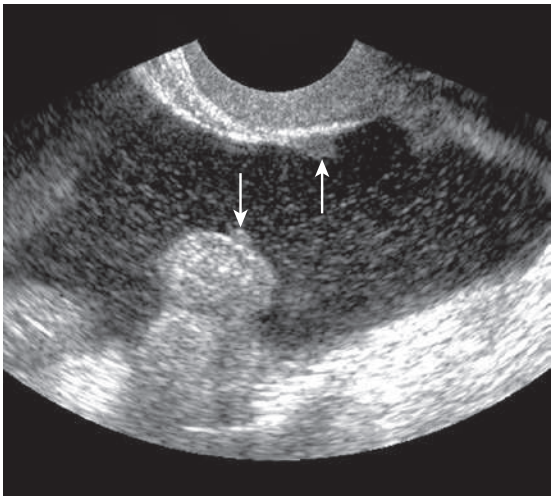

FIG. 14.21 Peritoneal Carcinomatosis From Ovarian Cancer. Oblique sagittal TVS shows small (<5 mm), parietal (near-field), and visceral (far-field) peritoneal implants *(arrows),* surrounded by particulate ascites.

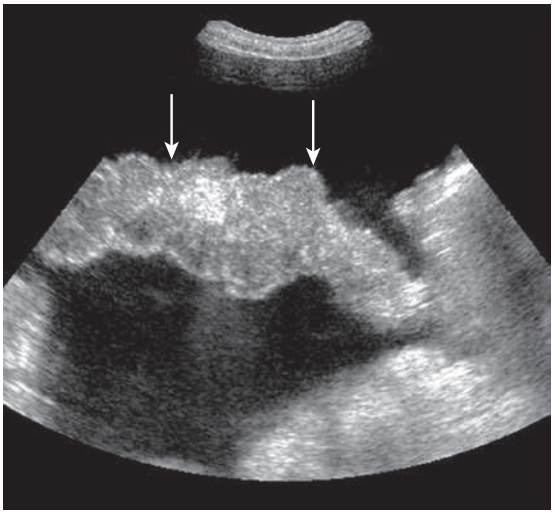

FIG. 14.22 Free-Floating "Omental Cake." Sagittal ultrasound image of the lower midline abdomen shows an omental cake *(arrows)* floating freely in the ascitic fluid. Note the free edge of the abnormal greater omentum inferiorly.

Patients with pseudomyxoma peritonei present with abdominal pain and distention. Ultimately, the bowel becomes encased with mucinous material, and bowel obstruction may occur. Repeated surgical intervention to remove the accumulated mucinous material remains the treatment of choice.[52] Perioperative intraperitoneal chemotherapy may add additional benefit.[53] Because patients present with abdominal symptoms, the diagnosis is frequently made preoperatively by ultrasound or CT.[54] Sonography frequently shows complex ascites reflecting the gelatinous nature of the fluid. The echogenic foci within the fluid are nonmobile, and the bowel loops, instead of floating freely, are displaced centrally and posteriorly by the surrounding mass, giving a characteristic "starburst" appearance[55] (Fig. 14.29). Scalloping of the liver is another typical feature of pseudomyxoma peritonei.[56] Ultrasound may be helpful to guide paracentesis in these patients because less viscous areas may be identified, with a greater likelihood of successful aspiration.

INFLAMMATORY DISEASE OF PERITONEUM

Peritonitis is defined as diffuse inflammation of the parietal and visceral peritoneum, with both infectious and noninfectious causes.[3] Infectious causes include bacteria (including tuberculosis), viruses, fungi, and parasites. Noninfectious causes are less common and include **chemical peritonitis** (secondary to gastric or pancreatic juice or bile), **granulomatous peritonitis** (secondary to foreign bodies such as talc), and **sclerosing peritonitis** associated with **continuous ambulatory peritoneal dialysis.**

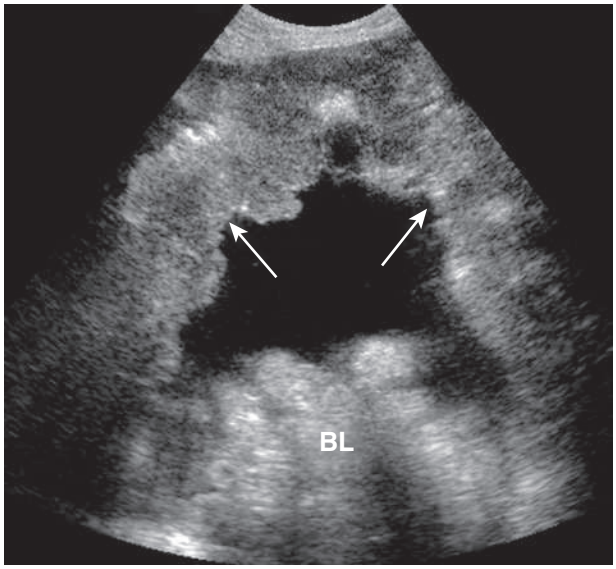

FIG. 14.23 Omental Cake Adherent to Parietal Peritoneum. Transverse ultrasound image of the midabdomen shows an omental cake *(arrows)* in the near field, adherent to the parietal peritoneum. Small bowel loops *(BL)* are visible in the far field, outlined by ascites.

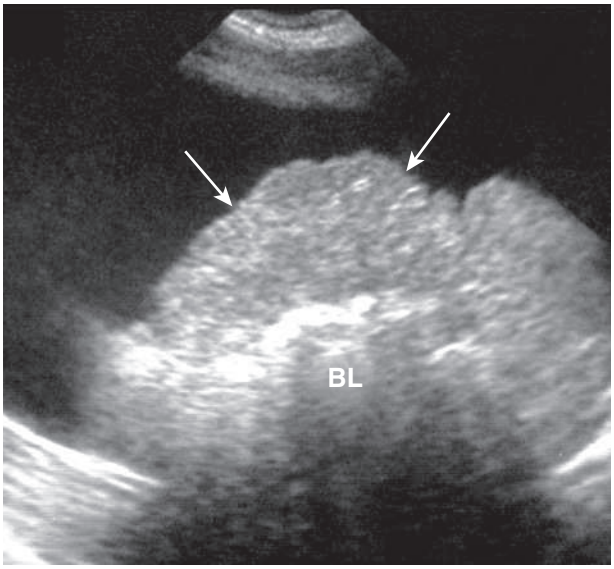

FIG. 14.24 Omental Cake Adherent to Visceral Peritoneum. Transverse ultrasound image of the midabdomen shows a thick omental cake *(arrows)* adherent to the visceral peritoneum and encasing gas-filled small bowel loops *(BL)*.

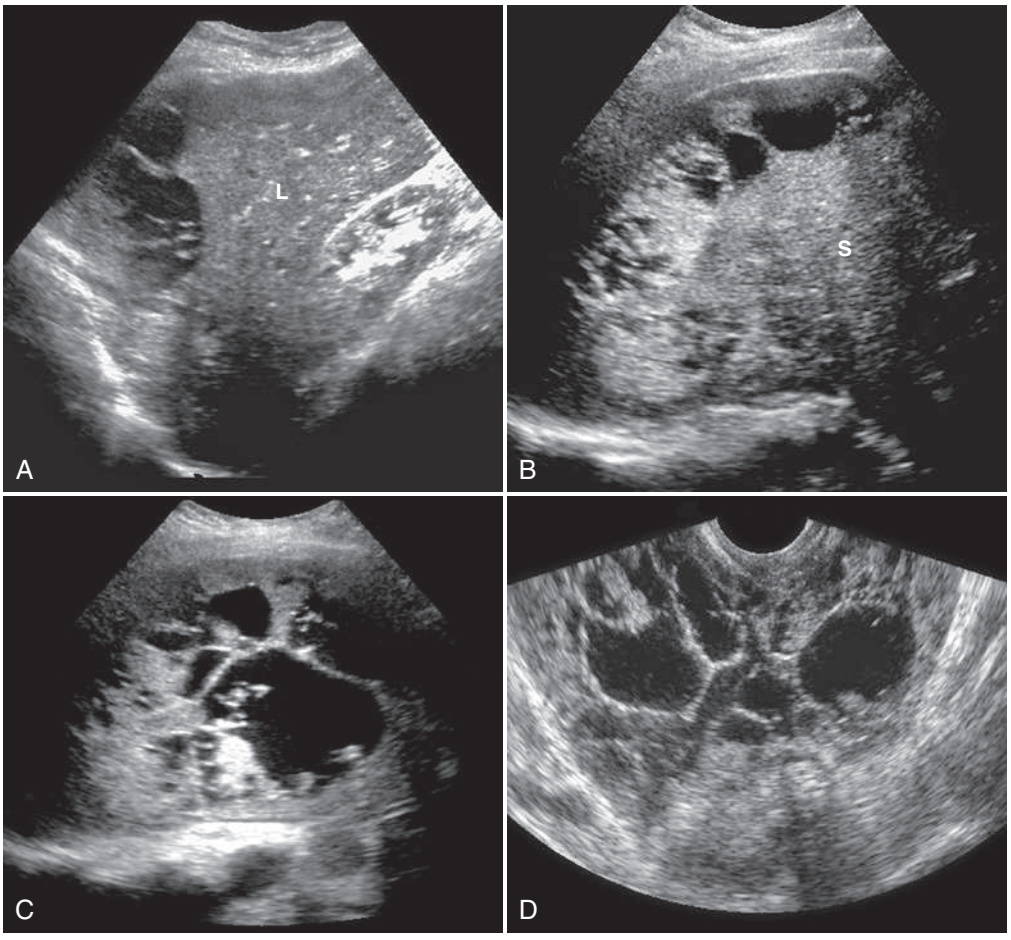

FIG. 14.25 Primary Peritoneal Serous Papillary Carcinoma. (A) Sagittal ultrasound image shows a highly complex peritoneal mass between the right hemidiaphragm and the liver *(L)*. The liver border is scalloped. **(B)** Sagittal ultrasound image in the left upper quadrant shows a similar complex peritoneal mass over the convexity of the spleen *(S)*. **(C)** Midabdominal image shows a complex peritoneal cystic and solid mass of enormous size. **(D)** TVS image taken in the pouch of Douglas shows no normal tissue. The entire pouch is filled with a complex cystic and solid tumor. (Reproduced from Wilson SR. Pseudomyxoma peritonei. In: Cohen HL, editor. Gastrointestinal disease, test and syllabus. Reston, VA: American College of Radiology; 2004. pp. 73-84.[28])

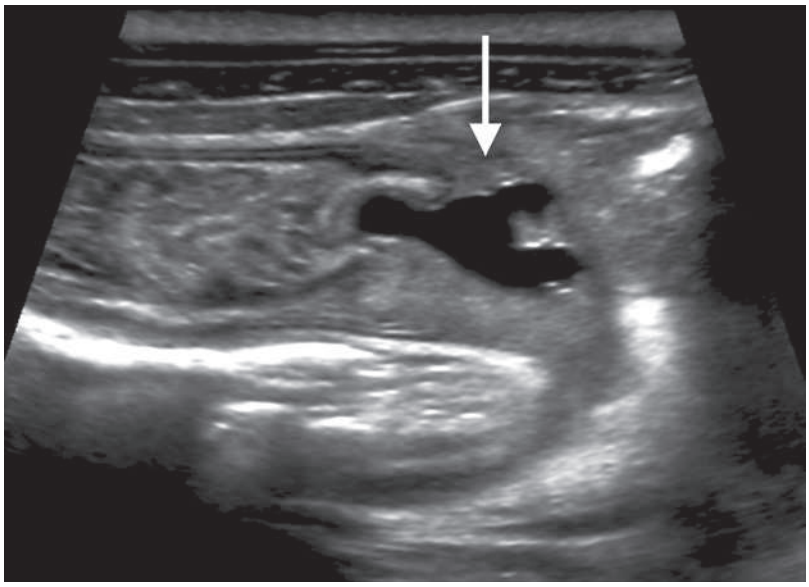

FIG. 14.26 Peritoneal Mesothelioma. Sagittal ultrasound image of the midabdomen shows hypoechoic thickening of the visceral peritoneum with a pocket of loculated fluid *(arrow)* separating small bowel loops. See also Video 14.7.

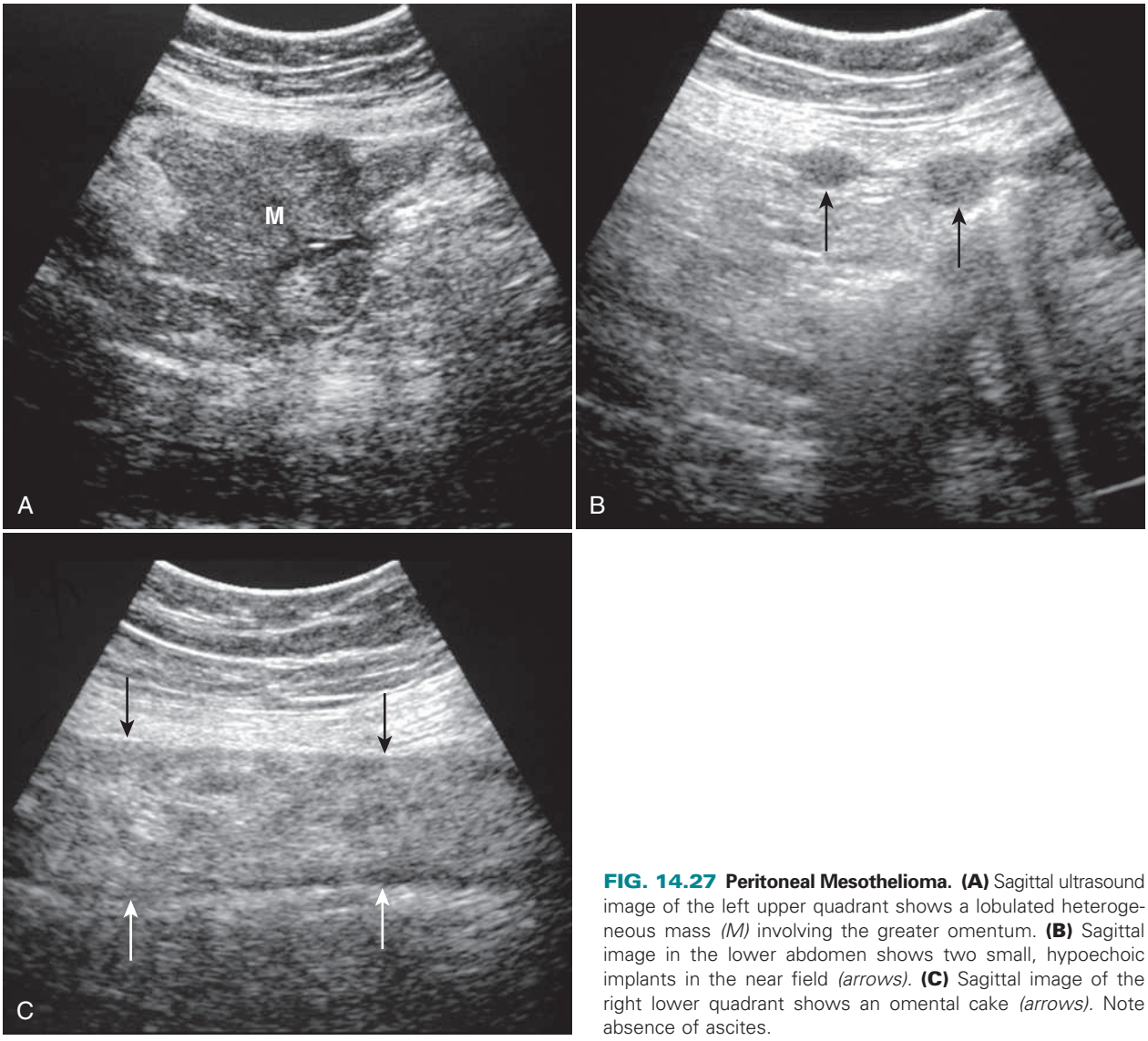

FIG. 14.27 Peritoneal Mesothelioma. (A) Sagittal ultrasound image of the left upper quadrant shows a lobulated heterogeneous mass *(M)* involving the greater omentum. **(B)** Sagittal image in the lower abdomen shows two small, hypoechoic implants in the near field *(arrows)*. **(C)** Sagittal image of the right lower quadrant shows an omental cake *(arrows)*. Note absence of ascites.

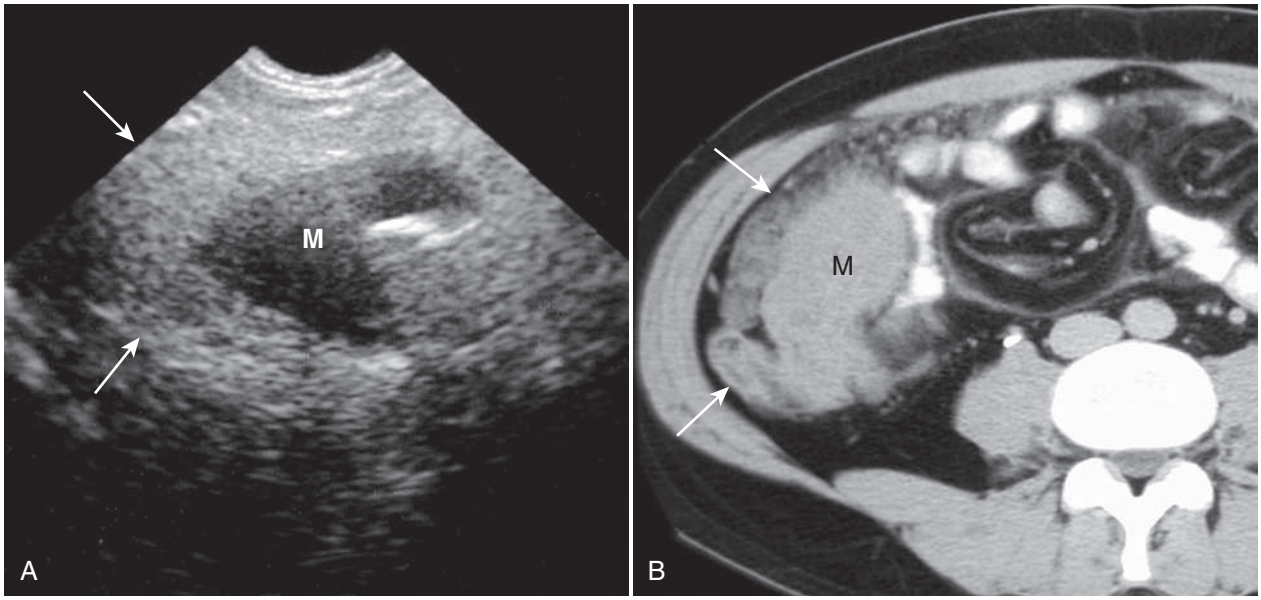

FIG. 14.28 Non-Hodgkin Lymphoma of the Peritoneum. (A) Transverse ultrasound image and **(B)** axial CT image of the right lower quadrant show a mass *(M)* displacing bowel loops medially. Infiltrated fat *(arrows)* is seen lateral to the mass as echogenic mass effect on the sonogram.

Most cases of **infective peritonitis** are **bacterial, secondary to complications** of disease processes involving intraabdominal organs. Common causes include bowel necrosis secondary to ischemia, perforated appendicitis, perforated diverticulitis, perforated duodenal ulcer, inflammatory bowel disease, and postoperative leaks. Culture of the exudate generally reveals a mixed flora in this setting, with gram-negative bacilli and anaerobes predominating.

Primary or **spontaneous bacterial peritonitis** occurs much less often, predominantly in association with cirrhosis and nephrotic syndrome. The clinical findings are often subtle, and correct diagnosis requires a high index of suspicion. Spontaneous bacterial peritonitis should be considered in any cirrhotic patient with ascites, fever, and an unexplained clinical deterioration. Culture of the ascitic fluid will characteristically reveal a single organism, usually *Escherichia coli.*

The sonographic appearance of infective peritonitis varies but may include particulate ascites (Fig. 14.30A), loculated ascites, or ascitic fluid containing septations (Fig. 14.31), debris, or gas.[57] Diffuse thickening of the parietal and visceral peritoneum (Fig. 14.30B), mesentery, and omentum may also be observed, and heterogeneous exudate may be seen interposed between bowel loops.

Peritonitis secondary to viruses, fungi, or parasites is rare and usually occurs in immunocompromised patients (Fig. 14.32) or patients on continuous ambulatory peritoneal dialysis. **Echinococcal disease** may involve the peritoneum.[58] A hepatic or splenic cyst may rupture, resulting in diffuse seeding of the peritoneal cavity. Ultrasound may reveal one or more of the typical appearances of hydatid cysts, including daughter cysts, the sonographic "water lily" sign, or multiple, closely folded echogenic membranes within the cyst cavity.

Abscess

Abscesses may occur at the site of a localized perforation or may result from delayed treatment of peritonitis, in which case they often develop in dependent areas of the abdomen and pelvis. The subphrenic or subhepatic spaces and the pouch of Douglas are common locations. Ultrasound is often limited in detecting intraabdominal abscesses, particularly in postoperative patients. These patients are less mobile because of their recent surgery and frequently have open wounds and dressings, limiting access for the ultrasound probe. In addition, visibility is often limited by extensive bowel gas, a result of paralytic ileus. In this setting, it may prove extremely difficult to distinguish between a dilated, aperistaltic, fluid-filled or gas-filled bowel loop and an extraluminal abscess collection.

Recognized features of intraabdominal abscesses include round or oval fluid collections with well-defined and irregular walls. They usually contain internal debris and septations (Figs.14.33 and 14.34) and occasionally small pockets of gas that appear as echogenic foci with ultrasound, often with posterior reverberation artifact. The presence of gas within a collection is virtually diagnostic of infection.[59] Ultrasound-guided or CT-guided percutaneous drainage is generally the treatment of choice, and follow-up sonographic examinations are helpful at assessing response to therapeutic intervention.

Tuberculous Peritonitis

Tuberculosis (TB) is still prevalent in developing countries, with a recent resurgence in the developed world, particularly among **AIDS** patients and immigrant populations.[60] Other groups at risk include patients with **alcoholism** and **cirrhosis.** Of all non-AIDS patients with TB, extrapulmonary disease occurs in only

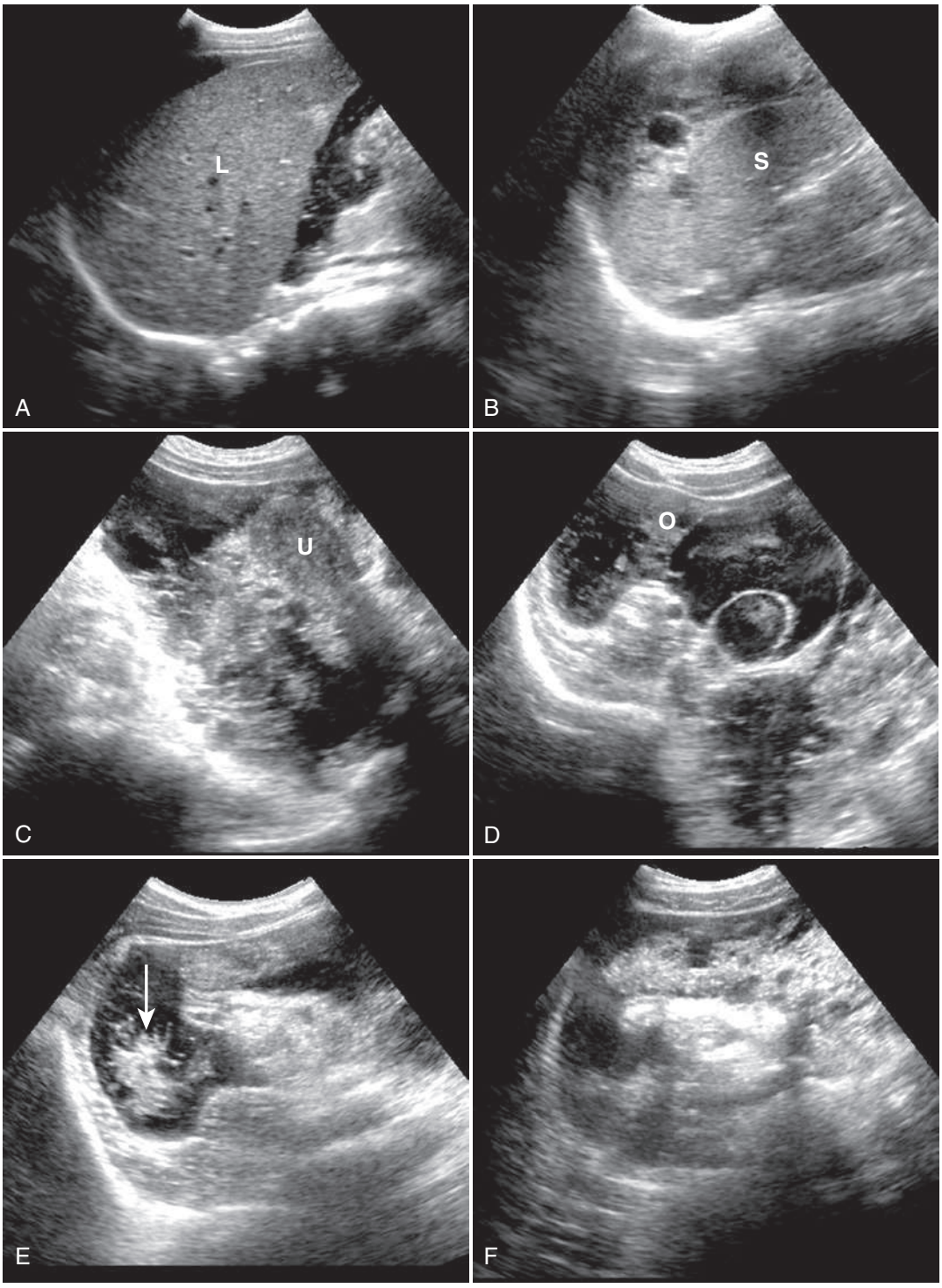

FIG. 14.29 Pseudomyxoma Peritonei. (A) Sagittal ultrasound image of the right upper quadrant shows complex fluid surrounding the liver *(L)* shows very mild and subtle scalloping of the deep border of the liver. **(B)** Sagittal ultrasound image of the left upper quadrant shows the spleen *(S)* surrounded by highly complex and echogenic fluid. The echogenic components of the fluid do not move with gravity. There is an indentation on the convexity of the spleen where the peritoneal process appears to invaginate the splenic parenchyma. **(C)** Sagittal transabdominal pelvic sonogram shows a normal anteverted uterus *(U)*. The pouch of Douglas is filled with highly complex fluid. **(D)** Oblique sagittal ultrasound image of the right abdomen at the pelvic brim shows a thin-walled intraperitoneal cyst with intracystic septations. This is not within the normal appearing right ovary *(O)*. The normal left ovary was seen elsewhere. **(E)** Transverse image in the right paracolic gutter shows a "starburst" within the fluid *(arrow)*. This is associated, in our experience, with the presence of mucin in the peritoneal cavity. **(F)** Highly echogenic plaque-like structure anteriorly represents a very thick and abnormal omentum, an "omental cake." There are hypoechoic nodules within the cake that are highly suggestive of tumor deposits. (Reproduced from Wilson SR. Pseudomyxoma peritonei. In: Cohen HL, editor. Gastrointestinal disease, test and syllabus. Reston, VA: American College of Radiology; 2004. pp. 73-84.[28])

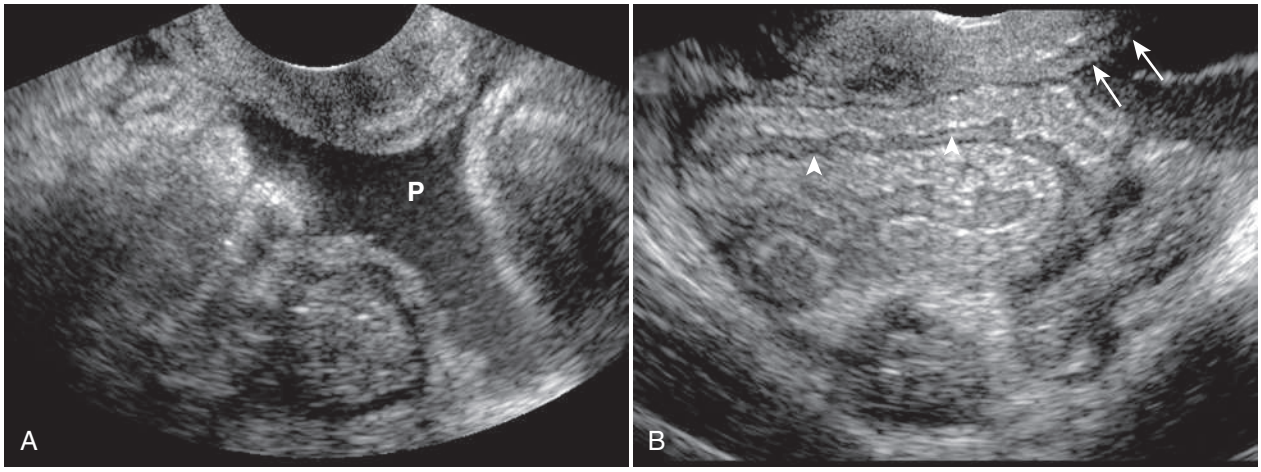

FIG. 14.30 Suppurative Peritonitis. (A) Transverse TVS of the pouch of Douglas shows particulate free fluid (P). **(B)** Transverse TVS more anteriorly in the pelvis shows diffuse thickening of both the parietal *(arrows)* and the visceral *(arrowheads)* peritoneum. An S-shaped small bowel loop is seen meandering through the thickened visceral peritoneum.

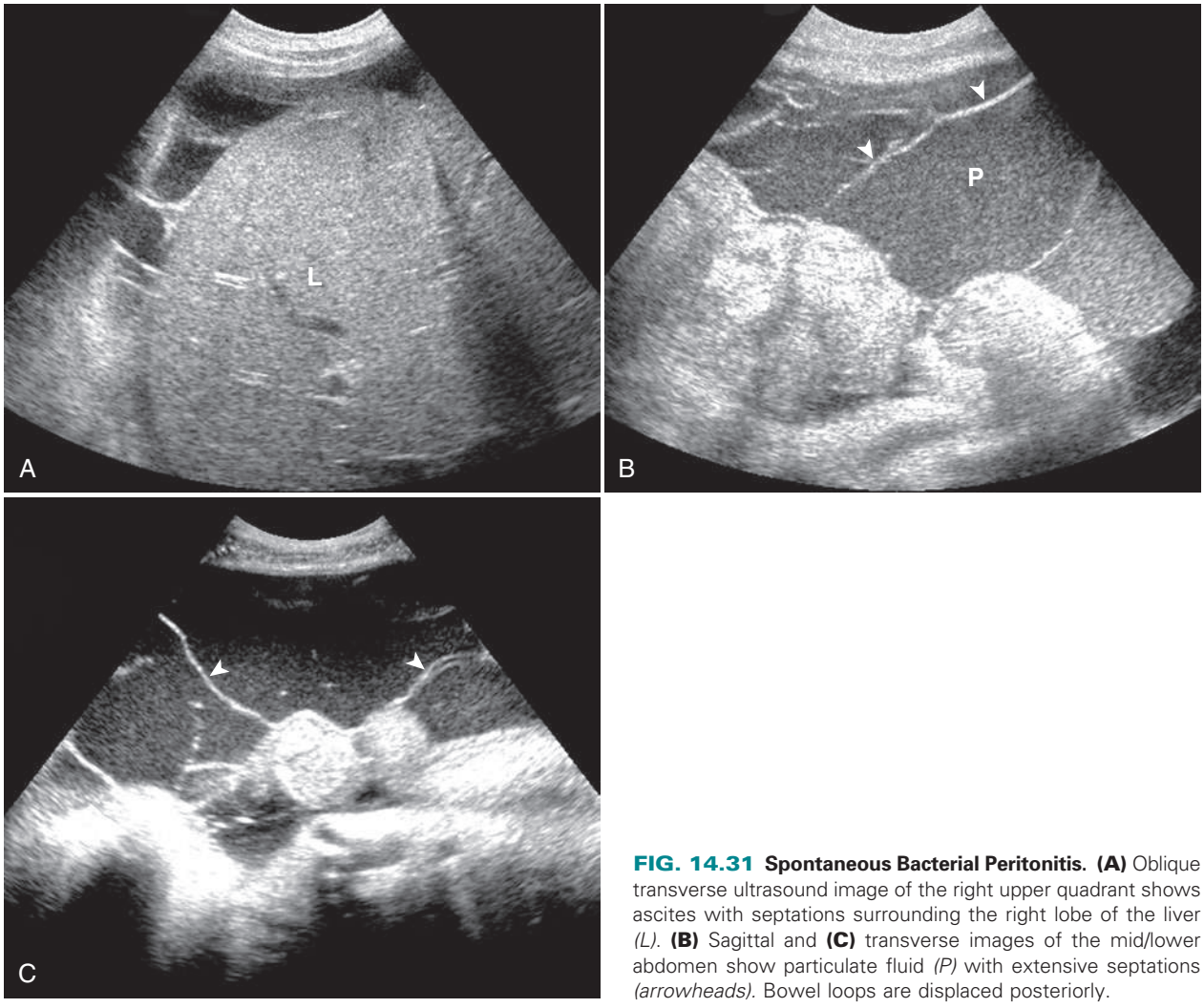

FIG. 14.31 Spontaneous Bacterial Peritonitis. (A) Oblique transverse ultrasound image of the right upper quadrant shows ascites with septations surrounding the right lobe of the liver *(L)*. **(B)** Sagittal and **(C)** transverse images of the mid/lower abdomen show particulate fluid *(P)* with extensive septations *(arrowheads)*. Bowel loops are displaced posteriorly.

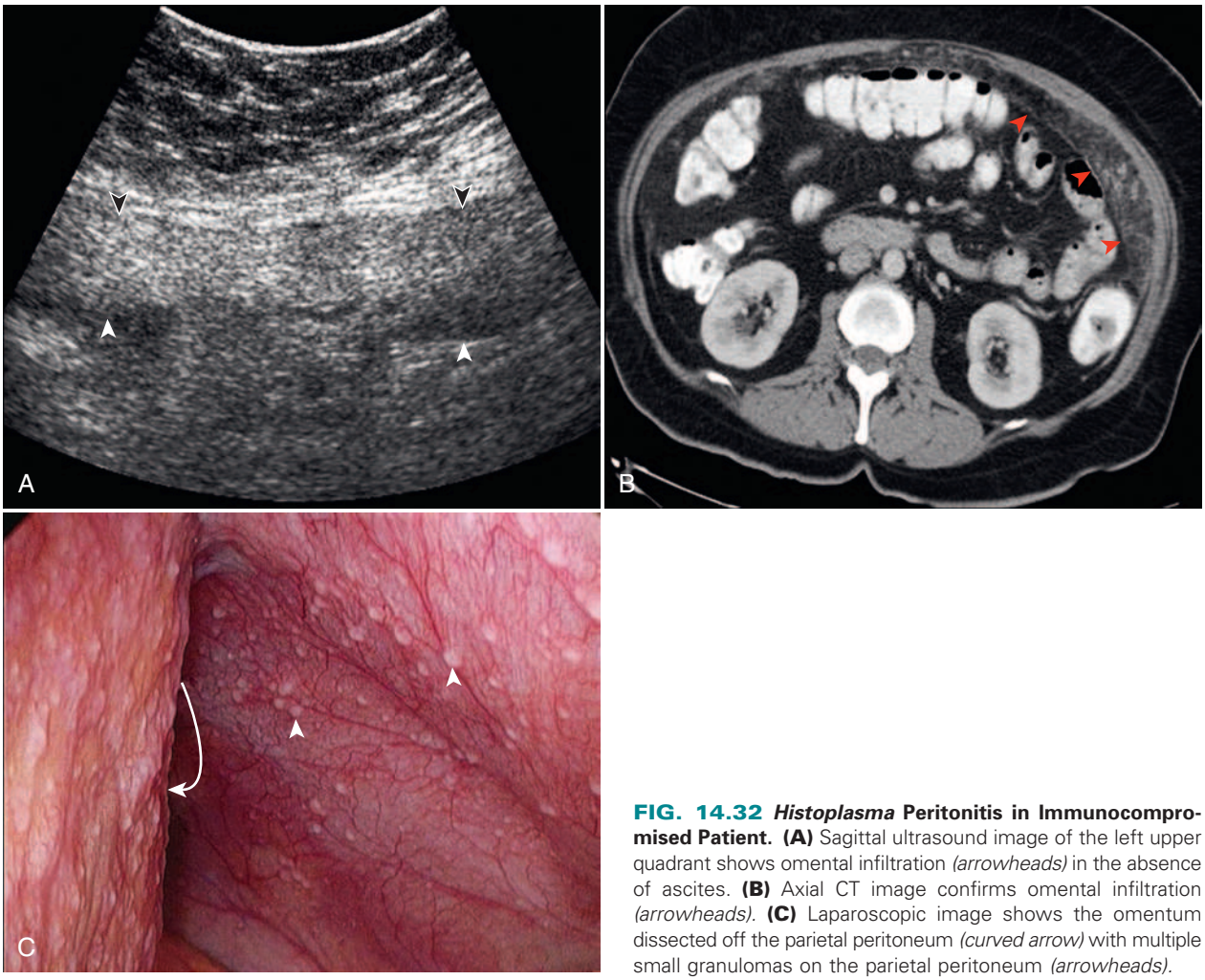

FIG. 14.32 *Histoplasma* Peritonitis in Immunocompromised Patient. (A) Sagittal ultrasound image of the left upper quadrant shows omental infiltration *(arrowheads)* in the absence of ascites. **(B)** Axial CT image confirms omental infiltration *(arrowheads)*. **(C)** Laparoscopic image shows the omentum dissected off the parietal peritoneum *(curved arrow)* with multiple small granulomas on the parietal peritoneum *(arrowheads)*.

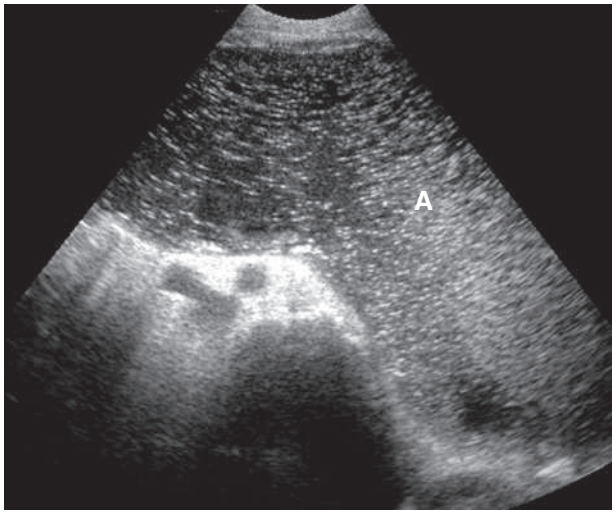

FIG. 14.33 Abscess. Transverse ultrasound image of the midabdomen shows a large abscess collection *(A)*.

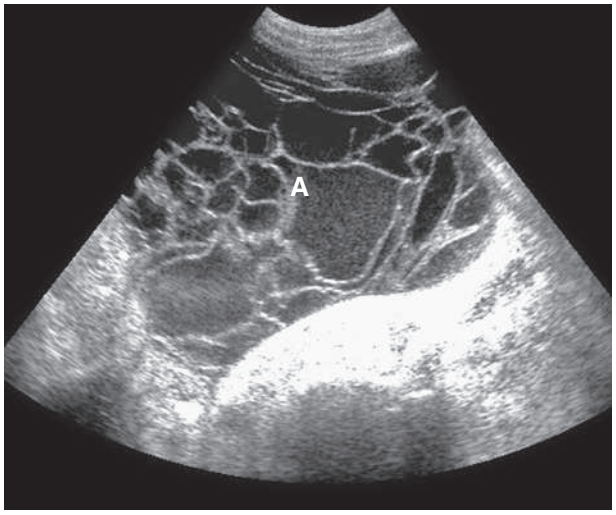

FIG. 14.34 Abscess. Sagittal ultrasound image of the right lower quadrant shows a large abscess collection with internal septations *(A)*.

10% to 15%; this increases to more than 50% in AIDS patients.[61] The peritoneum is a common site of extrapulmonary involvement,[62] but the chest radiograph will show evidence of pulmonary TB in only 14% of these patients. Therefore a high index of suspicion, particularly in high-risk groups, and knowledge of the common sonographic features allow for earlier diagnosis of this potentially curable disease, thus reducing morbidity and mortality.

There are no pathognomonic sonographic features for **TB peritonitis** but, in the proper clinical setting, a diffuse peritoneal process may strongly suggest the diagnosis. Ascites is frequently present and may be free or loculated. It may be anechoic or more frequently particulate and may contain fine, mobile strands composed of fibrin. These strands may produce a latticelike pattern. Irregular and nodular hypoechoic thickening of the peritoneum, mesentery, and omentum is another feature (Fig. 14.35).[63] Associated **lymphadenopathy** in the mesentery and retroperitoneum is a common feature and is more common than in peritoneal carcinomatosis.[64-66] The nodes may be discrete or conglomerate because of periadenitis. Caseation may give rise to a hypoechoic center within the node, although a similar appearance can be seen with metastatic lymph nodes undergoing necrosis. Echogenic nodes caused by fat deposition may suggest the diagnosis of TB. Sonographic assessment of the solid viscera may show involvement, particularly hypoechoic masses in the spleen. Ultrasound helps guide diagnostic paracentesis in TB peritonitis and may also guide fine-needle aspiration of enlarged nodes.[67] Sonography can also readily document response to treatment.

Sclerosing Peritonitis

Sclerosing peritonitis is a major complication of **continuous ambulatory peritoneal dialysis** and is characterized by the formation of a connective tissue membrane covering the peritoneum and eventually encasing and strangulating bowel loops.[68,69] Patients initially complain of abdominal pain and loss of ultrafiltration. Ultimately, bowel obstruction occurs. Surgery is often difficult in these patients, and the prognosis is poor. Early diagnosis of sclerosing peritonitis may be important in reducing mortality.

Ultrasound is extremely helpful in the diagnosis.[70] Increased peristalsis in multiple bowel loops is one of the earliest findings in sclerosing peritonitis. Ascites, both free and loculated, is common. With time, the fluid becomes more complex with **stranding** (Fig. 14.36). Bowel loops become matted together and are tethered to the posterior abdominal wall by a characteristic enveloping membrane. This membrane can be seen with ultrasound as a uniformly echogenic layer measuring 1 to 4 mm in thickness.

LOCALIZED INFLAMMATORY PROCESS OF PERITONEAL CAVITY

The CT appearance and significance of inflamed peritoneal fat are familiar to sonographers. If ultrasound is to be successful at investigating patients with abdominal symptoms, the sonographic appearance of inflamed fat must become just as familiar.

Inflamed perienteric fat appears as an echogenic "mass effect," with ultrasound frequently displacing bowel loops out of the scanning plane. Compression sonography may greatly enhance the detection of focally inflamed fat, and gentle palpation with the transducer over this area will frequently show that it is the site of the patient's maximal tenderness. Frequently, an associated underlying abnormality, such as an abnormal bowel segment, can be identified with ultrasound[71] (Fig. 14.37). **Appendicitis** and **diverticulitis** are the most common acute processes giving rise to focally inflamed fat. Other possibilities include inflammatory bowel disease, pancreatitis, and complicated acute cholecystitis. Progression to phlegmon typically shows development of a hypoechoic region within the echogenic fat without fluid content (Fig. 14.38). If untreated, this may progress to abscess formation. Color Doppler imaging frequently shows increased blood flow in the area of inflammation.[72]

RIGHT-SIDED SEGMENTAL OMENTAL INFARCTION

Right-sided segmental omental infarction is a rare clinical entity that usually presents with right-sided abdominal pain and is often mistaken for appendicitis. It is important to make the correct diagnosis because the condition is self-limiting and resolves spontaneously with supportive measures. Omental infarction occurs in all age groups and is thought to result from an embryologic variant in the blood supply to the right inferior portion of the omentum, leaving it prone to infarction. Precipitating factors include straining and eating a large meal.

Ultrasound reveals an echogenic, ovoid, or cakelike mass in the right midabdomen at the site of the patient's tenderness[73,74] (Fig. 14.39). Careful assessment will reveal no underlying bowel abnormality. The typical location of right-sided omental infarction is anterolateral to the hepatic flexure of the colon, and it corresponds to a circumscribed fatty mass on CT, with areas of stranding. The mass often adheres to the parietal peritoneum, with bowel moving deep to it on respiration.

ENDOMETRIOSIS

Endometriosis is a common condition affecting predominantly premenopausal women and occurs when functional endometrium is located outside of the uterus. Patients may be asymptomatic but frequently present with pelvic pain, dyspareunia, or infertility. The ovaries and suspensory ligaments of the uterus are the sites most often affected, but endometriotic implants can involve the bowel, urinary bladder, peritoneum, chest, or soft tissues.[75]

Sonographic evaluation is often normal in patients with endometriosis. If **endometriomas** are present, TVS is very sensitive at detecting and characterizing the masses, often showing the typical "chocolate" cysts with uniform, low-level internal echoes (Fig. 14.40, Video 14.8). There may be associated complex free fluid with stranding. Occasionally, tiny echogenic foci may be identified along the pelvic peritoneal surfaces. These foci are not specific for endometriosis and may also be seen with serous papillary ovarian neoplasms. Clinical correlation is essential,

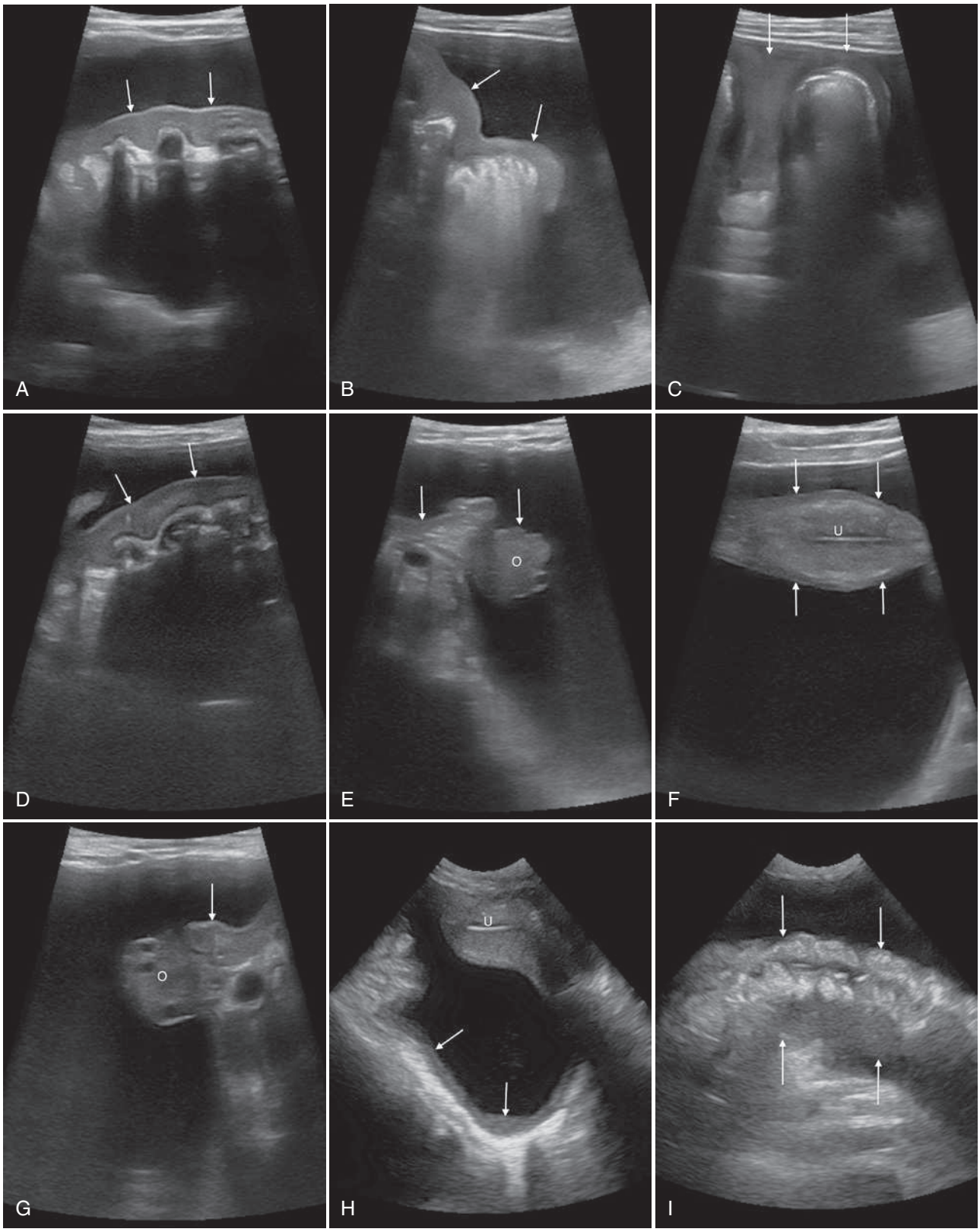

FIG. 14.35 Tuberculous Peritonitis. (A)-(D) Ultrasound images show a large volume of free fluid and striking smooth, hypoechoic, plaque-like thickening of the visceral peritoneum *(arrows)*. **(E)-(G)** Transverse ultrasound images of the pelvis show a large volume of free fluid surrounding the uterus *(U)* and ovaries *(O)*. Note smooth hypoechoic thickening of the peritoneum *(arrows)*. **(H)** Sagittal ultrasound image of the midpelvis with a large field of view shows the uterus *(U)*, a large volume of free fluid and hypoechoic thickening of the parietal peritoneum *(arrows)*. **(I)** Sagittal ultrasound image of the midabdomen shows a markedly thickened and heterogeneous omentum *(arrows)* and free fluid.

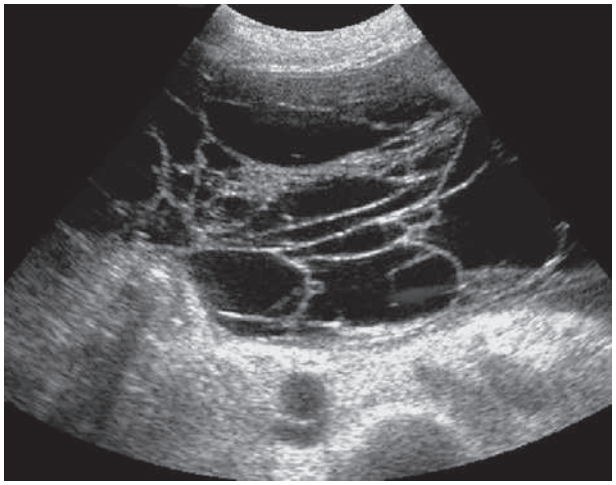

FIG. 14.36 Sclerosing Peritonitis. Transverse ultrasound image of the midabdomen shows extensive, complex, septated ascites.

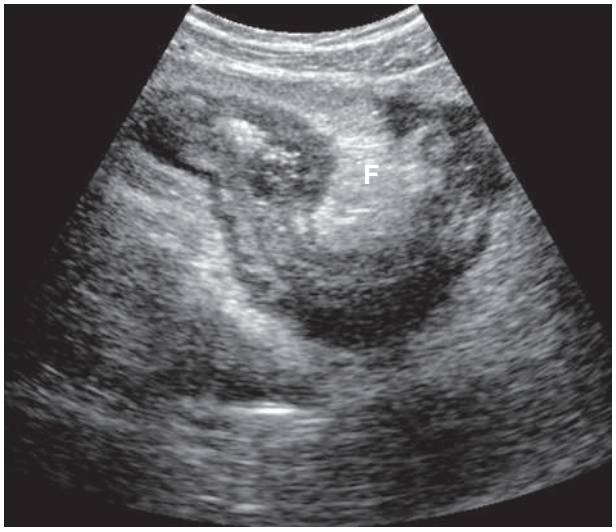

FIG. 14.37 Inflamed Fat. Transverse ultrasound image of the right lower quadrant shows echogenic inflamed fat *(F)* associated with a long segment of thickened terminal ileum in patient with Crohn disease.

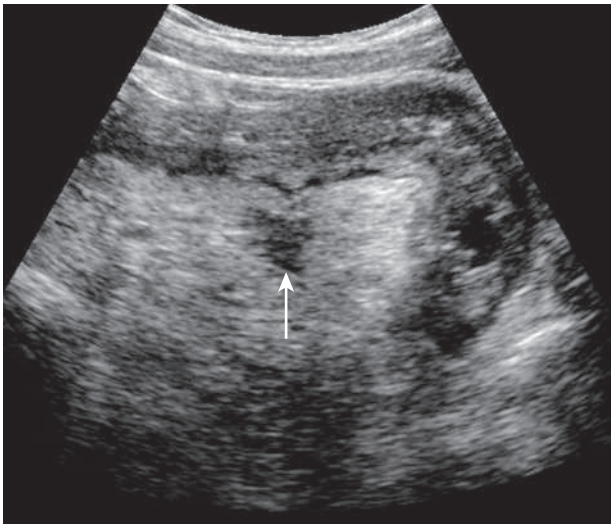

FIG. 14.38 Inflamed Fat With Phlegmon. Oblique sagittal ultrasound image of the right lower quadrant shows the thickened terminal ileum with echogenic inflamed fat and hypoechoic perienteric phlegmon formation *(arrow)*.

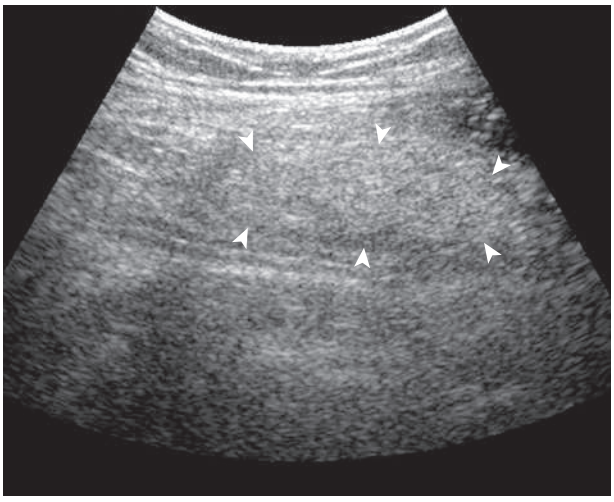

FIG. 14.39 Right-Sided Segmental Omental Infarction. Sagittal image of the right midabdomen shows an ovoid echogenic mass *(arrowheads)*. This was the site of the patient's maximal tenderness.

and occasionally laparoscopic evaluation may be necessary, with biopsy of the peritoneum to rule out tumor.

Another possible sonographic finding in endometriosis is the presence of hypoechoic **endometrial plaques** on the serosal surface of pelvic bowel loops or urinary bladder. These plaques may tether the wall of the affected organ and show flow with color Doppler imaging. They are best demonstrated with the transvaginal probe (Fig. 14.41, Videos 14.9 and 14.10). "The sliding sign" is proving useful at predicting pouch of Douglas obliteration in women caused by endometriosis.[76-78]

LEIOMYOMATOSIS PERITONEALIS DISSEMINATA

Leiomyomatosis peritonealis disseminata is a relatively rare clinical entity characterized by multiple nodules, mainly the result of smooth muscle proliferation over the surface of the peritoneal cavity.[79] Leiomyomatosis peritonealis disseminata often mimics a malignant process, but the diagnosis is easily made with biopsy.

Typically, leiomyomatosis peritonealis disseminata is an incidental finding at imaging or during procedures such as laparoscopy, cesarean section, laparotomy, and postpartum tubal ligation.[29] It occurs mainly in women, primarily during the reproductive period. Exposure to estrogen seems to play an etiologic role. Many patients have uterine leiomyomas as well. Conservative care is generally indicated. When leiomyomatosis peritonealis disseminata occurs during pregnancy or with the oral contraceptive use, it may regress spontaneously after delivery or with oral contraceptive discontinuation. Malignant transformation of leiomyomatosis peritonealis disseminata remains uncertain. In a few isolated cases, malignant leiomyosarcomas have been

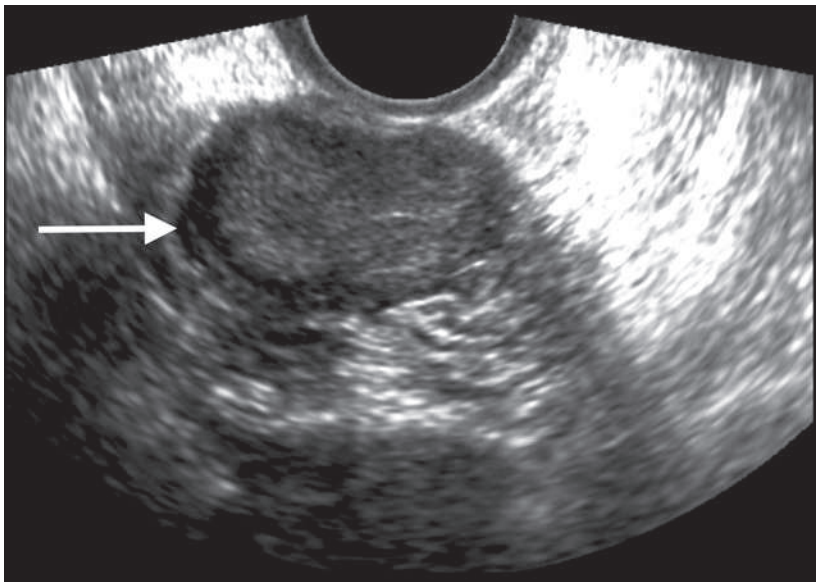

FIG. 14.40 Endometrioma in the Pouch of Douglas. Sagittal TVS shows a hypoechoic nodule deep in the pouch of Douglas *(arrow)* separate from the uterus and ovaries. This nodule could only be visualized by elevating the examining hand holding the probe. See also Video 14.8.

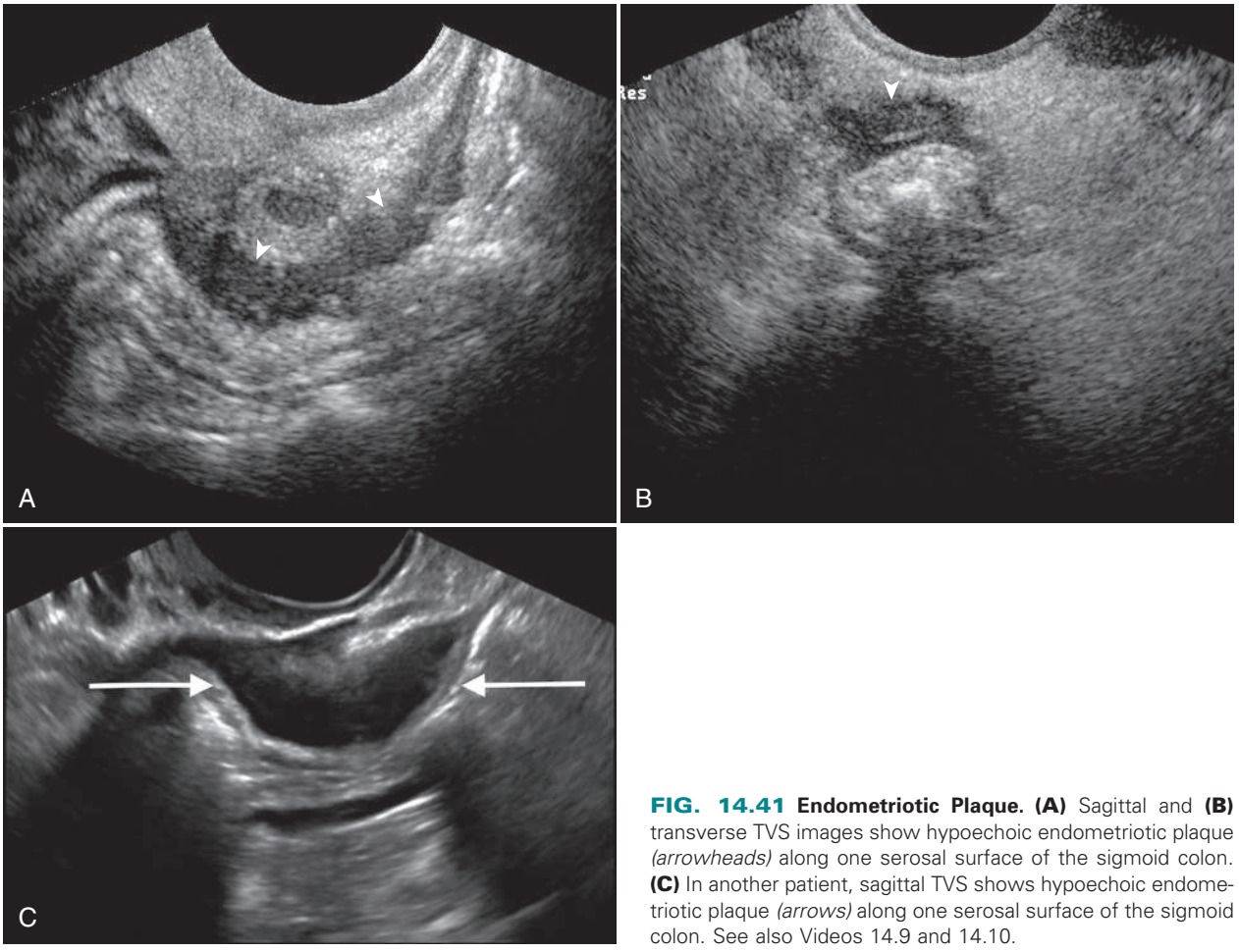

FIG. 14.41 Endometriotic Plaque. (A) Sagittal and **(B)** transverse TVS images show hypoechoic endometriotic plaque *(arrowheads)* along one serosal surface of the sigmoid colon. **(C)** In another patient, sagittal TVS shows hypoechoic endometriotic plaque *(arrows)* along one serosal surface of the sigmoid colon. See also Videos 14.9 and 14.10.

described shortly after making the diagnosis of leiomyomatosis peritonealis disseminata. A clear association, however, has not been established. Sonographic evaluation may show multiple small, hypoechoic nodules throughout the peritoneal cavity (Fig. 14.42).

PNEUMOPERITONEUM

CT is regarded as the standard for detecting, localizing, and quantifying free air.[80] Plain radiographs are also sensitive at detecting free air, with even 1 mL potentially visible on an erect

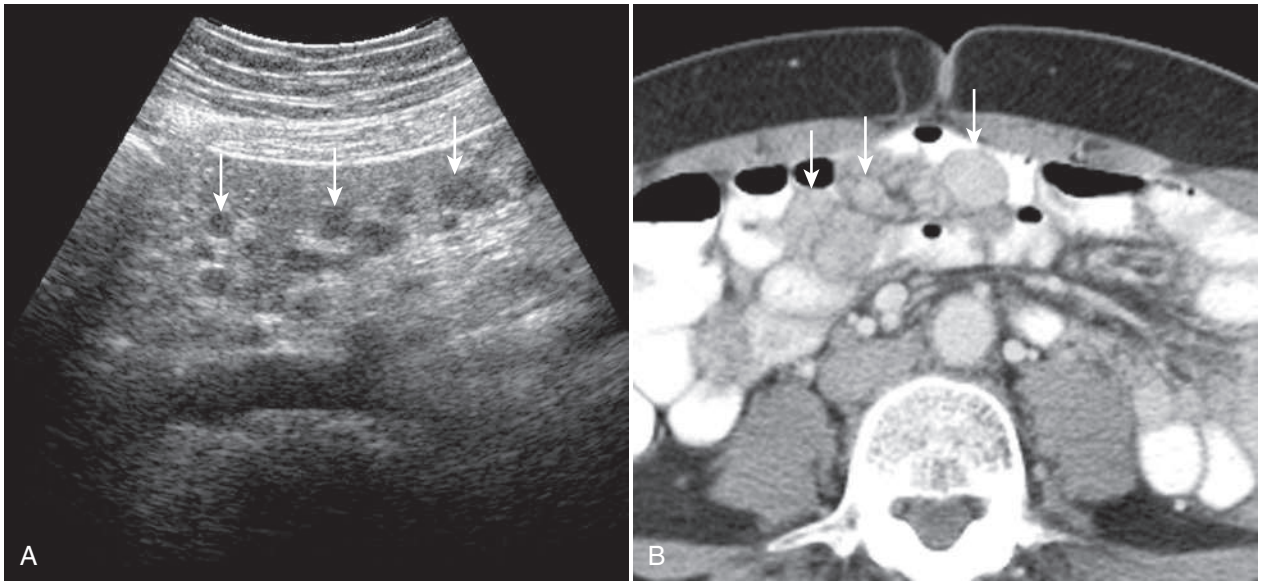

FIG. 14.42 Leiomyomatosis Peritonealis Disseminata. (A) Sagittal ultrasound and **(B)** axial CT, images show multiple small, hypoechoic, enhancing peritoneal nodules *(arrows)*.

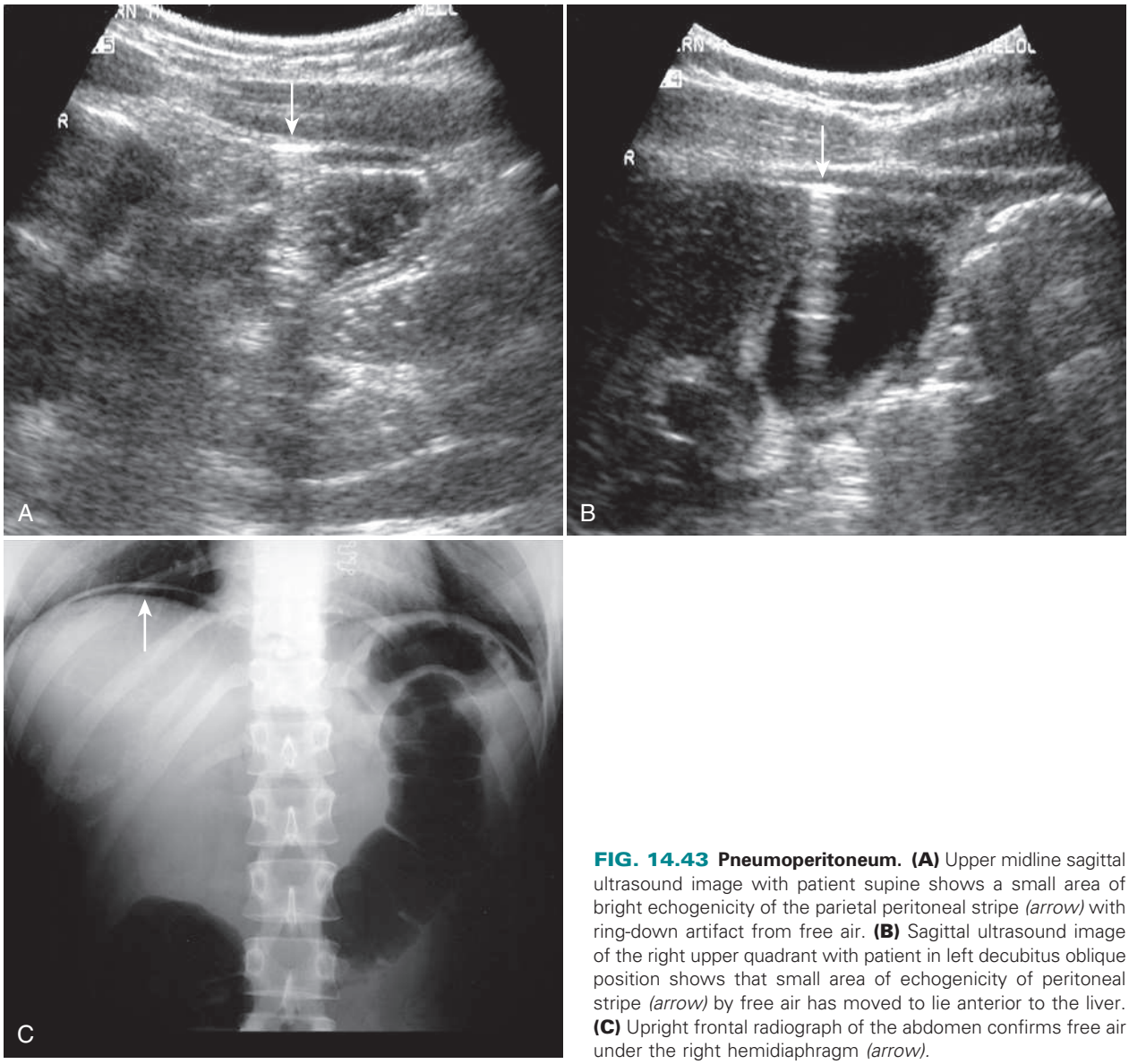

FIG. 14.43 Pneumoperitoneum. (A) Upper midline sagittal ultrasound image with patient supine shows a small area of bright echogenicity of the parietal peritoneal stripe *(arrow)* with ring-down artifact from free air. **(B)** Sagittal ultrasound image of the right upper quadrant with patient in left decubitus oblique position shows that small area of echogenicity of peritoneal stripe *(arrow)* by free air has moved to lie anterior to the liver. **(C)** Upright frontal radiograph of the abdomen confirms free air under the right hemidiaphragm *(arrow)*.

chest radiograph. Ultrasound is often the initial imaging modality requested to assess abdominal pain, however, so the identification of free air is an extremely important finding.

Sonographic technique is critical when assessing for free air. The patient should be scanned in the supine and steep left posterior oblique positions, paying particular attention to the epigastrium and right upper quadrants, respectively.[81,82] **Free air** in the epigastrium, with the patient lying supine, will frequently shift to the right upper quadrant with the patient lying in a left posterior oblique position (Fig. 14.43). Free air is most often seen just deep to the parietal peritoneum, is best appreciated with a linear array transducer, and appears as a region of extreme echogenicity of the parietal peritoneal line, often with posterior ring-down artifact.[83] Another sonographic sign of pneumoperitoneum in patients with ascites is gas bubbles in the ascitic fluid. Gas bubbles may appear as tiny, floating echogenic foci and have a high association with gut perforation and infection of the peritoneal fluid. When free air is detected, ultrasound will frequently reveal the underlying cause, so the remainder of the abdomen and pelvis should be carefully assessed for evidence of inflammation or tumor.[82]

CONCLUSION

Assessment of the peritoneum is easily performed with ultrasound in the majority of patients and should not add significantly to scanning time when the peritoneum is normal. There are limitations in extremely obese and postoperative patients, but in general, most peritoneal diseases can be readily detected and characterized with ultrasound. Many patterns of peritoneal disease are nonspecific, however, and sonographic findings must be interpreted in light of the patient's clinical symptoms, physical findings, and laboratory investigations. When fluid or tissue is required to reach a specific diagnosis, ultrasound is an efficient, cost-effective modality for guidance.[84] It is also a safe, readily available, and relatively inexpensive modality for monitoring disease progression and response to treatment. In patients with ovarian cancer, ultrasound is invariably performed as part of the patient's initial clinical workup. Because peritoneal dissemination is the major determinant of both prognosis and treatment choices, we recommend including the peritoneal cavity in the sonographic assessment of this patient population.

REFERENCES

1. Jeong YJ, Kim S, Kwak SW, et al. Neoplastic and nonneoplastic conditions of serosal membrane origin: CT findings. Radiographics. 2008;28(3):801-817.
2. Pickhardt PJ, Bhalla S. Primary neoplasms of peritoneal and sub-peritoneal origin: CT findings. Radiographics. 2005;25(4):983-995.
3. Elsayes KM, Staveteig PT, Narra VR, et al. MRI of the peritoneum: spectrum of abnormalities. AJR Am J Roentgenol. 2006;186(5):1368-1379.
4. Low RN. Gadolinium-enhanced MR imaging of liver capsule and peritoneum. Magn Reson Imaging Clin N Am. 2001;9(4):803-819, vii.
5. Low RN. MR imaging of the peritoneal spread of malignancy. Abdom Imaging. 2007;32(3):267-283.
6. Hanbidge AE, Lynch D, Wilson SR. US of the peritoneum. Radiographics. 2003;23(3):663-684, discussion 684-685.
7. Tirkes T, Sandrasegaran K, Patel AA, et al. Peritoneal and retroperitoneal anatomy and its relevance for cross-sectional imaging. Radiographics. 2012;32(2):437-451.
8. Healy JC, Reznek RH. The peritoneum, mesenteries and omenta: normal anatomy and pathological processes. Eur Radiol. 1998;8(6):886-900.
9. Derchi LE, Solbiati L, Rizzatto G, De Pra L. Normal anatomy and pathologic changes of the small bowel mesentery: US appearance. Radiology. 1987;164(3):649-652.
10. Damani N, Wilson SR. Nongynecologic applications of transvaginal US. Radiographics. 1999;19(Spec No):S179-S200.
11. Serafini G, Gandolfo N, Gandolfo N, et al. Transvaginal ultrasonography of nongynecologic pelvic lesions. Abdom Imaging. 2001;26(5):540-549.
12. Wang J, Gao L, Tang S, et al. A retrospective analysis on the diagnostic value of ultrasound-guided percutaneous biopsy for peritoneal lesions. World J Surg Oncol. 2013;11:251.
13. Goldberg BB, Goodman GA, Clearfield HR. Evaluation of ascites by ultrasound. Radiology. 1970;96(1):15-22.
14. Nichols JE, Steinkampf MP. Detection of free peritoneal fluid by transvaginal sonography. J Clin Ultrasound. 1993;21(3):171-174.
15. Meyers MA. The spread and localization of acute intraperitoneal effusions. Radiology. 1970;95(3):547-554.
16. Inadomi J, Cello JP, Koch J. Ultrasonographic determination of ascitic volume. Hepatology. 1996;24(3):549-551.
17. Edell SL, Gefter WB. Ultrasonic differentiation of types of ascitic fluid. AJR Am J Roentgenol. 1979;133(1):111-114.
18. Goerg C, Schwerk WB. Peritoneal carcinomatosis with ascites. AJR Am J Roentgenol. 1991;156(6):1185-1187.
19. Chiu WC, Cushing BM, Rodriguez A, et al. Abdominal injuries without hemoperitoneum: a potential limitation of focused abdominal sonography for trauma (FAST). J Trauma. 1997;42(4):617-623.
20. Kimura A, Otsuka T. Emergency center ultrasonography in the evaluation of hemoperitoneum: a prospective study. J Trauma. 1991;31(1):20-23.
21. Rozycki GS, Ochsner MG, Schmidt JA, et al. A prospective study of surgeon-performed ultrasound as the primary adjuvant modality for injured patient assessment. J Trauma. 1995;39(3):492-498.
22. Sirlin CB, Casola G, Brown MA, et al. Patterns of fluid accumulation on screening ultrasonography for blunt abdominal trauma: comparison with site of injury. J Ultrasound Med. 2001;20(4):351-357.
23. Wherrett LJ, Boulanger BR, McLellan BA, et al. Hypotension after blunt abdominal trauma: the role of emergent abdominal sonography in surgical triage. J Trauma. 1996;41(5):815-820.
24. Franklin JT, Azose AA. Sonographic appearance of chylous ascites. J Clin Ultrasound. 1984;12(4):239-240.
25. Hibbeln JF, Wehmueller MD, Wilbur AC. Chylous ascites: CT and ultrasound appearance. Abdom Imaging. 1995;20(2):138-140.
26. Hoffer FA, Kozakewich H, Colodny A, Goldstein DP. Peritoneal inclusion cysts: ovarian fluid in peritoneal adhesions. Radiology. 1988;169(1):189-191.
27. Kim JS, Lee HJ, Woo SK, Lee TS. Peritoneal inclusion cysts and their relationship to the ovaries: evaluation with sonography. Radiology. 1997;204(2):481-484.
28. Wilson SR. Pseudomyxoma peritonei. In: Cohen HL, editor. Gastrointestinal disease, test and syllabus. Reston, VA: American College of Radiology; 2004. pp. 73-84.
29. Levy AD, Arnáiz J, Shaw JC, Sobin LH. From the archives of the AFIP: primary peritoneal tumors: imaging features with pathologic correlation. Radiographics. 2008;28(2):583-607.
30. Arraiza M, Metser U, Vajpeyi R, et al. Primary cystic peritoneal masses and mimickers: spectrum of diseases with pathologic correlation. Abdom Imaging. 2014;40(4):875-906.
31. de Perrot M, Brundler M, Totsch M, et al. Mesenteric cysts. Toward less confusion? Dig Surg. 2000;17(4):323-328.
32. Egozi EI, Ricketts RR. Mesenteric and omental cysts in children. Am Surg. 1997;63(3):287-290.
33. Konen O, Rathaus V, Dlugy E, et al. Childhood abdominal cystic lymphangioma. Pediatr Radiol. 2002;32(2):88-94.
34. Meyers MA, Oliphant M, Berne AS, Feldberg MA. The peritoneal ligaments and mesenteries: pathways of intraabdominal spread of disease. Radiology. 1987;163(3):593-604.

35. Rioux M, Michaud C. Sonographic detection of peritoneal carcinomatosis: a prospective study of 37 cases. Abdom Imaging. 1995;20(1):47-51.
36. Koutselini HA, Lazaris AC, Thomopoulou G, et al. Papillary serous carcinoma of peritoneum: case study and review of the literature on the differential diagnosis of malignant peritoneal tumors. Adv Clin Path. 2001;5(3): 99-104.
37. Halperin R, Zehavi S, Langer R, et al. Primary peritoneal serous papillary carcinoma: a new epidemiologic trend? A matched-case comparison with ovarian serous papillary cancer. Int J Gynecol Cancer. 2001;11(5):403-408.
38. Chopra S, Laurie LR, Chintapalli KN, et al. Primary papillary serous carcinoma of the peritoneum: CT-pathologic correlation. J Comput Assist Tomogr. 2000;24(3):395-399.
39. Furukawa T, Ueda J, Takahashi S, et al. Peritoneal serous papillary carcinoma: radiological appearance. Abdom Imaging. 1999;24(1):78-81.
40. Morita H, Aoki J, Taketomi A, et al. Serous surface papillary carcinoma of the peritoneum: clinical, radiologic, and pathologic findings in 11 patients. AJR Am J Roentgenol. 2004;183(4):923-928.
41. Voultsinos V, Semelka RC, Elias Jr J, et al. Primary peritoneal carcinoma: computed tomography and magnetic resonance findings. J Comput Assist Tomogr. 2008;32(4):541-547.
42. Zissin R, Hertz M, Shapiro-Feinberg M, et al. Primary serous papillary carcinoma of the peritoneum: CT findings. Clin Radiol. 2001;56(9): 740-745.
43. Moertel CG. Peritoneal mesothelioma. Gastroenterology. 1972;63(2): 346-350.
44. Guest PJ, Reznek RH, Selleslag D, et al. Peritoneal mesothelioma: the role of computed tomography in diagnosis and follow up. Clin Radiol. 1992;45(2):79-84.
45. Reuter K, Raptopoulos V, Reale F, et al. Diagnosis of peritoneal mesothelioma: computed tomography, sonography, and fine-needle aspiration biopsy. AJR Am J Roentgenol. 1983;140(6):1189-1194.
46. Runyon BA, Hoefs JC. Peritoneal lymphomatosis with ascites. A characterization. Arch Intern Med. 1986;146(5):887-888.
47. Lynch MA, Cho KC, Jeffrey Jr RB, et al. CT of peritoneal lymphomatosis. AJR Am J Roentgenol. 1988;151(4):713-715.
48. O'Connell JT, Tomlinson JS, Roberts AA, et al. Pseudomyxoma peritonei is a disease of MUC2-expressing goblet cells. Am J Pathol. 2002;161(2): 551-564.
49. Hart WR. Ovarian epithelial tumors of borderline malignancy (carcinomas of low malignant potential). Hum Pathol. 1977;8(5):541-549.
50. Yan H, Pestieau SR, Shmookler BM, Sugarbaker PH. Histopathologic analysis in 46 patients with pseudomyxoma peritonei syndrome: failure versus success with a second-look operation. Mod Pathol. 2001;14(3):164-171.
51. Fox H. Pseudomyxoma peritonei. Br J Obstet Gynaecol. 1996;103(3): 197-198.
52. Mann Jr WJ, Wagner J, Chumas J, Chalas E. The management of pseudomyxoma peritonei. Cancer. 1990;66(7):1636-1640.
53. Sugarbaker PH. Cytoreductive surgery and perioperative intraperitoneal chemotherapy as a curative approach to pseudomyxoma peritonei syndrome. Tumori. 2001;87(4):S3-S5.
54. Walensky RP, Venbrux AC, Prescott CA, Osterman Jr FA. Pseudomyxoma peritonei. AJR Am J Roentgenol. 1996;167(2):471-474.
55. Que Y, Tao C, Wang X, et al. Pseudomyxoma peritonei: some different sonographic findings. Abdom Imaging. 2012;37(5):843-848.
56. Seshul MB, Coulam CM. Pseudomyxoma peritonei: computed tomography and sonography. AJR Am J Roentgenol. 1981;136(4):803-806.
57. Yeh HC, Wolf BS. Ultrasonography in ascites. Radiology. 1977;124(3): 783-790.
58. Prousalidis J, Tzardinoglou K, Sgouradis L, et al. Uncommon sites of hydatid disease. World J Surg. 1998;22(1):17-22.
59. Gazelle GS, Mueller PR. Abdominal abscess. Imaging and intervention. Radiol Clin North Am. 1994;32(5):913-932.
60. Snider Jr DE, Roper WL. The new tuberculosis. N Engl J Med. 1992;326(10): 703-705.
61. Marshall JB. Tuberculosis of the gastrointestinal tract and peritoneum. Am J Gastroenterol. 1993;88(7):989-999.
62. Vanhoenacker FM, De Backer AI, Op de BB, et al. Imaging of gastrointestinal and abdominal tuberculosis. Eur Radiol. 2004;14(Suppl. 3):E103-E115.
63. Akhan O, Pringot J. Imaging of abdominal tuberculosis. Eur Radiol. 2002;12(2):312-323.
64. Kedar RP, Shah PP, Shivde RS, Malde HM. Sonographic findings in gastrointestinal and peritoneal tuberculosis. Clin Radiol. 1994;49(1):24-29.
65. Lee DH, Lim JH, Ko YT, Yoon Y. Sonographic findings in tuberculous peritonitis of wet-ascitic type. Clin Radiol. 1991;44(5):306-310.
66. von Hahn T, Bange FC, Westhaus S, et al. Ultrasound presentation of abdominal tuberculosis in a German tertiary care center. Scand J Gastroenterol. 2013; 49(2):184-190.
67. Malik A, Saxena NC. Ultrasound in abdominal tuberculosis. Abdom Imaging. 2003;28(4):574-579.
68. Cohen O, Abrahamson J, Ben-Ari J, et al. Sclerosing encapsulating peritonitis. J Clin Gastroenterol. 1996;22(1):54-57.
69. Hollman AS, McMillan MA, Briggs JD, et al. Ultrasound changes in sclerosing peritonitis following continuous ambulatory peritoneal dialysis. Clin Radiol. 1991;43(3):176-179.
70. Krestin GP, Kacl G, Hauser M, et al. Imaging diagnosis of sclerosing peritonitis and relation of radiologic signs to the extent of the disease. Abdom Imaging. 1995;20(5):414-420.
71. Sarrazin J, Wilson SR. Manifestations of Crohn disease at US. Radiographics. 1996;16(3):499-520.
72. McDonnell 3rd CH, Jeffrey Jr RB, Vierra MA. Inflamed pericholecystic fat: color Doppler flow imaging and clinical features. Radiology. 1994;193(2): 547-550.
73. McClure MJ, Khalili K, Sarrazin J, Hanbidge A. Radiological features of epiploic appendagitis and segmental omental infarction. Clin Radiol. 2001;56(10):819-827.
74. Puylaert JB. Right-sided segmental infarction of the omentum: clinical, US, and CT findings. Radiology. 1992;185(1):169-172.
75. Woodward PJ, Sohaey R, Mezzetti Jr TP. Endometriosis: radiologic-pathologic correlation. Radiographics. 2001;21(1):193-216.
76. Holland TK, Cutner A, Saridogan E, et al. Ultrasound mapping of pelvic endometriosis: does the location and number of lesions affect the diagnostic accuracy? A multicentre diagnostic accuracy study. BMC Womens Health. 2013;13:43.
77. Koninckx PR, Ussia A, Adamyan L, et al. Deep endometriosis: definition, diagnosis, and treatment. Fertil Steril. 2012;98(3):564-571.
78. Reid S, Lu C, Casikar I, et al. Prediction of pouch of Douglas obliteration in women with suspected endometriosis using a new real-time dynamic transvaginal ultrasound technique: the sliding sign. Ultrasound Obstet Gynecol. 2012;41(6):685-691.
79. Bekkers RL, Willemsen WN, Schijf CP, et al. Leiomyomatosis peritonealis disseminata: does malignant transformation occur? A literature review. Gynecol Oncol. 1999;75(1):158-163.
80. Baker SR. Imaging of pneumoperitoneum. Abdom Imaging. 1996;21(5): 413-414.
81. Braccini G, Lamacchia M, Boraschi P, et al. Ultrasound versus plain film in the detection of pneumoperitoneum. Abdom Imaging. 1996;21(5):404-412.
82. Lee DH, Lim JH, Ko YT, Yoon Y. Sonographic detection of pneumoperitoneum in patients with acute abdomen. AJR Am J Roentgenol. 1990;154(1):107-109.
83. Muradali D, Wilson S, Burns PN, et al. A specific sign of pneumoperitoneum on sonography: enhancement of the peritoneal stripe. AJR Am J Roentgenol. 1999;173(5):1257-1262.
84. Gottlieb RH, Tan R, Widjaja J, et al. Extravisceral masses in the peritoneal cavity: sonographically guided biopsies in 52 patients. AJR Am J Roentgenol. 1998;171(3):697-701.

CHAPTER 15

The Uterus

Douglas Brown and Deborah Levine

SUMMARY OF KEY POINTS

- Transvaginal ultrasound is usually needed for optimal assessment of the uterus.
- Uterine enlargement in a nonpregnant patient is most commonly caused by fibroids or adenomyosis.
- Adenomyosis should be considered when there is an enlarged globular shape of the uterus; heterogeneity or asymmetrical thickening of the myometrium; indistinct interface between the endometrium and myometrium; or cysts, echogenic striations, or echogenic nodules in the myometrium.
- Leiomyosarcomas of the uterus overlap in appearance with much more common leiomyomas and are difficult to diagnose by ultrasound.
- If an intrauterine device (IUD) is low in the uterus, one should suspect that one or both arms of the IUD are embedded in the myometrium.
- Assessment of the fundal contour of the myometrium and endometrium in the coronal plane using three-dimensional (3-D) ultrasound is important for diagnosing the most common müllerian duct anomalies.
- Infrequently the endometrium will not be fully seen on ultrasound; when this occurs, one should state that it cannot be reliably measured.

CHAPTER OUTLINE

INTRODUCTION AND SCANNING TECHNIQUES
NORMAL UTERINE FINDINGS
MÜLLERIAN DUCT ANOMALIES
ABNORMALITIES OF THE MYOMETRIUM
Leiomyoma
Leiomyosarcoma
Adenomyosis
ABNORMALITIES OF THE CERVIX
ABNORMALITIES OF THE ENDOMETRIUM
Postmenopausal Endometrium
Hormone Use
Postmenopausal Bleeding
The Obstructed Uterus: Hydrometrocolpos and Hematometrocolpos
Endometrial Hyperplasia
Endometrial Polyps
Endometrial Carcinoma
Endometrial Sarcoma
Endometrial Adhesions
Endometrial Ablation
SONOGRAPHY OF CONTRACEPTIVE DEVICES
Intrauterine Contraceptive Devices
Tubal Occlusion Devices
POSTPARTUM FINDINGS
Normal Findings
Bleeding Postpartum
Retained Products of Conception
Endometritis
Arteriovenous Malformation
Findings After Cesarean Section
Acknowledgment

INTRODUCTION AND SCANNING TECHNIQUES

Sonography plays an integral role in evaluation of the uterus. Both transabdominal sonography (TAS) and transvaginal sonography (TVS) are well-established techniques for assessing the enlarged uterus and patients with abnormal vaginal bleeding. The anterior surface of the uterine fundus and body is covered by peritoneum. The peritoneal space anterior to the uterus is the **vesicouterine pouch,** or **anterior cul-de-sac.** This space is usually empty, but it may contain small bowel. Posteriorly, the peritoneal reflection extends to the posterior fornix of the vagina, forming the **rectouterine recess,** or **posterior cul-de-sac.** Laterally, the peritoneal reflection forms the **broad ligaments,** which extend from the lateral aspect of the uterus to the lateral pelvic side walls (Fig. 15.1). The **round ligaments** arise from the uterine cornua anterior to the fallopian tubes in the broad ligaments, extend anterolaterally, and course through the inguinal canals to insert into the fascia of the labia majora.

The **cervix** is located posterior to the bladder and opens into the upper vagina through the external os. The **vagina** is a fibromuscular canal that lies in the midline and runs from the cervix to the vestibule of the external genitalia. The cervix projects into the proximal vagina, creating a space between

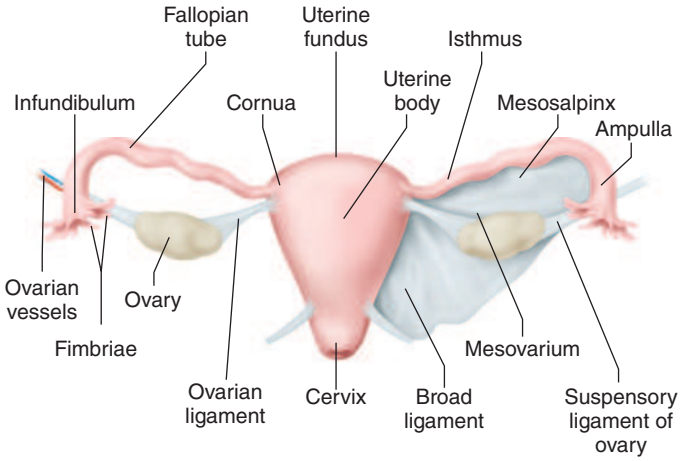

FIG. 15.1 Normal Gynecologic Organs. Diagram of uterus, ovaries, fallopian tubes, and related structures. On left side of the image, the broad ligament has been removed.

the vaginal walls and the surface of the cervix called the **vaginal fornix.**

The arterial blood supply to the uterus comes primarily from the **uterine artery,** a major branch of the anterior trunk of the internal iliac artery. The uterine artery ascends along the lateral margin of the uterus in the broad ligament and, at the level of the uterine cornua, runs laterally to anastomose with the ovarian artery. The uterine arteries anastomose extensively across the midline through the anterior and posterior arcuate arteries, which run within the broad ligament and then enter the myometrium.[1] The uterine plexus of veins accompanies the arteries.

The uterus is usually best imaged with TVS, with as high a frequency as possible that also allows sound to adequately penetrate the uterus. However, scanning with TAS is often helpful when the uterus is enlarged and/or fibroids are located very superiorly or laterally; in such instances TVS alone may miss important findings. Thus it is important to look, albeit sometimes briefly, with TAS regardless of the degree of fullness of the urinary bladder.

Advantages of Transvaginal Sonography

Use of higher-frequency transducers with better resolution
Examination of patients who are unable to fill their bladder
Examination of obese patients
Evaluation of a retroverted or retroflexed uterus
Better characterization of the internal characteristics of a pelvic mass
Better detail of a pelvic lesion
Better detail of the endometrium

Doppler ultrasound evaluation, most often with conventional color Doppler or power Doppler, is helpful in some patients. It can be used to evaluate for the presence of vascular flow and in select cases can provide an assessment of the degree and character of vascularity. As true for any application of color or power Doppler imaging, small pixels of color that are not part of a distinct vessel should have spectral Doppler evaluation to distinguish arterial or venous flow from noise.

Three-dimensional ultrasound (3-D ultrasound), usually performed with a transvaginal transducer, is most useful for evaluating **müllerian** anomalies of the uterus and for assessment of abnormal position of an **intrauterine device** (IUD).[2] 3-D ultrasound may also be helpful in other instances such as defining the relationship of uterine lesions to the endometrial cavity and may be useful to document findings during sonohysterography (SHG).

Sonohysterography can provide assessment of endometrium or submucosal myometrial lesions, by distending the endometrial cavity. Most studies on infusion techniques have used sterile saline.[3-6] However, gel infusion is now also being used at some centers.[7,8] SHG is not routinely needed but may be helpful if the endometrium is not adequately evaluated by TVS or TAS and may also be helpful in women with abnormal bleeding when a focal lesion is not visualized sonographically. Other indications may include evaluation of endometrial or intracavitary abnormalities detected by TVS, infertility,[9] suspected congenital uterine malformations,[10] and evaluation of women taking tamoxifen.[11]

The procedure involves placement of a sterile speculum, cleansing of the external cervical os with an aseptic solution, and placement of a sterile catheter through the cervix into the endometrial cavity. Several catheters are available, including some with a balloon (to help prevent leakage of the saline back out the cervix) and some without a balloon. If a balloon catheter is used, it should also be filled with saline, as using air may obscure part of the endometrium. Once the speculum has been removed and the transvaginal transducer inserted, sterile saline is slowly injected during ultrasound observation while fully scanning the entire endometrial cavity. If a balloon catheter is used, one should be careful that it does not obscure part of the endometrium; this generally requires deflation of the balloon at the end of the procedure. For premenopausal women, SHG should generally be performed at about day 4 to 10 of the menstrual cycle, when the patient is no longer bleeding but is still early in the menstrual cycle when the endometrium tends to be thin, allowing for avoidance of normal changes in the latter part of the menstrual cycle that can simulate pathology.[12] In postmenopausal women receiving sequential **hormone replacement therapy** (HRT), SHG is performed shortly after the monthly bleeding period. In postmenopausal women not receiving HRT, the procedure can be performed at any time. SHG should not be performed in patients who are pregnant or who have acute pelvic inflammatory disease. Prophylactic antibiotics may be considered in some women, such as those with chronic pelvic inflammatory disease,[12,13] including those in whom a hydrosalpinx is discovered at the time of the study.

Other sonographic methods are used infrequently. Transrectal ultrasound may occasionally be useful to evaluate portions of the uterus if TVS is inadequate, if the patient is a virgin, or if additional imaging is needed for better assessment of the endometrium or pelvic floor.[14,15] Translabial or transperineal scanning, although helpful for abnormalities of the pelvic floor,[16] is rarely useful to evaluate the uterus in a nonpregnant patient. Use of

intravenous ultrasound contrast agents to evaluate the uterus is still in its infancy but there are possible applications in such areas as endometrial lesions.[17] Elastography could potentially help in the evaluation of fibroids, adenomyosis, or sarcomas.[18] Both of these techniques need further investigation before routine clinical use.

NORMAL UTERINE FINDINGS

The uterus is typically divided into at least three sections anatomically, although precise boundaries may be difficult to determine with ultrasound. The **fundus** of the uterus is the most superior portion of uterus, often defined as that portion superior to the ostia of the fallopian tubes. The **body of the uterus** is the largest portion and lies between the fundus and the cervix. The term "isthmus" or "lower uterine segment" is sometimes used, usually referring to the region where the body of the uterus becomes slightly thinner just superior to the cervix. The **cervix** is the inferior portion of the uterus between the external cervical os and internal cervical os. The internal cervical os is often difficult to precisely locate in the nonpregnant uterus.

The position of the uterus is variable and can change with the degree of bladder and/or rectal distension (Fig. 15.2). It may also change during the course of the ultrasound examination in response to pressure from the transvaginal transducer or pressure from the examiner's hand on the lower abdominal wall. The term "version" is used to describe the sagittal axis of the cervix with respect to the sagittal axis of the vagina. The term "flexion" is used to describe the sagittal axis of the uterine body with respect to the sagittal axis of the cervix. These are usually subjective determinations; objective criteria have been suggested but are not widely accepted.[19] The direction of flexion and version

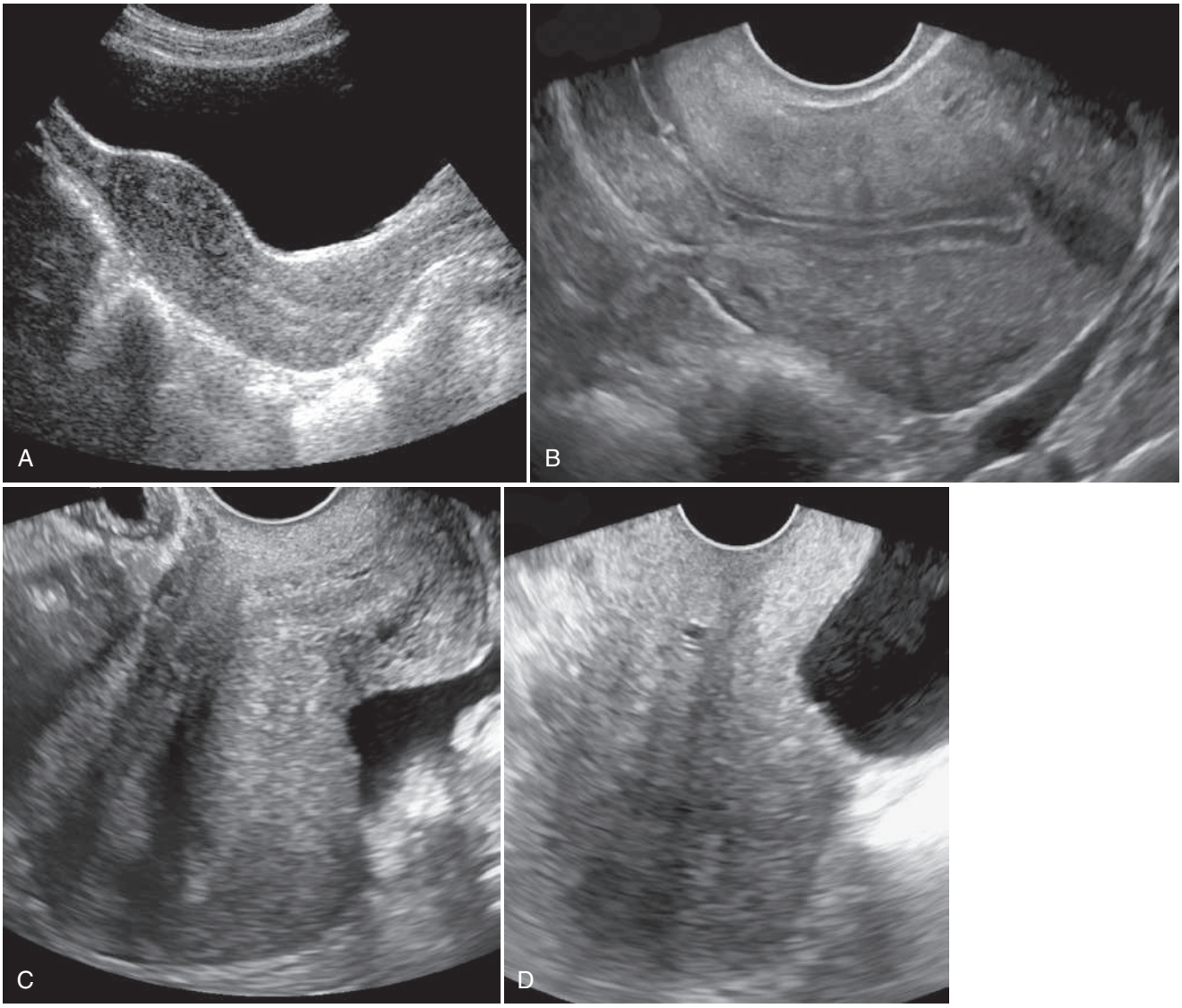

FIG. 15.2 Uterine Positions in the Sagittal Plane. (A) Anteverted, anteflexed position on TAS. **(B)** Retroverted, retroflexed position on TVS. **(C)** Anteverted, retroflexed position on TVS. The uterine body and fundus may be poorly seen with such a uterine position, as in this case. **(D)** Axial uterine position on TVS. The uterus is usually poorly seen when in this position.

are usually the same and the uterus is most frequently anteverted and anteflexed.[19] Anteverted, retroflexed position has been associated with prior cesarean section.[19] Occasionally the sagittal axis of the uterus is the same as the sagittal axis of the vagina. Such a position usually limits TVS evaluation of the uterus. Variable terms have been used to describe this latter position of the uterus, including "axial," "vertical," "midposition," or "partly retroverted."[19-21] One can try to change the uterine position by moving the transducer into the anterior or posterior vaginal fornix and applying gentle pressure with the transducer and/or the nonscanning hand on the lower abdominal wall.

Uterine size varies depending on patient age and gravidity.[13,22-24] In nulliparous adult women, a normal uterus has a pear-shaped appearance, with the diameter and length of the body about double that of the cervix.[25] In general, it measures less than about 8 cm in length, 5 cm in width, and 4 cm in anteroposterior (AP) diameter. **Parity** (pregnancy) can increase the normal size by 1 to 2 cm in each dimension.[23,22,26] After menopause the uterus atrophies, with the most rapid decrease in size occurring in the first 10 years after cessation of menstruation.[23] In patients older than 65 years, the uterus ranges from 3.5 to 6.5 cm in length and 1.2 to 1.8 cm in AP diameter.[26]

In premenopausal patients the endometrium varies in appearance and thickness during the menstrual cycle[27-32] (Fig. 15.3). The endometrium is composed of a **superficial functional layer** and a **deep basal layer.** The functional layer thickens throughout the menstrual cycle and is shed with menses. The basal layer remains intact during the cycle and contains the spiral arteries, which become tortuous and elongated to supply the functional layer as it thickens. The **proliferative phase** of the cycle before ovulation is under the influence of estrogen, whereas progesterone is mainly responsible for maintenance of the endometrium in the **secretory phase** following ovulation.

When obtaining an **endometrial thickness measurement,** one should make the measurement in the sagittal plane of the uterus, perpendicular to the long axis of the endometrium, at the endometrium's thickest point, including both the anterior and posterior layers.[33] If fluid is present in the endometrial cavity, it should be excluded from the measurement. If one cannot see the entire endometrium, which may occur in up to 10% of patients, a thickness measurement should not be reported and instead one should report that it cannot be reliably measured.[33] Such limited assessment of the endometrium may occur for various reasons including fibroids, marked obesity, and uterine position.[34] SHG may be helpful in these patients.

During the **menstrual phase** the endometrium is usually a thin hyperechoic line but may be irregular or contain a small amount of fluid from blood. During the **proliferative phase** the endometrium thickens slightly, and later in the proliferative phase develops a multilayered appearance, also known as trilaminar or triple layer. This appearance is due to the thin echogenic line centrally that represents the opposed endometrial mucosal surfaces, the functional layer of the endometrium that becomes relatively hypoechoic, and a thin echogenic outer line. The thin echogenic outer line may be the basal layer of the endometrium or the interface between the endometrium and the myometrium. One potential pitfall in measuring the endometrium is to mistake the hypoechoic inner myometrium as part of the endometrium. One can usually make the distinction because the multilayered appearance of the proliferative phase has a distinct outer echogenic line, whereas the hypoechoic inner myometrium has no such defining outer echogenic line. After ovulation, in the **secretory phase** the functional layer of the endometrium becomes hyperechoic, usually starting on the outer edge and progressing inward. It generally becomes uniformly hyperechoic by the mid to late secretory phase.[29-32] The endometrium tends to have more distal acoustic enhancement in the secretory phase, which can potentially be mistaken for the endometrium itself when the endometrium is poorly seen. The secretory endometrium may measure up to 16 to 20 mm (though there is no accepted upper limit of normal), and the appearance may be heterogeneous. One may occasionally see endometrial folds that can simulate polyps during the secretory phase.[33,34] One should be cautious before diagnosing polyps or an abnormally thick endometrium during this phase of the menstrual cycle and consider follow-up ultrasound in the proliferative phase.

In postmenopausal women the endometrium is normally homogeneously hyperechoic in appearance. In postmenopausal women without vaginal bleeding, the upper limit of acceptable thickness is 8 to 11 mm.[35-40] It should be noted that these limits are greater than expected for an atrophic endometrium and that polyps or hyperplasia could be present. However, because cancer tends to bleed early, this higher threshold in postmenopausal women who are not bleeding is acceptable in order to limit the number of endometrial biopsies for benign disease. When there is abnormal vaginal bleeding, the upper limit of normal thickness is based on the trade-off between sensitivity and specificity, and thresholds of 3 to 5 mm have been suggested. These are described in more detail in the section on endometrial bleeding.

The myometrium is normally homogeneous in echogenicity. The normal **myometrium** consists of three layers, although they are not distinctly separated from one another. The **intermediate layer** is the thickest and has a uniformly homogeneous texture of low to moderate echogenicity. The **inner layer** of myometrium is thin, compact, and relatively hypovascular.[41,42] This inner layer, which is hypoechoic and surrounds the relatively echogenic endometrium, has also been referred to as the **subendometrial halo.** It should be noted that this is not necessarily the same as the junctional zone on magnetic resonance imaging (MRI).[43] The thin **outer layer** is slightly less echogenic than the intermediate layer and is separated from it by the arcuate vessels.

The **arcuate arteries** lie between the outer and intermediate layers of the myometrium and branch into the **radial arteries,** which run in the intermediate layer to the level of the inner layer. The radial arteries then branch into the **spiral arteries,** which enter the endometrium and supply the functional layer. The **uterine veins** are larger than the accompanying arcuate arteries and are frequently identified as small, focal anechoic or hypoechoic areas on both TAS and TVS.[44] These veins can occasionally be prominent and simulate cystic areas (Fig. 15.4). Although Doppler imaging may be helpful in confirming the vascular nature of these spaces, the flow may be too slow to be detected by color Doppler imaging. Power Doppler imaging may be helpful in this instance; however, observation of these spaces

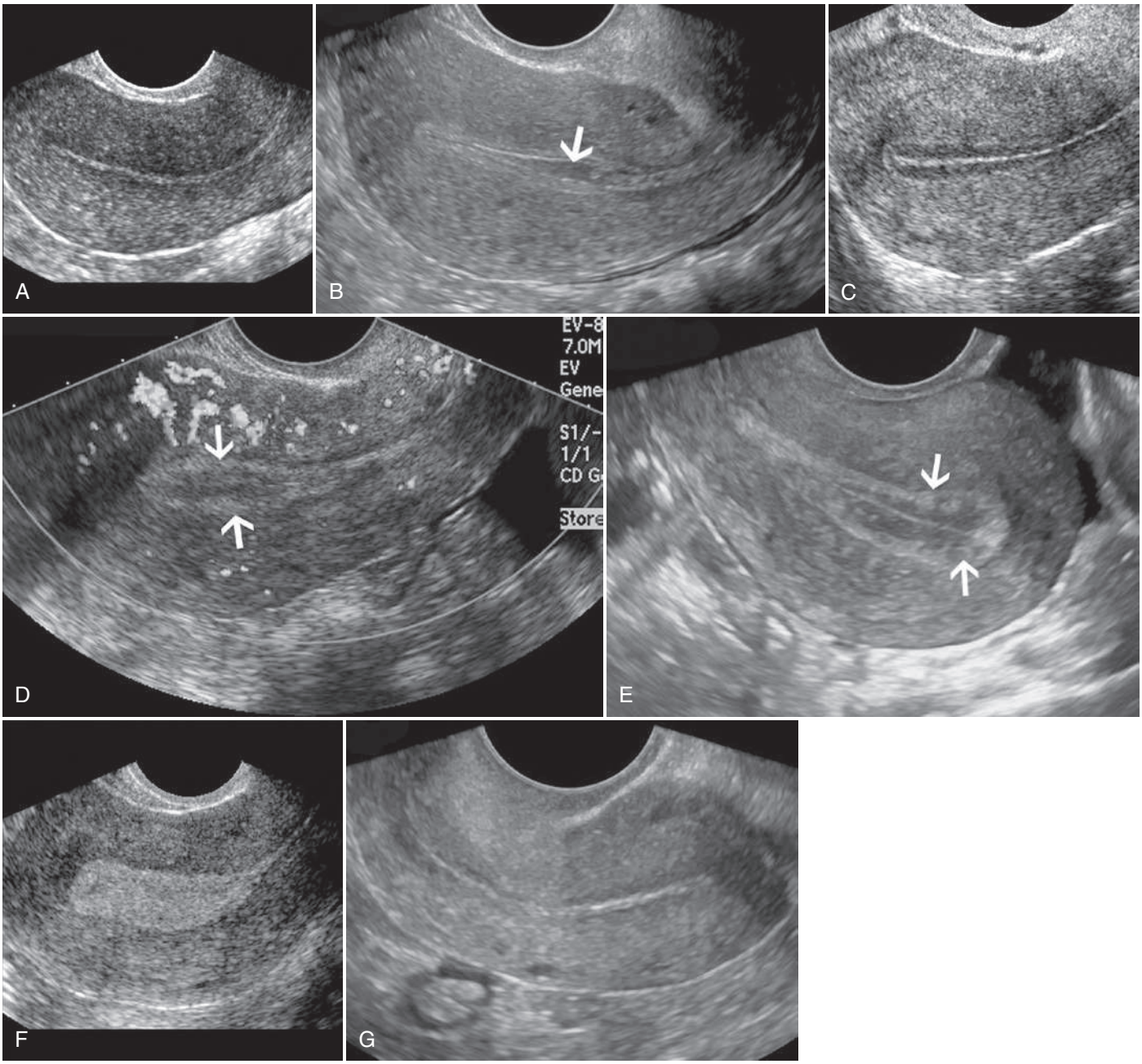

FIG. 15.3 Endometrium—Normal Appearances. All images were obtained with sagittal TVS. **(A)** Normal thin endometrium that may be seen in the menstrual phase or very early proliferative phase. A similar appearance is normal in postmenopausal women. **(B)** Normal thin endometrium with trace fluid *(arrow)* in the endometrial cavity in the menstrual phase. **(C)** Multilayered, also known as "triple-layered" or "trilaminar" (or sandwich sign), appearance typical of the mid to late proliferative phase. **(D)** In the secretory phase, the endometrium begins to become hyperechoic, usually beginning at the outer edge *(arrows)* and progressing inward. **(E)** As the endometrium becomes hyperechoic in the secretory phase, it sometimes does so in an irregular fashion, which can simulate polyps. These have been referred to as **endometrial moguls** or **pseudopolyps** *(arrows)*. Repeat scanning in the proliferative phase of the menstrual cycle can be helpful in such cases. **(F)** Uniformly hyperechoic appearance of the endometrium in the late secretory phase. **(G)** Normal thin postmenopausal endometrium, in this case measuring 2 mm in thickness.

with real-time gray-scale imaging, perhaps with increased gain settings, will usually show the movement of echoes in these veins with slow flow, confirming their vascular nature. Small calcifications may be present in the outer myometrium (Fig. 15.5), thought to be in arcuate arteries, and are most commonly seen in postmenopausal women.[45,46] Although it has been suggested that these calcifications might be more common in women with systemic diseases such as diabetes mellitus and renal failure, the literature thus far describes only a small number of patients.[13,45,46] The peripheral location and diffuse linear nature of these vascular calcifications should help distinguish them from calcified fibroids.

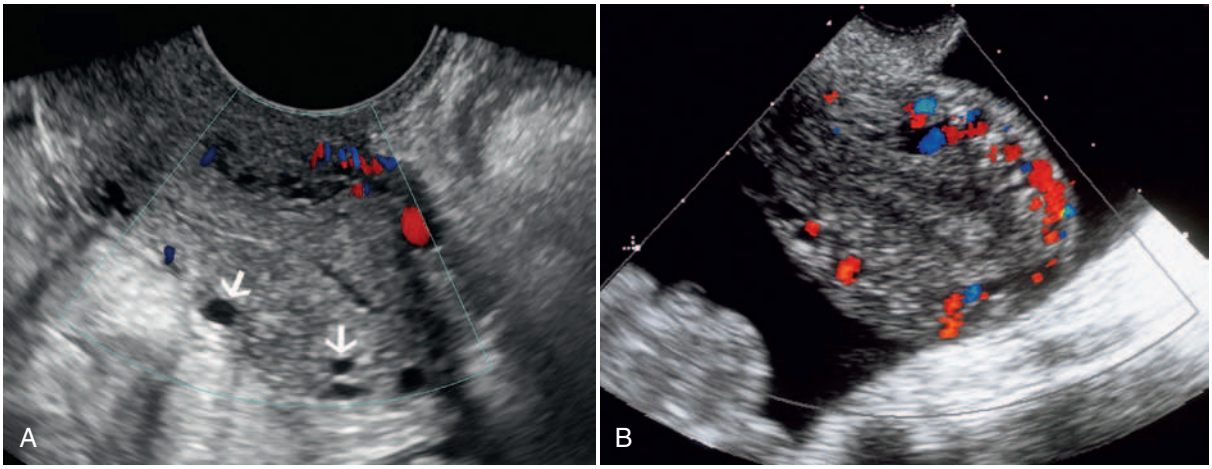

FIG. 15.4 Myometrial Veins. (A) Sagittal TVS shows prominent veins in the outer myometrium. A few had flow demonstrated on Doppler imaging, but many did not have detectable flow on Doppler (two indicated by *arrows*), owing to slow velocity of flow. Real-time imaging showed movement of echoes within these veins. **(B)** Another similar example. There is fluid in the pelvis surrounding the uterus.

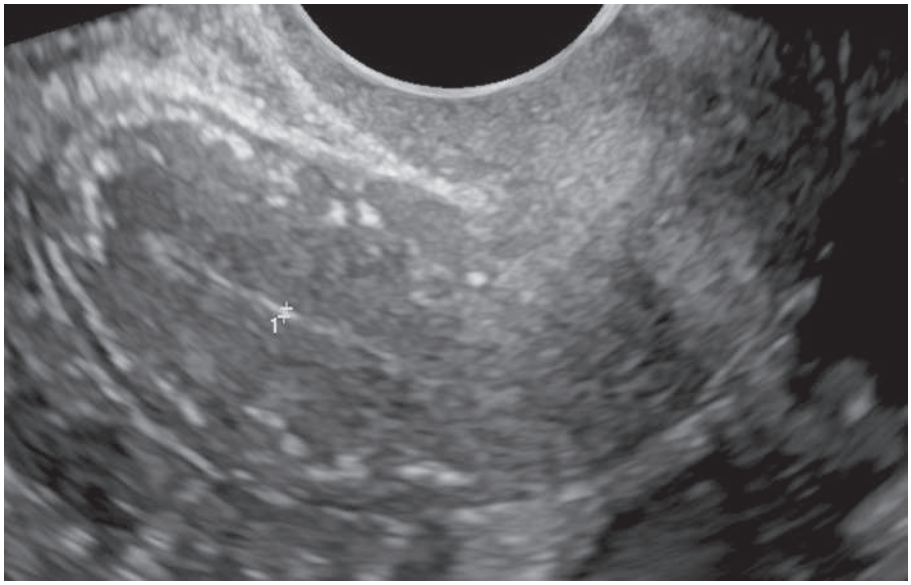

FIG. 15.5 Arcuate Artery Calcifications. Sagittal TVS demonstrates multiple echogenic foci in the outer myometrium due to arcuate artery calcifications. A normal thin endometrium is also noted in this postmenopausal patient (*calipers* centrally).

Myometrial contractions, although more commonly seen during pregnancy, can occasionally be seen in the inner myometrium of nonpregnant women.[47] However, these are subtle contractions and in general not as large or as likely to be mistaken for pathology as may occur during pregnancy.

Tiny echogenic foci, often without acoustic shadowing, may be present in the inner myometrium near the endometrial/myometrial interface (Fig. 15.6). Few data are available for this finding, but it seems to be of no clinical importance and may be due to dystrophic calcification related to prior uterine instrumentation.[48]

The cervix frequently contains cysts, most of which are mucous retention cysts and are commonly termed **nabothian cysts.** They often appear as simple cysts but may occasionally have internal echoes in the cyst fluid (Fig. 15.7). Although variable in size and number, most nabothian cysts are small and of no clinical importance.[49] Mucosal folds in the cervix, termed **plicae palmatae,** are more commonly seen with MRI but may occasionally be seen with TVS (see Fig. 15.7E). Tiny echogenic foci may also be seen in the inner portion of the cervix and are likely due to punctate calcifications (see Fig. 15.7F). These may be related to prior uterine instrumentation and are considered a benign finding.[50] The inner part of the cervix may also appear slightly hypoechoic compared with the outer cervix and possibly simulate a mass (Fig. 15.8). The uniform elongated nature of this finding should help distinguish it from a true mass.

MÜLLERIAN DUCT ANOMALIES

The fused caudal ends of the two müllerian **(paramesonephric)** ducts form the uterus, cervix, and upper two-thirds of the vagina. Fusion typically occurs in the medial portion of the ducts and

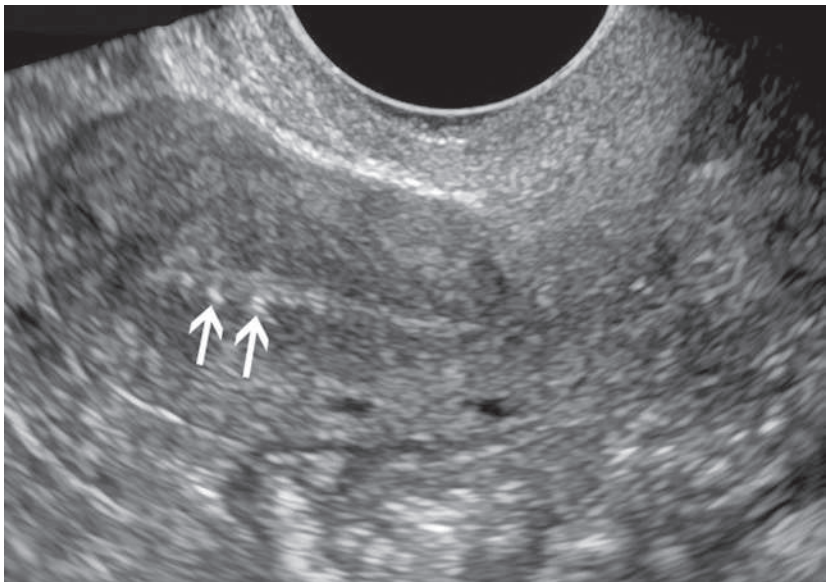

FIG. 15.6 Calcifications at Endometrial/Myometrial Interface. Sagittal TVS shows a few punctate echogenic foci *(arrows),* likely due to calcifications, at the interface of the myometrium and endometrium. This finding is of doubtful importance and may be related to prior uterine instrumentation.

proceeds in either a cephalad or a caudal direction or both.[51,52] The median septum formed by the medial walls of the müllerian ducts then resorbs, leaving a single uterine cavity.

Arrested development of the müllerian ducts, failure of fusion of the müllerian ducts, and/or failure of resorption of the median septum results in variable forms of müllerian duct anomalies (MDAs). MDAs have an estimated prevalence ranging from up to 6% in the general population to up to 15% in populations with recurrent pregnancy losses.[53] Whereas minor anomalies (arcuate uterus with just a mild fundal indentation) probably have no clinical consequence, others are associated with pregnancy loss (septate uterus)[54] and various obstetric complications such as premature delivery (bicornuate uterus).

The anomalies are typically categorized based on their embryology and morphology, and the most commonly used classification is one from 1988 by the American Fertility Society, now known as the American Society for Reproductive Medicine[55] (Fig. 15.9). Failure of fusion of the müllerian ducts results in **uterus didelphys** or **bicornuate uterus,** and failure of resorption of the uterine septum results in a **septate uterus** (the most common MDA).[56] Other anomalies may be seen in patients exposed to **diethylstilbestrol** (DES) *in utero*, although this is seen less frequently now since its use was stopped in the early 1970s. In DES exposure, sonography may demonstrate a diffuse decrease in the size of the uterus and an irregular T-shaped uterine cavity.[57,58]

The aforementioned classification system is problematic, however, because vaginal anomalies are not included, not all anomalies fit the classification, and there are no specific imaging features defined for diagnosis. Various imaging criteria have been proposed. We will focus on the more commonly used criteria, realizing there is no clear agreement on the best criteria. Alternative classification systems of MDAs have been suggested.[59-61] Some patients will have complex anomalies that do not fit neatly into classification systems; accurate description of the various components of the anomaly is important in such cases, with measurements such as fundal indentation, septal thickness, and myometrial thickness, being potentially helpful.

The coronal view of the uterus is important for many of the MDAs (Fig. 15.10, Videos 15.1 and 15.2), particularly when trying to diagnose the more common anomalies such as septate uterus. One cannot usually obtain a view of the uterus in its coronal plane with two-dimensional (2-D) TVS, although occasionally one can obtain a coronal view of the uterus with TAS when there is little fluid in the urinary bladder, and the uterus is sufficiently anteflexed. In general, 3-D ultrasound is needed for determining the type of MDA.[52,62] A recent meta-analysis for accuracy and diagnosis of MDAs (based on studies that predominately used the 1988 classification system[55]) showed that the highest degrees of mean diagnostic accuracy were, in decreasing order, as follows: 3-D ultrasound, 97.6%; SHG, 96.5%; hysterosalpingography (HSG), 86.9%; and 2-D ultrasound, 86.6%.[53]

The most common distinction to be made in clinical practice is when the endometrium appears slightly divided on 2-D ultrasound and one needs to determine whether this is an arcuate, septate, or bicornuate uterus. This is an important distinction to make because (particularly for infertility patients) when the MDA is thought to have reproductive consequences, a **septate uterus** will in general be treated surgically (because the septum may have a poor blood supply and can contain fibrous and/or myometrial tissue[63,64] and is associated with recurrent miscarriage), whereas a bicornuate uterus will in general not be treated surgically. Using the 3-D TVS reconstructed coronal view of the uterus, one should evaluate the contour of the myometrium in the fundus of the uterus. If the fundal myometrium is outwardly convex or has an inwardly concave indentation of less than 1 cm (from a

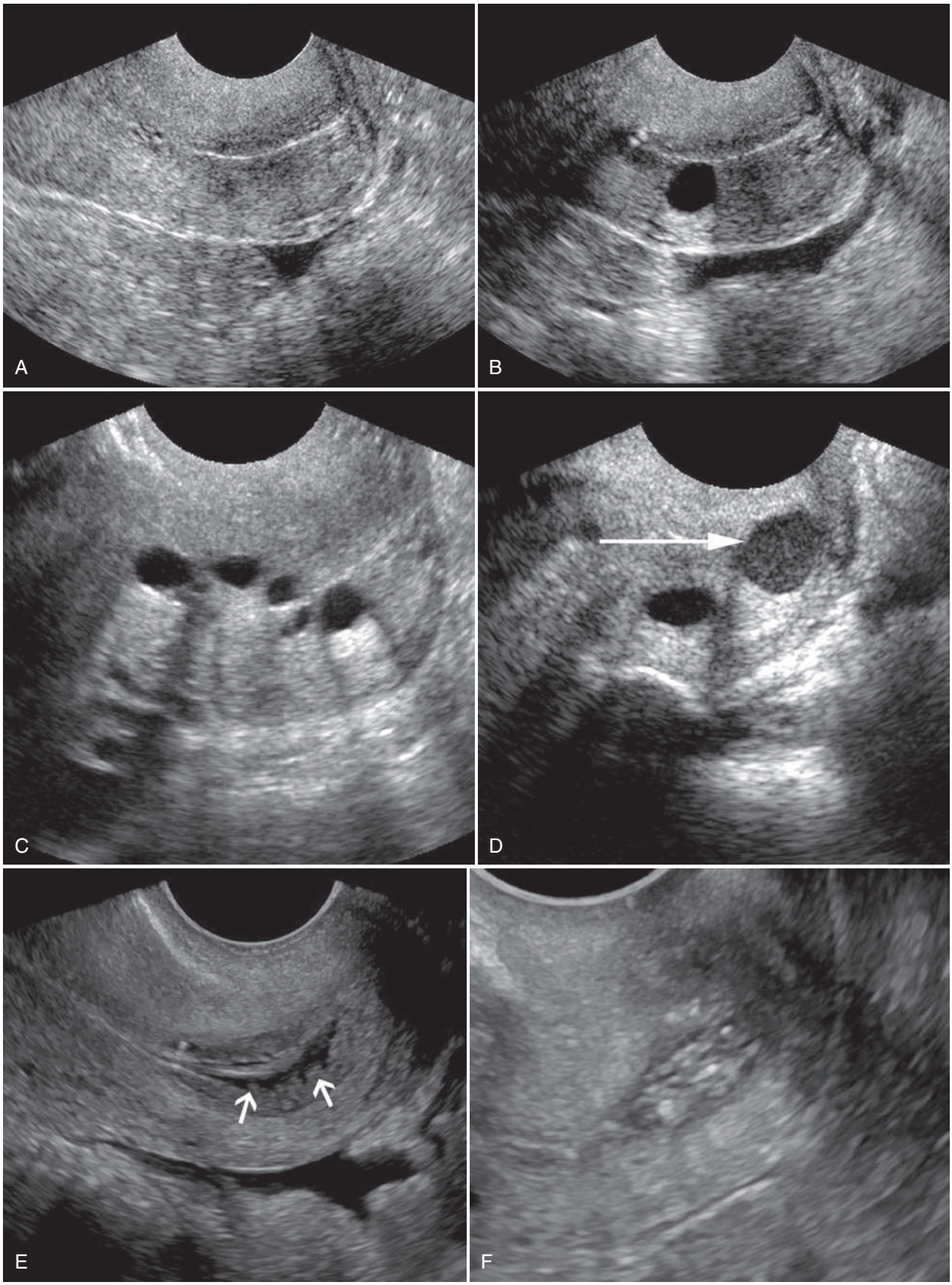

FIG. 15.7 Normal and Insignificant Cervical Findings. All images are sagittal TVS. **(A) Normal cervix. (B)** Single **nabothian cyst. (C)** Multiple nabothian cysts. **(D)** Nabothian cyst with internal echoes *(arrow)* likely due to proteinaceous material or hemorrhage. There is also a simple nabothian cyst. **(E) Cervical folds.** A small amount of fluid in the endocervical canal helps outline a few undulations (two of which are indicated by *arrows*), due to cervical folds, also known as **plicae palmatae.** They may be more easily seen when there is a small amount of fluid in the endocervical canal, as in this case. **(F)** Several tiny echogenic foci in the inner portion of the cervix.

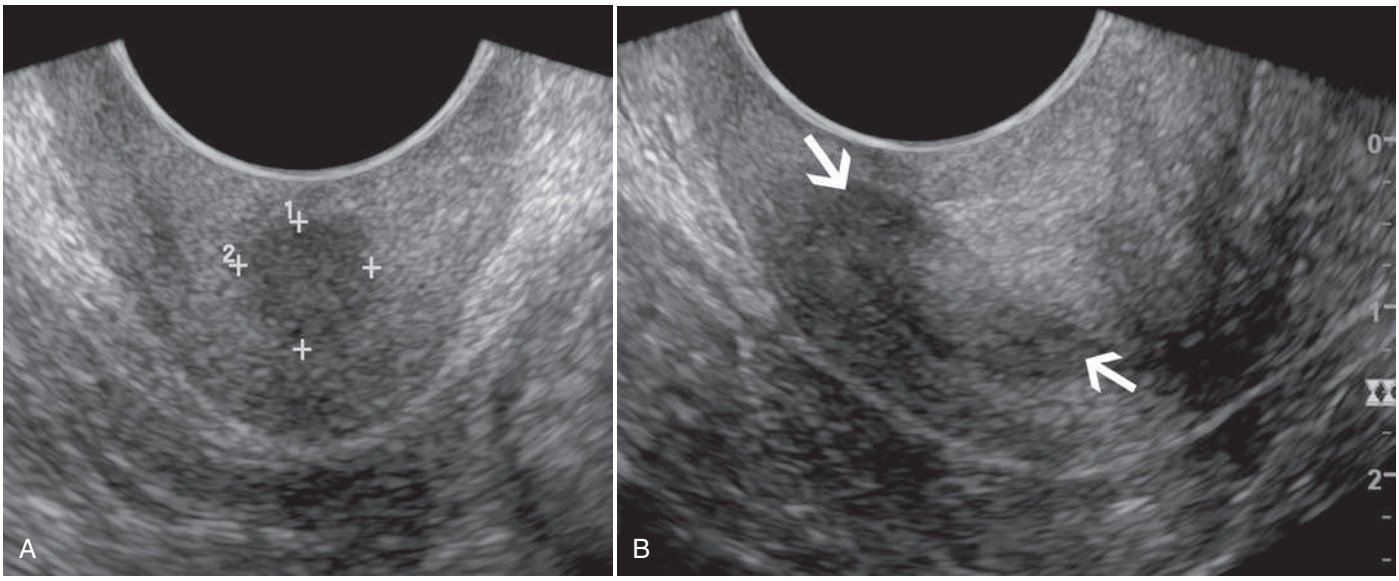

FIG. 15.8 Cervical Pseudomass. (A) Transverse TVS of cervix shows central hypoechoic area simulating a mass *(calipers).* **(B)** Sagittal TVS in same patient shows the smooth elongated nature of the inner portion of the cervix (between *arrows*) in a retroverted uterus. The inner portion of cervix is sometimes relatively hypoechoic to the outer portion and can simulate a mass.

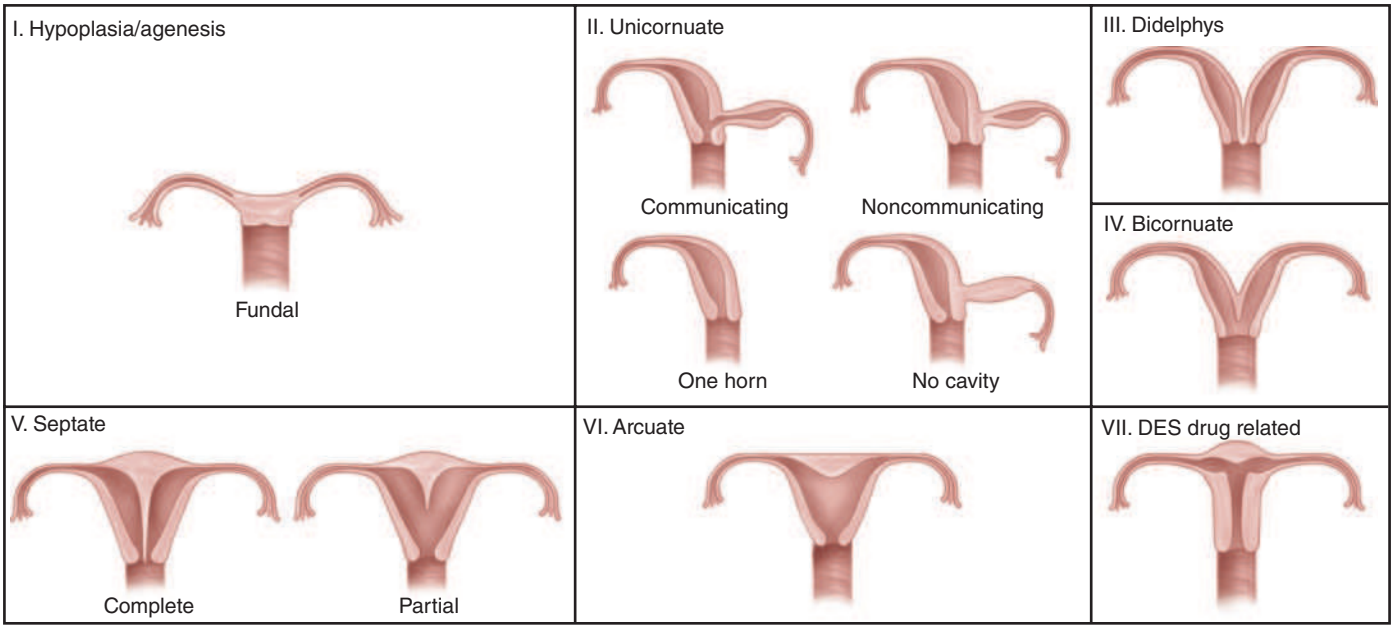

FIG. 15.9 Drawing of Müllerian Abnormalities. *DES,* Diethylstilbestrol. (Reprinted by permission from the American Society for Reproductive Medicine. The American Fertility Society classifications of adnexal adhesions, distal tubal occlusion, tubal occlusion secondary to tubal ligation, tubal pregnancies, mullerian anomalies and intrauterine adhesions. Fertil Steril. 1988;49(6):944-955.[55])

reference line across the superior aspect of the myometrial edge in the two cornual regions), the distinction narrows to a septate (or subseptate) versus arcuate uterus. The term "subseptate" or "partial septate" is sometimes used when the septum does not extend all the way from the fundus to the cervix. The 1-cm fundal cleft criterion to distinguish septate (or arcuate) from bicornuate uterus is a commonly used criterion, although other methods have been suggested.[54,56,65,66]

The significance of and diagnostic criteria for an arcuate uterus are unclear. Arcuate uterus refers to slight indentation of the fundal myometrium into the endometrium. There is debate about whether it is truly an anomaly or just a normal variant, and further debate about whether it has clinical importance.[56,67] Part of the difficulty in sorting out these questions arises from uncertainty in what criteria one uses for the diagnosis. We are also unaware of criteria for distinguishing mild arcuate uterus from a normal uterus. Suggested criteria for diagnosis of an arcuate uterus are an angle greater than 90 degrees at the end point of the fundal indentation[65] or a less than 1-cm indentation of myometrium into the endometrium (from a reference line

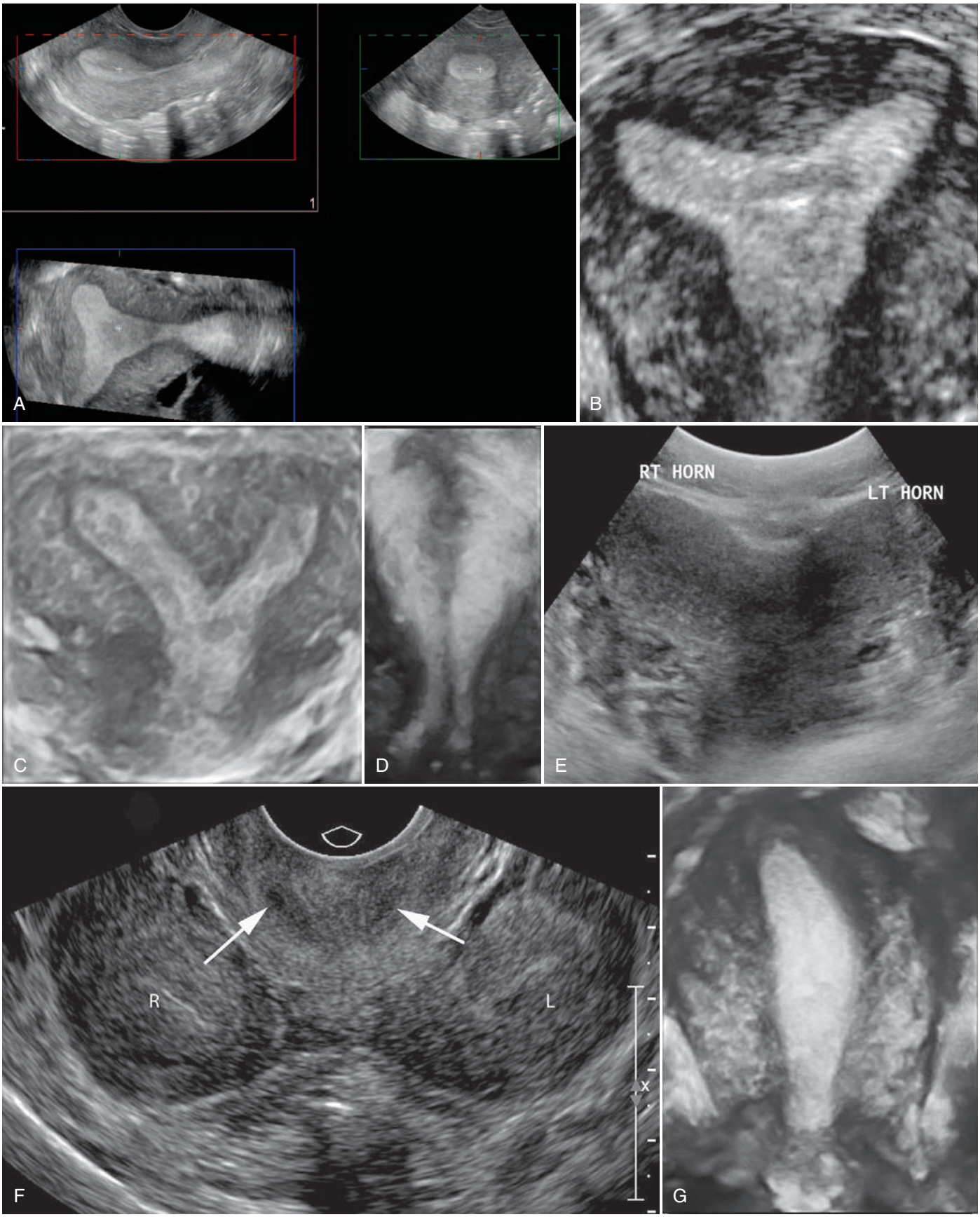

FIG. 15.10 Coronal Images of Normal Uterus and Müllerian Duct Anomalies. (A) Normal uterus with three-dimensional (3-D) views. It is often helpful to reconstruct the coronal plane when assessing for müllerian duct anomalies. **(B), (D),** and **(G)** are reconstructed 3D coronal images. **(E)** and **(F)** are coronal images obtained directly from two-dimensional (2-D) imaging. **(B) Arcuate uterus. (C) Subseptate uterus. (D)** Complete **septate uterus. (E) Bicornuate uterus** (note how the two horns come together). **(F) Uterus didelphys** (note two separate uterine cavities *[R, L]* and two cervices *[arrows]*). The endometrial cavities were always separate. **(G) Unicornuate uterus.** See also Video 15.1 for unicornuate uterus and Video 15.2 for bicornuate uterus.

across the superior aspect of the endometrial edge in the two cornual regions).[68]

In general, if there is an indentation of greater than 1 cm in the fundal myometrium, one then needs to distinguish between a bicornuate uterus and uterus didelphys. In bicornuate uterus, the two endometrial cavities join at some point, usually just above the cervix. There can be either one cervix (bicornis unicollis) or two cervices (bicornis bicollis). In uterus didelphys, there are two separate uterine horns and two cervices. However, the distinction between a bicornuate uterus with two cervices versus uterus didelphys may be difficult, and perhaps not clinically relevant. In a newer classification system the overlap between septate and bicornuate uterus is better described[53]; however, septate uterus is probably overdiagnosed by these definitions.[69]

Arrested development of one müllerian duct results in variable forms of a **unicornuate uterus.** In general, unicornuate uterus is easily recognized on 3-D ultrasound because the single horn configuration, sometimes referred to as "banana-shaped," is usually obvious on the reconstructed coronal plane. The single horn configuration of the endometrium, with absence of one cornual region, is easy to overlook on 2-D ultrasound unless one pays close attention. A unicornuate uterus may be deviated to one side of the pelvis, but this uterine deviation can be overlooked on 2-D ultrasound. When a unicornuate uterus is seen, it is important to determine if there is a rudimentary horn and if that rudimentary horn contains endometrium, as such determination will typically affect management of the patient.[54,70] About a third of patients with unicornuate uterus will not have a rudimentary horn. For the approximate two-thirds of patients with a unicornuate uterus who have a rudimentary horn, about half will have endometrium in the rudimentary horn.[54,70] In most patients with a **rudimentary horn** that has endometrium, the rudimentary horn does not communicate with the other horn. These latter patients are at increased risk for endometriosis and rudimentary horn pregnancy, which has a high likelihood of rupture. Hydrometra in the rudimentary horn may be mistaken for a uterine or adnexal mass. Surgical resection of a rudimentary horn that contains endometrium, especially if noncommunicating, is often recommended.[54] It is not clear how reliably ultrasound, whether 2-D or 3-D, can exclude the presence of a rudimentary horn because they are sometimes small and may be obscured by bowel gas. If a rudimentary horn is not seen on ultrasound, one should consider MRI to be more confident there is truly no rudimentary horn.

There are variable and often complex forms of **uterine hypoplasia** or agenesis. One may not be able to perform TVS in such patients, and MRI may be needed to fully define the anatomy as small uterine remnants may be present and difficult to identify sonographically. The most common form is Mayer-Rokitansy-Kuster-Hauser syndrome, with most patients having uterine and vaginal agenesis.[56]

Vaginal septa may be transverse or longitudinal in orientation and are most commonly seen with uterus didelphys, although they can occur with other MDAs. A transverse septum may cause obstruction and result in **hematocolpos** or **hematometrocolpos.** A duplicated cervix is a component of uterus didelphys but can occur with other anomalies. Other than clearly separated cervices, it can be difficult to distinguish true cervical duplication from a cervix divided by a septum. With this in mind, in women with a double cervix it is important to evaluate the full uterine anatomy because a complete septate uterus is at least as common as uterus didelphys.[71]

The kidneys should be evaluated in patients with MDAs because renal anomalies occur with increased frequency in such patients compared with the general population.[54] The most common renal anomalies are absent or ectopic kidney. The most common types of MDAs to have associated renal anomalies are uterus didelphys (often with renal agenesis ipsilateral to an obstructed horn) and unicornuate uterus (usually renal agenesis ipsilateral to the side of the absent or rudimentary horn).

ABNORMALITIES OF THE MYOMETRIUM

Leiomyoma

Uterine **leiomyomas,** commonly referred to as **fibroids,** are common benign neoplasms of the uterus. They are composed of varying amounts of smooth muscle and fibrous tissue. The lifetime prevalence of uterine leiomyomas is greater than 80% among black women and approaches 70% in white women.[72] Some women with leiomyomas are asymptomatic but leiomyomas can cause abnormal vaginal bleeding, pain, or "bulk" symptoms such as bowel or bladder dysfunction.[72]

Causes of Uterine Enlargement

Normal variant
Fibroids
Adenomyosis
Obstructed uterus
Malignancy
Endometrial cancer
Uterine sarcoma
Cervical cancer

Leiomyomas can be classified by location: submucosal (abutting the endometrium), intramural (within the myometrium) and subserosal (involving the serosal surface of the uterus). Some subserosal leiomyomas are pedunculated, with a common definition having the center of the leiomyoma outside the uterus and attached to the uterus by a stalk narrower than 50% of the diameter of the leiomyoma.[73] Pedunculated subserosal leiomyomas may be difficult to distinguish from a solid ovarian neoplasm if the ipsilateral ovary is not identified. In such cases, it is often helpful to use color or power Doppler imaging to search for vessels connecting the leiomyoma to the uterus (Fig. 15.11). Leiomyomas occasionally occur in the cervix. Submucosal leiomyomas, many of which can be treated hysteroscopically, are often subclassified into type 0 (completely within the endometrial cavity), type I (more than 50% in the endometrial cavity), and type II (less than 50% in the endometrial cavity).[74] This distinction is important

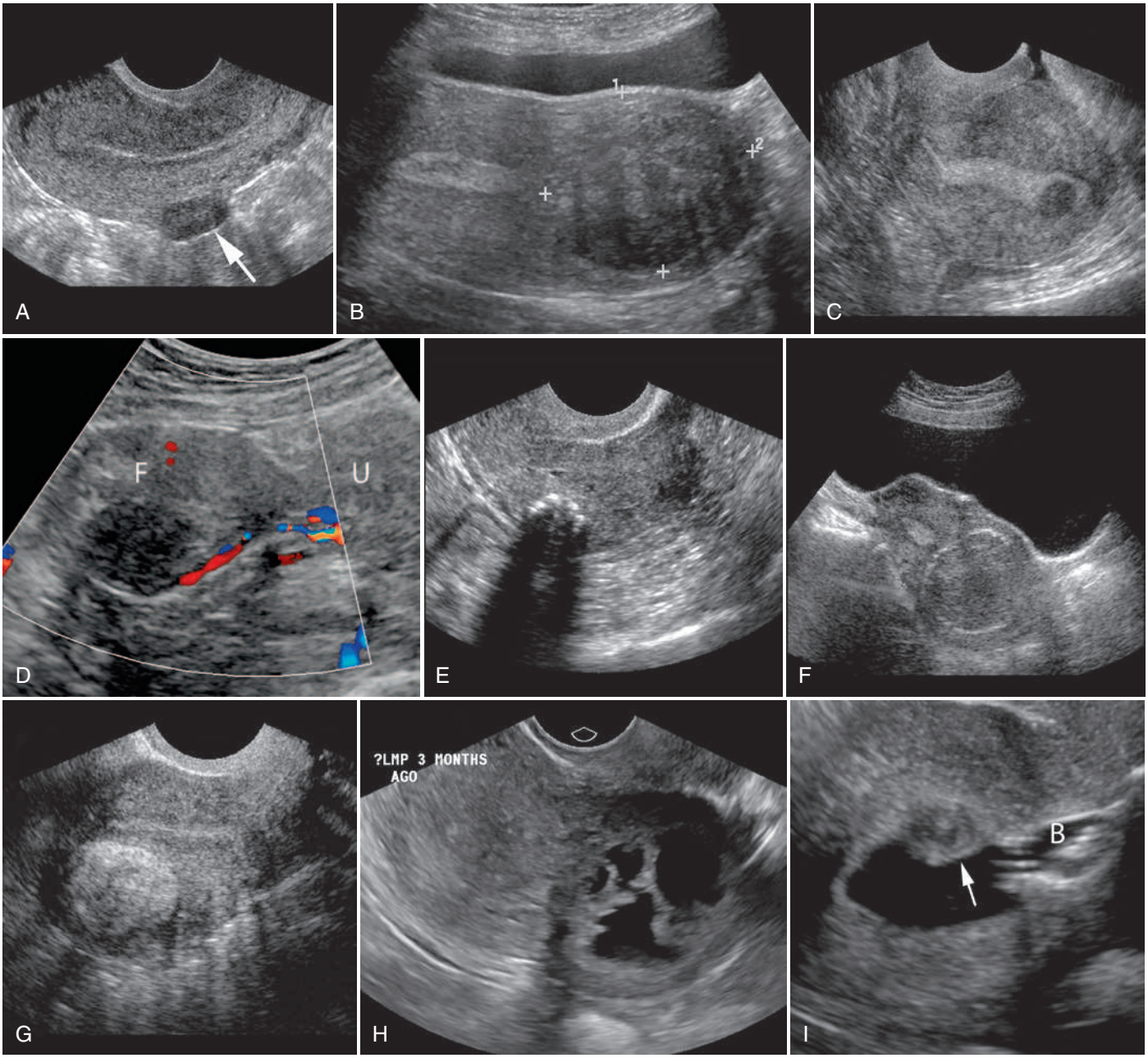

FIG. 15.11 Leiomyomas, Variable Appearances. (A) Sagittal TVS shows a hypoechoic **subserosal leiomyoma** *(arrow).* **(B)** Transverse TAS demonstrates a heterogeneous hypoechoic intramural fibroid *(calipers).* **(C)** Sagittal TVS shows a hypoechoic submucosal leiomyoma, almost entirely within the endometrial cavity. **(D)** TAS with color Doppler imaging shows vessels connecting the fibroid *(F)* to the uterus *(U),* confirming a **pedunculated subserosal leiomyoma. (E)** TVS of a leiomyoma with globular calcification with shadowing. **(F)** Sagittal TAS image of a leiomyoma with peripheral calcification. **(G)** Transverse TVS shows a hyperechoic mass, typical of a **lipoleiomyoma. (H)** Sagittal TVS demonstrates a leiomyoma with cystic degeneration. When pedunculated from the uterus, such a leiomyoma can be mistaken for an ovarian mass. See also Video 15.3. **(I)** Sagittal TVS from a sonohysterogram shows the endometrium *(arrow)* overlying the **submucosal fibroid.** Note the balloon catheter *(B).*

because when fibroids are more than 50% within the endometrial cavity, they can frequently be removed hysteroscopically. The location of some leiomyomas spans several of these more general groups, and a more detailed classification of leiomyoma location has been suggested.[75,76] Thus when fibroids are seen to distort the endometrium, it is frequently helpful to estimate the percentage within the endometrial cavity in addition to using whatever classification system is preferred by the referring clinicians. Although TVS is often adequate when fibroids are small and/or few in number, it is important to also assess the patient with TAS. Large fibroids, fibroids located superiorly in an enlarged uterus, or pedunculated subserosal leiomyomas may be incompletely seen or entirely overlooked if only TVS is performed.

Leiomyomas: Sonographic Features

Hypoechoic or heterogeneous solid mass, occasionally hyperechoic
Round or oval shape
Distortion of external uterine contour or endometrium, depending on size and location
Attenuation or shadowing
Calcification
Cystic areas from degeneration or necrosis

Fibroids may have variable appearances (see Fig. 15.11, Video 15.3) but most often appear as well-defined, spherical to ovoid, solid masses that are hypoechoic compared with normal myometrium. They are frequently heterogeneous and tend to produce mass effect on adjacent structures depending on size and location. Leiomyomas may attenuate sound deep to the entire mass, but also commonly have bandlike areas of shadowing originating from nonhyperechoic areas within the mass, termed "refractory shadowing."[77] Calcification occurs in a minority of leiomyomas. The calcification is usually in one or more focal areas and has associated acoustic shadowing. Less frequently, rim calcification may occur and in general is seen after hemorrhagic degeneration or after **uterine artery embolization** (UAE). Occasionally, leiomyomas are isoechoic or hyperechoic compared with myometrium. When one encounters a hyperechoic leiomyoma, a **lipoleiomyoma** should be considered,[78,79] although it is likely that not all hyperechoic leiomyomas are lipoleiomyomas. The fat in a lipoleiomyoma is probably due to adipocyte differentiation rather than a degenerative change.[80] Lipoleiomyomas are most frequently noted in postmenopausal women[78] and usually have a benign clinical course.[80,81]

Uterine leiomyomas occasionally undergo various forms of benign degeneration. Many types of degeneration are not evident sonographically and may be better detected on MRI.[82] Cystic spaces within a leiomyoma usually indicate **cystic degeneration** but may also be seen with **myxoid degeneration.** Hyaline, hemorrhagic, and hydropic degeneration are usually difficult to diagnose by ultrasound. **Hemorrhagic degeneration** may not produce any change in appearance, although homogeneity, a hyperechoic rim, and lack of detectable flow by Doppler imaging have been described.[76] In a patient with acutely degenerating fibroid (typically during rapid growth in pregnancy or as a result of UAE), pain will usually be localized to the fibroid(s) undergoing degeneration, and thus the diagnosis can be suggested during the sonographic examination, even if the sonographic appearance of degeneration is not yet evident.

Fortunately, the vast majority of myometrial masses are due to leiomyomas. There are other uncommon forms of myometrial neoplasms, such as **cellular leiomyomas** and **smooth muscle tumors of uncertain malignant potential** (STUMPs), but we are not aware of any specific sonographic features to diagnose such entities.[76] Rarely, leiomyomas have unusual growth patterns such as **intravenous leiomyomatosis, disseminated peritoneal leiomyomatosis, benign metastasizing leiomyomas,** and **parasitic leiomyomas;** the leiomyomas in these rare entities have a similar appearance to the more usual leiomyomas but are in vastly different locations.[76,82]

After noninvasive treatment with UAE most fibroids remain hypoechoic, although cystic change or increased echogenicity occasionally occurs; diminished or absent flow on Doppler imaging is expected.[83] Tubular hyperechoic structures thought to be due to thrombosed uterine artery branches have been described after UAE.[84] Echogenic foci due to gas may occur in leiomyomas as a normal finding after UAE, and clinical assessment is needed to help distinguish this from a **pyomyoma.**[82] Submucosal fibroids may prolapse and thus a mass may be seen in the endometrial cavity, cervix, or vagina.[85] Little has been reported about the appearance of leiomyomas after MRI-guided focused ultrasound ablation.

Leiomyosarcoma

Uterine **sarcomas** are uncommon. Although some forms of uterine sarcoma arise in the endometrium, the more common leiomyosarcomas arise in the myometrium. Risk factors for **leiomyosarcoma** include pelvic irradiation, tamoxifen, and rare genetic syndromes.[72] Unfortunately, it is difficult to diagnose leiomyosarcomas by ultrasound or other imaging modalities because their appearance and growth rate overlap with the much more common leiomyomas. Other than evidence of metastasis, no currently known imaging feature is reliably predictive. Leiomyosarcomas tend to be large and heterogeneous and to have cystic change (Fig. 15.12), but such changes are also common in leiomyomas.[82] Doppler imaging has not proven reliable. Rapid growth, particularly in a postmenopausal patient, has been considered a worrisome sign for leiomyosarcomas but "rapid" is not well defined and the usefulness of rapid growth is unclear. Diagnosis of leiomyosarcoma by MRI is also challenging, although diffusion-weighted imaging may be helpful.[86,87] Serum lactate dehydrogenase levels may be helpful for diagnosis of leiomyosarcoma.[87a,87b]

Adenomyosis

Adenomyosis is a benign condition wherein endometrial glands and stroma are present in the myometrium. In general, the histologic diagnosis of adenomyosis requires the presence of endometrial glands or stroma to be located more than 2.5 or 3 mm away from the outer edge of the endometrium.[88,89] It may cause pain, abnormal vaginal bleeding, or infertility, although some patients are asymptomatic. The prevalence of adenomyosis is uncertain; there are widely varying estimates from 5% to 70%.[90] Adenomyosis and

Adenomyosis: Sonographic Features

Diffuse, sometimes globular-shaped, uterine enlargement
Diffusely heterogeneous myometrium
Asymmetrical thickening of myometrium
Indistinct hypoechoic areas
Myometrial cysts
Poor definition of endometrial-myometrial border
Focal tenderness elicited when scanning over the uterus
Subendometrial echogenic linear striations
Subendometrial echogenic nodules

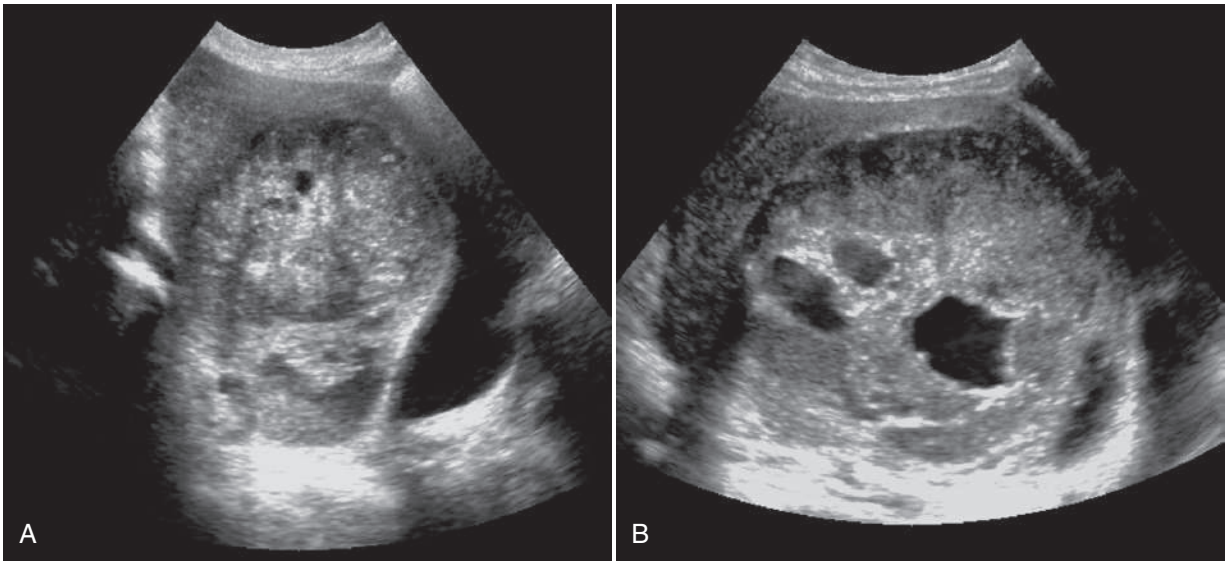

FIG. 15.12 Leiomyosarcoma. (A) Sagittal and **(B)** transverse TAS show a large heterogeneous uterine mass that is mostly solid but contains cystic areas. It is difficult to distinguish this from a benign leiomyoma with cystic degeneration because the appearance of leiomyomas and leiomyosarcomas overlap.

endometriosis may coexist; 22% to 49% of women with endometriosis are reported to also have adenomyosis.[91]

Adenomyosis most often affects the myometrium diffusely. Occasionally it occurs in a focal form (sometimes called "focal adenomyosis" when involving only part of the myometrium or an "adenomyoma" when more distinct)[92] and rarely can take the form of a cyst ("cystic adenomyoma").[76] Ultrasound is an accurate diagnostic test for adenomyosis, although about 9% of affected patients have normal ultrasound findings.[93] Sonographic findings that are suggestive of diffuse adenomyosis include enlarged globular shape of the uterus, heterogeneous myometrium, asymmetrical thickening of the myometrium, indistinct interface between the endometrium and myometrium, myometrial cysts, and echogenic striations or nodules in the myometrium (Fig. 15.13, Video 15.4).[94-97] Heterogeneity of the myometrium has been reported as the most common finding but has poor specificity[96]; this may be related to the subjective nature of determining heterogeneity. Thus it is important to look for other sonographic features when one identifies a heterogeneous myometrium. Echogenic linear striations, myometrial cysts, globular uterine shape, and asymmetrical myometrial thickness have all been reported to have high specificity.[94,96,97] Although not generally performed to diagnose adenomyosis, SHG may show communication between the lesions of adenomyosis and the endometrial cavity.[98] Rarely, adenomyosis can appear as an isolated cystic mass, larger than the small myometrial cysts typically seen in adenomyosis, and has been termed a **juvenile cystic adenomyoma.**[99] However, these isolated larger myometrial cysts may instead represent a rare, recently proposed type of MDA, an **accessory and cavitated uterine mass** (ACUM). Specific criteria to diagnose ACUM have been proposed.[100,101]

Adenomyosis and leiomyomas often coexist; 15% to 57% of women with leiomyomas are reported to also have adenomyosis in surgical series.[102] It can sometimes be difficult to distinguish these two entities, or determine if both are present, by ultrasound. Focal adenomyosis is usually the form most difficult to distinguish from leiomyomas. Distinct borders are typical of leiomyomas, whereas indistinct borders suggest adenomyosis. It has been suggested that color or power Doppler may be helpful in making the distinction, with adenomyosis tending to have more central vascularity and leiomyomas tending to have mostly peripheral vascularity.[92] However, the reliability of Doppler findings to make this distinction has not been adequately evaluated. In patients in whom one is uncertain whether the findings represent adenomyosis or leiomyomas or both (when making this distinction is important for clinical care), MRI is helpful.

Although adenomyosis is usually considered to occur mostly in premenopausal women, it can be seen in postmenopausal women.[103] Women with breast cancer who are treated with tamoxifen have a higher incidence of adenomyosis. It may be that the estrogen agonist effects of tamoxifen on endometrial tissue cause adenomyosis or reactivate preexisting adenomyosis.[90]

Occasionally one may encounter one or a few small cysts at the endometrial/myometrial border, in the absence of other sonographic findings of adenomyosis. The significance of such an isolated finding is not clear. As mentioned previously, the histologic diagnosis of adenomyosis generally requires the presence of endometrial glands or stroma to be located more than 2.5 or 3 mm away from the outer edge of the endometrium.[88,89] Thus we would be reluctant to diagnose adenomyosis based solely on one or a few small cysts at the endometrial/myometrial border, in the absence of other sonographic features of adenomyosis.

ABNORMALITIES OF THE CERVIX

After a supracervical hysterectomy, one expects to see most or all of the cervix remaining, and should not mistake the remaining cervix for a mass (Fig. 15.14A). Occasionally one may observe a cervical polyp on ultrasound (Fig. 15.14B), although many of

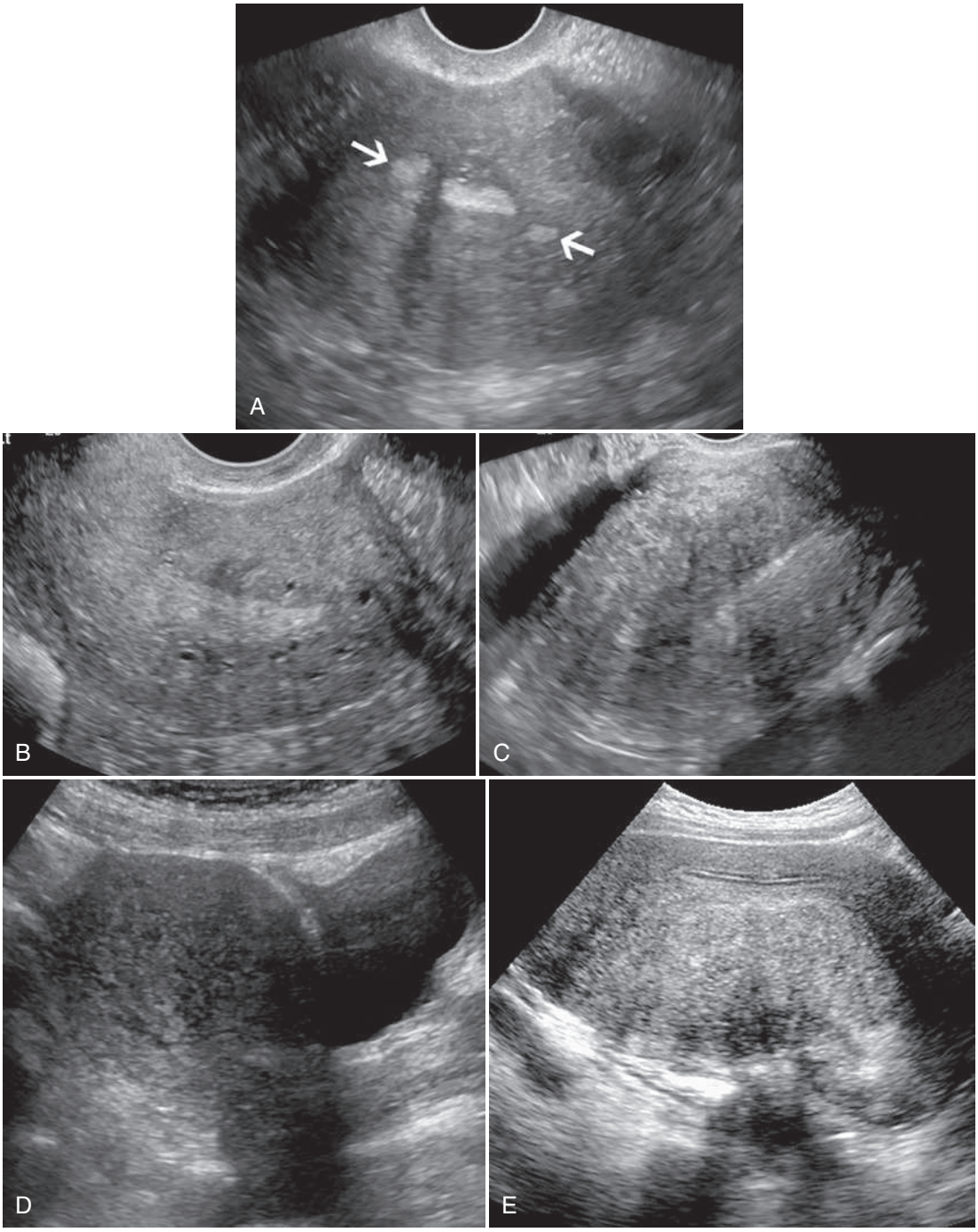

FIG. 15.13 Adenomyosis. (A) Transverse TVS shows echogenic nodules *(arrows).* The central echogenic area in this image is the endometrium. Striations and nodules are likely the same feature, with the term "striations" being used when more elongated in shape and "nodules" when more spherical. **(B)** Sagittal TVS reveals multiple small cysts in the myometrium. **(C)** Sagittal TVS shows diffuse myometrial heterogeneity. In addition, the endometrium is poorly defined. **(D)** Sagittal TAS demonstrates globular shape of the uterus. **(E)** Sagittal TAS shows asymmetrical myometrial thickness, with the posterior myometrium thicker and heterogeneous compared with the anterior myometrium. See also Video 15.4.

these are evident on clinical examination. Small cervical polyps may be difficult to identify sonographically unless there is surrounding fluid. At times, endometrial polyps (or endocavitary leiomyomas) will prolapse into the cervix. The diagnosis can be made based on visualization of the vascular stalk leading to the prolapsed lesion in the endocervical canal (Fig. 15.14C–D, Video 15.5).

Cervical carcinoma is usually diagnosed without imaging, but occasionally one may incidentally encounter a patient with cervical carcinoma. Cervical carcinoma typically appears as a heterogeneously hypoechoic solid mass (Fig. 15.14E). It may be difficult to distinguish from a leiomyoma by ultrasound, although increased vascularity on Doppler imaging has been described.[104]

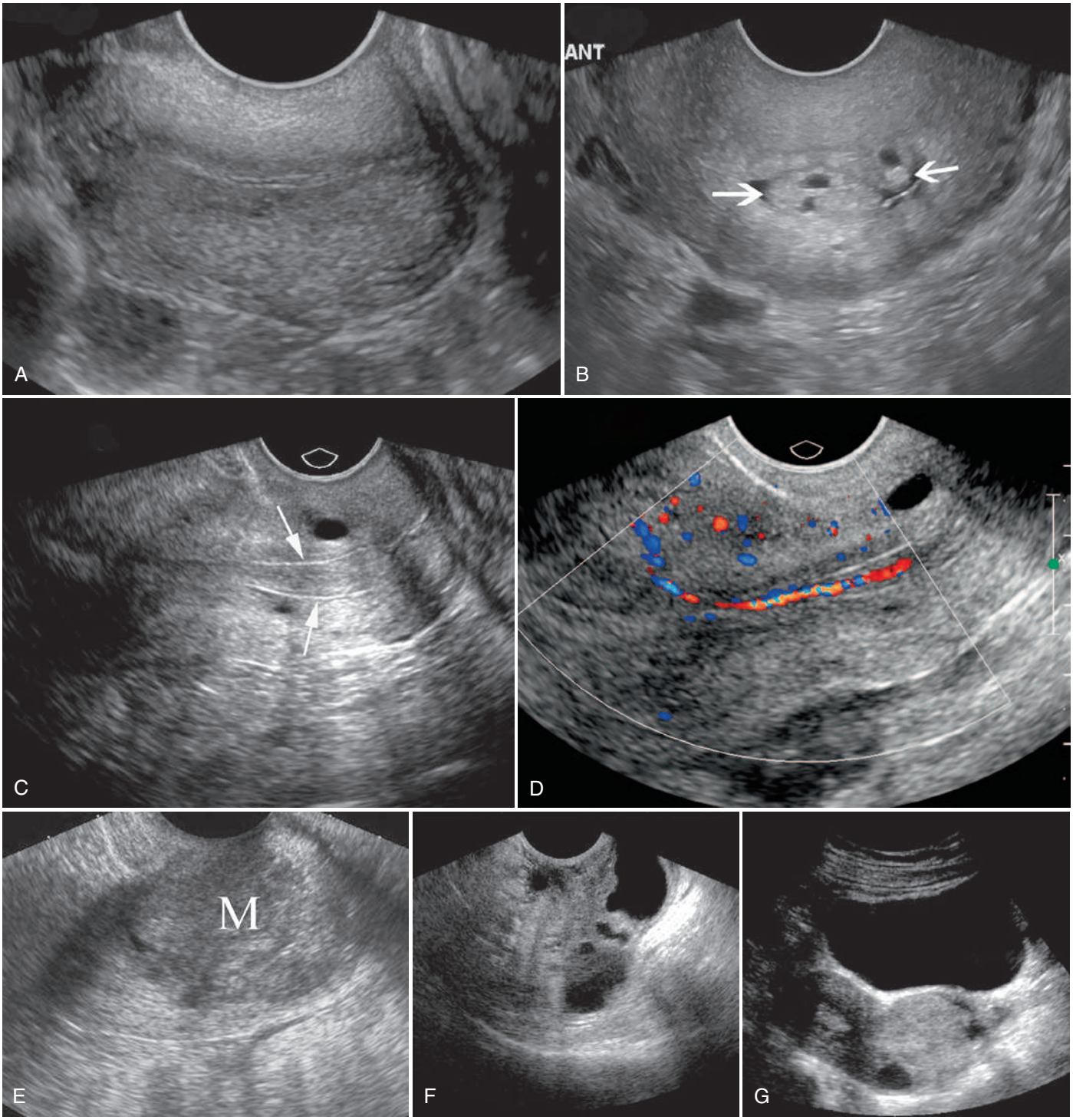

FIG. 15.14 Cervical Lesions. (A) Supracervical hysterectomy. Sagittal TVS shows the remaining normal cervix in a patient after supracervical hysterectomy. **(B) Cervical polyp.** Transverse TVS demonstrates a cervical polyp (between *arrows*). This polyp contains small cystic spaces that might be mistaken for nabothian cysts, but in this instance a small amount of fluid in the endocervical canal helps define borders of the polyp. **(C)** Sagittal gray-scale and **(D)** color Doppler TVS in patient with **endometrial polyp prolapsing into the cervix.** Note the vascular pedicle of the polyp extending from the endometrial cavity into the cervical region. See also Video 15.5. **(E) Cervical carcinoma.** Sagittal TVS shows a hypoechoic solid mass *(M)* due to cervical carcinoma. **(F)** Sagittal TVS and **(G)** sagittal TAS images from a patient with **adenoma malignum** show a mixed cystic and solid mass.

Adenoma malignum, also termed **minimal deviation adenocarcinoma,** is an uncommon type of cervical carcinoma that has been associated with **Peutz-Jeghers syndrome.** Watery vaginal discharge has been described as a common symptom. Sonographically these are most often multiloculated cystic masses with a solid component or completely solid masses (Fig. 15.14F–G).[105] Multiple adjacent nabothian cysts might simulate this lesion, but when a solid component is present, particularly with flow by Doppler imaging, one should consider this uncommon neoplasm.

ABNORMALITIES OF THE ENDOMETRIUM

Because of its improved resolution, TVS is better able to image and depict subtle abnormalities within the endometrium and clearly define the endometrial/myometrial interface than is TAS.[106] Knowledge of the varied normal sonographic appearances of the endometrium that vary with respect to time of the menstrual cycle, patient menopausal status, and hormone use allows for recognition of pathologic conditions manifested by endometrial thickening because the expected upper limits of normal thickness will vary with these factors. Many endometrial pathologies, such as **hyperplasia, polyps,** and **carcinoma,** can cause abnormal bleeding. Abnormal bleeding can be due to abnormally heavy menstrual periods at the expected time of the menstrual cycle (menorrhagia, for example due to fibroids or adenomyosis), abnormal bleeding at an unexpected time of the cycle (metrorrhagia), or both (menometrorrhagia).

Causes of Metrorrhagia

Pregnancy
Systemic disease (liver disease, blood dyscrasias)
Endometrial polyps or hyperplasia
Endometrial cancer
Intrauterine device (IUD) malposition
Cesarean section scar defect

Although heavy vaginal bleeding is typically from a myometrial or endometrial cause, abnormal bleeding can at times arise from other sources such as bleeding from the vulva or vagina (lacerations, infection, or cancer), from the cervix (polyps, fibroids, or cancer), from the fallopian tubes (salpingitis, tumors, or tubal pregnancy), or be secondary to ovarian pathology (estrogen-producing tumor, cancer, functional ovarian cysts).

SHG can be of great value in further evaluating the abnormally thickened endometrium.[5,6,107-110] SHG can distinguish between focal and diffuse endometrial abnormalities and help guide further management. If the abnormality is diffuse, a blind, nondirected biopsy can be done, but a focal process, such as a polyp, typically requires hysteroscopy with directed biopsy or excision.[5,110] SHG may also be able to help distinguish benign from malignant endometrial processes.[111,112] Patients with endometrial cancer may have poorly distensible endometrial cavities.[112]

Causes of Endometrial Thickening

Pregnancy
Retained products of conception
Fibroids (submucosal or intracavitary)
Endometritis
Adhesions
Hyperplasia
Polyps
Cancer

Postmenopausal Endometrium

Hormone Use

When assessing the postmenopausal endometrium, it is important to know if the patient is taking any exogenous hormones **(hormone replacement therapy).** These hormones used to be given long term to prevent osteoporosis and alleviate menopausal symptoms. Because unopposed estrogen replacement is associated with an increased risk of endometrial hyperplasia and carcinoma, estrogen therapy is frequently combined with progesterone in continuous combined or in sequential regimens. However, these hormones are no longer frequently used for long-term therapy owing to the known increased risk of thromboembolism, breast cancer, adverse cardiac events, and stroke (which are not offset by benefits of lower rates of colorectal cancer and hip fractures).[113] They may be given for a short time around the time of menopause to help alleviate menopausal symptoms. Use of continuous combined estrogen should lead to a thin atrophic-appearing endometrium. Use of sequential estrogen and progesterone may lead to a changing appearance of the endometrium similar to that of premenopausal women with increased thickness in the latter half of the hormonal cycle.[114] Women who are taking unopposed estrogen need to be monitored, given the known increased risk of endometrial cancer.

Effects of Hormones on the Postmenopausal Endometrium

Hormone Regimen	Expected Endometrial Appearance
No hormones	Thin, atrophic
Unopposed estrogen	Thick, maybe heterogeneous
Daily estrogen/progesterone	Thin, atrophic
Sequential estrogen/progesterone	Thickness varies with phase of cycle
Tamoxifen	Thick, cystic spaces (some changes are in the myometrium)

Tamoxifen and other hormonal treatments for breast cancer can have estrogenic effects in the uterus. An **increased risk of endometrial carcinoma** has been reported in patients receiving tamoxifen therapy,[115] as well as an increased risk of **endometrial hyperplasia** and **polyps.**[116,117] A correlation exists between increased endometrial thickness and cumulative dose of tamoxifen.[118] On sonography, tamoxifen-related endometrial changes are nonspecific and similar to those described in hyperplasia,

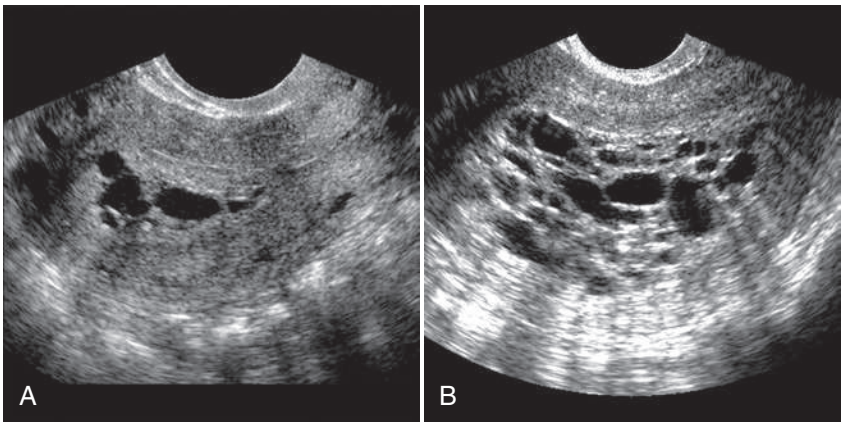

FIG. 15.15 Tamoxifen-Related Changes on TVS. (A) Thick, cystic endometrium caused by **endometrial hyperplasia** in patient taking tamoxifen. **(B)** Thick, cystic endometrium caused by a large **polyp** in patient receiving tamoxifen.

polyps, and carcinoma.[117,119,120] Cystic changes within the thickened endometrium are frequently seen (Fig. 15.15). Polyps are frequently present, have a higher incidence in women receiving tamoxifen than in untreated women, and can be quite large.[118,121] However, because cancer occurs in polyps in a higher percentage of women taking tamoxifen than in the general population, focal lesions in these women should be investigated.[122] As mentioned previously, in some women taking tamoxifen, the cystic changes are subendometrial in location and represent reactivation of adenomyosis in the inner layer of myometrium.[123] Because it is difficult to distinguish the endometrial/myometrial border in many of these patients, SHG may be valuable in determining whether an abnormality is endometrial or subendometrial.[11,124] It is also important to recognize that this adenomyosis-like change is a diagnosis of exclusion. When a cystic endometrial appearance is seen in a woman taking tamoxifen, although the effects of tamoxifen should be mentioned as part of the differential diagnosis, polyps, hyperplasia, and cancer also need to be considered.

Postmenopausal Bleeding

Postmenopausal bleeding is considered to be any vaginal bleeding that occurs in a postmenopausal woman other than the expected cyclic bleeding with sequential HRT. Because the prevalence of endometrial cancer is low and endometrial atrophy accounts for a large proportion of cases of postmenopausal bleeding, the negative predictive value of a thin endometrium is high; therefore a thin endometrium can be reliably used to exclude cancer. Several studies have shown that in patients with postmenopausal bleeding who have had endometrial sampling, an endometrial measurement of up to 3 mm,[125] up to 4 mm,[126-128] or up to 5 mm[129-131] can be considered normal. The bleeding in these patients is often related to an atrophic endometrium.

The majority of women with postmenopausal uterine bleeding have **endometrial atrophy.**[127-132] On TVS, an atrophic endometrium is thin and homogeneous. Histologically, the endometrial glands may be dilated, but the cells are cuboidal or flat and the stroma is fibrotic. A thin endometrium with cystic changes on TVS is consistent with a diagnosis of cystic atrophy, but when the endometrium is thick, the appearance is indistinguishable from that of cystic hyperplasia.[133]

A meta-analysis of 35 published studies that included 5892 women showed that an endometrial thickness of 5 mm or greater detected 96% of endometrial cancer and 92% of any endometrial disease.[134] For a postmenopausal woman with vaginal bleeding with a 10% pretest probability of cancer, her probability of cancer is 1% following a normal TVS result. However, many of the studies used in the meta-analysis were biased by only including those patients who underwent biopsy. In a recent study by Wong and colleagues of 4383 women who all underwent an ultrasound and biopsy after having postmenopausal bleeding, 3 mm was found to be the optimal threshold. The sensitivities for the detection of endometrial cancer at 3-, 4-, and 5-mm cutoffs were 97.0%, 94.1%, and 93.5%, respectively. The corresponding estimates of specificity at these thresholds were 45.3%, 66.8%, and 74.0%.[125] However, it should be noted that the incidence of endometrial cancer was low in this population (3.8%, which is much lower than the expected rate of 10% in postmenopausal women with bleeding), so results might not be reproducible in other populations. Local practice will likely dictate the threshold that is acceptable to patients and their physicians. It may also be that in the future, individualized risk ratios will be used, assessing risk factors such as increasing age, older age at menopause, body mass index, nulliparity, and diabetes.[135] Regardless, if a woman has continued postmenopausal bleeding after a normal sonogram, then biopsy is typically recommended.

Transvaginal assessment of endometrial thickness has been shown to be highly reproducible, with excellent intraobserver and good interobserver agreement.[136] If the endometrium cannot be visualized in its entirety or its margins are indistinct, the examination should be considered "nondiagnostic" and lead to further investigation (e.g., SHG, hysteroscopy).[137] Some recommend that all women with postmenopausal bleeding should undergo SHG, even if the TVS findings are normal[138,139]; however, if the endometrium is well seen on TVS and is thin with no morphologic abnormality, we feel this is usually adequate. Dubinsky and colleagues found that of 81 postmenopausal women with bleeding and thickness greater than 4 mm within 1 month after aspiration biopsy, endoluminal masses were present in 45 (56%) and that 41 of these were false-negative biopsy results.[140] The important question is whether finding and treating these

benign conditions (such as small polyps or fibroids) improves the patient's quality of life, morbidity, and survival; further investigation is warranted.[137]

Other studies have assessed the endometrium in asymptomatic postmenopausal patients and concluded that an endometrium of 8 mm or less can be considered normal.[35-39] Most of these reports have included a mixed group of patients, with some undergoing HRT and some not undergoing HRT. In a theoretical cohort of postmenopausal women aged 50 years or older who were not bleeding or receiving HRT, Smith-Bindman and colleagues[40] recommended that biopsy should be considered if the endometrium measures greater than 11 mm, because the risk of cancer is 6.7% (similar to that of a postmenopausal woman with bleeding and endometrial thickness >5 mm). If the endometrium measures 11 mm or less, biopsy is not needed because the risk of cancer is extremely low.[40] Using this cutoff provides an acceptable trade-off between cancer detection and unnecessary biopsies prompted by an incidental finding. In a recent study by Jokubkiene and colleagues, it was confirmed that even if endometrial focal lesions are present, there is likely no malignancy. In that study of 510 asymptomatic postmenopausal women, 11% had workup for endometrium of 5 mm or greater, and 34 (7%) underwent hysteroscopic surgery or ultrasound surveillance. There were 14.5 surgical procedures per premalignant lesion (endometrial hyperplasia) diagnosed, and two women developed severe complications from hysteroscopy.[141] At our institutions we currently use the more sensitive but less specific threshold of 8 mm.

The Obstructed Uterus: Hydrometrocolpos and Hematometrocolpos

Obstruction of the genital tract results in the accumulation of secretions and blood in the uterus *(metro)* and/or vagina *(colpos)*, with the location depending on the amount and level of obstruction. Before puberty, the accumulation of secretions in the vagina and uterus is referred to as **hydrometrocolpos.** After menstruation, **hematometrocolpos** results from the presence of retained menstrual blood. The obstruction may be congenital and is usually caused by an **imperforate hymen.** Other congenital causes include a **vaginal septum** or **vaginal atresia,** or a **noncommunicating rudimentary uterine horn.**[142] Hydrometra and hematometra may also be acquired as a result of cervical stenosis from endometrial or cervical tumors or from **postradiation fibrosis.**[143,144]

Causes of Endometrial Fluid

Congenital (imperforate hymen, vaginal septum, müllerian anomaly)
Current menstruation
Pregnancy
Recent instrumentation or trauma
Prior radiation
Infection
Cervical stenosis
Obstructing lesion (endometrial or cervical cancer)

Sonographically, if the obstruction is at the vaginal level, there is marked distention of the vagina and endometrial cavity with fluid. If seen before puberty, the accumulation of secretions is often anechoic. After menstruation, the presence of old blood results in echogenic material in the fluid (Fig. 15.16). There may also be layering of the echogenic material, resulting in a fluid-fluid level. Infrequently, blood may distend only the cervix, which has been termed **hematotrachelos.**[145]

Acquired hydrometra or hematometra usually shows a distended, fluid-filled endometrial cavity that may contain echogenic material (Fig. 15.17). Superimposed infection **(pyometra)** is difficult to distinguish from hydrometra on sonography, and this diagnosis is usually made clinically in the presence of hydrometra.[144]

In postmenopausal women endometrial fluid is of particular concern given their increased risk of endometrial cancer owing to age. However, even in this population the accumulation of endometrial fluid is more likely to be from a benign than from a malignant cause. A small amount of fluid within the endometrial canal, detected on TVS, may be a normal finding in asymptomatic

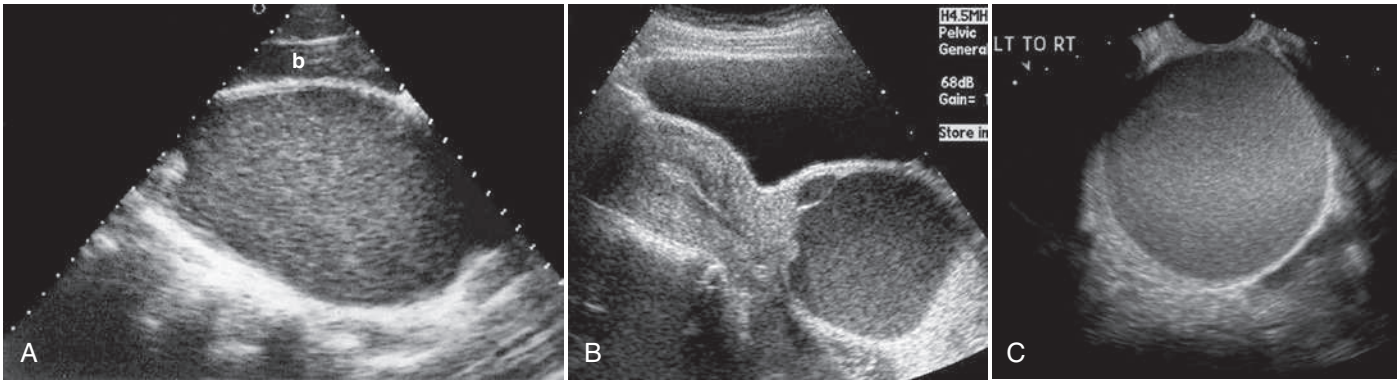

FIG. 15.16 Hematocolpos. (A) Sagittal TAS in a young patient with imperforate hymen shows the vagina distended with moderately echogenic material due to blood, compressing the bladder (b) anteriorly. **(B)** and **(C)** Fluid with internal echoes due to blood distends the vagina in a 26-year-old patient with benign vaginal stenosis. **(B)** is a TAS image and **(C)** is a translabial ultrasound image.

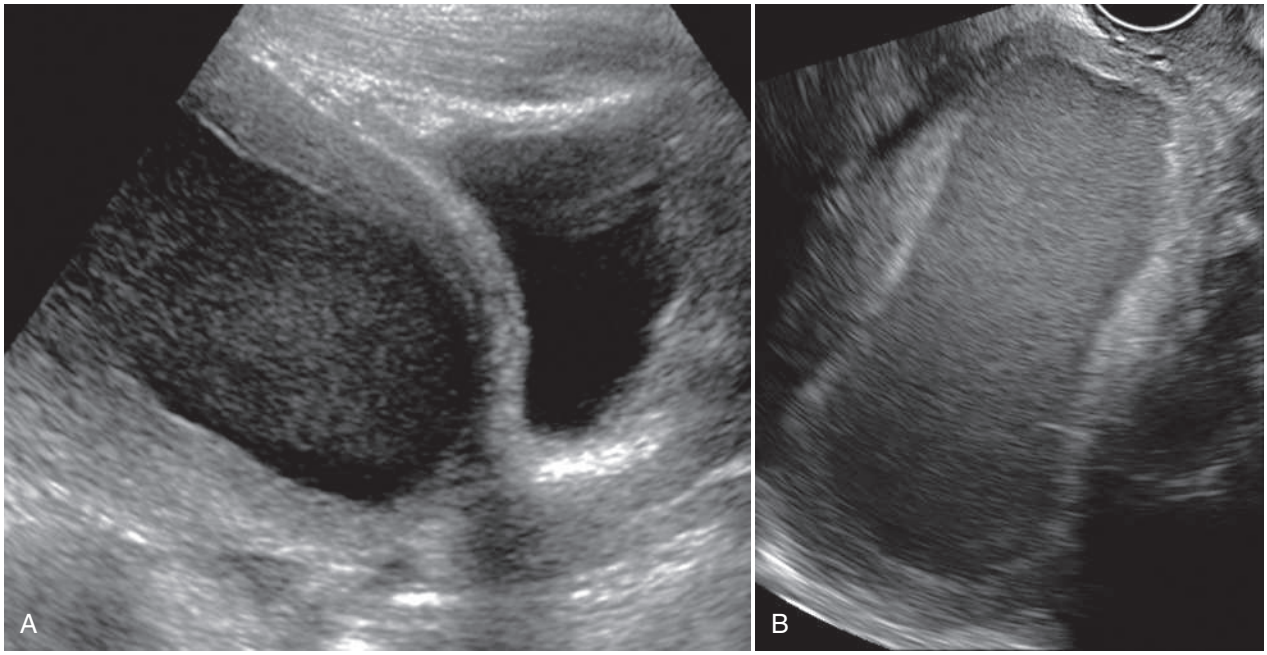

FIG. 15.17 Hematometra in Patient With Cervical Stenosis Due to Cervical Carcinoma. (A) TAS and **(B)** TVS show distended endometrial cavity filled with moderately echogenic material due to blood. The cancer was obstructing at the level of the cervix and is not shown on these images.

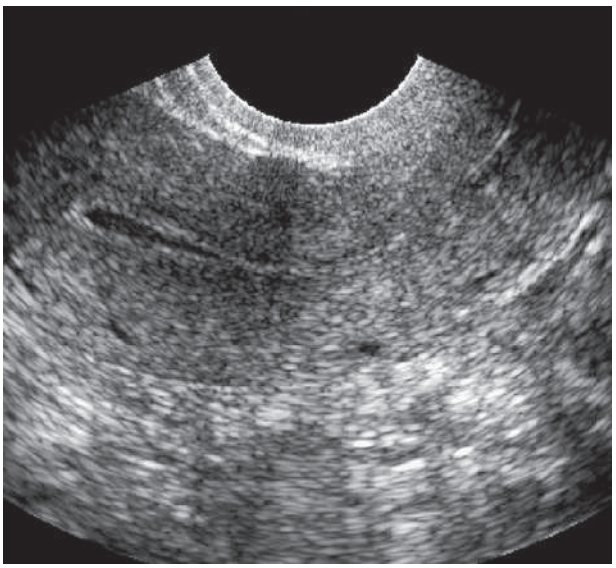

FIG. 15.18 Normal Postmenopausal Endometrium. Sagittal TVS shows a small amount of fluid in the endometrial cavity.

patients[146] (Fig. 15.18). Larger amounts of fluid may be associated with benign conditions, most often related to cervical stenosis.[143,147]

In a study of 1074 asymptomatic postmenopausal women, endometrial fluid was found in 134 (12%).[148] Biopsy was attempted in 131. Cervical stenosis precluded sampling in 12 and an additional 32 women had some degree of cervical stenosis (44/131 = 34%). Pathology included two polyps, and one case each of cystic hyperplasia, adenomatous hyperplasia, and carcinoma. Thus there were only two concerning endometrial lesions in the 131 patients (1.5%) in whom biopsy was attempted.

Endometrial Hyperplasia

Hyperplasia of the endometrium is defined as a proliferation of glands of irregular size and shape, with an increase in the gland-to-stroma ratio compared with the normal proliferative endometrium.[149] The process is typically diffuse but at times may simulate a broad-based polypoid lesion. Histologically, endometrial hyperplasia can be divided into hyperplasia without cellular atypia and hyperplasia with cellular atypia **(atypical hyperplasia).** Long-term follow-up studies have shown that about 25% of atypical hyperplasia will progress to carcinoma, versus less than 2% of hyperplasia without cellular atypia.[149] Each of these types may be further subdivided into **simple** or **complex** hyperplasia, depending on the amount of glandular complexity and crowding. In simple **(cystic)** hyperplasia, the glands are cystically dilated and surrounded by abundant cellular stroma, whereas in complex **(adenomatous)** hyperplasia, the glands are crowded together with little intervening stroma.

Endometrial hyperplasia is a common cause of abnormal uterine bleeding. Hyperplasia develops from unopposed estrogen stimulation which could be due to use of unopposed estrogen HRT, persistent anovulatory cycles (such as with polycystic ovarian syndrome) and in obese women with increased production of endogenous estrogens. Hyperplasia may also be seen in women with estrogen-producing tumors, such as ovarian granulosa cell tumors and thecomas.

Sonographically, the endometrium is usually diffusely thick and echogenic, with well-defined margins (Fig. 15.19). Focal or asymmetrical thickening can also occur. Small cysts may be

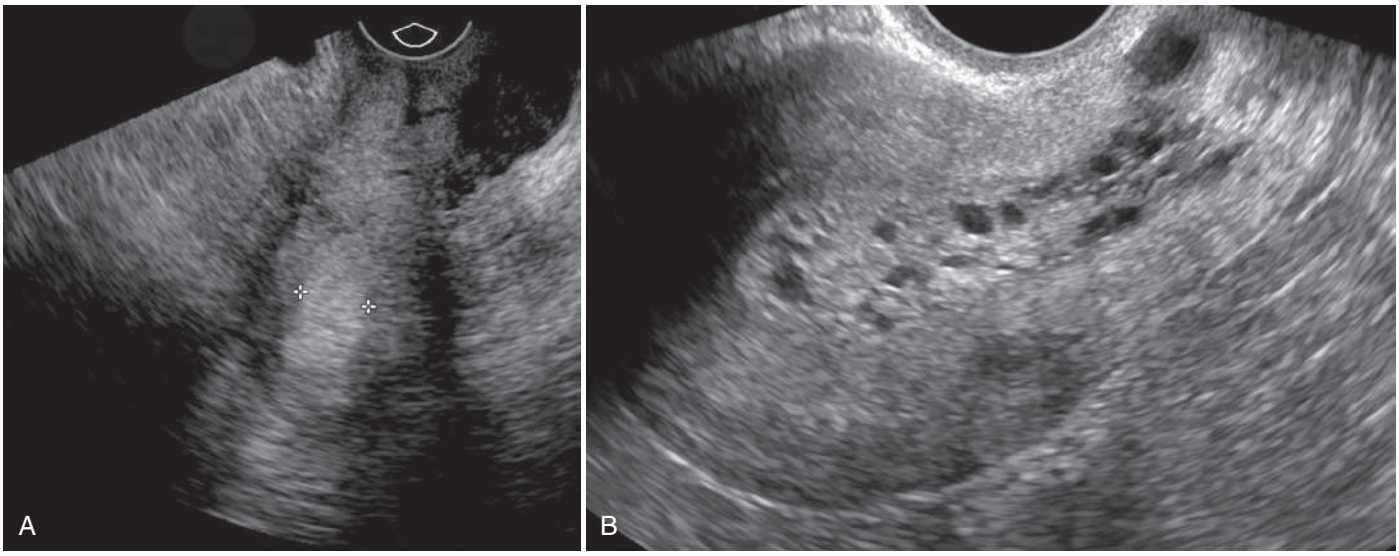

FIG. 15.19 Endometrial Hyperplasia in Two Patients. (A) Endometrial hyperplasia in a 58-year-old woman not taking hormones with abnormal bleeding. Sagittal TVS shows uniform hyperechoic thickening (*calipers*, 14 mm). **(B)** Complex endometrial hyperplasia without atypia in a 52-year-old postmenopausal woman with vaginal bleeding. Sagittal TVS shows numerous small cystic spaces diffusely in an endometrium that measured 16 mm in thickness.

seen within the endometrium in **cystic hyperplasia;** however, a similar appearance may be seen in **cystic atrophy,** and cystic changes can also be seen in endometrial **polyps.** These cystic areas represent the dilated cystic glands seen at histology.[150,151] Although cystic changes within a thickened endometrium are more frequently seen in benign conditions, they can also be seen in endometrial **carcinoma.**[133] Because hyperplasia has a nonspecific sonographic appearance, biopsy is necessary for diagnosis.

Endometrial Polyps

Endometrial polyps are common benign lesions frequently seen in perimenopausal and postmenopausal women. Polyps may cause bleeding at any point in the menstrual cycle, although many are asymptomatic. Histologically, polyps are localized overgrowths of endometrial tissue covered by epithelium and projecting above the adjacent surface epithelium.[149] They may be pedunculated or broad based, or may have a thin stalk. Approximately 20% of endometrial polyps are multiple. Malignant degeneration is uncommon. Occasionally a polyp will have a long stalk, allowing it to protrude into the cervix or even into the vagina.

On sonography, polyps may appear as nonspecific echogenic endometrial thickening, which may be diffuse or focal. However, they may also appear as a focal, round, echogenic mass within the endometrial cavity[152] (Fig. 15.20, Video 15.6). At times they will have a cystic appearance and distend the endometrial cavity (Video 15.7). This specific diagnosis of a polyp is much more easily made when there is fluid within the endometrial cavity outlining the mass and in premenopausal patients is better seen during the proliferative phase when the endometrium is typically less echogenic than the polyp. Because fluid is instilled into the endometrial cavity during SHG, this technique is ideal for demonstrating polyps (Fig. 15.20C–D). SHG is also a valuable technique when TVS is unable to differentiate an **endometrial polyp** from a **submucosal leiomyoma.** A polyp can be seen arising from the endometrium, whereas a normal layer of endometrium may be seen overlying a submucosal fibroid (see Fig. 15.11I). Cystic areas may be seen within a polyp representing the histologically dilated glands.[150,151] A feeding artery in the pedicle can frequently be seen with color Doppler ultrasound (pedicle artery sign).[153] The hyperechoic line sign may also be useful for identifying a polyp, helping one to recognize that there is a focal abnormality of the endometrium.[154]

Endometrial polyps may not be diagnosed on endometrial biopsy because a polyp on a pliable stalk may be missed by the curette. If abnormal bleeding persists after nondiagnostic dilation and curettage (D&C) in a postmenopausal woman with an endometrial thickness greater than 8 mm, hysteroscopy with direct visualization of the endometrial cavity is recommended.[155]

Endometrial Carcinoma

Endometrial carcinoma is the most common gynecologic malignancy in North America. The National Institute of Health estimated that there were 54,870 cases of endometrial cancer in the United States in 2015, with 10,170 deaths. There is an 82% overall 5-year survival rate. For endometrial cancer, 67% are diagnosed at the local stage. The 5-year survival for these localized cancers is 95.3%.[156]

Most endometrial carcinomas (75%-80%) occur in postmenopausal women. The most common clinical presentation is uterine bleeding, although only about 10% of women with postmenopausal bleeding will have endometrial carcinoma. There is a strong association with estrogen replacement therapy in postmenopausal women and anovulatory cycles in premenopausal women. Other risk factors include obesity, diabetes, hypertension, and low parity. Approximately 25% of patients with atypical endometrial hyperplasia will progress to develop well-differentiated endometrial carcinoma.[149]

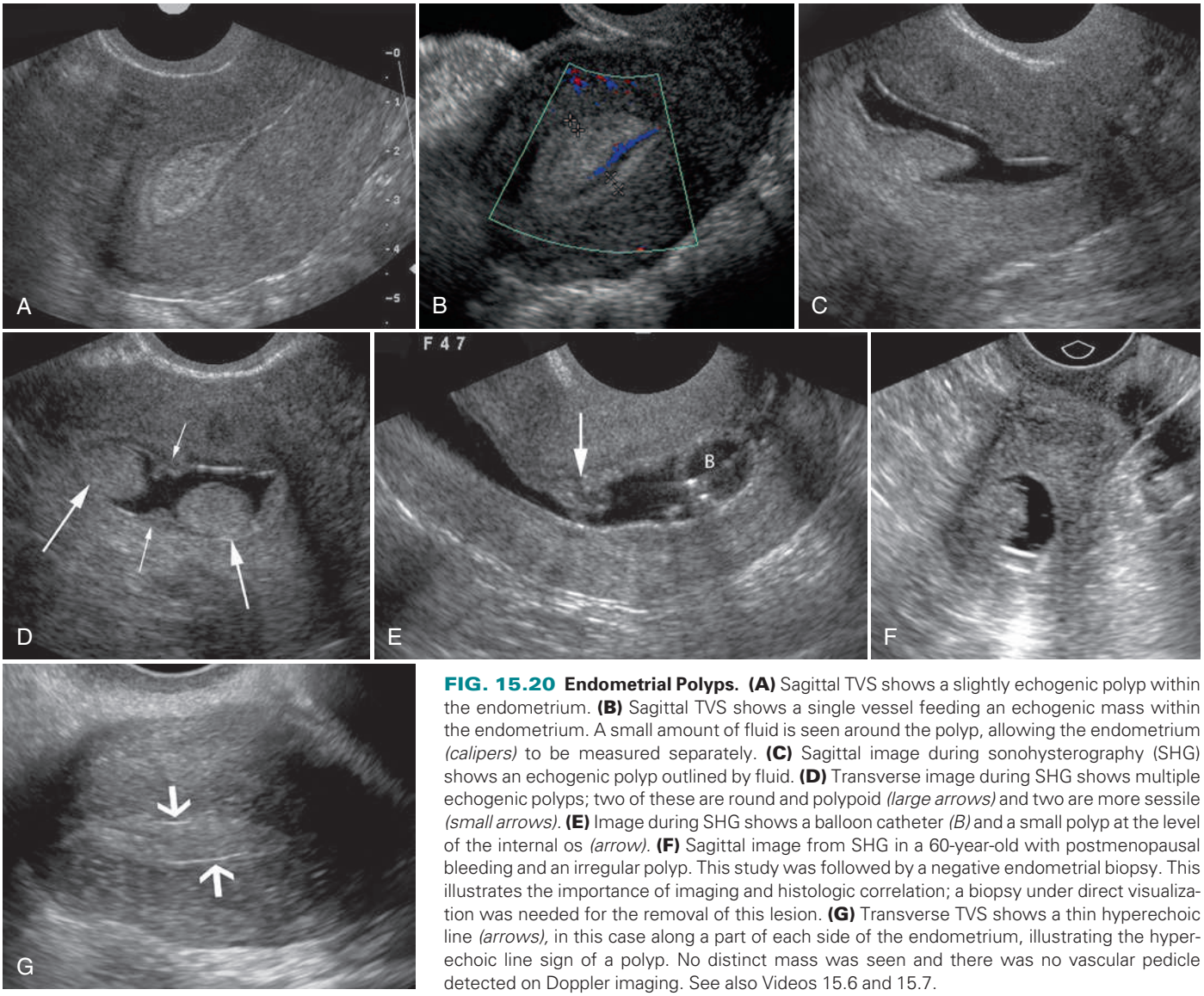

FIG. 15.20 Endometrial Polyps. (A) Sagittal TVS shows a slightly echogenic polyp within the endometrium. **(B)** Sagittal TVS shows a single vessel feeding an echogenic mass within the endometrium. A small amount of fluid is seen around the polyp, allowing the endometrium *(calipers)* to be measured separately. **(C)** Sagittal image during sonohysterography (SHG) shows an echogenic polyp outlined by fluid. **(D)** Transverse image during SHG shows multiple echogenic polyps; two of these are round and polypoid *(large arrows)* and two are more sessile *(small arrows)*. **(E)** Image during SHG shows a balloon catheter *(B)* and a small polyp at the level of the internal os *(arrow)*. **(F)** Sagittal image from SHG in a 60-year-old with postmenopausal bleeding and an irregular polyp. This study was followed by a negative endometrial biopsy. This illustrates the importance of imaging and histologic correlation; a biopsy under direct visualization was needed for the removal of this lesion. **(G)** Transverse TVS shows a thin hyperechoic line *(arrows),* in this case along a part of each side of the endometrium, illustrating the hyperechoic line sign of a polyp. No distinct mass was seen and there was no vascular pedicle detected on Doppler imaging. See also Videos 15.6 and 15.7.

Sonographic findings in endometrial cancer include a thickened endometrium, poor definition of the endometrial/myometrial interface, and an indistinct endometrium in an enlarged uterus. The thickened endometrium may be well defined, uniformly echogenic, and indistinguishable from hyperplasia and polyps. Cancer is more likely when the endometrium has a heterogeneous echotexture with irregular or poorly defined margins (Fig. 15.21, Videos 15.8 and 15.9). When invasion is clearly identified into the myometrium, then malignancy is almost certainly present. Cystic changes within the endometrium are more frequently seen in endometrial atrophy, hyperplasia, and polyps, but can also be seen with carcinoma. Endometrial carcinoma may also obstruct the endometrial canal, resulting in hematometra. Although certain sonographic appearances tend to favor a benign or malignant etiology, there are overlapping features, and endometrial biopsy is usually required for a definitive diagnosis.

The role of color and spectral Doppler ultrasound in the diagnosis of endometrial carcinoma is still controversial. Blood flow may be difficult to detect in the normal endometrium. In endometrial cancer, abnormal-appearing vessels may be seen (Fig. 15.21E). Initial studies using TVS color and spectral Doppler ultrasound suggested that endometrial carcinoma could be differentiated from a normal or benign postmenopausal endometrium by the presence of low-resistance flow in the uterine arteries in women with endometrial cancer, compared with high-resistance flow in women with normal or benign endometria.[157,158] Subsequent reports, however, have shown no significant difference in uterine blood flow between benign and malignant endometrial processes.[159-161] Low-resistance flow in the uterine artery has also been reported in association with uterine fibroids.[158] Some reports have shown low-resistance flow in the subendometrial and endometrial arteries in malignant endometrial lesions,[38,162] whereas others have found no statistically significant difference.[160,161,163] Sladkevicius and colleagues[161] found that endometrial thickness is a better method for discriminating between normal and pathologic or benign and malignant endometrium than Doppler ultrasound of the uterine, subendometrial, or intraendometrial arteries.[161]

Sonography can be used in the preoperative evaluation of a patient with known endometrial carcinoma to determine

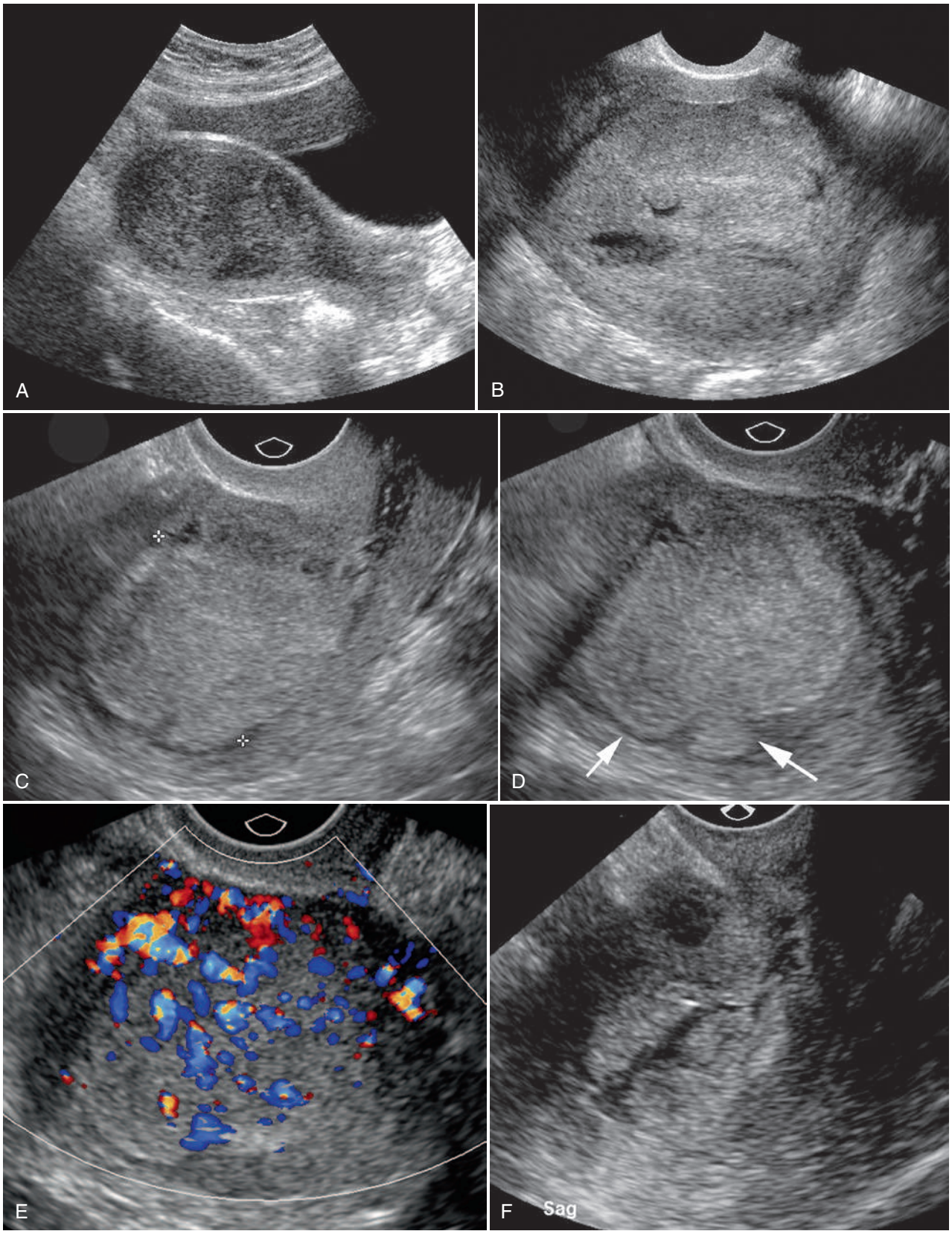

FIG. 15.21 Endometrial Carcinoma. (A) TAS and **(B)** TVS from same patient show a large, heterogeneous endometrial mass compressing the myometrium. Images **(C)-(E)** are from another patient with endometrial cancer. **(C)** The endometrium measures 33 mm *(calipers)*. **(D)** Areas of myometrial invasion are seen posteriorly *(arrows)*. **(E)** Color Doppler imaging shows irregular hypervascular tumor. **(F)** Another patient with multiple irregular polypoid lesions due to endometrial carcinoma. See also Videos 15.8 and 15.9.

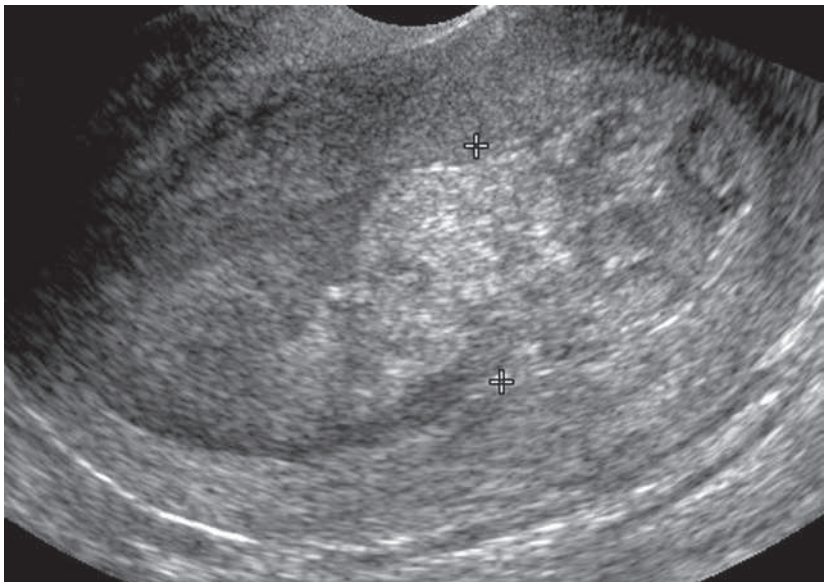

FIG. 15.22 Endometrial Carcinosarcoma. TVS shows a heterogeneous endometrial mass *(calipers)* that measures 27 mm in thickness.

myometrial invasion.[164-166] An intact **subendometrial halo** (inner layer of myometrium) usually indicates no more than superficial invasion, whereas obliteration of the halo indicates deep invasion.[166] Several objective sonographic parameters have been evaluated for staging, but subjective assessment of myometrial or cervical invasion has been shown to be as good or better than objective measurements.[167] TVS and unenhanced T2-weighted MRI have been reported to have similar accuracy,[168] but contrast-enhanced MRI has been shown to be superior to both in demonstrating myometrial invasion.[169-172] In stage IA, cancer is in the endometrium only or less than halfway through the myometrium. In stage IB, the tumor is still localized to the uterus but has spread halfway or more into the myometrium. In stage II, cancer has spread into connective tissue of the cervix, but has not spread outside the uterus. In stage III, the cancer has spread outside of the uterus or into nearby tissues in the pelvic area. In stage IV, the cancer has spread to the inner surface of the urinary bladder or the rectum (lower part of the large intestine), to lymph nodes in the groin, and/or to distant organs, such as the bones, omentum, or lungs.[173] MRI can also assess cervical extension (stage II) and extrauterine extension (stages III and IV).

Endometrial Sarcoma

Uterine sarcomas are a rare and heterogeneous group of malignancies.[174] Leiomyosarcomas have been discussed previously. Other uterine sarcomas may arise from the endometrium and include **carcinosarcomas** (also termed "malignant mixed müllerian tumors," and many now consider this a subtype of carcinoma rather than a sarcoma) (Fig. 15.22), **endometrial stromal sarcoma,** adenosarcomas, and undifferentiated sarcomas.[174,175] There is little information available regarding the sonographic appearance of these rare tumors and no specific appearance is known. Endometrial stromal sarcoma may appear as a diffuse or focal mass; may involve the myometrium, hampering determination of the origin of the lesion; and can be mistaken for a leiomyoma.[174,176]

Endometrial Adhesions

Endometrial adhesions **(synechiae)** are posttraumatic, postinfection, or postsurgical in nature and may be a cause of infertility or recurrent pregnancy loss. **Asherman syndrome** is the combination of synechiae that lead to menstrual dysfunction or infertility. The endometrium usually appears normal on TAS and TVS, although adhesions may be seen transvaginally as irregularities or a hypoechoic bridgelike band within the endometrium.[177] This is best seen during the secretory phase, when the endometrium is hyperechoic. The sonographic diagnosis is difficult unless there is endometrial fluid. SHG is an excellent technique for demonstrating adhesions.[178] Thick, broad-based adhesions may prevent distention of the uterine cavity,[108] and thus the patient may experience pain when fluid is being instilled. Synechiae appear as bridging bands of tissue that distort the cavity (Fig. 15.23, Video 15.10) or as thin, undulating membranes best seen on real-time sonography.[4] The adhesions can be divided under hysteroscopy.

Endometrial Ablation

The endometrium is typically indistinct after global **endometrial ablation** procedures (Fig. 15.24A).[179] Complications may arise when there is residual nonablated endometrium (which is common after endometrial ablation) and adjacent endometrial scarring.[180] This can result in a **cornual hematometra** (localized to the cornual region) or central hematometra (within the uterine cavity), and either may cause pain (Fig. 15.24B). **Postablation tubal sterilization syndrome** is a delayed complication of endometrial ablation that may occur in patients who previously had tubal ligation; these patients usually have pain due to a hematosalpinx of the proximal tubal stump and a cornual hematometra.[180,181] When

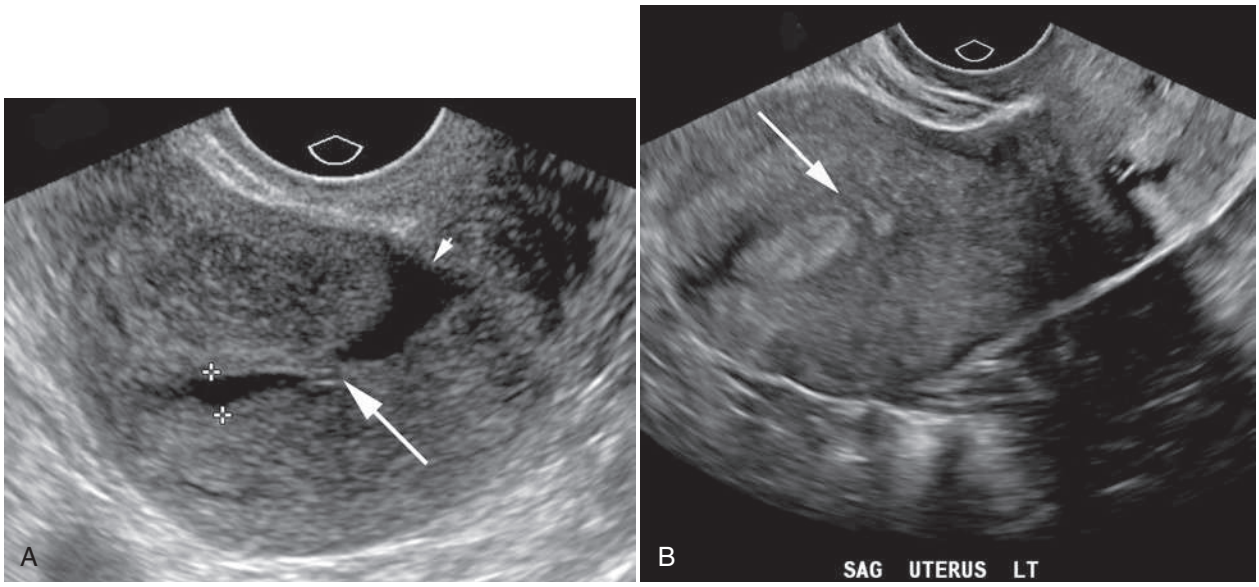

FIG. 15.23 Synechia. (A) During sonohysterography (SHG) a bridging band of tissue *(long arrow)* is seen within the fluid in the endometrial cavity. Fluid also extends into the cesarean section defect *(short arrow)*. Patients often experience pain during SHG owing to nondistensibility of the endometrial cavity when many adhesions are present. *Calipers* show the fluid in the endometrial cavity. **(B)** TVS in secretory phase shows a band of tissue similar in echogenicity to myometrium *(arrow)* spanning anterior to posterior. Note that a uterine septum would be oriented in the vertical plane extending from the fundus downward. A band of tissue in the short axis of the uterus therefore is not due to a müllerian abnormality. See also Video 15.10.

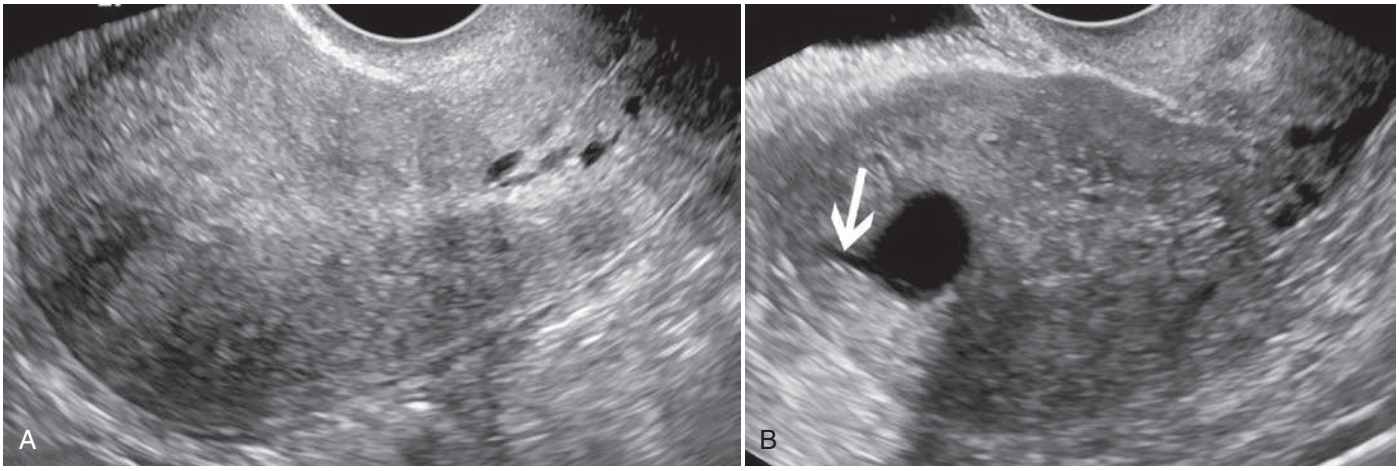

FIG. 15.24 Endometrial Ablation. (A) Sagittal TVS shows no distinct endometrial borders, a common finding after endometrial ablation. **(B)** Sagittal TVS on left side of uterus shows fluid collection due to a cornual hematometra. In this patient, there is also trace fluid extending into the intramural portion of the fallopian tube *(arrow)*.

evaluating for these complications, it may be helpful to perform imaging when the patient is symptomatic, because fluid in the obstructed area may be resorbed during the rest of the menstrual cycle.[180]

SONOGRAPHY OF CONTRACEPTIVE DEVICES

Intrauterine Contraceptive Devices

Intrauterine contraceptive devices (IUCDs or IUDs) are usually easily identified with ultrasound (Fig. 15.25). Most devices encountered in North America are T-shaped, although a circular IUD has been used in China and one may rarely still encounter a patient with a Lippes loop IUD (Ortho Pharmaceutical, Raritan, NJ).[182] The copper IUD (ParaGard, Teva Women's Health, North Wales, PA) can be left in place for up to 10 years. A levonorgestrel-releasing IUD (Mirena, Bayer HealthCare Pharmaceuticals, Pittsburgh, PA) can also be used to treat abnormal uterine bleeding rather than primarily for contraception and can be left in place for up to 5 years. Another levonorgestrel-releasing IUD (Skyla, Bayer HealthCare Pharmaceuticals) is slightly smaller than the Mirena IUD and can be left in place for up to 3 years.

In general, the shaft of an IUD is brightly echogenic and easily identified, although the levonorgestrel-releasing IUDs may

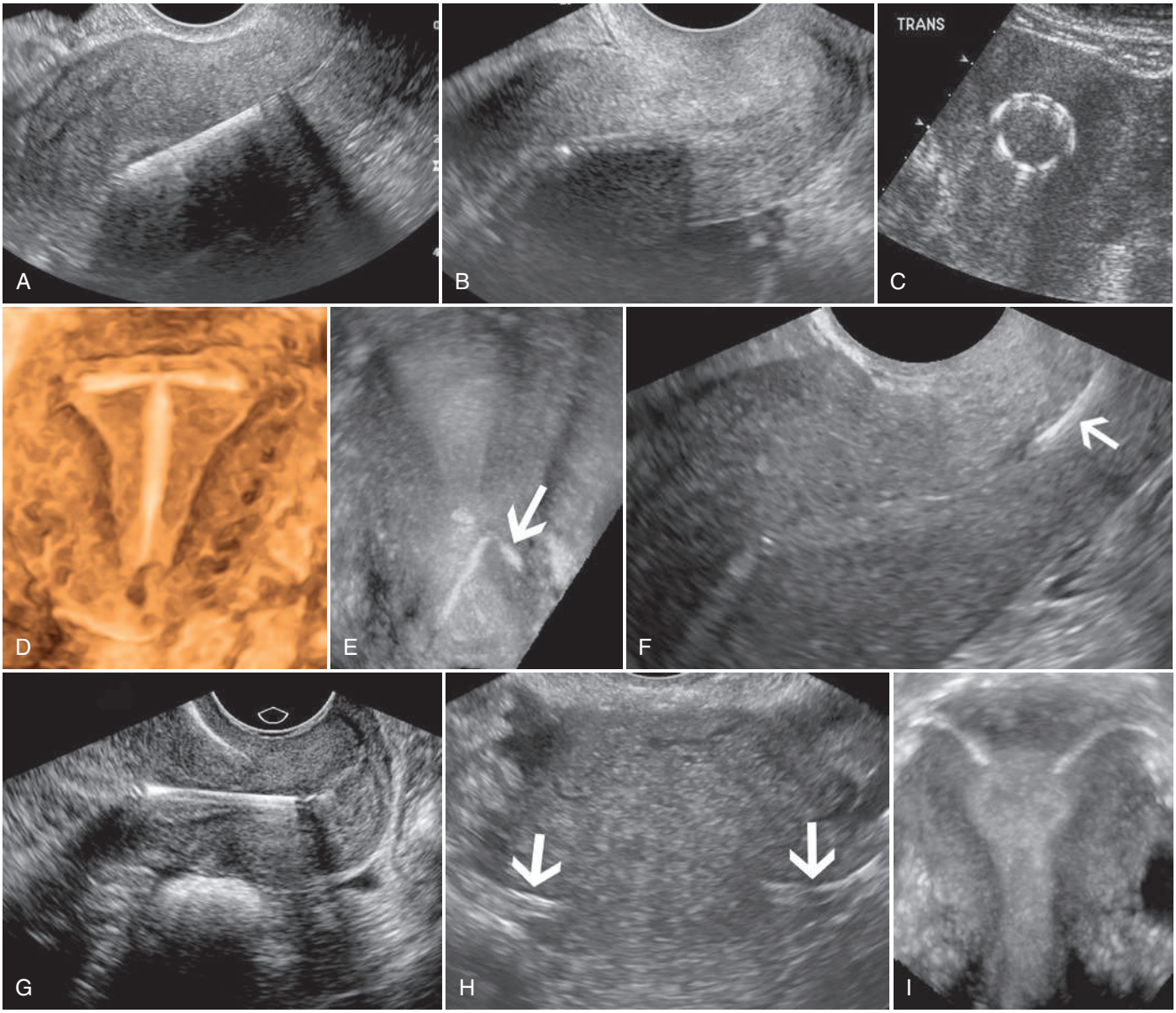

FIG. 15.25 Devices in the Uterus. (A) Sagittal TVS shows copper intrauterine device (IUD), with marked acoustic shadowing, in normal position. **(B)** Sagittal TVS shows a levonorgestrel-releasing IUD in normal position. Compared with copper IUDs, these IUDs are often not as echogenic and may have less intense acoustic shadowing. **(C)** Transverse TAS shows a circular IUD that had been placed in China. **(D)** Coronal reconstructed image from three-dimensional (3-D) ultrasound shows a levonorgestrel-releasing IUD in appropriate position. **(E)** Coronal reconstructed image from 3-D ultrasound shows an IUD that is low, being in the cervix and lower uterine segment, with the left arm *(arrow)* of the IUD embedded in the myometrium and cervical stroma. **(F)** String *(arrow)* of the IUD is seen in the cervix. IUD was normally positioned and is not visible in this image. Care should be taken to not mistake the string for the IUD itself. **(G)** TVS shows an IUD in low position, extending from the midcervix into the lower uterus. See also Video 15.11. **(H)** Transverse TVS shows tubal occlusion device *(arrows)* in their expected location in the cornual region of the uterus bilaterally. **(I)** Coronal reconstructed image from 3-D ultrasound shows tubal occlusion devices in their expected location in the cornual region of the uterus bilaterally.

be more difficult to identify than the copper IUD on 2-D ultrasound.[183] If a brightly echogenic interface of a levonorgestrel-releasing IUD is not seen, one should look carefully for acoustic shadowing originating from the shaft or arms to help in locating the IUD. Occasionally one may encounter endometrial calcifications that simulate an IUD, but the discontinuous nature of the calcifications should help prevent confusion. The upper end of the IUD and the arms of the IUD should normally be in the superior most portion of the endometrium. If the IUD is located lower in the uterus (Video 15.11), one should suspect that one or both arms of the IUD are embedded in the myometrium. 3-D ultrasound may help in identifying abnormal position of IUDs.[184] The most common location of a malpositioned IUD is the lower uterus or cervix.[185] The string of many IUDs is brightly echogenic and should not be confused for the shaft (Fig. 15.25F).

If an IUD is not seen on ultrasound and not known to have been expelled, one should evaluate the adnexa sonographically (Fig. 15.25G). However, if the IUD has perforated and is in the pelvis, it might be difficult to identify sonographically owing to bowel gas. A radiograph of the abdomen and pelvis should then be done to determine if the IUD is present in the peritoneal cavity.

Tubal Occlusion Devices

Tubal occlusion devices may be placed hysteroscopically into the fallopian tube to provide permanent sterilization. The Essure device (Bayer HealthCare Pharmaceuticals) has been most frequently used. These devices normally appear as curvilinear hyperechoic structures in the cornual region bilaterally (Fig. 15.25H–I).[186,187] Ideally the device spans the uterotubal junction, extending slightly into the endometrial cavity and into the fallopian tube.[188]

The Adiana device (Hologic, Bedford, MA) is a nonabsorbable silicone matrix that is inserted into the proximal fallopian tube. The product has been discontinued, although one may still encounter women with this device, which may appear as a small hyperechoic area in the cornual region of the uterus.[189]

POSTPARTUM FINDINGS

Normal Findings

The uterus will be enlarged initially after delivery and usually returns to its nongravid size by about 6 to 8 weeks after delivery. The uterus is often soft and easily compressible by the transducer during the first few days after delivery. TAS alone is often adequate to evaluate the uterus in the first few postpartum weeks, as the enlarged uterus usually provides an adequate sonographic window. TVS is more often needed later in the postpartum period. The inner myometrium may be hyperechoic relative to the outer myometrium in the early postpartum period and can potentially be mistaken for the endometrium (Fig. 15.26A).[190] Echogenic foci due to air are normal and can persist for up to 3 weeks.[191] Small amounts of fluid and heterogeneous tissue due to clot are commonly seen in the early postpartum period (Fig. 15.26B).

Bleeding Postpartum

Some amount of bleeding postpartum is expected and is normal; therefore visualization of blood and debris within the postpartum uterus is a normal finding. When patients have an abnormal amount of bleeding, pain, and/or fever, then sonographic evaluation is typically used to assess for causes such as **retained products of conception** (RPOC) or **endometritis.**

Retained Products of Conception

At times the calcified appearance of the term placenta will be visualized and the diagnosis of RPOC will be obvious. When there is vascularized (based on detectable flow on Doppler imaging) tissue in the endometrial cavity (Fig. 15.27), this is usually indicative of RPOC. If there is tissue that is not vascularized, this could be due to either blood clot or devascularized RPOC. The size of the suspected RPOC is important because that may guide therapy. For example, at one of our institutions, medical management is typically initiated for smaller regions of RPOC (usually 2 cm or less) whereas D&C is typically performed for larger areas which are felt to be unlikely to respond to medical therapy. If RPOC are seen and they extend beyond the expected endometrial cavity into myometrium, this is indicative of an invasive placental condition such as placenta accreta. This is an important diagnosis to suggest because the placenta will not be easily removed at D&C and the patient will be at increased risk

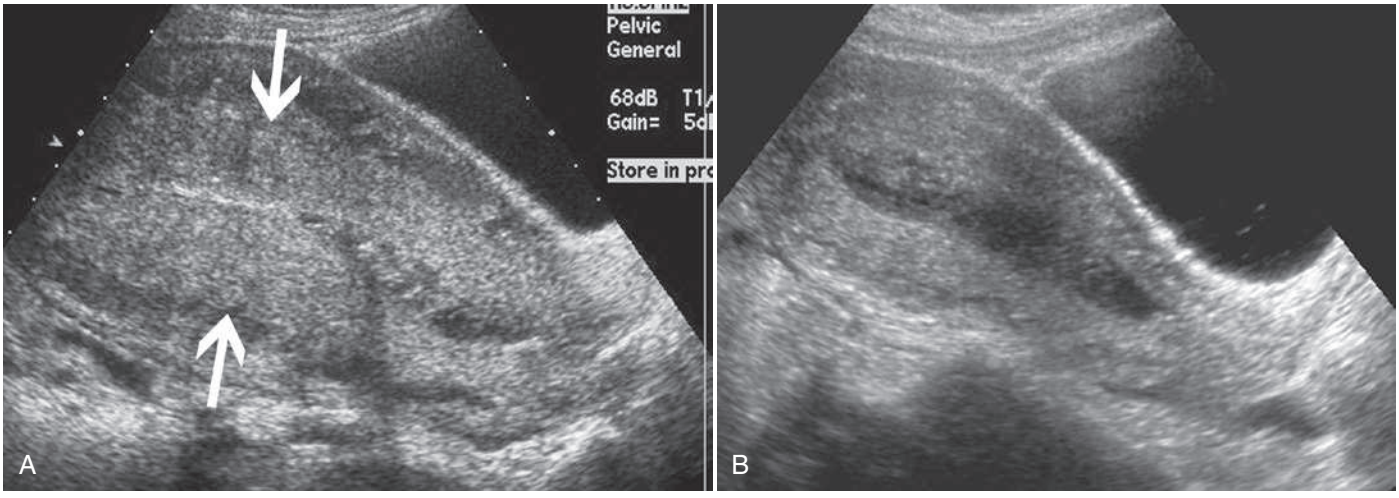

FIG. 15.26 Normal Postpartum Findings. (A) Normal hyperechoic myometrium. Sagittal TAS image from a patient 4 days after vaginal delivery shows hyperechoic appearance of inner portion of myometrium (between *arrows*). One could potentially misinterpret this entire area as endometrium. **(B)** Normal endometrial fluid. Sagittal TAS image from a patient 9 days after vaginal delivery shows a small amount of fluid in the endometrial cavity, a common finding in postpartum women.

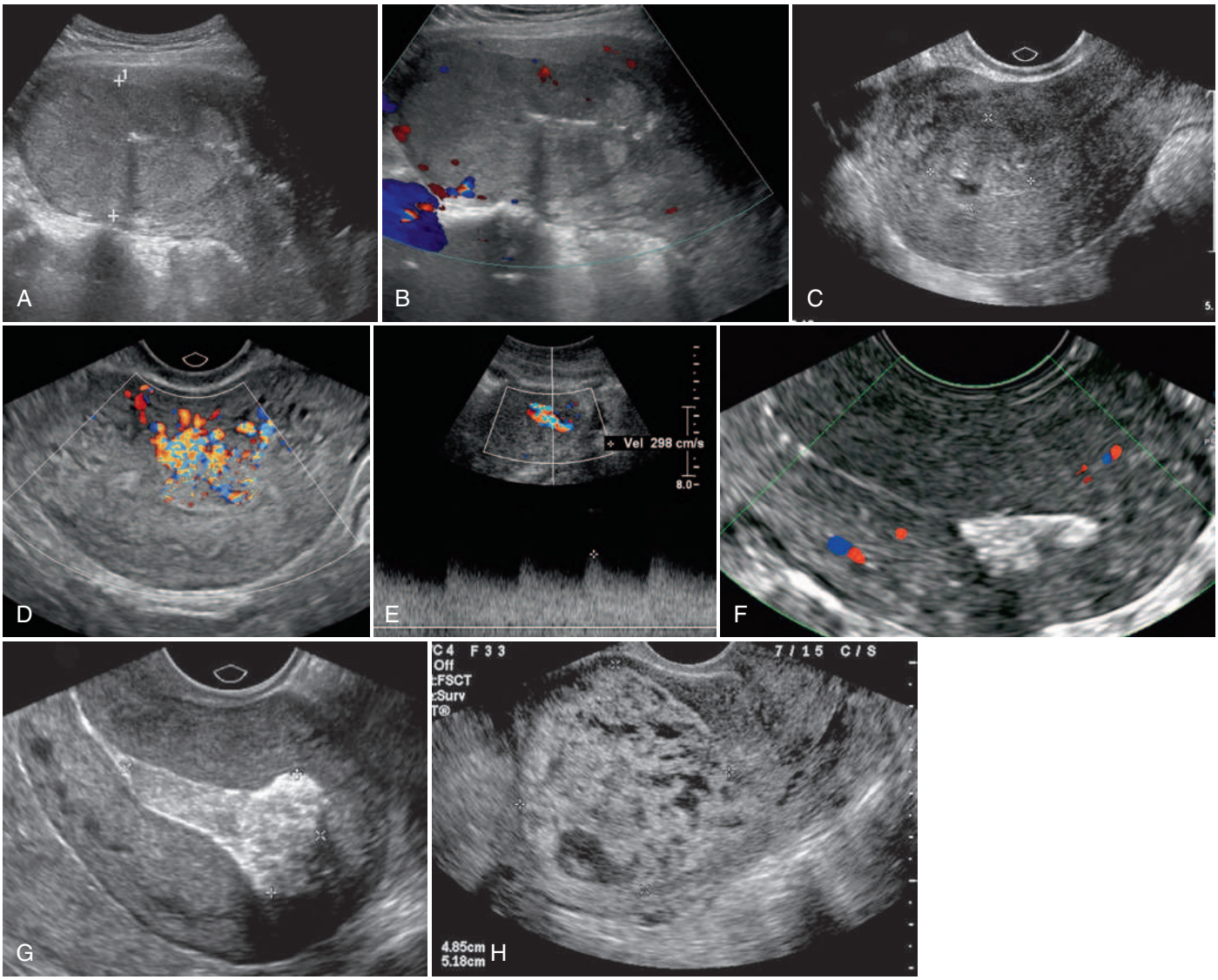

FIG. 15.27 Retained Products of Conception (RPOC). (A) and **(B)** Sagittal TAS scans in a patient 6 days after vaginal delivery. **(A)** There is a hyperechoic mass *(calipers)* in superior region of the uterus. **(B)** Color Doppler image shows a few areas of flow in the periphery of the mass. (**A** and **B** courtesy of Shannon Sheedy, MD.) **(C)-(E)** Retained products of conception 1 month after a miscarriage. **(C)** There is a hyperechoic mass *(calipers)* in the endometrial cavity. **(D)** Color Doppler shows substantial flow from the myometrium extending into the RPOC. **(E)** Angle-corrected spectral Doppler shows peak systolic velocity of 298 cm/sec. See also Video 15.12. **(F)** and **(G)** Sagittal TVS from two different patients, each a few months after delivery with calcified RPOC. **(H)** Sagittal sonogram shows a large area of RPOC after a cesarean section. The thin myometrium suggests placental invasion, in this case due to **placenta accreta.**

for uterine rupture. At times the myometrium and endometrium are heavily vascularized by RPOC (Fig. 15.27C–D, Video 15.12). In these cases, one study suggested that if there is higher-velocity flow (which they defined as >60 cm/sec), surgical removal of the residual tissue may be performed using sonographic guidance.[192] However, these were not angle-corrected velocity measurements, limiting the usefulness of relying on a specific velocity threshold.

Placental site trophoblastic tumor (PSTT) is an uncommon cause of postpartum bleeding but should be considered when there are persistently low serum levels of human chorionic gonadotropin (hCG) and/or elevated levels of human placental lactogen.[193] The hCG levels tend to be low, sometimes only minimally elevated, compared with the more common forms of gestational trophoblastic neoplasia. The sonographic appearance of PSTT is most commonly a heterogeneous predominately solid mass involving the endometrium and/or myometrium; occasionally it can be predominately cystic with marked vascularity simulating an arteriovenous malformation.[194] This is discussed in more depth in Chapter 30.

Endometritis

Endometritis should be considered as a potential diagnosis in the postpartum period when patients have fever and/or pain.

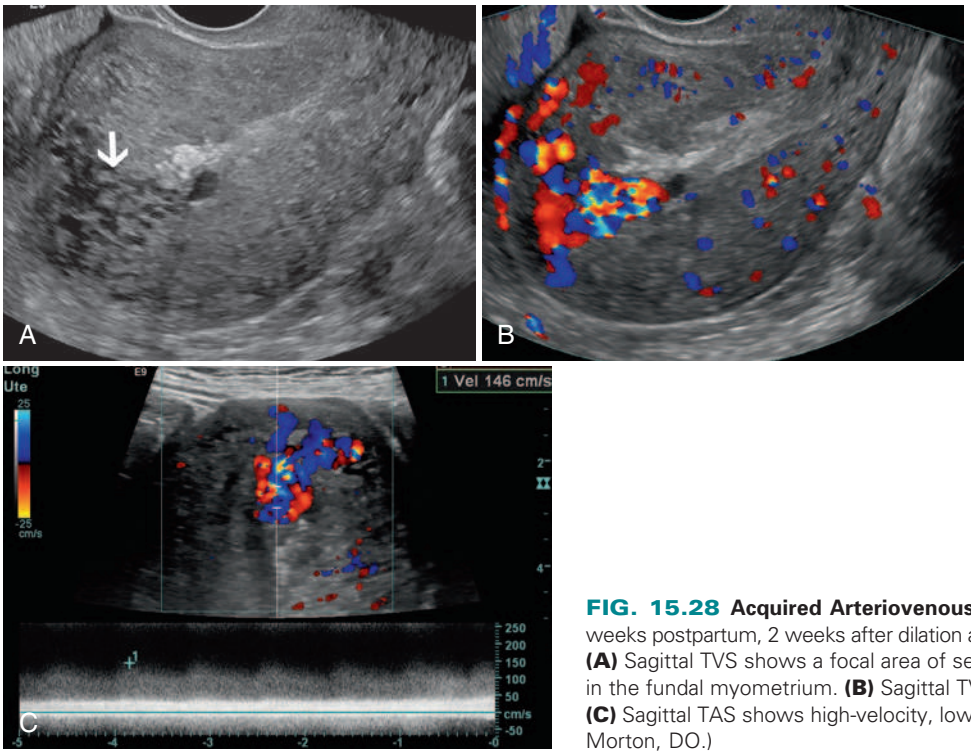

FIG. 15.28 Acquired Arteriovenous Malformation (AVM). AVM in a patient 9 weeks postpartum, 2 weeks after dilation and curettage, with continued vaginal bleeding. **(A)** Sagittal TVS shows a focal area of serpiginous cystic-appearing structures *(arrow)* in the fundal myometrium. **(B)** Sagittal TVS shows flow in the serpiginous structures. **(C)** Sagittal TAS shows high-velocity, low-resistance arterial flow. (Courtesy of Marilyn Morton, DO.)

Endometritis is a clinical diagnosis. The sonographic findings are variable and may be normal.[190] Fluid and/or air may be seen in the endometrial cavity in patients with endometritis, but these are also common normal findings in the first few postpartum weeks, limiting their usefulness.

Arteriovenous Malformation

Arteriovenous malformations (AVMs) are rare. In general, they are acquired lesions resulting from prior uterine instrumentation. Although they can be seen at other times, they are often diagnosed during the postpartum period or after a miscarriage, and patients usually have abnormal vaginal bleeding on presentation. It is important to diagnose AVM so that inappropriate treatment does not worsen the hemorrhage.[13]

Sonographically, AVMs should be considered when there is focal area of serpiginous tubular structures in the myometrium.[195,196] Color or power Doppler imaging will typically show exuberant flow in the AVM (Fig. 15.28), and spectral Doppler imaging will demonstrate low-resistance arterial flow. It has been suggested that the arterial velocities in the AVM may guide treatment, with higher velocities (>83 cm/sec) suggesting the need for embolization and lower velocities allowing for more conservative management.[197] However, in most published studies the reported velocities are not true velocities because angle correction was not used, confounding the usefulness of such measurements.

Uterine AVMs can be easily overdiagnosed in the postpartum and postmiscarriage periods.[198] Findings similar to true AVMs can be due to **subinvolution of the placental bed.**[199] Thus in stable patients one should try for conservative management because many of these seeming AVMs will resolve spontaneously. Focal areas of low-resistance arterial flow may also be seen in the myometrium in patients with RPOC and **gestational trophoblastic disease,** similar to an AVM.[200] A negative serum hCG may be helpful because hCG is typically elevated in patients with gestational trophoblastic disease.[13] Serum hCG level may not be as helpful for RPOC; about half of patients with RPOC are reported to have a negative or only minimally positive hCG level.[201]

Findings After Cesarean Section

Most patients undergoing a cesarean delivery will have a transverse incision in the lower uterine segment. In the initial postpartum period after a cesarean section, one typically will see small echogenic foci, due to sutures and/or gas, in the anterior myometrium of the lower uterine segment (Fig. 15.29A, Video 15.13). It is uncertain how long these can normally be seen but likely for several weeks or months. One may also see heterogeneity in this region of the myometrium, probably due to small areas of hemorrhage. For the minority of cesarean section patients who have a classic hysterotomy with a longitudinal incision higher in the uterus, one may see similar heterogeneity and/or echogenic foci in that region of the myometrium in the postpartum period.

Bladder flap hematomas, due to bleeding at the incision site, may occur in the lower uterine segment of the uterus or between it and the urinary bladder. Sonographically, they appear as a mass of variable echogenicity (see Fig. 15.29B, Video 15.13). Small hematomas are common and may not be clinically

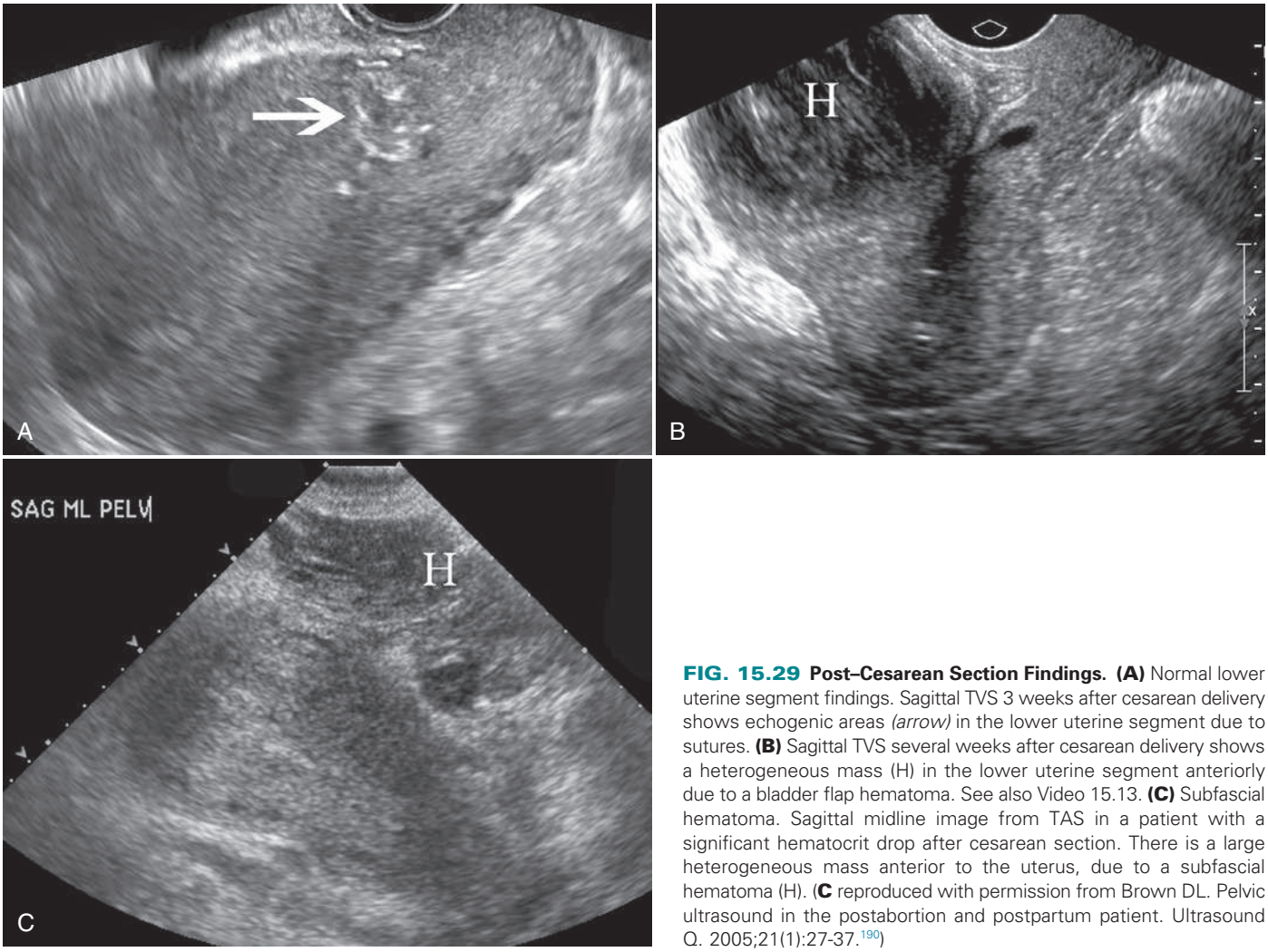

FIG. 15.29 Post–Cesarean Section Findings. (A) Normal lower uterine segment findings. Sagittal TVS 3 weeks after cesarean delivery shows echogenic areas *(arrow)* in the lower uterine segment due to sutures. **(B)** Sagittal TVS several weeks after cesarean delivery shows a heterogeneous mass (H) in the lower uterine segment anteriorly due to a bladder flap hematoma. See also Video 15.13. **(C)** Subfascial hematoma. Sagittal midline image from TAS in a patient with a significant hematocrit drop after cesarean section. There is a large heterogeneous mass anterior to the uterus, due to a subfascial hematoma (H). (**C** reproduced with permission from Brown DL. Pelvic ultrasound in the postabortion and postpartum patient. Ultrasound Q. 2005;21(1):27-37.[190])

significant. The size above which hematomas tend to be clinically important is uncertain, although it has been suggested that hematomas smaller than 4 cm[202] are unlikely to be clinically significant. **Subfascial hematomas** are thought to be due to disruption of inferior epigastric vessels and are located extraperitoneally.[203] They can appear as a mass of variable echogenicity, located posterior to the rectus abdominal muscles of the lower abdominal wall (see Fig. 15.29C). Subfascial and bladder flap hematomas may occur in the same patient, but it is important to distinguish them if surgical treatment is planned, because the approach is different.[203,204]

After several months, when healing is complete, a thin linear echo representing the hysterotomy scar can often be seen in the lower uterine segment[205] and is a normal, expected finding (Fig. 15.30A). More than one scar may be seen in patients with multiple prior cesarean deliveries. The myometrium superior to the scar, or between two adjacent scars, may have a convex outer contour and potentially be mistaken for a leiomyoma[204,206] (Fig. 15.30B–C). Fluid sometimes accumulates in the scar, either spontaneously or during SHG. Variable terminology has been used to describe this collection of fluid in the scar: **cesarean scar diverticuli, cesarean scar pouch, cesarean scar defect, uterine niche, and isthmocele.**[207-211] In general, this entity is considered present when fluid extends into a triangular defect in the anterior lower uterine segment (Fig. 15.30D); however, there is no standard definition.[211] It is also unclear whether such a "defect" is necessarily abnormal because many patients are asymptomatic.[211] However, these may cause intermenstrual bleeding and can be treated surgically.[211] Cesarean scar defects might also be a cause of dysmenorrhea, chronic pelvic pain, or infertility.[211] Larger defects, with thinner myometrium, seem to be associated with a higher likelihood of uterine rupture or dehiscence in a subsequent pregnancy, but it is not yet clear how this should affect clinical practice.[212]

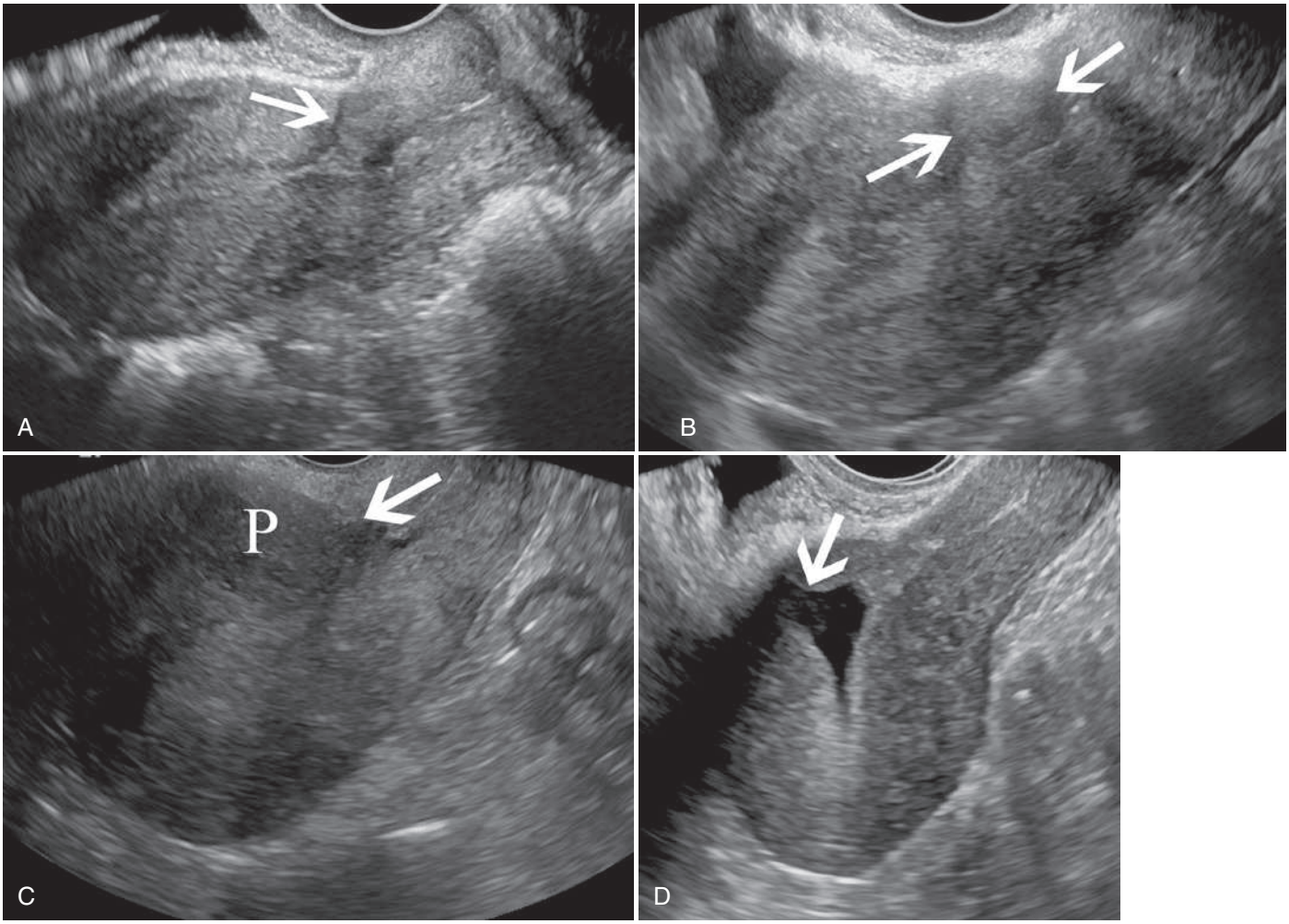

FIG. 15.30 Cesarean Section Scars Remote From Time of Surgery on Transvaginal Sonography (TVS). (A) Normal cesarean section scar *(arrow)* in anterior lower uterine segment. **(B)** Pseudomass due to bulbous area of myometrium, in this instance located between two cesarean sections scars *(arrows)*. This could be mistaken for a leiomyoma. **(C)** Pseudomass *(P)* due to bulbous area of myometrium superior to a cesarean section scar *(arrow)*. **(D)** Fluid *(arrow)* extends into the cesarean section scar in the anterior lower uterine segment. Variable terms, including "isthmocele," have been used to describe this finding.

Acknowledgment

The authors would like to acknowledge Dr. Shia Salem for use of the prior version of his chapter for this current edition.

REFERENCES

1. Williams PL, Warwick R, editors. Gray's anatomy. 37th ed. Edinburgh: Churchill Livingstone; 1989.
2. Benacerraf BR, Abuhamad AZ, Bromley B, et al. Consider ultrasound first for imaging the female pelvis. Am J Obstet Gynecol. 2015;212(4): 450-455.
3. Becker Jr E, Lev-Toaff AS, Kaufman EP, et al. The added value of transvaginal sonohysterography over transvaginal sonography alone in women with known or suspected leiomyoma. J Ultrasound Med. 2002;21(3): 237-247.
4. Cullinan JA, Fleischer AC, Kepple DM, Arnold AL. Sonohysterography: a technique for endometrial evaluation. Radiographics. 1995;15(3): 501-514.
5. Davis PC, O'Neill MJ, Yoder IC, et al. Sonohysterographic findings of endometrial and subendometrial conditions. Radiographics. 2002;22(4): 803-816.
6. Gaucherand P, Piacenza JM, Salle B, Rudigoz RC. Sonohysterography of the uterine cavity: preliminary investigations. J Clin Ultrasound. 1995;23(6):339-348.
7. Dueholm M, Moller C, Rydbjerg S, et al. An ultrasound algorithm for identification of endometrial cancer. Ultrasound Obstet Gynecol. 2014;43(5):557-568.
8. Werbrouck E, Veldman J, Luts J, et al. Detection of endometrial pathology using saline infusion sonography versus gel instillation sonography: a prospective cohort study. Fertil Steril. 2011;95(1):285-288.
9. Jokubkiene L, Sladkevicius P, Valentin L. Appearance of the endometrium at saline contrast sonohysterography in the luteal phase of the menstrual cycle: a prospective observational study. Ultrasound Obstet Gynecol. 2015;45(3):339-345.
10. American Institute of Ultrasound in Medicine (AIUM). AIUM practice guidelines for the performance of sonohysterography. Laurel, MD: AUIM; 2007.
11. Hann LE, Gretz EM, Bach AM, Francis SM. Sonohysterography for evaluation of the endometrium in women treated with tamoxifen. AJR Am J Roentgenol. 2001;177(2):337-342.
12. Allison SJ, Horrow MM, Kim HY, Lev-Toaff AS. saline-infused sonohysterography: tips for achieving greater success. Radiographics. 2011;31(7): 1991-2004.

13. Salem S. Gynecology. In: Rumack CM, Wilson SR, Charboneau JW, Levine D, editors. Diagnostic ultrasound. 4th ed. Philadelphia: Elsevier; 2011. p. 547-612.
14. Wachsberg RH. Transrectal ultrasonography for problem solving after transvaginal ultrasonography of the female internal reproductive tract. J Ultrasound Med. 2003;22(12):1349-1356.
15. Vitton V, Vignally P, Barthet M, et al. Dynamic anal endosonography and MRI defecography in diagnosis of pelvic floor disorders: comparison with conventional defecography. Dis Colon Rectum. 2011;54(11): 1398-1404.
16. Dietz HP, Jarvis SK, Vancaillie TG. The assessment of levator muscle strength: a validation of three ultrasound techniques. Int Urogynecol J Pelvic Floor Dysfunct. 2002;13(3):156-159.
17. Liu ZZ, Jiang YX, Dai Q, et al. Imaging of endometrial carcinoma using contrast-enhanced sonography. J Ultrasound Med. 2011;30(11): 1519-1527.
18. Stoelinga B, Hehenkamp WJ, Brolmann HA, Huirne JA. Real-time elastography for assessment of uterine disorders. Ultrasound Obstet Gynecol. 2014;43(2):218-226.
19. Sanders RC, Parsons AK. Anteverted retroflexed uterus: a common consequence of cesarean delivery. AJR Am J Roentgenol. 2014;203(1): W117-W124.
20. Goldstein SR. The endometrial echo revisited: have we created a monster? Am J Obstet Gynecol. 2004;191(4):1092-1096.
21. Ozcan T, Dogra V. The normal pelvis on ultrasonic imaging and anatomic correlations. In: Fielding JR, Brown DL, Thurmond AS, editors. Gynecologic imaging. Philadelphia: Elsevier; 2011. p. 5-20.
22. Merz E, Miric-Tesanic D, Bahlmann F, et al. Sonographic size of uterus and ovaries in pre- and postmenopausal women. Ultrasound Obstet Gynecol. 1996;7(1):38-42.
23. Platt JF, Bree RL, Davidson D. Ultrasound of the normal nongravid uterus: correlation with gross and histopathology. J Clin Ultrasound. 1990;18(1): 15-19.
24. Verguts J, Ameye L, Bourne T, Timmerman D. Normative data for uterine size according to age and gravidity and possible role of the classical golden ratio. Ultrasound Obstet Gynecol. 2013;42(6):713-717.
25. Orsini LF, Salardi S, Pilu G, et al. Pelvic organs in premenarcheal girls: real-time ultrasonography. Radiology. 1984;153(1):113-116.
26. Miller EI, Thomas RH, Lines P. The atrophic postmenopausal uterus. J Clin Ultrasound. 1977;5(4):261-263.
27. Fleischer AC, Kalemeris GC, Entman SS. Sonographic depiction of the endometrium during normal cycles. Ultrasound Med Biol. 1986;12(4): 271-277.
28. Forrest TS, Elyaderani MK, Muilenburg MI, et al. Cyclic endometrial changes: US assessment with histologic correlation. Radiology. 1988;167(1): 233-237.
29. Bakos O, Lundkvist O, Bergh T. Transvaginal sonographic evaluation of endometrial growth and texture in spontaneous ovulatory cycles—a descriptive study. Hum Reprod. 1993;8(6):799-806.
30. Lenz S, Lindenberg S. Ultrasonic evaluation of endometrial growth in women with normal cycles during spontaneous and stimulated cycles. Hum Reprod. 1990;5(4):377-381.
31. Nalaboff KM, Pellerito JS, Ben-Levi E. Imaging the endometrium: disease and normal variants. Radiographics. 2001;21:1409-1424.
32. Randall JM, Fisk NM, McTavish A, Templeton AA. Transvaginal ultrasonic assessment of endometrial growth in spontaneous and hyperstimulated menstrual cycles. Br J Obstet Gynaecol. 1989;96(8):954-959.
33. Leone FP, Timmerman D, Bourne T, et al. Terms, definitions and measurements to describe the sonographic features of the endometrium and intrauterine lesions: a consensus opinion from the International Endometrial Tumor Analysis (IETA) group. Ultrasound Obstet Gynecol. 2010;35(1): 103-112.
34. Goldstein SR. Abnormal uterine bleeding: the role of ultrasound. Radiol Clin North Am. 2006;44(6):901-910.
35. Lin MC, Gosink BB, Wolf SI, et al. Endometrial thickness after menopause: effect of hormone replacement. Radiology. 1991;180(2):427-432.
36. Osmers R, Volksen M, Schauer A. Vaginosonography for early detection of endometrial carcinoma? Lancet. 1990;335(8705):1569-1571.
37. Shipley CF 3rd, Simmons CL, Nelson GH. Comparison of transvaginal sonography with endometrial biopsy in asymptomatic postmenopausal women. J Ultrasound Med. 1994;13(2):99-104.
38. Aleem F, Predanic M, Calame R, et al. Transvaginal color and pulsed Doppler sonography of the endometrium: a possible role in reducing the number of dilatation and curettage procedures. J Ultrasound Med. 1995;14(2): 139-145.
39. Giannella L, Mfuta K, Setti T, et al. Diagnostic accuracy of endometrial thickness for the detection of intra-uterine pathologies and appropriateness of performed hysteroscopies among asymptomatic postmenopausal women. Eur J Obstet Gynecol Reprod Biol. 2014;177:29-33.
40. Smith-Bindman R, Weiss E, Feldstein V. How thick is too thick? When endometrial thickness should prompt biopsy in postmenopausal women without vaginal bleeding. Ultrasound Obstet Gynecol. 2004;24: 558-565.
41. Fleischer AC, Kalemeris GC, Machin JE, et al. Sonographic depiction of normal and abnormal endometrium with histopathologic correlation. J Ultrasound Med. 1986;5(8):445-452.
42. Farrer-Brown G, Beilby JO, Tarbit MH. The blood supply of the uterus. 2. Venous pattern. J Obstet Gynaecol Br Commonw. 1970;77(8):682-689.
43. Mitchell DG, Schonholz L, Hilpert PL, et al. Zones of the uterus: discrepancy between US and MR images. Radiology. 1990;174(3 Pt 1):827-831.
44. DuBose TJ, Hill LW, Hennigan Jr HW, et al. Sonography of arcuate uterine blood vessels. J Ultrasound Med. 1985;4(5):229-233.
45. Atri M, de Stempel J, Senterman MK, Bret PM. Diffuse peripheral uterine calcification (manifestation of Monckeberg's arteriosclerosis) detected by ultrasonography. J Clin Ultrasound. 1992;20(3):211-216.
46. Occhipinti K, Kutcher R, Rosenblatt R. Sonographic appearance and significance of arcuate artery calcification. J Ultrasound Med. 1991;10(2): 97-100.
47. de Vries K, Lyons EA, Ballard G, et al. Contractions of the inner third of the myometrium. Am J Obstet Gynecol. 1990;162(3):679-682.
48. Burks DD, Stainken BF, Burkhard TK, Balsara ZN. Uterine inner myometrial echogenic foci. Relationship to prior dilatation and curettage and endocervical biopsy. J Ultrasound Med. 1991;10(9):487-492.
49. Casey PM, Long ME, Marnach ML. Abnormal cervical appearance: what to do, when to worry? Mayo Clin Proc. 2011;86(2):147-150.
50. Duffield C, Gerscovich EO, Gillen MA, et al. Endometrial and endocervical micro echogenic foci: sonographic appearance with clinical and histologic correlation. J Ultrasound Med. 2005;24(5):583-590.
51. Ergun A, Pabuccu R, Atay V, et al. Three sisters with septate uteri: another reference to bidirectional theory. Hum Reprod. 1997;12(1): 140-142.
52. Deutch TD, Abuhamad AZ. The role of 3-dimensional ultrasonography and magnetic resonance imaging in the diagnosis of müllerian duct anomalies: a review of the literature. J Ultrasound Med. 2008;27(3):413-423.
53. Grimbizis GF, Di Spiezio Sardo A, Saravelos SH, et al. The Thessaloniki ESHRE/ESGE consensus on diagnosis of female genital anomalies. Hum Reprod. 2016;31(1):2-7.
54. Troiano RN, McCarthy SM. Müllerian duct anomalies: imaging and clinical issues. Radiology. 2004;233(1):19-34.
55. American Fertility Society. The American Fertility Society classifications of adnexal adhesions, distal tubal occlusion, tubal occlusion secondary to tubal ligation, tubal pregnancies, müllerian anomalies and intrauterine adhesions. Fertil Steril. 1988;49(6):944-955.
56. Olpin JD, Heilbrun M. Imaging of müllerian duct anomalies. Clin Obstet Gynecol. 2009;52(1):40-56.
57. Viscomi GN, Gonzalez R, Taylor KJ. Ultrasound detection of uterine abnormalities after diethylstilbestrol (DES) exposure. Radiology. 1980;136(3):733-735.
58. Lev-Toaff AS, Toaff ME, Friedman AC. Endovaginal sonographic appearance of a DES uterus. J Ultrasound Med. 1990;9(11):661-664.
59. Acien P, Acien M, Sanchez-Ferrer M. Complex malformations of the female genital tract. New types and revision of classification. Hum Reprod. 2004;19(10):2377-2384.
60. Grimbizis GF, Gordts S, Di Spiezio Sardo A, et al. The ESHRE/ESGE consensus on the classification of female genital tract congenital anomalies. Hum Reprod. 2013;28(8):2032-2044.

61. Oppelt P, Renner SP, Brucker S, et al. The VCUAM (vagina cervix uterus adnex–associated malformation) classification: a new classification for genital malformations. Fertil Steril. 2005;84(5):1493-1497.
62. Bermejo C, Martinez Ten P, Cantarero R, et al. Three-dimensional ultrasound in the diagnosis of müllerian duct anomalies and concordance with magnetic resonance imaging. Ultrasound Obstet Gynecol. 2010;35(5):593-601.
63. Pellerito JS, McCarthy SM, Doyle MB, et al. Diagnosis of uterine anomalies: relative accuracy of MR imaging, endovaginal sonography, and hysterosalpingography. Radiology. 1992;183(3):795-800.
64. Zreik TG, Troiano RN, Ghoussoub RA, et al. Myometrial tissue in uterine septa. J Am Assoc Gynecol Laparosc. 1998;5(2):155-160.
65. Salim R, Woelfer B, Backos M, et al. Reproducibility of three-dimensional ultrasound diagnosis of congenital uterine anomalies. Ultrasound Obstet Gynecol. 2003;21(6):578-582.
66. Wall DJ, Javitt MC, Glanc P, et al. ACR appropriateness Criteria® infertility. Ultrasound Q. 2015;31(1):37-44.
67. Saravelos SH, Cocksedge KA, Li TC. Prevalence and diagnosis of congenital uterine anomalies in women with reproductive failure: a critical appraisal. Hum Reprod Update. 2008;14(5):415-429.
68. Agrawal G, Riherd JM, Busse RF, et al. Evaluation of uterine anomalies: 3D FRFSE cube versus standard 2D FRFSE. AJR Am J Roentgenol. 2009;193(6):W558-W562.
69. Ludwin A, Ludwin I. Comparison of the ESHRE-ESGE and ASRM classifications of müllerian duct anomalies in everyday practice. Hum Reprod. 2015;30(3):569-580.
70. Brody JM, Koelliker SL, Frishman GN. Unicornuate uterus: imaging appearance, associated anomalies, and clinical implications. AJR Am J Roentgenol. 1998;171(5):1341-1347.
71. Smith BC, Brown DL, Carter RE, Famuyide AO. Double cervix: clarifying a diagnostic dilemma. Am J Obstet Gynecol. 2014;211(1):26.e1-26.e5.
72. Stewart EA. Clinical practice. Uterine fibroids. N Engl J Med. 2015;372(17):1646-1655.
73. Goodwin SC, Bonilla SM, Sacks D, et al. Reporting standards for uterine artery embolization for the treatment of uterine leiomyomata. J Vasc Interv Radiol. 2001;12(9):1011-1020.
74. McLucas B. Diagnosis, imaging and anatomical classification of uterine fibroids. Best Pract Res Clin Obstet Gynaecol. 2008;22(4):627-642.
75. Munro MG, Critchley HO, Broder MS, Fraser IS. FIGO classification system (PALM-COEIN) for causes of abnormal uterine bleeding in nongravid women of reproductive age. Int J Gynaecol Obstet. 2011;113(1):3-13.
76. Van den Bosch T, Dueholm M, Leone FP, et al. Terms, definitions and measurements to describe sonographic features of myometrium and uterine masses: a consensus opinion from the Morphological Uterus Sonographic Assessment (MUSA) group. Ultrasound Obstet Gynecol. 2015;46(3):284-298.
77. Caoili EM, Hertzberg BS, Kliewer MA, et al. Refractory shadowing from pelvic masses on sonography: a useful diagnostic sign for uterine leiomyomas. AJR Am J Roentgenol. 2000;174(1):97-101.
78. Maebayashi T, Imai K, Takekawa Y, et al. Radiologic features of uterine lipoleiomyoma. J Comput Assist Tomogr. 2003;27(2):162-165.
79. Prieto A, Crespo C, Pardo A, et al. Uterine lipoleiomyomas: US and CT findings. Abdom Imaging. 2000;25(6):655-657.
80. Wang X, Kumar D, Seidman JD. Uterine lipoleiomyomas: a clinicopathologic study of 50 cases. Int J Gynecol Pathol. 2006;25(3):239-242.
81. Akbulut M, Gundogan M, Yorukoglu A. Clinical and pathological features of lipoleiomyoma of the uterine corpus: a review of 76 cases. Balkan Med J. 2014;31(3):224-229.
82. Brown DL. Uterine leiomyomas. In: Fielding JR, Brown DL, Thurmond AS, editors. Gynecologic imaging. Philadelphia: Elsevier; 2011. p. 237-250.
83. Ghai S, Rajan DK, Benjamin MS, et al. Uterine artery embolization for leiomyomas: pre- and postprocedural evaluation with US. Radiographics. 2005;25(5):1159-1172.
84. Ahmad I, Ray Jr CE, Conyers C. Transvaginal sonographic appearance of thrombosed uterine arteries after uterine artery embolization: the "white snake" sign. J Clin Ultrasound. 2003;31(8):401-406.
85. Matytsina-Quinlan L, Matytsina L. Submucosal uterine fibroid prolapsed into vagina in a symptomatic patient with IUS. BMJ Case Rep. 2014;2014.
86. Sato K, Yuasa N, Fujita M, Fukushima Y. Clinical application of diffusion-weighted imaging for preoperative differentiation between uterine leiomyoma and leiomyosarcoma. Am J Obstet Gynecol. 2014;210(4):368.e1-368.e8.
87. Thomassin-Naggara I, Dechoux S, Bonneau C, et al. How to differentiate benign from malignant myometrial tumours using MR imaging. Eur Radiol. 2013;23(8):2306-2314.
87a. Nagai T, Takai Y, Akahori T, et al. Novel uterine sarcoma preoperative diagnosis score predicts the need for surgery in patients presenting with a uterine mass. Springerplus. 2014;3:678.
87b. Goto A, Takeuchi S, Sugimura K, Maruo T. Usefulness of Gd-DTPA contrast-enhanced dynamic MRI and serum determination of LDH and its isozymes in the differential diagnosis of leiomyosarcoma from degenerated leiomyoma of the uterus. Int J Gynecol Cancer. 2002;12(4):354-361.
88. Zaloudek C, Hendrickson MR. Mesenchymal tumors of the uterus. In: Kurman RJ, editor. Blaustein's pathology of the female genital tract. 5th ed. New York: Springer-Verlag; 2002. p. 561-615.
89. Bergholt T, Eriksen L, Berendt N, et al. Prevalence and risk factors of adenomyosis at hysterectomy. Hum Reprod. 2001;16(11):2418-2421.
90. Taran FA, Stewart EA, Brucker S. Adenomyosis: epidemiology, risk factors, clinical phenotype and surgical and interventional alternatives to hysterectomy. Geburtshilfe Frauenheilkd. 2013;73(9):924-931.
91. Di Donato N, Montanari G, Benfenati A, et al. Prevalence of adenomyosis in women undergoing surgery for endometriosis. Eur J Obstet Gynecol Reprod Biol. 2014;181:289-293.
92. Chopra S, Lev-Toaff AS, Ors F, Bergin D. Adenomyosis: common and uncommon manifestations on sonography and magnetic resonance imaging. J Ultrasound Med. 2006;25(5):617-627.
93. Meredith SM, Sanchez-Ramos L, Kaunitz AM. Diagnostic accuracy of transvaginal sonography for the diagnosis of adenomyosis: systematic review and metaanalysis. Am J Obstet Gynecol. 2009;201(1):107 e1-107.e6.
94. Atri M, Reinhold C, Mehio AR, et al. Adenomyosis: US features with histologic correlation in an in-vitro study. Radiology. 2000;215(3):783-790.
95. Bromley B, Shipp TD, Benacerraf B. Adenomyosis: sonographic findings and diagnostic accuracy. J Ultrasound Med. 2000;19(8):529-534.
96. Kepkep K, Tuncay YA, Goynumer G, Tutal E. Transvaginal sonography in the diagnosis of adenomyosis: which findings are most accurate? Ultrasound Obstet Gynecol. 2007;30(3):341-345.
97. Sun YL, Wang CB, Lee CY, et al. Transvaginal sonographic criteria for the diagnosis of adenomyosis based on histopathologic correlation. Taiwan J Obstet Gynecol. 2010;49(1):40-44.
98. Reeves MF, Goldstein RB, Jones KD. Communication of adenomyosis with the endometrial cavity: visualization with saline contrast sonohysterography. Ultrasound Obstet Gynecol. 2010;36(1):115-119.
99. Takeuchi H, Kitade M, Kikuchi I, et al. Diagnosis, laparoscopic management, and histopathologic findings of juvenile cystic adenomyoma: a review of nine cases. Fertil Steril. 2010;94(3):862-868.
100. Acien P, Acien M, Fernandez F, et al. The cavitated accessory uterine mass: a müllerian anomaly in women with an otherwise normal uterus. Obstet Gynecol. 2010;116(5):1101-1109.
101. Acien P, Bataller A, Fernandez F, et al. New cases of accessory and cavitated uterine masses (ACUM): a significant cause of severe dysmenorrhea and recurrent pelvic pain in young women. Hum Reprod. 2012;27(3):683-694.
102. Taran FA, Weaver AL, Coddington CC, Stewart EA. Characteristics indicating adenomyosis coexisting with leiomyomas: a case-control study. Hum Reprod. 2010;25(5):1177-1182.
103. Ozkan ZS, Kumbak B, Cilgin H, et al. Coexistence of adenomyosis in women operated for benign gynecological diseases. Gynecol Endocrinol. 2012;28(3):212-215.
104. Chu LC, Coquia SF, Hamper UM. Ultrasonography evaluation of pelvic masses. Radiol Clin North Am. 2014;52(6):1237-1252.
105. Park SB, Moon MH, Hong SR, et al. Adenoma malignum of the uterine cervix: ultrasonographic findings in 11 patients. Ultrasound Obstet Gynecol. 2011;38(6):716-721.
106. Mendelson EB, Bohm-Velez M, Joseph N, Neiman HL. Endometrial abnormalities: evaluation with transvaginal sonography. AJR Am J Roentgenol. 1988;150(1):139-142.

107. Lev-Toaff AS, Toaff ME, Liu JB, et al. Value of sonohysterography in the diagnosis and management of abnormal uterine bleeding. Radiology. 1996;201(1):179-184.
108. Parsons AK, Lense JJ. Sonohysterography for endometrial abnormalities: preliminary results. J Clin Ultrasound. 1993;21(2):87-95.
109. Dubinsky TJ, Parvey HR, Gormaz G, Makland N. Transvaginal hysterosonography in the evaluation of small endoluminal masses. J Ultrasound Med. 1995;14(1):1-6.
110. Jorizzo JR, Riccio GJ, Chen MY, Carr JJ. Sonohysterography: the next step in the evaluation of the abnormal endometrium. Radiographics. 1999;Spec No. 19:S117-S130.
111. Dubinsky TJ, Stroehlein K, Abu-Ghazzeh Y, et al. Prediction of benign and malignant endometrial disease: hysterosonographic-pathologic correlation. Radiology. 1999;210(2):393-397.
112. Laifer-Narin SL, Ragavendra N, Lu DS, et al. Transvaginal saline hysterosonography: characteristics distinguishing malignant and various benign conditions. AJR Am J Roentgenol. 1999;172(6):1513-1520.
113. Rossouw JE, Anderson GL, Prentice RL, et al. Risks and benefits of estrogen plus progestin in healthy postmenopausal women: principal results from the Women's Health Initiative randomized controlled trial. JAMA. 2002;288(3):321-333.
114. Levine D, Gosink BB, Johnson LA. Change in endometrial thickness in postmenopausal women undergoing hormone replacement therapy. Radiology. 1995;197(3):603-608.
115. Malfetano JH. Tamoxifen-associated endometrial carcinoma in postmenopausal breast cancer patients. Gynecol Oncol. 1990;39(1):82-84.
116. Kedar RP, Bourne TH, Powles TJ, et al. Effects of tamoxifen on uterus and ovaries of postmenopausal women in a randomised breast cancer prevention trial. Lancet. 1994;343(8909):1318-1321.
117. Lahti E, Blanco G, Kauppila A, et al. Endometrial changes in postmenopausal breast cancer patients receiving tamoxifen. Obstet Gynecol. 1993;81(5 Pt 1):660-664.
118. Hann LE, Giess CS, Bach AM, et al. Endometrial thickness in tamoxifen-treated patients: correlation with clinical and pathologic findings. AJR Am J Roentgenol. 1997;168(3):657-661.
119. Cohen I, Rosen DJ, Tepper R, et al. Ultrasonographic evaluation of the endometrium and correlation with endometrial sampling in postmenopausal patients treated with tamoxifen. J Ultrasound Med. 1993;12(5):275-280.
120. Hulka CA, Hall DA. Endometrial abnormalities associated with tamoxifen therapy for breast cancer: sonographic and pathologic correlation. AJR Am J Roentgenol. 1993;160(4):809-812.
121. Ascher SM, Imaoka I, Lage JM. Tamoxifen-induced uterine abnormalities: the role of imaging. Radiology. 2000;214(1):29-38.
122. Cohen I, Bernheim J, Azaria R, et al. Malignant endometrial polyps in postmenopausal breast cancer tamoxifen-treated patients. Gynecol Oncol. 1999;75(1):136-141.
123. Goldstein SR. Unusual ultrasonographic appearance of the uterus in patients receiving tamoxifen. Am J Obstet Gynecol. 1994;170(2):447-451.
124. Fong K, Kung R, Lytwyn A, et al. Endometrial evaluation with transvaginal US and hysterosonography in asymptomatic postmenopausal women with breast cancer receiving tamoxifen. Radiology. 2001;220(3):765-773.
125. Wong AW, Lao TH, Cheung CW, et al. Reappraisal of endometrial thickness for the detection of endometrial cancer in postmenopausal bleeding: a retrospective cohort study. BJOG. 2016;123(3):439-446.
126. Varner RE, Sparks JM, Cameron CD, et al. Transvaginal sonography of the endometrium in postmenopausal women. Obstet Gynecol. 1991;78(2):195-199.
127. Karlsson B, Granberg S, Wikland M, et al. Transvaginal ultrasonography of the endometrium in women with postmenopausal bleeding—a Nordic multicenter study. Am J Obstet Gynecol. 1995;172(5):1488-1494.
128. Ferrazzi E, Torri V, Trio D, et al. Sonographic endometrial thickness: a useful test to predict atrophy in patients with postmenopausal bleeding. An Italian multicenter study. Ultrasound Obstet Gynecol. 1996;7(5):315-321.
129. Granberg S, Wikland M, Karlsson B, et al. Endometrial thickness as measured by endovaginal ultrasonography for identifying endometrial abnormality. Am J Obstet Gynecol. 1991;164(1 Pt 1):47-52.
130. Nasri MN, Shepherd JH, Setchell ME, et al. The role of vaginal scan in measurement of endometrial thickness in postmenopausal women. Br J Obstet Gynaecol. 1991;98(5):470-475.
131. Goldstein SR, Nachtigall M, Snyder JR, Nachtigall L. Endometrial assessment by vaginal ultrasonography before endometrial sampling in patients with postmenopausal bleeding. Am J Obstet Gynecol. 1990;163(1 Pt 1):119-123.
132. Choo YC, Mak KC, Hsu C, et al. Postmenopausal uterine bleeding of nonorganic cause. Obstet Gynecol. 1985;66(2):225-228.
133. Atri M, Nazarnia S, Aldis AE, et al. Transvaginal US appearance of endometrial abnormalities. Radiographics. 1994;14(3):483-492.
134. Smith-Bindman R, Kerlikowske K, Feldstein VA, et al. Endovaginal ultrasound to exclude endometrial cancer and other endometrial abnormalities. JAMA. 1998;280(17):1510-1517.
135. Breijer M, Molb B. Transvaginal ultrasound measurement of the endometrium remains the first line test for investigating postmenopausal bleeding but integration of patient characteristics into testing may further improve diagnostic algorithms. BJOG. 2016;123(3):447.
136. Delisle MF, Villeneuve M, Boulvain M. Measurement of endometrial thickness with transvaginal ultrasonography: is it reproducible? J Ultrasound Med. 1998;17(8):481-484.
137. Goldstein RB, Bree RL, Benson CB, et al. Evaluation of the woman with postmenopausal bleeding: Society of Radiologists in Ultrasound–Sponsored Consensus Conference statement. J Ultrasound Med. 2001;20(10):1025-1036.
138. Bree RL, Bowerman RA, Bohm-Velez M, et al. US evaluation of the uterus in patients with postmenopausal bleeding: a positive effect on diagnostic decision making. Radiology. 2000;216(1):260-264.
139. Laifer-Narin S, Ragavendra N, Parmenter EK, Grant EG. False-normal appearance of the endometrium on conventional transvaginal sonography: comparison with saline hysterosonography. AJR Am J Roentgenol. 2002;178(1):129-133.
140. Dubinsky TJ, Parvey HR, Gormaz G, et al. Transvaginal hysterosonography: comparison with biopsy in the evaluation of postmenopausal bleeding. J Ultrasound Med. 1995;14(12):887-893.
141. Jokubkiene L, Sladkevicius P, Valentin L. Transvaginal ultrasound examination of the endometrium in postmenopausal women without vaginal bleeding. Ultrasound Obstet Gynecol. 2016;48(3):390-396.
142. Wilson DA, Stacy TM, Smith EI. Ultrasound diagnosis of hydrocolpos and hydrometrocolpos. Radiology. 1978;128(2):451-454.
143. Breckenridge JW, Kurtz AB, Ritchie WG, Macht Jr EL. Postmenopausal uterine fluid collection: indicator of carcinoma. AJR Am J Roentgenol. 1982;139(3):529-534.
144. Scott Jr WW, Rosenshein NB, Siegelman SS, Sanders RC. The obstructed uterus. Radiology. 1981;141(3):767-770.
145. Pretorius DH, Dennis MA, Manco-Johnson ML, Gottesfeld KR. Ultrasound diagnosis of hematotrachelos: a case report. Am J Obstet Gynecol. 1985;151(8):1080-1082.
146. Lewit N, Thaler I, Rottem S. The uterus: a new look with transvaginal sonography. J Clin Ultrasound. 1990;18(4):331-336.
147. McCarthy KA, Hall DA, Kopans DB, Swann CA. Postmenopausal endometrial fluid collections: always an indicator of malignancy? J Ultrasound Med. 1986;5(11):647-649.
148. Vuento MH, Pirhonen JP, Makinen JI, et al. Endometrial fluid accumulation in asymptomatic postmenopausal women. Ultrasound Obstet Gynecol. 1996;8(1):37-41.
149. Kurman RJ, editor. Blaustein's pathology of the female genital tract. 5th ed. New York: Springer-Verlag; 2002.
150. Sheth S, Hamper UM, Kurman RJ. Thickened endometrium in the postmenopausal woman: sonographic-pathologic correlation. Radiology. 1993;187(1):135-139.
151. Hulka CA, Hall DA, McCarthy K, Simeone JF. Endometrial polyps, hyperplasia, and carcinoma in postmenopausal women: differentiation with endovaginal sonography. Radiology. 1994;191(3):755-758.
152. Kupfer MC, Schiller VL, Hansen GC, Tessler FN. Transvaginal sonographic evaluation of endometrial polyps. J Ultrasound Med. 1994;13(7):535-539.

153. Timmerman D, Verguts J, Konstantinovic ML, et al. The pedicle artery sign based on sonography with color Doppler imaging can replace second-stage tests in women with abnormal vaginal bleeding. Ultrasound Obstet Gynecol. 2003;22(2):166-171.
154. Baldwin MT, Dudiak KM, Gorman B, Marks CA. Focal intracavitary masses recognized with the hyperechoic line sign at endovaginal US and characterized with hysterosonography. Radiographics. 1999;19(4):927-935.
155. Karlsson B, Granberg S, Hellberg P, Wikland M. Comparative study of transvaginal sonography and hysteroscopy for the detection of pathologic endometrial lesions in women with postmenopausal bleeding. J Ultrasound Med. 1994;13(10):757-762.
156. National Cancer Institute Surveillance, Epidemiology, and End Results Program (SEER). SEER Stat Fact Sheets: Eendometrial cancer. 2015. Available from: http://seer.cancer.gov/statfacts/html/corp.html.
157. Bourne TH, Campbell S, Steer CV, et al. Detection of endometrial cancer by transvaginal ultrasonography with color flow imaging and blood flow analysis: a preliminary report. Gynecol Oncol. 1991;40(3):253-259.
158. Weiner Z, Beck D, Rottem S, et al. Uterine artery flow velocity waveforms and color flow imaging in women with perimenopausal and postmenopausal bleeding. Correlation to endometrial histopathology. Acta Obstet Gynecol Scand. 1993;72(3):162-166.
159. Chan FY, Chau MT, Pun TC, et al. Limitations of transvaginal sonography and color Doppler imaging in the differentiation of endometrial carcinoma from benign lesions. J Ultrasound Med. 1994;13(8):623-628.
160. Carter JR, Lau M, Saltzman AK, et al. Gray scale and color flow Doppler characterization of uterine tumors. J Ultrasound Med. 1994;13(11):835-840.
161. Sladkevicius P, Valentin L, Marsal K. Endometrial thickness and Doppler velocimetry of the uterine arteries as discriminators of endometrial status in women with postmenopausal bleeding: a comparative study. Am J Obstet Gynecol. 1994;171(3):722-728.
162. Kurjak A, Shalan H, Sosic A, et al. Endometrial carcinoma in postmenopausal women: evaluation by transvaginal color Doppler ultrasonography. Am J Obstet Gynecol. 1993;169(6):1597-1603.
163. Sheth S, Hamper UM, McCollum ME, et al. Endometrial blood flow analysis in postmenopausal women: can it help differentiate benign from malignant causes of endometrial thickening? Radiology. 1995;195(3):661-665.
164. Cacciatore B, Lehtovirta P, Wahlstrom T, Ylostalo P. Preoperative sonographic evaluation of endometrial cancer. Am J Obstet Gynecol. 1989;160(1):133-137.
165. Gordon AN, Fleischer AC, Reed GW. Depth of myometrial invasion in endometrial cancer: preoperative assessment by transvaginal ultrasonography. Gynecol Oncol. 1990;39(3):321-327.
166. Fleischer AC, Dudley BS, Entman SS, et al. Myometrial invasion by endometrial carcinoma: sonographic assessment. Radiology. 1987;162(2):307-310.
167. Mascilini F, Testa AC, Van Holsbeke C, et al. Evaluating myometrial and cervical invasion in women with endometrial cancer: comparing subjective assessment with objective measurement techniques. Ultrasound Obstet Gynecol. 2013;42(3):353-358.
168. DelMaschio A, Vanzulli A, Sironi S, et al. Estimating the depth of myometrial involvement by endometrial carcinoma: efficacy of transvaginal sonography vs MR imaging. AJR Am J Roentgenol. 1993;160(3):533-538.
169. Yamashita Y, Mizutani H, Torashima M, et al. Assessment of myometrial invasion by endometrial carcinoma: transvaginal sonography vs contrast-enhanced MR imaging. AJR Am J Roentgenol. 1993;161(3):595-599.
170. Kinkel K, Kaji Y, Yu KK, et al. Radiologic staging in patients with endometrial cancer: a meta-analysis. Radiology. 1999;212(3):711-718.
171. Frei KA, Kinkel K, Bonel HM, et al. Prediction of deep myometrial invasion in patients with endometrial cancer: clinical utility of contrast-enhanced MR imaging—a meta-analysis and Bayesian analysis. Radiology. 2000;216(2):444-449.
172. Lalwani N, Dubinsky T, Javitt MC, et al. American College of Radiology (ACR). Appropriateness Criteria: pretreatment evaluation and follow-up of endometrial cancer. Ultrasound Q. 2014;30(1):21-28.
173. American Cancer Society. Endometrial (uterine) cancer. 2015. Available from: http://www.cancer.org/cancer/endometrialcancer.
174. Sohaib SA, Verma H, Attygalle AD, Ind TE. Imaging of uterine malignancies. Semin Ultrasound CT MR. 2010;31(5):377-387.
175. D'Angelo E, Prat J. Uterine sarcomas: a review. Gynecol Oncol. 2010;116(1):131-139.
176. Kim JA, Lee MS, Choi JS. Sonographic findings of uterine endometrial stromal sarcoma. Korean J Radiol. 2006;7(4):281-286.
177. Fedele L, Bianchi S, Dorta M, Vignali M. Intrauterine adhesions: detection with transvaginal US. Radiology. 1996;199(3):757-759.
178. Salle B, Gaucherand P, de Saint Hilaire P, Rudigoz RC. Transvaginal sonohysterographic evaluation of intrauterine adhesions. J Clin Ultrasound. 1999;27(3):131-134.
179. Alhilli MM, Wall DJ, Brown DL, et al. Uterine ultrasound findings after radiofrequency endometrial ablation: correlation with symptoms. Ultrasound Q. 2012;28(4):261-268.
180. Sharp HT. Endometrial ablation: postoperative complications. Am J Obstet Gynecol. 2012;207(4):242-247.
181. McCausland AM, McCausland VM. Long-term complications of endometrial ablation: cause, diagnosis, treatment, and prevention. J Minim Invasive Gynecol. 2007;14(4):399-406.
182. Nowitzki KM, Hoimes ML, Chen B, et al. Ultrasonography of intrauterine devices. Ultrasonography. 2015;34(3):183-194.
183. Moschos E, Twickler DM. Does the type of intrauterine device affect conspicuity on 2D and 3D ultrasound? AJR Am J Roentgenol. 2011;196(6):1439-1443.
184. Benacerraf BR, Shipp TD, Bromley B. Three-dimensional ultrasound detection of abnormally located intrauterine contraceptive devices which are a source of pelvic pain and abnormal bleeding. Ultrasound Obstet Gynecol. 2009;34(1):110-115.
185. Braaten KP, Benson CB, Maurer R, Goldberg AB. Malpositioned intrauterine contraceptive devices: risk factors, outcomes, and future pregnancies. Obstet Gynecol. 2011;118(5):1014-1020.
186. Khati NJ, Parghi CR, Brindle KA. Multimodality imaging of the Essure permanent birth control device: emphasis on commonly overlooked abnormalities. AJR Am J Roentgenol. 2011;196(5):W648-W658.
187. Wittmer MH, Brown DL, Hartman RP, et al. Sonography, CT, and MRI appearance of the Essure microinsert permanent birth control device. AJR Am J Roentgenol. 2006;187(4):959-964.
188. Legendre G, Gervaise A, Levaillant JM, et al. Assessment of three-dimensional ultrasound examination classification to check the position of the tubal sterilization microinsert. Fertil Steril. 2010;94(7):2732-2735.
189. Guelfguat M, Gruenberg TR, Dipoce J, Hochsztein JG. Imaging of mechanical tubal occlusion devices and potential complications. Radiographics. 2012;32(6):1659-1673.
190. Brown DL. Pelvic ultrasound in the postabortion and postpartum patient. Ultrasound Q. 2005;21(1):27-37.
191. Wachsberg RH, Kurtz AB. Gas within the endometrial cavity at postpartum US: a normal finding after spontaneous vaginal delivery. Radiology. 1992;183(2):431-433.
192. Van den Bosch T, Van Schoubroeck D, Timmerman D. Maximum peak systolic velocity and management of highly vascularized retained products of conception. J Ultrasound Med. 2015;34(9):1577-1582.
193. Kim SJ. Placental site trophoblastic tumour. Best Pract Res Clin Obstet Gynaecol. 2003;17(6):969-984.
194. Zhou Y, Lu H, Yu C, et al. Sonographic characteristics of placental site trophoblastic tumor. Ultrasound Obstet Gynecol. 2013;41(6):679-684.
195. Huang MW, Muradali D, Thurston WA, et al. Uterine arteriovenous malformations: gray-scale and Doppler US features with MR imaging correlation. Radiology. 1998;206(1):115-123.
196. O'Brien P, Neyastani A, Buckley AR, et al. Uterine arteriovenous malformations: from diagnosis to treatment. J Ultrasound Med. 2006;25(11):1387-1392.
197. Timmerman D, Wauters J, Van Calenbergh S, et al. Color Doppler imaging is a valuable tool for the diagnosis and management of uterine vascular malformations. Ultrasound Obstet Gynecol. 2003;21(6):570-577.
198. Mungen E. Vascular abnormalities of the uterus: have we recently overdiagnosed them? Ultrasound Obstet Gynecol. 2003;21(6):529-531.

199. Weydert JA, Benda JA. Subinvolution of the placental site as an anatomic cause of postpartum uterine bleeding: a review. Arch Pathol Lab Med. 2006;130(10):1538-1542.
200. Kamaya A, Petrovitch I, Chen B, et al. Retained products of conception: spectrum of color Doppler findings. J Ultrasound Med. 2009;28(8): 1031-1041.
201. Van den Bosch T, Van Schoubroeck D, Lu C, et al. Color Doppler and gray-scale ultrasound evaluation of the postpartum uterus. Ultrasound Obstet Gynecol. 2002;20(6):586-591.
202. diFlorio-Alexander R, Harris RD. Postpartum complications. In: Fielding JR, Brown DL, Thurmond AS, editors. Gynecologic imaging. Philadelphia: Elsevier; 2011. p. 381-398.
203. Wiener MD, Bowie JD, Baker ME, Kay HH. Sonography of subfascial hematoma after cesarean delivery. AJR Am J Roentgenol. 1987;148(5): 907-910.
204. Rodgers SK, Kirby CL, Smith RJ, Horrow MM. Imaging after cesarean delivery: acute and chronic complications. Radiographics. 2012;32(6): 1693-1712.
205. Armstrong V, Hansen WF, Van Voorhis BJ, Syrop CH. Detection of cesarean scars by transvaginal ultrasound. Obstet Gynecol. 2003;101(1): 61-65.
206. Kirby CL, Horrow MM. Pitfalls in gynecologic ultrasound. In: Fielding JR, Brown DL, Thurmond AS, editors. Gynecologic imaging. Philadelphia: Elsevier; 2011. p. 21-36.
207. Erickson SS, Van Voorhis BJ. Intermenstrual bleeding secondary to cesarean scar diverticuli: report of three cases. Obstet Gynecol. 1999;93(5 Pt 2):802-805.
208. Fabres C, Aviles G, De La Jara C, et al. The cesarean delivery scar pouch: clinical implications and diagnostic correlation between transvaginal sonography and hysteroscopy. J Ultrasound Med. 2003;22(7):695-700.
209. Florio P, Filippeschi M, Moncini I, et al. Hysteroscopic treatment of the cesarean-induced isthmocele in restoring infertility. Curr Opin Obstet Gynecol. 2012;24(3):180-186.
210. Monteagudo A, Carreno C, Timor-Tritsch IE. Saline infusion sonohysterography in nonpregnant women with previous cesarean delivery: the "niche" in the scar. J Ultrasound Med. 2001;20(10):1105-1115.
211. Tower AM, Frishman GN. Cesarean scar defects: an underrecognized cause of abnormal uterine bleeding and other gynecologic complications. J Minim Invasive Gynecol. 2013;20(5):562-572.
212. Vikhareva Osser O, Valentin L. Clinical importance of appearance of cesarean hysterotomy scar at transvaginal ultrasonography in nonpregnant women. Obstet Gynecol. 2011;117(3):525-532.

CHAPTER 16

The Adnexa

Rochelle Filker Andreotti and Lori A. Deitte

SUMMARY OF KEY POINTS

- The normal sonographic appearance of the ovaries changes with the menstrual cycle because of the influence of gonadotropins. These changes cease to occur as late menopause is reached and developing follicles are no longer present.
- Nonneoplastic lesions of the ovary and adnexa are usually simple cysts or cysts that contain blood products and are often physiologic. These include hemorrhagic physiologic cysts and endometriomas that can often be differentiated based on the sonographic appearance of the type of blood products. Other common nonneoplastic cysts include paraovarian cysts, hydrosalpinges, and peritoneal inclusion cysts.
- Ovarian torsion, a condition caused by rotation of the ovarian pedicle on its axis, is a surgical emergency and sonography is valuable in making the diagnosis.
- Morphologic and Doppler sonographic findings in neoplasms can be highly accurate in differentiating benign from malignant masses.

CHAPTER OUTLINE

NORMAL ANATOMY
Technique
Normal Sonographic Appearance of the Ovary and Fallopian Tube
Changes During the Menstrual Cycle
Postmenopausal Ovary
Postmenopausal Cysts
NONNEOPLASTIC LESIONS
Functional Cysts
Ovarian Remnant Syndrome
Pregnancy-Associated Ovarian Lesions
Surface Epithelial Inclusion Cysts
Paraovarian and Paratubal Cysts
Peritoneal Inclusion Cysts
Polycystic Ovarian Syndrome
Endometriosis
Adnexal Torsion
NEOPLASMS
Ovarian Cancer
Surface Epithelial–Stromal Tumors
Serous Cystadenoma and Cystadenocarcinoma
Mucinous Cystadenoma and Cystadenocarcinoma
Borderline (Low Malignant Potential) Tumors
Endometrioid Tumor
Clear Cell Tumor
Transitional Cell Tumor
Germ Cell Tumors
Cystic Teratoma
Dysgerminoma
Yolk Sac Tumor
Sex Cord–Stromal Tumors
Granulosa Cell Tumor
Sertoli-Leydig Cell Tumor
Thecoma and Fibroma
Metastatic Tumors
FALLOPIAN TUBE
Pelvic Inflammatory Disease
Tubal Torsion
Fallopian Tube Carcinoma
VASCULAR ABNORMALITIES IN THE ADNEXA
Ovarian Vein Thrombosis or Thrombophlebitis
Pelvic Congestion Syndrome
SONOGRAPHIC EVALUATION OF AN ADNEXAL MASS IN ADULT WOMEN
NONGYNECOLOGIC ADNEXAL MASSES
Postoperative Pelvic Masses
Gastrointestinal Tract Masses
Urinary Tract Masses

Sonography is the modality of choice for imaging the pelvis, including the adnexa, because it is noninvasive, radiation free, cost effective, and widely available. Sonography allows for accurate delineation of uterine and ovarian architecture and assessment of vascular flow. **Transvaginal sonography** (TVS) is a fundamental part of pelvic ultrasound examinations because of the use of higher frequency transducers (up to 10 MHz) and the vaginal probe's proximity to the uterus and adnexa. However, **transabdominal sonography** (TAS) continues to be the mainstay when structures are high in the pelvis, out of the field of view of the TVS probe; in pediatric patients; and in those who have difficulty tolerating TVS. Color and spectral **Doppler** sonography allow for assessment of normal and pathologic blood flow. Doppler ultrasound can also distinguish vascular structures from non-vascular structures, such as dilated fallopian tubes or fluid-filled bowel loops.

NORMAL ANATOMY

Bilaterally, the broad and round ligaments, fallopian tubes, ovaries and their associated vascularity extend from lateral uterine corpus forming the pelvic adnexa. Laterally, the peritoneal reflection

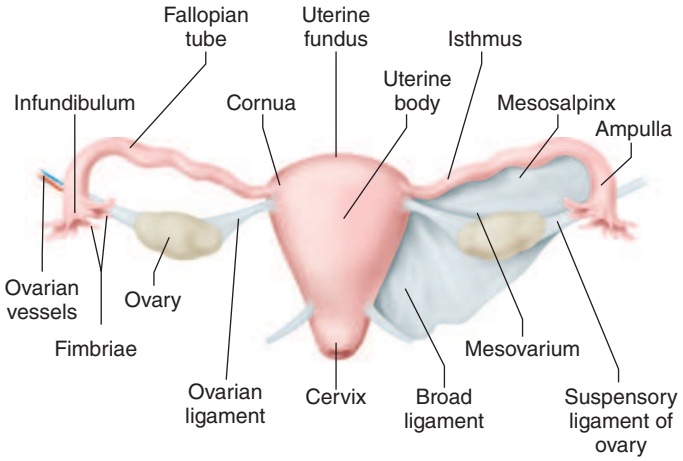

FIG. 16.1 Normal Gynecologic Organs. Diagram of uterus, ovaries, tubes, and related structures. On left side, broad ligament has been removed.

forms the **broad ligaments,** which extend from the lateral aspect of the uterus to the lateral pelvic side walls (Fig. 16.1). Encompassing the superior and lateral margin of the broad ligament is the **suspensory** (infundibulopelvic) **ligament.** The free border of the broad ligament contains the fallopian tube within its superior margin, which is referred to as the **mesosalpinx.** The ovary is attached to the posterior layer of broad ligament by reflections of peritoneum called the **mesovarium.** The **round ligaments** arise from the uterine cornua anterior to the fallopian tubes in the broad ligaments, extend anterolaterally, and course through the inguinal canals to insert into the fascia of the labia majora.[1]

Each **fallopian tube** varies from 7 to 12 cm in length and is divided into intramural, isthmic, ampullary, and infundibular portions. The intramural, or **interstitial,** portion is approximately 1 cm long, is contained within the muscular wall of the uterus, and is the narrowest part of the tube. The **isthmus,** constituting the medial third, is slightly wider, round, cordlike, and continuous with the **ampulla,** which is tortuous and forms approximately one-half the length of the tube. The ampulla terminates in the most distal portion, the **infundibulum,** or fimbriated end, which is funnel shaped and opens into the peritoneal cavity.[2]

The **ovaries** are elliptical in shape, with the long axis usually oriented vertically. The surface of the ovary is not covered by peritoneum but by a single layer of cuboidal or columnar cells called the **germinal epithelium,** which becomes continuous with the peritoneum at the hilum of the ovary. The internal structure of the ovary is divided into an outer **cortex** and inner **medulla.** The cortex consists of an interstitial framework, or stroma, which is composed of reticular fibers and spindle-shaped cells and which contains the ovarian follicles and corpus lutea. Beneath the germinal epithelium, the connective tissue of the cortex is condensed to form a fibrous capsule, the **tunica albuginea.** The medulla, which is smaller in volume than the cortex, is composed of fibrous tissue and blood vessels. In the nulliparous female, the ovary is located in a depression on the lateral pelvic wall called the *ovarian fossa*, which is bounded anteriorly by the obliterated umbilical artery, posteriorly by the ureter and the internal iliac artery, and superiorly by the external iliac vein.[2] The fimbriae of the fallopian tube lie superior and lateral to the

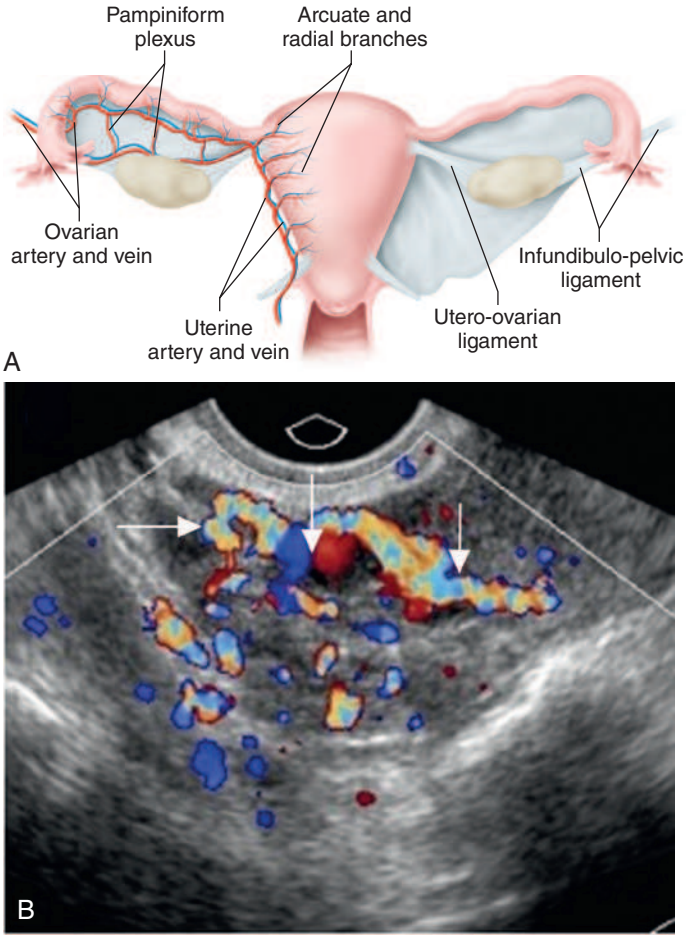

FIG. 16.2 Adnexal Vascularity. (A) Diagram of uterine artery along the lateral margin of the uterus and the ovarian artery seen lateral to the ovary within the right adnexa, both joining to form the pampiniform plexus anterior to the ovary. **(B)** Transverse color Doppler image demonstrating the ovarian artery *(right arrow),* uterine artery *(left arrow),* and pampiniform plexus *(middle arrow)* of the right adnexa.

ovary. The anterior surface of the ovary is attached to the posterior surface of the broad ligament by the short **mesovarium.** The upper pole of the ovary is attached to the lateral wall of the pelvis by the lateral extension of the broad ligament, the **suspensory (infundibulopelvic) ligament** of the ovary. Arising from the uterine cornu posteriorly to the tubes and attaching to the inferior aspect of the ovary is the **utero-ovarian ligament.** These ligaments are not rigid, and therefore the ovary can be quite mobile, especially in women who have had pregnancies and/or who have had a hysterectomy.

The vascularity to the adnexa consists of a dual blood supply. The ovary is chiefly supplied by the **ovarian artery,** a branch of the hypogastric (internal iliac) artery but usually receives additional arterial flow from the ovarian branches of the **uterine artery** (Fig. 16.2). The veins tend to parallel the arteries. From the ovarian **pampiniform plexus,** the right ovarian vein drains directly into the inferior vena cava, while the left ovarian vein empties into the left renal vein. The ovarian ligaments that include the **broad ligament,** the **ovarian ligament,** and the **infundibulopelvic ligament** contain vascular, lymphatic, and nervous supplies to the organs. The ovarian nerves and vessels

course with the suspensory (infundibulopelvic) ligament and the utero-ovarian ligament. The lymph vessels of the ovary accompany the ovarian artery to the lateral aortic and periaortic lymph nodes. Coursing superior and adjacent to the utero-ovarian ligament that arises from the uterine cornu posteriorly to the tubes and attaches to the inferior aspect of the ovary in the utero-ovarian ligament is the ovarian branch of the uterine artery. Derived from the main ovarian artery and the ovarian branch of the uterine artery are numerous arterioles extending to the capsule of the ovary and small penetrating arteries within the ovary itself. The ovarian blood supply may vary from five to six branches that penetrate the capsule to two large branches with multiple twigs.[2]

Although not considered part of the adnexal structures, the rectouterine recess **(posterior cul-de-sac)** is often involved in adnexal processes. It is the most posterior and inferior reflection of the peritoneal cavity and is located between the rectum and vagina and is also known as the **pouch of Douglas.** The posterior fornix of the vagina is closely related to the posterior cul-de-sac and is separated by the thickness of the vaginal wall and the peritoneal membrane. The cul-de-sac is a potential space, and because of its location, it is frequently the initial site for intraperitoneal fluid collection. As little as 5 mL of fluid has been detected by TVS.[3]

Technique

The standard examination of the pelvic adnexa is included in the routine pelvic sonogram and is composed of the traditional TAS combined with the TVS, frequently using color and spectral Doppler. TAS uses a distended bladder as window to pelvic structures for a global view and may be advantageous when ovaries are high in the pelvis, outside of the field of view of the TVS probe. However, using TAS, visualization of pelvic organs may be limited because of attenuation from the body wall and the distance from the area of interest of the transducer. As a result, it is not often possible to use higher frequency transducers and benefit from their inherent higher axial and lateral resolution. **TVS** gives a more detailed evaluation of adnexal architecture using higher frequency transducers at closer proximity to pelvic structures and should be used whenever feasible. Still, TVS should not be performed in premenarchal patients, in the majority of virginal patients, or in any patient who does not willingly consent to vaginal examination. Because TVS is typically performed, routine bladder distention is not required unless there is a reason for additional TAS images, or unless the woman declines vaginal scanning. Initial imaging with TAS is performed using the patient's bladder distention at presentation followed by a full TVS. When TVS is not going to be performed, then we require a full bladder for best visualization of the uterus, endometrium, and adnexa.

TVS with abdominal compression is a valuable technique for improving adnexa visibility. Abdominal pressure with one hand, while holding the transducer with the other hand, is used to displace bowel, bring structures closer to the transducer, and identify focal areas of tenderness. The pressure of the transducer between two adjacent structures in the pelvis can be used to determine if they move together or slide past each other as separate entities. This is often referred to as the **"sliding organ sign."** Examples of the value of this technique include its use to confirm that an adnexal mass is unattached to the ovary or a mass is ovarian and not uterine in origin.

Spectral and color and power Doppler are routinely used to characterize vascularity to the ovaries and fallopian tubes, helping to narrow the differential considerations. This is especially useful when there is suspicion of neoplasia or in patients presenting with pelvic pain with diagnostic considerations that include pelvic inflammatory disease (PID), ovarian torsion, or functional cysts. Because color or power Doppler signal may be produced artifactually, it is important to always confirm flow by demonstrating a spectral waveform.

Normal Sonographic Appearance of the Ovary and Fallopian Tube

The ovary can be quite variable in position and may be located high in the pelvis or in the cul-de-sac because of the laxity of the ligamentous attachments. Uterine location influences the position of the ovaries. The normal ovaries are usually identified laterally or posterolaterally to the anteflexed midline uterus. When the uterus lies to one side of the midline due to exogenous pressure by a mass or a normal variant, the ipsilateral ovary often lies superior to the uterine fundus. In a retroflexed uterus, the ovaries tend to be located laterally and superiorly, near the uterine fundus. When the uterus is enlarged, the ovaries may be displaced more superiorly and laterally. After hysterectomy, the ovaries tend to be located more medially and directly superior to the vaginal cuff. A common location of the ovaries, especially in nulliparous patients, is **Waldeyer fossa.** In this location, the ellipsoid configuration of the ovary has its craniocaudad axis paralleling the internal iliac vessels, which lie posteriorly and serve as a helpful reference (Fig. 16.3). Waldeyer fossa is also bounded by the obliterated umbilical artery anteriorly, the ureter posteriorly, and the external iliac vein superiorly. Superiorly or extremely laterally placed ovaries may not be visualized by the TVS approach because they may be outside of the field of view of the TVS probe.

Because of the variability in shape, **ovarian volume** has been considered the best method for determining ovarian size. The volume measurement is based on the formula for a prolate ellipse ($0.523 \times \text{length} \times \text{width} \times \text{height}$). In women of reproductive age, a normal ovary may have a volume as large as 22 mL. Cohen et al.[4] assessed 866 normal ovaries by TAS and reported a mean ovarian volume of 9.8 ± 5.8 mL, with an upper limit of 21.9 mL.[4] Another study of 406 patients with normal ovaries used TVS and reported a mean ovarian volume of 6.8 mL, with an upper limit of 18.0 mL.[5] There is no significant parity-related change in ovarian volume in premenopausal women.[6]

Punctate echogenic foci are commonly seen in an otherwise normal-appearing ovary (Fig. 16.4). Many are tiny (1-3 mm) nonshadowing foci, usually multiple and peripherally located, although they can be diffuse. Kupfer et al.[7] examined five patients with peripherally distributed echogenic ovarian foci who subsequently underwent bilateral oophorectomy for other clinical indications. All 10 ovarian specimens showed multiple surface epithelial inclusion cysts and associated psammomatous

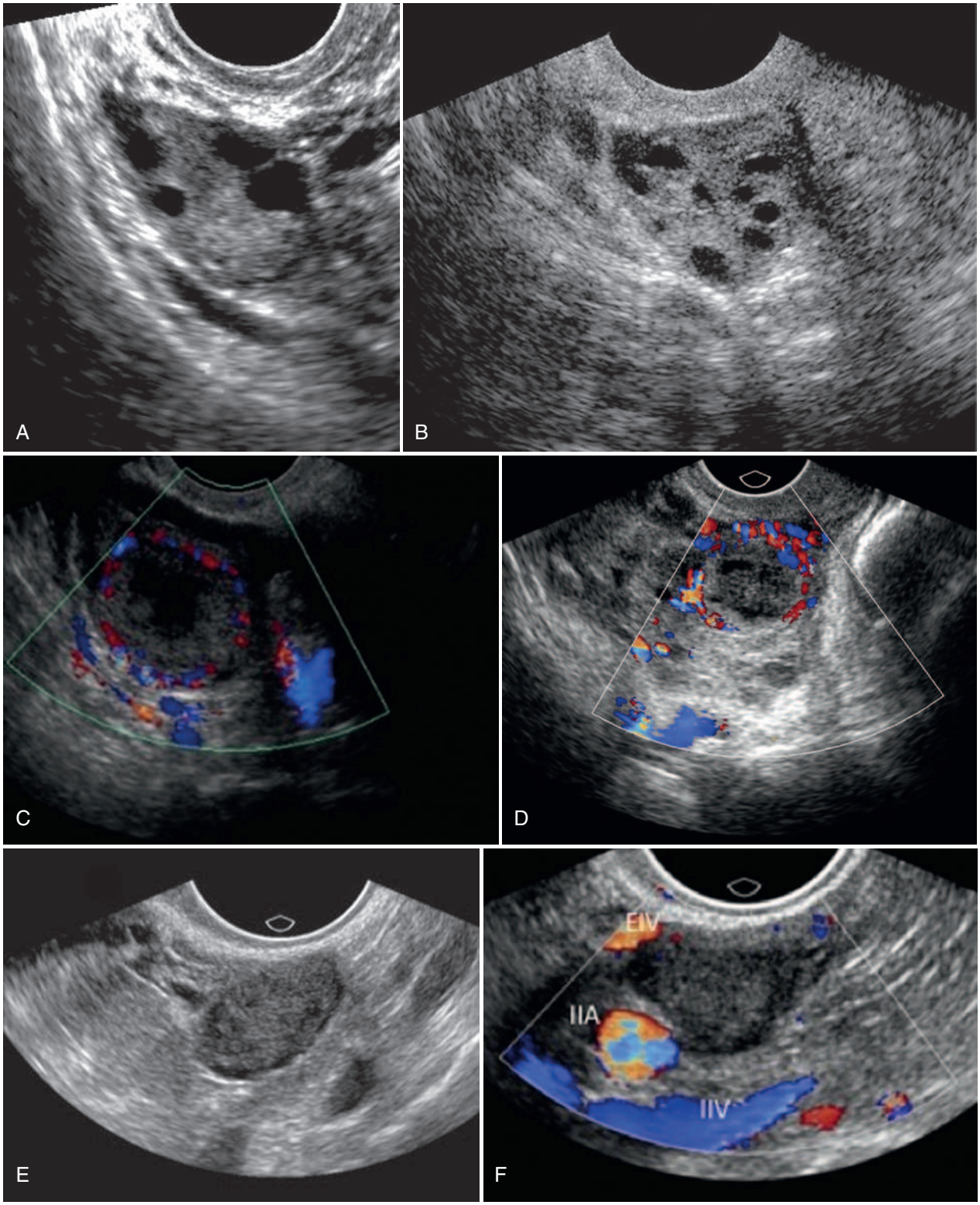

FIG. 16.3 Normal Ovary. (A) and **(B)** TVS images show normal ovaries in the follicular phase containing a few developing follicles in two patients. Internal iliac vein is posterior to ovary. **(C)** and **(D)** TVS color Doppler images of the early and late corpus luteum. Both demonstrate peripheral color Doppler flow. The early corpus luteum contains internal low-level echoes consistent with hemorrhage whereas the late corpus luteum has collapsed. **(E)** Transverse gray-scale and **(F)** sagittal color Doppler TVS images of the same patient show a normal postmenopausal ovary in the left adnexa anterior and medial to the internal iliac artery *(IIA)* and vein *(IIV)* and inferior to the external iliac vein *(EIV)* in the Waldeyer fossa. The ovary is small in size and lacks follicles.

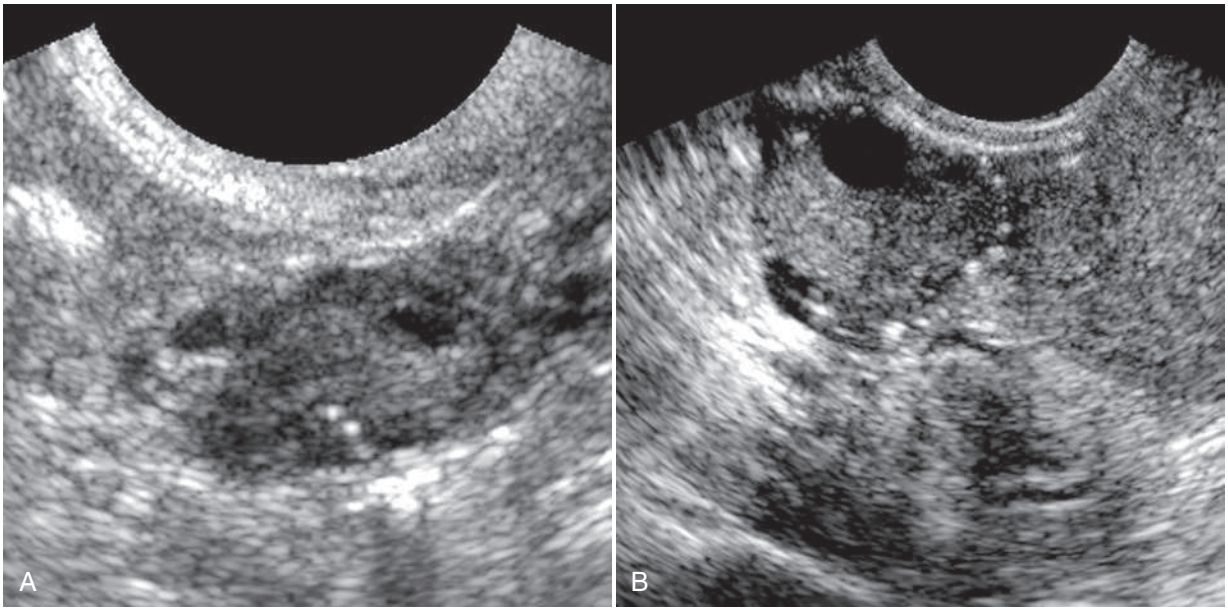

FIG. 16.4 Punctate Echogenic Foci in the Ovary. TVS images of two patients. **(A)** Two tiny echogenic foci in normal-appearing ovary. **(B)** Multiple peripheral tiny echogenic foci (back walls of tiny unresolved cysts).

calcifications. In another study with histopathologic correlation in seven normal ovaries with echogenic foci, Muradali et al.[8] showed that these foci are caused by a specular reflection from the walls of tiny unresolved cysts below the spatial resolution of ultrasound rather than calcification. These echogenic foci do not indicate significant underlying disease, so no further investigation or follow-up is necessary. Brandt et al.[9] reported that echogenic foci with associated shadowing consistent with **focal calcification** may occasionally be seen in an otherwise normal-appearing ovary. At histologic analysis, 4 of 17 ovaries analyzed (24%) were associated with benign neoplasms, whereas the remaining ovaries were unremarkable. It was proposed that these represent stromal reaction to previous hemorrhage or infection. Zeligs et al.[10] recently reported echogenic ovarian foci with atypical morphologic characteristics and distribution in addition to extraovarian echogenic foci. These proved to be calcifications associated with a serous borderline ovarian tumor with extraovarian noninvasive implants. This finding is unusual, however, as the vast majority of punctate ovarian calcifications without associated mass are of benign etiology. When there is an associated mass or morphology or distribution of calcifications is atypical, additional imaging is recommended.

The fallopian tubes are musculomembranous structures measuring up to 12 cm in length and consisting of the intramural, isthmic, and ampullary portions. Although documentation of fallopian tubes is not a routine part of a normal pelvic examination, at least a portion of each tube can be demonstrated in most patients. Sonographically, the length of the fallopian tube can be identified by its tubular structure containing a linear echogenic lumen that can be followed to the uterine cornua.

Changes During the Menstrual Cycle

The appearance of the ovary changes with age and phase of the menstrual cycle. Under the influence of follicle-stimulating hormone (FSH), human follicular development begins with a follicular size of approximately 0.03 mm with potential ovulation after more than 150 days of growth. It is only after follicles reach approximately 4 mm that they are routinely visualized by ultrasound. During the menstrual cycle, multiple immature, less than 1-cm follicles appear in the early follicular phase before day 10. Subsequently, one or more ovulatory follicles become dominant, increasing in size to 18 to 25 mm in average diameter. The average size of the dominant follicle is 20 mm in diameter at ovulation, which usually occurs on day 14 of a normal 28-day menstrual cycle. The other follicles become atretic. The disappearance of the dominant follicle with associated free fluid in the pelvis signifies ovulation. Other, less specific and sensitive findings may include irregularity of the cyst wall with internal echoes.[11] A **follicular cyst** develops if ovulation does not occur and follicular growth continues because of the lack of the luteinizing hormone surge and excessive stimulation by FSH.

Following release of the ovum and collapse of the dominant follicle, the postovulatory **corpus luteum** is formed, a crenulated thick-walled cyst demonstrating peripheral color Doppler signal. The corpus luteum may bleed internally as a result of vascularization of the inner granulosa layer following ovulation forming a **hemorrhagic corpus luteum** (see Fig. 16.3C and D). As the corpus luteum ages, it collapses and progressively transforms into a more solid, fatty structure, a **corpus albicans,** usually not well visualized sonographically. However, if pregnancy ensues, the corpus luteum continues to be maintained for hormonal support until approximately 10 to 13 weeks' gestation when placental hormone production can support the pregnancy.

Fluid in the cul-de-sac (Fig. 16.5) is a normal finding in asymptomatic women and can be seen during all phases of the menstrual cycle. Possible sources include blood or fluid caused by follicular rupture, blood from retrograde menstruation, and increased capillary permeability of the ovarian surface caused

FIG. 16.5 Fluid in Cul-De-Sac. TVS shows echogenic fluid in cul-de-sac caused by blood.

by the influence of estrogen.[12,13] Pathologic fluid collections in the pouch of Douglas may be seen in association with generalized **ascites, blood** resulting from a ruptured ectopic pregnancy or hemorrhagic cyst, or **pus** from infection. Sonography can aid in differentiating the type of fluid, because blood, pus, mucin, and malignant exudates usually contain echoes within the fluid, whereas serous fluid (either physiologic or pathologic) is usually anechoic. Clotted blood may be very echogenic, mimicking a solid mass.[14]

Postmenopausal Ovary

Differentiation of **perimenopause** and early **postmenopause** is often difficult. The postmenopausal period begins when at least 1 year or more has elapsed since the final menstrual period.[15] In early postmenopause (1 to 5 years since final menstrual period) ovulatory cycles may occur infrequently and folliculogenesis may continue. Once late postmenopause is reached (more than 5 years since final menstrual period),[16] folliculogenesis ceases, the ovary atrophies, and the follicles disappear, with the ovary decreasing in size with increasing age.[6,17-19] Because of its smaller size and lack of follicles, the postmenopausal ovary may be difficult to visualize sonographically (see Fig. 16.3E and F). A stationary loop of bowel may be mistaken for a normal ovary; therefore scanning must be done slowly to look for peristalsis (Video 16.1). However, because the colon does not always peristalse during a sonographic exam, lack of peristalsis is not sufficient for differentiation. Sonographic visualization of normal postmenopausal ovaries varies greatly in the literature, from a low of 20% to a high of 99%, using either the TAS or TVS.[5,17-22] The variation is likely caused by differences in technique and length of time since menopause, and the series with very high percentages of visualization likely include some loops of bowel rather than ovaries. The ovary decreases in size with increasing age, and therefore the ability to see the ovaries decreases as the length of time since menopause increases.[23] Also, the absence of the uterus may play a role in the visualization of ovaries that are less likely to be seen following hysterectomy because of the loss of normal anatomic landmarks.[23]

In 290 postmenopausal ovaries known to be present, Wolf et al.[23] visualized only 41% of ovaries through use of TVS, 58% through use of TAS, and 68% using both techniques. Highly placed ovaries may be out of the field of view of TVS transducers, and TAS may not image very small or deeply placed ovaries. Although nonvisualization of an ovary does not exclude an ovarian lesion, it can be a fairly reassuring finding since most ovarian neoplasms are cystic, and an ovarian mass will usually displace adjacent bowel loops and be more easily visible.

Mean postmenopausal ovarian volume ranges are reported from 1.2 to 5.8 mL.[4,5,17-21] The mean values in these studies may be somewhat high because nonvisualized ovaries were not included. One study assessing 563 patients with normal postmenopausal ovaries by TVS reported a mean ovarian volume of 2.0 mL with an upper limit of normal of 8.0 mL.[5] A postmenopausal ovarian volume of more than 8.0 mL should be considered abnormal. Because normal size varies widely, some authors suggest that an ovarian volume more than twice that of the opposite side should also be considered abnormal.[18,20]

Postmenopausal Cysts

As patients progress from early to late menopause, small simple cysts, defined as thin-walled, round or oval anechoic cysts with posterior acoustic enhancement, no internal solid component or septation, and no internal color Doppler flow, become less frequently observed. While follicles may still be present in the early menopause, other cysts may be paraovarian or paratubal in origin or ovarian **surface epithelial inclusion cysts.**

One report suggests that simple cysts of all sizes may be seen in up to 15% of postmenopausal ovaries and are not related to age, length of time since menopause, or hormone use[23] (Fig. 16.6). Smaller cysts are more frequently seen by TVS with its improved resolution, but in some women, especially those with hysterectomy or highly placed ovaries, the cysts may be seen only by TAS. Most of these cysts either disappear or decrease in size over time.[24-26] Other reports suggest that even in late menopause, when folliculogenesis is unlikely, small simple cysts are seen in up to 21% of women.[27,28]

Several studies have shown a very low incidence of malignancy in unilocular postmenopausal cysts less than 5 cm in diameter and without septations or solid components.[25,26,29-32] In surgical lesions that are inclined to be larger cysts and/or those in postmenopausal patients, 84% of simple ovarian cysts have been found to be cystadenomas.[33] Although it has been shown that an ovarian cystadenoma may be a precursor of borderline tumors (those of low malignant potential and low-grade carcinomas), there is an extremely slow rate of transformation so that these lesions can be considered benign and are safe to watch over time rather than remove surgically.[32,34] Ekerhovd et al.[32] found four borderline or malignant tumors in 247 postmenopausal women (1.6%) who underwent surgery for simple ovarian cysts detected by TVS. These four tumors were all greater than 7.5 cm in diameter. It is generally recommended that asymptomatic postmenopausal women with simple ovarian cysts less than 7 cm

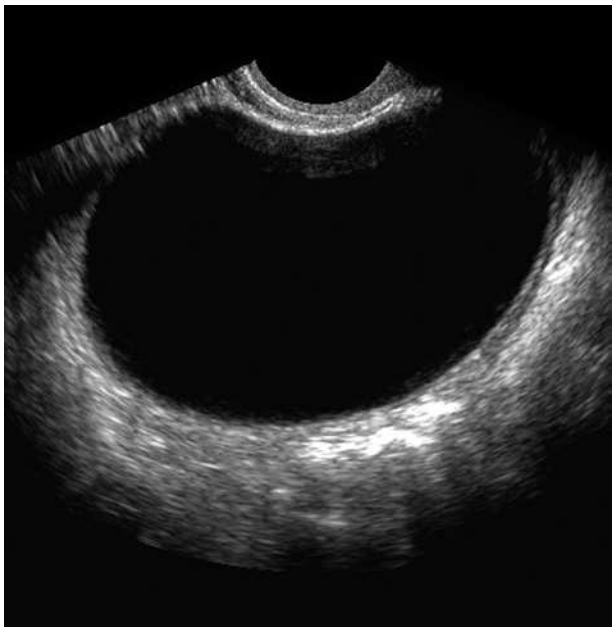

FIG. 16.6 Postmenopausal Large Ovarian Cyst. TVS image of a 7-cm ovarian cyst that contains no internal echoes or septations and had not changed in size over 4 years.

and greater than 1 cm in diameter be followed by serial yearly sonographic examinations without surgical intervention unless there is an increase in size or change in the characteristics of the lesion. Cysts measuring less than 1 cm are felt to be almost certainly benign and follow-up is not necessary. Surgery is usually recommended for postmenopausal simple cysts greater than 7 cm and for those containing multiple internal septations or one or more solid nodules. However, magnetic resonance imaging (MRI) is better able to characterize these larger cysts in which small mural nodules can be missed by ultrasound and thus may be a reasonable alternative to surgery.[28]

NONNEOPLASTIC LESIONS

Functional Cysts

Functional cysts are physiologic and not neoplastic lesions of the ovary whose appearance and disappearance is hormonally driven. These cysts may be simple or hemorrhagic and are commonly divided into three categories: follicular, corpus luteum, and theca lutein cysts. Acute abdominal pain caused by internal hemorrhage, rupture, or leakage is the most common symptom, but pelvic discomfort may simply be the result of the large size, greater than 2.5 to 3.0 cm.

A follicular cyst develops when a mature follicle fails to ovulate or to involute. Because normal follicles can vary from a few millimeters up to 2.5 cm, a follicular cyst cannot be diagnosed with certainty until it is larger than 2.5 cm. Therefore a simple cyst less than 2.5 cm in a premenopausal woman should be referred to as a *follicle* and considered to be normal. Follicles and follicular cysts are usually unilateral, asymptomatic, and frequently detected incidentally on sonographic examination. Follicular cysts usually regress spontaneously.

After ovulation, the corpus luteum develops and may be identified sonographically as a small, hypoechoic or isoechoic structure within the ovary. The corpus luteum usually contains low-level internal echoes, frequently with a thicker wall than a follicle and a crenulated appearance. It typically has a peripheral rim of color around the wall on color Doppler ultrasound (ring of fire; see Fig. 16.3C). The corpus luteum usually involutes before menstruation but may persist because of failure of absorption or internal bleeding. Timor-Tritsch and Goldstein[35] recommend using the term *corpus luteum* rather than *corpus lutein cyst* unless it is greater than 4 cm. Corpus lutein cysts are less common than follicular cysts but tend to be larger and more symptomatic. Pain is the major symptom. These cysts are usually unilateral and are prone to hemorrhage and, less commonly, rupture. If the ovum is fertilized, the corpus luteum continues as the corpus luteum of pregnancy, which may become enlarged with a simpler cystic appearance than the original corpus luteum. Maximum size is reached at 8 to 10 weeks of gestation, and by 16 weeks the cyst has usually resolved.[36]

Theca lutein cysts are associated with high beta–human chorionic gonadotropin (B-hCG) levels and are the largest of the functional ovarian cysts, increasing the risk of ovarian torsion. These cysts typically occur in patients with gestational trophoblastic disease but can also be seen as a complication of drug therapy for infertility causing ovarian hyperstimulation syndrome. Sonographically, theca lutein cysts are usually bilateral, multilocular, and very large. Similar to other functional cysts, they may undergo hemorrhage or rupture.

Although hemorrhage may occur in all types of functional cysts, it is most frequently seen in corpus luteal cysts. Women with hemorrhagic cysts frequently present with acute onset of pelvic pain. Hemorrhagic cysts show a spectrum of findings because of the variable sonographic appearance of blood (Fig. 16.7, Video 16.2). The appearance depends on the amount of hemorrhage and the time of the hemorrhage relative to the time of the sonographic examination.[37-39] The internal architecture is much better appreciated on TVS when compared to TAS because of its superior resolution. An acute hemorrhagic cyst is usually hyperechoic and may mimic a solid mass. However, it usually has a smooth posterior wall and shows posterior acoustic enhancement, indicating the cystic nature of the lesion. Diffuse low-level internal echoes may be appreciated, although this appearance is more frequently seen in endometriomas. As the clot hemolyzes, a reticular-type pattern is demonstrated internally containing intertwining linear internal echoes representing fibrin strands.[40] These should not be confused with septations, which are thicker. As the clot retracts, it will have a concave outer margin with angularity compared with a solid mural nodule, which will have a convex outer margin. Color Doppler ultrasound will show no flow within the clot but will demonstrate peripheral vascularity within the cyst wall. Care should be taken when assessing for flow in hemorrhagic cysts, because a clot can move and show color without true vascularity. Spectral Doppler can be helpful in these cases. Patel et al.[40] found that a specific diagnosis could be made in approximately 90% of hemorrhagic cysts by demonstrating the presence of a reticular pattern or a retractile clot. The presence of echogenic, free intraperitoneal fluid in the

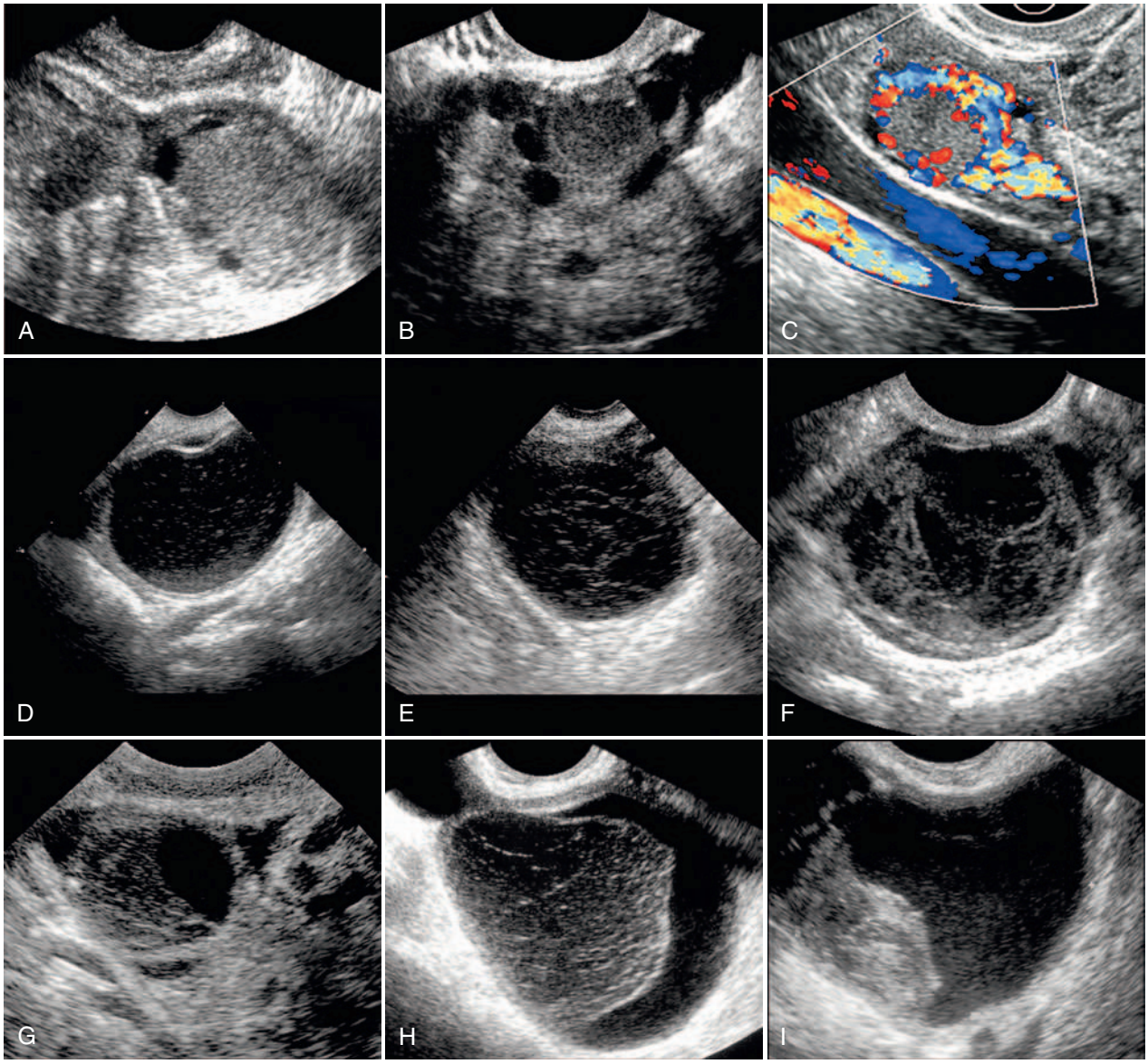

FIG. 16.7 Hemorrhagic Cysts on TVS Scans: Spectrum of Appearances. (A) Acute hyperechoic hemorrhagic cyst. **(B)** Acute hemorrhagic cyst mimicking a solid lesion. **(C)** Color Doppler ultrasound shows peripheral ring of vascularity **(ring of fire),** typical of a corpus luteum, but no vascularity within the cyst. **(D)** Large cyst containing low-level internal echoes. **(E)** Reticular pattern of internal echoes and septations within cyst. **(F)** Reticular pattern. **(G)-(I)** Variations in clot retraction. Concave margins in G are a sign of retracting clot. The blood products in I suggest a solid mass. Lack of color Doppler ultrasound signal supports its benign nature. See also Video 16.2.

cul-de-sac helps confirm the diagnosis of a leaking or ruptured hemorrhagic cyst. Rupture or leakage of a hemorrhagic cyst with associated peritoneal irritation in the setting of a positive serum B-hCG level may mimic a ruptured ectopic pregnancy, both clinically and sonographically.

Functional cysts are the most common cause of ovarian enlargement in young women. Because these cysts typically resolve within one to two menstrual cycles, follow-up is usually not required for small, simple cysts or typical hemorrhagic cysts less than 5 cm in asymptomatic patients. However, follow-up of larger cysts and those in symptomatic patients can be performed following a normal menstrual cycle, usually in 6 weeks. Because ultrasound may be unable to identify small mural nodules within larger cysts, surgical intervention or further characterization using MRI is generally recommended for cysts greater than 7 cm.[28]

Ovarian Remnant Syndrome

Infrequently, a cystic mass may be encountered in a patient who has undergone bilateral oophorectomy due to a small amount of residual ovarian tissue has been unintentionally left behind. The surgery has usually been technically difficult because of adhesions from endometriosis, PID, or tumor.[41] The residual ovarian tissue can develop functional cysts and produce pelvic pain and/or extrinsic compression of the distal ureter. Sonographically, the cysts vary in size and can be both simple and hemorrhagic.[42,43] A thin rim of ovarian tissue is usually present in the wall of the cyst.[43]

Pregnancy-Associated Ovarian Lesions

Ovarian lesions associated with pregnancy include hyperstimulated ovaries, ovarian hyperstimulation syndrome, theca lutein cysts, hyperreactio luteinalis, and the rare luteoma of pregnancy.[36] Most are related to the normal or abnormal response to serum hCG levels. **Hyperstimulated ovaries** are a normal response to elevated circulating levels of hCG. Ovarian hyperstimulation is most common in women undergoing ovulation induction. Sonographically, the ovaries are enlarged with multiple cysts, some of which may be hemorrhagic. The enlarged ovaries may undergo torsion.[44] They usually regress spontaneously during the pregnancy.

The term **ovarian hyperstimulation syndrome** (OHS) is used when the hyperstimulation is accompanied by fluid shifts[45] (Fig. 16.8). Clinically, three degrees of OHS are described: mild, moderate, and severe. The **mild** form is associated with lower abdominal discomfort, but no significant weight gain. The ovaries are enlarged, but less than 5 cm in average diameter. **Moderate** OHS presents with weight gain of 5 to 10 pounds and ovarian enlargement 5 to 12 cm. The patient may have nausea and vomiting. With **severe** OHS, there is weight gain of more than 10 pounds and the patient typically has severe abdominal pain and distention. The ovaries are greatly enlarged (>12 cm in diameter) and contain numerous large, thin-walled cysts, which may replace most of the ovary. The associated ascites and pleural effusions may lead to depletion of intravascular fluids and electrolytes, resulting in hemoconcentration with hypotension, oliguria, and electrolyte imbalance.[46] Severe OHS is usually treated conservatively to correct the depleted intravascular volume and electrolyte imbalance and usually resolves within 2 to 3 weeks.

Theca lutein cysts are the largest of the functional ovarian cysts and are associated with high hCG levels. These cysts typically occur in patients with gestational trophoblastic disease. However, theca lutein cysts are typically not seen in first-trimester diagnosis of gestational trophoblastic disease, because the hCG level will not have been sufficiently high for a long enough time for them to develop.[47] Theca lutein cysts can also be seen in OHS as a complication of drug therapy for infertility. Sonographically, theca lutein cysts are usually bilateral, multilocular, and very large. They may undergo hemorrhage, rupture, and torsion.

Hyperreactio luteinalis is caused by an abnormal response to circulating hCG in the absence of ovulation induction therapy. Approximately 60% of hyperreactio luteinalis cases occur in singleton pregnancies with normal circulating levels of hCG. Hyperreactio luteinalis usually occurs in the third trimester or less often in the puerperium. The majority of patients are asymptomatic, although maternal virilization may be seen in up to 25% of patients. The incidence of hyperreactio luteinalis increases in women with polycystic ovarian disease.[48] In contrast to OHS, body fluid shifts are rare. Sonographically, there are bilaterally enlarged ovaries with multiple cysts similar to OHS, although the ovaries tend not to be as large and the condition occurs later in pregnancy. Hyperreactio luteinalis is a self-limited condition that resolves spontaneously.

Luteoma of pregnancy is the only solid mass in this group of pregnancy-related processes. It is a rare benign process unique to pregnancy that is due to stromal cells that may become hormonally active, producing androgens and replacing the normal ovarian parenchyma. Most patients are asymptomatic, although maternal virilization may occur in up to 30%. These patients have a 50% risk of virilization of the female fetus.[49] Sonographically, luteomas usually present as nonspecific, heterogeneous, predominantly hypoechoic masses that may be highly vascular. An ovarian mass in a pregnant patient with signs of virilization should suggest this diagnosis, because luteoma is the most common cause of maternal virilization during pregnancy. Surgery is not indicated since the condition resolves spontaneously, typically after delivery.

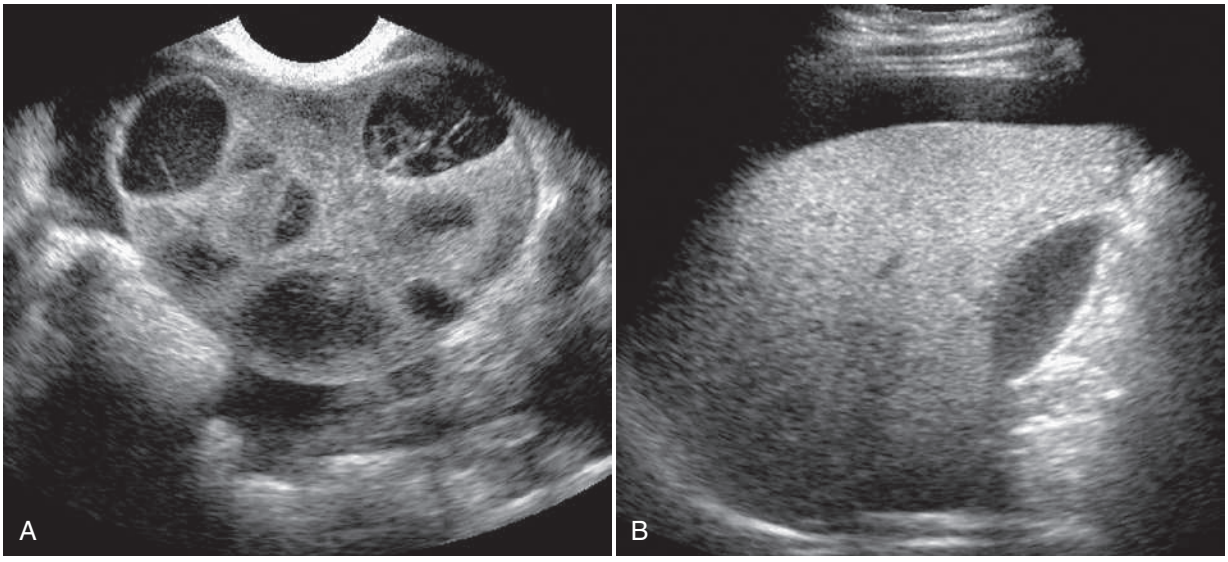

FIG. 16.8 Ovarian Hyperstimulation Syndrome. (A) TVS shows a greatly enlarged ovary with multiple cysts, some hemorrhagic. **(B)** Sagittal sonogram in right upper quadrant shows large volume of free intraperitoneal fluid.

Surface Epithelial Inclusion Cysts

Surface epithelial inclusion cysts are nonfunctional cysts usually seen in postmenopausal women, although they may be seen at any age, and are usually located peripherally in the cortex. They arise from cortical invaginations of the ovarian surface epithelium.[50] When very small, the cysts themselves may not be seen, but rather they may appear as punctate echogenicities in the surface of the ovary. Although usually tiny, unilocular, and thin walled, these cysts can measure up to several centimeters in diameter. Occasionally, surface epithelial inclusion cysts may be hemorrhagic, particularly if torsion has occurred.

Paraovarian and Paratubal Cysts

Paraovarian and **paratubal cysts** are wolffian or müllerian duct remnants in the mesosalpinx, often located superior to the uterine fundus. They are generally epithelium-lined simple cysts, rarely multiloculated or containing small wall nodularities. Echoes may also be occasionally seen with the cyst sonographically because of hemorrhage. They show no cyclic changes. There is an estimated incidence of 3%, accounting for about 10% to 20% of all adnexal masses. Typically, these cysts are small but may range in size up to 8 cm. They may occur at any age but are most commonly visualized in the third and fourth decades. Most are asymptomatic although patients with large cysts may have pelvic pain or the cysts may act as a fulcrum for torsion.[51-53] A specific diagnosis of a paraovarian cyst is possible only by demonstrating a normal ipsilateral ovary adjacent to, but separate from, the cyst.[54,55]

Benign neoplasms such as cystadenomas and cystadenofibromas of paraovarian origin are uncommon. Malignancy has been reported in 2% to 3% of parovarian cystic masses on histopathologic examination,[56,57] although it occurs even less often in masses smaller than 5 cm.[54,58]

Peritoneal Inclusion Cysts

Peritoneal inclusion cysts are seen in patients with peritoneal adhesions, occurring mostly in premenopausal women with a history of previous abdominal surgery, but they may also be seen in patients with a history of trauma, PID, or endometriosis. In patients with peritoneal adhesions, fluid produced by the ovary (which is the main producer of peritoneal fluid in women[13]) may accumulate within the adhesions and entrap the ovaries, resulting in an adnexal mass.[59-62] Peritoneal inclusion cysts are lined with mesothelial cells. Clinically, most patients present with pain and/or a pelvic mass.

On sonography, peritoneal inclusion cysts are multiloculated cystic adnexal masses, often with a bizarre shape frequently described as a spider web pattern[63] (Fig. 16.9). The diagnostic finding is the presence of an intact ovary positioned eccentrically amid septations and fluid.[60-62] The septations represent mesothelial and fibrous strands. The fluid is usually anechoic but may contain echoes in some compartments as a result of hemorrhage or proteinaceous fluid. Doppler evaluation may demonstrate vascularity within septations, at times mimicking a malignancy.

Peritoneal inclusion cysts must be differentiated from other extraovarian conditions such as parovarian cysts and a hydrosalpinx. Paraovarian cysts are separate from the ovary, whereas the ovary lies inside a peritoneal inclusion cyst. **Parovarian cysts** are usually round or ovoid and not associated with a history of pelvic surgery, trauma, or inflammation. A **hydrosalpinx** appears as a tubular or ovoid cystic structure often with visible folds, and the ovary is demonstrated as a separate entity. Accurate diagnosis of peritoneal inclusion cysts is important because the risk of recurrence after surgical resection is 30% to 50%.[64] Conservative therapy, such as ovarian suppression with oral contraceptives or fluid aspiration, is recommended.[62]

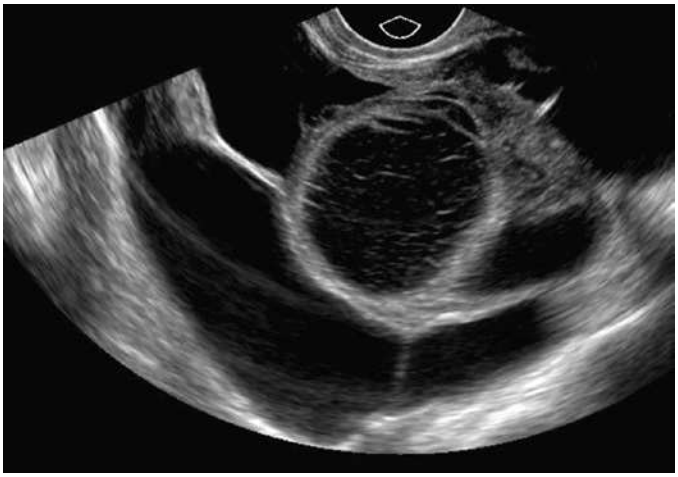

FIG. 16.9 Peritoneal Inclusion Cyst. TVS image shows a multilocular cyst with linear septations attached to the right ovary that projects within the structure and contains a hemorrhagic cyst. This represents adhesions attached to the right ovary.

Polycystic Ovarian Syndrome

Polycystic ovarian syndrome (PCOS) is now known to be a multifaceted endocrinologic disorder of ovarian dysfunction that includes abnormal estrogen and/or androgen production resulting in chronic anovulation and hyperandrogenism. Pathologically, the ovaries contain an increased number of follicles in various stages of maturation and atresia, and increased local concentration of androgens produces stromal abnormality. PCOS is a common cause of infertility and a higher-than-usual rate of early pregnancy loss.[65,66] Clinical manifestations of PCOS range from mild signs of hyperandrogenism in thin, normally menstruating women to the classic **Stein-Leventhal syndrome** (oligomenorrhea or amenorrhea, hirsutism, and obesity).

The typical sonographic findings of PCOS are bilaterally enlarged ovaries containing multiple small, 2- to 9-mm follicles and increased stromal echogenicity (Fig. 16.10). The ovaries have a rounded shape, with the follicles usually located peripherally ("string of pearls"), although they can also occur randomly throughout the ovarian parenchyma. Because of its superior resolution, TVS is more sensitive than TAS in detecting the small follicles. However, many women with PCOS will not have these typical sonographic findings. Ovarian volume may be normal in 30% of patients.[67,68] Using TVS, increased stromal echogenicity has also been reported as a sensitive and specific sign of polycystic ovaries.[69,70] In a small number of patients, the sonographic findings may be unilateral.[66,71]

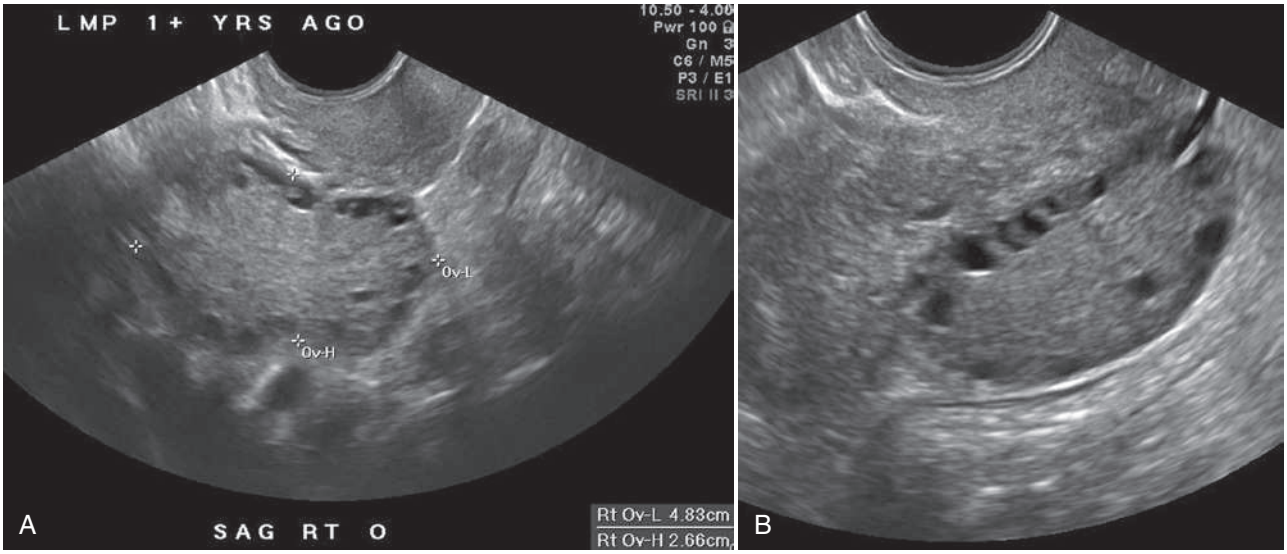

FIG. 16.10 Polycystic Ovaries: Typical Appearance on TVS in Woman With Hirsutism and Oligomenorrhea. (A) and **(B)** Enlarged ovaries *(cursors)* with mildly increased stromal echogenicity and multiple peripheral follicles, "string of pearls" sign.

A 2003 consensus meeting of the American Society for Reproductive Medicine and European Society of Human Reproduction and Embryology defined PCOS as requiring two of three criteria: (1) oligo-ovulation and/or anovulation, (2) hyperandrogenism (clinical and/or biochemical), and (3) polycystic ovaries.[72] An elevated serum luteinizing hormone (LH) level and insulin resistance have also been characteristic features. Historically, an elevated serum LH level and elevated LH/FSH ratio had been used as diagnostic tools. However, based on data that include the variability of LH depending on proximity to ovulation and its questionable importance in management, recommendations no longer support its necessity for clinical diagnosis.[73]

According to decisions made at the 2003 Rotterdam consensus workshop, the sonographic findings of polycystic ovaries should include either 12 or more follicles within the entire ovary measuring 2 to 9 mm in diameter[72] or increased ovarian volume greater than 10 mL. Although increased stromal echogenicity has been considered specific for polycystic ovaries, because of its subjective nature it was not included in the criteria. The consensus makers thought that measurement of ovarian volume worked as well as stromal evaluation in clinical practice. These criteria are not considered valid if the patient is taking oral contraceptives or has a dominant follicle greater than 10 mm. More recently, it has been reported that with the use of newer, higher resolution ultrasound technology and an offline reliable grid system to count follicles, a significantly higher follicle count threshold within the entire ovary is necessary to support the diagnosis of PCOS. Lujan et al.[74] advocated the use of a count of 26 and Christ et al.[75] a count of 28 follicles measuring 2 to 9 mm within the entire ovary as a better predictor of PCOS.

Because anovulation plays a key role in this disorder, the follicles will persist on serial studies. Long-term follow-up is recommended in patients with PCOS because the resulting high-unopposed estrogen levels can be associated with an increased risk of endometrial and breast carcinoma.

Endometriosis

Endometriosis is considered the most common benign gynecologic disorder. It is estimated that endometriosis affects between 5% and 45% of women in the reproductive age group, causes significant morbidity, and represents a major public health concern.[76,77] Clinical symptoms include pelvic pain, dysmenorrhea, dyspareunia, dyschezia, urinary symptoms, and infertility.[78]

The process is defined as the presence of functioning endometrial tissue outside the uterus. Endometriosis may present in different forms that include adnexal cysts (endometriomas), peritoneal plaques and adhesions, and deep infiltrating endometriosis consisting of implants or nodules that contain glands and stroma. Besides the ovary, the most commonly involved areas in the pelvis are the fallopian tube, broad ligament, and posterior cul-de-sac, but endometriosis can occur almost anywhere in the body, including the bladder and bowel.

The correct diagnosis and evaluation of the extent of disease are key in determining the best treatment approach. Ultrasound is well accepted as the initial imaging modality of choice, whereas MRI is considered the problem-solving tool.

The most common manifestation of endometriotic tissue is the **endometrioma,** which is readily diagnosed by its appearance sonographically with diffuse homogenous low level internal echoes. Endometriomas, often referred to as **chocolate cysts,** are frequently multiple, with a variety of appearances, from an anechoic cyst to a solid-appearing mass caused by the degradation of blood products over time.[79] The characteristic sonographic appearance is that of a well-defined, unilocular or multilocular, predominantly cystic mass containing diffuse, homogeneous, low-level internal echoes (Fig. 16.11, Video 16.3).[80] Color Doppler typically shows little if any vascularity within cyst walls (as opposed to the corpus luteum, which typically has pronounced flow). The low-level internal echoes may be seen diffusely throughout the mass or in the dependent portion. Occasionally, a fluid-fluid level may be seen, particularly if the woman has been lying in a similar position for sufficient time for the blood

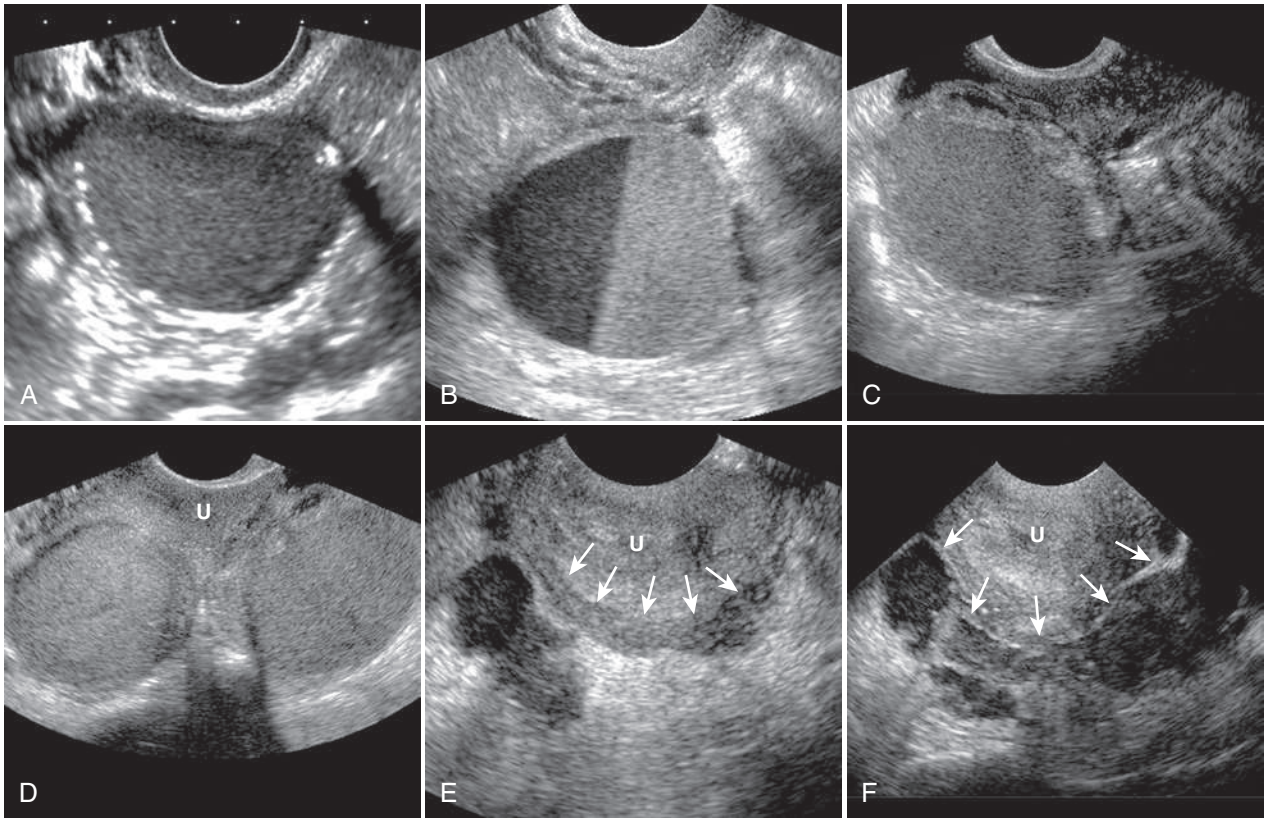

FIG. 16.11 Endometriosis: Spectrum of Appearances. TVS images. **(A)-(D)** Uniform low-level echoes within a cystic ovarian mass. **(A)** Typical peripheral echogenic foci. **(B)** Fluid-fluid level. **(C)** Avascular marginal echogenic nodules. **(D)** Bilateral disease. **(E)** Deep penetrating implant on posterior surface of uterus *(arrows)*. **(F)** Filling the pouch of Douglas *(arrows)*. *U,* Uterus. See also Videos 16.3, 16.4, and 16.5.

products to settle into layers. In a retrospective study, Patel et al.[81] found diffuse, low-level internal echoes in 95% of endometriomas. They concluded that this finding in the absence of neoplastic features is highly likely to be an endometrioma, especially if multilocularity or hyperechoic wall foci are present, whereas an endometrioma is highly unlikely when no component of the mass contains low-level echoes. A prospective study by Dogan et al.[82] found a positive predictive value of 97% for typically appearing endometriomas with low-level internal echoes, regular margins, round shape, and thick walls.

Differentiation of endometriosis from benign and malignant neoplasms is occasionally required. Papillary wall projections have been frequently described. Patel et al. demonstrated small, linear, hyperechoic foci sometimes present in the wall of the cyst that were thought to represent cholesterol deposits accumulating in the cyst wall.[81] Guerriero et al.[83] described papillations projecting within the cyst with a height of greater than 3 mm and no internal Doppler flow that were felt to represent adjacent fibrin or blood products (Video 16.4). In rare cases in pregnant women, decidualization of the wall of an endometrioma may occur, resulting in a solid vascular mural mass that cannot be differentiated from malignancy[84,85] (Fig. 16.12). Calcification is occasionally present in an endometrioma and can be confused with a dermoid.[86] Endometriomas may serve as precursors of borderline endometrioid and clear cell tumors that may eventually become low-grade invasive carcinoma and therefore, if not surgically removed, these are followed yearly.[50,87]

Endometriomas may be present in postmenopausal women, although their appearance generally differs. Instead of the unilocular cyst containing low-level echoes, the postmenopausal endometrioma more often has the appearance of a multilocular mass. When cyst fluid is present, it is more frequently anechoic or comprised of a more heterogeneous echogenicity.[88]

The appearance of an endometrioma may be similar to a **hemorrhagic ovarian cyst** because both are cystic masses that contain blood products of variable age. However, a hemorrhagic cyst more frequently demonstrates a reticular internal pattern rather than the pattern of homogeneous low-level echoes and is more frequently associated with free fluid in the cul-de-sac. A hemorrhagic cyst will resolve or show a significant decrease in size over the next few menstrual cycles, whereas endometriomas tend to show little change in size and internal echo pattern. Clinically, most women with a symptomatic hemorrhagic cyst present with acute pelvic pain, whereas women with an endometrioma have more chronic discomfort associated with their menses.

Endometriosis is frequently accompanied by the presence of pelvic adhesions. The evaluation of adhesions of the uterus and ovaries as well as obliteration of the pouch of Douglas can be challenging with ultrasound although techniques have been reported that can be performed successfully by experienced operators.[89,90] Movement of the normally mobile uterus and ovaries by abdominal palpation or pressure with the abdominal probe can show adherence of these structures to the adjacent

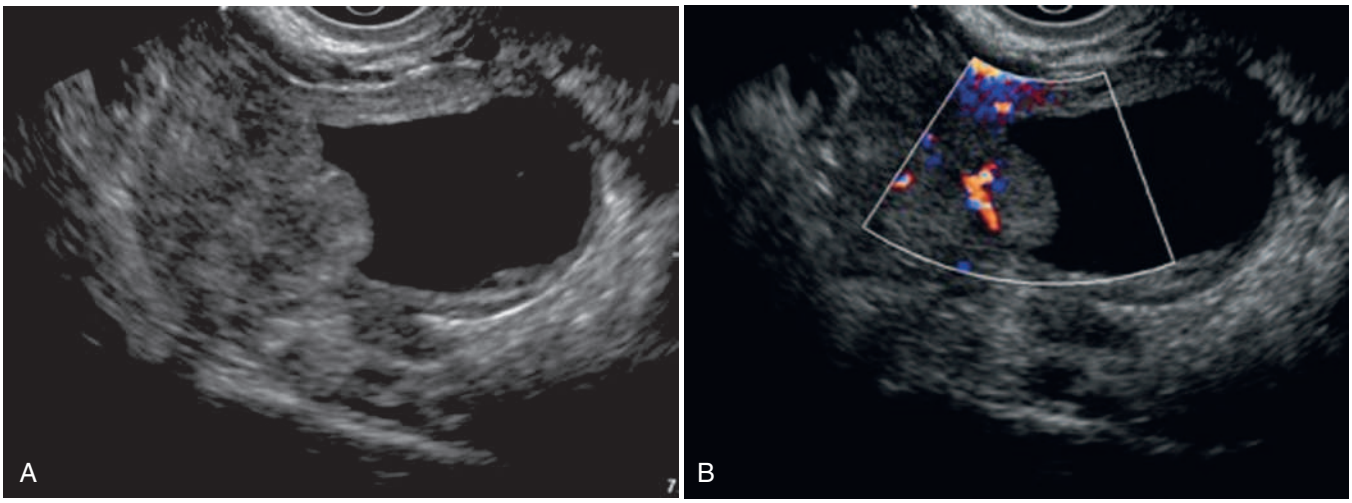

FIG. 16.12 Decidualization of Endometrioma in Pregnancy. (A) and **(B)** Sagittal gray-scale and color Doppler TVS images of a cyst containing low-level echoes and a peripheral echogenic nodule. The nodule demonstrates color Doppler flow, a finding seen in a borderline neoplasm or a decidualized endometrioma in a pregnant patient.

broad ligament, pouch of Douglas, bladder, rectum, or peritoneum. The use of the sliding sign on TVS has been described to diagnose the obliteration of the pouch of Douglas.[91,92] This procedure entails the placement of gentle pressure against the cervix with the TVS probe to determine if the posterior cervix slides easily along the anterior rectal and vaginal wall. Additionally, if fluid is present within the pelvis, fine linear structures representing adhesions may be seen joining the ovary with attached endometrioma, uterus and cul-de-sac peritoneum.

Deep infiltrating endometriosis is the most severe form of the disease although the extent of disease based laparoscopic staging may not correlate with the severity of symptoms.[78] Variable accuracy of TVS in the identification of deep infiltrating endometriosis has been reported. Most implants are found in dependent areas of the pelvis that is divided into the anterior and posterior compartment according to the deep infiltrating endometriosis classification by Chapron et al.[93] The **anterior compartment** is composed of the urinary bladder, and the **posterior compartment** includes the cul-de-sac, the uterosacral ligament, bowel wall, rectum and recto-sigmoid junction, vagina, and rectovaginal septum. Sonographically, implants appear as hypoechoic nodules or as diffuse or nodular retroperitoneal thickening. Within the bowel wall, the lesion often takes on the appearance of a fusiform swelling (Fig. 16.11E and F, Video 16.5). Few, if any, vessels are apparent using color Doppler evaluation.[94-97]

Adnexal Torsion

Adnexal torsion is a relatively infrequent gynecologic emergency requiring prompt surgical intervention with a reported incidence of 3% in some series. The process primarily affects women of reproductive age or younger and is uncommon in the postmenopausal age group.[98,99] Initially, there is twisting of the ovary, the fallopian tube, or both structures, causing venous and lymphatic compromise with resulting ovarian edema and adnexal enlargement. However, until venous and arterial thrombosis has occurred, reperfusion may permit complete recovery. Complete and unalleviated torsion can progress rapidly from interference with venous and lymphatic drainage to arterial occlusion and eventually necrosis. Torsion may be partial or complete, and acute or chronic. Not infrequently, torsion may be intermittent with periods of spontaneous remission of symptoms. The diagnosis of torsion is complicated by its vague clinical presentation. The most consistent presenting symptom is abdominal and pelvic pain, with other nonspecific signs and symptoms such as fever and nausea and vomiting more variably present. Early diagnosis and intervention prior to infarction permit ovarian preservation and prevent peritonitis.

Because the only consistent symptom cited in most studies is abdominal pain, usually intense and progressive, and localized to a lower quadrant, differential considerations include other gynecologic causes such as PID, ovarian cysts, and ectopic pregnancy as well as nongynecologic causes. Although often difficult to palpate, a demonstrable mass may be present. A right-sided predominance also exists that is attributed to the protective presence of the sigmoid colon on the left and the hypermobility of the right-sided cecum. As a result, the presentation of ovarian torsion may mimic that of appendicitis.[100,101]

Most cases of ovarian torsion (50%-80%) are associated with adnexal pathologic conditions such as ovarian tumors or cysts. This usually involves an ipsilateral ovarian mass 5 to 10 cm in diameter that acts as a fulcrum to potentiate torsion due to increased ovarian volume or weight within adnexal structures. Although associated with a neoplasm in as many as 50% of cases, previous studies have indicated that the lesions are usually benign since the inflammatory and invasive changes caused by malignant lesions may be protective against ovarian mobility.[102] It is associated with 1 in 1800 pregnancies, most commonly in the first trimester or immediately postpartum.[103] Women undergoing ovulation induction are at high risk secondary to the development of large theca lutein cysts.[100]

The initial role of sonography in the evaluation of patients at risk for ovarian torsion is to not only diagnose torsion but also exclude other causes of acute abdominal pain such as appendicitis,

PID, ruptured ovarian cyst, and ectopic pregnancy. The most consistent finding of ovarian torsion is an enlarged edematous ovary (Fig. 16.13) or ovarian complex of ovary and adnexal mass. The location of the ovary is frequently medial and superior to its usual location (Fig. 16.14A).[104] If the fallopian tube is involved, a hydrosalpinx will usually be demonstrated.

Peripherally placed follicles and homogeneous echoes seen centrally consistent with areas of edema within enlarged ovaries have also been reported,[105,106] although these descriptors are nonspecific (Video 16.6). Entities such as endometriomas, polycystic ovaries, hemorrhagic cysts, tubo-ovarian complexes, and hyperstimulated ovaries undergoing ovulation induction are often similarly described. The irregular internal texture of the ovary seems to correlate with intraovarian hemorrhage. Free fluid within the cul-de-sac is another nonspecific finding frequently associated with cases of ovarian torsion. The fluid may be a transudate from the ovarian capsule secondary to obstruction of veins and lymphatic vessels.[107]

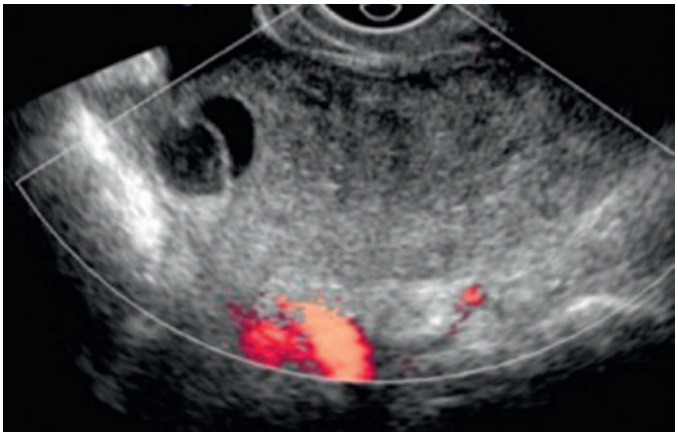

FIG. 16.13 Ovarian Torsion: Doppler Evaluation of Enlarged Ovaries. TVS color Doppler image of a young woman presenting with acute pelvic pain shows no evidence of color Doppler flow within an enlarged ovary containing irregular parenchyma; flow is demonstrated distally within the iliac artery. See also Video 16.6.

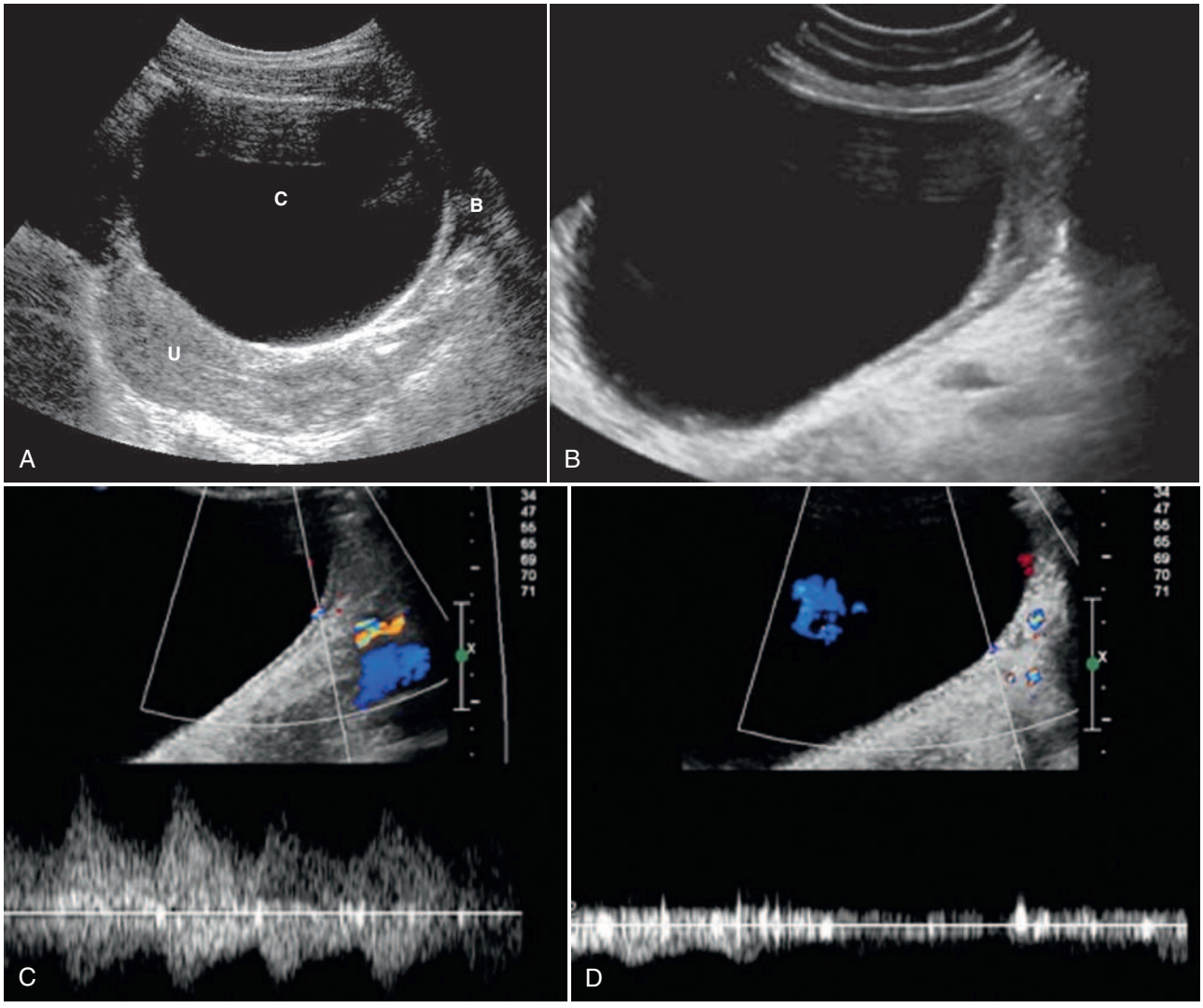

FIG. 16.14 Ovarian Torsion With Cyst as Fulcrum. (A) TAS sagittal image of a young woman with acute pain shows a large, simple cyst *(C)* that lies anterior to the uterus *(U)* and cephalad to the bladder *(B)*. This unusual position should raise the suspicion of torsion. **(B)-(D)** Another young female patient who is postpartum presenting with acute pelvic pain. **(B)** TAS shows a large simple ovarian cyst superior to the uterus. **(C)** and **(D)** TAS spectral Doppler images show normal arterial and venous waveforms within the wall of the cyst.

Doppler findings vary depending on degree of torsion and its chronicity. Lack of arterial and venous Doppler flow should enable confident diagnosis although false positive diagnoses may be obtained as a result of the depth of penetration being greater than the capabilities of the ultrasound beam, improper Doppler or gray-scale priority settings, and too high filter pulse repetition frequency (PRF) settings.[108] Thus it is helpful to scan the asymptomatic ovary first to ensure that Doppler settings are appropriate. Conversely, both arterial and venous ovarian spectral Doppler signal has been frequently reported in cases of surgically proven torsion. Absent venous Doppler flow has a positive predictive value as high as 94% for ovarian torsion despite persistence of arterial signal.[107] Explanations proposed include venous occlusion leading to symptoms before arterial occlusion occurs and that persistent adnexal arterial flow is related to the dual-ovarian arterial blood supply (ovarian artery and ovarian branches of uterine artery).[109] Occasionally, a twisted vascular pedicle (consisting of broad ligament, fallopian tube, and adnexal and ovarian branches of uterine artery and vein) may be demonstrated as a round hyperechoic structure with multiple concentric hypoechoic stripes (target appearance) or as an ellipsoid or tubular structure with internal heterogeneous echoes.[110] Using color or power Doppler ultrasound, the presence of circular or coiled twisted vessels within the vascular pedicle (whirlpool sign) is helpful in diagnosing torsion.[110] Absence of blood flow within the vascular pedicle suggests a nonviable ovary.[110,111] Comparison with the morphologic appearance and flow patterns of the contralateral ovary can also be helpful since decreased or abnormal flow may be present in the torsed ovary.[107,112]

Massive edema of the ovary is a rare condition resulting from partial or intermittent torsion of the ovary, causing venous and lymphatic obstruction but not arterial occlusion, leading to marked stromal edema. The few cases described in the literature show a large, edematous multicystic adnexal mass.[113-115]

The use of duplex and color Doppler imaging is most useful in making the diagnosis in the absence of Doppler flow although the presence of Doppler signal cannot eliminate the diagnosis. In the appropriate clinical setting, an enlarged ovary or ovary and adnexal mass complex should suggest torsion even in the presence of ovarian Doppler flow[112,116] Torsion is extremely unlikely if the ovary is morphologically normal and of normal size regardless of Doppler findings.

NEOPLASMS

Ovarian Cancer

Ovarian cancer is the fifth leading cause of cancer death among US women and causes more deaths than any other cancer of the female reproductive system. The American Cancer Society estimated 21,980 new cases of ovarian cancer in the United States in 2014, with about 14,270 deaths.[117] Between 1987 and 2010, the incidence decreased at a rate of 0.9% a year.[117,118] Ovarian cancer represents approximately 25% of all gynecologic malignancies, with peak incidence in the sixth decade of life. Ovarian cancer has the highest mortality rate of all gynecologic malignancies, mostly a result of late diagnosis. Because there are few clinical symptoms, 60% to 70% of women have advanced disease (stages III or IV) at diagnosis. The overall 5-year survival rate is 20% to 30%, but with early detection in stage I, the rate rises to 80% to 90%. Therefore efforts have been directed at developing methods of early diagnosis of ovarian cancer.

Increasing age, nulliparity, a family history of ovarian cancer, and a patient history of breast, endometrial, or colon cancer are associated with increased risk of ovarian cancer. The lifetime risk of a woman developing ovarian cancer is 1 in 70 (1.4%). However, if a woman has a first-degree relative (mother, daughter, sister) or second-degree relative (aunt or grandmother) who has had ovarian cancer, the risk is 5%. With two or more relatives who have had ovarian cancer, the lifetime risk increases to 7%.[119] About 3% to 5% of women with a family history of ovarian cancer have a hereditary ovarian cancer syndrome. The three main hereditary syndromes associated with ovarian cancer are the **breast-ovarian cancer syndrome,** the most common, caused by mutations in the suppressor genes BRCA1 and BRCA2, with a high frequency of both cancers; the **hereditary nonpolyposis colorectal cancer syndrome (Lynch II),** in which ovarian cancer occurs in association with nonpolyposis colorectal cancer or endometrial cancer, or both; and **site-specific ovarian cancer syndrome,** the least common, without an excess of breast or colorectal cancer.[120] Hereditary ovarian cancer syndromes are thought to have an autosomal dominant inheritance, and the lifetime risk of ovarian cancer in these patients is 40% to 50%. They have an earlier age of onset (10-15 years earlier) than do other ovarian cancers.[120] Therefore oophorectomy is commonly advocated after child-bearing in these women.

A number of clinical screening trials of asymptomatic women have been reported using TVS (either alone or in combination with Doppler sonography) and/or biologic markers such as cancer antigen (CA) 125.[121-126] **CA 125** is a high-molecular-weight glycoprotein recognized by the OC 125 monoclonal antibody. It has proved extremely useful in following the clinical course of patients undergoing chemotherapy and in detecting recurrent subclinical disease.[127,128] Although serum CA 125 is elevated in approximately 80% of women with epithelial ovarian cancer, it detects less than 50% of stage I disease and is insensitive to mucinous and germ cell tumors.[128] Other malignancies, as well as many benign conditions, are associated with elevated serum CA 125. The use of serum CA 125 and/or sonography as a screening test for ovarian cancer is not currently recommended for routine clinical use.[129] Routine screening has resulted in unnecessary surgery with its attendant risks.[129] The largest screening trial to date is the United Kingdom Collaborative Trial of Ovarian Cancer Screening (UKCTOCS), a randomized study evaluating annual screening using either TVS or serum CA 125 with TVS as a second-line test (multimodal screening). Preliminary results are encouraging, with superior sensitivity and positive predictive value reported with the multimodal screening strategy compared to TVS alone for detecting primary invasive epithelial ovarian and fallopian tube cancers.[130]

Histologically, **epithelial neoplasms** represent 65% to 75% of ovarian tumors and 90% of ovarian malignancies[50] (Table 16.1). The remaining neoplasms consist of **germ cell tumors** (15%-20%), **sex cord–stromal tumors** (5%-10%), and **metastatic**

TABLE 16.1 Ovarian Neoplasms

Tumor	Incidence	Examples
Surface epithelial–stromal tumors	65%-75%	Serous cystadenoma/carcinoma Mucinous cystadenoma/carcinoma Endometrioid carcinoma Clear cell carcinoma Transitional cell tumor
Germ cell tumors	15%-20%	Teratoma Dysgerminoma Yolk sac tumor
Sex cord–stromal tumors	5%-10%	Granulosa cell tumor Sertoli-Leydig cell tumor Thecoma and fibroma
Metastatic tumors	5%-10%	Uterus Stomach, colon, breast Lymphoma

tumors (5%-10%). Sonographically, ovarian cancer usually presents as an adnexal mass. Well-defined anechoic cysts are more likely to be benign, whereas lesions with irregular walls, thick irregular septations, mural nodules, and solid elements with flow are more likely to be malignant.[131,132] Many scoring systems and mathematical models based on the morphologic characteristics have been proposed for distinguishing between benign and malignant masses. However, **subjective evaluation** of the ultrasound morphologic features **(pattern recognition)** by an experienced interpreting physician has been shown to be the superior method.[133,134] Using this method, a physician should be able to distinguish benign from malignant masses in approximately 90% of cases.[135]

Color and pulsed Doppler sonography have been advocated for distinguishing benign from malignant ovarian masses. Support is based on the premise that malignant masses, because of internal neovascularization, will have high diastolic flow. Malignant tumor growth depends on angiogenesis, with the development of abnormal tumor vessels.[136] These abnormal vessels lack smooth muscle within their walls, which, along with arteriovenous shunting, leads to decreased vascular resistance and thus higher diastolic flow velocity. Therefore the pulsatility index (PI) and resistive index (RI) should be lower in malignant lesions. Although many reports have found a tendency for both PI and RI to be lower in malignant lesions, there is too much overlap to differentiate reliably between benign and malignant lesions in individual patients.[137-142] Other parameters such as vessel location have been suggested to improve the specificity of Doppler ultrasound assessment of ovarian masses.[143] Malignant lesions tend to have more central flow, whereas benign lesions tend to have more peripheral flow. However, Stein et al.[138] found considerable overlap, with 21% of malignant lesions having only peripheral flow and 31% of benign lesions having central flow. Guerriero et al.[144] found a higher accuracy in predicting malignancy when color Doppler ultrasound demonstrated arterial flow within the solid portions of the mass.

Studies comparing the morphologic features on sonography with the Doppler findings found that Doppler ultrasound showed no more diagnostic information than morphologic assessment alone.[133,139,140,145] Valentin[133] concluded that, in experienced hands, morphologic assessment is the best method for discriminating between benign and malignant masses. The main advantage of adding Doppler ultrasound would be to increase the confidence with which a correct diagnosis is made. Others have found that Doppler ultrasound, when added to sonographic morphologic assessment, improves specificity and positive predictive value.[142,146-148] Brown et al.[149] found that a nonhyperechoic solid component was the most statistically significant predictor of malignancy. Schelling et al.[150] also found that a solid component in an adnexal mass with central vascularity achieved high accuracy, sensitivity, and specificity in predicting malignancy. A meta-analysis of 46 published studies concluded that ultrasound techniques that combine morphologic assessment with color Doppler flow imaging is significantly better in characterizing ovarian masses than morphologic assessment, color Doppler flow imaging, or Doppler indices alone.[151] Doppler ultrasound is probably not needed if the mass has a characteristic benign morphology, because morphologic assessment is highly accurate in this group of lesions.[138,141] Doppler ultrasound is likely valuable in assessing the mass that is morphologically indeterminate or suggestive of malignancy. Doppler findings should be combined with morphologic assessment, clinical findings, patient age, and phase of menstrual cycle for optimal evaluation of an adnexal mass.[152]

Recently, contrast-enhanced TVS (CE-TVS) has been used to evaluate ovarian tumor neovascularity. With dynamic CE-TVS, malignant tumor neovascularity usually demonstrates more prolonged contrast washout compared with benign tumors. The difference in contrast enhancement patterns between benign and malignant ovarian masses results in potential improvement in differentiating benign from malignant lesions with CE-TVS compared with conventional TVS.[153]

Surface Epithelial–Stromal Tumors

In the past, epithelial-stromal tumors were generally considered to arise from the surface epithelium that covers the ovary and the underlying ovarian stroma. It has since been proposed that epithelial ovarian cancer is a collection of diseases arising from varying cells of origin. Evidence suggests that the majority of primary ovarian cancers (in particular, high-grade serous cancers) are derived from the fallopian tube rather than the ovary. A dualistic model that categorizes ovarian cancer into two groups (type I and type II) has been described. Type I tumors usually present at a low stage and include low-grade serous, low-grade endometrioid, clear cell, and mucinous carcinomas. Type II tumors include high-grade serous carcinomas, high-grade endometrioid carcinomas, carcinosarcomas, and undifferentiated carcinomas. Type I tumors tend to be clinically indolent, whereas type II tumors are typically highly aggressive.[154,155]

Epithelial-stromal tumors can be divided into five broad categories based on epithelial differentiation: **serous, mucinous, endometrioid, clear cell,** and **transitional cell (Brenner).**[50] This group of tumors accounts for 65% to 75% of all ovarian neoplasms and 80% to 90% of all ovarian malignancies. The mode of spread

of the malignant tumors is primarily intraperitoneal, although direct extension to contiguous structures can occur. Lymphatic spread is predominantly to the paraortic nodes. Hematogenous spread usually occurs late in the course of the disease.

Serous Cystadenoma and Cystadenocarcinoma

Serous tumors are the most common surface epithelial–stromal tumors, representing 30% of all ovarian neoplasms. Approximately 50% to 70% of serous tumors are benign. Serous **cystadenomas** account for about 25% of all benign ovarian neoplasms, and serous **cystadenocarcinomas** account for about 50% of all malignant ovarian neoplasms.[50] The peak incidence of serous cystadenomas is in the fourth and fifth decades, whereas serous cystadenocarcinomas most frequently occur in perimenopausal and postmenopausal women. Approximately 20% of benign serous tumors and 50% of malignant serous tumors are bilateral. Their sizes vary greatly, but in general they are smaller than mucinous tumors.

Sonographically, **serous cystadenomas** are usually large, thin-walled cysts. They are typically unilocular, but may contain thin septations (Fig. 16.15A and B). Papillary projections are occasionally seen. **Serous cystadenocarcinomas** may be quite large and usually present as multilocular cystic masses containing multiple papillary projections arising from the cyst walls and septa (Fig. 16.15G-I) The septa and walls may be thick. Echogenic solid material may be seen within the loculations. Papillary

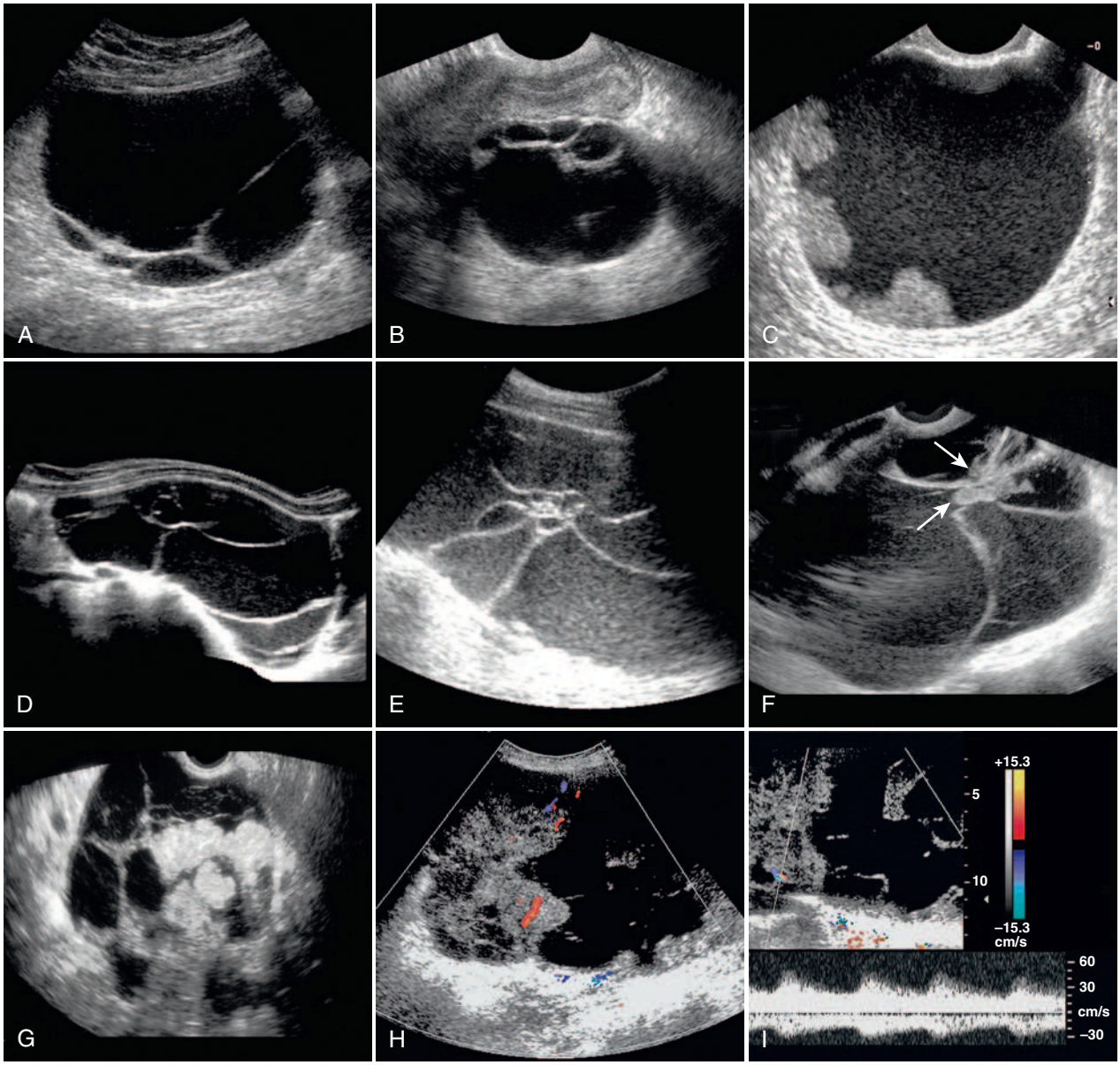

FIG. 16.15 Epithelial Ovarian Neoplasms: Spectrum of Appearances. (A) and **(B) Serous cystadenomas. (A)** Septations within a cystic mass are fairly thin. **(B)** Septations are thicker. **(C) Serous cystadenoma of low malignant potential.** Low-level echogenic particles and mural nodules. **(D)** and **(E) Mucinous cystadenomas. (F) Mucinous cystadenocarcinoma.** Large size and septations are characteristic; septal nodularity is marked *(arrows)*. **(G)-(I)** Patient with **serous cystadenocarcinoma.** Extensive nodularity shows vascularity, confirming the morphologic suspicion of a malignant mass. There is high diastolic flow resulting in a low resistive index.

FIG. 16.16 Mucinous Cystadenoma. Gross pathologic specimen shows multiple cystic loculations.

projections may form on the surface of the cyst and surrounding organs, resulting in fixation of the mass. Ascites is frequently seen.

Mucinous Cystadenoma and Cystadenocarcinoma

Mucinous tumors are the second most common ovarian epithelial tumor, accounting for 20% to 25% of ovarian neoplasms. Mucinous **cystadenomas** constitute 20% to 25% of all benign ovarian neoplasms, and mucinous **cystadenocarcinomas** make up 5% to 10% of all primary malignant ovarian neoplasms.[50] Mucinous cystadenomas occur most often in the third to sixth decades but may be seen in very young women, whereas mucinous cystadenocarcinomas most frequently occur in the fourth to seventh decades. Mucinous tumors are less frequently bilateral than their serous counterparts, with only 5% of the benign and 15% to 20% of the malignant lesions occurring on both sides. A high percentage, 80% to 85%, of mucinous tumors are benign.[156]

M**ucinous cystadenomas** can be huge cystic masses, measuring up 30 cm and filling the entire pelvis and abdomen (Figs. 16.15D and E and 16.16). Multiple thin septa are present, and low-level echoes caused by the mucoid material may be seen in the loculations. Papillary projections are less frequently seen than in the serous counterpart. **Mucinous cystadenocarcinomas** are usually large, multiloculated cystic masses containing papillary projections and echogenic material; they generally have a sonographic appearance similar to that of serous cystadenocarcinomas (Fig. 16.15F).

Penetration of the tumor capsule or rupture may lead to intraperitoneal spread of mucin-secreting cells that fill the peritoneal cavity with a gelatinous material. This condition, known as **pseudomyxoma peritonei,** may be similar sonographically to ascites or may contain multiple septations or floating debris in the fluid that fills much of the pelvis and abdomen. This condition may occur in mucinous cystadenomas and in mucinous cystadenocarcinomas. A ruptured mucocele of the appendix and mucinous tumors of the appendix and colon can also lead to pseudomyxoma peritonei.

Borderline (Low Malignant Potential) Tumors

There is an intermediate group of epithelial tumors that are histologically categorized as "borderline" or of "low malignant potential." They occur in about 10% to 15% of serous and mucinous tumors. These tumors have cytologic features of malignancy but do not invade the stroma and, although malignant, have a much better prognosis. They present at an earlier age than cystadenocarcinomas and have 5-year and 20-year survival of 95% and 80%, respectively. They may be treated by ovary-sparing surgery to preserve fertility.

Sonographic features suggestive of low malignant potential tumors are a small- to medium-sized cyst containing low-level echoes (similar to an endometrioma) with vascular mural nodules (Figs. 16.15C) or a cystic mass with a well-defined multilocular (honeycomb) nodule.[157,158] Normal ovarian tissue may be seen adjacent to the lesion and may be helpful in excluding invasive ovarian cancer.[157,159] This has been referred to as the **ovarian crescent sign.**[159] Although the presence of this sign decreases the likelihood of invasive adnexal malignancy, it was found to be a poor discriminator between benign and malignant adnexal masses in a prospective study by Van Holsbeke et al.[160]

Endometrioid Tumor

Almost all endometrioid tumors are malignant. They are the second most common epithelial malignancy, representing 20% to 25% of ovarian malignancies; 25% to 30% are bilateral, and they occur most frequently in the fifth and sixth decades. Their histologic characteristics are identical to those of endometrial adenocarcinoma, and approximately 30% of patients have associated endometrial adenocarcinoma, which is thought to represent an independent primary tumor. Approximately 15% to 20% of endometrioid cancer is associated with endometriosis, which may occur within the endometriosis, the ipsilateral or contralateral ovary.[50] The endometrioid tumor has a better prognosis than other epithelial malignancies, probably related to diagnosis at an earlier stage. Sonographically, it usually presents as a cystic mass containing papillary projections, although some endometrioid tumors are predominantly a solid mass that may contain areas of hemorrhage or necrosis.[156]

Clear Cell Tumor

This tumor is considered to be of müllerian duct origin and a variant of endometrioid carcinoma. Clear cell tumor is almost always malignant and constitutes 5% to 10% of primary ovarian carcinomas. It occurs most frequently in the fifth to seventh decades and is bilateral in about 20% of patients. Associated pelvic endometriosis is present in 50% to 70% of clear cell carcinomas, and approximately one-third arise within the lining of endometriomas.[50] Sonographically, it usually presents as a nonspecific, complex, predominantly cystic mass (Fig. 16.17, Video 16.7).[156]

Transitional Cell Tumor

Also known as **Brenner tumor,** transitional cell tumor is derived from the surface epithelium that undergoes metaplasia to form typical uroepithelial-like components.[156] It is uncommon, accounting for 2% to 3% of all ovarian neoplasms, and is almost always benign; 6% to 7% are bilateral. Most patients are asymptomatic, and the tumor is discovered incidentally on sonographic examination or at surgery. About 30% are associated with cystic neoplasms,

FIG. 16.17 Clear Cell Carcinoma in Endometrioma. TVS shows a complex cyst with homogenous low-level internal echoes centrally and solid nodules peripherally. See also Video 16.7

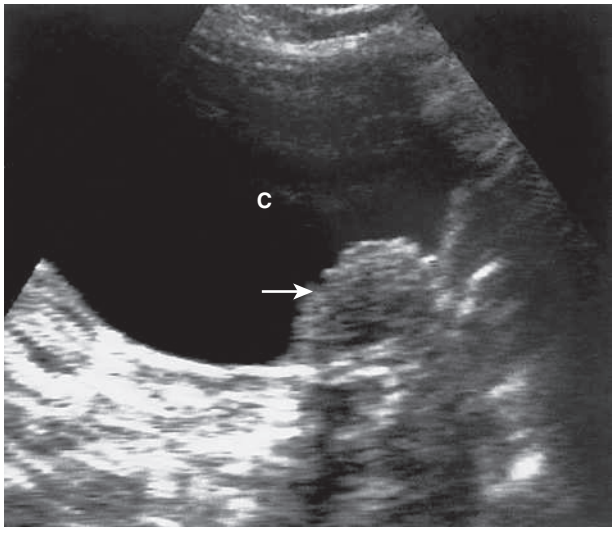

FIG. 16.18 Transitional Cell (Brenner) Tumor in Wall of Mucinous Cystadenoma. TAS shows a large, well-defined cystic mass *(C)* with a solid hypoechoic mural nodule *(arrow)*. Pathologic examination showed a Brenner tumor within the wall of a large, mucinous cystadenoma.

usually serous or mucinous cystadenomas or cystic teratomas, frequently in the ipsilateral ovary[161] (Fig. 16.18). Sonographically, Brenner tumors are hypoechoic solid masses. Calcification may occur in the outer wall. A cystic component is uncommon, but when present, usually results from a coexistent cystadenoma.[156,162] Pathologically, transitional cell masses are solid tumors composed of dense fibrous stroma. They appear similar to ovarian fibromas and thecomas and to uterine leiomyomas, both sonographically and pathologically.

Germ Cell Tumors

Germ cell tumors are derived from the primitive germ cells of the embryonic gonad. They account for 15% to 20% of ovarian neoplasms, with 95% being **benign cystic teratomas (dermoids).** The others, including **dysgerminomas** and **endodermal sinus** (yolk sac) **tumors,** occur mainly in children and young adults and are almost always malignant. Germ cell tumors are the most common ovarian malignancies in children and young adults. When a large, predominantly solid ovarian mass is present in a girl or young woman, the diagnosis of a malignant germ cell tumor should be strongly considered[163] (Video 16.8).

Cystic Teratoma

Cystic teratomas make up approximately 15% to 25% of ovarian neoplasms; 10% to 15% are bilateral. They are composed of well-differentiated derivatives of the **three germ layers:** ectoderm, mesoderm, and endoderm. Because **ectodermal elements** generally predominate, cystic teratomas are virtually always benign. Cystic teratomas are frequently seen in the reproductive years but can occur at any age and can be seen in postmenopausal women. These tumors may present as a palpable mass. Cystic teratomas are usually asymptomatic and often are discovered incidentally during sonography. In approximately 10% of cases, the tumor is diagnosed during pregnancy.[50] Torsion is the most common complication, whereas rupture is uncommon, occurring in 1% of patients and causing a secondary chemical peritonitis. Malignant transformation is also uncommon, occurring in 2% of patients, usually older women,[50] and is almost exclusively due to squamous cell carcinoma.[28]

Sonographically, cystic teratomas have a variable appearance ranging from completely anechoic to completely hyperechoic. However, certain features are considered specific (Fig. 16.19). These include a predominantly cystic mass with a highly echogenic mural nodule, the **dermoid plug.**[164] The dermoid plug usually contains hair, teeth, or fat and frequently casts an acoustic shadow. In many cases the cystic component is pure **sebum** (which is liquid at body temperature) rather than simple fluid.[165]

Cystic Teratomas: Sonographic Features

Dermoid plug
"Tip of the iceberg" sign
Dermoid mesh
Mobile spherules (rare)
Fat-fluid level

A mixture of matted hair and sebum is highly echogenic because of multiple tissue interfaces, and it produces poorly defined acoustic shadowing that obscures the posterior wall of the lesion. This has been termed the **"tip of the iceberg"** sign[166] (Fig. 16.19B). Highly echogenic foci with well-defined acoustic shadowing may arise from other elements, including teeth and bone. Multiple linear hyperechogenic interfaces, often described as lines and dots, may be seen floating within the cyst and have been shown to be hair fibers.[167] This is also considered a specific sign and has been referred to as the **dermoid mesh**[168] (Fig. 16.19G). A **fat-fluid** or **hair-fluid level** may also be seen (Fig. 16.19D and E). In most cases, as in other lesions such as endometriomas and hemorrhagic cysts, the dependent layer will be more echogenic. However, in approximately 30% of dermoids,

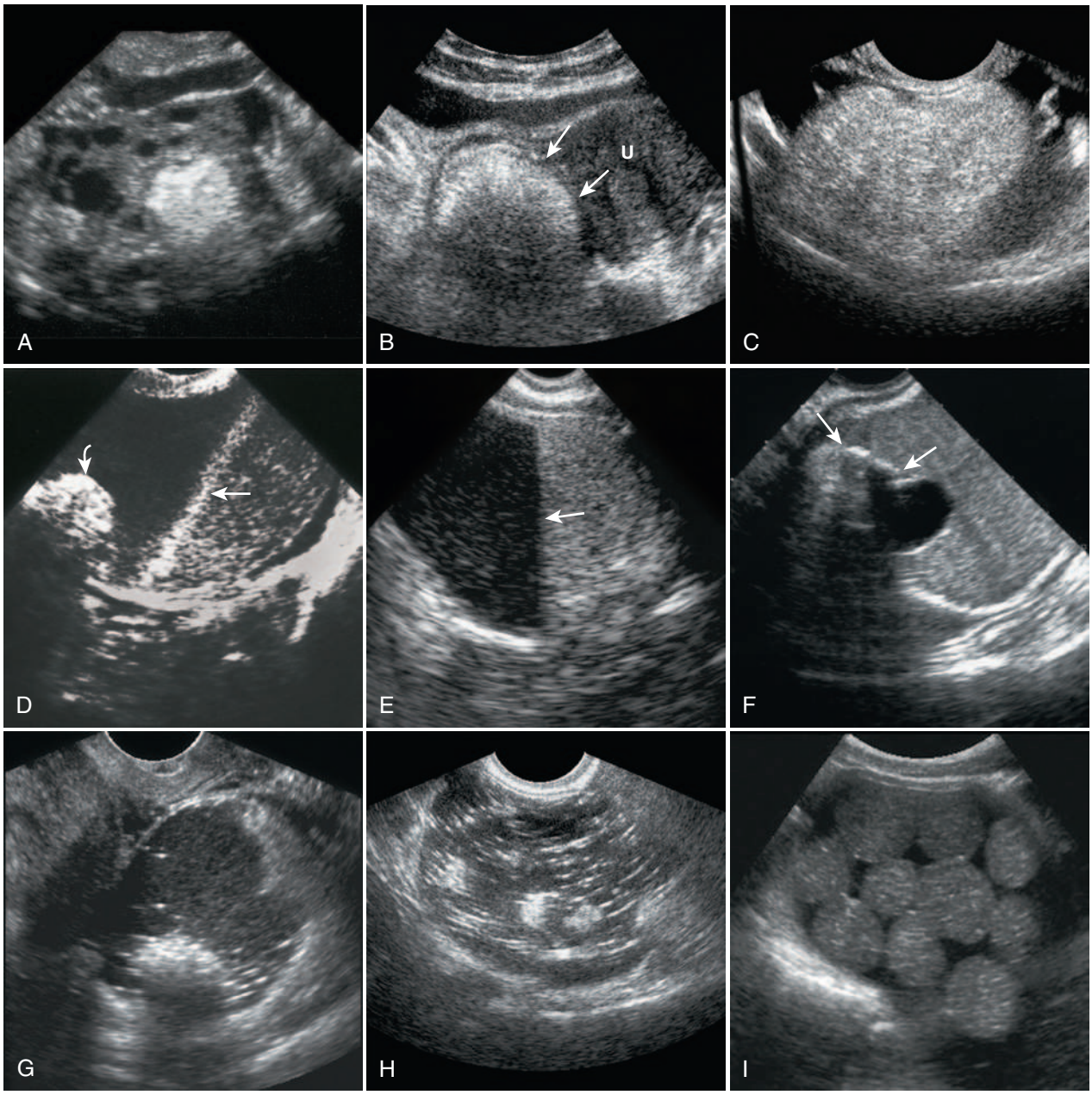

FIG. 16.19 Dermoid Cysts: Spectrum of Appearances. (A) Small, highly echogenic mass in an otherwise normal ovary. **(B)** Transverse TAS shows the uterus *(U)*. In the right adnexal region, there is a highly echogenic and attenuating mass *(arrows)*, the "tip of the iceberg" sign. **(C)** Highly echogenic intraovarian mass with no normal ovarian tissue. **(D)** Mass of varying echogenicity with **hair-fluid level** *(straight arrow)* and highly echogenic, fat-containing **dermoid plug** *(curved arrow)* with shadowing. **(E)** Mass with **fat-fluid level** *(arrow)*, with dependent layer more echogenic. **(F)** Mass containing uniform echoes, small cystic area, and calcification *(arrows)* with shadowing. **(G)** Combination of **dermoid mesh** and **dermoid plug** appearances. **(H) Dermoid mesh**, multiple linear hyperechogenic interfaces (lines and dots) floating within cystic mass. **(I)** Multiple mobile spherical echogenic structures floating in a large, cystic pelvic mass.

the nondependent layer will be more echogenic.[169] Another rare but characteristic feature is multiple mobile spherical echogenic structures floating in a large, cystic pelvic mass[170] (Fig. 16.19I). These spheres are typically composed of desquamative keratin-containing fibrin, hemosiderin, and hair.

Patel et al.[171] found that an adnexal mass showing two or more characteristic sonographic dermoid features had a positive predictive value of 100%. Pitfalls in the diagnosis of cystic teratomas have been described.[172] Acute hemorrhage into an ovarian cyst or an endometrioma may be so echogenic that it resembles a dermoid plug. However, posterior sound enhancement is usually seen with acute hemorrhage, whereas the dermoid plug tends to attenuate sound. Other pitfalls include pedunculated fibroids, especially lipoleiomyomas, and perforated appendicitis with an appendicolith. An echogenic dermoid may appear similar to bowel gas and may be overlooked. If a definite pelvic mass is clinically palpable and the sonogram appears normal, the patient should be reexamined, to carefully assess for a dermoid.

Doppler evaluation of a benign teratoma may show peripheral flow, but malignancy should be considered if flow is seen centrally and/or within solid areas. Additional findings suggesting malignancy include isoechoic branching structures within the lesion and invasion into adjacent organs.[28]

Struma ovarii is a teratoma composed entirely or predominantly of thyroid tissue. It occurs in 2% to 3% of teratomas. Color Doppler sonography detected central blood flow in solid tissue in four reported cases of struma ovarii, compared with absent central blood flow in benign cystic teratomas.[173] This is likely caused by the highly vascularized thyroid tissue in struma ovarii, compared with the avascular fat and hair found in benign cystic teratomas. Although associated hormonal effects are rare, sonography may be valuable in identifying a pelvic lesion in a hyperthyroid patient when there is no evidence of a thyroid lesion in the neck.[174]

Immature teratoma is uncommon, representing less than 1% of all teratomas, and contains immature tissue from all three germ-cell layers. It is a rapidly growing malignant tumor that most often occurs in the first two decades of life. Sonographically, the tumor usually presents as a solid mass, but cystic structures of varying size may also be seen.[163] Calcifications are typically present.

Dysgerminoma

Dysgerminomas are malignant germ cell tumors that constitute 1% to 2% of primary ovarian neoplasms and 3% to 5% of ovarian malignancies.[50] They are composed of undifferentiated germ cells and are morphologically identical to the male testicular **seminoma.** Dysgerminomas are highly radiosensitive and have a 5-year survival of 75% to 90%. This tumor occurs predominantly in women younger than 30 years and is bilateral in approximately 15% of cases.

Sonographically, they are solid masses that are predominantly echogenic but that may contain small anechoic areas caused by hemorrhage or necrosis[163] (Fig. 16.20). CT and MRI have shown these solid masses to be lobulated with fibrovascular septa between the lobules.[175] A report using color Doppler ultrasound in three dysgerminomas showed prominent arterial flow within the fibrovascular septa of a multilobulated, solid, echogenic mass.[176]

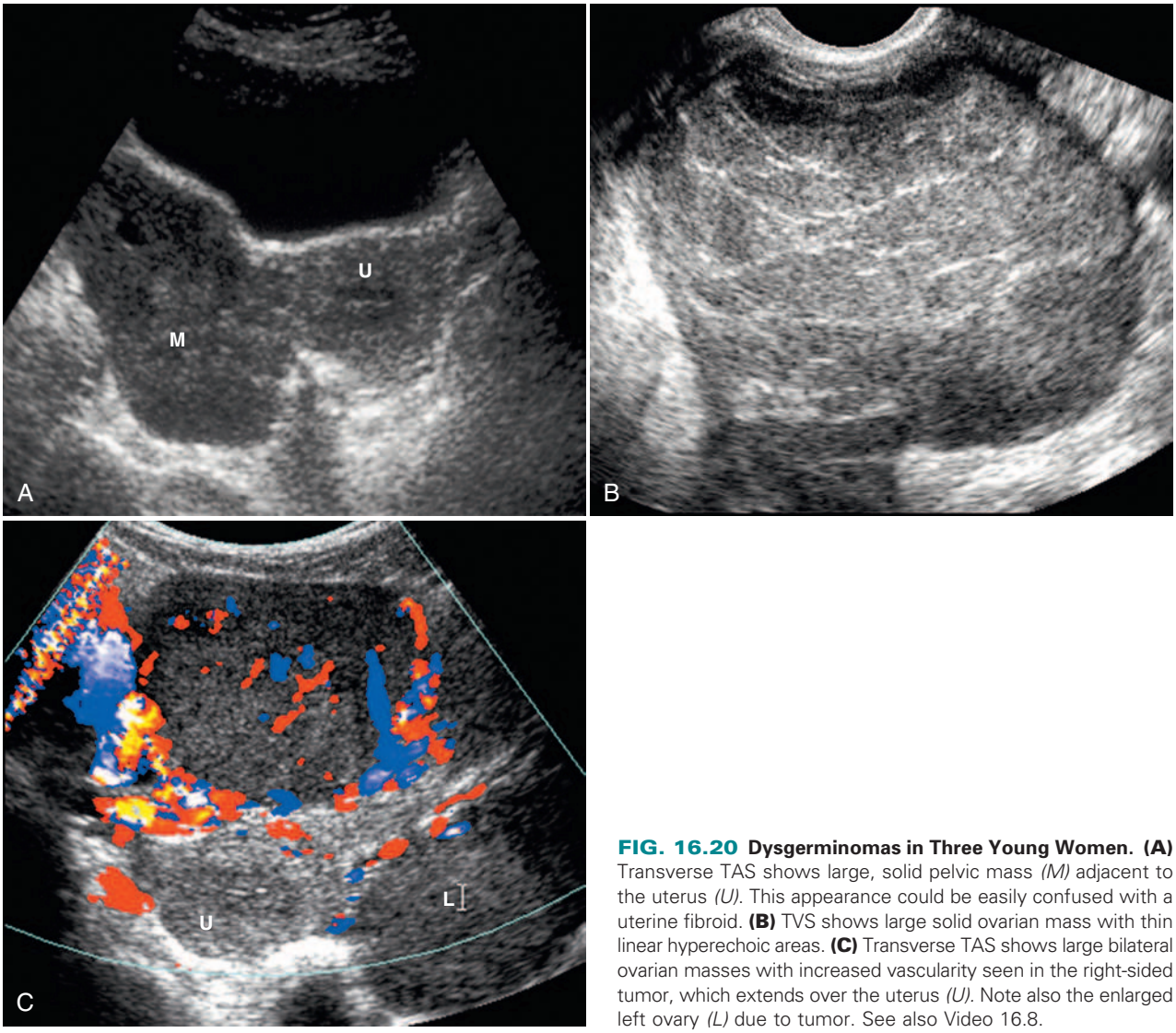

FIG. 16.20 Dysgerminomas in Three Young Women. (A) Transverse TAS shows large, solid pelvic mass *(M)* adjacent to the uterus *(U)*. This appearance could be easily confused with a uterine fibroid. **(B)** TVS shows large solid ovarian mass with thin linear hyperechoic areas. **(C)** Transverse TAS shows large bilateral ovarian masses with increased vascularity seen in the right-sided tumor, which extends over the uterus *(U)*. Note also the enlarged left ovary *(L)* due to tumor. See also Video 16.8.

Yolk Sac Tumor

This rare, rapidly growing tumor, also called **endodermal sinus tumor,** is the second most common malignant ovarian germ cell neoplasm after dysgerminoma. Yolk sac tumor has a poor prognosis. It is thought to arise from the undifferentiated, multipotential embryonal carcinoma by selective differentiation toward yolk sac or vitelline structures.[50] It usually occurs in females under 20 years of age and is almost always unilateral. Increased levels of serum alpha-fetoprotein may be seen in association with endodermal sinus tumor. The sonographic appearance is similar to that of the dysgerminoma[163] (see Video 16.8).

Sex Cord–Stromal Tumors

Sex cord–stromal tumors arise from the sex cords of the embryonic gonad and from the ovarian stroma. The main tumors in this group include **granulosa cell tumor, Sertoli-Leydig cell tumor (androblastoma), thecoma,** and **fibroma.** This group accounts for 5% to 10% of all ovarian neoplasms and 2% of all ovarian malignancies.

Granulosa Cell Tumor

Representing 1% to 2% of ovarian neoplasms, granulosa cell tumor has a low malignant potential. About 95% are of the **adult type** and occur predominantly in postmenopausal women; almost all are unilateral. Granulosa cell tumors are the most common estrogenically active ovarian tumor,[50] and clinical signs of estrogen production can occur, including development of endometrial carcinoma (in 10%-15%). The **juvenile type** makes up 5% of granulosa cell tumors, occurring mainly in patients younger than 30 years. Granulosa cell tumors have a variable appearance, ranging from small solid masses to tumors with variable degrees of hemorrhage or fibrotic changes, to multilocular cystic lesions.[177]

Sertoli-Leydig Cell Tumor

This rare tumor, also called **androblastoma and arrhenoblastoma,** constitutes less than 0.5% of ovarian neoplasms. It generally occurs in women younger than 30 years of age; almost all are unilateral. Malignancy occurs in 10% to 20% of these tumors. The malignant tumors tend to recur relatively soon after initial diagnosis, with few recurrences after 5 years.[178] Clinically, signs and symptoms of virilization occur in about 30% of patients, although about half will have no endocrine manifestations.[50] Occasionally, these tumors may be associated with estrogen production. Sonographically, Sertoli-Leydig cell tumors usually appear as solid hypoechoic masses or may be similar in appearance to granulosa cell tumors.[178]

Thecoma and Fibroma

Thecoma and fibroma arise from the ovarian stroma and may be difficult to distinguish from each other pathologically. Tumors with an abundance of thecal cells are classified as **thecomas,** whereas those with fewer thecal cells and abundant fibrous tissue are classified as **thecofibromas** and **fibromas. Thecomas** constitute approximately 1% of all ovarian neoplasms, and 70% occur in postmenopausal females. They are unilateral, almost always benign, and frequently show clinical signs of estrogen production.

Fibromas represent about 4% of ovarian neoplasms, are benign, usually unilateral, and occur most often in perimenopausal and postmenopausal women. Unlike thecomas, fibromas are rarely associated with estrogen production and therefore are frequently asymptomatic, despite reaching a large size. Ascites is present in up to 50% of patients with fibromas larger than 5 cm in diameter.[179] **Meigs syndrome** (associated ascites and pleural effusion) occurs in 1% to 3% of patients with ovarian fibromas but is not specific, having been reported in association with other ovarian neoplasms as well. Fibromas also occur in approximately 17% of patients with the **basal cell nevus (Gorlin) syndrome.** In this condition the fibromas are usually bilateral, calcified, and occur in younger women (mean age, 30 years).[178]

Sonographically, these tumors have a characteristic appearance of a fibrous lesion (Fig. 16.21). A hypoechoic mass with marked posterior attenuation of the sound beam is seen.[179] The main differential diagnosis is a pedunculated uterine fibroid. Not all fibromas and thecomas show this characteristic appearance, and a variety of sonographic appearances have been noted, probably because edema and cystic degeneration tend to occur within these tumors.[180]

Metastatic Tumors

About 5% to 10% of ovarian neoplasms are metastatic in origin. The most common primary sites of ovarian metastases are tumors of the breast and gastrointestinal tract. The term **Krukenberg tumor** should be reserved for those tumors containing the typical mucin-secreting "signet ring" cells, usually of gastric or colonic origin. Endometrial carcinoma frequently metastasizes to the ovary, but it may be difficult to distinguish from primary endometrioid carcinoma, as discussed earlier. Sonographically, **ovarian metastases** are usually bilateral solid masses (Fig. 16.22A-C), but they may become necrotic and may have a complex, predominantly cystic appearance that simulates primary cystadenocarcinoma[181,182] Testa et al.[183] found that almost all ovarian metastases from primary tumors of the breast, stomach, and uterus were solid, whereas those from the colon and rectum were more heterogeneous, most being multicystic with irregular borders. Ascites may be seen in either primary or metastatic tumors. **Lymphoma** may involve the ovary, usually in a diffuse, disseminated form that is frequently bilateral. The sonographic appearance is that of a solid hypoechoic mass similar to lymphoma elsewhere in the body (Fig. 16.22D-F).

FALLOPIAN TUBE

With careful TVS examination, a normal fallopian tube may be identified as an undulating structure measuring less than 10 mm in thickness that extends from the uterine cornu posterolaterally to the ipsilateral ovary. This assessment is not included as part of a routine pelvic sonogram. Identification becomes easier when the fallopian tube is dilated or surrounded by fluid. The contour of the lumen is not seen unless it is obstructed and fluid-filled[184] (Fig. 16.23). Diagnosis of an asymptomatic hydrosalpinx is important because it allows for what might otherwise be considered to be a concerning adnexal cyst to be ignored rather than followed (Videos 16.9 and 16.10). Developmental

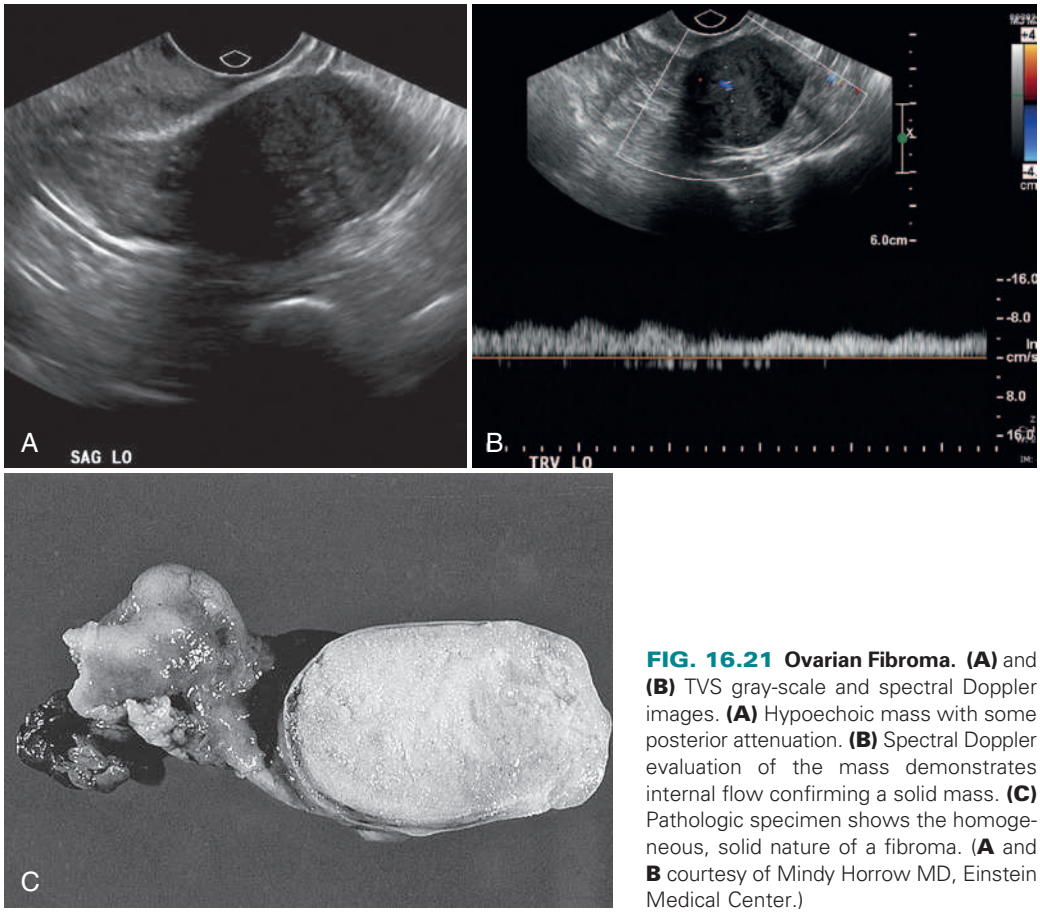

FIG. 16.21 Ovarian Fibroma. (A) and **(B)** TVS gray-scale and spectral Doppler images. **(A)** Hypoechoic mass with some posterior attenuation. **(B)** Spectral Doppler evaluation of the mass demonstrates internal flow confirming a solid mass. **(C)** Pathologic specimen shows the homogeneous, solid nature of a fibroma. (**A** and **B** courtesy of Mindy Horrow MD, Einstein Medical Center.)

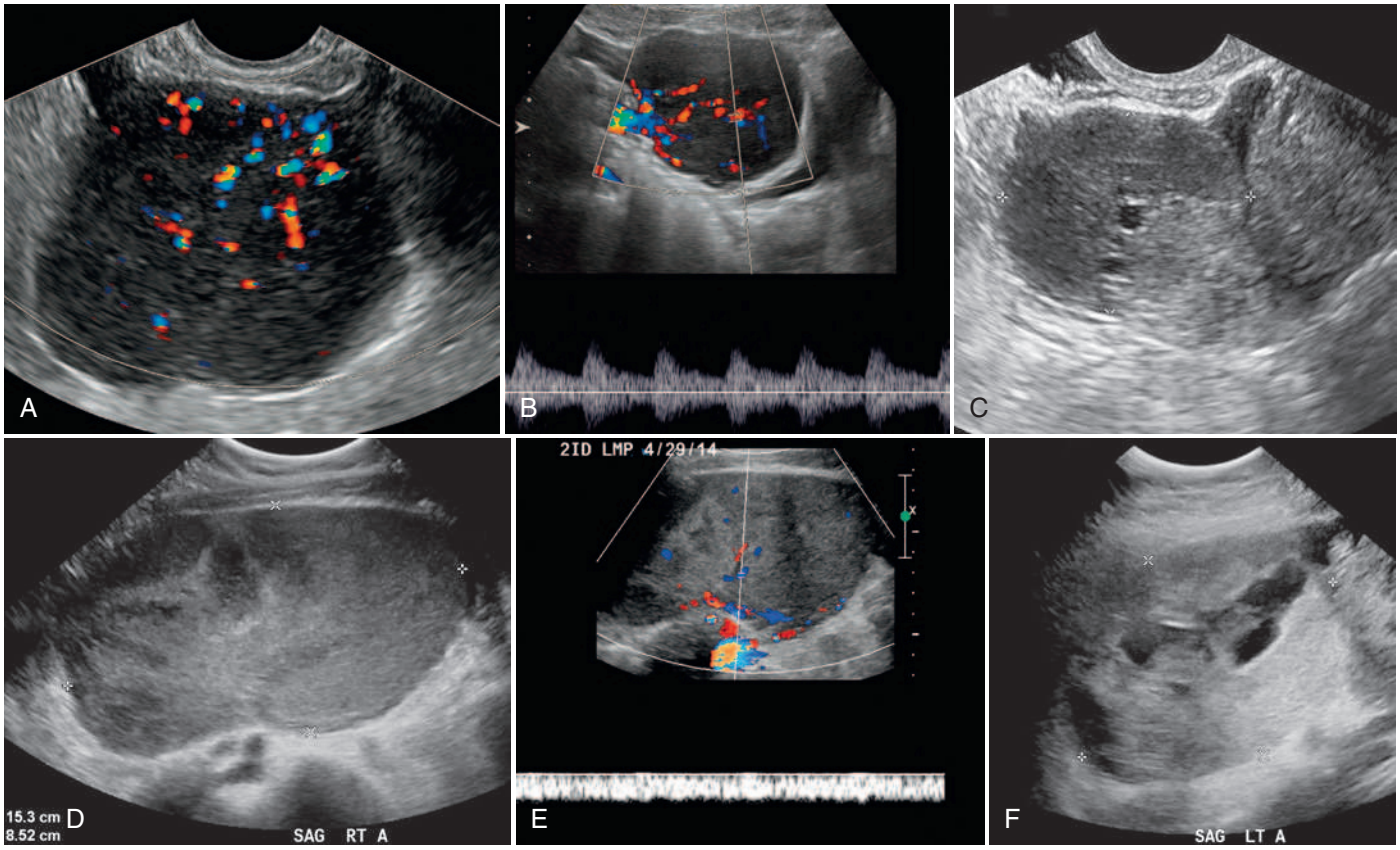

FIG. 16.22 Solid Malignant Adnexal Masses in Two Patients: Metastatic Disease and Lymphoma. (A)-(C) Bilateral solid ovarian masses or Krukenberg tumors in young woman with colon cancer (**A** and **B,** right ovary; **C,** left ovary). **(D)-(F)** Bilateral predominantly solid masses in young woman with lymphoma (**D** and **E,** right ovary; **F,** left ovary).

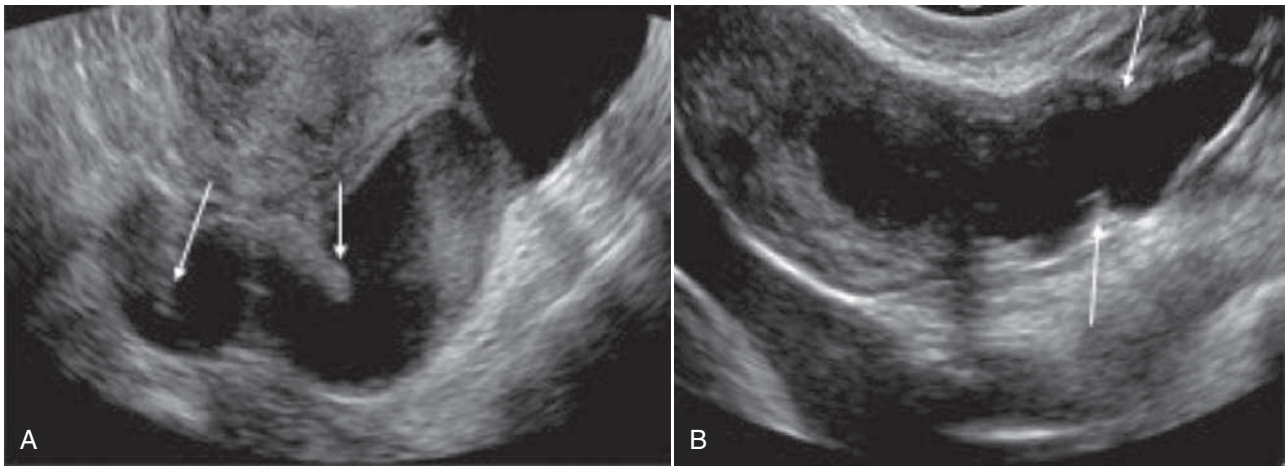

FIG. 16.23 Hydrosalpinx. TVS images show tubular fluid-filled structures with sonographic characteristics of the fallopian tube. **(A)** Incomplete septation related to the folding of the tube *(arrows)*. **(B)** A waist sign also associated with tubal folds *(arrows)* and endosalpingeal folds forming surface nodularities. See also Videos 16.9 and 16.10.

abnormalities of the fallopian tube are rare. Abnormalities of the tube include pregnancy, infection, torsion, and neoplasm as well as scarring and obstruction due to other causes.

Pelvic Inflammatory Disease

PID is a common condition that is increasing in frequency. It consists of inflammation of the endometrium, fallopian tubes, pelvic peritoneum, and adjacent structures. Typically, the primary infection is a sexually transmitted disease most often associated with gonorrhea and chlamydia, although with previous disruption of endometrial and tubal tissue due to prior infection, or postsurgical or postpartum changes, the patient can be infected by her own vaginal flora. The infection typically spreads by ascent from the cervix and endometrium. The disease is manifested by tubo-ovarian complexes, peritonitis, and abscess formation and is usually bilateral. Long-term sequelae include chronic pelvic pain, infertility, and increased risk of ectopic pregnancy.

Less common causes include direct extension from appendiceal, diverticular, or postsurgical abscesses that have ruptured into the pelvis, as well as puerperal and postabortion complications. Hematogenous spread is rare but can occur from tuberculosis. When caused by direct extension of an adjacent inflammatory process, it is most often unilateral. The presence of an intrauterine device (IUD) increases the risk of PID, although only during a period of a few weeks following its placement. PID may be unilateral in patients with IUDs.

Patients usually present clinically with pain, fever, cervical motion tenderness, and vaginal discharge. A pelvic mass may be palpated. TVS with color or power Doppler is highly specific in the diagnosis of the disease process.[185] However, because the success of the technique is dependent on the level of operator expertise and also because early changes can be subtle, TVS usually only detects complications of the disease. The sonographic findings may be normal early in the course of PID.[186] Increased echogenicity of peritoneal fat and indistinctness of the uterus may be seen early in the disease process but may be difficult to appreciate. Sonographic findings of the fallopian tubes are the most specific and conspicuous indicators of PID (Table 16.2).

TABLE 16.2 Sonographic Findings of Pelvic Inflammatory Disease

Endometritis	Endometrial thickening Intracavitary fluid
Purulent material in cul-de-sac	Fluid containing low-level echoes
Periovarian inflammation	Enlarged ovaries with multiple cysts and indistinct margins
Salpingitis	Fluid-filled fallopian tube with (pyosalpinx) or without (hydrosalpinx) internal echoes Increased echogenicity of peritoneal fat Indistinctness of the uterus
Tubo-ovarian complex	Fusion of inflamed, fluid-distended tube and ovary
Tubo-ovarian abscess	Multiloculated mass with variable septations, irregular margins, and low-level internal echoes

When imaging a normal appearing fallopian tube, hypervascularity with color Doppler flow within the tubal wall is a valuable early finding. As the disease progresses, a spectrum of findings may occur (Fig. 16.24). With inflammation, the tube swells and endosalpingeal folds thicken. With progressive inflammation and distal occlusion of the lumen, the tube fills with purulent echogenic fluid, becoming a **pyosalpinx.** In the presence of a fluid-distended fallopian tube, common findings include wall thickness greater than 5 mm, incomplete septa seen as the tube folds back on itself, and thickening of endosalpingeal folds **(cogwheel sign).**[187,188] Color or power Doppler allows for detection of hyperemia in the walls and incomplete septi associated with fallopian tube inflammation (Fig. 16.24B).[189] On TAS, dilated tubes appear as complex, predominantly cystic masses that are often indistinguishable from other adnexal masses. However, TVS allows for depiction of the fluid-filled tube with a tubular shape, somewhat

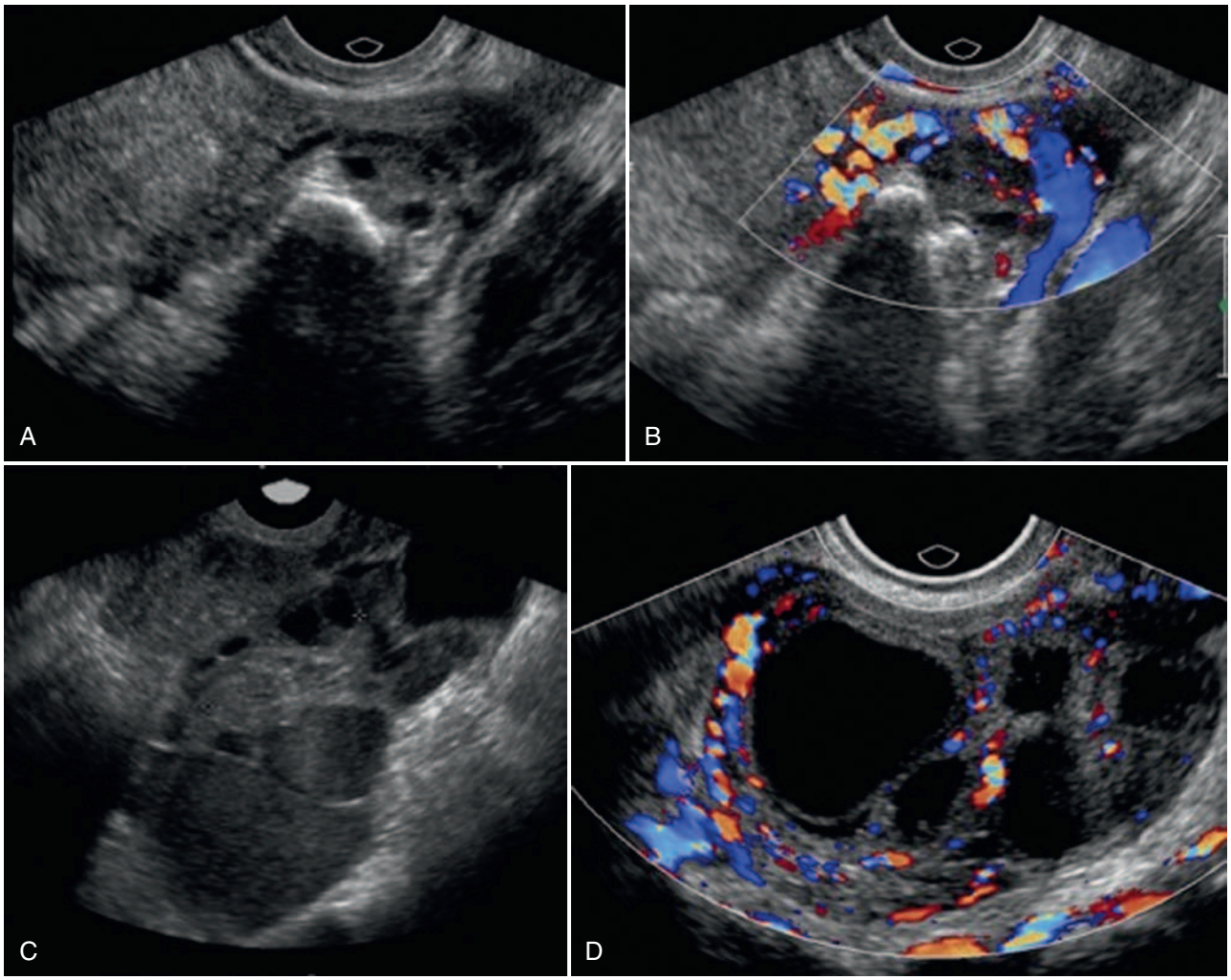

FIG. 16.24 Progression of Pelvic Inflammatory Disease. (A) TVS gray-scale and **(B)** color Doppler images show a normal appearing left fallopian tube by gray-scale imaging but markedly increased associated vascularity using color Doppler, consistent with salpingitis. **(C)** TVS image of a tubo-ovarian complex, a complex mass of fallopian tube and ovary that can still be identified as separate structures. **(D)** TVS color Doppler image of a tubo-ovarian abscess, a cystic, vascular mass containing thick septations in which the fallopian tube and ovary are no longer identifiable. See also Video 16.11.

folded configuration, and well-defined walls.[190] The dilated tube can be distinguished from a fluid-filled bowel loop by the lack of peristalsis. A fluid-pus level may occasionally be seen (Fig. 16.24A). Anechoic fluid within the tube indicates hydrosalpinx. In assessing 14 acute and 60 chronic cases of PID, Timor-Tritsch et al.[188] described three appearances of tubal wall structure: (1) **cogwheel sign,** an anechoic cogwheel-shaped structure visible in the cross section of the tube with thick walls, seen mainly in acute disease; (2) **"beads on a string" sign,** hyperechoic mural nodules measuring 2 to 3 mm on cross section of the fluid-filled distended tube, caused by degenerated and flattened endosalpingeal fold remnants and seen only in chronic disease; and (3) **incomplete septa,** hyperechoic septa that originate as a triangular protrusion from one of the walls, but do not reach the opposite wall, seen frequently in both acute and chronic disease and not discriminatory. Patel et al.[191] found that the presence of a tubular fluid-filled mass with diametrically opposed indentations in the wall **("waist sign")** had the highest likelihood ratio in discriminating hydrosalpinx from other adnexal masses (Fig. 16.23B).[191] Other findings include thick tubal walls and bilateral adnexal masses appearing as small solid masses or thick-walled cystic masses.[192] Nonspecific findings of PID include fluid in the endometrial cavity and/or cul-de-sac, and ill-defined ovarian enlargement often. Endometrial thickening or fluid may indicate endometritis. Fluid containing low-level echoes may be demonstrated in the cul-de-sac consistent with purulent material.

With progression of disease, there is exudation of pus from the distal fallopian tube, periovarian adhesions may form, with fusion of the inflamed dilated tube and ovary, forming an inflammatory **tubo-ovarian complex** (Fig. 16.24C, Video 16.11). The ovary is still recognizable but cannot be separated from the tube by applied pressure using the vaginal transducer.[186] Further progression results in complete breakdown of tubal and ovarian architecture so that separate structures are no longer identified and there is obscuration of the posterior and lateral margins of the uterus resulting in a **tubo-ovarian abscess** (Fig. 16.24D). Sonographically, this appears as a multiloculated mass with incomplete septations, irregular margins, and low-level internal

echoes. There is usually posterior acoustic enhancement, and a fluid-debris level or gas may occasionally be seen within the mass. The sonographic appearance may be indistinguishable from other benign and malignant adnexal masses. Clinical correlation is necessary to suggest the correct diagnosis. Regions of identifiable ovarian tissue may be seen within the inflammatory mass by TVS since the ovaries are relatively resistant to infection.[3]

Both TAS and TVS are useful in making the initial diagnosis in patients with PID and determining management. The TAS approach is helpful in assessing the extent of the disease, whereas the TVS approach is more sensitive in detecting dilated tubes, periovarian inflammatory change, and the internal characteristics of tubo-ovarian abscesses.[186,193] However, because of cervical motion tenderness, it may be quite difficult to perform a good quality TVS examination.

Although the use of outpatient antibiotic therapy has become the standard of care for mild to moderate cases of PID, according to guidelines from the Centers for Disease Control and Prevention,[185] hospitalization for intravenous antibiotic therapy would be prompted by the presence of a tubo-ovarian abscess. By making this diagnosis, TVS is pivotal in determining management.

Sonography is also used to follow the disease process following antibiotic therapy. If antibiotic therapy fails, sonographically guided drainage of tubo-ovarian abscesses in combination with antibiotics has been shown to be highly successful.[194] This initial approach allows for decreased need for surgical intervention.

Tubal Torsion

Tubal torsion is usually seen in conjunction with ovarian torsion, but isolated torsion of the fallopian tube is an infrequent finding. This may be seen in cases of paratubal cysts but also can be seen in association with chronic hydrosalpinx.[195] The patient usually presents with sudden onset of severe pelvic pain. Hydrosalpinx and tubal torsion have also been reported as late complications in patients who have undergone tubal ligation.[196]

Fallopian Tube Carcinoma

The fallopian tube is now thought to be the location for the initial development of high-grade serous cystadenocarcinomas. Thus whereas fallopian tube cancer used to be considered a rare finding, it is now managed similarly to ovarian cancer. Serous tubal intraepithelial carcinoma, a lesion too small to visualize using imaging modalities, represents the acknowledged precursor of these neoplasms.[154]

A minority of patients have a profuse watery discharge, known as **hydrops tubae profluens.** The tumor usually involves the distal end, but it may involve the entire length of the tube. Sonographically, carcinoma of the fallopian tube has been described as a sausage-shaped, solid, or cystic mass with papillary projections.[197-200] Patlas et al.[201] stated that this diagnosis should be considered when a solid vascular mass corresponding to the expected location of the fallopian tube is seen in association with normal ovaries, especially if the mass is mobile.[201]

VASCULAR ABNORMALITIES IN THE ADNEXA

Ovarian Vein Thrombosis or Thrombophlebitis

Ovarian vein thrombosis or thrombophlebitis is an uncommon condition that is usually seen 48 to 96 hours postpartum (Fig. 16.25). Symptoms include fever, lower abdominal pain, and a palpable mass. The underlying cause is venous stasis and spread of bacterial infection from endometritis. The right ovarian vein is involved in 90% of cases. Retrograde venous flow occurs in the left ovarian vein during the puerperium, which protects this side from bacterial spread from the uterus.[50] The condition may be diagnosed by sonography although CT and MRI usually perform better in this diagnosis.[202,203] Sonography may demonstrate an inflammatory mass lateral to the uterus and anterior to the psoas muscle. The ovarian vein may be seen as a tubular structure directed cephalad from the mass and containing echogenic thrombus. The thrombus usually affects the most cephalic portion of the right ovarian vein and can be demonstrated sonographically at the junction of the right ovarian vein with the inferior vena cava, sometimes extending into the inferior vena cava.[204] Doppler ultrasound will demonstrate complete or

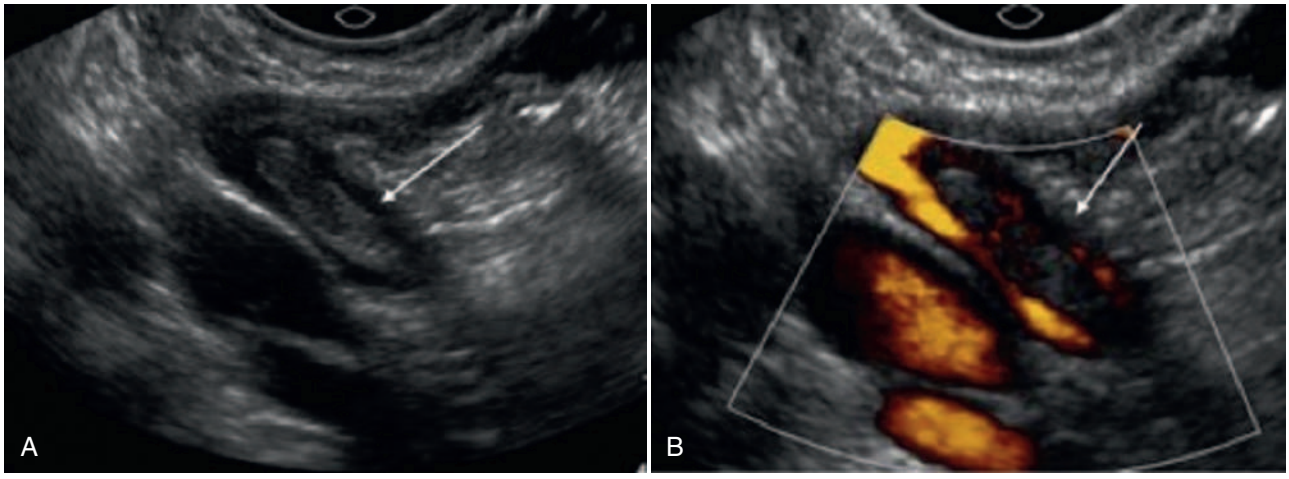

FIG. 16.25 Ovarian Vein Thrombophlebitis. (A) Transverse gray-scale and **(B)** color Doppler images of the right ovarian vein containing echogenic material representing thrombus. Color Doppler image shows Doppler signal surrounding the thrombus.

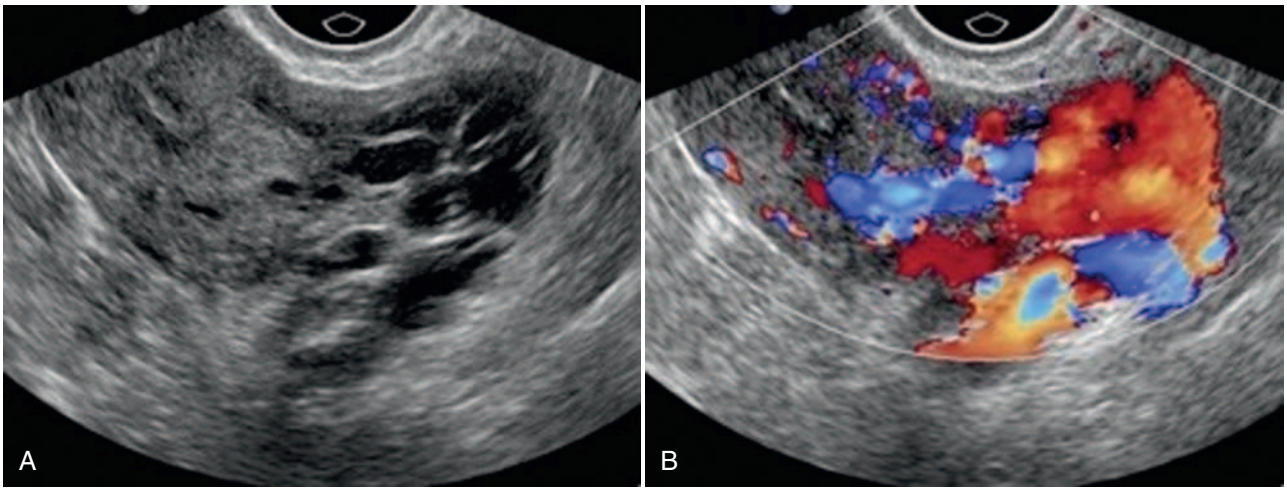

FIG. 16.26 Pelvic Congestion Syndrome. Transverse TVS images, **(A)** without and **(B)** with color Doppler, of the left adnexa demonstrating multiple large vascular structures consistent with varices.

partial absence of flow in these veins.[205] Most patients respond to anticoagulant and antibiotic therapy, and follow-up sonography may show resolution of the thrombus and normal flow by duplex and color Doppler imaging.

Pelvic Congestion Syndrome

Pelvic congestion syndrome is a condition that consists of dilatation of pelvic veins (pelvic varices) and reduced venous return causing dull chronic pain that is exacerbated by prolonged standing and relieved by lying down and elevating the legs. Although venography remains the reference standard for diagnosis, sonography can demonstrate an ovarian vein diameter of greater than 5 to 10 mm with reflux, uterine vein engorgement, congestion of ovarian plexuses (tortuous and dilated pelvic venous plexuses in the adnexa with individual varices measuring greater than 5 mm in diameter, Fig. 16.26), filling of the pelvic veins across the midline, or filling of vulvovaginal and thigh varicosities.[206] Dilated arcuate veins may also be seen crossing the myometrium. Spectral Doppler evaluation of ovarian veins may demonstrate reversed caudal flow.

SONOGRAPHIC EVALUATION OF AN ADNEXAL MASS IN ADULT WOMEN

Sonography in the setting of certain clinical features is often used to evaluate an ovarian/adnexal mass. Clinical features to be considered when evaluating an adnexal mass include symptoms, patient age, menstrual status, and family history. Comparison with previous examinations, if available, is often critical and may save the patient a surgical intervention, since many of these masses are hormonally driven and will resolve. A prior study will also demonstrate if there has been any change in size or internal characteristics.

When a mass is found by sonography, it should be characterized by the following:

- Location (intraovarian or extraovarian)
- Size
- External contour (thin or thick walled and regularity of borders)
- Internal consistency (cystic unilocular or multilocular with or without solid components, predominantly solid, or solid)

Generally, ovarian masses are predominantly cystic, whereas uterine masses are usually solid tumors, benign leiomyomas. Even solid adnexal masses are usually exophytic or interligamentous leiomyomas. Demonstrating a uterine origin by gray-scale and color Doppler is diagnostic and excludes a solid ovarian tumor. Occasionally, it may be difficult to determine the exact origin of the mass by sonography in which case MRI may be a problem-solving tool.

In 2010 the Society of Radiologists in Ultrasound published results of a consensus conference regarding the reporting and follow-up needed for asymptomatic adnexal cysts (Table 16.3). Use of these guidelines allows for decreased need for follow-up of benign adnexal cysts.[207,208] The vast majority of ovarian masses are functional in nature. Ovarian masses that are simple cysts are almost always benign. In premenopausal asymptomatic women, simple cysts or typical hemorrhagic cysts less than 5 cm can be considered functional. The simple adnexal cyst less than or equal to 1 cm in a postmenopausal woman is also very likely benign. These findings should be considered of no clinical significance in asymptomatic women and do not require follow-up. Simple cysts greater than 5 cm in premenopausal women are also likely functional, but resolution should be confirmed with a follow-up examination. In postmenopausal women, simple cysts greater than 1 cm are most often benign cystadenomas or hydrosalpinges or paraovarian/paratubal cysts that demonstrate no significant malignant potential. Cysts that are greater than 7 cm cannot be adequately evaluated sonographically for mural nodules, so MRI or surgical evaluation is recommended.[28]

Larger masses, especially those greater than 10 cm, and those with solid components have a higher incidence of malignancy. Solid ovarian masses that are not classic for fibromas are typically surgically removed because of association with malignancy. Cystic

TABLE 16.3 Society of Radiologists in Ultrasound Recommendations for Follow-Up of Asymptomatic Adnexal Cysts

Patient Population	Description in Report	Recommended Follow-Up
Premenopausal women	Simple or hemorrhagic cysts 3-5 cm	Simple or hemorrhagic cysts > 5 cm, 6 weeks to document resolution
Postmenopausal women	Cysts > 1 cm	Yearly
Any age	Hydrosalpinx	No follow-up needed
Any age	Dermoid, endometrioma	Yearly

With permission from Levine D, Brown DL, Andreotti RF, et al. Management of asymptomatic ovarian and other adnexal cysts imaged at US: Society of Radiologists in Ultrasound Consensus Conference Statement. Radiology. 2010;256(3):943-954.[28]

masses with solid components may be either benign or malignant and should be further assessed for wall contour, septations, and mural nodules. Irregular borders, thick irregular septations, papillary projections, and echogenic solid nodules favor malignancy. Color and spectral Doppler ultrasound may demonstrate vascularity within the septa or nodules. Although ascites may be associated with benign masses such as the mucinous cystadenoma or fibroma, it is more commonly seen with malignant disease. Malignant ascites often contains echogenic particulate matter.

If a pelvic mass is suspected of being malignant, the abdomen should also be evaluated for evidence of ascites and peritoneal implants, obstructive uropathy, lymphadenopathy, and hepatic and splenic metastases. Hepatic and splenic metastases are uncommon in ovarian carcinoma, but when they occur, they are usually peripheral on the surface of the liver or spleen as a result of peritoneal implantation. Hematogenous metastases within the liver or splenic parenchyma may occur late in the course of the disease.

Attempts have been made to standardize reporting of adnexal features and preoperatively classify these masses. The largest study to date analyzing features of ovarian and adnexal masses has been performed by the International Ovarian Tumor Analysis (IOTA) group.[209] Timmerman et al.[210] used these ultrasound-based features to develop simple rules that can correctly classify the majority of masses as benign or malignant (Table 16.4). If one or more of the malignant (M) rules or one or more of the benign (B) rules are present, the mass is classified as benign or malignant. If both M and B rules are present or no rules are present, the mass cannot be classified.

TABLE 16.4 Ten Simple Rules for Identifying a Benign or Malignant Tumor

Rules for Predicting a Malignant Tumor (M-Rules)	Rules for Predicting a Benign Tumor (B-Rules)
M1 Irregular solid tumor	B1 Unilocular
M2 Presence of ascites	B2 Presence of solid components where the largest solid component has a largest diameter <7 mm
M3 At least four papillary structures	B3 Presence of acoustic shadows
M4 Irregular multilocular solid tumor with largest diameter ≥100 mm	B4 Smooth multilocular tumor with largest diameter <100 mm
M5 Very strong blood flow	B5 No blood flow

If one or more M-rules apply in the absence of a B-rule, the mass is classified as malignant. If one or more B-rules apply in the absence of an M-rule, the mass is classified as benign. If both M-rules and B-rules apply, the mass cannot be classified. If no rule applies, the mass cannot be classified.
With permission from Timmerman D, Testa AC, Bourne T, et al. Simple ultrasound-based rules for the diagnosis of ovarian cancer. Ultrasound Obstet Gynecol. 2008;31(6):681-690.[210]

NONGYNECOLOGIC ADNEXAL MASSES

Pelvic masses and pseudomasses may not be of gynecologic origin. To make this diagnosis, it is important to visualize the uterus and ovaries separately from the mass. This is frequently not possible because of displacement of the normal pelvic structures by the mass. Nongynecologic pelvic masses most frequently originate from the gastrointestinal or urinary tract or may develop after surgery. These include bladder diverticulum, urachal cysts, gut duplication cysts, and Tarlov cysts.

Postoperative Pelvic Masses

Postoperative masses may be **abscesses, hematomas, lymphoceles, urinomas,** or **seromas.** Sonographically, **abscesses** are ovoid-shaped, hypoechoic masses with thick, irregular walls and posterior acoustic enhancement. Variable internal echogenicity may be seen, and high-intensity echoes with shadowing caused by gas may be demonstrated. With optimized settings, color Doppler usually demonstrates vascularity within the wall of the abscess. **Hematomas** show a spectrum of sonographic findings, varying with time.[211] During the initial hyperacute phase, hematomas are anechoic. After organization and clot formation, they become highly echogenic. With lysis of the clot, hematomas develop a reticular pattern and/or concave margins due to retracting clot, until finally, with complete lysis, they are again anechoic. An abscess may be indistinguishable from a hematoma sonographically requiring clinical correlation to make the final diagnosis.

Pelvic **lymphoceles** occur after surgical disruption of lymphatic channels, usually after pelvic lymph node dissection or renal transplantation. Sonographically, lymphoceles are anechoic, having an appearance similar to that of **urinomas,** which are localized collections of urine, or **seromas,** which are collections of serum. Sonography-guided aspiration may be necessary to differentiate these conditions.

Gastrointestinal Tract Masses

The most frequent pelvic pseudomasses are fecal material in the rectum simulating a complex mass in the cul-de-sac and a fluid-filled rectosigmoid colon presenting as a cystic adnexal mass. TVS can usually distinguish the pseudomass from a true mass, but when it cannot, a repeat examination or MRI may be necessary. **Bowel neoplasms,** especially those involving the rectosigmoid, cecum, and ileum, may simulate an adnexal mass. These tumors frequently show the characteristic target sign of a gastrointestinal mass, consisting of a central echogenic focus caused by air within the lumen, surrounded by a thickened hypoechoic wall.[212] **Abscesses** related to inflammatory disease of the gastrointestinal tract may also present as an adnexal mass. On the right side, this is most frequently caused by appendicitis or Crohn disease, whereas abscesses on the left side are usually caused by diverticular disease and are seen in an older age group.

Urinary Tract Masses

Patients with a **pelvic kidney** may present with a clinically palpable mass. This is readily recognized sonographically by the typical reniform appearance and the absence of a kidney in the normal location. Occasionally, a greatly distended bladder may be mistaken for an ovarian cyst. When a cystic pelvic mass is identified, it is imperative that the bladder be seen separately from the mass. If the origin of the cystic mass continues to be in question, having the patient void or draining the bladder with a Foley catheter can ensure a decompressed bladder. **Bladder diverticula** may also simulate a cystic adnexal mass. The diagnosis can be confirmed by demonstrating communication with the bladder and a changing appearance after voiding. **Dilated distal ureters** may simulate adnexal cysts on transverse scans; however, sagittal scans show their tubular appearance and continuity with the bladder.

REFERENCES

1. Gardner ED, O'Rahilly R, Müller F, Gardner ED. Gardner-Gray-O'Rahilly anatomy: a regional study of human structure. 5th ed. Philadelphia: Saunders; 1986.
2. Williams PL, Warwick R. Gray's anatomy. 37th ed. London: Churchill Livingstone; 1989.
3. Mendelson EB, Bohm-Velez M, Neiman HL, Russo J. Transvaginal sonography in gynecologic imaging. Semin Ultrasound CT MR. 1988;9(2):102-121.
4. Cohen HL, Tice HM, Mandel FS. Ovarian volumes measured by US: bigger than we think. Radiology. 1990;177(1):189-192.
5. van Nagell Jr JR, Higgins RV, Donaldson ES, et al. Transvaginal sonography as a screening method for ovarian cancer. A report of the first 1000 cases screened. Cancer. 1990;65(3):573-577.
6. Merz E, Miric-Tesanic D, Bahlmann F, et al. Sonographic size of uterus and ovaries in pre- and postmenopausal women. Ultrasound Obstet Gynecol. 1996;7(1):38-42.
7. Kupfer MC, Ralls PW, Fu YS. Transvaginal sonographic evaluation of multiple peripherally distributed echogenic foci of the ovary: prevalence and histologic correlation. AJR Am J Roentgenol. 1998;171(2):483-486.
8. Muradali D, Colgan T, Hayeems E, et al. Echogenic ovarian foci without shadowing: are they caused by psammomatous calcifications? Radiology. 2002;224(2):429-435.
9. Brandt KR, Thurmond AS, McCarthy JL. Focal calcifications in otherwise ultrasonographically normal ovaries. Radiology. 1996;198(2):415-417.
10. Zeligs KP, Javitt MC, Barner R, Hamilton CA. Atypical ovarian calcifications associated with bilateral borderline ovarian tumors. J Ultrasound Med. 2013;32(6):1059-1061.
11. Ecochard R, Marret H, Rabilloud M, et al. Sensitivity and specificity of ultrasound indices of ovulation in spontaneous cycles. Eur J Obstet Gynecol Reprod Biol. 2000;91(1):59-64.
12. Davis JA, Gosink BB. Fluid in the female pelvis: cyclic patterns. J Ultrasound Med. 1986;5(2):75-79.
13. Koninckx PR, Renaer M, Brosens IA. Origin of peritoneal fluid in women: an ovarian exudation product. Br J Obstet Gynaecol. 1980;87(3):177-183.
14. Jeffrey RB, Laing FC. Echogenic clot: a useful sign of pelvic hemoperitoneum. Radiology. 1982;145(1):139-141.
15. Seungdamrong A, Weiss G. Ovulation in a postmenopausal woman. Fertil Steril. 2007;88(5):1438.e1-1438.e2.
16. Soules MR, Sherman S, Parrott E, et al. Executive summary: Stages of Reproductive Aging Workshop (STRAW). Fertil Steril. 2001;76(5):874-878.
17. Goswamy RK, Campbell S, Royston JP, et al. Ovarian size in postmenopausal women. Br J Obstet Gynaecol. 1988;95(8):795-801.
18. Granberg S, Wikland M. A comparison between ultrasound and gynecologic examination for detection of enlarged ovaries in a group of women at risk for ovarian carcinoma. J Ultrasound Med. 1988;7(2):59-64.
19. Andolf E, Jorgensen C, Svalenius E, Sunden B. Ultrasound measurement of the ovarian volume. Acta Obstet Gynecol Scand. 1987;66(5):387-389.
20. Hall DA, McCarthy KA, Kopans DB. Sonographic visualization of the normal postmenopausal ovary. J Ultrasound Med. 1986;5(1):9-11.
21. Fleischer AC, McKee MS, Gordon AN, et al. Transvaginal sonography of postmenopausal ovaries with pathologic correlation. J Ultrasound Med. 1990;9(11):637-644.
22. DiSantis DJ, Scatarige JC, Kemp G, et al. A prospective evaluation of transvaginal sonography for detection of ovarian disease. AJR Am J Roentgenol. 1993;161(1):91-94.
23. Wolf SI, Gosink BB, Feldesman MR, et al. Prevalence of simple adnexal cysts in postmenopausal women. Radiology. 1991;180(1):65-71.
24. Levine D, Gosink BB, Wolf SI, et al. Simple adnexal cysts: the natural history in postmenopausal women. Radiology. 1992;184(3):653-659.
25. Goldstein SR, Subramanyam B, Snyder JR, et al. The postmenopausal cystic adnexal mass: the potential role of ultrasound in conservative management. Obstet Gynecol. 1989;73(1):8-10.
26. Conway C, Zalud I, Dilena M, et al. Simple cyst in the postmenopausal patient: detection and management. J Ultrasound Med. 1998;17(6):369-372.
27. Healy DL, Bell R, Robertson DM, et al. Ovarian status in healthy postmenopausal women. Menopause. 2008;15(6):1109-1114.
28. Levine D, Brown DL, Andreotti RF, et al. Management of asymptomatic ovarian and other adnexal cysts imaged at US: Society of Radiologists in Ultrasound Consensus Conference Statement. Radiology. 2010;256(3):943-954.
29. Bailey CL, Ueland FR, Land GL, et al. The malignant potential of small cystic ovarian tumors in women over 50 years of age. Gynecol Oncol. 1998;69(1):3-7.
30. Modesitt SC, Pavlik EJ, Ueland FR, et al. Risk of malignancy in unilocular ovarian cystic tumors less than 10 centimeters in diameter. Obstet Gynecol. 2003;102(3):594-599.
31. Nardo LG, Kroon ND, Reginald PW. Persistent unilocular ovarian cysts in a general population of postmenopausal women: is there a place for expectant management? Obstet Gynecol. 2003;102(3):589-593.
32. Ekerhovd E, Wienerroith H, Staudach A, Granberg S. Preoperative assessment of unilocular adnexal cysts by transvaginal ultrasonography: a comparison between ultrasonographic morphologic imaging and histopathologic diagnosis. Am J Obstet Gynecol. 2001;184(2):48-54.
33. Castillo G, Alcazar JL, Jurado M. Natural history of sonographically detected simple unilocular adnexal cysts in asymptomatic postmenopausal women. Gynecol Oncol. 2004;92(3):965-969.
34. Tavassoli FA, Devilee P. Pathology and genetics of tumours of the breast and female genital organs. Lyon, France: IARC; 2003.
35. Timor-Tritsch IE, Goldstein SR. The complexity of a "complex mass" and the simplicity of a "simple cyst." J Ultrasound Med. 2005;24(3):255-258.
36. Glanc P, Salem S, Farine D. Adnexal masses in the pregnant patient: a diagnostic and management challenge. Ultrasound Q. 2008;24(4):225-240.

37. Baltarowich OH, Kurtz AB, Pasto ME, et al. The spectrum of sonographic findings in hemorrhagic ovarian cysts. AJR Am J Roentgenol. 1987;148(5): 901-905.
38. Yoffe N, Bronshtein M, Brandes J, Blumenfeld Z. Hemorrhagic ovarian cyst detection by transvaginal sonography: the great imitator. Gynecol Endocrinol. 1991;5(2):123-129.
39. Jain KA. Sonographic spectrum of hemorrhagic ovarian cysts. J Ultrasound Med. 2002;21(8):879-886.
40. Patel MD, Feldstein VA, Filly RA. The likelihood ratio of sonographic findings for the diagnosis of hemorrhagic ovarian cysts. J Ultrasound Med. 2005;24(5):607-614.
41. Price FV, Edwards R, Buchsbaum HJ. Ovarian remnant syndrome: difficulties in diagnosis and management. Obstet Gynecol Surv. 1990;45(3):151-156.
42. Phillips HE, McGahan JP. Ovarian remnant syndrome. Radiology. 1982;142(2):487-488.
43. Fleischer AC, Tait D, Mayo J, et al. Sonographic features of ovarian remnants. J Ultrasound Med. 1998;17(9):551-555.
44. Wiser A, Levron J, Kreizer D, et al. Outcome of pregnancies complicated by severe ovarian hyperstimulation syndrome (OHSS): a follow-up beyond the second trimester. Hum Reprod. 2005;20(4):910-914.
45. Foulk RA, Martin MC, Jerkins GL, Laros RK. Hyperreactio luteinalis differentiated from severe ovarian hyperstimulation syndrome in a spontaneously conceived pregnancy. Am J Obstet Gynecol. 1997;176(6): 1300-1302.
46. Golan A, Ron-el R, Herman A, et al. Ovarian hyperstimulation syndrome: an update review. Obstet Gynecol Surv. 1989;44(6):430-440.
47. Lazarus E, Hulka C, Siewert B, Levine D. Sonographic appearance of early complete molar pregnancies. J Ultrasound Med. 1999;18(9):589-594.
48. Manganiello PD, Adams LV, Harris RD, Ornvold K. Virilization during pregnancy with spontaneous resolution postpartum: a case report and review of the English literature. Obstet Gynecol Surv. 1995;50(5):404-410.
49. Choi JR, Levine D, Finberg H. Luteoma of pregnancy: sonographic findings in two cases. J Ultrasound Med. 2000;19(12):877-881.
50. Kurman RJ, editor. Blaustein's pathology of the female genital tract. 5th ed. New York: Springer-Verlag; 2002.
51. Kiseli M, Caglar GS, Cengiz SD, et al. Clinical diagnosis and complications of paratubal cysts: review of the literature and report of uncommon presentations. Arch Gynecol Obstet. 2012;285(6):1563-1569.
52. Athey PA, Cooper NB. Sonographic features of parovarian cysts. AJR Am J Roentgenol. 1985;144(1):83-86.
53. Alpern MB, Sandler MA, Madrazo BL. Sonographic features of parovarian cysts and their complications. AJR Am J Roentgenol. 1984;143(1): 157-160.
54. Stein AL, Koonings PP, Schlaerth JB, et al. Relative frequency of malignant parovarian tumors: should parovarian tumors be aspirated? Obstet Gynecol. 1990;75(6):1029-1031.
55. Kim JS, Woo SK, Suh SJ, Morettin LB. Sonographic diagnosis of paraovarian cysts: value of detecting a separate ipsilateral ovary. AJR Am J Roentgenol. 1995;164(6):1441-1444.
56. Honoré LH, O'Hara KE. Serous papillary neoplasms arising in paramesonephric parovarian cysts. A report of eight cases. Acta Obstet Gynecol Scand. 1980;59(6):525-528.
57. Genadry R, Parmley T, Woodruff JD. The origin and clinical behavior of the parovarian tumor. Am J Obstet Gynecol. 1977;129(8):873-880.
58. Savelli L, Ghi T, De Iaco P, et al. Paraovarian/paratubal cysts: comparison of transvaginal sonographic and pathological findings to establish diagnostic criteria. Ultrasound Obstet Gynecol. 2006;28(3):330-334.
59. Hoffer FA, Kozakewich H, Colodny A, Goldstein DP. Peritoneal inclusion cysts: ovarian fluid in peritoneal adhesions. Radiology. 1988;169(1): 189-191.
60. Sohaey R, Gardner TL, Woodward PJ, Peterson CM. Sonographic diagnosis of peritoneal inclusion cysts. J Ultrasound Med. 1995;14(12):913-917.
61. Kim JS, Lee HJ, Woo SK, Lee TS. Peritoneal inclusion cysts and their relationship to the ovaries: evaluation with sonography. Radiology. 1997;204(2):481-484.
62. Jain KA. Imaging of peritoneal inclusion cysts. AJR Am J Roentgenol. 2000;174(6):1559-1563.
63. Savelli L, de Iaco P, Ghi T, et al. Transvaginal sonographic appearance of peritoneal pseudocysts. Ultrasound Obstet Gynecol. 2004;23(3):284-288.
64. Ross MJ, Welch WR, Scully RE. Multilocular peritoneal inclusion cysts (so-called cystic mesotheliomas). Cancer. 1989;64(6):1336-1346.
65. Balen AH, Tan SL, Jacobs HS. Hypersecretion of luteinising hormone: a significant cause of infertility and miscarriage. Br J Obstet Gynaecol. 1993;100(12):1082-1089.
66. Eden JA, Warren P. A review of 1019 consecutive cases of polycystic ovary syndrome demonstrated by ultrasound. Australas Radiol. 1999;43(1): 41-46.
67. Yeh HC, Futterweit W, Thornton JC. Polycystic ovarian disease: US features in 104 patients. Radiology. 1987;163(1):111-116.
68. Hann LE, Hall DA, McArdle CR, Seibel M. Polycystic ovarian disease: sonographic spectrum. Radiology. 1984;150(2):531-534.
69. Pache TD, Wladimiroff JW, Hop WC, Fauser BC. How to discriminate between normal and polycystic ovaries: transvaginal US study. Radiology. 1992;183(2):421-423.
70. Ardaens Y, Robert Y, Lemaitre L, et al. Polycystic ovarian disease: contribution of vaginal endosonography and reassessment of ultrasonic diagnosis. Fertil Steril. 1991;55(6):1062-1068.
71. Battaglia C, Regnani G, Petraglia F, et al. Polycystic ovary syndrome: it is always bilateral? Ultrasound Obstet Gynecol. 1999;14(3):183-187.
72. Jonard S, Robert Y, Dewailly D. Revisiting the ovarian volume as a diagnostic criterion for polycystic ovaries. Hum Reprod. 2005;20(10):2893-2898.
73. Balen AH, Laven JS, Tan SL, Dewailly D. Ultrasound assessment of the polycystic ovary: international consensus definitions. Hum Reprod Update. 2003;9(6):505-514.
74. Lujan ME, Jarrett BY, Brooks ED, et al. Updated ultrasound criteria for polycystic ovary syndrome: reliable thresholds for elevated follicle population and ovarian volume. Hum Reprod. 2013;28(5):1361-1368.
75. Christ JP, Willis AD, Brooks ED, et al. Follicle number, not assessments of the ovarian stroma, represents the best ultrasonographic marker of polycystic ovary syndrome. Fertil Steril. 2014;101(1):280-287.
76. Giudice LC. Clinical practice. Endometriosis. N Engl J Med. 2010;362(25):2389-2398.
77. Nnoaham KE, Hummelshoj L, Webster P, et al. Impact of endometriosis on quality of life and work productivity: a multicenter study across ten countries. Fertil Steril. 2011;96(2):366-373.e8.
78. Koninckx PR, Meuleman C, Demeyere S, et al. Suggestive evidence that pelvic endometriosis is a progressive disease, whereas deeply infiltrating endometriosis is associated with pelvic pain. Fertil Steril. 1991;55(4): 759-765.
79. Asch E, Levine D. Variations in appearance of endometriomas. J Ultrasound Med. 2007;26(8):993-1002.
80. Kupfer MC, Schwimer SR, Lebovic J. Transvaginal sonographic appearance of endometriomata: spectrum of findings. J Ultrasound Med. 1992;11(4):129-133.
81. Patel MD, Feldstein VA, Chen DC, et al. Endometriomas: diagnostic performance of US. Radiology. 1999;210(3):739-745.
82. Dogan MM, Ugur M, Soysal SK, et al. Transvaginal sonographic diagnosis of ovarian endometrioma. Int J Gynaecol Obstet. 1996;52(2):145-149.
83. Guerriero S, Ajossa S, Mais V, et al. The diagnosis of endometriomas using colour Doppler energy imaging. Hum Reprod. 1998;13(6):1691-1695.
84. Sammour RN, Leibovitz Z, Shapiro I, et al. Decidualization of ovarian endometriosis during pregnancy mimicking malignancy. J Ultrasound Med. 2005;24(9):1289-1294.
85. Fruscella E, Testa AC, Ferrandina G, et al. Sonographic features of decidualized ovarian endometriosis suspicious for malignancy. Ultrasound Obstet Gynecol. 2004;24(5):578-580.
86. Jain KA. Endometrioma with calcification simulating a dermoid on sonography. J Ultrasound Med. 2006;25(9):1237-1241.
87. Lalwani N, Shanbhogue AK, Vikram R, et al. Current update on borderline ovarian neoplasms. AJR Am J Roentgenol. 2010;194(2):330-336.
88. Van Holsbeke C, Van Calster B, Guerriero S, et al. Endometriomas: their ultrasound characteristics. Ultrasound Obstet Gynecol. 2010;35(6): 730-740.

89. Guerriero S, Ajossa S, Garau N, et al. Diagnosis of pelvic adhesions in patients with endometrioma: the role of transvaginal ultrasonography. Fertil Steril. 2010;94(2):742-746.
90. Holland TK, Yazbek J, Cutner A, et al. Value of transvaginal ultrasound in assessing severity of pelvic endometriosis. Ultrasound Obstet Gynecol. 2010;36(2):241-248.
91. Hudelist G, Fritzer N, Staettner S, et al. Uterine sliding sign: a simple sonographic predictor for presence of deep infiltrating endometriosis of the rectum. Ultrasound Obstet Gynecol. 2013;41(6):692-695.
92. Reid S, Lu C, Casikar I, et al. Prediction of pouch of Douglas obliteration in women with suspected endometriosis using a new real-time dynamic transvaginal ultrasound technique: the sliding sign. Ultrasound Obstet Gynecol. 2013;41(6):685-691.
93. Chapron C, Fauconnier A, Vieira M, et al. Anatomical distribution of deeply infiltrating endometriosis: surgical implications and proposition for a classification. Hum Reprod. 2003;18(1):157-161.
94. Piketty M, Chopin N, Dousset B, et al. Preoperative work-up for patients with deeply infiltrating endometriosis: transvaginal ultrasonography must definitely be the first-line imaging examination. Hum Reprod. 2009;24(3):602-607.
95. Hudelist G, Ballard K, English J, et al. Transvaginal sonography vs. clinical examination in the preoperative diagnosis of deep infiltrating endometriosis. Ultrasound Obstet Gynecol. 2011;37(4):480-487.
96. Vimercati A, Achilarre MT, Scardapane A, et al. Accuracy of transvaginal sonography and contrast-enhanced magnetic resonance-colonography for the presurgical staging of deep infiltrating endometriosis. Ultrasound Obstet Gynecol. 2012;40(5):592-603.
97. Holland TK, Cutner A, Saridogan E, et al. Ultrasound mapping of pelvic endometriosis: does the location and number of lesions affect the diagnostic accuracy? A multicentre diagnostic accuracy study. BMC Womens Health. 2013;13:43.
98. Hibbard LT. Adnexal torsion. Am J Obstet Gynecol. 1985;152(4):456-461.
99. Burnett LS. Gynecologic causes of the acute abdomen. Surg Clin North Am. 1988;68(2):385-398.
100. Lee CH, Raman S, Sivanesaratnam V. Torsion of ovarian tumors: a clinicopathological study. Int J Gynaecol Obstet. 1989;28(1):21-25.
101. Warner MA, Fleischer AC, Edell SL, et al. Uterine adnexal torsion: sonographic findings. Radiology. 1985;154(3):773-775.
102. Sommerville M, Grimes DA, Koonings PP, Campbell K. Ovarian neoplasms and the risk of adnexal torsion. Am J Obstet Gynecol. 1991;164(2):577-578.
103. Cappell MS, Friedel D. Abdominal pain during pregnancy. Gastroenterol Clin North Am. 2003;32(1):1-58.
104. Bertolotto M, Serafini G, Tomà P, et al. Adnexal torsion. Ultrasound Clin. 2008;3(1):109-119.
105. Graif M, Itzchak Y. Sonographic evaluation of ovarian torsion in childhood and adolescence. AJR Am J Roentgenol. 1988;150(3):647-649.
106. Graif M, Shalev J, Strauss S, et al. Torsion of the ovary: sonographic features. AJR Am J Roentgenol. 1984;143(6):1331-1334.
107. Albayram F, Hamper UM. Ovarian and adnexal torsion: spectrum of sonographic findings with pathologic correlation. J Ultrasound Med. 2001;20(10):1083-1089.
108. Fleischer AC, Stein SM, Cullinan JA, Warner MA. Color Doppler sonography of adnexal torsion. J Ultrasound Med. 1995;14(7):523-528.
109. Rosado Jr WM, Trambert MA, Gosink BB, Pretorius DH. Adnexal torsion: diagnosis by using Doppler sonography. AJR Am J Roentgenol. 1992;159(6):1251-1253.
110. Lee EJ, Kwon HC, Joo HJ, et al. Diagnosis of ovarian torsion with color Doppler sonography: depiction of twisted vascular pedicle. J Ultrasound Med. 1998;17(2):83-89.
111. Vijayaraghavan SB. Sonographic whirlpool sign in ovarian torsion. J Ultrasound Med. 2004;23(12):1643-1649.
112. Chang HC, Bhatt S, Dogra VS. Pearls and pitfalls in diagnosis of ovarian torsion. Radiographics. 2008;28(5):1355-1368.
113. Kapadia R, Sternhill V, Schwartz E. Massive edema of the ovary. J Clin Ultrasound. 1982;10(9):469-471.
114. Lee AR, Kim KH, Lee BH, Chin SY. Massive edema of the ovary: imaging findings. AJR Am J Roentgenol. 1993;161(2):343-344.
115. Hill LM, Pelekanos M, Kanbour A. Massive edema of an ovary previously fixed to the pelvic side wall. J Ultrasound Med. 1993;12(10):629-632.
116. Shadinger LL, Andreotti RF, Kurian RL. Preoperative sonographic and clinical characteristics as predictors of ovarian torsion. J Ultrasound Med. 2008;27(1):7-13.
117. American Cancer Society. Cancer facts & figures 2014. Atlanta: American Cancer Society; 2014. Available from: http://www.cancer.org/acs/groups/content/@research/documents/webcontent/acspc-042151.pdf.
118. American Cancer Society. Cancer facts and figures. New York: American Cancer Society; 2008.
119. Kerlikowske K, Brown JS, Grady DG. Should women with familial ovarian cancer undergo prophylactic oophorectomy? Obstet Gynecol. 1992;80(4):700-707.
120. Lynch HT, Watson P, Lynch JF, et al. Hereditary ovarian cancer. Heterogeneity in age at onset. Cancer. 1993;71(2 Suppl.):573-581.
121. Jacobs I, Davies AP, Bridges J, et al. Prevalence screening for ovarian cancer in postmenopausal women by CA 125 measurement and ultrasonography. BMJ. 1993;306(6884):1030-1034.
122. DePriest PD, Gallion HH, Pavlik EJ, et al. Transvaginal sonography as a screening method for the detection of early ovarian cancer. Gynecol Oncol. 1997;65(3):408-414.
123. Kurjak A, Shalan H, Kupesic S, et al. An attempt to screen asymptomatic women for ovarian and endometrial cancer with transvaginal color and pulsed Doppler sonography. J Ultrasound Med. 1994;13(4):295-301.
124. Bourne TH, Campbell S, Reynolds KM, et al. Screening for early familial ovarian cancer with transvaginal ultrasonography and colour blood flow imaging. BMJ. 1993;306(6884):1025-1029.
125. Karlan BY, Raffel LJ, Crvenkovic G, et al. A multidisciplinary approach to the early detection of ovarian carcinoma: rationale, protocol design, and early results. Am J Obstet Gynecol. 1993;169(3):494-501.
126. Weiner Z, Beck D, Shteiner M, et al. Screening for ovarian cancer in women with breast cancer with transvaginal sonography and color flow imaging. J Ultrasound Med. 1993;12(7):387-393.
127. Bast Jr RC, Klug TL, St John E, et al. A radioimmunoassay using a monoclonal antibody to monitor the course of epithelial ovarian cancer. N Engl J Med. 1983;309(15):883-887.
128. Jacobs I, Bast Jr RC. The CA 125 tumour-associated antigen: a review of the literature. Hum Reprod. 1989;4(1):1-12.
129. NIH consensus conference. Ovarian cancer. Screening, treatment, and follow-up. NIH Consensus Development Panel on Ovarian Cancer. JAMA. 1995;273(6):491-497.
130. Menon U, Griffin M, Gentry-Maharaj A. Ovarian cancer screening—current status, future directions. Gynecol Oncol. 2014;132(2):490-495.
131. Moyle JW, Rochester D, Sider L, et al. Sonography of ovarian tumors: predictability of tumor type. AJR Am J Roentgenol. 1983;141(5):985-991.
132. Granberg S, Wikland M, Jansson I. Macroscopic characterization of ovarian tumors and the relation to the histological diagnosis: criteria to be used for ultrasound evaluation. Gynecol Oncol. 1989;35(2):139-144.
133. Valentin L. Prospective cross-validation of Doppler ultrasound examination and gray-scale ultrasound imaging for discrimination of benign and malignant pelvic masses. Ultrasound Obstet Gynecol. 1999;14(4):273-283.
134. Timmerman D, Schwarzler P, Collins WP, et al. Subjective assessment of adnexal masses with the use of ultrasonography: an analysis of interobserver variability and experience. Ultrasound Obstet Gynecol. 1999;13(1):11-16.
135. Valentin L, Ameye L, Jurkovic D, et al. Which extrauterine pelvic masses are difficult to correctly classify as benign or malignant on the basis of ultrasound findings and is there a way of making a correct diagnosis? Ultrasound Obstet Gynecol. 2006;27(4):438-444.
136. Folkman J, Watson K, Ingber D, Hanahan D. Induction of angiogenesis during the transition from hyperplasia to neoplasia. Nature. 1989;339(6219):58-61.
137. Brown DL, Frates MC, Laing FC, et al. Ovarian masses: can benign and malignant lesions be differentiated with color and pulsed Doppler US? Radiology. 1994;190(2):333-336.

138. Stein SM, Laifer-Narin S, Johnson MB, et al. Differentiation of benign and malignant adnexal masses: relative value of gray-scale, color Doppler, and spectral Doppler sonography. AJR Am J Roentgenol. 1995;164(2): 381-386.
139. Jain KA. Prospective evaluation of adnexal masses with endovaginal gray-scale and duplex and color Doppler US: correlation with pathologic findings. Radiology. 1994;191(1):63-67.
140. Levine D, Feldstein VA, Babcook CJ, Filly RA. Sonography of ovarian masses: poor sensitivity of resistive index for identifying malignant lesions. AJR Am J Roentgenol. 1994;162(6):1355-1359.
141. Salem S, White LM, Lai J. Doppler sonography of adnexal masses: the predictive value of the pulsatility index in benign and malignant disease. AJR Am J Roentgenol. 1994;163(5):1147-1150.
142. Buy JN, Ghossain MA, Hugol D, et al. Characterization of adnexal masses: combination of color Doppler and conventional sonography compared with spectral Doppler analysis alone and conventional sonography alone. AJR Am J Roentgenol. 1996;166(2):385-393.
143. Fleischer AC, Jones HW 3rd. Color Doppler sonography of ovarian masses: the importance of a multiparameter approach. Gynecol Oncol. 1993;50(1):1-2.
144. Guerriero S, Alcazar JL, Coccia ME, et al. Complex pelvic mass as a target of evaluation of vessel distribution by color Doppler sonography for the diagnosis of adnexal malignancies: results of a multicenter European study. J Ultrasound Med. 2002;21(10):1105-1111.
145. Bromley B, Goodman H, Benacerraf BR. Comparison between sonographic morphology and Doppler waveform for the diagnosis of ovarian malignancy. Obstet Gynecol. 1994;83(3):434-437.
146. Carter J, Saltzman A, Hartenbach E, et al. Flow characteristics in benign and malignant gynecologic tumors using transvaginal color flow Doppler. Obstet Gynecol. 1994;83(1):125-130.
147. Reles A, Wein U, Lichtenegger W. Transvaginal color Doppler sonography and conventional sonography in the preoperative assessment of adnexal masses. J Clin Ultrasound. 1997;25(5):217-225.
148. Fleischer AC, Cullinan JA, Kepple DM, Williams LL. Conventional and color Doppler transvaginal sonography of pelvic masses: a comparison of relative histologic specificities. J Ultrasound Med. 1993;12(12):705-712.
149. Brown DL, Doubilet PM, Miller FH, et al. Benign and malignant ovarian masses: selection of the most discriminating gray-scale and Doppler sonographic features. Radiology. 1998;208(1):103-110.
150. Schelling M, Braun M, Kuhn W, et al. Combined transvaginal B-mode and color Doppler sonography for differential diagnosis of ovarian tumors: results of a multivariate logistic regression analysis. Gynecol Oncol. 2000;77(1):78-86.
151. Kinkel K, Hricak H, Lu Y, et al. US characterization of ovarian masses: a meta-analysis. Radiology. 2000;217(3):803-811.
152. Laing FC. US analysis of adnexal masses: the art of making the correct diagnosis. Radiology. 1994;191(1):21-22.
153. Fleischer AC, Lyshchik A, Hirari M, et al. Early detection of ovarian cancer with conventional and contrast-enhanced transvaginal sonography: recent advances and potential improvements. J Oncol. 2012;2012:302858.
154. Kurman RJ, Shih IeM. The origin and pathogenesis of epithelial ovarian cancer: a proposed unifying theory. Am J Surg Pathol. 2010;34(3): 433-443.
155. Moss EL, Evans T, Pearmain P, et al. Should all cases of high-grade serous ovarian, tubal, and primary peritoneal carcinomas be reclassified as tubo-ovarian serous carcinoma? Int J Gynecol Cancer. 2015;25(7):1201-1207.
156. Wagner BJ, Buck JL, Seidman JD, McCabe KM. From the archives of the AFIP. Ovarian epithelial neoplasms: radiologic-pathologic correlation. Radiographics. 1994;14(6):1351-1374.
157. Alfuhaid TR, Rosen BP, Wilson SR. Low-malignant-potential tumor of the ovary: sonographic features with clinicopathologic correlation in 41 patients. Ultrasound Q. 2003;19(1):13-26.
158. Yazbek J, Raju KS, Ben-Nagi J, et al. Accuracy of ultrasound subjective 'pattern recognition' for the diagnosis of borderline ovarian tumors. Ultrasound Obstet Gynecol. 2007;29(5):489-495.
159. Yazbek J, Aslam N, Tailor A, et al. A comparative study of the risk of malignancy index and the ovarian crescent sign for the diagnosis of invasive ovarian cancer. Ultrasound Obstet Gynecol. 2006;28(3):320-324.
160. Van Holsbeke C, Van Belle V, Leone FP, et al. Prospective external validation of the 'ovarian crescent sign' as a single ultrasound parameter to distinguish between benign and malignant adnexal pathology. Ultrasound Obstet Gynecol. 2010;36(1):81-87.
161. Athey PA, Siegel MF. Sonographic features of Brenner tumor of the ovary. J Ultrasound Med. 1987;6(7):367-372.
162. Green GE, Mortele KJ, Glickman JN, Benson CB. Brenner tumors of the ovary: sonographic and computed tomographic imaging features. J Ultrasound Med. 2006;25(10):1245-1251.
163. Brammer HM 3rd, Buck JL, Hayes WS, et al. From the archives of the AFIP. Malignant germ cell tumors of the ovary: radiologic-pathologic correlation. Radiographics. 1990;10(4):715-724.
164. Quinn SF, Erickson S, Black WC. Cystic ovarian teratomas: the sonographic appearance of the dermoid plug. Radiology. 1985;155(2):477-478.
165. Sheth S, Fishman EK, Buck JL, et al. The variable sonographic appearances of ovarian teratomas: correlation with CT. AJR Am J Roentgenol. 1988;151(2):331-334.
166. Guttman Jr PH. In search of the elusive benign cystic ovarian teratoma: application of the ultrasound "tip of the iceberg" sign. J Clin Ultrasound. 1977;5(6):403-406.
167. Bronshtein M, Yoffe N, Brandes JM, Blumenfeld Z. Hair as a sonographic marker of ovarian teratomas: improved identification using transvaginal sonography and simulation model. J Clin Ultrasound. 1991;19(6): 351-355.
168. Malde HM, Kedar RP, Chadha D, Nayak S. Dermoid mesh: a sonographic sign of ovarian teratoma. AJR Am J Roentgenol. 1992;159(6):1349-1350.
169. Kim HC, Kim SH, Lee HJ, et al. Fluid-fluid levels in ovarian teratomas. Abdom Imaging. 2002;27(1):100-105.
170. Kawamoto S, Sato K, Matsumoto H, et al. Multiple mobile spherules in mature cystic teratoma of the ovary. AJR Am J Roentgenol. 2001;176(6): 1455-1457.
171. Patel MD, Feldstein VA, Lipson SD, et al. Cystic teratomas of the ovary: diagnostic value of sonography. AJR Am J Roentgenol. 1998;171(4): 1061-1065.
172. Hertzberg BS, Kliewer MA. Sonography of benign cystic teratoma of the ovary: pitfalls in diagnosis. AJR Am J Roentgenol. 1996;167(5): 1127-1133.
173. Zalel Y, Caspi B, Tepper R. Doppler flow characteristics of dermoid cysts: unique appearance of struma ovarii. J Ultrasound Med. 1997;16(5): 355-358.
174. O'Malley BP, Richmond H. Struma ovarii. J Ultrasound Med. 1982;1(4): 177-178.
175. Tanaka YO, Kurosaki Y, Nishida M, et al. Ovarian dysgerminoma: MR and CT appearance. J Comput Assist Tomogr. 1994;18(3):443-448.
176. Kim SH, Kang SB. Ovarian dysgerminoma: color Doppler ultrasonographic findings and comparison with CT and MR imaging findings. J Ultrasound Med. 1995;14(11):843-848.
177. Ko SF, Wan YL, Ng SH, et al. Adult ovarian granulosa cell tumors: spectrum of sonographic and CT findings with pathologic correlation. AJR Am J Roentgenol. 1999;172(5):1227-1233.
178. Outwater EK, Wagner BJ, Mannion C, et al. Sex cord-stromal and steroid cell tumors of the ovary. Radiographics. 1998;18(6):1523-1546.
179. Stephenson WM, Laing FC. Sonography of ovarian fibromas. AJR Am J Roentgenol. 1985;144(6):1239-1240.
180. Athey PA, Malone RS. Sonography of ovarian fibromas/thecomas. J Ultrasound Med. 1987;6(8):431-436.
181. Athey PA, Butters HE. Sonographic and CT appearance of Krukenberg tumors. J Clin Ultrasound. 1984;12(4):205-210.
182. Shimizu H, Yamasaki M, Ohama K, et al. Characteristic ultrasonographic appearance of the Krukenberg tumor. J Clin Ultrasound. 1990;18(9): 697-703.
183. Testa AC, Ferrandina G, Timmerman D, et al. Imaging in gynecological disease (1): ultrasound features of metastases in the ovaries differ depending on the origin of the primary tumor. Ultrasound Obstet Gynecol. 2007;29(5): 505-511.
184. Timor-Tritsch IE, Rottem S. Transvaginal ultrasonographic study of the fallopian tube. Obstet Gynecol. 1987;70(3 Pt 1):424-428.

185. Workowski KA, Berman S. Centers for Disease Control and Prevention. Sexually transmitted disease treatment guidelines, 2010. MMWR Recomm Rep. 2010;59(RR-12):1-116.
186. Patten RM, Vincent LM, Wolner-Hanssen P, Thorpe Jr E. Pelvic inflammatory disease. Endovaginal sonography with laparoscopic correlation. J Ultrasound Med. 1990;9(12):681-689.
187. Taipale P, Tarjanne H, Ylostalo P. Transvaginal sonography in suspected pelvic inflammatory disease. Ultrasound Obstet Gynecol. 1995;6(6): 430-434.
188. Timor-Tritsch IE, Lerner JP, Monteagudo A, et al. Transvaginal sonographic markers of tubal inflammatory disease. Ultrasound Obstet Gynecol. 1998;12(1):56-66.
189. Molander P, Sjoberg J, Paavonen J, Cacciatore B. Transvaginal power Doppler findings in laparoscopically proven acute pelvic inflammatory disease. Ultrasound Obstet Gynecol. 2001;17(3):233-238.
190. Tessler FN, Perrella RR, Fleischer AC, Grant EG. Endovaginal sonographic diagnosis of dilated fallopian tubes. AJR Am J Roentgenol. 1989;153(3): 523-525.
191. Patel MD, Acord DL, Young SW. Likelihood ratio of sonographic findings in discriminating hydrosalpinx from other adnexal masses. AJR Am J Roentgenol. 2006;186(4):1033-1038.
192. Romosan G, Valentin L. The sensitivity and specificity of transvaginal ultrasound with regard to acute pelvic inflammatory disease: a review of the literature. Arch Gynecol Obstet. 2014;289(4):705-714.
193. Bulas DI, Ahlstrom PA, Sivit CJ, et al. Pelvic inflammatory disease in the adolescent: comparison of transabdominal and transvaginal sonographic evaluation. Radiology. 1992;183(2):435-439.
194. Goharkhay N, Verma U, Maggiorotto F. Comparison of CT- or ultrasound-guided drainage with concomitant intravenous antibiotics vs. intravenous antibiotics alone in the management of tubo-ovarian abscesses. Ultrasound Obstet Gynecol. 2007;29(1):65-69.
195. Sherer DM, Liberto L, Abramowicz JS, Woods Jr JR. Endovaginal sonographic features associated with isolated torsion of the fallopian tube. J Ultrasound Med. 1991;10(2):107-109.
196. Russin LD. Hydrosalpinx and tubal torsion: a late complication of tubal ligation. Radiology. 1986;159(1):115-116.
197. Subramanyam BR, Raghavendra BN, Whalen CA, Yee J. Ultrasonic features of fallopian tube carcinoma. J Ultrasound Med. 1984;3(9): 391-393.
198. Ajjimakorn S, Bhamarapravati Y. Transvaginal ultrasound and the diagnosis of fallopian tubal carcinoma. J Clin Ultrasound. 1991;19(2):116-119.
199. Slanetz PJ, Whitman GJ, Halpern EF, et al. Imaging of fallopian tube tumors. AJR Am J Roentgenol. 1997;169(5):1321-1324.
200. Kurjak A, Kupesic S, Ilijas M, et al. Preoperative diagnosis of primary fallopian tube carcinoma. Gynecol Oncol. 1998;68(1):29-34.
201. Patlas M, Rosen B, Chapman W, Wilson SR. Sonographic diagnosis of primary malignant tumors of the fallopian tube. Ultrasound Q. 2004;20(2):59-64.
202. Wilson PC, Lerner RM. Diagnosis of ovarian vein thrombophlebitis by ultrasonography. J Ultrasound Med. 1983;2(4):187-190.
203. Savader SJ, Otero RR, Savader BL. Puerperal ovarian vein thrombosis: evaluation with CT, US, and MR imaging. Radiology. 1988;167(3): 637-639.
204. Grant TH, Schoettle BW, Buchsbaum MS. Postpartum ovarian vein thrombosis: diagnosis by clot protrusion into the inferior vena cava at sonography. AJR Am J Roentgenol. 1993;160(3):551-552.
205. Baran GW, Frisch KM. Duplex Doppler evaluation of puerperal ovarian vein thrombosis. AJR Am J Roentgenol. 1987;149(2):321-322.
206. Giacchetto C, Catizone F, Cotroneo GB, et al. Radiologic anatomy of the genital venous system in female patients with varicocele. Surg Gynecol Obstet. 1989;169(5):403-407.
207. Ghosh E, Levine D. Recommendations for adnexal cysts: have the Society of Radiologists in Ultrasound consensus conference guidelines affected utilization of ultrasound? Ultrasound Q. 2013;29(1):21-24.
208. Rosenkrantz AB, Kierans AS. US of incidental adnexal cysts: adherence of radiologists to the 2010 Society of Radiologists in Ultrasound guidelines. Radiology. 2014;271(1):262-271.
209. Timmerman D, Valentin L, Bourne TH, et al. Terms, definitions and measurements to describe the sonographic features of adnexal tumors: a consensus opinion from the International Ovarian Tumor Analysis (IOTA) Group. Ultrasound Obstet Gynecol. 2000;16(5):500-505.
210. Timmerman D, Testa AC, Bourne T, et al. Simple ultrasound-based rules for the diagnosis of ovarian cancer. Ultrasound Obstet Gynecol. 2008;31(6):681-690.
211. Wicks JD, Silver TM, Bree RL. Gray scale features of hematomas: an ultrasonic spectrum. AJR Am J Roentgenol. 1978;131(6):977-980.
212. Salem S, O'Malley BP, Hiltz CW. Ultrasonographic appearance of gastrointestinal masses. J Can Assoc Radiol. 1980;31(3):163-167.

CHAPTER 17

Ultrasound-Guided Biopsy of Chest, Abdomen, and Pelvis

Theodora A. Potretzke, Thomas D. Atwell, J. William Charboneau, and Carl Reading

SUMMARY OF KEY POINTS

- Ultrasound is a key method of guidance for biopsy and fluid drainage because of its real-time needle visualization and the ability to image and intervene in multiple anatomic locations and planes.
- Effective periprocedural antithrombotic management requires an understanding of specific antithrombotic agents as well as the balance of the potential risk of hemorrhage from a given procedure versus the risk of a thrombotic event if a blood thinner is discontinued.
- Ultrasound typically offers excellent guidance for superficial biopsies, paracentesis, thoracentesis, and most solid organ biopsies in the abdomen including liver, kidney, and spleen. CT guidance is often utilized for adrenal, retroperitoneal, and certain deep pelvic biopsies or deep drain placement.
- Familiarity with both trocar and Seldinger techniques is useful for ultrasound-guided drain placement.

CHAPTER OUTLINE

PERCUTANEOUS NEEDLE BIOPSY
Indications and Contraindications
Periprocedural Antithrombotic Management
Imaging Methods
Ultrasound
Computed Tomography
Needle Selection
Biopsy Procedure
Needle Visualization
Specific Anatomic Applications
Liver
Pancreas
Kidney
Adrenal Gland
Spleen
Lung
Complications
ULTRASOUND-GUIDED DRAINAGE
Indications and Contraindications
Imaging Methods
Catheter Selection
Patient Preparation
Diagnostic Aspiration
Catheter Placement
Drainage Procedure
Follow-Up Care
Catheter Removal
Abdominal and Pelvic Abscesses: General
Specific Anatomic Applications
Liver
Biliary Tract
Pancreas
Spleen
Kidney
PERCUTANEOUS CYST MANAGEMENT
Renal Cyst
Liver Cyst
Ovarian Cyst

Percutaneous biopsy and fluid drainage are invaluable diagnostic and therapeutic procedures for the management of patients. Ultrasound is a central method of guidance for these interventional techniques because it allows real-time needle visualization and the ability to image and intervene in multiple anatomic locations and planes. An approach to this topic requires knowledge of the current fundamental methods and applications of these procedures in general and in terms of specific anatomic locations.

PERCUTANEOUS NEEDLE BIOPSY

Because of its relatively low cost and wide availability, ultrasound-guided biopsy has become one of the most important methods of tissue diagnosis in radiology practices worldwide. Ultrasound-guided biopsy is a safe and accurate technique for confirmation of suspected malignant masses and characterization of benign lesions in locations throughout the body.[1,2] In addition, minimally invasive tissue confirmation decreases patient costs by obviating the need for a surgical diagnosis and decreasing duration of hospital stay and number of ancillary diagnostic tests. In addition, lack of ionizing radiation and real-time imaging during the procedure make the procedure safer.

Indications and Contraindications

In most cases a biopsy is performed in the setting of possible malignancy, for either initial diagnosis of cancer, confirmation of metastatic disease, or to obtain tissue for molecular profiling and targeted treatment planning. In other patients, biopsy is performed to gauge the presence of parenchymal disease in a

native organ or rejection in a transplanted organ. Occasionally, biopsy is indicated simply to determine the nature of an incidentally discovered mass.

Relative contraindications to percutaneous needle biopsy include severe uncorrectable coagulopathy, lack of a safe biopsy route, and an uncooperative patient. To assess for inherent **coagulopathy,** the most valuable information comes from the patient history,[3] including bleeding tendency or need for transfusion or a family history of bleeding diathesis. Patient medications should also be reviewed for recent use of antithrombotic agents.

The second relative contraindication is the **lack of a safe biopsy route.** A biopsy path extending through large vessels such as the splenic or extrahepatic portal vein increases the risk of hemorrhage. A biopsy path free of overlying stomach or bowel is also a preferable route, although such biopsies have been safely performed using smaller (21-gauge) needles.[4] Biopsies performed through ascites have also proved to be safe, although drainage of ascites prior to biopsy may increase target accessibility.[5,6]

The third relative contraindication to needle biopsy is an **uncooperative patient** in whom uncontrolled motion during needle placement increases the risk of unanticipated injury and hemorrhage. This is a particularly common problem in pediatric patients, and deeper sedation may be required.

Periprocedural Antithrombotic Management

An effective approach to the management of **periprocedural antithrombotics** depends on an understanding of the balance of hemorrhagic and thrombotic complications. That is, the potential risk of hemorrhage from biopsy or drainage in a patient on an antithrombotic agent versus the risk in that same patient of a thrombotic event if a blood thinner is discontinued. Significant thromboembolic events, including myocardial infarction and ischemic stroke, have been shown to occur in 1% to 4% of select patients in whom aspirin or warfarin is withheld without bridging therapy.[7-11] Although decisions on periprocedural antithrombotic management are best made in collaboration with the referring clinician, the performing radiologist typically makes the ultimate judgment of whether and when to perform a procedure for a patient on an antithrombotic agent. It is therefore important for the radiologist to have a general knowledge of common anticoagulants and antiplatelet agents as well as the bleeding risks associated with certain procedures. However, any withdrawal of a therapeutic agent should be deferred to the ordering clinical provider, often following a discussion with the radiologist regarding procedure-specific bleeding risk.

Although helpful institutional and society guidelines have been put forth on the topic of periprocedural antithrombotic management, true consensus and uniformity in practice remain elusive. This is due to the expanding pharmacy of **antiplatelet agents** and **anticoagulation** as well as to evolving literature showing lower bleeding risks for some procedures than previously thought. In general, our own practice has leaned toward liberalizing guidelines; that is, foregoing preprocedural labs in certain patients for lower-risk procedures (superficial biopsies such as thyroid and superficial lymph nodes as well as thoracentesis, paracentesis, and superficial abscess drainage) and performing certain lower-risk procedures, especially if urgent, without discontinuing antithrombotic agents.

The most commonly encountered antithrombotics in both inpatient and outpatient populations are the antiplatelet agents aspirin and clopidogrel (Plavix), the vitamin K antagonist warfarin, and the clotting factor inhibitor heparin (unfractionated or low-molecular-weight). Anticoagulants using other mechanisms such as direct thrombin inhibitors (e.g., dabigatran), direct factor Xa inhibitors (e.g., fondaparinux), and glycoprotein IIb/IIIa inhibitors (e.g., abciximab) are being increasingly utilized and may also be encountered in practice. General familiarity with mechanisms and metabolism of these agents is important for decision making. For example, the direct thrombin inhibitor dabigatran has a half-life of 12 to 14 hours but is excreted by the kidneys; therefore the period of preprocedural discontinuation, if pursued for a nonurgent deep biopsy, should be extended in a patient with renal impairment (6-7 days vs. 4-5 days if normal renal function in our practice).

For low-risk procedures, such as thoracentesis and paracentesis, we have found little impact on bleeding risk from therapeutic anticoagulation or aspirin use. Bleeding complication rates in coagulopathic and thrombocytopenic patients (international normalized ratio [INR] > 1.6 and/or platelets < 50×10^9/L) after thoracentesis or paracentesis are very low (up to 1%).[12-15] Patients often benefit greatly from these procedures. Accordingly, we have eliminated routine complete blood count prior to these procedures for most patients and request warfarin be held only if patient is at low risk for thromboembolic event. If patients will be taking warfarin at the time of the procedure, an INR should be obtained within 24 hours prior to procedure to ensure they are not supratherapeutic. Additional labs may be requested by the radiologist at their discretion, but we have found this is rarely needed. Aspirin may also be continued in our practice for thoracentesis or paracentesis. A similar approach is used for superficial biopsies and superficial drain placement.

Higher-risk procedures include liver and kidney biopsy as well as mesenteric, retroperitoneal, or deep pelvic lymph node biopsy, and deep abscess drainage. Although called "higher risk" this is relative to other procedures, and the true risk of postprocedural bleeding, even for these procedures, is low.

Native renal parenchymal biopsies have the highest risk of postbiopsy bleeding with reported rates of significant bleeding of 0.3% to 6.6%.[16-23] Liver and renal transplant biopsy bleeding rates are generally lower and at our own institution are 0.5% and 0.2%, respectively.[16] If a higher-risk biopsy is nonurgent or elective, aspirin can be held for 5 days beforehand if the risk of thromboembolic event is acceptably low and then restarted at 24 hours after biopsy. However, our clinical experience has shown little if any association of recent aspirin use on significant postprocedural bleeding. In a study of 15,181 percutaneous core biopsies, the incidence of bleeding in patients taking aspirin within 10 days before biopsy was 0.6% and that of patients not taking aspirin was 0.4% ($p = .34$).[24] This study included 585 liver biopsies performed in patients with recent aspirin use with a 0.3% risk of major hemorrhage (not significantly different to the 0.5% in those not taking aspirin). Consequently, we continue to

perform many solid organ biopsies in patients on aspirin and rarely postpone or cancel a biopsy because of aspirin usage. Exceptions to this practice include elective biopsies, especially in a local patient who will be able to easily reschedule the procedure, and in some cases native kidney biopsies that already confer an increased risk of bleeding. The incidence of major hemorrhage after native or transplant renal biopsy in patients taking aspirin was slightly higher when compared to those not taking aspirin (1.0% vs. 0.6%) although this difference was not statistically significant ($p = .08$).[24] For warfarin and heparin, we recommend holding prior to a higher-risk biopsy if possible—5 days for warfarin (to INR ≤ 1.5), 4 hours for therapeutic dose intravenous (IV) unfractionated heparin, 24 hours for therapeutic dose low-molecular-weight heparin, and 12 to 24 hours for prophylactic dose unfractionated or low-molecular-weight heparin.

If the history suggests a bleeding disorder but the patient is not on an antithrombotic agent, prothrombin time (PT), activated partial thromboplastin time (aPTT), and platelet count should be obtained if a higher-risk procedure is planned.[25] The role of bleeding time measurement is of uncertain value in determining bleeding risk; in most cases, no good evidence supports the value of the bleeding time to predict bleeding.[3,26] For core biopsies or drains, platelets greater than 50×10^9/L and an INR of 1.6 or less are the suggested thresholds but biopsy may be pursued even if patients fall outside these parameters at the discretion of the performing radiologist and the referring clinician after weighing the risks and benefits. Data have shown that a platelet count of 50×10^9/L or less is a statistically significant risk factor for major bleeding after liver biopsy (2.2% vs. 0.5% rate of significant bleeding, $p = .04$).[27] Interestingly, in the same study group, no patients with an INR of 1.6 or greater ($n = 43$, range 1.6-1.9) had a significant postbiopsy hemorrhage.[27]

Some coagulopathies can be corrected with the transfusion of appropriate blood products although there is unpredictable impact of this on postprocedural bleeding rates for certain procedures such as thoracentesis.[12] For higher-risk biopsies, however, we continue to believe that there is benefit to transfusing to reach previously mentioned thresholds of platelets greater than 50×10^9/L and INR of 1.6 or less in thrombocytopenic and coagulopathic patients if possible. Desmopressin (DDAVP) can be given to a uremic patient to improve functioning platelet activity.[28] Postbiopsy embolization of the needle track has been reported to control hemorrhage in patients at high risk for bleeding and in whom the need for biopsy outweighs any risk, but it is not routinely performed in our practice.[29,30]

Imaging Methods

Both ultrasound and computed tomography (CT) can be used to guide percutaneous needle intervention. The choice of method depends on multiple factors, including lesion size and location, relative lesion conspicuity on the two modalities, equipment availability, and personal preference.

Ultrasound

Ultrasound has several strengths as a means of guiding percutaneous intervention. It is readily available, relatively inexpensive, and portable. Ultrasound uses no ionizing radiation and can provide guidance in almost any anatomic plane. The greatest advantage, however, is that sonography allows the real-time visualization of the needle tip as it passes through tissue into the target. This allows precise and confident needle placement and avoidance of important intervening structures. In addition, **color Doppler flow imaging** (CDFI) may help prevent complications of needle placement by identifying the vascular nature of a mass and by allowing the clinician to avoid vascular structures lying within the needle path.

Ultrasound guidance can be used for the biopsy of many organs and regions of the body. The technique is optimal for lesions located superficially or at moderate depth in a thin to average-sized person such as the omentum (Video 17.1), as well as for lesions within organs prone to respiratory motion (e.g., liver, kidney) (Video 17.2). In the latter scenario, the advantage of real-time ultrasound-guidance allows continuous visualization of the target during the biopsy. Lesions located within or behind bone or gas-filled bowel cannot be visualized because of near-complete reflection of sound from the bone or air interface.

Theoretically, any mass that is well visualized with ultrasound is amenable to ultrasound-guided needle biopsy. In our practice, most liver and kidney biopsies are performed with ultrasound guidance, as are biopsies of the thyroid and parathyroid glands. Superficial lymph nodes are also particularly well suited to real-time ultrasound-guided biopsy. Occasionally, the pancreas (particularly pancreas transplants) and other sites in the abdomen and pelvis undergo biopsy with ultrasound guidance if lesion visualization is adequate.

Compared with CT, ultrasound-guided procedures require less time to perform and can be more cost-effective.[31-33] Ultrasound-guided biopsy has been shown to be more accurate than CT, with a lower false-negative rate.[32,34]

Computed Tomography

CT is well established as an accurate guidance method for percutaneous biopsy of most regions in the body. It provides excellent spatial resolution of structures between the skin surface and targeted lesion, and it provides an accurate image of the needle tip. In addition, lesions located deep in the abdomen or within bone are better seen with CT than with ultrasound. In our practice, many pelvic, adrenal, pancreatic, retroperitoneal, and bone biopsies are performed with CT guidance because these structures are often best seen with this imaging method.

Historically, CT was limited by its lack of continuous visualization of the needle during insertion and biopsy. In the past decade, CT **fluoroscopy** has allowed real-time visualization of needle positioning. This has reduced the time required for interventional procedures at the cost of increased radiation dosage.[35]

Needle Selection

A variety of needles with a spectrum of calibers, lengths, and tip designs are commercially available for use in percutaneous biopsy. Needle caliber is based on outer diameter, with larger-caliber needles having a lower gauge number. Conceptually, needles can be grouped into small-caliber (20 gauge or smaller) or large-caliber (19 gauge or larger) sizes. **Small-caliber needles**

are traditionally used to obtain cells for cytologic analysis by using a procedure commonly referred to as **fine-needle aspiration** (FNA). However, small pieces of tissue may be obtained for histologic examination as well. With these small-caliber needles, masses behind loops of bowel can be punctured with minimal likelihood of infection.[4] The smaller samples yielded by small-caliber needles are appropriate to confirm tumor recurrence or metastasis in a patient known to have a previous primary malignancy. Even if the sample is small, the pathologist is usually able to make an accurate diagnosis by comparing the biopsy specimen with the original tissue.

Large-caliber needles can be used to obtain greater amounts of tissue for more thorough histologic and cytologic analysis. Larger needles may be necessary to obtain sufficient tissue to diagnose and subtype some types of malignancies (e.g., lymphoma), many benign lesions, and most chronic diffuse parenchymal diseases (e.g., hepatic cirrhosis, renal glomerulonephritis, renal allograft rejection).[36] The large-caliber tissue sample can also be used to generate an additional "touch prep" specimen, whereby the tissue is manually swiped across a glass pathology slide, leaving a cellular sample on the slide for cytologic analysis.[37]

The preference and level of expertise of the pathologist involved in the interpretation of biopsy specimens are considerations in the selection of needle size and type. **Cytopathologists** specialize in the interpretation of cellular samples, rendering a diagnosis based on the cells provided. Unfortunately, some clinical facilities do not offer cytopathologic interpretation. **Histopathologists,** in contrast, often prefer a large biopsy specimen for interpretation. For example, a large biopsy specimen from a metastatic lesion often allows a more reliable prediction of the primary site of the malignancy than a tiny sample or a cytologic aspirate. Determination of the primary site allows the oncologist to tailor subsequent treatment.

Biopsy Procedure

Before any invasive procedure is performed, the procedure, risks, alternatives, and benefits should be explained in terms that the patient can understand so that informed consent can be obtained. The performing physician must address patient apprehension about potential pain during the procedure and possible complications of the biopsy. After discussing the procedure, any patient questions should be answered fully.

Biopsies are frequently performed on an outpatient basis. Discomfort during the procedure is rarely severe and is usually controlled by appropriate administration of local anesthetic after the skin is cleaned and draped. An IV access may be established before the biopsy in the event that fluid or medications are necessary during the procedure. Premedication is usually not necessary. Sedatives and analgesics such as midazolam or fentanyl can be administered intravenously after consent has been obtained.[38] In patients with an increased risk of bleeding, a larger or second IV access site may be prudent.

There are two options to **sterilize the transducer.** The transducer may be covered with a sterile plastic sheath, although this may degrade image quality and make the transducer more difficult to handle. Alternatively, the transducer itself may be directly sterilized and placed directly on the skin. Sterile gel is used as an acoustic coupling agent. After the biopsy, the transducer is soaked for 10 minutes in a bactericidal dialdehyde solution.

Most ultrasound-guided biopsies are performed under continuous real-time visualization. **Needle guidance systems** designed to facilitate proper needle placement are commercially available. These guides attach to the transducer and direct the needle to various depths from the transducer surface, depending on the preselected angle of the guide relative to the transducer (Fig. 17.1A,B). Many radiologists prefer the **"freehand" technique** in which the needle is inserted through the skin directly into the view of the transducer without the use of a guide (Fig. 17.1C). The needle is then independently directed to the target lesion by the operator under real-time ultrasound visualization (Videos 17.3 and 17.4).

In contrasting these two biopsy techniques, one can appreciate the technical ease provided by the needle guidance method. This can decrease the time to perform a biopsy, particularly in the hands of a novice operator.[39] However, the freehand technique allows greater flexibility to the operator in performing subtle adjustments to the needle path in the event of patient movement, particularly with respiration.

FNA biopsies are performed by placing the tip of the needle into the target lesion and rapidly "bobbing" the needle within the mass, collecting cellular samples within the lumen of the small needle. Some biopsy devices include a syringe on the end to provide negative pressure within the lumen, increasing the cellular yield.

Large-caliber needles are used to obtain cores of tissue. With the typical spring-loaded core biopsy device (biopsy "gun"), the needle tip is advanced to the margin of the target lesion. Careful attention is made to the anticipated excursion of the device to prevent injury to deeper structures. Some biopsy devices allow initial manual advancement of the stylet through the target lesion to the desired depth. When the spring-loaded cutting sheath is activated, the sheath advances over the stylet, but there is no additional forward motion of the needle (Fig. 17.2).

Most biopsies are performed by making one or more passes into a mass with a single needle. Occasionally, two needles are used in a **coaxial** manner, whereby a larger introducer needle is first placed into the mass. The inner stylet of this needle is then removed, and a longer, smaller-caliber needle is placed through its lumen. Multiple samples can then be obtained with the smaller needle without the need to reposition the larger introducer needle. This technique allows a large amount of tissue to be obtained with only one puncture of the organ capsule, although gas introduced during the procedure may interfere with ultrasound imaging. Although intuitively this should decrease bleeding complications, this has not been conclusively demonstrated in real practice.[40] This may be related to the large caliber of the introducer needle or the extended time during which the introducer needle lies within the organ, potentially tearing the capsule.

After the biopsy is performed, the patient is typically observed in the radiology department for a period commensurate with procedure risk. Longer observation may be appropriate if there

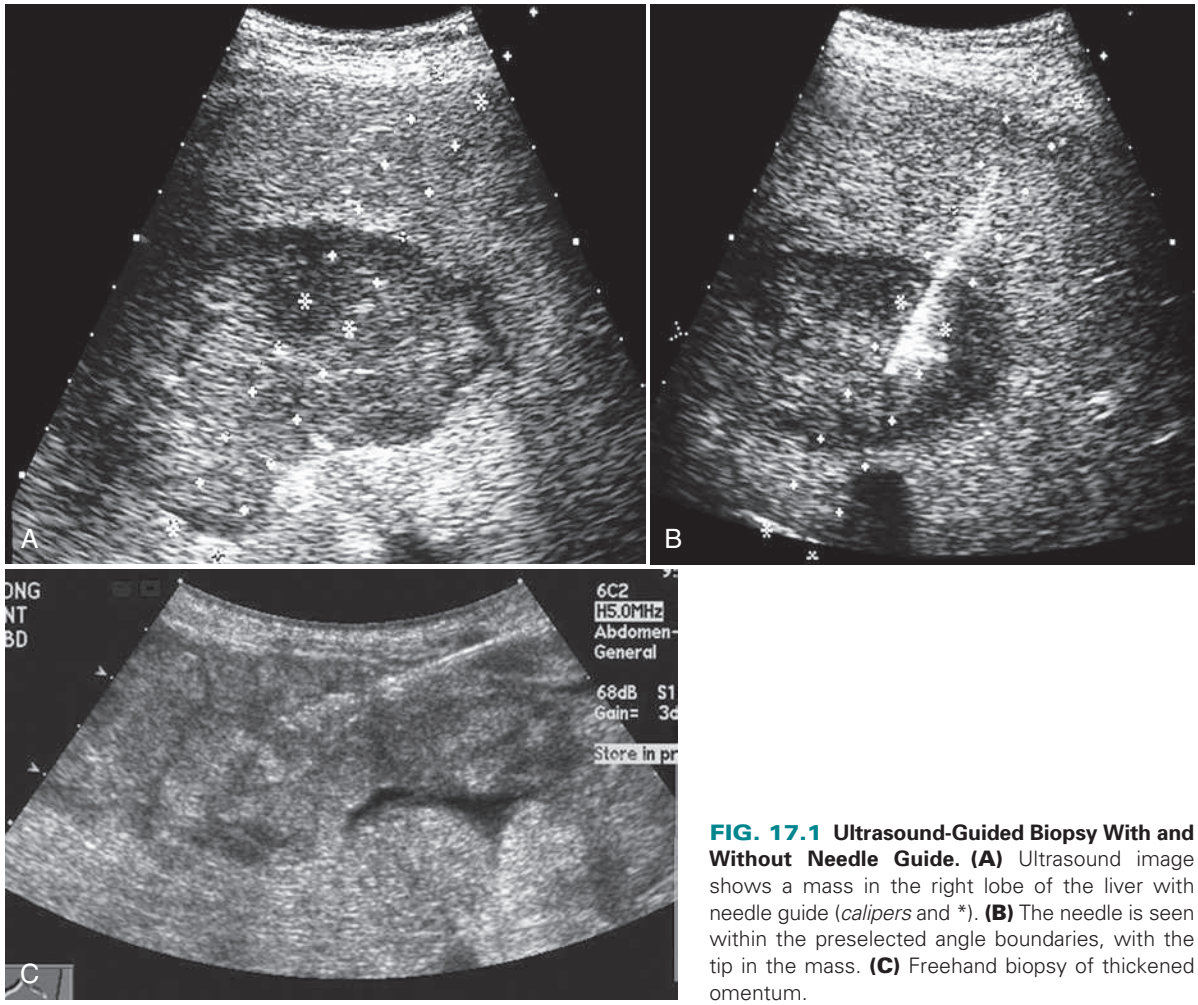

FIG. 17.1 Ultrasound-Guided Biopsy With and Without Needle Guide. (A) Ultrasound image shows a mass in the right lobe of the liver with needle guide (*calipers* and *). **(B)** The needle is seen within the preselected angle boundaries, with the tip in the mass. **(C)** Freehand biopsy of thickened omentum.

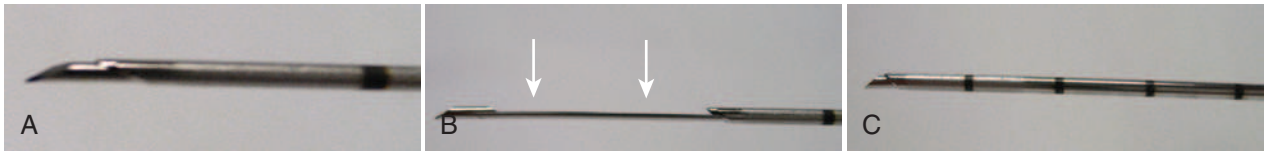

FIG. 17.2 Biopsy Needle With Central Stylet. (A) Biopsy needle tip before stylet deployment. **(B)** Stylet is deployed, with the biopsy trough *(arrows)* evident on the exposed stylet. **(C)** Outer cannula is fired over the stylet, allowing tissue to be obtained in the trough.

is clinical concern about a potential complication. In many medical centers, initial cytologic results are available within this time. If the results of the initial cytologic analysis are not conclusive, a **repeat biopsy** may be performed while the patient is in the department. When core biopsy tissue samples are obtained, frozen-section analysis may be performed for diagnosis if the touch-prep cytology specimen is inconclusive. In this case, additional samples may be necessary if permanent fixation or special staining is required.

Needle Visualization

Continuous real-time visualization of needle tip advancement is one of ultrasound's greatest strengths as a biopsy guidance method. Unfortunately, this is frequently the most technically difficult aspect of ultrasound-guided biopsy for many radiologists. Beginners may choose to practice on a homemade ultrasound biopsy phantom to develop the coordination necessary for ultrasound-guided procedures.[41,42]

The most common reason for nonvisualization of the needle tip is **improper alignment** of the needle tip and transducer. To visualize the entire needle, the needle and central ultrasound beam of the transducer must be in the same plane. This allows the entire shaft of the needle to be visualized. Although malalignment rarely occurs with the use of a mechanical needle guide, such parallel placement can be challenging using the freehand technique, particularly when the radiologist is focused on the ultrasound image. In many cases the radiologist can simply look at the alignment of the needle with the transducer to allow gross correction of path deviation (Fig. 17.3), and then fine-tune the needle alignment with ultrasound imaging.

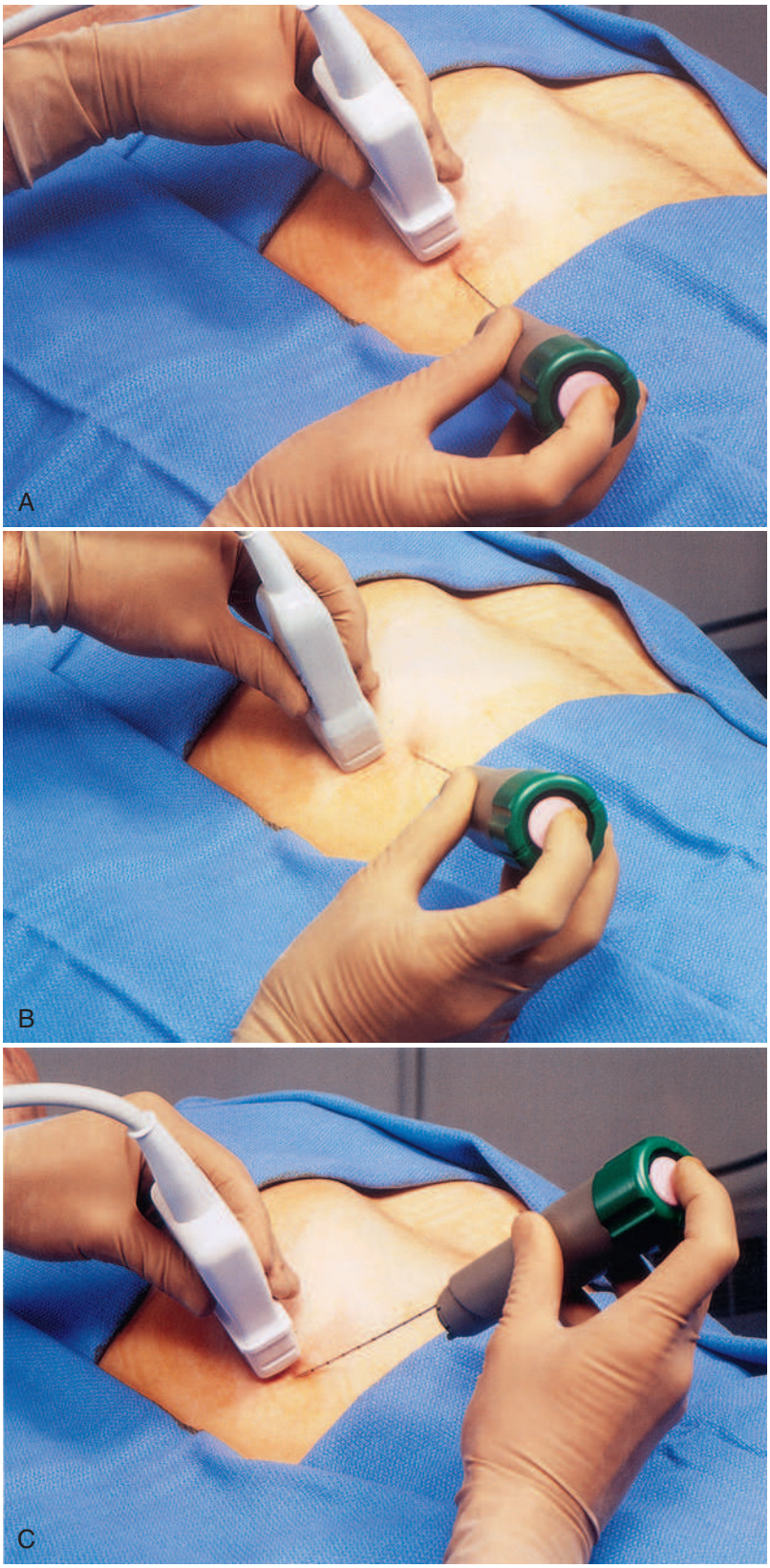

FIG. 17.3 Freehand Alignment of Biopsy Needle With Ultrasound Transducer. (A) Correct alignment for optimal sonographic visualization. Biopsy needle is aligned precisely within the central plane of the transducer. **(B)** Incorrect alignment. Biopsy needle is aligned off-center relative to the transducer. **(C)** Incorrect alignment. Biopsy needle is aligned correctly with the center of the transducer but is angled away from the central plane.

A **bobbing** or in-and-out jiggling movement of the biopsy needle during insertion improves needle visualization. This bobbing motion causes deflection of the soft tissues adjacent to the needle and makes the trajectory of the needle much more discernible within the otherwise stationary field. Alternatively, if using a coaxial system, the inner, smaller needle can be "pumped" or moved in and out within the larger cannula.

Needle visualization can also be improved by **increasing the reflectivity** of the biopsy needle. Large-caliber needles are more readily visualized than small-caliber needles. Keeping the bevel of the needle directed toward the transducer may also increase the conspicuity of the needle tip. Some authors have found CDFI helpful to visualize needle motion,[43] although we have not routinely incorporated Doppler ultrasound into our practice. Modifications in needle tip design to enhance needle visualization include scoring the needle tip and using a screw stylet. Extrareflective needles specifically designed for ultrasound guidance are commercially available. Most needles, however, are sufficiently visible sonographically as long as the needle and transducer are aligned.

The **echogenicity** of the parenchyma of the organ undergoing biopsy also affects the visibility of the biopsy needle. If the parenchyma is relatively hypoechoic, such as liver, kidney, or spleen, the echogenic needle can usually be identified easily. Conversely, if the organ or soft tissues are relatively hyperechoic, it is usually difficult to visualize the echogenic needle tip in this background. This is particularly relevant in the biopsy of masses in obese patients or masses surrounded by complex fat, as in the retroperitoneum.

Linear or curved array transducers are frequently used for guiding procedures because of their good near-field resolution, which allows visualization of the needle after relatively little tissue penetration. The **focal zone of the ultrasound beam should also be placed in the near field** for better needle visualization. Sector transducers are often used if there is a small acoustic window or if there is a deep lesion where a steep needle approach will be needed.

Clear visualization of the biopsy needle is an important element in the success of ultrasound-guided needle biopsies. The various techniques described here can be used to enhance needle visualization. However, considerable real-time scanning **experience** remains the key factor to the successful performance of ultrasound-guided biopsies.

Specific Anatomic Applications

Liver

The liver is the abdominal organ in which percutaneous biopsy is most frequently performed. Common indications for biopsy include nonsurgical confirmation of metastatic disease, characterization of focal liver mass(es) with inconclusive imaging, and diagnosis of parenchymal disease, although random parenchymal biopsies have decreased at our own institution as a result of increasing utilization of elastography for liver fibrosis evaluation. Biopsy of large or superficial lesions is most easily done. With experience, deep lesions and lesions smaller than 1 cm can undergo accurate biopsy[44,45] (Fig. 17.4).

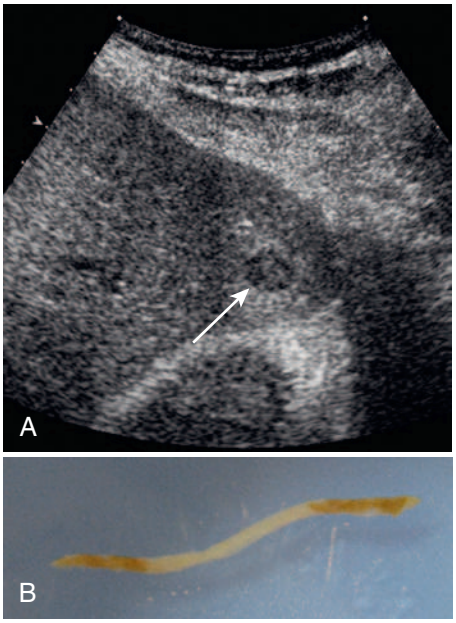

FIG. 17.4 Ultrasound-Guided Biopsy of Small Hepatic Metastasis. (A) Longitudinal ultrasound image of inferior right lobe of the liver shows a 1-cm mass *(arrow)*. **(B)** Gross photograph of the core biopsy sample shows the typical white core of pathologic tissue *(arrows)* bordered by typical-appearing normal liver parenchyma *(arrowheads)*.

In our practice, liver biopsy is almost universally performed under ultrasound guidance because of the real-time visualization of the needle. This advantage becomes particularly obvious when there is significant movement of the liver caused by respiration and diaphragm excursion.

Lesions in the left lobe of the liver and in the inferior portion of the right lobe can usually undergo biopsy through a subcostal approach. Lesions located superiorly in the dome of the liver present a technical challenge for traditional CT-guided biopsy, but real-time, off-axial imaging with ultrasound allows for accurate needle targeting of such tumors, often through an intercostal approach. Although the intercostal approach may violate the pleural space, aerated lung is rarely punctured because it is well visualized sonographically and can be avoided. We usually place the patient in a left posterior oblique rather than supine position when an intercostal approach is used to improve visibility of the liver. If working along the right side of the patient, such a position also prevents the patient from watching needle manipulation. As feasible, **orienting the transducer along the longitudinal axis** of the patient is preferable. Such orientation minimizes the interference of respiration, because the tumor and needle remain in the field of view throughout the procedure.

Benign hepatic lesions such as focal fatty infiltration, focal areas of normal liver within a fatty infiltrated liver, cavernous hemangiomas, focal nodular hyperplasia, and even atypical hemangiomas can usually be confidently characterized as benign by magnetic resonance imaging (MRI) of the liver. However, they occasionally mimic the appearance of malignancy on imaging studies. Biopsy of these processes can be done with ultrasound guidance to exclude malignancy and to confirm their benign nature if MRI findings are equivocal and especially if the

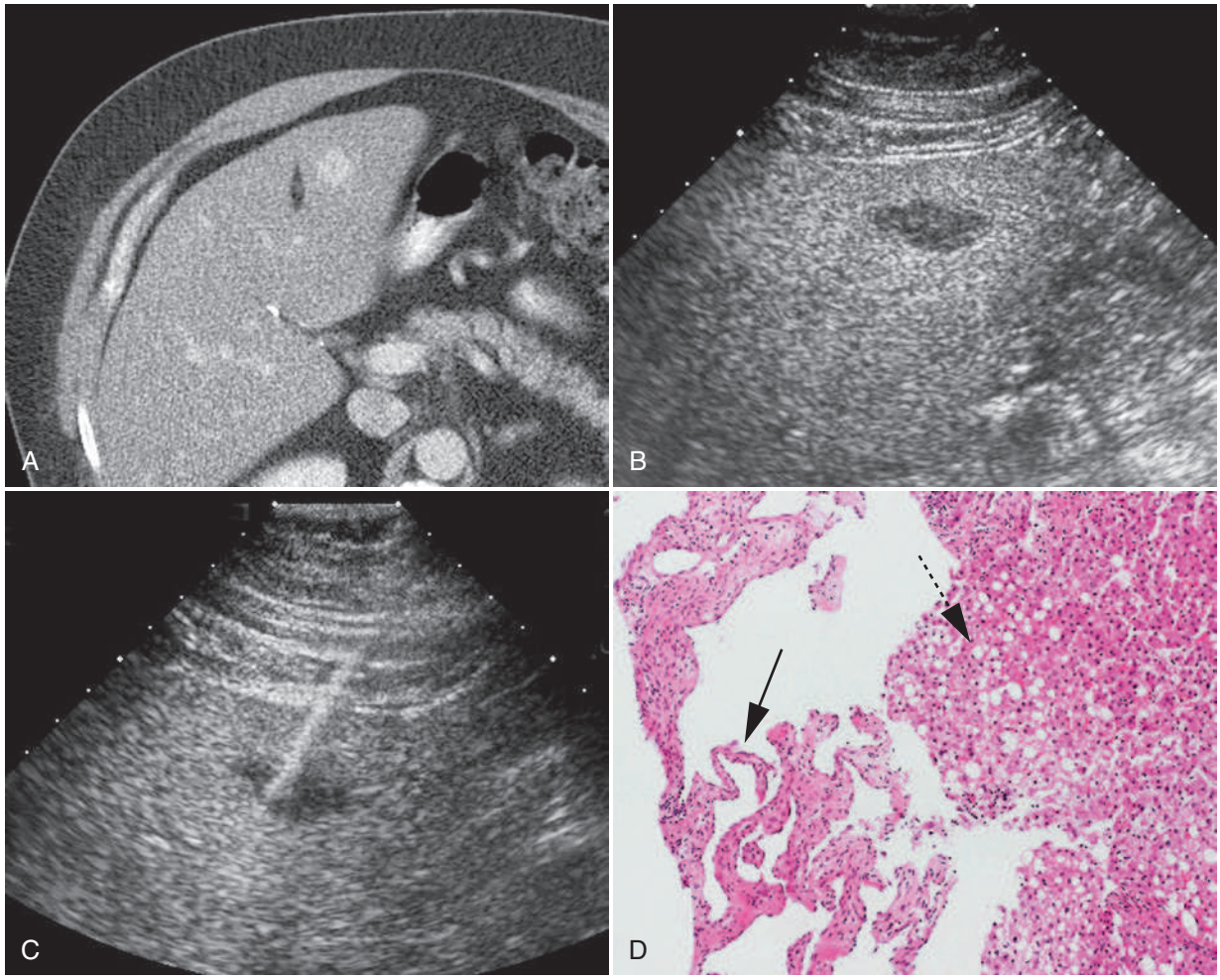

FIG. 17.5 Biopsy of Cavernous Hemangioma. (A) Contrast-enhanced CT scan shows a 1.5-cm vascular mass in left lobe of the liver. **(B)** Transverse ultrasound demonstrates a hypoechoic ellipsoid mass in a fatty infiltrated liver. **(C)** Ultrasound-guided biopsy using an 18-gauge needle. **(D)** Histologic specimen shows endothelial-lined vascular spaces *(arrow)* diagnostic of cavernous hemangioma, as well as small, round, fat globules *(dashed arrow)* within hematoxylin and eosin–stained hepatocytes.

patient has a known primary malignancy (Fig. 17.5). Although **cavernous hemangiomas** are vascular lesions, these masses have undergone successful percutaneous biopsy without significant complications.[46-48] Particular care must be taken to avoid direct puncture of cavernous hemangiomas without intervening liver parenchyma because this may result in significant bleeding.[49] Normal overlying liver may tamponade potential bleeding from the hemangioma in these cases. Significant bleeding after direct puncture of hypovascular liver masses is less of a concern.

There has been increasing interest in biopsy of suspected **hepatic adenomas** as a result of evolving classification schemes and subtyping. Different subtypes carry different potential for bleeding and malignant transformation and this has implications for patient management.[50] Although biopsy of hepatic adenoma is safe, there remains a small risk of discordant pathology results between initial biopsy and either subsequent biopsy or surgical resection specimen based on pitfalls in pathologic interpretation and occasional overlap in histologic features between adenoma, focal nodular hyperplasia, and hepatocellular carcinoma. In a series that included biopsy of 60 suspected hepatic adenomas, 6 (10%) showed discordant at time of follow-up pathology, including 4 later diagnosed as focal nodular hyperplasia and two later diagnosed as hepatocellular carcinoma.[51]

Percutaneous ultrasound-guided biopsy of **portal vein thrombus** has proved to be a safe and accurate diagnostic procedure for staging of hepatocellular carcinoma, although also performed less frequently in the context of advanced MRI techniques.[52]

Liver biopsies are relatively safe, with an overall significant complication rate of less than 1%.[16,24,53-59] Hemorrhage is most common. Such significant bleeding complications are more likely to occur in the biopsy of patients with malignancy and those with acute liver failure, chronic active hepatitis, or cirrhosis.[58,60,61] Most complications occur soon after the biopsy procedure, with about 60% occurring within 2 hours and 80% within 10 hours.[58] Several large series report mortality of percutaneous liver biopsy as 0.1% or less.[27,58-60]

Pancreas

Despite the growing use of **endoscopic ultrasound** (EUS) and EUS-guided FNA, percutaneous biopsy of pancreatic tumors remains necessary in some cases when the tumor is in the tail

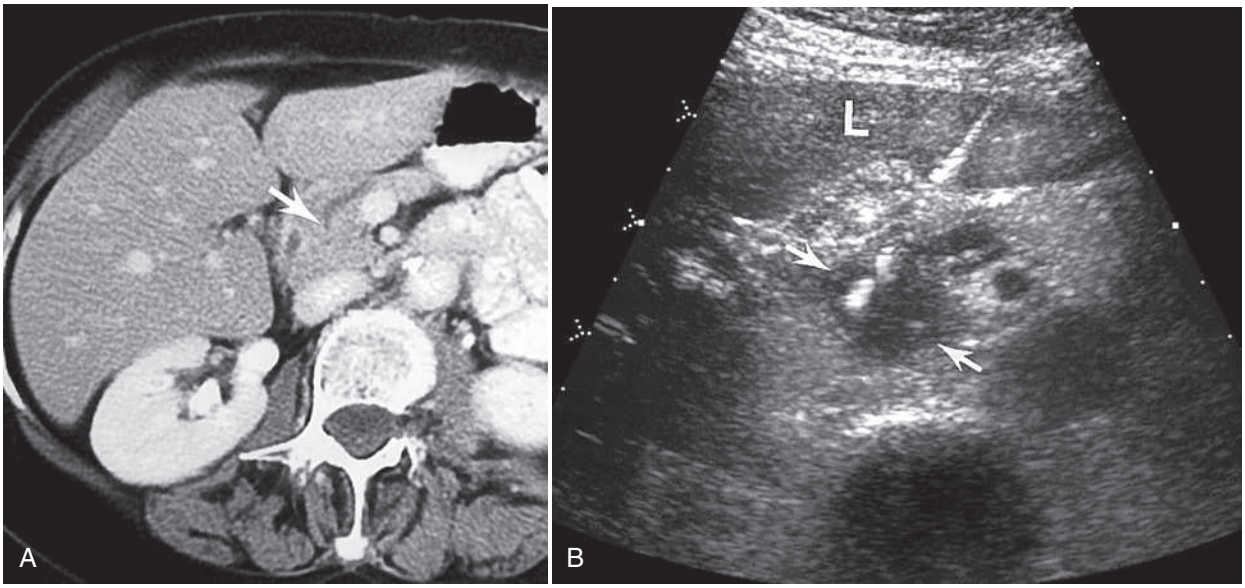

FIG. 17.6 Ultrasound-Guided Pancreatic Biopsy. (A) Contrast-enhanced CT scan shows a mildly dilated pancreatic duct with abrupt termination in the head of the pancreas *(arrow).* No definite mass is identified on CT scan. **(B)** Ultrasound for guided biopsy shows a 19-gauge needle passing through left lobe of the liver *(L),* with needle tip within a 2-cm hypoechoic mass in the head of the pancreas *(arrows).* The biopsy was positive for adenocarcinoma.

of the pancreas or when EUS is unavailable. Biopsy is occasionally required to document malignancy or differentiate malignancy from a benign condition, such as focal pancreatitis.

At our institution, most pancreatic biopsies are done with CT guidance because depth of the pancreas and presence of overlying bowel gas and hyperechoic abdominal fat can make visualization of the needle difficult. Nevertheless, biopsy of pancreatic masses in normal-size and slender patients can be done accurately under ultrasound guidance (Fig. 17.6).

The **gastrointestinal (GI) tract** may be traversed when biopsying the pancreas. With ultrasound, the stomach or bowel is either displaced or compressed. Brandt et al.[4] demonstrated the safety of traversing the GI tract (stomach, small bowel, colon) in performing percutaneous biopsies in 66 procedures. Most of these biopsies were performed using a 21-gauge needle, with no complications related to the biopsy route in these patients.

A particular advantage of ultrasound over CT is the ability to biopsy pancreatic masses in an off-axis plane, which is very useful if overlying vessels are present on CT. Ultrasound-guided biopsy has 93% to 95% accuracy, compared with 86% to 100% accuracy for CT guidance.[4,62,63]

In some series, the biopsy success rate for the diagnosis of pancreatic carcinoma has been lower than the success rate for the diagnosis of malignant lesions in other organs of the abdomen.[4,64,65] This may be related to sampling error, because significant desmoplastic reaction often accompanies pancreatic adenocarcinoma. By targeting the central hypoechoic portion of the pancreatic mass, the clinician can improve the diagnostic yield. In addition, core biopsy, either alone or in addition to FNA, results in improved diagnostic performance compared with FNA alone.[63]

The differentiation between **benign serous** and potentially **malignant mucinous pancreatic tumors** can be difficult with imaging alone. Unfortunately, cystic pancreatic malignancies are difficult to accurately diagnose with percutaneous biopsy; a definitive diagnosis was achieved in only 60% of patients in one study.[66] In biopsy of a cystic pancreatic lesion, it is critical to obtain **epithelial cells,** either in the wall of the lesion or within the cyst fluid. Analysis of **percutaneous fluid aspirates** from a cystic lesion has also been proposed as an aid to distinguish cystic neoplasms from pseudocysts.[66-68] A high amylase level is consistent with a pseudocyst. The presence of tumor markers with the cyst fluid may also be helpful in suggesting a cystic neoplasm.

The safety of percutaneous biopsy of the pancreas has been well established, with a complication rate of 0.8% to 2%.[4,16,24,69] A historic review reported six deaths related to pancreas biopsy.[70] Five of these deaths were attributed to pancreatitis and one to sepsis. No pancreatic cancer was found in either the biopsy specimen or the postmortem examination of these patients, suggesting an increased risk for developing pancreatitis after biopsy of normal pancreas. In this same large review of percutaneous biopsies, 10 of 23 cases of needle track seeding occurred after the biopsy of pancreatic malignancies. For this reason, biopsy may not be indicated in patients who are surgical candidates.

Kidney

Biopsy of the kidney is performed to assess intrinsic parenchymal disease or to characterize a renal mass (Fig. 17.7). Although there has been long-standing acceptance of **renal mass biopsy** for suspected metastasis, lymphoma, abscess, or unresectable suspected renal cell carcinoma, biopsy of potentially resectable suspected renal cell carcinoma has historically been controversial because of concerns regarding accuracy and safety as well as questionable impact on patient management.[71] In recent years, however, incidental detection of potentially benign small renal

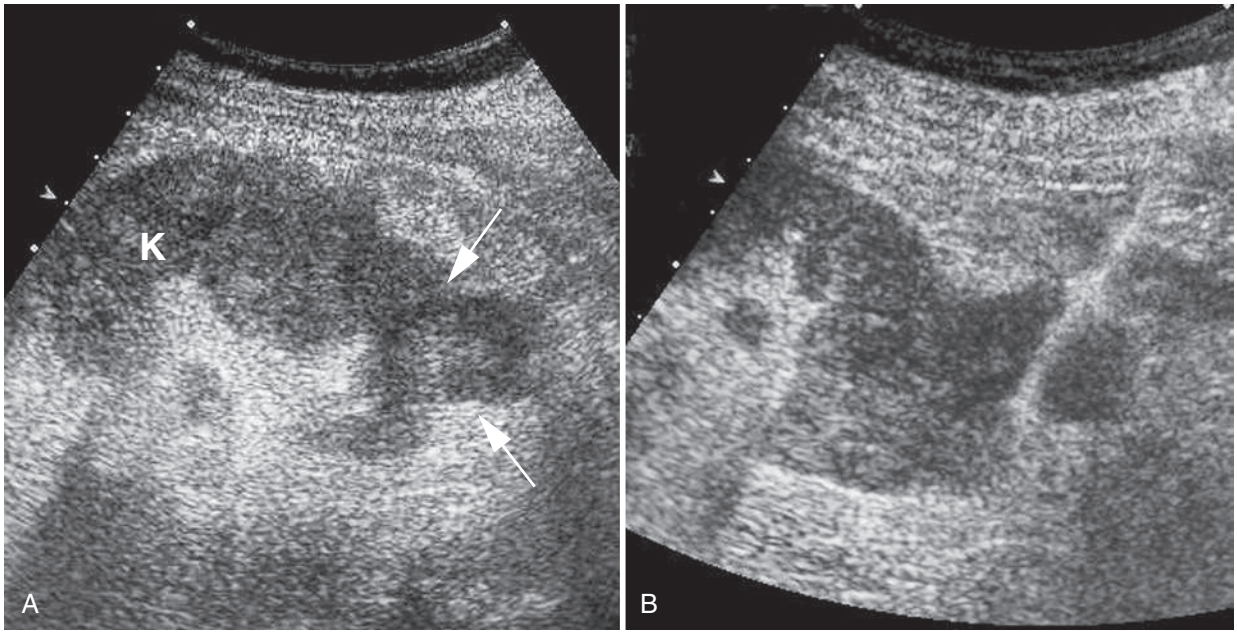

FIG. 17.7 Ultrasound-Guided Biopsy of Renal Mass. (A) Longitudinal image shows a 2-cm solid mass *(arrows)* extending from lower pole of the left kidney *(K)*. **(B)** Mass was biopsied using an 18-gauge biopsy device, confirming renal cell carcinoma.

masses has increased and both biopsy accuracy and safety profiles have improved. Current literature shows diagnostic rates for renal mass biopsy of 85% to 92%.[72,73] Other authors have also shown exceptional results,[74-76] but these studies are in some cases limited by the mode of determining true-negative results, which is based on stability on imaging follow-up. However, we know that the lack of growth in a renal mass does not imply a true-negative result, because 25% of renal tumors will not grow.[77] Nondiagnostic biopsies are more common in cystic or nonenhancing masses especially if small (<4 cm) or deep (>13 cm skin-to-tumor distance).[73]

It is helpful to keep in mind that the smaller the renal mass is, the more likely it is to be benign.[78,79] In one large series, 46% of tumors less than 1 cm were benign.[78] Cross-sectional imaging has allowed accurate characterization of many benign renal masses, notably benign **cysts** and fat-containing **angiomyolipomas.** The problem is with the indeterminate, small, enhancing renal mass, specifically the **oncocytoma, small renal cell carcinoma, and lipid-poor angiomyolipoma,** which cannot be reliably differentiated by imaging.[80] For these reasons and because a wider range of treatment options, including active surveillance and ablation, is available to patients, renal mass biopsy is being increasingly utilized. The current guidelines of the American Urological Association state that renal mass biopsy is appropriate for patients with a clinical stage 1 renal mass (confined to the kidney and ≤7 cm) in whom a wide range of management options are under consideration, ranging from surgery to observation. When performed in the appropriate circumstances, biopsy may affect a change in clinical management in 40% of patients.[74]

Sonographic guidance can be used in the biopsy of kidneys with **diffuse parenchymal disease.** Insertion of the needle into the cortex of the lower-pole renal parenchyma with tip directed away from the central hilum under continuous real-time guidance results in few complications and produces a tissue sample of excellent quality for analysis. An **18-gauge biopsy needle** provides a specimen that is equivalent in diagnostic quality to the biopsy specimen obtained by the traditional 14-gauge cutting needle.[81] In fact, Hergesell et al.[19] found a 99% success rate in obtaining diagnostic tissue using an 18-gauge needle, with only 0.36% of patients experiencing a significant bleeding complication. In this series, postbiopsy ultrasound revealed a clinically occult hematoma greater than 2 cm in 2% of patients. Similarly, asymptomatic hemorrhage may be detected by CT in up to 90% of patients after uncomplicated kidney biopsy.[82] **Arteriovenous (AV) fistulas** may be seen in about 10% of patients immediately after kidney biopsy and usually resolve spontaneously (Fig. 17.8).

Clinically important bleeding is the most serious complication after kidney biopsy, occurring in 0.3% to 6.6% of patients.[16,17,23] Gross hematuria may occur in 5% to 7% and usually stops within 6 to 12 hours.[83] Microscopic hematuria occurs in up to 100% of patients and should not be regarded as a complication.

Adrenal Gland

The most common indication for adrenal biopsy is to **confirm metastatic disease** in a patient with an adrenal mass and a known primary malignancy elsewhere. Currently, CT and MRI characterization of adrenal masses has supplanted biopsy in many cases in establishing benignity of an adrenal mass. Nevertheless, occasional histologic diagnosis is required. In this case, CT guidance is generally the preferred adrenal biopsy technique because of the deep location of the adrenal glands in the retroperitoneum. Percutaneous biopsy can yield a diagnosis in more than 93% of patients.[84,85]

The right adrenal gland is more accessible to ultrasound-guided biopsy than the left adrenal gland because the right lobe of the liver provides a sonographic window to optimize imaging (Fig. 17.9). Bright, echogenic, fat-containing adrenal masses and homogeneous, thin-walled, fluid-filled adrenal masses may not

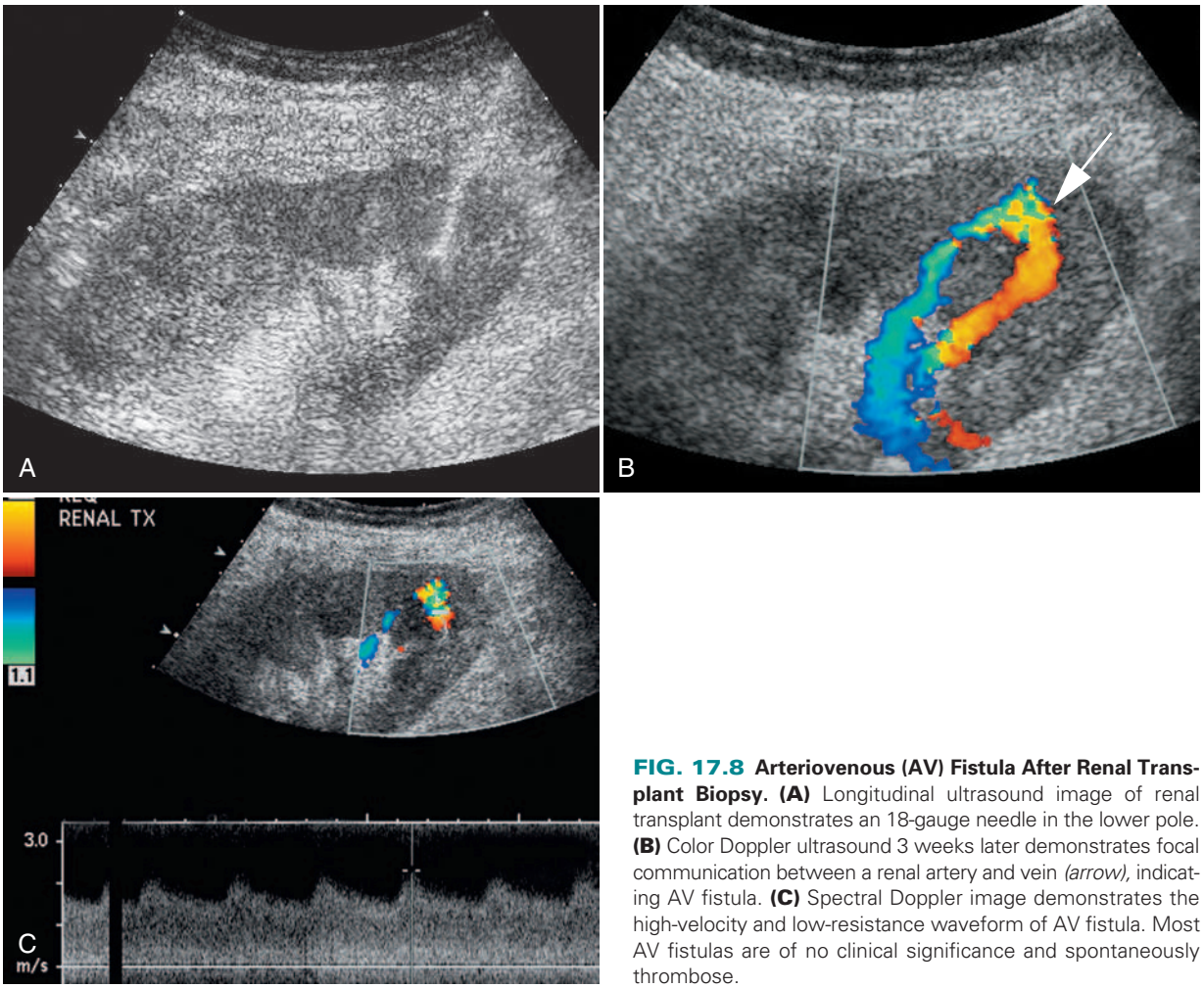

FIG. 17.8 Arteriovenous (AV) Fistula After Renal Transplant Biopsy. (A) Longitudinal ultrasound image of renal transplant demonstrates an 18-gauge needle in the lower pole. **(B)** Color Doppler ultrasound 3 weeks later demonstrates focal communication between a renal artery and vein *(arrow),* indicating AV fistula. **(C)** Spectral Doppler image demonstrates the high-velocity and low-resistance waveform of AV fistula. Most AV fistulas are of no clinical significance and spontaneously thrombose.

require biopsy because these should represent benign adrenal **myelolipomas** and **cysts,** respectively. CT or MRI can be performed to confirm this before considering biopsy.

Although **benign adenomas** can be larger than 3 cm, the likelihood of silent adrenal carcinoma increases significantly if an incidentally discovered adrenal mass is larger than 4 cm.[86] In this setting, surgical excision is recommended because biopsy will yield insufficient tissue to differentiate a benign adenoma from adrenocortical carcinoma.

Radiologists performing adrenal biopsies should be familiar with the management of a hypertensive crisis after inadvertent biopsy of a **pheochromocytoma.**[87] Although adrenal pheochromocytomas have been safely biopsied without premedication,[84] if the clinical history suggests pheochromocytoma, further laboratory tests, not biopsy, should establish the diagnosis. If biopsy is necessary, consultation with an endocrine specialist and pretreatment with alpha-adrenergic blockers and metyrosine should be considered.[88]

Spleen

The spleen is the abdominal organ that undergoes biopsy **least** often. First, isolated metastases to the spleen are exceptionally rare. In most cases, when the splenic tumor is visualized, there is concomitant disease in other abdominal organs, such as the liver or lymph nodes, in which a biopsy can be performed. Second, the spleen is a highly vascular organ, and the risk of needle biopsy would seem to be high. The reported rate of significant hemorrhage from needle biopsy varies from no hemorrhage up to 8%.[89-98] In some cases, splenectomy is required.[91,99] Pneumothorax may also occur as a complication after spleen biopsy.[97]

At this time, the main clinical reason for performing percutaneous biopsy of the spleen is to differentiate recurrent **lymphoma, metastasis,** and **infection** in a patient who has a new splenic lesion but no disease elsewhere in the abdomen (Fig. 17.10). In the immunocompromised patient, differentiation between **malignancy** and **fungal infection** can be critical in patient management. Percutaneous biopsy can yield a specific diagnosis in approximately 90% of patients.[90,91,100]

Lung

Percutaneous biopsy of the lung is typically performed with CT guidance. However, ultrasound has proved to be effective in the biopsy of masses that abut the chest wall, without the imaging interference of aerated lung parenchyma[101,102] (Fig. 17.11). Such lesions include **pulmonary, pleural,** and **mediastinal** masses. Notable advantages of ultrasound in the lung include (1) real-time guidance during patient respiration, (2) ability to biopsy efficiently in the off-axial plane, (3) ability to biopsy lesions in patients

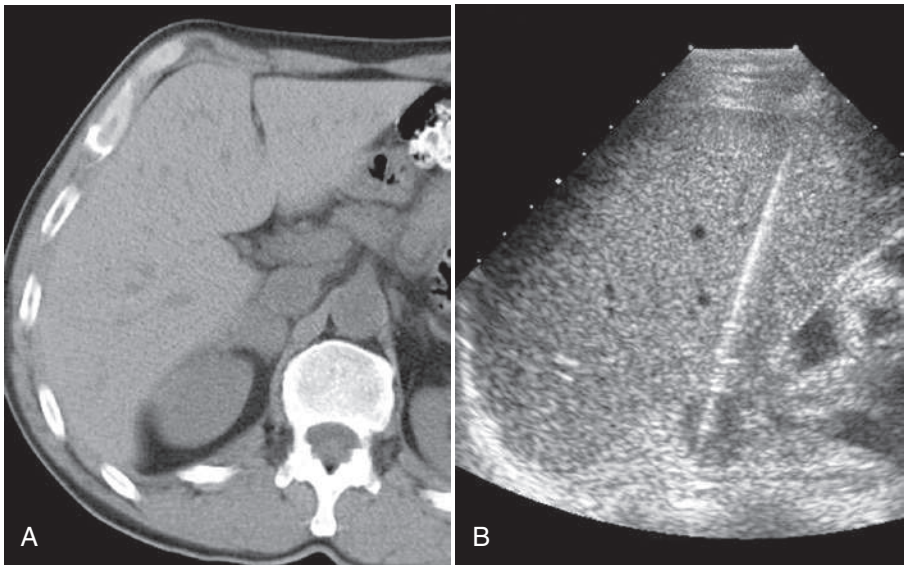

FIG. 17.9 Ultrasound-Guided Biopsy of Adrenal Mass. (A) CT scan without contrast demonstrates a 2-cm mass in the right adrenal gland. **(B)** Longitudinal ultrasound image shows value of the liver as a biopsy path to the right adrenal gland.

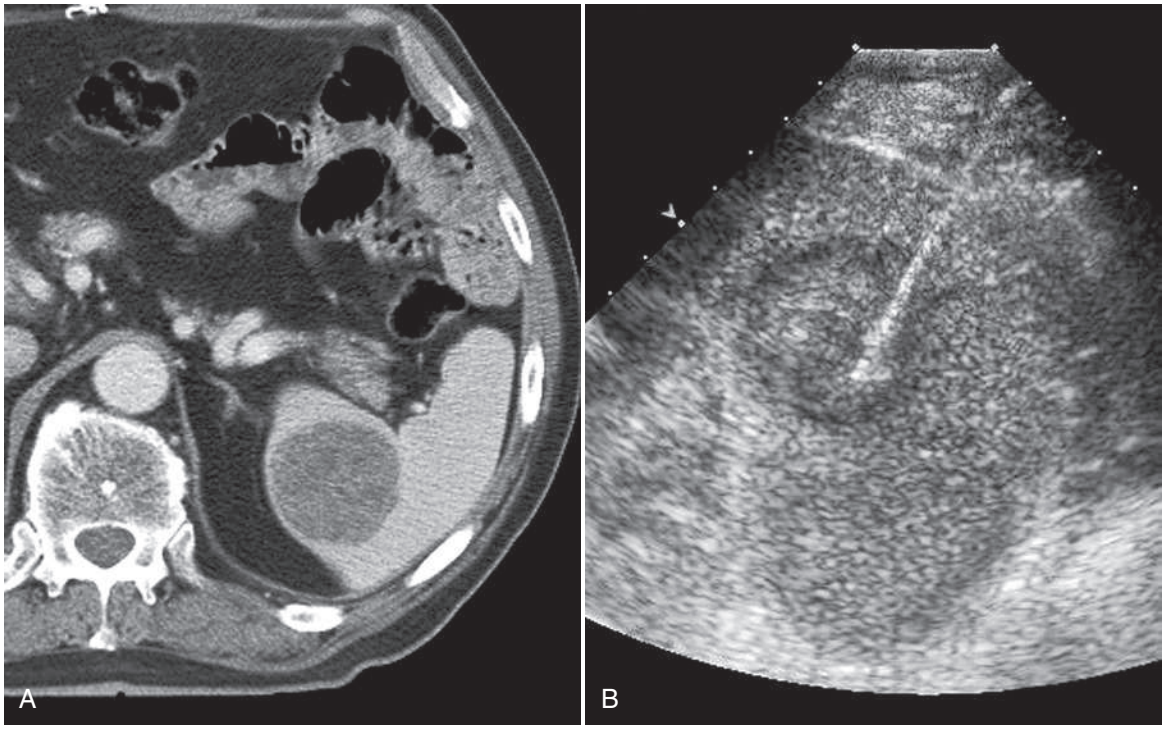

FIG. 17.10 Ultrasound-Guided Biopsy of Melanoma Metastasis to the Spleen. (A) Contrast-enhanced CT shows a 4-cm mass in the spleen. **(B)** Transverse ultrasound demonstrates the 18-gauge biopsy needle within the mass.

who would otherwise have difficulty cooperating, and (4) absence of ionizing radiation.[103] Ultrasound biopsy of mediastinal masses can be performed if the mass is visible. Mediastinal vessels in the path of the needle may be avoided with the use of color Doppler ultrasound before needle placement.

Complications

Image-guided percutaneous needle biopsy is a widely accepted mode of obtaining tissue for diagnosis, in part because of its well-documented safety. Several large reviews using multi-institutional questionnaires have reported major complication rates of 0.05% to 0.5% and mortality rates of 0.008% to 0.038%.[16,24,70,104-106]

Although rare, **hemorrhage** is the most common major complication of solid-organ biopsy and accounts for most biopsy-associated deaths. If hemorrhage is suspected after biopsy and the patient is hemodynamically stable, CT should be obtained. CT is more accurate than ultrasound to evaluate for hemorrhage.[82] On ultrasound, fresh blood has an echogenicity similar to that of surrounding tissues and can be overlooked (Fig. 17.12).

The difference in the complication rates associated with the use of larger-caliber core biopsy needles and small-caliber needles

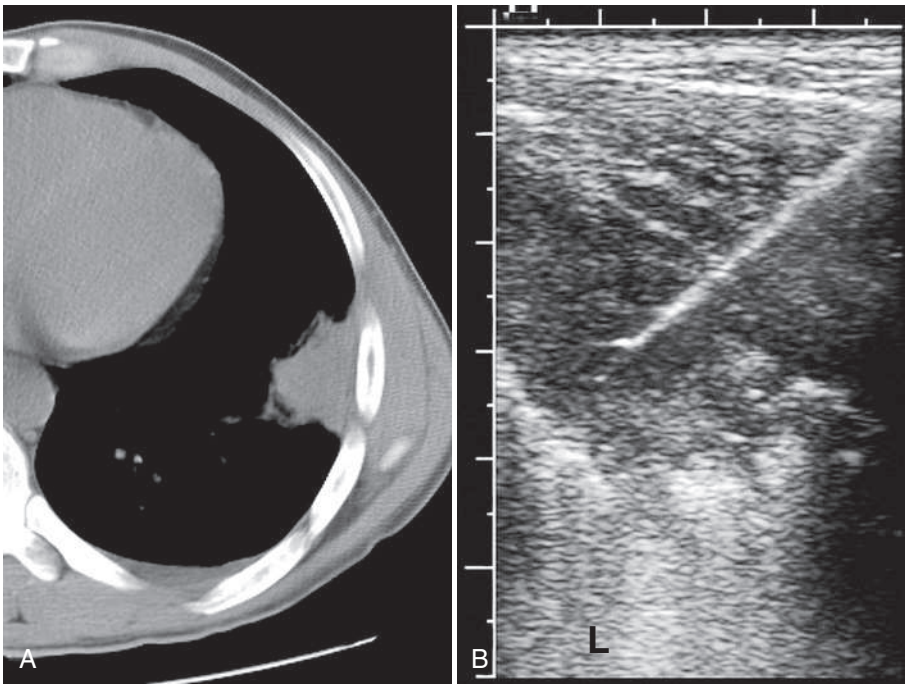

FIG. 17.11 Ultrasound-Guided Biopsy of Peripheral Lung Mass. (A) Noncontrast-enhanced CT demonstrates an indeterminate peripheral left lung mass. **(B)** Oblique ultrasound image shows a 20-gauge biopsy needle isolated within the hypoechoic mass, which is surrounded by aerated lung *(L)*. Biopsy confirmed histoplasmosis.

is not as great as might be expected. An early comparative study found complication rates of 0.8% with fine needles (22 gauge) and 1.4% with large-caliber needles (14 and 18 gauge); this difference was not statistically significant.[107] In addition, the larger needles provided a diagnostic tissue in 90% of biopsies compared with 65% in fine-needle biopsies. Welch et al.[108] found equal rates of complications from the use of 18-gauge and 21-gauge biopsy needles (0.3%).

Other major complications secondary to biopsy include **pneumothorax, pancreatitis, bile leakage, peritonitis,** and **infection** (Fig. 17.13). An exceedingly rare complication (0.003%),[70] **needle track seeding** has been reported after biopsy of various malignancies, including those arising from the pancreas, prostate, liver, kidney, lung, neck, pleura, and retroperitoneum.[70,109-120] Because seeding is so rare, in most cases it should not affect the decision to perform percutaneous biopsy.

Minor complications more often encountered include **vasovagal reactions** and **pain.**

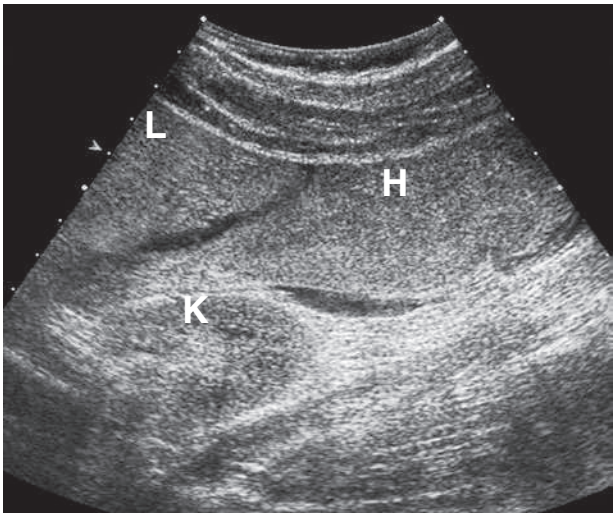

FIG. 17.12 Isoechoic Hematoma After Biopsy of Pancreas Transplant. Large, fresh, postbiopsy intraperitoneal hematoma *(H)* is isoechoic with the adjacent liver *(L)* and right kidney *(K)*. Newly evolving clot (<30 min) can be echogenic and therefore overlooked.

ULTRASOUND-GUIDED DRAINAGE

As with needle biopsy, percutaneous aspiration and drainage procedures have gained wide acceptance in clinical practice because of their safety, simplicity, and effectiveness. Ultrasound provides precise needle guidance to allow for needle aspiration or catheter drainage of superficial and deep fluid collections throughout the body.

Indications and Contraindications

Original criteria for percutaneous drainage specified that the fluid collection be unilocular with no communications, and surgical backup was considered essential.[121,122] Currently, percutaneous abscess drainage is performed safely for solitary, multilocular, and multifocal fluid collections with or without communication to the GI tract.[122,123] Such collections include complex solid-organ **abscesses,** enteric-related abdominal abscesses (e.g., caused by **appendicitis** and **diverticulitis**), **tubo-ovarian abscesses,** and **percutaneous cholecystostomy** for an inflamed gallbladder. Percutaneous drainage is more likely to be successful in abscesses with air-fluid levels or superficial gas collections, whereas abscesses with deep, trapped gas bubbles are less likely to be successfully managed with percutaneous drainage.[124] Poorly defined fluid in the peritoneum with an

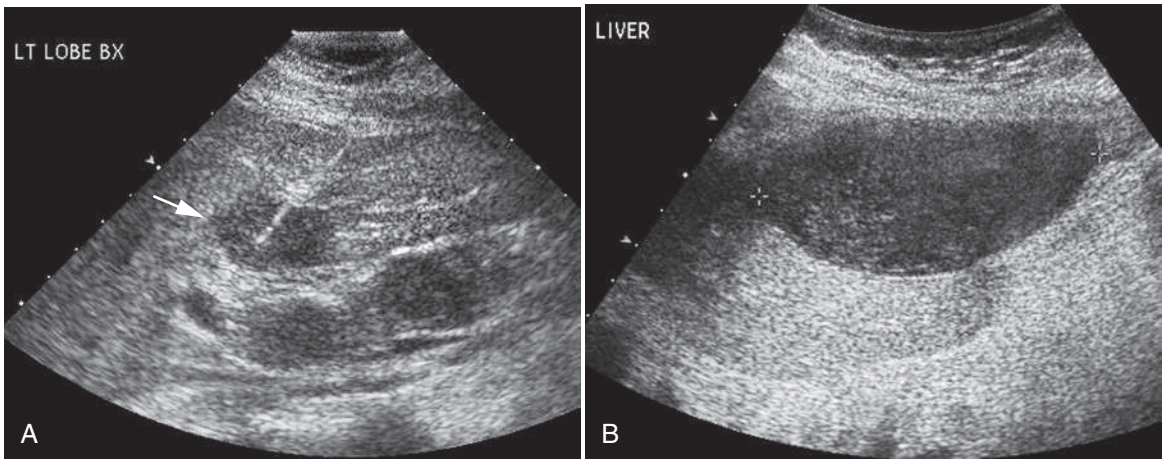

FIG. 17.13 Abscess After Liver Mass Biopsy. (A) Transverse ultrasound image shows an 18-gauge biopsy needle in a 3-cm metastasis *(arrow)*. **(B)** Longitudinal image obtained 2 weeks later demonstrates a 6-cm debris-containing fluid collection, anterior to left lobe of the liver, at biopsy site. Subsequent aspiration and drain placement confirmed abscess.

underlying surgically correctable abnormality (e.g., perforated bowel) is better treated with surgery.

Most percutaneous abscess drainage is performed to achieve a cure without the need for surgery. In other patients, it is a temporizing procedure that either postpones definitive surgery until the patient is stable (e.g., periappendiceal abscess drainage) or permits a single-stage rather than a multistage surgery (e.g., peridiverticular abscess drainage). This is particularly desirable in high-risk, medically complicated patients who present with sepsis.

Contraindications to image-guided percutaneous catheter drainage are all relative and are similar to those for percutaneous biopsy. Although uncommon, lack of a safe route for percutaneous drainage precludes the procedure. Unlike percutaneous biopsy, in which bowel may be traversed without complication, fluid aspiration and percutaneous abscess drainage through bowel should be avoided. Initial advancement of the drain through normally contaminated bowel may seed a sterile fluid collection, resulting in iatrogenic infection. In addition, drain placement through bowel may result in not only significant perforation but also enteric fistula.

Bleeding diathesis should be maximally corrected before drain placement, and appropriate sedation (local and systemic) should be given.

Imaging Methods

Selection of ultrasound or CT for guidance of aspiration and drainage is influenced by several factors, including the location of the fluid collection and the strengths and weaknesses of each imaging modality, as discussed earlier. For example, a **simple paracentesis** is best performed under ultrasound guidance (Fig. 17.14). More complicated drainage procedures in the retroperitoneum or pelvis are best performed with CT guidance. More **superficial abdominal fluid collections** may be aspirated or drained easily with ultrasound guidance. Obtaining a CT scan before the procedure often provides a more detailed view of potentially deeper components to the collection and an anatomic map for planning a safe access route.

FIG. 17.14 Ultrasound-Guided Paracentesis. Longitudinal image shows a 5-French angiocatheter with side holes in the left lower peritoneal cavity during a paracentesis.

In certain anatomic areas, such as the gallbladder, biliary tract, and kidneys, combined ultrasound and **fluoroscopic guidance** of catheter placement may be preferred. The combined use of ultrasound for initial needle placement and fluoroscopy for catheter placement, using the **guidewire exchange technique** (Seldinger), optimizes the strengths of both guidance modalities. Fluoroscopy can then be used to opacify the area drained and confirm final catheter placement and adequacy of drainage.

No single method of guidance for percutaneous drainage is appropriate for all abdominal fluid collections or abscesses. The approach to any fluid collection or potential abscess must be tailored to the patient, procedure, and specific circumstances.

Catheter Selection

Various catheters and introducing systems are available for percutaneous abscess drainage; choice depends mainly on operator preference. As with most interventional procedures, the clinician or radiologist must be familiar and comfortable with the system

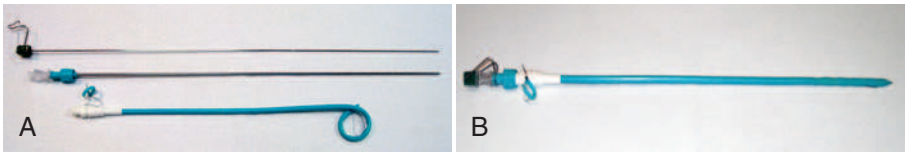

FIG. 17.15 Locking-Loop Drainage Catheter. (A) Three components of the locking-loop catheter are sharpened inner stylet *(top),* stiffener *(middle),* and catheter with distal locking loop *(bottom).* **(B)** Assembled catheter is ready for placement using trocar technique.

chosen. In general, thicker fluid is best drained with larger-caliber catheters. A 10- to 14-French catheter provides adequate drainage for most abscesses. Smaller (6-8 French) catheters are adequate for less viscous collections. Catheters with retention devices, such as a locking loop, are frequently used to prevent catheter dislodgement (Fig. 17.15).

Patient Preparation

The procedure and risks should be explained to the patient and informed consent obtained. The patient's hemostatic status should be assessed through clinical history, and recent coagulation studies should be available. We routinely require platelets and PT for drainage procedures. IV access is obtained in all patients for administration of medications and for emergency access, in the event of a complication, such as hemorrhage, sepsis, or hypotension. Patients often receive broad-spectrum antibiotics intravenously to decrease the risk of sepsis. Satisfactory analgesia is necessary throughout the procedure to provide optimal patient comfort and cooperation. Local anesthesia is usually sufficient for needle aspiration; however, IV sedatives and analgesics such as midazolam (Versed) or fentanyl (Sublimaze) are beneficial for percutaneous catheter insertion; dilation of the drain tract can be extremely painful to the patient.

Diagnostic Aspiration

Because fluid collections often have a nonspecific appearance, diagnostic aspiration is the first step. A fine needle is guided into the fluid collection by the selected imaging modality. This needle insertion defines a precise and safe route to the fluid collection. A small amount of fluid is aspirated and sent for appropriate microbiologic evaluation. The resulting culture and sensitivity data are used to direct the antibiotic therapy. If the fluid does not appear infected (i.e., clear, colorless, and odorless), the radiologist may elect to aspirate the cavity completely and not perform the drainage procedure. This is important, because a catheter placed in a sterile fluid collection will eventually serve as a nidus of infection, with subsequent infection of the collection. If pus is aspirated, care should be taken to aspirate only a small amount of fluid, because any decrease in the cavity size may make subsequent catheter placement more difficult.

Catheter Placement

Catheter insertion can be performed using the trocar or the Seldinger technique; the choice usually depends on operator preference. In the **trocar technique** the catheter fits over a stiffening cannula, and a sharp inner stylet is placed within the cannula for insertion (see Fig. 17.15). The catheter assembly is advanced into the fluid collection. The catheter is then pushed from the cannula, and the distal loop is formed and tightened to secure the catheter within the fluid collection. This method works best for large and superficial fluid collections.

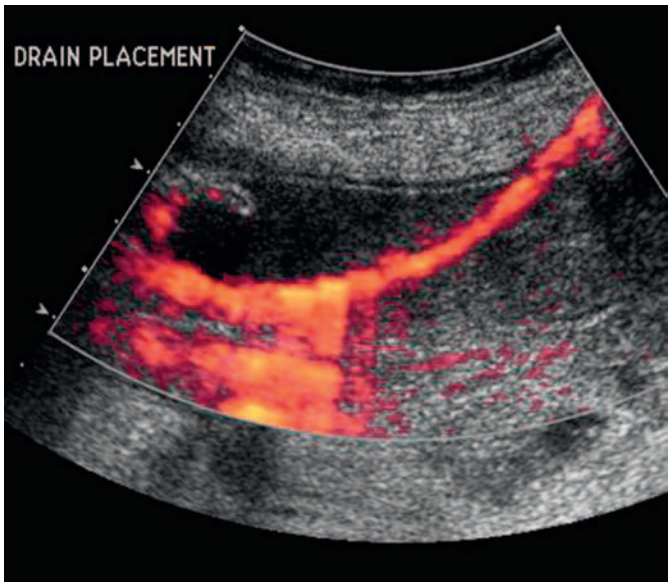

FIG. 17.16 Drain Within Deep Pelvic Abscess. With aspiration of the abscess and subsequent fluid motion within the drain, longitudinal transperineal Doppler ultrasound image shows a color shift, allowing good visualization of the catheter.

With the **Seldinger technique** (guidewire exchange technique), a guidewire is advanced through the aspiration needle and coiled within the fluid collection. The needle is then removed, and the guidewire is used as an anchor for passage of a dilator to widen the catheter track. The catheter-cannula assembly is placed over the guidewire into the fluid collection. The guidewire and inner cannula are removed as the catheter is simultaneously advanced. The distal locking loop of the catheter is re-formed to prevent catheter dislodgement. If the catheter is difficult to see with ultrasound, the use of CDFI may improve conspicuity. During aspiration or irrigation, Doppler shifts improve catheter visualization (Fig. 17.16, Video 17.5).

Final positioning of the catheter is important in maximizing the effectiveness of drainage. For this purpose, ultrasound and CT are complementary and at times should be used together. CT provides an anatomic road map for ideal catheter placement. Because this ideal position seldom lies in the true axial plane, ultrasound can be used to direct the needle, guidewire, and catheter into the ideal position. Final placement can then be verified with CT.

Drainage Procedure

After the drainage catheter is placed, the cavity is completely aspirated and gently irrigated. Care should be taken not to distend the cavity during the irrigation because this may increase the risk of bacteremia. Repeat images are obtained to determine the size of the residual cavity, the position of the drainage tube, and whether the entire abscess communicates with the drainage tube. If the abscess cavity has not completely resolved, the drainage catheter may need to be repositioned, or a second drain may need to be placed. Such manipulations are often performed under fluoroscopy the day after initial drain placement. Correct catheter position and adequate catheter size are the most important factors for successful drainage.

Follow-Up Care

All drains must be **irrigated regularly.** Injection and aspiration of 10 mL of isotonic sterile saline three or four times daily is usually sufficient. If drainage is especially tenacious or the abscess is large, more frequent irrigations with greater volumes of saline may be necessary. The flu id collection can be drained dependently or by low, intermittent suction. The character and volume of the output should be recorded each nursing shift and checked daily on rounds by the radiology service. If the drainage changes significantly in volume or character or if fever recurs, the patient should be reexamined to check for fistulas, catheter blockage, reaccumulation of the abscess, or a previously undiagnosed collection.

From 24 to 48 hours after tube placement, a sinogram may be performed to look at the abscess cavity size, completeness of drainage, and catheter position and to look for fistulas. Simple abscess cavities may drain for 5 to 10 days. Abscesses secondary to fistulas from bowel, biliary, or urinary tracts may drain for 6 weeks or longer. Follow-up sinograms can be performed as clinically indicated based on collection complexity and amount and character of drainage. Many patients can be cared for on an outpatient basis once stable.

Catheter Removal

The three criteria for catheter removal are as follows:

1. Negligible drainage over 24 hours
2. Afebrile patient
3. Minimal residual cavity

Drains in small, superficial abscess cavities can be pulled all at once, whereas drains in large, deeper cavities may be gradually removed over a few days, which promotes healing by secondary intention.

Abdominal and Pelvic Abscesses: General

Most abdominal and pelvic abscesses are secondary to underlying bowel disease or seen after surgery. Percutaneous abscess drainage for postoperative abdominal abscesses has become the accepted primary treatment of choice, with cure being the expected goal. Percutaneous drainage has also played a principal role in the treatment of **diverticular, appendiceal,** and **Crohn disease**–related abscesses.[125-127] Drainage of abscesses in these acutely ill patients can help alleviate sepsis and allow the necessary curative surgery to be performed on an elective basis.

Drainage of **abdominal abscesses** is often best performed with CT guidance, which allows the best visualization and avoids adjacent bowel loops. CT also provides an overview of the entire abdomen, to ensure all collections are drained. Ultrasound can provide excellent guidance for percutaneous abscess drainage; however, careful review of CT imaging assists in planning an optimal approach free of intervening bowel. Unlike CT, ultrasound is especially valuable in the treatment of critically ill patients who cannot be transported to the radiology department.

Pelvic abscesses are of variable origin and have been notoriously difficult to access because of their deep location, overlying bowel, blood vessels, and urinary bladder. Traditional approaches include an **anterior transperitoneal** approach or a **posterior transgluteal** approach. The transgluteal approach is relatively painful, and care must be taken to avoid the sciatic nerve. Small, deep pelvic abscesses may be difficult to access safely using traditional approaches.

Ultrasound-guided **transvaginal drainage** has been established as a viable alternative to these traditional approaches[128,129] (Fig. 17.17). Needle guides are available for endovaginal probes that help guide the needle into the fluid collection (Videos 17.6 and 17.7). This transvaginal approach can be used to drain tuboovarian abscesses unresponsive to medical treatment. The trocar technique may also be used successfully for transvaginal drain placement. **Transrectal** ultrasound-guided drainage has also been described in the drainage of pelvic fluid collections,[130] but such an approach is infrequently used.

For **nonpurulent pelvic collections,** immediate catheter drainage is not necessarily indicated. Many of these patients respond to a one-step aspiration, lavage, and antibiotic therapy based on results of cultures of the aspirates.[131,132]

Enteric abscesses often have communication with the GI tract. For these abscesses to be drained successfully, the GI communication first must be recognized, then allowed to heal and close before removal of the catheter. Fistulas will not close if there is distal obstruction, tumor, or persistent infection. Even with the most aggressive techniques, however, success in treating abscesses with enteric communication is lower than for noncommunicating abscesses.[133,134] A particular challenge exists in the percutaneous treatment of Crohn disease–related abscesses. Obviating surgery in the short term can only be achieved in about 50% of patients, with a much lower success rate in patients with preexisting bowel fistulas.[127,135] **Enterocutaneous fistulas** may develop along the drain tract in these patients.

Specific Anatomic Applications

Liver

In addition to antibiotics, percutaneous aspiration or drainage should be considered as a primary treatment for most **pyogenic liver abscesses** (Fig. 17.18). Pyogenic liver abscesses are most often caused by (1) hematogenous seeding from intestinal sources, such as **appendicitis** or **diverticulitis;** (2) direct extension from **cholecystitis** or **cholangitis** (Fig. 17.19); or (3) surgery or trauma.

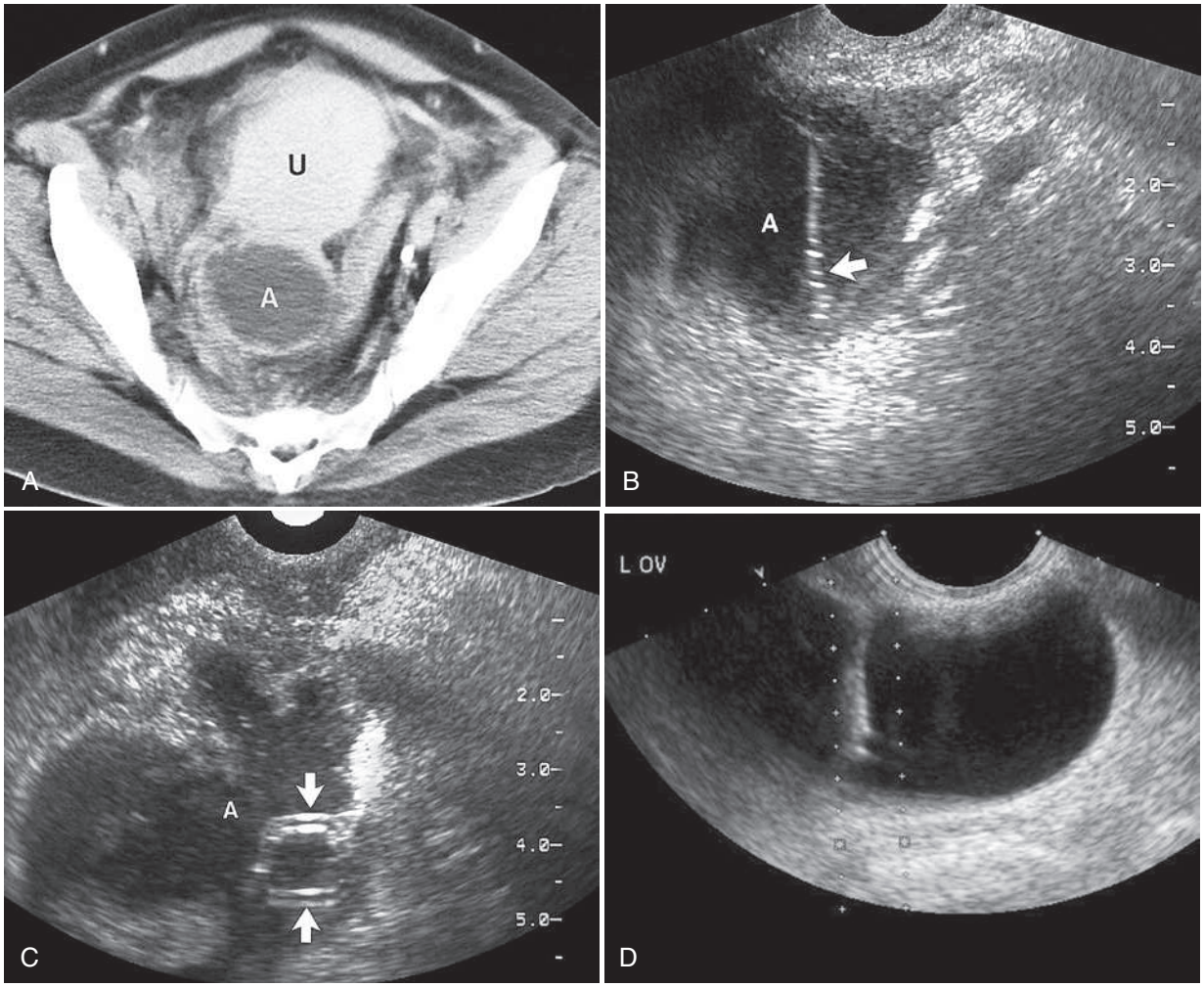

FIG. 17.17 Ultrasound-Guided Transvaginal Drainage of Pelvic Abscess. (A) Contrast-enhanced CT scan shows an abscess *(A)* deep in the pelvis, posterior to the uterus *(U)*. **(B)** TVS shows needle tip *(arrow)* in abscess cavity *(A)*. **(C)** With the catheter exchange technique, a locking-loop catheter *(arrows)* was inserted into the abscess cavity for drainage. **(D)** In a different patient, TVS shows needle within adnexal cyst at time of aspiration centered within needle guide markers.

As with abscesses elsewhere in the body, the sonographic appearance of hepatic abscess is usually a complex fluid collection. Both ultrasound and CT provide excellent guidance for percutaneous aspiration or drainage of hepatic abscesses, with a 67% to 94% cure rate.[133,136-138]

Some suggest treating pyogenic liver abscesses with antibiotics and percutaneous needle aspiration alone, without catheter drainage, although multiple aspiration procedures may be required.[139] Such an approach is particularly reasonable in smaller abscesses, less than 5 cm.[140,141] Multiple small (<1 cm) **microabscesses** are typically treated with antibiotics alone after diagnostic aspiration.[142] Final cure often depends on identification and appropriate treatment of the infectious source.

Amebic liver abscesses are caused by *Entamoeba histolytica*. Most amebic liver abscesses are effectively treated with metronidazole alone with 85% to 95% success.[143,144] However, percutaneous abscess drainage of amebic abscesses is indicated if the diagnosis is uncertain, the cavity is large (>5 cm) or enlarging, pyogenic superinfection is a concern, or there are signs of abscess cavity rupture.[144,145] Catheter drainage in these situations is safe and generally provides a rapid cure.

Historically, liver **hydatid abscesses** caused by *Echinococcus granulosus* were considered a contraindication to percutaneous abscess drainage because of the concern of **anaphylactic reaction** to cyst contents. More recently, these abscesses have been successfully treated with percutaneous aspiration combined with appropriate anthelmintic therapy.[146]

Complications of percutaneous hepatic abscess drainage include sepsis, hemorrhage, and catheter transgression of the pleura. Sepsis may occur in up to 25% of patients, even with antibiotic therapy.[141] Intercostal placement of a drain should be avoided; such a path could introduce bacteria into the pleural space.

Biliary Tract

Gallbladder. Percutaneous **cholecystostomy** has evolved into a favorable alternative to surgery in critically ill patients with **acute calculous** and **acalculous cholecystitis.** In contrast to

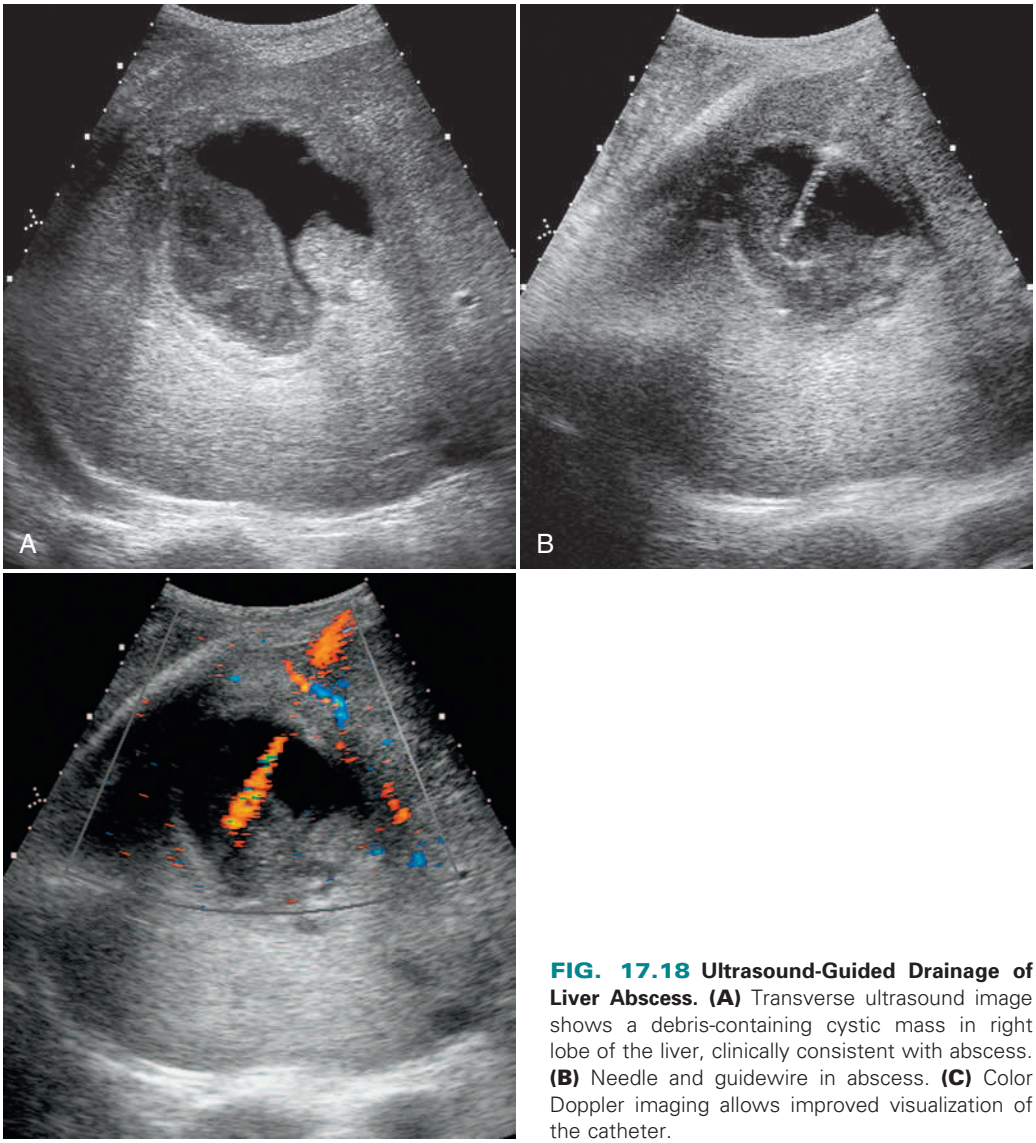

FIG. 17.18 Ultrasound-Guided Drainage of Liver Abscess. (A) Transverse ultrasound image shows a debris-containing cystic mass in right lobe of the liver, clinically consistent with abscess. **(B)** Needle and guidewire in abscess. **(C)** Color Doppler imaging allows improved visualization of the catheter.

surgical cholecystostomy, a major advantage of ultrasound-guided cholecystostomy is that the procedure can be performed at the patient's bedside. Thus critically ill patients need not be moved to the operating room or the radiology department. Similar to other drainage procedures, the cholecystostomy catheter is easily placed with ultrasound guidance using a transhepatic route and either the trocar method or guidewire exchange (Seldinger) technique (Fig. 17.20).

Cholecystostomy can be successfully performed in up to 100% of cases, with rapid clinical improvement in 56% to 95% of patients.[147-149] Because of the severe comorbidities of these patients, mortality rates of 36% to 59% have been reported in hospitalized patients after cholecystostomy tube placement.[147,149]

Gallbladder aspiration alone may also be considered in treating the noncritically ill patient with acute cholecystitis who is a high surgical risk (Fig. 17.21). Given that positive blood cultures are present in less than 50% of patients with acute cholecystitis, continuous drainage may not be as critical in the management of this condition. One study showed a 77% clinical response in high-risk surgical patients using aspiration alone, compared with a 90% response in those treated with percutaneous cholecystostomy.[150] Care must be taken to avoid direct puncture of the gallbladder wall without intervening hepatic parenchyma in patients with biliary obstruction because of the risk of significant bile leakage.[151]

Bile Ducts. Percutaneous **transhepatic cholangiography** and drainage is traditionally performed using "blind" cholangiography with fluoroscopy for initial needle placement. However, the combined use of ultrasound for the initial needle puncture and fluoroscopy for final catheter placement using the guidewire exchange technique optimizes the advantages of both guidance systems for transhepatic cholangiography, biliary drainage, and other invasive procedures. Select ducts may be punctured under ultrasound guidance for transhepatic cholangiography or as the site of definitive catheter placement. In patients with segmental biliary obstruction, a blind technique allows initial opacification

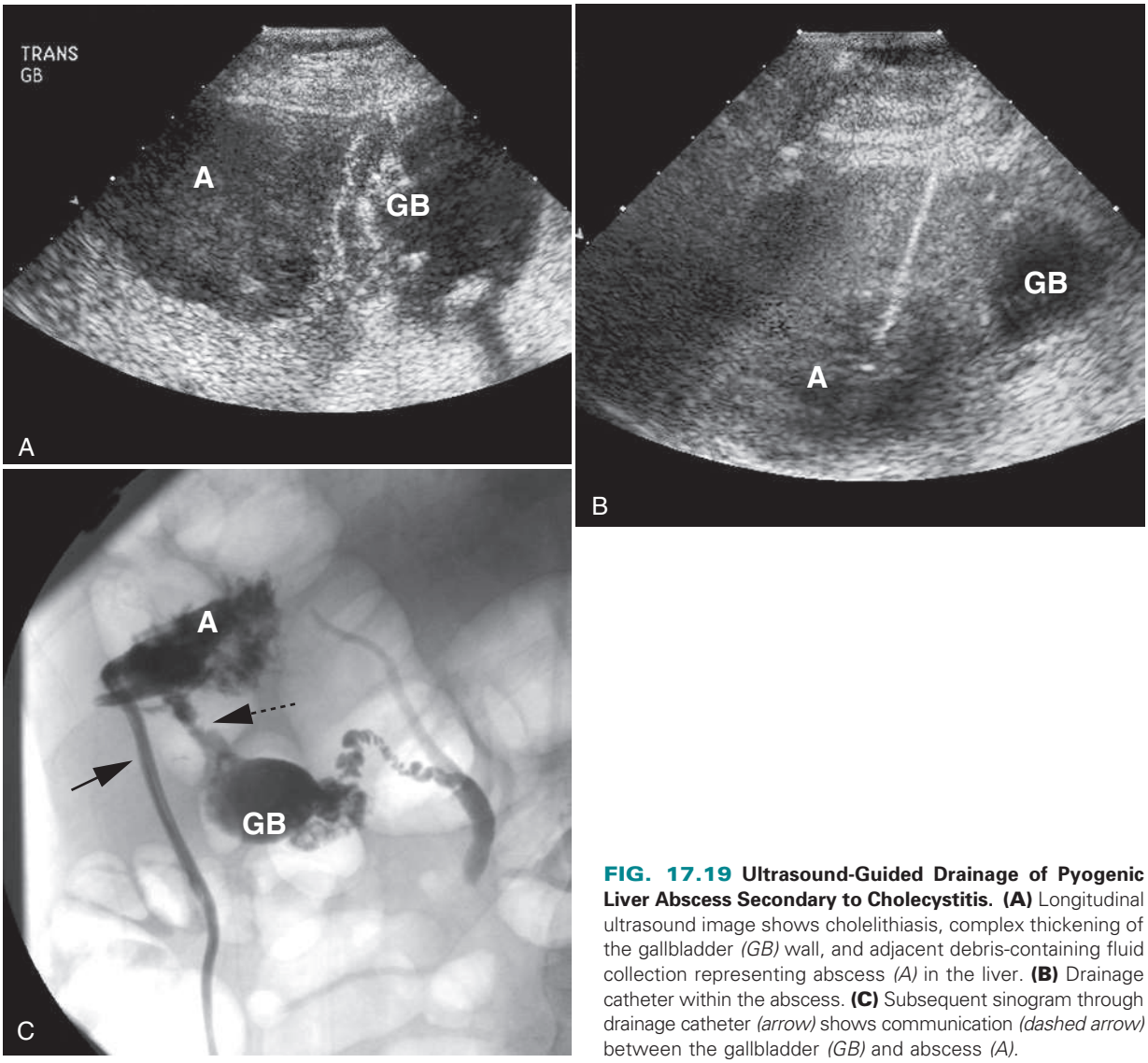

FIG. 17.19 Ultrasound-Guided Drainage of Pyogenic Liver Abscess Secondary to Cholecystitis. (A) Longitudinal ultrasound image shows cholelithiasis, complex thickening of the gallbladder *(GB)* wall, and adjacent debris-containing fluid collection representing abscess *(A)* in the liver. **(B)** Drainage catheter within the abscess. **(C)** Subsequent sinogram through drainage catheter *(arrow)* shows communication *(dashed arrow)* between the gallbladder *(GB)* and abscess *(A)*.

of the biliary system only by "chance," whereas ultrasound allows guided, direct puncture of the appropriate bile duct.

Pancreas

Percutaneous aspiration or drainage of pancreatic fluid collections typically arises in the setting of pancreatitis. In the absence of infection or obstruction of an adjacent hollow viscus, acute pancreatis-related peripancreatic fluid collections require no therapy.[152] Similarly, sterile pancreatic necrosis does not usually require treatment.

Infected **pancreatic necrosis** and some **pseudocysts** eventually require percutaneous intervention. Although CT is superior to ultrasound in evaluation of pancreatitis, ultrasound provides easy guidance for percutaneous interventional procedures (e.g., fluid aspiration) in these patients. Standard management of infected pancreatic necrosis is surgical debridement.[153] However, percutaneous drainage may provide short-term control of sepsis in almost 75% and cure in 50% of patients. Such a procedure typically involves very-large-bore catheters with frequent, vigorous irrigation, essentially resulting in a "percutaneous necrosectomy."[154]

Pancreatic pseudocysts arise in about 6% of patients following an episode of acute pancreatitis.[155] About half of pseudocysts will resolve spontaneously (but only a third of those >6 cm).[156,157] Simple aspiration of pancreatic pseudocysts is associated with a high rate of recurrence; therefore catheter drainage is preferred in select cases[156-159] (Fig. 17.22). Depending on location, endoscopic cystogastrostomy is another commonly used technique. Indications for pancreatic pseudocyst drainage include the following[160]:

- Symptoms related to pseudocyst
- Complication of infection or bleeding
- Increase in size during the observation period
- A diameter of 6 cm or more
- No decrease in size during last 6 weeks of observation

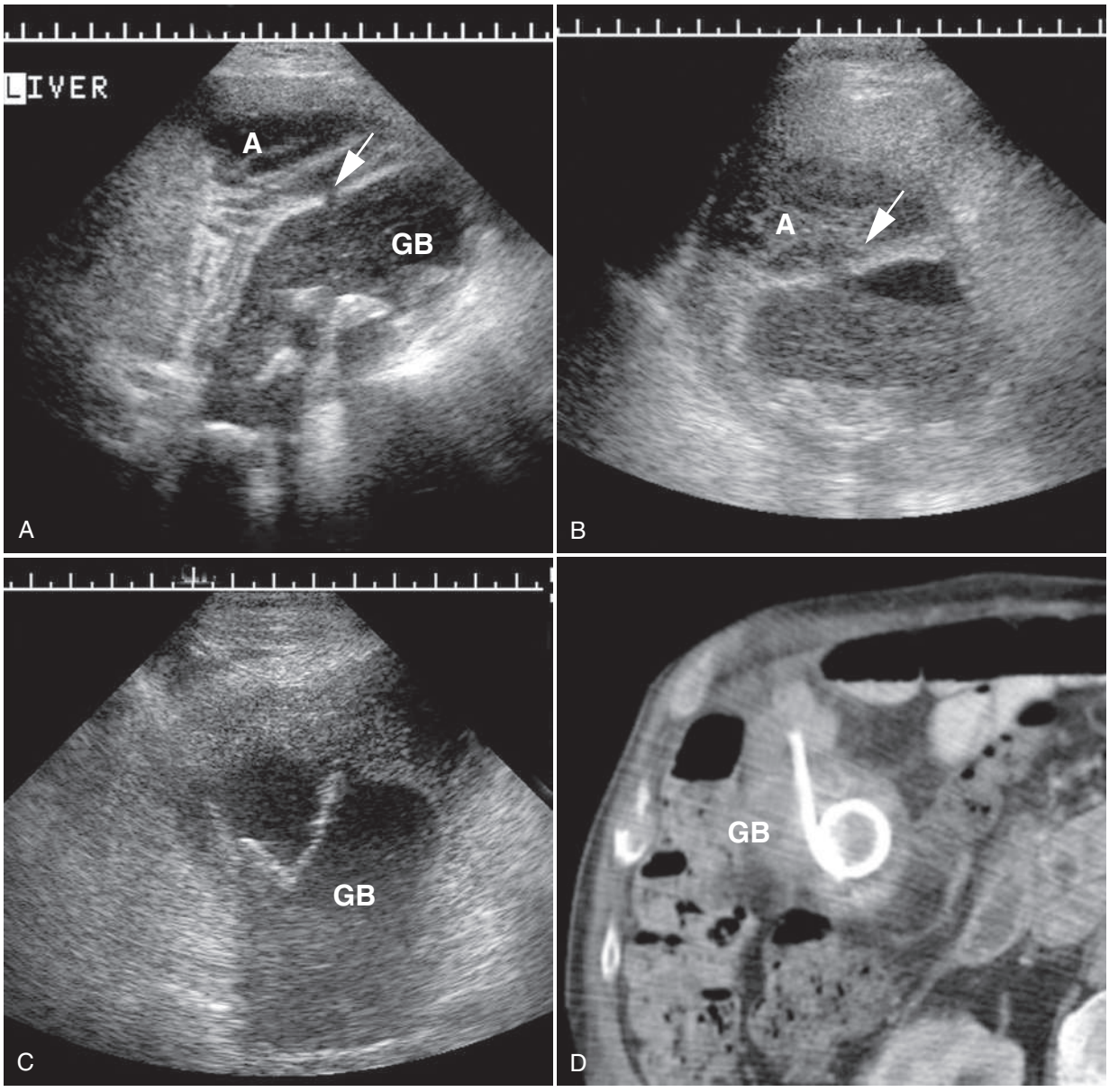

FIG. 17.20 Cholecystostomy Using Ultrasound Guidance. (A) Longitudinal and **(B)** transverse ultrasound images show stones within the gallbladder *(GB)* and adjacent debris-containing fluid collection representing abscess *(A)*. Perforation of gallbladder wall is identified *(arrow)*. **(C)** Drainage catheter was placed using ultrasound guidance. **(D)** Subsequent CT confirms catheter placement within gallbladder lumen.

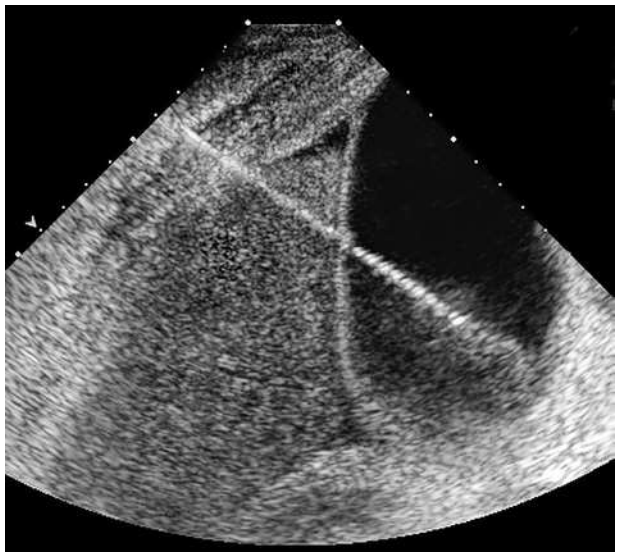

FIG. 17.21 Ultrasound-Guided Gallbladder Aspiration. Using freehand technique, a needle is advanced transhepatically into the lumen of a sludge-filled gallbladder.

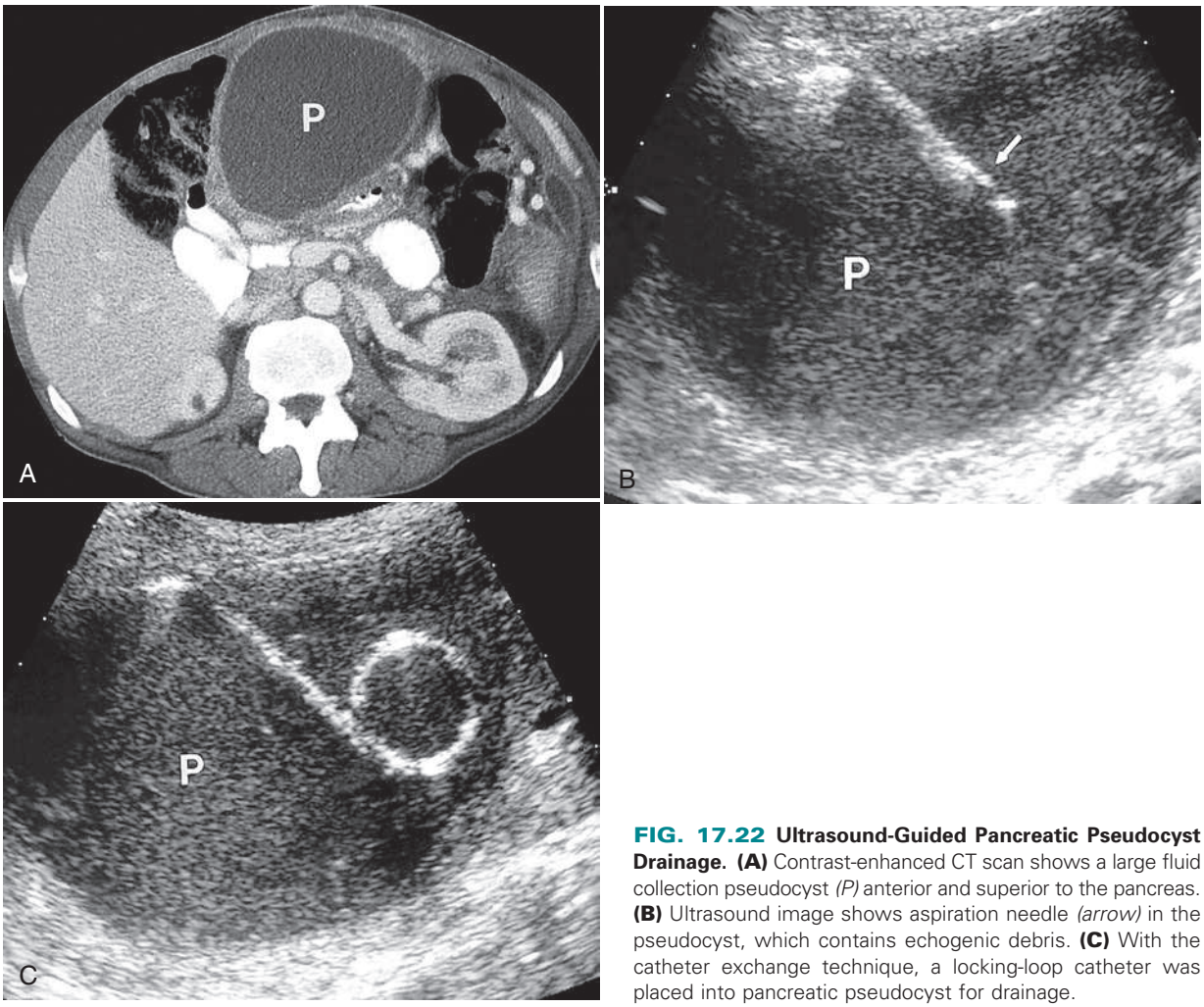

FIG. 17.22 Ultrasound-Guided Pancreatic Pseudocyst Drainage. (A) Contrast-enhanced CT scan shows a large fluid collection pseudocyst *(P)* anterior and superior to the pancreas. **(B)** Ultrasound image shows aspiration needle *(arrow)* in the pseudocyst, which contains echogenic debris. **(C)** With the catheter exchange technique, a locking-loop catheter was placed into pancreatic pseudocyst for drainage.

Success of percutaneous pseudocyst drainage ranges from 70% to 100%.[158] Ultimate success is associated with the integrity of the pancreatic duct.[161]

Spleen

Splenic abscesses are uncommon, and in the past they were often managed surgically. However, with increasing experience in percutaneous abscess management, image-guided drain placement into select splenic abscesses has been successfully performed in up to 100% of patients.[162-164] With smaller (≤3 cm) infected splenic fluid collections, a trial of aspiration may be reasonable, with drain placement if reaccumulation of fluid occurs. More complex, multiloculated abscesses or deep-seated collections should be managed surgically. The primary risk of spleen drainage is bleeding.[99]

Kidney

Most **renal abscesses** can be successfully managed with percutaneous drainage combined with systemic antibiotics (Fig. 17.23). The size of the abscess should be considered when determining the type of treatment. For abscesses smaller than 3 cm, antibiotics alone are typically sufficient for treatment.[165] Success in the percutaneous drainage of larger abscesses ranges from 70% to 90%, with better results in treating smaller abscesses.[165]

PERCUTANEOUS CYST MANAGEMENT

Renal Cyst

Simple aspiration of large, symptomatic or obstructing renal cysts is ineffective in the long-term management of renal cysts because of rapid reaccumulation of cyst fluid within the cavity.[166] This has led to interest in **aspiration combined with sclerosis** to provide more permanent ablation of the cyst (Fig. 17.24).

The procedure involves placing a 6- to 8-French drain into the cyst with aspiration of the cyst fluid. If the cyst's true benign nature is in doubt, the fluid may be sent for cytology and other chemical markers to confirm a serous nature of the fluid. If there is no evidence of malignancy, the cyst is then injected with contrast material under fluoroscopy to exclude a communication with the urinary collecting system; sclerosis should not be performed

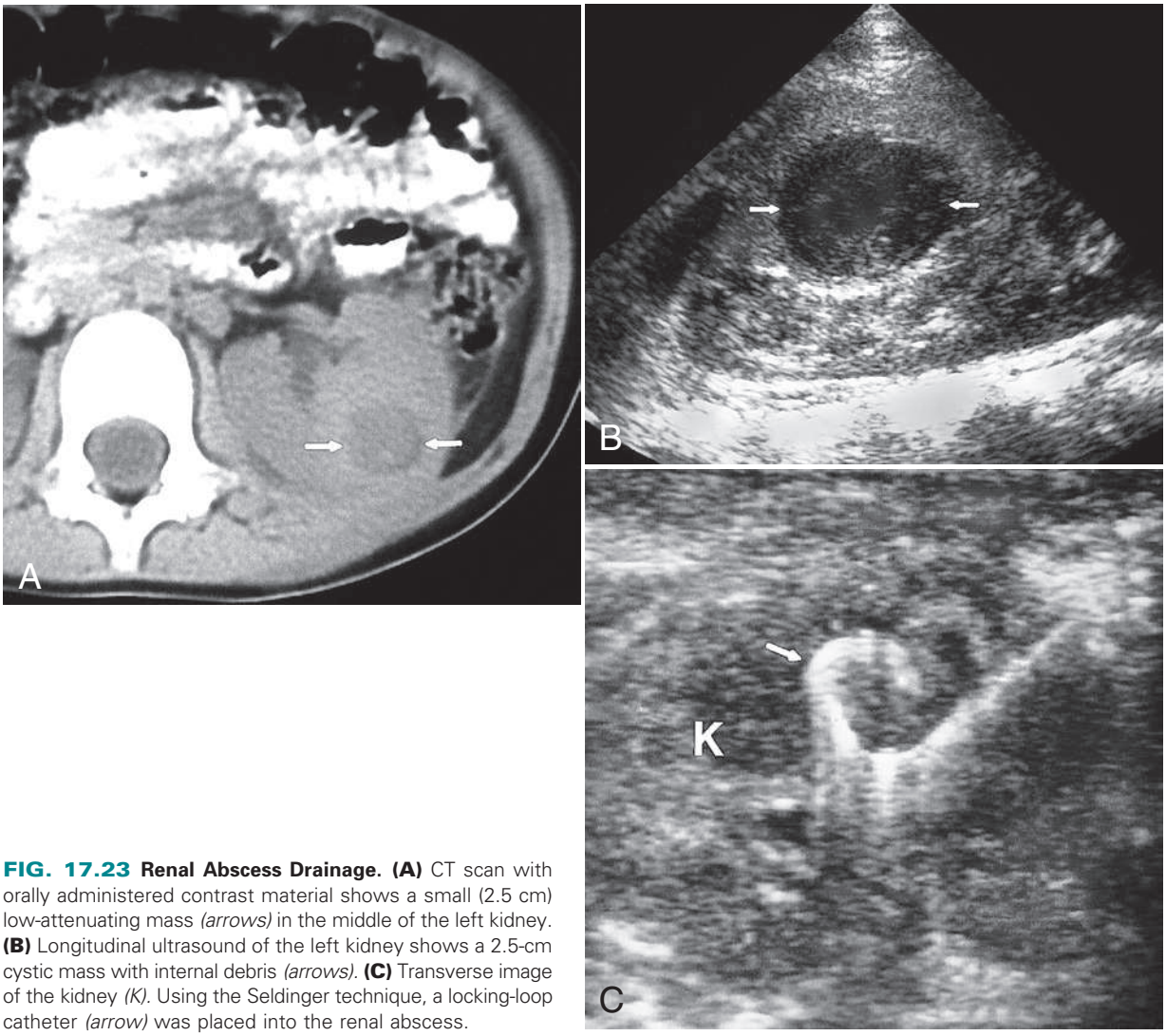

FIG. 17.23 Renal Abscess Drainage. (A) CT scan with orally administered contrast material shows a small (2.5 cm) low-attenuating mass *(arrows)* in the middle of the left kidney. **(B)** Longitudinal ultrasound of the left kidney shows a 2.5-cm cystic mass with internal debris *(arrows)*. **(C)** Transverse image of the kidney *(K)*. Using the Seldinger technique, a locking-loop catheter *(arrow)* was placed into the renal abscess.

if such a communication exists. The cyst is then injected with 95% alcohol at half the cyst volume, not to exceed 100 mL.[167] Injection of lidocaine with the alcohol minimizes the burning pain that often accompanies alcohol i njection. The patient is turned in various positions over a 20-minute period to facilitate exposure of the cyst wall to the sclerosing agent. The alcohol is aspirated and the drain removed or placed to continuous suction. Repeat injections may be performed over the subsequent 2 to 3 days to maximize sclerosis. This technique is successful in more than 95% of patients.[166,168] Although alcohol is the sclerosing agent typically used, other agents include tetracycline, doxycycline, talc, and iodine.

Liver Cyst

Similar to renal cysts, hepatic cysts can be effectively sclerosed to provide long-term relief of symptoms. A communication to the biliary tract is usually excluded by injecting the cyst with contrast under fluoroscopy. A smaller amount of alcohol (25% cyst volume) has been proposed.[169] In one study, investigators used alcohol and/or tetracycline or doxycycline in successfully treating 85% of symptomatic hepatic cysts.[170]

Ovarian Cyst

Historically, surgical extirpation of symptomatic ovarian cysts has been the standard of care. Percutaneous management has been discouraged because of the concern about seeding malignant cells in the inadvertent aspiration of a low-grade neoplasm and the poor sensitivity in characterizing aspirated cyst fluid.[171,172] However, given the well-recognized sonographic criteria of benign ovarian cysts, the confidence level in percutaneous aspiration of such symptomatic simple cysts has improved.

Ultrasound-guided aspiration of symptomatic, benign ovarian cysts is highly effective in alleviating patient symptoms.[173] A thorough ultrasound examination should be performed initially to fully characterize the symptomatic cyst. If the cyst can be confidently characterized as benign with no worrisome features, aspiration can be performed. Some recommend obtaining

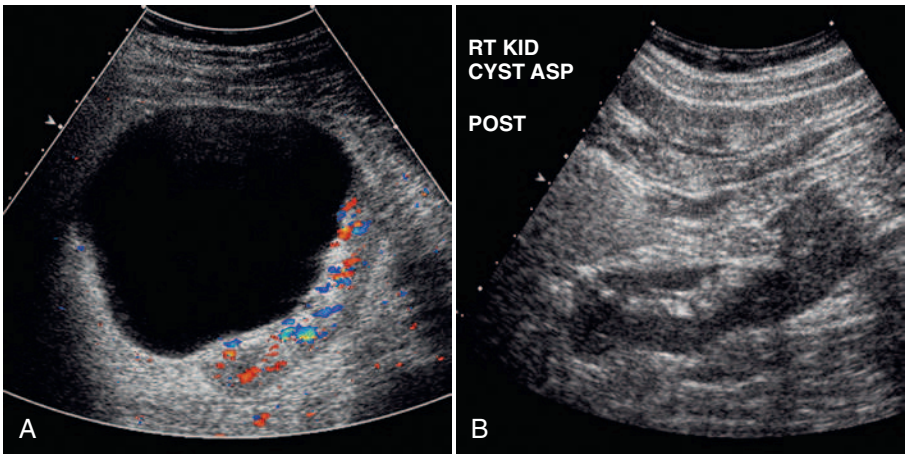

FIG. 17.24 Renal Cyst Sclerosis. (A) Longitudinal image of the right kidney shows a large, benign cyst. **(B)** After aspiration and sclerosis, the cyst is completely decompressed.

preprocedural serum tumor markers to help exclude malignancy.[174] Using either a transabdominal or an endovaginal approach, a 20-gauge or 22-gauge needle can be used to aspirate the cyst completely, with 100% relief in one series.[173] Fluid should be sent for appropriate studies, including cytology. Recurrence of the cyst may be seen in 11% to 26% of patients.[175,176]

REFERENCES

1. Ojalehto M, Tikkakoski T, Rissanen T, Apaja-Sarkkinen M. Ultrasound-guided percutaneous thoracoabdominal biopsy. Acta Radiol. 2002;43(2):152-158.
2. Winter TC, Lee Jr FT, Hinshaw JL. Ultrasound-guided biopsies in the abdomen and pelvis. Ultrasound Q. 2008;24(1):45-68.
3. Peterson P, Hayes TE, Arkin CF, et al. The preoperative bleeding time test lacks clinical benefit: College of American Pathologists' and American Society of Clinical Pathologists' position article. Arch Surg. 1998;133(2):134-139.
4. Brandt KR, Charboneau JW, Stephens DH, et al. CT- and US-guided biopsy of the pancreas. Radiology. 1993;187(1):99-104.
5. Little AF, Ferris JV, Dodd GD 3rd, Baron RL. Image-guided percutaneous hepatic biopsy: effect of ascites on the complication rate. Radiology. 1996;199(1):79-83.
6. Murphy FB, Barefield KP, Steinberg HV, Bernardino ME. CT- or sonography-guided biopsy of the liver in the presence of ascites: frequency of complications. AJR Am J Roentgenol. 1988;151(3):485-486.
7. Collet JP, Himbet F, Steg PG. Myocardial infarction after aspirin cessation in stable coronary artery disease patients. Int J Cardiol. 2000;76(2-3):257-258.
8. Douketis JD, Berger PB, Dunn AS, et al. The perioperative management of antithrombotic therapy: American College of Chest Physicians Evidence-Based Clinical Practice Guidelines (8th Edition). Chest. 2008;133(6 Suppl.):299S-339S.
9. Biondi-Zoccai GG, Lotrionte M, Agostoni P, et al. A systematic review and meta-analysis on the hazards of discontinuing or not adhering to aspirin among 50,279 patients at risk for coronary artery disease. Eur Heart J. 2006;27(22):2667-2674.
10. Sibon I, Orgogozo JM. Antiplatelet drug discontinuation is a risk factor for ischemic stroke. Neurology. 2004;62(7):1187-1189.
11. Wahl MJ. Dental surgery in anticoagulated patients. Arch Intern Med. 1998;158(15):1610-1616.
12. Hibbert RM, Atwell TD, Lekah A, et al. Safety of ultrasound-guided thoracentesis in patients with abnormal preprocedural coagulation parameters. Chest. 2013;144(2):456-463.
13. Kurup AN, Lekah A, Reardon ST, et al. Bleeding rate for ultrasound-guided paracentesis in thrombocytopenic patients. J Ultrasound Med. 2015;34(10):1833-1838.
14. McVay PA, Toy PT. Lack of increased bleeding after paracentesis and thoracentesis in patients with mild coagulation abnormalities. Transfusion. 1991;31(2):164-171.
15. Patel MD, Joshi SD. Abnormal preprocedural international normalized ratio and platelet counts are not associated with increased bleeding complications after ultrasound-guided thoracentesis. AJR Am J Roentgenol. 2011;197(1):W164-W168.
16. Atwell TD, Spanbauer JC, McMenomy BP, et al. The timing and presentation of major hemorrhage after 18,947 image-guided percutaneous biopsies. AJR Am J Roentgenol. 2015;205(1):190-195.
17. Korbet SM, Volpini KC, Whittier WL. Percutaneous renal biopsy of native kidneys: a single-center experience of 1,055 biopsies. Am J Nephrol. 2014;39(2):153-162.
18. Kriegshauser JS, Patel MD, Young SW, et al. Risk of bleeding after native renal biopsy as a function of preprocedural systolic and diastolic blood pressure. J Vasc Interv Radiol. 2015;26(2):206-212.
19. Hergesell O, Felten H, Andrassy K, et al. Safety of ultrasound-guided percutaneous renal biopsy-retrospective analysis of 1090 consecutive cases. Nephrol Dial Transplant. 1998;13(4):975-977.
20. Meola M, Barsotti G, Cupisti A, et al. Free-hand ultrasound-guided renal biopsy: report of 650 consecutive cases. Nephron. 1994;67(4):425-430.
21. Parrish AE. Complications of percutaneous renal biopsy: a review of 37 years' experience. Clin Nephrol. 1992;38(3):135-141.
22. Shidham GB, Siddiqi N, Beres JA, et al. Clinical risk factors associated with bleeding after native kidney biopsy. Nephrology (Carlton). 2005;10(3):305-310.
23. Whittier WL, Korbet SM. Timing of complications in percutaneous renal biopsy. J Am Soc Nephrol. 2004;15(1):142-147.
24. Atwell TD, Smith RL, Hesley GK, et al. Incidence of bleeding after 15,181 percutaneous biopsies and the role of aspirin. AJR Am J Roentgenol. 2010;194(3):784-789.
25. Silverman SG, Mueller PR, Pfister RC. Hemostatic evaluation before abdominal interventions: an overview and proposal. AJR Am J Roentgenol. 1990;154(2):233-238.
26. Rodgers RP, Levin J. A critical reappraisal of the bleeding time. Semin Thromb Hemost. 1990;16(1):1-20.
27. Boyum JH, Atwell TD, Schmit GD, et al. Incidence and risk factors for adverse events related to image-guided liver biopsy. Mayo Clin Proc. 2016;91(3):329-335.
28. Peter FW, Benkovic C, Muehlberger T, et al. Effects of desmopressin on thrombogenesis in aspirin-induced platelet dysfunction. Br J Haematol. 2002;117(3):658-663.

29. Smith TP, McDermott VG, Ayoub DM, et al. Percutaneous transhepatic liver biopsy with tract embolization. Radiology. 1996;198(3):769-774.
30. Zins M, Vilgrain V, Gayno S, et al. US-guided percutaneous liver biopsy with plugging of the needle track: a prospective study in 72 high-risk patients. Radiology. 1992;184(3):841-843.
31. Sheafor DH, Paulson EK, Kliewer MA, et al. Comparison of sonographic and CT guidance techniques: does CT fluoroscopy decrease procedure time? AJR Am J Roentgenol. 2000;174(4):939-942.
32. Sheafor DH, Paulson EK, Simmons CM, et al. Abdominal percutaneous interventional procedures: comparison of CT and US guidance. Radiology. 1998;207(3):705-710.
33. Kliewer MA, Sheafor DH, Paulson EK, et al. Percutaneous liver biopsy: a cost-benefit analysis comparing sonographic and CT guidance. AJR Am J Roentgenol. 1999;173(5):1199-1202.
34. Dameron RD, deLong DM, Fisher AJ, et al. Indeterminate findings on imaging-guided biopsy: should additional intervention be pursued? AJR Am J Roentgenol. 1999;173(2):461-464.
35. Kirchner J, Kickuth R, Laufer U, et al. CT fluoroscopy-assisted puncture of thoracic and abdominal masses: a randomized trial. Clin Radiol. 2002;57(3):188-192.
36. Erwin BC, Brynes RK, Chan WC, et al. Percutaneous needle biopsy in the diagnosis and classification of lymphoma. Cancer. 1986;57(5):1074-1078.
37. Hahn PF, Eisenberg PJ, Pitman MB, et al. Cytopathologic touch preparations (imprints) from core needle biopsies: accuracy compared with that of fine-needle aspirates. AJR Am J Roentgenol. 1995;165(5):1277-1279.
38. Miller DL, Wall RT. Fentanyl and diazepam for analgesia and sedation during radiologic special procedures. Radiology. 1987;162(1 Pt 1): 195-198.
39. Phal PM, Brooks DM, Wolfe R. Sonographically guided biopsy of focal lesions: a comparison of freehand and probe-guided techniques using a phantom. AJR Am J Roentgenol. 2005;184(5):1652-1656.
40. Hatfield MK, Beres RA, Sane SS, Zaleski GX. Percutaneous imaging-guided solid organ core needle biopsy: coaxial versus noncoaxial method. AJR Am J Roentgenol. 2008;190(2):413-417.
41. Fornage BD. A simple phantom for training in ultrasound-guided needle biopsy using the freehand technique. J Ultrasound Med. 1989;8(12): 701-703.
42. McNamara Jr MP, McNamara ME. Preparation of a homemade ultrasound biopsy phantom. J Clin Ultrasound. 1989;17(6):456-458.
43. Hamper UM, Savader BL, Sheth S. Improved needle-tip visualization by color Doppler sonography. AJR Am J Roentgenol. 1991;156(2):401-402.
44. Yu SC, Liew CT, Lau WY, et al. US-guided percutaneous biopsy of small (< or = 1-cm) hepatic lesions. Radiology. 2001;218(1):195-199.
45. Buscarini L, Fornari F, Bolondi L, et al. Ultrasound-guided fine-needle biopsy of focal liver lesions: techniques, diagnostic accuracy and complications. A retrospective study on 2091 biopsies. J Hepatol. 1990;11(3):344-348.
46. Caturelli E, Rapaccini GL, Sabelli C, et al. Ultrasound-guided fine-needle aspiration biopsy in the diagnosis of hepatic hemangioma. Liver. 1986;6(6):326-330.
47. Cronan JJ, Esparza AR, Dorfman GS, et al. Cavernous hemangioma of the liver: role of percutaneous biopsy. Radiology. 1988;166(1 Pt 1):135-138.
48. Tung GA, Cronan JJ. Percutaneous needle biopsy of hepatic cavernous hemangioma. J Clin Gastroenterol. 1993;16(2):117-122.
49. Terriff BA, Gibney RG, Scudamore CH. Fatality from fine-needle aspiration biopsy of a hepatic hemangioma. AJR Am J Roentgenol. 1990;154(1): 203-204.
50. Shanbhogue AK, Prasad SR, Takahashi N, et al. Recent advances in cytogenetics and molecular biology of adult hepatocellular tumors: implications for imaging and management. Radiology. 2011;258(3):673-693.
51. Doolittle DA, Atwell TD, Sanchez W, et al. Safety and outcomes of percutaneous biopsy of 61 hepatic adenomas. AJR Am J Roentgenol. 2016;206(4): 1-6.
52. Dodd GD 3rd, Carr BI. Percutaneous biopsy of portal vein thrombus: a new staging technique for hepatocellular carcinoma. AJR Am J Roentgenol. 1993;161(2):229-233.
53. van der Poorten D, Kwok A, Lam T, et al. Twenty-year audit of percutaneous liver biopsy in a major Australian teaching hospital. Intern Med J. 2006;36(11):692-699.
54. Bilreiro C, Noruegas MJ, Goncalves I, Moreira A. Ultrasound-guided liver biopsies in children–a single center experience and risk factors for minor bleeding. J Pediatr Gastroenterol Nutr. 2017. [Epub ahead of print.]
55. Bolia R, Matta J, Malik R, Hardikar W. Outpatient liver biopsy in children: safety, feasibility and economic impact. J Pediatr Gastroenterol Nutr. 2017. [Epub ahead of print.]
56. Firpi RJ, Soldevila-Pico C, Abdelmalek MF, et al. Short recovery time after percutaneous liver biopsy: should we change our current practices? Clin Gastroenterol Hepatol. 2005;3(9):926-929.
57. Garcia-Tsao G, Boyer JL. Outpatient liver biopsy: how safe is it? Ann Intern Med. 1993;118(2):150-153.
58. Piccinino F, Sagnelli E, Pasquale G, Giusti G. Complications following percutaneous liver biopsy. A multicentre retrospective study on 68,276 biopsies. J Hepatol. 1986;2(2):165-173.
59. Van Thiel DH, Gavaler JS, Wright H, Tzakis A. Liver biopsy. Its safety and complications as seen at a liver transplant center. Transplantation. 1993;55(5):1087-1090.
60. McGill DB, Rakela J, Zinsmeister AR, Ott BJ. A 21-year experience with major hemorrhage after percutaneous liver biopsy. Gastroenterology. 1990;99(5):1396-1400.
61. Terjung B, Lemnitzer I, Dumoulin FL, et al. Bleeding complications after percutaneous liver biopsy. An analysis of risk factors. Digestion. 2003;67(3): 138-145.
62. Paulsen SD, Nghiem HV, Negussie E, et al. Evaluation of imaging-guided core biopsy of pancreatic masses. AJR Am J Roentgenol. 2006;187(3): 769-772.
63. Matsubara J, Okusaka T, Morizane C, et al. Ultrasound-guided percutaneous pancreatic tumor biopsy in pancreatic cancer: a comparison with metastatic liver tumor biopsy, including sensitivity, specificity, and complications. J Gastroenterol. 2008;43(3):225-232.
64. Hall-Craggs MA, Lees WR. Fine-needle aspiration biopsy: pancreatic and biliary tumors. AJR Am J Roentgenol. 1986;147(2):399-403.
65. Lees WR, Hall-Craggs MA, Manhire A. Five years' experience of fine-needle aspiration biopsy: 454 consecutive cases. Clin Radiol. 1985;36(5): 517-520.
66. Carlson SK, Johnson CD, Brandt KR, et al. Pancreatic cystic neoplasms: the role and sensitivity of needle aspiration and biopsy. Abdom Imaging. 1998;23(4):387-393.
67. Lewandrowski K, Lee J, Southern J, et al. Cyst fluid analysis in the differential diagnosis of pancreatic cysts: a new approach to the preoperative assessment of pancreatic cystic lesions. AJR Am J Roentgenol. 1995;164(4):815-819.
68. Yong WH, Southern JF, Pins MR, et al. Cyst fluid NB/70K concentration and leukocyte esterase: two new markers for differentiating pancreatic serous tumors from pseudocysts. Pancreas. 1995;10(4):342-346.
69. Paulsen SD, Nghiem HV, Negussie E, et al. Evaluation of imaging-guided core biopsy of pancreatic masses. AJR Am J Roentgenol. 2006;187(3): 769-772.
70. Smith EH. Complications of percutaneous abdominal fine-needle biopsy. Review. Radiology. 1991;178(1):253-258.
71. Silverman SG, Gan YU, Mortele KJ, et al. Renal masses in the adult patient: the role of percutaneous biopsy. Radiology. 2006;240(1):6-22.
72. Marconi L, Dabestani S, Lam TB, et al. Systematic review and meta-analysis of diagnostic accuracy of percutaneous renal tumour biopsy. Eur Urol. 2015. doi:10.1016/j.eururo.2016.04.027.
73. Prince J, Bultman E, Hinshaw L, et al. Patient and tumor characteristics can predict nondiagnostic renal mass biopsy findings. J Urol. 2015;193(6): 1899-1904.
74. Wood BJ, Khan MA, McGovern F, et al. Imaging guided biopsy of renal masses: indications, accuracy and impact on clinical management. J Urol. 1999;161(5):1470-1474.
75. Caoili EM, Bude RO, Higgins EJ, et al. Evaluation of sonographically guided percutaneous core biopsy of renal masses. AJR Am J Roentgenol. 2002;179(2):373-378.
76. Richter F, Kasabian NG, Irwin Jr RJ, et al. Accuracy of diagnosis by guided biopsy of renal mass lesions classified indeterminate by imaging studies. Urology. 2000;55(3):348-352.
77. Kunkle DA, Crispen PL, Chen DY, et al. Enhancing renal masses with zero net growth during active surveillance. J Urol. 2007;177(3):849-853.

78. Frank I, Blute ML, Cheville JC, et al. Solid renal tumors: an analysis of pathological features related to tumor size. J Urol. 2003;170(6 Pt 1): 2217-2220.
79. Lane BR, Babineau D, Kattan MW, et al. A preoperative prognostic nomogram for solid enhancing renal tumors 7 cm or less amenable to partial nephrectomy. J Urol. 2007;178(2):429-434.
80. Dechet CB, Zincke H, Sebo TJ, et al. Prospective analysis of computerized tomography and needle biopsy with permanent sectioning to determine the nature of solid renal masses in adults. J Urol. 2003;169(1):71-74.
81. Bogan ML, Kopecky KK, Kraft JL, et al. Needle biopsy of renal allografts: comparison of two techniques. Radiology. 1990;174(1):273-275.
82. Ralls PW, Barakos JA, Kaptein EM, et al. Renal biopsy-related hemorrhage: frequency and comparison of CT and sonography. J Comput Assist Tomogr. 1987;11(6):1031-1034.
83. Wickre CG, Golper TA. Complications of percutaneous needle biopsy of the kidney. Am J Nephrol. 1982;2(4):173-178.
84. Paulsen SD, Nghiem HV, Korobkin M, et al. Changing role of imaging-guided percutaneous biopsy of adrenal masses: evaluation of 50 adrenal biopsies. AJR Am J Roentgenol. 2004;182(4):1033-1037.
85. Welch TJ, Sheedy PF 2nd, Stephens DH, et al. Percutaneous adrenal biopsy: review of a 10-year experience. Radiology. 1994;193(2):341-344.
86. Mantero F, Terzolo M, Arnaldi G, et al. A survey on adrenal incidentaloma in Italy. Study Group on Adrenal Tumors of the Italian Society of Endocrinology. J Clin Endocrinol Metab. 2000;85(2):637-644.
87. Casola G, Nicolet V, vanSonnenberg E, et al. Unsuspected pheochromocytoma: risk of blood-pressure alterations during percutaneous adrenal biopsy. Radiology. 1986;159(3):733-735.
88. Steinsapir J, Carr AA, Prisant LM, Bransome Jr ED. Metyrosine and pheochromocytoma. Arch Intern Med. 1997;157(8):901-906.
89. Olson MC, Atwell TD, Harmsen WS, et al. Safety and accuracy of percutaneous image-guided core biopsy of the spleen. AJR Am J Roentgenol. 2016;206(3):655-659.
90. Lieberman S, Libson E, Maly B, et al. Imaging-guided percutaneous splenic biopsy using a 20- or 22-gauge cutting-edge core biopsy needle for the diagnosis of malignant lymphoma. AJR Am J Roentgenol. 2003;181(4): 1025-1027.
91. Tam A, Krishnamurthy S, Pillsbury EP, et al. Percutaneous image-guided splenic biopsy in the oncology patient: an audit of 156 consecutive cases. J Vasc Interv Radiol. 2008;19(1):80-87.
92. Keogan MT, Freed KS, Paulson EK, et al. Imaging-guided percutaneous biopsy of focal splenic lesions: update on safety and effectiveness. AJR Am J Roentgenol. 1999;172(4):933-937.
93. Lucey BC, Boland GW, Maher MM, et al. Percutaneous nonvascular splenic intervention: a 10-year review. AJR Am J Roentgenol. 2002;179(6): 1591-1596.
94. Jansson SE, Bondestam S, Heinonen E, et al. Value of liver and spleen aspiration biopsy in malignant diseases when these organs show no signs of involvement in sonography. Acta Med Scand. 1983;213(4): 279-281.
95. Solbiati L, Bossi MC, Bellotti E, et al. Focal lesions in the spleen: sonographic patterns and guided biopsy. AJR Am J Roentgenol. 1983;140(1):59-65.
96. Soderstrom N. How to use cytodiagnostic spleen puncture. Acta Med Scand. 1976;199(1-2):1-5.
97. Caraway NP, Fanning CV. Use of fine-needle aspiration biopsy in the evaluation of splenic lesions in a cancer center. Diagn Cytopathol. 1997;16(4):312-316.
98. Patel N, Dawe G, Tung K. Ultrasound-guided percutaneous splenic biopsy using an 18-G core biopsy needle: our experience with 52 cases. Br J Radiol. 2015;88(1055):20150400.
99. Lucey BC, Boland GW, Maher MM, et al. Percutaneous nonvascular splenic intervention: a 10-year review. AJR Am J Roentgenol. 2002;179(6): 1591-1596.
100. Civardi G, Vallisa D, Berte R, et al. Ultrasound-guided fine needle biopsy of the spleen: high clinical efficacy and low risk in a multicenter Italian study. Am J Hematol. 2001;67(2):93-99.
101. Liao WY, Chen MZ, Chang YL, et al. US-guided transthoracic cutting biopsy for peripheral thoracic lesions less than 3 cm in diameter. Radiology. 2000;217(3):685-691.
102. Sheth S, Hamper UM, Stanley DB, et al. US guidance for thoracic biopsy: a valuable alternative to CT. Radiology. 1999;210(3):721-726.
103. Douglas BR, Charboneau JW, Reading CC. Ultrasound-guided intervention: expanding horizons. Radiol Clin North Am. 2001;39(3):415-428.
104. Nolsoe C, Nielsen L, Torp-Pedersen S, Holm HH. Major complications and deaths due to interventional ultrasonography: a review of 8000 cases. J Clin Ultrasound. 1990;18(3):179-184.
105. Livraghi T, Damascelli B, Lombardi C, Spagnoli I. Risk in fine-needle abdominal biopsy. J Clin Ultrasound. 1983;11(2):77-81.
106. Fornari F, Civardi G, Cavanna L, et al. Complications of ultrasonically guided fine-needle abdominal biopsy. Results of a multicenter Italian study and review of the literature. The Cooperative Italian Study Group. Scand J Gastroenterol. 1989;24(8):949-955.
107. Martino CR, Haaga JR, Bryan PJ, et al. CT-guided liver biopsies: eight years' experience. Work in progress. Radiology. 1984;152(3):755-757.
108. Welch TJ, Sheedy PF 2nd, Johnson CD, et al. CT-guided biopsy: prospective analysis of 1,000 procedures. Radiology. 1989;171(2):493-496.
109. Bergenfeldt M, Genell S, Lindholm K, et al. Needle-tract seeding after percutaneous fine-needle biopsy of pancreatic carcinoma. Case report. Acta Chir Scand. 1988;154(1):77-79.
110. Caturelli E, Rapaccini GL, Anti M, et al. Malignant seeding after fine-needle aspiration biopsy of the pancreas. Diagn Imaging Clin Med. 1985;54(2): 88-91.
111. Haddad FS, Somsin AA. Seeding and perineal implantation of prostatic cancer in the track of the biopsy needle: three case reports and a review of the literature. J Surg Oncol. 1987;35(3):184-191.
112. Greenstein A, Merimsky E, Baratz M, Braf Z. Late appearance of perineal implantation of prostatic carcinoma after perineal needle biopsy. Urology. 1989;33(1):59-60.
113. Onodera H, Oikawa M, Abe M, et al. Cutaneous seeding of hepatocellular carcinoma after fine-needle aspiration biopsy. J Ultrasound Med. 1987;6(5):273-275.
114. Kiser GC, Totonchy M, Barry JM. Needle tract seeding after percutaneous renal adenocarcinoma aspiration. J Urol. 1986;136(6):1292-1293.
115. Muller NL, Bergin CJ, Miller RR, Ostrow DN. Seeding of malignant cells into the needle track after lung and pleural biopsy. Can Assoc Radiol J. 1986;37(3):192-194.
116. Fajardo LL. Breast tumor seeding along localization guide wire tracks. Radiology. 1988;169(2):580-581.
117. Glasgow BJ, Brown HH, Zargoza AM, Foos RY. Quantitation of tumor seeding from fine needle aspiration of ocular melanomas. Am J Ophthalmol. 1988;105(5):538-546.
118. Hidai H, Sakuramoto T, Miura T, et al. Needle tract seeding following puncture of retroperitoneal liposarcoma. Eur Urol. 1983;9(6):368-369.
119. Raftopoulos Y, Furey WW, Kacey DJ, Podbielski FJ. Tumor implantation after computed tomography-guided biopsy of lung cancer. J Thorac Cardiovasc Surg. 2000;119(6):1288-1289.
120. Shinohara S, Yamamoto E, Tanabe M, et al. Implantation metastasis of head and neck cancer after fine needle aspiration biopsy. Auris Nasus Larynx. 2001;28(4):377-380.
121. Haaga JR, Alfidi RJ, Havrilla TR, et al. CT detection and aspiration of abdominal abscesses. AJR Am J Roentgenol. 1977;128(3):465-474.
122. vanSonnenberg E, D'Agostino HB, Casola G, et al. Percutaneous abscess drainage: current concepts. Radiology. 1991;181(3):617-626.
123. Gazelle GS, Mueller PR. Abdominal abscess. Imaging and intervention. Radiol Clin North Am. 1994;32(5):913-932.
124. Hui GC, Amaral J, Stephens D, et al. Gas distribution in intraabdominal and pelvic abscesses on CT is associated with drainability. AJR Am J Roentgenol. 2005;184(3):915-919.
125. Sahai A, Belair M, Gianfelice D, et al. Percutaneous drainage of intra-abdominal abscesses in Crohn's disease: short and long-term outcome. Am J Gastroenterol. 1997;92(2):275-278.
126. Lorenz JM, Al-Refaie WB, Cash BD, et al. ACR appropriateness criteria radiologic management of infected fluid collections. J Am Coll Radiol. 2015;12(8):791-799.
127. Men S, Akhan O, Koroglu M. Percutaneous drainage of abdominal abscess. Eur J Radiol. 2002;43(3):204-218.

128. Saokar A, Arellano RS, Gervais DA, et al. Transvaginal drainage of pelvic fluid collections: results, expectations, and experience. AJR Am J Roentgenol. 2008;191(5):1352-1358.
129. McGahan JP, Wu C. Sonographically guided transvaginal or transrectal pelvic abscess drainage using the trocar method with a new drainage guide attachment. AJR Am J Roentgenol. 2008;191(5):1540-1544.
130. Nosher JL, Needell GS, Amorosa JK, Krasna IH. Transrectal pelvic abscess drainage with sonographic guidance. AJR Am J Roentgenol. 1986;146(5): 1047-1048.
131. Kuligowska E, Keller E, Ferrucci JT. Treatment of pelvic abscesses: value of one-step sonographically guided transrectal needle aspiration and lavage. AJR Am J Roentgenol. 1995;164(1):201-206.
132. Feld R, Eschelman DJ, Sagerman JE, et al. Treatment of pelvic abscesses and other fluid collections: efficacy of transvaginal sonographically guided aspiration and drainage. AJR Am J Roentgenol. 1994;163(5):1141-1145.
133. Lambiase RE, Deyoe L, Cronan JJ, Dorfman GS. Percutaneous drainage of 335 consecutive abscesses: results of primary drainage with 1-year follow-up. Radiology. 1992;184(1):167-179.
134. Schuster MR, Crummy AB, Wojtowycz MM, McDermott JC. Abdominal abscesses associated with enteric fistulas: percutaneous management. J Vasc Interv Radiol. 1992;3(2):359-363.
135. Gervais DA, Hahn PF, O'Neill MJ, Mueller PR. Percutaneous abscess drainage in Crohn disease: technical success and short- and long-term outcomes during 14 years. Radiology. 2002;222(3):645-651.
136. Johnson RD, Mueller PR, Ferrucci Jr JT, et al. Percutaneous drainage of pyogenic liver abscesses. AJR Am J Roentgenol. 1985;144(3):463-467.
137. vanSonnenberg E, Mueller PR, Ferrucci Jr JT. Percutaneous drainage of 250 abdominal abscesses and fluid collections. Part I: results, failures, and complications. Radiology. 1984;151(2):337-341.
138. Wong WM, Wong BC, Hui CK, et al. Pyogenic liver abscess: retrospective analysis of 80 cases over a 10-year period. J Gastroenterol Hepatol. 2002;17(9):1001-1007.
139. Giorgio A, Tarantino L, Mariniello N, et al. Pyogenic liver abscesses: 13 years of experience in percutaneous needle aspiration with US guidance. Radiology. 1995;195(1):122-124.
140. Zerem E, Hadzic A. Sonographically guided percutaneous catheter drainage versus needle aspiration in the management of pyogenic liver abscess. AJR Am J Roentgenol. 2007;189(3):W138-W142.
141. Thomas J, Turner SR, Nelson RC, Paulson EK. Postprocedure sepsis in imaging-guided percutaneous hepatic abscess drainage: how often does it occur? AJR Am J Roentgenol. 2006;186(5):1419-1422.
142. Shankar S, van Sonnenberg E, Silverman SG, Tuncali K. Interventional radiology procedures in the liver. Biopsy, drainage, and ablation. Clin Liver Dis. 2002;6(1):91-118.
143. Krige JE, Beckingham IJ. ABC of diseases of liver, pancreas, and biliary system. BMJ. 2001;322(7285):537-540.
144. vanSonnenberg E, Mueller PR, Schiffman HR, et al. Intrahepatic amebic abscesses: indications for and results of percutaneous catheter drainage. Radiology. 1985;156(3):631-635.
145. Gervais DA, Brown SD, Connolly SA, et al. Percutaneous imaging-guided abdominal and pelvic abscess drainage in children. Radiographics. 2004;24(3):737-754.
146. Paksoy Y, Odev K, Sahin M, et al. Percutaneous treatment of liver hydatid cysts: comparison of direct injection of albendazole and hypertonic saline solution. AJR Am J Roentgenol. 2005;185(3):727-734.
147. Davis CA, Landercasper J, Gundersen LH, Lambert PJ. Effective use of percutaneous cholecystostomy in high-risk surgical patients: techniques, tube management, and results. Arch Surg. 1999;134(7):727-731.
148. Granlund A, Karlson BM, Elvin A, Rasmussen I. Ultrasound-guided percutaneous cholecystostomy in high-risk surgical patients. Langenbecks Arch Surg. 2001;386(3):212-217.
149. Sugiyama M, Tokuhara M, Atomi Y. Is percutaneous cholecystostomy the optimal treatment for acute cholecystitis in the very elderly? World J Surg. 1998;22(5):459-463.
150. Chopra S, Dodd GD 3rd, Mumbower AL, et al. Treatment of acute cholecystitis in non-critically ill patients at high surgical risk: comparison of clinical outcomes after gallbladder aspiration and after percutaneous cholecystostomy. AJR Am J Roentgenol. 2001;176(4):1025-1031.
151. Phillips G, Bank S, Kumari-Subaiya S, Kurtz LM. Percutaneous ultrasound-guided puncture of the gallbladder (PUPG). Radiology. 1982;145(3): 769-772.
152. AGA Institute medical position statement on acute pancreatitis. Gastroenterology. 2007;132(5):2019-2021.
153. Forsmark CE, Baillie J. AGA Institute technical review on acute pancreatitis. Gastroenterology. 2007;132(5):2022-2044.
154. Freeny PC, Hauptmann E, Althaus SJ, et al. Percutaneous CT-guided catheter drainage of infected acute necrotizing pancreatitis: techniques and results. AJR Am J Roentgenol. 1998;170(4):969-975.
155. Beger HG, Rau B, Mayer J, Pralle U. Natural course of acute pancreatitis. World J Surg. 1997;21(2):130-135.
156. Pitchumoni CS, Agarwal N. Pancreatic pseudocysts. When and how should drainage be performed? Gastroenterol Clin North Am. 1999;28(3): 615-639.
157. Yeo CJ, Bastidas JA, Lynch-Nyhan A, et al. The natural history of pancreatic pseudocysts documented by computed tomography. Surg Gynecol Obstet. 1990;170(5):411-417.
158. Neff R. Pancreatic pseudocysts and fluid collections: percutaneous approaches. Surg Clin North Am. 2001;81(2):399-403, xii.
159. Grosso M, Gandini G, Cassinis MC, et al. Percutaneous treatment (including pseudocystogastrostomy) of 74 pancreatic pseudocysts. Radiology. 1989;173(2):493-497.
160. Isaji S, Takada T, Kawarada Y, et al. JPN Guidelines for the management of acute pancreatitis: surgical management. J Hepatobiliary Pancreat Surg. 2006;13(1):48-55.
161. Nealon WH, Walser E. Main pancreatic ductal anatomy can direct choice of modality for treating pancreatic pseudocysts (surgery versus percutaneous drainage). Ann Surg. 2002;235(6):751-758.
162. Kang M, Kalra N, Gulati M, et al. Image guided percutaneous splenic interventions. Eur J Radiol. 2007;64(1):140-146.
163. Chou YH, Tiu CM, Chiou HJ, et al. Ultrasound-guided interventional procedures in splenic abscesses. Eur J Radiol. 1998;28(2):167-170.
164. Thanos L, Dailiana T, Papaioannou G, et al. Percutaneous CT-guided drainage of splenic abscess. AJR Am J Roentgenol. 2002;179(3):629-632.
165. Siegel JF, Smith A, Moldwin R. Minimally invasive treatment of renal abscess. J Urol. 1996;155(1):52-55.
166. Fontana D, Porpiglia F, Morra I, Destefanis P. Treatment of simple renal cysts by percutaneous drainage with three repeated alcohol injection. Urology. 1999;53(5):904-907.
167. Lohela P. Ultrasound-guided drainages and sclerotherapy. Eur Radiol. 2002;12(2):288-295.
168. Mohsen T, Gomha MA. Treatment of symptomatic simple renal cysts by percutaneous aspiration and ethanol sclerotherapy. BJU Int. 2005;96(9): 1369-1372.
169. Moorthy K, Mihssin N, Houghton PW. The management of simple hepatic cysts: sclerotherapy or laparoscopic fenestration. Ann R Coll Surg Engl. 2001;83(6):409-414.
170. vanSonnenberg E, Wroblicka JT, D'Agostino HB, et al. Symptomatic hepatic cysts: percutaneous drainage and sclerosis. Radiology. 1994;190(2): 387-392.
171. Higgins RV, Matkins JF, Marroum MC. Comparison of fine-needle aspiration cytologic findings of ovarian cysts with ovarian histologic findings. Am J Obstet Gynecol. 1999;180(3 Pt 1):550-553.
172. Martínez-Onsurbe P, Ruiz Villaespesa A, Sanz Anquela JM, Valenzuela Ruiz PL. Aspiration cytology of 147 adnexal cysts with histologic correlation. Acta Cytol. 2001;45(6):941-947.
173. Troiano RN, Taylor KJ. Sonographically guided therapeutic aspiration of benign-appearing ovarian cysts and endometriomas. AJR Am J Roentgenol. 1998;171(6):1601-1605.
174. Mathevet P, Dargent D. Role of ultrasound guided puncture in the management of ovarian cysts]. J Gynecol Obstet Biol Reprod (Paris). 2001;30(1 Suppl.):S53-S58.
175. Lee CL, Lai YM, Chang SY, et al. The management of ovarian cysts by sono-guided transvaginal cyst aspiration. J Clin Ultrasound. 1993;21(8): 511-514.
176. Balat O, Sarac K, Sonmez S. Ultrasound guided aspiration of benign ovarian cysts: an alternative to surgery? Eur J Radiol. 1996;22(2):136-137.

CHAPTER 18

Organ Transplantation

Derek Muradali and Tanya Punita Chawla

SUMMARY OF KEY POINTS

- To perform an ultrasound assessment of a transplanted organ, the sonographer should be aware of the surgical technique used including the type and location of vascular and nonvascular anastomoses.
- Gray-scale parenchymal changes often reflect the vascular status of the allograft (e.g., echogenic intraluminal material within a dilated biliary tree of a transplanted liver may result from sloughing of the biliary epithelium as a result of hepatic arterial narrowing or thrombosis).
- Evaluation of the tissues surrounding the allograft is just as important as assessment of the allograft itself.
- Any presumed cyst identified in the parenchyma of the allograft or in the region of the hilum should be assessed with color Doppler to exclude the possibility of a pseudoaneurysm.
- The criteria for arterial stenosis are similar with different allografts in that high-turbulence flow is detected at the region of narrowing with a distal tardus-parvus waveform.
- When assessing transplanted veins (portal vein, renal vein, inferior vena cava), a threefold to fourfold velocity increase at the site of stenosis relative to the prestenotic segment on spectral interrogation represents a hemodynamically significant stenosis.
- Elevated resistive indices may be of limited value depending on the allograft being interrogated—in renal transplants they are a nonspecific marker of renal dysfunction; in liver transplants they are of no clinical relevance; and in pancreatic transplants that are failing, the resistive indices may not be elevated owing to the lack of a pancreatic capsule.

CHAPTER OUTLINE

LIVER TRANSPLANTATION
Surgical Technique
Normal Liver Transplant Ultrasound
Biliary Complications
Biliary Strictures
Bile Leaks
Recurrent Sclerosing Cholangitis
Biliary Sludge and Stones
Dysfunction of the Sphincter of Oddi
Arterial Complications
Hepatic Artery Thrombosis
Hepatic Artery Stenosis
Elevated Hepatic Arterial Resistive Index
Hepatic Artery Pseudoaneurysms
Celiac Artery Stenosis
Portal Vein Complications
Inferior Vena Cava Complications
Hepatic Vein Stenosis
Extrahepatic Fluid Collections
Adrenal Hemorrhage
Intrahepatic Fluid Collections
Abscess Versus Infarct
Intrahepatic Solid Masses
RENAL TRANSPLANTATION
Surgical Technique
Normal Renal Transplant Ultrasound
Gray-Scale Assessment
Doppler Assessment
Abnormal Renal Transplant
Parenchymal Pathology
Acute Tubular Necrosis and Acute Rejection
Chronic Rejection
Infection
Prerenal Vascular Complications
Arterial Thrombosis
Renal Artery Stenosis
Venous Thrombosis
Renal Vein Stenosis
Postrenal Collecting System Obstruction
Arteriovenous Malformations and Pseudoaneurysms
Fluid Collections
PANCREAS TRANSPLANTATION
Surgical Technique
Venous Drainage
Arterial Supply
Normal Pancreas Transplant Ultrasound
Role of Contrast-Enhanced Ultrasound
Abnormal Pancreas Transplant
Thrombosis
Arteriovenous Fistula and Pseudoaneurysms
Rejection
Pancreatitis
Fluid Collections
Miscellaneous Complications
POST TRANSPLANT LYMPHOPROLIFERATIVE DISORDER
Treatment Options

Organ transplantation is the preferred treatment for patients with end-stage liver, renal, and pancreatic disease. Patients with fulminant liver failure have no other treatment option apart from orthotopic liver transplantation. Although patients with renal or pancreatic failure may be treated with dialysis or medical therapy, their long-term survival and quality of life are far superior with organ transplantation. Recent improvements in graft survival have been attributed to a combination of better donor-recipient matching,[1] more effective immunosuppressive therapy, improvements in surgical technique, and early recognition

of transplant-related complications. These improvements have resulted in a 1-year patient survival rate of over 80% for each of these organ transplants.[2,3]

Because the clinical presentation of posttransplant complications varies widely and is often nonspecific, imaging studies are essential for monitoring the status of the allograft. If diagnosis is delayed, the function of the allograft may be permanently compromised, and in severe cases with complete loss of function, retransplantation may be warranted. However, the chronic shortage of suitable donor organs may delay or preclude immediate retransplantation, with devastating clinical consequences. Therefore preservation of the allograft function and early detection of complications, with institution of appropriate treatment, are essential in the clinical management of these patients.

Ultrasound has revolutionized the practice of organ transplantation. Liver, renal, and pancreatic transplants should be assessed with gray-scale, color Doppler, and spectral Doppler interrogation. Gray-scale sonography permits optimal assessment of the textural and morphologic changes of the parenchyma, and color and spectral Doppler ultrasound permit evaluation of both parenchymal perfusion and the status of the major transplanted artery and vein. This chapter focuses on the ultrasound appearances of the normal organ transplant, acute and chronic transplant-related complications, and potential errors of interpretation that can lead to misdiagnoses.

LIVER TRANSPLANTATION

From January 1, 1988 to June 30, 2016 in the United States, 143,856 patients underwent liver transplantation.[4] One-year survival in liver transplant patients is approximately 87%, with 1-year graft survival of 80.3%. Patients are selected for transplantation when their life expectancy without transplantation is less than their life expectancy after the procedure. **Hepatitis C** is the most common disease requiring transplantation, followed by **alcoholic liver disease** and **cryptogenic cirrhosis.** Other end-stage liver disorders treated by transplantation include **chronic cholestatic diseases,** such as primary biliary cirrhosis and primary sclerosing cholangitis; **metabolic diseases,** including hemochromatosis and Wilson disease; and **other hepatitides,** such as autoimmune hepatitis, chronic hepatitis B, and acute liver failure. Patients with end-stage hepatitis B cirrhosis were initially regarded as poor transplant candidates because of the high rate of recurrence of infection in the implant, associated with rapid progression to cirrhosis. The use of hyperimmunoglobulins and nucleoside analogues has changed these expectations to a more favorable outcome.[5]

Most centers consider transplantation only in patients with **early-stage hepatocellular carcinoma** (HCC) or rarely **neuroendocrine metastasis.** The generally accepted guidelines for transplantation in patients with HCC are the Milan criteria: (1) no lesion greater than 5 cm in diameter or (2) no more than three lesions greater than 3 cm in diameter.[5,6]

Contraindications for liver transplantation include compensated cirrhosis without complications, extrahepatic malignancy, cholangiocarcinoma, active untreated sepsis, advanced cardiopulmonary disease, active alcoholism or substance abuse, or an anatomic abnormality precluding the surgical procedure. Although portal vein thrombosis is not an absolute contraindication to liver transplantation, its presence makes the surgery more complex, and posttransplantation patients show higher morbidity and mortality rates.[5]

Surgical Technique

Traditionally, most adult liver transplants involve explantation of the recipient liver and replacement with a cadaveric allograft. The surgery requires four **vascular anastomoses** (suprahepatic vena cava, infrahepatic vena cava, hepatic artery, portal vein) as well as a **biliary anastomosis** (Fig. 18.1).

The **hepatic artery** is reconstructed with a "fish-mouth" anastomosis between the donor common hepatic artery and either the bifurcation of the right and left hepatic arteries or the branch point of the common hepatic artery into the gastroduodenal and proper hepatic arteries of the recipient. When the native hepatic artery is small in diameter or shows minimal flow, a donor iliac artery or splenic artery interposition graft may be anastomosed directly to the supraceliac or infrarenal aorta.[7] The end-to-end attachment of these patulous arterial ends leads to a normally expected mild widening at the arterial anastomosis.

The **portal vein anastomosis** is usually end to end between the donor and recipient portal veins. In cases of extensive recipient portal vein thrombosis, a venous jump graft from the donor portal vein or the iliac vein may be used, to the portomesenteric confluence, superior mesenteric vein (SMV), or a collateral vein, or as a last resort, an anastomosis between both the portal vein and the hepatic artery of the donor and the arterial vessels of the recipient.[7,8]

During hepatectomy, the **inferior vena cava** (IVC) of the recipient usually is transected above and below the intrahepatic

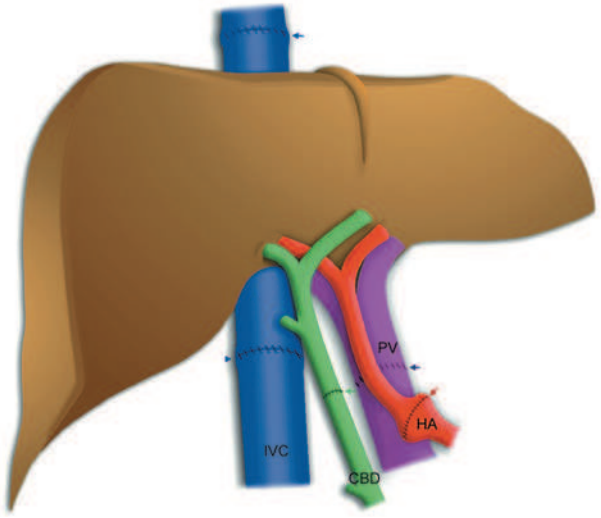

FIG. 18.1 Normal Liver Transplant: Surgical Approach. The transplanted liver shows four vascular anastomoses and a biliary anastomosis. The inferior vena cava *(IVC, blue)* is transplanted with a suprahepatic and infrahepatic anastomosis. An end-to-end anastomosis is often used for the common bile duct *(CBD, green)* and portal vein *(PV, purple),* whereas the hepatic artery *(HA, red)* is reconstructed with a "fish-mouth" anastomosis.

portion. The donor IVC is then anastomosed with two end-to-end suprahepatic and infrahepatic anastomoses. In an attempt to preserve the recipient retrohepatic IVC, some techniques advocate creation of an anastomosis between the donor and recipient IVC in an end-to-side or side-to-side configuration ("piggyback" anastomosis) or an end-to-end anastomosis between the donor IVC and a common stump of the three hepatic veins.[7] This piggyback anastomosis also prevents the need for venovenous bypass and retrocaval dissection, which are required for interposition of the donor IVC.

The donor and recipient **common bile duct** (CBD) are usually anastomosed end to end, after cholecystectomy. With this technique the sphincter of Oddi is preserved and acts as a barrier to the spread of infection. A T tube is typically left in situ for about 3 months and permits access for cholangiography or other biliary procedures. The use of a T tube has, however, decreased owing to an increased risk of bile leak.

When the recipient common hepatic duct is diseased (e.g., **sclerosing cholangitis**), too short, or too narrow in diameter, a **choledochojejunostomy** is performed.[7] This procedure involves an end-to-side anastomosis between the donor bile duct and a 40-cm recipient jejunal loop. It is associated with a higher risk of bile leaks, bleeding, enteric reflux and recurrent cholangitis compared with an end-to-end anastomosis.

The growing discrepancy between the number of patients awaiting transplantation and the number of available cadaveric donor organs has led to a progressive increase in the number of living related donor transplantations as well as split liver grafts from deceased donors. The recipient liver is replaced with the right lobe of a living donor. In the pediatric population, the lateral segment of the left lobe or the entire left lobe has been used successfully; the relatively small size of the left lobe is not sufficient, however, to sustain adequate liver function in an adult. Another advantage of using a right lobe (vs. left lobe) as the donor portion for transplantation is the relative ease of positioning the right lobe in the right subphrenic space, allowing a technically less challenging hepatic venous anastomosis, with a decrease in the incidence of torsion, compared with left lobe grafts.[9]

For **living related transplants,** donor surgery consists of cholecystectomy followed by right hepatectomy, removing segments V, VI, VII, and VIII as well as the right hepatic vein. Occasionally an extended right hepatectomy may be done to include a portion of segment IV and the middle hepatic vein. However, most surgeons prefer not to remove the middle hepatic vein, but to leave it intact in the donor because of the intimate relationship of the middle and left hepatic veins near their drainage into the IVC.[9]

In a **split liver graft from a deceased donor,** an adult recipient typically receives a trisegmental graft including the right lobe and segment IV and a pediatric recipient receives the left lateral segments. This technique is useful in increasing the numbers of transplants available but is more complex than when there is a single recipient.

Regardless of the type of liver transplantation, routine imaging evaluation of each anastomosis must be assessed with gray-scale ultrasound, color Doppler, and spectral Doppler interrogation. To interpret the gray-scale appearance and Doppler features of these anastomotic regions, the sonographer should be aware of the surgical techniques used in liver transplantation.

Normal Liver Transplant Ultrasound

The normal liver transplant has a homogeneous or slightly heterogeneous echotexture on gray-scale ultrasound, appearing identical to a normal, nontransplanted liver. In the early postoperative period, there is usually a small amount of free intraperitoneal fluid or small, perihepatic seromas or hematomas, which tend to resolve within 7 to 10 days.

The **biliary tree** should have a normal appearance, with an anechoic lumen and thin, imperceptible walls. If a T tube is in situ, the adjacent duct wall may appear mildly prominent secondary to irritation and edema. Ideally, the biliary anastomosis (end to end or biliary enteric) should be visualized and inspected for changes in caliber or wall thickness.

Pneumobilia is often observed in patients with choledochojejunostomy and appears as bright, echogenic foci with or without posterior acoustic shadowing in the bile duct lumen. The disappearance of previously documented pneumobilia should alert the sonographer to possible interval development of a biliary stricture at the biliary-enteric anastomosis. In addition, the sonographer should be aware that **intraductal biliary air** may be confused with tiny biliary stones or adjacent hepatic arterial calcifications because these structures can appear identical on gray-scale imaging (Fig. 18.2).

Vascular patency of the transplanted vessels (hepatic artery, portal vein, hepatic veins, IVC) is assessed by (1) direct inspection for narrowing of the diameter, (2) presence of thrombus within the vessel lumen, and (3) documentation of normal spectral waveforms with appropriate directional flow. Particular attention should be paid to the anastomotic regions because these areas have a higher propensity to develop a hemodynamically significant stenosis compared with the remaining vessel. Because intrahepatic segmental stenoses or occlusions can develop, the hepatic artery and main portal vein, as well as their major right and left branches, should be investigated with color and spectral Doppler (Fig. 18.3).

The **normal hepatic artery** shows a rapid systolic upstroke, with an acceleration time (AT; time from end diastole to first systolic peak) of less than 100 cm/sec, and continuous flow throughout diastole, with a resistive index (RI) of 0.5 to 0.7. A **normal portal vein** is typically smooth in contour, has an anechoic lumen, and may show a subtle change in caliber at the surgical anastomosis. The portal veins show continuous, monophasic, hepatopetal flow with mild velocity variations caused by respiration. The Doppler appearance of the **hepatic veins** shows a phasic waveform, reflecting physiologic changes in blood flow during the cardiac cycle.

Biliary Complications

Biliary tract complications are an important cause of morbidity and mortality in 15% to 30% of patients with liver transplantation.[10-12] Complications related to biliary-enteric anastomoses usually manifest within the first month of surgery and include anastomotic breakdown, bleeding, and an increased risk of ascending cholangitis from bacterial overgrowth.

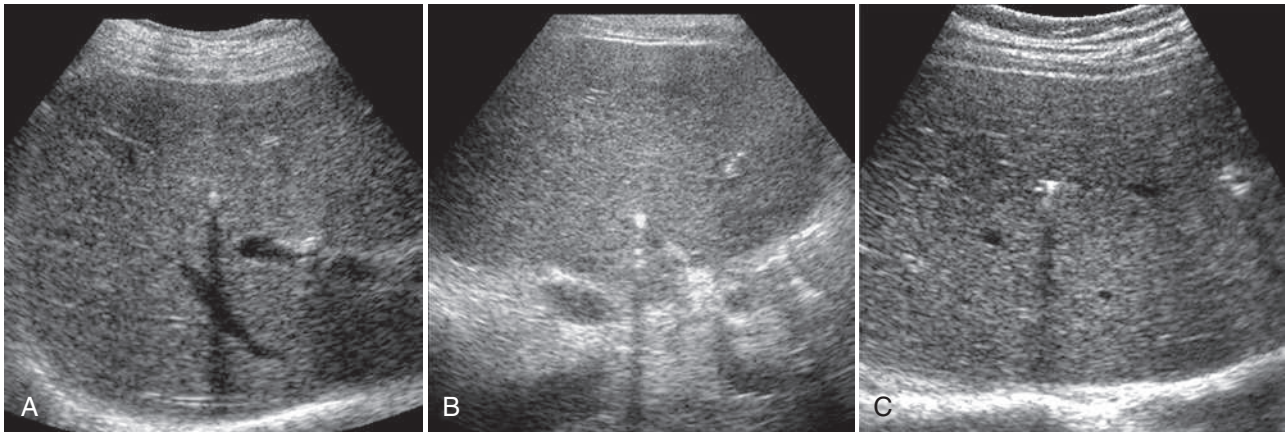

FIG. 18.2 Echogenic Foci in Liver Transplant. Transverse sonograms show similar bright echogenic foci with posterior acoustic shadowing secondary to **(A)** intrahepatic calcification; **(B)** hepatic arterial calcifications; and **(C)** pneumobilia. Note the ring-down artifact associated with the pneumobilia.

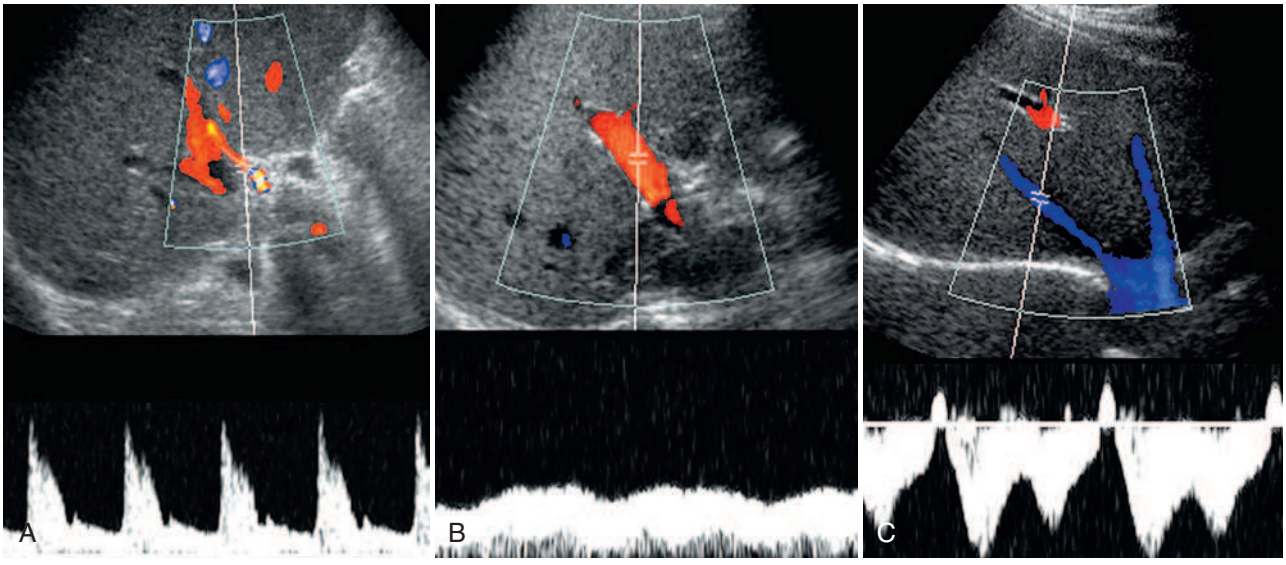

FIG. 18.3 Normal Liver Transplant: Color and Spectral Doppler. Color and spectral Doppler images of normal **(A)** hepatic artery, **(B)** main portal vein, and **(C)** right hepatic vein. (With permission from Crossin JD, Muradali D, Wilson SR. US of liver transplants: normal and abnormal. Radiographics. 2003;23[5]:1093-1114.[5])

Choledochocholedochostomy-related complications most frequently manifest after the first posttransplantation month and are often managed by endoscopic retrograde cholangiopancreatography (ERCP).[11] Regardless of the type of anastomoses used, biliary tract complications can be broadly classified as those related to leaks, strictures, intraluminal sludge or stones, dysfunction of the sphincter of Oddi, and recurrent disease.

Biliary Strictures

Early diagnosis of biliary tree complications may be difficult because transplant recipients do not typically experience colic; the transplanted liver has a poor supply of nerves.[13] Therefore patients with biliary strictures may be asymptomatic or may have painless obstructive jaundice or abnormalities in liver function test (LFT) results.[11] These strictures can be categorized based on location and pathophysiology as anastomotic (extrahepatic) and intrahepatic strictures (Fig. 18.4).

Anastomotic strictures are the most common cause of biliary obstruction after transplantation[14,15] and arise from postsurgical scarring, resulting in retraction of the duct wall and narrowing of the luminal diameter.[16] These strictures are more common in patients with a Roux-en-Y choledochojejunostomy than in patients with an end-to-end biliary anastomosis. On ultrasound, a focal narrowing can sometimes be observed at the anastomoses, associated with dilation of the intrahepatic bile ducts, with a normal-sized or near-normal-sized distal CBD.

Intrahepatic strictures occur proximal to the anastomosis and may be unifocal or multifocal. The arterial supply of the distal CBD (recipient duct) is rich because of prominent collateral flow, whereas the reconstructed hepatic artery is the only blood supply to the proximal CBD and intrahepatic bile ducts (donor ducts).[11,17] Therefore most intrahepatic duct strictures result from ischemia caused by **hepatic artery occlusion** (thrombosis or significant stenosis). In rare cases, biliary ischemia may also be

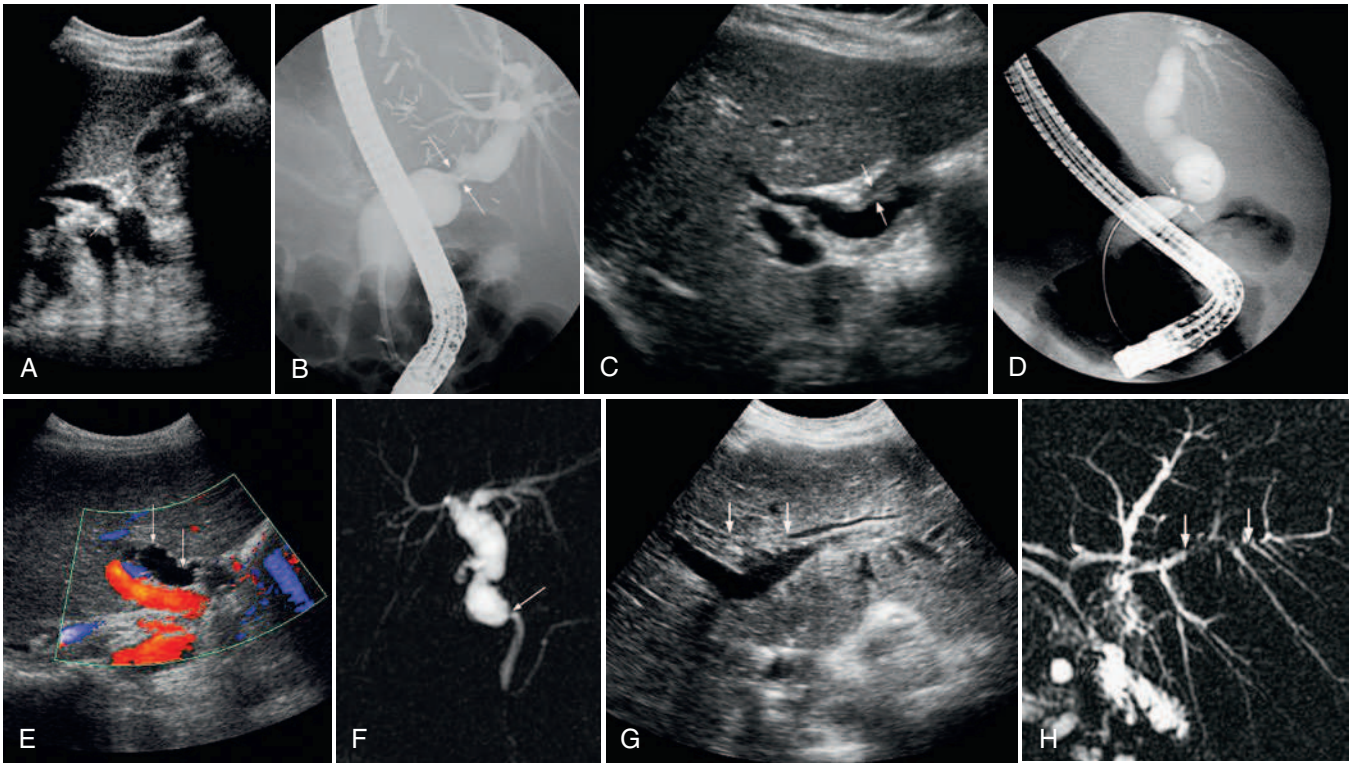

FIG. 18.4 Bile Duct: Strictures in Four Patients. *Patient 1:* **(A)** Gray-scale sonogram and **(B)** endoscopic retrograde cholangiopancreatography (ERCP) of common bile duct (CBD) anastomotic stricture *(arrows). Patient 2:* **(C)** Gray-scale sonogram and **(D)** ERCP show grossly thickened CBD walls *(arrows),* secondary to ascending cholangitis, a consequence of an anastomotic stricture. *Patient 3:* **(E)** Transverse sonogram shows central biliary dilation *(arrows).* **(F)** Magnetic resonance cholangiopancreatography (MRCP) image shows anastomotic stricture *(arrow). Patient 4:* **(G)** Transverse sonogram and **(H)** radial T2-weighted MRCP image show left intrahepatic bile duct stricture *(between arrows),* secondary to ischemia from hepatic artery stenosis. (**A** and **B** with permission from Crossin JD, Muradali D, Wilson SR. US of liver transplants: normal and abnormal. Radiographics. 2003;23[5]:1093-1114.[5])

caused by **prolonged cold preservation time** of the donor organ.[16,18] Other causes of intrahepatic strictures include immunogenic injury produced by chronic rejection, recurrent sclerosing cholangitis, ascending cholangitis, and cytomegalovirus (CMV) infections.

Ultrasound findings include focal areas of narrowing in the intrahepatic or proximal CBD and segmental dilation of the intrahepatic bile ducts, without evidence of an obstructing mass. The presence of echogenic intraluminal material within a dilated biliary tree is an ominous sign, sometimes caused by severe biliary ischemia, resulting in sloughing of the entire biliary epithelium. In this scenario the **intraluminal echogenic material** represents a combination of biliary sludge or stones, sloughed biliary epithelium, and intraluminal hemorrhage[16] (Fig. 18.5).

Bile Leaks

The incidence of bile leaks in patients with cadaveric liver transplants is 5% to 23%. The biliary complication rate is substantially higher in living related transplant recipients, possibly because of (1) leaks caused by division of the liver at retrieval, (2) variant biliary anatomy resulting in more than one bile duct orifice at the resection margin, and (3) ischemia of the right biliary tree.[19] Overall, biliary leaks can be categorized as occurring (1) at the anastomotic site, (2) at the T-tube exit site, (3) as a result of bile duct necrosis, and (4) secondary to percutaneous liver biopsies[20] (Fig. 18.6).

Most anastomotic leaks and T-tube exit site leaks occur within the first postsurgical month. **Anastomotic leaks** may be related to surgical technique or may result from ischemia caused by hepatic artery compromise. Clinically, anastomotic leaks are associated with bile peritonitis or intraabdominal sepsis and may manifest on ultrasound as a large periportal collection, a subhepatic collection, or ascites. **T-tube exit leaks** are related to technical errors when placing the T-tube and are usually detected incidentally at cholangiography. The resulting biloma is usually small, and patients with these types of bile leaks are usually asymptomatic.[20]

Leaks from **bile duct necrosis** usually occur after the first postsurgical month and are a result of severe hepatic artery stenosis or hepatic artery thrombosis. This condition is often associated with progressive hepatic dysfunction and a poor clinical course, eventually necessitating retransplantation. On ultrasound, the biliary tree may be dilated and thick walled and may communicate with multiple surrounding bilomas.[20]

In rare cases, bile leaks can occur as a result of bile duct injury from **percutaneous liver biopsies.** Bile may leak from the needle track into the peritoneal cavity. These leaks can resolve without

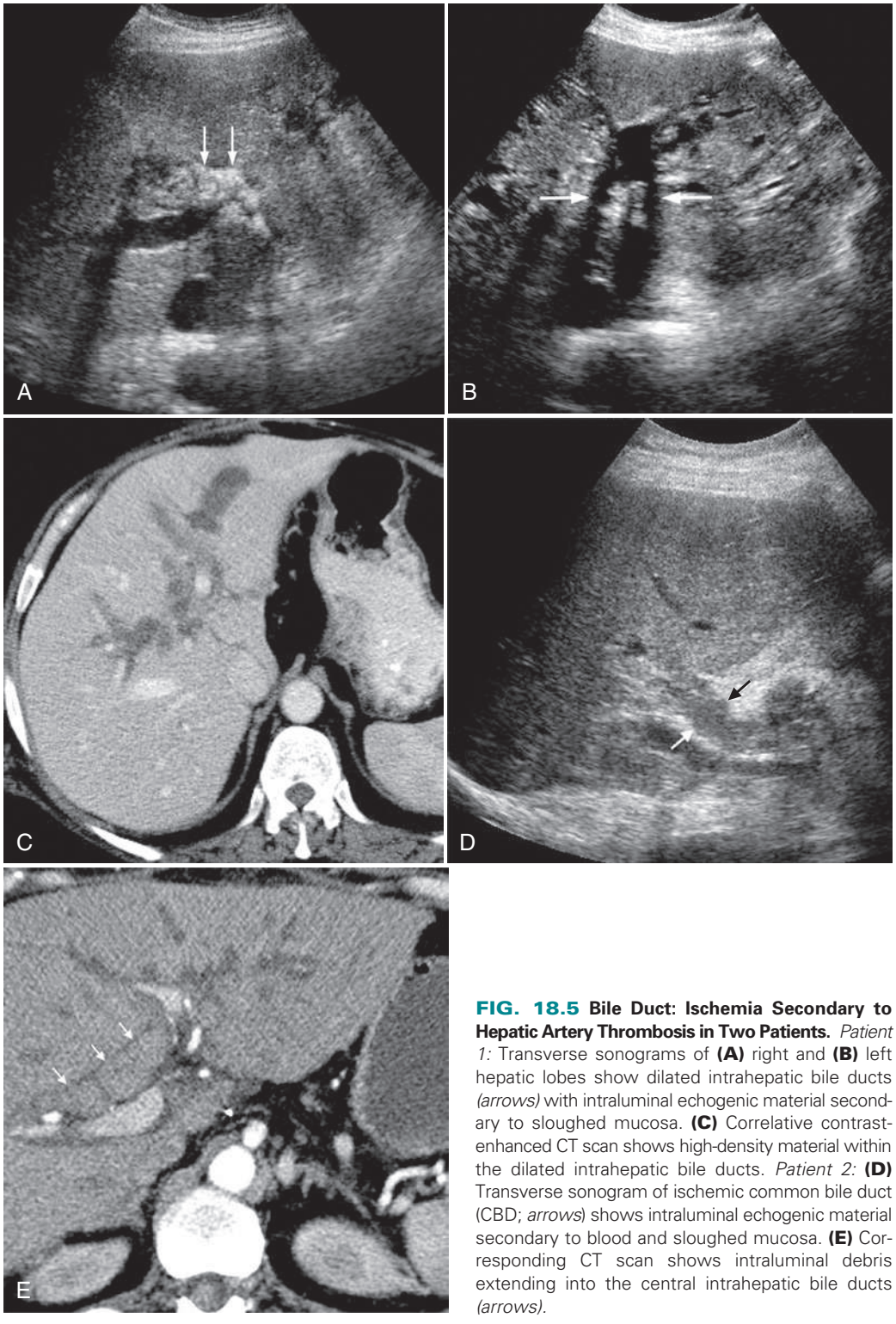

FIG. 18.5 Bile Duct: Ischemia Secondary to Hepatic Artery Thrombosis in Two Patients. *Patient 1:* Transverse sonograms of **(A)** right and **(B)** left hepatic lobes show dilated intrahepatic bile ducts *(arrows)* with intraluminal echogenic material secondary to sloughed mucosa. **(C)** Correlative contrast-enhanced CT scan shows high-density material within the dilated intrahepatic bile ducts. *Patient 2:* **(D)** Transverse sonogram of ischemic common bile duct (CBD; *arrows*) shows intraluminal echogenic material secondary to blood and sloughed mucosa. **(E)** Corresponding CT scan shows intraluminal debris extending into the central intrahepatic bile ducts *(arrows)*.

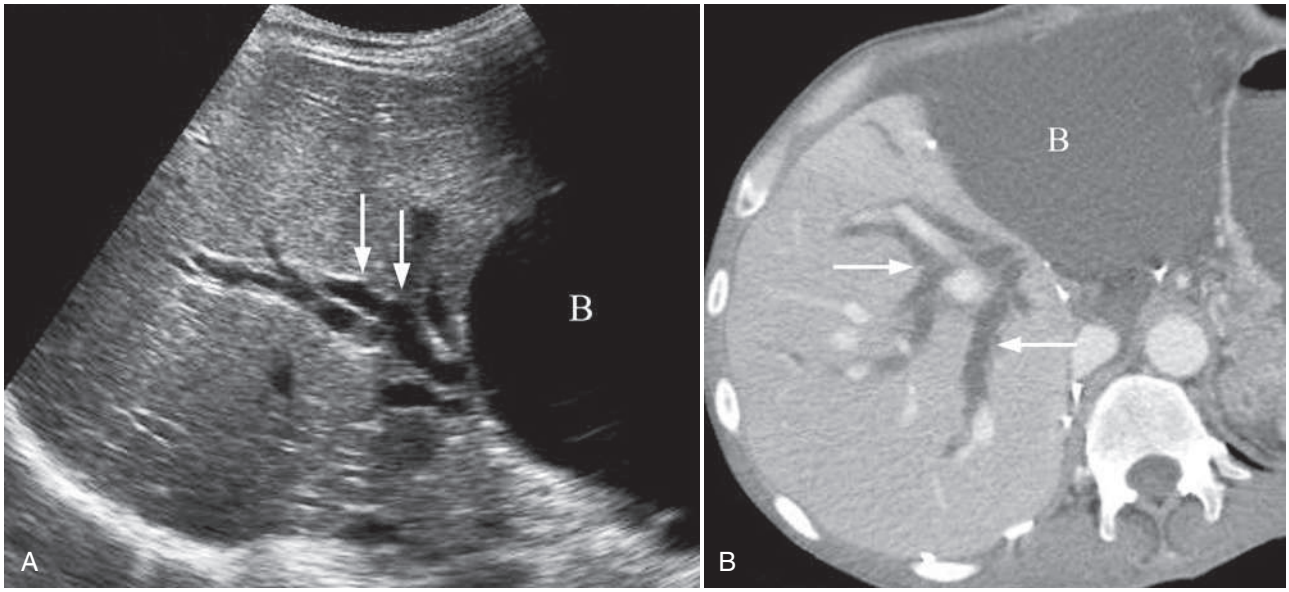

FIG. 18.6 Bile Duct: Anastomotic Leak. (A) Transverse sonogram and **(B)** correlative CT scan show large biloma *(B)* abutting the surgical margin of a living related donor transplant, secondary to anastomotic leak. The **biloma** exerts mass effect on the anastomosis, producing intrahepatic bile duct dilation *(arrows)*.

treatment or may persist and become clinically noticeable if distal biliary obstruction is present.[20]

Recurrent Sclerosing Cholangitis

Recurrent sclerosing cholangitis occurs in up to 20% of recipients undergoing orthotopic transplantation for sclerosing cholangitis, with a mean interval of 350 days.[5,8,21] Ultrasound findings include diffuse mural thickening of the intrahepatic bile duct and CBD and diverticulum-like outpouchings of the CBD[16,22] (Fig. 18.7). Recurrent disease should be suspected in patients who have undergone transplantation for end-stage primary sclerosing cholangitis and who have biliary dilation and mural thickening in the presence of a normal hepatic arterial waveform.

Occasionally, patients with ascending cholangitis show a similar ultrasound appearance. Infectious causes include both enteric flora and opportunistic infections (e.g., CMV, *Cryptosporidium*).[16]

Biliary Sludge and Stones

Biliary sludge can be detected within the hepatobiliary tree in 10% to 29% of liver transplant patients, as early as 6 days or as late as 8 years after surgery. The pathogenesis of biliary sludge in these patients is uncertain, although it has been related to ischemia, infection, rejection, mechanical obstruction, biliary leaks, and presence of stents or T tubes and is more common in patients with hepaticojejunostomy.[13] Once in the donor or recipient biliary tree, sludge can cause biliary obstruction and life-threatening ascending cholangitis (Fig. 18.8). The detection of biliary sludge is an ominous sign that should prompt meticulous evaluation of the CBD to rule out an obstructing lesion or leak, evaluation of the hepatic artery to ensure an optimal arterial supply, and a detailed clinical assessment to check for infection.

Intraductal stones are rare but may result from cyclosporine-induced changes in bile composition inciting crystal formation in the CBD, with subsequent stone development. Other causes include retained donor stones and stones secondary to biliary stasis from mechanical obstruction (e.g., stricture, dysfunctional T-tubes, mucocele formation in cystic duct remnant, kinking in redundant CBD)[23-25] (Fig. 18.9).

Dysfunction of the Sphincter of Oddi

In a minority of patients who have undergone a biliary end-to-end anastomosis, hepatic dysfunction is observed in the presence of diffuse dilation of the donor and recipient bile ducts in the absence of biliary stenosis. The cause of this is uncertain but may be related to devascularization or denervation of the ampulla of Vater, resulting in dysfunction of the sphincter of Oddi. Patients are usually treated with ERCP-guided sphincterotomy, which has been shown to normalize LFT values and decompress the biliary tree.[11,14]

Arterial Complications

At explantation, extrahepatic arterial vessels that supply the liver, such as the parabiliary arteries, are disrupted.[26] This results in the transplanted hepatic artery becoming the only arterial blood supply to intrahepatic biliary epithelium. Any compromise of the hepatic arterial perfusion can result in biliary ischemia and, potentially, biliary necrosis. Biliary necrosis is incompatible with graft survival and is an absolute indication for retransplantation, but uncomplicated biliary ischemia (i.e., without necrosis) can be reversible if hepatic arterial flow is reinstituted.[27] Thus the detection of hepatic arterial dysfunction before the development of biliary necrosis is paramount in the management of liver transplant patients.

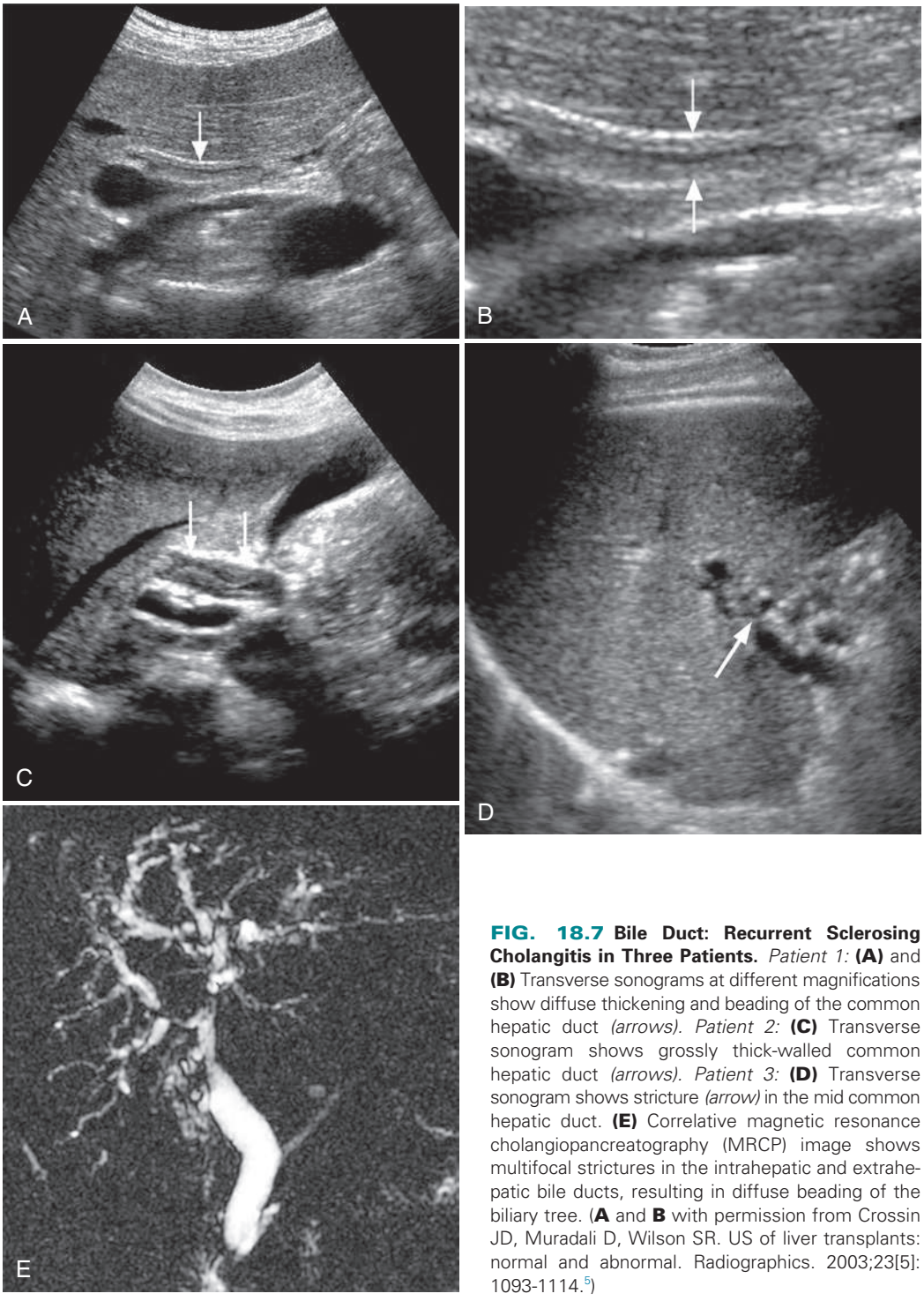

FIG. 18.7 Bile Duct: Recurrent Sclerosing Cholangitis in Three Patients. *Patient 1:* **(A)** and **(B)** Transverse sonograms at different magnifications show diffuse thickening and beading of the common hepatic duct *(arrows). Patient 2:* **(C)** Transverse sonogram shows grossly thick-walled common hepatic duct *(arrows). Patient 3:* **(D)** Transverse sonogram shows stricture *(arrow)* in the mid common hepatic duct. **(E)** Correlative magnetic resonance cholangiopancreatography (MRCP) image shows multifocal strictures in the intrahepatic and extrahepatic bile ducts, resulting in diffuse beading of the biliary tree. (**A** and **B** with permission from Crossin JD, Muradali D, Wilson SR. US of liver transplants: normal and abnormal. Radiographics. 2003;23[5]: 1093-1114.[5])

FIG. 18.8 Bile Duct: Sludge. Oblique sonogram shows intraluminal sludge, secondary to ascending cholangitis, in the CBD *(arrow),* with extension into the right hepatic duct *(arrowhead).*

Hepatic Artery Thrombosis

Hepatic artery thrombosis is the most important vascular complication of liver transplantation, with an incidence of 2.5% to 6.8% and mortality as high as 35%.[28] If retransplantation is not performed for these patients, mortality can increase to 73%.[29]

The pathophysiology is often difficult to decipher. Risk factors include patients requiring complex vascular reconstruction (caused by multiple arterial supply to the liver or small donor and recipient vessels), rejection, severe stenosis, increased cold ischemic time of the donor liver, and ABO blood type incompatibility.[8,30]

After transplantation, the donor bile duct is entirely dependent on the transplanted hepatic artery, particularly the right, for its arterial blood supply. Therefore patients with hepatic artery thrombosis can present clinically with delayed biliary leak, fulminant hepatic failure, or intermittent episodes of sepsis thought to be secondary to liver abscess formation within infarcted tissue.[30] However, the clinical presentation, imaging findings, and patient outcomes are related to the **timing of thrombosis** of the hepatic artery. Hepatic artery thrombosis occurring within 1 month of transplantation can be classified as **early** hepatic artery thrombosis. This is often associated with biliary tract necrosis, bacteremia, acute fulminant hepatic failure, and a high patient morbidity rate.[29] Gray-scale sonography may show the hepatic artery at the porta hepatis; however, no flow is detected on color or spectral Doppler in the hilum or parenchyma.

Hepatic artery thrombosis occurring after 1 month of transplantation can be classified as **late** hepatic artery thrombosis. This is usually associated with a milder clinical course, with patients remaining either asymptomatic for months to years or showing an insidious course eventually involving biliary tract complications, relapsing fevers, or bacteremia. It is thought that the development of collateral arterial vessels, as early as 2 weeks after surgery, accounts for the survival of the transplant in these patients. Although resection of all vascular connections in the transplant can hinder development of collateral circulation, arterial collateral vessels could develop from the angiogenic potential of the omentum and mesentery. On ultrasound, a **tardus-parvus arterial waveform** (RI < 0.5; AT > 100 ms) is detected within the hepatic parenchyma (Fig. 18.10). Within the hilum, no arterial flow is demonstrated, or if periportal arterial collaterals are present, a tardus-parvus waveform may be detected. Therefore demonstration of arterial flow in the hepatic parenchyma does not exclude the presence of hepatic arterial thrombosis, and meticulous inspection of the parenchymal waveform is warranted[29,30] (see Fig. 18.10).

Occasionally, a false-positive diagnosis of hepatic artery thrombosis can occur with severe hepatic edema, systemic hypotension, and high-grade hepatic artery stenosis.[8] In situations with poor visibility of the porta hepatis because of abdominal girth or overlying bowel gas, lack of detectable flow within the hepatic artery should be viewed with caution and confirmed on computed tomography angiography (CTA).

Hepatic Artery Stenosis

Hepatic artery stenosis has been reported in up to 11% of transplant recipients and most often occurs at or within a few centimeters of the surgical anastomosis. Risk factors for development of stenosis include faulty surgical technique, clamp injury, rejection, and intimal trauma caused by perfusion catheters.[27] Clinically, patients have biliary ischemia and/or abnormal LFT values.

Doppler ultrasound can provide direct and indirect evidence of hepatic artery stenosis. **Direct** evidence involves identifying and localizing a hemodynamically significant narrowing within the vessel. The porta hepatis should be initially screened with color Doppler ultrasound to detect a focal region of color aliasing within the hepatic artery, which indicates high-velocity turbulent flow produced by the stenotic segment. If the stenosis is hemodynamically significant, spectral tracing will reveal peak systolic velocity (PSV) of greater than 2 to 3 m/sec, with associated turbulent flow distally. **Indirect** evidence of hepatic artery stenosis includes a tardus-parvus waveform anywhere within the hepatic artery (RI < 0.5; AT > 100 ms). This waveform suggests the presence of a more proximally located stenotic region.[27] Indirect evidence of stenosis is much more common in clinical practice than documentation of the stenosis itself (Figs. 18.11 and 18.12).

The presence of an intraparenchymal tardus-parvus waveform indicates alterations in the intrahepatic arterial bed from impaired arterial perfusion of the liver. Although it is detected most often in patients with hepatic artery stenosis, tardus-parvus waveform may also result from collateral vessels arising from hepatic artery thrombosis or, less frequently, from severe aortoiliac atherosclerosis. Therefore an intraparenchymal tardus-parvus waveform cannot distinguish between hepatic artery stenosis and thrombosis if the hepatic arterial trunk is not visualized and meticulously investigated.[31]

Mild degrees of hepatic artery narrowing may also be present without Doppler abnormalities. Therefore if clinical suspicion is high, a normal Doppler study should not preclude further

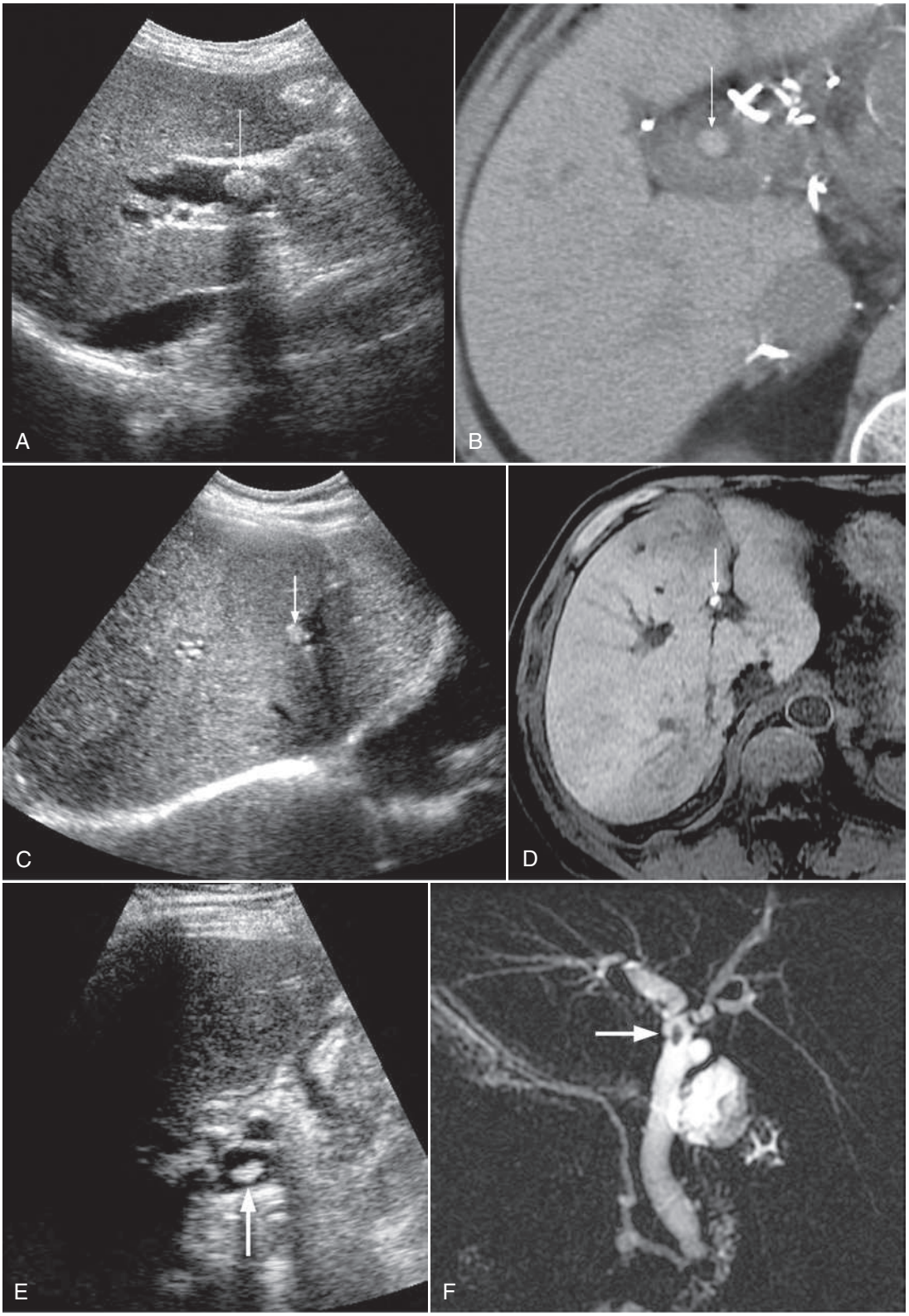

FIG. 18.9 Bile Duct: Stones. (A) Sonogram and **(B)** correlative noncontrast-enhanced CT show the presence of a large obstructing stone *(arrow)* in the common hepatic duct. **(C)** Transverse sonogram shows an echogenic focus *(arrow)* consistent with an intraductal calculus in this patient with recurrent primary sclerosing cholangitis. **(D)** Corresponding axial SPGR (spoiled gradient echo) T1-weighted pregadolinium-enhanced magnetic resonance image shows intraductal high-frequency signal *(arrow)* consistent with a stone. **(E)** Transverse sonogram at level of the common hepatic duct shows a nonshadowing echogenic focus *(arrow)* in the duct, consistent with a soft stone. **(F)** Corresponding T2-weighted magnetic resonance image shows a well-defined filling defect *(arrow),* confirming the presence of a calculus within the proximal common duct.

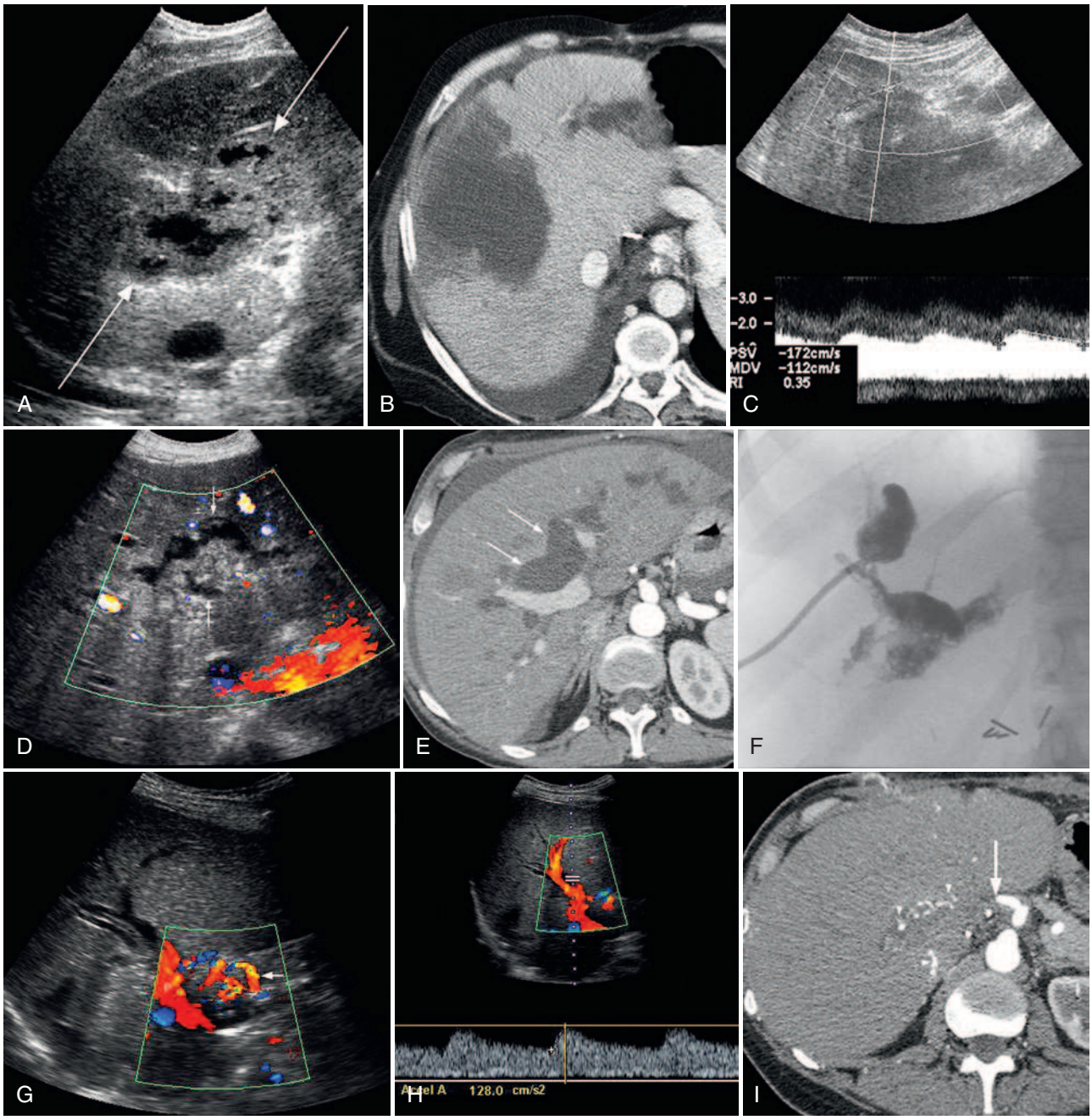

FIG. 18.10 Hepatic Artery: Thrombosis in Three Patients. *Patient 1:* **(A)** Transverse sonogram shows a right lobe infarct appearing as a solid-cystic region *(arrows),* resulting from hepatic arterial thrombosis. **(B)** Corresponding CT scan shows the infarct as a low-attenuating wedge-shaped region. **(C)** On spectral Doppler, no flow could be detected in the main hepatic artery. A tardus-parvus waveform detected within the liver indicates an upstream hepatic arterial problem—in this case, hepatic artery thrombosis with collateral arterial vessels supplying the hepatic tissue. *Patient 2:* **(D)** Transverse sonogram shows a greatly distended bile duct *(arrows)* with echogenic material within the lumen secondary to sloughed mucosa and blood. **(E)** Corresponding CT scan shows dramatically dilated intrahepatic bile ducts *(arrows).* The biliary necrosis is less well appreciated on CT. **(F)** Percutaneous cholangiogram shows contrast filling shaggy, intrahepatic ducts with multiple filling defects. The filling defects correspond to the sloughed biliary mucosa. *Patient 3:* **(G)** Transverse sonogram demonstrates multiple collateral vessels *(arrow)* at the porta hepatis. **(H)** Spectral Doppler sonogram within the liver shows a tardus-parvus waveform. **(I)** CT angiogram shows occlusion of the hepatic artery *(arrow)* caused by acute thrombosis. Multiple arterial collateral vessels *(arrowheads)* are identified, as seen on **(G).**

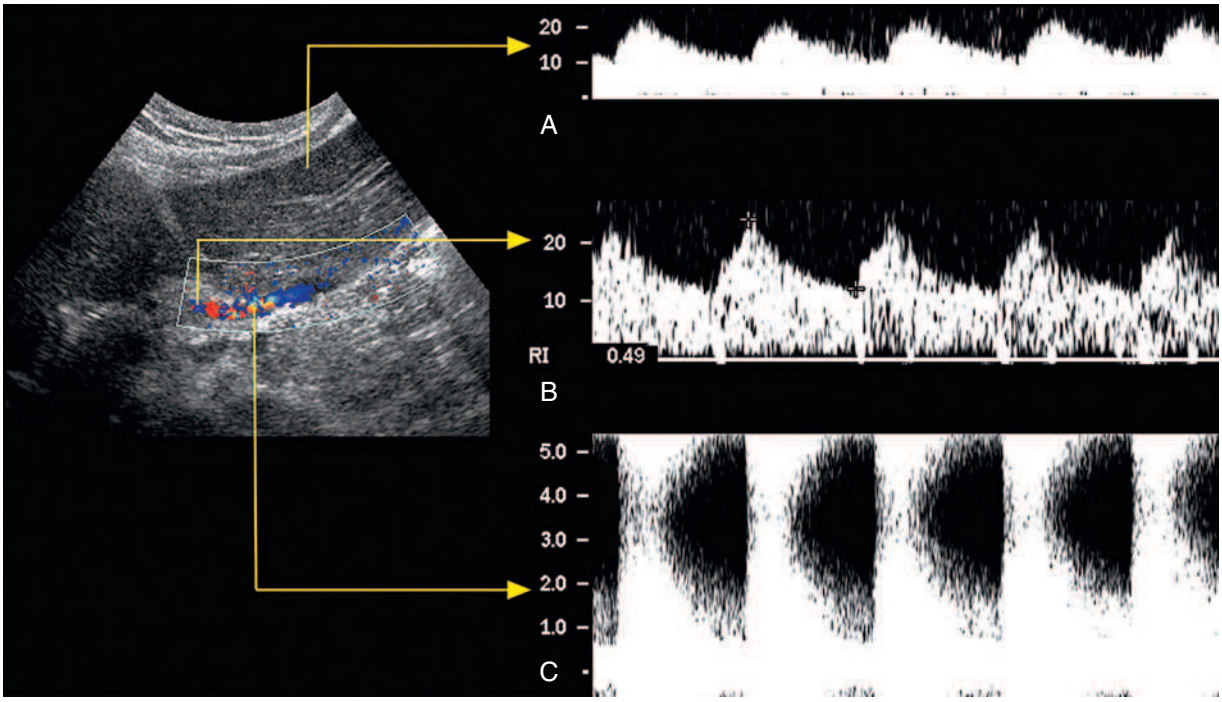

FIG. 18.11 Hepatic Artery Stenosis: Doppler Features. (A) Intrahepatic spectral waveform and **(B)** hepatic artery waveform at porta hepatis show a prolonged acceleration time and low resistance, a tardus-parvus waveform, suggesting an upstream problem. **(C)** Spectral waveform at the anastomosis shows high-velocity flow greater than 400 cm/sec. The corresponding color Doppler sonogram shows aliasing as turquoise and yellow between the red and blue at the stenosis, with turbulence beyond.

investigation with other cross-sectional techniques, although the stenosis, if detected, may be mild in these patients.

Although detection of a tardus-parvus waveform should incite further assessment, false-positive diagnoses can occur, particularly in the early postoperative period (within 48 hour of surgery), possibly because of postoperative edema. In one study, approximately 30% of false-positive tardus-parvus waveforms were idiopathic and not associated with any causative factors.[32]

Elevated Hepatic Arterial Resistive Index

In the early postoperative period, a normal hepatic artery may display a high-resistance arterial flow (RI > 0.8) or a complete lack of flow in diastole (RI = 1.0) on Doppler interrogation. In these patients the flow within the hepatic artery usually returns to normal in a few days. The cause of this waveform is uncertain, although it may be related to older donor age or prolonged cold ischemic time of the graft. RIs may also be higher in normal grafts with an infrarenal aortohepatic anastomosis compared with those grafts with an end-to-end anastomosis. Thus a high RI of the hepatic artery on Doppler assessment frequently has no clinical relevance and should not be misinterpreted as a sign of a hepatic artery abnormality.[33,34]

Hepatic Artery Pseudoaneurysms

Hepatic artery pseudoaneurysms are uncommon complications of transplantation (1%) and occur most frequently at the vascular anastomosis or as a result of prior angioplasty. **Intrahepatic** pseudoaneurysms are rare, usually peripherally located, and associated with percutaneous needle biopsies, infection, or biliary procedures. Intrahepatic aneurysms are often asymptomatic but can cause life-threatening arterial hemorrhage or, in mycotic pseudoaneurysms, produce fistulas between the aneurysm and the biliary tree or portal veins.[8] **Extrahepatic** pseudoaneurysms occur at the donor-recipient arterial anastomosis and may be caused by infection or technical failure.

Gray-scale ultrasound of hepatic artery pseudoaneurysms shows a hypoechoic structure (at times simulating a cyst), typically following the course of the hepatic artery, with intense swirling flow on color Doppler and a disorganized spectral waveform (Fig. 18.13). Management options are dictated by the location of the pseudoaneurysm. Extrahepatic pseudoaneurysms can be treated by surgery, transcatheter embolization, or stent insertion, whereas intrahepatic pseudoaneurysms are often treated with endovascular coil embolization.

Celiac Artery Stenosis

Celiac artery stenosis may be caused by **atheromatous disease** or impingement of the celiac axis by the **median arcuate ligament** of the diaphragm. If severe, celiac stenosis can result in decreased arterial flow to the allograft. Patients are often asymptomatic before transplantation, presumably because of rich collateral networks, usually through the pancreaticoduodenal arcade. After transplantation, patients may become symptomatic, with evidence of biliary ischemia and abnormalities in serum LFT values, a result of the greater flow demand imposed on the celiac artery by the newly transplanted liver.

Doppler ultrasound may be normal or may reveal a low-resistance tardus-parvus waveform in the transplanted hepatic

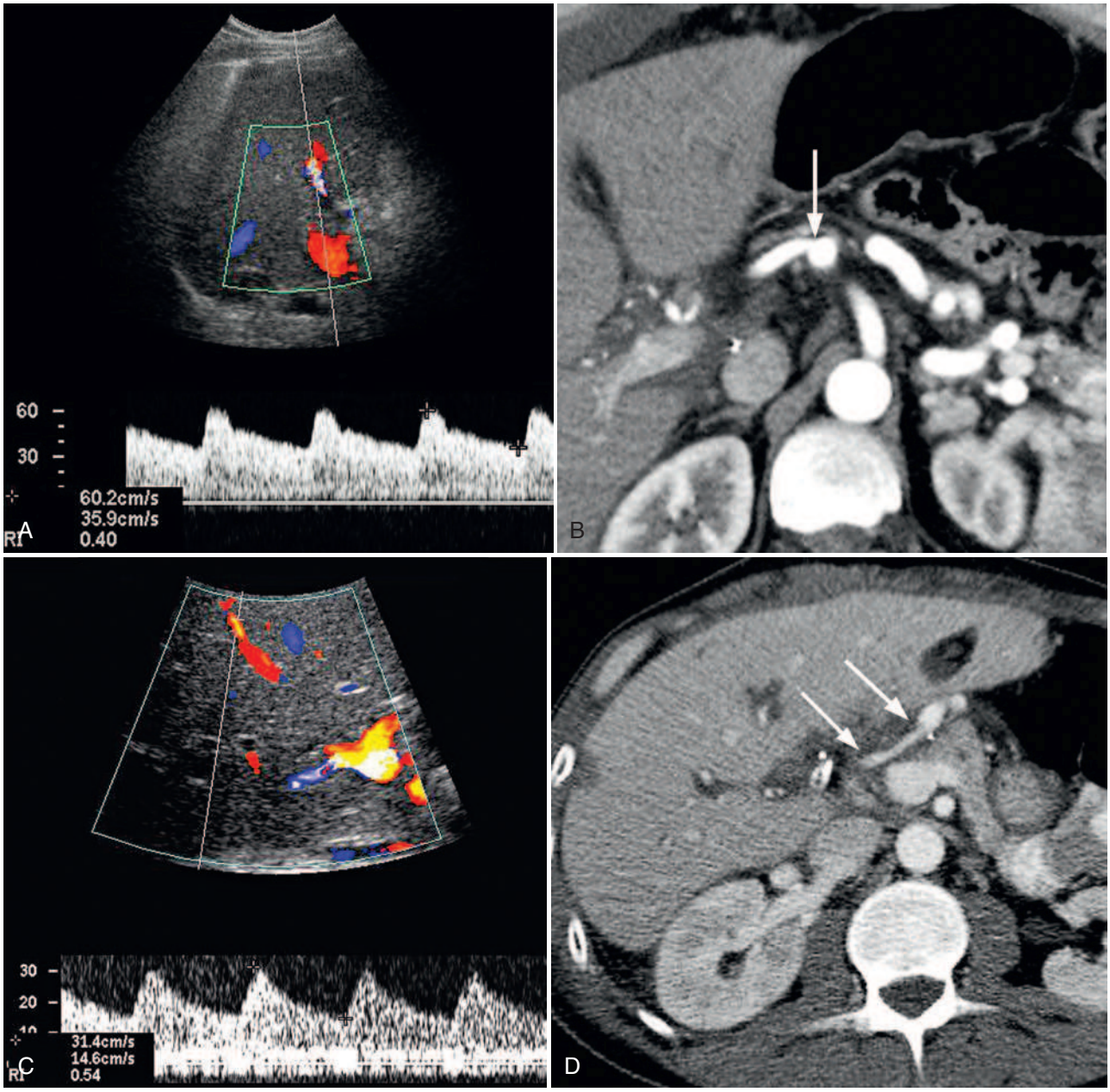

FIG. 18.12 Hepatic Artery Stenosis in Two Patients. *Patient 1:* **(A)** Intraparenchymal spectral Doppler ultrasound shows a low-resistance waveform (resistive index [RI] = 0.4). **(B)** Corresponding contrast-enhanced CT angiogram shows subtle stenosis of the proximal hepatic artery *(arrow). Patient 2:* **(C)** Intraparenchymal spectral Doppler shows a tardus-parvus, low-resistance waveform with a delayed acceleration time of 120 ms. **(D)** Corresponding CT angiogram shows long stenosis of the hepatic artery *(between arrows).*

artery and high-velocity jet across the celiac stenosis. Patients are treated with division of the median arcuate ligament or, in the case of atheromatous disease, an aortohepatic interposition bypass graft[35,36] (Fig. 18.14).

Portal Vein Complications

Portal vein **stenosis** or **thrombosis** is uncommon, with a reported incidence of 1% to 13%.[30,37,38] Risk factors include faulty surgical technique, misalignment of vessels, excessive vessel length, hypercoagulable states, and previous portal vein surgery.[30] Factors extrinsic to the portal vein may also contribute, such as increased downstream resistance caused by a suprahepatic stricture of the IVC or diminished portal venous blood flow. Clinical presentations include hepatic failure and signs of portal hypertension (gastrointestinal hemorrhage from varices or massive ascites).

Gray-scale ultrasound of **portal vein stenosis** may show narrowing of the vessel lumen, usually at the anastomosis. Doppler interrogation shows a focal region of color aliasing, reflecting turbulent, high-velocity flow, with a threefold to fourfold velocity

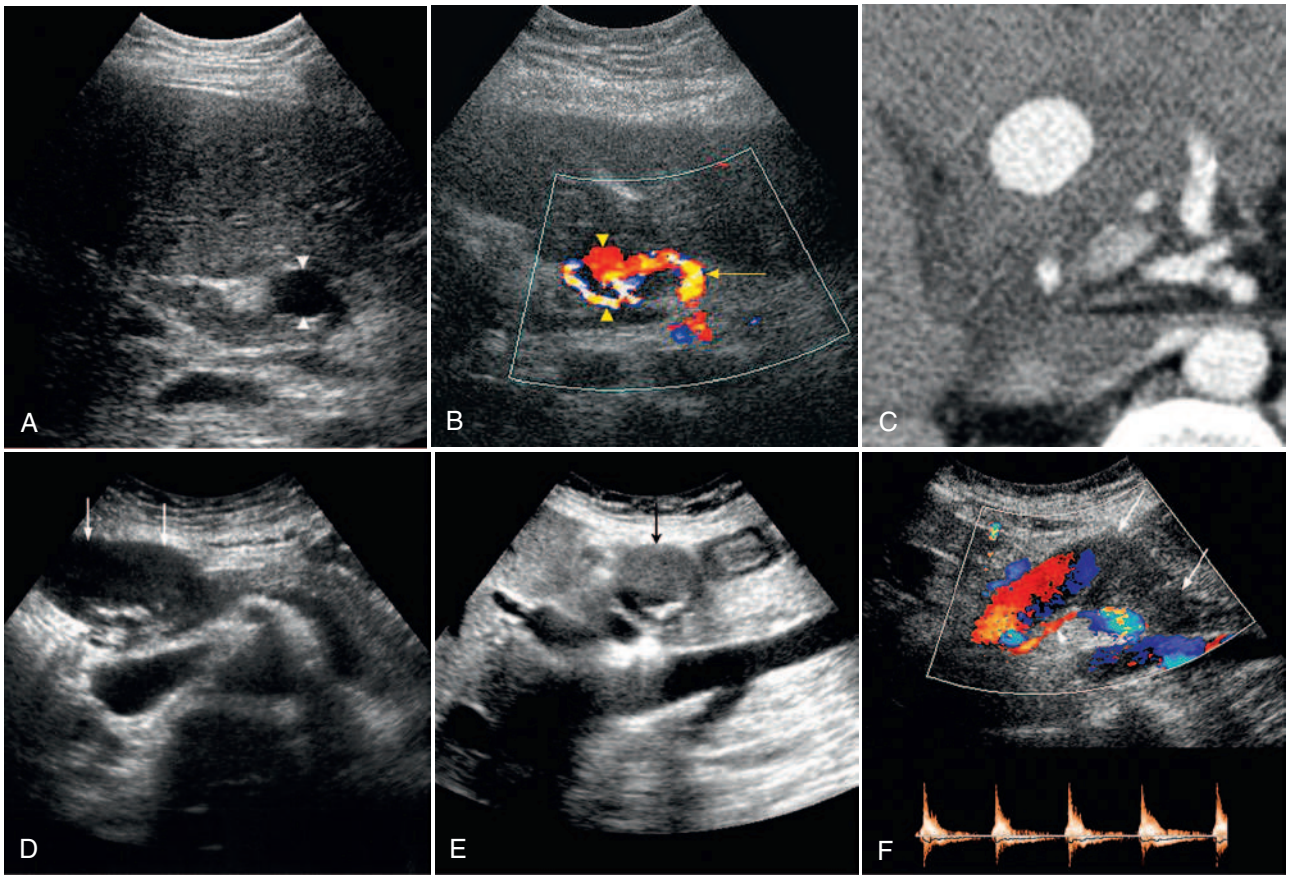

FIG. 18.13 Hepatic Artery Pseudoaneurysms in Two Patients. *Patient 1:* **(A)** Gray-scale sonogram shows a small cystic mass close to the porta hepatis *(arrowheads).* **(B)** Color Doppler ultrasound confirms vascularity within the pseudoaneurysm *(arrowheads)* arising from the hepatic artery *(arrow).* **(C)** Corresponding enhanced CT confirms the pseudoaneurysm arising at the hepatic artery anastomosis. *Patient 2:* **(D)** Transverse and **(E)** sagittal sonograms show a midline oval mass *(arrows).* **(F)** On color and spectral Doppler ultrasound, disorganized flow is identified in a portion of the mass, representing a partially thrombosed pseudoaneurysm. Arrows mark the thrombosed portion of the pseudoaneurysm. (**A-C** with permission from Crossin JD, Muradali D, Wilson SR. US of liver transplants: normal and abnormal. Radiographics. 2003;23[5]:1093-1114.[5])

increase at the site of stenosis relative to the prestenotic segment on spectral interrogation (Fig. 18.15). Chong and colleagues[39] showed that the presence of elevated portal vein anastomotic velocities greater than 125 cm/sec, or a velocity ratio of 3:1 at the anastomosis, was greater than 95% specific for portal vein stenosis.

True portal vein stenosis must be distinguished from a **pseudostenosis** of the portal vein. This entity is seen when the recipient portal vein is larger than the donor portal vein and no associated differential gradient exists across the site of narrowing.

Portal vein thrombosis manifests as echogenic solid material within the portal vein lumen (Figs. 18.16 and 18.17). In the acute state the thrombus may be anechoic, making detection difficult on gray-scale ultrasound and emphasizing the necessity for careful Doppler assessment of the entire portal venous system. As with portal vein thrombosis in the native liver, the thrombus may decrease in size and eventually recanalize, showing multiple venous flow channels within the thrombus. Treatment options for portal vein thrombosis or stenosis include thrombectomy, segmental portal vein resection, percutaneous thrombolysis, stent placement, and balloon angioplasty.

Inferior Vena Cava Complications

Stenosis of the IVC is a rare complication of liver transplantation and may occur at the suprahepatic or infrahepatic anastomosis. IVC stenosis occurs more frequently in pediatric recipients and patients undergoing retransplantation.[40] Causes of IVC stenosis include anastomotic discrepancy, IVC kinking, fibrosis, or neointimal hyperplasia. On gray-scale ultrasound, the IVC may show obvious narrowing at the site of anastomosis, associated with a focal region of aliasing on color Doppler. On spectral interrogation, a threefold to fourfold greater velocity gradient is observed across the stenosis compared with the prestenotic segment. The hepatic veins may show reversal of flow or may lose their normal phasicity, with a monophasic waveform[8] (Figs. 18.18 and 18.19).

Thrombosis of the IVC has been reported in less than 3% of recipients and is caused by technical difficulties at surgery, hypercoagulable states, or compression from adjacent fluid

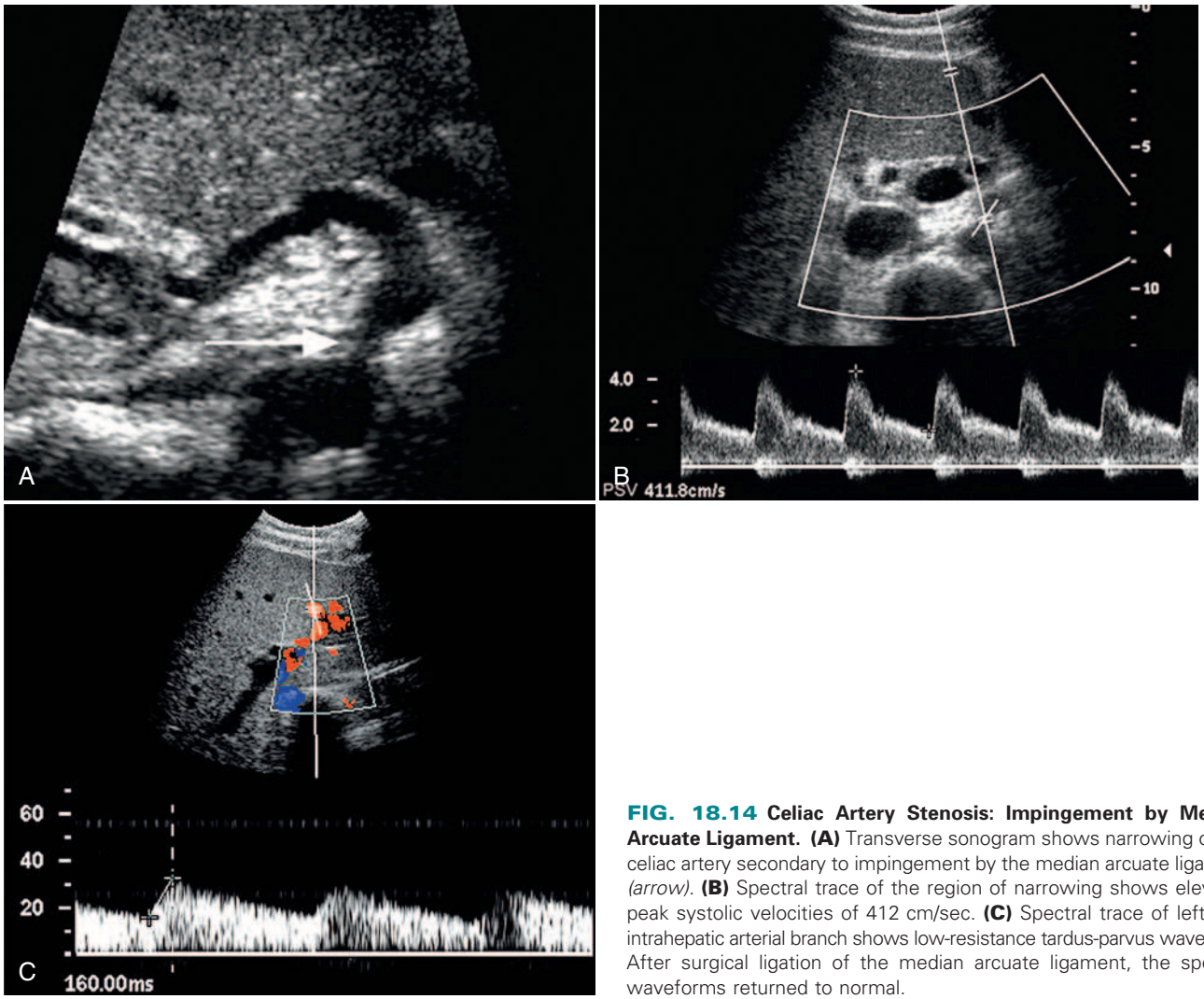

FIG. 18.14 Celiac Artery Stenosis: Impingement by Median Arcuate Ligament. (A) Transverse sonogram shows narrowing of the celiac artery secondary to impingement by the median arcuate ligament *(arrow)*. **(B)** Spectral trace of the region of narrowing shows elevated peak systolic velocities of 412 cm/sec. **(C)** Spectral trace of left lobe intrahepatic arterial branch shows low-resistance tardus-parvus waveform. After surgical ligation of the median arcuate ligament, the spectral waveforms returned to normal.

collections.[26,40] Gray-scale ultrasound shows echogenic thrombus within the IVC that may continue into the hepatic veins. In cases of recurrent HCC, tumor thrombus may extend from the hepatic veins into the IVC (Fig. 18.20).

Hepatic Vein Stenosis

Hepatic vein stenosis occurs with a frequency of 1% in **orthotopic liver transplant** and 2% to 5% in **living donor transplants.** This discrepancy in frequency is primarily related to different surgical techniques. In orthotopic liver transplants, an anastomosis is performed between the donor and recipient IVC without touching the hepatic veins. In living donor transplants, however, the donor hepatic vein is anastomosed to either the hepatic vein stump or the IVC of the recipient. This results in the hepatic veins being rigidly fixed in position, such that any movement of the graft produces a buckling and narrowing of the hepatic veins. In addition, progressive growth of partial liver grafts after surgery may result in stretching or twisting of the hepatic veins, further contributing to narrowing of the venous outlet.[41,42]

Clinically, hepatic vein stenosis manifests with liver congestion, hepatomegaly, ascites, and/or pleural effusions. Hepatic venous obstruction in the **early postoperative state** is a surgical emergency, and reoperation is usually necessary for correction or for retransplantation, if substantial hepatic necrosis has occurred. **Late-onset hepatic venous obstruction** may be associated with a more insidious deterioration in liver function. These patients may benefit from metallic stent insertion or balloon venoplasty, because surgical correction is often difficult as a result of fibrotic changes around the anastomotic sites.[41,42]

Direct signs of hepatic vein stenosis include focal narrowing on gray-scale ultrasound associated with turbulent flow on color and spectral Doppler interrogation (Fig. 18.21). A persistent, monophasic spectral waveform is suggestive of, but not diagnostic of, hepatic vein stenosis; monophasic waveforms may also be present in normal, nonobstructed hepatic veins. However, the presence of a triphasic or biphasic waveform rules out clinically important hepatic vein stenosis.[42]

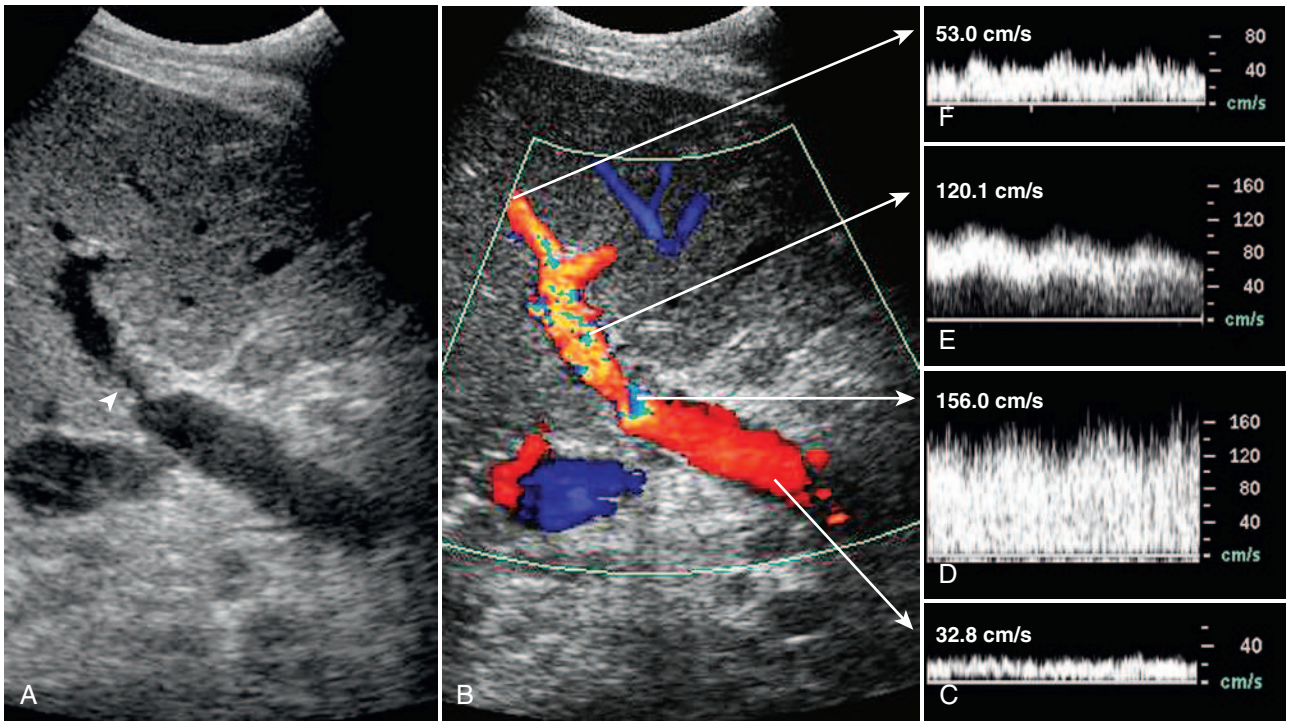

FIG. 18.15 Portal Vein Stenosis: Anastomotic Stricture. (A) Gray-scale sonogram of main portal vein shows narrowing at the anastomosis *(arrowhead).* **(B)** Color Doppler shows aliasing at the region of stenosis caused by high-velocity turbulent flow. **(C)** Spectral Doppler shows velocities of 32.8 cm/sec proximal to the stenosis. **(D)** Velocities at the stenosis are elevated at 156 cm/sec. **(E)** Poststenotic high-velocity turbulent flow is identified, measuring 120.1 cm/sec. **(F)** Beyond the turbulent flow, velocities of 53 cm/sec are obtained. This represents a threefold increased velocity gradient across the anastomosis, indicating that the stenosis is hemodynamically significant.

Extrahepatic Fluid Collections

Perihepatic fluid collections and ascites are frequently observed after transplantation. In the early postoperative period a small amount of free fluid or a right pleural effusion may be observed, but these usually resolve in a few weeks. **Fluid collections** and **hematomas** are common in the areas of vascular anastomosis (hepatic hilum and adjacent to IVC) and biliary anastomosis, in the lesser sac, and in the perihepatic and subhepatic spaces.[7] Because the peritoneal reflections surrounding the liver are ligated at transplantation, fluid collections can occur around the **bare area** of the liver, a location for fluid that is not encountered in the preoperative liver[5] (Fig. 18.22).

Ultrasound is highly sensitive in detecting these fluid collections, although it lacks specificity with regard to etiology because bile, blood, pus, and lymphatic fluid can all have a similar sonographic appearance. The presence of internal echoes in a fluid collection suggests blood or infection. Particulate ascites may also be observed in peritoneal carcinomatosis, although this would seem less likely in the transplant recipient population.[5]

Adrenal Hemorrhage

Right-sided adrenal hemorrhage may be observed in the immediate postoperative period and results from (1) venous engorgement caused by ligation of the right adrenal vein during the removal of a portion of the IVC or (2) a coagulopathy caused by the patient's preexisting liver disease.[26] On ultrasound, adrenal hemorrhage may be seen as a hypoechoic nodular structure or as a fluid collection in the right suprarenal region (Fig. 18.23).

Intrahepatic Fluid Collections

Sterile postoperative fluid collections are often located along the falciform ligament and ligamentum venosum, usually appearing as fluid-filled anechoic collections surrounding the echogenic ligaments (Fig. 18.24). **Bilomas** may manifest as a hypoechoic or complex cyst. **Intraparenchymal hematomas** may result from the transplant surgery or percutaneous biopsy or may be a sequela of donor trauma (e.g., motor vehicle crash).

Abscess Versus Infarct

In the early stages it may be difficult to differentiate a liver abscess from an infarct. Initially, both abscesses and infarcts may appear as a subtle hypoechoic region, associated with a localized coarsening of the parenchymal echotexture. **Infarcts** may subsequently organize into avascular round or wedge-shaped lesions, which can eventually develop central hypoechoic areas reflecting liquefaction and necrosis. A focal liver infarct should be diagnosed with accompanying Doppler evidence of hepatic arterial compromise.

As with infarcts, the ultrasound appearance of a **liver abscess** also varies with its maturation. The classic appearance of a mature transplant liver abscess is a complex, cystic structure with thick,

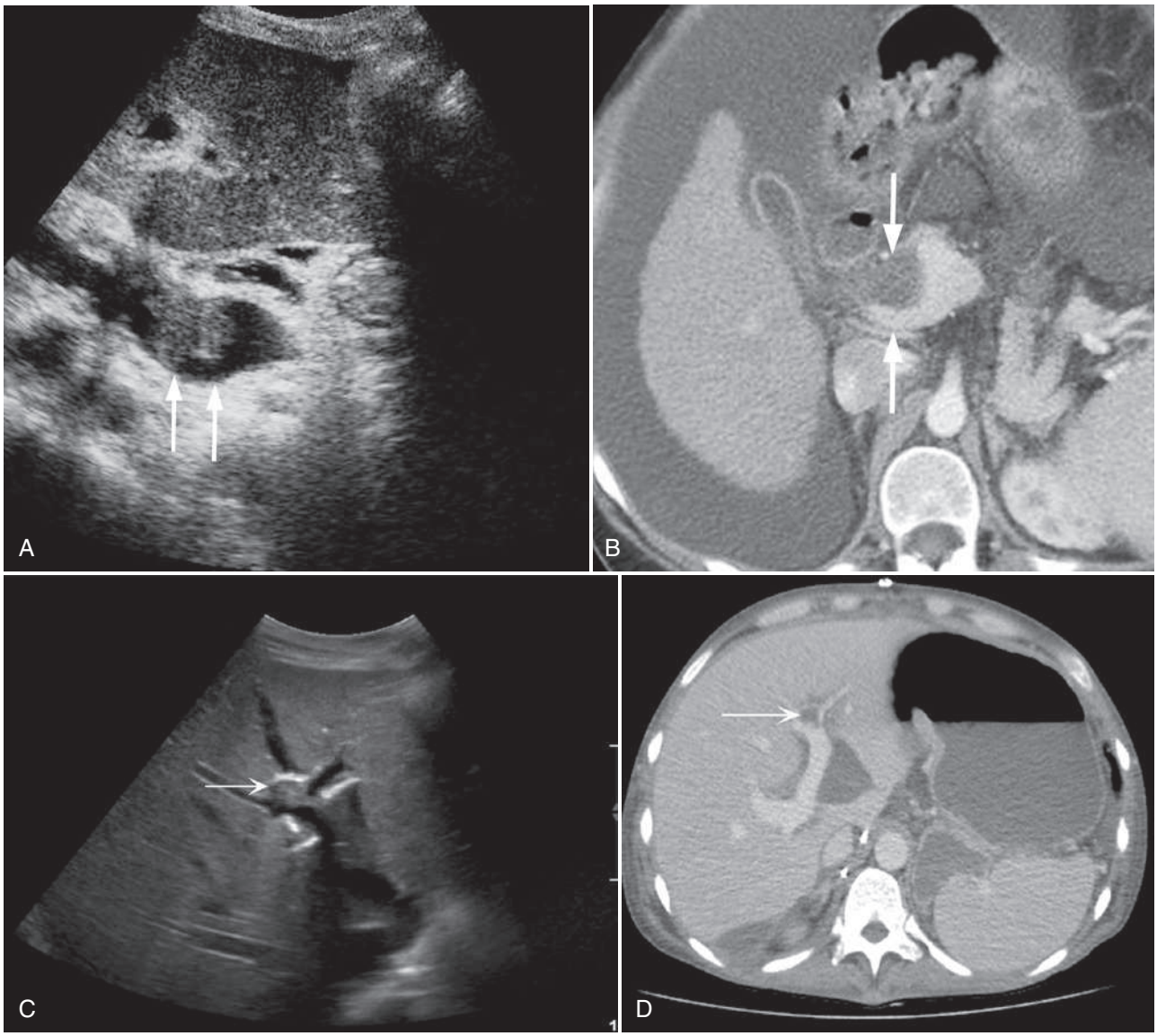

FIG. 18.16 Portal Vein: Bland Thrombus in Two Patients. *Patient 1:* **(A)** Transverse sonogram and **(B)** corresponding contrast-enhanced CT show nonocclusive thrombus in the main portal vein *(arrows). Patient 2:* **(C)** Transverse sonogram and **(D)** corresponding contrast-enhanced CT scan show nonocclusive thrombus in the ascending ramus of the left portal vein *(arrows).*

irregular walls and particulate internal fluid, with or without associated septations.

Both infarcts and abscesses may contain bubbles of air, visualized as bright echogenic foci with or without posterior acoustic shadowing (Fig. 18.25). Occasionally, bubbles of air within the lumen of an intraparenchymal abscess can be confused with benign pneumobilia or may be mistaken for air outside the liver within the gastrointestinal tract. A high index of suspicion is critical in patients at risk for either abscess or infarct to avoid these misinterpretations.

Intrahepatic Solid Masses

The differential diagnosis of a solitary mass in the transplanted liver is similar to that in the native liver. For example, benign lesions, such as hemangiomas and cysts, are relatively common in the transplanted liver, with the same range of appearances as described for the native liver. However, several pathologies unique to the transplanted liver may also appear as a solid or complex mass on gray-scale ultrasound, including infarcts (Fig. 18.26), abscesses, hematomas, recurrent or metastatic HCC, and post-transplant lymphoproliferative disorder (PTLD).

Recurrent hepatocellular carcinoma is a serious complication that can potentially develop after transplantation in patients with a preoperative history of end-stage cirrhosis with known or occult hepatomas. The most common site of recurrent HCC is the lung, presumably caused by embolization with tumor cells through the hepatic veins before or during transplantation. The second most common location of recurrent hepatomas is within the allograft, followed by regional or distant lymph nodes. Early detection of **recurrent hepatomas** in the transplanted liver is

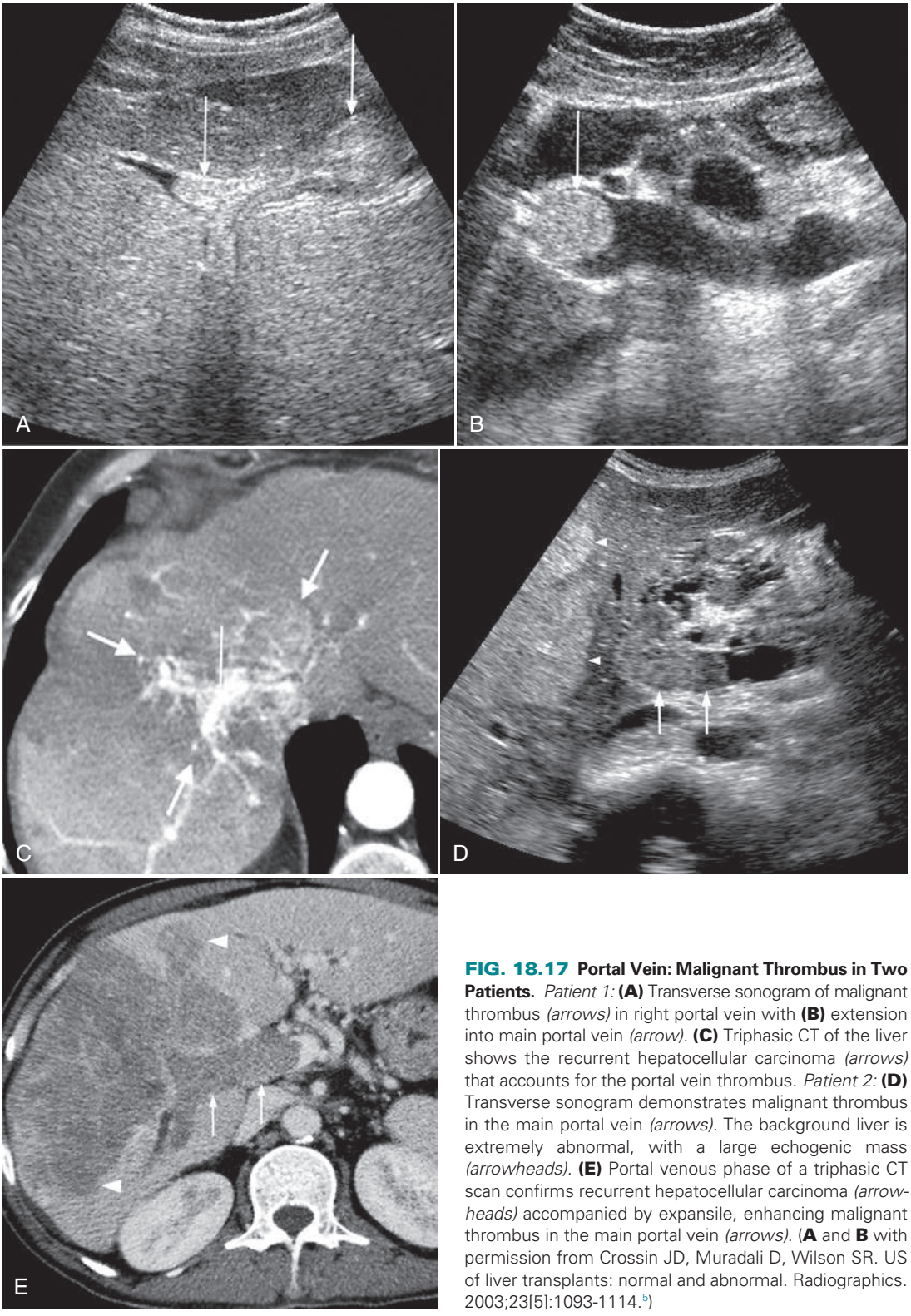

FIG. 18.17 Portal Vein: Malignant Thrombus in Two Patients. *Patient 1:* **(A)** Transverse sonogram of malignant thrombus *(arrows)* in right portal vein with **(B)** extension into main portal vein *(arrow).* **(C)** Triphasic CT of the liver shows the recurrent hepatocellular carcinoma *(arrows)* that accounts for the portal vein thrombus. *Patient 2:* **(D)** Transverse sonogram demonstrates malignant thrombus in the main portal vein *(arrows).* The background liver is extremely abnormal, with a large echogenic mass *(arrowheads).* **(E)** Portal venous phase of a triphasic CT scan confirms recurrent hepatocellular carcinoma *(arrowheads)* accompanied by expansile, enhancing malignant thrombus in the main portal vein *(arrows).* (**A** and **B** with permission from Crossin JD, Muradali D, Wilson SR. US of liver transplants: normal and abnormal. Radiographics. 2003;23[5]:1093-1114.[5])

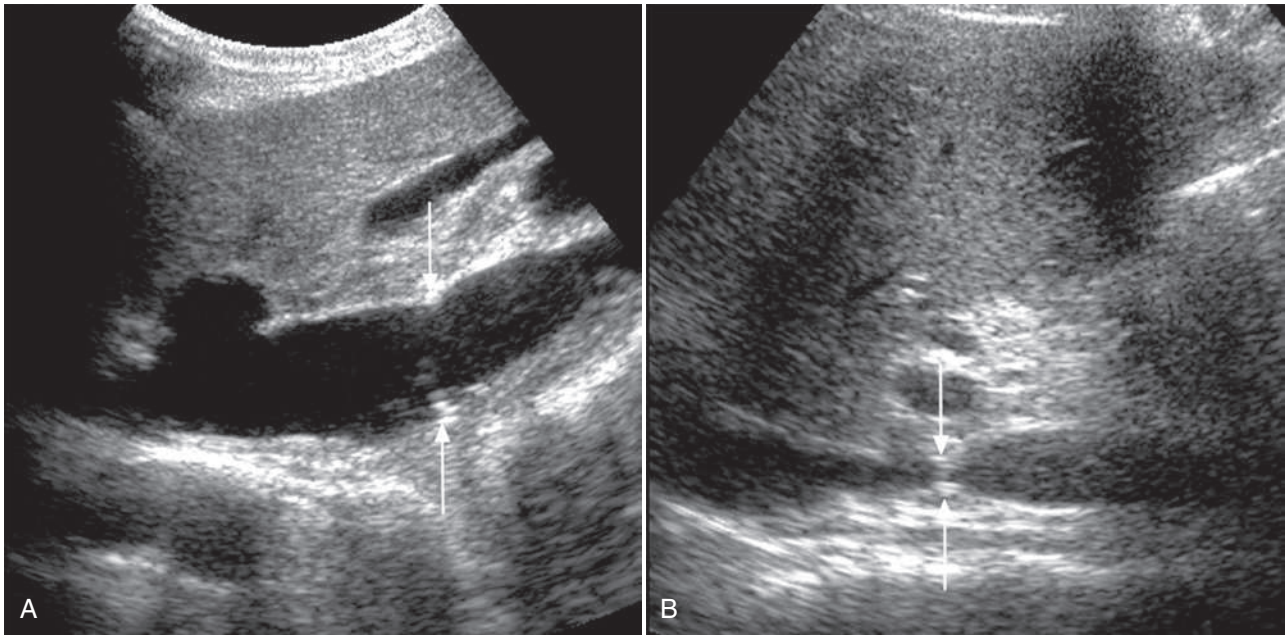

FIG. 18.18 Inferior Vena Cava (IVC) Infrahepatic Anastomosis: Normal and Abnormal in Two Patients. Sagittal sonograms of IVC show **(A)** a normal caliber at the anastomosis *(arrows)* and **(B)** narrowing at the anastomosis *(arrows)*.

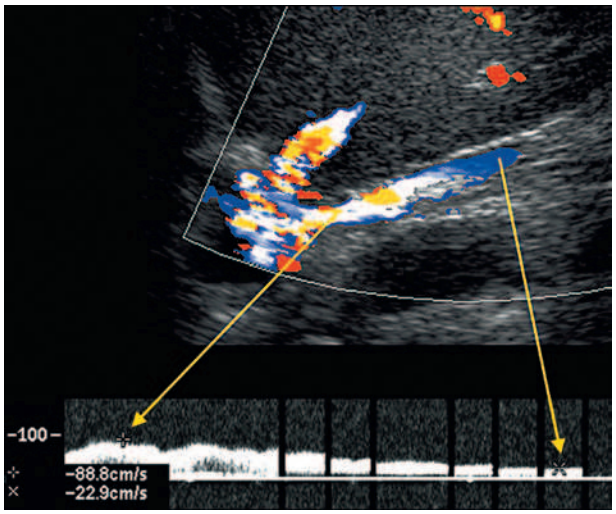

FIG. 18.19 Inferior Vena Cava (IVC) Suprahepatic Anastomotic Stricture. Sagittal color Doppler sonogram of a stenosed segment of the IVC shows aliasing produced by high-velocity turbulent flow in both the IVC and the hepatic vein. Spectral tracing shows a greater than threefold velocity increase at the stenotic region *(left arrow)*.

essential to facilitate early resection, ablation, or chemotherapy[26,43] (Fig. 18.27). As in the general population, transplant recipients can develop any type of primary or secondary neoplasm within the liver.

RENAL TRANSPLANTATION

Transplantation is the treatment of choice for many patients with **chronic renal failure** (CRF) severe enough to warrant dialysis. The only contraindications to transplantation are unsuitability for general anesthesia or surgery, preexisting infection or malignancy, and a risk of recurrent renal disease (e.g., active vasculitis or oxalosis). Before transplantation, a suitable donor must be obtained with appropriate human lymphocyte antigen (HLA) matching with the recipient.[44]

As the number of patients with CRF continues to rise, the major limitation for expanding transplant programs is the shortage of suitable donor kidneys. This organ shortage has resulted in an increasing number of renal transplantations from living related donors. These donors may include family members or close friends with a long-standing relationship with the recipient. The average life expectancy for a cadaveric allograft is 7 to 10 years, whereas that for a live donor allograft is 15 to 20 years.[44]

Regardless of whether a cadaveric or live donor allograft is used, the cost-benefit ratio of a functioning successful transplant far outweighs that of a patient with persistent CRF, so multiple health care resources are targeted to ensure high rates of success. Ultrasound is the most valuable noninvasive imaging modality in monitoring the renal transplant.

Surgical Technique

Detailed sonography of the renal transplant requires knowledge of the surgical procedure used in most institutions as well as the postsurgical anatomic relationships. The right or left lower quadrant is selected for the incision, based on the patient's prior surgical history and the surgeon's preference. Usually, the right lower quadrant is selected because the right iliac vein is more superficial and horizontal on this side of the pelvis, facilitating creation of a vascular anastomosis.[45,46]

The type of **arterial anastomosis** used depends on whether the allograft is cadaveric or living related and on the number

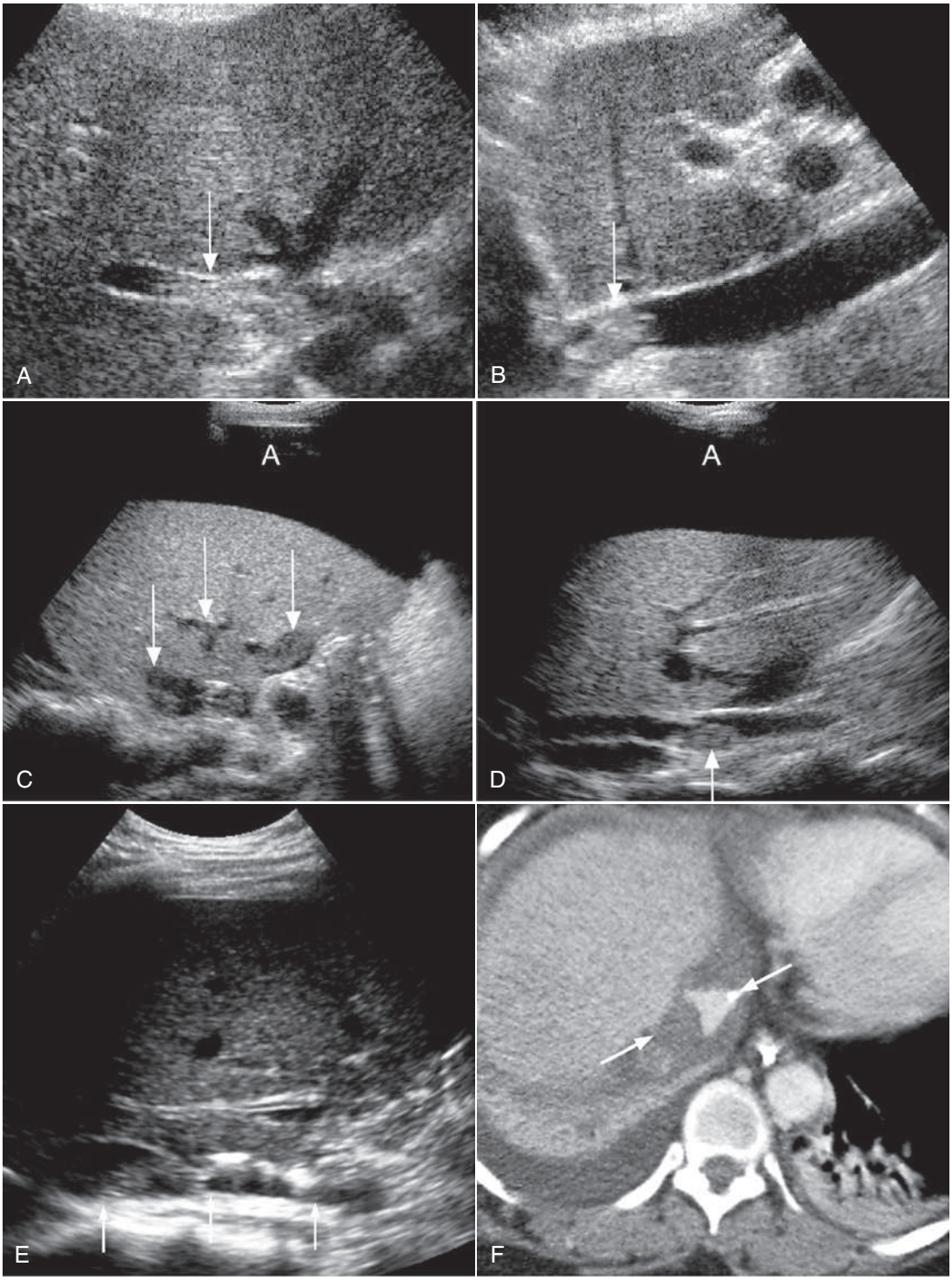

FIG. 18.20 Inferior Vena Cava (IVC) Thrombosis in Three Patients. (A) Transverse and **(B)** sagittal sonograms show malignant IVC and hepatic vein thrombus *(arrows)* in a patient with recurrent hepatocellular carcinoma after transplantation. **(C)** Transverse sonogram of the hepatic veins and **(D)** sagittal sonogram of IVC show bland thrombus *(arrows)* in each. **(E)** Sagittal sonogram and **(F)** corresponding contrast-enhanced CT show bland thrombus in the IVC *(arrows). A,* Ascites. (**A** and **B** with permission from Crossin JD, Muradali D, Wilson SR. US of liver transplants: normal and abnormal. Radiographics. 2003;23[5]:1093-1114.[5])

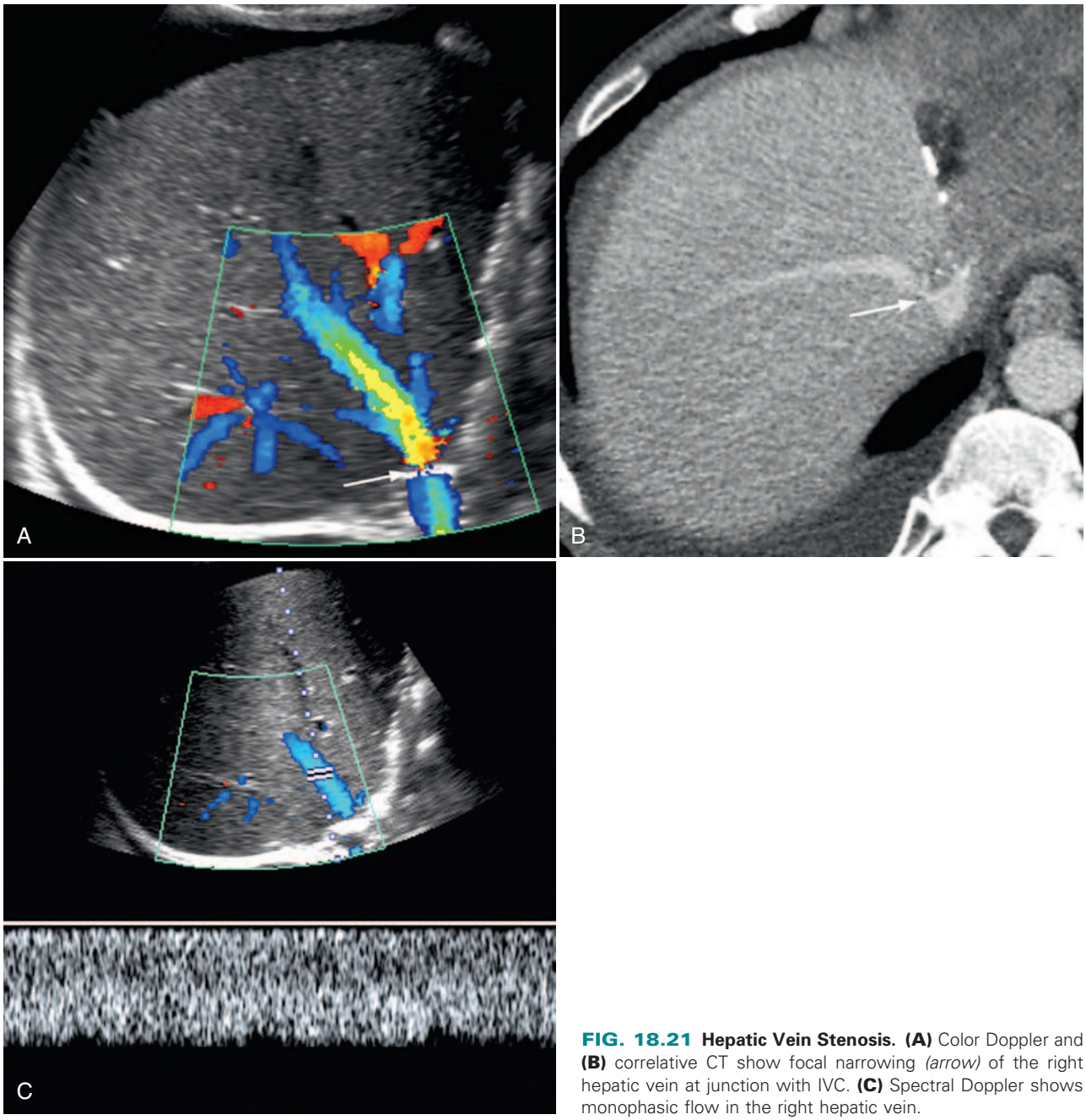

FIG. 18.21 Hepatic Vein Stenosis. (A) Color Doppler and **(B)** correlative CT show focal narrowing *(arrow)* of the right hepatic vein at junction with IVC. **(C)** Spectral Doppler shows monophasic flow in the right hepatic vein.

and size of donor renal arteries. In patients with cadaveric transplants, the donor artery, along with a portion of the aorta (Carrel patch) are anastomosed end to side to the external iliac artery. In patients with living donor transplants, the donor renal artery is anastomosed to either the internal iliac artery (end to end) or the external iliac artery (end to side) of the recipient. Multiple donor arteries of similar size may be joined together with a side-to-side anastomosis to form a common ostium. Alternatively, multiple arteries may be anastomosed as a Carrel patch, or anastomosed separately to the external iliac artery.[45,46]

The **donor renal vein** is almost always anastomosed end to side to the external iliac vein. In the case of multiple renal veins, the smaller veins are usually ligated, resulting in a single donor vein.[46]

The **ureter** is usually anastomosed to the superolateral wall of the urinary bladder through a neocystostomy. Several techniques are used to create a neocystostomy, but the basic procedure involves tunneling the ureter through the bladder wall to prevent reflux to the transplant. For patients undergoing repeat surgery on the collecting system and those with complex surgeries, the recipient's ureter may be used as a conduit to the bladder[45] (Fig. 18.28).

Because of the chronic shortage of donor organs, **paired cadaveric kidneys** from young (<5 years old) donors may be

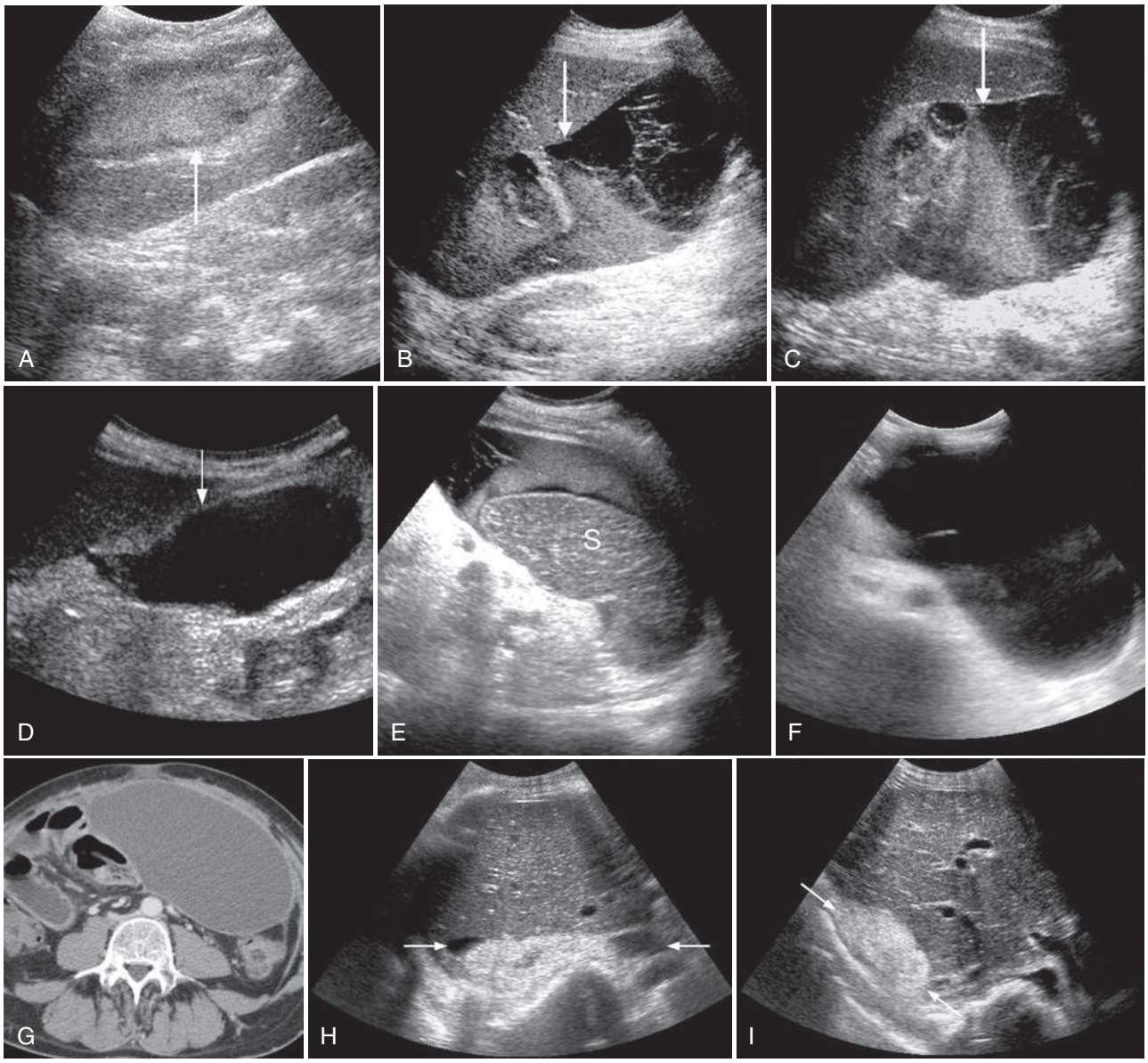

FIG. 18.22 Extrahepatic Fluid Collection. (A)-(D) Hematoma at surgical margin of a right lobe in living related transplant. **(A)** Transverse sonogram shows acute hematoma that appears echogenic, heterogeneous, and solid. **(B)** and **(C)** Hematoma liquefies after 3 weeks, with internal strands and a fluid-debris level. **(D)** After 2 months, further liquefaction of the hematoma appears as a smaller, anechoic collection. *Arrows* mark boundary of hematoma with liver. **(E)** Sagittal sonogram shows **hemoperitoneum** around spleen *(S),* with fluid-fluid level and internal strands. **(F)** and **(G) Anastomotic leak from roux-en-Y.** Transverse sonogram and correlative CT show large fluid collection in the left lower quadrant. **(H)** and **(I) Biloma secondary to anastomotic leak.** Sagittal sonogram and transverse sonogram show complex subphrenic echogenic collection *(arrows).*

transplanted en bloc in an attempt to provide a functional renal mass analogous to the renal mass of a single cadaveric kidney transplanted from an adult. At harvesting, both kidneys are removed en bloc with preservation of the ureters and main renal arteries and veins, as well as segments of the suprarenal and infrarenal abdominal aorta and IVC. The donor aorta and IVC are oversewn just cephalad to the origin of the renal arteries and veins, and the caudal ends anastomosed end to side to the recipient's external iliac artery and vein. The donor ureters are implanted into the urinary bladder through individual or common ureteroneocystostomies.[47] This surgery is more common in the pediatric population than in adults (see Fig. 18.28).

Normal Renal Transplant Ultrasound

Gray-Scale Assessment

Sonography of the renal transplant is usually easily performed because of the superficial location of the kidney in either the right or the left lower quadrant. Because the allograft is held in place by its pedicle, a variety of orientations may be encountered.

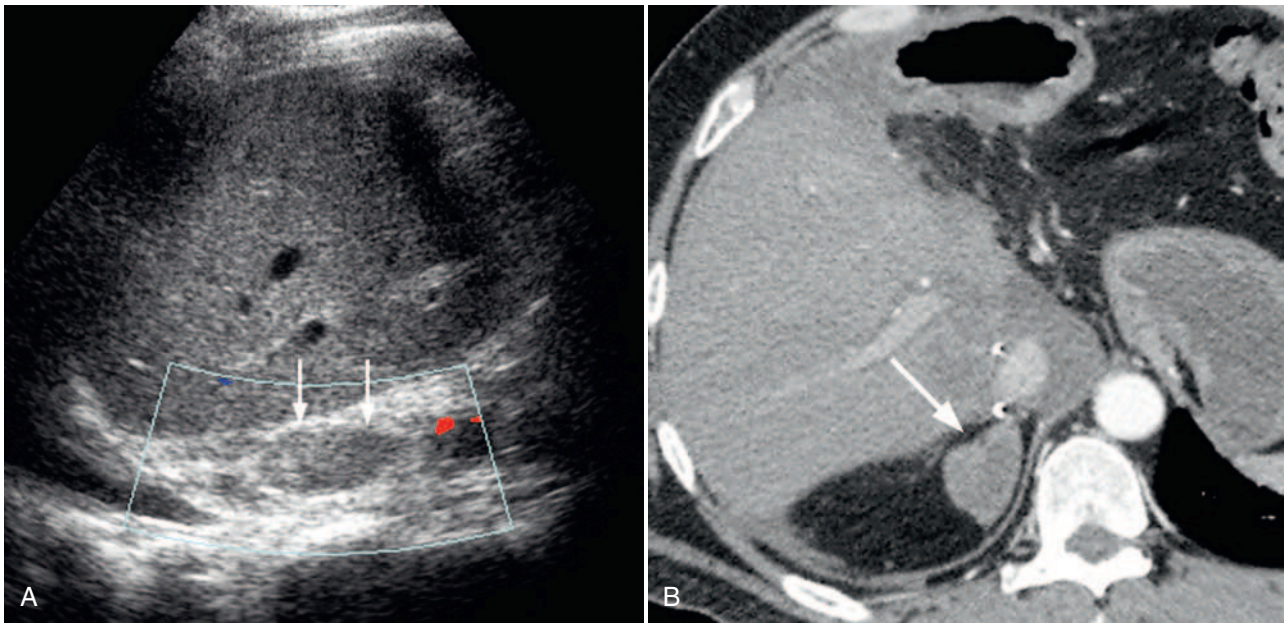

FIG. 18.23 Right Adrenal Hemorrhage. (A) Sagittal sonogram and **(B)** CT show a small right adrenal mass *(arrows).*

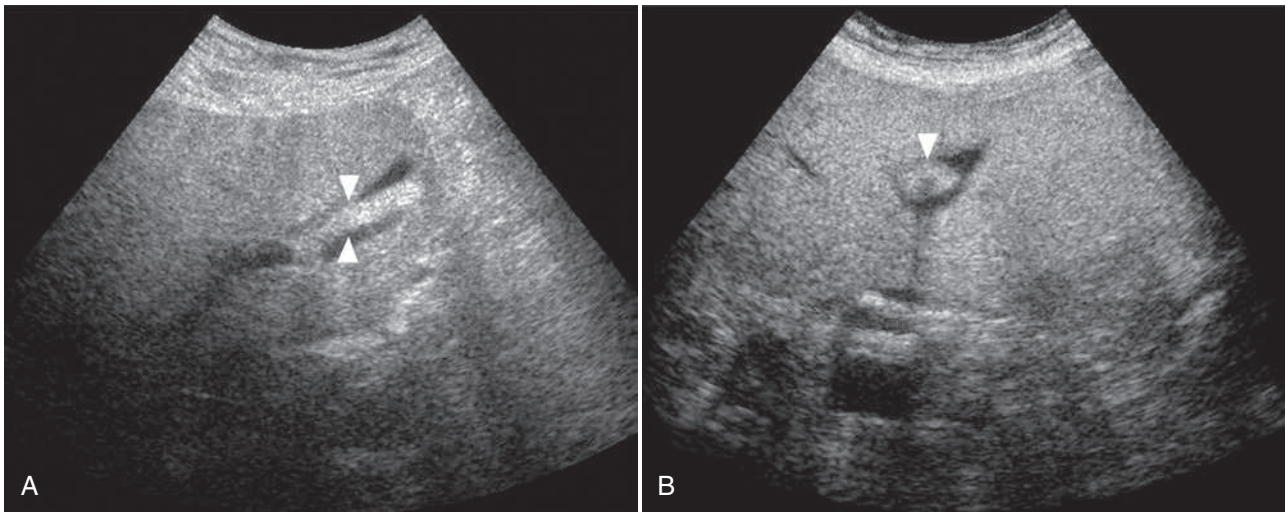

FIG. 18.24 Intrahepatic Fluid Collection. (A) Transverse and **(B)** sagittal sonograms show anechoic fluid surrounding echogenic falciform ligament *(arrowheads).*

Most often, the kidney is aligned with its long axis parallel to the surgical incision, with the hilum oriented inferiorly and posteriorly. Occasionally, in obese patients, the long axis may lie in an anterior-to-posterior plane.[48]

Longitudinal and transverse measurements of the transplant should be obtained with the kidney imaged through the hilum. Although there are no normative data for comparison, these measurements serve as a useful baseline for future reference to assess for interval changes in volume of the allograft. The transplant kidney may hypertrophy by up to 15% within the first 2 weeks after surgery, and eventually may increase in volume by 40%, with the final size attained at about 6 months.[49-51]

The transplanted kidney appears morphologically similar to the native kidney, with many of the subtle differences attributed to the improved resolution from proximity of the allograft to the skin surface (Fig. 18.29, Video 18.1 and Video 18.2). The normal renal cortex is well defined, hypoechoic, and easily differentiated from the highly reflective, central echogenic renal sinus fat. Apart from this improved corticomedullary differentiation, the renal pyramids of the allograft are more easily visualized than in the native kidney, appearing as wedge-shaped structures that are hypoechoic to the surrounding parenchyma.[44]

The collecting system should be assessed for the presence of hydronephrosis. If a stent is present, its proximal and distal

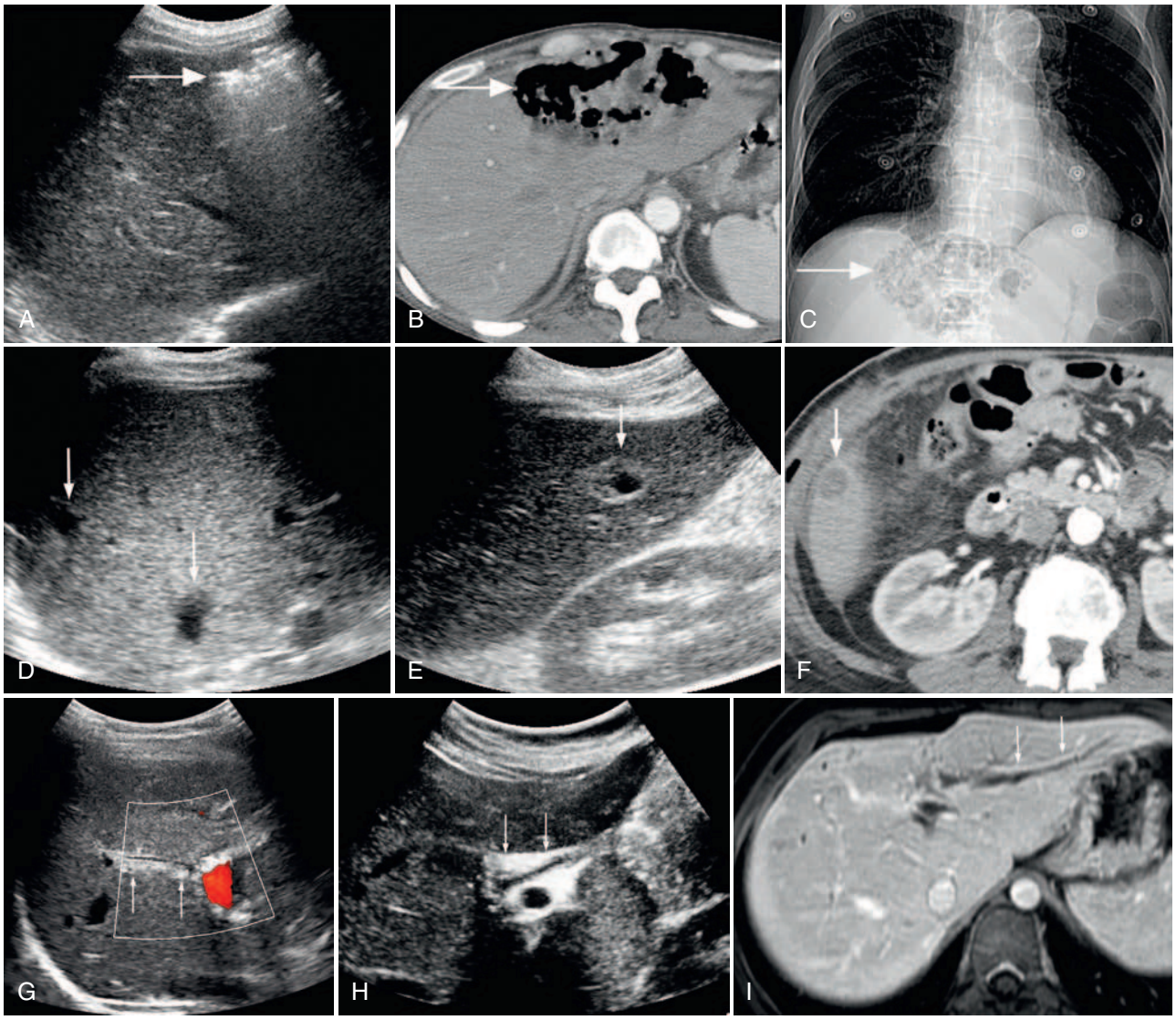

FIG. 18.25 Liver Infections in Three Patients: Solitary Abscess. (A)-(C) Air-containing abscess *(arrows)* in segment IV of liver. **(A)** Transverse ultrasound, **(B)** CT, and **(C)** plain film show air within the abscess, on ultrasound appearing as an echogenic interface associated with dirty shadowing. **(D)-(F) Multifocal abscess. (D)** Transverse and **(E)** sagittal sonograms show multiple small parenchymal collections *(arrows).* **(F)** Corresponding CT scan shows subtle rim enhancement *(arrow).* **(G)-(I) Ascending cholangitis. (G)** Transverse sonogram shows increased periductal echogenicity *(arrows)* of a right intrahepatic bile duct. **(H)** Oblique sonogram shows thickening of the common hepatic duct, with increased echogenicity of the periductal fat *(arrows).* **(I)** T1-weighted contrast-enhanced magnetic resonance image shows periductal enhancement *(arrows).*

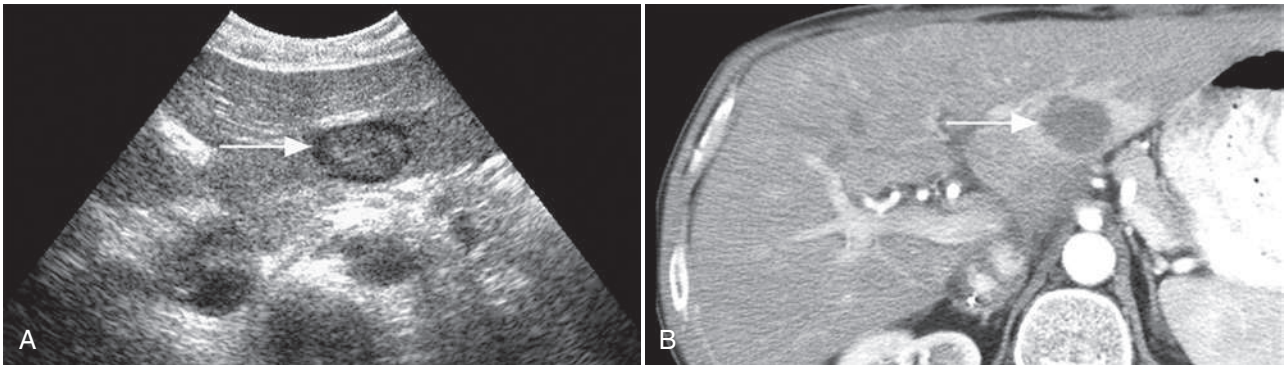

FIG. 18.26 Atypical Infarct. (A) Transverse sonogram shows an atypical infarct *(arrow)* appearing as a round mass associated with a surrounding hypoechoic halo. **(B)** Correlative CT shows that the infarct *(arrow)* is avascular, with a surrounding parenchymal blush. (With permission from Crossin JD, Muradali D, Wilson SR. US of liver transplants: normal and abnormal. Radiographics. 2003;23[5]:1093-1114.[5])

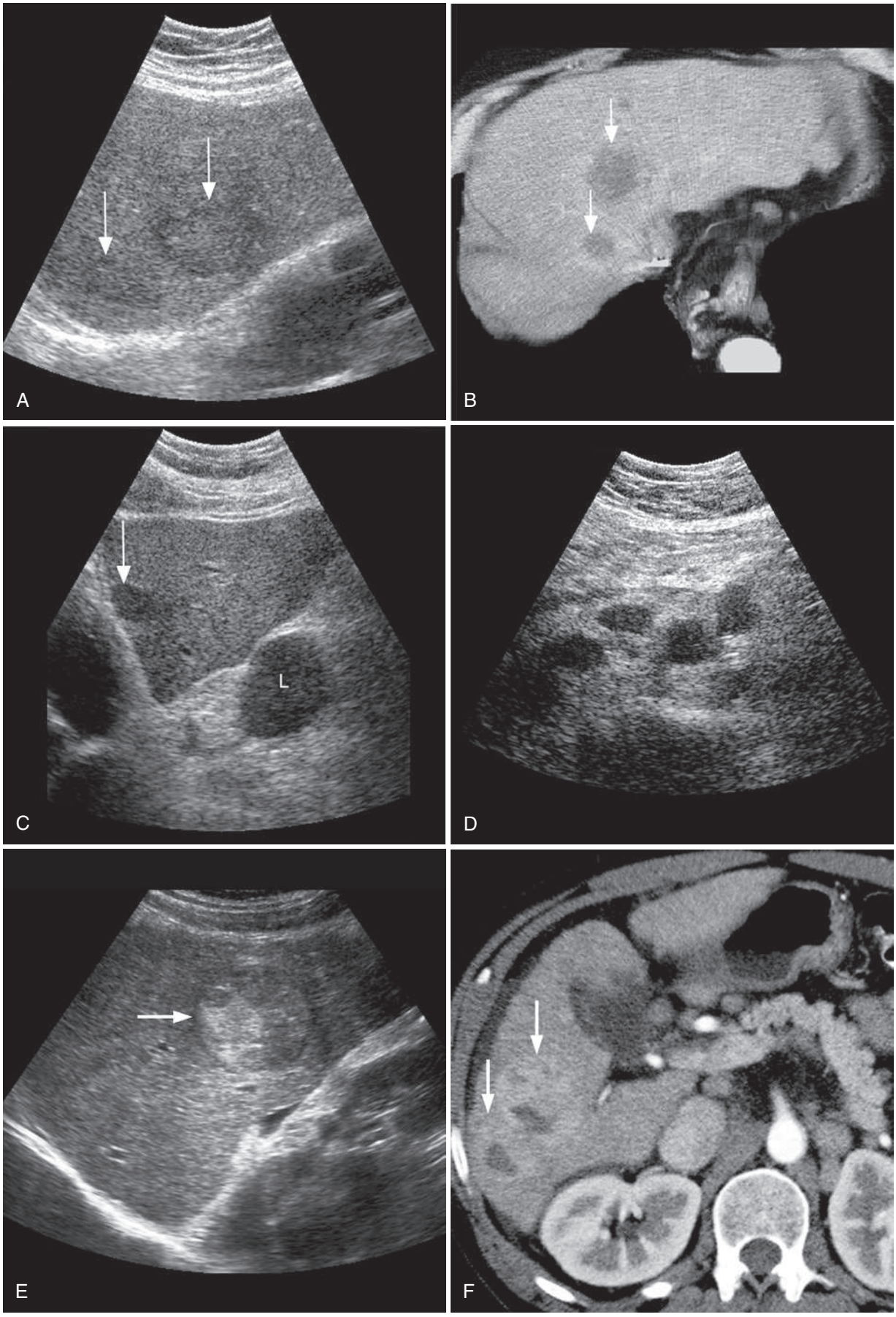

FIG. 18.27 Recurrent Hepatocellular Carcinoma (HCC) in Two Patients. *Patient 1:* **(A)** Transverse sonogram shows two malignant-appearing masses *(arrows)* secondary to recurrent HCC. **(B)** Correlative arterial phase CT shows peripheral enhancement of the masses *(arrows).* **(C)** Sagittal sonogram shows a third HCC in the medial segment of the left lobe *(arrow)* and a large metastatic lymph node *(L).* **(D)** Transverse midline sonogram shows multiple enlarged metastatic lymph nodes. *Patient 2:* **(E)** Sagittal sonogram shows solid mass *(arrow)* with echogenic and hypoechoic regions. **(F)** Correlative arterial phase CT scan shows hypervascular masses *(arrows),* consistent with recurrent HCC.

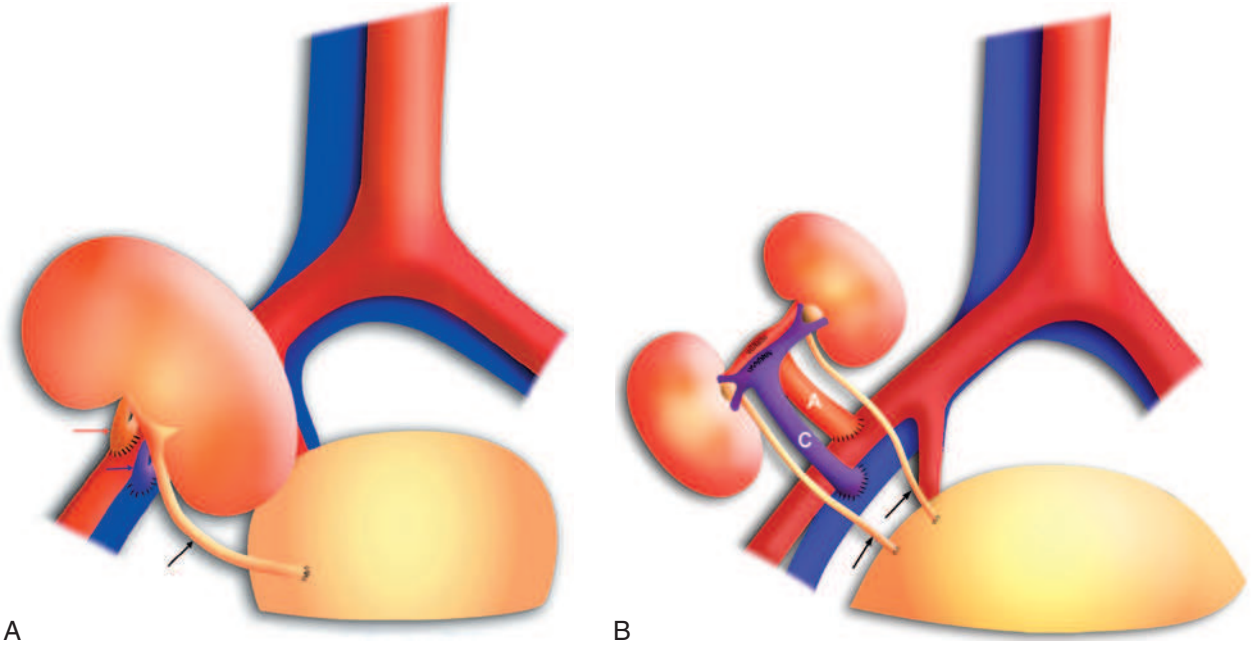

FIG. 18.28 Renal Transplant Surgery. (A) Single cadaveric transplant. The main renal artery *(red arrow)* and main renal vein *(purple arrow)* are anastomosed to the external iliac artery and vein, respectively. The ureter *(black arrow)* is anastomosed to the superolateral bladder wall. **(B)** Double cadaveric transplant. The aorta *(A)* and inferior vena cava *(C)* are anastomosed to the external iliac artery and vein, respectively. The ureters *(black arrows)* are anastomosed to the superolateral bladder wall.

FIG. 18.29 Normal Gray-Scale Ultrasound of Renal Transplant. See also Video 18.1 and Video 18.2.

positions should be documented. Transverse and sagittal images of the bladder should also be recorded. The perinephric space and surrounding regions should be assessed for the presence of fluid collections or free fluid.[52]

The sonographer should be aware that the transplanted kidney might show pathology that was likely present at the time of donation, such as benign cysts, angiomyolipomas, and medullary sponge kidney (Figs. 18.30 and 18.31).

Doppler Assessment

Color Doppler gives a global assessment of the intraparenchymal perfusion and is useful in localizing the main renal artery and vein. The renal parenchyma should be screened initially with color Doppler to check for focal regions of hypoperfusion and locate the interlobar arteries for spectral interrogation.[44]

Spectral traces of the interlobar arteries should be obtained from the upper-pole, middle-pole, and lower-pole regions with low filter settings, maximal gain, and the smallest scale demonstrating the PSV. The normal waveform is low impedance with a brisk upstroke and continuous diastolic flow; RI of 0.6 to 0.8 is normal. An intraparenchymal RI between 0.8 and 0.9 is considered equivocal, and greater than 0.9 is classified as abnormal, suggesting increased intraparenchymal resistance. Overall, an **elevated resistive index** is a nonspecific marker of transplant dysfunction but is not helpful in determining the cause of the dysfunction.[53]

The number of main renal arteries should be documented, and if there is more than one arterial anastomosis, then each anastomosis should be interrogated separately. Doppler assessment should also be performed of the external iliac artery and vein cephalad to the surgical anastomosis.[52] Provided that flow in the recipient common iliac artery is normal, the velocity of the transplanted main renal artery should be less than 250 cm/sec[53,54] (Figs. 18.32 and 18.33).

The intraparenchymal and extraparenchymal renal veins show either monophasic continuous flow or phasicity with the cardiac cycle. There are no accepted normal peak velocity values for these vessels. Documentation of the presence or absence of flow within the transplant and main renal vein, with an appropriate velocity gradient across the venous anastomosis, is of prime importance in the management of these patients.

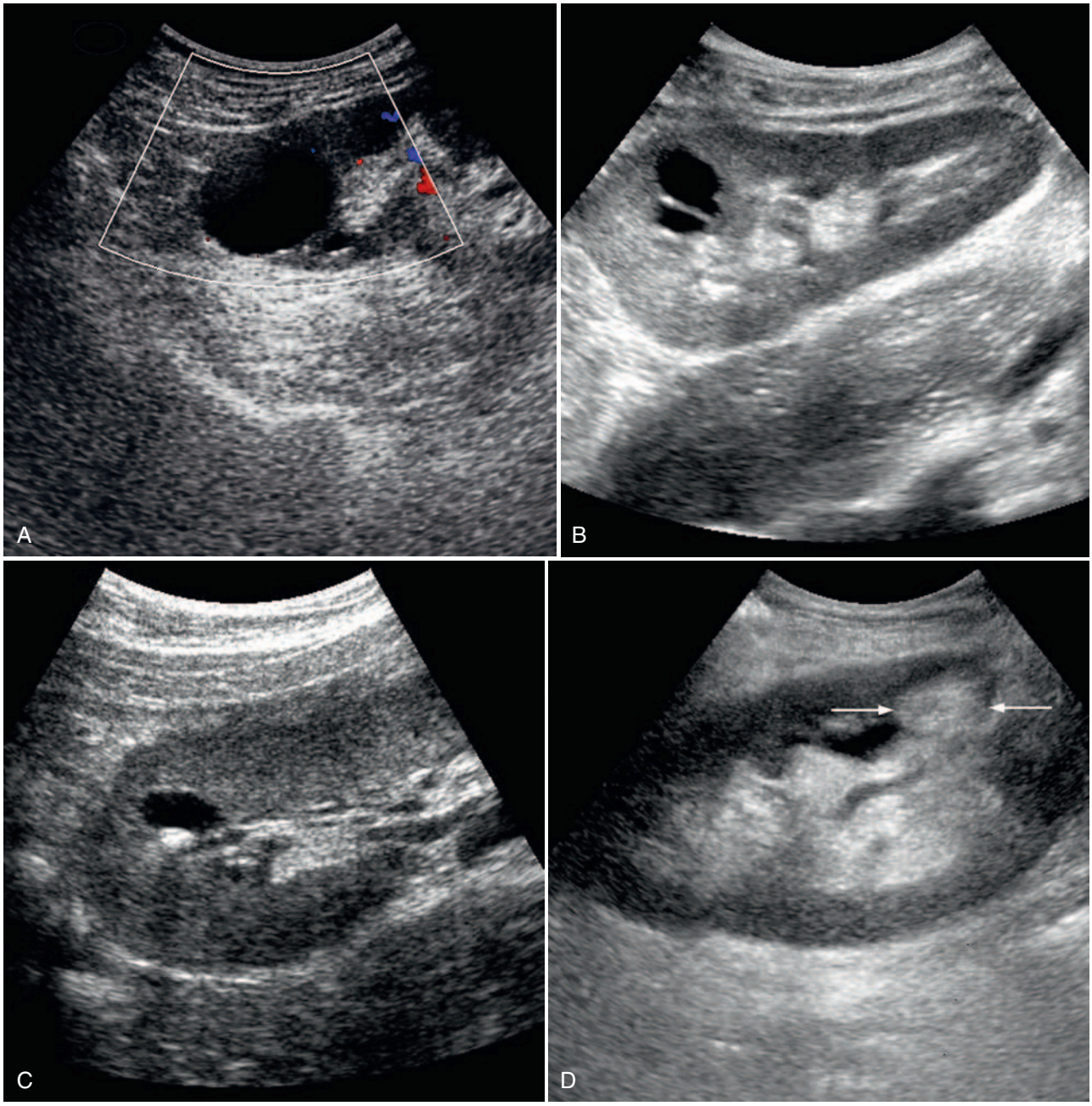

FIG. 18.30 Benign Renal Cysts in Four Patients. Sagittal sonograms of transplant kidneys. **(A)** Simple upper-pole cyst, which is avascular on color Doppler ultrasound. **(B)** Upper-pole cyst with a single thin strand. **(C)** Milk of calcium cyst with dependent calcification. **(D)** Marsupialized renal cyst *(arrows)* appearing as an echogenic mass.

Abnormal Renal Transplant

Renal transplants are routinely evaluated with sonography as either a component of a screening protocol or a workup for renal dysfunction based on a rising serum creatinine level or a decreased urine output. Postoperative complications have been reported in up to 20% of renal transplant recipients.[46] When encountered in a graft with a clinical suspicion of dysfunction, the sonographer should approach the possible causes in terms of (1) parenchymal pathology, (2) prerenal causes, and (3) postrenal complications. Parenchymal transplant pathology includes acute tubular necrosis (ATN), acute and chronic rejection, and infection. Prerenal problems include all factors affecting blood flow to the kidney or venous drainage from the graft. Postrenal complications include intrinsic or extrinsic lesions that can obstruct either a component of the calyceal system or the transplanted ureter.

Parenchymal Pathology

Acute Tubular Necrosis and Acute Rejection

Acute tubular necrosis results from donor organ ischemia either before vascular anastomosis or secondary to perioperative

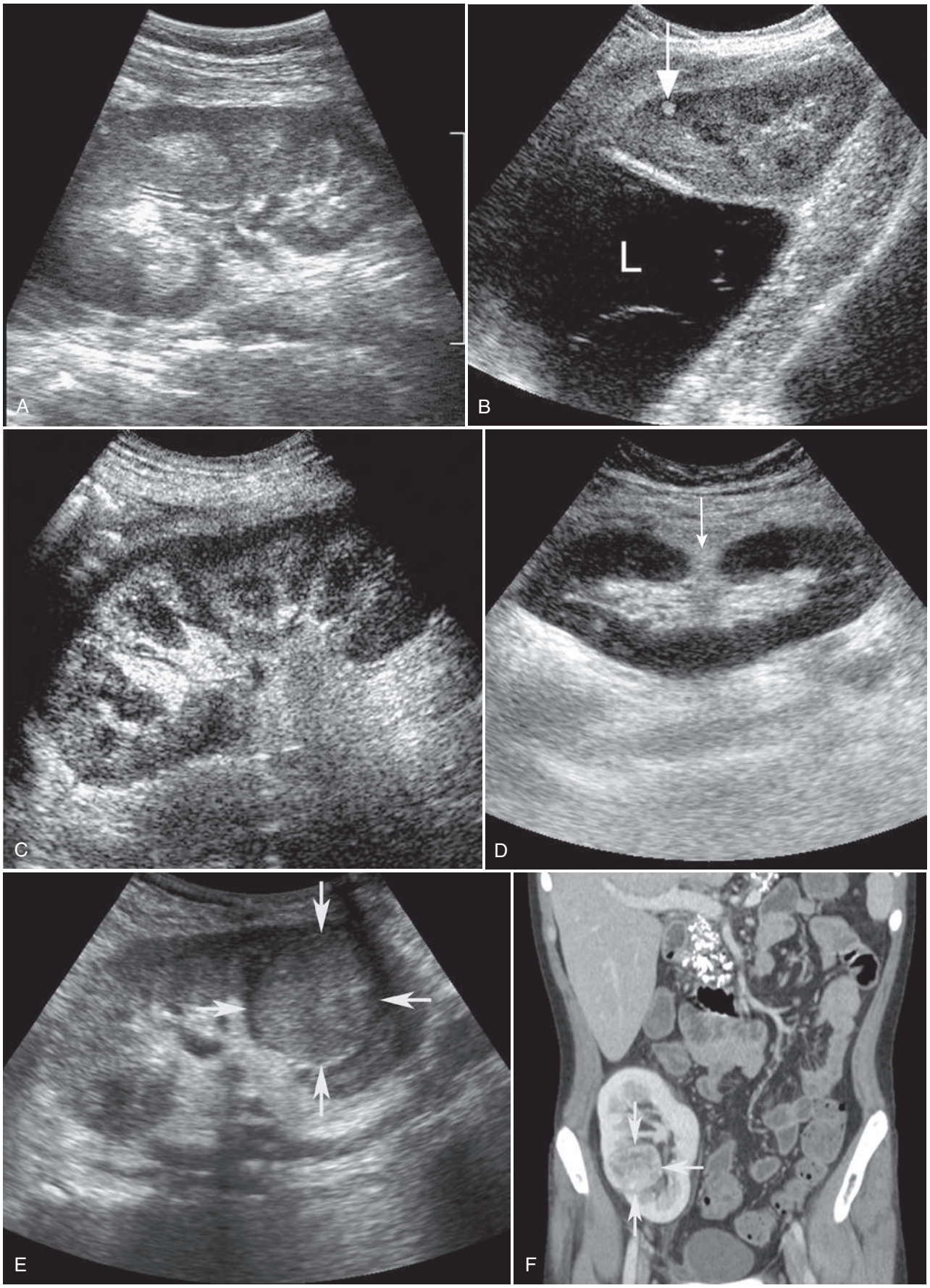

FIG. 18.31 Donor Pathology in Four Patients. Sagittal sonograms of transplant kidneys. **(A)** Nephrocalcinosis with calcifications in the renal medulla. **(B)** Tiny angiomyolipoma *(arrow). L,* Lymphocele. **(C)** Anderson-Carr morphology with echogenic borders around the medullary pyramids. **(D)** Midpole scar *(arrow).* **(E)** and **(F)** Renal cell carcinoma *(arrows)* on ultrasound **(E)** and CT **(F)**.

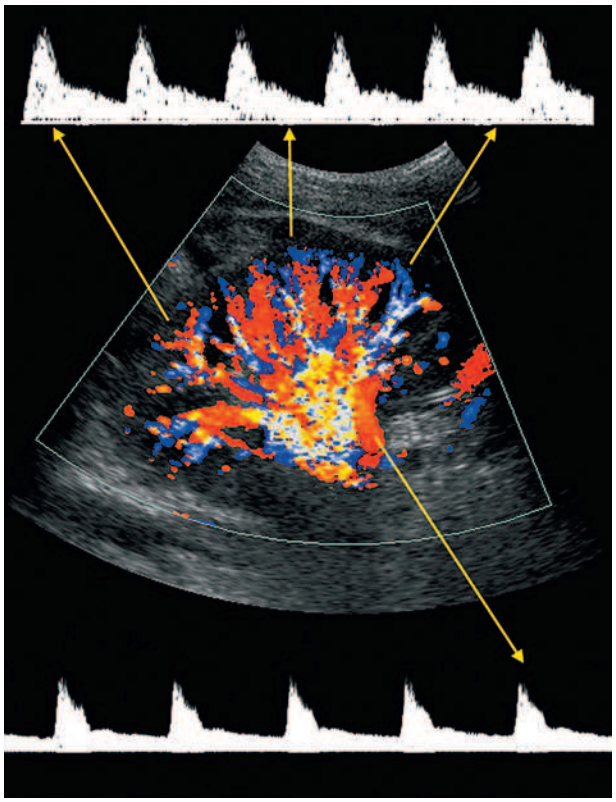

FIG. 18.32 Normal Renal Transplant Doppler. Color Doppler shows flow throughout kidney *(top)*. Intrarenal spectral traces of upper, middle, and lower poles show a resistive index of less than 0.8 and continuous flow throughout diastole. The main renal artery shows continuous flow with peak velocities less than 200 cm/sec *(bottom)*.

hypotension. It is most common in the early postoperative period and is the major cause of delayed graft function (defined as the need for dialysis within the first week of transplantation).[45,55] In patients requiring dialysis, recovery is usually in the first 2 weeks of transplantation but may be delayed by up to 3 months. ATN occurs in most cadaveric grafts and is observed infrequently in living related renal transplants because of the relatively short cold ischemic time of the donor kidney.[44]

Transplants affected by **hyperacute rejection** are rarely imaged because graft failure occurs immediately at the vascular anastomosis during surgery.[45] **Acute rejection** occurs in up to 40% of patients in the early transplant period, peaking at 1 to 3 weeks after surgery, and is an adverse long-term prognostic indicator. Most patients with acute rejection are asymptomatic, but a small proportion may have flulike symptoms, malaise, fever, and graft tenderness. Provided that the diagnosis can be rapidly established, acute rejection usually can be promptly reversed with high-dose steroids or antibiotic therapy.[44,56]

The imaging features of ATN and acute rejection are almost identical on gray-scale and Doppler ultrasound. Both conditions can produce increases in renal volume of the allograft. However, precise volumetric comparisons between interval studies can prove difficult; subtle changes in two-dimensional (2-D) measurements have not been adopted as a strong clinical sign of potential dysfunction. Other gray-scale findings include increased cortical thickness, increased or decreased cortical echogenicity, reduction of the corticomedullary differentiation, loss of the renal sinus echoes, and prominence of the pyramids (Fig. 18.34).

Color Doppler assessment may be normal or may occasionally show diffuse decreased blood flow. The RI of the intraparenchymal arteries is also nonspecific in these conditions and may be normal or elevated. In severe cases, there may be a complete lack of flow in diastole or a reversal of diastolic flow[44] (Fig. 18.35). Despite the lack of specificity of gray-scale and Doppler ultrasound in these acute conditions, **serial spectral Doppler** measurements, in combination with clinical assessments and biochemical findings, provide a useful guide to the clinician in terms of monitoring the allograft function and in determining the need for percutaneous biopsy.

Chronic Rejection

Chronic rejection is defined as a reduction in allograft function starting at least 3 months after transplantation in association with fibrous intimal thickening, interstitial fibrosis, and tubular atrophy on histology. It is the most common cause of late graft loss. The most frequent predisposing risk factor for development of chronic rejection is recurrent previous episodes of acute rejection.[44,45] On ultrasound, there is progressive thinning of the renal cortex, prominence of the central renal sinus fat, and a reduction in the overall size of the transplant. **Dystrophic calcifications** may be seen scattered throughout the residual parenchyma. In the end-stage renal transplant, the entire renal cortex can become calcified, appearing as a sharp echogenic interface associated with clean distal shadowing (Fig. 18.36).

Infection

Over 80% of patients with renal allografts will experience an episode of infection within the first year after transplant surgery.[57] Transplant pyelonephritis can result from an ascending infection, hematologic seeding, or contiguous spread from an adjacent infected fluid collection. Ultrasound findings include a focal or diffusely granular, echogenic renal cortex associated with loss of the corticomedullary junction; increased echogenicity and thickening of the perirenal fat secondary to extension of inflammation or infection into the surrounding tissue; and uroepithelial thickening (Fig. 18.37).

Pyonephrosis may occur occasionally in a chronically obstructed transplanted kidney. In the early stages, the lumen of the dilated collecting system appears anechoic. Once the lumen becomes filled with purulent material, low-level echoes develop within the calyceal system and ureter, sometimes associated with fluid-debris levels. Echogenic material within the collecting system may also result from intraluminal blood or other filling defects, or it may be artifactual as a result of scatter or s1ide-lobe artifact (see Fig. 18.37).

Abscesses can arise from infection of a previously sterile collection. On ultrasound, abscesses appear as a complex cystic structure and may be associated with fluid-fluid levels or intraluminal air (Fig. 18.38).

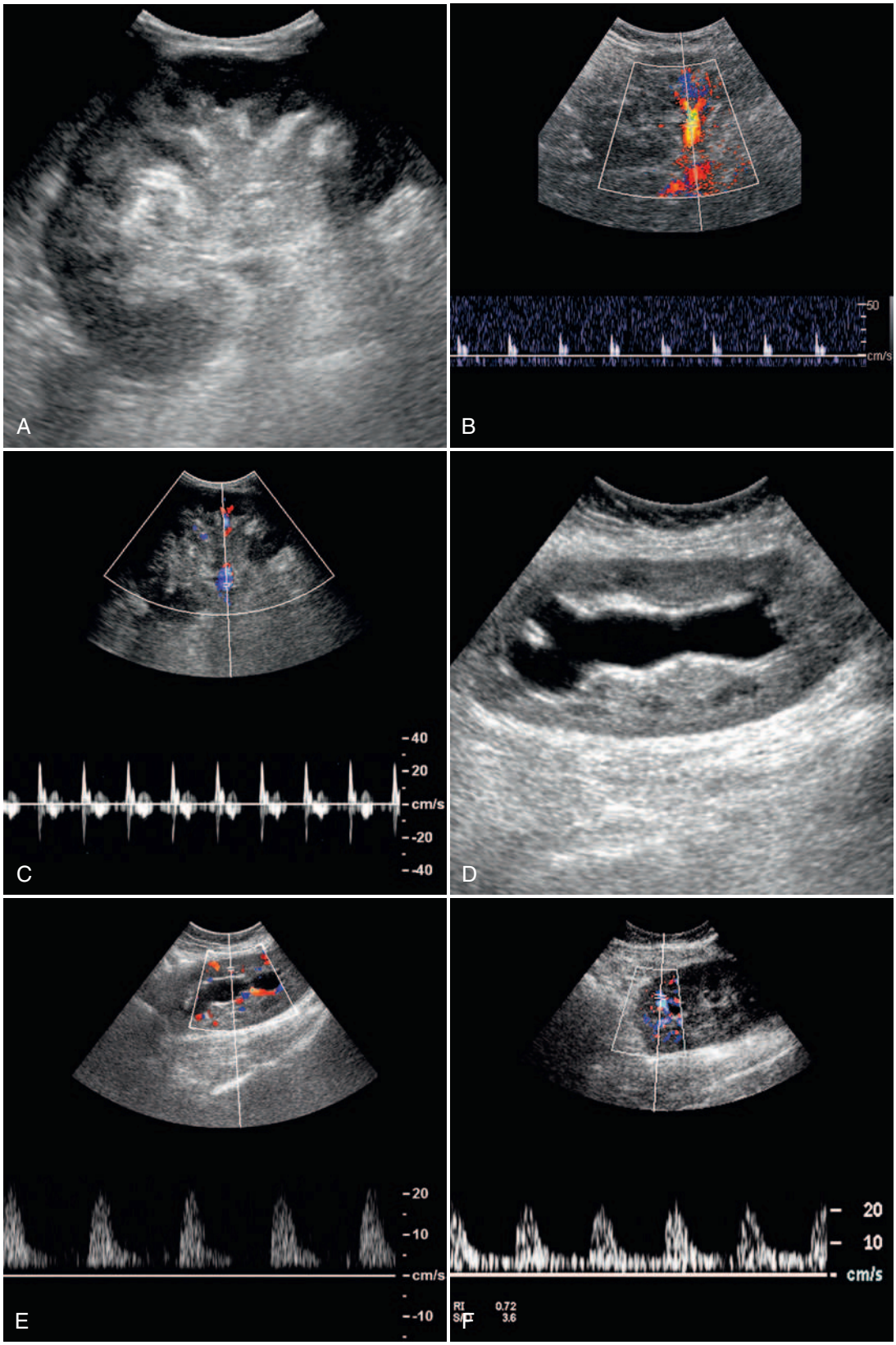

FIG. 18.33 Elevated Resistive Indices (RIs) in Two Patients. (A)-(C) Acute rejection. (A) Sagittal sonogram shows increased cortical echogenicity. **(B)** Spectral Doppler ultrasound done initially shows no flow in diastole and thus an RI of 1.0. **(C)** Follow-up spectral Doppler ultrasound 1 week later shows reversal of flow in diastole, which coincided with the clinical deterioration of the patient. **(D)-(F) Collecting system obstruction. (D)** Sagittal scan shows grade 3 pelvocaliectasis secondary to ureteral stricture (not shown). **(E)** Spectral Doppler shows RI of 1.0. **(F)** Spectral Doppler ultrasound performed after resolution of the pelvocaliectasis shows a normal RI of 0.72.

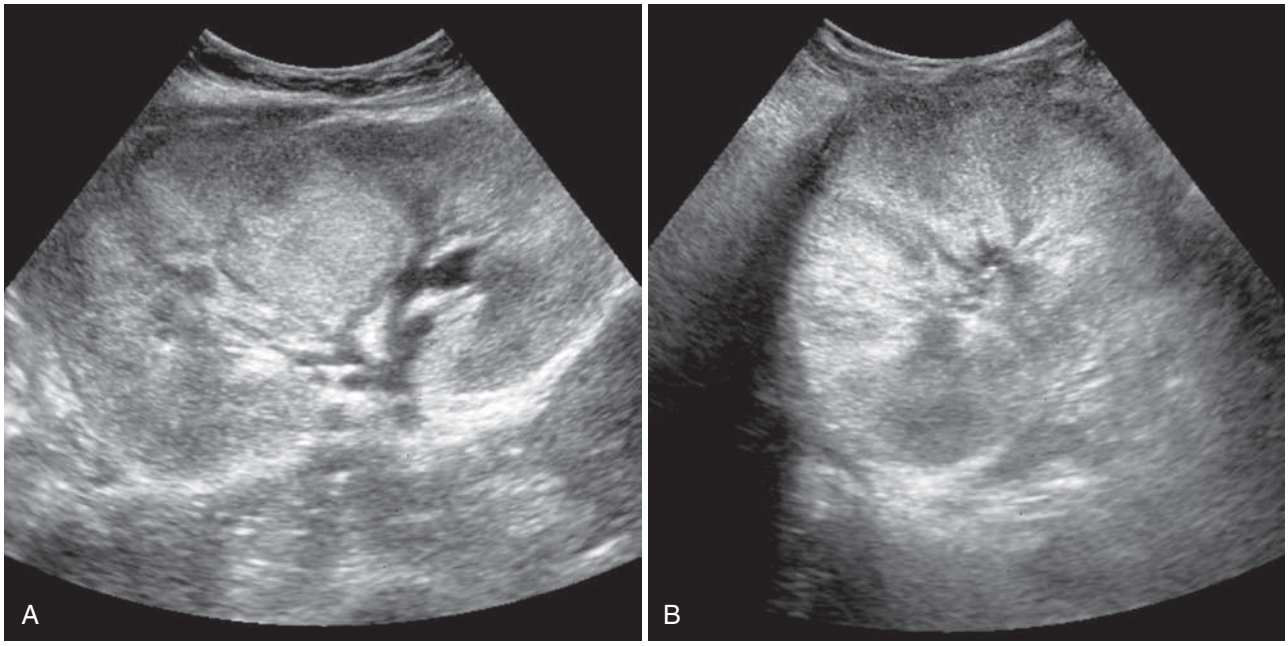

FIG. 18.34 Acute Tubular Necrosis. (A) Sagittal and **(B)** transverse sonograms show increased cortical thickness and echogenicity as well as loss of the normal corticomedullary differentiation.

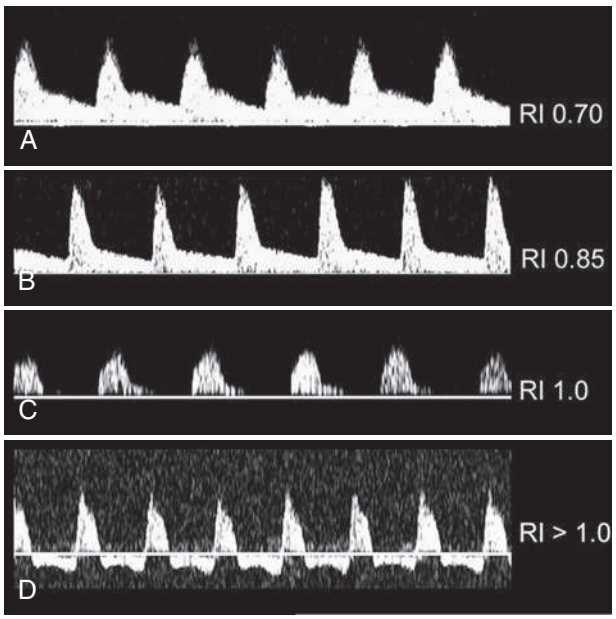

FIG. 18.35 Intrarenal Spectral Waveforms in Four Patients. (A) Normal waveform shows resistive index (RI) of 0.70. **(B)** RI in a gray zone (0.85). **(C)** RI elevated (1.0) with no flow in diastole. **(D)** Elevated RI (>1.0) with reversal of flow in diastole. This is seen with severely increased vascular resistance in the kidney from rejection or renal vein thrombosis.

Gas can be observed within the collecting system in **emphysematous pyelonephritis,** appearing as a bright echogenic focus with distal dirty shadowing. **Milk of calcium cysts** can produce dirty shadowing, mimicking an intrarenal abscess. Scanning the patient in a decubitus position allows for differentiation; gas rises to the nondependent portion of the lumen, whereas milk of calcium does not (Fig. 18.39).

Prerenal Vascular Complications

Arterial Thrombosis

Renal artery thrombosis occurs in less than 1% of transplants, usually within the first month of surgery, and is often initially asymptomatic. The most common cause is hyperacute or acute rejection, which results in occlusion of the intraparenchymal arterioles with retrograde main renal artery thrombosis. Other predisposing factors include a young pediatric donor kidney, atherosclerotic emboli, acquired renal artery stenosis, hypotension, vascular kinking, cyclosporine, hypercoagulable states, intraoperative vascular trauma, and poor intimal anastomosis.[58]

Global infarction of the allograft occurs when there is occlusive thrombosis of the main renal artery, with no perfusion to the renal parenchyma. On gray-scale ultrasound, the kidney may appear diffusely hypoechoic and enlarged. On color and spectral Doppler ultrasound, complete absence of arterial and venous flow distal to the occlusion, within both the hilar and the intraparenchymal vessels, is observed. Although surgical thrombectomy with arterial repair is often attempted, nephrectomy is frequently indicated in these patients.[46]

Segmental infarction of the allograft may occur in transplants with a single main renal artery with thrombosis of a major arterial branch (Fig. 18.40), in transplants with multiple renal arteries where a single artery is thrombosed, and in patients with systemic vasculitis. On gray-scale sonography, a segmental infarct may appear as a poorly defined hypoechoic region, a hypoechoic mass, or a hypoechoic mass with a well-defined echogenic wall.

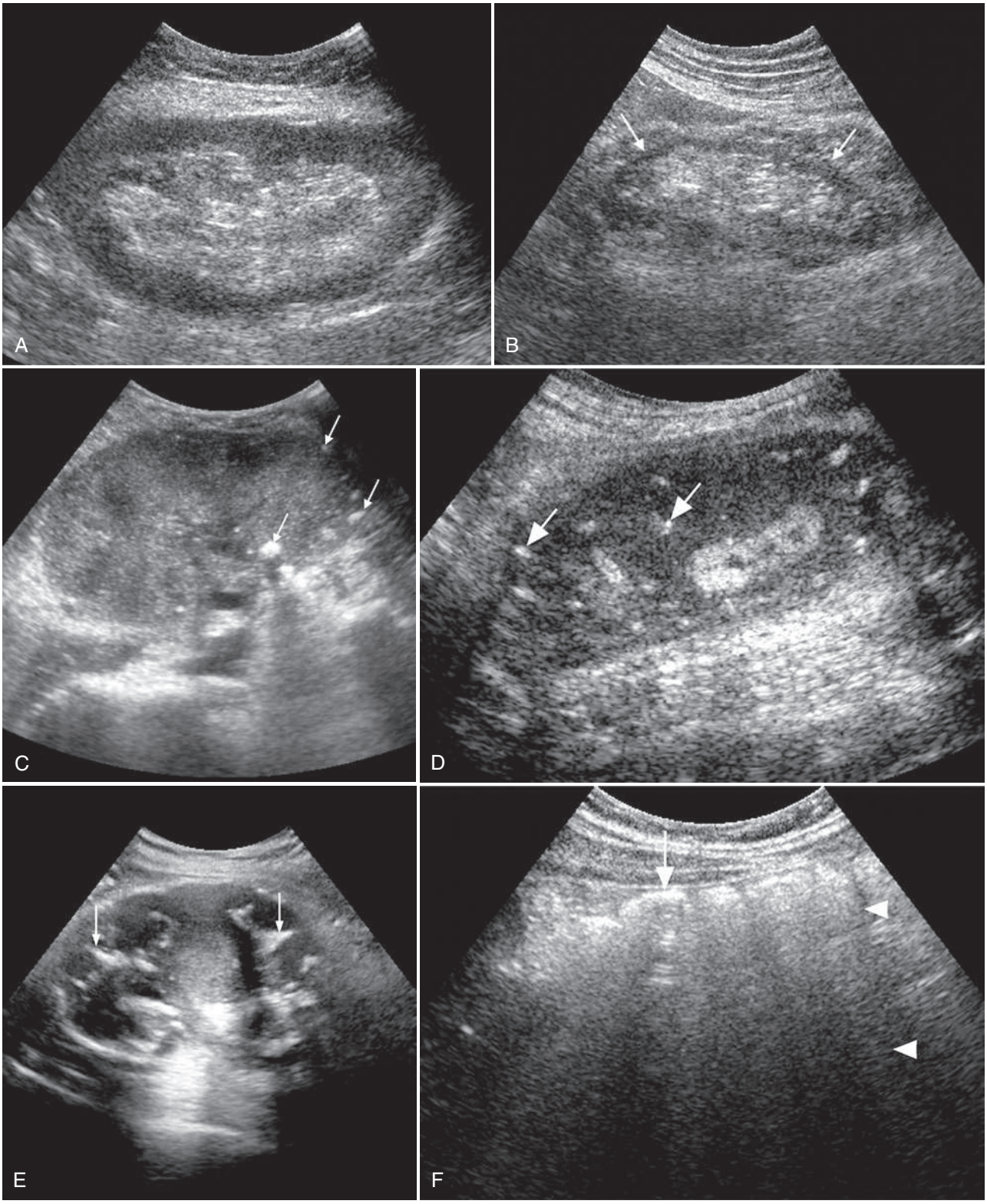

FIG. 18.36 Chronic Renal Failure in Six Patients. (A) and **(B) Cortical thinning. (A)** Sagittal scan shows moderate cortical thinning with abundant renal sinus fat. **(B)** With progression, the kidney *(arrows)* becomes smaller and the cortex thinner. **(C)-(F) Dystrophic calcifications.** Sagittal sonograms show **(C)** a few punctuate peripheral cortical calcifications *(arrows);* **(D)** multiple peripheral and central cortical calcifications *(arrows);* and **(E)** linear calcifications that extend from the peripheral to deep cortex *(arrows).* **(F)** The end-stage kidney becomes calcified, appearing as an echogenic interface *(arrow)* associated with dirty shadowing *(arrowheads).* The kidney is frequently not identified on sonography at this stage.

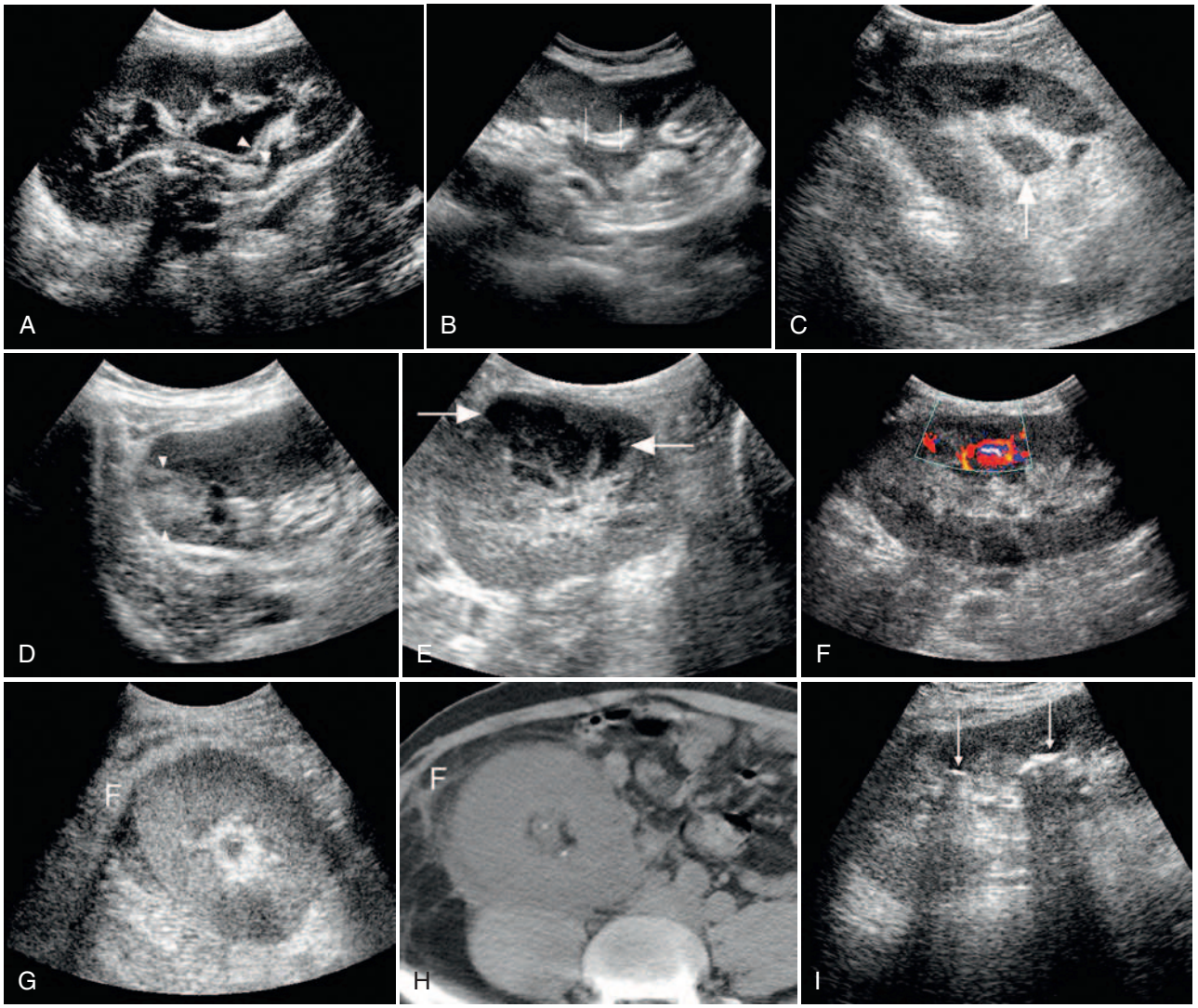

FIG. 18.37 Renal Transplant-Related Infections. (A) Uroepithelial thickening. Sagittal sonogram shows mild uroepithelial thickening *(arrowheads).* **(B)** Sagittal scan shows mild uroepithelial thickening *(arrows)* surrounding a mildly dilated collecting system with internal echoes, secondary to early pyonephrosis. **(C)** Transverse sonogram shows moderate to severe uroepithelial thickening *(arrow),* which can be misinterpreted as a mass in the renal pelvis. **(D)-(F) Focal pyelonephritis. (D)** Sagittal sonogram shows subtle, focal echogenic region in the upper-pole cortex *(arrowheads).* **(E)** Intraparenchymal phlegmon appearing as a hypoechoic mass within the renal cortex *(arrows).* **(F)** On color Doppler, the phlegmon seen in image **(E)** is vascular. **(G)** and **(H) Diffuse pyelonephritis. (G)** Transverse sonogram shows a generous kidney with echogenic granular renal cortex, surrounded by inflamed echogenic perinephric fat *(F).* **(H)** Corresponding CT shows inflamed fat *(F)* as perinephric streaking. **(I) Emphysematous pyelonephritis.** Sagittal sonogram shows air *(arrows)* within collecting system, appearing as bright, echogenic linear foci with distal dirty shadowing.

On Doppler sonography, the infarcted region appears as a wedge-shaped area devoid of flow on color or spectral interrogation.[57] Interpretation of the gray-scale and Doppler findings should not be influenced by urine output of the allograft or laboratory data, because segmental infarction may occur in the presence of preserved renal function.

The absence of blood flow on Doppler interrogation in the kidney parenchyma may be observed in conditions other than arterial thrombosis, including **hyperacute rejection** and **renal vein thrombosis.** In these conditions, however, the main renal artery is patent on spectral Doppler ultrasound and may exhibit reversal of diastolic flow.[44]

Renal Artery Stenosis

Renal artery stenosis, the most common vascular complication of transplantation, occurs in up to 10% of patients within the first year, is more frequent in living donor allografts compared with cadaveric allografts, and should be suspected in cases of severe hypertension refractory to medical therapy. Transplants with multiple renal arteries are now being used more frequently

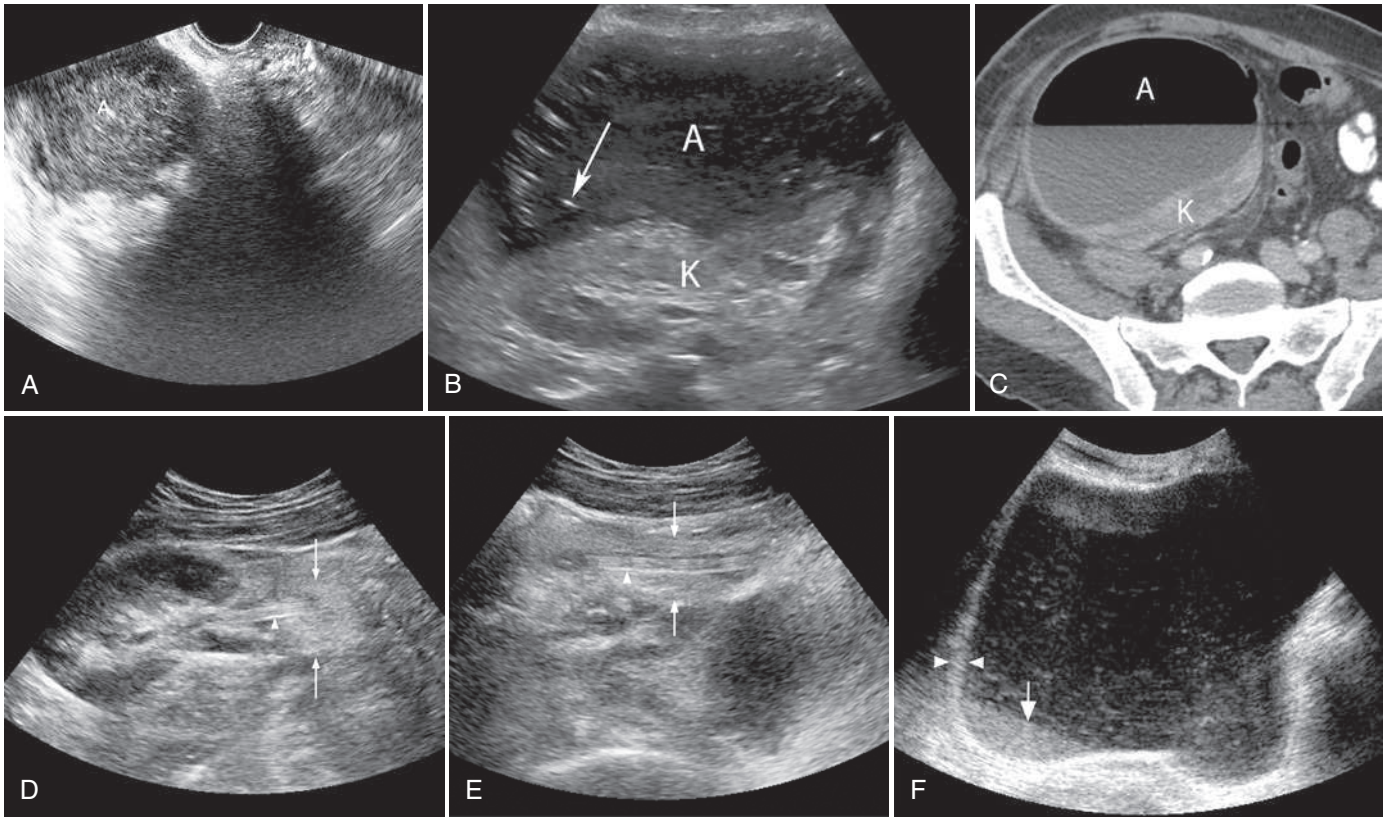

FIG. 18.38 Renal Transplant-Related Infections. (A) Perirenal *Candida* abscess. Transabdominal sagittal scan shows abscess *(A)* abutting the lower pole of the transplant kidney. **(B)** and **(C)** Subcapsular abscess on ultrasound and CT. Note the heterogeneous abscess *(A)* with gas *(arrow)* compressing the kidney *(K)*. **(D)** and **(E) Ureteritis.** Sagittal sonograms of proximal **(D)** and midline **(E)** ureter show inflamed echogenic periureteral fat *(arrows)* secondary to an infected ureteral stent *(arrowhead)*. **(F) Cystitis.** Transverse sonogram shows internal echoes and fluid-debris level *(arrow)* in urinary bladder, secondary to cystitis. *Arrowheads* show thickened bladder wall.

and show a very slightly higher rate of renal artery stenosis compared with those renal allografts with a single artery. Stenosis may occur in one of three regions of the transplanted artery: the **donor** portion (Fig. 18.41), most frequently observed in end-to-side anastomoses and thought to arise from either rejection or difficult surgical technique; the **recipient** portion (Fig. 18.42), which is more uncommon and usually the result of intraoperative clamp injury or intrinsic atherosclerotic disease; and the **anastomosis** (Fig. 18.43), which is more frequent in end-to-end anastomoses and is directly related to surgical technique or may be secondary to rejection.[54,58-60]

Initially, color Doppler ultrasound should be used to determine the location of the anastomosis, as well as to document focal regions of aliasing, which would indicate the presence of high-velocity turbulent flow and serve as a guide for meticulous spectral interrogation. A spectral tracing should then be obtained at the anastomosis and in any area where color aliasing is detected to determine the PSV in that region.

The upper limit of normal for arterial PSV is unclear. Assigning a PSV upper limit of 200 cm/sec for diagnosing renal artery stenosis may result in a relatively high false-positive rate. Thus some authors have suggested using an arterial threshold PSV of 250 cm/sec for the diagnosis of renal artery stenosis.[54,61]

However, high velocities in the renal artery may be secondary to changes in the external iliac artery. Therefore the renal artery–external iliac artery PSV ratio can be calculated to determine if renal artery velocity measurements are a result of narrowing or high flow rates from the external iliac artery. A renal artery–external iliac artery PSV ratio greater than 1.8:1 is suggestive of renal artery stenosis.[54,62] In addition, within the renal parenchyma, a tardus-parvus spectral waveform can be observed in the intraparenchymal arteries in patients with renal artery stenosis.[46,57] If no flow abnormality is detected within the main renal artery after color and spectral Doppler interrogation, significant stenosis can be excluded.[63]

Doppler Criteria for Renal Artery Stenosis

Color aliasing at the stenotic segment
Distal turbulent flow
Peak systolic velocity > 250 cm/sec
Velocity gradient between the renal artery and external iliac artery greater than 1.8:1

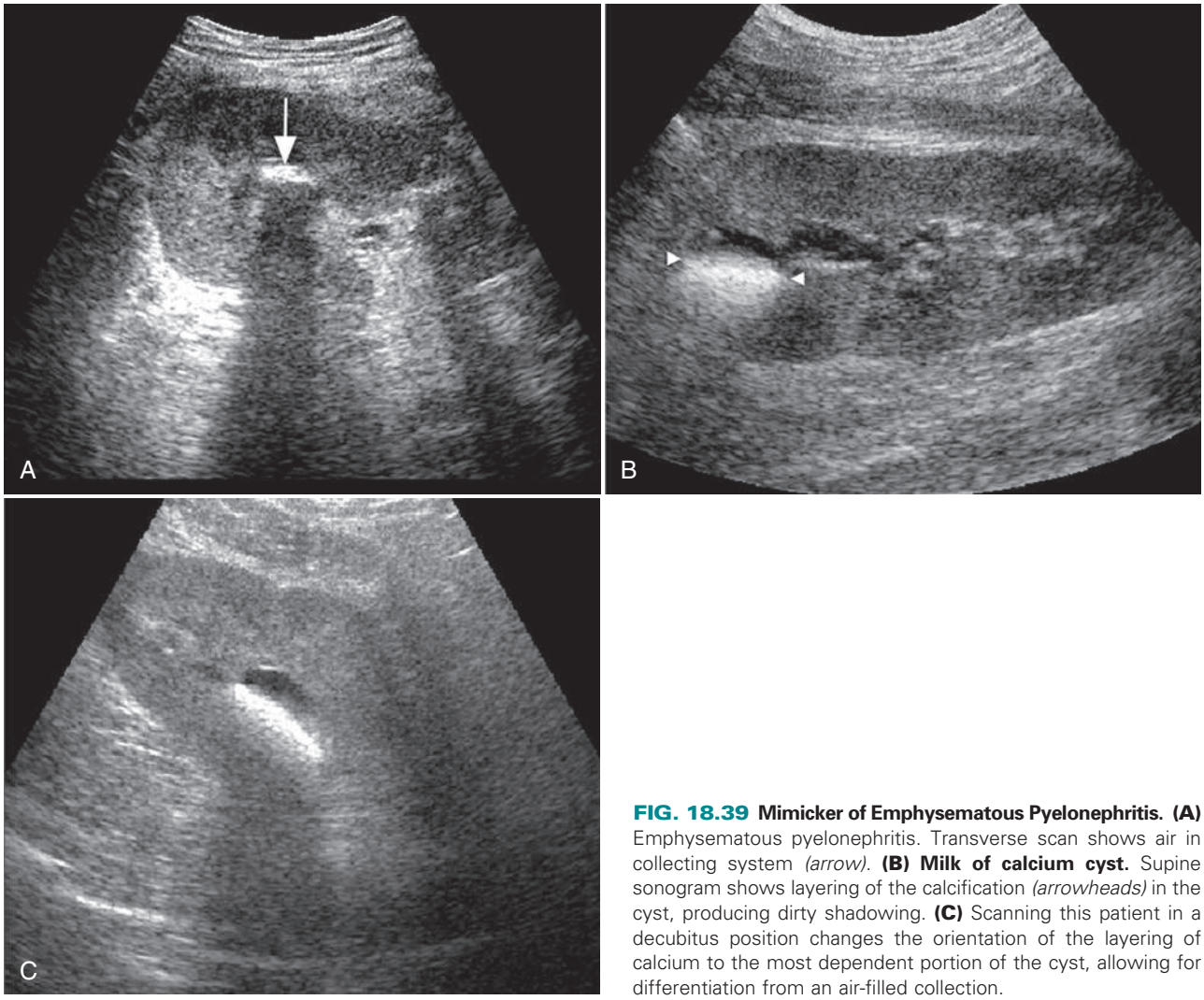

FIG. 18.39 Mimicker of Emphysematous Pyelonephritis. (A) Emphysematous pyelonephritis. Transverse scan shows air in collecting system *(arrow)*. **(B) Milk of calcium cyst.** Supine sonogram shows layering of the calcification *(arrowheads)* in the cyst, producing dirty shadowing. **(C)** Scanning this patient in a decubitus position changes the orientation of the layering of calcium to the most dependent portion of the cyst, allowing for differentiation from an air-filled collection.

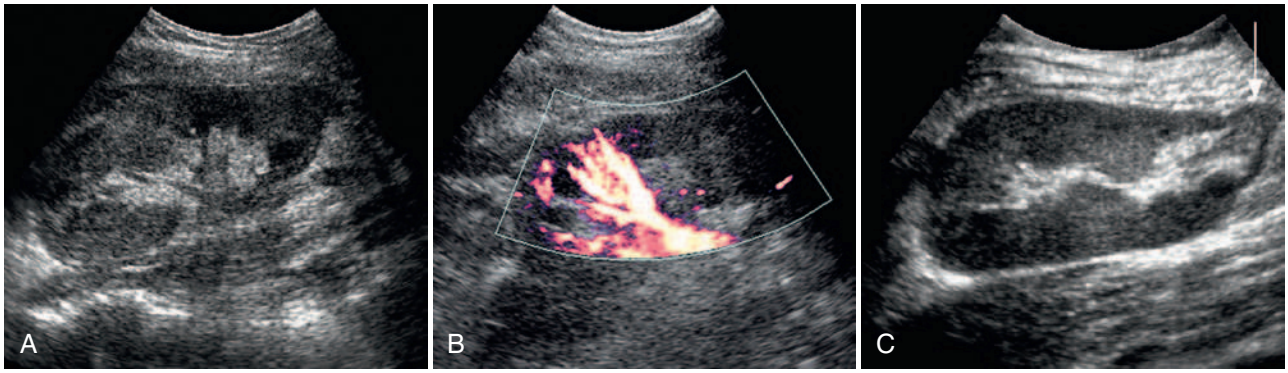

FIG. 18.40 Renal Artery Thrombosis. (A) Sagittal sonogram shows normal gray-scale ultrasound on postoperative day 1. **(B)** However, power Doppler shows no flow in the lower pole because of thrombosis of a segmental artery. **(C)** Three months later, there is secondary scarring of the entire lower pole *(arrow)*.

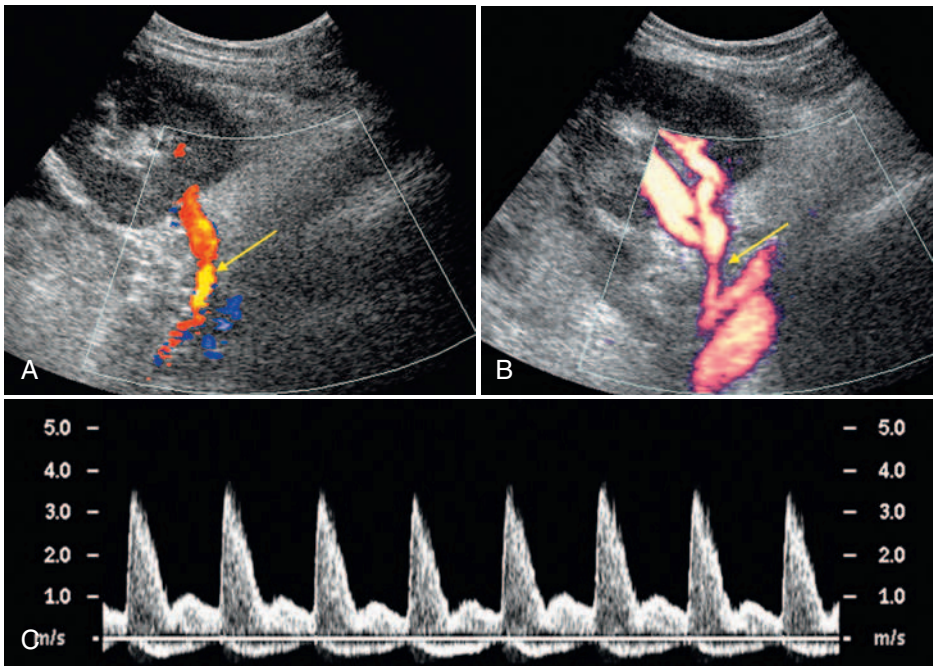

FIG. 18.41 Renal Artery Stenosis: Donor Portion. (A) Color Doppler ultrasound of donor renal artery anastomosis shows focal area of aliasing *(arrow).* **(B)** Power Doppler shows area of narrowing in this region *(arrow).* **(C)** Spectral Doppler shows elevated angle-corrected velocities at the site of the arrow, greater than 400 cm/sec.

Intraparenchymal arterial stenosis may be observed in chronic rejection as a result of scarring in the tissues surrounding the involved vessels. On spectral Doppler ultrasound, a prolonged AT may be observed in the segmental and interlobar arteries, with a normal main renal artery waveform.[45]

Treatment options for renal artery stenosis include percutaneous transluminal angioplasty, endovascular stent placement, and surgery. Surgical management of these transplants involves resection and revision of the stenosis with insertion of a patch graft at the stenotic segment.[46]

A **false-positive Doppler diagnosis** of renal artery stenosis can occur if there is an abrupt turn in the main renal artery, if the artery is severely tortuous, or if there are errors in Doppler technique (Fig. 18.44). Inadvertent compression of the main renal artery by the sonographer while performing spectral interrogation may also produce transient narrowing of the artery and elevated PSV readings. Turning the patient in a decubitus position such that the anterior abdominal or pelvic wall tissues are displaced from lying over the transplant can reduce external pressure on the allograft during scanning.

Venous Thrombosis

Occlusive renal vein thrombosis is slightly more common than arterial thrombosis, occurring in up to 4% of transplants, and is associated with acute pain, swelling of the allograft, and an abrupt cessation of renal function between the third and eighth postoperative day. Risk factors include technical difficulties at surgery, hypovolemia, propagation of femoral or iliac thrombosis, and compression by fluid collections.[58,64]

On gray-scale ultrasound, the allograft may appear enlarged, and in rare cases intraluminal thrombus may be detected in a dilated main renal vein or within the intraparenchymal venous system. Spectral and color Doppler ultrasound will show a lack of venous flow in the renal parenchyma, absence of flow in the main renal vein, and reversal of diastolic flow in the main renal artery, as well as sometimes in the intraparenchymal arteries[65,66] (Fig. 18.45). The sonographer should be aware that **reversal of flow in diastole in the main renal artery** or the intraparenchymal arterial branches is highly suggestive of renal vein thrombosis only in the absence of venous flow in the renal parenchyma and main renal vein.

Reversed diastolic arterial flow, with preservation of venous flow, is a nonspecific finding indicating extremely high vascular resistance in the small intrarenal vessels or main hilar vessels. The outcome for these patients is generally poor, with allograft loss rates of 33% to 55%. Potential causes of reversed diastolic flow include acute rejection, ATN, peritransplant hematomas (compressing renal graft or hilar vessels), and glomerulosclerosis.[67]

Renal Vein Stenosis

Renal vein stenosis most often occurs from perivascular fibrosis or external compression by adjacent fluid collections. The renal cortex appears either normal or hypoechoic, and on color Doppler, aliasing is identified at the stenotic region because of focal, high-velocity turbulent flow. On spectral Doppler sonography, a threefold to fourfold increase in velocity across the region of

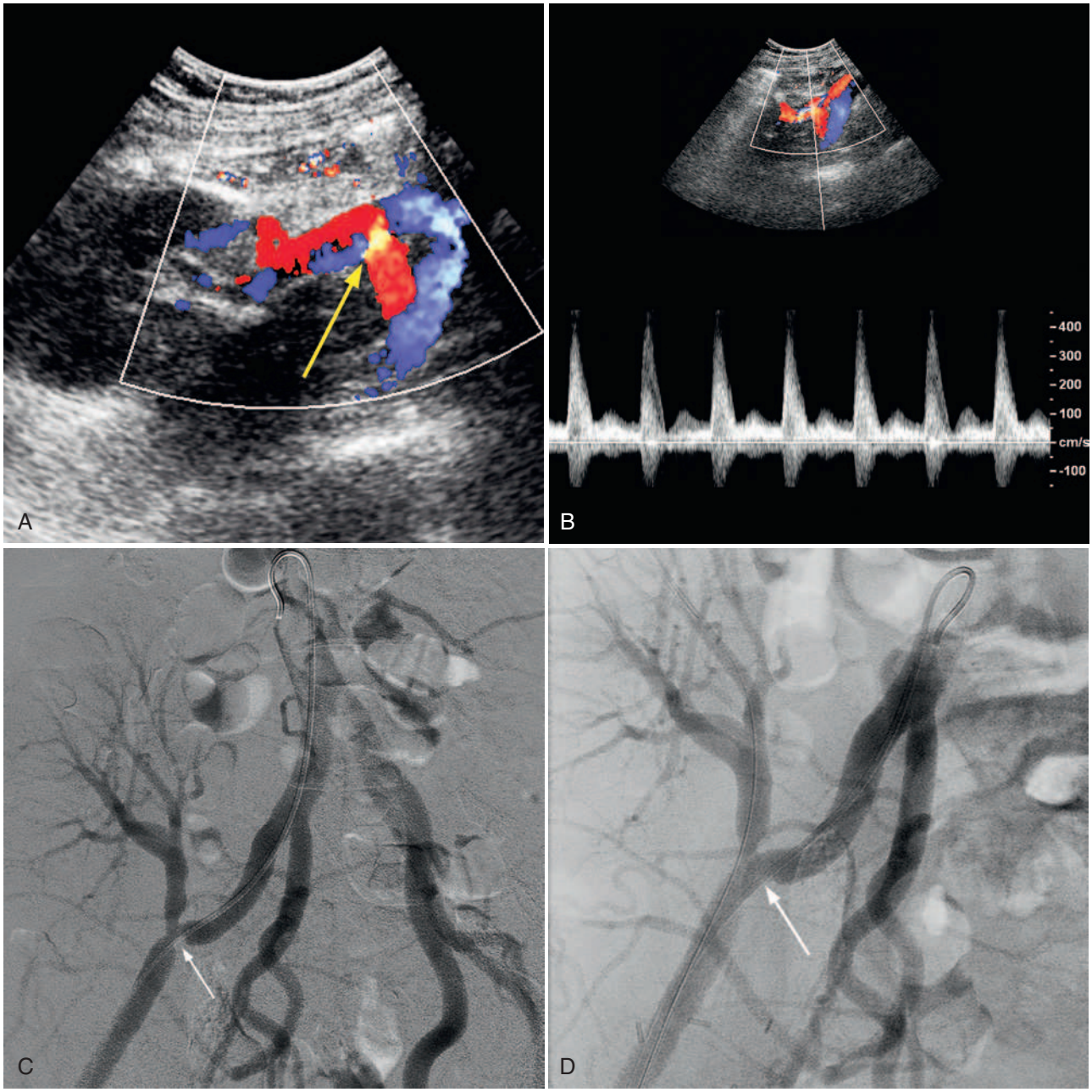

FIG. 18.42 Renal Artery Stenosis: Recipient Portion. (A) Color Doppler ultrasound shows focal area of aliasing *(arrow)* proximal to the renal artery anastomosis. **(B)** Spectral Doppler of the region of aliasing seen in image **(A)** shows angle-corrected peak velocities of 400 cm/sec. **(C)** Angiography shows a focal area of stenosis *(arrow)* arising from the external iliac artery. **(D)** Angiogram performed after angioplasty shows resolution of the stenotic region *(arrow)*.

narrowing indicates a hemodynamically significant stenosis[63] (Fig. 18.46).

Postrenal Collecting System Obstruction

Collecting system obstruction is unusual in renal transplants, occurring in less than 5% of patients.[45,63] Because the allograft is denervated, the collecting system dilates without clinical signs of pain or discomfort. The diagnosis is often made as an incidental finding on routine screening sonography or in the workup of the transplant patient for asymptomatic deterioration of renal function parameters.

The most common cause of **ureteral obstruction** is from ischemic strictures, usually involving the terminal ureter at the ureterovesical junction. The transplanted ureter is particularly susceptible to ischemic events because of its limited vascular supply from the renal artery. The ureterovesical junction is usually the region of most pronounced involvement because it is farthest anatomically from the renal

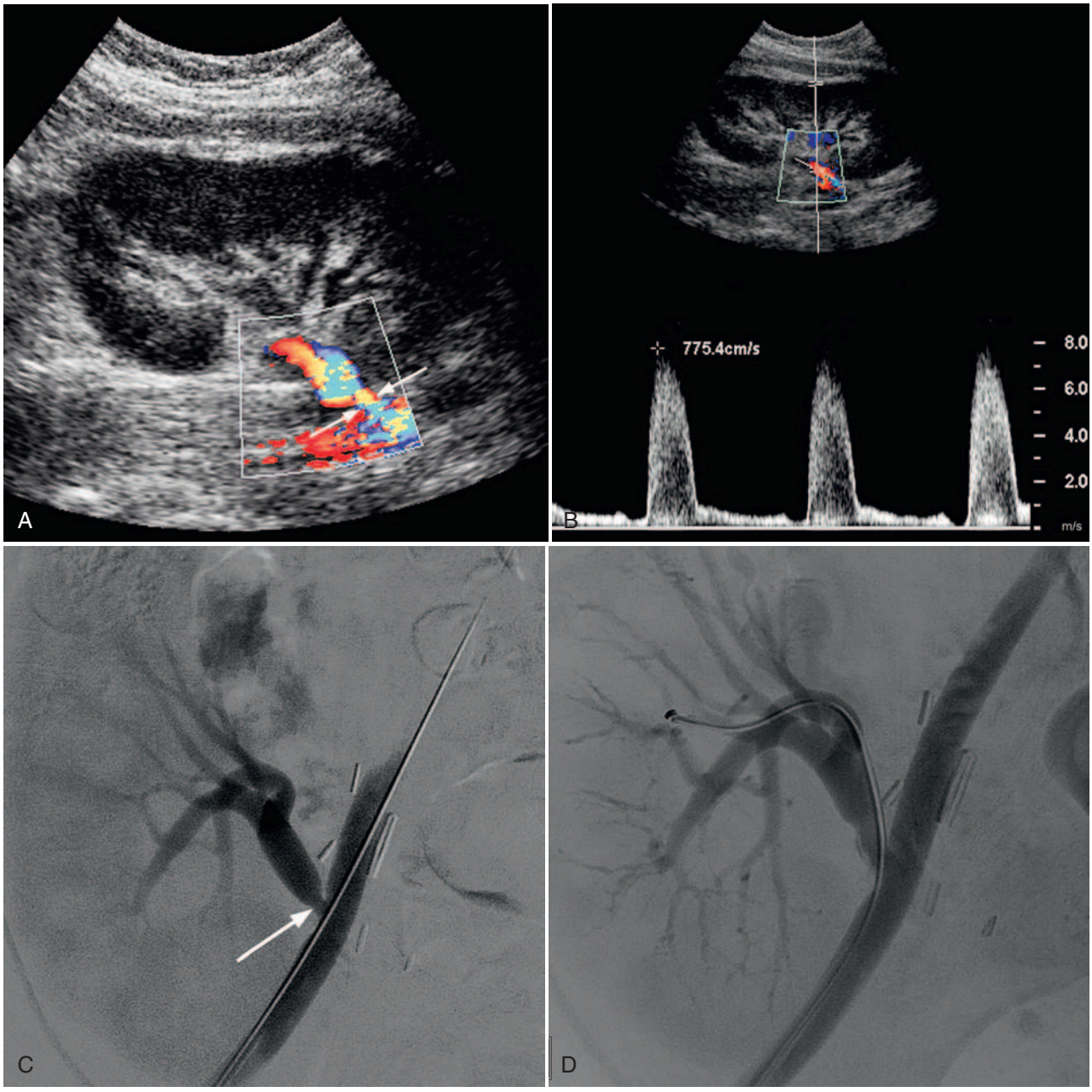

FIG. 18.43 Renal Artery Stenosis: Anastomosis. (A) Color Doppler ultrasound shows focal area of narrowing and aliasing at the anastomosis *(arrows).* **(B)** Spectral Doppler at the anastomosis shows elevated angle-corrected velocity of 775.4 cm/sec. **(C)** Renal arterial angiogram confirms stenosis at the anastomosis *(arrow).* **(D)** Angiogram performed after angioplasty shows resolution of the anastomotic stenosis.

hilum, where the ureteral branch originates.[46] Other causes of ureteral obstruction include strictures from iatrogenic injury, intraluminal lesions (e.g., stones, blood clots, sloughed papillae), perigraft fibrosis, and ureteral kinking (Figs. 18.47 and 18.48). Extrinsic compression of the ureter from peritransplant collections can also result in collecting system obstruction.

Patients with renal transplants are at higher risk for stone development compared with the general population. In approximately 15% of these patients, the stone development is related to hypercalcemia. Because the transplant is denervated, patients with stone-related collecting system obstruction may not have typical symptoms of renal colic.[54]

Evaluation of the collecting system with fundamental gray-scale imaging may be difficult because of side-lobe and scatter artifact, which can potentially obscure optimal evaluation of the calyceal system and ureter. Harmonic imaging, however, uses a narrower ultrasound beam with smaller side lobes and is less susceptible to scatter artifact. These parameters make harmonic imaging ideal for evaluating anechoic structures,

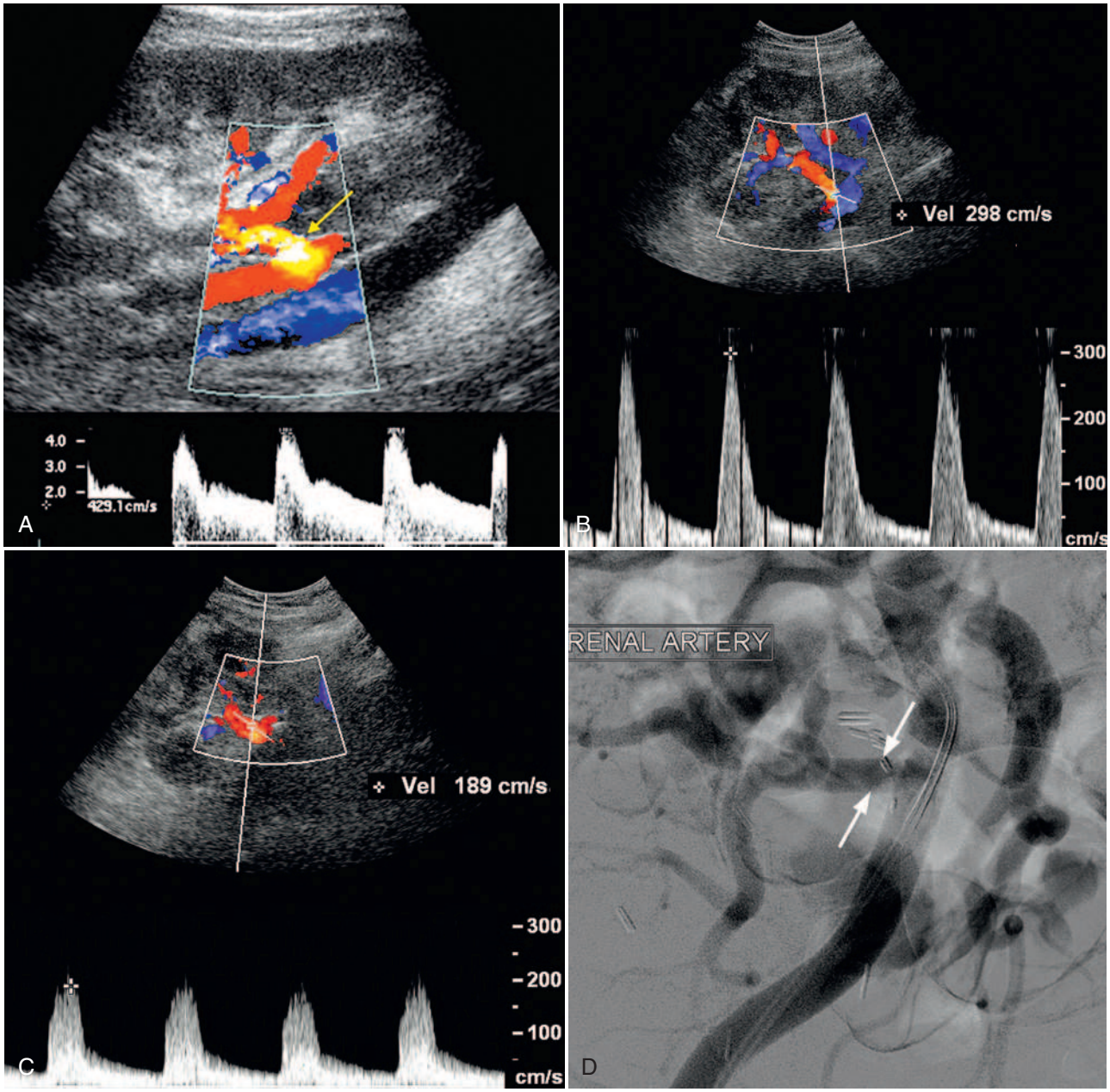

FIG. 18.44 Mimickers of Renal Artery Stenosis. (A) Abrupt turn in renal artery. On color Doppler ultrasound, aliasing is identified in this region *(arrow),* with peak systolic velocities of 429 cm/sec on spectral Doppler. **(B)-(D) Misaligned angle correction. (B)** Initial spectral Doppler shows elevated renal artery anastomotic velocity of 298 cm/sec. This elevated velocity reading is artifactual because the spectral angle correction is not aligned with the direction of the renal artery. **(C)** Follow-up spectral Doppler ultrasound shows a normal renal artery velocity of 189 cm/sec, with appropriate angle correction in the direction of the artery. **(D)** Renal angiogram confirms a normal renal artery *(arrows)* with no evidence of stenosis.

such as the renal collecting system for regions of subtle dilation, and the presence of **small intraluminal stones** (Fig. 18.49).

Mild pelvicaliectasis may be secondary to nonobstructive causes such as overhydration, decreased ureteric tone (from denervation of transplant), and ureteric-vesical reflux or can occur transiently in the immediate postoperative period from perianastomotic edema.[45,68] In addition, multiple parapelvic cysts can mimic a dilated collecting system (Fig. 18.50).

Arteriovenous Malformations and Pseudoaneurysms

Intraparenchymal arteriovenous malformations (AVMs) result from vascular trauma to both artery and vein during percutaneous biopsies and are usually asymptomatic with few clinical sequelae. Because most of these are small and resolve spontaneously, the incidence of posttransplant AVMs is unknown, although rates of 1% to 18% have been reported. In rare cases, large AVMs may manifest with bleeding, high-output cardiac failure, or decreased

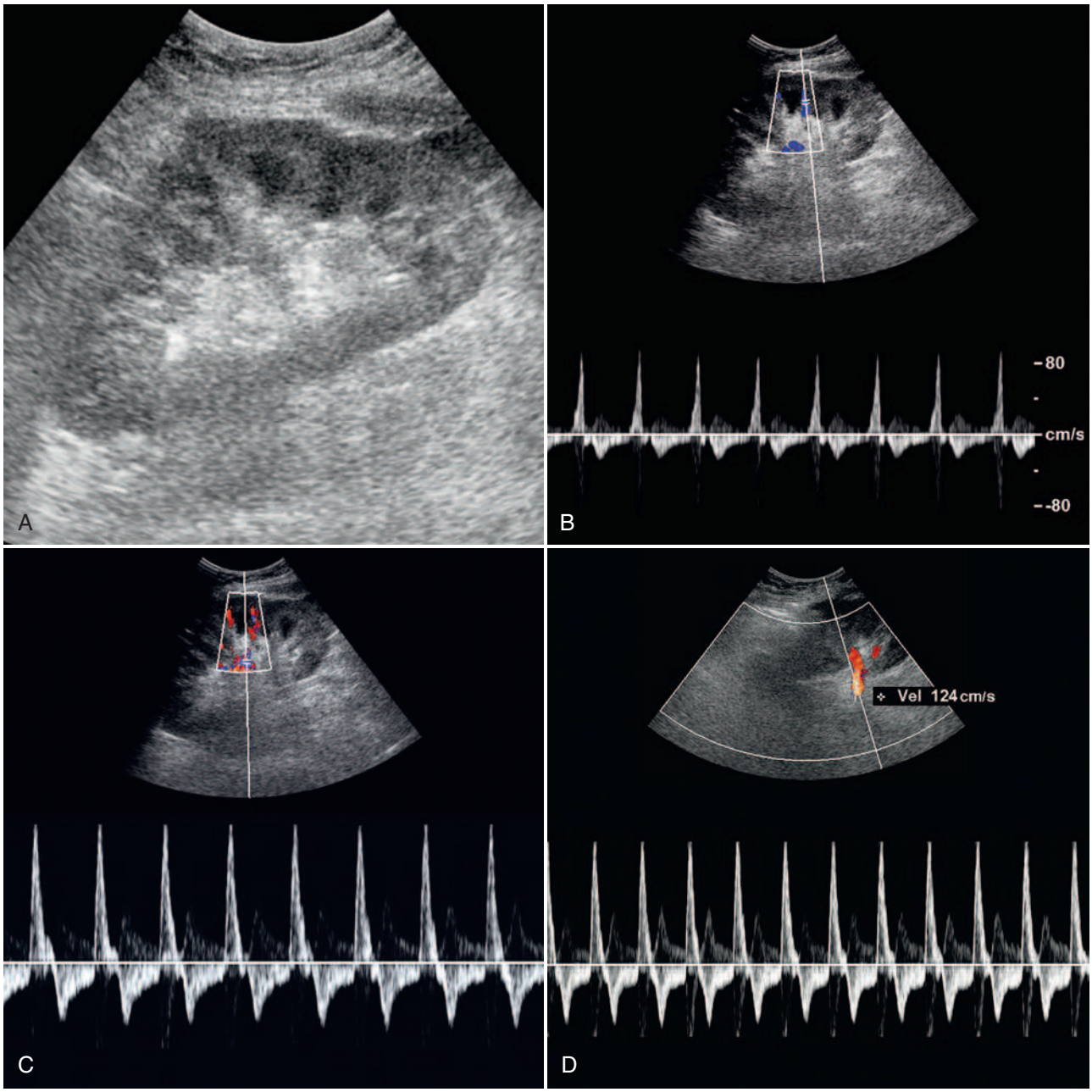

FIG. 18.45 Renal Vein Thrombosis. (A) Sagittal sonogram shows increased cortical echogenicity with a coarse echotexture. **(B)-(D)** Spectral Doppler ultrasound images of **(B)** cortical arteries, **(C)** renal sinus arterial branches, and **(D)** main renal artery show reversal of flow in diastole. No venous flow was detected in the transplant.

renal perfusion caused by the large shunt. In these patients, treatment usually involves percutaneous embolization therapy.[44]

Gray-scale ultrasound may not reveal small AVMs. Color Doppler sonography shows a focal region of aliasing with myriad intense colors, often associated with a prominent feeding artery or draining vein. Turbulent flow within the AVM produces vibration of the perivascular tissues, resulting in these tissues being assigned a color signal outside the borders of the renal vasculature. Spectral Doppler ultrasound is typical of that for all AVMs, with low-resistance, high-velocity flow and difficulty differentiating between artery and vein within the malformation. If a dominant draining vein is detected, the waveform may be pulsatile or arterialized[58,68-70] (Fig. 18.51, Video 18.3).

On color Doppler ultrasound, focal regions of cortical dystrophic calcifications or small stones can mimic an AVM by producing an intense color signal known as a *twinkling artifact*.[71] These artifacts can be differentiated from a true AVM on spectral tracing because both calcifications and stones produce characteristic linear bands on spectral interrogation. In our clinical experience, we have also observed a linear band of color posterior to these regions of calcium that extend to the limits of the color box. We have not observed this phenomenon with AVMs and

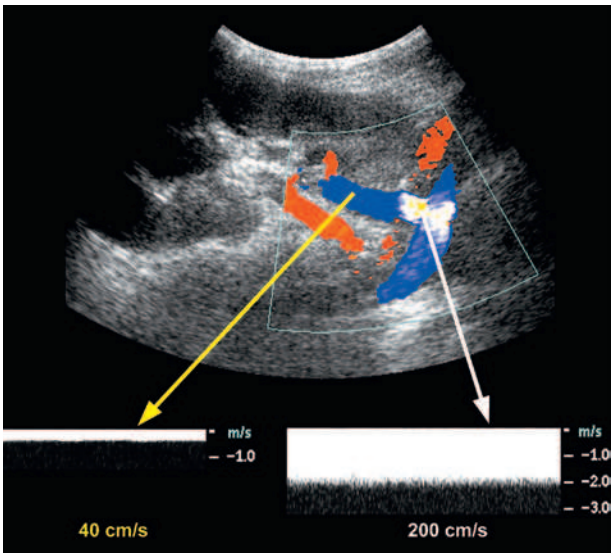

FIG. 18.46 Renal Vein Stenosis. Color Doppler of renal vein anastomosis shows focal area of aliasing *(white arrow)*. Spectral interrogation in region of aliasing shows velocities of 200 cm/sec. Spectral interrogation proximal to aliasing shows velocities of 40 cm/sec *(yellow arrow),* indicating a hemodynamically significant stenosis of the renal vein.

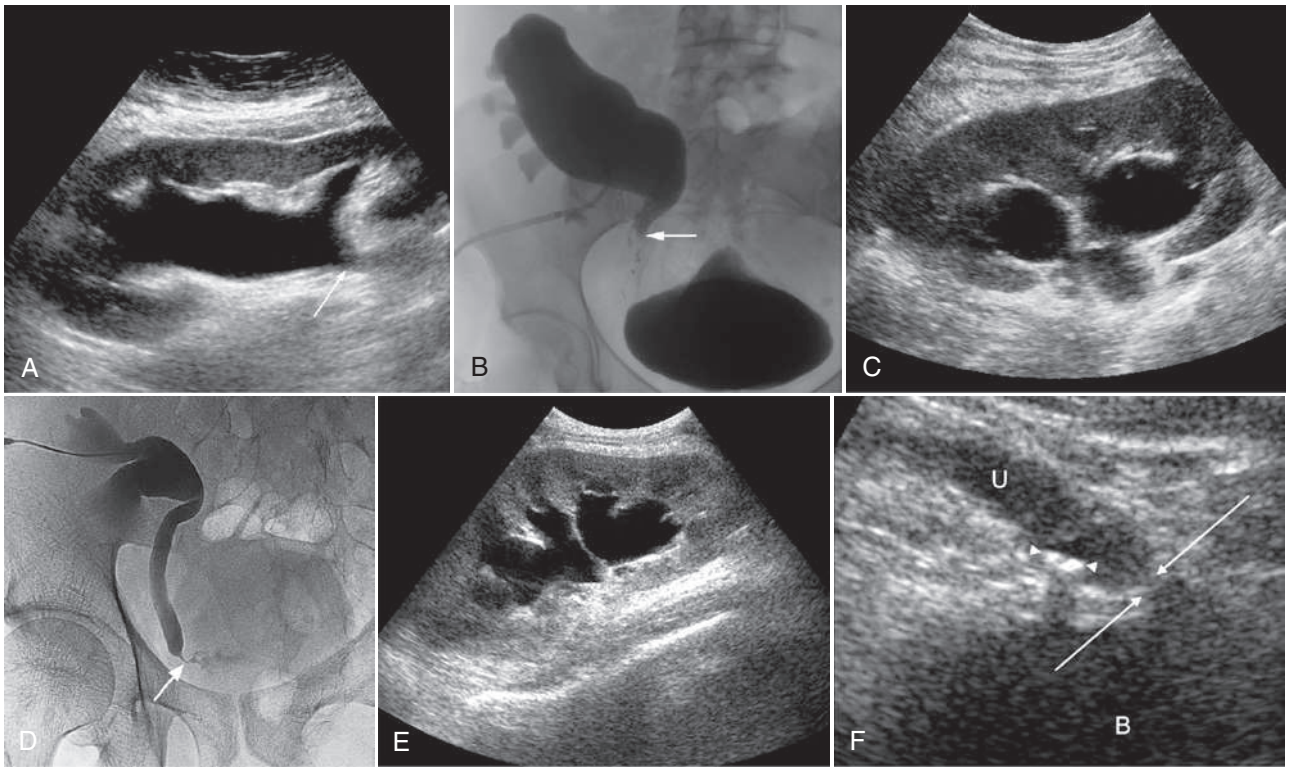

FIG. 18.47 Ureteral Strictures. (A) Sagittal sonogram and **(B)** percutaneous nephrostogram show grade 3 pelvocaliectasis secondary to a stricture at the **ureteropelvic junction** *(arrow).* **(C)** Sagittal sonogram shows grade 4 pelvocaliectasis. The distal ureter was not seen on ultrasound. **(D)** Percutaneous nephrostogram shows a stricture at the **ureterovesicular junction** *(arrow).* **(E)** Sagittal sonogram shows grade 3 pelvocaliectasis, produced by **(F)** a stricture at the **ureterovesicular junction** *(arrows). arrowheads,* Tiny nonobstructing stone; *B,* bladder; *U,* ureter.

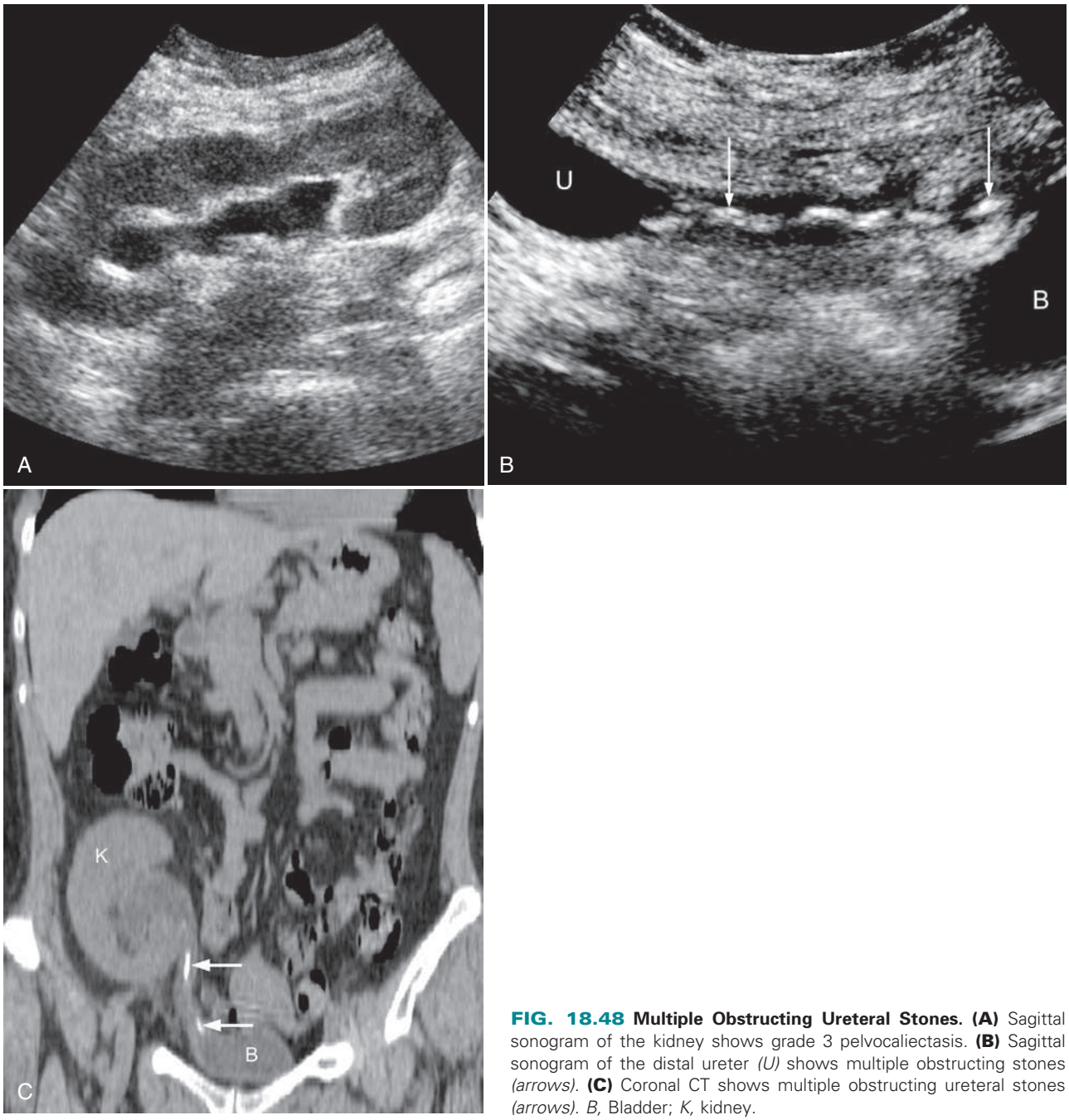

FIG. 18.48 Multiple Obstructing Ureteral Stones. (A) Sagittal sonogram of the kidney shows grade 3 pelvocaliectasis. **(B)** Sagittal sonogram of the distal ureter *(U)* shows multiple obstructing stones *(arrows)*. **(C)** Coronal CT shows multiple obstructing ureteral stones *(arrows)*. *B,* Bladder; *K,* kidney.

have found it a useful tool in differentiating vascular malformations from focal calcifications (Fig. 18.52).

Pseudoaneurysms result from vascular trauma to the arterial system during percutaneous biopsy or, more frequently, occur at the site of the vascular anastomosis. They may be intrarenal or extrarenal (Figs. 18.53 and 18.54,Video 18.4). Pseudoaneurysms located in the renal hilum are somewhat more concerning than intrarenal pseudoaneurysms owing to their increased risk of rupture. On gray-scale sonography, pseudoaneurysms can mimic a simple or complex cyst. On color Doppler ultrasound, flow can easily be obtained in the lumen of patent pseudoaneurysms, often with a swirling pattern, whereas on spectral Doppler, a central to-and-fro waveform or a disorganized arterial tracing may be obtained.[45,54] Presumed cysts in the renal parenchyma or in the region of the hilum should be assessed with color Doppler to exclude the possibility of a pseudoaneurysm.

Fluid Collections

Perinephric collections are demonstrated in up to 50% of transplant recipients.[72,73] The most common collections include

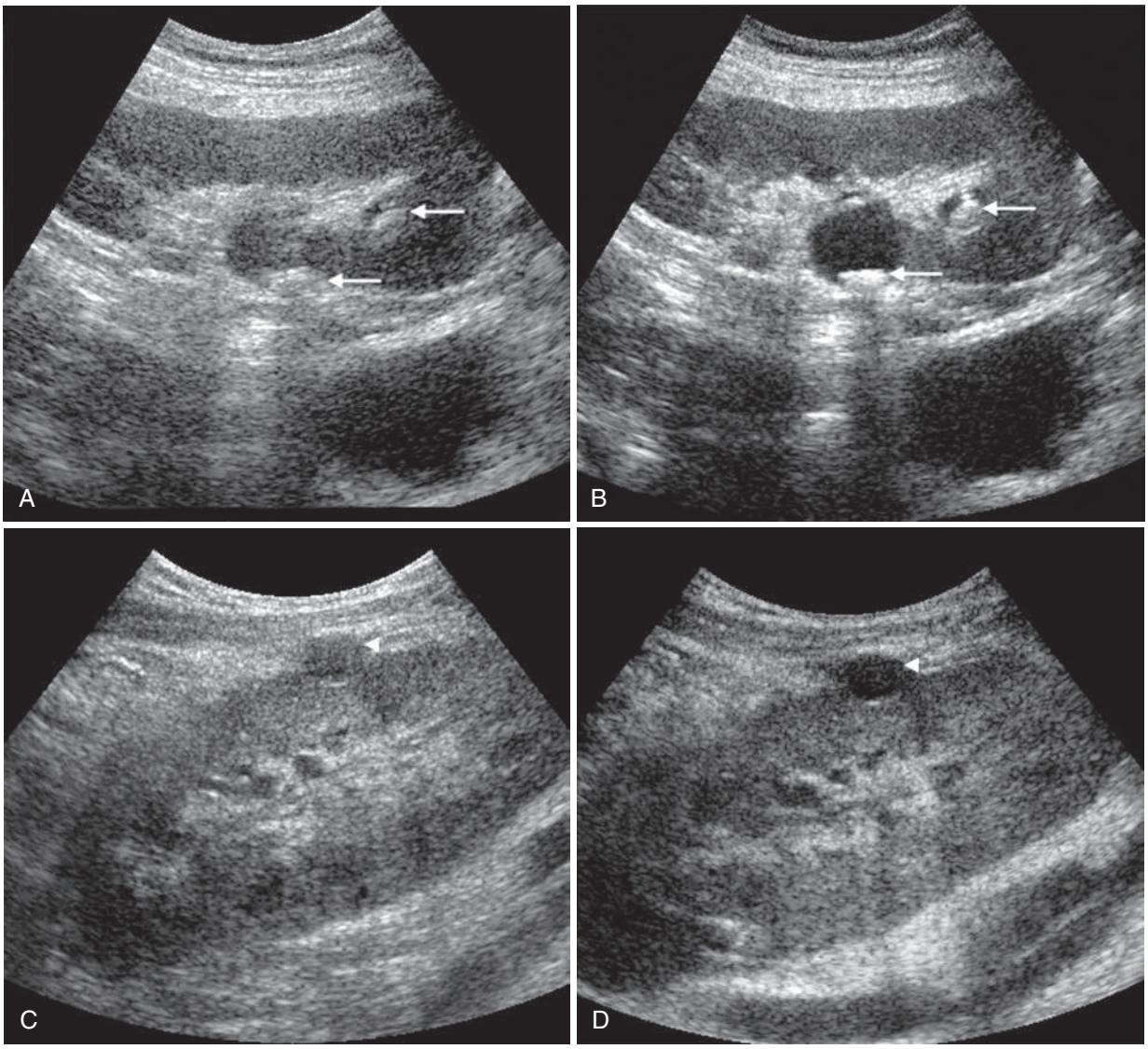

FIG. 18.49 Harmonic Imaging in Two Patients. (A) Sagittal fundamental image shows barely detectable stones *(arrows)* and a dilated collecting system. **(B)** Harmonic image shows improved resolution of stones *(arrows),* now seen associated with distal acoustic shadowing, within anechoic dilated collecting system. **(C)** Fundamental image shows cortical cyst *(arrowhead)* with internal echoes and minimal through transmission. **(D)** Harmonic image shows cyst *(arrowhead)* to be anechoic and simple, now associated with an appropriate amount of through transmission.

hematoma, urinoma, lymphocele, and abscess. The ultrasound appearances of these peritransplant collections are often nonspecific, and clinical findings are warranted to determine their cause. However, the presence of air within a perirenal collection, without a history of recent percutaneous intervention, is highly suggestive of an **abscess.** The size and location of each collection should be documented on baseline scans because an increase in size may indicate the need for surgical intervention.

Postoperative **hematomas** are variable in size but are often small, perirenal in location, and insignificant clinically and often resolve spontaneously.[68] Their ultrasound appearance depends on the age of the collection. An acute hematoma will appear as an echogenic heterogeneous solid mass. With time the hematoma will liquefy, becoming a complex fluid collection with internal echoes, strands, or pseudoseptations. Postbiopsy hematomas have a morphology similar to that of their postoperative counterparts (Figs. 18.55 and 18.56).

Urine leaks, or **urinomas,** have been reported in up to 6% of renal transplants and occur within the first 2 weeks after surgery.[44] They are usually secondary to either anastomotic leaks or ureteric ischemia. Rarely, urinomas can result from high-grade collecting system obstruction (Fig. 18.57). On sonography, urinomas are well defined and anechoic, may be associated with hydronephrosis, and in some cases can increase rapidly in size.[57] Large urine leaks may result in widespread extravasation and gross intraperitoneal urinary ascites.

Lymphoceles result from surgical disruption of the iliac lymphatics and have been reported in up to 20% of patients. They most often occur 4 to 8 weeks after surgery but may develop years after transplantation. Although most are discovered

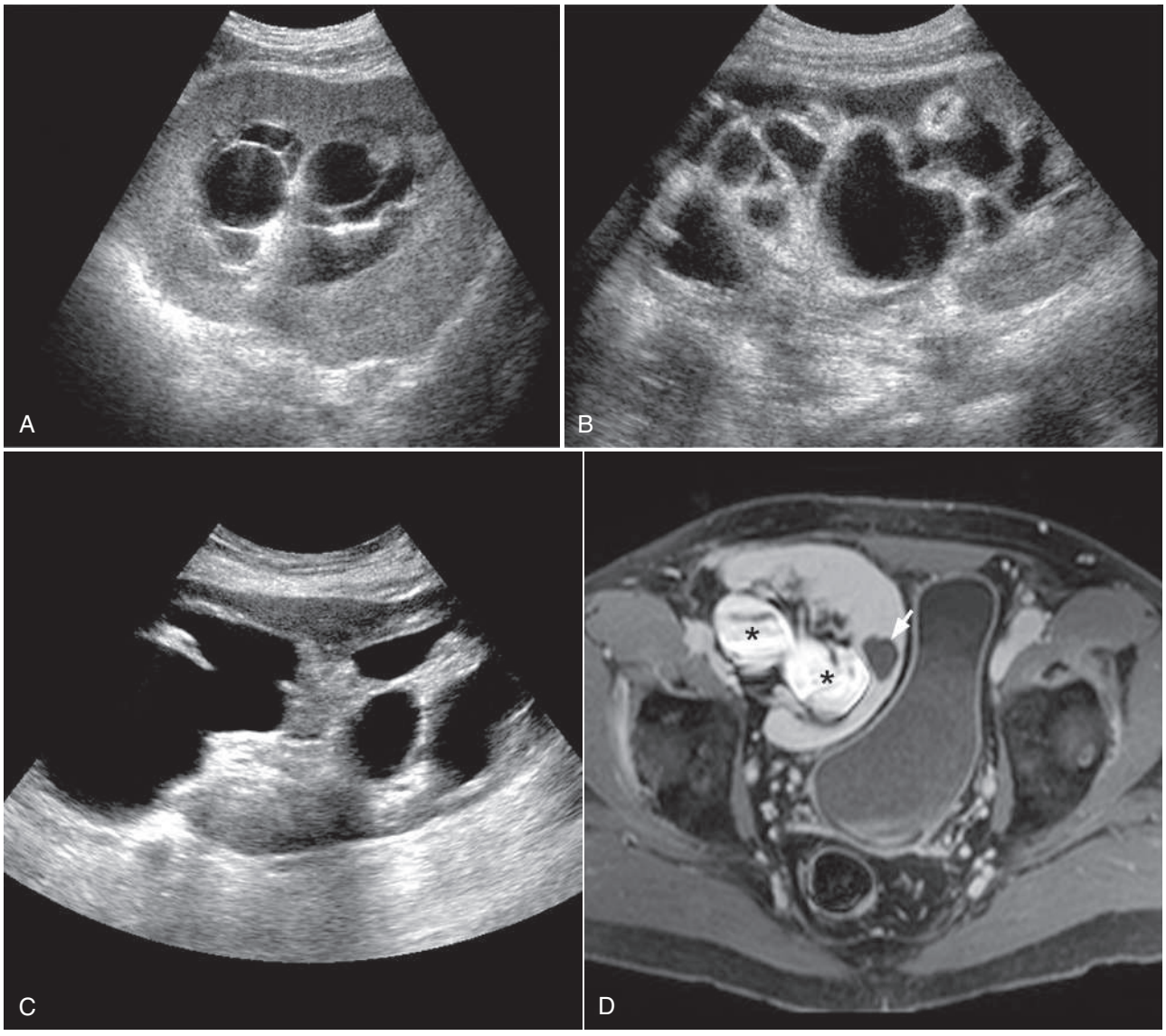

FIG. 18.50 Parapelvic Cysts Versus Pelvocaliectasis in Two Patients. *Patient 1:* **Parapelvic cysts. (A)** Transverse and **(B)** sagittal sonograms show multiple parapelvic cysts mimicking pelvocaliectasis. *Patient 2:* **Grade 3 pelvocaliectasis mimicking parapelvic cysts. (C)** Sagittal sonogram shows multiple anechoic structures in the central aspect of the kidney, initially interpreted as multiple parapelvic cysts. **(D)** Contrast-enhanced magnetic resonance image shows contrast filling grossly dilated calyces (*). A single parapelvic cyst *(arrow)* is present.

incidentally and are asymptomatic, lymphoceles are the most common fluid collection to result in ureteric obstruction. Lymphoceles can become infected or can obstruct venous drainage, resulting in edema of the lower limb, scrotum, or labia.[45] Symptomatic collections are drained (surgically or percutaneously) or undergo marsupialization. On sonography, lymphoceles are well-defined collections that are anechoic or that may contain fine internal strands (Figs. 18.58 and 18.59).

PANCREAS TRANSPLANTATION

Pancreatic transplantation is performed in select patients who have major complications related to type 1 diabetes. Pancreas transplant represents the only form of self-regulating endocrine replacement therapy, with more than 80% of recipients becoming free of exogenous insulin requirements within 1 year of surgery. Since 1988 in the United States, more than 15,000 kidney-pancreas transplants and 6000 pancreas transplants have been performed, with 1-year patient survival greater than 90%.[3,74]

Pancreatic transplantation aims to restore an adequate functioning beta cell mass and therefore to regain physiologic normoglycemic function, typically in the setting of insulin dependent diabetes. Recipients are typically type 1 diabetics in end-stage renal failure with other sequelae of long-term diabetes including neuropathy and atherosclerotic disease. Improvement in glycemic control diminishes the risk of long-term complications in diabetic patients.[75] In particular, simultaneous pancreas

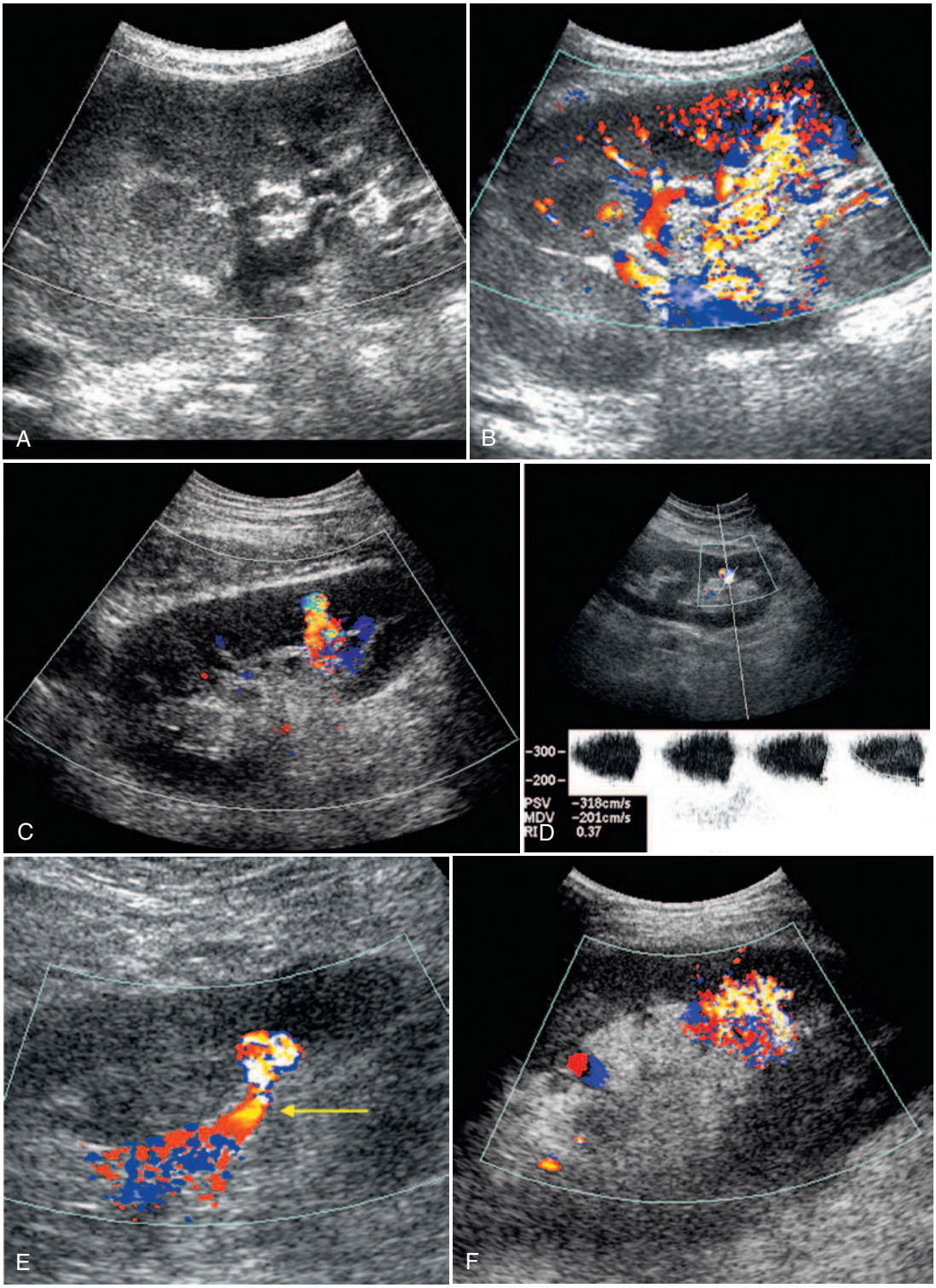

FIG. 18.51 Arteriovenous Malformations (AVMs). (A) Gray-scale ultrasound; AVM not detectable. **(B)** Corresponding color Doppler image shows large AVM. **(C)** Sagittal sonogram shows lower-pole AVM. **(D)** Spectral Doppler of AVM in image **(C)** shows high-velocity, low-resistance waveform. **(E)** Sagittal sonogram shows AVM with feeding vessel *(arrow).* **(F)** Sagittal scan shows lower-pole AVM with surrounding tissue vibration. See also Video 18.3.

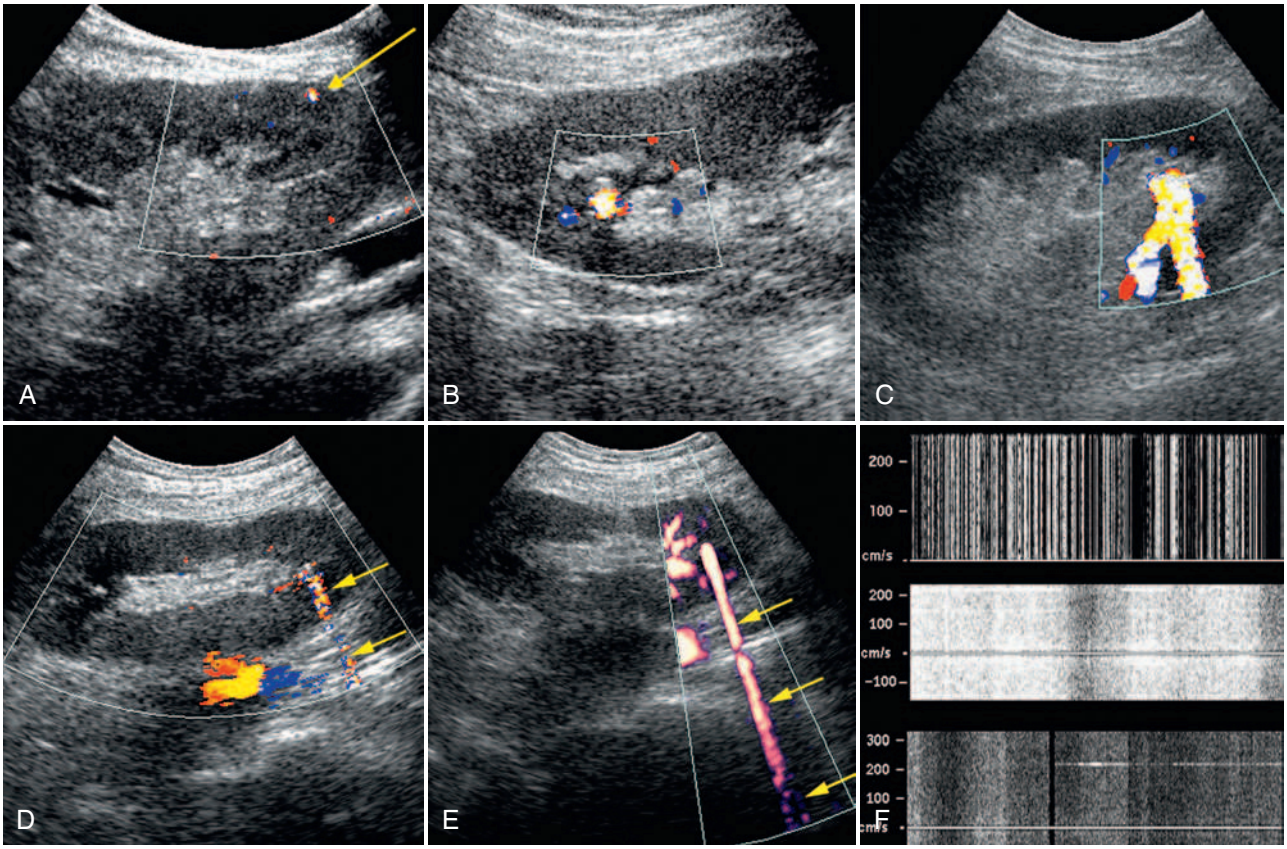

FIG. 18.52 Arteriovenous Malformation: Mimicker. (A)-(C) Sagittal sonograms show **twinkling artifact** produced by **(A)** lower-pole dystrophic cortical calcification *(arrow);* **(B)** upper-pole stone; and **(C)** lower-pole stone. **(D)-(F) Differentiation from AVM.** On **(D)** color Doppler and **(E)** power Doppler, color artifact *(arrows)* may be seen posterior to border of kidney. Size of twinkling artifact varies with size of the color box. **(F)** On spectral Doppler ultrasound, the twinkling artifact shows linear bands as on these three spectral traces.

transplant in the setting of kidney transplants has been known to improve long-term patient survival.

Surgical Technique

The simultaneous pancreas-kidney transplant is the most common form of pancreas transplantation in the United States and accounts of 80% of all pancreatic transplant procedures. To achieve optimum functioning beta cell mass, the procedure is a whole-organ pancreas transplant performed in conjunction with a kidney transplant. Best results are achieved if the procedure is performed before the need for dialysis. This approach allows serum creatinine to be used not only as a marker of renal rejection, but also as a surrogate marker of pancreatic graft rejection. This is particularly important because serum amylase and lipase are not sensitive or specific markers of pancreatic rejection. Serum amylase has only 50% sensitivity for detection of rejection, and lipase may be elevated in both rejection and pancreatitis. The ultimate diagnosis of graft dysfunction is often made on biopsy.

There are several further strategies for pancreas transplantation. A pancreas transplant can be performed as a second step following a successful renal transplant. The latter will typically be a living donor kidney and is usually advised for diabetic patients younger than age 5 with ongoing severe complications. The most severe complication is hypoglycemic unawareness wherein a patient may be wholly lacking the normal stigmata or warning signs of a low glucose level (such as trembling, sweating, and tachycardia).[76] This is the second most common mode of pancreatic transplant and contributes about 25% of all transplants in the United States.

Finally, pancreas-only transplantation can be performed in diabetic patients who have no evidence of diabetic nephropathy. Only a minority of diabetic patients are eligible for this approach because it is limited to patients whose hypoglycemic awareness is challenging to manage medically.

There are two well-established techniques for pancreas transplantation. Use of the bladder for exocrine drainage (duodenocystostomy) and use of the iliac vessels for arterial and venous supply were considered safer with regard to postoperative infection. This more traditional surgery, **exocrine bladder drainage,** involved anastomosing the donor duodenum to the urinary bladder and the donor portal vein to the recipient external iliac vein (systemic venous-endocrine drainage)[77] (Fig. 18.60). In this circumstance the pancreas graft is placed in the right hemipelvis and the renal graft on the left. The chronic loss of pancreatic secretions into the bladder can result in problems with dehydration, metabolic acidosis, and allograft pancreatitis.[3] There is also a higher risk of chemical cystitis secondary to the high amylase and lipase levels of pancreatic secretions. This can result in

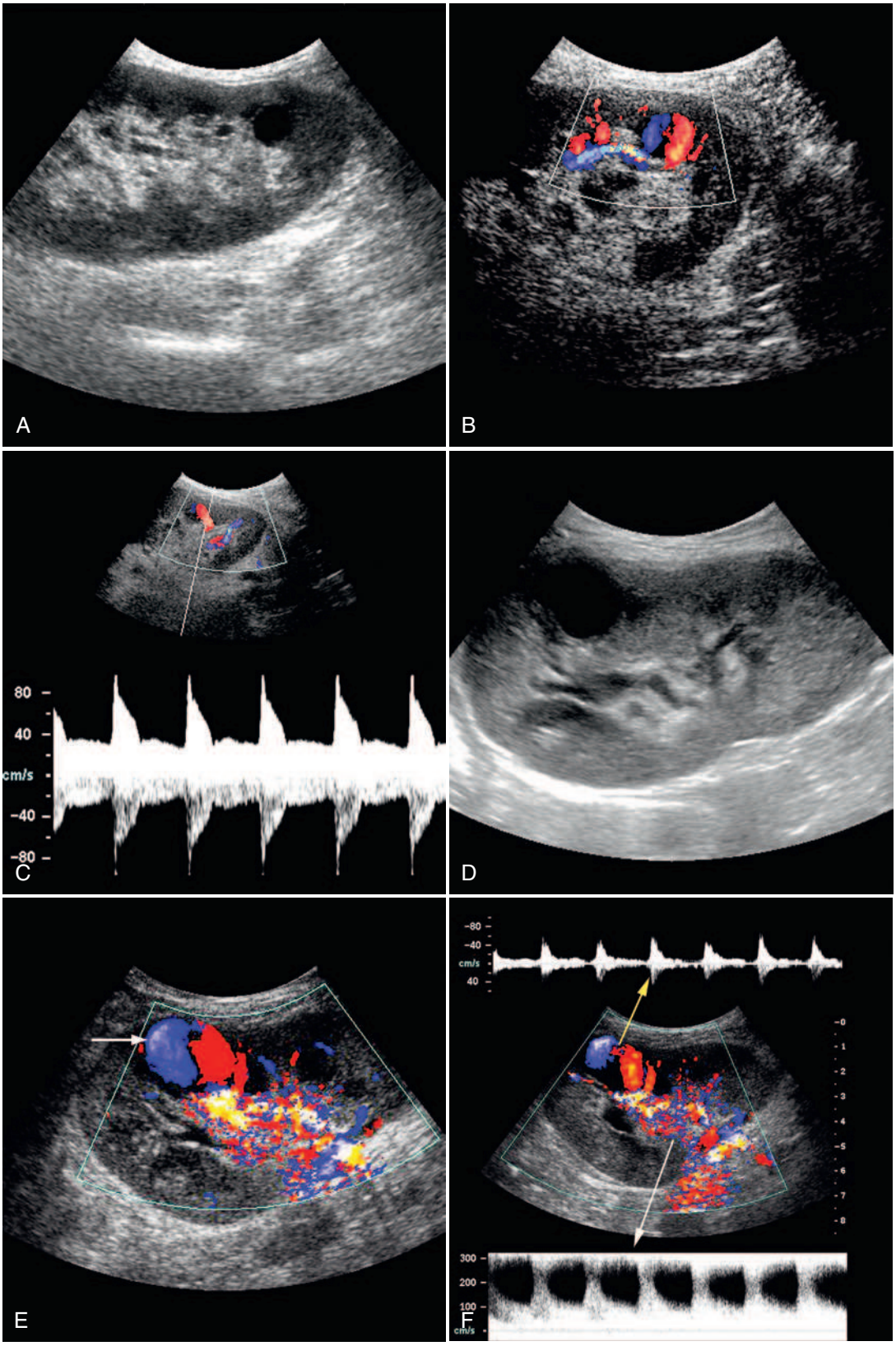

FIG. 18.53 Intrarenal Pseudoaneurysms in Two Patients. *Patient 1:* **(A)** Sagittal sonogram shows lower-pole anechoic structure, mimicking a simple cyst. **(B)** On color Doppler ultrasound, however, swirling flow is identified in this structure, indicating that it represents a pseudoaneurysm. **(C)** Spectral Doppler ultrasound shows disorganized swirling flow within the pseudoaneurysm identified on image **B.** *Patient 2:* **(D)** Sagittal sonogram shows upper-pole anechoic structure. **(E)** On color Doppler ultrasound, swirling flow is identified in the anechoic structure identified on image **(D)** *(arrow).* This is adjacent to a large central arteriovenous malformation (AVM). **(F)** Spectral Doppler ultrasound shows disorganized flow in the pseudoaneurysm *(yellow arrow)* and low-resistance high-velocity flow in the central AVM *(white arrow).*

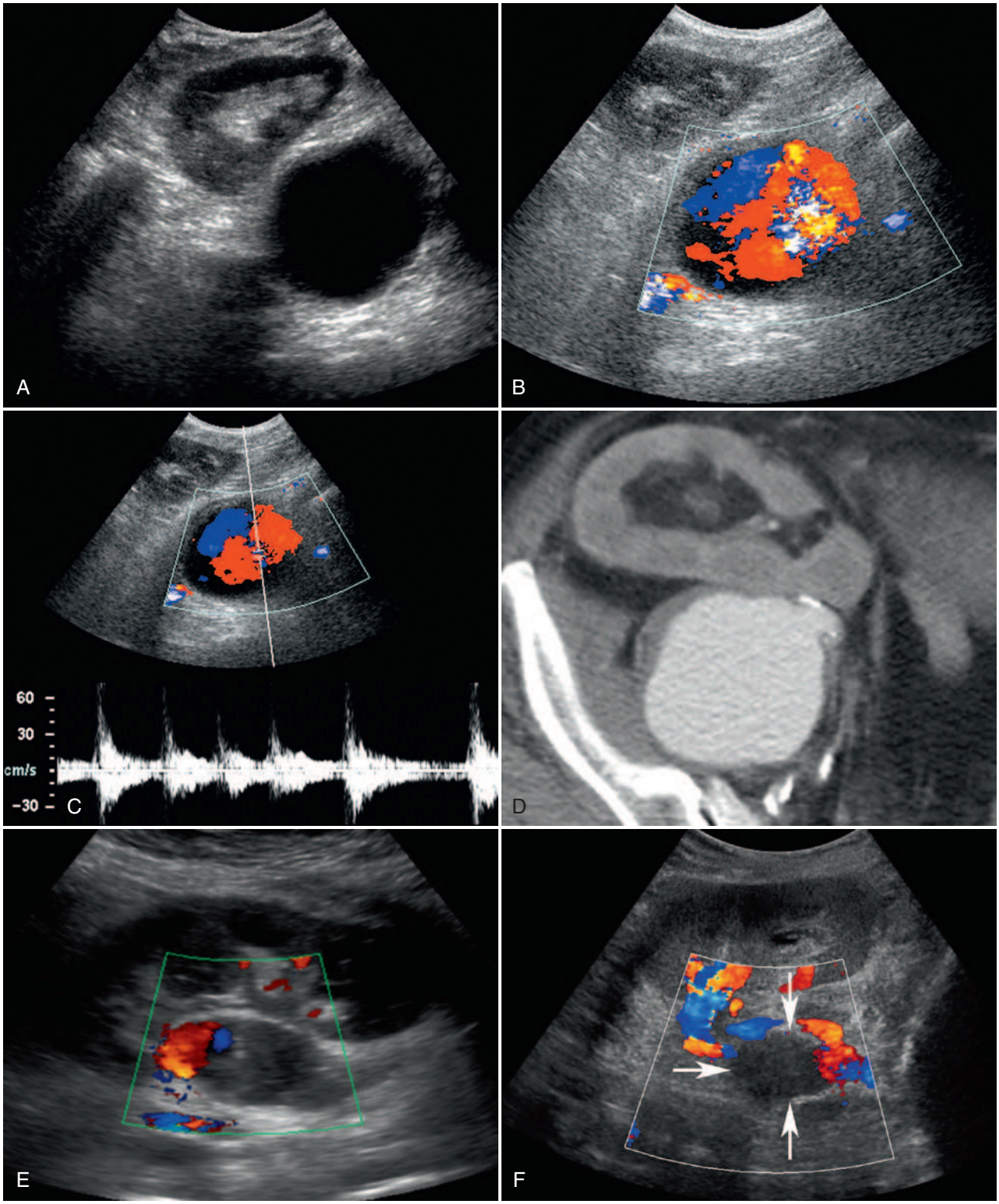

FIG. 18.54 Extrarenal Pseudoaneurysm of Renal Artery. (A) Transverse sonogram shows anechoic structure adjacent to renal hilum. **(B)** Color Doppler ultrasound shows that this structure contains swirling flow and represents a pseudoaneurysm. **(C)** Spectral Doppler ultrasound shows disorganized internal flow within pseudoaneurysm. **(D)** CT shows pseudoaneurysm arising from site of renal artery anastomosis. **(E)** and **(F)** In another patient, color Doppler images show a partially thrombosed pseudoaneurysm *(arrows).* See also Video 18.4.

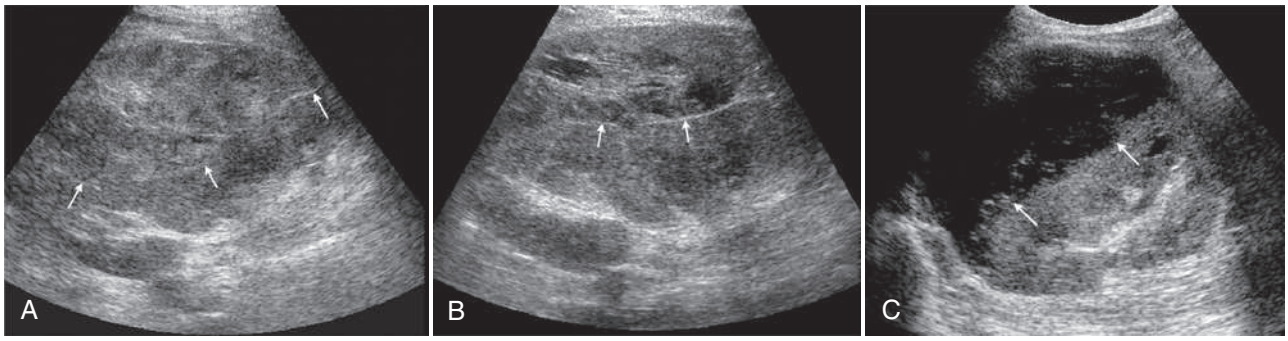

FIG. 18.55 Renal Transplant Subcapsular Hematoma Secondary to Biopsy. (A) Sagittal sonogram shows acute hematoma appearing as solid heterogeneous structure. **(B)** After 1 week, cystic regions have developed within the hematoma. **(C)** After 1 month, hematoma has liquefied and is larger because of a hyperosmolar effect. *Arrows* mark the junction of the renal cortex and hematoma.

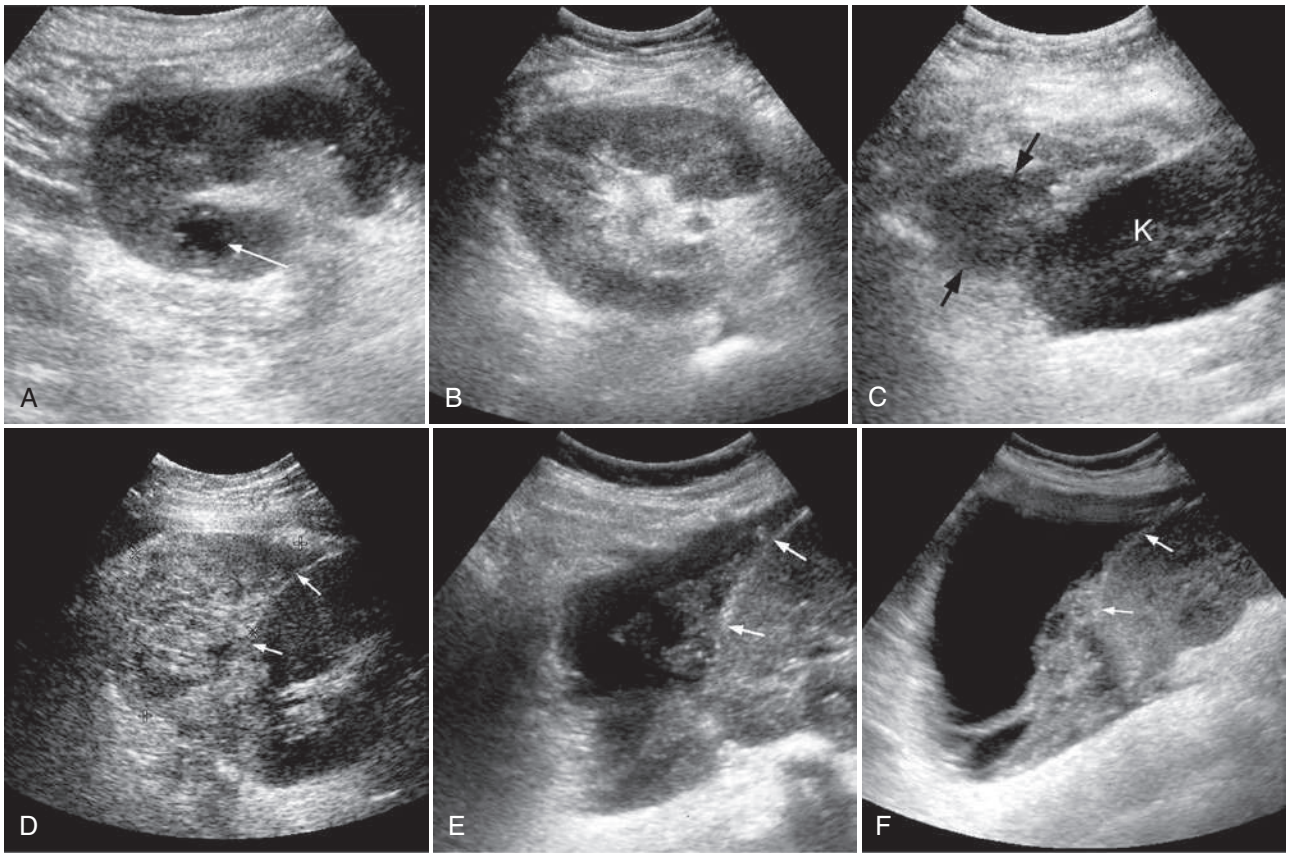

FIG. 18.56 Hematomas in Three Patients. *Patient 1:* **(A)** Transverse sonogram shows an intraparenchymal hematoma appearing as an anechoic cyst with mildly irregular walls *(arrow).* **(B)** Eight months later, the cyst has resolved. *Patient 2:* **(C)** Sagittal sonogram shows a hypoechoic solid-appearing mass *(arrows)* abutting the upper pole of the transplant kidney *(K). Patient 3:* **(D)-(F) Postoperative perirenal hematoma. (D)** Sagittal sonogram shows hematoma 1 day after surgery, appearing as a solid echogenic heterogeneous mass. **(E)** Four weeks later, hematoma has begun to liquefy, with interspersed solid components. **(F)** Six weeks later, hematoma is almost completely liquefied; arrows mark the junction of the hematoma and renal cortex.

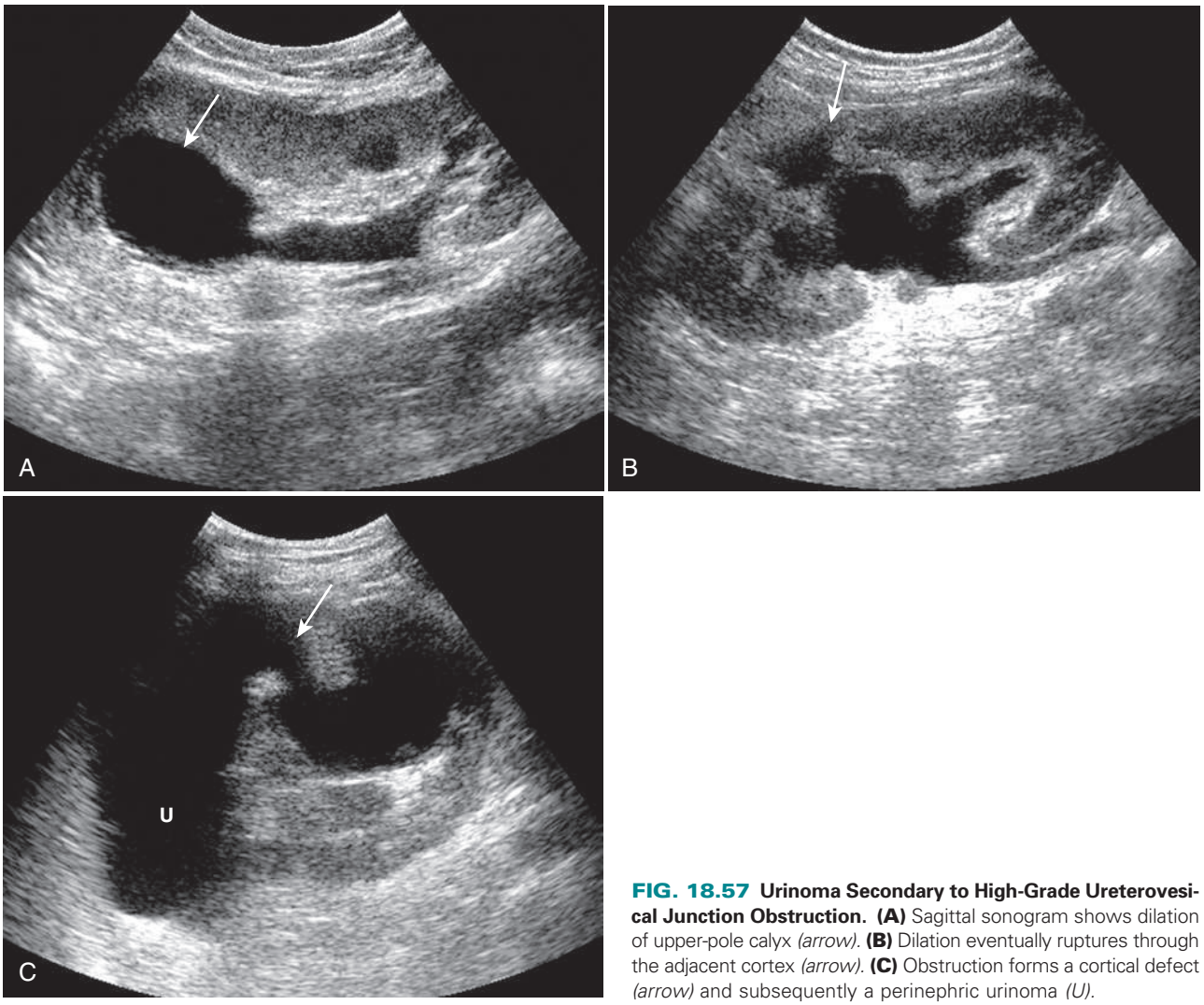

FIG. 18.57 Urinoma Secondary to High-Grade Ureterovesical Junction Obstruction. (A) Sagittal sonogram shows dilation of upper-pole calyx *(arrow)*. **(B)** Dilation eventually ruptures through the adjacent cortex *(arrow)*. **(C)** Obstruction forms a cortical defect *(arrow)* and subsequently a perinephric urinoma *(U)*.

recurrent urinary tract infections and hematuria. In male patients there is a higher risk of urethral infections and **balanitis,** which in turn may lead to urethral strictures.

These complication risks have resulted in a move toward the intestinal or **enteric-based drainage** procedure whereby a duodenojejunostomy is created for **exocrine** drainage of pancreatic secretions. This is performed as either a side-to-side anastomosis or a Roux-en-Y anastomosis.

The **endocrine drainage** is either systemic (anastomosis of donor portal vein to right common iliac vein or distal IVC) or portal venous (anastomosis of donor portal vein to SMV) (Fig. 18.61). This type of surgery provides a more physiologic transplant than the more traditional techniques and is not associated with dehydration or metabolic acidosis. In addition, it provides more appropriate glycemic control, with lower fasting insulin levels, and may be associated with a lower incidence of transplant rejection than the more traditional systemic venous-bladder drainage allografts.[3,78] Table 18.1 shows the major differences between two types of pancreatic transplants (exocrine bladder drainage and exocrine enteric drainage).

Venous Drainage

The two methods for venous drainage can be categorized as **systemic,** wherein the transplanted portal vein is anastomosed to an iliac vein or vena cava, or alternately as using the **portal** technique, whereby it drains into the SMV of the recipient. The latter technique has over time been shown to confer no additional advantage in terms of outcome compared with the systemic technique.

Arterial Supply

In both techniques (systemic and portal venous drainage) the arterial blood supply to the graft is via the donor common iliac artery being attached to the common or external iliac artery of the recipient. Most commonly at our institution, an arterial Y graft of the donor common iliac artery and external and internal iliac artery is anastomosed end to end with two separate anastomoses to the donor superior mesenteric and splenic arteries. There are some alternate methods, however, which include forming a single donor iliac arterial conduit (comprising either the common iliac and either the external or internal iliac artery),

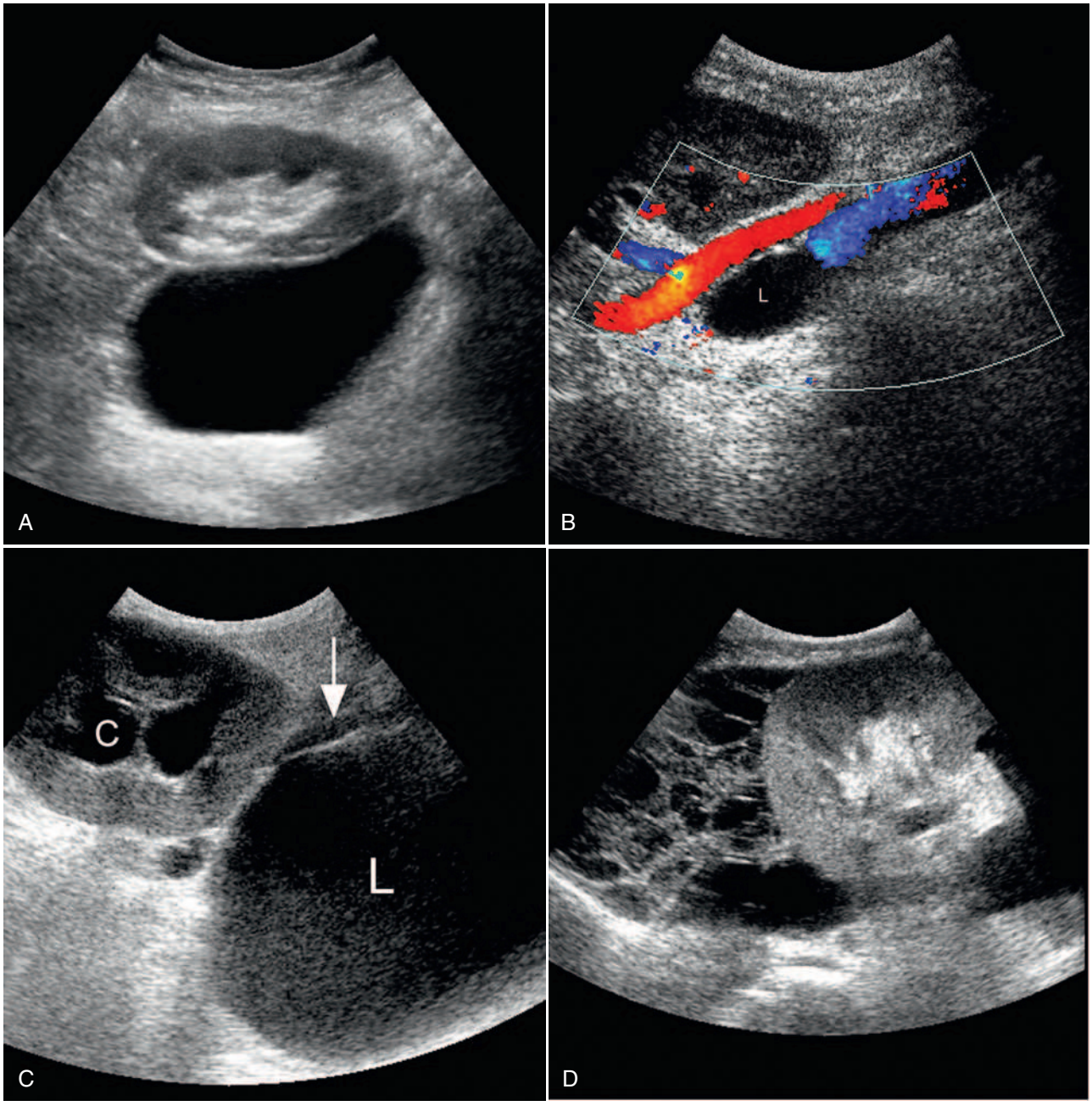

FIG. 18.58 Sterile Lymphoceles in Four Patients. (A) Sagittal sonogram shows large, simple lymphocele abutting the transplant. **(B)** Sagittal scan shows small lymphocele *(L)* adjacent to the external iliac artery and vein. **(C)** Anechoic lymphocele *(L)* causes obstruction of the midureter *(arrow)* and dilation of the calyceal system *(C)*. **(D)** Transverse sonogram shows septated perinephric lymphocele.

TABLE 18.1 Surgical Techniques for Pancreatic Transplantation

	Systemic Venous-Bladder Drainage	Portal Venous-Enteric Drainage
Location	Right lower quadrant	Right upper quadrant
Pancreatic orientation	Head caudad	Tail caudad
Arterial supply	Y-shaped donor arterial graft anastomosed to recipient common iliac artery	Donor splenic artery to recipient common iliac artery
Venous drainage	Donor portal vein is attached to external iliac vein	Donor portal vein anastomosed to superior mesenteric vein
Endocrine drainage	Systemic venous	Portal venous
Exocrine drainage	En bloc donor duodenal stump to recipient bladder	Duodenal segment anastomosed to Roux-en-Y loop of jejunum

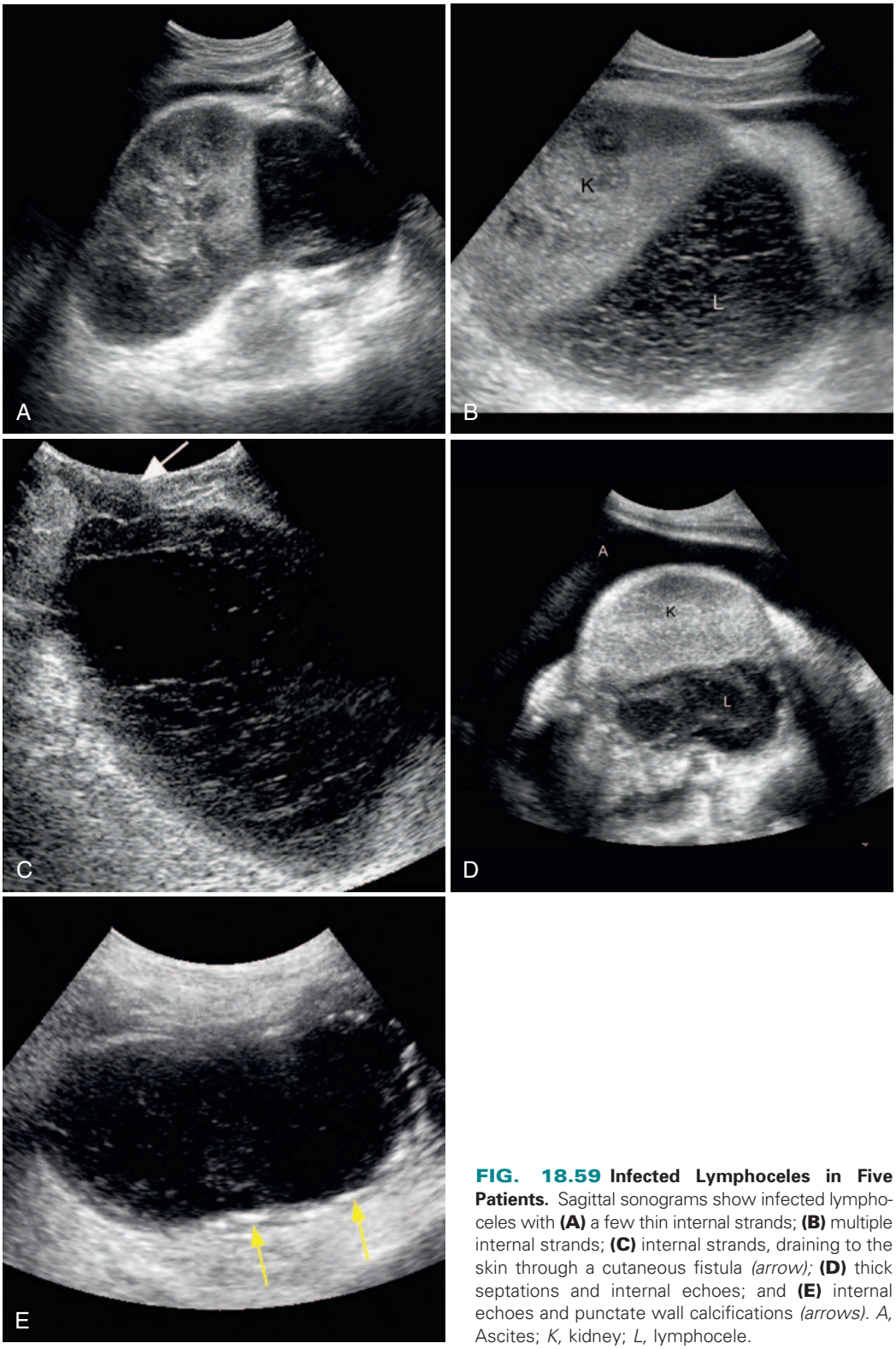

FIG. 18.59 Infected Lymphoceles in Five Patients. Sagittal sonograms show infected lymphoceles with **(A)** a few thin internal strands; **(B)** multiple internal strands; **(C)** internal strands, draining to the skin through a cutaneous fistula *(arrow);* **(D)** thick septations and internal echoes; and **(E)** internal echoes and punctate wall calcifications *(arrows). A,* Ascites; *K,* kidney; *L,* lymphocele.

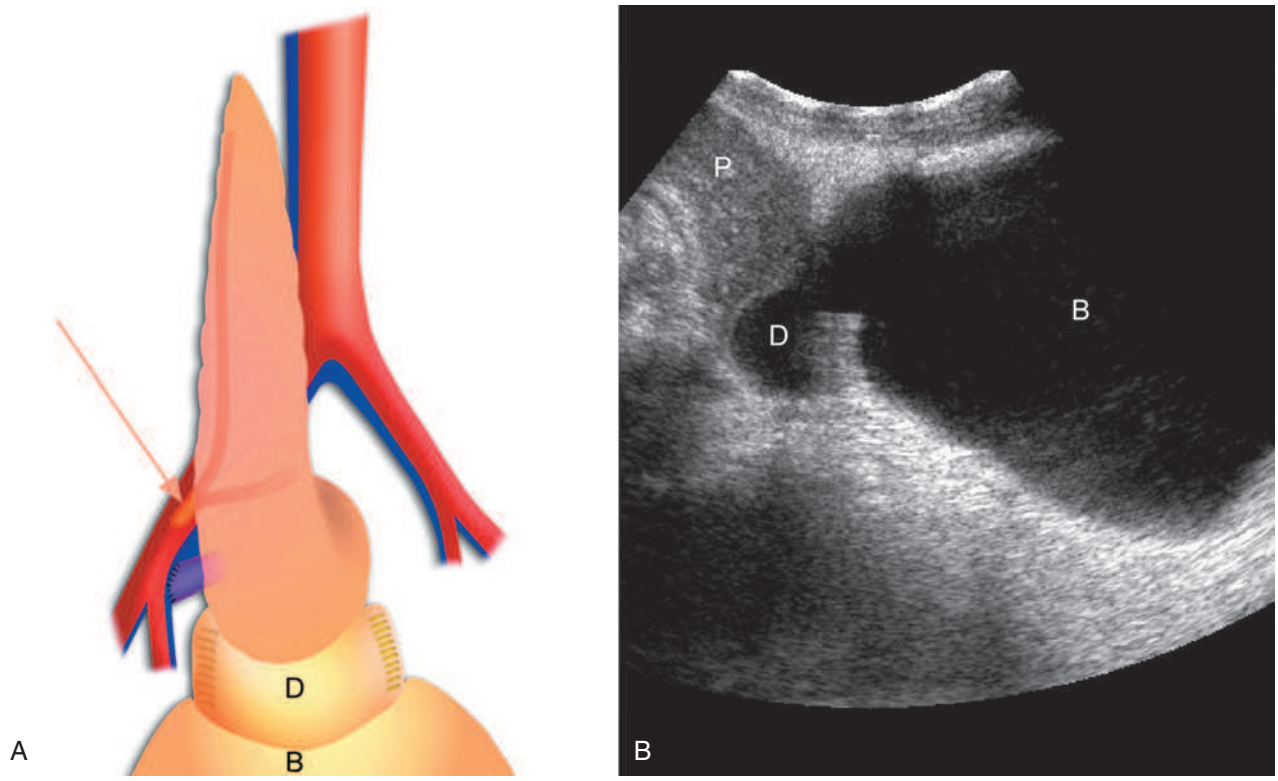

FIG. 18.60 Pancreas Transplant: Systemic Venous-Bladder Drainage (Traditional Surgery). (A) Donor portal vein *(purple)* is anastomosed to the external iliac vein, and donor artery Y graft *(coral arrow)* to the external iliac artery. Duodenal stump *(D)* is anastomosed to the bladder *(B).* **(B)** Sagittal sonogram shows duodenal stump anastomosed to the bladder *(B). P,* Pancreas.

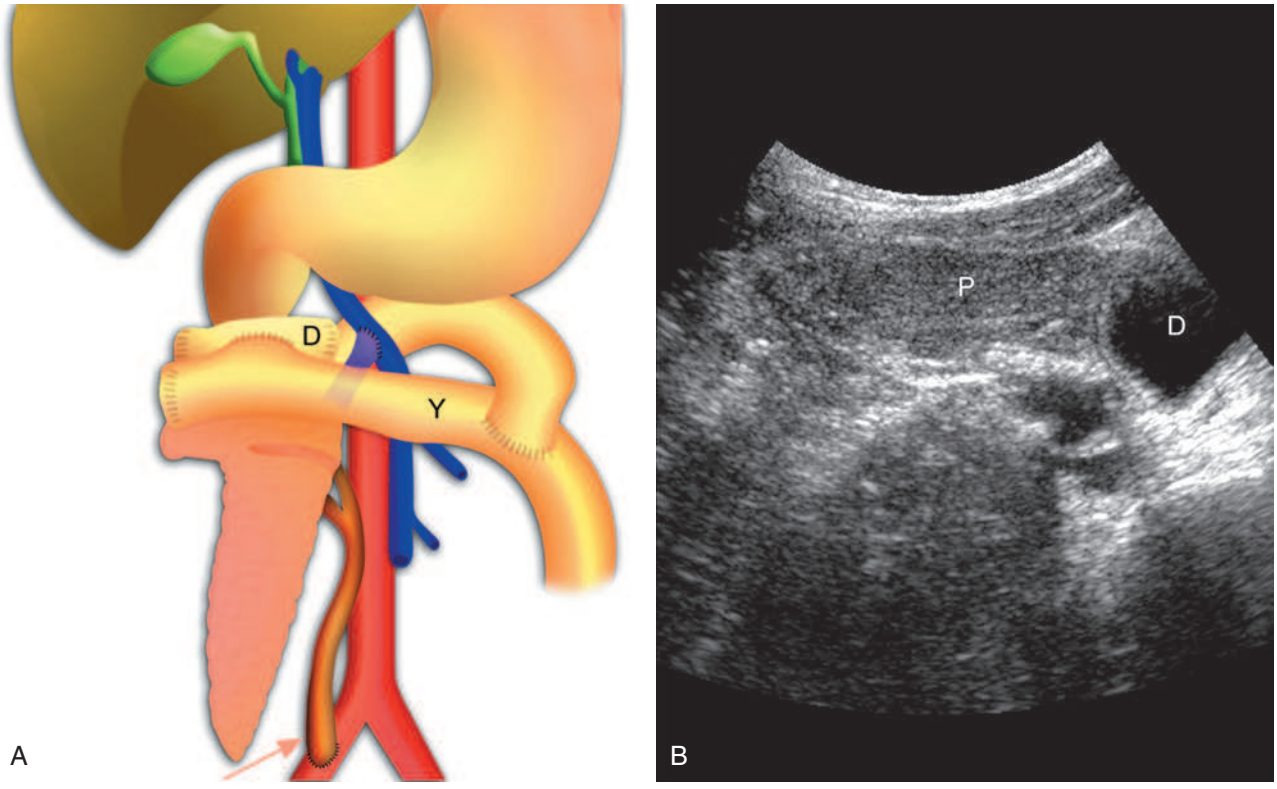

FIG. 18.61 Pancreas Transplant: Portal Venous-Enteric Drainage (New Technique). (A) Donor portal vein *(purple)* is anastomosed to the superior mesenteric vein *(blue),* and donor artery *(arrow)* is anastomosed to the common iliac artery. Duodenal stump *(D)* is anastomosed to a Roux-en-Y *(Y).* **(B)** Transverse sonogram shows pancreas transplant *(P)* with fluid-filled duodenal stump *(D).*

which is then anastomosed in an end-to-end fashion to the donor superior mesenteric artery (SMA) and end donor splenic artery to side donor iliac artery anastomosis. If the graft is portally drained, the arterial conduit is much longer than in a systemically drained graft.

Normal Pancreas Transplant Ultrasound

To perform an ultrasound assessment of a transplanted pancreas, the sonographer should be aware of the surgical technique used, the position of the allograft in the abdomen at surgery, and the sites of vascular anastomosis. This often entails a detailed review of the intraoperative surgical notes or discussion with the surgeon before scanning the patient.

With the **systemic venous** technique, the pancreatic head is placed in the iliac fossa, with the body and tail placed obliquely in the midabdomen. The pancreatic tail is therefore positioned superior to the head.

With the **portal venous** technique, the orientation of the graft is such that the pancreatic head lies superiorly and the body and tail lie inferiorly. The graft is positioned within the right side of the abdomen within the inferior mesocolic space. This allows the recipient's SMV to be anastomosed to the portal vein of the graft. In some instances the graft may be oriented in the transverse midline such that the recipient SMV is sagittally oriented to the transplant portal vein.

The normal allograft retains the normal gray-scale morphology of a native pancreas with well-defined margins; a homogeneous echotexture, isoechoic or minimally echogenic to liver; and a thin, nondilated pancreatic duct (Fig. 18.62, Video 18.5 and Video 18.6). The peripancreatic fat shows a normal echogenicity. Occasionally a trace amount of peripancreatic fluid may be observed and usually resolves without complication. Color Doppler ultrasound is useful for locating the mesenteric vessels, particularly when the graft is poorly visualized because of overlying bowel gas. Spectral Doppler sonography of the normal graft shows continuous monophasic venous flow and low-resistance arterial waveforms.

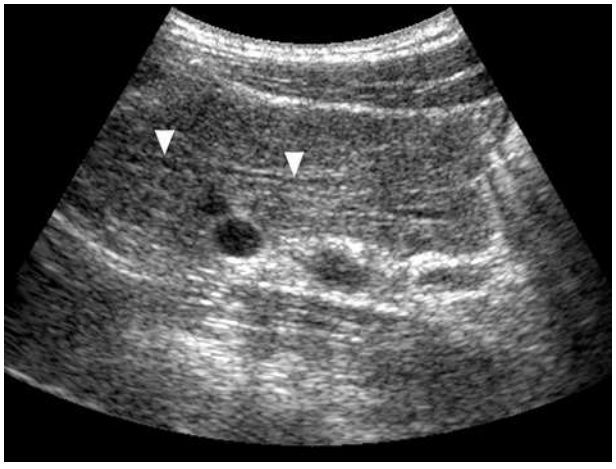

FIG. 18.62 Normal Pancreas Transplant. Gray-scale ultrasound of pancreas transplant shows normal echogenicity and echotexture of allograft, with nondilated pancreatic duct *(arrowheads)*. See also Video 18.5 and Video 18.6.

If patient habitus is slim and the graft lies in a relatively superficial location within the right iliac fossa, a high-frequency linear probe in the range of 5 to 12 MHz can be used for interrogation. Probe compression as well as placement of the patient in a right anterior oblique position will help to displace overlying bowel gas. Color and power Doppler ultrasound are useful for locating the parenchymal and graft vessels, particularly when the graft is poorly visualized because of overlying bowel gas. Spectral Doppler sonography of the normal graft shows continuous monophasic venous flow and low-resistance arterial waveforms, with a rapid systolic upstroke and continuous diastolic flow.

Role of Contrast-Enhanced Ultrasound

CT and MRI are often used for problem solving in the setting of postoperative complications; however, in the setting of associated renal impairment in this vulnerable patient group, the impact of iodinated contrast agents must be considered. Similarly, the potential risk of nephrogenic systemic fibrosis needs to be weighed against any possible diagnostic benefit when performing contrast-enhanced MRI, particularly in patients with elevated creatinine.

Contrast-enhanced ultrasound (CEUS) circumvents any underlying issues with renal impairment and facilitates the conspicuity of the graft relative to the surrounding tissues. It also allows assessment of areas of hypoperfusion. Its other inherent advantages have been well described and include safety, patient tolerance, and lack of ionizing radiation. Because the graft pancreas is highly vascularized, CEUS allows for visualization of areas of reduced or absent microcirculation. The contrast agent remains entirely intravascular, so focal areas of diminished perfusion or necrosis can be seen, and biopsy readily performed under ultrasound guidance. CEUS may also potentially allow an earlier diagnosis of graft rejection.[79]

Abnormal Pancreas Transplant

The graft vasculature consists of the following:

1. The iliac arterial graft is connected to the donor SMA and splenic artery. A Doppler arterial waveform is usually obtained from the SMA, the proximal and distal splenic artery, the intrapancreatic arcade, and the transverse vessels. The waveform is assessed for peak systolic flow velocity as well as being evaluated for vascular resistance within the graft. A normal graft should have arterial flow with a sharp systolic upstroke and continuous antegrade diastolic flow. This is seen in conjunction with an RI of 0.5 to 0.7, which implies a relatively low intragraft vascular resistance. Because there is no capsule enveloping the graft pancreas, normal resistance may be seen in a transplanted pancreas with edema (in the setting of either pancreatitis or rejection). This is in contradistinction to the graft kidney, wherein intrarenal edema results in elevation of vascular resistance.
2. The graft splenic vein and SMV join together to form the donor portal vein. This can be anastomosed to the recipient iliac vein, vena cava (systemic drainage), or SMV (portal drainage). Cardiac phasicity can be seen in the venous waveform when there is systemic venous drainage. Relative flattening of the venous waveform at the site of the donor portal vein

anastomosis to the recipient iliac or SMV is not an uncommon finding and is related to mild narrowing at this site.

The most common complications are venous thrombosis and arterial pseudoaneurysm.

Potential symptoms of graft thrombosis include unexplained hyperglycemia, graft tenderness, and, in the context of systemic-bladder drainage technique, hematuria and diminished urinary amylase levels. Potential complications of graft thrombosis include graft dysfunction and necrosis, pancreatitis, leakage of pancreatic secretions, and sepsis.

Thrombosis

Graft thrombosis, including both venous and arterial thrombosis, occurs in 2% to 19% of patients and is the second leading cause of transplant loss, after rejection. Pancreatic transplants are more vulnerable to graft thrombosis than renal transplants because the rate of blood flow in the transplanted pancreas is slower than that in a transplanted kidney.[80,81] Although the clinical signs and symptoms of graft thrombosis are nonspecific, detection of vascular thrombosis is imperative for both salvaging the transplant and preventing life-threatening sequelae, such as sepsis and cardiovascular collapse. Venous thrombosis, which occurs with an estimated incidence of 5%, is a particular concern because of the increased risk of hemorrhagic pancreatitis, tissue necrosis, infection, thrombus propagation, and pulmonary embolism.[81]

Graft thrombosis can be categorized as early or late, depending on the time of diagnosis after surgery. **Early** graft thrombosis occurs within 1 month of transplantation and is secondary to either microvascular injury during preservation of the graft or technical error during surgery. **Late** graft thrombosis occurs 1 month after transplant surgery and is usually caused by **alloimmune arteritis,** in which gradual occlusion of the small blood vessels eventually culminates in complete proximal vessel occlusion.[80] Other technical factors predisposing to graft thrombosis include coagulopathies, long preservation time, poor donor vessels, left-sided graft placement resulting in a deeper anastomosis, and the use of a venous extension graft.[81]

Prompt surgical intervention may be required depending on the severity of the thrombosis. Thrombosis of the graft splenic artery and vein results in infarction of the graft pancreatic body and tail. If there is thrombosis of the graft SMA and SMV, it may result in infarction of the pancreatic head and transplanted duodenum. In the context of acute thrombosis the graft may appear enlarged, whereas in more chronic thrombosis the graft appears diffusely atrophic.

Venous thrombosis is far more common than arterial thrombosis and is either completely or partially occlusive. It can be localized to the SMV, the splenic vein, or both vessels. A venous thrombosis may form owing to a phlebitis related to an underlying pancreatitis. Alternate mechanisms include stasis caused by a perianastomotic fluid collection or a torque on the venous anastomosis related to a shift in position of the graft resulting in stretching or twisting. Stasis in a stump of the SMV distal to the pancreaticoduodenal vessels may be a nidus for venous thrombosis.

Venous thrombi within the pancreatic graft may remain localized and not propagate into the portal vein, the iliac vein, or the IVC (systemic venous drainage) or the SMV (portal venous drainage). Normal graft function can therefore be maintained.[82] However, the potential for propagation of venous thrombi always exists, and if not well seen on ultrasound may need to be imaged dynamically in the venous phase on multiphase computed tomography (CT) or magnetic resonance imaging (MRI).

Splenic vein thrombosis results in reversal of arterial diastolic flow and absence of splenic venous flow on Doppler ultrasound. Diffuse narrowing of the transplanted portal vein can be visualized with either technique and is typically seen in association with elevation of venous pressure within the graft.

A combination of systemic anticoagulation and/or thrombolytic therapy may be necessary to treat complete splenic vein occlusion.[83] Endovascular thrombectomy may also be performed for partial or occlusive thrombus, provided there is no underlying pancreatitis or extrinsic vascular compression.[84]

Pseudoaneurysms occur at anastomotic sites or elsewhere as a result of pancreatitis or underlying infections or abscess. They can also occur secondary to biopsy or surgical trauma. The iatrogenic pseudoaneurysms may be seen in association with arteriovenous fistulas. Similar to the stump venous thrombi described earlier, stasis in low-flow surgically created vascular stumps can occur in peripheral superior mesenteric and splenic arterial segments and contributes to formation of stump thrombi.

Arterial thrombosis involves the graft SMA, the graft splenic artery, or the donor Y construct. The pancreas has a smaller microcirculatory blood flow in comparison with other graft types, and this increases its risk for thrombosis. It is usually mitigated by the formation of intrapancreatic arterial collaterals, which means that patency of only one allograft artery (SMA or splenic artery) is sufficient for graft survival and function. These collaterals are often better appreciated on a modality such as CT owing to the relatively diminutive caliber of the vessels.

Thrombosis is least common in the simultaneous pancreas-kidney transplant as compared with the other techniques, as well as being less likely when the systemic-bladder drainage technique is used as compared with the portal-enteric drainage technique. However, kinking of the Y graft is more likely in the portal enteric technique and is related to the length of the vessel (the graft is placed higher in the abdomen).

Many of these arterial complications can be managed via endovascular intervention, including coil embolization and covered stents. Surgical resection of aneurysms and grafting are usually reserved for patients who have infected grafts and pseudoaneurysms in the setting of abscesses in the transplant bed.

On ultrasound, occlusive or nonocclusive thrombus may be visualized within the lumen of the transplanted arteries or veins (Fig. 18.63). We have also observed several cases of thrombus occurring at the suture line of blind-ending arteries or veins (Fig. 18.64). On spectral Doppler, no arterial flow is detected in transplants with occlusive arterial thrombus. In grafts with occlusive venous thrombus, a lack of venous flow is detected on spectral tracing, with high-resistance arterial flow showing either no flow in diastole (RI = 1) or reversal of diastolic flow.[81] Surgically ligated arteries containing thrombus may show a cyclic pattern of flow adjacent to the thrombus, which we presume is secondary

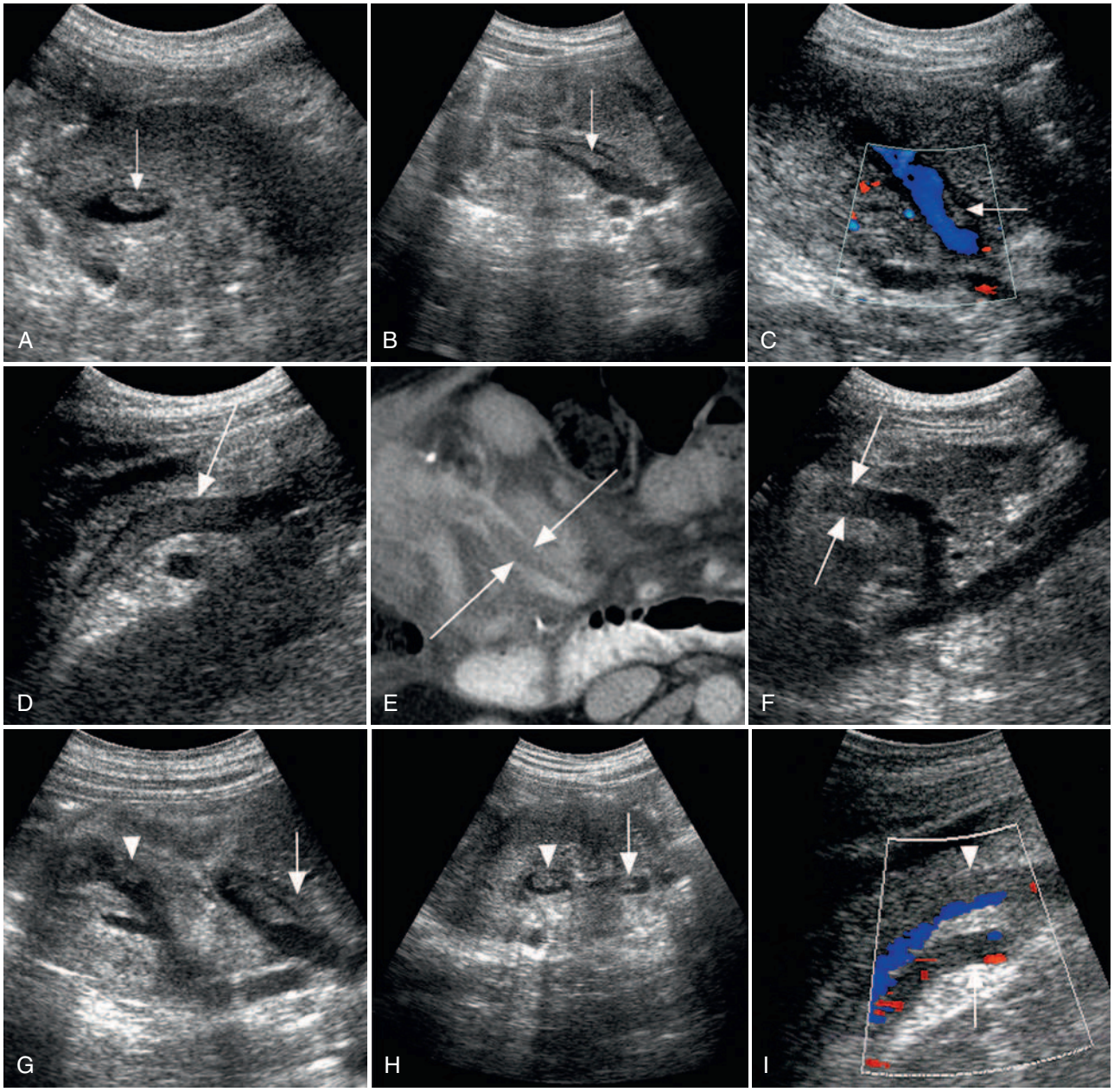

FIG. 18.63 Graft Thrombosis in Different Patients. (A) Transverse sonogram, **(B)** sagittal sonogram, and **(C)** color Doppler image show nonocclusive venous thrombus *(arrows).* **(D)** Gray-scale ultrasound *(arrow)* and **(E)** correlative CT *(arrows)* show nonocclusive venous thrombus. **(F)** Sagittal sonogram shows occlusive arterial thrombus *(arrows).* **(G)** Sagittal sonogram, **(H)** transverse sonogram, and **(I)** color Doppler image show nonocclusive venous *(arrowhead)* and arterial *(arrow)* thrombus in the same transplant.

to local eddy currents, with a normal arterial waveform more proximally.

Arteriovenous Fistula and Pseudoaneurysms

Arteriovenous fistulas and pseudoaneurysms are rare complications of pancreatic transplants and may be related to the blind ligation of mesenteric vessels along the inferior border of the pancreas during retrieval. In some patients, mycotic pseudoaneurysms may occur in the setting of graft infection.[85]

On gray-scale ultrasound, **arterial malformations** may not be detectable. On color Doppler sonography, however, a mosaic of intense colors may be identified, produced by the tangle of vessels within the malformation and adjacent tissue vibration. Spectral Doppler ultrasound reveals high-velocity, low-resistance flow within the lesion, which is typical of arteriovenous shunting (Fig. 18.65). On gray-scale ultrasound, **pseudoaneurysms** usually appear as anechoic spherical structures, although mural-based intraluminal thrombus may be detected. On spectral Doppler ultrasound, the classic to-and-fro pattern may be observed.

Rejection

Rejection is the most common cause of pancreatic graft loss after transplantation. This condition affects up to 40% of grafts and can be hyperacute, acute, or chronic.[77] Early recognition of transplant rejection remains a challenge because clinical

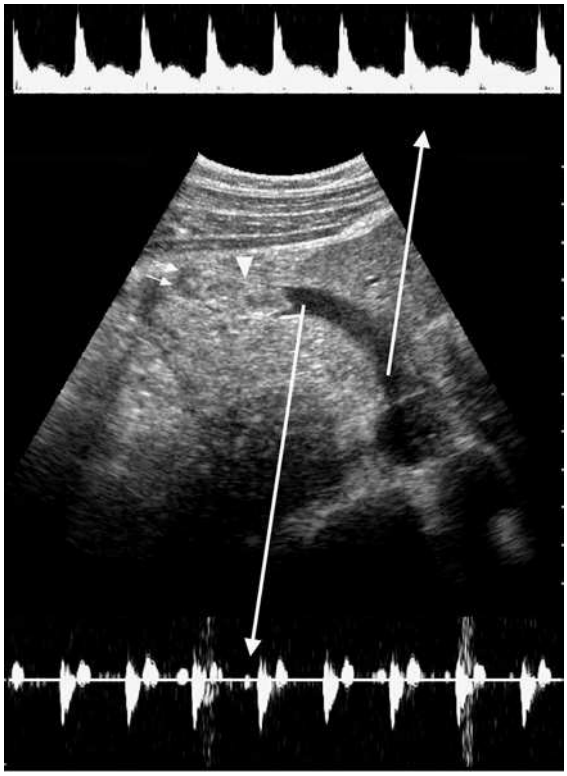

FIG. 18.64 Thrombus Adjacent to Suture Line. Echogenic thrombus *(arrowhead)* at suture line *(small arrows)* of blind-ending ligated artery. Spectral trace adjacent to thrombus shows to-and-fro waveform *(bottom)*, whereas spectral trace *(top)* more distally is normal.

parameters used to evaluate pancreas graft dysfunction have low sensitivity and specificity in detection of rejection. In particular, there is no individual biochemical marker that would permit acute rejection to be distinguished from vascular thrombosis or pancreatitis.

Although current advances in immunosuppressives have had an impact on acute rejection rates, chronic rejection remains one of the major causes of long-term graft failure.

Hyperacute rejection is rare and occurs in the immediate postsurgical period, usually as a result of preformed circulating cytotoxic antibodies in the recipient's blood. Thrombosis and immediate graft loss occur with this condition.

Acute rejection occurs as a result of an autoimmune vasculitis and develops 1 week to 3 months after transplantation. There is small vessel occlusion, which results in diminished perfusion and long-term infarction if not treated early.[86] Recurrent episodes of inadequately treated or unrecognized rejection result in chronic rejection, with progressive endarteritis of small vessels with acinar atrophy, and eventually with fibrosis and parenchymal atrophy. Chronic rejection occurs in 4% to 10% of patients and is seen as gradual decline in exocrine and then endocrine function.

On gray-scale ultrasound, the allograft may appear hypoechoic or may contain multiple anechoic regions, and the parenchymal echotexture may be patchy and heterogeneous[87,88] (Fig. 18.66). In addition, there may be abnormal graft size, typically enlargement in acute rejection and atrophy in chronic rejection. Pancreatic enlargement in acute rejection has a sensitivity of 58% and a specificity of 100%.[89]

The usefulness of arterial RIs as an indicator of rejection is controversial. It has been shown that RIs of the arteries supplying the pancreatic transplant cannot differentiate allografts with mild or moderate rejection from normal transplants without rejection.[90] The reason may be that the pancreatic transplant does not contain a discrete investing capsule, and therefore swelling from transplant rejection may not necessarily result in increased parenchymal pressures or elevated vascular resistance.[91] Grossly elevated RIs greater than 0.8 have been observed in pancreatic allografts with biopsy-proven acute severe rejection. Although these elevated RIs may be sensitive, they are not specific in the detection of severe pancreatic transplant rejection.[90] Similarly, graft enlargement and heterogeneity may be seen in acute pancreatitis and ischemia.

In a small series of patients, CEUS played a useful role in the surveillance of pancreatic grafts and in particular helped in the earlier diagnosis of rejection. Time-intensity curves in patients during rejection showed a significantly slower ascent and diminished maximum intensity. Overall, there was a significantly reduced maximum intensity and time to reach peak intensity. After successful treatment of the episode of rejection, these parameters near normalized to initial values.

Ultimately, image-guided biopsy is the reference standard for confirming and grading the severity of rejection.

Pancreatitis

Almost all patients develop symptoms of pancreatitis immediately after surgery, presumably caused by reperfusion injury and ischemia.[91] This typically involves the entire graft.

A temporary elevation of serum amylase 48 to 96 hours posttransplantation is therefore common and usually of no clinical consequence. There is also a mild transient elevation in amylase.

Focal edema of the donor mesenteric fat attached to the arterial stump of the SMA should not be misdiagnosed as a focal pancreatitis. This finding is related to ligation of the donor's lymphatic vessels. Other causes of pancreatitis include partial or complete occlusion of the pancreatic duct, poor perfusion of the allograft, and, in patients with systemic venous-bladder drainage, reflux-related pancreatitis.[87]

Long term, graft pancreatitis is seen in up to 35% of transplants. Underlying predisposing factors include prolonged warm ischemia time, graft handling, and reperfusion injury. The major differential diagnoses to consider include graft rejection and ischemia.

The ultrasound appearance of pancreatitis in the allograft is similar to that of pancreatitis in the native gland (Fig. 18.67). Gray-scale findings include a normal-sized or bulky edematous pancreas, poorly defined margins, increased echogenicity of the peripancreatic fat secondary to surrounding inflammation, peripancreatic fluid, and thickening of the adjacent gut wall. In cases of pancreatitis resulting from ductal obstruction, a dilated pancreatic duct may be observed.[87,91] In nonacute cases of pancreatitis, pseudocysts adjacent to or distal from the transplant may be identified, usually appearing as a well-circumscribed fluid collection with minimal adjacent inflammatory changes. Needle aspiration of this structure typically demonstrates fluid with high amylase content.

Pancreatitis may be seen in association with vascular sequelae such as a focal arterial aneurysm or venous thrombosis. Similarly,

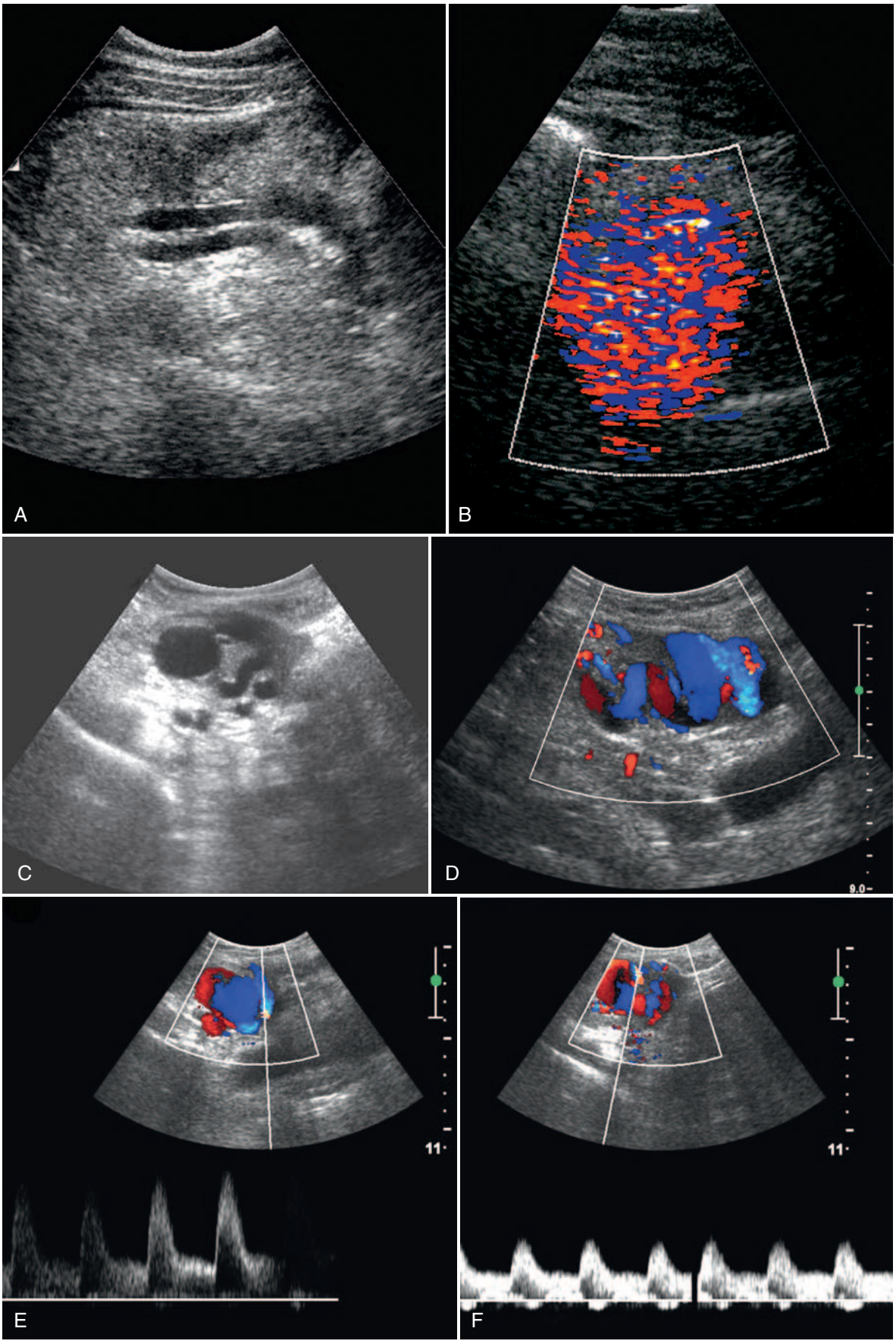

FIG. 18.65 Pancreas Transplant Vascular Malformations. (A) and **(B) Parenchymal arteriovenous malformation** (AVM). Transverse gray-scale ultrasound shows no abnormality. **(B)** Color Doppler ultrasound, however, shows an intense mosaic of color within the pancreas, secondary to a parenchymal AVM. **(C)-(F)** Transplant-related arteriovenous fistula (AVF). Gray-scale **(C)** and color Doppler **(D)** show dilated vessels with arterial **(E)** and mixed atrial and venous **(F)** waveforms.

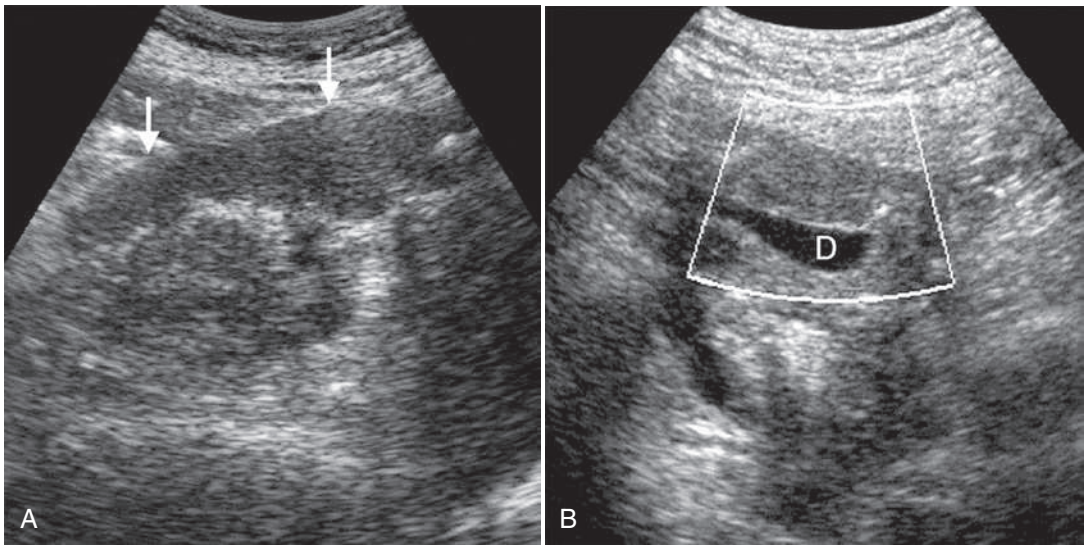

FIG. 18.66 Pancreas Transplant Rejection. (A) Transverse sonogram shows hypoechoic pancreas *(arrows)*. The pancreatic parenchyma is also atrophied. **(B)** Oblique sonogram shows dilated pancreatic duct *(D)* secondary to surrounding parenchymal atrophy.

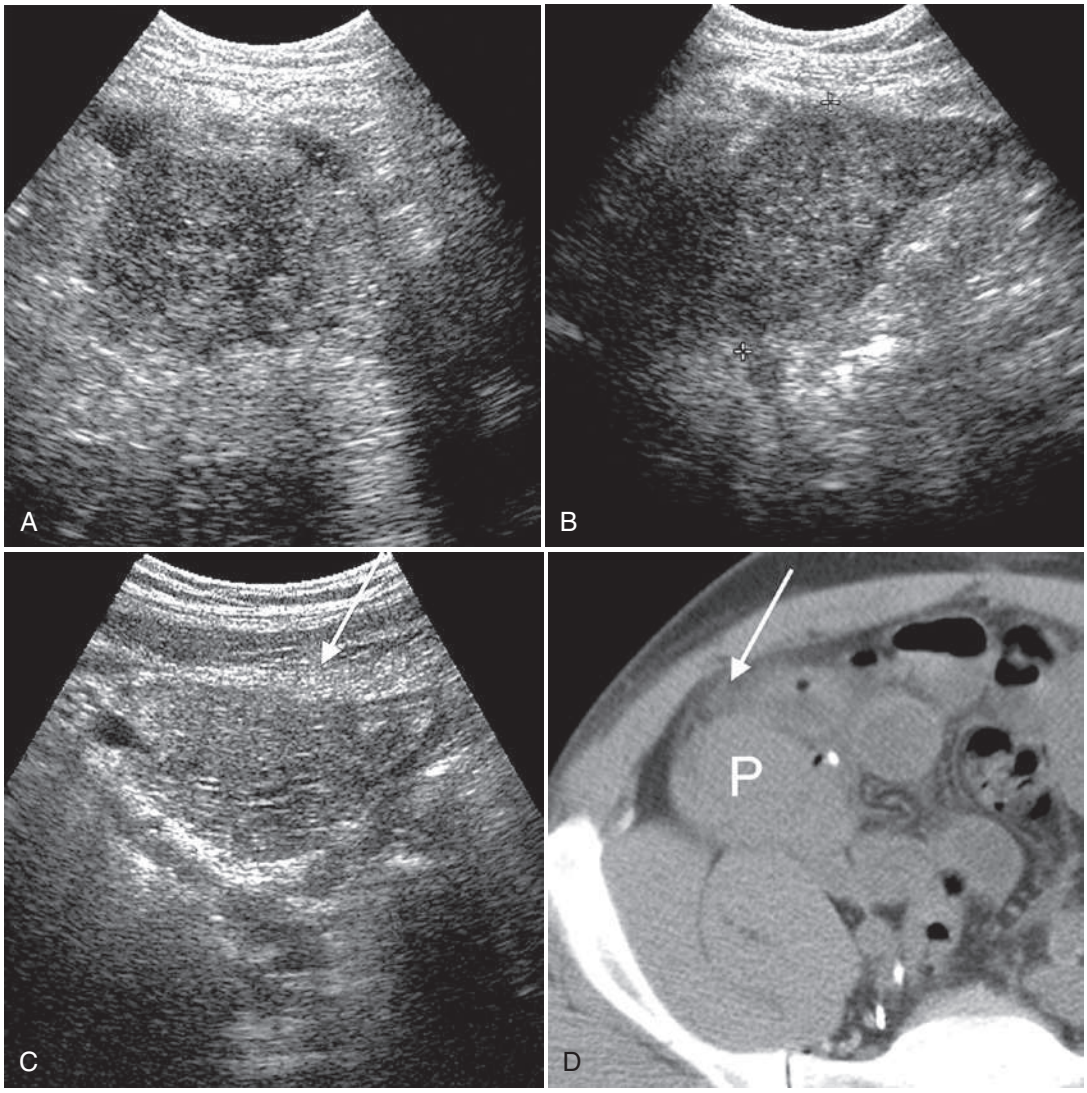

FIG. 18.67 Pancreatitis. (A) Transverse and **(B)** oblique images show bulky, edematous allograft. **(C)** Oblique ultrasound shows echogenic inflamed peripancreatic fat *(arrow)*. **(D)** This appears as "stranding" in the peripancreatic fat on CT *(arrow)*. *P,* Pancreas transplant.

severe graft pancreatitis is associated with a range of complications akin to those seen in a native pancreas such as pancreatic hemorrhage and necrosis, peripancreatic fluid collections, pseudocysts, abscesses, and pseudoaneurysms.

Ultrasound can be used to guide aspiration of potential fluid collections and help discriminate pseudocysts from abscesses or seromas. If infection is demonstrated at the time of ultrasound-guided aspiration, CT is often performed to assess the graft in its entirety and in particular to evaluate for areas of duct disruption as well as to demonstrate the location of fluid collections in relation to the duodenal C loop and duodenojejunostomy. Early fluid collections are often surgically managed.

Fluid Collections

Peripancreatic transplant-related fluid collections are associated with an increased likelihood of loss of allograft function and overall increased mortality and morbidity. Early diagnosis and characterization of these collections are imperative, because treatment in the acute stages is associated with improved graft function and decreased recipient morbidity.[92]

In the immediate postoperative period, peritransplant fluid may be caused by leakage of pancreatic fluid from transected ductules and lymphatics, an inflammatory exudate, blood, or urine (Fig. 18.68). These collections may require either close serial imaging follow-up or drainage, depending on the clinical status of the patient.

Duodenal leaks in **systemic venous-bladder drainage** transplants occur from dehiscence of the duodenal-bladder anastomosis and result in the formation of urinomas, frequently at the medial aspect of the transplant. Urinomas may also result from infection or necrosis of the graft.[92]

Duodenal leaks in **portal venous-enteric drainage** transplants occur at the blind end of the donor duodenum or from the anastomosis with the recipient Roux-en-Y loop. On ultrasound, gross ascites, duodenal wall thickening, or free intraperitoneal air may be observed in patients with breakdown of the duodenal anastomoses. These leaks may result in overwhelming sepsis and can be life-threatening. Furthermore, the presence of digestive enzymes in contact with the graft may lead to substantial tissue necrosis.[91]

Patients with pancreatic transplants are also susceptible to **infection** because of their immunosuppressive therapy, as well as their underlying diabetes mellitus. Abscesses are occasionally identified and are often associated with hematomas, urinary tract infections, and pancreatitis. Although gas within a fluid collection may indicate the presence of a gas-forming organism, bubbles of air within a collection may also result from the presence of a fistula or tissue necrosis in cases of vascular thrombosis.

On sonography these collections may demonstrate a thick irregular wall with peripheral hyperemia on Doppler interrogation. If gas is present, it typically is seen as echogenic foci with posterior reverberation artifact. Adjacent changes in the fat include increased echogenicity and fluid. In the posttransplant period, the development of a new collection or change in the sonographic morphology of the collection may result from a variety of causes, including infection; malfunction of the pancreatic duct, stent, or external drain; hemorrhage; or associated tissue infarction.[92]

Miscellaneous Complications

Other complications of pancreatic transplants include intussusception of the Roux-en-Y loop, small bowel obstruction from adhesions, internal hernias (due to the surgically created mesenteric defect), and volvulus along the long axis of the graft. Because the patient is immunocompromised, there is a higher incidence of entities such as typhlitis or *Clostridium difficile* colitis.

POST TRANSPLANT LYMPHOPROLIFERATIVE DISORDER

The global improvement in survival after transplantation can be attributed to a parallel improvement in immunosuppressant regimens. The depressed immune response to oncoviruses such as the Epstein-Barr virus (EBV) results in increased vulnerability of these patients to malignancies that are mediated by such oncoviruses. This contributes to a threefold to eightfold increased malignancy risk in transplant patients as compared with the baseline population.[93-95]

PTLD is the second most common malignancy in adult transplant patients, following skin malignancy (nonmelanoma).[96] PTLD encompasses myriad disease processes ranging from lymphoid hyperplasia to poorly differentiated lymphoma. Biopsy is required to discriminate among the various subtypes. Many patients are asymptomatic or have vague symptomatology, resulting in a delayed diagnosis. It can be hard to discriminate PTLD from infection or allograft rejection. Imaging is therefore important in establishing the diagnosis, enabling tissue sampling, and monitoring response to treatment.

EBV infection is relatively prevalent, with 90% to 95% of adults being seropositive; however, most immunocompetent hosts can eradicate B cells that display EBV antigens by using T cells. However, in immunocompromised patients as well as a small group of immunocompetent hosts, a small number of EBV-infected B cells escape and survive with resultant latent EBV infection.[97]

After solid organ transplantation, cytotoxic EBV-specific T cells may be completely lost within 6 months of transplantation as a result of immunosuppressive medication.[98] Latently infected B cells have the potential to proliferate, resulting in PTLD.[99]

A variety of genetic mutations (including ***p53, NRAS***) can result in PTLD. These genes are involved in the division, proliferation, and death of cells. Overproduction of cytokines such as interleukin-6 has also been implicated in the genesis of PTLD. Similarly, CMV-seronegative patients have a higher risk of developing PTLD after solid organ transplantation.[100]

The incidence of PTLD is thought to be related to the degree of immunosuppression and the type of allograft. The aggressive immunosuppressive therapy required to prevent heart-lung transplant rejection has resulted in a reported incidence of PTLD as high as 4.6%. However, the milder immunosuppression used in patients with liver transplant or renal transplant has resulted in a lower incidence of PTLD, reported as 2.2% and 1%, respectively.[101,102]

In addition, the numbers of lymphoid aggregates are higher in intestinal and lung transplants, both of which are associated with some of the highest incidences of PTLD.[103] It is therefore

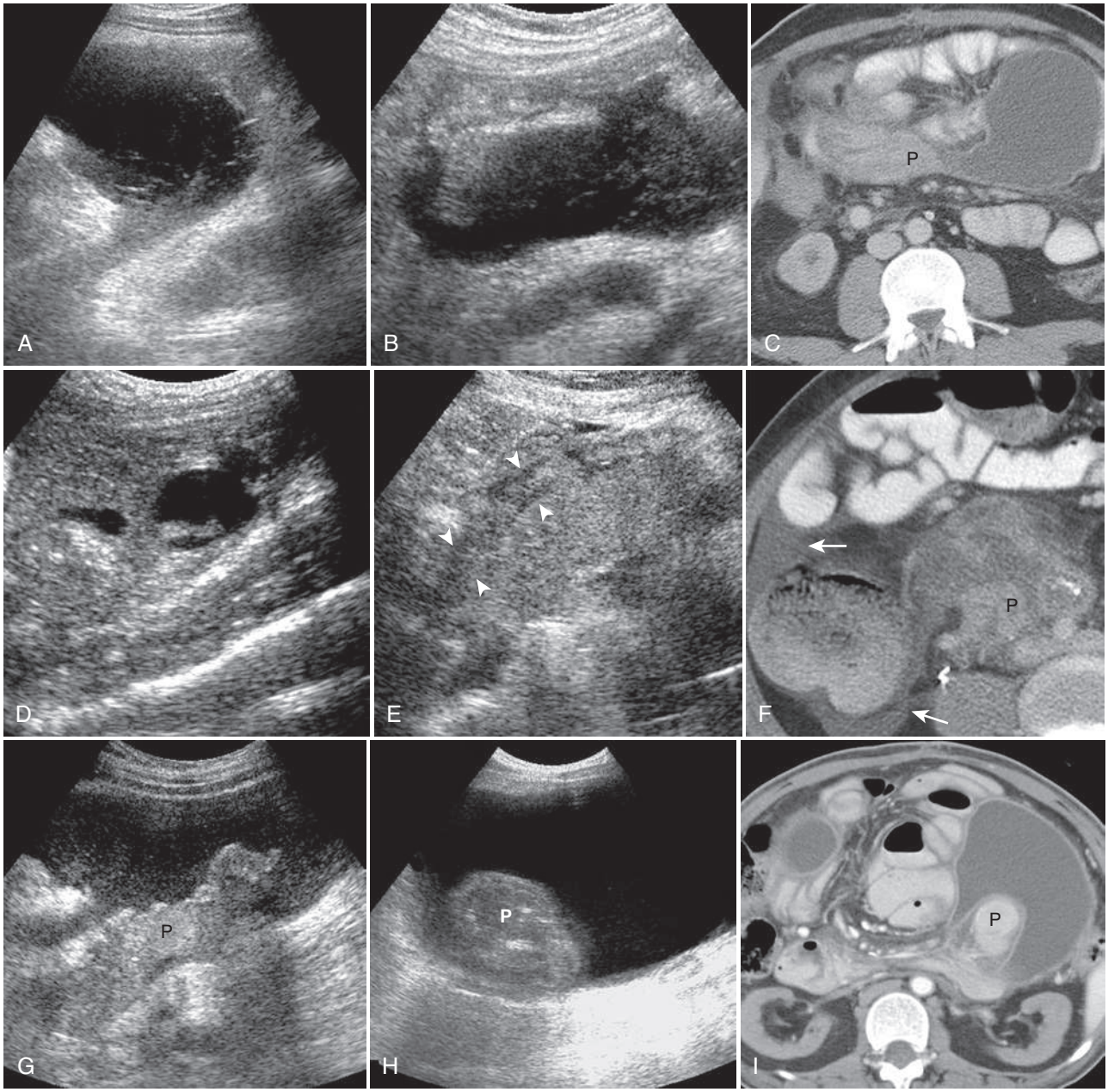

FIG. 18.68 Fluid Collections. (A)-(C) Hematoma. (A) Sagittal and **(B)** transverse sonograms show complex collection with internal echoes and strands. **(C)** Correlative CT shows hematoma in left upper quadrant that extends to pancreas *(P)*. **(D)-(I) Pseudocysts in three patients.** *Patient 1:* **(D)** Sagittal sonogram shows complex epigastric cyst with internal septation. *Patient 2:* **(E)** Sagittal sonogram shows complex collection adjacent to pancreas *(arrowheads)*. **(F)** Correlative CT scan shows collection extending into pancreatic head *(P)* and associated with free fluid *(arrows)*. *Patient 3:* **(G)** Sagittal sonogram shows large pseudocyst with internal echoes surrounding pancreatic tail *(P)*. **(H)** and **(I) Seroma.** Transverse sonogram and correlative CT scan show large, anechoic cystic structure surrounding pancreatic body *(P)*. The wall enhanced on CT scan. The collection was sterile on aspiration.

not surprising that agents that suppress T-cell activity are associated with a higher risk of PTLD. By the same token, a larger total number of immunosuppressant agents used by a patient may result in an increased risk of PTLD.[104]

The incidence of PTLD is bimodal, with the initial peak in the first year after transplantation and the second peak approximately 4 to 5 years after transplantation.[105] Biologically, the two peaks have a very different clinical course. The early-onset disease has a more favorable course, is pleomorphic in subtype, and has a positive response to reducing the level of immunosuppression. Late-onset disease is more commonly seen in conjunction with EBV infection, a monomorphic subtype, and an aggressive disease course. There is a higher mortality, and the disease is often resistant to chemotherapy.[106]

PTLD can be categorized depending on its primary location into either nodal disease (22%) or extranodal disease (81%). Nodal disease is either mediastinal or retroperitoneal in location. The involved lymph nodes have an abnormal appearance, showing a hypoechoic thickened cortex with an absent or flattened fatty hilum (Figs. 18.69 to 18.72). Extranodal disease

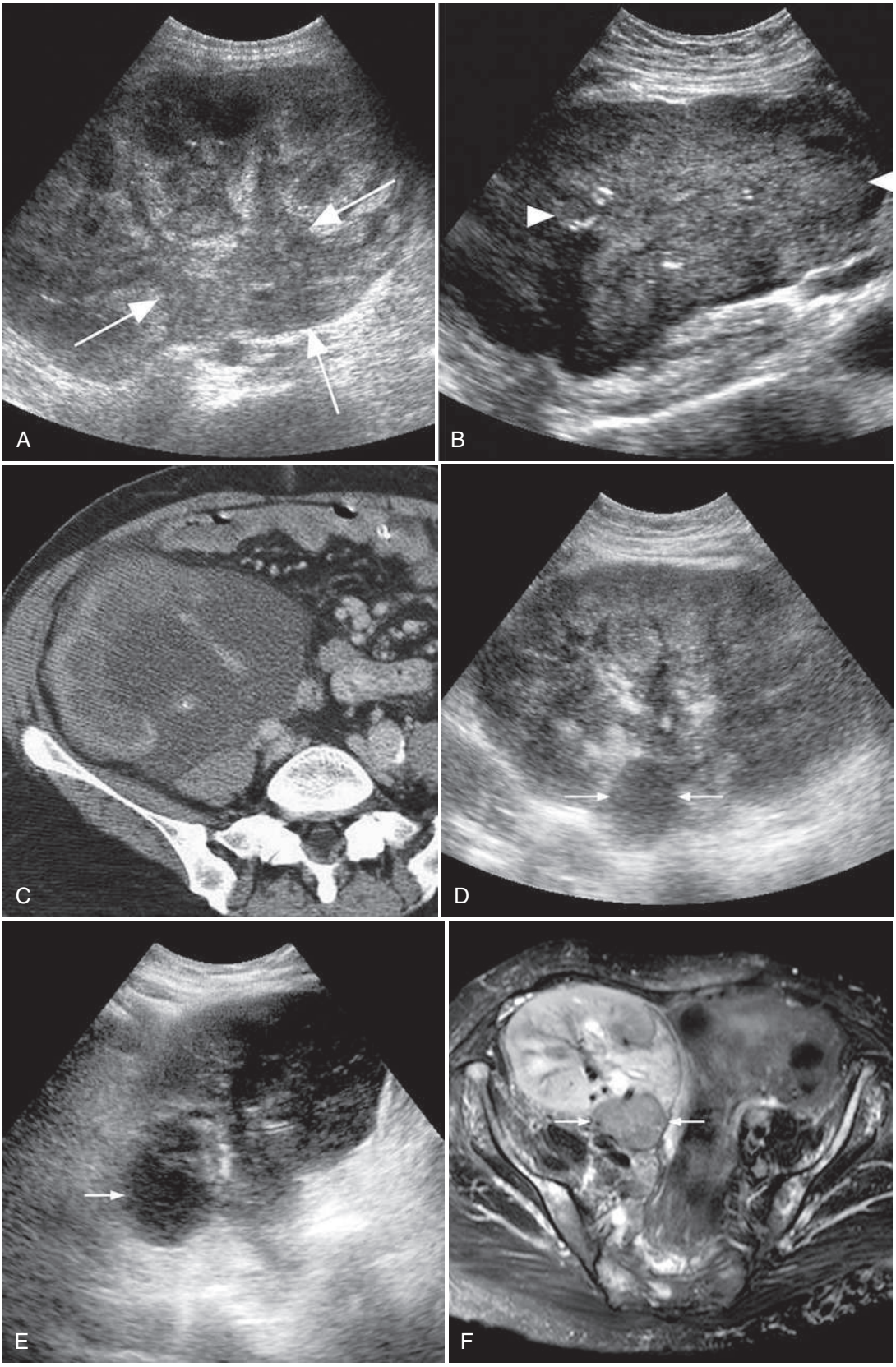

FIG. 18.69 Renal Posttransplant Lymphoproliferative Disorder in Two Patients. *Patient 1:* **(A)** Sagittal sonogram shows infiltrative mass *(arrows)* in renal hilum. **(B)** Six months later, the mass *(arrowheads)* has infiltrated into the renal cortex. **(C)** Correlative CT shows hilar mass infiltrating into renal cortex. *Patient 2:* **(D)** Sagittal and **(E)** transverse sonograms show a hypoechoic to anechoic structure with low-level echoes *(arrows)* in the renal hilum that could be interpreted as a complex cyst. **(F)** Contrast-enhanced MRI shows that this structure represents a solid mass *(arrows)*.

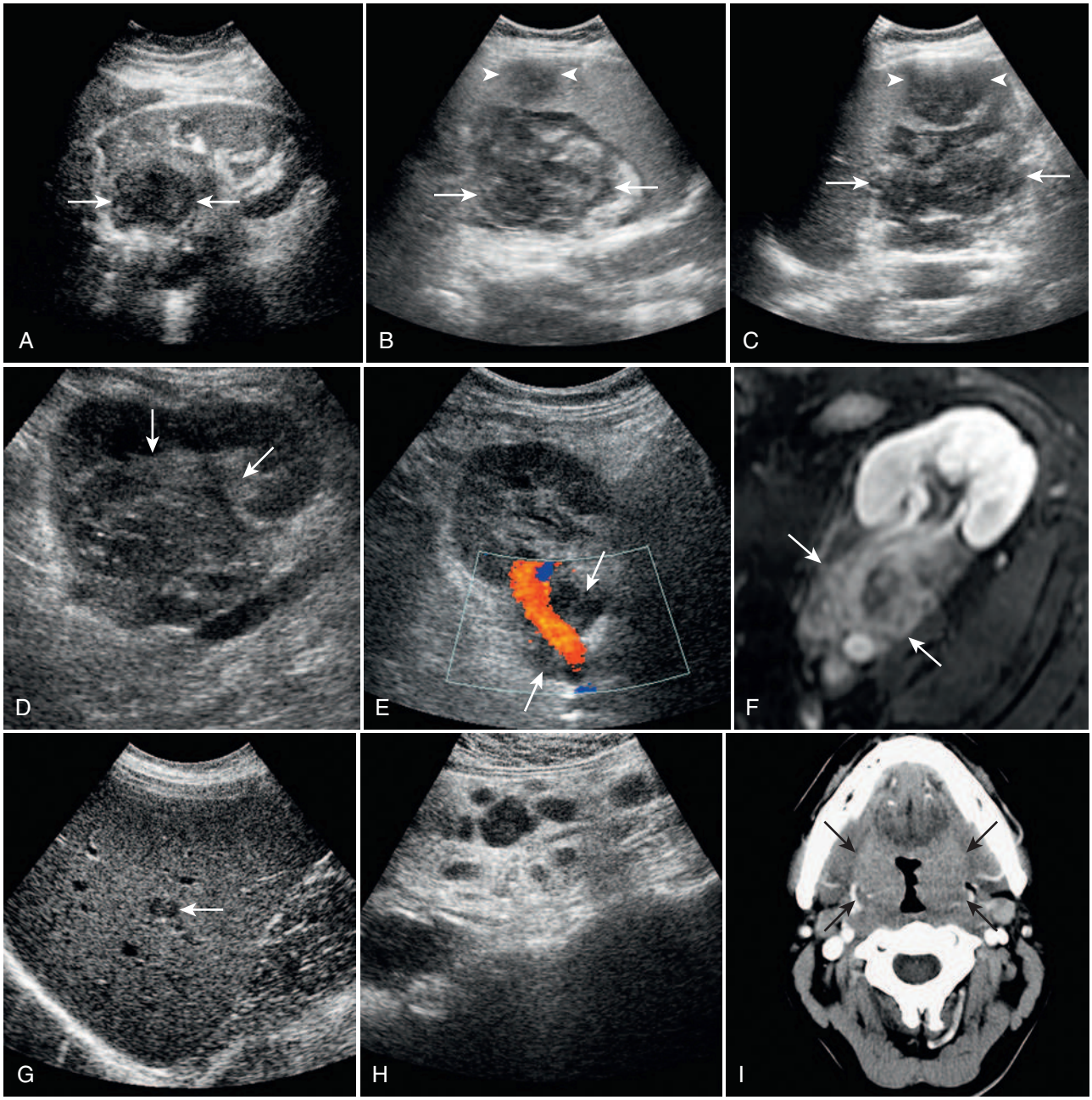

FIG. 18.70 Renal Posttransplant Lymphoproliferative Disorder (PTLD): Extrarenal Manifestations in Two Patients. *Patient 1:* **(A)** Sagittal sonogram shows a hypoechoic renal hilar mass *(arrows)*. **(B)** Sagittal and **(C)** transverse sonograms of the spleen show a mass in the hilum *(arrows)* as well as an intraparenchymal mass *(arrowheads)*. *Patient 2:* **(D)** Sagittal sonogram shows hilar mass *(arrows)*. **(E)** Transverse sonogram shows that mass *(arrows)* encases transplanted renal artery. **(F)** Correlative magnetic resonance image shows hilar mass *(arrows)* encasing renal vessels. **(G)** Transverse sonogram shows malignant-appearing hepatic nodule *(arrow)*. **(H)** Sagittal sonogram shows malignant lymphadenopathy. **(I)** CT shows tonsillar adenopathy in Waldeyer ring *(arrows)* secondary to PTLD.

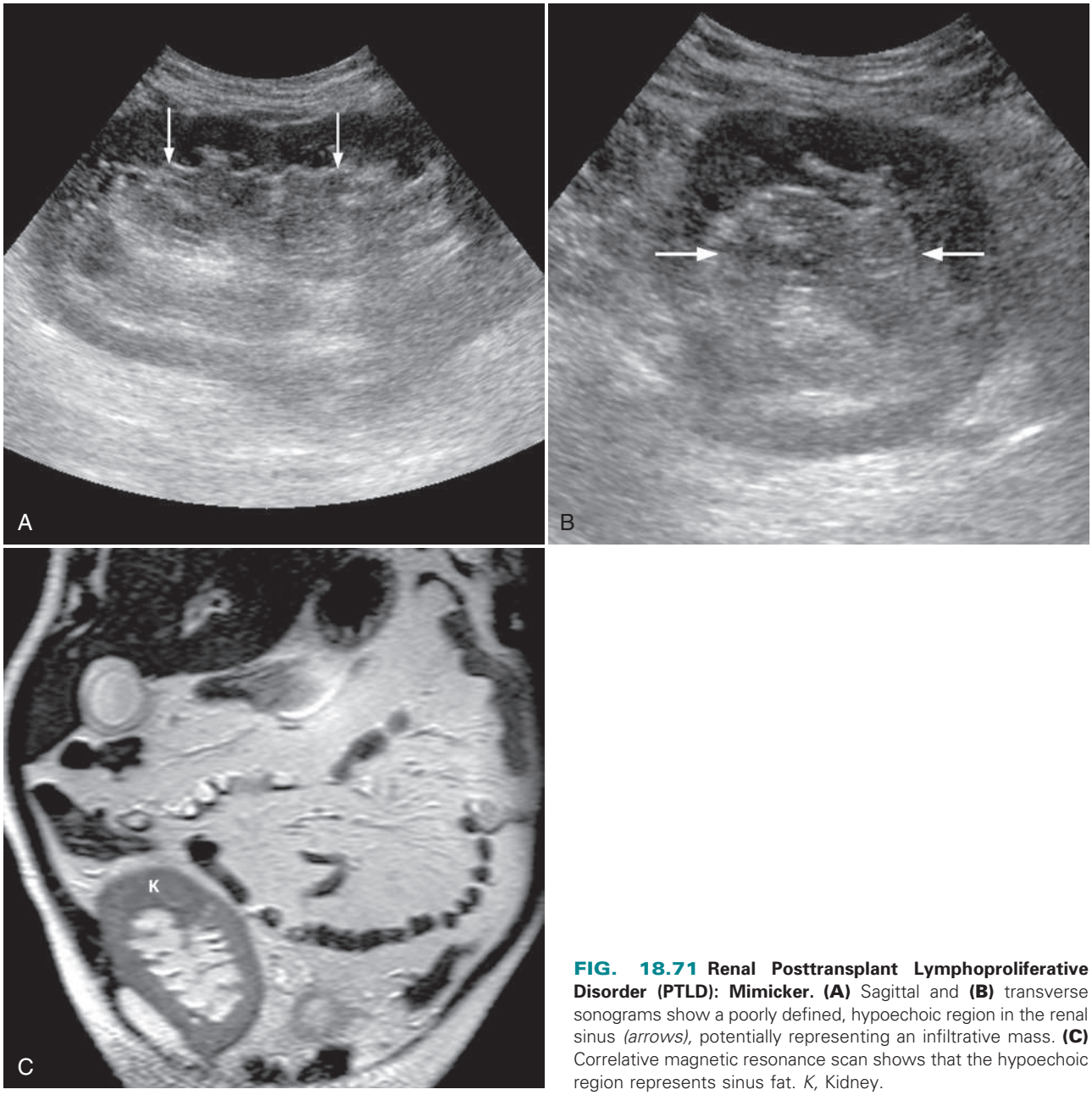

FIG. 18.71 Renal Posttransplant Lymphoproliferative Disorder (PTLD): Mimicker. (A) Sagittal and **(B)** transverse sonograms show a poorly defined, hypoechoic region in the renal sinus *(arrows),* potentially representing an infiltrative mass. **(C)** Correlative magnetic resonance scan shows that the hypoechoic region represents sinus fat. *K,* Kidney.

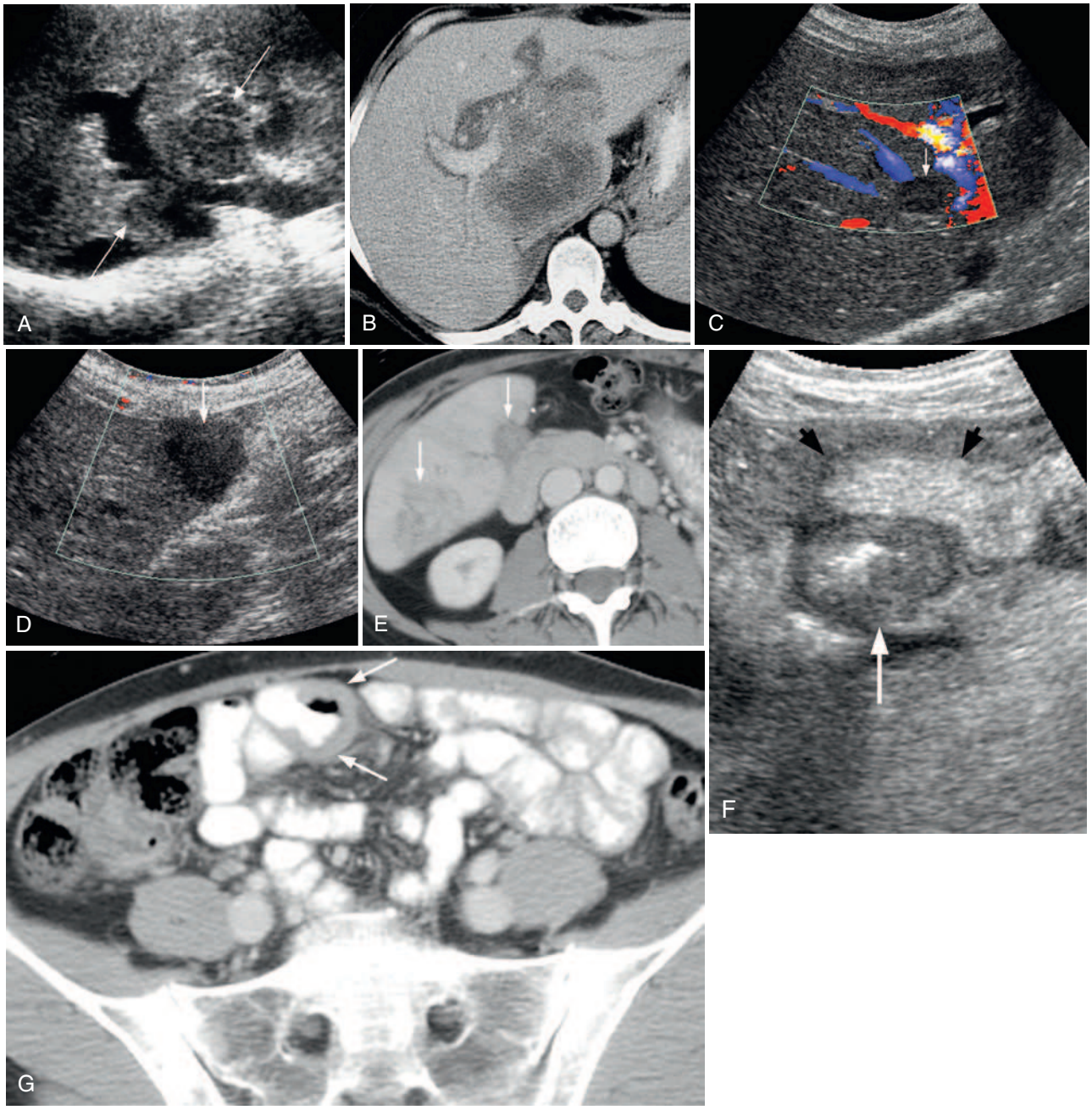

FIG. 18.72 Hepatic Posttransplant Lymphoproliferative Disorder (PTLD) in Three Patients. *Patient 1:* **(A)** Oblique sonogram shows malignant mass *(arrows)* encasing and narrowing main portal vein. **(B)** Correlative CT shows mass infiltrating liver. *Patient 2:* **(C)** Transverse and **(D)** sagittal color Doppler sonograms show avascular solid nodules *(arrow).* **(E)** Correlative CT scan shows solid hypovascular masses *(arrows). Patient 3:* **(F)** Transverse sonogram shows thick-walled gut *(white arrow)* adjacent to inflamed echogenic fat *(black arrows).* **(G)** Correlative CT scan shows thick-walled loop of small bowel *(arrows).*

by definition involves three main sites—the central nervous system, solid organs, or the gastrointestinal tract. The liver is the most common site of intraabdominal involvement, occurring in 30% to 45% of patients with PTLD. In rare cases, intraosseous lesions may be present, with imaging features on CT and MRI similar to those of metastatic disease, infection, or primary bone lymphoma. Overall, PTLD should be considered in the differential diagnosis of any transplant patient with lymphadenopathy or a new lesion within a solid viscus or the skeletal system.[107-110]

When the solid organs are involved, there are four main patterns of disease:

1. **Infiltrative pattern:** There is an ill-defined mass or masses that are extrinsic to the hilum and can result in secondary mass effect and/or vascular compromise. For instance, within the liver it may cause biliary obstruction and obstruction of blood flow within the periportal space. In renal involvement the mass typically is located extrinsic to the renal pelvis with resultant mass effect and obstruction of the vessels and the collecting system. In both instances the mass is usually relatively hypoenhancing but fluorodeoxyglucose (FDG) avid on positron emission tomography (PET) imaging.
2. **Parenchymal pattern:** This is characterized by multiple lesions that are disseminated throughout the affected organ. These also tend to be hypoenhancing. In the lung they are typically solid and may rarely cavitate. There may also be ill-defined alveolar infiltrates.
3. **Solitary mass:** A solitary mass in the affected organ is seen on ultrasound as a hypoechoic lesion with no Doppler signal on color Doppler imaging. Calcification is unusual but seen in the context of posttreatment changes or tumor necrosis.
4. **Infiltrative lesion:** This lesion involves the organ in question but also extends to involve regional structures such as the chest, abdominal wall, and adjacent solid organs. As a secondary manifestation, there may be dysfunction of the other organ(s) that are involved. Pancreatic PTLD tends to produce diffuse glandular enlargement, with an appearance that is indistinguishable from pancreatitis or rejection.[111]

Gastrointestinal disease can involve either bowel or the peritoneal cavity. When there is peritoneal disease, it can be nodular or diffusely infiltrating.[112] PTLD involving the gastrointestinal tract is seen in association with mural thickening, aneurysmal dilatation, ulceration, intussusception, and polypoidal lesions. Perforation is a rare manifestation of intestinal PTLD; the decline in perforation rates has been attributed to improved diagnosis and treatment of PTLD. As with any other lymphomatous-type lesions of the gut, obstruction of the bowel segments is rare.

Treatment Options

Stratification and patient management are determined by the subtype of PTLD, the distribution of disease, and the type of allograft. Potential management options include modification of immunosuppression, chemotherapy, radiation, and rituximab therapy as well as surgical resection of isolated lesions. Rituximab is a monoclonal antibody against B cell receptors, has a low toxicity profile, and has a response rate on the order of 60%. Preservation of graft function is an important goal of management while treating the PTLD.[113,114]

PET-CT has a pivotal role to play in monitoring response to therapy, particularly in patients in whom there are persistent focal lesions. In this scenario, FDG uptake allows discrimination between residual tumor and fibrosis.

REFERENCES

1. Takemoto S, Terasaki PI, Cecka JM, et al. Survival of nationally shared, HLA-matched kidney transplants from cadaveric donors. The UNOS Scientific Renal Transplant Registry. N Engl J Med. 1992;327(12):834-839.
2. Berthoux FC, Jones EH, Mehls O, Valderrabano F. Transplantation report. 1: Renal transplantation in recipients aged 60 years or older at time of grafting. The EDTA-ERA Registry. European Dialysis and Transplant Association–European Renal Association. Nephrol Dial Transplant. 1996;11(Suppl. 1):37-40.
3. Cattral MS, Bigam DL, Hemming AW, et al. Portal venous and enteric exocrine drainage versus systemic venous and bladder exocrine drainage of pancreas grafts: clinical outcome of 40 consecutive transplant recipients. Ann Surg. 2000;232(5):688-695.
4. United Network for Organ Sharing. National data. Transplants by organ type January 1, 1988–June 30, 2016. Available from: https://www.unos.org/data. Accessed 2016 July 18.
5. Crossin JD, Muradali D, Wilson SR. US of liver transplants: normal and abnormal. Radiographics. 2003;23(5):1093-1114.
6. Mazzaferro V, Regalia E, Doci R, et al. Liver transplantation for the treatment of small hepatocellular carcinomas in patients with cirrhosis. N Engl J Med. 1996;334(11):693-699.
7. Quiroga S, Sebastia MC, Margarit C, et al. Complications of orthotopic liver transplantation: spectrum of findings with helical CT. Radiographics. 2001;21(5):1085-1102.
8. Nghiem HV. Imaging of hepatic transplantation. Radiol Clin North Am. 1998;36(2):429-443.
9. Kamel IR, Kruskal JB, Raptopoulos V. Imaging for right lobe living donor liver transplantation. Semin Liver Dis. 2001;21(2):271-282.
10. Wolfsen HC, Porayko MK, Hughes RH, et al. Role of endoscopic retrograde cholangiopancreatography after orthotopic liver transplantation. Am J Gastroenterol. 1992;87(8):955-960.
11. Keogan MT, McDermott VG, Price SK, et al. The role of imaging in the diagnosis and management of biliary complications after liver transplantation. AJR Am J Roentgenol. 1999;173(1):215-219.
12. Letourneau JG, Castaneda-Zuniga WR. The role of radiology in the diagnosis and treatment of biliary complications after liver transplantation. Cardiovasc Intervent Radiol. 1990;13(4):278-282.
13. Barton P, Maier A, Steininger R, et al. Biliary sludge after liver transplantation: 1. Imaging findings and efficacy of various imaging procedures. AJR Am J Roentgenol. 1995;164(4):859-864.
14. Miller WJ, Campbell WL, Zajko AB, et al. Obstructive dilatation of extrahepatic recipient and donor bile ducts complicating orthotopic liver transplantation: imaging and laboratory findings. AJR Am J Roentgenol. 1991;157(1):29-32.
15. Zajko AB, Campbell WL, Bron KM, et al. Cholangiography and interventional biliary radiology in adult liver transplantation. AJR Am J Roentgenol. 1985;144(1):127-133.
16. Sheng R, Zajko AB, Campbell WL, Abu-Elmagd K. Biliary strictures in hepatic transplants: prevalence and types in patients with primary sclerosing cholangitis vs those with other liver diseases. AJR Am J Roentgenol. 1993;161(2):297-300.
17. Ward EM, Wiesner RH, Hughes RW, Krom RA. Persistent bile leak after liver transplantation: biloma drainage and endoscopic retrograde cholangiopancreatographic sphincterotomy. Radiology. 1991;179(3):719-720.
18. McDonald V, Matalon TA, Patel SK, et al. Biliary strictures in hepatic transplantation. J Vasc Interv Radiol. 1991;2(4):533-538.

19. Yeh BM, Coakley FV, Westphalen AC, et al. Predicting biliary complications in right lobe liver transplant recipients according to distance between donor's bile duct and corresponding hepatic artery. Radiology. 2007;242(1): 144-151.
20. Sheng R, Sammon JK, Zajko AB, Campbell WL. Bile leak after hepatic transplantation: cholangiographic features, prevalence, and clinical outcome. Radiology. 1994;192(2):413-416.
21. Gow PJ, Chapman RW. Liver transplantation for primary sclerosing cholangitis. Liver. 2000;20(2):97-103.
22. Chen LY, Goldberg HI. Sclerosing cholangitis: broad spectrum of radiographic features. Gastrointest Radiol. 1984;9(1):39-47.
23. Ciaccia D, Branch MS. Disorders of the biliary tree related to liver transplantation. In: DiMarino AJBS, editor. Gastrointestinal diseases: an endoscopic approach. Boston: Blackwell Scientific; 1997. p. 918-927.
24. Zajko AB, Campbell WL, Bron KM, et al. Diagnostic and interventional radiology in liver transplantation. Gastroenterol Clin North Am. 1988;17(1):105-143.
25. Starzl TE, Putnam CW, Hansbrough JF, et al. Biliary complications after liver transplantation: with special reference to the biliary cast syndrome and techniques of secondary duct repair. Surgery. 1977;81(2):212-221.
26. Ito K, Siegelman ES, Stolpen AH, Mitchell DG. MR imaging of complications after liver transplantation. AJR Am J Roentgenol. 2000;175(4):1145-1149.
27. Dodd GD 3rd, Memel DS, Zajko AB, et al. Hepatic artery stenosis and thrombosis in transplant recipients: Doppler diagnosis with resistive index and systolic acceleration time. Radiology. 1994;192(3):657-661.
28. Horrow MM, Blumenthal BM, Reich DJ, Manzarbeitia C. Sonographic diagnosis and outcome of hepatic artery thrombosis after orthotopic liver transplantation in adults. AJR Am J Roentgenol. 2007;189(2):346-351.
29. Gunsar F, Rolando N, Pastacaldi S, et al. Late hepatic artery thrombosis after orthotopic liver transplantation. Liver Transpl. 2003;9(6):605-611.
30. Wozney P, Zajko AB, Bron KM, et al. Vascular complications after liver transplantation: a 5-year experience. AJR Am J Roentgenol. 1986;147(4): 657-663.
31. De Gaetano AM, Cotroneo AR, Maresca G, et al. Color Doppler sonography in the diagnosis and monitoring of arterial complications after liver transplantation. J Clin Ultrasound. 2000;28(8):373-380.
32. Park YS, Kim KW, Lee SJ, et al. Hepatic arterial stenosis assessed with Doppler US after liver transplantation: frequent false-positive diagnoses with tardus parvus waveform and value of adding optimal peak systolic velocity cutoff. Radiology. 2011;260(3):884-891.
33. Garcia-Criado A, Gilabert R, Salmeron JM, et al. Significance of and contributing factors for a high resistive index on Doppler sonography of the hepatic artery immediately after surgery: prognostic implications for liver transplant recipients. AJR Am J Roentgenol. 2003;181(3): 831-838.
34. De Candia A, Como G, Tedeschi L, et al. Color Doppler sonography of hepatic artery reconstruction in liver transplantation. J Clin Ultrasound. 2002;30(1):12-17.
35. Dravid VS, Shapiro MJ, Needleman L, et al. Arterial abnormalities following orthotopic liver transplantation: arteriographic findings and correlation with Doppler sonographic findings. AJR Am J Roentgenol. 1994;163(3): 585-589.
36. Fukuzawa K, Schwartz ME, Katz E, et al. The arcuate ligament syndrome in liver transplantation. Transplantation. 1993;56(1):223-224.
37. Langnas AN, Marujo W, Stratta RJ, et al. Hepatic allograft rescue following arterial thrombosis. Role of urgent revascularization. Transplantation. 1991;51(1):86-90.
38. Raby N, Karani J, Thomas S, et al. Stenoses of vascular anastomoses after hepatic transplantation: treatment with balloon angioplasty. AJR Am J Roentgenol. 1991;157(1):167-171.
39. Chong WK, Beland JC, Weeks SM. Sonographic evaluation of venous obstruction in liver transplants. AJR Am J Roentgenol. 2007;188(6): W515-W521.
40. Pfammatter T, Williams DM, Lane KL, et al. Suprahepatic caval anastomotic stenosis complicating orthotopic liver transplantation: treatment with percutaneous transluminal angioplasty, Wallstent placement, or both. AJR Am J Roentgenol. 1997;168(2):477-480.
41. Kubo T, Shibata T, Itoh K, et al. Outcome of percutaneous transhepatic venoplasty for hepatic venous outflow obstruction after living donor liver transplantation. Radiology. 2006;239(1):285-290.
42. Ko EY, Kim TK, Kim PN, et al. Hepatic vein stenosis after living donor liver transplantation: evaluation with Doppler US. Radiology. 2003;229(3): 806-810.
43. Ferris JV, Baron RL, Marsh Jr JW, et al. Recurrent hepatocellular carcinoma after liver transplantation: spectrum of CT findings and recurrence patterns. Radiology. 1996;198(1):233-238.
44. Baxter GM. Ultrasound of renal transplantation. Clin Radiol. 2001; 56(10):802-818.
45. Brown ED, Chen MY, Wolfman NT, et al. Complications of renal transplantation: evaluation with US and radionuclide imaging. Radiographics. 2000;20(3):607-622.
46. Kobayashi K, Censullo ML, Rossman LL, et al. Interventional radiologic management of renal transplant dysfunction: indications, limitations, and technical considerations. Radiographics. 2007;27:1109-1130.
47. Memel DS, Dodd GD 3rd, Shah AN, et al. Imaging of en bloc renal transplants: normal and abnormal postoperative findings. AJR Am J Roentgenol. 1993;160(1):75-81.
48. O'Neill WC, Baumgarten DA. Ultrasonography in renal transplantation. Am J Kidney Dis. 2002;39(4):663-678.
49. Lachance SL, Adamson D, Barry JM. Ultrasonically determined kidney transplant hypertrophy. J Urol. 1988;139(3):497-498.
50. Babcock DS, Slovis TL, Han BK, et al. Renal transplants in children: long-term follow-up using sonography. Radiology. 1985;156(1):165-167.
51. Absy M, Metreweli C, Matthews C, Al Khader A. Changes in transplanted kidney volume measured by ultrasound. Br J Radiol. 1987;60(714): 525-529.
52. American College of Radiology (ACR), Society for Pediatric Radiology (SPR), Society of Radiologists in Ultrasound (SRU), American Institute of Ultrasound in Medicine (AIUM). AIUM practice guideline for the performance of an ultrasound examination of solid-organ transplants. J Ultrasound Med. 2014;33(7):1309-1320.
53. Tublin ME, Bude RO, Platt JF. Review. The resistive index in renal Doppler sonography: where do we stand? AJR Am J Roentgenol. 2003;180(4): 885-892.
54. Weber TM, Lockhart ME. Renal transplant complications. Abdom Imaging. 2013;38(5):1144-1154.
55. Rigg KM. Renal transplantation: current status, complications and prevention. J Antimicrob Chemother. 1995;36(Suppl. B):51-57.
56. Pirsch JD, Ploeg RJ, Gange S, et al. Determinants of graft survival after renal transplantation. Transplantation. 1996;61(11):1581-1586.
57. Akbar SA, Jafri SZ, Amendola MA, et al. Complications of renal transplantation. Radiographics. 2005;25(5):1335-1356.
58. Dodd GD 3rd, Tublin ME, Shah A, Zajko AB. Imaging of vascular complications associated with renal transplants. AJR Am J Roentgenol. 1991;157(3): 449-459.
59. Jordan ML, Cook GT, Cardella CJ. Ten years of experience with vascular complications in renal transplantation. J Urol. 1982;128(4):689-692.
60. Hanto DW, Simmons RL. Renal transplantation: clinical considerations. Radiol Clin North Am. 1987;25(2):239-248.
61. Baxter GM, Ireland H, Moss JG, et al. Colour Doppler ultrasound in renal transplant artery stenosis: which Doppler index? Clin Radiol. 1995;50(9): 618-622.
62. de Morais RH, Muglia VF, Mamere AE, et al. Duplex Doppler sonography of transplant renal artery stenosis. J Clin Ultrasound. 2003;31(3): 135-141.
63. Tublin ME, Dodd GD 3rd. Sonography of renal transplantation. Radiol Clin North Am. 1995;33(3):447-459.
64. Penny MJ, Nankivell BJ, Disney AP, et al. Renal graft thrombosis. A survey of 134 consecutive cases. Transplantation. 1994;58(5):565-569.
65. Baxter GM, Morley P, Dall B. Acute renal vein thrombosis in renal allografts: new Doppler ultrasonic findings. Clin Radiol. 1991;43(2): 125-127.
66. Reuther G, Wanjura D, Bauer H. Acute renal vein thrombosis in renal allografts: detection with duplex Doppler US. Radiology. 1989;170(2): 557-558.

67. Lockhart ME, Wells CG, Morgan DE, et al. Reversed diastolic flow in the renal transplant: perioperative implications versus transplants older than 1 month. AJR Am J Roentgenol. 2008;190(3):650-655.
68. Pozniak MA, Dodd GD 3rd, Kelcz F. Ultrasonographic evaluation of renal transplantation. Radiol Clin North Am. 1992;30(5):1053-1066.
69. Middleton WD, Kellman GM, Melson GL, Madrazo BL. Postbiopsy renal transplant arteriovenous fistulas: color Doppler US characteristics. Radiology. 1989;171(1):253-257.
70. Huang MW, Muradali D, Thurston WA, et al. Uterine arteriovenous malformations: gray-scale and Doppler US features with MR imaging correlation. Radiology. 1998;206(1):115-123.
71. Rahmouni A, Bargoin R, Herment A, et al. Color Doppler twinkling artifact in hyperechoic regions. Radiology. 1996;199(1):269-271.
72. Letourneau JG, Day DL, Ascher NL, Castaneda-Zuniga WR. Imaging of renal transplants. AJR Am J Roentgenol. 1988;150(4):833-838.
73. Silver TM, Campbell D, Wicks JD, et al. Peritransplant fluid collections. Ultrasound evaluation and clinical significance. Radiology. 1981;138(1): 145-151.
74. Data from the Organ Procurement and Transplantation Network and the U.S. Scientific Registry of Transplant Recipients. In United Network for Organ Sharing and Scientific Registry Data, 2008. Available from: https://optn.transplant.hrsa.gov/data/view-data-reports/national-data/#.
75. White SA, Shaw JA, Sutherland DE. Pancreas transplantation. Lancet. 2009;373(9677):1808-1817.
76. Hariharan S, Pirsch JD, Lu CY, et al. Pancreas after kidney transplantation. J Am Soc Nephrol. 2002;13(4):1109-1118.
77. Pozniak MA, Propeck PA, Kelcz F, Sollinger H. Imaging of pancreas transplants. Radiol Clin North Am. 1995;33(3):581-594.
78. Freund MC, Steurer W, Gassner EM, et al. Spectrum of imaging findings after pancreas transplantation with enteric exocrine drainage: Part 1, post-transplantation anatomy. AJR Am J Roentgenol. 2004;182(4):911-917.
79. Kersting S, Ludwig S, Ehehalt F, et al. Contrast-enhanced ultrasonography in pancreas transplantation. Transplantation. 2013;95(1):209-214.
80. Krebs TL, Daly B, Wong JJ, et al. Vascular complications of pancreatic transplantation: MR evaluation. Radiology. 1995;196(3):793-798.
81. Foshager MC, Hedlund LJ, Troppmann C, et al. Venous thrombosis of pancreatic transplants: diagnosis by duplex sonography. AJR Am J Roentgenol. 1997;169(5):1269-1273.
82. Vandermeer FQ, Manning MA, Frazier AA, Wong-You-Cheong JJ. Imaging of whole-organ pancreas transplants. Radiographics. 2012;32(2): 411-435.
83. Stockland AH, Willingham DL, Paz-Fumagalli R, et al. Pancreas transplant venous thrombosis: role of endovascular interventions for graft salvage. Cardiovasc Intervent Radiol. 2009;32(2):279-283.
84. Barth MM, Khwaja K, Faintuch S, Rabkin D. Transarterial and transvenous embolotherapy of arteriovenous fistulas in the transplanted pancreas. J Vasc Interv Radiol. 2008;19(8):1231-1235.
85. Hagspiel KD, Nandalur K, Burkholder B, et al. Contrast-enhanced MR angiography after pancreas transplantation: normal appearance and vascular complications. AJR Am J Roentgenol. 2005;184(2):465-473.
86. Drachenberg CB, Papadimitriou JC. Spectrum of histopathological changes in pancreas allograft biopsies and relationship to graft loss. Transplant Proc. 2007;39(7):2326-2328.
87. Patel B, Markivee CR, Mahanta B, et al. Pancreatic transplantation: scintigraphy, US, and CT. Radiology. 1988;167(3):685-687.
88. Yuh WT, Wiese JA, Abu-Yousef MM, et al. Pancreatic transplant imaging. Radiology. 1988;167(3):679-683.
89. Wong JJ, Krebs TL, Klassen DK, et al. Sonographic evaluation of acute pancreatic transplant rejection: morphology—Doppler analysis versus guided percutaneous biopsy. AJR Am J Roentgenol. 1996;166(4):803-807.
90. Aideyan OA, Foshager MC, Benedetti E, et al. Correlation of the arterial resistive index in pancreas transplants of patients with transplant rejection. AJR Am J Roentgenol. 1997;168(6):1445-1447.
91. Heyneman LE, Keogan MT, Tuttle-Newhall JE, et al. Pancreatic transplantation using portal venous and enteric drainage: the postoperative appearance of a new surgical procedure. J Comput Assist Tomogr. 1999;23:283-290.
92. Patel BK, Garvin PJ, Aridge DL, et al. Fluid collections developing after pancreatic transplantation: radiologic evaluation and intervention. Radiology. 1991;181(1):215-220.
93. Howard RJ, Patton PR, Reed AI, et al. The changing causes of graft loss and death after kidney transplantation. Transplantation. 2002;73(12): 1923-1928.
94. Briggs JD. Causes of death after renal transplantation. Nephrol Dial Transplant. 2001;16(8):1545-1549.
95. Apel H, Walschburger-Zorn K, Haberle L, et al. De novo malignancies in renal transplant recipients: experience at a single center with 1882 transplant patients over 39 yr. Clin Transplant. 2013;27(1):E30-E36.
96. Penn I. Post-transplant malignancy: the role of immunosuppression. Drug Saf. 2000;23(2):101-113.
97. Parker A, Bowles K, Bradley JA, et al. Diagnosis of post-transplant lymphoproliferative disorder in solid organ transplant recipients—BCSH and BTS guidelines. Br J Haematol. 2010;149(5):675-692.
98. Haque T, Crawford DH. Role of donor versus recipient type Epstein-Barr virus in post-transplant lymphoproliferative disorders. Springer Semin Immunopathol. 1998;20(3-4):375-387.
99. Babcock GJ, Decker LL, Freeman RB, Thorley-Lawson DA. Epstein-Barr virus–infected resting memory B cells, not proliferating lymphoblasts, accumulate in the peripheral blood of immunosuppressed patients. J Exp Med. 1999;190(4):567-576.
100. Opelz G, Daniel V, Naujokat C, et al. Effect of cytomegalovirus prophylaxis with immunoglobulin or with antiviral drugs on post-transplant non-Hodgkin lymphoma: a multicentre retrospective analysis. Lancet Oncol. 2007;8(3): 212-218.
101. Nalesnik MA, Makowka L, Starzl TE. The diagnosis and treatment of posttransplant lymphoproliferative disorders. Curr Probl Surg. 1988;25(6): 367-472.
102. Vrachliotis TG, Vaswani KK, Davies EA, et al. CT findings in posttransplantation lymphoproliferative disorder of renal transplants. AJR Am J Roentgenol. 2000;175(1):183-188.
103. Tsao L, Hsi ED. The clinicopathologic spectrum of posttransplantation lymphoproliferative disorders. Arch Pathol Lab Med. 2007;131(8): 1209-1218.
104. Opelz G, Dohler B. Lymphomas after solid organ transplantation: a collaborative transplant study report. Am J Transplant. 2004;4(2):222-230.
105. Vegso G, Hajdu M, Sebestyen A. Lymphoproliferative disorders after solid organ transplantation—classification, incidence, risk factors, early detection and treatment options. Pathol Oncol Res. 2011;17(3):443-454.
106. Dotti G, Fiocchi R, Motta T, et al. Epstein-Barr virus–negative lymphoproliferate disorders in long-term survivors after heart, kidney, and liver transplant. Transplantation. 2000;69(5):827-833.
107. Donnelly LF, Frush DP, Marshall KW, White KS. Lymphoproliferative disorders: CT findings in immunocompromised children. AJR Am J Roentgenol. 1998;171(3):725-731.
108. Penn I. Cancers complicating organ transplantation. N Engl J Med. 1990;323(25):1767-1769.
109. Pickhardt PJ, Siegel MJ. Abdominal manifestations of posttransplantation lymphoproliferative disorder. AJR Am J Roentgenol. 1998;171(4): 1007-1013.
110. Kaushik S, Fulcher AS, Frable WJ, May DA. Posttransplantation lymphoproliferative disorder: osseous and hepatic involvement. AJR Am J Roentgenol. 2001;177(5):1057-1059.
111. Meador TL, Krebs TL, Cheong JJ, et al. Imaging features of posttransplantation lymphoproliferative disorder in pancreas transplant recipients. AJR Am J Roentgenol. 2000;174(1):121-124.
112. Pickhardt PJ, Siegel MJ. Posttransplantation lymphoproliferative disorder of the abdomen: CT evaluation in 51 patients. Radiology. 1999;213(1): 73-78.
113. Allen U, Hebert D, Moore D, et al. Epstein-Barr virus–related post-transplant lymphoproliferative disease in solid organ transplant recipients, 1988-97: a Canadian multi-centre experience. Pediatr Transplant. 2001;5(3): 198-203.
114. Swinnen LJ. Diagnosis and treatment of transplant-related lymphoma. Ann Oncol. 2000;11(Suppl. 1):45-48.

CHAPTER 19

The Thyroid Gland

Luigi Solbiati, J. William Charboneau, Vito Cantisani, Carl Reading, and Giovanni Mauri

SUMMARY OF KEY POINTS

- Ultrasound is the best imaging modality to study the thyroid gland for both diffuse and nodular disease.
- The overwhelming majority of thyroid nodules are benign. Thyroid cancer is rare and accounts for less than 1% of all malignant neoplasms.
- Approximately 80% of nodular thyroid disease is caused by hyperplasia. When hyperplasia leads to an overall increase in size or volume of the gland, the term "goiter" is used.
- Most hyperplastic or adenomatous nodules are isoechoic compared with normal thyroid tissue, but may become hyperechoic because of the numerous interfaces between cells and colloid substance.
- Hyperfunctioning (autonomous) nodules often exhibit an abundant perinodular and intranodular vascularity.
- Purely anechoic areas are caused by serous or colloid fluid.
- Adenomas represent only 5% to 10% of all nodular disease of the thyroid and are seven times more common in women than men. In general, the cytologic features of follicular adenomas are indistinguishable from those of follicular carcinoma.
- Solid consistency, hypoechogenicity, microcalcifications, taller-than-wide appearance, hypervascularity, irregular margins, invasion of adjacent structures, and presence of cervical lymph node metastases are suspicious signs of thyroid malignancy.
- Ultrasound-guided fine-needle aspiration is the most effective method for diagnosing malignancy in a thyroid nodule.
- After partial or near-total thyroidectomy for carcinoma, sonography is the preferred method for follow-up, by detecting residual, recurrent, or metastatic disease in the neck.
- The Thyroid Imaging Reporting and Data System (TIRADS) can be used to stratify the risk of malignancy of a thyroid nodule according to its ultrasonographic characteristics.
- Ultrasound-guided ablation with chemical agents (ethanol) or thermal energy (radiofrequency and laser ablation) can be used to treat thyroid adenoma, benign cold nodules, and even nodal metastases of thyroid cancers.

CHAPTER OUTLINE

INSTRUMENTATION AND TECHNIQUE
ANATOMY
CONGENITAL THYROID ABNORMALITIES
NODULAR THYROID DISEASE
Pathologic Features and Sonographic Correlates
Hyperplasia and Goiter
Adenoma
Carcinoma
Lymphoma
Thyroid Metastases
Fine-Needle Aspiration Biopsy
Sonographic Applications
Detection of Thyroid Masses
Differentiation of Benign and Malignant Nodules
Thyroid Imaging Reporting and Data System
Contrast-Enhanced Ultrasound and Elastography
Guidance for Needle Biopsy
Guidance for Percutaneous Treatment
The Incidentally Detected Nodule
DIFFUSE THYROID DISEASE
Acknowledgment

Because of the superficial location of the thyroid gland, high-resolution real-time gray-scale and color Doppler sonography can demonstrate normal thyroid anatomy and pathologic conditions with remarkable clarity. As a result, ultrasound plays an increasingly important role in the diagnostic evaluation of thyroid disease, although it is only one of several diagnostic methods currently available. To use ultrasound effectively and economically, it is important to understand its current capabilities and limitations.

INSTRUMENTATION AND TECHNIQUE

High-frequency transducers (7.5-15.0 MHz) currently provide both deep ultrasound penetration—up to 5 cm—and high-definition images, with a resolution of 0.5 to 1.0 mm. No other clinically used imaging method can achieve this degree of spatial resolution. Linear array transducers with either rectangular or trapezoidal scan format are preferred to sector transducers because of the wider near field of view and the capability to combine

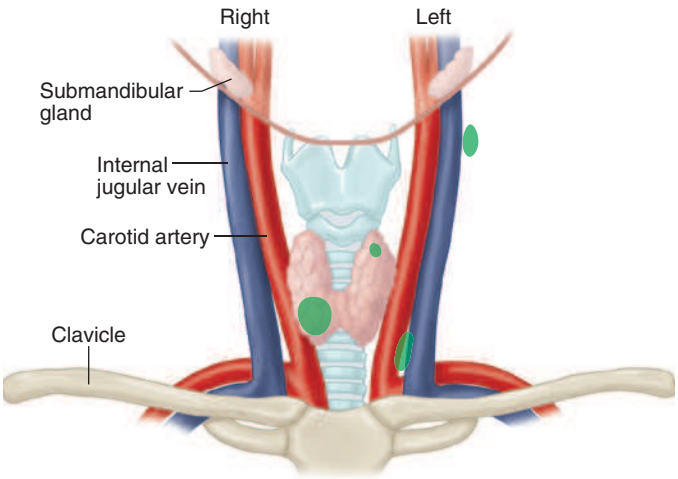

FIG. 19.1 Cervical "Map." Such diagrams help communicate relationships of pathology to clinicians and serve as a reference for follow-up examinations.

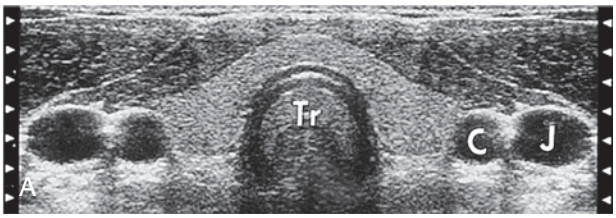

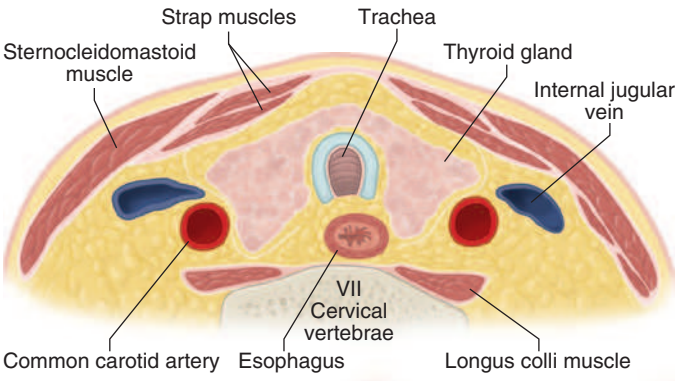

FIG. 19.2 Normal Thyroid Gland. (A) Transverse sonogram made with 7.5-MHz linear array transducer. **(B)** Corresponding anatomic drawing. *C,* Common carotid artery; *J,* jugular vein; *Tr,* tracheal air shadow.

high-frequency gray-scale and color Doppler images. The thyroid gland is one of the most vascular organs of the body. As a result, Doppler examination may provide useful diagnostic information in some thyroid diseases.

Two newer techniques used for the sonographic study of the thyroid gland are contrast-enhanced sonography and elastography. **Contrast-enhanced sonography** using second-generation contrast agents and very low mechanical index can provide useful information for the diagnosis of select cases of nodular disease and for ultrasound-guided therapeutic procedures. **Elastography** is based on the principle that when body tissues are compressed, the softer parts deform more easily than the harder parts. The amount of displacement at various depths is determined by the ultrasound signals reflected by tissues before and after they are compressed, and the corresponding strains are calculated from these displacements and displayed visually.

The patient is typically examined in the supine position, with the neck extended. A small pad may be placed under the shoulders to provide better exposure of the neck, particularly in patients with a short, stocky habitus. The thyroid gland must be examined thoroughly in both transverse and longitudinal planes. Imaging of the lower poles can be enhanced by asking the patient to swallow, which momentarily raises the thyroid gland in the neck. The entire gland, including the isthmus, must be examined. The examination must also be extended laterally to include the region of the carotid artery and jugular vein to identify enlarged jugular chain lymph nodes, superiorly to visualize submandibular adenopathy, and inferiorly to define any pathologic supraclavicular lymph nodes.

In addition to the images recorded during the examination, some operators include in the permanent record a diagrammatic representation of the neck showing the location(s) of any abnormal findings (Fig. 19.1). This cervical "map" helps to communicate the anatomic relationships of the pathology more clearly to the referring clinician and the patient. It also serves as a useful reference for the radiologist and sonographer for follow-up examinations.

ANATOMY

The thyroid gland is located in the anteroinferior part of the neck (infrahyoid compartment) in a space outlined by muscle, trachea, esophagus, carotid arteries, and jugular veins (Fig. 19.2). The thyroid gland is made up of **two lobes** located along either side of the trachea and connected across the midline by the **isthmus,** a thin structure draping over the anterior tracheal wall at the level of the junction of the middle and lower thirds of the thyroid gland. From 10% to 40% of normal patients have a small thyroid **(pyramidal)** lobe arising superiorly from the isthmus and lying in front of the thyroid cartilage.[1] It can be regularly visualized in younger patients, but it undergoes progressive atrophy in adulthood and becomes invisible. The size and shape of the thyroid lobes vary widely in normal patients. In tall individuals the lateral lobes have a longitudinally elongated shape on the sagittal scans, whereas in shorter individuals the gland is more oval. In the newborn the thyroid gland is 18 to 20 mm long, with an anteroposterior (AP) diameter of 8 to 9 mm. By 1 year of age, the mean length is 25 mm and AP diameter is 12 to 15 mm.[2] In adults the mean length is approximately 40 to 60 mm, with mean AP diameter of 13 to 18 mm. The mean thickness of the isthmus is 4 to 6 mm.[3]

Sonography is an accurate method for calculating **thyroid volume.** In about one-third of cases, the sonographic measurement of volume differs from the estimated physical size on examination.[4] Thyroid volume measurements may be useful for goiter size determination to assess the need for surgery, permit calculation of the dose of iodine-131 (^{131}I) needed for treating thyrotoxicosis, and evaluate response to suppression treatments.[5] Thyroid volume can be calculated with linear parameters or more precisely with mathematical formulas. Among the linear

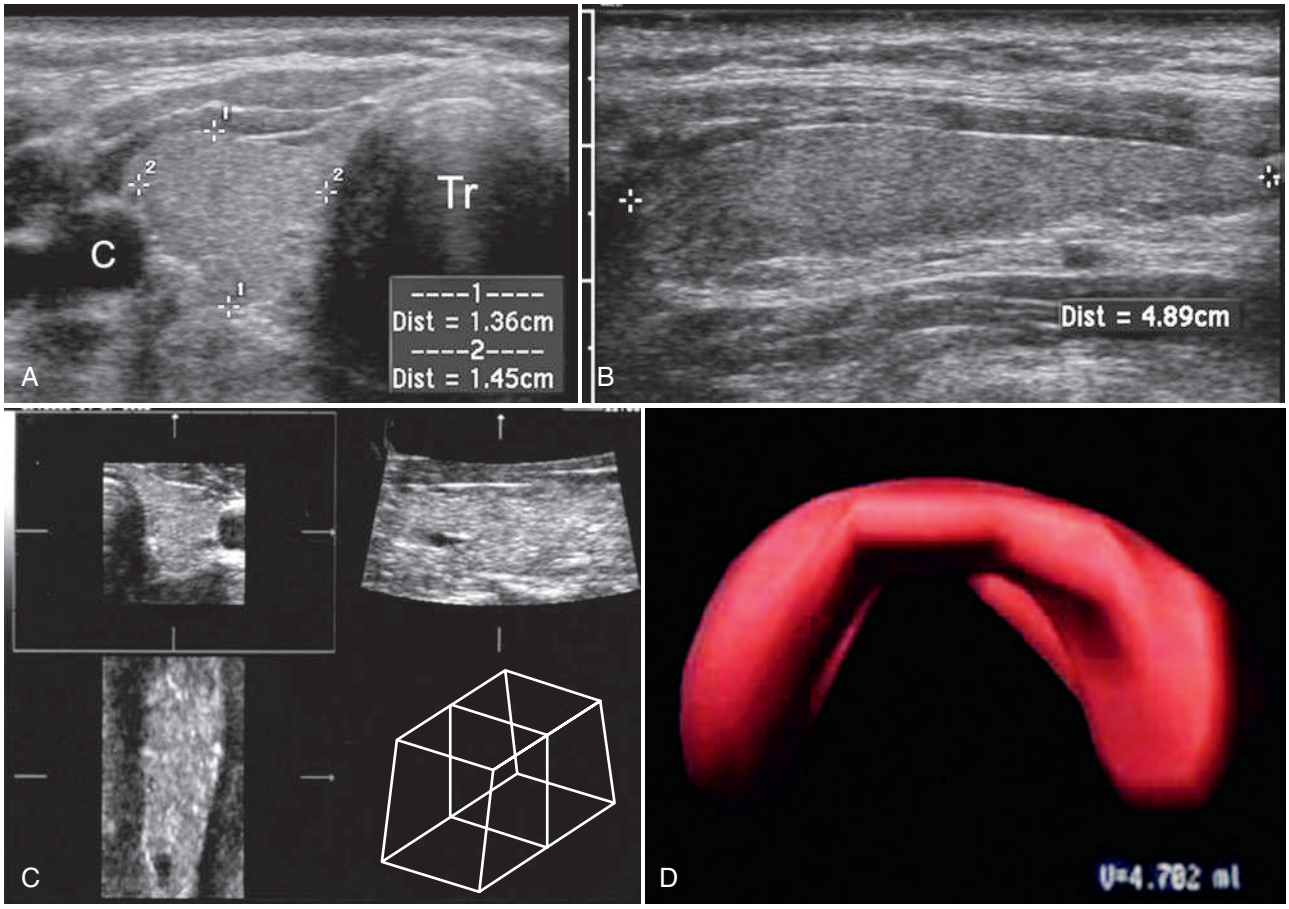

FIG. 19.3 Volume Measurement of Thyroid Gland. (A) Transverse and **(B)** longitudinal images show calipers at the boundaries of thyroid gland. *C,* Carotid artery; *Tr,* trachea air shadow. The calculated thyroid volume is based on the ellipsoid formula with a correction factor (length × width × thickness × 0.52 for each lobe). In this case, the volume is 10 mL (or grams), which is within normal limits for this female patient. **(C)** Images from real-time three-dimensional study of normal thyroid lobe, visualized simultaneously in axial *(top left),* longitudinal *(top right),* and coronal *(bottom left)* planes. **(D)** Volumetric reconstruction of gland.

parameters, the AP diameter is the most precise because it is relatively independent of possible dimensional asymmetry between the two lobes. When the AP diameter is more than 2 cm, the thyroid gland may be considered "enlarged."

The most common mathematical method to calculate thyroid volume is based on the ellipsoid formula with a correction factor (length × width × thickness × 0.529 for each lobe)[6] (Fig. 19.3A-B). With use of this method, the mean estimated error is approximately 15%. The most precise mathematical method is the integration of the cross-sectional areas of the thyroid gland, achieved through evenly spaced sonographic scans.[7] With this method the mean estimated error is 5% to 10%.[8] Modern three-dimensional (3-D) ultrasound technology allows one to simultaneously obtain the three orthogonal planes of thyroid lobes and then to calculate the volume either automatically or manually[9] (Fig. 19.3C-D).

In neonates, thyroid volume ranges from 0.40 to 1.40 mL, increasing by 1.0 to 1.3 mL for each 10 kg of body weight, up to a normal volume in adults of 10 to 11 ± 3 mL.[7] In general, thyroid volume is larger in patients living in regions with iodine deficiency and in patients who have acute hepatitis or chronic renal failure. Volume is smaller in patients who have chronic hepatitis or have been treated with thyroxine or radioactive iodine.[5,7]

Normal thyroid parenchyma has a homogeneous, medium- to high-level echogenicity that makes detection of focal cystic or hypoechoic thyroid lesions relatively easy in most cases. The thin, hyperechoic line around the thyroid lobes is the **capsule,** which is often identifiable on ultrasound. It may become calcified in patients who have uremia or disorders of calcium metabolism. With currently available high-sensitivity Doppler instruments, the rich vascularity of the gland can be seen homogeneously distributed throughout the entire parenchyma (Fig. 19.4). The **superior thyroid artery and vein** are found at the upper pole of each lobe. The **inferior thyroid vein** is found at the lower pole (Fig. 19.5), and the **inferior thyroid artery** is located posterior to the lower third of each lobe. The mean diameter of the arteries is 1 to 2 mm; the lower veins can be up to 8 mm in diameter. Normally, peak systolic velocities reach 20 to 40 cm/sec in the major thyroid arteries and 15 to 30 cm/sec in intraparenchymal arteries. These are the highest velocities found in blood vessels supplying superficial organs.

The **sternohyoid** and **omohyoid muscles** (strap muscles) are seen as thin, hypoechoic bands anterior to the thyroid gland (see Fig. 19.2). The **sternocleidomastoid muscle** is seen as a larger oval band that lies lateral to the thyroid gland. An important anatomic landmark is the **longus colli muscle,** located posterior to each thyroid lobe, in close contact with the prevertebral space.

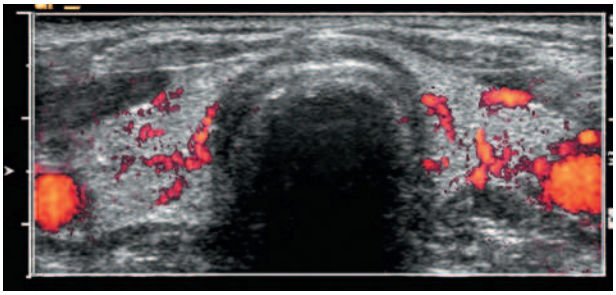

FIG. 19.4 Normal Thyroid Vascularity on Power Doppler Ultrasound.

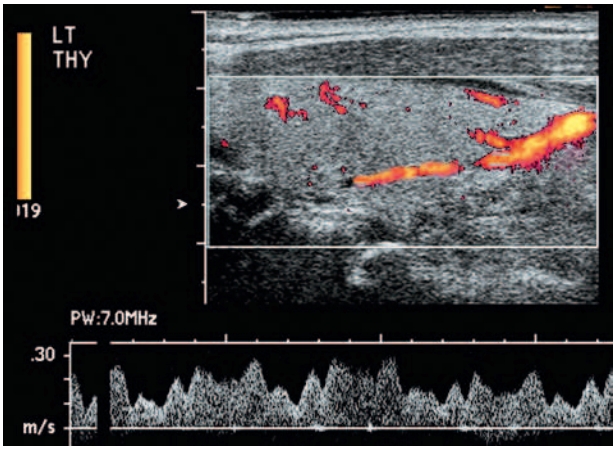

FIG. 19.5 Normal Inferior Thyroid Vein. Longitudinal power Doppler image shows a large inferior thyroid vein with associated normal venous spectral waveform.

The **recurrent laryngeal nerve** and the inferior thyroid artery pass in the angle among the trachea, esophagus, and thyroid lobe. On longitudinal scans, the recurrent laryngeal nerve and inferior thyroid artery may be seen between the thyroid lobe and esophagus on the left and between the thyroid lobe and longus colli muscle on the right. The **esophagus,** primarily a midline structure, may be found laterally and is usually on the left side. It is clearly identified by the target appearance of bowel in the transverse plane and by its peristaltic movements when the patient swallows.

CONGENITAL THYROID ABNORMALITIES

Congenital conditions of the thyroid gland include **aplasia** of one lobe or the whole gland, varying degrees of **hypoplasia,** and **ectopia** (Fig. 19.6). Sonography can be used to help establish the diagnosis of hypoplasia by demonstrating a diminutive gland. High-frequency ultrasound can also be used in the study of **congenital hypothyroidism** (CH), a relatively common disorder occurring in about 1 in 3000 to 4000 live births. Determining the cause of CH (dysgenesis, dyshormonogenesis, or pituitary or hypothalamic hypothyroidism) is clinically important because prognosis and therapy differ. Early initiation of therapy can prevent mental retardation and delayed bone development.[10,11]

Measurement of thyroid lobes can be used to differentiate aplasia (absent gland) from **goitrous hypothyroidism** (gland enlargement). Radionuclide scans are more often used to detect **ectopic thyroid tissue** (e.g., in a lingual or suprahyoid position).

NODULAR THYROID DISEASE

Many thyroid diseases can manifest clinically with one or more thyroid nodules. Such nodules represent common and controversial clinical problems. Epidemiologic studies estimate that

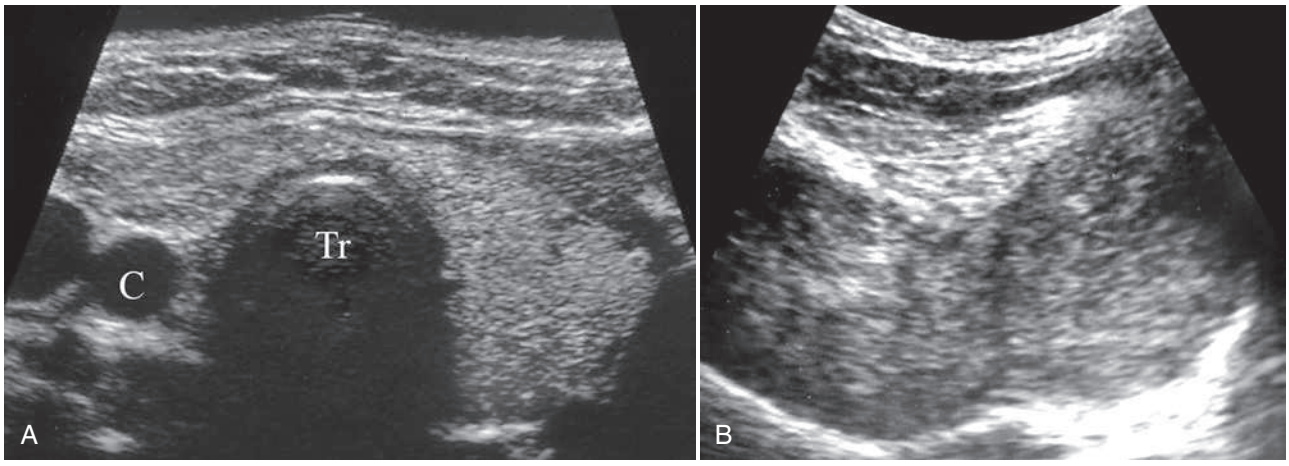

FIG. 19.6 Congenital Thyroid Abnormalities. (A) Hypoplasia of right thyroid lobe. *C,* Carotid artery; *Tr,* tracheal air shadow. **(B) Ectopic (sublingual)** thyroid gland. Transverse ultrasound image inferior to the base of the tongue shows a U-shaped parenchymal structure.

4% to 7% of adults in the United States have palpable thyroid nodules, with women affected more frequently than men.[12,13] Exposure to ionizing radiation increases the incidence of benign and malignant nodules, with 20% to 30% of a radiation-exposed population having palpable thyroid disease.[14,15]

Although nodular thyroid disease is relatively common, **thyroid cancer** is rare and accounts for less than 1% of all malignant neoplasms.[16] The overwhelming majority of thyroid nodules are benign. The clinical challenge is to distinguish the few clinically significant malignant nodules from the many benign nodules and thus identify patients who need surgical excision. This task is complicated because nodular disease of the thyroid gland often is clinically occult (<10-15 mm), although it can be readily detected by high-resolution sonography. The important question of how to manage these small nodules discovered incidentally by sonography is addressed later in this chapter.

Nodular Thyroid Disease: Sonographic Evaluation

- Determine location of palpable neck mass (e.g., thyroid or extrathyroid)
- Characterize benign versus malignant nodule features
- Detect occult nodule in patient with history of head and neck irradiation or multiple endocrine neoplasia (MEN) type II syndrome
- Determine extent of known thyroid malignancy
- Detect residual, recurrent, or metastatic carcinoma
- Guide fine-needle aspiration of thyroid nodule or cervical lymph nodes
- Guide percutaneous-thermal ablation of thyroid nodules, parathyroids, or lymph nodes

Pathologic Features and Sonographic Correlates

Hyperplasia and Goiter

Approximately 80% of nodular thyroid disease is caused by **hyperplasia** of the gland and occurs in up to 5% of any population.[17] Its etiology includes **iodine deficiency** (endemic), **disorders of hormonogenesis** (hereditary familial forms), and **poor utilization of iodine** as a result of medication. When hyperplasia leads to an overall increase in size or volume of the gland, the term **goiter** is used. The peak age of patients with goiter is 35 to 50 years, and women are affected three times more often than men.

Histologically, the initial stage is cellular hyperplasia of the thyroid acini, followed by micronodule and macronodule formation, often indistinguishable from normal thyroid parenchyma, even at histology. Hyperplastic nodules often undergo liquefactive degeneration with the accumulation of blood, serous fluid, and colloid substance (Fig. 19.7, Video 19.1). Pathologically, they are often referred to as **hyperplastic, adenomatous,** or **colloid** nodules. Many (if not all) cystic thyroid lesions are hyperplastic nodules that have undergone extensive liquefactive degeneration. Pathologically, true epithelial-lined cysts of the thyroid gland are rare. In the course of this cystic degenerative process,

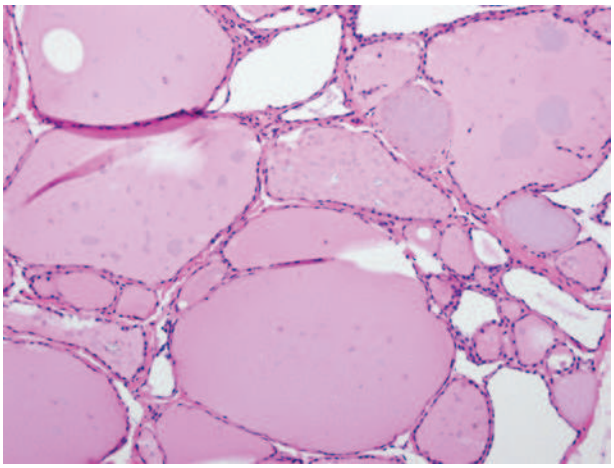

FIG. 19.7 Histology of Hyperplastic (Adenomatous) Change of Thyroid Gland. Histologic specimen shows many large dilated follicles that are filled with colloid material.

calcification, which is often coarse and perinodular, may occur.[3,5] Hyperplastic nodule function may have decreased, may have remained normal, or may have increased (toxic nodules).

Sonographically, most hyperplastic or adenomatous nodules are **isoechoic** compared with normal thyroid tissue (Fig. 19.8A) but may become **hyperechoic** because of the numerous interfaces between cells and colloid substance[5,18] (Fig. 19.8B-C). Less frequently, a hypoechoic spongelike or **honeycomb** pattern is seen (Fig. 19.9, Video 19.2). When the nodule is isoechoic or hyperechoic, a thin peripheral **hypoechoic halo** is typically seen, most likely caused by perinodular blood vessels and mild edema or compression of the adjacent normal parenchyma. Perinodular blood vessels are typically detected with color Doppler sonography; with current high-sensitivity Doppler technology, intranodular vascularity can also be seen.[5,19,20] **Hyperfunctioning** (autonomous) nodules often exhibit an abundant perinodular and intranodular vascularity; however, because of the hypervascular pattern shown in most solid thyroid nodules on high-sensitivity Doppler systems, this feature does not allow detection of hyperfunctioning nodules within multinodular goiters with sonography.[19,20]

The degenerative changes of goitrous nodules correspond to their sonographic appearances (Fig. 19.10). Purely anechoic areas are caused by **serous or colloid fluid.** Echogenic fluid or moving fluid-fluid levels correspond to **hemorrhage.**[21] Bright echogenic foci with **comet-tail artifacts** are likely caused by **microcrystals** or aggregates of colloid substance, which may also move slowly, like snowflakes, within the fluid collection.[22] **Thin, intracystic septations** probably correspond to attenuated strands of thyroid tissue and appear completely avascular on color Doppler ultrasound. These degenerative processes may also lead to the formation of calcifications, which may be either **thin, peripheral shells** ("eggshell") or **coarse, highly reflective foci** with associated acoustic shadows, scattered throughout the gland[8] (Fig. 19.11).

Intracystic solid projections, or papillae, usually containing color Doppler signals, may appear similar to the rare cystic papillary thyroid carcinoma (PTC).[20,21] In some cases, sonography and color Doppler imaging cannot differentiate the septations

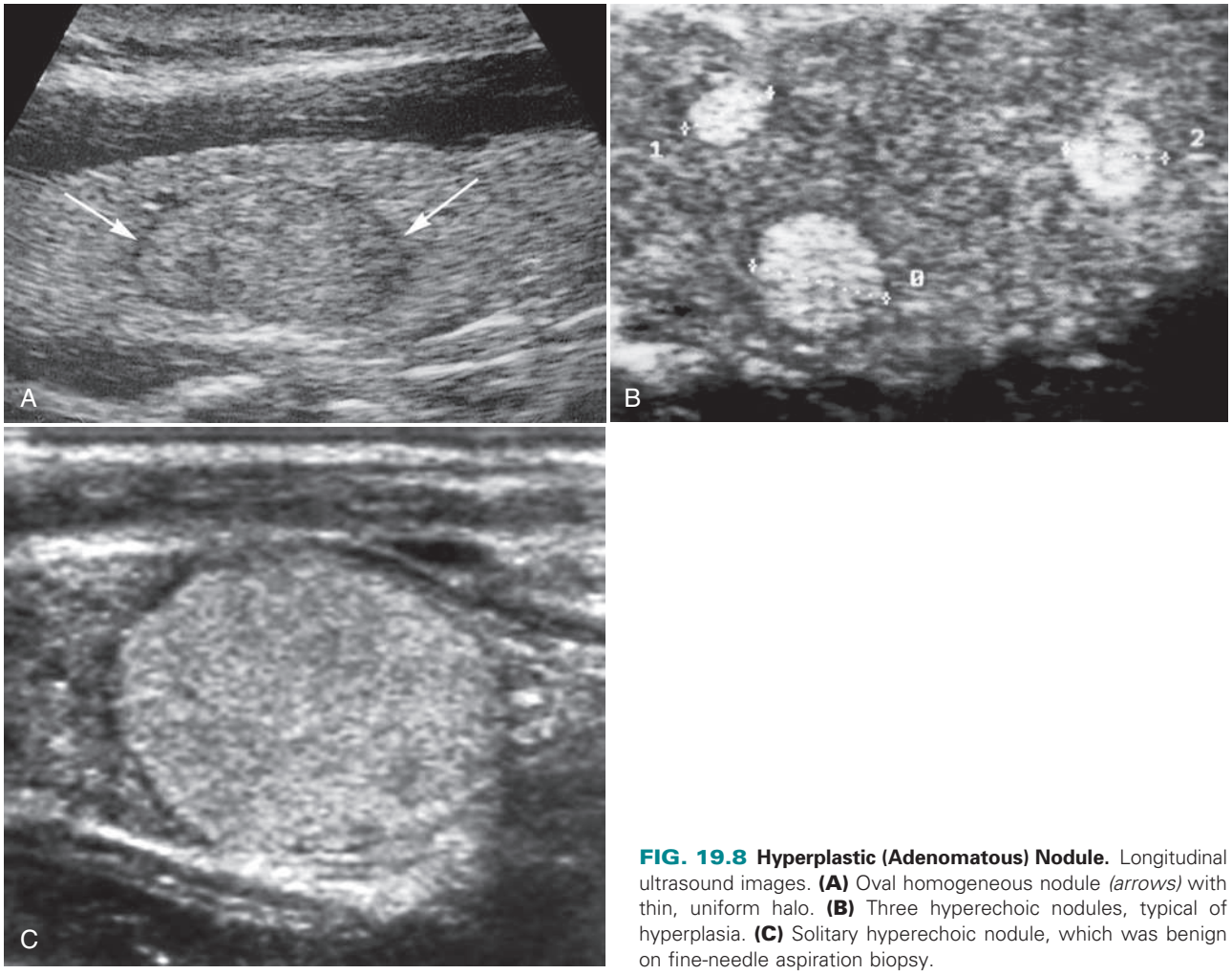

FIG. 19.8 Hyperplastic (Adenomatous) Nodule. Longitudinal ultrasound images. **(A)** Oval homogeneous nodule *(arrows)* with thin, uniform halo. **(B)** Three hyperechoic nodules, typical of hyperplasia. **(C)** Solitary hyperechoic nodule, which was benign on fine-needle aspiration biopsy.

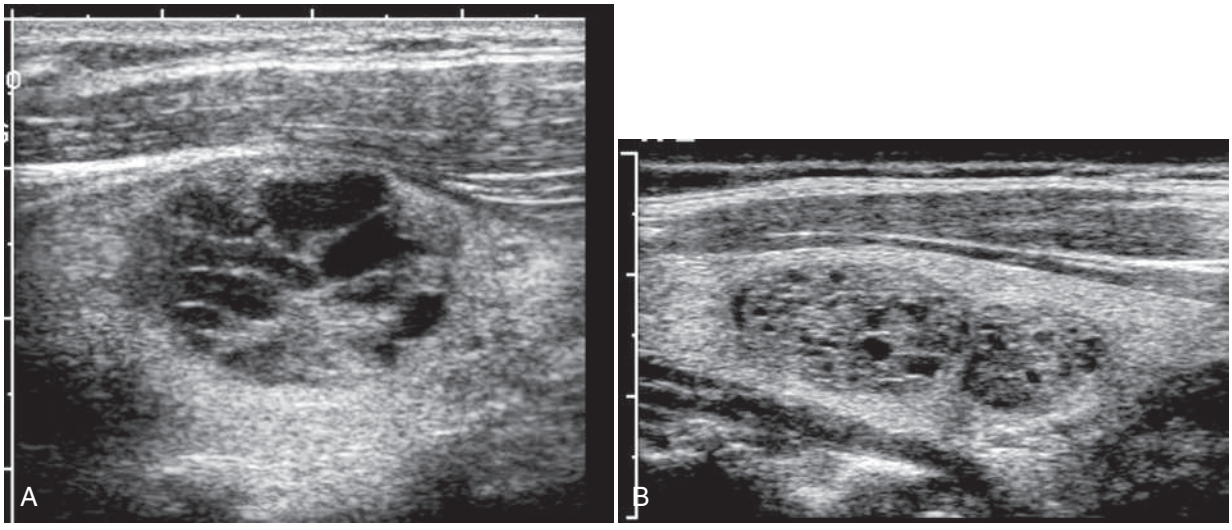

FIG. 19.9 Benign Nodule Feature. Longitudinal images. Extensive honeycomb-like or cystic changes, with nodules showing **(A)** larger cystic spaces and **(B)** smaller cystic spaces. These features indicate a very high probability of a benign process.

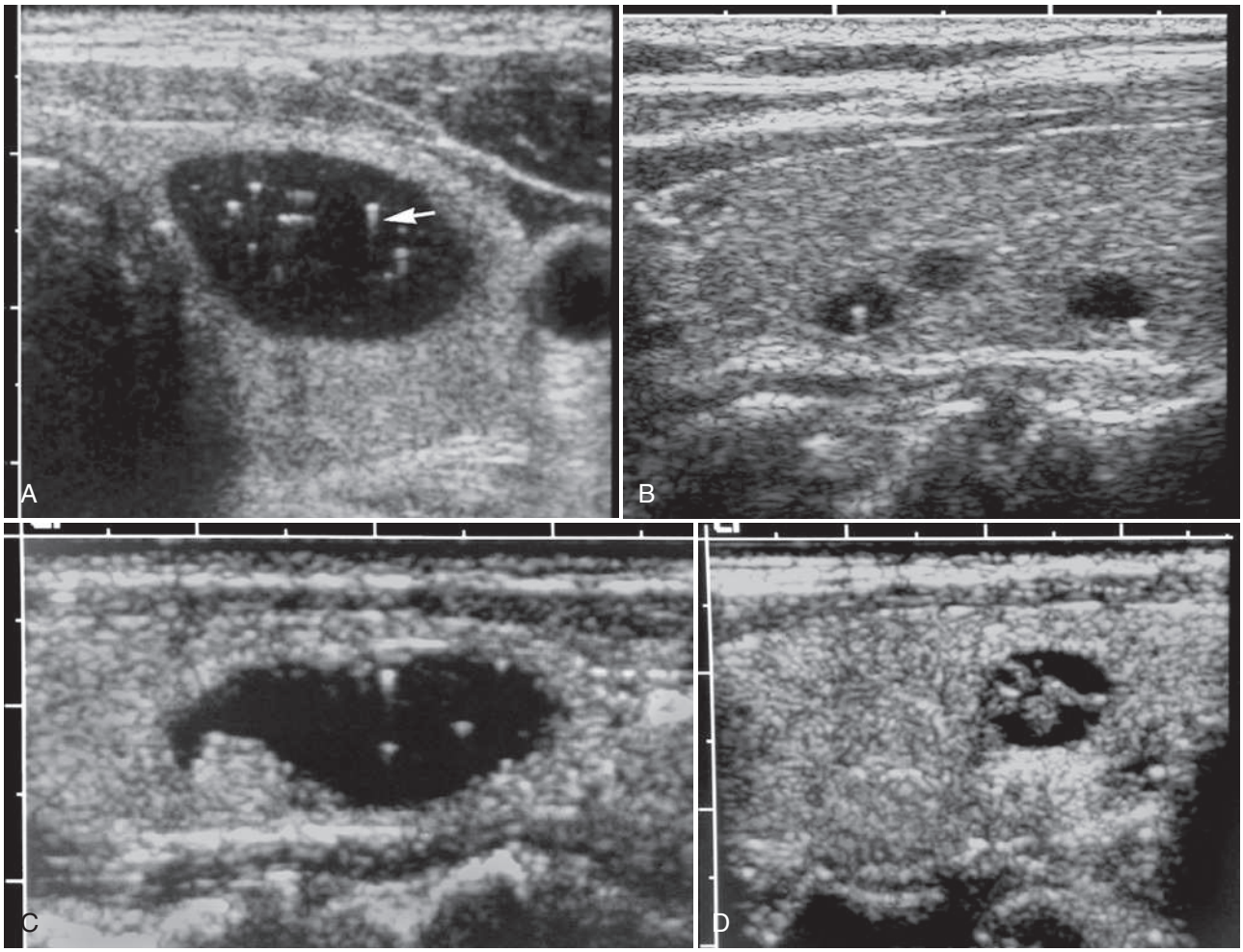

FIG. 19.10 Colloid Cysts. Transverse **(A)** and longitudinal **(B)-(D)** images of four patients show the typical appearance of colloid cysts. Some of the nodules have tiny echogenic foci that are thought to be microcrystals. A few of these foci are associated with comet-tail artifacts (*arrow* in **[A]**) posteriorly. Nodules that are mostly cystic, such as these, are considered benign. Colloid cysts often contain internal echoes.

of colloid hyperplastic nodules from the vegetations seen in papillary carcinomas; before moving to aspiration cytology studies, contrast-enhanced sonography with second-generation microbubbles and nondisruptive imaging can be used. **Benign septa** and **intracystic contents** do not show enhancement (and "disappear" in harmonic mode) (Fig. 19.12), whereas **malignant vegetations** show intense enhancement in arterial phase with relatively fast wash-out.

Adenoma

Adenomas represent only 5% to 10% of all nodular disease of the thyroid and are seven times more common in women than men.[5] Most result in no thyroid dysfunction; a minority (<10%) hyperfunction, develop autonomy, and may cause thyrotoxicosis. Most adenomas are solitary, but they may also develop as part of a multinodular process.

The **benign follicular adenoma** is a true thyroid neoplasm, characterized by compression of adjacent tissues and fibrous encapsulation. Various subtypes of follicular adenoma include the **fetal adenoma, Hürthle cell adenoma,** and **embryonal adenoma,** each distinguished according to the type of cell proliferation. The cytologic features of follicular adenomas are generally indistinguishable from those of follicular carcinoma. Vascular and capsular invasion are the hallmarks of **follicular carcinoma,** identified by histologic rather than cytologic analysis. Needle biopsy is therefore not a reliable method to distinguish between follicular carcinoma and cellular adenoma. Therefore such tumors are usually surgically removed.

Sonographically, adenomas are usually solid masses that may be hyperechoic, isoechoic, or hypoechoic (Fig. 19.13, Video 19.3). They often have a thick, smooth peripheral hypoechoic halo resulting from the fibrous capsule and blood vessels, which can be readily seen by color Doppler imaging. Often, vessels pass from the periphery to the central regions of the nodule, sometimes creating a "spoke and wheel" appearance. This vascular pattern is usually seen in both hyperfunctioning and poorly functioning adenomas and thus does not allow the detection of hyperfunctioning lesions.

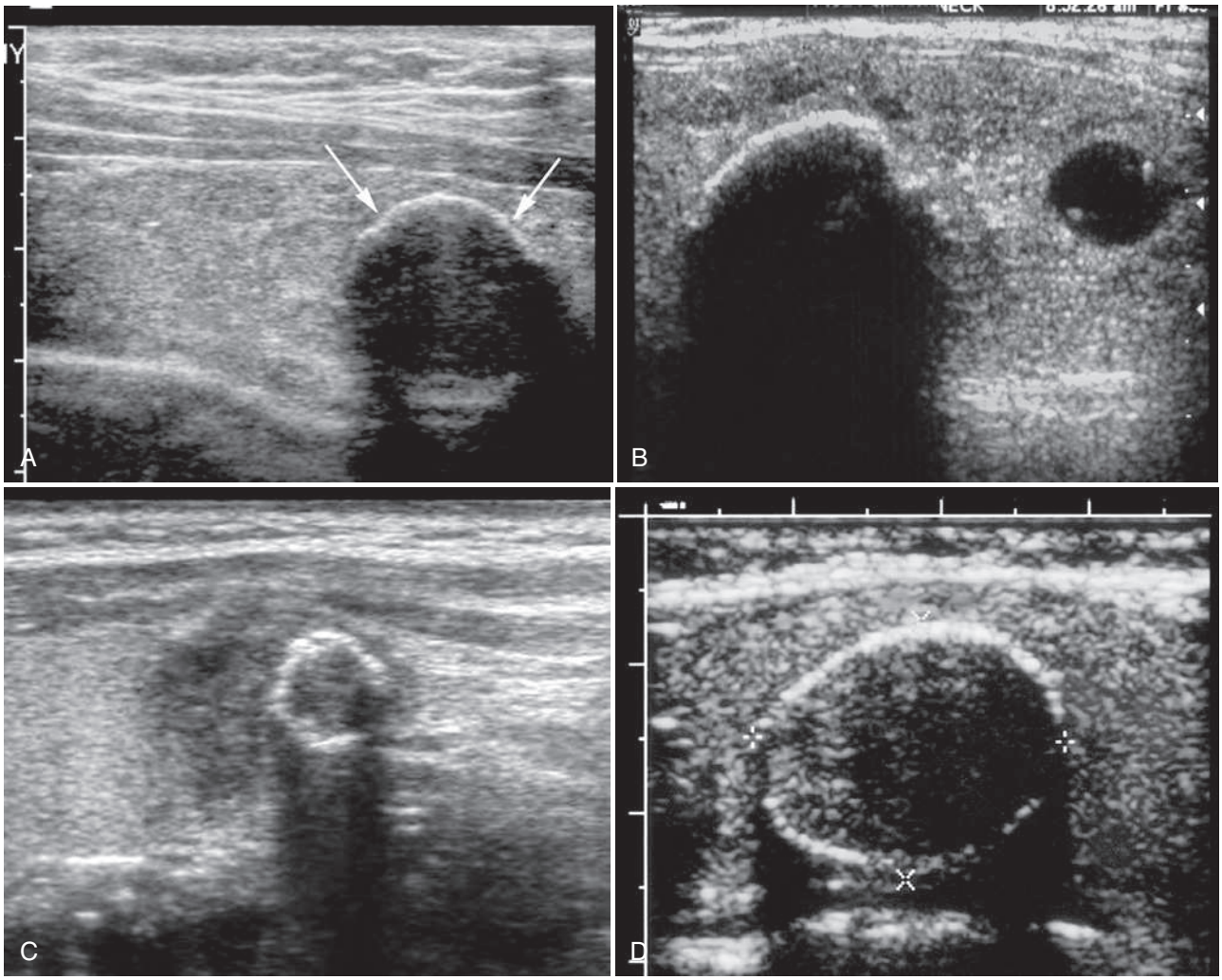

FIG. 19.11 "Eggshell" Calcification. Peripheral (eggshell) calcification was previously thought to indicate a benign nodule, but malignant nodules may have the appearance shown on these longitudinal images. **(A)** Coarse peripheral calcification *(arrows)* casts a large acoustic shadow. **(B)** Eggshell calcification and a typical appearance of colloid cyst on the right side in another patient. **(C)** Hypoechoic solid mass caused by papillary carcinoma surrounds area of eggshell calcification. **(D)** Peripheral shell (eggshell) calcification *(calipers)*.

Carcinoma

Most **primary thyroid cancers** are of epithelial origin and are derived from follicular or parafollicular cells.[16] Malignant thyroid tumors of mesenchymal origin are exceedingly rare, as are metastases to the thyroid. Most thyroid cancers are well differentiated, and papillary carcinoma (including so-called mixed papillary and follicular carcinoma) accounts for 75% to 90% of all cases.[16,23] In contrast, medullary, follicular, and anaplastic carcinomas (combined) represent only 10% to 25% of all thyroid carcinomas currently diagnosed in North America.

Papillary Carcinoma of Thyroid. Although it can occur in patients of any age, prevalence of PTC peaks in both the third and the seventh decades of life.[16] Women are affected more often than men. On microscopic examination, the tumor is multicentric within the thyroid gland in at least 20% of cases.[24] Round, laminated calcifications **(psammoma bodies)** in the cytoplasm of papillary cancer cells are seen in approximately 35% of patients. The major route of spread of papillary carcinoma is through the lymphatics to nearby cervical lymph nodes. In fact, a patient with PTC may have enlarged cervical nodes and a palpably normal thyroid gland.[25,26] Interestingly, the presence of nodal metastasis in the neck generally does not appear to worsen the prognosis for this malignancy. Distant metastases are very rare (2%-3%) and occur mostly in the mediastinum and lung. After 20 years, the cumulative mortality from PTC is typically only 4% to 8%.[25]

Papillary carcinoma has peculiar histologic (fibrous capsule, microcalcifications) and cytologic ("ground glass" nuclei, cytoplasmic inclusions in nucleus, indentations of nuclear membrane) features, which often allow a relatively easy pathologic diagnosis.[27] In particular, microcalcifications, which result from the deposition of calcium salts in the psammoma bodies, are frequently present in both the primary tumor and the cervical

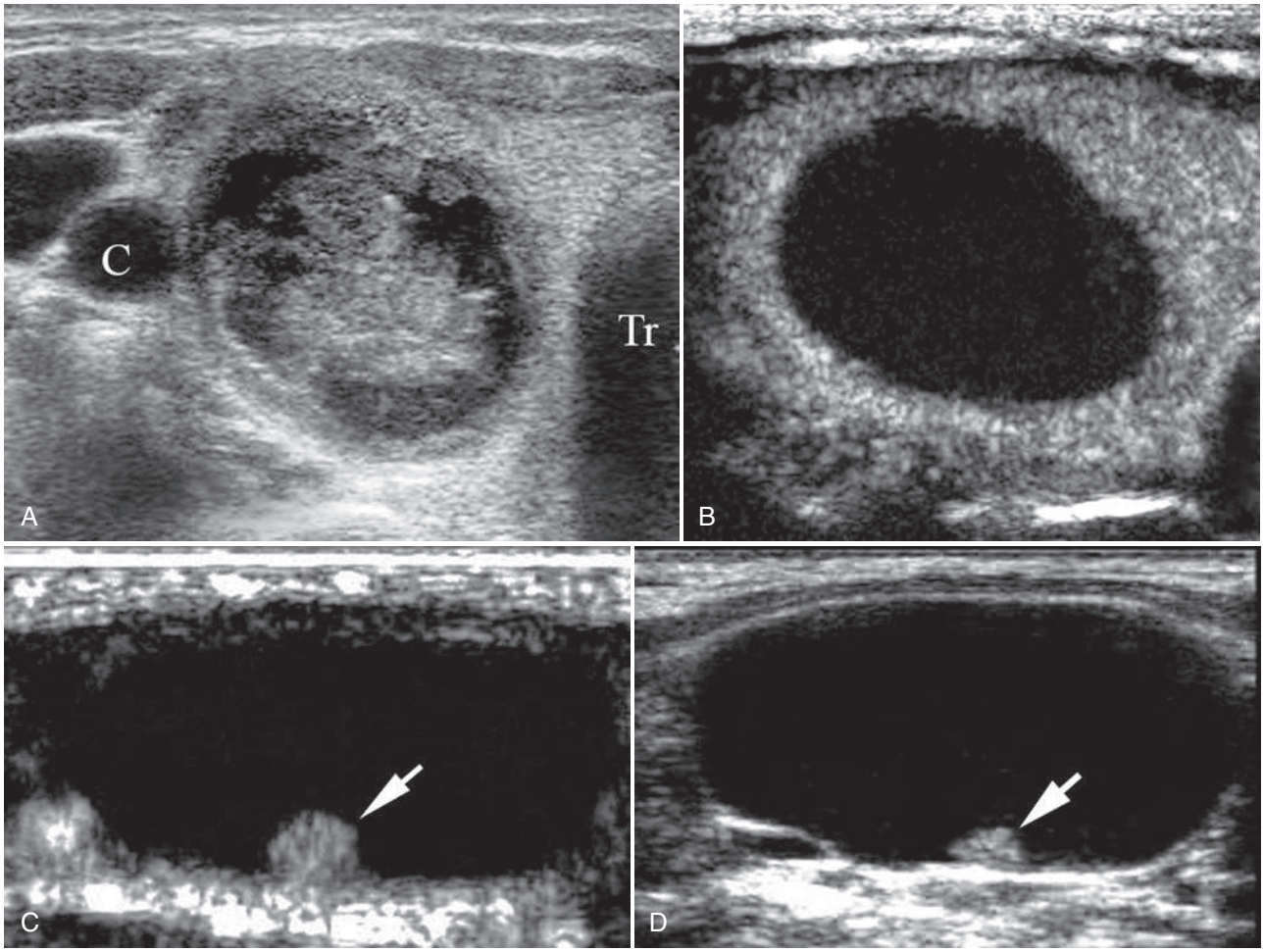

FIG. 19.12 Contrast-Enhanced Sonography to Differentiate Benign From Malignant Fluid-Filled Thyroid Nodules With Internal Septations or Solid Projections. (A) Conventional B-mode sonogram of right thyroid lobe demonstrates large, mixed solid and cystic nodule. *C,* Common carotid artery; *Tr,* tracheal air shadow. **(B)** Contrast-enhanced sonogram. After administration of contrast material, the internal contents are no longer visible because they lack enhancement, indicating that the contents were likely colloid and blood products. **(C)** Conventional B-mode sonogram in longitudinal plane demonstrates a nodule *(arrow)* arising from the posterior wall. **(D)** Contrast-enhanced longitudinal sonogram shows that the nodule remains visible, indicating enhancement after contrast enhancement. The lesion was a cystic papillary carcinoma.

lymph node metastases[26,28] (Fig. 19.14, Video 19.4 and Video 19.5). Similar to the pathologic features, sonographic characteristics of papillary carcinoma usually are relatively distinctive (Figs. 19.15 and 19.16):

- Hypoechogenicity (90% of cases), resulting from closely packed cell content, with minimal colloid substance.
- Microcalcifications, appearing as tiny, punctate hyperechoic foci, either with or without acoustic shadows. In rare but usually aggressive cases of papillary carcinomas of childhood, microcalcifications may be the only sonographic sign of the neoplasm, even without evidence of a nodular lesion[3,20,29,30] (see Fig. 19.15B).
- Hypervascularity (90% of cases), with disorganized vascularity, mostly in well-encapsulated forms[30] (see Fig. 19.16).
- Cervical lymph node metastases, which may contain tiny, punctate echogenic foci caused by microcalcifications (Fig. 19.17). These are mainly located in the caudal half of the deep jugular chain. Occasionally, metastatic nodes may be cystic as a result of extensive degeneration (Fig. 19.17H).

Cystic nodal metastases show a thickened outer wall, internal nodularity, and septations in most cases, although they may appear purely cystic in younger patients.[26] Cystic lymph node metastases in the neck occur almost exclusively in association with PTC, but occasionally with nasopharyngeal carcinomas.[31] On power Doppler sonography, noncystic nodes often show diffuse hypervascularity with tortuous vessels, arteriovenous (AV) shunts, and high vascular resistance (resistive index [RI] > 0.8). In some cases, however, these nodes may show only prominent hilar vascularity, similar to that of reactive nodes, and low RIs.[30]

Papillary carcinoma rarely displays extensive cystic change (Fig. 19.18). In our review of the amount of cystic change found in 360 thyroid carcinomas, a large amount of cystic change occurred in less than 3% of cases.[32] The overwhelming majority

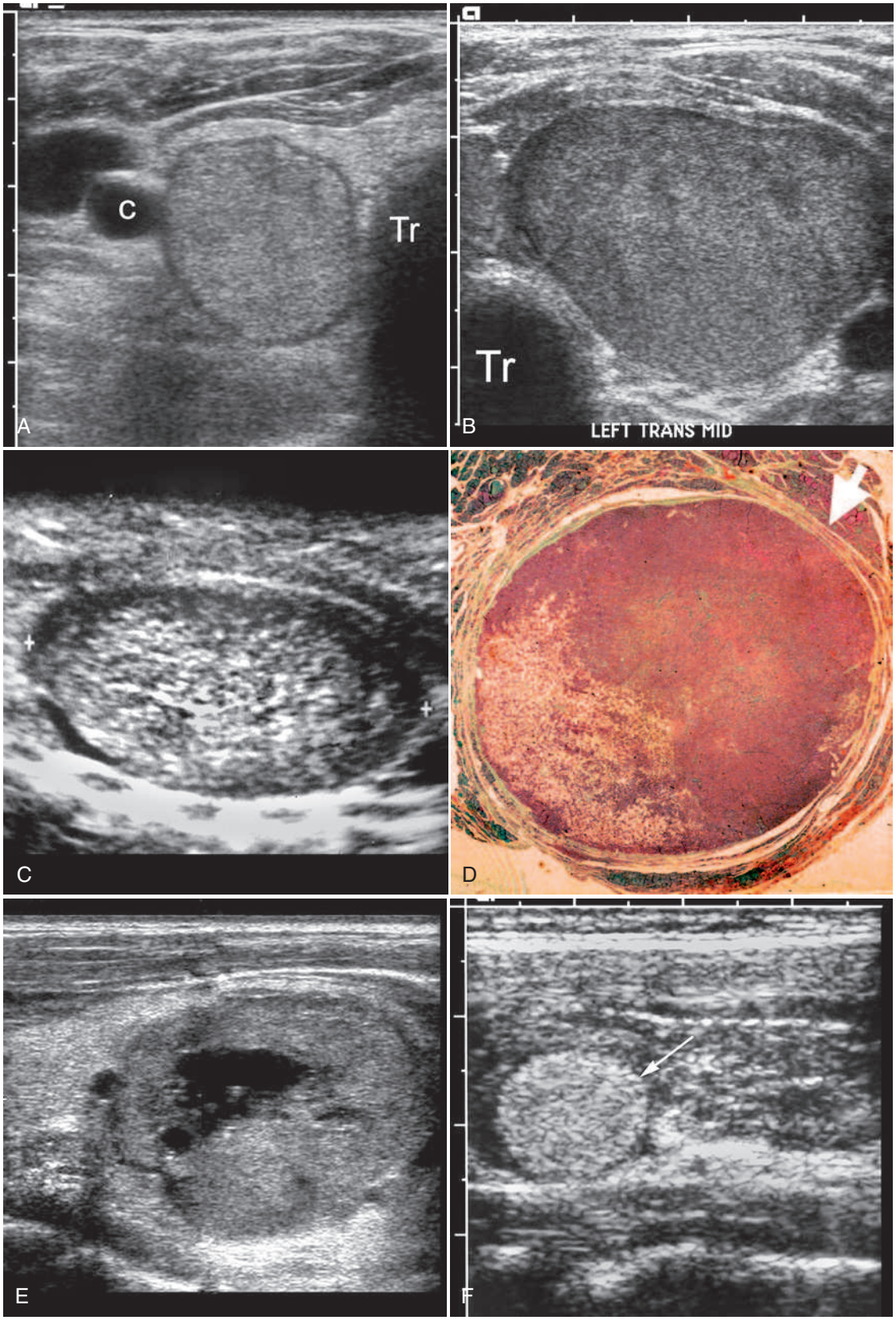

FIG. 19.13 Benign Follicular Adenoma: Spectrum of Appearances. Transverse images of **(A)** right lobe and **(B)** left lobe of thyroid gland in two patients show homogeneous, hypoechoic, round to oval masses with a surrounding thin halo, the capsule of the adenoma. *C,* Carotid artery; *Tr,* tracheal air shadow. **(C)** Longitudinal image shows oval hyperechoic lesion with thick peripheral halo. **(D)** Histology of lesion in **(C).** Note the uniform capsule *(arrow)* of the mass. **(E)** Longitudinal image shows oval mass with internal cystic component. **(F)** Longitudinal image shows round, hyperechoic homogeneous mass *(arrow)* in patient with Hashimoto thyroiditis.

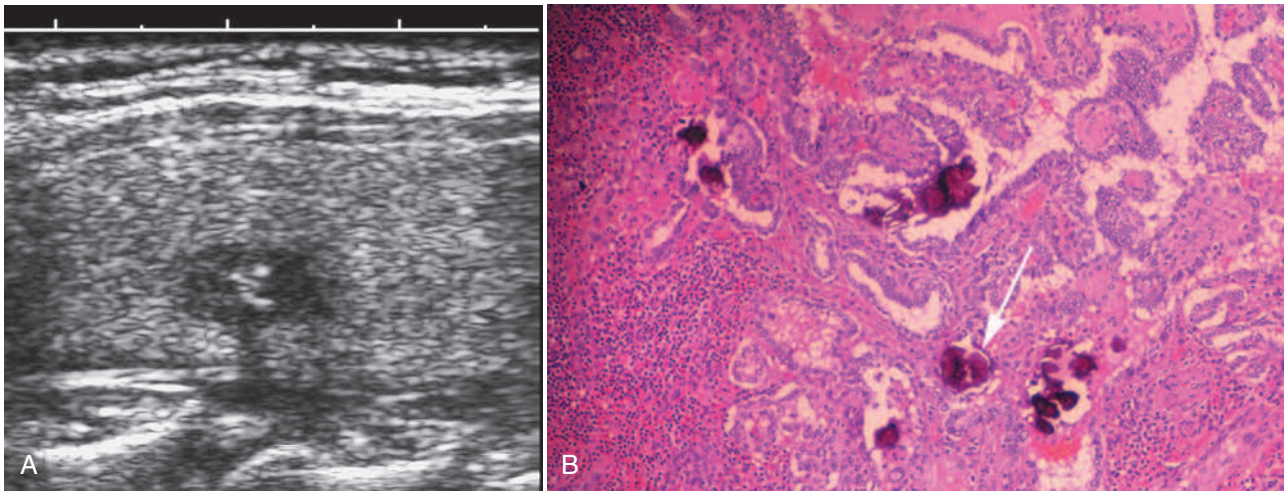

FIG. 19.14 Papillary Carcinoma: Small Cancer With Microscopic Correlation. (A) Longitudinal image shows 7-mm, hypoechoic solid nodule containing microcalcifications. **(B)** Microscopic pathologic image shows microcalcifications, or psammoma bodies *(arrow)*.

of papillary carcinomas appear as a predominantly solid mass. **Invasion of adjacent muscles** is infrequently visualized by ultrasound but indicates that the mass is malignant (Fig. 19.19). A **follicular variant** accounts for 10% of cases of papillary carcinoma and appears similar to a follicular neoplasm on gross pathologic inspection and ultrasound (Fig. 19.20). High-power microscopic studies show that the nuclear features are those of papillary carcinoma, and it is classified as a "follicular variant of papillary carcinoma." The clinical course and treatment are the same as for typical PTC.

Papillary microcarcinoma is a rare, nonencapsulated sclerosing tumor measuring 1 cm or less in diameter (Fig. 19.21). Most patients (80%) have enlarged cervical nodes and a palpably normal thyroid gland.[25,27] Papillary microcarcinoma can be imaged by high-frequency ultrasound in approximately 70% of cases, either as a small, hyperechoic patch (fibrotic-like) under the capsule with thickening and retraction of the capsule, or as a minute hypoechoic nodule with blurred irregular outline with no visible microcalcifications, but often with intense vascular signals within and around the lesion.

Follicular Carcinoma. Follicular carcinoma is the second subtype of well-differentiated thyroid cancer. It accounts for 5% to 15% of all cases of thyroid cancer, affecting women more often than men.[16] The two variants of follicular carcinoma differ greatly in histology and clinical course.[16,23,27] The **minimally invasive** follicular carcinomas are encapsulated, and only the histologic demonstration of focal invasion of capsular blood vessels of the fibrous capsule itself permits differentiation from follicular adenoma. The **widely invasive** follicular carcinomas are not well encapsulated, and invasion of the vessels and the adjacent thyroid is more easily demonstrated. Both variants of follicular carcinoma tend to spread through the bloodstream rather than the lymphatics, and distant metastases to bone, lung, brain, and liver are more likely than metastases to cervical lymph nodes. The widely invasive follicular carcinoma variant metastasizes in about 20% to 40% of cases, and the minimally invasive type metastasizes in only 5% to 10%. Mortality from follicular carcinoma is 20% to 30% at 20 years postoperatively.[16,25]

No unique sonographic features allow differentiation of follicular carcinoma from adenoma, which is not surprising, given the cytologic and histologic similarities of these two tumors (Figs. 19.22 and 19.23). Similarly, fine-needle aspiration (FNA) is not reliable in differentiating benign from malignant follicular neoplasms because the pathologic diagnosis is not based on cellular appearance but rather on capsular and vascular invasion. Therefore most follicular nodules must be surgically removed for accurate pathologic diagnosis. Features that suggest follicular carcinoma are rarely seen but include irregular tumor margins, a thick irregular halo, and a tortuous or chaotic arrangement of internal blood vessels on color Doppler imaging.[19,31]

Medullary Carcinoma. Medullary carcinoma accounts for about 5% of all malignant thyroid diseases. It is derived from the parafollicular cells, or C cells, and typically secretes the hormone **calcitonin,** which can be a useful serum marker. This cancer is frequently familial (20%) and is an essential component of the **multiple endocrine neoplasia (MEN) type II syndromes.**[33] The disease is multicentric and/or bilateral in about 90% of the familial cases[16] (Fig. 19.24). There is a high incidence of metastatic involvement of lymph nodes. The prognosis for patients with medullary cancer is somewhat worse than for follicular cancer.

Follicular Thyroid Carcinoma: Sonographic Features

Irregular tumor margins
Thick, irregular halo
Tortuous or chaotic arrangement of internal blood vessels

Text continued on p. 707.

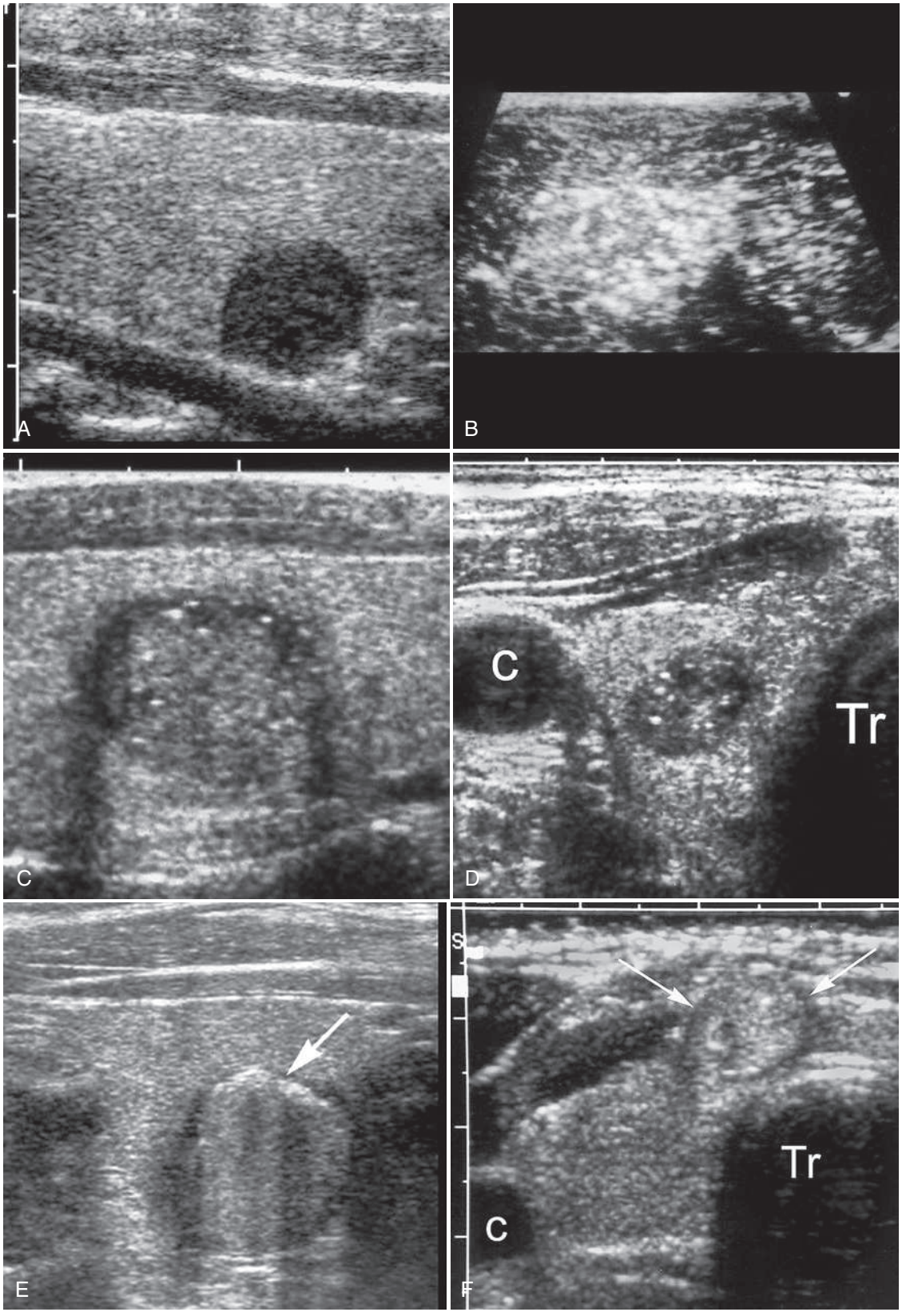

FIG. 19.15 Papillary Thyroid Carcinoma: Spectrum of Appearances. (A) Longitudinal image demonstrates extremely hypoechoic solid nodule without evidence of calcification. **(B)** Longitudinal image of the thyroid of a 6-year-old patient shows extensive diffuse microcalcifications without discrete mass. This is a very rare appearance and is more often encountered in children than adults. **(C)** Longitudinal and **(D)** transverse images show hypoechoic nodules that contain echogenic foci caused by microcalcification. **(E)** Longitudinal image shows hypoechoic solid nodule with thick, irregular halo and linear calcifications at anterior margin *(arrow)*. **(F)** Transverse image shows heterogeneous but isoechoic mass in the isthmus *(arrows)* that contains microcalcifications and has a thick, irregular halo. *C,* Carotid artery; *Tr,* tracheal air shadow.

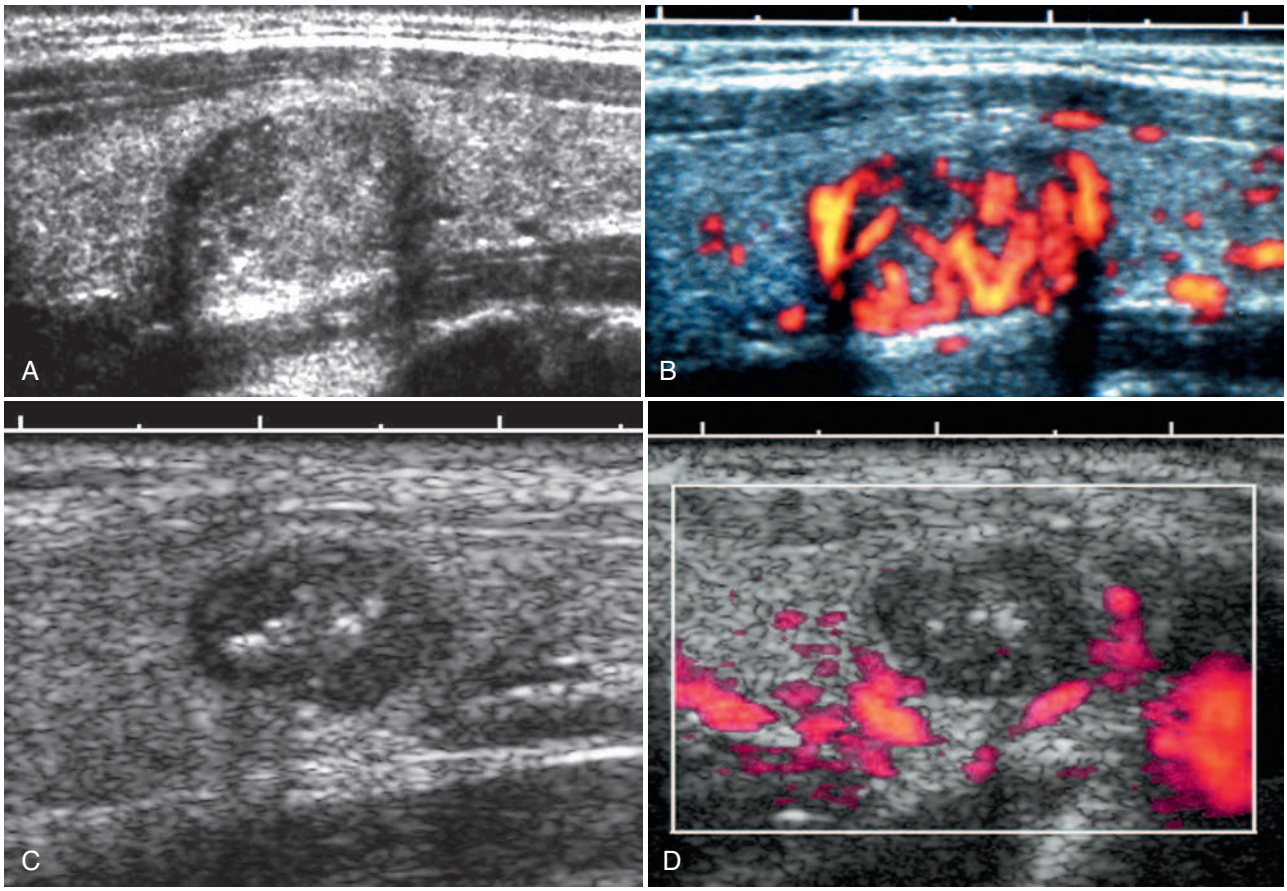

FIG. 19.16 Papillary Carcinoma: Power Doppler Appearances. Blood flow within cancer is often, but not always, increased. **(A)** Longitudinal image shows 1.5-cm nodule with a thick, irregular halo. **(B)** Power Doppler image shows that nodule is hypervascular and has flow in the center and at the periphery. **(C)** Longitudinal image shows hypoechoic nodule with microcalcifications. **(D)** Power Doppler image shows no blood flow within the cancer.

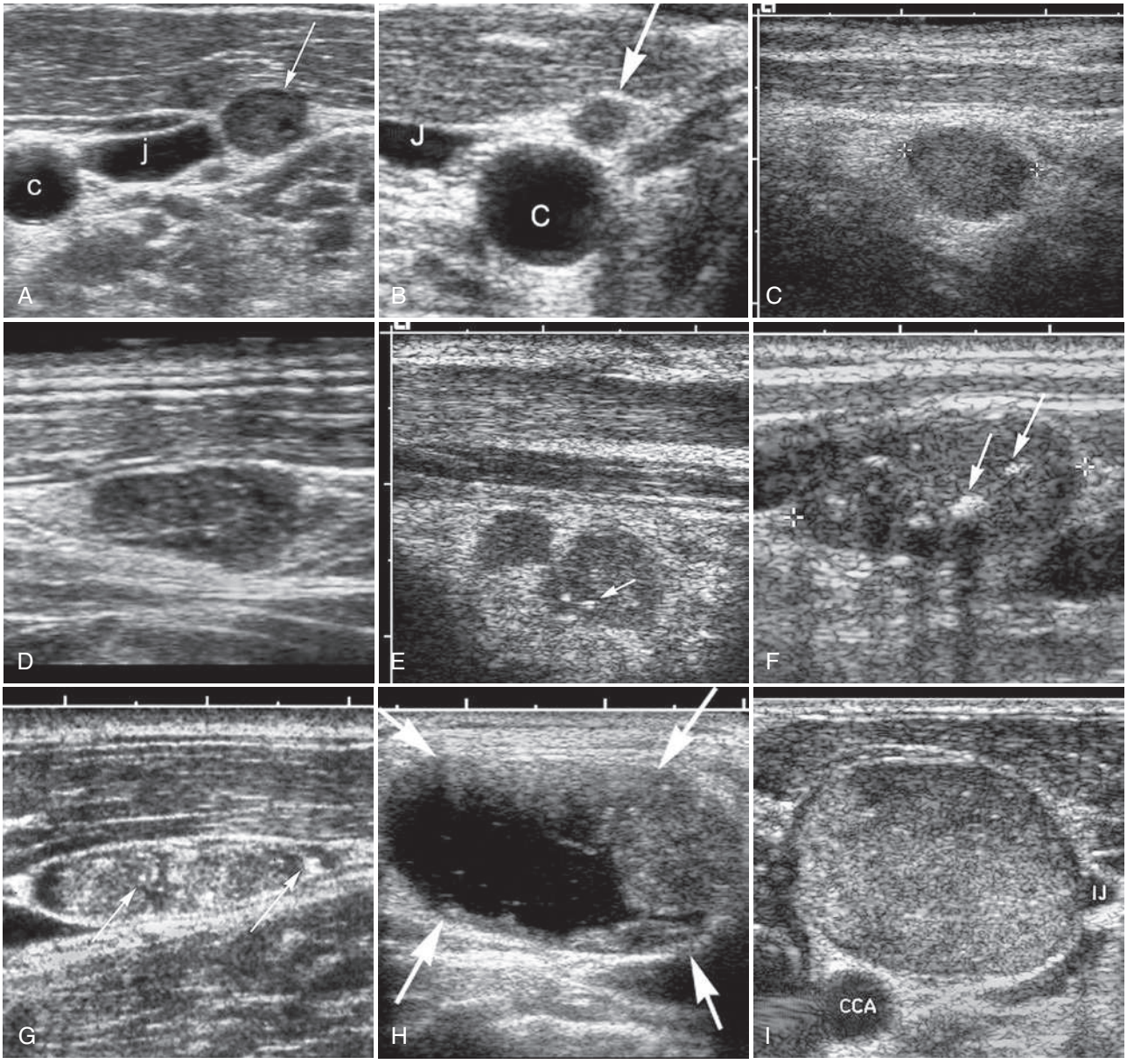

FIG. 19.17 Metastases Involving Cervical Lymph Nodes: Spectrum of Appearances. (A) and **(B)** Transverse images near the carotid artery *(C)* and jugular vein *(J)* show small, round, hypoechoic lymph nodes *(arrows).* Despite their small size (~4 mm), the round shape and the hypoechoic appearance are highly indicative of metastasis. **(C)** and **(D)** Longitudinal images show oval hypoechoic nodes. **(E)** Longitudinal image of thyroid bed after thyroidectomy shows two abnormal lymph nodes, one of which contains microcalcifications *(arrow).* **(F)** and **(G)** Longitudinal images show heterogeneous lymph nodes containing calcification *(arrows).* **(H)** Longitudinal image shows a large lymph node *(arrows)* containing cystic change. Cystic change in a cervical lymph node is almost always caused by metastatic papillary carcinoma. **(I)** Transverse image shows a large, round lymph node between the internal jugular vein *(IJ)* and the common carotid artery *(CCA).*

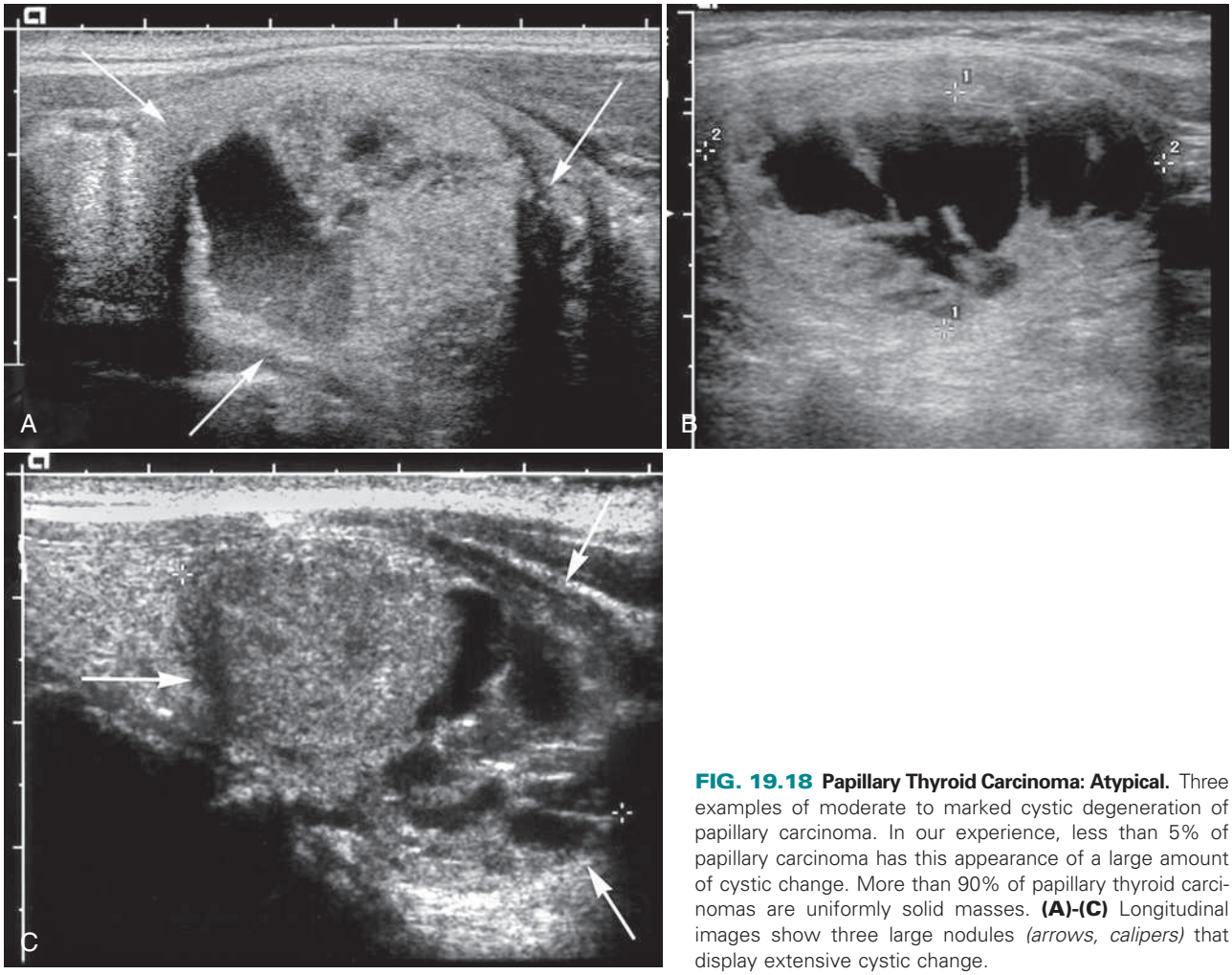

FIG. 19.18 Papillary Thyroid Carcinoma: Atypical. Three examples of moderate to marked cystic degeneration of papillary carcinoma. In our experience, less than 5% of papillary carcinoma has this appearance of a large amount of cystic change. More than 90% of papillary thyroid carcinomas are uniformly solid masses. **(A)-(C)** Longitudinal images show three large nodules *(arrows, calipers)* that display extensive cystic change.

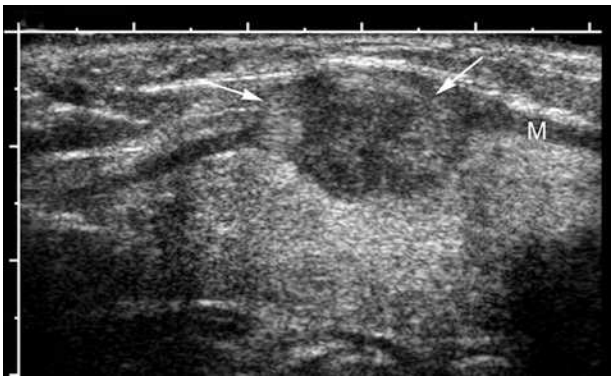

FIG. 19.19 Papillary Carcinoma Invades Muscle. Longitudinal image shows hypoechoic mass arising from anterior surface of the thyroid. This mass invades *(arrows)* adjacent strap muscle *(M)*. Muscular invasion is very rare.

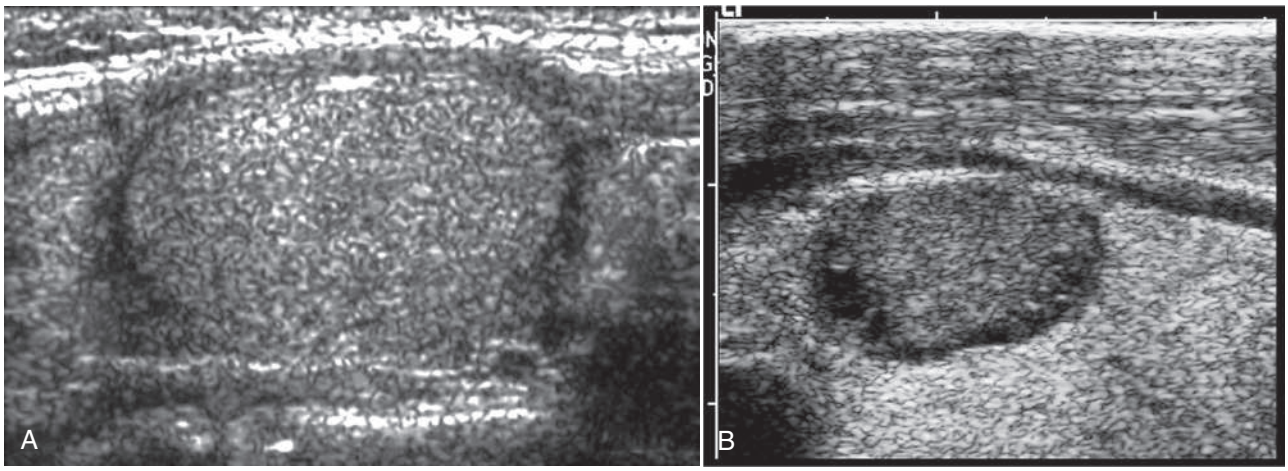

FIG. 19.20 Atypical Papillary Thyroid Carcinoma. Longitudinal images show two examples of the follicular variant of papillary thyroid carcinoma. **(A)** Oval isoechoic and **(B)** hypoechoic masses that look similar to the typical ultrasound appearance of a follicular neoplasm. This follicular variant is uncommon, accounting for 10% of cases of papillary carcinoma. The clinical course and treatment are the same as for typical papillary thyroid carcinoma.

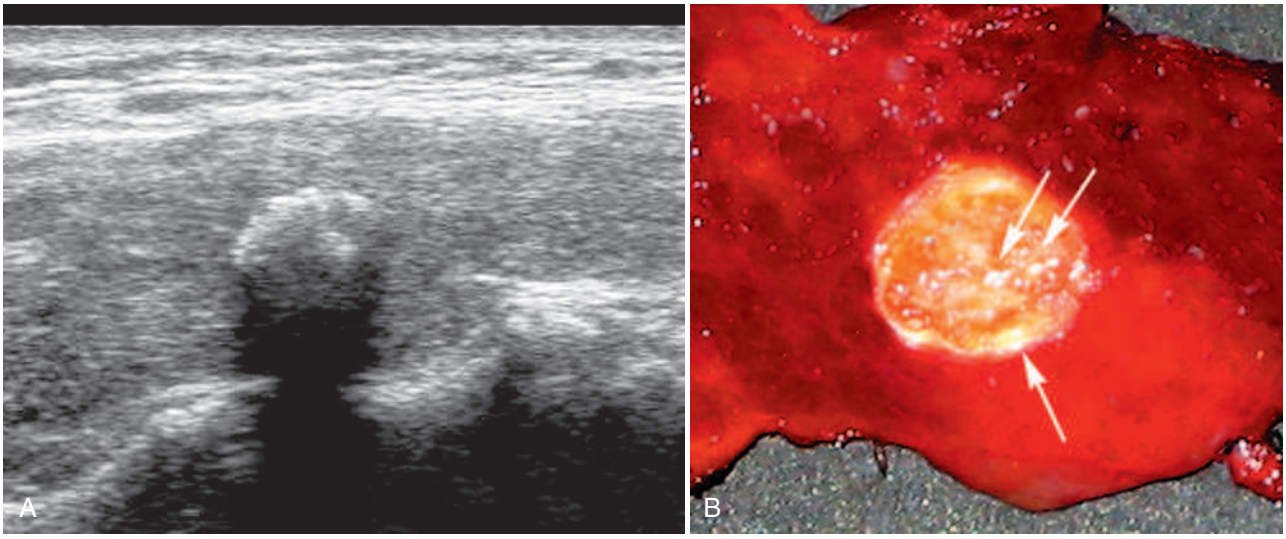

FIG. 19.21 Atypical Papillary Carcinoma. (A) Longitudinal image shows coarse calcification without mass effect, seen at the periphery and internally. **(B)** Gross pathologic specimen of **(A)** shows round nodule that contains multiple areas of grossly visible calcifications *(arrows)*. This is a rare sclerosing form of papillary carcinoma that contains a large amount of fibrosis and calcification.

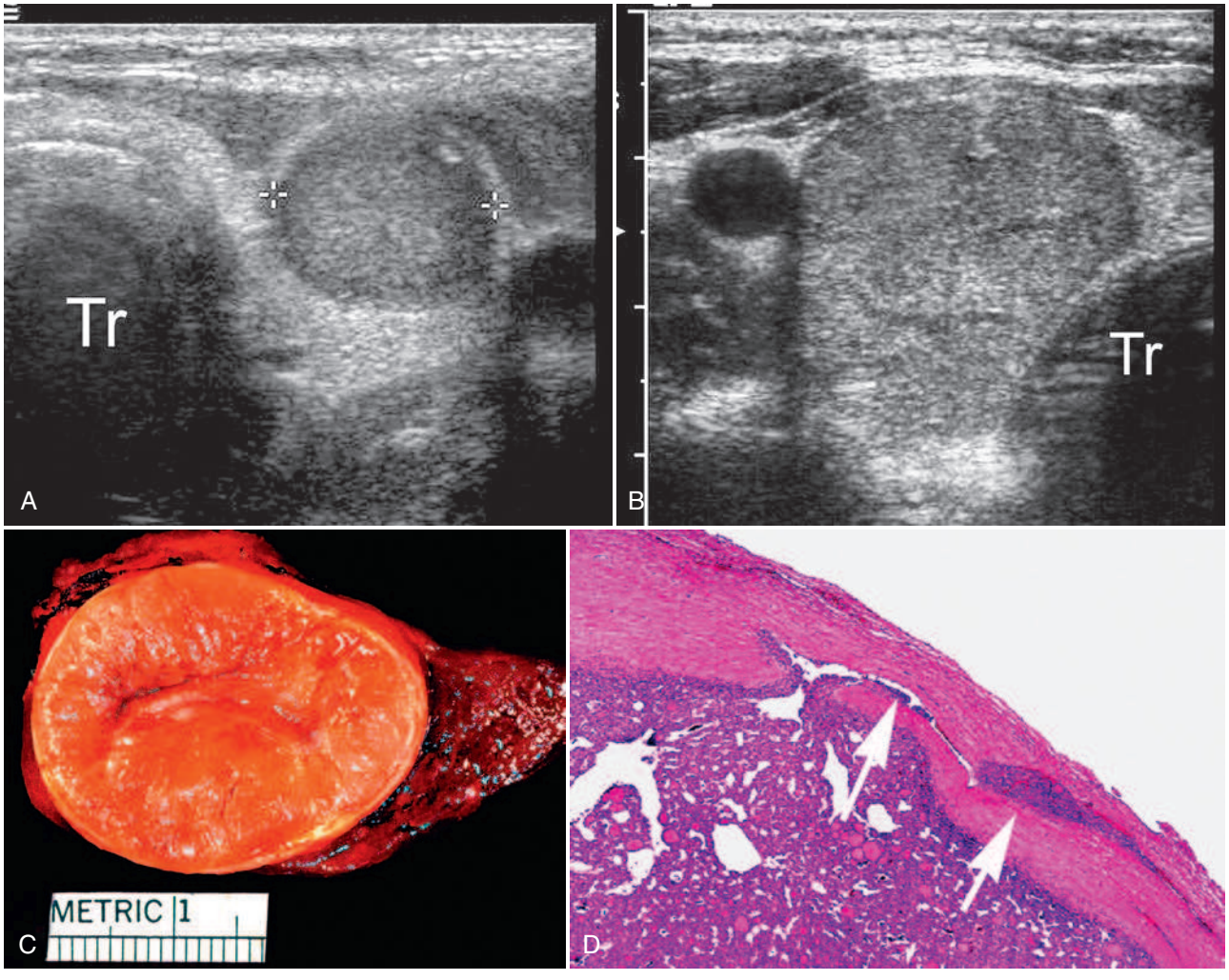

FIG. 19.22 Follicular Neoplasms: Benign and Malignant in Same Patient. (A) Left lobe and **(B)** right lobe of the thyroid show round, homogeneous hypoechoic masses that appear identical except for size differences on transverse images. *Tr,* tracheal air shadow. The smaller mass was malignant and the larger mass benign. **(C)** Gross pathologic specimen of follicular neoplasm shows a homogeneous tumor with a thin capsule. This capsule is present in both benign and malignant follicular neoplasms and is often seen on ultrasound. **(D)** Microscopic appearance of the capsule shows invasion of the follicular cells into the capsule *(arrows)*. This is one of the microscopic features that allows a pathologic diagnosis of malignancy but is not visible by ultrasound.

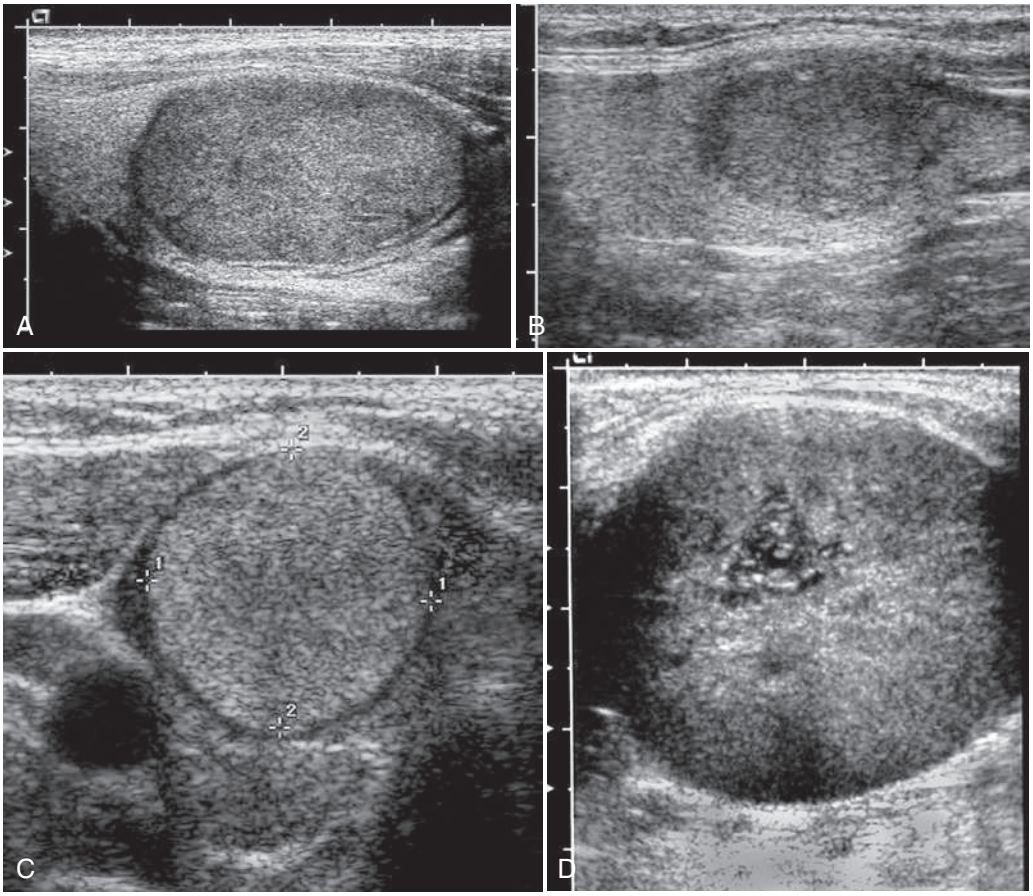

FIG. 19.23 Malignant Follicular Neoplasms. (A) and **(B)** Longitudinal images of two patients with oval homogeneous hypoechoic masses. **(C)** and **(D)** Transverse images of two other patients with round homogeneous masses. These four carcinomas appear identical to the benign follicular neoplasms (see Fig. 19.13), and surgical removal is required to exclude or establish malignancy of most follicular tumors.

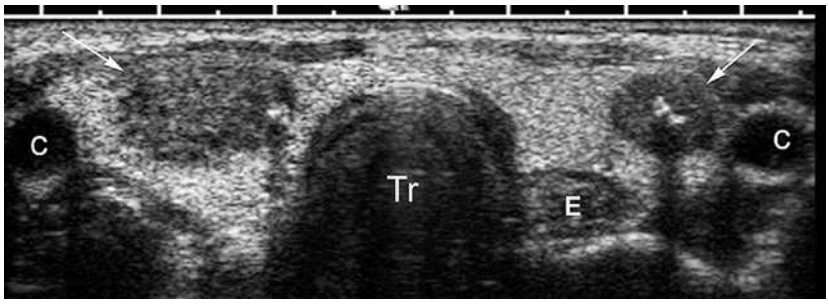

FIG. 19.24 Multicentric Medullary Thyroid Carcinoma. Transverse dual image in patient with multiple endocrine neoplasia type II (MEN II) shows bilateral hypoechoic masses *(arrows)* that contain areas of coarse calcification. *C,* Carotid arteries; *E,* esophagus; *Tr,* trachea.

The sonographic appearance of medullary carcinoma is usually similar to that of papillary carcinoma and is seen most often as a hypoechoic solid mass. Calcifications are often seen (histologically caused by calcified nests of amyloid substance) and tend to be more coarse than the calcifications of typical papillary carcinoma[34] (Fig. 19.25). Calcifications can be seen not only in the primary tumor but also in lymph node metastases and even in hepatic metastases.

Anaplastic Thyroid Carcinoma. Anaplastic thyroid carcinoma is typically a disease of elderly persons; it represents one of the most lethal of solid tumors. Although it accounts for less than 2% of all thyroid cancers, it carries the worst prognosis, with a 5-year mortality rate of more than 95%.[35] The tumor typically manifests as a rapidly enlarging mass extending beyond the gland and invading adjacent structures. It is often inoperable at presentation. Anaplastic carcinomas are often associated with papillary or follicular carcinomas, presumably representing a dedifferentiation of the neoplasm. They tend not to spread via the lymphatics but instead are prone to aggressive local invasion of muscles and vessels.[27]

Sonographically, anaplastic thyroid carcinomas are usually hypoechoic and often encase or invade blood vessels and neck muscles (Fig. 19.26). Often these tumors cannot be adequately examined by ultrasound because of their large size. Instead,

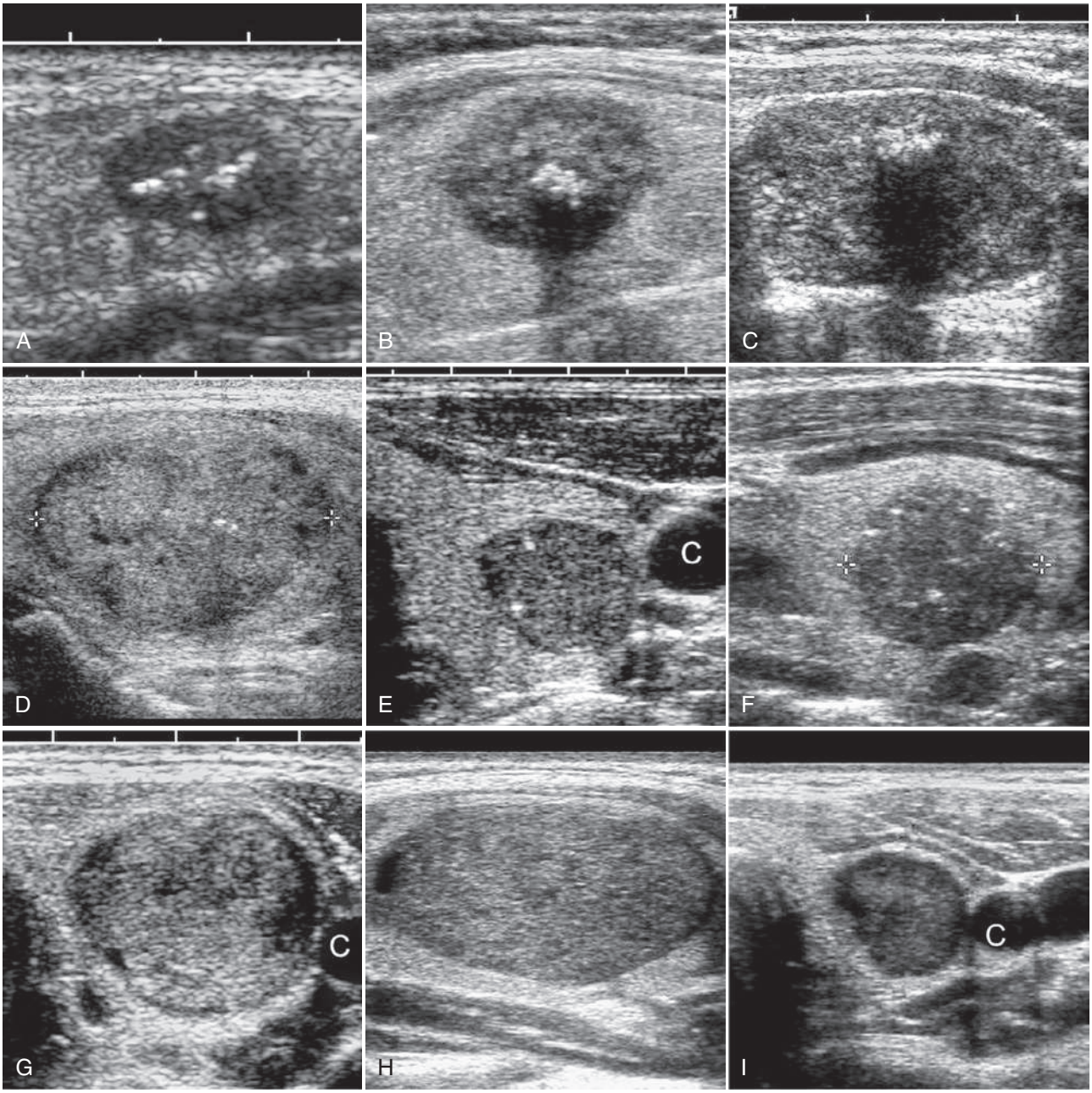

FIG. 19.25 Medullary Thyroid Carcinoma: Spectrum of Appearances. (A)-(C) Hypoechoic solid nodules with coarse internal calcifications. **(D)-(F)** Hypoechoic solid nodules with fine internal calcifications. **(G)-(I)** Hypoechoic solid nodules without calcification and with a similar appearance as follicular neoplasms. *C,* Carotid artery.

computed tomography (CT) or magnetic resonance imaging (MRI) of the neck usually demonstrates the extent of disease more accurately.

Anaplastic Thyroid Carcinoma: Sonographic Features

Large, hypoechoic mass
Encase or invade blood vessels
Invade neck muscles

Lymphoma

Lymphoma accounts for approximately 4% of all thyroid malignancies. It is mostly of the non-Hodgkin type and usually affects older women. The typical clinical sign is a rapidly growing mass that may cause symptoms of obstruction such as dyspnea and dysphagia.[36] In 70% to 80% of patients, lymphoma arises from a preexisting **chronic lymphocytic thyroiditis (Hashimoto thyroiditis)** with subclinical or overt hypothyroidism. The prognosis is highly variable and depends on the stage of the disease. Five-year survival ranges from almost 90% in early-stage cases to less than 5% in advanced, disseminated disease.

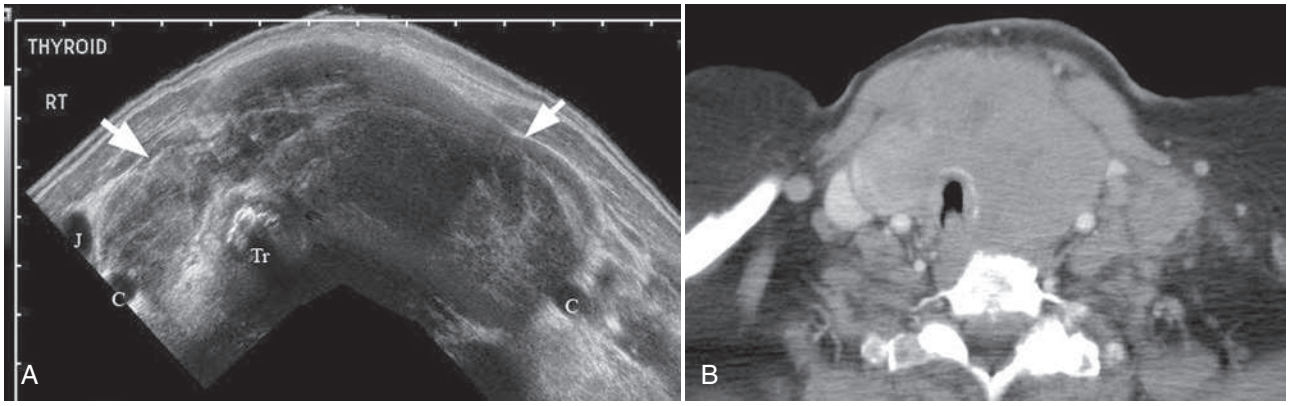

FIG. 19.26 Anaplastic Thyroid Carcinoma. (A) Transverse image shows large hypoechoic mass *(arrows)* involving the entire gland, greater on the left, which causes deviation of the trachea to the right. *C,* Common carotid artery; *J,* jugular vein; *Tr,* tracheal air shadow. **(B)** Contrast-enhanced computed tomography scan of the patient shows the large mass and its relationship to adjacent structures.

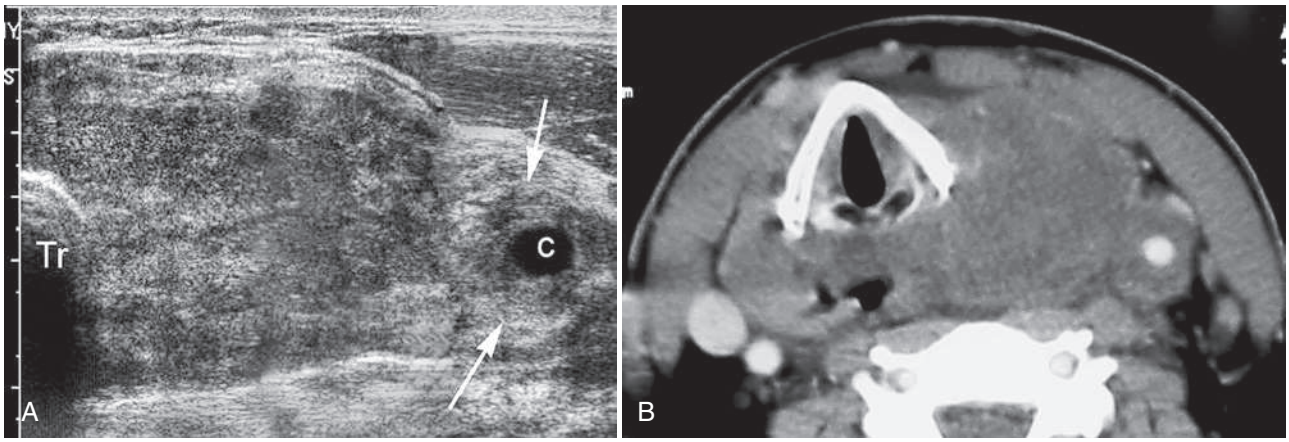

FIG. 19.27 Lymphoma. (A) Transverse image of left lobe of the thyroid shows diffuse mass enlarging the lobe and extending into the soft tissues *(arrows)* surrounding the common carotid artery *(c). Tr,* Tracheal air shadow. **(B)** Contrast-enhanced computed tomography scan shows a hypovascular mass in the left thyroid lobe and soft tissue encasement of the carotid artery.

Sonographically, lymphoma of the thyroid appears as an extremely hypoechoic and lobulated mass. Large areas of cystic necrosis may occur, as well as encasement of adjacent neck vessels[37] (Fig. 19.27). On color Doppler imaging, both nodular and diffuse thyroid lymphomas may appear mostly hypovascular or may show blood vessels with chaotic distribution and AV shunts. The adjacent thyroid parenchyma may be heterogeneous as a result of associated chronic thyroiditis.[38]

Thyroid Metastases

Metastases to the thyroid are infrequent, occurring late in the course of neoplastic diseases as the result of hematogenous spread or less frequently a lymphatic route. Metastases usually are from **melanoma** (39%), **breast** (21%), and **renal cell** (10%) carcinoma. Metastases may appear as solitary, well-circumscribed nodules or as diffuse involvement of the gland. On sonography, thyroid tumors are solid, homogeneously hypoechoic masses, without calcifications[39] (Fig. 19.28).

Fine-Needle Aspiration Biopsy

Once a thyroid nodule has been detected, the fundamental challenge is to determine if it is benign or malignant. Short of surgical excision, several methods for nodule characterization are in common use, including radionuclide imaging, sonography, and FNA biopsy. Each of these techniques has advantages and limitations, and the choice in any specific clinical setting depends largely on available instrumentation and expertise.

It is generally recognized that FNA biopsy is the most effective method for diagnosing malignancy in a thyroid nodule.[40-42] In many clinical practices, FNA under direct palpation is the first diagnostic examination performed on any clinically palpable nodule. Neither isotopic nor sonographic imaging is used routinely, instead reserved for special situations or difficult cases. FNA has had a substantial impact on the management of thyroid nodules because it provides more direct information than any other available diagnostic technique. It is safe and inexpensive and results in better selection of patients for surgery. The successful use of FNA in clinical practice, however, depends heavily on the presence of an experienced aspirationist and an expert cytopathologist.

Fine-needle thyroid aspirates are often classified cytopathologically into the following four categories:

1. Negative (no malignant cells)
2. Positive for malignancy

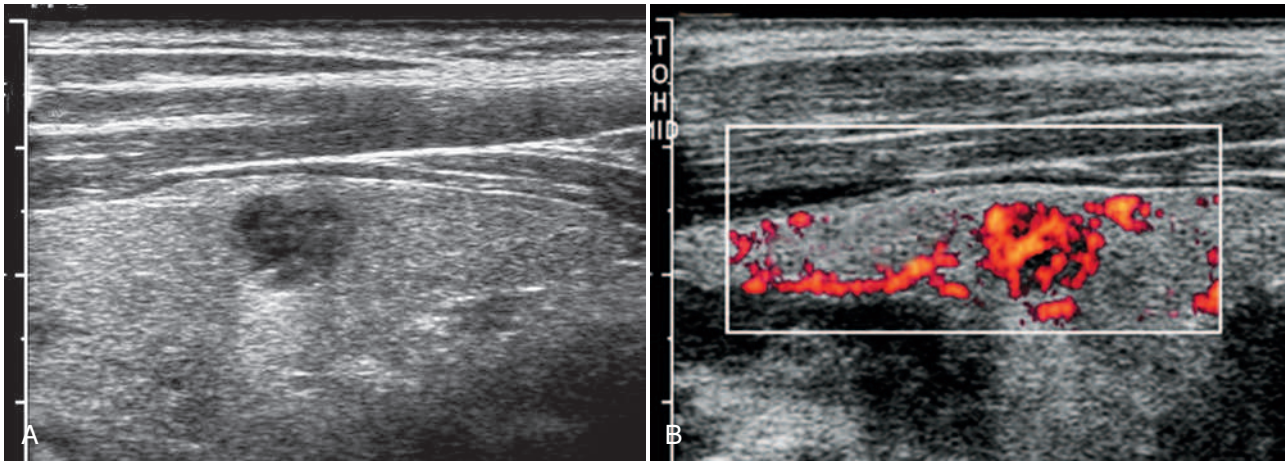

FIG. 19.28 Thyroid Metastasis From Renal Cell Carcinoma. (A) Longitudinal (gray-scale) and **(B)** power Doppler images show a 1-cm solid vascular mass.

TABLE 19.1 Diagnostic Yield of Thyroid Fine-Needle Aspiration (FNA)

Series	No. of Cases	FN rate	FP rate	Sensitivity	Specificity
Hawkins et al.[44]	1399	2.4%	4.6%	86%	95%
Khafagi et al.[45]	618	4.1%	7.7%	87%	72%
Hall et al.[46]	795	1.3%	3.0%	84%	90%
Altavilla et al.[47]	2433	6.0%	0.0%	71%	100%
Gharib and Goellner[43]	10,971	2.0%	0.7%	98%	99%
Ravetto et al.[48]	2014	11.2%	0.7%	89%	99%

FN, False-negative; *FP,* false-positive.
Modified from Gharib H, Goellner JR. Fine-needle aspiration biopsy of the thyroid: an appraisal. Ann Intern Med. 1993;118(4):282-289.[43]

3. Suggestive of malignancy
4. Nondiagnostic

If a nodule is classified in either of the first two categories, the results are highly sensitive and specific.[42] The major limitation of the technique is the lack of specificity in the third group—results are suggestive of malignancy—primarily because of the inability to distinguish follicular or Hürthle cell adenomas from their malignant counterparts. In these cases, surgical excision is required for diagnosis. In addition, up to 20% of aspirates may be nondiagnostic, approximately half of which result from inadequate cell sampling of cystic lesions. In these cases, repeat FNA under sonographic guidance can be performed for **selective sampling** of the solid elements of the mass. In the world literature, FNA of thyroid nodules has a sensitivity range of 65% to 98% and specificity of 72% to 100%, with a false-negative rate of 1% to 11% and a false-positive rate of 1% to 8%[43-49] (Table 19.1). In a study based on more than 5000 cytologic examinations, the most frequent cause of false-negative findings was the failure to recognize the follicular variant of papillary carcinoma.[49] In our practices, the overall accuracy of FNA exceeds 95%, and therefore it is currently the most accurate and cost-effective method for initial evaluation of patients with nodular thyroid disease. Since the introduction of FNA into routine clinical practice, the percentage of patients undergoing thyroidectomy has substantially decreased (to ~25%), and the cost of thyroid nodule care has been reduced by 25%.[43]

The evaluation of thyroid nodules primarily by FNA is common in North America and northern Europe. In other European countries and Japan, where goiter is prevalent, the initial evaluation often relies on radionuclide and sonographic imaging because of the need to select nodules that must undergo FNA.

Sonographic Applications

Although FNA is the most reliable diagnostic method for evaluating clinically palpable thyroid nodules, high-resolution sonography has four primary clinical applications[50-52]:

- Detection of thyroid and other cervical masses before and after thyroidectomy
- Differentiation of benign from malignant masses on the basis of their sonographic appearance
- Guidance for FNA biopsy
- Guidance for the percutaneous treatment of nonfunctional and hyperfunctioning benign thyroid nodules and of lymph node metastases from papillary carcinoma

Detection of Thyroid Masses

A practical use of sonography is to establish the precise anatomic location of a palpable cervical mass. The determination of whether

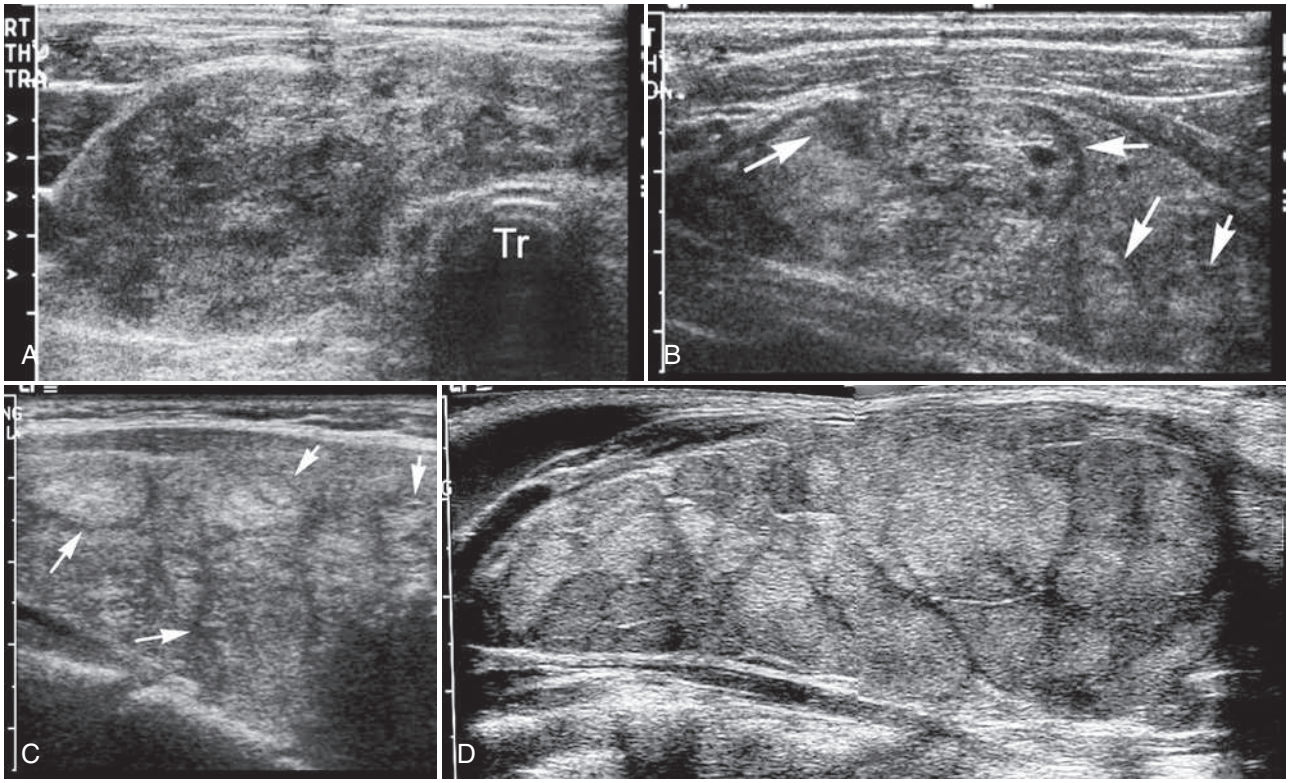

FIG. 19.29 Multinodular Goiter. (A) Transverse image shows enlargement of the right lobe and isthmus by multiple confluent hypoechoic and hyperechoic nodules. *Tr,* Tracheal air shadow. **(B)** and **(C)** Longitudinal images show multiple confluent nodules *(arrows).* **(D)** Longitudinal dual image shows enlargement of a lobe by multiple nodules.

such a mass is within or adjacent to the thyroid cannot always be made on the basis of the physical examination alone. Sonography can readily differentiate thyroid nodules from other cervical masses, such as cystic hygromas, thyroglossal duct cysts, and enlarged lymph nodes. Alternatively, sonography may help to confirm the presence of a thyroid nodule when the findings on physical examination are equivocal.

Sonography may be used to detect occult thyroid nodules in patients who have a **history of head and neck irradiation** during childhood as well as those with a **family history of MEN II syndrome;** both groups have a known increased risk for development of thyroid malignancy. If a nodule is discovered, a biopsy can be performed under sonographic guidance. It is unknown, however, whether the detection of a thyroid cancer before it becomes clinically palpable will change the ultimate clinical outcome for a given patient.

In the past, when thyroid nodules were evaluated primarily with isotope scintigraphy, it was generally accepted that a "solitary cold" nodule carried a probability of malignancy of 15% to 25%, whereas a "cold" nodule in a multinodular gland was malignant in less than 1% of cases.[53] However, benign goiter is multinodular in 70% to 80% of cases, and 70% of nodules considered "solitary" on scintigraphy or physical examination are actually *multiple* when assessed with high-frequency ultrasound[21,54] (Fig. 19.29).

It has been suggested, therefore, that sonography may be used to detect additional occult nodules in patients with clinically solitary lesions, thereby implying that the dominant palpable mass is benign. Such a conclusion is unwarranted, however, because pathologically, benign nodules often coexist with malignant nodules. In a series of 1500 consecutive patients undergoing surgery for papillary carcinoma, 33% had coexistent benign nodules at surgery.[55] In addition, PTC is recognized to be multicentric in at least 20% of cases and occult (<1.5 cm in diameter) in up to 48% of cases.[23,53] In a previous study, almost two-thirds (64%) of patients with thyroid cancer had at least one nodule in addition to the dominant nodule detected sonographically.[56] Pathologically, these extra nodules can be benign or malignant. Therefore in patients with a clinically solitary nodule, the sonographic detection of a few additional nodules is not a reliable sign for excluding malignancy.

An ultrasound-guided FNA biopsy is performed for patients with **multinodular goiter** when there is a dominant nodule. A **dominant nodule** is the largest nodule or has ultrasound features different from the other nodules or features suggestive of carcinoma.

In patients with known thyroid cancer, sonography can be useful to **determine the extent of disease,** both preoperatively and postoperatively. In most patients a sonographic examination is not performed routinely before thyroidectomy, but it can be useful in those with large cervical masses for evaluation of nearby structures, such as the carotid artery and internal jugular vein for evidence of direct invasion or encasement by the tumor. Alternatively, in patients with cervical lymphadenopathy caused by PTC but in whom the thyroid gland is palpably normal, sonography may be used preoperatively to detect an occult, nonpalpable primary focus within the gland.

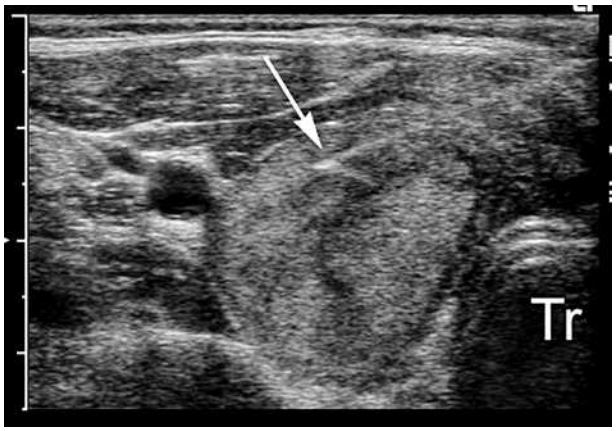

FIG. 19.30 Fine-Needle Aspiration of Thyroid Nodule Caused by Follicular Neoplasm. Transverse image shows a large nodule replacing the right thyroid lobe. *Tr,* Tracheal air shadow. The tip of the 25-gauge needle is highly visible *(arrow),* and the shaft of the needle is faintly visible.

After partial or near-total thyroidectomy for carcinoma, sonography is the preferred method for follow-up, by detecting **residual, recurrent, or metastatic disease** in the neck.[57] In patients who have had subtotal thyroidectomy, the sonographic appearance of the remaining thyroid tissue may serve as an important factor in deciding whether complete thyroidectomy is recommended. If a mass is identified, its nature can be determined by ultrasound-guided FNA (Fig. 19.30). If no masses are seen, the clinician may choose to follow the patient with periodic sonographic studies. For patients who have had total or near-total thyroidectomy, sonography has proved to be more sensitive than physical examination in detecting recurrent disease within the thyroid bed or metastatic disease in cervical lymph nodes.[58] Patients with a history of thyroid cancer often undergo periodic sonographic examinations of the neck to detect nonpalpable recurrent or metastatic disease. When a mass is identified, FNA under sonographic guidance can establish a diagnosis of malignancy and help in surgical planning.

Differentiation of Benign and Malignant Nodules

According to several reports, for the differentiation of benign from malignant thyroid nodules, sonography has sensitivity rates of 63% to 94%, specificity of 61% to 95%, and overall accuracy of 78% to 94%.[4,5,59-65] Currently, no single sonographic criterion distinguishes benign thyroid nodules from malignant nodules with complete reliability.[5,59-61,65] Nevertheless, certain sonographic features are seen more often with one type of histology or another type, thus establishing general diagnostic trends[31] (Table 19.2).

The fundamental anatomic features of a thyroid nodule on high-resolution sonography are as follows:

- Internal consistency (solid, mixed solid and cystic, or purely cystic)
- Echogenicity relative to adjacent thyroid parenchyma
- Margin
- Shape
- Presence and pattern of calcification

TABLE 19.2 Reliability of Sonographic Features in Differentiation of Benign From Malignant Thyroid Nodules

	PATHOLOGIC DIAGNOSIS	
Feature	**Benign**	**Malignant**
SHAPE		
Wider than tall	+++	++
Taller than wide	+	++++
INTERNAL CONTENTS		
Purely cystic content	++++	+
Cystic with thin septa	++++	+
Mixed solid and cystic	+++	++
Comet-tail artifact	+++	+
ECHOGENICITY		
Hyperechoic	++++	+
Isoechoic	+++	++
Hypoechoic	+++	+++
Markedly hypoechoic	+	++++
HALO		
Thin halo	++++	++
Thick, incomplete halo	+	+++
Absent	+	+++
MARGIN		
Well defined	+++	++
Poorly defined	++	+++
Spiculated	+	++++
CALCIFICATION		
Eggshell calcification	+++	++
Coarse calcification	+++	+
Microcalcification	++	++++
DOPPLER		
Peripheral flow pattern	+++	++
Internal flow pattern	++	+++
SONOELASTOGRAPHY		
Patterns 1 and 2	++++	+
Patterns 3 and 4	+	+++

+, Rare (<1%); ++, low probability (<15%); +++, intermediate probability (16%-84%); ++++, high probability (>85%).
Data from authors' experience and literature reports.

- Peripheral sonolucent halo
- Presence and distribution of blood flow signals

Internal Contents. In our experience, approximately 70% of thyroid nodules are solid, whereas the remaining 30% exhibit various amounts of cystic change. A nodule that has a significant cystic component is usually a **benign adenomatous (colloid) nodule** that has undergone degeneration or hemorrhage. When detected by older, lower-resolution ultrasound machines, these lesions were called "cysts" because the presence of internal debris and a thick wall could not be appreciated. Pathologically, a true

epithelium-lined, simple thyroid cyst is extremely rare. Virtually all cystic thyroid lesions seen with high-resolution ultrasound demonstrate some wall irregularity and internal solid elements or debris caused by nodule degeneration (see Figs. 19.9 and 19.10). When high-frequency gray-scale sonography and color Doppler imaging cannot differentiate debris and septa from neoplastic intracystic vegetations, contrast-enhanced sonography can sometimes resolve the problem by demonstrating the arterial enhancement in tumoral projections and the complete lack of enhancement of benign septa and debris (see Fig. 19.12). **Comet-tail artifacts** are frequently encountered in cystic thyroid nodules and are likely related to the presence of microcrystals (see Fig. 19.10). In a published series of 100 patients with this feature, FNA biopsy was benign in all cases.[22] These comet-tail artifacts can be located in the cyst walls and internal septations or in the cyst fluid. When a more densely echogenic fluid is gravitationally layered in the posterior portion of a cystic cavity, the likelihood of hemorrhagic debris is very high. Frequently, patients with hemorrhagic debris clinically demonstrate a rapidly growing, often tender neck mass. The **spongiform appearance** of thyroid nodules, related to the presence of tiny colloid changes, is an extremely uncommon finding in malignant nodules, particularly when it is associated with other findings such as well-defined margins and isoechogenicity. This pattern is highly predictive of a benign nodule (see Fig. 19.9).

Papillary carcinomas rarely exhibit varying amounts of cystic change, appearing almost indistinguishable from benign cystic nodules.[66-68] In cystic papillary carcinomas, however, the frequent sonographic detection of solid elements or projections (≥1 cm with blood flow signals and/or microcalcifications) into the lumen can lead to suspicion of malignancy (see Fig. 19.18). Cervical metastatic lymph nodes from either a solid or a cystic primary papillary cancer may also demonstrate a cystic pattern; this is likely pathognomonic of malignant adenopathy.

Shape. A taller-than-wide shape, in which the AP diameter is equal to or less than the transverse diameter on a transverse or longitudinal plane, is specific for differentiating malignant nodules from benign nodules, likely because malignant neoplasms (taller than wide) grow across normal tissue planes, whereas benign nodules grow parallel to normal tissue planes.[59,65,66]

Echogenicity. Thyroid cancers are usually hypoechoic relative to the adjacent normal thyroid parenchyma (see Fig. 19.15). Unfortunately, many benign thyroid nodules are also hypoechoic. In fact, most **hypoechoic nodules** are benign because benign nodules are so much more common than malignant nodules. However, marked hypoechogenicity is highly specific for diagnosing malignant nodules, whereas the hypoechogenicity often found in benign lesions is usually less marked.[65] A predominantly **hyperechoic nodule,** although relatively uncommon, is more likely to be benign.[21] The **isoechoic nodule,** visible because of a peripheral sonolucent rim that separates it from the adjacent normal parenchyma, has an intermediate to low risk of malignancy. Isoechogenicity has low sensitivity but high specificity and positive predictive value for the diagnosis of benign nodules.[65]

Halo. A peripheral sonolucent halo that completely or incompletely surrounds a thyroid nodule is present in 60% to 80% of benign nodules and 15% of thyroid cancers.[21,69] Histologically, it is thought to represent the capsule of the nodule, but hyperplastic nodules that have no capsule often have this sonographic feature. The hypothesis that it represents compressed normal thyroid parenchyma seems acceptable, especially for rapidly growing thyroid cancers, which often have thick, irregular, and incomplete halos (see Fig. 19.15C) that are hypovascular or avascular on color Doppler scans. Color and power Doppler imaging demonstrates that the thin, complete peripheral halo, which is strongly suggestive of benign nodules, represents blood vessels coursing around the periphery of the lesion—the "basket pattern."

Margin. Benign thyroid nodules tend to have sharp, well-defined margins, whereas malignant lesions tend to have irregular, spiculated, or poorly defined margins. For any given nodule, however, the appearance of the outer margin cannot reliably predict the histologic features because many exceptions to these general trends have been identified, even if the association of spiculated margins with malignant nodules has been demonstrated as highly specific.[65]

Calcification. Calcification can be detected in about 10% to 15% of thyroid nodules, but the location and pattern of the calcification have a more predictive value in distinguishing benign from malignant lesions.[21] **Peripheral shell (eggshell) calcification,** although rarely present, has traditionally been considered a characteristic of a benign nodule (see Fig. 19.11). As recently reported, however, **thickened and interrupted peripheral calcifications,** particularly if associated with hypoechoic halo, have very high sensitivity for the diagnosis of malignant nature.[70,71] Scattered echogenic foci of calcification with or without associated acoustic shadows are more common. When these calcifications are **large and coarse** (usually related to fibrosis and degeneration), the nodule is more likely to be a benign nodule, with long disease duration. When the calcifications are **fine and punctate,** however, malignancy is more likely. Pathologically, these fine calcifications may be caused by psammoma bodies, typically seen in papillary cancers (see Figs. 19.14 and 19.15).

Medullary thyroid carcinomas often exhibit bright echogenic foci either within the primary tumor or within metastatically involved cervical lymph nodes.[33] The larger echogenic foci are usually associated with acoustic shadowing (see Fig. 19.25). Pathologically, these densities are caused by reactive fibrosis and calcification around amyloid deposits, which are characteristic of medullary carcinoma. In the appropriate clinical setting (e.g., MEN II syndrome, increased serum calcitonin level), the finding of echogenic foci within a hypoechoic thyroid nodule or a cervical node can be highly suggestive of **medullary carcinoma.**

Kakkos and colleagues[72] found a strong association between sonographically detected thyroid calcifications and thyroid malignancy, particularly in young patients or those with a solitary thyroid nodule. Patients younger than 40 with calcified nodules constitute a high-risk group, four times more likely to harbor thyroid malignancies than patients of the same age but without intranodular calcifications. Similarly, the presence of calcifications within a solitary nodule increases the incidence of malignancy. Therefore these patients must be further evaluated or followed.

According to multiple studies of the various sonographic features seen in thyroid nodules, **microcalcifications** show the highest accuracy (76%), specificity (93%), and positive predictive value (70%) for malignancy as a single sign. However, sensitivity is low (36%) and insufficient to be reliable for detection of malignancy.[29,65,72,73]

Doppler Flow Pattern. It is well known from histologic studies that most hyperplastic nodules are hypovascular lesions and are less vascular than normal thyroid parenchyma. On the contrary, most **well-differentiated thyroid carcinomas** are generally hypervascular, with irregular tortuous vessels and AV shunting (see Fig. 19.16). **Poorly differentiated and anaplastic carcinomas** are often hypovascular because of the extensive necrosis associated with their rapid growth (see Fig. 19.26).

Quantitative analysis of flow velocities is not accurate in differentiating benign from malignant nodules, so the only Doppler feature that may be useful is the distribution of vessels. With current technology, no thyroid nodule appears totally avascular or extremely hypovascular on color and power Doppler imaging. The two main categories of vessel distribution are nodules with peripheral vascularity and nodules with internal vascularity (with or without a peripheral component).[19,20,74] Studies have demonstrated that 80% to 95% of hyperplastic, goitrous, and adenomatous nodules display **peripheral vascularity,** whereas 70% to 90% of thyroid malignancies display **internal vascularity,** with or without a peripheral component.[3,5,74-76] In addition, the RI of intranodular vessels was significantly higher in malignant nodules. Consequently, the vascular pattern and RI have been reported to provide high sensitivity (92.3%) and specificity (88%) for the differentiation between benign and malignant tumors.[76] According to other reports, however, color Doppler imaging was not a reliable aid in the sonographic diagnosis of thyroid nodules.[77-79] With the current generation of Doppler instruments, which have extremely high sensitivity to blood flow, the overlapping of the two populations of nodules significantly increased, significantly reducing the diagnostic reliability of Doppler findings.[80]

Findings on gray-scale and color Doppler ultrasound become highly predictive for malignancy only when multiple signs are simultaneously present in a nodule.[59,60,65] In a series the combination of **absent halo sign plus microcalcifications plus intranodular flow pattern** achieved a 97.2% specificity for the diagnosis of thyroid malignancy.[59] In a large study the presence of at least one malignant sonographic finding (taller-than-wide shape, spiculated margin, marked hypoechogenicity, microcalcification and macrocalcification) had sensitivity of 83.3%, specificity of 74.0%, and diagnostic accuracy of 78.0%.[65] The presence of other findings (e.g., rim calcification) showed no statistical significance in the differentiation of a malignant nodule from a benign nodule. In a recent pictorial review based on the ultrasound classification of the British Thyroid Association, benign and malignant features of thyroid nodules have been highlighted and discussed.[81]

Thyroid Imaging Reporting and Data System

To facilitate interpretation and standardization among specialists, recently a standardized system for analyzing and reporting thyroid ultrasound and for risk stratification (Thyroid Imaging Reporting and Data System [TIRADS]) was proposed,[82,83] following the BIRADS system widely used for mammography.

According to this system, thyroid nodules can be categorized in six different risk groups according to their ultrasonographic characteristics:

- TIRADS 1: normal thyroid gland.
- TIRADS 2: benign conditions (0% malignancy), including simple cyst, spongiform nodules, and isolated macrocalcifications.
- TIRADS 3: probably benign nodules (<5% malignancy).
- TIRADS 4: suspicious nodules (5%-80% malignancy rate). Nodules in this group can be further categorized as 4a (malignancy 5%-10%) and 4b (malignancy 10%-80%).
- TIRADS 5: probably malignant nodules (malignancy > 80%).
- TIRADS 6: biopsy-proven malignant nodules.

Contrast-Enhanced Ultrasound and Elastography

Ultrasound elastography and contrast-enhanced ultrasound (CEUS) are advanced techniques for thyroid nodule characterization, with a substantial amount of research in the last decade. CEUS may depict the macrovascularization and microvascularization of thyroid nodules, providing both qualitative and quantitative evaluation. Nodules show heterogeneous enhancement depending on histology. Malignant nodules most frequently have isohypovascular contrast enhancement and slower wash-out than thyroid parenchyma, whereas benign nodules show hypervascular enhancement and a rimlike pattern.[84] A recent meta-analysis based on seven studies regarding CEUS evaluation of thyroid nodules concluded that CEUS, with pooled sensitivity, specificity, and positive and negative likelihood ratio (LR) of 0.853, 0.876, 5.822, and 0.195, respectively, is accurate to differentiate benign from malignant nodules,[85] but studies with larger sample sizes are needed to confirm these preliminary data.

Elastography has also been applied to the study of thyroid nodules. Elastography provides information on tissue elasticity, based on the premise that pathologic processes such as cancer alter the physical characteristics of the involved tissue. The purpose is to acquire two sonographic images (before and after tissue compression) and track tissue displacement by assessing the propagation of the beam, providing accurate measurement of tissue distortion.[86,87]

Elastography applied to the thyroid gland uses principally two different approaches according to the type of compression force (excitation) and elasticity evaluation: (1) freehand ultrasound strain elastography, with its qualitative (based on colorimetric maps and divided into four or five classes)[88] and semiquantitative variants (strain ratio value); and (2) quantitative approach with transducer-induced high acoustic pulse and measures of the speed of the shear wave generated (shear wave elastography [SWE]). SWE can be performed using acoustic radiation force impulse (ARFI) technology either in a small region of interest (ROI) (point–shear wave elastography, p-SWE) or over a larger field of view using color-coding to visually display the stiffness values (two-dimensional shear wave elastography [2D-SWE]). An additional semiquantitative variant of strain elastography uses the internal (physiologic) pulsation of the carotid artery (*in vivo* quasi-static elastography). In this approach, no external

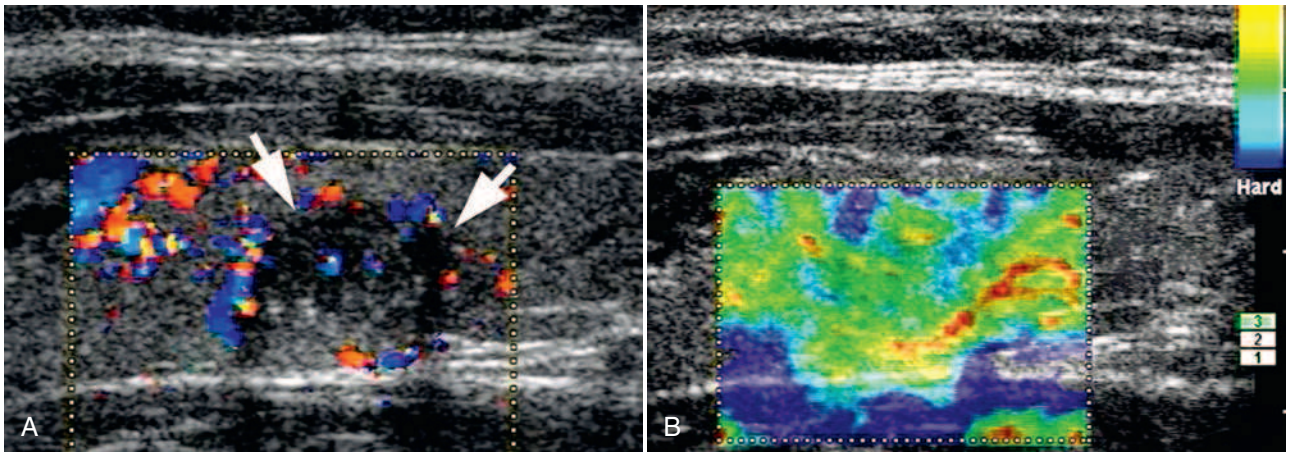

FIG. 19.31 Use of Ultrasound Elastography on Thyroid Nodule: Benign Nodular Hyperplasia (Pattern 1). (A) Conventional longitudinal B-mode sonogram with color Doppler shows a hypoechoic solid nodule *(arrows)* with peripheral halo, internal comet-tail artifacts, and perilesional blood flow pattern. **(B)** Longitudinal ultrasound elastography at same location demonstrates a "soft" color pattern.

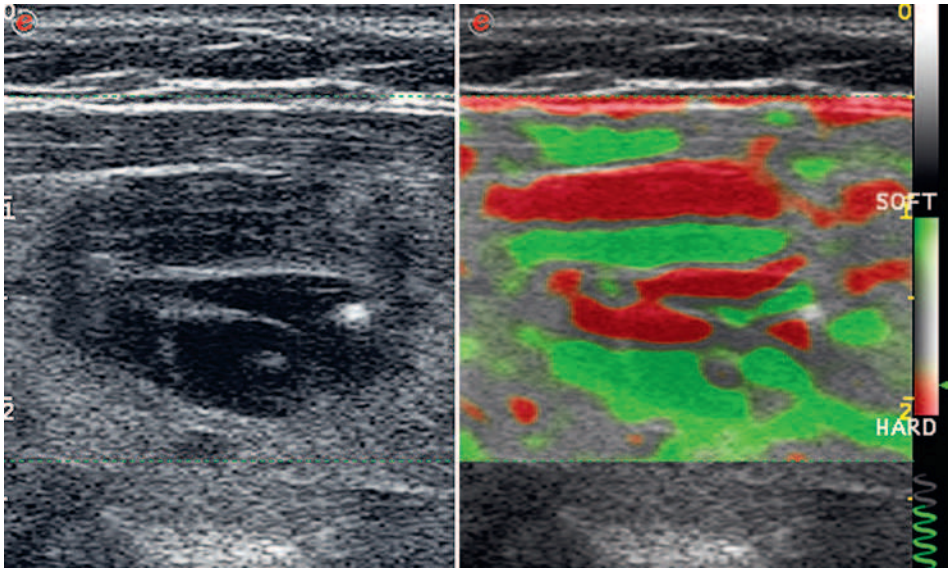

FIG. 19.32 Use of Ultrasound Elastography on Thyroid Nodule: Benign Nodular Hyperplasia With Cystic Changes (Pattern 2). Left half of image shows a cystic, poorly defined nodule on conventional B-mode gray-scale sonogram. Right half of elastogram of the nodule shows a predominantly elastic *(green)* pattern with a few internal anelastic bandlike areas.

pressure is required and pulsations of the carotid artery induce the displacement necessary to assess tissue elasticity.[89] Several papers and recent meta-analyses show very interesting results of qualitative and quantitative elastography.[90-93]

Four elastographic patterns have been classified as follows[86,87,94,95]:

Pattern 1: Elasticity in the whole nodule (Fig. 19.31)

Pattern 2: Elasticity in a large part of the nodule, with inconstant appearance of anelastic areas (Fig. 19.32)

Pattern 3: Constant presence of large unelastic areas at the periphery (Fig. 19.33)

Pattern 4: Uniformly unelastic (Fig. 19.34)

In literature reports, 78% to 100% of benign nodules had a score of 1 to 2, whereas 88% to 96% of malignant nodules had a score of 3 to 4. Sensitivity was 82% to 97%, specificity 78% to 100%, positive predictive value 64% to 81%, and negative predictive value 91% to 98%.[87-98] Specificity and sensitivity are relatively independent of the nodule size. However, the best accuracy is achieved in small nodules and when FNA biopsy is nondiagnostic or suggests a follicular lesion, provided the nodule is solid and devoid of coarse calcifications. Both strain elastography and SWE should be performed as additional tools to conventional ultrasound and to guide follow-up of lesions previously diagnosed as benign at FNA because multiparametric sonographic assessment can increase the accuracy of the ultrasound evaluation (Fig. 19.35), avoiding unnecessary biopsies or surgery.

Guidance for Needle Biopsy

Sonographically guided percutaneous needle biopsy of cervical masses has become an important technique in many clinical situations. Its main advantage is that it affords continuous real-time visualization of the needle, a crucial requirement for the biopsy of small lesions. Most physicians use a 25-gauge needle, employing either capillary action or minimal suction with a

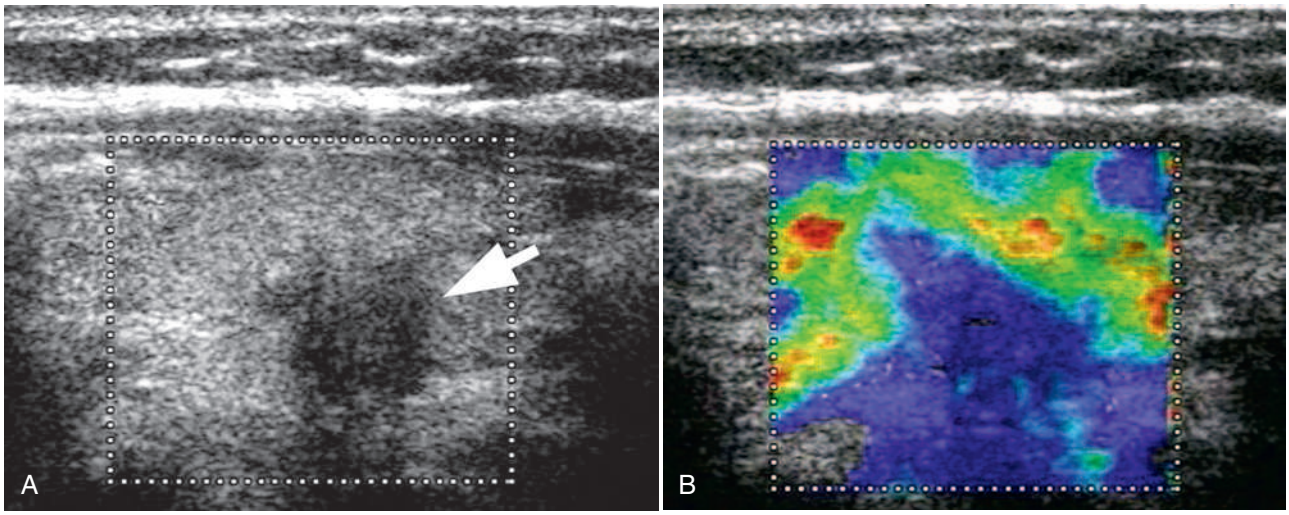

FIG. 19.33 Use of Ultrasound Elastography on Thyroid Nodule: Papillary Thyroid Carcinoma (Pattern 3). (A) Conventional longitudinal B-mode sonogram demonstrates a hypoechoic papillary carcinoma with irregular, poorly defined margins *(arrow)*. **(B)** Ultrasound elastography shows a predominantly inelastic *(blue)* pattern with a few small, elastic *(green)* areas in the posterior portion.

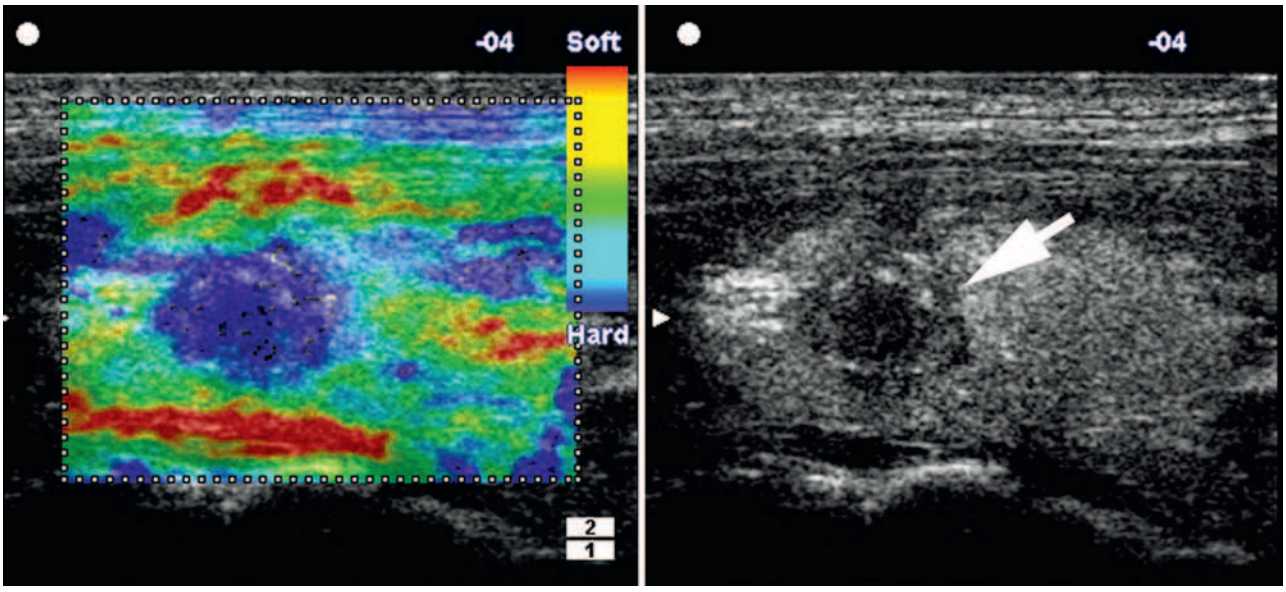

FIG. 19.34 Use of Ultrasound Elastography on Thyroid Nodule: Papillary Thyroid Carcinoma (Pattern 4). Right half of image shows a hypoechoic solid nodule *(arrow)* with microcalcifications, typical of papillary carcinoma. Left half of image shows that on ultrasound elastography, the nodule is almost entirely inelastic *(blue)* pattern 4. The small, elastic areas in the posterior portion of the lesion are artifacts caused by pulsations of the underlying carotid artery.

syringe (Video 19.6). There are reports of the usefulness of large-gauge, automated cutting needles for improved pathologic diagnosis.[99,100] Sonographic guidance is generally suggested for all thyroid aspiration biopsies, but it is strongly recommended in three settings. The first situation is the questionable or inconclusive physical examination in which a nodule is suggested but cannot be palpated with certainty. In these patients, sonography is used to confirm the presence of a nodule and to provide guidance for accurate biopsy. The second setting involves patients at high risk for thyroid cancer with a normal gland on physical examination but a sonographically demonstrated nodule. This group includes patients with a previous history of head and neck irradiation, a positive family history of MEN II syndrome, or a previous subtotal thyroid resection for malignancy. The third situation for ultrasound FNA guidance involves patients who have had a nondiagnostic or inconclusive biopsy performed under direct palpation. Usually about 20% of specimens obtained by palpation guidance are cytologically inconclusive, most often because of the aspiration of nondiagnostic fluid from cystic lesions. Sonography may be used in these cases to guide the needle selectively into a solid portion of the mass. The diagnostic accuracy of FNA is very high, with sensitivity approximately 85% and specificity of 99% in centers with extensive experience performing these procedures.[41-48,101]

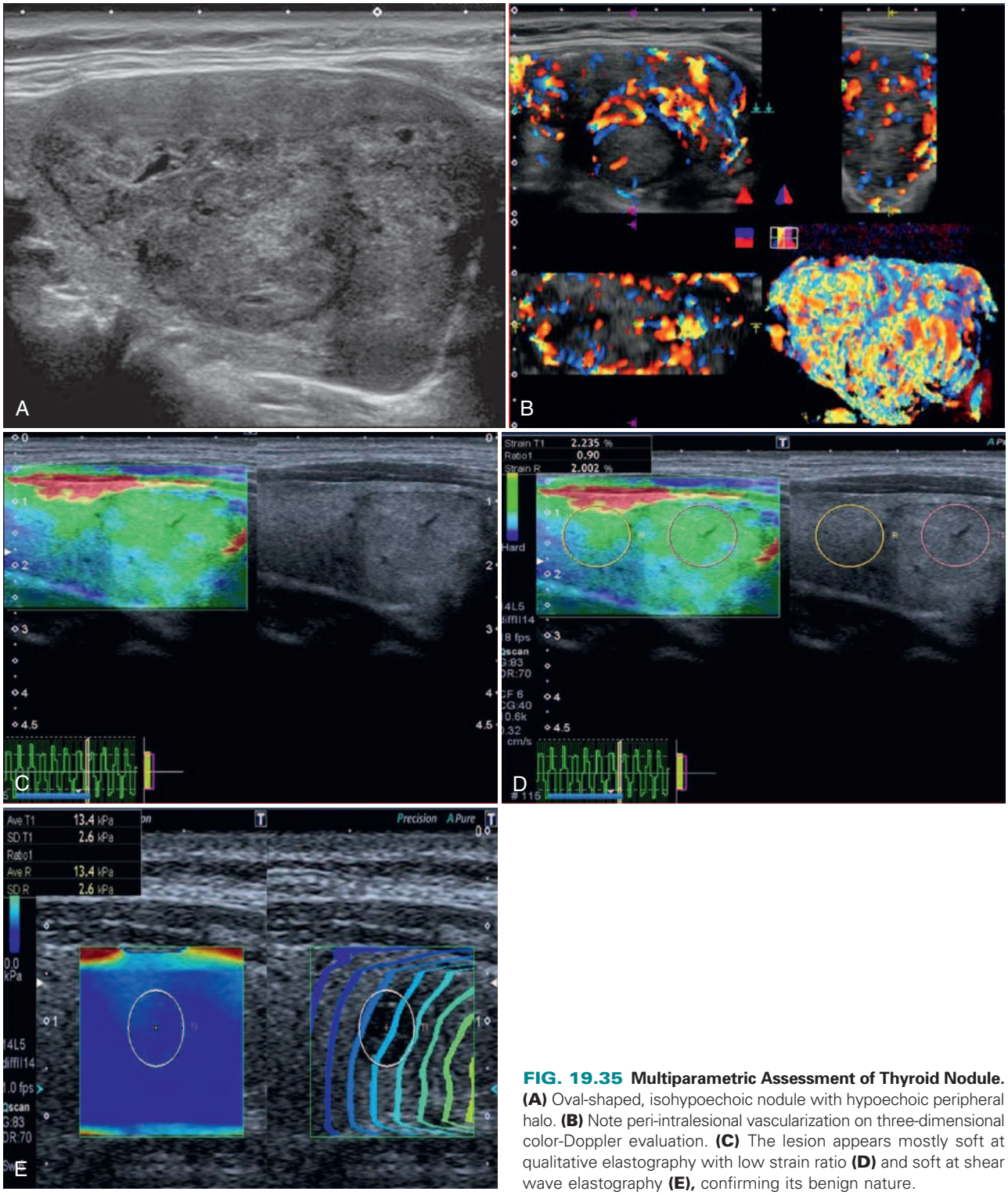

FIG. 19.35 Multiparametric Assessment of Thyroid Nodule. **(A)** Oval-shaped, isohypoechoic nodule with hypoechoic peripheral halo. **(B)** Note peri-intralesional vascularization on three-dimensional color-Doppler evaluation. **(C)** The lesion appears mostly soft at qualitative elastography with low strain ratio **(D)** and soft at shear wave elastography **(E),** confirming its benign nature.

In patients who have undergone a previous thyroid resection for carcinoma, sonographically guided FNA has become an important method in the early diagnosis of recurrent or metastatic disease in the neck (Fig. 19.36). In patients who have undergone hemithyroidectomy for a benign nodule, with the detection of one or more foci of occult malignant tumor in the surgical specimen, ultrasound evaluation of the contralateral lobe is warranted to exclude the existence of a residual nodule.

Cervical lymph nodes, both normal and abnormal, can be readily visualized by high-resolution sonography. They tend to lie along the internal jugular chain, extending from the level of the clavicles to the angle of the mandible, or to be in the region of the thyroid bed. **Benign cervical lymph nodes** usually have

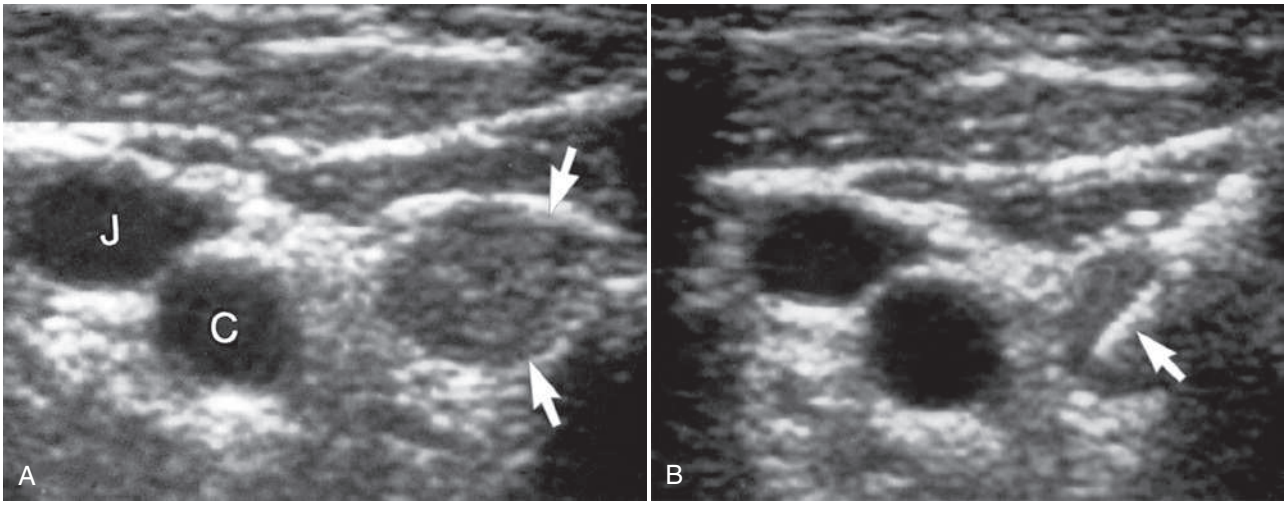

FIG. 19.36 Biopsy of Recurrent Papillary Carcinoma in Thyroid Bed After Thyroidectomy. (A) Transverse scan of right side of the neck shows a 1-cm solid mass *(arrows)* medial to carotid artery *(C)* and jugular vein *(J)*. **(B)** Sonographically guided fine-needle aspiration with needle seen within mass *(arrow)*.

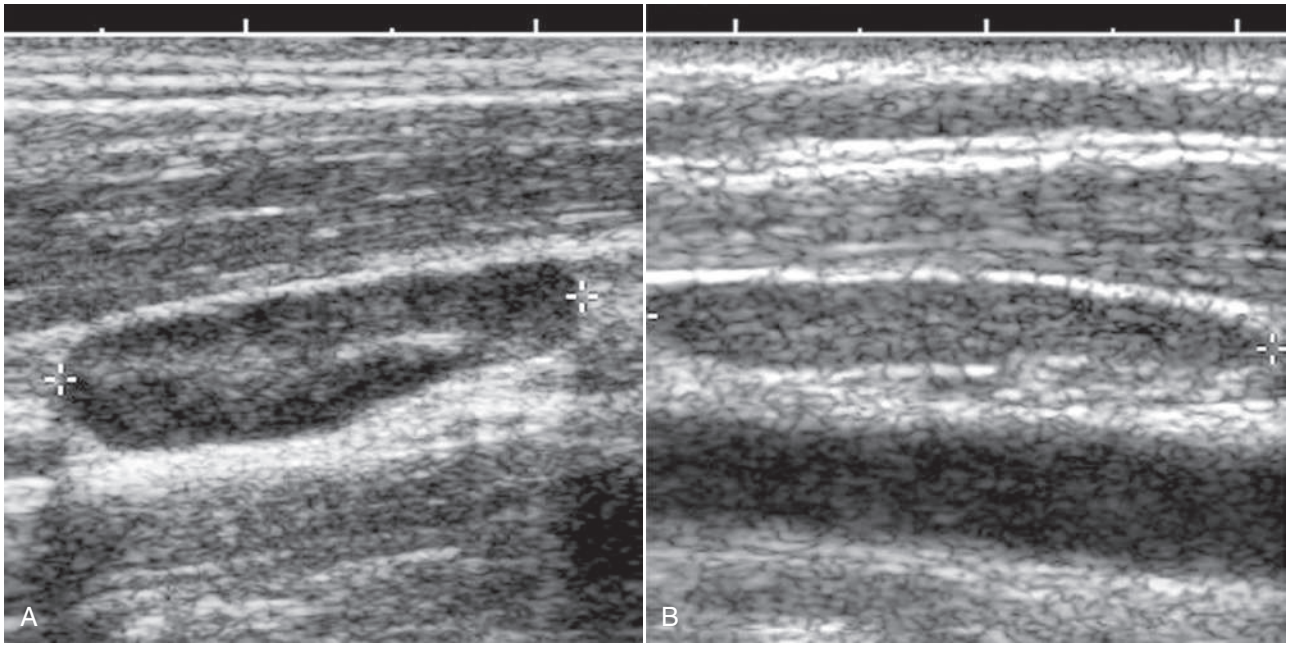

FIG. 19.37 Normal Cervical Lymph Nodes: Elongated Shape Is Typical. Longitudinal images. **(A)** Slender node *(calipers)* is homogeneous except for central echogenic hilum. **(B)** Normal homogeneous slender node *(calipers)* near the jugular vein without a visible hilum.

a slender, oval shape and often exhibit a central echogenic band that represents the fatty hilum (Fig. 19.37). **Malignant lymph nodes,** on the other hand, are more often located in the lower third of the neck and are usually rounder and have no echogenic hilum, presumably because of obliteration by tumor infiltration (see Fig. 19.17). Although often hypoechoic, malignant nodes may be diffusely echogenic, may be heterogeneous, and may contain calcifications and cystic changes. Calcifications can be seen in nodal metastases from papillary and medullary thyroid malignancies, and cystic changes are very characteristic in metastatic papillary carcinoma.[102] In addition, Lyshchik and colleagues[103] reported that with use of elastography, cervical lymph nodes with a strain index greater than 1.5 are usually malignant (85% sensitivity and 98% specificity).

When the differentiation between benign and malignant lymph nodes is not feasible with sonography, FNA under sonographic guidance is often used. In our experience, biopsy can be done with a high degree of accuracy in cervical nodes that are as small as 0.5 cm in diameter.[58] In addition to cytologic analysis, the "wash-out" of the aspirate can be sent for thyroglobulin assay, which is highly accurate for the diagnosis of metastatic papillary and follicular cancer.[104]

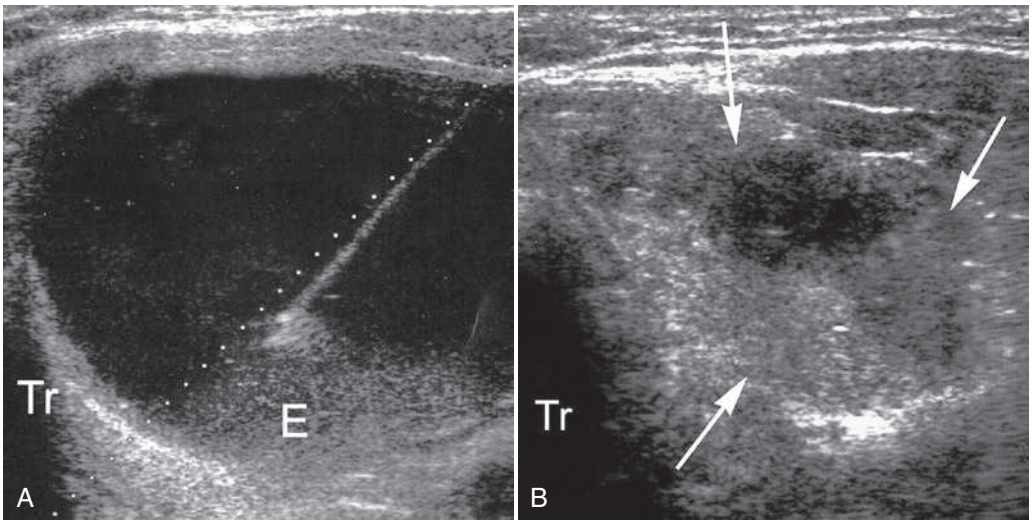

FIG. 19.38 Ethanol Treatment of Large Colloid Cyst. (A) Transverse image shows large colloid cyst with needle. Injected ethanol appears as low-level echoes *(E). Tr,* Tracheal air shadow. **(B)** Follow-up image 1 month later shows that the large cystic component has mostly resolved, leaving a slightly enlarged residual gland *(arrows).*

Guidance for Percutaneous Treatment

Ethanol Injection of Benign Cystic Thyroid Lesions. Lesions containing fluid (usually colloid cysts) account for 31% of thyroid nodules found on sonography, but less than 1% of these are pure epithelial-lined cysts.[5] Management of cystic thyroid nodules relies first on FNA biopsy to rule out malignancy. Simple aspiration may result in permanent shrinkage of the lesion, but the recurrence rate after aspiration is high, 10% to 80%, depending on the number of aspirations and the cyst volume; the greater the volume, the greater the recurrence risk.[105,106]

Prevention of cyst recurrence requires intranodular injection of a sclerosing agent. Ethanol has been used successfully for the past 20 years, with accurate placement using real-time sonographic guidance. Ethanol is distributed within tissues by diffusion and induces cellular dehydration and protein denaturation, followed by coagulation necrosis and reactive fibrosis. The cyst fluid is completely aspirated with a fine needle, and then sterile 95% ethanol is injected under ultrasound guidance, in an amount varying from 30% to 60% of the aspirated fluid[107,108] (Fig. 19.38). Subsequently, ethanol can be either reaspirated in 1 to 2 days or permanently left in place. In large cystic cavities, this procedure can be repeated once or twice after several weeks. The volume reduction of the cyst is more substantial if a larger amount of ethanol is injected; thus a relationship exists between the volume of ethanol instilled and the ablative effect.

Ethanol injection is usually well tolerated by the patient. Transient mild to moderate local pain is the most common complication, a result of ethanol leaking into subcutaneous tissue. Rare complications of **ethanol sclerotherapy** are transient hyperthyroidism, hoarseness, hematoma, and dyspnea.

Reported success rates (total disappearance or volume reduction greater than 70% of initial volume) of this treatment range from 72% to 95% at long-term follow-up,[107-110] achieved without a change in thyroid function. Ethanol injection is considered the percutaneous treatment of choice for cystic lesions of the thyroid gland at some institutions.

Ethanol Injection of Autonomously Functioning Thyroid Nodules. Thyroid nodules with independent secretory and proliferative activity are defined as **autonomous** thyroid nodules. On radionuclide scans, these nodules appear "hot," in contrast to the low or absent extranodular uptake, likely related to the avidity of iodine trapping and the degree of thyroid hyperfunction. The patient's condition may be toxic or nontoxic, depending on the amount of thyroid hormones secreted. The level of hyperthyroidism is usually proportional to the nodule volume. Therefore autonomous thyroid nodules can cause a range of functional abnormalities, from euthyroidism (compensated) to subclinical hyperthyroidism (pretoxic) and clinical hyperthyroidism (toxic).

The currently available treatments of autonomous nodules include surgery and radioactive iodine therapy. Surgery is effective but has the disadvantage of anesthesiology and surgical risks. Radioactive iodine therapy may require repeated sessions before achieving euthyroidism.

Percutaneous ethanol injection under ultrasound guidance, first proposed by Livraghi and colleagues[111] in 1990, is an alternative therapy. The diffusion of ethanol causes direct damage. Cell dehydration is followed by immediate coagulation necrosis and subsequent fibrotic changes. Sterile 95% ethanol is injected through a 21- or 22-gauge spinal needle with closed conical tip and three terminal side holes. This allows the injection of a large amount of ethanol, reduces the total number of sessions, increases the treated volume, and minimizes the risk of laryngeal nerve damage because of the lateral diffusion of ethanol. Several treatment sessions are needed (usually four to eight), typically performed at 2-day to 2-week intervals. The total amount of ethanol delivered is usually 1.5 times the nodular volume.

Color Doppler imaging and, if available, contrast-enhanced sonography are extremely valuable to assess the results of ethanol injection. The reduction (up to complete disappearance) of vascularity and contrast enhancement is directly related to the ethanol-induced necrosis. In addition, residual vascularity after

treatment can be targeted to achieve complete ablation.[112] **Complete cure** is defined as normalization of serum free thyroid hormones and serum thyrotropin and scintigraphic reactivation of extranodular tissue. **Partial cure** occurs when serum free thyroid hormones and thyrotropin levels are normalized, but the nodule is still visible on scintigraphy.[111,113]

Percutaneous ethanol injection is generally well tolerated. The common side effect is a brief burning sensation or moderate pain at the injection site, radiating to the mandibular or retroauricular regions. The slow withdrawal of the needle and use of the multihole needle reduce this side effect. In some patients with larger nodules, when the amount of necrosis is high, fever lasting 2 to 3 days develops after the initial treatments. The only important complication is transient damage of the recurrent laryngeal nerve, reported in 1% to 4% of cases.[80,94] Nerve damage is induced chemically or by compression. Full nerve recovery is likely because, in contrast to surgery, there is no anatomic nerve interruption.

Efficacy of response is inversely proportional to the nodule volume; the smaller the nodule, the more complete the response. Complete cure is achieved in 68% to 100% of pretoxic nodules and 50% to 89% of toxic nodules.[111-116] Ultrasound-guided percutaneous ethanol injection is the treatment of choice in older patients with contraindications to surgery, in pregnant patients, and in patients with large autonomous nodules (>40 mL), in addition to medical treatment to obtain euthyroidism more rapidly.

More recently, the use of **radiofrequency ablation** (RFA) with either internally cooled or multipronged electrodes has been reported in the treatment of autonomously functioning thyroid nodules, mostly for large nodules causing compressive symptoms. A significant decrease in size (≥50%) of the treated lesions was reported in all cases, and complete normalization of thyroid function was achieved in 24% to 44% of patients.[117,118] Also **laser ablation** has been used in the treatment of large toxic nodular goiter and has been proposed as combined treatment with ^{131}I to fasten the volumetric reduction and reduce the radioactive dose administered to the patient.[119]

Percutaneous Treatment of Solitary Solid Benign "Cold" Thyroid Nodules. In patients with solitary solid, biopsy-proven, benign "cold" thyroid nodules, ethanol injection, interstitial laser photocoagulation, and RFA have been proposed as ultrasound-guided percutaneous treatments, to achieve marked shrinkage of the nodule to a small, fibrous-calcified mass. With percutaneous ethanol injection, a mean nodule volume reduction of 84% (range, 73%-98%) has been reported after 3 to 10 treatments.[120] With low-power interstitial laser photocoagulation, mean thyroid nodule volumes decreased by 40% to 50% after 6 months, with improvement of local clinical symptoms in approximately 80% of patients and no side effects.[121-124]

RFA with internally cooled electrodes and low power (20-70 W) has also been employed for the treatment of benign cold thyroid nodules, with only one ablation session for a single nodule. A significant volume reduction of the treated nodules without adverse effects has been reported at follow-up, but studies with longer follow-up are needed to assess efficacy and safety.[125,126]

Treatment of Cervical Nodal Metastases From Papillary Carcinoma. RFA, laser ablation, and ethanol injection have been proposed for the treatment of recurrent disease and metastatic lymph nodes in patients who have previously undergone surgery. Percutaneous ethanol injection is an effective and safe method of treatment for limited lymph node metastasis from thyroid cancer. In a 2002 report from the Mayo Clinic, 14 patients who had undergone thyroidectomy for PTC had 29 metastatic lymph nodes on follow-up sonographic imaging.[127] Each node was treated with direct injection of ethanol using ultrasound guidance. Follow-up examination at 2 years showed a 95% decrease in the size of treated nodes. There were no major complications (e.g., recurrent laryngeal nerve palsy, bleeding) in the Mayo Clinic series or in 187 patients with papillary cancer nodes treated with percutaneous ethanol injection at the Ito Hospital in Japan.[128,129]

The percutaneous ethanol injection technique is similar to the method used for percutaneous ethanol therapy of parathyroid adenomas. A 25-gauge needle is attached to a tuberculin syringe containing up to 1 mL of 95% ethanol. The needle is placed with ultrasound guidance using a freehand technique that allows fine positioning of the needle within the node (Fig. 19.39). Each node is injected in several sites. The portion of the node that is injected becomes hyperechoic owing to the formation of microbubbles of gas. After usually less than 1 minute, the hyperechoic zone decreases. The needle is repositioned in the node, and several injections are made until the node appears adequately treated. Patients may experience mild to moderate pain at injection, but this resolves within minutes. For small nodes about 5 mm in diameter, a single injection may be sufficient. For larger nodes, a reinjection the following day is needed for complete therapy. Follow-up ultrasound at 3 to 6 months will show a reduction in size of the node in most cases. If blood flow was visualized in the node before therapy, it will often be substantially decreased or absent on follow-up. If on follow-up the size of the node has not decreased, or if there is residual blood flow on power Doppler examination, a repeat injection is performed.

Thermal ablation of nodal recurrent thyroid cancer has also been tested, with both RFA and laser ablation. In particular, laser ablation seems to be particularly promising in the treatment of nodal metastases from thyroid carcinoma; it is performed using thin (21-gauge) needles, and the energy can be delivered with great precision, allowing avoidance of damage to critical surrounding structures.[130-132]

The Incidentally Detected Nodule

Although using high-frequency sonography to detect small, nonpalpable thyroid nodules may be beneficial in certain clinical settings, it may actually introduce problems in other situations. What should one do with the many thyroid nodules detected incidentally during carotid, parathyroid, and other sonographic examinations of the neck? The goal should be to avoid extensive and costly evaluations in the majority of patients with benign disease, without missing the minority of patients who have clinically significant thyroid cancer. In our literature review, the incidence of thyroid nodules in patients can be estimated by method of detection: autopsy (49%), sonography (47%), palpation

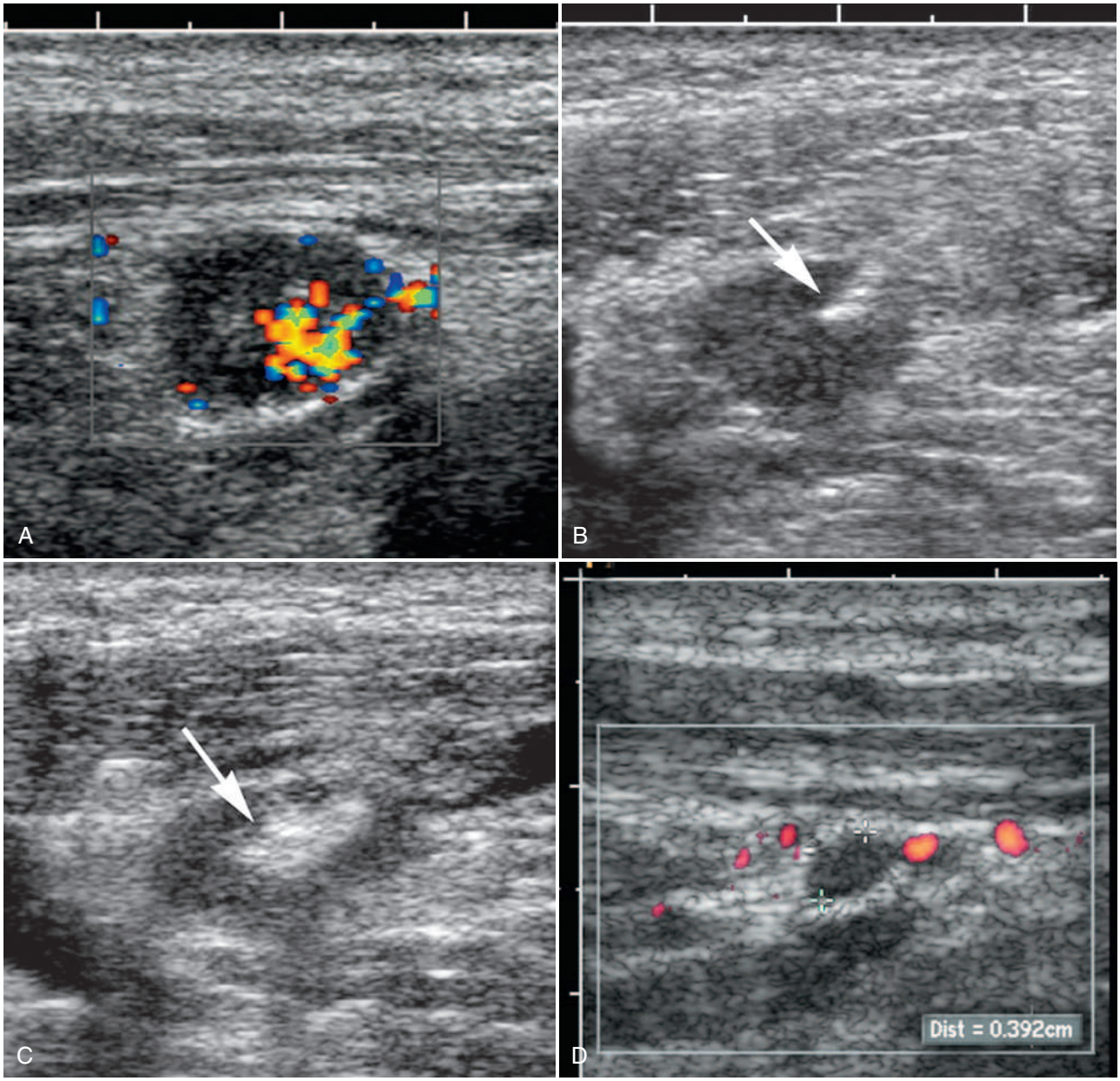

FIG. 19.39 Ethanol Treatment of Thyroid Metastasis in a Cervical Lymph Node. (A) Longitudinal color Doppler image shows a round, 1.6-cm, pathologic-appearing node with moderate vascularity. **(B)** The tip of a 25-gauge needle *(arrow)* is in the lymph node. **(C)** The ethanol effect is visible as a focal hyperechoic area *(arrow)* at injection and is caused by microbubbles that form from the interaction of ethanol with the tissues. This hyperechoic appearance will last from several seconds to several minutes and will be followed by a normal or near-normal appearance. During the injection, the hyperechogenicity is a useful marker to identify the areas treated. **(D)** Follow-up power Doppler image 6 months after ethanol injection shows that the lymph node has dramatically decreased in size (0.4 cm) and is no longer vascular. No further therapy is needed except to follow every 6 to 12 months to confirm lack of change.

(7%), occult cancer at autopsy (2%), and annual cancer incidence (0.005%).

Understanding the challenge of selecting nodules for workup requires background information in the following four areas:

1. The epidemic of thyroid nodules has resulted mostly from ultrasound imaging.

On physical palpation, an estimated 7% of the North American population has at least one thyroid nodule. In contrast, there is an "epidemic" of thyroid nodules detected by ultrasound, with studies showing up to 67% of patients having a nodule.[133] Our study of 1000 consecutive patients imaged with 10-MHz ultrasound transducers showed a prevalence of 41%.[134] This study also showed an increasing prevalence with advancing age, which parallels autopsy rates of prevalence compared with patient age (Fig. 19.40).

From these studies it is reasonable to estimate that more than 100 million Americans have thyroid nodules on ultrasound. The problem of the high rate of incidentally detected thyroid nodules, the so-called "incidentaloma," has led some to ask if it is "time to turn off the ultrasound machines."[135] The morbidity and cost

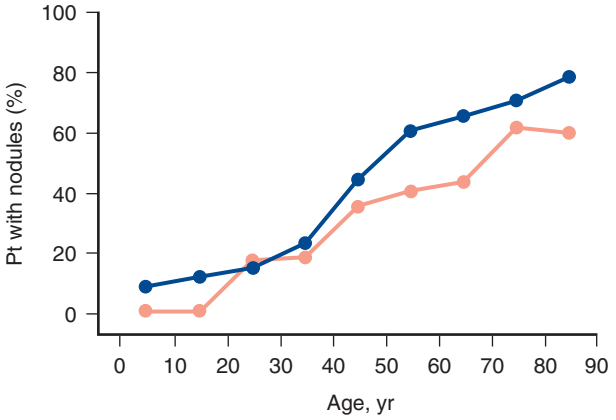

FIG. 19.40 Prevalence of Thyroid Nodules on Autopsy and Sonography. Autopsy *(blue circles)* revealed thyroid nodules on average in 49% of patients in 1955, and sonography *(orange circles)* detected thyroid nodules in 41% in 1985, with both shown here as a function of patient age. (With permission from Horlocker T, Hay I, James E. Prevalence of incidental nodular thyroid disease detected during high-resolution parathyroid ultrasonography. In: Medeiros-Neto G, Gaitan E, editors. Frontiers in thyroidology. New York: Plenum; 1986. p. 1209-1312.[134])

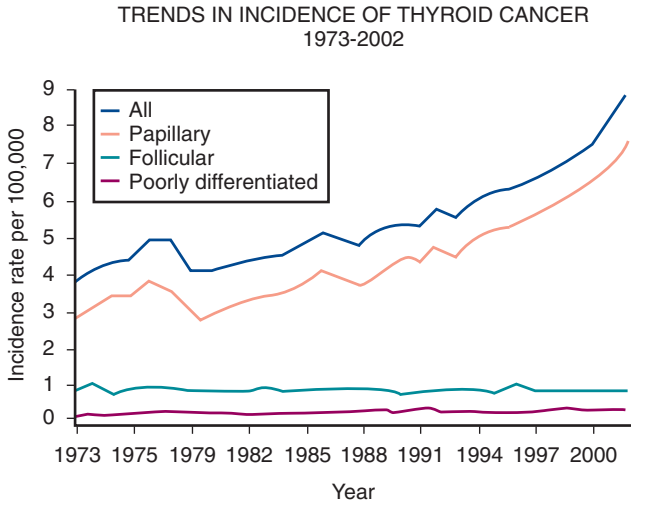

FIG. 19.41 Thyroid Cancer: Incidence. Graph shows the increasing incidence of thyroid cancer in North America during the past three decades. Note that the type of thyroid malignancy is almost entirely papillary carcinoma. The increasing incidence results from the increased rate of detection by diagnostic imaging methods such as ultrasound, rather than from an increase in the true occurrence of thyroid cancer. (Modified from Davies L, Welch HG. Increasing incidence of thyroid cancer in the United States, 1973-2002. JAMA. 2006;295[18]: 2164-2167.[138])

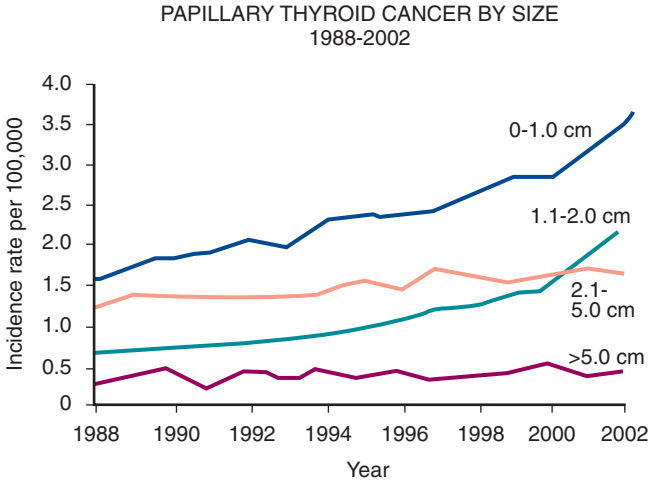

FIG. 19.42 Thyroid Cancer: Incidence by Size of Tumor. Note that the increased incidence of thyroid carcinoma is primarily the result of the detection of smaller tumors. (Adapted from Davies L, Welch HG. Increasing incidence of thyroid cancer in the United States, 1973-2002. JAMA. 2006;295[18]:2164-2167.[138])

to patients and society from workup of these nodules may far outweigh the benefit of detecting an occult thyroid cancer, because the vast majority of thyroid cancers behave in a benign manner. Specifically, patients with PTC have a 99% 10-year survival and approximately a 95% overall 30-year survival.[55,136]

2. The incidence of thyroid cancer is increasing.

Over 50 years ago, pathologists reported that clinically insignificant thyroid cancer was a common finding at autopsy. In the 1980s, Harach and colleagues[137] studied thinly sectioned thyroid glands at autopsy and found that 36% had occult thyroid cancer. They stated that had they sectioned the glands even more finely, almost every person would harbor a thyroid cancer. They concluded that occult PTC was a "normal" finding at autopsy.

Over the last three decades, the reported incidence of thyroid cancer in North America has more than doubled.[138] This raises the question of whether the increase represents a real increased incidence of thyroid cancer or is simply a result of an increased rate of detection by diagnostic imaging methods such as ultrasound. Analyzing the data, Davies and Welch[138] found that the increased incidence resulted from increased detection of subclinical disease rather than from an increase in the true occurrence of thyroid cancer. Their work showed that PTC accounts for virtually the entire increase in incidence (Fig. 19.41). They also showed that the increased rate of detection is caused by small, subclinical thyroid cancer (Fig. 19.42). Furthermore, although the prevalence of thyroid cancer more than doubled over 30 years, the mortality rate remained unchanged (Fig. 19.43). According to Ross,[139] "Considering the anxiety, costs and complications suffered by many of these patients, one can reasonably question the benefits of increased cancer detection."

3. What are the costs of frequent use of FNA biopsy for management of incidentally detected thyroid nodules?

If FNA biopsy were used as the automatic next step after nodule detection, the costs to patients and society would be great. Whereas FNA biopsy is considered the "reference standard" for nodule diagnosis, it is an imperfect technique for many reasons. First, the results are nondiagnostic in 10% to 20% of cases.[101,140] Second, there is a false-negative rate of 3% to 5%.[141] Third, interpretative skills vary widely regarding cytopathology of the thyroid nodule. Unfortunately, in less experienced centers, the report of "follicular cells are present, cannot exclude follicular neoplasm" occurs more frequently than in centers with greater interpretive experience. This report typically leads to the need for surgical excision. Given these considerations, an estimated 18% of all patients who have FNA biopsy ultimately undergo

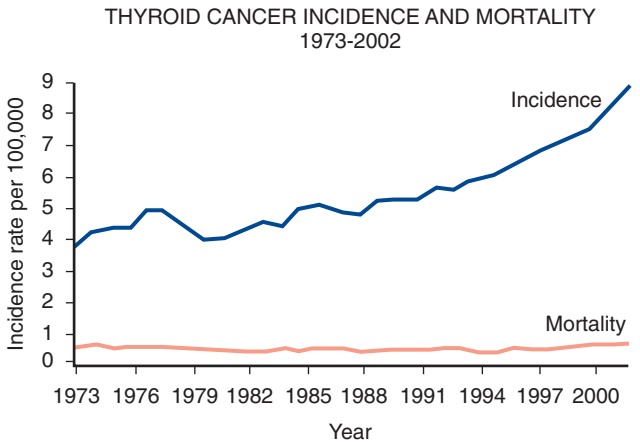

FIG. 19.43 Thyroid Cancer: Incidence Versus Mortality. Although the rate of occurrence of thyroid cancer has more than doubled in the last 30 years, the mortality rate is unchanged over that period. (Adapted from Davies L, Welch HG. Increasing incidence of thyroid cancer in the United States, 1973-2002. JAMA. 2006;295[18]:2164-2167.[138])

surgery for nodule excision based on positive, suspicious, or nondiagnostic results, and most of these nodules are benign.[101,142,143] Of these surgical patients, only 15% to 32% have cancer.[101,142] Therefore the majority of patients who undergo surgery for thyroid nodule excision will have had an operation for clinically insignificant, benign nodular disease.

The potential cost of the FNA biopsy workup of these nodules must be considered. For discussion purposes, assume that 1 million of the estimated 300 million people in the United States undergo a high-frequency ultrasound thyroid examination, and that one or more thyroid nodules are detected in approximately 40%. Therefore 400,000 people will have one or more thyroid nodules detected by ultrasound imaging. Assuming a cost of approximately $1500 for an ultrasound-guided FNA and cytologic analysis, $600 million could theoretically be spent to exclude or detect thyroid cancer in this group. If 18% of these FNA biopsies result in suspicious or nondiagnostic results, 72,000 procedures could occur at a cost of almost $20,000 each, for an additional cost of $1.44 billion. Finally, approximately 5%, or almost 3600 patients, could experience significant postsurgical morbidity, including hoarseness, hypoparathyroidism, and long-lasting pain.[144] Clearly, this type of aggressive management of thyroid nodules would entail massive health care expenditures and could have an extremely negative clinical impact.[145]

4. Which incidentally discovered nodules should be pursued? Because of the many nodules detected on ultrasound, the therapeutic approach should allow most patients with clinically significant cancers to go on to further investigations. More important, it should allow most patients with benign lesions to avoid further costly, potentially harmful workup. With this goal in mind, many practices, including ours, have found that it is both impractical and imprudent to pursue the diagnosis for most of the small nodules detected incidentally on ultrasound. If technically possible, we usually obtain FNA biopsy of lesions that exhibit sonographic features strongly associated with malignancy, such as marked hypoechogenicity, taller-than-wide shape, and thick irregular margins, as well as lesions containing microcalcifications.

Evaluation of Nodules Incidentally Detected by Sonography

Sonographic Findings	Follow-Up
Nodules < 1.5 cm	Followed by palpation at next physical examination
Nodules > 1.5 cm	Evaluation, usually by fine-needle aspiration
Nodules that have malignant features (marked hypoechogenicity, taller-than-wide shape, thick irregular margins, and/or calcifications or microcalcifications)	Evaluation by fine-needle aspiration

DIFFUSE THYROID DISEASE

Several thyroid diseases are characterized by diffuse rather than focal involvement. This usually results in generalized enlargement of the gland **(goiter)** and no palpable nodules. Specific conditions that produce such diffuse enlargement include chronic autoimmune lymphocytic **thyroiditis (Hashimoto thyroiditis), colloid or adenomatous goiter,** and **Graves disease.** These conditions are usually diagnosed on the basis of clinical and laboratory findings and occasionally FNA biopsy. Sonography is seldom indicated. However, high-resolution sonography can be helpful when the underlying diffuse disease causes **asymmetrical thyroid enlargement,** which suggests a mass in the larger lobe. The sonographic finding of generalized parenchymal abnormality may alert the clinician to consider diffuse thyroid disease as the underlying cause. FNA, with sonographic guidance if necessary, can be performed if a nodule is detected. Recognition of diffuse thyroid enlargement on sonography can often be facilitated by noting the thickness of the isthmus, normally a thin bridge of tissue measuring only a few millimeters in AP dimension. With diffuse thyroid enlargement, the isthmus may be up to 1 cm or more in thickness.

Diffuse Thyroid Diseases

Acute suppurative thyroiditis
Subacute granulomatous thyroiditis
Hashimoto thyroiditis (chronic lymphocytic thyroiditis)
Adenomatous or colloid goiter
Painless (silent) thyroiditis

Each type of thyroiditis, including acute suppurative thyroiditis, subacute granulomatous thyroiditis (de Quervain disease), and chronic lymphocytic thyroiditis (Hashimoto disease) has distinctive clinical and laboratory features.[146] **Acute suppurative thyroiditis** is a rare inflammatory disease usually caused by bacterial

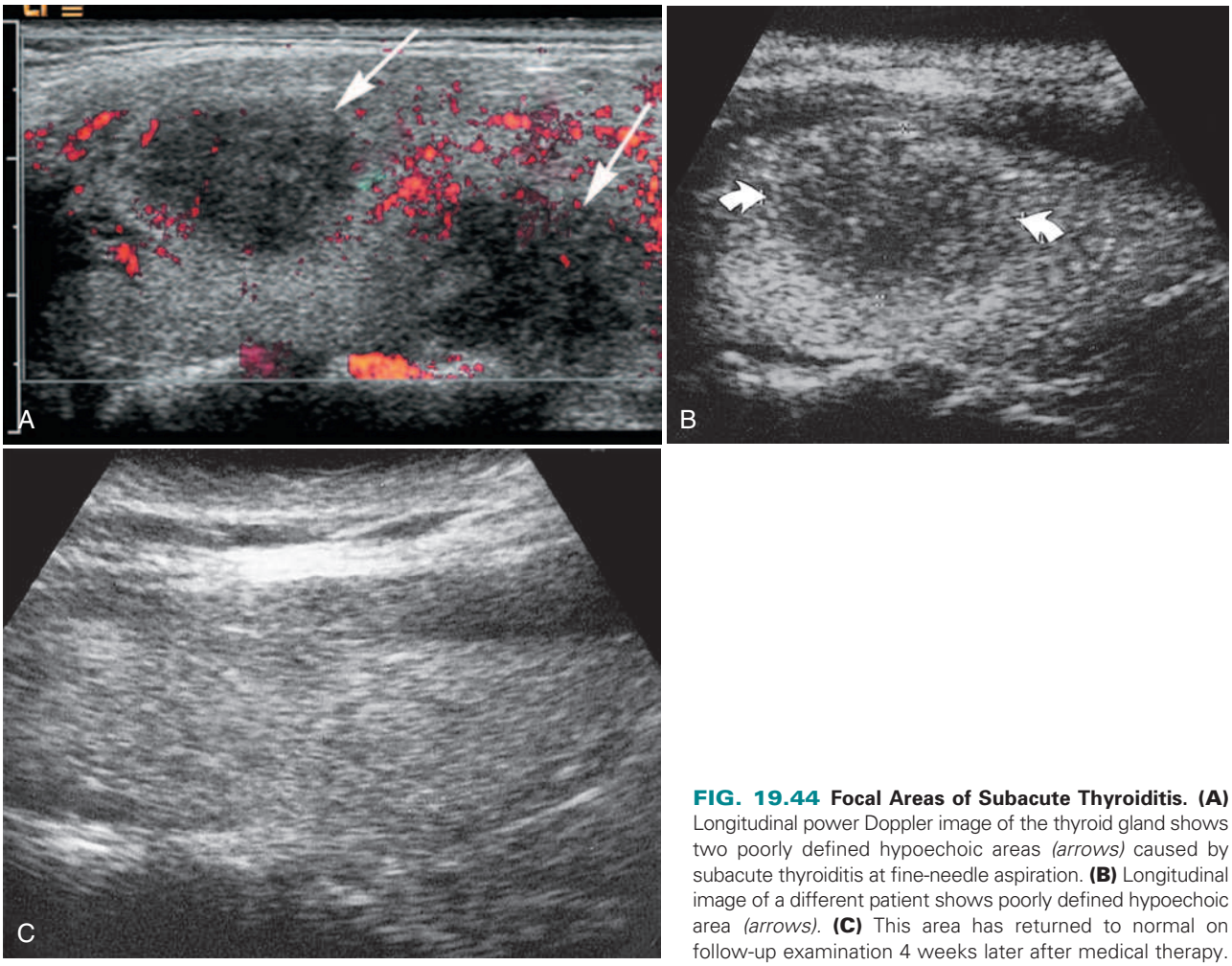

FIG. 19.44 Focal Areas of Subacute Thyroiditis. (A) Longitudinal power Doppler image of the thyroid gland shows two poorly defined hypoechoic areas *(arrows)* caused by subacute thyroiditis at fine-needle aspiration. **(B)** Longitudinal image of a different patient shows poorly defined hypoechoic area *(arrows)*. **(C)** This area has returned to normal on follow-up examination 4 weeks later after medical therapy.

infection and affecting children. Sonography can be useful in select patients to detect the development of a frank thyroid abscess. The infection usually begins in the perithyroidal soft tissues. On ultrasound images, an abscess is seen as a poorly defined, hypoechoic heterogeneous mass with internal debris, with or without septa and gas. Adjacent inflammatory nodes are often present.

Subacute granulomatous thyroiditis or De Quervain disease is a spontaneously remitting inflammatory disease probably caused by viral infection. The clinical findings include fever, enlargement of the gland, and pain on palpation. Sonographically, the gland may appear enlarged and hypoechoic, with normal or decreased vascularity caused by diffuse edema of the gland, or the process may appear as focal hypoechoic regions[147,148] (Fig. 19.44). Although usually not necessary, sonography can be used to assess evolution of de Quervain disease after medical therapy.

The most common type of thyroiditis is **chronic autoimmune lymphocytic thyroiditis, or Hashimoto thyroiditis.** It typically occurs as a painless, diffuse enlargement of the thyroid gland in a young or middle-aged woman, often associated with hypothyroidism. It is the most common cause of hypothyroidism in North America. Patients with this autoimmune disease develop antibodies to their own thyroglobulin as well as to the major enzyme of thyroid hormonogenesis, thyroid peroxidase. The typical sonographic appearance of Hashimoto thyroiditis is diffuse, coarsened, parenchymal echotexture, generally more hypoechoic than a normal thyroid[144] (Fig. 19.45). In most cases the gland is enlarged. Multiple, discrete **hypoechoic micronodules** from 1 to 6 mm in diameter are strongly suggestive of chronic thyroiditis; this appearance has been called **micronodulation** (see Fig. 19.45, Video 19.7). Micronodulation is a highly sensitive sign of chronic thyroiditis, with a positive predictive value of 94.7%.[149] Histologically, micronodules represent lobules of thyroid parenchyma that have been infiltrated by lymphocytes and plasma cells. These lobules are surrounded by multiple linear echogenic fibrous septations (Fig. 19.46). These fibrotic septations may give the parenchyma a "pseudolobulated" appearance. Both benign and malignant thyroid nodules may coexist with chronic lymphocytic thyroiditis, and FNA is often necessary to establish the final diagnosis[150] (Figs. 19.47 to 19.49). As with other autoimmune disorders, there is an increased risk of malignancy, with a B-cell malignant lymphoma most often arising within the gland.

The vascularity on color Doppler imaging is normal or decreased in most patients with the diagnosis of Hashimoto thyroiditis (see Fig. 19.45). Occasionally, hypervascularity similar to the "thyroid inferno" of Graves disease occurs. One study

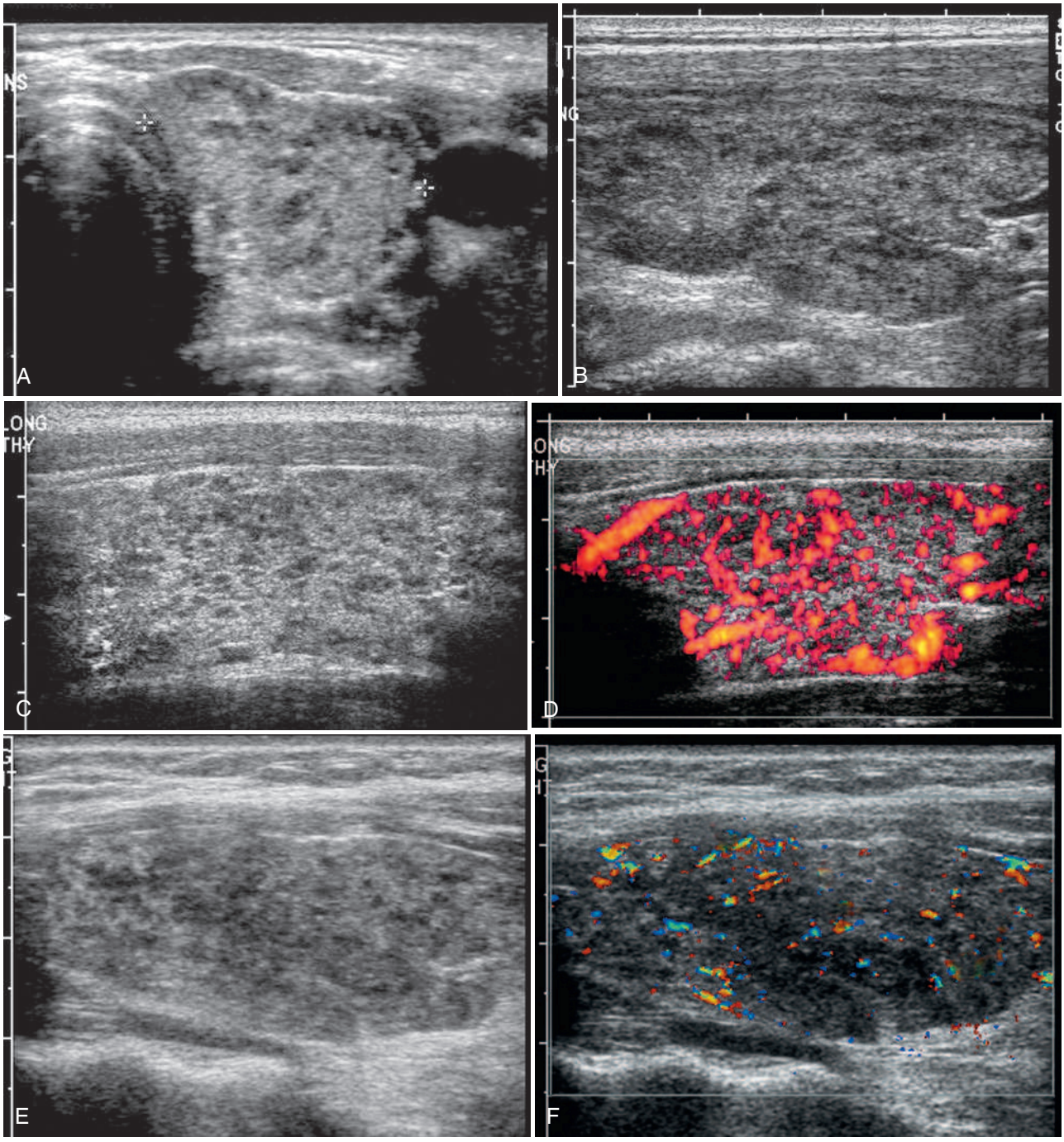

FIG. 19.45 Hashimoto Thyroiditis: Micronodularity. (A) Transverse and **(B)** longitudinal images of the left lobe demonstrate multiple small hypoechoic nodules that are lymphocyte infiltration of the parenchyma. **(C)** and **(D)** Longitudinal images of another patient show multiple tiny hypoechoic nodules and increased flow on power Doppler. This increased flow may indicate an acute phase of the thyroiditis. **(E)** and **(F)** Longitudinal images of a different patient show multiple tiny hypoechoic nodules and decreased flow on color Doppler scan. The blood flow is normal or diminished in most cases of Hashimoto thyroiditis.

suggested that hypervascularity occurs when hypothyroidism develops, perhaps related to stimulation from the associated high serum levels of thyrotropin (TSH).[151] Often, cervical lymphadenopathy is present, most evident near the lower pole of the thyroid gland (Fig. 19.50). The end stage of chronic thyroiditis is atrophy, when the thyroid gland is small, with poorly defined margins and heterogeneous texture caused by progressive fibrosis. Blood flow signals are absent. Occasionally, discrete nodules occur, and FNA biopsy is needed to establish the diagnosis.[150]

Painless (silent) thyroiditis has the typical histologic and sonographic pattern of chronic autoimmune thyroiditis (hypoechogenicity, micronodulation, and fibrosis), but clinical findings resemble classic subacute thyroiditis, with the exception of node tenderness. Moderate hyperthyroidism with thyroid

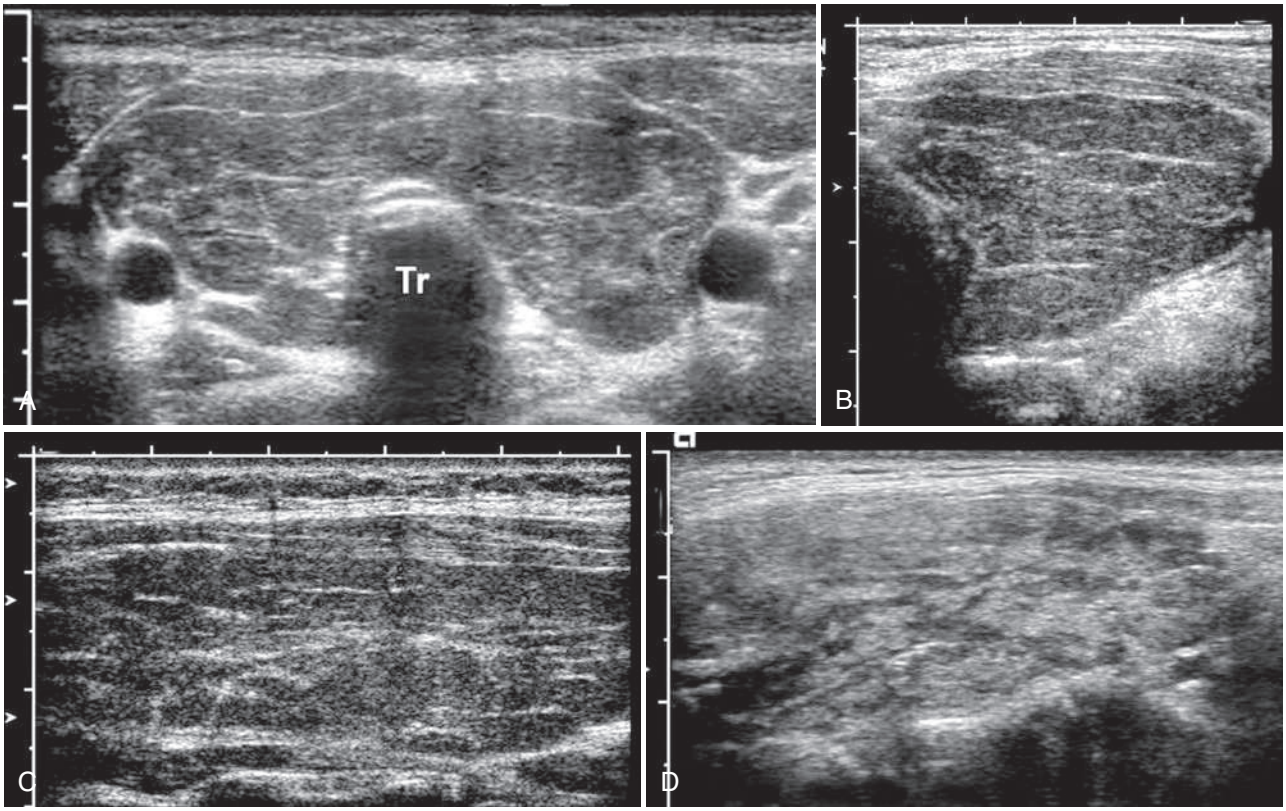

FIG. 19.46 Hashimoto Thyroiditis: Coarse Septations. (A) Transverse dual image of the thyroid shows marked diffuse enlargement of both lobes and the isthmus. Multiple linear bright echoes throughout the hypoechoic parenchyma are caused by lymphocytic infiltration of the gland with coarse septations from fibrous bands. *Tr,* Tracheal air shadow. **(B)** Transverse and **(C)** longitudinal images of another patient demonstrate linear echogenic septations throughout the gland. **(D)** Longitudinal image of another patient shows thicker echogenic linear areas that separate hypoechoic regions.

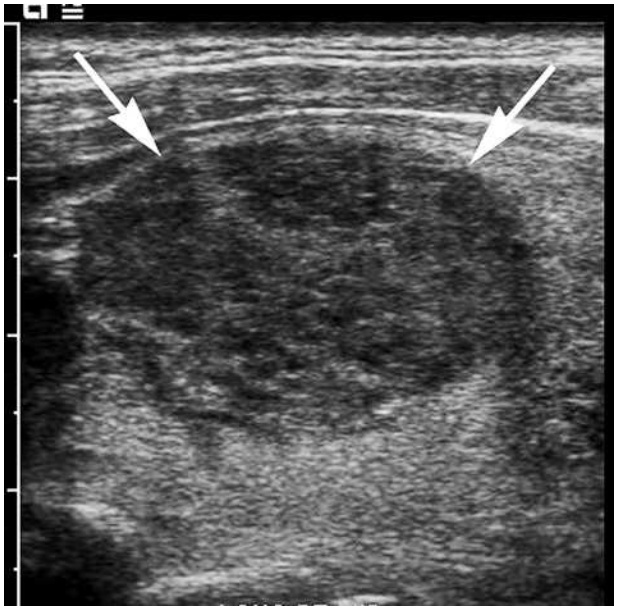

FIG. 19.47 Hashimoto Thyroiditis: Nodule. Longitudinal image shows a discrete hypoechoic nodule *(arrows)* that proved to be Hashimoto thyroiditis at fine-needle aspiration biopsy.

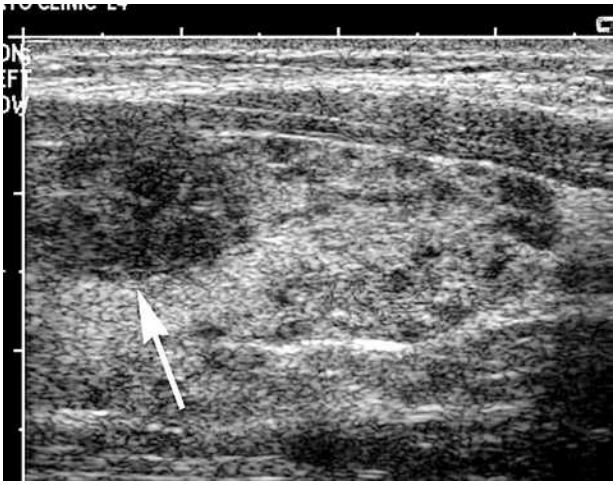

FIG. 19.48 Hashimoto Thyroiditis With Papillary Thyroid Cancer. Longitudinal image shows classic Hashimoto thyroiditis (micronodularity) and a hypoechoic dominant nodule *(arrow)* in the upper pole caused by papillary thyroid carcinoma. A dominant nodule in Hashimoto thyroiditis should be considered "indeterminate" and fine-needle aspiration performed.

FIG. 19.49 Lymphoma in Hashimoto Thyroiditis. Transverse image of the left lobe shows diffuse hypoechoic enlargement caused by lymphoma in a gland with Hashimoto thyroiditis. *Tr,* Tracheal air shadow.

FIG. 19.50 Hashimoto Thyroiditis With Hyperplastic Enlarged Lymph Nodes. Longitudinal image shows micronodularity of Hashimoto thyroiditis and an enlarged lymph node *(arrow)* inferior to the lower pole.

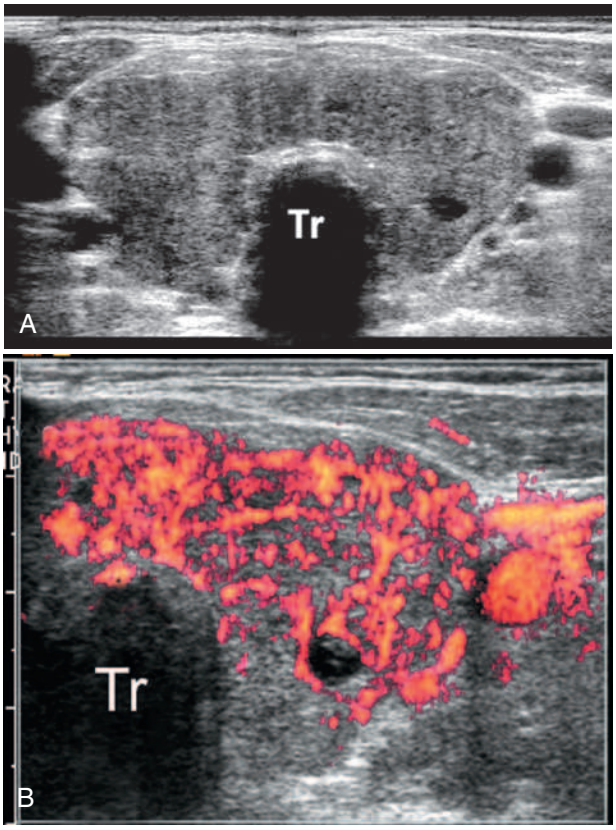

FIG. 19.51 Hyperthyroidism: Graves Disease. (A) Transverse dual image of the thyroid gland shows marked diffuse enlargement of both thyroid lobes and the isthmus. The gland is diffusely hypoechoic. **(B)** Transverse color Doppler image of the left lobe shows increased vascularity, indicating an acute stage of the Graves disease process. *Tr,* Trachea.

enlargement usually occurs in the early phase, in some cases followed by hypothyroidism of variable degree. In **postpartum thyroiditis** the progression to hypothyroidism is more common. In most cases the disease spontaneously remits within 3 to 6 months, and the gland may return to a normal appearance.

Although the appearance of diffuse parenchymal inhomogeneity and micronodularity is typical of Hashimoto thyroiditis, other diffuse thyroid diseases, most frequently **multinodular** or **adenomatous goiter,** may have a similar sonographic appearance. Most patients with adenomatous goiter have multiple discrete nodules separated by otherwise normal-appearing thyroid parenchyma (see Fig. 19.29); others have enlargement with rounding of the poles of the gland, diffuse parenchymal inhomogeneity, and no recognizable normal tissue. Adenomatous goiter affects women three times more often than men.

Graves disease is a common diffuse abnormality of the thyroid gland and is usually biochemically characterized by hyperfunction (thyrotoxicosis). The echotexture may be more inhomogeneous than in diffuse goiter, mainly because of numerous large, intraparenchymal vessels. Furthermore, especially in young patients, the parenchyma may be diffusely hypoechoic because of the extensive lymphocytic infiltration or the predominantly cellular content of the parenchyma, which becomes almost devoid of colloid substance. Color Doppler sonography often demonstrates a hypervascular pattern referred to as the **thyroid inferno** (Fig. 19.51). Spectral Doppler will often demonstrate peak systolic velocities exceeding 70 cm/sec, which is the highest velocity found in thyroid disease. There is no correlation between the degree of thyroid hyperfunction assessed by laboratory studies and the extent of hypervascularity or blood flow velocities. Previous studies have shown that Doppler analysis can be used to monitor therapeutic response in patients with Graves disease.[152] A significant decrease in flow velocities in the superior and inferior thyroid arteries after medical treatment has been reported.

The rarest type of inflammatory thyroid disease is **invasive fibrous thyroiditis,** also called **Riedel struma.**[146] This disease primarily affects women and often progresses to complete destruction of the gland. Some cases may be associated with

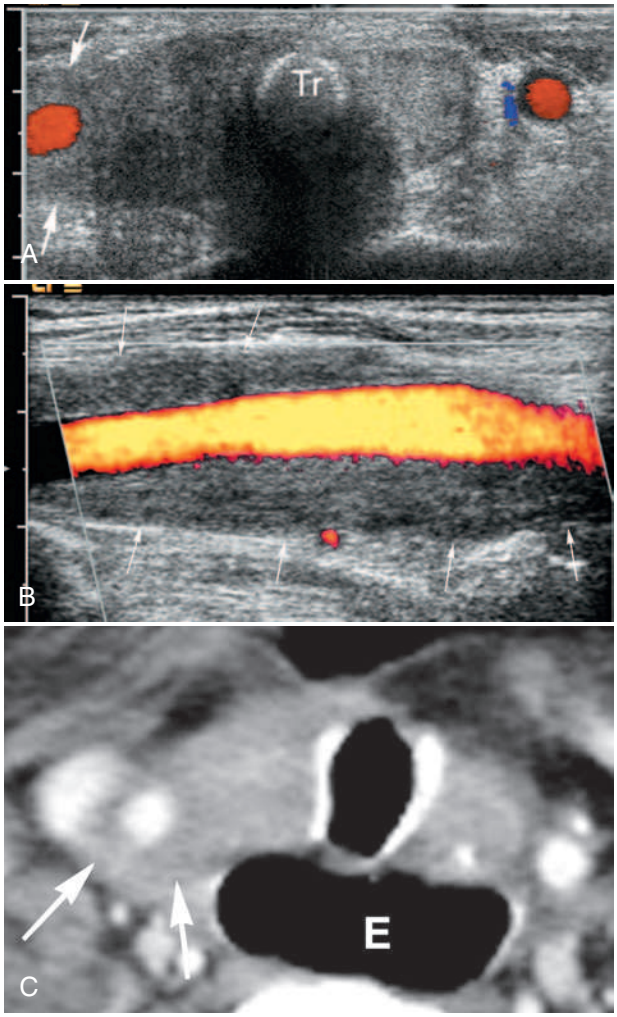

FIG. 19.52 Riedel Struma (Invasive Fibrous Thyroiditis). (A) Transverse dual-color Doppler ultrasound image of the thyroid shows a diffuse hypoechoic process in the right lobe extending around the common carotid artery *(arrows)*. *Tr,* Trachea. **(B)** Longitudinal power Doppler image of the right common carotid artery shows a hypoechoic soft tissue mass *(arrows)* encasing the vessel. **(C)** Contrast-enhanced CT scan shows mild enlargement of the right thyroid lobe and soft tissue thickening *(arrows)* around the right common carotid artery. Incidentally noted is dilation of the air-filled esophagus *(E)*.

mediastinal or retroperitoneal fibrosis or sclerosing cholangitis. In the few cases of invasive fibrous thyroiditis examined sonographically, the gland was diffusely enlarged and had an inhomogeneous parenchymal echotexture. The primary reason for sonography is to check for extrathyroid extension of the inflammatory process, with encasement of the adjacent vessels (Fig. 19.52). Such information can be particularly useful in surgical planning. Open biopsy is generally required to distinguish this condition from anaplastic thyroid carcinoma. The sonographic findings in these two diseases may be identical.

Acknowledgment

The authors would like to acknowledge the aid of Maija Radzina, MD, PhD, Institute of Diagnostic Radiology, Paula Stradins Clinical University Hospital, Riga, Latvia.

REFERENCES

1. Rogers WM. Anomalous development of the thyroid. In: Werner SC, Ingbar SH, editors. The thyroid. New York: Harper & Row; 1978. p. 416-420.
2. Toma P, Guastalla PP, Carini C, et al. Collo [The neck]. In: Fariello G, Perale R, Perri G, et al., editors. Ecografia Pediatrica. Milan: Ambrosiana; 1992. p. 139-162.
3. Solbiati L, Cioffi V, Ballarati E. Ultrasonography of the neck. Radiol Clin North Am. 1992;30(5):941-954.
4. Jarlov AE, Hegedus L, Gjorup T, Hansen JE. Accuracy of the clinical assessment of thyroid size. Dan Med Bull. 1991;38(1):87-89.
5. Kerr L. High-resolution thyroid ultrasound: the value of color Doppler. Ultrasound Q. 1994;12:21-43.
6. Shabana W, Peeters E, De Maeseneer M. Measuring thyroid gland volume: should we change the correction factor? AJR Am J Roentgenol. 2006;186(1): 234-236.
7. Hegedus L, Perrild H, Poulsen LR, et al. The determination of thyroid volume by ultrasound and its relationship to body weight, age, and sex in normal subjects. J Clin Endocrinol Metab. 1983;56(2):260-263.
8. Solbiati L, Osti V, Cova L, et al. The neck. In: Meire H, Cosgrove D, editors. Abdominal and general ultrasound. Edinburgh: Churchill Livingstone; 2001. p. 699-737.
9. Brandl H, Gritzky A, Haizinger M. 3D ultrasound: a dedicated system. Eur Radiol. 1999;9(Suppl. 3):S331-S333.
10. Ueda D, Mitamura R, Suzuki N, et al. Sonographic imaging of the thyroid gland in congenital hypothyroidism. Pediatr Radiol. 1992;22(2):102-105.
11. Chang YW, Hong HS, Choi DL. Sonography of the pediatric thyroid: a pictorial essay. J Clin Ultrasound. 2009;37(3):149-157.
12. Rojeski MT, Gharib H. Nodular thyroid disease. Evaluation and management. N Engl J Med. 1985;313(7):428-436.
13. Van Herle AJ, Rich P, Ljung BM, et al. The thyroid nodule. Ann Intern Med. 1992;96:221-232.
14. Favus MJ, Schneider AB, Stachura ME, et al. Thyroid cancer occurring as a late consequence of head-and-neck irradiation. Evaluation of 1056 patients. N Engl J Med. 1976;294(19):1019-1025.
15. DeGroot LJ, Reilly M, Pinnameneni K, Refetoff S. Retrospective and prospective study of radiation-induced thyroid disease. Am J Med. 1983;74(5): 852-862.
16. Grebe SK, Hay ID. Follicular cell-derived thyroid carcinomas. Cancer Treat Res. 1997;89:91-140.
17. Hennemann G. Non-toxic goitre. Clin Endocrinol Metab. 1979;8(1): 167-179.
18. Muller HW, Schroder S, Schneider C, Seifert G. Sonographic tissue characterisation in thyroid gland diagnosis. A correlation between sonography and histology. Klin Wochenschr. 1985;63(15):706-710.
19. Lagalla R, Caruso G, Midiri M, et al. Echo Doppler-couleur et pathologie thyroidienne. JEMU. 1992;13:44-47.
20. Solbiati L, Ballarati E, Cioffi V. Contribution of color-flow mapping to the differential diagnosis of the thyroid nodules. Proceedings 77th Annual Meeting of Radiological Society of North America, Chicago 1991. Radiology. 1991;181(P)(Suppl.):177-178.
21. Solbiati L, Volterrani L, Rizzatto G, et al. The thyroid gland with low uptake lesions: evaluation by ultrasound. Radiology. 1985;155(1):187-191.
22. Ahuja A, Chick W, King W, Metreweli C. Clinical significance of the comet-tail artifact in thyroid ultrasound. J Clin Ultrasound. 1996;24(3):129-133.
23. Schlumberger MJ, Filetti S, Hay ID. Nontoxic goiter and thyroid neoplasia. In: Larsen PR, Kronenberg HM, Melmed S, et al., editors. Williams textbook of endocrinology. 10th ed. Philadelphia: Saunders; 2003. p. 457-490.
24. Black BM, Kirk Jr TA, Woolner LB. Multicentricity of papillary adenocarcinoma of the thyroid: influence on treatment. J Clin Endocrinol Metab. 1960;20:130-135.
25. Hay ID, McConahey WM, Goellner JR. Managing patients with papillary thyroid carcinoma: insights gained from the Mayo Clinic's experience of treating 2512 consecutive patients during 1940 through 2000. Trans Am Clin Climatol Assoc. 2002;113:241-260.
26. Wunderbaldinger P, Harisinghani MG, Hahn PF, et al. Cystic lymph node metastases in papillary thyroid carcinoma. AJR Am J Roentgenol. 2002;178(3):693-697.

27. Pilotti S, Pierotti MA. Classificazione istologica e caratterizzazione molecolare dei tumori dell'epitelio follicolare della tiroide. Argomenti Oncol. 1992;13: 365-380.
28. Holtz S, Powers WE. Calcification in papillary carcinoma of the thyroid. Am J Roentgenol Radium Ther Nucl Med. 1958;80(6):997-1000.
29. Brkljacic B, Cuk V, Tomic-Brzac H, et al. Ultrasonic evaluation of benign and malignant nodules in echographically multinodular thyroids. J Clin Ultrasound. 1994;22(2):71-76.
30. Ahuja AT, Ying M, Yuen HY, Metreweli C. Power Doppler sonography of metastatic nodes from papillary carcinoma of the thyroid. Clin Radiol. 2001;56(4):284-288.
31. Solbiati L, Livraghi T, Ballarati E, et al. Thyroid gland. In: Solbiati L, Rizzatto G, editors. Ultrasound of superficial structures. Edinburgh: Churchill Livingstone; 1995. p. 49-85.
32. Henrichsen TL, Reading CC, Charboneau JW, et al. Cystic change in thyroid carcinoma: Prevalence and estimated volume in 360 carcinomas. J Clin Ultrasound. 2010;38(7):361-366.
33. Chong GC, Beahrs OH, Sizemore GW, Woolner LH. Medullary carcinoma of the thyroid gland. Cancer. 1975;35(3):695-704.
34. Gorman B, Charboneau JW, James EM, et al. Medullary thyroid carcinoma: role of high-resolution US. Radiology. 1987;162(1 Pt 1):147-150.
35. Nel CJ, van Heerden JA, Goellner JR, et al. Anaplastic carcinoma of the thyroid: a clinicopathologic study of 82 cases. Mayo Clin Proc. 1985;60(1): 51-58.
36. Hamburger JI, Miller JM, Kini SR. Lymphoma of the thyroid. Ann Intern Med. 1983;99(5):685-693.
37. Kasagi K, Hatabu H, Tokuda Y, et al. Lymphoproliferative disorders of the thyroid gland: radiological appearances. Br J Radiol. 1991;64(763): 569-575.
38. Takashima S, Morimoto S, Ikezoe J, et al. Primary thyroid lymphoma: comparison of CT and US assessment. Radiology. 1989;171(2):439-443.
39. Ahuja A, Evans R. The thyroid and parathyroid. Practical head and neck ultrasound. London: GMM; 2000.
40. Feld S, Barcia M, Baskic HJ, et al. AACE clinical practice guidelines for the diagnosis and management of thyroid nodules. Endocr Pract. 1996;2: 78-84.
41. Miller JM. Evaluation of thyroid nodules. Accent on needle biopsy. Med Clin North Am. 1985;69(5):1063-1077.
42. Hamberger B, Gharib H, Melton 3rd LJ, et al. Fine-needle aspiration biopsy of thyroid nodules. Impact on thyroid practice and cost of care. Am J Med. 1982;73(3):381-384.
43. Gharib H, Goellner JR. Fine-needle aspiration biopsy of the thyroid: an appraisal. Ann Intern Med. 1993;118(4):282-289.
44. Hawkins F, Bellido D, Bernal C, et al. Fine needle aspiration biopsy in the diagnosis of thyroid cancer and thyroid disease. Cancer. 1987;59(6): 1206-1209.
45. Khafagi F, Wright G, Castles H, et al. Screening for thyroid malignancy: the role of fine-needle biopsy. Med J Aust. 1988;149(6):302-303, 6-7.
46. Hall TL, Layfield LJ, Philippe A, Rosenthal DL. Sources of diagnostic error in fine needle aspiration of the thyroid. Cancer. 1989;63(4): 718-725.
47. Altavilla G, Pascale M, Nenci I. Fine needle aspiration cytology of thyroid gland diseases. Acta Cytol. 1990;34(2):251-256.
48. Ravetto C, Spreafico G, Colombo L. Cytological examination using needle aspiration in the early diagnosis of thyroid neoplasms. Comparison of clinical and scintigraphic data. Recenti Prog Med. 1977;63(3):258-274.
49. Sangalli G, Serio G, Zampatti C, et al. Fine needle aspiration cytology of the thyroid: a comparison of 5469 cytological and final histological diagnoses. Cytopathology. 2006;17(5):245-250.
50. James EM, Charboneau JW. High-frequency (10 MHz) thyroid ultrasonography. Semin Ultrasound CT MR. 1985;6:294-309.
51. Scheible W, Leopold GR, Woo VL, Gosink BB. High-resolution real-time ultrasonography of thyroid nodules. Radiology. 1979;133(2):413-417.
52. Simeone JF, Daniels GH, Mueller PR, et al. High-resolution real-time sonography of the thyroid. Radiology. 1982;145(2):431-435.
53. Brown CL. Pathology of the cold nodule. Clin Endocrinol Metab. 1981;10(2):235-245.
54. Brander A, Viikinkoski P, Nickels J, Kivisaari L. Thyroid gland: US screening in middle-aged women with no previous thyroid disease. Radiology. 1989;173(2):507-510.
55. Hay ID. Papillary thyroid carcinoma. Endocrinol Metab Clin North Am. 1990;19(3):545-576.
56. Hay ID, Reading CC, Weiland LH, et al. Clinicopathologic and high-resolution ultrasonographic evaluation of clinically suspicious or malignant thyroid disease. In: Medeiros-Neto G, Gaitan E, editors. Frontiers in thyroidology. New York: Plenum; 1986.
57. Simeone JF, Daniels GH, Hall DA, et al. Sonography in the follow-up of 100 patients with thyroid carcinoma. AJR Am J Roentgenol. 1987;148(1): 45-49.
58. Sutton RT, Reading CC, Charboneau JW, et al. US-guided biopsy of neck masses in postoperative management of patients with thyroid cancer. Radiology. 1988;168(3):769-772.
59. Kim EK, Park CS, Chung WY, et al. New sonographic criteria for recommending fine-needle aspiration biopsy of nonpalpable solid nodules of the thyroid. AJR Am J Roentgenol. 2002;178(3):687-691.
60. Koike E, Noguchi S, Yamashita H, et al. Ultrasonographic characteristics of thyroid nodules: prediction of malignancy. Arch Surg. 2001;136(3): 334-337.
61. Rago T, Vitti P, Chiovato L, et al. Role of conventional ultrasonography and color flow-Doppler sonography in predicting malignancy in 'cold' thyroid nodules. Eur J Endocrinol. 1998;138(1):41-46.
62. Watters DA, Ahuja AT, Evans RM, et al. Role of ultrasound in the management of thyroid nodules. Am J Surg. 1992;164(6):654-657.
63. Okamoto T, Yamashita T, Harasawa A, et al. Test performances of three diagnostic procedures in evaluating thyroid nodules: physical examination, ultrasonography and fine needle aspiration cytology. Endocr J. 1994;41(3): 243-247.
64. Leenhardt L, Tramalloni J, Aurengo H, et al. Echography of thyroid nodules. The echography specialist facing the clinician's requirements. Presse Med. 1994;23(30):1389-1392.
65. Moon WJ, Jung SL, Lee JH, et al. Benign and malignant thyroid nodules: US differentiation—multicenter retrospective study. Radiology. 2008;247(3): 762-770.
66. Alexander EK, Marqusee E, Orcutt J, et al. Thyroid nodule shape and prediction of malignancy. Thyroid. 2004;14(11):953-958.
67. Hammer M, Wortsman J, Folse R. Cancer in cystic lesions of the thyroid. Arch Surg. 1982;117(8):1020-1023.
68. Livolsi A. Pathology of thyroid disease. In: Falj SA, editor. Thyroid disease: endocrinology, surgery, nuclear medicine and radiotherapy. Philadelphia: Lippincott-Raven; 1997. p. 65-104.
69. Propper RA, Skolnick ML, Weinstein BJ, Dekker A. The nonspecificity of the thyroid halo sign. J Clin Ultrasound. 1980;8(2):129-132.
70. Kim BM, Kim MJ, Kim EK, et al. Sonographic differentiation of thyroid nodules with eggshell calcifications. J Ultrasound Med. 2008;27(10): 1425-1430.
71. Park M, Shin JH, Han BK, et al. Sonography of thyroid nodules with peripheral calcifications. J Clin Ultrasound. 2009;37(6):324-328.
72. Kakkos SK, Scopa CD, Chalmoukis AK, et al. Relative risk of cancer in sonographically detected thyroid nodules with calcifications. J Clin Ultrasound. 2000;28(7):347-352.
73. Solbiati L, Ierace T, Lagalla R, et al. Reliability of high-frequency US and color Doppler US of thyroid nodules: Italian multicenter study of 1042 pathologically confirmed cases-which role for scintigraphy and biopsy. Proceedings 81st Annual Meeting of Radiological Society of North America, Chicago 1995. Radiology. 1995;197(P)(Suppl.):270.
74. Fobbe F, Finke R, Reichenstein E, et al. Appearance of thyroid diseases using colour-coded duplex sonography. Eur J Radiol. 1989;9(1):29-31.
75. Argalia G, D'Ambrosio F, Lucarelli F, et al. [Echo Doppler in the characterization of thyroid nodular disease]. Radiol Med. 1995;89(5):651-657.
76. Chammas MC, Gerhard R, de Oliveira IR, et al. Thyroid nodules: evaluation with power Doppler and duplex Doppler ultrasound. Otolaryngol Head Neck Surg. 2005;132(6):874-882.
77. Spiezia S, Colao A, Assanti AP, et al. [Usefulness of color echo Doppler with power Doppler in the diagnosis of hypoechoic thyroid nodules: work in progress]. Radiol Med. 1996;91(5):616-621.

78. Clark KJ, Cronan JJ, Scola FH. Color Doppler sonography: anatomic and physiologic assessment of the thyroid. J Clin Ultrasound. 1995;23(4): 215-223.
79. Shimamoto K, Endo T, Ishigaki T, et al. Thyroid nodules: evaluation with color Doppler ultrasonography. J Ultrasound Med. 1993;12(11):673-678.
80. Frates MC, Benson CB, Doubilet PM, et al. Can color Doppler sonography aid in the prediction of malignancy of thyroid nodules? J Ultrasound Med. 2003;22(2):127-131.
81. Xie C, Cox P, Taylor N, LaPorte S. Ultrasonography of thyroid nodules: a pictorial review. Insights Imaging. 2016;7(1):77-86.
82. Horvath E, Majlis S, Rossi R, et al. An ultrasonogram reporting system for thyroid nodules stratifying cancer risk for clinical management. J Clin Endocrinol Metab. 2009;94(5):1748-1751.
83. Kwak JY, Han KH, Yoon JH, et al. Thyroid imaging reporting and data system for US features of nodules: a step in establishing better stratification of cancer risk. Radiology. 2011;260(3):892-899.
84. Cantisani V, Bertolotto M, Weskott HP, et al. Growing indications for CEUS: The kidney, testis, lymph nodes, thyroid, prostate, and small bowel. Eur J Radiol. 2015;84(9):1675-1684.
85. Yu D, Han Y, Chen T. Contrast-enhanced ultrasound for differentiation of benign and malignant thyroid lesions: meta-analysis. Otolaryngol Head Neck Surg. 2014;151(6):909-915.
86. Rago T, Vitti P. Role of thyroid ultrasound in the diagnostic evaluation of thyroid nodules. Best Pract Res Clin Endocrinol Metab. 2008;22(6): 913-928.
87. Rubaltelli L, Corradin S, Dorigo A, et al. Differential diagnosis of benign and malignant thyroid nodules at elastosonography. Ultraschall Med. 2009;30(2):175-179.
88. Cantisani V, Consorti F, Guerrisi A, et al. Prospective comparative evaluation of quantitative-elastosonography (Q-elastography) and contrast-enhanced ultrasound for the evaluation of thyroid nodules: preliminary experience. Eur J Radiol. 2013;82(11):1892-1898.
89. Cantisani V, Lodise P, Di Rocco G, et al. Diagnostic accuracy and interobserver agreement of quasistatic ultrasound elastography in the diagnosis of thyroid nodules. Ultraschall Med. 2015;36(2):162-167.
90. Cosgrove D, Piscaglia F, Bamber J, et al. EFSUMB guidelines and recommendations on the clinical use of ultrasound elastography. Part 2: Clinical applications. Ultraschall Med. 2013;34(3):238-253.
91. Liu BJ, Li DD, Xu HX, et al. Quantitative shear wave velocity measurement on acoustic radiation force impulse elastography for differential diagnosis between benign and malignant thyroid nodules: a meta-analysis. Ultrasound Med Biol. 2015;41(12):3035-3043.
92. Nell S, Kist JW, Debray TP, et al. Qualitative elastography can replace thyroid nodule fine-needle aspiration in patients with soft thyroid nodules. A systematic review and meta-analysis. Eur J Radiol. 2015;84(4):652-661.
93. Razavi SA, Hadduck TA, Sadigh G, Dwamena BA. Comparative effectiveness of elastographic and B-mode ultrasound criteria for diagnostic discrimination of thyroid nodules: a meta-analysis. AJR Am J Roentgenol. 2013;200(6): 1317-1326.
94. Ueno E, Ito A. Diagnosis of breast cancer by elasticity imaging. Eizo Joho Med. 2004;36:2-6.
95. Ferrari FS, Megliola A, Scorzelli A, et al. Ultrasound examination using contrast agent and elastosonography in the evaluation of single thyroid nodules: preliminary results. J Ultrasound. 2008;11(2):47-54.
96. Hong Y, Liu X, Li Z, et al. Real-time ultrasound elastography in the differential diagnosis of benign and malignant thyroid nodules. J Ultrasound Med. 2009;28(7):861-867.
97. Lyshchik A, Higashi T, Asato R, et al. Thyroid gland tumor diagnosis at US elastography. Radiology. 2005;237(1):202-211.
98. Rago T, Santini F, Scutari M, et al. Elastography: new developments in ultrasound for predicting malignancy in thyroid nodules. J Clin Endocrinol Metab. 2007;92(8):2917-2922.
99. Quinn SF, Nelson HA, Demlow TA. Thyroid biopsies: fine-needle aspiration biopsy versus spring-activated core biopsy needle in 102 patients. J Vasc Interv Radiol. 1994;5(4):619-623.
100. Taki S, Kakuda K, Kakuma K, et al. Thyroid nodules: evaluation with US-guided core biopsy with an automated biopsy gun. Radiology. 1997;202(3): 874-877.
101. Goellner JR, Gharib H, Grant CS, Johnson DA. Fine needle aspiration cytology of the thyroid, 1980 to 1986. Acta Cytol. 1987;31(5):587-590.
102. Kuna SK, Bracic I, Tesic V, et al. Ultrasonographic differentiation of benign from malignant neck lymphadenopathy in thyroid cancer. J Ultrasound Med. 2006;25(12):1531-1537.
103. Lyshchik A, Higashi T, Asato R, et al. Cervical lymph node metastases: diagnosis at sonoelastography—initial experience. Radiology. 2007;243(1): 258-267.
104. Snozek CL, Chambers EP, Reading CC, et al. Serum thyroglobulin, high-resolution ultrasound, and lymph node thyroglobulin in diagnosis of differentiated thyroid carcinoma nodal metastases. J Clin Endocrinol Metab. 2007;92(11):4278-4281.
105. Miller JM, Hamburger JI, Taylor CI. Is needle aspiration of the cystic thyroid nodule effective and safe treatment? In: Hamburger JI, Miller JM, editors. Controversies in clinical thyroidology. New York: Springer-Verlag; 1981.
106. Verde G, Papini E, Pacella CM, et al. Ultrasound guided percutaneous ethanol injection in the treatment of cystic thyroid nodules. Clin Endocrinol (Oxf). 1994;41(6):719-724.
107. Yasuda K, Ozaki O, Sugino K, et al. Treatment of cystic lesions of the thyroid by ethanol instillation. World J Surg. 1992;16(5):958-961.
108. Antonelli A, Campatelli A, Di Vito A, et al. Comparison between ethanol sclerotherapy and emptying with injection of saline in treatment of thyroid cysts. Clin Investig. 1994;72(12):971-974.
109. Lee SJ, Ahn IM. Effectiveness of percutaneous ethanol injection therapy in benign nodular and cystic thyroid diseases: long-term follow-up experience. Endocr J. 2005;52(4):455-462.
110. Raggiunti B, Fiore G, Mongia A, et al. A 7-year follow-up of patients with thyroid cysts and pseudocysts treated with percutaneous ethanol injection: volume change and cost analysis. J Ultrasound. 2009;12(3):107-111.
111. Livraghi T, Paracchi A, Ferrari C, et al. Treatment of autonomous thyroid nodules with percutaneous ethanol injection: preliminary results. Work in progress. Radiology. 1990;175(3):827-829.
112. Cerbone G, Spiezia S, Colao A, et al. Percutaneous ethanol injection under power Doppler ultrasound assistance in the treatment of autonomously functioning thyroid nodules. J Endocrinol Invest. 1999;22(10):752-759.
113. Goletti O, Monzani F, Caraccio N, et al. Percutaneous ethanol injection treatment of autonomously functioning single thyroid nodules: optimization of treatment and short term outcome. World J Surg. 1992;16(4):784-789.
114. Livraghi T, Paracchi A, Ferrari C, et al. Treatment of autonomous thyroid nodules with percutaneous ethanol injection: 4-year experience. Radiology. 1994;190(2):529-533.
115. Ozdemir H, Ilgit ET, Yucel C, et al. Treatment of autonomous thyroid nodules: safety and efficacy of sonographically guided percutaneous injection of ethanol. AJR Am J Roentgenol. 1994;163(4):929-932.
116. Pacella CM, Papini E, Bizzarri G, et al. Assessment of the effect of percutaneous ethanol injection in autonomously functioning thyroid nodules by colour-coded duplex sonography. Eur J Radiol. 1995;5:395-400.
117. Baek JH, Moon WJ, Kim YS, et al. Radiofrequency ablation for the treatment of autonomously functioning thyroid nodules. World J Surg. 2009;33(9): 1971-1977.
118. Deandrea M, Limone P, Basso E, et al. US-guided percutaneous radiofrequency thermal ablation for the treatment of solid benign hyperfunctioning or compressive thyroid nodules. Ultrasound Med Biol. 2008;34(5): 784-791.
119. Chianelli M, Bizzarri G, Todino V, et al. Laser ablation and 131-iodine: a 24-month pilot study of combined treatment for large toxic nodular goiter. J Clin Endocrinol Metab. 2014;99(7):E1283-E1286.
120. Goletti O, Monzani F, Lenziardi M, et al. Cold thyroid nodules: a new application of percutaneous ethanol injection treatment. J Clin Ultrasound. 1994;22(3):175-178.
121. Dossing H, Bennedbaek FN, Karstrup S, Hegedus L. Benign solitary solid cold thyroid nodules: ultrasound-guided interstitial laser photocoagulation—initial experience. Radiology. 2002;225:53-57.
122. Pacella CM, Bizzarri G, Spiezia S, et al. Thyroid tissue: US-guided percutaneous laser thermal ablation. Radiology. 2004;232(1):272-280.
123. Papini E, Guglielmi R, Bizzarri G, et al. Treatment of benign cold thyroid nodules: a randomized clinical trial of percutaneous laser ablation versus levothyroxine therapy or follow-up. Thyroid. 2007;17(3):229-235.

124. Pacella CM, Mauri G, Achille G, et al. Outcomes and risk factors for complications of laser ablation for thyroid nodules: a multicenter study on 1531 patients. J Clin Endocrinol Metab. 2015;100(10):3903-3910.
125. Jeong WK, Baek JH, Rhim H, et al. Radiofrequency ablation of benign thyroid nodules: safety and imaging follow-up in 236 patients. Eur Radiol. 2008;18(6):1244-1250.
126. Dupuy DE, Monchik JM, Decrea C, Pisharodi L. Radiofrequency ablation of regional recurrence from well-differentiated thyroid malignancy. Surgery. 2001;130(6):971-977.
127. Lewis BD, Hay ID, Charboneau JW, et al. Percutaneous ethanol injection for treatment of cervical lymph node metastases in patients with papillary thyroid carcinoma. AJR Am J Roentgenol. 2002;178(3):699-704.
128. Fukunari N. PEI therapy for thyroid lesions. Biomed Pharmacother. 2002;56:79-82.
129. Kim BM, Kim MJ, Kim EK, et al. Controlling recurrent papillary thyroid carcinoma in the neck by ultrasonography-guided percutaneous ethanol injection. Eur Radiol. 2008;18(4):835-842.
130. Kim JH, Yoo WS, Park YJ, et al. Efficacy and safety of radiofrequency ablation for treatment of locally recurrent thyroid cancers smaller than 2 cm. Radiology. 2015;276(3):909-918.
131. Mauri G, Cova L, Tondolo T, et al. Percutaneous laser ablation of metastatic lymph nodes in the neck from papillary thyroid carcinoma: preliminary results. J Clin Endocrinol Metab. 2013;98(7):E1203-E1207.
132. Papini E, Bizzarri G, Bianchini A, et al. Percutaneous ultrasound-guided laser ablation is effective for treating selected nodal metastases in papillary thyroid cancer. J Clin Endocrinol Metab. 2013;98(1):E92-E97.
133. Mazzaferri EL. Managing small thyroid cancers. JAMA. 2006;295(18):2179-2182.
134. Horlocker T, Hay I, James E. Prevalence of incidental nodular thyroid disease detected during high-resolution parathyroid ultrasonography. In: Medeiros-Neto G, Gaitan E, editors. Frontiers in thyroidology. New York: New York: Plenum; 1986. p. 1209-1312.
135. Cronan JJ. Thyroid nodules: is it time to turn off the US machines? Radiology. 2008;247(3):602-604.
136. Hay ID, Bergstralh EJ, Goellner JR, et al. Predicting outcome in papillary thyroid carcinoma: development of a reliable prognostic scoring system in a cohort of 1779 patients surgically treated at one institution during 1940 through 1989. Surgery. 1993;114(6):1050-1057.
137. Harach HR, Franssila KO, Wasenius VM. Occult papillary carcinoma of the thyroid. A "normal" finding in Finland. A systematic autopsy study. Cancer. 1985;56(3):531-538.
138. Davies L, Welch HG. Increasing incidence of thyroid cancer in the United States, 1973-2002. JAMA. 2006;295(18):2164-2167.
139. Ross DS. Editorial: predicting thyroid malignancy. J Clin Endocrinol Metab. 2006;91(11):4253-4255.
140. Burch HB. Evaluation and management of the solid thyroid nodule. Endocrinol Metab Clin North Am. 1995;24(4):663-710.
141. Goellner J. Fine-needle aspiration of the thyroid gland. In: Erosan YS, Bonfiglio TA, editors. Fine-needle aspiration of subcutaneous organs and masses. Philadelphia: Lippincott-Raven; 1996. p. 81-98.
142. Haas S, Trujillo A, Kunstle J. Fine needle aspiration of thyroid nodules in a rural setting. Am J Med. 1993;94(4):357-361.
143. Spiliotis J, Scopa CD, Gatopoulou C, et al. Diagnosis of thyroid cancer in southwestern Greece. Bull Cancer. 1991;78(10):953-959.
144. Songun I, Kievit J, Wobbes T, et al. Extent of thyroidectomy in nodular thyroid disease. Eur J Surg. 1999;165(9):839-842.
145. Reading CC, Charboneau JW, Hay ID, Sebo TJ. Sonography of thyroid nodules: a "classic pattern" diagnostic approach. Ultrasound Q. 2005;21(3):157-165.
146. Hay ID. Thyroiditis: a clinical update. Mayo Clin Proc. 1985;60(12):836-843.
147. Adams H, Jones MC. Ultrasound appearances of de Quervain's thyroiditis. Clin Radiol. 1990;42(3):217-218.
148. Birchall IW, Chow CC, Metreweli C. Ultrasound appearances of de Quervain's thyroiditis. Clin Radiol. 1990;41(1):57-59.
149. Yeh HC, Futterweit W, Gilbert P. Micronodulation: ultrasonographic sign of Hashimoto thyroiditis. J Ultrasound Med. 1996;15(12):813-819.
150. Takashima S, Matsuzuka F, Nagareda T, et al. Thyroid nodules associated with Hashimoto thyroiditis: assessment with US. Radiology. 1992;185(1):125-130.
151. Lagalla R, Caruso G, Benza I, et al. [Echo-color Doppler in the study of hypothyroidism in the adult]. Radiol Med. 1993;86(3):281-283.
152. Castagnone D, Rivolta R, Rescalli S, et al. Color Doppler sonography in Graves' disease: value in assessing activity of disease and predicting outcome. AJR Am J Roentgenol. 1996;166(1):203-207.

CHAPTER 20

The Parathyroid Glands

Bonnie J. Huppert and Carl Reading

SUMMARY OF KEY POINTS

- In the vast majority of cases, primary hyperparathyroidism is caused by hyperfunction of a single parathyroid gland due to adenoma, much less commonly due to multiple gland involvement.
- Surgical removal of the abnormal gland is the only definitive treatment for primary hyperparathyroidism, and selective, minimally invasive surgical techniques are most commonly used for first-time surgery.
- The role of parathyroid imaging is not in the diagnosis of primary hyperparathyroidism but rather to provide accurate adenoma localization to successfully direct selective surgical parathyroid resection.
- When used by an experienced examiner, parathyroid sonography can provide high-resolution anatomic imaging with good sensitivity and accuracy which is noninvasive, lacks radiation exposure, is relatively low cost, and has the added ability to assess for concomitant thyroid disease prior to surgery.
- In persistent or recurrent hyperparathyroidism, liberal use of multimodality preoperative imaging is particularly beneficial prior to reoperation.
- In selected cases, ultrasound can also be used to guide biopsy of suspected parathyroid adenomas to provide preoperative confirmation and to guide ablation of abnormal parathyroid glands in patients who are not surgical candidates.

CHAPTER OUTLINE

EMBRYOLOGY AND ANATOMY
PRIMARY HYPERPARATHYROIDISM
Prevalence
Diagnosis
Pathology
Treatment
SONOGRAPHIC APPEARANCE
Shape
Echogenicity and Internal Architecture
Vascularity
Size
Multiple Gland Disease
Carcinoma
ADENOMA LOCALIZATION
Sonographic Examination and Typical Locations
Ectopic Locations
Retrotracheal/Retroesophageal Adenoma
Mediastinal Adenoma
Intrathyroid Adenoma
Carotid Sheath/Undescended Adenoma
PERSISTENT OR RECURRENT HYPERPARATHYROIDISM
SECONDARY HYPERPARATHYROIDISM
PITFALLS IN INTERPRETATION
False-Positive Examination
False-Negative Examination
ACCURACY IN IMAGING
Ultrasound
Other Modalities
Importance of Imaging in Primary Hyperparathyroidism
INTRAOPERATIVE SONOGRAPHY
PERCUTANEOUS BIOPSY
ETHANOL ABLATION

High-frequency sonography is a well-established, noninvasive imaging method used in the evaluation and treatment of patients with parathyroid disease. Sonography is often used for the preoperative localization of enlarged parathyroid glands or adenomas in patients with hyperparathyroidism. Ultrasound is also used to guide the percutaneous biopsy of suspected parathyroid adenomas or enlarged glands, particularly in patients with persistent or recurrent hyperparathyroidism, as well as in some patients with suspected ectopic glands. In select patients, sonography can be used to guide the percutaneous ethanol ablation of parathyroid adenomas as an alternative to surgical treatment.

EMBRYOLOGY AND ANATOMY

The paired superior and inferior parathyroid glands have different embryologic origins, and knowledge of their development aids in understanding their ultimate anatomic locations.[1-3] The **superior parathyroid glands** arise from the paired fourth branchial pouches (clefts), along with the lateral lobes of the

thyroid gland. Minimal migration occurs during fetal development, and the superior parathyroids usually remain associated with the posterior aspect of the middle to upper portion of the thyroid gland. The majority of superior parathyroid glands (>80%) are found at autopsy within a 2-cm area located just superior to the crossing of the recurrent laryngeal nerve and the inferior thyroid artery.[4]

The **inferior parathyroid glands** arise from the paired third branchial pouches, along with the thymus.[2] During fetal development, these "parathymus glands" migrate caudally along with the thymus in a more anterior plane than their superior counterparts, bypassing the superior glands to become the inferior parathyroid glands.[3] Because of their greater caudal migration, the inferior parathyroid glands are more variable in location than the superior glands and can be found anywhere from the angle of the mandible to the pericardium. The majority of inferior parathyroid glands (>60%) come to rest at or just inferior to the posterior aspect of the lower pole of the thyroid[4] (Fig. 20.1).

A significant percentage of parathyroid glands lie in relatively or frankly **ectopic** locations in the neck or mediastinum. Symmetry to fixed landmarks occurs in 70% to 80%, so side-to-side comparisons can often be made.[3,4] The ectopic superior parathyroid gland usually lies posterior to the esophagus or in the tracheoesophageal groove, in the retropharyngeal space, or has continued its descent from the posterior neck into the posterosuperior mediastinum.[5,6] Superior glands are less often found higher in the neck, near the superior extent of the thyroid, or, in rare cases, surrounded by thyroid tissue within the thyroid capsule.[4] The inferior parathyroid gland is more frequently ectopic than its superior counterpart.[4,6] About 25% of the inferior glands fail to completely dissociate from the thymus and continue to migrate in an anterocaudal direction and are found in the low neck along the thyrothymic ligament or embedded within or adjacent to the thymus in the low neck and anterosuperior mediastinum. Less common ectopic positions of the inferior parathyroid glands include an undescended position high in the neck anterior to the carotid bifurcation associated with a remnant of thymus, and lower in the neck along or within the carotid sheath.[7] In other rare cases, ectopic glands have also been reported in the mediastinum posterior to the esophagus or carina, in the aortopulmonic window, within the pericardium, or even far laterally within the posterior triangle of the neck.

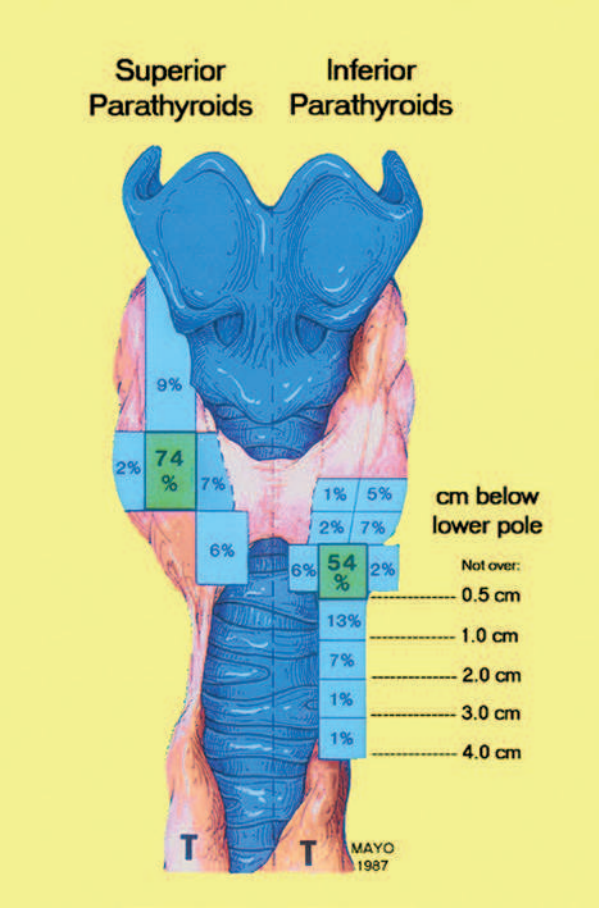

FIG. 20.1 Location of Parathyroid Glands. Frequency of the location of normal superior and inferior parathyroid glands. Anatomic drawing from 527 autopsies. *T,* Thymus. (Modified from Gilmour JR. The gross anatomy of the parathyroid glands. J Pathol 1938;46:133-148.[1])

Most adults have four parathyroid glands, two superior and two inferior, each measuring about 5 × 3 × 1 mm and weighing on average 35 to 40 mg (range, 10-78 mg).[3,8] **Supernumerary glands** (>4) may be present and result from the separation of parathyroid anlage when the glands pull away from the pouch structures during the embryologic branchial complex phase.[9,10] These supernumerary glands are often associated with the thymus in the anterior mediastinum, suggesting a relationship in their development with the inferior parathyroid glands.[11] Supernumerary glands have been reported in 13% of the population at autopsy studies[3,4]; however, many of these are small, rudimentary or split glands. "Proper" supernumerary glands (>5 mg and located well away from the other four glands) are found in 5% of cases. The presence of fewer than four parathyroid glands is rare clinically but has been reported in 3% at autopsy.

Normal parathyroid glands vary from a yellow to a red-brown color, depending on the degree of vascularity and the relative content of yellow parenchymal fat and chief cells.[8] The chief cells are the primary source for the production of **parathyroid hormone (PTH, parathormone).** The percentage of glandular fat typically increases with age or with disuse atrophy. Hyperfunctioning glands resulting from adenomas or hyperplasia contain relatively little fat and are vascular, thus more reddish. The glands are generally oval or bean shaped but may be spherical, lobular, elongated, or flattened. Although normal parathyroid glands are occasionally seen with high-frequency ultrasound,[12,13] typically they are not visualized, likely because of their small size, deep location, and poor conspicuity related to increased glandular fat. **Eutopic** parathyroid glands typically derive their major blood supply from branches of the inferior thyroid artery, with a lesser and variable contribution to the superior glands from the superior thyroid artery.[3,7]

PRIMARY HYPERPARATHYROIDISM

Prevalence

Primary hyperparathyroidism is a common endocrine disease, with prevalence in the United States of 1 to 2 per 1000

population.[14] Women are affected two to three times more frequently than men, particularly after menopause. More than half of patients with primary hyperparathyroidism are older than 50 years, and cases are rare in those younger than age 20.

Diagnosis

Primary hyperparathyroidism is usually suspected because an increased serum calcium level is detected on routine biochemical screening. Elevated ionized serum calcium level, **hypophosphatasia,** and **hypercalciuria** may be further biochemical clues to the disease. A serum PTH level that is "inappropriately high" for the corresponding serum calcium level confirms the diagnosis. Even when the PTH level is within the upper limits of the normal range in a hypercalcemic patient, the diagnosis of primary hyperparathyroidism should still be suspected, since **hypercalcemia** from other nonparathyroid causes (including malignancy) should suppress the glandular function and decrease the serum PTH level. Because of earlier detection by increasingly routine laboratory tests, the later "classic" signs of hyperparathyroidism, such as "painful bones, renal stones, abdominal groans, and psychic moans," are often not present. Many patients are diagnosed before severe manifestations of hyperparathyroidism, such as **nephrolithiasis, osteopenia, subperiosteal resorption,** and **osteitis fibrosis cystica.** In general, patients rarely have obvious symptoms unless their serum calcium level exceeds 12 mg/dL. However, subtle nonspecific symptoms, such as muscle weakness, malaise, constipation, dyspepsia, polydipsia, and polyuria, may be elicited from these otherwise asymptomatic patients by more specific questioning.

Pathology

Primary hyperparathyroidism is caused by a **single adenoma** in 80% to 90% of cases, by **multiple gland enlargement** in 10% to 20%, and by **carcinoma** in less than 1%.[6,15,16] A solitary adenoma may involve any one of the four glands. Multigland enlargement most often results from primary parathyroid hyperplasia and less often from multiple adenomas. Hyperplasia usually involves all four glands asymmetrically, whereas multiple adenomas may involve two or possibly three glands. An adenoma and hyperplasia cannot always be reliably distinguished histologically, and the sample may be referred to as "hypercellular parathyroid" tissue. Because of this inconsistent pattern of gland involvement, and because distinguishing hyperplasia from multiple adenomas is difficult pathologically, these two entities are often histologically considered together as "multiple gland disease."[17]

Causes of Primary Hyperparathyroidism

Type of Disease	Percentage
Single adenoma	80%-90%
Multiple gland disease	10%-20%
Carcinoma	<1%

Most cases of primary hyperparathyroidism are sporadic. However, **prior external neck irradiation** has been associated with the development of hyperparathyroidism in a small percentage of cases. Patients receiving **long-term lithium therapy** may also present with primary hyperparathyroidism. Up to 10% of cases may occur on a hereditary basis, most often caused by **multiple endocrine neoplasia syndrome,** type I **(MEN I).** This condition is an uncommon disorder that most typically follows an autosomal dominant pattern of inheritance and has a high penetrance, resulting in adenomatous parathyroid hyperplasia, as well as pancreatic islet cell tumors and pituitary adenomas. Multiple–parathyroid gland enlargement occurs in more than 90% of patients with MEN I.[18,19] Most MEN I patients present with hypercalcemia before their third or fourth decade of life. Not all the parathyroid glands may be grossly enlarged at these patients' initial operation, but all of them likely will ultimately be involved with hyperplasia. Patients with the **MEN IIA syndrome** less frequently develop parathyroid hyperplasia. Other, rarer familial syndromes may also be associated with primary hyperparathyroidism caused by hyperplasia, adenomas, or carcinoma. An important hereditary hyperparathyroidism that must be distinguished from primary hyperparathyroidism caused by hyperplasia or adenoma is **familial hypocalciuric hypercalcemia** (benign familial hypercalcemia). Most of these patients are asymptomatic, without the complications of primary hyperparathyroidism. Parathyroidectomy does not cure the hypercalcemia, and thus surgery is inappropriate.

Parathyroid carcinoma is a rare cause of primary hyperparathyroidism.[20-23] The histologic distinction from adenoma is difficult to establish with certainty because both carcinomas and atypical adenomas can exhibit increased mitotic activity and cellular atypia. Patients with parathyroid carcinoma usually present with a very high serum calcium level (>14 mg/dL). The diagnosis is often made at operation when the surgeon discovers an enlarged, firm gland that is adherent to the surrounding tissues due to local invasion. A thick, fibrotic capsule is often present. Treatment consists of en bloc resection without entering the capsule, to prevent tumor seeding. In many cases, cure may not be possible because of the invasive and metastatic nature of the disease. Generally, death occurs not from tumor spread but from complications associated with unrelenting hyperparathyroidism.

Treatment

No effective definitive medical therapies are available for the treatment of primary hyperparathyroidism. Medications utilized include short-term hypocalcemic agents such as calcitonin and **calcimimetics** (calcium-sensing receptor agonists) such as cinacalcet. The bisphosphonates aid in preventing bone mass loss. Synthetic vitamin D analogs such as paricalcitol are mainly used in the treatment of secondary hyperparathyroidism.

Surgery is the only definitive treatment for primary hyperparathyroidism. Studies demonstrate that surgical cure rates by an experienced surgeon are greater than 95%, and the morbidity and mortality rates are extremely low.[24,25] Therefore in symptomatic patients with primary hyperparathyroidism, the treatment of choice is surgical excision of the involved parathyroid gland or glands.

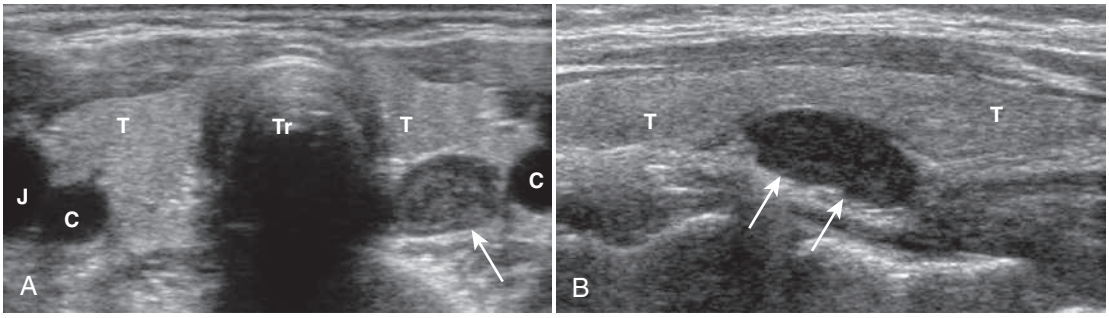

FIG. 20.2 Typical Parathyroid Adenoma. (A) Transverse and **(B)** longitudinal sonograms of a typical adenoma *(arrows)* located adjacent to the posterior aspect of the thyroid *(T). C,* Common carotid artery; *J,* internal jugular vein; *Tr,* trachea.

However, since in current practice, most cases of primary hyperparathyroidism are discovered in the early stages of the disease, some controversy exists as to whether asymptomatic patients with minimal hypercalcemia should be treated surgically, or followed medically with frequent measurements of bone density, serum calcium levels, and urinary calcium excretion and monitoring for nephrolithiasis.[26] Recommendations for the management of asymptomatic primary hyperparathyroidism have been outlined in various articles, many of which are based on International Workshop and National Institutes of Health (NIH) Consensus Conference statements and subsequent updates. This area continues to evolve, and approaches to treatment may differ slightly among clinical practices.[24-31]

SONOGRAPHIC APPEARANCE

Shape

Parathyroid adenomas are typically oval or bean shaped (Fig. 20.2). As parathyroid glands enlarge, they dissect between longitudinally oriented tissue planes in the neck and acquire a characteristic oblong shape. If this process is exaggerated, they can become tubular or flattened. There is often asymmetry in the enlargement, and the cephalic and/or caudal end can be more bulbous, producing a triangular, tapering, teardrop or bilobed shape.[19,32-34]

Echogenicity and Internal Architecture

The echogenicity of most **parathyroid adenomas** is substantially less than that of normal thyroid tissue (Fig. 20.3). The characteristic **hypoechoic** appearance of parathyroid adenomas is caused by the uniform hypercellularity of the gland with little fat content, which leaves few interfaces for reflecting sound. Occasionally, adenomas have a heterogeneous appearance, with areas of increased and decreased echogenicity. The rare, functioning **parathyroid lipoadenomas** are more echogenic than the adjacent thyroid gland because of their high fat content[35] (Fig. 20.3G). A great majority of parathyroid adenomas are **homogeneously solid.** About 2% have internal cystic components resulting from **cystic degeneration** (most often) or true simple cysts (less often)[36-38] (Fig. 20.3E and F, Video 20.1). Adenomas may rarely contain internal calcification (Fig. 20.3H and I).

Vascularity

Color flow, spectral, and power Doppler sonography of an enlarged parathyroid gland may demonstrate a hypervascular pattern with prominent diastolic flow (Fig. 20.4). An enlarged **extrathyroidal artery,** often originating from branches of the **inferior thyroidal artery,** may be visualized supplying the adenoma with its insertion along the long-axis pole.[39-44] A finding described in parathyroid adenomas is a **vascular arc,** which envelops 90 to 270 degrees of the mass. This vascular flow pattern may increase the sensitivity of initial detection of parathyroid adenomas and aid in confirming the diagnosis by allowing for differentiation from lymph nodes, which have a central hilar flow pattern. Asymmetric increased vascular flow may also be present in the thyroid gland adjacent to a parathyroid adenoma.

Size

Most parathyroid adenomas are 0.8 to 1.5 cm long and weigh 500 to 1000 mg. The smallest adenomas can be minimally enlarged glands that appear virtually normal during surgery but are found to be hypercellular on pathologic examination (Fig. 20.5, Video 20.2). Large adenomas can be 5 cm or more in length and weigh more than 10 g. Preoperative serum calcium levels are usually higher in patients with larger adenomas.[32]

Multiple Gland Disease

Multiple gland disease may be caused by diffuse hyperplasia or multiple adenomas. Individually, these enlarged glands may have the same sonographic and gross appearance as other parathyroid adenomas (Fig. 20.6, Videos 20.3 and 20.4). However, the glands may be inconsistently and asymmetrically enlarged, and the diagnosis of multigland disease can be difficult to make sonographically. For example, if one gland is much larger than the others, the appearance may be misinterpreted as solitary adenomatous disease. Alternatively, if multiple glands are only minimally enlarged, the diagnosis may be missed altogether.

Carcinoma

Carcinomas are usually larger than adenomas.[45-47] Carcinomas often measure more than 2 cm compared with about 1 cm for adenomas (Fig. 20.7). On ultrasound, carcinomas also frequently have a lobular contour, heterogeneous internal architecture, and internal cystic components. However, large adenomas may also

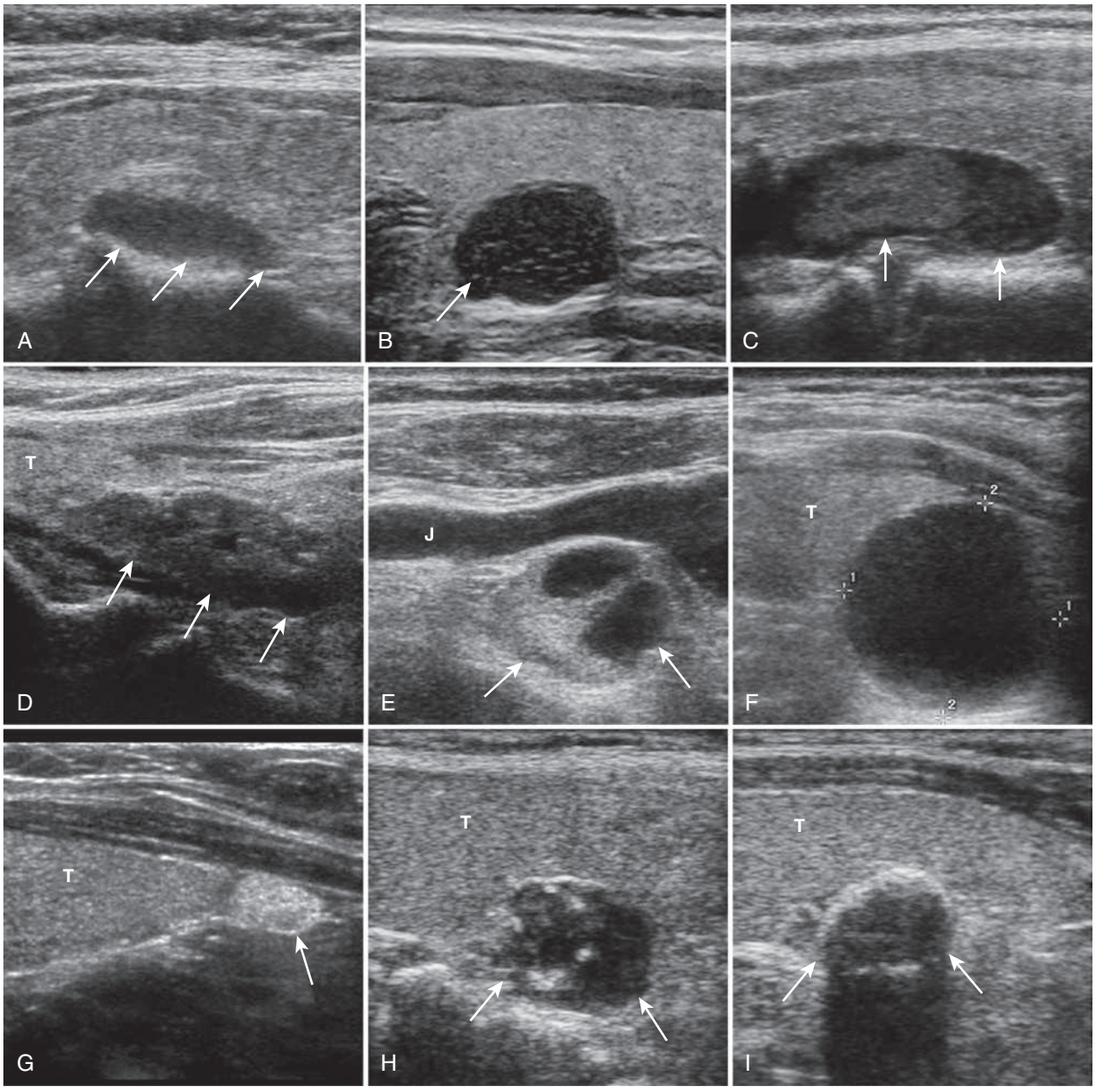

FIG. 20.3 Spectrum of Echogenicity and Internal Architecture of Parathyroid Adenomas and Enlarged Hyperplastic Glands. Longitudinal sonograms. **(A)** Typical homogeneous hypoechoic appearance of a parathyroid adenoma *(arrows)* with respect to the overlying thyroid tissue. **(B)** Highly hypoechoic solid **adenoma. (C)** Mixed-geographic echogenicity. The adenoma is hyperechoic in its cranial portion and hypoechoic in its caudal portion. **(D)** An adenoma with diffusely heterogeneous echogenicity. **(E)** Partial cystic change. An ectopic adenoma posterior to the jugular vein *(J)* has both solid and cystic components. **(F)** Completely cystic 2-cm adenoma *(calipers)* near the lower pole of the thyroid *(T)*. See also Video 20.1. **(G)** A **lipoadenoma** is more echogenic than the adjacent lower pole thyroid tissue. **(H)** Enlarged parathyroid gland with small, nonshadowing calcifications in the setting of **secondary hyperparathyroidism** related to chronic **renal failure**. **(I)** Enlarged parathyroid gland with densely shadowing peripheral calcifications in the setting of secondary hyperparathyroidism.

have these features. In many cases, carcinomas are indistinguishable sonographically from large, benign adenomas.[45] Some authors report that a depth-to-width ratio of 1 or greater is a sonographic feature more associated with carcinoma than with adenoma, with sensitivity and specificity of 94% and 95%, respectively.[47] Gross evidence of invasion of adjacent structures, such as vessels or muscles, is a reliable preoperative sonographic criterion for the diagnosis of malignancy, but this is an uncommon finding.

ADENOMA LOCALIZATION

Sonographic Examination and Typical Locations

The sonographic examination of the neck for parathyroid adenoma localization is performed with the patient supine. The patient's neck is hyperextended by a pad centered under the scapulae, and the examiner usually sits at the patient's head. High-frequency

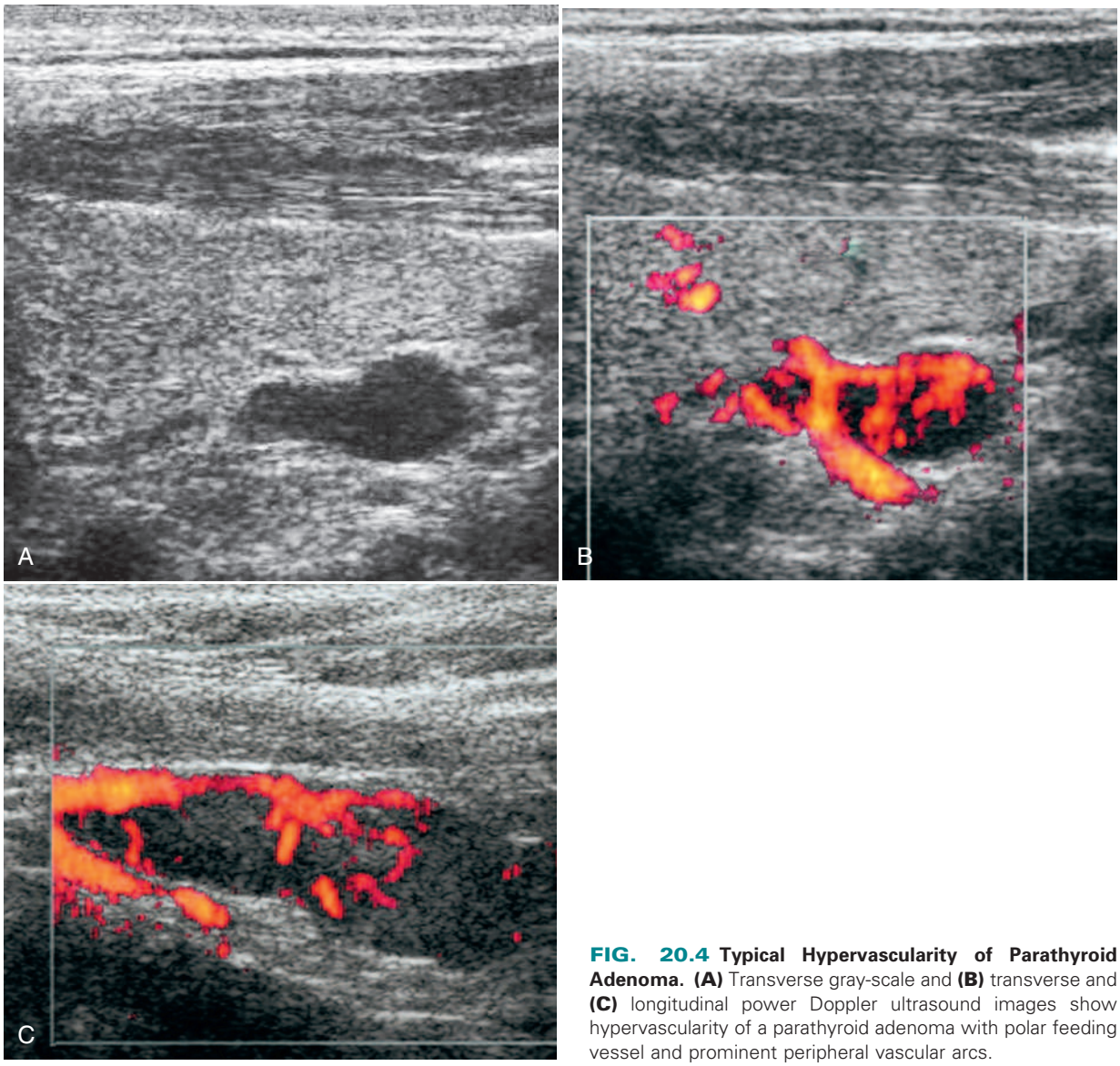

FIG. 20.4 Typical Hypervascularity of Parathyroid Adenoma. (A) Transverse gray-scale and **(B)** transverse and **(C)** longitudinal power Doppler ultrasound images show hypervascularity of a parathyroid adenoma with polar feeding vessel and prominent peripheral vascular arcs.

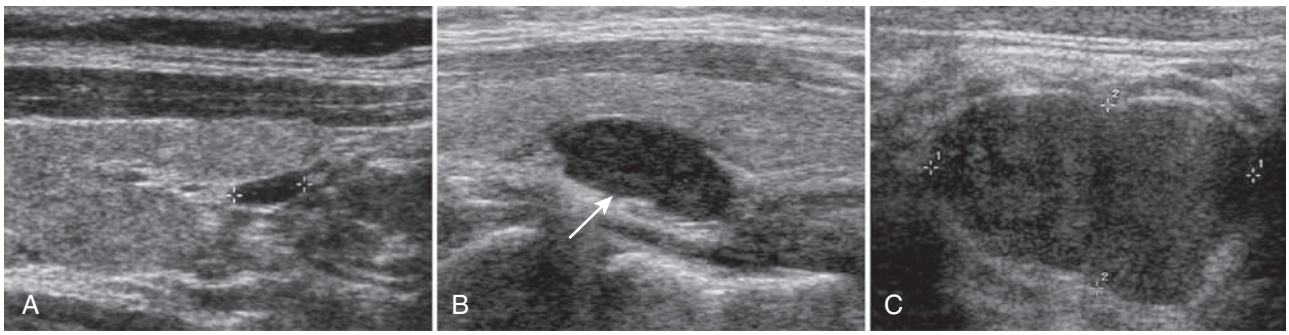

FIG. 20.5 Spectrum of Size of Parathyroid Adenomas. Longitudinal sonograms. **(A)** Minimally enlarged, 0.5 × 0.2–cm parathyroid adenoma *(calipers)*. See also Video 20.2. **(B)** Typical midsized, 1.5 × 0.6–cm, 400-mg adenoma *(arrow)*. **(C)** Large, 3.5 × 2–cm, >4000-mg adenoma *(calipers)*.

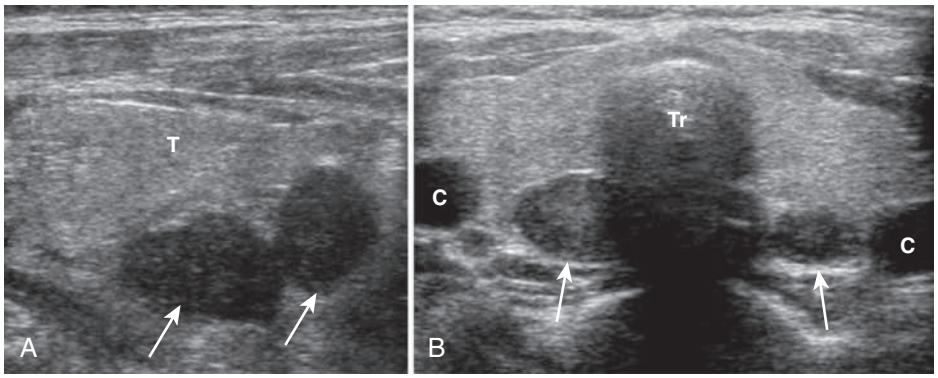

FIG. 20.6 Multiple Gland Disease. (A) Longitudinal sonogram of the right neck shows superior and inferior parathyroid gland enlargement *(arrows)* in the setting of secondary hyperparathyroidism, which can be difficult to distinguish from multiple adenomas. *T,* Thyroid. **(B)** Transverse sonogram in another patient shows enlargement of bilateral superior parathyroid glands in the setting of secondary hyperparathyroidism. *C,* Common carotid artery; *Tr,* trachea. See also Videos 20.3 and 20.4.

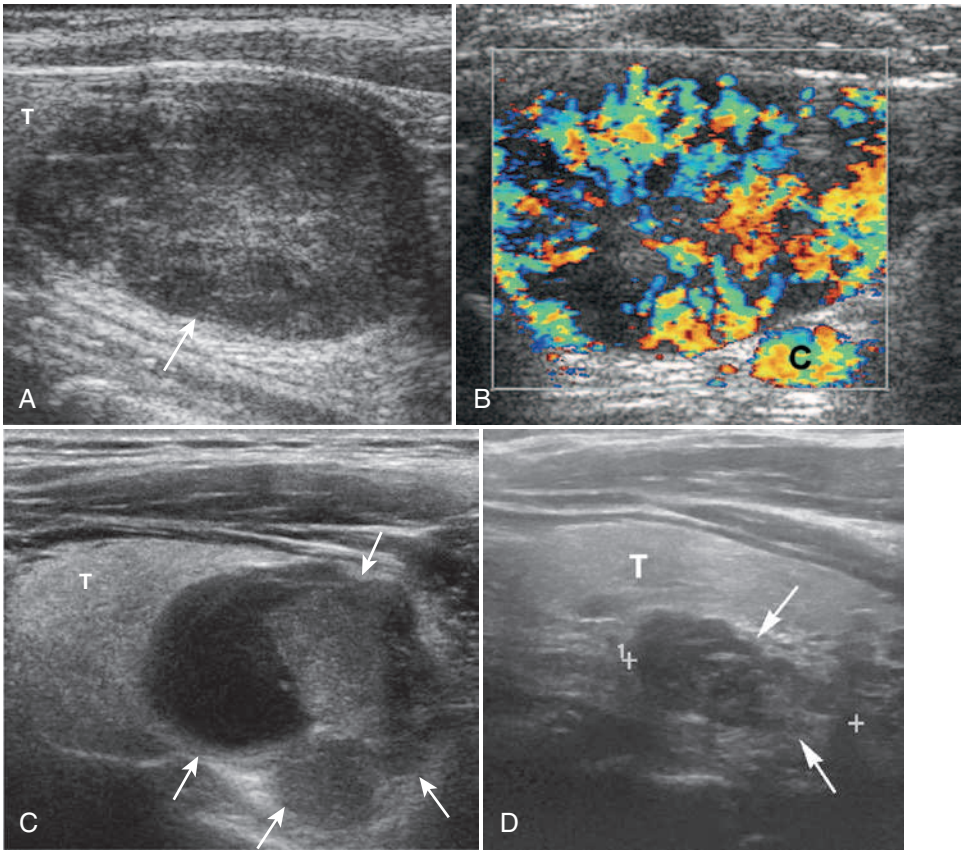

FIG. 20.7 Parathyroid Carcinoma. (A) Longitudinal sonogram shows heterogeneous 4-cm parathyroid carcinoma *(arrow)* located near tip of lower pole of the left thyroid lobe *(T).* **(B)** Transverse sonogram with color Doppler flow imaging shows prominent internal vascularity of the carcinoma. *C,* Common carotid artery. **(C)** Longitudinal sonogram in another patient shows lobulated, solid and cystic, 4-cm parathyroid carcinoma *(arrows)* adjacent to the lower pole of the thyroid. **(D)** Longitudinal sonogram in another patient shows a 3-cm heterogeneous solid low-grade parathyroid carcinoma (*calipers)* with irregular lobulated margins *(arrows)* posterior to the thyroid.

transducers (6-15 MHz and 8-18 MHz) are used to provide optimal spatial resolution and visualization in most patients; the highest frequency possible should be used that still allows for tissue penetration to visualize the deeper structures, such as the longus colli muscles. In obese patients with thick necks or with large multinodular thyroid glands, use of a 5- to 8-MHz transducer may be necessary to obtain adequate depth of penetration.

The pattern of the sonographic survey of the neck for adenoma localization can be considered in terms of the pattern of dissection and visualization that the surgeon uses in a thorough neck exploration. The typical **superior parathyroid adenoma** is usually adjacent to the posterior aspect of the midportion of the thyroid (Fig. 20.8, Videos 20.5 and 20.6). The location of the typical **inferior parathyroid adenoma** is more variable but usually lies

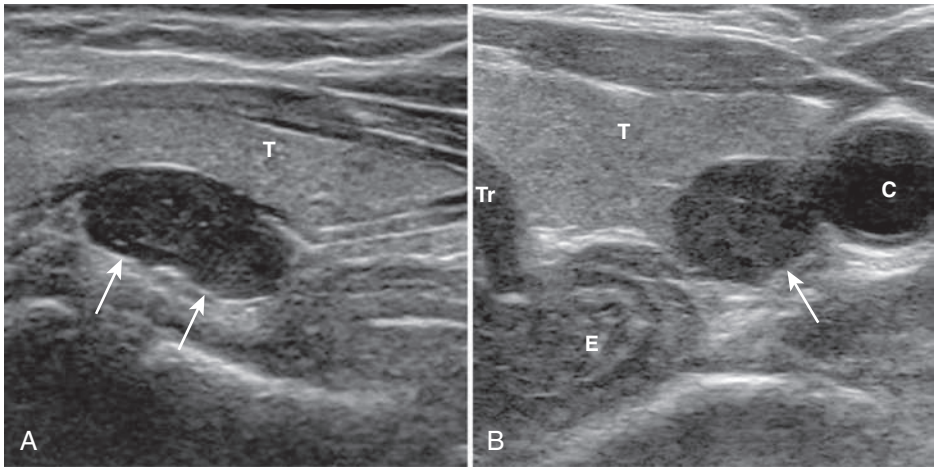

FIG. 20.8 Superior Parathyroid Adenoma. (A) Longitudinal and **(B)** transverse sonograms show an adenoma *(arrows)* adjacent to the posterior aspect of the midportion of the left lobe of the thyroid *(T). C,* Common carotid artery; *E,* esophagus; *Tr,* trachea. See also Videos 20.5 and 20.6.

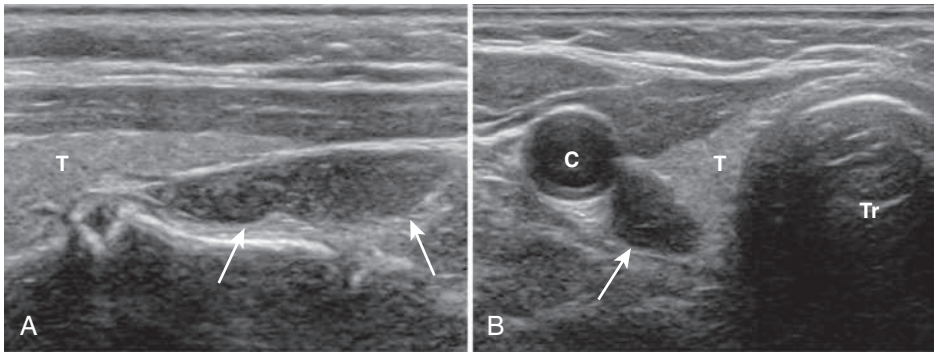

FIG. 20.9 Inferior Parathyroid Adenoma. (A) Longitudinal and **(B)** transverse sonograms show an adenoma *(arrows)* adjacent to lower pole of right lobe of the thyroid *(T). C,* Common carotid artery; *Tr,* trachea. See also Videos 20.7 and 20.8.

close to the lower pole of the thyroid (Fig. 20.9, Videos 20.7 and 20.8). Most of these inferior adenomas are adjacent to the posterior aspect of the lower pole of the thyroid, and the rest are in the soft tissues 1 to 2 cm inferior to the thyroid. Therefore the examination is initiated on one side of the neck, centered in the region of the thyroid gland, with the focal zone placed deep to the thyroid. High-resolution gray-scale images are obtained in the transverse (axial) and longitudinal (sagittal) planes. Any potential parathyroid adenomas detected in the transverse scan plane must be confirmed by longitudinal imaging to prevent mistaking other structures for an adenoma.

Some authors recommend the use of **compression** of the superficial soft tissues to aid in adenoma detection.[12,43,48] This has been described as "graded" compression with the transducer to effect minimal deformity of the overlying subcutaneous tissues and strap muscles and increase the conspicuity of deeper, smaller adenomas (<1 cm). Color flow and/or power Doppler sonography are also used to assess the vascularity of any potential adenoma, aid in detection, and support differentiation from other structures.[40-44,48] Hypervascularity may be evident with a polar insertion of a prominent extrathyroidal feeding artery, also with peripheral arcs of blood flow. After one side of the neck has been examined, a similar survey is conducted of the opposite side. However, 1% to 3% of parathyroid adenomas are frankly ectopic and not found in typical locations adjacent to the thyroid. Therefore the sonographic examination must be extended laterally along the carotid sheaths, superiorly from the level of the mandible, and inferiorly to the level of the sternal notch and clavicles. The four most common ectopic locations are considered separately next.

Ectopic Locations

Retrotracheal/Retroesophageal Adenoma

Superior adenomas tend to enlarge between tissue planes that extend toward the posterior mediastinum; the most common location of an ectopic superior adenoma is deep in the neck, posterior or posterolateral to the trachea or esophagus (Fig. 20.10, Video 20.9). Acoustic shadowing from air in the trachea can make evaluation of this area difficult. The transducer should be angled medially to visualize the tissues posterior to the trachea. Often the adenoma protrudes slightly from behind the trachea,

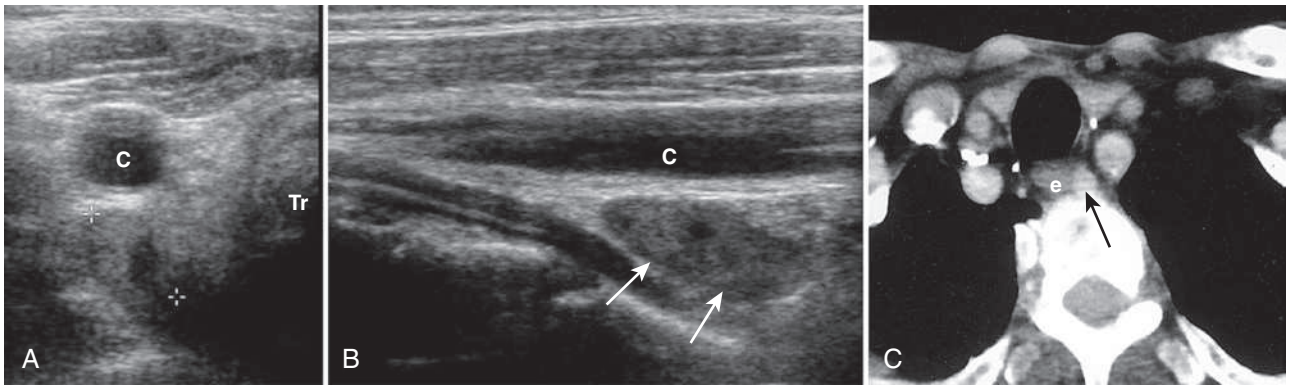

FIG. 20.10 Ectopic Superior Parathyroid Adenoma: Tracheoesophageal Groove. (A) Transverse sonogram reveals an adenoma *(calipers)* arising from the right tracheoesophageal groove located posteriorly in the neck. The patient's head is turned to the left, which deviates the adenoma laterally and aids in visualization. *C,* Common carotid artery; *Tr,* trachea. **(B)** Corresponding longitudinal sonogram shows the ectopic superior parathyroid adenoma *(arrows)* posterior in the low neck adjacent to the cervical spine. **(C)** CT scan of the low neck/upper mediastinum in another patient shows an ectopic adenoma *(arrow)* in the left tracheoesophageal groove adjacent to the esophagus *(e).* See also Video 20.9.

and only a portion of the mass will be visible. Turning the patient's head to the opposite side will accentuate the protrusion and provide better accessibility to the retrotracheal area. This process is then repeated on the other side of the neck to visualize the contralateral aspect of the retrotracheal area. This process is analogous to the maneuver that a surgeon uses to run a fingertip behind the trachea in an attempt to palpate a retrotracheal adenoma. Maximal turning of the head also often causes the esophagus to move to the opposite side of the trachea as it becomes compressed between the trachea and the cervical spine. If the examiner sees the esophagus move completely from one side of the trachea to the opposite side during maximal head turning, the esophagus has effectively "swept" the retrotracheal space and will have pushed any parathyroid adenoma in this location out from behind the trachea.

Mediastinal Adenoma

The most common location for ectopic inferior parathyroid adenomas is low within the neck or in the anterosuperior mediastinum[4,6,49,50] (Fig. 20.11). Parathyroid adenomas are sufficiently hypoechoic that they may be visualized as discrete structures separate from the thymus and surrounding tissues. To visualize this area optimally, the patient's neck is maximally hyperextended. With this technique and the transducer angled posterior and caudal to the clavicular heads, sonographic visualization is often possible to the level of the brachiocephalic veins. If the adenoma lies caudal to this level or far anterior, just deep to the sternum, it cannot be visualized sonographically.

Ectopic superior adenomas located in the mediastinum tend to stay in a more posterior plane than their ectopic inferior counterparts and are often not visible with traditional sonography. They usually lie deep in the low neck or posterior superior mediastinum, requiring use of a 5-MHz transducer for maximal penetration. Ectopic superior adenomas may be intimately associated with the posterior aspect of the trachea, and the head-turning maneuver described for retrotracheal adenomas in the neck can be applied here as well. With the patient's neck hyperextended and the transducer angled caudally, the posterior mediastinum may sometimes be visualized to the level of the apex of the aortic arch; adenomas lying caudal to this level cannot be visualized.

Intrathyroid Adenoma

Intrathyroid parathyroid adenomas are uncommon and have been described as either superior or inferior gland adenomas.[4,6,8] Most intrathyroid adenomas are in the posterior half of the middle to lower thyroid, are completely surrounded by thyroid tissue, and are oriented with their greatest dimension in the cephalocaudal direction (Fig. 20.12, Videos 20.10 and 20.11). Intrathyroid adenomas may be overlooked at surgery because they are soft and are similar to the surrounding thyroid tissue on palpation. A thyroidotomy or subtotal lobectomy may be needed to find an intrathyroid adenoma. Sonographically, however, parathyroid adenomas usually are well visualized because they are hypoechoic, in contrast to the echogenic thyroid parenchyma, and a polar feeding vessel is often present on color flow or power Doppler imaging.[51] The internal architecture and appearance of these adenomas are the same as for adenomas elsewhere in the neck. However, because intrathyroid parathyroid adenomas can be similar to thyroid nodules in appearance, percutaneous biopsy is often necessary to distinguish between these entities.

Some parathyroid adenomas lie under the pseudocapsule or sheath that covers the thyroid gland or within a sulcus of the thyroid, but these are not usually considered to be true intrathyroid adenomas. These adenomas may be difficult for the surgeon to visualize at surgery unless this sheath is opened.[4,8] Sonographically, these may appear the same as other parathyroid adenomas that lie immediately adjacent to the thyroid, although the typical thin, echogenic capsular interface often seen between the thyroid and a parathyroid adenoma may be absent.

Carotid Sheath/Undescended Adenoma

Rare ectopic adenomas can lie in a high position superior and lateral in the neck, near the **carotid bifurcation** at the level of

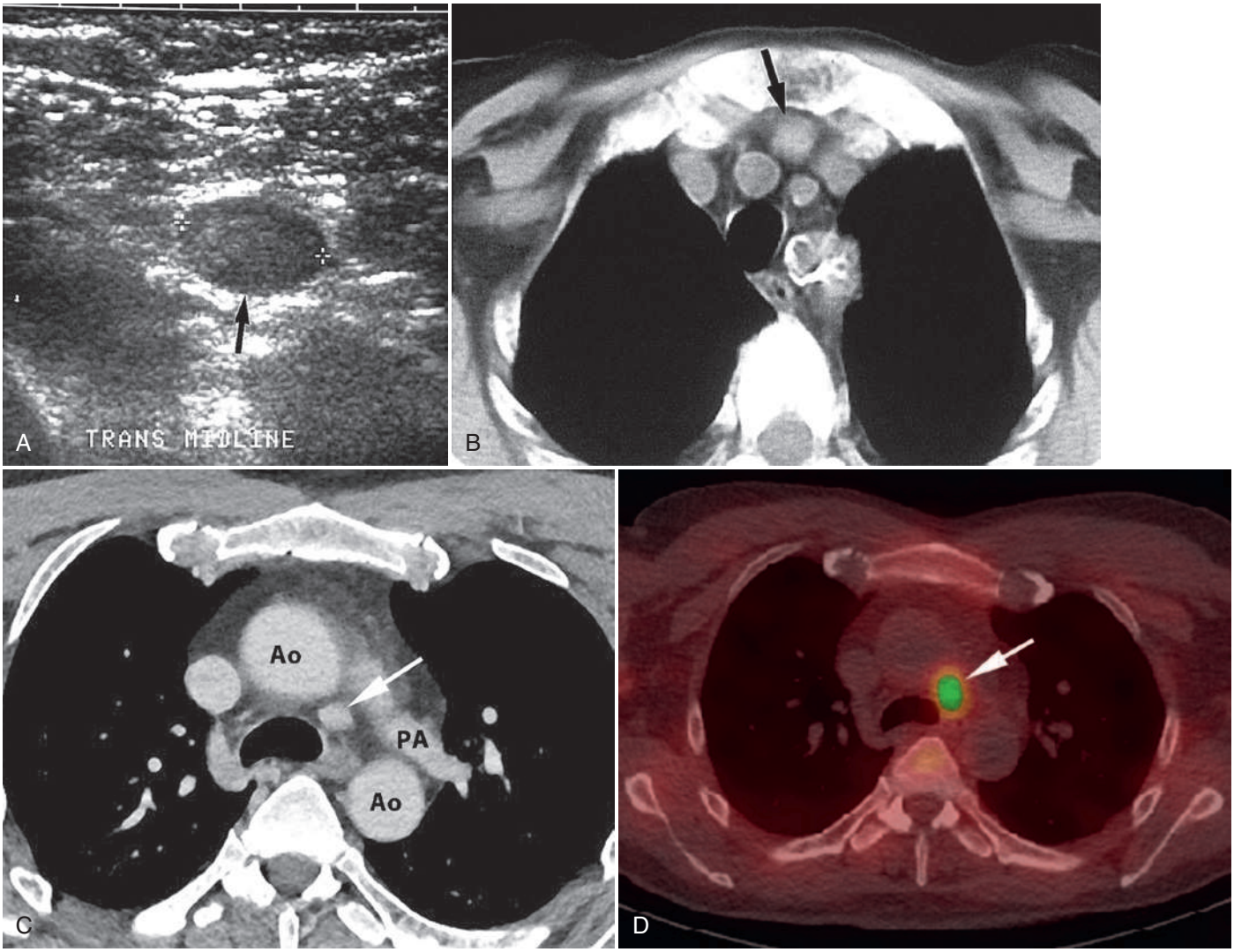

FIG. 20.11 Ectopic Parathyroid Adenoma: Mediastinum. (A) Transverse sonogram angled caudal to the clavicles shows an oval, 1-cm ectopic inferior parathyroid adenoma *(arrow)* in the soft tissues of the anterosuperior mediastinum. **(B)** CT scan of the upper mediastinum shows the ectopic adenoma in the anterosuperior mediastinum, deep to the manubrium and adjacent to the great vessels. **(C)** Enhanced axial CT performed in another patient shows an enhancing ectopic middle mediastinal parathyroid adenoma. *Ao,* Aorta; *PA,* left pulmonary artery. **(D)** Technetium-99m (^{99m}Tc) sestamibi axial single-photon emission computed tomography (SPECT)/CT scintigraphy shows the same ectopic adenoma in the middle mediastinum.

the hyoid bone and adjacent to the submandibular gland, or elsewhere within or along the carotid sheath[4,7,19,52-54] (Fig. 20.13, Video 20.12). These adenomas likely arise from inferior glands that are embryologically undescended, or partially descended, having come to reside within or adjacent to the carotid sheath that surrounds the carotid artery, jugular vein, and **vagus nerve.** They may be associated with a small amount of **ectopic thymic tissue.** These adenomas are frequently overlooked during surgery unless the surgeon specifically opens the carotid sheath and dissects within it.[6,7] Sonographically, these masses can appear similar to mildly enlarged lymph nodes in the jugular chain; correlative imaging and percutaneous biopsy are often necessary for confirmation before surgery. Ectopic undescended superior gland adenomas may be present high in the neck in a parapharyngeal location but frequently are not seen with traditional sonography.

PERSISTENT OR RECURRENT HYPERPARATHYROIDISM

Persistent hyperparathyroidism is the persistence of hypercalcemia after previous failed parathyroid surgery. This is frequently caused by an undiscovered ectopic parathyroid adenoma or unrecognized multiple gland disease, with failure to resect all the hyperfunctioning tissue during surgery.[55-57] **Recurrent hyperparathyroidism** is defined as hypercalcemia occurring after a 6-month interval of normocalcemia, resulting from the new development of hyperfunctioning parathyroid tissue from previously normal glands.[58] Recurrent hyperparathyroidism is often seen in patients with unrecognized MEN syndromes.

Because of scarring and fibrosis from previous surgery, the curative rate for repeat surgery is lower than for initial surgery; the risk of recurrent laryngeal nerve damage and postoperative

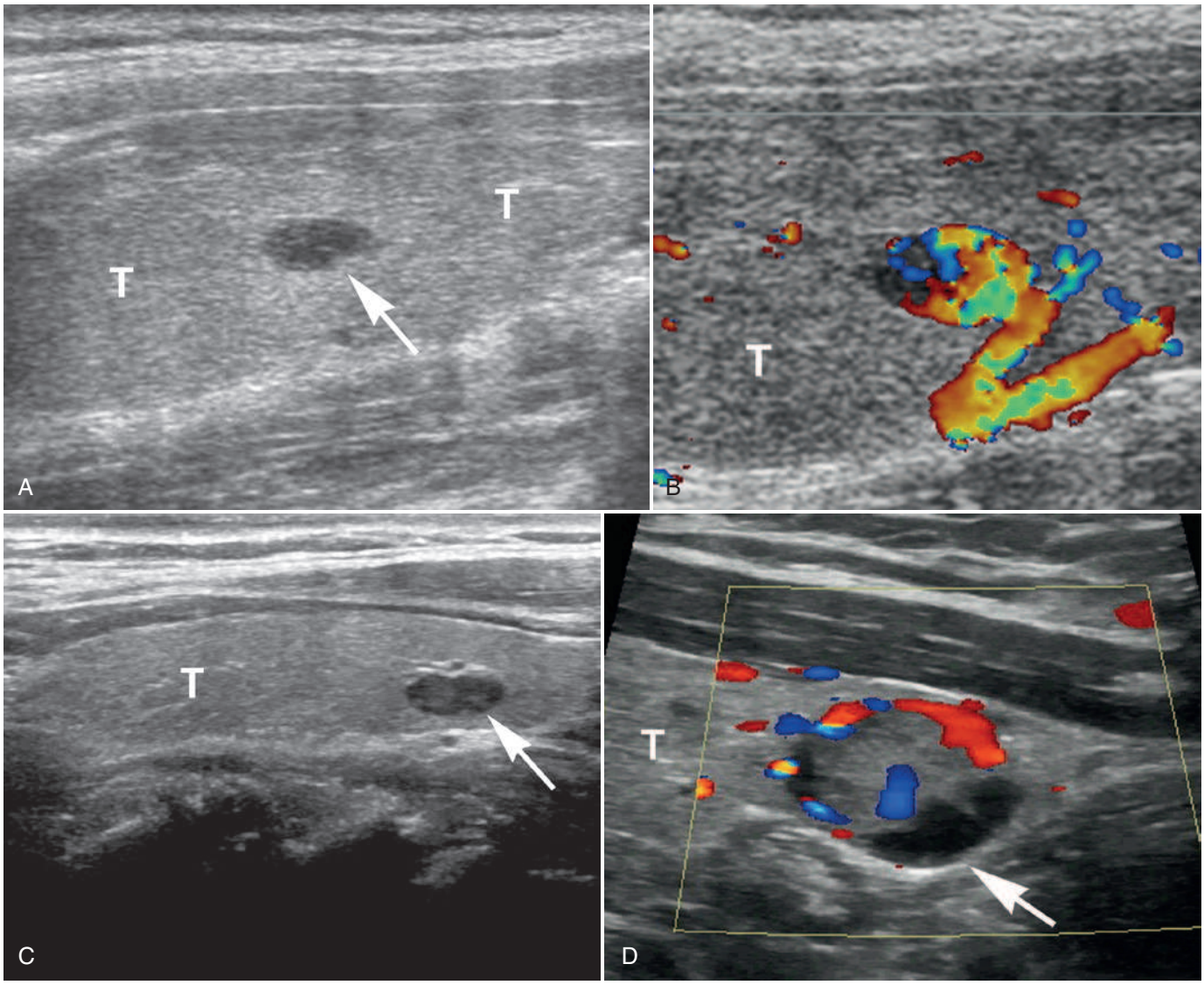

FIG. 20.12 Ectopic Parathyroid Adenoma: Intrathyroidal. (A) Longitudinal sonogram shows a subcentimeter hypoechoic intrathyroid parathyroid adenoma *(arrow)* in the midlobe completely surrounded by thyroid tissue. *T,* Thyroid. **(B)** Corresponding color Doppler flow imaging demonstrates typical hypervascularity with polar insertion of feeding vessel. **(C)** Longitudinal sonogram in another patient shows a subcentimeter hypoechoic intrathyroid parathyroid adenoma in the lower portion of the thyroid. **(D)** Longitudinal color Doppler flow sonogram in another patient shows a partially cystic intrathyroid parathyroid adenoma with prominent peripheral vascularity. See also Video 20.10.

hypocalcemia from hypoparathyroidism is also greater.[59,60] Imaging before reoperation is particularly beneficial.[57,60-64] Ultrasound is an effective first-line imaging modality in the preoperative and reoperative assessment of parathyroid disease, providing anatomic localization with a relatively inexpensive, noninvasive method that avoids the use of ionizing radiation.[43,44,63,64] During sonographic evaluation of reoperative patients, specific attention is paid to the most likely ectopic parathyroid locations—those associated with a gland that was not discovered at the initial neck dissection.

A small subgroup of patients who develop recurrent hyperparathyroidism underwent previous **autotransplantation** of parathyroid tissue in conjunction with previous total parathyroidectomy, typically for complications of chronic renal failure. Hyperparathyroidism in the setting of parathyroid autotransplantation is referred to as **graft-dependent hyperparathyroidism.** In parathyroid autotransplantation, a gland is sliced into fragments that are inserted into surgically prepared intramuscular pockets in the forearm or sternocleidomastoid muscle. Normal-functioning autotransplanted parathyroid grafts are typically too small and similar in echotexture to the surrounding muscle to be adequately visualized sonographically. However, graft-dependent recurrent hyperparathyroidism can be imaged sonographically, appearing as oval, sharply marginated, hypoechoic hypervascular nodules measuring 5 to 11 mm and similar in appearance to hyperfunctioning parathyroid glands or adenomas arising in the neck[65] (Fig. 20.14). The hyperfunctioning autotransplanted fragments usually can be found by the surgeon while the patient is under local anesthesia, and a portion of the grafted tissue can be excised to cure the hypercalcemia.

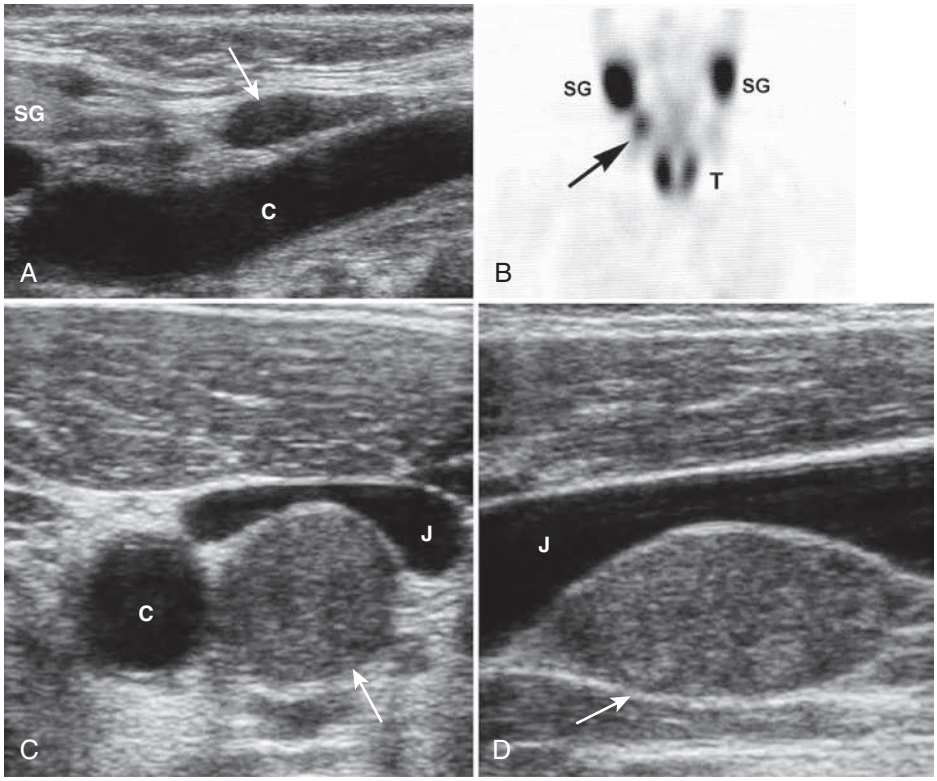

FIG. 20.13 Ectopic Parathyroid Adenoma: Near Carotid Sheath. (A) Longitudinal sonogram of the right side of the neck shows an ectopic undescended parathyroid adenoma *(arrow)* external to the carotid sheath, anterior to the common carotid artery *(C).* Ultrasound-guided biopsy confirmed parathyroid tissue before surgical exploration. *SG,* Submandibular gland. **(B)** ^{99m}Tc sestamibi coronal SPECT imaging shows a focal area of increased activity in right superior lateral neck, which corresponds to the ectopic adenoma. *SG,* Salivary glands; *T,* thyroid. **(C)** Transverse and **(D)** longitudinal sonograms in another patient show an ectopic left inferior adenoma located within the carotid sheath, posterior to the internal jugular vein *(J).* Ultrasound-guided biopsy confirmed parathyroid tissue before surgical exploration. At surgery, the adenoma was adherent to the vagus nerve. See also Video 20.12.

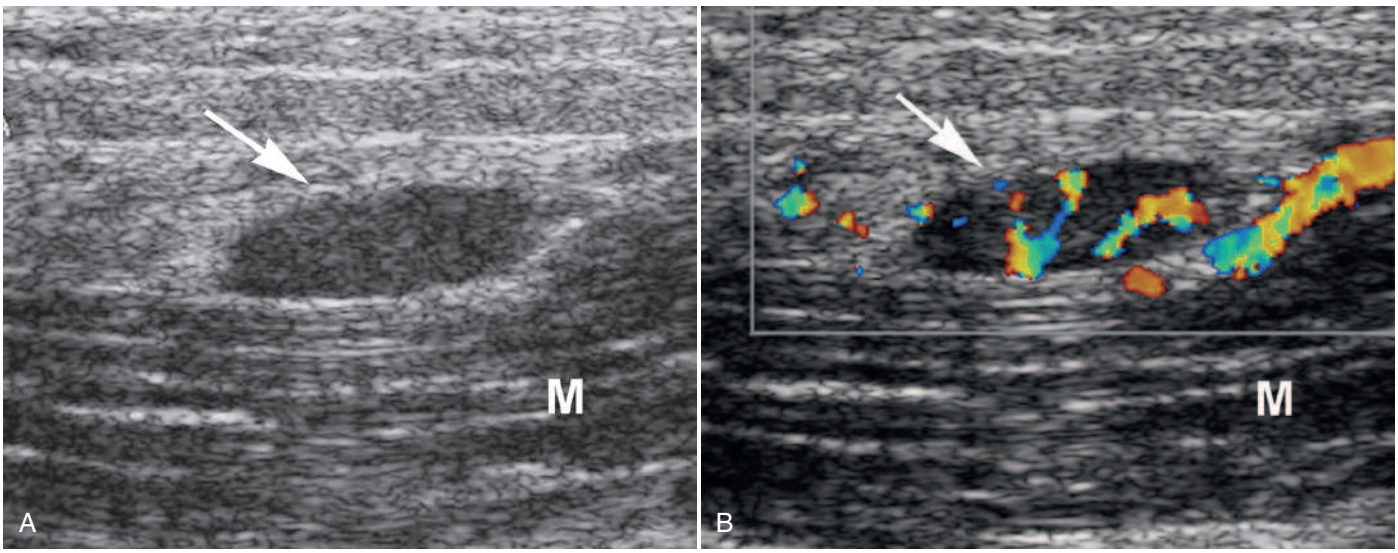

FIG. 20.14 Graft-Dependent Hyperparathyroidism. (A) Longitudinal sonogram of left forearm shows an oval, 2-cm hypoechoic nodule *(arrow)* resulting from hyperplasia of autotransplanted parathyroid tissue. *M,* Muscle. **(B)** Corresponding color Doppler flow sonogram shows hypervascularity of the hyperfunctioning parathyroid tissue in this patient with recurrent graft-dependent hyperparathyroidism.

Occasionally, for patients who are not candidates for repeat surgery, ultrasound-guided percutaneous ethanol injection may be used for ablation of recurrent hyperparathyroid disease in the neck or at a graft site (see "Ethanol Ablation").

A rare cause of persistent or recurrent hyperparathyroidism is **parathyromatosis,** a condition in which multiple foci of benign hyperfunctioning parathyroid tissue are present in the neck and/or mediastinum.[66,67] The theory of most common pathogenesis is inadvertent spillage and seeding of parathyroid cells during parathyroid excision. However, rare cases of hyperplasia of preexisting embryologic rests under the influence of physiologic stimuli have also been described.[66-70] The condition is most commonly seen in patients with a history of previous parathyroid surgery and those with secondary hyperparathyroidism resulting from chronic renal disease.[71] Sonographic imaging in the setting of recurrent hyperparathyroidism after previous parathyroid resection may demonstrate multiple hypoechoic to isoechoic neck nodules of varying size in locations atypical for missed parathyroid disease. Larger nodules may display hypervascularity, parasitized from local vessels[72] (Fig. 20.15, Video 20.13).

SECONDARY HYPERPARATHYROIDISM

Secondary hyperparathyroidism is characterized by pronounced parathyroid gland hyperfunction resulting from end-organ resistance to PTH and is most often found in patients with chronic

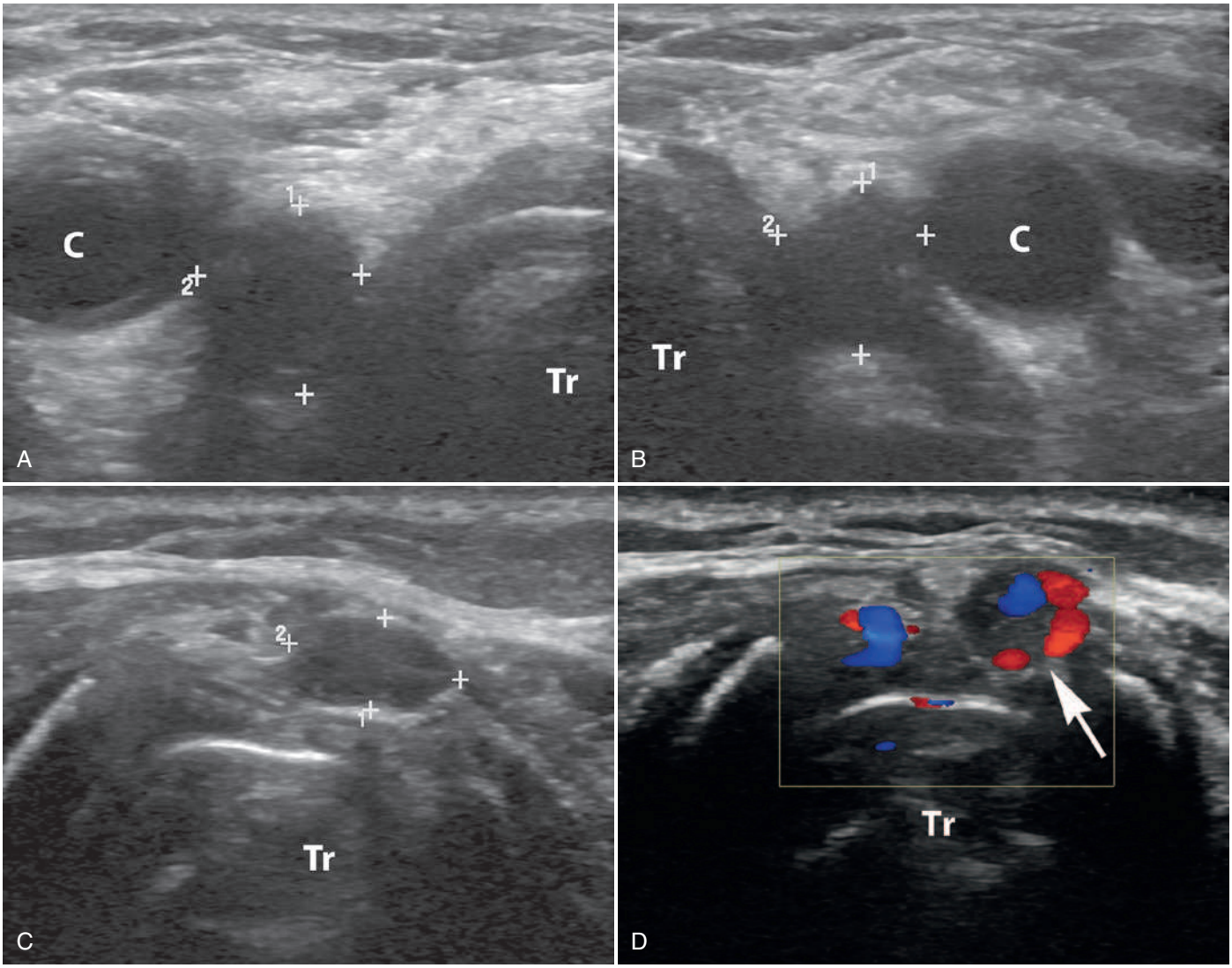

FIG. 20.15 Parathyromatosis in Persistent Primary Hyperparathyroidism. (A) Transverse sonogram of the right side of the neck in a patient with persistent primary hyperparathyroidism despite multiple surgeries for parathyroid and thyroid resection shows a 7-mm hypoechoic nodule *(calipers)* representing hyperfunctioning benign parathyroid tissue between the trachea *(Tr)* and common carotid artery *(C)*. **(B)** Transverse sonogram of the left side of the neck shows a similar-appearing 7-mm hypoechoic nodule *(cursors)* representing hyperfunctioning benign parathyroid tissue between the trachea and common carotid artery. **(C)** Transverse sonogram of the midline upper neck shows a 3 × 6–mm hypoechoic nodule representing hyperfunctioning benign parathyroid tissue. *T,* Trachea. **(D)** Corresponding color Doppler flow sonogram demonstrates peripheral parasitized hypervascularity *(arrow)*. See also Video 20.13.

renal failure. In these patients, chronic relative hypocalcemia is the result of multiple complex factors, including decreased synthesis of the active form of vitamin D, poor calcium and vitamin D absorption, persistent hyperphosphatemia, and skeletal resistance to the actions of PTH. These factors contribute to parathyroid hyperplasia. If untreated, secondary hyperparathyroidism can result in bone demineralization, soft tissue calcification, and acceleration of vascular calcification. Surgical treatment for secondary hyperparathyroidism is less common because of the success of renal transplantation, dialysis, and medical therapy, including the newer calcimimetics. However, in symptomatic patients who are refractory to these therapies, subtotal parathyroidectomy or total parathyroidectomy with autotransplantation are surgical options.[25,73-75]

Patients with secondary hyperparathyroidism have multiple enlarged glands. Individually, these glands may have the same sonographic appearance as other parathyroid adenomas (see Fig. 20.6, Videos 20.3 and 20.4). However, the glands may be asymmetrically enlarged and more lobular. Although imaging is not usually necessary, sonography can be used to evaluate the severity of parathyroid hyperplasia by assessing gland enlargement.[76,77] Patients with sonographically enlarged glands tend to have significantly worse symptoms, laboratory values, and radiographic signs of secondary hyperparathyroidism than patients without gland enlargement. Sonography can also be used to aid in localization of the enlarged parathyroid glands before surgical resection for secondary hyperparathyroidism. Ultrasound-guided percutaneous ethanol injection is also a treatment option for ablation of hyperplastic parathyroid glands in patients with refractory secondary hyperparathyroidism who are not surgical candidates (see "Ethanol Ablation").

PITFALLS IN INTERPRETATION

False-Positive Examination

Normal and pathologic cervical structures, such as lymph nodes, small veins adjacent to the thyroid gland, the esophagus, the longus colli muscles, and thyroid nodules, can simulate parathyroid adenomas, producing false-positive results during neck sonography.

Parathyroid Adenoma: Causes of Examination Errors

FALSE-POSITIVE RESULTS
Cervical lymph node
Prominent blood vessel
Esophagus
Longus colli muscle
Thyroid nodule

FALSE-NEGATIVE RESULTS
Minimally enlarged adenoma/gland
Multinodular thyroid goiter
Ectopic parathyroid adenoma

One source for a false-positive ultrasound study is confusion of **cervical lymph nodes** for a parathyroid adenoma.[32] Cervical lymph nodes are usually visualized sonographically in the lateral neck adjacent to the jugular vein and away from the thyroid. However, lymph nodes found adjacent to the carotid artery may occasionally simulate an ectopic adenoma. Lymph nodes may also be visualized within the central compartment near the inferior pole of the thyroid, simulating an inferior gland adenoma. Enlarged cervical lymph nodes may have an oval, hypoechoic appearance similar to parathyroid adenomas, but they often also have a central echogenic band or hilum composed of fat, vessels, and fibrous tissue, which differentiates them from parathyroid adenomas.[78] Nonetheless, ultrasound-guided biopsy may be necessary to distinguish a potential parathyroid adenoma from an atypical lymph node, particularly in the postoperative setting.

Many **small veins** lie immediately adjacent to the posterior and lateral aspects of both lobes of the thyroid, and a tortuous or segmentally dilated vein can simulate a small parathyroid adenoma. Scanning maneuvers to help establish the structure as a vein, not an adenoma, include (1) real-time imaging in multiple planes to show the tubular nature of the vein; (2) a Valsalva maneuver by the patient, which may cause transient engorgement of the vein; and (3) spectral or color Doppler sonography to show flow within the vein.

The **esophagus** may partially protrude from behind the posterolateral aspect of the trachea and simulate a mass or parathyroid adenoma (see Fig. 20.8B). Turning the patient's head to the opposite side will accentuate the protrusion. Careful inspection of this structure in the transverse plane shows that it has the typical concentric ring appearance of bowel, with a peripheral hypoechoic muscular layer and the central echogenic appearance of the mucosa and intraluminal contents. Using a longitudinal scan plane helps to demonstrate the tubular nature of this structure. Real-time imaging while the patient swallows will cause a stream of brightly echogenic mucus and microbubbles to flow through the lumen, which confirms that the structure is the esophagus.

The **longus colli muscle** lies adjacent to the anterolateral aspect of the cervical spine. When viewed in the transverse plane, it appears as a hypoechoic triangular mass that can simulate a large parathyroid adenoma located posterior to the thyroid gland. However, scanning in the longitudinal plane will show that this structure is long and flat and contains longitudinal echogenic striations typical of skeletal muscle. Real-time imaging while the patient swallows can be useful because swallowing will cause movement of the thyroid gland and adjacent thyroid structures, such as a parathyroid adenoma, but the longus colli muscle, which is attached to the spine, will remain stationary. Finally, comparison with the opposite side of the neck will demonstrate similar symmetric findings because the longus colli muscles are paired structures located on both sides of the cervical spine.

Thyroid nodules are also potential causes of false-positive ultrasound and scintigraphic imaging.[32,79] If a thyroid nodule protrudes from the posterior aspect of the thyroid, it can simulate a mass in the location of a parathyroid adenoma (Fig. 20.16). A

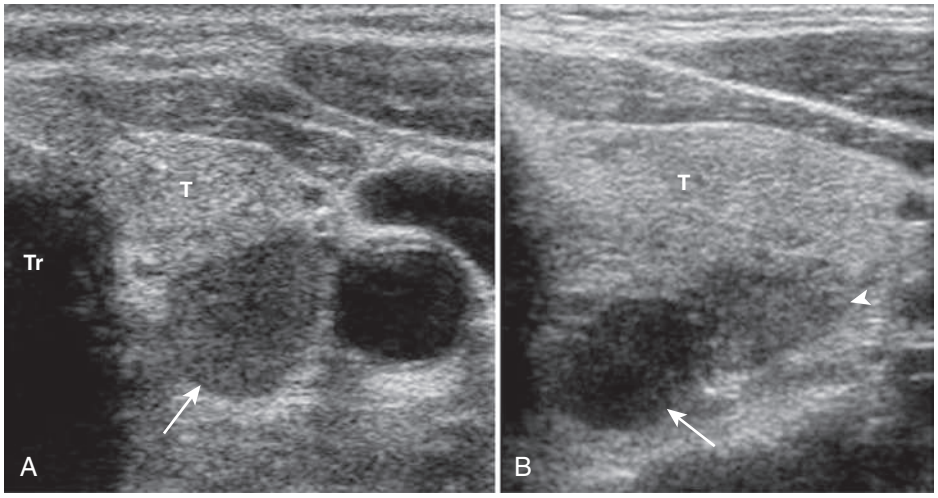

FIG. 20.16 Thyroid Nodules May Simulate Parathyroid Adenoma. (A) Transverse sonogram shows hypoechoic thyroid nodule *(arrow)* arising within the posterior aspect, left lobe of the thyroid *(T),* which could simulate a parathyroid adenoma. *Tr,* Trachea. **(B)** Transverse sonogram in another patient shows highly hypoechoic parathyroid adenoma *(arrow)* posterior to left lobe of the thyroid. An adjacent, slightly hypoechoic thyroid *(T)* nodule *(arrowhead)* is also present and might simulate a parathyroid adenoma.

useful sign in this situation is the thin, echogenic line of the capsular interface that separates the parathyroid adenoma (which usually arises outside the thyroid) from the thyroid gland itself (Video 20.14). Thyroid nodules, which arise within the thyroid gland, typically do not show this tissue plane of separation.[80] Morphologically, thyroid nodules, unlike parathyroid adenomas, are often partially cystic, and some are calcified. Also, thyroid nodules often are of a heterogeneous, mixed echogenicity, whereas parathyroid adenomas are typically of a homogeneous, hypoechoic echogenicity. When a parathyroid adenoma cannot be distinguished from a thyroid nodule by imaging criteria, ultrasound-guided percutaneous biopsy may be necessary.

False-Negative Examination

Minimally enlarged adenomas, adenomas displaced posteriorly and obscured by a greatly enlarged nodular thyroid, and ectopic adenomas may cause false-negative imaging results.

Minimally enlarged adenomas or **hyperplastic glands** are a common cause of error because they can be difficult to distinguish from the thyroid and adjacent soft tissues[32,81] (see Fig. 20.5A, Video 20.2). The abnormal but minimally enlarged gland can be encountered with single adenomas or with multigland disease caused by hyperplasia. **Multinodular thyroid goiters** interfere with parathyroid adenoma detection in two ways.[32,79,81] First, the thyroid gland enlargement displaces structures located adjacent to the posterior thyroid, away from the transducer. This can necessitate the use of 5-MHz transducers rather than higher-frequency transducers to obtain the necessary penetration, which decreases spatial resolution. Second, thyroid goiters may have a multinodular contour and irregular echotexture, which can cast refractive shadows, decrease the conspicuity and thereby hinder the detection of adjacent parathyroid gland enlargement (Videos 20.15 and 20.16). Some **ectopic adenomas,** such as retrotracheal adenomas or adenomas located deep in the mediastinum, will not be visible because of acoustic shadowing from overlying air and bone.

ACCURACY IN IMAGING

Ultrasound

Sonographic imaging provides a noninvasive and economical method to localize parathyroid adenomas in the preoperative setting of primary hyperparathyroidism, without the need for patient radiation exposure.[43,44,63,64,82-91] However, the success of parathyroid ultrasound depends on the use of high-frequency, higher-resolution technology and improves with operator experience and diligence. The sensitivity of sonographic parathyroid adenoma localization in primary hyperparathyroidism varies from 74% to 89% and improves with the use of higher-resolution sonography and in the hands of an experienced examiner.[42,43,63,85-88,92,93] The reported accuracy for ultrasound in detecting adenomatous disease is 74% to 94%, the specificity 96%, and the positive predictive value 93% to 98%.[42,43,82,86,87,92,93] However, the sensitivity of ultrasound to detect ectopic mediastinal adenomas is predictably much lower, and the accuracy, sensitivity, and specificity decrease in the setting of multigland disease.[42-44,82,84,88,92] Therefore the success of sonographic parathyroid adenoma localization also depends on the specific characteristics of the patient population imaged, including the prevalence of multigland and ectopic mediastinal parathyroid disease. However, overall successful localization of solitary or multiglandular parathyroid disease in the neck by an experienced examiner has been reported as 78%.[92]

As described later, ultrasound-guided **fine-needle aspiration (FNA) biopsy** is a valuable adjunct to the ultrasound examination and can be used to improve its accuracy. For any suspected adenoma mass, aspirates should be sent for PTH assay, in addition to cytologic analysis.[19,60,92,94-99] Another advantage of ultrasound is its ability to assess for concomitant thyroid disease during the evaluation for parathyroid disease, which may further impact surgical planning.

In persistent or recurrent hyperparathyroidism, sensitivity of sonography in adenoma localization varies widely. However,

sonography has demonstrated some of the highest sensitivities and accuracies of all modalities for adenoma detection in the reoperative setting, especially when combined with ultrasound-guided FNA biopsy of a suspected parathyroid adenoma.[57,59,60,62,64,100-103] Ultrasound augmented by FNA biopsy and PTH assay can lead to a specificity approaching 100%, a sensitivity of 84% to 90%, and an accuracy 82% to 84%.[60,103] It is important to understand that in most large clinical series of patients undergoing reoperation for hyperparathyroidism, the great majority of parathyroid adenomas are still found in the neck or are accessible through a neck incision.[59-61,64] Therefore a thorough ultrasound examination of the neck is important in these reoperative patients. If the adenoma is not visible sonographically, an ectopic mediastinal location must be considered. There should be a low threshold to utilize multiple imaging modalities, especially when initial imaging findings are ambiguous or the surgical risk is high.[57,60,61,64] This approach significantly improves the success rate and decreases the procedural time and cost in the reoperated patient.[57,59,60]

Other Modalities

Another widely used imaging modality for parathyroid localization is **scintigraphy** with technetium-99m (^{99m}Tc) labeled agents, providing combined functional and anatomic imaging in the primary preoperative imaging of patients with parathyroid disease.[44,81,85,88,104-111] ^{99m}Tc sestamibi scintigraphy, using single-isotope, dual-phase ("washout") imaging, or dual-isotope, single-phase ("subtraction") imaging, particularly when combined with single-photon emission computed tomography (SPECT) or SPECT/CT, has sensitivity similar to or better than ultrasound[44,62,81,85,104-109,111-116] (Fig. 20.17). Scintigraphy can demonstrate adenomas in areas that are missed by ultrasound, including the mediastinum and retrotracheal space. However, scintigraphy is more expensive than ultrasound and requires the use of ionizing radiation. As with ultrasound, parathyroid scintigraphy also appears to be less sensitive and accurate in multiglandular parathyroid disease, for smaller adenomas, and in the presence of multinodular thyroid disease.[92,93,111]

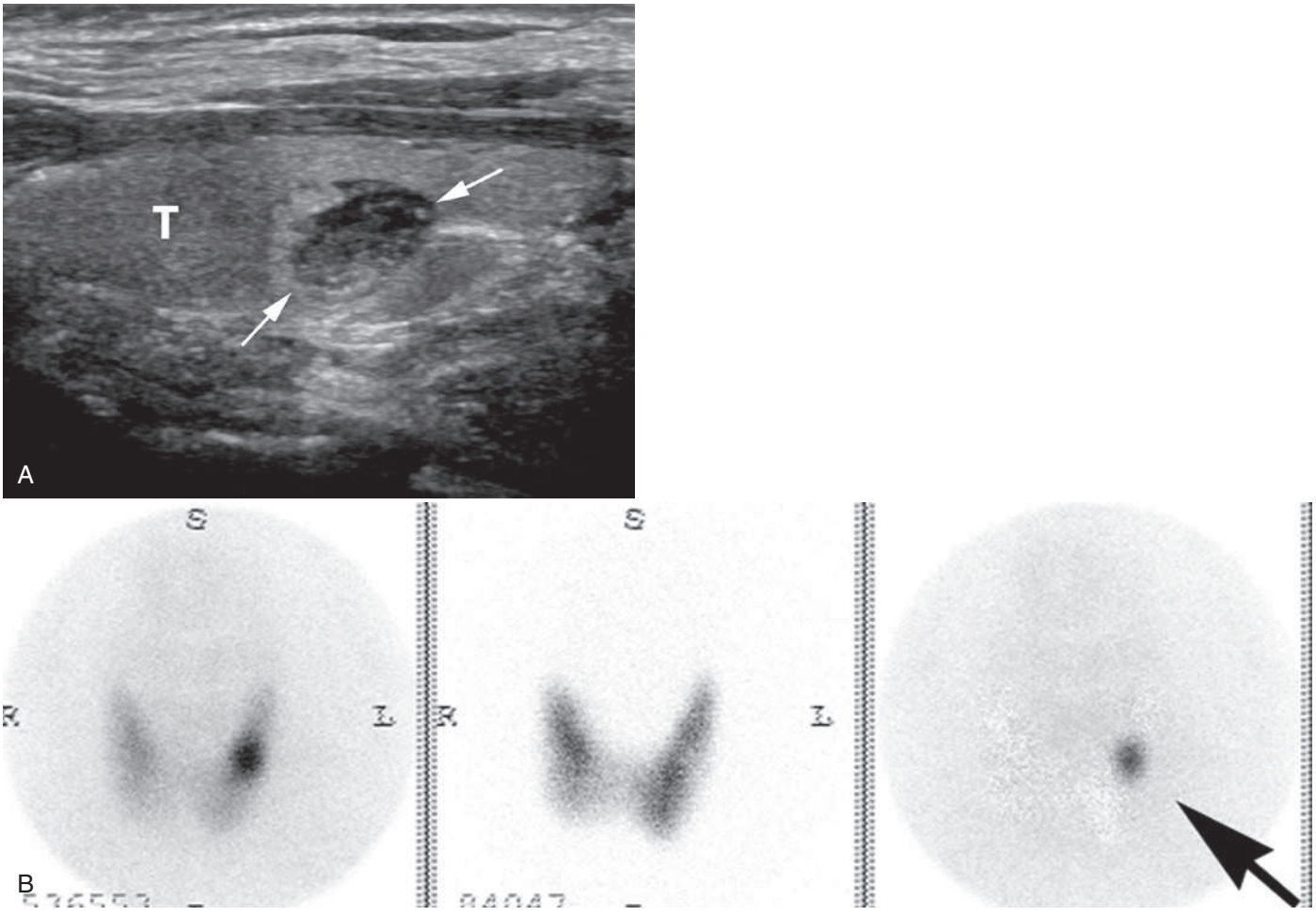

FIG. 20.17 Ectopic Intrathyroid Parathyroid Adenoma. Correlation of ultrasound and scintigraphy. **(A)** Longitudinal sonogram of the left neck in a patient with persistent hyperparathyroidism shows a heterogeneous ectopic intrathyroid parathyroid adenoma *(arrows). T,* Thyroid. **(B)** Corresponding anterior projection using ^{99m}Tc sestamibi *(left image)* and iodine-123 *(middle image)* dual-agent subtraction *(right image)* coronal SPECT imaging shows a concordant focal area of increased activity *(arrows)* in the left thyroid lobe, which corresponds to the ectopic intrathyroid parathyroid adenoma.

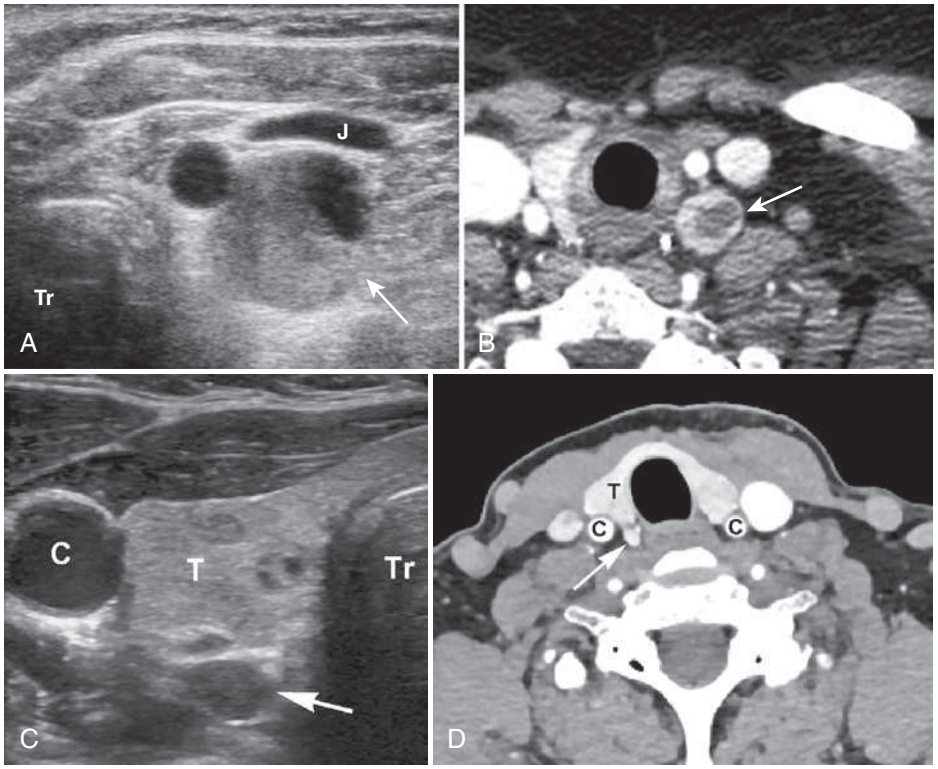

FIG. 20.18 Parathyroid Adenoma: Correlation of Ultrasound and CT. (A) Transverse sonogram shows a partially cystic ectopic supernumerary parathyroid adenoma *(arrow)* posterior to the left internal jugular vein *(J)* but external to the carotid sheath. Left superior and inferior parathyroid glands and the left thyroid lobe had previously been resected. *Tr,* Trachea. **(B)** Enhanced conventional axial CT image of the neck shows the same partially cystic parathyroid adenoma. **(C)** Transverse sonogram in another patient shows a subcentimeter parathyroid adenoma posterior to the right thyroid lobe *(T). C,* Common carotid artery. **(D)** Contrast enhanced axial CT of the neck shows the enhancing adenoma posterior to the right thyroid lobe.

Computed tomography (CT) is also used in the evaluation of parathyroid disease. More recently, thin-acquisition thickness, multidetector CT (MDCT) with reconstruction has been utilized with multiphase technique ("four-dimensional" ["4D"]), and provides high-resolution, multiplane diagnostic information based on the temporal perfusion characteristics of parathyroid tissue[117-122] (Fig. 20.18). Successful imaging requires experience in interpretation with close attention to exam technique; in such studies, preoperative lateralization of single gland parathyroid disease accuracies of 92% to 94%, sensitivities of 88% to 92%, and specificity of 93% have been reported, with sensitivity decreasing to 43% in the setting of multigland disease.[117-122] However, these examinations typically utilize multiphase, thin-acquisition thickness techniques, which lead to concerns of increased radiation exposure to the patient, despite dose reduction with protocol modifications. In addition, potential drawbacks of the technique include exam costs and the need to administer iodinated IV contrast material. Therefore it has not been widely supported in the literature as initial first-line preoperative imaging method to detect parathyroid disease.

Magnetic resonance imaging (MRI) is also a useful noninvasive modality in the evaluation of parathyroid disease but is not widely performed nor widely supported by the literature for first-line parathyroid imaging[44,111,123-127] (Fig. 20.19). As with ultrasound, MRI is performed without the need for patient radiation exposure; however, it is more expensive than ultrasound. MRI has demonstrated particular utility in localizing **mediastinal adenomas** and in the evaluation of the reoperative patient, especially in cases when other functional and cross-sectional imaging has been inconclusive.

The previously described modalities have largely replaced angiography and venous sampling in the imaging of parathyroid disease.[44,86,128] Selective **venous sampling** is more invasive, expensive, and technically demanding than other imaging modalities. However, it can be an occasional useful technique to lateralize parathyroid disease, particularly in a high-risk reoperative setting or when previous noninvasive imaging is inconclusive.[128]

The combination of multiple preoperative imaging studies demonstrates improved sensitivity compared with single-modality evaluation. Combined imaging with ultrasound and ^{99m}Tc sestamibi scintigraphy increases the sensitivity for the preoperative diagnosis of parathyroid disease.[44,85,90,104,110-112] When multiple studies are used, ultrasound is a good choice for initial preoperative imaging because of its noninvasiveness, lack of radiation exposure, relative low cost, high-resolution anatomic detail, ability to assess for concomitant thyroid disease, and competitive sensitivity and accuracy when used by an experienced examiner.[92,103,110,111,113,115,116,129]

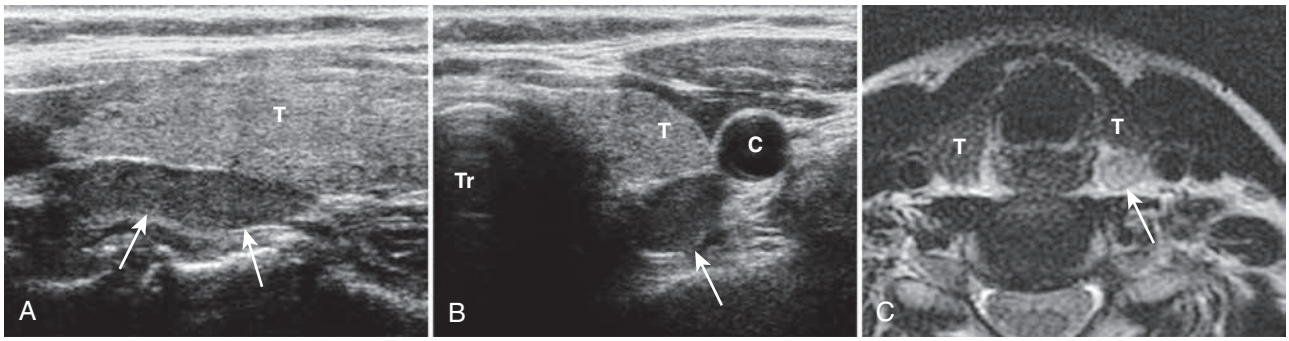

FIG. 20.19 Parathyroid Adenoma: Correlation of Ultrasound and MRI. (A) Longitudinal and **(B)** transverse sonograms show superior parathyroid adenoma *(arrows)* posterior to upper-middle portion of left lobe of the thyroid *(T). C,* Common carotid artery; *Tr,* trachea. **(C)** T2-weighted fast spin-echo axial MRI of the neck shows the same left superior parathyroid adenoma *(arrow),* which appears hyperintense compared with the thyroid gland.

Importance of Imaging in Primary Hyperparathyroidism

Primary hyperparathyroidism is commonly clinically recognized, and both clinicians and patients desire definitive treatment for it. Definitive cure of primary hyperparathyroidism requires surgical parathyroidectomy, which can be accomplished with a very high degree of success and minimal morbidity when performed by an experienced surgeon.[24,25,27] Historically, the standard surgical procedure involved open bilateral neck dissection with inspection of each parathyroid gland, and routine preoperative imaging was not considered necessary.

Minimally invasive surgical techniques, termed **minimal-access parathyroidectomy (MAP),** now predominate as standard surgical technique for first-time surgery in primary hyperparathyroidism.[24,27,130-133] In MAP the abnormal gland or adenoma is selectively removed through a small unilateral incision in the neck, thereby potentially improving cosmesis, reducing complication risks, and decreasing operative time, hospital stay, and overall cost, often without sacrificing significant operative efficacy when performed by an experienced surgeon (Fig. 20.20). Moreover, postsurgical fibrosis is limited to a smaller area, thus facilitating any necessary repeat surgery in the future. The successful institution of these minimally invasive techniques is predicated on the availability of (1) accurate preoperative imaging techniques to direct a focused surgical approach and (2) reliable, rapid (10-15 minutes) **intraoperative parathyroid hormone monitoring,** which facilitates the surgical determination of the need for further exploration. With intraoperative PTH monitoring the surgeon can quickly assess the success of a focused unilateral approach. If intraoperative PTH levels fail to normalize or decrease by at least 50%, multigland disease should be suspected, and the procedure may be converted to a bilateral dissection.

Many investigators promote the use of both anatomic and functional imaging, such as ultrasound and ^{99m}Tc sestamibi scintigraphy, to increase the preoperative certainty of unilateral disease and aid in excluding patients with multigland disease who are not candidates for MAP.[19,62,82,84-86,103,104,110,112,113,116,129] Proponents of preoperative imaging in primary hyperparathyroidism also note that some adenomas are found lower in the neck or mediastinum and that the initial operative approach may be changed or optimized if imaging shows parathyroid disease near the thymus.[24,60,87,91]

In patients with persistent or recurrent hyperparathyroidism, localization studies are liberally used because of the lower surgical success rate and the higher morbidity rate of reoperation. Preoperative localization studies in recurrent hyperparathyroidism contribute to both the success and the speed of the repeat surgery. In patients who had reexploration for persistent or recurrent hyperparathyroidism, the surgical cure rate was 88% to 89%, and it was thought that prospective localization studies contributed to this high rate of success and decreased surgical time.[57,59,60] Because most persistent and recurrent parathyroid adenomas are accessible in the neck or the upper mediastinum through a cervical incision, sonography and ^{99m}Tc sestamibi scintigraphy, particularly with SPECT or SPECT/CT, may be the initial localizing procedures of choice and, in select patients, can aid in directing a focused, minimal-access surgical approach[44,59,60,62,64,92,100,103,110,111,113,115,116,129] (Fig. 20.21). However, low threshold for additional diagnostic confirmation with ultrasound-guided biopsy, 4D MDCT, and/or MRI is supported.[103,110,111,118,120] (Fig. 20.22).

INTRAOPERATIVE SONOGRAPHY

Intraoperative sonography is occasionally a useful adjunct in the surgical detection of parathyroid adenomas, particularly in the reoperative setting.[19,134,135] Intraoperative scanning can be performed with a small, conventional, high-frequency (8-18 MHz) transducer draped with a sterile plastic sheath or with a dedicated sterilized intraoperative transducer. Intraoperative ultrasound appears to be most useful for localizing abnormal inferior and intrathyroid parathyroid glands.[135] Correlated with preoperative imaging, intraoperative sonography can also help guide a focused surgical resection to limit tissue damage associated with exploration in the reoperated patient; it also allows directed resection of ectopic adenomas in the mediastinum, thyroid, and carotid sheath. If an abnormal parathyroid gland is detected, surgical time can be shortened.

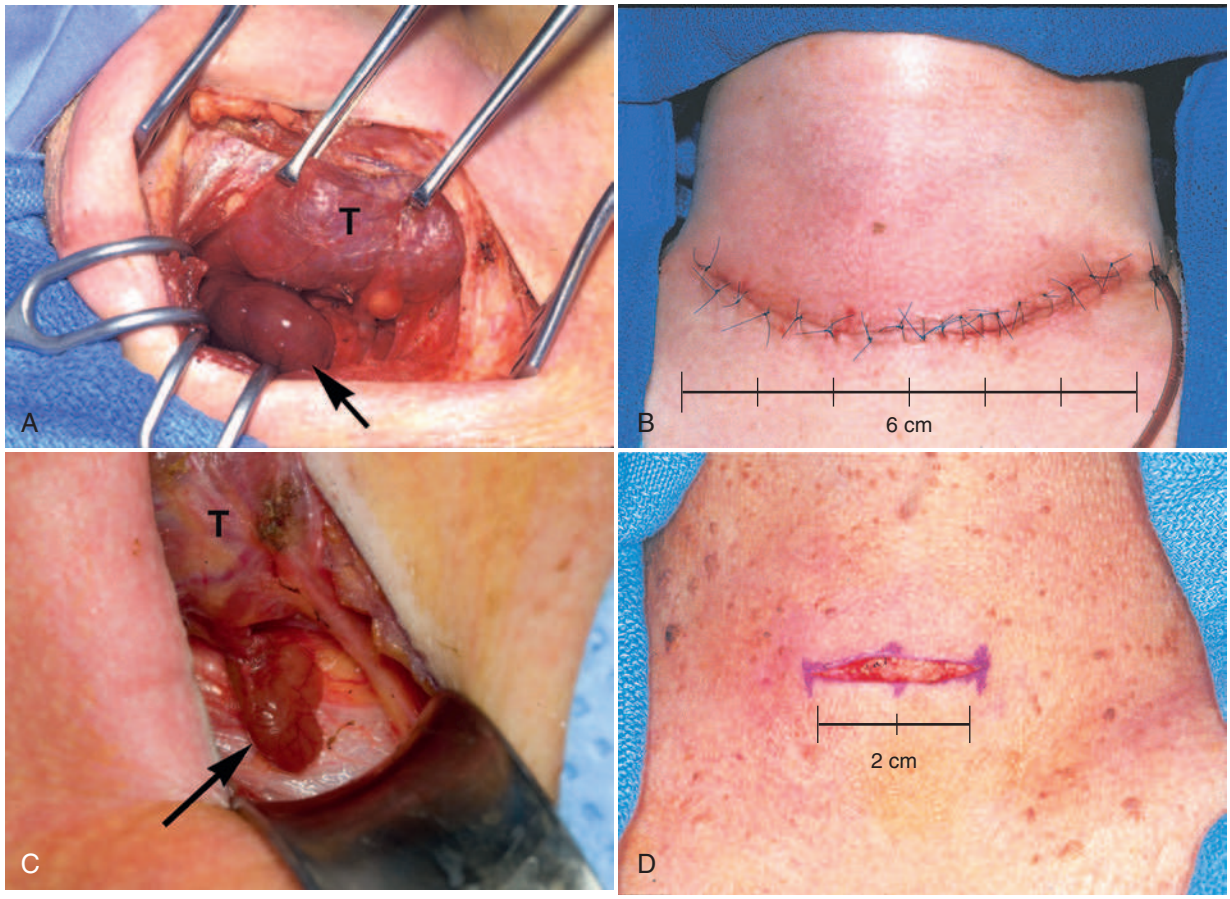

FIG. 20.20 Comparison of Surgical Procedures for Removal of Parathyroid Adenoma. (A) Intraoperative photograph during bilateral neck dissection for parathyroidectomy. The thyroid gland *(T)* is retracted back and a parathyroid adenoma *(arrow)* exposed. **(B)** Corresponding 6-cm "collar" incision with a surgical drain. **(C)** Intraoperative photograph during minimally invasive surgery uses a much smaller incision. Parathyroid adenoma is exposed adjacent to the thyroid *(T)*. **(D)** Minimally invasive surgical incision, approximately 2 cm. (Courtesy of Geoffrey B. Thompson, MD, Mayo Clinic, Rochester, Minn.)

PERCUTANEOUS BIOPSY

Sonographically guided percutaneous FNA biopsy can be used for preoperative confirmation of suspected abnormal parathyroid glands in selected cases, particularly in the candidate for reoperation.[59,60,94,96-102,136] This technique can decrease the false-positive rate and increase the specificity of sonography by permitting the reliable differentiation of parathyroid adenomas from other pathologic structures, such as thyroid nodules and cervical lymph nodes. In addition to its value to the surgeon, a positive biopsy may reassure the reluctant reoperative patient. FNA biopsy is also generally obtained for diagnostic confirmation before percutaneously injected ethanol ablation of a suspected abnormal gland.

If the suspected parathyroid adenoma is in a location remote from the thyroid gland, the main differential diagnostic consideration is a lymph node. Percutaneous biopsy is performed by using a standard noncutting 25- or 27-gauge needle to obtain aspirates that contain either parathyroid cells or lymphocytes (Fig. 20.23, Videos 20.17 and 20.18). The aspirate must also be analyzed for PTH because elevated levels indicate the presence of parathyroid tissue, even if the cytologic results are inconclusive.[19,96-99] After the aspirated material is expelled onto a slide for cytologic review, the residual sample in the needle hub is rinsed with a tiny amount of sterile saline, emptied into a tube, and placed on ice. This is repeated for each aspirate, diluting the sample for PTH assay into a total volume of 1 to 1.5 mL. Alternatively, three to four aspirates may be expelled and rinsed directly into a tube containing 1 to 1.5 mL of sterile saline, then placed on ice. When performed in this manner, positive aspirate assays yield PTH levels markedly higher than that of normal serum levels, and typically much higher than the patient's own inappropriately elevated serum PTH levels. If the suspected parathyroid adenoma lies adjacent to the thyroid, FNA biopsy may be necessary to differentiate parathyroid and thyroid tissue. These aspirates should also be analyzed for PTH because parathyroid and thyroid tissue can be very difficult to differentiate by cytology.[19,96-99] In addition, thyroid tissue sometimes must be traversed to access a parathyroid adenoma, causing possible sample contamination with thyroid cells.[19] A histologic specimen obtained with a small-caliber (20- to 22-gauge) cutting needle may provide more cellular material for analysis but usually is unnecessary if PTH assay is performed. In addition, the possibility of **postbiopsy periglandular fibrosis** complicating subsequent

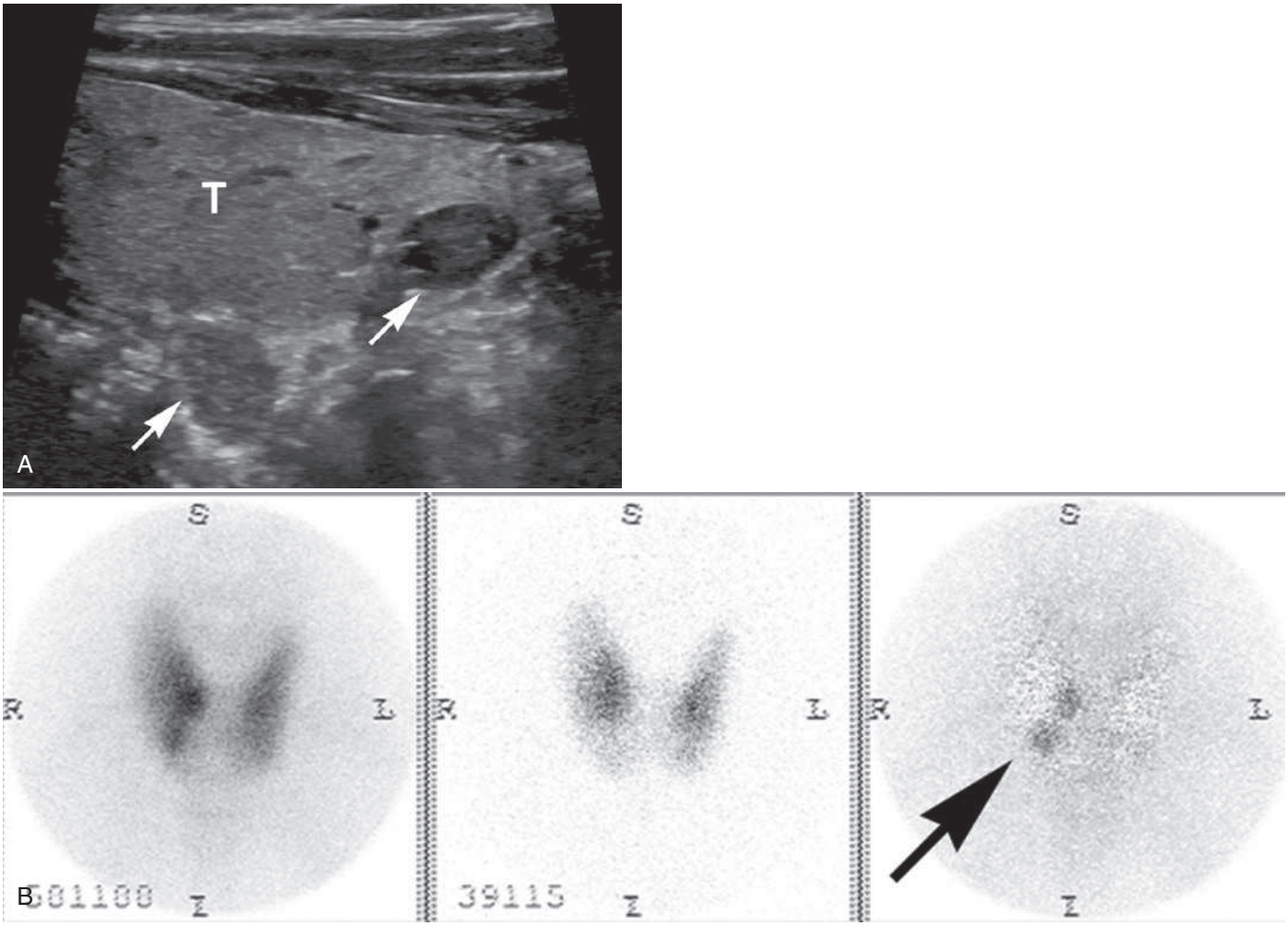

FIG. 20.21 Multimodality Imaging in Recurrent Hyperparathyroidism. (A) Longitudinal sonogram of the right neck in a patient with recurrent hyperparathyroidism shows two subcentimeter nodules *(arrows)* along the posterior surface of the thyroid *(T),* consistent with hyperplastic parathyroid tissue at the site of previous remote parathyroid resection for multiple gland disease. **(B)** Corresponding anterior projection from ^{99m}Tc sestamibi *(left image)* and iodine-123 *(middle image)* dual-agent subtraction *(right image)* coronal SPECT imaging shows two concordant focal areas of increased activity *(arrow).*

surgery may be greater with cutting-needle biopsy. FNA biopsy of suspected parathyroid adenomas is well tolerated, with few reported complications.[103] Although a theoretic consideration, parathyromatosis does not appear to be a complication of FNA biopsy.[137]

ETHANOL ABLATION

Sonography can be used to guide percutaneous injection of ethanol into abnormally enlarged parathyroid glands for chemical ablation.[138-151] Ethanol ablation is most often used in postoperative patients with recurrent or persistent hyperparathyroidism who have sonographically visible, biopsy-proven hyperfunctioning parathyroid tissue but who are poor surgical candidates.[141,144,146] Some dialysis patients with secondary hyperparathyroidism and patients with a history of multigland disease with recalcitrant recurrent hyperparathyroidism after previous subtotal surgery have also received this treatment.[141,146-151] Ethanol ablation has been shown to be very useful in patients with MEN I who have had previous subtotal parathyroidectomy and recurrent disease in their remaining residual half-gland in the neck.[141,152] A portion of the remaining gland can be ablated with ethanol to control hypercalcemia and avoid repeat surgery, which has a very high complication rate of postoperative hypoparathyroidism in these patients. Autografts in patients with recurrent graft-dependent hyperparathyroidism can be similarly treated[153] (Fig. 20.24, Video 20.19). Adenomatous hyperplasia with autonomously functioning glands **(tertiary hyperparathyroidism)** has also been treated with ultrasound-guided ethanol injection to reduce gland mass, but with unpredictable results.[154,155]

Ethanol ablation is generally performed under local anesthesia, typically after confirmation of parathyroid tissue with FNA biopsy. Under real-time ultrasound guidance, a standard 25-gauge needle attached to a 1-mL tuberculin syringe is inserted into the mass. With the tip in constant visualization, sterile 95% ethanol is injected into multiple regions of the mass, with a volume about

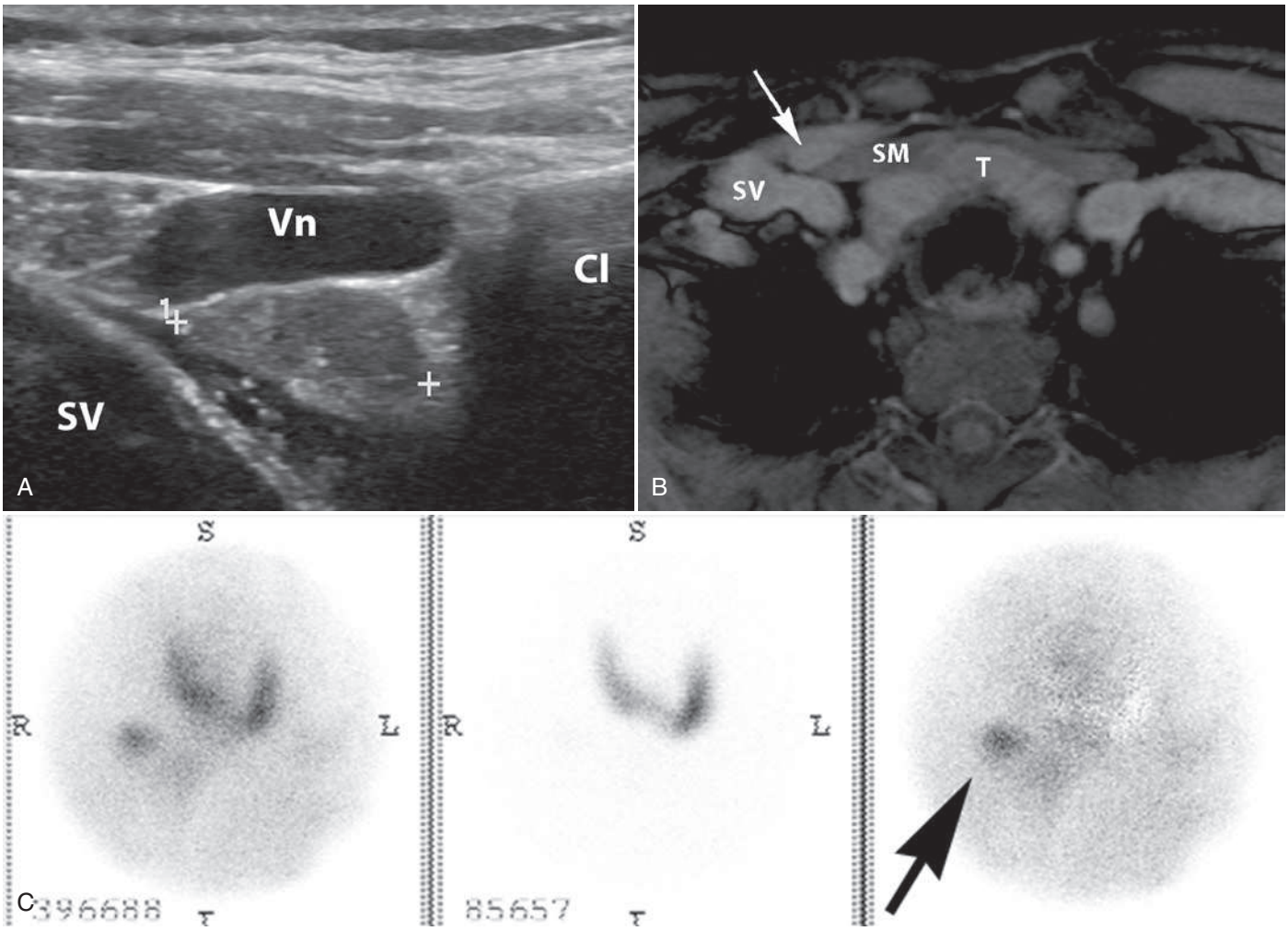

FIG. 20.22 Ectopic Parathyroid Adenoma: Multimodality Imaging in Persistent Hyperparathyroidism. (A) Longitudinal, sonogram demonstrates an ectopic parathyroid adenoma *(calipers)* adjacent to the right clavicle *(Cl),* overlying the subclavian vein *(SV)* and deep to a prominent collateral vein *(Vn).* **(B)** Artifact from the adjacent clavicle and IV contrast bolus limited CT evaluation (not shown), however, enhanced axial MRI demonstrates the enhancing ectopic parathyroid adenoma *(arrow)* overlying the strap musculature *(SM)* and the subclavian vein. *T,* Thyroid. **(C)** Corresponding right anterior oblique projection from ^{99m}Tc sestamibi *(left image)* and iodine-123 *(middle image)* dual-agent subtraction *(right image)* coronal SPECT imaging shows a concordant focal area of increased right periclavicular activity *(arrows)* which corresponds to the ectopic parathyroid adenoma.

half that of the mass, typically 0.1 to 1.0 mL. The tissue becomes highly echogenic at the moment of injection; the echogenicity slowly disappears over 1 minute. There is also a marked decrease in vascularity of the parathyroid adenoma after alcohol injection, presumably secondary to thrombosis and occlusion of parathyroid vessels (Fig. 20.24D). The injections are repeated every day or every other day until the serum calcium level reaches the normal range. In most patients, three or fewer injections are necessary. All patients undergoing parathyroid ethanol ablation require long-term close follow-up of serum calcium levels to detect subsequent hypoparathyroidism or, more often, recurrent hyperparathyroidism.

The reported adverse effects from ethanol ablation of parathyroid adenomas have been limited to temporary jaw pain during the procedure and dysphonia from vocal cord paralysis. Dysphonia is caused by recurrent laryngeal nerve palsy, which is typically a transient effect. Patients who have had prior subtotal parathyroid surgery are also theoretically at increased risk for postablation hypoparathyroidism, and conservative ablation of only a portion of the remaining gland is prudent.

The long-term efficacy of ethanol ablation as a treatment of hyperparathyroidism in patients with primary disease does not approach that of surgery.[139-142,144,146,152] In addition, postablation periglandular fibrosis may make future surgical procedures more difficult. Therefore ethanol ablation as a treatment of primary hyperparathyroidism is reserved for patients who cannot or will not undergo surgery. Studies on the outcomes of ethanol ablation in primary hyperparathyroidism report that most patients had either partial or complete biochemical improvement, although many of these patients will have recurrent disease.[141,142,146] Thus close clinical and biochemical follow-up is necessary, and repeat treatments may be required. Reasons for failure include (1) incomplete ablation of hyperfunctioning tissue within the treated adenoma and (2) residual

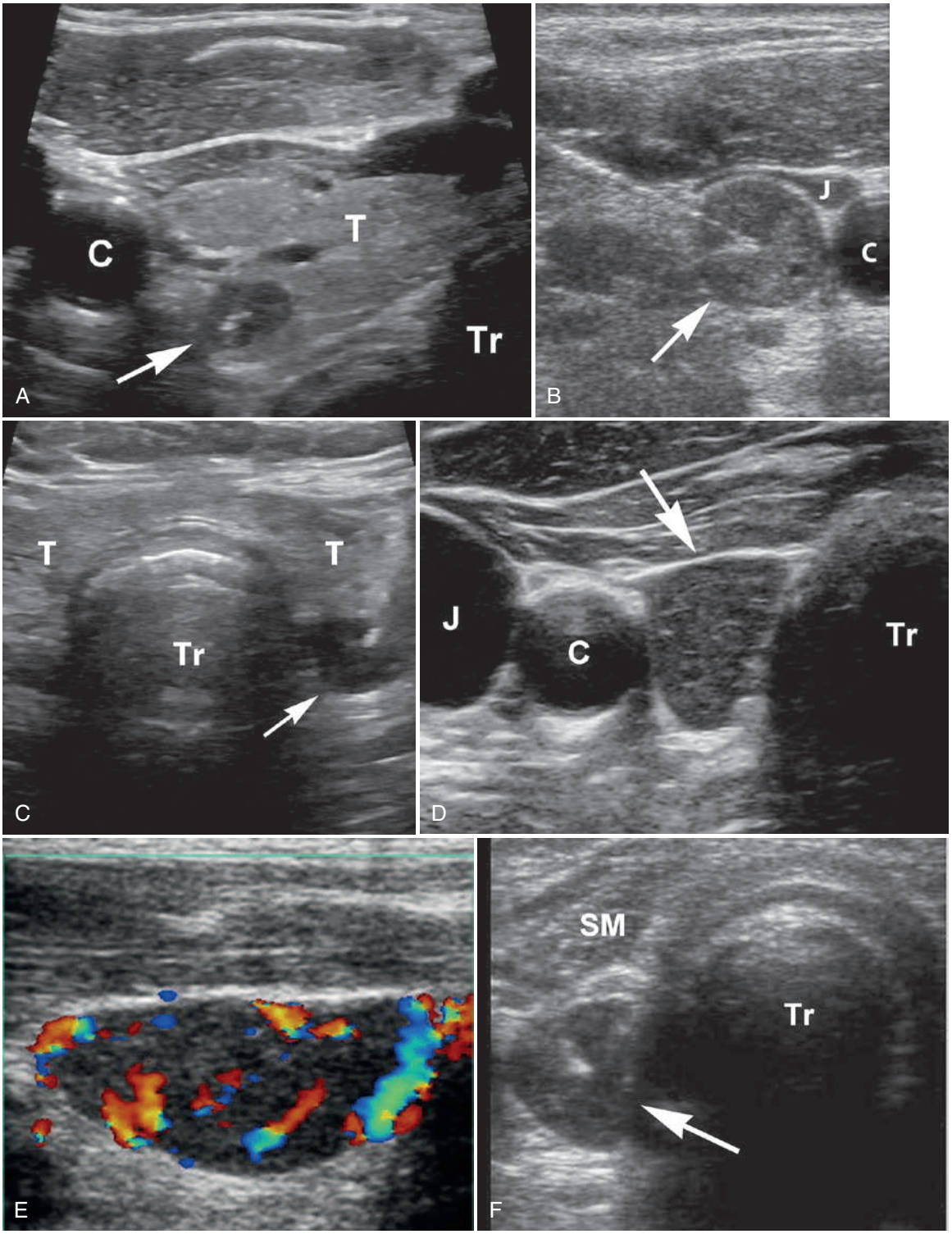

FIG. 20.23 Percutaneous Needle Biopsy of Parathyroid Adenoma Prior to Reoperation. (A) Transverse sonogram shows needle tip within a subcentimeter hypoechoic ectopic intrathyroid parathyroid adenoma *(arrow)* in a patient with persistent hyperparathyroidism. *C,* Common carotid artery; *T,* thyroid. *Tr,* trachea. **(B)** Transverse sonogram in another patient with persistent hyperparathyroidism shows needle biopsy of an ectopic inferior adenoma *(arrow)* located within the carotid sheath, posterior to the internal jugular vein *(J).* **(C)** Transverse sonogram in a patient with recurrent hyperparathyroidism shows biopsy of recurrent hyperplastic parathyroid tissue *(arrow)* at the site of previous remote parathyroid resection for multiple gland disease. **(D)** Transverse sonogram of a patient with hyperparathyroidism and prior subtotal thyroidectomy demonstrates hypoechoic tissue in the right thyroid bed *(arrow)* between the trachea *(Tr)* and common carotid artery *(C)* indeterminate for residual thyroid versus parathyroid tissue. **(E)** Longitudinal color Doppler flow sonogram in the same patient demonstrates indeterminate hypervascular tissue in the right thyroid bed. **(F)** Transverse sonogram in the same patient shows needle biopsy of the indeterminate tissue in the right thyroid bed *(arrow)* which confirmed parathyroid adenoma when multimodality imaging was equivocal for thyroid versus parathyroid tissue. *SM,* Strap muscle. See also Video 20.18.

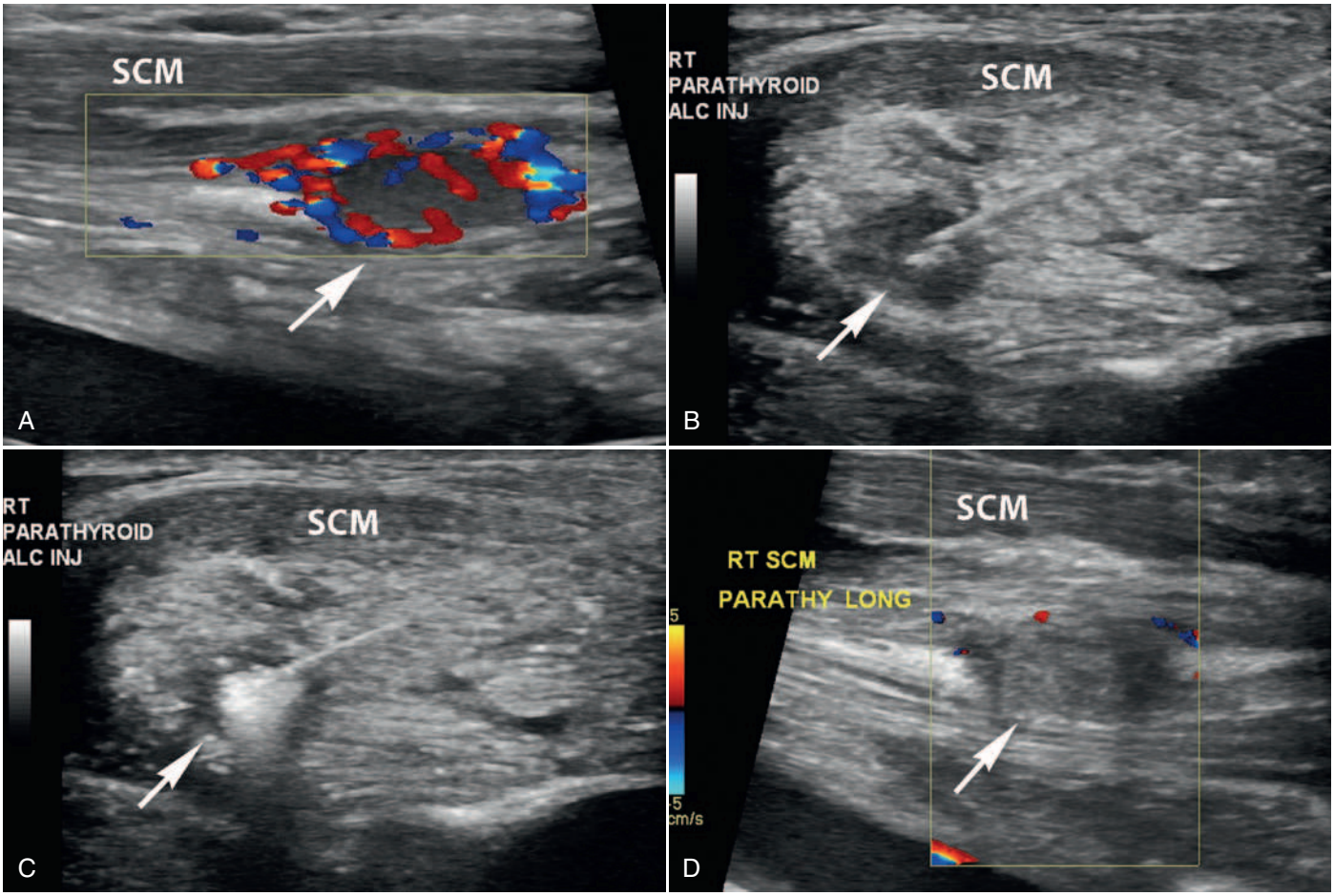

FIG. 20.24 Ethanol Ablation of Hyperplastic Autotransplanted Parathyroid Tissue. (A) Longitudinal color Doppler flow sonogram of the right neck shows a dominant vascular nodule that represents hyperfunctioning parathyroid tissue *(arrow)* in a patient with **recurrent graft-dependent hyperparathyroidism.** *SCM,* Sternocleidomastoid muscle. **(B)** Transverse sonogram shows a needle tip *(arrow)* is placed within the nodule. **(C)** Transverse sonogram shows ethanol is injected into portions of the nodule, which causes the tissues adjacent to the needle tip to become transiently, brightly echogenic *(arrow).* **(D)** Subsequent to ethanol ablation, longitudinal color Doppler flow sonogram shows decreased vascularity in the injected nodule *(arrow).* See also Video 20.19.

hyperfunctioning of other untreated glands in the patient with unrecognized multigland disease.

In theory, methods of thermal tissue ablation such as radiotherapy, cryotherapy, and laser therapy, which have been used to treat tumors elsewhere in the body, could also be applied to treat parathyroid disease in the neck. These methods are limited at present by the lack of ablation devices that can precisely treat very small amounts of tissue. In patients not considered surgical candidates, there have been reports of successful treatment of parathyroid adenomas using ultrasound-guided percutaneous laser ablation.[156-158] However, as with ethanol ablation, the clinical efficacy is transient and these methods of ablation are not definitive treatment of parathyroid disease.

REFERENCES

1. Gilmour JR. The gross anatomy of the parathyroid glands. J Pathol. 1938;46:133-148.
2. Weller JGL. Development of the thyroid, parathyroid and thymus glands in man. Carnegie Institution of Washington. Contrib Embryol. 1933;24:93-139.
3. Mansberger Jr AR, Wei JP. Surgical embryology and anatomy of the thyroid and parathyroid glands. Surg Clin North Am. 1993;73(4):727-746.
4. Akerstrom G, Malmaeus J, Bergstrom R. Surgical anatomy of human parathyroid glands. Surgery. 1984;95(1):14-21.
5. Edis AJ. Surgical anatomy and technique of neck exploration for primary hyperparathyroidism. Surg Clin North Am. 1977;57(3):495-504.
6. Thompson NW, Eckhauser FE, Harness JK. The anatomy of primary hyperparathyroidism. Surgery. 1982;92(5):814-821.
7. Edis AJ, Purnell DC, van Heerden JA. The undescended "parathymus." An occasional cause of failed neck exploration for hyperparathyroidism. Ann Surg. 1979;190(1):64-68.
8. Wang C. The anatomic basis of parathyroid surgery. Ann Surg. 1976;183(3):271-275.
9. Norris EH. The parathyroid glands and the lateral thyroid in man: their morphogenesis, histogenesis, topographic anatomy and prenatal growth. Carnegie Institution of Washington. Contrib Embryol. 1937;26:247-294.
10. Castleman B, Roth SI. Tumors of the parathyroid glands. In: Atlas of tumor pathology. Washington, DC: Armed Forces Institute of Pathology; 1978.
11. Russell CF, Grant CS, van Heerden JA. Hyperfunctioning supernumerary parathyroid glands. An occasional cause of hyperparathyroidism. Mayo Clin Proc. 1982;57(2):121-124.
12. Kamaya A, Quon A, Jeffrey RB. Sonography of the abnormal parathyroid gland. Ultrasound Q. 2006;22(4):253-262.

13. Huppert BJ, Reading CC. Parathyroid sonography: imaging and intervention. J Clin Ultrasound. 2007;35(3):144-155.
14. Heath 3rd H, Hodgson SF, Kennedy MA. Primary hyperparathyroidism. Incidence, morbidity, and potential economic impact in a community. N Engl J Med. 1980;302(4):189-193.
15. van Heerden JA, Beahrs OH, Woolner LB. The pathology and surgical management of primary hyperparathyroidism. Surg Clin North Am. 1977;57(3):557-563.
16. Wang CA. Surgery of the parathyroid glands. Adv Surg. 1971;5:109-127.
17. Black 3rd WC, Utley JR. The differential diagnosis of parathyroid adenoma and chief cell hyperplasia. Am J Clin Pathol. 1968;49(6):761-775.
18. van Heerden JA, Kent 3rd RB, Sizemore GW, et al. Primary hyperparathyroidism in patients with multiple endocrine neoplasia syndromes. Surgical experience. Arch Surg. 1983;118(5):533-536.
19. Shawker TH. Ultrasound evaluation of primary hyperparathyroidism. Ultrasound Q. 2000;16:73-87.
20. Wynne AG, van Heerden J, Carney JA, Fitzpatrick LA. Parathyroid carcinoma: clinical and pathologic features in 43 patients. Medicine (Baltimore). 1992;71(4):197-205.
21. Vetto JT, Brennan MF, Woodruf J, Burt M. Parathyroid carcinoma: diagnosis and clinical history. Surgery. 1993;114(5):882-892.
22. DeLellis RA. Tumors of the parathyroid gland. In: Atlas of tumor pathology. Washington, DC: Armed Forces Institute of Pathology; 1993.
23. Shane E, Bilezikian JP. Parathyroid carcinoma: a review of 62 patients. Endocr Rev. 1982;3(2):218-226.
24. Grant CS, Thompson G, Farley D, van Heerden J. Primary hyperparathyroidism surgical management since the introduction of minimally invasive parathyroidectomy: Mayo Clinic experience. Arch Surg. 2005;140(5):472-478.
25. Kearns AE, Thompson GB. Medical and surgical management of hyperparathyroidism. Mayo Clin Proc. 2002;77(1):87-91.
26. Silverberg SJ, Bilezikian JP, Bone HG, et al. Therapeutic controversies in primary hyperparathyroidism. J Clin Endocrinol Metab. 1999;84(7):2275-2285.
27. van Heerden JA, Grant CS. Surgical treatment of primary hyperparathyroidism: An institutional perspective. World J Surg. 1991;15(6):688-692.
28. Bilezikian JP, Khan AA, Potts Jr JT. Guidelines for the management of asymptomatic primary hyperparathyroidism: summary statement from the Third International Workshop. J Clin Endocrinol Metab. 2009;94(2):335-339.
29. Bilezikian JP, Brandi ML, Eastell R, et al. Guidelines for the management of asymptomatic primary hyperparathyroidism: summary statement from the Fourth International Workshop. J Clin Endocrinol Metab. 2014;99(10):3561-3569.
30. Udelsman R, Akerstrom G, Biagini C, et al. The surgical management of asymptomatic primary hyperparathyroidism: proceedings of the Fourth International Workshop. J Clin Endocrinol Metab. 2014;99(10):3595-3606.
31. Marcocci C, Bollerslev J, Khan AA, Shoback DM. Medical management of primary hyperparathyroidism: proceedings of the fourth International Workshop on the Management of Asymptomatic Primary Hyperparathyroidism. J Clin Endocrinol Metab. 2014;99(10):3607-3618.
32. Reading CC, Charboneau JW, James EM, et al. High-resolution parathyroid sonography. AJR Am J Roentgenol. 1982;139(3):539-546.
33. Randel SB, Gooding GA, Clark OH, et al. Parathyroid variants: US evaluation. Radiology. 1987;165(1):191-194.
34. Graif M, Itzchak Y, Strauss S, et al. Parathyroid sonography: diagnostic accuracy related to shape, location, and texture of the gland. Br J Radiol. 1987;60(713):439-443.
35. Obara T, Fujimoto Y, Ito Y, et al. Functioning parathyroid lipoadenoma—report of four cases: clinicopathological and ultrasonographic features. Endocrinol Jpn. 1989;36(1):135-145.
36. Krudy AG, Doppman JL, Shawker TH, et al. Hyperfunctioning cystic parathyroid glands: CT and sonographic findings. AJR Am J Roentgenol. 1984;142(1):175-178.
37. Gooding GA, Duh QY. Primary hyperparathyroidism: functioning hemorrhagic parathyroid cyst. J Clin Ultrasound. 1997;25(2):82-84.
38. Johnson NA, Yip L, Tublin ME. Cystic parathyroid adenoma: sonographic features and correlation with 99mTc-sestamibi SPECT findings. AJR Am J Roentgenol. 2010;195(6):1385-1390.
39. Doppman JL, Brennan MF, Kahn CR, Marx SJ. Circumscribing or periadenomal vessel: a helpful angiographic finding in certain islet cell and parathyroid adenomas. AJR Am J Roentgenol. 1981;136(1):163-165.
40. Gooding GA, Clark OH. Use of color Doppler imaging in the distinction between thyroid and parathyroid lesions. Am J Surg. 1992;164(1):51-56.
41. Wolf RJ, Cronan JJ, Monchik JM. Color Doppler sonography: an adjunctive technique in assessment of parathyroid adenomas. J Ultrasound Med. 1994;13(4):303-308.
42. Lane MJ, Desser TS, Weigel RJ, Jeffrey Jr RB. Use of color and power Doppler sonography to identify feeding arteries associated with parathyroid adenomas. AJR Am J Roentgenol. 1998;171(3):819-823.
43. Reeder SB, Desser TS, Weigel RJ, Jeffrey RB. Sonography in primary hyperparathyroidism: review with emphasis on scanning technique. J Ultrasound Med. 2002;21(5):539-552.
44. Johnson NA, Tublin ME, Ogilvie JB. Parathyroid imaging: technique and role in the preoperative evaluation of primary hyperparathyroidism. AJR Am J Roentgenol. 2007;188(6):1706-1715.
45. Edmonson GR, Charboneau JW, James EM, et al. Parathyroid carcinoma: high-frequency sonographic features. Radiology. 1986;161(1):65-67.
46. Daly BD, Coffey SL, Behan M. Ultrasonographic appearances of parathyroid carcinoma. Br J Radiol. 1989;62(743):1017-1019.
47. Hara H, Igarashi A, Yano Y, et al. Ultrasonographic features of parathyroid carcinoma. Endocr J. 2001;48(2):213-217.
48. Devcic Z, Jeffrey RB, Kamaya A, Desser TS. The elusive parathyroid adenoma: techniques for detection. Ultrasound Q. 2013;29(3):179-187.
49. Clark OH. Mediastinal parathyroid tumors. Arch Surg. 1988;123(9):1096-1100.
50. Thompson NW, Vinik AI, editors. Endocrine surgery update. New York: Grune & Stratton; 1983.
51. Heller MT, Yip L, Tublin ME. Sonography of intrathyroid parathyroid adenomas: are there distinctive features that allow for preoperative identification? Eur J Radiol. 2013;82(1):e22-e27.
52. Fraker DL, Doppman JL, Shawker TH, et al. Undescended parathyroid adenoma: an important etiology for failed operations for primary hyperparathyroidism. World J Surg. 1990;14(3):342-348.
53. Doppman JL, Shawker TH, Krudy AG, et al. Parathymic parathyroid: CT, US, and angiographic findings. Radiology. 1985;157(2):419-423.
54. Doppman JL, Shawker TH, Fraker DL, et al. Parathyroid adenoma within the vagus nerve. AJR Am J Roentgenol. 1994;163(4):943-945.
55. Irvin 3rd GL, Prudhomme DL, Deriso GT, et al. A new approach to parathyroidectomy. Ann Surg. 1994;219(5):574-579.
56. Levin KE, Clark OH. The reasons for failure in parathyroid operations. Arch Surg. 1989;124(8):911-914.
57. Grant CS, van Heerden JA, Charboneau JW, et al. Clinical management of persistent and/or recurrent primary hyperparathyroidism. World J Surg. 1986;10(4):555-565.
58. Clark OH, Way LW, Hunt TK. Recurrent hyperparathyroidism. Ann Surg. 1976;184(4):391-402.
59. Richards ML, Thompson GB, Farley DR, Grant CS. Reoperative parathyroidectomy in 228 patients during the era of minimal-access surgery and intraoperative parathyroid hormone monitoring. Am J Surg. 2008;196(6):937-942.
60. Thompson GB, Grant CS, Perrier ND, et al. Reoperative parathyroid surgery in the era of sestamibi scanning and intraoperative parathyroid hormone monitoring. Arch Surg. 1999;134(7):699-704.
61. Rodriquez JM, Tezelman S, Siperstein AE, et al. Localization procedures in patients with persistent or recurrent hyperparathyroidism. Arch Surg. 1994;129(8):870-875.
62. Feingold DL, Alexander HR, Chen CC, et al. Ultrasound and sestamibi scan as the only preoperative imaging tests in reoperation for parathyroid adenomas. Surgery. 2000;128(6):1103-1109.

63. Koslin DB, Adams J, Andersen P, et al. Preoperative evaluation of patients with primary hyperparathyroidism: role of high-resolution ultrasound. Laryngoscope. 1997;107(9):1249-1253.
64. Ghaheri BA, Koslin DB, Wood AH, Cohen JI. Preoperative ultrasound is worthwhile for reoperative parathyroid surgery. Laryngoscope. 2004;114(12): 2168-2171.
65. Winkelbauer F, Ammann ME, Langle F, Niederle B. Diagnosis of hyperparathyroidism with US after autotransplantation: results of a prospective study. Radiology. 1993;186(1):255-257.
66. Palmer JA, Brown WA, Kerr WH, et al. The surgical aspects of hyperparathyroidism. Arch Surg. 1975;110(8):1004-1007.
67. Reddick RL, Costa JC, Marx SJ. Parathyroid hyperplasia and parathyromatosis. Lancet. 1977;1(8010):549.
68. Rattner DW, Marrone GC, Kasdon E, Silen W. Recurrent hyperparathyroidism due to implantation of parathyroid tissue. Am J Surg. 1985;149(6): 745-748.
69. Fitko R, Roth SI, Hines JR, et al. Parathyromatosis in hyperparathyroidism. Hum Pathol. 1990;21(2):234-237.
70. Kollmorgen CF, Aust MR, Ferreiro JA, et al. Parathyromatosis: a rare yet important cause of persistent or recurrent hyperparathyroidism. Surgery. 1994;116(1):111-115.
71. Hage MP, Salti I, El-Hajj Fuleihan G. Parathyromatosis: a rare yet problematic etiology of recurrent and persistent hyperparathyroidism. Metabolism. 2012;61(6):762-775.
72. Tublin ME, Yim JH, Carty SE. Recurrent hyperparathyroidism secondary to parathyromatosis: clinical and imaging findings. J Ultrasound Med. 2007;26(6):847-851.
73. Richards ML, Wormuth J, Bingener J, Sirinek K. Parathyroidectomy in secondary hyperparathyroidism: Is there an optimal operative management? Surgery. 2006;139(2):174-180.
74. Milas M, Weber CJ. Near-total parathyroidectomy is beneficial for patients with secondary and tertiary hyperparathyroidism. Surgery. 2004;136(6): 1252-1260.
75. Leapman SB, Filo RS, Thomalla JV, King D. Secondary hyperparathyroidism. The role of surgery. Am Surg. 1989;55(6):359-365.
76. Takebayashi S, Matsui K, Onohara Y, Hidai H. Sonography for early diagnosis of enlarged parathyroid glands in patients with secondary hyperparathyroidism. AJR Am J Roentgenol. 1987;148(5):911-914.
77. Gladziwa U, Ittel TH, Dakshinamurty KV, et al. Secondary hyperparathyroidism and sonographic evaluation of parathyroid gland hyperplasia in dialysis patients. Clin Nephrol. 1992;38(3):162-166.
78. Sutton RT, Reading CC, Charboneau JW, et al. US-guided biopsy of neck masses in postoperative management of patients with thyroid cancer. Radiology. 1988;168(3):769-772.
79. Karstrup S, Hegedus L. Concomitant thyroid disease in hyperparathyroidism. Reasons for unsatisfactory ultrasonographical localization of parathyroid glands. Eur J Radiol. 1986;6(2):149-152.
80. Scheible W, Deutsch AL, Leopold GR. Parathyroid adenoma: accuracy of preoperative localization by high-resolution real-time sonography. J Clin Ultrasound. 1981;9(6):325-330.
81. Mazzeo S, Caramella D, Lencioni R, et al. Comparison among sonography, double-tracer subtraction scintigraphy, and double-phase scintigraphy in the detection of parathyroid lesions. AJR Am J Roentgenol. 1996;166(6): 1465-1470.
82. Soon PS, Delbridge LW, Sywak MS, et al. Surgeon performed ultrasound facilitates minimally invasive parathyroidectomy by the focused lateral mini-incision approach. World J Surg. 2008;32(5):766-771.
83. Meilstrup JW. Ultrasound examination of the parathyroid glands. Otolaryngol Clin North Am. 2004;37(4):763-778, ix.
84. Yeh MW, Barraclough BM, Sidhu SB, et al. Two hundred consecutive parathyroid ultrasound studies by a single clinician: the impact of experience. Endocr Pract. 2006;12(3):257-263.
85. Lumachi F, Ermani M, Basso S, et al. Localization of parathyroid tumours in the minimally invasive era: which technique should be chosen? Population-based analysis of 253 patients undergoing para-thyroidectomy and factors affecting parathyroid gland detection. Endocr Relat Cancer. 2001;8: 63-69.
86. van Dalen A, Smit CP, van Vroonhoven TJ, et al. Minimally invasive surgery for solitary parathyroid adenomas in patients with primary hyperparathyroidism: role of US with supplemental CT. Radiology. 2001;220(3):631-639.
87. Haber RS, Kim CK, Inabnet WB. Ultrasonography for preoperative localization of enlarged parathyroid glands in primary hyperparathyroidism: comparison with 99mtechnetium sestamibi scintigraphy. Clin Endocrinol (Oxf). 2002;57:241-249.
88. Ruda JM, Hollenbeak CS, Stack Jr BC. A systematic review of the diagnosis and treatment of primary hyperparathyroidism from 1995 to 2003. Otolaryngol Head Neck Surg. 2005;132(3):359-372.
89. Milas M, Stephen A, Berber E, et al. Ultrasonography for the endocrine surgeon: a valuable clinical tool that enhances diagnostic and therapeutic outcomes. Surgery. 2005;138(6):1193-1200.
90. Solorzano CC, Carneiro-Pla DM, Irvin 3rd GL. Surgeon-performed ultrasonography as the initial and only localizing study in sporadic primary hyperparathyroidism. J Am Coll Surg. 2006;202(1):18-24.
91. Van Husen R, Kim LT. Accuracy of surgeon-performed ultrasound in parathyroid localization. World J Surg. 2004;28(11):1122-1126.
92. Tublin ME, Pryma DA, Yim JH, et al. Localization of parathyroid adenomas by sonography and technetium tc 99m sestamibi single-photon emission computed tomography before minimally invasive parathyroidectomy: are both studies really needed? J Ultrasound Med. 2009;28(2): 183-190.
93. Siperstein A, Berber E, Mackey R, et al. Prospective evaluation of sestamibi scan, ultrasonography, and rapid PTH to predict the success of limited exploration for sporadic primary hyperparathyroidism. Surgery. 2004;136(4): 872-880.
94. Solbiati L, Montali G, Croce F, et al. Parathyroid tumors detected by fine-needle aspiration biopsy under ultrasonic guidance. Radiology. 1983;148(3): 793-797.
95. Charboneau JW, Grant CS, James EM, et al. High-resolution ultrasound-guided percutaneous needle biopsy and intraoperative ultrasonography of a cervical parathyroid adenoma in a patient with persistent hyperparathyroidism. Mayo Clin Proc. 1983;58(8):497-500.
96. Glenthøj A, Karstrup S. Parathyroid identification by ultrasonically guided aspiration cytology. Is correct cytological identification possible? APMIS. 1989;97(6):497-502.
97. Karstrup S, Glenthøj A, Hainau B, et al. Ultrasound-guided, histological, fine-needle biopsy from suspect parathyroid tumours: success-rate and reliability of histological diagnosis. Br J Radiol. 1989;62(743):981-985.
98. Bergenfelz A, Forsberg L, Hederström E, Ahrén B. Preoperative localization of enlarged parathyroid glands with ultrasonically guided fine needle aspiration for parathyroid hormone assay. Acta Radiol. 1991;32(5): 403-405.
99. Sacks BA, Pallotta JA, Cole A, Hurwitz J. Diagnosis of parathyroid adenomas: efficacy of measuring parathormone levels in needle aspirates of cervical masses. AJR Am J Roentgenol. 1994;163(5):1223-1226.
100. Reading CC, Charboneau JW, James EM, et al. Postoperative parathyroid high-frequency sonography: evaluation of persistent or recurrent hyperparathyroidism. AJR Am J Roentgenol. 1985;144(2):399-402.
101. Gooding GA, Clark OH, Stark DD, et al. Parathyroid aspiration biopsy under ultrasound guidance in the postoperative hyperparathyroid patient. Radiology. 1985;155(1):193-196.
102. MacFarlane MP, Fraker DL, Shawker TH, et al. Use of preoperative fine-needle aspiration in patients undergoing reoperation for primary hyperparathyroidism. Surgery. 1994;116(6):959-964.
103. Bancos I, Grant CS, Nadeem S, et al. Risks and benefits of parathyroid fine-needle aspiration with parathyroid hormone washout. Endocr Pract. 2012;18(4):441-449.
104. De Feo ML, Colagrande S, Biagini C, et al. Parathyroid glands: combination of (99m)Tc MIBI scintigraphy and US for demonstration of parathyroid glands and nodules. Radiology. 2000;214(2):393-402.
105. Mullan BP. Nuclear medicine imaging of the parathyroid. Otolaryngol Clin North Am. 2004;37(4):909-939, xi-xii.
106. Moka D, Voth E, Dietlein M, et al. Technetium 99m-MIBI-SPECT: a highly sensitive diagnostic tool for localization of parathyroid adenomas. Surgery. 2000;128(1):29-35.

107. Civelek AC, Ozalp E, Donovan P, Udelsman R. Prospective evaluation of delayed technetium-99m sestamibi SPECT scintigraphy for preoperative localization of primary hyperparathyroidism. Surgery. 2002;131(2): 149-157.
108. Lorberboym M, Minski I, Macadziob S, et al. Incremental diagnostic value of preoperative 99mTc-MIBI SPECT in patients with a parathyroid adenoma. J Nucl Med. 2003;44(6):904-908.
109. Jones JM, Russell CF, Ferguson WR, Laird JD. Pre-operative sestamibi-technetium subtraction scintigraphy in primary hyperparathyroidism: experience with 156 consecutive patients. Clin Radiol. 2001;56(7): 556-559.
110. Davis ML, Quayle FJ, Middleton WD, et al. Ultrasound facilitates minimally invasive parathyroidectomy in patients lacking definitive localization from preoperative sestamibi scan. Am J Surg. 2007;194(6):785-790.
111. Phillips CD, Shatzkes DR. Imaging of the parathyroid glands. Semin Ultrasound CT MR. 2012;33(2):123-129.
112. Lumachi F, Zucchetta P, Marzola MC, et al. Advantages of combined technetium-99m-sestamibi scintigraphy and high-resolution ultrasonography in parathyroid localization: comparative study in 91 patients with primary hyperparathyroidism. Eur J Endocrinol. 2000;143:755-760.
113. Mihai R, Simon D, Hellman P. Imaging for primary hyperparathyroidism—an evidence-based analysis. Langenbecks Arch Surg. 2009;394(5): 765-784.
114. Eslamy HK, Ziessman HA. Parathyroid scintigraphy in patients with primary hyperparathyroidism: 99mTc sestamibi SPECT and SPECT/CT. Radiographics. 2008;28(5):1461-1476.
115. Patel CN, Salahudeen HM, Lansdown M, Scarsbrook AF. Clinical utility of ultrasound and 99mTc sestamibi SPECT/CT for preoperative localization of parathyroid adenoma in patients with primary hyperparathyroidism. Clin Radiol. 2010;65(4):278-287.
116. Leupe PK, Delaere PR, Vander Poorten VL, Debruyne F. Pre-operative imaging in primary hyperparathyroidism with ultrasonography and sestamibi scintigraphy. B-ENT. 2011;7(3):173-180.
117. Rodgers SE, Hunter GJ, Hamberg LM, et al. Improved preoperative planning for directed parathyroidectomy with 4-dimensional computed tomography. Surgery. 2006;140(6):932-940.
118. Mortenson MM, Evans DB, Lee JE, et al. Parathyroid exploration in the reoperative neck: improved preoperative localization with 4D-computed tomography. J Am Coll Surg. 2008;206(5):888-895.
119. Hunter GJ, Schellingerhout D, Vu TH, et al. Accuracy of four-dimensional CT for the localization of abnormal parathyroid glands in patients with primary hyperparathyroidism. Radiology. 2012;264(3):789-795.
120. Chazen JL, Gupta A, Dunning A, Phillips CD. Diagnostic accuracy of 4D-CT for parathyroid adenomas and hyperplasia. AJNR Am J Neuroradiol. 2012;33(3):429-433.
121. Beland MD, Mayo-Smith WW, Grand DJ, et al. Dynamic MDCT for localization of occult parathyroid adenomas in 26 patients with primary hyperparathyroidism. AJR Am J Roentgenol. 2011;196(1):61-65.
122. Randall GJ, Zald PB, Cohen JI, Hamilton BE. Contrast-enhanced MDCT characteristics of parathyroid adenomas. AJR Am J Roentgenol. 2009;193(2):W139-W143.
123. Kang YS, Rosen K, Clark OH, Higgins CB. Localization of abnormal parathyroid glands of the mediastinum with MR imaging. Radiology. 1993;189(1):137-141.
124. McDermott VG, Fernandez RJ, Meakem 3rd TJ, et al. Preoperative MR imaging in hyperparathyroidism: results and factors affecting parathyroid detection. AJR Am J Roentgenol. 1996;166(3):705-710.
125. Gotway MB, Higgins CB. MR imaging of the thyroid and parathyroid glands. Magn Reson Imaging Clin N Am. 2000;8(1):163-182, ix.
126. Gotway MB, Leung JW, Gooding GA, et al. Hyperfunctioning parathyroid tissue: spectrum of appearances on noninvasive imaging. AJR Am J Roentgenol. 2002;179(2):495-502.
127. Gotway MB, Reddy GP, Webb WR, et al. Comparison between MR imaging and 99mTc MIBI scintigraphy in the evaluation of recurrent of persistent hyperparathyroidism. Radiology. 2001;218(3):783-790.
128. Reidel MA, Schilling T, Graf S, et al. Localization of hyperfunctioning parathyroid glands by selective venous sampling in reoperation for primary or secondary hyperparathyroidism. Surgery. 2006;140(6):907-913.
129. Wang TS, Cheung K, Farrokhyar F, et al. Would scan, but which scan? A cost-utility analysis to optimize preoperative imaging for primary hyperparathyroidism. Surgery. 2011;150(6):1286-1294.
130. Russell CF, Laird JD, Ferguson WR. Scan-directed unilateral cervical exploration for parathyroid adenoma: a legitimate approach? World J Surg. 1990;14(3):406-409.
131. Lorenz K, Nguyen-Thanh P, Dralle H. Unilateral open and minimally invasive procedures for primary hyperparathyroidism: a review of selective approaches. Langenbecks Arch Surg. 2000;385(2):106-117.
132. Udelsman R. Six hundred fifty-six consecutive explorations for primary hyperparathyroidism. Ann Surg. 2002;235(5):665-670.
133. Palazzo FF, Delbridge LW. Minimal-access/minimally invasive parathyroidectomy for primary hyperparathyroidism. Surg Clin North Am. 2004;84(3): 717-734.
134. Norton JA, Shawker TH, Jones BL, et al. Intraoperative ultrasound and reoperative parathyroid surgery: an initial evaluation. World J Surg. 1986;10(4):631-639.
135. Harris R, Ryu H, Vu T, et al. Modern approach to surgical intervention of the thyroid and parathyroid glands. Semin Ultrasound CT MR. 2012;33(2): 115-122.
136. Charboneau JW, Grant CS, James EM, et al. High-resolution ultrasound-guided percutaneous needle biopsy and intraoperative ultra-sonography of a cervical parathyroid adenoma in a patient with persistent hyperparathyroidism. Mayo Clin Proc. 1983;58:497-500.
137. Kendrick ML, Charboneau JW, Curlee KJ, et al. Risk of parathyromatosis after fine-needle aspiration. Am Surg. 2001;67(3):290-293.
138. Charboneau JW, Hay ID, van Heerden JA. Persistent primary hyperparathyroidism: successful ultrasound-guided percutaneous ethanol ablation of an occult adenoma. Mayo Clin Proc. 1988;63(9):913-917.
139. Karstrup S, Holm HH, Glenthøj A, Hegedus L. Nonsurgical treatment of primary hyperparathyroidism with sonographically guided percutaneous injection of ethanol: results in a selected series of patients. AJR Am J Roentgenol. 1990;154(5):1087-1090.
140. Karstrup S, Hegedus L, Holm HH. Ultrasonically guided chemical parathyroidectomy in patients with primary hyperparathyroidism: a follow-up study. Clin Endocrinol (Oxf). 1993;38(5):523-530.
141. Harman CR, Grant CS, Hay ID, et al. Indications, technique, and efficacy of alcohol injection of enlarged parathyroid glands in patients with primary hyperparathyroidism. Surgery. 1998;124(6):1011-1019.
142. Cercueil JP, Jacob D, Verges B, et al. Percutaneous ethanol injection into parathyroid adenomas: mid- and long-term results. Eur Radiol. 1998;8(9):1565-1569.
143. Reading CC. Ultrasound-guided percutaneous ethanol ablation of solid and cystic masses of the liver, kidney, thyroid, and parathyroid. Ultrasound Q. 1994;12:67-68.
144. Bennedbaek FN, Karstrup S, Hegedus L. Percutaneous ethanol injection therapy in the treatment of thyroid and parathyroid diseases. Eur J Endocrinol. 1997;136(3):240-250.
145. Lewis BD, Charboneau JW, Reading CC. Ultrasound-guided biopsy and ablation in the neck. Ultrasound Q. 2002;18(1):3-12.
146. Veldman MW, Reading CC, Farrell MA, et al. Percutaneous parathyroid ethanol ablation in patients with multiple endocrine neoplasia type 1. AJR Am J Roentgenol. 2008;191(6):1740-1744.
147. Solbiati L, Giangrande A, De Pra L, et al. Percutaneous ethanol injection of parathyroid tumors under US guidance: treatment for secondary hyperparathyroidism. Radiology. 1985;155(3):607-610.
148. Kakuta T, Fukagawa M, Fujisaki T, et al. Prognosis of parathyroid function after successful percutaneous ethanol injection therapy guided by color Doppler flow mapping in chronic dialysis patients. Am J Kidney Dis. 1999;33(6):1091-1099.
149. Takeda S, Michigishi T, Takazakura E. Successful ultrasonically guided percutaneous ethanol injection for secondary hyperparathyroidism. Nephron. 1992;62(1):100-103.
150. Kitaoka M, Fukagawa M, Ogata E, Kurokawa K. Reduction of functioning parathyroid cell mass by ethanol injection in chronic dialysis patients. Kidney Int. 1994;46(4):1110-1117.
151. Giangrande A, Castiglioni A, Solbiati L, Allaria P. Ultrasound-guided percutaneous fine-needle ethanol injection into parathyroid glands in

secondary hyperparathyroidism. Nephrol Dial Transplant. 1992;7(5): 412-421.
152. Singh Ospina N, Thompson GB, Lee RA, et al. Safety and efficacy of percutaneous parathyroid ethanol ablation in patients with recurrent primary hyperparathyroidism and multiple endocrine neoplasia type 1. J Clin Endocrinol Metab. 2015;100(1):E87-E90.
153. Takeda S, Michigishi T, Takazakura E. Ultrasonically guided percutaneous ethanol injection to parathyroid autografts for recurrent hyperparathyroidism. Nephron. 1993;65(4):651-652.
154. Cintin C, Karstrup S, Ladefoged SD, Joffe P. Tertiary hyperparathyroidism treated by ultrasonically guided percutaneous fine-needle ethanol injection. Nephron. 1994;68(2):217-220.
155. Fletcher S, Kanagasundaram NS, Rayner HC, et al. Assessment of ultrasound guided percutaneous ethanol injection and parathyroidectomy in patients with tertiary hyperparathyroidism. Nephrol Dial Transplant. 1998;13(12): 3111-3117.
156. Bennedbaek FN, Karstrup S, Hegedus L. Ultrasound guided laser ablation of a parathyroid adenoma. Br J Radiol. 2001;74(886):905-907.
157. Adda G, Scillitani A, Epaminonda P, et al. Ultrasound-guided laser thermal ablation for parathyroid adenomas: analysis of three cases with a three-year follow-up. Horm Res. 2006;65(5):231-234.
158. Andrioli M, Riganti F, Pacella CM, Valcavi R. Long-term effectiveness of ultrasound-guided laser ablation of hyperfunctioning parathyroid adenomas: present and future perspectives. AJR Am J Roentgenol. 2012;199(5): 1164-1168.

CHAPTER 21

The Breast

Jordana Phillips, Rashmi J. Mehta, and A. Thomas Stavros

SUMMARY OF KEY POINTS

- Breast ultrasound plays a key role in supplemental breast cancer screening, diagnostic imaging, and interventional breast procedures.
- All images should be annotated with the following: the side (left or right), clock face position, distance from the nipple in centimeters, and transducer orientation. All lesions should be scanned and measured in two orthogonal planes to assess the size, surface, internal characteristics, and shape.
- A negative whole-breast screening ultrasound examination should include a minimum of five images of each breast, including one image in one plane of each quadrant of the breast, typically at the same distance from the nipple, and one image of the retroareolar breast.
- For diagnostic ultrasound examinations, it is necessary to document that the area in question was imaged, even if no abnormality is seen. If the area is palpable, make sure to palpate the area and place the probe immediately over this location.
- The Breast Imaging Reporting and Data System (BI-RADS) is a required standardized lexicon for describing and classifying findings and their probability of malignancy.
- Suspicious findings include irregular shape; indistinct, speculated, angular, or microlobulated margins; orientation that is not parallel; acoustic shadowing; hypoechoic echotexture; and calcifications.
- For mammographic-sonographic correlation, it is important to confirm that the size, shape, location, and surrounding tissue density of the mammographic and sonographic findings are the same.
- Tools that can aid diagnosis include Doppler imaging and elastography. Three-dimensional imaging and contrast-enhanced ultrasound are currently being studied.

CHAPTER OUTLINE

APPLICATIONS OF BREAST ULTRASOUND
BREAST ANATOMY AND PHYSIOLOGY
SONOGRAPHIC EQUIPMENT
SONOGRAPHIC TECHNIQUE
Patient Position
Annotation
Documentation of Lesions
Split-Screen Imaging
Special Breast Techniques
Doppler Sonography
Elastography
Three-Dimensional Ultrasound
Contrast-Enhanced Ultrasound
REPORTING
SONOGRAPHIC FINDINGS
Normal Tissues and Variations
Cysts and Cystic Masses
Simple Cysts
Complicated Cysts
Complex Cystic and Solid Masses
Solid Masses
Suspicious Findings
Indistinct Margins
Spiculation or Thick Echogenic Rim
Angular Margins
Microlobulations
Not Parallel (Not Taller-Than-Wide) Orientation
Duct Extension
Acoustic Shadowing
Hypoechogenicity
Calcifications
Associated Features
Benign Findings
Hyperechoic Tissue
Parallel (Wider-Than-Tall) Orientation
Thin Echogenic Capsule
DIAGNOSTIC ULTRASOUND INDICATIONS
Symptomatic Breast
Breast Pain
Palpable Abnormality
Nipple Discharge
Mammographic Findings
Size Correlation
Shape Correlation
Location or Position Correlation
Surrounding Tissue Density Correlation
Sonographic-Mammographic Confirmation
NICHE APPLICATIONS FOR BREAST ULTRASOUND
Infection
Implants
Breast Cancer Staging
Sonographic–Magnetic Resonance Imaging Correlation
ULTRASOUND-GUIDED INTERVENTION

APPLICATIONS OF BREAST ULTRASOUND

There are four main roles for sonography in breast imaging: (1) primary screening; (2) supplemental screening (after mammography); (3) diagnosis—for example, evaluation of palpable mass or other breast-related symptoms; and (4) interventional breast procedures. Other uses include evaluation of problems associated with breast implants and treatment planning for radiation therapy.[1]

Sonography currently does not have a proven role in primary breast cancer screening, but the use of sonography in **supplemental screening** (after mammography, as an ancillary study), especially in women with dense breast tissue on mammography, has expanded in recent years and its use continues to grow. Multiple studies[2-5] have shown promising results for sonography as an adjunct to mammography for screening women with dense breast tissue. Early studies evaluating bilateral handheld sonography performed by either radiologist or technologist detected approximately three carcinomas that were missed by primary screening mammography per 1000 patients. These cancers were often less than 1 cm in size and had not yet involved the axillary lymph nodes (termed "node negative"). In addition, supplemental screening with whole-breast ultrasound significantly increased mammography's sensitivity by approximately 20% to 30%.

The American College of Radiology Imaging Network whole-breast ultrasound screening trial (ACRIN 6666) was designed to assess the role of bilateral whole-breast screening ultrasound in a group of patients at increased risk for breast cancer and with dense breast tissue on mammography using a standardized technique. Each patient had three scans over 3 years in addition to mammography. The results of the first prevalence scan showed that ultrasound detected 4.2 cancers per 1000, more than were detected by mammography, but at a high cost in benign biopsies compared with mammography.[6] Subsequent evaluation at years 2 and 3 demonstrated that an additional 3.7 cancers were detected with screening whole-breast ultrasound per 1000 patients screened.[7] Unfortunately, the identification of additional breast cancers is associated with an increase in the false-positive rate, with lower true-positive biopsy rates. This likely will decrease over time as technologists and radiologists become more accustomed to performing and interpreting whole-breast ultrasound screening examinations. Given that the probability of malignancy is much lower in a screening population compared with a diagnostic population, some findings that might be viewed with suspicion in a patient with a palpable lump or suspicious mammographic abnormality in the diagnostic setting can potentially be ignored in a screening setting. As radiologists learn this over time, the false-positive rate of screening ultrasound should improve.

The encouraging data regarding whole-breast ultrasound coincided with 2009 Connecticut legislation mandating radiologists to inform patients of their tissue density and the potential benefit of adjunct screening, possibly with ultrasound or breast magnetic resonance imaging (MRI). As a result, whole-breast screening ultrasound began to be implemented into clinical practice. Although an additional three cancers were found per 1000 women screened,[8,9] the challenges of screening ultrasound in the clinical setting began to surface. These included low compliance rates and the increased length of time necessary to perform the examination. Of those for whom supplemental whole-breast screening was offered, only 28% initially accepted.[8] The expectation is that this rate will improve as the workflow and culture for screening ultrasound improve.

To shorten the length of time for the examination and the radiologist time commitment during image acquisition, **automated whole-breast ultrasound** (ABUS) was introduced. **ABUS** is a system by which an ultrasound probe moves across a women's breast and ensures that all areas of the breast are imaged. The technologist helps direct the probe, but probe movement is largely automatic. The images then are stored for later interpretation. Unlike handheld ultrasound, in which the technologist takes representative images of each breast for radiologist review, ABUS allows the radiologist to review all imaging through each breast. Although the ultrasound examination is still lengthy, taking approximately 15 minutes per breast, the main benefit is that the radiologist does not need to be present at the time of image acquisition, similar to screening mammography. This provides more options for how to integrate ABUS into a screening setting.

Several dedicated automated breast ultrasound machines are being developed, the first of which was approved by the U.S. Food and Drug Administration (FDA) in 2012. Performance data have been very promising. Similar to handheld screening ultrasound, studies have shown that ABUS detects an additional 2 to 3 cancers per 1000 women screened. It has improved sensitivity as compared with mammography alone by 30% to 40%, and the identified cancers are often invasive and node negative.[10-13] As with earlier studies of handheld ultrasound, both call-back rates and false positives are higher than with mammography alone. Again, it is the expectation that these rates will decrease with experience.

The most widespread role for breast ultrasound is **diagnosis.** This is usually performed in a targeted fashion after mammography and clinical examination, to provide a more specific diagnosis than can be obtained from mammography or clinical examination alone. Palpable masses and mammographic abnormalities constitute the most common indications for targeted diagnostic breast ultrasound. Specific goals of targeted diagnostic sonography are to prevent biopsies and short-interval follow-up mammography of benign lesions, to guide interventions of all types, to give feedback that improves clinical and mammographic skills, and to find malignancies missed on mammography.

Ultrasound also plays a large role in **interventional breast procedures.** In general, procedures performed with ultrasound are relatively quicker, more comfortable for the patient, and less expensive than procedures performed with stereotaxis or MRI guidance.

BREAST ANATOMY AND PHYSIOLOGY

The breast is a modified sweat gland that is composed of varying number of lobes ranging from 4 to 20[14] that are not well delineated from one another; they overlap and vary greatly in size and distribution. Each lobe consists of parenchymal elements (lobar

duct, smaller branch ducts, and lobules) and supporting stromal tissues (compact interlobular stromal fibrous tissue, loose periductal and intralobular stromal fibrous tissue, and fat). Historically, it was believed that the lobar ducts converge in the subareolar region to form lactiferous sinuses that serve as reservoirs for milk storage during lactation. However, more recent data suggest that lactiferous sinuses do not exist.[14] As the lobar ducts extend deep into the breast, they divide into segmental and subsegmental ducts that lead to the terminal ducts and acini of the lobules. Each lobule consists of the intralobular segment of the terminal duct, ductules, acini, and loose intralobular stromal fibrous tissue. Acini are saclike structures that produce milk during lactation. The functional unit of the breast is the **terminal ductolobular unit** (TDLU), which consists of a lobule and its extralobular terminal duct.

TDLUs are important because they are the site of origin of most breast pathology and of **aberrations of normal development and involution** (ANDIs). Most breast carcinomas are thought to arise in the terminal duct near the junction of the intralobular and extralobular segments. Most **invasive ductal carcinomas** have **ductal carcinoma in situ** (DCIS) components that can use the ductal system as conduits for growth into other parts of the breast. Unlike TDLUs, lobar ducts give rise to few pathologic processes. They are the primary site of origin for large **duct papillomas** and the **duct ectasia–periductal mastitis complex.**

Each lobar duct has several rows of TDLUs arising from it. Anterior TDLUs tend to have long extralobular terminal ducts, whereas posterior TDLUs tend to have shorter extralobular terminal ducts. Some TDLUs lie at the distal end of the ductal system and are horizontally oriented. Anterior TDLUs are more numerous than posterior and terminal TDLUs, and over time the posterior TDLUs tend to regress, leaving a progressively larger percentage of anterior TDLUs. Because anterior TDLUs greatly outnumber posterior TDLUs, most breast pathology that arises from TDLUs occurs in the superficial half of the mammary zone, just deep to the anterior mammary fascia.

The breast can be divided into three zones (Fig. 21.1). The most superficial zone is the **premammary zone,** or **subcutaneous zone,** which lies between the skin and the anterior mammary fascia. The premammary zone is part of the integument, and processes that arise primarily within the premammary zone are usually not true breast lesions. Rather, these are lesions of the skin and/or subcutaneous tissues that are identical to those arising from skin and subcutaneous tissues covering any other part of the body (e.g., **lipomas, sebaceous cysts**). The **mammary zone** is the middle zone and lies between the anterior mammary fascia and the posterior mammary fascia. It contains the lobar ducts, their branches, most of the TDLUs, and most of the fibrous stromal elements of the breast. The deepest of the zones is the **retromammary zone.** It mainly contains fat, blood vessels, and lymphatics and is usually much less apparent on sonograms than on mammograms because sonographic compression flattens the retromammary zone against the chest wall. This differs greatly from mammography, in which mammographic compression pulls the retromammary fat away from the chest wall and expands it in the anteroposterior (AP) direction. Because most breast pathology arises from TDLUs and, to a lesser extent, from the mammary ducts, and because most of the ducts and lobules lie within the mammary zone, most true breast pathology arises from the mammary zone. Although lesions that arise within the premammary or retromammary zone are usually skin lesions, true breast lesions that arise within the mammary zone can secondarily involve the premammary and retromammary tissues.

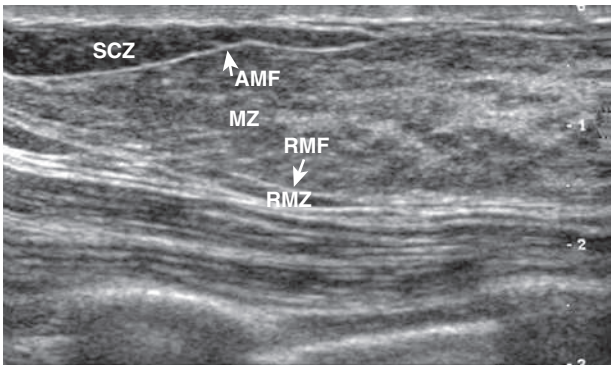

FIG. 21.1 Three Zones of the Breast. The premammary or **subcutaneous zone** *(SCZ),* **mammary zone** *(MZ),* and **retromammary zone** *(RMZ).* The mammary zone is where most of the ducts and lobules of the breast that give rise to breast pathology lie. The mammary zone is enveloped in thick, tough fascia. Anteriorly it is delineated from the subcutaneous fat by the premammary or anterior mammary fascia *(AMF)* and posteriorly from the retromammary fat by the posterior or retromammary fascia *(RMF).* The anterior mammary fascia is continuous with the **Cooper ligaments,** with each ligament being formed by two apposed layers of anterior mammary fascia. The retromammary zone is compressed during real-time sonography in the recumbent position and is relatively small and unapparent in comparison to its appearance on mammography.

The **mammary fascia** that envelops the mammary zone is tough and is relatively more resistant to invasive malignancy than are loose, stromal fibrous tissues. The anterior mammary fascia is continuous with the **Cooper ligaments.** At the point where it is continuous with a ligament, the anterior mammary fascia continues superficially obliquely through the subcutaneous fat, attaches to superficial fascia, and then courses back down through the subcutaneous fat, where it continues as the anterior mammary fascia. Each Cooper ligament is composed of two closely applied layers of anterior mammary fascia with a potential space inferiorly, where the two layers separate and course away from each other as anterior mammary fasciae (Fig. 21.2). This affects the sonographic appearance of invasive malignancies, as discussed later.

The normal anatomic structures of the breast span a spectrum of echogenicities, from midlevel gray to intensely hyperechoic. **Hyperechoic** normal structures include compact interlobular stromal fibrous tissue, anterior and posterior mammary fasciae, Cooper ligaments, and skin. Duct walls, when visible, also appear hyperechoic. **Isoechoic** normal structures that have midlevel echogenicity include fat, epithelial tissues in ducts and lobules, and loose, intralobular and periductal, stromal fibrous tissue.

Water density tissue on mammography corresponds to a variety of different normal tissues that can be shown sonographically. Consequently, although dense interlobular stromal fibrous tissue, loose periductal or intralobular stromal fibrous tissue,

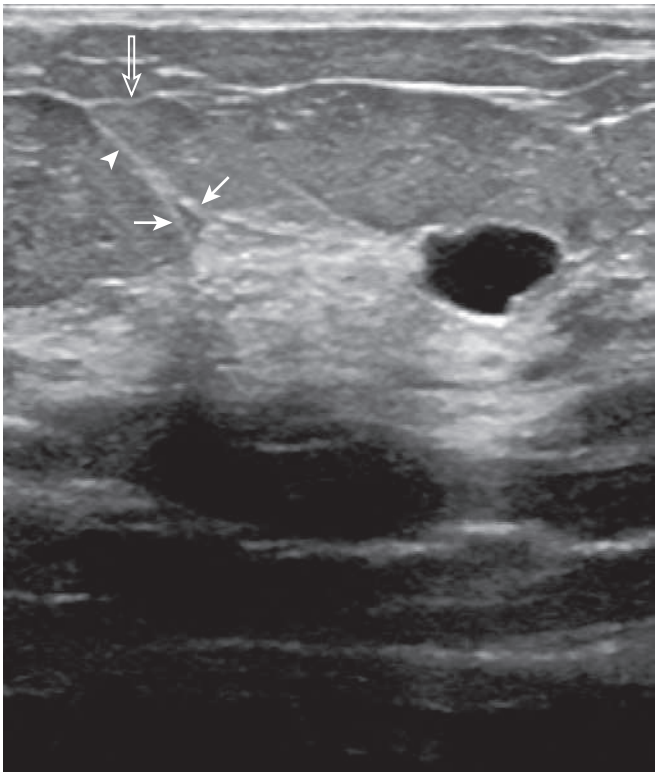

FIG. 21.2 Mammary Fasciae and Cooper Ligaments. Two layers of anterior mammary fascia *(arrows)* form the bases of a Cooper ligament *(white arrowhead),* which inserts into superficial fascia *(open arrow).* Invasive malignancies often develop angles as they invade the base of Cooper ligaments.

and epithelial elements in ducts and lobules all have different sonographic appearances, they all appear to be water density on mammography. **Mammographically dense tissue** can correspond to purely hyperechoic, purely isoechoic, or mixed hyperechoic and isoechoic tissues on sonography (Fig. 21.3). Most contain mixtures of fibrous and glandular elements interspersed with variable amounts of fat (Fig. 21.4). Over time, atrophy tends to occur more rapidly in the areas of the mammary zone that lie between Cooper ligaments, leaving progressively more of the residual fibroglandular elements within these ligaments (Fig. 21.5).

Normal mammary ducts that are not ectatic can appear in two ways sonographically. A mammary duct can appear purely isoechoic when the centrally located hyperechoic duct wall cannot be visualized because of poor angle of incidence or suboptimal transducer resolution and only the loose periductal stromal fibrous tissue is visible. A mammary duct can also be shown as a central, bright echo surrounded by isoechoic loose stromal fibrous tissue when the apposed walls of the central duct can be optimally demonstrated (Fig. 21.6A). It is common for a single duct to have both sonographic appearances, depending on the angle of incidence with the duct walls. Variable degrees of **ductal ectasia** become increasingly common with age, particularly in the subareolar region. In **ectatic ducts,** anechoic or hypoechoic fluid separates the two duct walls and compresses the loose periductal stromal tissues to variable degrees (Fig. 21.6B-C). Duct ectasia occurs commonly in women over age 50 and usually is asymptomatic.[15] In certain patients, however, ductal ectasia may be associated with nipple discharge or may lead to periductal mastitis and its acute and chronic complications.

The ducts within the nipple and immediate subareolar regions are poorly seen when scanned from straight anteriorly because they course almost parallel to the beam in those locations. However, special maneuvers designed to improve the angle of incidence enable adequate demonstration of the entire mammary duct throughout the subareolar region, even within the nipple when necessary. These maneuvers include the **peripheral compression technique, two-handed compression technique,** and **rolled nipple technique.** These maneuvers are most useful when evaluating patients with nipple discharge (Fig. 21.7) and in assessing malignant nodules for extensive intraductal involvement growing within the duct toward the nipple. The two-handed compression technique is also useful in assessing gynecomastia.

Individual TDLUs may be sonographically visible—under ideal conditions—as small isoechoic structures (Fig. 21.8). In patients who are pregnant or lactating and in patients with adenosis, not only are TDLUs enlarged, but they are also increased in number. In certain cases, TDLUs become large and numerous enough to form continuous sheets of isoechoic tissue. The variable prominence of TDLUs creates a continuous spectrum in the appearance of breast tissue from TDLUs that are not visible to breasts that appear to be totally isoechoic (Fig. 21.9). This most often occurs anteriorly, where lobules are most numerous, but in certain cases can fill and distend the entire mammary zone.

Lymphatic drainage from most of the breast is from deep to superficial, toward the subdermal lymphatic network, then to the periareolar plexus **(Sappey plexus),** and finally on to the axilla. Most drainage of the breast is to the axillary lymph nodes; however, some of the deep portions of the breast, particularly medially, preferentially drain along the chest wall to the **internal mammary lymph nodes.** As a result, most lymphatic metastases from the breast are to the axilla, with a minority occurring in the internal mammary lymph nodes. The three levels of axillary lymph nodes are determined by their location relative to the pectoralis minor muscle. Lymph nodes that lie peripheral to the inferolateral edge of the pectoralis minor are **level 1** lymph nodes; nodes that lie deep to the pectoralis minor muscle are **level 2** lymph nodes; and nodes that lie medial to the superomedial border of the pectoralis minor muscle are **level 3** lymph nodes or **infraclavicular nodes.** Lymphatic drainage to the axilla usually passes through level 1, then level 2, and finally to level 3 lymph nodes (Fig. 21.10). From level 3 nodes, metastases may progress to internal jugular or supraclavicular lymph nodes. **Rotter nodes** lie between the pectoralis major and pectoralis minor muscles. It is important to identify level 2 and 3 lymph nodes and Rotter lymph node metastases, because unrecognized and untreated metastases to these lymph nodes can be a source of recurrence.

Internal mammary nodes lie in a chain parallel to the internal mammary artery and veins along the deep side of the chest wall, just lateral to the edges of the sternum. Metastases most often

Text continued on p. 767.

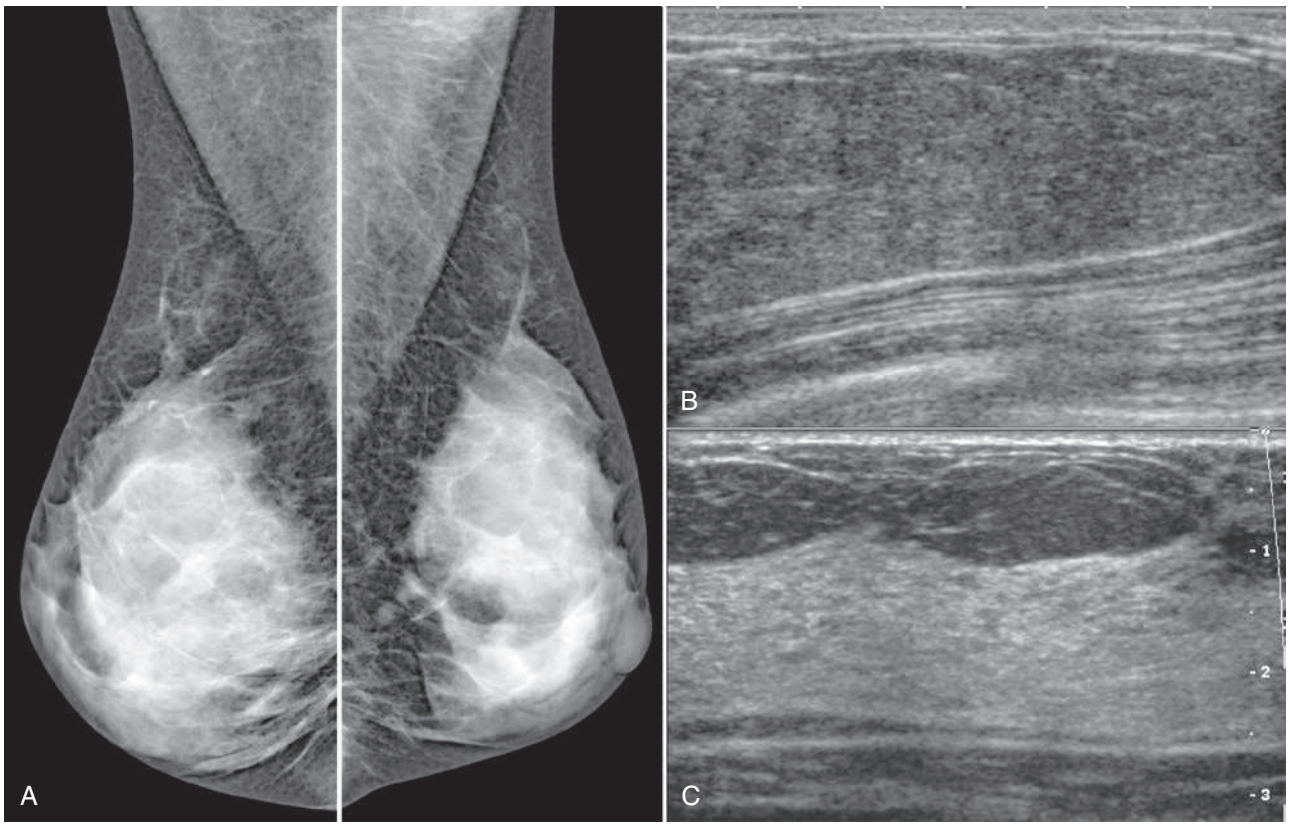

FIG. 21.3 Dense Breast Tissue: Radiographic-Sonographic Correlation. Radiographically dense (water density) tissue on mammograms **(A)** can correspond to two different types of tissue on sonography: **(B)** almost-isoechoic glandular tissue, and **(C)** intensely hyperechoic interlobular stromal fibrous tissue.

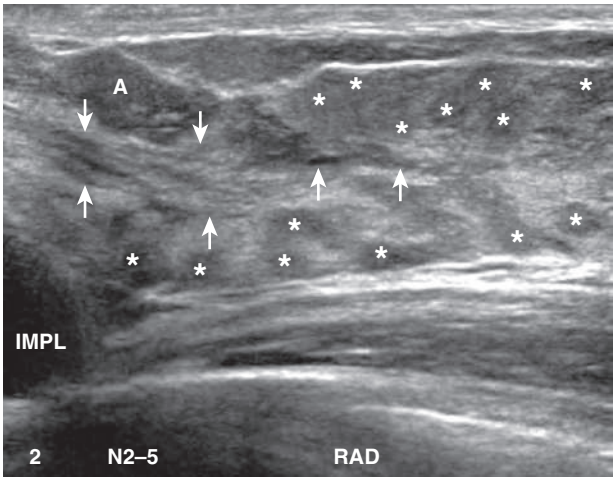

FIG. 21.4 Water Density Breast Tissue. Most water density tissue on mammography is not pure fibrous or glandular tissue, but a mixture of hyperechoic interlobular stromal fibrous tissue and isoechoic glandular or loose periductal and intralobular stromal tissue. Note that the lobar duct is mildly ectatic *(arrows)*. The round or taller-than-wide isoechoic elements (*) within the peripheral segments of the mammary zone represent epithelial and loose stromal tissues within terminal ductolobular units (TDLUs). Note that TDLUs are more numerous and prominent anteriorly than they are posteriorly.

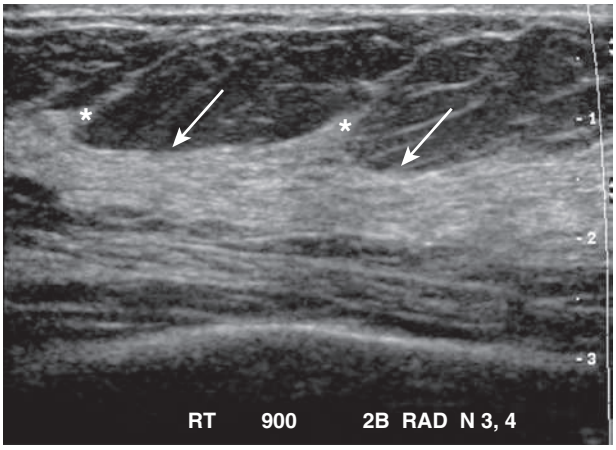

FIG. 21.5 Breast Atrophy. With advancing age, and particularly after full-term pregnancy and breastfeeding, the fibroglandular elements of the breast regress more rapidly in the areas of the mammary zone *(arrows)* that lie between Cooper ligaments than in the area within the ligaments. This eventually can leave much or all of the residual breast tissue entrapped within Cooper ligaments (*).

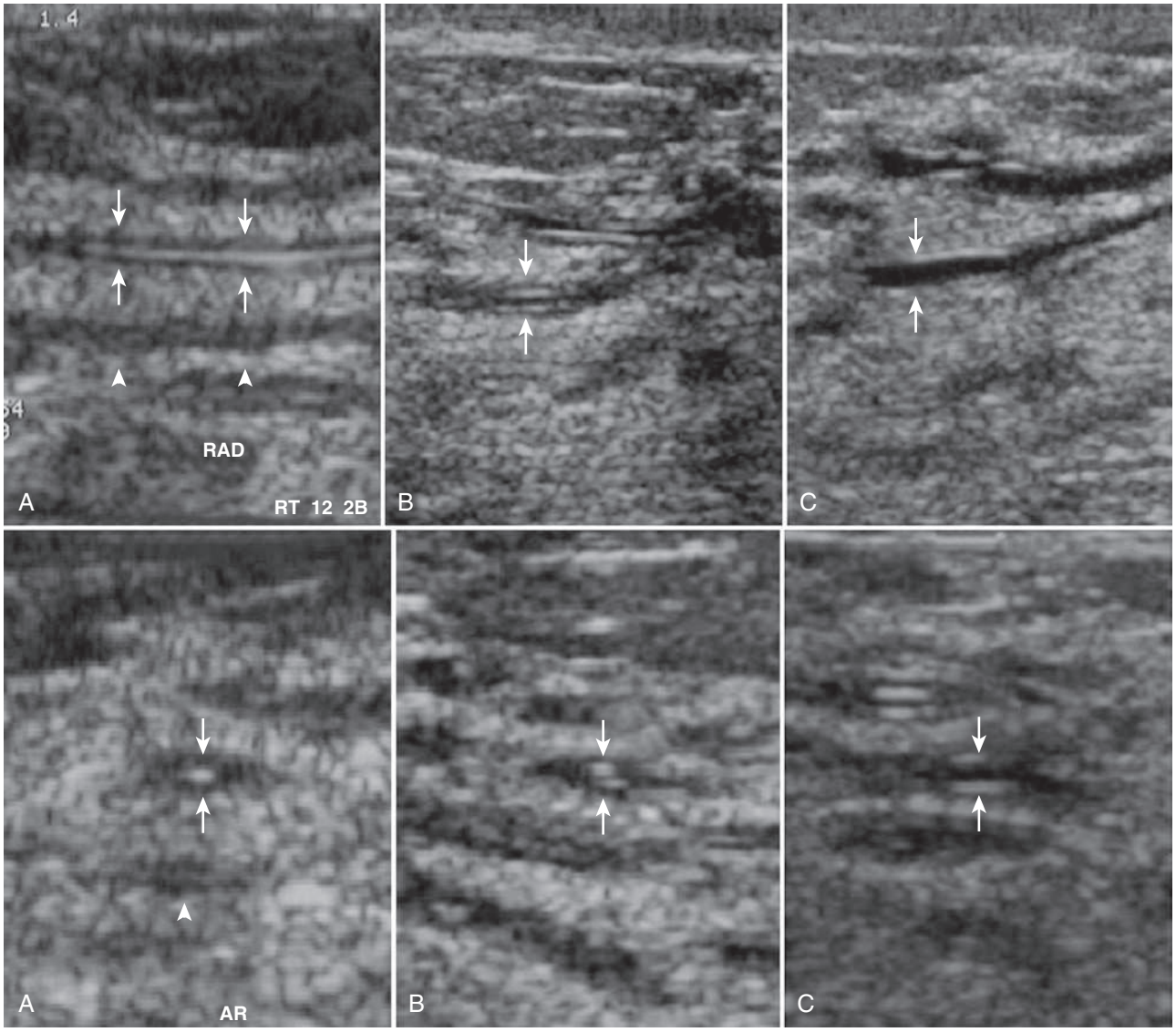

FIG. 21.6 Mammary Duct: Spectrum of Normal Appearances. (A) With high spatial resolution, 90-degree angle of incidence, and perfect centering, the duct appears to be composed of a central echogenic line *(arrows)* that represents the apposed walls of the collapsed mammary duct. The surrounding isoechoic tissue represents loose periductal stromal tissue. Unfortunately, only a minority of the ducts seen have this trilaminar appearance in the long axis and targetoid appearance in the short axis. Ducts that are slightly out of focus, coursing at an angle, or not perfectly centered within the beam have a different appearance. The deeper duct *(arrowheads)* is too deep for the short-axis focal length of the transducer. The central echo that represents the apposed walls of the collapsed duct is not seen. Only the isoechoic loose periductal stromal tissue can be identified. **(B)** This mildly ectatic duct *(arrows)* is shown in long axis *(upper image)* and short axis *(lower image)*. The duct is now represented by two hyperechoic lines that represent the anterior and posterior walls of the duct separated by secretions within the duct lumen. **(C)** This severely ectatic duct *(arrows)* is shown in long axis *(upper image)* and short axis *(lower image)*. As the degree of ductal ectasia increases, the walls of the duct become more separated, and the loose periductal stromal tissue becomes more compressed and less apparent. In severe ductal ectasia the periductal loose stromal tissue may no longer be visible.

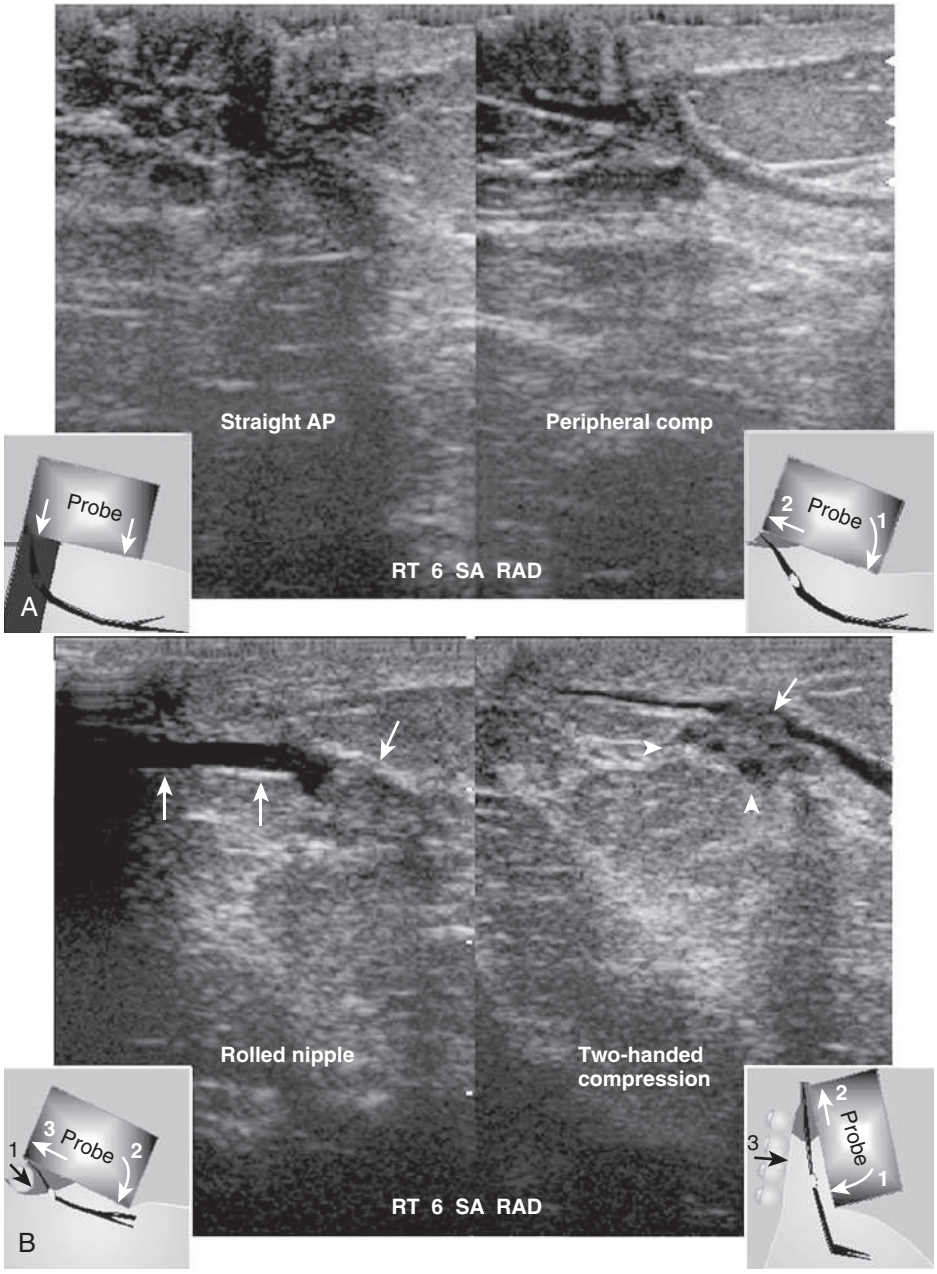

FIG. 21.7 Maneuvers for Demonstrating Subareolar and Intranipple Mammary Ducts. (A) *Left image,* The subareolar ducts are difficult to assess from a straight anterior approach because shadowing arises from the nipple and areola and the tissue planes of the nipple are parallel to the ultrasound beam. *Right image,* Peripheral compression technique. With vigorous compression on the peripheral end of the transducer and by sliding it over the nipple to push the nipple to the side, shadowing can be minimized, and the angle of incidence of the beam with the subareolar ducts can be improved. Lesions that lie in the immediate subareolar region can often be demonstrated. **(B)** *Left image,* Rolled nipple technique is the best way to demonstrate the ducts within the nipple and whether a lesion extends into the nipple from the subareolar ducts. *Right image,* Two-handed compression technique further improves the angle of incidence with the subareolar ducts and helps assess the compressibility of the ducts. This can help to distinguish echogenic, inspissated secretions from intraductal papillary lesions and determine whether the lesion *(arrows)* has penetrated through the duct wall *(arrowheads).* The rolled nipple technique shows that this **malignant intraductal papillary lesion** does not extend into the intranipple segment of the duct, but the two-handed compression maneuver shows that it has invaded through the posterior duct wall and is forming angles within the periductal tissues.

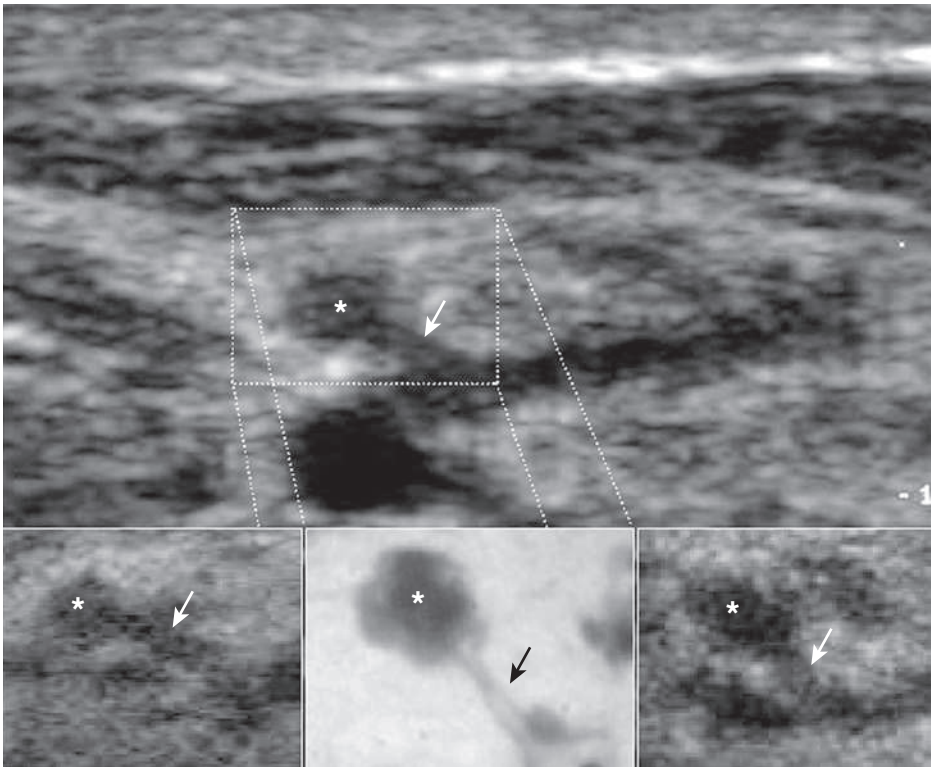

FIG. 21.8 Terminal Ductolobular Units (TDLUs). The TDLU includes the extralobular terminal duct and the lobule, which contains the intralobular terminal duct, ductules, and intralobular isoechoic loose stromal tissue. TDLUs appear as an isoechoic structure similar to a tennis racket; the head of the racket (*) represents the lobule, and the handle and neck of the racket *(arrows)* represent the extralobular terminal duct. Bottom center image is three-dimensional histology. (Courtesy of Hanne M. Jensen, MD.)

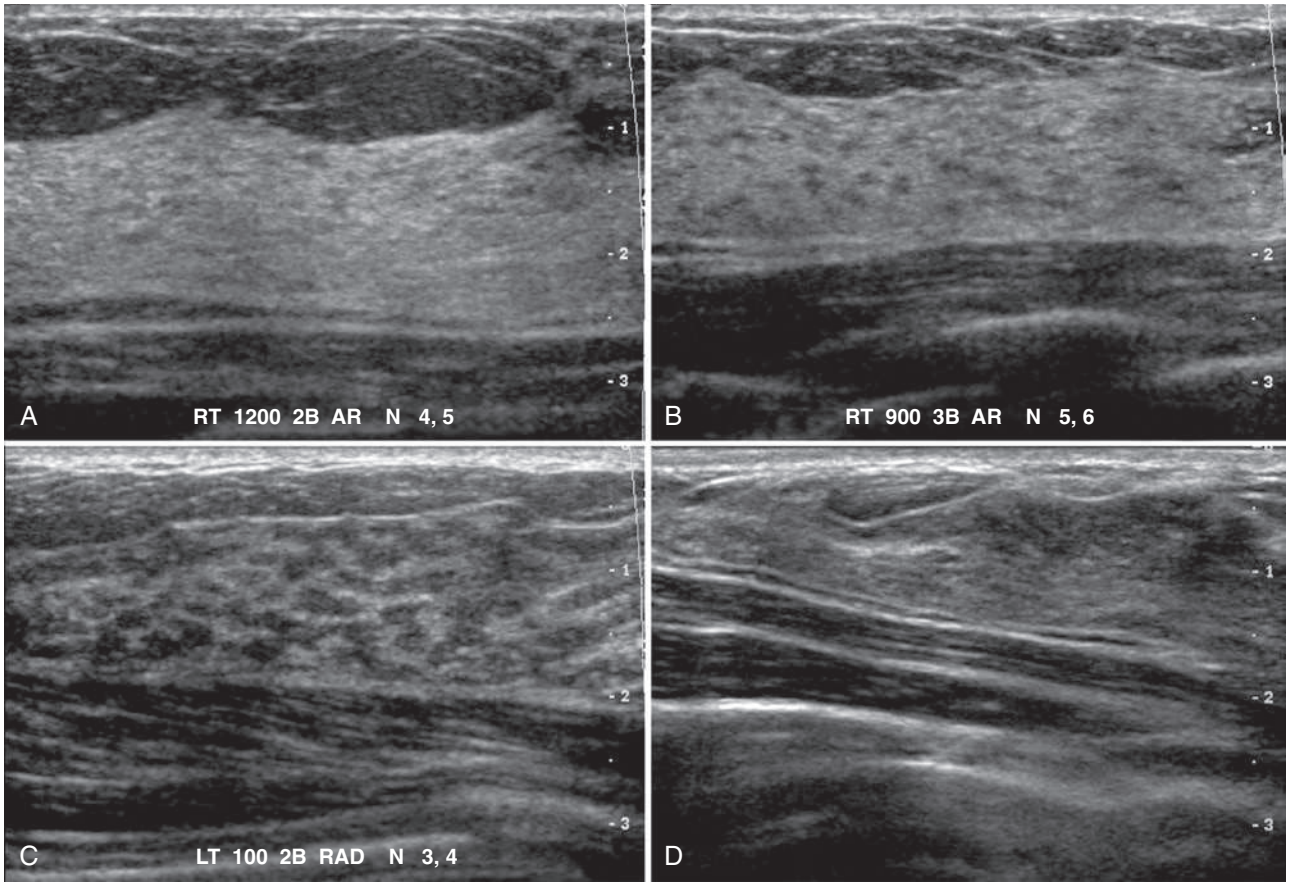

FIG. 21.9 Variable Prominence of Terminal Ductolobular Units (TDLUs). (A) Only a few scattered TDLUs may be visible. **(B)** As TDLUs become larger and more numerous in adenosis and adenosis of pregnancy, they may almost touch each other. Because anterior TDLUs are more numerous than posterior TDLUs, these changes tend to affect the superficial aspect of the mammary zone earlier and to a greater extent than they affect its deep aspect. **(C)** When lobular enlargement is pronounced, the entire superficial aspect of the mammary zone may appear isoechoic, with the deep half still being hyperechoic. **(D)** When lobular prominence is most pronounced, both superficial and deep aspects of the mammary zone may appear almost homogeneously isoechoic.

involve internal mammary lymph nodes in the second and third interspaces. Using color Doppler sonography to identify the internal mammary vessels can be helpful in finding abnormal internal mammary lymph nodes. Normal internal mammary lymph nodes can be identified under ideal circumstances, but not in all patients.

A significant percentage of patients have lymph nodes that lie within the breast and are called **intramammary lymph nodes.** These can lie anywhere within the breast but are most common in the axillary segment just below the axilla. They usually lie within a centimeter of the posterior mammary artery, a branch of the axillary artery that extends from the axilla toward the nipple. Intramammary lymph nodes can also be found occasionally in the medial edge of the breast superficial to the internal mammary lymph nodes. These medial lymph nodes are seen much less frequently on mammography than on sonography because mammographic compression can seldom pull them far enough away from the chest wall to be mammographically visible. Medial intramammary lymph nodes can be difficult to demonstrate sonographically without the use of an acoustic standoff because of their superficial location just beneath the skin.

Breast cancer metastases can involve the **supraclavicular lymph nodes,** but these nodes are positive only when lymph node metastases are extensive. Metastases often involve levels 1, 2, and 3 axillary lymph nodes or internal mammary and internal jugular lymph nodes before reaching the supraclavicular nodes.

The first lymph node to which lymphatic drainage flows and the first node involved by metastases has been termed the **sentinel lymph node.** The location of the sentinel node varies, depending on the location of the primary tumor within the breast. The sentinel lymph node is usually a level 1 axillary lymph node, but in certain cases it may be an intramammary node or even a level 2 node. Occasionally the sentinel node may be an internal mammary node.

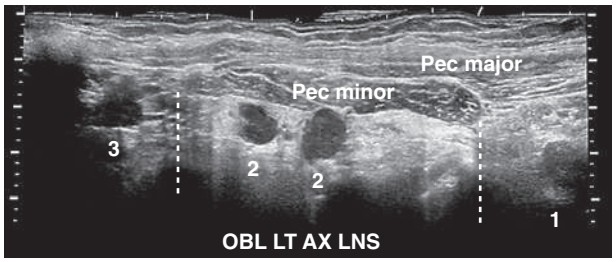

FIG. 21.10 Pectoralis Minor Muscle and Levels of Axillary Lymph Nodes. Extended–field-of-view (FOV) sonogram shows metastases to all three axillary lymph node levels on the left. The level of axillary lymph nodes is determined by the pectoralis minor muscle. Lymph nodes that lie inferior and lateral to the inferolateral edge of the pectoralis minor muscle are level 1 nodes; those that lie deep to the pectoralis minor muscle are level 2 lymph nodes; and those that lie superior and medial to the superomedial edge of the pectoralis minor muscles are level 3 (infraclavicular) lymph nodes.

SONOGRAPHIC EQUIPMENT

Breast ultrasound requires high-frequency transducers that are optimized for near-field imaging. Transducers used for breast sonography should be high-resolution, real-time, linear-array, broad-bandwidth transducers operating at a center frequency of at least 12 MHz and preferably higher. Other transducers may be used in special circumstances. Focal zones should be electronically adjustable. In general, the highest frequency capable of adequate penetration to the depth of interest should be used.[1] When evaluating more superficial lesions, such as those within the skin or those that are palpable and "pea-sized" or smaller, an acoustic standoff should be used (Fig. 21.11). This is either an acoustic standoff pad or a thick layer of acoustic gel that allows better characterization of these areas. In some patients, simply scanning with lighter compression can obviate the need for a standoff.

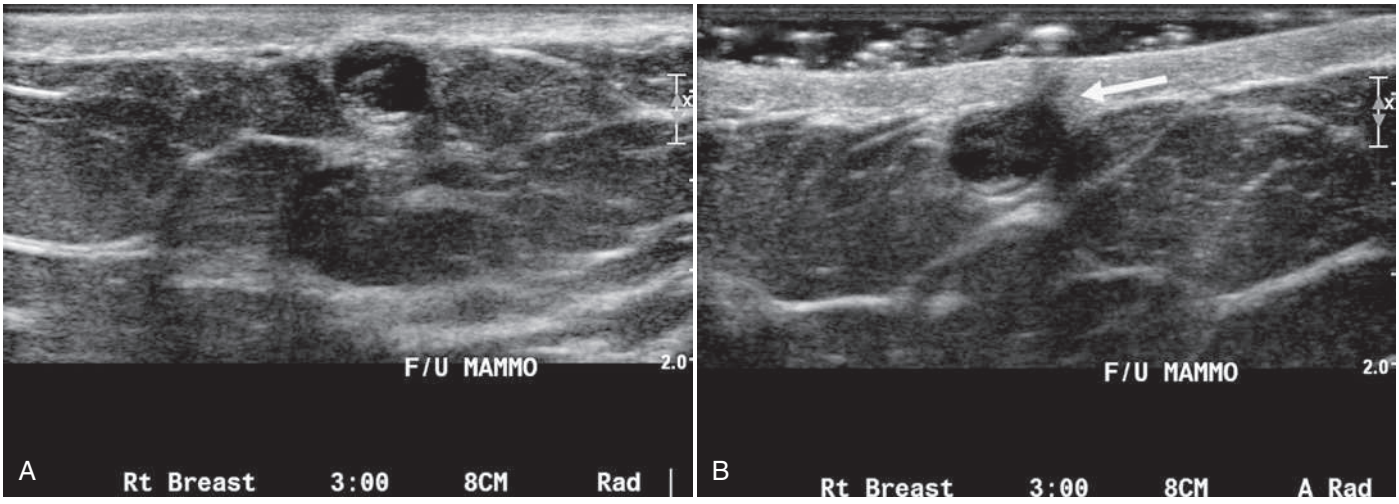

FIG. 21.11 Value of Standoff Pad. (A) Ultrasound evaluation of an **epidermal inclusion cyst** in the skin without a standoff pad did not delineate the obstructed gland neck. **(B)** A thick layer of acoustic gel was then used and clearly shows the obstructed gland neck extending to the skin surface *(arrow)*.

SONOGRAPHIC TECHNIQUE

For optimal scanning of the breast, the patient should be positioned supine with the arm on the side of interest relaxed up by the side of the head. Images should be acquired using the highest frequency probe that allows penetration of the targeted area. Initial images should include the pectoralis muscle to ensure that the entire depth of the breast has been imaged. The gain should be set such that the fat is a midlevel gray.

Patient Position

Breast sonographic evaluation depends heavily on special **dynamic** and **positional** maneuvers performed during the examination. Dynamic maneuvers include **varying compression** to assess compressibility and mobility. Lesions that are compressible are benign with a high degree of certainty and may represent either a normal fat lobule or a benign lipoma. Superficial venous thrombosis **(Mondor disease)** has a lack of flow on Doppler ultrasound and may be incompressible.[16] **Ballottement** (alternating compression and compression release) can be helpful to demonstrate mobility of echoes with ectatic ducts or complex cysts. Varying compression can also eradicate artifactual shadowing from critical angle shadowing off steeply oblique tissue planes. **Heeling and toeing of the transducer** can minimize critical angle shadowing arising from Cooper ligaments and better demonstrate the thin, echogenic capsule on the ends of solid nodules, an important sign of a noninvasive lesion margin. Heeling and toeing can also improve the angle of incidence with duct walls, allowing better demonstration of ductal anatomy and pathology, especially in the subareolar portions of the ducts. **Doppler ultrasound assessment** of the breast depends greatly on using as little compression pressure as possible (Video 21.1 and Video 21.2). Blood flow in a breast lesion can easily be decreased or even completely ablated if compression is too vigorous.

Positional changes are important in assessment of complex cysts. **Fluid-debris levels, milk of calcium,** and **fat-fluid levels** can all be shown to change sonographically between supine and upright or lateral decubitus positions. Some palpable abnormalities are clinically evident only in the upright position and therefore require that the scan be performed in the upright position. Even routine whole-breast scanning may require changing the position of the patient during the examination. Contralateral posterior oblique positions are better for evaluating the lateral half of the breast, whereas supine positioning is better for the medial half of the breast.

Annotation

The location of a scan plane in the breast or the location of a lesion in the breast should be annotated in compliance with American College of Radiology (ACR) ultrasound Breast Imaging Reporting and Data System (BI-RADS) lexicon.[17,18] The side (left and right), clock face position, distance from the nipple in centimeters, and transducer orientation must be recorded. Distance from the nipple should be measured from the nipple itself because the areolar width is variable among patients. Painting centimeter markers on the transducer can facilitate recording the distance from the nipple in centimeters, but the distance is usually estimated from the known lengths of linear high-frequency transducers, either 38 mm or 50 mm. The transducer orientation can be longitudinal, transverse, **radial,** or **antiradial,** which is orthogonal to the radial plane. The advantage of radial imaging is that the central ducts are radially oriented with respect to the nipple. Scanning in a plane that lies radial to the duct enables visualization of **DCIS** components of lesions growing within the ductal system of the breast. Identifying intraductal components of tumor can reduce the chances of mischaracterizing a malignant solid nodule as benign or "probably benign" and also facilitates demonstrating the true extent of DCIS components of mixed invasive and intraductal malignant lesions.

Thus a lesion at the 12 o'clock position of the right breast that lies 2 cm from the nipple when scanned radially could be annotated as "Right breast 12:00 2 cm Rad." This method of annotation allows reproducibility within and across practice sites. An icon of the right or left breast with a linear marker that demonstrates the position and orientation of the transducer is an acceptable alternative for annotation of scan location, and most ultrasound equipment manufacturers provide breast icons for this.

The farther from the nipple a lesion lies, the less likely the duct will course in a plane that is truly radial with respect to the nipple because of tortuosity of the duct, or because the duct of interest is a branch duct that is not oriented perfectly radially. In this scenario, the sonographer should think of *internal* radial planes versus the *external* true radial plane with respect to the nipple. The internal radial plane is parallel to the long axis of the ducts in the region of interest. If the internal plane of the duct of interest does not fall into a standard category of longitudinal, transverse, radial, or antiradial, one can opt to annotate this as an oblique view.

In addition to the ACR BI-RADS lexicon mandates,[17,18] some elect to record the depth of a lesion in addition to the parameters previously discussed. One option is to use three zones: **A** for the superficial third, **B** for the middle third, and **C** for the deep third of the breast.

Documentation of Lesions

All lesions should be scanned in their entirety in two orthogonal planes to assess the surface and internal characteristics as well as shape. These orthogonal planes could be longitudinal and transverse, but many practitioners prefer radial and antiradial planes. Each image plane should be recorded with and without calipers. It is important to document the maximum dimensions of the lesion in both planes because this is an important prognostic indicator. If the maximum diameter does not lie in one of the standard longitudinal, transverse, radial, or antiradial planes, an additional oblique view parallel to the long axis of the lesion should be obtained with and without calipers. Films without calipers are especially important in small lesions, where the calipers may interfere with assessment of surface characteristics. It is also recommended to document lesion vascularity using color or power Doppler imaging.

When performing a whole-breast screening ultrasound examination and when no abnormal imaging finding has been

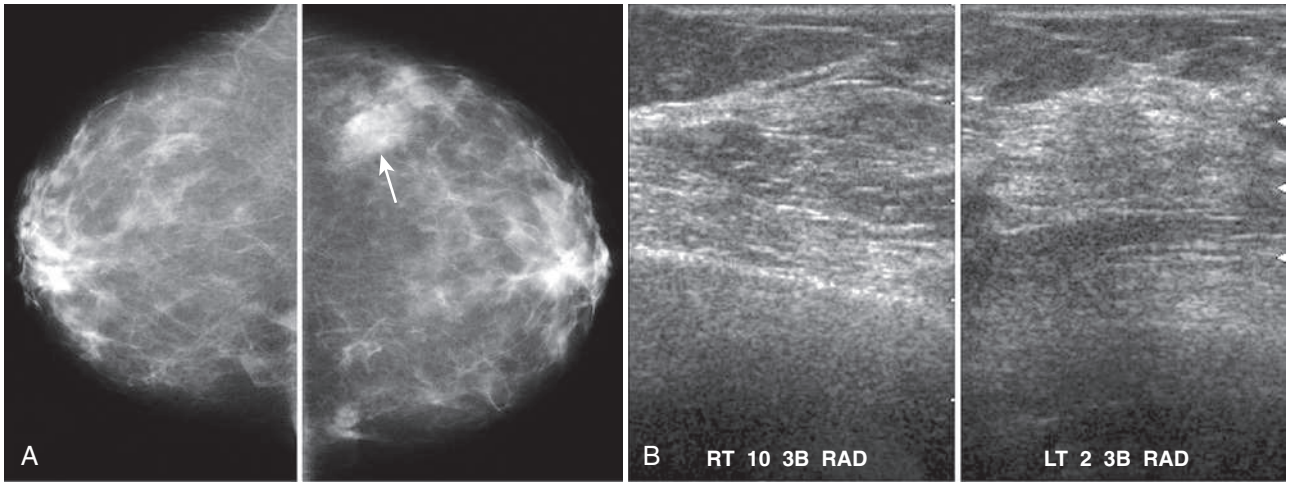

FIG. 21.12 Value of Split-Screen Mirror Ultrasound Image. (A) Mammography of both breasts showed a focal asymmetrical density in the left breast, upper outer quadrant on the craniocaudal (CC) view *(arrow).* **(B)** Split-screen mirror-image ultrasound images show focal fibrous tissue in the upper outer quadrant of the left breast that is markedly asymmetrical with the thickness of tissue in the mirror-image upper outer quadrant location of the right breast. This collection of **asymmetrical fibrous tissue** is the cause of the mammographic asymmetry.

identified, five images of each breast should be acquired.[18] These include one image in one plane of each quadrant of the breast, typically at the same distance from the nipple, and one image of the retroareolar breast. The axilla can be scanned, but this is not required.

When performing a targeted diagnostic ultrasound examination, it is necessary to document that the area in question was imaged. If the area is palpable, make sure to first evaluate for the palpable finding and place the probe immediately over this location. If a finding is seen, then documentation as described earlier is necessary. If no abnormal finding is seen—for example, in the case of a mammographic asymmetry corresponding to normal breast tissue—then documentation of that area showing normal breast tissue is still necessary.

Split-Screen Imaging

Split-screen imaging capability is invaluable in breast imaging. Split-screen images are most frequently used to compare mirror-image locations in the right and left breasts to document that **asymmetrical fibroglandular tissue** causes either a mammographic asymmetry or a palpable lump (Fig. 21.12). Split-screen imaging can also be used to document dynamic events, such as compressibility and mobility, on a single freeze-frame image and in simultaneous mode, to show both the gray-scale image on one side and the color or power Doppler image on the other. It may also be used to document a finding in both orthogonal views on the same screen.

Multiple lesions and lesions larger than the width of the transducer require special techniques for demonstration. Of several methods for demonstrating larger fields of view (FOVs), one can use combined split-screen images or extended-FOV imaging. Extended-FOV images can be helpful in demonstrating very large lesions, multifocal and multicentric malignant lesions, lymph node levels, implant integrity, or, as in Fig. 21.13, extensive fibrocystic change (FCC) with numerous cysts of variable size within the breast.

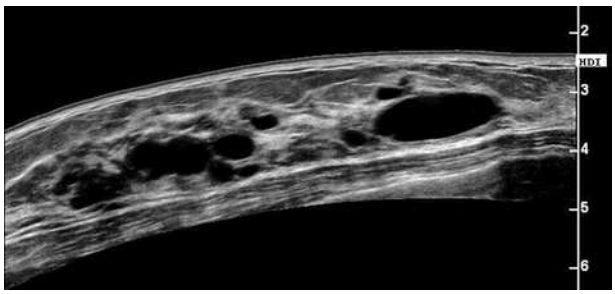

FIG. 21.13 Extended–field-of-view (FOV) images shows extensive **fibrocystic change** with numerous cysts of variable size within the breast.

Special Breast Techniques

Doppler Sonography

One of the main purposes of Doppler ultrasound is to help classify masses seen on ultrasound as benign or malignant. Once a breast malignancy exceeds about 3 mm in size, it must stimulate neovascularity to continue to grow. To accomplish this, tumors elaborate a variety of angiogenesis factors. A net of peripheral neovessels forms to nourish the rapidly proliferating periphery of the tumor. Studies have been performed evaluating the presence or absence of flow, the distribution and pattern of vessels, vessel density, peak systolic velocity (PSV), pulsatility index, and resistive index (RI) and have found conflicting results, some demonstrating that these measures could predict malignancy, but others showing substantial overlap of findings.[19-23] As a result, Doppler cannot be used independently to classify solid masses as benign or malignant but rather should be used to supplement the routine ultrasound evaluation.

That being said, Doppler ultrasound can be used to differentiate solid masses from those that are cystic. Some markedly hypoechoic solid nodules can have a pseudocystic appearance. Demonstrating

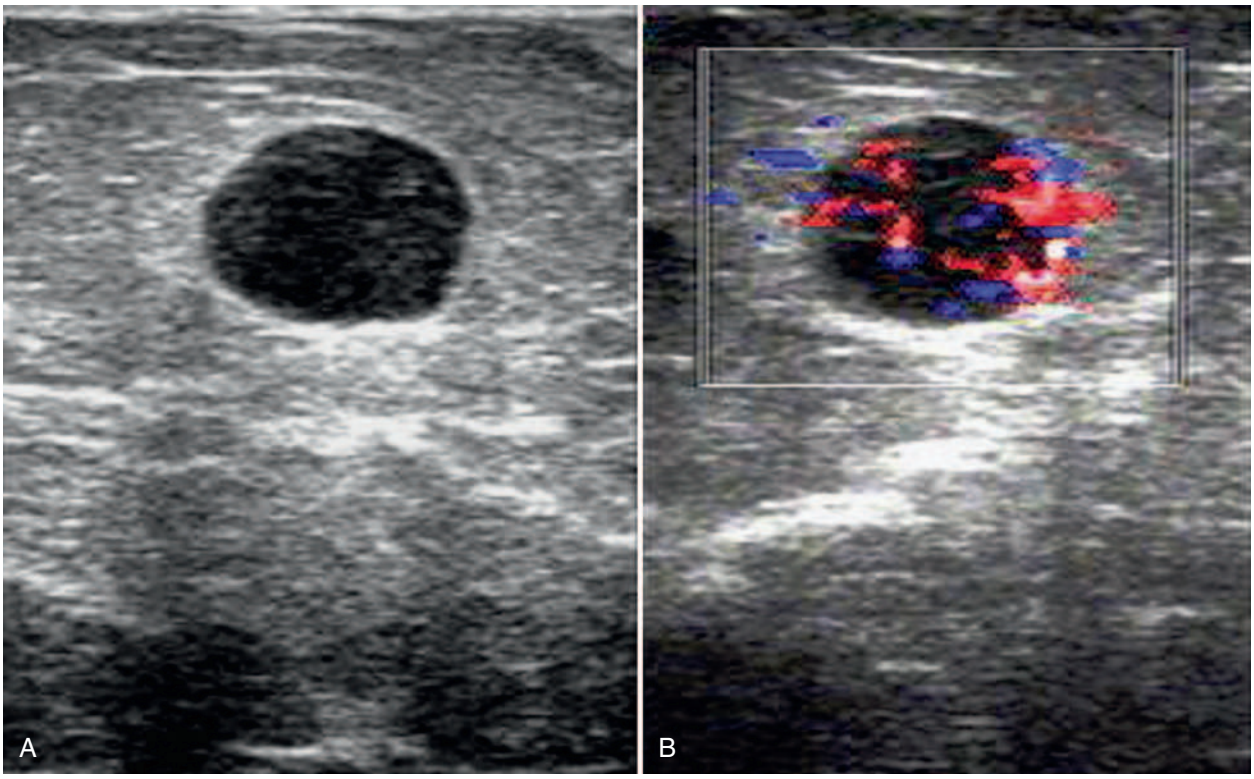

FIG. 21.14 Pseudocystic Solid Nodule Versus Complicated Cyst. Color Doppler ultrasound can be helpful in distinguishing between complex cysts and solid nodules when the distinction is uncertain based on the image alone. **(A) Metastatic leiomyosarcoma of the breast** shows a pseudocystic appearance on the sonogram. **(B)** Color Doppler sonography shows abundant internal flow, indicating that the lesion is solid.

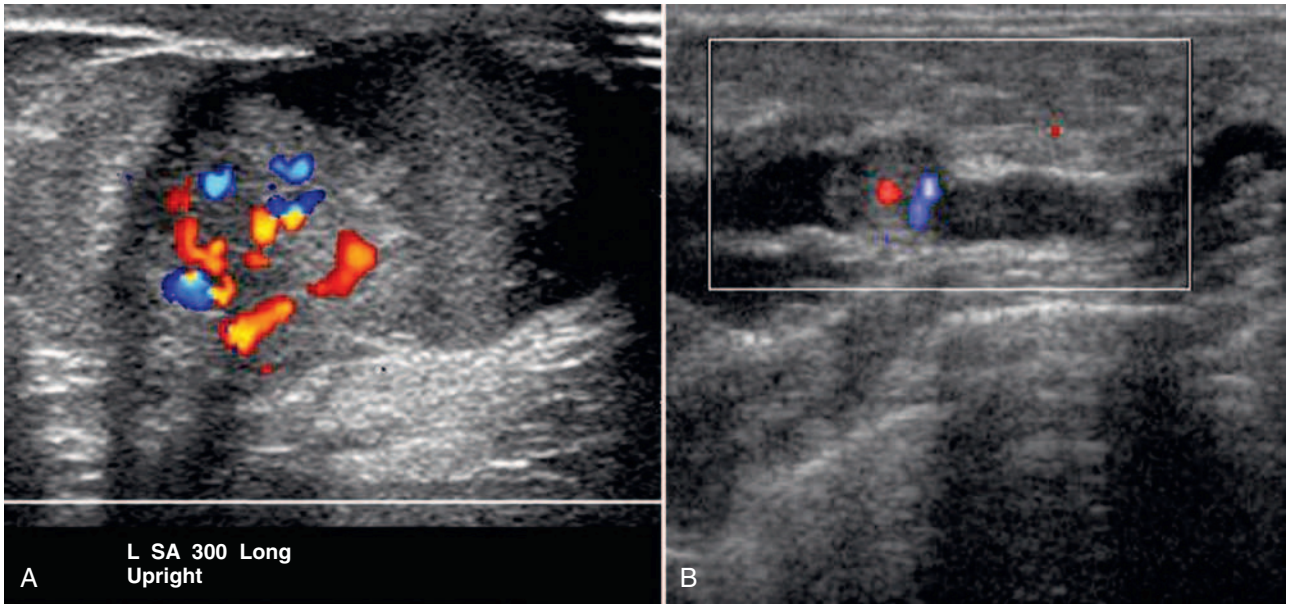

FIG. 21.15 Intracystic Papillary Lesions and Intraductal Papillomas. (A) Malignant lesion fed by multiple vessels. **(B)** Benign intraductal papillomas with a small vascular stalk demonstrable on color Doppler ultrasound.

an internal vessel on color Doppler ultrasound indicates that the lesion is either solid or a cyst completely filled by a papillary lesion (Fig. 21.14). Similarly, Doppler sonography can be useful in distinguishing between an echogenic lipid layer or tumefactive sludge within a cyst and a true intracystic papillary lesion. Intracystic papillary lesions, whether benign or malignant, are among the most vascular lesions of the breast and usually have a prominent vascular stalk that is demonstrable with color or power Doppler sonography (Fig. 21.15A). Benign intracystic papillomas tend to have a single, large feeding vessel within the vascular stalk, whereas malignant intracystic papillary lesions tend to be fed by multiple feeding vessels.

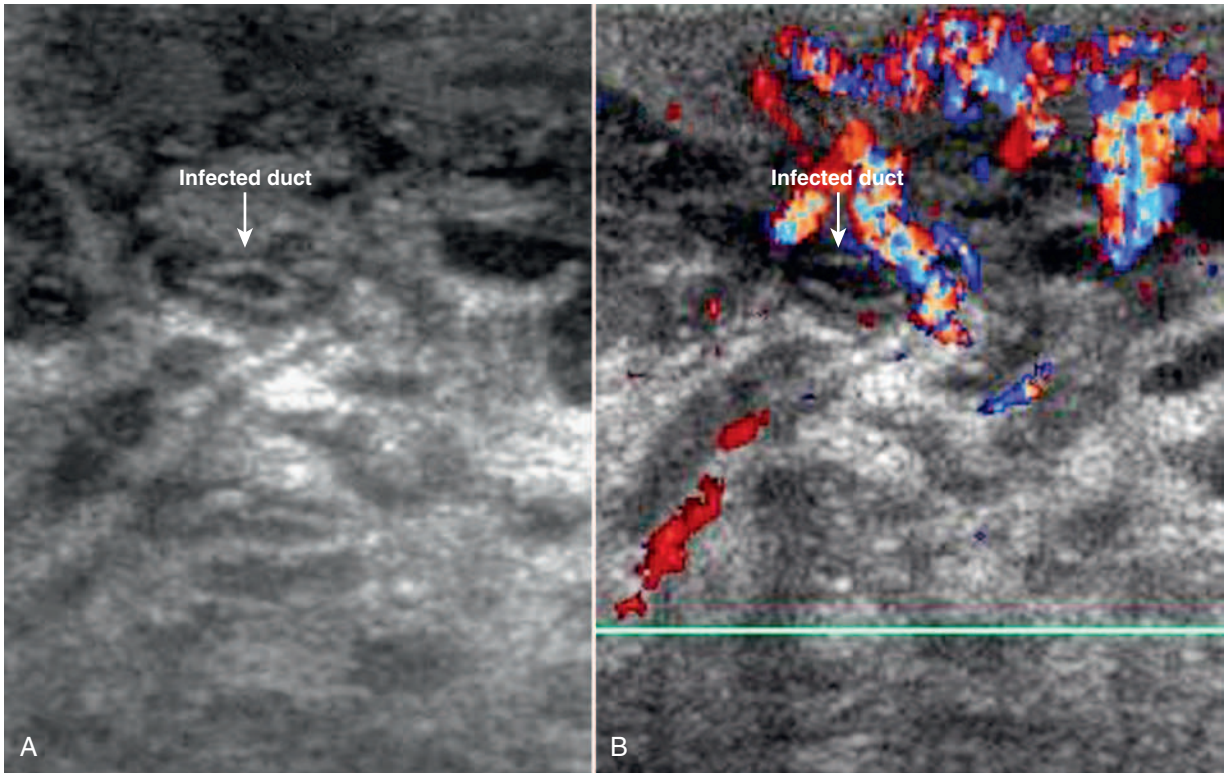

FIG. 21.16 Duct Wall Hyperemia in Acute Periductal Mastitis. (A) Gray-scale image shows uniform isoechoic wall thickening in the inflamed or infected duct *(arrow)*. The noninflamed ectatic duct just to the right has a normal, thin, echogenic wall. **(B)** Color Doppler sonogram shows marked hyperemia of the wall and tissues around the inflamed duct. The vessel is oriented parallel to the wall.

Ectatic ducts, like cysts, often contain echogenic secretions or blood that can be difficult to distinguish from intraductal papillomas or DCIS by gray-scale imaging alone. Ballottement of ectatic ducts that contain diffuse low-level echoes can cause the echoes to slosh back and forth within the duct. This can be appreciated on real-time gray-scale imaging or cine clips and can be documented on color Doppler sonography as well. The secretions tend to move posteriorly during compression and anteriorly during compression release, creating color signals of opposite color. Demonstrating such a "color swoosh" documents that the internal echoes are caused by inspissated secretions or blood rather than tumor. It is important that the color signal fills the duct because echogenic blood from an intraductal papillary lesion can lead to a color swoosh, but the underlying papillary lesion will cause a defect in the color signal. As with intracystic papillary lesions, intraductal papillary lesions are often vascular enough to have a demonstrable vascular stalk on color Doppler sonography (Fig. 21.15B). This helps to identify intraductal papillary lesions and to distinguish them from echogenic lipid or debris layers within the duct.

Doppler may also be useful to evaluate acute breast pain by helping to reveal an acute inflammatory etiology. Acutely **inflamed cysts** and acute **periductal mastitis** are the most common causes for this pain. The normally thin, echogenic wall of an acutely inflamed cyst or duct becomes thick, isoechoic, and hyperemic, which can be easily demonstrated by color or power Doppler ultrasound (Fig. 21.16). In comparison, the walls of noninflamed cysts and ducts have no demonstrable flow on color Doppler sonography. The direction in which the vessels course within the walls of inflamed cysts and ducts differs from the orientation of vessels that feed intracystic or intraductal papillary lesions. Vessels that lie within the walls of inflamed ducts or within the periductal tissues course *parallel* to the duct wall because they are feeding and draining the duct wall and periductal tissues. Vessels that feed intraductal papillary lesions are oriented *perpendicular* to the axis of the duct wall because the vessels are merely passing through the wall to feed a lesion inside the duct. Doppler ultrasound and other imaging findings in acutely inflamed or infected peri-implant capsules are similar to those in acutely inflamed cysts or ducts.

Doppler sonography can be helpful in assessing **lymph nodes** that are not normal but have nonspecific imaging findings that prevent determination of whether the node is merely inflamed or contains metastasis. The histologic and biologic behavior of lymph node metastases is usually identical to that of the primary lesion. A vascular primary tumor will tend to have a vascular lymph node metastasis. If the spectral waveforms obtained from the center of the primary are high impedance and have high and sharp systolic peaks, the waveforms obtained from lymph node metastases from that primary will have similar waveforms. Conversely, inflamed or reactive lymph nodes will usually have low-impedance waveforms with low, rounded systolic peaks. The

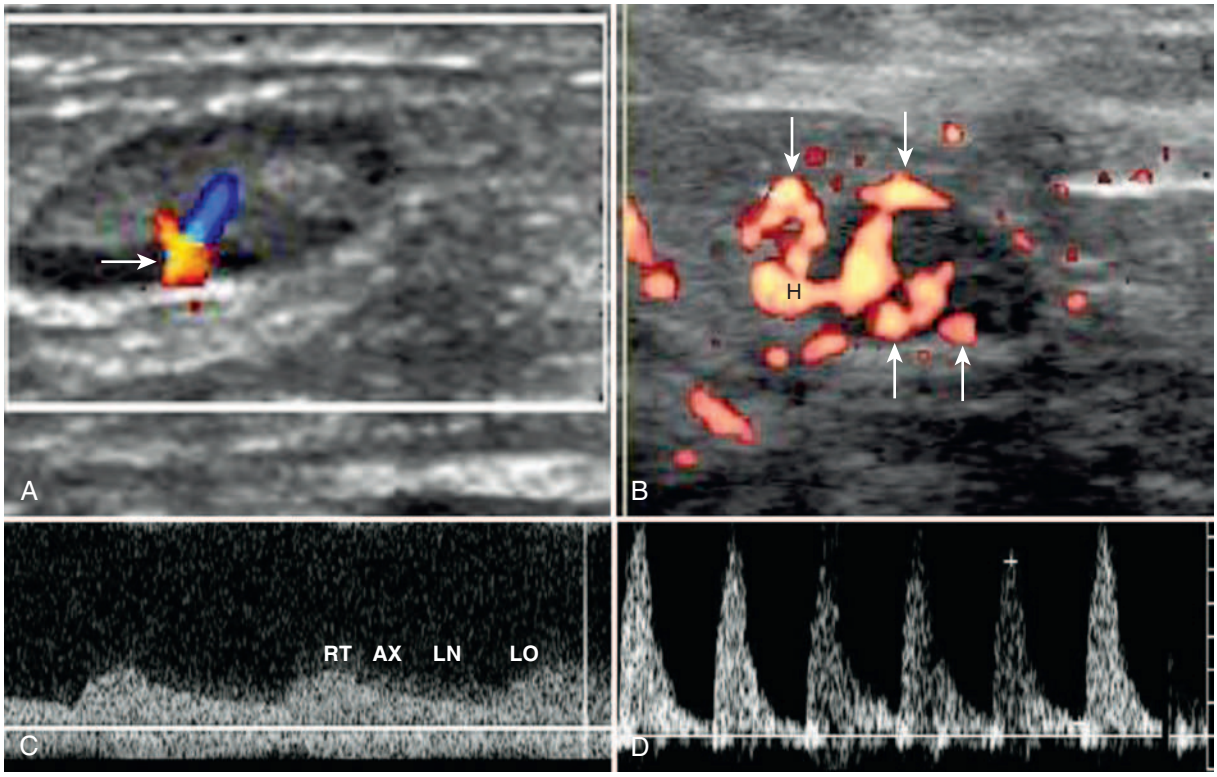

FIG. 21.17 Color Doppler Flow Patterns and Special Waveforms Help Distinguish Between Metastatic and Inflammatory Etiologies of Mild Lymphadenopathy. (A) Benign reactive lymph node is usually fed by a single hilar artery *(arrow).* **(B)** Lymph nodes that bear metastasis often develop transcapsular feeding vessels *(arrows)* in addition to having a normal hilar artery *(H).* **(C)** Pulsed Doppler spectral waveforms obtained from benign reactive nodes tend to have low resistive index (RI) and low peak systolic velocity (PSV) with rounded systolic peaks. **(D)** Waveforms obtained from metastasis-bearing lymph nodes tend to have high RI, high PSV, and sharp systolic peaks.

pattern of blood vessels within lymph nodes can also be helpful. Inflamed or reactive lymph nodes tend to be fed by a single hilar artery that arborizes to various degrees within the mediastinum of the lymph nodes (Fig. 21.17A). Well-differentiated and low-grade lymphomas can have a similar pattern. Metastases to lymph nodes can stimulate development of transcapsular tumor neovascularity (Fig. 21.17B).

Doppler sonography can also be useful for diagnosing vascular conditions such as **arteriovenous malformations, arteriovenous fistulas, venous malformations,** and **superficial venous thrombosis (Mondor disease).** Along these lines, Doppler can help identify blood vessels that should be avoided during interventional procedures.

When assessing blood flow in the breast, it is critical to use exceedingly light compression. Tumor vessels have no muscle or elastic to prop them open and are very soft. The transducer is hard, the chest wall is firm, and even the weight of the sonographer's arm on the transducer can compress a lesion between the probe and chest wall enough to decrease or even completely ablate flow within breast lesions (Fig. 21.18; see Videos 21.1 and 21.2). As a result, Doppler sonography must be performed with such light scan pressure that the transducer barely contacts the skin. In some cases, using a standoff of acoustic gel may be necessary so that Doppler ultrasound–detectable blood flow will not be affected.

Elastography

Elastography is a technique that uses the lesion's stiffness to inform the likelihood of malignancy. This phenomenon is captured quantitatively by Young's modulus, which measures stiffness, wherein E (elasticity) = stress/strain. Stress is the force that is applied to the mass during the imaging evaluation and strain is the amount of tissue displacement that occurs in response to this force. A less compressible mass has a higher Young's modulus and a greater likelihood of malignancy. There are two methods of performing elastography: strain and shear wave. **Strain elastography** requires the operator to provide gentle repetitive compression to the breast tissue either via repetitive motion or using the patient's own breathing or heartbeat. The strain of the tissue is measured through longitudinal displacement of the tissue before and after compression. Because the delivered force is variable, Young's modulus cannot be calculated. The result is predominantly qualitative information. The strain of the mass and surrounding normal tissue can be compared to create a strain ratio (Fig. 21.19). **Shear wave elastography** employs a force automatically applied by the transducer to the targeted mass, making it less operator dependent. Horizontal shear waves are then produced at variable speeds based on the mass's hardness, and the elasticity of the mass can be calculated.[24,25]

Stiffness measures for both strain and shear wave elastography are typically color-coded for quick interpretation. Although red

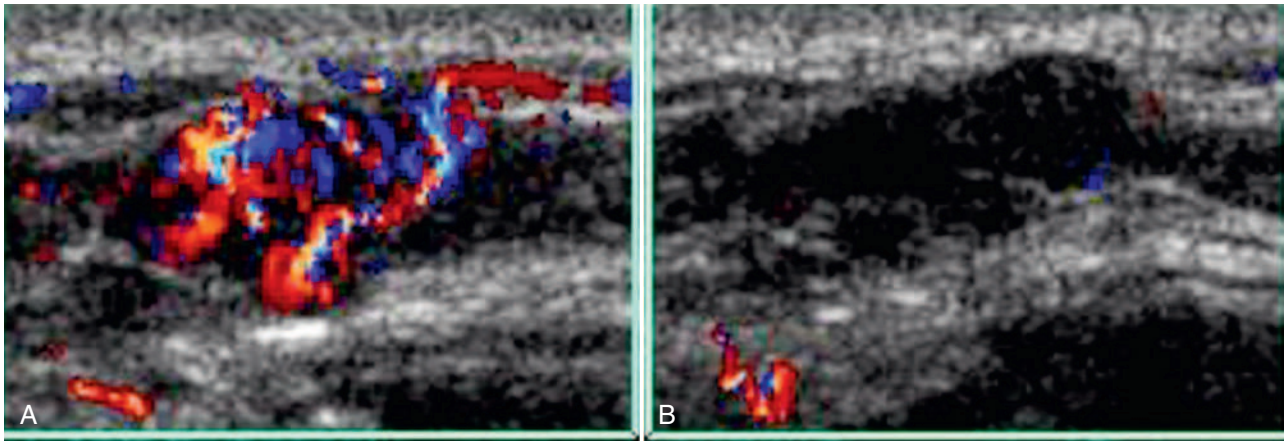

FIG. 21.18 Importance of Light Pressure for Color Doppler Examination. (A) Micropapillary ductal carcinoma in situ lesion appears exceedingly hypervascular when scanned with light pressure. **(B)** Lesion appears avascular when just the weight of the scanning arm is allowed to rest on the transducer during scanning.

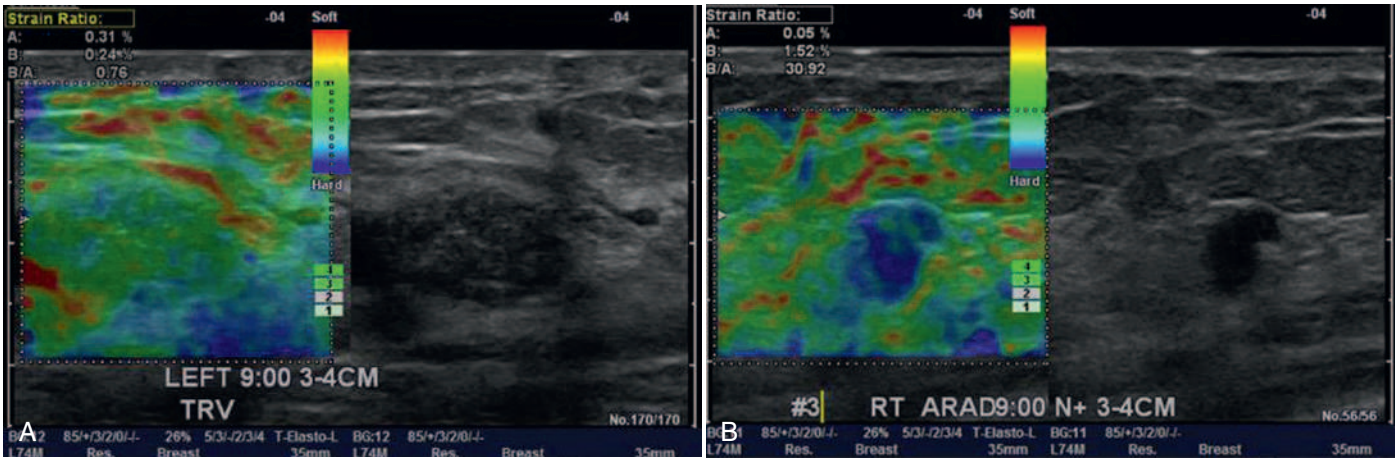

FIG. 21.19 Elastography Depicts Benign and Malignant Masses. (A) A benign-appearing hypoechoic macrolobulated mass has a strain value, which is similar to the strain value of the surrounding tissue. The ratio is therefore close to 1. **(B)** An irregular, spiculated, not parallel mass has a lower strain value as compared with surrounding tissue, consistent with malignancy. (Courtesy of Sughra Raza, MD.)

typically indicates increased stiffness and increased likelihood of malignancy and blue indicates less stiffness and increased likelihood of benignity, these color conventions have not been standardized. Elastography features including shape, size, heterogeneity, and stiffness all complement the features obtained during routine diagnostic ultrasound imaging. Quantitative values have also been advocated for improved standardization. Studies have shown that elastography can be helpful to improve specificity of diagnostic imaging and to identify more advanced malignancies.[26-29]

Limitations of elastography primarily relate to the lack of standardization of technique and implementation across vendors. Grading schemes,[30,31] quantification of signal,[28] and color-coding of lesions vary.[24,27] In addition, these techniques are based on compression, which can vary by user and, in turn, can affect elasticity measures.

Three-Dimensional Ultrasound

Three-dimensional (3-D) ultrasound captures volumetric information about breast lesions so they can be viewed in sagittal, coronal, and transverse planes. This is being studied with both hand-held and automated breast ultrasound methods to determine its added value above conventional ultrasound. Initially, 3-D ultrasound was not shown to be superior to conventional ultrasound[32,33]; however, more recent studies suggest that 3-D ultrasound may help with identifying cancer.[34]

Contrast-Enhanced Ultrasound

New vascular networks are created as malignant tumors grow. Doppler ultrasound is currently used to capture these areas of neovascularity. However, Doppler has not been shown to be sufficiently accurate in its ability to differentiate malignant from benign masses. As a result, contrast-enhanced ultrasound has

TABLE 21.1 Breast Imaging Reporting and Data System (BI-RADS) Categories[43]

BI-RADS Category	Description and Examples	Risk of Malignancy	Recommended Follow-Up
0	Incomplete examination; additional imaging is necessary to evaluate the finding or area of clinical concern		
1	Sonographically normal tissues that cause mammographic or clinical abnormalities	0%	Routine screening[a]
2	Benign entities: includes intramammary lymph nodes, ectatic ducts, all simple and some complicated cysts (milk of calcium), and definitively benign solid nodules, such as lipomas and hamartomas	0%	Routine screening[a]
3	"Probably benign" complicated and complex cystic and solid masses, some small intraductal masses possibly representing debris or papilloma, and a subset of fibroadenomas	≤2%	Short-interval follow-up recommendation with either mammography or ultrasound, typically 6 months[a]
4a	Mildly suspicious	>2-10%	Histologic sampling either with percutaneous biopsy or surgical excision
4b	Moderately suspicious	>10%-≤50%	
4c	Highly suspicious	>50%-<95%	
5	Very highly suspicious	≥95%	
6	Known malignancy		

[a]In the above BI-RADS description, should the patient have a palpable abnormality or other clinical finding and be rated as BI-RADS 1 or 2, the patient should also have a clinical follow-up in 6 weeks to 3 months to ensure that the clinical finding has not changed. If BI-RADS 3 characterization is associated with a stable lesion at first follow-up, then an additional 6-month follow-up is recommended. After 1 year of stability, an additional 1 year, and possibly 2 years, of imaging follow-up may be performed.

been increasingly used to better identify masses associated with neovascularity that more likely represent malignancy.[35-40] Additional studies have evaluated whether contrast-enhanced ultrasound can identify sentinel lymph nodes during the preoperative evaluation[41] and tumor response to chemotherapy.[42]

REPORTING

The ACR **Breast Imaging Reporting and Data System (BI-RADS)** was initially developed for mammography but has similar categories and descriptors for ultrasound[18] to standardize reporting and data. BI-RADS has developed a standardized lexicon for describing findings seen on ultrasound in addition to a system for classifying these findings and their probability of malignancy.[17] The BI-RADS assessment categories for classification of findings range from BI-RADS 0 through BI-RADS 6 (Table 21.1).

SONOGRAPHIC FINDINGS

When evaluating the breast by ultrasound, it is important to adhere to the BI-RADS descriptors of sonographic findings because they provide a standard lexicon for communicating results. In this section, we review common imaging findings and how to describe them according to the most recent edition of the ACR BI-RADS Atlas.[18]

The sonographic findings that correlate with mammographic abnormalities or areas of clinical concern can fall into several different categories: (1) ANDIs, (2) cysts, (3) solid masses, and (4) indeterminate (cystic vs. solid) lesions.

Normal Tissues and Variations

Normal breast tissues and variations of normal tissues, including duct ectasia, FCC, and benign proliferative disorders, can cause both mammographic and sonographic abnormalities. These changes have been termed "ANDIs" (aberrations of normal development and involution). ANDIs can appear sonographically not only as normal tissues but as cysts and solid nodules, accounting for some false-positive results at biopsy. Most sonographically normal tissues can be characterized as BI-RADS 1. That being said, ANDIs can cause a spectrum of abnormalities that can be characterized as BI-RADS 2, 3, or 4.[44]

Cysts and Cystic Masses

Simple Cysts

Simple cysts are anechoic, round or oval, and surrounded completely by a thin, echogenic wall or capsule with enhanced sound transmission and thin-edge shadows (Fig. 21.20, Video 21.3). They form from dilation of the acini in the TDLU. When multiple acini dilate, they can form a group of small microcysts. They can then coalesce together to form a solitary cyst. Cysts that meet strict criteria for being simple are "definitively benign" and do not require further follow-up. Aspiration of simple cysts is generally reserved for relief of pain and tenderness in very tense simple cysts.

Demonstrating that a benign simple cyst causes a palpable lump or mammographic nodule is by far the most valuable finding demonstrable on sonography because the negative predictive value is 100%.[45]

FIG. 21.20 Simple Cysts. Simple cysts are anechoic and have enhanced sound transmission, well-circumscribed borders, thin-edge shadows, and thin, echogenic walls. They are benign (Breast Imaging Reporting and Data System [BI-RADS] 2) and require no aspiration or follow-up. See also Video 21.3.

Complicated Cysts

Complicated cysts are cysts that contain debris. This manifests as echogenic fluid, fluid-debris levels, or fat-fluid levels without a solid vascular component. Cellular debris, epithelial cells, blood, proteinaceous material, and pus can all contribute to the appearance of low-level echoes within a complicated cyst. Complicated cysts are generally benign as part of the broad spectrum of benign **fibrocystic change,** but have a low risk of containing papillomas or carcinomas[46] and are therefore often classified as BI-RADS 3, for which follow-up is recommended.

There are some instances in which complicated cysts can be characterized as BI-RADS 2. This is the case when the complicated cyst can confidently be characterized as a specific benign lesion such as a galactocele (which is a cyst that contains milk and often demonstrates a fat-fluid level on ultrasound) or a cyst of skin origin such as an epidermal inclusion cyst.

Cysts can contain particles suspended in fluid that are so light that they can be moved by the energy of the B-mode imaging or color or power Doppler ultrasound beam. Such particles are subcellular in size and are often seen with uncomplicated FCC. In general, high-transmit power settings are necessary to cause such particles to move during real-time B-mode imaging. However, the energy of the color or power Doppler ultrasound beam is high enough to cause these particles to move at even default low-power settings, creating what has been termed **"color streaking."** Particles are forced posteriorly by the energy of the Doppler ultrasound beam, creating vertically oriented color streaks within the cyst as they move (Fig. 21.21). The particles that cause color streaking have been shown to be cholesterol crystals, which can be seen on cytologic evaluation as birefractive crystals when viewed with polarized light.

Milk of calcium is a BI-RADS 2 mammographic finding that has been directly applied to sonography. Milk of calcium is a collection of tiny calculi within the lumen of a cyst. Such calculi are very common in benign FCC and can be demonstrated definitively on horizontal beam mammographic films. Sonography can prove the presence of milk of calcium by demonstrating that the calcifications move within the cyst to new dependent positions created by lateral decubitus or upright positioning of the patient (Fig. 21.22). Although mammography can generally show smaller and more numerous calcifications, sonography has one advantage over mammography in demonstrating milk of calcium. Mammography requires dozens of small calcifications before the classic "teacup" appearance can be shown on horizontal beam films, whereas sonography can definitively demonstrate a single mobile calculus in a cyst (Fig. 21.23). Thus, although less sensitive than mammography for calcifications, sonography can be more specific than mammography for milk of calcium. This is particularly true when mammography shows a nonspecific cluster of punctate microcalcifications that might require biopsy, but sonography shows benign clustered microcysts, each containing one or more tiny calculi (Fig. 21.24).

Fat-fluid levels within cysts are definitively benign mammographic findings that have been directly applied to ultrasound. Fat-fluid levels are rarely demonstrated on mammography, and usually only within classic **galactoceles,** but are much more frequently demonstrated by sonography. The lipid layer appears echogenic compared with cyst fluid and floats on the fluid in the nondependent portion of the cyst. The lipid layer moves within the cyst to a new nondependent position with change in the patient's position from supine to lateral decubitus or upright (Fig. 21.25). As with tumefactive sludge, lipid layers tend to shift very slowly within a cyst when the patient's position is changed, requiring up to 5 minutes to document the shift of a fat-fluid level. During the shift in position, the shape of the interface between the lipid and fluid layers changes and is usually obliquely oriented with respect to the tabletop and has a sigmoid shape. The oblique orientation of the interface in combination with the sigmoid shape is characteristic of a fat-fluid level in the process of equilibrating to a new position and may represent a shortcut to waiting 5 minutes for the fat-fluid level to shift. Power Doppler ultrasound **fremitus** can also be used to distinguish a mural nodule from a fat-fluid level.[47] The lipid layer is not attached to the cyst wall, so the fremitus artifact will not pass through it. On the other hand, true papillary lesions that are attached to the cyst wall will vibrate and transmit the fremitus artifact on power Doppler; having the patient hum in a deep voice creates an orange artifact on power Doppler ultrasound (Fig. 21.26).

Lipid cysts or oil cysts are definitively benign mammographic findings. Unfortunately, lipid cysts usually appear more definitively benign on mammography than sonography. Most lipid cysts lack enhanced sound transmission and may actually have posterior shadowing due to calcified walls. Most have some additional suspicious features on sonography, such as (1) mural nodules; (2) thick septations; (3) thick walls; and (4) fluid debris levels (Fig. 21.27). This should not be surprising because most lipid

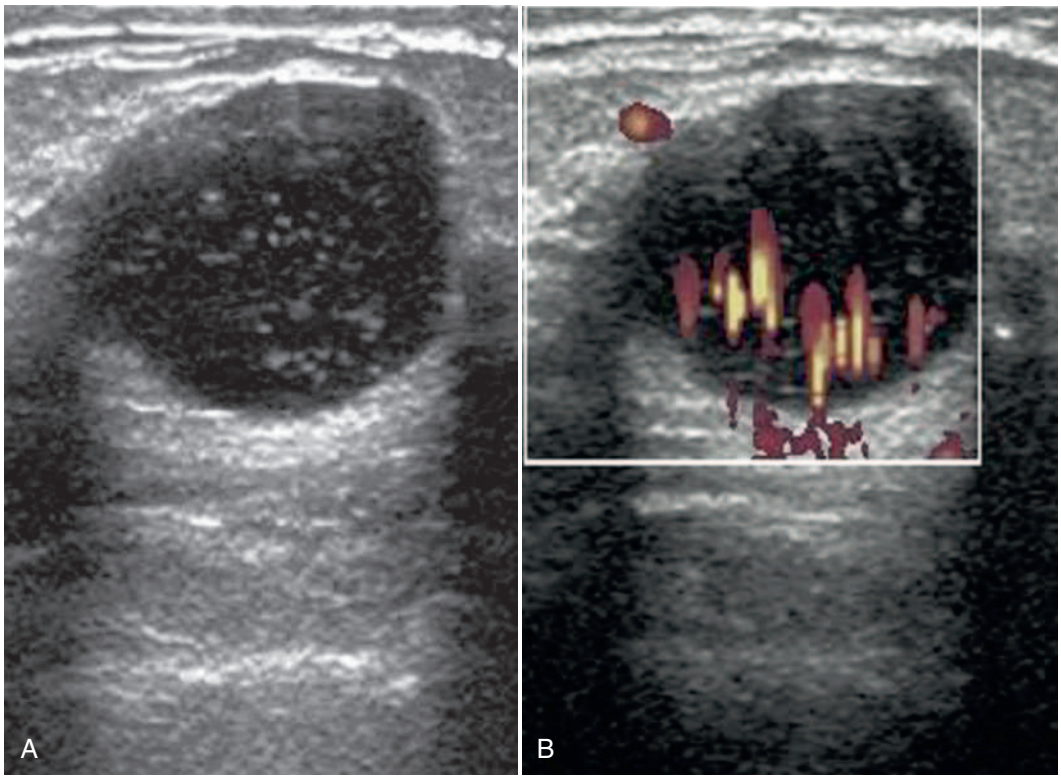

FIG. 21.21 Cyst With Scintillating Echoes and Color Streaking. (A) This complicated cyst contains floating punctate echoes that move posteriorly while being scanned, creating a scintillating appearance on gray-scale sonography. **(B)** Power Doppler ultrasound pushes the echoes posteriorly faster and with more energy than does the gray-scale beam. The echoes move fast enough that color persistence creates the appearance of "color streaking," an artifact that should not be confused with blood flow.

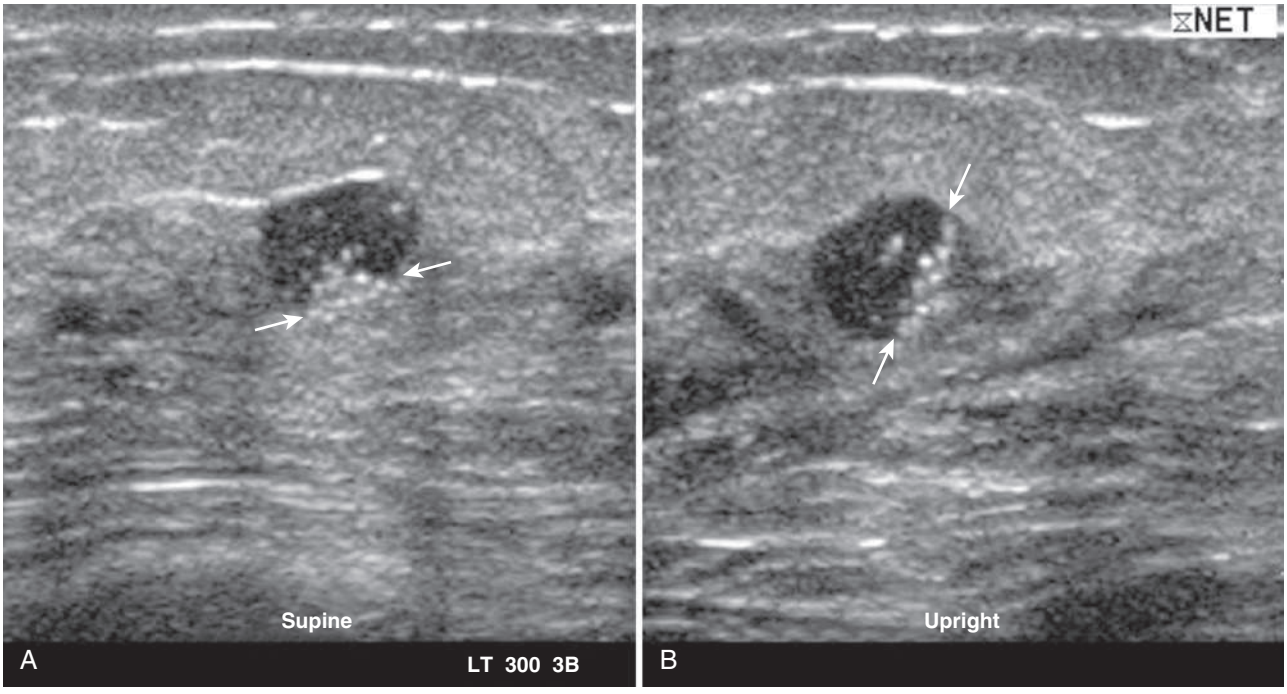

FIG. 21.22 Milk of Calcium. Milk of calcium is actually a dependent layer of tiny calculi *(between arrows)* within a breast cyst that moves when the patient changes position. **(A)** The calculi lie along the dependent posterior wall in the supine position. **(B)** The calculi fall to the dependent inferior position when the patient is in the upright position and scanned in the longitudinal plane.

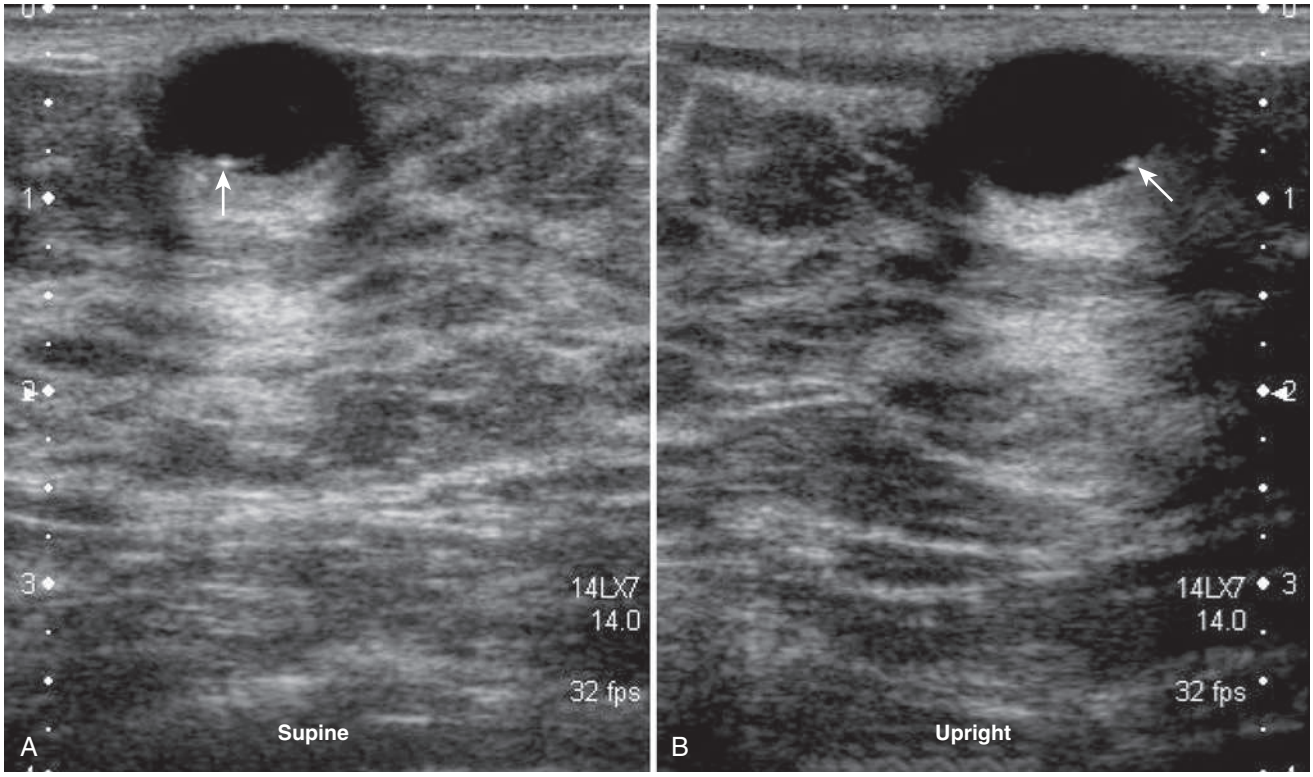

FIG. 21.23 Milk of Calcium Appearing as Single Calculus Within Cyst. (A) Sonogram shows a single stone *(arrow)* lying on the posterior wall of cyst in the supine position. **(B)** Stone falls to the dependent inferior wall of the cyst *(arrow)* when the patient is upright and the cyst is scanned in the longitudinal plane.

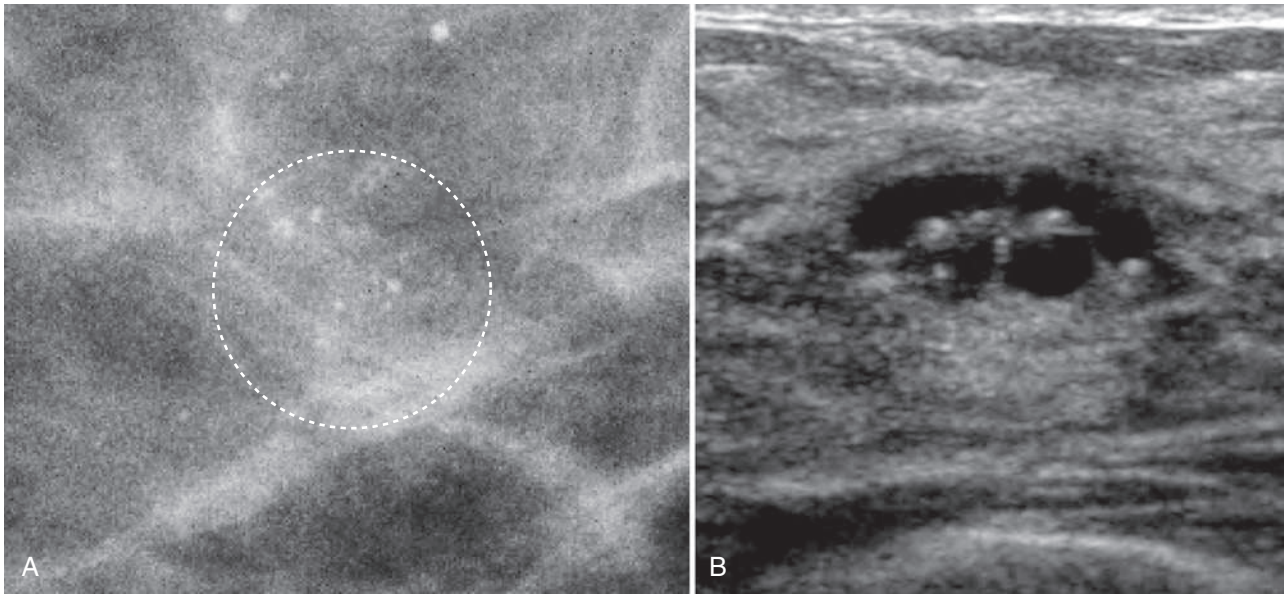

FIG. 21.24 Milk of Calcium Within Clustered Microcysts. (A) Mammogram shows a nonspecific cluster of punctate and granular calcifications indicated by *dashed circle*. **(B)** Sonography shows a cluster of microcysts (avascular on color Doppler), many of which contain single dependent calculi, that is definitively benign.

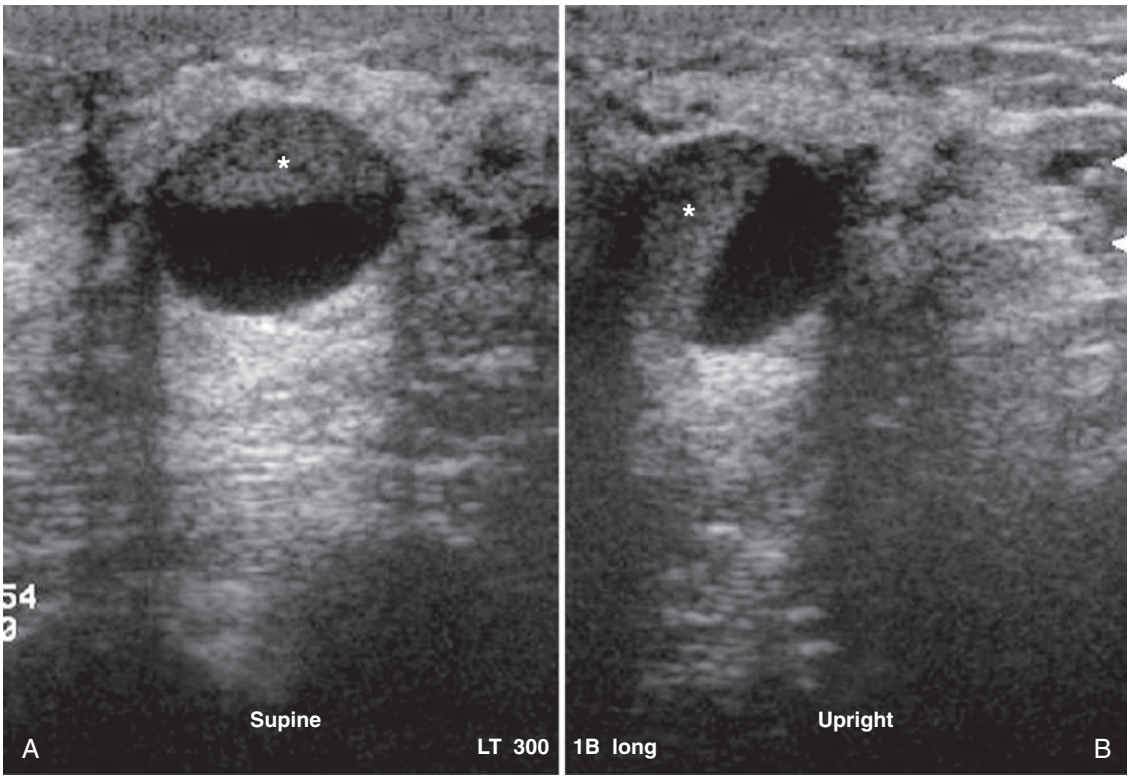

FIG. 21.25 Fat-Fluid Level. The lipid layer is echogenic compared with cyst fluid and moves within the cyst to its nondependent part when the patient changes position. **(A)** The echogenic lipid layer (*) floats to the nondependent anterior wall of the cyst, and the interface is oriented horizontally when the patient is scanned in the supine position. **(B)** The echogenic lipid layer has floated to the new nondependent superior wall, and the interface is oriented vertically when the patient is in the upright position and the cyst is scanned longitudinally.

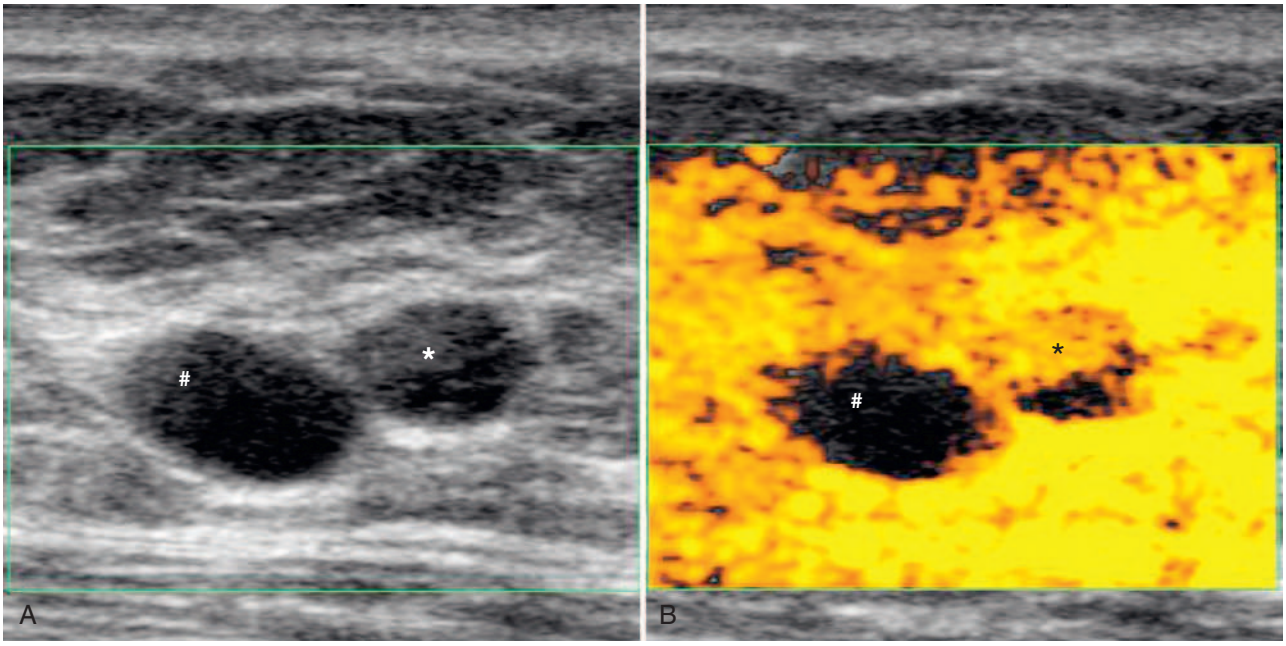

FIG. 21.26 Acorn Cysts of Two Different Types. (A) Sonogram shows two cysts that have crescentic echogenic thickening along the anterior wall, resembling the caps on acorns. The echogenic material in the left acorn cyst (#) is floating lipid debris, whereas the echogenic material along the anterior wall of the right acorn cyst (*) is **papillary apocrine metaplasia** (PAM). Unfortunately, the distinction cannot be made from a single image obtained in the supine position. Changing position can help but often takes 5 minutes; with power Doppler vocal fremitus, the distinction can be made virtually instantly. Having the patient hum in a deep voice creates an orange artifact on power Doppler in normal breast tissues and within any mural nodules or thick septations that are attached to the wall of the cyst, but not within unattached debris. **(B)** Power Doppler ultrasound image shows that the vocal fremitus artifact does not fill the echoes caused by the unattached debris level in the left acorn cyst (#) but does fill the attached echogenic PAM (*) within the right acorn cyst.

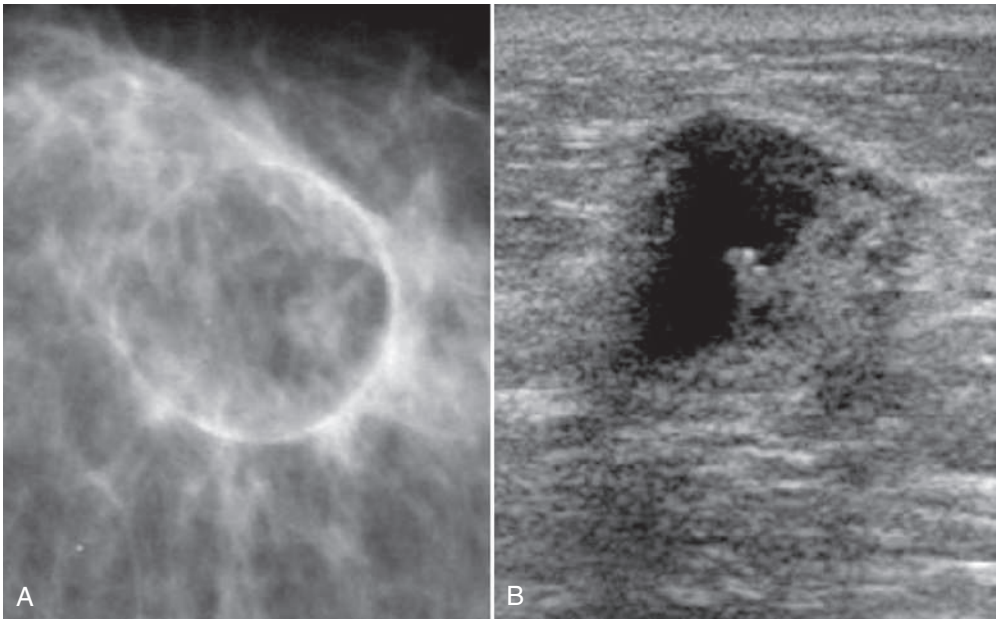

FIG. 21.27 Lipid Cyst. Mammographic spot compression views can more accurately characterize lipid cysts than sonography. On ultrasound images, **(A)** lesions that appear to be classic benign lipid cysts on mammography often have suspicious features, such as **(B)** thick irregular wall, thick isoechoic septations, and mural nodules. These sonographically suspicious features are typical of chronic hematomas, from which most lipid cysts arise.

cysts originate in chronic seromas or hematomas, which often manifest such findings. However, the suspicious sonographic findings in lipid cysts are avascular, unlike those in cysts containing true papillary lesions. Nevertheless, lipid cysts frequently appear more worrisome sonographically than on spot compression mammograms. Thus, when sonographic and mammographic findings are discordant, we rely more on the mammographic findings in this subset of patients, unless color Doppler ultrasound shows internal vascularity.

Eggshell calcifications are benign mammographic findings that have been applied directly to sonography. In general, eggshell calcifications are so definitively benign on mammography that they do not require sonographic assessment (Fig. 21.28A-B). Occasionally they will be seen on sonography in a patient who has not had mammography or for whom the mammograms are not available. Punctate calcifications that occur within the normal thin, echogenic cyst wall represent incomplete eggshell calcifications and therefore can be considered BI-RADS 2 sonographic findings (Fig. 21.28C). In such cases the sonographic findings are more definitively benign than the mammographic findings. Calcifications that are suspended within the lumen of a cyst cannot be characterized as BI-RADS 2. In most cases they occur with **papillary apocrine metaplasia** (PAM), but they can also occur in DCIS (Fig. 21.28D).

Clustered macrocysts are identical to thinly septated cysts (Fig. 21.29). The septations represent the residual walls of individual, cystically dilated ductules within an individual TDLU. Each cystically dilated ductule can be thought of as a simple cyst; a thinly septated cyst is typically a cluster of simple cysts, each having BI-RADS 2 characteristics.

Cysts of skin origin are benign and usually represent **sebaceous cysts** or **epidermal inclusion cysts.** Sebaceous cysts have three typical appearances: (1) a complex or solid-appearing lesion that lies entirely within the skin (Fig. 21.30); (2) a complicated cyst that lies mainly within the subcutaneous tissues but has clawlike hyperechoic skin wrapped around it (Fig. 21.30B); and (3) a lesion that lies entirely within the subcutaneous fat but has an associated, abnormally hypoechoic, thickened inflamed gland neck that courses through the skin (Fig. 21.30C). The gland neck is obliquely oriented and is often better demonstrated by heeling or toeing the transducer to change the angle of incidence. Because cysts of skin origin are so superficial in location, optimal demonstration of one of these three patterns usually requires that an acoustic standoff be used.

Foam cysts are cysts whose lumens are completely filled with low-level echoes (Fig. 21.31A). Other names include **gel cysts** and **inspissated cysts.** The foam cyst appearance can actually represent a spectrum of lesions, from those completely filled with PAM to those that contain only echogenic proteinaceous debris or lipid material.[48] Others may contain mixtures of PAM and proteinaceous or fatty debris. These lesions have sonographic features that overlap with those of fibroadenomas, and in about 3% of cases it is not possible to determine with certainty whether the lesion is cystic or solid. In this scenario, the clinician should characterize the mass using BI-RADS descriptors and make a recommendation based on the most suspicious finding. If the sonographic features suggest a low probability for malignancy, this mass—whether cystic with low-level echoes or solid—can be followed and classified as BI-RADS 3. Otherwise, sampling should be performed. Aspiration may be attempted first, followed by core biopsy if unsuccessful. When the internal echoes are all caused by PAM, the lesion cannot be aspirated. When the lesion is filled with proteinaceous or fatty debris, it can be completely aspirated. If partially filled with PAM, the lesion will be only partially aspirated. In this case, core biopsy of the residual material or additional short-term follow-up is recommended.

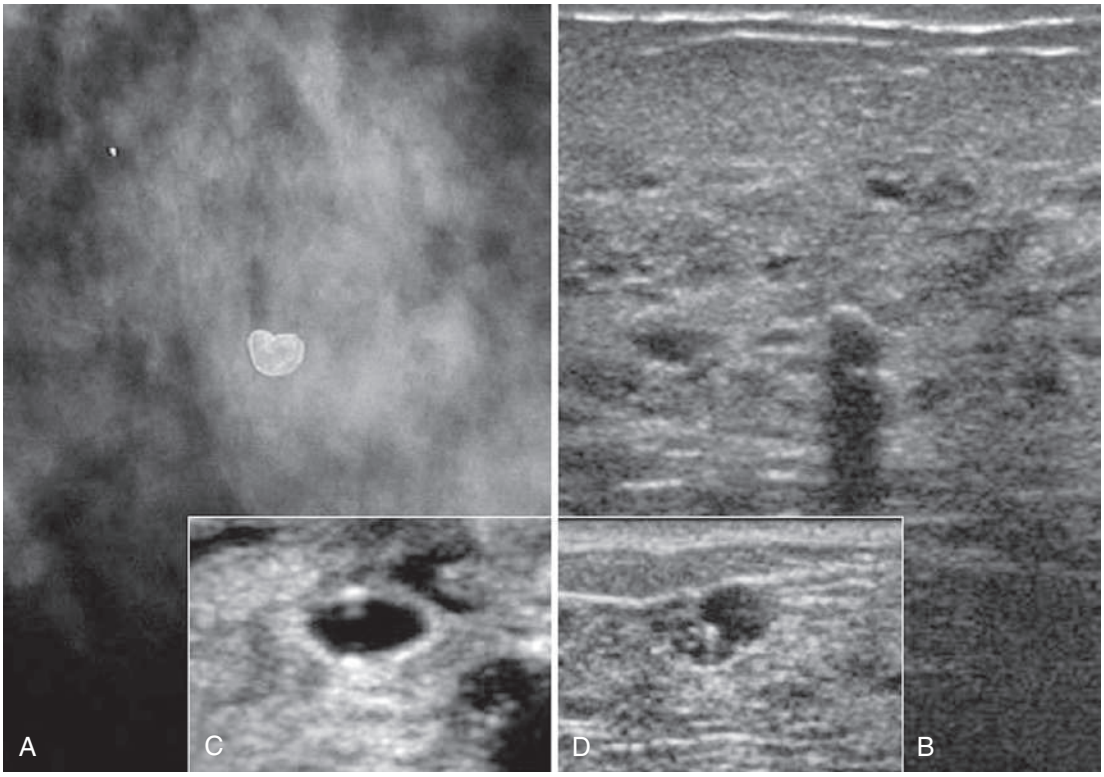

FIG. 21.28 Eggshell Calcification. (A) Eggshell calcifications are mammographic findings that are definitively benign. **(B)** Dense eggshell calcifications cause acoustic shadowing on ultrasound. **(C)** Punctate calcifications confined to the thin echogenic cysts walls can be thought of as incomplete eggshell calcifications and therefore are benign. **(D)** Nondependent and nonmobile punctate calcifications within the interior of the cyst are nonspecific and can be associated with papillary apocrine metaplasia (PAM) or ductal carcinoma in situ (DCIS).

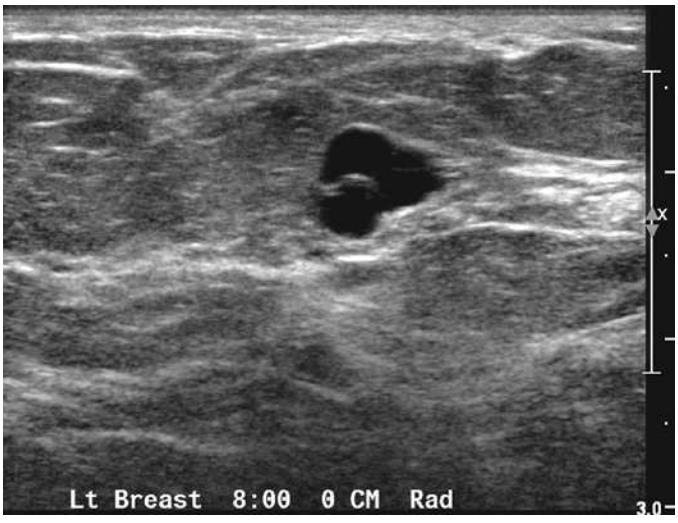

FIG. 21.29 Clustered Macrocysts. Thin, echogenic septations within cysts are not suspicious. Such septations represent residual walls of cystically dilated acini within a single terminal ductolobular unit (TDLU) and can be thought of as clusters of simple cysts.

Acorn cysts have a crescentic, eccentrically thickened wall caused by PAM that does not completely fill the cyst (see Fig. 21.31B). Unlike the echogenic crescent within cysts that contain fat-fluid levels, the echogenic crescent caused by PAM does not shift within the cyst when the patient changes position, regardless of duration (see Fig. 21.31C and D). In these cases the normal, thin, echogenic outer cyst wall is preserved along the entire thickened wall, and there is no vascular stalk (see Fig. 21.31E). It is important to confirm that none of the internal components is vascular or solid because this may be suggestive of a complex cystic and solid mass rather than an acorn cyst (see next section). If there is any question as to whether this represents a true mural nodule, biopsy should be performed. If no suspicious features are identified, then this can be followed and classified as BI-RADS 3.

The algorithm used for evaluation of nonsimple cysts has been derived from the mammographic and solid nodule algorithms. The BI-RADS lexicon should be used to characterize the mass. The presence of even a single suspicious finding requires exclusion from the BI-RADS 2 category, and possibly the BI-RADS 3 category. Although every effort should be made to characterize as many nonsimple cysts as BI-RADS 2 as possible, they must meet strict criteria before they can be characterized as such.

Complex Cystic and Solid Masses

Complex cystic and solid masses contain both solid and cystic components. They may have thick and irregular walls, mural nodules, thick septations, and internal blood flow (Fig. 21.32). These complex masses are at increased risk of containing papillomas or carcinomas such as DCIS, papillary carcinoma, or infiltrating ductal carcinoma, with or without necrosis. Since it is not always easy to determine whether the internal material is

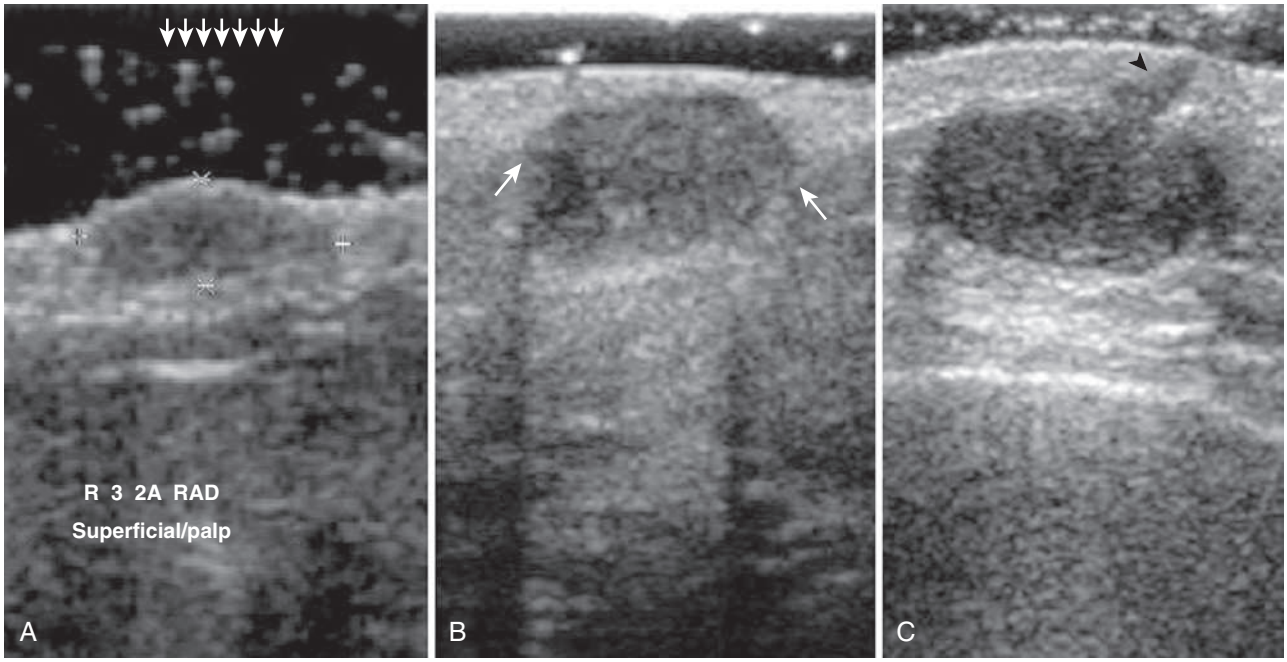

FIG. 21.30 Benign Sebaceous Skin Cysts. (A) Sebaceous cyst is entirely within the skin *(calipers)*. Extra gel has been used as a stand off pad for scanning *(arrows)*. **(B)** Cyst is primarily within the subcutaneous fat, but a thin "claw sign" of echogenic skin *(arrows)* can be shown to wrap around the cyst, confirming that it originates within the skin. **(C)** Cyst is entirely within the subcutaneous fat, but a dilated and obstructed gland neck can be seen coursing obliquely through the skin *(arrowhead)*. A standoff of acoustic gel is necessary to see these lesions. To show the obliquely oriented hair follicle, heeling or toeing of the transducer may be necessary.

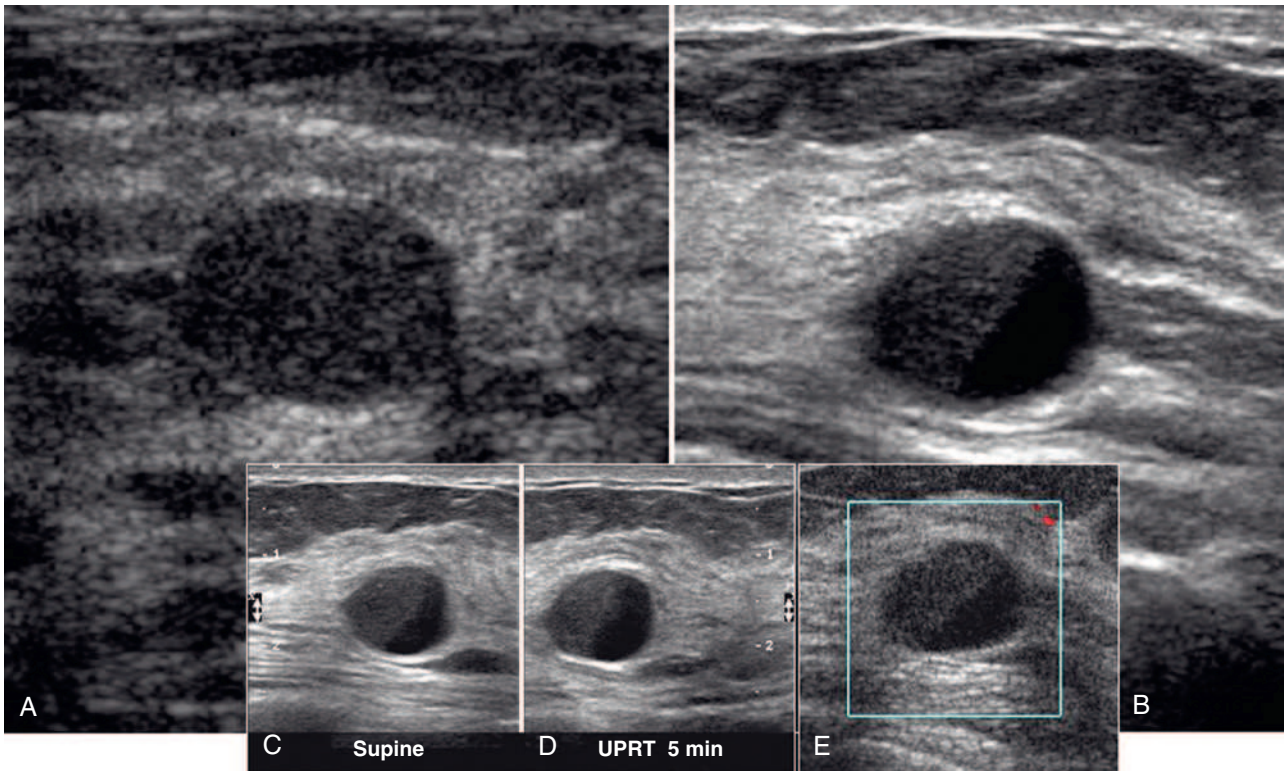

FIG. 21.31 Foam and Acorn Cysts. (A) Foam cysts are filled with diffuse low-level echoes and can be difficult to distinguish from solid nodules. Foam cysts have also been called **inspissated cysts, gel cysts,** and **mucoceles. (B)** Acorn cysts have an echogenic concave rim of **papillary apocrine metaplasia** (PAM) that appears similar to the cap on an acorn. Unlike similar-appearing lipid layers within cysts that have fat-fluid levels, the position of the PAM does not change from the supine **(C)** to the upright **(D)** or left lateral decubitus position. **(E)** Color Doppler ultrasound image shows that, unlike intracystic papillomas or carcinomas, PAM rarely has a demonstrable vascularity.

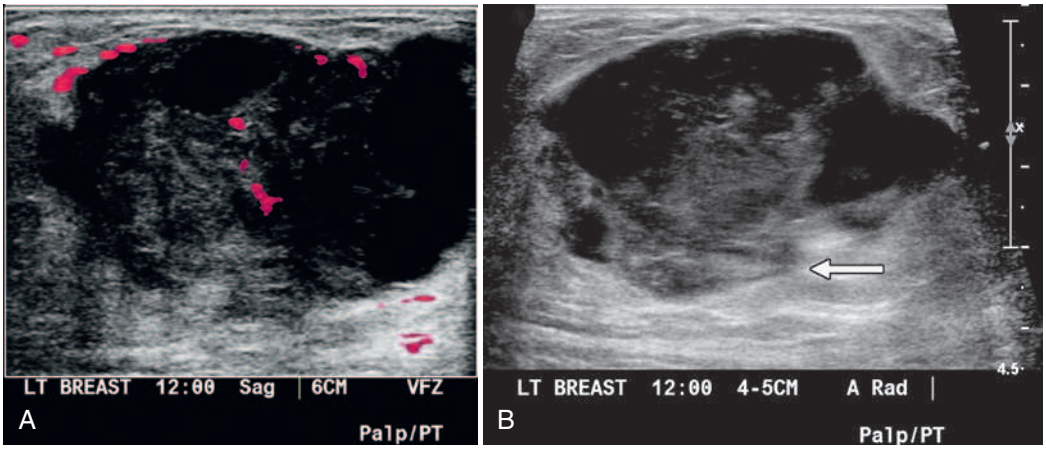

FIG. 21.32 Complex Cystic and Solid Mass. (A) This mass has both solid and cystic components. Color Doppler demonstrates that the thick internal septations are highly vascular, suggesting they represent solid material rather than internal debris, increasing the probability of malignancy. **(B)** Also note the extension of the solid component beyond the margin of the mass *(arrow),* most consistent with a malignant process.

solid or thick fluid, additional nonmalignant differential considerations for a cystic and solid appearing mass include hematoma, fat necrosis, abscess, or galactocele. Given the increased probability for malignancy for complex cystic and solid masses, they should be classified as BI-RADS 4 or BI-RADS 5 lesions and biopsy should be performed. When the mass is sampled, special attention should be paid to the solid component.

Papillary Lesions. Complex cystic and solid masses may involve intracystic or intraductal papillary lesions. Sonography does not distinguish benign from malignant intraductal or intracystic masses as effectively as it does for purely solid nodules because of the direction of invasion. Invasion arising from solid nodules is *outwardly* directed, greatly affecting the shape and the surface characteristics of the lesion. However, invasion arising from intracystic or intraductal lesions is *inwardly* directed, into the fibrovascular stalk of the lesion. As a result, the surface characteristics and shape are not distorted, making it more challenging to use sonographic descriptors to identify an abnormality. Any intracystic or intraductal papillary lesion with solid components should be characterized as BI-RADS 4a or higher and undergo histologic evaluation.

Findings that are suspicious for true intracystic or intraductal papillary lesions include thick isoechoic septations, mural nodules, a Doppler-demonstrable vascular stalk within a thick septation, and clustered complex microcysts. Thick, isoechoic septations are suspicious for **intracystic papilloma** or **intracystic carcinoma** (Fig. 21.33A), whereas thin echogenic septations merely represent **fibrocystic change** and the intact walls between multiple ductules with severe cystic dilation within an individual TDLU (Fig. 21.33B). Most **mural nodules** are caused by PAM, which is part of the benign FCC spectrum, or are pseudonodules caused by tumefactive sludge or lipid layers rather than papillomas or intracystic papillary carcinomas. Suspicious mural nodules demonstrate loss of the thin echogenic outer cyst wall along their points of attachment, extension beyond the circular or oval shape of the cyst into surrounding ducts (Fig. 21.34A), or angular margins at the point of attachment. Mural nodules that are caused by PAM remain confined within the circular or round shape of the cyst in which they lie and do not disrupt the thin, echogenic outer cyst wall (Fig. 21.34B). Regardless, biopsy of all these masses should be performed to ensure there is no malignancy present.

Papillomas and intracystic carcinomas are generally vascular and tend to develop easily demonstrable and prominent vascular stalks (Fig. 21.35A, Video 21.4), whereas mural nodules and thick internal septations caused by florid PAM rarely develop vascular stalks (Fig. 21.35B). Papillomas and intracystic carcinomas frequently undergo hemorrhagic infarction that can obscure vascularity. Most benign papillomas have a single feeding vessel, whereas malignant intracystic papillary lesions tend to incite the formation of multiple feeding vessels.[49] **Clustered microcysts** most frequently merely represent FCC and **apocrine metaplasia**[50] (Fig. 21.36A), but high–nuclear-grade micropapillary DCIS can also appear as clustered microcysts (Fig. 21.36B). The gray-scale appearances of microcysts caused by apocrine metaplasia and micropapillary DCIS can be virtually indistinguishable. However, clustered microcysts caused by micropapillary DCIS are usually vascular on color Doppler sonography, whereas microcysts caused by apocrine metaplasia, like mural nodules caused by apocrine metaplasia, are usually avascular on color Doppler ultrasound assessment (Fig. 21.36C). If even one suspicious finding is present, the cystic lesion should be characterized as BI-RADS 4a or higher and should be evaluated histologically.[45]

Inflammation and Infection. Nonsimple cysts may be caused by inflammation and/or infection. The findings that are suspicious for acute inflammation or infection are (1) uniform isoechoic thickening of the cyst wall, (2) fluid-debris levels (tumefactive sludge or layered pus), and (3) inflammatory hyperemia of cyst wall and surrounding tissues. Usually, all three findings coexist (Fig. 21.37A). Uniform isoechoic thickening is typical of inflammation, not tumor, so this finding does not raise much concern about malignancy. Debris levels can be shown to shift to the dependent portion of complex cysts when the patient is placed

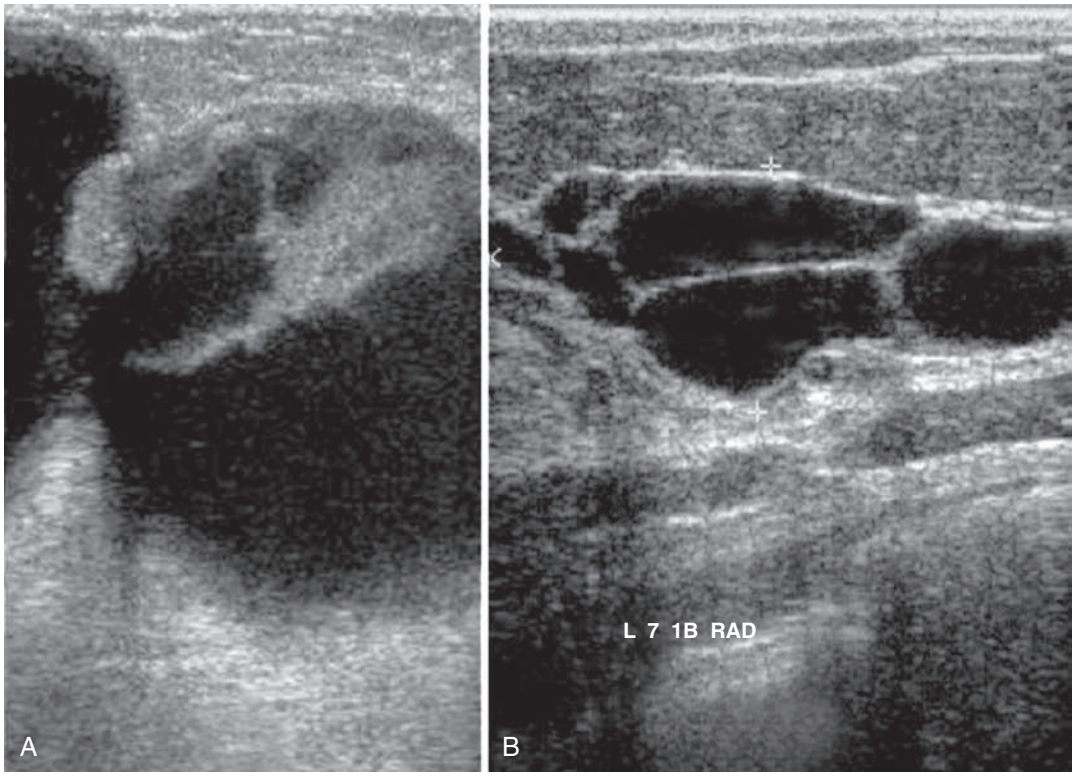

FIG. 21.33 Septations Within Cystic Masses. (A) Thick, isoechoic septations within complex cystic and solid masses are suspicious for intracystic papilloma or intracystic papillary carcinoma. **(B)** Thin, echogenic septations are not suspicious. Such septations represent residual walls of cystically dilated acini within a single terminal ductolobular unit (TDLU) and can be thought of as clusters of simple cysts.

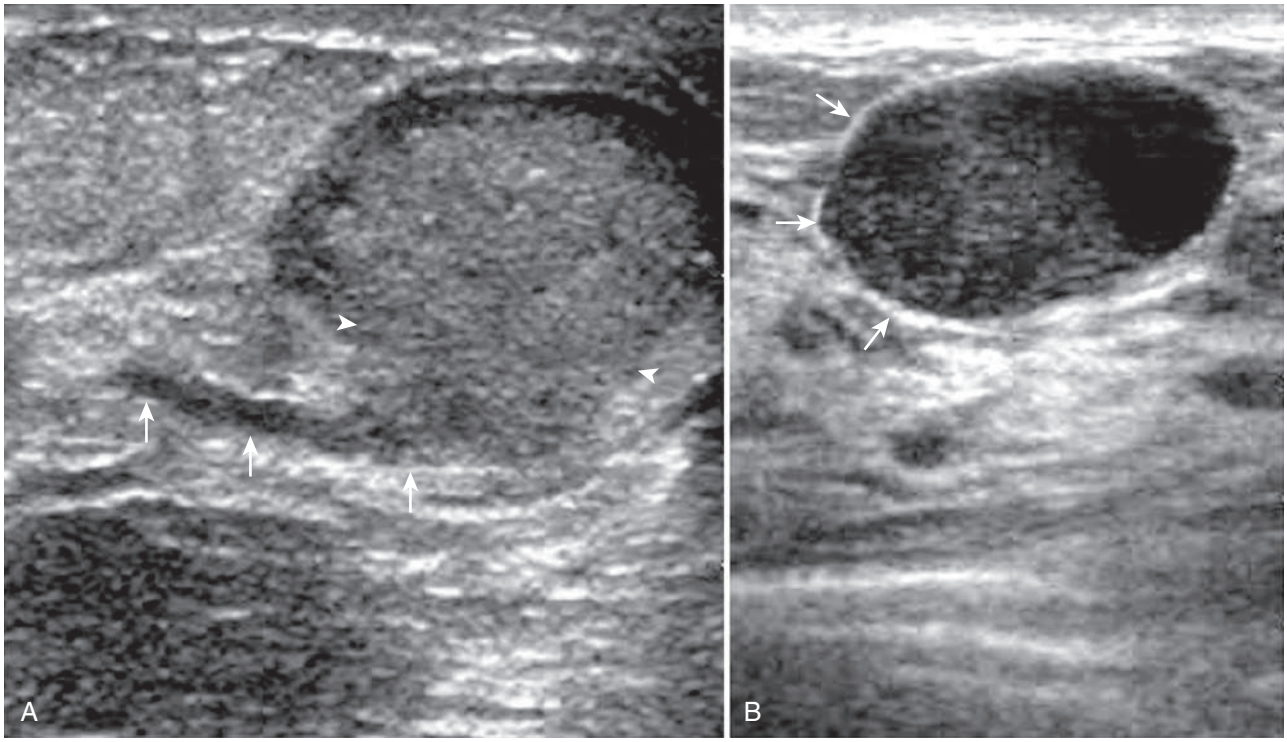

FIG. 21.34 Cysts With Mural Nodules. (A) Mural nodules that protrude beyond a circular or elliptical shape *(arrowheads),* lack a thin echogenic capsule at the point of attachment to the cyst wall, are angular at the point of attachment, or extend into surrounding ducts *(arrows)* are suspicious for intracystic papilloma or intracystic papillary carcinoma. **(B)** Mural nodules that are caused by papillary apocrine metaplasia remain confined within the circular or elliptical shape of the cyst. The thin, echogenic outer wall of the cyst is intact all along the attached surface of the mural nodule *(arrows).*

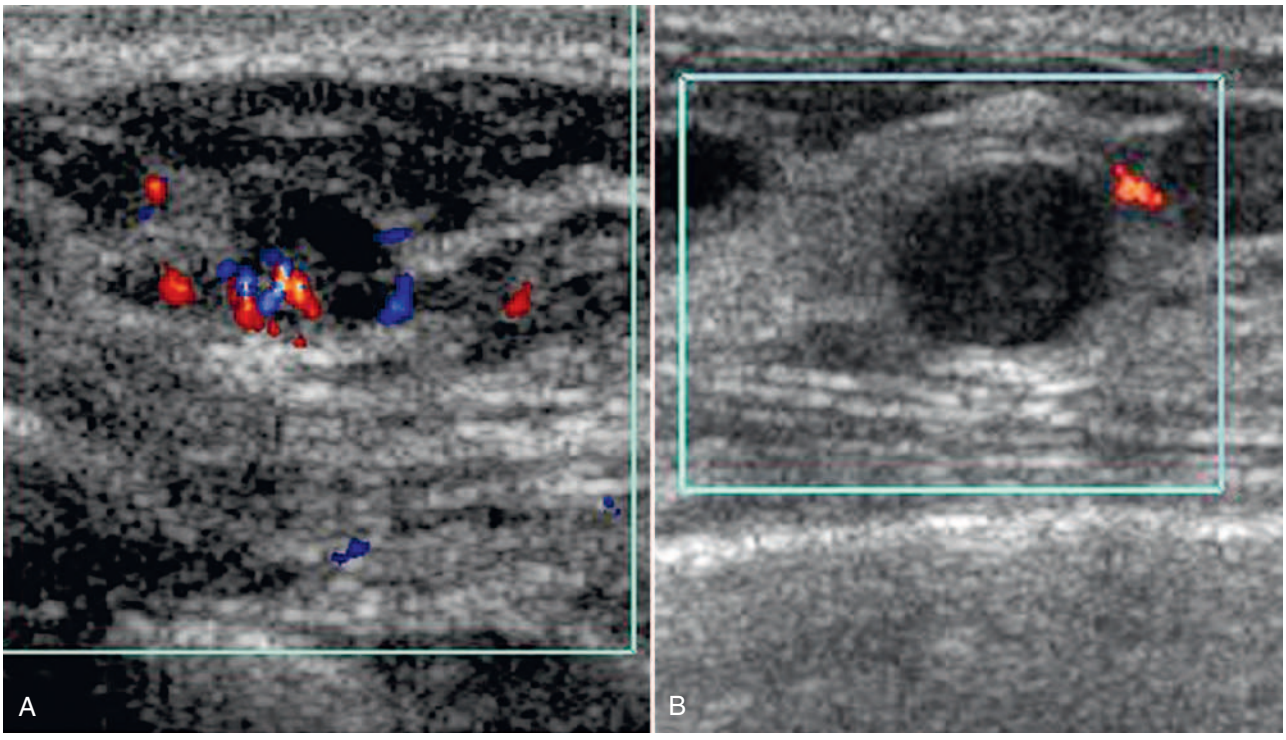

FIG. 21.35 Use of Color Doppler Ultrasound for Mural Nodules. (A) Mural nodules caused by intracystic carcinoma, as in this case, tend to be fed by multiple vessels. **(B)** Mural nodules caused by papillary apocrine metaplasia (PAM) rarely develop a fibrovascular stalk with demonstrable flow on color Doppler ultrasound.

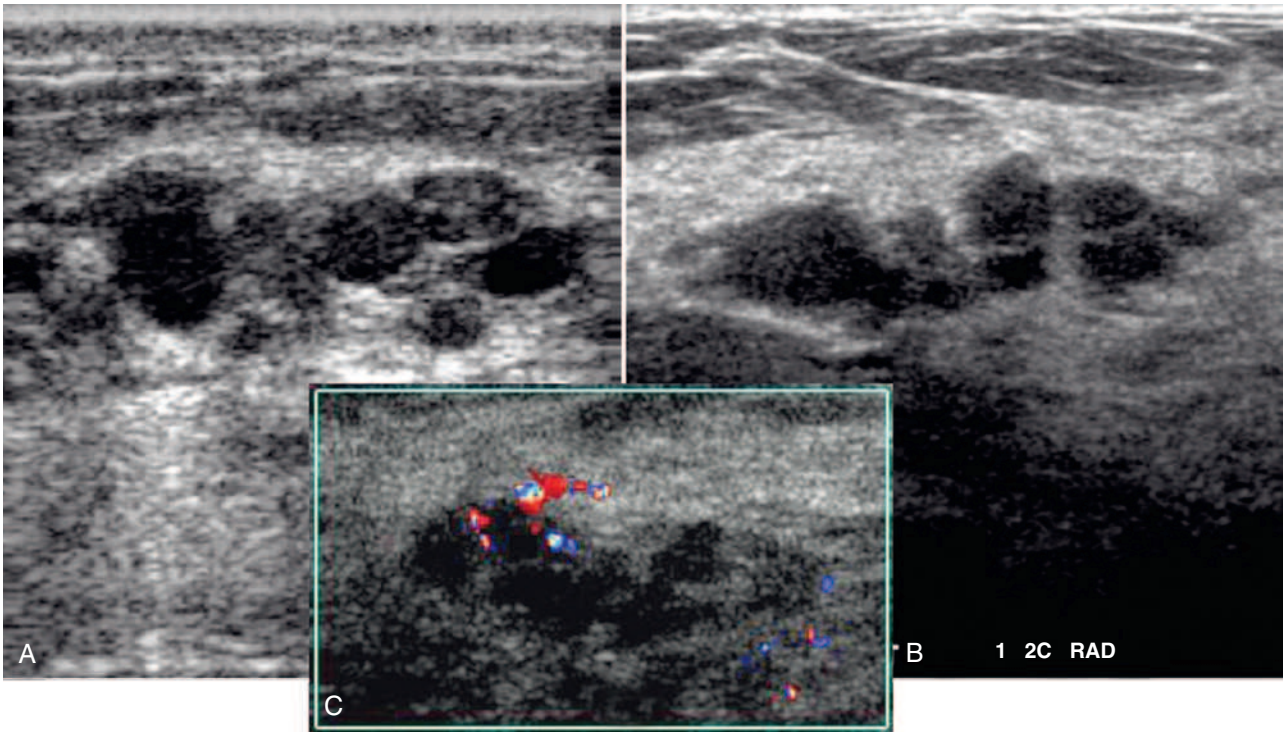

FIG. 21.36 Microcysts. Clustered microcysts can represent **(A)** fibrocystic change, in which the microcysts are caused by papillary apocrine metaplasia (PAM), or **(B)** neoplasm, in which the microcysts represent ducts distended with secretions and micropapillary ductal carcinoma in situ (DCIS). Unfortunately, the gray-scale appearances of fibrocystic change and DCIS may be indistinguishable. **(C)** However, clustered microcysts caused by micropapillary DCIS frequently show internal blood flow on color or power Doppler ultrasound, whereas clustered microcysts caused by PAM, as with mural nodules caused by PAM, rarely have demonstrable internal flow.

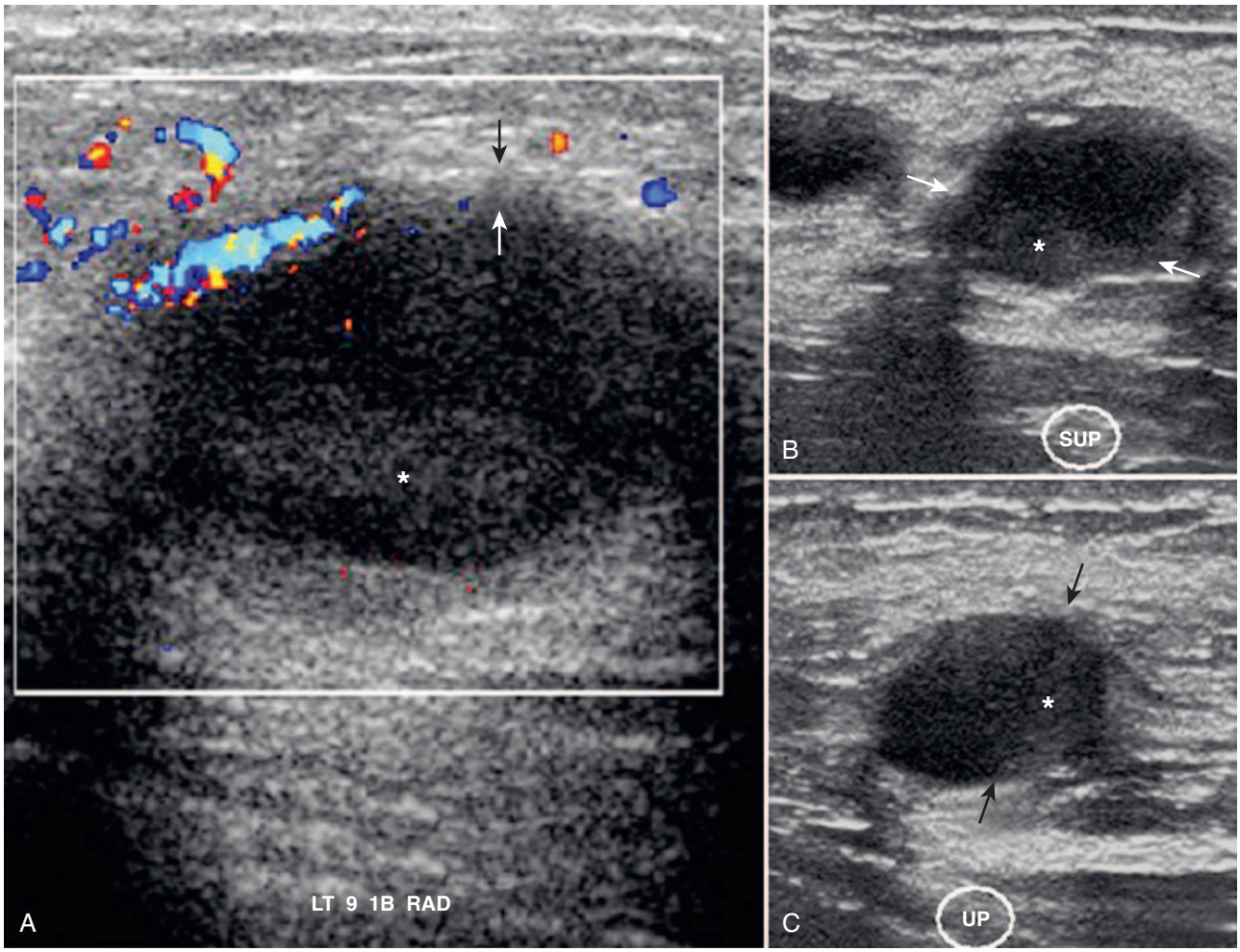

FIG. 21.37 Inflamed or Infected Cyst. (A) Acutely inflamed or infected cysts demonstrate three findings: (1) abnormal uniform isoechoic wall thickening *(between arrows),* (2) dependent debris (*), and (3) hyperemia of the thickened wall. **(B)** Supine and **(C)** upright images show the debris (*), resembling sludge within a gallbladder, shifting to the dependent part of the cyst when the position of the patient is changed from supine to upright or lateral decubitus position. Note the change in the position of the interface between the nondependent fluid and the dependent debris or pus *(arrows).*

in lateral decubitus or upright positions (Fig. 21.37B-C). However, tumefactive sludge may be so viscous that it requires 5 minutes or more to shift to the new dependent position. The hyperemic vessels in the wall of inflamed cysts course in a direction parallel to the cyst wall, in contrast to vessels that feed intracystic malignancies, which tend to course perpendicular to the cyst wall. These findings indicate acute inflammation, which is common in FCC, but do not necessarily indicate infection. Even after aspirating pus under ultrasound guidance, the clinician cannot determine whether the cyst is infected or merely inflamed. This requires Gram stain and culture. Many times, however, the key to differentiating inflammation from infection lies with the clinical examination. Often patients with infection will have tenderness, erythema, and warmth overlying the area of clinical concern.

Uniform wall thickening may also be seen in cysts with fibrotic walls, but in such cases, there is no hyperemia or tenderness of the thickened wall because cysts with fibrotic walls represent the healed phase of acute inflammation. The fluid and debris within acutely inflamed cysts usually can be completely aspirated, but the residually thickened cyst wall will persist. If the cyst was not infected, usually the fluid and debris do not reaccumulate, and the residually thickened wall gradually resolves over a few days. Because the sonographic appearances of acute inflammation are so characteristic and do not raise questions about neoplasm, we usually do not perform cytologic evaluation of the aspirated cyst fluid. Rather, if there is concern for infection, Gram stain and culture are recommended. Often patients will be provided with empiric antibiotic therapy while awaiting culture results.

Solid Masses

Initially, sonographic studies reported substantial overlap between the features of benign and malignant solid nodules that prevented a clear distinction to be made. These studies were performed with older, lower-frequency, lower-resolution equipment and generally assessed only single sonographic findings. Since then, the approach to characterizing solid nodules has substantially improved.

The key to developing a successful algorithm for characterizing solid nodules is having realistic goals. Distinguishing all benign from all malignant solid nodules is challenging, and therefore a more realistic goal is to identify a subpopulation of all solid

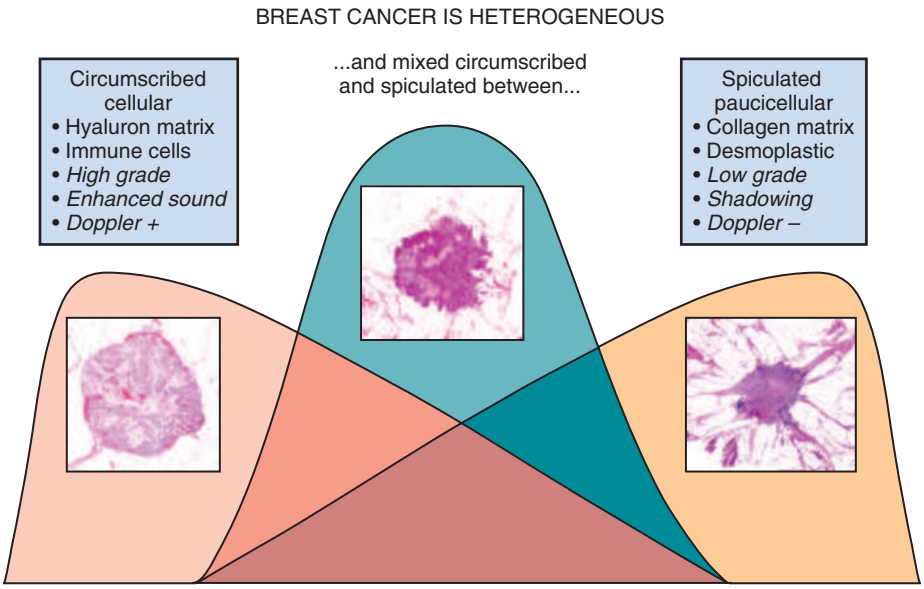

FIG. 21.38 Malignant Masses: Spectrum of Appearances. The appearance of breast cancer spans a spectrum from classic spiculated lesions to circumscribed carcinomas. There are also mixed spiculated and circumscribed lesions in the middle of the spectrum. Sonographic findings for circumscribed and spiculated lesions can be opposite from each other. Only by using multiple findings capable of identifying lesions at both ends of the spectrum can carcinomas be identified with the desired 98% or greater sensitivity.

nodules that is so likely to be benign that the patient can be offered the option of follow-up in addition to the option of biopsy. BI-RADS 3 lesions must have a 2% or lower risk of being malignant.

Before delving into the sonographic appearance of various solid nodules it is important to gain an understanding of what pathologic features contribute to the findings we see on ultrasound. Fig. 21.38 illustrates the **heterogeneity** of breast cancer, which can be thought of as spanning a spectrum from spiculated to circumscribed lesions. Not only is breast cancer heterogeneous from one mass to another, but it also can be heterogeneous within an individual mass, and thus there is a peak of mixed circumscribed-spiculated lesions in the center of the spectrum. These features should be considered when classifying a mass as probably benign (BI-RADS 3) or classifying a mass as suspicious and recommending a biopsy.

Spiculated and circumscribed cancers differ greatly. The histologic and gross morphologic features of the spiculated and circumscribed ends of the malignant spectrum differ in cellularity, constituents of the extracellular matrix, host reaction to the tumor, and water content. Spiculated or stellate malignant lesions tend to be low to intermediate in histologic grade, whereas circumscribed lesions tend to be either special-type tumors (e.g., colloid or medullary carcinoma) or high-grade invasive ductal carcinoma. The classic **spiculated breast carcinoma** is composed of tumor cells, collagenous extracellular matrix, and desmoplastic host response to the lesion. The usually low-grade spiculated carcinomas are paucicellular—a small percentage of the total volume of the lesion is composed of tumor cells. The paucicellular nature, collagenous matrix, and desmoplastic host response of spiculated malignant lesions makes them relatively water poor, so they often cause acoustic shadowing. **Circumscribed carcinomas,** usually high-grade invasive ductal carcinomas, on the other hand, are highly cellular. They have more hyaluronic acid in the matrix and manifest a primarily lymphoplasmacytic immune response. The high cellularity, hydrophilic hyaluronic acid matrix, and lymphoplasmacytic response in circumscribed lesions makes them water rich.[45] Thus circumscribed lesions usually manifest increased sound transmission.

Because breast tumors have varying histology, specific sonographic features do not universally apply to all malignancies. For example, **acoustic shadowing** can help clinicians detect lesions at the spiculated end of the spectrum and some of the mixed lesions in the middle of the spectrum, but it is much less effective at the circumscribed end of the spectrum. On the other hand, **Doppler** ultrasound is very helpful for circumscribed carcinomas because of their high tumor cellularity and associated abundant angiogenesis factors. In addition, the **lymphoplasmacytic immune-inflammatory response of circumscribed carcinomas** causes vasodilation of surrounding vessels. Doppler is not as helpful for spiculated lesions that have relatively few tumor cells that elaborate angiogenesis factors. These masses also have a collagen matrix and desmoplasia that require little blood flow. As a result, spiculated lesions often do not have perceptibly increased flow compared with benign lesions or normal tissue. The heterogeneity of breast cancer therefore requires that multiple different sonographic features be used to characterize masses to detect cancer with adequate sensitivity.

The algorithm that we use to evaluate lesions must account for internal heterogeneity by assessing the shape, orientation, margin, echo pattern and posterior features of the lesion for suspicious findings completely in two orthogonal planes (preferably radial and antiradial). In lesions that have a mixture of suspicious and nonsuspicious findings, it is important to focus on the most suspicious findings.

TABLE 21.2 Comparison of Morphologic and Histopathologic Features of Suspicious Sonographic Findings

Morphologic Features	Histopathologic Features
SURFACE CHARACTERISTICS AND MARGINS	**"HARD" FINDINGS**
Spiculation	Spiculation
Angular margins	Echogenic rim
Indistinct margin	Angular margins
Microlobulation	Acoustic shadowing
SHAPES	**MIXED FINDINGS**
Irregular	Hypoechogenicity
Not parallel	Not parallel
Duct extension	
INTERNAL CHARACTERISTICS	**"SOFT" FINDINGS**
Calcifications	Microlobulation
Acoustic shadowing	Duct extension
Hypoechogenicity	Microcalcifications

FIG. 21.39 Indistinct Margins in Invasive Ductal Carcinoma, Grade 3. An indistinct margin refers to the inability to delineate the margin of the breast mass. This feature, in combination with other suspicious features including hypoechoic and not parallel appearance, make this mass highly suspicious for malignancy.

Suspicious Findings

The suspicious sonographic features can be classified into subgroups by morphologic features or by histopathologic features (Table 21.2).

Table 21.2 shows the suspicious findings listed by their morphologic features: **shape** (irregular), **margins** (indistinct, spiculation, angular margins, and microlobulations); **orientation** (termed "not parallel" in ACR BI-RADS ultrasound lexicon[17]); duct changes; and **internal characteristics** (acoustic shadowing, hypoechoic echotexture, and calcifications). Histopathologic categories include **"hard" findings** that indicate the presence of invasion of surrounding tissues (angular margins, spiculation, thick echogenic rim, and acoustic shadowing); **"soft" findings** that indicate the presence of DCIS components of tumor (microlobulations, calcifications, and duct changes); and **mixed findings** that can be seen in association with either invasive or DCIS components of tumor (hypoechoic echotexture and not parallel orientation).

Soft suspicious findings help in three ways. First, soft findings can help clinicians detect pure DCIS, which rarely develops hard suspicious findings, and the most common breast carcinoma usually contains DCIS components. Second, including soft findings can help to detect and characterize the circumscribed invasive duct carcinomas that contain both invasive and DCIS components. In such cases, the new periphery of the lesion is where the DCIS components are located. Thus the surface characteristics and shapes of the lesion are created by the DCIS elements of the lesion, not by the centrally located invasive components. Finally, the use of soft findings can aid in accurately staging malignant breast lesions on sonography, because the DCIS components of the lesion that extend into the surrounding tissues for variable distances can be identified only by soft findings. Although soft findings do increase the sensitivity of the sonographic algorithm for detecting malignant disease, they also increase the false-positive rate, especially for lesions that contain only soft findings. Lesions that demonstrate only soft findings are most likely to be benign and include papillomas, fibroadenomas, and FCC. However, given that the risk of malignancy for solid masses that demonstrate only soft suspicious findings is greater than 2%, it is still important that such lesions be characterized as mildly suspicious (BI-RADS 4a) and that biopsy be performed.

Indistinct Margins

"Indistinct margins" refers to the inability to distinguish any portion of the margin of the mass from the surrounding tissue (Fig. 21.39). This also includes masses that have an echogenic rim, because the surrounding echogenic area prevents clear demarcation of the mass' margins.

Spiculation or Thick Echogenic Rim

Spiculation is a hard sonographic finding that corresponds to invasion of surrounding tissues and a desmoplastic host response to the lesion. Spiculation is a subcategory of the ACR BI-RADS category "Margin–Not Circumscribed"[17] and is a mammographic finding that can be directly applied to sonography (Fig. 21.40A). When the spiculations are coarse, they manifest as alternating hypoechoic and hyperechoic lines that radiate perpendicular to the surface of the nodule; the **hypoechoic** components represent either fingers of invasive tumor or DCIS components of tumor extending into the surrounding tissues, and the **hyperechoic** elements represent the interfaces between the spicules and surrounding breast tissues (Fig. 21.40B). In most cases, however, spicules are fine and manifest with only a single echogenicity.

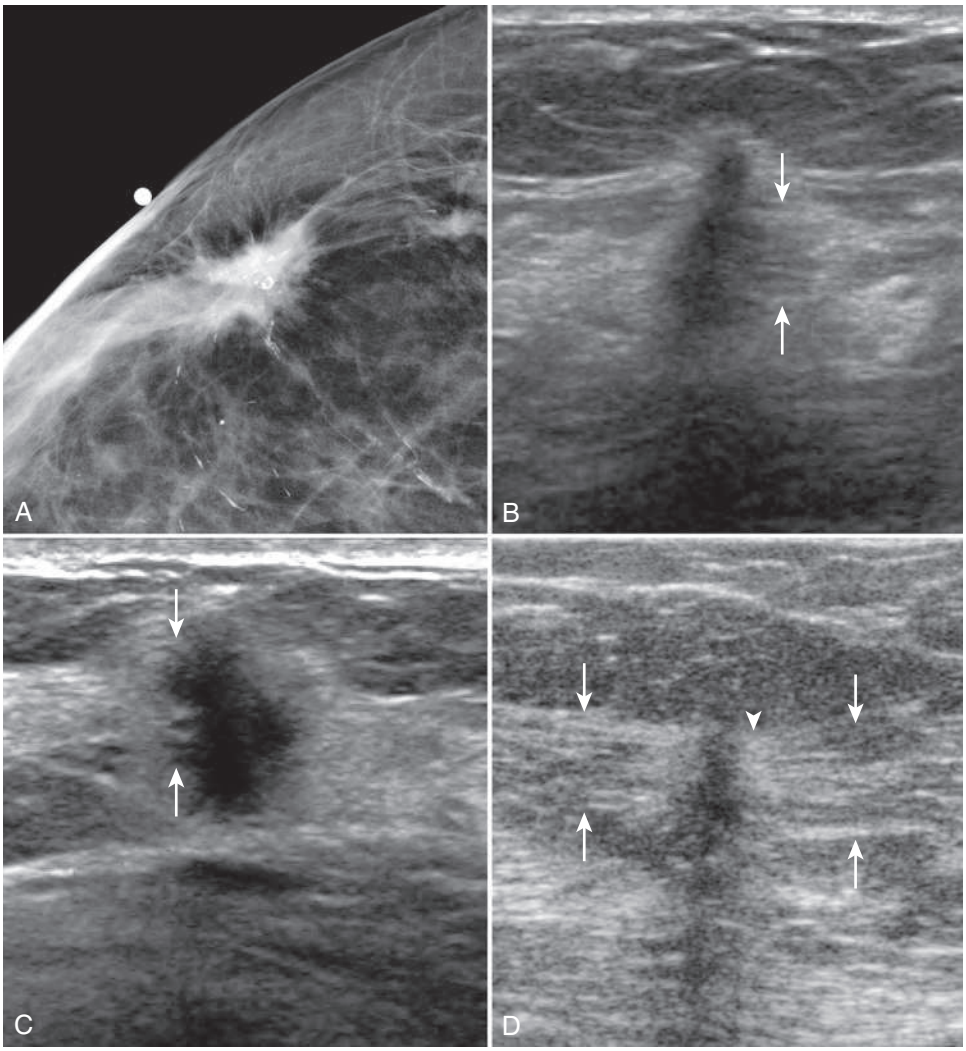

FIG. 21.40 Spiculation. (A) Spiculation is a "hard" mammographic finding that indicates invasion. **(B)** Coarse spiculations *(arrows)* appear as alternating hypoechoic and hyperechoic lines radiating from the nodule on ultrasound. The hypoechoic parts represent fingers of invasive tumor or ductal carcinoma in situ, and the hyperechoic lines represent the interface between the tumor and surrounding tissue. Most spicules are fine rather than coarse and appear with only a single echogenicity opposite that from the background tissues. **(C)** The spiculations extending from lesions surrounded by hyperechoic fibrous tissues are hypoechoic *(arrows).* **(D)** Fine spicules in lesions surrounded by fat appear hyperechoic *(arrows).* Note that spiculations are most prominent within the coronal plane along the sides of the nodule.

They appear to be either hyperechoic or hypoechoic depending on echogenicity of the tissue within which the lesion lies. The spicules in malignant nodules that are surrounded by hyperechoic fibrous tissues appear hypoechoic (Fig. 21.40C), whereas spicules in malignant nodules that are surrounded by fat appear hyperechoic (Fig. 21.40D).

The thick, echogenic rim that surrounds some malignant solid nodules represents spiculations that are too small to demonstrate sonographically. For this reason, either frank spiculations or the presence of a thick, echogenic rim should be considered as spiculations, which approximately doubles the sensitivity of spiculation for malignant nodules, from 36% to 70%. The classic thick echogenic rim often appears thicker along the edges of the nodule than on its anterior and posterior surfaces (Fig. 21.41). The presence of an echogenic rim can be used in conjunction with the BI-RADS descriptor "indistinct" when referring to margins.

Sonographic imaging in three dimensions is very helpful at demonstrating spiculations. Most spiculations are oriented in the coronal plane, so the reconstructed coronal plane is especially helpful. Thick, echogenic rims in standard planes can often be resolved as frank spiculations in the coronal plane. This is true for hand-held and automated breast scanners (Figs. 21.42 and 21.43).

Angular Margins

Angular margins are a subcategory of the ACR BI-RADS category "Margin–Not Circumscribed."[17] Angular margin represents a hard sonographic finding indicative of invasion. The angles of the lesion margins can be acute, right angle, or obtuse. Angles on the surface of the mass occur in regions of low resistance to invasion. In lesions surrounded by fat, angulations can occur on any surface of the nodule (Fig. 21.44A). In fibrous-surrounded lesions, angular margins tend to occur on the edges of the lesion,

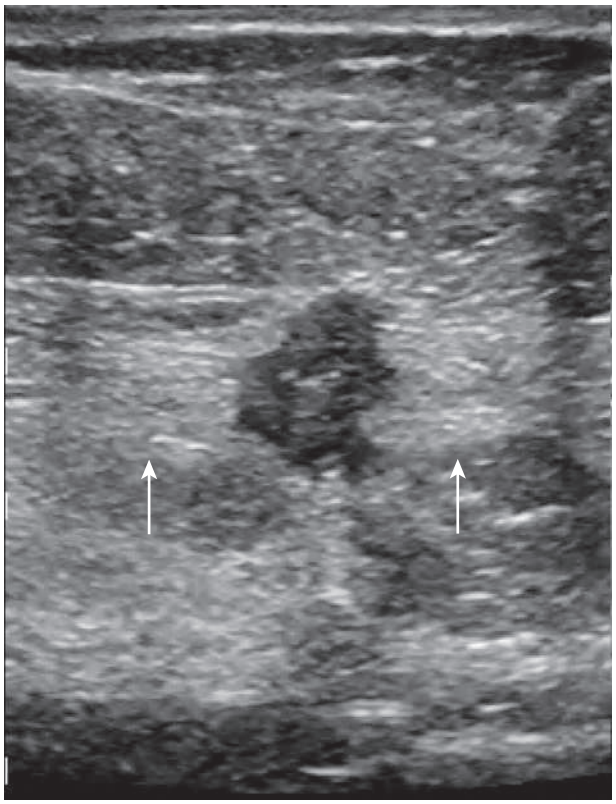

FIG. 21.41 Echogenic Rim With Hyperechoic Spicules. The thick, poorly defined echogenic rim that can be seen around some invasive malignant lesions surrounded by fat represents hyperechoic spicules too small to be resolved individually. The rim is more often seen and is thicker along the sides of the nodule within the coronal plane *(arrows)* because spicules are more common in the coronal plane and because the spicules that lie within the coronal plane are perpendicular to the ultrasound beam, where they make strong specular reflectors.

within loose periductal stromal tissues, and between tissue planes within the fibrous tissue (Fig. 21.44B-C). A single angle of any type on the surface of the lesion should be considered suspicious. **The presence of angular margins has the greatest individual sensitivity and overall accuracy of any of the features.**[45]

Microlobulations

Microlobulations are 1-mm to 2-mm lobulations that vary in number and distribution along the surface and within the substance of a mass. Microlobulations are a subcategory of the ACR BI-RADS category "Margin–Not Circumscribed."[17] They may occur over only a small percentage of the surface of a nodule. Microlobulation is a mixed finding that can be seen with both invasive and DCIS components of tumor, but more often represents *in situ* components of tumor. When microlobulations are angular and are associated with a thick echogenic rim, they usually represent fingers of invasive carcinoma[45] (Fig. 21.45A). When the microlobulations are rounded and associated with a thin echogenic capsule, they usually represent DCIS components of tumors. DCIS components can create microlobulations in two ways: involved lobules (Fig. 21.45B), or ductules or ducts that are distended with tumor and necrosis (Fig. 21.45C-D).

Not Parallel (Not Taller-Than-Wide) Orientation

Lesions that are larger in the AP dimension than in any horizontal dimension are considered not parallel and are suspicious for malignancy. Round masses are also viewed as not parallel in their orientation. Not parallel orientation is unique to sonography and is not seen on mammography. It is a subcategory of the ACR BI-RADS category "Orientation."[17] This is a mixed finding that can be seen with both invasive and DCIS lesions (Fig. 21.46). This orientation is primarily a feature of small, solid malignant

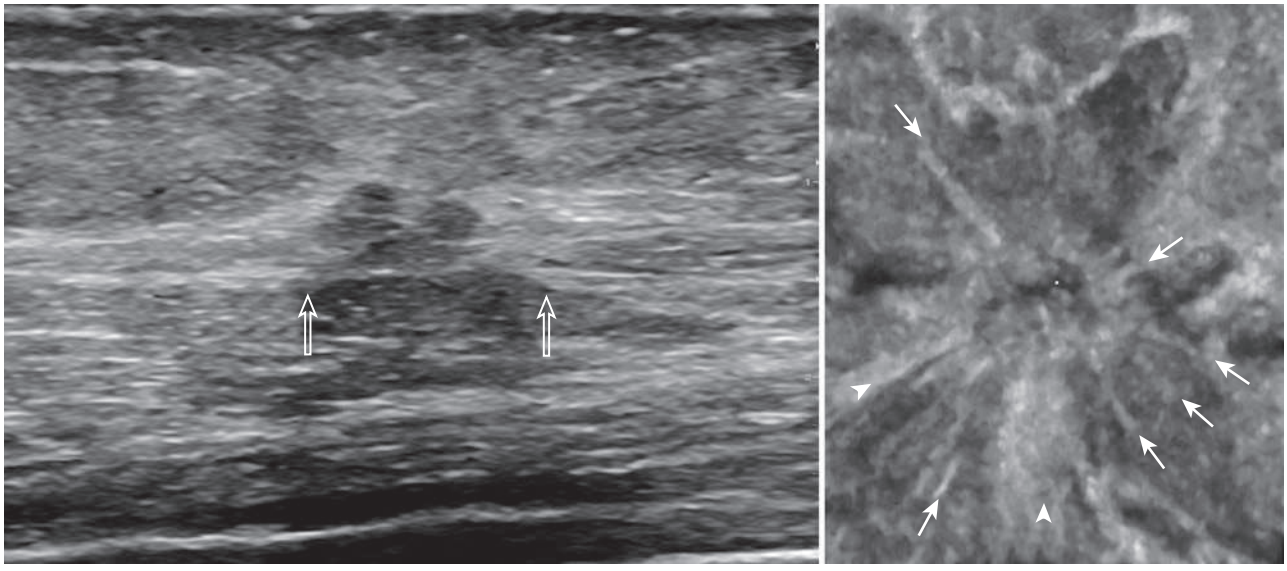

FIG. 21.42 Three-Dimensional or Volume Imaging With a Hand-Held Transducer. The coronal reconstructed plane can be especially useful in assessing for spiculations. What appears to be a poorly defined, thick, echogenic rim in radial or antiradial planes *(left, arrows),* can often be resolved as individual hyperechoic spicules in the reconstructed coronal plane *(right, arrows).* The coronal plane can also better demonstrate other architectural distortions, such as **thickened Cooper ligaments** *(right, arrowheads).*

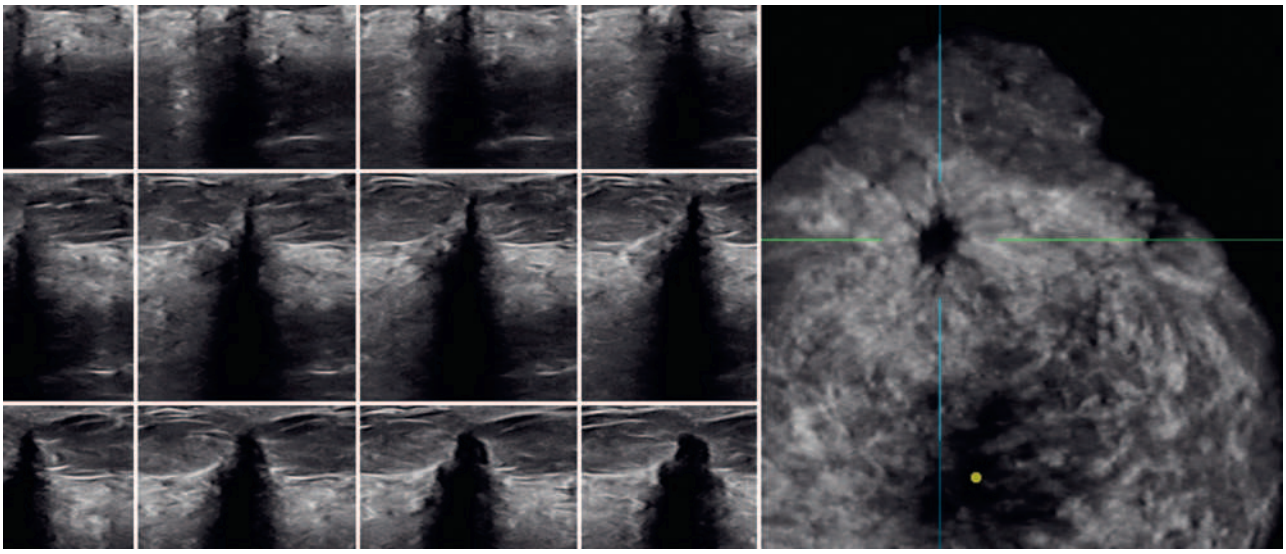

FIG. 21.43 Three-Dimensional or Volume Imaging With Automated Breast Scanner. Spiculations are better demonstrated on the reconstructed coronal plane *(right)* than on the serial native (original) plane images.

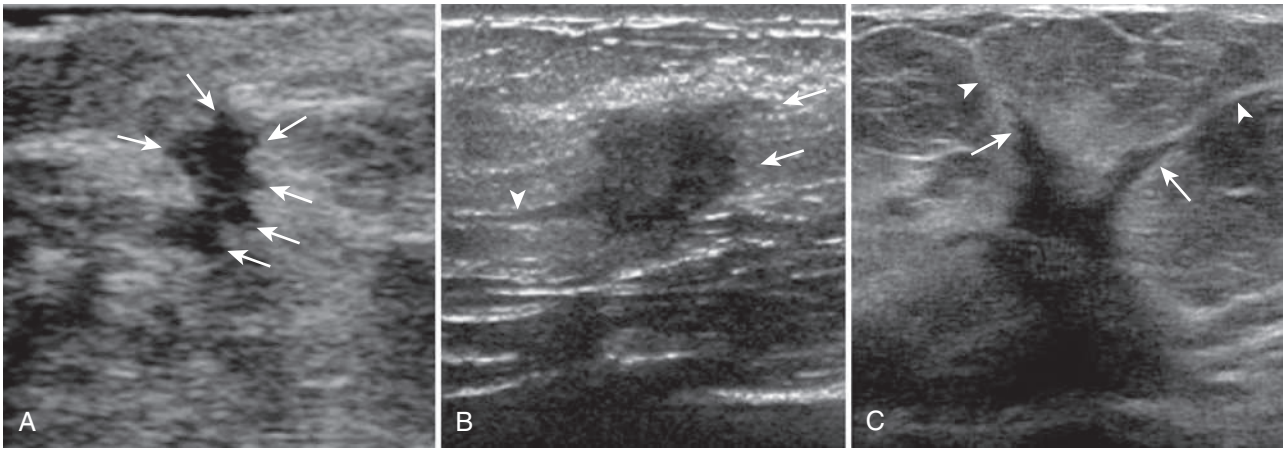

FIG. 21.44 Angular Margins Represent Invasion of Carcinoma Into Low-Resistance Pathways. (A) Fat offers little resistance to invasion, so malignant nodules surrounded by fat can develop angles along any surface *(arrows)*. **(B)** In lesions surrounded by hyperechoic fibrous tissues, paths of low resistance are along the periductal tissues *(arrowhead)* and horizontally along the tissue planes within the fibrous tissue *(arrows)*. **(C)** Following Cooper ligaments *(arrowheads)* down to their base, where they intersect the surface of the nodule, is the best way to detect angles *(arrows)* on the surface of malignant solid nodules.

nodules that have a volume of 1 cc or less. As lesions enlarge, they tend to become parallel (previously termed "wider-than-tall"). The best of several explanations for this finding is that the orientation of small carcinomas reflects the shape of the TDLUs within which the carcinoma arose. Most TDLUs lie anteriorly and are oriented in a not parallel axis. As malignant lesions expand into the lobar ductal system, which is oriented horizontally within the breast, they tend rapidly to become parallel (Fig. 21.47). Given that some carcinomas can have parallel orientation, orientation alone should not be the distinguishing feature between benign and malignant.

Duct Extension

Duct extension is a "soft" shape finding that correlates with the presence of DCIS components of tumor. Duct extension is a part of the ACR BI-RADS subcategory "Associated Features–Duct Changes."[17] Other changes that are part of this subcategory include ductal dilation, irregularities in caliber and/or arborizaton, and the presence of an intraductal mass, thrombus, or detritus. Duct extension correlates with mammographic calcification patterns that have been applied to components of solid nodules. Duct extension can best be demonstrated when the scan plane is oriented parallel to the long axis of the mammary ducts in the region of the mass. Duct extension usually manifests as a single projection of solid growth toward the nipple from the main mass (Fig. 21.48). Additional projections of the solid mass into multiple small ducts peripherally can also occur. Solid masses that have long duct extensions tend to have extensive intraductal DCIS components that increase the likelihood of local recurrence.

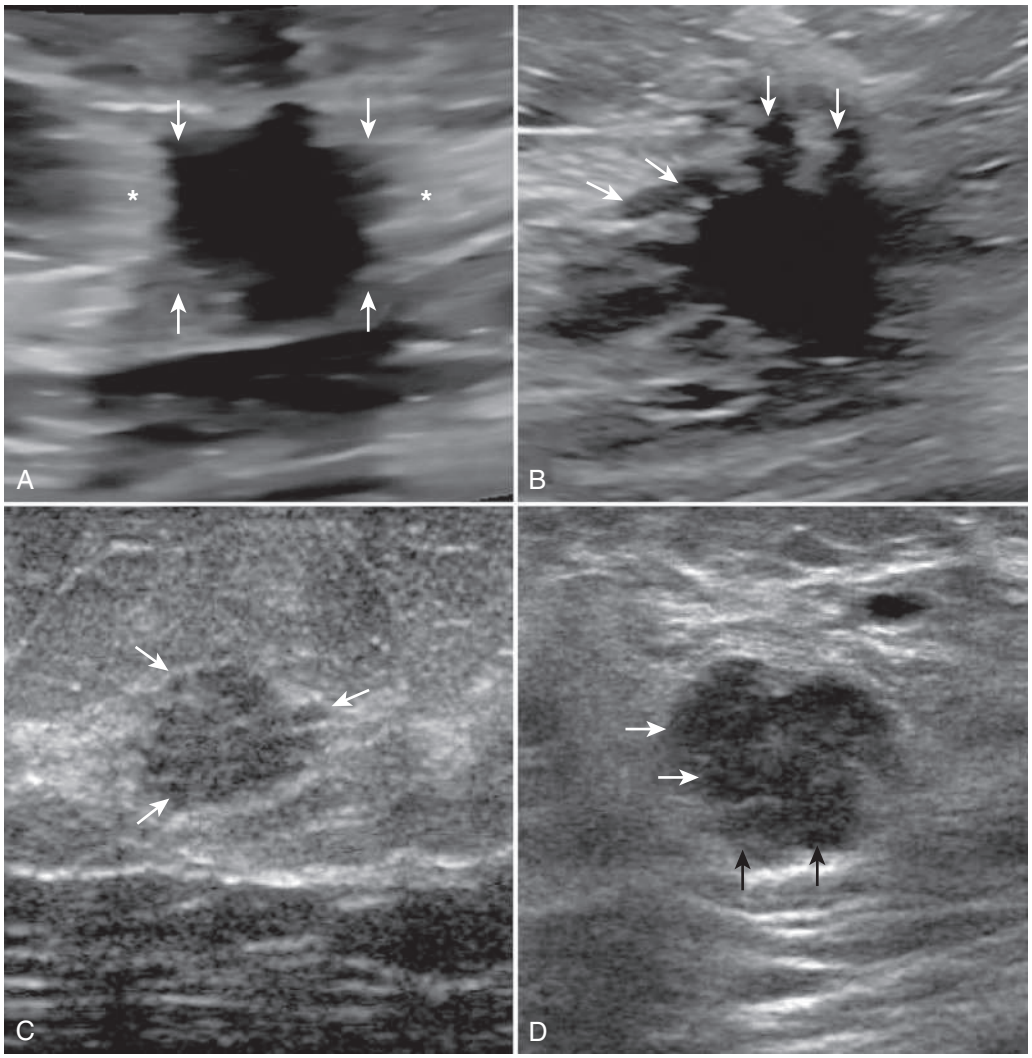

FIG. 21.45 Microlobulations. These can represent either angles of invasive tumor or ductal carcinoma in situ (DCIS) components of the lesion. **(A)** When microlobulations are pointed or angular *(arrows)* and associated with spiculations or thick, echogenic rim (*), they represent fingers of invasive tumor. **(B)** When microlobulations appear as small "tennis rackets" *(arrows)* projecting from the surface of the nodule, they represent surrounding lobules distended with DCIS or cancerous lobules. Microlobulations that are round or oval with thin, echogenic capsules represent tumor-distended ducts. The thin capsule represents the intact duct wall. **(C)** Small microlobulations *(arrows)* correspond to minimally distended ducts that are filled with low–nuclear-grade DCIS. **(D)** Large microlobulations *(arrows)* correspond to grossly distended ducts that contain high–nuclear-grade DCIS.

The presence of duct extension is not a specific sign of malignancy, but rather suggests an intraductal growth pattern. Benign intraductal lesions such as papillomas and chronic periductal mastitis and fibrosis can also demonstrate duct extension. Overall, it is important to recognize duct extension for two reasons: (1) to minimize false-negative characterization of pure DCIS and (2) to identify extensive intraductal components of tumor.

Acoustic Shadowing

Acoustic shadowing is a subcategory of the ACR BI-RADS category "Posterior Features."[17] Acoustic shadowing is a hard suspicious internal characteristic finding that suggests the presence of invasive malignancy. Acoustic shadowing tends to occur in solid nodules that lie on the spiculated end of the malignant spectrum and represent about one-third of all solid malignant nodules. The desmoplastic components of the tumor substance and spiculations cause the shadowing (Fig. 21.49). Because breast carcinomas can be internally heterogeneous, only part of a solid malignant nodule might give rise to acoustic shadowing. Other parts of the lesion might be associated with **normal** or **enhanced sound transmission.** High-grade invasive ductal carcinomas, the most common circumscribed malignant nodules, do not usually cause shadowing. In fact, they most often have associated enhanced sound transmission (Fig. 21.50A). Even pure DCIS that is high nuclear grade may be associated with enhanced through transmission. Many intermediate-grade lesions demonstrate normal sound transmission (Fig. 21.50B). Special-type tumors

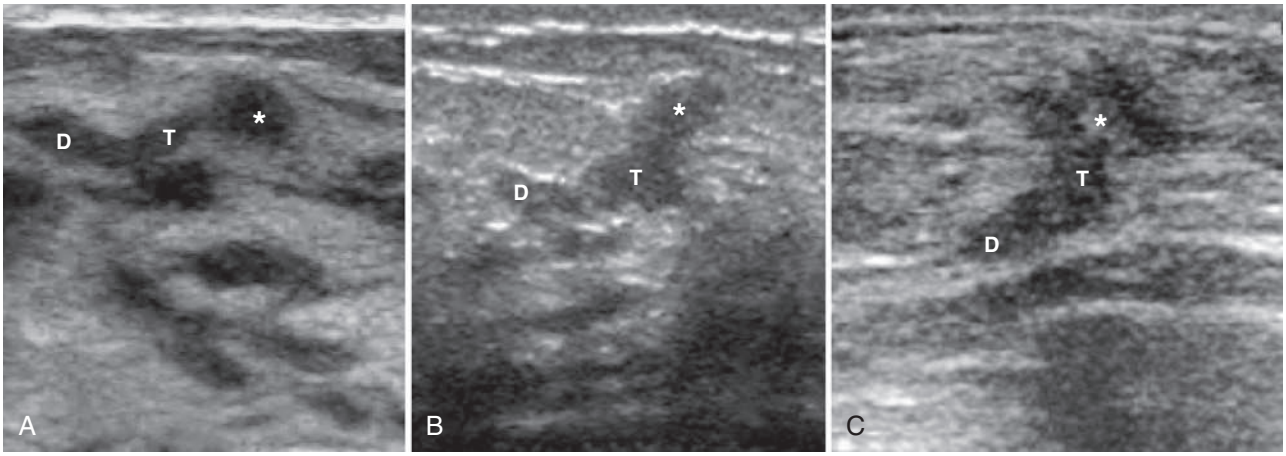

FIG. 21.46 Terminal Ductolobular Unit (TDLU) Carcinoma. Taller-than-wide orientation corresponds to a small, in situ or invasive carcinoma involving a single TDLU. **(A)** Normal lobule (*), its extralobular terminal duct *(T),* and part of the segmental duct *(D).* The TDLU orientation is taller than wide. **(B)** Small, intermediate–nuclear-grade ductal carcinoma in situ (DCIS) grossly distends the lobule and its extralobular terminal duct, remaining oriented in the taller-than-wide axis of the lobule from which it arose. **(C)** Small, low–nuclear-grade invasive ductal carcinoma more grossly distends and distorts the lobule and extralobular terminal duct from which it arose, but remains oriented taller than wide. Note the angles that indicate invasion into the surrounding tissues.

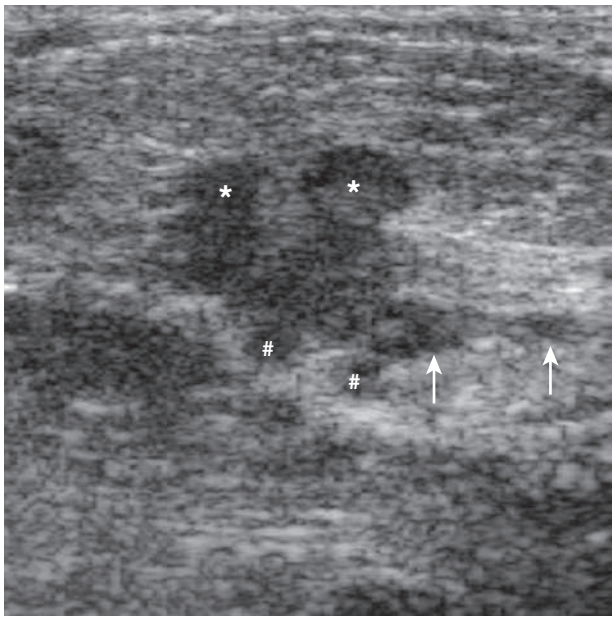

FIG. 21.47 Ductal Carcinoma in Situ (DCIS). Growth of DCIS changes shape to parallel. As malignant solid nodules enlarge, DCIS components grow down the lobar duct toward the nipple and develop cancerized adjacent lobules, changing from not parallel to parallel shape. Tumor-distended anterior lobules (*); tumor-distended but smaller posterior lobules (#); and tumor-distended lobar duct *(arrows)* are shown.

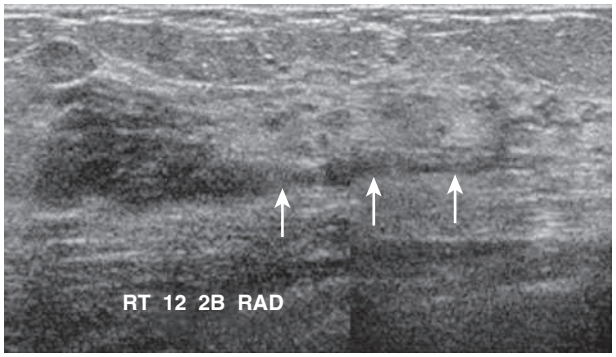

FIG. 21.48 Duct Extension of Ductal Carcinoma in Situ (DCIS). DCIS growing within the lobar duct toward nipple. Most invasive duct carcinomas contain DCIS components. In some cases the DCIS growing away from the tumor toward the nipple within the lobar duct may grossly distend the duct enough to allow recognition of duct extension sonographically *(arrows).* If such duct extensions are not recognized on ultrasound, they might be transected at surgery, leading to positive margins, local recurrence, and the need for reresection.

and invasive lobular carcinomas also tend to cause either acoustic shadowing or enhanced sound transmission.

The differential diagnosis for malignant masses that cause acoustic shadowing, in order of frequency, consists of (1) low-grade to intermediate-grade invasive ductal carcinoma, (2) invasive lobular carcinoma, (3) tubulolobular carcinoma, and (4) tubular carcinoma. The differential diagnosis for malignant masses associated with enhanced sound transmission includes high-grade malignancies, colloid carcinoma, medullary carcinoma, and invasive papillary carcinoma.[51-55]

Hypoechogenicity

Hypoechogenicity is a subcategory of the ACR BI-RADS category "Echo Pattern."[17] Marked hypoechogenicity of the substance of a solid mass (compared with fat) is a mixed suspicious internal characteristic sonographic feature of malignancy. It can be the result of several different tumor characteristics. High-grade invasive ductal carcinomas that are highly cellular and contain abundant hyaluronic acid in the extracellular matrix may appear hypoechoic because of the high water content. Pure DCIS may appear hypoechoic because of either necrosis or secretions within the lumina of tumor-distended ducts. Low-grade invasive ductal carcinomas can appear "markedly hypoechoic" because of acoustic

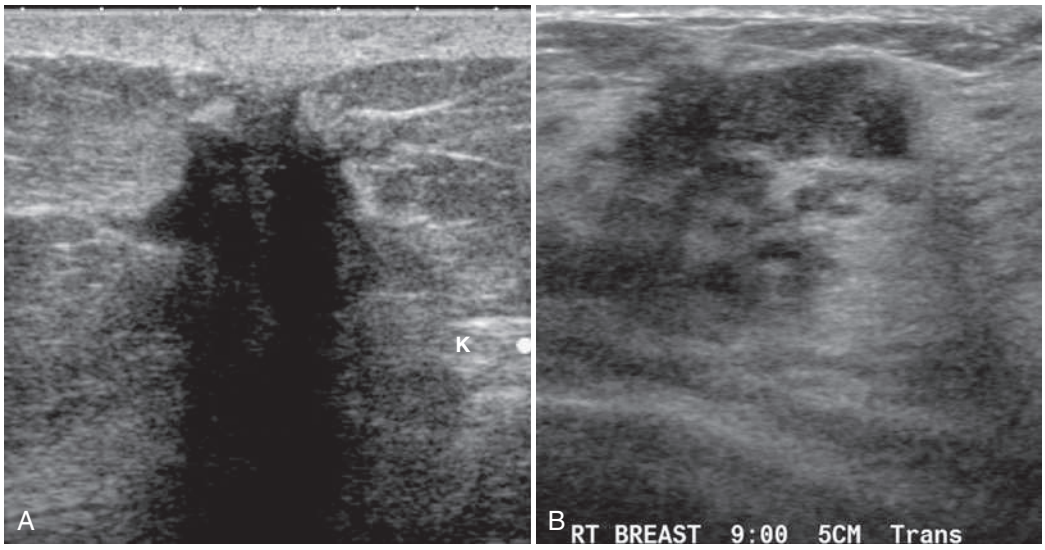

FIG. 21.49 Cancer Causing Acoustic Shadowing. Acoustic shadowing is a "hard" finding that suggests the presence of desmoplastic invasive tumor. Any acoustic shadowing should be considered suspicious—whether **(A)** complete, or **(B)** partial. Tumors that are becoming progressively more dedifferentiated and that are polyclonal or that contain mixtures of low-grade and intermediate-grade or high-grade components tend to create partial shadows.

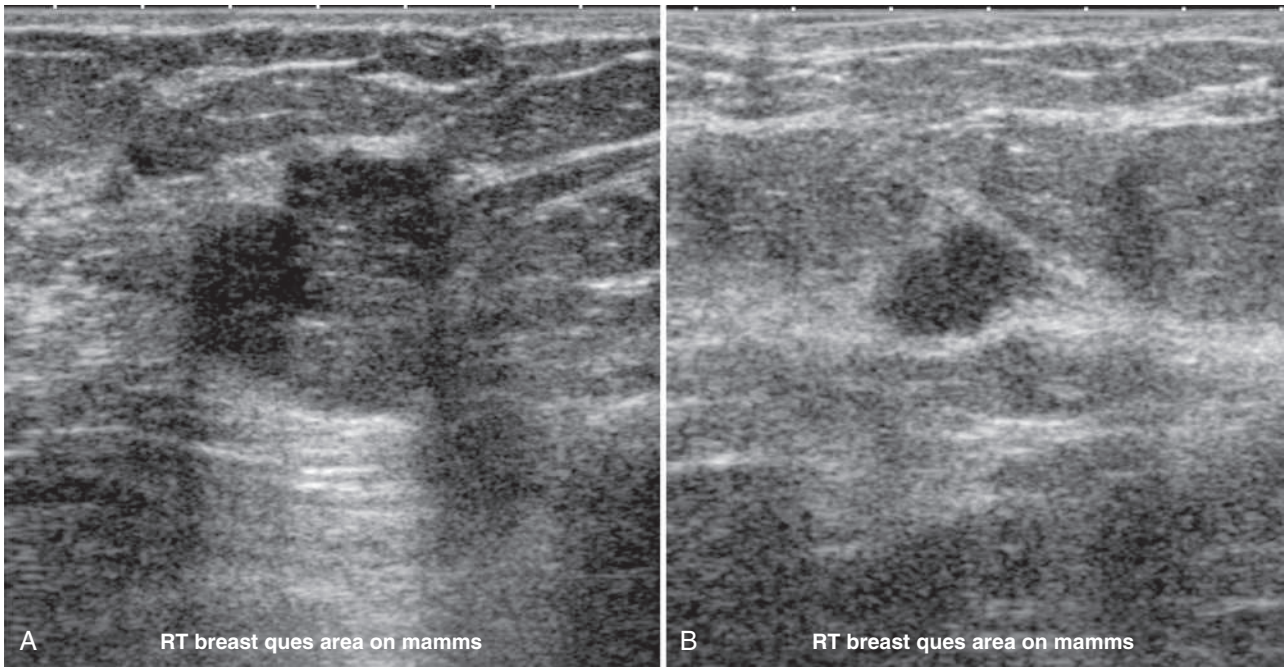

FIG. 21.50 Variable Sound Transmission Deep to Carcinomas. (A) High-grade invasive ductal carcinomas tend to be associated with enhanced sound transmission. **(B)** Intermediate-grade invasive duct carcinomas tend to be associated with normal or mixed sound transmission.

shadowing (Fig. 21.51). Digitally encoded harmonic ultrasound can make solid masses appear markedly hypoechoic compared with the surrounding fat (Fig. 21.52).

Calcifications

Calcifications within solid nodules are soft suspicious sonographic findings that suggest the presence of DCIS components. In the ACR BI-RADS ultrasound lexicon, calcifications are classified according to their location as either within a mass, outside a mass, or intraductal.[17] Calcifications can develop within necrotic debris within the center of the lumen of DCIS-distended ductules or ducts. Because microlobulations and duct extension represent DCIS components of the tumor distending ducts, malignant calcifications can often be found within the other soft findings that represent DCIS. Thus many malignant calcifications can be found within the center of microlobulations or duct extensions (Fig. 21.53).

The calcifications that are shown on sonography are smaller than the beam width and therefore are subject to volume averaging. They are usually in the 200- to 500-micron size range.

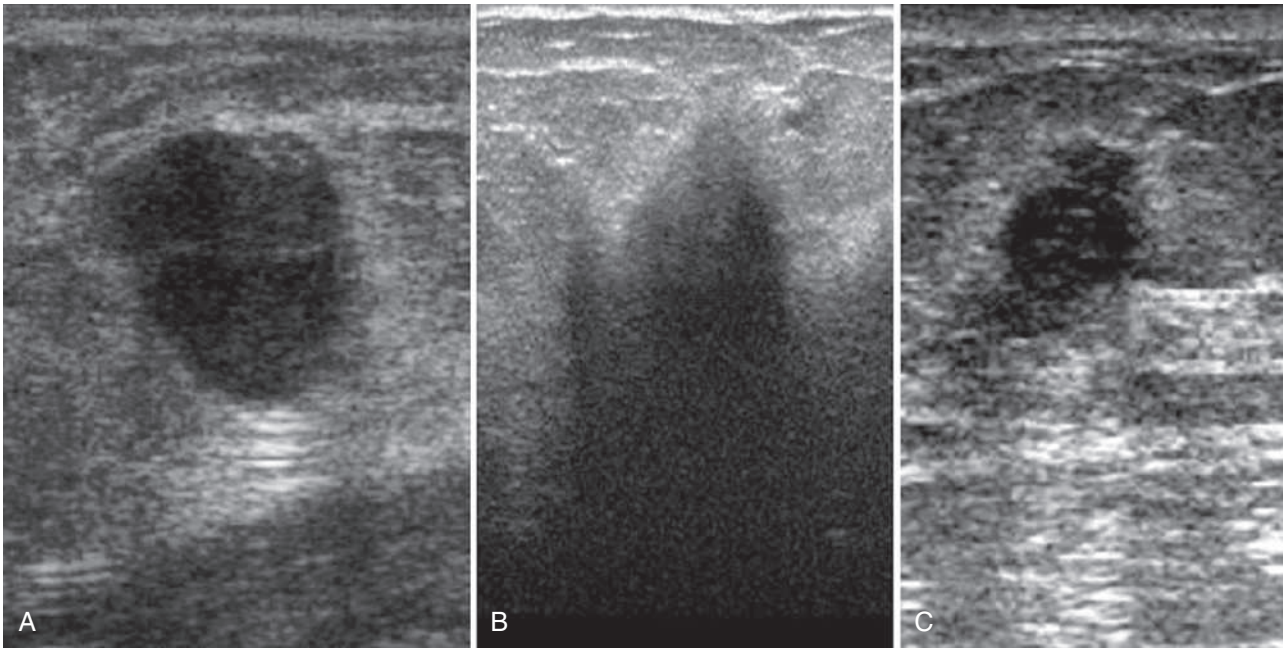

FIG. 21.51 Hypoechoic Carcinomas. Malignant nodules are often markedly hypoechoic in comparison to fat. Hypoechogenicity can be the result of **(A)** high cellularity and high content of hyaluronic acid within the extracellular matrix, or **(B)** intense acoustic shadowing associated with invasive carcinomas. **(C)** Necrosis within the lumen of tumor-containing ductules can cause marked hypoechogenicity in lesions composed of pure ductal carcinoma in situ (DCIS).

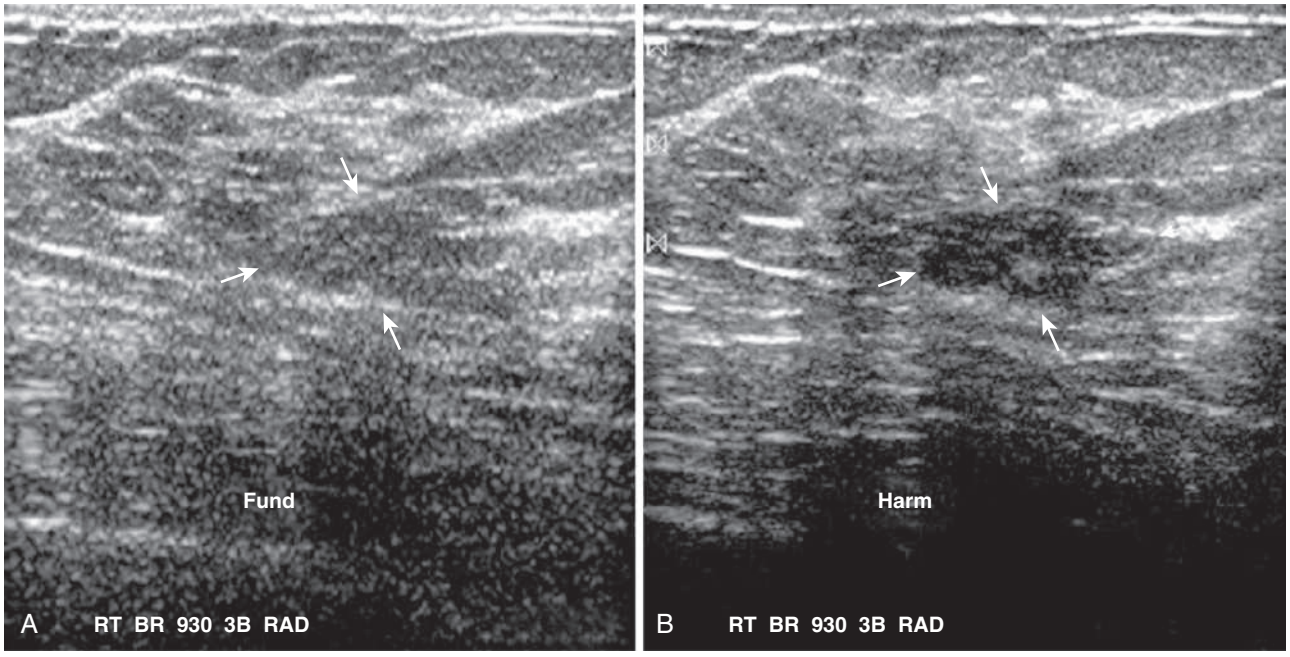

FIG. 21.52 Harmonic Imaging Improves Mass Visibility. (A) Nodules that are isoechoic with surrounding tissues and difficult to identify with fundamental imaging *(arrows)* often appear **(B)** markedly hypoechoic and more conspicuous *(arrows)* when viewed with harmonics.

Calcifications that are narrower than the beam width do not cast acoustic shadows, appear larger than their true size, and appear less echogenic than their true echogenicity. Most **benign calcifications** lie within a fairly echogenic background, so that when volume is averaged with the surrounding echogenic tissues, they are no longer bright enough to be identified sonographically. **Malignant calcifications** lie within rather homogeneously hypoechoic tumor substance and remain visible even though they are subject to volume averaging with surrounding tissues. Thus sonography can generally demonstrate a higher percentage of malignant than benign microcalcifications.

Associated Features

Other findings that can be associated with malignancy but are less specific than the suspicious features listed earlier include architectural distortion, skin changes, edema, and elasticity. These

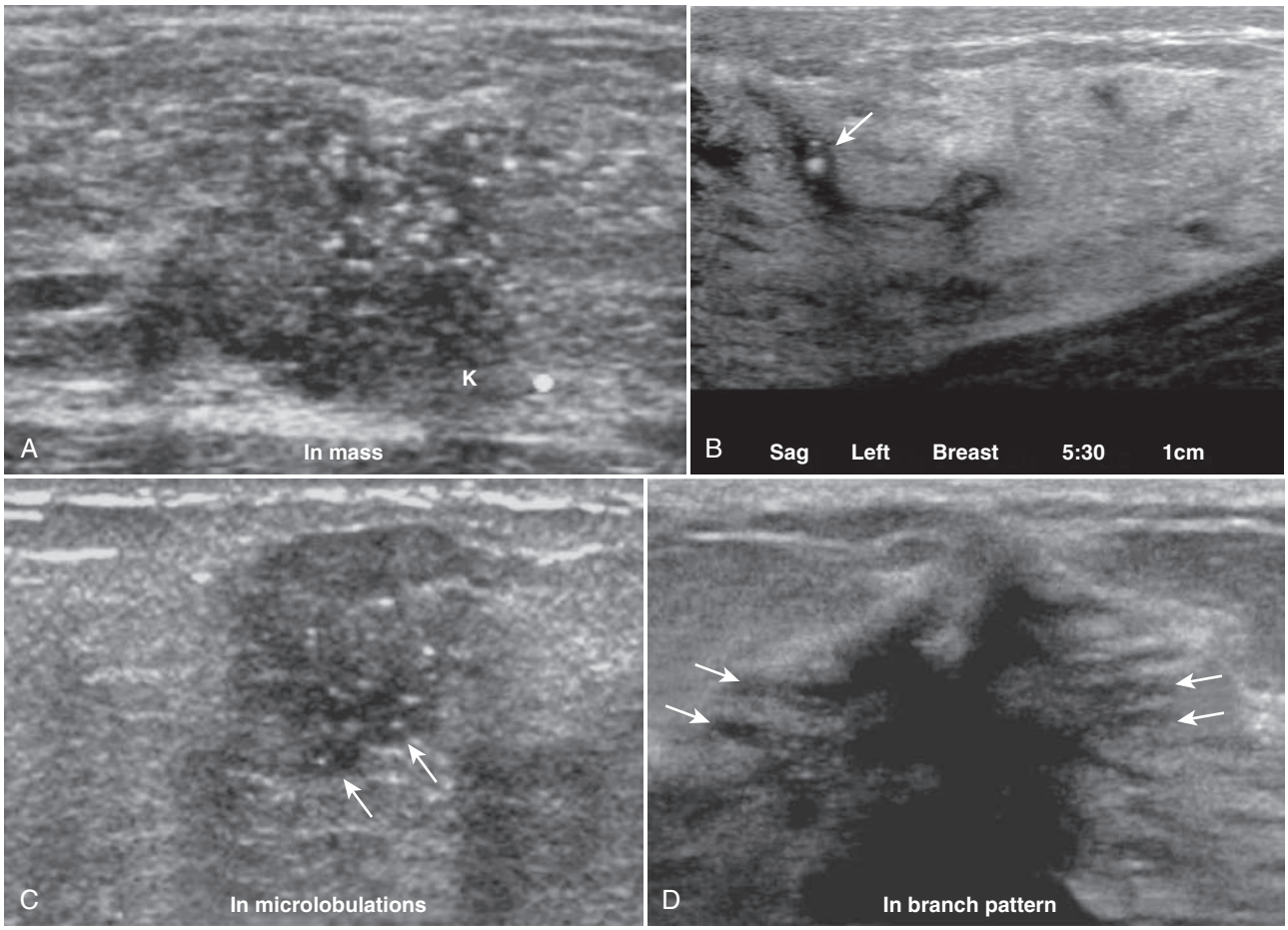

FIG. 21.53 Microcalcifications. These appear as bright echoes too small to create acoustic shadows. Microcalcifications are "soft" findings that suggest the presence of ductal carcinoma in situ (DCIS) elements. **(A)** Microcalcifications can occur amorphously within a mass. **(B)** However, most malignant breast calcifications occur within the necrotic debris in the center of the lumen of tumor-distended ducts. **(C)** Calcifications can also be found within microlobulations *(arrows)* or **(D)** within branch patterns *(arrows)*.

terms are found under the category "Associated Features" in the ACR BI-RADS lexicon.[17]

Architectural distortion associated with malignancy is caused by the effect of a mass on the surrounding tissues. These can manifest as compression of the surrounding tissues by the mass, obliteration of the tissue planes, changes to Cooper ligaments including thickening or straightening, and aberrations in the ductal pattern. Architectural distortion can also be present from benign causes such as radial scars or complex sclerosing lesions. Postsurgical change is an important iatrogenic cause of architectural distortion.

Skin changes include skin thickening and skin retraction. Skin thickening as defined by the ACR BI-RADS system is greater than 2 mm and can be focal or diffuse.[18] An important note is that skin in the periareolar area and inframammary folds can be up to 4 mm. Skin retraction is defined as a concave skin surface or a skin surface that appears ill defined and pulled in. Although skin changes can be present in benign processes such as infection or inflammation, prior surgery or biopsy, or radiation, skin changes can also be a sign of malignancy. Inflammatory breast cancer is an aggressive form of breast cancer that involves the skin through dermal lymphatic vessels and can result in skin thickening. Ductal carcinomas can also result in skin involvement. For example, some ductal carcinomas develop superficially in the peripheral zone and can extend into the skin.

Edema is suggested with increased echogenicity of breast tissue and interdigitating hypoechoic lines that may represent interstitial fluid or dilated lymphatics. Edema can be associated with inflammatory breast cancer but also with benign causes such as mastitis and congestive heart failure.

Elasticity assessment evaluates the stiffness of masses. Malignant masses are typically stiff or hard, whereas benign masses are more compressible. Descriptors for masses include soft, intermediate, and hard. This feature is far less important than the morphologic descriptors because there is significant overlap in appearance for benign and malignant masses.

Benign Findings

Benign findings should be sought only if no suspicious findings are present. The benign findings are (1) **pure and total hyperechogenicity,** which represents interlobular stromal fibrous tissue or fat; (2) an **oval circumscribed mass with parallel orientation,** completely encompassed by a thin, echogenic capsule; and (3) **an oval mass with gently lobulated margins** (three or fewer

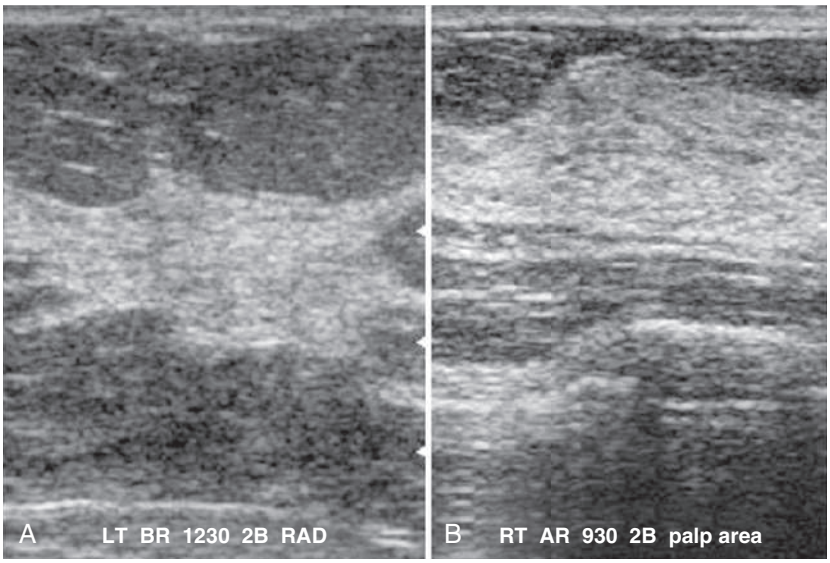

FIG. 21.54 Hyperechoic Fibrous Tissue Collections. Normal isolated collections of hyperechoic interlobular stromal fibrous tissue can cause **(A)** mammographic nodules and masses, or **(B)** palpable ridges.

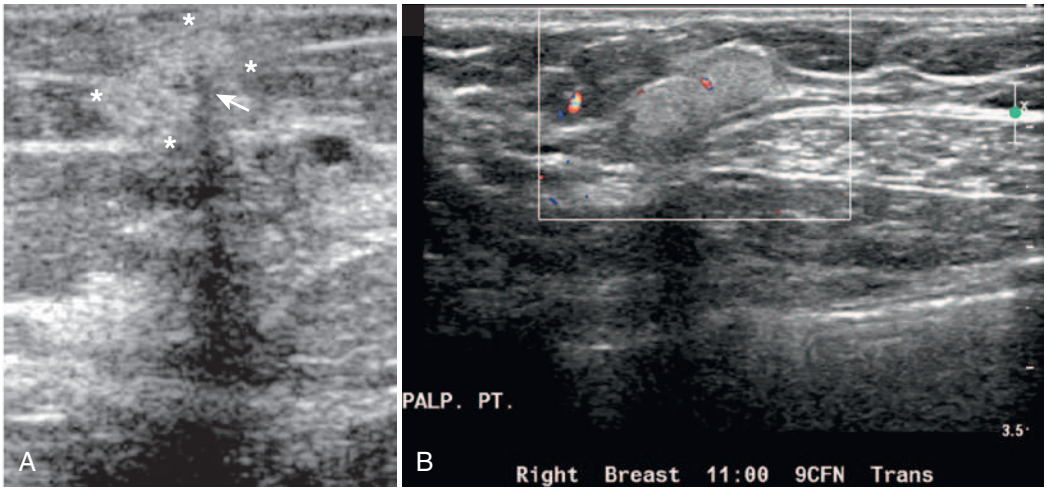

FIG. 21.55 Hyperechoic Malignancies. The negative predictive value of purely and intensely hyperechoic tissue is essentially 100%. However, collections of hyperechoic tissue should not contain any hypoechoic or isoechoic areas that are larger than normal ducts or terminal ductolobular units (TDLUs). **(A)** Certain small, invasive carcinomas can appear with tiny hypoechoic central foci *(arrow)* surrounded by a very thick, echogenic rim (*). Near-field volume averaging or tangential imaging through the thick, echogenic rim of such lesions can make them falsely appear to be purely hyperechoic. **(B)** In addition, hyperechoic masses with internal vascularity may also represent malignancy and should be sampled.

lobulations) and **parallel orientation** that is completely encompassed by a thin, echogenic capsule. If a nodule fits into one of these three categories, it can be characterized as BI-RADS 3, "probably benign."

Hyperechoic Tissue

Purely hyperechoic tissue is often normal interlobular stromal fibrous tissue or fat, which can cause either palpable or mammographic abnormalities (Fig. 21.54). To be considered benign, the hyperechoic tissue should contain normal-sized ducts or TDLUs without any isoechoic or hypoechoic structures larger than normal ducts or lobules. Purely hyperechoic carcinomas are exceedingly rare, but occasionally a carcinoma may have a very small, hypoechoic central nidus and a very thick, echogenic rim, and technical errors such as volume averaging or tangential imaging through the rim can make the lesion falsely appear to be purely hyperechoic (Fig. 21.55A).

It is important to correlate all hyperechoic masses with the mammographic findings. Hyperechoic masses that appear radiolucent on mammography are benign fat-containing masses, such as lipoma, oil cysts, or fat necrosis. Hyperechoic masses seen with a water density mass on mammography in the setting of trauma could represent fat necrosis or hematoma, and follow-up is warranted to ensure resolution. Biopsy of any hyperechoic mass that has any suspicious mammographic or sonographic feature should be performed. Similarly, although benign hyperechoic masses such as angiolipoma or pseudoangiomatous stromal hyperplasia can be vascular, any hyperechoic mass with increased

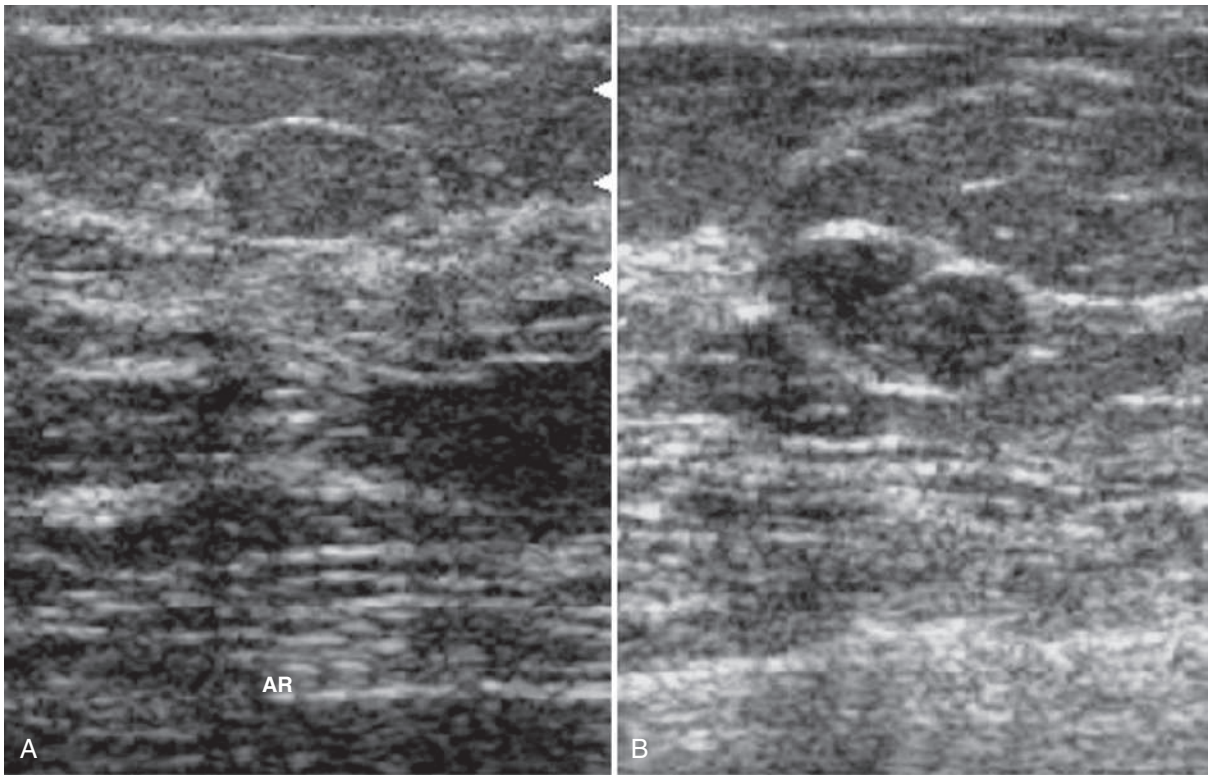

FIG. 21.56 Fibroadenoma. (A) Classic shape of benign fibroadenomas is elliptical. Such lesions are wider than tall and completely encompassed by a thin, echogenic capsule. **(B)** Second most common shape of benign fibroadenomas is gently lobulated. Classic lobulated fibroadenomas have three or fewer lobulations, are wider than tall, and are completely encompassed by a thin, echogenic capsule.

blood flow should be sampled to exclude malignancies such as invasive ductal carcinoma, lymphoma, or angiosarcoma[56] (Fig. 21.55B).

Parallel (Wider-Than-Tall) Orientation

An oval shape with parallel orientation is the classic appearance of a fibroadenoma (Fig. 21.56A). An oval mass with gently lobulated margins containing three or fewer lobulations and parallel orientation is the second most common shape of fibroadenomas (Fig. 21.56B). Masses that appear to be circumscribed in one view and gently lobulated in the orthogonal view are common. The negative predictive value of the oval shape is 97%, and the negative predictive value of the gently lobulated shape is 99%, in a population of masses with 33% malignancy.[45] Despite the high likelihood of benignity, these masses should always be followed or biopsy performed to ensure no malignancy is present.

Thin Echogenic Capsule

It is important to combine the circumscribed or gently lobulated margins with the presence of a complete, thin, echogenic capsule to minimize false-negative results in circumscribed carcinomas and in pure DCIS. Although carcinoma has an echogenic pseudocapsule and DCIS can have an echogenic surrounding duct wall, they almost never have an elliptical or gently lobulated shape. In addition, the thin echogenic pseudocapsule that can be seen around circumscribed carcinomas is often absent along part of the surface of the nodule. Carcinoma and DCIS are also usually associated with other suspicious findings, such as angular margins, not parallel orientation, microlobulations, or duct extension. By combining the presence of a **complete, thin, echogenic capsule with the oval circumscribed mass or oval gently lobulated mass** we can achieve a negative predictive value of greater than 99%.[45]

Rocking the transducer in its short axis and heeling and toeing the transducer along its long axis are often necessary to demonstrate the presence of a thin, echogenic capsule along the edges of the masses. Using less compression often helps to demonstrate the thin echogenic capsule in benign masses that are surrounded by hyperechoic fibrous tissue.

DIAGNOSTIC ULTRASOUND INDICATIONS

Most diagnostic breast ultrasound is performed in a targeted fashion to evaluate a particular symptom or mammographic abnormality.

Symptomatic Breast

Breast Pain

The evaluation of breast pain is based on whether the patient has focal pain or nonfocal pain. Although focal pain alone indicates a low likelihood of malignancy,[57] ultrasound is often performed to provide reassurance to the patient or to identify a benign cause that may be treatable. Ultrasound is not

recommended for diffuse unilateral or bilateral breast pain that may or may not be cyclic in nature.

Palpable Abnormality

The specific goal of targeted sonographic evaluation of palpable lumps is either (1) to find a malignant lesion that has been obscured by surrounding dense tissues on the mammogram or (2) to find normal or definitively benign causes of the lump that do not require biopsy or short-interval follow-up.

Ultrasound is most useful when there is dense tissue in the area of the palpable lump on mammography. Lesions that do not contain calcifications may be obscured by surrounding dense tissues on mammography. Sonography has much less to contribute to cases with a background of predominantly fat and only fatty density in the area of the palpable lump on mammography. It is unlikely that the mammogram missed anything significant, and the palpable lump is most likely to be either a fat lobule or a benign lipoma in such cases. The rare exception to this general rule occurs in cases of pea-sized or smaller palpable lumps when the skin line is overpenetrated on the mammogram and thus cannot be appreciated. These patients may have a tiny, superficial lesion just under the skin that is not adequately shown on the mammogram. This situation is much less common on digital mammograms with current tissue equalization techniques. Should the palpable lump be an asymmetric mixture of fat and water density in a predominantly fatty breast, sonographic evaluation should be aggressively performed, because this could represent a malignancy. When a palpable area correlates with a suspicious mass on ultrasound, the ultrasound evaluation can be used to help target the area for subsequent biopsy.

When used to confirm that a palpable abnormality is benign, ultrasound can help avoid biopsy or additional imaging follow-up. Should the mammogram reveal a finding in the area of clinical concern, ultrasound can be used to demonstrate whether the finding is benign such as a simple or complicated cyst. Should the mammogram be normal in the area of clinical concern, targeted ultrasound to that location should be performed as well. If only normal breast tissue is seen, then there is a high probability that the area is not malignant. Several studies have now shown an extremely high (≥99%) negative predictive value for the combination of normal mammography and normal or benign ultrasound findings.[58,59] That being said, should a patient have a new or increasing palpable area that is clinically suspicious, the clinicians can perform a blind biopsy of the area to confirm that it is not malignant. Accordingly, a notation for clinical follow-up is important as part of the management recommendations.

If sonography is to be effective at evaluating a palpable abnormality, it is essential that the abnormality be simultaneously palpated while being scanned. The image should be annotated with the word "palpable." An image could be acquired during the act of palpation wherein the finger is documented in the image (Fig. 21.57). Simply showing that normal tissue or a benign cyst exists in the same quadrant is insufficient proof that it is the cause of the palpable lump. For large lesions in compressible breasts, the operator can usually slide the nonscanning index finger under the transducer while scanning. For smaller lesions and firmer breasts, the index finger may lift the ends of the transducer so far off the skin that the lesion cannot be scanned with the finger between the transducer and skin. In such cases, trapping the lesion between the index and middle fingers and scanning the lesion while it is trapped may be useful (Fig. 21.58). For very small and superficial lesions, an opened paper clip can be used to palpate the lesion during scanning without lifting the ends of the transducer off the skin.

Nipple Discharge

Evaluation of nipple discharge begins with a review of the symptoms. Bilateral nonspontaneous milky nipple discharge is more often associated with hormonal changes that are either physiologic or are associated with prolactin-producing tumor, and imaging evaluation of the breast is not needed.

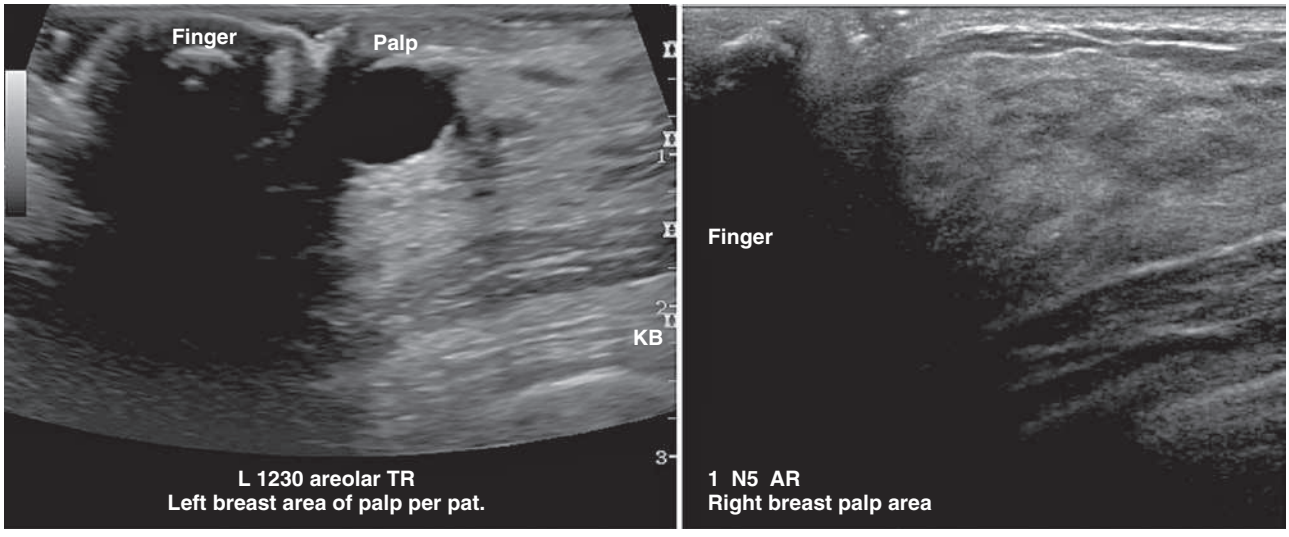

FIG. 21.57 Marking Palpable Lesions During Targeted Diagnostic Sonography Is Critical. *Left,* Small, simple cyst is palpated with the nonscanning index finger during imaging. *Right,* Fibroductal ridge is palpated during scanning.

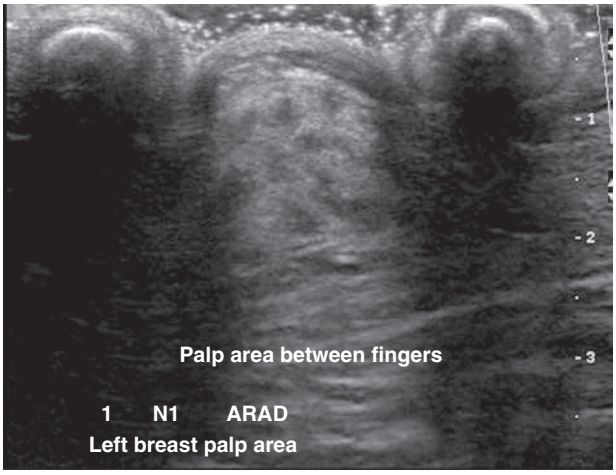

FIG. 21.58 Finger Trapping to Document Breast Lesion. Trapping the palpable abnormality between the index and middle fingers can be helpful in documenting the cause of the "lump."

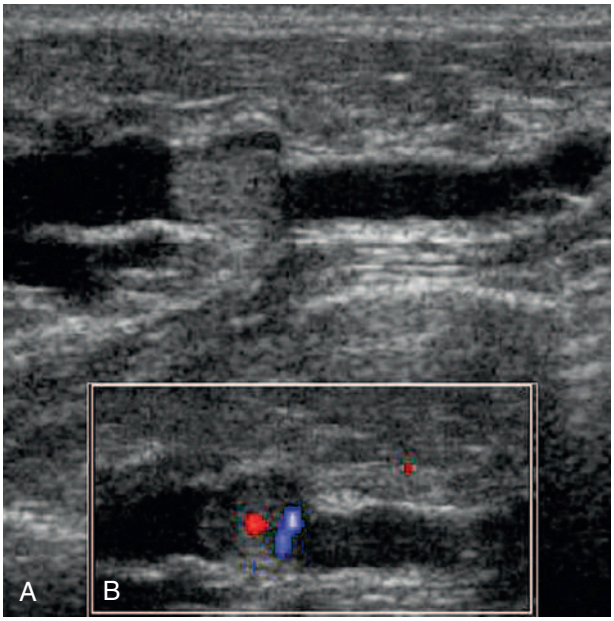

FIG. 21.59 Intraductal Papillary Lesion. (A) Small, ovoid intraductal papillary lesions that do not expand the duct represent benign large duct papillomas in more than 98% of cases. **(B)** Even small intraductal papillomas typically have a readily demonstrable vascular stalk.

Discharge that is more concerning for breast malignancy is unilateral and spontaneous. The discharge may be bloody, serosanguinous, or clear, although color alone should not lead one to dismiss the sign. Unilateral nipple discharge is most often caused by papillomas; however, carcinoma must be excluded. Other causes include duct ectasia, benign FCC with communicating cysts, or an idiopathic cause. Historically, imaging evaluation of unilateral nipple discharge was primarily with **galactography;** however, other tools including ultrasound are now more commonly used. Ultrasound can be performed during the initial diagnostic workup or can be used during a second-look evaluation after MRI or galactography.[60-62] As a first-line evaluation, retroareolar ultrasound is performed to identify an intraductal mass that may be causing the discharge. Because **intraductal papillary lesions** that cause nipple discharge often lie within the large mammary ducts under or near the areola, this is the area that should be targeted for the ultrasound evaluation.[49] Warm room temperature, warm acoustic gel, and special maneuvers, such as the two-handed compression maneuver and the rolled nipple technique, help minimize shadowing that can arise in the nipple and areola.

Papillomas appear to be isoechoic nodules (less echogenic than the duct wall) within ectatic fluid-filled ducts (Fig. 21.59). The appearance of papillomas varies with the degree and distribution of duct dilation, with the diameter and length of the lesion, and with involvement of branch ducts and TDLUs. In addition, papillary lesions that affect TDLUs are, by definition, **peripheral papillomas,** regardless of their distance from the nipple. Peripheral papillomas are at much higher risk for being malignant than large duct papillomas (Fig. 21.60). However, because ultrasound characteristics of malignant versus benign papilloma have not been well established, biopsy is performed on most intraductal masses and likely papilloma.

Sonography can show causes of nipple discharge other than large duct papilloma, such as **carcinoma, duct ectasia, communicating cysts,** and **hyperprolactinemia** (Fig. 21.61).

Mammographic Findings

Sonography is the best diagnostic tool for assessing mammographic abnormalities that do not contain suspicious calcifications. These mammographic abnormalities range from discrete masses to one-view asymmetries. It is important to complete the mammographic workup of these findings and determine the level of suspicion before beginning the ultrasound evaluation. This essentially becomes the pretest probability for identifying a malignancy and will help drive one's recommendations. Only in a small percentage of patients will sonography show findings that are more suspicious than those suggested by mammography. Completing the mammographic workup initially is most important for the scenario in which no ultrasound correlate is found and management must depend solely on the mammographic evaluation.

When completing the ultrasound evaluation, it is important to be sure that the sonographic finding explains the mammographic abnormality, and that there are not two completely disparate findings—a mammographic finding and a separate and incidental sonographic finding. To ensure that there is only a *single* finding and that the sonographic finding and mammographic finding are the same, the clinician must rigorously ensure that the size, shape, location, and surrounding tissue density of the mammographic and sonographic findings are the same. **Mammographic-sonographic correlation** of size, shape, location, and surrounding tissue density is best made between the craniocaudal (CC) mammographic view and the transverse sonographic view because there is little rotation and no obliquity of the x-ray beam on the mammographic CC view. If a mammographic lesion can be seen only on the mediolateral oblique (MLO) view, it is usually best to obtain a true mediolateral (ML)

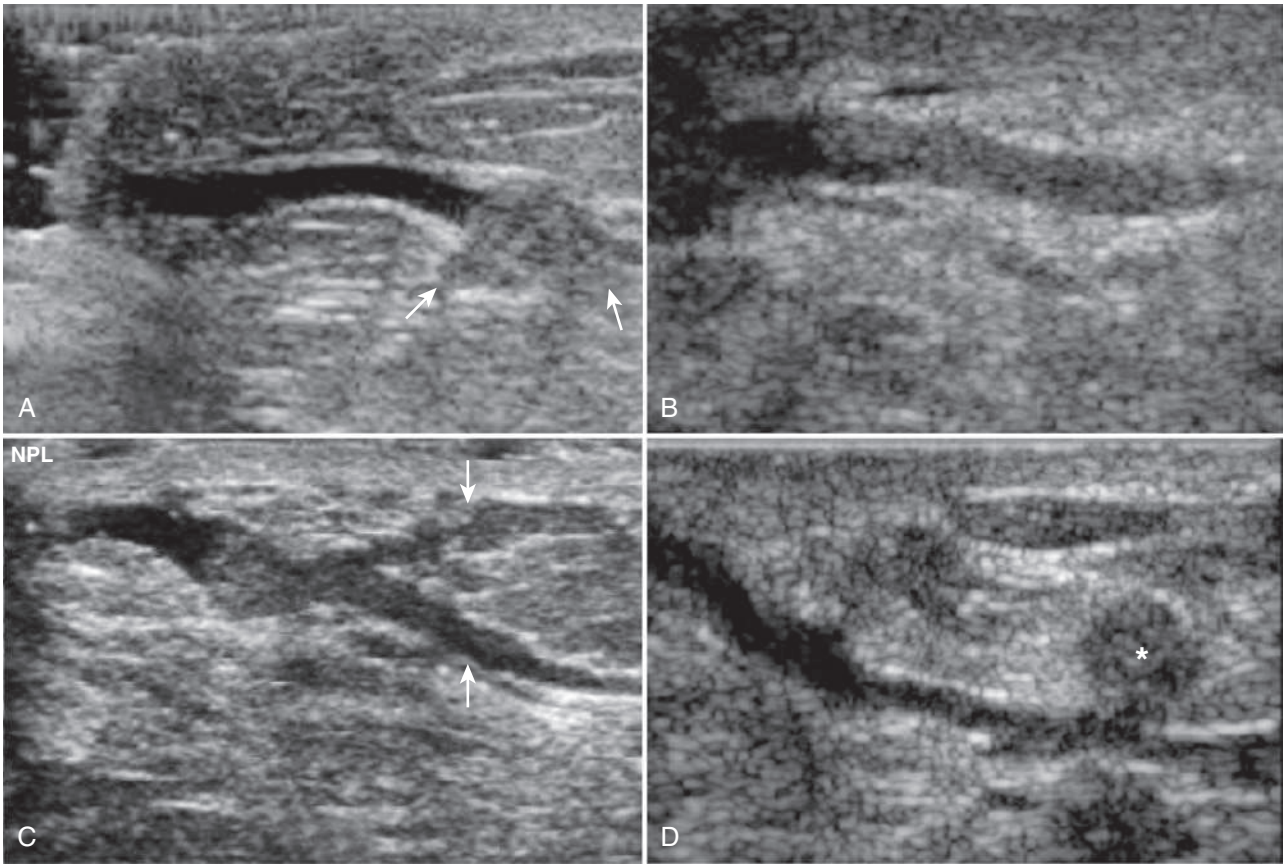

FIG. 21.60 Suspicious Intraductal Papillary Lesions. Intraductal papillary lesions that have greater than a 2% risk of being malignant and that should be characterized as Breast Imaging Reporting and Data System (BI-RADS) 4 and undergo biopsy include **(A)** lesions that expand the duct or breach *(arrows)* its wall, **(B)** lesions that are longer than 1.5 cm, **(C)** lesions that involve multiple peripheral branch ducts *(arrows),* and **(D)** lesions that involve terminal ductolobular units (TDLUs; *) **(peripheral papillomas).**

view, taking care not to rotate the breast during compression, and then obtain a true longitudinal ultrasound view to correlate with the mammographic ML view.

Size Correlation

Mammographic-sonographic correlation of size should take into account everything that is water density on the mammogram. Therefore an oval, 3-cm, circumscribed mass on mammography could correlate with multiple different types of masses on ultrasound that all measure 3 cm, such as (1) a cyst, (2) a solid nodule with a thin echogenic capsule, (3) a cyst that contains a mural nodule, (4) a 3-cm collection of fibroglandular tissue, (5) a smaller cyst, or (6) a solid nodule surrounded by fibroglandular tissue (Fig. 21.62). All six sonographic structures would constitute a perfect mammographic-sonographic size match. Measurements on ultrasound should be made outside-to-outside to include the capsule that surrounds the cyst or solid nodules, because the capsule is water density and will be included in the measurement of the lesion on the mammogram. Ideally, the lesion will be measured identically on both modalities to maximize sonographic-mammographic correlation.

Maximum diameter is used for sonographic-mammographic correlation rather than mean diameter, because many mammographic lesions are partially compressible. Lesions that appear to be spherical on mammography are often oval on ultrasound (Fig. 21.63). The mean diameter of partially compressible lesions will appear larger on mammography than on sonography.

Shape Correlation

Sonographic-mammographic correlation of shape must consider two phenomena: **partial compressibility** and **rotary forces** applied during compression. This can be demonstrated when a partially compressible spherical mass on mammography appears oval on ultrasound (see Fig. 21.63). When the mammographic lesion is spherical and *not* compressible, the shape will be spherical on sonography as well.

Mammographic compression and sonographic compression apply different rotatory forces on lesions that are not spherical. Mammographic compression not only pulls lesions away from the chest wall, but also tends to rotate the lesion so that its long axis lies perpendicular to the chest wall. Sonographic compression will push lesions closer to the chest wall and tends to rotate the lesion's long axis parallel to the chest wall. There is typically a 90-degree difference in the orientation of the long axis of lesions between the mammogram and the sonogram (Fig. 21.64). If this rotation is not considered, the breast sonographer may falsely conclude that the shape of the lesion is different on the mammographic and sonographic images.

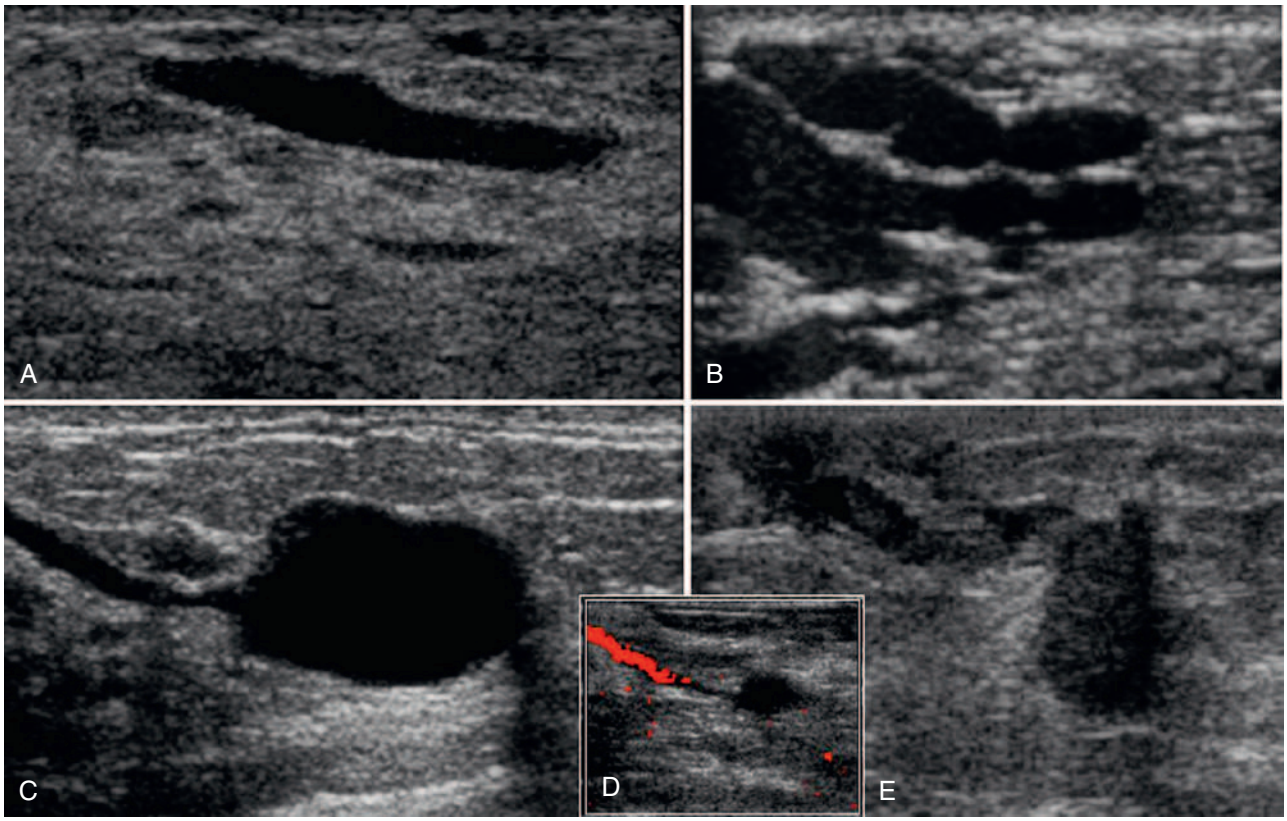

FIG. 21.61 Lesions Other Than Papillomas That Cause Nipple Discharge. Duct ectasia usually involves one lobar ductal system at a time. **(A)** Early in its course, only a single duct might be involved. **(B)** Over time, additional lobar ducts can become involved, leading to multiple dilated ducts. When all the ducts are severely involved, one must consider **hyperprolactinemia** as an underlying factor. **(C) Communicating cysts. (D)** Confirmation that the cyst truly communicates with the ductal system can be made by showing a "color-swoosh" with the communicating duct when the cyst undergoes ballottement with the transducer. **(E)** Pure ductal carcinoma in situ (DCIS) and invasive duct carcinomas that have DCIS components can also give rise to nipple discharge.

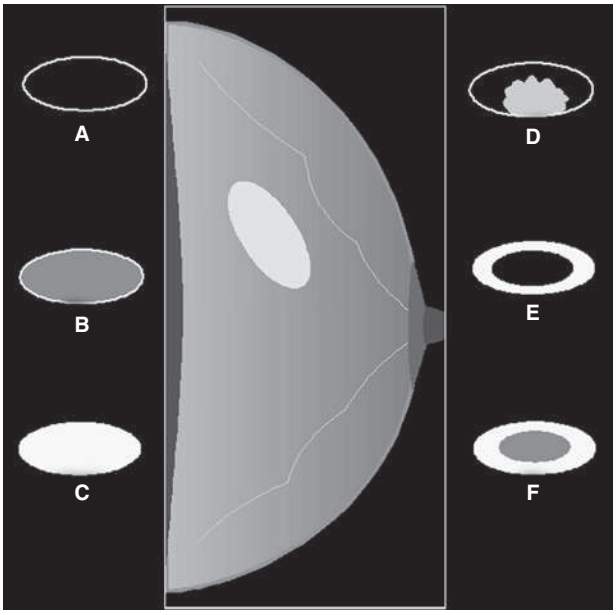

FIG. 21.62 Importance of Mammographic-Sonographic Correlation. Everything that is water density could contribute to the size of the mammographic lesion. Thus a 3-cm, ovoid, circumscribed mammographic mass could represent **(A)** a cyst, or **(B)** a solid nodule, surrounded by a thin echogenic capsule; **(C)** 3-cm collection of interlobular stromal fibrous tissue; **(D)** 3-cm cyst containing a mural nodule; or **(E)** smaller cyst, or **(F)** solid nodule, surrounded by fibrous or glandular tissue.

Location or Position Correlation

Because mammographic compression pulls a lesion away from the chest wall and sonographic compression pushes the lesion closer to the chest wall, lesions usually appear much closer to the chest wall on sonography than on mammography. Lesions that appear to lie several centimeters from the chest wall on mammography may appear to lie very close to the chest wall, even indenting the chest wall musculature, on sonography. If this routine apparent difference in depth of lesions on mammography and sonography is not understood, the clinician might falsely conclude that the sonographic lesion lies too deep to correspond to the mammographic lesion.

Surrounding Tissue Density Correlation

The final step in correlating the sonographic and mammographic findings is assessment of the density of surrounding tissues. A lesion that protrudes into the subcutaneous fat from the mammary zone, and that is surrounded by fat superficially and water density tissue along its deep margins on the mammogram, should lie at the junction of the subcutaneous fat and mammary zone on the sonogram. It should be surrounded by subcutaneous fat along its superficial margin and by either hyperechoic fibrous tissue or isoechoic glandular tissue along its deep border on the sonogram (Fig. 21.65).

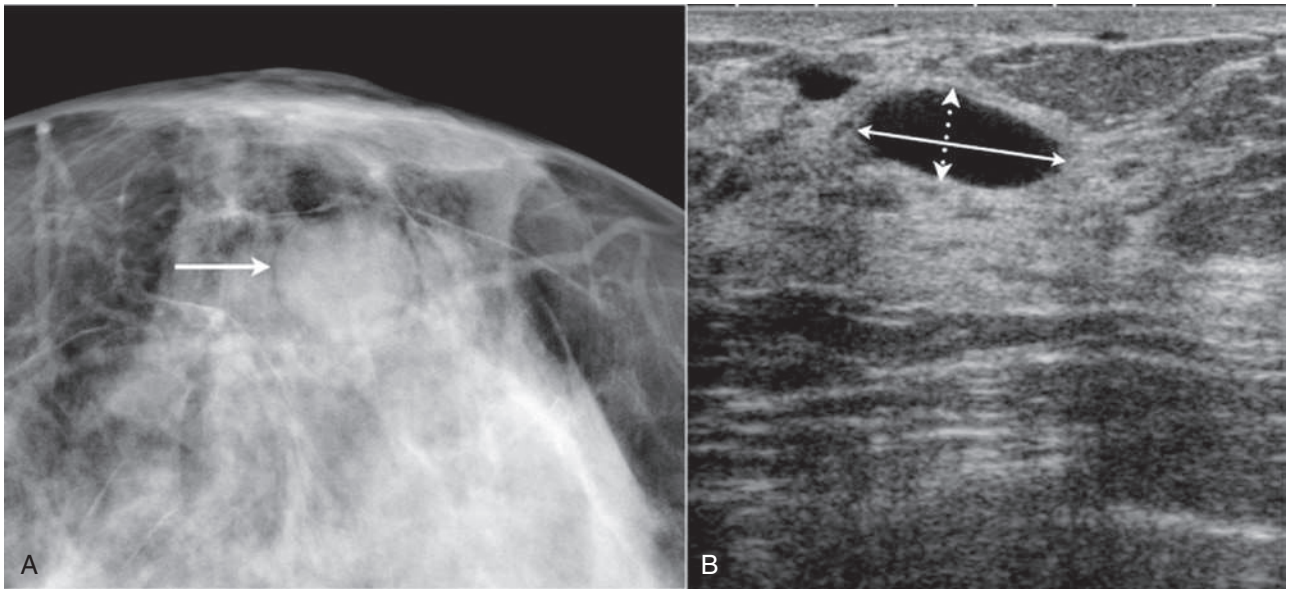

FIG. 21.63 Lesions That Appear Spherical on Mammography Often Appear Elliptical on Sonography. (A) Circumscribed isodense mammographic nodules appeared circular in both views (spherical) because the mammogram demonstrates only the axes of the cyst that lie perpendicular to the axis of compression and not the compressed axis. Sonography, however, does show the compressed axis. The mean diameter calculated from mammograms includes three large diameters that all lie in axes perpendicular to the axis of compression. **(B)** The mean diameter calculated from the sonographic views includes two large diameters that lie perpendicular to the axis of compression *(solid arrow)* and one smaller diameter that lies parallel to the axis of compression *(dotted arrow)*. For compressible lesions, the mean diameter obtained from sonograms is often smaller than the mean diameter obtained from mammography, but the maximum diameters from mammography and sonography will be similar.

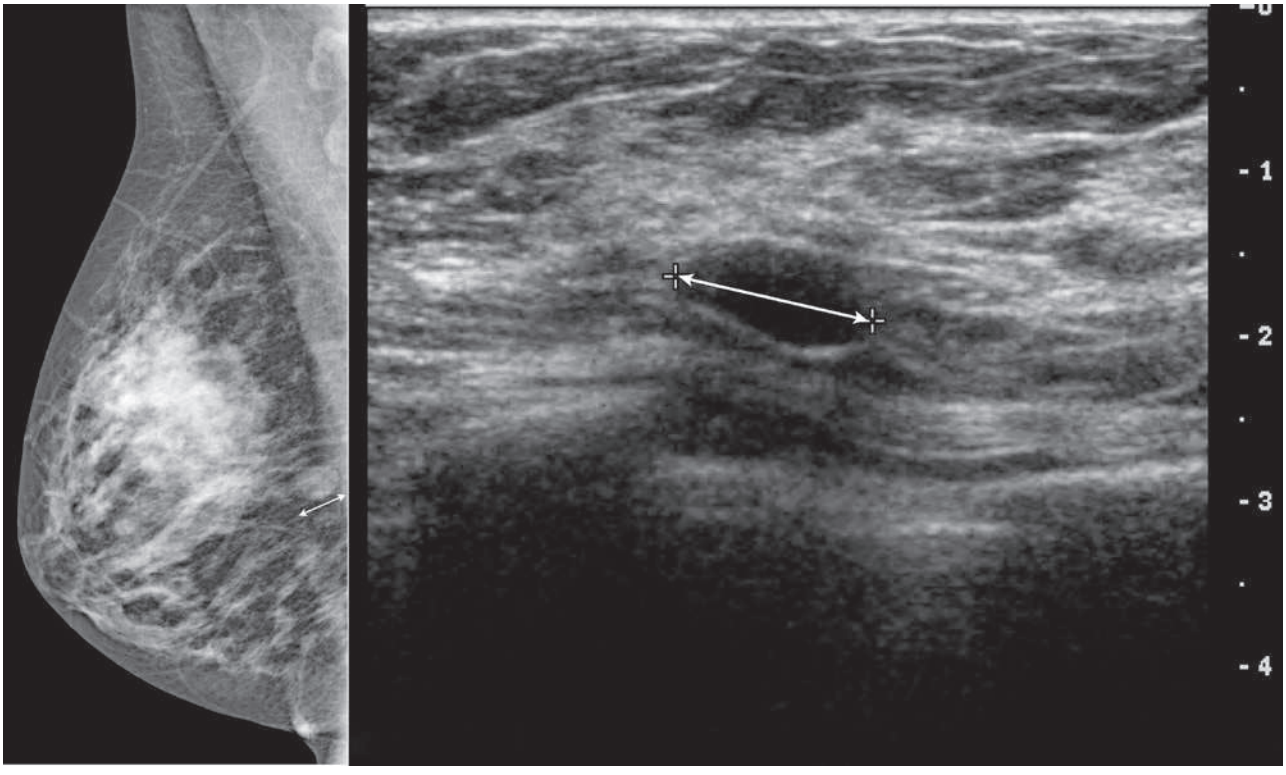

FIG. 21.64 Mammographic-Sonographic Compression and Lesion Orientation. Mammographic compression *(left)* tends to rotate the long axis of the lesion perpendicular to the chest wall, whereas sonographic compression *(right)* tends to rotate the long axis parallel to the chest wall. The long axes of lesions on mammography and sonography often differ by almost 90 degrees. The double-headed arrows show the long axis of the lesions.

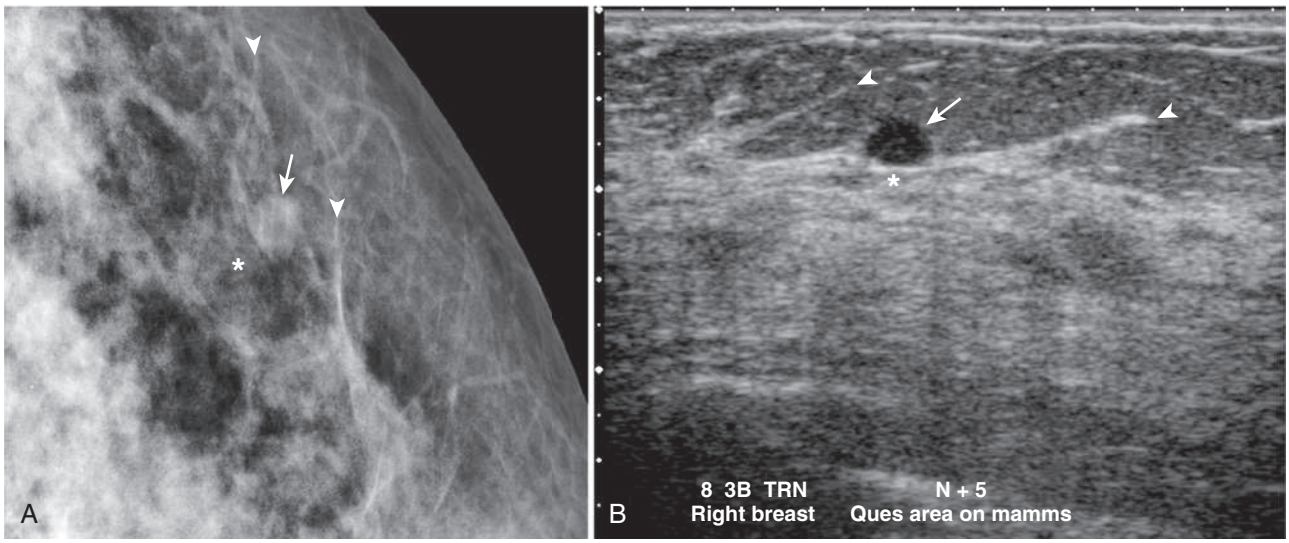

FIG. 21.65 Mammographic-Sonographic Correlation of Surrounding Tissue Density. (A) Mammogram shows a nodule projecting between two Cooper ligaments *(arrowheads)* and bulging anteriorly into the subcutaneous fat *(arrow)* from the mammary zone (*). **(B)** Sonogram shows that the mammographic nodule is a small cyst that protrudes out of fibrous tissue in the mammary zone (*) and into the subcutaneous fat *(arrow).* It lies between two Cooper ligaments *(arrowheads).*

Sonographic-Mammographic Confirmation

Correlating size, shape, location, and surrounding tissue density will allow the mammographic and sonographic findings to be definitively correlated in most cases, but in some cases may fail. If it cannot be determined with absolute certainty that the mammographic and sonographic lesions are indeed the same, minimally invasive sonographic procedures can be performed to confirm the correlation. If sonography shows the suspect mammographic lesion to be cystic, ultrasound-guided cyst aspiration can be performed and the mammogram repeated to see if the mammographic lesion has disappeared. If sonography shows the suspect lesion to be solid, ultrasound-guided placement of a small-gauge needle (e.g., 25 gauge) or removable wire can be performed and the mammogram repeated with the needle or wire in place, to document that the sonographic lesion and mammographic lesion are indeed in the same lesion. Alternatively, an ultrasound-guided core biopsy can be performed with placement of a radiopaque biopsy marker in the sampled area. Subsequent postprocedural mammography can confirm whether the lesion that underwent biopsy and the initially seen finding are the same.

NICHE APPLICATIONS FOR BREAST ULTRASOUND

Infection

The main uses of sonography in patients with **mastitis** is to determine whether there is an abscess, to determine its maturity, to determine if it is multiloculated, and to guide aspiration of, or drain placement into, the abscess in appropriate cases. The appearance of abscesses varies depending on whether the mastitis is puerperal or nonpuerperal and whether it is centrally or peripherally located.[49,63-65] **Peripheral abscesses** in **puerperal mastitis** usually arise in preexisting galactoceles (Fig. 21.66) and may contain milk by-products, whereas peripheral abscesses in **nonpuerperal mastitis often** arise within inflamed cysts. **Central abscesses,** whether arising from puerperal or nonpuerperal mastitis (Fig. 21.67), usually result from rupture of an inflamed or infected duct and tend to be elongated in a plane that is parallel to the inflamed duct. Initially, unilocular abscesses can be treated with sequential ultrasound-guided aspirations. If they continue to re-collect, infectious abscesses may require placement of a percutaneous drain or surgical drainage. However, some noninfectious collections such as those seen with **granulomatous mastitis** may not benefit from continued aspirations because this can result in fistula formation. Biopsy may be necessary to confirm this alternate diagnosis. In these scenarios, treatment may involve antibiotic or steroid therapy or surgical excision. In some cases,

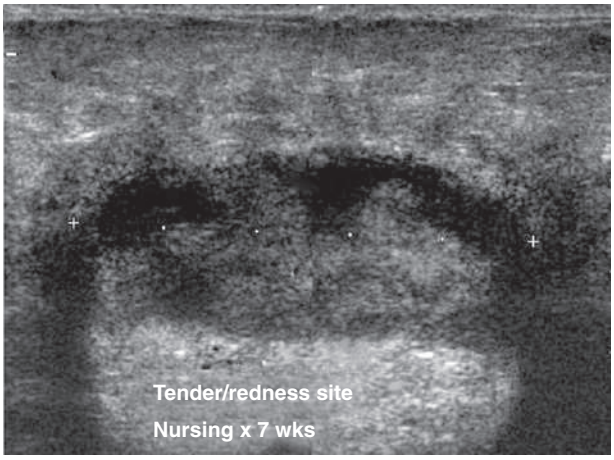

FIG. 21.66 Peripheral Puerperal Abscess. Often arising within preexisting galactoceles, peripheral puerperal abscesses *(calipers)* have very irregular walls and mixtures of fluid and echogenic debris.

sonography may be used to determine if there is an underlying inflammatory carcinoma.

Implants

In general, MRI is considered the modality of choice for evaluating breast implants.[66] However, most patients with implants at risk for **rupture** are within the mammographic screening cohort. Patients with implants may have palpable lumps and mammographic densities that require sonographic evaluation much more often than they require MRI evaluation of their implants. Thus sonographers must understand the wide variations of normal appearances in implants and must be able to identify intracapsular and extracapsular rupture, silicone granulomas, herniation, and capsular infection.

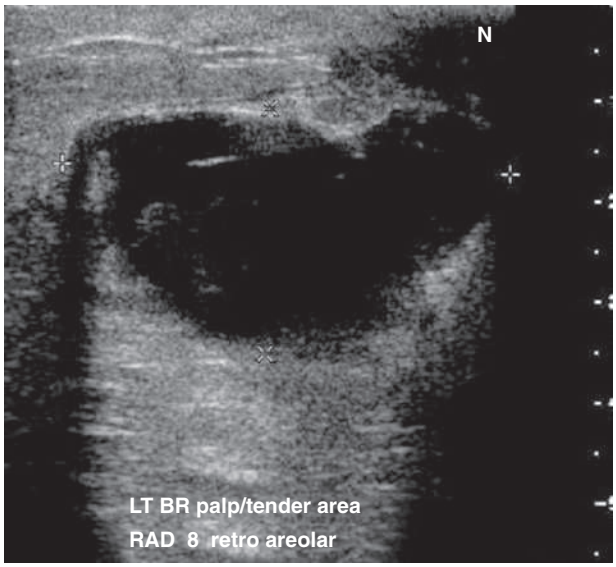

FIG. 21.67 Central Periareolar Abscess. Whether puerperal or nonpuerperal, central periareolar abscesses *(calipers)* usually arise when an inflamed or infected duct ruptures, spilling its contents into the periductal tissues. *N,* nipple.

Sonography allows identification of the type of implant, its implantation site, and many associated complications.[67-70] The **capsule** that surrounds the implant is fibrous and is a normal foreign body reaction to the implant. The capsule is abnormal only when (1) it becomes too thick and causes capsular contracture, (2) it develops a tear through which the implant can herniate, (3) it becomes inflamed or infected or (4) it develops an associated mass that could be either benign or malignant. The implant is filled with saline or silicone gel and is surrounded by a silicone elastomer shell. The **shell,** a part of the implant, must be distinguished from the capsule, which is living tissue formed by the patient in response to the implant.

Normal implants can give rise to palpable abnormalities in certain cases. **Radial folds** may be palpable when the patient is in certain positions. It is important to scan the patient when she is in the position where she feels the lump, because radial folds are dynamic and frequently occur only in certain positions, usually upright. Only anteriorly located radial folds will be palpable (Fig. 21.68A). Radial folds on the posterior surface of the implant are almost never palpable. In patients with saline implants, the **fill valve** can cause palpable abnormalities. In general, fill valves are placed behind the nipple. In certain cases, however, the valve may not be placed directly behind the nipple, or the implant may have rotated after placement. In such cases the valve may be palpable if overlying breast tissue is minimal. In other cases, valves become palpable years after the implant is placed because of eversion of the valve (Fig. 21.68B). **Eversion** is most likely to occur in implants that are under chronic pressure resulting from capsular contracture.

In **intracapsular rupture** the shell develops a tear through which silicone gel extravasates into the space between the shell and the capsule; the capsule remains intact. The classic findings of intracapsular rupture are the **stepladder sign** ("linguini" sign in MRI literature) and abnormally increased echogenicity in the extravasated gel that lies within the intracapsular extrashell space[67,71] (Fig. 21.69). Unfortunately, these signs have low sensitivity for intracapsular rupture because they are present only when

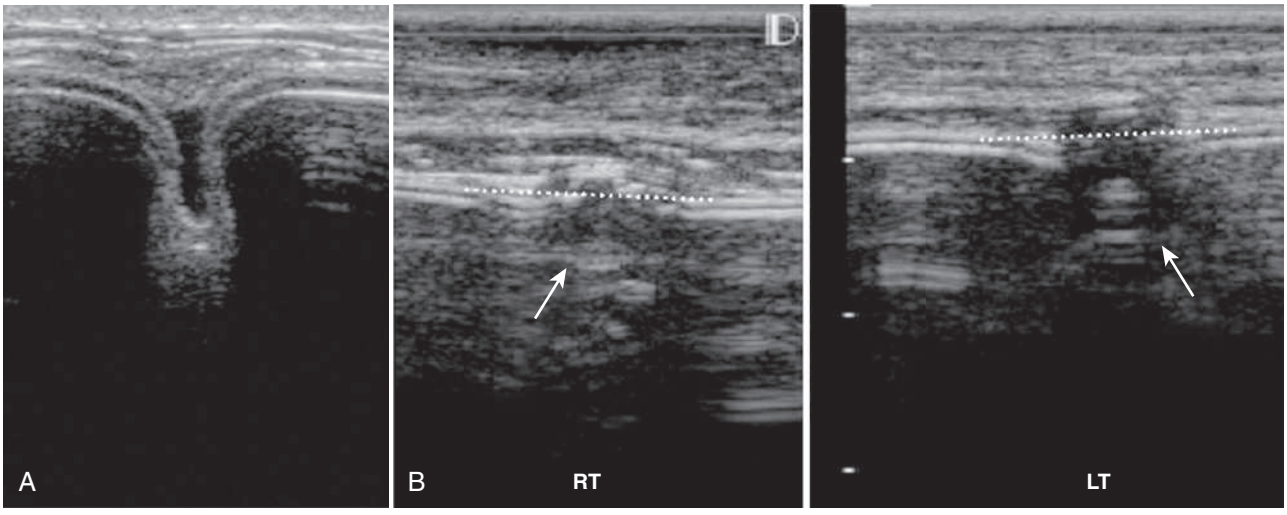

FIG. 21.68 Palpable Implant Components. (A) Anterior radial folds can cause palpable abnormalities; these folds often feel "crinkly." **(B)** Single-lumen saline implants have fill valves. In some cases, particularly with capsular contracture, increased pressure within the implant may cause the valve, which is normally flush with the outer surface of the implant shell *(RT, dotted line),* to evert and become palpable *(LT).*

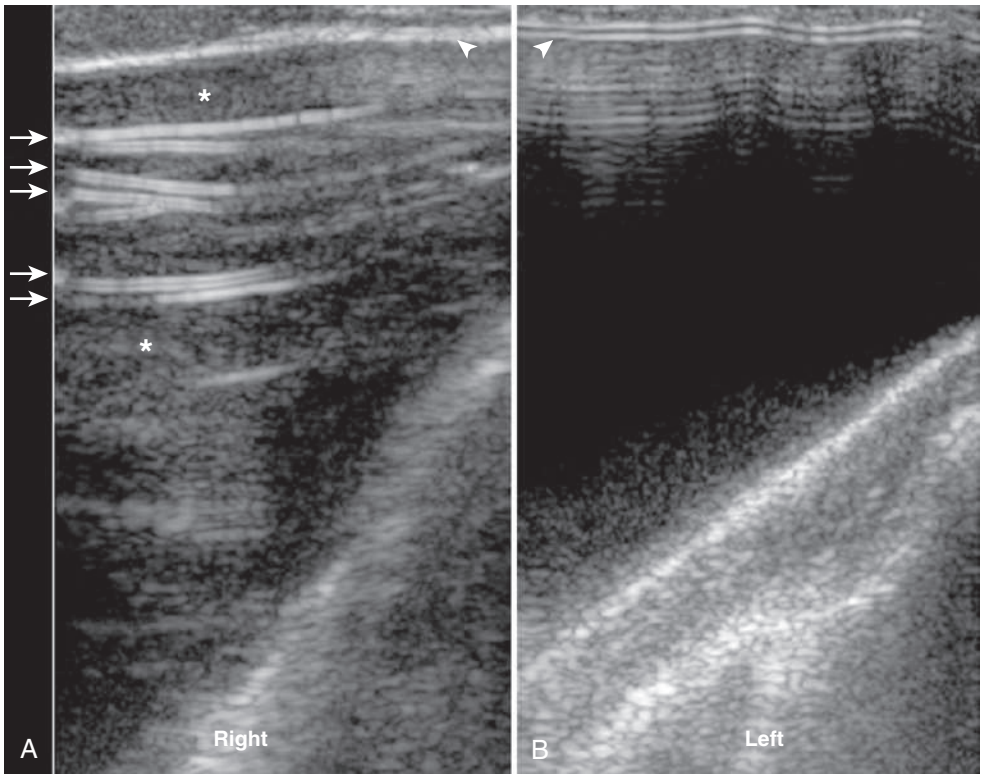

FIG. 21.69 Breast Implant Rupture. (A) Classic findings of intracapsular rupture of a single-lumen silicone gel implant are the "stepladder sign" *(arrows)*. Several linear, horizontally oriented echoes represent folds in a collapsed shell. Several of these are double echogenic lines that represent the inner and outer surfaces of each fold of the shell *(arrows)*. *Asterisk* (*) denotes silicone extravasated outside the implant shell but still within the capsule. **(B)** Normal left breast implant. Note that the superficial aspect of the unruptured left implant shows the double echogenic line *(white arrowhead)* of the shell at the anterior aspect of the silicone gel.

nearly all the silicone gel has extravasated from the shell and the shell is completely collapsed. Lesser degrees of collapse merely lead to abnormal, sheetlike separation of the shell inwardly away from the capsule. In general, there is a continuous spectrum of intracapsular collapse from involvement of a single radial fold to complete collapse. Radial folds are quite dynamic, forming when the patient is in one position, then disappearing when the patient assumes another position; the apex of radial folds therefore is prone to fatigue fractures. Because radial folds normally contain anechoic peri-implant effusion that is identical to silicone gel in echogenicity, for any individual radial fold, it is impossible to know whether the fluid within the fold is normal effusion or extravasated silicone gel from a fatigue fracture at the apex of the fold, unless the extravasated gel within the fold becomes hyperechoic. Radial folds should be considered normal unless they contain hyperechoic contents ("snowstorm" appearance).

In **extracapsular rupture** there is a tear in the capsule as well as in the shell, and silicone gel extravasates into the breast tissues outside the capsule. By definition, all cases of extracapsular rupture must be preceded by intracapsular rupture, although in many cases the intracapsular component is difficult to demonstrate sonographically. The classic finding is the **silicone granuloma** with a snowstorm appearance. Such granulomas are markedly hyperechoic and well circumscribed anteriorly but have an incoherent, "dirty" shadow posteriorly. Silicone granulomas can occur superficial to implants (Fig. 21.70A), but they most often occur at the edges of the implant, where the shell is thinnest and where fatigue fractures are more likely to occur (Fig. 21.70B). In certain cases, extravasated silicone gel forms a thin sheet over the outer surface of the implant rather than a discrete mass (Fig. 21.70C). In other cases, extravasated silicone gel can migrate away from the edge of the implant to the axilla, chest wall, back, or abdominal wall (Fig. 21.70D). Extravasated silicone gel can be picked up and carried by lymphatic vessels into the axillary lymph nodes, where it accumulates from the medullary sinuses within the mediastinum of the lymph node outwardly. Early **accumulation of silicone gel within lymph nodes** can be difficult to detect, although gel in the lymph node hilum will cause a subtle, dirty-appearing shadow.[72] As more silicone gel accumulates, the diagnosis of silicone gel accumulation within the lymph node becomes more obvious, and dirty shadowing arises from the entire lymph node (Fig. 21.70E).

Silicone granulomas have a spectrum of appearances. Not all have the classic snowstorm appearance. Large, acute accumulations of extracapsular silicone gel can appear complex and cystic (Fig. 21.71A). Over time, these may become solid appearing and isoechoic (Fig. 21.71B). The classic snowstorm appearance develops late, after the solid, isoechoic phase. Very late in the history of a silicone granuloma, so much foreign body granuloma may develop that the lesion can become hypoechoic, causing architectural distortion and more intense acoustic shadowing—findings that simulate those of stellate breast malignant lesions

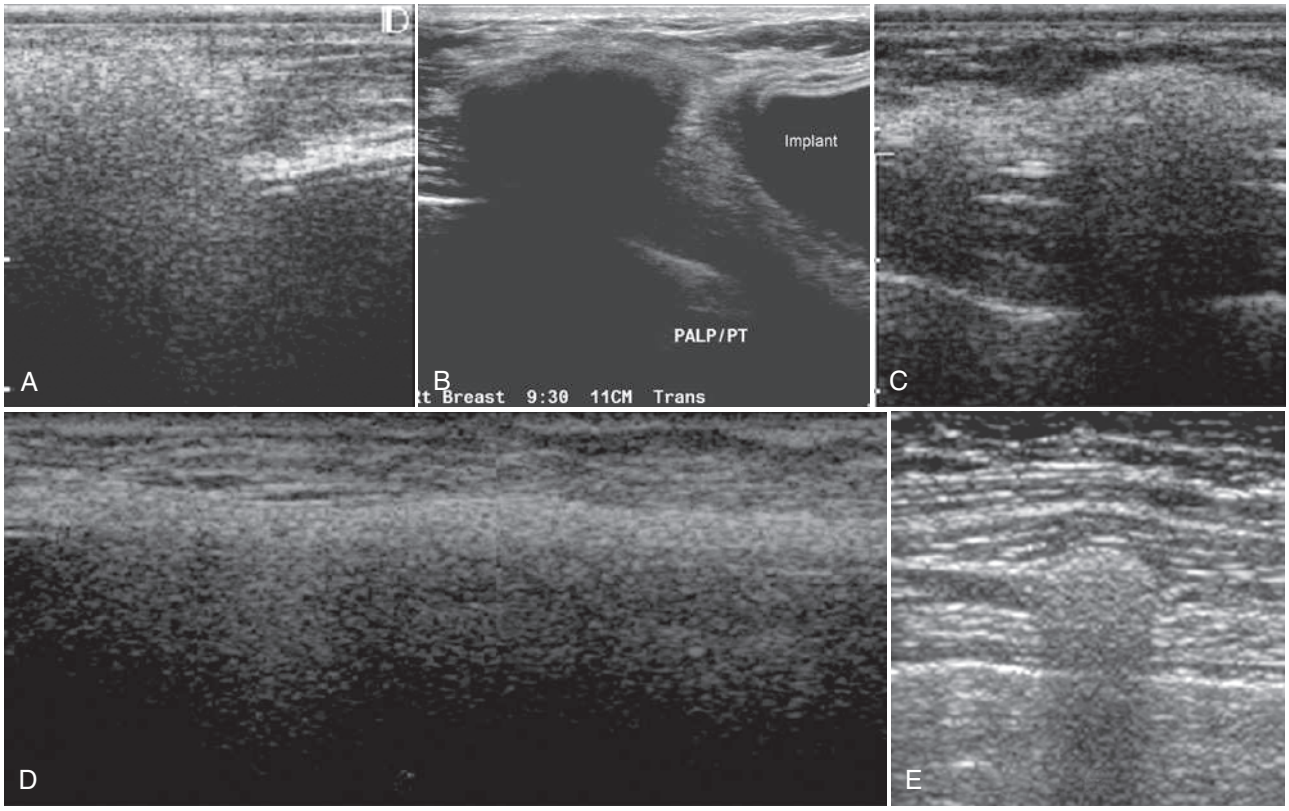

FIG. 21.70 Silicone Granulomas: Typical "Snowstorm" Appearance of Extracapsular Rupture. Silicone granulomas that manifest the snowstorm sign are hyperechoic and have a well-circumscribed superficial border and a posterior border obscured by "dirty" incoherent shadowing. **(A)** Silicone granulomas can occur anterior to the implant. **(B)** However, most occur along the edges of the implant, where the shell is thinner. **(C)** Silicone granulomas can spread over the surface of the implant in a thin sheet rather than forming a discrete mass. **(D)** Silicone granulomas can migrate away from the edge of the implant to lie on the chest or abdominal wall or in the axilla. **(E)** Extravasated silicone can be carried by lymphatics to regional lymph nodes, where it fills the lymph nodes with hyperechoic gel, giving a snowstorm appearance, from the medulla outward, as with this Rotter node that lies between the pectoralis major and pectoralis minor muscles.

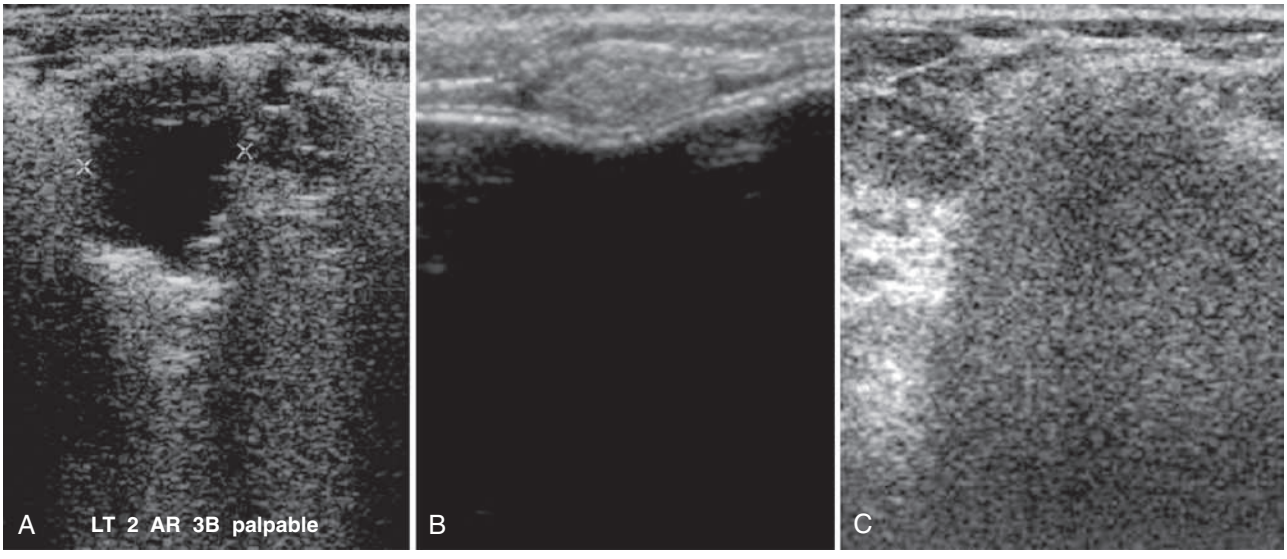

FIG. 21.71 Silicone Granulomas: Less Common Appearances of Extracapsular Rupture. (A) Large collections of acutely extravasated silicone gel can have a complex cystic appearance *(calipers)*. **(B)** Silicone granulomas of a few weeks to a few months' duration can appear to be isoechoic solid nodules. These usually progress to the snowstorm appearance within months. **(C)** Silicone granulomas that are many years old can develop so much foreign body reaction that they become intensely shadowing masses that simulate malignancy. Note also that, although most silicone granulomas result from extracapsular rupture, they can form between the capsule and the shell in certain patients, as in image **(B)**.

(Fig. 21.71C). The sensitivity of ultrasound for extracapsular rupture will be enhanced if the sonographer can recognize the entire spectrum of its sonographic appearances.

The presence of implants should not discourage necessary ultrasound-guided procedures. With ultrasound guidance, an angle of approach that is almost parallel to the surface of the implant can be used. A large amount of local anesthetic can be injected between the lesion and the implant to "hydrodissect" the lesion away from the implant and create a safe working space.

It is important to remember that patients with implants are subject to the same disease processes as patients without implants. Most patients are satisfied with their implants and experience no implant-related problems. The major problem for the sonographer is that the implants are distracting and a breast malignancy can be missed. Consequently, it is important to evaluate breast tissues *overlying* the implant before turning attention to the implants.

Breast Cancer Staging

When a patient is diagnosed with breast cancer, additional imaging may be performed to determine disease extent within the involved breast, disease involvement in the contralateral breast, and ipsilateral lymph node status. The most sensitive imaging study available is breast MRI, which identifies additional sites of malignancy in the ipsilateral breast in approximately 16% of patients and in the contralateral breast in 3% to 4% of patients[73] that would not have been seen on routine mammography. Ultrasound has been studied for evaluation of disease extent and has been shown to identify many of these additional sites, although not as many as breast MRI.[74-76] That being said, some institutions prefer ultrasound for breast cancer staging because histologic sampling of additional abnormalities can occur near simultaneously with the diagnostic evaluation.[77]

However, ultrasound *is* commonly used for evaluating lymph node status. Until recently, if invasive breast cancer was diagnosed, the patient would proceed with a sentinel lymph node biopsy of the ipsilateral axilla at the time of surgical excision to determine lymph node involvement. If positive lymph nodes were discovered, the patient would return for axillary dissection. To bypass this two-step process, preoperative ultrasound of the axilla was commonly performed to identify potentially involved lymph nodes. Should abnormal nodes be identified, histologic sampling could be performed before surgery. If the nodes were positive, then the patient could go straight to axillary dissection and avoid first having a sentinel node biopsy. If negative, the patient would still proceed with sentinel node sampling because the false-negative rate of axillary lymph node sampling is approximately 42%.[78]

A recent clinical trial has changed this routine. The American College of Surgeons Oncology Group Z0011 trial was a randomized, prospective study that compared survival and locoregional recurrence rates after sentinel node biopsy versus complete axillary dissection in women with clinical stage T1 or T2, N0, M0 breast cancer who were found to have one or two positive sentinel nodes at the time of lumpectomy.[79,80] The study revealed no significant difference between the two groups. Because of these findings, the role of preoperative ultrasound evaluation of the axilla is changing. Identifying lymph node metastasis preoperatively in patients who would otherwise meet the Z0011 criteria may no longer be necessary, because these patients may no longer proceed with axillary dissection. Consequently, some institutions no longer image the axilla at all, unless clinically relevant. Other institutions still image the axilla preoperatively but reserve histologic sampling for those patients in whom preoperative identification would change surgical management. Some studies suggest that preoperative lymph node sampling revealing malignant involvement is strongly correlated with tumor burden and the number of involved nodes.[81,82] Therefore some institutions are continuing to perform preoperative lymph node sampling and opting to proceed directly to axillary dissection in patients with positive results, even if they would otherwise quality for Z0011.

It is important to note, however, that the Z0011 results do not pertain to patients with stage 3 tumors, more than two positive sentinel nodes, or clinically positive axillary nodes or patients undergoing mastectomy, neoadjuvant chemotherapy, or partial-breast irradiation.[83] Ultrasound still plays a pivotal role in evaluating the axilla in these patients.

Ultrasound can easily evaluate the lymph node basins involved in breast cancer metastasis including axillary, internal mammary, and supraclavicular. Normal lymph nodes have a sonographic appearance similar to miniature kidneys. They are oval in the long axis, C-shaped in the short axis, and flat in the AP dimension (Fig. 21.72A). The **cortex** of the lymph node includes the marginal sinus, lymphoid follicles, and paracortex and is hypoechoic on ultrasound, whereas the **hilum** of the lymph node includes multiple blood vessels, fat, and the central sinus, which is hyperechoic on ultrasound.[84] As patients age, fatty infiltration of the lymph node may make the hypoechoic cortex very thin or barely visible (Fig. 21.72B). The flow of lymph passes through afferent lymphatic channels, which enter the lymph node from the periphery. The lymph then passes, in order, through the subcapsular sinusoids, cortical sinusoids, medullary sinusoids, and then out the efferent lymphatics, which exit through the hilum.

Many gray-scale criteria have evolved for evaluating lymph nodes, including size, shape, and echogenicity. Minimum diameters greater than 1 cm are considered abnormal. However, we have often seen morphologically abnormal metastatic lymph nodes with diameters less than 1 cm and normal atrophic lymph nodes with diameters well over 1 cm. Thus **size** is a poor criterion for metastasis. Metastatic lymph nodes tend to become **abnormally round,** but unfortunately this is a late finding. The cortex in some (not all) metastatic lymph nodes becomes **abnormally hypoechoic.** This finding may not be detected when using harmonics because harmonics routinely make the cortex appear more hypoechoic.

Morphologic assessment of the lymph node is more effective than evaluating its size, shape, and echogenicity. Lymph nodes that demonstrate **eccentric cortical thickening** should be considered suspicious for metastasis. Given that the lymphatics enter the node from the periphery, metastases initially implant within the subcapsular or cortical sinusoids, causing focal cortical thickening. The pattern of thickening depends on where

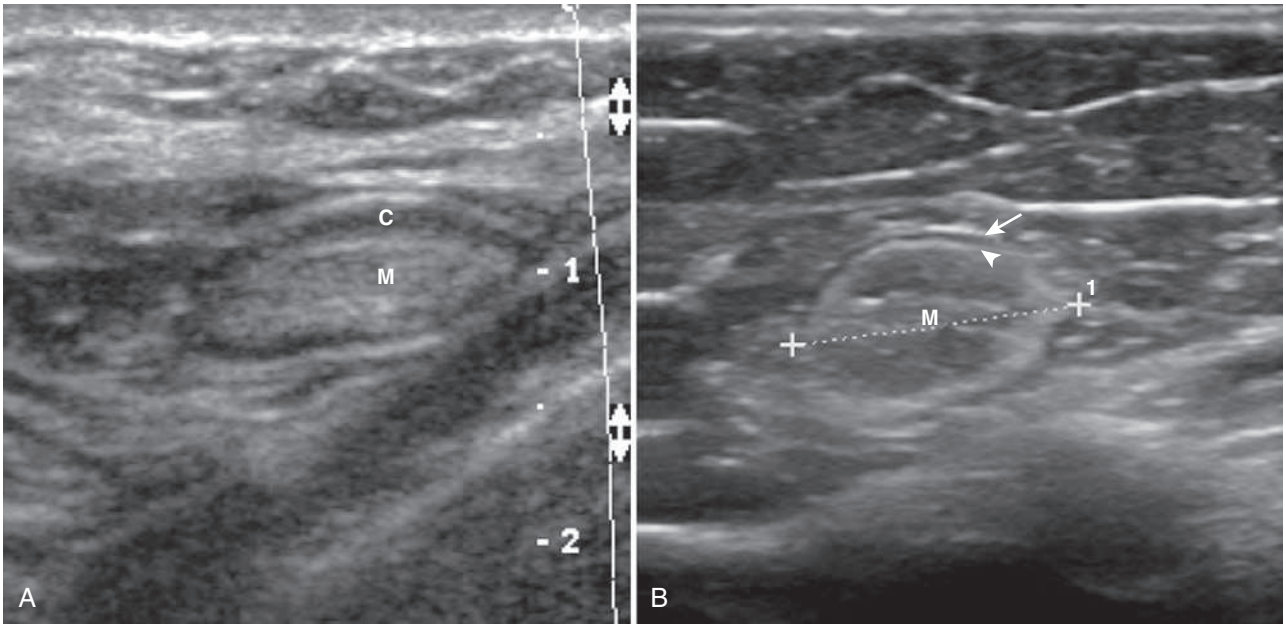

FIG. 21.72 Lymph Node: Spectrum of Normal Appearances. (A) In young patients the mediastinum of the lymph node tends to be uniformly hyperechoic because the medullary cords and sinuses fill the entire mediastinum *(M)*. *C* represents the lymph node cortex. **(B)** In older patients fatty infiltration of the lymph node may make the hypoechoic cortex very thin or barely visible (between the *arrowhead* and *arrow*).

specifically the metastases first implant within the cortex. Metastases that implant near the center of the cortical sinusoids tend to widen the cortex focally and equally in inward and outward directions (Fig. 21.73A). Metastases that implant in the subcapsular sinusoids tend to bulge outwardly, creating a "mouse ear" configuration (Fig. 21.73B). Metastases that implant toward the inner side of the cortical sinusoids tend to bulge into the lymph node hilum, creating "rat bite" defects in the hilum (Fig. 21.73C). When metastasis fills cortical sinusoids throughout the entire lymph node, the cortical thickening becomes uniform, an appearance that can be simulated by benign reactive lymph nodes (Fig. 21.73D). Metastases cause severe enough cortical thickening to obliterate the hilum, which occurs more frequently than inflammation (Fig. 21.73E). Lymph nodes that contain microcalcifications are metastatic until proven otherwise, especially when the primary breast lesion manifests with microcalcifications (Fig. 21.73F). Histologic sampling of the node should specifically target the area of the cortex that is focally thickened.

Lymph nodes that demonstrate mild to moderate, symmetrical cortical thickening of 3 mm or greater have a lower positive predictive value for metastasis than those with clear-cut eccentric cortical thickening, because they can be reactive or metastatic. Comparison versus adjacent lymph nodes is the best way to determine whether a lymph node with symmetrical cortical thickening is a benign reactive node or a metastatic node. Unless there is obvious evidence of inflammation in the ipsilateral breast or upper extremity, reactive lymph nodes are usually reacting to a systemic stimulus; thus all the lymph nodes will be reactive (Fig. 21.74A). However, if the adjacent node is sonographically normal, the node with symmetrical cortical thickening is more likely to be metastatic (Fig. 21.74B). Assessment of adjacent lymph nodes is not necessary when cortical thickening is so severe that the hilum is completely obliterated, because this occurs much more frequently in metastatic than reactive nodes (Fig. 21.74C). Although Doppler sonography can also be used to help determine whether a node with symmetrical cortical thickening is reactive or metastatic, gray-scale imaging of adjacent lymph nodes usually makes this unnecessary.

Although differences in morphology help determine whether lymph nodes are abnormal, clear criteria for classifying these changes have not been well established. Cortical thickness of 2.5 mm to 4 mm is used by some to differentiate normal from abnormal. Others use a cortex-to-hilum ratio; an increased probability for malignancy is associated with a maximum cortical thickness that is greater than the hilar thickness.[85-88]

Abnormal axillary lymph nodes are located most commonly within level 1 of the axilla, located lateral and inferior to the lateral edge of the pectoralis minor muscle. These are the first nodes involved by metastases, except in rare cases in which the sentinel lymph node is a level 2 node. Lymph nodes deep to the pectoralis minor muscle are level 2, and those that lie superior and medial to the medial edge of the pectoralis minor muscle are level 3, or infraclavicular, lymph nodes (Fig. 21.75). Rotter lymph nodes lie between the pectoralis major and minor muscles and lie anterior to and at the same level as level 2 lymph nodes (Fig. 21.76). If undetected and untreated, they can give rise to chest wall invasion. If level 3 nodes are positive, supraclavicular and jugular lymph nodes should be assessed. Internal mammary lymph nodes should be evaluated in all cases, but especially when the primary lesion is medial and deep, and when bulky axillary adenopathy may cause **tumor damming** and collateral flow medially (Fig. 21.77). Presence of metastasis to internal mammary lymph nodes is especially important to radiation oncologists. There is controversy regarding whether to prophylactically irradiate internal mammary lymph nodes when axillary nodes are positive for malignancy. However, if there are known

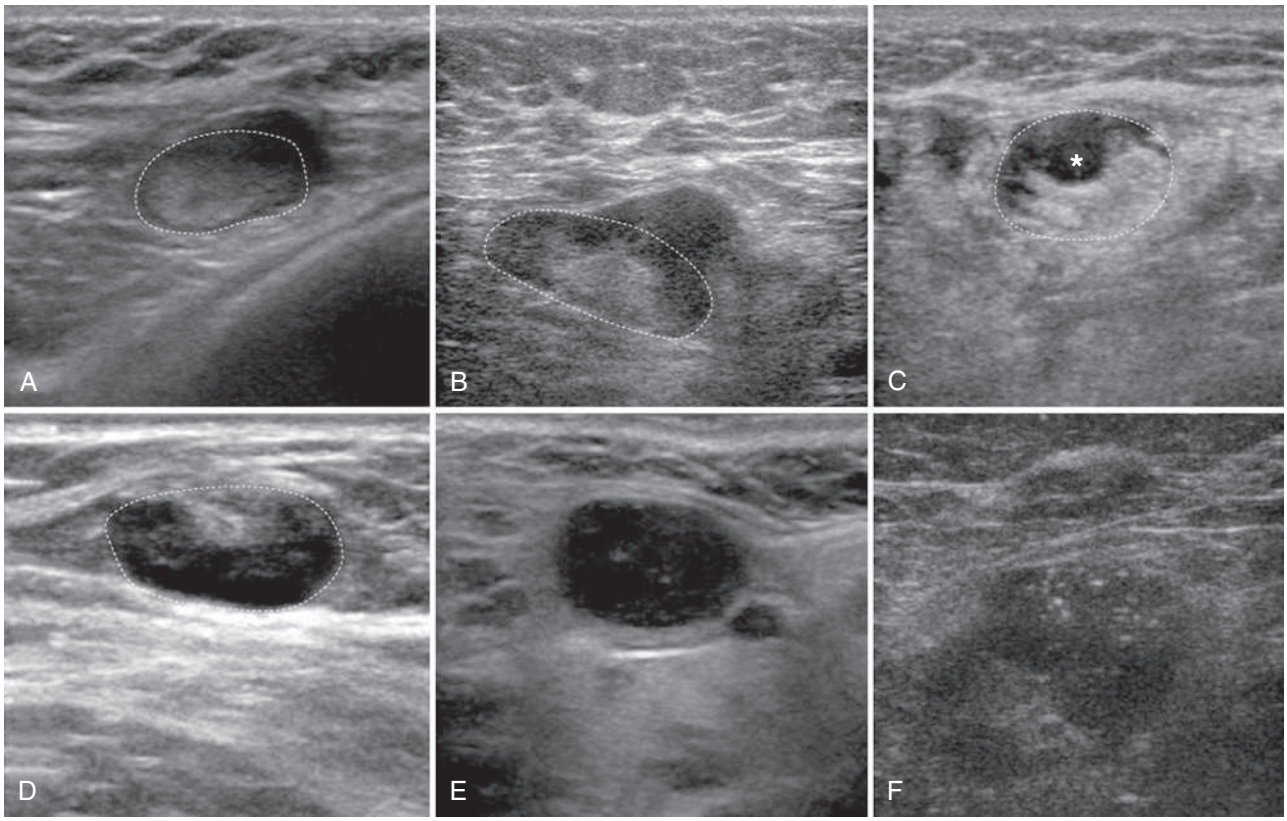

FIG. 21.73 Hallmark of Lymph Node Metastasis: Spectrum of Cortical Thickening. In **A–D,** the anticipated outline of a normal node is shown in dotted line. **(A)** Metastases that implant near the midcortical sinusoids tend to thicken the cortex focally and equally in inward and outward directions. **(B)** Metastases that implant within the subcapsular sinusoids tend to cause focal, outwardly bulging cortical thickening ("mouse ear"). **(C)** Metastases that implant toward the inner part of the cortical sinusoids cause focal cortical thickenings that bulge inwardly into the lymph node mediastinum ("rat bite" defect, *). **(D)** Metastases that implant extensively throughout the cortical sinusoids can cause symmetrical cortical thickening indistinguishable from the cortical thickening caused by inflammation. **(E)** Cortical thickening so severe that the hilum is obliterated is usually caused by metastasis and is strongly against the node being benign and reactive. **(F)** Microcalcifications within a lymph node indicate metastasis until proved otherwise, especially if the primary breast lesion has microcalcifications.

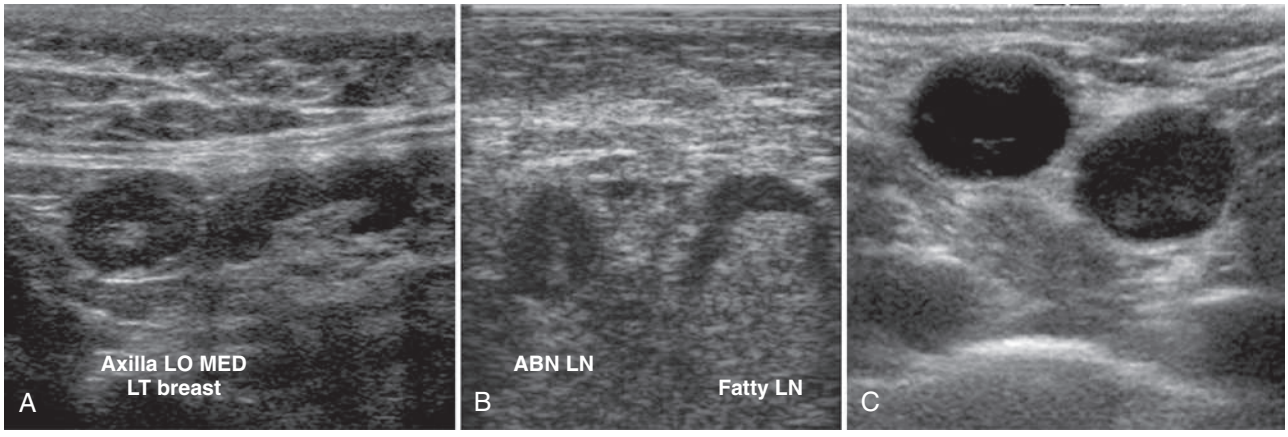

FIG. 21.74 Comparison With Adjacent Lymph Nodes to Assess Significance of Symmetrical Cortical Thickening. (A) When adjacent lymph nodes within the axilla show similar degrees of symmetrical cortical thickening, the lymph nodes are more likely reactive than metastatic. If contralateral axillary lymph nodes show similar degrees of thickening, the risk of metastasis is reduced even further. **(B)** If the adjacent lymph node shows normal cortical thickness, the risk of metastasis in the node with symmetrical cortical thickening is increased. **(C)** When the cortical thickening is so severe that the mediastinum of the lymph node is obliterated, the cause should be assumed to be metastatic, even when adjacent lymph nodes are involved to a similar degree.

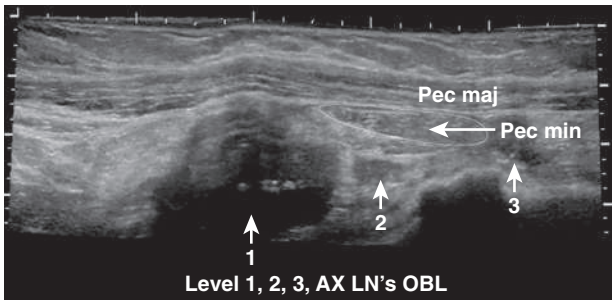

FIG. 21.75 Metastases to Three Lymph Node Levels. Extended–field-of-view (FOV), obliquely oriented sonogram shows metastasis to all three levels of axillary lymph nodes. Massive adenopathy and microcalcifications are seen in a level 1 lymph node that lies lateral and inferior to the pectoralis minor muscle *(dotted oval)*. A mildly enlarged level 2 lymph node lies posterior to the pectoralis muscle. A moderately enlarged level 3 lymph node with a microcalcification lies superior and medial to the pectoralis muscle.

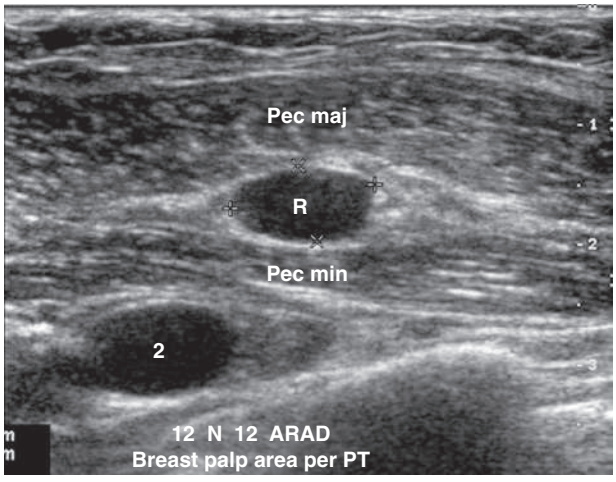

FIG. 21.76 Metastasis to Level 2 and Rotter Lymph Nodes. Rotter lymph nodes *(R)* lie between the pectoralis minor and major muscles at the same level as level 2 lymph nodes *(2)* and, if unrecognized, can be a source for chest wall invasion. This patient has gross metastasis that obliterates the mediastinum of level 2 and Rotter lymph nodes.

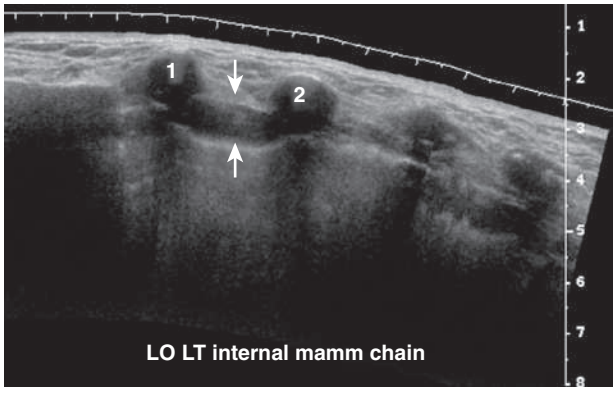

FIG. 21.77 Metastasis to Internal Mammary Lymph Nodes. Long-axis extended–field-of-view (FOV) image shows a gross internal mammary lymph node metastasis *(between arrows)* lying between the first *(1)* and second *(2)* costal cartilages.

internal mammary nodal metastases, the radiation oncologist will add an internal mammary field to the treatment. Internal mammary lymph node metastasis is most common in the first three interspaces just lateral to the sternum.

Sonographic–Magnetic Resonance Imaging Correlation

The role of contrast-enhanced MRI for breast cancer screening as well as diagnostic evaluation has expanded greatly in recent years, along with the role of ultrasound correlation after MRI. Because of the high rate of false-positive results with contrast-enhanced breast MRI, treatment decisions require histologic confirmation of the cause of abnormal enhancement. Thus image-guided biopsy of abnormal areas of enhancement is necessary. However, MRI-guided biopsies can be costly, time-consuming, less readily accessible, and uncomfortable for the patient. Therefore patients are often taken for second-look ultrasound of the targeted area to see if the biopsy can be performed with ultrasound instead. Second-look breast ultrasound can be very effective at confirming the presence of additional ipsilateral or contralateral foci of invasive breast cancer identified on MRI and targeting the finding for biopsy (Fig. 21.78). Similarly, if a probably benign lesion seen on MRI has an ultrasound correlate, this lesion can be followed with ultrasound instead of MRI.

The challenge of second-look ultrasound examinations is confirming that the finding seen on MRI truly correlates with the ultrasound finding. Approximately 50% to 70% of lesions seen on MRI can be found on second-look ultrasound.[89,90] Masses are more easily identified than nonmass enhancement.[89,90] Although it seems intuitive that larger masses would be more easily visualized than smaller masses, this has not been consistently shown in these studies. As a result, it is quite possible to perform a second-look ultrasound and not find an ultrasound correlate. Alternatively, it is also possible to mistakenly correlate an incidental ultrasound finding with the MRI target. If biopsy of this area is then performed with ultrasound, there is the chance of leaving the MRI target unsampled. Therefore it is worthwhile to pause before recommending a second-look ultrasound for smaller, subtle areas of nonmass enhancement seen on MRI, especially if one is sufficiently concerned regarding malignancy and believes that biopsy is warranted. It may be that MRI-guided breast biopsy is the preferred approach for these patients.

If a second-look ultrasound examination is performed for a suspicious MRI finding and identifies a correlate, there is a greater chance that this MRI finding is malignant.[91] Therefore it is worth sampling. This raises the issue of pretest probability for different types of ultrasound examinations. Breast ultrasound involves three different patient groups, each with a different prevalence of breast cancer (pretest probability): the screening group, the diagnostic group, and the MRI correlation group. Different sets of rules are needed for interpreting studies in these patients. In the screening group the risk of cancer will be about 3 to 6 per 1000 patients (0.3%-0.6%). In the diagnostic group the risk will be about 3% to 8%, and in the MRI correlation group the risk is 30% to 60%.[89,90,92] In the screening group, we must deemphasize

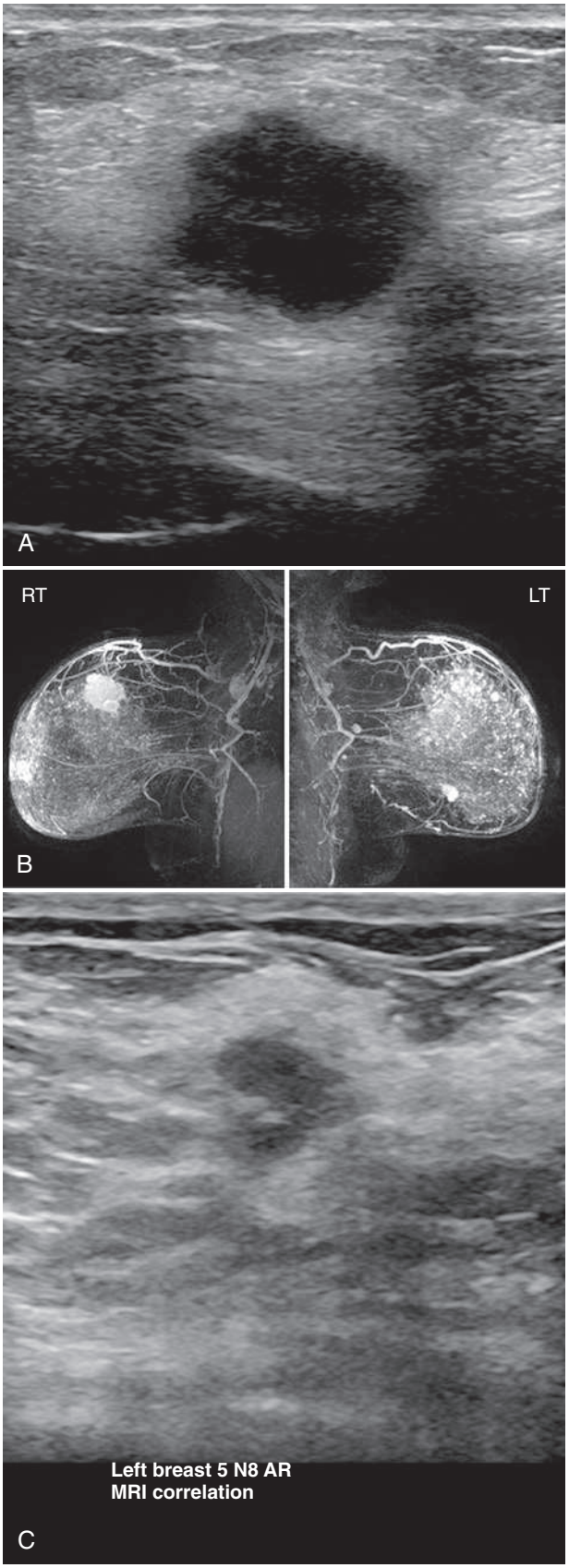

FIG. 21.78 Contralateral Invasive Carcinoma Detected on Magnetic Resonance Imaging (MRI) and Verified on "Second-Look" Ultrasound. (A) Targeted diagnostic sonogram of a high-grade invasive carcinoma in upper right breast that manifested as a palpable lump. Ultrasound-guided biopsy showed high-grade invasive carcinoma. **(B)** Staging MRI showed right breast carcinoma and an enhancing mass inferiorly in the contralateral left breast. **(C)** Second-look ultrasound showed irregular mass corresponding to the left breast lesion on MRI. Ultrasound-guided biopsy showed synchronous high-grade invasive duct carcinoma.

soft, subtle findings. In the diagnostic group, we weight soft and hard findings almost equally, and in the MRI correlation group, we weight soft findings heavily (Fig. 21.79).

ULTRASOUND-GUIDED INTERVENTION

The use of sonography for guiding interventional procedures is almost unlimited. Any type of interventional procedure for a lesion that is visible with sonography can be guided by sonography. Ultrasound can be used to guide cyst aspiration (Fig. 21.80), needle localization for surgical biopsy with specimen sonography (Fig. 21.81), sentinel node injection, sentinel node localization, abscess drainage, percutaneous ductography, foreign body removal (broken localization wires), percutaneous removal, and biopsy using fine needles, spring-loaded needles (Fig. 21.82), and vacuum assistance (Fig. 21.83). Sonography can be used to locate and orient the lumpectomy cavity for booster doses of external radiation, to guide placement of brachytherapy needles, and to place partial-breast irradiation balloons. It can also be used to guide lesion ablation using laser, radiofrequency, and cryotherapy. Sonographic guidance is usually quicker, more precise, and less expensive than mammographic, stereotaxic, or MRI guidance. Ultrasound guidance is truly a real-time procedure, whereas stereotaxic and MRI guidance are not.

When targeting a mass for histologic sampling, biopsy is the most preferred approach, and a 14-gauge biopsy device is sufficient. Different types of biopsy devices exist that have different mechanisms of action. Some function by having the biopsy device sample the breast tissue when it is fired in the breast (see Fig. 21.82; Video 21.5). These biopsy devices are associated with a throw of approximately 2 cm when fired. Others allow the 2-cm throw to occur outside of the patient's breast, and perform the actual sampling only while in the breast tissue. This is helpful for areas that are deep within the breast and there is concern for injuring the chest wall while firing the biopsy device. This also can be helpful if choosing to sample an axillary lymph node using a biopsy device because there is increased probability of injuring adjacent blood vessels and causing hematoma with a device that fires within the breast. Another form of biopsy device uses vacuum assistance wherein no firing is involved. The biopsy device is placed beneath the target. The vacuum then sucks the targeted area into the aperture and removes it (Fig. 21.83). This type of biopsy device does not need to be removed from the breast after each sample, and therefore there is less risk of losing

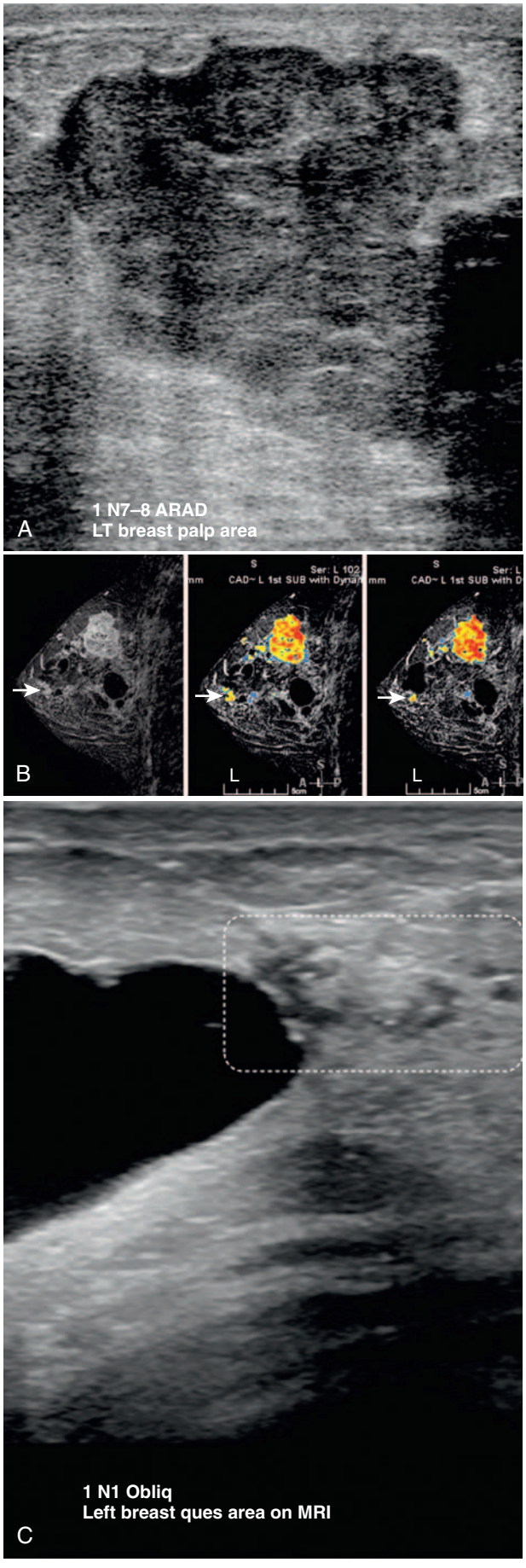

FIG. 21.79 High-Grade Invasive Duct Carcinoma With Second in Situ Lesion With Only "Soft" Finding at Presentation. (A) Targeted diagnostic ultrasound shows an irregularly shaped mass that appeared as a palpable lump. Ultrasound-guided biopsy showed high-grade invasive ductal carcinoma. **(B)** Magnetic resonance imaging (MRI) shows an ipsilateral nonmasslike area *(arrow)* of clumped enhancement farther inferiorly that lies just inferior to a large cyst. **(C)** Second-look ultrasound shows no mass. Only the soft findings of branching ducts and microcalcifications *(within dotted box)* next to a large, simple cyst correspond to clumped enhancement on MRI. Ultrasound-guided vacuum biopsy showed intermediate–nuclear-grade in situ carcinoma.

the target. This is most helpful for intraductal masses or complex cystic masses, in which the cystic component is likely to disappear after initial sampling, making the target less visible with each subsequent pass. Vacuum assistance can also be helpful for masses containing calcifications.

A marker should be placed after every ultrasound-guided biopsy. The reason is that if the biopsy reveals malignant or atypical histology, a needle localization excisional biopsy will frequently be necessary. This marker can be targeted by needle localization when the area is ultimately surgical excised. In addition, if the lesion is malignant, the patient may receive chemotherapy before surgery. After chemotherapy, all imaging evidence of the lesion may disappear, but the marker will continue to denote the area of prior cancer. Finally, the presence of markers placed in a benign lesion helps immensely in interpreting follow-up mammograms. Future imagers will know that the area has undergone biopsy and is benign.

Axillary lymph nodes can be sampled using fine-needle aspiration with smaller-gauge needles, often ranging from 22 to 25 gauge, or with core biopsy. The method of sampling is typically chosen based on radiologist and pathologist preference. Therapeutic and diagnostic aspiration of cysts can be performed with fine-needle aspiration, typically with a larger-gauge needle of 16 to 18 gauge. If the fluid is thick, even larger-gauge needles may be used, including the coaxial introducers from the biopsy device. If the aspirate is benign appearing with colors including black, green, yellow, and clear, then the fluid can be discarded. If the aspirate is bloody, then it should be sent to the cytology department for analysis and a marker should be placed in the breast. Should the aspirate be found to be atypical or malignant, the marker is then present to guide future surgery.

The recommended technique for most procedures, but most importantly for biopsies with devices that have a throw, is to place the **needle along the long axis of the transducer,** enabling the needle to be visualized along its entire course in real time throughout the entire procedure. This is most important to ensure that the biopsy device does not extend into the chest wall musculature during sampling. The main difficulty encountered during a long-axis approach is in keeping the needle and the long axis of the transducer exactly parallel to each other. Watching the ultrasound monitor before the needle has passed far enough into the breast to be within the ultrasound beam is the main cause of misalignment. It is best to watch one's hands until the needle is deep enough within the breast to be within the

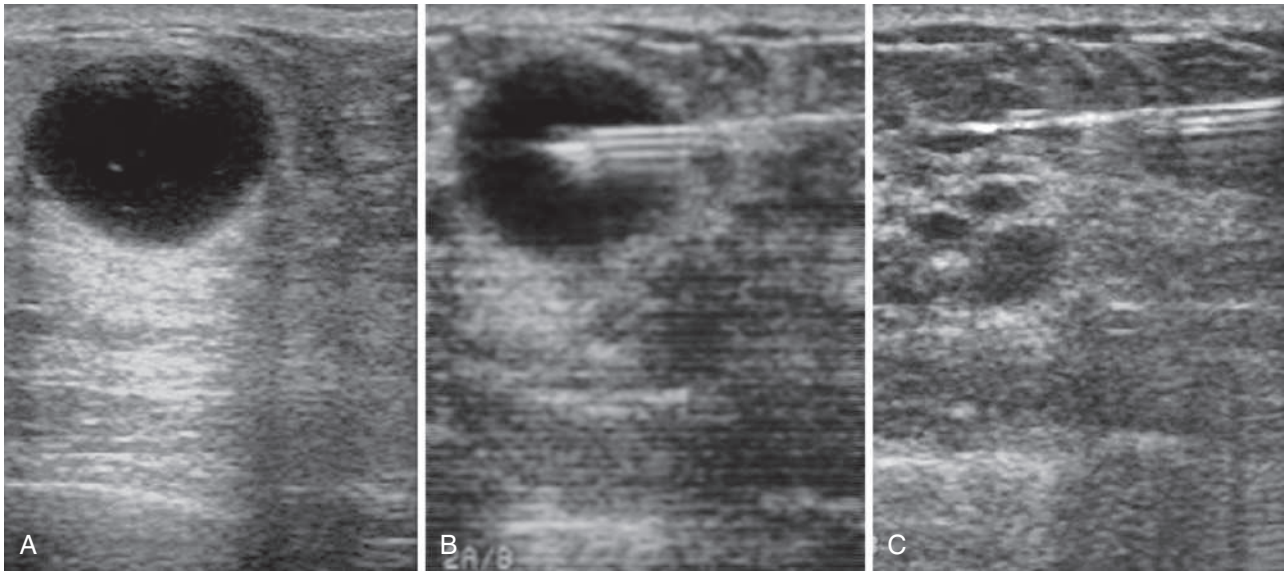

FIG. 21.80 Technique of Needle Aspiration and Biopsy. Ultrasound images show tender, simple tension cyst **(A)** before aspiration; **(B)** during aspiration; and **(C)** after aspiration. Ultrasound-guided interventional procedures of the breast are performed with the needle oriented along the long axis of the transducer, with angulation of the needle and appropriate heeling or toeing of the transducer to place the needle almost parallel to the transducer face and perpendicular to the ultrasound beam. A steeper angle can be used for aspirations because there is no throw associated with the procedure that might injure underlying chest wall structures.

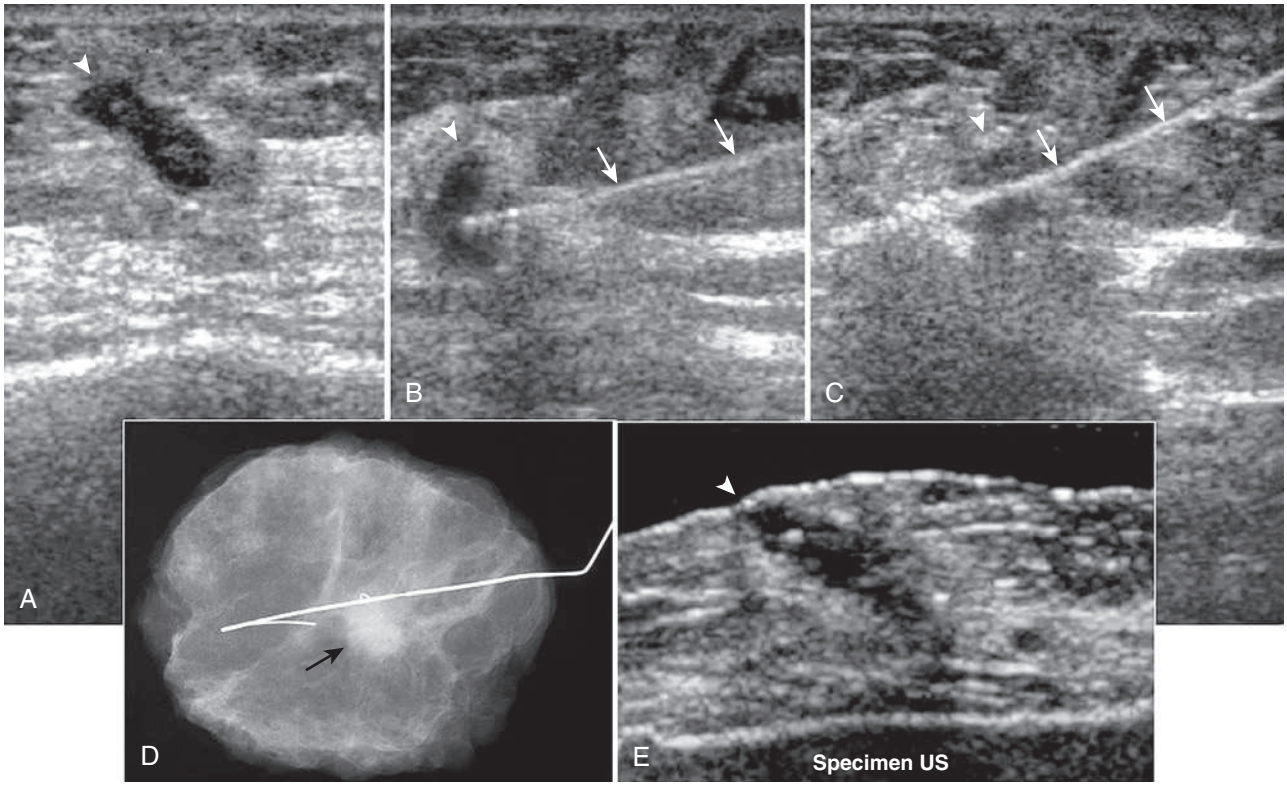

FIG. 21.81 Ultrasound-Guided Wire Localization for Excisional Biopsy. (A) Nodule *(arrowhead)* before the procedure. **(B)** Nodule *(arrowhead)* with the localization needle *(arrows)* in place. **(C)** Localization wire *(arrows)* in place after the needle is removed (*arrowhead,* nodule). **(D)** Specimen radiograph shows the nodule *(arrow)* in center of specimen. **(E)** Specimen sonogram, however, shows the nodule extending to superficial margin of specimen *(arrowhead).*

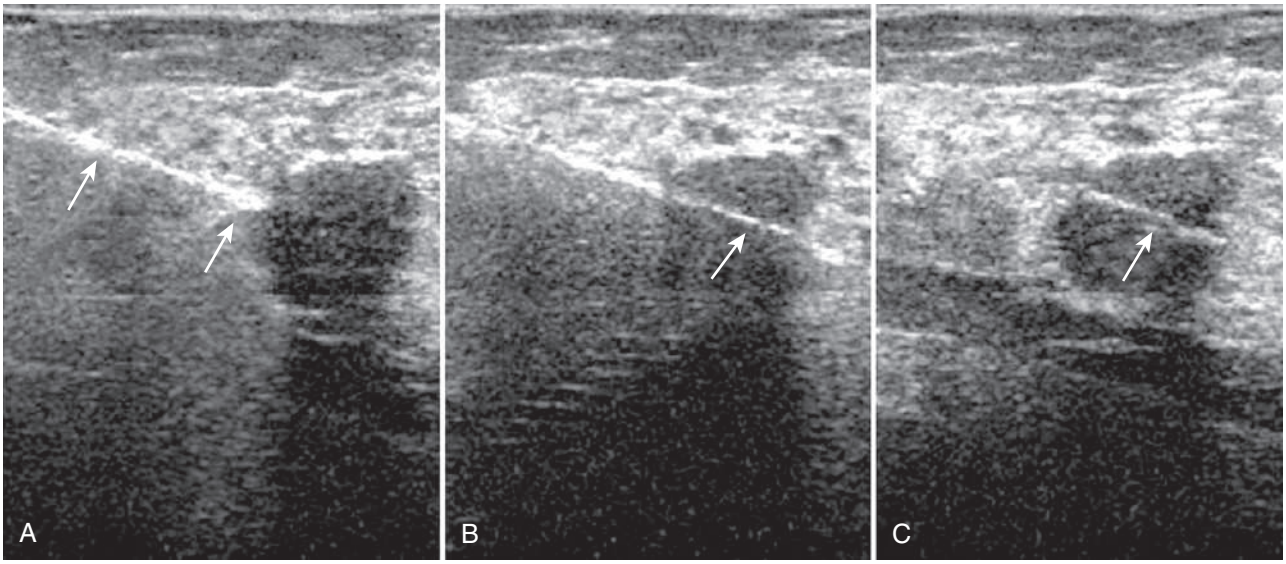

FIG. 21.82 Ultrasound-Guided Needle Biopsy With a 14-Gauge Needle. (A) Needle *(arrows)* has been advanced to the edge of the nodule in the prefire position. **(B)** Needle *(arrow)* has been fired through the nodule and now is in the postfire position. **(C)** Needle has been withdrawn, but a vapor trail of microbubbles *(arrow)* can still be seen within the needle tract, which documents that the needle did pass through the target nodule.

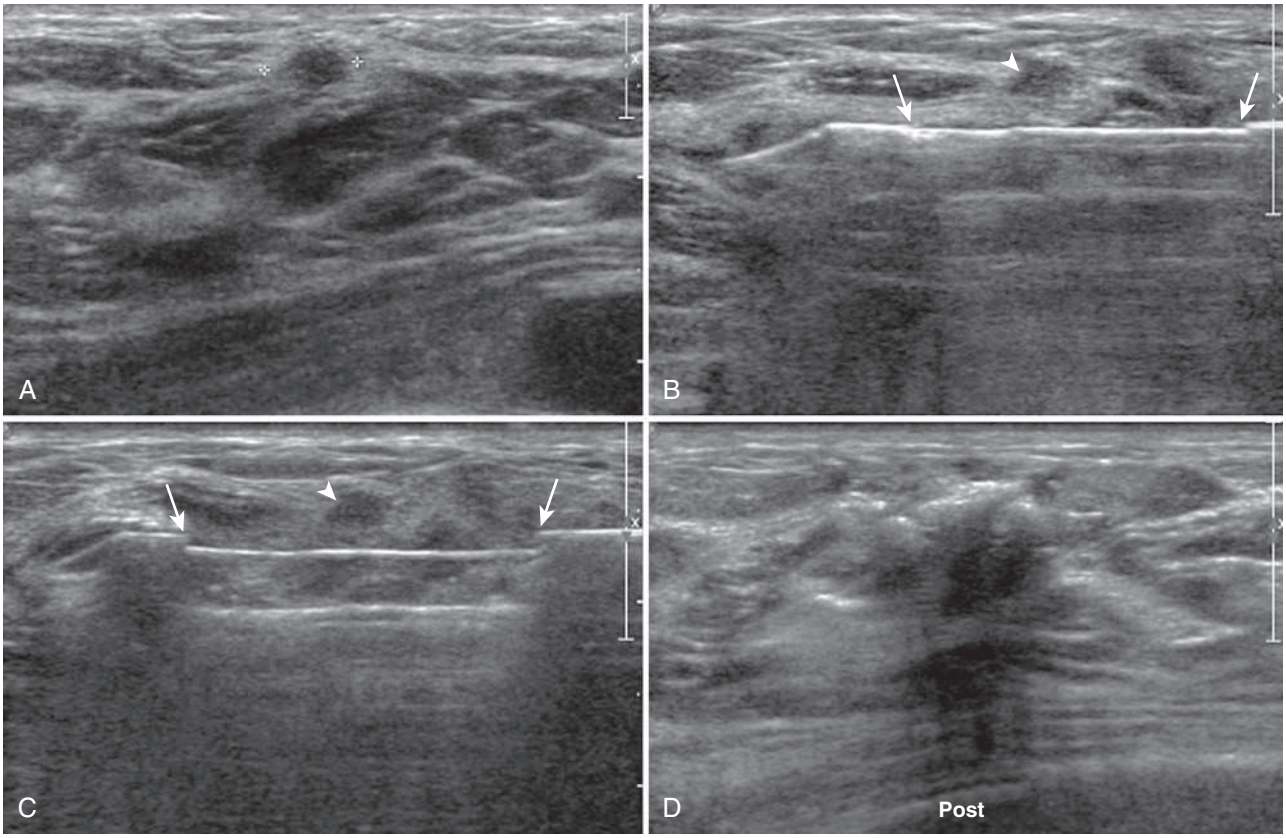

FIG. 21.83 Ultrasound-Guided Directional Vacuum-Assisted Biopsy With 10-Gauge Needle. (A) High-grade 5-mm invasive ductal carcinoma *(calipers)*. **(B)** Vacuum probe has been placed just deep to the lesion, with the closed aperture *(arrows)* just deep to the nodule *(arrowhead)*. **(C)** Aperture has been opened *(arrows)* and is beneath the mass *(arrowhead)*. There is ring-down artifact deep to the aperture created by the vacuum holes. **(D)** Lesion has been removed and a marker placed, consisting of air-impregnated pellets, one of which contains a metallic clip.

ultrasound beam before moving the eyes to the ultrasound monitor. Once the needle is within the beam, it is relatively easy to keep it precisely parallel to the beam. When performing cyst aspirations and fine-needle aspirations of lymph nodes, the needle can be placed at a steeper angle, because there is no firing involved and the needle does not advance past the target. As a result, there is less risk of injuring underlying chest wall structures. That being said, an angle that is too steep will make needle visualization more challenging.

REFERENCES

1. American College of Radiology (ACR). ACR practice parameter for the performance of a breast ultrasound examination. 2016. Accessed 8 October 2016. Available from: http://www.acr.org/~/media/ACR/Documents/PGTS/guidelines/US_Breast.pdf.
2. Kolb TM, Lichy J, Newhouse JH. Occult cancer in women with dense breasts: detection with screening US—diagnostic yield and tumor characteristics. Radiology. 1998;207(1):191-199.
3. Kolb TM, Lichy J, Newhouse JH. Comparison of the performance of screening mammography, physical examination, and breast US and evaluation of factors that influence them: an analysis of 27,825 patient evaluations. Radiology. 2002;225(1):165-175.
4. Kaplan SS. Clinical utility of bilateral whole-breast US in the evaluation of women with dense breast tissue. Radiology. 2001;221(3):641-649.
5. Buchberger W, DeKoekkoek-Doll P, Springer P, et al. Incidental findings on sonography of the breast: clinical significance and diagnostic workup. AJR Am J Roentgenol. 1999;173(4):921-927.
6. Berg WA, Blume JD, Cormack JB, et al. Combined screening with ultrasound and mammography vs mammography alone in women at elevated risk of breast cancer. JAMA. 2008;299(18):2151-2163.
7. Berg WA, Zhang Z, Lehrer D, et al. Detection of breast cancer with addition of annual screening ultrasound or a single screening MRI to mammography in women with elevated breast cancer risk. JAMA. 2012;307(13):1394-1404.
8. Weigert J, Steenbergen S. The Connecticut experiment: the role of ultrasound in the screening of women with dense breasts. Breast J. 2012;18(6):517-522.
9. Hooley RJ, Greenberg KL, Stackhouse RM, et al. Screening US in patients with mammographically dense breasts: initial experience with Connecticut Public Act 09-41. Radiology. 2012;265(1):59-69.
10. Kelly KM, Dean J, Comulada WS, Lee SJ. Breast cancer detection using automated whole breast ultrasound and mammography in radiographically dense breasts. Eur Radiol. 2010;20(3):734-742.
11. Kelly KM, Dean J, Lee SJ, Comulada WS. Breast cancer detection: radiologists' performance using mammography with and without automated whole-breast ultrasound. Eur Radiol. 2010;20(11):2557-2564.
12. Giger ML, Inciardi MF, Edwards A, et al. Automated breast ultrasound in breast cancer screening of women with dense breasts: reader study of mammography-negative and mammography-positive cancers. AJR Am J Roentgenol. 2016;206(6):1341-1350.
13. Brem RF, Tabar L, Duffy SW, et al. Assessing improvement in detection of breast cancer with three-dimensional automated breast US in women with dense breast tissue: the SomoInsight Study. Radiology. 2015;274(3):663-673.
14. Ramsay DT, Kent JC, Hartmann RA, Hartmann PE. Anatomy of the lactating human breast redefined with ultrasound imaging. J Anat. 2005;206(6):525-534.
15. Rahal RM, de Freitas-Junior R, Paulinelli RR. Risk factors for duct ectasia. Breast J. 2005;11(4):262-265.
16. Shetty MK, Watson AB. Mondor's disease of the breast: sonographic and mammographic findings. AJR Am J Roentgenol. 2001;177(4):893-896.
17. American College of Radiology (ACR). ACR BI-RADS-US lexicon classification form. Reston, VA: American College of Radiology; 2003. Available from: http://www.acr.org/~/media/acr/documents/pdf/qualitysafety/resources/birads/uslexiconclass.pdf. Accessed 9 October 2016.
18. Mendelson E, Böhm-Vélez M, Berg W, et al. ACR BI-RADS ultrasound. In: American College of Radiology, editor. ACR BI-RADS Atlas: breast imaging reporting and data system. 5th ed. Reston, VA: American College of Radiology; 2013.
19. Cosgrove DO, Kedar RP, Bamber JC, et al. Breast diseases: color Doppler US in differential diagnosis. Radiology. 1993;189(1):99-104.
20. Sehgal CM, Arger PH, Rowling SE, et al. Quantitative vascularity of breast masses by Doppler imaging: regional variations and diagnostic implications. J Ultrasound Med. 2000;19(7):427-440.
21. Davoudi Y, Borhani B, Rad M, Matin N. The role of Doppler sonography in distinguishing malignant from benign breast lesions. J Med Ultrasound. 2014;22(2):92-95.
22. Birdwell RL, Ikeda DM, Jeffrey SS, Jeffrey Jr RB. Preliminary experience with power Doppler imaging of solid breast masses. AJR Am J Roentgenol. 1997;169(3):703-707.
23. Chao TC, Lo YF, Chen SC, Chen MF. Color Doppler ultrasound in benign and malignant breast tumors. Breast Cancer Res Treat. 1999;57(2):193-199.
24. Lee SH, Chang JM, Cho N, et al. Practice guideline for the performance of breast ultrasound elastography. Ultrasonography. 2014;33(1):3-10.
25. Hooley RJ, Scoutt LM, Philpotts LE. Breast ultrasonography: state of the art. Radiology. 2013;268(3):642-659.
26. Berg WA, Cosgrove DO, Dore CJ, et al. Shear-wave elastography improves the specificity of breast US: the BE1 multinational study of 939 masses. Radiology. 2012;262(2):435-449.
27. Itoh A, Ueno E, Tohno E, et al. Breast disease: clinical application of US elastography for diagnosis. Radiology. 2006;239(2):341-350.
28. Athanasiou A, Tardivon A, Tanter M, et al. Breast lesions: quantitative elastography with supersonic shear imaging—preliminary results. Radiology. 2010;256(1):297-303.
29. Evans A, Whelehan P, Thomson K, et al. Invasive breast cancer: relationship between shear-wave elastographic findings and histologic prognostic factors. Radiology. 2012;263(3):673-677.
30. Tozaki M, Fukuma E. Pattern classification of ShearWave Elastography images for differential diagnosis between benign and malignant solid breast masses. Acta Radiol. 2011;52(10):1069-1075.
31. Fleury Ede F, Fleury JC, Piato S, Roveda Jr D. New elastographic classification of breast lesions during and after compression. Diagn Interv Radiol. 2009;15(2):96-103.
32. Kotsianos-Hermle D, Hiltawsky KM, Wirth S, et al. Analysis of 107 breast lesions with automated 3D ultrasound and comparison with mammography and manual ultrasound. Eur J Radiol. 2009;71(1):109-115.
33. Kotsianos-Hermle D, Wirth S, Fischer T, et al. First clinical use of a standardized three-dimensional ultrasound for breast imaging. Eur J Radiol. 2009;71(1):102-108.
34. Wilczek B, Wilczek HE, Rasouliyan L, Leifland K. Adding 3D automated breast ultrasound to mammography screening in women with heterogeneously and extremely dense breasts: report from a hospital-based, high-volume, single-center breast cancer screening program. Eur J Radiol. 2016;85(9):1554-1563.
35. Zhang XL, Guan J, Li MZ, et al. Adjunctive targeted contrast-enhanced ultrasonography for the work-up of Breast Imaging Reporting and Data System category 3 and 4 lesions. J Med Imaging Radiat Oncol. 2016;60(4):485-491.
36. Du J, Wang L, Wan CF, et al. Differentiating benign from malignant solid breast lesions: combined utility of conventional ultrasound and contrast-enhanced ultrasound in comparison with magnetic resonance imaging. Eur J Radiol. 2012;81(12):3890-3899.
37. Luo J, Chen JD, Chen Q, et al. Contrast-enhanced ultrasound improved performance of Breast Imaging Reporting and Data System evaluation of critical breast lesions. World J Radiol. 2016;8(6):610-617.
38. Xiao X, Dong L, Jiang Q, et al. Incorporating contrast-enhanced ultrasound into the BI-RADS scoring system improves accuracy in breast tumor diagnosis: a preliminary study in China. Ultrasound Med Biol. 2016;42(11):2630-2638.
39. Sridharan A, Eisenbrey JR, Dave JK, Forsberg F. Quantitative nonlinear contrast-enhanced ultrasound of the breast. AJR Am J Roentgenol. 2016;207(2):274-281.

40. Ma X, Liu R, Zhu C, et al. Diagnostic value of contrast-enhanced sonography for differentiation of breast lesions: a meta-analysis. J Ultrasound Med. 2016;35(10):2095-2102.
41. Sever AR, Mills P, Weeks J, et al. Preoperative needle biopsy of sentinel lymph nodes using intradermal microbubbles and contrast-enhanced ultrasound in patients with breast cancer. AJR Am J Roentgenol. 2012; 199(2):465-470.
42. Zhou SC, Le J, Fan YW, et al. Study on breast cancer animal model of tumor-micro vessel variation before and after the chemotherapy by contrast enhanced ultrasound quantitative analysis. Pak J Pharm Sci. 2016;29(4 Suppl.): 1407-1413.
43. D'Orsi C, Sickles E, Mendelson E, et al. ACR BI-RADS Atlas, breast imaging reporting and data system. Reston, VA: American College of Radiology; 2013.
44. Hughes LE, Mansel RE, Webster DJ. Aberrations of normal development and involution (ANDI): a new perspective on pathogenesis and nomenclature of benign breast disorders. Lancet. 1987;2(8571):1316-1319.
45. Stavros AT, Thickman D, Rapp CL, et al. Solid breast nodules: use of sonography to distinguish between benign and malignant lesions. Radiology. 1995;196(1):123-134.
46. Berg WA, Sechtin AG, Marques H, Zhang Z. Cystic breast masses and the ACRIN 6666 experience. Radiol Clin North Am. 2010;48(5): 931-987.
47. Kim MJ, Kim EK, Youk JH, et al. Application of power Doppler vocal fremitus sonography in breast lesions. J Ultrasound Med. 2006;25(7):897-906.
48. Laforga JB, Aranda FI, Sevilla F. Adenomyoepithelioma of the breast: report of two cases with prominent cystic changes and intranuclear inclusions. Diagn Cytopathol. 1998;19(1):55-58.
49. Eiada R, Chong J, Kulkarni S, et al. Papillary lesions of the breast: MRI, ultrasound, and mammographic appearances. AJR Am J Roentgenol. 2012;198(2):264-271.
50. Berg WA, Campassi CI, Ioffe OB. Cystic lesions of the breast: sonographic-pathologic correlation. Radiology. 2003;227(1):183-191.
51. Irshad A, Leddy R, Pisano E, et al. Assessing the role of ultrasound in predicting the biological behavior of breast cancer. AJR Am J Roentgenol. 2013;200(2): 284-290.
52. Zhang L, Li J, Xiao Y, et al. Identifying ultrasound and clinical features of breast cancer molecular subtypes by ensemble decision. Sci Rep. 2015;5: 11085.
53. Lam WW, Chu WC, Tse GM, Ma TK. Sonographic appearance of mucinous carcinoma of the breast. AJR Am J Roentgenol. 2004;182(4):1069-1074.
54. Meyer JE, Amin E, Lindfors KK, et al. Medullary carcinoma of the breast: mammographic and US appearance. Radiology. 1989;170(1 Pt 1):79-82.
55. Alsharif S, Daghistani R, Kamberoglu EA, et al. Mammographic, sonographic and MR imaging features of invasive micropapillary breast cancer. Eur J Radiol. 2014;83(8):1375-1380.
56. Gao Y, Slanetz PJ, Eisenberg RL. Echogenic breast masses at US: to biopsy or not to biopsy? Radiographics. 2013;33(2):419-434.
57. Leung JW, Kornguth PJ, Gotway MB. Utility of targeted sonography in the evaluation of focal breast pain. J Ultrasound Med. 2002;21(5):521-526.
58. Soo MS, Rosen EL, Baker JA, et al. Negative predictive value of sonography with mammography in patients with palpable breast lesions. AJR Am J Roentgenol. 2001;177(5):1167-1170.
59. Lehman CD, Lee CI, Loving VA, et al. Accuracy and value of breast ultrasound for primary imaging evaluation of symptomatic women 30-39 years of age. AJR Am J Roentgenol. 2012;199(5):1169-1177.
60. Cilotti A, Marini C, Marinari A, et al. [Correlation of ultrasound and galactography in the diagnosis of nipple discharge. Preliminary results]. Radiol Med. 1999;98(4):248-254.
61. Patel BK, Falcon S, Drukteinis J. Management of nipple discharge and the associated imaging findings. Am J Med. 2015;128(4):353-360.
62. Rissanen T, Reinikainen H, Apaja-Sarkkinen M. Breast sonography in localizing the cause of nipple discharge: comparison with galactography in 52 patients. J Ultrasound Med. 2007;26(8):1031-1039.
63. Lequin MH, van Spengler J, van Pel R, et al. Mammographic and sonographic spectrum of non-peurperal mastitis. Eur J Radiol. 1995;138-142.
64. Crowe DJ, Helvie MA, Wilson TE. Breast infection. Mammographic and sonographic findings with clinical correlation. Invest Radiol. 1995;30(10): 582-587.
65. Hayes R, Michell M, Nunnerley HB. Acute inflammation of the breast—the role of breast ultrasound in diagnosis and management. Clin Radiol. 1991;44(4):253-256.
66. Ahn CY, DeBruhl ND, Gorczyca DP, et al. Comparative silicone breast implant evaluation using mammography, sonography, and magnetic resonance imaging: experience with 59 implants. Plast Reconstr Surg. 1994;94(5):620-627.
67. Caskey CI, Berg WA, Anderson ND, et al. Breast implant rupture: diagnosis with US. Radiology. 1994;190(3):819-823.
68. Chung KC, Wilkins EG, Beil Jr RJ, et al. Diagnosis of silicone gel breast implant rupture by ultrasonography. Plast Reconstr Surg. 1996;97(1): 104-109.
69. DeBruhl ND, Gorczyca DP, Ahn CY, et al. Silicone breast implants: US evaluation. Radiology. 1993;189(1):95-98.
70. Leibman AJ, Kruse B. Breast cancer: mammographic and sonographic findings after augmentation mammoplasty. Radiology. 1990;174(1):195-198.
71. Gorczyca DP, Sinha S, Ahn CY, et al. Silicone breast implants in vivo: MR imaging. Radiology. 1992;185(2):407-410.
72. Yang N, Muradali D. The augmented breast: a pictorial review of the abnormal and unusual. AJR Am J Roentgenol. 2011;196(4):W451-W460.
73. Brennan ME, Houssami N, Lord S, et al. Magnetic resonance imaging screening of the contralateral breast in women with newly diagnosed breast cancer: systematic review and meta-analysis of incremental cancer detection and impact on surgical management. J Clin Oncol. 2009;27(33): 5640-5649.
74. Hlawatsch A, Teifke A, Schmidt M, Thelen M. Preoperative assessment of breast cancer: sonography versus MR imaging. AJR Am J Roentgenol. 2002;179(6):1493-1501.
75. Berg WA, Gutierrez L, NessAiver MS, et al. Diagnostic accuracy of mammography, clinical examination, US, and MR imaging in preoperative assessment of breast cancer. Radiology. 2004;233(3):830-849.
76. Moon WK, Noh DY, Im JG. Multifocal, multicentric, and contralateral breast cancers: bilateral whole-breast US in the preoperative evaluation of patients. Radiology. 2002;224(2):569-576.
77. Fornage BD. Local and regional staging of invasive breast cancer with sonography: 25 years of practice at MD Anderson Cancer Center. Oncologist. 2014;19(1):5-15.
78. Park SH, Kim EK, Park BW, et al. False negative results in axillary lymph nodes by ultrasonography and ultrasonography-guided fine-needle aspiration in patients with invasive ductal carcinoma. Ultraschall Med. 2013;34(6): 559-567.
79. Giuliano AE, Ballman K, McCall L, et al. Locoregional recurrence after sentinel lymph node dissection with or without axillary dissection in patients with sentinel lymph node metastases: long-term follow-up from the American College of Surgeons Oncology Group (Alliance) ACOSOG Z0011 Randomized Trial. Ann Surg. 2016;264(3):413-420.
80. Giuliano AE, Hunt KK, Ballman KV, et al. Axillary dissection vs no axillary dissection in women with invasive breast cancer and sentinel node metastasis: a randomized clinical trial. JAMA. 2011;305(6):569-575.
81. Cools-Lartigue J, Meterissian S. Accuracy of axillary ultrasound in the diagnosis of nodal metastasis in invasive breast cancer: a review. World J Surg. 2012;36(1):46-54.
82. Cools-Lartigue J, Sinclair A, Trabulsi N, et al. Preoperative axillary ultrasound and fine-needle aspiration biopsy in the diagnosis of axillary metastases in patients with breast cancer: predictors of accuracy and future implications. Ann Surg Oncol. 2013;20(3):819-827.
83. American Society of Breast Surgeons. Consensus statement on management of the axilla in patients with invasive breast cancer. 2011. Available from: https://www.breastsurgeons.org/new_layout/about/statements/PDF_Statements/Axillary_Management.pdf. Accessed on 10/1/16.
84. Whitman G, Lua T, Adejolu M, et al. Lymph node sonography. Ultrasound Clin. 2011;6:369-380.
85. Cho N, Moon WK, Han W, et al. Preoperative sonographic classification of axillary lymph nodes in patients with breast cancer: node-to-node correlation with surgical histology and sentinel node biopsy results. AJR Am J Roentgenol. 2009;193(6):1731-1737.

86. Bedi DG, Krishnamurthy R, Krishnamurthy S, et al. Cortical morphologic features of axillary lymph nodes as a predictor of metastasis in breast cancer: in vitro sonographic study. AJR Am J Roentgenol. 2008;191(3):646-652.
87. Mainiero MB, Cinelli CM, Koelliker SL, et al. Axillary ultrasound and fine-needle aspiration in the preoperative evaluation of the breast cancer patient: an algorithm based on tumor size and lymph node appearance. AJR Am J Roentgenol. 2010;195(5):1261-1267.
88. Song SE, Seo BK, Lee SH, et al. Classification of metastatic versus non-metastatic axillary nodes in breast cancer patients: value of cortex-hilum area ratio with ultrasound. J Breast Cancer. 2012;15(1):65-70.
89. Abe H, Schmidt RA, Shah RN, et al. MR-directed ("second-look") ultrasound examination for breast lesions detected initially on MRI: MR and sonographic findings. AJR Am J Roentgenol. 2010;194(2):370-377.
90. Demartini WB, Eby PR, Peacock S, Lehman CD. Utility of targeted sonography for breast lesions that were suspicious on MRI. AJR Am J Roentgenol. 2009;192(4):1128-1134.
91. Shin JH, Han BK, Choe YH, et al. Targeted ultrasound for MR-detected lesions in breast cancer patients. Korean J Radiol. 2007;8(6):475-483.
92. Candelaria R, Fornage BD. Second-look US examination of MR-detected breast lesions. J Clin Ultrasound. 2011;39(3):115-121.

CHAPTER 22

The Scrotum

Daniel Sommers and Thomas Winter

SUMMARY OF KEY POINTS

- Diagnostic ultrasound is an accurate means of evaluating most scrotal processes and can supplement the physical examination.
- Solid intratesticular lesions have a high likelihood of malignancy, whereas cystic extratesticular intrascrotal lesions are almost certainly benign.
- Doppler sonography is the most useful and most rapid technique to assess the patient with acute scrotal pain. Ultrasound can establish the diagnosis of testicular ischemia and help distinguish torsion from other causes of acute pain such as epididymitis and epididymo-orchitis.
- In the setting of acute scrotal trauma, sonography has a primary role to evaluate the continuity of the tunica albuginea and assess for testicular rupture, which requires early surgical intervention.
- Varicocele is the most common correctable cause of male infertility and is diagnosed by ultrasound by visualization of dilatation of the veins (>2-3 mm and increasing in size with Valsalva maneuver or standing) of the pampiniform plexus located posterior to the testis.

CHAPTER OUTLINE

SONOGRAPHIC TECHNIQUE
NORMAL ANATOMY
INTRATESTICULAR SCROTAL MASSES
Malignant Tumors
Germ Cell Tumors
Non–Germ Cell Tumors
Testicular Metastases
Lymphoma and Leukemia
Extramedullary Myeloma
Metastatic Disease
Benign Intratesticular Lesions
Cysts
Tubular Ectasia of Rete Testis
Cystic Dysplasia
Epidermoid Cysts
Abscess
Segmental Infarction
Adrenal Rests
Splenogonadal Fusion
Calcifications
EXTRATESTICULAR PATHOLOGIC LESIONS
Tunica Vaginalis
Hydrocele, Hematocele, and Pyocele
Paratesticular Masses
Hernia
Calculi
Varicocele
Fibrous Pseudotumor
Polyorchidism
Epididymal Lesions
Cystic Lesions
Tumors
Sperm Granuloma
Postvasectomy Changes in the Epididymis
Chronic Epididymitis
Sarcoidosis
ACUTE SCROTAL PAIN
Torsion
Epididymitis and Epididymo-orchitis
Fournier Gangrene
TRAUMA
CRYPTORCHIDISM

Diagnostic ultrasound is the most common imaging technique used to supplement the physical examination of the scrotum and is an accurate means of evaluating many scrotal processes. Technical advancements in high-resolution real-time sonography and the ability of color and power Doppler sonography to evaluate testicular perfusion have improved and expanded the clinical applications of scrotal sonography to include (among other indications) assessment of scrotal masses, evaluation of acute scrotal pain, evaluation of scrotal trauma, assessment of varicoceles in the infertility workup, assessment for tumors and metastatic disease, and evaluation of an undescended testis.

SONOGRAPHIC TECHNIQUE

Scrotal ultrasound examination is performed with the patient in the supine position. The scrotum is elevated on top of a towel draped over the thighs, and the penis is placed on the patient's abdomen and covered with a towel. Optimal results are typically obtained with a high-frequency (14-18 MHz) linear array transducer. If greater penetration is needed because of scrotal swelling, a lower-frequency transducer may be used. A direct-contact scan is performed using acoustic coupling gel. Images of both testes are obtained in transverse and sagittal planes. The

Scrotal Sonography: Current Uses

Evaluation of location and characteristics of scrotal masses
Evaluation of acute scrotal pain
Evaluation of scrotal trauma, including surgical or iatrogenic injury
Evaluation for varicoceles in infertile men
Evaluation of testicular ischemia with color and power Doppler sonography
Follow-up of patients with previous testicular neoplasms, lymphoma, or leukemia
Detection of occult primary tumor in patients with known metastatic disease
Localization of the undescended testis

size and appearance of each testis and epididymis should be noted and compared to the contralateral structures. Color and pulsed Doppler parameters should be optimized to evaluate for low flow velocities and to demonstrate blood flow in the testes and surrounding structures. Transverse images including portions of both testes should be acquired in gray-scale and color Doppler modes to demonstrate symmetry. Scrotal structures should be examined thoroughly to evaluate for extratesticular masses or processes. Additional techniques, such as upright positioning of the patient or performing the Valsalva maneuver, may be used to evaluate venous vascularity for varicocele or for inguinal hernia assessment.

NORMAL ANATOMY

The normal scrotal wall consists of the epidermis, superficial dartos muscle, dartos fascia, external spermatic fascia, cremasteric muscle and fascia, and internal spermatic fascia. The scrotum is a fibromuscular sac that is divided by the midline raphe, forming a right and left hemiscrotum. Each hemiscrotum contains a testis, epididymis, spermatic cord, and vascular and lymphatic networks (Fig. 22.1).

The two layers of the **tunica vaginalis** separate the testis from much of the scrotal wall and form an isolated mesothelial lined sac.[1,2] During embryologic development, the tunica vaginalis arises from the **processus vaginalis,** an outpouching of fetal peritoneum that accompanies the testis in its descent into the scrotum. The upper portion of the processus vaginalis, extending from the internal inguinal ring to the upper pole of the testis, is normally obliterated. The lower portion, the tunica vaginalis, remains as a closed pouch within each hemiscrotum, partially folded around the testis. Only the posterior aspect of the testis, the site of attachment of the testis and epididymis, is not in continuity with the tunica vaginalis.

The inner or visceral layer of the tunica vaginalis covers the testis, epididymis, and lower portion of the spermatic cord. The outer or parietal layer of the tunica vaginalis lines the walls of the scrotal pouch and is attached to the fascial coverings of the testis. A small amount of fluid is normally present between these two layers.[3]

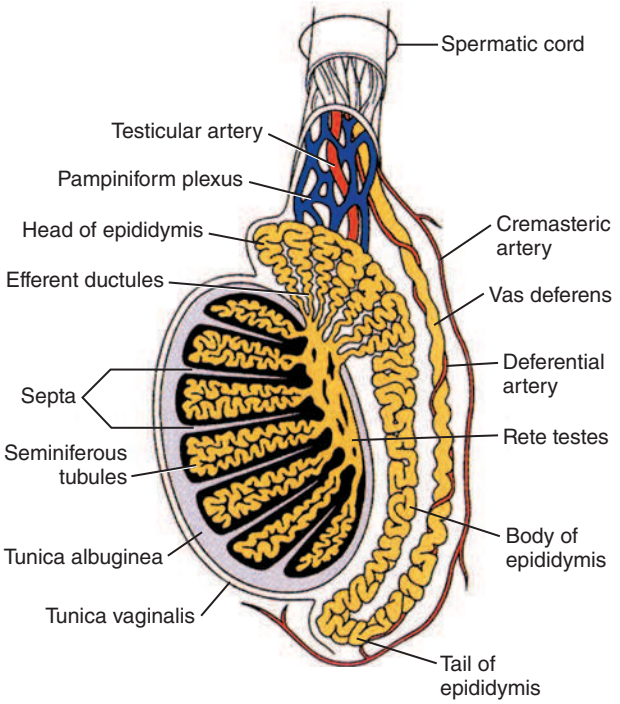

FIG. 22.1 Normal Intrascrotal Anatomy. (With permission from Sudakoff GS, Quiroz F, Karcaaltincaba M, Foley WD. Scrotal ultrasonography with emphasis on the extratesticular space: anatomy, embryology, and pathology. Ultrasound Q. 2002;18[4]:255-273.[78])

The fibrous **tunica albuginea** covers and protects the testis. Posteromedially, the tunica albuginea projects inward into the testis to form the mediastinum. Numerous fibrous septations project inward from the mediastinum, dividing the testis into 250 to 400 lobules. Each lobule consists of one to three seminiferous tubules supporting the Sertoli cells and spermatocytes. The Leydig cells are adjacent to the tubules, within the loose interstitial tissue, and are responsible for **testosterone** secretion.

The adult testes are ovoid glands measuring 3 to 5 cm in length, 2 to 4 cm in width, and 3 cm in anteroposterior dimension. Testicular size and weight decrease with age.[3,4] Sonographically, the **normal testis** has relatively homogeneous, medium-level, granular echotexture (Fig. 22.2A). Prepubertal testes are typically less echogenic than postpubertal testes secondary to incomplete maturation of the germ cell elements and tubules.[5] The tunica (**tunica vaginalis** and **tunica albuginea**) can often be seen as an echogenic outline of the testes. Where the tunica invaginates to form the mediastinum testis, the **mediastinum testis** is sometimes seen as a linear echogenic band extending craniocaudally within the testis (Fig. 22.2C). Its appearance varies according to the amount of fibrous and fatty tissue present. The fibrous septum, or **septula testis,** may be seen as a linear echogenic or hypoechoic structure (Fig. 22.2B).

The **seminiferous tubules** converge to form larger **tubuli recti,** which open into the dilated spaces of the rete testis. The normal **rete testis** can be identified in 20% of patients as a hypoechoic region near the mediastinum.[6] The rete testis drains into the epididymal head via 15 to 20 efferent ductules.

The **epididymis** is a curved structure measuring 6 to 7 cm in length and lying posterolateral to the testis. It is composed

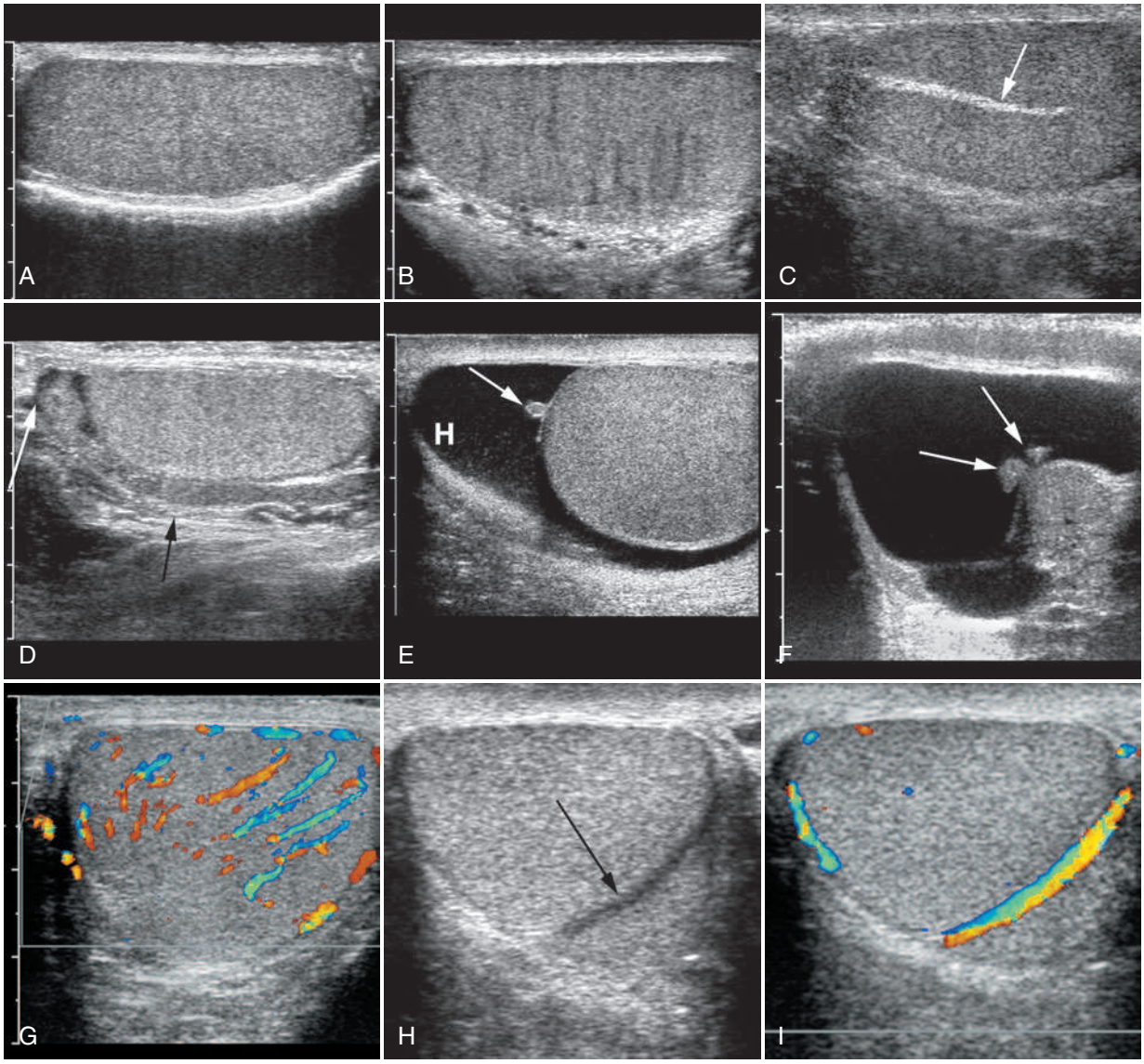

FIG. 22.2 Normal Intrascrotal Anatomy. Longitudinal scans show **(A)** normal homogeneous echotexture of the testis; **(B)** striated appearance of the **septula testis; (C) mediastinum testis** *(arrow)* as a linear echogenic band of fibrofatty tissue; **(D)** head *(white arrow)* and body *(black arrow)* of epididymis; **(E) hydrocele** *(H)* and **appendix testis** *(arrow);* and **(F) appendages of epididymis** *(arrows).* **(G)** Color Doppler scan shows normal testicular arteries. **(H)** Transverse scan shows hypoechoic band of **transmediastinal artery** *(arrow).* **(I)** Color Doppler scan shows transmediastinal artery.

of a head, a body, and a tail. The pyramid-shaped **epididymal head,** or **globus major,** is located at the superoposterior aspect of the testis, measuring 5 to 12 mm in diameter (Fig. 22.2D). It is formed by the efferent ductules from the rete testis, which join together to form a single convoluted duct, the **ductus epididymis.** This duct forms the body and the majority of the tail of the epididymis, measures approximately 6 m in length and follows a convoluted course from the head to the tail of the epididymis. The **body (corpus)** of the epididymis lies adjacent to the posterolateral margin of the testis. The **tail (globus minor)** is loosely attached to the lower pole of the testis by areolar tissue. The ductus epididymis forms an acute angle at the inferior aspect of the globus minor and courses cephalad as the **vas deferens** to the spermatic cord. Sonographically, the epididymal head is normally isoechogenic or slightly more echogenic than the testis, and its echotexture may be coarser. The body tends to be isoechoic or slightly less echogenic than the globus major and testis. The normal body measures less than 4 mm in diameter, averaging 1 to 2 mm.

The **appendix testis,** a remnant of the upper end of the paramesonephric (Müllerian) duct, is a small ovoid structure usually located on the superior pole of the testis or in the groove between the testis and the head of the epididymis. The appendix testis is identified sonographically in 80% of testes and is more readily visible when a hydrocele is present[7] (Fig. 22.2E). The appendix testis may appear stalklike and pedunculated, cystic, or even calcified.[8] The **appendices of the epididymis** are blind-ending tubules **(vasa aberrantia)** derived from the **mesonephric (Wolffian) duct;** they form small stalks, which may be duplicated, and project from the epididymis[9] (Fig. 22.2F). In rare cases,

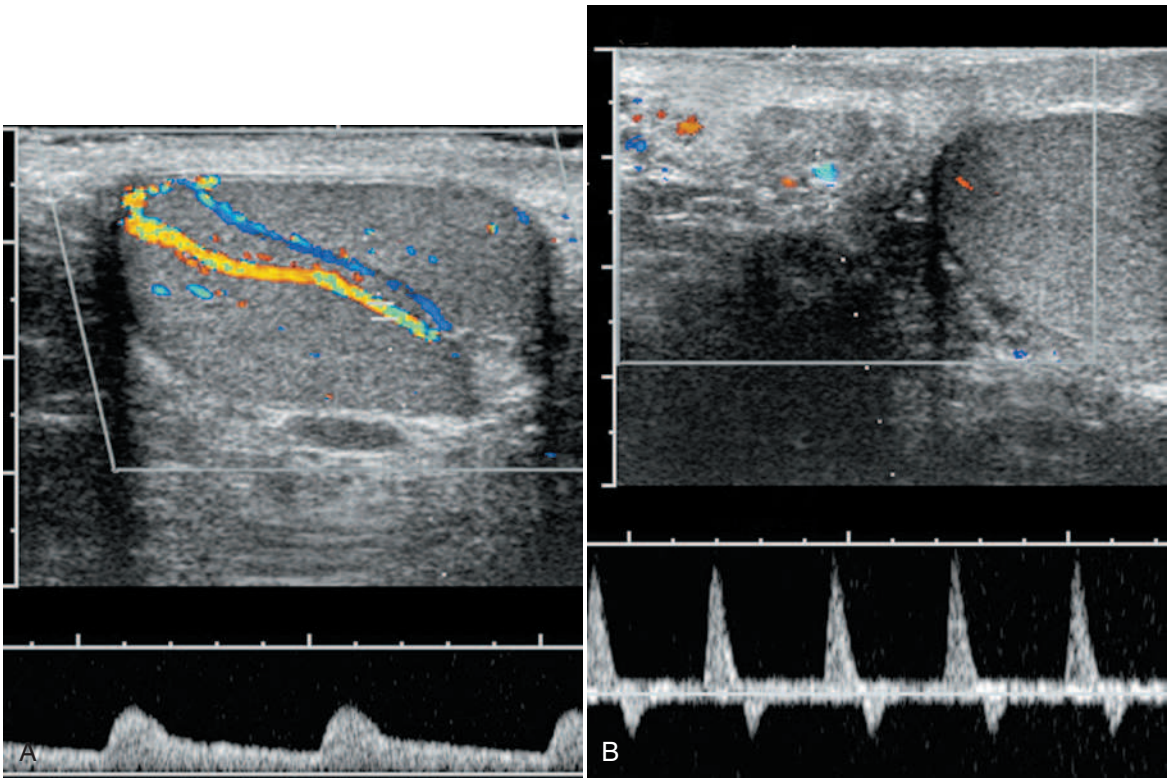

FIG. 22.3 Spectral Doppler of Normal Intratesticular and Extratesticular Arterial Flow. (A) Intratesticular artery has a low-impedance waveform with large amount of end diastolic flow. **(B)** Extratesticular scrotal arterial supply (cremasteric and deferential arteries) has high-impedance waveform with reversed flow in diastole.

other appendages, such as the **paradidymis (organ of Giraldés)** and the superior and **inferior vas aberrans of Haller,** may be seen.[10] The appendages of the epididymis are most often identified sonographically as separate structures when a hydrocele is present.

Knowledge of the arterial supply of the testis is important for interpretation of color flow Doppler sonography of the testis. Testicular blood flow is supplied primarily by the **testicular, deferential,** and **cremasteric (external spermatic) arteries.** The **testicular arteries** arise from the anterior aspect of the aorta immediately below the origin of the renal arteries. They course through the inguinal canal with the spermatic cord to the posterosuperior aspect of the testis. On reaching the testis, the testicular artery divides into branches that pierce the tunica albuginea where the **capsular arteries** form and arborize over the surface of the testis in a layer known as the **tunica vasculosa,** deep to the tunica albuginea. Centripetal branches arise from these capsular arteries; these branches course along the septa to converge on the mediastinum. From the mediastinum, these branches form recurrent rami that course into the testicular parenchyma, where they branch into arterioles and capillaries[11] (Fig. 22.2G). In about 50% of normal testes a **transmediastinal artery** supplies the testis, entering through the mediastinum and coursing toward the periphery of the gland to supply the capsular arteries, and is accompanied by a large vein, frequently seen as a hypoechoic band in the midtestis[11,12] (Fig. 22.2H and I). The transmediastinal artery may be associated with acoustic shadowing obscuring the distal aspect of the testis and giving rise to the "two-tone" testis appearance.[13] The **deferential artery** originates from the superior vesical artery and courses to the tail of the epididymis, where it divides and forms a capillary network. The **cremasteric artery** arises from the inferior epigastric artery. It courses with the remainder of the structures of the spermatic cord through the inguinal ring, continuing to the surface of the tunica vaginalis, where it anastomoses with capillaries of the testicular and deferential arteries.

The velocity waveforms of the **normal capsular** and **intratesticular arteries** show high levels of antegrade diastolic flow throughout the cardiac cycle, reflecting the low vascular resistance of the testis (Fig. 22.3A). Supratesticular arterial waveforms vary in appearance. Two main types of waveforms exist: a low-resistance waveform similar to that seen in the capsular and intratesticular arteries, reflecting the testicular artery; and a high-resistance waveform with sharp, narrow systolic peaks and little or no diastolic flow[14] (Fig. 22.3B). This high-resistance waveform is believed to reflect the high vascular resistance of the extratesticular tissues. The deferential and cremasteric arteries within the **spermatic cord** primarily supply the epididymis and extratesticular tissues, but they also supply the testis through anastomoses with the testicular artery.

The spermatic cord consists of the vas deferens; the testicular, cremasteric, and deferential arteries; a pampiniform plexus of veins; the lymphatics; and the nerves of the testis. It courses superiorly toward the superficial and deep (also called "internal") inguinal rings. Sonographically, the normal spermatic cord lies just beneath the skin and may be difficult to distinguish from

the adjacent soft tissues of the inguinal canal.[15] Distally, it may be visualized within the scrotum when a hydrocele is present or with the use of color flow Doppler sonography.

INTRATESTICULAR SCROTAL MASSES

When a scrotal mass is palpated, the concern is for the presence of a testicular neoplasm. With sonographic examination, intrascrotal masses can be detected with a sensitivity of nearly 100%.[16] Delineation between intratesticular and extratesticular processes is 98% to 100% accurate.[16-19] In general, intratesticular masses should be considered malignant.[19,20] If the mass is extratesticular and cystic, then this process is almost certainly benign, with the general accepted prevalence of malignancy of extratesticular lesions being 3% to 6%.[19,21-24]

Testicular neoplasms account for 1% to 2% of all malignant neoplasms in men and represent the most common nonhematologic malignancy in men in the 15- to 49-year-old age group.[25-27] Most (65%-94%) patients with testicular neoplasms present with painless unilateral testicular masses or diffuse testicular enlargement, and 4% to 14% present with symptoms of metastatic disease.[3,28,29] Approximately 10% to 15% of patients will present with pain and initially may be misdiagnosed as having epididymo-orchitis.[30]

Testicular tumors are subdivided into two major categories: germ cell and stromal tumors, with germ cell tumors accounting for 90% to 95% of all testicular tumors. **Germ cell tumors** arise from primitive germ cells and are further divided into **seminoma** and **nonseminomatous germ cell tumors** (NSGCTs). These tumors are uniformly malignant. Non–germ cell **(sex cord–stromal)** primary tumors of the testis derive from the sex cords **(Sertoli cells)** and the stroma **(Leydig cells)** and are malignant in approximately 10% of cases.[3,29] Nonprimary tumors include lymphoma, leukemia, and metastases and can present as intratesticular masses. Color Doppler imaging has limited ability to distinguish between malignant and benign solid intratesticular masses.[31]

Pathologic Classification of Testicular Tumors

GERM CELL TUMORS
- Seminoma
  - Classic
  - Spermatocytic
- Nonseminomatous germ cell tumors
  - Mixed malignant germ cell
  - Embryonal cell carcinoma
  - Yolk sac tumor (endodermal sinus tumor)
  - Teratoma
  - Choriocarcinoma
  - Placental site trophoblastic tumor
  - Trophoblastic tumor, unspecified
- Regressed tumor

STROMAL TUMORS
- Leydig cell (interstitial)
- Sertoli cell
- Granulosa cell
- Mixed undifferentiated sex cord

MIXED GERM CELL–STROMAL TUMORS
- Gonadoblastoma
- Germ cell–stromal–sex cord, unclassified

METASTATIC NEOPLASMS
- Lymphoma
- Leukemia
- Myeloma
- Carcinoma

OTHER[a]
- Adrenal rests
- Epidermoid cyst
- Malacoplakia
- Carcinoid tumor
- Mesenchymal tumor
- Granulomatous disease

[a]Rare tumors and nonneoplastic tumorous conditions.
Modified from Moch H, Cubilla AL, Humphrey PA, et al. The 2016 WHO classification of tumours of the urinary system and male genital organs-Part A: renal, penile, and testicular tumors. Eur Urol. 2016:70(10):93-105.[32]

Malignant Tumors

Germ Cell Tumors

Intratubular germ cell neoplasia is believed to be the precursor of most germ cell tumors and is the equivalent of carcinoma in situ. It is thought that these abnormal cells develop along a unipotential line and form seminoma, or develop along a totipotential line and form nonseminomatous tumors.[33,34] Seminomas are radiosensitive tumors, whereas NSGCTs respond better to surgery and chemotherapy.[27]

Approximately 95% of primary testicular neoplasms larger than 1.6 cm in diameter show increased vascularity on color flow Doppler examination. However, color Doppler findings do not appear to be important in the evaluation of adult testicular tumors.[35] Color flow may help to identify tumors that are relatively isoechoic with testicular parenchyma,[36] but focal or diffuse inflammatory lesions cannot be distinguished from neoplasms on the basis of color flow Doppler or spectral Doppler findings. Nonpalpable testicular tumors have also been detected with sonography in patients presenting for scrotal discomfort or infertility.[37-40] Incidentally discovered nonpalpable lesions are often benign, but 20% to 30% are malignant.[38,39,41]

Tumor markers have a role in diagnosis, staging, prognosis, and follow-up of a number of germ cell tumors, with three markers having clinical use: **α-fetoprotein, human chorionic gonadotropin,** and, less so, **lactate dehydrogenase.** α-Fetoprotein is produced by the fetal liver, gastrointestinal tract, and yolk sac and is elevated in yolk sac tumors or mixed germ cell tumors containing yolk sac elements. Human chorionic gonadotropin is a glycoprotein produced by syncytiotrophoblasts of the developing placenta. It is elevated in tumors containing syncytiotrophoblasts, including choriocarcinoma and seminoma. Lactate dehydrogenase, although not specific, correlates with bulk of disease and is used in staging.[20]

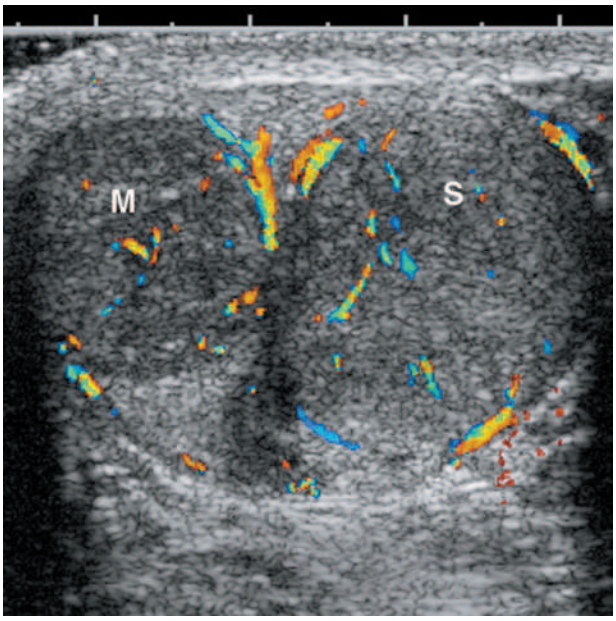

FIG. 22.4 Mixed Tumor. Transverse scan of coexistent solid masses—a mixed germ cell tumor *(M)* and a seminoma *(S)*.

Seminoma. Seminoma is the most common pure, or single cell–type, germ cell tumor in adults, accounting for 35% to 50% of all germ cell neoplasms.[20,30] It is also a common component of mixed germ cell tumors, occurring in 30% of these tumors. Seminomas tend to occur in slightly older patients than do other testicular neoplasms, with a peak incidence in the fourth and fifth decades, and they rarely occur before puberty.[3,42,43] They are typically confined within the tunica albuginea at presentation, with approximately 25% of patients having metastases at diagnosis. As a result of the radiosensitivity and chemosensitivity of the primary tumor and its metastases, seminomas have the most favorable prognosis of the malignant testicular tumors. A **second primary synchronous or metachronous germ cell tumor** occurs in 1% to 2.5% of patients with seminomas (Fig. 22.4).

Seminoma is the most common tumor type in **cryptorchid testes.** Between 8% and 30% of patients with seminoma have a history of undescended testes.[29,43] The risk of a seminoma developing is substantially increased in an undescended testis, even after orchiopexy. Patients with a normally located but atrophic testis have an increased risk of seminoma (Video 22.1). There is also an increased risk of malignancy developing in the contralateral, normally located testis. Therefore sonography is often used to screen for an occult tumor in both testes after orchiopexy.

Seminomas range from a small, well-circumscribed lesion to large masses replacing the testis. Macroscopically, cellular morphology resembles that of primitive germ cells, which are relatively uniform.[25] The sonographic features of pure seminoma parallel this homogeneous macroscopic appearance. Pure seminomas usually have predominantly uniform, low-level echoes without calcification, and they appear hypoechoic compared with normally echogenic testicular parenchyma (Fig. 22.5).[44] Larger tumors may have a more heterogeneous appearance. In rare cases, seminomas become necrotic and appear partly cystic on sonography (Fig. 22.5I).

Nonseminomatous Germ Cell Tumors. NSGCTs include **embryonal carcinomas, teratomas, yolk sac (endodermal sinus) tumors, choriocarcinomas,** and **mixed germ cell tumors.** These tumors occur more often in younger patients than do seminomas, with a peak incidence during the latter part of the second decade and the third decade. They are uncommon before puberty and after age 50. Approximately 70% of NSGCTs produce hormonal markers.[45] Up to 60% of germ cell tumors are mixed germ cell tumors, composed of at least two different cell types.[20,46] Pure NSGCTs are rare and occur more often in the pediatric population.[20] The sonographic appearance of NSGCTs reflects the histologic features and relative proportions of each component, although as a group these tumors are more heterogeneous than seminoma, demonstrating irregular margins, echogenic foci, and solid and cystic components (Fig. 22.6). These malignancies are more aggressive than seminomas, frequently invading the tunica albuginea and resulting in distortion of the testicular contour (see Fig. 22.6). Approximately 60% of NSGCTs have metastatic involvement at presentation.[46]

Mixed germ cell tumors are the most common germ cell tumors, constituting up to 60% of all germ cell tumors. They contain nonseminomatous germ cell elements in various combinations. Seminomatous elements may also be present but do not influence prognosis or treatment.[47] Embryonal carcinoma is the most common component, although any combination of cell types may occur. Imaging features are variable, reflecting the diversity of this group of tumors. Nonseminomatous tumors are not as radiosensitive as seminomas. **Embryonal carcinoma** is composed of primitive anaplastic cells that resemble early embryonic cells. It is present in 87% of mixed germ cell tumors, but in its pure form it is rare, accounting for only 2% to 3% of testicular germ cell neoplasms (Fig. 22.6C).[48] As with other NSGCTs, embryonal cell tumors occur in younger patients than seminomas do, with a peak incidence during the latter part of the second and third decades. The sonographic features of pure embryonal cell carcinoma are nonspecific, especially in children, in whom the only finding may be testicular enlargement without a defined mass.[36,49]

Totipotent germ cells that differentiate toward extraembryonic fetal membranes give rise to **yolk sac tumors,** or **endodermal sinus tumors.** Yolk sac tumors are the most common germ cell tumor in infants younger than 2 years, accounting for 80% of childhood testicular neoplasms.[49] Yolk sac tumor is rare in its pure form in adults, although it is present in 44% of adult cases of mixed germ cell tumor (Fig. 22.6D).[20] Yolk sac tumor is associated with elevated levels of α-fetoprotein in greater than 90% of infants. **Teratomas** constitute 5% to 10% of primary testicular neoplasms. They are defined according to the World Health Organization (WHO) classification on the basis of the presence of derivatives of the different germinal layers (endoderm, mesoderm, and ectoderm). Histologically, teratomas can be divided into mature and immature. The peak incidence is in infancy and early childhood, with another peak in the third decade of life. In infants and young children, teratomas are the second most common testicular tumor after yolk sac tumor and are considered benign, even when they are histologically immature.[43,50,51] Postpubertal testicular teratomas are malignant and

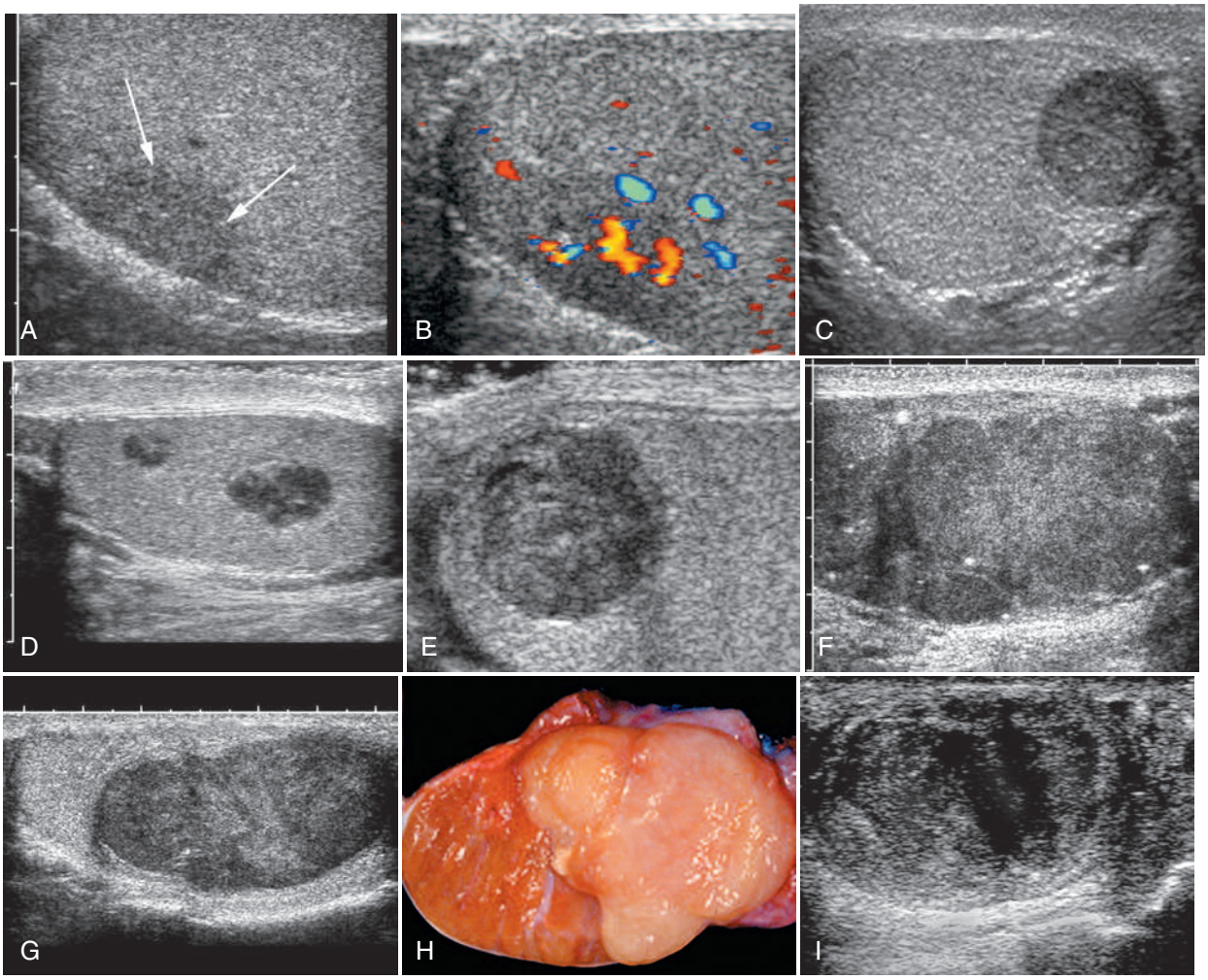

FIG. 22.5 Seminoma: Spectrum of Appearances. Longitudinal scans. **(A)** and **(B)** Subtle hypoechoic seminoma *(arrows)* with increased flow. **(C)** Typical homogeneous hypoechoic seminoma. **(D)** Two small foci of seminoma. **(E)** Slightly heterogeneous seminoma. **(F)** Seminoma associated with microlithiasis and coarser calcifications. **(G)** Seminoma occupying most of testis. Typical homogeneous hypoechoic sonographic appearance. **(H)** Gross specimen of seminoma in **G. (I)** Necrotic seminoma replacing testicle. See also Video 22.1.

have a higher metastatic rate, approximately 20%, than their ovarian counterpart.[52] Teratomas in their pure form are rare in adults, although teratomatous elements occur in approximately half of all adult cases of mixed germ cell tumor (Fig. 22.6B). Both mature and immature teratomas are generally associated with normal tumor markers, although elevated levels of α-fetoprotein or human chorionic gonadotropin may be found.[47] Sonographically, the teratoma is usually a well-defined, markedly heterogeneous mass containing cystic and solid areas of various sizes and appears similar to other NSGCTs. Dense echogenic foci causing acoustic shadowing are common, resulting from focal calcification, cartilage, immature bone, fibrosis, and non-calcific scarring (Fig. 22.6E).[44]

Choriocarcinoma accounts for less than 1% of malignant primary testicular tumors in its pure form but occurs in 8% of mixed germ cell tumors.[20,43,48,50] The peak incidence is in the second and third decades. These tumors are highly malignant and metastasize early by hematogenous and lymphatic routes. The primary tumor and metastases are often hemorrhagic, and patients may have symptoms resulting from hemorrhagic metastases, including hemoptysis, hematemesis, and central nervous system–related symptoms. Focal necrosis of the primary tumor secondary to hemorrhage is an almost invariable feature, and calcification may be present, giving a sonographic appearance similar to the other NSGCTs (Fig. 22.6F). The levels of human chorionic gonadotropin are elevated and cause gynecomastia in 10% of cases.[20,53] Choriocarcinoma has the worst prognosis of any of the germ cell tumors.[50]

Regressed Germ Cell Tumor. Sonography is an important diagnostic tool for patients who present with widespread metastatic testicular carcinoma (Fig. 22.7) even though the primary tumor has involuted (Fig. 22.8); ultrasound is an important component in the search for a primary testicular neoplasm. Mediastinal and central nervous system extragonadal tumors can often present as primary lesions, although retroperitoneal germ cell tumors are more likely to have a testicular origin.[54,55] The primary testicular tumor may regress, despite widespread advancing metastatic disease, resulting in an echogenic fibrous and possibly calcific scar. Regression may be caused by the high metabolic rate of the tumor and vascular compromise from the

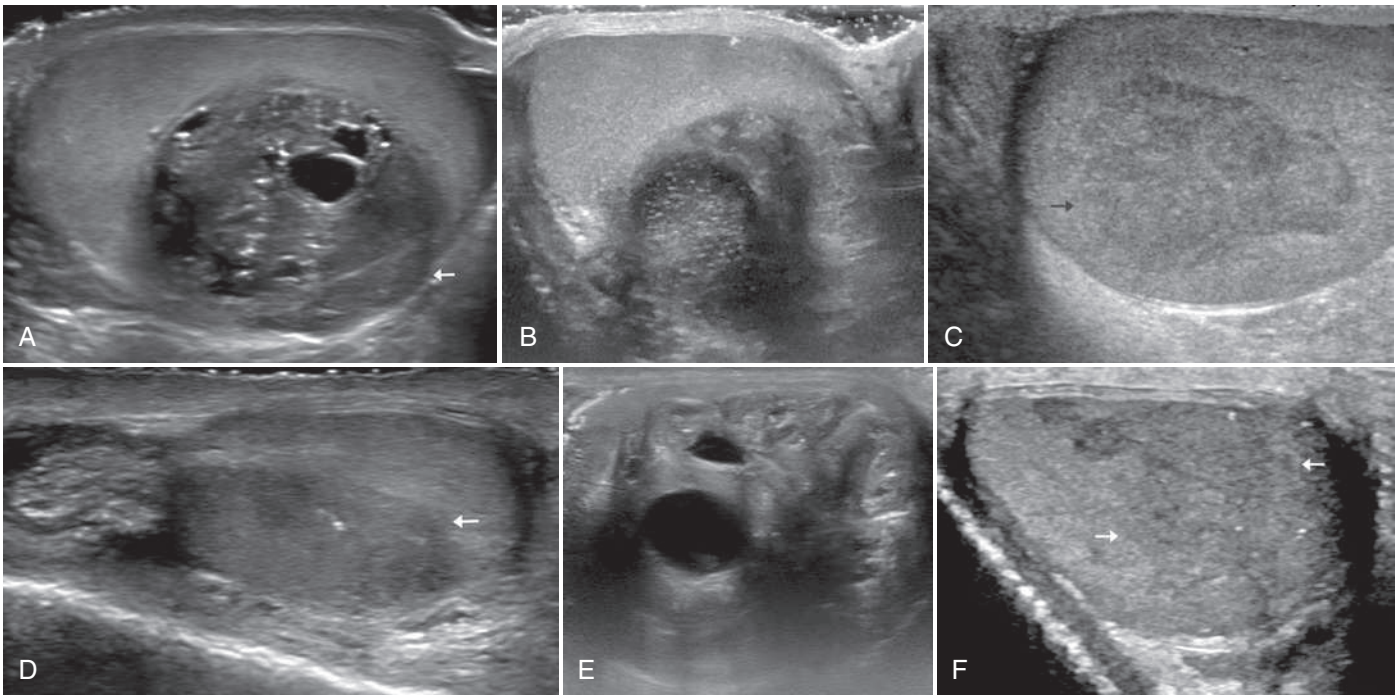

FIG. 22.6 Nonseminomatous Germ Cell Tumor: Spectrum of Appearances. (A) and **(B) Mixed germ cell tumor. (A)** Longitudinal scan shows a large tumor with cystic changes occupying most of the testis and invading the tunica *(arrow).* **(B)** Transverse scan shows a heterogeneous, mixed germ cell tumor that has 85% teratoma elements. **(C) Embryonal carcinoma.** Longitudinal scan shows relatively homogeneous tumor *(arrow).* **(D) Yolk sac, or Endodermal sinus tumor.** Longitudinal scan shows a mildly heterogenous tumor extending to the mediastinum *(arrow).* **(E) Teratoma.** Longitudinal scans shows a large heterogeneous mass with cystic foci and scattered calcifications. **(F) Choriocarcinoma.** Longitudinal scan shows a relatively homogeneous tumor *(arrows).*

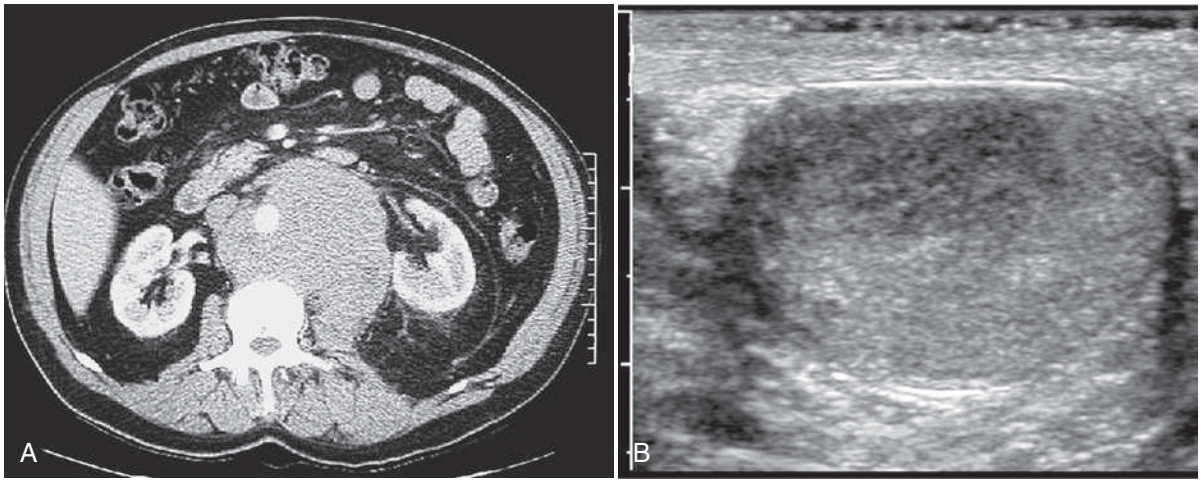

FIG. 22.7 Occult Testicular Seminoma With Retroperitoneal Metastases. (A) Contrast-enhanced CT scan shows extensive retroperitoneal adenopathy from seminoma. **(B)** Longitudinal sonographic scan shows occult homogeneous hypoechoic seminoma. The physical examination of the testis was negative.

tumor outgrowing its blood supply. Tumors are typically clinically occult with the affected testis normal or small on palpation. Histologic analysis may reveal no residual tumor, although intratubular malignant germ cells may be present.[25,28,54] These lesions, also known as **"Azzopardi tumors,"** have a variable sonographic appearance; they can be hypoechoic or hyperechoic or seen as focal calcifications. Although sonographic appearance is not specific for a "burned-out" or regressed tumor, findings are suggestive in the context of histologically proven testicular metastases.[56]

Non–Germ Cell Tumors

Sex Cord–Stromal Tumors. Sex cord–stromal tumors account for 3% to 6% of all testicular neoplasms. The prevalence is greater in the pediatric population where non–germ cell tumors account for 10% to 30% of all testicular neoplasms. The term

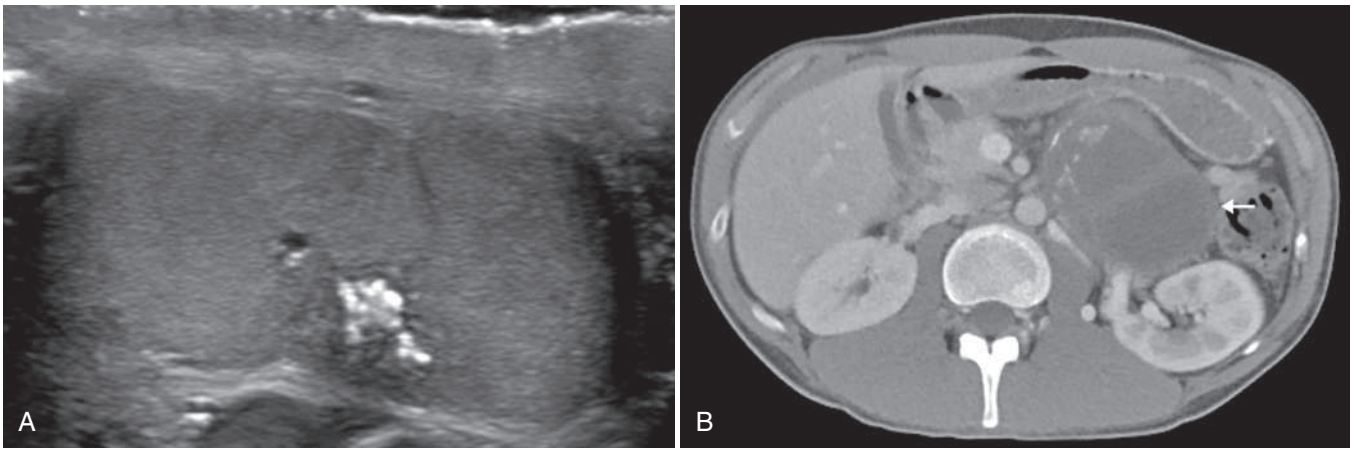

FIG. 22.8 Regressed, or "Burned-Out," Germ Cell Tumor. (A) Longitudinal scan shows a partly calcified nonviable germ cell tumor in a patient with retroperitoneal metastases. Notice the hypoechoic mass around the focus of calcification. **(B)** Contrast-enhanced CT scan in the same patient shows heterogeneous left retroperitoneal adenopathy *(arrow)* from regressed primary testicular teratoma.

sex cord–stromal tumor refers to a neoplasm containing Leydig, Sertoli, thecal, granulosa, or lutein cells and fibroblasts in various degrees of differentiation. These tumors may contain single or multiple cell types because of the totipotentiality of the gonadal stroma.[29]

The most common type of sex cord–stromal tumor is a **Leydig cell tumor,** accounting for 1% to 3% of all testicular neoplasms; these can occur in any age group, although predominantly in patients aged 20 to 50 years.[42,43,53] Patients most often present with painless testicular enlargement or a palpable mass. Approximately 30% of patients present with an endocrinopathy secondary to secretions of androgens or estrogens by the tumor, which may manifest as precocious virilization, impotence, or loss of libido. The tumor is bilateral in 3% of cases. From 10% to 15% of the tumors are malignant, having invaded the tunica at diagnosis. These gonadal tumors are usually small, solid, homogeneous hypoechoic masses on sonography and may show mainly peripheral flow on color Doppler imaging (Fig. 22.9A and B).[57] Foci of hemorrhage and necrosis are present in 25% of tumors,[42,53] and thus cystic spaces due to hemorrhage and/or necrosis are occasionally seen in larger lesions.

Sertoli cell tumors are rare and account for less than 1% of all testicular tumors; they occur with equal frequency in all age groups.[58] They can be of one of three histologic types: **Sertoli cell tumor not otherwise specified, sclerosing Sertoli cell tumor,** or **large cell calcifying Sertoli cell tumor.** The most common presentation is with a painless intratesticular mass. These tumors are less likely than Leydig cell tumors to be hormonally active, although gynecomastia may occur. Sertoli cell tumors may occur in **undescended testes,** in patients with **testicular feminization, Klinefelter syndrome,** and **Peutz-Jeghers syndrome.**[59] Sertoli cell tumors are typically well-circumscribed, unilateral, rounded to lobulated masses. Occasionally, hemorrhage or necrosis may occur, giving a more heterogeneous appearance on sonography. The large-cell calcifying Sertoli cell tumor is a subtype with distinctive clinical, histologic, and sonographic features.[59] These tumors are often bilateral and multifocal and may be almost completely calcified. **Carney complex,** a very rare autosomal dominant multiple endocrine neoplasia syndrome, is often associated with Sertoli cell tumors (Fig. 22.9C).

Additional, less common tumors in this category include **granulosa cell tumors, fibroma-thecomas, and mixed sex cord–stromal tumors** (Fig. 22.9D). Gonadal stromal tumors in conjunction with germ cell tumors are called **gonadoblastomas.** The majority of gonadoblastomas occur in the setting of **gonadal dysgenesis** and **intersex syndromes.**[43,60]

Testicular Metastases

Lymphoma and Leukemia

Lymphoma accounts for 5% of all testicular tumors and is the most common testicular tumor in men older than 60 years, where it can account for up to 50% of intratesticular masses. However, testicular involvement occurs in only 1% to 3% of patients with lymphoma.[29,61] The peak age at diagnosis of lymphoma is 60 to 70 years; 80% of the patients are older than 50 years at diagnosis. Malignant lymphoma is the most common bilateral testicular tumor, occurring bilaterally either in a synchronous or, more often, in a metachronous manner in up to 38% of cases.[60] One-half of bilateral testicular neoplasms are lymphoma.[29,42] Most lymphomas of the testis are B-cell lymphomas, with diffuse large cell lymphoma being the most common. Hodgkin lymphoma of the testis is extremely rare.

Testicular Metastases

LYMPHOMA
Mostly non-Hodgkin lymphoma

LEUKEMIA
Second most common
Acute leukemia: 40%-65%
"Sanctuary" site

NONLYMPHOMA METASTASES
Lung and prostate most common
Kidney, stomach, colon, pancreas, melanoma

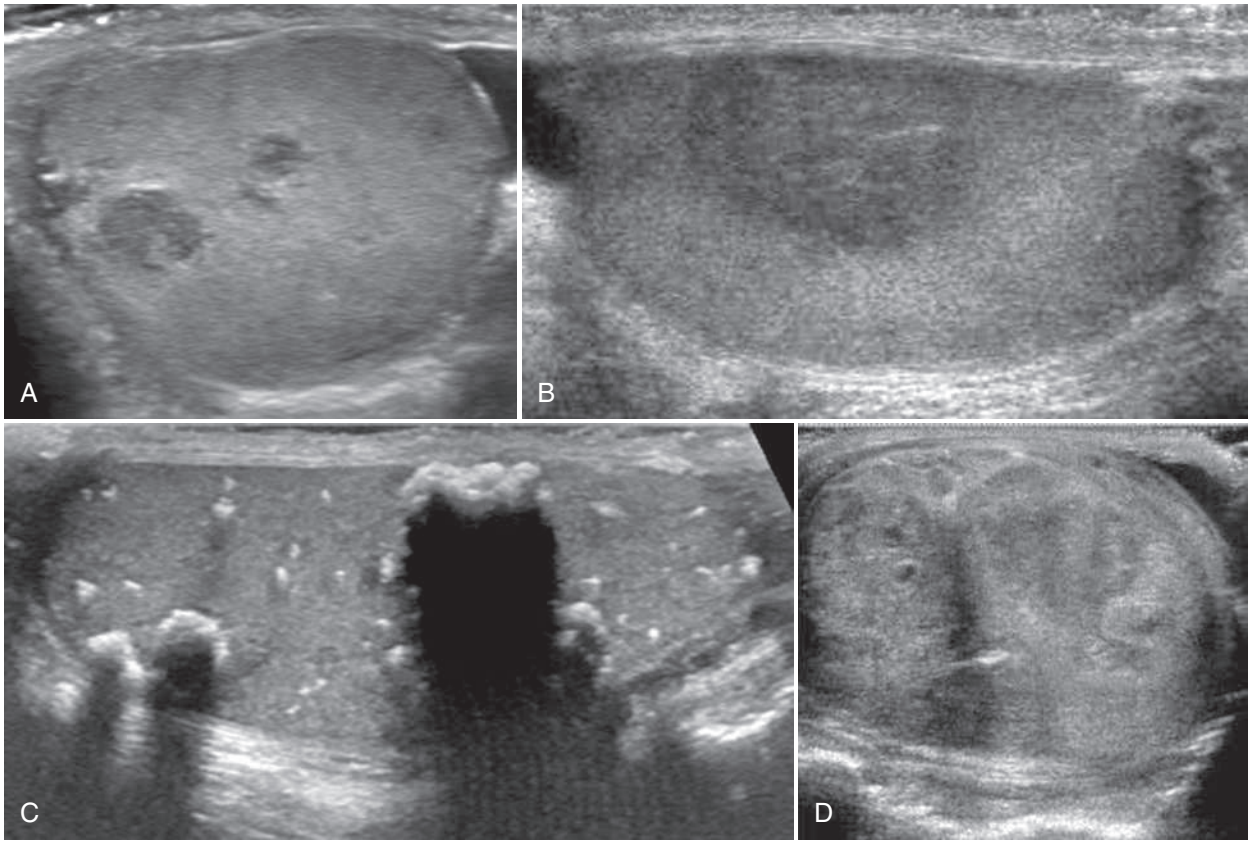

FIG. 22.9 Stromal Tumors: Spectrum of Appearances. (A) and **(B) Leydig cell tumor. (A)** Transverse scan shows several small, hypoechoic solid masses in the midtestis consistent with Leydig cell hyperplasia. **(B)** Longitudinal scan shows a hypoechoic solid mass in the midtestis. The patient had bilateral Leydig cell tumors. **(C)** Longitudinal scan of multifocal large-cell calcifying **Sertoli cell tumor. (D) Stromal tumor.** Transverse scan demonstrates a large, heterogeneous tumor (which was a stromal tumor, not otherwise specified) replacing the testis. (**C** courtesy of Theodora Potretzke, MD, Mayo Clinic.)

Testicular lymphoma most frequently occurs in association with disseminated disease, as the initial manifestation of occult nodal disease, or as a site of recurrent disease.[29] True primary lymphoma of the testis has not been conclusively documented.[47] Although most patients with lymphoma of the testis present with a painless intratesticular mass or diffuse testicular enlargement, approximately 25% of the patients have constitutional symptoms, such as fever, weakness, anorexia, or weight loss.

Lymphoma of the testis is often large at diagnosis. The tunica vaginalis is usually intact, but unlike germ cell tumors, extension into the epididymis and spermatic cord is common, occurring in up to 50% of cases.[62] The scrotal skin is rarely involved. Grossly, the tumor is not encapsulated but compresses the parenchyma to the periphery. The sonographic appearance of lymphoma is nonspecific, although generally appears as homogeneous, hypoechoic lesions which may diffusely infiltrate the testis[29]; however, focal hypoechoic lesions can occur (Fig. 22.10). Hemorrhage and necrosis are rare.

Color flow Doppler imaging shows increased vascularity in testicular lymphoma, regardless of lesion size, and the appearance may resemble diffuse inflammation[63] (Fig. 22.10C). Unlike inflammation, lymphoma is usually painless, and the testes are not tender to palpation.

Leukemia is the second most common metastatic testicular neoplasm. Primary testicular leukemia is rare, but leukemic infiltration of the testis during bone marrow remission is common in children.[29,64] The testis appears to act as a "sanctuary" site for leukemic cells during chemotherapy because of the **blood-testis barrier,** which inhibits concentration of chemotherapeutic agents.[64] The highest frequency of testicular involvement is found at autopsy in patients with acute leukemia (40%-65%). Approximately 20% to 35% of patients with chronic leukemia have testicular involvement.[65] Most cases of testicular involvement occur within 1 year of the discontinuation of long-term remission maintenance chemotherapy.

The sonographic appearance of leukemia is nonspecific and similar to lymphoma. Patients most frequently present with diffuse infiltration, which produces diffusely enlarged, hypoechoic testes (Fig. 22.10E).[63] The differential diagnosis includes inflammation.

Extramedullary Myeloma

Involvement of the testis is usually a manifestation of diffuse myeloma, although rarely the testis may be the site of primary **focal myeloma (plasmacytoma).**[66] The testis may have single or multiple nodules that appear hypoechoic and homogeneous

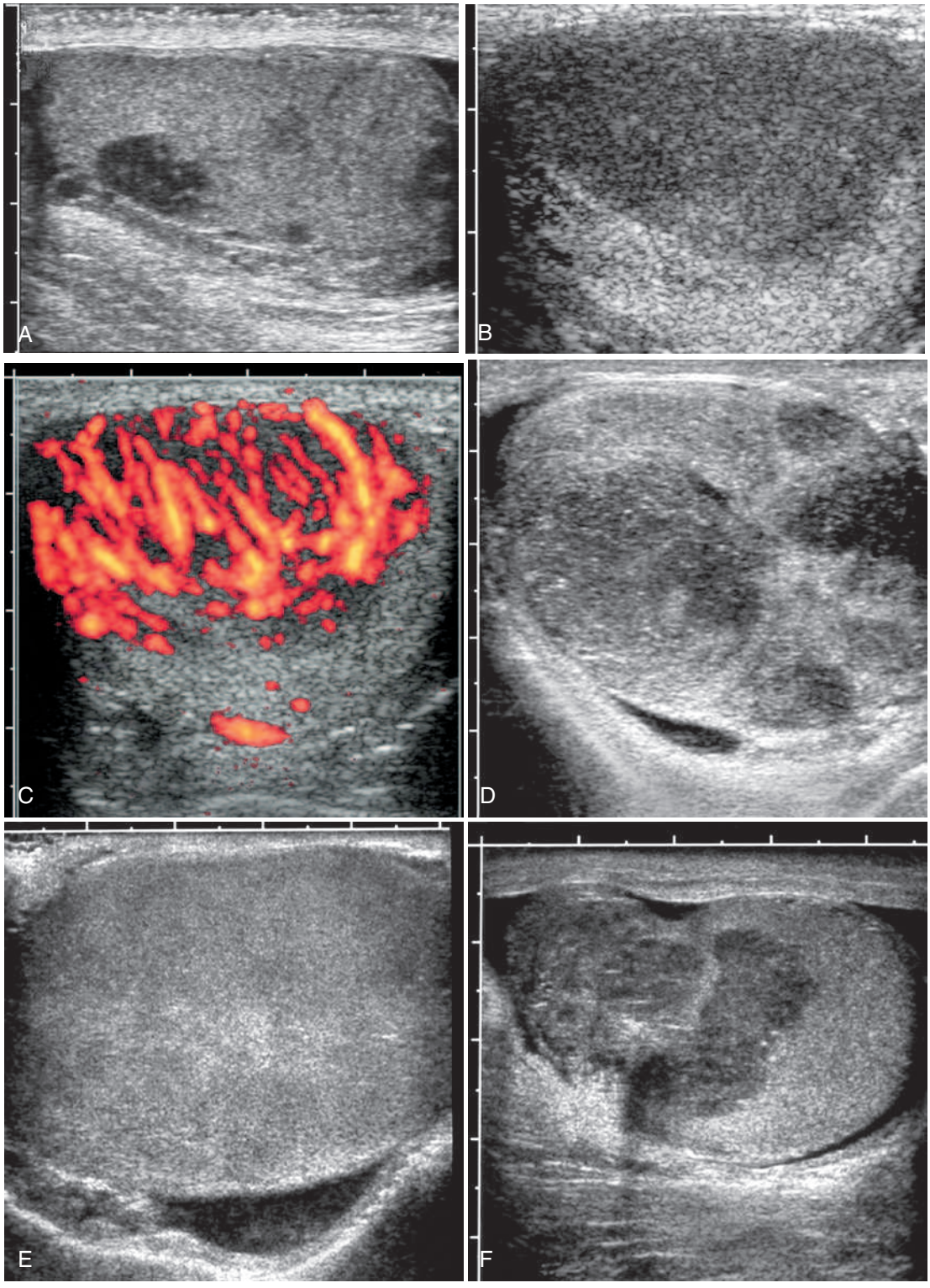

FIG. 22.10 Lymphoma, Leukemia, and Metastases. (A)-(D) Lymphoma. (A) Longitudinal scan shows two subtle hypoechoic foci of lymphoma. In another patient, sagittal gray-scale **(B)** and power Doppler **(C)** images show diffuse, homogeneous hypoechoic hypervascular mass. **(D)** Heterogeneous involvement of the testes in patient with lymphoma. **(E) Leukemia.** Longitudinal scan shows diffuse hypoechoic involvement. **(F) Melanoma metastasis.** Longitudinal scan shows a hypoechoic lobulated mass in the upper pole of the testis and epididymis.

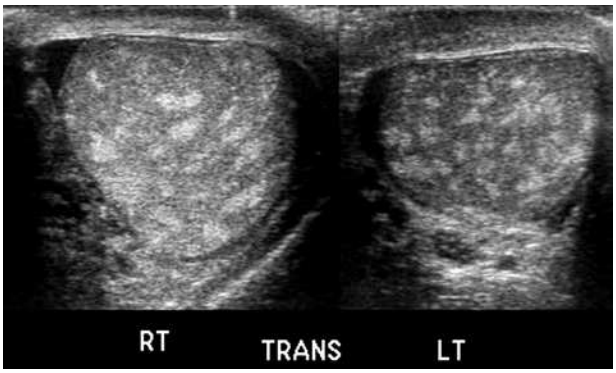

FIG. 22.11 Multiple Testicular Hamartomas in Cowden Disease. Dual transverse image shows multiple bilateral small echogenic hamartomas. The patient had Cowden disease, an inherited autosomal dominant disorder, which causes multiple hamartomas in the gastrointestinal tract.

on sonographic examination with marked hypervascularity.[67,68] Bilateral involvement occurs in approximately 20% of cases.[47]

Metastatic Disease

Nonlymphomatous metastases to the testes are uncommon, representing 0.02% to 5% of all testicular neoplasms.[69] The most frequent primary sites are the **lung** and **prostate gland.**[42] Other frequent primary sites for metastatic neoplasms include melanoma, kidney, colon, stomach, and pancreas.[70] Most metastases are clinically silent, being discovered incidentally at autopsy. Testicular metastases are most common in patients during the sixth and seventh decades.[3] They are usually multiple and are bilateral in 15% of cases.[42] Because primary germ cell tumors may also be multicentric and bilateral, these features are not helpful in distinguishing primary from metastatic testicular neoplasms. Widespread systemic metastases are usually present in patients with testicular metastases. Possible routes of metastases to the testis include retrograde venous, hematogenous, retrograde lymphatic, and direct tumor invasion. Metastases from sites remote from the testis, such as the lung and skin, most likely spread hematogenously. Retrograde venous extension through the testicular vein occurs in renal cell carcinoma and may also occur in urinary bladder and prostate tumors.[71] Neoplasms with metastases to the periaortic lymph nodes may involve the testis through retrograde lymphatic extension. Sonographic features of nonlymphomatous testicular metastases vary. The appearance is often hypoechoic but may be echogenic or complex[3] (Fig. 22.10F).

Other rare tumors of the testis include hamartoma (Fig. 22.11), dermoid tumor, hemangioma, intratesticular adenomatoid tumor, carcinoid tumor, carcinoma of the mediastinum testis, neuroectodermal tumor, leiomyoma, Brenner tumor, fibroma, fibrosarcoma, osteosarcoma, chondrosarcoma, and undifferentiated sarcoma, among others.

Benign Intratesticular Lesions

Cysts

Intratesticular cystic lesions are discovered incidentally on sonography in 8% to 10% of men.[72] Benign testicular cysts may be associated with the tunica albuginea, tunica vaginalis, or located within the parenchyma. Cystic testicular lesions are not always benign; testicular tumors (especially NSGCTs) can undergo cystic degeneration from hemorrhage or necrosis. The distinction between a benign cyst and a cystic neoplasm is of utmost clinical importance (Fig. 22.12). Simple intratesticular cysts can be managed conservatively without the need for surgical intervention.[73] Of the 34 cystic testicular masses discovered with sonography by Hamm et al.,[72] 16 were neoplastic, and all of these had sonographic features of complicated cysts. NCGCTs, especially those with teratoma elements, are the most common tumors to contain both cystic and solid components.

Testicular Cystic Lesions

BENIGN
Tunica albuginea cysts
Tunica vaginalis cysts
Intratesticular cysts
Tubular ectasia of rete testis
Cystic dysplasia
Epidermoid cysts
Abscess

MALIGNANT
Nonseminomatous germ cell tumor
Necrosis or hemorrhage in tumor
Tubular obstruction by tumor

Cysts of the tunica albuginea are located within the tunica, which surrounds the testis. They vary in size from 2 to 30 mm and are well defined. They are usually solitary and unilocular but may be multiple or multilocular[72,74] (Fig. 22.12A). The mean age at presentation is 40 years, but cysts also occur in the fifth and sixth decades.[75] The cysts may be asymptomatic, but patients frequently present with cysts that are clinically palpable, firm scrotal nodules. Histologically, they are simple cysts lined with cuboid or low columnar cells and filled with serous fluid.[76] Careful scanning in multiple planes allows delineation of the cyst as arising from the tunica albuginea and clarifies its benign nature. Complex tunica albuginea cysts may simulate a testicular neoplasm.[77]

Cysts of the tunica vaginalis are rare and arise from the visceral or parietal layer of the tunica vaginalis. They may be single or multiple. Sonographically, they usually appear anechoic but may have septations or may contain echoes caused by hemorrhage.[78]

Intratesticular cysts are simple cysts filled with clear serous fluid; they vary in size from 2 to 18 mm.[79] Sonographically, they are well-defined, anechoic cysts with thin, smooth walls and posterior acoustic enhancement. Hamm et al.[72] reported that in all 13 of their cases, the cysts were located near the mediastinum testis, supporting the theory that they originate from the rete testis, possibly secondary to posttraumatic or postinflammatory stricture formation (Fig. 22.12B).

Tubular Ectasia of Rete Testis

Tubular ectasia of the rete testis is a benign, normal variant that may be mistaken for a testicular neoplasm.[80-83] Dilatation of the

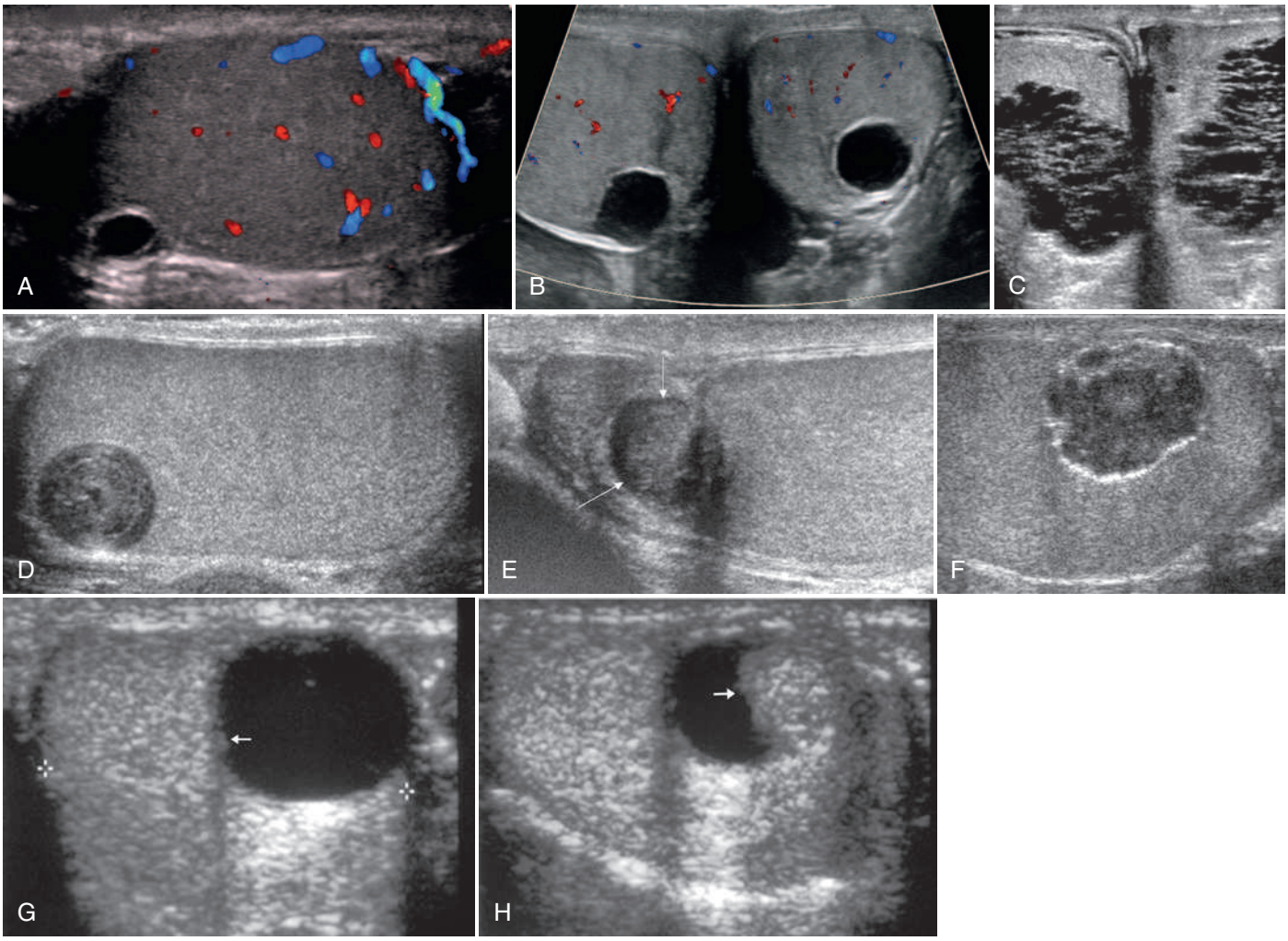

FIG. 22.12 Intratesticular Cystic Lesions. (A) Tunica albuginea cyst. Longitudinal scan shows a cyst arising from the tunica albuginea. These cysts are usually palpable. **(B) Intratesticular cyst.** Transverse scan shows bilateral benign intratesticular cysts. **(C) Cystic dilatation in rete testis.** Transverse scan shows dilated tubules of the rete testis in both testes. **(D)-(F) Epidermoid cyst** (benign). See also Video 12.2. **(D)** Typical whorled appearance; **(E)** heterogeneous hypoechoic lesion *(arrows);* **(F)** typical peripheral calcifications. **(G)** Transverse scan shows an intratesticular cystic lesion with minimal mural nodularity *(arrow)*. **(H)** Transverse scan at 6-month interval follow-up shows interval development of an isoechoic, solid mass *(arrow)* partially filling the cystic lesion, surgically proven to represent teratoma. (**G** and **H** courtesy of Shane Macauley, MD.)

rete testis is thought to result from obstruction in the efferent tubules or epididymis, with epididymal obstruction caused by inflammation, trauma, or surgery. Sonographic appearance is of multiple fluid-filled tubular structures in or adjacent to the mediastinum testis with no associated soft tissue abnormality and no flow on color flow Doppler imaging (Fig. 22.12C). Rete testis dilatation is often bilateral, asymmetric, and is frequently associated with a spermatocele. The characteristic sonographic appearance and location should allow recognition as a benign condition, thus preventing an orchiectomy. Characteristic findings of the dilated rete testis on magnetic resonance imaging (MRI) include intratesticular signal intensity similar to that of fluid in the region of the mediastinum testis.[80] This appearance is in contrast to the MRI appearance of testicular tumors, which typically have low signal intensity on T2-weighted imaging.

Cystic Dysplasia

Cystic dysplasia is a rare congenital malformation, usually occurring in infants and young children, although one case was reported in a 30-year-old man.[84,85] This lesion is thought to result from an embryologic defect that prevents connection of the tubules of the rete testis and the efferent ductules. Pathologically, the lesion consists of multiple, interconnecting cysts of various sizes and shapes, separated by fibrous septa. This lesion originates in the rete testis and extends into the adjacent parenchyma, resulting in pressure atrophy of the adjacent testicular parenchyma. The cysts are lined by a single layer of flat or cuboidal epithelium. Sonographically, the appearance is similar to acquired cystic dilatation of the rete testis. Renal agenesis or dysplasia frequently coexists with testicular cystic dysplasia.[85]

Epidermoid Cysts

An epidermoid cyst is an uncommon, benign, generally well-circumscribed tumor of germ cell origin, representing approximately 1% of all testicular tumors. These tumors occur at any age but are most common during the second to fourth decades.[42] Usually, patients present with a painless testicular nodule; one-third of the tumors are discovered incidentally on physical examination. Diffuse, painless testicular enlargement occurs in 10% of patients. Pathologically, epidermoid cysts are composed of keratinizing, stratified, squamous epithelium with a well-defined, fibrotic wall. Although the histogenesis of epidermoid cysts is controversial, the current prevailing theory is that these entities represent teratomas that have undergone monodermal differentiation. However, a complete absence of mesodermal or ectodermal components and absence of intraepithelial neoplasia, a histologic precursor of germ cell tumors, brings this theory into question. Additionally, unlike germ cell tumors, epidermoid cysts have an invariably benign course without recurrence or metastatic disease following resection.[86] Squamous metaplasia of seminiferous epithelium or rete testis is an alternative diagnosis.[87] These benign lesions can be differentiated from premalignant teratomas only through histologic examination.

Sonographically, epidermoid cysts are generally well-defined, round to ovoid, avascular masses and may be multiple or bilateral.[86] A characteristic whorled or laminated appearance, like the layers of an onion skin, corresponds to the alternating layers of compacted keratin and desquamated squamous cells seen histologically[88-90] (Fig. 22.12D, Video 22.2). This appearance, however, may not be pathognomonic because it is rarely seen with teratoma.[91] Another typical appearance of an epidermoid cyst is a well-defined hypoechoic mass with an echogenic capsule that may be calcified (Fig. 22.12F). There may be central calcification, giving a "bull's eye" or target appearance.[86] Epidermoid cysts may also have the nonspecific appearance of a hypoechoic mass with or without calcifications and may resemble germ cell tumors (Fig. 22.12E). Avascularity is a clue to the diagnosis.[89] Although the sonographic appearance is characteristic, it is not pathognomonic, and histologic confirmation should be obtained by a conservative testis-sparing approach with local excision (enucleation).[92] MRI has been used to support the sonographic diagnosis of epidermoid cysts as they have a target appearance with low signal capsule. The layers of keratinizing material are rich in water and lipid and can appear as areas of high signal intensity on both T1- and T2-weighted imaging.[93,94]

Abscess

Testicular abscesses are usually a complication of **epididymo-orchitis,** although they may also result from an undiagnosed **testicular torsion, testicular infarct, trauma,** a **gangrenous or infected tumor,** or a primary **pyogenic orchitis.** Infectious causes of abscess formation are **mumps, smallpox, scarlet fever, influenza, typhoid, sinusitis, osteomyelitis,** and **appendicitis.**[95] A testicular abscess may cross the mesothelial lining of the tunica vaginalis, resulting in formation of a **pyocele** or a fistula to the scrotal skin.

Most often, sonography demonstrates an irregularly marginated, hypoechoic or mixed echogenic intratesticular mass (Fig. 22.13). Testicular abscesses have no diagnostic sonographic features but can often be distinguished from tumors on the basis of clinical symptoms and short-term interval change.

In patients with **acquired immunodeficiency syndrome** (AIDS), distinguishing an abscess from a neoplastic process may be difficult on sonographic examination. Clinical findings may

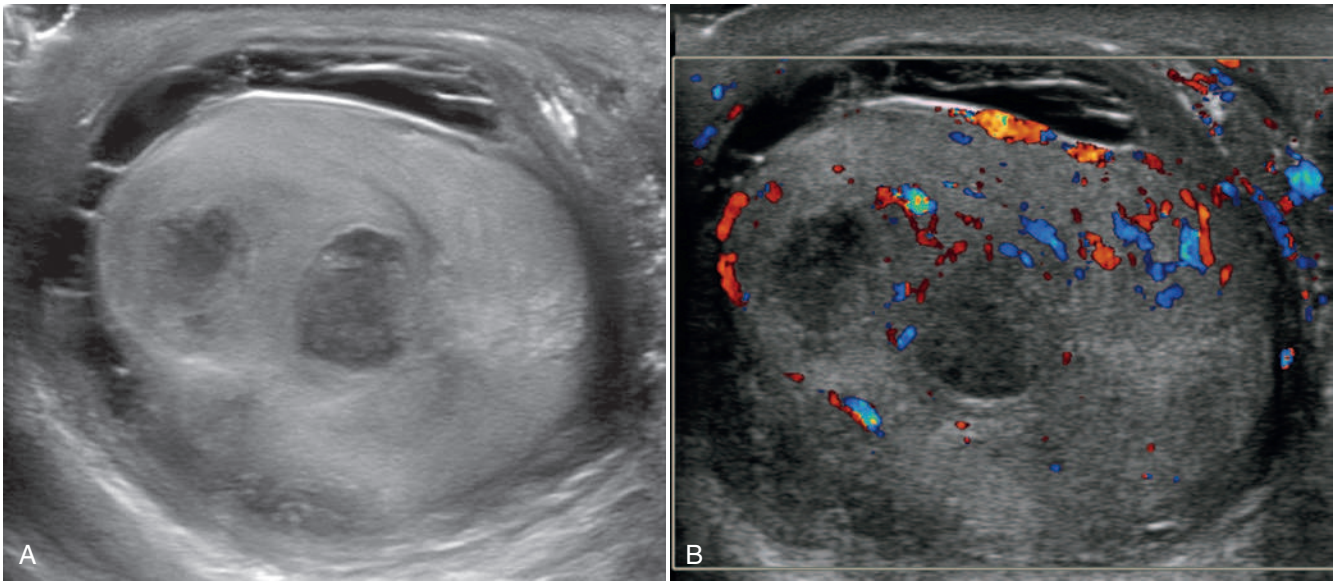

FIG. 22.13 Testicular Abscesses. (A) Transverse gray-scale image shows typical hypoechoic intratesticular abscesses, which may be indistinguishable from a tumor. However, heterogeneity of the parenchyma, skin thickening, and developing pyocele suggest that these masses represent abscesses. **(B)** Transverse color Doppler image shows echogenic and hypoechoic areas in the intratesticular abscesses with increased vascularity around the abscesses.

be helpful; however, orchiectomy is frequently necessary to obtain a histologic diagnosis.[96,97]

Segmental Infarction

Segmental testicular infarction may occur after **torsion, trauma, surgery, bacterial endocarditis, vasculitis, leukemia,** or **hypercoagulable states.**[98] Spontaneous infarction of the testis is rare. The sonographic appearance depends on the age of the infarction. Initially, a typical segmental infarct is seen as a focal, wedge-shaped or round hypoechoic mass, with approximately 80% occurring in the upper pole, likely secondary to vascular supply between the upper and lower poles.[99] The focal hypoechoic mass may not be distinguishable from a neoplasm on the basis of its gray-scale sonographic appearance.[100,101] These lesions should have reduced or absent blood flow, depending on the age of the infarction.[99] If a well-circumscribed, nonpalpable, relatively peripheral, hypoechoic mass shows a complete lack of vascularity on power Doppler imaging or after the administration of sonographic contrast agent, it may be possible to distinguish such benign infarctions from neoplasm[102,103] (Fig. 22.14). With time, the hypoechoic mass or the entire testis often decreases in size and develops areas of increased echogenicity because of fibrosis or dystrophic calcification.[104] The early sonographic appearance may be difficult to distinguish from a testicular neoplasm, but infarcts decrease substantially in size, whereas tumors characteristically enlarge with time.[3,101,105]

Adrenal Rests

Adrenal rests are a rare cause of intertesticular masses and can be seen in the setting of **congenital adrenal hyperplasia** (CAH), and rarely in the setting of **Cushing syndrome.** CAH is an autosomal recessive disease involving an adrenocortical enzyme defect. This disease typically becomes clinically obvious early in life or in early adulthood. Patients often present with a testicular mass or enlargement, **precocious puberty,** and with or without salt-depletion syndrome. Adrenal rests arise from aberrant adrenocortical cells that migrate with gonadal tissues in the fetus. They can form tumorlike masses in response to elevated levels

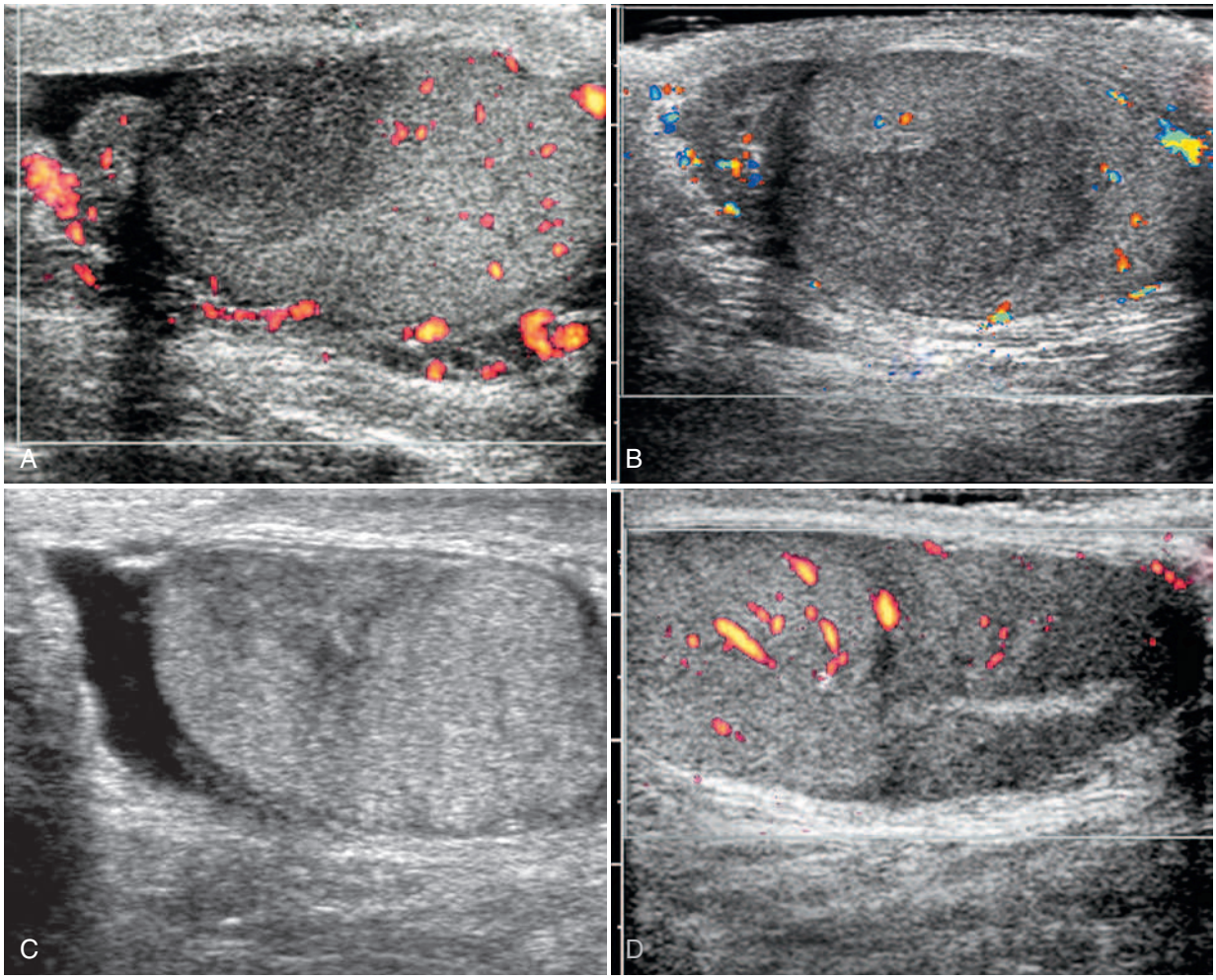

FIG. 22.14 Testicular Infarcts: Spectrum of Appearances. (A) and **(B) Acute infarct. (A)** Longitudinal power Doppler scan shows an avascular area at the upper pole from **partial torsion. (B)** Longitudinal color Doppler scan shows an avascular area in the midtestis caused by **vasculitis. (C)** and **(D) Chronic infarct. (C)** Longitudinal scan shows a peripheral wedge-shaped hypoechoic area caused by prior **mumps orchitis. (D)** Longitudinal power Doppler scan shows lack of vascularity in the lower pole.

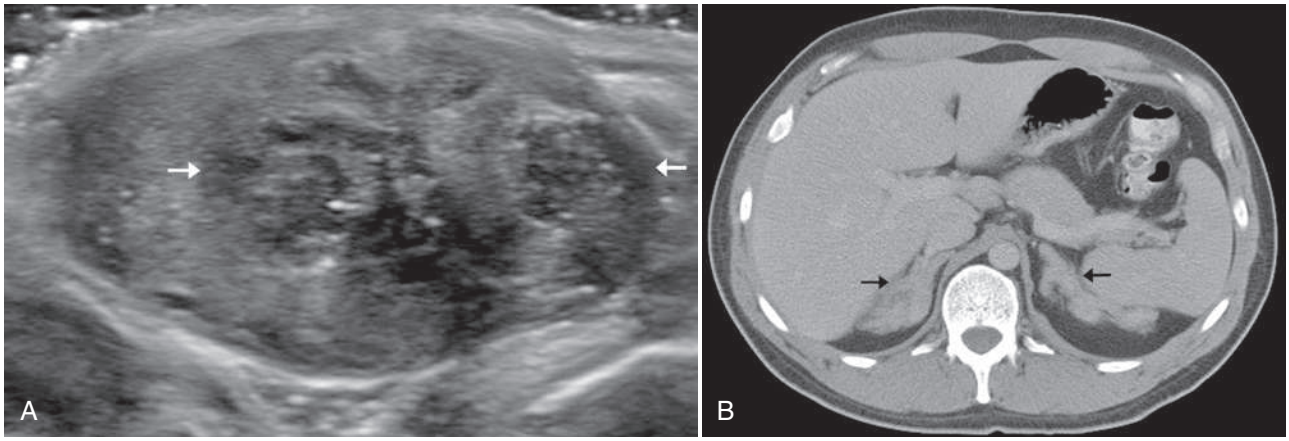

FIG. 22.15 Adrenal Rests in Patient With Congenital Adrenal Hyperplasia. (A) Longitudinal scan shows multifocal hypoechoic masses *(arrows)* within the testis that cannot be distinguished from tumor. **(B)** CT in same patient shows bilateral adrenal hyperplasia *(arrows)*.

of circulating adrenocorticotropic hormone in CAH and Cushing syndrome. These lesions are typically multifocal, bilateral, and eccentrically located. Sonographically, they are variable in appearance, typically presenting as hypoechoic masses, although they may be heterogeneous, hyperechoic masses with posterior acoustic shadowing (Fig. 22.15). Adrenal rests can demonstrate spokelike vascularity with multiple peripheral vessels radiating toward a central point within the mass. Usually, if the patient has the appropriate hormonal abnormalities associated with CAH and if sonography shows the appropriate findings, no further workup is necessary.[106,107] If confirmation of the diagnosis is required, a biopsy under ultrasound guidance may be obtained intraoperatively when the testis is exposed. Additionally, testicular vein sampling will show elevated cortisol levels compared with peripheral blood levels.[108] Treatment with glucocorticoid replacement therapy results in stabilization or regression of the masses.[109]

Splenogonadal Fusion

Splenogonadal fusion is a rare congenital anomaly in which there is fusion of the spleen and gonad. It typically occurs on the left side and is most often associated with cryptorchidism.[110] There are two types of splenogonadal fusion: continuous and discontinuous. In the more common **continuous** form, the gonad is linked to the spleen by a fibrous cord of splenic tissue. In the **discontinuous** form, ectopic splenic tissue is attached to the testis. Rarely, ectopic splenic tissue may occur on the epididymis or spermatic cord. Splenogonadal fusion may mimic testicular malignancy. The diagnosis may be established by documenting uptake on a technetium-99m sulfur colloid scan.

Calcifications

Scrotal calcifications may be seen within the parenchyma of the testis or epididymis, attached to the tunica, or freely located in the fluid between the layers of the tunica vaginalis. Large, smooth, curvilinear intratesticular calcifications without an associated soft tissue mass are characteristic of a large-cell calcifying **Sertoli cell tumor**[111] (see Fig. 22.9C). Scattered calcifications may be found in **tuberculosis, filariasis,** and **scarring** from **regressed germ cell tumor** or trauma.

Scrotal Calcifications

TESTICULAR
Solitary, postinflammatory granulomatous, vascular
Microlithiasis
Regressed, or "burned-out," germ cell tumor
Large-cell calcifying Sertoli cell tumor
Teratoma
Mixed germ cell tumor
Sarcoid
Tuberculosis
Chronic infarct
Posttraumatic

EXTRATESTICULAR
Tunica vaginalis, "scrotal pearls"
Torsed appendages
Chronic epididymitis
Schistosomiasis

Testicular microlithiasis is a condition in which calcifications are present within the seminiferous tubules of the testis either unilaterally or bilaterally. It is postulated that microlithiasis is caused by defective Sertoli cell phagocytosis of degenerating tubular cells, which then calcify within the seminiferous tubules.[112,113] Microlithiasis has been classified as diffuse and limited.[114] In the **diffuse** form, innumerable small, hyperechoic foci are diffusely scattered throughout the testicular parenchyma. These tiny (1-3 mm) foci rarely shadow and occasionally demonstrate a comet-tail appearance (Fig. 22.16). In the **limited** form, less than five hyperechoic foci are seen per image of the testis (Fig. 22.16B).

Microlithiasis is seen in 1% to 2% of patients referred for testicular sonography and has a reported prevalence in the general population of 0.6% to 0.9%.[115] Microlithiasis has been associated with **cryptorchidism, Klinefelter syndrome, Down syndrome, pulmonary alveolar microlithiasis, AIDS, neurofibromatosis, previous radiotherapy,** and **subfertility.**[112,115-117] Microlithiasis is typically an incidental finding on scrotal ultrasound, and if

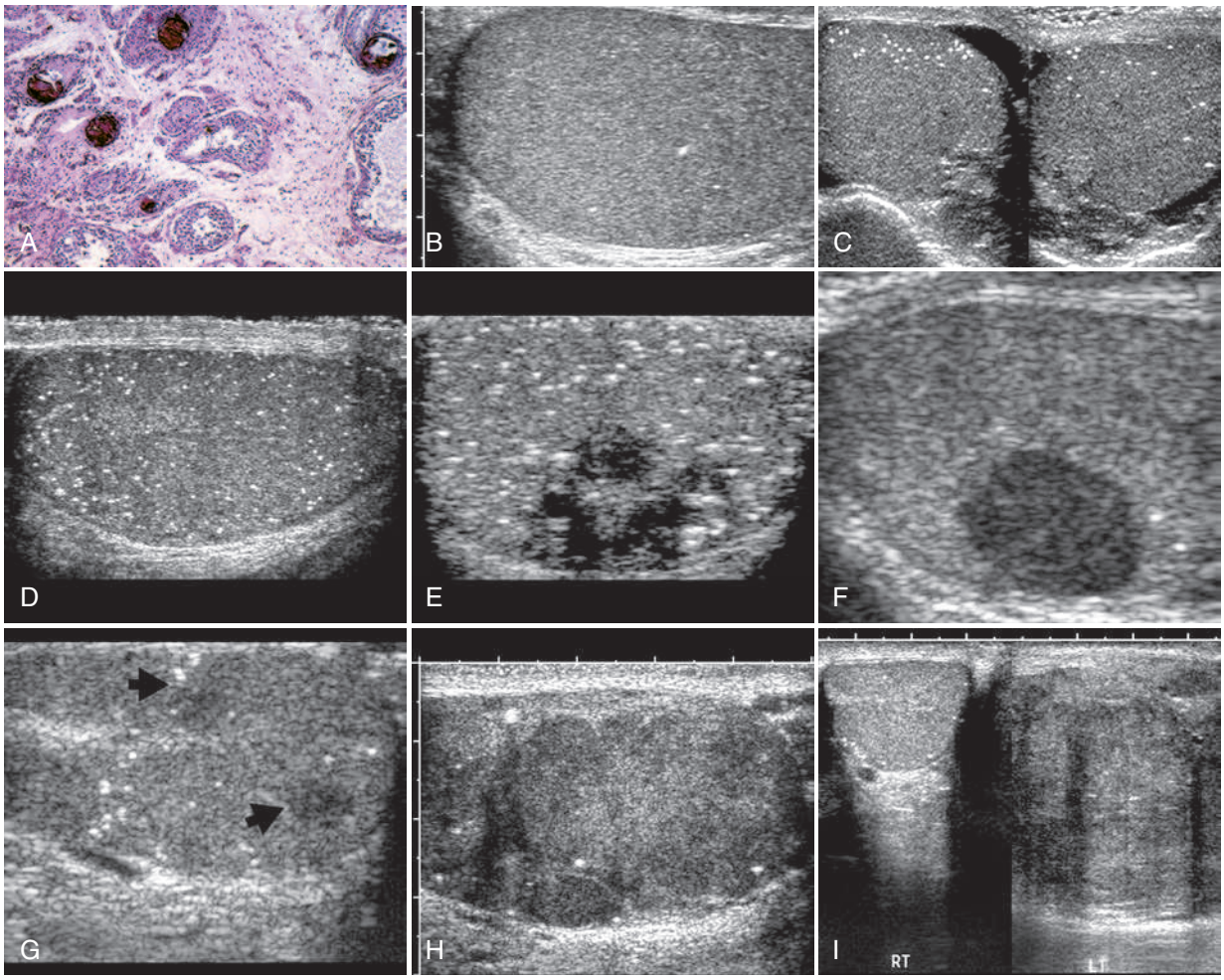

FIG. 22.16 Microlithiasis and Associated Testicular Tumors: Spectrum of Appearances. (A) Light microscopy examination shows multiple intratubular calcifications *(dark areas)* characteristic of microlithiasis. **(B)** Longitudinal scan shows a few tiny calcifications of limited microlithiasis. **(C)** and **(D)** Diffuse microlithiasis. **(E)** Transverse scan of testis shows microlithiasis and partially cystic mass caused by **mixed germ cell tumor. (F)** Limited microlithiasis with **seminoma.** Longitudinal scan shows a few tiny calcifications and a homogeneous hypoechoic mass. **(G)** Longitudinal scan shows microlithiasis and two hypoechoic homogeneous masses *(arrows)* due to seminoma. **(H)** Longitudinal scan shows large hypoechoic mass with multiple small and coarser calcifications. **(I)** Dual transverse image shows large hypoechoic left testicular mass and microcalcifications in the right testis.

associated with a mass, management is dictated by the intratesticular mass itself. It has been correlated with testicular carcinoma, although the extent of the risk for subsequent development of neoplasm and the recommended surveillance in the setting of microlithiasis remain controversial.[114,115,118] Annual physical examination and periodic self-examination have been suggested for those who have no additional risk factors.[114,115,119,120] Recent literature suggests that there is no causal link and that sonographic follow-up of microlithiasis should be determined by any additional risk factors and not the microlithiasis itself.[121]

EXTRATESTICULAR PATHOLOGIC LESIONS

Tunica Vaginalis

Hydrocele, Hematocele, and Pyocele

The normal scrotum contains a few milliliters of serous fluid between the layers of the tunica vaginalis, and this is usually visible on sonographic examination. Larger volumes of serous fluid, and blood, pus, or urine may also accumulate in the space between the parietal and visceral layers of the tunica vaginalis lining the scrotum. These fluid collections should be confined to the anterolateral portions of the scrotum because of the attachment of the testis to the epididymis and scrotal wall posteriorly (the **bare area**)[9] (Fig. 22.17).

Hydrocele is an abnormal accumulation of serous fluid between the layers of the tunica vaginalis. Hydrocele is the most common cause of painless scrotal swelling[14] and may be congenital or acquired. The **congenital type** results from incomplete closure of **the processus vaginalis,** with persistent open communication between the scrotal sac and the peritoneum, usually resolving by 18 months of age (Fig. 22.17D). **Acquired hydroceles** may be idiopathic or caused by **epididymitis, epididymo-orchitis, torsion,** or, in rare cases, tumors. Hydroceles associated with testicular tumors are usually small.[3,122,123] Sonography is useful in detecting a potential cause of the hydrocele by allowing evaluation of the testis when a

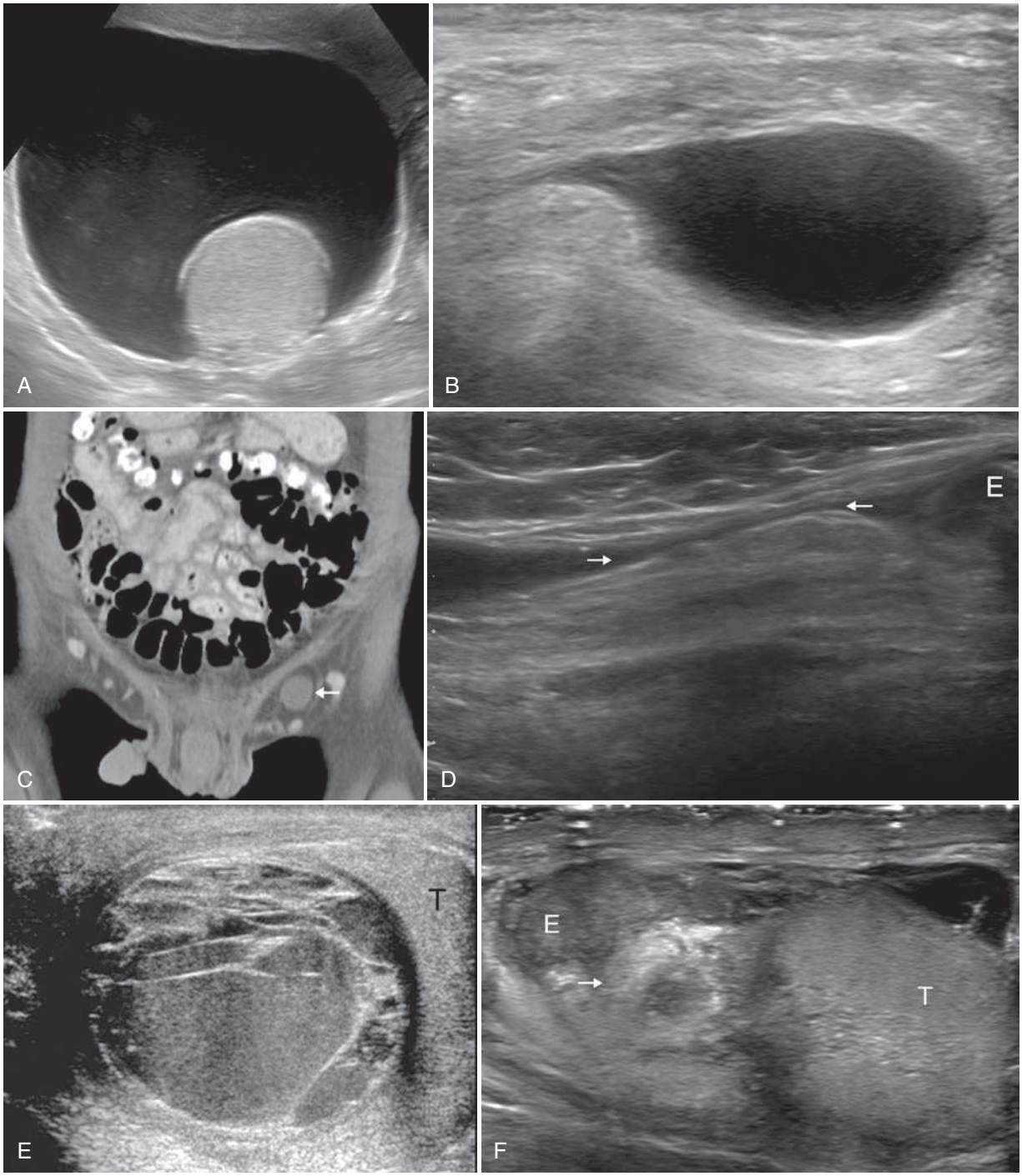

FIG. 22.17 Scrotal Fluid Collections: Spectrum of Appearances. (A) Hydrocele. Transverse scan shows a large hydrocele anterolaterally with testis partially enveloped by tunica vaginalis posteriorly. **(B) Encysted hydrocele.** Longitudinal scan along the spermatic cord shows a fluid collection present in the inguinal canal. **(C) Encysted hydrocele.** Coronal CT image of patient in **B** demonstrates a well circumscribed fluid collection *(arrow)* corresponding to sonographic examination. **(D) Patent processus vaginalis.** Longitudinal scan of inguinal region shows an elongated fluid collection *(arrows)* above the level of the testis and epididymis *(E)* in patient with chronic hydrocele. **(E) Hematocele.** Transverse scan shows loculated fluid with internal echoes and mass affect on the testis *(T)*. **(F) Pyocele.** Longitudinal scan shows an irregular, centrally hypodense, extratesticular (*T,* testis) collection *(arrow)* adjacent to the epididymis *(E)* in the setting of **epididymo-orchitis.**

large hydrocele hampers palpation. Hydroceles are characteristically anechoic collections with good sound transmission surrounding the anterolateral aspects of the testis. Low-level to medium-level echoes from fibrin bodies or cholesterol crystals may occasionally be visualized moving freely within a hydrocele.[124] Rarely, a large hydrocele may impede testicular venous drainage and cause absence of antegrade arterial diastolic flow.[122] Uncommonly, a hydrocele may be loculated around the spermatic cord above the testis and epididymis, representing a noncommunicating, encysted hydrocele; or the

collection communicates with the peritoneum but not the scrotum, a **funicular hydrocele**[125] (Fig. 22.17B and C).

Hematoceles and **pyoceles** are less common than simple hydroceles. Hematoceles (accumulation of blood within the tunica vaginalis) result from trauma, surgery, neoplasms, or torsion.[126] Pyoceles result from untreated epididymo-orchitis or rupture of an intratesticular abscess into the space between the layers of the tunica vaginalis. Both hematoceles and pyoceles appear as complex fluid collections with internal septations and loculations (Fig. 22.17). Thickening of the scrotal skin and calcifications may be seen in chronic cases.

Paratesticular Masses

Most extratesticular neoplasms in adults are benign, but extratesticular neoplasms in children are frequently malignant.[127]

Extratesticular Tumors/Masses

BENIGN
Hernia
Adenomatoid tumor
Fibroma/fibrous pseudotumor
Lipoma
Hemangioma
Leiomyoma
Neurofibroma
Cholesterol granuloma
Polyorchidism
Papillary cystadenoma
Adrenal rest

MALIGNANT
Fibrosarcoma
Liposarcoma
Rhabdosarcoma
Histiocytoma
Lymphoma
Metastases

Hernia

An inguinal hernia is a common paratesticular mass.[128] Although scrotal hernias are usually diagnosed on the basis of clinical history and physical examination, sonography is useful in the evaluation of atypical cases. Hernias are classified as either direct or indirect. An indirect hernia exits the abdominal cavity through the internal inguinal ring, can traverse the inguinal canal, and extend into the scrotum. Indirect hernias are associated with a patent processus vaginalis. A direct hernia represents a protrusion through the abdominal wall at Hesselbach triangle, an area of weakness bordered by the lateral border of the rectus sheath medially, the inferior epigastric artery laterally, and the inguinal ligament inferiorly.

Sonographic appearance of an inguinal hernia depends on its contents. Bowel will often be fluid filled with multiple internal bright echoes. Bowel gas may cause shadowing, a finding also seen with abscesses and thus potentially confusing. The presence of bowel loops within the hernia may be confirmed by the visualization of valvulae conniventes or haustrations and detection of peristalsis on real-time examination (Fig. 22.18A). The presence of highly echogenic material within the scrotum may result from a hernia containing omentum or other fatty masses such as lipomas, although lipomas are typically well defined and herniated omentum can typically be traced back to the inguinal canal (Fig. 22.18B). Sonographic examination of the inguinal canal into the scrotum is necessary to make the diagnosis.[129] Additional discussion of hernias can be found in Chapter 13.

Calculi

Extratesticular scrotal calculi are calcifications within the tunica vaginalis (Fig. 22.19). These fibrinoid loose bodies have been called **scrotoliths,** or **"scrotal pearls"** because of their macroscopic appearance, which is usually rounded, pearly white, and rubbery. Histologically, they consist of fibrinoid material deposited around a central nucleus of hydroxyapatite.[130] They may result from inflammatory deposits that form and then ultimately separate

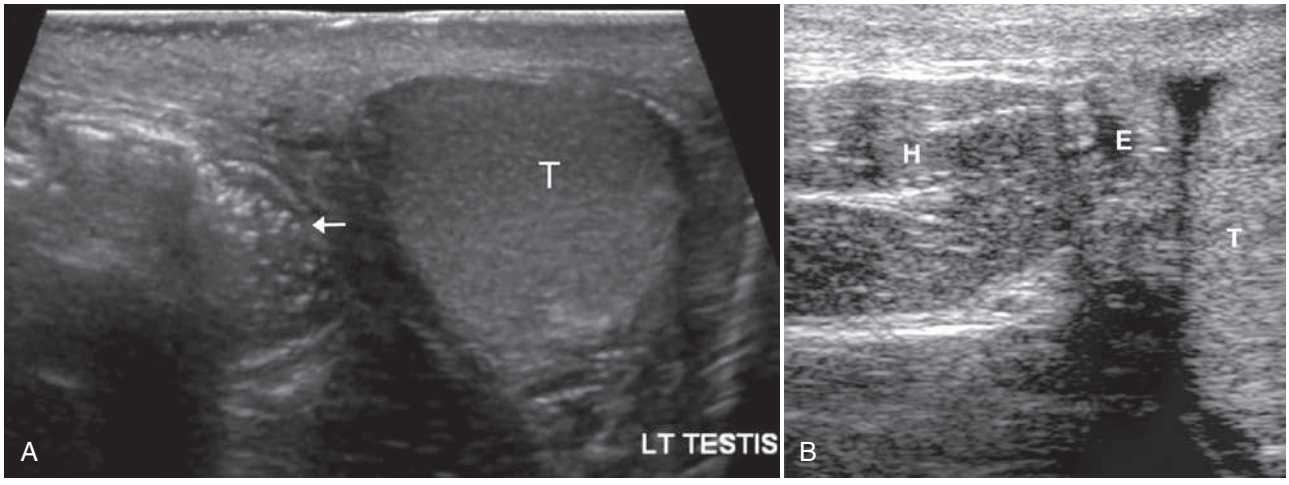

FIG. 22.18 Indirect Inguinal Hernias: Spectrum of Appearances. (A) Herniated small bowel. Oblique scan shows herniated small bowel *(arrow)* superior to and abutting the testis *(T).* **(B) Herniated mesenteric fat.** Longitudinal scan shows herniated fat *(H)* above testis *(T)* and epididymis *(E).*

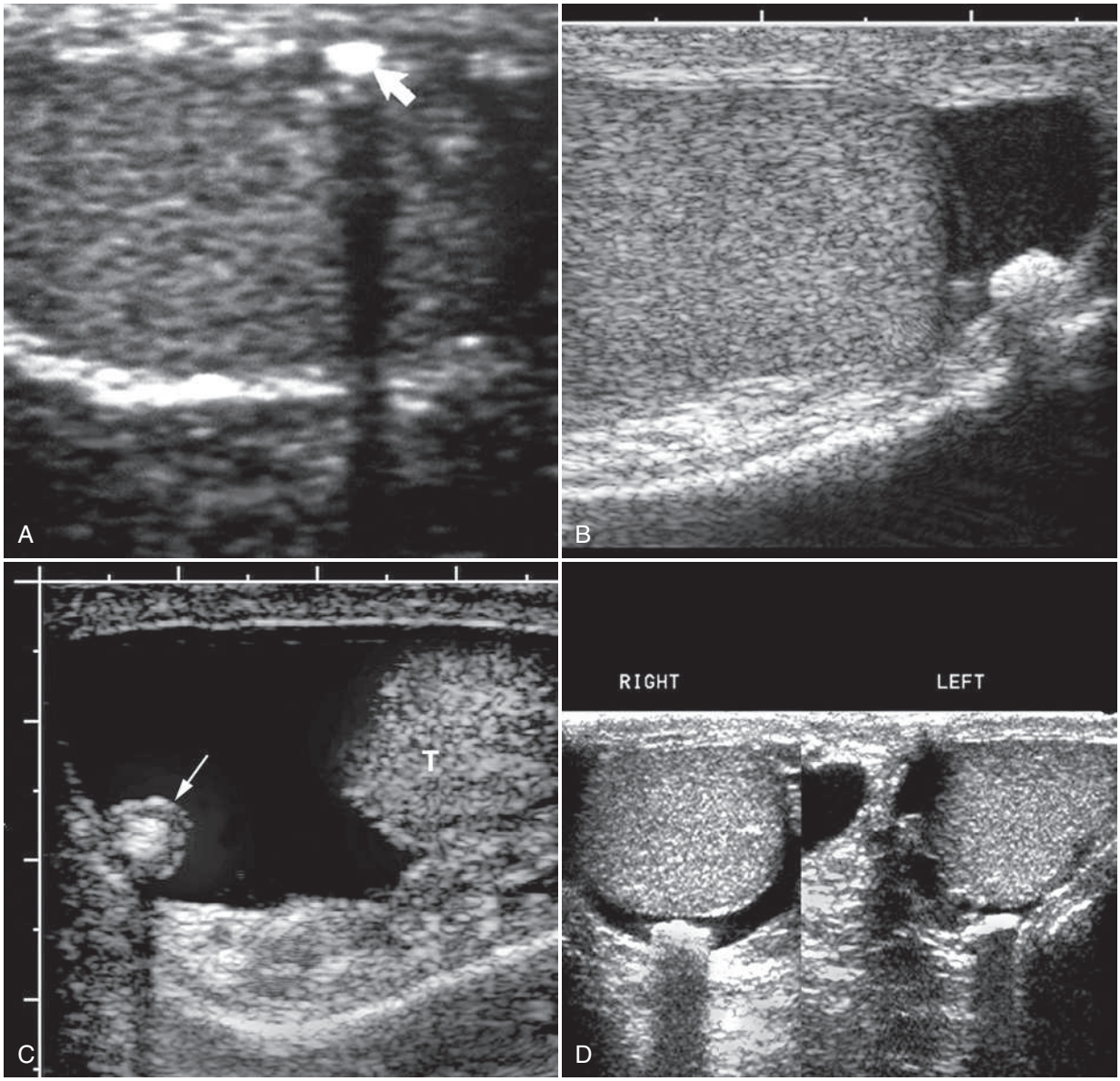

FIG. 22.19 Benign Intrascrotal Calcification. (A) Calcified tunica plaque *(arrow)* on the tunica vaginalis. **(B)-(D) Scrotal pearls. (B)** Mobile scrotal calcification in a small hydrocele. **(C)** Longitudinal scan shows a mostly calcified scrotal pearl *(arrow)* in a hydrocele. *T,* Testis. **(D)** Bilateral scrotal pearls.

from the tunica vaginalis, or from torsion of the appendix testis or appendix epididymis. Sonographically, they appear as free floating, echogenic calculi with posterior acoustic shadowing; can be multiple; and range in size from a few millimeters to larger than a centimeter. Hydroceles facilitate the sonographic diagnosis of scrotal calculi.

Varicocele

A varicocele is an abnormal dilatation of the veins of the pampiniform plexus located posterior to the testis, adjacent to the epididymis, and accompanying the vas deferens within the spermatic cord[14] (Fig. 22.20). A varicocele is the most frequently encountered mass of the spermatic cord. The veins of the pampiniform plexus normally range from 0.5 to 1.5 mm in diameter, with a main draining vein up to 2 mm in diameter. The size for normal varies, with some diagnosticians using greater than 2 mm as a guideline for the diagnosis of a varicocele and others using 3 mm.[131]

There are two types of varicoceles: primary (idiopathic) and secondary. The **idiopathic varicocele** is caused by incompetent valves in the internal spermatic vein, which results in impaired drainage of blood from the spermatic vein and pampiniform plexus with the patient in an upright position. Varicoceles affect approximately 15% of men but occur in up to 40% of men attending infertility clinics.[132,133] Varicocele is the most common correctable cause of male infertility.[134] Idiopathic varicoceles occur much more commonly on the left side and are most common in men aged 15 to 25 years. The left-sided predominance probably occurs because the left testicular vein is longer, with venous drainage into the left renal vein entering the renal vein

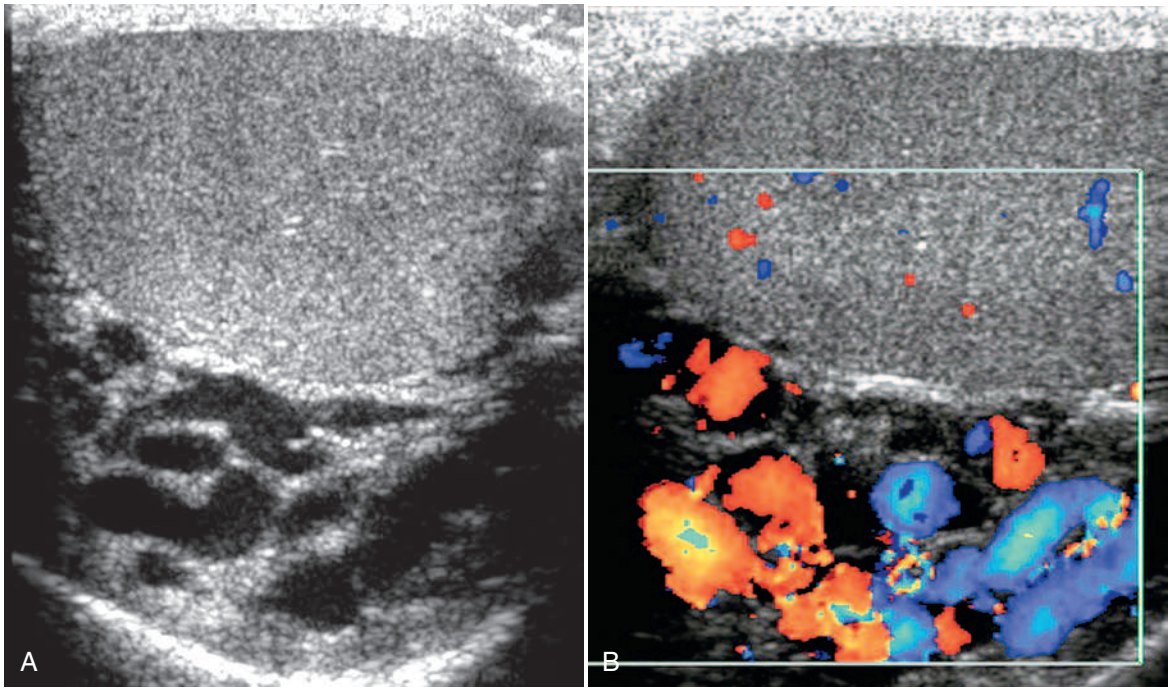

FIG. 22.20 Varicocele. (A) Longitudinal and **(B)** color Doppler images show serpentine, hypoechoic, dilated veins posterior to the testis. The blood flow in a varicocele is slow and may be detected only with low-flow Doppler settings or the Valsalva maneuver. See also Video 22.3.

at a right angle, as opposed to the right spermatic vein, which drains directly into the vena cava. Idiopathic varices normally distend when the patient is upright or performs the Valsalva maneuver and decompress when the patient is supine. Primary varicoceles are bilateral in up to 50% of cases.[135]

Secondary varicoceles result from increased pressure on the spermatic vein or its tributaries by marked hydronephrosis, an enlarged liver, abdominal neoplasms, or venous compression by a retroperitoneal mass.[43] Secondary varicoceles may also occur in **nutcracker syndrome (nutcracker phenomenon),** in which the superior mesenteric artery compresses the left renal vein.[136] A search for neoplastic obstruction of gonadal venous return must be undertaken in cases of a right-sided, nondecompressible, or newly discovered varicocele in a patient older than 40 years[14] (Fig. 22.21). The appearance of secondary varicoceles is not affected by patient position.

In infertile men, sonography aids in the diagnosis of clinically palpable and subclinical varicoceles. Sonography is also of value in assessing testicular size before and after treatment, because varicocele may be associated with a decreased testicular volume.[133] There is poor correlation between the size of the varicocele and the degree of testicular tissue damage leading to infertility, and surgical repair of subclinical varicoceles for infertility has been controversial.[137]

Sonographically, a varicocele consists of multiple, serpentine, anechoic structures more than 2 mm in diameter, creating a tortuous, multicystic collection located adjacent or proximal to the upper pole of the testis and head of the epididymis. A high-frequency transducer in conjunction with low-flow Doppler settings should be used to optimize slow-flow detection within varices. Slowly moving red blood cells may be visualized with high-frequency transducers, even when flow is too slow to be detected by Doppler imaging. Venous flow can be augmented with the patient in the upright position or during Valsalva maneuver (Video 22.3). Varicoceles follow the course of the spermatic cord into the inguinal canal and are easily compressed by the transducer.[3] Rarely, varicoceles may be intratesticular, either in a subcapsular location or around the mediastinum testis[138,139] (Fig. 22.22).

Fibrous Pseudotumor

Fibrous pseudotumor is a rare, nonneoplastic mass of reactive fibrous tissue that most commonly involves the tunica vaginalis. These masses are known by a number of names, including **fibroma, paratesticular fibrosis,** or **inflammatory pseudotumor,** and can become quite large and mimic neoplasms. Most patients present with a painless scrotal mass, possibly with a prior history of infection or trauma. Histologically, masses are composed of hyalinized collagen and granulation tissue and may be partially calcified. On sonography, fibrous pseudotumors may appear as one or more solid masses attached to or closely associated with the capsule of the testis. There may be an associated hydrocele. Echogenicity is variable and they may be seen as a hypoechoic, hyperechoic, or heterogeneous paratesticular mass with posterior acoustic shadowing depending on extent of calicfications[140-142] (Fig. 22.23A and B).

Polyorchidism

Polyorchidism, or **supernumerary testes,** is a rare entity thought to result from abnormal division of the genital ridge embryologically. The supernumery testes are intrascrotal in location in approximately 75% of cases and present as a painless scrotal

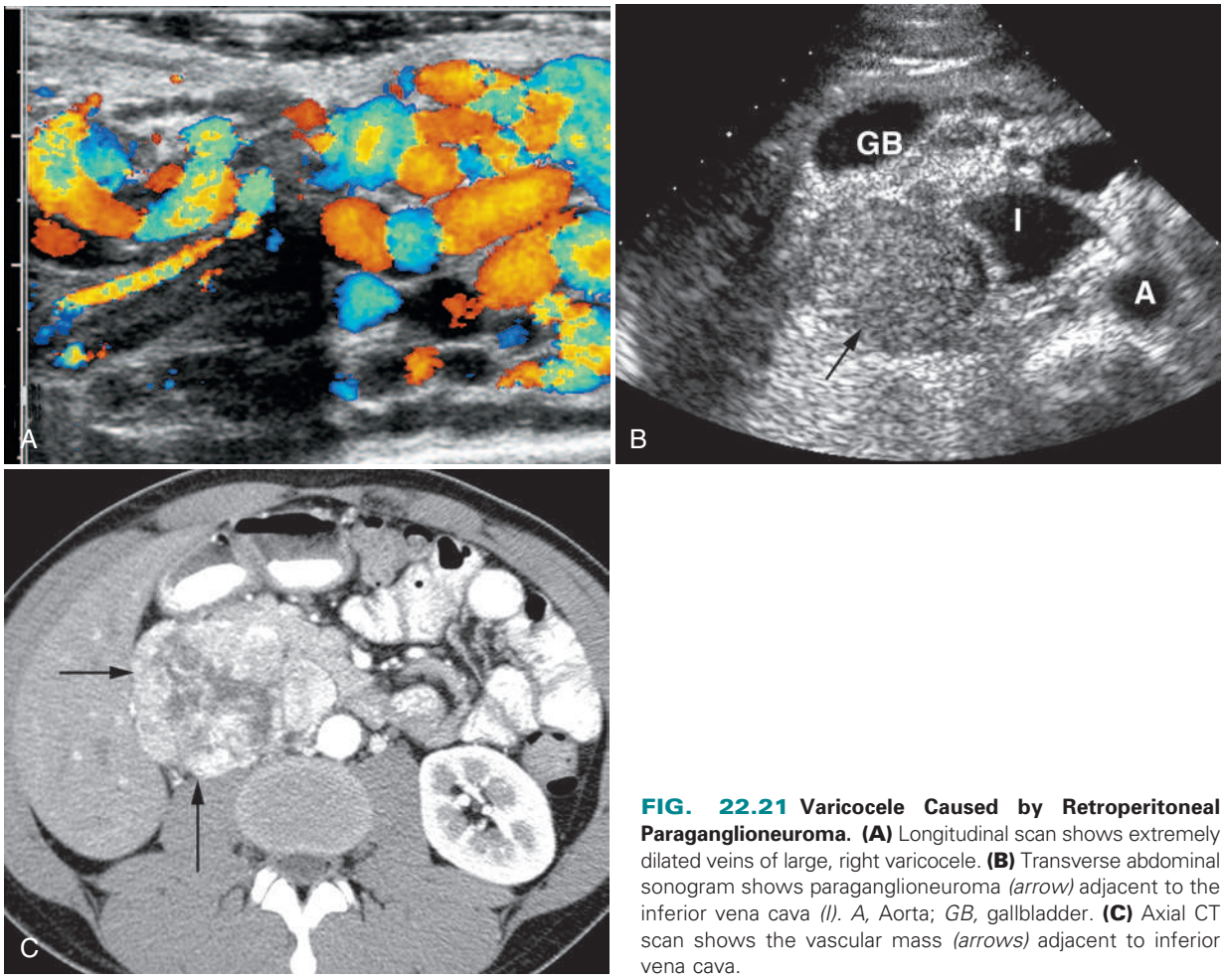

FIG. 22.21 Varicocele Caused by Retroperitoneal Paraganglioneuroma. (A) Longitudinal scan shows extremely dilated veins of large, right varicocele. **(B)** Transverse abdominal sonogram shows paraganglioneuroma *(arrow)* adjacent to the inferior vena cava *(I). A,* Aorta; *GB,* gallbladder. **(C)** Axial CT scan shows the vascular mass *(arrows)* adjacent to inferior vena cava.

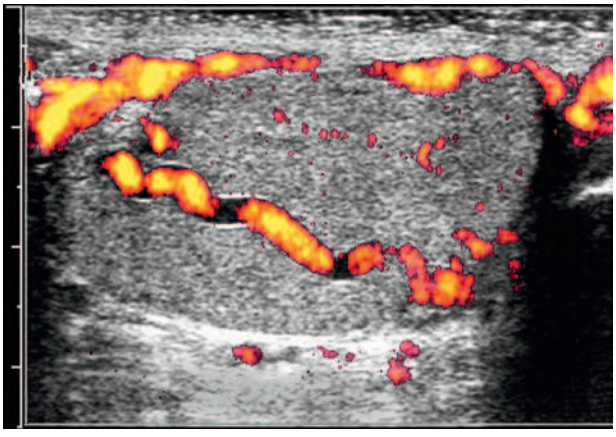

FIG. 22.22 Intratesticular Varicocele. Longitudinal scan shows the dilated intratesticular veins.

mass (Fig. 22.24). Twenty percent of supernumery testes are inguinal with the remaining retroperitoneal in location.[60] These supernumery testes have similar imaging characteristics to normal testes, but they are more mobile and therefore at increased risk of torsion. There has also been an increased risk of carcinoma reported.[131,135,137,143]

Epididymal Lesions

Cystic Lesions

The most common epididymal mass is a cyst, which includes **epididymal cysts** and **spermatoceles.** Both were seen in 20% to 40% of all asymptomatic patients studied by Leung et al.,[144] and were multiple in 30% of cases. Both epididymal cysts and spermatoceles are thought to result from dilatation of the epididymal ductules, but the contents of these masses differ.[14] Epididymal cysts contain clear serous fluid, whereas spermatoceles are filled with spermatozoa and sediment containing lymphocytes, fat globules, and cellular debris, giving the fluid a thick, milky appearance.[3] Both lesions may result from prior episodes of epididymitis or trauma. Spermatoceles and epididymal cysts appear identical on sonography: anechoic, circumscribed masses with no or few internal echoes. Loculations and septations are often seen (Fig. 22.25). In rare cases, a spermatocele may be hyperechoic.[9] Differentiation between a spermatocele and an epididymal cyst is rarely important clinically. Spermatoceles almost always occur in the head of the epididymis and represent cystic dilatation of efferent ductules, whereas epididymal cysts arise throughout the length of the epididymis.

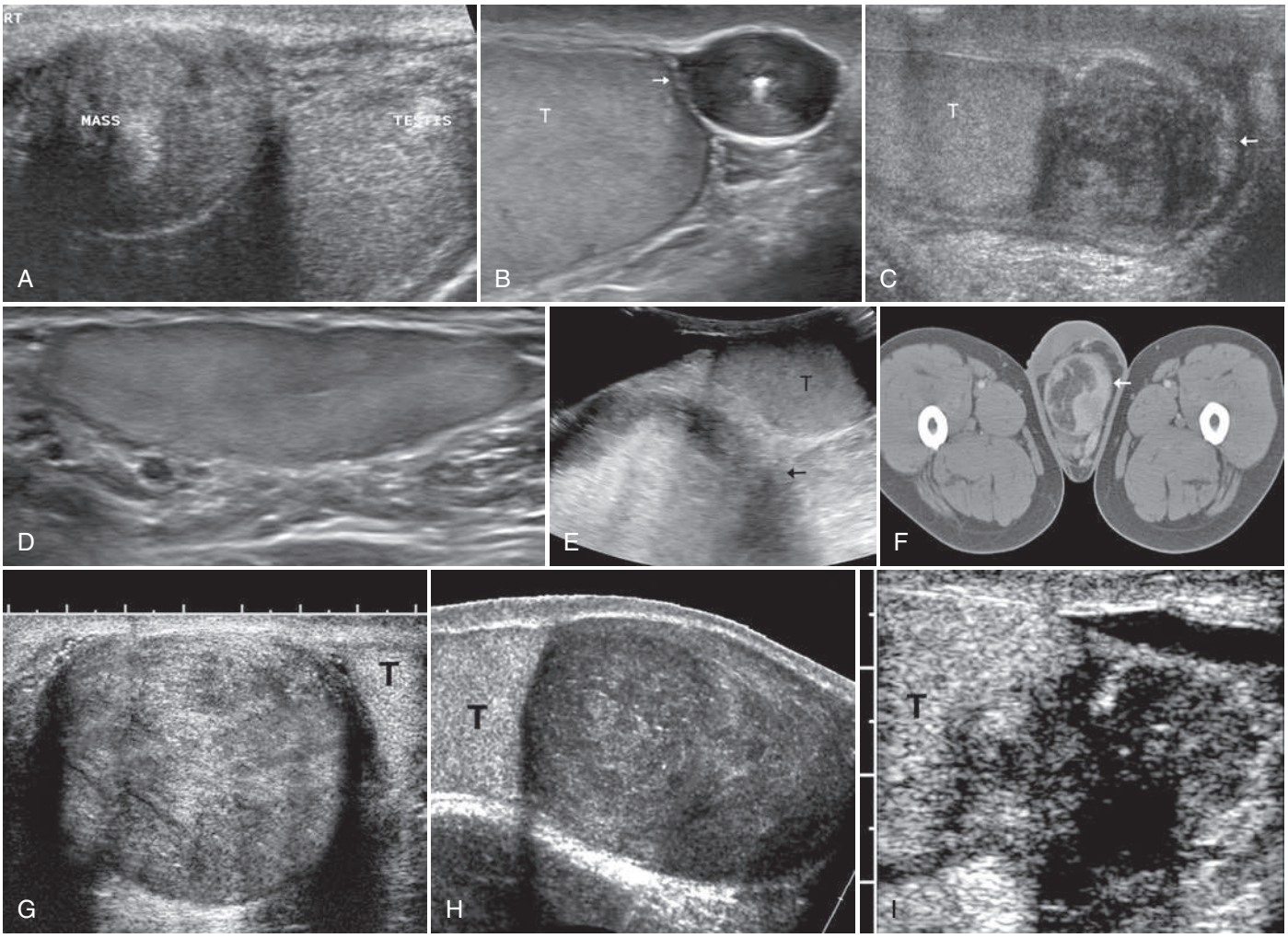

FIG. 22.23 Extratesticular Scrotal Solid Masses: Spectrum of Appearances. (A) Fibrous pseudotumor. Transverse scan shows a mass of mixed echogenicity lateral to and separate from the testis. **(B) Fibrous pseudotumor.** Longitudinal scan shows a lamellated extratesticular mass *(arrow)* with a central echogenic focus adjacent to the tunica of the testis *(T)*. **(C) Benign adenomatoid tumor of epididymis.** Longitudinal scan shows a hypoechoic mass *(arrow)* in the epididymal tail separate from the testis *(T)*. **(D) Spermatic cord lipoma.** Longitudinal scan shows an echogenic mass superior to the epididymis and testis, along the spermatic cord. **(E) Liposarcoma.** Transverse scan shows a large heterogeneous mass *(arrow)* deep to the testis *(T)* in the scrotal wall or spermatic cord. **(F) Liposarcoma.** Contrast-enhanced axial CT image shows a heterogeneous mass containing fat and solid components *(arrow)* associated with the spermatic cord in patient **E,** consistent with a liposarcoma. **(G) Leiomyoma of cord.** Longitudinal scan shows a solid mass superior to the testis. **(H) Rhabdomyosarcoma.** Longitudinal extended–field of view scan in a 12-year-old shows a large, paratesticular mass inferior to the testis. **(I) Metastasis from lung carcinoma.** Longitudinal scan shows a heterogenous mass with calcifications in the tail of the epididymis.

Tumors

The most common epididymal neoplasm is the **benign adenomatoid tumor,** which accounts for approximately 30% of all paratesticular neoplasms, second only to lipoma.[28] Although most frequently located in the tail (see Fig. 22.23C), adenomatoid tumors may occur anywhere in the epididymis and have also been reported in the spermatic cord, as well as the tunica albuginea, where they may grow intratesticularly. Adenomatoid tumor may occur at any age but most often affects patients aged 20 to 50 years.[3,145] Adenomatoid tumors are generally unilateral, solitary, well defined, and round or oval, rarely measuring more than 5 cm in diameter. Occasionally, they may appear plaquelike and poorly defined. Sonography usually shows a solid, well-circumscribed mass with echogenicity that is at least as great as the testis,[3] although they may also be hypoechoic.

Other benign extratesticular tumors are rare and include **lipomas** (see Fig. 22.23D), **leiomyomas** (see Fig. 22.23G), **fibromas, hemangiomas, neurofibromas,** and **cholesterol granulomas.** Adrenal rests may also be encountered in the spermatic cord, testis, epididymis, rete testis, and tunica albuginea, typically in the setting of CAH.

Papillary cystadenoma of the epididymis is a rare tumor with a strong association with **von Hippel–Lindau disease.** Up to 40% of cystadenomas are bilateral, a finding that is virtually pathognomic for von Hippel–Lindau disease. These tumors are benign epithelial tumors of the epididymis, occurring in the

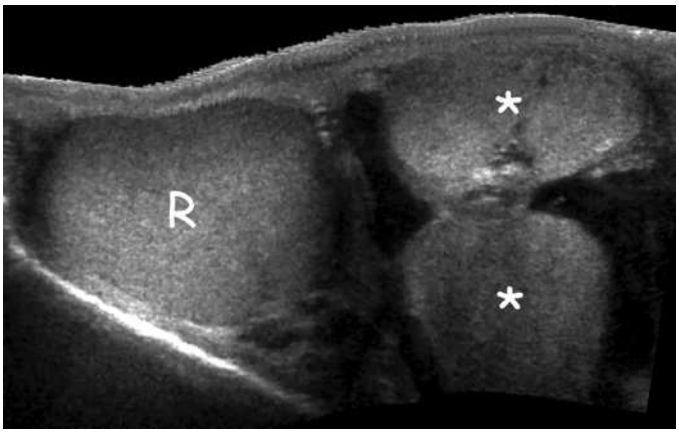

FIG. 22.24 Polyorchidism. Transverse extended field of view image of the right hemiscrotum shows a right testis *(R)* and two additional intrascrotal masses with similar imaging characteristics to the right testis (*) consistent with supernumery testes in an asymptomatic patient with a palpable mass.

efferent ductules of the epididymal head. They generally present as a hard, palpable mass, and at ultrasound appear as an echogenic, solid mass with distinct, small cystic spaces.

The majority of solid epididymal masses are benign. However, primary extratesticular scrotal malignant neoplasms do occur, including adenocarcinoma, **fibrosarcoma, liposarcoma** (see Fig. 22.23E and F), **histiocytoma,** and **lymphoma** in adults and **rhabdomyosarcoma** in children (see Fig. 22.23H). Metastatic tumors to the epididymis are also rare. The most common primary sites include the testis, stomach, kidney, prostate, colon, and, less often, the pancreas[146,147] (see Fig. 22.23I). Size of the lesion and the presence of color flow may be helpful in the diagnosis of extratesticular scrotal masses.[23,148] Larger masses (>1.5 cm) with prominent color flow that present without cl inical symptoms of inflammation are more likely to be malignant.[23,148]

Sperm Granuloma

Sperm granulomas are thought to arise from extravasation of spermatozoa into the soft tissues surrounding the epididymis, producing a necrotizing granulomatous response.[3] These lesions may be painful or asymptomatic, and they are most often found in patients after vasectomy. It is assumed that vasectomy produces increased pressure in the epididymal ductules, causing rupture with subsequent formation of sperm granulomas. Sperm granulomas may also be associated with prior epididymal infection or trauma. The typical sonographic appearance is that of a solid, hypoechoic or heterogeneous mass, usually located in or adjacent to the epididymis, although it may simulate an intratesticular lesion (Fig. 22.26A). Chronic sperm granulomas may contain calcification.[149]

Postvasectomy Changes in the Epididymis

Sonographic changes in the epididymis are very common in patients after vasectomy.[150,151] In addition to the formation of sperm granulomas, these findings include epididymal enlargement with ductular ectasia involving the epididymis (Fig. 22.26B) and rete testis, as well as the development of cysts (Video 22.4). A dilated vas deferens may be seen in addition to the enlarged epididymis. An unusual appearance described as **"dancing megasperm"** is occasionally seen in patients with vasectomy (Video 22.5). High reflective echoes within the dilated epididymis appear to move independently, shown histologically to be aggregations of spermatozoa and macrophages.[152]

Chronic Epididymitis

Chronic epididymitis is more commonly seen with conditions associated with **granulomatous reactions,** including **tuberculosis, brucellosis, syphilis,** and **parasitic** and **fungal infections.**[60] Tuberculosis epididymal infections are the most common of these and are believed to result from renal disease seeding the lower genitourinary tract, with 25% of patients having bilateral involvement.[153] Patients with chronic granulomatous epididymitis caused by spread of tuberculosis from the genitourinary tract complain of a hard, nontender scrotal mass.[14] Sonography most often shows a thickened tunica albuginea and a thickened, irregular epididymis with variable appearance (Fig. 22.27). Calcification may be identified within the tunica albuginea or epididymis.[3] Associated findings include hydroceles, scrotal wall thickening, and fistulas.[153] Untreated granulomatous epididymitis can spread to the testes, causing an epididymo-orchitis, although this is less common than isolated epididymal disease. Focal testicular involvement may demonstrate a variable sonographic appearance and may simulate the appearance of a testicular neoplasm on sonography. Patients may also develop chronic epididymitis after episodes of acute bacterial epididymitis that do not subside.

Sarcoidosis

Sarcoidosis is a noninfectious, chronic, granulomatous disease that may involve the genital tract.[154-156] In an autopsy series, approximately 5% of cases had genital tract involvement, with the epididymis most frequently involved.[60] The clinical presentation is acute or recurrent epididymitis or painless enlargement of the testis or epididymis. Sonographically, sarcoid lesions are irregular, hypoechoic solid masses in the testis or epididymis (Fig. 22.28). Occasionally, hyperechoic, calcific foci with acoustic shadowing may be seen. Distinguishing sarcoidosis from an inflammatory process or a neoplasm is difficult on sonography alone. Resection or orchiectomy may be necessary for definitive diagnosis. As noted previously, tuberculosis can also cause a chronic granulomatous reaction of the genital tract, typically a granulomatous epididymitis.

ACUTE SCROTAL PAIN

Acute scrotal pain may have numerous causes. More common causes include **torsion of the spermatic cord and testis, epididymitis or orchitis, torsion of a testicular appendage, acute hydrocele, strangulated hernia, idiopathic scrotal edema, Henoch-Schönlein purpura, abscess, traumatic hemorrhage, hemorrhage into a testicular neoplasm,** and **scrotal fat necrosis. Torsion of the spermatic cord** and **acute epididymitis** or **epididymo-orchitis** are the most common causes of acute scrotal pain. These entities cannot be distinguished by

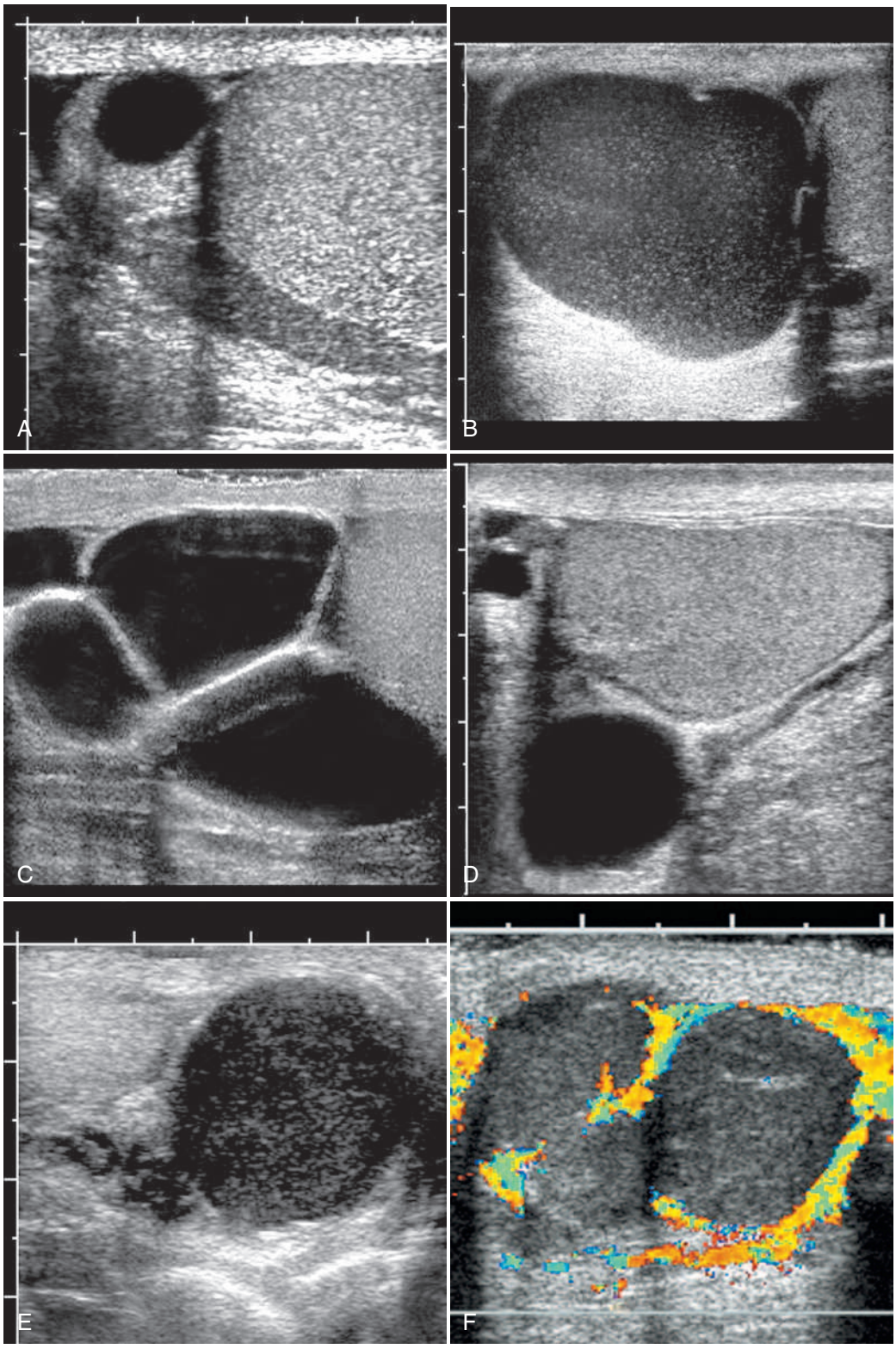

FIG. 22.25 Extratesticular Scrotal Cysts: Spectrum of Appearances. (A) Spermatocele. Longitudinal scan shows an anechoic cyst in head of the epididymis. **(B) Spermatocele.** Longitudinal scan shows a large cyst containing internal echoes in head of the epididymis. **(C) Septate spermatocele.** Longitudinal scan shows a septate cyst in head of the epididymis. **(D) Epididymal cyst.** Longitudinal scan shows a cyst in body of the epididymis. **(E) Cyst of vas deferens remnant.** Longitudinal scan shows a cyst with internal echoes inferior to the testis (surgically proven). **(F) Epidermoid inclusion cyst of epididymis.** Longitudinal color Doppler scan shows bilobed cystic mass in head of the epididymis surrounded by vessels.

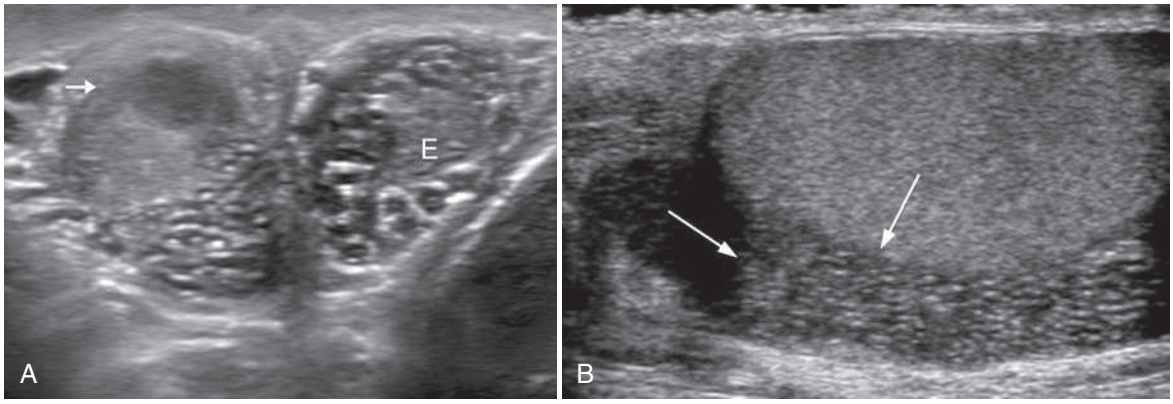

FIG. 22.26 Postvasectomy Changes. (A) Sperm granuloma. Transverse scan shows a heterogeneous mass *(arrow)* along the vas deferens and separate from the epididymis *(E)* in a postvasectomy patient. **(B) Postvasectomy changes in epididymis.** Longitudinal image of the scrotum shows ectasia of the ductules of the epididymis *(arrows)* in a patient who had a vasectomy. See also Videos 22.4 and 22.5.

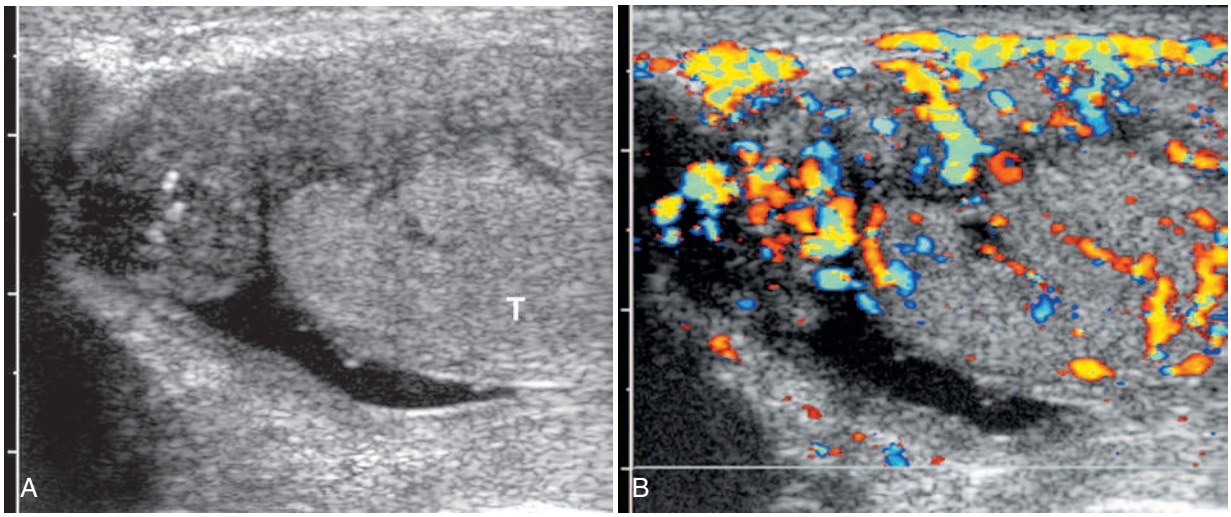

FIG. 22.27 Tuberculous Epididymo-orchitis. (A) Longitudinal scan shows a heterogeneous mass with calcification involving the head and body of the epididymis and the adjacent testis *(T)*. **(B)** Longitudinal color Doppler image shows increased vascularity in the epididymis and adjacent testis.

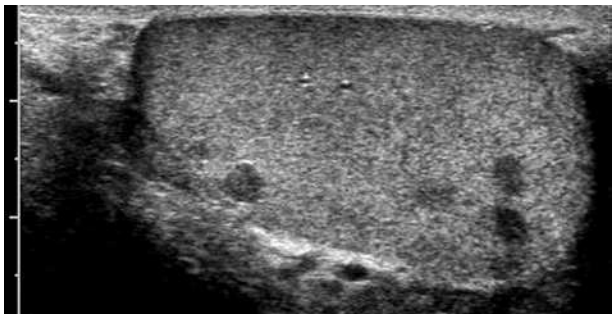

FIG. 22.28 Testicular Sarcoid. Longitudinal scan of the testis shows multiple, small, hypoechoic, solid masses resulting from sarcoid.

routine physical examination or laboratory tests in up to 50% of patients.[157] In the past, immediate surgical exploration was been advised in boys and young men with acute scrotal pain, unless a definitive diagnosis of epididymitis or orchitis was made. This aggressive approach resulted in an increased testicular salvage rate from torsion but also an increase in unnecessary surgical procedures. Real-time sonography, Doppler sonography, testicular radionuclide scintigraphy, and MRI have been used to increase the accuracy of distinguishing between infection and torsion.[158] Currently, sonography using color flow or power Doppler is the imaging study of choice to diagnose the cause of acute scrotal pain.

Causes of Acute Scrotal Pain

Torsion of the testis
Epididymo-orchitis
Testicular or epididymal appendage torsion
Strangulated hernia
Trauma
Idiopathic scrotal edema
Henoch-Schönlein purpura

Torsion

Torsion is more common in adolescent boys and represents approximately 20% of the acute scrotal pathologic phenomena in postpubertal males.[3] Prompt diagnosis is necessary because torsion requires immediate surgery to preserve the testis. The testicular salvage rate is over 80% if surgery is performed within 5 or 6 hours of the onset of pain, 70% if surgery is performed within 6 to 12 hours, and only 20% if surgery is delayed for more than 12 hours.[159]

Two types of testicular torsion have been described: intravaginal and extravaginal. **Extravaginal torsion** occurs prenatally and in newborns up to 30 days after delivery. Torsion occurs outside of the tunica vaginalis when the testis, **gubernaculum,** and tunica vaginalis are not fixed to the scrotal wall, allowing rotation of these structures as a unit and causing torsion of the cord at the level of the external ring. If this occurs prenatally, the affected neonate presents with a firm, painless mass in the scrotum, and swelling and discoloration of the affected side. The testis is typically infarcted and necrotic at birth. Postnatal testicular torsion is detected as a change in the testicular examination.[160,161] **Intravaginal torsion** is the more common type, arising within the tunica vaginalis and occurring most frequently at puberty. It results from anomalous suspension of the testis by a long stalk of spermatic cord mesentery, resulting in complete investment of the distal cord, testis, and epididymis by the tunica vaginalis. This allows the testis to swing and rotate within the tunica vaginalis like a clapper inside a bell, the so-called **bell-clapper deformity** (Fig. 22.29). Anomalous testicular suspension is bilateral in 50% to 80% of patients; hence the contralateral testis is usually fixed at the time of surgery as well. Sonography is considered the first step in evaluation of the acute scrotum, and its role is well established.[162-164] Sonographic findings vary with duration and degree of rotation. Gray-scale sonographic changes are nonspecific in the acute phase of torsion.[157,161,165] A torsed testis with normal, homogeneous echogenicity on gray-scale imaging has a high chance of successful salvage at surgery.[166] Testicular enlargement and decreased echogenicity are the most common findings 4 to 6 hours after the onset of torsion. With continued torsion, at 24 hours the testis can develop heterogeneous echotexture secondary to vascular congestion, hemorrhage, and infarction[167-169] (Fig. 22.30). A hypoechoic or heterogeneous echogenicity may indicate nonviability, although this is not specific.[166]

Torsion may change the position of the long axis of the testis. Extratesticular sonographic findings typically occur in torsion and are important to recognize. The spermatic cord immediately cranial to the testis and epididymis is twisted, causing a characteristic **torsion knot** or "whirlpool pattern" of concentric layers seen on sonography or MRI[161,170,171] (Fig. 22.30G and H). The epididymis may be enlarged and heterogeneous because of hemorrhage or ischemia, and may be difficult to separate from the torsion knot of the spermatic cord. This spherical epididymis-cord complex can be mistaken for epididymitis.[161] A reactive hydrocele and scrotal skin thickening are often seen with torsion. Large, echogenic, or complex extratesticular masses caused by hemorrhage in the tunica vaginalis or epididymis may be seen in patients with undiagnosed torsion.[172] The gray-scale findings of acute and subacute torsion are not specific and may be seen in testicular infarction caused by epididymitis, epididymo-orchitis, and traumatic testicular rupture or infarction.

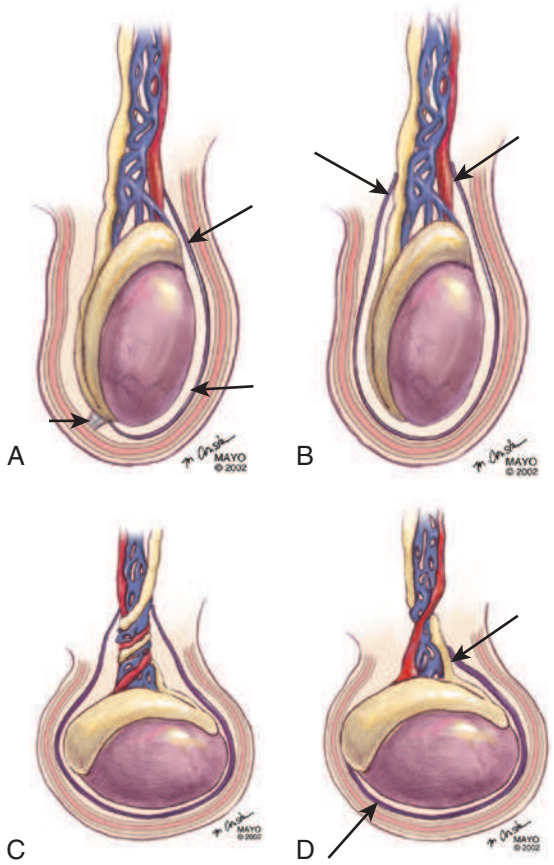

FIG. 22.29 "Bell-Clapper" Anomaly, Intravaginal Torsion, and Extravaginal Torsion. (A) Normal anatomy. The tunica vaginalis *(arrows)* does not completely surround the testis and epididymis, which are attached to the posterior scrotal wall *(short arrow).* **(B) Bell-clapper anomaly.** The tunica vaginalis *(arrows)* completely surrounds the testis, epididymis, and part of the spermatic cord, predisposing to torsion. **(C) Intravaginal torsion.** Bell-clapper anomaly with complete torsion of the spermatic cord, compromising the blood supply to the testis. **(D) Extravaginal torsion in a neonate.** Tunica vaginalis *(arrows)* is in normal position, but abnormal motility allows rotation of the testis, epididymis, and spermatic cord.

Doppler sonography is the most useful and most rapid technique to establish the diagnosis of testicular ischemia and to help distinguish torsion from epididymo-orchitis.[157,162,167] The absence of intratesticular blood flow at color and power Doppler ultrasound is considered diagnostic of ischemia (color and power techniques appear to have equivalent sensitivity in the diagnosis of torsion).[173-178] Meticulous scanning of the testicular parenchyma with the use of low-flow detection Doppler settings (low pulse repetition frequency, low wall filter, high Doppler gain, small color sampling box, lowest possible threshold setting) is important because intratesticular vessels are small and have low flow velocities, especially in prepubertal boys. Color flow Doppler sonography is more sensitive for showing decreased testicular flow in incomplete torsion than is nuclear scintigraphy, which is rarely

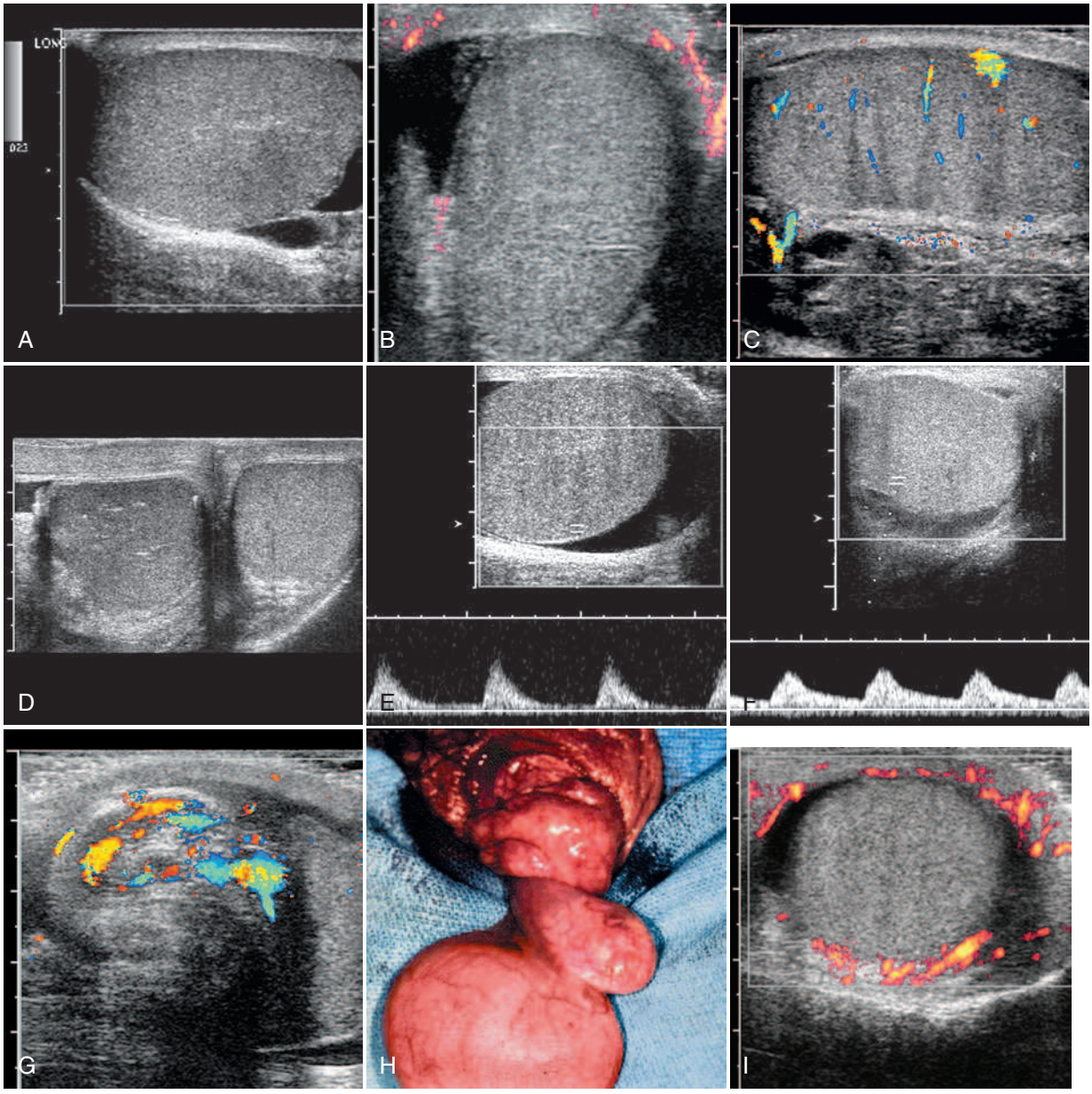

FIG. 22.30 Torsion of Spermatic Cord and Testis: Spectrum of Appearances. (A)-(D) Acute torsion. Longitudinal power Doppler scans show **(A)** no flow in the testis and **(B)** abnormal, transverse, and vertical orientation of the testis with no flow. **(C)** After manual detorsion of case in **B,** longitudinal color Doppler scan shows the normal orientation of the testis with blood flow present. The testis has a striated appearance caused by the previous ischemia. **(D)** Dual transverse gray-scale scan shows enlarged hypoechoic right testis resulting from torsion and skin thickening in the right hemiscrotum. **(E) Partial torsion.** Longitudinal scan with spectral Doppler shows a high-resistance testicular arterial waveform with little diastolic flow because of venous occlusion; a small, reactive hydrocele was found. **(F)** After spontaneous detorsion of case in **E,** longitudinal scan with spectral Doppler shows return of diastolic flow. **(G) Torsion knot.** Longitudinal scan with acute spermatic cord torsion shows the "torsion knot" complex of epididymis and spermatic cord. **(H) Acute torsion.** Intraoperative photograph shows the twisted spermatic cord that gives the torsion knot appearance on sonograph. **(I) Subacute torsion** (3 days of pain). Transverse power Doppler scan shows absent flow within the testis with surrounding hyperemia. (**H** with permission from Winter TC. Ultrasonography of the scrotum. Appl Radiol 2002;31[3]:9-18.[169])

used anymore to diagnose torsion.[179] In testicular torsion, color Doppler sonography has a sensitivity of 80% to 98%, specificity of 97% to 100%, and accuracy of 97%.[161,162,180] The use of intravascular contrast agents in sonography can improve the sensitivity and specificity of detecting blood flow in the scrotum.[175,181] In pediatric patients, it may be difficult to document flow in a normal testis.[182] In practice, many surgeons elect to explore the testis surgically if clinical symptoms and signs are suggestive and results of the sonographic examination are equivocal.

Torsion is not an all or none phenomenon. Potential pitfalls in using sonography in the diagnosis of torsion are **partial torsion, torsion/detorsion,** and **ischemia from orchitis.** Torsion of at least 540 degrees is necessary for complete arterial occlusion.[162,183] With partial torsion of 360 degrees or less, arterial flow may still

occur, but venous outflow is often obstructed, causing diminished diastolic arterial flow on spectral Doppler examination[184,185] (Fig. 22.30E). If spontaneous detorsion occurs, flow within the affected testis may be normal, or it may be increased and mimic orchitis.[186] Spontaneous detorsion can occur with sequelae including a segmental testicular infarction.[102,103] Segmental testicular infarction may also occur with **Henoch-Schönlein purpura** or with **orchitis** (see Fig. 22.14). Orchitis may also cause global ischemia of the testis and mimic torsion.[186]

In subacute or chronic torsion, Doppler sonography demonstrates no flow in the testis and increased flow in the paratesticular tissues, including the epididymis-cord complex and **dartos fascia** (Fig. 22.30I).

Torsion of the appendix testis or appendix epididymis can present with acute scrotal pain, potentially mimicking testicular torsion clinically, although there are no other clinical symptoms and the **cremasteric reflex** can still be elicited. Patients are rarely referred for imaging because the pain is usually not severe, and the twisted appendage may be evident on physical examination as a small firm nodule palpable at the superior aspect of the testis, with a bluish discoloration, or the **"blue dot" sign.**[187] Up to 95% of twisted appendages involve the appendix testis and occur most often in boys aged 7 to 14 years.[65] The sonographic appearance of the twisted testicular appendage has been described as an avascular hyperechoic mass with a central hypoechoic focus adjacent to the head of a normally perfused testis and surrounded by an area of increased color Doppler perfusion.[162,188] These cases are managed conservatively with pain typically resolving in 2 to 3 days with interval atrophy of the torsed appendage. The role of sonography is to exclude testicular torsion or epididymo-orchitis. **Idiopathic scrotal edema** typically affects prepubertal boys, with acute onset of relatively painless scrotal erythema and subcutaneous edema. Idiopathic scrotal edema typically resolves spontaneously in 1 to 3 days without sequelae.

Epididymitis and Epididymo-orchitis

Epididymitis is the most common cause of acute scrotal pain in postpubertal men. It may be acute or chronic, depending on the inciting organism and the duration of the process. Acute epididymitis usually results from a lower urinary tract infection and is less often hematogenous or traumatic in origin. The common causative organisms are ***Escherichia coli, Pseudomonas,*** and ***Klebsiella.*** Sexually transmitted organisms causing urethritis, such as ***Neisseria gonorrhoeae*** and ***Chlamydia trachomatis,*** are common causes of epididymitis in younger men. Less frequently, epididymitis may be caused by **tuberculosis, mumps,** or **syphilitic orchitis.**[153,189] The age of peak incidence is 40 to 50 years. Typically, patients present with the insidious onset of pain which increases over 1 or 2 days. Fever, dysuria, and urethral discharge may also be present.

In **acute epididymitis,** sonography characteristically shows enlargement of the epididymis, involving the tail initially and frequently spreading to the entire epididymis[190] (Fig. 22.31A and B). The echogenicity of the epididymis is usually decreased and its echotexture is often coarse and heterogeneous, likely secondary to edema, hemorrhage, or both. Color flow Doppler sonography usually shows increased blood flow in the epididymis or testis, or both, compared with the asymptomatic side.[191] Reactive hydrocele formation is common, and associated scrotal wall thickening may be seen.

Direct extension of epididymal inflammation to the testis, called **epididymo-orchitis,** occurs in up to 20% of patients with acute epididymitis. Isolated orchitis may also occur. In such cases, increased blood flow is localized to the testis (Fig. 22.31D and E, Video 22.6). Testicular involvement may be focal or diffuse. Characteristically, **focal orchitis** produces a hypoechoic area adjacent to an enlarged portion of the epididymis. Color Doppler shows increased flow in the hypoechoic area of the testis; increased flow in the tunica vasculosa may also be visible as lines of color signal radiating from the mediastinum testis.[192] These lines of color correspond to septal accentuation visible as hypoechoic bands on gray-scale sonography (Fig. 22.31H and I). Spectral Doppler shows increased diastolic flow in uncomplicated orchitis (Fig. 22.32A). If left untreated, the entire testis may become involved, appearing hypoechoic and enlarged. As pressure in the testis increases from edema, venous infarction with hemorrhage may occur, appearing hyperechoic initially and hypoechoic later.[192] Ischemia and subsequent infarction may also occur when the vascularity of the testis is compromised by venous occlusion or venous thrombosis.[193] When vascular disruption is severe, resulting in complete testicular infarction, the changes are indistinguishable from those seen in testicular torsion. Color Doppler sonography may show focal areas of reactive hyperemia and increased blood flow associated with relatively avascular areas of infarction in both the testis and the epididymis in patients with severe epididymo-orchitis. Diastolic flow reversal in the arterial waveforms of the testis is an ominous finding, associated with testicular infarction in severe epididymo-orchitis[194] (Fig. 22.32B).

In addition to infarction, other complications of acute epididymo-orchitis include intratesticular abscess formation and development of a pyocele (see Figs. 22.13 and 22.17F). Chronic changes may be seen in the epididymis or testis from clinically resolved epididymo-orchitis. Swelling of the epididymis may persist and appear as a heterogeneous mass on sonography. The testis may have a persistent, striated appearance of septal accentuation from fibrosis (Figs. 22.33 and 22.34). This striated appearance of the testis is nonspecific and may also be seen after ischemia from torsion or during a hernia repair.[192,195] A similar heterogeneous appearance in the testis may be seen in older patients because of **seminiferous tubule atrophy and sclerosis.**[196] Focal areas of infarction in the testis may persist as wedge-shaped or cone-shaped hypoechoic areas or may appear as hyperechoic scars.[192] If complete infarction of the testis has occurred because of epididymo-orchitis, the testis may become small, with a hypoechoic or heterogeneous echotexture.

Fournier Gangrene

Fournier gangrene is a **necrotizing fasciitis of the perineum,** external genitalia, and perianal area occurring most frequently in men aged 50 to 70 years. The origin is usually a disease process from the overlying skin, urinary tract, or colorectal area, frequently due to a synergistic polymicrobial infection.[197] Predisposing factors include systemic immunosuppression, diabetes mellitus,

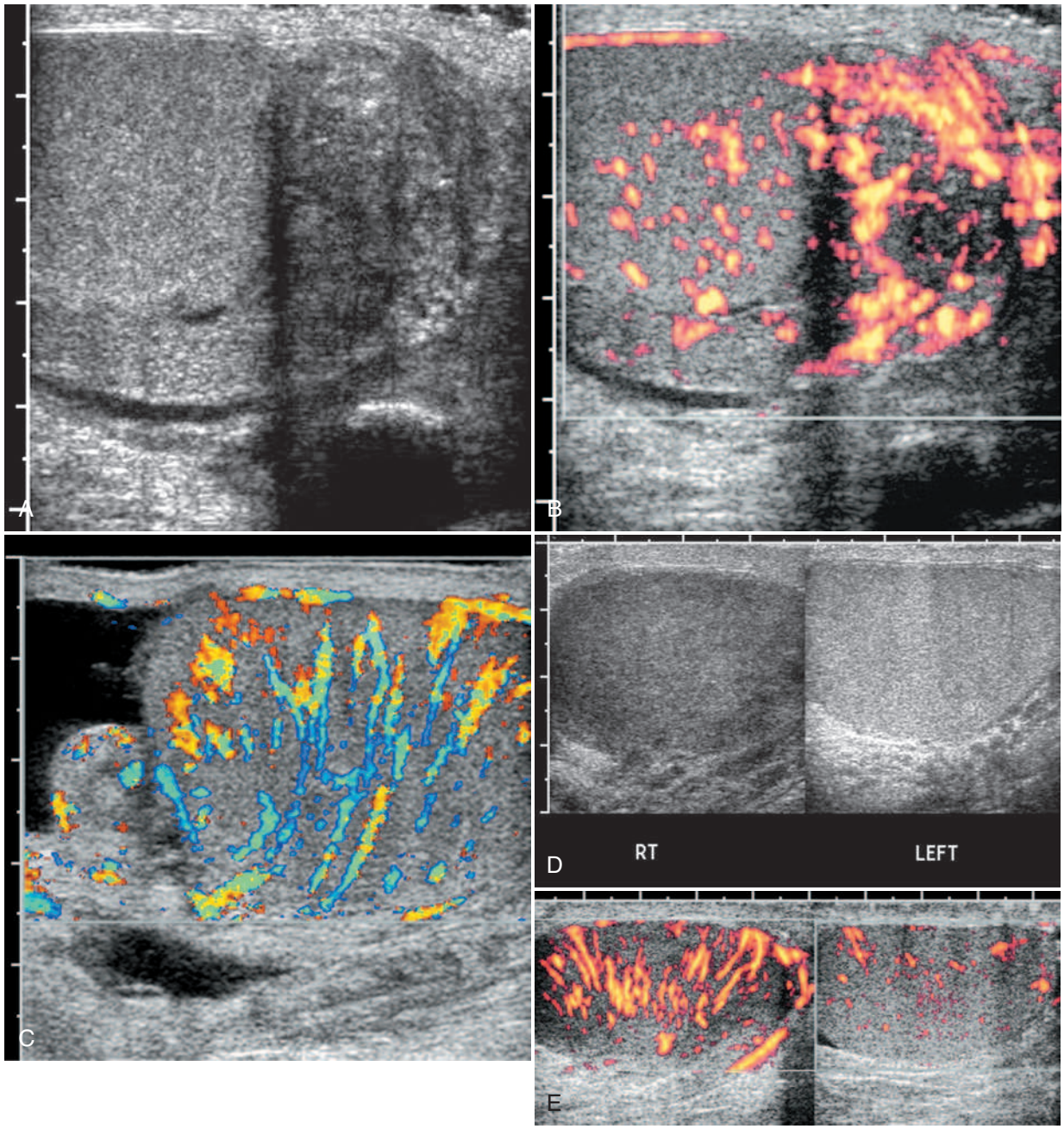

FIG. 22.31 Epididymo-orchitis, Epididymitis, and Orchitis: Spectrum of Appearances. (A) and **(B) Acute epididymitis.** Longitudinal gray-scale and color Doppler images show enlargement and a heterogeneous echotexture of tail of the epididymis, with greatly increased flow in tail of the epididymis and minimally increased flow in the adjacent testis. **(C) Acute epididymo-orchitis.** Longitudinal color Doppler scan shows increased flow in the epididymis and testis. **(D)** and **(E) Acute orchitis.** Longitudinal dual-image gray-scale and color Doppler images show that right testis is hypoechoic and has greatly increased flow.

chronic alcoholism, and steroid therapy.[152] Multiple organisms are usually involved, including *Klebsiella, Streptococcus, Proteus,* and *Staphylococcus.* Surgical debridement of devitalized tissue is usually required, and morbidity and mortality are high without prompt treatment. Ultrasound is helpful in diagnosis by demonstrating scrotal wall thickening containing gas with accompanying shadowing.

TRAUMA

When evaluating testicular integrity in the setting of acute trauma, the primary role of sonography is to assess for the continuity of the tunica albuginea: this determines clinical management. Disruption of the tunica albuginea indicates testicular rupture. Prompt diagnosis of a ruptured testis is crucial because of the

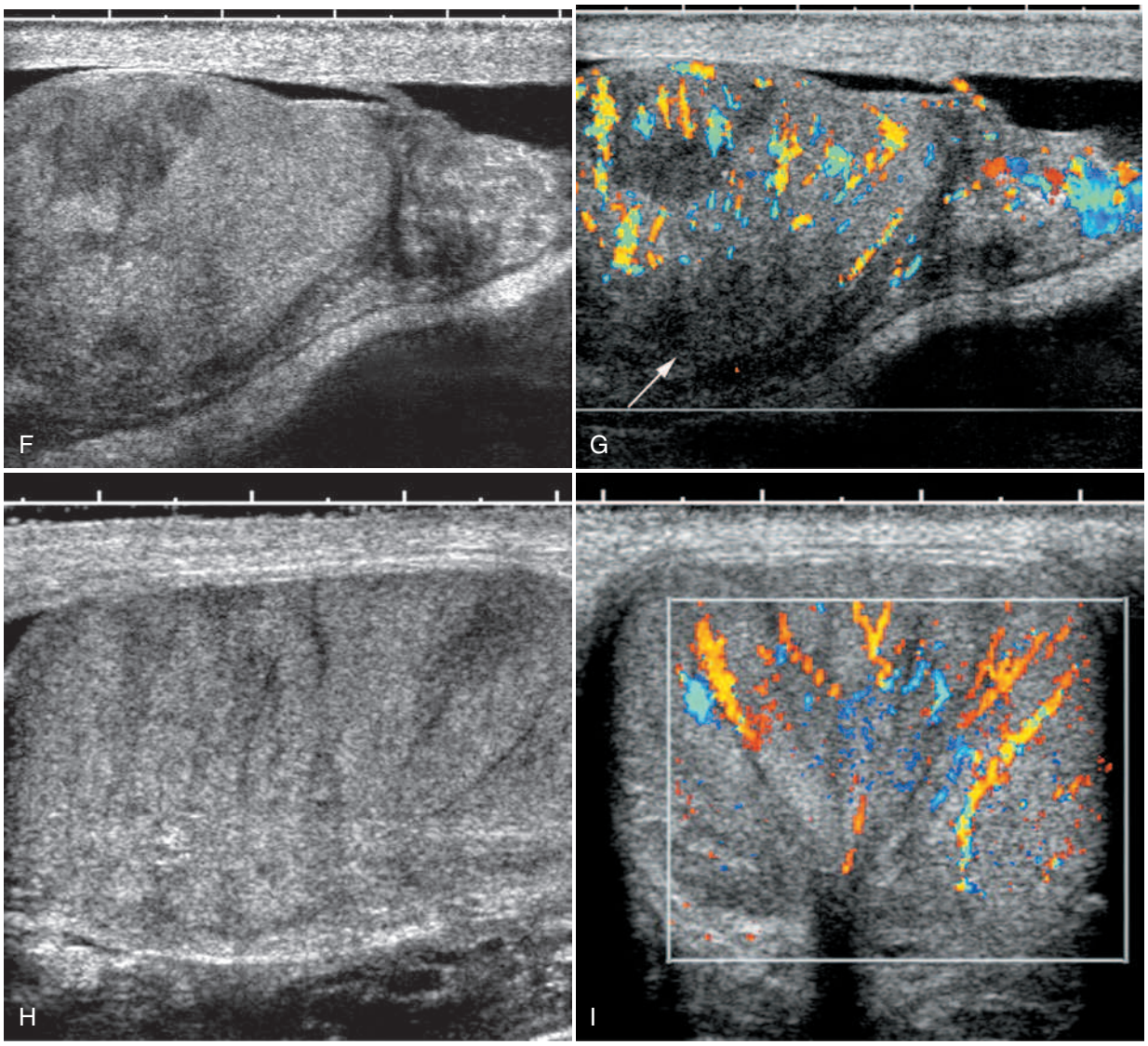

FIG. 22.31, cont'd. **(F)** Longitudinal gray-scale scan with 3 weeks of epididymo-orchitis unresolved with antibiotic therapy shows hypoechoic areas in the testis and an enlarged heterogeneous tail of the epididymis. **(G)** Color Doppler image shows increased flow in the testis and epididymis with an area of decreased flow due to ischemia *(arrow)*. **(H)** and **(I)** **Acute orchitis.** Longitudinal gray-scale and color Doppler images show hypoechoic bands caused by septal accentuation from edema and increased vascularity of the testis. See also Video 22.6.

direct relationship between early surgical intervention and testicular salvageability. Approximately 90% of ruptured testes can be saved if surgery is performed within the first 72 hours, whereas only 45% may be salvaged after 72 hours.[198]

Sonographic features of testicular rupture include focal areas of altered testicular echogenicity, corresponding to areas of hemorrhage or infarction, and hematocele formation in 33% of patients. A discrete fracture plane may not be identified. Tunical disruption associated with extrusion of the seminiferous tubules is specific for rupture (Fig. 22.35E, Video 22.7). However, the sensitivity of the diagnosis of rupture based on tunical disruption alone is only 50%. Heterogeneity of the testis with associated testicular contour irregularity may be helpful in making the diagnosis of rupture.[110,199,200] Color Doppler imaging can be helpful because rupture of the tunica albuginea is almost always associated with disruption of the tunica vasculosa and loss of blood supply to part or all of the testis.[110] Although not specific for a ruptured testicle, these features may suggest the diagnosis in the appropriate clinical setting, prompting immediate surgical exploration.

Clinical diagnosis is often impossible because of marked scrotal pain and swelling; thus sonography can be invaluable in the assessment of tunica albuginea integrity and the extent of testicular hematoma.[110,198-200] A visibly intact tunica albuginea should exclude rupture, but a complex intrascrotal hematoma may be difficult to distinguish from testicular rupture and may obscure the tunica[110,201] (Fig. 22.35A). Patients with large intrascrotal hematomas or hematoceles will often undergo surgical exploration because it is difficult to exclude rupture sonographically in the presence of surrounding complex fluid.[110] If a patient with a presumed intratesticular hematoma is not surgically explored,

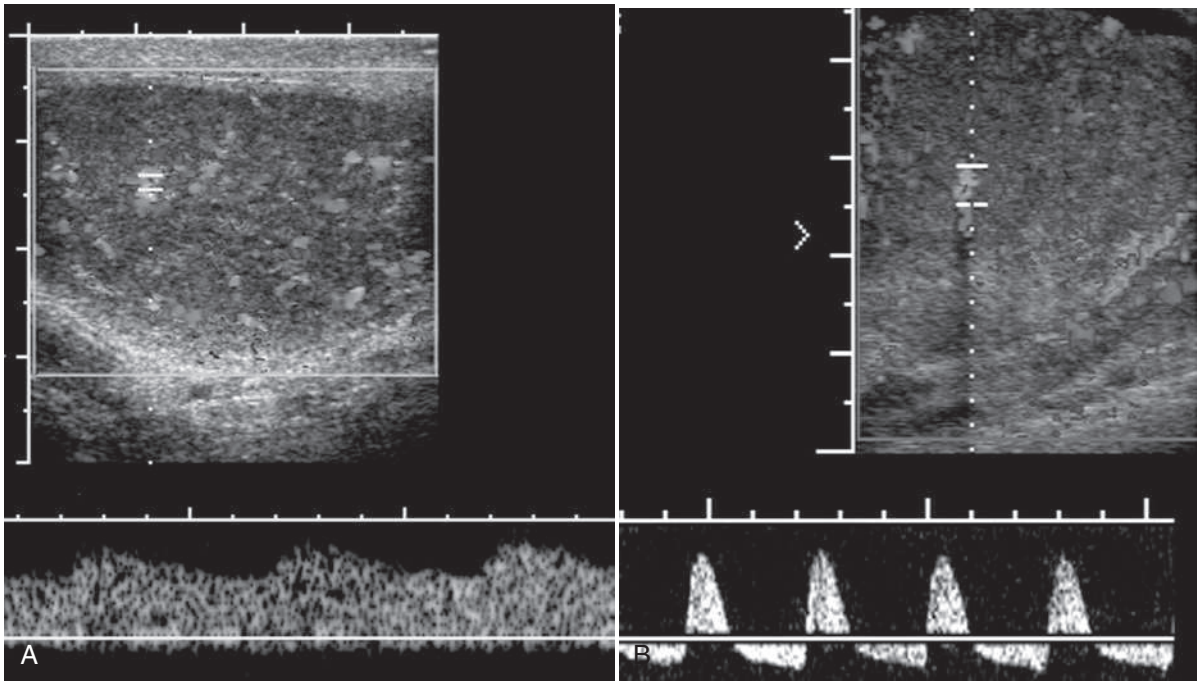

FIG. 22.32 Spectral Doppler Changes in Orchitis. (A) Uncomplicated orchitis. Longitudinal scan with spectral Doppler tracing shows increased diastolic flow in the testis. **(B) Orchitis with venous compromise.** Longitudinal scan with spectral Doppler tracing in more severe orchitis shows reversal of flow in diastole caused by edema impeding venous flow.

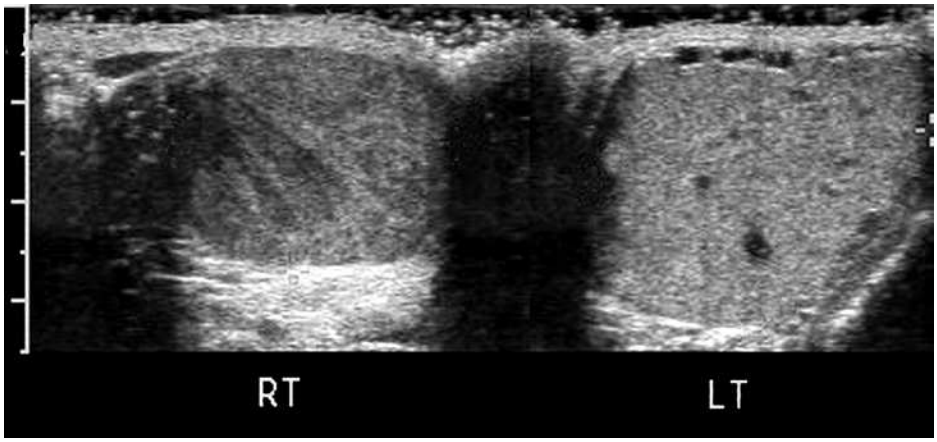

FIG. 22.33 Heterogeneous "Striped" Testis. Transverse dual image shows heterogeneity in the right testis with marked septal accentuation from previous orchitis. This appearance may also be seen after ischemia.

FIG. 22.34 Fibrosis of Testis After Orchitis. Pathologic specimen of testis shows linear bands of fibrosis *(white areas)* caused by previous severe orchitis. A similar "end-stage" testis could have this appearance due to ischemia.

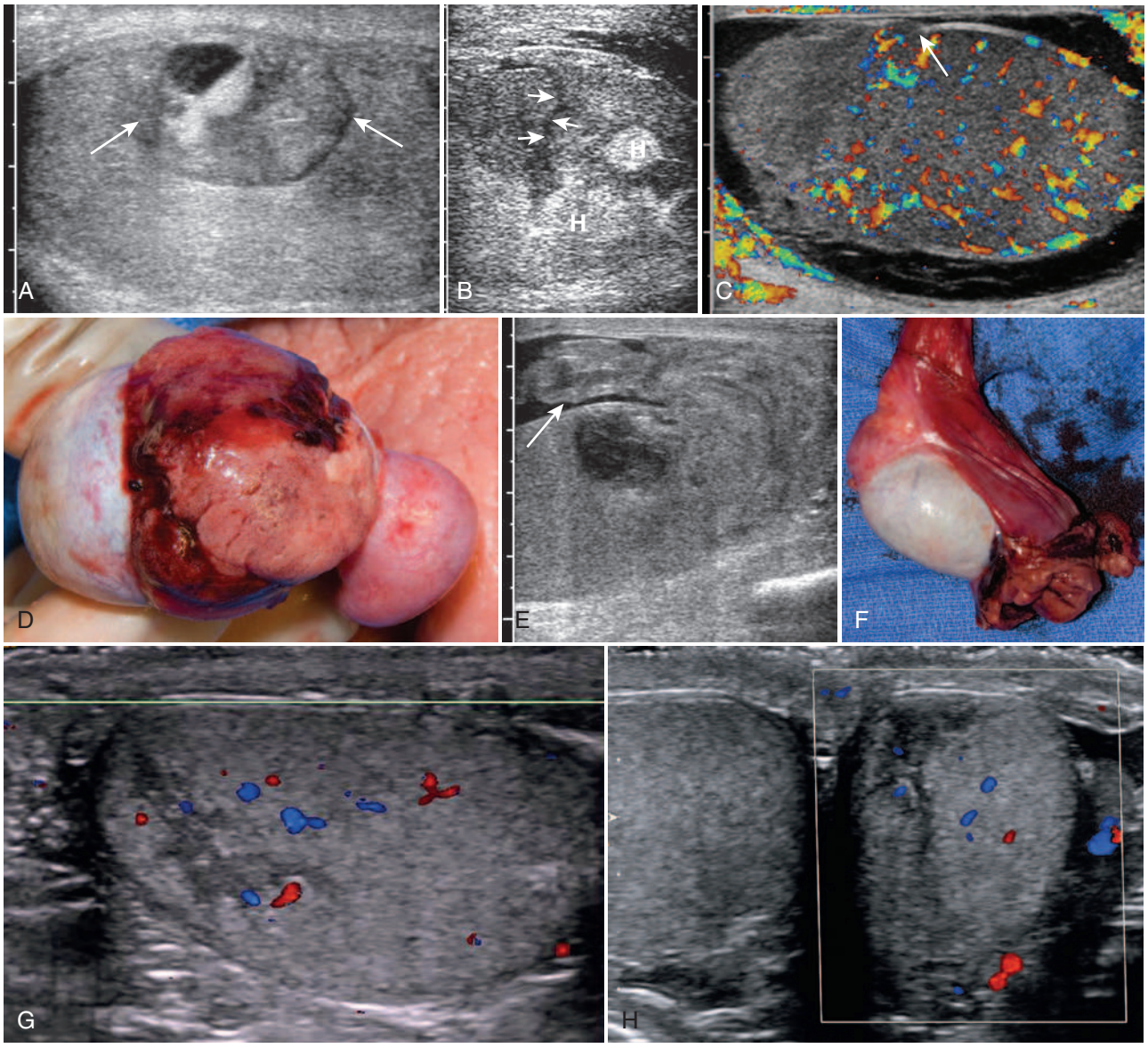

FIG. 22.35 Testicular Trauma: Spectrum of Appearances. (A) Hematoma. Longitudinal image shows hematoma *(arrows)* on the anterior surface of the testis. Tunica intact at surgery. **(B) Fracture of testis.** Transverse scan shows a heterogeneous testicle with a linear band *(arrows)* indicating a fracture. *H,* Testicular hematoma. **(C) Tunical tear.** Longitudinal color Doppler image shows contour irregularity of the testis with disruption of the tunica *(arrow).* Extruded testis parenchyma shows no color flow. **(D)** Same case as **C.** Photograph during surgery shows tunical tear in the exposed right testis. **(E) Rupture of testis.** Longitudinal image shows rupture of the testis with extrusion of seminiferous tubules *(arrow).* **(F)** In same case as **E,** photograph during surgery shows a tear in the tunica inferiorly with extrusion of seminiferous tubules. **(G)** and **(H) Fracture of testis.** Longitudinal and transverse color Doppler images of the left testis show an irregular linear, hypoechoic, avascular band representing a testicular fracture following acute blunt trauma. The tunica albuginea was intact. See also Video 22.7.

it is incumbent upon the clinician to follow the intratesticular abnormality to resolution because a testicular tumor can mimic an intratesticular hematoma and also predispose to rupture following relatively minor trauma.

Testicular fracture refers to discontinuity of normal testicular parenchyma, which may be present in the absence of disruption of the tunica albuginea. An associated intratesticular hematoma or hematocele may be present. Sonographically, the fracture appears as a linear, hypoechoic, avascular band extending across the testicular parenchyma (Fig. 22.35).

Sonography can also be used to discern the severity of scrotal trauma resulting from penetrating scrotal injury. Gunshot injury is the most common cause; other causes include stabbing, self mutilation, human and animal bites, and projectile injuries. Bilateral injuries are more common in the setting of penetrating trauma.[202] Penetrating trauma can disrupt the tunica albuginea, as well as penetrate the parenchyma, causing a fracturelike injury. Ultrasound can assess the degree of injury and evaluate for the presence of foreign bodies and for the presence of air, which may denote the path of the penetrating injury.[203] Doppler

sonography can assess for viability of the testis in the setting of penetrating trauma. A careful gray-scale and color flow Doppler evaluation of the epididymis should be performed in all examinations of blunt trauma. Traumatic epididymitis may be an isolated finding that should not be confused with an infectious process.[204]

CRYPTORCHIDISM

The testes remain near the deep inguinal ring until the seventh month of gestation when they normally begin their descent through the inguinal canal into the twin scrotal sacs.[1,2] The **gubernaculum testis** is a fibromuscular structure that extends from the inferior pole of the testis to the scrotum and guides the testis in its descent, a process normally completed before birth. **Undescended testis** is one of the most common genitourinary anomalies in male infants. At birth, 3.5% of male infants weighing more than 2500 g have an undescended testis; 10% to 25% of these cases are bilateral. This figure decreases to 0.8% by age 1 year because the testes descend spontaneously in most infants. The incidence of undescended testes increases to 30% in premature infants, approaching 100% in neonates who weigh less than 1000 g at birth. Complete descent is necessary for full testicular maturation.[205,206]

Malpositioned testes may be located anywhere along the pathway of descent from the retroperitoneum to the scrotum. Most (80%) undescended testes are palpable, lying distal to the external inguinal ring. **Anorchia** occurs in 4% of the remaining patients with impalpable testes.[206]

Localization of the undescended testis is important for the prevention of two potential complications of cryptorchidism: **infertility** and **cancer.** The undescended testis is more likely to undergo malignant change than is the normally descended testis.[3] The most common malignancy is **seminoma.** The risk of malignancy is increased in both the undescended testis after orchiopexy and the normally descended testis. Therefore careful serial examinations of both testes are essential.

Sonographically, the **undescended testis** is often smaller and slightly less echogenic than the contralateral, normally descended testis (Fig. 22.36). The pars infravaginalis gubernaculi, which is the distal bulbous segment of the gubernaculum testis, can be mistaken for the testis. After completion of testicular descent, the pars infravaginalis gubernaculi and the gubernaculum normally atrophy. If the testis remains undescended, both structures persist. The pars infravaginalis gubernaculi is located distal to the undescended testis, usually in the scrotum, but it may be found in the inguinal canal. Sonographically, the pars infravaginalis gubernaculi is a hypoechoic, cordlike structure of echogenicity similar to the testis, with the gubernaculum leading to it.[207]

Sonography is often used in the initial evaluation of cryptorchidism, although the value of this has been questioned because it is insensitive in detecting high intraabdominal testes.[208] MRI has also been used in cryptorchidism because it is more sensitive than ultrasound in detecting undescended testes in the retroperitoneum.[209,210] Nonvisualization of an undescended testis on sonography or MRI does not exclude its presence, and therefore laparoscopy or surgical exploration should be performed if clinically indicated.

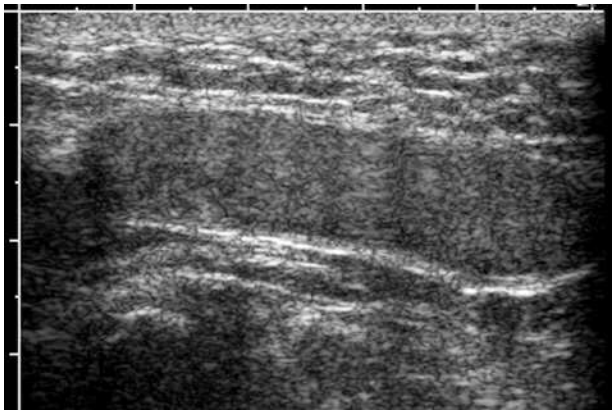

FIG. 22.36 Testis in Inguinal Canal. Longitudinal scan shows an elongated, ovoid, undescended testis.

REFERENCES

1. Larsen WJ. Human embryology. New York: Churchill Livingstone; 1993. p. 235-280.
2. Moore KL, Persaud TVN. The developing human: clinically oriented embryology. 5th ed. Philadelphia: Saunders; 1993.
3. Krone KD, Carroll BA. Scrotal ultrasound. Radiol Clin North Am. 1985;23(1): 121-139.
4. Trainer TD. Histology of the normal testis. Am J Surg Pathol. 1987;11(10): 797-809.
5. Siegel MJ. The acute scrotum. Radiol Clin North Am. 1997;35(4): 959-976.
6. Thomas RD, Dewbury KC. Ultrasound appearances of the rete testis. Clin Radiol. 1993;47(2):121-124.
7. Johnson KA, Dewbury KC. Ultrasound imaging of the appendix testis and appendix epididymis. Clin Radiol. 1996;51(5):335-337.
8. Sellars ME, Sidhu PS. Ultrasound appearances of the testicular appendages: pictorial review. Eur Radiol. 2003;13(1):127-135.
9. Black JA, Patel A. Sonography of the normal extratesticular space. AJR Am J Roentgenol. 1996;167(2):503-506.
10. Allen TD. Disorders of the male external genitalia. In: Kelalis PP, King LR, editors. Clinical pediatric urology. Philadelphia: Saunders; 1976. p. 636-668.
11. Middleton WD, Bell MW. Analysis of intratesticular arterial anatomy with emphasis on transmediastinal arteries. Radiology. 1993;189(1):157-160.
12. Fakhry J, Khoury A, Barakat K. The hypoechoic band: a normal finding on testicular sonography. AJR Am J Roentgenol. 1989;153(2):321-323.
13. Bushby LH, Sellars ME, Sidhu PS. The "two-tone" testis: spectrum of ultrasound appearances. Clin Radiol. 2007;62(11):1119-1123.
14. Middleton WD, Thorne DA, Melson GL. Color Doppler ultrasound of the normal testis. AJR Am J Roentgenol. 1989;152(2):293-297.
15. Gooding GA. Sonography of the spermatic cord. AJR Am J Roentgenol. 1988;151(4):721-724.
16. Benson CB, Doubilet PM, Richie JP. Sonography of the male genital tract. AJR Am J Roentgenol. 1989;153(4):705-713.
17. Rifkin MD, Kurtz AB, Pasto ME, Goldberg BB. Diagnostic capabilities of high-resolution scrotal ultrasonography: prospective evaluation. J Ultrasound Med. 1985;4(1):13-19.
18. Rifkin MD, Kurtz AB, Pasto ME, et al. The sonographic diagnosis of focal and diffuse infiltrating intrascrotal lesions. Urol Radiol. 1984;6(1): 20-26.
19. Carroll BA, Gross DM. High-frequency scrotal sonography. AJR Am J Roentgenol. 1983;140(3):511-515.
20. Woodward PJ, Sohaey R, O'Donoghue MJ, Green DE. From the archives of the AFIP: tumors and tumorlike lesions of the testis: radiologic-pathologic correlation. Radiographics. 2002;22(1):189-216.

21. Beccia DJ, Krane RJ, Olsson CA. Clinical management of non-testicular intrascrotal tumors. J Urol. 1976;116(4):476-479.
22. Frates MC, Benson CB, DiSalvo DN, et al. Solid extratesticular masses evaluated with sonography: pathologic correlation. Radiology. 1997;204(1): 43-46.
23. Alleman WG, Gorman B, King BF, et al. Benign and malignant epididymal masses evaluated with scrotal sonography: clinical and pathologic review of 85 patients. J Ultrasound Med. 2008;27(8):1195-1202.
24. Kenney PJ. Solid extratesticular masses. Radiology. 1998;206(1):290.
25. Grantham JG, Charboneau JW, James EM, et al. Testicular neoplasms: 29 tumors studied by high-resolution US. Radiology. 1985;157(3):775-780.
26. Siegel R, DeSantis C, Virgo K, et al. Cancer treatment and survivorship statistics, 2012. CA Cancer J Clin. 2012;62(4):220-241.
27. Kreydin EI, Barrisford GW, Feldman AS, Preston MA. Testicular cancer: what the radiologist needs to know. AJR Am J Roentgenol. 2013;200(6): 1215-1225.
28. Kirschling RJ, Kvols LK, Charboneau JW, et al. High-resolution ultrasonographic and pathologic abnormalities of germ cell tumors in patients with clinically normal testes. Mayo Clin Proc. 1983;58(10):648-653.
29. Javadpour N. Principles and management of testicular cancer. New York: Thieme; 1986.
30. Horwich A. Testicular cancer: investigation and management. 2nd ed. London: Chapman and Hall Medical; 1996.
31. Winter TC. There is a mass in the scrotum-what does it mean?: Evaluation of the scrotal mass. Ultrasound Q. 2009;25(4):195-205.
32. Moch H, Cubilla AL, Humphrey PA, et al. The 2016 WHO classification of tumours of the urinary system and male genital organs-Part A: renal, penile, and testicular tumors. Eur Urol. 2016;70(10):93-105.
33. Cotran RS, Kumar V, Collins T. Pathologic basis of disease. 6th ed. Philadelphia: Saunders; 1999. p. 1011-1034.
34. Heiken JP. Tumors of the testis and testicular adnexa. In: Pollack HM, McClennan BL, Dyer R, et al., editors. Clinical urography. 2nd ed. Philadelphia: Saunders; 2000. p. 1716-1741.
35. Horstman WG, Melson GL, Middleton WD, Andriole GL. Testicular tumors: findings with color Doppler US. Radiology. 1992;185(3):733-737.
36. Luker GD, Siegel MJ. Pediatric testicular tumors: evaluation with gray-scale and color Doppler US. Radiology. 1994;191(2):561-564.
37. Hindley RG, Chandra A, Saunders A, O'Brien TS. Impalpable testis cancer. BJU Int. 2003;92(6):572-574.
38. Powell TM, Tarter TH. Management of nonpalpable incidental testicular masses. J Urol. 2006;176(1):96-98.
39. Carmignani L, Gadda F, Gazzano G, et al. High incidence of benign testicular neoplasms diagnosed by ultrasound. J Urol. 2003;170(5):1783-1786.
40. Carmignani L, Morabito A, Gadda F, et al. Prognostic parameters in adult impalpable ultrasonographic lesions of the testicle. J Urol. 2005;174(3): 1035-1038.
41. Horstman WG, Haluszka MM, Burkhard TK. Management of testicular masses incidentally discovered by ultrasound. J Urol. 1994;151(5): 1263-1265.
42. Talerman A, Roth LM. Pathology of the testis and its adnexa. In: Talerman A, Roth LM, editors. Germ cell tumors. New York: Churchill Livingstone; 1986.
43. Jacobsen GK, Talerman A. Atlas of germ cell tumors. J Pathol. 1989;160:86-87.
44. Schwerk WB, Schwerk WN, Rodeck G. Testicular tumors: prospective analysis of real-time US patterns and abdominal staging. Radiology. 1987;164(2):369-374.
45. Akin EA, Khati NJ, Hill MC. Ultrasound of the scrotum. Ultrasound Q. 2004;20(4):181-200.
46. Geraghty MJ, Lee Jr FT, Bernsten SA, et al. Sonography of testicular tumors and tumor-like conditions: a radiologic-pathologic correlation. Crit Rev Diagn Imaging. 1998;39(1):1-63.
47. Damjanov I. Tumors of the testis and epididymis. In: Murphy WM, editor. Urological pathology. 2nd ed. Philadelphia: Saunders; 1997. p. 342-400.
48. Ulbright TM. Germ cell neoplasms of the testis. Am J Surg Pathol. 1993;17(11):1075-1091.
49. Frush DP, Sheldon CA. Diagnostic imaging for pediatric scrotal disorders. Radiographics. 1998;18(4):969-985.
50. Mostofi FK, Price EB. Tumors of the male genital system. Atlas of tumor pathology. Washington, DC: Armed Forces Institute of Pathology; 1973.
51. Rushton HG, Belman AB, Sesterhenn I, et al. Testicular sparing surgery for prepubertal teratoma of the testis: a clinical and pathological study. J Urol. 1990;144(3):726-730.
52. Carver BS, Al-Ahmadie H, Sheinfeld J. Adult and pediatric testicular teratoma. Urol Clin North Am. 2007;34(2):245-251.
53. Emory TH, Charboneau JW, Randall RV, et al. Occult testicular interstitial-cell tumor in a patient with gynecomastia: ultrasonic detection. Radiology. 1984;151(2):474.
54. Tasu JP, Faye N, Eschwege P, et al. Imaging of burned-out testis tumor: five new cases and review of the literature. J Ultrasound Med. 2003;22(5): 515-521.
55. Mindrup SR, Konety BR. Testicular recurrence from "primary" retroperitoneal germ cell tumor. Urology. 2004;64(5):1031.
56. Shawker TH, Javadpour N, O'Leary T, et al. Ultrasonographic detection of "burned-out" primary testicular germ cell tumors in clinically normal testes. J Ultrasound Med. 1983;2(10):477-479.
57. Maizlin ZV, Belenky A, Kunichezky M, et al. Leydig cell tumors of the testis: gray scale and color Doppler sonographic appearance. J Ultrasound Med. 2004;23(7):959-964.
58. Gabrilove JL, Freiberg EK, Leiter E, Nicolis GL. Feminizing and nonfeminizing Sertoli cell tumors. J Urol. 1980;124(6):757-767.
59. Young S, Gooneratne S, Straus FH 2nd, et al. Feminizing Sertoli cell tumors in boys with Peutz-Jeghers syndrome. Am J Surg Pathol. 1995;19(1): 50-58.
60. Ulbright TM, Amin MB, Young RH. Tumors of the testis, adnexa, spermatic cord, and scrotum. In: Rosai J, Sobin LH, editors. Atlas of tumor pathology, fasc 25, ser 3. Washington, DC: Armed Forces Institute of Pathology; 1999. p. 1-366.
61. Duncan PR, Checa F, Gowing NF, et al. Extranodal non-Hodgkin's lymphoma presenting in the testicle: a clinical and pathologic study of 24 cases. Cancer. 1980;45(7):1578-1584.
62. Mostofi FK, Sobin LH. Histological typing of testis tumours. International histological classification of tumors of the testes. Geneva: World Health Organization; 1977.
63. Mazzu D, Jeffrey Jr RB, Ralls PW. Lymphoma and leukemia involving the testicles: findings on gray-scale and color Doppler sonography. AJR Am J Roentgenol. 1995;164(3):645-647.
64. Rayor RA, Scheible W, Brock WA, Leopold GR. High resolution ultrasonography in the diagnosis of testicular relapse in patients with acute lymphoblastic leukemia. J Urol. 1982;128(3):602-603.
65. Dogra VS, Gottlieb RH, Oka M, Rubens DJ. Sonography of the scrotum. Radiology. 2003;227(1):18-36.
66. Iizumi T, Shinohara S, Amemiya H, et al. Plasmacytoma of the testis. Urol Int. 1995;55(4):218-221.
67. Bude RO. Testicular plasmacytoma: appearance on gray-scale and power Doppler sonography. J Clin Ultrasound. 1999;27(6):345-346.
68. Avitable AM, Gansler TS, Tomaszewski JE, et al. Testicular plasmacytoma. Urology. 1989;34(1):51-54.
69. Grignon DJ, Shum DT, Hayman WP. Metastatic tumours of the testes. Can J Surg. 1986;29(5):359-361.
70. Werth V, Yu G, Marshall FF. Nonlymphomatous metastatic tumor to the testis. J Urol. 1982;127(1):142-144.
71. Hanash KA, Carney JA, Kelalis PP. Metastatic tumors to testicles: routes of metastasis. J Urol. 1969;102(4):465-468.
72. Hamm B, Fobbe F, Loy V. Testicular cysts: differentiation with US and clinical findings. Radiology. 1988;168(1):19-23.
73. Shergill IS, Thwaini A, Kapasi F, et al. Management of simple intratesticular cysts: a single-institution 11-year experience. Urology. 2006;67(6): 1266-1268.
74. Martinez-Berganza MT, Sarria L, Cozcolluela R, et al. Cysts of the tunica albuginea: sonographic appearance. AJR Am J Roentgenol. 1998;170(1): 183-185.
75. Dogra VS, Gottlieb RH, Rubens DJ, Liao L. Benign intratesticular cystic lesions: US features. Radiographics. 2001;21:S273-S281.
76. Warner KE, Noyes DT, Ross JS. Cysts of the tunica albuginea testis: a report of 3 cases with a review of the literature. J Urol. 1984;132(1):131-132.

77. Poster RB, Spirt BA, Tamsen A, Surya BV. Complex tunica albuginea cyst simulating an intratesticular lesion. Urol Radiol. 1991;13(2):129-132.
78. Sudakoff GS, Quiroz F, Karcaaltincaba M, Foley WD. Scrotal ultrasonography with emphasis on the extratesticular space: anatomy, embryology, and pathology. Ultrasound Q. 2002;18(4):255-273.
79. Takihara H, Valvo JR, Tokuhara M, Cockett AT. Intratesticular cysts. Urology. 1982;20(1):80-82.
80. Tartar VM, Trambert MA, Balsara ZN, Mattrey RF. Tubular ectasia of the testicle: sonographic and MR imaging appearance. AJR Am J Roentgenol. 1993;160(3):539-542.
81. Brown DL, Benson CB, Doherty FJ, et al. Cystic testicular mass caused by dilated rete testis: sonographic findings in 31 cases. AJR Am J Roentgenol. 1992;158(6):1257-1259.
82. Weingarten BJ, Kellman GM, Middleton WD, Gross ML. Tubular ectasia within the mediastinum testis. J Ultrasound Med. 1992;11(7):349-353.
83. Older RA, Watson LR. Tubular ectasia of the rete testis: a benign condition with a sonographic appearance that may be misinterpreted as malignant. J Urol. 1994;152(2 Pt 1):477-478.
84. Cho CS, Kosek J. Cystic dysplasia of the testis: sonographic and pathologic findings. Radiology. 1985;156(3):777-778.
85. Keetch DW, McAlister WH, Manley CB, Dehner LP. Cystic dysplasia of the testis. Sonographic features with pathologic correlation. Pediatr Radiol. 1991;21(7):501-503.
86. Atchley JT, Dewbury KC. Ultrasound appearances of testicular epidermoid cysts. Clin Radiol. 2000;55(7):493-502.
87. Bruni SG, Glanc P. Bilateral epidermoid cysts of the testes: a characteristic appearance on ultrasonography. Ultrasound Q. 2015;31(3):205-207.
88. Sanderson AJ, Birch BR, Dewbury KC. Case report: multiple epidermoid cysts of the testes—the ultrasound appearances. Clin Radiol. 1995;50(6):414-415.
89. Malvica RP. Epidermoid cyst of the testicle: an unusual sonographic finding. AJR Am J Roentgenol. 1993;160(5):1047-1048.
90. Stein MM, Stein MW, Cohen BC, et al. Unusual sonographic appearance of an epidermoid cyst of the testis. J Ultrasound Med. 1999;18(10):723-726.
91. Maizlin ZV, Belenky A, Baniel J, et al. Epidermoid cyst and teratoma of the testis: sonographic and histologic similarities. J Ultrasound Med. 2005;24(10):1403-1409.
92. Eisenmenger M, Lang S, Donner G, et al. Epidermoid cysts of the testis: organ-preserving surgery following diagnosis by ultrasonography. Br J Urol. 1993;72(6):955-957.
93. Cho JH, Chang JC, Park BH, et al. Sonographic and MR imaging findings of testicular epidermoid cysts. AJR Am J Roentgenol. 2002;178(3):743-748.
94. Langer JE, Ramchandani P, Siegelman ES, Banner MP. Epidermoid cysts of the testicle: sonographic and MR imaging features. AJR Am J Roentgenol. 1999;173(5):1295-1299.
95. Hermansen MC, Chusid MJ, Sty JR. Bacterial epididymo-orchitis in children and adolescents. Clin Pediatr (Phila). 1980;19(12):812-815.
96. Korn RL, Langer JE, Nisenbaum HL, et al. Non-Hodgkin's lymphoma mimicking a scrotal abscess in a patient with AIDS. J Ultrasound Med. 1994;13(9):715-718.
97. Smith FJ, Bilbey JH, Filipenko JD, Goldenberg SL. Testicular pseudotumor in the acquired immunodeficiency syndrome. Urology. 1995;45(3):535-537.
98. Wu VH, Dangman BC, Kaufman Jr RP. Sonographic appearance of acute testicular venous infarction in a patient with a hypercoagulable state. J Ultrasound Med. 1995;14(1):57-59.
99. Bilagi P, Sriprasad S, Clarke JL, et al. Clinical and ultrasound features of segmental testicular infarction: six-year experience from a single centre. Eur Radiol. 2007;17(11):2810-2818.
100. Flanagan JJ, Fowler RC. Testicular infarction mimicking tumour on scrotal ultrasound—a potential pitfall. Clin Radiol. 1995;50(1):49-50.
101. Einstein DM, Paushter DM, Singer AA, et al. Fibrotic lesions of the testicle: sonographic patterns mimicking malignancy. Urol Radiol. 1992;14(3):205-210.
102. Ledwidge ME, Lee DK, Winter 3rd TC, et al. Sonographic diagnosis of superior hemispheric testicular infarction. AJR Am J Roentgenol. 2002;179(3):775-776.
103. Sriprasad S, Kooiman GG, Muir GH, Sidhu PS. Acute segmental testicular infarction: differentiation from tumour using high frequency colour Doppler ultrasound. Br J Radiol. 2001;74(886):965-967.
104. Mevorach RA, Lerner RM, Dvoretsky PM, Rabinowitz R. Testicular abscess: diagnosis by ultrasonography. J Urol. 1986;136(6):1213-1216.
105. Thompson JP, Bhatt S, Rubens D. Identify before orchiectomy: segmental testicular infarct. Ultrasound Q. 2015;31(3):198-201.
106. Avila NA, Premkumar A, Shawker TH, et al. Testicular adrenal rest tissue in congenital adrenal hyperplasia: findings at gray-scale and color Doppler US. Radiology. 1996;198(1):99-104.
107. Vanzulli A, DelMaschio A, Paesano P, et al. Testicular masses in association with adrenogenital syndrome: US findings. Radiology. 1992;183(2):425-429.
108. Shawker TH, Doppman JL, Choyke PL, et al. Intratesticular masses associated with abnormally functioning adrenal glands. J Clin Ultrasound. 1992;20(1):51-58.
109. Seidenwurm D, Smathers RL, Kan P, Hoffman A. Intratesticular adrenal rests diagnosed by ultrasound. Radiology. 1985;155(2):479-481.
110. Bhatt S, Dogra VS. Role of US in testicular and scrotal trauma. Radiographics. 2008;28(6):1617-1629.
111. Gierke CL, King BF, Bostwick DG, et al. Large-cell calcifying Sertoli cell tumor of the testis: appearance at sonography. AJR Am J Roentgenol. 1994;163(2):373-375.
112. Vegni-Talluri M, Bigliardi E, Vanni MG, Tota G. Testicular microliths: their origin and structure. J Urol. 1980;124(1):105-107.
113. Bieger RC, Passarge E, McAdams AJ. Testicular intratubular bodies. J Clin Endocrinol Metab. 1965;25(10):1340-1346.
114. Middleton WD, Teefey SA, Santillan CS. Testicular microlithiasis: prospective analysis of prevalence and associated tumor. Radiology. 2002;224(2):425-428.
115. Kim B, Winter 3rd TC, Ryu JA. Testicular microlithiasis: clinical significance and review of the literature. Eur Radiol. 2003;13(12):2567-2576.
116. Nistal M, Paniagua R, Diez-Pardo JA. Testicular microlithiasis in 2 children with bilateral cryptorchidism. J Urol. 1979;121(4):535-537.
117. Janzen DL, Mathieson JR, Marsh JI, et al. Testicular microlithiasis: sonographic and clinical features. AJR Am J Roentgenol. 1992;158(5):1057-1060.
118. Backus ML, Mack LA, Middleton WD, et al. Testicular microlithiasis: imaging appearances and pathologic correlation. Radiology. 1994;192(3):781-785.
119. Dagash H, Mackinnon EA. Testicular microlithiasis: what does it mean clinically? BJU Int. 2007;99(1):157-160.
120. Lam DL, Gerscovich EO, Kuo MC, McGahan JP. Testicular microlithiasis: our experience of 10 years. J Ultrasound Med. 2007;26(7):867-873.
121. Winter TC, Kim B, Lowrance W, Middleton W. Testicular microlithiasis: what should you recommend? AJR Am J Roentgenol. 2016;206(6):1164-1169.
122. Nye PJ, Prati Jr RC. Idiopathic hydrocele and absent testicular diastolic flow. J Clin Ultrasound. 1997;25(1):43-46.
123. Worthy L, Miller EI, Chinn DH. Evaluation of extratesticular findings in scrotal neoplasms. J Ultrasound Med. 1986;5(5):261-263.
124. Gooding GA, Leonhardt WC, Marshall G, et al. Cholesterol crystals in hydroceles: sonographic detection and possible significance. AJR Am J Roentgenol. 1997;169(2):527-529.
125. Rathaus V, Konen O, Shapiro M, et al. Ultrasound features of spermatic cord hydrocele in children. Br J Radiol. 2001;74(885):818-820.
126. Cunningham JJ. Sonographic findings in clinically unsuspected acute and chronic scrotal hematoceles. AJR Am J Roentgenol. 1983;140(4):749-752.
127. Sung T, Riedlinger WF, Diamond DA, Chow JS. Solid extratesticular masses in children: radiographic and pathologic correlation. AJR Am J Roentgenol. 2006;186(2):483-490.
128. Fitzgibbons Jr RJ, Forse RA. Clinical practice. Groin hernias in adults. N Engl J Med. 2015;372(8):756-763.
129. Bhosale PR, Patnana M, Viswanathan C, Szklaruk J. The inguinal canal: anatomy and imaging features of common and uncommon masses. Radiographics. 2008;28(3):819-835.

130. Linkowski GD, Avellone A, Gooding GA. Scrotal calculi: sonographic detection. Radiology. 1985;156(2):484.
131. Kim ED, Lipshultz LI. Role of ultrasound in the assessment of male infertility. J Clin Ultrasound. 1996;24(8):437-453.
132. Beddy P, Geoghegan T, Browne RF, Torreggiani WC. Testicular varicoceles. Clin Radiol. 2005;60(12):1248-1255.
133. Zucchi A, Mearini L, Mearini E, et al. Varicocele and fertility: relationship between testicular volume and seminal parameters before and after treatment. J Androl. 2006;27(4):548-551.
134. Gonda Jr RL, Karo JJ, Forte RA, O'Donnell KT. Diagnosis of subclinical varicocele in infertility. AJR Am J Roentgenol. 1987;148(1):71-75.
135. Doherty FJ. Ultrasound of the nonacute scrotum. Semin Ultrasound CT MR. 1991;12(2):131-156.
136. Graif M, Hauser R, Hirshebein A, et al. Varicocele and the testicular-renal venous route: hemodynamic Doppler sonographic investigation. J Ultrasound Med. 2000;19(9):627-631.
137. Howards SS. Treatment of male infertility. N Engl J Med. 1995; 332(5):312-317.
138. Tétreau R, Julian P, Lyonnet D, Rouvière O. Intratesticular varicocele: an easy diagnosis but unclear physiopathologic characteristics. J Ultrasound Med. 2007;26(12):1767-1773.
139. Atasoy C, Fitoz S. Gray-scale and color Doppler sonographic findings in intratesticular varicocele. J Clin Ultrasound. 2001;29(7):369-373.
140. Krainik A, Sarrazin JL, Camparo P, et al. Fibrous pseudotumor of the epididymis: imaging and pathologic correlation. Eur Radiol. 2000;10(10): 1636-1638.
141. al-Otaibi L, Whitman GJ, Chew FS. Fibrous pseudotumor of the epididymis. AJR Am J Roentgenol. 1997;168(6):1586.
142. Oliva E, Young RH. Paratesticular tumor-like lesions. Semin Diagn Pathol. 2000;17(4):340-358.
143. Thum G. Polyorchidism: case report and review of literature. J Urol. 1991;145(2):370-372.
144. Leung ML, Gooding GA, Williams RD. High-resolution sonography of scrotal contents in asymptomatic subjects. AJR Am J Roentgenol. 1984;143(1):161-164.
145. Pavone-Macaluso M, Smith PH, Bagshaw MA, editors. Testicular cancer and other tumors of the genitourinary tract. New York: Plenum Press; 1985.
146. Smallman LA, Odedra JK. Primary carcinoma of sigmoid colon metastasizing to epididymis. Urology. 1984;23(6):598-599.
147. Wachtel TL, Mehan DJ. Metastatic tumors of the epididymis. J Urol. 1970;103(5):624-627.
148. Yang DM, Kim SH, Kim HN, et al. Differential diagnosis of focal epididymal lesions with gray scale sonographic, color Doppler sonographic, and clinical features. J Ultrasound Med. 2003;22(2):135-142.
149. Oh C, Nisenbaum HL, Langer J, et al. Sonographic demonstration, including color Doppler imaging, of recurrent sperm granuloma. J Ultrasound Med. 2000;19(5):333-335.
150. Reddy NM, Gerscovich EO, Jain KA, et al. Vasectomy-related changes on sonographic examination of the scrotum. J Clin Ultrasound. 2004;32(8):394-398.
151. Ishigami K, Abu-Yousef MM, El-Zein Y. Tubular ectasia of the epididymis: a sign of postvasectomy status. J Clin Ultrasound. 2005;33(9):447-451.
152. Stewart VR, Sidhu PS. The testis: the unusual, the rare and the bizarre. Clin Radiol. 2007;62(4):289-302.
153. Chung JJ, Kim MJ, Lee T, et al. Sonographic findings in tuberculous epididymitis and epididymo-orchitis. J Clin Ultrasound. 1997;25(7): 390-394.
154. Carmody JP, Sharma OP. Intrascrotal sarcoidosis: case reports and review. Sarcoidosis Vasc Diffuse Lung Dis. 1996;13(2):129-134.
155. Winter 3rd TC, Keener TS, Mack LA. Sonographic appearance of testicular sarcoid. J Ultrasound Med. 1995;14(2):153-156.
156. Eraso CE, Vrachliotis TG, Cunningham JJ. Sonographic findings in testicular sarcoidosis simulating malignant nodule. J Clin Ultrasound. 1999;27(2): 81-83.
157. Mueller DL, Amundson GM, Rubin SZ, Wesenberg RL. Acute scrotal abnormalities in children: diagnosis by combined sonography and scintigraphy. AJR Am J Roentgenol. 1988;150(3):643-646.
158. Watanabe Y, Dohke M, Ohkubo K, et al. Scrotal disorders: evaluation of testicular enhancement patterns at dynamic contrast-enhanced subtraction MR imaging. Radiology. 2000;217(1):219-227.
159. Hricak H, Lue T, Filly RA, et al. Experimental study of the sonographic diagnosis of testicular torsion. J Ultrasound Med. 1983;2(8):349-356.
160. Pillai SB, Besner GE. Pediatric testicular problems. Pediatr Clin North Am. 1998;45(4):813-830.
161. Prando D. Torsion of the spermatic cord: sonographic diagnosis. Ultrasound Q. 2002;18(1):41-57.
162. Lerner RM, Mevorach RA, Hulbert WC, Rabinowitz R. Color Doppler US in the evaluation of acute scrotal disease. Radiology. 1990;176(2): 355-358.
163. Horstman WG, Middleton WD, Melson GL, Siegel BA. Color Doppler US of the scrotum. Radiographics. 1991;11(6):941-957.
164. Middleton WD, Siegel BA, Melson GL, et al. Acute scrotal disorders: prospective comparison of color Doppler US and testicular scintigraphy. Radiology. 1990;177(1):177-181.
165. Sidhu PS. Clinical and imaging features of testicular torsion: role of ultrasound. Clin Radiol. 1999;54(6):343-352.
166. Middleton WD, Middleton MA, Dierks M, et al. Sonographic prediction of viability in testicular torsion: preliminary observations. J Ultrasound Med. 1997;16(1):23-27.
167. Middleton WD, Melson GL. Testicular ischemia: color Doppler sonographic findings in five patients. AJR Am J Roentgenol. 1989;152(6): 1237-1239.
168. Chinn DH, Miller EI. Generalized testicular hyperechogenicity in acute testicular torsion. J Ultrasound Med. 1985;4(9):495-496.
169. Winter TC. Ultrasonography of the scrotum. App Radiol. 2002;31:3.
170. Vijayaraghavan SB. Sonographic differential diagnosis of acute scrotum: real-time whirlpool sign, a key sign of torsion. J Ultrasound Med. 2006;25(5): 563-574.
171. Trambert MA, Mattrey RF, Levine D, Berthoty DP. Subacute scrotal pain: evaluation of torsion versus epididymitis with MR imaging. Radiology. 1990;175(1):53-56.
172. Vick CW, Bird K, Rosenfield AT, et al. Extratesticular hemorrhage associated with torsion of the spermatic cord: sonographic demonstration. Radiology. 1986;158(2):401-404.
173. Barth RA, Shortliffe LD. Normal pediatric testis: comparison of power Doppler and color Doppler US in the detection of blood flow. Radiology. 1997;204(2):389-393.
174. Bader TR, Kammerhuber F, Herneth AM. Testicular blood flow in boys as assessed at color Doppler and power Doppler sonography. Radiology. 1997;202(2):559-564.
175. Coley BD, Frush DP, Babcock DS, et al. Acute testicular torsion: comparison of unenhanced and contrast-enhanced power Doppler US, color Doppler US, and radionuclide imaging. Radiology. 1996;199(2):441-446.
176. Luker GD, Siegel MJ. Scrotal US in pediatric patients: comparison of power and standard color Doppler US. Radiology. 1996;198(2): 381-385.
177. Albrecht T, Lotzof K, Hussain HK, et al. Power Doppler US of the normal prepubertal testis: does it live up to its promises? Radiology. 1997;203(1): 227-231.
178. Lee Jr FT, Winter DB, Madsen FA, et al. Conventional color Doppler velocity sonography versus color Doppler energy sonography for the diagnosis of acute experimental torsion of the spermatic cord. AJR Am J Roentgenol. 1996;167(3):785-790.
179. Fitzgerald SW, Erickson S, DeWire DM, et al. Color Doppler sonography in the evaluation of the adult acute scrotum. J Ultrasound Med. 1992;11(10): 543-548.
180. Burks DD, Markey BJ, Burkhard TK, et al. Suspected testicular torsion and ischemia: evaluation with color Doppler sonography. Radiology. 1990;175(3):815-821.
181. Hedayati V, Sellars ME, Sharma DM, Sidhu PS. Contrast-enhanced ultrasound in testicular trauma: role in directing exploration, debridement and organ salvage. Br J Radiol. 2012;85(1011):e65-e68.
182. Atkinson Jr GO, Patrick LE, Ball Jr TI, et al. The normal and abnormal scrotum in children: evaluation with color Doppler sonography. AJR Am J Roentgenol. 1992;158(3):613-617.

183. Bude RO, Kennelly MJ, Adler RS, Rubin JM. Nonpulsatile arterial waveforms: observations during graded testicular torsion in rats. Acad Radiol. 1995;2(10):879-882.
184. Dogra VS, Rubens DJ, Gottlieb RH, Bhatt S. Torsion and beyond: new twists in spectral Doppler evaluation of the scrotum. J Ultrasound Med. 2004;23(8):1077-1085.
185. Sanelli PC, Burke BJ, Lee L. Color and spectral Doppler sonography of partial torsion of the spermatic cord. AJR Am J Roentgenol. 1999;172(1): 49-51.
186. Alcantara AL, Sethi Y. Imaging of testicular torsion and epididymitis/orchitis: diagnosis and pitfalls. Emerg Radiol. 1998;5:394-402.
187. Dresner ML. Torsed appendage. Diagnosis and management: blue dot sign. Urology. 1973;1(1):63-66.
188. Hesser U, Rosenborg M, Gierup J, et al. Gray-scale sonography in torsion of the testicular appendages. Pediatr Radiol. 1993;23(7):529-532.
189. Basekim CC, Kizilkaya E, Pekkafali Z, et al. Mumps epididymo-orchitis: sonography and color Doppler sonographic findings. Abdom Imaging. 2000;25(3):322-325.
190. Gondos B, Wong TW. Non-neoplastic diseases of the testis and epididymis. In: Murphy WM, editor. Urological pathology. 2nd ed. Philadelphia: Saunders; 1997. p. 277-341.
191. Horstman WG, Middleton WD, Melson GL. Scrotal inflammatory disease: color Doppler US findings. Radiology. 1991;179(1):55-59.
192. Cook JL, Dewbury K. The changes seen on high-resolution ultrasound in orchitis. Clin Radiol. 2000;55(1):13-18.
193. Hourihane DO. Infected infarcts of the testis: a study of 18 cases preceded by pyogenic epididymoorchitis. J Clin Pathol. 1970;23(8):668-675.
194. Sanders LM, Haber S, Dembner A, Aquino A. Significance of reversal of diastolic flow in the acute scrotum. J Ultrasound Med. 1994;13(2): 137-139.
195. Casalino DD, Kim R. Clinical importance of a unilateral striated pattern seen on sonography of the testicle. AJR Am J Roentgenol. 2002;178(4): 927-930.
196. Harris RD, Chouteau C, Partrick M, Schned A. Prevalence and significance of heterogeneous testes revealed on sonography: ex vivo sonographic-pathologic correlation. AJR Am J Roentgenol. 2000;175(2):347-352.
197. Eke N. Fournier's gangrene: a review of 1726 cases. Br J Surg. 2000;87(6): 718-728.
198. Jeffrey RB, Laing FC, Hricak H, McAninch JW. Sonography of testicular trauma. AJR Am J Roentgenol. 1983;141(5):993-995.
199. Kim SH, Park S, Choi SH, et al. Significant predictors for determination of testicular rupture on sonography: a prospective study. J Ultrasound Med. 2007;26(12):1649-1655.
200. Buckley JC, McAninch JW. Use of ultrasonography for the diagnosis of testicular injuries in blunt scrotal trauma. J Urol. 2006;175(1):175-178.
201. Cohen HL, Shapiro ML, Haller JO, Glassberg K. Sonography of intrascrotal hematomas simulating testicular rupture in adolescents. Pediatr Radiol. 1992;22(4):296-297.
202. Cass AS, Ferrara L, Wolpert J, Lee J. Bilateral testicular injury from external trauma. J Urol. 1988;140(6):1435-1436.
203. Learch TJ, Hansch LP, Ralls PW. Sonography in patients with gunshot wounds of the scrotum: imaging findings and their value. AJR Am J Roentgenol. 1995;165(4):879-883.
204. Gordon LM, Stein SM, Ralls PW. Traumatic epididymitis: evaluation with color Doppler sonography. AJR Am J Roentgenol. 1996;166(6): 1323-1325.
205. Elder JS. Cryptorchidism: isolated and associated with other genitourinary defects. Pediatr Clin North Am. 1987;34(4):1033-1053.
206. Harrison JH, Gittes RF, Stamey TA, et al. Campbell's urology. 4th ed. Philadelphia: Saunders; 1979.
207. Rosenfield AT, Blair DN, McCarthy S, et al. Society of Uroradiology Award paper. The pars infravaginalis gubernaculi: importance in the identification of the undescended testis. AJR Am J Roentgenol. 1989;153(4):775-778.
208. Friedland GW, Chang P. The role of imaging in the management of the impalpable undescended testis. AJR Am J Roentgenol. 1988;151(6): 1107-1111.
209. Fritzsche PJ, Hricak H, Kogan BA, et al. Undescended testis: value of MR imaging. Radiology. 1987;164(1):169-173.
210. Kier R, McCarthy S, Rosenfield AT, et al. Nonpalpable testes in young boys: evaluation with MR imaging. Radiology. 1988;169(2):429-433.

CHAPTER 23

Overview of Musculoskeletal Ultrasound Techniques and Applications

Colm McMahon and Corrie Yablon

SUMMARY OF KEY POINTS

- A wide variety of inflammatory, degenerative, traumatic, and neoplastic conditions can be imaged accurately and cost-effectively with ultrasound.
- Understanding optimal imaging techniques and recognizing and avoiding common artifacts is essential to musculoskeletal ultrasound.
- Ultrasound can provide higher-resolution imaging of nerves and tendons compared with standard clinical magnetic resonance imaging examinations.
- Dynamic imaging may be performed with ultrasound, which can assist in the diagnosis of tendon and ligamentous injury.

CHAPTER OUTLINE

GENERAL CONSIDERATIONS
Doppler Imaging
Elastography
Extended Field of View Imaging
MUSCLES
TENDONS
LIGAMENTS
NERVES
JOINT ASSESSMENT
SOFT TISSUE MASSES
FOREIGN BODIES
SOFT TISSUE INFECTION
CONCLUSION

GENERAL CONSIDERATIONS

Ultrasound is becoming a central part of the diagnostic pathway for patients with musculoskeletal complaints. In many cases, ultrasound is performed as an alternative or complement to magnetic resonance imaging (MRI). Ultrasound has several advantages over MRI that have been described in the literature, succinctly by Nazarian in a 2008 perspective article.[1] Ultrasound is well tolerated by patients and can be performed in those with contraindications to MRI, such as implanted cardiac devices or other MRI-incompatible implants, large size, or claustrophobia. Ultrasound examinations often take less time to perform than the corresponding MRI examinations. Ultrasound provides higher-resolution imaging of tendons and ligaments than routine musculoskeletal MRI. Ultrasound also provides the ability to image dynamically, which can be important in the diagnosis of disorders of impingement and subluxation of nerves or tendons. It is excellent at determining the fundamental tissue characterization of solid versus cystic in the setting of a mass lesion—this type of characterization may otherwise require the administration of intravenous contrast when MRI is used to distinguish a T2-hyperintense solid mass from a simple cyst. In many cases, patients can be given results at the time of their examination.

As a general rule, a systematic approach to musculoskeletal ultrasound examination of the joints using defined protocols is preferred to a focal examination when time permits. Focused imaging of symptomatic areas of concern adds additional diagnostic information to the routine protocol.[2] When evaluating a foreign body or palpable soft tissue mass, focal assessment can be performed, with attention to the relationship to nearby anatomic structures, critical to treatment planning. As with MRI interpretation, it is imperative that the radiologist have a clear understanding of musculoskeletal anatomy before performing or interpreting a sonographic examination, especially when previous studies are not available for comparison.

High-frequency linear ultrasound probes (12-15 MHz) are recommended for musculoskeletal imaging. Higher-frequency probes (15-17 MHz) can be helpful for evaluating superficial anatomy, for example, ligaments and tendons in the fingers. Hockey stick–style high-frequency probes can be very useful for evaluation of fine structures, providing focused small field of view images and permitting good skin contact in the peripheral extremities. Lower-frequency (3-9 MHz) linear probes may be

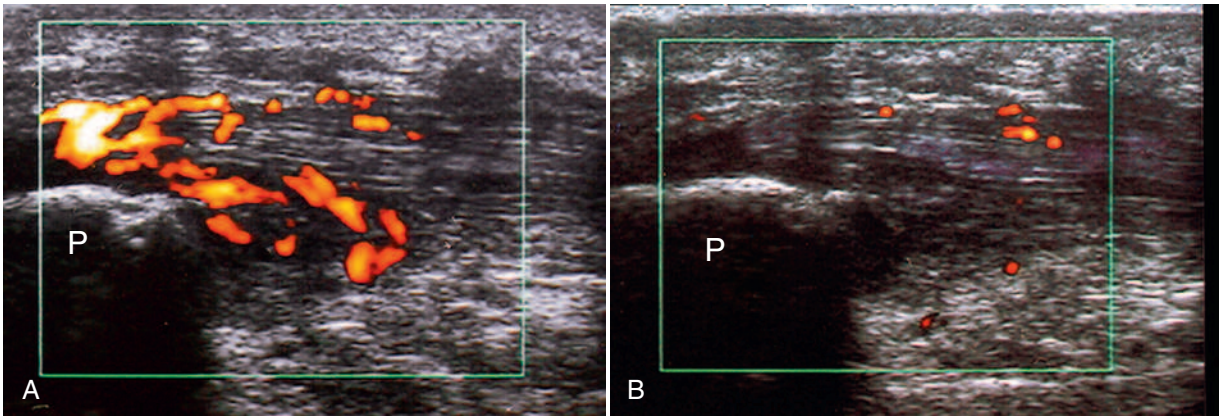

FIG. 23.1 Effect of Examination Technique on Power Doppler Findings. (A) Longitudinal sonogram obtained without pressure exerted on the tendon shows hypervascularity. **(B)** Longitudinal sonogram obtained with the usual pressure on the transducer shows the near complete disappearance of hypervascularity. *P,* Patella.

needed for greater tissue penetration in deeper structure evaluation or when attempting to determine the relationships of a deep pathologic process to the underlying bone and muscle. Although lower-frequency probes provide deeper penetration of soft tissues, there is a corresponding trade-off of lower resolution. In some cases, a low-frequency curvilinear probe may be necessary (2-5 MHz), for example, in the evaluation of the thigh and hip region or the examination of deep thigh or gluteal masses. By using more than one probe, the user may obtain complementary information about a single disease process. As is the case for all ultrasound imaging, careful attention to image optimization, such as positioning the focal zone at the appropriate depth, is important. Adequate ultrasound wave transduction is facilitated by good skin contact with the transducer and the use of ultrasound gel. A standoff pad can help for imaging very superficial structures.

Doppler Imaging

The role of Doppler imaging in musculoskeletal ultrasound includes characterization of neoplastic, inflammatory, and degenerative conditions.[3] Doppler ultrasound is helpful in confirming vascularization of solid masses in distinction from avascular cystic lesions. It is also helpful in characterization of inflammatory conditions, including synovitis, tenosynovitis, myositis, and soft tissue infection. Finally, tendon neovascularization is a sign occasionally seen with the development of degenerative tendinosis. As in other areas of the body, setting the appropriate Doppler gain is important, and imaging with a small sample volume will minimize motion artifacts. Because many structures of interest in musculoskeletal imaging are superficial, care should be taken to avoid excessive probe pressure during imaging, because this can limit flow detection in areas of vascularization (Fig. 23.1).

Elastography

An exciting recent development is imaging and quantification of tissue elasticity. This is defined by the tissue deformability and can be measured as a Young modulus for a given tissue expressed in kilopascals (kPa).[4] The range of Young modulus for musculoskeletal tissue ranges from 1 to 10 kPa. Depending on available hardware, ultrasound elastography may be performed using strain elastography or shear-wave elastography. In the musculoskeletal system, early application of elastography has shown substantial promise in the evaluation of tendinosis. In tendinosis, collagen disorganization and mucoid and lipoid degeneration result in tendon softening, which can be visualized and quantified with sonoelastography.[5] Other emerging applications include diagnosis of muscle disorders such as myositis[6] and characterization of soft tissue masses.[7]

Extended Field of View Imaging

Although high-resolution linear array probes are optimal for imaging relatively superficial musculoskeletal structures with fine anatomic detail, the overall field of view during imaging is limited. This may cause difficulty when viewing the images after acquisition, because the scale and anatomic position and orientation, which are intuitive when scanning real time, may be difficult to convey in the retained static images. This can be overcome by use of cine-clips and also with use of extended field of view (panorama) imaging. With this technique, an image is acquired while the probe is moved in the direction of the probe footprint long axis. The image acquired is a composite panoramic image of the anatomy scanned during the motion path of the probe. The scanners equipped with this technology recognize the degree of probe motion by the degree of frame shift during the movement of the probe. By utilizing knowledge of this motion vector, a blended image of successively acquired image frames during the probe sweep can be formed.[8] This technique can be extremely helpful in putting a specific finding in overall anatomic context, measuring a lesion that is larger than the probe field of view, and can also provide some diagnostic benefit—for example, in comparing the echogenicity and bulk of muscles of the rotator cuff.[9]

MUSCLES

Normal muscle is composed of multiple fascicles each embedded in perimysium, a thin layer of connective tissue and fat.[10] The

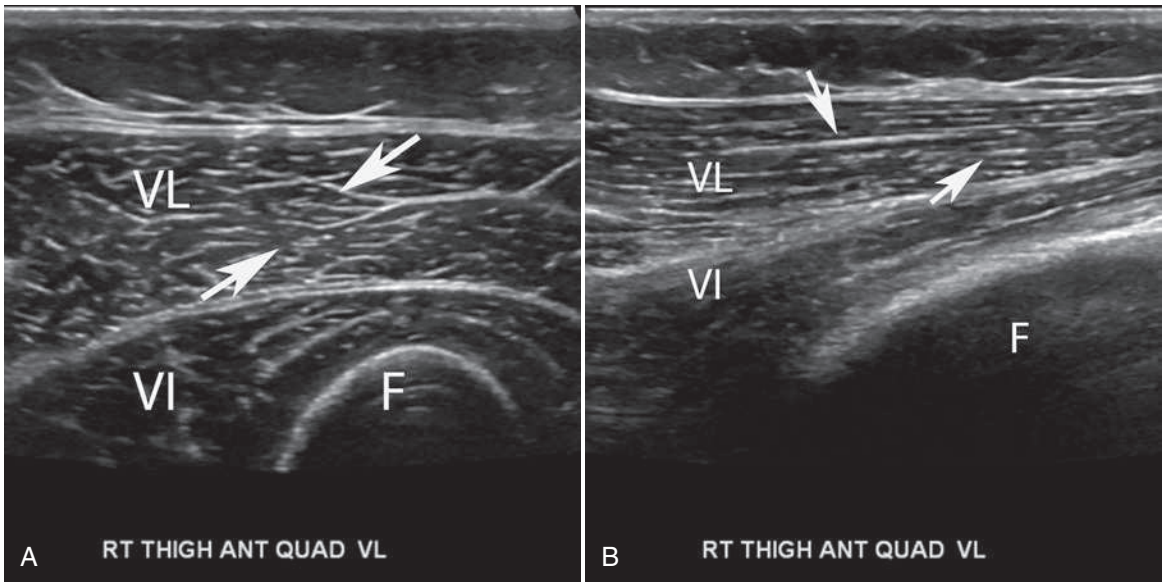

FIG. 23.2 Normal Muscle. (A) In short-axis view a normal vastus lateralis *(VL)* muscle demonstrates a speckled or "starry sky" appearance *(arrows).* **(B)** In long-axis view the normal muscle demonstrates a pennate appearance *(arrows). F,* Femur; *VI,* vastus intermedius.

ultrasound pattern of muscle is typically feathery, or pennate, with fiber orientation usually directed along the long axis of the muscle. In the short-axis view, the muscle fibers demonstrate a speckled appearance (Fig. 23.2). Fibers typically converge to the myotendinous junction and the muscle tapers in diameter at this point (Videos 23.1 and 23.2). A thin layer of fascia surrounds the muscle unit, separating it from adjacent muscles and subcutaneous fat. Muscle is usually overall hypoechoic, with more echogenic internal linear interfaces generated by the perimysium.

Muscle injuries of different grades can be identified with ultrasound.[11] A grade I injury is a minor strain and is depicted on ultrasound as just minimal fiber elongation and hypoechogenicity, but without detectible discontinuity. Ultrasound is less sensitive than MRI to these minor grades of injury, which are usually treated conservatively.[12] A grade II injury is a partial tear. Fiber discontinuity is seen, with a focal anechoic or hypoechoic gap, usually filled by more echogenic hematoma. Gentle probe pressure can demonstrate muscle fibers floating freely within fluid and hematoma, referred to as the "bell-clapper" sign. At the most severe end of the spectrum of muscle injury is a grade III injury, or complete tear (Fig. 23.3). In the case of a grade III injury, the muscle is completely interrupted with retraction of the muscle ends and an interposed gap, which should be measured. A large hematoma is expected in association with a complete tear.

A distinct form of muscle injury that deserves special mention is the avulsion of a muscle from its aponeurosis, a pattern of injury particularly common in the calf in the clinical spectrum of "tennis leg" (Fig. 23.4). In this injury the **medial gastrocnemius muscle** tears away from the aponeurosis with the underlying soleus muscle. Fluid and hematoma may dissect along the aponeurotic plane and there may be some retraction of the medial gastrocnemius. This usually occurs during forceful plantar flexion

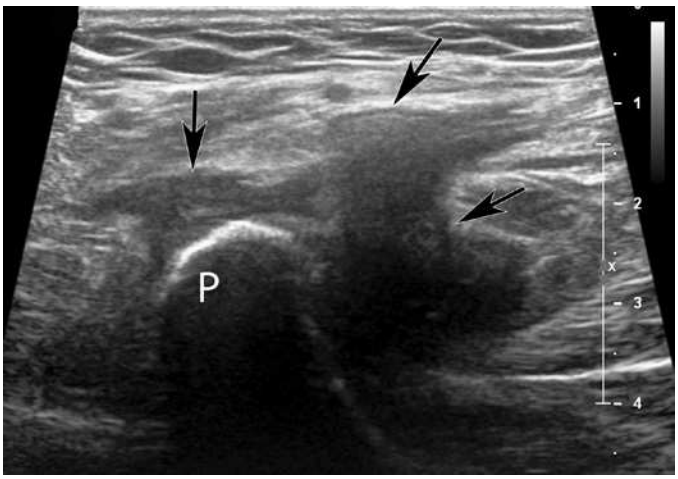

FIG. 23.3 Muscle Tear. Long-axis image of the medial groin region demonstrates hypoechoic fluid *(arrows)* at the pubic symphysis *(P)* origin of the adductor muscles, consistent with a grade III muscle tear.

during sports, for example, in a forceful lunge in tennis. This injury may be accompanied by a plantaris tendon tear.

Symptomatic **myofascial defects** lend themselves well to ultrasound evaluation. In this injury a defect in the muscular fascia allows herniation of muscle fibers, leading to a palpable and often painful mass (Fig. 23.5). In some cases, the patient may have associated neuropathy resulting from compression of adjacent nerves.[13] The mass may be more apparent to the patient during certain movements and activities that lead to muscle contraction, and these can be reproduced during scanning to assist in diagnosis. On ultrasound imaging, focused evaluation of the region of concern reveals focal bulging of muscle fibers through the otherwise smooth fascia. If this is equivocal or the patient reports symptoms only in certain positions such as

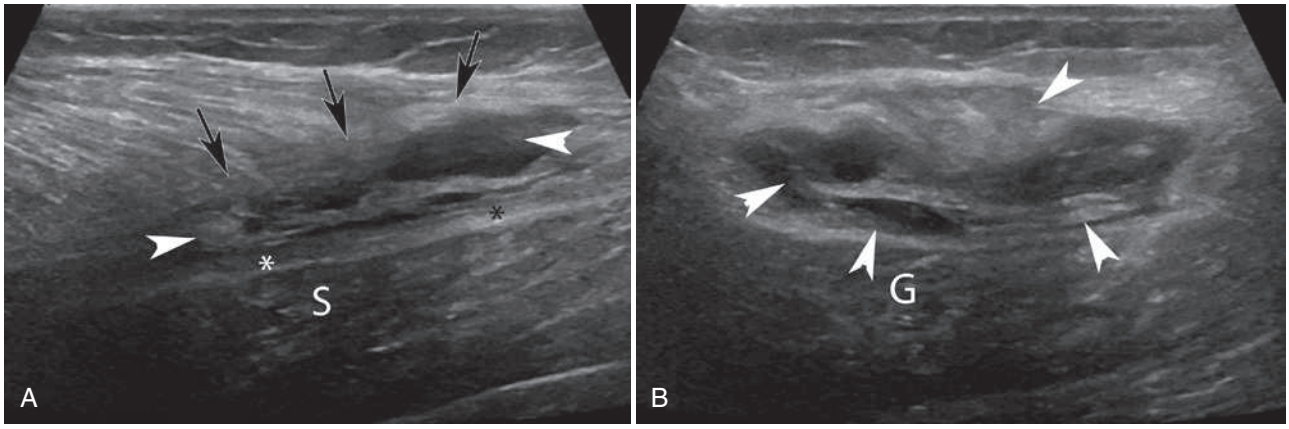

FIG. 23.4 Medial Head Gastrocnemius Tear From the Aponeurosis. (A) Long-axis image shows blunting and retraction of the medial head gastrocnemius fibers *(arrows)* from the aponeurosis (*) with an associated hematoma *(arrowheads)*. **(B)** Short-axis image shows effacement of the normal gastrocnemius muscle *(G)* architecture and a hematoma of mixed echogenicity at the site of the tear from the aponeurosis *(arrowheads)*. *S,* Soleus muscle.

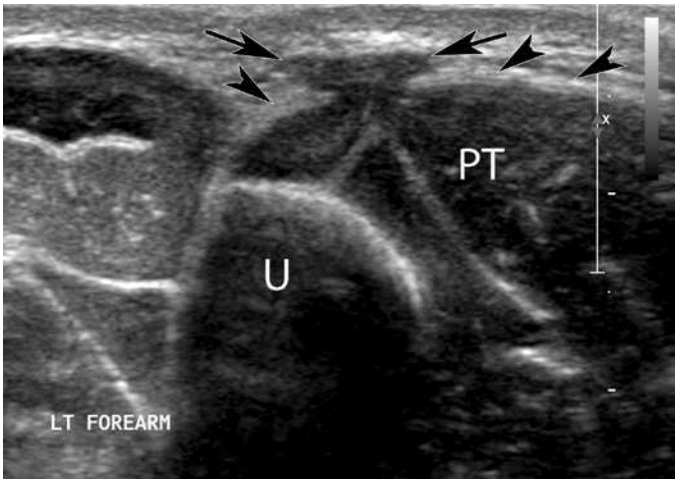

FIG. 23.5 Forearm Muscle Herniation. At the site of the palpable abnormality, there is focal herniation of a portion of the **pronator teres** muscle *(PT) (arrows)* through the muscle fascia *(arrowheads)*. This patient noticed a forearm bulge while weightlifting. *U,* Ulna.

standing, the area should be scanned with the patient reproducing the relevant position where possible.

Muscle atrophy can occur in response to denervation or chronic injury, for example, in the setting of a chronic complete rotator cuff tear. Muscle atrophy is characterized on ultrasound as a decrease in muscle bulk and a relative increase in echogenicity, reflecting replacement of muscle fibers with fatty tissue (Fig. 23.6). Comparison with adjacent muscles or the contralateral side can assist in subtle cases. As a result of increased echogenicity, the visibility of the central tendon at the myotendinous junction is diminished, and there is a loss of normal pennate pattern.[14]

TENDONS

Imaging the musculoskeletal system with ultrasound has built on early success in evaluation of tendons, with initial reports of Achilles tendon assessment.[15] Many tendons are ideally suited to ultrasound evaluation, as they are superficial and require the high-resolution imaging that ultrasound affords. Normal tendons are composed of longitudinally oriented bundles of collagen fibers, which give a highly organized echogenic linear fibrillar or striated pattern on ultrasound when viewed in long axis (Fig. 23.7). In short-axis view, normal tendons are usually smooth and ovoid in outline, with a homogenous stippled appearance, representing the tendon fibers viewed en face. Some tendons, such as the flexor and extensor tendons of the hand and wrist, are invested in a synovial lined sheath, whereas others, such as the Achilles tendon, are enveloped in a layer of loose areolar tissue called a **paratenon.**

It is critically important to understand the concept of **anisotropy** when performing the sonographic evaluation of tendons (Fig. 23.8). **Collagen bundles,** because of their smooth parallel organization within tendons, act as specular reflectors, such that sound waves are reflected in a single direction. When these specular reflectors are imaged with ultrasound, if the angle of insonation is not perpendicular to the tendon fibers, sound waves will be reflected away from the transducer, leading to the generation of an image with artifactual hypoechogenicity within the tendon.[16] This can be resolved by correcting the angle of insonation to 90 degrees when an area of hypoechogenicity is observed. The finding of focal persistent abnormal hypoechogenicity in a second plane with optimized imaging adds further corroboration to the observation of an apparent pathologic hypoechoic region.

Tendon injuries are usually caused by overuse and range from tendinosis to complete tear. The term **tendinosis** refers to intratendinous degeneration without tearing. Histologically, tendinosis consists of tendon expansion and loss of clear demarcation of collagen bundles, with increased mucoid ground substance among collagen bundles.[17] There is noninflammatory fibroblastic and myofibroblastic cellular proliferation. On ultrasound, tendinosis appears as an area of hypoechogenicity, without discontinuity, frequently associated with varying degrees of tendon thickening (Fig. 23.9). **Dystrophic calcification,** and even ossification, can be seen within affected tendons. An additional characteristic feature is the development of neovascularization,

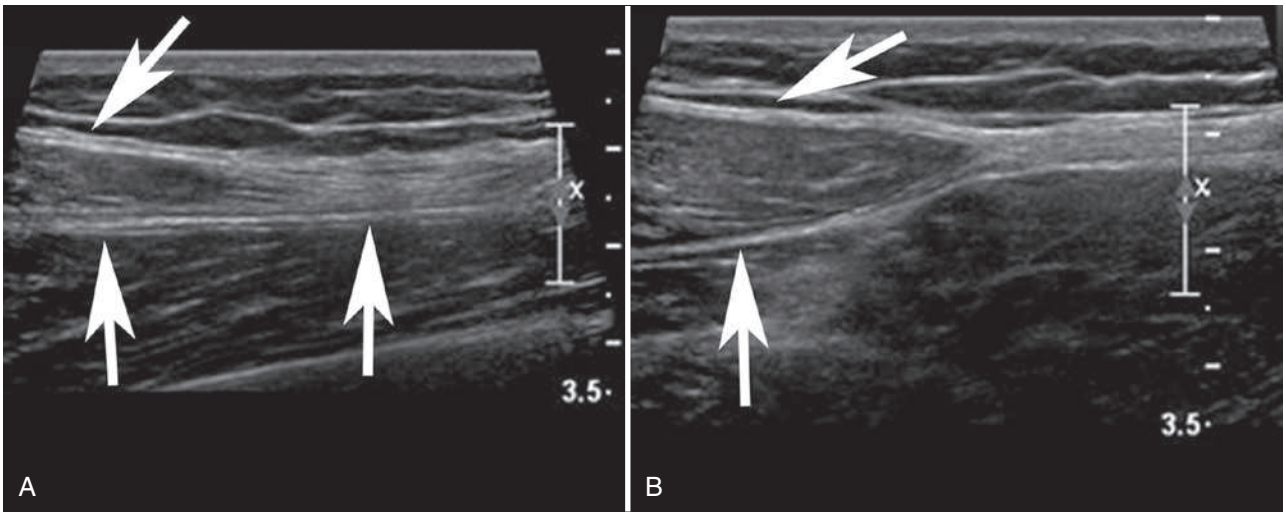

FIG. 23.6 Muscle Atrophy. Patient with a remote history of quadriceps injury presented with noticeable volume loss in his right anterior thigh. **(A)** Ultrasound of the abnormal right side shows marked volume loss in the rectus femoris muscle *(arrows)* with echogenic fatty infiltration of the remaining muscle. **(B)** The normal left side demonstrates normal muscle bulk and echotexture *(arrows).*

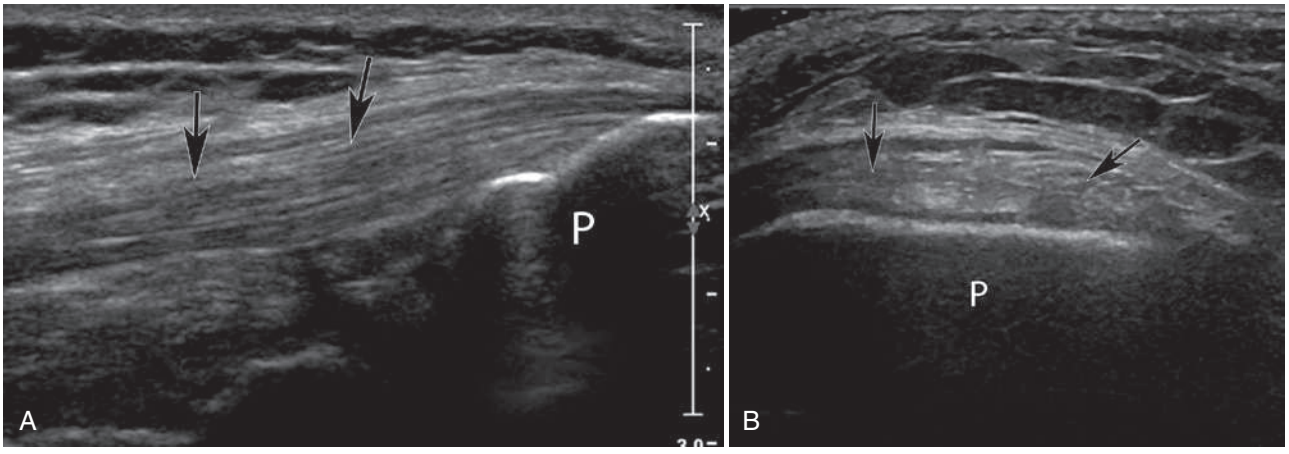

FIG. 23.7 Normal Quadriceps Tendon. (A) In long-axis view, the normal tendon demonstrates a fibrillar appearance *(arrows).* **(B)** In short-axis view, the tendon is ovoid and echogenic with a speckled appearance *(arrows). P,* Patella.

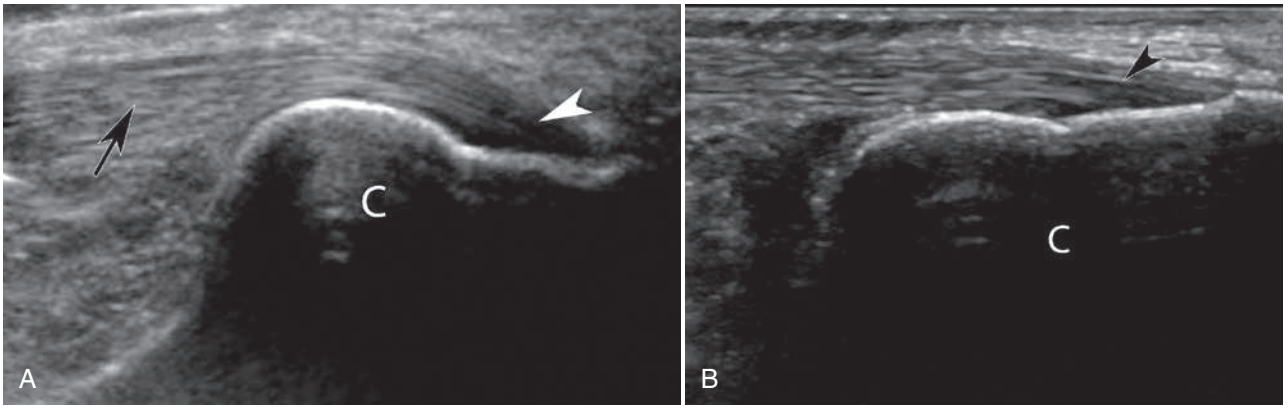

FIG. 23.8 Anisotropy. (A) In this long-axis scan of the Achilles insertion on the calcaneus, the proximal portion of the imaged tendon demonstrates a normal fibrillar appearance *(arrow),* whereas the distal tendon insertion is hypoechoic *(arrowhead).* **(B)** When the transducer is angled 90 degrees to the distal tendon insertion, the tendon then becomes fibrillar and is normal in appearance *(arrowhead). C,* Calcaneus.

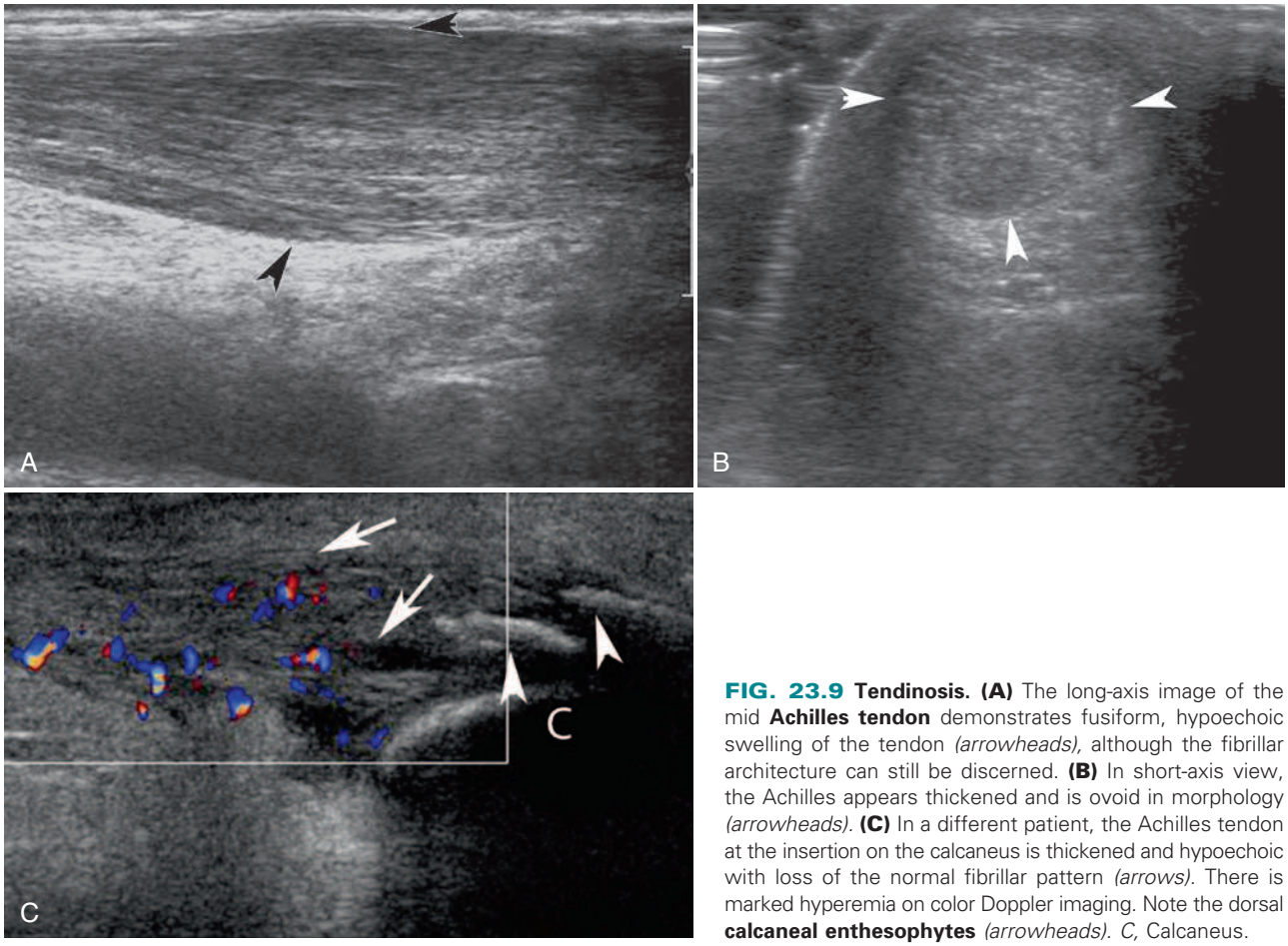

FIG. 23.9 Tendinosis. (A) The long-axis image of the mid **Achilles tendon** demonstrates fusiform, hypoechoic swelling of the tendon *(arrowheads),* although the fibrillar architecture can still be discerned. **(B)** In short-axis view, the Achilles appears thickened and is ovoid in morphology *(arrowheads).* **(C)** In a different patient, the Achilles tendon at the insertion on the calcaneus is thickened and hypoechoic with loss of the normal fibrillar pattern *(arrows).* There is marked hyperemia on color Doppler imaging. Note the dorsal **calcaneal enthesophytes** *(arrowheads). C,* Calcaneus.

which can be visualized on Doppler ultrasound in tendinosis but not in normal tendons.[18]

Tendinosis is common in the **Achilles tendon,** where it most commonly affects the midportion of the tendon, or "watershed," where there is overlapping blood supply. Tendon degeneration can also occur at the bone-tendon interface or enthesis, seen in the Achilles as insertional tendinosis at the calcaneus. Tendinosis at the tendon-bone interface is the most common pattern of degeneration seen in the common flexor and extensor origins at the medial and lateral humeral epicondyles at the elbow, forming part of the clinical spectrum of **epicondylitis.** Similar to tendinosis elsewhere, insertional tendinosis or enthesopathy is characterized by tendon expansion and hypoechogenicity.[19,20] Enthesitis, or inflammation at the enthesis, can occur in patients with rheumatoid arthritis, psoriatic arthritis, or spondyloarthropathy. The imaging features of enthesitis can overlap with tendinosis, with tendon expansion and hypoechogenicity, but neovascularization may be a more prominent feature and bony erosion may also be present.[21,22]

Patients with tendinosis are more prone to **tendon tears.** Tendon tears may be partial or complete. Partial tears may be transversely oriented (parallel to the short axis of the tendon) or longitudinally oriented (parallel to the long axis of the tendon, also referred to as a "longitudinal split tear"). Tears are manifested by anechoic or hypoechoic clefts, with focal tendon fiber discontinuity[23] (Fig. 23.10). When a complete rupture occurs, the tendon fibers are entirely discontinuous and some degree of tendon retraction may occur because of now-unopposed muscle contraction (Fig. 23.11). The extent of retraction is of importance for surgical planning and thus should be measured. In an acute tear, there may be complex fluid and hematoma within and about the tear site. When evaluating flexor and extensor tendons at the hand and wrist, passive and active motion can facilitate accurate identification of the tendon of interest and can provide mechanical correlation for the integrity of a tendon (Video 23.3).

Sonographic Signs of Tendon Tears

Discontinuity of fibers (partial or complete) with hypoechoic or anechoic gap
Focal thinning of the tendon
Hematoma (usually small)
Bone fragment (in cases of avulsion)
Nonvisualization of retracted tendon (in complete tear)

In tendons with surrounding tendon sheaths, inflammation of the tendon sheath **(tenosynovitis)** may occur as an overuse phenomenon or as a result of an inflammatory condition, such as rheumatoid arthritis. Tenosynovitis is manifest on ultrasound

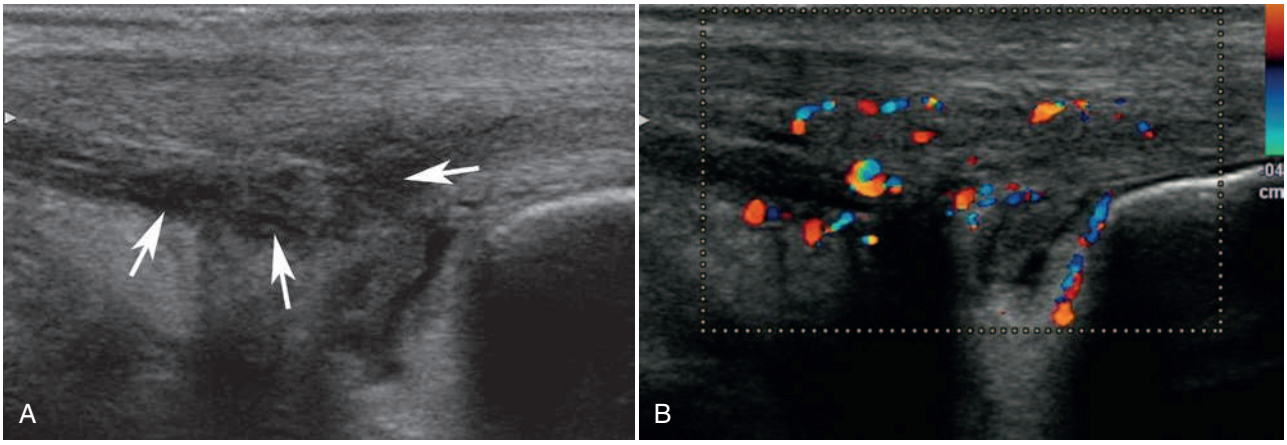

FIG. 23.10 Partial Tear of the Distal Achilles Tendon. (A) There is focal anechoic clefting of the anterior fibers of the Achilles distal insertion *(arrows)* although the posterior fibers remain intact. **(B)** Color Doppler imaging in the same patient demonstrates marked hyperemia in the injured tendon.

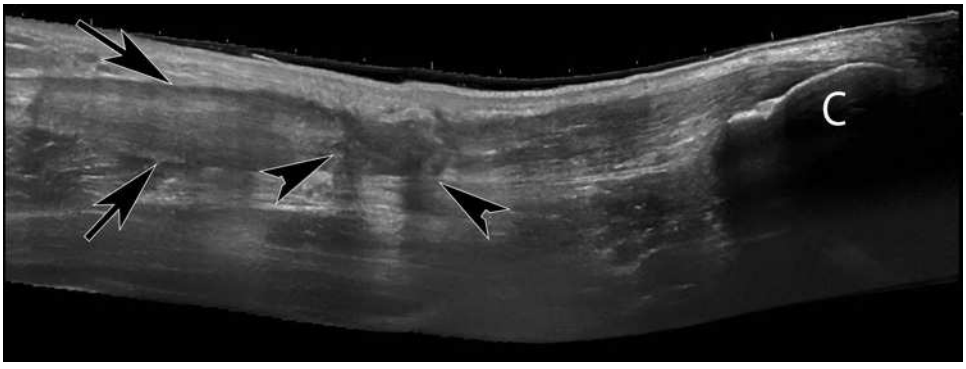

FIG. 23.11 Achilles Tendon Rupture. A panoramic view of the Achilles tendon demonstrates a rupture within the midportion of the tendon. The proximal aspect of the tendon is chronically thickened and hypoechoic *(arrows)*. Refraction artifact *(arrowheads)* is caused by the interfaces between the ruptured tendon edges and hemorrhage. *C,* Calcaneus.

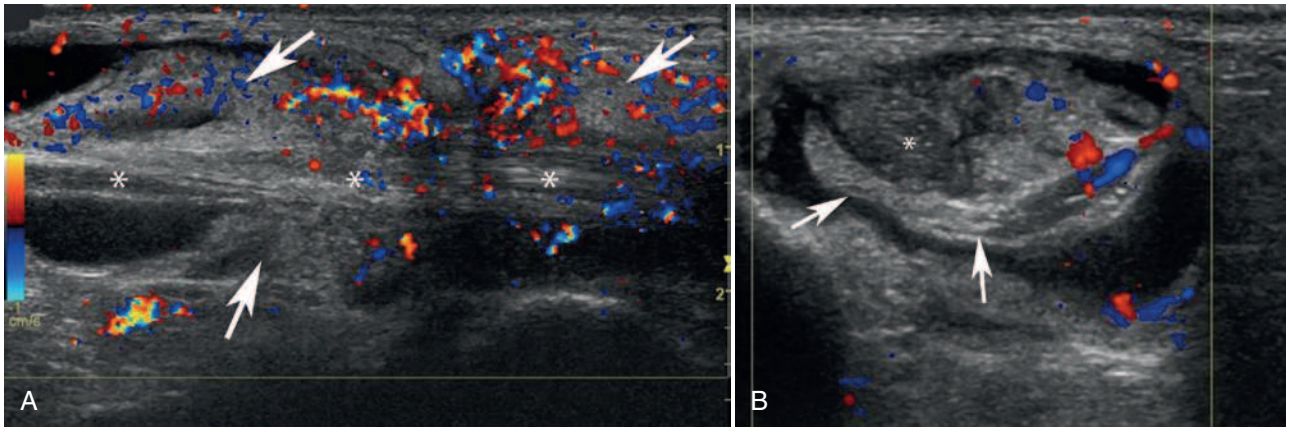

FIG. 23.12 Tenosynovitis. In this patient with rheumatoid arthritis and ankle pain, the peroneus brevis tendon (*) in long-axis **(A)** and short-axis **(B)** views is thickened and heterogeneous. The tendon sheath contains a large amount of echogenic synovium *(arrows),* hypoechoic fluid, and hyperemia on color Doppler imaging.

as an increase of fluid volume around a tendon within its sheath (Fig. 23.12). The tendon sheath itself can thicken and demonstrate hypervascularity on Doppler evaluation.[24] In patients with imaging findings of tenosynovitis and a history of penetrating injury or foreign body, septic tenosynovitis should be considered.[25]

LIGAMENTS

Ultrasound is an excellent technique for the evaluation of **ligamentous injuries,** with some advantages over MRI in this regard. Ultrasound permits high-resolution imaging of small ligaments

in planes that can be individualized to the structure of interest in any given patient, overcoming some intrinsic difficulties that can be encountered with scan plane prescription for MRI. In addition to static imaging, dynamic assessment may provide additional diagnostic information. Normal ligaments consist of interweaved bundles of collagen, extending between bones, usually restricting joint movements to prevent pathologic motion.[26] Ligament injury leads to pain and instability. Normal ligaments are linear bandlike structures and appear hyperechoic and fibrillar[27] (Fig. 23.13). Low-grade injuries consist of mild sprains, which typically have a good prognosis with conservative care. Mild sprains are characterized on ultrasound by swelling, hypoechogenicity, and some loss of fibrillar pattern (Fig. 23.14). Tears can be partial or complete. In the case of complete tears, there may be retraction of the torn ligament components from each other, a finding that can be exaggerated by dynamic imaging with stress maneuvers (Figs. 23.15 and 23.16). The use of stress maneuvers is somewhat controversial, however, because of concerns that a partial tear may be exacerbated or even converted to a complete tear by additional stress.[28,29]

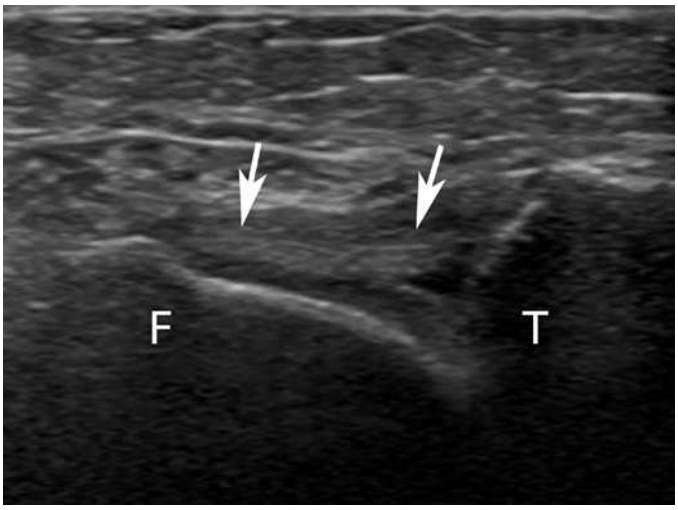

FIG. 23.13 Normal Anterior Talofibular Ligament. Note that the ligament *(arrows)* demonstrates a fibrillar appearance and that the fibers are more densely packed than those seen in a normal tendon. *F,* Fibula, *T,* talus.

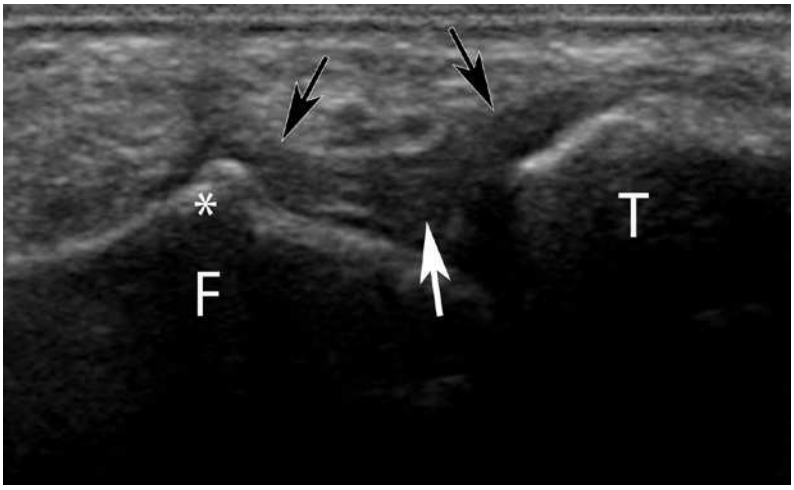

FIG. 23.14 Ligament Sprain. The anterior talofibular ligament *(arrows)* is diffusely thickened and hypoechoic, with intact fibers, consistent with sprain. Note the cortical irregularity at the lateral fibula (*) consistent with prior avulsion. *F,* Fibula, *T,* talus.

FIG. 23.15 Chronic Ligament Rupture. In this patient with a history of multiple ankle sprains, the anterior talofibular ligament is absent and the joint is widened on dynamic stress maneuver. Hypoechoic fluid (*) appears in the lateral recess. *F,* Fibula, *T,* talus.

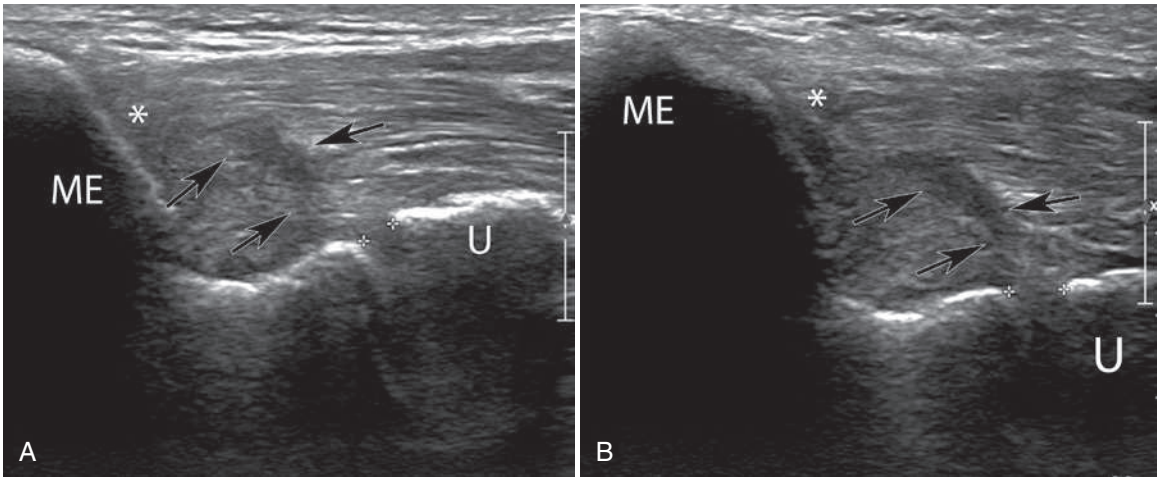

FIG. 23.16 Elbow Joint Widening on Dynamic Valgus Stress. (A) The medial joint is 2 mm *(calipers)* wide at rest in this patient with an ulnar collateral ligament (UCL) tear. Note the UCL is markedly thickened at the proximal humeral attachment and a hypoechoic cleft is present within the ligament consistent with a tear *(arrows)*. **(B)** With valgus stress, the medial joint space widens to 4 mm, confirming the presence of a UCL tear. The overlying common extensor tendon (*) is intact. *ME,* Medial epicondyle of the humerus; *U,* ulna.

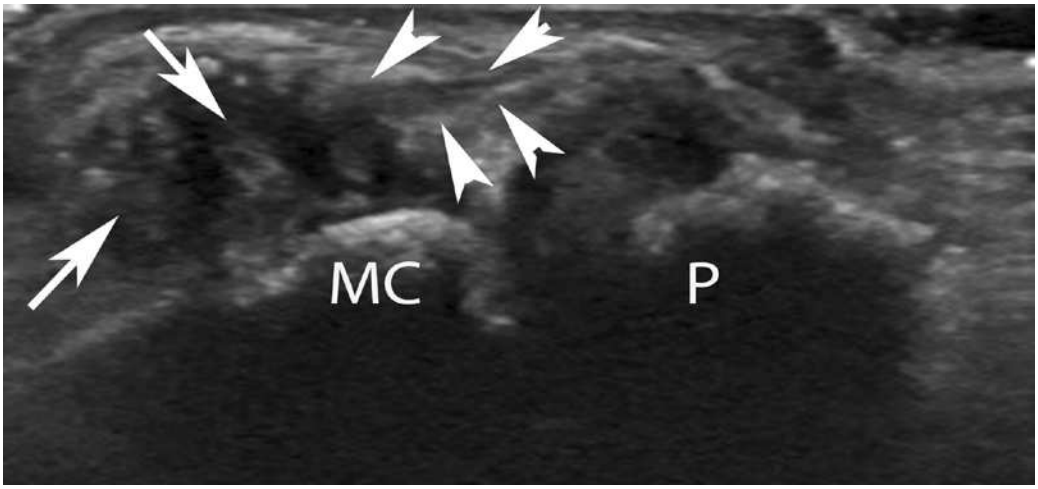

FIG. 23.17 Stener Lesion. The ulnar collateral ligament *(arrows)* of the thumb is torn and the stump is retracted proximal to the metacarpophalangeal joint and to the adductor aponeurosis *(arrowheads),* which is thickened and hypoechoic. *MC,* Metacarpal; *P,* proximal phalanx.

Ultrasound has been effectively utilized to diagnose injury of ligaments at the hand and wrist, notably the ulnar collateral ligament of the thumb metacarpophalangeal joint[28-30] in addition to the scapholunate ligament.[31] Other ligaments, such as the anterior oblique ligament of the thumb, have been identified with ultrasound, but the role of ultrasound in diagnosis has yet to be defined.[32,33] Ultrasound may also be used to evaluate the collateral ligaments of the elbow,[34-39] ankle ligaments,[40] and collateral ligaments of the knee.[41]

When evaluating ligamentous injury, it is important to assess nearby structures such as tendons, which may also have been injured (e.g., common flexor tendon origin injury in the setting of ulnar collateral ligament injury at the elbow) or which may be relevant to the ligamentous injury, as in the case of a **Stener lesion.** A Stener lesion occurs when a thumb metacarpal phalangeal ulnar collateral ligament tear entraps the adductor aponeurosis such that the ligament lies superficial to the aponeurosis (Fig. 23.17). This injury is important to recognize, as the treatment is surgical. The appearance of a Stener lesion on ultrasound is of retracted hypoechoic ligament fibers displaced over the linear aponeurosis, giving rise to the **"yo-yo on a string"** appearance.[28]

NERVES

Normal **peripheral nerves** are well visualized with high-resolution ultrasound. Nerves have a characteristic honeycomb morphology on ultrasound when imaged in short axis[42] (Fig. 23.18). Nerves are tubular structures, and on longitudinal axis, they demonstrate an internal striated pattern, somewhat similar to tendons but with a coarser pattern referred to as a "fascicular pattern."[43,44] This pattern consists of alternating internal hypoechoic and hyperechoic linear components. The hypoechoic components represent **fascicles** or groups of fascicles, whereas the hyperechoic parts correspond with the **epineurium.**[44] The epineurium consists of connective tissue that surrounds nerve fascicles, composed

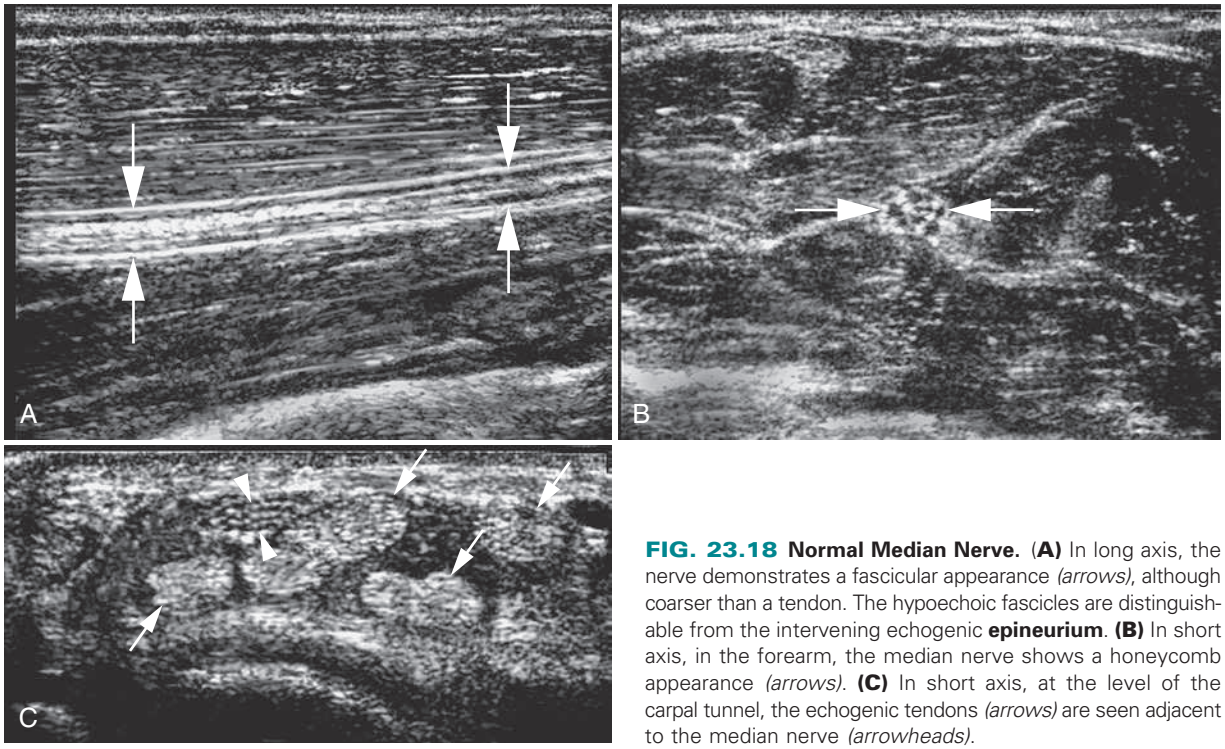

FIG. 23.18 Normal Median Nerve. (**A**) In long axis, the nerve demonstrates a fascicular appearance *(arrows)*, although coarser than a tendon. The hypoechoic fascicles are distinguishable from the intervening echogenic **epineurium**. **(B)** In short axis, in the forearm, the median nerve shows a honeycomb appearance *(arrows)*. **(C)** In short axis, at the level of the carpal tunnel, the echogenic tendons *(arrows)* are seen adjacent to the median nerve *(arrowheads)*.

of collagenous and adipose components, with small blood vessels and lymphatics. On short-axis view, peripheral nerves appear ovoid or round and have punctate internal hypoechoic fat representing nerve fascicles within the echogenic epineurium. Dynamic maneuvers including flexion and extension of the imaged region should show no substantial motion of a peripheral nerve, as distinct from tendons.

Assessment of peripheral nerves using ultrasound is performed primarily in the short-axis plane. The nerve is evaluated at a known anatomic location and followed proximally and distally as needed. Anisotropy is less problematic for peripheral nerves than for tendons.[23] Longitudinal scanning is helpful for providing an overview and illustrating relative caliber changes of peripheral nerves detected on transverse imaging. Caution should be exercised in primary interpretation of longitudinal sonographic images of peripheral nerves because of the potential to scan in a plane, which is not parallel to the nerve with potential artifactual changes in caliber and echogenicity.

Nerve dysfunction can result from compression by masses arising from or adjacent to the nerve, entrapment within fibro-osseous tunnels (such as the **carpal tunnel** in the case of median nerve compression at the wrist), or subluxation from fibro-osseous tunnels. Masses include neurogenic tumors, **neurofibromas** and **schwannomas,** considered more fully later. **Soft tissue ganglia,** usually appearing anechoic on ultrasound, may also cause nerve compression.[45-47] In the setting of nerve compression by any cause, the findings detectible on ultrasound relate to echotextural and caliber changes. Local compression causes venous congestion, which can lead to intraneural edema. Chronic compression can ultimately lead to intraneural fibrosis. These alterations in intraneural composition lead to loss of normal hyperechogenicity of the interfascicular epineural tissue, causing an overall hypoechoic appearance of the nerve in addition to poor definition or disappearance of the normal fascicular pattern.[43]

One of the most common clinical forms of entrapment neuropathy is **carpal tunnel syndrome.** In this condition, compression and flattening of the nerve occurs within the carpal tunnel, at the palmar aspect of the wrist, and the nerve is typically swollen and expanded just proximal to the carpal tunnel. The sonographic diagnosis of carpal tunnel syndrome is made by measuring the cross-sectional area of the median nerve at the level of the pronator quadratus and comparing this to the cross-sectional area of the median nerve in the carpal tunnel at the level of the pisiform. A difference of more than 2 mm^2 between the two measurements is highly associated with carpal tunnel syndrome[48] (Fig. 23.19). Variable cut-off values for the diagnosis of carpal tunnel syndrome based on single cross-sectional measurements of the median nerve in the carpal tunnel have been reported in the literature, in the 9- to 11-mm^2 range.[49-51] Bowing and thickening of the overlying **flexor retinaculum** can also be observed.[51]

Symptoms may also arise from dynamic **nerve subluxation** from fibro-osseous tunnels. One example of this is at the **cubital tunnel,** at the medial posterior aspect of the elbow. The **ulnar nerve** normally passes through this fibro-osseous tunnel at the posterior aspect of the humerus and is stabilized by an overlying retinaculum. This retinaculum normally passes between the olecranon and the medial epicondyle of the humerus. Developmental or posttraumatic deficiency of this retinaculum can allow the ulnar nerve to dynamically subluxate out of the cubital tunnel

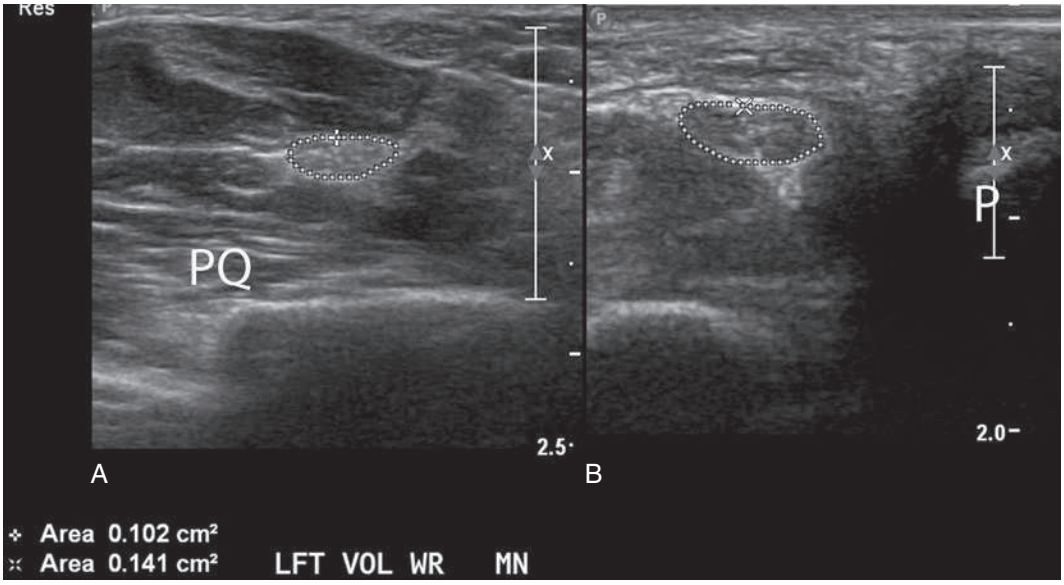

FIG. 23.19 Carpal Tunnel Entrapment of the Median Nerve. (A) Short-axis cross-sectional area of the median nerve obtained at the level of the pronator quadratus *(PQ)* at the distal forearm. **(B)** Cross-sectional area obtained in the carpal tunnel at the level of the pisiform *(P)*. The 4-mm² difference in area between the two images is consistent with **carpal tunnel syndrome.**

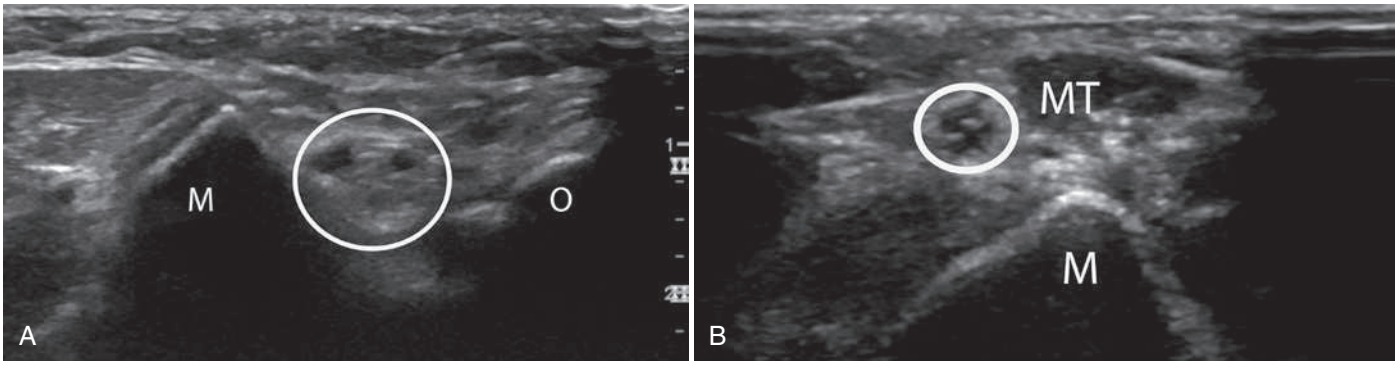

FIG. 23.20 Ulnar Nerve Dislocation at the Elbow. (A) At rest, with the elbow extended and the probe positioned between the medial epicondyle *(M)* and the ulnar olecranon *(O)*, the ulnar nerve *(circled)* is positioned posterior to the epicondyle. Note the ulnar nerve is enlarged at this location. **(B)** On flexion the ulnar nerve *(circled)* dislocates anterior to the medial epicondyle along with the medial head *(MT)* of the triceps muscle (known as **"snapping triceps"** syndrome). Most patients with ulnar dislocation do not exhibit medial head triceps dislocation. See also Video 23.4.

during elbow flexion, and this subluxation can be captured on dynamic imaging (Video 23.4). Scan technique is important in this diagnosis. The probe should be positioned in a transverse plane with respect to the medial posterior elbow. The nerve should normally be visible within the cubital tunnel with the elbow in an extended position. The osseous landmark of the medial epicondyle should be maintained in the visualized field as the patient slowly flexes the elbow. Excessive probe pressure should be avoided because this can limit dynamic motion of the nerve. The nerve should normally remain lateral to the medial epicondyle. Subluxation, where the nerve moves medially and anteriorly along the epicondyle, or dislocation, where the nerve snaps anteromedial to the medial epicondyle, may occur on flexion[52,53] (Fig. 23.20). Patients with ulnar nerve subluxation or dislocation may experience pain or transient numbness, but this dynamic instability can also be seen in asymptomatic in healthy controls, and the association with neuropathy is debated.[54,55]

JOINT ASSESSMENT

Ultrasound can play a helpful role in the diagnosis and follow-up of both inflammatory and noninflammatory arthropathy and may guide diagnostic and therapeutic procedures in patients with these disorders. Patients with **inflammatory arthropathy** such as **rheumatoid arthritis** present with joint pain, swelling, and stiffness. Ultrasound plays a complementary role to clinical history, physical examination, radiographs, and serology tests such as acute phase reactants (e.g., C-reactive protein, erythrocyte sedimentation rate, rheumatoid factor, and antinuclear antibody). In this role, when used systematically, ultrasound can substantially increase diagnostic certainty in patients with suspected inflammatory arthropathy.[56] Ultrasound also represents a great tool in the follow-up of these patients, allowing detection of subclinical relapse in patients with clinical remission and predicting relapse and joint deterioration.[57]

Joint effusions are frequently present in patients with **inflammatory arthritis** but are nonspecific as they may also occur in patients with osteoarthritis, with infection, and in the setting of trauma or internal derangement (Fig. 23.21). The diagnosis of an effusion rests on the visualization of increased volume of joint fluid. Joint fluid is typically anechoic but can contain some mobile low-level echoes. In addition, **joint fluid** is mobile and compressible.[58] Normal joints contain just a trace of fluid, so an increase in this fluid volume constitutes a **joint effusion.**

Synovitis is determined by the presence of intraarticular nondisplaceable hypoechoic to hyperechoic soft tissue, which usually demonstrates hyperemia on color Doppler assessment (Fig. 23.22). On Doppler assessment, the velocity filter should be set to detect low amounts of flow, and the gain settings should be adjusted to just below a level where noise is visualized.[59] Either color Doppler or power Doppler may be more sensitive to flow in the evaluation of synovitis, depending on individual machine, so familiarity with the hardware being used is important.[60] The quantity of synovial hyperemia can be graded as described by Szkudlarek et al.[61]: Grade I (low) hyperemia consists of the visualization of several single vessel dots. Grade II (moderate) hyperemia is shown when there are confluent vessel signals occupying less than half of the visualized synovial tissue. Grade III (high) represents confluent vessel signals in more than half of the synovium. Doppler ultrasound has shown high degrees of sensitivity and specificity in the diagnosis of synovitis at the metacarpophalangeal joints in patients with rheumatoid arthritis when compared with dynamic contrast-enhanced MRI.[61] Ultrasound has also been shown to have high interobserver and intraobserver reliability in detection of synovitis.[62]

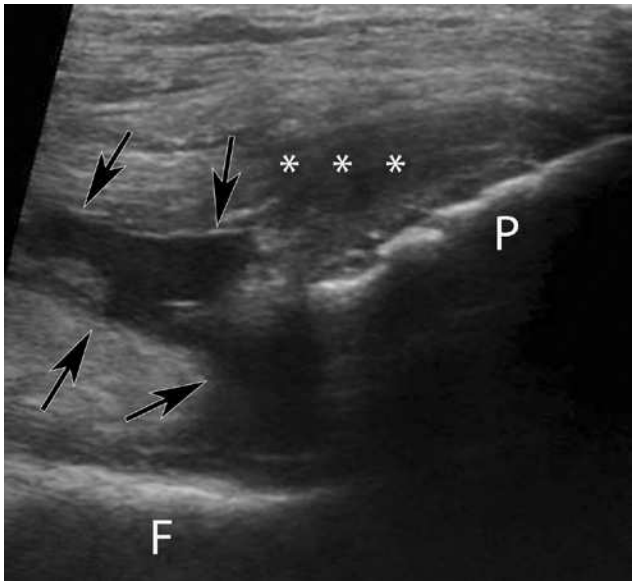

FIG. 23.21 Simple Knee Joint Effusion. Anechoic fluid is present within the suprapatellar recess of the knee *(arrows)*. There is concomitant quadriceps tendinosis (*). *F,* Distal femur; *P,* patella.

Bone erosion in **erosive inflammatory arthritis** such as rheumatoid arthritis can be depicted on ultrasound as a cortical defect visible in two perpendicular planes[63] (Fig. 23.23). Erosions may be graded as small (<2 mm), moderate (2-4 mm), or large (>4 mm).[64] Ultrasound is more sensitive than plain radiographs in the detection of bone erosion and thus may aid in diagnosis of early disease.[65] In addition to cortical discontinuity, there may be acoustic enhancement of marrow subjacent to the inflammatory bony erosion.[65] Patients with inflammatory arthropathy may also have associated **tenosynovitis, enthesitis,** and, in the case of rheumatoid arthritis, **inflammatory periarticular nodules (rheumatoid nodules)**[66] (Fig. 23.24).

Gout is a common inflammatory arthritis with a predilection for first metatarsophalangeal joint involvement, caused by precipitation of uric acid crystals within joints. In patients with gout, there may be **joint effusion, synovial hypertrophy** and hyperemia, soft tissue swelling, and juxtaarticular **erosions** that can be large.[67] Intraarticular crystals may be evidenced by the presence of a characteristic irregular hyperechoic line along the surface of the normally hypoechoic cartilage, termed the **"double contour sign"**[68] (Fig. 23.25). This is distinct from

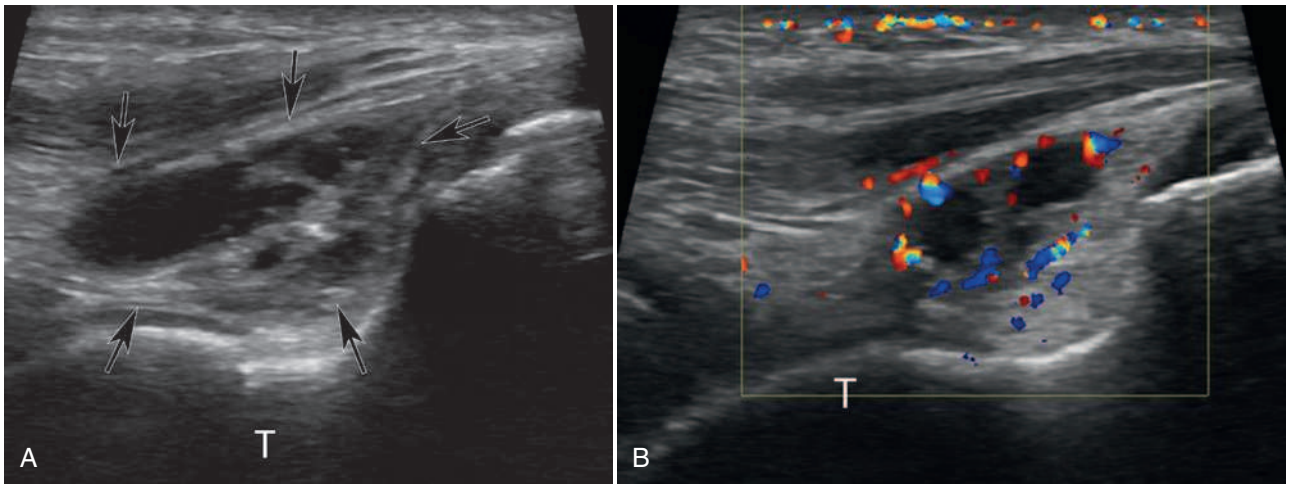

FIG. 23.22 Complex Ankle Joint Effusion in Rheumatoid Arthritis. (A) A long-axis image of the tibiotalar joint demonstrates a complex joint effusion *(arrows)* with both anechoic fluid and echogenic, thickened synovium consistent with synovitis. **(B)** Color Doppler imaging of the tibiotalar joint demonstrates marked hyperemia within the echogenic synovium. *T,* Talus.

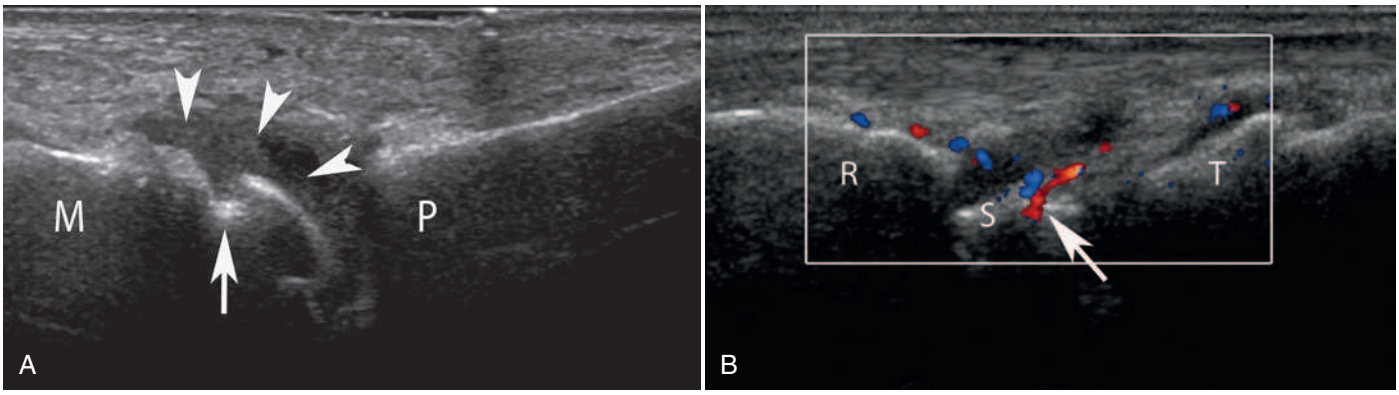

FIG. 23.23 Bone Erosions in Two Different Patients Rheumatoid Arthritis. (A) Long-axis gray-scale image at the fifth metatarsophalangeal joint demonstrates bone erosion in the fifth metatarsal head *(arrow)* with associated cortical irregularity and synovial hypertrophy *(arrowheads). M,* Metatarsal, *P,* proximal phalanx. **(B)** Color Doppler imaging of the dorsal wrist in long-axis view demonstrates hyperemia within the synovium and erosion *(arrow)* of the scaphoid *(S). R,* Distal radius, *T,* trapezium.

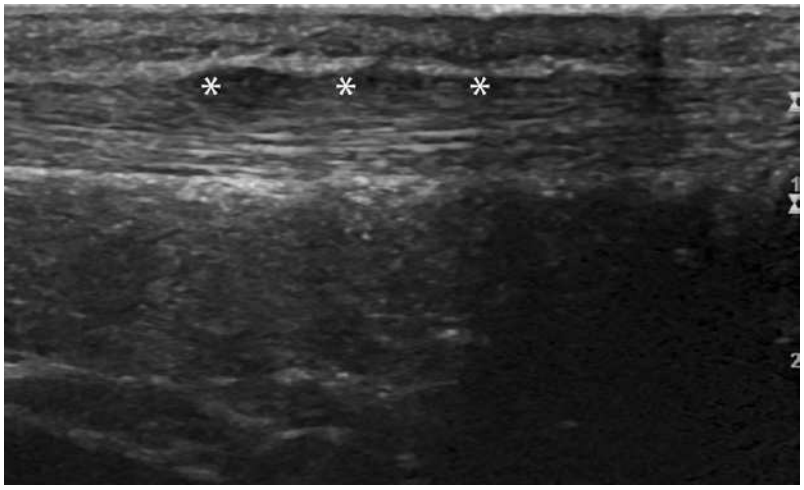

FIG. 23.24 Achilles Tendon With Rheumatoid Nodules. Long-axis image of the Achilles tendon demonstrates hypoechoic nodular thickening (*) of the posterior tendon surface, consistent with rheumatoid nodules. No hyperemia was seen on color Doppler imaging (not shown).

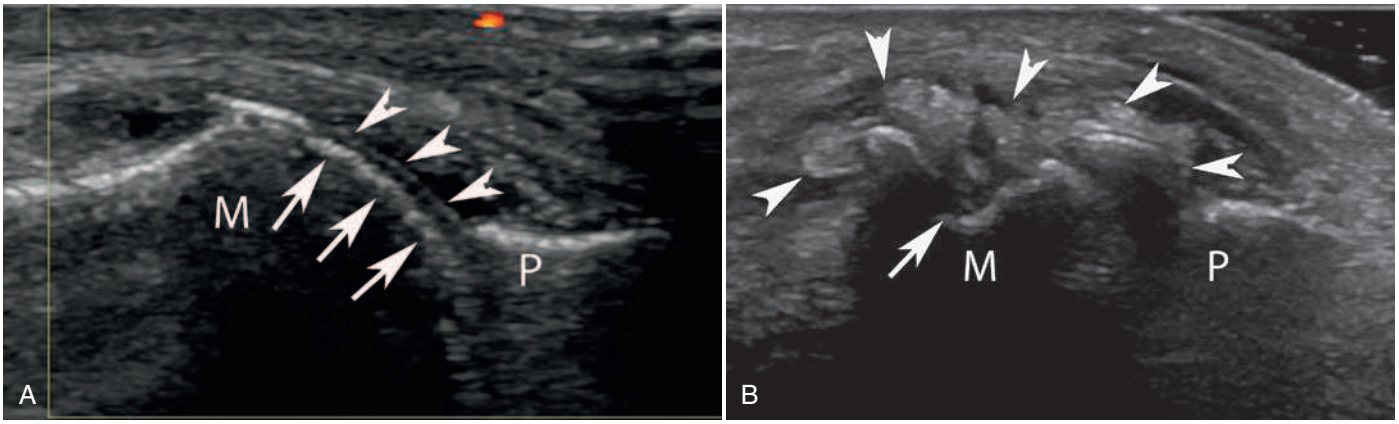

FIG. 23.25 Gout in Two Different Patients. (A) Long-axis gray-scale image of the first metatarsal phalangeal joint demonstrates the **"sugar icing"** appearance where echogenic urate crystals are deposited along the synovial lining of the joint *(arrowheads).* The **"double contour sign"** is formed by the echogenic urate crystals ("sugar icing") layering on the anechoic hyaline cartilage with the underlying echogenic cortex *(arrows).* **(B)** Long-axis gray-scale image of the fifth metatarsal phalangeal joint shows a large erosion *(arrow)* with a large amorphous **tophus** *(arrowheads),* part of which extends into the erosion. *M,* First metatarsal, *P,* first proximal phalanx.

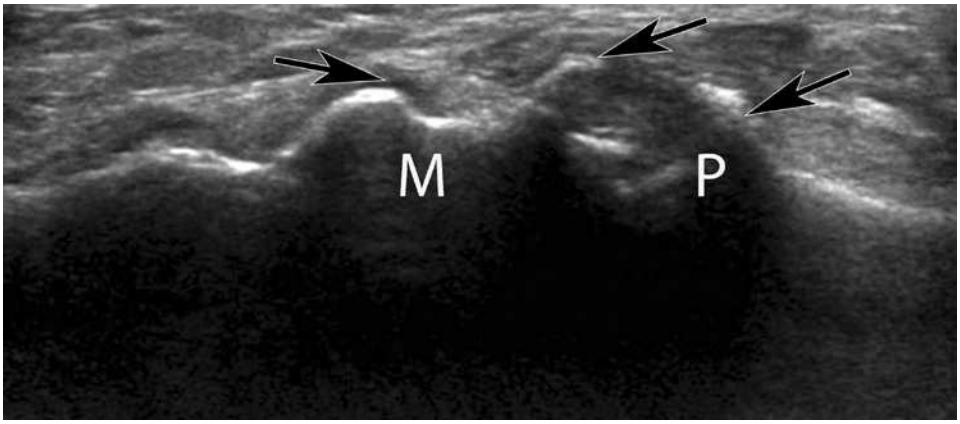

FIG. 23.26 Osteoarthritis. Long-axis gray-scale image of the fifth metatarsophalangeal joint demonstrates osteophyte formation *(arrows)* at both sides of the joint. *M,* Metatarsal, *P,* proximal phalanx.

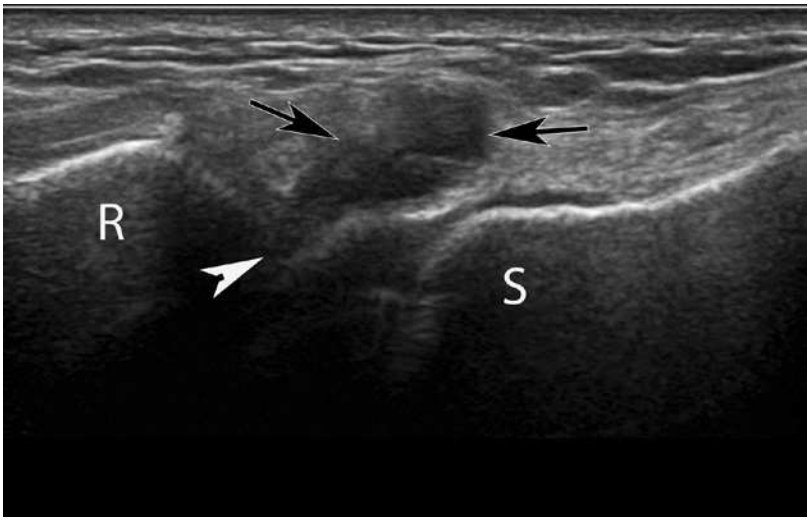

FIG. 23.27 Ganglion Cyst. Long-axis image of the radiocarpal joint at the radioscaphoid articulation demonstrates a lobulated, hypoechoic ganglion cyst *(arrows)* arising from the region of the scapholunate ligament. Note the neck *(arrowhead)* arising from the joint. *R,* Radius, *S,* scaphoid.

chondrocalcinosis in which cartilage calcification may be seen with an intracartilaginous echogenic line. Tophi are focal crystal accumulations, which occur around joints in some patients with gout, appearing as clumps of hyperechoic material, which may have a surrounding hypoechoic rim, an appearance has been referred to as "wet sugar clumps."[68] Bony erosions may be seen adjacent to these tophi.

In **osteoarthritis** (nonerosive), cartilage thinning and irregularity may be seen in addition to osteophytes and typically mild synovitis (Fig. 23.26). Osteophytes appear as cortical protrusions at the margin of the articular surface, with posterior acoustic shadowing.[69] **Synovitis** may be nodular or diffuse. **Joint effusions** may also be demonstrated in osteoarthritis, and although they may occur in the absence of synovitis, the presence and size of effusion correlate with the presence of synovitis and the extent of synovial thickening. Joint effusion and synovitis also correlate with clinical and radiographic disease severity.[70]

SOFT TISSUE MASSES

Palpable soft tissue masses are very common and represent a diagnostic dilemma for physicians. Although the vast majority of these masses are benign, discrimination between benign and malignant masses is not clinically possible. Ultrasound is a complementary modality to MRI in the workup of soft tissue masses. Although MRI has overall higher specificity, several soft tissue masses can be characterized as benign with ultrasound.[71,72] In indeterminate cases, contrast-enhanced MRI can be performed, and this two-tiered strategy may provide an overall cost savings to the health care system if appropriately implemented.

Ganglion cysts are mucin-filled lesions most often found at the wrist; they are usually closely related to a joint or tendon sheath. Approximately 10% of ganglion cysts occur secondary to trauma.[73] The most common location is adjacent to the scapholunate articulation (Fig. 23.27). A neck extending from the lesion to an underlying joint or tendon sheath should be

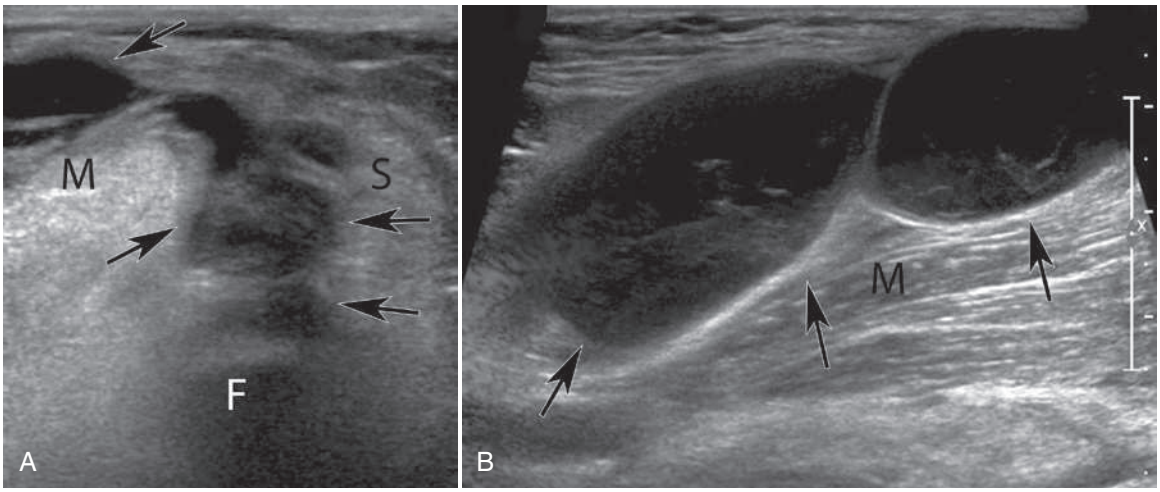

FIG. 23.28 Baker Cyst. (A) Short-axis image from the medial posterior knee shows a lobulated, septated, hypoechoic Baker cyst *(arrows)* communicating with the joint between the medial gastrocnemius muscle *(M)* and the semimembranosus tendon *(S). F,* Posterior medial femoral condyle. **(B)** In a different patient, long-axis image from the posterior medial knee demonstrates an ovoid, septated complex Baker cyst *(arrows)* with internal debris, lined with echogenic synovium. See also Video 23.5.

FIG. 23.29 Ruptured Baker Cyst. Longitudinal sonogram of the calf with extended field of view shows a complex mass *(arrows)* that is connected to a small amount of fluid in the popliteal fossa *(arrowheads),* representing the ruptured Baker cyst.

sought but is often not definable.[74] These lesions typically appear as well-circumscribed, oval or lobulated anechoic cystic masses, with accompanying through transmission.[75] Ganglion cysts may demonstrate low-level internal echoes and may be septated.[74] Ganglion cysts are typically noncompressible (as opposed to **bursae,** which are compressible). Ganglion cysts do not usually demonstrate internal flow on color Doppler evaluation.[76]

Baker cysts, occurring in the medial aspect of the popliteal fossa, deserve special mention, as they are extremely common. A Baker cyst is caused by fluid distention of the **semimembranosus-gastrocnemius bursa,** occurring between the distal semimembranosus tendon and the medial head of the gastrocnemius muscle with a narrow neck arising from the underlying knee joint (Fig. 23.28, Video 23.5). This usually occurs in the setting of an underlying cause of joint effusion, including osteoarthritis, but also in the setting of posterior horn **medial meniscal tear, inflammatory arthritis,** and internal derangement. Although common, they are not reliably diagnosed clinically.[77] Baker cysts are typically anechoic when uncomplicated, yet may have a variable appearance, with complex fluid and hemorrhage, internal septations and debris, and thick, echogenic, hyperemic synovium lining the cyst. The narrow neck can act as a valve, and fluid accumulation within the cyst can lead to rupture, resulting in acute pain, swelling, and erythema behind the knee and in the proximal calf.[78] When this occurs, the margin of the cyst is often irregular caudally and there may be associated medial calf subcutaneous edema, with fluid tracking distally about the medial head of the gastrocnemius (Fig. 23.29). The clinical presentation of this may mimic deep venous thrombosis or developing cellulitis.[79]

Lipomas are the most common palpable soft tissue masses (Table 23.1). These may occur within the subcutaneous tissues, muscle, or deep soft tissues. Simple lipomas are usually homogeneously isoechoic, or slightly hyperechoic to fat, with well-defined margins and internal wavy septations mimicking the surrounding fat[80] (Fig. 23.30). They should be painless, mobile, and compressible with transducer pressure.[81] Simple lipomas should not demonstrate internal complexity or hypervascularity; however, vessels may be seen passing through the lipoma. MRI with contrast should be performed to exclude underlying liposarcoma in the evaluation of any suspected lipoma with the following atypical features: deep acoustic shadowing, internal complexity or hypervascularity, size greater than 5 cm, deep or intramuscular location, pain, or history of enlargement.

TABLE 23.1 Fat-Containing Soft Tissue Lesions

Diagnosis	Sonographic Findings	Follow-Up
Simple lipoma	Similar echogenicity to subcutaneous fat Mobile Soft, compressible Painless Few, small vessels	Clinical follow-up sufficient if classic sonographic appearance
Indeterminate lipomatous lesion	Complex echogenicity Deep acoustic shadowing Hypervascularity Size > 5 cm Deep or intramuscular location Pain History of enlargement	MRI with contrast for further evaluation, with biopsy if needed
Fat-containing hernia	Change in appearance over time or with Valsalva maneuver	

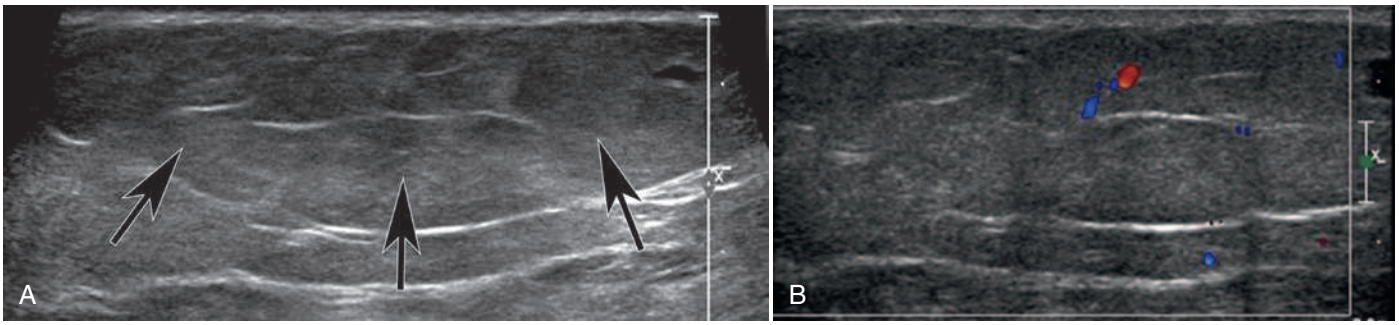

FIG. 23.30 Lipoma. (A) A simple lipoma *(arrows)* is isoechoic to the adjacent subcutaneous fat and contains thin echogenic septations that parallel the skin surface. **(B)** Color Doppler imaging demonstrates two small vessels traversing the lipoma. There is no hyperemia.

A pitfall in the diagnosis of lipoma is that a fat-containing hernia can have some overlapping ultrasound appearances, including similar echogenicity to subcutaneous fat and internal wavy septations.[80] Anatomic location, dynamic change in appearance, and movement with Valsalva maneuver can assist in the diagnosis of hernia. When appearances are typical for benign lipoma, periodic clinical follow-up can be performed rather than additional imaging or biopsy.

Nerve sheath tumors are common, usually benign masses, although malignant nerve sheath tumors may uncommonly occur. Nerve sheath tumors are usually well-circumscribed solid hypoechoic masses, ovoid or fusiform in shape, and have faint deep acoustic enhancement.[82] A contiguous nerve of origin of the lesion may be identified, either centrally within the lesion in the case of neurofibroma or peripherally related to the lesion in a schwannoma (however, these findings are not absolute) (Fig. 23.31). An echogenic capsule may be seen, and occasionally cystic spaces can occur in a degenerated schwannoma. A split-fat sign, although not entirely specific, is often seen in association with benign peripheral nerve sheath tumors. This sign comprises the presence of a rim of fat about the end of the lesion, representing fat normally present about the neurovascular bundle from which the lesion arises.[83] The imaging appearances of benign and malignant peripheral nerve sheath tumors overlap, but malignant lesions should be considered when a lesion is more poorly defined (reflecting its infiltrative nature), is increasing in size, or is internally heterogeneous in appearance as a result of internal necrosis and/or hemorrhage.[84] If lesions typical for benign nerve sheath tumors on imaging are not biopsied or resected, then imaging and clinical follow-up are warranted.

Various benign and malignant soft tissue lesions cannot be definitively discriminated by ultrasound alone. Lesions that remain indeterminate by ultrasound may then be evaluated with contrast-enhanced MRI. Lesions that remain worrisome for malignant neoplasm will typically undergo image-guided biopsy (most often with ultrasound guidance). Primary **soft tissue sarcomas** typically appear solid, with irregular borders, variable internal necrosis, and hemorrhage (Fig. 23.32). They may be partly calcified (especially synovial sarcomas).[85] The lesions usually demonstrate internal vascularization and may show local invasion of adjacent tissues. Secondary lesions (metastases) should be considered when a solid vascularized soft tissue lesion is found in a patient with known underlying malignancy. An important pitfall in the diagnosis of sarcoma is the clinical presentation with a hemorrhagic tumor, which can be incorrectly diagnosed as a bland hematoma, potentially leading to delay in correct diagnosis.[86] To further complicate the diagnosis, patients may report a history of trauma. A spontaneous hematoma in the absence of anticoagulant medication should be regarded with suspicion, as should an apparent hematoma disproportionate to the patient-reported trauma.[73] Such lesions should be evaluated carefully for vascularized components, which should be targeted for biopsy. If none are found, then repeat imaging should be performed in 6 weeks to document resolution of the hematoma. Following surgical

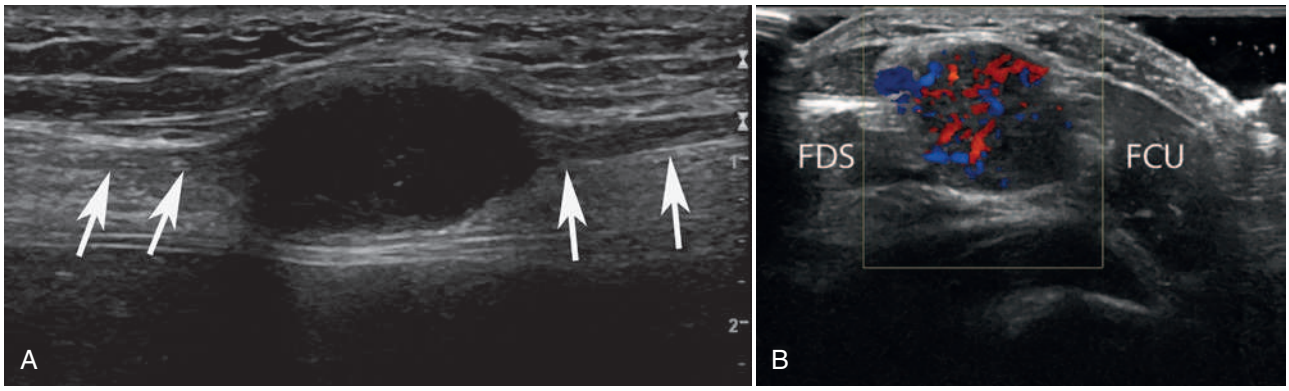

FIG. 23.31 Peripheral Nerve Sheath Tumor. (A) Long-axis image obtained at the site of a palpable mass shows an ovoid, hypoechoic mass with smooth borders, arising from the ulnar nerve. Note the ulnar nerve enters and exits the mass *(arrows).* **(B)** A short-axis image of the forearm demonstrates the mass in the expected location of the ulnar nerve. Color Doppler shows marked hyperemia within the mass. *FCU,* Flexor carpi ulnaris; *FDS,* flexor digitorum superficialis and profunda.

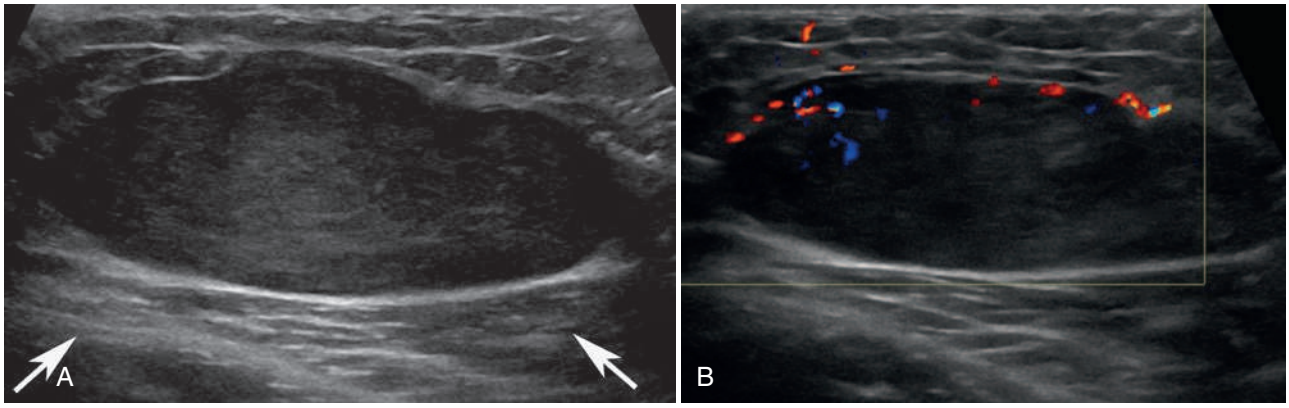

FIG. 23.32 Sarcoma. (A) A myxoid liposarcoma demonstrates mildly increased through transmission *(arrows)* due to the myxoid content. However, the mass is solid, with internal echoes. The superficial border is microlobulated. **(B)** Color Doppler imaging demonstrates increased blood flow within the mass.

resection of soft tissue sarcoma, ultrasound has been shown to have acceptable diagnostic accuracy but may miss a small number of recurrences. Ultrasound could play a complementary role to MRI in follow-up of these cases.[87,88]

FOREIGN BODIES

Embedded **soft tissue foreign bodies** are a common problem in both adult and pediatric populations. Whereas some materials, such as metal and glass, are radiopaque and can be seen on plain radiographs, other materials such as wood are not detected radiographically. In these cases, ultrasound is an effective means for diagnosis. Foreign bodies are typically highly echogenic and may have posterior acoustic shadowing (Fig. 23. 33). They may be surrounded by a hypoechoic halo, representing an inflammatory reaction[89] or hyperemia on color Doppler imaging. A large amount of associated fluid should prompt consideration of a secondary abscess.

From a practical standpoint, the patient can usually accurately direct the sonographer to the area of greatest concern, and observation of skin entry and/or exit sites is helpful to focus evaluation. Knowledge of the trajectory of foreign body entry is particularly helpful in assessment of thin linear objects such as wooden splinters, because they are often seen in nonanatomic oblique planes. Meticulous scanning is needed because small foreign bodies may be occult to cursory scanning in the hands and feet, where they may be obscured by adjacent ligaments, tendons, nerves, and vessels.[90] It is also important to determine the relationship of the object to these anatomic structures and to determine if there is associated injury to them. In addition to the visualization of nonradiopaque foreign bodies, ultrasound may help guide surgical planning by providing accurate three-dimensional localization of both radiopaque and nonradiopaque objects, and the overlying skin can be marked preprocedurally as an aid. Ultrasound can also be used to directly guide foreign body retrieval with real-time imaging.[91,92]

SOFT TISSUE INFECTION

Infection of the skin and subcutaneous soft tissue, **cellulitis,** is a common clinical problem, which can be effectively treated with antibiotics. On ultrasound, the skin and subcutaneous tissues are thickened and hyperechoic early in the process. Later, there may be interdigitating reticular strands of hypoechogenicity representing interstitial inflammatory exudate,[93] also known as the "cobblestone" appearance (Fig. 23.34).

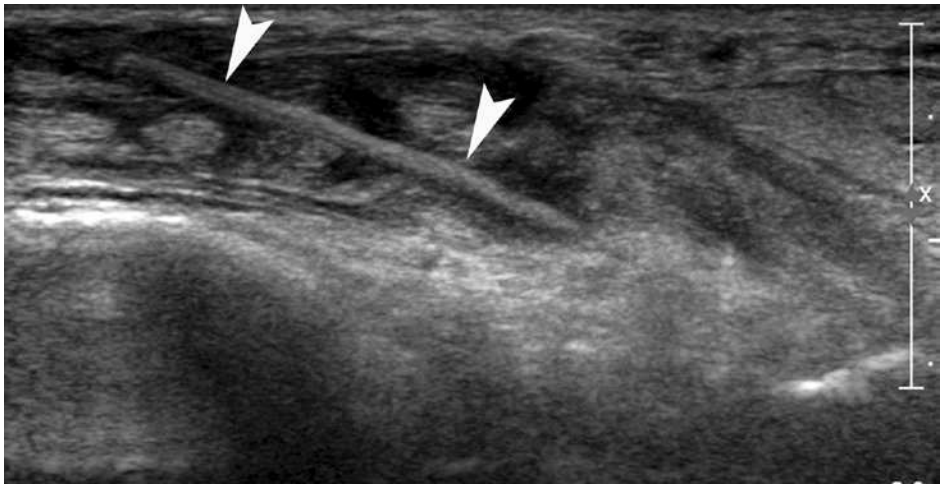

FIG. 23.33 Wood Foreign Body. A wood splinter is embedded within the dorsal soft tissues of the hand. The splinter *(arrowheads)* appears as a linear, echogenic structure.

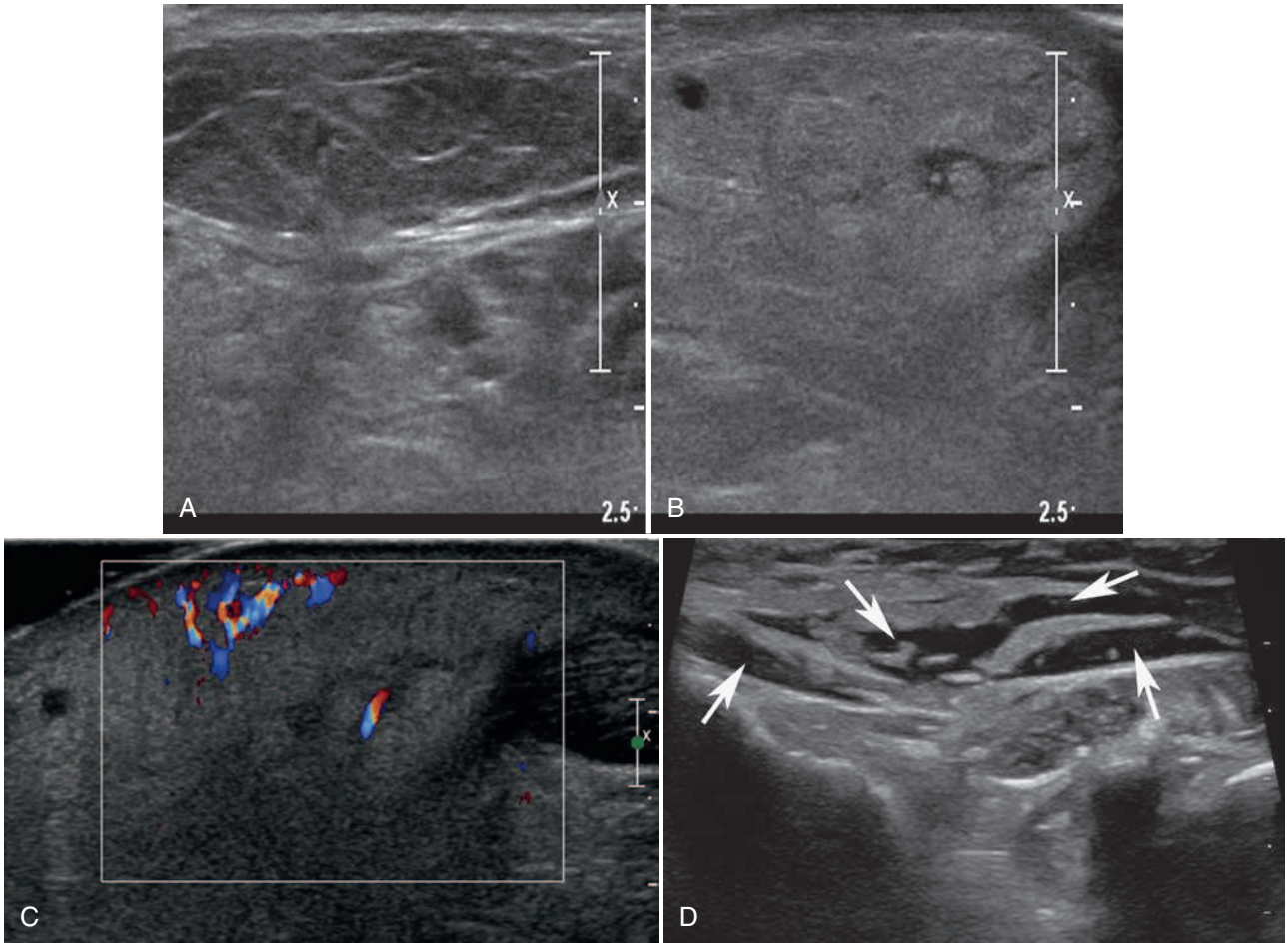

FIG. 23.34 Cellulitis. (A) Normal subcutaneous fat in the lateral nonaffected ankle is juxtaposed with the **(B)** abnormal contralateral ankle in the same patient with cellulitis. Note the hypoechoic echotexture of the normal fat *(left side of image)* versus the echogenic, swollen subcutaneous fat with obscuration of the normal internal septations *(right side of image).* **(C)** Color Doppler imaging demonstrates increased blood flow within the echogenic, swollen subcutaneous fat. **(D)** Gray-scale imaging in a different patient with cellulitis demonstrates anechoic fluid *(arrows)* within the echogenic cellulitic tissue.

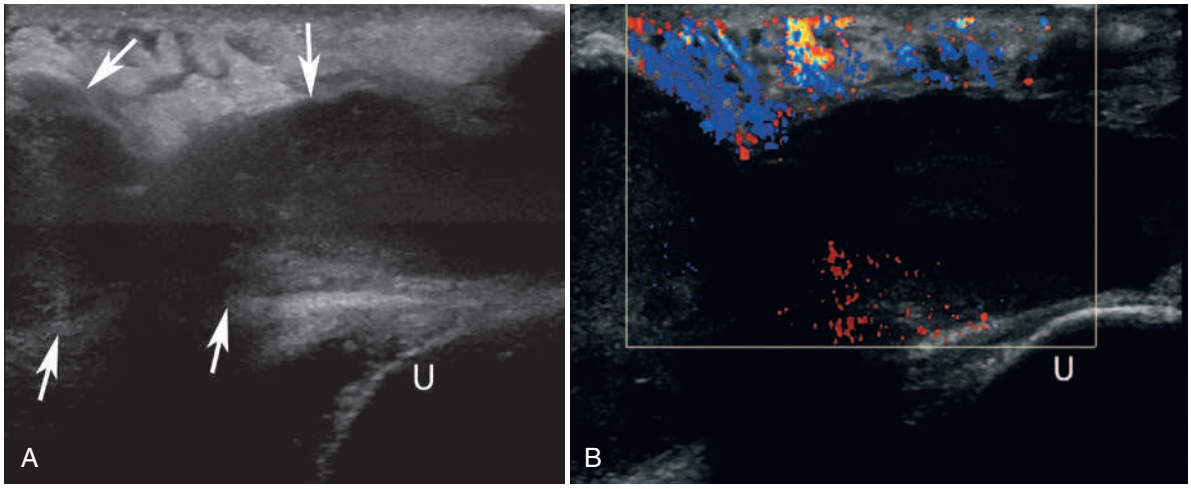

FIG. 23.35 Forearm Abscess. (A) Short-axis image of a complex fluid hypoechoic collection *(arrows)* with echogenic peripheral soft tissue rind and increased through transmission, consistent with an abscess. **(B)** Color Doppler image demonstrates hyperemia within the surrounding soft tissues. *U,* Ulna.

Cellulitis may progress to **abscess** formation. The development of an associated **abscess** is an important finding to diagnose, as this will typically not respond to antibiotics, instead requiring drainage, either surgical or image guided. Abscesses can have a variable appearance on ultrasound evaluation.[94] An abscess border may be well defined or poorly defined and infiltrative (Fig. 23.35). There may be a surrounding rim of hyperemic, thickened soft tissue. The internal liquefied material may demonstrate an anechoic, hypoechoic, or complex echogenic appearance, with internal septations and low-level echoes. Foci of echogenic gas, with associated ill-defined shadowing, may be present within the abscess. With dynamic compression, swirling of the echogenic debris within the abscess can be seen.

In cases of fluid collection, several other entities may be considered and differentiated from an abscess. A seroma can be distinguished from an abscess in that a seroma appears as a simple anechoic to hypoechoic fluid collection without peripheral hyperemia, and there may be increased through transmission. A hematoma may appear as a mixed echogenicity fluid collection, yet will have no internal color Doppler flow and will have scant peripheral hyperemia. A soft tissue sarcoma will demonstrate solid, hyperemic internal components, as well as posterior acoustic shadowing. If the sonographic diagnosis of the fluid collection is indeterminate, confirmation can be obtained with aspiration (sonographically guided, if needed) and microbiologic and histologic assessment of the aspirate.

CONCLUSION

Ultrasound is a cost-effective means by which to provide an accurate diagnosis in many scenarios of musculoskeletal pathology, including tendon and ligament injury, arthritis, and characterization of infection and some soft tissue masses. In addition to ongoing technical developments, critical to the use of this technology in the future will be technologist and physician education and appropriate and consistent incorporation of new technology into patient care pathways.

REFERENCES

1. Nazarian LN. The top 10 reasons musculoskeletal sonography is an important complementary or alternative technique to MRI. AJR Am J Roentgenol. 2008;190(6):1621-1626.
2. Jamadar DA, Jacobson JA, Caoili EM, et al. Musculoskeletal sonography technique: focused versus comprehensive evaluation. AJR Am J Roentgenol. 2008;190(1):5-9.
3. Teh J. Applications of Doppler imaging in the musculoskeletal system. Curr Probl Diagn Radiol. 2006;35(1):22-34.
4. Klauser AS, Miyamoto H, Bellmann-Weiler R, et al. Sonoelastography: musculoskeletal applications. Radiology. 2014;272(3):622-633.
5. Ooi CC, Malliaras P, Schneider ME, Connell DA. "Soft, hard, or just right?" Applications and limitations of axial-strain sonoelastography and shear-wave elastography in the assessment of tendon injuries. Skeletal Radiol. 2014;43(1):1-12.
6. Botar Jid C, Damian L, Dudea SM, et al. The contribution of ultrasonography and sonoelastography in assessment of myositis. Med Ultrason. 2010;12(2):120-126.
7. Magarelli N, Carducci C, Bucalo C, et al. Sonoelastography for qualitative and quantitative evaluation of superficial soft tissue lesions: a feasibility study. Eur Radiol. 2014;24(3):566-573.
8. Weng L, Tirumalai AP, Lowery CM, et al. US extended-field-of-view imaging technology. Radiology. 1997;203(3):877-880.
9. Kavanagh EC, Koulouris G, Parker L, et al. Does extended-field-of-view sonography improve interrater reliability for the detection of rotator cuff muscle atrophy? AJR Am J Roentgenol. 2008;190(1):27-31.
10. Harcke HT, Grissom LE, Finkelstein MS. Evaluation of the musculoskeletal system with sonography. AJR Am J Roentgenol. 1988;150(6):1253-1261.
11. Peetrons P. Ultrasound of muscles. Eur Radiol. 2002;12(1):35-43.
12. Draghi F, Zacchino M, Canepari M, et al. Muscle injuries: ultrasound evaluation in the acute phase. J Ultrasound. 2013;16(4):209-214.
13. Nguyen JT, Nguyen JL, Wheatley MJ, Nguyen TA. Muscle hernias of the leg: a case report and comprehensive review of the literature. Can J Plast Surg. 2013;21(4):243-247.
14. Strobel K, Hodler J, Meyer DC, et al. Fatty atrophy of supraspinatus and infraspinatus muscles: accuracy of US. Radiology. 2005;237(2):584-589.
15. Dillehay GL, Deschler T, Rogers LF, et al. The ultrasonographic characterization of tendons. Invest Radiol. 1984;19(4):338-341.
16. Crass JR, van de Vegte GL, Harkavy LA. Tendon echogenicity: ex vivo study. Radiology. 1988;167(2):499-501.
17. Khan KM, Bonar F, Desmond PM, et al. Patellar tendinosis (jumper's knee): findings at histopathologic examination, US, and MR imaging. Victorian Institute of Sport Tendon Study Group. Radiology. 1996;200(3):821-827.

18. Ohberg L, Lorentzon R, Alfredson H. Neovascularisation in Achilles tendons with painful tendinosis but not in normal tendons: an ultrasonographic investigation. Knee Surg Sports Traumatol Arthrosc. 2001;9(4):233-238.
19. Connell D, Burke F, Coombes P, et al. Sonographic examination of lateral epicondylitis. AJR Am J Roentgenol. 2001;176(3):777-782.
20. Dones 3rd VC, Grimmer K, Thoirs K, et al. The diagnostic validity of musculoskeletal ultrasound in lateral epicondylalgia: a systematic review. BMC Med Imaging. 2014;14:10.
21. Eder L, Barzilai M, Peled N, et al. The use of ultrasound for the assessment of enthesitis in patients with spondyloarthritis. Clin Radiol. 2013;68(3): 219-223.
22. Frediani B, Falsetti P, Storri L, et al. Ultrasound and clinical evaluation of quadricipital tendon enthesitis in patients with psoriatic arthritis and rheumatoid arthritis. Clin Rheumatol. 2002;21(4):294-298.
23. Martinoli C, Bianchi S, Dahmane M, et al. Ultrasound of tendons and nerves. Eur Radiol. 2002;12(1):44-55.
24. Breidahl WH, Stafford Johnson DB, Newman JS, Adler RS. Power Doppler sonography in tenosynovitis: significance of the peritendinous hypoechoic rim. J Ultrasound Med. 1998;17(2):103-107.
25. Jeffrey Jr RB, Laing FC, Schechter WP, et al. Acute suppurative tenosynovitis of the hand: diagnosis with US. Radiology. 1987;162(3):741-742.
26. Hodgson RJ, O'Connor PJ, Grainger AJ. Tendon and ligament imaging. Br J Radiol. 2012;85(1016):1157-1172.
27. Zbojniewicz AM. US for diagnosis of musculoskeletal conditions in the young athlete: emphasis on dynamic assessment. Radiographics. 2014;34(5): 1145-1162.
28. Ebrahim FS, De Maeseneer M, Jager T, et al. US diagnosis of UCL tears of the thumb and Stener lesions: technique, pattern-based approach, and differential diagnosis. Radiographics. 2006;26(4):1007-1020.
29. Noszian IM, Dinkhauser LM, Orthner E, et al. Ulnar collateral ligament: differentiation of displaced and nondisplaced tears with US. Radiology. 1995;194(1):61-63.
30. Melville DM, Jacobson JA, Fessell DP. Ultrasound of the thumb ulnar collateral ligament: technique and pathology. AJR Am J Roentgenol. 2014;202(2):W168.
31. Finlay K, Lee R, Friedman L. Ultrasound of intrinsic wrist ligament and triangular fibrocartilage injuries. Skeletal Radiol. 2004;33(2):85-90.
32. Gondim Teixeira PA, Omoumi P, Trudell DJ, et al. High-resolution ultrasound evaluation of the trapeziometacarpal joint with emphasis on the anterior oblique ligament (beak ligament). Skeletal Radiol. 2011;40(7):897-904.
33. Chiavaras MM, Harish S, Oomen G, et al. Sonography of the anterior oblique ligament of the trapeziometacarpal joint: a study of cadavers and asymptomatic volunteers. AJR Am J Roentgenol. 2010;195(6):W428-W434.
34. Ferreira FB, Fernandes ED, Silva FD, et al. A sonographic technique to evaluate the anterior bundle of the ulnar collateral ligament of the elbow: imaging features and anatomic correlation. J Ultrasound Med. 2015;34(3): 377-384.
35. Bica D, Armen J, Kulas AS, et al. Reliability and precision of stress sonography of the ulnar collateral ligament. J Ultrasound Med. 2015;34(3):371-376.
36. Jacobson JA, Chiavaras MM, Lawton JM, et al. Radial collateral ligament of the elbow: sonographic characterization with cadaveric dissection correlation and magnetic resonance arthrography. J Ultrasound Med. 2014;33(6): 1041-1048.
37. Nazarian LN, McShane JM, Ciccotti MG, et al. Dynamic US of the anterior band of the ulnar collateral ligament of the elbow in asymptomatic major league baseball pitchers. Radiology. 2003;227(1):149-154.
38. Jacobson JA, Propeck T, Jamadar DA, et al. US of the anterior bundle of the ulnar collateral ligament: findings in five cadaver elbows with MR arthrographic and anatomic comparison—initial observations. Radiology. 2003;227(2): 561-566.
39. Sasaki J, Takahara M, Ogino T, et al. Ultrasonographic assessment of the ulnar collateral ligament and medial elbow laxity in college baseball players. J Bone Joint Surg Am. 2002;84-A(4):525-531.
40. Hua Y, Yang Y, Chen S, Cai Y. Ultrasound examination for the diagnosis of chronic anterior talofibular ligament injury. Acta Radiol. 2012;53(10): 1142-1145.
41. De Maeseneer M, Vanderdood K, Marcelis S, et al. Sonography of the medial and lateral tendons and ligaments of the knee: the use of bony landmarks as an easy method for identification. AJR Am J Roentgenol. 2002;178(6): 1437-1444.
42. Fornage BD. Peripheral nerves of the extremities: imaging with US. Radiology. 1988;167(1):179-182.
43. Bianchi S. Ultrasound of the peripheral nerves. Joint Bone Spine. 2008;75(6):643-649.
44. Silvestri E, Martinoli C, Derchi LE, et al. Echotexture of peripheral nerves: correlation between US and histologic findings and criteria to differentiate tendons. Radiology. 1995;197(1):291-296.
45. Sole JS, Pingree MJ, Spinner RJ, et al. Saphenous neuropathy secondary to extraneural ganglion cyst 15 years after reconstruction of the anterior cruciate ligament. PM R. 2014;6(5):451-455.
46. Rawal A, Ratnam KR, Yin Q, et al. Compression neuropathy of common peroneal nerve caused by an extraneural ganglion: a report of two cases. Microsurgery. 2004;24(1):63-66.
47. Elias DA, Lax MJ, Anastakis DJ. Musculoskeletal images. Ganglion cyst of Guyon's canal causing ulnar nerve compression. Can J Surg. 2001;44(5):331-332.
48. Klauser AS, Halpern EJ, De Zordo T, et al. Carpal tunnel syndrome assessment with US: value of additional cross-sectional area measurements of the median nerve in patients versus healthy volunteers. Radiology. 2009;250(1): 171-177.
49. Wiesler ER, Chloros GD, Cartwright MS, et al. The use of diagnostic ultrasound in carpal tunnel syndrome. J Hand Surg Am. 2006;31(5): 726-732.
50. Duncan I, Sullivan P, Lomas F. Sonography in the diagnosis of carpal tunnel syndrome. AJR Am J Roentgenol. 1999;173(3):681-684.
51. Roll SC, Evans KD, Li X, et al. Screening for carpal tunnel syndrome using sonography. J Ultrasound Med. 2011;30(12):1657-1667.
52. Ozturk E, Sonmez G, Colak A, et al. Sonographic appearances of the normal ulnar nerve in the cubital tunnel. J Clin Ultrasound. 2008;36(6):325-329.
53. Okamoto M, Abe M, Shirai H, Ueda N. Morphology and dynamics of the ulnar nerve in the cubital tunnel. Observation by ultrasonography. J Hand Surg [Br]. 2000;25(1):85-89.
54. Van Den Berg PJ, Pompe SM, Beekman R, Visser LH. Sonographic incidence of ulnar nerve (sub)luxation and its associated clinical and electrodiagnostic characteristics. Muscle Nerve. 2013;47(6):849-855.
55. Campbell WW. Ulnar nerve subluxation. Muscle Nerve. 2013;48(6): 997-998.
56. Rezaei H, Torp-Pedersen S, af Klint E, et al. Diagnostic utility of musculoskeletal ultrasound in patients with suspected arthritis—a probabilistic approach. Arthritis Res Ther. 2014;16(5):448.
57. Ben Abdelghani K, Miladi S, Souabni L, et al. Role of ultrasound in assessing remission in rheumatoid arthritis. Diagn Interv Imaging. 2015;96(1): 3-10.
58. Wakefield RJ, Balint PV, Szkudlarek M, et al. Musculoskeletal ultrasound including definitions for ultrasonographic pathology. J Rheumatol. 2005;32(12):2485-2487.
59. Szkudlarek M, Court-Payen M, Strandberg C, et al. Power Doppler ultrasonography for assessment of synovitis in the metacarpophalangeal joints of patients with rheumatoid arthritis: a comparison with dynamic magnetic resonance imaging. Arthritis Rheum. 2001;44(9):2018-2023.
60. Torp-Pedersen S, Christensen R, Szkudlarek M, et al. Power and color Doppler ultrasound settings for inflammatory flow: impact on scoring of disease activity in patients with rheumatoid arthritis. Arthritis Rheumatol. 2015;67(2):386-395.
61. Szkudlarek M, Court-Payen M, Strandberg C, et al. Contrast-enhanced power Doppler ultrasonography of the metacarpophalangeal joints in rheumatoid arthritis. Eur Radiol. 2003;13(1):163-168.
62. Cheung PP, Dougados M, Gossec L. Reliability of ultrasonography to detect synovitis in rheumatoid arthritis: a systematic literature review of 35 studies (1,415 patients). Arthritis Care Res (Hoboken). 2010;62(3):323-334.
63. McGonagle D, Gibbon W, O'Connor P, et al. A preliminary study of ultrasound aspiration of bone erosion in early rheumatoid arthritis. Rheumatology (Oxford). 1999;38(4):329-331.
64. Wright SA, Filippucci E, McVeigh C, et al. High-resolution ultrasonography of the first metatarsal phalangeal joint in gout: a controlled study. Ann Rheum Dis. 2007;66(7):859-864.

65. Weidekamm C, Koller M, Weber M, Kainberger F. Diagnostic value of high-resolution B-mode and Doppler sonography for imaging of hand and finger joints in rheumatoid arthritis. Arthritis Rheum. 2003;48(2):325-333.
66. Fornage BD. Soft-tissue changes in the hand in rheumatoid arthritis: evaluation with US. Radiology. 1989;173(3):735-737.
67. Kang MH, Moon KW, Jeon YH, Cho SW. Sonography of the first metatarsophalangeal joint and sonographically guided intraarticular injection of corticosteroid in acute gout attack. J Clin Ultrasound. 2015;43(3):179-186.
68. Thiele RG, Schlesinger N. Diagnosis of gout by ultrasound. Rheumatology (Oxford). 2007;46(7):1116-1121.
69. Iagnocco A. Imaging the joint in osteoarthritis: a place for ultrasound? Best Pract Res Clin Rheumatol. 2010;24(1):27-38.
70. D'Agostino MA, Conaghan P, Le Bars M, et al. EULAR report on the use of ultrasonography in painful knee osteoarthritis. Part 1: prevalence of inflammation in osteoarthritis. Ann Rheum Dis. 2005;64(12):1703-1709.
71. Lakkaraju A, Sinha R, Garikipati R, et al. Ultrasound for initial evaluation and triage of clinically suspicious soft-tissue masses. Clin Radiol. 2009;64(6):615-621.
72. Hung EH, Griffith JF, Ng AW, et al. Ultrasound of musculoskeletal soft-tissue tumors superficial to the investing fascia. AJR Am J Roentgenol. 2014;202(6):W532-W540.
73. Carra BJ, Bui-Mansfield LT, O'Brien SD, Chen DC. Sonography of musculoskeletal soft-tissue masses: techniques, pearls, and pitfalls. AJR Am J Roentgenol. 2014;202(6):1281-1290.
74. Teefey SA, Dahiya N, Middleton WD, et al. Ganglia of the hand and wrist: a sonographic analysis. AJR Am J Roentgenol. 2008;191(3):716-720.
75. Bianchi S, Abdelwahab IF, Zwass A, Giacomello P. Ultrasonographic evaluation of wrist ganglia. Skeletal Radiol. 1994;23(3):201-203.
76. Wang G, Jacobson JA, Feng FY, et al. Sonography of wrist ganglion cysts: variable and noncystic appearances. J Ultrasound Med. 2007;26(10):1323-1328.
77. Akgul O, Guldeste Z, Ozgocmen S. The reliability of the clinical examination for detecting Baker's cyst in asymptomatic fossa. Int J Rheum Dis. 2014;17(2):204-209.
78. Rudikoff JC, Lynch JJ, Phillips E, Clapp PR. Ultrasound diagnosis of Baker cyst. JAMA. 1976;235(10):1054-1055.
79. Cronan JJ, Dorfman GS, Grusmark J. Lower-extremity deep venous thrombosis: further experience with and refinements of US assessment. Radiology. 1988;168(1):101-107.
80. Wagner JM, Lee KS, Rosas H, Kliewer MA. Accuracy of sonographic diagnosis of superficial masses. J Ultrasound Med. 2013;32(8):1443-1450.
81. Jacobson JA. Fundamentals of musculoskeletal ultrasound: Expert Consult-Online. Philadelphia: Elsevier Health Sciences; 2012.
82. Beggs I. Sonographic appearances of nerve tumors. J Clin Ultrasound. 1999;27(7):363-368.
83. Abreu E, Aubert S, Wavreille G, et al. Peripheral tumor and tumor-like neurogenic lesions. Eur J Radiol. 2013;82(1):38-50.
84. Murphey MD, Smith WS, Smith SE, et al. From the archives of the AFIP. Imaging of musculoskeletal neurogenic tumors: radiologic-pathologic correlation. Radiographics. 1999;19(5):1253-1280.
85. Widmann G, Riedl A, Schoepf D, et al. State-of-the-art HR-US imaging findings of the most frequent musculoskeletal soft-tissue tumors. Skeletal Radiol. 2009;38(7):637-649.
86. Brouns F, Stas M, De Wever I. Delay in diagnosis of soft tissue sarcomas. Eur J Surg Oncol. 2003;29(5):440-445.
87. Tagliafico A, Truini M, Spina B, et al. Follow-up of recurrences of limb soft tissue sarcomas in patients with localized disease: performance of ultrasound. Eur Radiol. 2015;25(9):2764-2770.
88. Choi H, Varma DG, Fornage BD, et al. Soft-tissue sarcoma: MR imaging vs sonography for detection of local recurrence after surgery. AJR Am J Roentgenol. 1991;157(2):353-358.
89. Montechiarello S, Miozzi F, Martinelli M, Giovagnorio F. Ultrasound picture of a wooden splinter evolved in phlegmon of the hand. J Ultrasound. 2010;13(1):38-40.
90. Shiels WE 2nd, Babcock DS, Wilson JL, Burch RA. Localization and guided removal of soft-tissue foreign bodies with sonography. AJR Am J Roentgenol. 1990;155(6):1277-1281.
91. Bradley M, Kadzombe E, Simms P, Eyes B. Percutaneous ultrasound guided extraction of non-palpable soft tissue foreign bodies. Arch Emerg Med. 1992;9(2):181-184.
92. Callegari L, Leonardi A, Bini A, et al. Ultrasound-guided removal of foreign bodies: personal experience. Eur Radiol. 2009;19(5):1273-1279.
93. Bureau NJ, Chhem RK, Cardinal E. Musculoskeletal infections: US manifestations. Radiographics. 1999;19(6):1585-1592.
94. Loyer EM, DuBrow RA, David CL, et al. Imaging of superficial soft-tissue infections: sonographic findings in cases of cellulitis and abscess. AJR Am J Roentgenol. 1996;166(1):149-152.

CHAPTER 24

The Shoulder

Colm McMahon and Corrie Yablon

SUMMARY OF KEY POINTS

- In the diagnosis of full-thickness rotator cuff tears, ultrasound is of comparable accuracy to magnetic resonance imaging, although it may be less accurate in the diagnosis of partial-thickness tears.
- The key to scanning the shoulder is meticulous technique using a protocol that systematically evaluates the entirety of the shoulder.
- Understanding of optimal patient positioning, probe orientation, and shoulder anatomy is critical to effective diagnostic shoulder ultrasound.
- Ultrasound allows dynamic assessment of subacromial and subcoracoid impingement, biceps subluxation, and rotator cuff integrity.

CHAPTER OUTLINE

CLINICAL PERSPECTIVE
SHOULDER ANATOMY
SCAN TECHNIQUE
Biceps Tendon Evaluation
Subscapularis Tendon Evaluation
Supraspinatus Evaluation
Infraspinatus, Teres Minor, and Posterior Shoulder Evaluation
Rotator Cuff Musculature Evaluation
ROTATOR CUFF DEGENERATION AND TEARS
Background
Tendinosis
Full-Thickness Rotator Cuff Tears
Partial-Thickness Rotator Cuff Tears
Postsurgical Rotator Cuff
Muscle Atrophy
Subacromial-Subdeltoid Bursa
Calcific Tendinitis
LONG HEAD BICEPS TENDON PATHOLOGY
ARTHROPATHY
Degenerative
Inflammatory
PITFALLS IN SHOULDER ULTRASOUND
CONCLUSION

CLINICAL PERSPECTIVE

The human **shoulder** represents an intricate balanced anatomic system capable of exerting force in multiple directions, in multiple different positions, all possible because of a number of static and dynamic structures, which when functioning well provide for the competing needs of movement and stability. Proper function of the shoulder is critical for activities ranging from the most basic of daily life to many sporting pursuits including those of the throwing athlete. The shoulder is, however, prone to injury, related to anatomic factors such as **subacromial impingement.**[1,2] Shoulder pain and limitation of motion are very common causes for quality-of-life impairment, medical resource use, and loss of workplace productivity.[3-7] In fact, about 50% of adults have at least one episode of shoulder pain yearly.[8] Clinical presentation varies from acute injury[9,10] to more chronic dysfunction, which is more common with advancing age.[11]

Although shoulder pain and dysfunction are common clinical complaints, the underlying etiology is variable, with causes including **rotator cuff pathology (degeneration, tears, calcific tendinosis),** long head biceps pathology, subacromial subdeltoid bursa pathology, arthropathy of the glenohumeral or acromioclavicular joint (which may be of inflammatory or degenerative cause), or osseous disease. Of these, **subacromial subdeltoid bursitis** and rotator cuff pathology are the most common causes of symptomatic shoulder disease.[12] Correct diagnosis is crucial for treatment decision making, allowing appropriate management with surgical or nonsurgical treatment, which may diminish the personal and societal effect of shoulder problems.[13,14] Of course, clinical history taking and examination are intrinsic parts of patient assessment, but the accuracy of clinical examination in diagnosis of the cause of shoulder pain is both modest and variable.[15-20]

In this clinical and socioeconomic setting, the advantages of ultrasound as a diagnostic test are myriad, as this technique is accurate, cost-effective, and well tolerated by patients. In the diagnosis of full-thickness rotator cuff tears, ultrasound is of comparable accuracy to magnetic resonance imaging (MRI), although it may be less accurate in the diagnosis of partial-thickness tears.[21-30] Ultrasound can also determine **muscle atrophy,** an important parameter in predicting successful surgical outcome of rotator cuff repair.[31] Ultrasound is a good alternative to MRI in patients who are claustrophobic, are of large size, or have

incompatible implanted metallic and electronic devices. Patients with shoulder pain tolerate ultrasound better than MRI owing to relatively increased patient comfort and diminished examination time.[32]

Ultrasound provides several benefits that MRI cannot. Ultrasound offers the possibility of dynamic assessment of the rotator cuff, allowing the patient to be imaged while engaging in the motion that causes pain or clicking. Ultrasound can assess **subacromial impingement, subcoracoid impingement,** and **biceps tendon subluxation** dynamically, in real time, and cine clips can be obtained. If there is a question as to pathology versus a normal variant, comparison to the contralateral side can be easily made. Dynamic compression of rotator cuff tears can aid in the assessment of cuff integrity. Ultrasound is also more sensitive than MRI to the detection of calcium deposits within the tendon. Finally, patients can receive the results of their examination instantaneously, and this adds tremendously to patients' satisfaction with the modality.[33]

It should be noted that ultrasound is not without limitations. In the clinical setting of instability, ligamentous injury, or suspected glenoid labral injury, MRI or MRI arthrography are preferred. Ultrasound is also of limited value in the evaluation of bony disorders, and plain radiography should be considered complementary in the assessment of patients with shoulder pain to further diagnosis of fracture, bone lesions, subacromial spurs, acromioclavicular osteophytes, acromiohumeral interval narrowing, glenohumeral and acromioclavicular alignment and joint space abnormality, and soft tissue calcification.

In view of these considerations, ultrasound should be considered a first-line investigation in patients with acute or chronic shoulder pain in whom rotator cuff tear is suspected. Imaging algorithms detailing the role of shoulder ultrasound in specific common scenarios have been published in a consensus statement by the Society of Radiologists in Ultrasound, a highly useful resource.[34]

SHOULDER ANATOMY

The shoulder consists of the osseous shoulder girdle with associated muscles and ligamentous structures.[35] Central to understanding the anatomy of the shoulder and scan technique is the anatomy of the **scapula** (Fig. 24.1). The scapula consists of a flat triangular bone with anterior and posterior surfaces in addition to the **glenoid fossa** laterally. The glenoid fossa is deepened by a fibrocartilaginous labrum, and lined with hyaline cartilage for articulation with the humerus at the synovial **glenohumeral joint.** The glenoid neck tapers to the flatter triangular body of the scapula. At the anterior aspect of the scapular body is the **subscapular fossa,** a concavity with oblique ridges that gives origin to the **subscapularis muscle.** The posterior surface of the scapula is convex posteriorly and divided into superior and inferior portions by the scapular spine. Above the spine is the **supraspinatus fossa,** which provides origin to the **supraspinatus muscle.** Below the spine is the **infraspinatus fossa,** with the **infraspinatus muscle** originating from the medial two-thirds, and the **teres minor** originating along the medial border. Extending superolaterally from the scapular spine is the **acromion,** a flattened hooklike structure that curves from posterior to anterior where it articulates with the **clavicle** at the **acromioclavicular joint.** The acromion and scapular spine give origin to the **deltoid muscle.** The acromion is important functionally and for the purpose of ultrasound technique as it overlies the supraspinatus and infraspinatus in the neutral position, prohibiting accurate visualization unless specific positioning maneuvers are undertaken. Also, osseous spurs **(subacromial spurs)** along the undersurface of the acromion may be a cause for **subacromial**

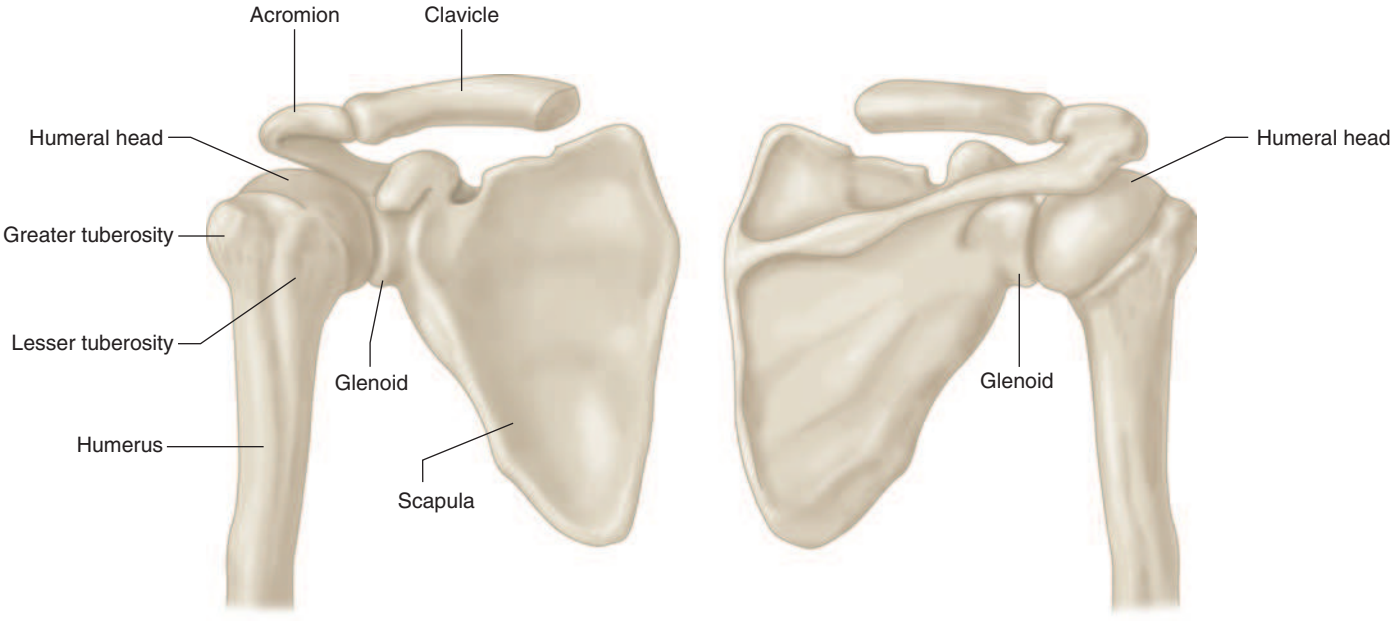

FIG. 24.1 **Illustration of the Scapula and Osseous Landmarks.**

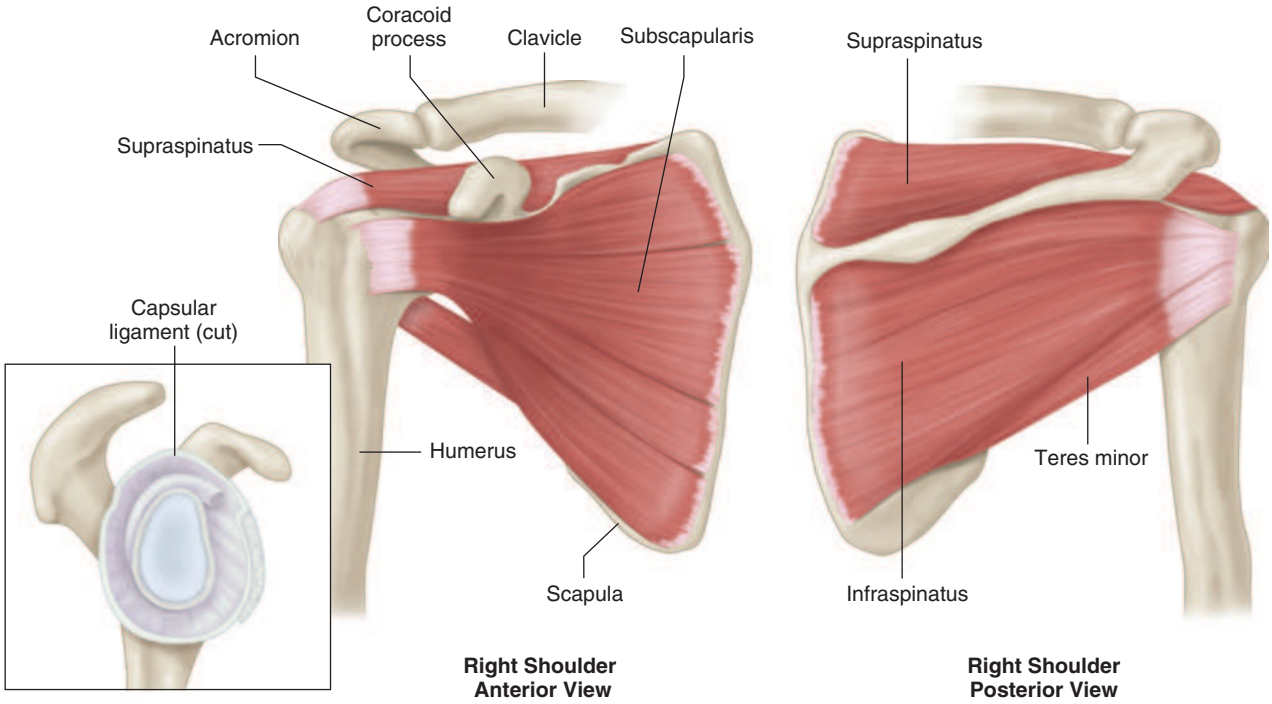

FIG. 24.2 Illustration of Rotator Cuff Anatomy.

impingement. These typically form at the attachment of the **coracoacromial ligament.** Furthermore, **osteoarthritis** at the acromioclavicular joint may result in osteophyte formation, which, when present inferiorly, may cause rotator cuff tendon impingement. The **coracoid process** is a fingerlike curved process extending anteriorly from the scapular neck, giving attachment to the short head of **biceps, coracobrachialis,** and **pectoralis minor muscles** in addition to the **coracohumeral ligament,** and also the **coracoclavicular ligaments,** which help stabilize the **acromioclavicular joint.**

The **rotator cuff** consists of four muscles: the subscapularis, supraspinatus, infraspinatus, and teres minor muscles (Fig. 24.2). These originate from the scapula and insert on the proximal humerus. Normal rotator cuff tendons are about 4 to 6 mm in thickness,[36] tapering out smoothly from medial to lateral along the insertional footprint at the greater tuberosity. The **subscapularis** muscle is a multipennate structure that originates from the anterior surface of the scapula, which converges to a flat tendon laterally to insert on the lesser tuberosity. Of note, the inferior one-third of the subscapularis remains muscular to the level of the lesser tuberosity.[37] The supraspinatus muscle originates from and occupies the supraspinatus fossa, with its tendon extending laterally to insert on the greater tuberosity of the humerus at its anterior aspect. The tendon has a more cordlike component anteriorly and is flatter and more quadrilateral in short axis at its mid and posterior fibers. The **infraspinatus** muscle originates at the infraspinatus fossa and passes laterally to insert on the posterosuperior aspect of the greater tuberosity. The fibers of the supraspinatus and infraspinatus tendons merge at their posterior and anterior borders, respectively, forming a conjoint insertion. The teres minor originates along the lateral border of the scapular body and inserts along the posterior aspect of the greater tuberosity, inferior to the infraspinatus.

The **long head of biceps tendon** originates from a bony tubercle at the superior glenoid, the supraglenoid tubercle, and from the superior labrum. It passes inferolaterally between the subscapularis and supraspinatus tendons, which form the inferior and superior borders of the **rotator interval** (Fig. 24.3). Within the rotator interval, the tendon is stabilized by a ligamentous sling formed by the coracohumeral and superior glenohumeral ligaments. Passing inferolaterally out of the rotator interval, the long head of biceps tendon becomes extraarticular and extends inferiorly in the bicipital or intertubercular groove, which lies between the greater and lesser tuberosities. The biceps tendon is stabilized in the groove by the transverse ligament, formed by tendinous fibers at the subscapularis insertion.[38]

The **subacromial-subdeltoid bursa** is a synovium-lined flat, thin structure that lies between the rotator cuff tendons and the overlying deltoid muscle and acromion.[39] It serves to reduce friction between the rotator cuff and the overlying structures, permitting smooth movement.

SCAN TECHNIQUE

For consistent and accurate shoulder ultrasound performance, a standard protocol is suggested with comprehensive evaluation in every case, rather than targeted scanning (Table 24.1).[40-44] The patient should be sitting upright if possible, either on a rotating stool or at the edge of a bed. A chair with a backrest should not be used, because this would interfere with patient positioning. Likewise, the sonographer should also sit on a rotating stool, with the seat position somewhat higher than the patient's, so

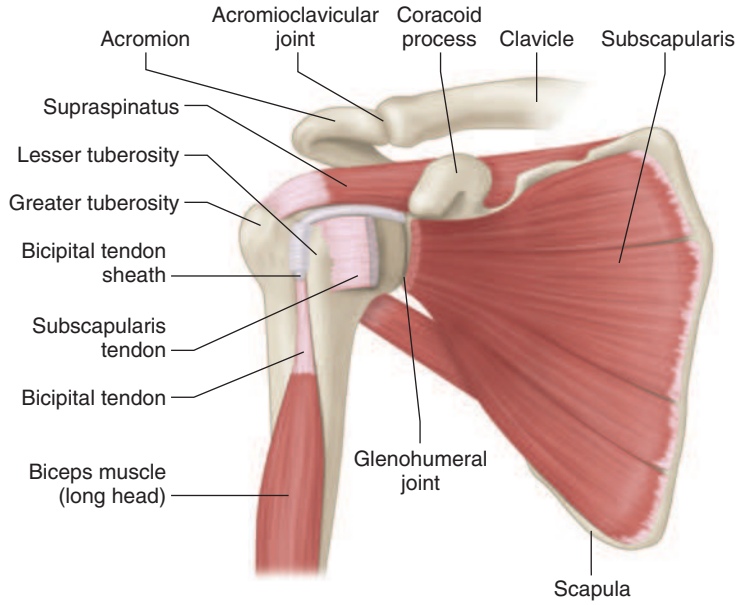

FIG. 24.3 **Illustration of the Long Head Biceps Tendon in the Rotator Interval and in the Bicipital Groove.**

TABLE 24.1 Routine Shoulder Ultrasound Protocol

Long head of biceps tendon	Long and short-axis static images
Subscapularis tendon	Long and short-axis static images Dynamic evaluation for subcoracoid impingement
Supraspinatus tendon	Long and short-axis static images Dynamic evaluation for subacromial impingement
Infraspinatus tendon	Long and short-axis static images
Teres minor tendon	Long and short-axis static images
Supraspinatus and infraspinatus muscles	Sagittal images—panorama if possible
Posterior shoulder	Axial plane image
Acromioclavicular joint	Coronal plane image

that the sonographer's arm can be held in a natural, ergonomic position. If a patient is wheelchair-bound, it is helpful if possible to temporarily remove the backrest. If the patient cannot sit upright, more limited scanning is possible with the patient lying supine, with the affected shoulder at the edge of the bed. A high-frequency 12- to 15-MHz linear array transducer is used to permit high-resolution scanning. Occasionally, in larger patients, a lower-frequency probe (9 MHz) may be needed to achieve tissue penetration to the required depth, but this incurs a reduction in resolution.

When scanning any tendon, care should be taken to maintain an angle of close to 90 degrees between the probe and the tendon of interest to avoid artifactual hypoechogenicity due to **anisotropy.** This is discussed in more detail later in the chapter.

Biceps Tendon Evaluation

Biceps tendon evaluation is best performed with the arm in a neutral position, resting the forearm on the patient's ipsilateral thigh, with elbow flexed and the palm up (Fig. 24.4). In this position, the biceps tendon is seen anteriorly.[45] The tendon can be imaged in its short axis within the bicipital groove by holding the probe transversely with respect to the upper arm and following the course of the tendon inferiorly where it passes deep to the pectoralis major tendon insertion on the humerus. In short axis, the tendon appears as a homogeneous, echogenic, round or ovoid structure that may be accompanied by a trace of fluid within its tendon sheath. The normal biceps tendon is 2 to 4 mm thick.[36] The tendon can be followed superiorly and medially into the rotator interval, by angling the probe more obliquely to remain orthogonal to its short axis. Finally, the probe can be rotated 90 degrees to view the tendon in its long axis where it should appear smooth and fibrillar.

Subscapularis Tendon Evaluation

The subscapularis is scanned with the patient's arm at the side, in external rotation with the palm facing up[44] (Fig. 24.5). The tendon should be evaluated in long axis, with the probe aligned with the subscapularis tendon, and in short axis, with the probe held perpendicular to the subscapularis tendon. The coracoid process of the scapula, medial to the subscapularis and palpable in many patients, is a useful anatomic landmark when locating the subscapularis tendon. The tendon fibers can be seen emanating from the broad multipennate muscle belly. The normal hypoechoic muscle should not be mistaken for fluid. In this position the patient's arm can be rotated from external rotation to neutral position, while observing the passage of the tendon fibers deep to the coracoid process to assess for subcoracoid impingement (Video 24.1). This dynamic maneuver is also useful to assess for long head biceps tendon subluxation from the bicipital groove.

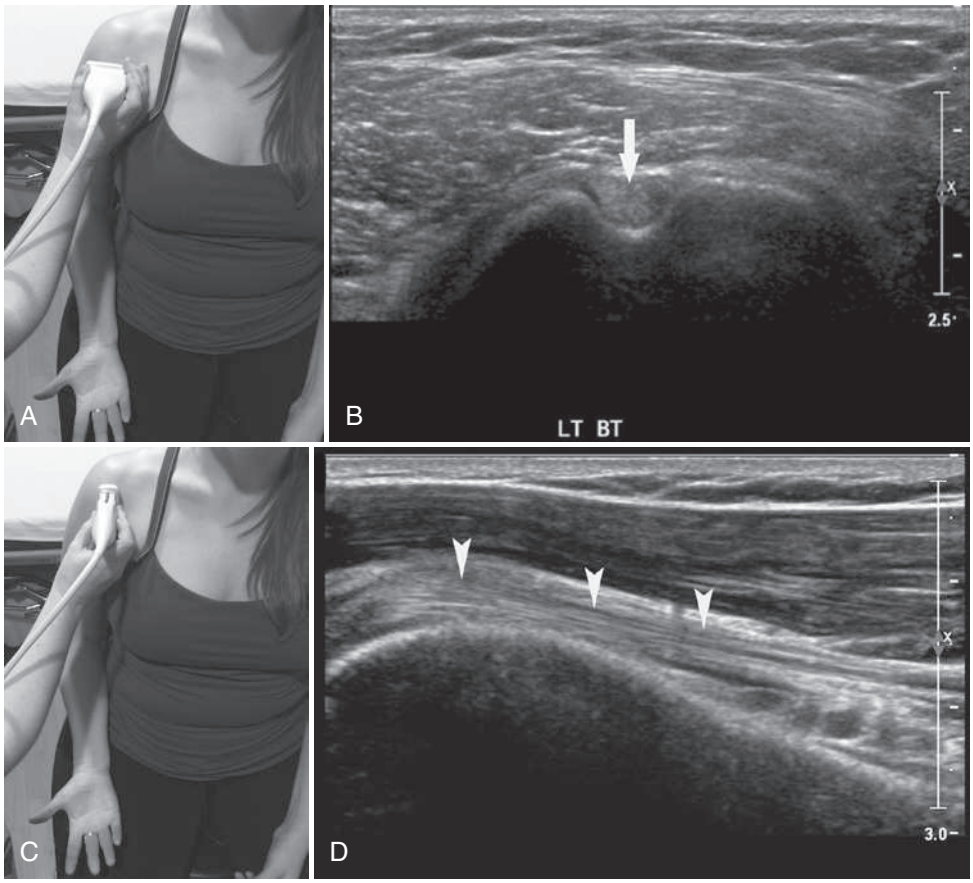

FIG. 24.4 Long Head Biceps Tendon (LHBT). (A) Photograph of the probe position for imaging the LHBT in short axis. The patient's shoulder is externally rotated, with the elbow flexed and held tight to the body, with the forearm palm up, resting on the patient's lap. This position rotates the LHBT anteriorly. **(B)** Short-axis image of LHBT *(arrow)*. **(C)** Photograph of probe position for imaging the LHBT in long axis. The probe is rotated 90 degrees to the short-axis starting position. Patient position remains the same as for the short-axis image. **(D)** Long-axis image of LHBT *(arrowheads)*.

Supraspinatus Evaluation

In neutral position the supraspinatus tendon is largely obscured from view by the overlying acromion. To draw the tendon out from under the acromion, specific maneuvers are needed. The position, originally described by Crass[46] (Fig. 24.6), consists of asking the patient to place his or her hand behind the back, reaching toward the opposite back pocket with the back of the hand. This results in flexion, internal rotation, and adduction of the shoulder. In this position, the greater tuberosity is located anteriorly, so the supraspinatus tendon courses anterolaterally to its insertion and is drawn out from under the acromion, allowing visualization. Patients with shoulder pain often find this position difficult to achieve and maintain, so an alternative position is the **"modified Crass position"** (Fig. 24.7) in which the patient puts the palm of the hand on the ipsilateral hip or buttock, with elbow flexed and directed posteriorly. In this position, the greater tuberosity is similarly positioned as in the original **Crass position,** but the maneuver is usually well tolerated by patients. The supraspinatus tendon will again course anterolaterally to the greater tuberosity.

To visualize the supraspinatus in long axis, the probe should parallel the long-axis orientation of the tendon, resulting in an oblique sagittal probe position relative to the patient, with the probe directed toward the patient's ear (see Fig. 24.7A). The long head biceps tendon in long axis with the patient in the **modified Crass position** is a useful landmark for locating the most anterior portion of the supraspinatus tendon (Fig. 24.8). If the probe in long axis is then moved posteriorly in the same plane, the entire supraspinatus will be assessed. Correctly imaged, the normal supraspinatus should appear smooth, echogenic, and fibrillar, tapering at its insertion or "footprint" with a so called "bird's beak appearance." Normal rotator cuff tendons possess a fibrocartilaginous interface at their bony attachment that may manifest as a thin hypoechoic band paralleling the insertional cortex, similar in echogenicity to hyaline cartilage.[37] This should not be mistaken for a tear.

The probe is then rotated 90 degrees to image the tendon in short axis. In this position, the more cordlike anterior fibers of the supraspinatus tendon are seen merging with the flatter quadrilateral mid and posterior fibers. While visualizing the supraspinatus tendon in short axis, it is important to move the probe anteriorly so that the long head biceps tendon is imaged in short axis. This ensures that the entire anterior leading edge of the supraspinatus has been evaluated. In short axis, the **rotator interval** is well seen

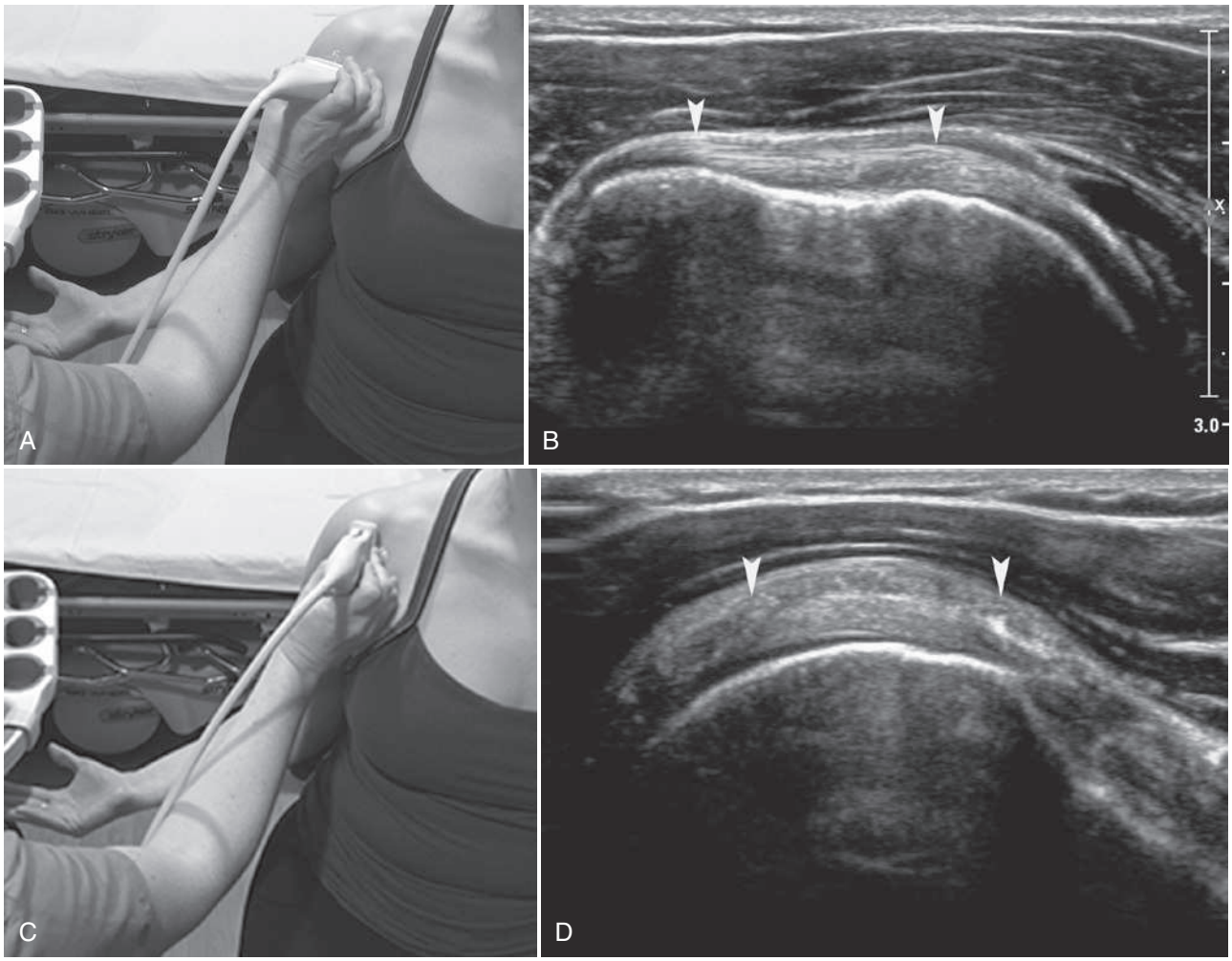

FIG. 24.5 Subscapularis Tendon. (A) Long-axis probe position. From the long head biceps tendon (LHBT) starting position, the patient now externally rotates the elbow, keeping the elbow tight to the body with the palm up. This position elongates the subscapularis tendon and rotates the tendon out from under the coracoid process, allowing visualization. The probe is placed across from the coracoid process. Note that the probe position is similar for imaging the LHBT in short axis, but the patient's position is different. **(B)** Long-axis image of subscapularis tendon *(arrowheads).* **(C)** Short-axis probe position. From the long-axis starting position, the probe is simply turned 90 degrees to image the subscapularis in short axis, with the patient remaining in the same position. Note that the probe position is similar to the LHBT long-axis probe position, but the patient's position is different. **(D)** Short-axis image of subscapularis tendon *(arrowheads).* See also Video 24.1.

anterior to the tendon, with the biceps tendon coursing through the interval, also in short axis, stabilized by the **coracohumeral ligament** and **superior glenohumeral ligament.**

As with all tendons, the supraspinatus should be scanned through its entirety from anterior to posterior in long axis and medial to lateral in short axis. When the posterior fibers of the supraspinatus tendon are reached, the more posteriorly oriented fibers of the infraspinatus tendon are routinely encountered; this is a helpful landmark to ensure the entire supraspinatus tendon has been studied. It is important to note that as the transducer is moved posteriorly, the greater tuberosity changes shape, from ledgelike to flat. This area of transition is where the anterior infraspinatus fibers overlap the posterior supraspinatus fibers. A discrete overlap of fibers can be visualized at this juncture (Fig. 24.9, Video 24.2). Continuing posteriorly from this overlap, the infraspinatus fibers can be evaluated in their entirety, looking for the similar normal fibrillar pattern in the long axis, and the echogenic appearance in the short axis.

The **rotator cable** is a thin fibrous band contiguous with the coracohumeral ligament that passes along the deep surface of the supraspinatus and infraspinatus tendons.[47] This bandlike structure is oriented perpendicular to the long axis of the rotator cuff, running in an anterior to posterior direction, and is felt to have a biomechanical role in stress distribution, likened to the cable of a suspension bridge.[48] It can be visualized consistently with ultrasound, seen in its short axis where it appears elliptical, when scanning the long axis of the supraspinatus and infraspinatus (Fig. 24.10). It is located about 1 cm (average 9 mm, range 4-15 mm[47]) medial to the rotator cuff insertion at the greater tuberosity.

Dynamic assessment for **subacromial impingement** of the supraspinatus can now be performed. The patient's arm rests in a neutral position at his or her side, and the probe is positioned in a coronal plane, with the acromion at the medial aspect of the field of view, and the greater tuberosity laterally. The patient then abducts the arm slowly, and the motion of the supraspinatus

FIG. 24.6 Crass Position. The patient places her arm behind her back with the dorsum of the hand resting on the contralateral back pocket. This position rotates the supraspinatus tendon from underneath the acromion.

tendon under the acromion is observed. The motion should be smooth and uninterrupted, without deformation of the tendon under the acromion, deformation of the bursa, or pooling of bursal fluid (Video 24.3).

A useful alternative technique to assess the supraspinatus has been described by Turrin and Cappello.[49] In this technique, the patient lies supine with the affected shoulder at the edge of the bed, but allows the arm to drop over the side of the bed, with the elbow extended and the forearm pronated. This can be particularly helpful in patients who are unable to sit—for example following cerebrovascular accident with hemiplegia, when associated shoulder pain is not uncommon, though of varied etiology (related to **subluxation, spasticity, adhesive capsulitis,** or **rotator cuff tears**), and standard positioning in the seated position may be difficult.[50]

Infraspinatus, Teres Minor, and Posterior Shoulder Evaluation

Several methods of evaluation of the infraspinatus have been described. The patient can remain in the modified Crass position, or with the arm hanging at the side, and scanning can simply

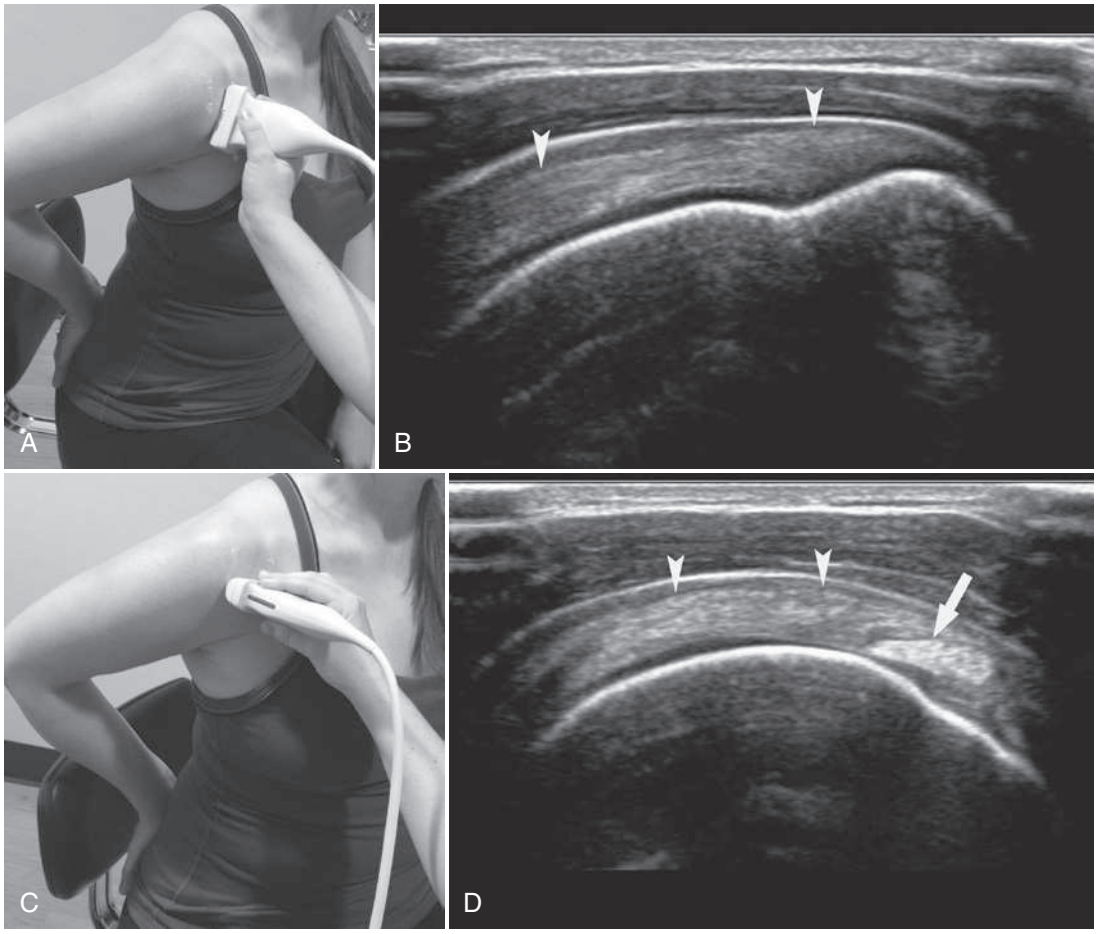

FIG. 24.7 Supraspinatus Tendon and Modified Crass Position. Probe position for supraspinatus in long axis, with the patient in the modified Crass position. The patient places her arm behind her back, palm on the ipsilateral back pocket, with the elbow straight back, as tight to the body as possible. This position rotates the supraspinatus from underneath the acromion. This position is usually better tolerated by patients who have a rotator cuff tear. **(A)** The probe is placed somewhat obliquely, directed toward the patient's ear. **(B)** Long-axis image of the supraspinatus tendon *(arrowheads).* **(C)** Short-axis probe position. The patient remains in the modified Crass position and the probe is rotated 90 degrees from the long-axis starting position. **(D)** Short-axis image of the supraspinatus tendon *(arrowheads).* Note that the long head of biceps tendon is visualized anterior to the supraspinatus tendon *(arrow).*

be continued posteriorly from the supraspinatus both in long and short axis.

An alternate position of scanning the infraspinatus has been described, in which the patient is asked to bring the arm forward across the chest, resting the hand on the contralateral shoulder.[44,51] These positions allow imaging of the infraspinatus tendon and muscle. The probe is held in an oblique transverse orientation, placed on the posterior shoulder to parallel the long axis of the infraspinatus tendon, using the inferior border of the scapular spine as a visual landmark (Fig. 24.11). In long axis the tendon appears similar to the supraspinatus in morphology, although having a more elongated tapered appearance at its insertion, lacking the bird's beak appearance seen at the supraspinatus footprint. The probe is then rotated 90 degrees, to the short axis of the infraspinatus, and the tendon and muscle are evaluated. The normal muscle is hypoechoic and positioned below the scapular spine in the infraspinatus fossa.

The teres minor tendon is also evaluated in this position and is seen inserting at the posterior aspect of the greater tuberosity, inferior to the infraspinatus insertion. The teres minor muscle can be seen arising from the posterolateral scapula, inferior to the infraspinatus muscle.

Also in this position, the posterior shoulder is seen, with visualization of glenohumeral joint fluid and limited views of the posterior labrum and spinoglenoid notch. Scanning the posterior shoulder with external rotation may aid visualization of a glenohumeral effusion.[52]

Rotator Cuff Musculature Evaluation

Using the scapular spine as a visual landmark, the supraspinatus muscle in the supraspinatus fossa can be imaged by placing the probe perpendicular to the scapular spine (Fig. 24.12). This demonstrates the muscle in its short axis. The normal muscle should be hypoechoic and convex in contour, and should fill the

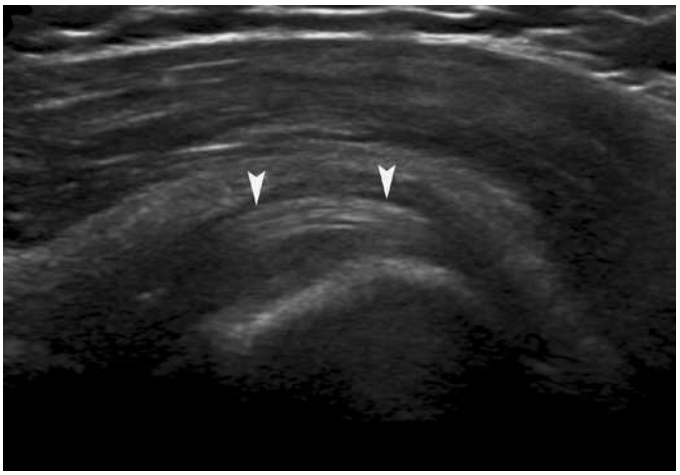

FIG. 24.8 Long-Axis Biceps Tendon Image, With Shoulder in the Modified Crass Position. This is a good starting point for imaging the supraspinatus tendon in long axis. Once the long head biceps tendon is seen well in long axis *(arrowheads),* the probe can simply be moved posteriorly to image the supraspinatus tendon.

FIG. 24.9 Overlap of Posterior Supraspinatus *(Arrow)* and Anterior Infraspinatus Fibers *(Arrowheads)* Seen in Long Axis. See also Video 24.2.

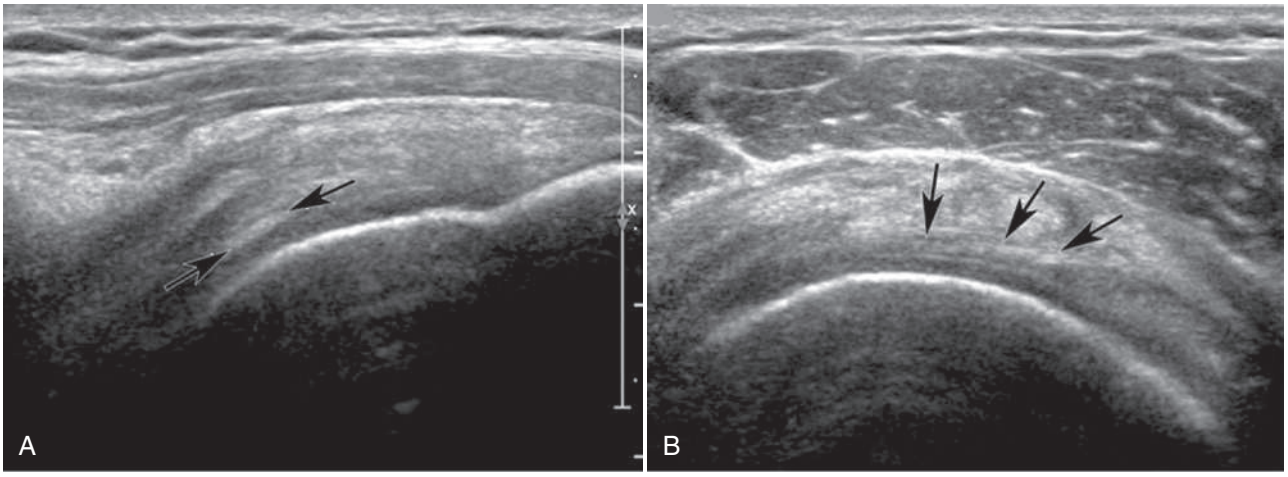

FIG. 24.10 Rotator Cable. (A) The rotator cable *(arrows)* is visualized in short axis along the articular surface of the supraspinatus tendon, when this tendon is imaged in long axis. **(B)** The rotator cable *(arrows)* is visualized as a linear structure in its long axis *(arrows)* along the articular surface of the supraspinatus tendon, when this tendon is imaged in short axis. (Courtesy of Dr. Yoav Morag, Ann Arbor, MI.)

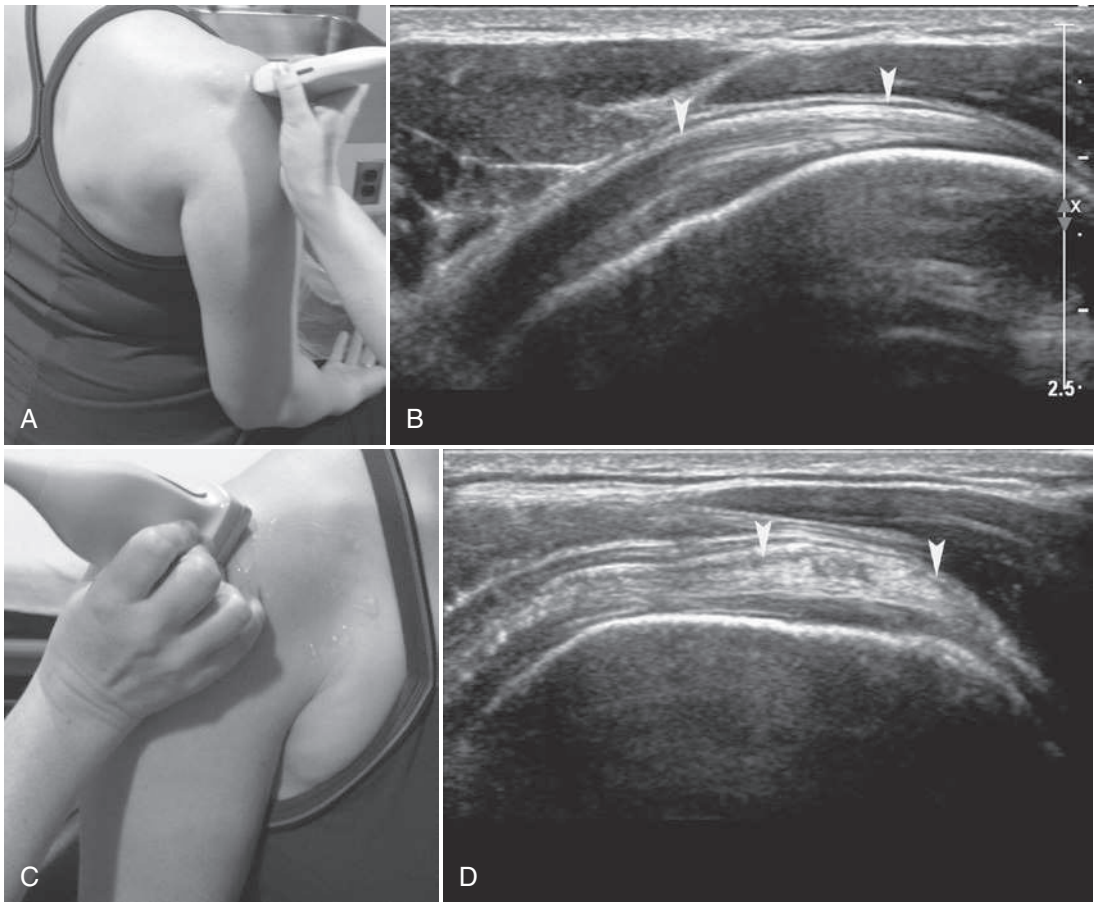

FIG. 24.11 Infraspinatus Tendon. (A) Long-axis probe position. The patient can simply rest the arm at the side, with the forearm palm up in the lap. The probe is placed under the scapular spine and moved laterally to see the distal insertion on the greater tuberosity. **(B)** Long-axis image of infraspinatus tendon *(arrowheads).* **(C)** Short-axis probe position. The probe is rotated 90 degrees to the infraspinatus long-axis starting position. **(D)** Short-axis image of infraspinatus tendon *(arrowheads).*

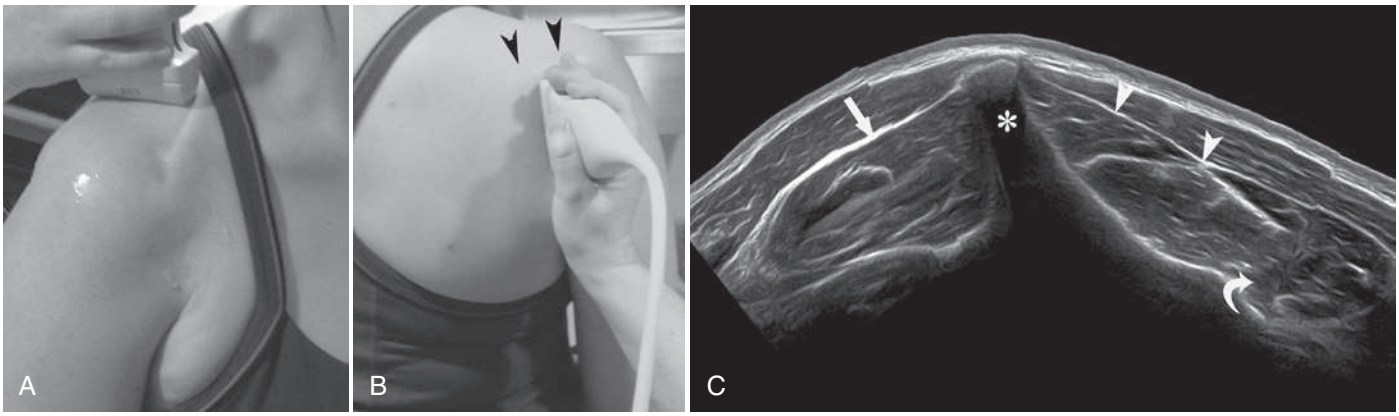

FIG. 24.12 Rotator Cuff Musculature. (A) Probe position for supraspinatus muscle. The probe is placed at the top of the shoulder, medial to the acromioclavicular joint, and posterior to the clavicle. **(B)** Probe position for infraspinatus and teres minor muscles. The probe is placed 90 degrees to the scapular spine, just inferior to the scapular spine *(arrowheads).* **(C)** Extended field-of-view image of supraspinatus *(straight arrow),* infraspinatus *(arrowheads),* and teres minor *(curved arrow).* Note the spine of the scapula (*) separating the supraspinatus and infraspinatus muscles.

supraspinatus fossa. The central tendon should be visible within the muscle.

To image the infraspinatus and teres minor muscles, the transducer is moved distal to the scapular spine, remaining perpendicular to the spine. A relative comparison and assessment of muscle volume and echogenicity can easily be made by using an extended field-of-view scan technique.

ROTATOR CUFF DEGENERATION AND TEARS

Background

Rotator cuff dysfunction, either due to tear or to tendon degeneration, is the most common cause of referral for evaluation of the shoulder.[53] Likewise, rotator cuff disease is the most frequent cause for referral for shoulder ultrasound. The supraspinatus tendon is the most commonly injured tendon in the rotator cuff.[54] The incidence of rotator cuff tears rises as patients age. Up to 22% of patients age 65 and older have rotator cuff tears.[55] It is interesting to note that 70% of imaged patients age 65 and older have asymptomatic rotator cuff defects.[56] Rotator cuff tears in patients younger than 40 are uncommon, but they do occur in the setting of acute trauma or sports-related injuries. Rotator cuff tears in patients older than 40 are usually secondary to tendon degeneration.

Tendinosis

Tendinosis of the rotator cuff is a degenerative process that may be associated with shoulder pain. Histologically, there is no inflammatory component (hence the term **"tendinitis"** is not appropriate for this condition), but rather **mucoid degeneration** and frequently **chondroid metaplasia** are present. On ultrasound, tendinosis appears heterogeneous or hypoechoic, with tendon thickening, and loss of the normal fibrillar pattern[57] (Fig. 24.13). Although discrete defects or tears are not encompassed by this diagnosis, they may coexist.

Full-Thickness Rotator Cuff Tears

Ultrasound is a reliable method for diagnosis of rotator cuff tears, with sensitivity and specificity over 90%[21,26,28,29,58,59] for full-thickness tears, and low interobserver variability.[60,61] Full-thickness tears are visualized as a hypoechoic or anechoic gap within the rotator cuff (Fig. 24.14), which may also have a concave contour at its bursal border.[30,62] Alternatively, a greatly retracted tear can result in nonvisualization of the rotator cuff tendon[62] (Fig. 24.15). This occurs because the tendon may retract deep to the acromion, and is likely in cases in which the degree of retraction exceeds 3 cm.[63] When a full-thickness tear is present, the gap between the retracted tendon end and the greater tuberosity or distal tendon stump may be filled with hypoechoic fluid or echogenic debris (Fig. 24.16) and granulation tissue. Alternatively, the subacromial-subdeltoid bursa (frequently thickened) and the deep surface of the deltoid muscle may occupy the defect created by the tear.[29]

Small foci of debris within the tear gap may give the appearance of mobile or "floating" bright spots.[59] Fluid within the tear gap my accentuate visualization of the underlying humeral head articular cartilage owing to enhanced through transmission of the ultrasound beam, referred to as the **"cartilage interface sign"**[64] (Fig. 24.17). Occasionally one may be uncertain as to whether abnormal echotexture in the location of the rotator cuff represents a partial tear or a full-thickness tear with intervening granulation tissue and debris. Dynamic compression of the abnormal area may clarify this confusion by causing complex fluid and debris to swirl within the rotator cuff tear.

It may be helpful to ascertain if a tear is more likely to be acute or chronic because acute tears are felt to have a greater chance of successful surgical outcome. In this regard, the findings of glenohumeral and bursal effusions are more common in acute tears. In addition, midsubstance tears, medial to the bone-tendon junction, are more likely to be acute. On the other hand, severely retracted tears are more likely to be chronic.[65] In chronic full-thickness tears, the tendon gap may be filled with

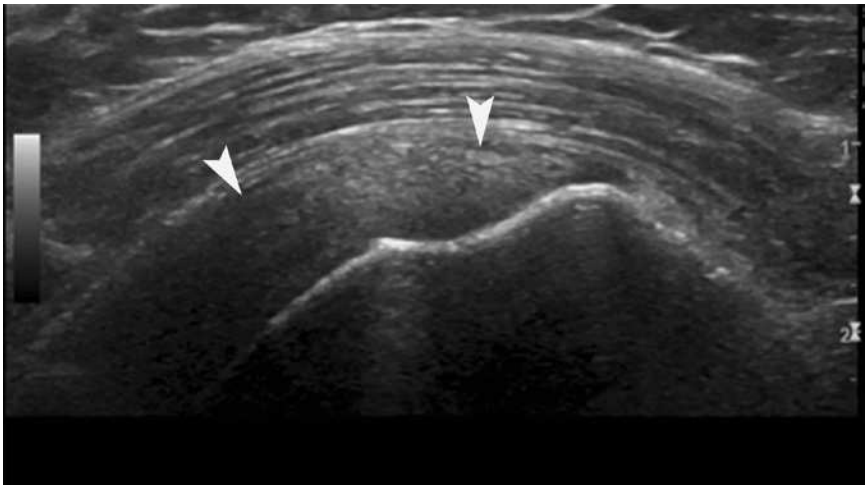

FIG. 24.13 Tendinosis of the Supraspinatus. Long-axis image of the supraspinatus tendon *(arrowheads)* demonstrates hypoechogenicity and diffuse loss of normal fibrillar echotexture.

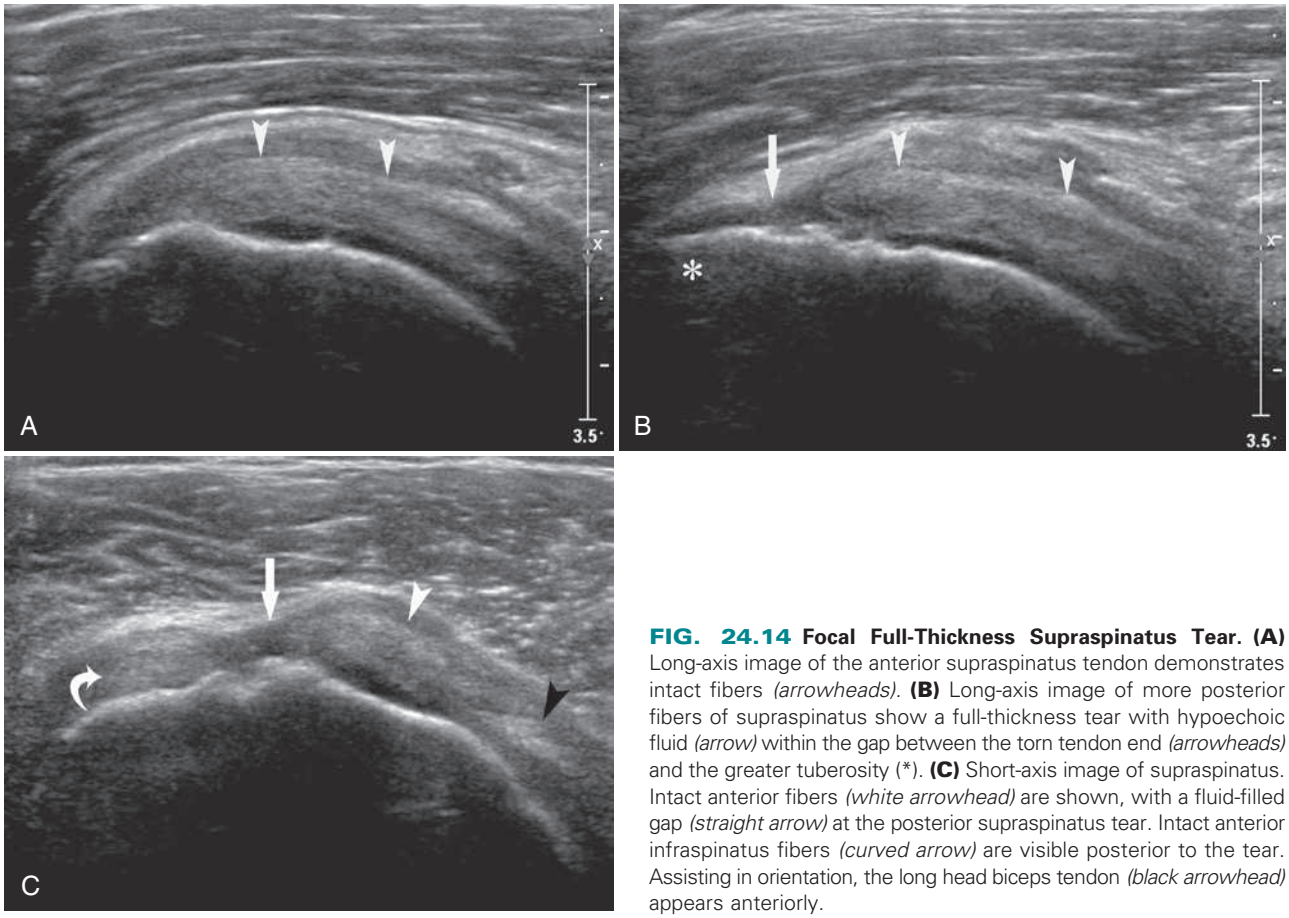

FIG. 24.14 Focal Full-Thickness Supraspinatus Tear. (A) Long-axis image of the anterior supraspinatus tendon demonstrates intact fibers *(arrowheads)*. **(B)** Long-axis image of more posterior fibers of supraspinatus show a full-thickness tear with hypoechoic fluid *(arrow)* within the gap between the torn tendon end *(arrowheads)* and the greater tuberosity (*). **(C)** Short-axis image of supraspinatus. Intact anterior fibers *(white arrowhead)* are shown, with a fluid-filled gap *(straight arrow)* at the posterior supraspinatus tear. Intact anterior infraspinatus fibers *(curved arrow)* are visible posterior to the tear. Assisting in orientation, the long head biceps tendon *(black arrowhead)* appears anteriorly.

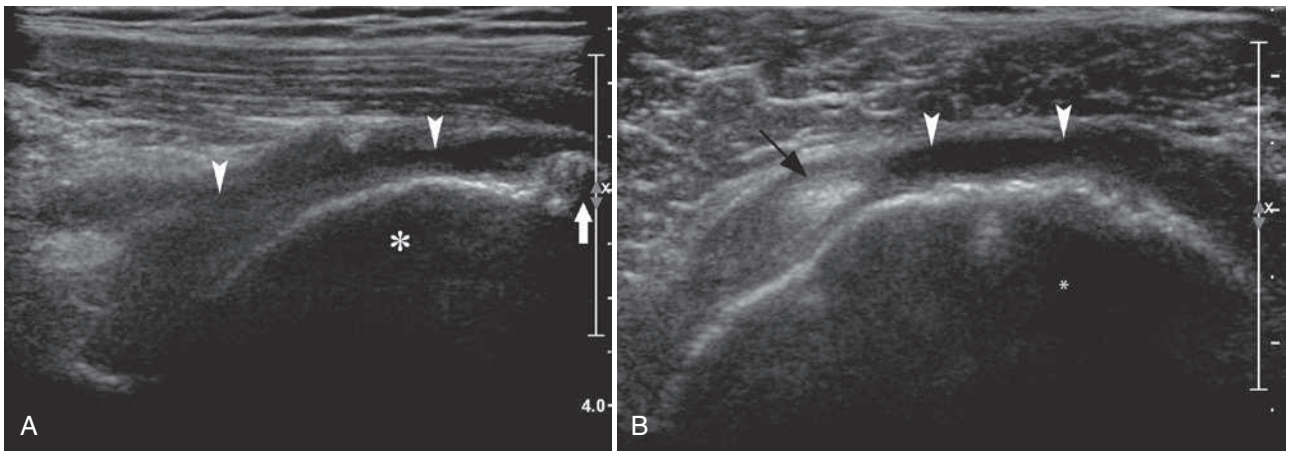

FIG. 24.15 Full-Thickness Supraspinatus Tear With Retraction of the Tendon Beneath the Acromion. Image in the expected location of the supraspinatus tendon in long **(A)** and short **(B)** axis demonstrates absence of the tendon above the humeral head (*) and greater tuberosity *(white arrow)*. Fluid and debris are seen in place of the normal tendon *(arrowheads)*. Note the intact long head biceps tendon anteriorly *(black arrow)*.

noncompressible, complex echogenic debris and granulation tissue that are contiguous with the subacromial subdeltoid bursa, and this may give the false impression of rotator cuff volume to the novice practitioner.

Partial-Thickness Rotator Cuff Tears

As with full-thickness rotator cuff tears, partial-thickness tears occur in both younger and older patients. Partial tears occur more commonly than full-thickness tears in younger patients, and most commonly occur in young athletes. Partial articular-sided supraspinatus tears are the most common subtype in the young athlete.[66] In the older patient population, partial-thickness tears also most commonly occur in the supraspinatus tendon, but the most common cause is tendon degeneration, with increased incidence as patients age.

FIG. 24.16 Focal Full-Thickness Tear of Supraspinatus Tendon. In this long-axis image of the supraspinatus tendon, there is a focal full-thickness tear, and the gap between the tendon retracted end and the greater tuberosity is filled with echogenic debris *(arrow)* and fluid.

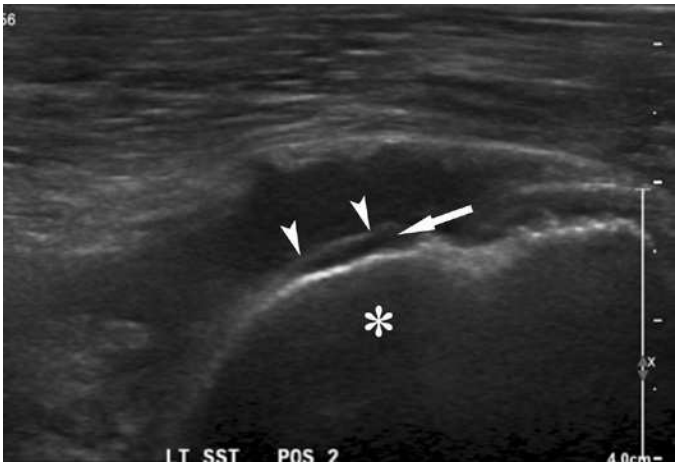

FIG. 24.17 Full-Thickness Supraspinatus Tear With Associated Cartilage Interface Sign. A hyperechoic line *(arrowheads)* is seen along the surface of the normal hypoechoic cartilage *(arrow),* along the superior aspect of the humeral head (*).

Partial-thickness tears are characterized by a focal area of hypoechogenicity or mixed echogenicity involving one side of the tendon, but not extending through the entire thickness.[58] There are several subtypes of partial-thickness tears of the rotator cuff (Figs. 24.18 and 24.19). **Bursal-sided partial-thickness tears** (Fig. 24.19A and B) occur superficially, just deep to the **subacromial subdeltoid bursa. Articular-sided tears** (see Fig. 24.19C and D) occur at the undersurface of the tendon in contiguity with the joint space. **Intrasubstance tears** (Fig. 24.19E) can occur either within the substance of the tendon footprint at the enthesis or longitudinally within the tendon fibers. These tendons may not be identified at arthroscopy because they do not communicate with either the bursal or the articular surfaces of the tendon.

A specific partial-thickness tear type is the **"rim-rent" tear** (see Fig. 24.19F), occurring at the articular side of the supraspinatus tendon, extending into the tendon footprint on the greater tuberosity.[67,68] This type of tear is most commonly seen in athletes who engage in overhead-throwing activities.

Partial-thickness tears vary from small, 1- to 2-mm tears to those involving more than 50% of tendon thickness. Although tears of 50% or greater have typically been referred for repair, patients with tears involving as little as 25% of the tendon may benefit from arthroscopic debridement.[69,70] Surgical decisions, however, are made in the context of the individual patient performance status, limitation by the injury, comorbidities, and patient preference. Partial tears occur most commonly along the articular side of the tendon in younger patients.[70] Care must be taken to adequately assess the anterior leading edge fibers of the supraspinatus tendon, where these tears can often occur.[71] Bursal-sided partial-thickness tears may manifest as flattening of the bursal contour of the tendon of varying severity.[29] This may lead to an hourglass-like diameter shift between areas of normal and attenuated tendon.[28]

An associated sign frequently observed in the setting of both partial- and full-thickness rotator cuff tears is the finding of cortical irregularity of the greater tuberosity, a finding with a 75% positive predictive value for the presence of an associated rotator cuff tear.[72] This is more severe in full-thickness tears and represents bony remodeling with irregularity, pitting, and erosion.[73] A second sign that can be seen in both partial articular-sided and full-thickness tears is the **"cartilage interface" sign,** mentioned earlier.

In analysis of partial- and full-thickness tears, it is important to quantify the extent of the tear in both its long and short axis (tear length and width); for example, in the case of a supraspinatus tendon tear, a measurement of the medial to lateral tear length should be made in long axis, and a measurement of the anterior to posterior tear width should be made on short-axis imaging.

Postsurgical Rotator Cuff

After surgical rotator cuff repair, the appearance of the rotator cuff and surrounding soft tissues is abnormal, as can be expected, with loss of normal soft tissue planes and abnormal echotexture of the rotator cuff tendon. Because of loss of normal interface with the overlying subacromial bursa, dynamic assessment may aid in identification and visualization of the supraspinatus tendon.[74] Bony irregularity at the site of anchor placement is expected, and echogenic suture material within the tendon may contribute to the heterogeneous appearance of the postoperative rotator cuff tendon (Fig. 24.20, Video 24.4). A gap within the tendon and nonvisualization of the tendon owing to retraction are the most reliable signs for a recurrent tear.[75,76] A thinned tendon or one with subtle contour abnormality is considered intact.

Muscle Atrophy

Ultrasound may also be used to assess for rotator cuff muscle atrophy, which may occur in the setting of a subacute or chronic rotator cuff tear. This is characterized by decreased muscle bulk and increased muscle echogenicity (related to increased fat interposed among muscle fibers[77] (Fig. 24.21). Ultrasound appearances also include lack of clarity of the muscle contour, and loss of visibility of the central tendon within the myotendinous

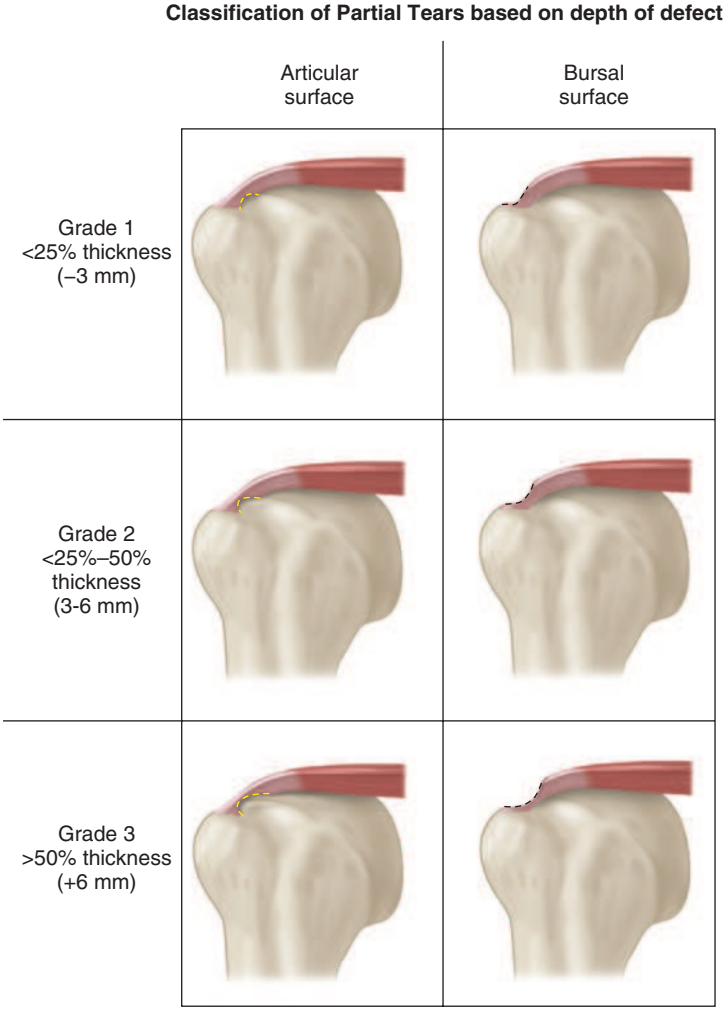

FIG. 24.18 Illustration of Partial Tear Subtypes.

junction.[78] Extended field-of-view imaging, whereby the rotator cuff muscles are imaged in short axis side by side, may assist in reducing interobserver variability in the ultrasound diagnosis of muscle atrophy, presumably by providing an internal control between muscles. Diagnosis of muscle atrophy is of importance in clinical management because the presence of muscle atrophy is considered a negative prognostic indicator with regard to the likelihood of successful surgical repair. It is worth remembering that atrophy may also occur because of denervation.

Muscle atrophy can be qualitatively graded from 0 to 4 as described by Goutallier and colleagues[79]: 0 = normal muscle, 1 = minimal fatty streaks, 2 = more muscle than fat, 3 = equal amounts of muscle and fat, 4 = more fat is present than muscle. This grading system was designed for MRI interpretation; therefore Strobel and colleagues described a modified grading system for ultrasound assessment of muscle atrophy whereby morphology and echogenicity are evaluated.[78] In this system, morphologic changes of atrophy are graded 0 to 2: grade 0 = normal, with clearly visible muscle contours, muscle fibers, and central tendon; grade 1 = only partially visible normal muscle features; grade 2 = normal structures no longer visible. Meanwhile, the echogenicity of muscle is graded in comparison with the deltoid from 0 to 2: grade 0 = isoechoic to deltoid; grade 1 = slightly hyperechoic to the deltoid muscle; grade 2 = markedly hyperechoic to deltoid muscle. Ultrasound grading of fatty atrophy has been shown to correlate well with MRI assessment.[31,80]

Subacromial-Subdeltoid Bursa

The subacromial-subdeltoid bursa is visualized superficial to the rotator cuff tendons, deep to the deltoid muscle and acromion.[39] At its inferolateral aspect, it extends beyond the lateral margin of the rotator cuff, lying superficial to the humeral shaft. This can be a helpful observation in distinguishing this structure from the superficial fibers of the rotator cuff. On ultrasound, the subacromial-subdeltoid bursa normally consists of a thin hypoechoic band measuring less than 2 mm where synovial fluid resides within the bursa, and a thin hyperechoic line superficial and deep to this, representing the wall of the bursa and peribursal fat (Fig. 24.22).

Abnormalities of the subacromial-subdeltoid bursa manifest with increased fluid within and distention of the bursa, and/or by bursal wall thickening (Fig. 24.23). Bursal abnormality detected

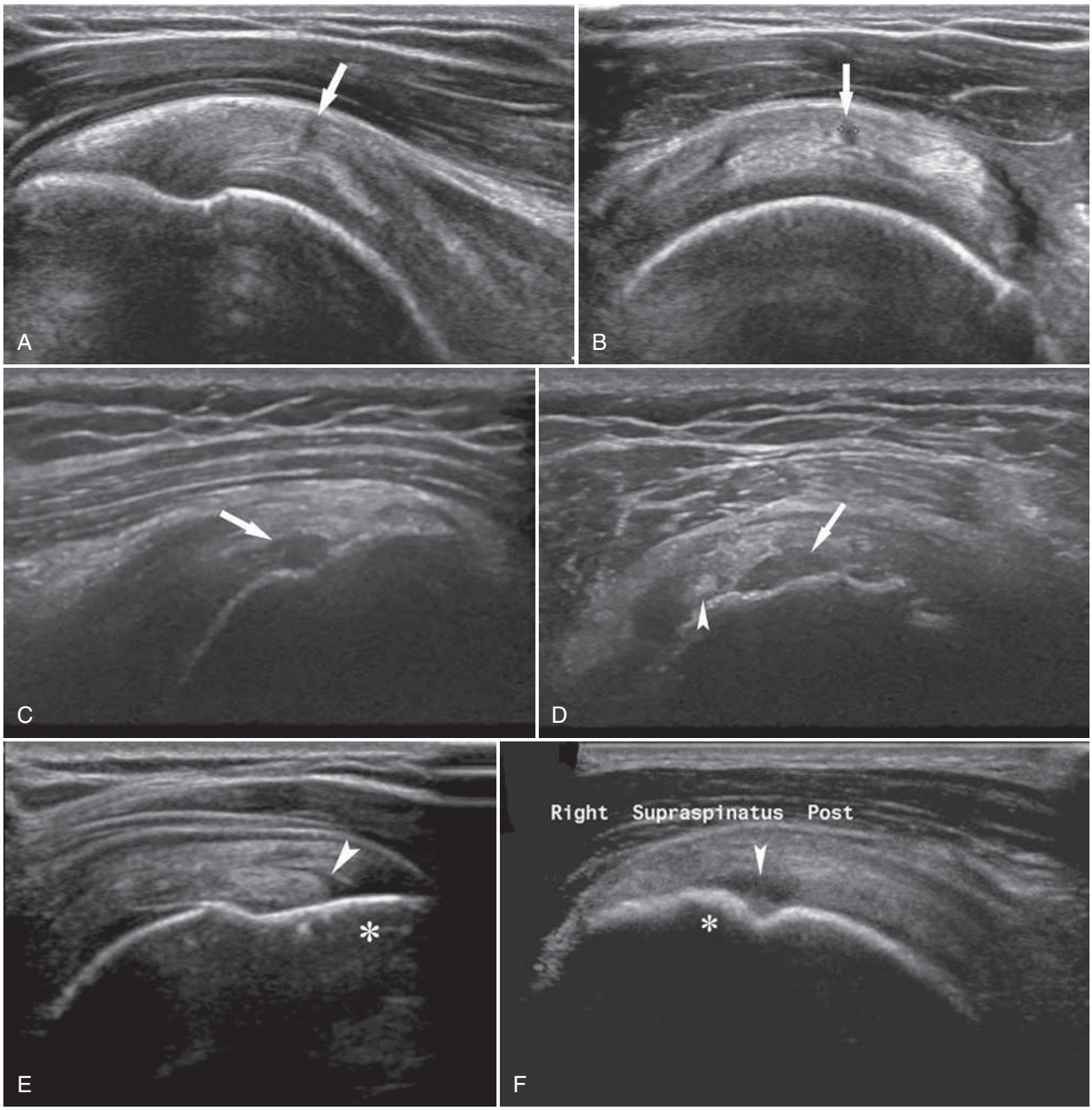

FIG. 24.19 Partial-Thickness Tears of the Rotator Cuff. (A) Bursal-sided tear—long-axis image. A focal hypoechoic area *(arrow)* is shown extending from the bursal surface of the supraspinatus tendon. **(B) Bursal-sided tear—**short-axis image. A focal hypoechoic area *(arrow)* is shown extending from the bursal surface of the supraspinatus tendon. **(C) Articular-sided tear—**a focal hypoechoic tear *(arrow)* is present along the articular side of the supraspinatus, shown here in long axis. **(D) Articular-sided tear—**a focal hypoechoic tear *(arrow)* is present along the articular side of the supraspinatus, seen here in short axis. Note the long head biceps tendon (LHBT) *(arrowhead)* anteriorly. **(E) Intrasubstance tear—**long-axis image of supraspinatus tendon demonstrates linear hypoechoic cleft *(arrowhead)* within the tendon, extending to the greater tuberosity (*) but not extending to either the bursal or articular surface of the tendon. **(F) Rim-rent tear—**long-axis image of the supraspinatus tendon demonstrates a hypoechoic tear *(arrowhead)* along the articular side of the tendon, at the insertional footplate on the greater tuberosity (*).

on ultrasound is highly associated with shoulder pain.[81] The most common cause for fluid distention of the bursa is an underlying rotator cuff tear, which may cause communication with the normally separate glenohumeral joint space. Uncommonly, fluid can also track through the adjacent acromioclavicular joint in this setting and into the soft tissues superficial to the acromioclavicular joint to form a **ganglion ("geyser sign")** (Fig. 24.24). In this case, patients will have a lump over the acromioclavicular joint, and they often do not relate it to background shoulder pain or immobility. Complete examination of the shoulder is indicated in such cases to evaluate for underlying communicating full-thickness rotator cuff tear. This is important

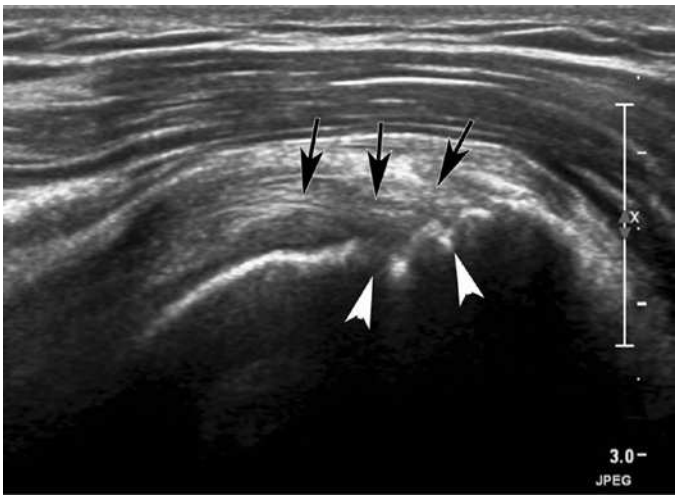

FIG. 24.20 Postoperative Supraspinatus Tendon. Long-axis image of supraspinatus shows a heterogeneous *(arrows)* but intact supraspinatus tendon, and irregularity of the greater tuberosity *(arrowheads)*. See also Video 24.4.

because the natural history of untreated asymptomatic rotator cuff tears is frequently the development of symptoms in addition to tear progression.[82]

Direct trauma to the shoulder can also cause thickening and distention of the subacromial-subdeltoid bursa, sometimes with more echogenic fluid representing blood. The bursa may be chronically irritated by friction related to subacromial impingement, and may worsen this clinical syndrome. Additional inflammatory causes of subacromial subdeltoid bursa thickening and distention include rheumatoid arthritis, polymyalgia rheumatica, and hydroxyapatite deposition **(calcific bursitis).** Infection of the bursa can also occur either through direct inoculation or via communication with underlying septic arthritis in the setting of concomitant full-thickness rotator cuff tear.

Calcific Tendinitis

Hydroxyapatite crystal deposition within rotator cuff tendons can be a cause of severe atraumatic pain. These deposits occur most frequently in the supraspinatus tendon, slightly more

FIG. 24.21 Fatty Atrophy of the Infraspinatus Muscle. Image obtained of the short axis of the infraspinatus tendon shows low-volume, hyperechoic infraspinatus muscle *(arrowheads),* compared with the normal echogenicity of the teres minor (*).

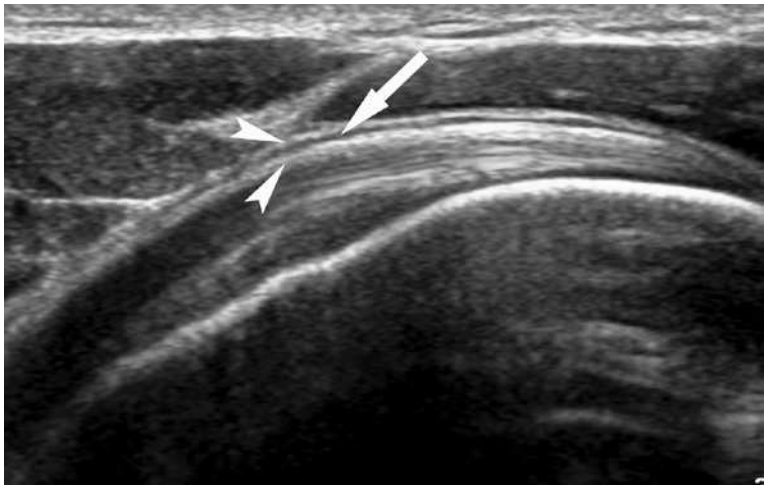

FIG. 24.22 Normal Subacromial-Subdeltoid Bursa. Overlying the infraspinatus tendon, in long axis, the subacromial subdeltoid bursa is visualized as a thin hypoechoic line *(arrow),* with thin hyperechoic borders superficial and deep to the bursa *(arrowheads).*

commonly than the infraspinatus tendon, and more uncommonly in the teres minor and subscapularis tendons.[83] Calcium deposits may undergo resorption, and it is during this resorptive phase that patients are most likely to be symptomatic. The hallmarks of this phase on ultrasound evaluation are fragmented, nodular or cystic echogenic deposits (Fig. 24.25), usually without shadowing, and there may be associated neovascularity on color Doppler assessment.[84] Associated bony osteolysis at the greater tuberosity may be present and denotes a more clinically severe syndrome, with more protracted pain and functional limitation.[85] More dense arclike echogenic calcific deposits with clear posterior acoustic shadowing are more likely to be asymptomatic or less symptomatic. Ultrasound-guided treatment with direct needling and barbotage leads to short- and long-term clinical improvement in this condition.[86,87]

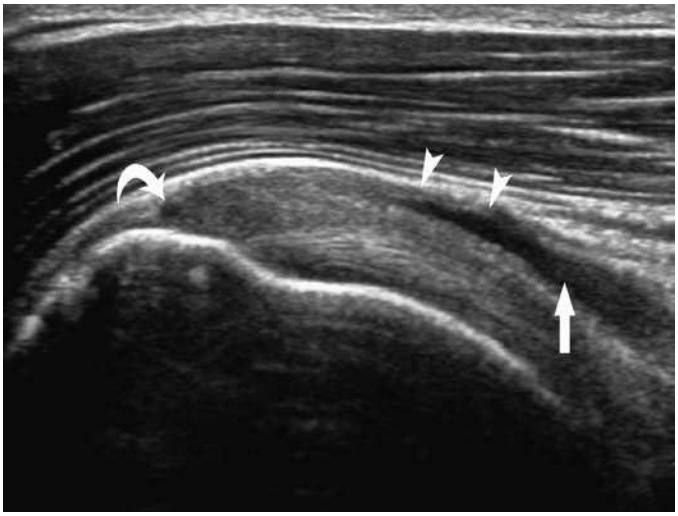

FIG. 24.23 Subacromial-Subdeltoid Bursal Thickening. Image shows increased fluid in the subacromial bursa *(straight arrow),* and thickening of the wall of the subacromial bursa *(arrowheads).* Note also a small bursal-sided tear of the supraspinatus at its insertion *(curved arrow).*

LONG HEAD BICEPS TENDON PATHOLOGY

The long head biceps tendon can be injured in the setting of concomitant rotator cuff tear, shoulder dislocation, or overhead sports. It has been noted by several authors that there is an association between pathologies of the long head biceps tendon and supraspinatus tendon, with coexistent injuries of these structures in 22% to 79% of cases of injury to either structure.[88]

The long head biceps tendon is partly intraarticular and is extrasynovial, with a tendon sheath at the intertubercular groove that communicates with the glenohumeral joint. Because of this, fluid in the tendon sheath may relate to intraarticular processes, particularly if associated with glenohumeral effusion. Inflammation of the tendon sheath **(tenosynovitis)** should be considered, however, if the tendon appears abnormal, if there is hyperemia on color Doppler imaging, if there is no sign of alternative

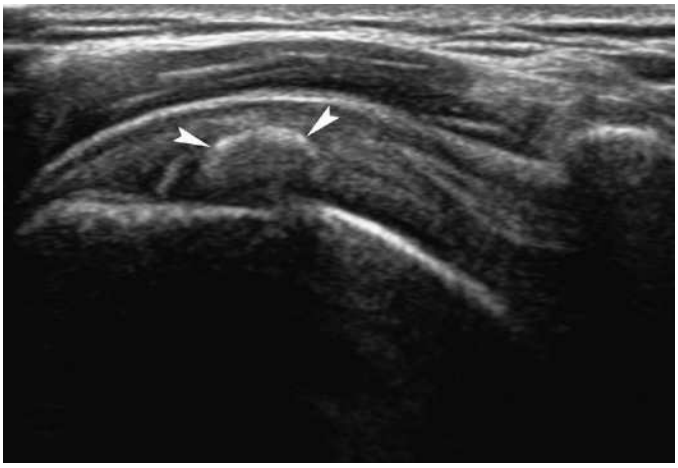

FIG. 24.25 Calcific Tendinitis of the Supraspinatus Tendon. Long-axis image of the supraspinatus image demonstrates a hyperechoic focus of calcification *(arrowheads)* within the supraspinatus tendon.

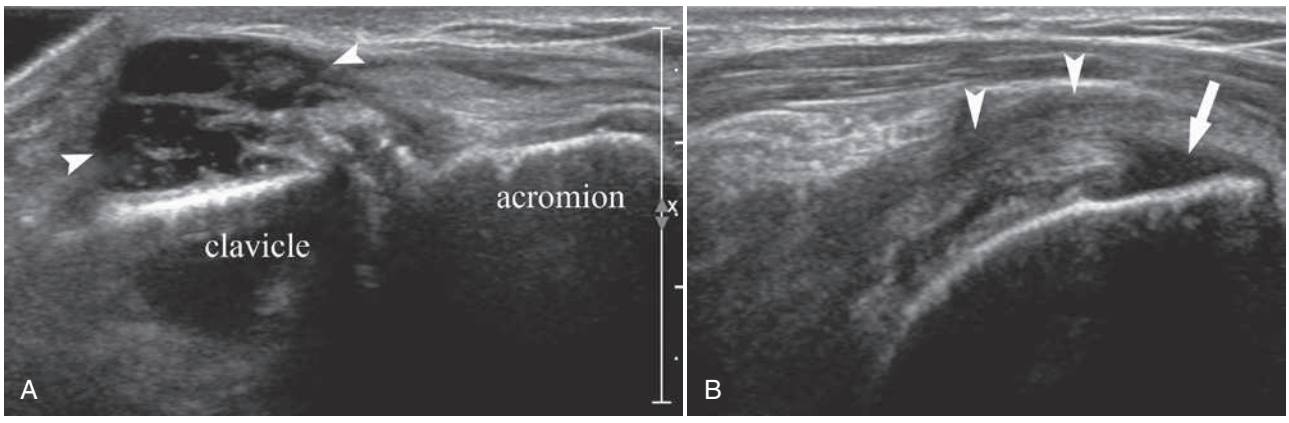

FIG. 24.24 Full-Thickness Supraspinatus Tendon Tear With Geyser Sign. (A) Image obtained at the acromioclavicular joint where the patient felt a mass. The mass corresponds with a heterogeneous hypoechoic lesion *(arrowheads)* with internal debris and septation compatible with a complex **ganglion. (B)** Long-axis image of the supraspinatus tendon in the same patient shows a full-thickness supraspinatus tendon tear *(arrow)* in addition to thickening of the subacromial bursa.

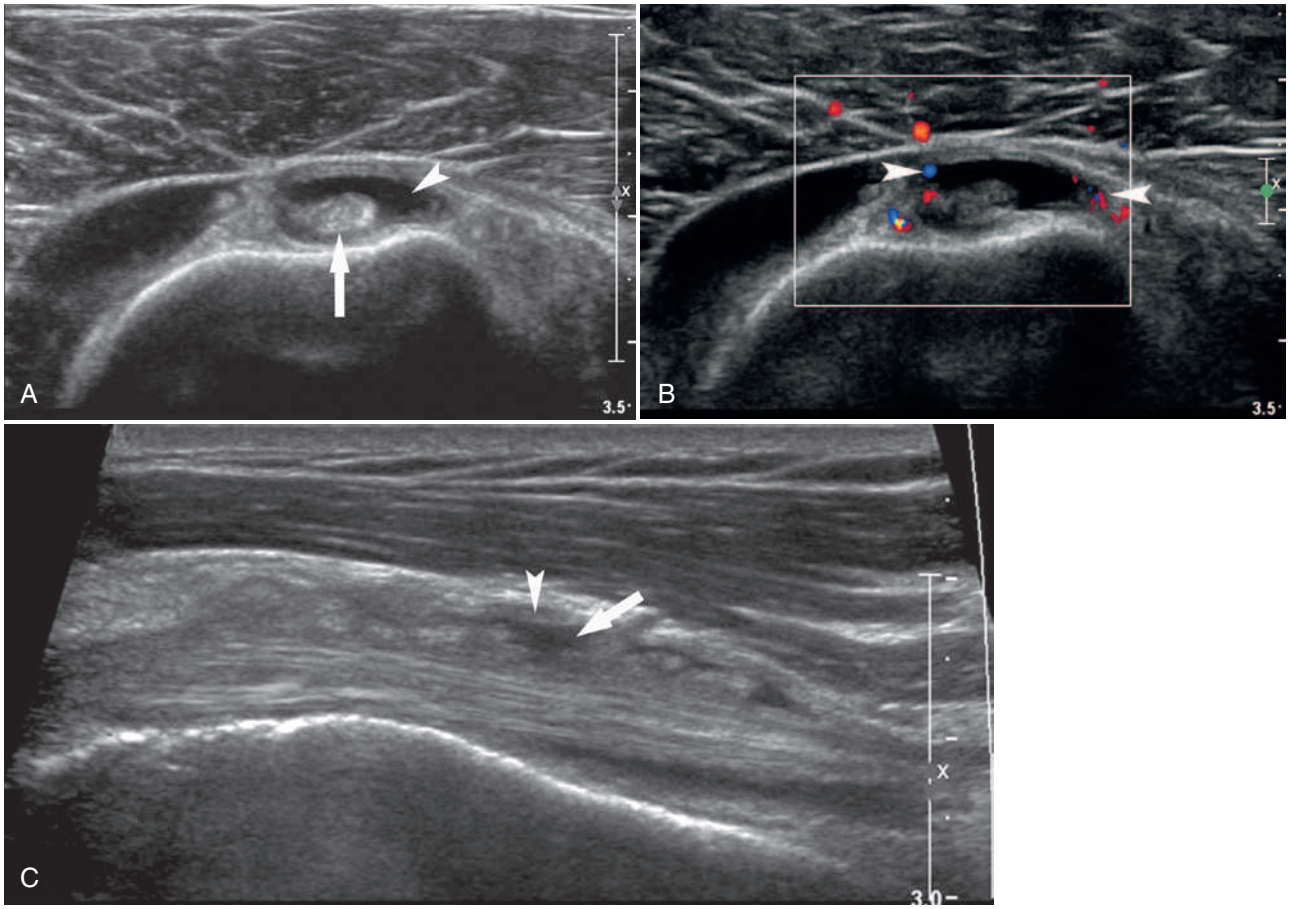

FIG. 24.26 Long Head of Biceps Tenosynovitis. (A) Short-axis image shows increased fluid within the long head biceps tendon sheath *(arrowhead),* surrounding the tendon *(arrow).* **(B)** Short-axis image shows hyperemia *(arrowheads)* in the long head of biceps tendon sheath. **(C)** In a different patient, long-axis image of the long head of biceps tendon shows thickening of the wall *(arrowhead)* of the tendon sheath and increased fluid *(arrow)* within the sheath.

glenohumeral pathology or effusion, or if there is localizing tenderness[89] (Fig. 24.26).

Long head biceps tendinosis is characterized by loss of normal tendon fibrillar pattern, abnormal hypoechogenicity, and often thickening.[90] Ultrasound is an accurate means for diagnosis of full-thickness biceps tendon tears, with more modest accuracy in the diagnosis of partial tears.[90,91] Partial-thickness tears are characterized by anechoic clefts within the tendon, without complete discontinuity. These tears are often longitudinally orientated, paralleling the tendon long axis, and may result in splitting the tendon into two distinct parallel components, termed a **longitudinal split tear** (Fig. 24.27). Long head biceps complete tears typically occur close to the tendon origin and may manifest with acute onset of contour deformity of the biceps muscle. The tendon will usually retract distally, often distal to the insertion of the pectoralis major, which usually inserts on the humerus just anterior to the long head biceps tendon course in the upper arm. A complete tear with retraction is typically diagnosed by nonvisualization of the tendon within the intertubercular groove,[45] but care should be taken to assess for medial dislocation of the tendon as an alternative cause if the tendon is not seen within the bicipital groove. The biceps tendon is normally stabilized within the tendon groove by the thin transverse ligament. Medially, displacement is resisted by the subscapularis tendon. If the subscapularis tendon is torn at its insertion, this may allow medial displacement of the biceps tendon, deep to the subscapularis tendon.[92] Alternatively, if the transverse ligament is torn, this may permit medial **dislocation of the biceps tendon,** which then lies superficial to the otherwise intact subscapularis tendon.

ARTHROPATHY

Degenerative

Osteoarthritis is common and characterized by the formation of marginal bone spurs—osteophytes—at the margin of articular surface. This is particularly common at the acromioclavicular joint (Fig. 24.28). There may be small associated joint effusions, and echogenic intraarticular bodies, which may be calcified, can be observed.

Inflammatory

The shoulder can be involved in **inflammatory arthropathies, including rheumatoid arthritis** and **ankylosing spondylitis.**[93,94] The shoulder involvement in rheumatoid arthritis occurs later than peripheral arthritis. Patients with inflammatory arthropathy

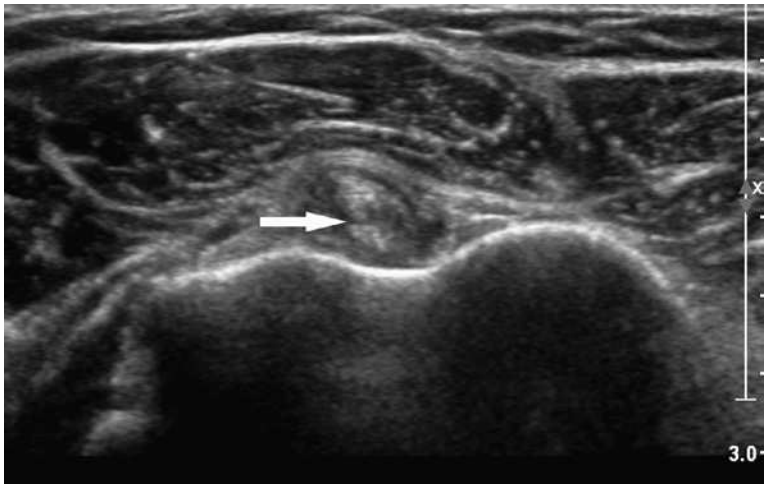

FIG. 24.27 Longitudinal Split Tear of the Long Head of Biceps Tendon. Short-axis image demonstrates a hypoechoic cleft *(arrow)* through the long head of biceps tendon, dividing it into two components.

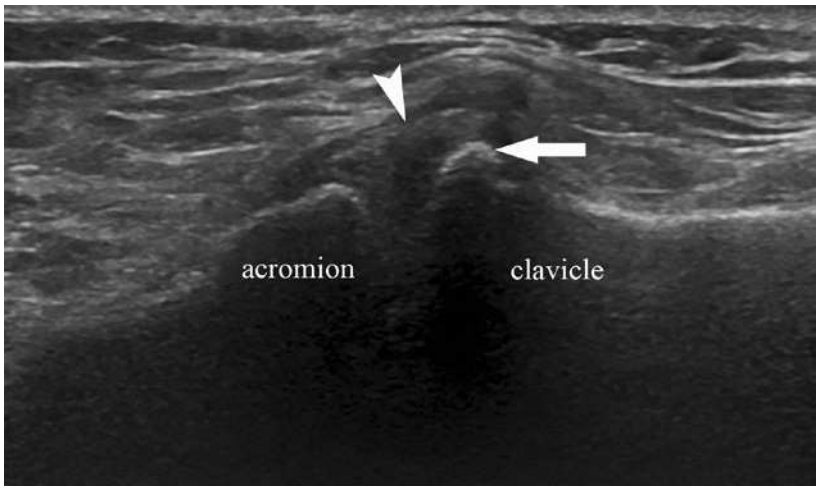

FIG. 24.28 Acromioclavicular Joint Osteoarthritis. Image of the acromioclavicular joint demonstrates osteophyte formation at the distal clavicle *(arrow)* and capsular thickening and hypertrophy *(arrowhead)*.

may have **glenohumeral effusion.** This is best assessed posteriorly, and a thickness of 3 mm or more from the humeral head to the capsule may represent effusion and/or synovial thickening[95] (Fig. 24.29). Ultrasound is particularly sensitive to detection of fluid in the posterior glenohumeral recess when patients are scanned with the arm in external rotation[52] (see Video 24.4). Use of color Doppler, particularly power Doppler,[96] is helpful to elucidate synovial hyperemia and can help separate thickened synovium from complex intraarticular fluid. Bone erosions may also be present, characterized by bony cortical surface rounded or steplike deformations, often at the humeral head margins.[97,98] Ultrasound may be used as a complementary technique to radiographs in assessment for erosions, because it may detect radiographically occult erosions,[94] although overall, MRI has greater sensitivity and can be used for problem solving.[99] In ankylosing spondylitis, acromioclavicular synovitis is common. Patients with inflammatory arthritis may also be affected by subacromial-subdeltoid bursitis, in addition to rotator cuff and biceps tendon tears.

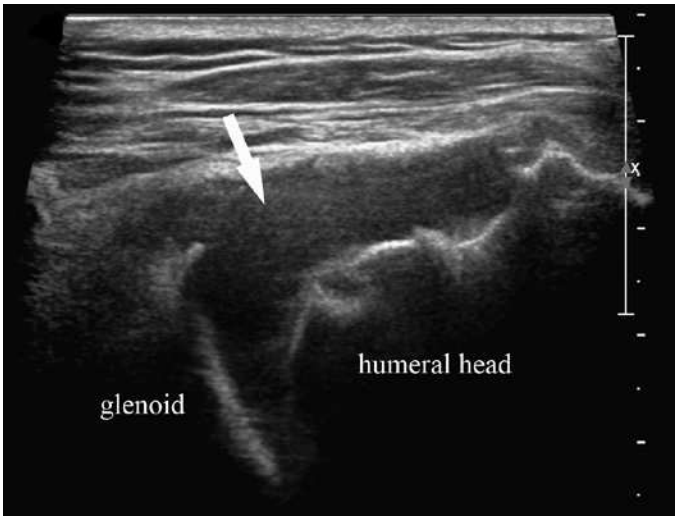

FIG. 24.29 Glenohumeral Joint Effusion. Image of the posterior shoulder shows increased fluid within the joint *(arrow)* in this patient with osteoarthritis.

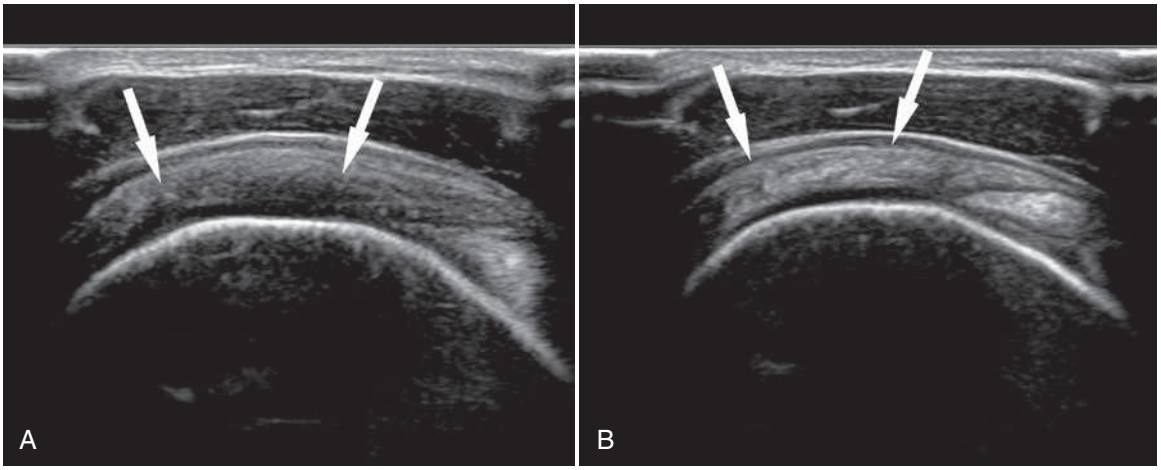

FIG. 24.30 Short-Axis Images of the Supraspinatus Tendon. (A) Artifactual hypoechogenicity of the supraspinatus tendon *(arrows)* may simulate tendinosis or tear. **(B)** Correction of angle of insonation to be perpendicular to the tendon permits visualization of the normal intact supraspinatus tendon *(arrows)*.

PITFALLS IN SHOULDER ULTRASOUND

Anisotropy is a common problem in diagnostic shoulder ultrasound, but thankfully one that can be easily rectified. It consists of artifactual hypoechogenicity within a tendon caused by scanning with the probe in a suboptimal angle with respect to the tendon. As a highly organized linear structure, a tendon reflects ultrasound waves, effectively giving a normal echogenic appearance when the angle of insonation is close to 90 degrees. However, deviation from this angle can result in reflection of sound waves away from the transducer, leading to apparent hypoechogenicity, which can be erroneously interpreted as tendinosis or tearing.[37] This can be corrected by attention to the angle of insonation of the tendon in question and by attempting to visualize any pathologic finding in more than one plane (Fig. 24.30, Video 24.5).

There are several additional scanning pitfalls frequently encountered by the inexperienced sonographer. Tears of the anterior-most fibers of the supraspinatus are easily missed if scanning does not extend anteriorly enough. One way to solve this problem is to use the anatomic landmark of the long head bicipital tendon as the starting point for scanning the supraspinatus tendon, both in short and long axis.

In the hands of novice operators, chronic full-thickness rotator cuff tears with echogenic granulation tissue may be confused for intact, abnormal tendon. Careful evaluation with dynamic compression, and differentiation of bursal tissue from rotator cuff tissue should be performed. In addition, inexperienced operators may mistake the junction of the posterior supraspinatus and anterior infraspinatus, where the tendon fibers overlap, as pathology. Careful angling of the probe with respect to the long axis of the fibers, and direct correlation to short-axis images should ameliorate this misperception.

If the long head biceps tendon is not seen in the bicipital groove, one should not automatically assume that the tendon is torn. It is important to ensure that the transducer is perpendicular to the tendon, as otherwise the tendon may appear artifactually hypoechoic owing to anisotropy. The transducer should then be moved medially to visualize the coracoid process, to look for a medially dislocated tendon. Lastly, one should scan distally to the pectoralis junction to see if the tendon has torn and retracted distally.

Soft tissue distortion by bony abnormality can cause confusion during imaging and can be rectified by referring to a concurrent radiograph.[100] This is particularly the case in the setting of recent trauma wherein an underlying fracture can cause considerable distortion, especially if the greater tuberosity is involved.

As is the case for learning any skill, there is a learning curve involved when performing diagnostic shoulder ultrasound. Accuracy is lower when operators are unfamiliar with the technique, but the learning curve plateaus between 50 and 100 cases,[101] which should be considered when undertaking this examination for the first time and when training and mentoring other sonographers.

CONCLUSION

In conclusion, ultrasound is an accurate and cost-effective technique for diagnosing soft tissue pathology at the shoulder and is well tolerated by patients. Ultrasound confers many advantages over MRI in the evaluation of the rotator cuff. Adequate experience in this technique is important, in addition to correlation with other imaging modalities when available.

REFERENCES

1. Chopp-Hurley JN, O'Neill JM, Dickerson CR. Distribution of bone and tissue morphological properties related to subacromial space geometry in a young, healthy male population. Surg Radiol Anat. 2016;38(1):135-146.
2. Craik JD, Mallina R, Ramasamy V, Little NJ. Human evolution and tears of the rotator cuff. Int Orthop. 2014;38(3):547-552.
3. Takura T, Ushida T, Kanchiku T, et al. The societal burden of chronic pain in japan: an Internet survey. J Orthop Sci. 2015;20(4):750-760.
4. White JJ, Titchener AG, Fakis A, et al. An epidemiological study of rotator cuff pathology using the health improvement network database. Bone Joint J. 2014;96-B(3):350-353.
5. Virta L, Joranger P, Brox JI, Eriksson R. Costs of shoulder pain and resource use in primary health care: a cost-of-illness study in Sweden. BMC Musculoskelet Disord. 2012;13:17.

6. Shanahan EM, Sladek R. Shoulder pain at the workplace. Best Pract Res Clin Rheumatol. 2011;25(1):59-68.
7. Bostrom M, Dellve L, Thomee S, Hagberg M. Risk factors for generally reduced productivity—a prospective cohort study of young adults with neck or upper-extremity musculoskeletal symptoms. Scand J Work Environ Health. 2008;34(2):120-132.
8. Brox JI. Regional musculoskeletal conditions: shoulder pain. Best Pract Res Clin Rheumatol. 2003;17(1):33-56.
9. Lazarides AL, Alentorn-Geli E, Choi JH, et al. Rotator cuff tears in young patients: a different disease than rotator cuff tears in elderly patients. J Shoulder Elbow Surg. 2015;24(11):1834-1843.
10. Valkering KP, Stokman RD, Bijlsma TS, et al. Prevalence of symptomatic rotator cuff ruptures after shoulder trauma: a prospective cohort study. Eur J Emerg Med. 2014;21(5):349-353.
11. Teunis T, Lubberts B, Reilly BT, Ring D. A systematic review and pooled analysis of the prevalence of rotator cuff disease with increasing age. J Shoulder Elbow Surg. 2014;23(12):1913-1921.
12. Micheroli R, Kyburz D, Ciurea A, et al. Correlation of findings in clinical and high resolution ultrasonography examinations of the painful shoulder. J Ultrason. 2015;15(60):29-44.
13. Moosmayer S, Lund G, Seljom US, et al. Tendon repair compared with physiotherapy in the treatment of rotator cuff tears: a randomized controlled study in 103 cases with a five-year follow-up. J Bone Joint Surg Am. 2014;96(18):1504-1514.
14. Mather 3rd RC, Koenig L, Acevedo D, et al. The societal and economic value of rotator cuff repair. J Bone Joint Surg Am. 2013;95(22):1993-2000.
15. Hughes PC, Taylor NF, Green RA. Most clinical tests cannot accurately diagnose rotator cuff pathology: a systematic review. Aust J Physiother. 2008;54(3):159-170.
16. Park HB, Yokota A, Gill HS, et al. Diagnostic accuracy of clinical tests for the different degrees of subacromial impingement syndrome. J Bone Joint Surg Am. 2005;87(7):1446-1455.
17. Malhi AM, Khan R. Correlation between clinical diagnosis and arthroscopic findings of the shoulder. Postgrad Med J. 2005;81(960):657-659.
18. Holtby R, Razmjou H. Accuracy of the Speed's and Yergason's tests in detecting biceps pathology and slap lesions: comparison with arthroscopic findings. Arthroscopy. 2004;20(3):231-236.
19. Palmer K, Walker-Bone K, Linaker C, et al. The Southampton examination schedule for the diagnosis of musculoskeletal disorders of the upper limb. Ann Rheum Dis. 2000;59(1):5-11.
20. Itoi E, Kido T, Sano A, et al. Which is more useful, the "full can test" or the "empty can test," in detecting the torn supraspinatus tendon? Am J Sports Med. 1999;27(1):65-68.
21. Roy JS, Braen C, Leblond J, et al. Diagnostic accuracy of ultrasonography, MRI and MR arthrography in the characterisation of rotator cuff disorders: a meta-analysis. Br J Sports Med. 2015;49(20):1316-1328.
22. Smith TO, Back T, Toms AP, Hing CB. Diagnostic accuracy of ultrasound for rotator cuff tears in adults: a systematic review and meta-analysis. Clin Radiol. 2011;66(11):1036-1048.
23. Vlychou M, Dailiana Z, Fotiadou A, et al. Symptomatic partial rotator cuff tears: diagnostic performance of ultrasound and magnetic resonance imaging with surgical correlation. Acta Radiol. 2009;50(1):101-105.
24. Naqvi GA, Jadaan M, Harrington P. Accuracy of ultrasonography and magnetic resonance imaging for detection of full thickness rotator cuff tears. Int J Shoulder Surg. 2009;3(4):94-97.
25. de Jesus JO, Parker L, Frangos AJ, Nazarian LN. Accuracy of MRI, MR arthrography, and ultrasound in the diagnosis of rotator cuff tears: a meta-analysis. AJR Am J Roentgenol. 2009;192(6):1701-1707.
26. Al-Shawi A, Badge R, Bunker T. The detection of full thickness rotator cuff tears using ultrasound. J Bone Joint Surg Br. 2008;90(7):889-892.
27. Milosavljevic J, Elvin A, Rahme H. Ultrasonography of the rotator cuff: a comparison with arthroscopy in one-hundred-and-ninety consecutive cases. Acta Radiol. 2005;46(8):858-865.
28. Zehetgruber H, Lang T, Wurnig C. Distinction between supraspinatus, infraspinatus and subscapularis tendon tears with ultrasound in 332 surgically confirmed cases. Ultrasound Med Biol. 2002;28(6):711-717.
29. Teefey SA, Hasan SA, Middleton WD, et al. Ultrasonography of the rotator cuff. A comparison of ultrasonographic and arthroscopic findings in one hundred consecutive cases. J Bone Joint Surg Am. 2000;82(4):498-504.
30. Crass JR, Craig EV, Feinberg SB. Ultrasonography of rotator cuff tears: a review of 500 diagnostic studies. J Clin Ultrasound. 1988;16(5):313-327.
31. Wall LB, Teefey SA, Middleton WD, et al. Diagnostic performance and reliability of ultrasonography for fatty degeneration of the rotator cuff muscles. J Bone Joint Surg Am. 2012;94(12):e83.
32. Middleton WD, Payne WT, Teefey SA, et al. Sonography and MRI of the shoulder: comparison of patient satisfaction. AJR Am J Roentgenol. 2004;183(5):1449-1452.
33. Nazarian LN. The top 10 reasons musculoskeletal sonography is an important complementary or alternative technique to MRI. AJR Am J Roentgenol. 2008;190(6):1621-1626.
34. Nazarian LN, Jacobson JA, Benson CB, et al. Imaging algorithms for evaluating suspected rotator cuff disease: Society of Radiologists in Ultrasound consensus conference statement. Radiology. 2013;267(2):589-595.
35. Gray H. Anatomy of the human body, 1918. 20th edition. Available from: http://www.bartleby.com/107/50.html. Accessed 6 September 2015.
36. Karthikeyan S, Rai SB, Parsons H, et al. Ultrasound dimensions of the rotator cuff in young healthy adults. J Shoulder Elbow Surg. 2014;23(8):1107-1112.
37. Seibold CJ, Mallisee TA, Erickson SJ, et al. Rotator cuff: evaluation with US and MR imaging. Radiographics. 1999;19(3):685-705.
38. MacDonald K, Bridger J, Cash C, Parkin I. Transverse humeral ligament: does it exist? Clin Anat. 2007;20(6):663-667.
39. van Holsbeeck M, Strouse PJ. Sonography of the shoulder: evaluation of the subacromial-subdeltoid bursa. AJR Am J Roentgenol. 1993;160(3):561-564.
40. Jacobson JA, Shoulder US. anatomy, technique, and scanning pitfalls. Radiology. 2011;260(1):6-16.
41. Corazza A, Orlandi D, Fabbro E, et al. Dynamic high-resolution ultrasound of the shoulder: how we do it. Eur J Radiol. 2015;84(2):266-277.
42. Beggs I. Shoulder ultrasound. Semin Ultrasound CT MR. 2011;32(2):101-113.
43. European Society of Musculoskeletal Radiology. European society of Musculoskeletal Radiology—musculoskeletal ultrasound technical guidelines. 1. Shoulder. 2015. Available from: http://www.essr.org/html/img/pool/shoulder.pdf. Accessed 6 September 2015.
44. Thain LM, Adler RS. Sonography of the rotator cuff and biceps tendon: technique, normal anatomy, and pathology. J Clin Ultrasound. 1999;27(8):446-458.
45. Farin PU. Sonography of the biceps tendon of the shoulder: normal and pathologic findings. J Clin Ultrasound. 1996;24(6):309-316.
46. Crass JR, Craig EV, Feinberg SB. The hyperextended internal rotation view in rotator cuff ultrasonography. J Clin Ultrasound. 1987;15(6):416-420.
47. Morag Y, Jamadar DA, Boon TA, et al. Ultrasound of the rotator cable: prevalence and morphology in asymptomatic shoulders. AJR Am J Roentgenol. 2012;198(1):W27-W30.
48. Gyftopoulos S, Bencardino J, Nevsky G, et al. Rotator cable: MRI study of its appearance in the intact rotator cuff with anatomic and histologic correlation. AJR Am J Roentgenol. 2013;200(5):1101-1105.
49. Turrin A, Cappello A. Sonographic anatomy of the supraspinatus tendon and adjacent structures. Skeletal Radiol. 1997;26(2):89-93.
50. Lee IS, Shin YB, Moon TY, et al. Sonography of patients with hemiplegic shoulder pain after stroke: correlation with motor recovery stage. AJR Am J Roentgenol. 2009;192(2):W40-W44.
51. Crass JR, Craig EV, Thompson RC, Feinberg SB. Ultrasonography of the rotator cuff: surgical correlation. J Clin Ultrasound. 1984;12(8):487-491.
52. Zubler V, Mamisch-Saupe N, Pfirrmann CW, et al. Detection and quantification of glenohumeral joint effusion: reliability of ultrasound. Eur Radiol. 2011;21(9):1858-1864.
53. Oh LS, Wolf BR, Hall MP, et al. Indications for rotator cuff repair: a systematic review. Clin Orthop Relat Res. 2007;455:52-63.
54. Millstein ES, Snyder SJ. Arthroscopic evaluation and management of rotator cuff tears. Orthop Clin North Am. 2003;34(4):507-520.

55. Fehringer EV, Sun J, VanOeveren LS, et al. Full-thickness rotator cuff tear prevalence and correlation with function and co-morbidities in patients sixty-five years and older. J Shoulder Elbow Surg. 2008;17(6):881-885.
56. Milgrom C, Schaffler M, Gilbert S, van Holsbeeck M. Rotator-cuff changes in asymptomatic adults. The effect of age, hand dominance and gender. J Bone Joint Surg Br. 1995;77(2):296-298.
57. Crass JR, Craig EV, Feinberg SB. Clinical significance of sonographic findings in the abnormal but intact rotator cuff: a preliminary report. J Clin Ultrasound. 1988;16(9):625-634.
58. van Holsbeeck MT, Kolowich PA, Eyler WR, et al. US depiction of partial-thickness tear of the rotator cuff. Radiology. 1995;197(2):443-446.
59. Yen CH, Chiou HJ, Chou YH, et al. Six surgery-correlated sonographic signs for rotator cuff tears: emphasis on partial-thickness tear. Clin Imaging. 2004;28(1):69-76.
60. Middleton WD, Teefey SA, Yamaguchi K. Sonography of the rotator cuff: analysis of interobserver variability. AJR Am J Roentgenol. 2004;183(5):1465-1468.
61. Rutten MJ, Jager GJ, Kiemeney LA. Ultrasound detection of rotator cuff tears: observer agreement related to increasing experience. AJR Am J Roentgenol. 2010;195(6):W440-W446.
62. Hodler J, Fretz CJ, Terrier F, Gerber C. Rotator cuff tears: correlation of sonographic and surgical findings. Radiology. 1988;169(3):791-794.
63. Kluger R, Mayrhofer R, Kroner A, et al. Sonographic versus magnetic resonance arthrographic evaluation of full-thickness rotator cuff tears in millimeters. J Shoulder Elbow Surg. 2003;12(2):110-116.
64. Moosikasuwan JB, Miller TT, Burke BJ. Rotator cuff tears: clinical, radiographic, and us findings. Radiographics. 2005;25(6):1591-1607.
65. Teefey SA, Middleton WD, Bauer GS, et al. Sonographic differences in the appearance of acute and chronic full-thickness rotator cuff tears. J Ultrasound Med. 2000;19(6):377-378.
66. Zbojniewicz AM, Maeder ME, Emery KH, Salisbury SR. Rotator cuff tears in children and adolescents: experience at a large pediatric hospital. Pediatr Radiol. 2014;44(6):729-737.
67. Tuite MJ, Turnbull JR, Orwin JF. Anterior versus posterior, and rim-rent rotator cuff tears: prevalence and MR sensitivity. Skeletal Radiol. 1998;27(5):237-243.
68. Schaeffeler C, Mueller D, Kirchhoff C, et al. Tears at the rotator cuff footprint: prevalence and imaging characteristics in 305 MR arthrograms of the shoulder. Eur Radiol. 2011;21(7):1477-1484.
69. Franceschi F, Papalia R, Del Buono A, et al. Repair of partial tears of the rotator cuff. Sports Med Arthrosc. 2011;19(4):401-408.
70. Payne LZ, Altchek DW, Craig EV, Warren RF. Arthroscopic treatment of partial rotator cuff tears in young athletes. A preliminary report. Am J Sports Med. 1997;25(3):299-305.
71. Cullen DM, Breidahl WH, Janes GC. Diagnostic accuracy of shoulder ultrasound performed by a single operator. Australas Radiol. 2007;51(3):22622-22629.
72. Wohlwend JR, van Holsbeeck M, Craig J, et al. The association between irregular greater tuberosities and rotator cuff tears: a sonographic study. AJR Am J Roentgenol. 1998;171(1):229-233.
73. Jiang Y, Zhao J, van Holsbeeck MT, et al. Trabecular microstructure and surface changes in the greater tuberosity in rotator cuff tears. Skeletal Radiol. 2002;31(9):522-528.
74. Mack LA, Nyberg DA, Matsen 3rd FR, et al. Sonography of the postoperative shoulder. AJR Am J Roentgenol. 1988;150(5):1089-1093.
75. Crass JR, Craig EV, Feinberg SB. Sonography of the postoperative rotator cuff. AJR Am J Roentgenol. 1986;146(3):561-564.
76. Prickett WD, Teefey SA, Galatz LM, et al. Accuracy of ultrasound imaging of the rotator cuff in shoulders that are painful postoperatively. J Bone Joint Surg Am. 2003;85-A(6):1084-1089.
77. Sofka CM, Haddad ZK, Adler RS. Detection of muscle atrophy on routine sonography of the shoulder. J Ultrasound Med. 2004;23(8):1031-1034.
78. Strobel K, Hodler J, Meyer DC, et al. Fatty atrophy of supraspinatus and infraspinatus muscles: accuracy of US. Radiology. 2005;237(2):584-589.
79. Goutallier D, Postel JM, Gleyze P, et al. Influence of cuff muscle fatty degeneration on anatomic and functional outcomes after simple suture of full-thickness tears. J Shoulder Elbow Surg. 2003;12(6):550-554.
80. Khoury V, Cardinal E, Brassard P. Atrophy and fatty infiltration of the supraspinatus muscle: sonography versus MRI. AJR Am J Roentgenol. 2008;190(4):1105-1111.
81. Draghi F, Scudeller L, Draghi AG, Bortolotto C. Prevalence of subacromial-subdeltoid bursitis in shoulder pain: an ultrasonographic study. J Ultrasound. 2015;18(2):151-158.
82. Moosmayer S, Tariq R, Stiris M, Smith HJ. The natural history of asymptomatic rotator cuff tears: a three-year follow-up of fifty cases. J Bone Joint Surg Am. 2013;95(14):1249-1255.
83. Sansone V, Consonni O, Maiorano E, et al. Calcific tendinopathy of the rotator cuff: the correlation between pain and imaging features in symptomatic and asymptomatic female shoulders. Skeletal Radiol. 2016;45(1):49-55.
84. Chiou HJ, Chou YH, Wu JJ, et al. Evaluation of calcific tendonitis of the rotator cuff: role of color Doppler ultrasonography. J Ultrasound Med. 2002;21(3):289-295.
85. Porcellini G, Paladini P, Campi F, Pegreffi F. Osteolytic lesion of greater tuberosity in calcific tendinitis of the shoulder. J Shoulder Elbow Surg. 2009;18(2):210-215.
86. Serafini G, Sconfienza LM, Lacelli F, et al. Rotator cuff calcific tendonitis: short-term and 10-year outcomes after two-needle US-guided percutaneous treatment—nonrandomized controlled trial. Radiology. 2009;252(1):157-164.
87. del Cura JL, Torre I, Zabala R, Legorburu A. Sonographically guided percutaneous needle lavage in calcific tendinitis of the shoulder: short- and long-term results. AJR Am J Roentgenol. 2007;189(3):W128-W134.
88. Redondo-Alonso L, Chamorro-Moriana G, Jimenez-Rejano JJ, et al. Relationship between chronic pathologies of the supraspinatus tendon and the long head of the biceps tendon: systematic review. BMC Musculoskelet Disord. 2014;15:377.
89. Ptasznik R, Hennessy O. Abnormalities of the biceps tendon of the shoulder: sonographic findings. AJR Am J Roentgenol. 1995;164(2):409-414.
90. Skendzel JG, Jacobson JA, Carpenter JE, Miller BS. Long head of biceps brachii tendon evaluation: accuracy of preoperative ultrasound. AJR Am J Roentgenol. 2011;197(4):942-948.
91. Armstrong A, Teefey SA, Wu T, et al. The efficacy of ultrasound in the diagnosis of long head of the biceps tendon pathology. J Shoulder Elbow Surg. 2006;15(1):7-11.
92. Chan TW, Dalinka MK, Kneeland JB, Chervrot A. Biceps tendon dislocation: evaluation with MR imaging. Radiology. 1991;179(3):649-652.
93. Ali Ou Alla S, Bahiri R, Amine H, et al. Ultrasound features of shoulder involvement in patients with ankylosing spondylitis: a case-control study. BMC Musculoskelet Disord. 2013;14:272.
94. Ottaviani S, Gill G, Palazzo E, et al. Ultrasonography of shoulders in spondyloarthritis and rheumatoid arthritis: a case-control study. Joint Bone Spine. 2014;81(3):247-249.
95. Alasaarela E, Leppilahti J, Hakala M. Ultrasound and operative evaluation of arthritic shoulder joints. Ann Rheum Dis. 1998;57(6):357-360.
96. Stegbauer J, Rump LC, Weiner SM. Sites of inflammation in painful rheumatoid shoulder assessed by musculoskeletal ultrasound and power Doppler sonography. Rheumatol Int. 2008;28(5):459-465.
97. Alasaarela E, Suramo I, Tervonen O, et al. Evaluation of humeral head erosions in rheumatoid arthritis: a comparison of ultrasonography, magnetic resonance imaging, computed tomography and plain radiography. Br J Rheumatol. 1998;37(11):1152-1156.
98. Amin MF, Ismail FM, El Shereef RR. The role of ultrasonography in early detection and monitoring of shoulder erosions, and disease activity in rheumatoid arthritis patients; comparison with MRI examination. Acad Radiol. 2012;19(6):693-700.
99. Hermann KG, Backhaus M, Schneider U, et al. Rheumatoid arthritis of the shoulder joint: comparison of conventional radiography, ultrasound, and dynamic contrast-enhanced magnetic resonance imaging. Arthritis Rheum. 2003;48(12):3338-3349.
100. Middleton WD, Reinus WR, Melson GL, et al. Pitfalls of rotator cuff sonography. AJR Am J Roentgenol. 1986;146(3):555-560.
101. Alavekios DA, Dionysian E, Sodl J, et al. Longitudinal analysis of effects of operator experience on accuracy for ultrasound detection of supraspinatus tears. J Shoulder Elbow Surg. 2013;22(3):375-380.

CHAPTER 25

Musculoskeletal Interventions

Ronald S. Adler

SUMMARY OF KEY POINTS

- Choose transducer geometry and entry site to visualize the needle as a specular reflector.
- Orient transducer to maximize tendon echogenicity (anisotropy).
- Injected corticosteroid/anesthetic suspension often displays a contrast effect, which can help localize injected mixture.
- Patients with diabetes should be cautioned that they may develop a transient hyperglycemia that may last up to 5 days following therapeutic injection.
- Most small joints and superficial tendon sheaths of hand and foot can be injected using a short-axis approach.
- Shoulder and hip joints can be injected using long-axis approach.
- Ganglion and paralabral cyst fluid can be very viscous or gelatinous and may require a large-bore needle.
- Choose needle trajectory to avoid neurovascular structures.
- Intratendinous injections of platelet-rich plasma (PRP) should be performed in combination with intratendinous fenestration to promote bleeding and initiate an inflammatory response. The patient should avoid nonsteroidal antiinflammatory drugs (NSAIDs) for 1 week before and 2 weeks after the procedure.
- Use of coaxial technique can be of value in performing ablative therapy and core biopsies to minimize extralesional soft tissue damage.

CHAPTER OUTLINE

TECHNICAL CONSIDERATIONS
INJECTION TECHNIQUE
INJECTION MATERIALS
INJECTION OF JOINTS
SUPERFICIAL PERITENDINOUS AND PERIARTICULAR INJECTIONS
Foot and Ankle
Hand and Wrist
INJECTION OF DEEP TENDONS
Biceps Tendon
Iliopsoas Tendon
Abductor and Hamstring Tendons
BURSAL, GANGLION CYST, AND PARALABRAL INJECTIONS
Calcific Tendinitis
INTRATENDINOUS INJECTIONS: PERCUTANEOUS TENOTOMY
PERINEURAL INJECTIONS
CONCLUSION

The real-time nature of ultrasound makes it ideally suited to provide guidance for a variety of musculoskeletal interventional procedures.[1-10] Continuous observation of needle position ensures proper placement and allows continuous monitoring of the distribution of injected and aspirated material. The adverse effects of improper needle placement during corticosteroid administration are well documented.[11-16] Likewise, decompression of fluid-filled lesions and fragmentation of calcific deposits may be performed.

The current generation of high-frequency transducers for sonography of small parts allows excellent depiction of soft tissue detail and articular surfaces, particularly in the hand, wrist, foot, and ankle.[17] This allows needle placement in nonfluid-distended structures, such as a nondistended joint, tendon sheath, or bursa. The injected agent also produces a **contrast** effect, which can improve delineation of surrounding structures (e.g., labral morphology) and provide additional information regarding the agent's distribution.[18,19] Ultrasound guidance has broad appeal because it does not involve ionizing radiation; this feature is particularly advantageous in the pediatric population and during pregnancy.

Ultrasound-guided injections in the musculoskeletal system include injection of joints, tendon sheaths, bursae, and ganglion cysts. The chapter emphasizes the most common injections performed at my institution, an orthopedic and rheumatology specialty hospital. The most common clinical indication for ultrasound-guided injections generally relates to pain that does not respond to other conservative measures, regardless of the anatomic site. The pain may result from a chronic repetitive injury in the work environment, a sports-related injury, or an underlying inflammatory disorder, such as rheumatoid arthritis.

TECHNICAL CONSIDERATIONS

Diagnostic and subsequent interventional examinations are often performed using either linear or curved, phased array transducers,

based on depth and local geometry. Needle selection is based on specific anatomic conditions (i.e., depth and size of region of interest). We use a freehand technique in which the basic principle is to ensure needle visualization as a specular reflector.[7] This relies on orienting the needle so that it is perpendicular (or nearly so) to the insonating beam (Fig. 25.1). The needle then becomes a specular reflector, often having a strong ring-down artifact. Although needle guides are available and may be of value, a freehand technique allows greater flexibility in adjusting needle position during a procedure. Furthermore, needle visualization can be enhanced by injecting a small amount of anesthetic and observing the corresponding moving echoes in either gray-scale or color flow sonographic imaging.[1]

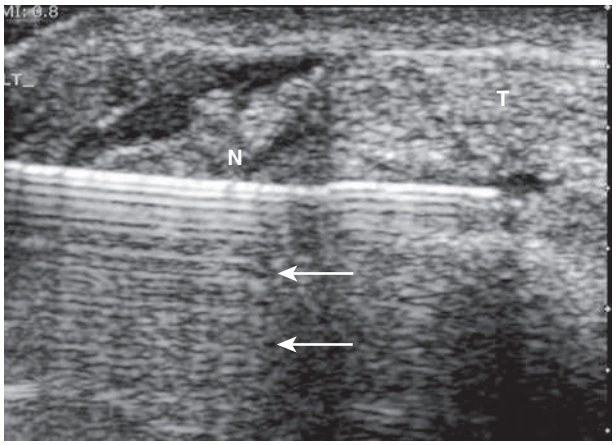

FIG. 25.1 Needle as Specular Reflector With Reverberation Artifact. A 25-gauge needle *(N)* has been positioned into the retrocalcaneal bursa deep to the Achilles tendon *(T)*. Note that the needle is a specular reflector with a characteristic reverberation artifact *(arrows)*.

Patient positioning should be assessed first to ensure comfort and optimal visualization of the anatomy. It is important to keep in mind that tendons display inherent **anisotropy;** they will look hypoechoic if the transducer footprint is not parallel to the tendon.[17] Therefore the transducer must be oriented to maximize tendon echogenicity to avoid false interpretation of the tendon as being complex fluid or synovium. An offset may be required at the skin entry point of the needle relative to the transducer to allow for the appropriate needle orientation. Deep structures, such as tendons about the hip, are often better imaged using a curved linear or sector transducer, operating at center frequencies of about 3.5 to 7.5 MHz. Superficial, linearly oriented structures, such as in the wrist or ankle, are best approached using a linear array transducer with higher center frequencies (>10 MHz). Transducers with a small footprint ("hockey stick") are particularly well suited to superficial injections. These factors should be assessed before skin preparation.

The immiscible nature of the steroid anesthetic mixture may likewise produce temporary contrast effect (Fig. 25.2, Video 25.1). *In vitro* experiments suggest that this property is caused by alterations in acoustic impedance by the scattering material, formed by the suspension of steroid in an aqueous background; this results in an increase in echo intensity of about 20 dB.[19] This contrast effect has the advantage of increasing the conspicuity of the delivered agent during real time, enabling the operator to better define the distribution of delivered agent during ultrasound-guided therapy.

INJECTION TECHNIQUE

We use a sterile technique; the area in question is cleaned with iodine-based solution and draped with a sterile drape. The transducer is cleaned with iodine-based or alcohol-based solutions

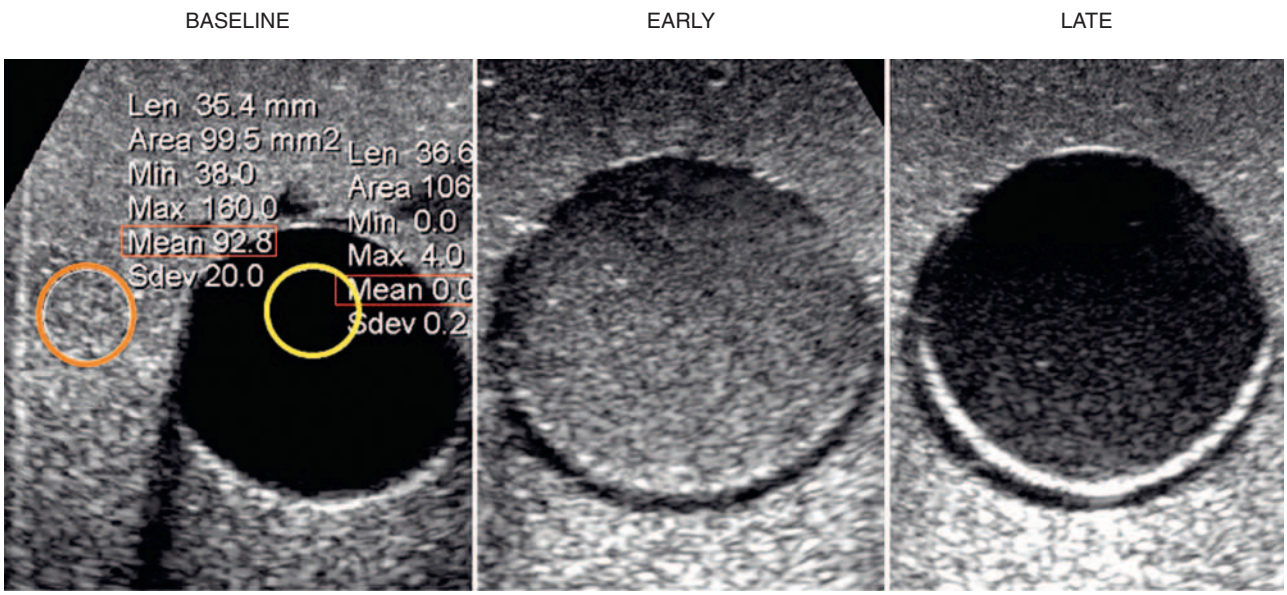

FIG. 25.2 Contrast Effect. A suspension of anesthetic and triamcinolone has been injected into a cyst phantom. *Baseline:* Before injection, anechoic "cyst" is shown in a scattering medium, with baseline pixel intensities listed. *Early:* The early mixing phase is obtained immediately after injection. A contrast effect is evident, in which the cyst becomes almost isoechoic to the background. *Late:* 20 minutes after injection. In the late phase, apparent gravitational effect results in settling of the suspension toward the dependent portions of the cyst phantom and development of a contrast gradient.

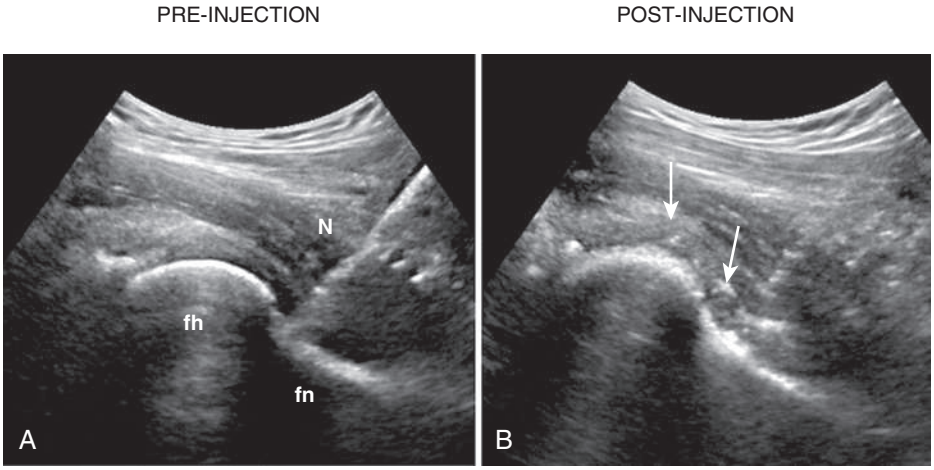

FIG. 25.3 Long-Axis Approach: Injection of Left Hip. The long-axis approach is suitable for deep joint injections, such as the hip or shoulder. **(A)** Before injection, 22-gauge spinal needle *(N)* has been positioned at the femoral head-neck junction in a 50-year-old woman with a labral tear demonstrated on magnetic resonance imaging *(not shown),* to assess relief after therapeutic injection. **(B)** After injection, confirmation of intraarticular deposition of injected material is obtained by the presence of microbubbles *(arrows)* deep to the joint capsule. *fh,* Femoral head; *fn,* femoral neck. See also Video 25.1.

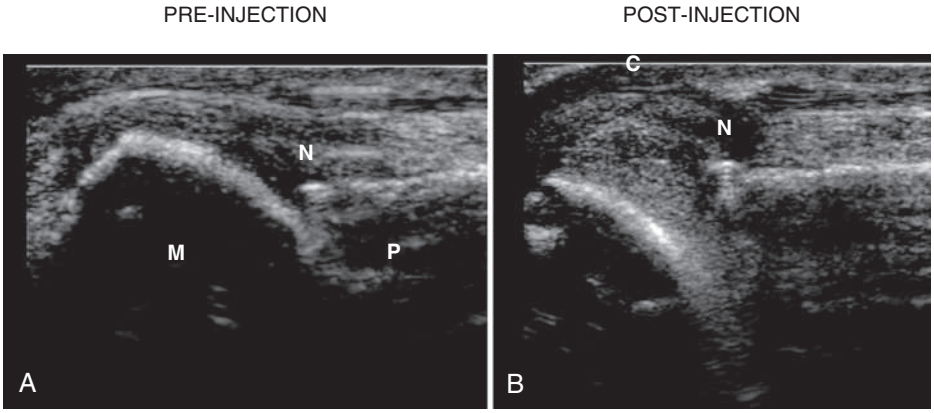

FIG. 25.4 Short-Axis Approach for Injection of First Metatarsophalangeal (MTP) Joint. (A) Long-axis view shows 25-gauge needle positioned in MTP joint of 53-year-old woman with plantar plate injury; needle *(N)* is seen in cross section. *M,* Metatarsal head; *P,* proximal phalanx. **(B)** While monitoring the injection in real time, the joint capsule distends and fills with echogenic material. *C,* Capsule.

and surrounded by a sterile drape. A drape is also placed over portions of the ultrasound unit. A sonographer or radiologist positions the transducer; a radiologist positions the needle and performs the procedure. We use 1% lidocaine and bupivacaine (0.25%-0.75%) for local anesthesia. Once the needle is in position, the procedure is undertaken while imaging in real time. Depending on anatomic location, a 1.5-inch or spinal needle with stylet is used to administer the anesthetic-corticosteroid mixture, generally consisting of local long-acting anesthetic and one of the standard injectable corticosteroid derivatives (e.g., triamcinolone).

Two approaches to performing injections are long axis and short axis, which relate needle orientation to the structure being injected.[9] The **long-axis approach** refers to needle placement in the plane parallel to the structure of interest (Fig. 25.3). For example, longitudinal imaging of the hip to display a hip effusion might be used as the plane to direct the needle for ultrasound-guided aspiration. Alternatively, the **short-axis approach** refers to needle entry in the plane perpendicular to the long axis of a structure (Fig. 25.4). For example, injection of the retrocalcaneal bursa or metatarsophalangeal (MTP) joint might use a lateral approach. In my experience, the short-axis approach works well when performing injections or aspirations in small joints and tendon sheaths of the hand and foot. The long-axis approach appears better suited for deep joint injections, such as in the hip or shoulder. It is important to recognize, however, that such approaches serve merely as guidelines and that no single method necessarily applies to any specific injection.

INJECTION MATERIALS

Most injections involve use of a long-acting corticosteroid in combination with a local anesthetic in relatively small volumes. **Injectable steroids** usually come in either a **crystalline** form, associated with a slower rate of absorption, or a **soluble** form, characterized by rapid absorption.[20-22] Crystalline agents include triamcinolone and methylprednisolone acetate (Depo-Medrol). A common soluble agent is Celestone, which includes a rapidly absorbed betamethasone salt. A reactive inflammatory response or flushing response may occur with crystalline steroids, but typically not with soluble agents.[13]

The most significant complications associated with injectable steroid use in the musculoskeletal system relate to **chondrolysis** (when used in weight-bearing joints), **depigmentation, fat necrosis,** and **impaired healing response** (when used in soft tissues).[11-14] Impaired healing has been associated with tendon, ligament, and plantar fascia rupture. The most frequently used mixtures contain insoluble particles, so a systemic injection could theoretically result in an "embolic phenomenon," which has been implicated as a mechanism for neurologic complications associated with transforaminal epidural injections. We have not encountered this as a complication when performing injections in the appendicular skeletal system.

The most common **anesthetics** are lidocaine (Xylocaine) and bupivacaine (Marcaine).[22,23] Both are characterized as "local injectable anesthetics" but differ in the onset of effect and duration. Lidocaine is characterized by early onset (seconds) and short duration (1-2 hours). Bupivacaine becomes effective in 5 to 10 minutes, and its effects generally last 4 to 6 hours. In addition to allergic reactions, potential adverse effects include neurotoxicity and cardiotoxicity; these are generally rare when small doses are used under image guidance, taking care to avoid an intravascular injection. Bupivacaine has also been associated with chondrolysis when used for intraarticular applications, but only with constant infusions during arthroscopy and *in vitro*.[24] Chondrolysis is probably not an issue with the small, fixed volumes of bupivacaine typically used during injections in the musculoskeletal system.

INJECTION OF JOINTS

A high-frequency linear transducer is used for hand, wrist, elbow, foot, and ankle injections. A short-axis approach is often technically easier for small joint injections. The needle should enter the skin parallel to the plane of the joint space. Superficial joints usually appear as separations between the normally continuous specular echoes produced by cortical surfaces. As in other fluid-containing structures, the presence of an effusion is a helpful feature in visualizing the needle as it enters the joint, because it provides a fluid standoff.

The short-axis approach entails scanning across the joint and looking for the transition from one cortical surface to the next, marking the skin (with a surgical marker), and then placing a needle into the joint using ultrasound guidance. When imaging the joint in long axis, the needle will be seen in cross section (Fig. 25.5). Needle placement is confirmed by injecting a small amount of 1% lidocaine, which should display distention of the joint, as well as echoes filling the joint. Small joint injections generally require 0.5 to 1 mL of the therapeutic mixture. In my experience, this approach works well in the **metatarsophalangeal** (MTP) or **metacarpophalangeal** (MCP) and **interphalangeal** (IP) joints, midfoot, ankle, and elbow. Occasionally a long-axis approach may be efficacious, as in the radiocarpal joint or lateral gutter of the ankle. Ultrasound guidance allows the clinician to negotiate osteophytes and joint bodies. It allows identification of capsular outpouching, thereby affording a more convenient, indirect approach into a joint than slipping a needle into a small joint space.

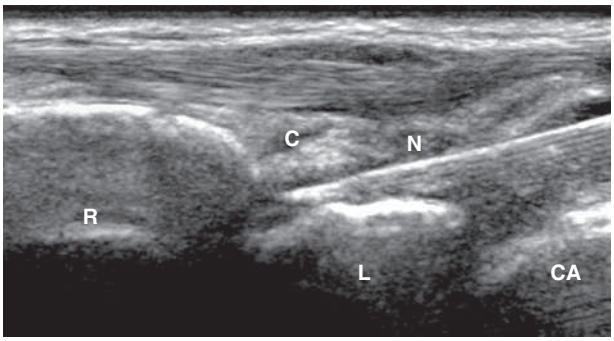

FIG. 25.5 Long-Axis Approach for Therapeutic Radiocarpal Joint Injection. A 25-gauge needle *(N)* has been positioned deep to the dorsal capsule *(C)* and above the lunate bone *(L)* of a 19-year-old female patient with chronic wrist pain, to assess relief. *CA,* Capitate; *R,* radius.

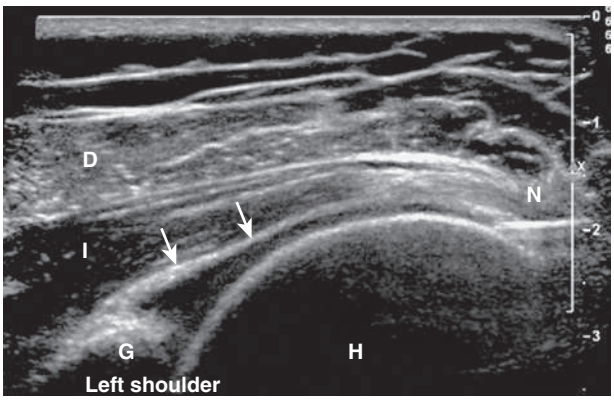

FIG. 25.6 Long-Axis Approach for Glenohumeral Joint Injection. A 22-gauge needle *(N)* has been positioned deep to the posterior capsule *(arrows)* during a glenohumeral joint injection in 42-year-old woman with adhesive capsulitis. Mild fluid distention of the posterior recess of the joint is evident. *D,* Deltoid muscle; *G,* glenoid; *H,* humeral head; *I,* infraspinatus muscle.

A long-axis approach and a spinal needle are used when performing injections of large joints such as the hip or shoulder (Fig. 25.6). A greater volume is usually injected, typically 5 mL of the steroid-anesthetic mixture. In the case of adhesive capsulitis, significantly larger volumes of local anesthetic (5-10 mL) may be added to provide additional joint distention. We generally approach the glenohumeral joint using a posterior approach, with the patient in a decubitus position and the arm placed in cross-adduction. An intermediate-frequency, linear or curvilinear transducer will suffice in most cases. A linear transducer often results in better anatomic detail than curved arrays. The interface of the glenohumeral joint is usually seen with the patient in the decubitus position, as well as the hypoechoic articular cartilage overlying the humeral head. We perform this injection using a long-axis approach, with the needle directed toward the joint along the articular cartilage and deep to the posterior capsule. A test injection with 1% lidocaine should show bright echoes filling the posterior recess or distributed along the articular cartilage.

The hip is approached similarly in long axis, with the transducer placed over the proximal anterior thigh at the level of the joint[25] (see Fig. 25.3, Video 25.1). The approach is similar to that

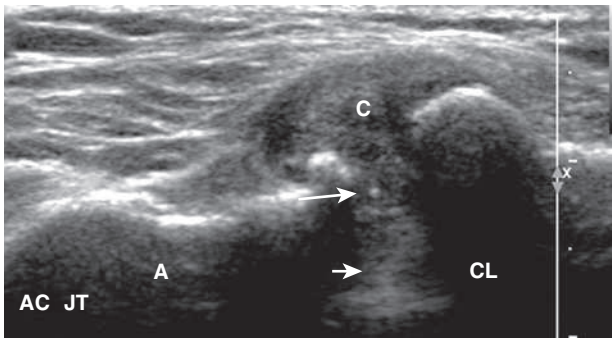

FIG. 25.7 Short-Axis Approach to Injection of Acromioclavicular (AC) Joint. A 25-gauge needle *(long thin arrow)* is seen in cross section in a distended hypertrophic AC joint during therapeutic injection in 73-year-old woman with pain centered over AC joint. The joint appears widened, containing echogenic material caused by the contrast effect *(short thick arrow)* of the therapeutic agent. *A,* Acromion; *C,* distended capsule; *CL,* clavicle.

used in evaluating the joint for an effusion. Ideally, the anterior capsule is imaged at the head-neck junction of the femur. In this approach the scan plane is lateral to the neurovascular bundle. The needle may be directed into the joint while maintaining its position in the scan plane of the transducer. A test injection of 1% lidocaine confirms the intraarticular needle position, and the therapeutic injection follows.

Fibrous joints, such as the **acromioclavicular** (AC) joint, can likewise be injected using ultrasound guidance (Fig. 25.7). A short-axis technique is employed similar to that used in the foot. The majority of these injections can be performed using a 1.5-inch needle with a small volume (0.5-1.0 mL) of therapeutic mixture. In addition to the AC joint, this approach is useful in the sternoclavicular joint and pubic symphysis.

SUPERFICIAL PERITENDINOUS AND PERIARTICULAR INJECTIONS

Peritendinous injection of anesthetic and long-acting corticosteroid is an effective means to treat tenosynovitis, bursitis, and ganglion cysts in the hand, foot, and ankle. These structures are superficially located and well delineated on sonography. Ultrasound-guided injections are an effective means to ensure correct localization of therapeutic agents.

Foot and Ankle

In my experience, peritendinous injections in the foot and ankle are most often requested for patients with chronic **achillodynia** or those with medial or lateral ankle pain caused by posterior tibial or peroneal **tendinosis** or **tenosynovitis.** Less often, patients are referred to help differentiate pain from posterior impingement and stenosing tenosynovitis of the flexor hallucis longus (FHL) tendon.[26] This distinction can be difficult, sometimes requiring diagnostic and therapeutic injection of the corresponding tendon sheath. Patients with plantar foot pain caused by **plantar fasciitis** and forefoot pain resulting from painful neuromas are also frequently referred for ultrasound-guided injections.[27,28]

The large majority of patients with achillodynia have pain referable to the enthesis, with associated retrocalcaneal bursitis and Achilles tendinosis. **Enthesis** is the site of attachment of a muscle or ligament to bone where the collagen fibers are mineralized and integrated into bone. A **retrocalcaneal bursal injection** may help alleviate local pain and inflammation (Fig. 25.8). I scan the patient in a prone position with the ankle in mild dorsiflexion, using a linear transducer of 10 MHz or higher frequency. A 1.5-inch needle usually suffices in these patients, with placement using a short-axis approach. The deep retrocalcaneal bursa is usually well seen. A small amount of anesthetic will help confirm position by active distention of the bursa in real time.

We similarly approach posterior **tibial** or **peroneal** tendons in short axis (Fig. 25.9). Patients with pain in this distribution have been shown to benefit from local tendon sheath injections. The presence of preexisting tendon sheath fluid can facilitate needle visualization. However, careful scanning should be done before the procedure to assess the needle trajectory relative to adjacent neurovascular structures. Use of color or power Doppler imaging can facilitate visualization of the neurovascular bundle. The posterior tibial nerve is closely related to adjacent vascular structures and is usually well seen before bifurcating into medial and lateral plantar branches. Fluid frequently is seen in relation to the posterior tibial tendon, in the submalleolar region. The location of the peroneal tendon is less predictable. Use of power Doppler sonography in conjunction with real-time guidance can help localize areas of inflammation for guided injection. In **stenosing tenosynovitis** the tendons may be surrounded only by a thickened retinaculum, proliferative synovium, or scar tissue. In this case, use of a test injection of local anesthesia can be invaluable to confirm the distribution of the therapeutic agent within the tendon sheath in real time.

The **flexor hallucis longus** (FHL) tendon poses a more challenging problem because of its close relation to the neurovascular bundle of the posterior medial ankle. One helpful feature in performing FHL tendon sheath injections is that tendon sheath effusions tend to localize at the posterior recess of the tibiotalar joint. The neurovascular bundle is easily circumvented by placing the needle lateral to the Achilles tendon while scanning medially (Fig. 25.10). This approach allows flexibility in needle placement while maintaining the needle perpendicular to the insonating beam.

Ultrasound diagnosis of **plantar fasciitis** includes thickening of the medial band of the plantar fascia and fat pad edema. One treatment option for severe plantar fasciitis is regional corticosteroid injection, typically performed using anatomic landmarks. However, "blind" injections into the heel have been associated with rupture of the plantar fascia and failure of the longitudinal arch.[13] Ultrasound can be used to guide a needle along the plantar margin of the fascia, thus avoiding direct intrafascial injection.[26] The plantar fascia is imaged with the patient prone and the foot mildly dorsiflexed, using a long-axis approach. The transducer is centered over the medial band, which is most often implicated in these patients. A mark is placed over the posterior aspect of the heel and the needle advanced superficial to the plantar fascia, approximately to the margin of the medial tubercle (Fig. 25.11). I perform a perifascial injection using this approach, monitoring the distribution of injected material in real time.

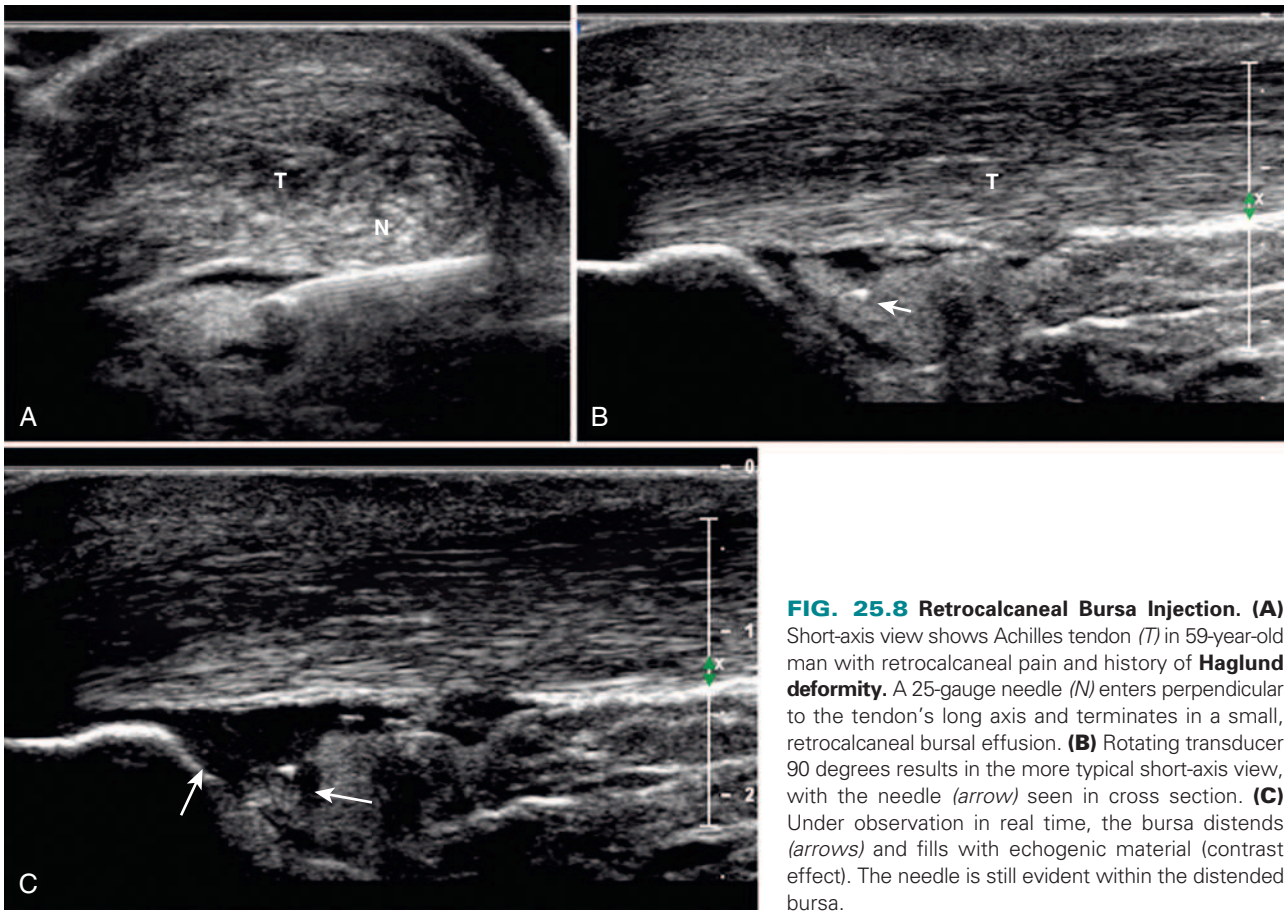

FIG. 25.8 Retrocalcaneal Bursa Injection. (A) Short-axis view shows Achilles tendon *(T)* in 59-year-old man with retrocalcaneal pain and history of **Haglund deformity.** A 25-gauge needle *(N)* enters perpendicular to the tendon's long axis and terminates in a small, retrocalcaneal bursal effusion. **(B)** Rotating transducer 90 degrees results in the more typical short-axis view, with the needle *(arrow)* seen in cross section. **(C)** Under observation in real time, the bursa distends *(arrows)* and fills with echogenic material (contrast effect). The needle is still evident within the distended bursa.

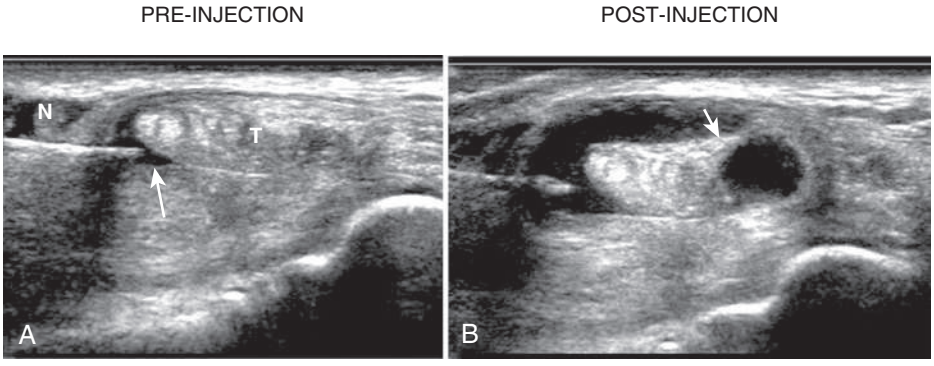

FIG. 25.9 Tendon Sheath Injection Using Short-Axis Approach. A 17-year-old female patient with medial ankle pain was referred for ultrasound-guided injection of posterior tibial tendon sheath. **(A)** Preinjection view shows 25-gauge needle *(N)* within a small tendon sheath effusion *(long arrow)* in the inframalleolar portion of the tendon *(T)*. The tendon, which is inhomogeneous, is seen in cross section. **(B)** Postinjection view shows that the tendon sheath is distended, confirming appropriate deposition of the injected material. Note that the tendon margins are better delineated because of a tenosonographic effect of the injected fluid. The vascular pedicle *(short arrow)* of the tendon is evident.

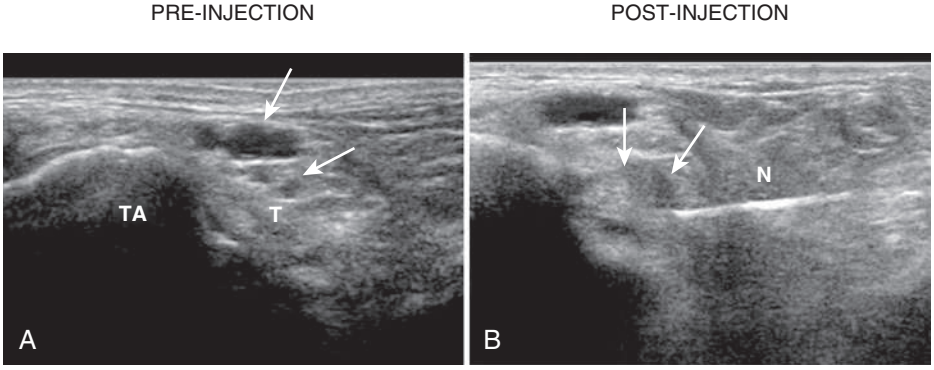

FIG. 25.10 Flexor Hallucis Longus (FHL) Tendon Sheath Injection. Short-axis approach with ultrasound guidance in 31-year-old professional dancer with posteromedial ankle pain during plantar flexion. **(A)** Preinjection image depicts the tendon *(T)* at the level of the posterior sulcus of the talus *(TA)*. The arrows show relationship of the tendon to the neurovascular structures. **(B)** Postinjection image depicts 25-gauge needle *(N)* situated within the distended tendon sheath *(arrows)* below the neurovascular structures.

Interdigital (Morton) neuromas, a common cause of forefoot pain especially in women, have been described at sonography as hypoechoic masses replacing the normal hyperechoic fat in the interdigital web spaces. Occasionally a dilated hypoechoic tubular structure can be seen associated with the neuroma, reflecting the enlarged feeding interdigital nerve. The second and third web spaces are most often involved. I generally inject Morton neuromas using a dorsal approach while imaging the neuroma in long axis[28] (Fig. 25.12). This approach is well tolerated by the majority of patients. In certain patients, however, a plantar approach to injecting the nodule is preferred, such as those with severe subluxation at the MTP joint. In either case, the needle is positioned directly within the neuroma and/or adjacent intermetatarsal bursa (if present) and a small volume of therapeutic mixture injected, similar to that used for a small joint injection (0.5-0.75 mL).

Hand and Wrist

In the hand and wrist, **de Quervain tendinosis** is a frequently encountered tendinopathy involving the abductor pollicis longus and extensor pollicis brevis tendons that respond to local administration of antiinflammatory agents (Fig. 25.13). Injections are also frequently requested for patients with **rheumatoid arthritis** or **psoriatic arthritis.** These patients typically experience severe tenosynovitis, which can lead to secondary tendon rupture and deformity. The approach is similar to that used for superficial structures in the foot and ankle. A short-axis approach avoids the surrounding neurovascular structures, and the corresponding tendon sheaths are injected.

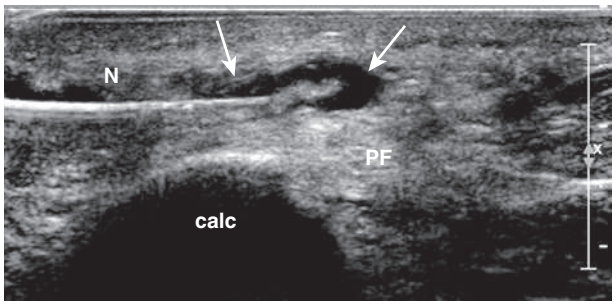

FIG. 25.11 Plantar Fascia Injection. The proximal medial band of the plantar fascia *(PF)* is thickened and inhomogeneous in a 36-year-old man with hindfoot pain. *calc,* Calcaneus. A 25-gauge needle *(N)* has been positioned superficial to this plantar fascia and a perifascial injection performed. The injected material *(arrows)* loculates along the superficial margin of the medial band.

INJECTION OF DEEP TENDONS

Frequently requested deep tendon injections include those for the **bicipital tendon sheath, iliopsoas tendon, gluteal tendon insertion onto the greater trochanter,** and **hamstring tendon** origin.

Biceps Tendon

Anterior shoulder pain with radiation into the arm may be secondary to bicipital tendinitis or tenosynovitis.[29] The biceps tendon can be palpated, but if nondistended, the sheath may offer less than 2 mm of clearance to place a needle. This is complicated by the caudal extension of the subacromial subdeltoid bursa, which may overlie the bicipital tendon sheath. A nonimage-guided injection could therefore result in delivery into an extratendinous synovial space, or possibly result in an intratendinous injection. Ultrasound guidance enables localization of therapeutic agent to the biceps tendon sheath.[10]

The patient is placed recumbent with the forearm supinated and the shoulder mildly elevated. The bicipital groove is oriented anteriorly. A linear transducer, typically 7.5 MHz, is used with a lateral approach and 25- or 22-gauge needle (Fig. 25.14). The long head of the biceps tendon is scanned in short axis. When fluid distends the bicipital tendon sheath, the tip is directed into the fluid. Otherwise, the needle is directed along the superficial margin of the tendon, and a test injection of local anesthetic is used to confirm local distention of the sheath, which is then followed by administration of the long-acting corticosteroid. The

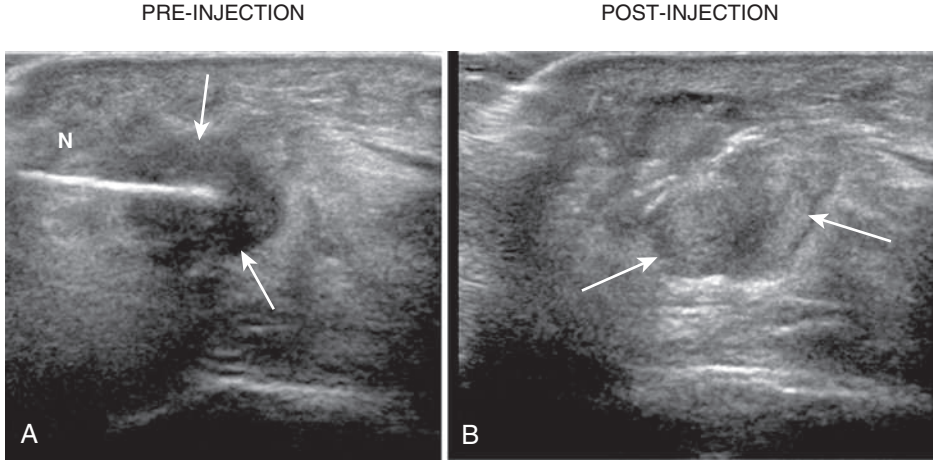

FIG. 25.12 Morton Neuroma Injection. (A) Preinjection image shows 25-gauge needle *(N)* positioned in a third web space neuroma using a dorsal approach in 45-year-old woman with forefoot pain. Neuroma appears as a heterogeneous hypoechoic nodule *(arrows)* within the normal echogenic fat. **(B)** After injection and needle removal, the nodule appears expanded and echogenic *(arrows).* The injected material often decompresses into an adjacent adventitial bursa, which frequently accompanies these nodules.

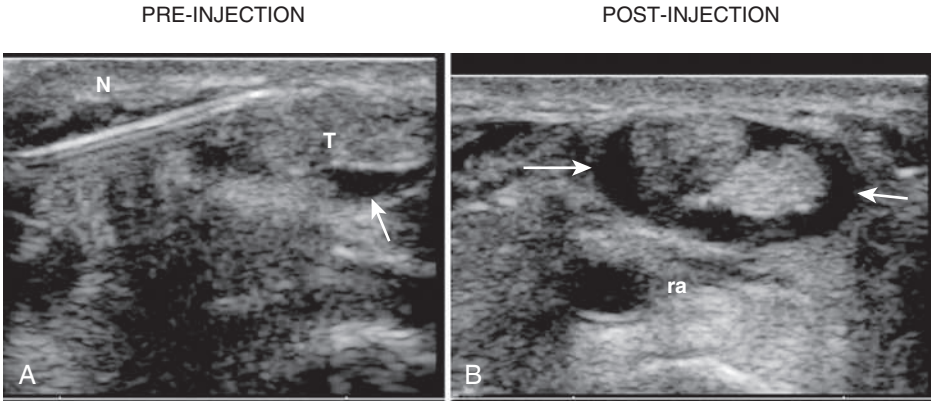

FIG. 25.13 Injection of First Dorsal Compartment of Wrist. This 70-year-old woman with **de Quervain tendinosis** had clinical symptoms of wrist pain radiating along the extensor surface of the forearm. **(A)** Preinjection image shows 25-gauge needle *(N)* positioned in the first dorsal compartment tendon sheath under ultrasound guidance. The tendons *(T)* are inhomogeneous, with a small effusion evident *(arrows)* in the dependent part of the tendon sheath. **(B)** After injection and needle removal, the injected material distends the sheath *(arrows),* producing a tenosonographic effect; the intrinsic tendon abnormalities become more conspicuous. *ra,* Radial artery.

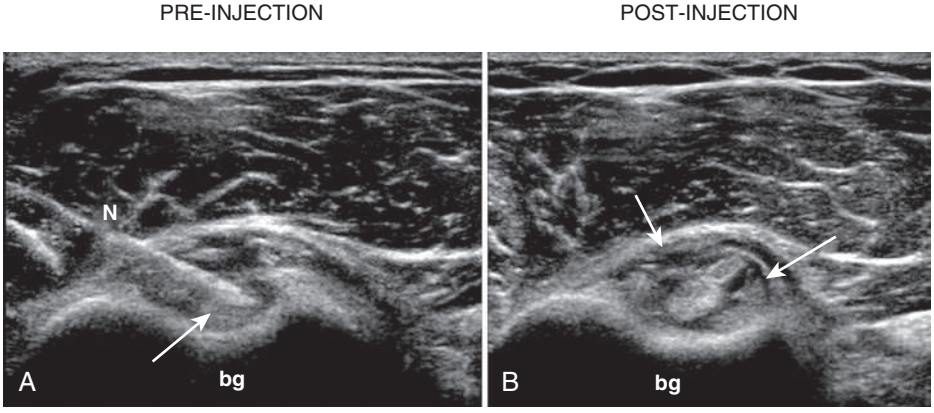

FIG. 25.14 Biceps Tendon Sheath Injection. Biceps tendinosis was clinically suspected and a biceps tendon sheath injection requested for this 41-year-old man with development of anterior shoulder pain after arthroscopic surgery for labral tear. **(A)** Preinjection image shows 25-gauge needle *(N)* placed superficial to the long head of the biceps tendon *(arrow).* **(B)** After injection and needle removal, there is distention of the tendon sheath by fluid *(arrows)* containing low-level echoes caused by contrast effect. *bg,* Bicipital groove.

presence of fluid distention of the sheath with superficially located microbubbles helps to confirm a successful injection. A technique to obviate the need to directly approach the tendon sheath, which can sometimes be challenging in the absence of an effusion, entails direct positioning of the needle within the rotator interval adjacent to the intraarticular portion of the biceps tendon and deep to the biceps pulley mechanism.[30] Stone and Adler reported 100% success in distending the sheath in their series.[30] Therapeutic mixture was also noted to distribute within the rotator interval (Fig. 25.15, Video 25.2).

Iliopsoas Tendon

The iliopsoas tendon lies superficial to and along the medial margin of the anterior capsule of the hip. The tendon inserts onto the lesser trochanter. A bursa that frequently communicates with the hip is present in this location and may be distended because of underling joint pathology or a primary iliopsoas bursitis. Alternatively, iliopsoas tendinosis may occur in the absence of a preexisting bursitis for which a peritendinous injection is requested.[31] A lateral approach to the tendon often requires use of a lower-frequency transducer and curved linear or sector geometry. The neurovascular bundle lies medial and superficial to the tendon, so it is advantageous to approach from the lateral margin of the tendon and perform a small test injection to confirm needle position. A successful injection will show the appearance of fluid or microbubbles distending a bursa that follows the course of the long axis of the tendon (Fig. 25.16).

Abductor and Hamstring Tendons

The most commonly requested peritendinous injections in my experience are about the abductor tendon insertion and hamstring tendon origin. In the first two of these injections, the needle is directed to the greater trochanteric bursa. These injections can be fairly straightforward when the bursa is distended. They become more challenging when there is no preexisting bursal distention. One must then employ anatomic landmarks and test injections with anesthetic for localization (Figs. 25.17 and 25.18). Injections at the hamstring origin are generally peritendinous because no true anatomic bursa exists. An adventitial bursa may be present over the ischium. A lateral approach while scanning the tendons in short axis is preferred for each of these injections, directing

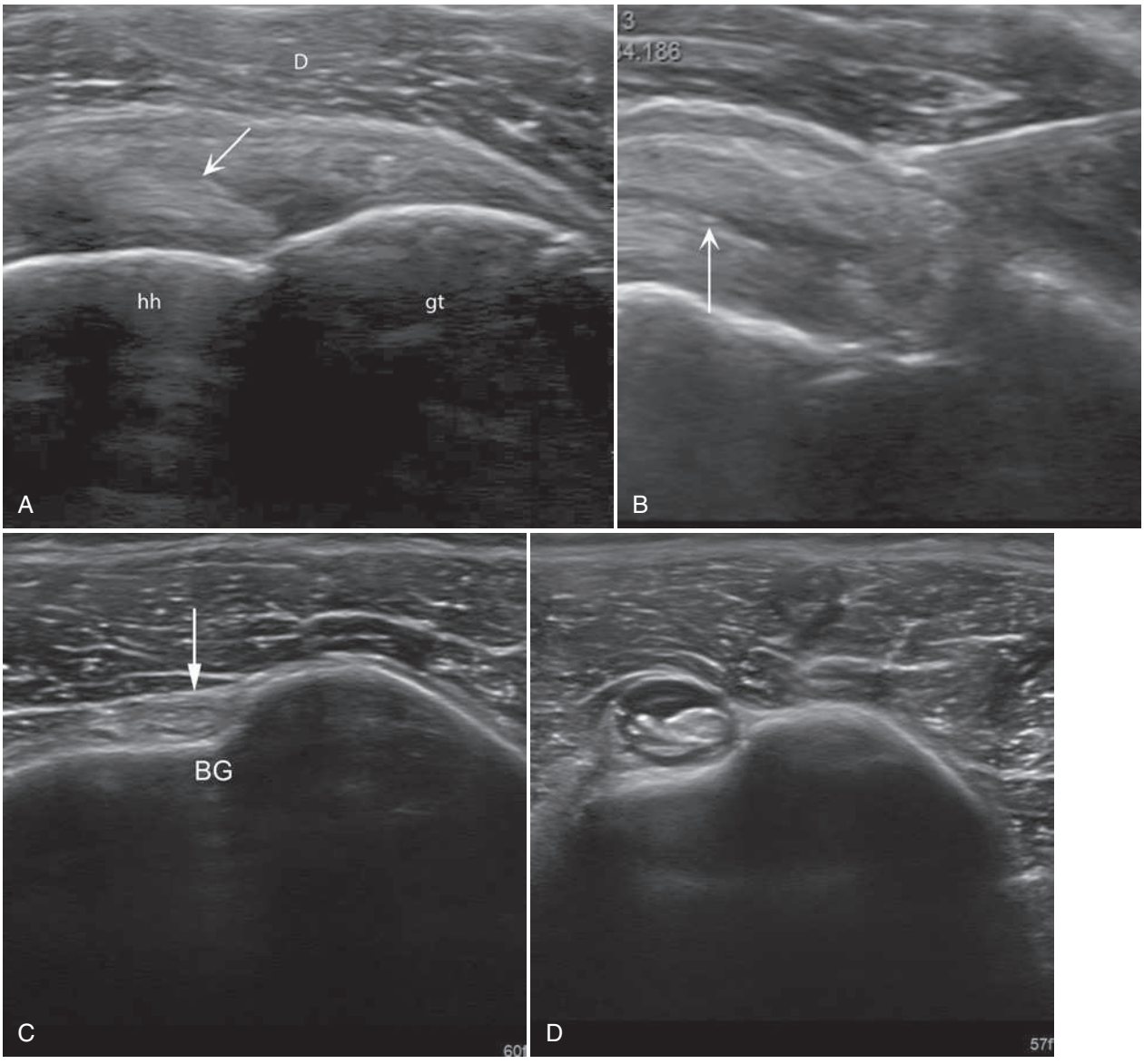

FIG. 25.15 Biceps Tendon Sheath Injection: Rotator Interval Approach. A 44-year-old woman with anterior shoulder pain. **(A)** Gray-scale ultrasound image obtained slightly oblique to the intraarticular biceps tendon *(arrow).* The greater tuberosity *(gt),* humeral head *(hh),* and deltoid *(D)* are labeled. **(B)** A 25-gauge needle is positioned using a short-axis lateral approach adjacent to the margin of the biceps tendon within the rotator interval. The tip of the needle is indicated *(arrow).* A test injection with anesthetic is performed to ensure appropriate needle position. Fluid should not accumulate by the needle tip and the needle position should be adjusted accordingly. **(C)** Short-axis view of the biceps tendon within the sheath before needle placement and injection. The tendon *(arrow)* and bicipital groove *(BG)* are labeled. **(D)** Postinjection image at approximately the same anatomic level as **(C)** depicting the distended biceps tendon sheath. See also Video 25.2.

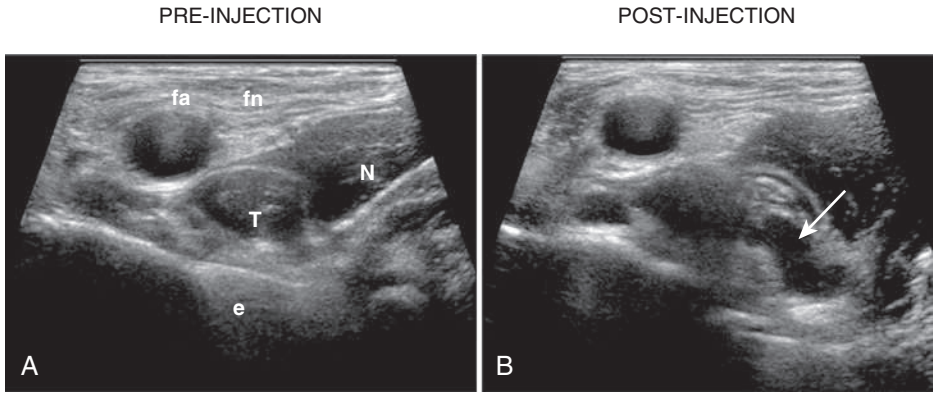

FIG. 25.16 Ultrasound-Guided Iliopsoas Bursa Injection for Pain Relief. This 66-year-old woman with a total hip arthroplasty had developed pain with hip flexion. **(A)** Preinjection image shows 22-gauge spinal needle *(N)* positioned deep to the tendon *(T)* at the level of the iliopectineal eminence *(e),* using a short-axis approach. *fa,* Femoral artery; *fn,* femoral nerve. **(B)** After injection and needle removal, fluid surrounds the tendon within the distended iliopsoas bursa *(arrow).*

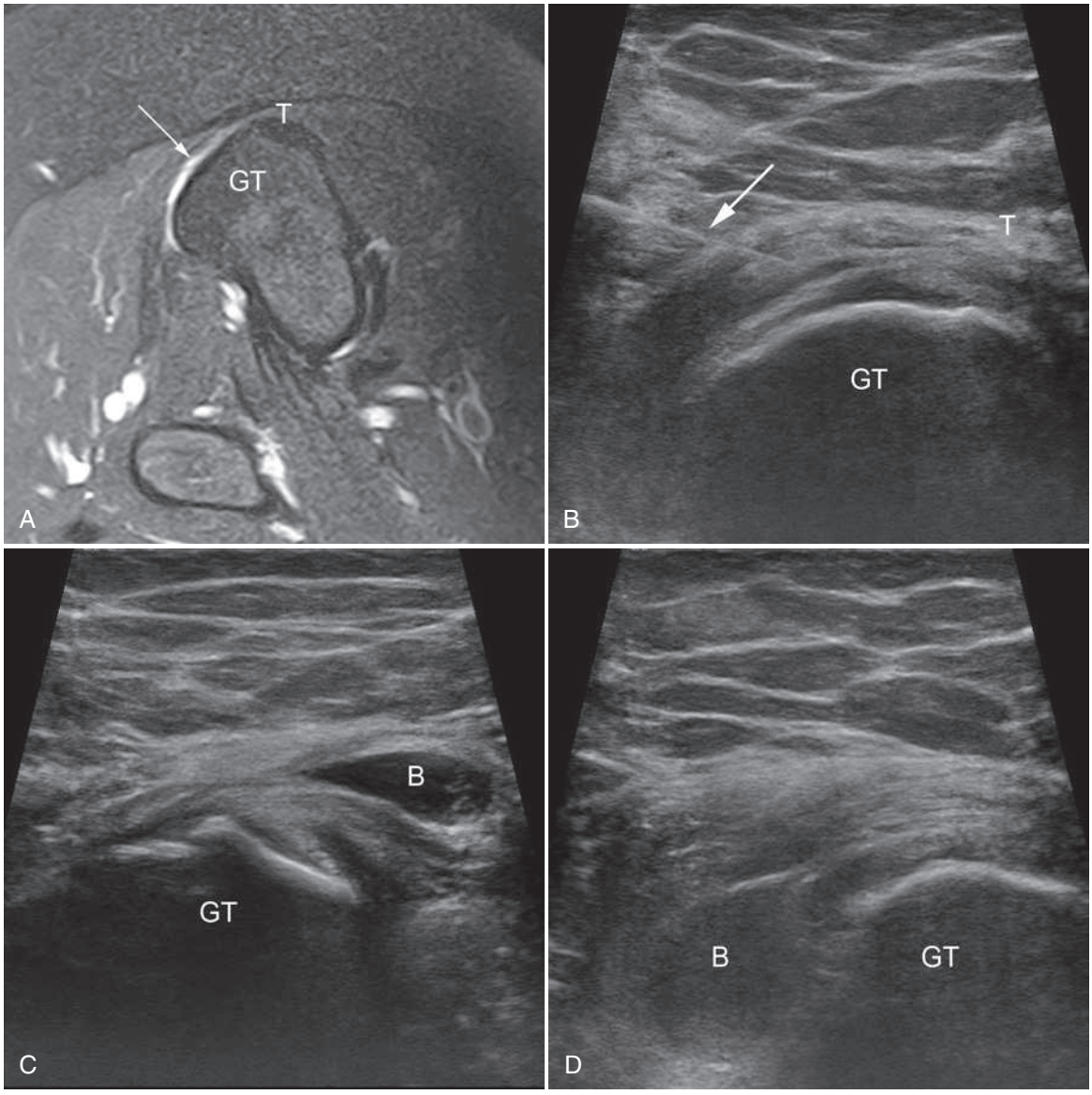

FIG. 25.17 Ultrasound-Guided Greater Trochanteric Bursal Injection. A 53-year-old woman with right lateral hip pain. **(A)** Axial T2-weighted fat-suppressed image depicts the greater trochanter *(GT)* and abductor tendon complex *(T)*. The image is oriented similar to the manner in which it would be viewed during an injection with the patient in a lateral decubitus position. A trace amount of T2-bright fluid *(arrow)* is present in the bursa. **(B)** A 22-gauge spinal needle *(arrow)* is positioned near the posterior margin of the greater trochanter, superficial to the gluteus medius tendon and deep to the gluteus maximus. A test injection with local anesthetic helps ensure appropriate needle placement, which is followed by injection of the therapeutic mixture. **(C)** Short-axis postinjection image at the greater trochanter shows anterior extension of the greater trochanteric bursa *(B)* at the level of the anterior facet. **(D)** Postinjection short-axis image centered more posteriorly over the lateral and posterior facets depicts the posterior extension of the bursa *(B)* abutting the posterior facet of the greater trochanter, also referred to as the "bare area" of the greater trochanter. I usually inject a large volume (10 mL).

the needle toward the posterior facet of the greater trochanter in the case of a trochanteric bursal injection, or adjacent to the margin of the hamstring origin if a peritendinous injection is requested.

BURSAL, GANGLION CYST, AND PARALABRAL INJECTIONS

Distended bursae around tendinous insertions provide anatomic localization for therapeutic agents. Injection of these areas is often requested for the patient with localized **bursitis** and abnormality of the adjacent tendon. Examples include the retrocalcaneal, iliopsoas, greater trochanteric, and ischial bursae (Fig. 25.19). Alternatively, the presence of a bursitis, distended synovial cyst, or ganglion cyst may cause mechanical impingement of adjacent tendons. The decompression of these cysts with subsequent administration of a therapeutic agent may alleviate these symptoms[32] (Fig. 25.20). **Ganglion cysts** typically contain clear gelatinous material, most often occurring in the hand, wrist, foot, and ankle. Not infrequently they may come in close proximity to neurovascular structures and may extend along nerves as perineural ganglia. This occurs most often in the knee, at the

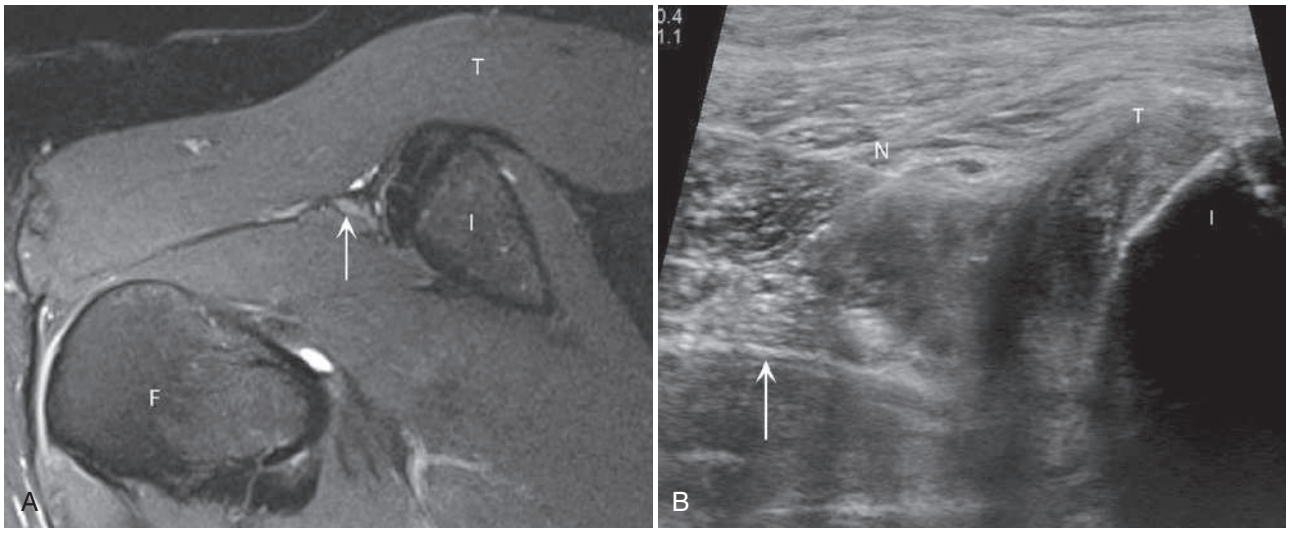

FIG. 25.18 Ultrasound-Guided Hamstring Peritendinous Injection. A 50-year-old female runner with left buttock pain. **(A)** Axial fat-suppressed T2-weighted sequence positioned in a manner similar to that viewed by a sonographer. The hamstring origin *(T)* and ischium *(I)* are labeled. The sciatic nerve *(arrow)* appears as a mildly hyperintense ellipse lateral to the ischium and superficial to the quadratus femoris. *F,* Femur. **(B)** A 22-gauge spinal needle *(N)* is positioned in short axis, using a lateral approach, adjacent to the margin of the hamstring tendon origin *(T).* The sciatic nerve *(arrow)* and ischium *(I)* are labeled.

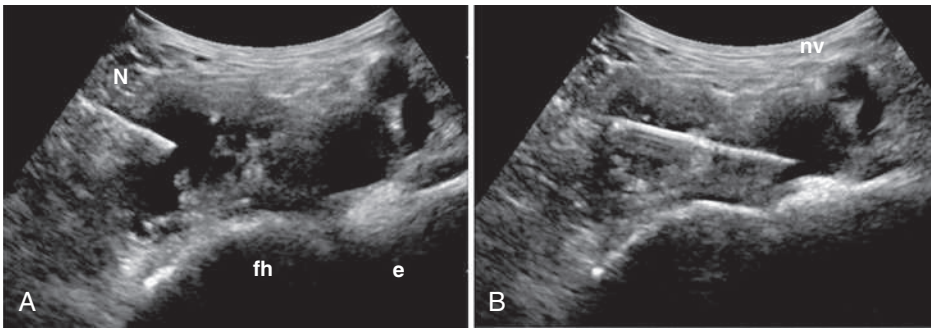

FIG. 25.19 Ultrasound-Guided Aspiration and Injection of Multiloculated Iliopsoas Bursa. (A) Image shows 22-gauge spinal needle *(N)* positioned into the lateral component of the bursa in a 65-year-old woman with groin pain. *e,* Iliopectineal eminence; *fh,* femoral head. **(B)** After aspiration of the lateral component, the needle has been advanced into the medial component for aspiration and subsequent injection with therapeutic mixture. *nv,* Neurovascular structures.

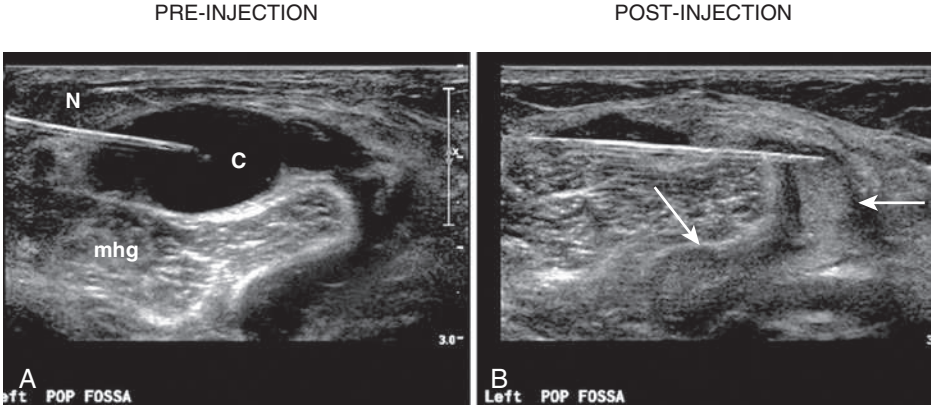

FIG. 25.20 Ultrasound-Guided Aspiration and Injection of Clinically Suspected Baker Cyst. (A) Preinjection image shows 22-gauge needle *(N)* positioned in the cyst *(C)* under ultrasound guidance in 59-year-old woman with posterior knee pain and swelling. *mhg,* Medial head of gastrocnemius muscle. **(B)** After cyst aspiration and injection of the therapeutic mixture, the anechoic fluid is replaced by echogenic fluid resulting from contrast effect *(arrows).*

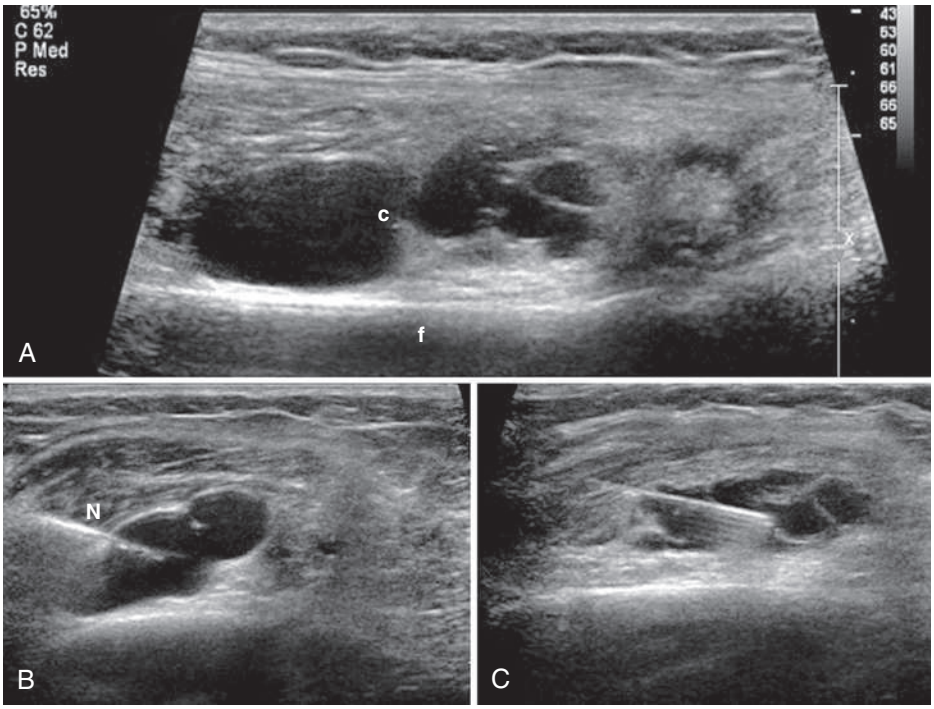

FIG. 25.21 Ultrasound-Guided Aspiration and Injection of Multiloculated Ganglion Cyst. (A) Baseline sonogram shows a multiloculated cyst *(c)* within the vastus lateralis muscle of the left knee and superficial to the lateral margin of the femur *(f)* in a 41-year-old woman. **(B)** A 20-gauge spinal needle *(N)* was initially positioned into the proximal component of the cyst. **(C)** Subsequently the needle was redirected into the distal component. Multiple lavages and aspiration enabled complete decompression of the cyst *(not shown)*.

tibiofibular joint.[33,34] Ultrasound guidance allows the clinician to avoid intratendinous injections as well as adjacent neurovascular structures. Furthermore, the needle may be redirected as necessary in the presence of a multiloculated cyst (Fig. 25.21). We find that performing a lavage technique similar to that employed in treating calcific tendinosis results in progressive dilution of the cyst contents, thereby permitting complete aspiration. In the upper extremity, where cosmesis may also be an issue, use of a rapidly absorbed corticosteroid may reduce potential complications, such as depigmentation and local atrophy. Similar considerations apply when aspirating and injecting **parameniscal and paralabral cysts.** These cysts occur at sites of torn and/or degenerated fibrocartilage and are most often present in the knee, hip, and shoulder. These cysts are similar to ganglion cysts in consistency but often contain additional echogenic debris. In the shoulder, paralabral cysts have been associated with development of a compressive neuropathy, because they can occur in close proximity to the suprascapular nerve.[35] The approach used in aspirating these cysts is variable, depending on location and orientation, as well as location of adjacent neurovascular structures (Figs. 25.22 and 25.23, Video 25.3).

Calcific Tendinitis

The presence of symptomatic intratendinous calcification involves the deposition of **calcium hydroxyapatite.** This often appears as a nodular echogenic mass within the tendon, which may or may not display posterior acoustic shadowing.[36] Although most often affecting the shoulder, this may occur elsewhere in the musculoskeletal system. Ultrasound-guided fragmentation and lavage, also known as **barbotage,** has been described as an excellent method to fenestrate the calcification and reduce the level of calcification and to deposit therapeutic agents.[37-40] Single- and dual-needle techniques have been described and appear to be comparably effective. I currently use a single-needle technique, with the needle acting as inflow for anesthetic and sterile saline and as an outflow for the calcium solution (Fig. 25.24). The elasticity of the pseudocapsule encasing the calcification is sufficient to decompress the calcific mass in the majority of cases (Video 25.4). After multiple lavages, the needle is used to inject the anesthetic and antiinflammatory mixture. The injected mixture is distributed within the adjacent subdeltoid bursa in most cases. If the calcification is too small or fragmented, precluding lavage and decompression, the single needle is used to fenestrate the calcium deposit, and a peritendinous therapeutic injection has been shown to be effective.

INTRATENDINOUS INJECTIONS: PERCUTANEOUS TENOTOMY

Image guidance can be useful for performing percutaneous tenotomy and intratendinous injections with either autologous blood or platelet-rich plasma (PRP).[41-45] These methods are associated with secondary release of local growth factors, such as platelet-derived growth factor, which in turn may produce a direct healing response.[44] Preliminary data show significant promise in promoting ultrasound-guided tendon repair. "Dry needling" techniques have been employed successfully in patients with lateral epicondylitis refractory to other conservative

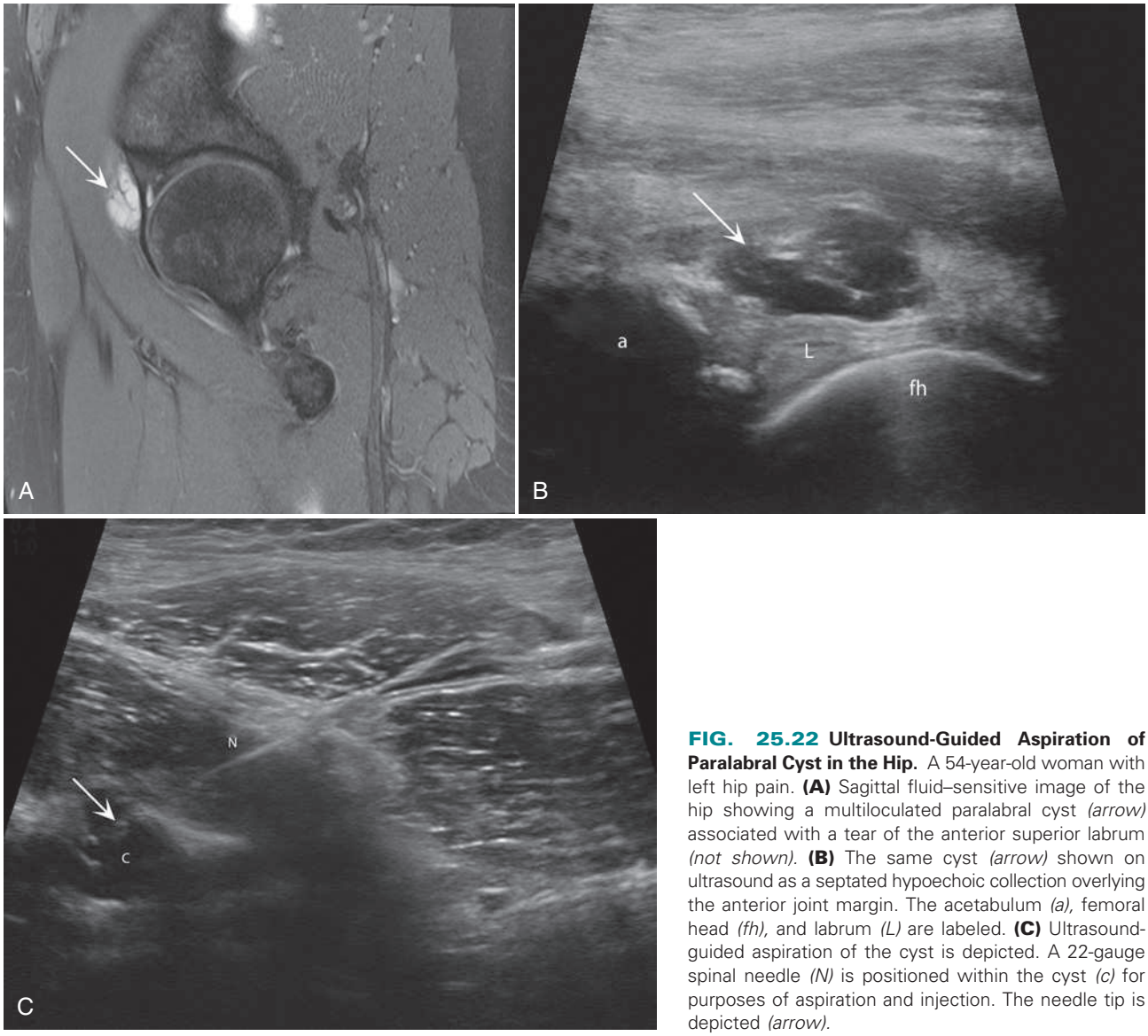

FIG. 25.22 Ultrasound-Guided Aspiration of Paralabral Cyst in the Hip. A 54-year-old woman with left hip pain. **(A)** Sagittal fluid–sensitive image of the hip showing a multiloculated paralabral cyst *(arrow)* associated with a tear of the anterior superior labrum *(not shown)*. **(B)** The same cyst *(arrow)* shown on ultrasound as a septated hypoechoic collection overlying the anterior joint margin. The acetabulum *(a)*, femoral head *(fh)*, and labrum *(L)* are labeled. **(C)** Ultrasound-guided aspiration of the cyst is depicted. A 22-gauge spinal needle *(N)* is positioned within the cyst *(c)* for purposes of aspiration and injection. The needle tip is depicted *(arrow)*.

measures.[41] Likewise, autologous blood injections and PRP injections have been successfully used in both the elbow and the knee[42-44] (Figs. 25.25 and 25.26, Video 25.5). The advantage of performing these injections under ultrasound guidance becomes evident when the clinician wants to generalize such techniques to include tendons close to neurovascular structures, such as the hamstring tendon origin. Newer technology is now available that allows sonographically directed emulsification of focal tendinosis, calcifications, and enthesopathic spurs followed by removal during the course of the procedure.[46] The technique employs a coaxial system with a mechanically active hollow tip that disrupts the tissue and is connected to vacuum suction, while the outer tube supplies sterile water to cool the tip and remove debris as part of the suctioned material (Fig. 25.27, Video 25.6). This technique is relatively new, and no definitive long-term trials are available to assess efficacy, but preliminary results appear promising.

PERINEURAL INJECTIONS

Ultrasound has shown promise in evaluating and treating patients with painful lesions of peripheral nerves due to compressive neuropathies, such as in carpal or cubital tunnel syndromes, or in cases of posttraumatic or postsurgical neuromas.[35] These injections can include nerve blocks with long-acting anesthetic, therapeutic injections using an injectable steroid, or neurolytic therapy with an agent that promotes cellular death such as absolute ethanol.[47,48] A rapidly absorbed injectable steroid, such as dexamethasone, may be preferable for superficial lesion to minimize potential complications, such as depigmentation or atrophy of the subcutaneous fat.

A thorough knowledge of the normal sonographic appearances of nerves and their anatomic course is a prerequisite.[35,36] In the case of small sensory nerves, which can be difficult to visualize, knowledge of the anatomic relationships of the nerves to adjacent

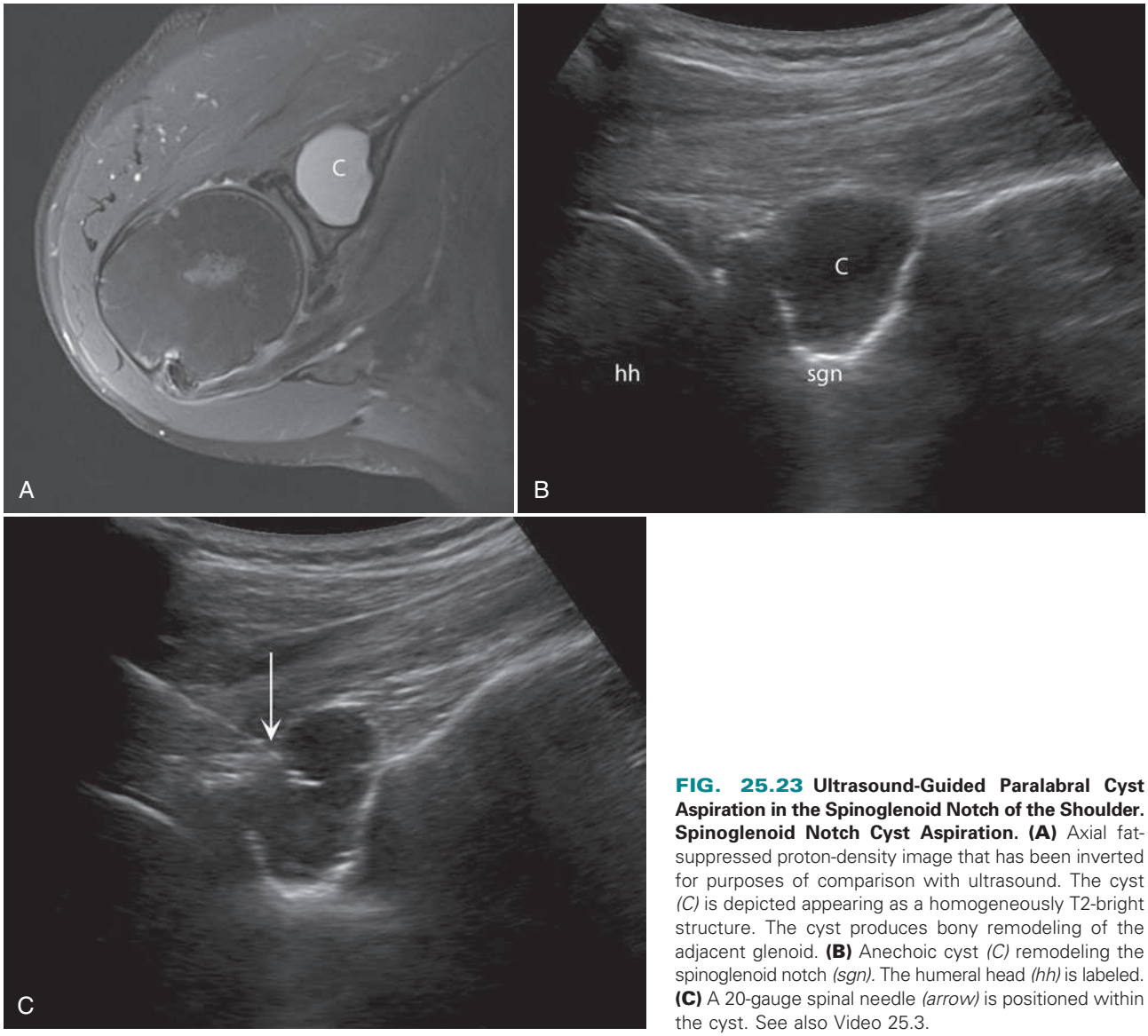

FIG. 25.23 Ultrasound-Guided Paralabral Cyst Aspiration in the Spinoglenoid Notch of the Shoulder. Spinoglenoid Notch Cyst Aspiration. (A) Axial fat-suppressed proton-density image that has been inverted for purposes of comparison with ultrasound. The cyst *(C)* is depicted appearing as a homogeneously T2-bright structure. The cyst produces bony remodeling of the adjacent glenoid. **(B)** Anechoic cyst *(C)* remodeling the spinoglenoid notch *(sgn)*. The humeral head *(hh)* is labeled. **(C)** A 20-gauge spinal needle *(arrow)* is positioned within the cyst. See also Video 25.3.

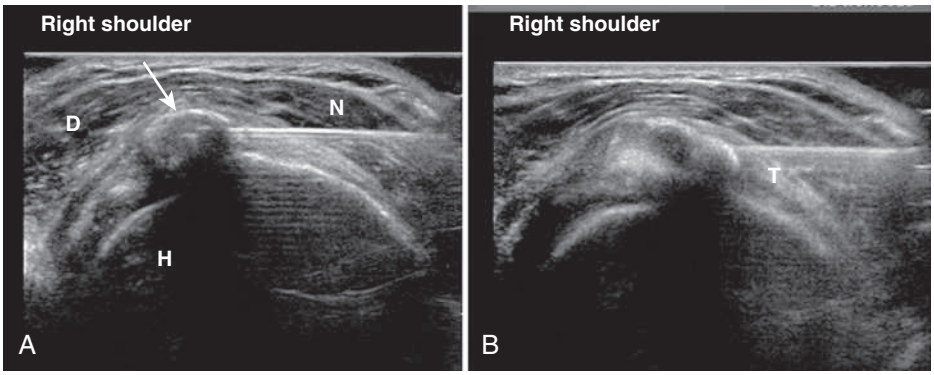

FIG. 25.24 Ultrasound-Guided Aspiration and Injection for Calcific Tendinosis. (A) Image shows 20-gauge spinal needle *(N)* positioned into the calcification *(arrow)* under ultrasound guidance in 42-year-old man with shoulder pain. *D,* Deltoid; *H,* humeral head. **(B)** Series of repeat lavage and aspirations of the calcification are performed, with the calcification eventually largely replaced by fluid contents within the surrounding pseudocapsule of the calcific mass. *T,* Rotator cuff tendons. Note that the degree of posterior acoustic shadowing has diminished and that the center of the calcification (*arrow* on **A**) is partially replaced by fluid. After numerous lavages, the calcification is typically fenestrated, and a therapeutic mixture is injected and often decompresses into the subdeltoid bursa *(not shown)*.

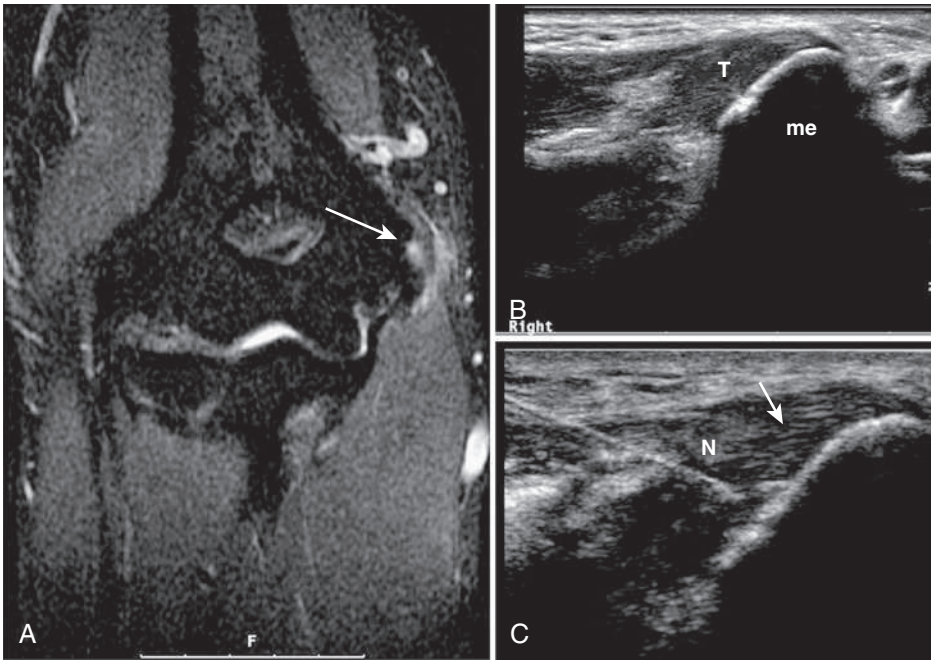

FIG. 25.25 Ultrasound-Guided Injection of Autologous Blood to Induce Healing Response. (A) Coronal inversion-recovery magnetic resonance imaging scan of the affected elbow in a 43-year-old man with medial epicondylitis shows increased signal intensity *(arrow)* of the common flexor tendon mass and adjacent collateral ligament. **(B)** Long-axis ultrasound image of the tendon *(T)* and adjacent medial epicondyle *(me)* shows that tendon is predominantly hypoechoic, reflecting underlying tendinosis. **(C)** Image shows 22-gauge needle *(N)* placed within the common flexor tendon mass, for purposes of mechanical fenestration, and injection of 5 mL of autologous blood, obtained from an antecubital vein. Tendon echogenicity *(small arrow)* is increased by microbubbles within the injected blood.

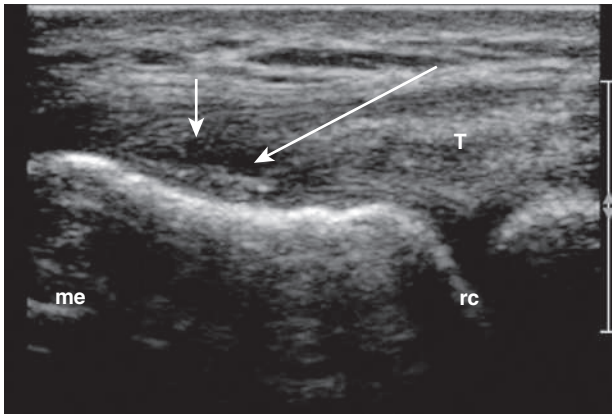

FIG. 25.26 Baseline Image Before Autologous Blood Injection. Common extensor tendon mass *(T)* in 50-year-old woman with partial tear of the deep portion of the tendon (*short arrow,* extensor carpi radialis brevis) as it inserts on the medial epicondyle *(me); rc,* radiocapitellar joint; *long arrow,* plane of needle entry for percutaneous tenotomy and autologous blood injection. See also Video 25.5.

anatomic compartments is of value. Nerves are best visualized in short axis as clusters of hypoechoic fascicles with echogenic septations (internal epineurium), which have a surrounding echogenic epineurial sleeve (external epineurium). An enlarged hypoechoic nerve may indicate neuritis, whereas a focal hypoechoic nodule seen in relationship to the nerve may represent a neuroma in the appropriate clinical setting.

Ultrasound allows direct targeting of the perineural soft tissue or a neuroma for injection (Fig. 25.28, Video 25.7). The nerve is best approached in short axis, usually with a 1.5-inch 25-gauge needle or occasionally a spinal needle. In the case of a perineural injection, it is helpful to position the needle in close proximity to the nerve, injecting small amounts of anesthetic until a clear-cut fluid plane outlining the epineurium is evident. When this is achieved, the therapeutic mixture can be instilled. The same procedure is used when performing ultrasound-guided neurolytic therapy. I typically inject a mixture of long-acting anesthetic (0.75% bupivacaine) with a total of 0.5 to 1 mL of absolute ethanol for peripheral nerve lesions. In my experience, absolute ethanol may require multiple injections and can produce a marked postinjection inflammatory response that can last for several days. The volume injected can be variable and in general does not exceed 1 mL. Multiple small injections have been advocated to be efficacious for Morton neuromas (0.25-0.5 mL).

CONCLUSION

Ultrasound offers distinct advantages in providing guidance for delivery of therapeutic injections. Most important, ultrasound allows the operator to visualize the needle and make adjustments in real time, to ensure that medication is delivered to the appropriate location. Current ultrasound technology provides excellent depiction of relevant musculoskeletal anatomy. The needle has a unique sonographic appearance and can be monitored with

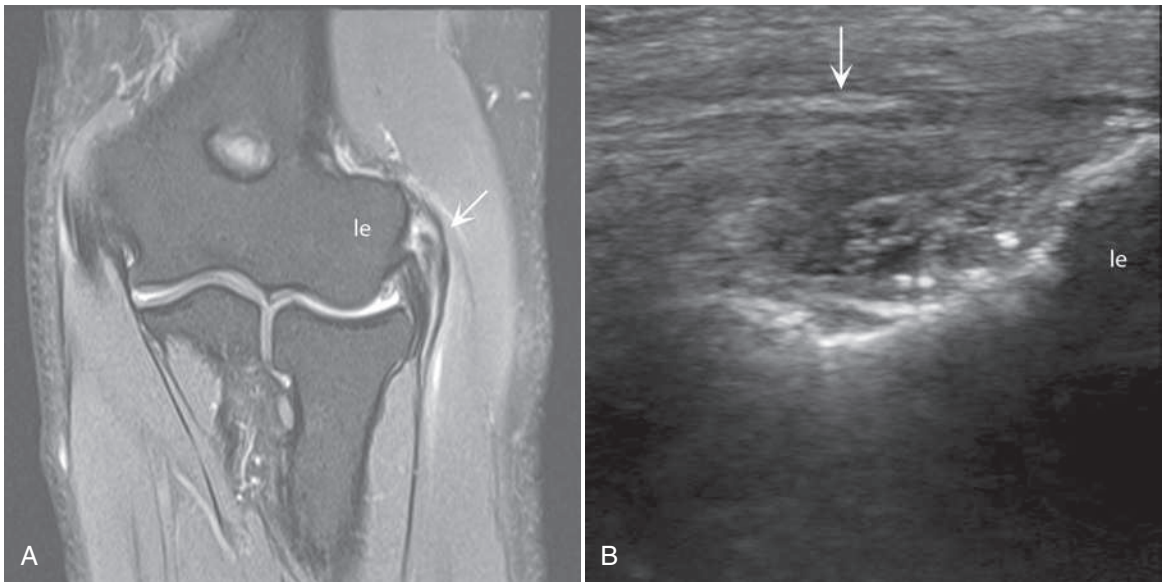

FIG. 25.27 Percutaneous Tenotomy Using Tenex Device. A 47-year-old man with lateral epicondylitis. **(A)** Coronal fat-suppressed proton-density image depicting a partial torn and degenerated common extensor tendon and radial collateral ligament *(arrow).* The lateral epicondyle *(le)* is labeled. **(B)** The common extensor mechanism *(arrow)* is shown in long axis. Hypoechoic areas within the tendon represent interstitial tearing. In addition, punctate echogenic foci within the tendon substance are characteristic for dystrophic calcification. The lateral epicondyle *(le)* is labeled. See also Video 25.6.

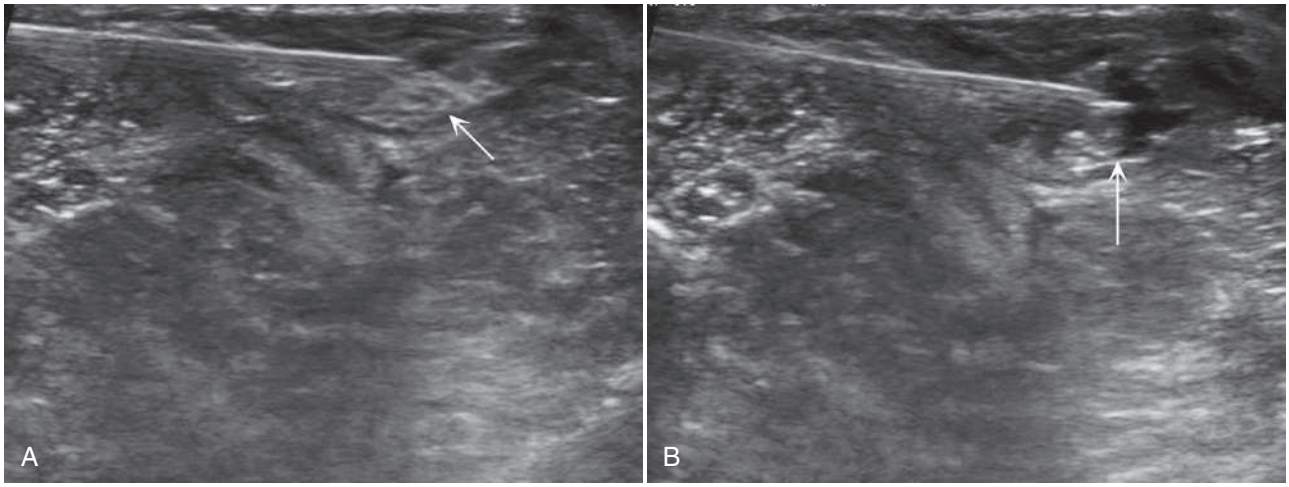

FIG. 25.28 A 58-Year-Old Woman With Postoperative Sural Nerve Entrapment and Neuropathic Pain. (A) A 1.5-inch 25-gauge needle is positioned adjacent to the outer epineurium of the sural nerve *(arrow).* **(B)** Hypoechoic fluid consisting of anesthetic and corticosteroid surrounds the nerve. Ideally, fluid hydrodissection of the epineurial fat from the adjacent perineural soft tissues is achieved. See also Video 25.7.

real-time imaging, as can the steroid-anesthetic mixture. Given these advantages, ultrasound guidance should become the method of choice to perform a large variety of guided musculoskeletal interventions.

REFERENCES

1. Christensen RA, Van Sonnenberg E, Casola G, Wittich GR. Interventional ultrasound in the musculoskeletal system. Radiol Clin North Am. 1988;26(1):145-156.
2. Cunnane G, Brophy DP, Gibney RG, FitzGerald O. Diagnosis and treatment of heel pain in chronic inflammatory arthritis using ultrasound. Semin Arthritis Rheum. 1996;25(6):383-389.
3. Brophy DP, Cunnane G, Fitzgerald O, Gibney RG. Technical report: ultrasound guidance for injection of soft tissue lesions around the heel in chronic inflammatory arthritis. Clin Radiol. 1995;50(2):120-122.
4. Cardinal E, Chhem RK, Beauregard CG. Ultrasound-guided interventional procedures in the musculoskeletal system. Radiol Clin North Am. 1998;36(3):597-604.
5. Koski JM. Ultrasound guided injections in rheumatology. J Rheumatol. 2000;27(9):2131-2138.
6. Grassi W, Farina A, Filippucci E, Cervini C. Sonographically guided procedures in rheumatology. Semin Arthritis Rheum. 2001;30(5):347-353.
7. Sofka CM, Collins AJ, Adler RS. Use of ultrasonographic guidance in interventional musculoskeletal procedures: a review from a single institution. J Ultrasound Med. 2001;20(1):21-26.
8. Sofka CM, Adler RS. Ultrasound-guided interventions in the foot and ankle. Semin Musculoskelet Radiol. 2002;6(2):163-168.
9. Adler RS, Sofka CM. Percutaneous ultrasound-guided injections in the musculoskeletal system. Ultrasound Q. 2003;19(1):3-12.
10. Adler RS, Allen A. Percutaneous ultrasound-guided injections in the shoulder. Tech Shoulder Elbow Surg. 2004;5(2):122-133.

11. Unverferth LJ, Olix ML. The effect of local steroid injections on tendon. J Sports Med. 1973;1(4):31-37.
12. Ford LT, DeBender J. Tendon rupture after local steroid injection. South Med J. 1979;72(7):827-830.
13. Gottlieb NL, Riskin WG. Complications of local corticosteroid injections. JAMA. 1980;243(15):1547-1548.
14. Oxlund H, Manthorpe R. The biochemical properties of tendon and skin as influenced by long term glucocorticoid treatment and food restriction. Biorheology. 1982;19(5):631-646.
15. Stapczynski JS. Localized depigmentation after steroid injection of a ganglion cyst on the hand. Ann Emerg Med. 1991;20(7):807-809.
16. Shrier I, Matheson GO, Kohl 3rd HW. Achilles tendonitis: are corticosteroid injections useful or harmful? Clin J Sport Med. 1996;6(4):245-250.
17. Bouffard JA, Eyler WR, Introcaso JH, van Holsbeeck M. Sonography of tendons. Ultrasound Q. 1993;11:259-286.
18. Koski JM, Saarakkala SJ, Heikkinen JO, Hermunen HS. Use of air-steroid-saline mixture as contrast medium in greyscale ultrasound imaging: experimental study and practical applications in rheumatology. Clin Exp Rheumatol. 2005;23(3):373-378.
19. Luchs JS, Sofka CM, Adler RS. Sonographic contrast effect of combined steroid and anesthetic injections: in vitro analysis. J Ultrasound Med. 2007;26(2):227-231.
20. Curatolo M, Bogduk N. Pharmacologic pain treatment of musculoskeletal disorders: current perspectives and future prospects. Clin J Pain. 2001;17(1):25-32.
21. Caldwell JR. Intra-articular corticosteroids. Guide to selection and indications for use. Drugs. 1996;52(4):507-514.
22. Kannus P, Jarvinen M, Niittymaki S. Long- or short-acting anesthetic with corticosteroid in local injections of overuse injuries? A prospective, randomized, double-blind study. Int J Sports Med. 1990;11(5):397-400.
23. Cox B, Durieux ME, Marcus MA. Toxicity of local anaesthetics. Best Pract Res Clin Anaesthesiol. 2003;17(1):111-136.
24. Gomoll AH, Kang RW, Williams JM, et al. Chondrolysis after continuous intra-articular bupivacaine infusion: an experimental model investigating chondrotoxicity in the rabbit shoulder. Arthroscopy. 2006;22:813-819.
25. Sofka CM, Saboeiro G, Adler RS. Ultrasound-guided adult hip injections. J Vasc Interv Radiol. 2005;16(8):1121-1123.
26. Mehdizade A, Adler RS. Sonographically guided flexor hallucis longus tendon sheath injection. J Ultrasound Med. 2007;26(2):233-237.
27. Tsai WC, Wang CL, Tang FT, et al. Treatment of proximal plantar fasciitis with ultrasound-guided steroid injection. Arch Phys Med Rehabil. 2000;81(10):1416-1421.
28. Sofka CM, Adler RS, Ciavarra GA, Pavlov H. Ultrasound-guided interdigital neuroma injections: short-term clinical outcomes after a single percutaneous injection—preliminary results. HSS J. 2007;3:44-49.
29. Middleton WD, Reinus WR, Totty WG, et al. US of the biceps tendon apparatus. Radiology. 1985;157(1):211-215.
30. Stone TJ, Adler RS. Ultrasound-guided biceps peritendinous injections in the absence of a distended tendon sheath: a novel rotator interval approach. J Ultrasound Med. 2015;34(12):2287-2292.
31. Adler RS, Buly R, Ambrose R, Sculco T. Diagnostic and therapeutic use of sonography-guided iliopsoas peritendinous injections. Am J Roentgenol. 2005;185(4):940-943.
32. Breidahl WH, Adler RS. Ultrasound-guided injection of ganglia with corticosteroids. Skeletal Radiol. 1996;25(7):635-638.
33. Martinoli C, Bianchi S, Derchi LE. Tendon and nerve sonography. Radiol Clin North Am. 1999;37(4):691-711, viii.
34. Bianchi S. Ultrasound of the peripheral nerves. Joint Bone Spine. 2008;75(6):643-649.
35. Tung GA, Entzian D, Stern JB, Green A. MR imaging and MR arthrography of paraglenoid labral cysts. AJR Am J Roentgenol. 2000;174(6):1707-1715.
36. Farin PU, Jaroma H. Sonographic findings of rotator cuff calcifications. J Ultrasound Med. 1995;14(1):7-14.
37. Farin PU, Jaroma H, Soimakallio S. Rotator cuff calcifications: treatment with US-guided technique. Radiology. 1995;195(3):841-843.
38. Farin PU, Rasanen H, Jaroma H, Harju A. Rotator cuff calcifications: treatment with ultrasound-guided percutaneous needle aspiration and lavage. Skeletal Radiol. 1996;25(6):551-554.
39. Aina R, Cardinal E, Bureau NJ, et al. Calcific shoulder tendinitis: treatment with modified US-guided fine-needle technique. Radiology. 2001;221(2):455-461.
40. Lin JT, Adler RS, Bracilovic A, et al. Clinical outcomes of ultrasound-guided aspiration and lavage in calcific tendinosis of the shoulder. HSS J. 2007;3(1):99-105.
41. McShane JM, Nazarian LN, Harwood MI. Sonographically guided percutaneous needle tenotomy for treatment of common extensor tendinosis in the elbow. J Ultrasound Med. 2006;25(10):1281-1289.
42. James SL, Ali K, Pocock C, et al. Ultrasound guided dry needling and autologous blood injection for patellar tendinosis. Br J Sports Med. 2007;41(8):518-521.
43. Connell DA, Ali KE, Ahmad M, et al. Ultrasound-guided autologous blood injection for tennis elbow. Skeletal Radiol. 2006;35(6):371-377.
44. Mishra A, Pavelko T. Treatment of chronic elbow tendinosis with buffered platelet-rich plasma. Am J Sports Med. 2006;34(11):1774-1778.
45. Gamradt SC, Rodeo SC, Warren RF. Platelet-rich plasma in rotator cuff repair. Tech Orthop. 2007;22:26-33.
46. Barnes D. Ultrasonic energy in tendon treatment. Oper Tech Orthop. 2013;23(2):78-83.
47. Tagliafico A, Serafini G, Lacelli F, et al. Ultrasound-guided treatment of meralgia paresthetica (lateral femoral cutaneous neuropathy): technical description and results of treatment in 20 consecutive patients. J Ultrasound Med. 2011;30(10):1341-1346.
48. Lee J, Lee YS. Percutaneous chemical nerve block with ultrasound-guided intraneural injection. Eur Radiol. 2008;18(7):1506-1512.

CHAPTER 26

The Extracranial Cerebral Vessels

Edward I. Bluth, Stephen I. Johnson, and Laurie Troxclair

SUMMARY OF KEY POINTS

- The combination of gray-scale, color-flow Doppler, and Doppler spectral analysis is highly accurate in determining plaque characterization and degree of carotid stenosis.
- Accurate diagnosis of carotid stenosis is critical for patients who would benefit from surgical and interventional treatment.
- Clinicians can accurately follow changes in noncritical carotid stenosis or plaque using ultrasound.
- The assessment of the vertebral arteries is an integral component of the carotid ultrasound examination. However, the degree of stenosis of the vertebral arteries cannot be accurately assessed.
- Carotid atherosclerotic plaque with resultant stenosis usually involves the internal carotid artery within 2 cm of the carotid bifurcation.
- Homogenous plaque, which is stable, has uniform echo pattern with a smooth surface. The amount of sonolucency is less than 50%.
- Heterogeneous plaque, which can be unstable, has a more complex echo pattern with sonolucent areas of more than 50%.
- Either the consensus table by the Society of Radiologists in Ultrasound or other standard reporting tables and criteria can be used to grade carotid stenosis as long as there is appropriate quality outcome feedback for accuracy.

CHAPTER OUTLINE

INTRODUCTION: INDICATIONS FOR CAROTID ULTRASOUND EXAMINATION
CAROTID ARTERY ANATOMY
CAROTID ULTRASOUND EXAMINATION
CAROTID ULTRASOUND INTERPRETATION
Visual Inspection of Gray-Scale Images
Vessel Wall Thickness and Intima-Media Thickening
Plaque Characterization
Ultrasound Plaque Classification System
Plaque Ulceration
Gray-Scale Evaluation of Stenosis
Doppler Spectral Analysis
Standard Examination
Spectral Broadening
Pitfalls in Interpretation
High-Velocity Blood Flow Patterns
Color Doppler Ultrasound
Optimal Settings for Low-Flow Vessel Evaluation
Advantages and Pitfalls
Power Doppler Ultrasound
Pitfalls and Adjustments
Internal Carotid Artery Occlusion
Follow-Up of Stenosis
Preoperative Strategies for Patients With Carotid Artery Disease
Postoperative Ultrasound
Carotid Artery Stents and Revascularization
Grading Carotid Intrastent Restenosis
NONATHEROSCLEROTIC CAROTID DISEASE
Pulsatile Neck Masses in the Carotid Region
TRANSCRANIAL DOPPLER SONOGRAPHY
VERTEBRAL ARTERY
Anatomy
Sonographic Technique and Normal Examination
Subclavian Steal
Stenosis and Occlusion
INTERNAL JUGULAR VEINS
Sonographic Technique
Thrombosis
Acknowledgment

INTRODUCTION: INDICATIONS FOR CAROTID ULTRASOUND EXAMINATION

Stroke secondary to atherosclerotic disease is the third leading cause of death in the United States. Many stroke victims survive the catastrophic event with some degree of neurologic impairment depending on collateral flow.[1,2] Annually, stroke kills more than 130,000 people in the United States with an incidence of more than 795,000 cases of cerebrovascular accident (CVA).[3,4] Ischemia from severe, flow-limiting stenosis caused by atherosclerotic disease involving the extracranial carotid arteries is implicated in 20% to 30% of strokes with a decreasing incidence due to improved control of hypertension and hyperlipidemia with medications.[3,5] An estimated 80% of CVAs are thromboembolic in origin, often with carotid plaque as the embolic source.[6] **Cardioembolic stroke** carries a higher risk of death, recurrent

stroke, hospital readmission, and severe disability than other types of stroke.[6]

Carotid atherosclerotic plaque with resultant stenosis usually involves the **internal carotid artery** (ICA) within 2 cm of the carotid bifurcation. This location is readily amenable to examination by sonography as well as surgical intervention. **Carotid endarterectomy** (CEA) initially proved to be more beneficial than medical therapy in symptomatic patients with carotid stenoses of more than 70%, as reported in the **North American Symptomatic Carotid Endarterectomy Trial** (NASCET) and the **European Carotid Surgery Trial** (ECST).[7,8]

Subsequent NASCET results for moderate stenoses have shown a net benefit for surgical intervention with carotid narrowing between 50% and 69% of vessel diameter. A 15.7% reduction in the 5-year ipsilateral stroke rate was seen in patients treated surgically versus 22.2% stroke reduction in those treated medically. These results are not as compelling as those for the higher degree of stenosis seen in the earlier NASCET trial. The benefit from surgery was greatest in men, patients with recent stroke, and those with hemispheric symptoms. In addition, the NASCET trials dealing with moderate carotid stenoses required rigorous surgical expertise, such that the risks for disabling stroke or death should not exceed 2% to achieve the statistical surgical benefit.[9] The **Asymptomatic Carotid Atherosclerosis Study** (ACAS) trials published in 1995 reported a reduction in ipsilateral stroke in asymptomatic patients with greater than 60% ICA stenoses who undergo CEA.[3] However, these results were less clear-cut than the NASCET trials. According to the Carotid Revascularization Endarterectomy Versus Stenting Trial (CREST), carotid artery stenting has been shown to be comparable to CEA with respect to rates of ipsilateral stroke and death. However, there are increased adverse effects in women and elevated stroke rates and deaths in older patients.[10] With implementation of new medical management regimens—including aspirin, clopidogrel, statins, antihypertensive medications, diabetic management, smoking cessation, and lifestyle changes—future trials may change how carotid disease is treated.[10]

Accurate diagnosis of carotid stenosis clearly is critical to identify patients who would benefit from surgical treatment. In addition, ultrasound can assess plaque morphology, such as determining heterogeneous or homogeneous plaque, known to be an independent risk factor for stroke and **transient ischemic attack** (TIA).

Carotid sonography is the principal screening method for suspected extracranial carotid atherosclerotic disease. Gray-scale examination, color Doppler, power Doppler, and pulsed Doppler imaging techniques are routinely employed in the evaluation of patients with neurologic symptoms and suspected extracranial cerebral disease.[11,12] Ultrasound is an inexpensive, noninvasive, and highly accurate method of diagnosing carotid stenosis. **Magnetic resonance angiography** (MRA) and computed tomography angiography (CTA) are additional noninvasive screening tools for the identification of carotid bifurcation disease as well as for clarification of ultrasound findings. **Angiography** is often now reserved for those patients for whom the ultrasound or MRA was equivocal or inadequate.

Other carotid ultrasound applications include the evaluation of carotid bruits, monitoring the progression of known atherosclerotic disease,[11,13,14] assessment during or after CEA or stent placement,[15] screening before major vascular surgery, and evaluation after the detection of retinal cholesterol emboli.[11] Also, **nonatherosclerotic carotid diseases** can be evaluated, including follow-up of carotid dissection,[16-21] examination of fibromuscular dysplasia or Takayasu arteritis,[22-24] assessment of malignant carotid artery invasion,[25,26] and workup of pulsatile neck masses and carotid body tumors.[27-29]

Indications for Carotid Ultrasound

- Evaluation of patients with hemispheric neurologic symptoms, including stroke, transient ischemic attack, and amaurosis fugax
- Evaluation of patients with a carotid bruit
- Evaluation of pulsatile neck masses
- Evaluation of patients scheduled for major cardiovascular surgical procedures
- Evaluation of nonhemispheric or unexplained neurologic symptoms
- Follow-up of patients with proven carotid disease
- Evaluation of patients after carotid revascularization, including stenting
- Intraoperative monitoring of vascular surgery
- Evaluation of suspected subclavian steal syndrome
- Evaluation of a potential source of retinal emboli
- Follow-up of carotid dissection
- Follow-up of radiation therapy to the neck in select patients

CAROTID ARTERY ANATOMY

The first major branch of the aortic arch is the innominate or brachiocephalic artery, which divides into the right subclavian artery and right **common carotid artery** (CCA). The second major branch is the left CCA, which is generally separate from the third major branch, the left subclavian artery (Fig. 26.1).

The right and left CCAs ascend into the neck posterolateral to the thyroid gland and lie deep to the jugular vein and sternocleidomastoid muscle. The CCAs have different proximal configurations, with the right originating at the bifurcation of the innominate (brachiocephalic) artery into the common carotid and subclavian arteries. The left CCA usually originates directly from the aortic arch but often arises with the brachiocephalic trunk. This is known as a **"bovine arch"** configuration. The CCA usually has no branches in its cervical region. Occasionally, however, it may give off the superior thyroid artery, vertebral artery, ascending pharyngeal artery, and occipital or inferior thyroid artery. At the carotid bifurcation, the CCA divides into the **external carotid artery** (ECA) and the **internal carotid artery** (ICA). The ICA usually has no branching vessels in the neck. The ECA, which supplies the facial musculature, has multiple branches in the neck. The ICA may demonstrate an ampullary region of mild dilation just beyond its origin.

CAROTID ULTRASOUND EXAMINATION

Carotid artery ultrasound examinations are performed with the patient supine, the neck slightly extended, and the head turned away from the side being examined. Some operators prefer to perform the examination at the patient's side, whereas others prefer to sit at the patient's head. The examination sequence also varies with operator preference. This sequence includes the gray-scale examination, Doppler spectral analysis, and color Doppler blood flow interrogations. Power Doppler sonography may or may not be employed. A 5- to 12-MHz transducer is used for gray-scale imaging and a 3- to 7-MHz transducer for Doppler sonography; the choice depends on the patient's body habitus and technical characteristics of the ultrasound machine. Color Doppler flow imaging and power Doppler imaging may be performed with 5- to 10-MHz transducers. In cases of critical stenosis, the Doppler parameters should be optimized to detect extremely slow flow.

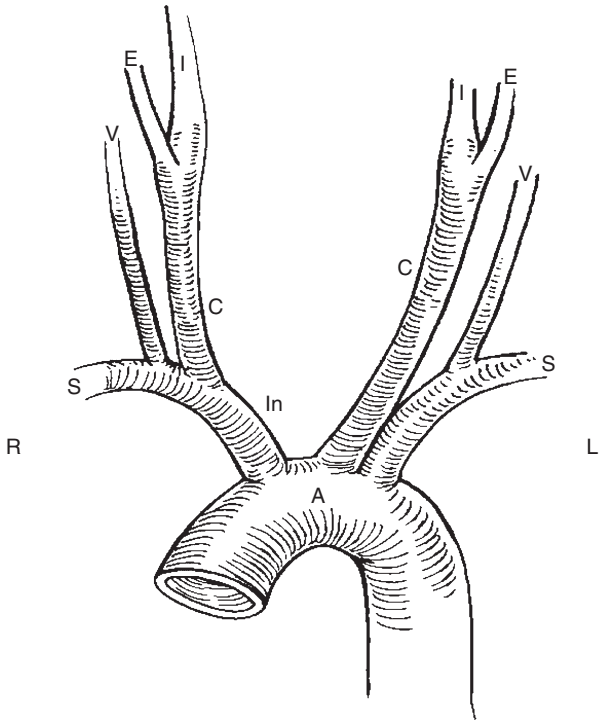

FIG. 26.1 Branches of Aortic Arch and Extracranial Cerebral Arteries. *A,* Aortic arch; *C,* common carotid artery; *E,* external carotid artery; *I,* internal carotid artery; *In,* innominate artery; *L,* left side; *R,* right side; *S,* subclavian artery; *V,* vertebral artery.

Gray-scale sonographic examination begins in the transverse projection. Scans are obtained along the entire course of the cervical carotid artery, from the supraclavicular notch cephalad to the angle of the mandible (Fig. 26.2). Inferior angulation of the transducer in the supraclavicular area images the CCA origin. The left CCA origin is deeper and more difficult to image consistently than the right. The **carotid bulb** is identified as a mild widening of the CCA near the bifurcation. Transverse views of the **carotid bifurcation** establish the orientation of the external and internal carotid arteries and help define the optimal longitudinal plane in which to perform Doppler spectral analysis (Video 26.1). When the transverse ultrasound images demonstrate occlusive atherosclerotic disease, the percentage of "diameter stenosis" or "area stenosis" can be calculated directly using electronic calipers and software analytic algorithms available on most duplex equipment.

After transverse imaging, longitudinal scans of the carotid artery are obtained. The examination plane necessary for optimal longitudinal scans is determined by the course of the vessels demonstrated on the transverse study. In some patients, the optimal longitudinal orientation will be nearly coronal, whereas in others it will be almost sagittal. In most cases, the optimal longitudinal scan plane will be oblique, between sagittal and coronal. In approximately 60% of patients, both vessels above the carotid bifurcation and the CCA can be imaged in the same plane (Fig. 26.3); in the remainder, only a single vessel will be imaged in the same plane as the CCA. Images are obtained to display the relationship of both branches of the carotid bifurcation to the visualized plaque disease, and the cephalocaudal extent

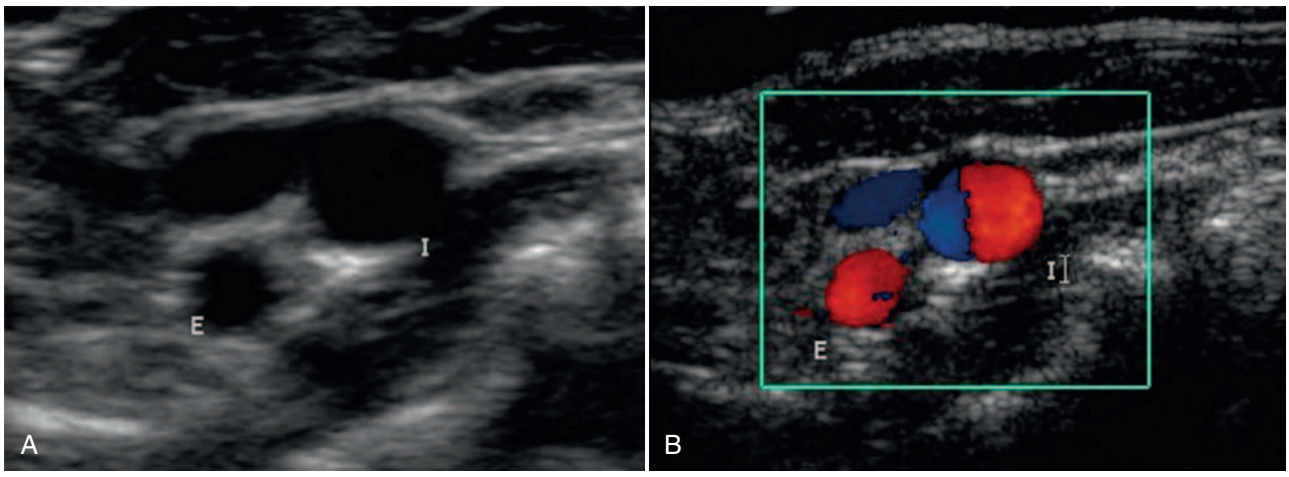

FIG. 26.2 Carotid Sonographic Anatomy. (A) Transverse image of the left internal carotid artery *(I)* and external carotid artery *(E).* The internal carotid artery is lateral and larger in relation to the external carotid artery. **(B)** Color Doppler image of the left internal carotid artery *(I)* and the external carotid artery *(E).* Note normal color-flow separation in the internal carotid artery.

of the plaque is measured. Several anatomic features differentiate the ICA from the ECA. In about 95% of patients, the ICA is posterior and lateral to the ECA. This may vary considerably, and the ICA may be medial to the ECA in 3% to 9% of people.[15] The ICA frequently has an ampullary region of dilation just beyond its origin and is usually larger than the ECA.

One reliable distinguishing feature of the ECA is that it has **branching vessels** (Fig. 26.4A). A useful method to identify the ECA is the tapping of the ipsilateral superficial temporal artery in the preauricular area, the **temporal tap.** The pulsations are transmitted back to the ECA where they cause a **sawtooth** appearance on the spectral waveform (Fig. 26.4B). Although the tap helps identify the ECA, this tap deflection may be transmitted into the CCA and even the ICA in certain rare situations.

The **superior thyroid artery** is often seen as the first branch of the ECA after the bifurcation of the CCA. Occasionally, an aberrant superior thyroid artery branch will arise from the distal CCA. The ICA usually has no branches in the neck, although in rare cases the ICA gives rise to the ascending pharyngeal, occipital, facial, laryngeal, or meningeal arteries. In some patients, a considerable amount of the ICA will be visible, but in others, only the immediate origin of the vessel will be accessible. Very rarely, the bifurcation may not be visible at all.[28] Rarely, the ICA may be hypoplastic or congenitally absent.[30,31]

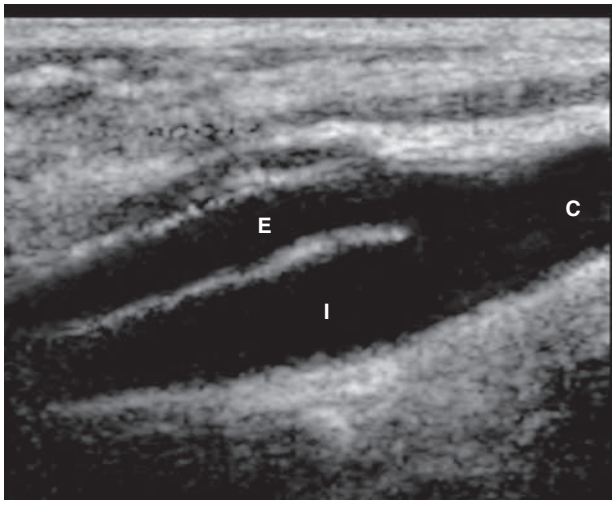

FIG. 26.3 Carotid Bifurcation. Longitudinal image demonstrates common carotid artery *(C);* external carotid artery *(E);* and large, posterior internal carotid artery *(I).*

CAROTID ULTRASOUND INTERPRETATION

Each facet of the carotid sonographic examination is valuable in the final determination of the presence and extent of disease. In most cases, the gray-scale, color Doppler, and power Doppler sonographic images and assessments will agree. However, when there are discrepancies between Doppler ultrasound imaging findings and measured velocities, every attempt should be made to discover the source of the disagreement. The more closely the image and spectral Doppler findings correlate, the higher the degree of confidence in the diagnosis. Generally, gray-scale and color or power Doppler images better demonstrate and quantify low-grade stenoses, whereas high-grade occlusive disease is more accurately defined by Doppler spectral analysis. For **plaque** characterization, assessment must be made in gray-scale only, without color or power Doppler ultrasound.

Visual Inspection of Gray-Scale Images

Vessel Wall Thickness and Intima-Media Thickening

Longitudinal views of the layers of the normal carotid wall demonstrate **two nearly parallel echogenic lines,** separated by a hypoechoic to anechoic region (Fig. 26.5). The first echo, bordering the vessel lumen, represents the lumen-intima interface; the second echo is caused by the media-adventitia interface. The media is the anechoic/hypoechoic zone between the echogenic lines. The distance between these lines represents the combined thickness of the **intima and media (I-M complex).** The far wall of the CCA is measured. Many consider measurement of

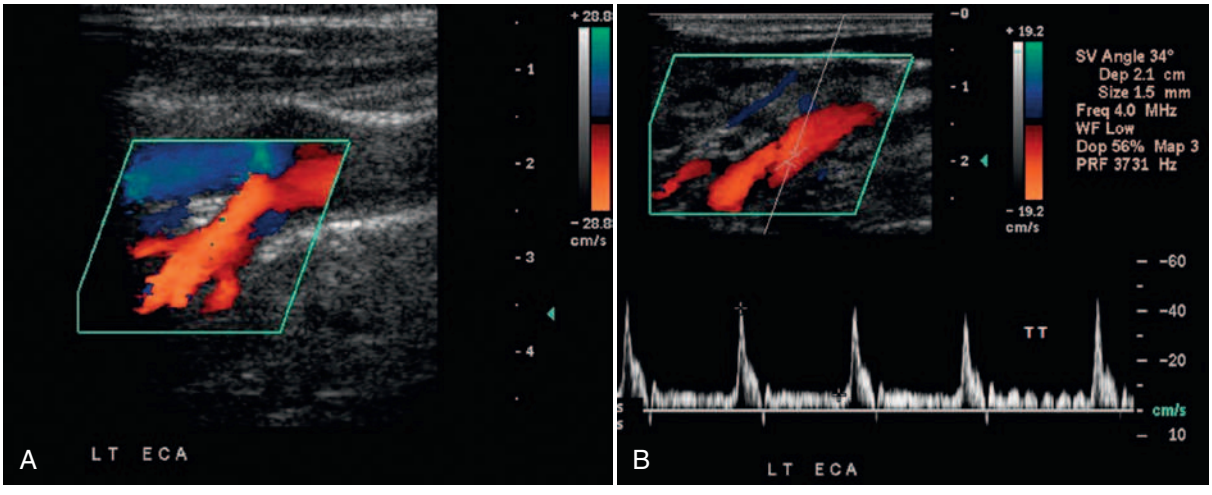

FIG. 26.4 Normal External Carotid Artery (ECA). (A) Color Doppler ultrasound of bifurcation demonstrates two small arteries originating from the ECA. **(B)** ECA spectral Doppler shows the reflected temporal tap *(TT)* as a serrated (sawtooth) flow disturbance.

intima-media thickness (IMT) to be a surrogate marker for atherosclerotic disease in the *whole* arterial system, not only the cerebrovascular system.[32,33] Some believe that thickening of the I-M complex greater than 0.8 mm is abnormal and may represent the earliest changes of atherosclerotic disease. However, because thickness of the I-M increases with age, absolute measurements of IMT for any given person may not be a reliable indicator of atherosclerotic risk factors[34] (Fig. 26.6).

Carotid artery IMT is an independent predictor of new cardiovascular events in persons without a history of cardiovascular disease.[35] Numerous studies support the relationship between IMT and increased risk for myocardial infarction or stroke in asymptomatic patient populations.[19,36-43] Assessment of IMT has been advocated as a means of assessing effectiveness of medical interventions to reduce the progression of I-M thickening or even reverse carotid wall thickening. However, because of concerns regarding minimal impact on prediction models and difficulty in standardizing measurement technique, the 2013 American College of Cardiology/American Heart Association (ACC/AHA) Guideline on the Assessment of Cardiovascular Risk does not recommend the carotid IMT test.[44]

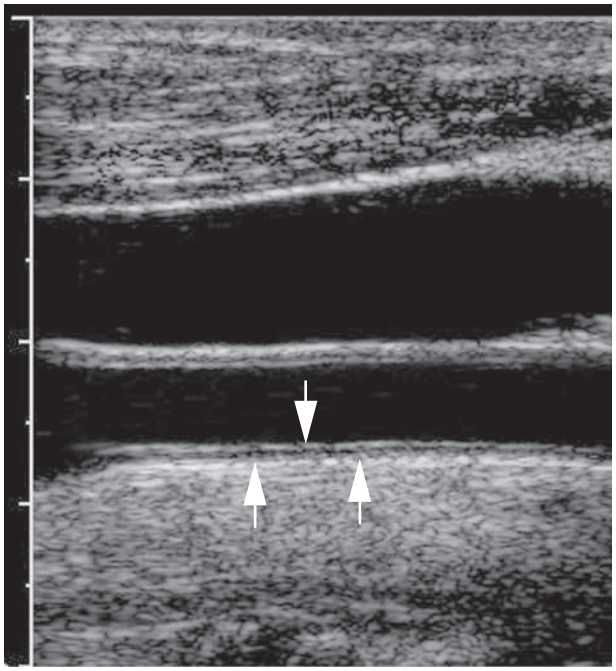

FIG. 26.5 Normal Intima-Media (I-M) Complex of Common Carotid Artery. The I-M complex *(arrows)* is seen in a left common carotid artery.

Plaque Characterization

Atheromatous carotid plaques should be carefully evaluated to determine plaque extent, location, surface contour, and texture, as well as to assess luminal stenosis.[45] The plaque should be scanned and evaluated in both the sagittal and the transverse projections.[46] The most common cause of TIAs is **embolism,** not flow-limiting stenosis; less than half of patients with documented TIA have hemodynamically significant stenosis. It is important to identify low-grade atherosclerotic lesions that may contain hemorrhage or ulceration, which can serve as a nidus for emboli that cause both TIAs and stroke.[1] Polak et al.[47] showed that plaque is an independent risk factor for developing a stroke. Of patients with hemispheric stroke symptoms, 50% to 70% demonstrate hemorrhagic or ulcerated plaque. Plaque analysis of CEA specimens has implicated intraplaque hemorrhage as an important factor in the development of neurologic symptoms.[48-55] However, the relationship between sonographic plaque morphology and the onset of symptoms is controversial.

Currently, substantial gaps in knowledge of the mechanisms involved in **atherosclerotic plaque rupture** exist and this is a critical barrier to developing methodologies for the prevention of myocardial infarction and stroke. Myocardial infarction and stroke, complications of atherosclerosis, are the most common causes of death in developed countries and are caused by inflammation-driven rupture of atherosclerotic plaques. Stable plaques are characterized by a necrotic core with an overlying fibrous cap composed of vascular smooth muscle cells in a

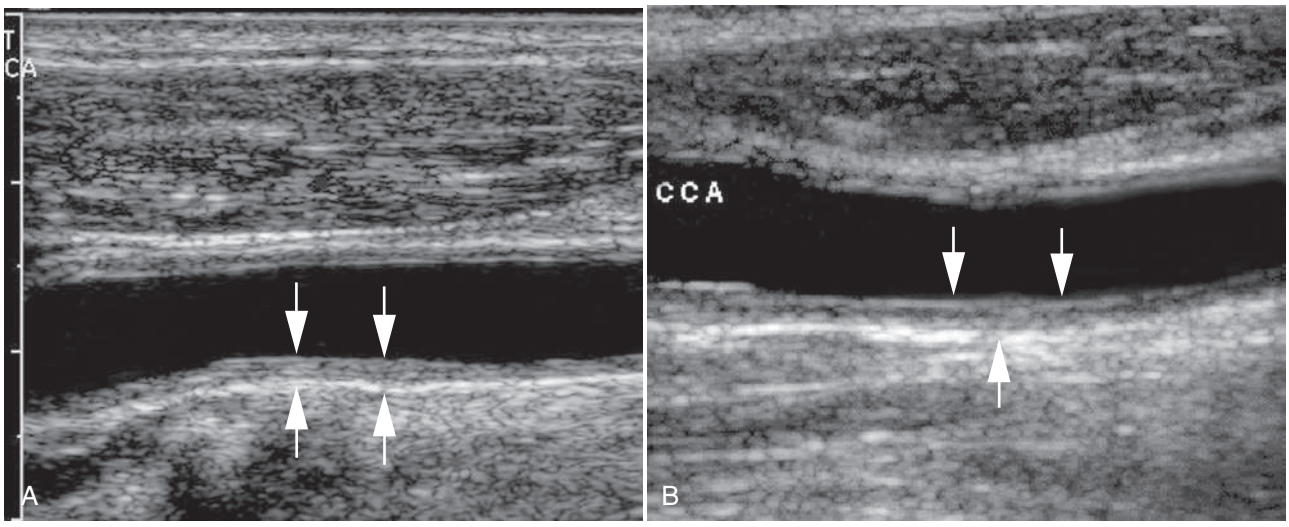

FIG. 26.6 Abnormal Intima-Media (I-M) Complex of Common Carotid Artery (CCA). (A) Early I-M hyperplasia with loss of the hypoechoic component of the I-M complex and thickening *(arrows).* **(B)** Thickening of the I-M complex with hyperplasia *(arrows).*

collagen-rich matrix.[56,57] In **vulnerable/ruptured plaques,** the fibrous cap has thinned, exhibiting fewer vascular smooth muscle cells, decreased collagen, and increased inflammatory cells.

Heterogeneous plaque has been suggested as unstable and vulnerable, in contrast to homogeneous plaque. Some have suggested that environmental factors and toxins cause abnormal flow patterns, damaging the internal structure of the vessels.[58] This can lead to intimal proliferation and potential wall ischemia and the degradation of the vasa vasorum.[58] Because the vasa vasorum do not have a muscular media, these vessels are subsequently at risk to rupture, perhaps leading, in part, to intraplaque hemorrhage.[58] Others have suggested that a bacterial infection etiology may play a role in inflammatory angiogenesis.[58]

Recently, several groups have demonstrated that microRNAs play a key role in the development and thinning of the **fibrous cap.**[59-69] **MicroRNAs** are a class of noncoding RNAs (ncRNAs) that are approximately 21 nucleotides in length and are potent effectors of gene expression, doing so by binding to messenger RNA and inhibiting protein translation. A role for ncRNA in cardiovascular diseases is emerging, including microRNAs (miRNAs) and their inhibition by circular RNA (circRNAs). MicroRNA-221 and microRNA-222 (miR-221/miR-222) are short ncRNAs that inhibit the expression of the cyclin-dependent kinase inhibitor $p27^{Kip1}$, promoting vascular smooth muscle cell proliferation and intimal thickening. Bazan et al. recently demonstrated an important role for the downregulation of miR-221/222 in the shoulder region of carotid plaques shortly after rupture[70] through increased $p27^{Kip1}$ and propose that vascular smooth muscle cell volume is lost, leading to intimal thinning.

Ultrasound Plaque Classification System

Plaque texture is generally classified as homogeneous or heterogeneous.[14,38,41,45,46,48-50,71-75] The accurate evaluation of plaque can only be made with gray-scale ultrasound, without the use of

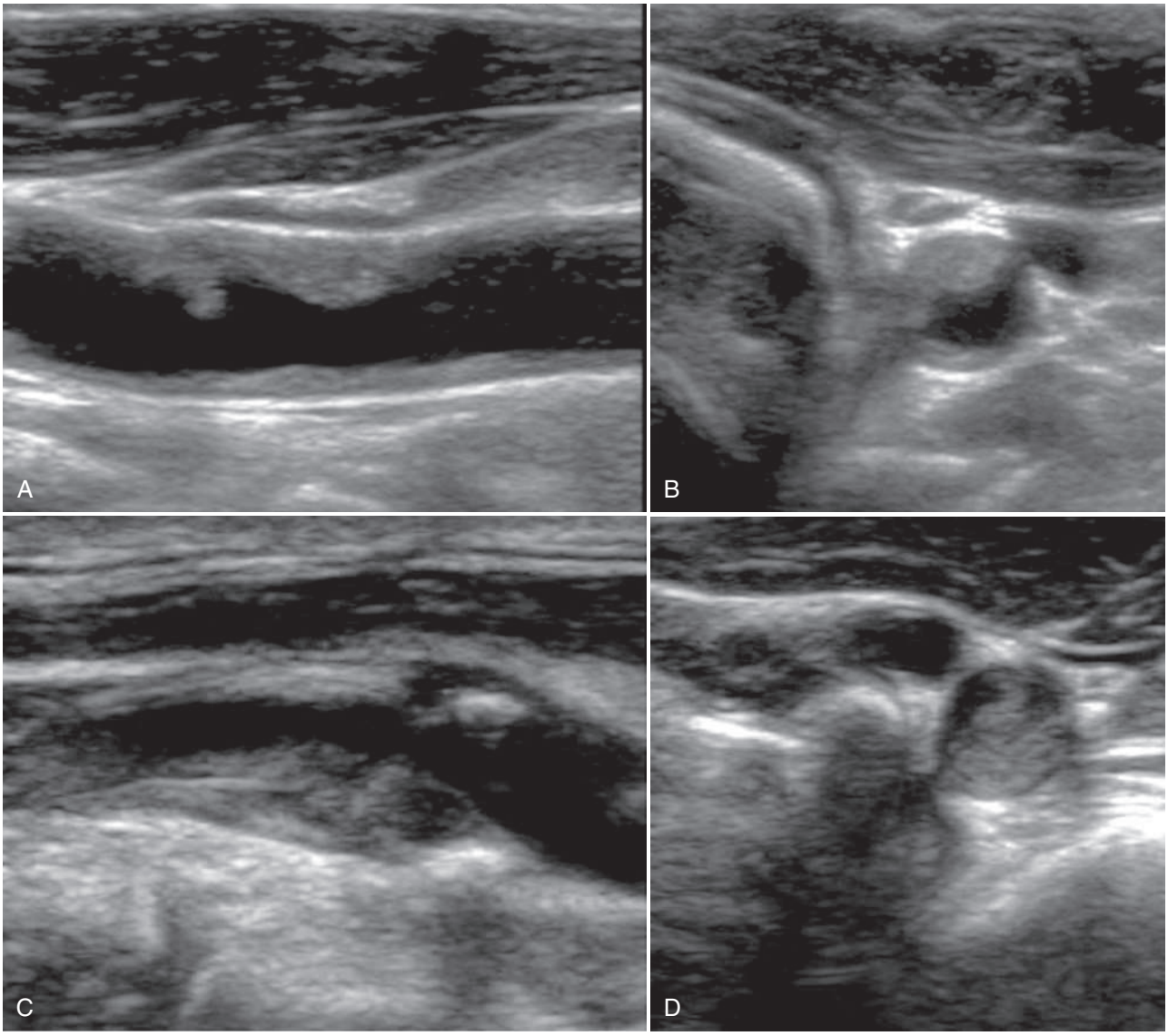

FIG. 26.7 Spectrum of Patterns of Homogeneous Plaque. (A) Sagittal and **(B)** transverse images show homogeneous plaque in left common carotid artery (type 4). Note the uniform echo texture. **(C)** Sagittal and **(D)** transverse images show homogeneous plaque in proximal left internal carotid artery (type 3). Note the focal hypoechoic area within the plaque, estimated at less than 50% of plaque volume.

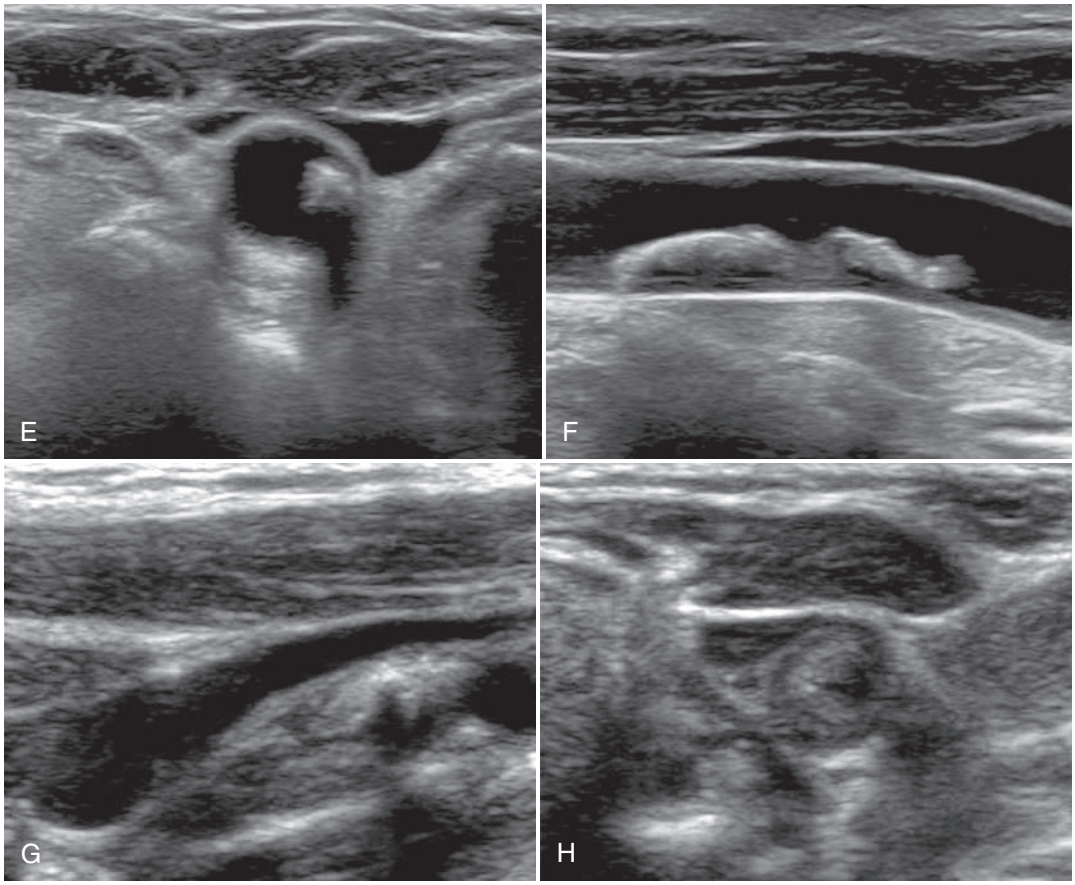

FIG. 26.7, cont'd **(E)** Sagittal and **(F)** transverse images demonstrate homogeneous plaque (type 3). Associated calcifications best seen on image E obscure uniformity of plaque. **(G)** Sagittal and **(H)** transverse images demonstrate homogeneous plaque (type 3) in the carotid bifurcation. The sonolucent areas are less than 50% of the volume of the plaque.

color or power Doppler. The plaque must be evaluated in both sagittal and transverse planes.[46] **Homogeneous plaque** has a generally uniform echo pattern and a smooth surface (Fig. 26.7). Sonolucent areas may be seen, but the amount of sonolucency is less than 50% of the plaque volume. The uniform acoustic texture corresponds pathologically to **dense fibrous connective tissue** (Videos 26.2 through 26.4). **Calcified plaque** produces posterior acoustic shadowing and is common in asymptomatic individuals (Fig. 26.8, Video 26.5). **Heterogeneous** plaque has a more complex echo pattern and contains one or more focal sonolucent areas corresponding to more than 50% of the plaque volume (Fig. 26.9, Videos 26.6 through 26.11). Heterogeneous plaque is characterized pathologically by containing **intraplaque hemorrhage** and deposits of lipid, cholesterol, and proteinaceous material.[15,73] Homogeneous plaque is identified much more often than heterogeneous plaque, occurring in 80% to 85% of patients examined.[47] Sonography accurately determines the presence or absence of intraplaque hemorrhage (sensitivity, 90%-94%; specificity, 75%-88%).[48,54,73,76-80]

Some sources suggest classifying plaque according to four types. Plaque **types 1 and 2,** similar to heterogeneous plaque and much more likely to be associated with intraplaque hemorrhage and ulceration, are considered unstable and subject to abrupt increases in plaque size after hemorrhage or embolization.[14,46,74,81-84] Types 1 and 2 plaque are typically found in symptomatic patients with stenoses greater than 70% of diameter. Plaque **types 3 and 4** are generally composed of fibrous tissue and calcification. These plaque types are similar to homogeneous plaque. These are generally more benign, stable plaques typically seen in asymptomatic individuals (see Fig. 26.8).

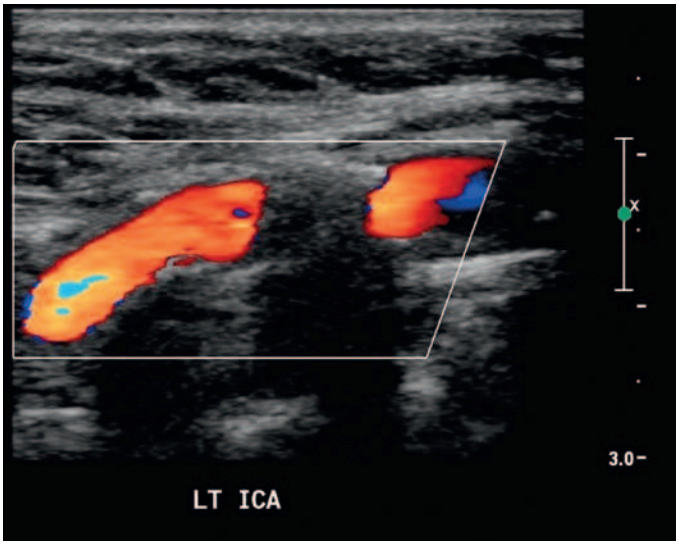

FIG. 26.8 Calcified Plaque. The calcified plaque creates a shadow that obscures characterization of plaque in the left internal carotid artery.

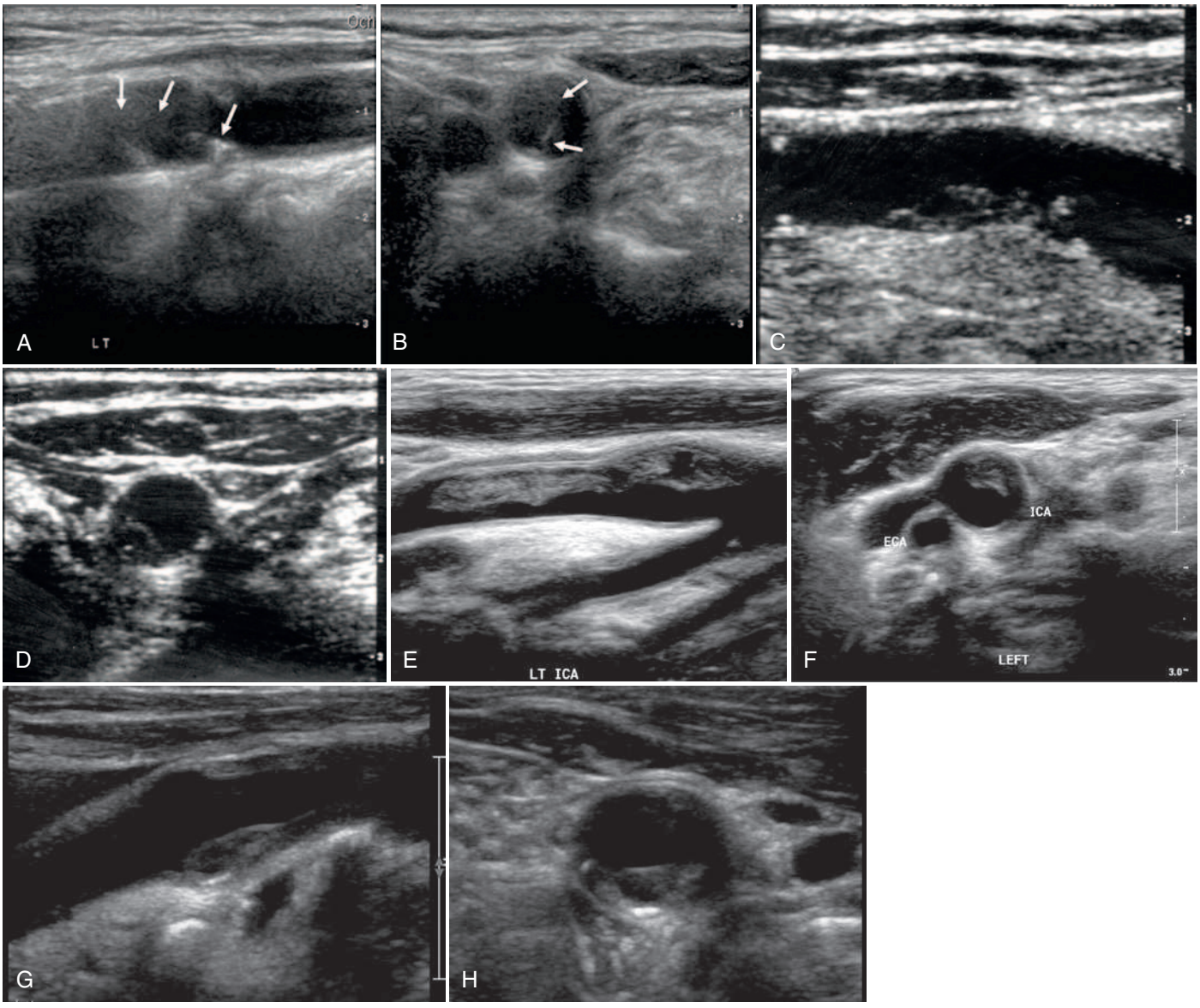

FIG. 26.9 Spectrum of Patterns of Heterogeneous Plaque in the Internal Carotid Artery (ICA). (A) Sagittal and **(B)** transverse images show plaque *(arrows)* virtually completely sonolucent, consistent with heterogeneous plaque (type 1). Note smooth plaque surface. **(C)** Sagittal and **(D)** transverse images show focal sonolucent areas within the plaque greater than 50% of plaque volume, corresponding to heterogeneous plaque (type 2). Note the irregular surface of the plaque. **(E)** Sagittal image demonstrates heterogeneous plaque in the carotid bulb and homogeneous plaque in the internal carotid artery (type 2). **(F)** Transverse image demonstrates heterogeneous plaque (type 2). **(G)** and **(H)** Sagittal and transverse images demonstrate subtle heterogeneous plaque (type 2).

Ultrasound Types of Plaque Morphology

Type 1: Predominantly echolucent, with a thin echogenic cap
Type 2: Substantially echolucent with small areas of echogenicity (>50% sonolucent)
Type 3: Predominantly echogenic with small areas of echolucency (<50% sonolucent)
Type 4: Uniformly echogenic

Other methods are being introduced to characterize plaque in a more automated and reproducible manner. Reiter et al.[85] developed a **gray-scale median level** for echolucency of plaque after standardizing and adjusting the B-mode images. They obtained standardized gray-scale median levels for asymptomatic patients with greater than 30% stenosis and found that decreasing echolucency of carotid plaques over 6 to 9 months is predictive of major cardiovascular events affecting coronary, peripheral, and cerebrovascular circulation. However, absolute gray-scale median levels were not associated with a specific risk.[85]

Plaque Ulceration

Sonography has a low sensitivity (38%) and high specificity (92%) for plaque ulceration.[86] However, when identified, all ulcerated plaques fit into the heterogeneous plaque pattern.[46,81,87,88] Sonographic findings that suggest **plaque ulceration** include a focal depression or break in the plaque surface, causing an irregular surface or an anechoic area within the plaque that extends to the plaque surface without an intervening echo between the vessel lumen and the anechoic plaque region. Color and power Doppler ultrasound may improve sonographic identification of plaque ulceration.[88] Color or power Doppler ultrasound or B-flow imaging (a proprietary non-Doppler imaging technique) may demonstrate slow-moving eddies of color within an anechoic region in plaque, which would suggest ulceration[78,88] (Fig. 26.10). The demonstration of these flow vortices was 94% accurate in predicting ulcerative plaque at surgery in one study.[89] Contrast-enhanced ultrasound represents a promising tool in the characterization of vulnerable carotid plaque with improved detection of intraplaque vascularization and ulceration.[90-92]

Ultrasound Features Suggestive of Plaque Ulceration

Focal depression or break in plaque surface
Anechoic region within plaque extending to vessel lumen
Eddies of color within plaque

A potential pitfall in the diagnosis of plaque ulceration results from a mirror-image artifact producing **pseudoulceration** of the carotid artery. Highly reflective plaque can produce a color Doppler ghost artifact simulating ulceration. However, the region of color within the plaque can be recognized as artifactual because the spectral waveform and color shading within the pseudoulceration are of lower amplitude, but otherwise identical to those within the true carotid lumen.[93] Conversely, pulsed Doppler traces from within **ulcer craters** show low-velocity dampened waveforms (Fig. 26.11).

Although the diagnosis of ulceration varies, the ability to predict intraplaque hemorrhage reliably, with its associated clinical implications, underscores the importance of ultrasound plaque characterization. The presence of heterogeneous, irregular plaque should be noted because of the association of heterogeneous plaque, and intraplaque hemorrhage even in a stenosis of less than 50% may warrant medical therapy. Many now consider heterogeneous plaque to be the "vulnerable," unstable form of plaque that should be treated differently than the more stable homogeneous form of plaque.[94] Plaque characterization should be considered when determining the type of therapy to use in carotid intervention. Angioplasty and subsequent stenting of carotid vessels might be safer if performed in patients with homogeneous plaque than those with heterogeneous plaque.[94]

Gray-Scale Evaluation of Stenosis

Measurements of carotid diameter and area stenosis should be made in the transverse plane, perpendicular to the long axis of the vessel, using gray-scale, B-flow, or power Doppler sonographic imaging[45] (Fig. 26.12, Videos 26.12 and 26.13). Measurements made on longitudinal scans may overestimate or underestimate the severity of stenosis by partial "voluming" through an eccentric plaque. The percentage of diameter stenosis and the percentage of area stenosis are not always linearly related. Clinical records should state the type of stenosis measured. Asymmetrical stenoses are most appropriately assessed with "percentage of area stenosis" measurements,[45] although these are often time consuming and technically difficult. The cephalocaudal extent and length of plaques should be noted, along with the presence of **tandem plaques.** Recently, three-dimensional ultrasound has been used

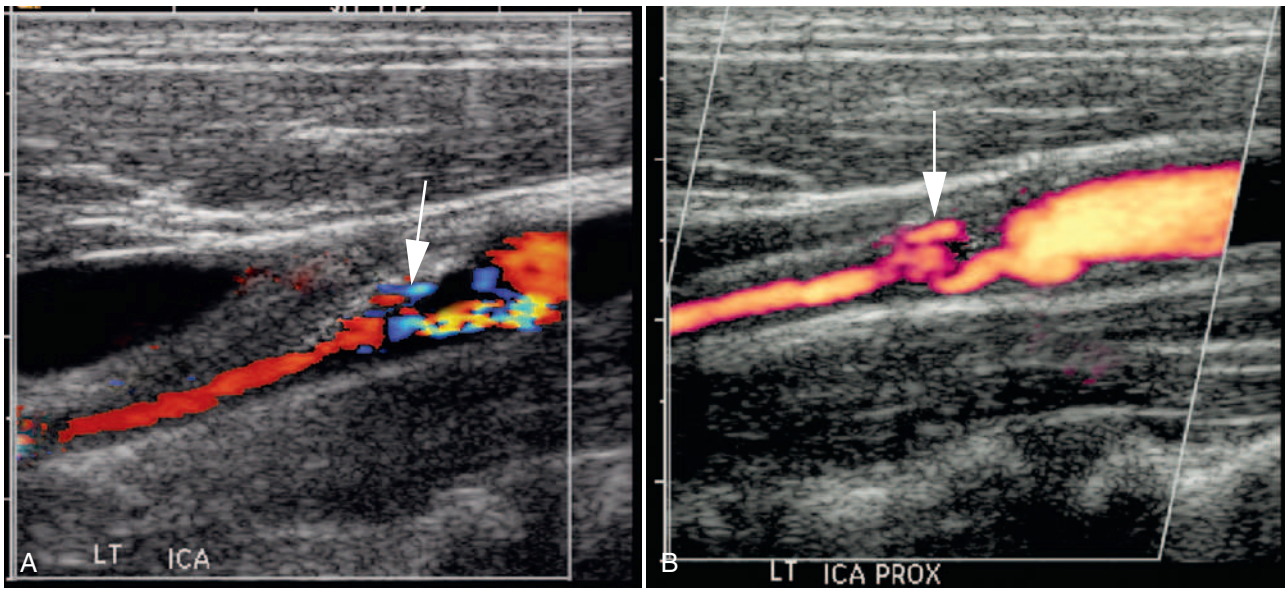

FIG. 26.10 Plaque Ulceration. (A) Color Doppler and **(B)** power Doppler longitudinal images show blood flow *(arrow)* into hypoechoic ulcerated plaque.

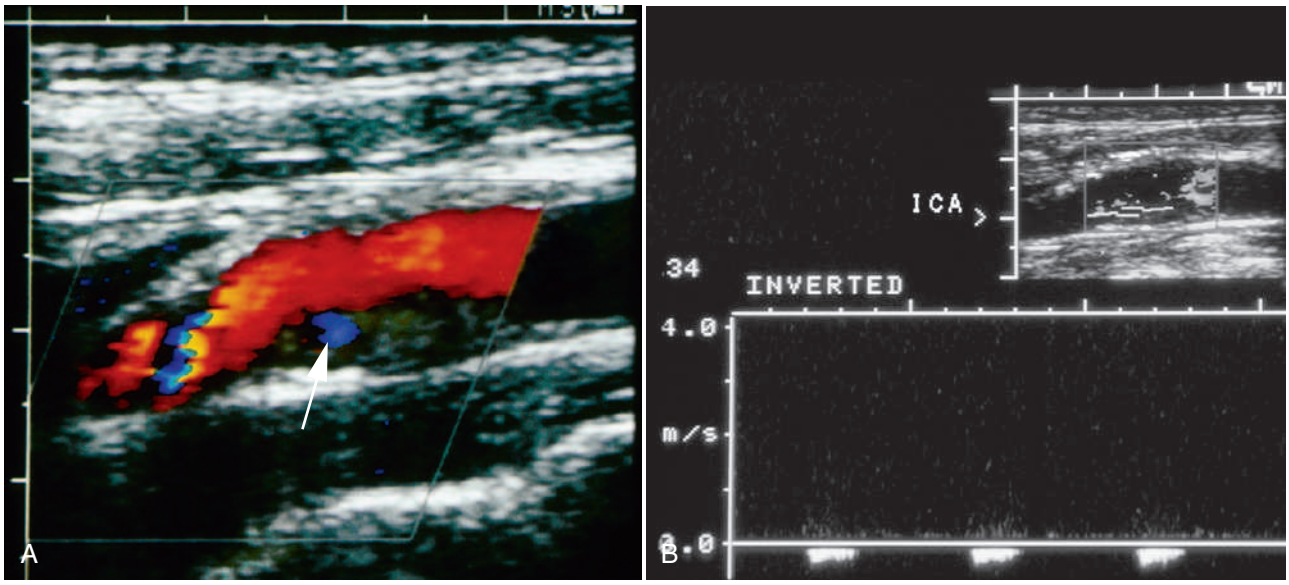

FIG. 26.11 Plaque Ulceration and Abnormal Flow. (A) Longitudinal image of the proximal right internal carotid artery (ICA) demonstrates heterogeneous plaque with an associated area of reversed low-velocity eddy flow within an ulcer *(arrow)*. **(B)** Pulsed Doppler waveforms in this ulcer crater demonstrate the extremely dampened low-velocity reversed flow, not characteristic of that seen within the main vessel lumen of the ICA.

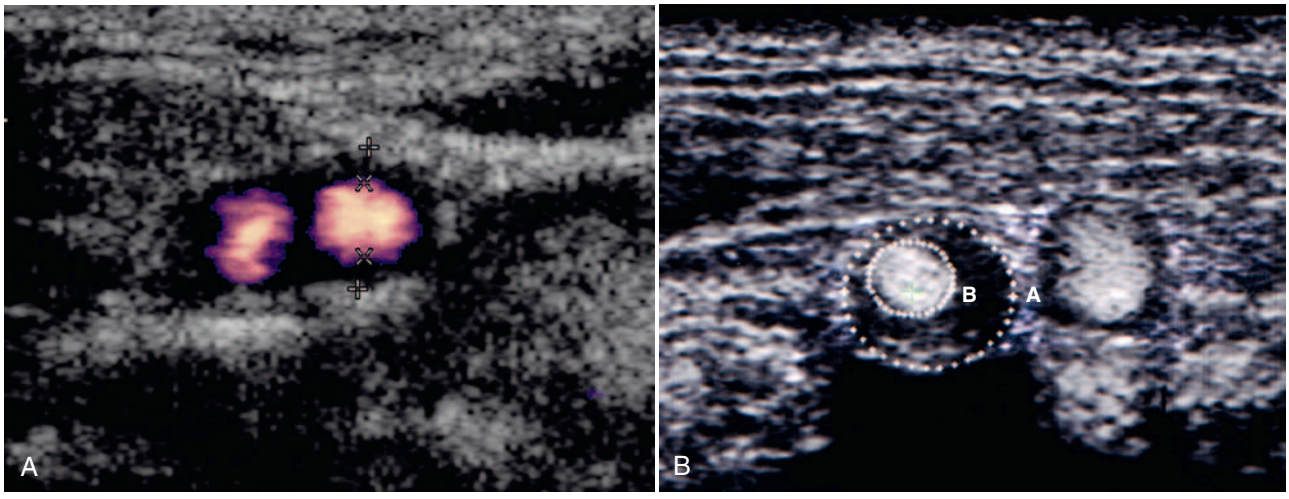

FIG. 26.12 Measurement of Carotid Artery Diameter. (A) Power Doppler transverse image shows a less than 50% diameter stenosis *(cursors)*. **(B)** Transverse B-mode flow image of the right carotid bifurcation shows measurement of stenosis *(B)* in area of internal carotid artery (ICA). *A,* Outer ICA area.

to measure plaque volume with good intraobserver and interobserver variability as well as plaque characterization.[95,96]

As the severity of a stenosis increases, the quality of the real-time image deteriorates.[93,97] Several factors work against successful image assessment of high-grade stenosis. Plaque calcification and irregularity produce shadowing, which obscures the vessel lumen. Heterogeneous plaque often has acoustic properties similar to flowing blood, producing anechoic plaques or thrombi that are difficult to visualize on gray-scale images. In the most extreme cases, vessels can show little visible plaque yet be totally occluded (see Fig. 26.9E and F). Color Doppler sonography readily identifies such phenomena. For these reasons, real-time gray-scale ultrasound is best suited for the evaluation of nonrate-limiting lesions and not for quantifying high-grade stenoses, which are more accurately determined by spectral analysis.[98,99] The gray-scale findings and Doppler spectral analysis values must be integrated and correlated for a complete ultrasound assessment of the carotid vessels (Video 26.14).

It is probably unnecessary to make a quantitative assessment of the amount of plaque. Rather, a **qualitative** assessment of the amount of plaque should be made and compared to the Doppler spectral findings to ensure accuracy in grading stenoses. A mismatch between the qualitative assessment of the amount of plaque and the Doppler findings should alert the examiner to a possible technical error. If these cannot be resolved, further assessment with CTA or MRA should be considered.

Doppler Spectral Analysis

The **Doppler spectrum** is a quantitative graphic display of the velocities and directions of moving red blood cells (RBCs) present in the Doppler sample volume. The Doppler spectral display represents velocities on the *y* axis and time on the *x* axis. By convention, flow toward the transducer is displayed above the zero-velocity baseline, and flow away from the transducer is below. For ease of analysis, spectra that project below the baseline are often inverted and placed above the baseline, always keeping in mind the true direction of flow within the vessel. The amplitude of each velocity component (number of RBCs with each velocity component) is used to modulate the brightness of the traces. This is also known as a **gray-scale velocity plot.** In the normal carotid artery, the frequency spectrum is narrow in systole and somewhat wider in early and late diastole (Videos 26.15 through 26.18). There is usually a black zone between the spectral line and the zero-velocity baseline called the **spectral window**[100,101] (Fig. 26.13).

The ICA and ECA branches of the CCA have distinctive spectral waveforms (Fig. 26.14). The **external carotid artery** supplies the high-resistance vascular bed of the facial musculature, so its flow resembles that of other peripheral arterial vessels. Flow velocity rises sharply during systole and falls rapidly during diastole, approaching zero or transiently reversing direction. The **internal carotid artery** supplies the low-resistance circulation of the brain and demonstrates flow similar to that in vessels supplying other blood-hungry organs, such as the liver, kidneys, and placenta. The common feature in all low-resistance arterial waveforms is that a large quantity of forward flow continues

FIG. 26.13 Normal Internal Carotid Artery (ICA) Waveform. Normal low resistive ICA waveform with clear spectral window indicating the absence of spectral broadening.

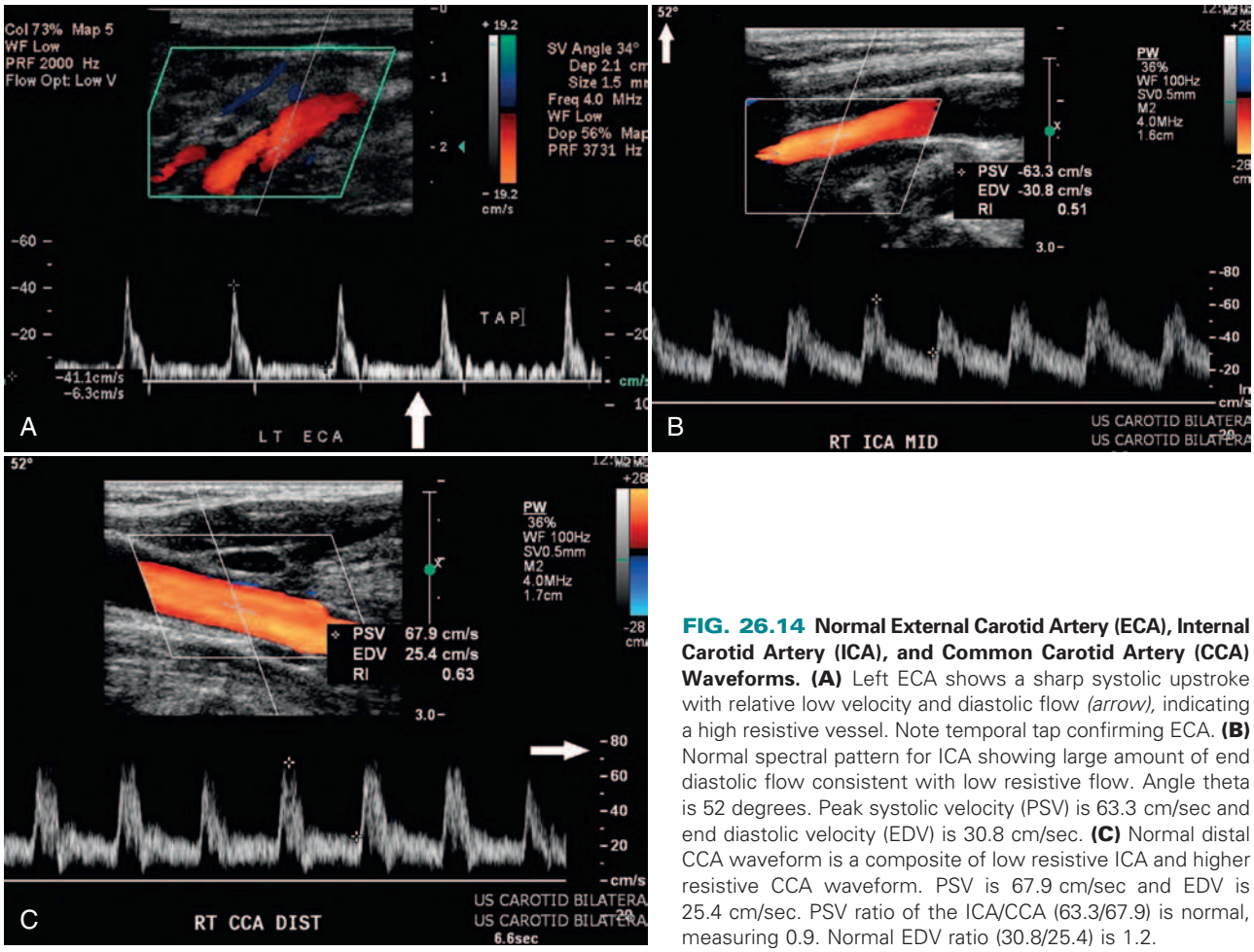

FIG. 26.14 Normal External Carotid Artery (ECA), Internal Carotid Artery (ICA), and Common Carotid Artery (CCA) Waveforms. (A) Left ECA shows a sharp systolic upstroke with relative low velocity and diastolic flow *(arrow),* indicating a high resistive vessel. Note temporal tap confirming ECA. **(B)** Normal spectral pattern for ICA showing large amount of end diastolic flow consistent with low resistive flow. Angle theta is 52 degrees. Peak systolic velocity (PSV) is 63.3 cm/sec and end diastolic velocity (EDV) is 30.8 cm/sec. **(C)** Normal distal CCA waveform is a composite of low resistive ICA and higher resistive CCA waveform. PSV is 67.9 cm/sec and EDV is 25.4 cm/sec. PSV ratio of the ICA/CCA (63.3/67.9) is normal, measuring 0.9. Normal EDV ratio (30.8/25.4) is 1.2.

throughout diastole (see Videos 26. through 26.17). The CCA waveform is a composite of the internal and external waveforms, but most often the CCA flow pattern more closely resembles that of the ICA, and diastolic flow is generally above the baseline (see Video 26.18). Approximately 80% of the blood flowing from the CCA goes through the ICA into the brain, whereas 20% goes through the ECA into the head musculature. The relative decrease in blood flow through the ECA will cause it to have a generally lower amplitude gray-scale waveform than in either the ICA or the CCA.[15]

Standard Examination

Virtually all state-of-the-art ultrasound equipment offers color and power Doppler, as well as gray-scale capabilities and pulsed Doppler, for the carotid examination (Video 26.19). A rapid color Doppler screen allows the detection of abnormal flow patterns, which allows the pulsed Doppler signal volume to be placed in areas that are abnormal, especially those with **high-velocity jets** (Video 26.20). These high-velocity jets are located in the region of and immediately distal to a high-grade stenosis (Figs. 26.15 and 26.16). In cases where both gray-scale and color and power Doppler images of an entire carotid artery are normal, only representative spectral tracings from the CCA, ICA, and ECA are necessary to complete the examination.

The standard Doppler spectral examination consists of traces obtained from the proximal and distal CCA, carotid bulb, and proximal ECA; samples in the proximal, middle, and distal ICA; and a representative trace from the vertebral artery. Normal velocities are higher in the proximal CCA and lower in the distal vessel; normal ICA velocities tend to increase from proximal to distal. In addition, blood flow velocities are obtained immediately proximal to, at, and just beyond regions of maximal visible stenosis and at 1-cm intervals distal to the visualized plaque as far cephalad as possible. Positioning the Doppler angle cursor parallel to the vessel walls determines angle theta, used to convert frequency information into velocity values (see Fig. 26.14B). **Doppler angle theta** is defined as the angle between the Doppler transducer line of sight and the direction of blood flow. The ideal angle theta is 0 degrees, as the cosine of this angle is 1, thus resulting in the greatest possible detectable frequency shift. Because this angle is rarely achievable in the clinical setting, angles from 30 to 60 degrees are considered acceptable for carotid spectral analysis.

Certain schools of ultrasound use a technique in which the Doppler angle is set at 60% and the transducer is "heel and toed" to parallel the carotid artery for Doppler spectral analysis. In our experience, it is frequently not possible to optimize cursor placement in the midportion of the vessel using this technique in tortuous vessels. Therefore our technique involves selecting the site of spectral analysis and paralleling the wall of the vessel at that point, making certain that the Doppler angle does not exceed 60 degrees. Although either technique can be used, results obtained using these different methodologies can result in different velocities. Thus if the first technique is used, a different set of velocity criteria should be expected than if the second is used. This is one of the factors responsible for the differences in velocity spectral criteria used in different laboratories (Fig. 26.16). When angle theta exceeds 60 to 70 degrees, the accuracy of velocity measurement declines precipitously (Fig. 26.17), to the point that virtually no velocity change is detected at angle theta of 90 degrees. The entire course of the CCA and ICA should be

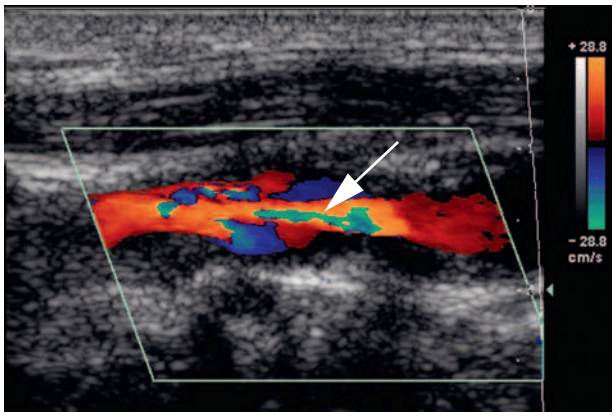

FIG. 26.15 Color Doppler Jet. High-velocity jet *(arrow)* or aliasing color demonstrates the area of highest velocity in the area of stenosis.

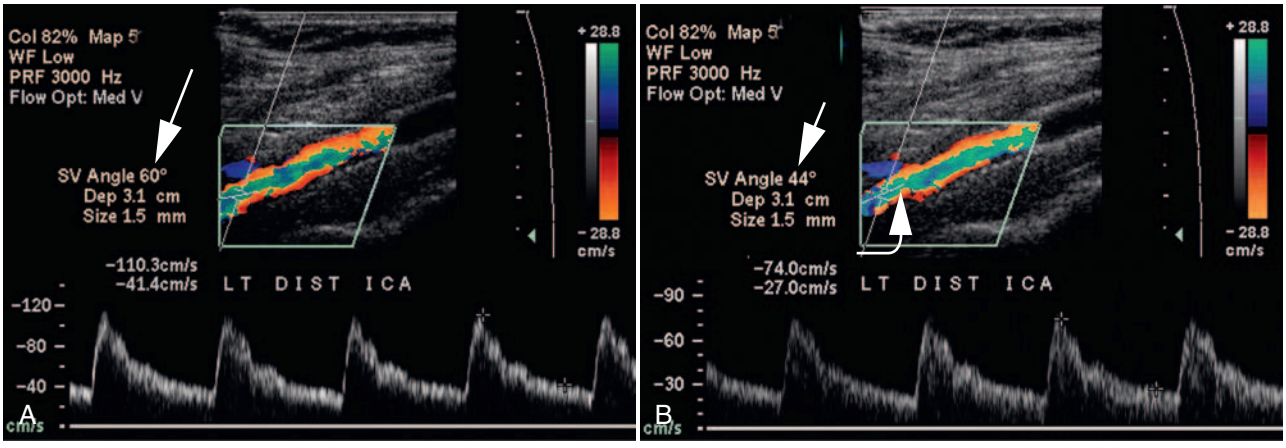

FIG. 26.16 Doppler Angle Theta Measurement. (A) Velocity obtained in the distal internal carotid artery with angle theta of 60 degrees is higher than that obtained at 44 degrees *(arrow)*. **(B)** However, the sample angle does not parallel the vessel wall at 60 degrees. Note central color aliasing in the region of highest velocity *(curved arrow)*.

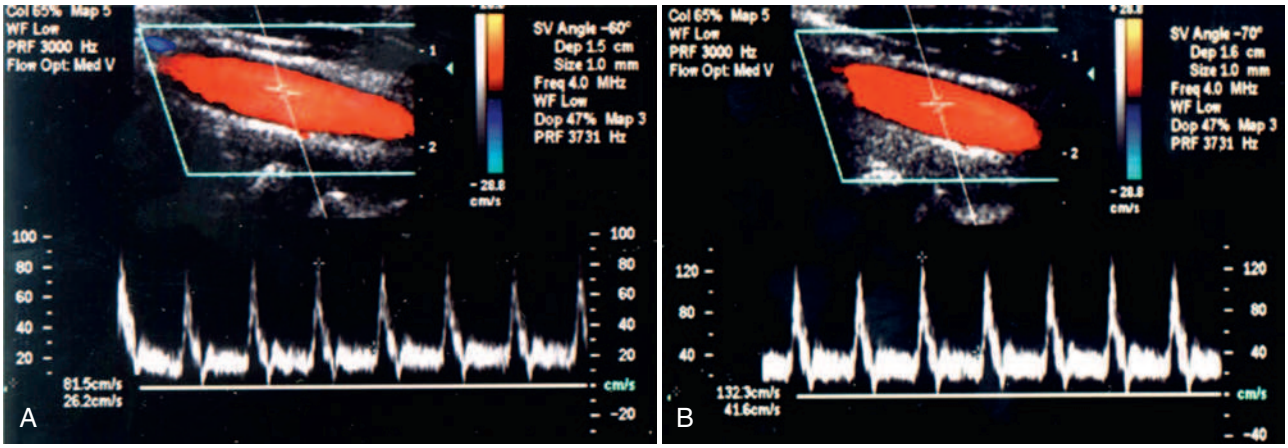

FIG. 26.17 Incorrect Doppler Angle Theta. Velocity obtained in the internal carotid artery (ICA) with angle theta of 60 degrees **(A)** is less accurate than the velocity obtained from the same area of the same ICA with an angle theta of 70 degrees **(B)**.

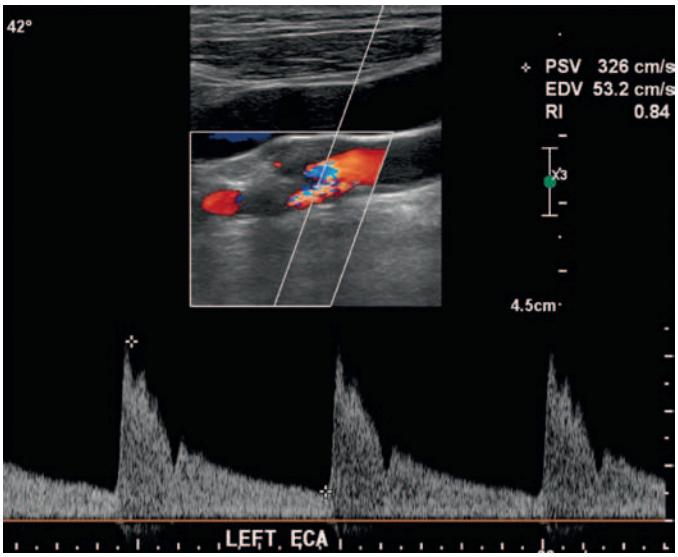

FIG. 26.18 High-Grade External Carotid Artery (ECA) Stenosis. Elevated velocities and visible narrowing. Spectral broadening is present. Color Doppler spectral broadening is also seen.

interrogated with a **consistent angle theta** between the transducer and the vessel maintained throughout the examination, when possible. Generally, only the origin of the ECA is evaluated because occlusive plaque is less common here than in the ICA and is rarely clinically important. A stenosis of the ECA should be noted because it may account for a worrisome cervical bruit when the ICA is normal.[30]

Spectral Broadening

Atheromatous plaque projecting into the arterial lumen disturbs the normal, smooth laminar flow of erythrocytes. The RBCs move with a wider range of velocities, so the spectral line becomes wider, filling in the normally black spectral window. This phenomenon, termed *spectral broadening,* increases in proportion to the severity of carotid artery stenosis[102-104] (Fig. 26.18, Video 26.21). Some duplex machines allow the operator to measure the spectral spread between the maximal and minimal velocities (bandwidth) and thus quantitate spectral broadening. The validity of these measurements remains unproved, however, and further correlative studies are needed to document the relationship of quantitative spectral broadening parameters to specific degrees of stenosis.[104] Most tables no longer include a measurement for spectral broadening when grading carotid stenosis. Nevertheless, a visible gestalt of the amount of spectral window obliteration, as well as color Doppler heterogeneity, provides a useful, if not quantitative, predictor of the severity of flow disturbance.

Pitfalls in Interpretation

Pseudospectral broadening can be caused by technical factors, such as too high a gain setting. In such cases the background around the spectral waveform often contains noise. Whenever spectral broadening is suspected, the gain should be lowered to see if the spectral window clears. Similarly, spectral broadening caused by vessel wall motion can occur when the Doppler sample volume is too large or positioned too near the vessel wall. Decreasing the size of the sample volume and placing it midstream should eliminate this potential pitfall.

Altered flow patterns can normally be found at certain sites in the carotid system. For example, it is normal to find flow separation at the site of branching vessels, such as where the CCA branches into the ECA and ICA.[105] Flow disturbances also occur at sites where there is an abrupt change in the vessel diameter. For example, flow disturbances and bizarre waveforms caused by **flow separation** may be encountered in a normal carotid bulb where the CCA terminates in a localized area of dilation as it divides into the ECA and ICA[15] (Fig. 26.19).

The tendency for spectral broadening increases in direct proportion to the velocity of blood flow. For example, spectral broadening can be observed in a normal ECA, vertebral arteries, and CCA supplying circulation contralateral to an occluded contralateral ICA. Increased velocity may also account for the disturbed flow that is sometimes observed in the normal extracranial carotid arteries of young athletes with normal cardiac outputs or in patients in pathologically high cardiac output states. It is also seen in arteries supplying **arteriovenous fistulas and malformations.**[15,106,107] Postoperative spectral broadening

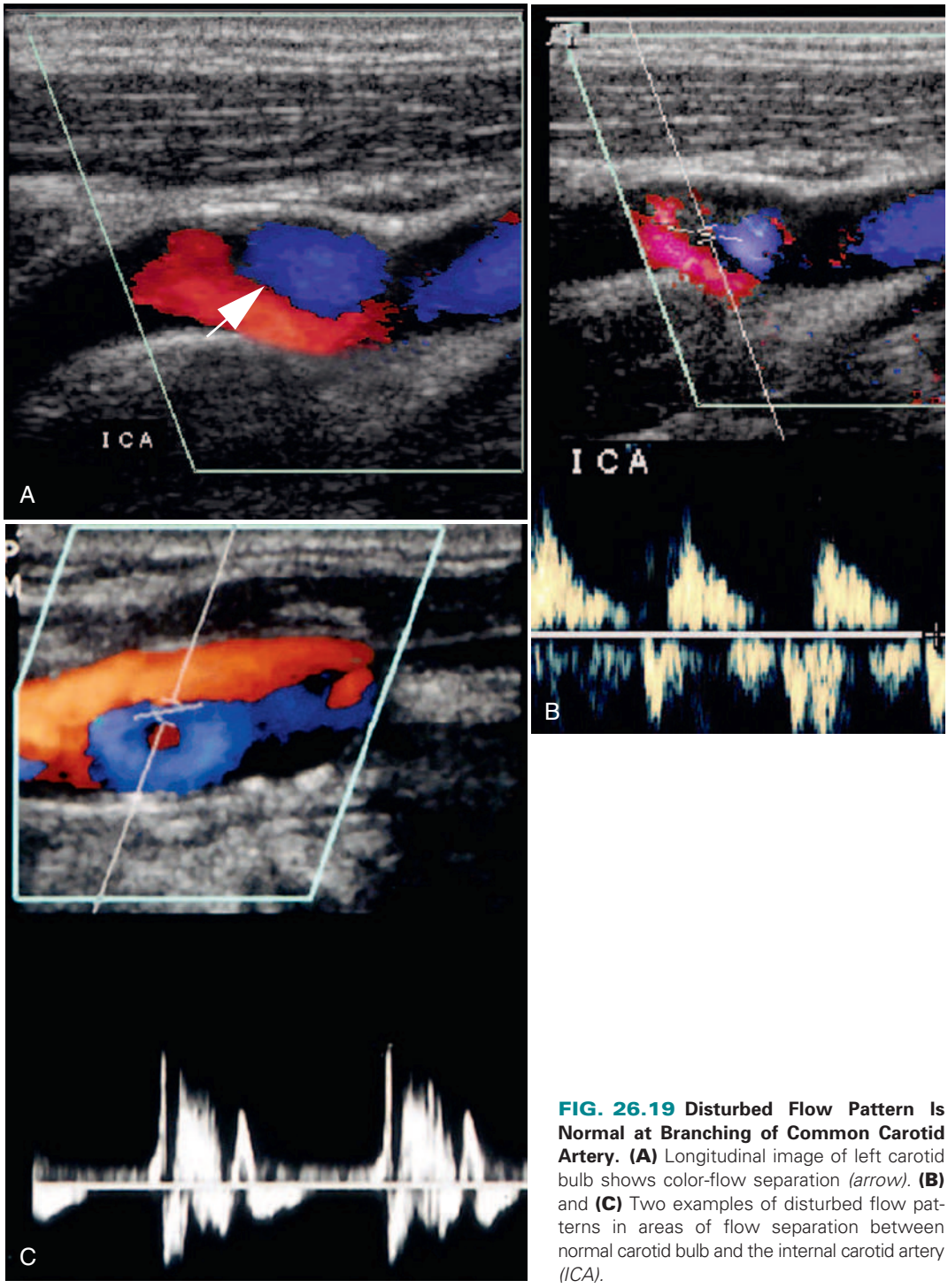

FIG. 26.19 Disturbed Flow Pattern Is Normal at Branching of Common Carotid Artery. (A) Longitudinal image of left carotid bulb shows color-flow separation *(arrow)*. **(B)** and **(C)** Two examples of disturbed flow patterns in areas of flow separation between normal carotid bulb and the internal carotid artery *(ICA)*.

may persist for months after CEA in the absence of significant residual or recurrent disease, possibly from changes in wall compliance.

Tortuous carotid vessels can demonstrate spectral broadening and asymmetrical high-velocity flow jets in the absence of plaque disease. Other nonatheromatous causes of disturbed blood flow in the extracranial carotid arteries include **aneurysms, arterial wall dissections,** and **fibromuscular dysplasia.**

High-Velocity Blood Flow Patterns

Carotid stenoses usually begin to cause velocity changes when they exceed 50% diameter (70% cross-sectional area)[1] (Fig. 26.20). Velocity elevations generally increase as the severity of the stenosis increases. At **critical stenoses** (>95%), the velocity measurements may actually decrease, and the waveform becomes dampened.[99,108]

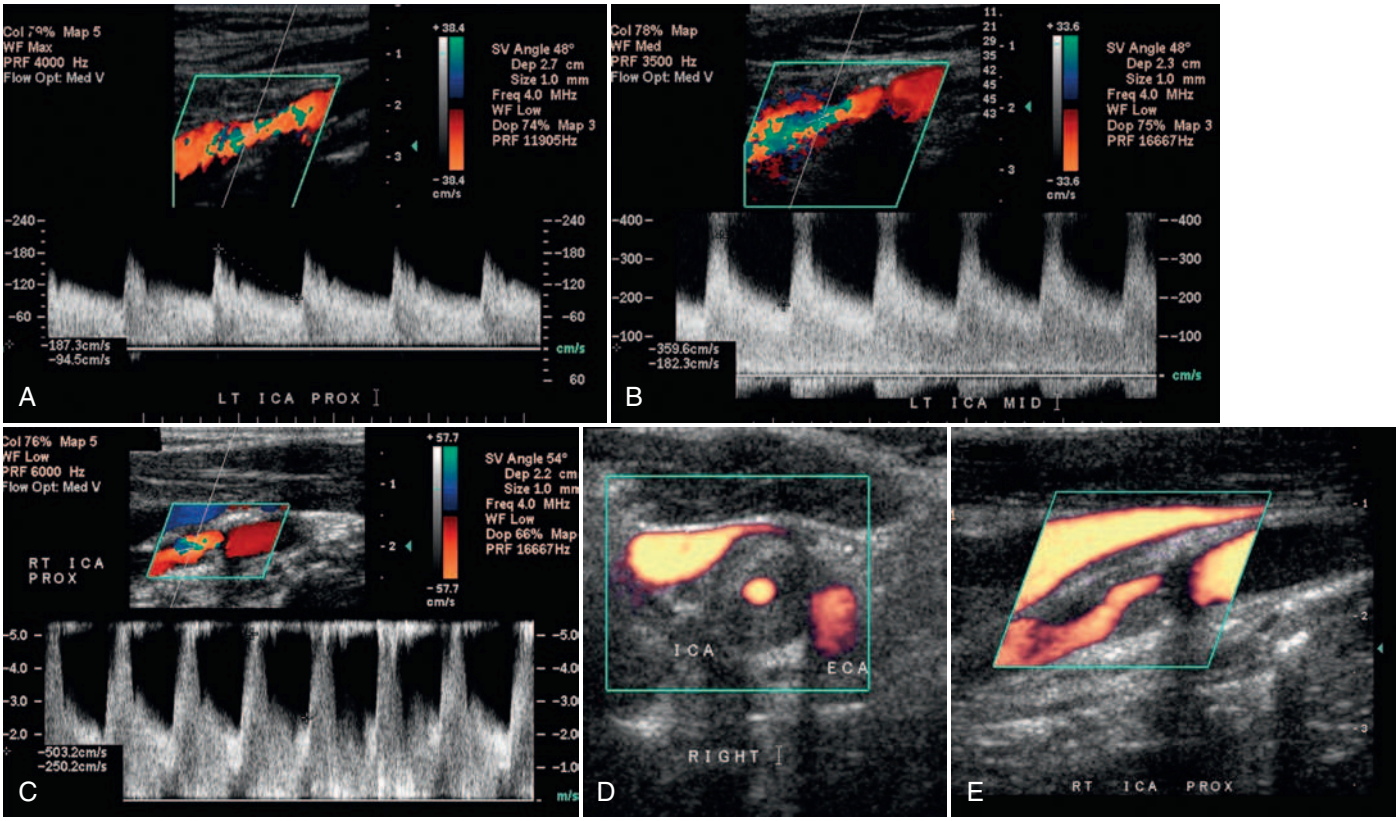

FIG. 26.20 Internal Carotid Artery (ICA) Stenosis. (A) ICA stenosis of 50% to 69% diameter shows a peak systolic velocity (PSV) of 187 cm/sec. **(B)** Left ICA demonstrates a visible high-grade stenosis on color Doppler with end diastolic velocities (EDVs) of greater than 180 cm/sec and PSVs that alias at greater than 350 cm/sec. This is consistent with a very high-grade stenosis. **(C)** Right carotid bulb seen in longitudinal projection with color Doppler demonstrates a high-grade narrowing and spectral broadening with an approximately 500 cm/sec velocity in peak systole and 250 cm/sec in end diastole, consistent with an 80% to 95% stenosis. **(D)** and **(E)** Power transverse and long images demonstrate high-grade stenosis of the ICA.

In these cases, correlation with color or power Doppler imaging is essential to diagnose correctly the severity of the stenoses. Velocity increases are focal and most pronounced in and immediately distal to a stenosis, emphasizing the importance of sampling directly in these regions. Moving further distal from a stenosis, flow begins to reconstitute and assume a more normal pattern, provided a tandem lesion does not exist distal to the initial site of stenosis. Spectral broadening results in the jets of high-velocity flow associated with carotid stenosis; however, correlation with gray-scale and color Doppler images can define other causes of spectral broadening. An awareness of normal flow spectra combined with appropriate Doppler techniques can obviate many potential diagnostic pitfalls.

The degree of **carotid stenosis** that is considered **clinically significant** in the symptomatic or asymptomatic patient is in evolution. Initially, it was thought that lesions causing 50% diameter stenosis were significant; this perception changed as more information was gathered from two large clinical trials. As noted earlier, NASCET demonstrated that CEA was more beneficial than medical therapy in symptomatic patients with 70% to 99% ICA stenosis.[7] ECST demonstrated a CEA benefit when the degree of stenosis was greater than 60%.[8] Interestingly, the method used to grade stenoses in the ECST study was substantially different than that used in the NASCET trials. The NASCET trials compared the severity of the ICA stenosis on arteriogram with the residual lumen of a presumably more normal distal ICA. The ECST methodology entailed assessment of the severity of stenosis with a "guesstimation" of the lumen of the carotid artery at the level of the stenosis. The ECST assessment is more comparable to ultrasound's visible assessment of the degree of narrowing, whereas velocity tables currently in use have been derived to correspond to the NASCET angiographic determinations for stenosis. The ECST method for grading carotid artery stenosis tends to give a more severe assessment of narrowing than the NASCET technique (Fig. 26.21).

The initial NASCET trials retrospectively compared velocity data obtained on the Doppler examination with angiographic measurements of stenosis. No standardized ultrasound protocol was employed by the numerous centers involved in the trials. Despite the lack of uniformity, moderate sensitivity and specificity ranging from 65% to 77% were obtained for grading ICA stenoses using Doppler velocities. If ultrasound technique is standardized and criteria are validated in a given laboratory, **peak systolic velocity** (PSV) and peak systolic ratios have proved to be an accurate method for determining carotid stenosis.[109] The ECST group compared three different angiographic measurement

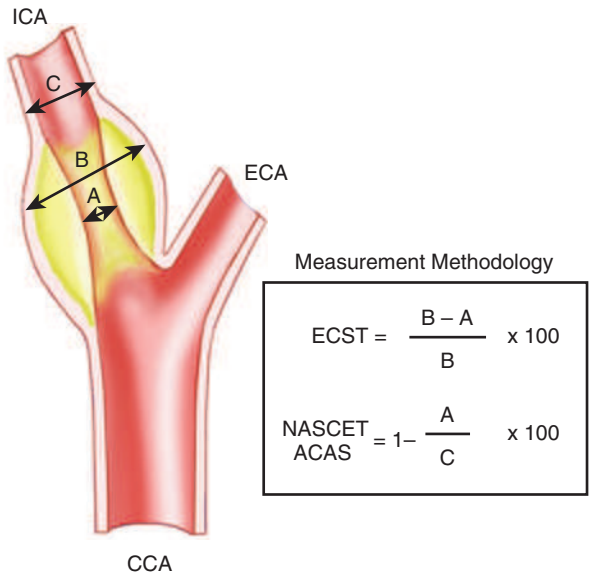

FIG. 26.21 Comparative Measurement Methodology. Different methodologies for grading internal carotid artery stenoses, from the North American Symptomatic Carotid Endarterectomy Trial *(NASCET),* Asymptomatic Carotid Atherosclerosis Study *(ACAS),* and European Carotid Surgery Trial *(ECST). CCA,* Common carotid artery; *ECA,* external carotid artery; *ICA,* internal carotid artery.

techniques: the NASCET, the ECST, and a technique comparing distal CCA measurements with those of ICA stenosis. Researchers concluded that the ECST and NASCET techniques were similar in their prognostic value, whereas the CCA/stenosis measurement was the most reproducible of the three techniques. They also concluded that the CCA method, although reproducible, would be invalidated by the presence of CCA disease.[110] Virtually all investigators advocate using the NASCET angiographic measurement technique.

The results of these trials, as well as the more recent ACAS and moderate NASCET studies, have generated reappraisals of the Doppler velocity criteria that most accurately define 70% or greater stenosis and, more recently, greater than 50% diameter stenoses.[111] Attempts have been made to determine the Doppler parameters or combination of parameters that most reliably identify a certain-diameter stenosis. Most sources agree that the best parameter is the PSV of the ICA in the region of a stenosis.[108] Using multiple parameters can improve diagnostic confidence, particularly when combined with color and power Doppler imaging (see Video 26.19).

The degree of stenosis is best assessed using the gray-scale and pulsed Doppler parameters, including ICA PSV, ICA **end diastolic velocity** (EDV), CCA PSV, CCA EDV, **peak systolic ICA/CCA ratio,** and **peak end diastolic ICA/CCA ratio** (EDR)[108,109,112] (Videos 26.21 and 26.22).[108,109,112] PSV has proved accurate for quantifying high-grade stenoses.[98,109] The relationship of PSV to the degree of luminal narrowing is well defined and easily measured.[113,114] Although Doppler velocities have proved reliable for defining 70% or greater stenosis, Grant et al.[109] showed less favorable results for substenosis classification between 50% to 69% using PSV and ICA/CCA PSV ratios. In our experience, however, using all four parameters and determining a correct category for the degree of stenosis is the most efficacious way to ensure accuracy. Agreement for all four parameters for a clinical situation is most common. When there is an outlying parameter, further assessment and careful attention to technique and detail are required. EDV and EDR are particularly useful in distinguishing between high grades of stenosis. Additionally, correlating the visual estimation of the degree of stenosis and the velocity numbers will help in correctly grading stenosis, particularly when the degree of stenosis is "near occlusion" (Figs. 26.22 and 26.23; see also Fig. 26.20D and E). On rare occasions, alternate imaging methodologies (e.g., MRA, CTA) may need to be recommended.

No criteria for grading **external carotid artery stenoses** have been established. A good general rule is that if the ECA velocities do not exceed 200 cm/sec, no significant stenosis is present. However, we usually rely on a visible assessment of the degree of narrowing associated with velocity changes. Occlusive plaque involving the ECA is less common than in the ICA and is rarely clinically significant.

Similarly, velocity criteria used to grade **common carotid artery stenoses** have not been well established.[115,116] However, if one is able to visualize 2 cm proximal and 2 cm distal to a visible CCA stenosis, a PSV ratio obtained 2 cm proximal to the stenosis (vs. in region of greatest visible stenosis) can be used to grade the "percent diameter stenosis" in a manner similar to that used in peripheral artery studies. A doubling of the PSV across a lesion would correspond to at least a 50% diameter stenosis, and a velocity ratio in excess of 3.5 corresponds to a greater than 75% stenosis.

One persistent problem with duplex Doppler with gray-scale ultrasound evaluation of the carotid arteries is that different institutions use PSVs ranging from 130 cm/sec[117] to 325 cm/sec[111] to diagnose greater than 70% ICA stenosis.[118,119] Factors adding to these discrepancies include technique and equipment.[120] While there is a strong level of correlation between techniques and criteria, the choice of criteria has a significant impact on which patients go to surgery.[119] This wide range of PSVs reinforces the need for individual ultrasound laboratories to determine which Doppler parameters are most reliable in their own institution.[120] Correlation of the velocity ranges obtained by ultrasound with angiographic and surgical results is necessary to achieve accurate, reproducible examinations in a particular ultrasound laboratory.[121]

The Society of Radiologists in Ultrasound, representing multiple medical and surgical specialties, held a consensus conference in 2002 to consider carotid Doppler ultrasound.[122] In addition to guidelines for performing and interpreting carotid ultrasound examinations, panelists devised a set of criteria widely applicable among vascular laboratories (Table 26.1).[122] Although the conference did not recommend all established laboratories with internally validated velocity charts alter their practices, they suggested physicians establishing new laboratories consider using the consensus criteria; those with preexisting charts might consider comparing in-house criteria with those provided by the consensus conference. Velocity criteria corresponding to specific degrees of vascular stenosis are listed in the tables. Our

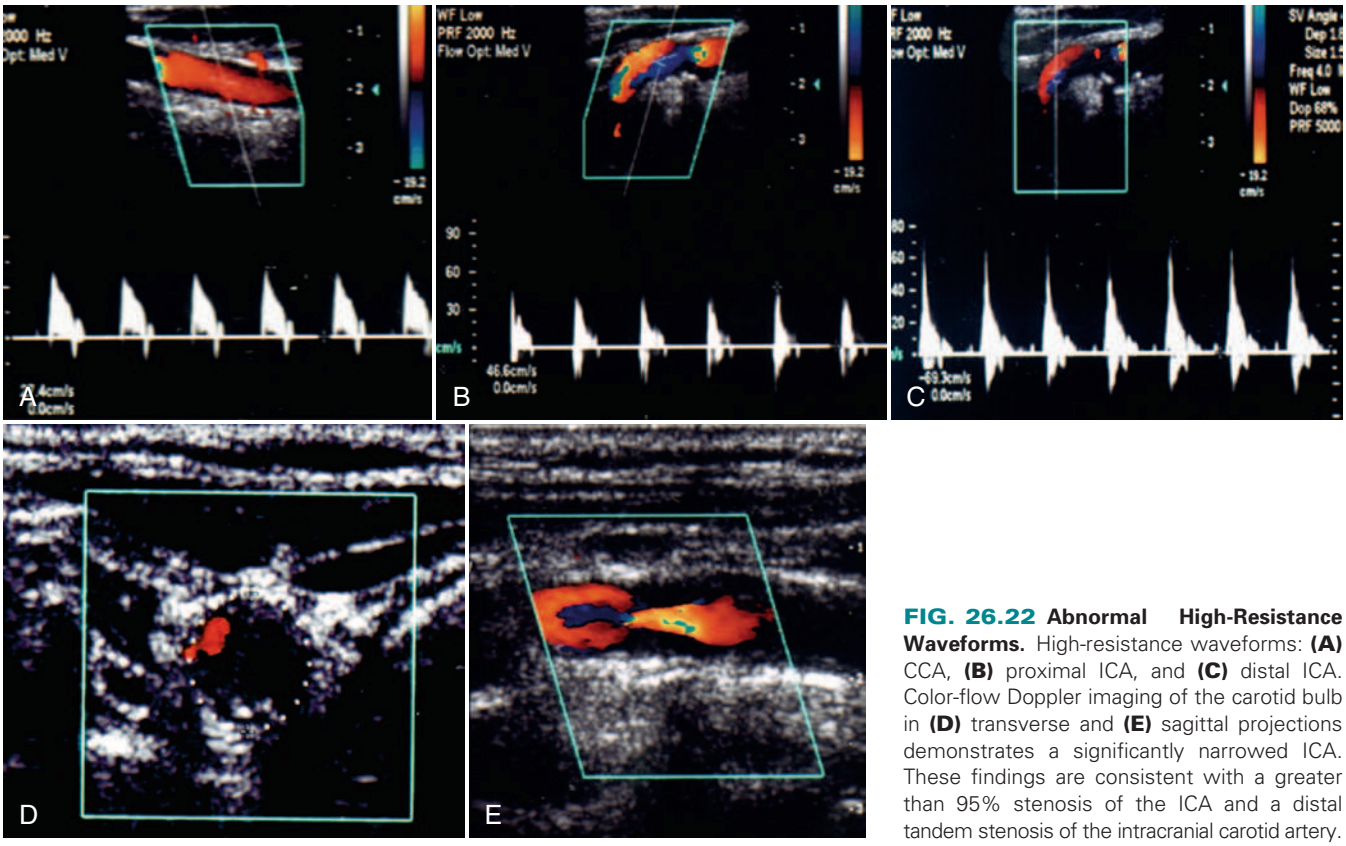

FIG. 26.22 Abnormal High-Resistance Waveforms. High-resistance waveforms: **(A)** CCA, **(B)** proximal ICA, and **(C)** distal ICA. Color-flow Doppler imaging of the carotid bulb in **(D)** transverse and **(E)** sagittal projections demonstrates a significantly narrowed ICA. These findings are consistent with a greater than 95% stenosis of the ICA and a distal tandem stenosis of the intracranial carotid artery.

TABLE 26.1 Diagnostic Criteria for Carotid Ultrasound Examinations

	ICA PSV	Plaque	ICA/CCA PSV Ratio	ICA EDV
Normal	<125 cm/sec	None	<2.0	<40 cm/sec
<50%	<125 cm/sec	<50% diameter reduction	<2.0	<40 cm/sec
50%-69%	125-230 cm/sec	≥50% diameter reduction	2.0-4.0	40-100 cm/sec
≥70% to near occlusion	>230 cm/sec	≥50% diameter reduction	>4.0	>100 cm/sec
Near occlusion	May be low or undetectable	Visible	Variable	Variable
Total occlusion	Undetectable	Visible, no detectable lumen	Not applicable	Not applicable

CCA, Common carotid artery; *EDV,* end diastolic velocity; *ICA,* internal carotid artery; *PSV,* peak systolic velocity.
With permission from Grant EG, Benson CB, Moneta GL, et al. Carotid artery stenosis: gray-scale and Doppler US diagnosis—Society of Radiologists in Ultrasound Consensus Conference. Radiology. 2003;229(2):340-346.[122]

TABLE 26.2 Alternative Diagnostic Criteria for Estimating Carotid Artery Disease

Diameter Stenosis	Peak Systolic Velocity (cm/sec)	Peak Diastolic Velocity (cm/sec)	Systolic Velocity Ratio (VICA/VCCA)	Diastolic Velocity Ratio (VICA/VCCA)
0% (normal)	<110	<40	<2.0	<2.6
1%-39% (mild)	<110	<40	<2.0	<2.6
40%-59% (moderate)	<170	<40	<2.0	<2.6
60%-79% (severe)	>170	>40	>2.0	>2.6
80%-95% (critical)	>250	>100	>3.7	>5.5
96%-99%	Velocities demonstrate variability and may be low			
100% (occlusion)	No flow detected			

VCCA, Velocity common carotid artery; *VICA,* velocity internal carotid artery.
Based on the European Carotid Surgery Trial's methodology of measuring residual lumen to outer vessel margin. Bluth EI, Stavros AT, Marich KW, et al. Carotid duplex sonography: a multicenter recommendation for standardized imaging and Doppler criteria. Radiographics. 1988;8(3):487-506[45]; Carpenter JP, Lexa FJ, Davis JT. Determination of sixty percent or greater carotid artery stenosis by duplex Doppler ultrasonography. J Vasc Surg. 1995;22(6):697-703.[123]

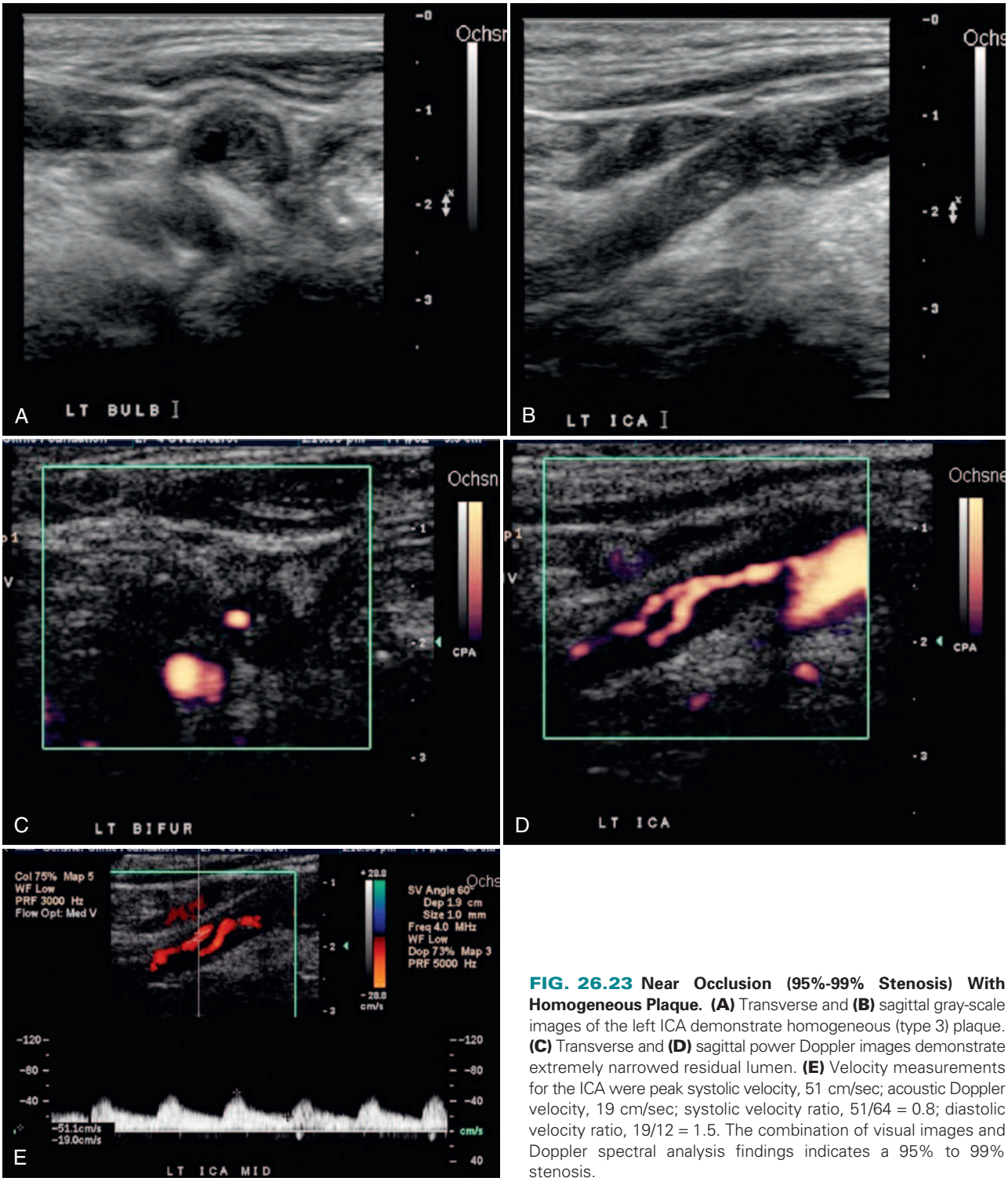

FIG. 26.23 Near Occlusion (95%-99% Stenosis) With Homogeneous Plaque. (A) Transverse and **(B)** sagittal gray-scale images of the left ICA demonstrate homogeneous (type 3) plaque. **(C)** Transverse and **(D)** sagittal power Doppler images demonstrate extremely narrowed residual lumen. **(E)** Velocity measurements for the ICA were peak systolic velocity, 51 cm/sec; acoustic Doppler velocity, 19 cm/sec; systolic velocity ratio, 51/64 = 0.8; diastolic velocity ratio, 19/12 = 1.5. The combination of visual images and Doppler spectral analysis findings indicates a 95% to 99% stenosis.

institution uses Table 26.2, which has a category for 80% to 95% stenoses; our surgeons are more inclined to consider surgery for patients with asymptomatic stenoses greater than 80% than for those with less severe stenoses.[45,123]

The ICA values should be obtained at or just distal to the point of maximum visible stenosis and at the point of greatest color Doppler spectral abnormality. Values from the CCA should be obtained 2 cm proximal to the widening in the region of the carotid bulb. Because velocities normally decrease from proximal to distal in the CCA and increase from proximal to distal in the ICA, it is important that standardized levels be used routinely for obtaining the ICA/CCA velocity ratio.

Color Doppler Ultrasound

Color Doppler ultrasound displays blood flow information in real time over the entire image or a selected area. Stationary soft

tissue structures, which lack a detectable phase or frequency shift, are assigned an amplitude value and displayed in a gray-scale format with flowing blood in vessels superimposed in color. Color assignments depend on the direction of blood flow relative to the Doppler transducer. Blood flow toward the transducer appears in one color and blood flow away from the transducer is in another. These color assignments are arbitrary. Color saturation displays indicate the variable velocity of blood flow. Deeper shades usually indicate low velocities centered around the zero-velocity color-flow baseline. As velocity increases, the shades become lighter or are assigned a different color hue. Some systems allow selected frequency shifts to be displayed in a contrasting color, such as green. This **green-tag feature** provides a real-time estimation of the presence of high-velocity flow.

Setting the color Doppler scale can also be used to create an aliasing artifact corresponding to the highest-velocity flow within a vessel (see Figs. 26.16B, 26.18, and 26.21). These **high-velocity jets** pinpoint areas for spectral analysis. Color assignments are a function of both the mean frequency shift produced by moving RBC ensembles and the Doppler angle theta. If the vessel is tortuous or diving, angle theta between the transducer and vessel will change along the course of the vessel, resulting in **changing color assignments** that are unrelated to the change in RBC velocity. The color assignments will reverse in tortuous vessels as their course changes relative to the Doppler transducer, even though the absolute direction of flow is unchanged. Portions of a vessel that **parallel the Doppler beam** when angle theta is 90 degrees will have little or no frequency shift detected, and no color will be seen.

Optimal Settings for Low-Flow Vessel Evaluation

Color Doppler flow studies should be performed with optimal flow sensitivity and gain settings. Color flow should fill the entire vessel lumen but not spill over into adjacent soft tissues. The **pulse repetition frequency** (PRF) and frame rates should be set to allow visualization of flow phenomena anticipated in a vessel. Frame rates will vary as a function of the width of the area chosen for color Doppler display and for depth of the region of interest. The greater the color image area is, the slower the frame rate will be. The deeper the posterior boundary of the color image is, the slower the PRF will be. Color Doppler sensitivity should be adjusted to detect anticipated velocities, such that if slow flow in a preocclusive carotid lesion is sought, low-flow settings with decreased sampling rates are employed. However, the system will then alias at lower velocities because of the decrease in PRF. In addition to changes in the PRF, optimization of the Doppler angle, increases in gain and power settings, decrease in the wall filter, increase in persistence, and increase in ensemble or dwell time can be used to optimize low-flow detection.

Optimization of Color Doppler Low-Flow Vessel Evaluation

Use low pulse repetition frequency
Use Doppler angle of less than 60 degrees
Increase gain setting
Increase power setting
Decrease wall filter
Increase persistence
Increase dwell time

Flowing blood becomes, in effect, its own contrast medium, with color or power Doppler outlining the patent vessel lumen. This allows determination of the true course of the vessel, facilitating positioning of the Doppler cursor and thus providing more reliable velocity determinations. Furthermore, color Doppler facilitates Doppler spectral analysis by rapidly identifying areas of flow abnormalities. The highest velocities in the region of and immediately distal to a stenosis are seen as **aliasing** high-velocity jets of color. Color Doppler ultrasound facilitates placing the pulsed Doppler range gate in the region of these most striking color abnormalities for pulsed Doppler spectral analysis. The presence of a stenosis can be determined by color Doppler changes in the vessel lumen as well as by visible luminal narrowing. Although color Doppler can be used to determine the presence of hypoechoic plaque, it cannot be used optimally to determine the area of patent lumen in transverse projection because the optimal angle for measuring the area or diameter of narrowing is at 90 degrees to the long axis of the vessel, which is the worst angle for color Doppler imaging. Gray-scale assessment, power Doppler, or B-flow imaging should be used to assess the diameter/area of the patent carotid lumen (see Fig. 26.12). If a stenosis produces a **bruit** or **thrill,** the resultant perivascular tissue vibrations may be seen as transient speckles of color in the adjacent soft tissues, more prominent during systole[124] (Fig. 26.24).

Comparisons of color Doppler ultrasound with conventional duplex Doppler sampling techniques and angiography have shown relatively similar accuracy, sensitivity, and specificity.[125,126] However, color Doppler offers many benefits, including a reduction in examination time by pinpointing areas of color Doppler abnormality for pulsed Doppler spectral analysis.[126] Branches of the ECA are readily detected, facilitating differentiation from the ICA. The real-time flow information over a large cross-sectional area provides a global overview of flow abnormalities and allows ready determination of the course of a vessel. Furthermore, color Doppler improves diagnostic confidence and reproducibility of ultrasound studies, thereby avoiding many potential diagnostic pitfalls.

The laminar blood flow is disrupted in the region of the carotid bifurcation where there is a **normal transient flow reversal** opposite the origin of the ECA (see Fig. 26.19). Color Doppler displays this normal flow separation as an area of flow reversal located along the outer wall of the carotid bulb, which appears either at early systole or in peak systole and persists for a variable period into the diastolic part of the cardiac cycle.[127,128] This flow reversal can produce some strikingly bizarre pulsed Doppler waveforms; however, the color Doppler appearance readily discerns the nature of these waveform changes. Furthermore, the absence of this flow reversal may be abnormal and may

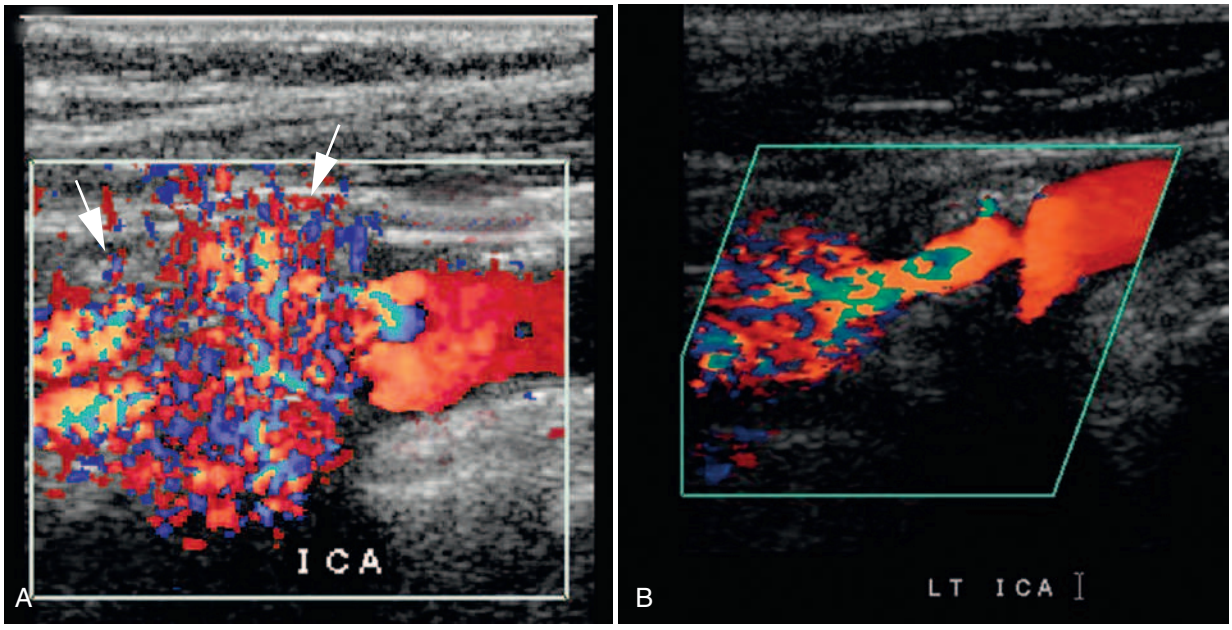

FIG. 26.24 Color Doppler Bruit. (A) Extensive soft tissue color Doppler bruit *(arrows)* surrounds the carotid bifurcation with a 90% internal carotid artery *(ICA)* stenosis. **(B)** ICA demonstrates a small bruit, not as significant as in view A, but nevertheless a bruit showing the appropriate area to place the cursor for Doppler flow evaluation of the significant stenosis.

represent one of the earliest changes of atherosclerotic disease.[127] The flow reversal seen in the region of the carotid bifurcation is clearly different than that seen with color Doppler aliasing. Contiguous saturated areas of red and blue are seen in this low-velocity flow separation versus the very different contiguous color hues representing the highest color assignments for forward and reversed flow.

Helical flow in the CCA may be an indirect indication of proximal arterial stenosis but can occur as a normal variant. Color Doppler sonography graphically displays the eccentric spiraling of flow up the CCA.

Advantages and Pitfalls

Color Doppler ultrasound may help avoid potential diagnostic pitfalls. Alterations in cardiovascular physiology, tandem lesions, contralateral carotid disease, arrhythmias, postoperative changes, and tortuous vessels can lead to underestimation or overestimation of the degree of stenosis. In such cases, color Doppler ultrasound can provide direct visualization of the patent lumen in a fashion analogous to angiography.[129] In fact, because angiography images only the vessel lumen and not the vessel wall, color Doppler and power Doppler ultrasound imaging have the potential to evaluate stenoses even more completely than angiography. Because flow patterns are displayed with color Doppler imaging, the local hemodynamic consequences of the lesion are readily discerned. Color and power Doppler ultrasound have particular value in detecting small residual channels of flow in areas of high-grade carotid stenoses[124,125,129-134] (Fig. 26.25). Power Doppler ultrasound offers a comparable advantage and has the theoretical potential to be more sensitive for detecting extremely low-amplitude, low-velocity flow. Finally, color Doppler and power Doppler ultrasound have the potential to clarify image Doppler mismatches, further improving diagnostic accuracy and confidence.

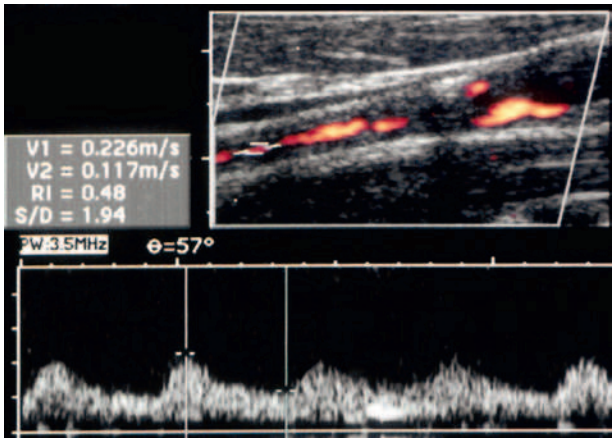

FIG. 26.25 High-Grade "String Sign" Stenosis of Internal Carotid Artery. Tardus-parvus waveform with low velocity in a long segment.

Color Doppler Evolution of Carotid Stenosis

ADVANTAGES

Reduction in examination time
Quick identification of areas of stenosis/high velocity, which facilitates spectral analysis to artifacts
Improved diagnostic reproducibility and confidence
Distinguishes occlusion from "string sign"
Simultaneous hemodynamic and anatomic information, velocity, and directional blood flow information
Improved accuracy in quantitating stenoses
Clarifies pulsed Doppler/image mismatch

DISADVANTAGES

Prone to angle dependence
Resolution less than with gray-scale
Slower frame rates information
Cannot characterize plaque

Although color Doppler ultrasound offers many advantages, it is angle dependent and prone to artifacts, such as aliasing. The spatial resolution of color Doppler ultrasound is less than that of gray-scale imaging, and the Doppler resolution is inferior to pulsed Doppler spectral analysis. Color saturation cannot be equated with velocity.[120] The color image is corrected for only one angle, so changes in color saturation may simply reflect changes in the vessel course and the relative Doppler angle. Color systems generally compute the mean velocity to produce the color pixel in the image. However, the examiner is usually interested in determining the maximum velocity; therefore pulsed Doppler spectral analysis remains necessary for precise quantification of a hemodynamically significant stenosis.

Power Doppler Ultrasound

The color signal in power Doppler ultrasound is generated from the integrated power Doppler spectrum. The amplitude of the reflected echoes determines the brightness and color tone of the color signal. This amplitude depends on the density of RBCs flowing within the sample volume. Power Doppler ultrasound uses a larger dynamic range with a better signal-to-noise ratio than color Doppler ultrasound. Because power Doppler ultrasound does not evaluate frequencies but rather amplitude (or power), artifacts such as aliasing do not occur. Power Doppler sonography, unlike color Doppler ultrasound, is largely angle independent. These features combine to make power Doppler ultrasound exquisitely sensitive to detecting a **residual string of flow** in the region of a suspected carotid occlusion.[130,135]

It is also hypothesized that power Doppler ultrasound has better edge definition than color Doppler ultrasound. The combination of improved edge definition and relative angle-independent flow imaging offers the potential for better visual assessment of the degree of stenosis using power Doppler.[136] Better edge definition may also allow power Doppler ultrasound to define plaque surface characteristics more clearly[137] (see Fig. 26.10B).

Despite the many potential benefits of power Doppler ultrasound, it does not provide velocity or directional flow information.[138] Also, power Doppler is very motion sensitive, which may result in a **pseudostring** of flow. If the vibrations of soft tissue at an echogenic interface exceed the clutter filter level, color information may be displayed in areas where there is no blood flow. Pulsed Doppler evaluation of a color or power string should always be performed to confirm the presence of real flow.

Power Doppler screening may produce an accurate and cost-effective method for patients at risk for carotid disease.[139-141] In one study, power Doppler imaging used independent of spectral analysis was effectively performed in 89 of 100 patients.[139] The sensitivity for the detection of 40% or greater stenoses using power Doppler was 91%, with 79% specificity. This would be reasonable for a screening test, allowing patients with greater than 40% stenosis to undergo more expensive spectral analysis. Some believe that using this less expensive power Doppler screening could result in a more cost-effective approach to carotid Doppler screening. In addition, carotid power Doppler imaging, as well as carotid B-flow imaging, is ideally suited to combined use with vascular contrast agents that may be widely available in the future. However, after evaluating the literature, the US Preventative Task Force has given this a Grade D recommendation and recommends not screening for asymptomatic carotid artery stenosis in the general adult population.[142]

Power Doppler Evaluation of Carotid Stenosis

ADVANTAGES

Produces no aliasing
Potentially increases accuracy of grading stenoses
Aids in distinguishing preocclusive from occlusive lesions
Potentially provides superior depiction of plaque surface morphology
Yields increased sensitivity to detecting low-velocity, low-amplitude blood flow
Is angle independent

DISADVANTAGES

Does not provide direction or velocity flow information
Is very motion sensitive (poor temporal resolution)

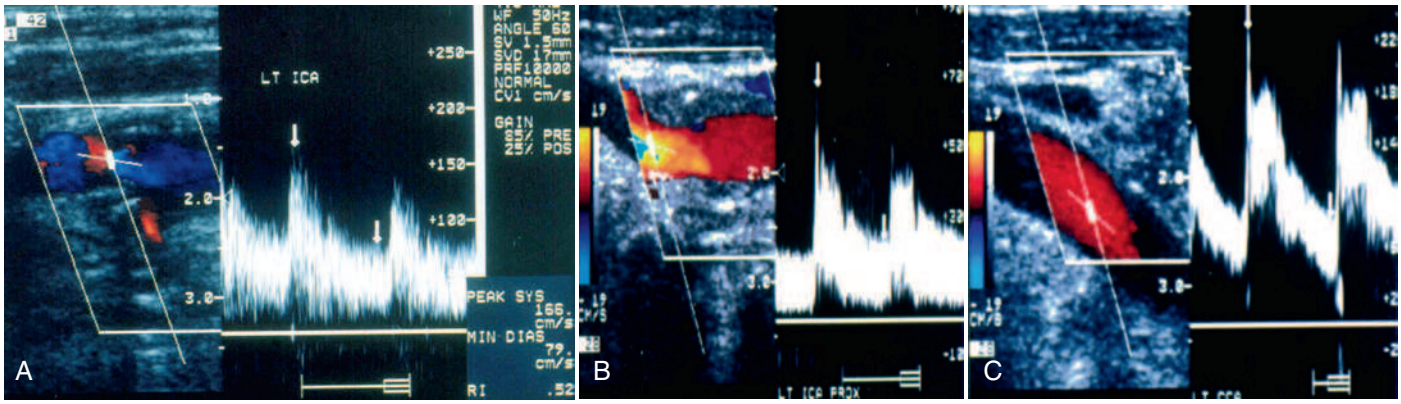

FIG. 26.26 Value of ICA/CCA Ratio. (A) Increased velocity ICA and CCA in a patient with hypertension. ICA PSV is 166 cm/sec; EDV is 79 cm/sec. CCA velocities: PSV = 96 cm/sec, EDV = 36 cm/sec. ICA/CCA systolic velocity ratio is 1.7, and diastolic velocity ratio is 2.2, corresponding to a degree of stenosis less than 50%. **(B)** Low velocities in left ICA: PSV = 67 cm/sec, EDV = 23 cm/sec. **(C)** In left CCA, PSV = 23 cm/sec, EDV = 8 cm/sec. ICA/CCA systolic velocity ratio is 2.9, and diastolic velocity ratio is 2.9, corresponding to a 50% to 69% stenosis in patient with cardiomyopathy.

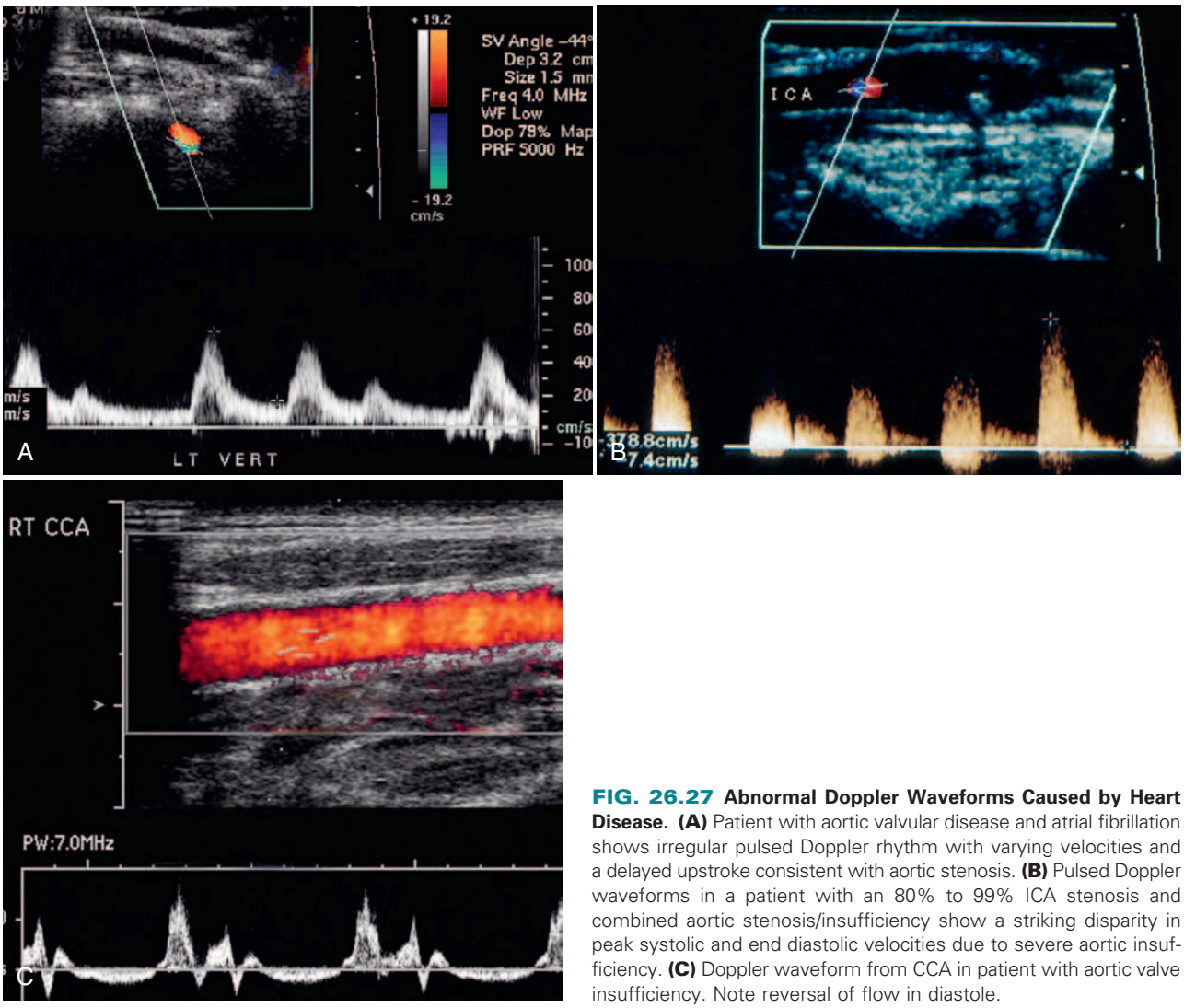

FIG. 26.27 Abnormal Doppler Waveforms Caused by Heart Disease. (A) Patient with aortic valvular disease and atrial fibrillation shows irregular pulsed Doppler rhythm with varying velocities and a delayed upstroke consistent with aortic stenosis. **(B)** Pulsed Doppler waveforms in a patient with an 80% to 99% ICA stenosis and combined aortic stenosis/insufficiency show a striking disparity in peak systolic and end diastolic velocities due to severe aortic insufficiency. **(C)** Doppler waveform from CCA in patient with aortic valve insufficiency. Note reversal of flow in diastole.

Pitfalls and Adjustments

Although absolute velocity determinations are valuable in assessing the degree of vascular stenosis, these measurements are less reliable in certain patients.[1] Variations in cardiovascular physiology may affect carotid velocity measurements.[143,144] For example, velocities produced by a stenosis in a **hypertensive patient** may be higher than those in a normotensive individual with comparable narrowing, especially in the setting of a wide-pulsed pressure.[145] On the other hand, a **reduction in cardiac output** will diminish both systolic and diastolic velocities (Fig. 26.26). **Cardiac arrhythmias, aortic valvular lesions,** and **severe cardiomyopathies** can cause significant aberrations in the shape of carotid flow waveforms and alter systolic and diastolic velocity readings[146] (Fig. 26.27). Use of an **aortic balloon pump** can also distort the Doppler velocity spectrum[147] (Fig. 26.28). These alterations can invalidate the use of standard Doppler parameters to quantify stenoses. **Bradycardia,** for example, produces increased stroke volume, causing systolic velocities to increase, whereas **prolonged diastolic runoff** causes spuriously decreased end diastolic values resulting in underestimation of carotid stenosis.[148]

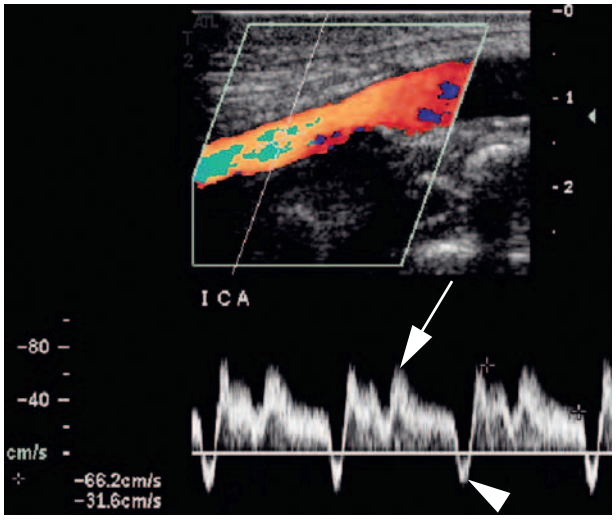

FIG. 26.28 Abnormal Doppler Waveform Caused by Aortic Balloon Pump. ICA pulsed Doppler trace shows the effect of an aortic balloon pump on carotid waveforms. Inflation of the device in systole *(arrow)* produces a second systolic peak, whereas deflation produces flow reversal *(arrowhead)* in end diastole.

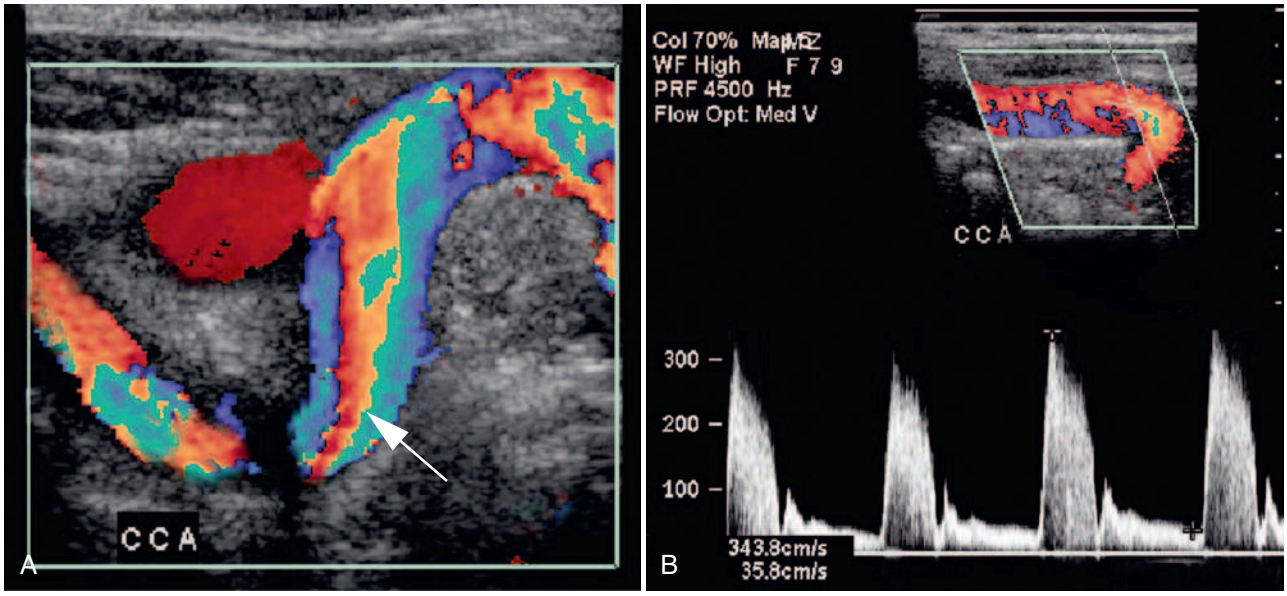

FIG. 26.29 Abnormal Doppler Flow Caused by Tortuous Vessel. (A) Tortuous common carotid artery *(CCA)* displays color Doppler eccentric jets of flow *(arrow).* **(B)** Spuriously elevated velocity is caused by an eccentric jet in a tortuous proximal left CCA without any visible stenosis.

Patients with isolated **severe or critical aortic stenosis** may demonstrate duplex waveform abnormalities, including prolonged acceleration time, decreased peak velocity, delayed upstroke, and rounded waveforms.[149] However, **mild or moderate aortic stenosis** usually results in little or no sonographic abnormality. **Tortuous or kinked carotid arteries** represent either congenital or acquired changes in the carotid artery. The clinical significance of these is debatable; however, the **vascular tortuosity** frequently results in eccentric jets of high-velocity flow, which may show elevated velocities in the absence of significant stenosis[150-152] (Fig. 26.29). Conversely, if the carotid bulb is capacious, a large plaque burden may still fail to produce anticipated velocity increases. The relative difference in area between the distal CCA and the residual patent lumen of the large bulb is not sufficient to produce a greater than 50% velocity change. Some refer to this as **nonstenotic (homogeneous) plaque** (Fig. 26.30). Frequently, an **image/Doppler mismatch** alerts the examiner to potential pitfalls.

Causes of Image/Doppler Mismatch

Cardiac arrhythmia
Cardiac valvular disease, cardiomyopathy
Severe aortic stenosis
Hypotension or hypertension
Tandem lesions
Contralateral carotid stenosis
Nonstenotic plaque
Long-segment, concentric high-grade stenosis
Carotid dissection
Preocclusive lesion
Tortuous vessels
Calcified plaque, hypoechoic or anechoic plaque
Anatomic variants

Color Doppler can be used to overcome diagnostic dilemmas in these situations, particularly when "cine loop" playback capabilities are present. Cine loop allows the computer to store portions of the previous color Doppler flow recording for playback at the real-time rate or frame by frame. This allows the clinician to assess the filling of all parts of the vessel lumen. **Obstructive lesions in one carotid can affect velocities in the contralateral vessel.** For example, severe unilateral ICA stenosis or occlusion may cause shunting of increased flow through the contralateral carotid system. This increased flow artificially increases velocity measurements in the contralateral vessel, particularly in areas of stenosis.[150,153-156] Conversely, a proximal common carotid or innominate artery stenosis may reduce flow, with consequent reduction of velocity measurements in a stenosis that is distal to the point of obstruction **(tandem lesion)** (see Fig. 26.22).

Velocity ratios that compare velocity values in the ICA to those in the ipsilateral CCA can help avoid some pitfalls.[99] Of particular value are the **peak systolic ratio** (PSV in ICA vs. PSV in CCA)[104,157] and the **end diastolic ratio** (ICA/CCA EDV).[112] Grant et al. have shown that PSV ICA/CCA ratios are comparable in accuracy to PSV values for determining the degree of ICA stenosis.[109] Although the PSV and peak systolic ICA/CCA velocity ratio have shown relative comparable sensitivities and specificities, at times the velocity ratio will more correctly identify the degree of stenosis and the absolute velocity. Velocity ratios should always be employed when unusually high or low CCA velocities or significant asymmetry of CCA velocities is detected. Long-segment, high-grade stenoses frequently will not demonstrate the anticipated degree of ICA velocity elevation. In such situations, the velocity ratio coupled with the gray-scale/color/power Doppler appearance may provide insight into the actual degree of narrowing. As discussed for spectral broadening, color and power Doppler sonography are invaluable in the avoidance of pitfalls related to spurious Doppler spectral traces.

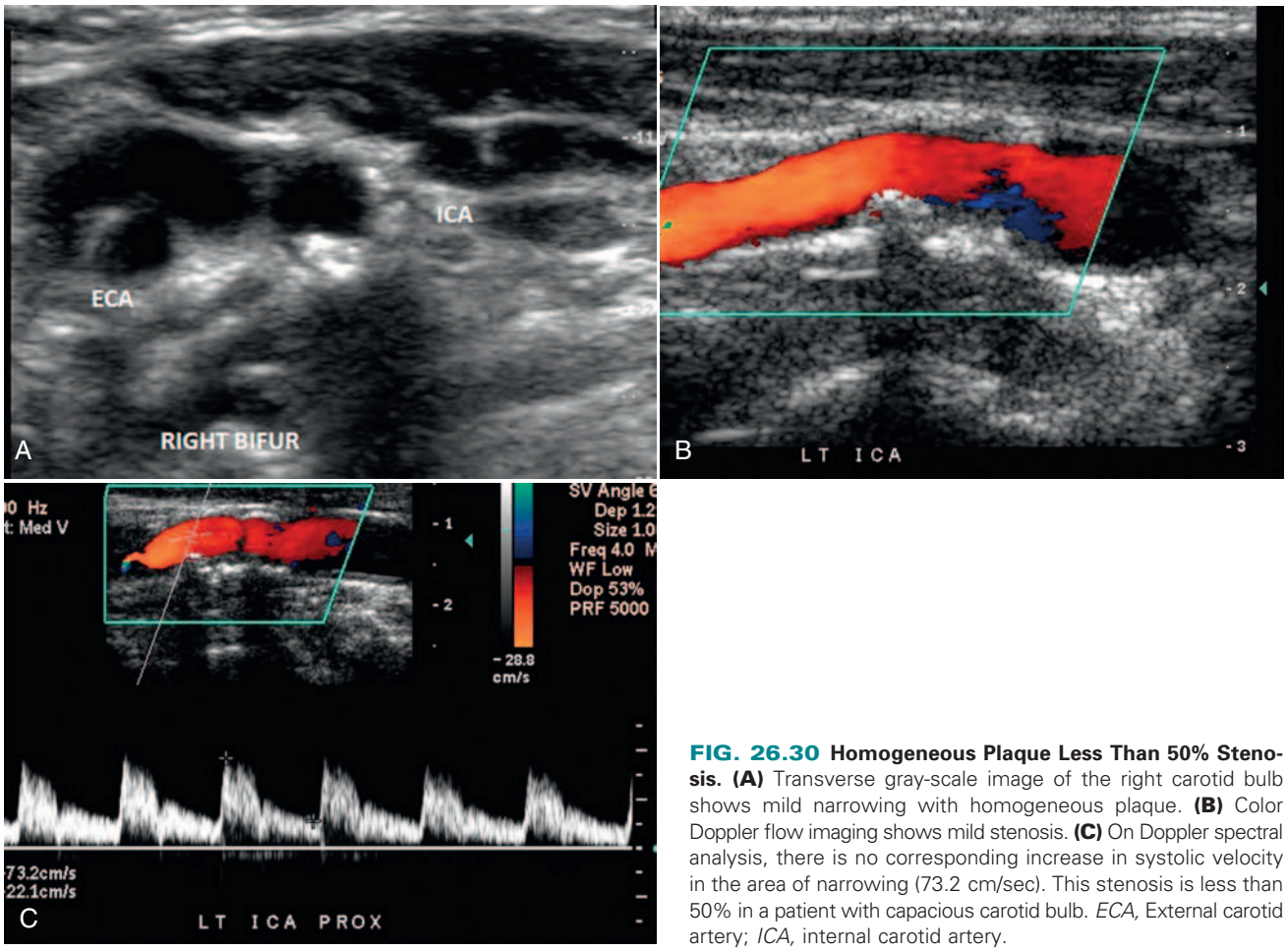

FIG. 26.30 Homogeneous Plaque Less Than 50% Stenosis. (A) Transverse gray-scale image of the right carotid bulb shows mild narrowing with homogeneous plaque. **(B)** Color Doppler flow imaging shows mild stenosis. **(C)** On Doppler spectral analysis, there is no corresponding increase in systolic velocity in the area of narrowing (73.2 cm/sec). This stenosis is less than 50% in a patient with capacious carotid bulb. *ECA,* External carotid artery; *ICA,* internal carotid artery.

Although high-grade stenoses usually produce increased velocity in the region of a plaque and distal to it, high-grade intracranial or extracranial occlusive **lesions in tandem may reduce anticipated velocity shifts** and produce an atypical high-resistance ICA waveform (see Fig. 26.22). Vessels should be examined as far cephalad as possible to avoid missing a distal tandem lesion. Flow immediately distal to stenosis of greater than 95% frequently demonstrates very-low-velocity **tardus-parvus waveforms** versus the anticipated high velocities seen in a high-grade stenosis (see Fig. 26.25). **High-grade vascular narrowings,** particularly those of a circumferential nature that occur over a long segment of a vessel, may also produce dampened waveforms without a high-velocity frequency shift. Although no definite velocity elevations are present in such a long, circumferential narrowing, spectral broadening and disturbed flow distal to such a narrowing are usually apparent. In addition, the fusiform narrowings are usually detected with the real-time color Doppler image. **Innominate artery occlusions** may result in tardus-parvus waveforms, asymmetric, elevated left common carotid to right common carotid ratios, and even carotid steal patterns similar to those noted in the vertebral artery[134] (Fig. 26.31).

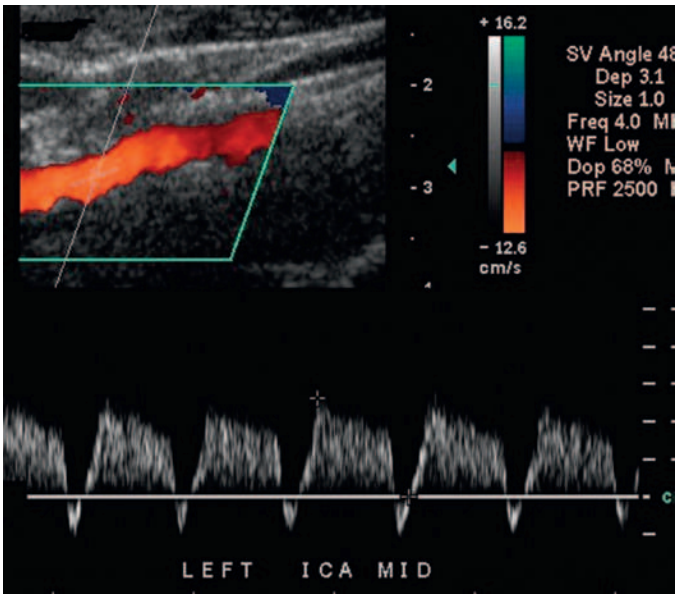

FIG. 26.31 Abnormal CCA Velocity Caused by Innominate Artery Stenosis. Low left ICA velocities with presteal waveform distal to the severe innominate artery stenosis.

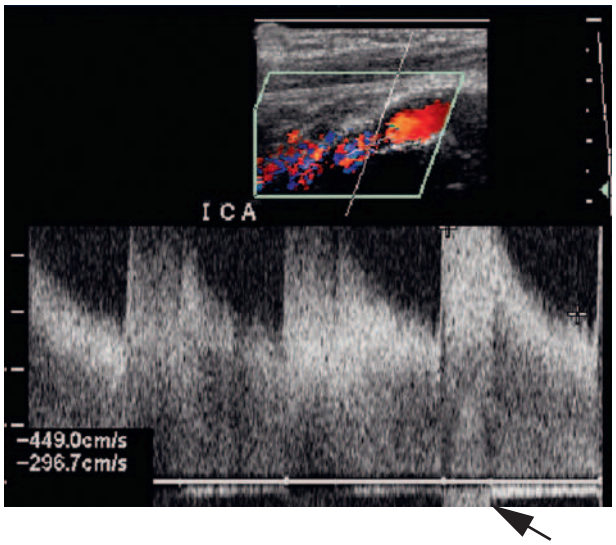

FIG. 26.32 Aliasing of Doppler Waveform in the Region of a High-Grade (80%-95%) Stenosis. Highest velocities are wrapped around *(arrow)* and displayed below the zero-velocity baseline. *ICA,* Internal carotid artery.

Another source of error in pulsed Doppler ultrasound analysis is **aliasing,** which is caused by the inability to detect the true PSV because the Doppler sampling rate, the PRF, is too low. The maximal detectable frequency shift can be no greater than half the PRF. With aliasing, the tips of the time velocity spectrum (representing high velocities) are cut off and wrap around to appear below the baseline (Fig. 26.32). If aliasing occurs, **continuous wave probes** used in conjunction with duplex pulsed Doppler can readily demonstrate the true peak velocity shift. Aliasing can also be overcome or decreased by **increasing the angle theta** (the angle of Doppler insonation), thereby reducing the detected Doppler shift, or by decreasing the insonating sound beam frequency. **Increasing the PRF** increases the detectable frequency shift, but the PRF increase is limited by the depth of the vessel as well as the center frequency of the transducer.[45,101,158] One can also **shift the zero baseline** and reassign a larger range of velocities to forward flow to overcome aliasing. It is also valid to **add velocity values above and below the baseline** to obtain an accurate velocity value, provided that multiple wraparounds do not occur, as seen in extremely high velocities. Aliasing may sometimes be useful in color Doppler image interpretation, where color-flow Doppler aliasing can accent the severity of flow disturbances as well as define the patent lumen.

Internal Carotid Artery Occlusion

Distinguishing between a **string sign** and a **totally occluded carotid artery** has major clinical consequences.[88] Grubb et al.[159] showed that untreated preocclusive lesions carry about a 5% per year risk for stroke. Thus intervention in this patient population is particularly important.

Carotid occlusion is diagnosed when no flow is detected in a vessel. Occasionally, transmitted pulsations into an occluded ICA may mimic abnormal flow in a patent vessel. The pulsed Doppler cursor should be clearly located in the ICA lumen, and arterial pulsatile flow should be identified. Close attention should be paid to the direction of flow and the nature of pulsations. **True center-stream sampling** should be documented by transverse scanning, and the sample volume reduced in size as much as possible. Extraneous pulsations are seldom transmitted to the center of the thrombus.[102]

As a high-grade stenosis approaches occlusion, the high-velocity jet is reduced to a mere trickle. It may be difficult to locate the small residual string of flow within a largely occluded lumen using gray-scale imaging alone, particularly if the adjacent plaque or thrombus is anechoic, making the residual lumen difficult to visualize during real-time examination, or if calcified plaque obscures visualization. In critical high-grade stenoses (>95%), standard-sensitivity color Doppler settings may fail to demonstrate a string of residual flow. Thus it is always prudent to employ the **slow-flow sensitivity settings** on color Doppler to discriminate between critical stenoses and occlusions.[86,125,129] Alternatively, power Doppler ultrasound (with its increased sensitivity to detecting low-amplitude, slow-velocity signals) may be used to visualize a **residual string of blood flow** (Fig. 26.33). Color Doppler is 95% to 98% accurate in distinguishing high-grade stenosis from complete occlusion on angiography when appropriate technical parameters are employed.[160-162]

The presence of a high-grade ICA stenosis or occlusion can often be inferred from inspection of the ipsilateral CCA on a pulsed Doppler waveform or color/power Doppler image (see Fig. 26.31). The pulsed Doppler waveforms in the ipsilateral CCA and ICA proximal to a lesion frequently demonstrate an asymmetrical, high-resistance signal with decreased, absent, or reversed diastolic flow, except when there are **ECA collaterals to the intracranial circulation** (Fig. 26.34). The main intracranial/extracranial collateral pathway exists between the orbital and ophthalmic arteries. Other collateral pathways include the occipital branch of the ECA to the vertebral artery and cervical branches off the arch with the vertebral artery. Similarly, color or power Doppler images may show a flash of color flow in systole but a conspicuous decrease or absence of color flow in diastole, which is asymmetrical compared to the contralateral side. The diagnosis of carotid occlusion versus a string sign is made more accurately with color and power Doppler than with gray-scale duplex scanning and may obviate the need for angiography to confirm a sonographically diagnosed ICA occlusion; however, if ambiguity persists, CTA, MRA, or angiography can be helpful.[88,160,161]

Internal Carotid Artery Occlusion

Internalization of ipsilateral ECA waveform
Absence of flow in ICA by color Doppler, power Doppler, or pulsed Doppler ultrasound
Reversal of flow in segment of ICA or CCA proximal to occluded segment
Thrombus or plaque completely filling lumen of ICA on gray-scale, color Doppler, or power Doppler images
Dampened high-resistance waveform in ipsilateral CCA or proximal ICA
Possibly significantly higher velocities in contralateral CCA than in ipsilateral CCA

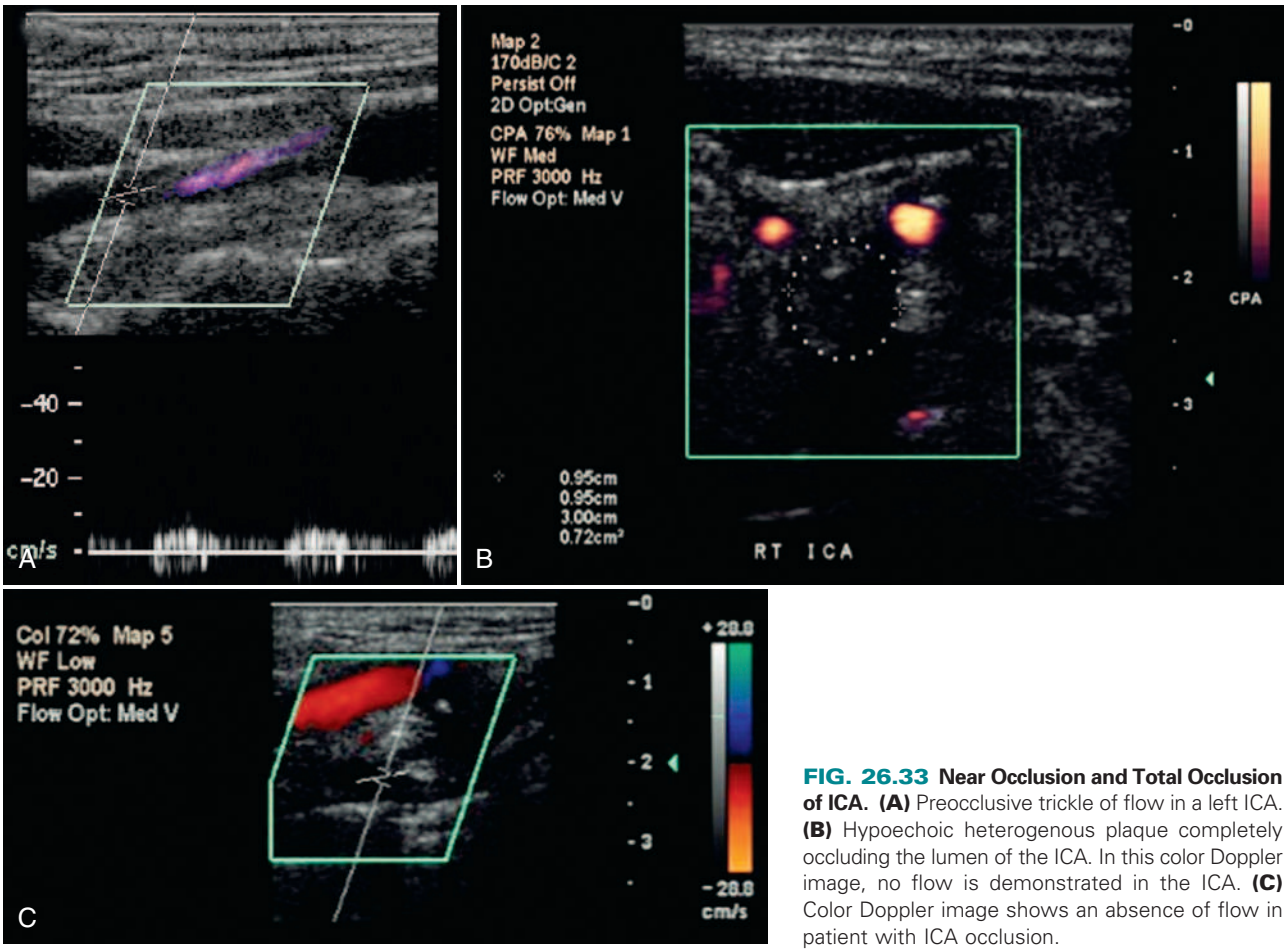

FIG. 26.33 Near Occlusion and Total Occlusion of ICA. (A) Preocclusive trickle of flow in a left ICA. **(B)** Hypoechoic heterogenous plaque completely occluding the lumen of the ICA. In this color Doppler image, no flow is demonstrated in the ICA. **(C)** Color Doppler image shows an absence of flow in patient with ICA occlusion.

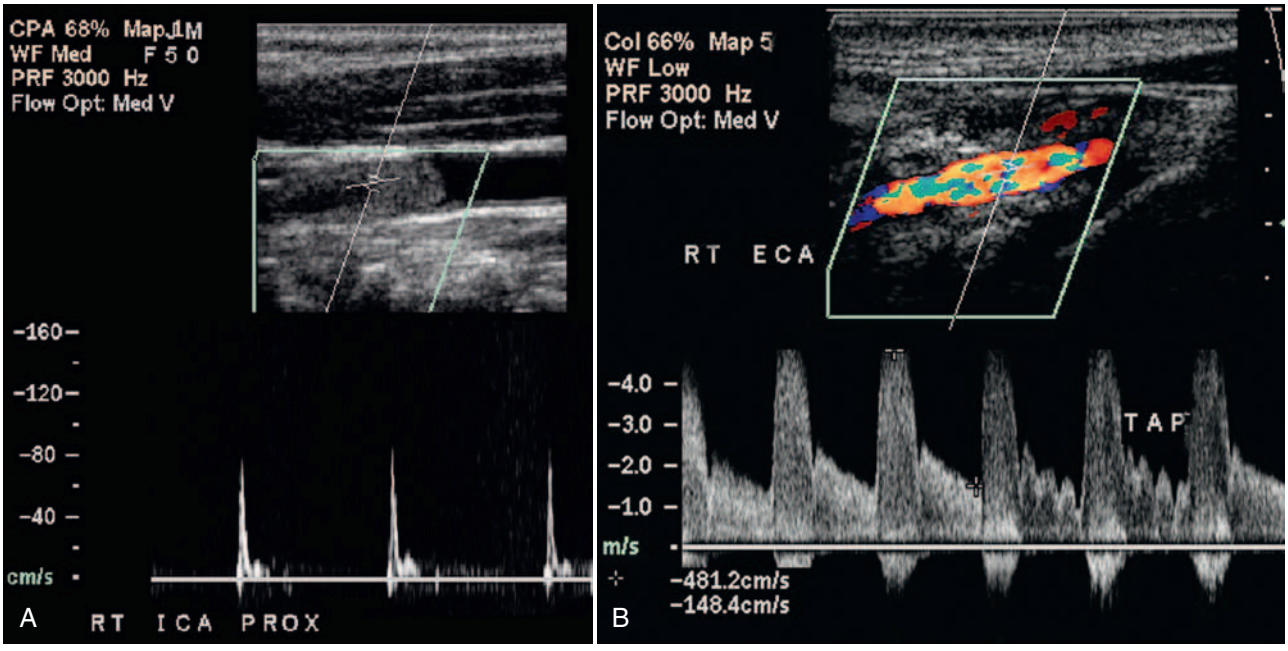

FIG. 26.34 ICA Occlusion. (A) Complete right ICA occlusion shows a spiked waveform consistent with an occlusion. **(B)** Proximal right ECA tracing shows a low-resistance waveform consistent with collaterals to intracranial circulation, as well as increased velocity caused by a stenosis. *TAP,* Temporal artery tap.

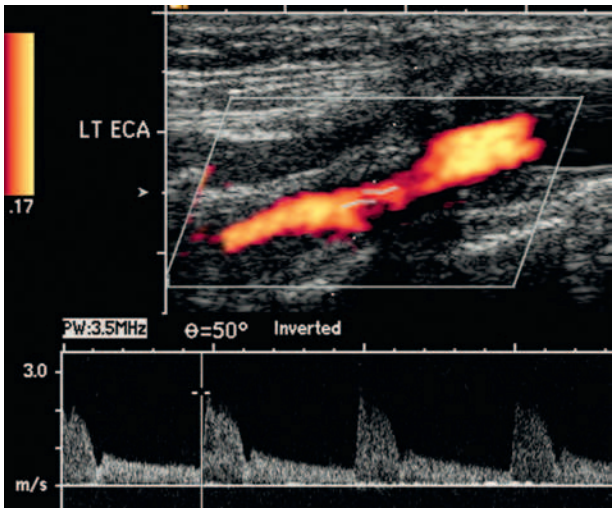

FIG. 26.35 Internalization of ECA Waveform in Association With ICA Occlusion. Long-standing ICA occlusion results in low-resistance waveform in the ECA.

Another pitfall in the diagnosis of a totally occluded ICA is **mistaking a patent ECA** (or one of its branches) **for the ICA.** The situation is especially confusing when the ECA/ICA collaterals open in response to long-standing ICA disease, and the ECA acquires a low-resistance waveform (internalization) (Fig. 26.35). One technique that can aid in identifying the ECA is scanning at the origin of the vessel while simultaneously tapping the temporal artery. Percussion of the superficial temporal artery often results in a serrated distortion of the Doppler waveform in the ECA (80% of ECAs percussed in one study[162]) (see Fig. 26.4B). However, this maneuver should be interpreted with caution because the temporal tap can also be seen in the CCA and ICA, although less frequently (54% and 33%, respectively) than in the ECA.[163] Branching vessels are a unique feature of the ECA, which can also be used to differentiate this vessel from the ICA. Color Doppler sonography can facilitate the identification of such branching vessels (see Fig. 26.4A). Usually, the combination of vessel size, position, waveform shape, presence of branches, and the temporal tap response can correctly identify the ECA.

Although distal propagation of the thrombus almost invariably occurs after an ICA occlusion, CCA occlusions are often localized. Flow may be maintained in the ECA and ICA but must be reversed in one of the two vessels. Sonography is the preferred method for evaluating the maintenance of flow around the carotid bifurcation after proximal CCA occlusion. Most often, retrograde flow in the ECA will supply antegrade flow in the ipsilateral ICA. Occasionally, the opposite flow pattern will be encountered[102,164,165] (Fig. 26.36).

Follow-Up of Stenosis

Although there is a considerable amount of published literature regarding cutoff criteria for determining the degree of stenosis as well as recommendations for interventions, little has been written regarding the appropriate follow-up for stenosis not requiring intervention. There is no accepted national or international consensus regarding surveillance intervals for monitoring stenosis less than 60%.[58] As a result of this lack of national and international consensus, we at Ochsner Clinic Foundation, following discussions with the Cardiology and Vascular Surgery Departments, have come up with our own internal consensus for the follow-up of patients with different degrees of stenosis, differences regarding symptomatology, and different types of plaque (Table 26.3). Patients with heterogeneous plaque and those who are symptomatic are recommended to have shorter interval follow-up studies to watch for more rapid progression compared to others with the same degree of stenosis.

Preoperative Strategies for Patients With Carotid Artery Disease

The preoperative workup of carotid disease is evolving in response to NASCET, ECST, and ACAS results.[7,8,166] The issue of numbers to be used for a carotid ultrasound examination depends on the intent of the examination. Why are we doing the study? How will we use the results? If the examination is a screening test, are we evaluating all patients or only symptomatic patients? If we intend to select patients for surgery on the basis of the ultrasound alone, then a different set of variables is likely to produce the desired outcome. The purpose of a carotid examination and the patient population being screened will impact the selection of velocity thresholds. For example, screening of high-risk, asymptomatic patients might best be performed with high-velocity thresholds with increased specificity, whereas symptomatic patients more likely to undergo surgery for optimal treatment would dictate lower thresholds with increased sensitivity.

Although many still consider angiography as the standard, its critics cite significant intraobserver variability and frequent underestimation of the degree of stenosis.[167,168] Comparisons of angiographic and sonographic estimations of carotid stenosis reveal a closer surgical correlation with the ultrasound measurements.[1] Carotid ultrasound has proved highly accurate in detecting high-grade stenoses, as well as differentiating critical stenoses from occlusion.

MRA is currently demonstrating comparable accuracy as ultrasound and angiography for the detection and quantification of carotid stenosis. During the past 15 years, magnetic resonance imaging (MRI) has also been shown to be useful in the characterization and risk stratification of carotid disease. MRI can accurately identify intraplaque hemorrhage, lipid-rich necrotic core, and thinning and rupture of the fibrous cap, which are associated with increased risk of future stroke and TIA.[169-172] MRA can also evaluate intracranial circulation; however, cost, time, and availability limit MRA as a first-line choice of evaluation of carotid disease.[173] MRA may be helpful in situations where calcified plaque obscures the underlying carotid lumen from insonation. CTA is a fast, widespread modality that can accurately detect ulceration and calcification but cannot differentiate intraplaque hemorrhage and lipid-rich necrotic core.[173] The overall concordance rate between Doppler ultrasound, contrast-enhanced MRA, and CTA is very similar for evaluating carotid stenosis.[174,175]

Many investigators now suggest replacing preoperative angiography with a combination of carotid sonography and MRA. They advocate utilizing angiography only in cases where MRA

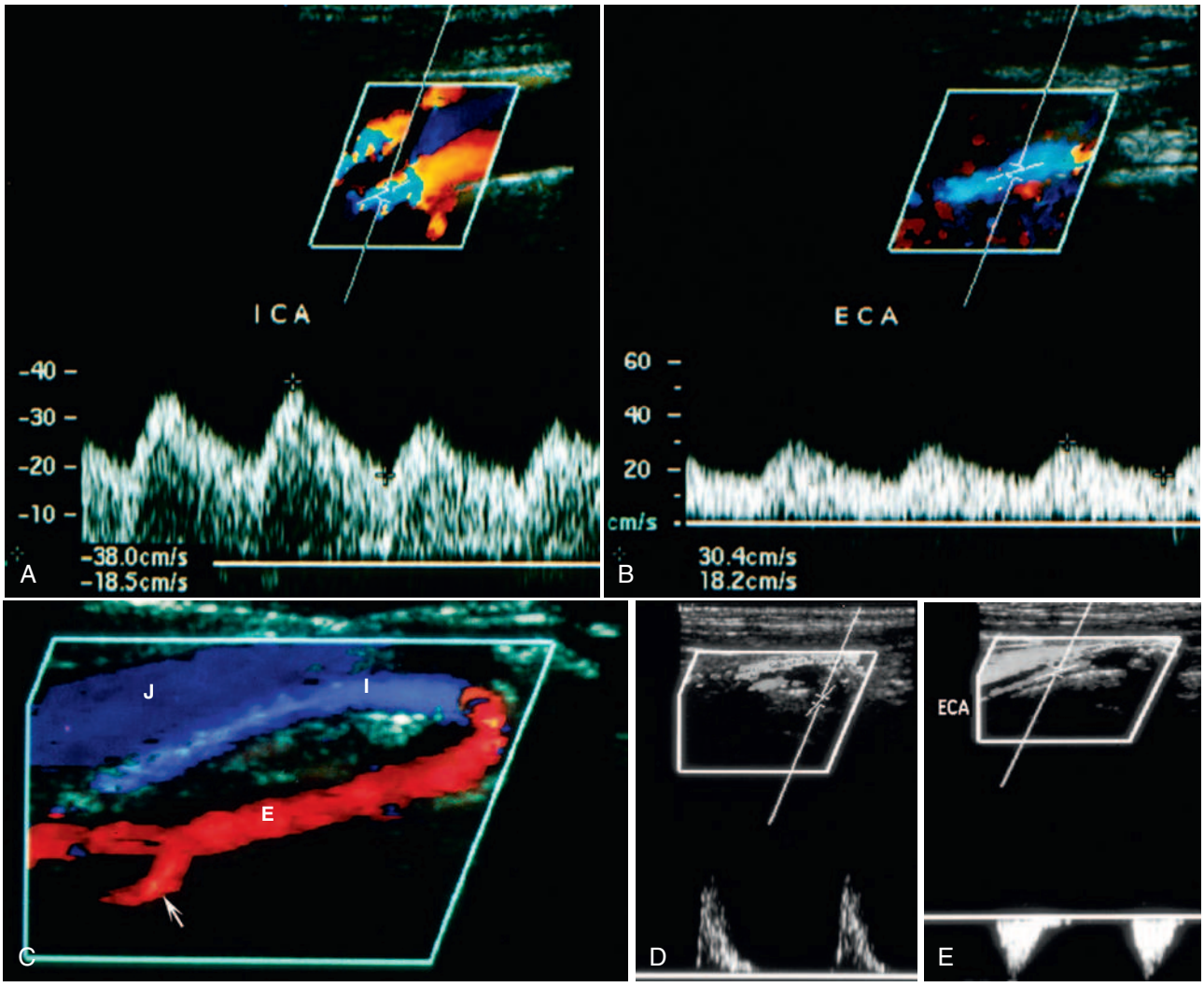

FIG. 26.36 CCA Occlusion Causes Abnormal ICA Waveform. (A) Antegrade tardus-parvus waveform is seen in an ICA distal to a CCA occlusion. **(B)** Retrograde ECA flow with a tardus-parvus waveform caused by collateral flow from the contralateral ECA to supply the ipsilateral ICA distal to a CCA occlusion. **(C)** Color Doppler image shows antegrade ECA flow *(E)* with an ECA branch *(arrow)* and retrograde ICA flow *(I)*. *J,* Internal jugular vein. **(D)** Spectral Doppler image shows high-resistance retrograde right ICA flow. **(E)** High-resistance antegrade flow in the right ECA distal to a CCA occlusion.

and carotid ultrasound have discordant results or they are inadequate.[176-180] Other studies support the use of carotid ultrasound alone before endarterectomy.[177,178,181-185] Numerous studies show that more than 90% of surgical candidates can be adequately screened using clinical assessment and ultrasound alone. However, in suspected aortic arch proximal vessel disease or in cases of suspected complete occlusion, some practitioners still advocate preoperative angiography.

Postoperative Ultrasound

The carotid artery after endarterectomy **(post-CEA)** demonstrates many characteristic features[186,187] (Fig. 26.37). A discrete wedge between the normal I-M complex and the endarterectomized surface is frequently seen, as are periodically spaced echogenic sutures. The absent I-M complex has also been shown to regrow. One study showed that 6% of CEA patients had carotid flaps, residual moderate to moderately severe stenoses, or occluded ECAs.[188] Two of these patients with postoperative abnormalities on ultrasound sustained perioperative stroke. Patients without defects on the postoperative ultrasound had no perioperative sequelae or need for a repeat of procedures. Patients with preoperative stenoses greater than 75% have a greater risk for residual stenoses. Ultrasound appears useful in the symptomatic postoperative population, but its role in the asymptomatic patient population is debatable.[189] Routine follow-up with ultrasound every 6 months after CEA for 2 years and then annually or possibly just once 12 months after CEA has been recommended; however, more research needs to be done.[190,191]

Carotid Artery Stents and Revascularization

Percutaneous transluminal **carotid artery stenting** (CAS) in association with carotid angioplasty is becoming an increasing popular and common means of carotid revascularization. Between 1998 and 2004, the incidence of CEA decreased 17%, whereas

TABLE 26.3 Recommendations for Follow-Up Based on Ultrasound Assessment

	ASYMPTOMATIC		SYMPTOMATIC	
	Heterogeneous Plaque	**Homogeneous Plaque**	**Heterogeneous Plaque**	**Homogeneous Plaque**
1%-39%[b] (1%-50%)[c]	3 months ×2 Then 6 months Then yearly Medical prescription (Rx)[a]	2-5 years depending on degree of plaque and other risk factors	3 months ×2 Then 6 months Then yearly Medical therapy[a]	1-3 years depending on degree of plaque and other risk factors Refer for evaluation for other sources such as cardioembolic disease or neurovascular sources of symptoms
40%-59%[b]	3 months ×2 Then every 6 months until converted to homogeneous or degree of stenosis increases Medical Rx[a]	Yearly Medical Rx[a]	3 months ×2 Then every 6 months until converted to homogeneous or degree of stenosis increases Medical Rx[a]	6 months ×2 Then yearly Medical Rx[a]
60%-79%[b] (50%-70%)[c]	Refer to vascular specialist[d] Medical Rx[a] (Alternatively, if no intervention, follow-up every 3 months to assess stability)	6-month follow-up ×2 for stability, then annually Medical Rx[a]	Refer to vascular specialist[d] Medical Rx[a] (Alternatively, if no intervention, follow-up every 3 months to assess stability)	Refer to vascular specialist[d] Medical Rx[a]
80%-99%[b] (>70%)[c]	Refer to vascular specialist[b] Medical Rx[a]			

[a]Medical Rx includes antiplatelet Rx, statin Rx, smoking cessation, and good blood pressure control.
[b]Bluth et al. criteria.[45]
[c]SRU criteria.[122]
[d]Vascular specialist could be a vascular surgeon, interventional cardiologist, or interventional neuroradiologist or neurosurgeon, depending on the skill set of providers in any given area. Treatment recommended by these specialists could be endovascular stent, endarterectomy, or intensive medical Rx.

incidence of CAS increased 149%.[192] While CAS has emerged as a less-invasive treatment than CEA, several randomized clinical trials and the Society of Vascular Surgery have shown CAS to be associated with lower perioperative morbidity, particularly myocardial infarction, but with an increased incidence of stroke.[193-195] Careful patient selection is critical if the potential benefits of carotid revascularization are to be realized.[193,194] Ultrasound may be helpful in (1) assessing the presence and severity of stenosis; (2) characterizing the carotid bifurcation; and (3) assessing anatomic variants, vessel tortuosity, and plaque calcification before stent placement (Fig. 26.38).

The role of ultrasound in determining patient selection also remains controversial. Certainly, the accuracy of duplex ultrasound in grading flow-limiting stenosis is well established, with a sensitivity of 94% and a specificity of 92%, and is universally accepted as an important criterion in patient selection.[193,194,196] However, although the role of plaque characterization in patient selection remains controversial, it is becoming more important as **vulnerable plaque,** as a cause of stroke, becomes more appreciated. Vulnerable plaque appears to correlate with heterogeneous or echolucent type 1 or 2 plaque. This type of plaque is associated with intraplaque hemorrhage and is thought to have strong embolic potential. Using **intravascular ultrasound,** Diethrich et al.[197] showed a strong correlation between intravascular ultrasound plaque characterization and histologic examination of the plaque after endarterectomy. Considering the accuracy of ultrasound characterization, when intraplaque hemorrhage or vulnerable plaque is identified, CEA rather than CAS might be the preferred method of revascularization to reduce the risk of embolic complications. However, Reiter et al.[85] were unable to use plaque echolucency as a criterion for those at increased risk for post-CAS neurologic events and therefore did not recommend this type of risk stratification. The use of plaque characterization to determine the type of therapeutic intervention needs further assessment.

Grading Carotid Intrastent Restenosis

Sonography allows accurate evaluation of stent placement within the carotid vessels.[198] Carotid **stents** are readily visualized with ultrasound, allowing sonographers to assess disease before, along,

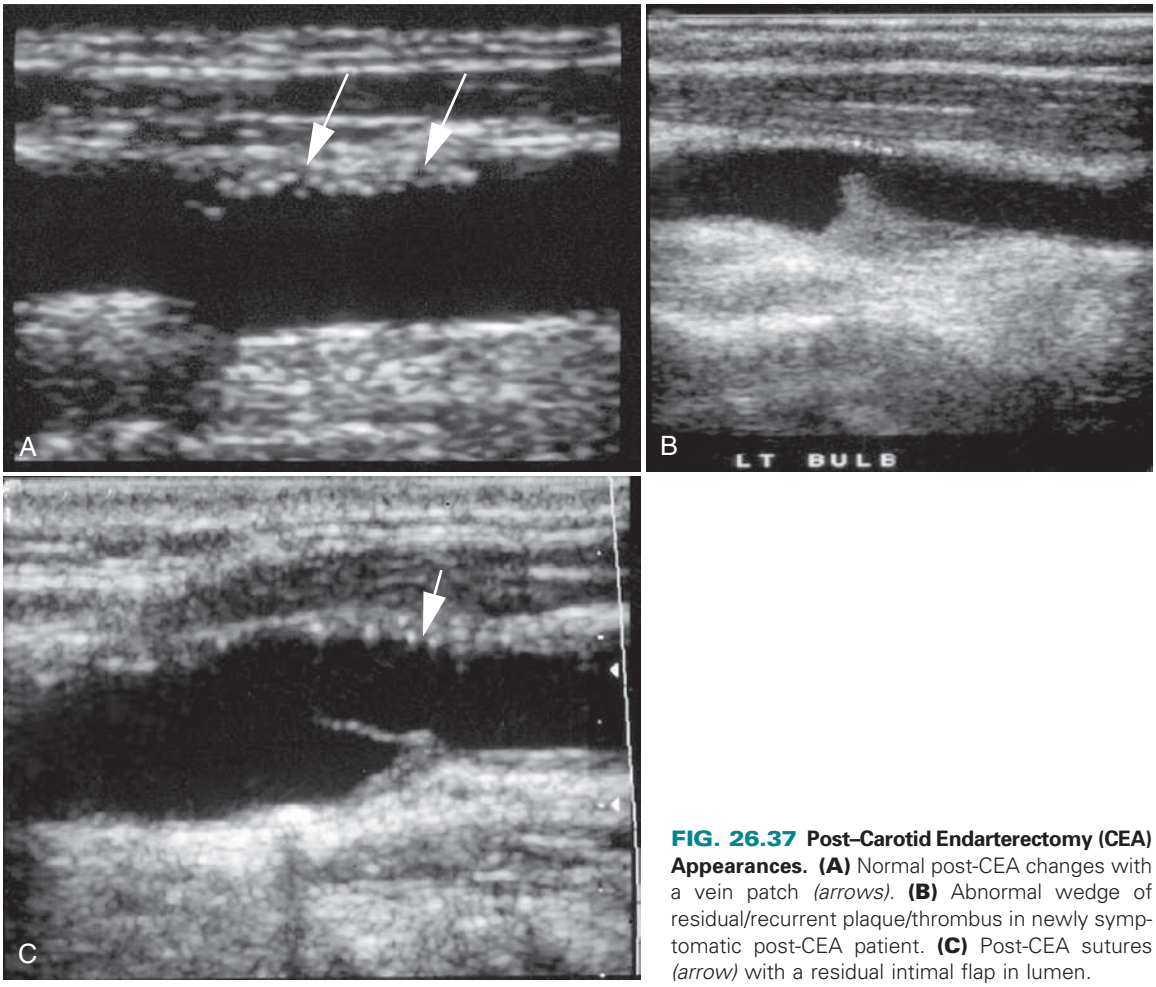

FIG. 26.37 Post–Carotid Endarterectomy (CEA) Appearances. (A) Normal post-CEA changes with a vein patch *(arrows)*. **(B)** Abnormal wedge of residual/recurrent plaque/thrombus in newly symptomatic post-CEA patient. **(C)** Post-CEA sutures *(arrow)* with a residual intimal flap in lumen.

and distal to the stent. The rate of post-CAS restenosis has been reported as between 1.9% and 16%.[198-203] Velocity criteria for grading stenoses in a stent may not be the same as for those in the native carotid artery.[204,205] Some investigators have shown that velocities along the stent are routinely higher than those in a nonstented vessel. Velocity elevations in the range of 125 to 140 cm/sec are fairly common in widely patent stents. In addition, sonographers normally see an increase in velocity in the distal ICA beyond the deployed stent. At present, slight increases in velocity in a stent that appears widely patent on power or color Doppler are unlikely to indicate significant narrowing or warrant further assessment or intervention.

Fleming et al.[198] and Chahwan et al.[206] showed that normal Doppler ultrasound reliably identifies arteriographically normal carotid arteries after CAS. They also reported that post-CAS carotid velocities did not always correlate with the prestent flow-limiting stenosis assessments and that the velocities are disproportionately elevated in mild and moderately restenotic vessels. The disproportionate velocity elevations along the stent may be caused by several factors, including changes in vessel wall compliance and shunting of blood flow away from the ECA. Also, the technique used in many stent trials, which require strict adherence to the 60-degree angle theta technique for Doppler interrogation, may result in systematic velocity increases. As such, it was realized that new tables must be established and validated for the follow-up of patients after CAS. Multiple proposals for grading post-CAS parameters have been suggested[207-211] (Table 26.4).

NONATHEROSCLEROTIC CAROTID DISEASE

Nonatherosclerotic carotid disease is much less common than plaque disease. **Fibromuscular dysplasia,** a noninflammatory process with hypertrophy of muscular and fibrous arterial walls separated by abnormal zones of fragmentation, involves the middle and distal ICA more frequently than other carotid segments. A characteristic "string of beads" appearance has been described on angiography. Only a few reports describe sonographic features of fibromuscular dysplasia.[212-214] Many patients with fibromuscular dysplasia demonstrate nonspecific or no obvious abnormalities on ultrasound; however, some patients may demonstrate redundancy of the mid to distal ICA causing an S-shaped curve.[215] Fibromuscular dysplasia may be asymptomatic or can result in

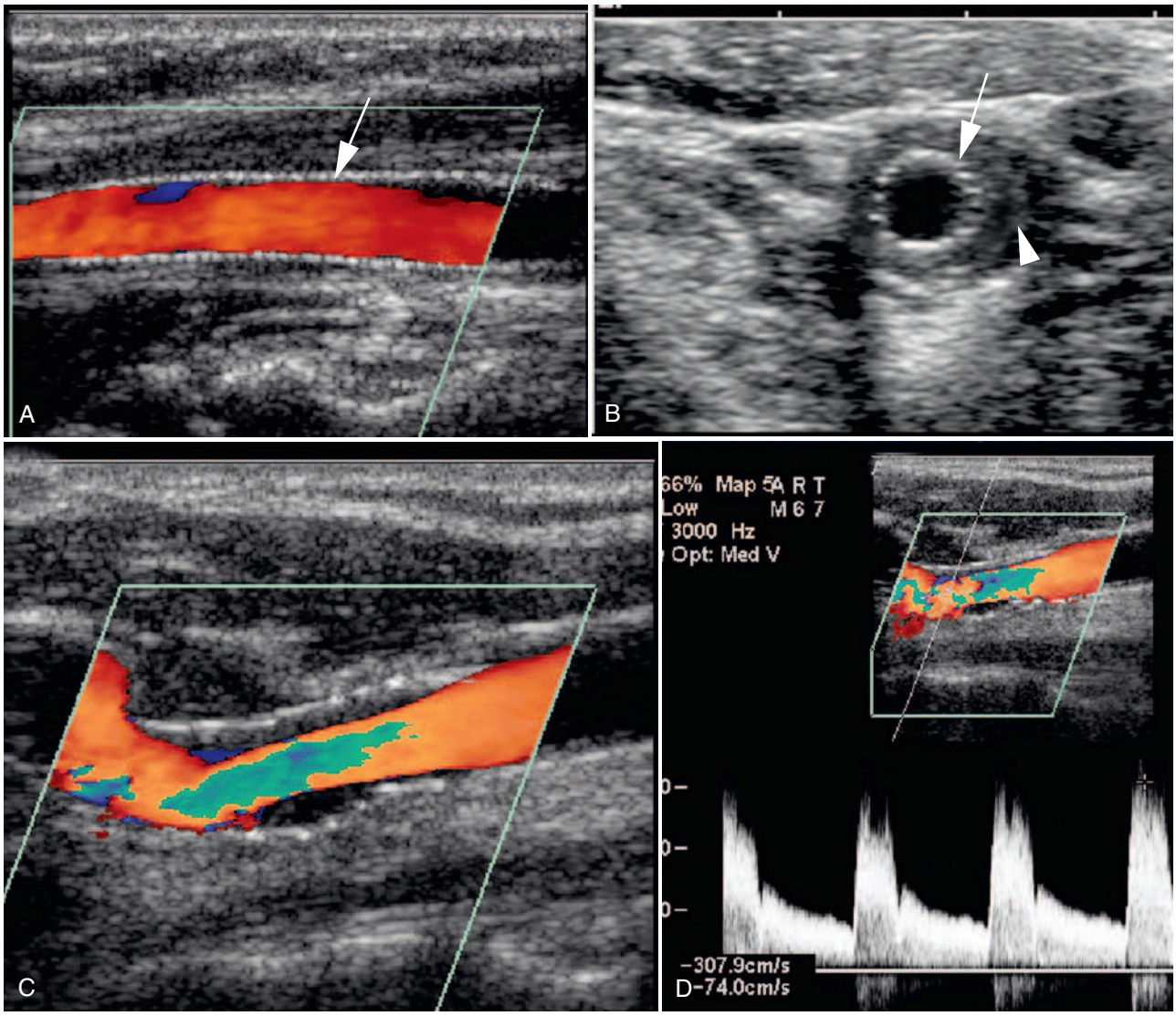

FIG. 26.38 Carotid Stent. (A) Normal right carotid stent *(arrow)* shows complete filling on color Doppler examination. **(B)** Transverse image of carotid stent *(arrow)* in the carotid bulb shows residual plaque *(arrowhead)* in the lumen. **(C)** and **(D)** Left carotid stent shows visible narrowing on color Doppler **(C)** and elevated velocities **(D)** consistent with a greater than 70% stenosis using standard carotid velocity criteria.

TABLE 26.4 Carotid Artery Stenosis Grading After Stent

Study	Degree of Stenosis	PSV (cm/sec)	EDV (cm/sec)	ICA/CCA PSV Ratio
Setacci et al.[207]	<30%	≤104		
	30%-50%	105-174		
	50%-70%	175-299		
	≥70%	≥300	≥140	≥3.8
Zhou et al.[208]	>70%	>300	>90	>4
Lal et al.[209]	≥20%	≥150	>2.15	
	≥50%	≥220	≥2.7	
	≥80%	>340	≥4.15	
Armstrong et al.[210]	>50%	>150	>2	
	>75%	>300	>125	>4
Chi et al.[211]	≥50%	240	2.45	
	≥70%	450	4.3	

CCA, Common carotid artery; *EDV,* end diastolic velocity; *ICA,* internal carotid artery; *PSV,* peak systolic velocity.
Modified from Chahwan S, Miller MT, Pigott JP, et al. Carotid artery velocity characteristics after carotid artery angioplasty and stenting. J Vasc Surg. 2007;45(3):523-526[206]; Fleming SE, Bluth EI, Milburn J. Role of sonography in the evaluation of carotid artery stents. J Clin Ultrasound. 2005;33(7):321-328.[198]

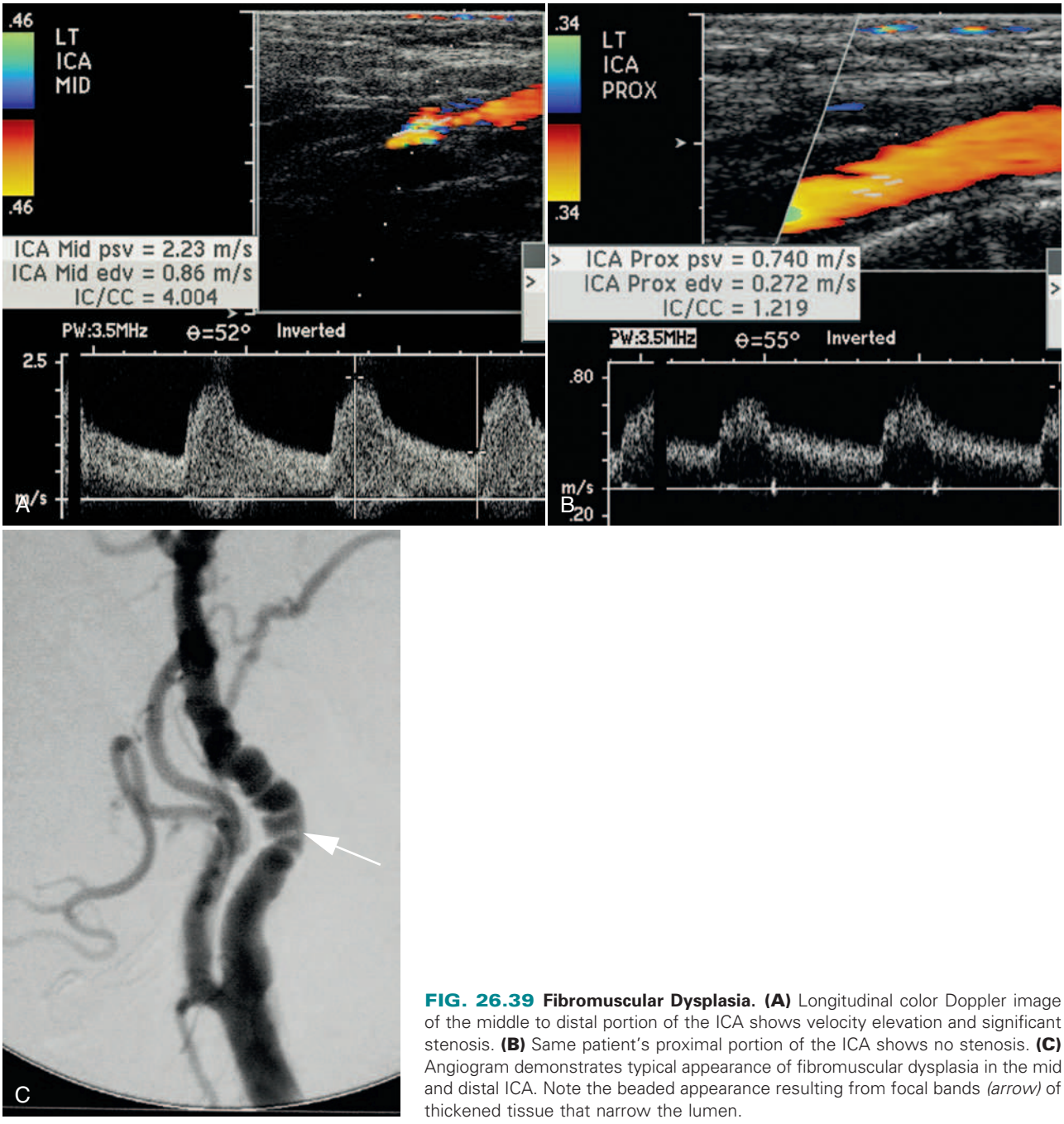

FIG. 26.39 Fibromuscular Dysplasia. (A) Longitudinal color Doppler image of the middle to distal portion of the ICA shows velocity elevation and significant stenosis. **(B)** Same patient's proximal portion of the ICA shows no stenosis. **(C)** Angiogram demonstrates typical appearance of fibromuscular dysplasia in the mid and distal ICA. Note the beaded appearance resulting from focal bands *(arrow)* of thickened tissue that narrow the lumen.

carotid dissection or subsequent thromboembolic events (Fig. 26.39). **Arteritis** resulting from autoimmune processes (e.g., Takayasu arteritis, temporal arteritis) or radiation changes can produce diffuse concentric thickening of carotid walls, which most frequently involves the CCA[23,216,217] (Fig. 26.40).

Cervical trauma can produce carotid dissections or aneurysms. **Carotid artery dissection** results from a tear in the intima, allowing blood to dissect into the wall of the artery, which produces a false lumen. The false lumen may be blind ended or may reenter the true lumen. The false lumen may occlude or narrow the true lumen, producing symptoms similar to carotid plaque disease. Dissections may arise spontaneously or secondary to trauma or to intrinsic disease with elastic tissue degeneration (e.g., **Marfan syndrome**) or may be related to atherosclerotic plaque disease.[20] The ultrasound examination of a carotid dissection may reveal a mobile or fixed **echogenic intimal flap,** with or without thrombus formation.[218] Frequently, there is a striking image/Doppler mismatch with a paucity of gray-scale abnormalities seen in association with marked flow abnormalities (Fig. 26.41).

Color or power Doppler ultrasound can readily clarify the source of this mismatch by demonstrating abrupt tapering of the patent, filled lumen to the point of an ICA occlusion. When the ICA is occluded, the proximal ipsilateral CCA will demonstrate

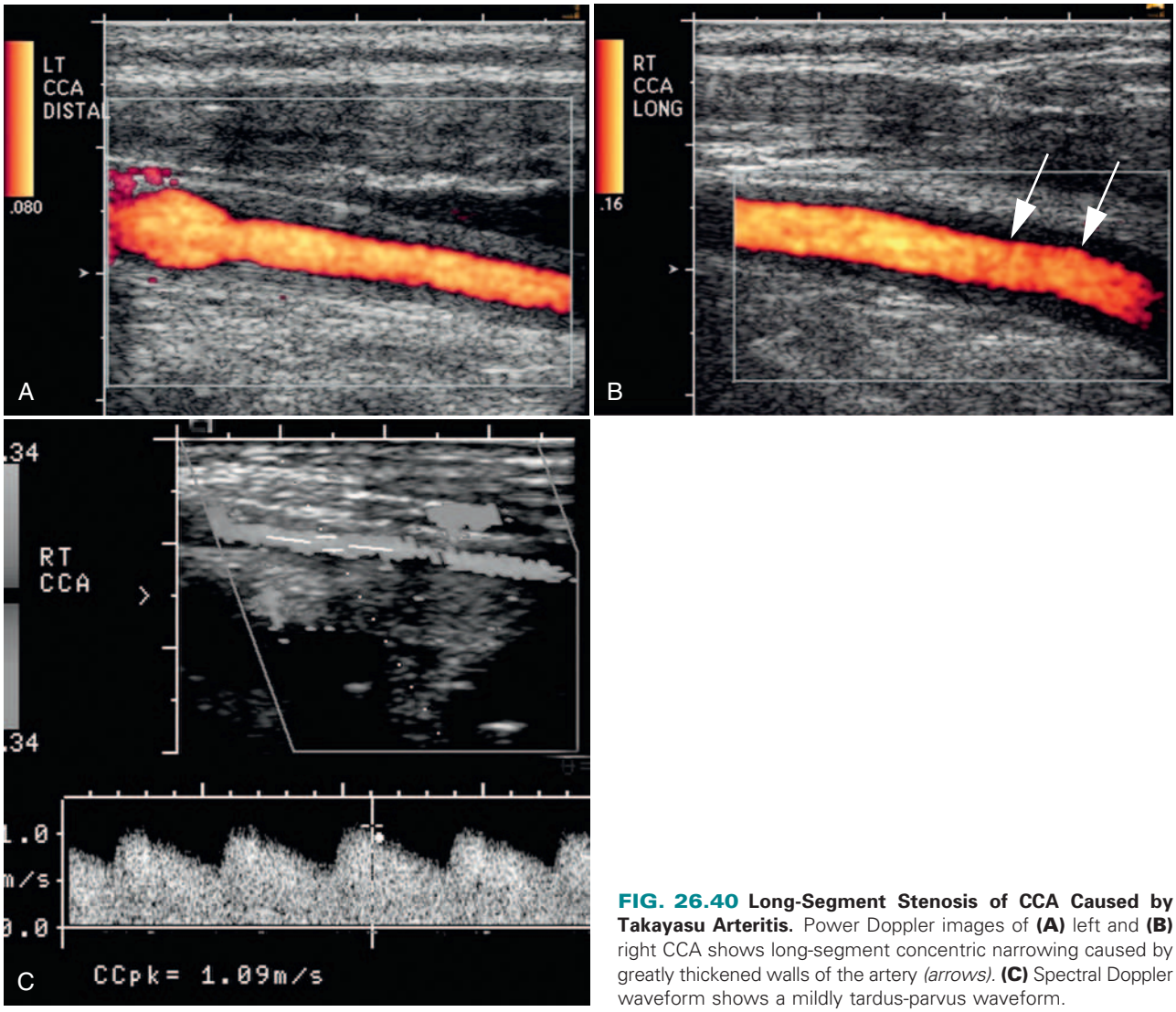

FIG. 26.40 Long-Segment Stenosis of CCA Caused by Takayasu Arteritis. Power Doppler images of **(A)** left and **(B)** right CCA shows long-segment concentric narrowing caused by greatly thickened walls of the artery *(arrows)*. **(C)** Spectral Doppler waveform shows a mildly tardus-parvus waveform.

Internal Carotid Artery Dissection: Spectrum of Findings

INTERNAL CAROTID ARTERY
Absent flow or occlusion
Echogenic intimal flap, with or without thrombus
Hypoechoic thrombus, with or without luminal narrowing
Normal appearance

COMMON CAROTID ARTERY
High-resistance waveform
Dampened flow
Normal appearance

a high-resistance waveform. When the ICA is severely narrowed (secondary to hemorrhage and a thrombus in the area of the false lumen), flow in the ICA may demonstrate high velocities. In these nonoccluded ICA cases, flow velocity waveforms in the CCA may be normal. Although conventional angiography, MRA, or CTA can be used initially to diagnose a dissection, ultrasound can be used to follow patients to assess the therapeutic response to anticoagulation. Repeat sonographic evaluation of patients with ICA dissection after anticoagulation therapy reveals recanalization of the artery in as many as 70% of cases.[219-221] It is important to consider the diagnosis of dissection as a cause of neurologic symptoms, particularly when the clinical presentation, age, and patient history are atypical for that of atherosclerotic disease or hemorrhagic stroke.

Pulsatile Neck Masses in the Carotid Region

The most common **CCA aneurysm** occurs in the region of the carotid bifurcation. These aneurysms may result from atherosclerosis, infection, trauma, surgery, or contagious disease, such as **syphilis.** The normal CCA usually measures no more than 1 cm in diameter. **Carotid body tumors,** one of several **paragangliomas** that involve the head and neck, are usually benign,

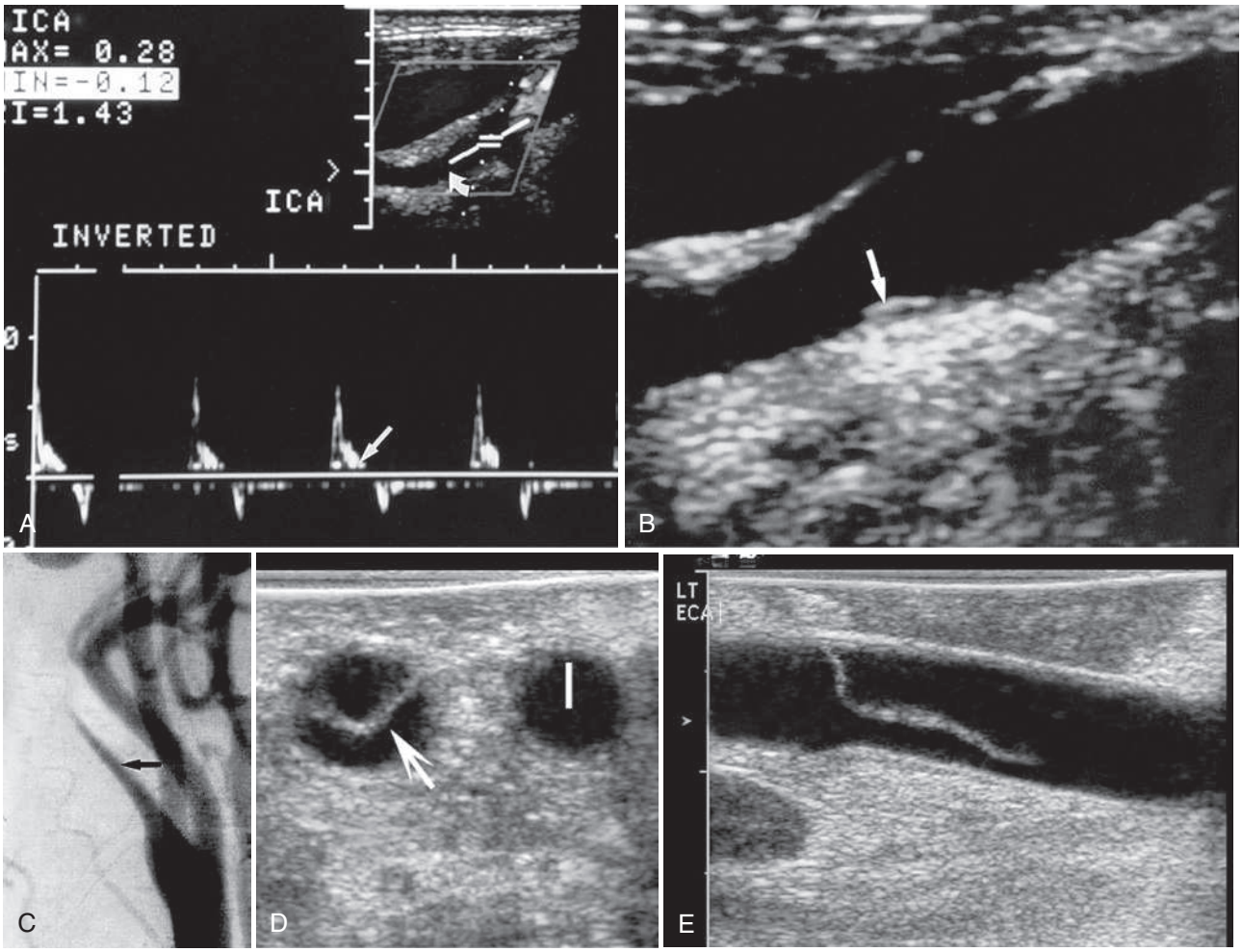

FIG. 26.41 Carotid Artery Dissection. (A) Abnormal high-resistance waveforms *(arrow)* at the origin of the right ICA with no evidence of flow distal to this point *(curved arrow)*. **(B)** Gray-scale evaluation of the vessel in the area of the occlusion demonstrates only a small, linear echogenic structure *(arrow)* without evidence of significant atherosclerotic narrowing. **(C)** Subsequent angiogram demonstrates the characteristic tapering to the point of occlusion *(arrow)* associated with carotid artery dissection and thrombotic occlusion. **(D)** Transverse and **(E)** longitudinal images of another patient show an intimal flap *(arrow)* in an ECA. *I,* Internal carotid artery.

well-encapsulated masses located at the carotid bifurcation.[29] These tumors may be bilateral, particularly in the familial variant, and are very vascular, often producing an audible bruit.[29] Some of these tumors produce catecholamines, leading to sudden changes in blood pressure during or after surgery. Color Doppler ultrasound demonstrates an extremely vascular soft tissue mass at the carotid bifurcation[29] (Fig. 26.42). Color Doppler ultrasound can also be used to monitor embolization or surgical resection of carotid body tumors. A classic nonmass is the **ectatic innominate/proximal CCA,** frequently occurring as a pulsatile supraclavicular mass in older women. The request to rule out a carotid aneurysm almost invariably shows the classic normal features of these tortuous vessels (Fig. 26.43).

Extravascular masses (e.g., lymph node masses [Fig. 26.44], hematomas, abscesses) that compress or displace the carotid arteries can be readily distinguished from primary vascular masses, such as aneurysms or pseudoaneurysms. **Posttraumatic pseudoaneurysms** can usually be distinguished from true carotid aneurysms by the characteristic to-and-fro waveforms in the neck of the pseudoaneurysm, as well as the internal variability (yin-yang) characteristic of a pseudoaneurysm (Fig. 26.45).

TRANSCRANIAL DOPPLER SONOGRAPHY

In transcranial Doppler (TCD) ultrasound, a low-frequency 2-MHz transducer is used to evaluate blood flow within the intracranial carotid and vertebrobasilar system and the circle of Willis. Access is achieved through the orbits, foramen magnum, or, most often, the region of temporal calvarial thinning **(transtemporal window).**[222,223] However, many patients (up to 55% in one series[224]) may not have access to an interpretable TCD examination. Women, particularly African American women, have a thick temporal bone through which it is difficult to insonate the basal cerebral arteries.[224,225] This difficulty limits the feasibility of TCD imaging as a routine part of the noninvasive cerebrovascular workup.[223,224]

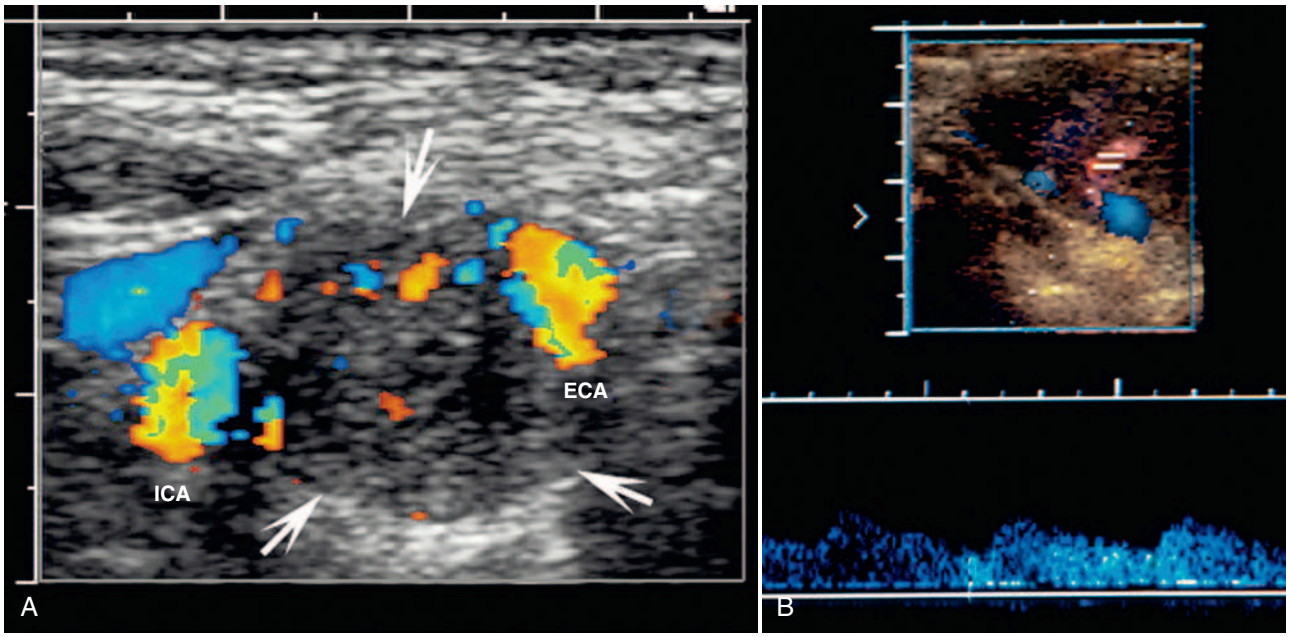

FIG. 26.42 Carotid Body Tumor. (A) Transverse image of the carotid bifurcation shows a mass *(arrows)* splaying the internal carotid artery *(ICA)* and external carotid artery *(ECA)*. **(B)** Pulsed Doppler traces of the carotid body tumor show typical arteriovenous shunt (low-resistance) waveform.

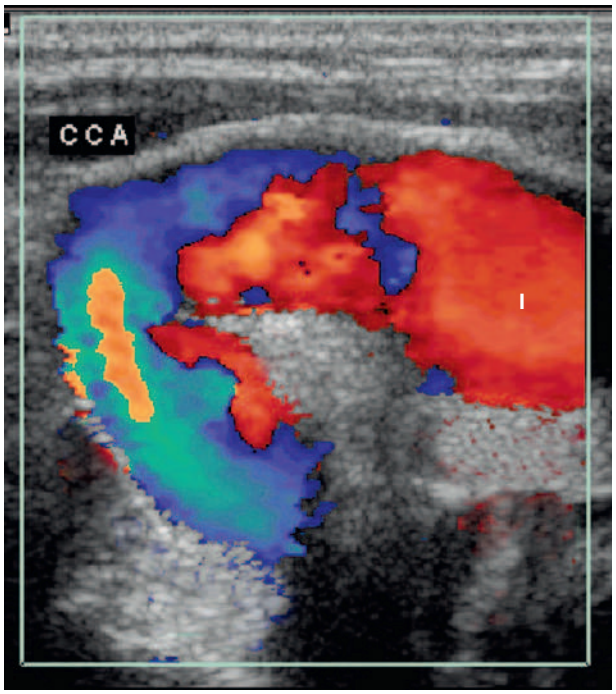

FIG. 26.43 Ectatic CCA. Color Doppler image shows ectatic proximal common carotid artery *(CCA)* arising from the innominate artery *(I)* and responsible for a pulsatile right supraclavicular mass.

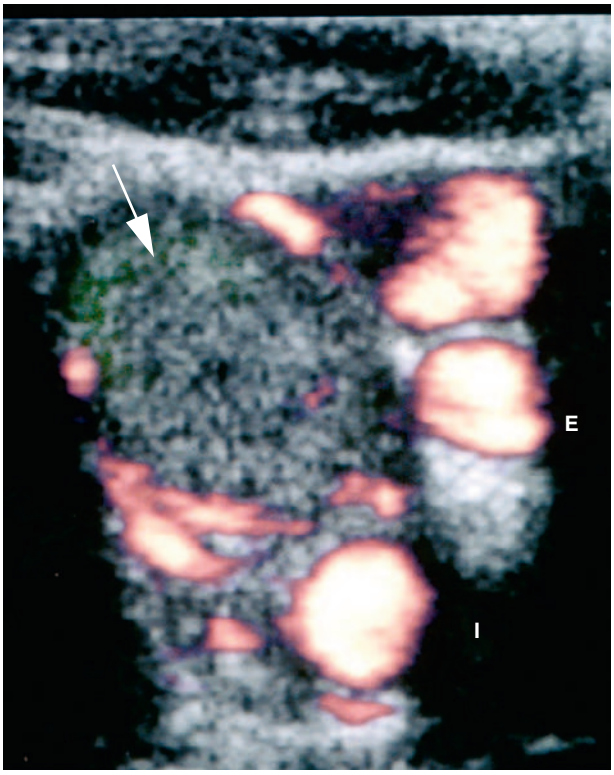

FIG. 26.44 Pathologic Lymph Node Near Carotid Bifurcation. Power Doppler image shows a malignant lymph node *(arrow)* lateral to the carotid bifurcation. *E,* External carotid artery; *I,* internal carotid artery.

By using spectral analysis, various parameters are determined, including mean velocity, PSV, EDV, and the pulsatility and resistive indices of the blood vessels. Color or power Doppler ultrasound can improve velocity determination by providing better angle theta determination and localizing the course of vessels.[222] TCD applications include (1) evaluation of intracranial stenoses and collateral circulation, (2) detection and follow-up of vasoconstriction from subarachnoid hemorrhage, (3) determination of brain death, (4) evaluation of patients with sickle cell disease, and (5) identification of arteriovenous malformation.[219-223,226,227] TCD is most reliable in diagnosing stenoses of the middle cerebral artery, with sensitivities as high as 91% reported. TCD is less reliable for detecting stenoses of the intracranial vertebrobasilar system, anterior and posterior cerebral arteries, and terminal ICA. However, TCD is helpful in assessing vertebral artery patency and flow direction when no flow is detected in the extracranial vertebral artery (Fig. 26.46). Diagnosis of an intracranial stenosis is based on an increase in the mean velocity of blood flow in the affected vessel compared to that of the contralateral vessel at the same location.[223-225]

Advantages of TCD ultrasound also include its availability for monitoring patients in the operating room or angiographic suite for potential cerebrovascular complications.[225] Intraoperative TCD monitoring can be performed with the transducer strapped over the transtemporal window, allowing evaluation of blood flow in the middle cerebral artery during CEA. The adequacy of cerebral perfusion can be assessed while the carotid artery is clamped.[225,228] TCD is also capable of detecting **intraoperative microembolization,** which produces high-amplitude spikes (high-intensity transient signals ["HITS"]) on the Doppler spectrum.[223,224,227,229-231] The technique can be used for the serial evaluation of **vasospasms.** This diagnosis is usually based on serial examinations of the relative increase in blood flow velocity and resistive index changes resulting from a decrease in the lumen of the vessel caused by vasospasms.[225] More description of transcranial Doppler is in Chapter 47.

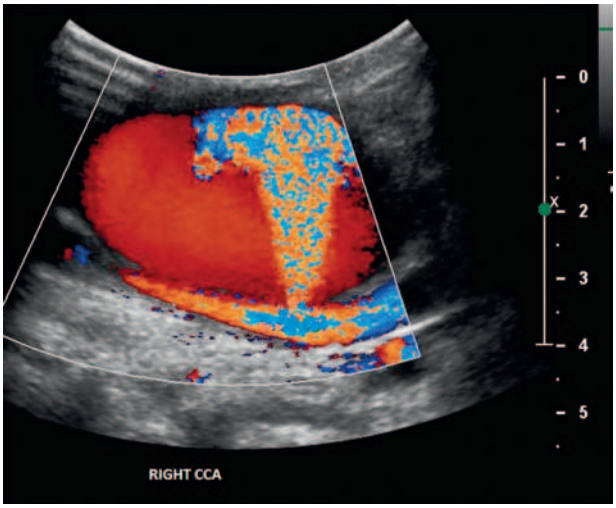

FIG. 26.45 Pseudoaneurysm of the Common Carotid Artery (CCA). Transverse image of the right CCA demonstrates a jet of flow into a pseudoaneurysm, which resulted from an attempted central venous line placement.

VERTEBRAL ARTERY

The vertebral arteries supply the majority of the posterior brain circulation. Through the circle of Willis, the vertebral arteries also provide collateral circulation to other portions of the brain

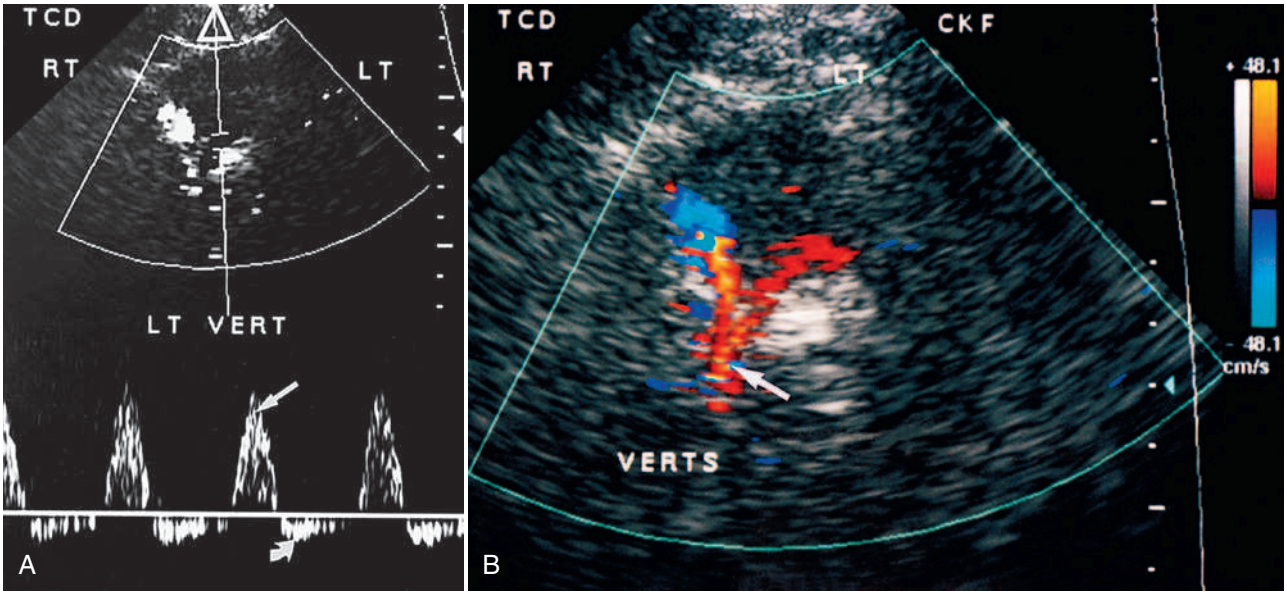

FIG. 26.46 Transcranial Doppler Imaging. (A) Transcranial duplex scan of the posterior fossa in a patient with an incomplete left subclavian steal syndrome demonstrates retrograde systolic flow *(arrow)* and antegrade diastolic flow *(curved arrow).* The scan is obtained in a transverse projection from the region of the foramen magnum *(open arrowhead).* **(B)** Color Doppler image obtained in the same patient demonstrates that there is retrograde flow not only within the left vertebral artery but also within the basilar artery *(arrow).*

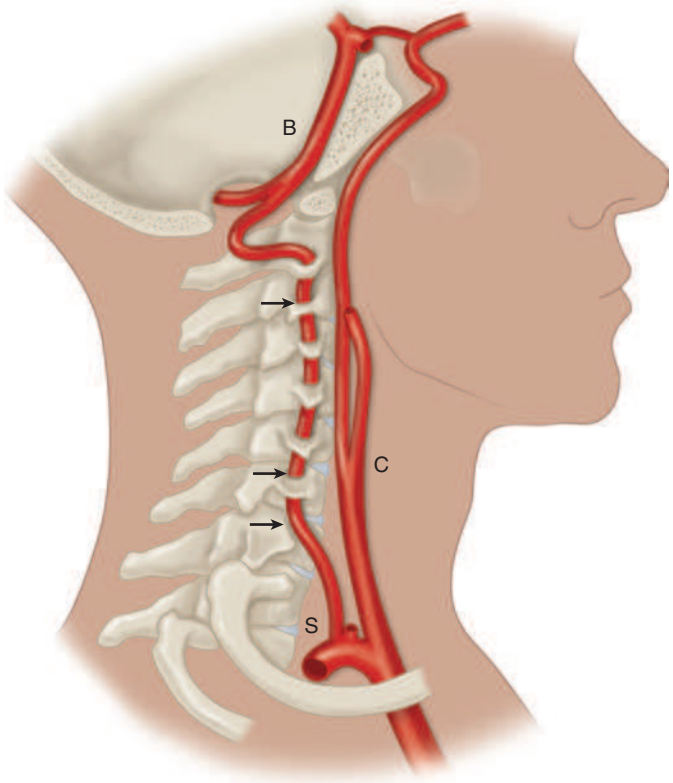

FIG. 26.47 Vertebral Artery Course. Lateral diagram of vertebral artery *(arrows)* shows its course through the cervical spine transverse foramina en route to joining the contralateral vertebral artery to form the basilar artery *(B). C,* Carotid artery; *S,* subclavian artery.

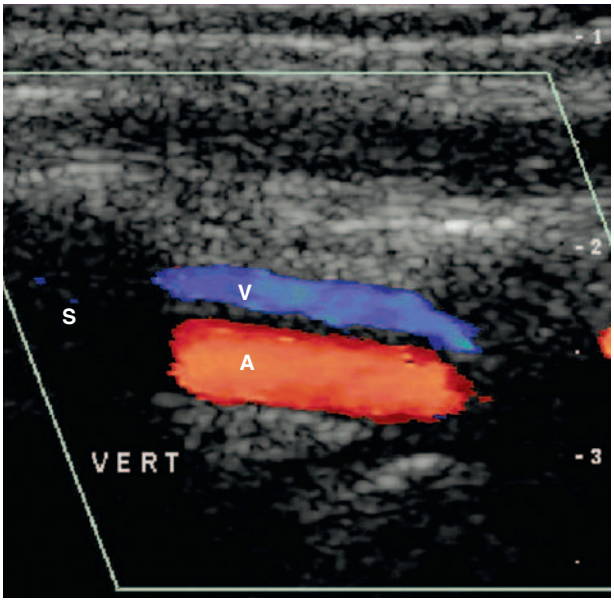

FIG. 26.48 Normal Vertebral Artery and Vein. Longitudinal color Doppler image shows a normal vertebral artery *(A)* and vein *(V)* running between the transverse processes of the second to sixth cervical vertebrae (C2-C6), which are identified by their periodic acoustic shadowing *(S).*

in patients with carotid occlusive disease. Evaluation of the extracranial vertebral artery seems a natural extension of carotid duplex and color Doppler imaging.[232,233] Historically, however, these arteries have not been studied as intensively as the carotids. Symptoms of **vertebrobasilar insufficiency** also tend to be rather vague and poorly defined compared with symptoms referable to the carotid circulation. It is often difficult to make an association confidently between a lesion and symptoms. Furthermore, interest in surgical correction of vertebral lesions has been limited. The anatomic variability, small size, deep course, and limited visualization resulting from overlying transverse processes make the vertebral artery more difficult to examine accurately with ultrasound.[232,234-236] The clinical utility of vertebral artery duplex scanning in diagnosing subclavian steal and presteal phenomena is well established.[237-239] Less clear-cut is the use of vertebral duplex scanning in evaluating vertebral artery stenosis, dissection, or aneurysm.[240]

Anatomy

The vertebral artery is usually the first branch off the subclavian artery (Fig. 26.47). However, variation in the origin of the vertebral arteries is common. In 6% to 8% of people, the left vertebral artery arises directly from the aortic arch proximal to the left subclavian artery.[234,241] In 90%, the proximal vertebral artery ascends superomedially, passing anterior to the transverse process of the seventh cervical vertebra (C7), and enters the transverse foramen at the C6 level. The rest of the vertebral arteries enter into the transverse foramen at the C5 or C7 level and, rarely, at the C4 level. The size of vertebral arteries is variable, with the left larger than the right in 42%, the two vertebral arteries equal in size in 26%, and the right larger than the left in 32% of cases.[242] One vertebral artery may even be congenitally absent. Usually, the vertebral arteries join at their confluence to form the **basilar artery.** Rarely, the vertebral artery may terminate in a posterior inferior cerebellar artery.

Sonographic Technique and Normal Examination

Vertebral artery visualization with Doppler flow analysis can be obtained in 92% to 98% of vessels[232,243] (Fig. 26.48). Vertebral artery duplex examinations are performed by first locating the CCA in the longitudinal plane. The direction of flow in the CCA and jugular vein is determined. A gradual sweep of the transducer laterally demonstrates the vertebral artery and vein running between the transverse processes of C2 to C6, which are identified by their periodic acoustic shadowing. Angling the transducer caudad allows visualization of the vertebral artery origin in 60% to 70% of the arteries, in 80% on the right side, and in 50% on the left. This discrepancy may relate to the left vertebral artery origin being deeper and arising directly from the aortic arch in 6% to 8% of cases.[234,241]

The presence and direction of flow should be established. Visible plaque should be assessed. The vertebral artery usually has a low-resistance flow pattern similar to that of the CCA, with continuous flow in systole and diastole; however, wide variability in waveform shape has been noted in angiographically

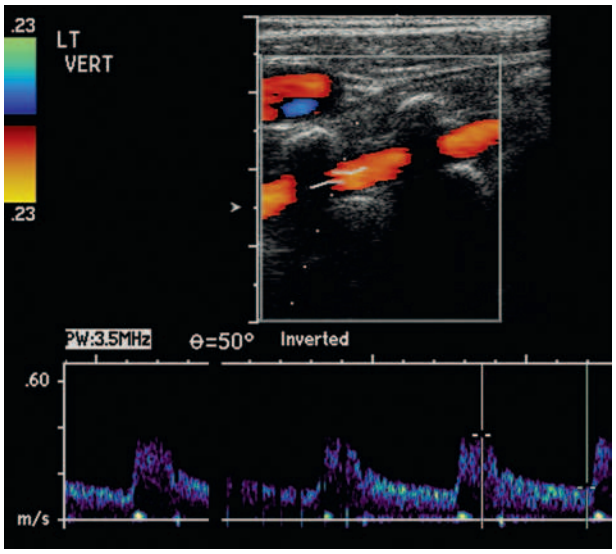

FIG. 26.49 Normal Vertebral Artery Waveform. Normal low-resistance waveform of the vertebral artery with filling of the spectral window.

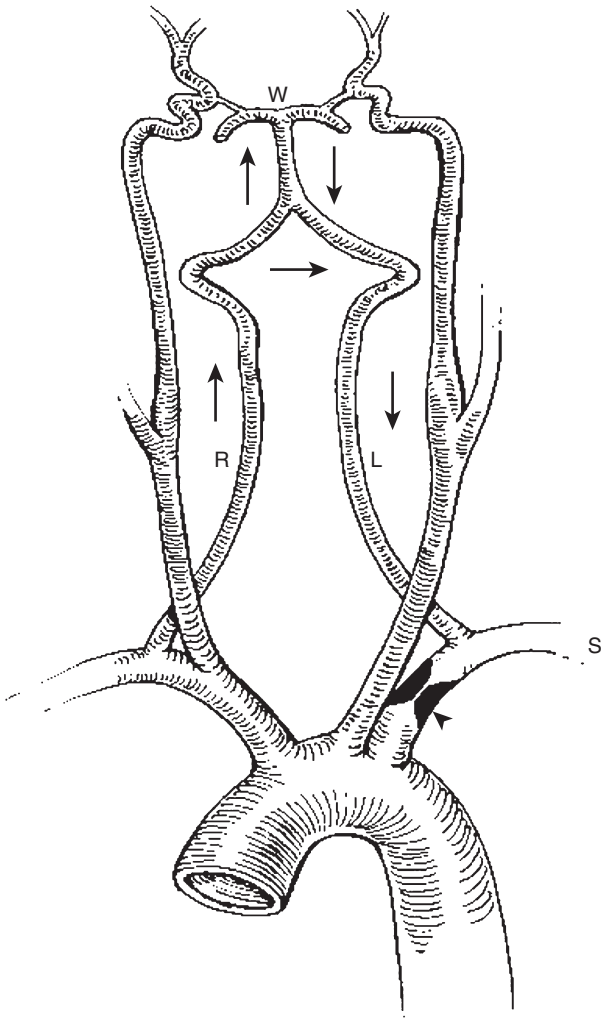

FIG. 26.50 Hemodynamic Pattern in Subclavian Steal Syndrome. Proximal left subclavian artery occlusive lesion *(arrowhead)* decreases flow to the distal subclavian artery *(S)*. This produces retrograde flow *(large arrows)* down the left vertebral artery *(L)* and stealing from the right vertebral artery *(R)* and other intracranial vessels through the circle of Willis *(W)*.

normal vessels.[244] Because the vessel is small, flow tends to demonstrate a broader spectrum. The clear spectral window seen in the normal carotid system is often filled in the vertebral artery[102] (Fig. 26.49).

The **vertebral vein** (often a plexus of veins) runs parallel and adjacent to the vertebral artery. Care must be taken not to mistake its flow for that of the adjacent artery, particularly if the venous flow is pulsatile. Comparison with jugular venous flow during respiration should readily distinguish between vertebral artery and vein. At times, the ascending cervical branch of the thyrocervical trunk can be mistaken for the vertebral artery. This can be avoided by looking for landmark transverse processes that accompany the vertebral artery and by paying careful attention to the waveform of the visualized vessel. The ascending cervical branch has a high-impedance waveform pattern similar to that of the ECA.[237]

TCD sonographic examination of the vertebrobasilar artery system can be performed as an adjunct to the extracranial evaluation. The examination is conducted with a 2-MHz transducer with the patient sitting, using a suboccipital midline nuchal approach, or with the patient supine, using a retromastoidal approach. Color or power Doppler facilitates TCD imaging of the vertebrobasilar system.[245]

Subclavian Steal

The **subclavian steal phenomenon** occurs when there is high-grade stenosis or occlusion of the proximal subclavian or innominate arteries with patent vertebral arteries bilaterally. The artery of the ischemic limb "steals" blood from the vertebrobasilar circulation through retrograde vertebral artery flow, which may result in symptoms of vertebrobasilar insufficiency (Fig. 26.50). Symptoms are usually most pronounced during exercise of the upper extremity but can be produced by changes in head position. However, there is often poor correlation between vertebrobasilar symptoms and the subclavian steal phenomenon. In most cases, flow within the basilar artery is unaffected unless severe stenosis of the vertebral artery supplying the steal exists.[245] Also, surgical or angioplastic restoration of blood flow may not result in relief of symptoms.[246] The subclavian steal phenomenon is most often caused by atherosclerotic disease, although traumatic, embolic, surgical, congenital, and neoplastic factors have also been implicated. Although the proximal subclavian stenosis or occlusion may be difficult to image, particularly on the left, the vertebral artery waveform abnormalities correlate with the severity of the subclavian disease.

Doppler evaluation of the vertebral artery reveals four distinct abnormal waveforms that correlate with subclavian or vertebral

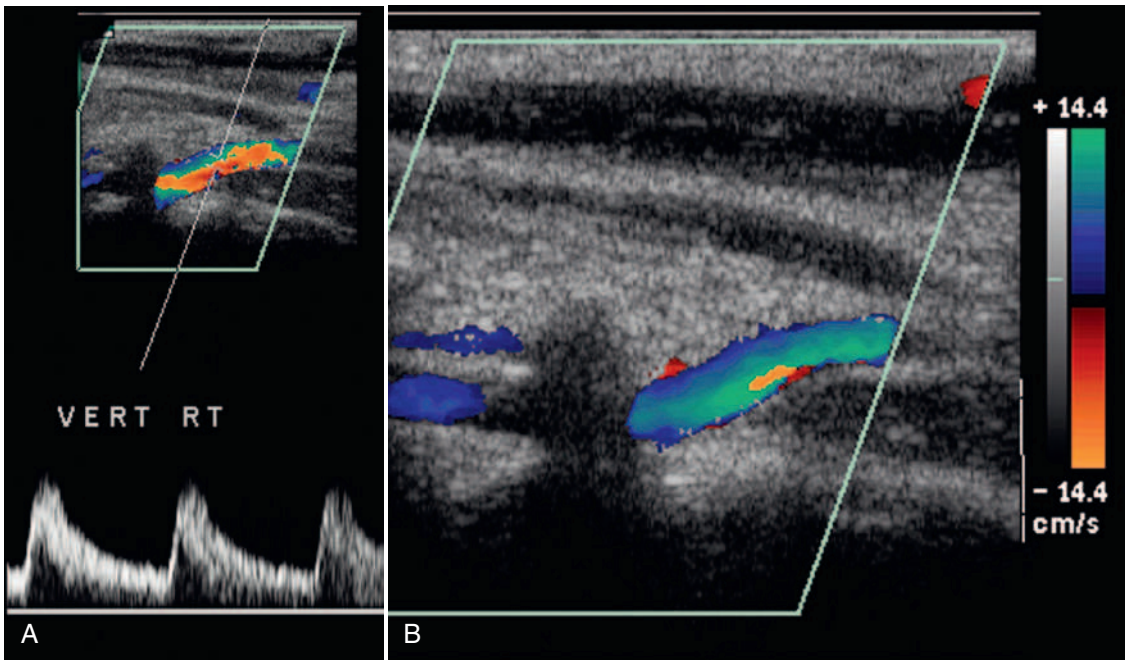

FIG. 26.51 Reversal of Vertebral Artery Flow in Subclavian Steal. Subclavian steal causes reversed flow in vertebral artery. Spectral Doppler **(A)** demonstrates complete vertebral artery flow reversal due to right subclavian artery occlusion. Color-flow Doppler **(B)** demonstrates flow toward the transducer.

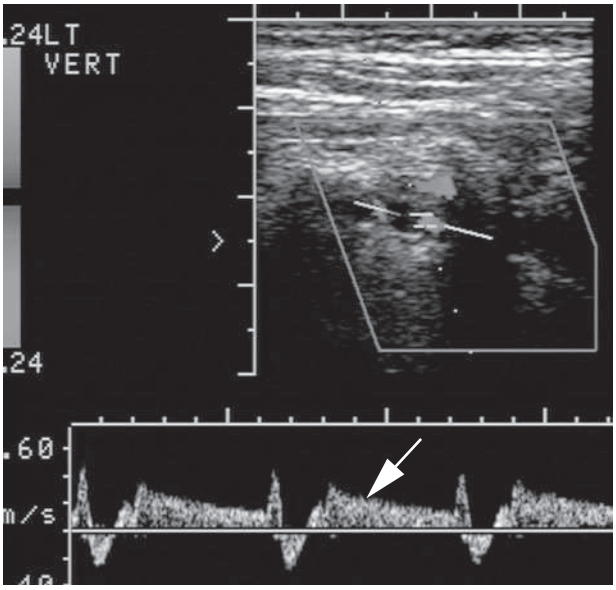

FIG. 26.52 Incomplete Subclavian Steal. Flow in early systole is antegrade, flow in peak systole is retrograde, and flow in late systole and diastole *(arrow)* is again antegrade.

Abnormal Vertebral Artery Waveforms

COMPLETE SUBCLAVIAN STEAL
Reversal of flow within vertebral artery ipsilateral to stenotic or occluded subclavian or innominate artery

INCOMPLETE OR PARTIAL SUBCLAVIAN STEAL
Transient reversal of vertebral artery flow during systole
May be converted into a complete steal using provocative maneuvers
Suggests stenotic, not occlusive, lesion

PRESTEAL PHENOMENON
"Bunny" waveform: systolic deceleration less than diastolic flow
May be converted into partial steal by provocative maneuvers
Seen with proximal subclavian stenosis

TARDUS-PARVUS (DAMPENED) WAVEFORM
Seen with vertebral artery stenosis

artery pathology on angiography. These include the complete subclavian steal, partial or incomplete steal, presteal phenomenon, and tardus-parvus vertebral artery waveforms.[239,244] In a **complete subclavian steal,** flow within the vertebral artery is completely reversed (Fig. 26.51). **Incomplete steal** or **partial steal** demonstrate transient reversal of vertebral flow during systole[239,245] (Fig. 26.52). Incomplete steal suggests high-grade stenosis of the subclavian or innominate artery rather than occlusion. Provocative maneuvers, such as exercising the arm for 5 minutes or 5-minute inflation of a sphygmomanometer on the arm to induce rebound hyperemia on the side of the subclavian or innominate lesion, can enhance the sonographic findings and convert an incomplete steal to a complete steal.[155,185]

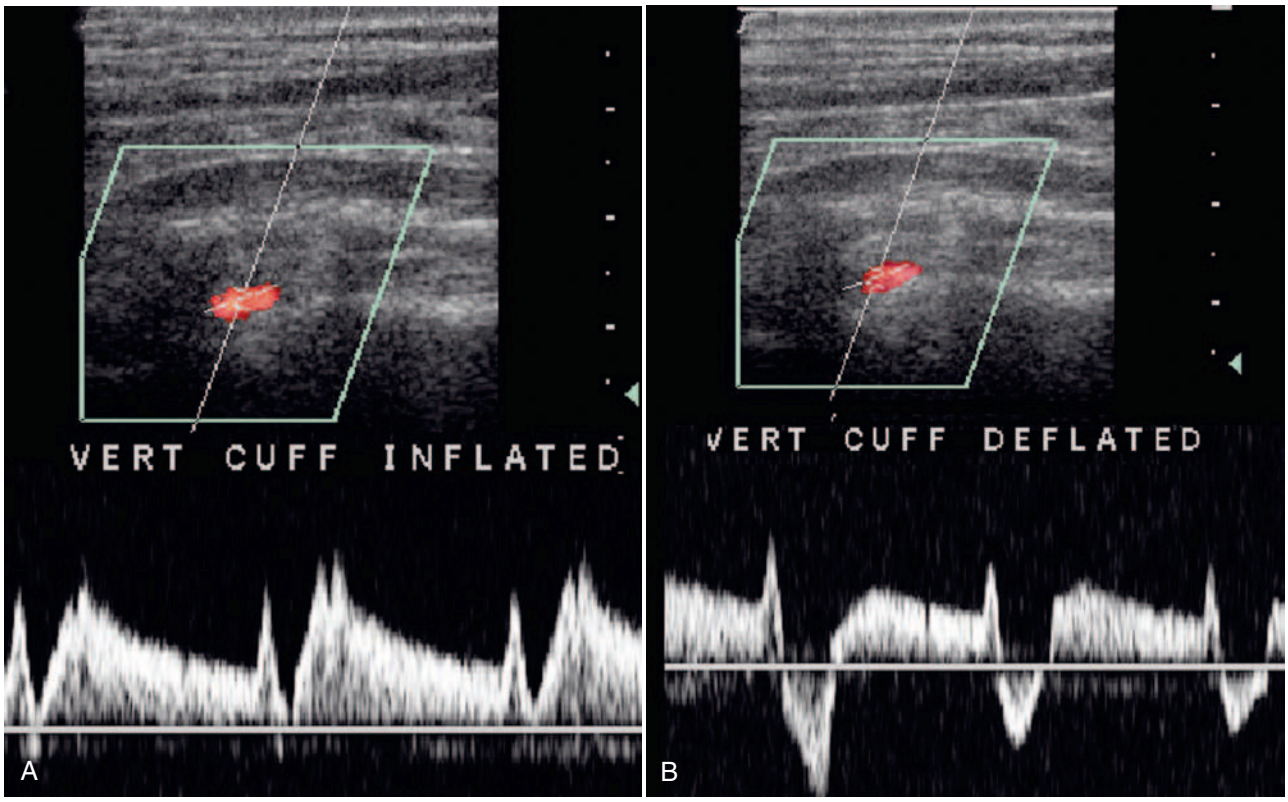

FIG. 26.53 Incomplete Subclavian Steal and Provocative Maneuver. (A) Presteal left vertebral artery waveform. Flow decelerates in peak systole but does not reverse. **(B)** After provocative maneuver, there is reversal of flow in peak systole in response to a decrease in peripheral arterial pressure.

The **presteal** ("bunny") **waveform** shows antegrade flow but with a striking deceleration of velocity in peak systole to a level less than EDV. This is seen in patients with proximal subclavian stenosis, which is usually less severe than in those with partial steal waveform.[239] The bunny waveform can be converted into a partial steal or complete steal waveform by provocative maneuvers (Fig. 26.53). A **tardus-parvus waveform** (also called a dampened waveform) can be seen in patients with high-grade proximal vertebral stenosis.[238,239]

With a subclavian steal, color Doppler may show two similarly color-encoded vessels between the transverse processes, representing the vertebral artery and vein.[129] Transverse images of the vertebral artery with color Doppler show reversed flow compared with those of the CCA. A Doppler spectral waveform must be produced in all such cases to avoid mistaking flow reversal within an artery for flow in a pulsatile vertebral vein.[129,237]

Stenosis and Occlusion

Diagnosis of **vertebral artery stenosis** is more difficult than diagnosis of flow reversal. Most hemodynamically significant stenoses occur at the vertebral artery origin, situated deep in the upper thorax and seen in only 60% to 70% of patients.[234,243,241] Even if the vertebral artery origin is visualized, optimal adjustments of the Doppler angle for accurate velocity measurements may be difficult because of the deep location and vessel tortuosity. No accurate reproducible criteria for evaluating vertebral artery stenosis exist. Because flow is normally turbulent within the vertebral artery, spectral broadening cannot be used as an indicator of stenosis. Velocity measurements are not reliable as criteria for stenosis because of the wide normal variation in vertebral artery diameter. Although velocities greater than 100 cm/sec often indicate stenosis, they can occur in angiographically normal vessels. For example, high-flow velocity may be present in a vertebral artery that is serving as a major collateral pathway for cerebral circulation in cases of carotid occlusion[34,188,247] (Fig. 26.54). Thus only a **focal increase in velocity of at least 50%, visible stenosis on gray-scale or color Doppler, or a striking tardus-parvus vertebral artery waveform** is likely to indicate significant vertebral stenosis. The variability of resistive indices in normal and abnormal vertebral arteries precludes the use of this parameter as an indicator of vertebral disease.[244]

Diagnosis of **vertebral artery occlusion** is also difficult. Often, the inability to detect arterial flow results from a small or congenitally absent vertebral artery or a technically difficult examination. The differentiation of severe stenosis from occlusion is difficult for the same reasons. Extremely dampened blood flow velocity in high-grade stenoses may result in a Doppler

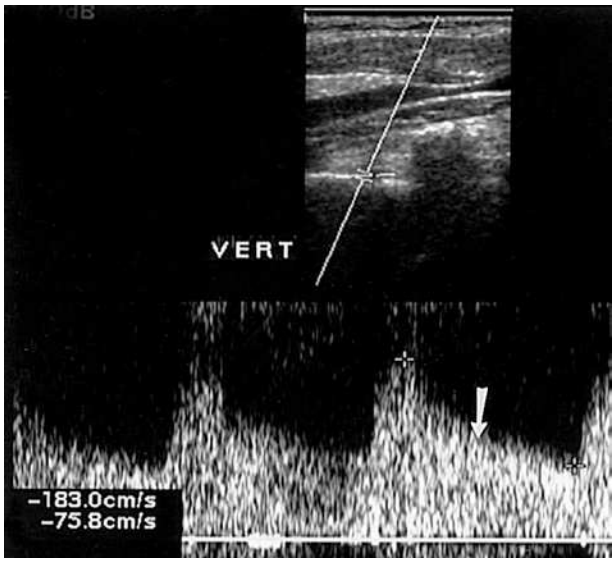

FIG. 26.54 Increased Flow Velocity in Vertebral Artery. Pulsed Doppler spectral trace from a left vertebral artery demonstrates strikingly high velocities and disturbed flow *(arrow)*. Although this degree of velocity elevation and flow disturbance could be associated with a focal stenosis, in this case there was increased velocity throughout the vertebral artery from bilateral internal carotid artery occlusion and increased collateral flow into the vertebral artery.

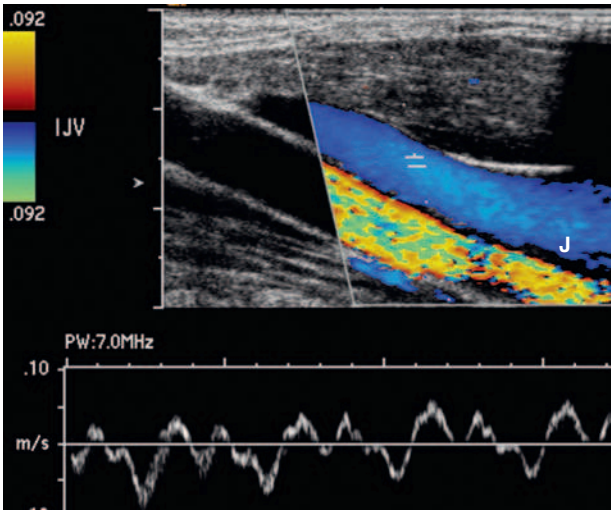

FIG. 26.55 Normal Jugular Vein. Complex venous pulsations in a normal jugular vein *(J)* reflect the cycle of events in the right atrium.

signal with amplitude too low to be detected.[235] Power Doppler imaging may prove useful in this situation. Visualization of only a vertebral vein may indicate vertebral artery occlusion or congenital absence.

INTERNAL JUGULAR VEINS

The internal jugular veins are the major vessels responsible for the return of venous blood from the brain. The most common clinical indication for duplex and color Doppler flow ultrasound of the internal jugular vein is the evaluation of suspected **jugular venous thrombosis.**[248-256] Thrombus formation may be related to central venous catheter placement. Other indications include a diagnosis of jugular venous ectasia[254,255,257,258] and guidance for internal jugular or subclavian vein cannulation,[259-265] particularly in difficult situations where vascular anatomy is distorted.

Sonographic Technique

The normal internal jugular vein is easily visualized. The vein is scanned with the neck extended and the head turned to the contralateral side. Longitudinal and transverse scans are obtained with light transducer pressure on the neck to avoid collapsing the vein. A coronal view from the supraclavicular fossa is used to image the lower segment of the internal jugular vein and the medial segment of the subclavian vein as they join to form the brachiocephalic vein.

The jugular vein lies lateral and anterior to the CCA, lateral to the thyroid gland, and deep to the sternocleidomastoid muscle. The vessel has sharply echogenic walls and a hypoechoic or anechoic lumen. Normally, a valve can be visualized in its distal portion.[251,260,266] The right internal jugular vein is usually larger than the left.[259]

Real-time ultrasound demonstrates **venous pulsations related to right heart contractions,** as well as changes in venous diameter that vary with changes in intrathoracic pressure. Doppler examination graphically depicts these flow patterns (Fig. 26.55). On inspiration, negative intrathoracic pressure causes flow toward the heart and the jugular veins to decrease in diameter. During expiration and during Valsalva maneuver, increased intrathoracic pressure causes a decrease in the blood return, and the veins enlarge, with minimal or no flow noted. The walls of the normal jugular vein collapse completely when moderate transducer pressure is applied. Sudden patient sniffing reduces intrathoracic pressure, causing momentary collapse of the vein on real-time ultrasound, accompanied by a brief increase in venous flow toward the heart as shown by Doppler.[250,252,254]

Thrombosis

Clinical features of jugular venous thrombosis include a tender, poorly defined, nonspecific neck mass or swelling. The correct diagnosis may not be immediately obvious.[251] Thrombosis of the internal jugular vein can be completely asymptomatic because of the deep position of the vein and the presence of abundant collateral circulation.[254] Internal jugular thrombosis most often results from complications of **central venous catheterization.**[249,253,254] Other causes include intravenous drug abuse, mediastinal tumor, hypercoagulable states, neck surgery, and local inflammation or adenopathy.[251] Some cases are idiopathic or spontaneous.[251] Possible complications of jugular venous thrombosis include suppurative thrombophlebitis, clot propagation, and pulmonary embolism.[251,255]

Real-time examination reveals an enlarged, noncompressible vein, which may contain a visible echogenic intraluminal thrombus. An **acute thrombus** may be anechoic and

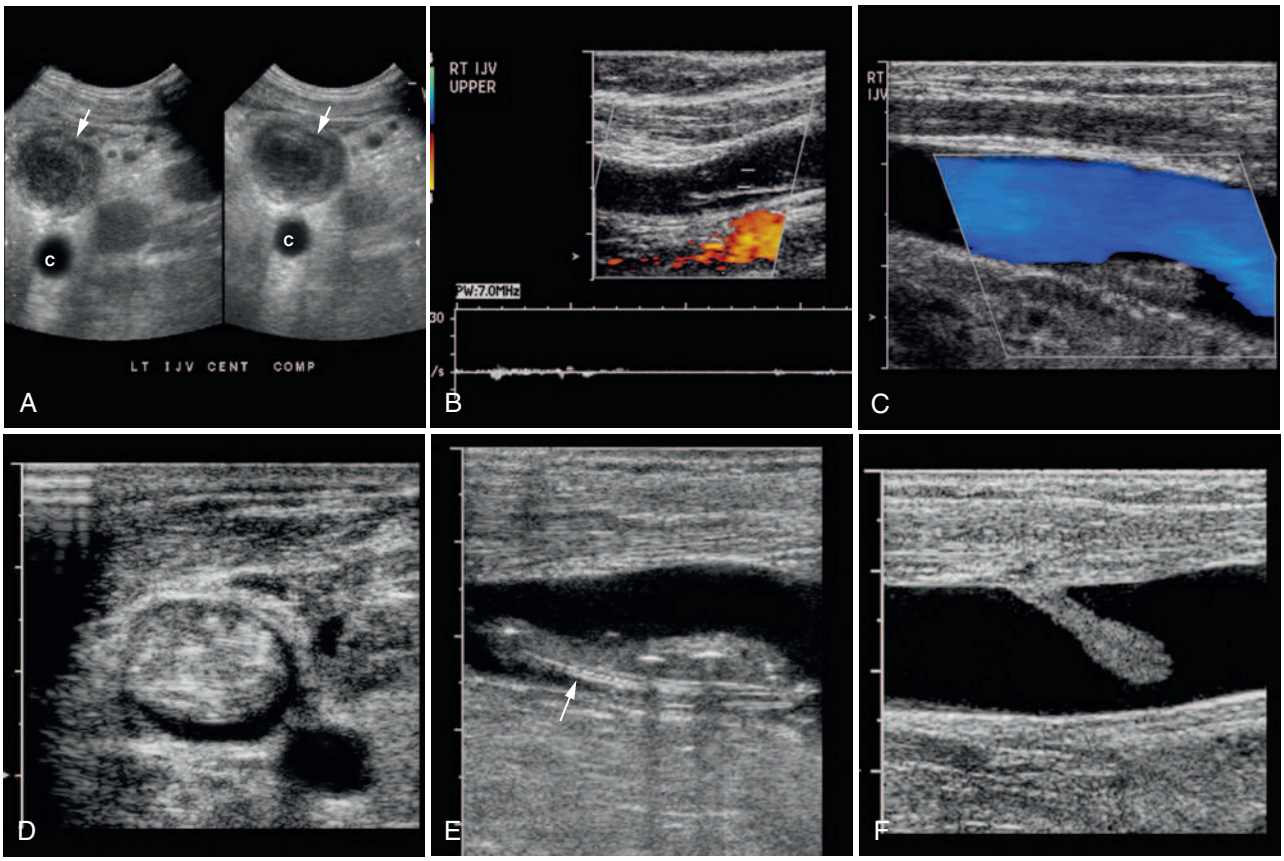

FIG. 26.56 Internal Jugular Vein (IJV) Thrombosis: Spectrum of Appearances. (A) Transverse image of an acute left internal jugular vein thrombus *(arrow).* The vein is distended and noncompressible. *C,* Common carotid artery. **(B)** Longitudinal image of a different patient demonstrates a hypoechoic thrombus and no Doppler signal. **(C)** Longitudinal color Doppler image shows a small amount of thrombus arising from the posterior wall of the IJV. **(D)** Transverse image shows an echogenic thrombus, indicating chronic thrombus in IJV. **(E)** Longitudinal image demonstrates a thrombus *(arrow)* around jugular vein catheter. **(F)** Longitudinal images show a thrombus arising from anterior wall. This thrombus probably results from previous catheter placement in this region.

indistinguishable from flowing blood; however, the characteristic lack of compressibility and absent Doppler or color Doppler flow in the region of a thrombus quickly lead to the correct diagnosis. In addition, there is visible loss of vein response to respiratory maneuvers and venous pulsation. Spectral and color Doppler interrogations reveal absent flow (Fig. 26.56). Collateral veins may be identified, particularly in cases of chronic internal jugular vein thrombosis. Central liquefaction or other heterogeneity of the thrombus also suggests chronicity. **Chronic thrombi** may be difficult to visualize because they tend to organize and are difficult to separate from echogenic perivascular fatty tissue.[260] The absence of cardiorespiratory plasticity in a patent jugular or subclavian vein can indicate a more central, nonocclusive thrombus (Fig. 26.57). The confirmation of bilateral loss of venous pulsations strongly supports a more central thrombus, which can be documented by angiographic or magnetic resonance venography.

A thrombus that is related to catheter insertion is often demonstrated at the tip of the catheter, although it may be seen anywhere along the course of the vein. The catheter can be visualized as two parallel echogenic lines separated by an anechoic region. Flow is not usually demonstrated in the catheter, even if the catheter itself is patent.

Sonography is a reliable means of diagnosing jugular and subclavian vein thrombosis. Sonography has limited access and cannot image all portions of the jugular and subclavian veins, especially those located behind the mandible or below the clavicle, although knowledge of the full extent of a thrombus is not typically a critical factor in treatment planning.[251,255] Serial sonographic examination to evaluate response to therapy after the initial assessment can be performed safely and inexpensively. Sonography can also document venous patency before vascular line placement, facilitating safer and more successful catheter insertion.

Acknowledgment

Thanks to Kathleen McFadden and Barbara Siede for their assistance with manuscript preparation.

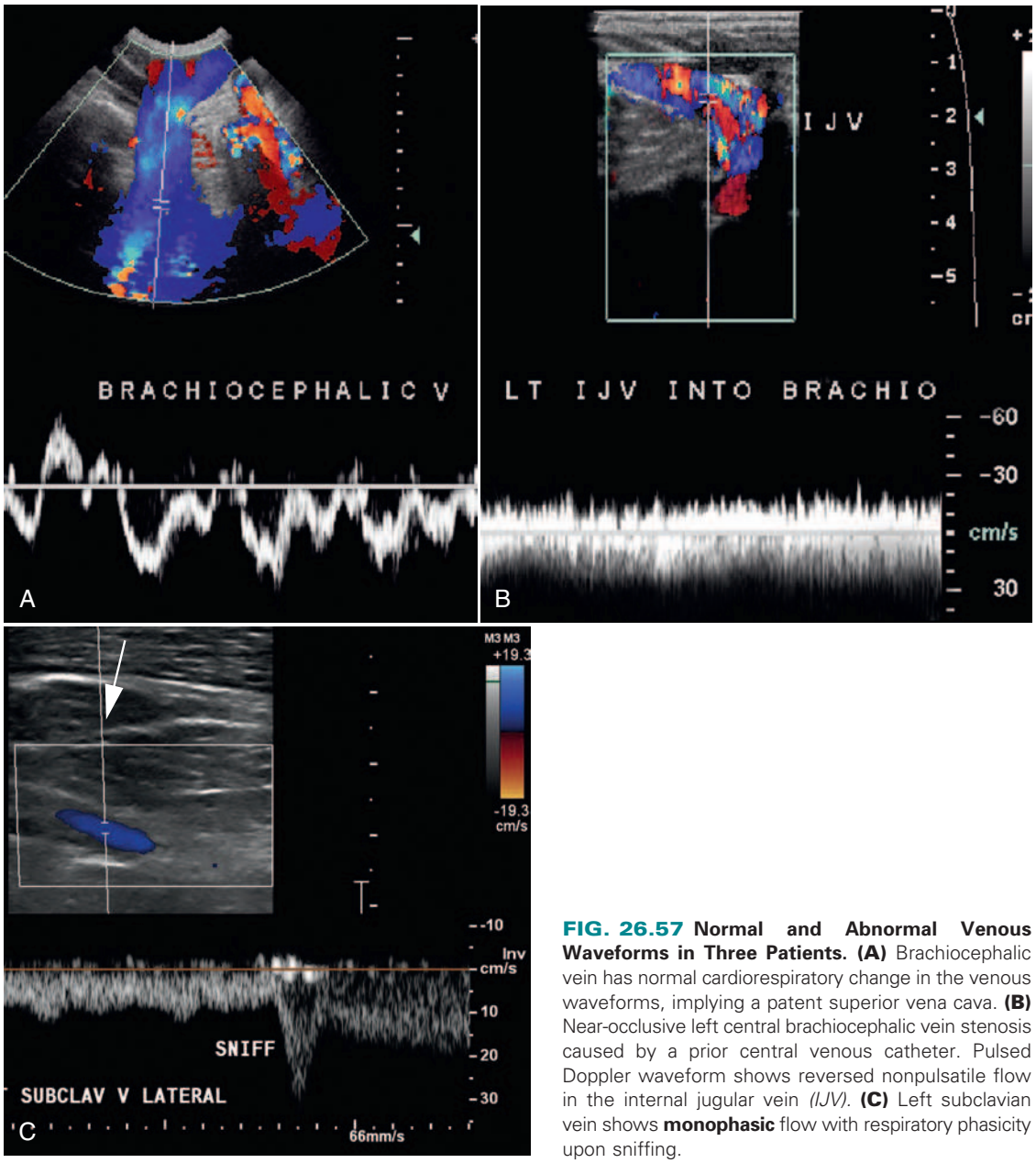

FIG. 26.57 Normal and Abnormal Venous Waveforms in Three Patients. (A) Brachiocephalic vein has normal cardiorespiratory change in the venous waveforms, implying a patent superior vena cava. **(B)** Near-occlusive left central brachiocephalic vein stenosis caused by a prior central venous catheter. Pulsed Doppler waveform shows reversed nonpulsatile flow in the internal jugular vein *(IJV)*. **(C)** Left subclavian vein shows **monophasic** flow with respiratory phasicity upon sniffing.

REFERENCES

1. Carroll BA. Carotid sonography. Radiology. 1991;178(2):303-313.
2. Menon BK, Campbell BC, Levi C, Goyal M. Role of imaging in current acute ischemic stroke workflow for endovascular therapy. Stroke. 2015;46(6):1453-1461.
3. Executive Committee for the Asymptomatic Carotid Atherosclerosis Study. Endarterectomy for asymptomatic carotid artery stenosis. Executive Committee for the Asymptomatic Carotid Atherosclerosis Study. JAMA. 1995;273(18):1421-1428.
4. National Center for Chronic Disease Prevention and Health Promotion, Division for Heart Disease and Stroke Prevention. Centers for Disease Control and Prevention. Stroke facts. 2015. Available from: http://www.cdc.gov/stroke/facts.htm.
5. Bogiatzi C, Hackam DG, McLeod AI, Spence JD. Secular trends in ischemic stroke subtypes and stroke risk factors. Stroke. 2014;45(11):3208-3213.
6. Fontenelle LJ, Simper SC, Hanson TL. Carotid duplex scan versus angiography in evaluation of carotid artery disease. Am Surg. 1994;60(11):864-868.
7. North American Symptomatic Carotid Endarterectomy Trial C. Beneficial effect of carotid endarterectomy in symptomatic patients with high-grade carotid stenosis. N Engl J Med. 1991;325(7):445-453.
8. European Carotid Surgery Trialists' Collaborative Group. MRC European Carotid Surgery Trial: interim results for symptomatic patients with severe (70-99%) or with mild (0-29%) carotid stenosis. Lancet. 1991;337(8752):1235-1543.
9. Barnett HJ, Taylor DW, Eliasziw M, et al. Benefit of carotid endarterectomy in patients with symptomatic moderate or severe stenosis. North American Symptomatic Carotid Endarterectomy Trial Collaborators. N Engl J Med. 1998;339(20):1415-1425.
10. Bae C, Szuchmacher M, Chang JB. Comparative review of the treatment methodologies of carotid stenosis. Int J Angiol. 2015;24(3):215-222.

11. Bluth EI, Bertino RE, Grant EG, et al. ACR guideline for the performance of an ultrasound examination of the extracranial cerebrovascular system. Am Coll Radiol. 2007;1037-1040.
12. ACR Guidelines and Standards Committee of the ACR Commission on Ultrasound in collaboration with the AIUM and the SRU. ACR–AIUM–SRU practice parameter for the performance of an ultrasound examination of the extracranial cerebrovascular system. 2015.
13. Derdeyn CP, Powers WJ, Moran CJ, et al. Role of Doppler US in screening for carotid atherosclerotic disease. Radiology. 1995;197(3):635-643.
14. Merritt CR, Bluth EI. The future of carotid sonography. Am J Roentgenol. 1992;158(1):37-39.
15. Taylor KJW. Clinical applications of carotid Doppler ultrasound. In: Taylor KJW, Burns PN, Wells PNT, editors. Clinical applications of Doppler ultrasound. New York: Raven Press; 1988. p. 120-161.
16. Bluth EI, Shyn PB, Sullivan MA, Merritt CR. Doppler color flow imaging of carotid artery dissection. J Ultrasound Med. 1989;8(3):149-153.
17. Hennerici M, Steinke W, Rautenberg W. High-resistance Doppler flow pattern in extracranial carotid dissection. Arch Neurol. 1989;46(6): 670-672.
18. Rothrock JF, Lim V, Press G, Gosink B. Serial magnetic resonance and carotid duplex examinations in the management of carotid dissection. Neurology. 1989;39(5):686-692.
19. O'Leary DH, Polak JF, Kronmal RA, et al. Carotid-artery intima and media thickness as a risk factor for myocardial infarction and stroke in older adults. Cardiovascular Health Study Collaborative Research Group. N Engl J Med. 1999;340(1):14-22.
20. Sidhu PS, Jonker ND, Khaw KT, et al. Spontaneous dissections of the internal carotid artery: appearances on colour Doppler ultrasound. Br J Radiol. 1997;70:50-57.
21. Katoh H, Nozue T, Nagamine H, et al. A case of carotid artery dissection after surgical repair of aortic dissection successfully treated with endovascular therapy using intravascular ultrasound. Cardiovasc Interv Ther. 2014;29(3):237-242.
22. Perren F, Urbano L, Rossetti AO, et al. Ultrasound image of a single symptomatic carotid stenosis disclosed as fibromuscular dysplasia. Neurology. 2004;62(6):1023-1024.
23. Schmidt WA. Ultrasound in vasculitis. Clin Exp Rheumatol. 2014;32(1 Suppl. 80):S71-S77.
24. Schmidt WA. Role of ultrasound in the understanding and management of vasculitis. Ther Adv Musculoskelet Dis. 2014;6(2):39-47.
25. Gritzmann N, Grasl MC, Helmer M, Steiner E. Invasion of the carotid artery and jugular vein by lymph node metastases: detection with sonography. Am J Roentgenol. 1990;154(2):411-414.
26. Gooding GA, Langman AW, Dillon WP, Kaplan MJ. Malignant carotid artery invasion: sonographic detection. Radiology. 1989;171(2):435-438.
27. Steinke W, Hennerici M, Aulich A. Doppler color flow imaging of carotid body tumors. Stroke. 1989;20(11):1574-1577.
28. Grant EG, Wong W, Tessler F, Perrella R. Cerebrovascular ultrasound imaging. Radiol Clin North Am. 1988;26(5):1111-1130.
29. Dematte S, Di Sarra D, Schiavi F, et al. Role of ultrasound and color Doppler imaging in the detection of carotid paragangliomas. J Ultrasound. 2012;15(3):158-163.
30. Ide C, De Coene B, Mailleux P, et al. Hypoplasia of the internal carotid artery: a noninvasive diagnosis. Eur Radiol. 2000;10(12):1865-1870.
31. Tasar M, Yetiser S, Tasar A, et al. Congenital absence or hypoplasia of the carotid artery: radioclinical issues. Am J Otolaryngol. 2004;25(5): 339-349.
32. Naqvi TZ, Lee MS. Carotid intima-media thickness and plaque in cardiovascular risk assessment. JACC Cardiovasc Imaging. 2014;7(10): 1025-1038.
33. van den Oord SC, Sijbrands EJ, ten Kate GL, et al. Carotid intima-media thickness for cardiovascular risk assessment: systematic review and meta-analysis. Atherosclerosis. 2013;228(1):1-11.
34. Polak JF, O'Leary DH, Kronmal RA, et al. Sonographic evaluation of carotid artery atherosclerosis in the elderly: relationship of disease severity to stroke and transient ischemic attack. Radiology. 1993;188(2):363-370.
35. Stein JH. Carotid intima-media thickness and cardiovascular events. N Engl J Med. 2011;365(17):1640, author reply 1-2.
36. Veller MG, Fisher CM, Nicolaides AN, et al. Measurement of the ultrasonic intima-media complex thickness in normal subjects. J Vasc Surg. 1993;17(4):719-725.
37. Bots ML, Mulder PG, Hofman A, et al. Reproducibility of carotid vessel wall thickness measurements. The Rotterdam Study. J Clin Epidemiol. 1994;47(8):921-930.
38. Csányi A, Egervári A. Simple clinical method of average intima-media thickness measurement in the common carotid artery. Vasa. 1996;25(3): 242-248.
39. Bots ML, Hoes AW, Koudstaal PJ, et al. Common carotid intima-media thickness and risk of stroke and myocardial infarction: the Rotterdam Study. Circulation. 1997;96(5):1432-1437.
40. Kanters SD, Algra A, van Leeuwen MS, Banga JD. Reproducibility of in vivo carotid intima-media thickness measurements: a review. Stroke. 1997;28(3):665-671.
41. Dwyer JH, Sun P, Kwong-Fu H, et al. Automated intima-media thickness: the Los Angeles Atherosclerosis Study. Ultrasound Med Biol. 1998;24(7):981-987.
42. Aminbakhsh A, Frohlich J, Mancini GB. Detection of early atherosclerosis with B mode carotid ultrasonography: assessment of a new quantitative approach. Clin Invest Med. 1999;22(6):265-274.
43. Greenland P, Abrams J, Aurigemma GP, et al. Prevention Conference V: Beyond secondary prevention: identifying the high-risk patient for primary prevention: noninvasive tests of atherosclerotic burden: Writing Group III. Circulation. 2000;101(1):E16-E22.
44. Goff Jr DC, Lloyd-Jones DM, Bennett G, et al. 2013 ACC/AHA guideline on the assessment of cardiovascular risk: a report of the American College of Cardiology/American Heart Association Task Force on Practice Guidelines. J Am Coll Cardiol. 2014;63(25 Pt B):2935-2959.
45. Bluth EI, Stavros AT, Marich KW, et al. Carotid duplex sonography: a multicenter recommendation for standardized imaging and Doppler criteria. Radiographics. 1988;8(3):487-506.
46. Bluth EI. Evaluation and characterization of carotid plaque. Semin Ultrasound CT MR. 1997;18(1):57-65.
47. Polak JF, Shemanski L, O'Leary DH, et al. Hypoechoic plaque at US of the carotid artery: an independent risk factor for incident stroke in adults aged 65 years or older. Cardiovascular Health Study. Radiology. 1998;208(3): 649-654.
48. Langsfeld M, Gray-Weale AC, Lusby RJ. The role of plaque morphology and diameter reduction in the development of new symptoms in asymptomatic carotid arteries. J Vasc Surg. 1989;9(4):548-557.
49. Leahy AL, McCollum PT, Feeley TM, et al. Duplex ultrasonography and selection of patients for carotid endarterectomy: plaque morphology or luminal narrowing? J Vasc Surg. 1988;8(5):558-562.
50. Reilly LM, Lusby RJ, Hughes L, et al. Carotid plaque histology using real-time ultrasonography. Clinical and therapeutic implications. Am J Surg. 1983;146(2):188-193.
51. Persson AV, Robichaux WT, Silverman M. The natural history of carotid plaque development. Arch Surg. 1983;118(9):1048-1052.
52. Lusby RJ, Ferrell LD, Ehrenfeld WK, et al. Carotid plaque hemorrhage. Its role in production of cerebral ischemia. Arch Surg. 1982;117(11): 1479-1488.
53. Edwards JH, Kricheff II, Gorstein F, et al. Atherosclerotic subintimal hematoma of the carotid artery. Radiology. 1979;133(1):123-129.
54. Imparato AM, Riles TS, Gorstein F. The carotid bifurcation plaque: pathologic findings associated with cerebral ischemia. Stroke. 1979;10(3):238-245.
55. Zavodni AE, Wasserman BA, McClelland RL, et al. Carotid artery plaque morphology and composition in relation to incident cardiovascular events: the Multi-Ethnic Study of Atherosclerosis (MESA). Radiology. 2014;271(2): 381-389.
56. Ross R, Wight TN, Strandness E, Thiele B. Human atherosclerosis. I. Cell constitution and characteristics of advanced lesions of the superficial femoral artery. Am J Pathol. 1984;114(1):79-93.
57. Libby P. Mechanisms of acute coronary syndromes and their implications for therapy. N Engl J Med. 2013;368(21):2004-2013.
58. Pellerito J, Polak J. Introduction to vascular ultrasonography: Expert Consult. 6th ed. Philadelphia: Saunders; 2012.

59. Cheng Y, Liu X, Yang J, et al. MicroRNA-145, a novel smooth muscle cell phenotypic marker and modulator, controls vascular neointimal lesion formation. Circ Res. 2009;105(2):158-166.
60. Fan P, Chen Z, Tian P, et al. miRNA biogenesis enzyme Drosha is required for vascular smooth muscle cell survival. PLoS ONE. 2013;8(4):e60888.
61. Jin W, Reddy MA, Chen Z, et al. Small RNA sequencing reveals microRNAs that modulate angiotensin II effects in vascular smooth muscle cells. J Biol Chem. 2012;287(19):15672-15683.
62. Li P, Liu Y, Yi B, et al. MicroRNA-638 is highly expressed in human vascular smooth muscle cells and inhibits PDGF-BB-induced cell proliferation and migration through targeting orphan nuclear receptor NOR1. Cardiovasc Res. 2013;99(1):185-193.
63. Liu X, Cheng Y, Chen X, et al. MicroRNA-31 regulated by the extracellular regulated kinase is involved in vascular smooth muscle cell growth via large tumor suppressor homolog 2. J Biol Chem. 2011;286(49):42371-42380.
64. Liu X, Cheng Y, Yang J, et al. Cell-specific effects of miR-221/222 in vessels: molecular mechanism and therapeutic application. J Mol Cell Cardiol. 2012;52(1):245-255.
65. Merlet E, Atassi F, Motiani RK, et al. miR-424/322 regulates vascular smooth muscle cell phenotype and neointimal formation in the rat. Cardiovasc Res. 2013;98(3):458-468.
66. Norata GD, Pinna C, Zappella F, et al. MicroRNA 143-145 deficiency impairs vascular function. Int J Immunopathol Pharmacol. 2012;25(2):467-474.
67. Song L, Duan P, Guo P, et al. Downregulation of miR-223 and miR-153 mediates mechanical stretch-stimulated proliferation of venous smooth muscle cells via activation of the insulin-like growth factor-1 receptor. Arch Biochem Biophys. 2012;528(2):204-211.
68. Bazan H, Coleman C, Smith T, et al. The pro-proliferative and anti-apoptotic micro-RNA 221 is decreased in vulnerable carotid atherosclerotic plaques. J Vasc Surg. 2012;55(Suppl. 6):75S-76S.
69. Coleman CB, Lightell Jr DJ, Moss SC, et al. Elevation of miR-221 and -222 in the internal mammary arteries of diabetic subjects and normalization with metformin. Mol Cell Endocrinol. 2013;374(1-2):125-129.
70. Bazan HA, Hatfield SA, O'Malley CB, et al. Acute loss of miR-221 and miR-222 in the atherosclerotic plaque shoulder accompanies plaque rupture. Stroke. 2015;46(11):3285-3287.
71. Geroulakos G, Ramaswami G, Nicolaides A, et al. Characterization of symptomatic and asymptomatic carotid plaques using high-resolution real-time ultrasonography. Br J Surg. 1993;80(10):1274-1277.
72. Holdsworth RJ, McCollum PT, Bryce JS, Harrison DK. Symptoms, stenosis and carotid plaque morphology. Is plaque morphology relevant? Eur J Vasc Endovasc Surg. 1995;9(1):80-85.
73. Bluth EI, Kay D, Merritt CR, et al. Sonographic characterization of carotid plaque: detection of hemorrhage. Am J Roentgenol. 1986;146(5):1061-1065.
74. Merritt CRB, Bluth EI. Ultrasonographic characterization of carotid plaque. In: Labs KH, editor. Diagnostic vascular ultrasound. London: Hodder & Stoughton; 1991.
75. Bluth EI. B-mode evaluation and characterization of carotid plaque. In: Tegler CH, Babikian VL, Gomez CR, editors. Neurosonology. St Louis: Mosby-Year Book; 1991. p. 62-67.
76. Sterpetti AV, Schultz RD, Feldhaus RJ, et al. Ultrasonographic features of carotid plaque and the risk of subsequent neurologic deficits. Surgery. 1988;104(4):652-660.
77. Weinberger J, Marks SJ, Gaul JJ, et al. Atherosclerotic plaque at the carotid artery bifurcation. Correlation of ultrasonographic imaging with morphology. J Ultrasound Med. 1987;6(7):363-366.
78. Stahl JA, Middleton WD. Pseudoulceration of the carotid artery. J Ultrasound Med. 1992;11(7):355-358.
79. Michel JB, Virmani R, Arbustini E, Pasterkamp G. Intraplaque haemorrhages as the trigger of plaque vulnerability. Eur Heart J. 2011;32(16):1977-1985, 1985a-1985c.
80. Picano E, Paterni M. Ultrasound tissue characterization of vulnerable atherosclerotic plaque. Int J Mol Sci. 2015;16(5):10121-10133.
81. Bluth EI. Extracranial carotid arteries: intraplaque hemorrhage and surface ulceration. Minerva Cardioangiol. 1998;46(3):81-85.
82. Bluth EI. Plaque morphology as a risk factor for stroke. JAMA. 2000;284(2):177.
83. Brinjikji W, Huston 3rd J, Rabinstein AA, et al. Contemporary carotid imaging: from degree of stenosis to plaque vulnerability. J Neurosurg. 2016;124(1):27-42.
84. AbuRahma AF, Wulu Jr JT, Crotty B. Carotid plaque ultrasonic heterogeneity and severity of stenosis. Stroke. 2002;33(7):1772-1775.
85. Reiter M, Effenberger I, Sabeti S, et al. Increasing carotid plaque echolucency is predictive of cardiovascular events in high-risk patients. Radiology. 2008;248(3):1050-1055.
86. Saba L, Caddeo G, Sanfilippo R, et al. CT and ultrasound in the study of ulcerated carotid plaque compared with surgical results: potentialities and advantages of multidetector row CT angiography. AJNR Am J Neuroradiol. 2007;28(6):1061-1066.
87. Bluth EI, McVay 3rd LV, Merritt CR, Sullivan MA. The identification of ulcerative plaque with high resolution duplex carotid scanning. J Ultrasound Med. 1988;7(2):73-76.
88. Tahmasebpour HR, Buckley AR, Cooperberg PL, Fix CH. Sonographic examination of the carotid arteries. Radiographics. 2005;25(6):1561-1575.
89. Ballard JL, Deiparine MK, Bergan JJ, et al. Cost-effective evaluation and treatment for carotid disease. Arch Surg. 1997;132(3):268-271.
90. Furst H, Hartl WH, Jansen I, et al. Color-flow Doppler sonography in the identification of ulcerative plaques in patients with high-grade carotid artery stenosis. AJNR Am J Neuroradiol. 1992;13(6):1581-1587.
91. Schinkel AF, Kaspar M, Staub D. Contrast-enhanced ultrasound: clinical applications in patients with atherosclerosis. Int J Cardiovasc Imaging. 2016;32(1):35-48.
92. Varetto G, Gibello L, Castagno C, et al. Use of contrast-enhanced ultrasound in carotid atherosclerotic disease: limits and perspectives. Biomed Res Int. 2015;2015:293163.
93. Abildgaard A, Egge TS, Klow NE, Jakobsen JA. Use of sonicated albumin (Infoson) to enhance arterial spectral and color Doppler imaging. Cardiovasc Intervent Radiol. 1996;19(4):265-271.
94. Bluth EI. Value of US in selecting patients for carotid angioplasty and stent placement. Radiology. 2005;237(1):374-375, author reply 5.
95. Lee W. General principles of carotid Doppler ultrasonography. Ultrasonography. 2014;33(1):11-17.
96. Spence JD, Parraga G. Three-dimensional ultrasound of carotid plaque. Neuroimaging Clin N Am. 2016;26(1):69-80.
97. Comerota AJ, Cranley JJ, Cook SE. Real-time B-mode carotid imaging in diagnosis of cerebrovascular disease. Surgery. 1981;89(6):718-729.
98. Zwiebel WJ, Austin CW, Sackett JF, Strother CM. Correlation of high-resolution, B-mode and continuous-wave Doppler sonography with arteriography in the diagnosis of carotid stenosis. Radiology. 1983;149(2):523-532.
99. Jacobs NM, Grant EG, Schellinger D, et al. Duplex carotid sonography: criteria for stenosis, accuracy, and pitfalls. Radiology. 1985;154(2):385-391.
100. Taylor KJ, Holland S, Doppler US, Part I. Basic principles, instrumentation, and pitfalls. Radiology. 1990;174(2):297-307.
101. Carroll BA, von Ramm OT. Fundamental of current Doppler technology. Ultrasound Q. 1988;6:275-298.
102. Kassam M, Johnston KW, Cobbold RS. Quantitative estimation of spectral broadening for the diagnosis of carotid arterial disease: method and in vitro results. Ultrasound Med Biol. 1985;11(3):425-433.
103. Douville Y, Johnston KW, Kassam M. Determination of the hemodynamic factors which influence the carotid Doppler spectral broadening. Ultrasound Med Biol. 1985;11(3):417-423.
104. Garth KE, Carroll BA, Sommer FG, Oppenheimer DA. Duplex ultrasound scanning of the carotid arteries with velocity spectrum analysis. Radiology. 1983;147(3):823-827.
105. Phillips DJ, Greene Jr FM, Langlois Y, et al. Flow velocity patterns in the carotid bifurcations of young, presumed normal subjects. Ultrasound Med Biol. 1983;9(1):39-49.
106. Lichtman JB, Kibble MB. Detection of intracranial arteriovenous malformation by Doppler ultrasound of the extracranial carotid circulation. J Ultrasound Med. 1987;6(10):609-612.

107. Rothoerl RD, Schebesch KM, Woertgen C, Brawanski A. Ultrasonic blood flow volume assessment in the extracranial internal carotid artery in arteriovenous malformations. Neurol Res. 2005;27(2):209-211.
108. Robinson ML, Sacks D, Perlmutter GS, Marinelli DL. Diagnostic criteria for carotid duplex sonography. Am J Roentgenol. 1988;151(5): 1045-1049.
109. Grant EG, Duerinckx AJ, El Saden SM, et al. Ability to use duplex US to quantify internal carotid arterial stenoses: fact or fiction? Radiology. 2000;214(1):247-252.
110. Rothwell PM, Gibson RJ, Slattery J, Warlow CP. Prognostic value and reproducibility of measurements of carotid stenosis. A comparison of three methods on 1001 angiograms. European Carotid Surgery Trialists' Collaborative Group. Stroke. 1994;25(12):2440-2444.
111. Moneta GL, Edwards JM, Chitwood RW, et al. Correlation of North American Symptomatic Carotid Endarterectomy Trial (NASCET) angiographic definition of 70% to 99% internal carotid artery stenosis with duplex scanning. J Vasc Surg. 1993;17:152-157.
112. Friedman SG, Hainline B, Feinberg AW, et al. Use of diastolic velocity ratios to predict significant carotid artery stenosis. Stroke. 1988;19(7):910-912.
113. Kohler TR, Langlois Y, Roederer GO, et al. Variability in measurement of specific parameters for carotid duplex examination. Ultrasound Med Biol. 1987;13(10):637-642.
114. Hunink MG, Polak JF, Barlan MM, O'Leary DH. Detection and quantification of carotid artery stenosis: efficacy of various Doppler velocity parameters. Am J Roentgenol. 1993;160(3):619-625.
115. Slovut DP, Romero JM, Hannon KM, et al. Detection of common carotid artery stenosis using duplex ultrasonography: a validation study with computed tomographic angiography. J Vasc Surg. 2010;51(1):65-70.
116. Pisimisis GT, Katsavelis D, Mandviwala T, et al. Common carotid artery peak systolic velocity ratio predicts high-grade common carotid stenosis. J Vasc Surg. 2015;62(4):951-957.
117. Faught WE, Mattos MA, van Bemmelen PS, et al. Color-flow duplex scanning of carotid arteries: new velocity criteria based on receiver operator characteristic analysis for threshold stenoses used in the symptomatic and asymptomatic carotid trials. J Vasc Surg. 1994;19:818-827.
118. Jogestrand T, Fredén-Lindqvist J, Lindqvist M, et al. Discrepancies in recommended criteria for grading of carotid stenosis with ultrasound. Clin Physiol Funct Imaging. 2016;36(4):326-329.
119. Gray C, Murray SA, Connolly M, et al. The implications of different criteria for grading carotid artery stenosis by duplex ultrasound. J Clin Ultrasound. 2015;43(9):563-566.
120. Kuntz KM, Polak JF, Whittemore AD, et al. Duplex ultrasound criteria for the identification of carotid stenosis should be laboratory specific. Stroke. 1997;28(3):597-602.
121. Alexandrov AV, Vital D, Brodie DS, et al. Grading carotid stenosis with ultrasound. An interlaboratory comparison. Stroke. 1997;28(6): 1208-1210.
122. Grant EG, Benson CB, Moneta GL, et al. Carotid artery stenosis: gray-scale and Doppler US diagnosis—Society of Radiologists in Ultrasound Consensus Conference. Radiology. 2003;229(2):340-346.
123. Carpenter JP, Lexa FJ, Davis JT. Determination of sixty percent or greater carotid artery stenosis by duplex Doppler ultrasonography. J Vasc Surg. 1995;22(6):697-703.
124. Middleton WD, Erickson S, Melson GL. Perivascular color artifact: pathologic significance and appearance on color Doppler US images. Radiology. 1989;171(3):647-652.
125. Erickson SJ, Mewissen MW, Foley WD, et al. Stenosis of the internal carotid artery: assessment using color Doppler imaging compared with angiography. Am J Roentgenol. 1989;152(6):1299-1305.
126. Adla T, Adlova R. Multimodality imaging of carotid stenosis. Int J Angiol. 2015;24(3):179-184.
127. Middleton WD, Foley WD, Lawson TL. Flow reversal in the normal carotid bifurcation: color Doppler flow imaging analysis. Radiology. 1988;167(1): 207-210.
128. Zierler RE, Phillips DJ, Beach KW, et al. Noninvasive assessment of normal carotid bifurcation hemodynamics with color-flow ultrasound imaging. Ultrasound Med Biol. 1987;13(8):471-476.
129. Erickson SJ, Mewissen MW, Foley WD, et al. Color Doppler evaluation of arterial stenoses and occlusions involving the neck and thoracic inlet. Radiographics. 1989;9(3):389-406.
130. Middleton WD, Foley WD, Lawson TL. Color-flow Doppler imaging of carotid artery abnormalities. Am J Roentgenol. 1988;150(2):419-425.
131. Branas CC, Weingarten MS, Czeredarczuk M, Schafer PF. Examination of carotid arteries with quantitative color Doppler flow imaging. J Ultrasound Med. 1994;13(2):121-127.
132. Grant EG, El-Saden SM, Madrazo BL, et al. Innominate artery occlusive disease: sonographic findings. Am J Roentgenol. 2006;186(2):394-400.
133. Gaitini D, Soudack M. Diagnosing carotid stenosis by Doppler sonography: state of the art. J Ultrasound Med. 2005;24(8):1127-1136.
134. Grant EG, Benson CB, Moneta GL, et al. Carotid artery stenosis: grayscale and Doppler ultrasound diagnosis—Society of Radiologists in Ultrasound consensus conference. Ultrasound Q. 2003;19(4):190-198.
135. Jung EM, Kubale R, Ritter G, et al. Diagnostics and characterisation of preocclusive stenoses and occlusions of the internal carotid artery with B-flow. Eur Radiol. 2007;17(2):439-447.
136. Steinke W, Ries S, Artemis N, et al. Power Doppler imaging of carotid artery stenosis. Comparison with color Doppler flow imaging and angiography. Stroke. 1997;28(10):1981-1987.
137. Bluth EI, Althans LE, Sullivan M, et al. Comparison of plaque characterization with grayscale imaging and 3-D power Doppler imaging: can more be learned about intraplaque hemorrhage? J Echocardiol Med Ultrasons. 1999;20:11-15.
138. Griewing B, Morgenstern C, Driesner F, et al. Cerebrovascular disease assessed by color-flow and power Doppler ultrasonography. Comparison with digital subtraction angiography in internal carotid artery stenosis. Stroke. 1996;27(1):95-100.
139. Bluth EI, Sunshine JH, Lyons JB, et al. Power Doppler imaging: initial evaluation as a screening examination for carotid artery stenosis. Radiology. 2000;215(3):791-800.
140. Bluth EI. Screening test for carotid disease. Semin Ultrasound CT MR. 2003;24(1):55-61.
141. Bluth EI. Power Doppler imaging to evaluate flow-limiting stenoses. Radiology. 2001;221(2):557-558.
142. Weyer GW, Davis AM. Screening for asymptomatic carotid artery stenosis. JAMA. 2015;313(2):192-193.
143. Zbornikova V, Lassvik C. Duplex scanning in presumably normal persons of different ages. Ultrasound Med Biol. 1986;12(5):371-378.
144. Spencer EB, Sheafor DH, Hertzberg BS, et al. Nonstenotic internal carotid arteries: effects of age and blood pressure at the time of scanning on Doppler US velocity measurements. Radiology. 2001;220(1):174-178.
145. Okura T, Watanabe S, Miyoshi K, et al. Intrarenal and carotid hemodynamics in patients with essential hypertension. Am J Hypertens. 2004;17(3): 240-244.
146. Kaproth-Joslin KA, Bhatt S, Scoutt LM, Rubens DJ. The essentials of extracranial carotid ultrasonographic imaging. Radiol Clin North Am. 2014;52(6):1325-1342.
147. Applebaum RM, Wun HH, Katz ES, et al. Effects of intraaortic balloon counterpulsation on carotid artery blood flow. Am Heart J. 1998;135(5 Pt 1):850-854.
148. Ratchford EV, Salameh MJ, Morrissey NJ. Underestimation of carotid stenosis in bradycardia. Vascular. 2009;17(1):51-54.
149. O'Boyle MK, Vibhakar NI, Chung J, et al. Duplex sonography of the carotid arteries in patients with isolated aortic stenosis: imaging findings and relation to severity of stenosis. Am J Roentgenol. 1996;166(1):197-202.
150. Macchi C, Gulisano M, Giannelli F, et al. Kinking of the human internal carotid artery: a statistical study in 100 healthy subjects by echocolor Doppler. J Cardiovasc Surg (Torino). 1997;38(6):629-637.
151. Mumoli N, Cei M. Asymptomatic carotid kinking. Circ J. 2008;72(4): 682-683.
152. Matteo Ciccone M, K Sharma R, Scicchitano P, et al. Dolichocarotids: echo-color Doppler evaluation and clinical role. J Atheroscler Thromb. 2014;21(1):56-63.
153. Busuttil SJ, Franklin DP, Youkey JR, Elmore JR. Carotid duplex overestimation of stenosis due to severe contralateral disease. Am J Surg. 1996;172(2): 144-147.

154. AbuRahma AF, Richmond BK, Robinson PA, et al. Effect of contralateral severe stenosis or carotid occlusion on duplex criteria of ipsilateral stenoses: comparative study of various duplex parameters. J Vasc Surg. 1995;22(6):751-761.
155. van Everdingen KJ, van der Grond J, Kappelle LJ. Overestimation of a stenosis in the internal carotid artery by duplex sonography caused by an increase in volume flow. J Vasc Surg. 1998;27(3):479-485.
156. Preiss JE, Itum DS, Reeves JG, et al. Carotid duplex criteria for patients with contralateral occlusion. J Surg Res. 2015;193(1):28-32.
157. Blackshear WM, Phillips DJ, Chikos PM, et al. Carotid artery velocity patterns in normal and stenotic vessels. Stroke. 1980;11(1):67-71.
158. Rubens DJ, Bhatt S, Nedelka S, Cullinan J. Doppler artifacts and pitfalls. Radiol Clin North Am. 2006;44(6):805-835.
159. Grubb Jr RL, Derdeyn CP, Fritsch SM, et al. Importance of hemodynamic factors in the prognosis of symptomatic carotid occlusion. JAMA. 1998;280(12):1055-1060.
160. Berman SS, Devine JJ, Erdoes LS, Hunter GC. Distinguishing carotid artery pseudo-occlusion with color-flow Doppler. Stroke. 1995;26(3): 434-438.
161. Gortler M, Niethammer R, Widder B. Differentiating subtotal carotid artery stenoses from occlusions by colour-coded duplex sonography. J Neurol. 1994;241(5):301-305.
162. AbuRahma AF, Pollack JA, Robinson PA, Mullins D. The reliability of color duplex ultrasound in diagnosing total carotid artery occlusion. Am J Surg. 1997;174(2):185-187.
163. Kliewer MA, Freed KS, Hertzberg BS, et al. Temporal artery tap: usefulness and limitations in carotid sonography. Radiology. 1996;201(2):481-484.
164. Bebry AJ, Hines GL. Total occlusion of the common carotid artery with a patent internal carotid artery; identification by duplex ultrasonography: report of a case. J Vasc Surg. 1989;10(4):469-470.
165. Blackshear Jr WM, Phillips DJ, Bodily KC, Strandness Jr DE. Ultrasonic demonstration of external and internal carotid patency with common carotid occlusion: a preliminary report. Stroke. 1980;11(3):249-252.
166. Lee DH, Gao FQ, Rankin RN, et al. Duplex and color Doppler flow sonography of occlusion and near occlusion of the carotid artery. AJNR Am J Neuroradiol. 1996;17(7):1267-1274.
167. Alexandrov AV, Bladin CF, Maggisano R, Norris JW. Measuring carotid stenosis. Time for a reappraisal. Stroke. 1993;24(9):1292-1296.
168. Beach KW, Leotta DF, Zierler RE. Carotid Doppler velocity measurements and anatomic stenosis: correlation is futile. Vasc Endovascular Surg. 2012;46(6):466-474.
169. Gupta A, Baradaran H, Schweitzer AD, et al. Carotid plaque MRI and stroke risk: a systematic review and meta-analysis. Stroke. 2013;44(11): 3071-3077.
170. Saam T, Hetterich H, Hoffmann V, et al. Meta-analysis and systematic review of the predictive value of carotid plaque hemorrhage on cerebrovascular events by magnetic resonance imaging. J Am Coll Cardiol. 2013;62(12):1081-1091.
171. McLaughlin MS, Hinckley PJ, Treiman SM, et al. Optimal prediction of carotid intraplaque hemorrhage using clinical and lumen imaging markers. AJNR Am J Neuroradiol. 2015;36(12):2360-2366.
172. Yuan C, Parker DL. Three-dimensional carotid plaque MR imaging. Neuroimaging Clin N Am. 2016;26(1):1-12.
173. Brinjikji W, Rabinstein AA, Lanzino G, et al. Ultrasound characteristics of symptomatic carotid plaques: a systematic review and meta-analysis. Cerebrovasc Dis. 2015;40(3-4):165-174.
174. Randoux B, Marro B, Koskas F, et al. Carotid artery stenosis: prospective comparison of CT, three-dimensional gadolinium-enhanced MR, and conventional angiography. Radiology. 2001;220(1): 179-185.
175. Nonent M, Serfaty JM, Nighoghossian N, et al. Concordance rate differences of 3 noninvasive imaging techniques to measure carotid stenosis in clinical routine practice: results of the CARMEDAS multicenter study. Stroke. 2004;35(3):682-686.
176. Polak JF, Kalina P, Donaldson MC, et al. Carotid endarterectomy: preoperative evaluation of candidates with combined Doppler sonography and MR angiography. Work in progress. Radiology. 1993;186(2):333-338.
177. Johnston DC, Goldstein LB. Clinical carotid endarterectomy decision making: noninvasive vascular imaging versus angiography. Neurology. 2001;56(8):1009-1015.
178. Kuntz KM, Skillman JJ, Whittemore AD, Kent KC. Carotid endarterectomy in asymptomatic patients—is contrast angiography necessary? A morbidity analysis. J Vasc Surg. 1995;22(6):706-714.
179. DeMarco JK, Spence JD. Plaque assessment in the management of patients with asymptomatic carotid stenosis. Neuroimaging Clin N Am. 2016;26(1):111-127.
180. Spence JD. Management of asymptomatic carotid stenosis. Neurol Clin. 2015;33(2):443-457.
181. Mattos MA, Hodgson KJ, Faught WE, et al. Carotid endarterectomy without angiography: is color-flow duplex scanning sufficient? Surgery. 1994;116(4):776-782.
182. Cartier R, Cartier P, Fontaine A. Carotid endarterectomy without angiography. The reliability of Doppler ultrasonography and duplex scanning in preoperative assessment. Can J Surg. 1993;36(5):411-416.
183. Thusay MM, Khoury M, Greene K. Carotid endarterectomy based on duplex ultrasound in patients with and without hemispheric symptoms. Am Surg. 2001;67(1):1-6.
184. Welch HJ, Murphy MC, Raftery KB, Jewell ER. Carotid duplex with contralateral disease: the influence of vertebral artery blood flow. Ann Vasc Surg. 2000;14(1):82-88.
185. Chen JC, Salvian AJ, Taylor DC, et al. Can duplex ultrasonography select appropriate patients for carotid endarterectomy? Eur J Vasc Endovasc Surg. 1997;14(6):451-456.
186. Johnson BL, Gupta AK, Bandyk DF, et al. Anatomic patterns of carotid endarterectomy healing. Am J Surg. 1996;172(2):188-190.
187. Kagawa R, Okada Y, Shima T, et al. B-mode ultrasonographic investigations of morphological changes in endarterectomized carotid artery. Surg Neurol. 2001;55(1):50-56.
188. Jackson MR, D'Addio VJ, Gillespie DL, O'Donnell SD. The fate of residual defects following carotid endarterectomy detected by early postoperative duplex ultrasound. Am J Surg. 1996;172(2):184-187.
189. Ricotta JJ, DeWeese JA. Is routine carotid ultrasound surveillance after carotid endarterectomy worthwhile? Am J Surg. 1996;172(2):140-142.
190. Lal BK. Recurrent carotid stenosis after CEA and CAS: diagnosis and management. Semin Vasc Surg. 2007;20(4):259-266.
191. Kallmayer M, Tsantilas P, Zieger C, et al. Ultrasound surveillance after CAS and CEA: what's the evidence? J Cardiovasc Surg (Torino). 2014;55(2 Suppl. 1):33-41.
192. Goodney PP, Lucas FL, Travis LL, et al. Changes in the use of carotid revascularization among the Medicare population. Arch Surg. 2008;143(2): 170-173.
193. Murad MH, Shahrour A, Shah ND, et al. A systematic review and meta-analysis of randomized trials of carotid endarterectomy vs stenting. J Vasc Surg. 2011;53(3):792-797.
194. Ricotta JJ, Aburahma A, Ascher E, et al. Updated Society for Vascular Surgery guidelines for management of extracranial carotid disease: executive summary. J Vasc Surg. 2011;54(3):832-836.
195. Chaer RA, Derubertis BG, Trocciola SM, et al. Safety and efficacy of carotid angioplasty and stenting in high-risk patients. Am Surg. 2006;72(8): 694-698.
196. Wolff T, Guirguis-Blake J, Miller T, et al. Screening for carotid artery stenosis: an update of the evidence for the U.S. Preventive Services Task Force. Ann Intern Med. 2007;147(12):860-870.
197. Diethrich EB, Pauliina Margolis M, Reid DB, et al. Virtual histology intravascular ultrasound assessment of carotid artery disease: the Carotid Artery Plaque Virtual Histology Evaluation (CAPITAL) study. J Endovasc Ther. 2007;14(5):676-686.
198. Fleming SE, Bluth EI, Milburn J. Role of sonography in the evaluation of carotid artery stents. J Clin Ultrasound. 2005;33(7):321-328.
199. Peterson BG, Longo GM, Kibbe MR, et al. Duplex ultrasound remains a reliable test even after carotid stenting. Ann Vasc Surg. 2005;19(6): 793-797.
200. Roffi M, Greutmann M, Eberli FR, et al. Starting a carotid artery stenting program is safe. Catheter Cardiovasc Interv. 2008;71(4):469-473.

201. Zhou W, Lin PH, Bush RL, et al. Management of in-sent restenosis after carotid artery stenting in high-risk patients. J Vasc Surg. 2006;43(2): 305-312.
202. Daou B, Chalouhi N, Starke RM, et al. Predictors of restenosis after carotid artery stenting in 241 cases. J Neurointerv Surg. 2016;8(7):677-679.
203. Miyazaki Y, Mori T, Iwata T, et al. Continuous daily use of cilostazol prevents in-stent restenosis following carotid artery stenting: serial angiographic investigation of 229 lesions. J Neurointerv Surg. 2016;8(5):471-475.
204. Robbin ML, Lockhart ME, Weber TM, et al. Carotid artery stents: early and intermediate follow-up with Doppler US. Radiology. 1997;205(3): 749-756.
205. Barros P, Felgueiras H, Pinheiro D, et al. Restenosis after carotid artery stenting using a specific designed ultrasonographic protocol. J Stroke Cerebrovasc Dis. 2014;23(6):1416-1420.
206. Chahwan S, Miller MT, Pigott JP, et al. Carotid artery velocity characteristics after carotid artery angioplasty and stenting. J Vasc Surg. 2007;45(3): 523-526.
207. Setacci C, Chisci E, Setacci F, et al. Grading carotid intrastent restenosis: a 6-year follow-up study. Stroke. 2008;39(4):1189-1196.
208. Zhou W, Felkai DD, Evans M, et al. Ultrasound criteria for severe in-stent restenosis following carotid artery stenting. J Vasc Surg. 2008;47(1): 74-80.
209. Lal BK, Hobson RW 2nd, Tofighi B, et al. Duplex ultrasound velocity criteria for the stented carotid artery. J Vasc Surg. 2008;47(1):63-73.
210. Armstrong PA, Bandyk DF, Johnson BL, et al. Duplex scan surveillance after carotid angioplasty and stenting: a rational definition of stent stenosis. J Vasc Surg. 2007;46(3):460-465.
211. Chi YW, White CJ, Woods TC, Goldman CK. Ultrasound velocity criteria for carotid in-stent restenosis. Catheter Cardiovasc Interv. 2007;69(3): 349-354.
212. Furie DM, Tien RD. Fibromuscular dysplasia of arteries of the head and neck: imaging findings. Am J Roentgenol. 1994;162(5):1205-1209.
213. Kliewer MA, Carroll BA. Ultrasound case of the day. Internal carotid artery web (atypical fibromuscular dysplasia). Radiographics. 1991;11(3): 504-505.
214. Arning C, Grzyska U. Color Doppler imaging of cervicocephalic fibromuscular dysplasia. Cardiovasc Ultrasound. 2004;2:7.
215. Sethi SS, Lau JF, Godbold J, et al. The S curve: a novel morphological finding in the internal carotid artery in patients with fibromuscular dysplasia. Vasc Med. 2014;19(5):356-362.
216. Maeda H, Handa N, Matsumoto M, et al. Carotid lesions detected by B-mode ultrasonography in Takayasu's arteritis: "macaroni sign" as an indicator of the disease. Ultrasound Med Biol. 1991;17(7):695-701.
217. Ralls PW. Takayasu arteritis. Ultrasound Q. 2010;26(3):133-134.
218. Sallustio F, Di Legge S, Rossi C, Stanzione P. Ultrasound evaluation of early changes in arterial dissection. J Stroke Cerebrovasc Dis. 2010;19(2): 167-168.
219. Sturzenegger M. Spontaneous internal carotid artery dissection: early diagnosis and management in 44 patients. J Neurol. 1995;242(4): 231-238.
220. Sturzenegger M, Mattle HP, Rivoir A, Baumgartner RW. Ultrasound findings in carotid artery dissection: analysis of 43 patients. Neurology. 1995;45(4):691-698.
221. Steinke W, Rautenberg W, Schwartz A, Hennerici M. Noninvasive monitoring of internal carotid artery dissection. Stroke. 1994;25(5):998-1005.
222. Lupetin AR, Davis DA, Beckman I, Dash N. Transcranial Doppler sonography. Part 1. Principles, technique, and normal appearances. Radiographics. 1995;15(1):179-191.
223. LaRovere KL, O'Brien NF. Transcranial Doppler sonography in pediatric neurocritical care: a review of clinical applications and case illustrations in the pediatric intensive care unit. J Ultrasound Med. 2015;34(12): 2121-2132.
224. Comerota AJ, Katz ML, Hosking JD, et al. Is transcranial Doppler a worthwhile addition to screening tests for cerebrovascular disease? J Vasc Surg. 1995;21(1):90-95.
225. Rorick MB, Nichols FT, Adams RJ. Transcranial Doppler correlation with angiography in detection of intracranial stenosis. Stroke. 1994;25(10): 1931-1934.
226. Kwiatkowski J. Ultrasound screening helps prevent stroke in children with sickle cell disease. Science Centric. 2008;7.
227. Kalanuria A, Nyquist PA, Armonda RA, Razumovsky A. Use of transcranial Doppler (TCD) ultrasound in the neurocritical care unit. Neurosurg Clin N Am. 2013;24(3):441-456.
228. Lupetin AR, Davis DA, Beckman I, Dash N. Transcranial Doppler sonography. Part 2. Evaluation of intracranial and extracranial abnormalities and procedural monitoring. Radiographics. 1995;15(1):193-209.
229. Lin SK, Ryu SJ, Chu NS. Carotid duplex and transcranial color-coded sonography in evaluation of carotid-cavernous sinus fistulas. J Ultrasound Med. 1994;13(7):557-564.
230. Mast H, Mohr JP, Thompson JL, et al. Transcranial Doppler ultrasonography in cerebral arteriovenous malformations: diagnostic sensitivity and association of flow velocity with spontaneous hemorrhage and focal neurological deficit. Stroke. 1995;26:1024-1027.
231. Gaunt ME, Martin PJ, Smith JL, et al. Clinical relevance of intraoperative embolization detected by transcranial Doppler ultrasonography during carotid endarterectomy: a prospective study of 100 patients. Br J Surg. 1994;81(10):1435-1439.
232. Bendick PJ, Glover JL. Hemodynamic evaluation of vertebral arteries by duplex ultrasound. Surg Clin North Am. 1990;70(1):235-244.
233. Lewis BD, James EM, Welch TJ. Current applications of duplex and color Doppler ultrasound imaging: carotid and peripheral vascular system. Mayo Clin Proc. 1989;64(9):1147-1157.
234. Visona A, Lusiani L, Castellani V, et al. The echo-Doppler (duplex) system for the detection of vertebral artery occlusive disease: comparison with angiography. J Ultrasound Med. 1986;5(5):247-250.
235. Davis PC, Nilsen B, Braun IF, Hoffman Jr JC. A prospective comparison of duplex sonography vs angiography of the vertebral arteries. AJNR Am J Neuroradiol. 1986;7(6):1059-1064.
236. Yurdakul M, Tola M. Doppler criteria for identifying proximal vertebral artery stenosis of 50% or more. J Ultrasound Med. 2011;30(2): 163-168.
237. Bluth EI, Merritt CR, Sullivan MA, et al. Usefulness of duplex ultrasound in evaluating vertebral arteries. J Ultrasound Med. 1989;8(5):229-235.
238. Walker DW, Acker JD, Cole CA. Subclavian steal syndrome detected with duplex pulsed Doppler sonography. AJNR Am J Neuroradiol. 1982;3(6):615-618.
239. Kliewer MA, Hertzberg BS, Kim DH, et al. Vertebral artery Doppler waveform changes indicating subclavian steal physiology. Am J Roentgenol. 2000;174(3):815-819.
240. Gottesman RF, Sharma P, Robinson KA, et al. Imaging characteristics of symptomatic vertebral artery dissection: a systematic review. Neurologist. 2012;18(5):255-260.
241. Ackerstaff RG, Grosveld WJ, Eikelboom BC, Ludwig JW. Ultrasonic duplex scanning of the prevertebral segment of the vertebral artery in patients with cerebral atherosclerosis. Eur J Vasc Surg. 1988;2(6):387-393.
242. Elias DA, Weinberg PE. Angiography of the posterior fossa. In: Taverask JM, Ferrucci JT, editors. Radiology: diagnosis-imaging-intervention. Philadelphia: Lippincott; 1989.
243. Bendick PJ, Jackson VP. Evaluation of the vertebral arteries with duplex sonography. J Vasc Surg. 1986;3(3):523-530.
244. Carroll BA, Holder CA. Vertebral artery duplex sonography (abstract). J Ultrasound Med. 1990;9:S27-S28.
245. de Bray JM, Zenglein JP, Laroche JP, et al. Effect of subclavian syndrome on the basilar artery. Acta Neurol Scand. 1994;90(3):174-178.
246. Thomassen L, Aarli JA. Subclavian steal phenomenon. Clinical and hemodynamic aspects. Acta Neurol Scand. 1994;90(4):241-244.
247. Nicolau C, Gilabert R, Garcia A, et al. Effect of internal carotid artery occlusion on vertebral artery blood flow: a duplex ultrasonographic evaluation. J Ultrasound Med. 2001;20(2):105-111.
248. Williams CE, Lamb GH, Roberts D, Davies J. Venous thrombosis in the neck. The role of real time ultrasound. Eur J Radiol. 1989;9(1):32-36.
249. Hubsch PJ, Stiglbauer RL, Schwaighofer BW, et al. Internal jugular and subclavian vein thrombosis caused by central venous catheters. Evaluation using Doppler blood flow imaging. J Ultrasound Med. 1988;7(11): 629-636.

250. Gaitini D, Kaftori JK, Pery M, Engel A. High-resolution real-time ultrasonography. Diagnosis and follow-up of jugular and subclavian vein thrombosis. J Ultrasound Med. 1988;7(11):621-627.
251. Albertyn LE, Alcock MK. Diagnosis of internal jugular vein thrombosis. Radiology. 1987;162(2):505-508.
252. Falk RL, Smith DF. Thrombosis of upper extremity thoracic inlet veins: diagnosis with duplex Doppler sonography. Am J Roentgenol. 1987;149(4):677-682.
253. Weissleder R, Elizondo G, Stark DD. Sonographic diagnosis of subclavian and internal jugular vein thrombosis. J Ultrasound Med. 1987;6(10): 577-587.
254. de Witte BR, Lameris JS. Real-time ultrasound diagnosis of internal jugular vein thrombosis. J Clin Ultrasound. 1986;14(9):712-717.
255. Wing V, Scheible W. Sonography of jugular vein thrombosis. Am J Roentgenol. 1983;140(2):333-336.
256. Chin EE, Zimmerman PT, Grant EG. Sonographic evaluation of upper extremity deep venous thrombosis. J Ultrasound Med. 2005;24(6): 829-838.
257. Gribbin C, Raghavendra BN, Ginsburg HB. Ultrasound diagnosis of jugular venous ectasia. N Y State J Med. 1989;89(9):532-533.
258. Hughes PL, Qureshi SA, Galloway RW. Jugular venous aneurysm in children. Br J Radiol. 1988;61(731):1082-1084.
259. Jasinski RW, Rubin JM. CT and ultrasonographic findings in jugular vein ectasia. J Ultrasound Med. 1984;3(9):417-420.
260. Stevens RK, Fried AM, Hood Jr TR. Ultrasonic diagnosis of jugular venous aneurysm. J Clin Ultrasound. 1982;10(2):85-87.
261. Lee W, Leduc L, Cotton DB. Ultrasonographic guidance for central venous access during pregnancy. Am J Obstet Gynecol. 1989;161(4):1012-1013.
262. Bond DM, Champion LK, Nolan R. Real-time ultrasound imaging aids jugular venipuncture. Anesth Analg. 1989;68(5):700-701.
263. Machi J, Takeda J, Kakegawa T. Safe jugular and subclavian venipuncture under ultrasonographic guidance. Am J Surg. 1987;153(3):321-323.
264. Oh C, Lee S, Seo JM, Lee SK. Ultrasound guided percutaneous internal jugular vein access in neonatal intensive care unit patients. J Pediatr Surg. 2016;51(4):570-572.
265. Vezzani A, Manca T, Vercelli A, et al. Ultrasonography as a guide during vascular access procedures and in the diagnosis of complications. J Ultrasound. 2013;16(4):161-170.
266. Dresser LP, McKinney WM. Anatomic and pathophysiologic studies of the human internal jugular valve. Am J Surg. 1987;154(2):220-224.

CHAPTER 27

Peripheral Vessels

Mark E. Lockhart, Heidi R. Umphrey, Therese M. Weber, and Michelle L. Robbin

SUMMARY OF KEY POINTS

- Key aspects of vascular Doppler imaging include knowledge of anatomy and waveform morphology, scanning technique, and attention to detail.
- Spectral Doppler velocity criteria can characterize stenosis detected by gray-scale and color Doppler.
- Doppler evaluation of peripheral artery disease can provide diagnostic information and enable surgical planning and evaluation of bypass grafts.
- Extremity aneurysm and pseudoaneurysm have typical Doppler findings similar to other areas of the arterial system.
- Evaluation of the upper and lower extremity venous system is primarily performed with sonography.
- Differentiation of acute from residual or chronic deep venous thrombosis (DVT) with imaging and clinical parameters is often difficult.
- Controversial venous issues include clinical criteria for treatment of DVT, when to recommend a follow-up examination, calf vein evaluation, and two-point or focused examination approach.
- Preoperative sonographic mapping of upper extremity and thigh vessels assists surgical planning for placement of hemodialysis arteriovenous fistula (AVF) and grafts.
- Postoperative evaluation of hemodialysis AVF and grafts with ultrasound aids the assessment of AVF maturation, as well as evaluation for access stenosis, steal, thrombus, and focal complications.

CHAPTER OUTLINE

PERIPHERAL ARTERIES
Sonographic Examination Technique
Stenosis Evaluation
Lower Extremity Arteries
Normal Anatomy
Ultrasound Examination and Imaging Protocol
Peripheral Arterial Occlusion
Peripheral Arterial Stenosis
Aneurysm
Pseudoaneurysm
Arteriovenous Fistula
Lower Extremity Vein Bypass Grafts
Upper Extremity Arteries
Normal Anatomy
Ultrasound Examination and Imaging Protocol
Arterial Occlusion, Aneurysm, and Pseudoaneurysm
Arterial Stenosis
Subclavian Stenosis
Thoracic Outlet Syndrome
Radial Artery Evaluation for Coronary Bypass Graft

PERIPHERAL VEINS
Sonographic Examination Technique
Lower Extremity Veins
Normal Anatomy
Ultrasound Examination and Imaging Protocol
Acute Deep Venous Thrombosis
Residual (Chronic) Deep Venous Thrombosis
Potential Pitfalls
Complete Venous Doppler Versus More Limited Examinations
Recommendations for Deep Venous Thrombosis Follow-Up
Venous Insufficiency
Venous Mapping
Upper Extremity Veins
Normal Anatomy
Ultrasound Examination and Imaging Protocol
Upper Extremity Acute Deep Venous Thrombosis
Differentiation of Acute From Residual or Chronic Venous Thrombosis
Potential Pitfalls

HEMODIALYSIS
Sonographic Examination Technique
Vascular Mapping Before Hemodialysis Access
Upper Extremity
Ultrasound Examination and Imaging Protocol
Arteriovenous Fistula and Graft
Arteriovenous Fistula
Graft
Palpable Focal Masses Near Arteriovenous Fistula and Graft
Arteriovenous Fistula Maturation Evaluation
Arteriovenous Fistula and Graft Stenosis
Arterial Steal
Arm and Leg Swelling With Arteriovenous Fistula or Graft
Arteriovenous Fistula and Graft Occlusion

CONCLUSION

Prior chapters have described details of physics of Doppler analysis and use of ultrasound in the assessment of the vasculature supplying the head and neck. In this chapter we describe assessment of the peripheral arteries and veins, as well as arteriovenous fistula (AVF) and grafts. In general, these areas are readily evaluated by Doppler ultrasound. Because they are usually located at depths of 6 cm or less, the extremity vessels are more consistently imaged than those in the abdomen or thorax. Availability of sufficient imaging windows allows the transducer to be placed over the vascular area of interest with overlying tissue containing bone or gas. Transducers with frequencies greater than 5 MHz can typically be used.

Gray-scale sonography is useful for evaluating the presence of atherosclerotic plaque or confirming extravascular masses. Color flow Doppler imaging allows for a rapid survey of the area of interest, and then spectral Doppler can be used to characterize blood flow patterns.

Standardized protocols, such as those provided by the American College of Radiology (ACR), American Institute of Ultrasound in Medicine, and Society of Radiologists in Ultrasound should be followed.[1,2] It is recommended that examinations be performed in an accredited laboratory with participation in one of the vascular accreditation programs, such as the ACR or the Intersocietal Commission for the Accreditation of Vascular Laboratories, in order to achieve a national standard of excellence and to improve the chance of success of peripheral arterial and venous ultrasound examinations.[3] In the setting of a dedicated staff and with physician support, ultrasound can be used to diagnose many peripheral vascular abnormalities definitively and avoid the need for ionizing radiation or intravenous contrasted cross-sectional studies.

PERIPHERAL ARTERIES

A variety of symptoms and signs can be evaluated by arterial ultrasound. Sonographic examination is relatively rapid and has benefits over other modalities, such as real-time technique, lack of ionizing radiation, and relatively low expense. In the last two decades, the number of indications for peripheral artery ultrasound has expanded. The most recent ACR practice parameter on the topic lists indications for the examination, which include claudication and/or rest pain in the lower extremities to evaluate for arterial stenosis or occlusion.[2] Patients with pain, discoloration, or ulcer formation in the extremities (most commonly lower) may have tissue ischemia or necrosis from arterial stenosis or occlusion. Additional symptoms of numbness or cold extremity may be noted. However, symptomatology may vary depending on the rapidity of onset and whether collaterals have developed to decrease the effects of stenosis on the tissues. In some patients, vascular abnormalities may be subclinical and found incidentally on imaging for other indications. Once an abnormality has been identified, ultrasound can monitor progression of disease, determine success or failure after intervention, and identify acceptable vessels for bypass graft creation.

Other extremity abnormalities can be evaluated sonographically. Focal masses can be assessed to exclude vascular causes such as aneurysm or fistula with venous enlargement. When chronic positional upper extremity symptoms are present, ultrasound can evaluate for thoracic outlet syndrome. More peripherally, Doppler can document patency of the palmar arch in surgical planning for bypass graft harvesting, and it can assess the radial artery before and after vascular access.

In the acute setting, traumatic injuries can be evaluated to determine adjacent arterial patency. Pseudoaneurysms and dissections are visible by ultrasound in these patients. Specific levels of embolic disease can also be depicted.

Sonographic Examination Technique

Gray-scale evaluation of the peripheral arteries is important to determine the amount of atherosclerotic disease or thrombus present. The highest frequency transducer that allows good penetration and visualization should be applied, typically a 5- to 12-MHz linear array transducer, with a higher frequency transducer used in areas where the arteries are more superficial. Occasionally, a 3- to 5-MHz sector or curved array probe may be necessary in large patients or those with large amounts of edema.

Occasionally, atherosclerotic plaque or thrombus is hypoechoic, and color Doppler is extremely useful to evaluate residual lumen, with the gain adjusted so color does not overlap into adjacent tissues. The spectral Doppler gate is adjusted within the lumen of the artery to allow adequate signal. The scale and gain should be optimized to show strong flow signals that use most of the scale to display the waveform. Normally, a medium or high wall filter is used in arterial evaluation. If there is slow flow, a low wall filter may be used to improve detection. In general, for detection of small channels of slow flow in areas of near-occlusion, power Doppler may be more sensitive than color Doppler.[4] However, the advances in color Doppler may have reduced this difference in recent years.

The components of the sonographic evaluation differ based on the indication. For example, imaging for suspected arterial stenosis or occlusion is very different from evaluation of a focal mass or aneurysm. The technical components of the examination have been recently described in the ACR practice parameters.[2]

Stenosis Evaluation

Color and spectral Doppler imaging are key to **stenosis** evaluation, using a combination of waveform morphology and velocity characteristics. On gray-scale imaging, a focal stenosis or occlusion may be visible, but this should be confirmed by Doppler. Collaterals should also prompt additional attention with Doppler. Any areas of visible narrowing or turbulent color Doppler signal should be further characterized with spectral Doppler. A change in spectral waveform morphology from one arterial segment to the next should also be further evaluated with color and spectral Doppler to locate a point of transition (Fig. 27.1). Spectral Doppler should be performed in the longitudinal plane and should be angle corrected 60% or less from the center beam. If a jet at or downstream from a stenosis is seen, angle correction parallel to the orientation of the jet should be performed to more accurately measure peak systolic velocity (PSV). Using this technique, waveform morphology and peak velocity should be evaluated at any suspected area of stenosis, as well as the feeding vessel

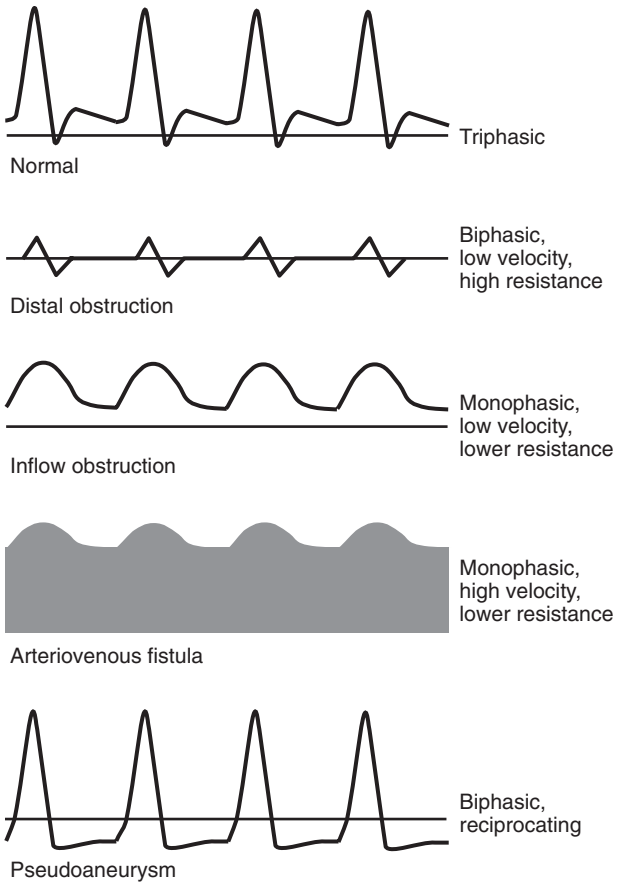

FIG. 27.1 Diagrams of Doppler Flow Patterns in Normal and Abnormal Scenarios. The normal **Doppler spectrum** of flowing blood **in the lower extremity** arteries typically has a **triphasic pattern:** (1) forward flow during systole, (2) a short period of flow reversal in early diastole, and (3) low-velocity flow during the remainder of diastole. Arterial Doppler signals are altered depending on the pathologic change. The four other patterns are examples of common arterial pathologies: distal obstruction, inflow obstruction, arteriovenous fistula, and pseudoaneurysm.

within 4 cm upstream, and the draining artery within 4 cm downstream. The inflow velocity is used as a reference to assess for increased peak velocity at the stenosis, and the downstream location is evaluated for peak velocity drop, decreased resistance, and **tardus parvus** morphology. The same concepts apply to bypass grafts, when looking for stenosis and occlusion, with additional evaluation at the anastomoses, which are common sites of abnormality. Ultrasound is the primary screening for bypass abnormalities but can be a time-consuming study if used to cover all areas of concern in a patient with diffuse atherosclerotic disease. If diffuse atherosclerotic disease is suspected, other imaging techniques such as computed tomography (CT) or magnetic resonance angiography may be able to survey large areas more effectively.

Lower Extremity Arteries

Normal Anatomy

Each lower extremity arterial system is primarily supplied from the **common femoral artery,** which originates from the **external iliac artery** at the level of the inguinal ligament and extends caudally a few centimeters until it divides into the **superficial femoral artery** (SFA) and **profunda femoris artery.** The profunda femoris artery supplies the femoral head and the deep muscles of the thigh through perforators, as well as the medial circumflex artery and the lateral circumflex artery. The **SFA** continues along the medial thigh to the adductor canal in parallel with the femoral vein (FV). Below the adductor canal, it becomes the **popliteal artery,** coursing posterior to the knee and supplying branches of the calf.

The popliteal artery branches into the **anterior tibial artery** and the **tibioperoneal trunk.** The anterior tibial artery courses laterally, perforating through the interosseous membrane between the tibia and fibula into the anterior compartment of the lower leg. The anterior tibial artery becomes the **dorsalis pedis artery** in the dorsum of the ankle and along the first intertarsal space of the foot. The tibioperoneal trunk divides after approximately 3 to 4 cm into the **posterior tibial artery** and the **peroneal artery.** The posterior tibial artery courses posterior to the medial malleolus of the ankle. The peroneal artery courses through the interosseous membrane above the ankle, and then supplies branches of the lateral ankle and foot.

Ultrasound Examination and Imaging Protocol

Lower extremity arterial inflow from the external iliac artery is assessed by groin insonation in supine position, and then each major vessel in the leg is directly evaluated throughout its entire course. **Normal arteries** have thin smooth walls with anechoic lumens and lack of atherosclerotic plaques or stenosis on gray-scale imaging (Fig. 27.2). After gray-scale evaluation, long arterial segments can be screened rapidly with color Doppler to find areas of suspected stenosis. Color Doppler is set to barely fill the lumen in a normal area of the artery. Color aliasing can alert the sonographer to areas of luminal narrowing that need to be evaluated further with spectral Doppler to determine significance. For evaluation of focal abnormalities other than stenosis, the examination may be limited to the general region of concern.

The ACR-AIUM-SRU practice parameter for the performance of peripheral arterial ultrasound suggests that lower extremity ultrasound should examine the common femoral artery; the proximal, mid, and distal SFA; and the popliteal artery above and below the knee.[2] Other arteries are examined as deemed clinically appropriate. The practice parameter states that these may include "iliac, deep femoral, tibioperoneal trunk, anterior tibial, posterior tibial, peroneal, and dorsalis pedis arteries." The guideline further suggests that angle-corrected longitudinal Doppler and/or gray-scale imaging should be documented in each normal and at any abnormal segment. Angle-corrected spectral Doppler is recommended proximal to, at, and beyond any suspected stenosis.[2] Supine position of the patient is acceptable for the thigh vessels, but a decubitus position may aid evaluation of the popliteal artery. Depending on the symptoms and findings of these arteries, imaging of the iliac arterial system may look for inflow disease, or imaging of the calf arteries may be indicated.

Normal outer diameters of the common femoral artery, SFA, popliteal artery, posterior tibial artery, and anterior tibial artery

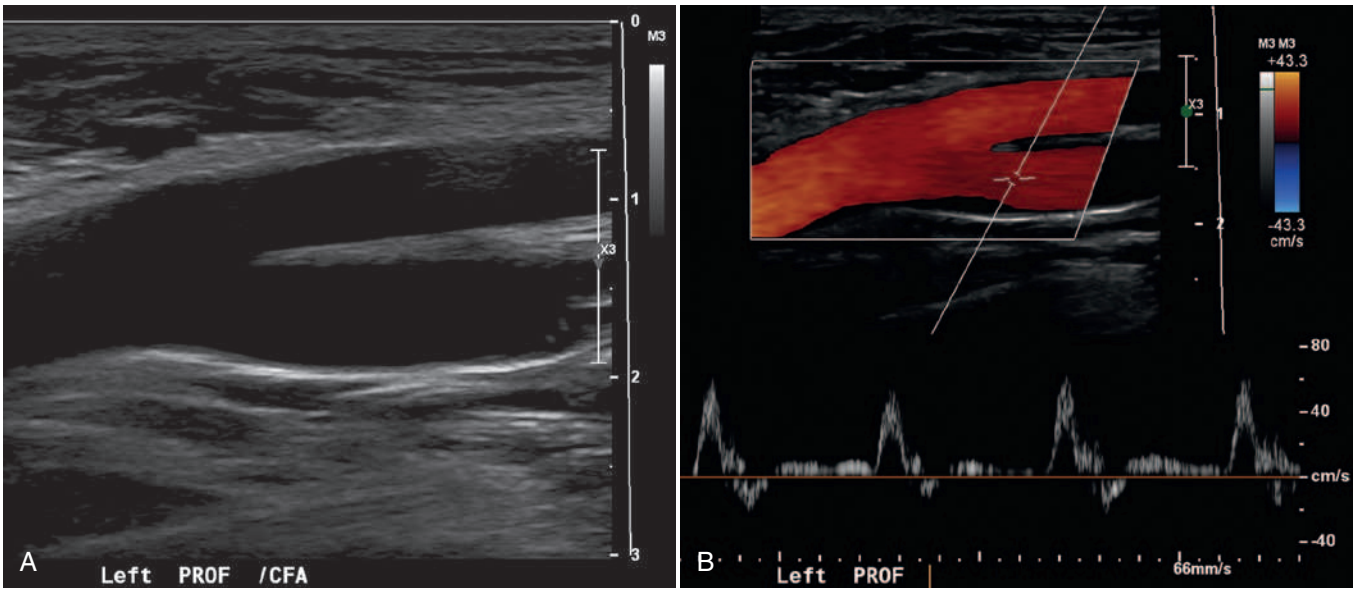

FIG. 27.2 Normal Common Femoral Artery Bifurcation. (A) Gray-scale imaging shows the normal appearance of arterial wall with lack of plaque. **(B)** Color and spectral Doppler normal triphasic spectral waveform in the profunda femoris artery.

are 8.1 mm, 6.1 mm, 6.0 mm, 2.1 mm, and 2.0 mm, respectively, and these vessels are slightly larger in males.[5] The common femoral artery, SFA, and popliteal artery become slightly larger with age, whereas the calf arteries become smaller.[5] **Laminar flow** is present without turbulence or aliasing on color Doppler. A high-resistance **triphasic waveform** with sharp upstroke and transient flow reversal is typically present in the normal lower extremity arteries on spectral Doppler. A monophasic waveform morphology that does not return to baseline can occur after exercise in normal patients, but can be also seen in lower extremity atherosclerotic disease. For differentiation, the PSV will decrease in the ischemic limb of a patient with peripheral artery disease after exercise, whereas it will increase in a patient with a healthy arterial system.

For calf assessment, a posterior medial approach is used for the posterior tibial artery in the midcalf with longitudinal Doppler, and then the artery can be followed proximally and distally. Alternatively, it can be found at the medial malleolus at the ankle and followed cranially. An anterior transducer placement is applied for the anterior tibial artery with the patient lying supine. The anterior tibial artery is well seen along the interosseous membrane near the fibula. The peroneal artery can also be seen from this anterior probe placement; it is more deeply located posterior to the interosseous membrane. A posterior lateral approach may also be used to locate the peroneal artery.

Peripheral Arterial Occlusion

Acute **arterial occlusion** is an emergent situation that can generate severe symptomatology and requires immediate attention. It is usually present in the setting of atherosclerotic disease, although traumatic dissection or embolic disease can occur (Fig. 27.3, Video 27.1). Use of Doppler allows for sensitive and specific demonstration of absent flow, and can differentiate occlusion from stenosis in the lower extremity with 98% accuracy.[6] In another study, sensitivities for occlusion of the SFA and popliteal artery were 97% and 83%, respectively.[7] In the lower leg, Doppler performs better in the anterior and posterior tibial arteries than in the peroneal. Doppler sensitivity for patency of the tibial artery was 93% in a recent study, but with many false positives related to angiography.[8]

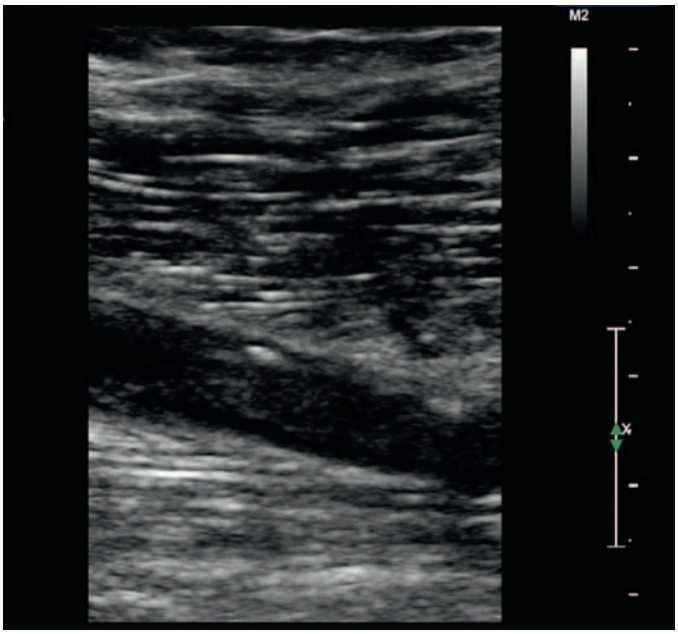

FIG. 27.3 Acute Thrombus in the Superficial Femoral Artery. Note the echogenic material within the arterial lumen. See also Video 27.1, which shows the thrombus to be slightly mobile.

On gray-scale imaging, the anechoic lumen is typically filled with medium-echogenicity thrombus. Using a similar technique as generally performed for detection of deep venous thrombus, the artery can be externally compressed by the transducer to show focal thrombus that is noncompressible. However, if the artery walls completely coapt, then the findings are likely artifactual. On color and spectral Doppler of an occluded artery,

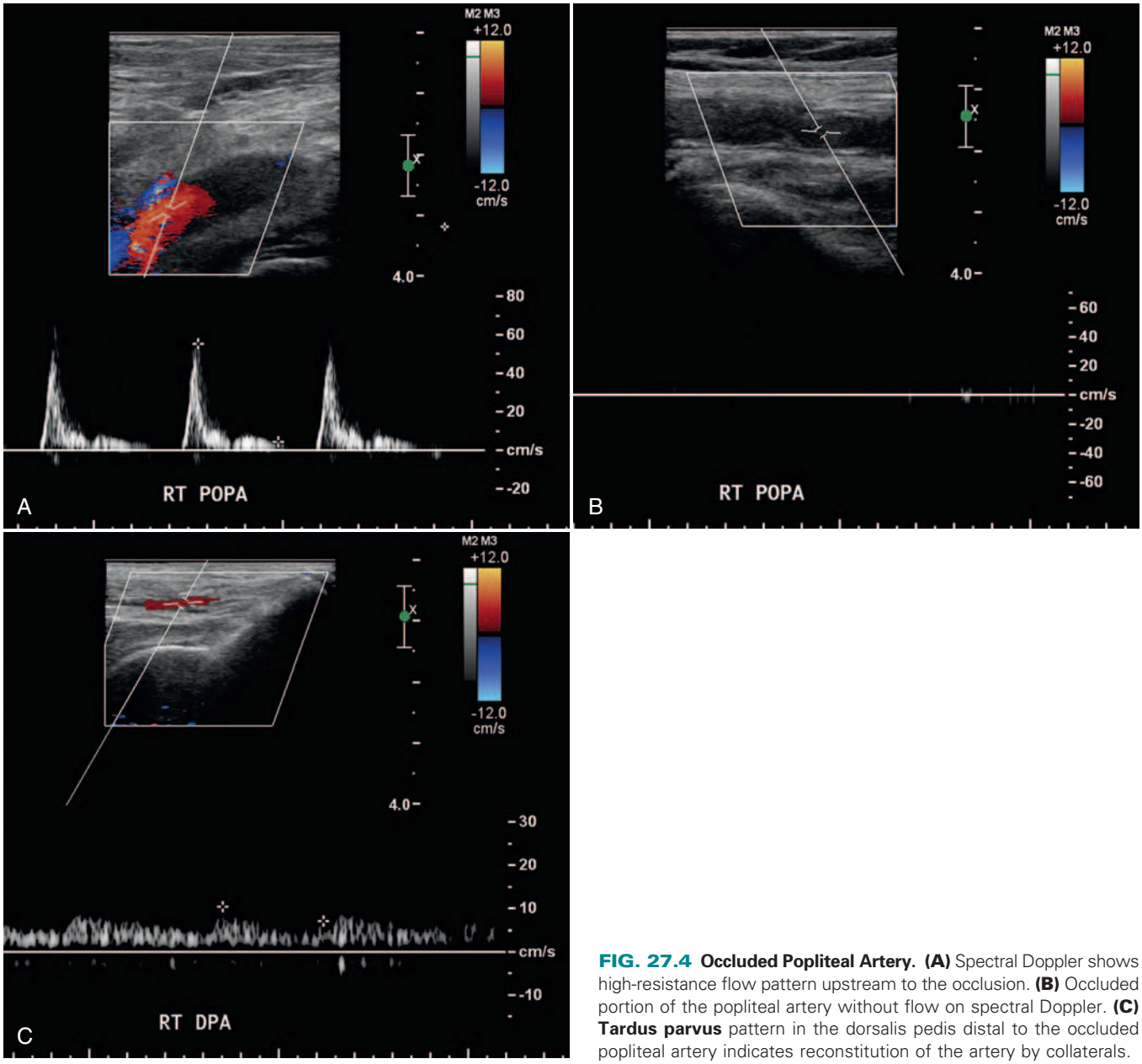

FIG. 27.4 Occluded Popliteal Artery. (A) Spectral Doppler shows high-resistance flow pattern upstream to the occlusion. **(B)** Occluded portion of the popliteal artery without flow on spectral Doppler. **(C) Tardus parvus** pattern in the dorsalis pedis distal to the occluded popliteal artery indicates reconstitution of the artery by collaterals.

no flow signal should be detectable (Fig. 27.4). Collaterals suggest chronic occlusion, but there may be a superimposed acute-on-chronic thrombotic component (Fig. 27.5, Video 27.2).

Peripheral Arterial Stenosis

Detection of **stenosis** in the setting of **atherosclerotic disease** is important owing to its role as a precursor to occlusion. Ultrasound is the primary screening tool for detection of stenosis, using a combination of gray-scale, color, and spectral Doppler. Duplex Doppler should be performed in these patients because of its superior performance relative to segmental Doppler pressures.[9] In a study of 151 lower extremities, duplex Doppler demonstrated 78% to 95% sensitivity and 97% to 100% specificity for high-grade lower extremity arterial stenosis. Spectral broadening can be seen in nonflow-limiting stenoses less than 50%, with an otherwise normal waveform (Fig. 27.6). As regional measurements are made in the arteries of the lower extremity, there may be a change noted from normal triphasic arterial morphology to a pulsatile but monophasic waveform that does not return to baseline or demonstrate transient reversal (Fig. 27.7). When this transition is encountered, the artery between these two measurements should be more closely evaluated by color and spectral Doppler to locate a focal velocity elevation associated with visible narrowing of the artery. Gray-scale can characterize overall plaque burden, but calcifications may limit sonographic penetration into the artery lumen (Fig. 27.8, Video 27.3).

In a patient with diffuse atherosclerotic disease and generalized calcifications, there may be numerous mild stenoses that have a combined effect to reduce flow pressures to the lower leg without a dominant stenosis. Gray-scale imaging is limited in its ability

to measure narrowing of the vessel, and velocity and waveform criteria are more widely applied. Color Doppler improves the examination by rapidly depicting areas of turbulent or high-velocity flow that can be further sampled by spectral Doppler for velocity characterization.

The main criteria for characterizing arterial stenosis involve waveform morphology, PSV, and end-diastolic velocity (EDV). For velocity criteria, the absolute values and the peak velocity ratio (defined as peak velocity at or in the downstream jet divided by peak velocity of the artery 2 cm upstream) have both been applied effectively. In a study of 338 arterial segments, focal increase in the PSV ratio at the stenosis relative to the adjacent nonstenotic artery exceeding 2.0 is consistent with at least 50% diameter stenosis when combined with spectral broadening and loss of transient flow reversal in the artery[10] (Fig. 27.9). The distal artery waveform will be abnormal with tardus parvus waveforms in the setting of stenosis greater than 50% (Fig. 27.10) but is typically normal if a lesser degree of stenosis is present.[10] Direct measurement of PSVs can also be performed. For the femoral-popliteal region of native vessels, a combination of thresholds of PSV greater than 200 cm/sec and ratio above 2:1 have been suggested as criteria for greater than 70% stenosis with sensitivity of 79% and specificity of 99%[11] (Fig. 27.11).

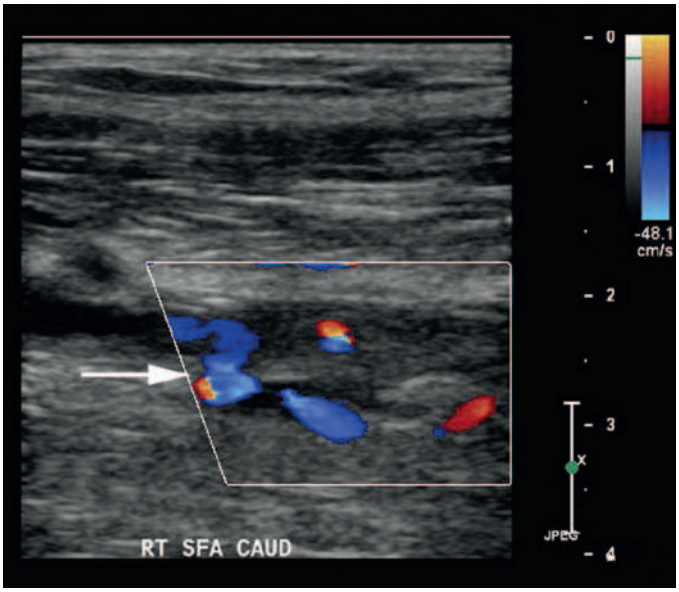

FIG. 27.5 Occlusion of the Superficial Femoral Artery With a Large Collateral Exiting Proximal to the Occlusion *(Arrow).* The presence of a collateral suggests chronic occlusion. See also Video 27.2.

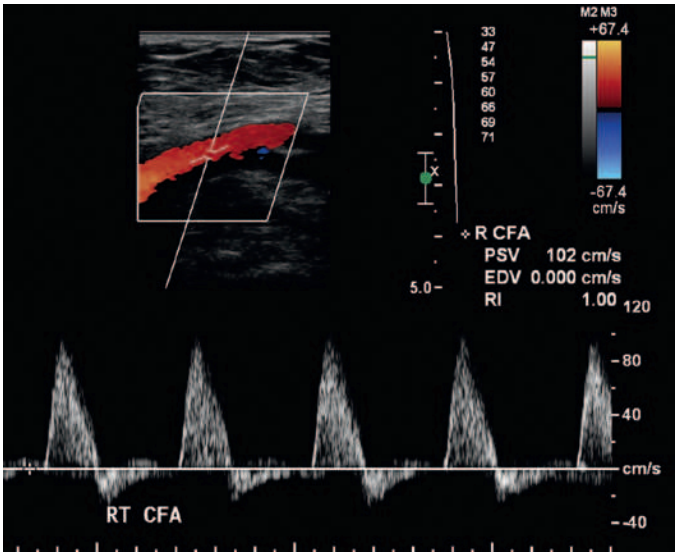

FIG. 27.6 Common Femoral Artery Stenosis. Color and spectral Doppler shows normal biphasic waveform, with fill-in of the waveform spectral envelope, indicating some degree of stenosis but less than 50%.

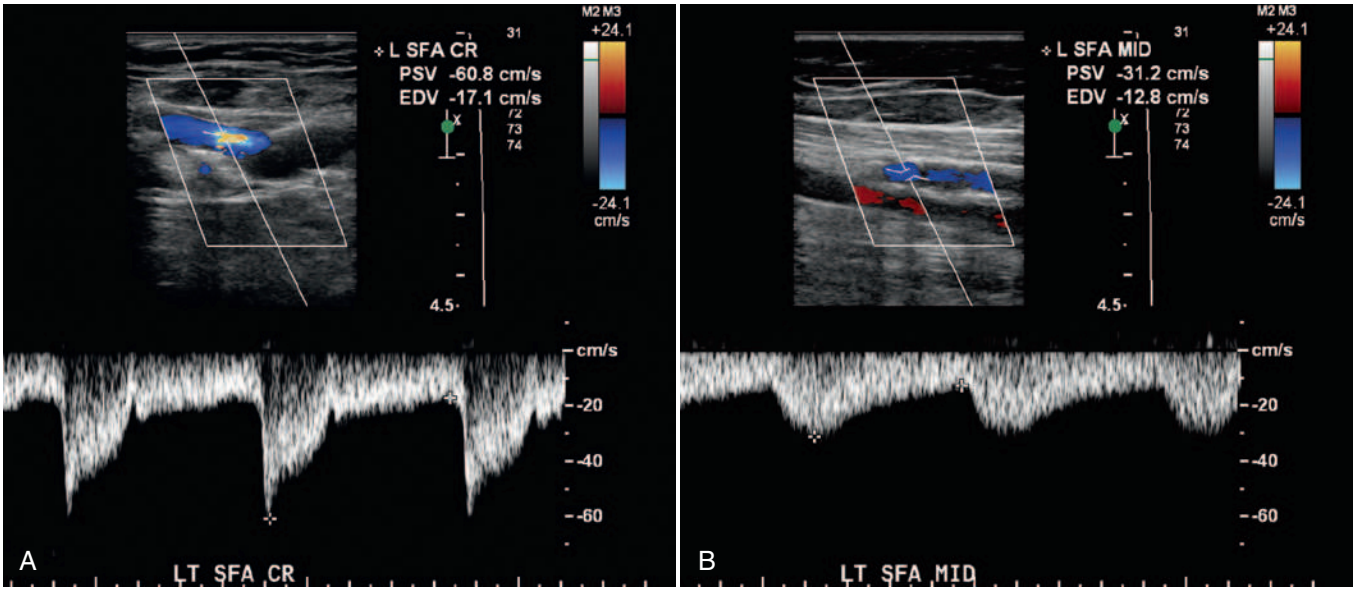

FIG. 27.7 Focal High-Grade Stenosis in the Proximal Superficial Femoral Artery (SFA). (A) Elevated peak systolic velocity at a focal high-grade stenosis in the proximal SFA. **(B)** Tardus parvus pattern downstream.

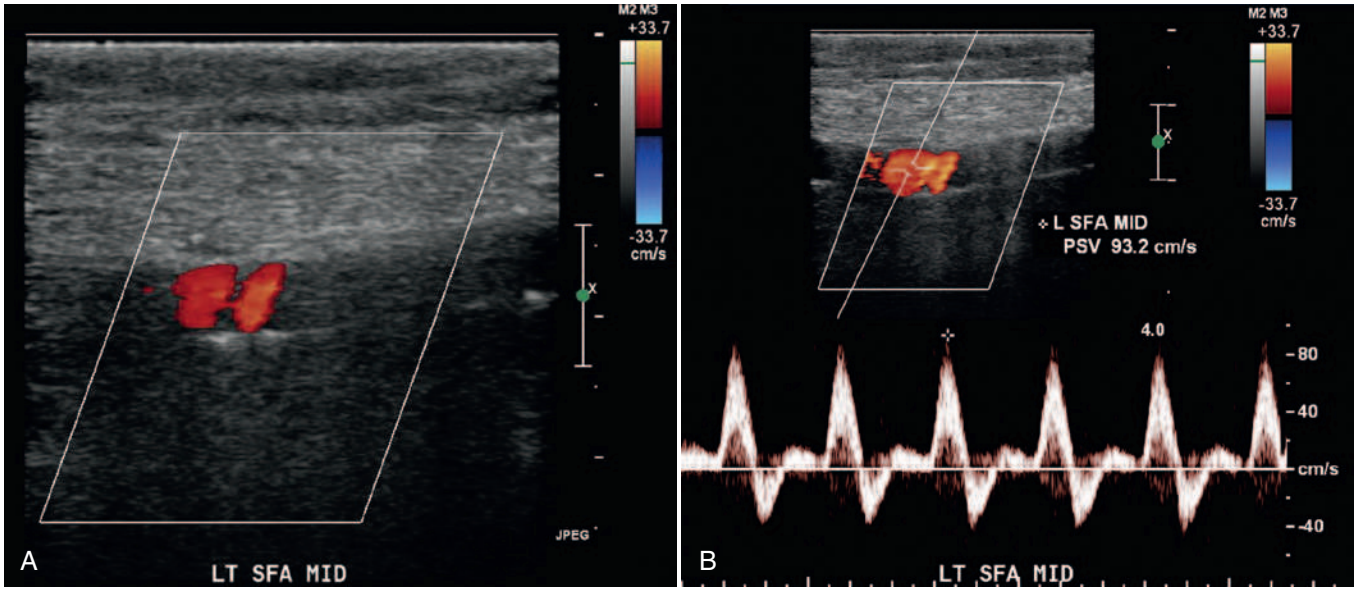

FIG. 27.8 Calcification of the Superficial Femoral Artery (SFA). (A) Severe calcification of the SFA limits ability to see within the artery lumen with gray-scale imaging. Color Doppler is useful to locate a place where spectral Doppler can be sampled. **(B)** Spectral Doppler of the artery has mild spectral broadening but otherwise normal triphasic waveform, without significant stenosis in this location. See also Video 27.3.

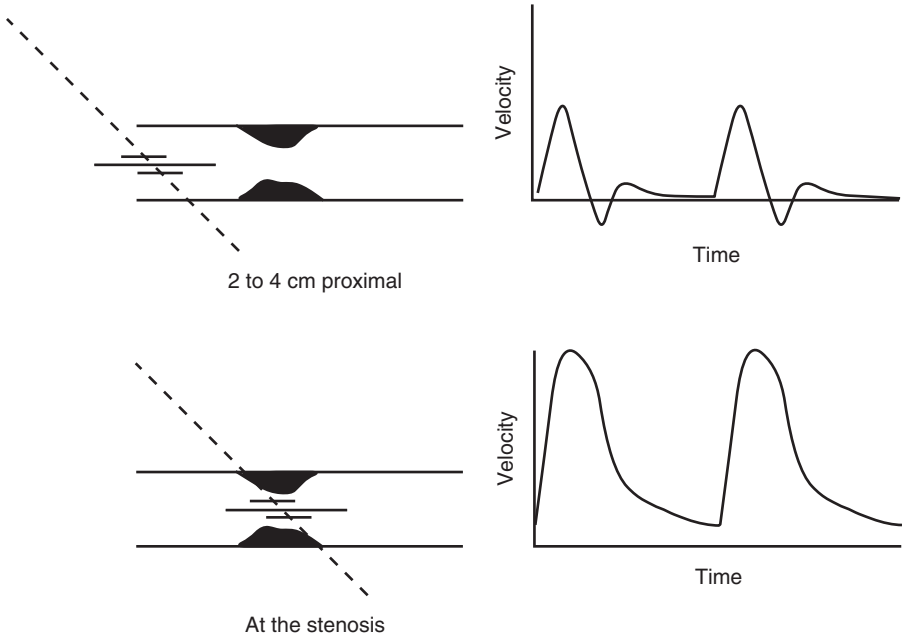

FIG. 27.9 Blood Flow Velocity Alterations Occur With Stenosis of at Least 50%. Proximal to the lesion, the flow pattern is normal. At the stenosis, the peak systolic velocity increases in proportion to the degree of stenosis. Alterations in the diastolic portion of the Doppler waveform sampled at the lesion depend on the state of the distal arteries and the severity and geometry of the lesion; diastolic flow may increase dramatically or may be almost absent.

Ultrasound can direct intervention in these patients. Patients with nonacute conditions can benefit from ultrasound to characterize subacute occlusion or embolic disease versus chronic ischemic disease to help the surgeon decide among therapies such as thrombectomy or bypass procedure.[12,13] Mapping with Doppler before bypass is very useful. Lesions are characterized by severity using the Trans-Atlantic Inter-Society Consensus (TASC) guidelines.[14] Isolated and short category A and B lesions typically are directed to endovascular repair, whereas more complex or longer lesions, C and D, in general require bypass. In one study of 622 TASC C or D lesions, Doppler mapping successfully identified lesions for intervention with sensitivity of 97% and specificity of 99%.[15] Similar high accuracy has been shown in other studies as well.[16,17]

Doppler can also predict which lesions are suitable for percutaneous transluminal angioplasty with good success.[18,19] However, duplex assessment may underestimate the length of **stenosis.** The lesions treated by angioplasty are generally short

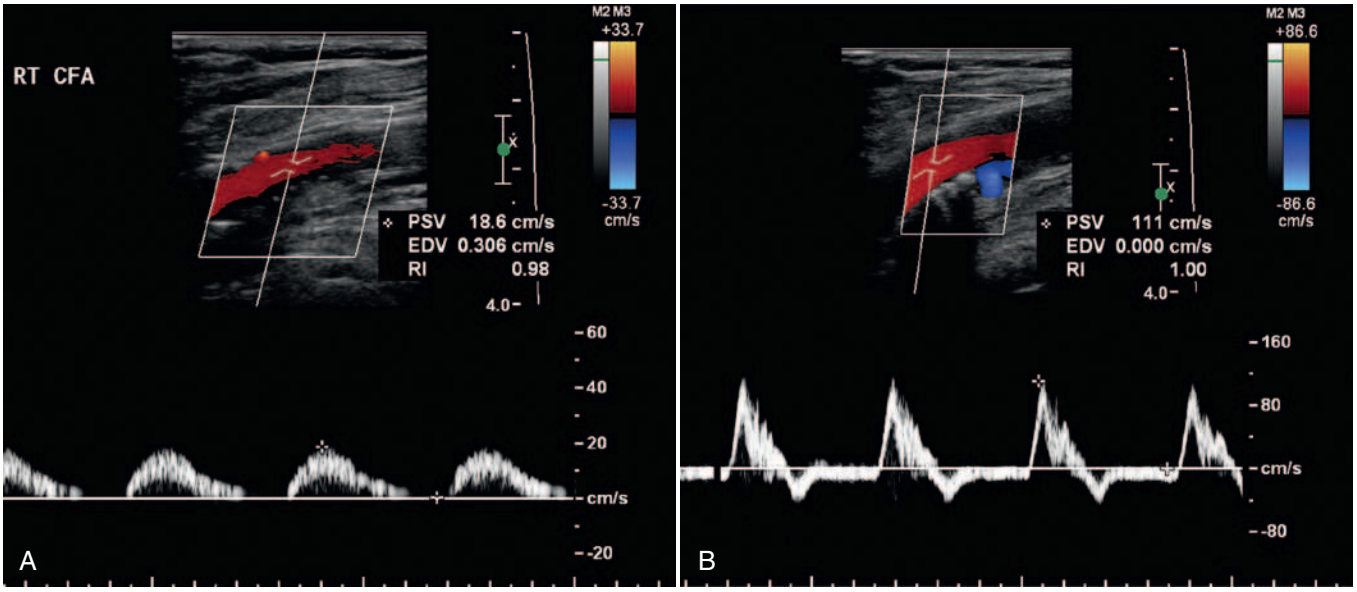

FIG. 27.10 Iliac Artery Stenosis With Tardus Parvus Waveform. (A) Tardus parvus waveform in the right common femoral artery indicates severe upstream stenosis or occlusion. **(B)** Normal velocity biphasic waveform of the contralateral left common femoral artery indicates atherosclerotic disease is in right common or external iliac artery, and not in the aorta (unilateral abnormal waveform).

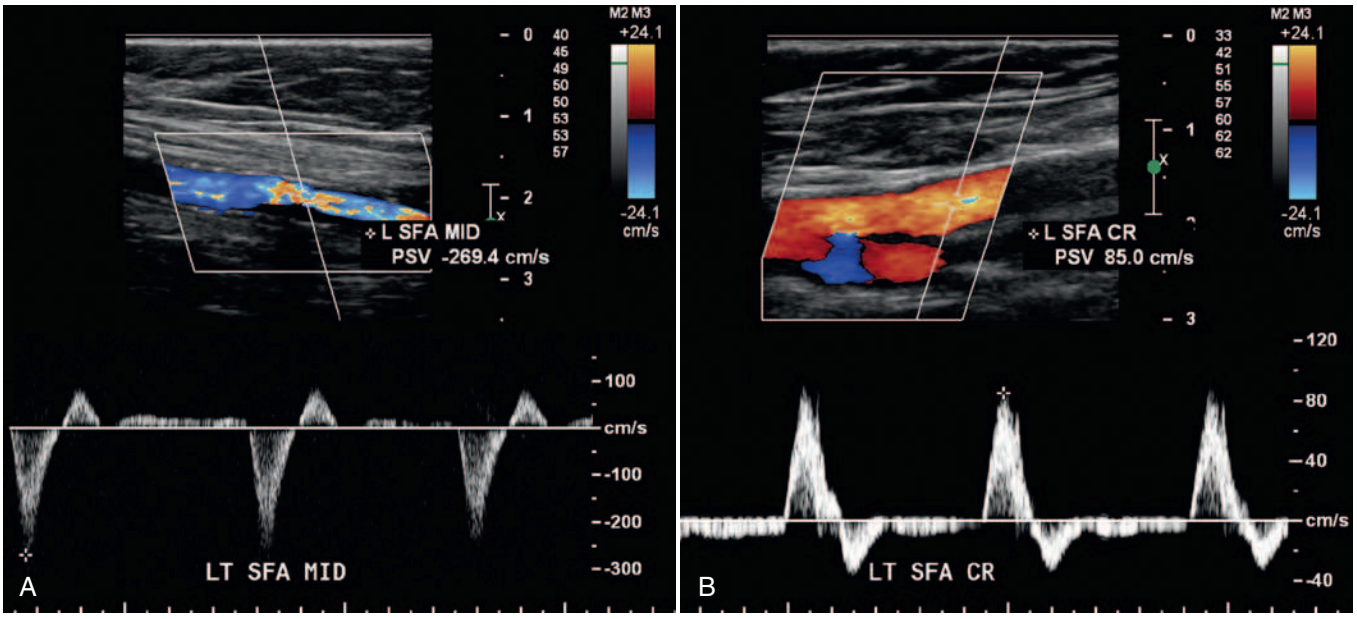

FIG. 27.11 Superficial Femoral Artery (SFA) With >70% Stenosis. (A) Moderately severe stenosis in the SFA with a peak systolic velocity (PSV) of 269 cm/sec. **(B)** At 4 cm upstream from the stenosis the PSV is 85.0 cm/sec, for a ratio exceeding 3:1, indicative of greater than 70% stenosis.

and isolated and have a diameter reduction of greater than 50%. In patients with endovascular intervention and stenting, Doppler can monitor success of the procedure and survey for recurrent stenosis at follow-up. In patients treated for critical limb ischemia, Doppler follow-up should occur every 3 months for the first year.[20] Normal triphasic waveforms at the ankle help exclude stenosis, but spectral Doppler is still performed even in the absence of symptoms. For evaluation of stenosis within a stented artery, the best Doppler criteria to characterize SFA in-stent stenosis of 80% or greater include a combination of PSV above 275 cm/sec and PSV ratio (the ratio of the highest PSV within the stent to the PSV in a disease-free arterial segment 3 cm above the stented area) above 3.5.[21] In patients with stent repair of SFA stenosis, Doppler and CT angiography have strong agreement.[22]

Aneurysm

An **aneurysm** occurs when weakness of the arterial layers allows expansion of the arterial caliber beyond normal limits. Aneurysms of the peripheral arteries are uncommon, but most are found in

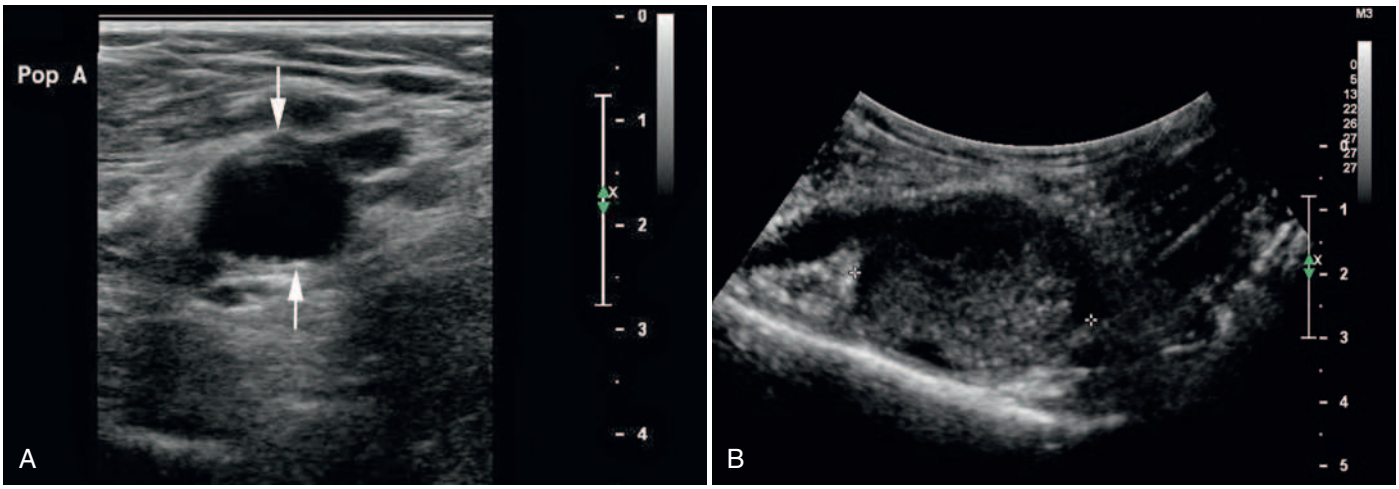

FIG. 27.12 Popliteal Artery Aneurysms. (A) Popliteal artery aneurysm measures 1.2 cm diameter *(arrows)*. **(B)** In a different patient, a 3.7-cm popliteal artery aneurysm contains low-level echoes and is partially thrombosed *(cursors)*.

the popliteal regions.[23] Less commonly, aneurysms are present in the SFA. In more than half of patients with popliteal artery aneurysm, they are bilateral. An association exists between popliteal artery aneurysms and abdominal aortic aneurysm, and thus if a popliteal artery aneurysm is found, the abdominal aorta should be evaluated. There is also an association among peripheral artery aneurysm, tobacco use, and hypertension. Peripheral artery aneurysms may contain clot, which may result in distal emboli with or without soft tissue ischemia and infarction. In these cases, intervention is necessary regardless of aneurysm size. The walls of an aneurysm may calcify, and the presence of calcifications may have some protective effects against rupture.

On gray-scale ultrasound, an aneurysm may appear as a fusiform anechoic or hypoechoic mass along the course of an artery. The Doppler signal depends on the amount of thrombus, the size of the neck of the aneurysm, and presence of calcification. Aneurysms may be saccular and commonly occur at branch points. The normal popliteal artery measures 4 to 6 mm in diameter.[24] A bulge or focal enlargement of 20% of the vessel diameter constitutes a simple functional definition of an aneurysm (Fig. 27.12). Empirically, a 2-cm cutoff has been used to determine need for intervention.[25] For popliteal artery aneurysm, surgical exclusion (ligation of the aneurysm) is the traditional treatment and has high rates of success.[26] However, a recent meta-analysis showed that endovascular repair has similar success.[27] Doppler ultrasound can be used to monitor the success of the intervention.[28] Aneurysm exclusion with covered stents is an increasingly used therapy in place of surgical intervention. Doppler ultrasound can be used to monitor the patency of the stent and confirm the exclusion of the aneurysm from the circulation.[29,30]

Pseudoaneurysm

Pseudoaneurysm describes disruption of an artery with flow in a space beyond the vessel wall. It may arise from any arterial structure and may occur with direct trauma or tumor or inflammatory erosion. Pseudoaneurysms are found in less than 1% of diagnostic angiography examinations and more commonly in coronary angiography.[31] Pathologically, the arterial wall has been at least partially breached. Outer arterial layers, perivascular tissues, clot, or reactive fibrosis contain the pseudoaneurysm sac.[32] The mechanism of pseudoaneurysm formation has been well characterized. A hematoma forms adjacent to the artery at the point of injury. Eventual lysis of the clot results in pseudoaneurysm.

A pseudoaneurysm is different from an aneurysm in that at least one layer of wall is disrupted. It differs from active extravasation in that blood within the pseudoaneurysm flows back into the feeding artery through a narrowed opening rather than into adjacent tissues. Arteriovenous communication, when present, is used to guide appropriate therapy. In patients with arteriovenous communication, thrombin repair is contraindicated owing to the potential for embolization of the thrombin into the venous system with resultant unintended regions of thrombosis.

Gray-scale ultrasound is typically performed first to identify the abnormality. The pseudoaneurysm can appear as a round or oval anechoic structure with or without associated thrombus. When present, thrombus appears isoechoic or hypoechoic; it may be located along the edge of the pseudoaneurysm lumen. Attention should be directed to these areas of extraluminal hematoma or any anechoic collections to determine if there are areas of flow with color Doppler. If flow is detected, spectral Doppler is next performed to characterize arterial versus venous flow and to exclude a superimposed AVF. In the patent portion of a pseudoaneurysm, there may be turbulent or disorganized intraaneurysmal flow with a "yin-yang" appearance. Communication of the sac with the adjacent artery occurs through a neck with a typical "to-and-fro" biphasic flow on spectral Doppler[33] (Fig. 27.13, Video 27.4). Measurement of the neck length and diameter of the neck off the artery is performed as part of the assessment before thrombin injection. A neck with larger diameter has clinical implications because these are less successfully treated by thrombin injection. If the sac is thrombosed, the neck may represent the only patent portion of the pseudoaneurysm. At least one-third of pseudoaneurysm require repair, but spontaneous closure is common for pseudoaneurysm smaller than 1.8 cm in diameter.[34] If the sac is patent, ultrasound-guided thrombin

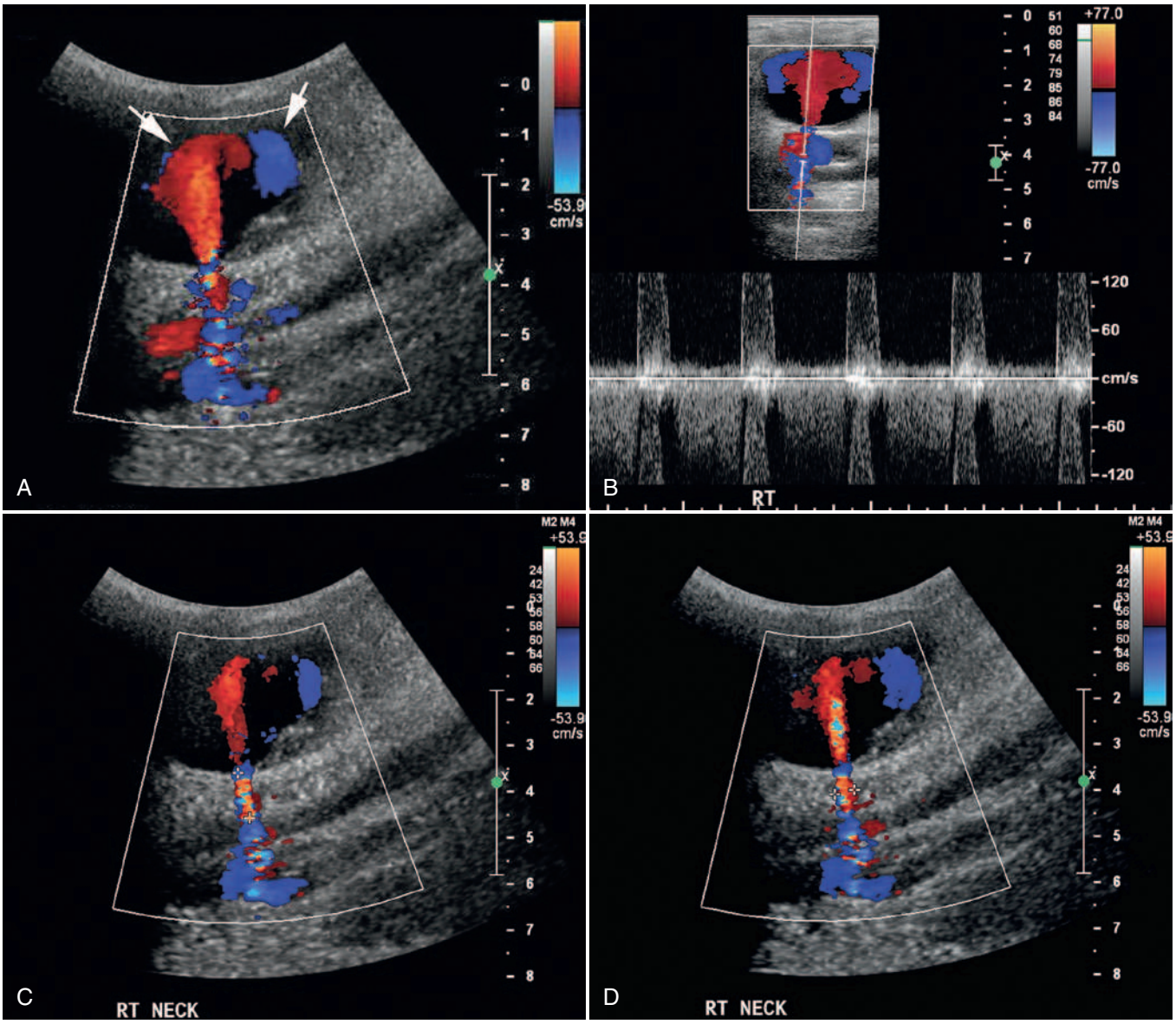

FIG. 27.13 Common Femoral Artery Pseudoaneurysm. (A) Common femoral artery pseudoaneurysm with "yin-yang" color flow pattern in the pseudoaneurysm *(arrows)*. **(B)** Spectral Doppler of the pseudoaneurysm neck shows a high-velocity "to-and-fro" pattern. **(C)** Measurement of the length of the neck from the common femoral artery to the pseudoaneurysm *(calipers)*. **(D)** Measurement of the diameter of the neck *(calipers)* off of the common femoral artery indicates size of hole in artery; a "rent" in the artery is less amenable to thrombin injection. It is preferable to measure the diameter in gray-scale because color may overestimate the diameter, but sometimes the neck cannot be seen without color (as in this case). See also Video 27.4.

injection into the pseudoaneurysm to thrombose is commonly performed, with a success rate of 94% to 97% without surgical intervention.[35-37] Treatment with sonographically guided direct compression has been used in the past but is less successful (up to 85% pseudoaneurysm thrombosis).[38]

Arteriovenous Fistula

The term **"fistula"** describes an abnormal communication between the arterial and venous circulations. There is disruption through all layers of the arterial wall as well as a focal disruption of a nearby venous structure, allowing communication from high–arterial pressure to low-pressure veins. This communication bypasses the capillary bed. It can be congenital, acquired, or rarely spontaneous in nature. Fistulas may be seen after autologous vein bypass grafting[39] and do not appear to affect patency of the graft.[40] In the absence of bypass graft, most are acquired and usually associated with a history of trauma.[41] A **traumatic arteriovenous fistula** may course from normal artery to normal vein in the setting of trauma, but congenital **arteriovenous malformations** (AVMs) may occur with associated abnormal vascular structures. Many are asymptomatic. However, symptomatic AVFs do not typically spontaneously resolve and often require surgery.[42]

Gray-scale imaging may show very little arterial abnormality in a traumatic fistula, but the cluster of dilated structures of an AVM can be identified. In either abnormality, there may be venous

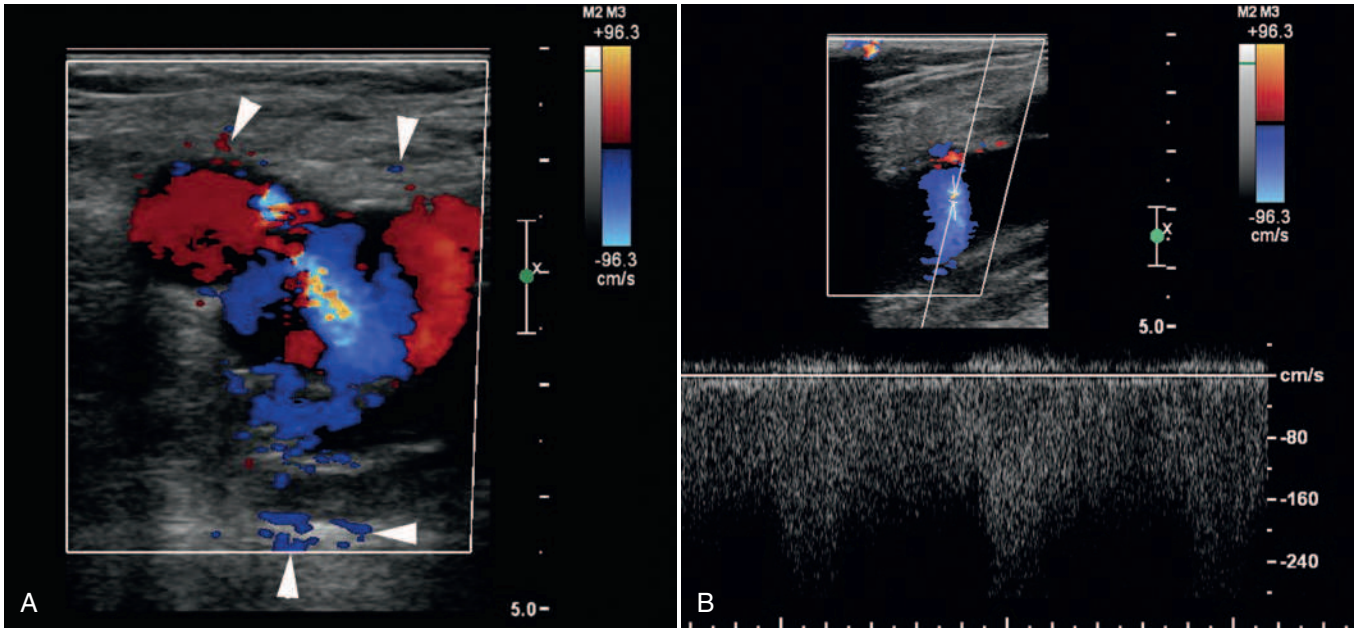

FIG. 27.14 Common Femoral Artery to Common Femoral Vein Arteriovenous Fistula (AVF). (A) Color Doppler shows common femoral artery to common femoral vein AVF. Note the adjacent tissue vibration artifact *(arrowheads)*. **(B)** Arterialized turbulent flow is seen within the vein just downstream to the AVF. See also Video 27.5.

dilation. Color Doppler ultrasound is the best noninvasive imaging modality to evaluate AVF or AVM and may show a large cluster of tortuous vessels with abnormal hyperemic flow. Spectral Doppler waveforms of the inflow arteries feeding the AVF may show low-resistance flow because they bypass the capillary bed. Doppler can show arterialized waveforms in the venous structures near the AVF. **Tissue vibration artifact** is commonly seen with AVFs, consisting of color pixels erroneously placed in the adjacent soft tissue by the ultrasound scanner because of the marked turbulence of the AVF. If the tissue vibration artifact is seen, a search should be made for an AVF. The arterialized waveform may be better seen during the Valsalva maneuver because with the increased thoracic pressure it causes, normal antegrade venous flow is decreased (Fig. 27.14, Video 27.5).

Lower Extremity Vein Bypass Grafts

Bypass grafts may use arterial segments or veins for arterial revascularization. Like bypass conduits in other portions of the body, these have potential complications that can limit their functionality. Failures soon after surgery may result from poor bypass conduit selection or surgical technical factors such as poor selection of the sites for anastomosis. In addition, the valves of an autologous vein may not be fully lysed during surgical preparation. Although completion imaging is commonly performed at the time of surgery, a recent study showed no improvement in graft survival in patients with intraoperative completion angiography or ultrasound.[43,44] In the longer term, fibrosis may occur at the site of a vein valve, or there may be intimal hyperplasia at an anastomotic region. If the bypass survives long enough, the underlying atherosclerotic disease may affect the bypass and inflow vessels to limit function. For synthetic grafts, the characterization of occlusion is similar to the native vessels, with absence of flow on color or spectral Doppler. Echogenic thrombus may be identified within the graft on gray-scale technique.

Ultrasound is a good technique to identify lesions that are likely to result in native vein bypass graft failure. Once the arterial bypass graft has been created, ultrasound is the primary screening modality; Doppler surveillance with revisions when needed is cost-effective.[45] The diagnosis depends on visible identification of **stenosis** on gray-scale imaging in combination with characterization by color and spectral Doppler. Normal triphasic or biphasic waveforms in the ankle arteries distal to the bypass suggest patency of the bypass. Generalized reduced or monophasic flow velocities in a graft are concerning for disease, and further search for a focal abnormality should be performed. Color Doppler sonography can be used to search for areas of aliasing, and subsequent spectral Doppler evaluation for velocity changes is then performed. When a stenosis is detected in a nonbranching vessel, a velocity ratio can be applied to evaluate significance. The PSV ratio is calculated by dividing the PSV at the stenotic site by peak velocity in the graft 2 cm upstream. A PSV ratio of at least 2.0 corresponds to at least 50% diameter stenosis.[46,47] Likewise, a PSV above 180 cm/sec has been associated with stenosis of greater than 50% diameter[47] in lower extremity bypass vein grafts (Fig. 27.15, Video 27.6).

Several ultrasound parameters, including PSV ratio, are associated with future bypass **graft dysfunction.** Once the PSV ratio measures at least 3.5 to 4.0, showing severe stenosis, treatment should be considered if it has not been performed at less severe degrees of stenosis, even in less symptomatic patients.[46,47] A recent study of Doppler and CT showed that patients with PSV ratio above 3.5 were at high risk for graft failure, whereas high-grade stenosis on CT did not correlate as well with graft failure.[48] Velocity criteria for severe stenosis used by Wixon and

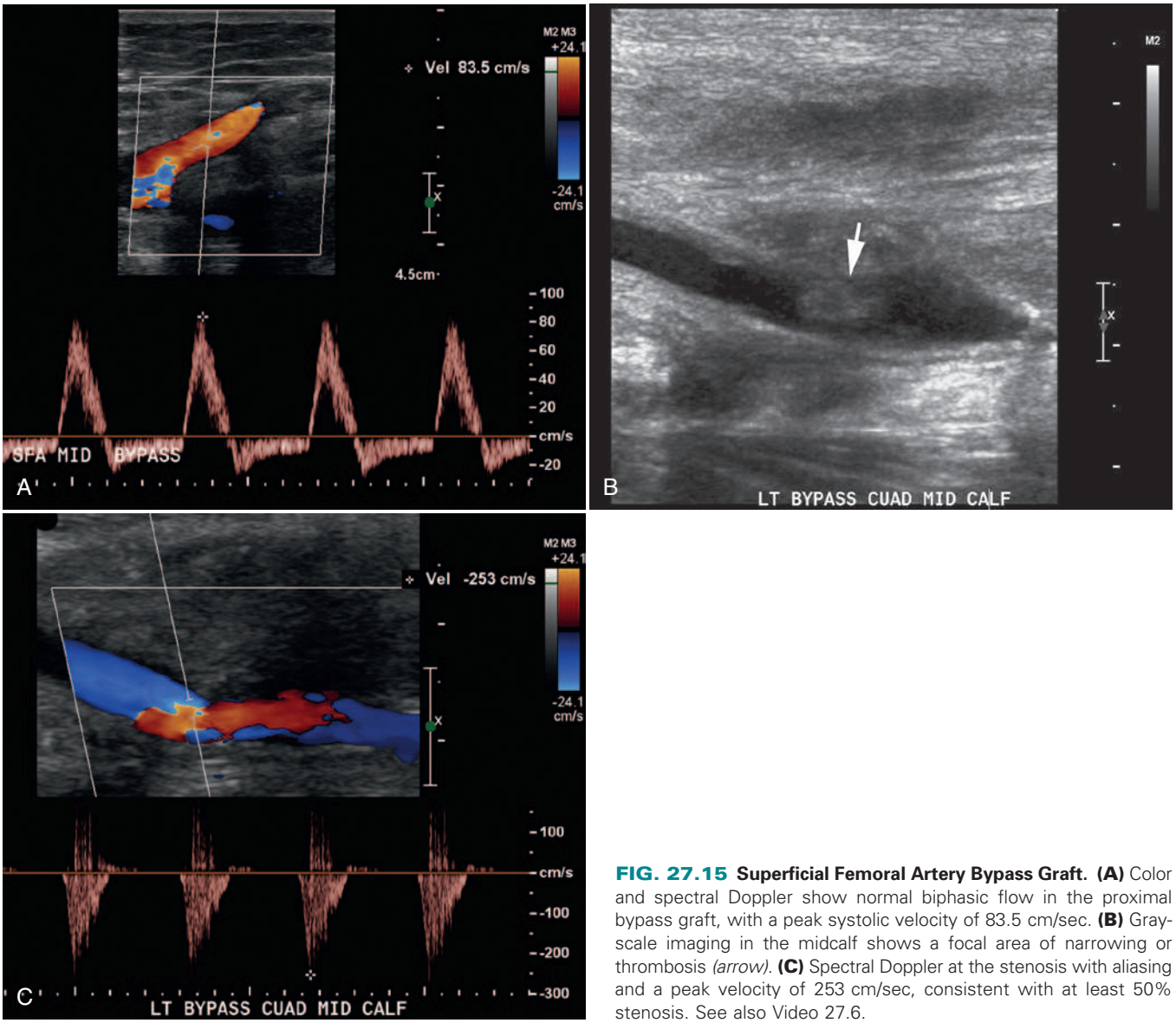

FIG. 27.15 Superficial Femoral Artery Bypass Graft. (A) Color and spectral Doppler show normal biphasic flow in the proximal bypass graft, with a peak systolic velocity of 83.5 cm/sec. **(B)** Gray-scale imaging in the midcalf shows a focal area of narrowing or thrombosis *(arrow)*. **(C)** Spectral Doppler at the stenosis with aliasing and a peak velocity of 253 cm/sec, consistent with at least 50% stenosis. See also Video 27.6.

colleagues suggest that PSV above 300 cm/sec and PSV ratio above 3.5 should direct the patient to intervention of a vein graft stenosis. In patients who meet these criteria, the intervention should be immediate if flow velocity within the graft falls below 45 cm/sec.[45] Decreased flow relative to a prior study is also a worrisome finding on spectral Doppler. In surveillance of vein grafts by Doppler with intervention on stenotic lesions, there is increased survival of the surveillance group. In patients with greater than 70% stenosis, 100% of grafts failed without revision, but only 10% failed with ultrasound detection and a subsequent revision pathway.[49]

Patients with venous bypass graft may form pseudoaneurysms or true aneurysms, but these are rare. When present, they occur most frequently in the anastomotic regions. In a study of saphenous vein grafts, only 10 of 260 (4%) developed true arterial aneurysm,[50] with higher incidence in patients with preexisting aneurysm and in males. The average time to diagnosis was 7 years after graft placement.[51]

Upper Extremity Arteries

Normal Anatomy

Each **upper extremity arterial system** is supplied from either the **brachiocephalic artery** (right) or the **subclavian artery** (left) in patients without normal anatomic variations. The artery is anterior to the vein when insonated from the supraclavicular fossa. The subclavian artery courses laterally and becomes the **axillary artery** once it is beyond the lateral margin of the first rib. The axillary artery courses medially over the proximal humeral head to the inferior margin of the pectoralis muscle, where it becomes the **brachial artery.** The brachial artery typically courses along the medial upper arm to the antecubital fossa and divides into the radial, ulnar, and smaller interosseous arteries.

Occasionally, there is high brachial artery bifurcation above the antecubital fossa[52] (Fig. 27.16). Regardless of the level of origin, the radial and ulnar branches extend to the wrist. On gray-scale imaging, normal upper extremity arteries have smooth

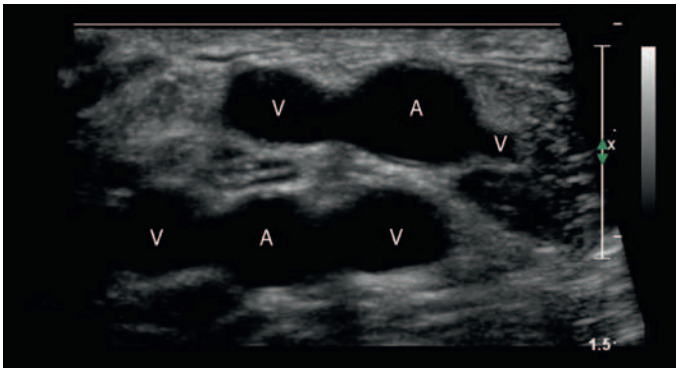

FIG. 27.16 High Brachial Artery Bifurcation. High brachial artery bifurcation, with two arteries *(A)* (radial and ulnar) and their paired accompanying veins *(V)*, above the antecubital fossa.

walls with anechoic lumens and lack of atherosclerotic plaques or stenosis, similar to lower extremity arteries. Laminar flow is present without turbulence or aliasing on color Doppler. A similar high-resistance triphasic waveform with sharp upstroke and transient flow reversal is typically present in the upper extremity arteries on spectral Doppler.

Ultrasound Examination and Imaging Protocol

Higher frequency imaging is usually possible owing to decreased size of the arm with respect to the leg. The subclavian artery, axillary artery, and brachial artery are evaluated to the level of the elbow. Both upper extremities should usually be insonated so that the symptomatic side can be compared with the asymptomatic. The ipsilateral innominate artery should be evaluated to determine an abnormal inflow etiology of the problem when the subclavian artery waveform is abnormal. In the forearm, imaging of the radial and ulnar arteries is the key to most diagnoses.

The ACR-AIUM-SRU practice parameter for the performance of peripheral arterial ultrasound suggests that upper extremity ultrasound should examine the subclavian artery, axillary artery, and brachial artery.[2] Other arteries are examined as deemed clinically appropriate. It states that these may include "innominate, radial, and ulnar arteries, and the palmar arch." The guideline further suggests that angle-corrected longitudinal Doppler and/or gray-scale imaging should be documented in each normal and at any abnormal segment. Angle-corrected spectral Doppler is recommended proximal to, at, and beyond any suspected stenosis.[2]

Arterial Occlusion, Aneurysm, and Pseudoaneurysm

Upper arm arterial **occlusion** is usually the result of trauma, often iatrogenic. The rate of radial artery occlusion after artery access for coronary angiography may be as high as 30.5%, although lower rates are also reported in the literature.[53] For surgical bypass harvest planning, documentation of patency of the **palmar arch** is an additional component. For detection and characterization of arterial aneurysm, the maximal outer diameters of the aneurysm should be measured in transverse (short axis) with gray-scale technique. Doppler can differentiate the patent component from mural thrombus. In **pseudoaneurysm** characterization, the size and Doppler components are also measured, but the pseudoaneurysm neck is also evaluated with spectral Doppler as detailed earlier in the section on lower extremity arteries (Fig. 27.17, Video 27.7 and Video 27.8). If there is concern for AVF, both the arterial inflow portion and venous outflow should be characterized by duplex Doppler within several centimeters of the pseudoaneurysm, because the characteristic arterialization of the downstream venous waveform may be dampened farther away from the fistula. Turbulent flow through the fistula may affect surrounding tissues causing a tissue reverberation artifact, which may be the first clue that an AVF is present.

Arterial Stenosis

Atherosclerotic disease can cause upper extremity **stenosis** but is a less common problem in the arm than encountered in the lower extremities. Gray-scale findings are similar to the lower extremities and include intimal plaques and/or visible irregularity of the vessel lumen. Color Doppler may show aliasing with turbulent flow similar to those findings seen in lower extremity arterial stenosis. On spectral Doppler, velocity criteria are not well defined for the upper extremity arteries. However, for a stenosis in most nonbranching arteries, a greater than 2:1 PSV ratio of the stenosis relative to the upstream artery within 2 to 4 cm is consistent with at least 50% diameter stenosis. Depending on the timing and whether collaterals have formed, this degree of stenosis may or may not be symptomatic or clinically significant (Fig. 27.18).

Subclavian Stenosis

Subclavian stenosis most commonly occurs proximal to the origin of the left vertebral artery. In a subset of patients, flow to the arm is provided by filling through the vertebral artery via retrograde flow. If this reversed flow is significant, there can be a steal phenomenon **("subclavian steal")** from the brain, leading to dizziness with certain arm movements as additional flow is diverted to the arm. In these patients, the vertebral artery waveform should be insonated (Fig. 27.19, Video 27.9). Transient early systolic deceleration with resultant transient cessation of antegrade flow or transient reversal of flow (Fig. 27.20) correlated with subclavian artery mean diameter stenosis of 72% and 78%, respectively.[54] Similar stenosis can occur in the right subclavian artery, but less frequently. If these abnormal vertebral artery waveforms are seen, an attempt should be made to directly visualize a stenosis by gray-scale and duplex Doppler in the subclavian artery itself.

Thoracic Outlet Syndrome

In distal upper extremity ischemic symptoms, embolic or traumatic injury (commonly iatrogenic) to the artery should also be considered. If embolic phenomena are seen, evaluation for **thoracic outlet syndrome** should be considered. In patients with symptoms elicited by specific positioning of the arm, thoracic outlet syndrome is a form of arterial stenosis that should be considered. It occurs by external compression of the artery by adjacent muscles during abduction of the arm, and this narrowing

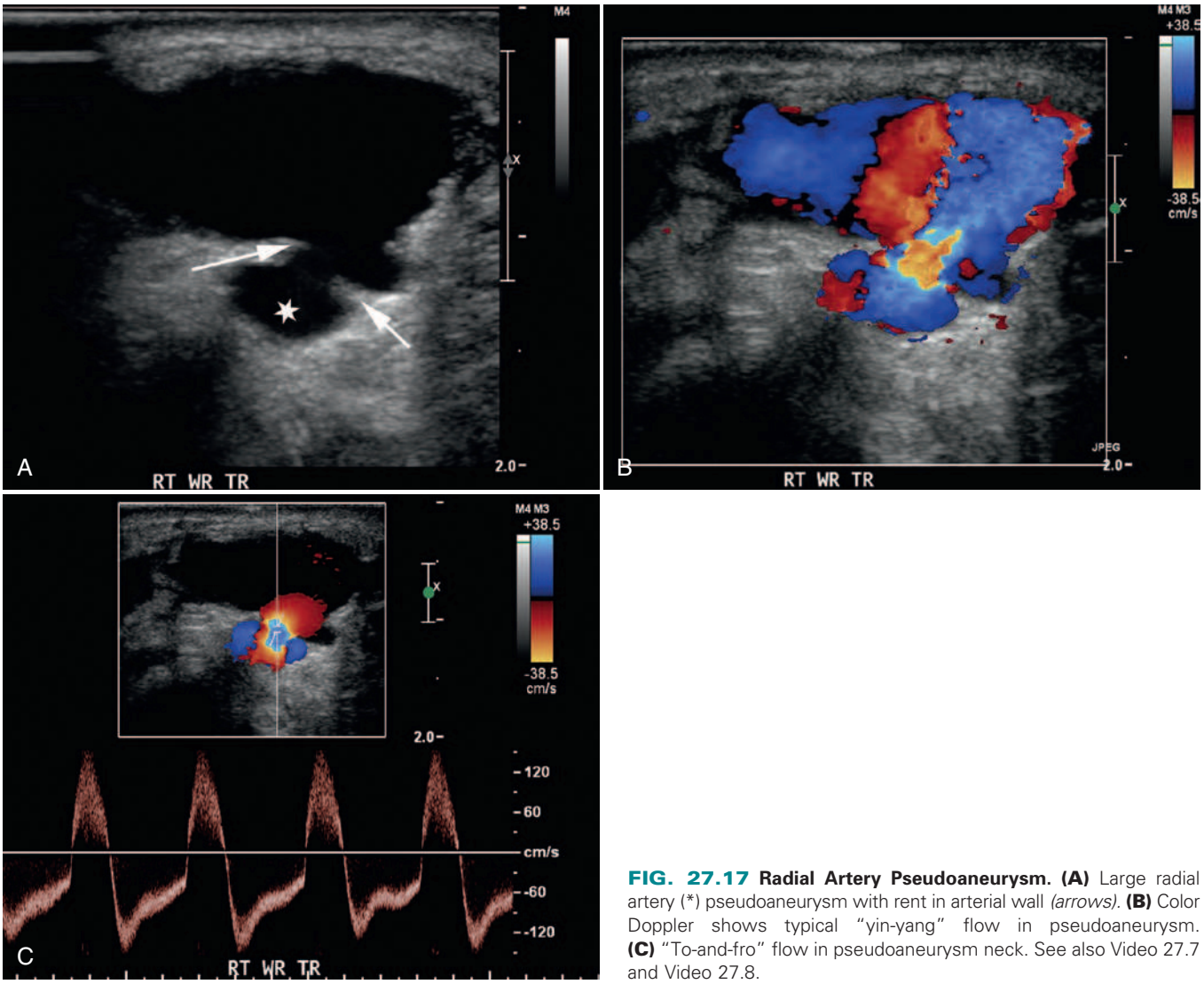

FIG. 27.17 Radial Artery Pseudoaneurysm. (A) Large radial artery (*) pseudoaneurysm with rent in arterial wall *(arrows)*. **(B)** Color Doppler shows typical "yin-yang" flow in pseudoaneurysm. **(C)** "To-and-fro" flow in pseudoaneurysm neck. See also Video 27.7 and Video 27.8.

can affect the waveform morphology of the downstream arteries.[55] Bone and rib anomalies frequently contribute to the pathology.[56] The velocities in the artery should be evaluated during adduction or neutral position then compared with velocities and waveforms in abduction. Over time, the artery may become injured, and this can lead to occlusion and formation of emboli, which may also be visible sonographically. These emboli can then migrate distally within the upper extremity to cause pain in regions such as the hand. For sonographic evaluation of thoracic outlet syndrome in the proper clinical presentation, it is important to begin by insonating the arteries with the arm in neutral position for baseline waveform characterization. Waveforms are acquired from the forearm arteries with the patient sitting comfortably in an upright, seated position. Once the baseline morphology is clearly defined, the arm is moved into the inciting position, usually with abduction and elevation of the arm with external rotation. A combination of inspiration, breath holding, neck extension, and neck turn to the affected side, known as the **Adson maneuver,** may elicit a positive finding on Doppler.[57] The waveform is monitored as the arm is moved into a variety of positions to elicit symptoms. If abnormal waveforms are not readily apparent, a variety of positions should be tested (Fig. 27.21). If positive, a diminished waveform should be apparent in the arteries of the forearm. Once this has been identified, it may be helpful to repeat the baseline and positive results to show reproducibility of the findings. Further support of the diagnosis includes visible narrowing identified in the subclavian artery, or the presence of an aneurysm in this region, if found.[58] Pseudoaneurysms are frequently present in the setting of thoracic outlet syndrome and can lead to embolic events. Care must be taken in the diagnosis because hyperextension can produce arterial flow abnormality in up to 20% of normal volunteers.[59]

Radial Artery Evaluation for Coronary Bypass Graft

Another use of Doppler in bypass patients is to determine suitability of the **radial artery** for **coronary artery grafting.** The ulnar artery typically provides the dominant source of blood

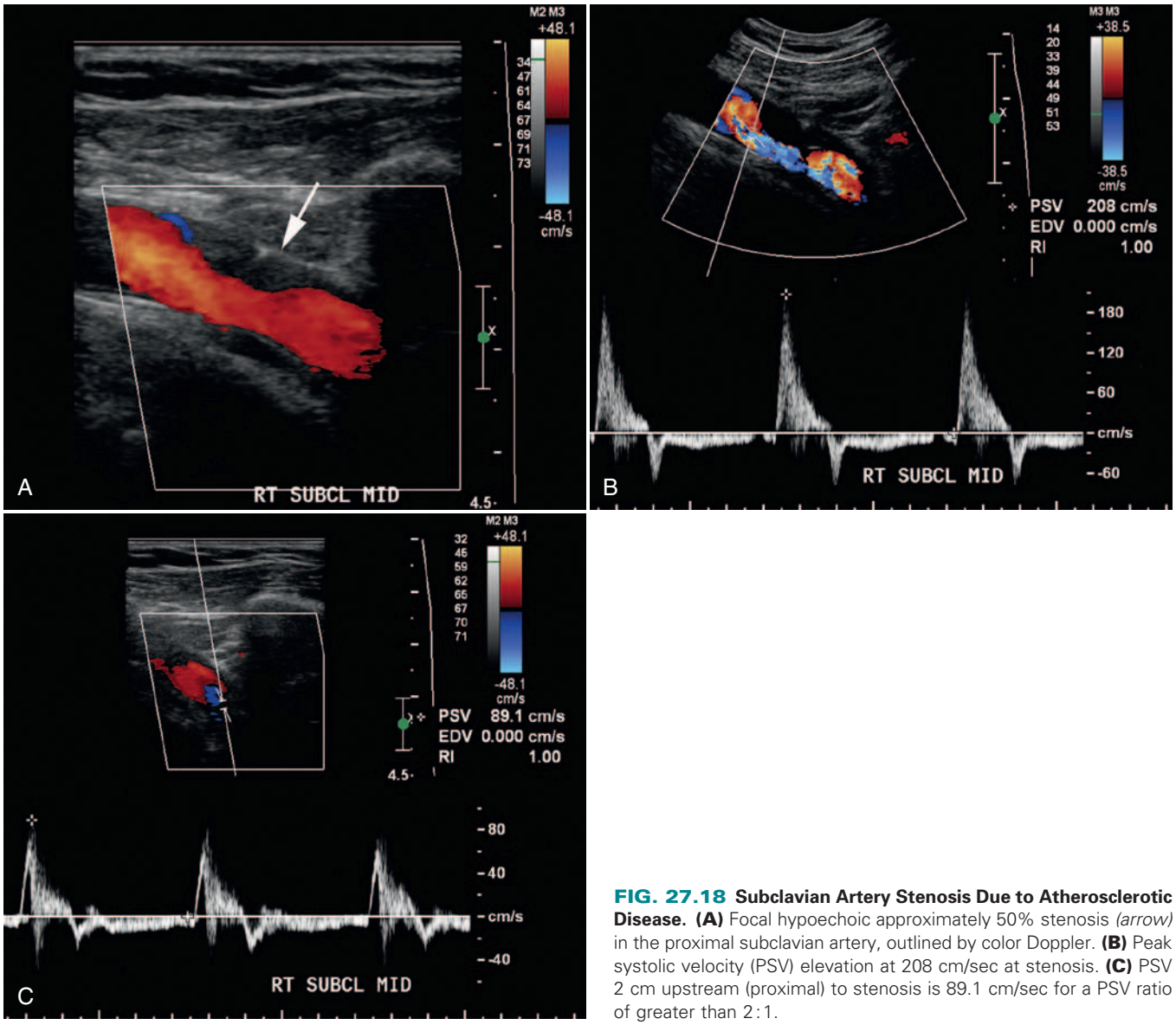

FIG. 27.18 Subclavian Artery Stenosis Due to Atherosclerotic Disease. (A) Focal hypoechoic approximately 50% stenosis *(arrow)* in the proximal subclavian artery, outlined by color Doppler. **(B)** Peak systolic velocity (PSV) elevation at 208 cm/sec at stenosis. **(C)** PSV 2 cm upstream (proximal) to stenosis is 89.1 cm/sec for a PSV ratio of greater than 2:1.

flow to the hand. The ulnar artery supplies the superficial **palmar arch,** which is often incomplete. The radial artery supplies the deep palmar arch, which is more commonly complete, in communication with the ulnar artery. If the superficial palmar arch in the hand is patent, thus allowing flow to the entire hand through the ulnar artery, then the radial artery is harvested. Thus evaluation of palmar arch patency is necessary before harvest. Doppler evaluation of patency is more accurate than the modified Allen test on physical examination, because only about 5 of 43 (12%) patients with an abnormal modified Allen test result will have abnormal Doppler findings.[60]

A small linear array 12- to 15-MHz "hockey stick" transducer initially is used to determine antegrade flow of the ulnar artery and radial artery at the wrist. With duplex Doppler, arterial flow to the hand in the superficial palmar arch at the thenar eminence near the crease of the base of the thumb is characterized first with normal distal radial artery inflow. Subsequently, the radial artery is transiently occluded by direct compression of the radial artery at the wrist, and the resultant spectral Doppler waveform is evaluated. Care should be taken during examination not to hyperextend the hand with regard to the wrist, because a false-negative examination finding may incorrectly suggest lack of patency of the arch. In patients with a patent superficial palmar arch, there should be reversed flow of the radial artery in the hand, measured at the thenar eminence or in the region of the snuff box between the first metacarpal and second carpal bone.[61,62] If there is no flow or absent reversed flow, then the radial artery of that upper extremity is not suitable for harvest owing to an incomplete arch (Fig. 27.22). Increased flow in the ulnar artery may also occur during radial artery compression if the arch is patent.[63]

PERIPHERAL VEINS

Evaluation of the upper and lower extremity venous system is primarily performed with sonography. Useful applications

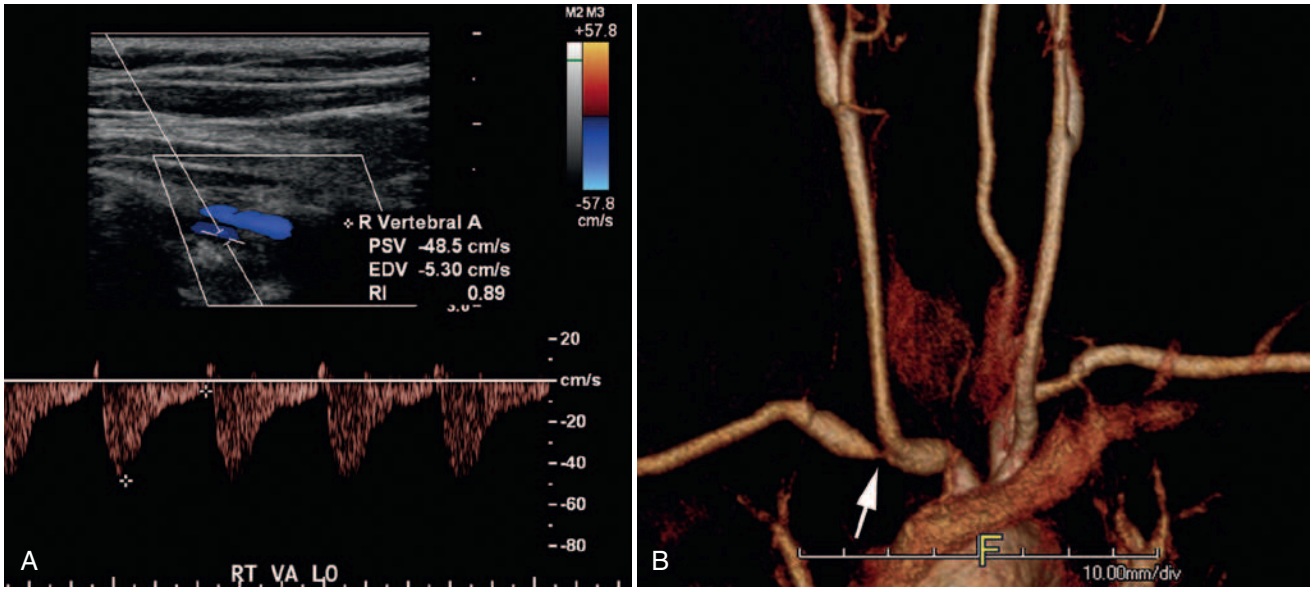

FIG. 27.19 Subclavian Steal Phenomenon. (A) Reversed flow in the right vertebral artery. Note that artery and vein are the same color, indicating abnormal flow direction in one of the vessels. **(B)** Magnetic resonance imaging confirms significant stenosis in the subclavian artery just distal to the vertebral artery *(arrow)*. See also Video 27.9.

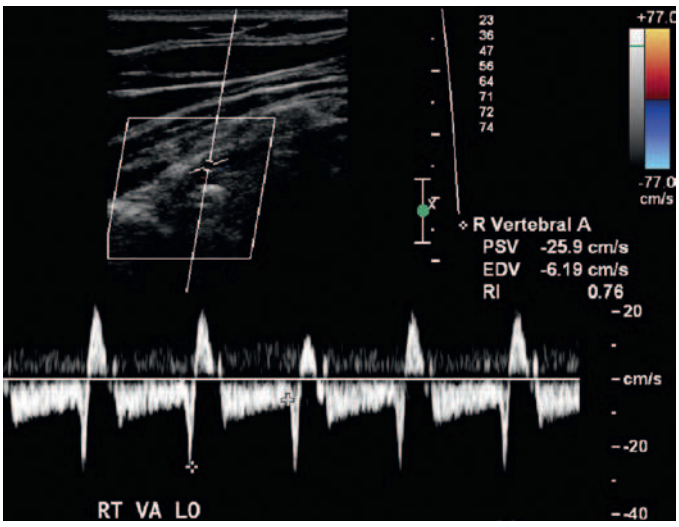

FIG. 27.20 Subclavian Steal With Transient Flow Reversal in the Vertebral Artery.

include evaluation for thrombus, localization for venous access procedures, preoperative venous mapping for hemodialysis AVF and graft placement, and postoperative hemodialysis AVF and graft assessment. Key aspects of venous Doppler imaging include knowledge of anatomy, scanning technique, and attention to detail.

The most common indication for venous Doppler ultrasound is to identify deep venous thrombosis (DVT). Undiagnosed and untreated DVT can result in fatal pulmonary embolism (PE). Sudden death is the first symptom in about 25% of people who have PE[64] (Fig. 27.23). Clinical evaluation of the peripheral venous system is frequently difficult, nonspecific, and often inaccurate. Clinical decision rules to improve pretest probability are recommended by the American College of Physicians and the American Academy of Family Physicians.[65-67] The Wells criteria generate a score for certain physical examination findings and pertinent clinical history.[68] Clinical factors associated with increased probability of DVT include active cancer, immobilization, localized tenderness along the distribution of the deep venous system, swollen extremity, pitting edema localized to the symptomatic extremity, collateral superficial veins, and previously documented DVT.

A modification of the **Wells score** creates two groups: DVT unlikely or DVT likely.[69] Current guidelines recommend a D-dimer test for those with low risk.[70,71] The D-dimer test measures a degradation product of fibrin and has a high negative predictive value that is sensitive, but not specific for DVT.[72] If the D-dimer test result is positive, the patient should be evaluated with venous Doppler. As with patients without cancer, the combination of low probability and negative D-dimer result can exclude DVT in cancer patients.[73,74] In practice, many patients do not undergo this workup.[75] Going directly to sonography is frequently faster than waiting for workup results and may offer an alternative musculoskeletal diagnosis such as popliteal fossa cyst. Also, in cases of technically limited sonographic evaluation of the more central deep venous system (iliac veins and inferior vena cava [IVC]), magnetic resonance venography or CT venography may be more sensitive.[76]

Sonographic Examination Technique

The superficial location of the upper and lower venous system allows the use of linear, higher frequency transducers. The highest frequency linear transducer that still gives adequate penetration should be used to optimize spatial resolution. Typically the examination is best performed using a 5- to 10-MHz linear array transducer, with application of the higher frequency range in upper arm, forearm, calf, and more superficial veins. A curved array or sector probe in the 3- to 5-MHz range may be necessary

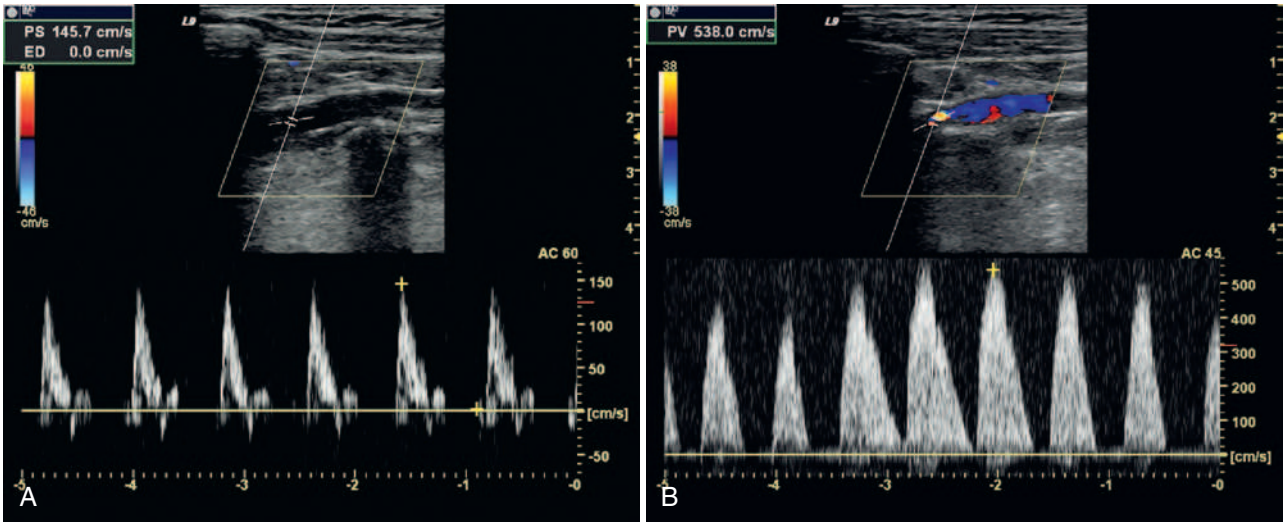

FIG. 27.21 Thoracic Outlet Syndrome. (A) Normal baseline subclavian artery waveform. **(B)** Altered waveform during hyperextension, with compression against the clavicle causing stenosis.

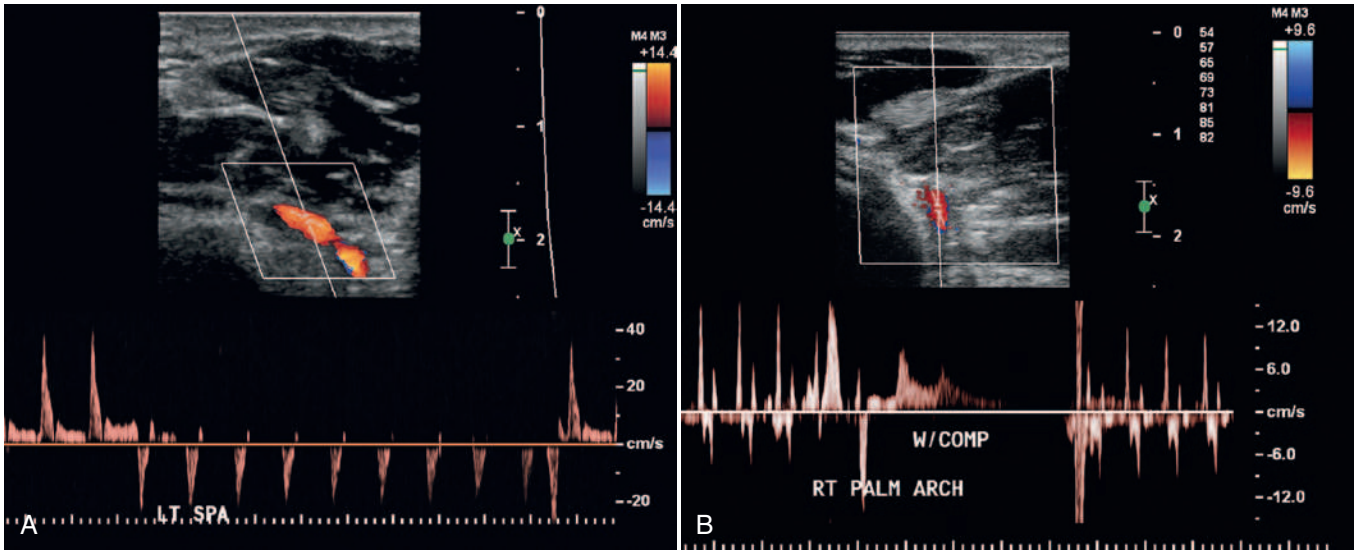

FIG. 27.22 Radial Artery Evaluation for Coronary Bypass Graft. (A) Patent palmar arch, with reversal of flow in the superficial palmar arch on radial artery compression at the wrist. **(B) Incomplete palmar arch,** with lack of flow in the superficial palmar arch on radial artery compression at the wrist.

in very large patients or those with substantial extremity edema. Gray-scale imaging should include compression and should be performed in the transverse plane.

Color flow and spectral analysis are the most common applications of Doppler sonography, with occasional use of power Doppler. Both techniques evaluate the disease process in the peripheral veins and give additional information regarding altered venous hemodynamics. Anatomic and functional detail makes sonography a valuable tool. Color Doppler sonography can be used to evaluate venous segments that cannot be directly assessed by compression, such as the subclavian veins. Power Doppler provides improved detection of very slow flow, especially in small veins. All spectral Doppler waveforms should be obtained in the longitudinal plane.

Lower Extremity Veins

Normal Anatomy

Deep Venous System. The venous anatomy of the leg is illustrated in Fig. 27.24. The **common femoral vein** (CFV) begins at the level of the inguinal ligament as the continuation of the external iliac vein and extends caudally to the bifurcation into the **femoral vein** (FV) and the **profunda femoris vein,** which lie medial to the adjacent artery. The FV courses medially to the adjacent artery through the adductor canal in the caudal thigh. The term "femoral vein," previously called the "superficial femoral vein," should be used to avoid clinical confusion regarding the deep versus superficial venous system.[77] The **popliteal vein** (PV) represents the continuation of the FV after its exit from the adductor canal in the posterior caudal thigh. The PV is located superficial

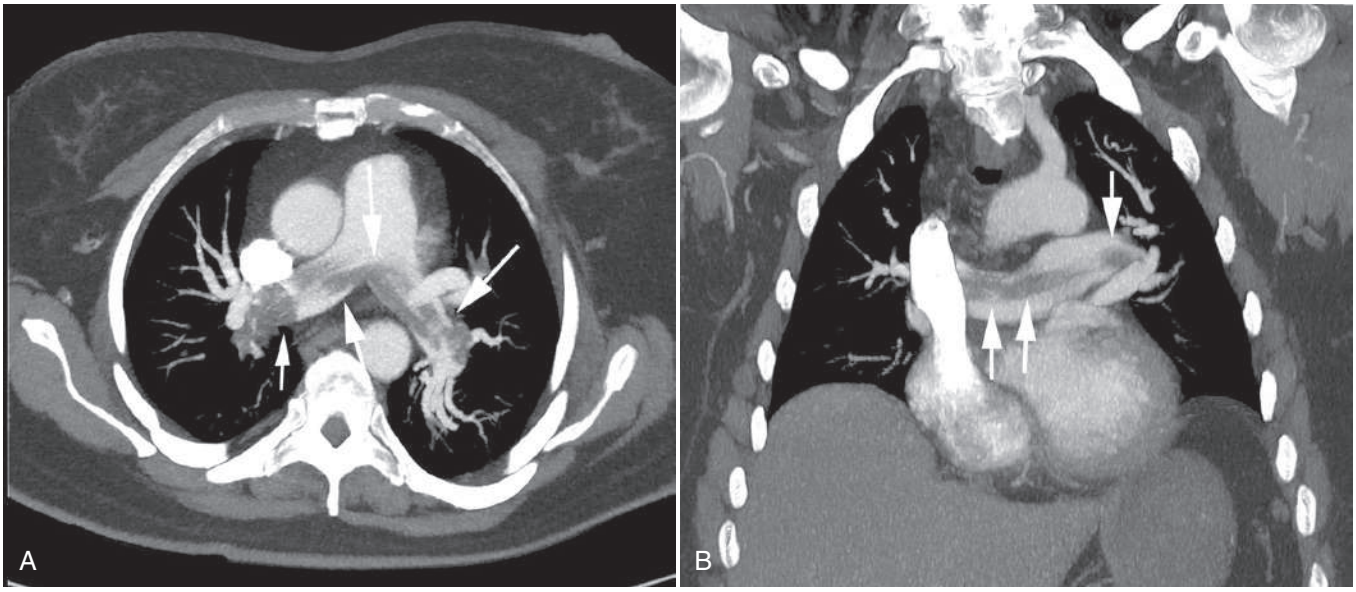

FIG. 27.23 Pulmonary Emboli. (A) Axial CT with contrast shows a large saddle pulmonary embolus extending into the left and right pulmonary arteries *(arrows)*. **(B)** Maximum-intensity projection coronal CT with contrast in the same patient shows extent of bilateral pulmonary emboli *(arrows)*.

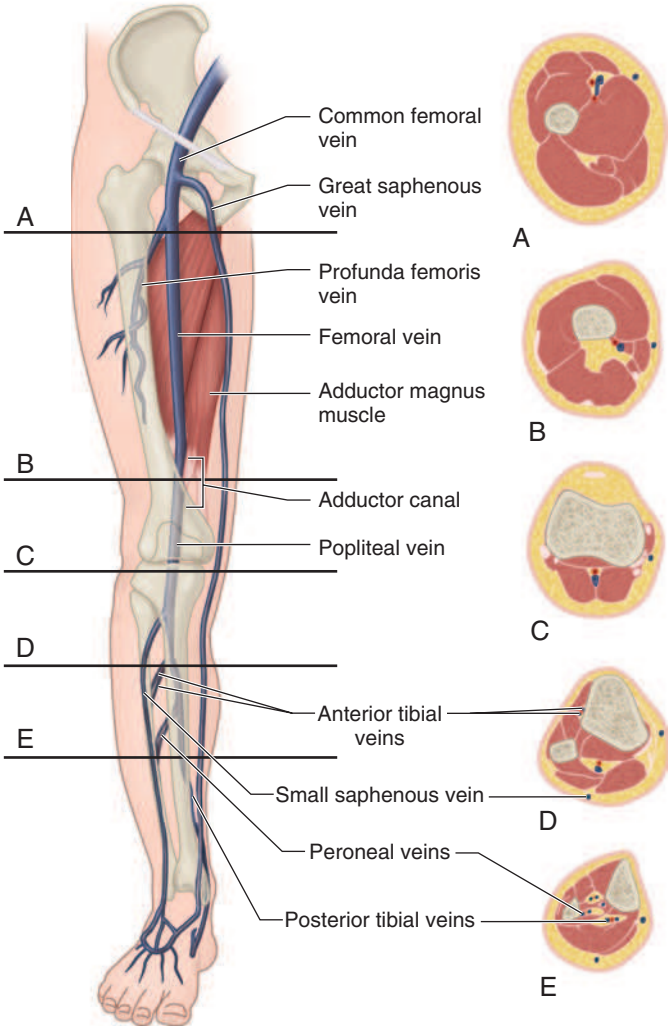

FIG. 27.24 Venous Anatomy of the Lower Extremity.

to the artery and courses through the popliteal space into the proximal calf. Duplication of the FV can be seen in about 30% of patients.[78] Duplication of the FV can also be segmental. It has been shown that these anatomic variants are associated with increased incidence of DVT.[79,80] About 40% of patients with multiple vessels within the popliteal fossa arise from a high confluence of the posterior tibial and peroneal veins, rather than true PV duplication.[78] Description of these anatomic variants assists in avoiding a missed diagnosis on follow-up examinations.

The paired **anterior tibial veins** arise from the PV and course laterally along the anterior calf to the dorsum of the foot. The **tibioperoneal trunk** originates from the PV slightly caudal to the anterior tibial veins and bifurcates into the paired **posterior tibial veins** and **peroneal veins.** The peroneal veins course medial to the posterior aspect of the fibula, whereas the posterior tibial veins course through the posterior calf muscles posterior to the tibia and along the medial malleolus. Deep veins in the gastrocnemius and soleus calf muscles do not have an adjacent artery and are a common site of acute calf vein thrombus in postoperative or high-risk patients.[81]

Superficial Venous System. Anatomic terminology for the lower extremity superficial venous system was standardized in 2002. The great and small saphenous veins and their branches comprise the superficial venous system of the lower extremities.[82] The **great saphenous vein** (GSV) empties into the medial aspect of the CFV in the proximal thigh superior to the bifurcation of the CFV. The GSV courses along the medial thigh and calf. The normal GSV typically is 1 to 3 mm in diameter at the level of the ankle and 3 to 5 mm in diameter at the saphenofemoral junction. These measurements are important when performing saphenous vein mapping for harvesting an autologous vein graft. The **small saphenous vein** has a variable insertion into the posterior aspect of the PV and courses along the dorsal calf to the ankle. Measurements for the small saphenous vein are typically

1 to 2 mm in diameter inferiorly and 2 to 4 mm at the saphenopopliteal junction. In cases of **superficial venous insufficiency,** both the GSV and small saphenous vein can become abnormally enlarged and tortuous.

Ultrasound Examination and Imaging Protocol

The choice of transducer depends on the patient's body habitus and depth of the vessel to be studied. Typically a high-resolution 5- to 7.5-MHz linear array transducer will be used. For larger patients a lower-frequency (2.5- or 3.5-MHz) curvilinear transducer may be needed. Appropriate gain settings are needed to ensure that the vessels show no artifactual internal echoes and that thrombus is not mistaken for echoes caused by slow-flowing blood. Color Doppler imaging settings must be optimized for sensitivity to slow, low-volume flow.

The lower extremity deep venous system should be evaluated from just above the inguinal ligament to the bifurcation of the PV in the upper calf, including compression, color, and spectral Doppler sonography with assessment of respiratory phasicity. The cranial profunda femoris vein and cranial GSV should also be examined. Ultrasound evaluation of the **external iliac veins and IVC** is helpful to determine extent of documented CFV when the top of the thrombus is not seen in the CFV.

The patient is examined in the supine position with the leg abducted and externally rotated with slight flexion of the knee. The most important portion of the examination is venous gray-scale compression. The veins of the deep system are compressed in the transverse plane and evaluated in a stepwise fashion every 1 to 2 cm through the level of the adductor canal (Fig. 27.25, Video 27.10). Pressure on the skin with the transducer should be applied to collapse the vein. If the adjacent artery is deforming, pressure application is adequate. Color Doppler is then performed in selected segments to evaluate for patency and any nonocclusive or hypoechoic thrombus not seen on the gray-scale images. The spectral Doppler waveform obtained is assessed for respiratory phasicity and cardiac pulsatility. The PV is best evaluated with the patient's leg bent in a frog leg position. Applying hand pressure to the posterior surface of the leg when imaging the adductor canal or creating simulated augmentation by asking the patient to "step on the gas" may aid in visualizing the vein if the veins are difficult to see because of slow flow, increased depth, or significant edema.[83]

Ultrasound evaluation of the **calf veins** remains controversial owing to uncertain clinical value and cost-effectiveness. The ACR practice guidelines do not require evaluation of the calf veins. At a minimum, all symptomatic areas should be evaluated, including the calf, to determine the source of symptoms such as superficial varicosities, and thrombophlebitis. Some institutions that routinely evaluate the calf veins start at the PV and track the paired anterior tibial veins, posterior tibial veins, and peroneal veins to the ankle. Calf imaging has become more common and is required for accreditation by the Intersocietal Accreditation Commission,[84] but there is not a standard study protocol.[85] The American College of Chest Physicians guideline for antithrombotic therapy does not favor routine venous Doppler of the calf veins.[65] The more benign natural history of calf venous thrombosis favors management with serial sonographic examination with treatment only if proximal DVT is demonstrated. If calf venous thrombosis is detected, the interpreting physician may not know whether a patient with calf venous thrombosis will be treated. A suggested general statement may include, "If this calf venous thrombosis is not treated, a follow-up in 1 week is recommended to evaluate for progression."[85]

Imaging Protocol. The lower extremity venous imaging protocol includes the following images for each deep venous segment:

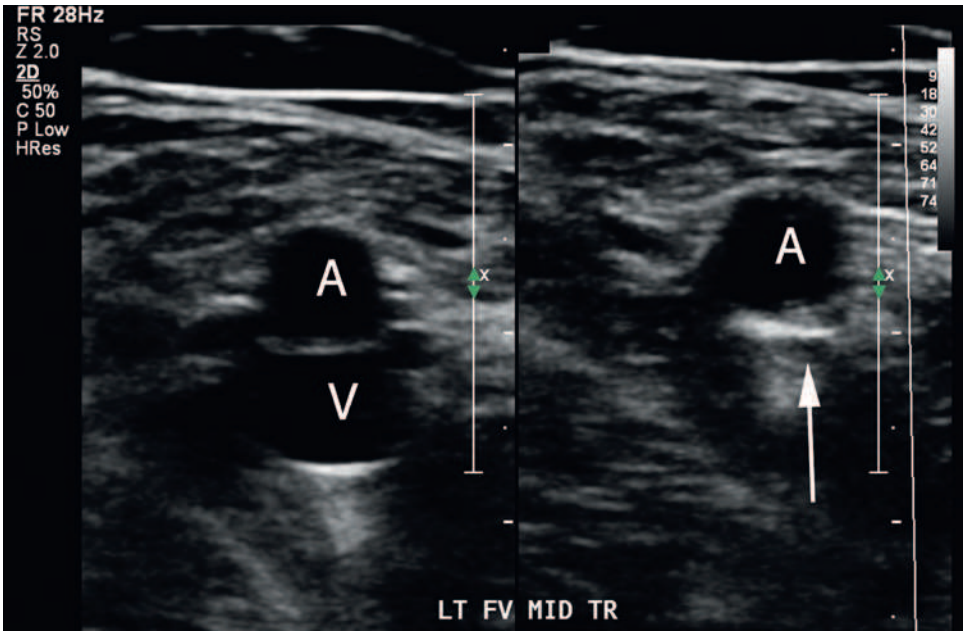

FIG. 27.25 Normal Femoral Vein (FV) Compression. Dual transverse image showing noncompressed *(left)* and compressed FV. (FV is completely compressed in right panel and thus not seen; location marked by arrow.) Accompanying Video 27.10 shows the compression maneuver. *A,* Superficial femoral artery; *V,* femoral vein.

1. Transverse gray-scale image at rest and with compression, or a cine clip of the compression maneuver, of the saphenofemoral junction, CFV, FV (at minimum proximal and distal), and PV.
2. Longitudinal color Doppler with spectral waveform analysis.
   a. CFV at the level of the saphenofemoral junction and distal portions. If only a unilateral examination is requested, the contralateral CFV is also evaluated.
   b. PV at a minimum. Consider recording FV as well.
   c. A separate compression image of the profunda femoris vein at the bifurcation with the FV is not typically obtained, but patency is evaluated on the longitudinal color and spectral Doppler waveform of the CFV bifurcation into the proximal FV and profunda femoris vein.
   d. If a thrombus is seen in the CFV, the most proximal extent of thrombus should be demonstrated with inclusion of the external iliac veins and IVC in the evaluation.
   e. Document additional musculoskeletal findings (such as popliteal cyst, knee joint effusion, or hematoma if present in the region being evaluated).

Acute Deep Venous Thrombosis

There are four findings of acute venous thrombosis: (1) intraluminal material that is deformable during compression, (2) dilation of the vein, (3) smooth intraluminal material, and (4) free tail floating proximally from the attachment of the clot on the vein wall.[85] The classic gray-scale findings of acute DVT are noncompressibility of the vessel with direct visualization of the thrombus. With complete acute vein thrombosis, the vein will typically enlarge. Thrombi may completely or partially occlude the lumen, may be adherent to the wall, or may be free floating (Fig. 27.26, Video 27.11). Compression ultrasound for DVT has been shown to have 95% accuracy with 98% specificity.[86]

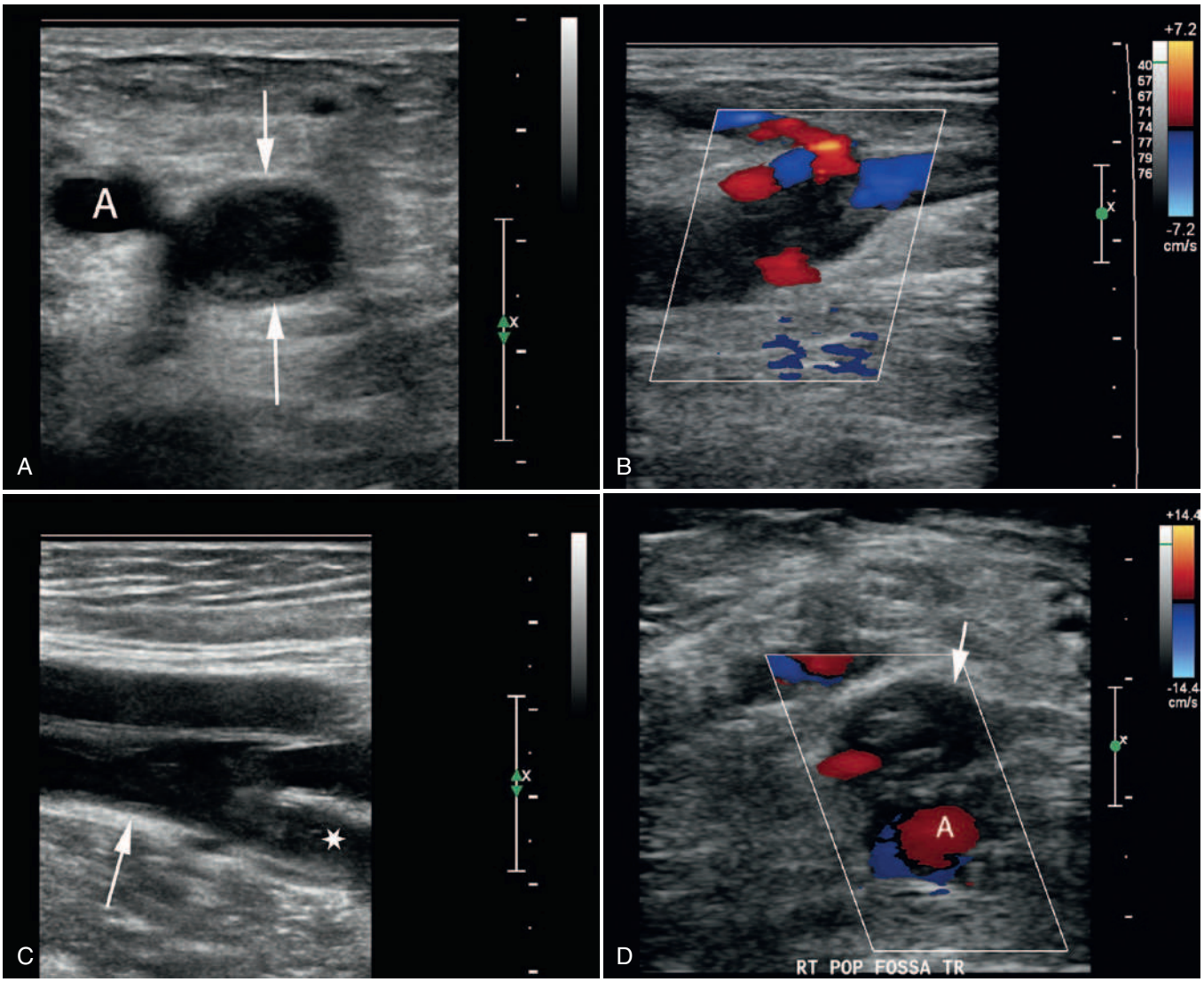

FIG. 27.26 Acute Deep Venous Thrombosis (DVT). (A) Acute common femoral vein (CFV) thrombus: Compression image in the transverse plane shows acute CFV thrombus. Note that the vein *(arrows)* is larger than the adjacent artery *(A)*. **(B)** Longitudinal color Doppler image in the same patient shows acute nearly occlusive common femoral vein thrombus with little flow. See also Video 27.11. **(C)** Longitudinal image of acute DVT in the profunda femoris vein (*), with nonocclusive extension into the CFV *(arrow),* and a small amount of thrombus in the femoral vein as well. **(D)** Transverse color image of acute popliteal vein DVT, with expansion of the vein *(arrow)* relative to the popliteal artery *(A)*.

Thrombus within the proximal GSV may be treated as a DVT if within several centimeters of the insertion of the GSV, or more than 5 cm long, according to physician preference.[65] If the thrombus within the GSV extends into the CFV, it should be treated as a DVT (Fig. 27.27, Video 27.12). If the top of the thrombus is not seen in the CFV or external iliac vein, an IVC and iliac vein examination should be considered to assess for more central thrombus (Fig. 27.28, Video 27.13).

Residual (Chronic) Deep Venous Thrombosis

Differentiation of acute from residual or chronic DVT with imaging and clinical parameters is often difficult. With compression ultrasound, both acute and chronic DVT may show noncompressibility of the vessel. Wall thickening and smaller caliber vein suggest residual or chronic DVT (Fig. 27.29). Because vein noncompressibility can be seen in both acute and chronic DVT, an attempt to differentiate the two is important for the appropriate therapeutic decision. As the thrombus evolves, it loses bulk and the vein may return to normal size or may become smaller in caliber owing to scarring (Fig. 27.30, Video 27.14). Residual thrombus will become broadly adherent to the vein wall. Additional chronic findings that may assist in differentiating chronic from acute DVT are echogenic weblike filling defects within the vein (Fig. 27.31), collateral vessels (Fig. 27.32, Video 27.15), and valvular damage with reflux and subsequent chronic deep venous insufficiency.[23] Differentiation of acute versus residual or chronic thrombus cannot be performed on thrombus echogenicity alone, although if calcifications are present, there is at least an element of chronic thrombus present[87] (Fig. 27.33). If the thrombus is small (several centimeters or less), measurement may be helpful to aid the clinician in determining clinical importance, especially after catheter removal.

Potential Pitfalls

Lower extremity **potential pitfalls** to avoid include the following:

1. Very slowly flowing blood may mimic the appearance of clot (Fig. 27.34, Video 27.16 and Video 27.17); however, compression will be normal.

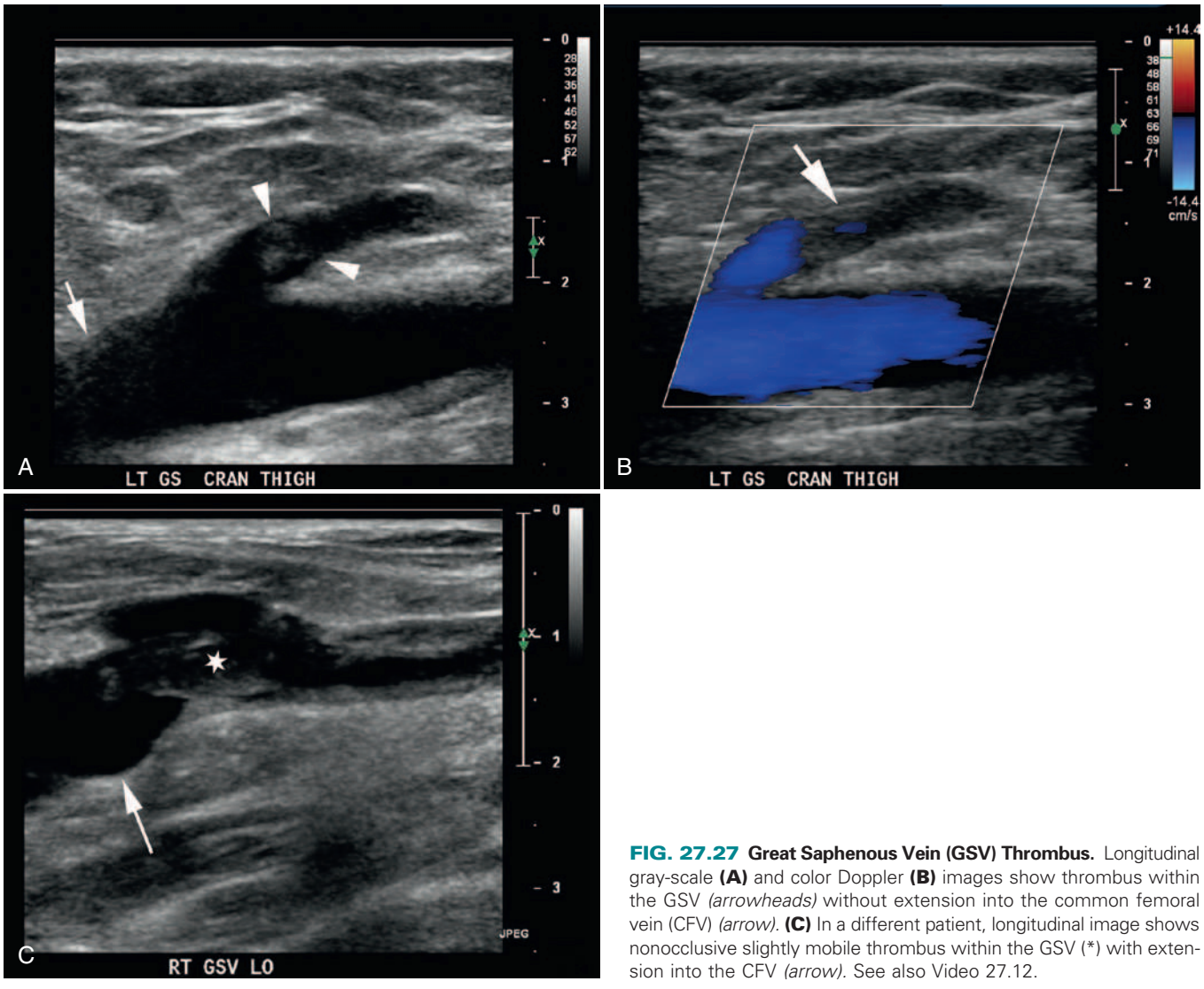

FIG. 27.27 Great Saphenous Vein (GSV) Thrombus. Longitudinal gray-scale **(A)** and color Doppler **(B)** images show thrombus within the GSV *(arrowheads)* without extension into the common femoral vein (CFV) *(arrow)*. **(C)** In a different patient, longitudinal image shows nonocclusive slightly mobile thrombus within the GSV (*) with extension into the CFV *(arrow)*. See also Video 27.12.

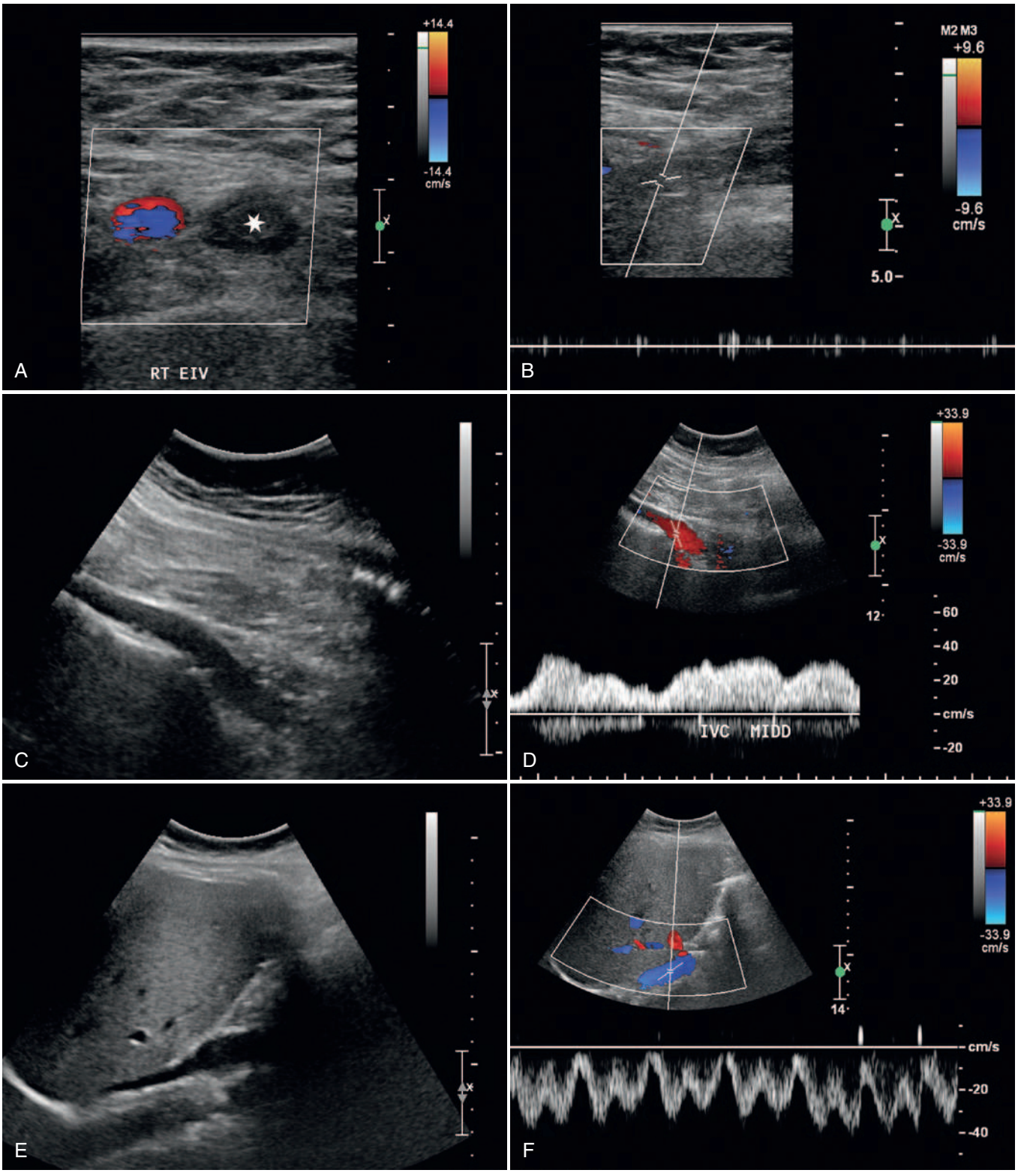

FIG. 27.28 Acute Deep Venous Thrombosis (DVT). (A) Transverse duplex Doppler image shows external iliac vein without demonstrable venous flow (*). The top of the thrombus is not seen, so sonographic evaluation continues to the common iliac vein and inferior vena cava (IVC). **(B)** Longitudinal image of occluded external iliac vein shows large amount of low-level echoes within the vein, without flow on spectral or color Doppler imaging. **(C)** Longitudinal image of caudal IVC shows no definite echoes on gray-scale imaging, confirmed with duplex Doppler imaging *(not shown).* **(D)** Duplex Doppler longitudinal image of the mid IVC shows no thrombus. **(E)** Longitudinal gray-scale image of the intrahepatic IVC shows no thrombus. **(F)** Duplex Doppler longitudinal image of the intrahepatic IVC without thrombus, with normal spectral Doppler waveform. Because the spectral waveform in the left common femoral vein was normal *(not shown),* thrombus in this patient extended into either the right external or common iliac vein, but not into the IVC. See also Video 27.13.

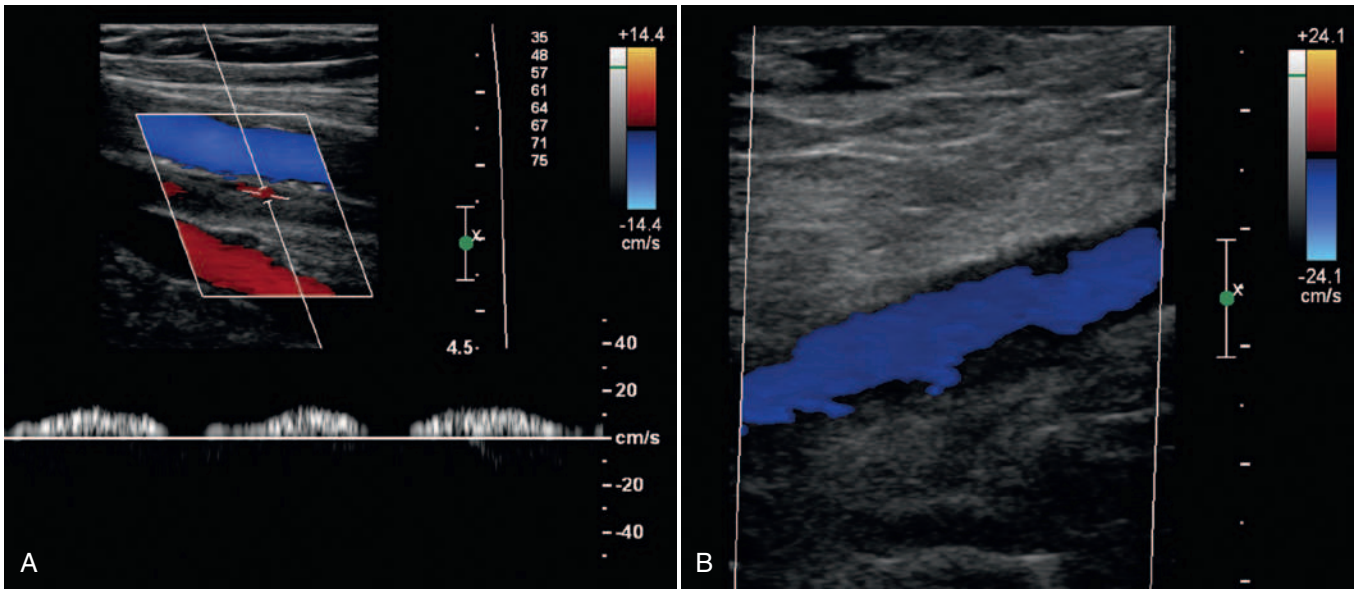

FIG. 27.29 Chronic Deep Venous Thrombosis (DVT). (A) Duplex Doppler longitudinal image of chronic femoral vein DVT, with small vein and peripheral nonocclusive flow. **(B)** Duplex Doppler longitudinal image of chronic DVT and scarring in a patent popliteal vein, with peripheral irregular residual thrombus.

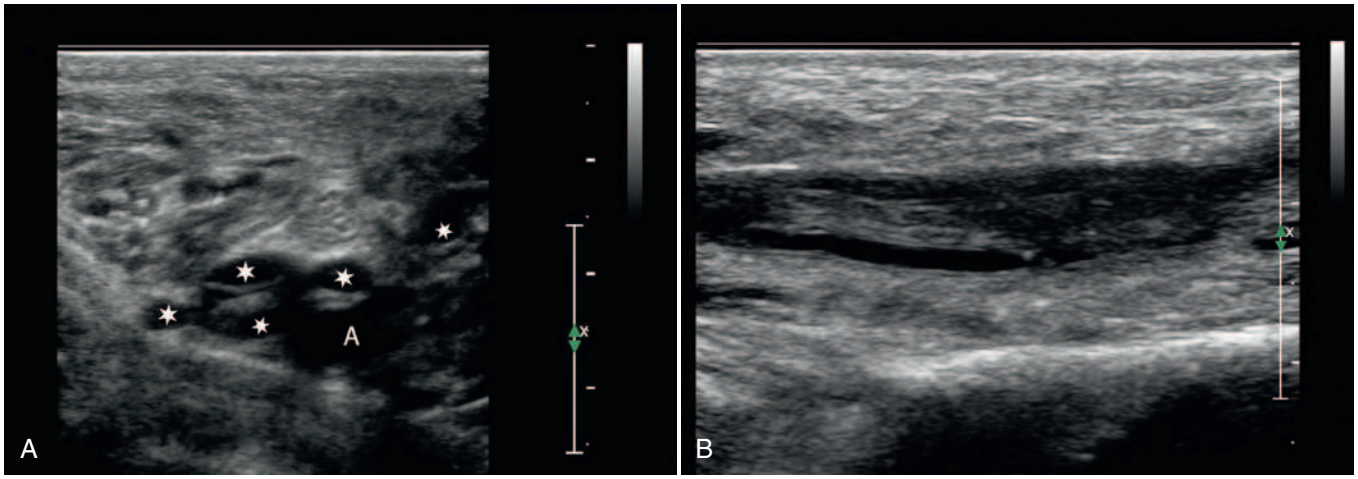

FIG. 27.30 Chronic Vein Occlusion With Collaterals. (A) Transverse image of the popliteal fossa shows multiple small collateral veins (*) in the region of the popliteal vein, adjacent to the popliteal artery *(A)* in the setting of chronic popliteal vein deep venous thrombosis (DVT) and scarring. **(B)** Longitudinal image of chronic DVT and scarring in the popliteal vein shows mildly compressible nonocclusive thrombus with some portions adhering to the wall, in a small vein. See also Video 27.14.

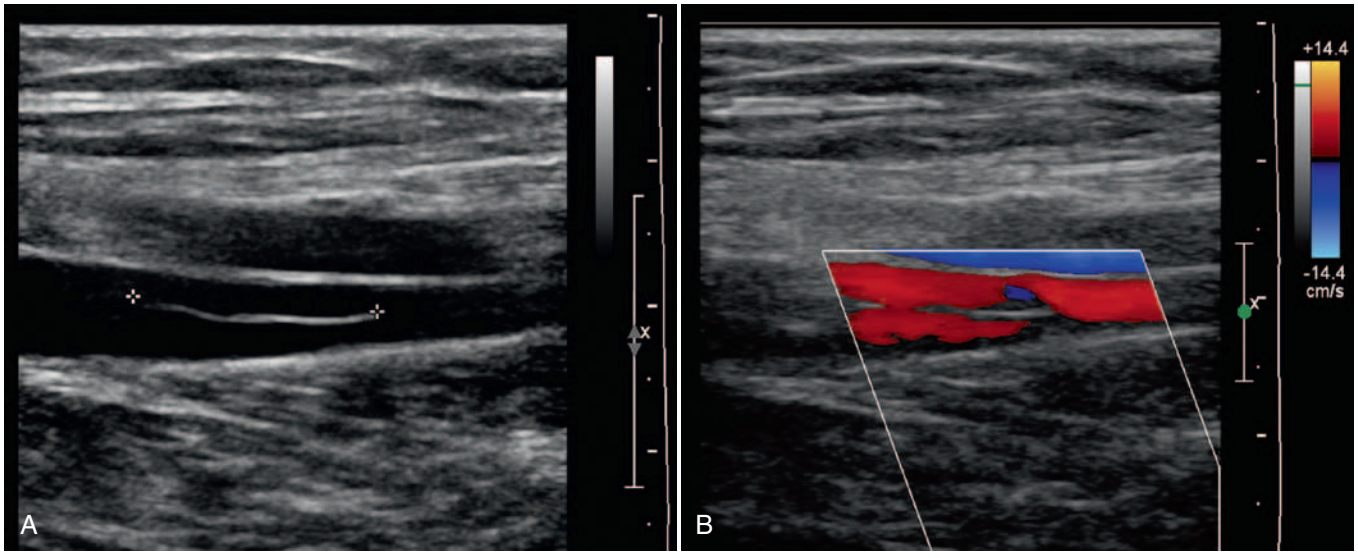

FIG. 27.31 Chronic Deep Venous Thrombosis (DVT) With Vein Web. Longitudinal gray-scale **(A)** and color Doppler **(B)** images show linear weblike chronic DVT *(cursors)* with patent channels around the web.

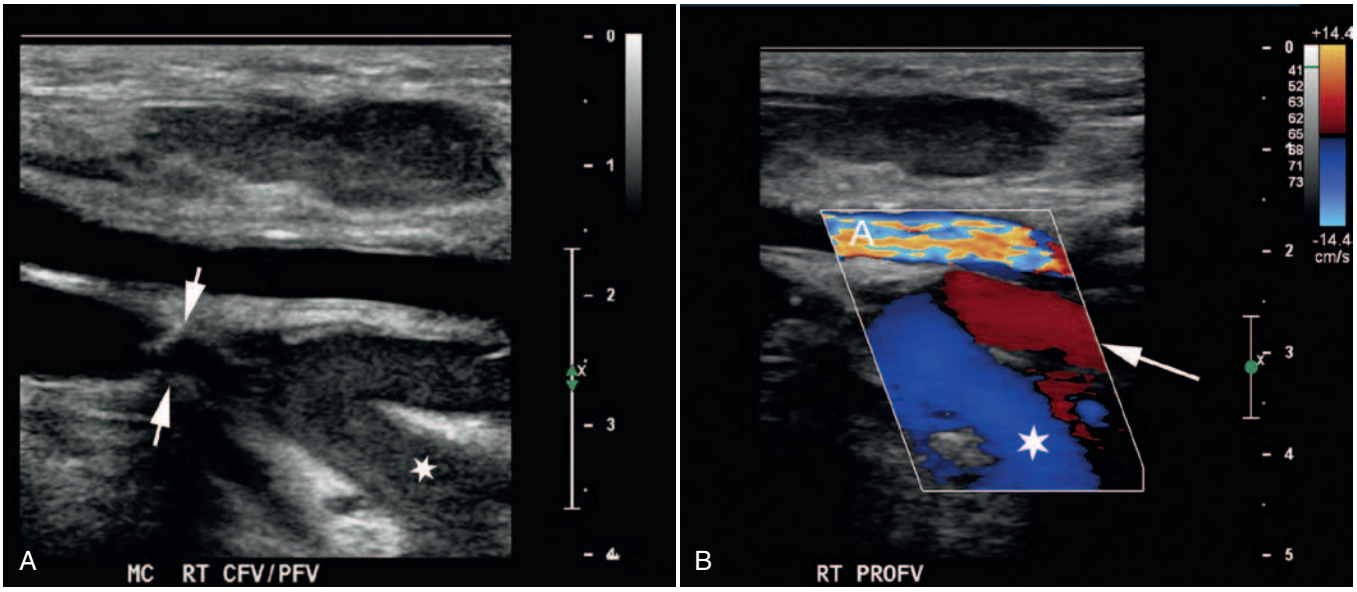

FIG. 27.32 Chronic Common Femoral Vein (CFV) Occlusion With Flow Reversal in the Profunda Femoris Vein (PFV). Longitudinal gray-scale **(A)** and color Doppler **(B)** images show chronic CFV occlusion *(arrows)* and flow reversal in the PFV (*). The artery *(A)* is located anteriorly. See also Video 27.15.

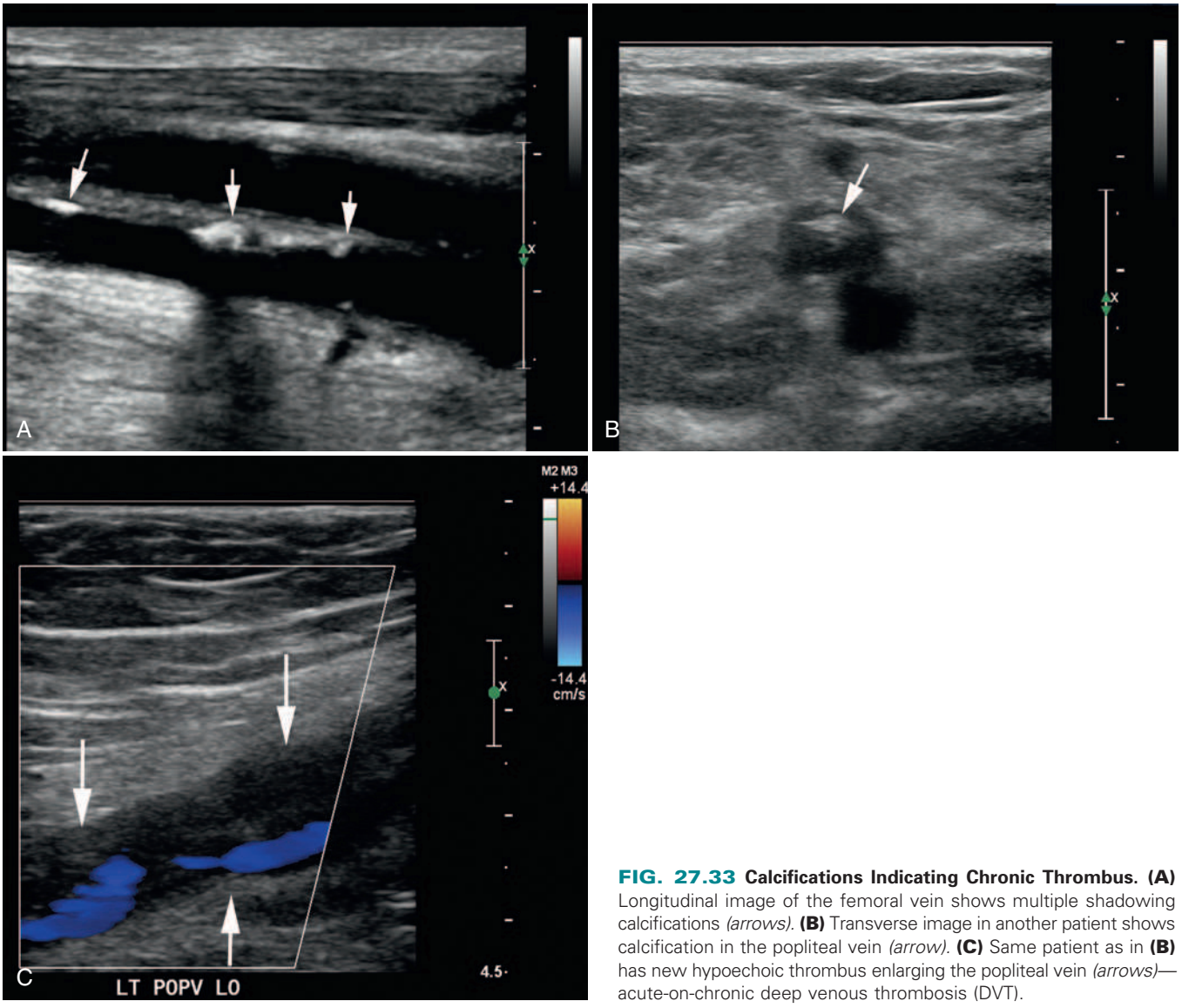

FIG. 27.33 Calcifications Indicating Chronic Thrombus. (A) Longitudinal image of the femoral vein shows multiple shadowing calcifications *(arrows)*. **(B)** Transverse image in another patient shows calcification in the popliteal vein *(arrow)*. **(C)** Same patient as in **(B)** has new hypoechoic thrombus enlarging the popliteal vein *(arrows)*—acute-on-chronic deep venous thrombosis (DVT).

2. Small nonocclusive thrombi in the profunda femoris vein may be missed if not carefully assessed. It is important to remember that DVT may initially be demonstrated in the profunda femoris vein only.
3. Thrombosis of a duplicated FV may be challenging to detect. It is useful to record the presence of this common anatomic variant in the report for comparison in a subsequent study, when only one of several FVs may be thrombosed (Fig. 27.35, Video 27.18).
4. Proximal iliac vein thrombosis may be difficult to demonstrate because of overlying bowel gas. Loss of respiratory phasicity should be recognized as a secondary sign suggesting more proximal thrombosis or obstructive compression by masses or fluid collections (Fig. 27.36). False-negative examination results may occur when the Valsalva maneuver is used while the pelvic veins are evaluated in patients with nonocclusive thrombus in the iliac veins who have well-developed pelvic venous collaterals.

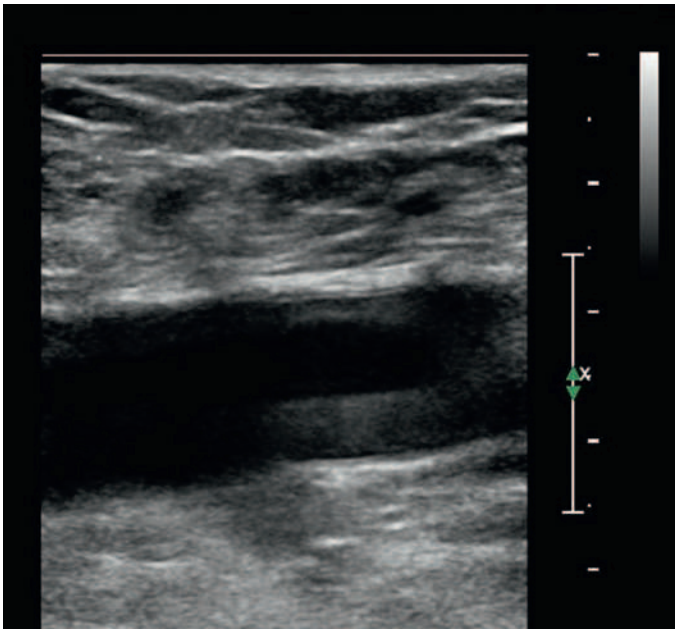

FIG. 27.34 Slow Flow in Patent, Compressible Vein Without Deep Venous Thrombosis (DVT). Accompanying Videos 27.16 and 27.17 show slow flow in longitudinal plane, and no DVT with compression.

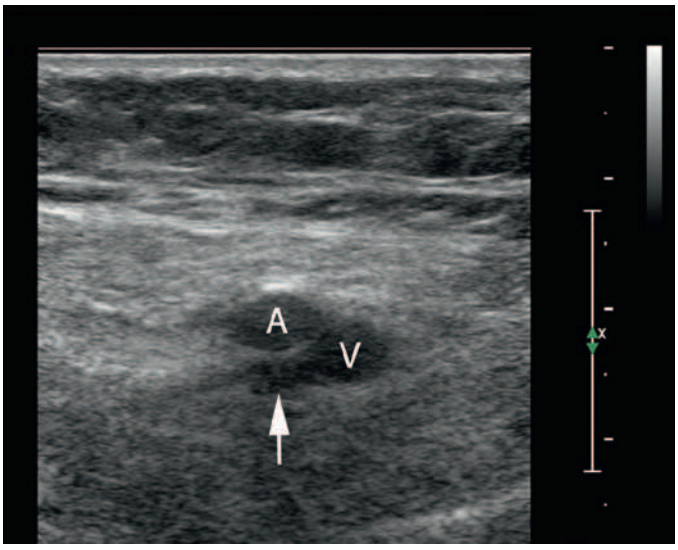

FIG. 27.35 Thrombus in One of Paired Femoral Veins. Transverse image of compressed paired femoral veins shows that one of the veins does not compress because of deep venous thrombosis (DVT). Arrow shows position of one femoral vein, which is completely compressed and thus not seen. See also Video 27.18. *A,* Superficial femoral artery; *V,* thrombus in other (paired) femoral vein.

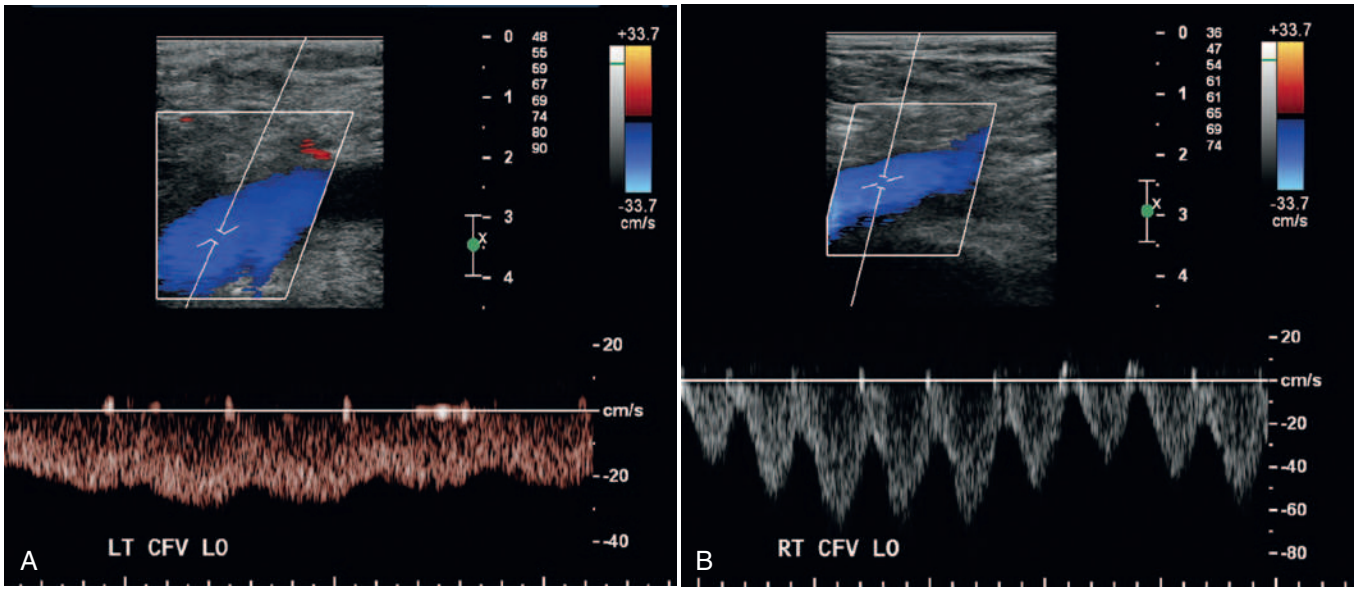

FIG. 27.36 (A) Patient with large pelvic mass compressing the left external iliac vein *(not shown).* Monophasic flow in left common femoral vein (CFV). **(B)** Normal phasic flow in right CFV.

5. Occasionally only the actual coapting of the vein walls is seen during compression, the so-called vessel "wink." The FV can sometimes be difficult to visualize throughout its entire extent. However, isolated FV thrombus is relatively uncommon, reported to occur in fewer than 1% to 4% of patients.[83]

Complete Venous Doppler Versus More Limited Examinations

Complete compression venous Doppler from the inguinal area to the popliteal area is accurate, with less than 1% venous thromboembolic disease at 3-month follow-up in recent analyses.[88,89] Limited, less detailed examinations have recently been proposed. A variety of specialties are performing this type of examination in office settings, intensive care units, and emergency departments. The two-point ultrasonography examination of the CFV and the PV using the compression technique has shown that most, but not all, proximal DVTs are detected.[90,91] However, this approach requires a serial examination 1 week later to detect propagation of calf thrombus into proximal DVT. Two negative study results, 1 week apart, have shown a low likelihood of DVT in the months following the tests.[89] The two-point technique has a 2% to 5.7% chance of detecting DVT on a repeat examination at 2 weeks.[89,90] A carefully performed complete thigh venous ultrasound as detailed earlier remains the standard of care.

Recommendations for Deep Venous Thrombosis Follow-Up

If the patient's clinical condition worsens, follow-up venous Doppler is warranted. In patients with documented DVT on therapy, a repeat venous Doppler during treatment is rarely warranted. Repeat Doppler should not be requested unless there is a clinical change.[85,92] DVT typically lyses or fibroses over 6 to 18 months. Reevaluation near the anticipated end of anticoagulation should be encouraged to establish a new baseline for patients who return with new symptoms suggesting recurrent thrombus, especially those at high risk for recurrent DVT.[85]

In patients with isolated calf DVT, a follow-up Doppler examination at 1 week is warranted if the patient is not treated. In patients with scarring, pregnant women, patients with technically limited examinations, or patients with calf pain wherein DVT is not identified, it may be prudent to suggest follow-up in 1 week. It has been established that use of two limited examinations, 1 week apart, is a safe strategy.[90] In an otherwise normal report, it may be prudent, as a helpful reminder, to state, "If there remains suspicion for DVT or the clinical condition worsens, a follow-up should be considered."[85]

Venous Insufficiency

The cause of deep venous insufficiency in many patients is venous valvular damage after DVT, which occurs in about 50% of patients with acute DVT.[93] The physiology of venous insufficiency entails direct transmission of the hydrostatic pressure of the standing column of fluid in the venous system to the caudal lower extremity. Clinical manifestations include lower extremity swelling, chronic skin and pigmentation changes, woody induration, and eventually nonhealing venous stasis ulcers.

Superficial venous insufficiency has a much better prognosis than deep venous insufficiency and is associated with extensive varicosities. Perforating veins communicate between the superficial and deep system and may also become incompetent owing to chronic deep venous insufficiency.

For assessment of venous insufficiency, the patient is placed in an upright or semi-upright position, with the body's weight supported by the contralateral lower extremity. This positioning produces the hydrostatic pressure needed to reproduce venous insufficiency. Spectral analysis is obtained at several levels of the deep and superficial venous system during Valsalva and other provocative maneuvers in the CFV, proximal aspect of the GSV, PV, and saphenopopliteal junction. Distal augmentation is more reproducible and easier when performed by a single examiner.[94]

Normal veins after brisk distal augmentation will show antegrade flow, with a very short period of flow reversal as returning blood closes the first competent venous valve (Fig. 27.37, Video 27.19). Distal augmentation can be performed manually and more reproducibly with automated devices that inflate every 5 to 10 seconds. Insufficient veins show greater degree of reversed flow for a longer duration (Fig. 27.38). It is important that each vascular laboratory validate its protocol and quantification schemes.

Venous Mapping

Vein mapping of superficial leg or arm veins is performed to determine patency, size, condition, and course of superficial veins to be used for vein grafts. Ultrasound mapping is also helpful when a vein is harvested as autologous graft material for a peripheral arterial bypass graft. Any superficial vein can be used, but the GSV is most often suitable for graft purposes. The examination is performed with the patient in the supine or reverse Trendelenburg position. The GSV is identified from the level of

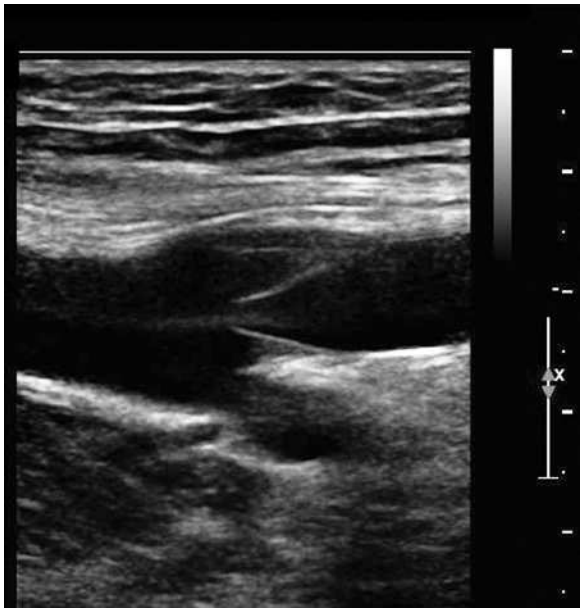

FIG. 27.37 Normal Femoral Vein Valve. Accompanying Video 27.19 shows normal coapting of valve, which prevents retrograde flow.

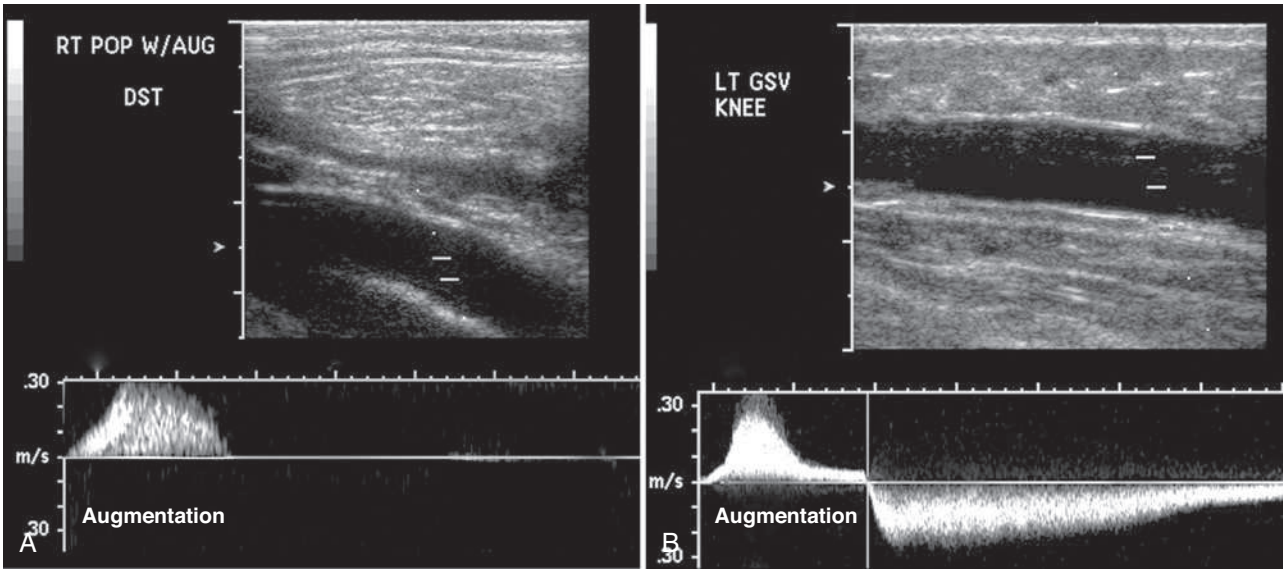

FIG. 27.38 Venous Insufficiency. (A) Duplex spectral analysis of the popliteal vein shows a normal waveform with distal augmentation. Note no reversal of flow following distal augmentation. **(B)** Duplex spectral analysis of the great saphenous vein shows **prolonged reflux** after distal augmentation, consistent with severe superficial venous insufficiency.

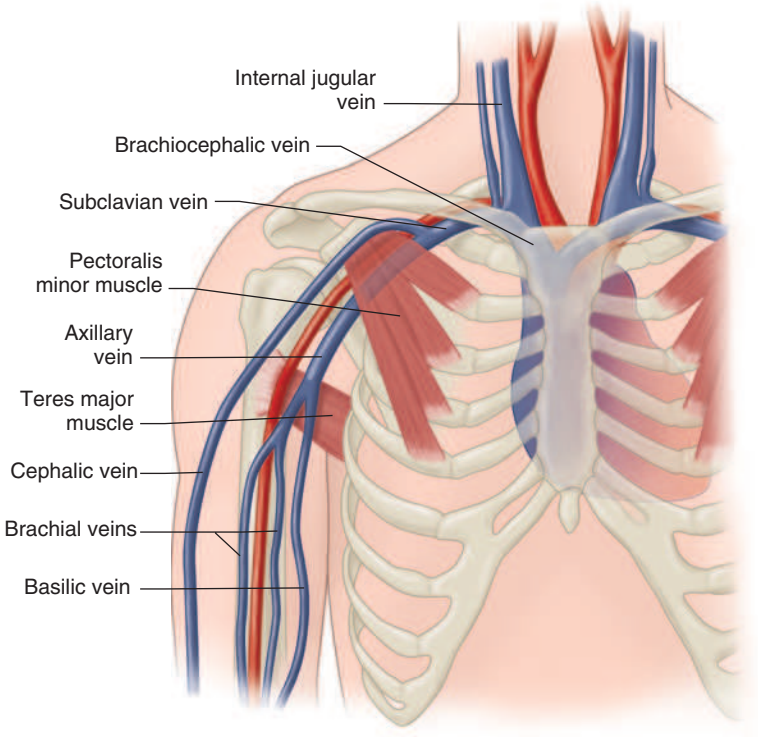

FIG. 27.39 Venous Anatomy of the Upper Extremity Veins.

the saphenofemoral junction to as far inferiorly as possible. A superficial vein typically needs to be larger than 3 mm in diameter, but not varicose, to be suitable graft material.[95] The small saphenous vein and cephalic and basilic veins are secondary choices and can be used if the GSV has already been harvested or is inadequate.

Upper Extremity Veins

Normal Anatomy

The venous anatomy of the neck and arm is illustrated in (Fig. 27.39). The deep venous system includes the paired **radial and ulnar veins** in the forearm, which unite distal to the level of the

elbow to form the **brachial veins.** The brachial veins in the upper arm join with the **basilic vein** at a variable location, typically at the level of the teres major muscle. The confluence of the brachial and basilic veins continues as the **axillary vein,** which passes through the axilla from the teres major muscle to the first rib. As the axillary vein crosses the first rib, it becomes the lateral portion of the **subclavian vein.** The medial portion of the subclavian vein receives the smaller external jugular vein and the larger **internal jugular vein** (IJV) to form the **brachiocephalic (innominate) vein.**

Most ultrasound laboratories define the central veins as the brachiocephalic veins and superior vena cava, which often are difficult to visualize sonographically. Because some angiographers include the subclavian vein when they describe the central veins, it is important to be very specific about the vein segment examined when describing sonographic findings. The presence or absence of clinically important central stenosis or thrombosis may be inferred by evaluating the transmitted cardiac pulsatility and respiratory phasicity in the medial subclavian vein and distal IJV.[96]

The cephalic and basilic veins comprise the most important superficial named veins of the upper extremity. The more laterally located cephalic vein traverses in the superficial soft tissues of the shoulder to drain into the axillary vein in the lateral chest. The basilic vein is located more medially, and typically joins the brachial veins to form the axillary vein.

Ultrasound Examination and Imaging Protocol

Upper extremity Duplex evaluation consists of gray-scale compression and color and spectral Doppler assessment of all the visualized portions of the IJV and subclavian, axillary, and innominate veins, as well as compression gray-scale ultrasound of the brachial, basilic, and cephalic veins in the upper arm to the elbow. A high-frequency, small-footprint transducer can be applied to the suprasternal notch to better demonstrate the brachiocephalic junction and IVC, often difficult to see because of overlying sternum and lung. Venous compression is applied to accessible veins in the transverse plane with adequate pressure on the skin to completely obliterate the normal vein lumen.

The patient is scanned in a supine position with the examined arm abducted from the chest, with the patient's head turned slightly away from the examined arm. Typically a 5- to 10-MHz linear array transducer will be used, with a higher frequency transducer chosen for more superficial veins. A curved array transducer or sector transducer may be more effective in larger patients, especially in the axillary area, because of its increased depth of penetration and larger field of view. All veins are examined with compression every 1 to 2 cm in the transverse plane. Gray-scale transverse images with and without compression or cine clips during compression are obtained from the cranial aspect of the IJV in the neck to the thoracic inlet caudally (Fig. 27.40, Video 27.20). Longitudinal color and spectral images are obtained.

The subclavian vein is evaluated from its medial to lateral aspect with longitudinal color and spectral images, assessing for transmitted respiratory variability, cardiac pulsatility, and color fill-in. To demonstrate the superior brachiocephalic vein and the medial portion of the subclavian vein, an inferiorly angled, supraclavicular approach with color Doppler is necessary. A small-footprint sector probe in or near the suprasternal notch may improve visualization of the brachiocephalic veins and the cranial aspect of the superior vena cava (Fig. 27.41). The midportion of the subclavian vein, located deep to the clavicle, frequently is incompletely imaged. An infraclavicular, superiorly angled approach can be used to demonstrate the lateral aspect of the

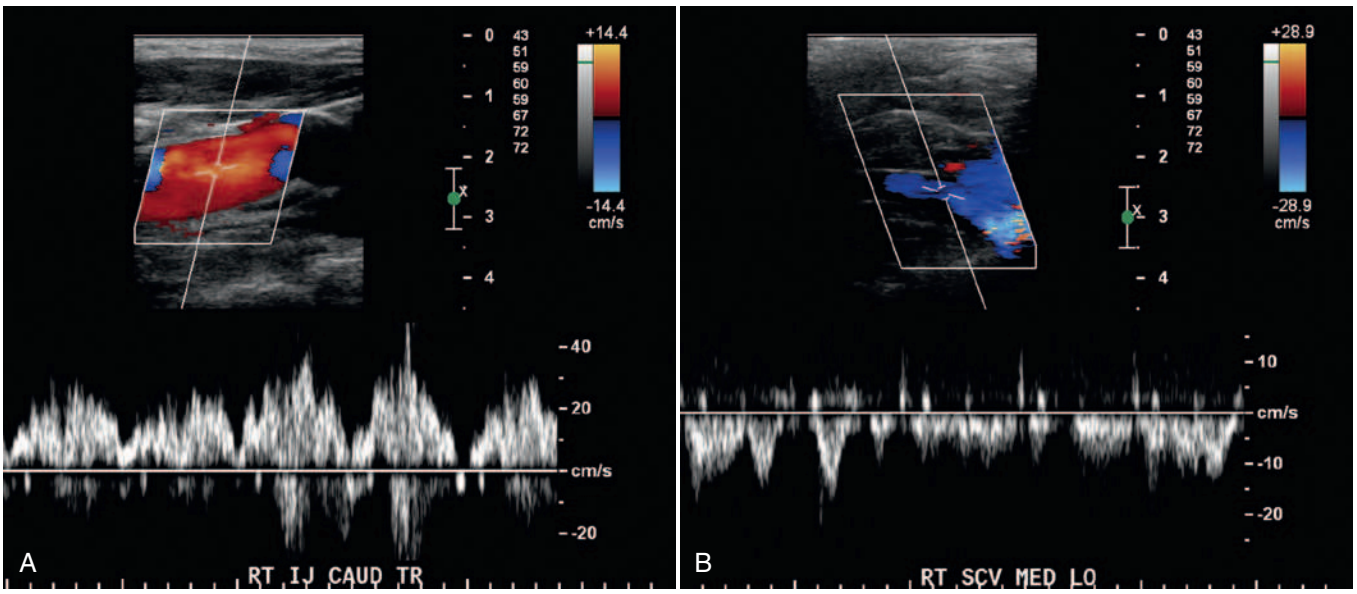

FIG. 27.40 Normal Internal Jugular Vein (IJV) and Subclavian Vein (SCV) Spectral Doppler Waveforms. (A) Normal IJV spectral Doppler waveform, with transmitted cardiac pulsatility and respiratory phasicity, with spectral waveform going to the baseline. Accompanying Video 27.20 shows normal IJV compression. **(B)** Normal medial SCV spectral Doppler, with transmitted cardiac pulsatility and respiratory phasicity, and spectral waveform going to the baseline.

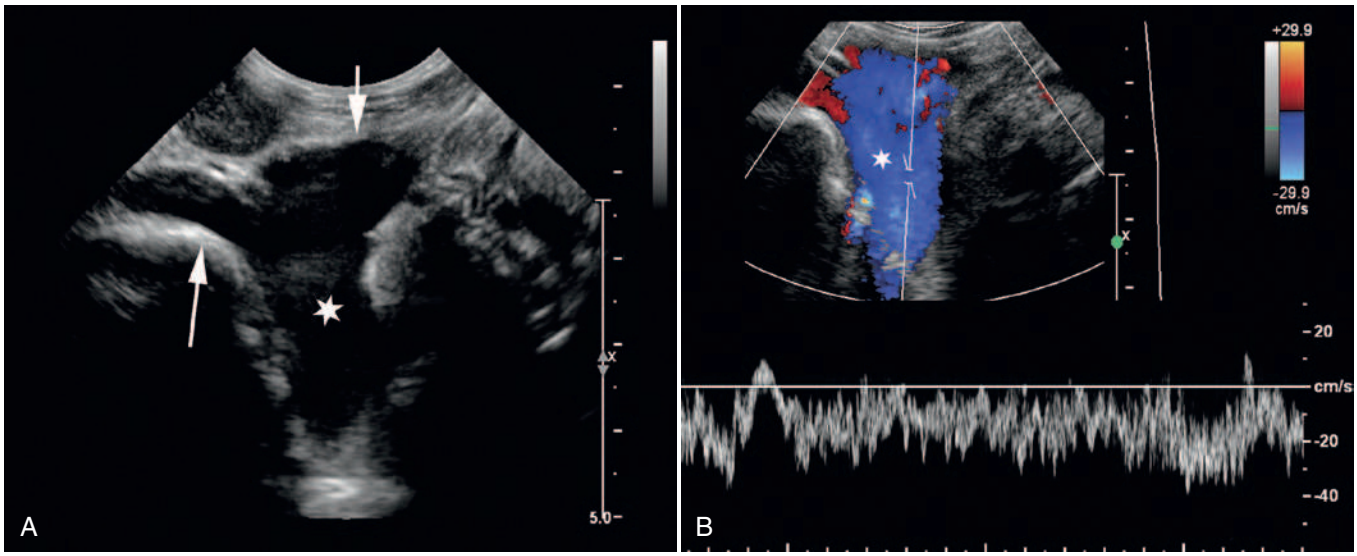

FIG. 27.41 Normal Brachiocephalic Veins. Gray-scale **(A),** and color and spectral Doppler **(B)** of left and right brachiocephalic veins *(arrows)* and cranial superior vena cava (SVC; *).

subclavian vein. In many cases the subclavian vein can be compressed.

Accurate spectral waveform evaluation is critical to this examination. Documentation of normal flow in the medial subclavian vein confirms patency of the brachiocephalic vein and superior vena cava, which cannot be examined directly. Each spectral image obtained in the longitudinal plane of the vessel with angle of insonation maintained at less than 60 degrees is evaluated for spontaneous, phasic, and pulsatile flow. Demonstration of transmitted cardiac pulsatility and respiratory phasicity is necessary in the spectral analysis of the caudal IJV and medial subclavian vein. A normal spectral tracing should return to baseline. Absence of pulsatility may be caused by a more central venous stenosis or obstruction (Fig. 27.42).[97]

Spectral tracings from the medial subclavian vein should be compared with tracings from the lateral subclavian vein. A change between these two tracings suggests midsubclavian vein stenosis. Response to a brisk inspiratory sniff or Valsalva maneuver may assist evaluation of venous patency. During a sniff, the normal IJV or subclavian vein normally decreases in diameter or collapses completely. The Valsalva maneuver will increase the vein diameter, demonstrating response to the increased thoracic pressure and documenting communication with the central vasculature. Patients with significant stenosis or obstruction of the central brachiocephalic vein of the superior vena cava will lose this response.[97]

The upper extremity venous **imaging protocol** includes the following images for each deep venous segment:

1. Transverse gray-scale image at rest and with compression, or a cine clip of the compression maneuver of the proximal and distal IJV, subclavian, axillary, and brachial veins. The basilic and cephalic veins are evaluated in the upper arm to the elbow.
2. Longitudinal color Doppler with spectral waveform analysis is performed of the IJV, both proximal and distal portions, as well as the subclavian vein, both medially and laterally, and the axillary vein. If only a unilateral examination is requested, the contralateral subclavian vein is also evaluated.
3. Evaluation of focal symptomatic areas if present, including the forearm.

Upper Extremity Acute Deep Venous Thrombosis

Current literature shows the sensitivity and specificity of venous Doppler ultrasound for upper extremity DVT to range from 78% to 100% and 82% to 100%, respectively.[96,98-102] The classic ultrasound finding in acute upper extremity DVT is an enlarged, tubular structure filled with thrombus showing variable echogenicity and absence of color Doppler flow (Fig. 27.43, Video 27.21). Nonocclusive thrombus may show flow outlining the thrombus, with a variable appearance depending on whether the nonocclusive thrombus is acute or chronic. Nonocclusive thrombus usually does not result in enlargement of the vein (Fig. 27.44). When the obstruction is incomplete, nonphasic flow is demonstrated when the luminal narrowing is significant enough to affect the transmitted cardiac pulsatility and respiratory phasicity from the thorax. Attention to detail is important in the normally paired brachial veins to avoid overlooking thrombus in one of the veins (Fig. 27.45, Video 27.22).

Evaluation of central thrombus relies on spectral analysis. The presence of a nonpulsatile waveform (similar to portal venous flow) that does not cross the baseline strongly suggests central venous thrombosis, stenosis, or extrinsic compression from an adjacent mass.[96] A suspicious waveform should always be compared with the contralateral side to assess a unilateral versus bilateral process. Patel and colleagues[103] found that absent or reduced cardiac pulsatility was a more sensitive parameter in patients who had unilateral venous thrombosis, even though respiratory phasicity often was asymmetric. In cases of bilateral subclavian vein or superior vena cava occlusion, a high level of suspicion must be maintained to detect central thrombus or stenosis. Of importance, because of high-volume flow, there may

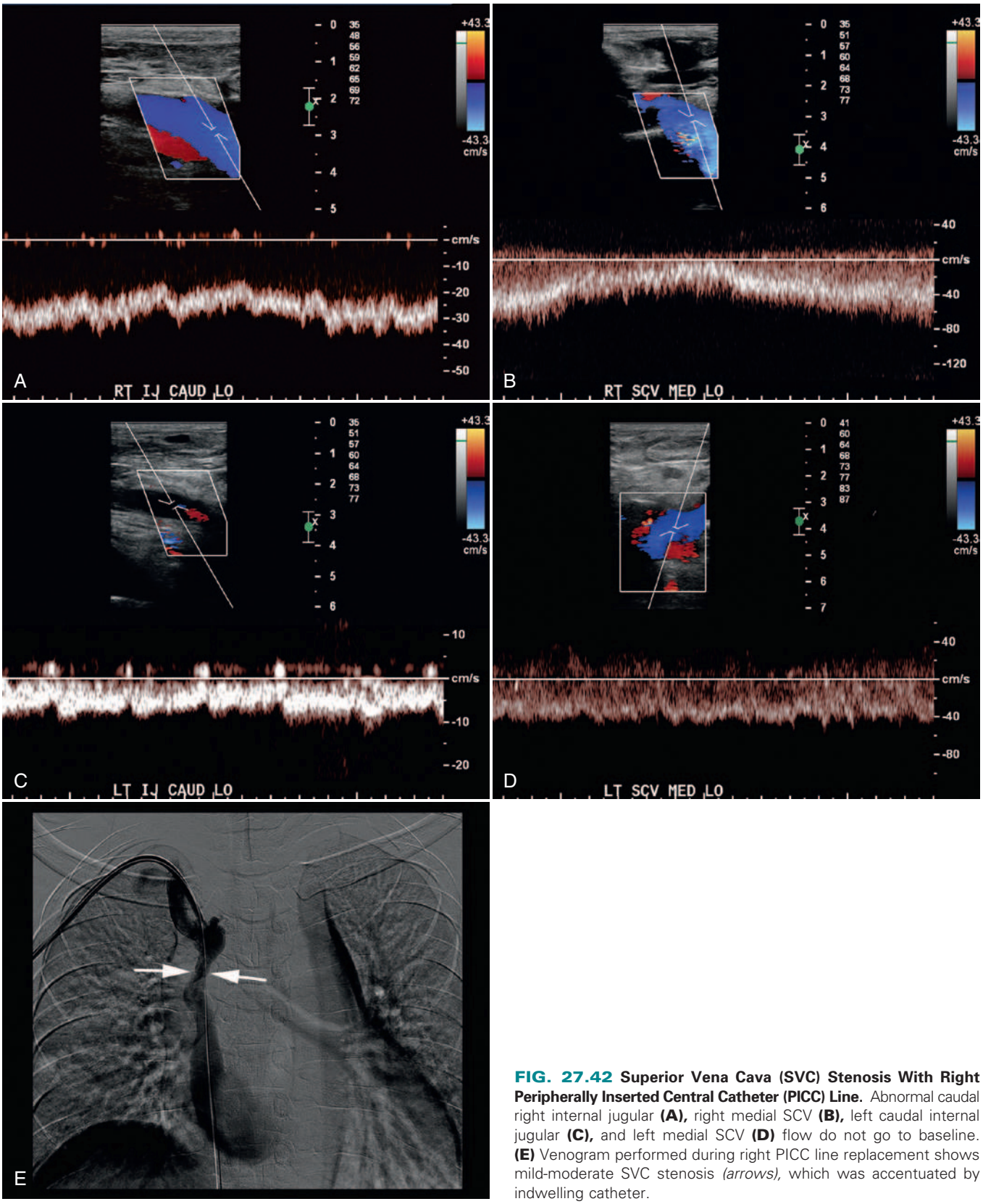

FIG. 27.42 Superior Vena Cava (SVC) Stenosis With Right Peripherally Inserted Central Catheter (PICC) Line. Abnormal caudal right internal jugular **(A),** right medial SCV **(B),** left caudal internal jugular **(C),** and left medial SCV **(D)** flow do not go to baseline. **(E)** Venogram performed during right PICC line replacement shows mild-moderate SVC stenosis *(arrows),* which was accentuated by indwelling catheter.

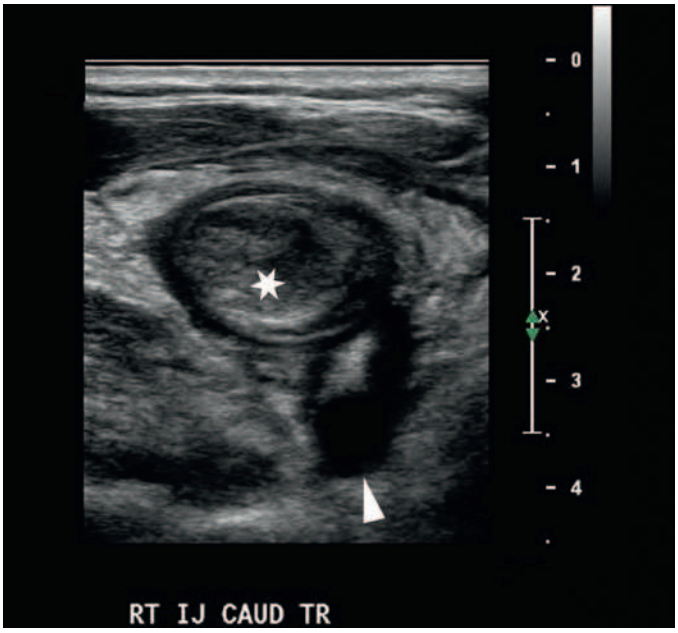

FIG. 27.43 Acute Internal Jugular Thrombus. Transverse image of a noncompressible internal jugular vein filled with thrombus (*). *Arrowhead* shows carotid artery. See also Video 27.21.

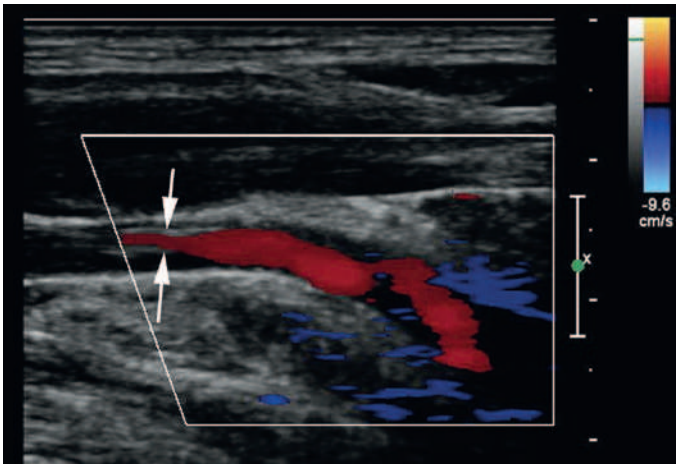

FIG. 27.44 Nonocclusive Chronic Internal Jugular Thrombus. Longitudinal color Doppler image of the small-caliber proximal internal jugular vein with irregular thrombus adjacent to wall, with thickened valves *(arrows)*.

be absence of phasicity without stenosis in the central veins if a hemodialysis graft or AVF is present in the upper arm.

Unlike the lower extremity, most cases of upper extremity DVT are related to the presence of a central venous catheter or electrode leads from an implanted cardiac device. Approximately 35% to 75% of patients who have upper extremity venous catheters develop thrombosis, and approximately 75% are asymptomatic[104-106] (Fig. 27.46, Video 27.23 and Video 27.24).

Frequently a fibrin sheath is found adjacent to the catheter and may be seen after catheter removal. It is important to look carefully at the valves for adherent thrombus. Whether the catheter access site is the subclavian vein or the IJV affects the complication rate. Trerotola and colleagues[107] examined only patients who had symptomatic upper extremity DVT and found a greater incidence of DVT in patients who had subclavian venous access than in those who had internal jugular access. The placement of large-bore catheters into the subclavian vein should be avoided, especially in patients who have end-stage renal disease (ESRD) for whom dialysis access is being considered. Subsequent development of subclavian vein stenosis or thrombosis would limit dialysis access possibilities for that upper extremity.

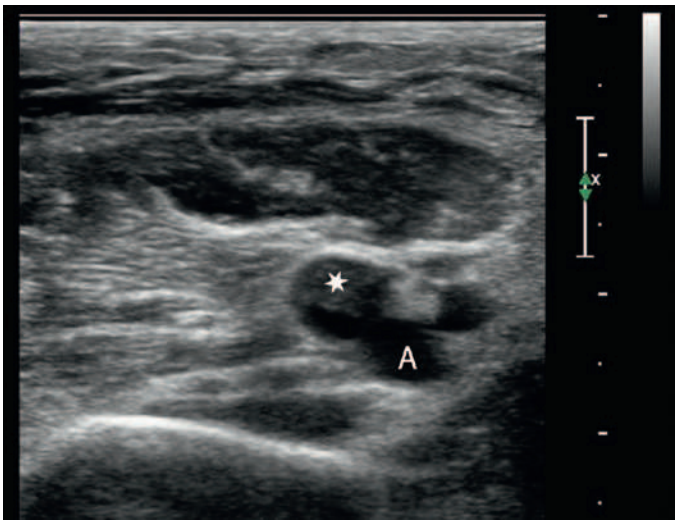

FIG. 27.45 Nonocclusive Thrombus in Brachial Vein. Transverse noncompressed image of nonocclusive thrombus (*) in one brachial vein in the paired brachial veins. *A,* Brachial artery. See also Video 27.22.

Only 12% to 16% of patients who have upper extremity DVT develop PE.[108,109] In comparison, 44% of patients who developed proximal lower extremity DVT detected by sonography had a subsequent PE diagnosed clinically.[110] Acute pulmonary emboli in patients who have upper extremity DVT tend to occur in untreated patients.[111,112] As expected, there is greater risk of PE in catheter-related upper extremity DVT than in upper extremity DVT from other causes.[113] Venous stasis and insufficiency caused by venous thrombosis, more commonly seen with LE DVT, are less common and less severe in the upper extremity. The deep venous system in the arm has less exposure to the physiologic hydrostatic high-pressure pump mechanism that is seen in the lower extremity.[114,115] Development of extensive collateral venous pathways in the arm and chest after venous thrombosis or obstruction contributes to these differences and may cause greater technical challenge in performing the upper extremity venous Doppler examination, as compared with the lower extremity.

Differentiation of Acute From Residual or Chronic Venous Thrombosis

Findings suggesting residual or chronic DVT in the upper extremity include fixed valve leaflets, synechiae, fibrin sheaths, small-caliber veins with noncompressible, thickened walls, and multiple serpiginous veins not paralleling the artery (Fig. 27.47). In some cases of residual or chronic thrombosis, the vein may not be seen in the expected location owing to fibrosis or scarring.

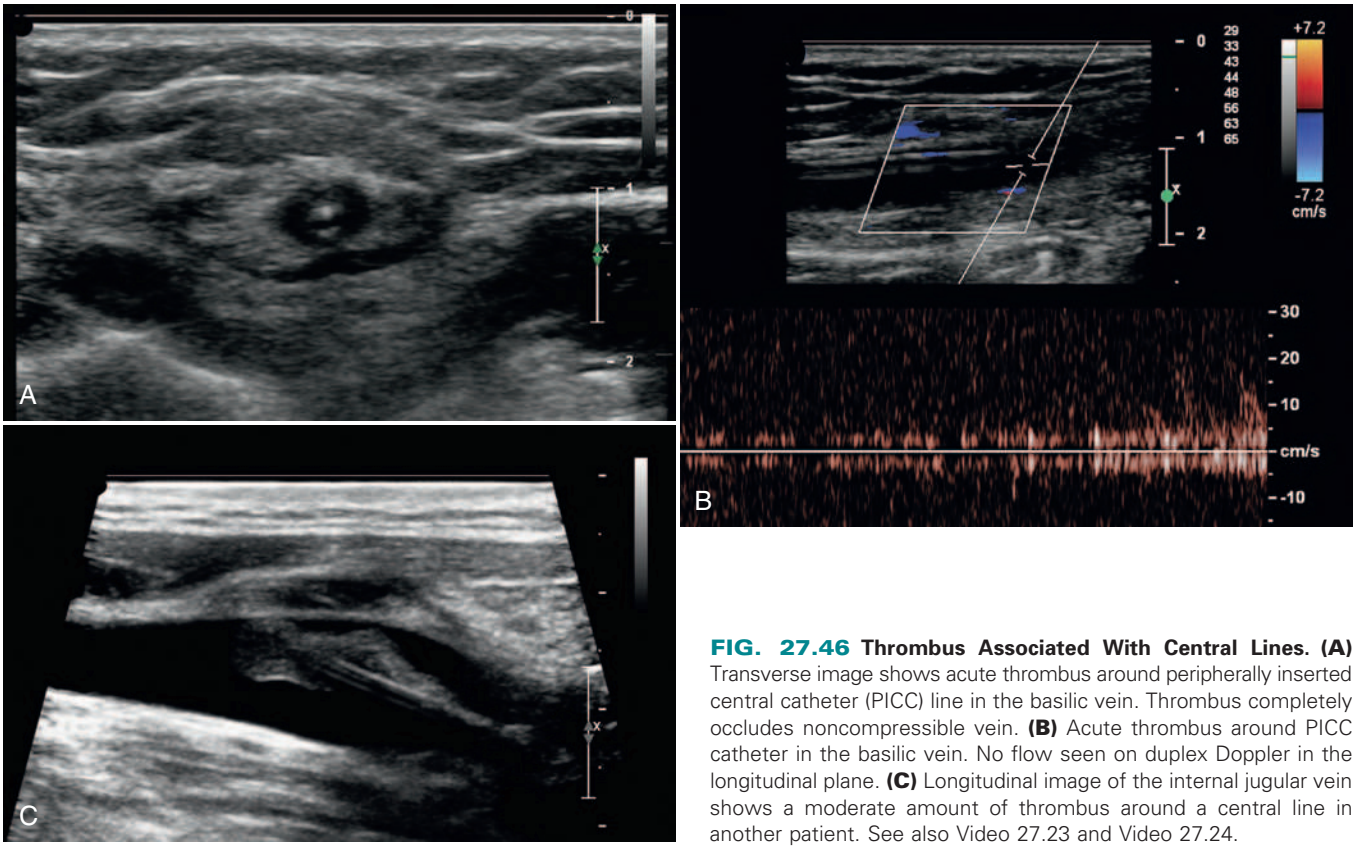

FIG. 27.46 Thrombus Associated With Central Lines. (A) Transverse image shows acute thrombus around peripherally inserted central catheter (PICC) line in the basilic vein. Thrombus completely occludes noncompressible vein. **(B)** Acute thrombus around PICC catheter in the basilic vein. No flow seen on duplex Doppler in the longitudinal plane. **(C)** Longitudinal image of the internal jugular vein shows a moderate amount of thrombus around a central line in another patient. See also Video 27.23 and Video 27.24.

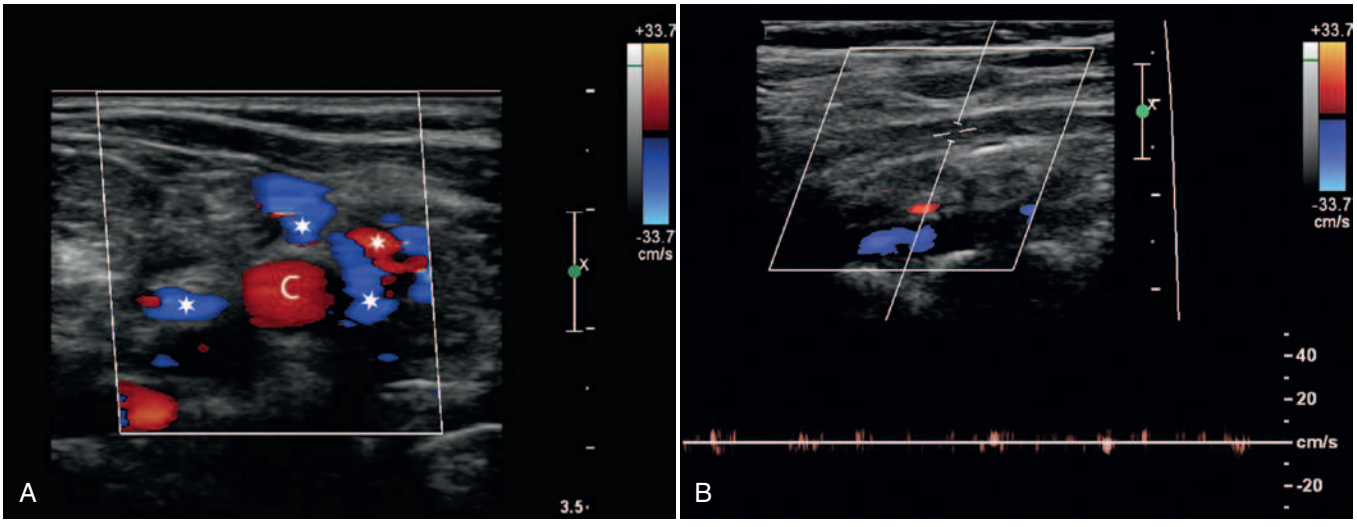

FIG. 27.47 Collateral Formation in the Upper Extremity After Deep Venous Thrombosis (DVT). (A) Transverse images of many serpiginous veins (*) in the region of the chronically occluded proximal internal jugular vein near the base of the neck. *C,* Carotid. **(B)** Longitudinal duplex Doppler image shows no spectral flow in the small, occluded distal internal jugular vein.

An excellent example is demonstration of only one brachial vein because of chronic scarring from prior DVT of the paired brachial veins[116] (Fig. 27.48).

Potential Pitfalls

Upper extremity pitfalls to avoid include the following[117-119]:

1. Axillary versus cephalic vein: The axillary vein of the deep venous system empties into the subclavian vein. The cephalic vein of the superficial venous system empties into the axillary vein and will not have an adjacent artery along its course. Access to the axilla is generally improved by bending the patient's elbow and placing the hand near the patient's head, with an outstretched arm. Excessive abduction may alter the venous waveform, falsely suggesting a more central venous stenosis or obstruction; however, this will resolve with change in position.

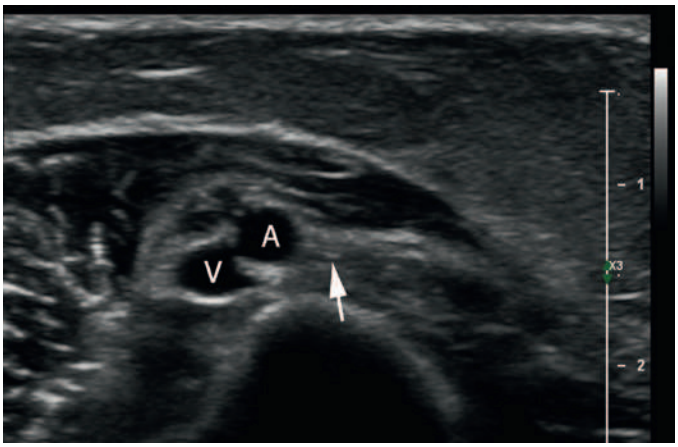

FIG. 27.48 Chronic Clot in Brachial Vein. One of the paired brachial veins is small and chronically occluded *(arrow). A,* Brachial artery; *V,* other, normal brachial vein.

2. Distal occlusion of IJV: The distal aspect of the IJV must be demonstrated flowing into the junction with the medial subclavian vein in the area of the brachiocephalic vein. If the vein being traced is located more than a few millimeters away from the carotid artery, it probably represents a collateral vessel, rather than the IJV. Well-developed collaterals may demonstrate normal respiratory phasicity, an additional pitfall. Collateral vessels tend to be multiple and serpiginous and to follow the occluded vein.

HEMODIALYSIS

There were 661,648 patients being treated for ESRD by the end of 2013 in the United States, with 117,162 new cases that year.[1] Approximately 64% of these patients were undergoing hemodialysis.[120] A major cause of morbidity among ESRD patients is related to vascular access procedures and associated complications that increase health care costs in patients undergoing hemodialysis.[121] There are two options for permanent access placement for ESRD patients requiring hemodialysis—an **arteriovenous fistula** (AVF) or a **synthetic arteriovenous graft.** Mature AVFs are the preferred access when appropriate, because of the lower rates of infection and thrombosis than with graft or catheter access.[122-124]

Several studies have shown that **preoperative ultrasound** evaluation of the upper extremity veins and arteries may increase the number of successful AVF placements through optimization of surgical planning[125-127] as well as before graft placement in the thigh.[128] Although sonographic postoperative hemodialysis access evaluation may be beneficial in assessing AVF maturation,[129-131] the role of **postoperative ultrasound** evaluation for the detection of access pathology and early intervention to improve the longevity of a particular access is still being studied.[132-139]

Ultrasound is useful in evaluation of palpable masses adjacent to the vascular access to differentiate hematoma from pseudoaneurysm. It is also used in the evaluation of the swollen upper extremity in a patient with an AVF or graft, or a swollen lower extremity in a patient with a thigh graft, assessing for outflow vein stenosis and DVT. Ultrasound is also used in the evaluation of patients with arm and hand pain after access placement to evaluate for symptomatic steal.

The surgical creation of an AVF is preferred over a graft when surgically and clinically feasible. Placement of access in the nondominant upper extremity is preferred to allow continuance of daily activities of life while the access site heals; however, a dominant arm AVF is preferred to a graft in most patients. Possible sites of hemodialysis access in order of preference are as follows: (1) forearm AVF (radiocephalic AVF or transposed forearm basilic vein to radial artery AVF); (2) upper arm brachiocephalic AVF; (3) transposed brachiobasilic AVF; (4) forearm loop graft; (5) upper arm straight graft (brachial artery to upper basilic or axillary vein); (6) upper arm axillary artery to axillary vein loop graft; and (7) thigh graft (Fig. 27.49). The cephalic vein is preferred over a basilic vein transposition for fistula formation because the cephalic vein procedure involves less dissection and venous manipulation. Additional, less common access configurations may also be placed based on surgical experience.[140]

Sonographic Examination Technique

Both gray-scale and color Doppler ultrasound techniques should be optimized for venous and arterial imaging as previously discussed in this chapter. A high-frequency linear array 12- to 15-MHz transducer provides optimal spatial resolution and adequate depth penetration to successfully evaluate superficial vascular structures. A lighter-weight transducer with a smaller footprint, such as a hockey stick configuration, can increase the speed and ease of the examination. A lower-frequency linear array 9- to 12-MHz transducer may be needed for adequate penetration in larger patients. A small-footprint curved array transducer may be useful for evaluation of the brachiocephalic vein and distal SVC.

It is important to apply light pressure and use plenty of gel so as not to deform the circular shape of the vessels during the mapping examination for accurate vessel diameters. All diameter measurements are of the inner lumen measured in the anteroposterior dimension in the transverse plane. Color and spectral Doppler evaluation are performed in the longitudinal plane with angle correction of 60 degrees or less. Blood flow rate measurements are performed in the longitudinal plane in a straight area that is not curvy. In blood flow rate measurement, the Doppler gate is increased in size to encompass the entire vessel diameter, and is angle corrected to 60 degrees or less, parallel to the posterior vessel wall. Three to five spectral Doppler waveforms are analyzed, using the automatic blood flow rate calculation in most ultrasound scanners, using the formula of time-averaged mean velocity multiplied by the inner vessel diameter. Three measurements at the same location are performed and averaged, to ensure measurement reliability.

Vascular Mapping Before Hemodialysis Access

Upper Extremity

Attention to technical detail is necessary for optimum ultrasound evaluation for hemodialysis access planning.[126,130,141-143] In general,

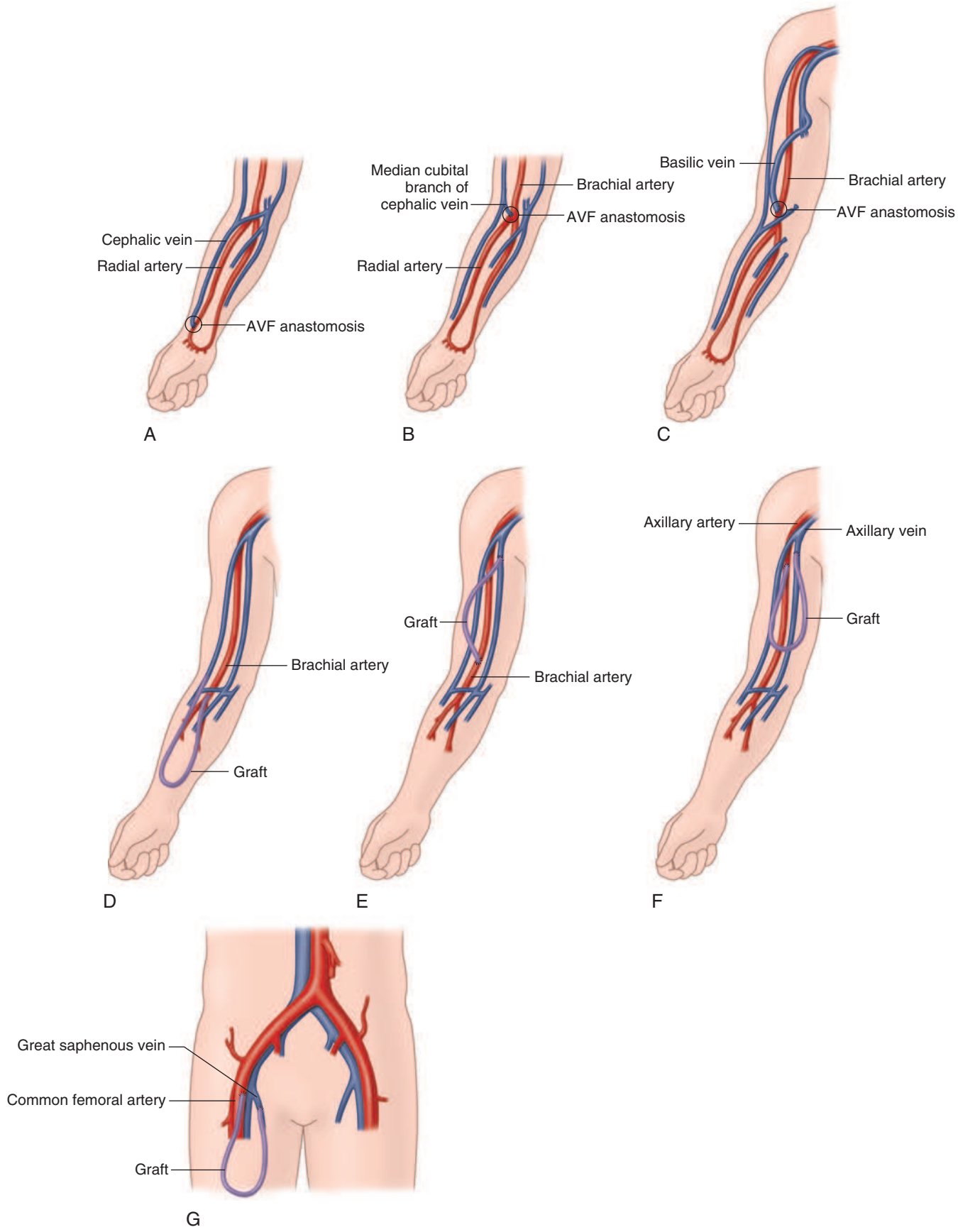

FIG. 27.49 Most Common Arteriovenous Fistula *(AVF)* and Graft Placements. (A) Forearm cephalic vein–radial artery AVF. **(B)** Upper arm cephalic vein–brachial artery AVF, using the median cubital branch of the cephalic vein for the anastomosis. **(C)** Upper arm basilic vein–brachial artery AVF. **(D)** Forearm loop graft. **(E)** Upper arm straight graft. **(F)** Upper arm loop graft. **(G)** Thigh loop graft. (Reproduced with permission from Robbin ML, Lockhart ME. Ultrasound evaluation before and after hemodialysis access. In: Zweibel WJ, Pellerito JS, editors. Introduction to vascular ultrasonography. 5th ed. Philadelphia: Elsevier; 2005. p. 325-340.[158])

FIG. 27.50 Sonographic Evaluation of the Forearm Veins With Patient's Arm Comfortably Resting on a Surgical Stand.

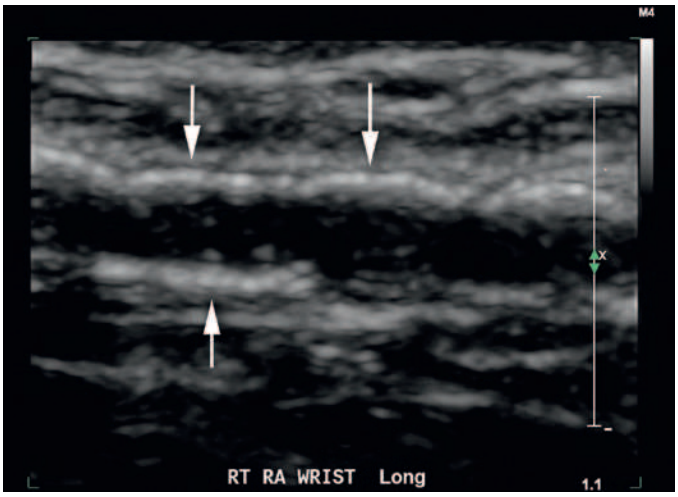

FIG. 27.51 Heavily Calcified Radial Artery at the Wrist. Longitudinal image shows heavy arterial wall calcification *(arrows)*.

it is easier to map all the upper extremity arteries and veins on the same side at one sitting so the surgeon has adequate information if vessel character at surgery is suboptimal and another access site needs to be chosen. If a suitable site for AVF creation is not found on the arm evaluated, the other arm is evaluated. The patient should be sitting upright for optimal evaluation of the upper extremity arteries and veins, with the forearm resting comfortably on a table or armrest. A tourniquet should be placed after arterial assessment, to assess vein caliber and distention[144] (Fig. 27.50). Central venous evaluation to include the IJV and subclavian vein should then be performed with the patient supine, for easier and potentially more accurate waveform assessment.

Sonographic assessment of the arterial wall should evaluate the amount of calcification and degree of stenosis or occlusion, if present. Vein walls should be described with as much detail as possible to assess for wall thickening and thrombus, which may limit future venous distention. The literature suggests that preoperative criteria include a minimum intraluminal arterial diameter of 2.0 mm and a minimal intraluminal venous diameter of 2.5 mm to allow successful AVF creation, and a minimum intraluminal venous diameter of 4.0 mm and a minimum arterial diameter threshold of 2.0 mm for grafts.[145,146]

At least the caudal third of the brachial artery and the entire radial artery are evaluated for intimal thickening, calcification, stenosis, or occlusion, with more extensive evaluation of the brachial and ulnar arteries as warranted, as well as the axillary artery. The severity of arterial calcification may be categorized, depending on surgeon preference, because it may be difficult to suture into a heavily calcified artery, and the risk of emboli at surgery may be higher[123] (Fig. 27.51). The arterial waveform is evaluated for a normal triphasic or biphasic high-resistance flow pattern, and PSV is measured in these regions (Fig. 27.52). A high brachial artery bifurcation is a common anatomic variant and should be suspected when two arteries with accompanying paired veins are seen in the upper arm[52] (Fig. 27.53). The two arteries should be followed into the forearm to the wrist to confirm the presence of a high brachial artery bifurcation and to exclude a prominent arterial branch supplying the elbow, less commonly seen.

For assessment of veins, the upright-seated position ensures venous distention owing to hydrostatic pressure. For optimal venous distention, the tourniquet should be placed on the arm cranial to the area of interrogation so that the veins are distended. Each vein should be inspected, with compression performed along the entire venous length to exclude thrombus (Fig. 27.54). The tourniquet is first placed in the midforearm. The region of the cephalic vein at the wrist is percussed for about 2 minutes for maximal venous distention, and the cephalic vein inner diameter is measured at multiple points in the forearm (Fig. 27.55, Video 27.25). Thereafter, the tourniquet is placed at the antecubital fossa, and then the proximal upper arm, after segmental vein diameter measurement. Cephalic vein anterior wall distance from the skin can be measured because if the cephalic vein is too deep for easy cannulation, it may need to be superficialized in a subsequent surgery (Fig. 27.56). It is not necessary to measure the distance of the basilic vein from the skin; the vein needs to be transposed for easier access. The median antecubital vein typically connects the cephalic vein to the basilic vein and is often part of the AVF draining vein. The median antecubital vein also can be used in creating an upper arm basilic or cephalic vein AVF and so is commonly evaluated at the mapping ultrasound procedure. The axillary vein, subclavian vein, and IJV should be assessed for compressibility (when possible) and normal waveforms (see Fig. 27.40).

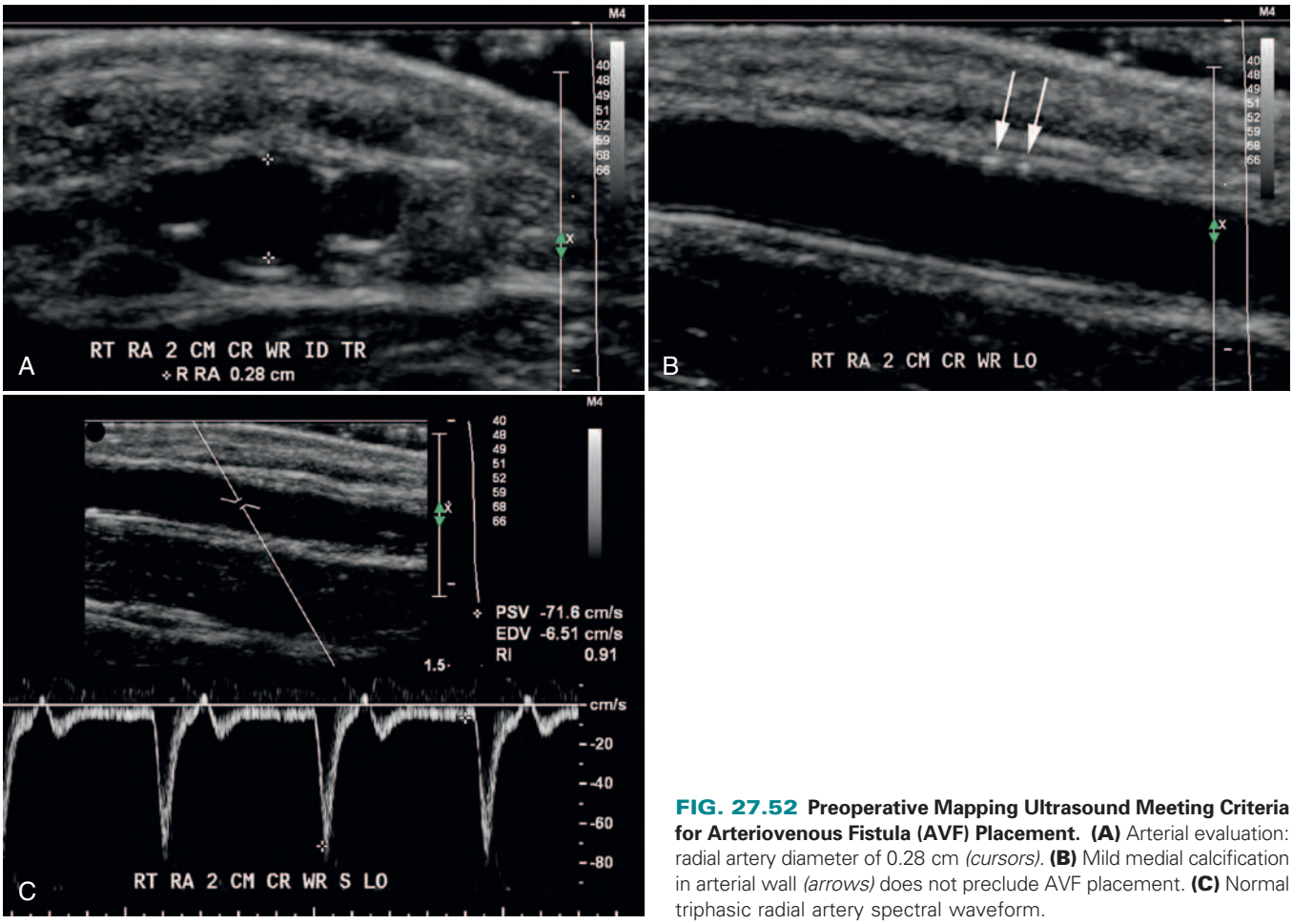

FIG. 27.52 Preoperative Mapping Ultrasound Meeting Criteria for Arteriovenous Fistula (AVF) Placement. (A) Arterial evaluation: radial artery diameter of 0.28 cm *(cursors)*. **(B)** Mild medial calcification in arterial wall *(arrows)* does not preclude AVF placement. **(C)** Normal triphasic radial artery spectral waveform.

FIG. 27.53 High Brachial Artery Bifurcation. Radial and ulnar arteries *(A)* and accompanying paired veins *(V)*.

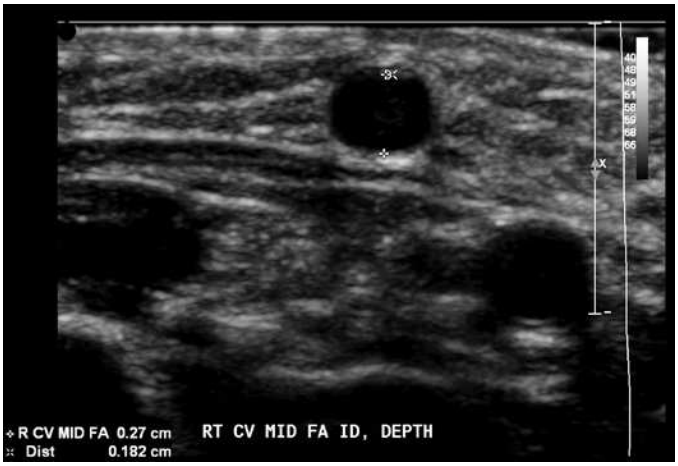

FIG. 27.54 Preoperative Mapping Ultrasound Meeting Criteria for Arteriovenous Fistula (AVF) Placement. Venous evaluation: cephalic vein in the midforearm is 0.27 cm *(+ cursors)*. Anterior vein wall depth is 0.18 cm from skin *(X cursor)*.

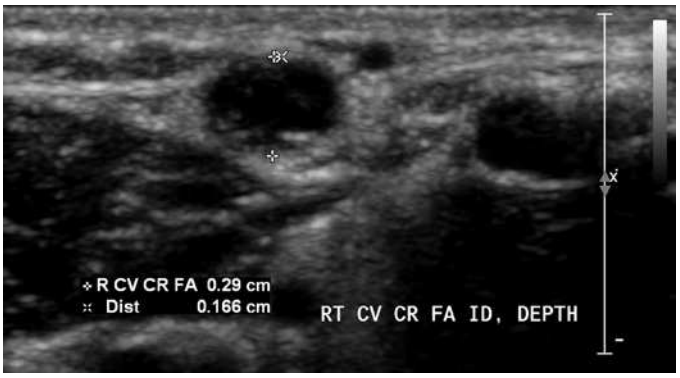

FIG. 27.55 Thick-Walled Cephalic Vein With Chronic Thrombus. This vein may not dilate normally after arteriovenous fistula (AVF) placement and should not be chosen for a potential AVF draining vein. See accompanying Video 27.25.

FIG. 27.56 Cephalic vein is quite deep from the skin surface (0.9 cm; *X cursor*), and may need to be superficialized after arteriovenous fistula creation.

Ultrasound Examination and Imaging Protocol

Upper Extremity. After assessment of the brachial and radial arteries, the inner luminal diameter of the brachial artery 2 cm proximal to the antecubital fossa, and the radial artery at the wrist are measured, along with the axillary artery diameter. Using sequential tourniquet placement and after wrist percussion of the cephalic vein region, the cephalic vein inner diameter is measured at the wrist, midforearm, and proximal forearm (approximately 4 cm from the antecubital fossa). The proximal forearm measurement is used to evaluate the length of vein available to surgically move the vein from the forearm to the brachial artery in upper arm AVF creation.

The cephalic and basilic vein diameters are measured at the antecubital fossa and mid and cranial upper arm. Distance of the anterior wall of the cephalic vein to the skin surface is measured. The axillary vein diameter is measured. The subclavian vein and IJV are assessed in the longitudinal plane with color and spectral Doppler assessment, and IJV compression is performed to assess for thrombus, stenosis, and occlusion. Subclavian and internal jugular spectral Doppler waveforms are assessed for respiratory phasicity and transmitted cardiac pulsatility.

Thigh. Once options to place AVF and grafts in the upper extremity are exhausted, the thigh graft becomes a viable option. Thigh grafts are similar to upper extremity grafts in length of time to permanent failure, with a trend toward increased loss because of infection.[147] Thigh grafts are superior to dialysis via a catheter.[148] If heavy arterial common femoral or superficial femoral arterial calcification is found at ultrasound, pelvic CT may be useful to determine the degree of atherosclerotic disease present. Careful sonographic assessment of atherosclerotic calcification and stenosis may limit immediate graft failure at surgical placement.[128] Thigh graft creation has typically been at the common femoral artery and vein (Fig. 27.57). An alternate place to anastomose the venous end of the graft is the GSV, to preserve the CFV when graft revision is necessary. However, to preserve proximal vasculature for graft revision, and potentially because of fewer infectious complications, midthigh grafts are now being increasingly placed in the mid SFA and superficial femoral vein.[149]

Technical considerations for mapping the arteries and veins of the thigh for hemodialysis graft placement are similar to mapping the upper extremity as described earlier, although a lower-frequency linear transducer may be necessary because of greater thigh size. Evaluation of the degree of arterial calcification and the presence of thrombus is carefully performed in the thigh. More central stenosis or obstruction is assessed by spectral Doppler evaluation of the CFV and common femoral artery. Distance of the vein to the skin is not measured, because typically only thigh grafts are surgically created. A tourniquet is not used in sonographic thigh graft mapping.

The common femoral artery and vein inner luminal diameters are measured, and evaluated for the degree of atherosclerotic calcification. Spectral and color Doppler evaluation of the common femoral artery and vein are performed to evaluate for more proximal stenosis or occlusion. SFA waveforms are also assessed for normalcy. The length of the GSV, which is at least 0.4 cm inner diameter, is measured from its insertion into the CFV extending distally. Inner diameter measurements of the proximal and mid superficial femoral artery and FV are obtained. Compressibility of the veins assessing for thrombus and wall thickening is performed.[128]

Arteriovenous Fistula and Graft

A surgically created hemodialysis access can have a variety of complications, and most of these can be successfully evaluated by ultrasound. Operative notes and pertinent patient history should be reviewed before sonographic evaluation of hemodialysis access. An overall ultrasound scan is performed initially to obtain an overview of the access anatomy and anastomoses. When the general layout is known, sonographic assessment is performed with duplex Doppler sonography, typically in a seated patient with his or her arm resting comfortably on a table. The caudal third of the feeding artery is assessed for stenosis, and the intraluminal diameter is measured in the transverse plane using gray-scale techniques. The feeding artery is further assessed with

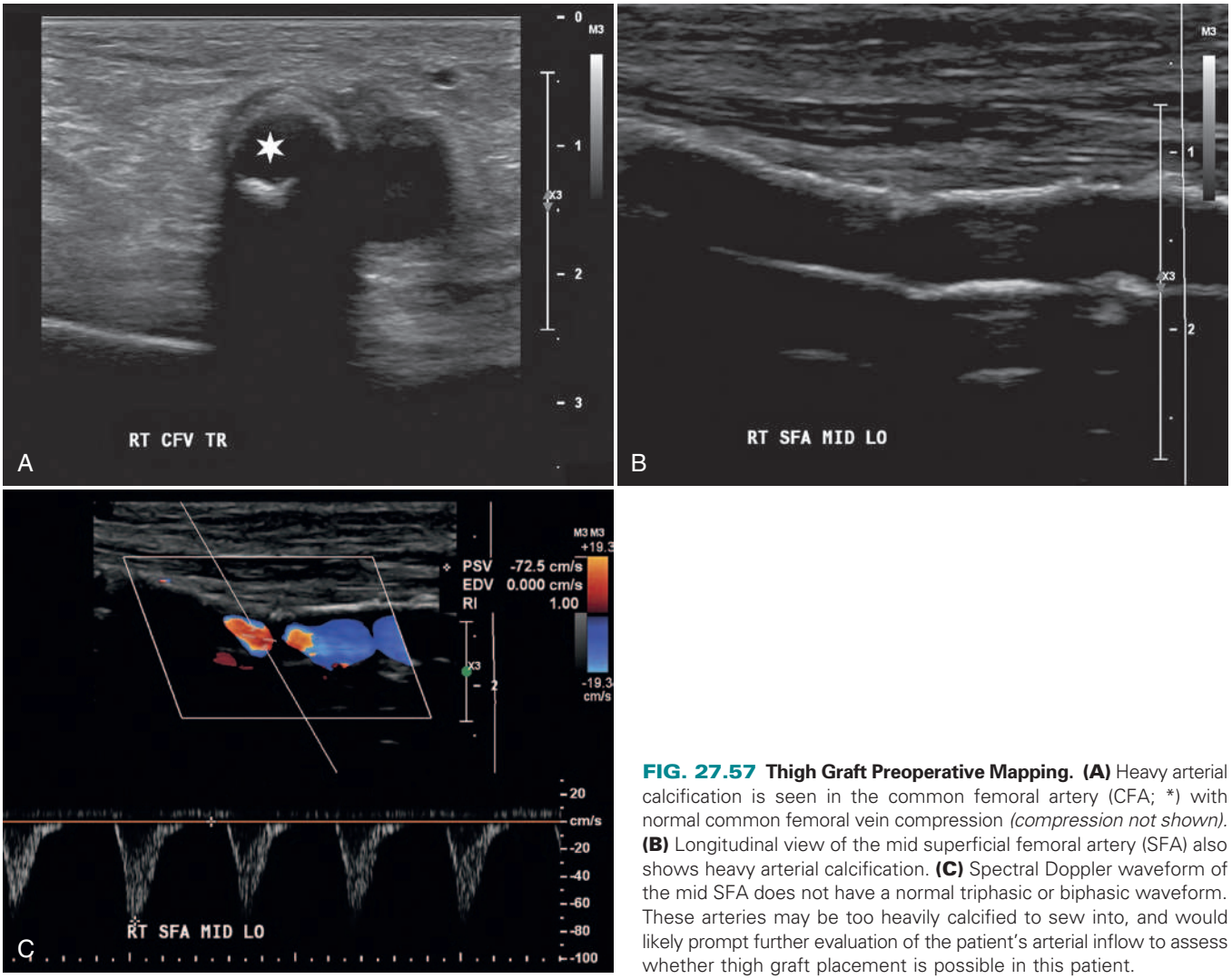

FIG. 27.57 Thigh Graft Preoperative Mapping. (A) Heavy arterial calcification is seen in the common femoral artery (CFA; *) with normal common femoral vein compression *(compression not shown).* **(B)** Longitudinal view of the mid superficial femoral artery (SFA) also shows heavy arterial calcification. **(C)** Spectral Doppler waveform of the mid SFA does not have a normal triphasic or biphasic waveform. These arteries may be too heavily calcified to sew into, and would likely prompt further evaluation of the patient's arterial inflow to assess whether thigh graft placement is possible in this patient.

color and spectral Doppler in the longitudinal plane to document normal low-resistance flow (Fig. 27.58). Measurements of PSV and EDV can be obtained in the feeding artery, and at least at the anastomosis(es). There may be multiple anastomoses in the case of a graft. The draining vein of the AVF or graft is inspected for wall thickening, stenosis, and thrombosis along its entire length.[143]

If a stenosis is seen, the highest PSV either within the stenosis or in the jet downstream from the stenosis is measured, using angle correction parallel to the jet if different from the angle with the posterior vascular wall, keeping the angle to 60 degrees or less. The PSV 2 cm upstream to the stenosis is measured, and a PSV ratio of the PSV at the stenosis divided by the upstream PSV is calculated. A longitudinal gray-scale image is obtained to document any intraluminal thrombus identified within a draining vein or graft. Duplex Doppler should be performed to confirm absence of flow, with use of the more sensitive power Doppler as needed. Description of artery and vein location with regard to the AVF and graft can be difficult. Terminology including cranial and caudal location with regard to a particular anastomosis, and upstream or downstream position, may be more useful than the conventional proximal and distal terminology.

Arteriovenous Fistula

The feeding artery luminal diameter is measured. Spectral and color Doppler evaluations of the feeding artery are performed to evaluate for arterial stenosis or occlusion. The anastomosis is assessed for visible narrowing with subsequent spectral and color Doppler evaluation. The AVF draining vein diameter is evaluated at several levels from the anastomosis to 15 cm cranial to the anastomosis. The intraluminal draining vein diameter and the depth of the vein from the skin surface are measured at several points cranial to the arteriovenous anastomosis. Access challenges may result with a depth greater than 5 to 6 mm and require superficialization.[131,150] The draining vein is interrogated for accessory branches (Fig. 27.59). Intraluminal diameter and distance from the anastomosis are recorded for each identified accessory vein within 10 to 15 cm of the anastomotic site. The flow volume rate measurements are obtained within the midportion of the draining vein of an AVF, typically at 10 cm cranial to the anastomosis. Optimal flow volume measurement is obtained

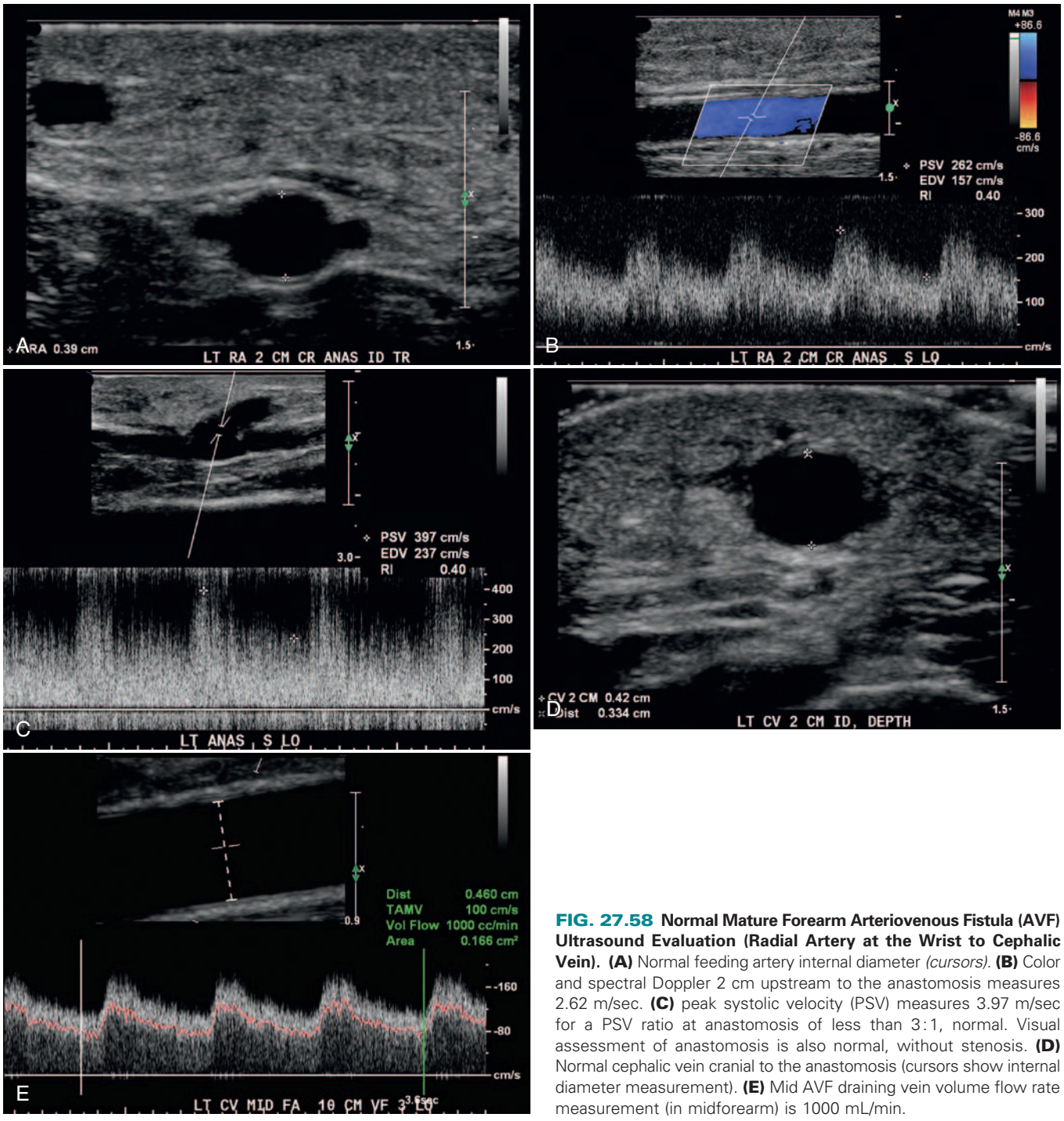

FIG. 27.58 Normal Mature Forearm Arteriovenous Fistula (AVF) Ultrasound Evaluation (Radial Artery at the Wrist to Cephalic Vein). (A) Normal feeding artery internal diameter *(cursors).* **(B)** Color and spectral Doppler 2 cm upstream to the anastomosis measures 2.62 m/sec. **(C)** peak systolic velocity (PSV) measures 3.97 m/sec for a PSV ratio at anastomosis of less than 3:1, normal. Visual assessment of anastomosis is also normal, without stenosis. **(D)** Normal cephalic vein cranial to the anastomosis (cursors show internal diameter measurement). **(E)** Mid AVF draining vein volume flow rate measurement (in midforearm) is 1000 mL/min.

in an area with parallel vessel walls, minimal vessel tortuosity, and no stenosis (Fig. 27.60).

Graft

Sonographic evaluation of the forearm or thigh graft is similar to that of the AVF. A normal graft is seen as two echogenic lines that represent strong specular reflection from polytetrafluoroethylene material. A low-resistance flow (arterialized flow) should be seen within a graft. Duplex Doppler evaluation of the feeding artery (including luminal diameter), arterial-graft anastomosis, graft (arterial side and venous side if loop graft), and venous anastomosis is performed, as well as draining vein and central vein evaluation. Flow volume is assessed within the midgraft (Fig. 27.61), and both arterial and venous limbs if a loop graft. Any points of visible narrowing are further assessed with spectral and color Doppler.

Palpable Focal Masses Near Arteriovenous Fistula and Graft

Hematoma. Avascular, hypoechoic lesions adjacent to the AVF or graft often represent postaccess or postprocedure hematomas (Fig. 27.62, Video 27.26). These collections should

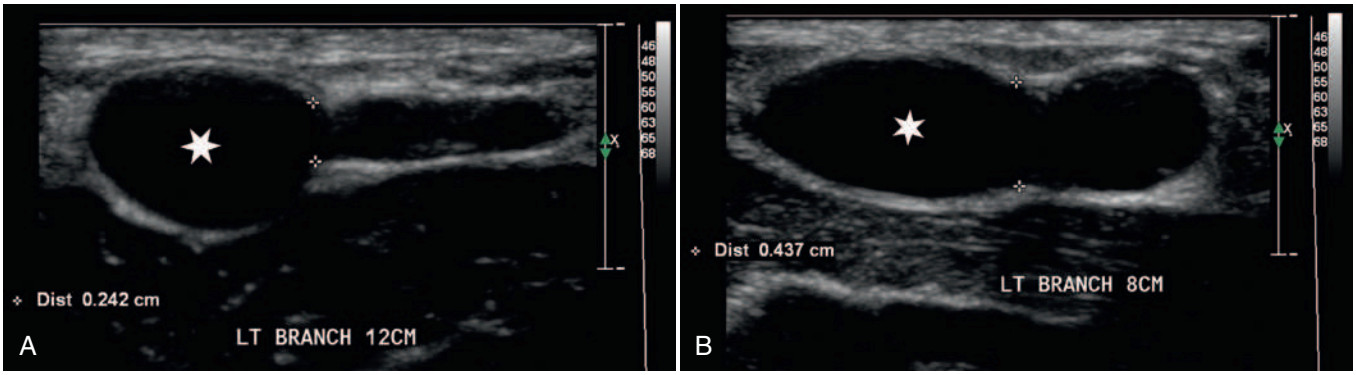

FIG. 27.59 Accessory Arteriovenous Fistula (AVF) Branch Measurement. (A) Transverse image of the AVF draining vein (*) shows a branch of 0.24 cm *(cursors)*. **(B)** Larger accessory AVF branch *(cursors)* of 0.44 cm may be large enough to sump blood away from the AVF draining vein (*).

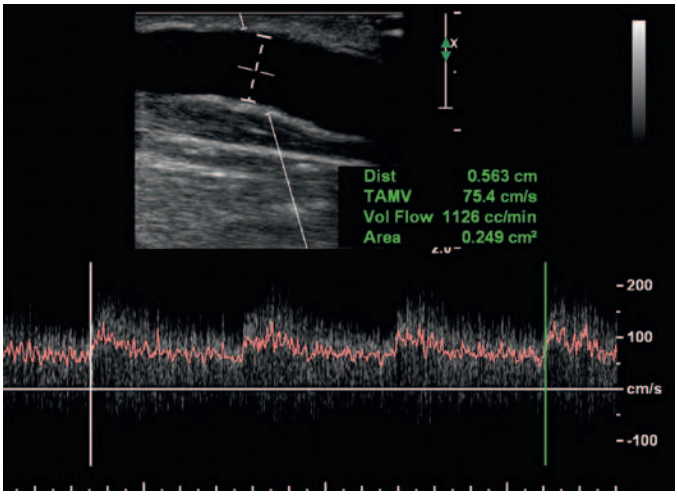

FIG. 27.60 Volume Flow in a Fairly Straight Area of an Arteriovenous Fistula (AVF) Draining Vein.

be inspected for echogenic foci or gas. Fluid collections with echogenic foci associated with shadowing suspicious for gas may represent abscess in certain clinical settings.

Aneurysm and Pseudoaneurysm. Focal or diffuse aneurysmal dilation of the AVF draining vein may occur as a result of repeated puncture (Fig. 27.63). Pseudoaneurysms may develop within a fistula or graft and often are related to suboptimal compression after cannulation. Color Doppler of a **pseudoaneurysm** reveals a circular flow pattern termed "yin-yang" (Fig. 27.64, Video 27.27). There may be "to-and-fro" flow identified in the pseudoaneurysm neck. Evaluation of the depth of the anterior wall of the pseudoaneurysm from the skin surface is important to evaluate those pseudoaneurysms in danger of imminent rupture. A unique complication of grafts is the degeneration of graft synthetic material. Irregularity of the graft wall is present, which may be associated with diffuse or focal pseudoaneurysms along the length of the graft wall (Fig. 27.65, Video 27.28).

Arteriovenous Fistula Maturation Evaluation

A 6-week postoperative AVF ultrasound is used in some clinical centers for routine evaluation of the AVF to determine its development toward usability.[130] A functioning AVF has a volume flow of at least 300 to 800 mL/min.[129,151] Robbin and colleagues showed that when an AVF had a minimum draining vein of 4 mm or larger or a blood flow rate of 500 mL/min or higher, approximately 70% of AVFs were able to be used for hemodialysis. The likelihood of fistula maturation was 95% if both criteria were met. If neither of these criteria was met, only 33% of fistulas were used for hemodialysis.[129] Sonographic criteria published by the National Kidney Foundation Kidney Disease Outcomes Quality Initiative suggestive of maturation include a draining vein greater than 6 mm diameter, blood flow rate greater than 600 mL/min, and less than 6 mm skin depth. These criteria may exclude many fistulas that could subsequently provide hemodialysis access. Active investigation is underway with larger, multicenter trials to test these criteria. Etiology of failure to mature such as anastomotic or AVF draining vein stenosis, large accessory veins, or arterial inflow stenosis can be identified and ultrasound used to triage the AVF for intervention.[131]

Arteriovenous Fistula and Graft Stenosis

AVF. Stenoses associated with AVFs are most frequently juxta-anastomotic, followed in frequency by AVF draining vein, with central venous and feeding artery stenosis less common but not infrequent. Stenoses may be clinically relevant owing to resultant flow decrease and can be associated with subsequent thrombosis. Potential sites for AVF stenosis include the feeding artery, juxta-anastomotic region, draining vein, and central veins. Early after placement, juxta-anastomotic stenoses are the most common. Later, AVF draining vein and central vein stenoses are more common, including a "cephalic arch" stenosis in which the cephalic vein enters the subclavian vein in the cephalic vein AVF. A careful directed search to common areas of stenosis is important during the sonographic examination, because stenoses may be short and therefore overlooked.

Fistula stenosis is characterized by two criteria: (1) visual narrowing of greater than 50% as assessed on gray-scale imaging, and (2) an elevated PSV ratio of the PSV at or just distal to the stenosis as compared with the PSV measured 2 cm upstream from the site of stenosis. A juxta-anastomotic stenosis is defined by a location within 2 cm of the anastomosis, encompassing both the feeding artery and the draining

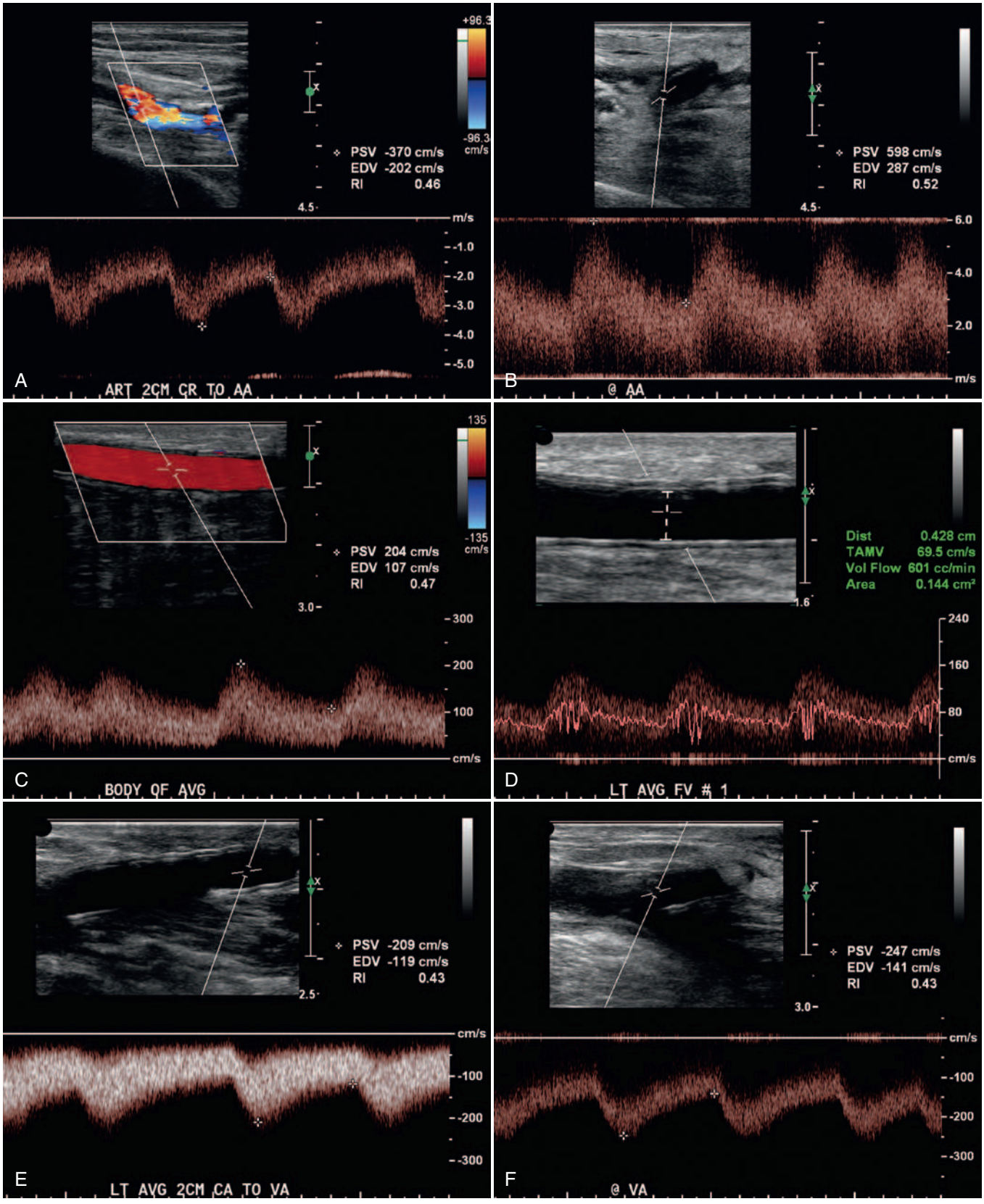

FIG. 27.61 Assessment of Upper Arm Graft (Brachial Artery to Axillary Vein Graft) With Peak Systolic Velocity (PSV) Measurement. (A) Normal color and spectral Doppler images show artery feeding the graft 2 cm cranial to the arterial anastomosis; PSV measures 3.7 m/sec. **(B)** Arterial anastomosis: PSV is 5.98 m/sec. PSV ratio is <3:1, normal, corroborating with no visual stenosis. **(C)** Midgraft body. No abnormal area of stenosis is seen. **(D)** Flow volume rate measurement of 601 mL/min in midgraft. **(E)** Within the graft, 2 cm upstream from venous anastomosis, PSV measures 2.09 m/sec. **(F)** At the venous anastomosis, PSV measures 2.47 m/sec. PSV ratio is <2:1, normal, corroborating with no visual anastomotic stenosis.

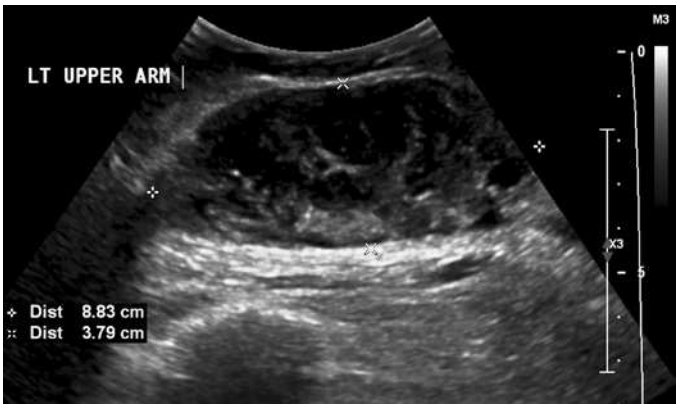

FIG. 27.62 Large Hematoma Adjacent to Arteriovenous Fistula (AVF). Gray-scale image shows hematoma *(calipers)*. No flow was seen on color or spectral Doppler *(not shown)*. See also Video 27.26 for adjacent patent AVF.

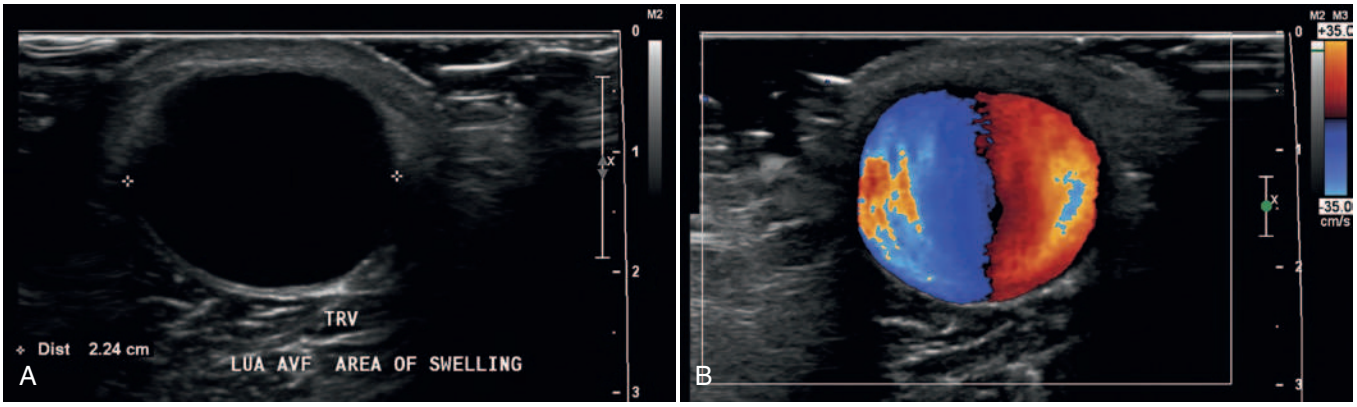

FIG. 27.63 Helical Flow in the Aneurysmal Dilation of Arteriovenous Fistula (AVF). (A) Aneurysmal dilation of the AVF draining vein in the area of palpable swelling. No pseudoaneurysm seen. **(B)** "Yin-yang" flow pattern on color Doppler due to swirling blood.

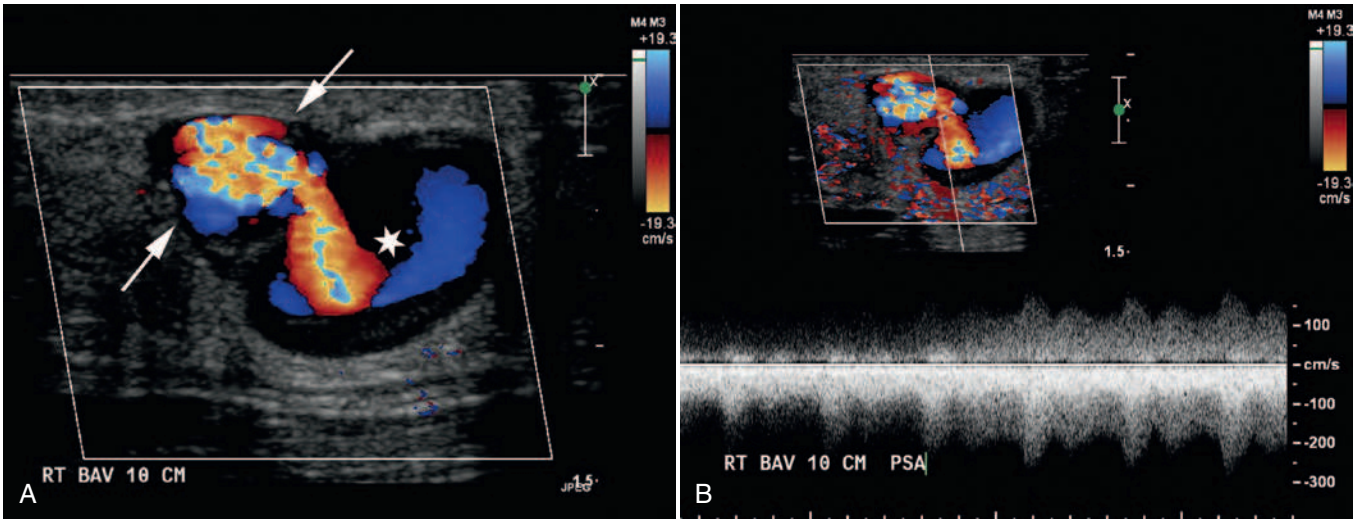

FIG. 27.64 Small Basilic Vein Pseudoaneurysm. (A) Basilic vein arteriovenous fistula (*) with pseudoaneurysm *(arrows)*. **(B)** Spectral Doppler in the pseudoaneurysm neck shows typical "to-and-fro" pattern. See also Video 27.27.

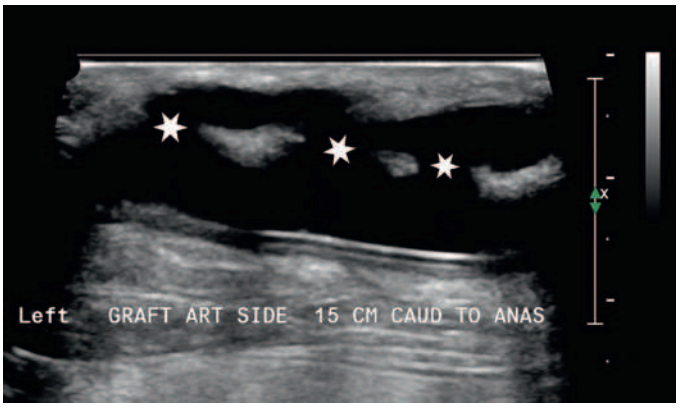

FIG. 27.65 Graft Wall Irregularity and Degeneration From Repeated Punctures. Note bright linear parallel walls posteriorly seen in polytetrafluoroethylene hemodialysis grafts. Stars (*) denote areas of degeneration. See also Video 27.28.

vein.[152,153] The juxta-anastomotic stenosis will show visible narrowing and a PSV ratio of greater than or equal to 3:1 (Fig. 27.66). A draining vein stenosis is defined by visible narrowing and a PSV ratio of 2:1 identified within the draining vein 2 cm cranial to the anastomosis[141] (Fig. 27.67). Feeding artery stenosis greater than 2 cm proximal to the anastomosis is uncommon; these are characterized by a PSV ratio of 2:1 with visible narrowing. Poststenotic waveforms show delayed systolic upstrokes that may suggest proximal arterial stenosis and prompt further direct evaluation of the feeding artery more cranially.

Graft. Graft abnormalities are similar to those described earlier for AVF, with differing diagnostic thresholds and criteria. Several studies have indicated that grafts with decreased blood flow are at increased risk for thrombosis.[141,154,155] The four sonographic criteria used to characterize graft stenosis are (1) luminal narrowing on gray-scale imaging, (2) a high-velocity jet on color Doppler, (3) a PSV ratio greater than 2:1 for the venous anastomosis or draining vein, and (4) a PSV ratio greater than 3:1 for the arterial anastomosis. The most common site of graft stenosis is the venous anastomosis. Other, less frequently used sites are the draining vein, intragraft region, arterial anastomosis, and central veins (Fig. 27.68, Video 27.29).

Arterial Steal

Arterial steal is defined as flow reversal in the native artery caudal to the anastomosis and may be asymptomatic, or associated with clinical findings such as hand pain and paresthesias that can worsen during hemodialysis.[156] In severe cases, ischemia or tissue necrosis of the fingers can occur. Sonographic evaluation may show reversal of flow in the distal artery, and rarely shows an arterial occlusion (Fig. 27.69). Brief manual compression of the graft can demonstrate a change in the reversed arterial flow, producing an antegrade high-resistance flow pattern toward the hand.[157]

It is important to note that asymptomatic flow reversal in the artery downstream from the arterial anastomosis is frequently seen, particularly in the AVF. In severe cases of arterial steal, surgical revision may be necessary.

Arm and Leg Swelling With Arteriovenous Fistula or Graft

When there is upper extremity swelling associated with an AVF or graft, the ipsilateral axillary, subclavian vein, and IJV should be included in the postoperative sonographic evaluation. Occasionally, a DVT of the brachial, axillary, or subclavian vein is the cause of arm swelling in a patient with an AVF or graft. If an upper extremity DVT is not found, spectral Doppler imaging of the IJV and subclavian vein may provide indirect evaluation of the brachiocephalic veins.

As discussed earlier in this chapter, monophasic venous waveforms of the subclavian vein and IJV suggest central venous stenosis or occlusion (Fig. 27.70). The absence of phasicity in the central veins is less specific for central venous occlusion in patients with a graft than in patients with an AVF because of the larger blood flow volume rate within grafts. Findings suggestive of central stenosis or occlusion are visible narrowing, focal turbulence, focally elevated velocity, and collaterals. If a central stenosis or occlusion is suspected, central vein assessment with magnetic resonance imaging (MRI) or venography may be useful because a central stenosis severe enough to cause arm swelling may be present despite adequate or high AVF flow.

Arteriovenous Fistula and Graft Occlusion

Access occlusion can be determined by physical examination. However, in the case of significant arm swelling or an inexperienced examiner, ultrasound evaluation may be useful. Thrombosis can be visualized within the vessel lumen on gray-scale imaging (Fig. 27.71) and confirmed by lack of color or spectral Doppler flow within the affected portion of the AVF, graft, or draining vein. Slow flow may be identified with power Doppler when nonocclusive thrombus is present. Arterial inflow will typically be high resistance flow in the occluded AVF or graft.

CONCLUSION

Ultrasound plays an important role in evaluating the peripheral vasculature. Although peripheral artery ultrasound is commonly considered for its uses in peripheral artery atherosclerotic disease, the technique can be applied in numerous clinical scenarios. For evaluation of stenosis in native or bypassed vessels, the concepts are similar, although threshold values may differ. For evaluation of aneurysm, pseudoaneurysm, or AVF, the examination can be more localized in its scope to determine the size of the abnormality by gray-scale and the use of Doppler to focus on the inflow and outflow characteristics.

For the upper and lower extremity deep venous system, ultrasound is the initial imaging modality of choice. In the occasional case where sonographic findings are equivocal or nondiagnostic, especially when there is concern for central thrombosis, correlation with MRI, CT, or catheter venography may be helpful. Ultrasound can provide an accurate, rapid, portable, low-cost, noninvasive method for screening,

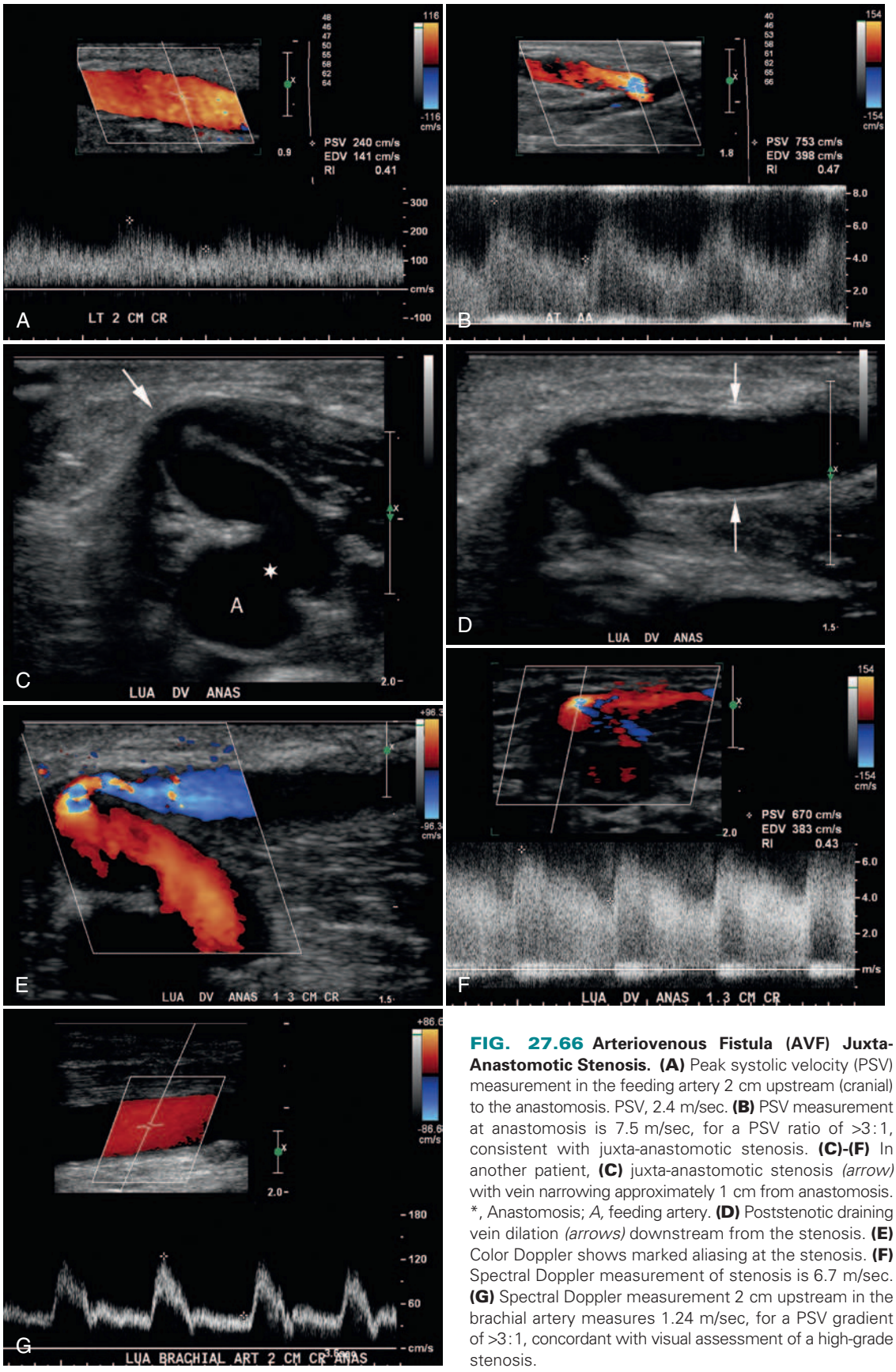

FIG. 27.66 Arteriovenous Fistula (AVF) Juxta-Anastomotic Stenosis. (A) Peak systolic velocity (PSV) measurement in the feeding artery 2 cm upstream (cranial) to the anastomosis. PSV, 2.4 m/sec. **(B)** PSV measurement at anastomosis is 7.5 m/sec, for a PSV ratio of >3:1, consistent with juxta-anastomotic stenosis. **(C)-(F)** In another patient, **(C)** juxta-anastomotic stenosis *(arrow)* with vein narrowing approximately 1 cm from anastomosis. *, Anastomosis; *A,* feeding artery. **(D)** Poststenotic draining vein dilation *(arrows)* downstream from the stenosis. **(E)** Color Doppler shows marked aliasing at the stenosis. **(F)** Spectral Doppler measurement of stenosis is 6.7 m/sec. **(G)** Spectral Doppler measurement 2 cm upstream in the brachial artery measures 1.24 m/sec, for a PSV gradient of >3:1, concordant with visual assessment of a high-grade stenosis.

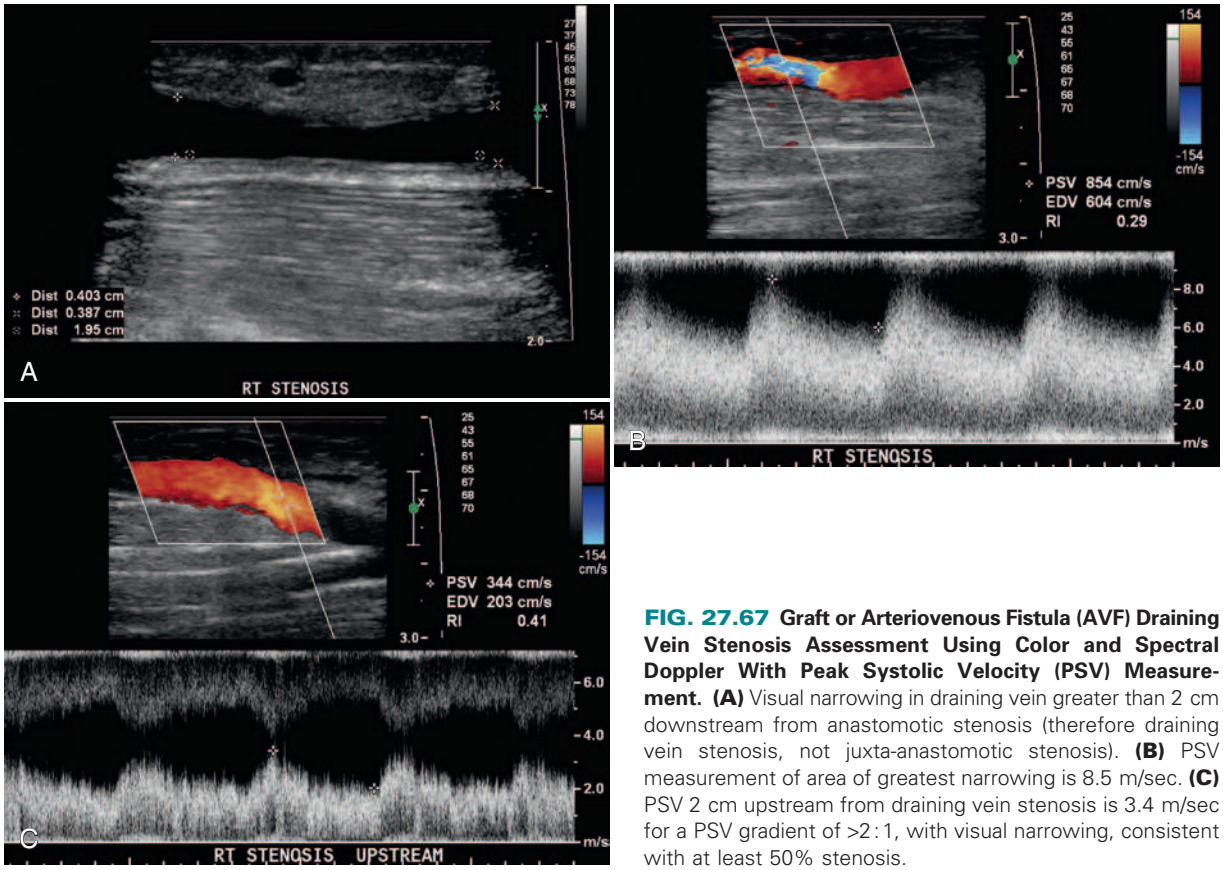

FIG. 27.67 Graft or Arteriovenous Fistula (AVF) Draining Vein Stenosis Assessment Using Color and Spectral Doppler With Peak Systolic Velocity (PSV) Measurement. (A) Visual narrowing in draining vein greater than 2 cm downstream from anastomotic stenosis (therefore draining vein stenosis, not juxta-anastomotic stenosis). **(B)** PSV measurement of area of greatest narrowing is 8.5 m/sec. **(C)** PSV 2 cm upstream from draining vein stenosis is 3.4 m/sec for a PSV gradient of >2:1, with visual narrowing, consistent with at least 50% stenosis.

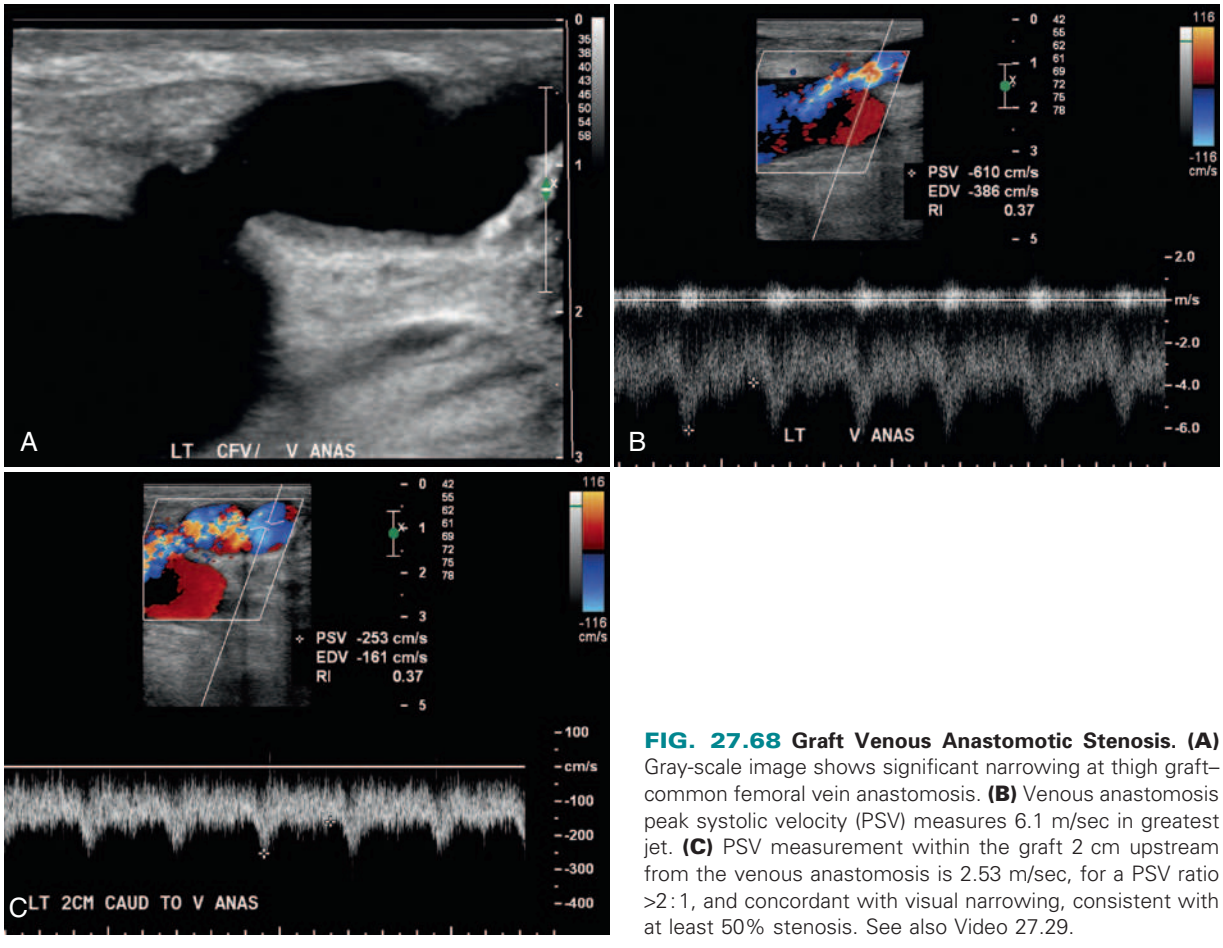

FIG. 27.68 Graft Venous Anastomotic Stenosis. (A) Gray-scale image shows significant narrowing at thigh graft–common femoral vein anastomosis. **(B)** Venous anastomosis peak systolic velocity (PSV) measures 6.1 m/sec in greatest jet. **(C)** PSV measurement within the graft 2 cm upstream from the venous anastomosis is 2.53 m/sec, for a PSV ratio >2:1, and concordant with visual narrowing, consistent with at least 50% stenosis. See also Video 27.29.

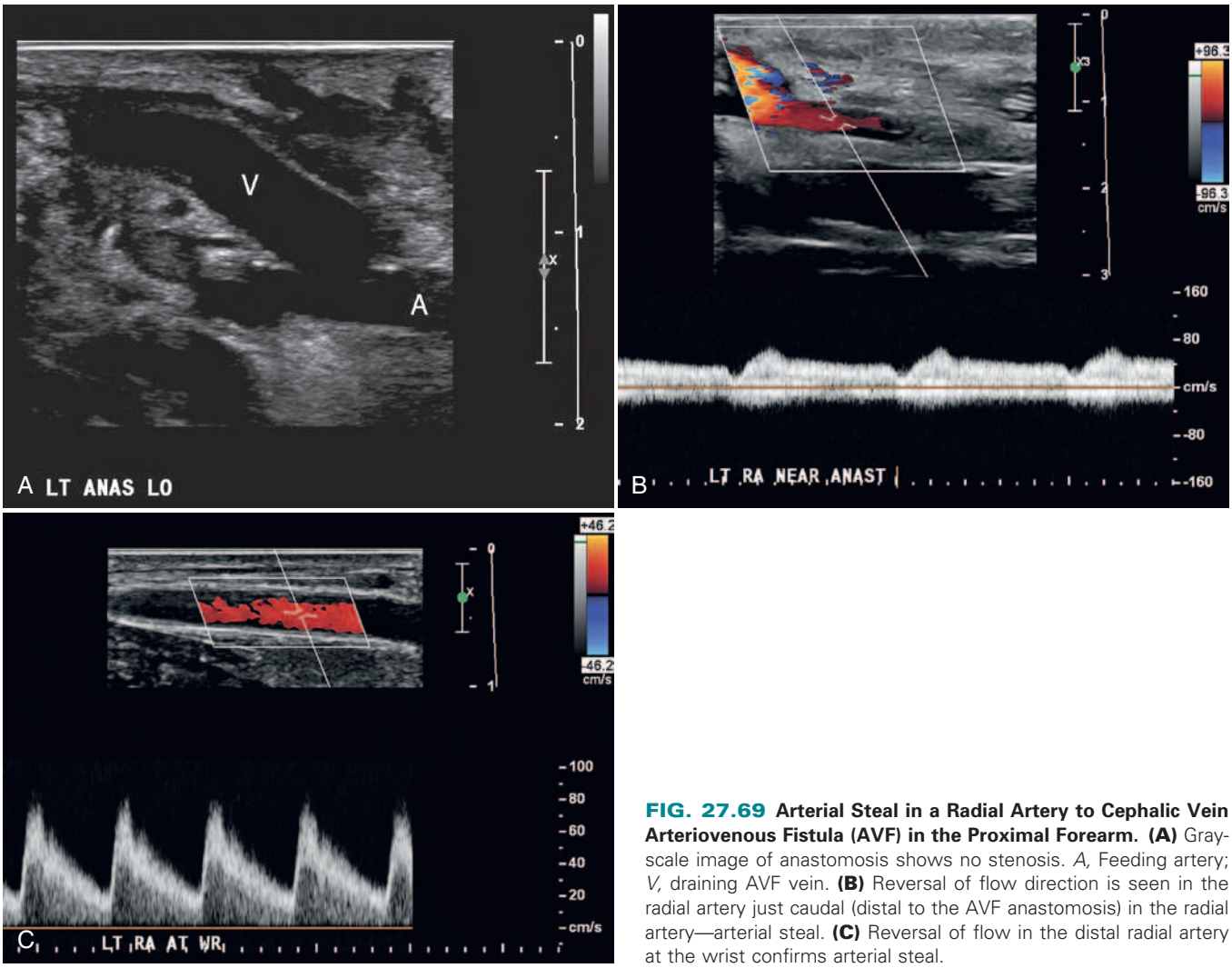

FIG. 27.69 Arterial Steal in a Radial Artery to Cephalic Vein Arteriovenous Fistula (AVF) in the Proximal Forearm. (A) Gray-scale image of anastomosis shows no stenosis. *A,* Feeding artery; *V,* draining AVF vein. **(B)** Reversal of flow direction is seen in the radial artery just caudal (distal to the AVF anastomosis) in the radial artery—arterial steal. **(C)** Reversal of flow in the distal radial artery at the wrist confirms arterial steal.

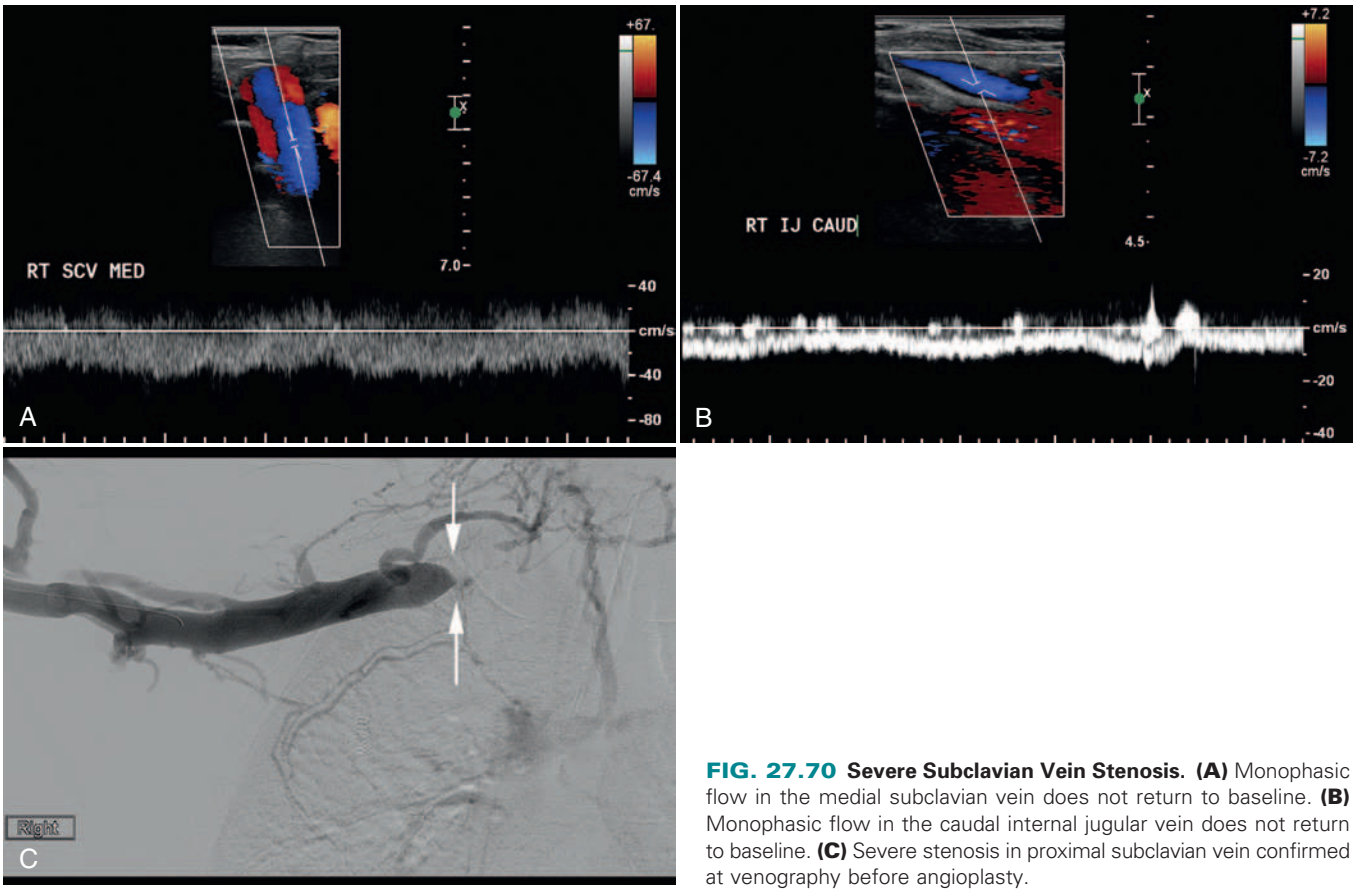

FIG. 27.70 Severe Subclavian Vein Stenosis. (A) Monophasic flow in the medial subclavian vein does not return to baseline. **(B)** Monophasic flow in the caudal internal jugular vein does not return to baseline. **(C)** Severe stenosis in proximal subclavian vein confirmed at venography before angioplasty.

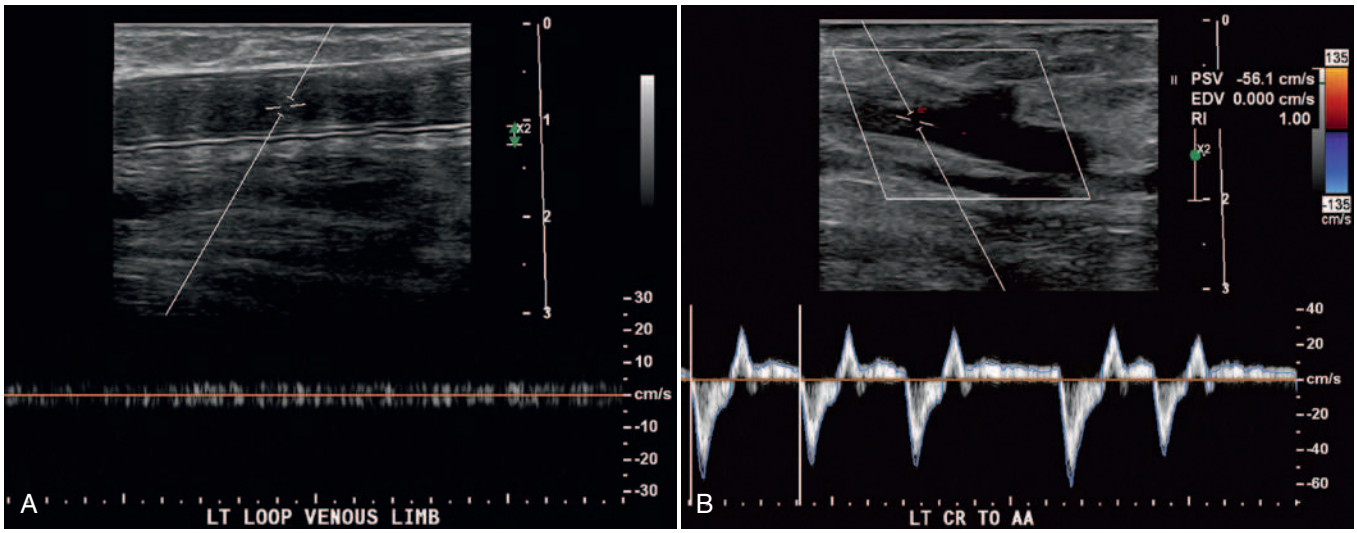

FIG. 27.71 Thrombosed Hemodialysis Graft. (A) No flow seen on spectral Doppler (no flow on color Doppler; *not shown*). **(B)** Color and spectral Doppler of artery upstream (cranial) from graft takeoff shows high-resistance waveform expected in graft thrombosis.

mapping, and surveillance of the upper and lower extremity venous system.

Preoperative ultrasound evaluation of the veins and arteries before both upper extremity and thigh hemodialysis access placement may decrease complications related to access procedures and improve overall access utility. After access placement, ultrasound is useful in the assessment of complications including stenosis, pseudoaneurysm, steal, and AVF nonmaturation.

REFERENCES

1. American College of Radiology (ACR), American Institute of Ultrasound in Medicine (AIUM), Society of Pediatric Radiology (SPR), Society of Radiologists in Ultrasound (SRU). ACR-AIUM-SPR-SRU Practice parameter for the performance of peripheral venous ultrasound examinations 2015. Available from: http://www.acr.org/~/media/ACR/Documents/PGTS/guidelines/US_Peripheral_Venous.pdf.
2. American College of Radiology (ACR), American Institute of Ultrasound in Medicine (AIUM), Society of Radiologists in Ultrasound (SRU). Practice parameter for the performance of peripheral arterial ultrasound using color and spectral Doppler. Peripheral arterial US. 2014. Available from: https://www.acr.org/~/media/ACR/Documents/PGTS/guidelines/US_Peripheral_Arterial.pdf.
3. Sanyal R, Kraft B, Alexander LF, et al. Scanner-based protocol-driven ultrasound: an effective method to improve efficiency in an ultrasound department. AJR Am J Roentgenol. 2016;1-5.
4. AbuRahma AF, Jarrett K, Hayes DJ. Clinical implications of power Doppler three-dimensional ultrasonography. Vascular. 2004;12(5):293-300.
5. Czyzewska D, Ustymowicz A, Krysiuk K, et al. Ultrasound assessment of the caliber of the arteries in the lower extremities in healthy persons—the dependency on age, sex and morphological parameters of the subjects. J Ultrason. 2012;12(51):420-427.
6. Moneta GL, Yeager RA, Antonovic R, et al. Accuracy of lower extremity arterial duplex mapping. J Vasc Surg. 1992;15(2):275-283.
7. Hatsukami TS, Primozich JF, Zierler RE, et al. Color Doppler imaging of infrainguinal arterial occlusive disease. J Vasc Surg. 1992;16(4):527-531.
8. Mustapha JA, Saab F, Diaz-Sandoval L, et al. Comparison between angiographic and arterial duplex ultrasound assessment of tibial arteries in patients with peripheral arterial disease: on behalf of the Joint Endovascular and Non-Invasive Assessment of LImb Perfusion (JENALI) Group. J Invasive Cardiol. 2013;25(11):606-611.
9. Moneta GL, Yeager RA, Lee RW, Porter JM. Noninvasive localization of arterial occlusive disease: a comparison of segmental Doppler pressures and arterial duplex mapping. J Vasc Surg. 1993;17(3):578-582.
10. Jager KA, Phillips DJ, Martin RL, et al. Noninvasive mapping of lower limb arterial lesions. Ultrasound Med Biol. 1985;11(3):515-521.
11. Khan SZ, Khan MA, Bradley B, et al. Utility of duplex ultrasound in detecting and grading de novo femoropopliteal lesions. J Vasc Surg. 2011;54(4):1067-1073.
12. Elbadawy A, Aly H, Ibrahim M, Bakr H. Impact of duplex arterial mapping on decision making in non-acute ischemic limb patients. Int Angiol. 2015;34(6):538-544.
13. Fontcuberta J, Flores A, Orgaz A, et al. Reliability of preoperative duplex scanning in designing a therapeutic strategy for chronic lower limb ischemia. Ann Vasc Surg. 2009;23(5):577-582.
14. Norgren L, Hiatt WR, Dormandy JA, et al. Inter-Society Consensus for the Management of Peripheral Arterial Disease (TASC II). J Vasc Surg. 2007;45(Suppl.S):S5-S67.
15. Sultan S, Tawfick W, Hynes N. Ten-year technical and clinical outcomes in Trans-Atlantic Inter-Society Consensus II infrainguinal C/D lesions using duplex ultrasound arterial mapping as the sole imaging modality for critical lower limb ischemia. J Vasc Surg. 2013;57(4):1038-1045.
16. Davies AH, Willcox JH, Magee TR, et al. Colour duplex in assessing the infrainguinal arteries in patients with claudication. Cardiovasc Surg. 1995;3(2):211-212.
17. Legemate DA, Teeuwen C, Hoeneveld H, et al. The potential of duplex scanning to replace aorto-iliac and femoro-popliteal angiography. Eur J Vasc Surg. 1989;3(1):49-54.
18. Edwards JM, Coldwell DM, Goldman ML, Strandness Jr DE. The role of duplex scanning in the selection of patients for transluminal angioplasty. J Vasc Surg. 1991;13(1):69-74.
19. Lai DT, Huber D, Glasson R, et al. Colour-coded duplex ultrasonography in selection of patients for transluminal angioplasty. Australas Radiol. 1995;39(3):243-245.
20. Hodgkiss-Harlow KD, Bandyk DF. Interpretation of arterial duplex testing of lower-extremity arteries and interventions. Semin Vasc Surg. 2013;26(2-3):95-104.
21. Baril DT, Rhee RY, Kim J, et al. Duplex criteria for determination of in-stent stenosis after angioplasty and stenting of the superficial femoral artery. J Vasc Surg. 2009;49(1):133-138.
22. Langenberger H, Schillinger M, Plank C, et al. Agreement of duplex ultrasonography vs. computed tomography angiography for evaluation of

native and in-stent SFA re-stenosis—findings from a randomized controlled trial. Eur J Radiol. 2012;81(9):2265-2269.
23. Hamper UM, DeJong MR, Scoutt LM. Ultrasound evaluation of the lower extremity veins. Radiol Clin North Am. 2007;45(3):525-547, ix.
24. Stiegler H, Brandl R. Importance of ultrasound for diagnosing peripheral arterial disease. Ultraschall Med. 2009;30(4):334-374.
25. Shortell CK, DeWeese JA, Ouriel K, Green RM. Popliteal artery aneurysms: a 25-year surgical experience. J Vasc Surg. 1991;14(6):771-776.
26. Dorigo W, Pulli R, Alessi Innocenti A, et al. A 33-year experience with surgical management of popliteal artery aneurysms. J Vasc Surg. 2015;62(5):1176-1182.
27. von Stumm M, Teufelsbauer H, Reichenspurner H, Debus ES. Two decades of endovascular repair of popliteal artery aneurysm—a meta-analysis. Eur J Vasc Endovasc Surg. 2015;50(3):351-359.
28. Mehta M, Champagne B, Darling 3rd RC, et al. Outcome of popliteal artery aneurysms after exclusion and bypass: significance of residual patent branches mimicking type II endoleaks. J Vasc Surg. 2004;40(5):886-890.
29. Rajasinghe HA, Tzilinis A, Keller T, et al. Endovascular exclusion of popliteal artery aneurysms with expanded polytetrafluoroethylene stent-grafts: early results. Vasc Endovascular Surg. 2006;40(6):460-466.
30. Antonello M, Frigatti P, Battocchio P, et al. Endovascular treatment of asymptomatic popliteal aneurysms: 8-year concurrent comparison with open repair. J Cardiovasc Surg (Torino). 2007;48(3):267-274.
31. Lumsden AB, Miller JM, Kosinski AS, et al. A prospective evaluation of surgically treated groin complications following percutaneous cardiac procedures. Am Surg. 1994;60(2):132-137.
32. Schoen FJ. Blood vessels. In: Kumar V, Abbas AK, Fausto N, editors. Robbins and cotran pathologic basis of disease. 7th ed. Philadelphia, PA: Elsevier Saunders; 2005. p. 511-554.
33. Middleton WD, Dasyam A, Teefey SA. Diagnosis and treatment of iatrogenic femoral artery pseudoaneurysms. Ultrasound Q. 2005;21(1):3-17.
34. Kent KC, McArdle CR, Kennedy B, et al. A prospective study of the clinical outcome of femoral pseudoaneurysms and arteriovenous fistulas induced by arterial puncture. J Vasc Surg. 1993;17(1):125-131.
35. La Perna L, Olin JW, Goines D, et al. Ultrasound-guided thrombin injection for the treatment of postcatheterization pseudoaneurysms. Circulation. 2000;102(19):2391-2395.
36. Shah KJ, Halaharvi DR, Franz RW, Jenkins Ii J. Treatment of iatrogenic pseudoaneurysms using ultrasound-guided thrombin injection over a 5-year period. Int J Angiol. 2011;20(4):235-242.
37. Paulson EK, Nelson RC, Mayes CE, et al. Sonographically guided thrombin injection of iatrogenic femoral pseudoaneurysms: further experience of a single institution. AJR Am J Roentgenol. 2001;177(2):309-316.
38. Franklin JA, Brigham D, Bogey WM, Powell CS. Treatment of iatrogenic false aneurysms. J Am Coll Surg. 2003;197(2):293-301.
39. Wolodiger F, Dardik H, Johnson F, Ibrahim IM. Rupture of arteriovenous fistula after in situ saphenous vein bypass. J Vasc Surg. 1991;13(4):503-505.
40. Lundell A, Nyborg K. Do residual arteriovenous fistulae after in situ saphenous vein bypass grafting influence patency? J Vasc Surg. 1999;30(1):99-110.
41. Davidovic L, Lotina S, Vojnovic B, et al. Post-traumatic AV fistulas and pseudoaneurysms. J Cardiovasc Surg (Torino). 1997;38(6):645-651.
42. Straton CS, Tisnado J. Spontaneous arteriovenous fistulas of the lower extremities: angiographic demonstration in five patients with peripheral vascular disease. Cardiovasc Intervent Radiol. 2000;23(4):318-321.
43. Woo K, Palmer OP, Weaver FA, et al. I. Outcomes of completion imaging for lower extremity bypass in the Vascular Quality Initiative. J Vasc Surg. 2015;62(2):412-416.
44. Tan TW, Rybin D, Kalish JA, et al. Routine use of completion imaging after infrainguinal bypass is not associated with higher bypass graft patency. J Vasc Surg. 2014;60(3):678-685 e2.
45. Wixon CL, Mills JL, Westerband A, et al. An economic appraisal of lower extremity bypass graft maintenance. J Vasc Surg. 2000;32(1):1-12.
46. Mills JL Sr, Wixon CL, James DC, et al. The natural history of intermediate and critical vein graft stenosis: recommendations for continued surveillance or repair. J Vasc Surg. 2001;33(2):273-278.
47. Gonsalves C, Bandyk DF, Avino AJ, Johnson BL. Duplex features of vein graft stenosis and the success of percutaneous transluminal angioplasty. J Endovasc Surg. 1999;6(1):66-72.
48. Rehfuss J, Scali S, He Y, et al. The correlation between computed tomography and duplex evaluation of autogenous vein bypass grafts and their relationship to failure. J Vasc Surg. 2015;62(6):1546-1554 e1.
49. Idu MM, Blankenstein JD, de Gier P, et al. Impact of a color-flow duplex surveillance program on infrainguinal vein graft patency: a five-year experience. J Vasc Surg. 1993;17(1):42-52.
50. Szilagyi DE, Elliott JP, Hageman JH, et al. Biologic fate of autogenous vein implants as arterial substitutes: clinical, angiographic and histopathologic observations in femoro-popliteal operations for atherosclerosis. Ann Surg. 1973;178(3):232-246.
51. Cassina PC, Hailemariam S, Schmid RA, Hauser M. Infrainguinal aneurysm formation in arterialized autologous saphenous vein grafts. J Vasc Surg. 1998;28(5):944-948.
52. McCormack LJ, Cauldwell EW, Anson BJ. Brachial and antebrachial arterial patterns; a study of 750 extremities. Surg Gynecol Obstet. 1953;96(1):43-54.
53. Uhlemann M, Mobius-Winkler S, Mende M, et al. The Leipzig prospective vascular ultrasound registry in radial artery catheterization: impact of sheath size on vascular complications. JACC Cardiovasc Interv. 2012;5(1):36-43.
54. Kliewer MA, Hertzberg BS, Kim DH, et al. Vertebral artery Doppler waveform changes indicating subclavian steal physiology. AJR Am J Roentgenol. 2000;174(3):815-819.
55. Longley DG, Yedlicka JW, Molina EJ, et al. Thoracic outlet syndrome: evaluation of the subclavian vessels by color duplex sonography. AJR Am J Roentgenol. 1992;158(3):623-630.
56. Wadhwani R, Chaubal N, Sukthankar R, et al. Color Doppler and duplex sonography in 5 patients with thoracic outlet syndrome. J Ultrasound Med. 2001;20(7):795-801.
57. Lee AD, Agarwal S, Sadhu D. Doppler Adson's test: predictor of outcome of surgery in non-specific thoracic outlet syndrome. World J Surg. 2006;30(3):291-292.
58. Criado E, Berguer R, Greenfield L. The spectrum of arterial compression at the thoracic outlet. J Vasc Surg. 2010;52(2):406-411.
59. Chen H, Doornbos N, Williams K, Criado E. Physiologic variations in venous and arterial hemodynamics in response to postural changes at the thoracic outlet in normal volunteers. Ann Vasc Surg. 2014;28(7):1583-1588.
60. Abu-Omar Y, Mussa S, Anastasiadis K, et al. Duplex ultrasonography predicts safety of radial artery harvest in the presence of an abnormal Allen test. Ann Thorac Surg. 2004;77(1):116-119.
61. Habib J, Baetz L, Satiani B. Assessment of collateral circulation to the hand prior to radial artery harvest. Vasc Med. 2012;17(5):352-361.
62. Kochi K, Sueda T, Orihashi K, Matsuura Y. New noninvasive test alternative to Allen's test: snuff-box technique. J Thorac Cardiovasc Surg. 1999;118(4):756-758.
63. Pola P, Serricchio M, Flore R, et al. Safe removal of the radial artery for myocardial revascularization: a Doppler study to prevent ischemic complications to the hand. J Thorac Cardiovasc Surg. 1996;112(3):737-744.
64. Lucena J, Rico A, Vazquez R, et al. Pulmonary embolism and sudden-unexpected death: prospective study on 2477 forensic autopsies performed at the Institute of Legal Medicine in Seville. J Forensic Leg Med. 2009;16(4):196-201.
65. Bates SM, Jaeschke R, Stevens SM, et al. Diagnosis of DVT: antithrombotic therapy and prevention of thrombosis, 9th ed: American College of Chest Physicians evidence-based clinical practice guidelines. Chest. 2012;141(2 Suppl.):e351S-e418S.
66. Ageno W, Squizzato A, Wells PS, et al. The diagnosis of symptomatic recurrent pulmonary embolism and deep vein thrombosis: guidance from the SSC of the ISTH. J Thromb Haemost. 2013;11(8):1597-1602.
67. Wilbur J, Shian B. Diagnosis of deep venous thrombosis and pulmonary embolism. Am Fam Physician. 2012;86(10):913-919.
68. Wells PS. Integrated strategies for the diagnosis of venous thromboembolism. J Thromb Haemost. 2007;5(Suppl. 1):41-50.

69. Le Gal G, Carrier M, Rodger M. Clinical decision rules in venous thromboembolism. Best Pract Res Clin Haematol. 2012;25(3):303-317.
70. Qaseem A, Snow V, Barry P, et al. Current diagnosis of venous thromboembolism in primary care: a clinical practice guideline from the American Academy of Family Physicians and the American College of Physicians. Ann Fam Med. 2007;5(1):57-62.
71. Segal JB, Eng J, Tamariz LJ, Bass EB. Review of the evidence on diagnosis of deep venous thrombosis and pulmonary embolism. Ann Fam Med. 2007;5(1):63-73.
72. Wells PS, Anderson DR, Rodger M, et al. Evaluation of D-dimer in the diagnosis of suspected deep-vein thrombosis. N Engl J Med. 2003;349(13):1227-1235.
73. Carrier M, Lee AY, Bates SM, et al. Accuracy and usefulness of a clinical prediction rule and D-dimer testing in excluding deep vein thrombosis in cancer patients. Thromb Res. 2008;123(1):177-183.
74. Geersing GJ, Zuithoff NP, Kearon C, et al. Exclusion of deep vein thrombosis using the Wells rule in clinically important subgroups: individual patient data meta-analysis. BMJ. 2014;348:g1340.
75. Squizzato A, Micieli E, Galli M, et al. Diagnosis and management of venous thromboembolism: results of a survey on current clinical practice. Thromb Res. 2010;125(2):134-136.
76. Spritzer CE. Progress in MR imaging of the venous system. Perspect Vasc Surg Endovasc Ther. 2009;21(2):105-116.
77. Bundens WP, Bergan JJ, Halasz NA, et al. The superficial femoral vein. A potentially lethal misnomer. JAMA. 1995;274(16):1296-1298.
78. Quinlan DJ, Alikhan R, Gishen P, Sidhu PS. Variations in lower limb venous anatomy: implications for US diagnosis of deep vein thrombosis. Radiology. 2003;228(2):443-448.
79. Simpson WL, Krakowsi DM. Prevalence of lower extremity venous duplication. Indian J Radiol Imaging. 2010;20(3):230-234.
80. Dona E, Fletcher JP, Hughes TM, et al. Duplicated popliteal and superficial femoral veins: incidence and potential significance. Aust N Z J Surg. 2000;70(6):438-440.
81. Lautz TB, Abbas F, Walsh SJ, et al. Isolated gastrocnemius and soleal vein thrombosis: should these patients receive therapeutic anticoagulation? Ann Surg. 2010;251(4):735-742.
82. Caggiati A, Bergan JJ, Gloviczki P, et al. Nomenclature of the veins of the lower limbs: an international interdisciplinary consensus statement. J Vasc Surg. 2002;36(2):416-422.
83. Lockhart ME, Sheldon HI, Robbin ML. Augmentation in lower extremity sonography for the detection of deep venous thrombosis. AJR Am J Roentgenol. 2005;184(2):419-422.
84. Intersocietal Accreditation Commission (IAC). IAC standards and guidelines for vascular testing accreditation. IAC. Available from: http://www.intersocietal.org/vascular/standards/IACVascularTestingStandards2016.pdf.
85. Needleman L. Update on the lower extremity venous ultrasonography examination. Radiol Clin North Am. 2014;52(6):1359-1374.
86. Cronan JJ. Venous thromboembolic disease: the role of US. Radiology. 1993;186(3):619-630.
87. Rubin JM, Xie H, Kim K, et al. Sonographic elasticity imaging of acute and chronic deep venous thrombosis in humans. J Ultrasound Med. 2006;25(9):1179-1186.
88. Johnson SA, Stevens SM, Woller SC, et al. Risk of deep vein thrombosis following a single negative whole-leg compression ultrasound: a systematic review and meta-analysis. JAMA. 2010;303(5):438-445.
89. Guanella R, Righini M. Serial limited versus single complete compression ultrasonography for the diagnosis of lower extremity deep vein thrombosis. Semin Respir Crit Care Med. 2012;33(2):144-150.
90. Birdwell BG, Raskob GE, Whitsett TL, et al. The clinical validity of normal compression ultrasonography in outpatients suspected of having deep venous thrombosis. Ann Intern Med. 1998;128(1):1-7.
91. Bernardi E, Camporese G, Buller HR, et al. Serial 2-point ultrasonography plus D-dimer vs whole-leg color-coded Doppler ultrasonography for diagnosing suspected symptomatic deep vein thrombosis: a randomized controlled trial. JAMA. 2008;300(14):1653-1659.
92. Society for Vascular Medicine. Five things physicians and patients should question. Choosing Wisely. 2014:1-2. Available from: http://www.choosingwisely.org/doctor-patient-lists/society-for-vascularmedicine/.
93. van Haarst EP, Liasis N, van Ramshorst B, Moll FL. The development of valvular incompetence after deep vein thrombosis: a 7 year follow-up study with duplex scanning. Eur J Vasc Endovasc Surg. 1996;12(3):295-299.
94. Thorisson HM, Pollak JS, Scoutt L. The role of ultrasound in the diagnosis and treatment of chronic venous insufficiency. Ultrasound Q. 2007;23(2):137-150.
95. Human P, Franz T, Scherman J, et al. Dimensional analysis of human saphenous vein grafts: implications for external mesh support. J Thorac Cardiovasc Surg. 2009;137(5):1101-1108.
96. Chin EE, Zimmerman PT, Grant EG. Sonographic evaluation of upper extremity deep venous thrombosis. J Ultrasound Med. 2005;24(6):829-838.
97. Gooding GA, Hightower DR, Moore EH, et al. Obstruction of the superior vena cava or subclavian veins: sonographic diagnosis. Radiology. 1986;159(3):663-665.
98. Baarslag HJ, van Beek EJ, Koopman MM, Reekers JA. Prospective study of color duplex ultrasonography compared with contrast venography in patients suspected of having deep venous thrombosis of the upper extremities. Ann Intern Med. 2002;136(12):865-872.
99. Knudson GJ, Wiedmeyer DA, Erickson SJ, et al. Color Doppler sonographic imaging in the assessment of upper-extremity deep venous thrombosis. AJR Am J Roentgenol. 1990;154(2):399-403.
100. Baxter GM, Kincaid W, Jeffrey RF, et al. Comparison of colour Doppler ultrasound with venography in the diagnosis of axillary and subclavian vein thrombosis. Br J Radiol. 1991;64(765):777-781.
101. Bernardi E, Piccioli A, Marchiori A, et al. Upper extremity deep vein thrombosis: risk factors, diagnosis, and management. Semin Vasc Med. 2001;1(1):105-110.
102. Fraser JD, Anderson DR. Venous protocols, techniques, and interpretations of the upper and lower extremities. Radiol Clin North Am. 2004;42(2):279-296.
103. Patel MC, Berman LH, Moss HA, McPherson SJ. Subclavian and internal jugular veins at Doppler US: abnormal cardiac pulsatility and respiratory phasicity as a predictor of complete central occlusion. Radiology. 1999;211(2):579-583.
104. Bonnet F, Loriferne JF, Texier JP, et al. Evaluation of Doppler examination for diagnosis of catheter-related deep vein thrombosis. Intensive Care Med. 1989;15(4):238-240.
105. McDonough JJ, Altemeier WA. Subclavian venous thrombosis secondary to indwelling cathers. Surg Gynecol Obstet. 1971;133(3):397-400.
106. Luciani A, Clement O, Halimi P, et al. Catheter-related upper extremity deep venous thrombosis in cancer patients: a prospective study based on Doppler US. Radiology. 2001;220(3):655-660.
107. Trerotola SO, Kuhn-Fulton J, Johnson MS, et al. Tunneled infusion catheters: increased incidence of symptomatic venous thrombosis after subclavian versus internal jugular venous access. Radiology. 2000;217(1):89-93.
108. Monreal M, Lafoz E, Ruiz J, et al. Upper-extremity deep venous thrombosis and pulmonary embolism. A prospective study. Chest. 1991;99(2):280-283.
109. Becker DM, Philbrick JT, Walker FB. Axillary and subclavian venous thrombosis. Prognosis and treatment. Arch Intern Med. 1991;151(10):1934-1943.
110. Kearon C. Natural history of venous thromboembolism. Circulation. 2003;107(23 Suppl. 1):I22-I30.
111. Horattas MC, Wright DJ, Fenton AH, et al. Changing concepts of deep venous thrombosis of the upper extremity—report of a series and review of the literature. Surgery. 1988;104(3):561-567.
112. Mustafa S, Stein PD, Patel KC, et al. Upper extremity deep venous thrombosis. Chest. 2003;123(6):1953-1956.
113. Kooij JD, van der Zant FM, van Beek EJ, Reekers JA. Pulmonary embolism in deep venous thrombosis of the upper extremity: more often in catheter-related thrombosis. Neth J Med. 1997;50(6):238-242.
114. Meissner MH, Moneta G, Burnand K, et al. The hemodynamics and diagnosis of venous disease. J Vasc Surg. 2007;46(Suppl.S):4S-24S.

115. Recek C. Calf pump activity influencing venous hemodynamics in the lower extremity. Int J Angiol. 2013;22(1):23-30.
116. Weber TM, Lockhart ME, Robbin ML. Upper extremity venous Doppler ultrasound. Radiol Clin North Am. 2007;45(3):513-524, viii-ix.
117. Kremkau FW, Taylor KJ. Artifacts in ultrasound imaging. J Ultrasound Med. 1986;5(4):227-237.
118. Reading CC, Charboneau JW, Allison JW, Cooperberg PL. Color and spectral Doppler mirror-image artifact of the subclavian artery. Radiology. 1990;174(1):41-42.
119. Pozniak MA, Zagzebski JA, Scanlan KA. Spectral and color Doppler artifacts. Radiographics. 1992;12(1):35-44.
120. U.S. Renal Data System (USRDS). 2015 USRDS annual data report: epidemiology of kidney disease in the United States. Bethesda, MD: National Institutes of Health; 2015.
121. Feldman HI, Kobrin S, Wasserstein A. Hemodialysis vascular access morbidity. J Am Soc Nephrol. 1996;7(4):523-535.
122. Vascular Access Work Group. Clinical practice guidelines for vascular access, pt 1. Am J Kidney Dis. 2006;48(Suppl. 1):S176-S247.
123. Hodges TC, Fillinger MF, Zwolak RM, et al. Longitudinal comparison of dialysis access methods: risk factors for failure. J Vasc Surg. 1997;26(6): 1009-1019.
124. Allon M, Robbin ML. Increasing arteriovenous fistulas in hemodialysis patients: problems and solutions. Kidney Int. 2002;62(4):1109-1124.
125. Allon M, Lockhart ME, Lilly RZ, et al. Effect of preoperative sonographic mapping on vascular access outcomes in hemodialysis patients. Kidney Int. 2001;60(5):2013-2020.
126. Robbin ML, Gallichio MH, Deierhoi MH, et al. US vascular mapping before hemodialysis access placement. Radiology. 2000;217(1):83-88.
127. Gibson KD, Caps MT, Kohler TR, et al. Assessment of a policy to reduce placement of prosthetic hemodialysis access. Kidney Int. 2001;59(6): 2335-2345.
128. Little MD, Allon M, McNamara MM, et al. Risk evaluation of immediate surgical failure during thigh hemodialysis graft placement by sonographic screening. J Ultrasound Med. 2015;34(9):1613-1619.
129. Robbin ML, Chamberlain NE, Lockhart ME, et al. Hemodialysis arteriovenous fistula maturity: US evaluation. Radiology. 2002;225(1):59-64.
130. Robbin ML, Greene T, Cheung AK, et al. Arteriovenous fistula development in the first 6 weeks after creation. Radiology. 2015;150385.
131. Singh P, Robbin ML, Lockhart ME, Allon M. Clinically immature arteriovenous hemodialysis fistulas: effect of US on salvage. Radiology. 2008; 246(1):299-305.
132. Allon M, Bailey R, Ballard R, et al. A multidisciplinary approach to hemodialysis access: prospective evaluation. Kidney Int. 1998;53(2): 473-479.
133. Robbin ML, Oser RF, Lee JY, et al. Randomized comparison of ultrasound surveillance and clinical monitoring on arteriovenous graft outcomes. Kidney Int. 2006;69(4):730-735.
134. Lumsden AB, MacDonald MJ, Kikeri D, et al. Prophylactic balloon angioplasty fails to prolong the patency of expanded polytetrafluoroethylene arteriovenous grafts: results of a prospective randomized study. J Vasc Surg. 1997;26(3): 382-390.
135. Ram SJ, Work J, Caldito GC, et al. A randomized controlled trial of blood flow and stenosis surveillance of hemodialysis grafts. Kidney Int. 2003;64(1):272-280.
136. Malik J, Slavikova M, Svobodova J, Tuka V. Regular ultrasonographic screening significantly prolongs patency of PTFE grafts. Kidney Int. 2005;67(4): 1554-1558.
137. Dember LM, Holmberg EF, Kaufman JS. Randomized controlled trial of prophylactic repair of hemodialysis arteriovenous graft stenosis. Kidney Int. 2004;66(1):390-398.
138. Tonelli M, James M, Wiebe N, et al. Ultrasound monitoring to detect access stenosis in hemodialysis patients: a systematic review. Am J Kidney Dis. 2008;51(4):630-640.
139. Allon M, Robbin ML. Hemodialysis vascular access monitoring: current concepts. Hemodial Int. 2009;13(2):153-162.
140. Jennings WC, Sideman MJ, Taubman KE, Broughan TA. Brachial vein transposition arteriovenous fistulas for hemodialysis access. J Vasc Surg. 2009;50(5):1121-1126.
141. Robbin ML, Oser RF, Allon M, et al. Hemodialysis access graft stenosis: US detection. Radiology. 1998;208(3):655-661.
142. Lockhart ME, Robbin ML. Hemodialysis access ultrasound. Ultrasound Q. 2001;17(3):157-167.
143. Umphrey HR, Abts CA, Robbin ML. Dialysis grafts and fistulae: planning and assessment. Ultrasound Clin. 2011;6(4):477-490.
144. Lockhart ME, Robbin ML, Fineberg NS, et al. Cephalic vein measurement before forearm fistula creation: does use of a tourniquet to meet the venous diameter threshold increase the number of usable fistulas? J Ultrasound Med. 2006;25(12):1541-1545.
145. Glass CJM, DiGragio W, Illig KA. A meta-analysis of preoperative duplex ultrasound vessel diameters for successful radiocephalic fistula placement. J Vasc Ultrasound. 2009;65-68(4).
146. Sidawy AN, Spergel LM, Besarab A, et al. The Society for Vascular Surgery: clinical practice guidelines for the surgical placement and maintenance of arteriovenous hemodialysis access. J Vasc Surg. 2008;48(5 Suppl.):2S-25S.
147. Miller CD, Robbin ML, Barker J, Allon M. Comparison of arteriovenous grafts in the thigh and upper extremities in hemodialysis patients. J Am Soc Nephrol. 2003;14(11):2942-2947.
148. Ong S, Barker-Finkel J, Allon M. Long-term outcomes of arteriovenous thigh grafts in hemodialysis patients: a comparison with tunneled dialysis catheters. Clin J Am Soc Nephrol. 2013;8(5):804-809.
149. Scott JD, Cull DL, Kalbaugh CA, et al. The mid-thigh loop arteriovenous graft: patient selection, technique, and results. Am Surg. 2006; 72(9):825-828.
150. National Kidney Foundation. KDOQI clinical practice guidelines and clinical practice recommendations for vascular access 2006. Am J Kidney Dis. 2006;48(Suppl. 1):S176-S322.
151. Falk A. Maintenance and salvage of arteriovenous fistulas. J Vasc Interv Radiol. 2006;17(5):807-813.
152. Clark TW, Hirsch DA, Jindal KJ, et al. Outcome and prognostic factors of restenosis after percutaneous treatment of native hemodialysis fistulas. J Vasc Interv Radiol. 2002;13(1):51-59.
153. Beathard GA, Arnold P, Jackson J, et al. Aggressive treatment of early fistula failure. Kidney Int. 2003;64(4):1487-1494.
154. May RE, Himmelfarb J, Yenicesu M, et al. Predictive measures of vascular access thrombosis: a prospective study. Kidney Int. 1997;52(6): 1656-1662.
155. Shackleton CR, Taylor DC, Buckley AR, et al. Predicting failure in polytetrafluoroethylene vascular access grafts for hemodialysis: a pilot study. Can J Surg. 1987;30(6):442-444.
156. Leake AE, Winger DG, Leers SA, et al. Management and outcomes of dialysis access-associated steal syndrome. J Vasc Surg. 2015;61(3):754-760.
157. Valji K, Hye RJ, Roberts AC, et al. Hand ischemia in patients with hemodialysis access grafts: angiographic diagnosis and treatment. Radiology. 1995;196(3):697-701.
158. Robbin ML, Lockhart ME. Ultrasound evaluation before and after hemodialysis access. In: Zweibel WJ, Pellerito JS, editors. Introduction to vascular ultrasonography. 5th ed. Philadelphia: Elsevier; 2005. p. 325-340.

This page intentionally left blank

APPENDIX

Ultrasound Artifacts: A Virtual Chapter

Korosh Khalili, Hojun Yu, Alexander Jesurum, and Deborah Levine

SUMMARY OF KEY POINTS

- Artifacts are common in ultrasound imaging.
- Knowledge of artifacts can aid in diagnosis.
- Understanding ultrasound physics allows for correction of artifacts that distort the visualized anatomy.

CHAPTER OUTLINE

ASSUMPTIONS IN GRAY-SCALE IMAGING
Velocity of Sound
Attenuation of Sound
Path of Sound
Beam Profile
PROPAGATION VELOCITY ARTIFACT
ATTENUATION ERRORS
Shadowing
Increased Through Transmission
PATH OF SOUND-RELATED ARTIFACTS
Mirror Image Artifact
Comet-Tail Artifact
Refraction
Anisotropy
Reverberation Artifact
GAS-RELATED ARTIFACTS
Reverberation Artifact
Ring-Down Artifact
Dirty Shadowing Artifact
BEAM PROFILE–RELATED ARTIFACTS
Side Lobe and Grating Lobe Artifacts
Partial Volume Averaging
DOPPLER IMAGING ARTIFACTS
Loss or Distortion of Doppler Information
Artifactual Vascular Flow
Tissue Vibration Artifact
Aliasing and Velocity Scale Errors
Spectral Broadening
Blooming Artifact
Twinkle Artifact
Acknowledgment

Almost all ultrasound images contain artifacts. Many of these artifacts go unrecognized because they are contained within (and contribute to) the background noise. However, when artifacts substantially alter the signal, they become recognizable on images. Certain artifacts distort the images and must be recognized in order to improve image quality or prevent a false diagnosis. Other artifacts add useful data and thus are important for understanding the composition, anatomy, and pathology of the image being visualized. We hope you enjoy this virtual chapter, which encompasses animated illustrations of how artifacts are produced as well as multiple examples of images and videos from the text.

ASSUMPTIONS IN GRAY-SCALE IMAGING

Several assumptions about the propagation of sound waves are made when ultrasound equipment maps echoes onto the image.[1] When one or more of these assumptions prove invalid, artifacts result.

Velocity of Sound

The speed of sound throughout the tissues is assumed to be uniform at 1540 m/sec. When the waves travel through tissues that substantially alter sound velocity, propagation velocity artifacts occur.

Attenuation of Sound

Sound waves normally become fainter—that is, their intensity decreases—as they travel through tissues. The equipment assumes that this attenuation of intensity occurs at a constant rate. If the waves travel through tissues that either do not attenuate as much or attenuate more than the adjacent tissues, attenuation errors such as increased through transmission or shadowing arise.

Path of Sound

In creating the image, the equipment assumes that the generated sound wave travels from the surface of the probe in a straight line, is reflected off a reflector only once, and returns directly back to the probe at the same angle exactly to the point from which it left the probe. If the sound waves undergo more than one reflection, then artifacts such as mirror image, reverberation,

or comet-tail occur. And if the direction of the beam or its echo is altered, refraction or anisotropy artifact may be produced.

Beam Profile

An assumption is made that the sound beam generated by the transducer is a narrow line. When the beam is not sufficiency narrow in the imaging plane or in the elevation plane (i.e., along the short axis of the transducer), side lobe or grating lobe or partial volume averaging artifacts may occur.

PROPAGATION VELOCITY ARTIFACT

Ultrasound image processing assumes that the speed of sound in tissue is a constant 1540 m/sec. However, when a sufficiently large structure composed of tissue that propagates speed at a different velocity is encountered, then propagation velocity artifact can occur.[1] In the case of a fatty lesion, the slower speed of propagation (approximately 1450 m/sec) means that the echo will take longer to return to the transducer; thus the lesion is displayed deeper in the image than its true location. Some newer ultrasound machines with multibeam (spatial compounding) features and improved signal processing can minimize this artifact.

Click here to see an explanatory video of **propagation velocity artifact** (Video A.1).

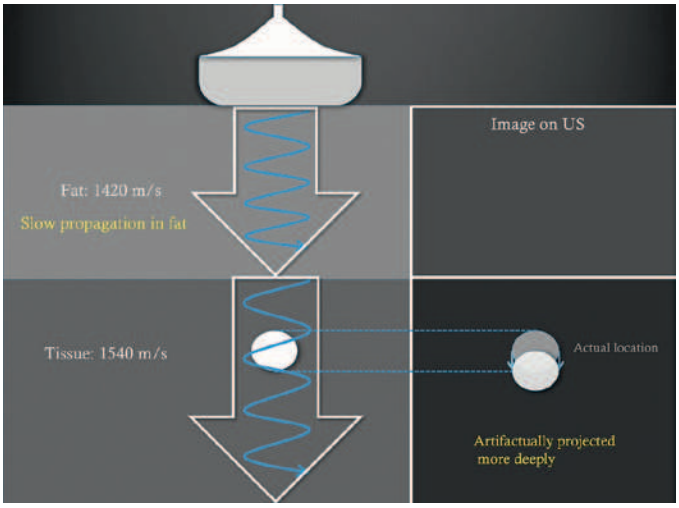

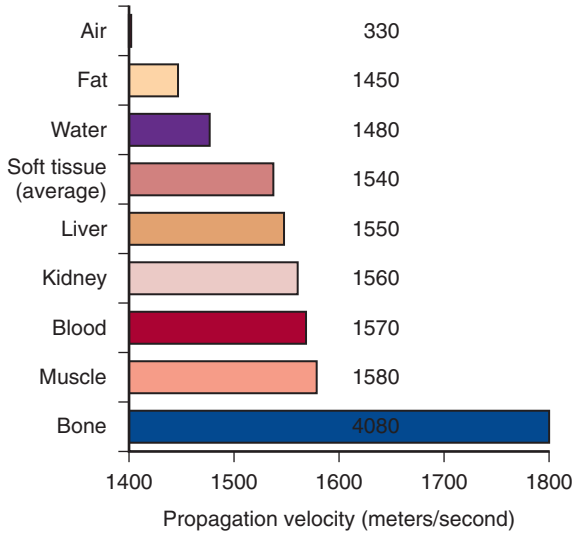

FIG. A.1 Propagation Velocity. Propagation velocity of different body tissues.[2] (See Chapter 1, Fig. 1.2.)

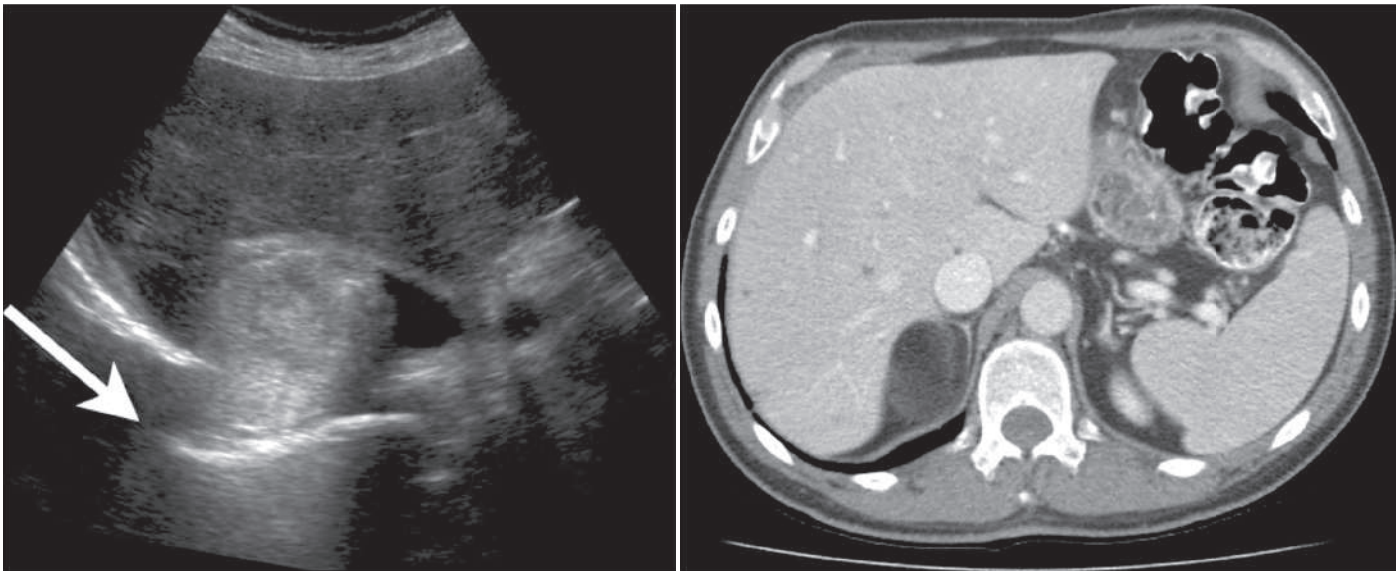

FIG. A.2 Propagation Velocity. When sound passes through a fatty mass, in this case a myelolipoma, its speed slows down to 1450 m/sec. Because the ultrasound scanner assumes that sound is being propagated at the average velocity of 1540 m/sec, the delay in echo return is interpreted as indicating a deeper target. Therefore the final image shows a **misregistration artifact** in which the diaphragm *(arrow)* is shown in a deeper position than expected in this patient with a right adrenal myelolipoma. The computed tomography image depicts the myelolipoma, confirming its fatty nature.

ATTENUATION ERRORS

When the ultrasound beam encounters a focal lesion that attenuates the sound to a greater or lesser extent than the surrounding tissues, the intensity of the beam deep to the lesion will be either weaker (shadowing) or stronger (increased through transmission) than in the surrounding tissues.

Click here to see an explanatory video of **attenuation-related artifacts** (Video A.2).

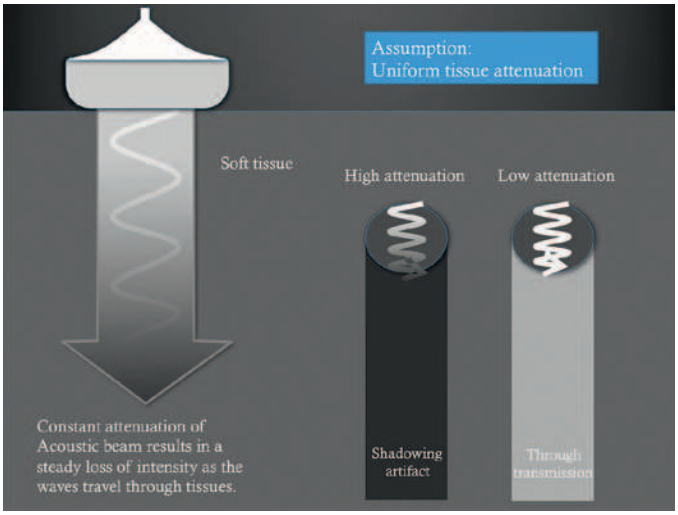

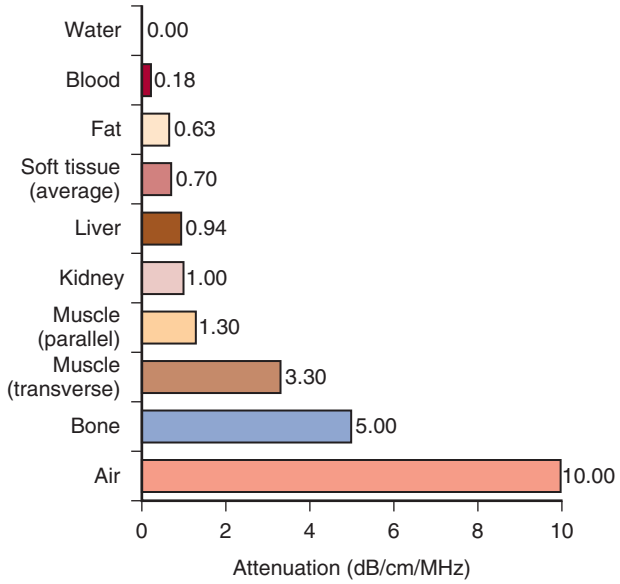

FIG. A.3 As sound passes through tissue, it loses energy through the transfer of energy to tissue by heating, reflection, and scattering. Attenuation is determined by the insonating frequency and the nature of the attenuating medium. Attenuation values for normal tissues show considerable variation. Attenuation also increases in proportion to insonating frequency, resulting in less penetration at higher frequencies.[2] (See Chapter 1, Fig. 1.9.)

Shadowing

Shadowing results when there is a marked reduction in the intensity of the ultrasound deep to a strong reflector, attenuator, or refractor. Clean dark shadows will be seen behind calcified objects when the focal zone is at or just below the structure.

Click here to see an explanatory video of **shadowing** (Video A.3).

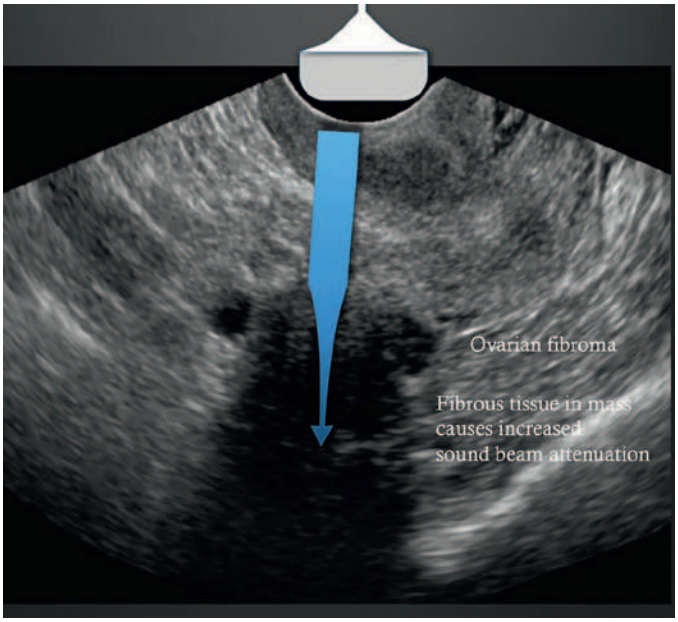

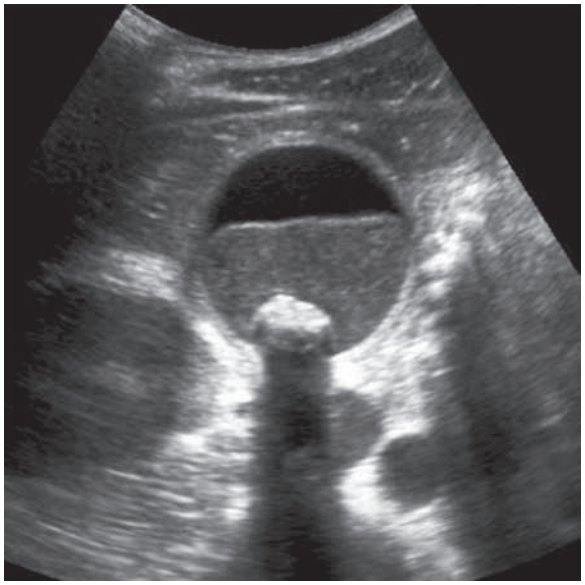

FIG. A.4 Gallstone With Shadowing. Note the dark, well-defined shadow.[3] (See Chapter 6, Fig. 6.39C.)

FIG. A.5 Shadowing From Hernia Repair Mesh.

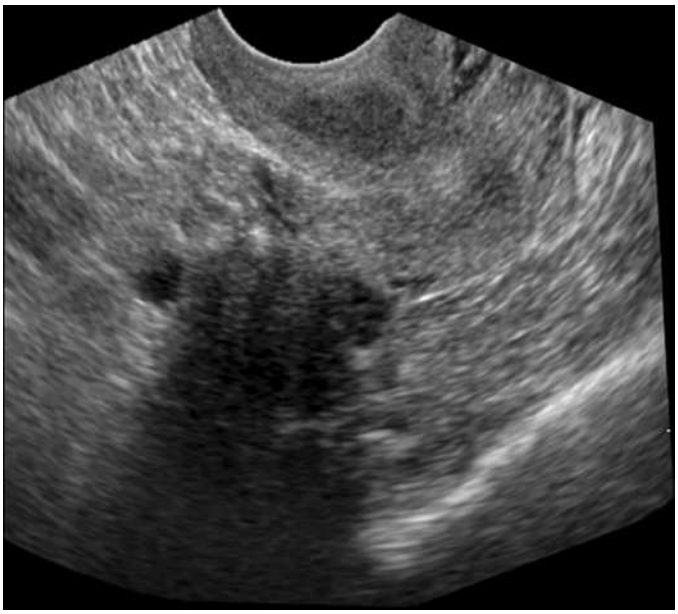

FIG. A.6 Shadowing From Ovarian Fibroma. This is a slightly less "clean" shadow since the fibroma is not as dense as a calcified stone.

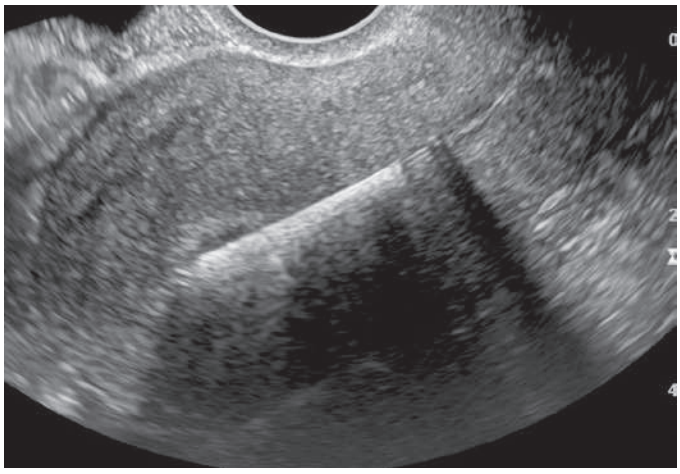

FIG. A.7 Shadowing From an Intrauterine Device.[4] (See Chapter 15, Fig. 15.25A.)

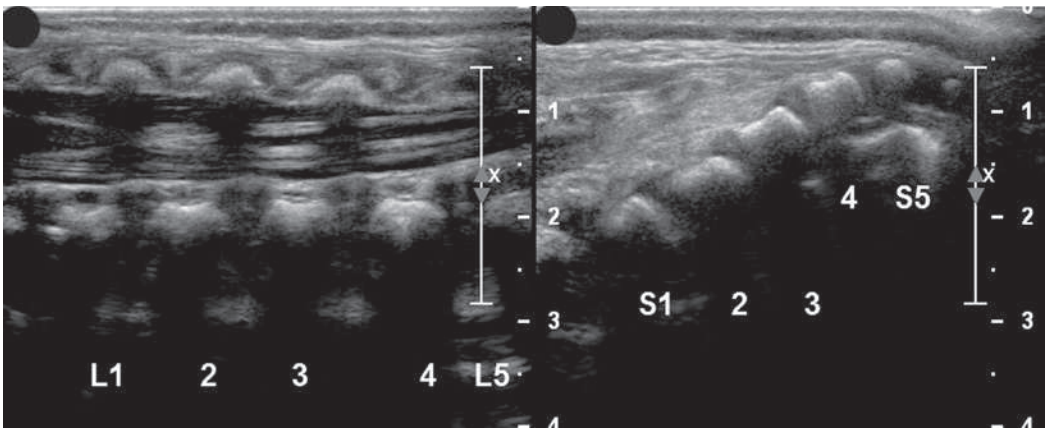

FIG. A.8 Shadowing. Coned down view of distal neonatal spine shows **shadowing** from vertebral bodies that interrupt the linear appearance of the nerve roots.[5] (See Chapter 49, Fig. 49.3.)

Click here to see real-time cine clip of showing in region of cauda equina (Video A.4).[5]

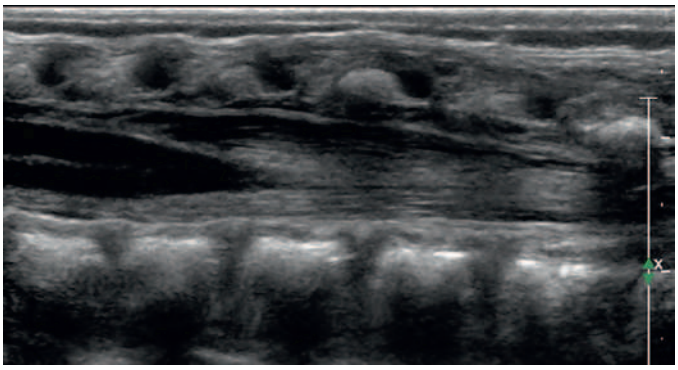

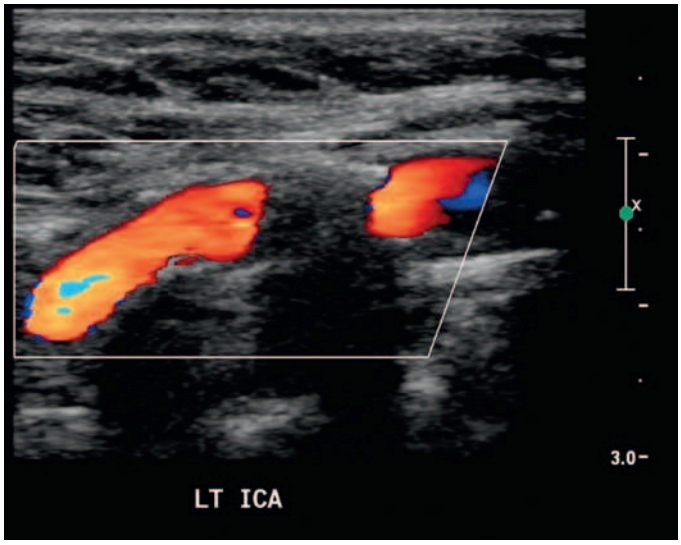

FIG. A.9 Shadowing. Shadowing from dense plaque prevents assessment of color flow in that region. Note that there must be flow present because similar color is visualized before and after the shadow.[6] (See Chapter 26, Fig. 26.8.)

Edge shadowing is caused by excessive refraction and commonly occurs from the edges vessels, cystic structures, and bones.

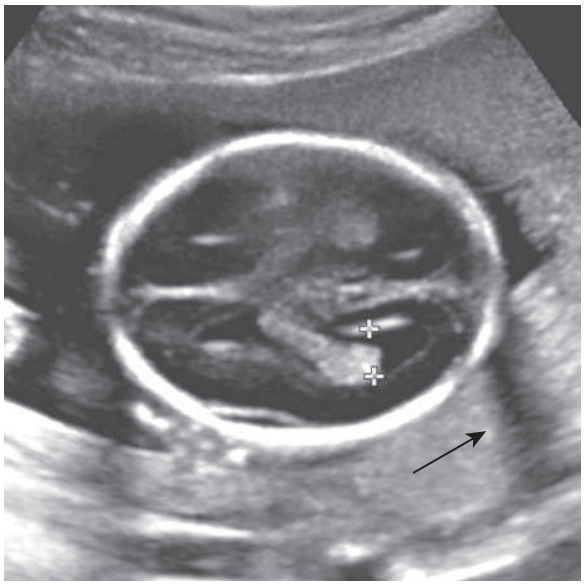

FIG. A.10 Edge Shadowing. Note the **edge shadowing** artifact behind the posterior aspect of the fetal skull. The beam bends at curved surface and loses intensity, producing a shadow *(arrow)*.[7] (See Chapter 34, Fig. 34.3.)

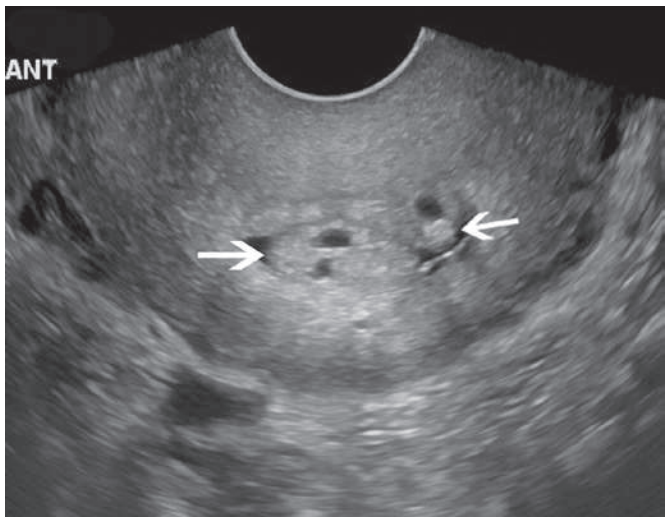

FIG. A.11 Edge Shadowing 2. Endometrial polyp shows both **through transmission** behind the cystic spaces and **edge shadowing** at the margins of the cysts.[4] (See Chapter 15, Fig. 15.14B.)

Increased Through Transmission

Increased through transmission occurs when an object (such as a cyst) attenuates the sound waves less than the surrounding tissues.

Click here to an explanatory video of **increased through transmission** (Video A.5).

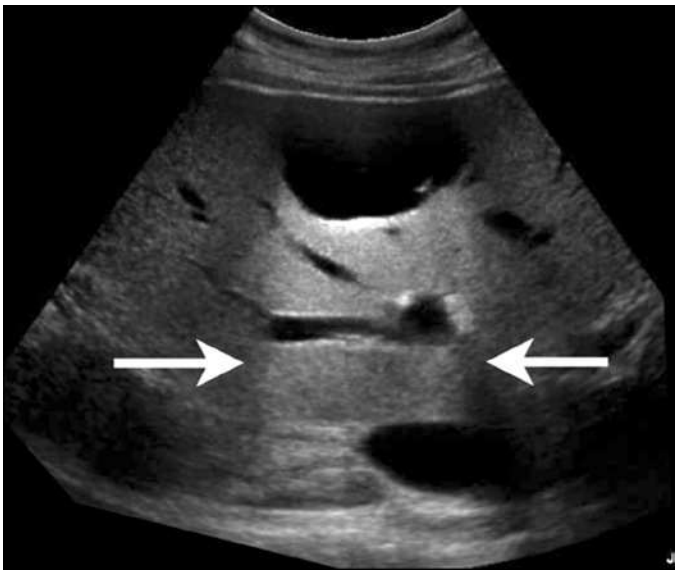

FIG. A.13 Increased Through Transmission. The hepatic parenchyma distal to the cysts is falsely displayed as increased in echogenicity *(arrows)* secondary to increased through-transmission artifact.

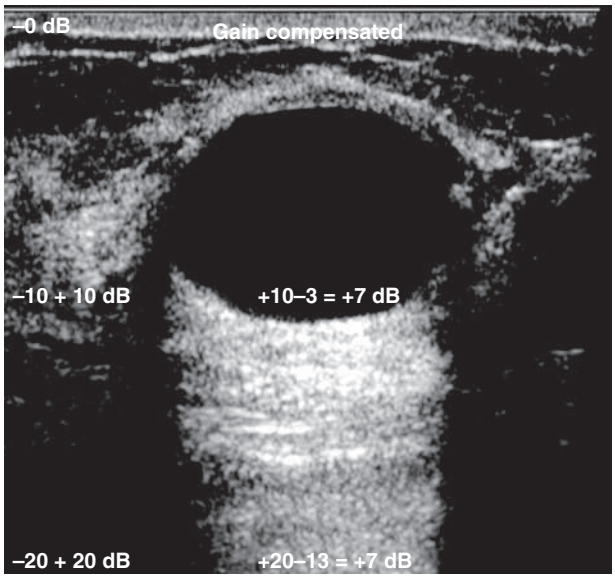

FIG. A.12 Increased Through Transmission. The cyst attenuates 7 dB less than the normal tissue, and time gain curve correction for normal tissue results in overamplification of the signals deep to the cyst, producing **increased through transmission** of these tissues.[2] (See Chapter 1, Fig. 1.31C.)

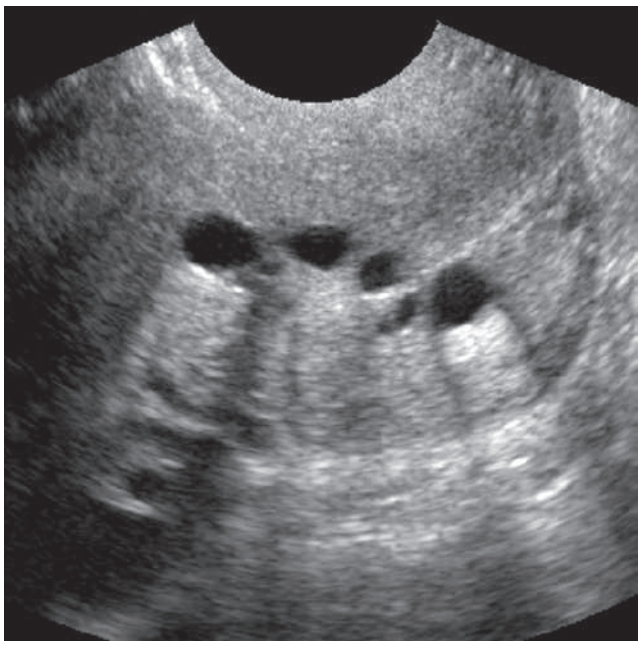

FIG. A.14 Increased Through Transmission. Nabothian cysts show both **increased through transmission** behind the cysts and **edge shadowing** at the margins of the cysts.[4] (See Chapter 15, Fig. 15.7C.)

PATH OF SOUND-RELATED ARTIFACTS

In mapping a returning echo onto the generated image, an assumption is made that it originated from the same part of the transducer from which it was produced. Also, an assumption is made that the echo is the result of a single reflection. The depth of the reflector is calculated based on the time it took for the sound wave to travel from the transducer to the reflector and back, assuming a single reflection. When these assumptions do not hold, various types of artifacts occur.

Click here to see an explanatory video of **path of sound assumption** (Video A.6).

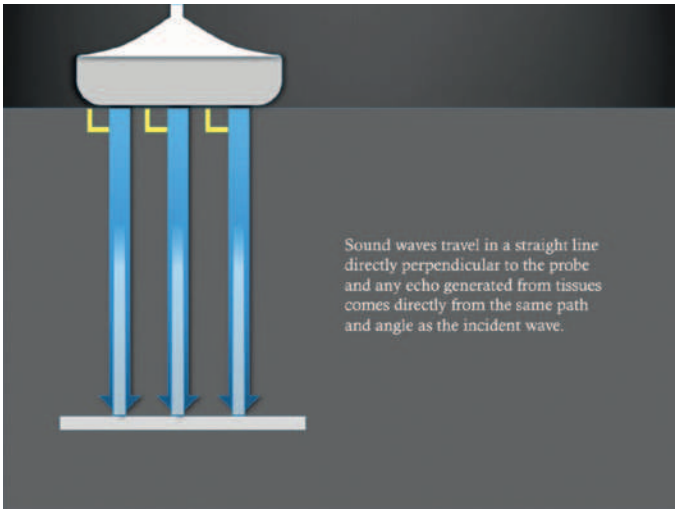

Mirror Image Artifact

A mirror image artifact is created when the primary beam encounters a highly reflective surface that acts like a mirror. The reflected echoes then encounter other reflectors and bounce back onto the mirror before being directed to the transducer. The result is artifactually inverted projection of the reflectors deeper to the surface of the mirror. The image is displayed deeper because of the longer path of the reflected sound. If the mirror image artifact causes confusion, it can be decreased or eliminated by moving the transducer to center it on the region of interest and/or placing the focal zone at the level of interest in the real structure.

Click here to see an explanatory video of **mirror image artifact** (Video A.7).

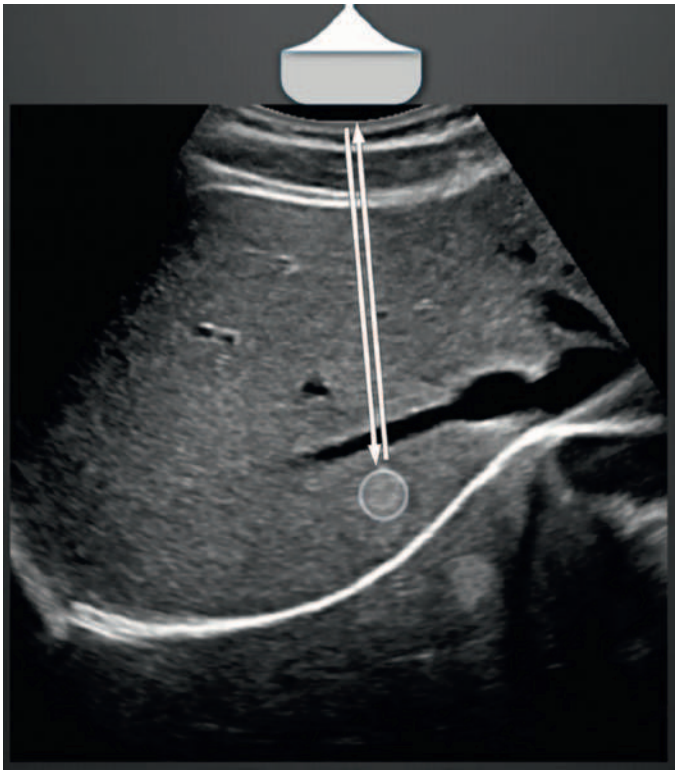

FIG. A.15 Mirror Image. Picture of reflection in water—similar to mirror image artifact.

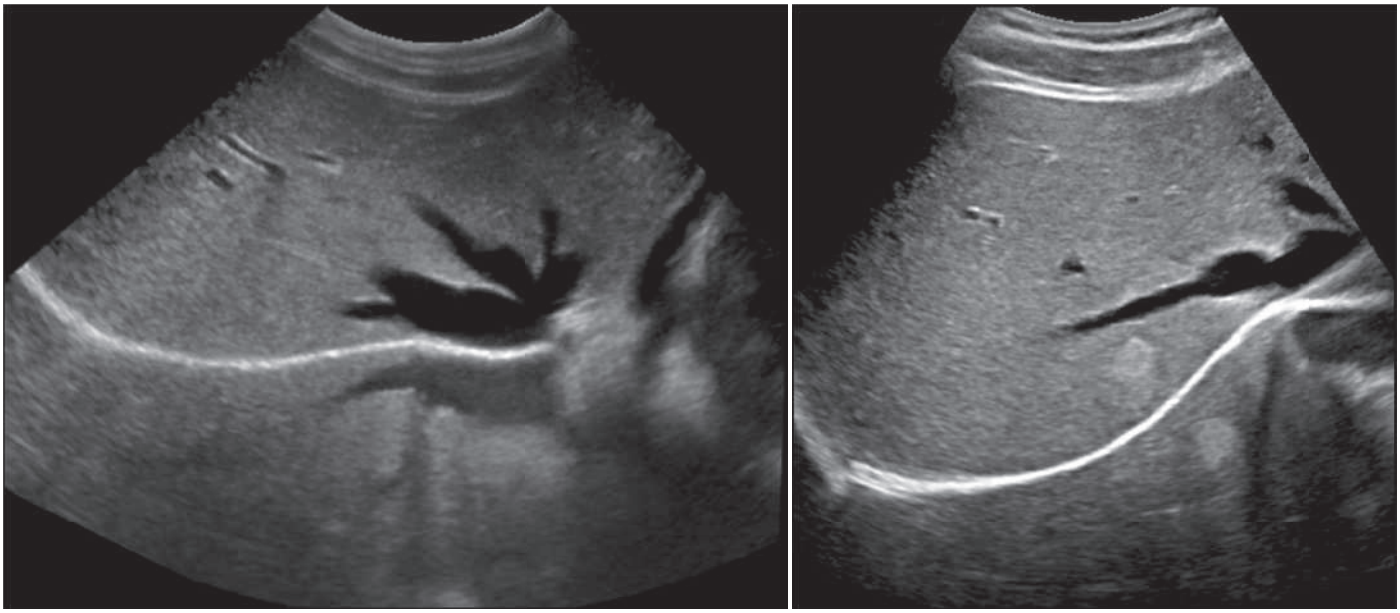

FIG. A.16 Mirror Image Artifact. Soft tissue–gas interfaces, such as the diaphragm, are excellent reflectors of the sound beam owing to the large difference in the acoustic impedance between the two materials. Therefore hepatic structures are frequently seen mirrored beyond the diaphragm onto the lungs. These two figures show liver parenchyma, hepatic veins in part A, and a hepatic hemangioma in part B all inversely projected onto lung.

Comet-Tail Artifact

Comet-tail artifact is a type of reverberation artifact.[8] The repetitive reflections occur within very small structures, such as tiny cysts in the case of von Meyenburg complexes and tiny crypts in the wall of the gallbladder in the case of adenomyomatosis. Accordingly, the reverberated echoes may not be individually visible. The tapered, comet-tail appearance is due to the decreasing amplitude of each reverberation as a result of beam attenuation.

Click here to see the explanatory video of **comet-tail artifact** in adenomyomatosis (Video A.8).

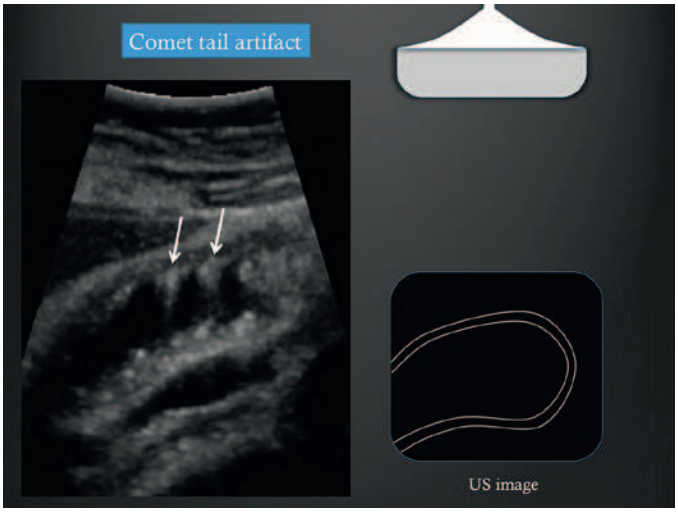

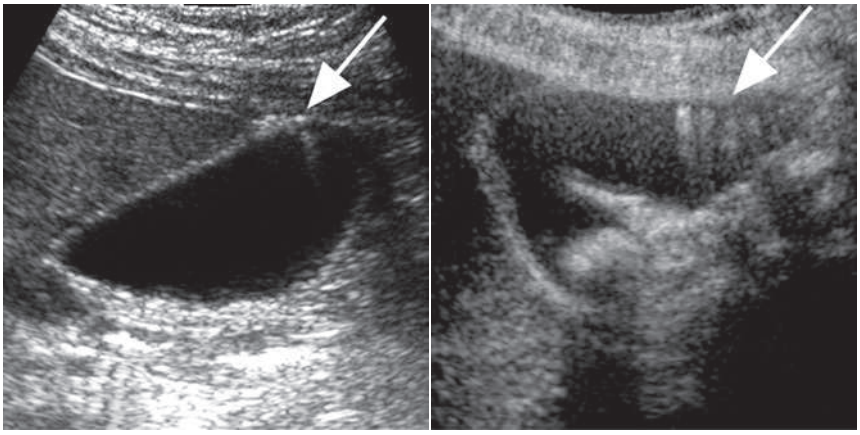

FIG. A.17 Comet-Tail Artifact in Association With Adenomyomatosis. This is felt to be due to cholesterol crystals within the prominent Rokitansky-Aschoff sinuses.[3] (See Chapter 6, Fig. 6.45.)

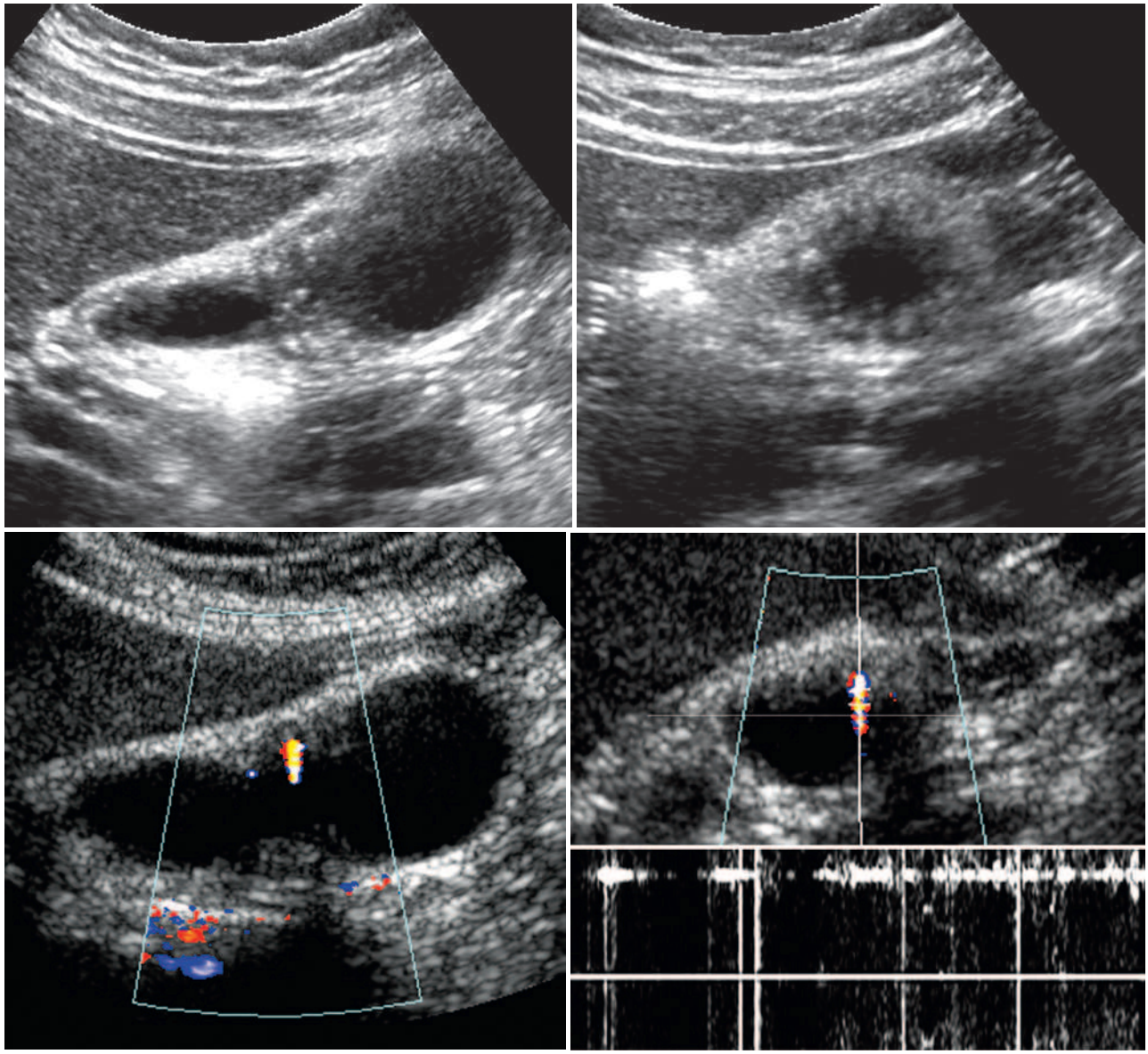

FIG. A.18 Comet-Tail Artifact. On color and spectral Doppler this can look like a twinkle artifact, but it is a color representation of the comet-tail. (See section on color Doppler artifacts for description of the twinkling.[3]) (See Chapter 6, Fig. 6.46.)

FIG. A.19 Adenomyomatosis and Comet-Tail Artifact.

Click here to see real time scanning of **comet-tail artifact** in adenomyomatosis (Video A.9).

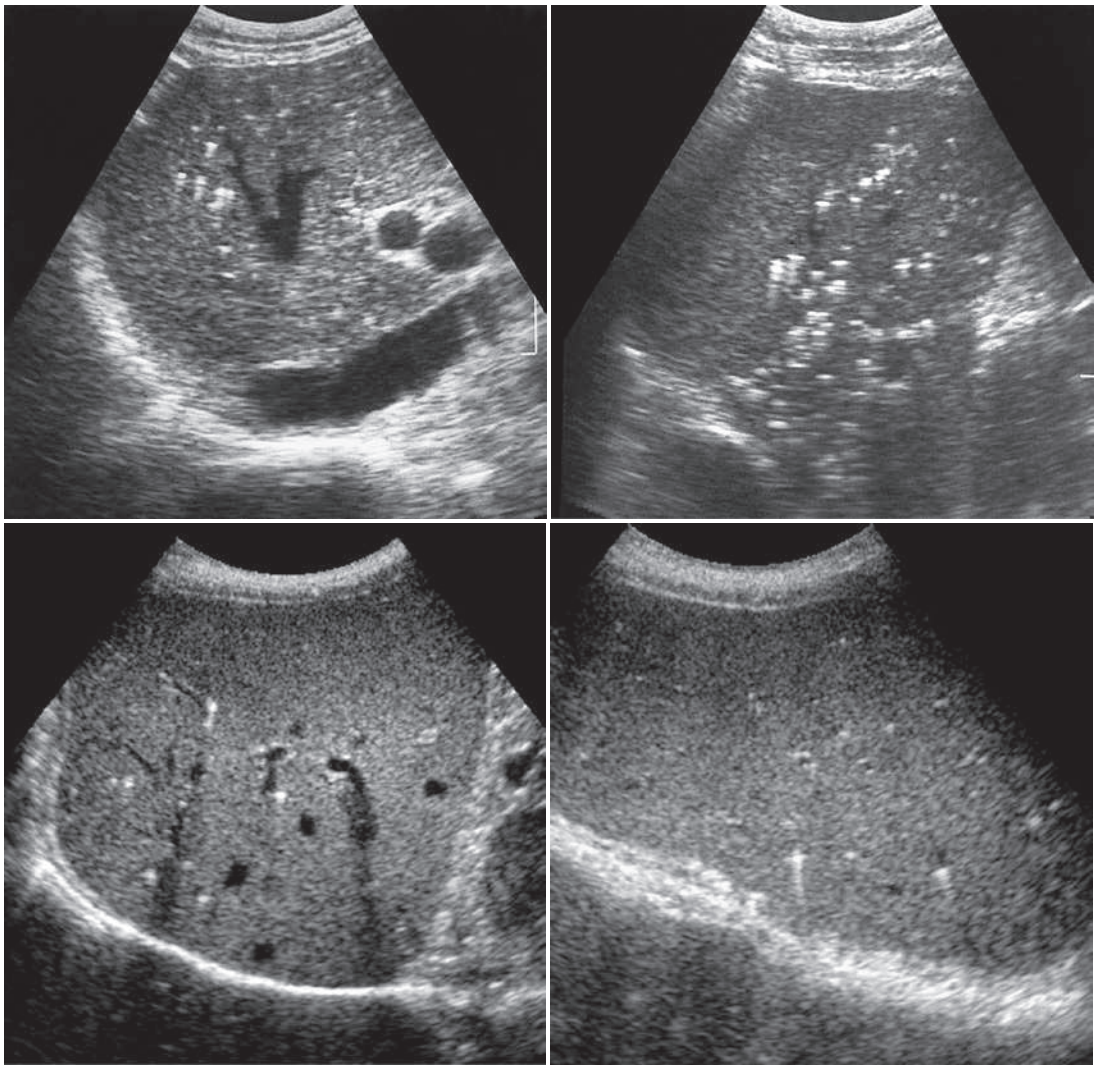

FIG. A.20 Comet-Tail Artifact Behind von Meyenburg Complex in Two Patients.[9] (See Chapter 4, Fig. 4.16.)

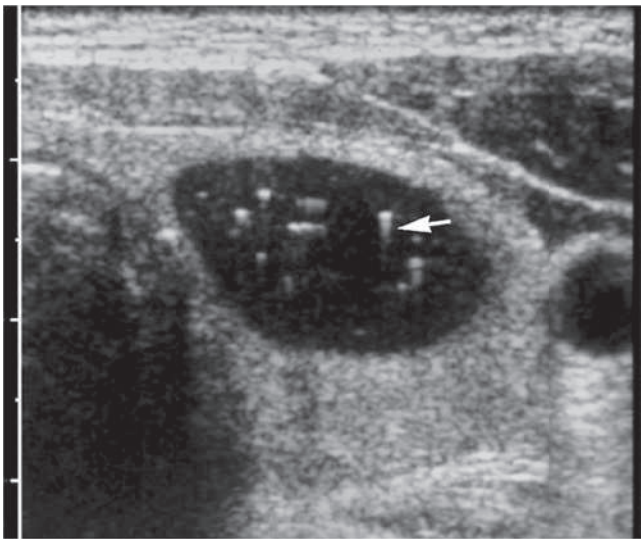

FIG. A.21 Colloid Cyst in Thyroid Gland With Characteristic Comet-Tail Artifact *(Arrow).*[10] (See Chapter 19, Fig. 19.10A.)

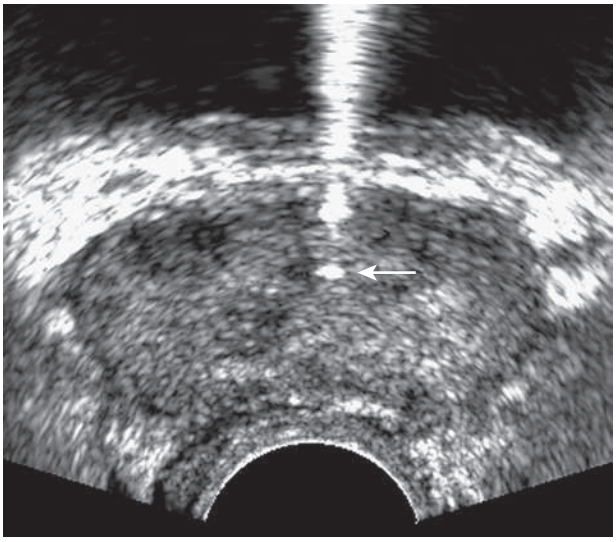

FIG. A.22 Strong Comet-Tail Artifact Due to Fiducial Marker in Patient With Prostate Cancer.[11] (See Chapter 10, Fig. 10.13.)

Refraction

As sound moves between tissues with different propagation velocities, such as from muscle to fat, it changes its direction at their interface as a result of refraction. The physical properties of refraction are explained by Snell's law, as demonstrated in Figs. A.23[12] and A.24. The change in the direction of the sound waves results in violation of the assumption made by the ultrasound equipment that the incident and reflected waves travel in a straight line. Therefore, with refraction, structures insonated by the bent path of sound waves are artifactually translated to appear as if the sound waves had traveled along a straight path. If refraction is suspected, it can be minimized by increasing the scan angle so that sound waves travel perpendicular to the interface.

Click here to see an explanatory video of **refraction** from the anterior abdominal wall (Video A.10).

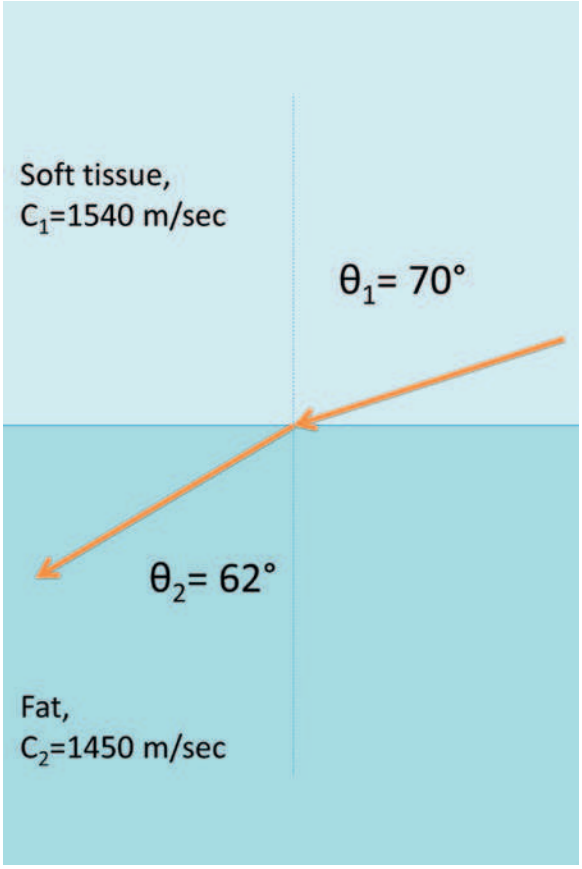

FIG. A.23 Refraction. Refraction can be due to tissues with different propagation velocities. When sound passes from soft tissue with propagation velocity (C_1) of 1540 m/sec to fat with a propagation velocity (C_2) of 1450 m/sec, there is a change in the direction of the sound wave because of refraction. The degree of change is related to the ratio of the propagating velocities of the media forming the interface ($\sin\theta_1/\sin\theta_2 = C_1/C_2$)[2]. Note that when the incident angle is changed to zero degrees—that is, the incident beam is perpendicular to the interface ($\theta_1 = 0°$)—the artifact disappears.

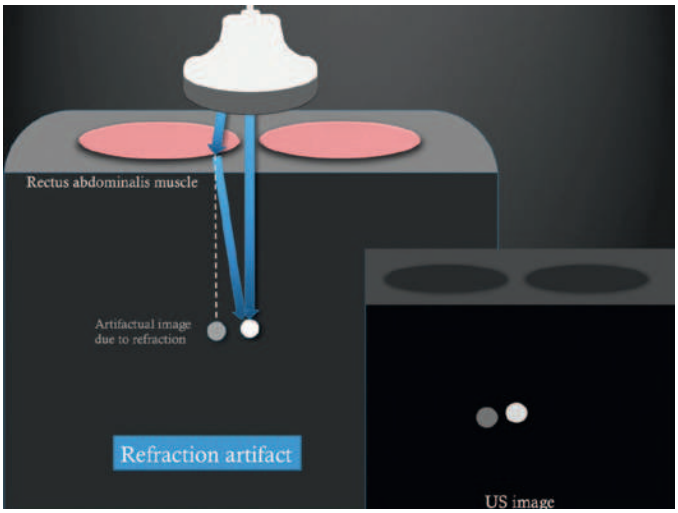

FIG. A.24 Refraction. Image of a straw in water. Refraction has occurred owing to the difference between air and water, causing an offset in the appearance of the straw. Note also how the straw appears larger in the water because of distortion of the image.

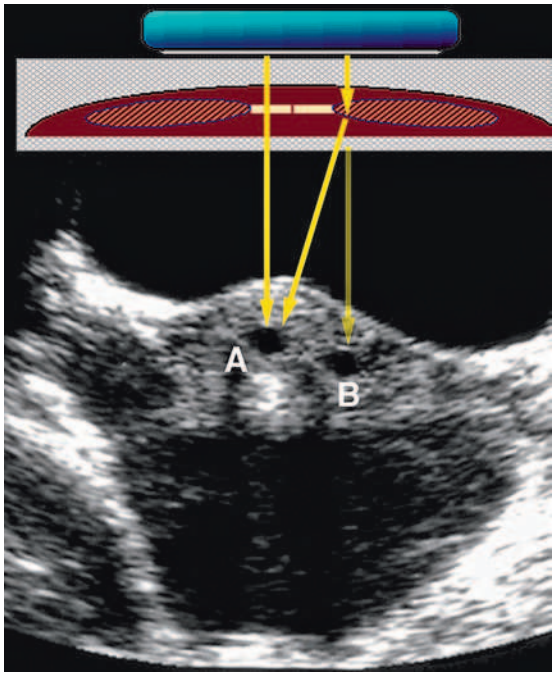

FIG. A.25 Refraction. This figure shows what appears to be a second gestational sac due to refraction artifact. This is sometimes called **"ghosting."**[2] (See Chapter 1, Fig. 1.8.)

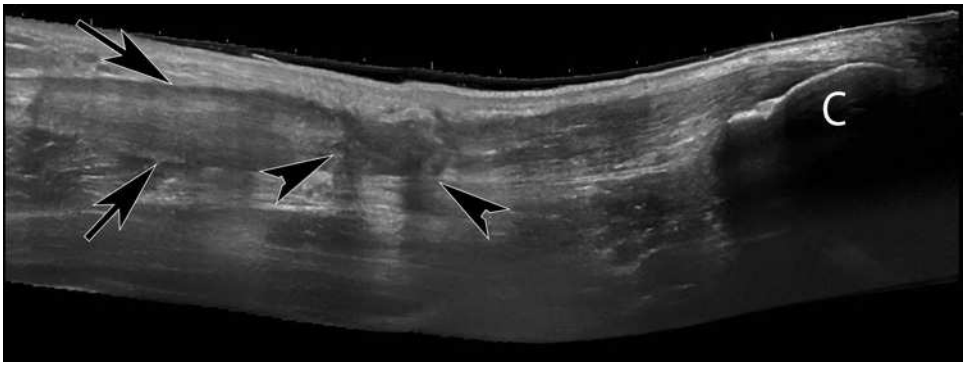

FIG. A.26 Refraction. A panoramic view of the Achilles tendon demonstrates a rupture within the midportion of the tendon. The proximal aspect of the tendon is chronically thickened and hypoechoic *(arrows)*. **Refraction artifact** *(arrowheads)* is caused by the interfaces between the ruptured tendon edges and hemorrhage. *C,* Calcaneus.[13] (See Chapter 23, Fig. 23.11.)

Anisotropy

Anisotropy is an artifact caused by structures that are composed of bundles of highly reflective fibers running parallel to each other, such as tendons and ligaments. If the sound beam hits the tendon or ligament fibers perpendicular to their length, it is reflected directly back, resulting in an echogenic appearance. But if the angle of insonation is not perpendicular to the tendon fibers, the beam is reflected away from the transducer, leading to the generation of an image with artifactual hypoechogenicity within the tendon.

Click here to see an explanatory video of **anisotropy** (Video A.11).

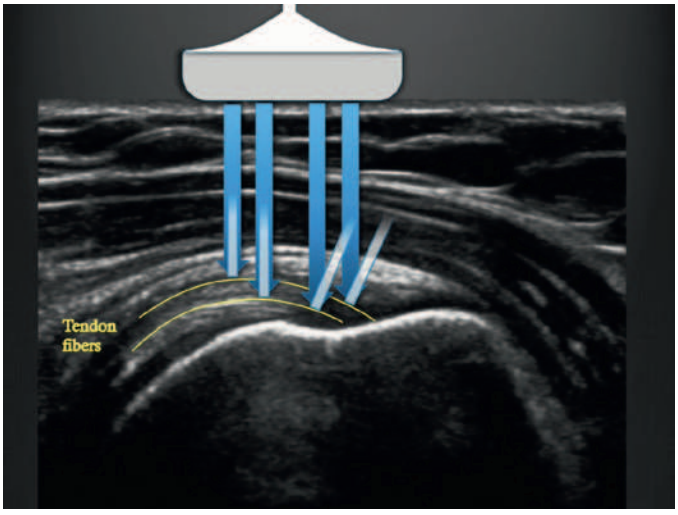

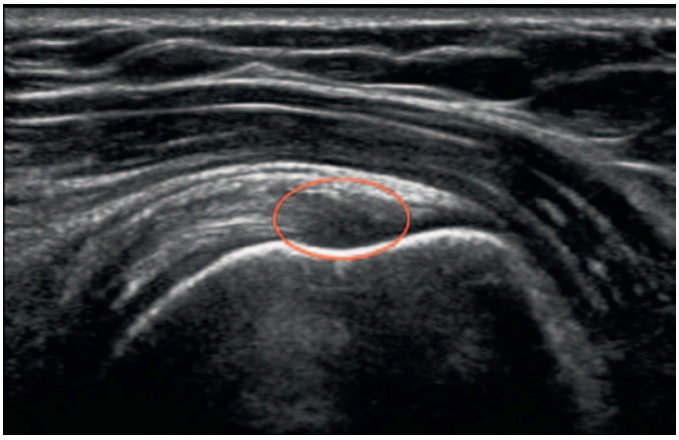

FIG. A.27 Anisotropy. The insertion of supraspinatus tendon artifactually appears hypoechoic due to anisotropy.

Click here for video of real-time scanning of **anisotropy** at supraspinatus insertion (Video A.12).

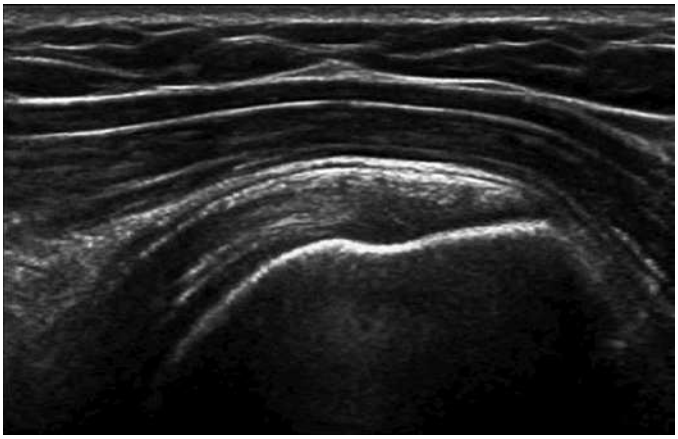

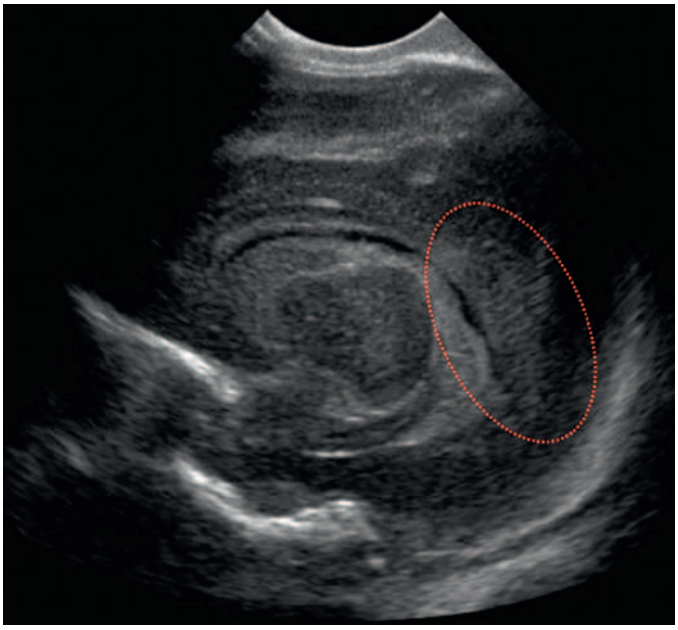

FIG. A.28 Anisotropy. The peritrigonal region of the white matter *(ellipse)* appears relatively echogenic, also called "peritrigonal blush." This **anisotropic effect** artifact occurs because in the trigone region, the parallel white matter fibers run perpendicular to the incident sound beam, causing increased reflection.[14] The artifact is visible only in the region of the trigone when the anterior fontanelle is used as a scanning window.

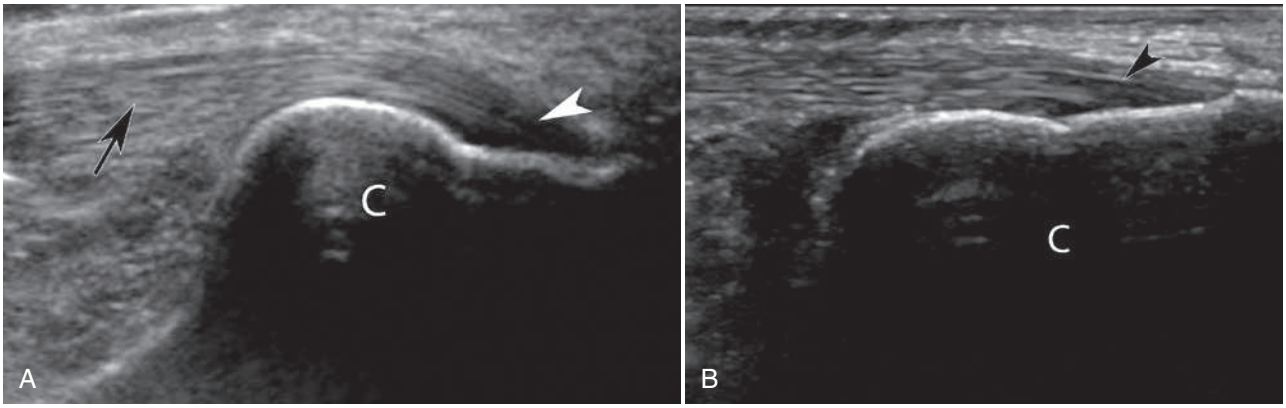

FIG. A.29 Anisotropy. (A) In this long-axis scan of the Achilles insertion on the calcaneus, the proximal portion of the imaged tendon demonstrates a normal fibrillar appearance *(arrow),* whereas the distal tendon insertion is hypoechoic *(arrowhead). (B)* When the transducer is angled 90 degrees to the distal tendon insertion, the tendon then becomes fibrillar and is normal in appearance *(arrowhead). C,* Calcaneus.[13] (See Chapter 23, Fig. 23.8.)

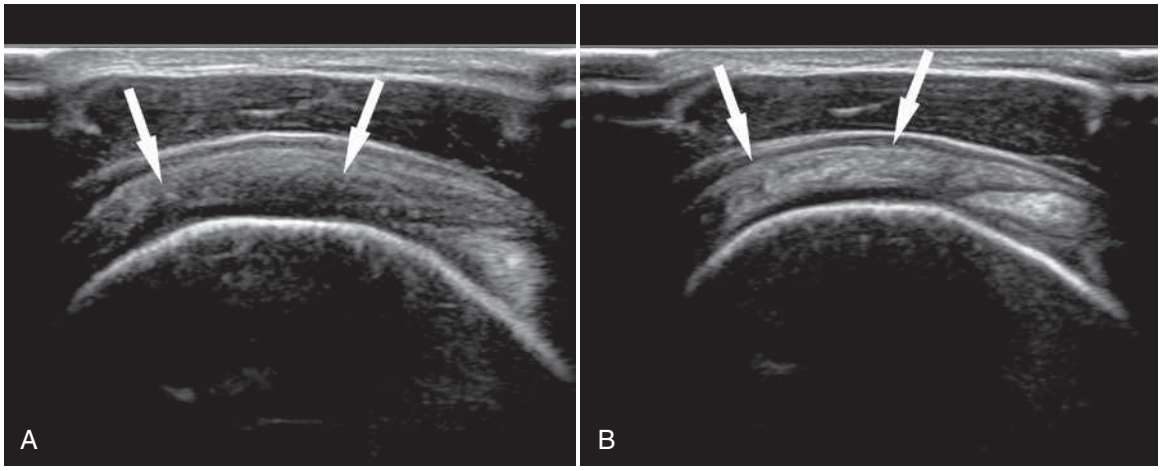

FIG. A.30 Anisotropy. Short-axis images of the supraspinatus tendon. **(A)** Artifactual hypoechogenicity of the supraspinatus tendon *(arrows)* may simulate tendinosis or tear. **(B)** Correction of angle of insonation to be perpendicular to the tendon permits visualization of the normal intact tendon.[15] (See Chapter 24, Fig. 24.30.)

Reverberation Artifact

Reverberation artifact occurs when a strong reflector runs perpendicular to the direction of the beam (i.e., parallel to the probe surface), usually close to the skin surface.[1] The sound waves may then get partially "trapped" between the reflector and skin, reverberating back and forth and causing the appearance of multiple regular lines when some of the waves eventually reach the probe. Often the reflectors are the skin and subcutaneous fascia (see Fig. A.31). Reverberation artifact is angle dependent, so moving the transducer slightly will cause a decrease in or elimination of the artifact. Reverberation can be helpful during biopsies, to see a needle. If it is distracting, try changing the angle of insonation, using a different window, or decreasing the gain.

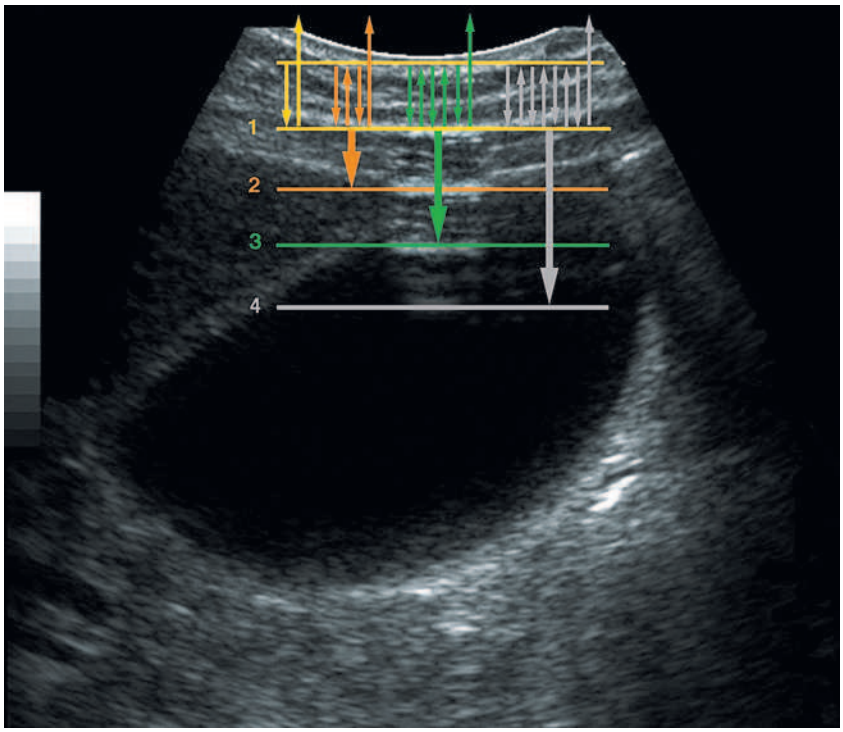

FIG. A.31 Reverberation Artifact. Reverberation artifacts arise when the ultrasound signal reflects repeatedly between highly reflective interfaces near the transducer, resulting in delayed echo return to the transducer. This appears in the image as a series of regularly spaced echoes at increasing depth.[2] (See Chapter 1, Fig. 1.27.)

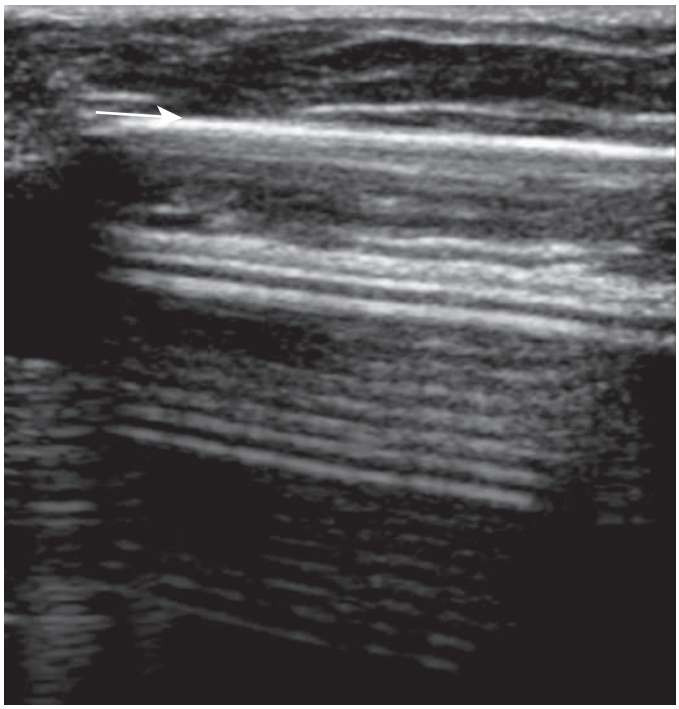

FIG. A.32 Mirror Image and Reverberation Artifacts Behind a Pacemaker. The highly reflective and mirrorlike surface of the pacemaker *(arrow)* results in repeated bouncing of sound wave among the probe surface, pacemaker, and skin.

For reverberation due to gas, see next section.

GAS-RELATED ARTIFACTS

Several physical properties of gases lead to unique artifacts in ultrasound that help identify gas but also may hinder visualization of other organs. These properties include the very dissimilar acoustic impedance of gas compared with soft tissues, making them highly reflective surfaces. The varied and ever-changing shape of gas in the body, including foam, leads to variability of its appearance even in the same field. The very low density of gases makes them quite compressible, and they can undergo resonant oscillation in response to sound waves, leading to amplification of echoes. These properties result in three distinct artifacts, which can be present at the same time: **reverberation, ring-down,** and **dirty shadowing.**[16]

Reverberation Artifact

The physical pressure of the probe on the soft tissues, such as the abdominal wall, flattens their shape in the near field, making them perpendicular to the surface of the probe and the incident sound beam. Because gases conform to the shape of their containers, they too will form a linear and perpendicular interface to the incident sound beam, especially when in the form of a large bubble. The highly reflective gas interface will act like a mirror, resulting in reverberation artifacts.

Click here to see an explanatory video of **reverberation artifact due to gas** (Video A.13).

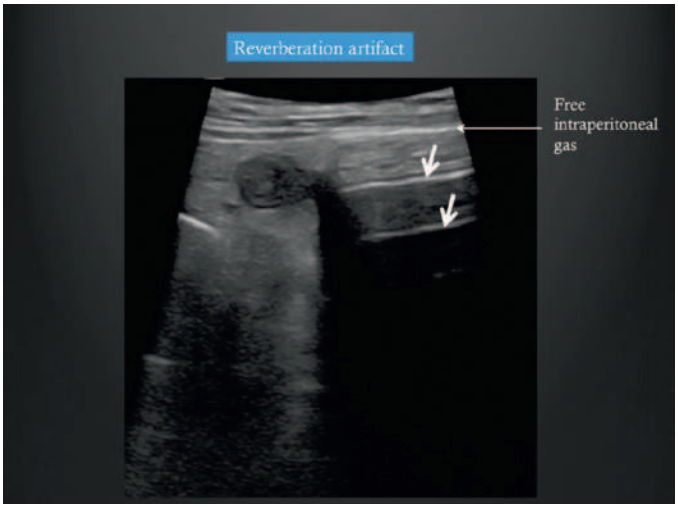

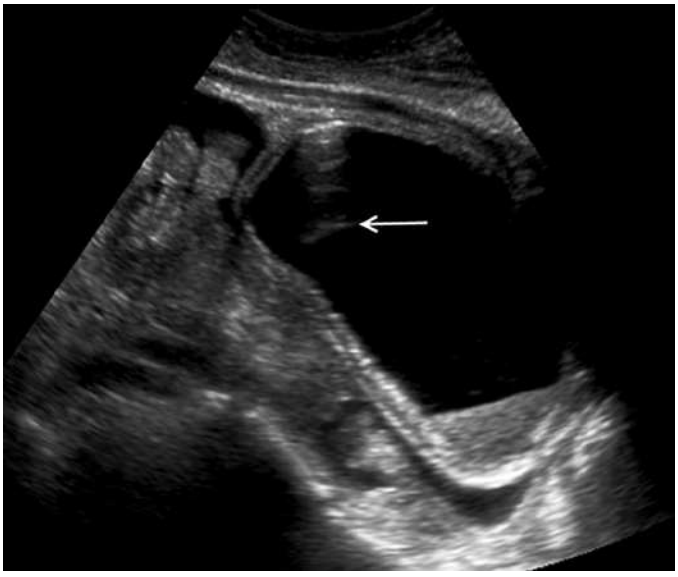

FIG. A.33 Reverberation Artifact. Small amount of gas within the bladder is recognizable by the reverberation artifact *(arrow)*.

Ring-Down Artifact

Ring-down artifact occurs when the ultrasound waves cause oscillation within fluid trapped by a tetrahedron of gas bubbles.[17] These oscillations create a continuous sound wave that is transmitted back to the transducer. What will be seen is a line or series of parallel bands extending posterior to a gas collection. Although this has the appearance of reverberation artifact, it actually has a different mechanism.

Click here to see an explanatory video of **ring-down artifact** (Video A.14).

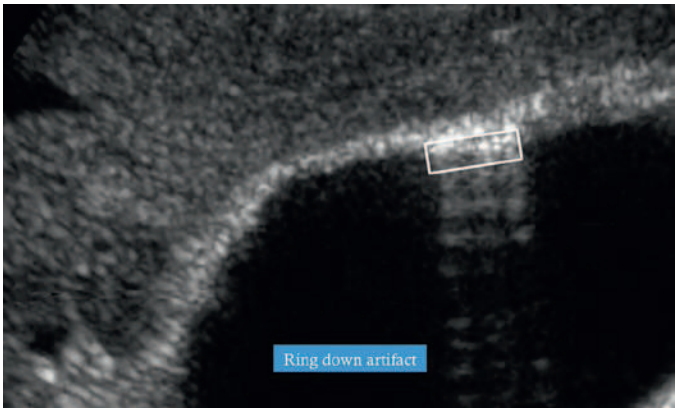

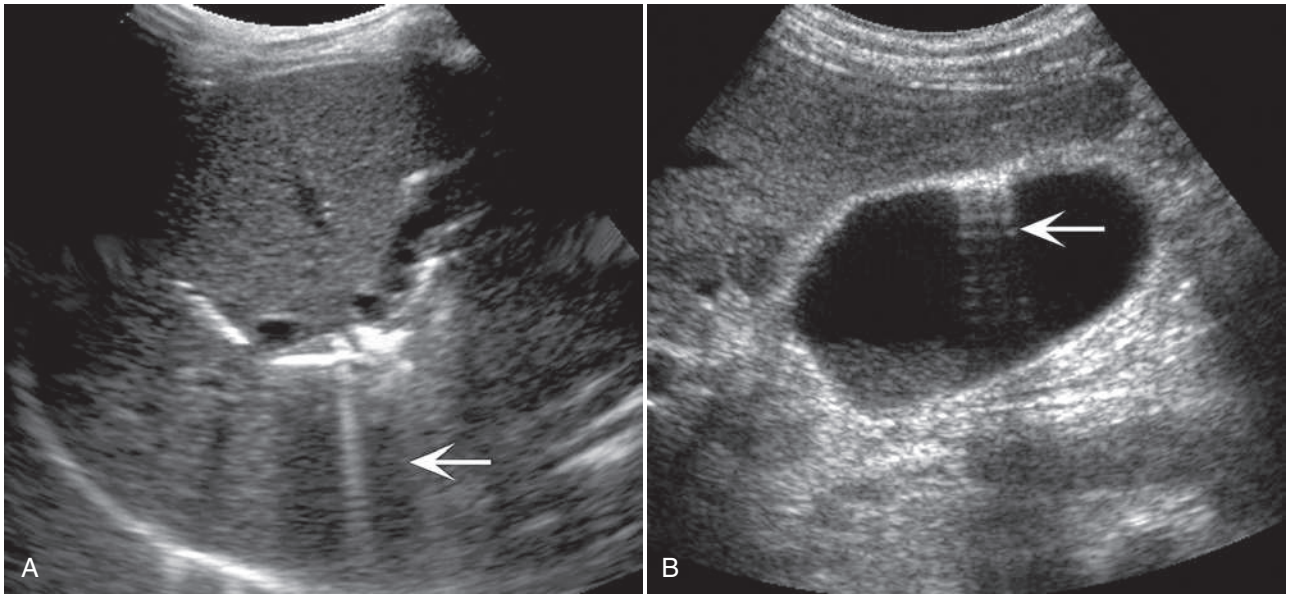

FIG. A.34 Ring-Down Artifact. Pneumobilia causing **ring-down artifact** in the biliary tree **(A)** and gallbladder **(B).**[3] (See Chapter 6, Fig. 6.13.)

Click here to see a video clip of **ring-down artifact** in peripheral ducts of the liver (Video A.15).

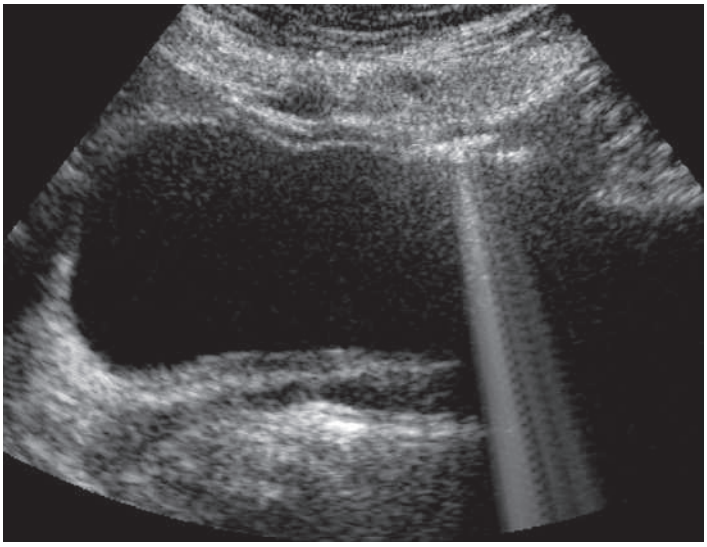

FIG. A.35 Ring-Down Artifact. Iatrogenic air in the bladder introduced at cystoscopy appears as a nondependent bright region with **ring-down artifact.**[18] (See Chapter 9, Fig. 9.36.)

Dirty Shadowing Artifact

Dirty shadowing results from a combination of reflection, reverberation, and ring-down artifacts arising from multiple variably sized bubbles in foam.[16]

Click here to see an explanatory video of **dirty shadowing** artifact (Video A.16).

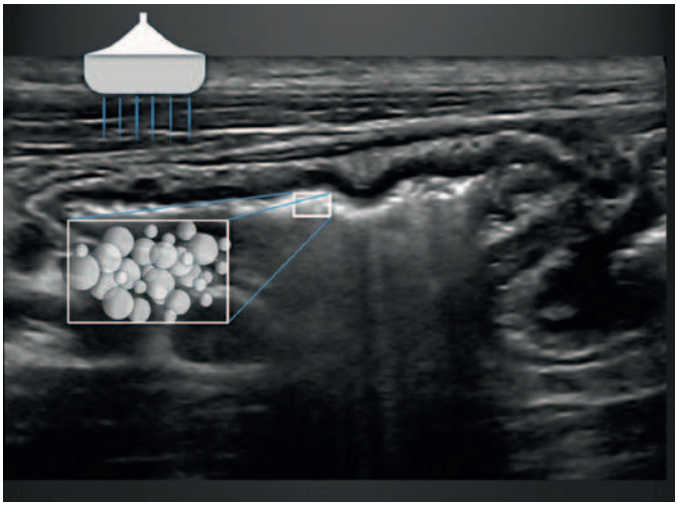

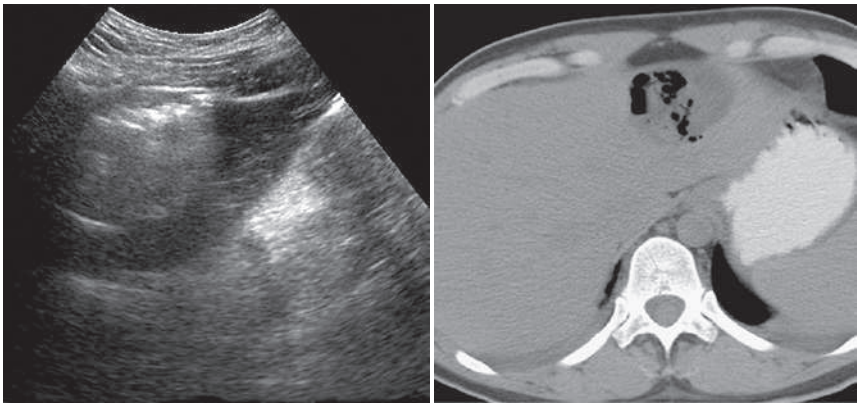

FIG. A.36 Dirty Shadowing. Sonographic image of the liver shows gas in liver mass with reverberation artifact filling the cavity. See comparison computed tomography scan.[9] (See Fig. 4.19.)

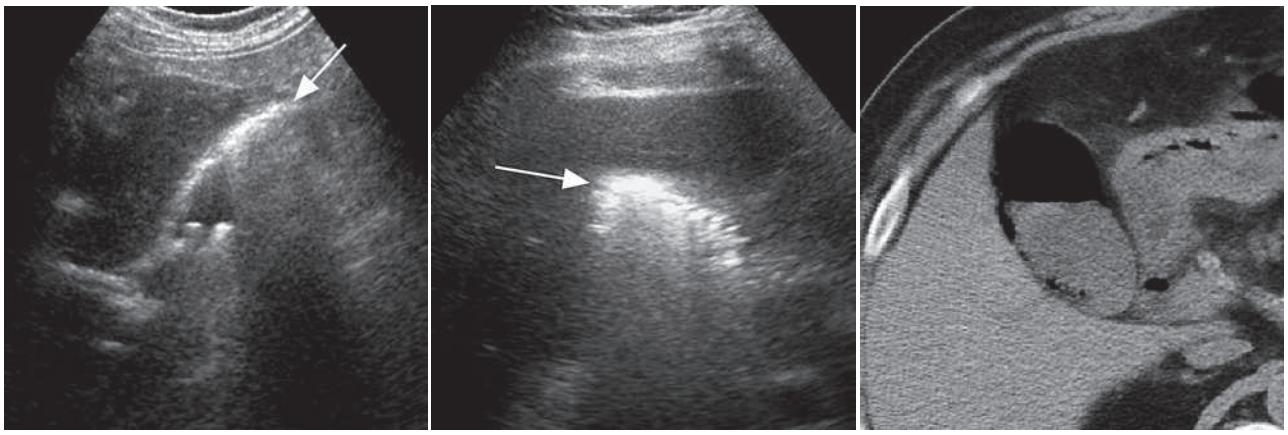

FIG. A.37 Dirty Shadowing Posterior to Emphysematous Cholecystitis.[3] (See Chapter 6, Fig. 6.40.)

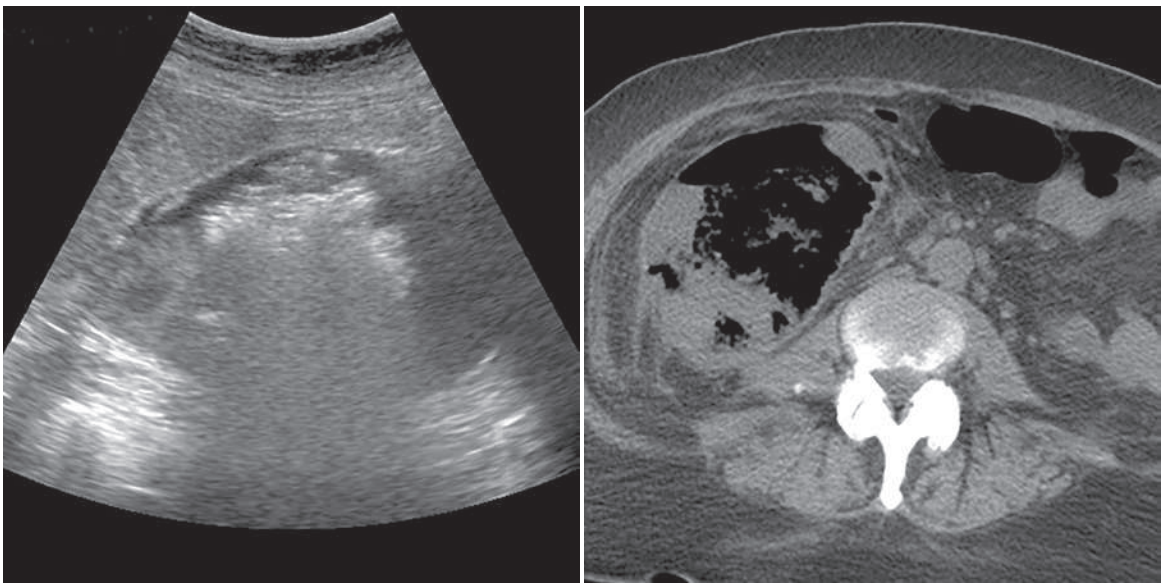

FIG. A.38 Dirty Shadowing in the Kidney Due to Emphysematous Pyelonephritis.[18] (See Chapter 9, Fig. 9.22.)

BEAM PROFILE–RELATED ARTIFACTS

Frequently echoes are seen within what should be an anechoic structure. This can occur as a result of side lobe or grating lobe artifacts in which information from the side of the image projects centrally, or because of partial volume averaging (owing to the thickness of the ultrasound beam (resolution in the Z plane).

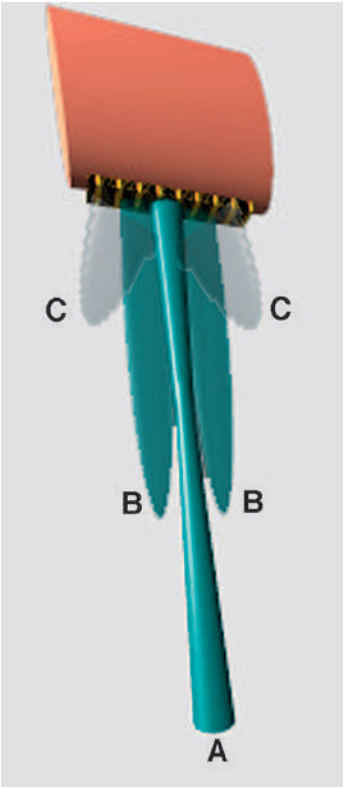

FIG. A.39 The ultrasound beam is not a narrow straight line but has a complex profile that varies depending on the type and shape of the transducer. Although most of the energy generated by a transducer is emitted in a beam along the central axis of the transducer *(A)*, some energy is also emitted at the periphery of the primary beam (*B* and *C*). These are called "side lobes" *(B)* or "grating lobes" *(C)* and are lower in intensity than the primary beam. Side lobes or grating lobes may interact with strong reflectors that lie outside of the scan plane and produce artifacts that are displayed in the ultrasound image.[2] They are more evident when the misplaced echoes overlap an expected anechoic structure. (See Chapter 1, Fig. 1.28.)

Side Lobe and Grating Lobe Artifacts

Click here to see an explanatory video of **side lobe artifact** (Video A.17).

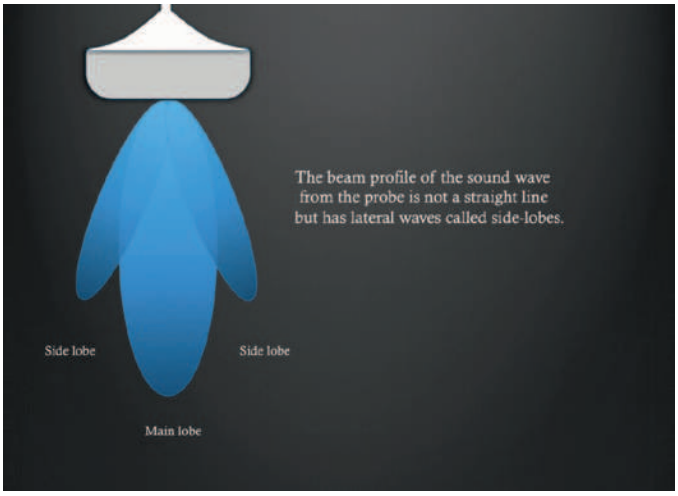

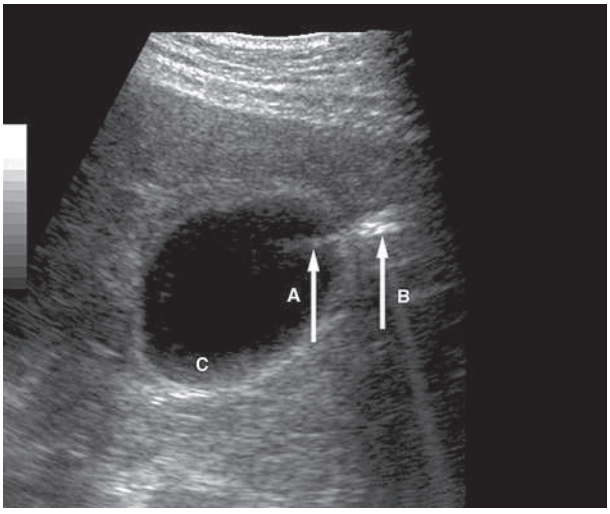

FIG. A.40 Side or Grating Lobe 1. Transverse image of the gallbladder reveals a bright internal echo *(A)* that suggests a band or septum within the gallbladder. This is a side lobe artifact related to the presence of a strong out-of-plane reflector *(B)* medial to the gallbladder. The low-level echoes in the dependent portion of the gallbladder *(C)* are also artifactual and are caused by the same phenomenon. Side lobe and slice thickness artifacts are of clinical importance because they may create the impression of debris in fluid-filled structures.[2] (See Chapter 1, Fig. 1.29.)

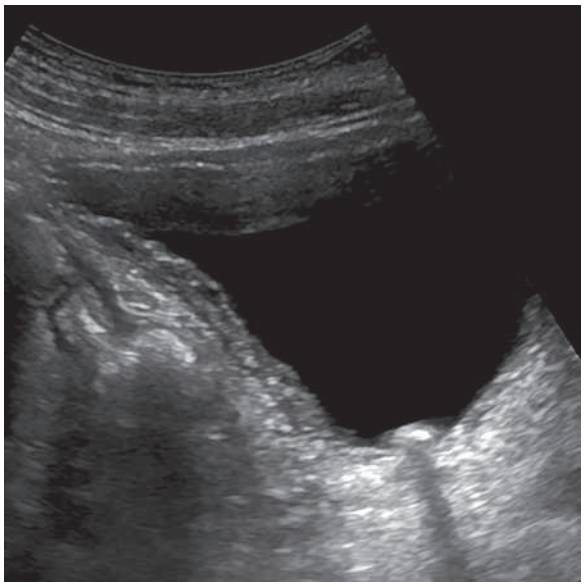

FIG. A.41 Side or Grating Lobe. In this patient with a ureterovesical junction stone there are echoes seen in the nondependent portion of the bladder. These are due to **grating lobe artifact,** wherein off-axis signal projects into the field of view.[18] Note also the **shadowing** behind the bladder stone.[18] (See Chapter 9, Fig. 9.43.)

Partial Volume Averaging

The ultrasound beam not only has a complex shape in the imaging plane but also has a real profile in the third dimension, called the "elevation plane" or "Z plane." The ultrasound image appears as a flat two-dimensional image, but the brightness of each pixel is representative of the average sum of all the echoes received within the thickness of the beam in the elevation plane. This results in echoes being projected in structures that should be anechoic.

Click here to see an explanatory video of **partial volume averaging** (Video A.18).

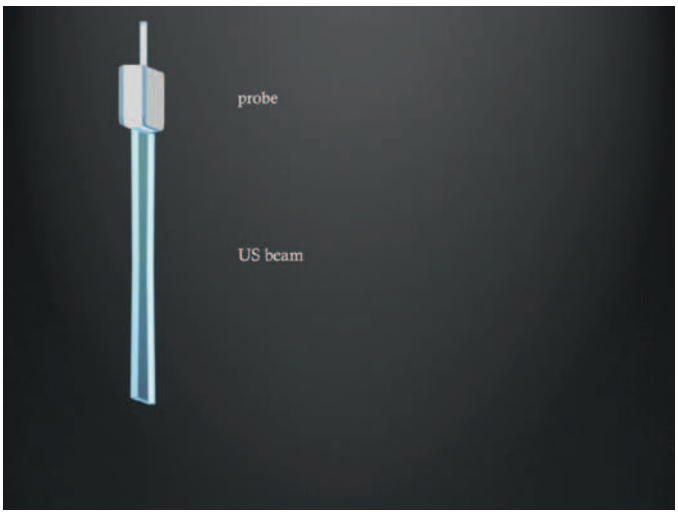

FIG. A.42 Partial Volume Averaging. The bladder wall is indistinct in region of this image. It is unclear if there are masses or if this is due to **grating lobe artifact** or **partial volume artifact** or both. Moving the patient or transducer to avoid bowel gas and putting the focal zone in the region in question should aid in evaluation. For the area closer to the patient's anterior abdominal wall, a higher-frequency transducer might be helpful.[18] (See Chapter 9, Fig. 9.57.)

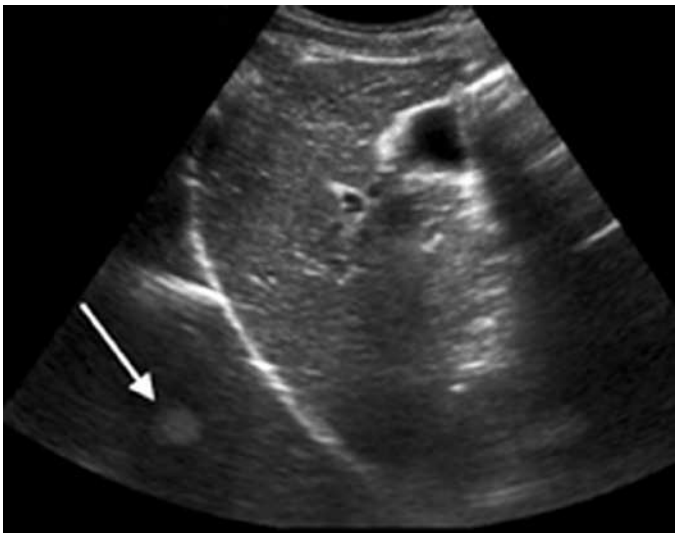

FIG. A.43 Partial Volume Averaging. A radiofrequency ablation zone present in the liver just outside the scanning plane is depicted onto the lungs through both partial volume averaging and mirror image artifacts.

DOPPLER IMAGING ARTIFACTS

The appearance of color Doppler signal is affected by several variables including color-write priority, gray-scale gain, and pulse repetition frequency. If the color gain is too low, flow might not be visualized. If the gain is too high, artifactual flow may be seen in adjacent soft tissues, and thrombus within the vessel might be missed.

Loss or Distortion of Doppler Information

Incorrect gain, wall-filter, and velocity scale can all lead to loss or distortion of Doppler signal. A rule of thumb for gain adjustment in Doppler imaging is to turn up the color gain until noise is encountered and then back off just until the noise clears from the image. In estimating frequency, the rule of thumb is to use a Doppler angle less than 60 degrees (but not 0). Wall filters eliminate low-frequency noise, but a high setting can lead to loss of signal. In general, wall filters should be kept at the lowest practical level, typically in the range of 50 to 100 Hz.

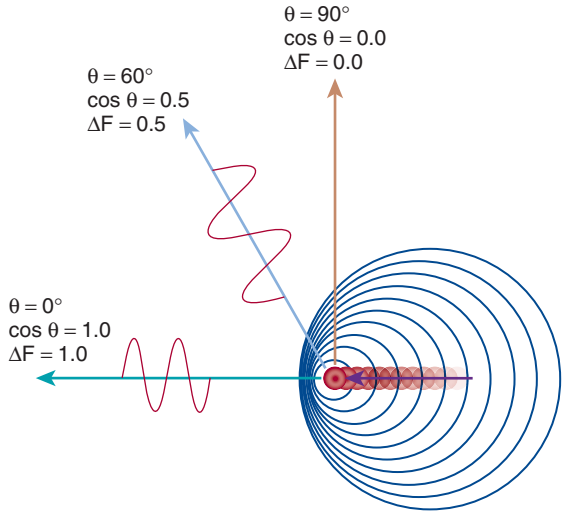

FIG. A.44 Effect of Doppler Angle on Frequency Shift. At an angle of 60 degrees, the detected frequency shift detected by the transducer is only 50% of the shift detected at an angle of 0 degrees. At 90 degrees, there is no relative movement of the target toward or away from the transducer, and no frequency shift is detected. The detected Doppler frequency shift is reduced in proportion to the cosine of the Doppler angle. Because the cosine of the angle changes rapidly at angles above 60 degrees, the use of Doppler angles of less than 60 degrees is recommended in making velocity estimates.[2] (See Chapter 1, Fig. 1.35.)

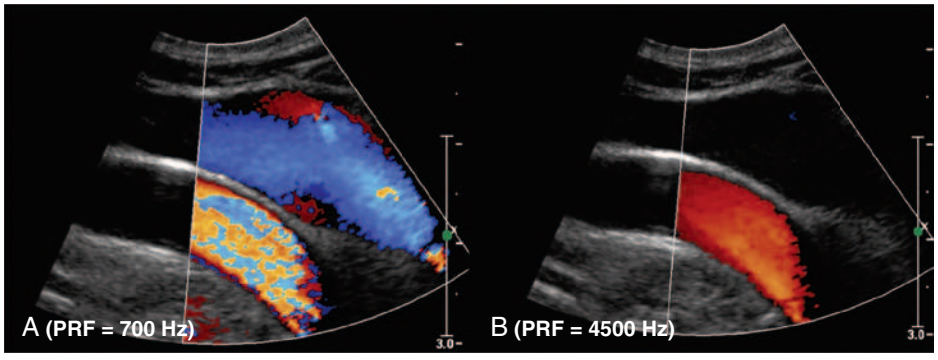

FIG. A.45 Artifactual Lack of Flow. Color Doppler image of a carotid artery and jugular vein. In **(A),** the pulse repetition frequency *(PRF)* is 700 Hz and there is aliasing in the carotid artery, but slow flow in the jugular vein is seen. In **(B),** the PRF is 4500 Hz, eliminating aliasing in the artery but also suppressing the display of the low Doppler frequencies in the internal jugular vein.[2] (See Chapter 1, Fig. 1.43.)

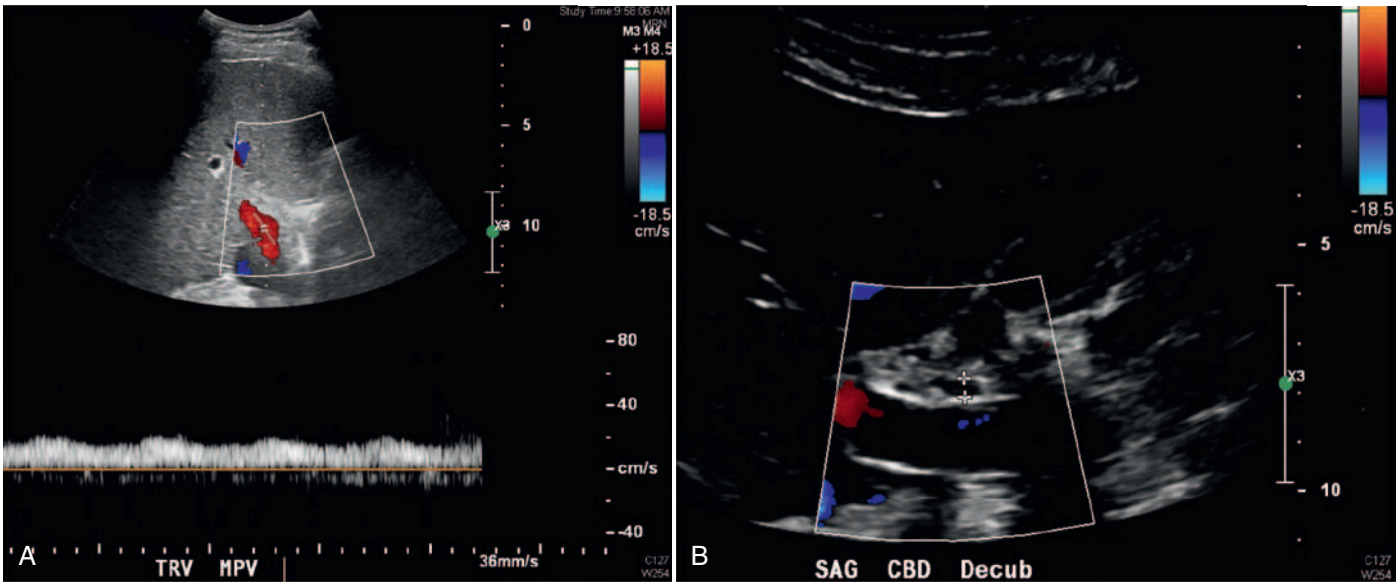

FIG. A.46 Artifactual Lack of Flow. (A) Color Doppler image shows flow in the portal vein. **(B)** When a color image is taken to assess the common duct, no flow is visible in the portal vein. Note the difference in overall gain in image **B.**

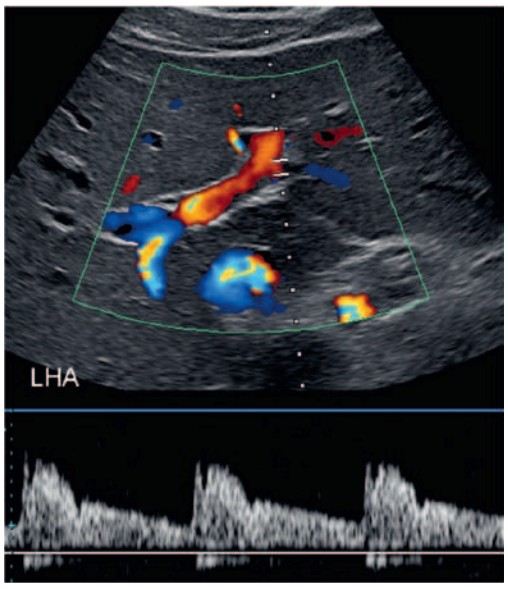

FIG. A.47 Color Direction. Shown in color is a portion of the portal venous system. Note how the flow direction appears to change in the region of branching, but this is merely a result of the orientation of flow with respect to the mid transducer. Note the aliasing in the posterior branch of the right portal vein. This is due to the curve of the vein and change in Doppler angle.[19] (See Chapter 51, Fig. 51.22.)

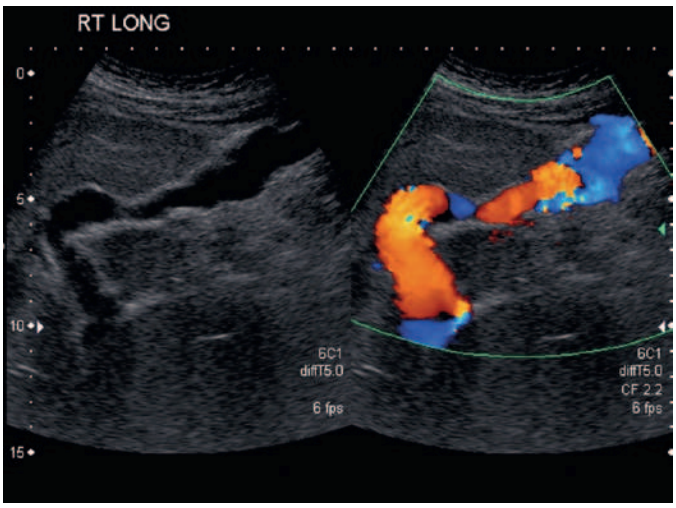

FIG. A.48 Color Direction as Shown in Recanalized Umbilical Vein. Flow on color Doppler will sometimes appear to change direction, but the flow needs to be assessed with respect to the transducer in order to determine if it is in the appropriate direction or not. In this example, transverse paramedian gray-scale and color Doppler sonograms show left lobe of liver in a child with cirrhosis and portal hypertension.[19] The recanalized umbilical vein is always flowing in relatively the same direction out of the liver, but at times, due to tortuosity, appears to change flow direction. Note that the flow changes from red (toward the transducer) to blue (away from the midpoint of the transducer), but at each interface there is a black region where the Doppler angle is 90. (See Chapter 51, Fig. 51.28.)

Artifactual Vascular Flow

The Doppler effect (shift) is not specific to vascular flow and occurs with movement of any reflector toward or away from the ultrasound beam. Fluid or solid tissue motion can mimic vascular flow. Transmitted pulsations, especially close to the heart or major arteries, can therefore result in artifactual appearance of flow within thrombosed veins or avascular areas. Artifactual vascular flow can also be visualized if the color gain is too high or the color-write priority is too high.

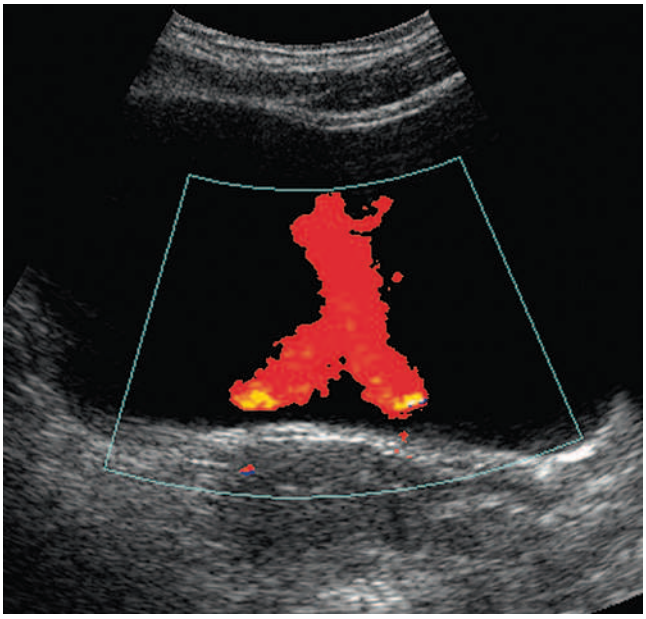

FIG. A.49 Artifactual Vascular Flow. Color Doppler jets in the bladder use color motion to indicate that there is flow from each ureteral orifice.[18] (See Chapter 9, Fig. 9.42A.)

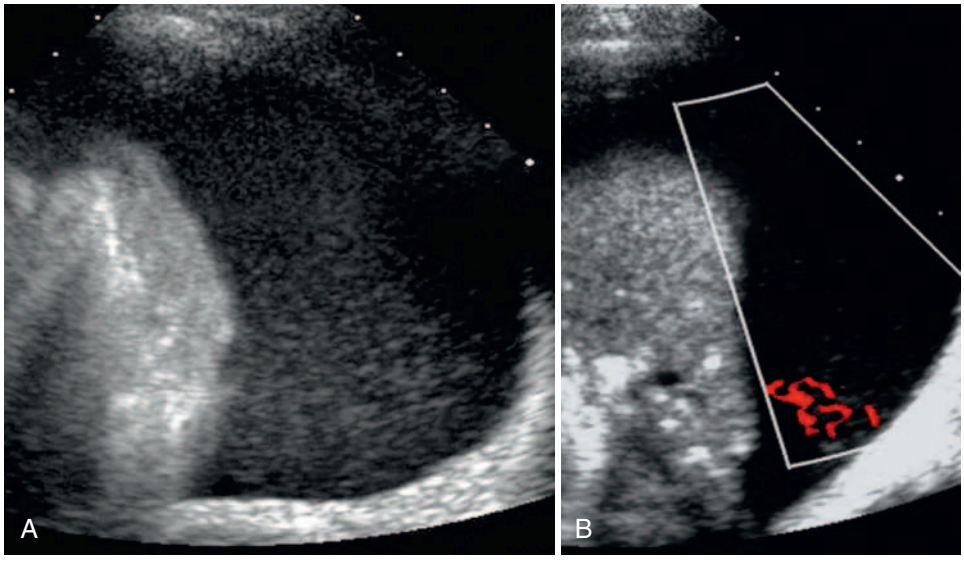

FIG. A.50 Artifactual Vascular Flow. Color flow Doppler signal in pleural fluid with debris. **(A)** Gray-scale sonogram shows left pleural fluid with much debris. **(B)** Color flow Doppler signal.[20] (See Chapter 50, Fig. 50.14.)

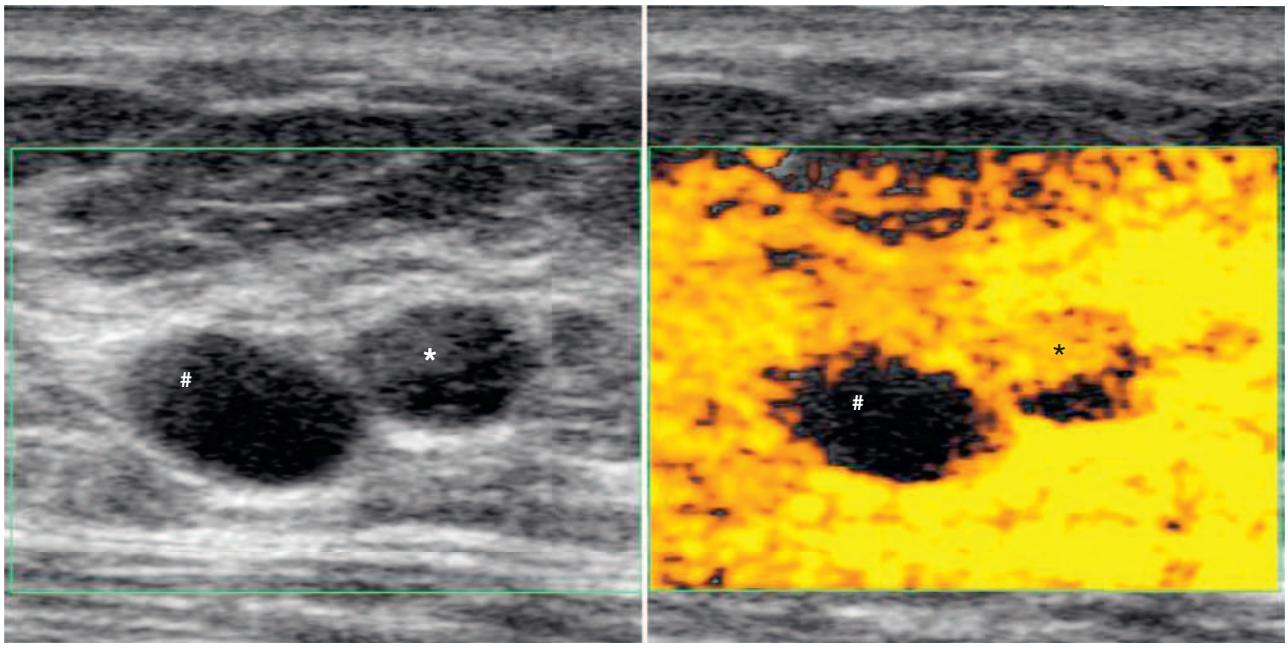

FIG. A.51 Artifactual Vascular Flow. Power Doppler ultrasound **vocal fremitus** can be used to distinguish a mural nodule from a fat-fluid level. The lipid layer is not attached to the cyst wall, so the fremitus artifact will not pass through it. On the other hand, true papillary lesions that are attached to the cyst wall will vibrate and transmit the fremitus artifact on power Doppler; having the patient hum in a deep voice creates a color artifact on power Doppler ultrasound.[21] (See Chapter 21, Fig. 21.26.)

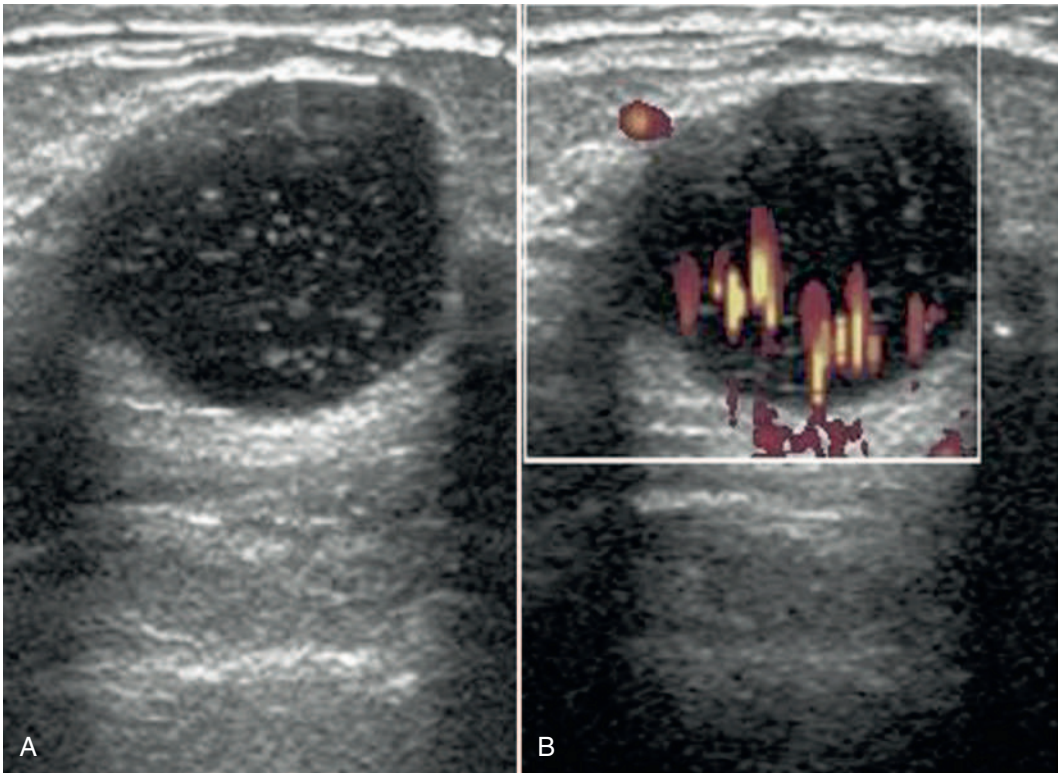

FIG. A.52 Color Streaking Artifact. (A) This complicated cyst contains floating punctate echoes that move posteriorly while being scanned, creating a scintillating appearance on gray-scale sonography. **(B)** Power Doppler ultrasound pushes the echoes posteriorly faster and with more energy than does the gray-scale beam. The echoes move fast enough that color persistence creates the appearance of **"color streaking"** artifact.[21] (See Chapter 21, Fig. 21.21.)

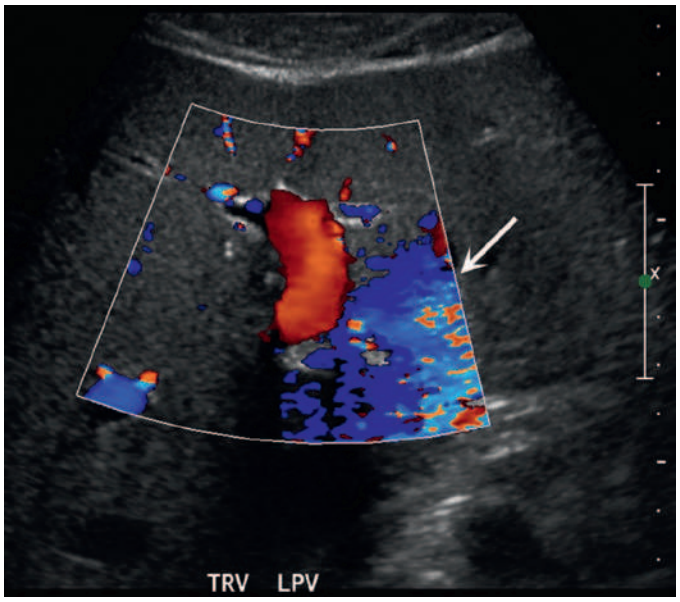

FIG. A.53 Flash Artifact From Pulsation. In this image of the left portal vein, note how transmitted pulsation from the heart causes artifactual flow in the adjacent liver owing to motion.

Tissue Vibration Artifact

Tissue vibration artifact consists of color pixels erroneously placed in the adjacent soft tissue by the ultrasound scanner because of the transmitted vibration from a region of marked turbulence. It is commonly seen with shunts, tight stenoses of large arteries, and especially arteriovenous fistulas. If tissue vibration artifact is seen, a search should be made for an arteriovenous fistula.

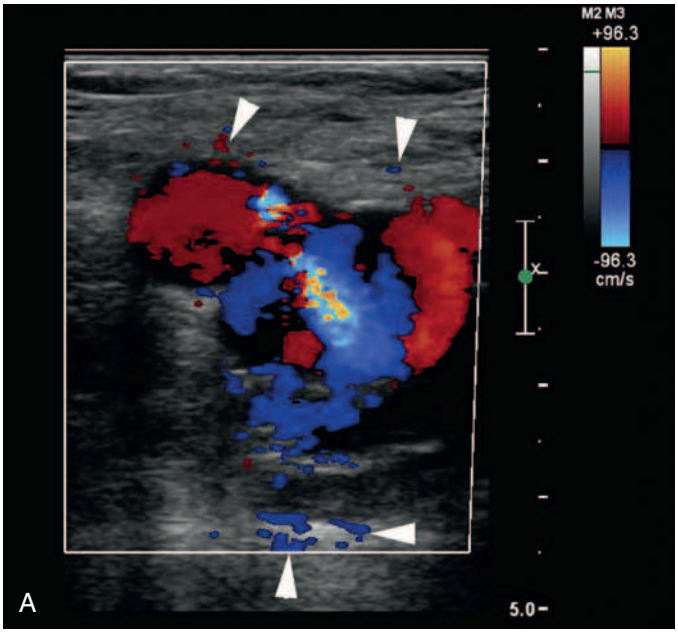

FIG. A.54 Tissue Vibration Artifact From Common Femoral Artery to Common Femoral Vein Arteriovenous Fistula. Turbulent flow through the fistula may affect surrounding tissues, causing a tissue vibration artifact, which may be the first clue that an arteriovenous fistula (AVF) is present. **Common femoral artery to common femoral vein AVF. (A)** Color Doppler shows common femoral artery to common femoral vein AVF. Note the adjacent tissue vibration artifact *(arrowheads)*. (See Chapter 27, Fig. 27.14.)

Click here to see the video of **tissue vibration** (Video A.19).

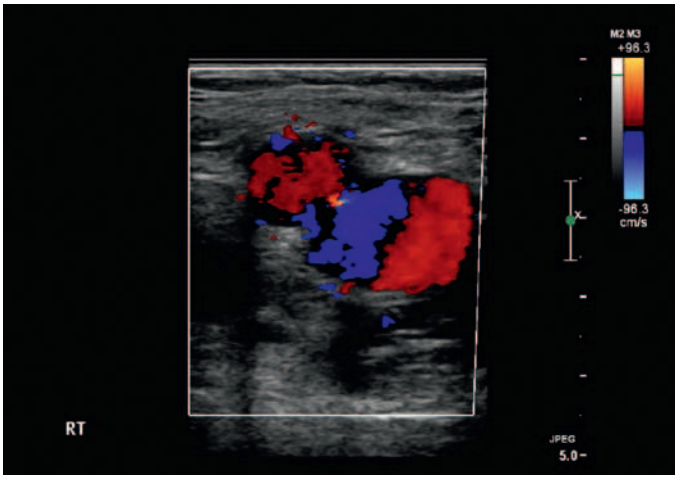

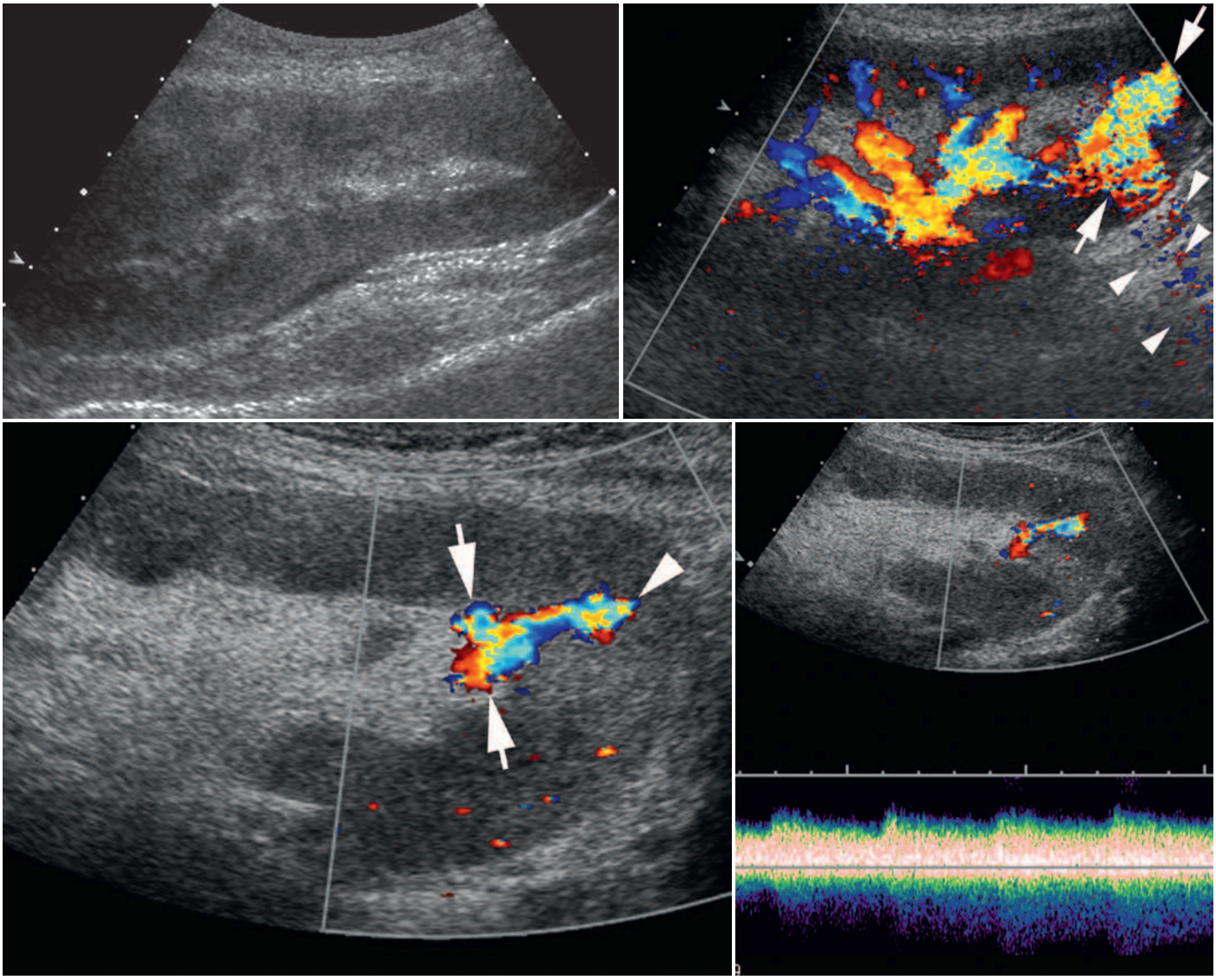

FIG. A.55 Tissue Vibration Artifact. Postbiopsy arteriovenous fistula. Color Doppler image shows markedly increased lower-pole blood flow *(arrows)* with adjacent soft tissue color artifact related to tissue vibration *(arrowheads)*.[22] (See Chapter 52, Fig. 52.49.)

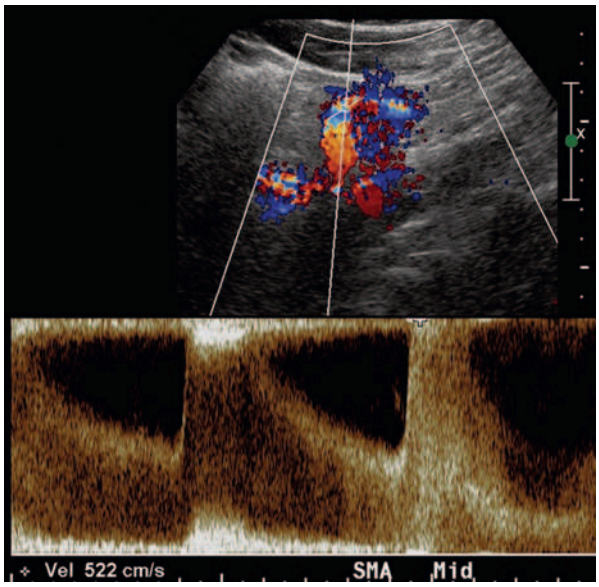

FIG. A.56 Tissue Vibration Artifact. Spectral waveform at site of superior mesenteric artery stenosis shows very high systolic velocity, and diastolic velocities of greater than 500 cm/sec. Color portion of the image shows **color bruit** consisting of color outside the vessel near the stenosis site. Color bruit is believed to be caused by tissue vibration.[23] (See Chapter 12, Fig. 12.27A.)

Click for video showing **tissue vibration artifact** in patient with **stenotic superior mesenteric artery with color bruit** (Video A.20). (See also Video 12.11.)

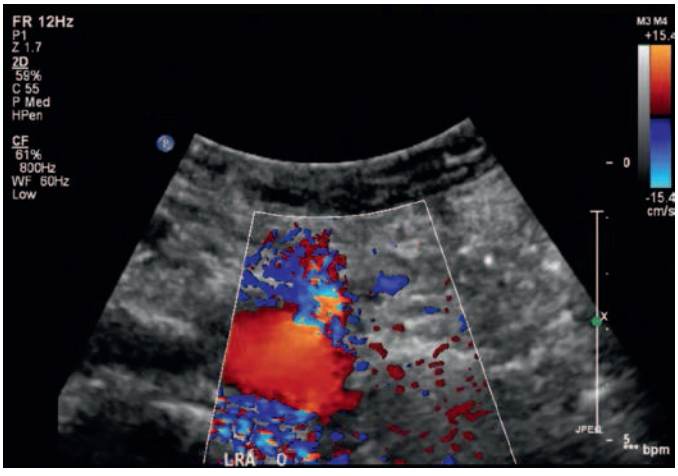

Aliasing and Velocity Scale Errors

Aliasing is an artifact due to undersampling of Doppler signal, resulting in incorrect estimation of flow velocity. To measure the Doppler frequency shift appropriately by pulsed Doppler, at least two samples from the cycle are required (Nyquist limit). If the pulse repetition frequency is less than twice the maximum frequency shift produced by movement of the target, aliasing results. The Doppler signal wraps around either the spectrum (spectral Doppler) or the color scale (color Doppler). The most common methods for correcting for aliasing are to shift the baseline down or up, or increase the pulse repetition frequency (or velocity scale). A lower-frequency transducer can also be used to help in correcting for aliasing. As angulation approaches 90 degrees, directional ambiguity can occur, suggesting bidirectional flow. Errors in Doppler angle correction can also lead to misleading assessments of flow velocity.

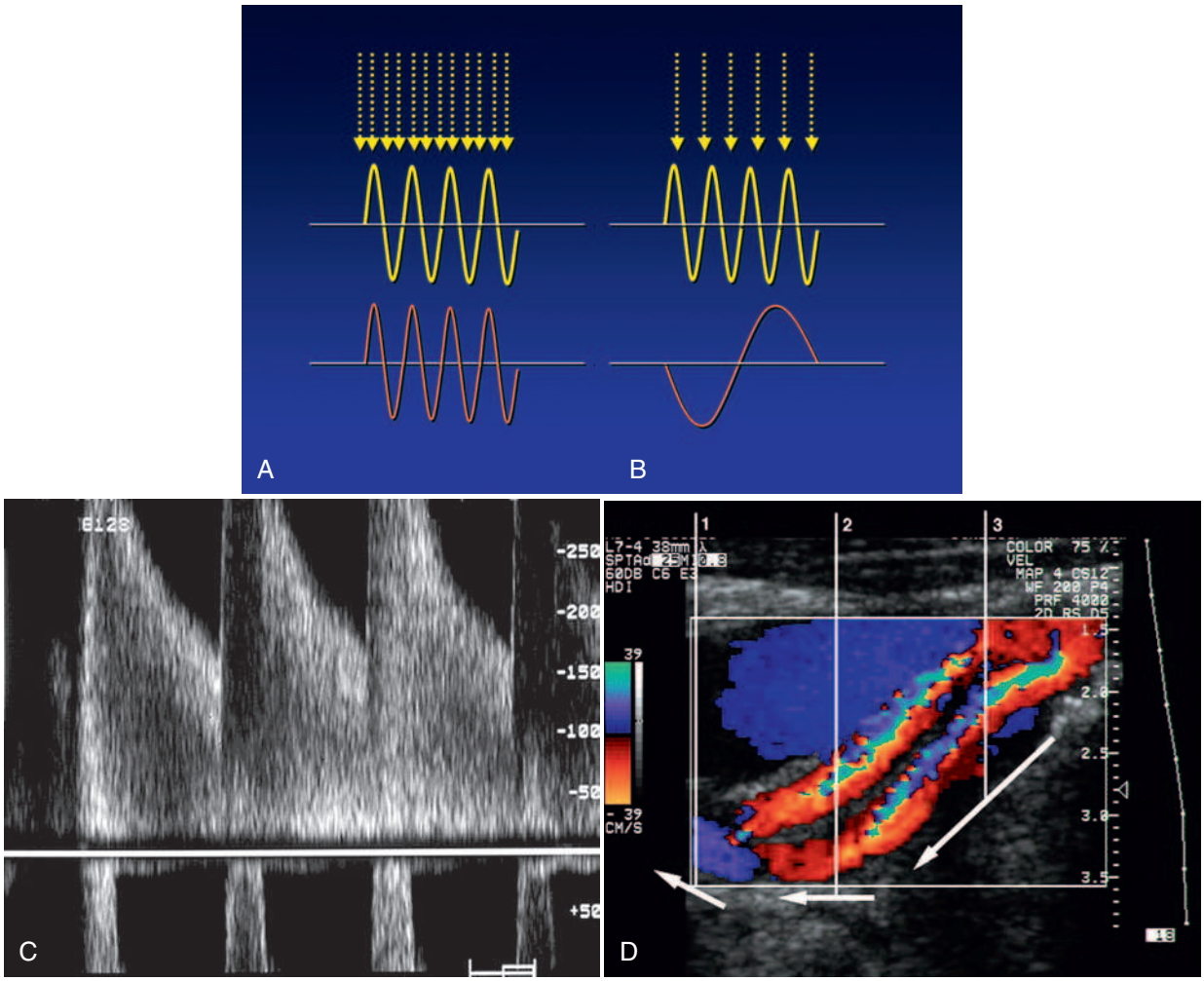

FIG. A.57 Aliasing. Pulse repetition frequency (PRF) determines the sampling rate of a given Doppler frequency. **(A)** If PRF *(arrows)* is sufficient, the sampled waveform *(orange curve)* will accurately estimate the frequency being sampled *(yellow curve)*. **(B)** If PRF is less than half the frequency being measured, **undersampling** will result in a lower-frequency shift being displayed *(orange curve)*. **(C) Aliasing** appears in the spectral display as a "wraparound" of the higher frequencies to display below the baseline. **(D)** In color Doppler display, aliasing results in a wraparound of the frequency color map from one flow direction to the opposite direction.[2] Unlike a true direction of flow change, with aliasing there will be no transition of unsaturated color. (See Chapter 1, Fig. 1.46.)

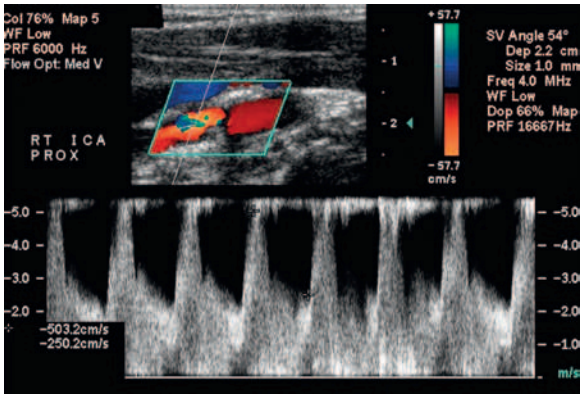

FIG. A.58 Aliasing. Note that aliasing prevents precise calculation of the maximum systolic velocity. However, because it is greater than 500 cm/sec, the precise number is not needed. The aliasing in the image allows for easier identification of the region of highest velocity for placement of the spectral Doppler gate.[6] (See Chapter 26, Fig. 26.20.)

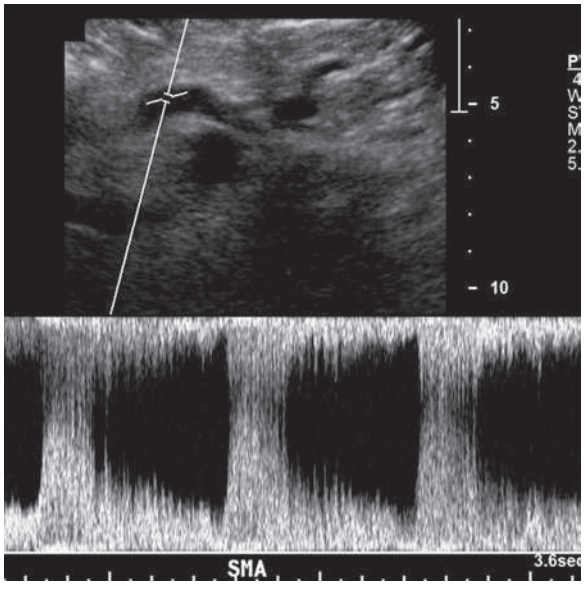

FIG. A.59 Aliasing in Superior Mesenteric Artery (*SMA*) Due to High-Velocity Flow.[23] (See Chapter 12, Fig. 12.28.)

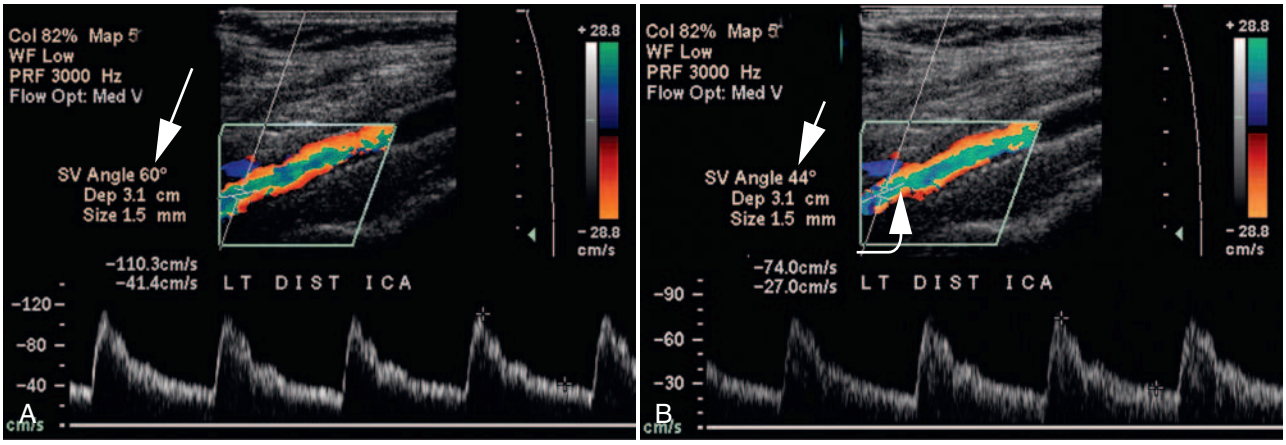

FIG. A.60 Aliasing Due to Doppler Angle Theta Changes. (A) Velocity obtained in the distal internal carotid artery with angle theta of 60 degrees is higher than that obtained at 44 degrees *(arrow)*. **(B)** However, the sample angle does not parallel the vessel wall at 60 degrees. Note central color aliasing in the region of highest velocity *(curved arrow)*.[6] (See Chapter 26, Fig. 26.16.)

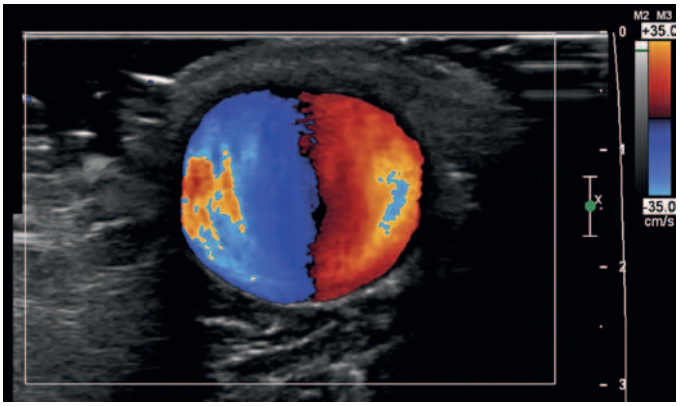

FIG. A.61 Aliasing in Pseudoaneurysm. Note the swirling flow in a pseudoaneurysm, resulting in a yin-yang appearance.[24] At the midline border of red and blue, there is a black line where the Doppler angle is 90 degrees. Here the flow is perpendicular to the sound beam, and so it is not detected. At 3 and 9 o'clock positions, there is aliasing within the blue and red areas. Here the Doppler angle is zero degrees with the flow directly toward and away from the transducer, thus appearing with maximal velocity. As the velocity exceeds the selected 35-cm/sec Doppler velocity range, aliasing results with artifactual opposite direction color signal. (See Chapter 27, Fig. 27.63.)

Click here to see the pseudoaneurysm video clip showing even more dramatic aliasing in the femoral artery (Video A.21).[24] (See also Chapter 27, Video 27.5.)

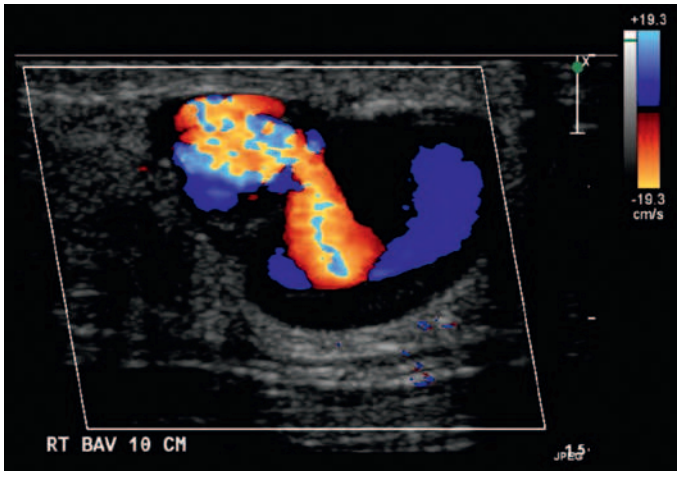

Spectral Broadening

Spectral broadening occurs when there are multiple different velocities of flow within a vessel. This can be a sign of stenosis. However, artifactual spectral broadening can occur owing to improper positioning of the sample volume near the vessel wall, use of an excessively large sample volume, or excessive system gain.

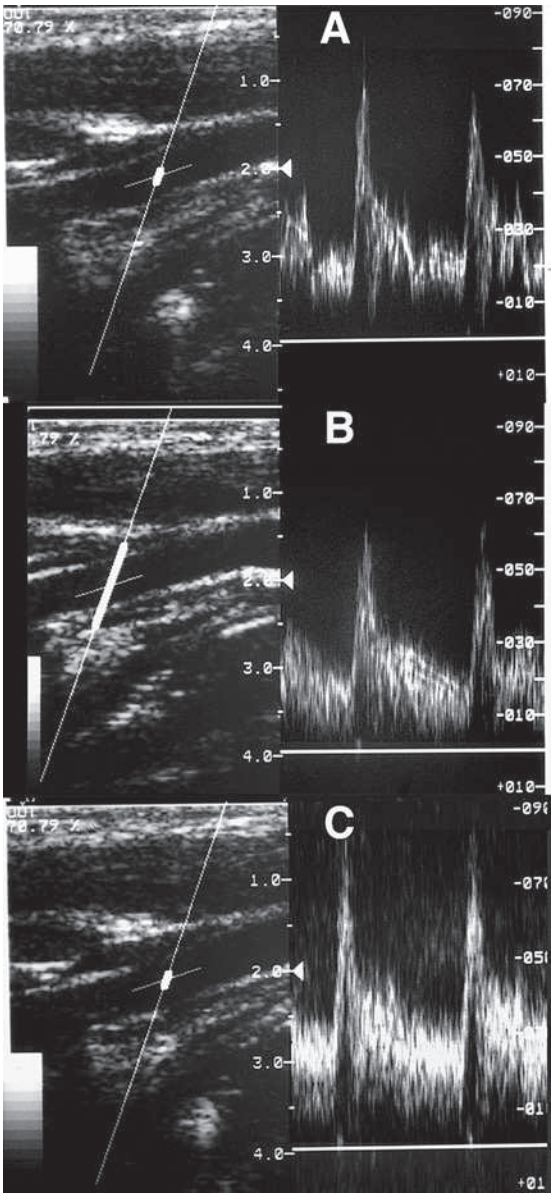

FIG. A.62 Spectral Broadening. The range of velocities detected at a given time in the pulse cycle is reflected in the Doppler spectrum as spectral broadening. **(A) Normal spectrum.** Spectral broadening may arise from turbulent flow in association with vessel stenosis. **(B** and **C) Artifactual spectral broadening** may be produced by improper positioning of the sample volume near the vessel wall, use of an excessively large **sample volume (B), or excessive system gain (C).**[2] (See Chapter 1, Fig. 1.45.)

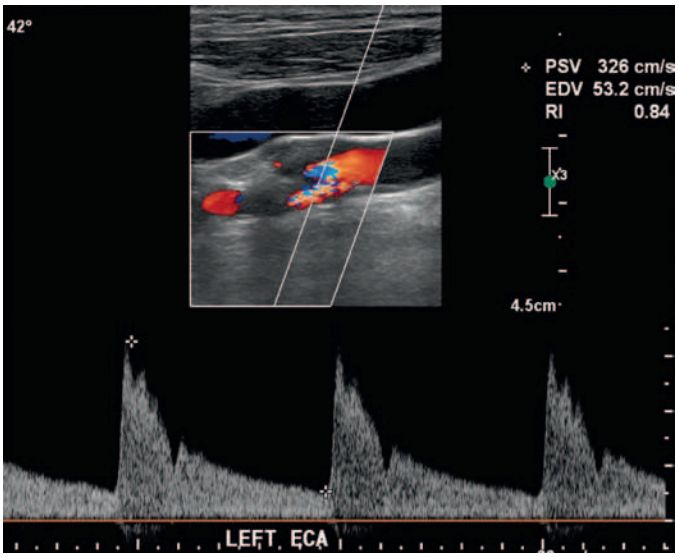

FIG. A.63 Spectral Broadening. True spectral broadening due to ECA stenosis.[6] (See Chapter 26, Fig. 26.18.)

Blooming Artifact

Blooming artifact occurs when color reaches beyond the vessel wall, making the vessels look larger than expected. It is gain dependent in that lowering the gain will decrease blooming. It is also wall filter and color-overwrite dependent, in that increasing the wall filter will decrease the artifact.

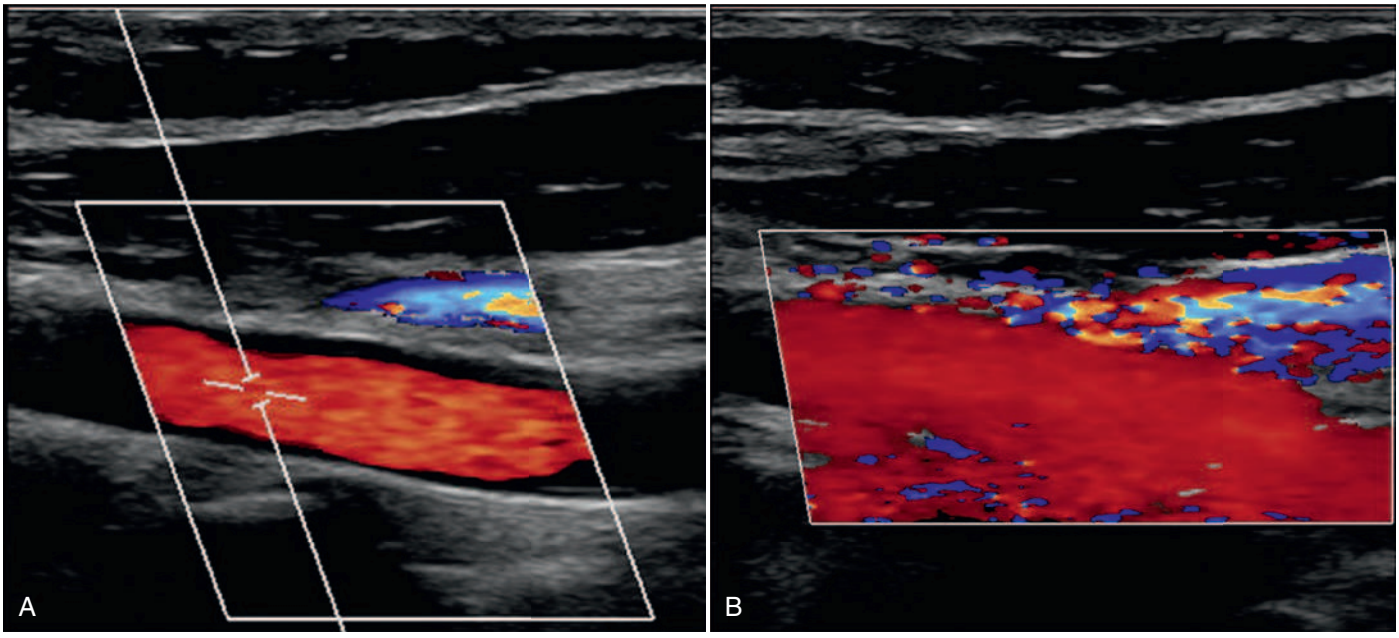

FIG. A.64 Blooming Artifact. Two images of the same carotid artery. In **(A)** the gain and wall filter are appropriate to show the flow centrally in the vessel. In **(B)** the gain and wall filter have been changed (in a manner beyond what would be used in clinical imaging) to demonstrate how these can make the vessel "bloom" and appear larger.

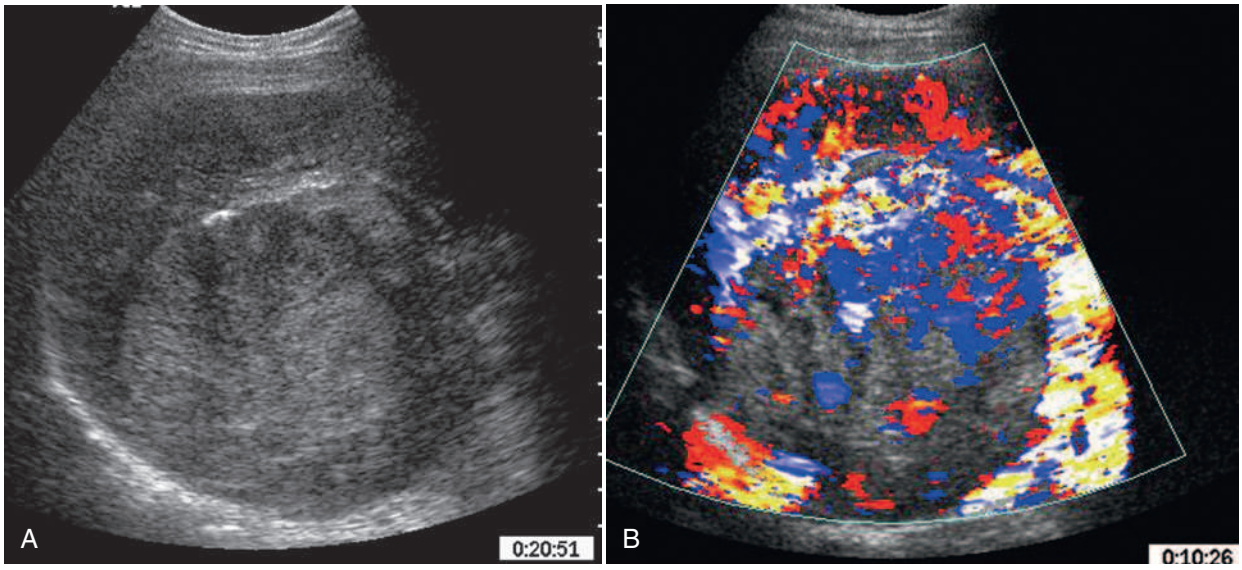

FIG. A.65 Blooming artifact due to use of contrast and tissue motion. **(A)** Use of contrast material creates color Doppler artifacts owing to blooming and tissue motion. **(B)** Contrast-specific imaging shows blood vessels not seen with Doppler.[25] (See Chapter 3, Fig. 3.7.)

Twinkle Artifact

Twinkle artifact is the artifactual depiction of color signal on crystalline materials in the body. It appears as discrete foci of alternating colors with or without an associated color comet-tail artifact. The appearance of twinkle artifact is highly dependent on machine settings and is likely generated by a narrow-band, intrinsic machine noise called "phase (or clock) jitter." This, along with a strongly reflecting, rough surface such as a renal stone, results in a high-amplitude, broadband signal appearing as random motion on color Doppler sonography. The twinkle artifact is quite useful clinically because it can aid in the detection of small stones, calcifications, and other crystalline material within the body.

View the PowerPoint illustration of **twinkle artifact** here (Video A.22).

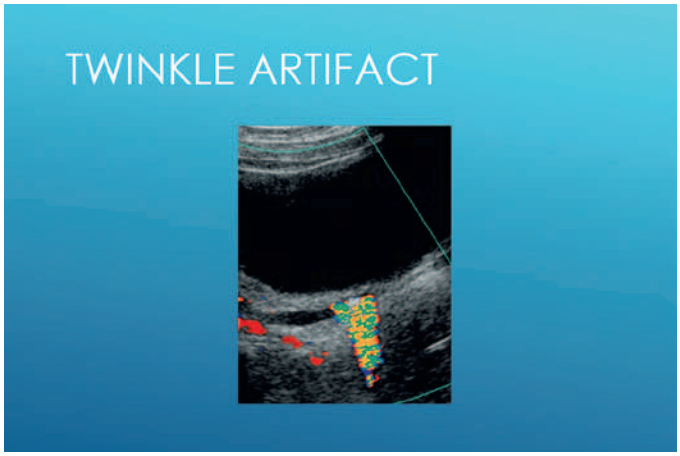

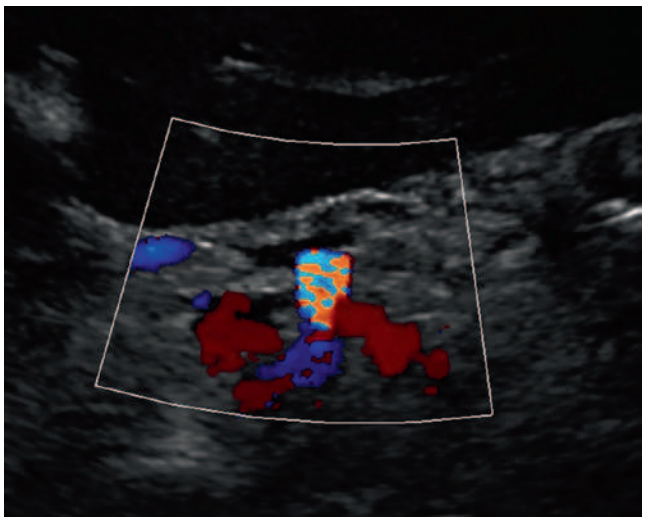

FIG. A.66 Twinkle Artifact Posterior to Pancreatic Duct Stone.[26] (See Chapter 7, Fig. 7.48D.)

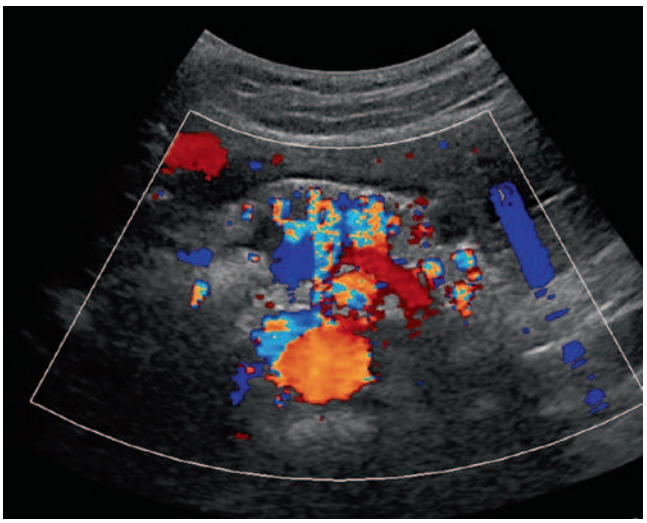

FIG. A.67 Calcifications in Chronic Pancreatitis With Twinkle Artifact.[26] (See Chapter 7, Fig. 7.49B.)

Click here for associated cine clip (Video A.23).[26] (See also Chapter 7, Video 7.5.)

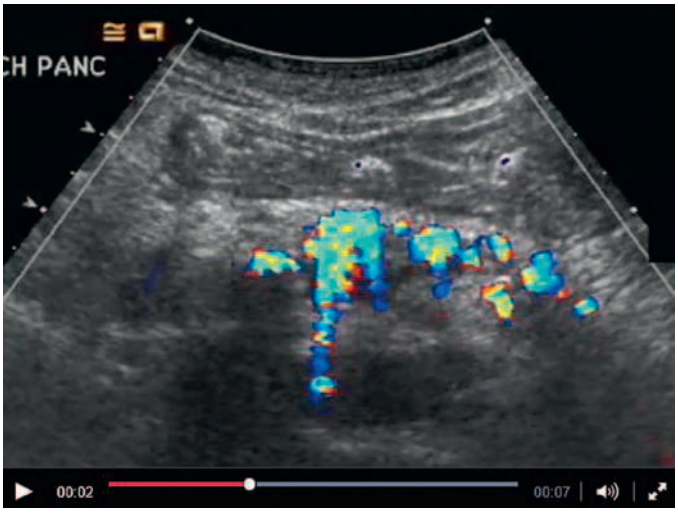

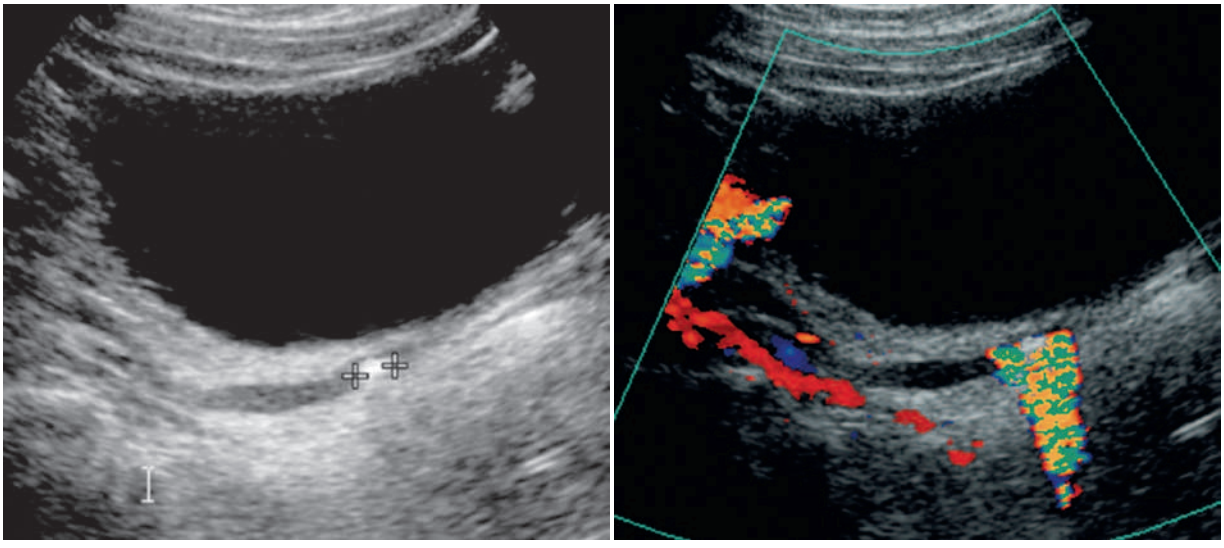

FIG. A.68 Twinkle Behind Distal Ureterovesical Junction Stone.[27] (See Chapter 54, Fig. 54.61.)

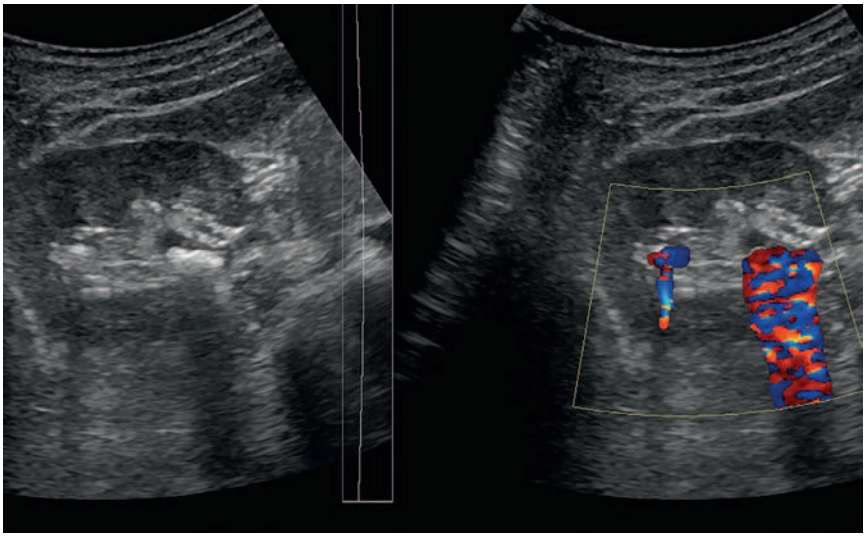

FIG. A.69 Twinkle Behind a Kidney Stone.[18] (See Chapter 9, Fig. 9.38.)

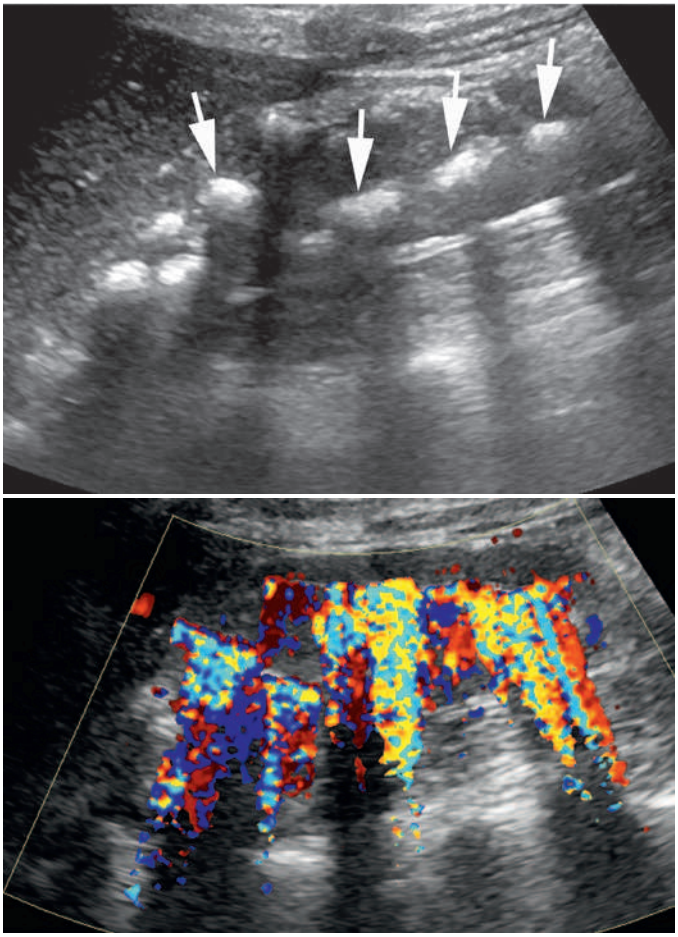

FIG. A.70 Twinkle Behind Multiple Kidney Stones.[22] (See Chapter 52, Fig. 52.37.)

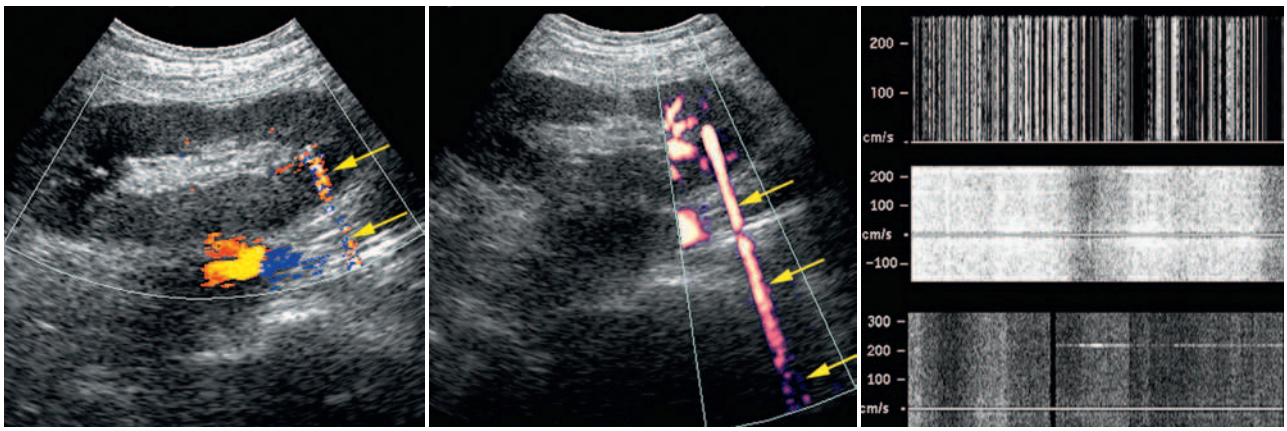

FIG. A.71 Appearances of Twinkle Artifact on Color, Power, and Pulsed Wave Doppler. Note how the spectral Doppler tracing of a twinkle artifact shows lines going through the tracing, which allow distinction from true blood flow.[28] (See Chapter 18, Fig. 18.52.)

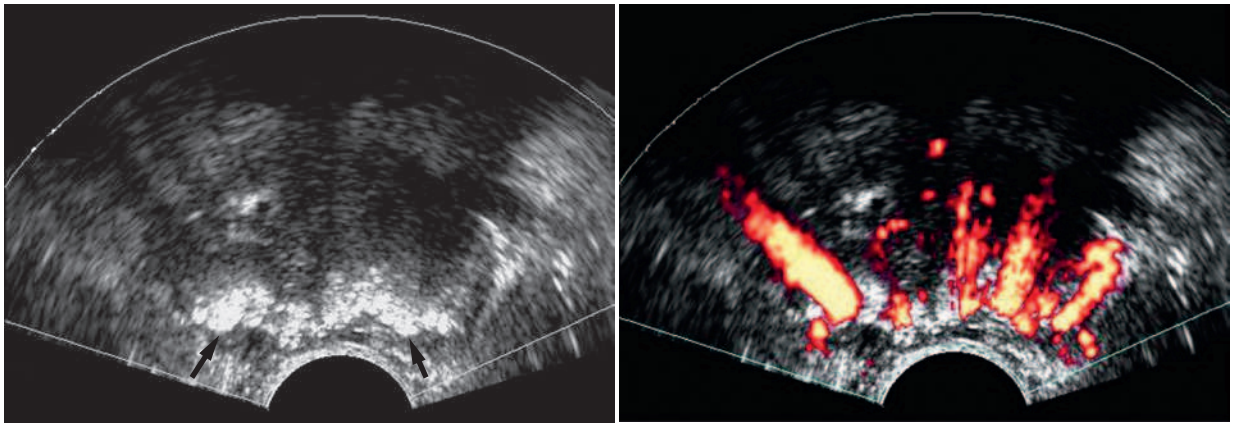

FIG. A.72 Power Doppler Image of Twinkle Behind Prostatic Calcifications.[11] (See Chapter 10, Fig. 10.7.)

Acknowledgment

Most of the images in this virtual chapter were obtained from chapters in the fifth edition of Diagnostic Ultrasound. We thank the authors for the use of their work.

REFERENCES

1. Hoskins P, Martin K, Thrush A. Diagnostic ultrasound: physics and equipment. 2nd ed. Cambridge, UK: Cambridge University Press; 2010.
2. Merritt C. Physics of ultrasound. In: Levine D, Rumack C, editors. Diagnostic ultrasound. 5th ed. Philadelphia: Elsevier; 2017.
3. Khalili K, Wilson S. The biliary tree and gallbladder. In: Levine D, Rumack C, editors. Diagnostic ultrasound. 5th ed. Philadelphia: Elsevier; 2017.
4. Brown D, Levine D. The uterus. In: Levine D, Rumack C, editors. Diagnostic ultrasound. 5th ed. Philadelphia: Elsevier; 2017.
5. Castro I, Levine D, Rumack C. The pediatric spinal canal. In: Levine D, Rumack C, editors. Diagnostic ultrasound. 5th ed. Philadelphia: Elsevier; 2017.
6. Bluth E, Troxclair L, Johnson S. The extracranial cerebral vessels. In: Levine D, Rumack C, editors. Diagnostic ultrasound. 5th ed. Philadelphia: Elsevier; 2017.
7. Toi A, Levine D. The fetal brain. In: Levine D, Rumack C, editors. Diagnostic ultrasound. 5th ed. Philadelphia: Elsevier; 2017.
8. Feldman MK, Katyal S, Blackwood MS. US artifacts. Radiographics. 2009;29(4):1179-1789.
9. Wilson S, Withers C. The liver. In: Levine D, Rumack C, editors. Diagnostic ultrasound. 5th ed. Philadelphia: Elsevier; 2017.
10. Solbiati L, Charboneau J, Reading C, et al. The thyroid gland. In: Levine D, Rumack C, editors. Diagnostic ultrasound. 5th ed. Philadelphia: Elsevier; 2017.
11. Toi A. The prostate and transrectal ultrasound. In: Levine D, Rumack C, editors. Diagnostic ultrasound. 5th ed. Philadelphia: Elsevier; 2017.
12. Vandeman FN, Meilstrup JW, Nealey PA. Acoustic prism causing sonographic duplication artifact in the upper abdomen. Invest Radiol. 1990;25(6): 658-663.
13. McMahon C, Yablon C. Overview of musculoskeletal ultrasound techniques and applications. In: Levine D, Rumack C, editors. Diagnostic ultrasound. 5th ed. Philadelphia: Elsevier; 2017.
14. DiPietro MA, Brody BA, Teele RL. Peritrigonal echogenic "blush" on cranial sonography: pathologic correlates. AJR Am J Roentgenol. 1986;146(5): 1067-1072.
15. McMahon C, Yablon C. The shoulder. In: Levine D, Rumack C, editors. Diagnostic ultrasound. 5th ed. Philadelphia: Elsevier; 2017.
16. Wilson SR, Burns PN, Wilkinson LM, et al. Gas at abdominal US: appearance, relevance, and analysis of artifacts. Radiology. 1999;210(1):113-123.
17. Avruch L, Cooperberg PL. The ring-down artifact. J Ultrasound Med. 1985;4(1):21-28.
18. Tublin M, Levine D, Thurston W, Wilson S. The kidney and urinary tract. In: Levine D, Rumack C, editors. Diagnostic ultrasound. 5th ed. Philadelphia: Elsevier; 2017.
19. O'Hara S. The pediatric liver and spleen. In: Levine D, Rumack C, editors. Diagnostic ultrasound. 5th ed. Philadelphia: Elsevier; 2017.
20. Shah C, Greenberg S. The pediatric chest. In: Levine D, Rumack C, editors. Diagnostic ultrasound. 5th ed. Philadelphia: Elsevier; 2017.
21. Phillips J, Mehta R. The breast. In: Levine D, Rumack C, editors. Diagnostic ultrasound. 5th ed. Philadelphia: Elsevier; 2017.
22. Paltiel H, Babcock D. The pediatric kidney and adrenal glands. In: Levine D, Rumack C, editors. Diagnostic ultrasound. 5th ed. Philadelphia: Elsevier; 2017.
23. Bertino R, Mustafaraj E. The retroperitoneum. In: Levine D, Rumack C, editors. Diagnostic ultrasound. 5th ed. Philadelphia: Elsevier; 2017.
24. Lockhart M, Umphrey H, Weber T, Robbin M. Peripheral vessels. In: Levine D, Rumack C, editors. Diagnostic ultrasound. 5th ed. Philadelphia: Elsevier; 2017.
25. Burns P. Contrast agents for ultrasound imaging and Doppler. In: Levine D, Rumack C, editors. Diagnostic ultrasound. 5th ed. Philadelphia: Elsevier; 2017.
26. Winter T, Sun M. The pancreas. In: Levine D, Rumack C, editors. Diagnostic ultrasound. 5th ed. Philadelphia: Elsevier; 2017.
27. Kotlus Rosenberg H, Simpson Jr W, Chaudhry H. Pediatric pelvic sonography. In: Levine D, Rumack C, editors. Diagnostic ultrasound. 5th ed. Philadelphia: Elsevier; 2017.
28. Muradali D, Chawla T. Organ transplantation. In: Levine D, Rumack C, editors. Diagnostic ultrasound. 5th ed. Philadelphia: Elsevier; 2017.

Index

A
AA anastomoses. *See* Arterial/arterial anastomoses
AAA. *See* Abdominal aortic aneurysm
Aase syndrome, 1401
Abciximab, 598
Abdomen. *See also* Acute abdomen
  abscess of, drainage of, 612, 613*f*
  blunt trauma to, small bowel obstruction from, 1843
  calcifications of, meconium peritonitis and, 1313, 1314*f*
  ectopic pregnancy implantation in, 1074, 1075*f*
  fetal
    circumference of, in gestational age determination, 1448, 1450*f*
    circumference of, in second-trimester, 1023*f*
    musculature of, absent, in prune belly syndrome, 1361–1362
    routine sonographic views of, 1021, 1026*f*
  lymphangiomas of, pediatric, 1862, 1864*f*
  pediatric, systemic veins of, flow patterns in, 1750
Abdominal aorta. *See also* Iliac veins; Inferior vena cava; Mesenteric artery(ies); Renal artery(ies)
  anatomy of, 433, 433*f*
  dilation of, 439–441
    aneurysm causing, 433–439
    aortic ectasia causing, 440
    arteriomegaly causing, 440
    inflammatory AAAs causing, 439–440, 443*f*
    penetrating ulcer causing, 441, 444*f*
    pseudoaneurysm causing, 441
  diseases of, 445–464
  dissection complications with, renal artery stenosis and, 447, 448*f*
  endovascular aortic repair for ruptured, 438
  stenotic disease of, 441–445, 445*f*
Abdominal aortic aneurysm (AAA), 433–439
  definition of, 433–434, 434*f*
  endoleaks after repair of, 438–439, 440*f*–442*f*
  inflammatory, 439–440, 443*f*
  medical therapy for, 434
  mortality from, 433
  natural history of, 434
  pathophysiology of, 434
  postoperative ultrasound assessment for, 438–439, 440*f*–442*f*
  rupture of, evaluation of, ultrasound compared to CT for, 438, 439*f*
  screening for, 434–435
    CT in, 437
    false-positive/false-negative results in, 437*f*–438*f*, 438
    recent studies in, 434–435
    ultrasound approach to, 435
Abdominal aortic aneurysm (AAA) *(Continued)*
  surveillance of, 435–437
    CT in, 437
    sonographic technique for, 436–437, 436*f*–437*f*
  treatment planning for, 438
Abdominal cervical cerclage, 1506, 1506*f*
Abdominal ectopia cordis, 1295
Abdominal ectopic pregnancy, 1074, 1075*f*
Abdominal wall
  defects in, thickened NT in, 1095–1096
  hernias of anterior, dynamic ultrasound of contents of, 472–473
    entities stimulating, 500–501, 502*f*
    maneuvers for, 473–474, 474*f*–475*f*
    technical requirements for, 471
    types of, 471, 471*f*
    ventral, 488–494
Abdominal wall, fetal, 1322–1330
  amniotic band syndrome and, 1330, 1330*f*
  bladder exstrophy and, 1326, 1328*f*
  body stalk anomaly and, 1329
  cloacal exstrophy and, 1328–1329, 1329*f*
  ectopia cordis and, 1329, 1329*f*
  embryology of, 1322, 1323*f*
  gastroschisis and, 1322–1325
    associated conditions of, 1324–1325
    epidemiology of, 1322–1323
    management of, 1325
    pathogenesis of, 1323
    prenatal diagnosis of, 1323–1324, 1324*f*
  maternal serum alpha-fetoprotein and defects of, 1322
  omphalocele and, 1325–1326, 1326*f*
    associated conditions with, 1325, 1327*f*
    epidemiology of, 1325
    management of, 1325–1326
    prenatal diagnosis of, 1325, 1327*f*
  pentalogy of Cantrell and, 1329
Abductor tendon, injection for, 905–907, 907*f*
Ablation. *See also* Ethanol ablation
  adrenal, 428
  endometrial, 551–552, 552*f*
Abscess(es)
  abdominal, drainage of, 612
  adrenal, bacterial, 423
  amebic liver, 613
  appendiceal, pediatric, 1871*f*
    hemorrhagic ovarian cyst differentiated from, 1877
  branchial sinus, type IV, 1643–1645, 1645*f*, 1651, 1653*f*
  breast, 803–804, 803*f*–804*f*
  cellulitis leading to, 874, 874*f*
  complicated lymphadenitis with, in children, 1634, 1658–1660
  costochondral junction, pediatric, aspiration and drainage of, 1963*f*
  in Crohn disease, 275–276, 278*f*–279*f*
  empyemas differentiated from, pediatric, 1725, 1726*f*
  enteric, 612
Abscess(es) *(Continued)*
  gastrointestinal, 592
  hydatid, 613
  of kidneys
    acute pyelonephritis and, 325, 325*f*
    drainage of, 617, 618*f*
    pediatric, complicating acute pyelonephritis, 1792–1793
    transplantation complications with, 651, 656*f*
  liver
    drainage of pyogenic, 612–613, 614*f*–615*f*
    after liver transplantation, 638–639, 646*f*
    pyogenic, 85–86, 87*f*
  liver, pediatric, 1746–1748
    parasitic, 1747–1748
    pyogenic, 1746–1747, 1751*f*
  lung, pediatric, 1711, 1713*f*
  pancreatic, acute pancreatitis complications with, 230
  parenchymal, pediatric renal transplantation and, 1812
  parotid, pediatric, 1632–1633, 1633*f*
  pediatric drainage of, interventional sonography for, 1953
    transrectal, 1953–1954, 1954*f*
  pelvic, 283, 591
    drainage of, 612, 613*f*
  percutaneous needle biopsy complications with, 609, 610*f*
  perforated appendicitis and, pediatric, 1857, 1861*f*
  perianal, perianal inflammatory disease and, 305–306
  perinephric
    acute pyelonephritis and, 325
    pediatric renal transplantation and, 1812
    after renal transplantation, 664–665
  perinephric fluid collections and, 1809
  peritonitis and, 517, 520*f*
  prostate, 389, 390*f*, 392
  splenic, 148, 151*f*
    drainage of, 617
    pediatric, 1769
  stitch, after herniorrhaphy, 494–496, 495*f*
  subphrenic, 1716
  testicular, 831–832, 831*f*
  tubo-ovarian, in pelvic inflammatory disease, 588–589, 588*f*
ABUS. *See* Automated whole-breast ultrasound
ACA. *See* Anterior cerebral artery
Acalculous cholecystitis, 200
Acardiac twins, hydrops and, 1429
ACAS. *See* Asymptomatic Carotid Atherosclerosis Study
Accessory and cavitated uterine mass (ACUM), 541
Accessory arteries, 445–446
Accessory lobes, of placenta, 1480–1481, 1481*f*
Accessory spleen, 158–159, 160*f*, 1771*f*
Acetabular dysplasia, familial, 1921

Page numbers followed by *f* indicate figures; *t*, tables; *b*, boxes.

Volume I pp 1–1014 • Volume II pp 1015–1968

Acetabulum
  description of, in evaluation of infant at risk, 1927–1929
  development of, 1923
Acetylcholinesterase (AChE), in neural tube defect screening, 1228
Achilles tendon
  rheumatoid nodules in, 867, 868*f*
  tendinosis in, 861, 861*f*
Achillodynia, peritendinous injections of foot and ankle for, 902, 903*f*
Achondrogenesis, 1383*f*, 1391
  diagnosis of, 1376–1377
  type 1, 1391
  type 2, 1391, 1391*f*
Achondroplasia
  heterozygous, 1396–1398, 1398*f*
    detection of, gestational age for, 1381
    inheritance pattern for, 1379–1380
  homozygous, thanatophoric dysplasia differentiated from, 1389, 1389*f*
  "trident hand" configuration in, 1407, 1408*f*
Achondroplasia, megalencephaly associated with, 1194–1195
Acinic cell carcinoma, parotid gland, pediatric, 1638, 1639*f*
Acinus, 78
ACN. *See* Acute cortical necrosis
ACOG. *See* American College of Obstetricians and Gynecologists
Acorn cysts, in breast, 778*f*
Acoustic attenuation, in uterine fibroids, 539*f*, 540, 540*b*
Acoustic cavitation, 35
  bubbles generated from, 41–42, 42*f*
  considerations for acoustic output increases and, 44
  contrast agents and, 43, 44*b*
  effects of, 40–46
  inertial, 40
  lithotripters as evidence of, 42–43, 42*f*
  in lung and intestine, 43
  mechanical index for, 44–45, 45*f*
  potential sources of, 40–42, 42*f*
  sonochemistry and, 42, 42*f*
Acoustic enhancement, pleural fluid producing, 1709–1710
Acoustic frequency, 2
Acoustic impedance, 3–4
Acoustic power, 5
Acoustic radiation force imaging (ARFI), 1764, 1765*f*
Acoustic shadowing, 786
  breast sonography and, 791–792, 793*f*
  carcinoma causing, 791–792, 793*f*
  decreased/absent, in skeletal dysplasias, 1381–1382
  malignant masses causes, differential diagnosis for, 792
  by rib, in pediatric chest sonography, 1710
Acoustic standoff, in breast tumor imaging, 767, 767*f*
Acoustics
  attenuation of sound energy in, 5–7, 7*f*
  basics of, 2–7
  distance measurement in, 3, 4*f*
  frequency and wavelength in, 2, 2*f*
  impedance of, 3–4
  microbubble behavior and, 57*t*, 58–59, 59*f*
  reflection in, 4, 5*f*
  refraction in, 5, 6*f*
  sound propagation in, 2–3, 3*f*
Acquired cystic kidney disease, 364, 364*f*
  renal cell carcinoma and, 340
Acquired immunodeficiency syndrome (AIDS)
  acute typhlitis and, 287–288, 289*f*
  gastrointestinal tract infections and, 296
  genitourinary infections in, 331–333, 332*f*–333*f*
  lymphoma related to, 266, 266*f*
  Pneumocystis carinii opportunistic infection of liver and, 91, 91*f*
Acrania, 1179
Acromelia, 1381, 1381*b*, 1382*f*
Acromioclavicular joint, 878–879, 878*f*
  injection of, 902, 902*f*
  osteoarthritis of, 893, 894*f*
Acromion, 878–879, 878*f*
Active surveillance, for prostate cancer, 401
ACUM. *See* Accessory and cavitated uterine mass
Acute abdomen. *See also* Diverticulitis, acute
  fluid collections in, 281
  free intraperitoneal gas in, 277–281, 282*f*
  gastrointestinal tract and, 277–290
  left lower quadrant pain in, 288–290
    from acute diverticulitis, 288–290
  mesenteric adenopathy in, 282
  perienteric soft tissues in, 281–282
  pneumatosis intestinalis in, 277–281
  right lower quadrant pain in, 282–288
    from acute appendicitis, 282–285
    from acute typhlitis, 287–288, 289*f*
    from Crohn appendicitis, 285, 287*f*
    from mesenteric adenitis, 288
    from right-sided diverticulitis, 285–287, 288*f*
    from right-sided segmental omental infarction, 288, 289*f*
  sonographic evaluation of, 277–282, 281*b*, 282*f*
Acute cortical necrosis (ACN), 370, 372*f*, 1795–1796
Acute interstitial nephritis, 370
Acute kidney injury (AKI), 1795–1796, 1796*b*, 1797*f*
Acute pancreatitis, microlithiasis and, 221
Acute suppurative thyroiditis, 723–724
Acute tubular necrosis (ATN), 370
  acute kidney injury and, 1795–1796, 1797*f*
  renal transplantation complication with, 649–651, 653*f*, 1809
Addisonian crisis, 426–427
Adduction, Barlow test with, in dynamic examination
  in coronal/flexion view, 1927
  in transverse/flexion view, 1927
Adenitis, mesenteric
  pediatric, 1858–1860, 1862*f*
  right lower quadrant pain in acute abdomen from, 288
Adenocarcinoma(s). *See also* Pancreas, carcinoma of
  of bladder, 348
  colorectal, 261–264, 263*f*–264*f*
  gastrointestinal, 261–264, 263*f*–264*f*
  genitourinary, 348
  pancreatic, 172*f*
  pancreatic ductal, 236–238
  prostate, 395
  of renal pelvis, 348
  urachal, 355
  of ureter, 348
Adenoid cystic carcinoma, salivary gland, pediatric, 1638
Adenolymphomas, pediatric, parotid gland, 1638
Adenoma(s)
  adrenal, 418–420, 418*b*
    in Conn syndrome, 419
    in Cushing disease and Cushing syndrome, 419
    functioning, 419
    imaging considerations for, 418–420, 419*f*
Adenoma(s) *(Continued)*
    nonfunctioning, 419
    percutaneous needle biopsy of, 607
  benign follicular, 697
  bleeding and, 117, 118*f*
  CEUS for diagnosis of, 116–117, 117*f*
  FNH differentiated from, 116–117
  of gallbladder, 203–204, 205*f*
  in GSD, 1740*f*
  of liver, 115–117, 116*f*–118*f*
    inborn errors of metabolism and, pediatric, 1738
    pediatric, 1746
  malignum, 544
  parathyroid
    carcinomas differentiated from, 735–736, 738*f*
    carotid sheath/undescended, 740, 742*f*
    combined modalities for accuracy with, 748
    compression for detection of, 739
    CT accuracy for, 748, 748*f*
    echogenicity of, 735, 736*f*
    ectopic locations of, 739–741
    false-negative examination for, 745*b*, 746
    false-positive examination for, 745–746, 745*b*
    fine-needle aspiration biopsy accuracy for, 746
    hypoechoic, 735
    imaging accuracy with, 746–749
    inferior, 738–739, 739*f*
    internal architecture of, 735, 736*f*
    intrathyroid, 740, 742*f*
    localization of, 736–741
    mediastinal, 740, 741*f*, 748
    MRI accuracy in, 748, 749*f*
    multiple gland disease in, 735, 738*f*
    pediatric, 1650, 1650*f*
    percutaneous needle biopsy of, 750–751, 753*f*
    pitfalls in examination of, 745–746, 745*b*
    retrotracheal/retroesophageal, 739–740, 740*f*
    scintigraphy accuracy for, 747, 747*f*
    shape of, 735, 735*f*
    size of, 735, 737*f*
    sonographic appearance of, 735–736
    sonographic examination and typical locations in, 736–739, 739*f*
    superior, 738–739, 739*f*
    surgical removal of, 749, 750*f*
    ultrasound accuracy for, 746–747, 748*f*
    vascularity of, 735, 737*f*
  pleomorphic, salivary gland, pediatric, 1636–1638, 1638*f*
  primary hyperparathyroidism caused by, 734, 734*b*
  thyroid
    follicular, pediatric, 1646–1648, 1647*f*
    nodular disease and, 697, 700*f*
Adenomatoid tumor(s)
  paratesticular, 1904
  scrotal, 840, 840*f*
Adenomyomas, of gallbladder, 202–204, 204*f*–205*f*
Adenomyomatosis, gallbladder, 202, 203*f*–205*f*
Adenomyosis, 540–541, 540*b*, 542*f*
Adenovirus infection, fetal, hydrops from, 1431–1432
Adhesions, endometrial, 551, 552*f*
ADI. *See* Agent detection imaging
Adnexa. *See also* Fallopian tube(s); Ovary(ies); Round ligament(s)
  anatomy of, 564–570, 565*f*
  cysts of, in pregnancy, 1020
  mass of, ectopic pregnancy and, 1072, 1073*f*
  mass of, pediatric, in ectopic pregnancy, 1884–1885, 1898*f*
  pediatric, torsion of, 1875–1876
  sonography for, 564
    technique for, 566
  torsion of, 576–578, 577*f*

Adnexa *(Continued)*
transvaginal ultrasound for assessment of, 566
vascular abnormalities in, 589–590
ovarian vein thrombosis and thrombophlebitis as, 589–590, 589*f*
pelvic congestion syndrome as, 590, 590*f*
vascularity of, 565–566, 565*f*
ADPKD. *See* Autosomal dominant polycystic kidney disease
Adrenal ablation, 428
Adrenal cortex
carcinoma of, 424–425, 426*f*
functions of, 417
Adrenal gland(s)
anatomy of, 416–417, 417*f*
benign neoplasms of, 418–424
adenomas as, 418–420, 418*b*, 419*f*, 607
cysts as, 421–422, 422*b*, 423*f*
hemorrhage as, 422–424, 424*f*
management of, 428
myelolipomas as, 420–421, 420*b*, 420*f*
pheochromocytomas as, 421, 422*f*
rare, 427–428
calcification of, 423, 425*f*
causes of, 424*b*
cysts of, 421–422, 422*b*, 423*f*
fetal
congenital hyperplasia of, genitalia in, 1367–1368
masses in, 1353–1354, 1353*f*, 1353*t*
normal, 1353, 1353*f*
hemorrhage in, 422–424, 424*f*
after liver transplantation, 638, 645*f*
histoplasmosis of, 423
hypertrophy of, 416–417
immunosuppression and, 423
infectious diseases of, 423–424, 425*f*
interventions for neoplasms of, 428–429
endoscopic ultrasound for, 428–429, 429*f*
intraoperative ultrasound for, 429
ultrasound-guided biopsy for, 428, 429*f*
left, 416–417, 417*f*
multiplanar scanning of, 418
malignant neoplasms of, 424–427
adrenocortical carcinomas as, 424–425, 426*f*
lymphomas as, 426–427, 427*f*
management of, 428
metastases as, 425–426, 426*f*–427*f*
rare, 427–428
pediatric
adrenocortical neoplasms of, 1827, 1827*f*
carcinoma of, 1827, 1827*f*
congenital hyperplasia of, 1822–1824, 1824*f*, 1900–1901
hemorrhage into, neonatal, 1824–1825, 1825*f*
measurements of, in neonates, 1820–1821, 1823*t*
neuroblastoma and, 1825–1826, 1826*f*
normal anatomy of, 1820–1822, 1824*f*
pheochromocytoma and, 1826–1827, 1827*f*
sonography of, 1820–1827
percutaneous needle biopsy of, 606–607, 608*f*
physiology of, 416–417, 417*f*
right, 416–417, 417*f*
multiplanar scanning of, 417–418, 418*f*
sonographic imaging and technique for, 417–418, 418*f*
tuberculosis of, 423
Adrenal insufficiency, 426–427
Adrenal medulla, functions of, 417
Adrenal rests, testicular, 832–833, 833*f*, 1824
pediatric, 1900–1901
Adrenarche, pseudoprecocious puberty and, 1888
Adrenocortical neoplasms, pediatric, 1827, 1827*f*
Adson maneuver, 976–977
Afferent loop obstruction, mechanical bowel and, 293
AFI. *See* Amniotic fluid index
Age. *See* Gestational age; Maternal age
Age, pediatric
kidney length and
comparison of, 1776–1778, 1777*f*
reference values for, 1776–1778, 1778*t*
with single functioning kidney, 1779*t*
kidney volume according to
reference values for, 1776–1778, 1778*t*
with single functioning kidney, 1779*t*
Agent detection imaging (ADI), 66
Agnathia, 1154, 1159*f*
Agyria, in lissencephaly, 1195
Aicardi syndrome
choroid plexus papillomas in, 1209
corpus callosum agenesis and, 1526–1528
AIDS. *See* Acquired immunodeficiency syndrome
AIDS cholangitis, 181
Air bronchograms, sonographic
in atelectatic lung, 1714, 1716*f*
in consolidated lung, 1711, 1714*f*–1715*f*
pneumonia and, 1702, 1703*f*, 1708*f*
round, 1712, 1715*f*
Air bubbles, encapsulated, as blood pool contrast agents, 55–56, 55*t*
AIUM. *See* American Institute of Ultrasound in Medicine
AKI. *See* Acute kidney injury
Alagille syndrome, pediatric, 1737
ALARA, 31, 1041–1042
Albunex, 55–56
Aldosterone, secretion of, 417
Aliasing
in color Doppler ultrasound, 28, 29*f*, 966
high-velocity jets and, 933
in Doppler ultrasound, 29*b*, 32*f*
in pediatric abdominal vessel imaging, 1749
in pulsed Doppler ultrasound, 939, 939*f*
in renal artery duplex Doppler sonography, 449
Alkaline-encrusted pyelitis, 324–325
Allantois, 1059, 1337*f*, 1338
Allergy, milk, gastric mucosa thickening and, 1839–1840
Allograft nephropathy, chronic, 1810, 1812*f*
Alloimmune arteritis, after pancreas transplantation, 677
Alloimmune thrombocytopenia, intracranial hemorrhage and, 1206
Alpha angle, in hip joint classification, 1924, 1924*f*–1925*f*
Alpha-fetoprotein, maternal serum, 1117
elevated, causes of, 1226, 1226*b*, 1228
fetal abdominal wall defects and, 1322
gestational age compared to levels of, 1227*f*
spina bifida screening and, 1221, 1226–1228, 1226*b*, 1227*f*
17-alpha hydroxy-progesterone caproate (17α-OHPC), vaginal progesterone compared to, 1507
Alport syndrome, CKD and, 1796–1798
Alternating current, 8
Ambient cistern, fetal, normal sonographic appearance of, 1168
Amebiasis, hepatic, 87–88, 89*f*
in children, 1747–1748
Amebic liver abscesses, 613
Amelia, definition of, 1399
Amenorrhea, primary, causes of, 1887
American College of Obstetricians and Gynecologists (ACOG), 1107
American Institute of Ultrasound in Medicine (AIUM), 1041
on bioeffects
of diagnostic ultrasound with gas body contrast agents, 43, 44*b*
in gas bodies, 45–46, 46*b*
safety statements of, general, 47, 47*b*
thermal, 40, 40*b*–41*b*
Thermal Index Working Group of, 38–40
Amniocentesis
diagnostic, in NTD screening, 1228
genetic, 1108–1109, 1108*f*
in multifetal pregnancy, 1125–1126
therapeutic, in fetal hydrops, 1436
Amnion
chorion separation from, 1469, 1469*f*
early pregnancy failure and size of, 1066, 1067*f*–1068*f*
normal sonographic appearance of, 1057, 1059*f*–1060*f*
unfused, 1057
Amnion inclusion cyst, 1061
Amnionicity, in multifetal pregnancy, 1057, 1058*f*, 1115–1116, 1116*f*
sonographic determination of, 1117, 1119*t*
triplets and, 1122*f*
Amniotic band sequence
amputations caused by, 1401, 1403*f*
anencephaly differentiated from, 1179
fetal brain and, 1180*f*, 1182–1183
terminal transverse limb defects and, 1400
Amniotic band syndrome, 1057
facial clefts in, 1152–1153
fetal abdominal wall and, 1330, 1330*f*
Amniotic bands
circumvallate placenta confused with, 1479–1480
constrictive, 1182–1183
Amniotic cavity, formation of, 1051, 1052*f*
Amniotic fluid
assessment of, 1339*b*
volume of, 1339–1340
Amniotic fluid index (AFI), 1339
method for obtaining, 1340
values for, in normal pregnancy, 1341*t*
A-mode ultrasound, 9
Amplitude
evaluation of, power Doppler in, 935
modulation imaging, 64, 65*f*
Ampulla, 565
Amputations, from amniotic band sequence, 1401, 1403*f*
Amyand hernias, 472–473, 473*f*
Amyloidosis, renal failure in, 372
Anabolic steroid therapy, hepatic adenomas and, 1746
Anal atresia, 1311
Anal canal, endosonography of, 302–307, 304*f*–307*f*, 306*b*
Anal dimple, 1311–1312, 1311*f*
fetal cloacal exstrophy and, 1328
Analgesia, TRUS-guided biopsy and, 407
Anaplastic carcinoma, of thyroid gland, 707–708, 708*b*, 709*f*
Anasarca, fetal, in hydrops, 1417, 1420*f*
Anastomotic pseudoaneurysms, 438
Anastomotic strictures, bladder augmentation and, 1912–1913
Anderson-Carr-Randall theory of stone progression, 339, 1798–1799
Androblastoma, 585
Androgens, secretion of, 417
Anechoic cysts, 331

Anemia
  fetal, hydrops from, 1431
  pediatric, Fanconi, 1746
Anencephaly, 1218
  CDH and, 1263
  detection of, early, 1018–1019, 1019*f*
  embryonic, 1077
  in fetal brain, 1179, 1180*f*
  temperature increase in utero and, 1037
  thickened NT and, 1096*f*
Anesthetics
  local, for pediatric interventional sonography, 1951, 1952*f*
  for musculoskeletal injections, 901
Aneuploidy. *See also* Trisomy 21
  background risk for, 1088, 1089*f*
  definition of, 1088
  fetal echogenic bowel and, 1315–1316, 1315*f*
  fetal gastroschisis and, 1324–1325
  fetal liver calcifications and, 1316–1318
  hand and foot abnormalities in, 1404, 1406*f*
  identification of, fluorescent in situ hybridization in, 1433–1434
  pyelectasis as marker for, 1355
  risk of, NT in assessing for, 1018–1019, 1019*f*, 1049
  screening for, first-trimester, 1089–1097
    with cell-free DNA, 1107
    combined, 1090–1091
    contingent, 1091
    cystic hygroma in, 1093, 1093*f*
    integrated, 1091
    in multifetal pregnancy, 1091
    nasal bone in, 1093–1095, 1094*b*, 1094*f*
    NT in trisomy 13 and 18, 1093
    NT in trisomy 21 and, 1089, 1090*f*
    NT measurement technique and, 1091–1093, 1092*b*
    reversed flow in ductus venosus in, 1095, 1095*f*
    sequential, 1091
    serum biochemical markers in, 1089–1090
    thickened NT in congenital heart defects and, 1095–1097, 1096*f*
    tricuspid regurgitation in, 1095
  skeletal findings with, 1407–1409
Aneurysm(s). *See also* Abdominal aortic aneurysm
  abdominal aortic, 433–439
  atrial septal, 1295
  in AVF for hemodialysis, 1003, 1005*f*
  carotid flow disturbances in, 928
  common carotid artery, 947–948
  hepatic artery, after liver transplantation, 1768, 1769*f*–1770*f*
  of peripheral arteries
    lower extremity, 971–972, 972*f*
    upper extremity, 976
  portal vein, 103–104
    after liver transplantation, 1768, 1769*f*–1770*f*
  renal artery, 369, 369*f*, 451
  in synthetic arteriovenous graft for hemodialysis, 1003
  umbilical artery, 1483
  vein of Galen, 1204, 1206*f*
    arachnoid cysts differentiated from, 1192–1193
    cavum veli interpositi cysts differentiated from, 1170
    in neonatal/infant brain, duplex Doppler sonography of, 1583–1584, 1585*f*–1586*f*
  ventricular, congenital, 1294
Angiogenesis, in yolk sac wall, 1057
Angiography, in carotid stenosis diagnosis, 916
Angiomas, littoral cell, splenic, 153–156, 156*f*
Angiomyolipomas
  of liver, 117–118, 119*f*
  renal, 351–352, 351*f*–352*f*
    pediatric, 1820, 1822*f*
Angiosarcoma
  hepatic, 123
  splenic lesions in, 153, 155*f*
Angle of incidence, 5
Angle of insonation, 4
Angle of refraction, 5
Angle theta
  consistent, in carotid spectral analysis, 926–927
  Doppler
    definition of, 926
    measurement of, 926–927, 926*f*
  increasing, to overcome aliasing, 939
Angular margins, in breast sonography, 788–789, 790*f*
Aniridia, sporadic, Wilms tumor screening with, 1818
Anisospondyly, in dyssegmental dysplasia, 1399
Anisotropic effect, in HPS sonography, 1838, 1838*b*, 1839*f*
Anisotropic effect artifact, 1517
Anisotropy
  shoulder ultrasound and, 895, 895*f*
  tendon, 859, 860*f*, 899
Ankle, injection of, 901
  superficial peritendinous and periarticular, 902–904, 903*f*–904*f*
Annular constricting lesions, 261–264, 263*f*
Annular pancreas, fetal, 1320, 1321*f*
Anomalous pulmonary venous return (APVR), 1280, 1282*f*, 1290, 1291*f*
  total compared to partial, 1290
Anophthalmia, 1140, 1145*f*
Anorchidism, 1890
Anorectal malformations, fetal, 1310–1312, 1311*f*
Anterior cerebral artery (ACA)
  of infant, RI in, 1576, 1577*t*
  of infant, RI in, fontanelle compression in hydrocephalus and, 1582, 1584*f*
  stenosis of, SCD and, 1607*f*
  TCD sonography for collateral flow in, 1610, 1611*f*
  as transtemporal approach landmark, 1592, 1593*f*–1594*f*
Antibiotic prophylaxis, TRUS-guided biopsy and, 407, 408*f*
Antibiotics, for pediatric interventional sonography, 1951
Anticoagulants, deficiency of physiologic, dural sinus thrombosis from, 1205–1206
Antley-Bixler syndrome, craniosynostosis in, 1136–1138
Antral dyskinesia, 1836–1838
Antral foveolar hyperplasia, prostaglandin-induced, 1839–1840
Antral web, pediatric, 1839, 1840*f*
Anus
  ectopic, pediatric, 1847–1848, 1850*f*
  imperforate, 1310–1311
    block vertebrae with, 1689, 1692*f*
    high, pediatric, risk of spinal dysraphism with, 1689
    pediatric, 1847–1848, 1850*f*
Aorta
  coarctation of, 1291, 1292*f*
    fetal, hydrops from, 1423–1424
    hypoplastic left heart syndrome with, 1287
  fetal, continuity of, 1278*f*
  small, in Turner syndrome, 1106*f*, 1107
Aortic arch
  fetal, 1275, 1279*f*
  pediatric, cervical, 1658
Aortic balloon pump, carotid flow waveforms and, 936–937, 936*f*
Aortic coarctation, renal artery stenosis and, 447, 449*f*
Aortic root, fetal, diameter of, 1277*f*
Aortic stenosis, 1292
  carotid flow waveforms and, 936–937
  fetal, hydrops from, 1423–1424
Aortic valve, lesions of, carotid flow waveforms and, 936–937
Aortoenteric fistulas, 438
Apert syndrome
  craniosynostosis in, 1136–1138
  midface hypoplasia in, 1148
Aplasia
  pulmonary, 1245–1246
  of thyroid gland, 694, 694*f*
Apnea, sleep, pediatric TCD sonography for, 1611
Aponeurosis, torn, in spigelian hernia, 483–484, 487*f*
Appendices epiploicae, torsion of, 290
Appendicitis
  acute
    clinical misdiagnosis of, 283–285
    pathophysiology of, 283
    right lower quadrant pain from, 282–285
    sonographic diagnosis of, 283, 283*b*
    symptoms of, 283
    transvaginal ultrasound for diagnosis of, 283, 285*f*
  Crohn, 285, 287*f*
  focally inflamed fat in, 521
  pediatric, 1855–1860
    acute, 1857, 1859*f*
    Meckel diverticulum resembling, 1858–1860, 1862*f*
    normal appearance of, 1857, 1858*f*
    perforated, 1857, 1857*b*, 1861*f*
    sonographic signs of, 1857*b*
Appendicolith, 283
Appendix. *See also* Appendicitis
  inflammation of, 282–285
  mucocele of, 299, 299*f*
  pediatric
    abscess of, 1871*f*, 1877
    abscess of, drainage of, 1956, 1960*f*
    gangrenous, 1857, 1861*f*
    normal, 1857, 1858*f*
  perforations of, 283–285, 285*b*, 286*f*
Appendix epididymis, pediatric, 1897, 1897*f*
Appendix testis, 820–821, 820*f*
  pediatric, 1897
"Apple peel" jejunal atresia, 1310
Aprosencephaly, 1186
APVR. *See* Anomalous pulmonary venous return
Aqueduct of Sylvius
  in rhombencephalosynapsis, 1192
  stenosis of
    obstructive hydrocephalus from, 1538, 1540*f*
    VM and, 1177, 1177*f*
Arachnoid cyst(s)
  cavum veli interpositi cysts differentiated from, 1170
  corpus callosum agenesis and, 1526–1528
  fetal brain and, 1192–1193, 1193*f*
  of neonatal/infant brain, 1563–1565, 1565*b*
  spinal canal and, pediatric, 1695–1697, 1696*f*
Arachnoid granulations, 1177
Arcuate arteries, calcifications of, 531–532, 533*f*
Arcuate uterus, 534, 536–538, 536*f*–537*f*
Area cerebrovasculosa, in anencephaly, 1179
Area membranacea, 1189
Areflexia, detrusor, 372–374, 373*f*
ARFI. *See* Acoustic radiation force imaging
ARPKD. *See* Autosomal recessive polycystic kidney disease

Arrays, transducer, 11–12
Arrhenoblastoma, 585
  pediatric, 1880
Arrhythmia(s)
  early pregnancy loss and, 1069
  Ebstein anomaly with, 1286
  fetal heart, 1295–1297
    bradycardia as, 1297, 1297*f*
    CHD and, 1270–1273
    congenital heart block as, 1297, 1297*f*
    hydrops from, 1424, 1425*f*
    PACs and PVCs as, 1295–1296
    tachycardia as, 1296–1297, 1296*f*
Arsenic, 123
Arterial venous (AV) anastomoses, 1125, 1125*f*
Arterial/arterial (AA) anastomoses, 1125, 1125*f*
Arteriomegaly, 440
Arteriovenous fistulas (AVFs)
  arteries supplying, spectral broadening in, 927–928
  of common femoral artery, 974*f*
  dural, TCD sonography assessing, 1614
  hemodialysis and
    aneurysms near, 1003, 1005*f*
    arm and leg swelling with, 1006, 1009*f*
    hematomas near, 1002–1003, 1005*f*
    maturation of, evaluating, 1003
    occlusion of, 1006
    palpable focal masses near, 1002–1003
    placement of, 996, 997*f*
    pseudoaneurysms near, 1003, 1005*f*
    stenoses associated with, 1003–1006, 1007*f*–1008*f*
    ultrasound evaluation of, 1000–1006, 1002*f*–1003*f*
  of lower extremity peripheral arteries, 973–974, 974*f*
  after pancreas transplantation, 678, 680*f*
  pediatric, of neck, 1658
  renal, 366–367
    percutaneous needle biopsy of, 606, 607*f*
  renal biopsies and, Doppler assessment of, 1809, 1810*f*
  traumatic, 973
Arteriovenous graft, synthetic, hemodialysis and
  arm and leg swelling with, 1006, 1009*f*
  hematomas near, 1002–1003
  occlusion of, 1006, 1010*f*
  palpable focal masses near, 1002–1003
  placement of, 996, 997*f*
  ultrasound evaluation of, 1002, 1004*f*
Arteriovenous malformations (AVMs)
  arteries supplying, spectral broadening in, 927–928
  cerebral, pediatric, TCD sonography detecting, 1614, 1615*f*
  fetal hydrops from, 1430–1431
  of lower extremity peripheral arteries, 973
  pediatric, of neck, 1657–1658, 1659*f*
  pial, 1204–1205
  postpartum recognition of, 556, 556*f*
  renal, 366–367, 367*f*
    renal transplantation complications from, 661–664, 667*f*–670*f*
    twinkling artifacts mimicking, 662–664, 668*f*
Arteriovenous shunting, in fetal sacrococcygeal teratoma, 1238–1239
Arteritis
  alloimmune, after pancreas transplantation, 677
  of common carotid artery, 944–946, 947*f*
  Takayasu, aortic stenosis in, 444
Artery(ies). *See specific arteries*
Arthritis
  osteoarthritis, 869, 869*f*
    acromioclavicular joint, 893, 894*f*
Arthritis *(Continued)*
  psoriatic, of hand and wrist, injections for, 904
  rheumatoid, 866
    erosive, 867, 868*f*
    gout and, 867–869, 868*f*
    of hand and wrist, injections for, 904
    joint effusion in, 867, 867*f*
  septic, pediatric, 1936, 1937*f*
Arthrogryposis multiplex congenita
  elbow and knee dislocation and, 1933–1934
  findings in, 1382
  as limb reduction defect, 1401–1404, 1405*f*
  teratologic hip dislocation and, 1932
Arthropathy
  inflammatory, 866
    shoulder and, 893–894, 894*f*
  shoulder and, 893–894
    degenerative, 893, 894*f*
    inflammatory, 893–894, 894*f*
Articular-sided rotator cuff tears, 888, 890*f*
Artifacts
  anisotropic effect, 1517
  blooming, 60–61
  comet-tail, 202, 695
    in benign and malignant thyroid nodule differentiation, 712–713
    in degenerative cysts of thyroid, 1646, 1647*f*
  Doppler ultrasound sources of, 29*b*
  empty stomach, 1838, 1839*f*
  enhancement as, 21, 22*f*
  flash, 60–61
  loss of information from, 19–21
  misregistration, 3*f*, 420–421
  multipath, 19–21, 21*f*
  propagation velocity, 3, 3*f*, 420–421
  refraction, 5, 6*f*
  reverberation, 19, 20*f*
    posterior, liver abscess and, 85–86, 87*f*
  ring-down, 266, 266*f*
  shadowing as, 19–21, 22*f*
  side lobe, 19, 20*f*
  tangential imaging, of pyloric muscle, 1834–1835, 1836*f*
  TGC settings and, 19–21
  thump, 60
  tissue vibration, 973–974, 974*f*
  twinkling
    bezoars and, 1840
    mimicking AVMs after renal transplantation, 662–664, 668*f*
    renal calculi indicated by, 336, 337*f*
Ascariasis
  biliary, 181
  intestinal, pediatric, 1853, 1853*f*
Ascites
  chylous, 508
  exudate, 506–507
  fetal
    cloacal exstrophy and, 1328
    in hydrops, 1413, 1415*f*–1416*f*, 1435, 1436*f*
    meconium peritonitis and massive, 1418–1419, 1421*f*
    parvovirus infection and massive, 1418–1419
    urinary, from bladder rupture in posterior urethral valves, 1361, 1361*f*
  from gastrointestinal tract metastases, 266, 267*f*
  meconium peritonitis and, 1313
  particulate, 507
  pediatric, pleural fluid differentiated from, 1709
  peritoneum and, 506–508, 507*f*–509*f*
  small bowel mesentery assessment with, 505, 505*f*
  transudate, 506–507
ASD. *See* Atrial septal defect
ASH. *See* Asymmetrical septal hypertrophy
Asherman syndrome, 551
Aspergillosis, neonatal chylothorax from, 1704*f*
Asphyxia
  intrauterine, near-total, acute, in diffuse cerebral edema, 1553–1554, 1555*f*
  neonatal/infant brain and, duplex Doppler sonography of, 1580
  pediatric, TCD sonography in, 1614, 1616*f*
Asphyxiating thoracic dysplasia, 1398
Asphyxiating thoracic dystrophy, 1396
  polydactyly in, 1382
Aspiration, for pyogenic liver abscesses, 1746–1747
Aspirin, 598–599
Asplenia, 159–160
  in cardiosplenic syndrome, 1292, 1293*b*
  fetal, 1320
  univentricular heart with, 1287–1288
Assisted reproductive technology, multifetal pregnancy incidence and, 1115
Astrocytomas, neonatal/infant brain and, 1562
Asymmetrical fibroglandular tissue, split-screen imaging and, 769, 769*f*
Asymmetrical septal hypertrophy (ASH), 1292, 1294–1295
Asymptomatic Carotid Atherosclerosis Study (ACAS), 916
Atelectasis, pediatric, 1714, 1716*f*
Atelencephaly, 1186
  hydranencephaly differentiated from, 1208
Atelosteogenesis, 1396
Atheromatous carotid plaques, characterization of, 919
Atherosclerosis, 432–433
  renovascular disease and, 368
Atherosclerotic disease, peripheral arterial stenosis in, 968, 976, 978*f*
Atherosclerotic disease, renal artery stenosis and, 447
Atherosclerotic plaque rupture, 919–920
Athletes, direct inguinal hernias in, 485–486
Athletic pubalgia. *See* Sports hernias
ATN. *See* Acute tubular necrosis
Atrazine, fetal gastroschisis and, 1322–1323
Atretic cephalocele, 1180
Atretic meningocele, tethered cord and, 1679
Atrial fibrillation, fetal, 1296
  hydrops from, 1424
Atrial flutter, fetal, 1296
  hydrops from, 1424
Atrial pacemaker, 1295–1296
Atrial septal aneurysm, PACs and, 1295
Atrial septal defect (ASD), 1277–1280, 1282*f*–1283*f*
  coronary sinus, 1280
  ostium primum, 1279–1280, 1282*f*–1283*f*
  ostium secundum, 1279–1280, 1282*f*
  prenatal diagnosis of, 1280
  sinus venosus, 1280, 1282*f*
  types of, 1282*f*
Atrioventricular block (AVB), 1297
Atrioventricular (A-V) canal
  defects of, 1284
  in trisomy 21, 1098*f*
Atrioventricular septal defect (AVSD), 1279, 1282*f*, 1284–1286, 1284*f*–1285*f*
  balanced compared to unbalanced, 1285
  complete compared to incomplete, 1284–1285, 1285*f*
  in trisomy 21, 1101, 1284
Atrioventricular valves, of fetal heart, 1274–1275
Atrium of lateral ventricles, neonatal/infant, in coronal imaging, 1515

Attenuation
coefficient, 36
of sound energy, 5–7, 7*f*, 35
Atypical hips, pediatric, 1932, 1933*f*
Auditory response, in obstetric sonography, 1038
Auricular hillocks, 1134
Autoimmune cholangiopathy, 182
Autoimmune cholangitis, 182
Autoimmune pancreatitis, 236, 237*f*
Autoimmune vasculitis, Henoch-Schönlein purpura and, 1853
Automated whole-breast ultrasound (ABUS), 760
Autopsy, in hydrops diagnosis, 1435
Autosomal dominant polycystic kidney disease (ADPKD), 83, 243, 361, 362*f*, 1346, 1348–1350, 1349*f*–1350*f*
pediatric, 1814–1815, 1815*f*
Autosomal recessive polycystic kidney disease (ARPKD), 359, 361*f*, 1799
pediatric, 1812–1813, 1814*f*
AV anastomoses. *See* Arterial venous anastomoses
A-V canal. *See* Atrioventricular canal
A-V canal defects, 1284
AVB. *See* Atrioventricular block
AVFs. *See* Arteriovenous fistulas
AVMs. *See* Arteriovenous malformations
AVSD. *See* Atrioventricular septal defect
Axial resolution, 16–19, 18*f*
Axillary artery, 975
Axillary vein, 990–991, 990*f*
Azimuth planes, 12*f*
Azimuth resolution, 19, 19*f*
Azoospermia, prostate and, 393
Azzopardi tumors, 824–825

B

Bacille Calmette-Guérin (BCG), 390, 390*f*
Backscatter, 3–4
CEUS increasing, 107, 111*f*
Doppler ultrasound and, 21–22, 23*f*, 35
Bacteria
pediatric infections from
cervical lymphadenopathy in, 1660–1663
parotid gland, 1632–1633, 1632*f*
thyroid, 1643–1645, 1645*f*
pyogenic, liver abscesses from, 85–86, 87*f*
pediatric, 1746–1747, 1751*f*
Bacterial epididymitis, 841, 843*f*
Baker cyst(s)
injection for, 907–909, 908*f*
ruptured, 870, 870*f*
ultrasound techniques for, 870, 870*f*
Ballottement, compression and, 768
Banana sign, in Chiari II malformation, 1183–1185, 1184*f*
spina bifida screening and, 1221, 1228, 1230–1232
Band, of frequencies, 7
Band heterotopia, 1196
Bandwidth, 7–8
Barbotage, 909
Bardet-Biedl syndrome, hyperechogenic kidneys in, 1351
Bare area
of liver, 77
sign, as pleural fluid sonographic sign, 1709, 1709*f*
Barlow test
with adduction, in dynamic examination
in coronal/flexion view, 1927
in transverse/flexion view, 1927
in determining hip stability, 1923
Basal cell nevus syndrome, 585
rhabdomyosarcoma associated with, 1908
Basal ganglia
fetal, normal sonographic appearance of, 1168
vasculopathy, neonatal/infant brain and, 1556–1557
Basilar artery, 951
Basilic vein, anatomy of, 990–991, 990*f*
Bat wing configuration, in Chiari II malformation, 1526, 1527*f*
Battledore placenta, 1484
B-cell lymphoma, AKI and, 1796
BCG. *See* Bacille Calmette-Guérin
"Beads on a string" sign, 587–588
Beam steering, 10–11, 11*f*
Beam width, 35
Beare-Stevenson syndrome, craniosynostosis in, 1136–1138
Beckwith-Wiedemann syndrome
adrenocortical neoplasms and, 1827
CDH and, 1263
fetal
hepatomegaly and, 1316
omphalocele and, 1325, 1327*f*
pancreatic cysts and, 1320
hepatoblastomas and, 1746
macroglossia in, 1153
megalencephaly associated with, 1194–1195
mesenchymal dysplasia of placenta in, 1479, 1479*f*
nesidioblastosis and, 1865
neuroblastoma with, pediatric, 1825
Wilms tumor screening with, 1818
Beemer-Langer syndrome, 1396
Behavioral changes, obstetric sonography and, 1040–1041
Bell-clapper deformity, 844, 844*f*
pediatric, 1325
Benign ductal ectasia, prostate and, 387, 388*f*
Benign follicular adenoma, 697
Benign mixed-cell tumors, 1638
Benign prostatic hyperplasia (BPH), 384, 385*f*–386*f*, 387–388
Bent-limb dysplasia, 1395
Beta angle, in hip joint classification, 1924, 1924*f*–1925*f*
β-hCG. *See* Human chorionic gonadotropin
Bezoars
of gastrointestinal tract, 300
pediatric, 1840, 1841*f*
Biceps tendon, 878–879
dislocation of, 893
injection of, 904–905, 905*f*–906*f*
long head of, 879, 880*f*–881*f*
longitudinal split tear of, 893, 894*f*
pathology of, 892–893
tenosynovitis and, 892–893, 893*f*
ultrasound evaluation of, 880, 881*f*
Bicornuate uterus, 534, 536*f*–537*f*, 538, 1881, 1881*f*
Bifid lamina, 1688
Bifid scrotum, fetal, 1367
Bilateral hernias, 1262
Bile
calcium, milk of, 194, 195*f*
flow
extrahepatic obstruction to, 1734
stasis of, stone formation and, 1741
leakage of, after liver transplantation, 627–629, 629*f*
limey, 194, 195*f*
Bile duct(s)
aberrant, 167, 168*f*
dilation of, in Caroli disease, 1736–1737, 1736*f*
drainage of, 614–615
interlobular, paucity of, jaundice from, 1737
ischemia of, from post-liver transplant hepatic artery thrombosis, 628*f*
Bile duct(s) *(Continued)*
necrosis of, post-liver transplantation, bile leaks from, 627
normal, 166–168, 166*f*
spontaneous rupture of, neonatal jaundice caused by, 1734, 1737
strictures in, after liver transplantation, 626–627, 627*f*–628*f*
Biliary atresia
extrahepatic, 1319
neonatal jaundice and, 1734–1735, 1737, 1738*f*
Biliary cirrhosis, 92–93, 182
pediatric, 1741
Biliary cystadenomas, 82, 83*f*
Biliary hamartomas, 83, 83*f*–84*f*
Biliary rhabdomyosarcoma, in pediatric liver, 1746, 1749*f*
Biliary sludge
acute pancreatitis and, 221
complicating liver transplantation, 629, 631*f*
gallbladder and, 194–195, 196*f*
Biliary system, fetal, 1318–1319
Biliary tree, 166–188. *See also* Cholangiocarcinoma
anatomy of, 166–168
ascariasis and, 181
autoimmune cholangitis and, 182
branching pattern of, 167, 167*f*
Caroli disease of, 171, 171*f*
cholangiocarcinoma and, 184–188
choledochal cysts of, 168–170, 169*f*–170*f*
choledocholithiasis in, 172–173, 182
common bile duct stones and, 173–174, 173*f*
intrahepatic, 173, 173*f*
cirrhosis and, 182
clonorchiasis and, 178–179, 179*f*
dilation of, in acute cholangitis, 176
fascioliasis and, 176–178, 177*f*–178*f*
harmonic imaging of, 168, 169*f*
hemobilia and, 174, 175*f*
HIV cholangiopathy and, 181–182, 181*f*
immune-related diseases of, 182–184
infection of, 176–182
liver flukes and, 176–179, 177*f*–179*f*
after liver transplantation
complications involving, 625–629, 1767–1768, 1769*f*–1770*f*
normal appearance of, 625
strictures in, 626–627, 627*f*–628*f*
metastases to, 188, 192*f*
Mirizzi syndrome and, 174, 174*f*
obstruction of
acute cholangitis and, 176, 177*f*
causes of, 172*b*
overview of, 171–172, 172*f*
opisthorchiasis and, 178–179
pneumobilia and, 175–176, 176*f*
primary sclerosing cholangitis and, 182, 183*f*, 184
recurrent pyogenic cholangitis and, 179–181, 180*f*
sonographic technique for, 168, 169*f*
trauma to, hemobilia from, 174, 175*f*
variants of normal, 166–168
Bilobed placenta, 1481, 1482*f*
Bilobed testis, 1891
Biloma, after liver transplantation, 638
Bioeffects. *See also* Acoustic cavitation; Thermal index
acoustic cavitation and, 40–46
AIUM on
of diagnostic ultrasound with gas body contrast agents, 43, 44*b*
in gas bodies, 45–46, 46*b*
safety statements of, general, 47, 47*b*
thermal, 40, 40*b*–41*b*

Bioeffects *(Continued)*
epidemiology of, 48
of HIFU, 31–33, 33*f*
mechanical, 32
of obstetric sonography
animal research and, 1038–1039
behavioral changes and, 1040–1041
birth weight and, 1040
childhood malignancies and, 1041
congenital malformations and, 1041
delayed speech and, 1040
Doppler ultrasound and, 1041
dwell time and, 1036
dyslexia and, 1040
human studies on, 1039–1041
instrument outputs and, 1035–1036
mechanical, 1038
neurologic development and, 1040–1041
nonright-handedness and, 1040
scanning mode and, 1035
system setup and, 1035–1036, 1035*f*–1037*f*
thermal, 1036–1038
operating modes and, 30–31
output control and, 48–50, 49*t*
output display standard and, 46–47, 46*f*
output regulation and, 34–35
physical effects of sound and, 35
thermal, 32, 35–40
AIUM summary statement on, 40, 40*b*–41*b*
bone heating and, 37, 37*f*, 37*t*
estimating, 40
hyperthermia and safety and, 38, 38*f*
mechanism of, 35
in obstetric sonography, 1036–1038
soft tissue heating and, 37–38, 37*f*
spatial focusing and, 35
temporal considerations in, 36, 36*f*
tissue type and, 36, 36*f*
ultrasound output and, regulation of, 34–35
user concerns and, 31
Biometry, second-trimester, 1021, 1023*f*
Biophysical profile (BPP), 1456–1458, 1457*f*, 1457*t*
Biopsy(ies). *See also* Transrectal ultrasound, biopsy guided by
chest wall lesion, ultrasound-guided, 1724–1725
fine-needle aspiration
parathyroid adenoma and accuracy of, 746
of thyroid gland, 709–710, 710*t*, 722
interventional sonography devices for, 1950
liver, percutaneous, 132–133
post-transplant bile leaks from, 627–629
mediastinal mass, pediatric, 1956, 1959*f*
percutaneous needle, 597–609
abscess complications with, 609, 610*f*
of adrenal gland, 606–607, 608*f*
of breast nodules, ultrasound-guided, 811–815, 813*f*–814*f*
for cervical lymph nodes, 717–718, 718*f*
color Doppler ultrasound for, 599
complications of, 608–609
computed tomography for, 599
contraindications to, 597–598
"freehand" technique for, 600, 602*f*
hemorrhage complications with, 608, 609*f*
imaging methods for, 599
indications for, 597–598
infection complications with, 609
of kidney, 605–606, 606*f*–607*f*
of liver, 603–604, 603*f*–604*f*
of lung, 607–608, 609*f*
needle selection for, 599–600
needle visualization in, 601–603, 602*f*
of pancreas, 604–605, 605*f*
of parathyroid adenomas, 750–751, 753*f*
Biopsy(ies) *(Continued)*
periprocedural antithrombotic management and, 598–599
procedure for, 600–601, 601*f*
of spleen, 607, 608*f*
for thyroid gland, 715–720, 718*f*–719*f*, 721*f*
transducer sterilization for, 600
prostate
PSA-directed, 395
ultrasound-guided, 407–411, 408*f*
renal, pediatric, Doppler assessment of, 1809, 1810*f*–1811*f*
of renal cell carcinoma staging, 343–344, 345*f*
targeted organ lesion, 1961, 1961*f*–1962*f*
ultrasound-guided
of adrenal glands, 428, 429*f*
of spleen, 161
Biparietal diameter (BPD)
corrected, in gestational age determination, 1447, 1447*t*, 1448*f*
femur length compared to, in heterozygous achondroplasia, 1398, 1398*f*
in gestational age determination, 1446, 1447*f*
long-bone lengths and, at different menstrual ages, 1379*t*
nasal bones in trisomy 21 and, 1099–1100
in second-trimester, 1023*f*
BI-RADS. *See* Breast Imaging Reporting and Data System
Birth, preterm. *See* Preterm birth
Birth weight
discordance, in multifetal pregnancy, 1123
obstetric sonography and, 1040
Birt-Hogg-Dubé, hereditary oncocytosis, 348–350
Bladder. *See also* Cystitis
adenocarcinoma of, 348
agenesis of, 322
anatomy of, 314
calculi in, 338–339, 339*f*
pediatric, 1908
carcinomas of
squamous cell, 348
transitional cell, 347–348, 350*f*
cavernous hemangiomas of, 356
development of, 311, 312*f*
congenital anomalies related to, 322
diverticula, 374, 374*f*
identification of, 592
drainage to, in pancreas transplantation, 668–672, 675*f*
duplication of, 322
endometriosis of, 372, 372*f*
exstrophy of, 322
fetal, 1339, 1340*f*
cloacal exstrophy and inability to visualize, 1328
exstrophy of, 1365–1366, 1366*f*
maximum volume of, 1339
nonvisualized, 1365, 1365*b*
routine sonographic view of, 1026*f*
rupture of, from posterior urethral valves, 1361, 1361*f*
fistulas of, 334, 335*f*
function of, in spina bifida, 1233
leiomyomas of, 356
leiomyosarcoma of, 356
lymphomas of, 353, 354*f*
malacoplakia and, 333, 333*f*
mesenchymal tumors of, 356
metastases to, 354–355, 355*f*
neck of, 314
neurofibromas of, 356
neurogenic, 372–374, 373*f*
Bladder *(Continued)*
pediatric
augmentation of, 1912–1913, 1913*f*
calculi in, 1908
dysfunctional, 1907–1908
neurogenic, 1907–1908
postoperative, 1912–1913, 1913*f*
spontaneous rupture of, 1912
pheochromocytomas of, 356
rare tumors of, 356
rhabdomyosarcomas of, 356
schistosomiasis of, 331, 331*f*
sonographic technique for, 314–315
trauma to, 366
urachal anomalies of, 322, 323*f*
wall of
causes of thickening of, 333*b*
interstitial cystitis and thickening of, 372, 373*f*
prune belly syndrome and thin walled, 1361–1362
Bladder, pediatric. *See also* Urinary tract, pediatric
exstrophy of, hydronephrosis and, 1791, 1791*f*
neurogenic, pediatric hydronephrosis and, 1788
normal anatomy of, 1783, 1783*f*
outlet of, obstruction of, pediatric hydronephrosis and, 1788, 1789*f*–1790*f*
postvoid scanning of, 1872
rhabdomyosarcoma of, 1820, 1823*f*
tumors of, 1820, 1823*f*
pediatric hydronephrosis and, 1788
volume of
determination of, 1778, 1780*f*
shape and correction coefficient for, 1780*t*
wall thickness of, determination of, 1778–1781, 1780*f*
Bladder exstrophy, fetal, 1326, 1328*f*
Bladder flap hematomas, cesarean sections and, 556–557, 557*f*
Bladder outlet obstruction, pediatric
causes of, 1905–1906, 1905*b*
epididymitis and, 1897
Blake pouch
cerebellum and, 1189
cyst of
arachnoid cysts differentiated from, 1192–1193
sonographic appearance of, 1170, 1173*f*
Dandy-Walker malformation differentiated from, 1190
formation of, 1167
Blastocyst, 1049
Blastocyte stage, 1051, 1051*f*
Bleeding
adenoma and, 117, 118*f*
endometrial abnormalities with, 544, 544*b*
postmenopausal bleeding as, 545–546
intraamniotic, fetal echogenic bowel and, 1316
in placenta previa, 1469
uterine postpartum findings with, 554
vaginal, hydatidiform molar pregnancy and, 1078
Block vertebrae
imperforate anus with, 1689, 1692*f*
in scoliosis and kyphosis, 1235
Blood
autologous, intratendinous injection of, 909–910, 912*f*
fetal, sampling of
in hydrops diagnosis, 1434–1435, 1435*f*
in immune hydrops, 1421
incompatible, immune hydrops from, 1419–1421

Blood flow. *See also* Cerebral blood flow, neonatal/infant
in carotid arteries
internal, residual string of, detection of, 939, 940*f*
normal transient reversal of, 933–934
patterns of, altered, misinterpretation of, 927, 928*f*
patterns of, high-velocity, in stenoses, 928–932, 929*f*–931*f*, 931*t*
pseudostring of, on power Doppler, 935
residual string of, in occlusion, detection of, 935
in MCA, PSV and, 1421–1423, 1421*b*, 1422*t*
reversed, in ductus venosus, in aneuploidy screening, 1095, 1095*f*
trophoblastic, 1083
venous
absence of, in DVT, 992–994
slow moving, without DVT, 984, 988*f*
Blood pool contrast agents, 55–56
encapsulated air bubbles as, 55–56, 55*t*
free gas bubbles as, 55
second-generation, 56
selective uptake, 56, 57*f*
Blood vessels. *See also* Carotid artery(ies); Internal jugular vein; Vascular malformations; Vertebral artery
adrenal, 416–417, 417*f*
cerebral
extracranial, 917*f*
IJV as, 955–956
malformations of, TCD sonography in, 1614, 1615*f*
vertebral artery as, 950–955
chest, pediatric, 1716–1723, 1721*f*–1724*f*
of fetal brain, malformations of, 1204–1208, 1206*f*
hepatic, abnormalities in, 96–104
patency of, after liver transplantation, 625
renal
aberrant, 321–322
Doppler ultrasound of, 366
stenosis of, high-grade, waveforms in, 938
Blood-testis barrier, 827
Blooming artifacts, 60–61
"Blue dot" sign, 846
Blue rubber bleb nevus syndrome, in venous malformations of neck, 1657
Blue-dot sign, 1897
B-mode ultrasound, real-time, gray-scale, 9–10, 10*f*
Bochdalek hernia, 1258
Body stalk anomaly, fetal, 1329
Bone marrow transplantation, for SCD, 1598
Bone(s)
heating of, 37, 37*f*, 37*t*
shear waves created in, 39
thermal index for, in late, 1039
wormian, 1139, 1139*b*, 1139*f*
Bone(s), fetal
appearance of, abnormal, sonographic evaluation for, 1381–1382
long
abnormal length of, sonographic evaluation for, 1380–1384, 1381*b*, 1382*f*–1384*f*
bowing of, 1381–1382
BPD and, at different menstrual ages, 1379*t*
sonographic assessment of, 1387*b*–1388*b*
Bone Thermal Index (TIB), 39
Bony septum, in spinal cord in diastematomyelia, 1234–1235, 1236*f*
Boomerang dysplasia, 1396
Borderline tumors, ovarian, 580*f*, 581
Bosniak classification, malignant potential of renal cysts and, 359
Bossing, frontal, in skeletal dysplasias, 1382
"Bovine arch" configuration, 916
Bowel. *See also* Echogenic bowel; Mechanical bowel obstruction; Small bowel
dilated, fetal, 1313
dilated loops of, 1310, 1311*f*
fetal gastroschisis and, 1323–1324
echogenic
fetal, 1310, 1313–1316, 1315*f*
in trisomy 21, 1100*f*, 1101
fetal, obstruction of, cloacal malformation and, 1363
function of, in spina bifida, 1233
ischemic disease of, 297
neoplasms of, 592
obstruction of mechanical, 293
pediatric
interventional sonography and anatomy of, 1950
necrosis of, with perforation, in NEC, 1854–1855
TRUS-guided biopsy and preparation of, 407
Bowing
of femur, osteogenesis imperfecta type I and, 1380*f*
of fetal long bones, 1381–1382
BPD. *See* Biparietal diameter
BPH. *See* Benign prostatic hyperplasia
BPP. *See* Biophysical profile
BPS. *See* Bronchopulmonary sequestration
Brachial artery, 975
high, bifurcation of, 975–976, 976*f*, 998, 999*f*
Brachial plexus injury, pediatric, 1934–1936, 1936*f*–1937*f*
Brachial vein
anatomy of, 990–991, 990*f*
DVT and
chronic, 994–995, 996*f*
nonocclusive, 994*f*
Brachiocephalic artery, 916, 975
Brachiocephalic vein
anatomy of, 990–991, 990*f*
ultrasound examination of, 992*f*
Brachmann-de Lange syndrome, CDH and, 1263
Brachycephaly, 1136, 1137*f*
Brachydactyly, fetal, 1407, 1408*f*
Brachytherapy, for prostate cancer, TRUS-guided, 401, 402*f*
Bradycardia
carotid flow waveforms and, 936–937
embryonic, 1068–1069, 1068*f*
fetal, 1297, 1297*f*
hydrops from, 1423–1424
sinus, 1297
Brain, fetal. *See also* Ventriculomegaly
abnormalities of, 1179
acrania and, 1179
Blake pouch cyst of, 1170, 1173*f*
cavum veli interpositi of, 1170–1174, 1174*f*
choroid plexus cysts of, 1170, 1173*f*
cortical development malformations and, 1193–1203
absence of septi pellucidi as, 1201–1203
cerebrohepatorenal syndrome as, 1196
chondrodysplasia punctata as, 1196
classification of, 1194*b*
corpus callosum agenesis/dysgenesis as, 1199–1201, 1202*f*, 1203*b*
focal changes in, 1196
hemimegalencephaly as, 1195
heterotopia as, 1196, 1199*f*
intracranial calcifications as, 1195*f*, 1203, 1204*f*
lissencephaly as, 1195–1196, 1196*f*–1197*f*
macrocephaly as, 1194–1195
megalencephaly as, 1194–1195
microcephaly as, 1194, 1195*f*
Brain, fetal *(Continued)*
polymicrogyria as, 1196, 1198*f*
schizencephaly as, 1196, 1199*f*
SOD as, 1201–1203, 1203*f*
TSC and, 1198, 1200*f*
development of, stages of, 1525*b*, 1525*f*
developmental anatomy of, 1167–1174, 1167*t*
dorsal induction errors and, 1179–1186
amniotic band sequence as, 1180*f*, 1182–1183
anencephaly as, 1179, 1180*f*
cephalocele as, 1179–1182
ciliopathies as, 1182
cranial changes in spina bifida as, 1183–1186, 1184*f*–1185*f*, 1185*t*–1186*t*
encephalocele as, 1179–1182, 1181*f*, 1182*t*
exencephaly as, 1179
Joubert syndrome as, 1182
limb-body wall complex as, 1182–1183
Meckel-Gruber syndrome as, 1182
embryology of, 1167, 1167*t*
hydrocephalus and, 1174–1178
infections of, 1203–1204, 1205*f*
MRI evaluation of, 1166–1167, 1172*f*
sonographic anatomy of, 1167–1170, 1168*f*, 1170*f*–1172*f*
cerebellar view of, 1168–1169, 1169*f*
median (midsagittal) view of, 1169, 1169*f*
thalamic view of, 1168, 1169*f*
ventricular view of, 1168, 1169*f*
split, 1196
tumors and, 1208–1210, 1209*f*–1210*f*
variants in (usually normal), 1170–1174
vascular malformations of, 1204–1208, 1206*f*
dural sinus thrombosis as, 1205–1206, 1206*f*
hydranencephaly as, 1208, 1208*f*
intracranial hemorrhage as, 1206, 1207*f*
ventral induction errors and, 1186–1203
arachnoid cysts as, 1192–1193, 1193*f*
in cerebellum, 1189–1192
Dandy-Walker malformation as, 1190, 1190*f*
HPE as, 1186–1189, 1187*b*, 1188*f*, 1189*b*
mega-cisterna magna as, 1192, 1193*f*
in posterior fossa, 1189–1192
rhombencephalosynapsis as, 1192
vermis hypoplasia or dysplasia as, 1190–1192, 1192*f*
VM and, 1174–1178
Brain, neonatal/infant. *See also* Hypoxic-ischemic events, neonatal/infant brain and
astrocytomas of, 1562, 1564*f*
calcar avis of, development of, 1523*f*, 1524
cavum septi pellucidi of, development of, 1521, 1521*f*–1522*f*
cavum veli interpositi of, development of, 1521–1522, 1521*f*
cavum vergae of, development of, 1521, 1521*f*–1522*f*
cellular migration disorders of, 1536–1537
cerebellar vermis of, development of, 1524
choroid plexus of
in coronal imaging, 1514–1515, 1514*f*
cysts of, 1565, 1566*f*
development of, 1522–1523, 1522*f*–1523*f*
papillomas of, 1562, 1565*f*
cisterna magna of, development of, 1524
cleavage disorders of, 1532–1536
color Doppler ultrasound for, 1573–1574
congenital malformations of, 1524–1526, 1525*b*
cystic encephalomalacia and, 1538, 1539*f*
cystic intracranial lesions of, 1562–1565, 1565*t*
cysts of
arachnoid, 1563–1565, 1565*b*
choroid plexus, 1565, 1566*f*
frontal horn, 1522, 1522*f*, 1566
periventricular, 1566, 1566*f*

Brain, neonatal/infant *(Continued)*
porencephalic, 1537, 1565
subependymal, 1566, 1567*f*
death of, duplex Doppler sonography and, 1580, 1583*f*
destructive lesions and, 1537–1538
developmental anatomy of, 1520–1524
diverticulation disorders and, 1532–1536
duplex Doppler sonography of, 1573–1576
approaches to, 1574, 1575*f*
arterial blood flow in, 1576, 1577*t*
asphyxia and, 1580
brain death and, 1580, 1583*f*
cerebral edema and, 1580
diffuse neuronal injury and, 1580
ECMO and, 1578–1580, 1579*f*
hemodynamics in, 1576–1580
HII and, 1580, 1581*f*–1582*f*
hydrocephalus and, 1581–1583, 1584*f*
intensive care therapies and, 1578–1580
intracranial hemorrhage and, 1580–1581, 1584*f*
intracranial tumors and, 1585, 1587*f*
measurements in, 1576, 1576*f*–1577*f*, 1576*t*
mechanical ventilation and, 1578, 1579*f*
near-field structures and, 1585, 1588*f*
optimization of, 1574, 1574*b*
pitfalls of, 1585–1589, 1589*f*
safety considerations for, 1574–1576
stroke and, 1580–1581, 1584*f*
uncommon applications of, 1585, 1588*f*
vascular malformations and, 1583–1585, 1585*f*–1587*f*
venous blood flow in, 1578, 1578*f*, 1578*t*
ependymomas of, 1562
germinal matrix of, development of, 1524, 1524*f*
HPE and, 1532–1536
alobar, 1534–1535, 1534*b*, 1536*f*
classification of, 1534*f*
lobar, 1535
midline interhemispheric form of, 1535–1536
semilobar, 1535
hydranencephaly and, 1538, 1538*f*
hydrocephalus and, 1538–1541
causes of, 1540*b*
cerebrospinal fluid production and circulation and, 1538–1541
hypoxic-ischemic injury to, 1541–1557
imaging of
coronal, technique for, 1513–1515, 1513*b*, 1513*f*–1515*f*
equipment for, 1512
mastoid fontanelle, 1512, 1517–1518, 1517*f*, 1519*f*
pitfalls in, 1523*b*
posterior fontanelle, 1512, 1517, 1517*f*–1518*f*
sagittal, 1515–1517, 1516*b*, 1516*f*–1517*f*
sonographic technique for, 1512–1518
standardized reports of, 1518–1520, 1520*b*
3-D ultrasound in, 1518
infections and, 1557–1560
acquired, 1560, 1561*f*–1563*f*
CMV, 1558–1560, 1559*f*
congenital, 1557–1560, 1559*f*
ventriculitis as, 1560, 1563*f*
lissencephaly and, 1537
in metabolic disorders, 1538
neural tube closure disorders of, 1526–1532
Chiari malformations and, 1526, 1526*b*, 1527*f*–1529*f*
corpus callosum agenesis and, 1526–1528, 1529*b*, 1530*f*–1533*f*
corpus callosum lipoma and, 1529, 1533*f*

Brain, neonatal/infant *(Continued)*
Dandy-Walker malformation and, 1529–1532, 1530*b*, 1533*f*–1534*f*
posttraumatic injury to, 1557, 1558*f*
power mode Doppler ultrasound for, 1573–1574
premature
coronal imaging of, 1515, 1515*f*
hypoxic-ischemic events and, 1541, 1541*t*
normal sonographic appearance of, 1521*f*
ultrasound screening in, optimal, 1543*b*
PVL and, 1550–1553, 1551*f*–1553*f*, 1566
schizencephaly and, 1536–1537, 1537*f*
SOD and, 1532–1534, 1535*f*
sulcation disorders of, 1536–1537
sulcus of, development of, 1520–1521, 1520*f*–1521*f*
teratomas and, 1562
tumors of, 1560–1566, 1562*b*, 1564*f*–1565*f*
primitive neuroectodermal, 1562
rhabdoid, 1562
supratentorial, 1562
vein of Galen malformations and, 1566, 1567*f*
Brain, pediatric. *See* Transcranial Doppler sonography, pediatric
Brain death
neonatal/infant brain and, duplex Doppler sonography of, 1580, 1583*f*
pediatric
coma differentiated from, 1618–1620, 1620*f*
TCD sonography and, 1618–1620, 1618*b*, 1619*f*–1620*f*
Brainstem, neonatal/infant, in diffuse cerebral edema, 1555*f*
Branchial arches, 1133–1134
anomalies of, 1651, 1651*f*–1653*f*
Branchial clefts, 1651
Branchial cysts
type I, pediatric, 1639, 1651, 1651*f*
type II, pediatric, 1639–1640, 1651, 1652*f*
type III, pediatric, 1651, 1652*f*
Branchial sinus abscess, type IV, 1643–1645, 1645*f*, 1651, 1653*f*
Branchio-oto-renal syndrome, MCDK and, 1815
Breast Imaging Reporting and Data System (BI-RADS), 768
reporting categories of, 774, 774*t*
Breast-ovarian cancer syndrome, 578
Breast(s)
abscesses of, 803–804, 803*f*–804*f*
anatomy of, 760–767
atrophy of, 763*f*
benign sonographic findings of, 795–797
hyperechoic tissue in, 796–797, 796*f*
parallel (wide-than-tall) orientation in, 797, 797*f*
thin echogenic capsule in, 797
BI-RADS reporting categories for, 774, 774*t*
cancer, staging of, 807–810, 808*f*–810*f*
CEUS for assessment of, 773–774
cysts of, 774–785
acorn, 778*f*
aspiration of, ultrasound-guided, 811, 813*f*
clustered macrocysts and, 779, 780*f*
clustered microcysts and, 782
with color streaking, 775, 776*f*
complex, 780–785, 782*f*
complicated, 775–780, 776*f*
Doppler ultrasound for differentiating, 769–770, 770*f*
eggshell calcification and, 779, 780*f*
fat-fluid levels in, 775, 778*f*
fibrocystic change and, 775
inflammation and infection of, 782–785, 785*f*
lipid, 775–779, 779*f*

Breast(s) *(Continued)*
microcysts and, 782, 784*f*
milk of calcium and, 775, 776*f*–777*f*
mural nodules and, PAM causing, 782, 783*f*–784*f*
papillary lesions and, 782
septations within, 782, 783*f*
simple, 774, 775*f*
of skin origin, 779, 781*f*
diagnostic ultrasound indications for, 797–803
breast pain as, 797–798
nipple discharge as, 798–799, 799*f*–801*f*
palpable lumps as, 769, 769*f*, 798, 798*f*
Doppler ultrasound for assessment of, 768–772, 770*f*–773*f*
echogenicities of, 761
elastography for assessment of, 772–773, 773*f*
implants of, evaluation of, 804–807, 804*f*–806*f*
interventions for, ultrasound-guided, 811–815, 813*f*–814*f*
lymphatic drainage of, 762–767, 767*f*
mammographic findings of, 799–803
dense tissue in, 761–762, 763*f*
location or position correlation in, 801
shape correlation in, 800, 802*f*–803*f*
size correlation in, 800, 801*f*–802*f*
sonographic-mammographic confirmation in, 803
surrounding tissue density correlation in, 801, 803*f*
nipple discharge and, 798–799, 799*f*–801*f*
pain in, 797–798
papillomas of, 769–771, 770*f*
intracystic, 782, 783*f*
intraductal, 799, 799*f*–800*f*
peripheral, 799, 800*f*
periductal mastitis of, 771, 771*f*
physiology of, 760–767
solid nodules of, 780–786, 782*f*
biopsy of, ultrasound-guided, 811–815, 813*f*–814*f*
circumscribed, 786
heterogenicity of, 786, 786*f*
papillary lesions and, 782
spiculated, 786
sonographic equipment for, 767, 767*f*
sonographic techniques for, 768–774
for annotation, 768
CEUS as, 773–774
color Doppler ultrasound as, 769–772, 770*f*–773*f*
Doppler ultrasound as, 768–772, 770*f*–773*f*
elastography as, 772–773, 773*f*
for lesion documentation, 768–769
patient position in, 768
special, 769–774
split-screen imaging for, 769, 769*f*
3-D ultrasound as, 773
suspicious sonographic findings of, 787–795, 787*t*
acoustic shadowing in, 791–792, 793*f*
angular margins in, 788–789, 790*f*
architectural distortion in, 795
associated features in, 794–795
calcifications in, 793–794, 795*f*
duct extension in, 790–791, 792*f*
edema in, 795
hypoechogenicity in, 792–793, 794*f*
indistinct margins in, 787, 787*f*
microlobulations in, 789, 791*f*
not parallel orientation (taller-than-wide) in, 789–790, 792*f*
skin changes in, 795
spiculation in, 787–788, 788*f*

Breast(s) *(Continued)*
thick echogenic rim, with hyperechoic spicules in, 787–788, 789*f*
TDLUs of, 760–761
sonographic appearance of, 762, 766*f*
3-D ultrasound for, 773
ultrasound examination of, 774–797
applications of, 760
automated whole-breast, 760
BI-RADS reporting categories for, 774, 774*t*
diagnosis in, 760
Doppler ultrasound for, 768–772, 770*f*–773*f*
equipment for, 767, 767*f*
for guided intervention, 811–815, 813*f*–814*f*
for implant evaluation, 804–807, 804*f*–806*f*
for infection, 803–804, 803*f*–804*f*
for interventional procedures, 760
for lymph node assessment, 807–810, 808*f*–810*f*
niche applications for, 803–811
normal tissue and variations in, 774
for sonographic-MRI correlation, 810–811, 811*f*–812*f*
suspicious findings in, 787–795, 787*t*
technique for, 768–774
three dimensional, 788, 789*f*–790*f*
water density tissue of, 761–762, 763*f*
zones of, 761, 761*f*
Breathing, sleep-disordered, 1611
Brenner tumor, 581–582, 582*f*
Breus mole, 1471
Broad ligaments, 564–565
Broad-bandwidth, 7–8
Bronchogenic cysts
fetal, 1255–1256, 1255*f*, 1255*t*
pediatric, 1650, 1716, 1718*f*
Bronchopulmonary foregut malformations, pediatric, 1716, 1718*f*
Bronchopulmonary sequestration (BPS), 1246, 1248*t*, 1250–1251, 1251*f*
extralobar, 1250
fetal, hydrops from, 1426
intralobar, 1250
Bruit, from carotid stenosis, color Doppler, 933, 934*f*
Brunn epithelial nests, in chronic cystitis, 333, 333*f*
Bubbles. *See also* Microbubbles
acoustic cavitation generation of, 41–42, 42*f*
behavior of, incident pressure and, 56–58, 57*t*
Budd-Chiari syndrome, 98–103, 100*f*–103*f*
in children, suprahepatic portal hypertension and, 1762–1763, 1763*f*
IVC and, 463
"Buddha position," fetal, 1401
Bulk modulus, 15–16
"Bunny" waveform, 953*b*, 954, 954*f*
Burkitt lymphoma, pediatric, 1860
"Burned-out" tumors. *See* Germ cell tumors, testicular, regressed
Bursal-sided partial-thickness rotator cuff tears, 888, 890*f*
Bursitis, bursal injections for, 907–909, 908*f*
Burst length, in output control, 48–50
Butterfly vertebrae, in scoliosis and kyphosis, 1235
Bypass graft(s)
coronary, radial artery evaluation for, 977–978, 980*f*
of lower extremity peripheral arteries, 974–975, 975*f*
PSV and dysfunction of, 974–975
of superficial femoral artery, 975*f*

C

CA. *See* Celiac artery
CA 125, in ovarian cancer, 578
Cadaveric kidneys, paired, in transplantation, 643–644, 648*f*
CAH. *See* Congenital adrenal hyperplasia
"Cake" kidneys, pediatric, 1785
CAKUT. *See* Congenital anomalies of kidney and urinary tract
Calcaneus, ossification of, 1377–1378
Calcar avis, neonatal/infant, development of, 1523*f*, 1524
Calcarine fissure, neonatal/infant, development of, 1520–1521, 1524
Calcific bursitis, 891
Calcific tendinitis
injections for, 909, 911*f*
of supraspinatus tendon, 891–892, 892*f*
Calcification(s). *See also* Nephrocalcinosis
abdominal, meconium peritonitis and, 1313, 1314*f*
of adrenal glands, 423, 425*f*
causes of, 424*b*
in breast sonography, 793–794, 795*f*
chronic DVT indicated by, 984, 987*f*
in chronic pancreatitis masses, 233–236, 236*f*
cystic meconium peritonitis with, 1842–1843, 1846*f*
DCIS and, 793, 795*f*
dystrophic, 339
pediatric urinary tract and, 1799
eggshell, breast cysts and, 779, 780*f*
of endometrium, 533, 534*f*
of gallbladder, 202, 202*f*
intracranial, fetal, 1195*f*, 1203, 1204*f*
liver, fetal, 1316–1318, 1317*f*, 1318*b*
of meconium periorchitis, focal, 1904, 1904*f*
of myometrium, 531–533, 533*f*–534*f*
ovarian, focal, 566–568
of prostate, 387, 388*f*
psammomatous, in peritoneal nodule, 510–511, 513*f*
of radial arteries, evaluation for, 998, 998*f*
renal artery, 336
of renal cysts, 358, 358*f*
of renal parenchyma, 339–340, 340*f*
scrotal, 833–834, 833*b*, 834*f*
of seminal vesicles, 392
splenic, 150, 153*f*
pediatric, 1769
of superficial femoral artery, 968, 970*f*
of tendons, 859–861
of thyroid cysts, 695
in thyroid nodules
diagnostic significance of, 713–714
in papillary carcinoma, 699, 702*f*
of urinary tract, pediatric, 1798–1801
cortical nephrocalcinosis and, 1798, 1798*b*, 1798*f*
dystrophic, 1799
medullary nephrocalcinosis and, 1798–1799, 1799*f*
renal vein thrombosis and, 1799, 1800*f*
urinary stasis and, 1799, 1800*f*
urolithiasis and, 1799–1801, 1799*f*
in uterine fibroids, 539*f*, 540, 540*b*
of vas deferens, 392
yolk sac, 1067, 1068*f*
Calcified metastases, of liver, 125, 128*f*
Calcimimetics, for secondary hyperparathyroidism, 734
Calcitonin, secretion of, in medullary carcinoma of thyroid, 701
Calcium bile, milk of, 194, 195*f*
Calcium hydroxyapatite, in calcific tendinitis, 909
Calculus(i)
bladder, 338–339, 339*f*
pediatric, 1908
caliceal, 334–335
Calculus(i) *(Continued)*
liver transplantation complications with, 629, 632*f*
renal, 334–336, 336*f*–337*f*
entities that mimic, 336, 337*b*, 337*f*
scrotal, extratesticular, 836–837, 837*f*
staghorn
tyrosinemia and, 1799, 1800*f*
in xanthogranulomatous pyelonephritis, 328, 329*f*
ureteral, 337–338, 338*f*–339*f*
bladder augmentation and, 1912–1913
complicating renal transplantation, 659–660, 663*f*–664*f*
urethral, pediatric, bladder outlet obstruction from, 1906, 1906*f*
Calf veins, ultrasound imaging of, 982
Caliceal calculi, 334–335
Callosomarginal sulcus, neonatal/infant, development of, 1520–1521
Calvarium, fetal, compressibility of
in osteogenesis imperfecta type II, 1382, 1392, 1393*f*
in skeletal dysplasia, 1382
Calyceal diverticula, renal milk of calcium and, 1799, 1800*f*
Calyces, dilation of, in hydronephrosis, 1354
Campomelic dysplasia, 1395, 1396*f*
bowing of long bones in, 1381–1382
pulmonary hypoplasia and, 1384*f*
ribs and, 1382–1384
sonographic appearance of, 1380*f*
thanatophoric dysplasia differentiated from, 1388–1389
Camptodactyly, fetal, 1404–1405, 1406*f*
Campylobacter, 1852
Canal of Nuck
cyst or hydrocele of, simulating groin hernia, 499–500, 501*f*
delayed closure of, indirect inguinal hernia from, 476–477, 477*f*
Canalization, in spine embryology, 1672, 1673*f*
Candida albicans
genitourinary tract infections from, 330–331, 331*f*
neonatal urinary tract infection from, 1794, 1795*f*
Candidiasis
hepatic, 86–87, 88*f*
hepatosplenic, splenic abscesses in, 150–152, 154*f*
neonatal, 1794, 1795*f*
Capillary malformations, tethered cord and, 1679
Capsular arteries, 821
Caput medusae, 1752
Carcinoid tumor, renal, 355–356
Carcinoma(s). *See also* Breast(s), solid nodules of; Ductal carcinoma in Situ; Hepatocellular carcinoma; Papillary carcinoma; Renal cell carcinoma; Transitional cell carcinoma
acinic cell, parotid gland, pediatric, 1638, 1639*f*
acoustic shadowing caused by, 791–792, 793*f*
adenoid cystic, salivary gland, pediatric, 1638
adrenal, pediatric, 1827, 1827*f*
adrenocortical, 424–425, 426*f*
of bladder
squamous cell, 348
transitional cell, 347–348, 350*f*
cervical, 542, 543*f*
hematometra in, 547*f*, 549
choriocarcinoma, testicular, 824, 825*f*
circumscribed, 786
clear cell, 581, 582*f*
colon, 261–264, 263*f*–264*f*
pediatric, 1880

Carcinoma(s) *(Continued)*
embryonal, 823, 825*f*
ovarian, 1880
pediatric, testicular, 1899
endometrial, 544, 548–551, 550*f*
polycystic ovarian disease and, 1877–1878
esophageal, staging of, endosonography in, 301
fallopian tube, 589
gallbladder, 206–207, 206*f*
gastric, endosonographic identification of, 301
mucoepidermoid, salivary gland, pediatric, 1638
of parathyroid glands
adenomas differentiated from, 735–736, 738*f*
primary hyperparathyroidism from, 734
primary peritoneal serous papillary, 511–513, 515*f*
prostate, transrectal sonography of, 302, 302*f*
rectal, staging of, endosonography in, 301–302, 301*f*–304*f*
spiculated, 786
TDLU, 789–790, 792*f*
of thyroid gland, 695
anaplastic, 707–708, 708*b*, 709*f*
follicular, 701, 701*b*, 706*f*–707*f*, 1648
incidence of, 722, 722*f*–723*f*
medullary, 701–707, 707*f*–708*f*, 1648
nodular disease and, 698–708
papillary, 698–701, 701*f*–705*f*, 713, 1648, 1649*f*
vaginal, pediatric, 1883
Carcinomatosis, peritoneal, 510–511, 510*f*–515*f*
Cardiac output, reduced, carotid flow waveforms and, 935*f*, 936–937
Cardioembolic stroke, 915–916
Cardiomyopathy(ies)
carotid flow waveforms and, 936–937, 936*f*
fetal, 1295*f*
adrenal glands and, 1353–1354
hydrops from, 1425
Cardiopulmonary bypass
partial, in neonatal/infant brain, duplex Doppler sonography and, 1578–1579, 1579*f*
pediatric TCD sonography in, 1621–1622
Cardiosplenic syndrome, 1292–1293, 1293*b*
Cardiovascular disease, 432–433
Carney complex, 826
Carney triad, pheochromocytomas with, 1826
Caroli disease
of biliary tree, 171, 171*f*
pediatric, 1735
bile duct dilation in, 1736–1737, 1736*f*
Carotid artery(ies). *See also* Plaque(s), carotid
anatomy of, 916, 917*f*
arthrosclerotic disease of, plaque characterization in, 919
color Doppler evaluation for stenosis of, 932–935
advantages and pitfalls of, 934–935, 934*b*, 934*f*
bruit from, 933, 934*f*
optimal settings in, low-flow vessel evaluation, 933–934, 933*b*, 934*f*
Takayasu arteritis of, 944–946, 947*f*
common, 916, 917*f*
aneurysm of, 947–948
carotid bifurcation and, 917–918, 918*f*
ectatic, 947–948, 949*f*
helical flow in, 934
occlusion of, abnormal internal carotid artery waveform and, 941, 942*f*
posttraumatic pseudoaneurysm of, 948, 950*f*
stenosis of, grading of, 930
waveform of, 925–926, 925*f*
disease of, preoperative strategies for, 941–942
dissection of, 946–947, 947*b*, 948*f*
Carotid artery(ies) *(Continued)*
distal internal, as transtemporal approach landmark, 1592, 1594*f*
Doppler spectral analysis for, 925–932
high-velocity blood flow patterns in, 928–932, 929*f*–931*f*, 931*t*
pitfalls in, 927–928, 928*f*
spectral broadening in, 927, 927*f*
standard examination in, 926–927, 926*f*
endarterectomized, sonographic features of, 942, 944*f*
external, 916
branching vessels of, 918, 918*f*
collaterals of, intracranial circulation and, 939, 940*f*
mistaking for internal carotid artery, 941, 941*f*
stenosis of, grading of, 930
waveform of, 925–926, 925*f*
flow pattern in
altered, misinterpretation of, 927, 928*f*
high-velocity, in stenoses, 928–932, 929*f*–931*f*, 931*t*
normal transient reversal of, 933–934
internal, 916
common carotid artery occlusion causing abnormal waveform in, 941, 942*f*
fibromuscular dysplasia of, 944–946, 946*f*
mistaking external carotid artery for, 941, 941*f*
stenosis of, grading, 928–929, 929*f*–930*f*
tardus-parvus waveforms in stenosis of, 934*f*, 938
waveform of, 925–926, 925*f*
internal, occlusion of, 939–941
external carotid collaterals to intracranial circulation in, 939, 940*f*
pitfall in diagnosis of, 941, 941*f*
sonographic findings in, 939*b*
string sign distinguished from, 939
kinked, carotid flow waveforms and, 936–937, 936*f*
lymph node masses near, 948, 949*f*
neck masses of, 947–948, 949*f*–950*f*
nonarthrosclerotic diseases of, 944–948
arteritis as, 944–946, 947*f*
carotid body tumors as, 947–948, 949*f*
from cervical trauma, 946, 948*f*
extravascular masses as, 948, 949*f*
fibromuscular dysplasia as, 944–946, 946*f*
posttraumatic pseudoaneurysms as, 948, 950*f*
ultrasound examination of, 916
postoperative ultrasound of, 942–944, 944*f*
power Doppler evaluation for stenosis of, 935–939, 935*b*
pitfalls and adjustments in, 935*f*–939*f*, 936–939, 937*b*
pseudoulceration of, 923
revascularization of, ultrasound after, 942–943, 945*f*
stenosis of
angiography and MRA for, 916
CEA for, 916
color Doppler evaluation of, 932–935
Doppler spectral analysis in, 925–932
external, grading of, 930
follow-up for, 941, 943*t*
gray-scale, 923–924, 924*f*
high-velocity blood flow patterns in, 928–932, 929*f*–931*f*, 931*t*
internal, grading of, 928–930, 929*f*–930*f*
internal, tardus-parvus waveforms in, 934*f*, 938
power Doppler evaluation of, 935–939, 935*b*
recurrent, grading of, 943–944, 945*t*
Carotid artery(ies) *(Continued)*
stroke from, 915–916
ultrasound diagnostic criteria for, 930–932, 931*t*
stenting of
restenosis in, grading of, 943–944, 945*t*
ultrasound after, 942–943, 945*f*
tandem lesions in, 937
TIA from embolism of, 919
tortuous
carotid flow waveforms and, 936–937, 937*f*
spectral broadening in, 928
transcranial Doppler sonography for, 948–950, 950*f*
ultrasound examination of
color Doppler evaluation for, 932–935
diagnostic criteria for, 930–932, 931*t*
Doppler spectral analysis for, 925–932
follow-up based on, 941, 943*t*
indications for, 915–916, 916*b*
interpretation of, 918–944
postoperative, 942–944, 944*f*
techniques for, 917–918, 917*f*–918*f*
transcranial Doppler sonography for, 948–950, 950*f*
visual inspection of gray-scale images in, 918–924
visual inspection of gray-scale images for, 918–924
for intima-media thickening, 918–919, 919*f*
for plaque characterization, 919–922, 920*f*–922*f*, 922*b*
for plaque ulceration, 923, 923*b*, 923*f*–924*f*
for stenosis evaluation, 923–924, 924*f*
for vessel wall thickness, 918–919
walls of, dissections in, flow disturbances in, 928
Carotid bifurcation, 917–918, 918*f*
pathologic lymph node near, 948, 949*f*
Carotid body tumors, 947–948, 949*f*
Carotid bulb, 917
Carotid endarterectomy (CEA)
for carotid stenosis, 916
pediatric, TCD sonography in, 1621
sonographic features following, 942, 944*f*
Carotid Revascularization Endarterectomy Versus Stenting Trial (CREST), 916
Carotid-cavernous fistulas, TCD sonography assessing, 1614
Carpal tunnel entrapment, of median nerve, 864–865, 866*f*
Carpal tunnel syndrome, 865, 866*f*
Carpenter syndrome, craniosynostosis in, 1136–1138
Cartilage, sonographic characteristics of, 1923
"Cartilage interface" sign, 886, 888, 888*f*
Cataracts
congenital, 1143, 1147*b*
temperature increase in utero and, 1037
Catheterization
central venous, IJV thrombosis complicating, 955
ESRD and, 994
Catheter(s)
central, peripherally inserted, pediatric, insertion of, 1953
drainage
for interventional sonography, 1948
placement of, 610–611, 611*f*
removal of, 612
selection of, 610–611, 611*f*
peripherally inserted central, 993*f*
interventional sonography, pediatric, 1954, 1955*f*–1957*f*
SVC, pediatric, position of, 1716–1721, 1722*f*

Cat-scratch disease, pediatric, 1633–1634
  causes of, 1938, 1938*f*
  lymphadenopathy in, 1660–1663
Cauda equina, formation of, 1673, 1673*f*
Caudal agenesis, 1674
  closed spinal dysraphism and, 1689, 1690*f*
  maternal diabetes mellitus and, 1689
  type 1, 1689, 1690*f*
  type 2, 1689
Caudal appendage, tethered cord and, 1679
Caudal cell mass, differentiation of, in spine embryology, 1674
Caudal neuropore, in spine embryology, 1217
Caudal regression
  defects, 1218
  fetal, 1237–1238, 1237*f*
  sequence, sacral agenesis in, 1237
  syndromes
    as limb reduction defect, 1401, 1404*f*
    skeletal dysplasia and, 1382
Caudate lobe, 75–76, 76*f*
Caudate nucleus, in sagittal imaging of neonatal/infant brain, 1515, 1517*f*
Caudothalamic groove, neonatal/infant
  in intraparenchymal hemorrhage, 1547, 1547*f*
  in sagittal imaging, 1516–1517, 1517*f*
Causality, criteria for judging, 48
Cavernoma, portal, in portal vein thrombosis, 1757, 1761*f*
Cavernous hemangiomas
  of bladder, 356
  CEUS characterization of, 111, 113*f*
  Doppler ultrasound characterization of, 109–110
  of liver, 108–112, 112*f*–113*f*
    percutaneous needle biopsy of, 603–604, 604*f*
Cavitation. *See* Acoustic cavitation
Cavum septi pellucidi
  fetal
    formation of, 1167
    normal sonographic appearance of, 1168–1169
    sonographic view of, 1024*f*
  neonatal/infant, development of, 1521, 1521*f*–1522*f*
Cavum veli interpositi
  arachnoid cysts differentiated from, 1192–1193
  fetal, 1170–1174, 1174*f*
  neonatal/infant, development of, 1521–1522, 1521*f*
Cavum Vergae
  formation of, 1167
  neonatal/infant
    in coronal imaging, 1514–1515
    development of, 1521, 1521*f*–1522*f*
CBAVD. *See* Congenital bilateral absence of the vas deferens
CCAM. *See* Congenital cystic adenomatoid malformation
CDH. *See* Congenital diaphragmatic hernia
CEA. *See* Carotid endarterectomy
Cebocephaly
  alobar HPE and, 1534–1535, 1536*f*
  hypotelorism and, 1140
Celiac artery (CA)
  anatomy of, 451
  duplex Doppler sonography of, 453–455, 455*f*
  in median arcuate ligament syndrome, 453, 453*f*
  occluded, 454–455, 458*f*
  stenosis of, after liver transplantation, 634–635, 637*f*
Celiac disease, in gastrointestinal tract, 300
Cell aggregation, in obstetric sonography, 1038
Cell membrane alteration, from obstetric sonography, 1038
Cell-free DNA, 1088–1089
  aneuploidy screening with, 1107
Cellular migration
  disorders of, neonatal/infant brain and, 1536–1537
  in organogenesis, 1524–1525
Cellulitis, 872–874, 873*f*–874*f*
  complicated lymphadenitis with, in children, 1658–1660, 1662*f*
Center-stream sampling, true, in carotid occlusion diagnosis, 939
Central echo complex, in pediatric kidney, in renal duplication, 1783, 1784*f*
Central hypoventilation syndrome, neuroblastoma with, pediatric, 1825
Central nervous system (CNS)
  anomalies of, 1166
  MRI evaluation of fetal, 1166–1167
Central venous access, for interventional sonography, pediatric, 1954
Central venous catheterization
  DVT related to, 935, 995*f*
  IJV thrombosis complicating, 955
Centrum semiovale, neonatal/infant, 1514
Centrum(a), of vertebral body
  in lateral longitudinal scan plane, 1223*f*
  in lateral transaxial scan plane, 1222*f*
  ossification of, 1218, 1219*f*
  in posterior longitudinal scan plane, 1224*f*
  in posterior transaxial scan plane, 1222*f*
Cephalic vein, 990*f*, 991
Cephalocele(s)
  atretic, 1180
  fetal brain and, 1179–1182
  as spinal dysraphism, 1139–1140
Cerclage, cervical, for cervical incompetence, 1505–1507, 1506*f*
Cerebellar hemispheres, fetal, normal sonographic appearance of, 1168–1169, 1169*f*
Cerebellar hemorrhage, neonatal/infant brain and, 1548–1550, 1549*f*
Cerebellar infarction, neonatal/infant brain and, 1555
Cerebellar vermis, 1167, 1515, 1516*f*
  neonatal/infant, development of, 1524
Cerebellum
  Blake pouch and, 1189
  Dandy-Walker malformation in, 1190, 1190*f*
  embryology of, 1167
  fetal, sonographic view of, 1024*f*
  hypoplasia of, 1190
  mega-cisterna magna and, 1192, 1193*f*
  neonatal/infant, in coronal imaging, 1514–1515, 1514*f*
  rhombencephalosynapsis in, 1192
  ventral induction errors in, 1189–1192
  vermis hypoplasia or dysplasia in, 1190–1192, 1192*f*
Cerebral artery. *See* Anterior cerebral artery; Middle cerebral artery; Posterior cerebral artery
Cerebral blood flow, neonatal/infant
  arterial, velocities in, range of, 1576, 1577*t*
  velocity of, determination of, 1576, 1576*f*
  venous, velocities in, range of, 1578, 1578*f*, 1578*t*
Cerebral blood vessels, extracranial, 917*f*. *See also* Internal jugular vein; Vertebral artery
  IJV as, 955–956
  vertebral artery as, 950–955
Cerebral cavernous malformation, in venous malformations of neck, 1657
Cerebral cortex. *See also* Cortical development malformations, fetal brain and
  development of, 1167
  malformations of, 1193–1203
Cerebral edema
  neonatal/infant, 1550–1556
    diffuse, 1553–1555, 1554*f*–1555*f*
    duplex Doppler studies of brain and, 1580
  pediatric, TCD sonography in, 1614, 1617*f*
Cerebral hemisphere, neonatal/infant, in sagittal imaging, 1517, 1517*f*
Cerebral infarction, neonatal/infant, 1550–1556
  focal, 1555–1556, 1556*b*, 1556*f*
  luxury perfusion and, 1580–1581, 1584*f*
Cerebral palsy
  pediatric, neurogenic bladder in, 1907
  periventricular leukomalacia and, 1550
Cerebral peduncles, 1518
  as transtemporal approach landmark, 1592, 1593*f*
Cerebral sinovenous thrombosis, 1547–1548
Cerebrohepatorenal syndrome
  cortical malformations in, 1196
  subependymal cysts from, 1566
Cerebroplacental ratio, MCA and, 1458, 1460*f*
Cerebrospinal fluid, hydrocephalus and production and circulation of, 1538–1541
Cerebrovascular accident, 915–916. *See also* Stroke
Cerebrovascular disease, SCD indicators for, 1598, 1599*b*
  MCA and, 1600*f*, 1604*f*–1605*f*
  ophthalmic artery flow as, 1599*f*
  stroke and, 1601*f*–1603*f*
Cervical aortic arch, 1658
Cervical canal, dilation of, spontaneous PTB and, 1503
Cervical carcinoma, iliac veins and, 461*f*
Cervical cerclage, for cervical incompetence, 1505–1507, 1506*f*
Cervical ectopia cordis, 1295
Cervical ectopic pregnancy, 1073–1074, 1074*f*
Cervical ectopic thymus, 1723
Cervical fascia, pediatric. *See also* Infrahyoid space, pediatric; Suprahyoid space, pediatric
  deep layers of, 1628, 1629*f*
    infrahyoid space in, 1628–1629, 1640–1650
    suprahyoid space in, 1628–1629
Cervical kyphosis, in campomelic dysplasia, 1381–1382
Cervical lymph node(s)
  parathyroid adenomas confused with, 745
  pediatric, inflammatory disease of, 1658–1663, 1661*f*–1663*f*
  percutaneous needle biopsies for, 717–718, 718*f*
Cervical teratoma
  fetal, 1159, 1161*f*
  pediatric, 1654, 1654*f*
Cervicothoracic vertebrae, campomelic dysplasia and, 1395
Cervix, 528–530
  abnormalities of, 541–544, 543*f*
    management protocols for, 1507, 1507*f*–1508*f*
    transvaginal ultrasound findings on, 1503*b*
  assessment of, 1503–1507
    for asymptomatic patients, 1503–1505
    in cervical incompetence and cervical cerclage, 1505–1507, 1506*f*
    fetal therapy and, 1505
    in general obstetric population screening, 1503–1504
    in high-risk obstetric population screening, 1504–1505
    in multiple gestations, 1504–1505
    in pervious cervical surgery, 1505
    in polyhydramnios, 1505
    in preterm premature rupture of membranes, 1505
    in prior PTB, 1504

Cervix *(Continued)*
for symptomatic patients, 1505–1507
in uterocervical anomalies, 1505
carcinoma of, 542, 543*f*
hematometra in, 547*f*, 549
duplicated, 538
dynamic changes in, spontaneous PTB and, 1501–1503, 1503*f*
ectopic pregnancy implantation in, 1073–1074, 1074*f*
funneling of, in spontaneous PTB prediction, 1501, 1502*f*
incompetence of, 1495–1496
cervical cerclage and, 1505–1507, 1506*f*
vaginal pessary and, 1507
length of, 1499–1500, 1499*f*
in prediction of spontaneous preterm birth, 1500–1501, 1501*t*
short, 1500–1501, 1500*f*, 1501*t*
nabothian cysts of, 533, 535*f*
in pregnancy, on second-trimester scan, 1021*f*
pseudomass in, 533, 536*f*
short, 1500–1501, 1500*f*, 1501*t*
shortening of, progressive, spontaneous PTB and, 1501
sonography of, 1496–1501
technical limitations and pitfalls of, 1498–1499, 1498*b*, 1499*f*
transabdominal approach to, 1496–1497, 1496*f*
transperineal/translabial approach to, 1497, 1497*f*
transvaginal approach to, 1497–1498, 1497*f*–1498*f*
surgery on, prior, cervical assessment and, 1505
trauma to, carotid artery damage from, 946, 948*f*
Cesarean section(s)
hematomas and
bladder flap, 556–557, 557*f*
subfascial, 556–557, 557*f*
pediatric pregnancy and, 1884
postpartum findings on, 556–557, 557*f*–558*f*
scars from, 557, 558*f*
ectopic pregnancy implantation and, 1073, 1075*f*
CEUS. *See* Contrast-enhanced ultrasound
CF. *See* Cystic fibrosis
CHAOS. *See* Congenital high airway obstruction
Charcot triad, in acute cholangitis, 176
CHARGE syndrome, coloboma in, 1143
CHD. *See* Congenital heart disease
Chemical peritonitis, 514
Chemical ventriculitis, in intraventricular hemorrhage, 1545–1547
Chemiluminescence, 42, 42*f*
Chest, fetal. *See also* Congenital diaphragmatic hernia; Congenital pulmonary airway malformation; Lung(s)
bronchogenic cysts in, 1255–1256, 1255*f*, 1255*t*
CHAOS and, 1253–1255, 1254*f*
congenital diaphragmatic hernia in, 1258–1264
development of structures in, 1243–1245
neurenteric cyst in, 1256
normal sonographic features of, 1244–1245, 1244*f*
pericardial effusion in, 1258, 1258*f*
pleural effusion in, 1256–1258, 1257*f*
pleuropulmonary blastoma and, 1252–1253
pulmonary development in, 1243
pulmonary hypoplasia and, 1245–1246
pulmonary lymphangiectasia and, 1258, 1259*f*
Chest, pediatric. *See also* Pneumonia, pediatric
atelectasis and, 1714, 1716*f*
bronchopulmonary foregut malformations and, 1716, 1718*f*
CPAM and, 1715–1716, 1717*f*
diaphragm disorders of, 1716, 1718*f*–1720*f*
empyema in, sonographic signs of, 1702–1711, 1707*f*
lung abscess in, 1711, 1713*f*
lung parenchyma and, 1711–1716
lymphatic malformations and, 1723
mediastinal masses in, 1723–1724
abnormal thymus location mimicking, 1723
anterior, 1723–1724
lymphadenopathy and, 1724
posterior, 1724
thymic index and, 1723, 1724*t*, 1725*f*, 1726*t*
parapneumonic collections in, 1710–1711
pleural effusions in, sonographic signs of, 1702–1711, 1704*f*–1708*f*
pleural fluid in, sonographic signs of, 1709, 1709*b*, 1709*f*–1710*f*
rib fractures in, 1727
sonography of
CT compared to, 1709, 1710*f*–1711*f*
indications for, 1701, 1702*b*
pitfalls in, 1709–1710, 1712*f*
technique for, 1701–1702, 1703*f*–1704*f*
ultrasound-guided interventional procedures in, 1724–1726, 1726*f*–1727*f*
vascular disorders of, 1716–1723
thrombosis, 1716–1721, 1721*f*–1723*f*
wall of, lesion of, ultrasound-guided biopsy of, 1724–1725
Chiari malformation(s)
I, 1526
II, 1190
banana sign in, 1183–1185, 1184*f*, 1221, 1228, 1230–1232
corpus callosum agenesis in, 1526, 1528*f*
lemon sign in, 1183–1185, 1184*f*, 1221, 1232–1233
myelomeningoceles with no, 1526, 1529*f*
normal sonographic appearance of fetal, 1168–1169
open spina bifida and fetal, 1183, 1184*f*
open spinal dysraphism with, pediatric, 1681–1682
sonographic findings in, 1526, 1526*b*, 1527*f*–1528*f*
in spina bifida screening, 1221, 1228
VM with, 1177
III, 1526
neonatal/infant neural tube closure disorders and, 1526, 1526*b*, 1527*f*–1529*f*
Chiba needles, 1948
Child life specialists, 1776–1781
Childhood malignancies, obstetric sonography and, 1041
Chlamydia trachomatis, 846, 1633–1634
Chlamydial perihepatitis, PID and, 1887
Chloroma
masseter muscle, 1641*f*
pediatric, neck, 1667*f*
Chocolate cysts, 574–575
Cholangiocarcinoma, 171
biliary tree and, 184–188
characterization of, with microbubble contrast agents, 106*f*
distal, 188, 192*f*
fluke infections and, 178–179
hilar, 185–188
CEUS assessment of, 188, 191*f*
criteria for unresectable, 187*b*
Cholangiocarcinoma *(Continued)*
Doppler ultrasound assessment for, 187–188, 189*f*–191*f*
treatment and staging for, 186–187
tumor growth patterns in, 186
intrahepatic, 184–185, 186*f*
intraductal, 185, 186*f*–187*f*
peripheral, 129
Cholangiography, transhepatic, 614–615
Cholangiohepatitis, Oriental, 179
Cholangiopathy
autoimmune, 182
HIV, 181–182, 181*f*
Cholangitis
acute (bacterial), 176, 177*f*
AIDS, 181
ascending, 629
autoimmune, 182
IgG4-related, 182–184, 185*f*
pyogenic, recurrent, 179–181, 180*f*
sclerosing
causes of secondary, 182*b*
primary, 182, 183*f*, 184
recurrent, after liver transplantation, 629, 630*f*
Cholecystectomy, gallbladder nonvisualization from, 190–194
Cholecystenteric fistula, 207
Cholecystitis
acalculous, 200
pediatric, 1741
acute, 195–200, 197*f*–199*f*, 197*t*, 201*f*
hyperemia in, 197*f*, 198–199
pediatric, 1741
prominent cystic artery in, 197*f*, 198–199
sonographic findings in, 196, 197*t*
chronic, 201–202
emphysematous, 175, 198*f*, 200
gallbladder nonvisualization from, 190–194, 193*f*
gangrenous, 198*f*, 200
hemorrhagic, 200
percutaneous cholecystostomy for, ultrasound-guided, 613–614, 616*f*
xanthogranulomatous, 202
Cholecystostomy, percutaneous, ultrasound-guided, 613–614, 616*f*
Choledochal cysts
of biliary tree, 168–170, 169*f*–170*f*
fetal duodenal atresia mistaken for, 1309
of fetal gallbladder, 1319, 1320*f*
neonatal jaundice and, 1735–1737, 1735*f*–1736*f*
pediatric pancreatitis and, 1862–1864
Choledochocele, pediatric, 1735
Choledochoduodenal fistula, 175–176, 177*f*
Choledochoenteric fistula, 175–176, 177*f*
Choledochojejunostomy, for liver transplantation, 625
Choledocholithiasis, in biliary tree, 172–173, 182
common bile duct stones and, 173–174, 173*f*
intrahepatic, 173, 173*f*
Cholelithiasis, pediatric, 1741, 1741*b*, 1743*f*
Chondrodysplasia punctata, 1399
cortical malformations in, 1196
sonographic appearance of, 1380*f*
Chondroectodermal dysplasia, 1398–1399
Chondrolysis, complicating injectable steroids, 901
Chorioamnionitis, maternal, PVL and, 1551
Chorioangioma, 1476, 1478*f*–1479*f*
Choriocarcinoma
ovarian, pediatric, 1880
pseudoprecocious puberty and, 1887
PTN and, 1080–1082, 1083*f*
testicular, 824, 825*f*, 1899
Chorion, amnion separation from, 1469, 1469*f*
Chorion frondosum, 1465–1466

Chorion laeve, 1465–1466
Chorionic bump, in gestational sac, 1065
Chorionic cavity, 1051, 1053*f*
Chorionic plate, 1465–1466
Chorionic sac fluid, 1054–1055, 1056*f*
Chorionic villi, 1465–1466
  formation of, 1051–1052, 1053*f*
Chorionic villus sampling (CVS), 1107–1108, 1108*f*
Chorionicity, in multifetal pregnancy, 1115–1116, 1116*f*
  sonographic determination of, 1117–1119, 1118*f*, 1119*t*, 1120*f*–1121*f*
  triplets and, 1122*f*
Choroid plexus
  fetal
    fetal brain and cysts of, 1170, 1173*f*
    sonographic view of, 1024*f*
    spina bifida and cysts of, 1233
    trisomy 18 and cyst of, 1103*f*, 1104
    trisomy 21 and cysts of, 1101
  neonatal/infant
    in coronal imaging, 1514–1515, 1514*f*
    cysts of, 1565, 1566*f*
    development of, 1522–1523, 1522*f*–1523*f*
    papillomas of, 1562, 1565*f*
  papillomas of
    Aicardi syndrome and giant pigmented nevi in, 1209
    in neonatal/infant brain, duplex Doppler sonography of, 1588*f*
    VM with, 1177–1178
Choroid(s)
  asymmetry of, in VM, 1178
  separation of, from medial ventricle wall, in VM evaluation, 1176, 1176*f*
Chromosomal abnormalities. *See also* Aneuploidy; Triploidy; Trisomy 13; Trisomy 18; Trisomy 21
  diagnostic testing for, 1107–1109, 1108*f*
  Ebstein anomaly with, 1286
  fetal, IUGR and, 1455
  fetal hydrops from, 1429–1430, 1430*f*
  maternal age-related risks of, 1088, 1089*f*
  primary amenorrhea in, 1887
  teratologic hip dislocation and, 1932
  triploidy as, 1104–1106, 1104*b*, 1105*f*
  trisomy 13 as, 1104
  trisomy 18 as, 1103–1104
  trisomy 21 as, 1097–1103
  Turner syndrome as, 1106–1107, 1106*f*
Chromosomal anomalies, in CHD, 1270
Chromosomal microarray analysis (CMA), 1097
Chromosome 11p13, hepatoblastomas and, 1746
Chronic allograft nephropathy, 1810, 1812*f*
Chronic autoimmune lymphocytic thyroiditis, 724, 725*f*–727*f*
Chronic epididymitis, 841, 843*f*
Chronic kidney disease (CKD), 1796–1798, 1797*t*, 1798*f*
Chronic prostatitis/chronic pelvic pain syndrome (CP/CPPS), 389–390, 390*f*
Chronic sclerosing pancreatitis, 236
Chylothorax
  congenital, fetal, hydrops from, 1425–1426
  fetal
    in hydrops, 1413–1416
    primary, 1256
  neonatal, radiopaque hemithorax in, 1704*f*
Chylous ascites, 508
Ciliopathies, 1182, 1346
Cingulate sulcus, 1515
  neonatal/infant, development of, 1520–1521, 1521*f*
Circumscribed carcinomas, 786
Circumvallate placenta, 1479–1480, 1480*f*–1481*f*
Cirrhosis
  biliary, 92–93, 182
    pediatric, 1741
  gallbladder wall thickening and, 199*f*
  hepatic vein strictures in, 95, 95*f*
  in inborn errors of metabolism, 1738
  of liver, 92–96
    Doppler ultrasound characteristics of, 95, 95*f*
    HCC and, 122, 122*t*
    intrahepatic portal hypertension from, 96
    morphologic patterns of, 92–95, 94*f*
    pseudocirrhosis of, 125–128, 129*f*
    sonographic features of, 95*b*
    SWE and, 95–96
  macronodular and micronodular, 92–93
  pediatric, 1741, 1742*f*
    causes of, 1760*b*
    intrahepatic portal hypertension and, 1759–1762
  post necrotic, 1741
Cistern, as transtemporal approach landmark, 1592, 1593*f*
Cisterna magna
  fetal
    effacement of, in Chiari II malformation, 1183–1185, 1184*f*
    normal sonographic appearance of, 1168–1169
  neonatal/infant
    clot in, in intraventricular hemorrhage, 1545, 1546*f*
    development of, 1524
    mega, Dandy-Walker malformation differentiated from, 1531, 1534*f*
CKD. *See* Chronic kidney disease
Classic diagnostic triad, for renal cell carcinoma, 340
Clavicle, 878–879, 878*f*
  growth of, normal, 1378
Clear cell carcinoma, 581, 582*f*
Cleavage, neonatal/infant brain and disorders of, 1532–1536. *See also* Holoprosencephaly
Cleft lip/palate
  associated signs of, 1152*b*
  bilateral, 1152, 1156*f*–1157*f*
    hypertelorism and, 1144*f*
    Roberts syndrome and, 1401
  complete compared to incomplete, 1151, 1153*f*–1154*f*
  deviation of vomer in, 1151
  differential diagnosis of, 1151*b*
  isolated clefts of secondary palate in, 1153
  median, 1152
  as midface abnormality, 1151–1153
  patterns of, 1152*f*
  Tessier category of, 1152–1153, 1153*f*
  trisomy 13 and 18 in, 1151
  unilateral, 1152, 1155*f*
    midface hypoplasia with, 1149*f*
Cleidocranial dysplasia
  ribs in, 1382–1384
  wormian bones in, 1139
Clinodactyly, fetal, 1404–1405, 1406*f*
Cliopathies, 1182
Clitoris, fetal, enlarged, 1367
CLO. *See* Congenital lobar overinflation
Cloaca, 1337*f*, 1338, 1674
Cloacal exstrophy
  fetal abdominal wall and, 1328–1329, 1329*f*
  pediatric, risk of spinal dysraphism with, 1689
  sacral agenesis in, 1237
Cloacal malformation, 1310–1311
  fetal, lower urinary tract obstruction and, 1363, 1363*f*
  pediatric, risk of spinal dysraphism with, 1689
Clonorchiasis, biliary tree and, 178–179, 179*f*
Clopidogrel (Plavix), 598
Closed-loop obstruction, mechanical bowel and, 293, 295*f*
Cloverleaf-shaped skull, 1136
  craniosynostosis with, 1137*f*–1138*f*
  in skeletal dysplasias, 1382
  in thanatophoric dysplasia type 2, 1388–1389, 1389*f*
Clubfoot
  fetal, 1407, 1407*f*
    body stalk anomaly and, 1329
    campomelic dysplasia and, 1395
    in skeletal dysplasia, 1382
    spina bifida and, 1233
  pediatric, 1932
Clubhand, fetal, 1407
  in skeletal dysplasias, 1382
Clustered macrocysts, in breast, 779, 780*f*
Clustered microcysts, in breast, 782
CMA. *See* Chromosomal microarray analysis
CMV. *See* Cytomegalovirus infection
CNS. *See* Central nervous system
CNVs. *See* Copy number variants
Coagulation necrosis, from HIFU, 32
Coagulopathies, small bowel obstruction from, 1843
Coarctation
  of aorta, 1291, 1292*f*
    fetal, hydrops from, 1423–1424
    hypoplastic left heart syndrome with, 1287
  of frontal horn, 1522, 1522*f*
  of lateral ventricles, 1566
Coccygeal dimples, 1679, 1680*f*
Coccyx
  agenesis of, 1689
  development of, in infants, 1677, 1680*f*
Cogwheel sign, 587–588
Colitis
  infectious, pediatric, 1852
  pseudomembranous, 296–297, 298*f*
  tuberculosis, 287–288
  ulcerative, 266–267
Collagen bundles, 859
Collagen vascular disease, maternal, fetal AVB from, 1297
Coloboma, 1143, 1146*f*
Colon
  carcinoma of, 261–264, 263*f*–264*f*
    pediatric, 1880
  diverticula of, 290, 291*f*
  fetal, 1308–1316
    anorectal malformations and, 1310–1312, 1311*f*
    MMIHS and, 1362–1363
  pediatric, 1847–1848
    ectopic or imperforate anus and, 1847–1848, 1850*f*
    interventional sonography and anatomy of, 1950
    normal anatomy of, 1847, 1850*f*
    sonographic technique for, 1847
Color assignments, changing, in color Doppler, 933
Color Doppler ultrasound, 24, 25*b*
  aliasing in, 28, 29*f*, 966
  for breast assessment, 769–772, 770*f*–773*f*
  for carotid stenosis evaluation, 932–935
    advantages and pitfalls of, 934–935, 934*b*, 934*f*
    bruit from, 933, 934*f*
    optimal settings in, low-flow vessel evaluation, 933–934, 933*b*, 934*f*
  color assignments in, changing, 933
  for Crohn disease, 268*t*, 269, 272*f*
  Doppler beam in, vessel paralleling, 933
  for epididymitis, pediatric, 1896, 1896*b*
  in fetal heart assessment, 1275–1277, 1282*f*

Color Doppler ultrasound *(Continued)*
green-tag feature in, 932–933
interpretation of, 28, 28*f*–29*f*
interventional sonography, pediatric and, 1945
limitations of, 25*b*
for neonatal/infant brain, 1573–1574
operating modes in, 30–31
for pancreatic carcinoma, 241, 241*b*, 241*f*–243*f*, 241*t*
for percutaneous needle biopsies, 599
in placenta accreta diagnosis, 1471
in placenta blood flow assessment, 1468–1469
in pleural fluid imaging, 1709, 1710*f*
power compared to conventional, 25, 26*f*
PRF in, 28, 29*f*, 30–31
process of, 24, 26*f*
prostate cancer and, 404*f*, 406
slow-flow sensitivity settings on, 939
for testicular torsion, pediatric, 1895–1899, 1896*b*
for testicular tumors, pediatric, 1901–1902
in ureteral calculi detection, 337, 339*f*
for ureteral jets evaluation, 1781*f*
weighted mean frequency in, 28
Color gain, in renal artery duplex Doppler sonography, 449
Color streaking, breast cysts with, 775, 776*f*
Colpocephaly, 1202*f*
in Chiari II malformation, 1526, 1527*f*
in corpus callosum agenesis, 1528, 1530*f*
Column of Bertin, in kidney development, 1781, 1783, 1784*f*
Coma, brain death differentiated from, 1618–1620, 1620*f*
Comet-tail artifacts, 202, 695
in benign and malignant thyroid nodule differentiation, 712–713
in degenerative cysts of thyroid, 1646, 1647*f*
Common bile duct
anastomosis of, for liver transplantation, 625
dilation of, cylindrical or saccular, pediatric, 1735, 1736*f*
diverticula of, 1735
stones in, 173–174, 173*f*
acute pancreatitis and, 221
liver transplantation complications with, 629, 632*f*
Common femoral vein
as landmark for femoral hernias, 482, 485*f*
normal anatomy of, 500, 981*f*
Complete molar pregnancy, 1078, 1079*f*
Complete subclavian steal, 952–953, 953*b*, 953*f*
Complete TGA, 1289, 1289*f*
Complicated cysts, of breast, 775–780, 776*f*
Compression
of amplitudes, 9
ballottement and, 768
for breast sonography, 768, 772, 773*f*
of femoral vein, normal, 982*f*
maneuvers, for dynamic ultrasound of hernia, 474, 475*f*
for parathyroid gland adenomas detection, 739
soft tissue ganglia causing, 865
in sound wave, 2, 2*f*
Compression sonography, 258–260, 261*f*
Computed tomography (CT)
in abdominal aortic aneurysm
rupture evaluation and, 438, 439*f*
for screening and surveillance, 437
treatment planning with, 438
in interventional sonography, pediatric, 1943, 1943*t*
parathyroid adenomas and accuracy of, 748, 748*f*
Computed tomography (CT) *(Continued)*
pediatric chest, sonography compared to, 1709, 1710*f*–1711*f*
for percutaneous needle biopsies, 599
three-dimensional, in skeletal dysplasia evaluation, 1384–1385
Concentric hypertrophy, 1294–1295
Conceptual age, definition of, 1443–1444
ConfirmMDx test, 396
Congenital adrenal hyperplasia (CAH)
adrenal rests in, 832–833, 833*f*, 1824, 1900–1901
pediatric, 1822–1824, 1824*f*, 1900–1901
Congenital anomalies of kidney and urinary tract (CAKUT), 1336
Congenital bilateral absence of the vas deferens (CBAVD), 394
Congenital coxa vara, atypical hips and, 1932
Congenital cystic adenomatoid malformation (CCAM), 1246, 1248*t*
fetal, hydrops from, 1426
Congenital diaphragmatic hernia (CDH), 1248*t*, 1258–1264
anomalies associated with, 1263
bilateral, 1262
fetal lung size and, 1244
FETO for, 1264
left-sided, 1258–1259, 1260*f*
morbidity and mortality from, 1264, 1264*t*
prognosis of, 1261–1262, 1262*b*
right-sided, 1259, 1261*f*
survival predictors in, 1262, 1262*b*
in utero therapy for, 1264
Congenital heart block, fetal, 1297, 1297*f*
hydrops from, 1425
Congenital heart defects, thickened NT in, 1095–1097, 1096*f*
Congenital heart disease (CHD)
chromosomal anomalies in, 1270
extracardiac malformations in, 1270
fetal arrhythmia and, 1270–1273
hydrops and, 1270
IVF and, 1270–1273
MCDA twins and, 1270–1273
risk factors associated with, 1270, 1271*t*–1272*t*
recurrence, in offspring, 1273*t*
recurrence, in siblings, 1273*t*
Congenital high airway obstruction (CHAOS), 1248*t*, 1253–1255, 1254*f*
hydrops from, 1426
Congenital hypothyroidism, 694
pediatric ovarian cysts and, 1875
Congenital infantile myofibromatosis, 1664, 1665*f*
Congenital lobar emphysema, 1246
Congenital lobar overinflation (CLO), 1246, 1251–1252, 1253*f*
Congenital malformations, obstetric sonography and, 1041
Congenital myopathy, atypical hips and, 1932
Congenital nephrotic syndrome, CKD and, 1796–1798
Congenital pulmonary airway malformation (CPAM)
classification of, 1248
differential diagnosis of, 1248*t*
fetal, 1246–1252
hydrops development and, 1248–1249, 1426, 1427*f*
pediatric, 1715–1716, 1717*f*
pleuropulmonary blastoma differentiated from, 1252–1253
sonographic diagnosis of, 1248, 1249*f*
volume ratio of, 1248, 1250
Congestive heart failure
gallbladder wall thickening and, 199*f*
neonatal/infant, 1566
Conglomerate masses, Crohn disease and, 269
Conjoined tendon insufficiency
direct inguinal hernia and, 479–481, 483*f*–484*f*
sports hernia and, 485–486, 489*f*
Conjoined twins, 1115–1116
complications with, 1129–1130, 1130*f*
Conn syndrome, adrenal adenomas in, 419
Connatal cysts, 1566
Connective tissue, dense fibrous, homogeneous plaque and, 920–921
Conradi-Hünermann syndrome, 1399
Constrictive amniotic bands, 1182–1183
Continuous ambulatory peritoneal dialysis, 521
Continuous wave (CW) devices, 8
Continuous wave Doppler, 24, 25*f*
Continuous wave probes, with duplex pulsed Doppler, 939
Continuous wave ultrasound, 36
Contraceptive devices, intrauterine, 529, 552–554, 553*f*
Contraceptives, oral, hepatic adenomas and, 1746
Contrast, speckle effect on, 13–15, 14*f*
Contrast agents, 41–42. *See also* Blood pool contrast agents
acoustic cavitation and, 43, 44*b*
avoidance of, in obstetric sonography, 1038
blood pool, 55–56
disruption-replenishment imaging and, 66–67, 67*f*
echo enhancing, 57*f*
harmonic imaging with, 58–64
in hydrosonovaginography, 1870–1871, 1871*f*
intermittent harmonic power Doppler imaging and, 66, 66*f*
intermittent imaging with, 64–67, 66*f*
intravenous Doppler, 1749–1750
intravenous ultrasound, 1746
microbubbles as, 53–54, 54*f*
behavior of, incident pressure and, 56–58, 57*t*
disruption of, 64–67, 66*f*
FNH characterization with, 106, 106*f*, 108*t*, 109*f*
future of technology for, 68–69, 69*f*–70*f*
HCC characterization with, 106, 106*f*
hemangioma characterization with, 106, 106*f*–107*f*, 108*t*
inertial cavitation and, 67–68
lesional enhancement with, 105, 106*f*–107*f*, 109*f*
liver mass characterization with, 105–106, 106*f*–107*f*, 108*t*, 109*f*–110*f*
MI and, 58, 58*b*, 105
need for, 56–58, 57*f*
regulation of, 68
safety of, 67–68
in musculoskeletal interventions, 898
nonlinear echoes and, 58–64
amplitude and phase modulation imaging and, 64, 65*f*
harmonic B-mode imaging and, 60
harmonic spectral and power Doppler and, 60–61, 60*f*–62*f*
plane-wave contrast imaging and, 64
pulse inversion Doppler imaging and, 63–64
pulse inversion imaging and, 62–63, 62*f*–63*f*
temporal maximum intensity projection imaging and, 64, 65*f*
tissue harmonic imaging and, 61–62
perfluorocarbons in, 56
for liver mass detection, 107, 111*f*
requirements for, 54–56

Contrast agents *(Continued)*
triggered imaging and, 65
types of, 54–56
in water enema technique, 1870–1871, 1871*f*
Contrast effect, of steroid anesthetic mixture, 899, 899*f*
Contrast pulse sequence (CPS), 64
Contrast-enhanced ultrasound (CEUS)
adenoma diagnosis with, 116–117, 117*f*
backscatter increased with, 107, 111*f*
for breast lesions, 773–774
cavernous hemangioma characterization with, 111, 113*f*
for Crohn disease, 269, 273*f*
Crohn disease identification with, pediatric, 1853, 1854*f*
in fatty liver diagnosis, 91–92
FNH diagnosis with, 113–115, 115*f*
gut wall and, 261
HCC detection with, 120–122, 123*f*
Hilar cholangiocarcinoma assessment with, 188, 191*f*
liver metastases diagnosis with, 128–129, 130*f*
for pancreas, 251
for pancreas transplantation, 676
for prostate cancer, 406
for thyroid gland assessment, 692, 714–715
Contrast-to-noise ratio, spatial compounding and, 13–15, 15*f*
Conus medullaris
determining position of, 1677, 1679*f*
fetal, location of, 1218–1221, 1221*f*, 1673, 1673*f*
low and tethered, caudal agenesis type II and, 1689
Conus septum, TOF and, 1288
Cooper ligaments, 761, 761*f*–763*f*
Copy number variants (CNVs), 1088
Coracoacromial ligament, 878–879
Coracobrachialis muscle, 878–879
Coracoclavicular ligaments, 878–879
Coracohumeral ligament, 878–879
Coracoid process, 878–879, 879*f*
Cordocentesis, 1434, 1434*f*
Cornelia de Lange syndrome, microcephaly in, 1194
Cornua
hematometra and, 551–552
"Cornual pregnancy", 1073
Coronary bypass graft, radial artery evaluation for, 977–978, 980*f*
Corpora amylacea, 387
Corpora quadrigemina, 1518
Corpus callosum
agenesis of
in Chiari II malformation, 1526, 1528*f*
fetal brain and, 1199–1201, 1202*f*, 1203*b*
neonatal/infant neural tube closure disorders and, 1526–1528, 1529*b*, 1530*f*–1533*f*
periventricular nodular heterotopia and, 1199*f*
VM and, 1177
dysgenesis of, fetal brain and, 1199–1201, 1203*b*
lipoma of, 1529, 1533*f*
in rhombencephalosynapsis, 1192
thinning of, in PVL, 1552
Corpus luteum
angiogenesis of, 1063
cysts of, 570
pediatric, 1875
development of, 568
formation of, 1049
Corrected TGA, 1290, 1290*f*
Cortical development malformations, fetal brain and, 1193–1203
absence of septi pellucidi as, 1201–1203
cerebrohepatorenal syndrome as, 1196
chondrodysplasia punctata as, 1196
Cortical development malformations, fetal brain and *(Continued)*
classification of, 1194*b*
corpus callosum agenesis/dysgenesis as, 1199–1201, 1202*f*, 1203*b*
focal changes in, 1196
hemimegalencephaly as, 1195
heterotopia as, 1196, 1199*f*
intracranial calcifications as, 1195*f*, 1203, 1204*f*
lissencephaly as, 1195–1196, 1196*f*–1197*f*
macrocephaly as, 1194–1195
megalencephaly as, 1194–1195
microcephaly as, 1194, 1195*f*
polymicrogyria as, 1196, 1198*f*
schizencephaly as, 1196, 1199*f*
SOD as, 1201–1203, 1203*f*
TSC and, 1198, 1200*f*
Cortical nephrocalcinosis, 339
pediatric, 1798, 1798*b*, 1798*f*
Corticosteroids, for musculoskeletal injections, 900
Cortisol, secretion of, 417
Couinaud anatomy, of liver, 76–77, 77*t*, 78*f*
Coxa vara, congenital, atypical hips and, 1932
Coxsackie virus, 1203–1204
Coxsackie virus infection, fetal hydrops from, 1431
Coxsackievirus B, endocardial fibroelastosis from, 1294
CPAM. *See* Congenital pulmonary airway malformation
CP/CPPPS. *See* Chronic prostatitis/chronic pelvic pain syndrome
CPS. *See* Contrast pulse sequence
Cranial Bone Thermal Index (TIC), 39–40
Cranial hairy tuft, diastematomyelia and, 1689
Cranial neuropore, in spine embryology, 1217
Craniocervical junction, in pediatric spine, 1674, 1675*f*
Cranioectodermal dysplasia, 1395
Craniolacunia, in Chiari II malformation, 1526
Craniopharyngioma, intracranial, fetal, 1208
Craniorachischisis, 1179, 1218
Cranioschisis, definition of, 1225*t*
Craniosynostosis
with cloverleaf-shaped skull deformity, 1137*f*–1138*f*
cranial contour indicating, 1382
intracranial compliance in, evaluation of, 1581–1582
metopic, 1137*f*
syndromes associated with, 1136–1139, 1137*f*–1138*f*
Cranium, in skeletal dysplasias, 1382
Crass position, for shoulder ultrasound
modified, 881, 883*f*–884*f*
original, 881, 883*f*
Creeping fat, Crohn disease and, 269, 271*f*
Cremasteric (external spermatic) artery, 821, 821*f*
Cremasteric reflex, 846
CREST. *See* Carotid Revascularization Endarterectomy Versus Stenting Trial
CRL. *See* Crown-rump length
Crohn disease
anatomy affected by, 268
appendicitis associated with, 285, 287*f*, 1862*f*
CEUS for, 269, 273*f*
classic features of, 269
color Doppler ultrasound for, 268*t*, 269, 272*f*
complications of, 269–276
fistula formation as, 276, 279*f*–280*f*
incomplete mechanical bowel obstruction as, 274, 276*f*
inflammatory masses as, 275–276, 278*f*–279*f*
localized perforation with phlegmon as, 274–275, 277*f*
perianal inflammation as, 276, 281*f*, 305–306
strictures as, 269–274, 275*f*–276*f*
Crohn disease *(Continued)*
conglomerate masses and, 269
creeping fat and, 269, 271*f*
diagnosis of, 267–268
gastrointestinal tract and, 266–269
gut wall thickening and, 269, 270*f*–271*f*
hyperemia and, 269, 272*f*–273*f*
intramural sinus tract in, 269, 274*f*
lymphadenopathy in, 269, 272*f*
management of, 266–267
mucosal abnormalities and, 269, 274*f*
pediatric, 1853, 1854*f*
sonographic assessment of, 268, 268*b*, 268*t*
transperineal scanning in, 276
Crossed-fused ectopia, 318, 318*f*
pediatric, 1784–1785, 1785*f*
Crouzon syndrome
craniosynostosis in, 1136–1138
midface hypoplasia in, 1148
Crown-rump length (CRL), 1054
accurate, criteria for, 1092, 1092*b*
early pregnancy failure and, no heartbeat and, 1063, 1064*f*
embryos with less than 7 mm, and no heartbeat, 1064
in gestational age determination, 1445, 1446*f*, 1446*t*
in gestational age estimation, 1062
gestational sac with small MSD in relationship to, early pregnancy failure and, 1066, 1067*f*
NT compared to, 1089, 1090*f*
Cryptorchid testes, 823
Cryptorchidism
testicular microlithiasis and, 1904
testis and, 851, 851*f*
pediatric, 826
Crystalline form, of injectable steroids, 900
CT. *See* Computed tomography
Cubital tunnel, 865–866
Cul-de-sac
anterior, 528
fluid in, 568–569, 569*f*
posterior, 528, 566
Cumulus oophorus, 1049
Currarino triad, 1689
Curved array transducers
beam steering in, 10–11, 11*f*
use and operation of, 12
Cushing disease, adrenal adenomas in, 419
Cushing syndrome, 832–833
adrenal adenomas in, 419
pediatric, adrenal rests in, 1900–1901
Cutaneous rapidly involuting congenital hemangiomas, 1742–1743
CVS. *See* Chorionic villus sampling
CW devices. *See* Continuous wave devices
Cyclopia, 1140
alobar HPE and, 1534–1535
Cystadenocarcinoma(s)
mucocele of appendix and, 299
ovarian
mucinous, 580*f*, 581
pediatric, 1880
serous, 580–581, 580*f*
Cystadenoma(s)
biliary, 82, 83*f*
epididymal, paratesticular, 1904
mucocele of appendix and, 299
ovarian
mucinous, 580*f*–581*f*, 581
pediatric, 1880
serous, 580–581, 580*f*
papillary, of epididymis, 840–841
Cystic adenomatoid malformations, pediatric, 1715

Cystic artery, 194
prominent, in acute cholecystitis, 197*f*, 198–199
Cystic dysplasia, testicular, 830
pediatric, 1891–1892, 1891*f*
Cystic encephalomalacia, 1538, 1539*f*
Cystic fibrosis (CF)
fatty infiltration of liver in, 1740*f*
fetal, hydrops from, 1428
fetal echogenic bowel and, 1316
fetal liver calcifications and, 1316–1318
gastrointestinal tract and, 300
ileal obstruction and, 1310
inborn errors of metabolism and, 1738
ovarian cysts and, pediatric, 1875
pediatric pancreatitis and, 1862–1864
Cystic hygroma(s). *See also* Lymphatic malformations
in aneuploidy screening, 1093, 1093*f*
hydrops from, 1425
thickened NT and, 1096*f*
in Turner syndrome, 1106–1107, 1106*f*
Cystic kidney disease, CKD and, 1796–1798
Cystic meconium peritonitis, 1842–1843, 1846*f*
Cystic metastases, 82
of liver, 125, 128*f*
Cystic periventricular leukomalacia, 1551–1552, 1552*f*
Cystic presacral lesions, pediatric, 1915
Cystic teratomas, ovarian, 582–584, 582*b*, 583*f*
Cystic tumor(s)
arachnoid cysts differentiated from, 1192–1193
cavum veli interpositi cysts differentiated from, 1170
Cystinosis, CKD and, 1796–1798
Cystitis
chronic, 333, 333*f*
cystica, pediatric, 1908
emphysematous, 333, 334*f*
genitourinary, 333
glandularis, pediatric, 1908
granulomatous, pediatric, 1908
hemorrhagic, pediatric, 1908, 1910*f*
infectious, 333, 334*f*
interstitial, 372, 373*f*
pediatric urinary tract infection and, 1794, 1796*f*–1797*f*, 1908, 1910*f*–1911*f*
pseudopolyps and, 333, 333*f*
Cystitis cystica, 333
Cystitis glandularis, 333
Cystogenesis, 1524, 1525*b*
Cystoscopy, for lower urinary tract obstruction, 1363–1365
Cyst(s). *See also* Dermoid cyst(s); Duplication cysts; Epidermoid cyst(s); Kidneys, fetal, cystic disease of; Kidneys, pediatric, cystic disease of; Kidney(s), cysts of; Pancreas, cystic neoplasms of; Pseudocyst(s)
in adenomyosis, 540*b*, 541, 542*f*
adnexal, in pregnancy, 1020
adrenal, 421–422, 422*b*, 423*f*
amnion inclusion, 1061
anechoic, 331
arachnoid
cavum veli interpositi cysts differentiated from, 1170
corpus callosum agenesis and, 1526–1528
fetal brain and, 1192–1193, 1193*f*
of neonatal/infant brain, 1563–1565, 1565*b*
spinal canal and, pediatric, 1695–1697, 1696*f*
Baker, 870, 870*f*
injection for, 907–909, 908*f*
Cyst(s) *(Continued)*
Blake pouch
arachnoid cysts differentiated from, 1192–1193
sonographic appearance of, 1170, 1173*f*
branchial
type I, pediatric, 1639, 1651, 1651*f*
type II, pediatric, 1639–1640, 1651, 1652*f*
type III, pediatric, 1651, 1652*f*
breast, 774–785
acorn, 778*f*
aspiration of, ultrasound-guided, 811, 813*f*
clustered macrocysts and, 779, 780*f*
clustered microcysts and, 782
with color streaking, 775, 776*f*
complex, 780–785, 782*f*
complicated, 775–780, 776*f*
Doppler ultrasound for differentiating, 769–770, 770*f*
eggshell calcification and, 779, 780*f*
fat-fluid levels in, 775, 778*f*
fibrocystic change and, 775
foam, 779, 781*f*
inflammation and infection of, 782–785, 785*f*
lipid, 775–779, 779*f*
microcysts and, 782, 784*f*
milk of calcium and, 775, 776*f*–777*f*
mural nodules and, PAM causing, 782, 783*f*–784*f*
papillary lesions and, 782
septations within, 782, 783*f*
simple, 774, 775*f*
of skin origin, 779, 781*f*
bronchogenic, pediatric, 1650, 1716, 1718*f*
chocolate, 574–575
choledochal
of biliary tree, 168–170, 169*f*–170*f*
fetal duodenal atresia mistaken for, 1309
of fetal gallbladder, 1319, 1320*f*
neonatal jaundice and, 1735–1737, 1735*f*–1736*f*
pediatric pancreatitis and, 1862–1864
choroid plexus
fetal brain and, 1170, 1173*f*
neonatal/infant brain and, 1565, 1566*f*
spina bifida and, 1233
in trisomy 18, 1103*f*, 1104
in trisomy 21, 1101
connatal, 1566
corpus lutein, 570
pediatric, 1875
daughter, 331, 332*f*
in *Echinococcosis*, 1748
decidual, 1054
dorsal midline, in corpus callosum agenesis, 1528, 1531*f*
ejaculatory duct, 392
embryonic, 1077, 1077*f*
endometrial, 547–548
epididymal, 839, 842*f*
pediatric, 1902–1903, 1903*f*
esophageal, pediatric, 1650
fetal
bronchogenic, 1255–1256, 1255*f*, 1255*t*
cortical, in renal dysplasia, 1347–1348
neurenteric, 1256
ovarian, 1369, 1369*f*
pancreatic, 1320
renal, 1346–1352
splenic, 1320–1322, 1322*f*
filar, in newborn, 1674–1675, 1678*f*
follicular, 568
pediatric, 1875
foregut, pediatric, 1650
Cyst(s) *(Continued)*
frontal horn, neonatal/infant brain and, 1522, 1522*f*, 1566
ganglion, 869–870, 869*f*
injection for, 907–909, 909*f*
Gartner, pediatric, 1883–1884
gastrointestinal
congenital, 297, 298*f*
pediatric, 1860–1862, 1863*f*–1864*f*
gel, 779, 781*f*
hydatid, 89, 89*f*–90*f*
in *Echinococcosis*, 1748
renal, 331, 332*f*
splenic, 147, 150*f*
inclusion
amnion, 1061
epidermal, 779
peritoneal, 508–509, 509*f*, 573, 573*f*
surface epithelial, 569, 573
vaginal, pediatric, 1883–1884
infrahyoid space, pediatric, 1650
inspissated, 779, 781*f*
interhemispheric, in corpus callosum agenesis, 1201
intratesticular, 829, 830*f*
of kidneys, 356–365
percutaneous management of, 617–618, 619*f*
of kidneys, pediatric, congenital, 1816–1818
dialysis and acquired, 1816–1818, 1817*f*
after liver transplantation, 1816–1818
in TSC, 1816, 1817*f*
in VHL disease, 1816
liver, 82, 82*f*–83*f*
autosomal dominant polycystic kidney disease and, 83
benign, 82
fetal, 1318, 1318*f*
percutaneous management of, 618
peribiliary, 82–83
mesenteric
fetal, ovarian cysts differentiated from, 1369
gastrointestinal cysts differentiated from, 1860, 1863*f*
pediatric, ovarian cysts differentiated from, 1875
peritoneal, 509–510, 510*f*
milk of calcium, 653, 657*f*
müllerian duct, 392
pediatric, 1908, 1910*f*
nabothian, 533, 535*f*, 1499
neurenteric, pediatric, 1686–1688, 1724
omental, pediatric ovarian cysts differentiated from, 1875
ovarian
dermoid, 582–584, 583*f*
fetal, 1369, 1369*f*
functional, 570–571, 571*f*
hemorrhagic, 570–571, 571*f*, 575
menstrual cycle and follicular, 568
neonatal, 1876*f*
paratubal, 573
parovarian, 573
percutaneous management of, 618–619
peritoneal inclusion, 573, 573*f*
postmenopausal, 569–570, 571*f*
surface epithelial inclusion, 569, 573
in triploidy, 1105*f*
ovarian, pediatric, 1873–1877
hemorrhagic, 1877, 1878*f*–1879*f*
in polycystic ovarian disease, 1877–1878, 1879*f*
torsion and, 1875–1876, 1876*b*, 1877*f*
pancreatic, 242–248, 243*f*
congenital, 1865
fetal, 1320

Cyst(s) *(Continued)*
simple, 243, 244*f*
VHL disease and, 243, 244*f*
paralabral, injection for, 907–909, 910*f*–911*f*
parameniscal, 907–909
paramesonephric duct, pediatric, 1883–1884
paraurethral, pediatric, 1883–1884
parovarian, pediatric, 1875, 1876*f*
percutaneous management of, 617–619, 619*f*
peritoneal
inclusion, 508–509, 509*f*
mesenteric, 509–510, 510*f*
periventricular, of neonatal/infant brain, 1566, 1566*f*
pineal, 1170
popliteal, pediatric, 1939
porencephalic, neonatal/infant brain and, 1537, 1565
posterior fossa subarachnoid, Dandy-Walker malformation differentiated from, 1190, 1531, 1531*b*
prostate, 388, 390–392, 391*f*
in renal cell carcinoma, 343, 343*f*
rhombencephalon, 1077, 1077*f*
round ligament, simulating groin hernias, 500, 501*f*
scrotal, extratesticular, 839, 842*f*
sebaceous, 779, 781*f*
seminal vesicle, 392, 393*f*
pediatric, 1908, 1910*f*
simulating groin hernias, 499–500, 501*f*
spermatic cord, pediatric, 1902–1903
splenic, 146–148, 146*b*, 148*f*–151*f*
endothelial-lined, 148
epidermoid, 146–147, 148*f*–149*f*
false, 146–147, 149*f*
fetal, 1320–1322, 1322*f*
hydatid, 147, 150*f*
pediatric, 1769
primary congenital, 146–147, 148*f*–149*f*
pseudocysts as, 146–147, 149*f*
subchorionic
maternal floor infarction with, 1474, 1476*f*
placental, 1474, 1477*f*
subependymal, 1543–1544
of neonatal/infant brain, 1566, 1567*f*
of suprahyoid space, pediatric, 1639–1640, 1640*b*, 1640*f*–1641*f*
tailgut, 297, 298*f*
testicular, 829, 829*b*
cystic dysplasia and, 830
epidermoid, 830*f*, 831
intratesticular, 829, 830*f*
simple, pediatric, 1901–1902
tubular ectasia of rete testis and, 829–830, 830*f*
theca lutein, 570, 572
pediatric, 1875
thymic, 1652, 1653*f*, 1723–1724
thyroglossal, duct, pediatric, 1640, 1643, 1644*f*–1645*f*
thyroid
calcifications of, 695
pediatric, 1646, 1647*f*
tunica albuginea, 829, 830*f*
tunica vaginalis, 829, 830*f*
pediatric, 1902–1903
umbilical cord, 1483, 1483*f*
sonographic appearance of, 1061, 1061*f*
in trisomy 18, 1103*f*
urachal, 322, 323*f*
ovarian cysts differentiated from, 1369
pediatric, 1907–1908, 1909*f*
pediatric hydronephrosis and, 1791, 1792*f*–1793*f*
pediatric ovarian cysts differentiated from, 1875
Cyst(s) *(Continued)*
utricle, 391*f*, 392
vallecula, pediatric, 1640, 1641*f*
of vas deferens, 842*f*
Cytogenesis, 1513*b*, 1524
Cytomegalovirus (CMV) infection, 91
in acute typhlitis, 287–288, 289*f*
congenital, neonatal/infant brain and, 1558–1560, 1559*f*
fetal
brain development and, 1203–1204, 1205*f*
hydrops from, 1431–1432
hyperechogenic kidneys in, 1351
fetal echogenic bowel and, 1315*f*
neonatal/infant, schizencephaly from, 1536–1537, 1558
Cytopathologists, definition of, 600
Cytotrophoblast cells, 1466*f*

D

Dabigatran, 598
Dacryocystocele, 1143, 1147*f*
Damping materials, in transducers, 8
"Dancing megasperm", 841
Dandy-Walker complex, VM and, 1177
Dandy-Walker continuum, 1190–1191
Dandy-Walker malformation, 1190
arachnoid cysts differentiated from, 1192–1193
in cerebellum, 1190, 1190*f*
corpus callosum agenesis and, 1526–1528
differential diagnosis of, 1190, 1192–1193, 1531–1532, 1531*b*
etiology of, 1530
mega-cisterna magna differentiated from, 1192
neonatal/infant neural tube closure disorders and, 1529–1532, 1530*b*, 1533*f*–1534*f*
sonographic findings of, 1530*b*
in triploidy, 1105*f*
ventriculoperitoneal shunting for, 1530
Dandy-Walker spectrum, 1530–1531
Dandy-Walker variant, 1190–1191, 1530
Dartos fascia, 846
Daughter cysts, 331, 332*f*
in *Echinococcosis*, 1748
DCIS. *See* Ductal carcinoma in Situ
DDH. *See* Development dysplasia of the hip
de la Chapelle dysplasia, 1396
de Morsier syndrome, 1201–1203. *See also* Septo-optic dysplasia
de Quervain disease, 724
de Quervain tendinosis, injection for, 904, 905*f*
de Quervain thyroiditis, 1645
Decibel, 5–7
Decidua, 1466*f*
Decidua basalis, 1054, 1465–1466
Decidua basalis–chorion frondosum, 1054
Decidua capsularis, 1054, 1465–1466
Decidua vera, 1054,
Decidual cysts, 1054
Decidual reaction, 1049
Deep venous thrombosis (DVT). *See also* Peripheral veins
acute
brachial veins and nonocclusive, 994*f*
in GSV, 984, 984*f*
lower extremity, 983–984, 983*f*–985*f*
upper extremity, 992–994, 994*f*–995*f*
blood flow and
absent, 992–994
slow, 984, 988*f*
of calf, 982
central venous catheterization related to, 935, 995*f*
chronic
in brachial vein, 994–995, 996*f*
calcifications indicating, 984, 987*f*
Deep venous thrombosis (DVT) *(Continued)*
of IJV, 994*f*
lower extremity, 984, 986*f*–987*f*
nonocclusive, 992, 994*f*
in profunda femoris vein, 987*f*
upper extremity, 994–995, 995*f*–996*f*
in femoral vein, duplicated, detecting, 988, 988*f*
follow-up recommendations for, 989
pulmonary embolism from
lower extremity, 979, 981*f*
upper extremity, 994
ultrasound examinations of
indications in, 979
limitations of, 989
venous insufficiency caused by, 989, 990*f*
Default output power, for obstetric sonography, 1035
Deferential artery, 821, 821*f*
Definity, 56
Deformations, definition of, 1399
Delivery. *See also* Preterm birth
fetal hydrops and, 1436
preterm, 1495–1496
Deltoid muscle, 878–879, 878*f*
Demineralization, of spine, in skeletal dysplasias, 1382
Depigmentation, complicating injectable steroids, 901
Depth gain compensation, 8
Dermal sinus tract
dorsal, pediatric, 1686, 1688*f*
focal, 1674
tethered cord and, 1679
Dermoid cyst(s)
hemorrhagic ovarian cyst differentiated from, 1877
neck, pediatric, 1652–1654, 1654*f*
ovarian, 582–584, 583*f*
in suprahyoid area, 1640
Dermoid mesh, 582–583, 583*f*
Dermoid plug, 582, 583*f*
DES. *See* Diethylstilbestrol
Desmoid tumors, simulating anterior abdominal wall hernias, 500–501, 502*f*
Desmoplastic small round cell tumors, 1860
Detrusor areflexia, 372–374, 373*f*
Detrusor hyperreflexia, 372–374, 373*f*
Development dysplasia of the hip (DDH), 1920–1930
causes of, 1921
clinical overview of, 1920–1921
dynamic sonographic technique for, 1922–1927
anterior view for, 1927, 1929*f*
coronal/flexion view for, 1925–1927, 1926*f*
coronal/neutral view for, 1923–1924, 1924*f*–1925*f*
history of, 1922
stress maneuvers for, 1923
technical factors in, 1922–1923
transverse/flexion view for, 1927, 1928*f*
transverse/neutral view for, 1927
evaluation during treatment and, 1929–1930
evaluation of infant at risk and, 1927–1929
incidence of, 1920–1921
mechanism of, 1921
minimum standard examination for, 1922*b*
risk factors of, 1921*b*
screening for, 1921
Dextrocardia, 1273
Dextroposition, 1273, 1274*f*
Dextrotransposition, of great arteries, 1289–1290
DFI. *See* Direction of flow index

Diabetes mellitus
chronic renal failure in, 372
maternal
caudal agenesis and, 1689
LGA fetus and, 1454, 1455*t*
NTDs from, 1218
Dialysis
acquired cystic kidney disease associated with, 364
acquired renal cysts in, pediatric, 1816–1818, 1817*f*
peritoneal, continuous ambulatory, 521
postoperative ultrasound evaluation for, 996
preoperative ultrasound for, 996
Diamond-Blackfan syndrome, 1401
Diaphragm
duodenal, 1841–1842, 1844*f*
eventration of, 1716
fetal
agenesis of, 1258
defect of anterior, pentalogy of Cantrell and, 1329
development of, 1244*f*, 1245
eventration of, 1258, 1262–1263
gastric, pediatric, 1839, 1840*f*
interventional sonography and anatomy of, pediatric, 1950, 1950*f*
pediatric
disorders of, 1716, 1718*f*–1720*f*
paralysis of, 1716, 1719*f*–1720*f*
rupture of, 1716, 1720*f*
Diaphragm sign, as pleural fluid sonographic sign, 1709
Diaphragmatic hernia
congenital, 1248*t*, 1258–1264
anomalies associated with, 1263
bilateral, 1262
fetal lung size and, 1244
FETO for, 1264
left-sided, 1258–1259, 1260*f*
morbidity and mortality from, 1264, 1264*t*
prognosis of, 1261–1262, 1262*b*
right-sided, 1259, 1261*f*
survival predictors in, 1262, 1262*b*
in utero therapy for, 1264
fetal, hydrops from, 1425
pediatric, 1716, 1718*f*
thickened NT in, 1095–1096
Diaphragmatic pericardium, pentalogy of Cantrell and, 1329
Diaphragmatic slips, 80
Diastasis recti abdominis, 489–490, 489*f*
Diastematomyelia, 1674, 1681
closed spinal dysraphism and, 1688–1689, 1688*f*
fetal, 1234–1235, 1236*f*
Diastolic runoff, prolonged, carotid flow waveforms and, 936–937
Diastrophic dwarfism
findings associated with, 1382
hitchhiker thumb in, 1382, 1406
Diastrophic dysplasia, 1398, 1398*f*
DICA. *See* Distal internal carotid artery
Dichorionic diamniotic twins, 1019*f*, 1115–1116, 1116*f*
growth discrepancy in, 1123*f*
placental findings in, 1119
sonographic findings of, chorionicity and, 1119, 1120*f*
Didelphys uterus, 534, 536*f*–537*f*, 1881
Diencephalon, 1077
Diethylstilbestrol (DES)
cervical assessment in, 1505
uterus exposure to, 534, 536*f*, 1881
Diffuse reflectors, 4, 5*f*
Diffuse steatosis, 91, 92*f*
Diffusion tensor imaging, in PVL, 1553
DiGeorge syndrome, 1196
neuroblastoma with, pediatric, 1825
DiGeorge syndrome, fetal thymus evaluation for, 1245
Digestive tube, embryology of, 1304–1305
Digital rectal examination (DRE), 381–382, 387
Dilated bowel, fetal, 1313
Dilated distal ureter, 592
Dilated loops of bowel, 1310, 1311*f*
fetal gastroschisis and, 1323–1324
Dilated loops of small bowel, 1311–1312
Dilated stomach, fetal, 1307, 1308*f*
Diploid karyotype, complete molar pregnancy and, 1078
Diplomyelia, in diastematomyelia, 1236*f*
Direct controls, 48, 49*t*
Direction of flow index (DFI), 1618
Discriminatory level, for seeing gestational sac, 1056
Disjunction, in spine embryology, 1672–1673
Dislocations, pediatric. *See also* Developmental dislocation and dysplasia of hip
frank, of hip, 1927
of hip, developmental, 1920–1930
Displaced-crus sign, as pleural fluid sonographic sign, 1709
Disruption-replenishment imaging, 66–67, 67*f*
Disruptions, definition of, 1376, 1377*t*, 1399
Dissection complications, renal artery stenosis and, 447, 448*f*
Distal cholangiocarcinoma, 188, 192*f*
Distal internal carotid artery (DICA)
SCD and stenosis of, 1606*f*
as transtemporal approach landmark, 1592, 1594*f*
Diuretic therapy, medullary nephrocalcinosis and, 1798
Diverticulation. *See also* Holoprosencephaly
neonatal/infant brain and disorders of, 1532–1536
in organogenesis, 1524, 1525*f*
Diverticulitis
acute, 288–290
classic features of, 288–290
muscular hypertrophy from, 290, 291*f*
pericolonic changes in, 290, 292*f*
sonography of, 290, 290*b*
focally inflamed fat in, 521
right-sided, 285–287, 288*f*
Diverticulosis, spastic, 288–290
Diverticulum(a)
bladder, 374, 374*f*
identification of, 592
calyceal, renal milk of calcium and, 1799, 1800*f*
colonic, 290, 291*f*
of common bile duct, 1735
Hutch, 310
Meckel
intussusception and, 1844–1845, 1849*f*
pediatric appendicitis differentiated from, 1858–1860, 1862*f*
urachal, 322, 323*f*
pediatric, 1907–1908, 1909*f*
urethral, 323, 323*f*
anterior, pediatric, bladder outlet obstruction from, 1906
urinary bladder, transitional cell carcinoma in, 348
ventricular, 1294
vesicourachal, pediatric, 1775, 1791
Dizygotic (fraternal) twins, 1115–1116, 1116*f*
Dolichocephaly, 1136
Donor renal vein, anastomosis, in renal transplantation, 643
Doppler angle, 21–22, 24*f*, 29*b*, 30
Doppler angle theta. *See* Angle theta, Doppler
Doppler beam, vessel paralleling, in color Doppler, 933
Doppler effect, 21–22, 23*f*
Doppler frequency, 29
Doppler frequency shift, 21–22, 23*f*–24*f*
Doppler gain, 30, 33*f*
Doppler indices, 27–28, 27*f*
Doppler spectrum, 925
interpretation of, 25–28, 27*f*
Doppler ultrasound. *See also* Carotid artery(ies), Doppler spectral analysis for; Color Doppler ultrasound; Duplex Doppler sonography; Kidneys, pediatric, vascular disease of, Doppler assessment of; Liver, pediatric, Doppler assessment of; Obstetric sonography; Power Doppler ultrasound; Transcranial Doppler sonography
aliasing in, 29*b*, 32*f*
artifact sources in, 29*b*
backscatter and, 21–22, 23*f*, 35
bioeffects of obstetric sonography and, 1041
for breast assessment, 768–772, 770*f*–773*f*
cysts in, 769–770, 770*f*
cavernous hemangiomas characterized by, 109–110
cirrhosis of liver characteristics in, 95, 95*f*
complete venous, for lower extremity peripheral veins, 989
continuous wave, 24, 25*f*
Doppler angle and, 21–22, 24*f*, 29*b*, 30
Doppler effect and, 21–22, 23*f*
Doppler equations and, 21–22, 23*f*–24*f*
Doppler frequency and, 29
Doppler frequency shift and, 21–22, 23*f*–24*f*
Doppler gain and, 30, 33*f*
Doppler indices and, 27–28, 27*f*
Doppler spectrum and, interpretation of, 25–28, 27*f*
for ductus venosus assessment, 1458, 1459*f*
for fetal well-being assessment, 1458–1460, 1459*f*–1460*f*
FNH characterized by, 113
gut wall evaluation with, 260–261, 262*f*
harmonic spectral and power, 60–61, 60*f*–62*f*
hilar cholangiocarcinoma assessment with, 187–188, 189*f*–191*f*
instrumentation for, 24–25, 25*b*, 25*f*–26*f*
for intussusception, pediatric, 1849*f*
of liver transplantation recipient, pediatric, 1764–1769
lymphadenopathy assessment with, 771–772, 772*f*
for MCA
in fetal alloimmunization detection, 1421, 1422*f*
fetal assessment of, 1458–1460, 1460*f*
for musculoskeletal system, 857, 857*f*
obstetric, sample volume and velocity range in, 1036
operating modes in, 30–31
overview and physics of, 21–30
pediatric kidney assessment with, 1778
pediatric liver assessment with, 1748–1764
placental vascularity and, 1467–1469
portal hypertension assessment with, 1748–1764
for PTN, 1083
pulse inversion, 63–64
pulsed wave, 24, 25*f*
testicular flow, 1890

Doppler ultrasound *(Continued)*
renal arterial stenosis diagnosis from, false-positive, 658, 661*f*
for renal cell carcinoma detection, 343, 344*f*
for renal transplant
assessment, 648, 651*f*–652*f*
pediatric, 1807–1812
renal vascular, 366
sample volume size and, 29*b*, 30
signal processing and display in, 23–24, 24*f*
spatial focusing and, 35
spectral, 60–61, 60*f*–62*f*
in carotid artery analysis, 925–932
for fetal heart assessment, 1275, 1281*f*
spectral broadening in, 24, 24*f*, 29, 29*b*, 31*f*
spectral display in, 25
technical considerations in, 28–30
thermal effects in, 31
for umbilical arteries assessment, 1458, 1459*f*
wall filters in, 29, 30*f*
Dorsal dermal sinus, pediatric, 1686, 1688*f*
Dorsal enteric fistula, pediatric, 1686–1688
Dorsal induction errors, fetal brain and, 1179–1186
amniotic band sequence as, 1180*f*, 1182–1183
anencephaly as, 1179, 1180*f*
cephalocele as, 1179–1182
ciliopathies as, 1182
cranial changes in spina bifida as, 1183–1186, 1184*f*–1185*f*, 1185*t*–1186*t*
encephalocele as, 1179–1182, 1181*f*, 1182*t*
exencephaly as, 1179
Joubert syndrome as, 1182
limb-body wall complex as, 1182–1183
Meckel-Gruber syndrome as, 1182
Dorsal midline cyst, in corpus callosum agenesis, 1528, 1531*f*
Dorsal rectum, in bladder development, 311, 312*f*
Dorsalis pedis artery, 966
DORV. *See* Double-outlet right ventricle
"Double contour sign", 867–869, 868*f*
"Double-bubble" sign, in fetal duodenal atresia, 1309, 1310*f*
Double-decidual sign, 1054, 1056*f*
"Double-duct" sign, 231, 231*f*
Double-outlet right ventricle (DORV), 1288–1289, 1289*f*
Down syndrome, testicular microlithiasis and, 1904. *See also* Trisomy 21
Drainage, ultrasound-guided, 609–617
of abscesses
abdominal, 612
liver, 612–613, 614*f*–615*f*
pediatric, 1953
pediatric, appendiceal, 1956, 1960*f*
pelvic, 612, 613*f*
renal, 617, 618*f*
splenic, 617
transrectal, 1953–1954, 1954*f*
of bile duct fluids, 614–615
of biliary tract fluids, 613–615
catheters for
for interventional sonography, 1948
placement of, 610–611, 611*f*
removal of, 612
selection of, 610–611, 611*f*
contraindications to, 609–610
diagnostic aspiration in, 611
of empyemas, pediatric, 1954, 1958*f*
follow-up care for, 612
of gallbladder fluids, 613–614, 616*f*
imaging methods for, 610, 610*f*
indications for, 609–610
of pancreatic pseudocysts, 615–617, 617*f*
patient preparation for, 611
percutaneous cholangiography and, 1956, 1959*f*
Drainage, ultrasound-guided *(Continued)*
of pleural and peritoneal fluids, pediatric, 1954–1956, 1958*f*
of pleural effusion, 1724–1725
procedure for, 612
DRE. *See* Digital rectal examination
Drop metastasis, 266, 267*f*
Drugs
fetal hydrops from, 1432
illicit use of, fetal gastroschisis and, 1322–1323
nephrotoxic, AKI and, 1796
toxicity of, renal transplantation abnormalities and, 1809
Duct extension, of DCIS, 790–791, 792*f*
Ductal arch, fetal, 1275, 1279*f*
Ductal carcinoma in Situ (DCIS), 789–790, 792*f*
calcifications and, 793, 795*f*
duct extension of, 790–791, 792*f*
Ductal ectasia, mammary ducts and, 762
Duct(s). *See also* Bile duct(s)
mammary
normal sonographic appearance of, 762, 764*f*
subareolar and intranipple, scanning of, 762, 765*f*
pancreatic, 215–218, 219*f*–220*f*
of Santorini, 218, 219*f*
thymopharyngeal, formation of, 1652
of Wirsung, 218, 219*f*
Ductus arteriosus, 1273–1274, 1275*f*
Ductus venosus, 1273–1274, 1275*f*
fetal, Doppler ultrasound assessment of, 1458, 1459*f*
reversed flow in, in aneuploidy screening, 1095, 1095*f*
Duodenal atresia, fetal
dilated fetal stomach differentiated from, 1307
"double-bubble" sign in, 1309, 1310*f*
echogenic bowel and, 1315*f*
small bowel obstruction and, 1308–1309, 1310*f*
Duodenal diaphragm, 1841–1842, 1844*f*
Duodenal duplication cysts, fetal duodenal atresia mistaken for, 1309
Duodenal leaks, after pancreas transplantation, 682
Duodenal stenosis, 1308–1309
Duodenal web, 1841, 1844*f*
Duodenum, 219
atresia of, in trisomy 21, 1097, 1098*f*
pediatric, 1841–1847
anatomy of, 1841, 1841*f*
atresia of, 1841, 1842*f*
congenital obstruction of, 1841–1842, 1842*f*–1844*f*
hematoma of, 1842, 1845*f*
sonographic technique for, 1841
stenosis of, 1841
ulcer in, perforated, gallbladder wall thickening signs in, 201*f*
Duplex Doppler sonography
in Budd-Chiari syndrome, 102–103
celiac artery, 453–455, 455*f*
mesenteric artery, 453–455, 455*f*
interpretation of, 454–455, 456*f*–458*f*
of neonatal/infant brain, 1573–1576
approaches to, 1574, 1575*f*
arterial blood flow in, 1576, 1577*t*
asphyxia and, 1580
brain death and, 1580, 1583*f*
cerebral edema and, 1580
diffuse neuronal injury and, 1580
ECMO and, 1578–1580, 1579*f*
hemodynamics in, 1576–1580
HII and, 1580, 1581*f*–1582*f*
hydrocephalus and, 1581–1583, 1584*f*
intensive care therapies and, 1578–1580
intracranial hemorrhage and, 1580–1581, 1584*f*
Duplex Doppler sonography *(Continued)*
intracranial tumors and, 1585, 1587*f*
measurements in, 1576, 1576*f*–1577*f*, 1576*t*
mechanical ventilation and, 1578, 1579*f*
near-field structures and, 1585, 1588*f*
optimization of, 1574, 1574*b*
pitfalls of, 1585–1589, 1589*f*
safety considerations for, 1574–1576
stroke and, 1580–1581, 1584*f*
uncommon applications of, 1585, 1588*f*
vascular malformations and, 1583–1585, 1585*f*–1587*f*
venous blood flow in, 1578, 1578*f*, 1578*t*
obesity and renal artery in, 447
in portal hypertension, 98
renal artery, 447–450, 450*f*
false-positive/false-negative results with, 450, 450*f*
interpretation of, 450
in ureteral calculi detection, 337–338
Duplex scanner, 24
Duplication anomalies, fetal, 1359–1360, 1359*f*, 1360*b*
Duplication cysts, 297
duodenal, fetal duodenal atresia mistaken for, 1309
enteric, fetal, 1312–1313, 1313*f*
ovarian cysts differentiated from, 1369
esophageal, 1256
gastrointestinal, pediatric, 1860, 1863*f*
ovarian cysts differentiated from, 1875
Dural sinus
fetal
malformations of, 1205
thrombosis of, 1205–1206, 1206*f*
neonatal/infant, thrombosis of, 1585
Duty factor, 36
DVT. *See* Deep venous thrombosis
Dwarfism, diastrophic
findings associated with, 1382
hitchhiker thumb in, 1382, 1406
Dwell time, 36
in obstetric sonography, 1036
Dynamic contrast-enhanced ultrasound, 66–67
Dynamic maneuvers, for hernia imaging, 473–474, 474*f*–475*f*
Dynamic range, of amplitudes, 9
Dysgerminomas, ovarian, 584, 584*f*
pediatric, 1880
pseudoprecocious puberty and, 1887
Dyslexia, obstetric sonography and, 1040
Dysostoses, definition of, 1376, 1377*t*
Dysplastic kidneys, pediatric, 1798, 1798*f*
Dysraphic hamartomas, 1682
Dysraphic lesions, 1679–1680
Dysraphism. *See* Spinal dysraphism, fetal; Spinal dysraphism, pediatric
Dyssegmental dysplasia, 1399
Dystrophic calcification, 339
pediatric urinary tract and, 1799
Dystrophic facies, in Miller-Dieker syndrome, 1195

E

Eagle-Barrett syndrome. *See* Prune belly syndrome
Early pregnancy failure. *See* Pregnancy, first trimester of, early failure of
Ear(s)
embryology of, 1134
fetal
abnormalities of, 1148, 1148*f*
length of, in trisomy 21, 1101
low-set, 1148
Ebstein anomaly, 1286–1287, 1286*f*
Echinococcal disease
adrenal, 423
genitourinary, 331, 332*f*

Echinococcal disease *(Continued)*
peritoneal, 517
splenic, 147, 150*f*
Echinococcosis, in pediatric liver, 1748
Echinococcus granulosus, 613
hepatic infestation by, 88–89
Echinococcus multilocularis, parasitic infestation by, 90
Echocardiography, fetal
five-chamber view in, 1275, 1279*f*
four-chamber view in
apical, 1274–1275, 1277*f*
subcostal, 1274–1275, 1277*f*
indications for, 1270–1273, 1273*b*
M-mode, 1275, 1280*f*–1281*f*
three-vessel and trachea view in, 1275, 1279*f*
timing of, 1274
Echoendoscope, 428–429
Echoes, 3–4. *See also* Nonlinear echoes
fundamental, 58–59
Echogenic bowel
fetal
aneuploidy and, 1315–1316, 1315*f*
bowel obstruction and, 1316
CF and, 1316
conditions associated with, 1315*b*
fetal growth restriction and fetal demise with, 1316
infection and, 1316
intraamniotic bleeding and, 1316
meconium peritonitis and, 1313
in trisomy 21, 1100*f*, 1101
Echogenic capsule, thin, in breast sonography, 797
Echogenic intimal flap, in carotid artery dissection, 946, 948*f*
Echogenic lines, nearly parallel, in normal carotid wall, 918–919, 919*f*
Echogenic metastases, of liver, 125, 128*f*
Echogenic rim, in breast sonography, with hyperechoic spicules, 787–788, 789*f*
Echogenicity, in liver mass detection, 106–107
Echo-ranging, 3
Echovist, 55–56
ECMO. *See* Extracorporeal membrane oxygenation
ECST. *See* European Carotid Surgery Trial
Ectasia, aortic, 440
Ectoderm layer, of trilaminar embryonic disc, 1216–1217, 1217*f*
Ectodermal-neuroectodermal tract, focal, 1674
Ectopia cordis, fetal
abdominal wall and, 1329, 1329*f*
pentalogy of Cantrell and, 1329
structural cardiac anomalies and, 1295, 1296*f*, 1329
Ectopic pregnancy, 1069–1076
abdominal, 1074, 1075*f*
cervical, 1073–1074, 1074*f*
clinical presentation of, 1069–1070
heterotopic gestation and, 1070–1071, 1072*f*
implantation sites of, 1072–1073
abdominal, 1074, 1075*f*
cervical, 1073–1074, 1074*f*
cesarean scar, 1073, 1075*f*
interstitial, 1073, 1074*f*
infertility and, 1070
interstitial, 1073, 1074*f*
management of, 1075–1076
conservative, 1076
failure of, 1076, 1076*f*
laparoscopy for, 1076
medical, 1076
nonspecific sonographic findings in, 1072–1073
adnexal mass and, 1072, 1073*f*
ectopic tubal ring as, 1072, 1073*f*
Ectopic pregnancy *(Continued)*
endometrium and, 1072–1073
free pelvic fluid and, 1072, 1073*f*
pediatric, 1884–1885, 1885*f*
prevalence of, 1070
risk of, 1070*b*
ruptures, hemoperitoneum in, 508*f*
serum β-hCG levels and, 1071
sonographic diagnosis of, 1070–1071, 1070*f*–1071*f*
specific sonographic findings in, 1071–1072, 1072*f*
of unknown location, 1075
Ectopic thyroid tissue, 694
Ectrodactyly, fetal, 1406–1407, 1406*f*
EDD. *See* Expected date of delivery
Edema
breast sonography and, 795
cerebral
neonatal/infant, 1550–1556, 1554*f*–1555*f*, 1580
pediatric, TCD sonography in, 1614, 1617*f*
gut, 295, 297*f*
of ovaries, massive, 578
pediatric, 1878–1879, 1879*f*
scrotal, idiopathic, 846
pediatric, 1898–1899, 1898*f*
subcutaneous, fetal, in hydrops, 1417, 1419*f*–1420*f*
Edematous cord, 1484*f*
Edwards syndrome. *See* Trisomy 18
EF. *See* Endocardial fibroelastosis
EFSUMB. *See* European Federation of Societies of Ultrasound in Medicine and Biology
Eggshell calcification, breast cysts and, 779, 780*f*
EHE. *See* Epithelioid hemangioendothelioma
Ejaculatory ducts, 382*f*–383*f*, 384
cysts of, 392
obstruction of, 393–394
transurethral resection of, 393
Elastography
basic points in, 15–16, 16*b*
for breast assessment, 772–773, 773*f*
gut wall and, 261
for musculoskeletal system, 857
for prostate cancer, 407
shear wave, 16, 17*f*–18*f*, 772
cirrhosis of liver and, 95–96
for pediatric liver, 1764, 1765*f*
strain, 16, 17*f*, 772
for thyroid gland assessment, 692, 714–715, 715*f*–716*f*
transient, 1764
Elbow
injection of, 901
pediatric, dislocations of, 1933–1934
ulnar nerve dislocation at, 865–866, 866*f*
Electronic beam steering, 10–11
"Elephant trunk" sign, fetal cloacal exstrophy and, 1328
Elevation planes, 12*f*
Elevation resolution, 19, 19*f*
Ellis-van Creveld syndrome, 1396, 1397*f*, 1398–1399
polydactyly in, 1382
Emboli showers, 1621–1622
Embolism
carotid artery, TIAs from, 919
pulmonary, DVT causing
lower extremity, 979, 981*f*
upper extremity, 994
Embolization, uterine artery, for uterine fibroids, 540
Embolus, renal artery stenosis and, 447
Embryo. *See also* Aneuploidy, screening for, first-trimester; Chromosomal abnormalities
abnormal, 1077
anencephaly in, 1077
cardiac activity of, normal sonographic appearance of, 1058–1059, 1060*f*
with CRL less than 7mm and no heartbeat, 1064
definition of, 1445
early pregnancy failure and gestational sac with no, 1063–1065, 1065*f*
evaluation of, 1076–1077
heartbeat of, in gestational age determination, 1445, 1445*f*, 1446*t*
intracranial cystic structures in, 1077, 1077*f*
normal development of, mimicking pathology, 1077, 1077*f*
normal sonographic appearance of, 1057, 1059*f*–1060*f*
physiologic anterior abdominal wall herniation in, 1077, 1077*f*, 1322, 1323*f*
omphalocele confused with, 1325, 1327*f*
sonographic appearance of, normal, 1018*f*
transfer, 1070
in yolk sac, 1058*f*
Embryonal carcinoma, 823, 825*f*
ovarian, 1880
pediatric, testicular, 1899
Embryonal rhabdomyosarcoma, pediatric, paratesticular, 1903–1904, 1903*f*
Embryonal sarcoma, undifferentiated, in pediatric liver, 1746, 1748*f*
Embryonic bradycardia, 1068–1069, 1068*f*
Embryonic disc, trilaminar, in spinal development, 1216–1217, 1217*f*
Embryonic period, 1053–1054
Emphysema, lobar, congenital, 1251, 1253*f*
Emphysematous cholecystitis, 175, 198*f*, 200
Emphysematous cystitis, 333, 334*f*
Emphysematous pyelitis, 326–327, 327*f*
Emphysematous pyelonephritis, 325–326, 326*f*
Empty stomach artifact, 1838, 1839*f*
Empyemas, pediatric, 1702–1711
abscess differentiated from, 1725, 1726*f*
drainage of, 1954, 1958*f*
lung abscess compared to, 1711, 1713*f*
parapneumonic collections and, 1710–1711
from pneumonia, 1707*f*
sonographic appearance of, 1707*f*
Encephalitis
CMV, neonatal, 1559*f*
pediatric, neurogenic bladder in, 1907
Encephalocele(s)
corpus callosum agenesis and, 1526–1528
fetal
amniotic band syndrome and, 1330
anencephaly differentiated from, 1179
fetal brain and, 1179–1182, 1181*f*, 1182*t*
pentalogy of Cantrell and, 1329
sloped forehead in, 1139–1140
Encephaloclastic schizencephaly, 1196
Encephalomalacia, cystic, 1538, 1539*f*
End diastolic ratio, in internal carotid artery stenosis evaluation, 937
End diastolic velocity
in assessing degree of carotid stenosis, 929
in mesenteric duplex Doppler sonography interpretation, 454
Endarterectomy, carotid
for carotid stenosis, 916
pediatric, TCD sonography in, 1621
sonographic features following, 942, 944*f*
Endocardial cushion defects, 1284

Endocardial cushion(s), 1279, 1282*f*
  development of, 1284, 1284*f*
Endocardial fibroelastosis (EF), 1292
  fetal, 1294, 1295*f*
  heart block and, 1425
Endocervical canal, normal sonographic appearance of, 1497*f*, 1499
Endocrine disorders, fetal hydrops from, 1432
Endocrine drainage, in pancreas transplantation, 672, 675*f*
Endocrine tumors, pancreatic, 248–249, 249*f*–250*f*, 249*t*
Endoderm layer, of trilaminar embryonic disc, 1216–1217, 1217*f*
Endodermal sinus tumor
  ovarian, 585
    pediatric, 1880
  testicular, 823–824, 825*f*
    pediatric, 1899
  vaginal, pediatric, 1883
Endoleaks, after AAA repair, 438–439, 440*f*–442*f*
Endoluminal graft, 438
Endometrial carcinoma, 544, 550*f*
  polycystic ovarian disease and, 1877–1878
Endometrial plaques, 523, 524*f*
Endometrioid tumors, ovarian, 581
Endometrioma(s)
  appearances of, 574–575, 575*f*
  in pouch of Douglas, 524*f*
  sonographic evaluation of, 521–523
Endometriosis
  of bladder, 372, 372*f*
  in ovaries, 574–576, 575*f*–576*f*
  in peritoneum, 521–523, 524*f*
Endometritis, 554
  PID and, 1885
  postpartum recognition of, 555–556
Endometrium
  abnormalities of, 544–552
    ablation as, 551–552, 552*f*
    adhesions as, 551, 552*f*
    atrophy as, 547–548
    bleeding as, 544, 544*b*
    carcinoma as, 544, 548–551, 550*f*
    hematometrocolpos as, 546–547, 546*f*
    hormone use and postmenopausal, 544–545, 544*b*, 545*f*
    hydrometrocolpos as, 546–547
    hyperplasia as, 544, 547–548, 548*f*
    polyps as, 544, 548, 549*f*
    postmenopausal bleeding as, 545–546
    postmenopausal fluid and, 546–547, 546*b*, 547*f*
    sarcoma as, 551, 551*f*
    thickening, 544, 544*b*
  calcifications of, 533, 534*f*
  cysts of, 547–548
  ectopic pregnancy and, 1072–1073
  layers of, sonographic appearance of, 531, 532*f*
  lining of, in menstrual cycle, 1050*f*
  phases of, sonographic appearance of, 531, 532*f*
  proliferation of, 1049, 1050*f*
  sonographic appearance of, 531, 532*f*
  thickness of
    measurement for, 531
    transvaginal ultrasound assessment for, 545–546
Endoscopic ultrasound
  for adrenal glands, 428–429, 429*f*
  for percutaneous needle biopsy of pancreas, 423
Endosonography, of gastrointestinal tract, 300–307
  for anal canal, 302–307, 304*f*–307*f*, 306*b*
  for rectum, 301–302, 301*f*–304*f*
  for upper gastrointestinal tract, 300–301
Endotracheal suctioning, in neonatal/infant brain, 1578
Endovascular aortic repair (EVAR), 438
End-stage renal disease (ESRD)
  catheterization and, 994
  hemodialysis for, 996
  reflux nephropathy and, 327, 327*f*
Enhancement artifacts, 21, 22*f*
Entamoeba histolytica, 613
  hepatic infection by, 87
Enteric drainage, in pancreas transplantation, 672
Enteric duplication cysts, fetal
  ovarian cysts differentiated from, 1369
  small bowel and, 1312–1313, 1313*f*
Enterobius vermicularis organisms, 1853
Enterocolitis, necrotizing, pediatric, 1854–1855, 1855*b*, 1856*f*
Enterocutaneous fistulas, 612
Entertainment videos, 49*b*, 50
Enthesis, 902
Eosinophilic gastritis, gastric mucosa thickening in, 1839–1840
Ependymomas, neonatal/infant brain and, 1562
Epicondylitis, 861
Epidermal inclusion cysts, 779
Epidermal nevus syndrome, hemimegalencephaly associated with, 1195
Epidermoid cyst(s)
  pediatric
    neck and, 1652–1654
    in suprahyoid area, 1640
    testicular, 1900–1901, 1901*f*
  splenic, 146–147, 148*f*–149*f*
  testicular, 830*f*, 831
Epidermolysis bullosa, pyloric atresia and, 1307
Epididymis
  anatomy of, 819–820, 820*f*
  appendices of, 820–821, 820*f*
  cystadenomas of, paratesticular, 1904
  cysts of, 839, 842*f*
  inflammation of, 846
  lesions of, 839–841
  papillary cystadenomas of, 840–841
  pediatric, 1890
    appendix, 1897, 1897*f*
    cysts of, 1902–1903, 1903*f*
  postvasectomy changes in, 841, 843*f*
  sarcoidosis and, 841, 843*f*
  sperm granuloma and, 841, 843*f*
  tumors of, extratesticular, 840–841, 840*f*
Epididymitis
  acute, 846
    scrotum pain from, 846, 847*f*–848*f*, 1895–1896, 1896*f*
  chronic, 841, 843*f*
  pediatric
    bladder outlet obstruction and, 1897
    chronic, 1896
    color Doppler ultrasound for, 1896, 1896*b*
    following trauma, 1897
    infarction and, 1896
    ischemia and, 1896
    orchitis and, 1896
    testicular torsion and, 1323–1324, 1895–1896, 1896*f*
Epididymo-orchitis, acute scrotal pain from, 846, 847*f*–849*f*
Epidural hematomas, neonatal/infant, 1557
Epigastric hernias, 488–491, 490*f*–491*f*
Epigastrium, free air in, 526
Epignathus, 1159
Epinephrine, secretion of, 417
Epineurium, 864–865, 865*f*
Epiphysis
  slipped capital femoral, 1931–1932
  stippled, 1399
Epiploic foramen, 211–212
Epispadias, bladder exstrophy with, 1326
Epispadias, fetal cloacal exstrophy and, 1328
Epithelial cell tumors, ovarian, pediatric, 1879
Epithelioid hemangioendothelioma (EHE), 123–124
Epstein-Barr virus
  diffuse lymphadenitis in, 1660, 1662*f*
  PTLD and, 682
Erb palsy, 1934
ERSPC (European Randomized Study of Screening for Prostate Cancer), 397
Erythroblastosis fetalis, 1419. *See also* Hydrops, fetal, immune
Escherichia coli, 846, 1852
Esophageal atresia, 1305–1306, 1305*f*–1306*f*, 1305*t*
Esophageal cysts, pediatric, 1650
Esophageal duplication cysts, 1256
Esophageal pouch sign, 1305–1306, 1306*f*
Esophagus
  carcinoma of, staging of, endosonography in, 301
  fetal, 1305–1306
    esophageal atresia and, 1305–1306, 1305*f*–1306*f*, 1305*t*
  parathyroid adenomas confused with, 745
  pediatric, 1833–1840
    anatomy of, 1834, 1834*f*
    sonographic technique for, 1833–1835
ESRD. *See* End-stage renal disease
ESWL. *See* Extracorporeal shockwave lithotripsy
Ethanol ablation
  of cervical nodal metastasis from papillary carcinoma, 720, 721*f*
  for secondary or recurrent hyperparathyroidism, 751–754, 754*f*
  for thyroid nodules
    autonomously functioning, 719–720
    benign functioning, 719, 719*f*
    solitary solid benign "cold", 720
Ethanol sclerotherapy, 719
Ethmocephaly
  alobar HPE and, 1534–1535
  hypotelorism and, 1140
European Carotid Surgery Trial (ECST), 916
European Federation of Societies of Ultrasound in Medicine and Biology (EFSUMB), 1041
European Randomized Study of Screening for Prostate Cancer (ERSPC), 397
EVAR. *See* Endovascular aortic repair
Ex utero intrapartum treatment (EXIT) procedure, 1159, 1255
Exencephaly, 1179, 1218
EXIT procedure. *See* Ex utero intrapartum treatment procedure
Exorbitism, 1140
  craniosynostosis and, 1136–1138
  hypertelorism with, in Pfeiffer syndrome, 1145*f*
Expected date of delivery (EDD)
  determination of, 1022
  ultrasound changing, 1022–1029
External beam radiotherapy, for prostate cancer, 400–401, 401*f*
External spermatic (cremasteric) artery, 821, 821*f*
Extracardiac malformations, in CHD, 1270
Extracorporeal membrane oxygenation (ECMO)
  complications of, 1548
  in neonatal/infant brain, duplex Doppler sonography and, 1578–1580, 1579*f*
  TCD sonography in monitoring, 1622
Extracorporeal shockwave lithotripsy (ESWL), 42
Extravaginal torsion, 844, 844*f*
Extremities
  fetal
    measurements of, 1378–1379, 1379*t*, 1380*f*–1381*f*
    routine sonographic views of, 1021, 1028*f*
  right lower, amputation of, 1403*f*

Exudate ascites, 506–507
Exudates, pleural, sonographic appearance of, 1702

F
Face
  abnormalities of, craniosynostosis and, 1136–1138
  midface abnormalities of, 1148–1153
Face, fetal. *See also* Midface abnormalities; Neck, fetal; Orbits, fetal
  embryology and development of, 1133–1134, 1134*f*
  forehead abnormalities in, 1137*f*, 1139–1140, 1139*b*, 1140*f*–1141*f*
  hemangiomas of, 1154, 1160*f*
  HPE changes to, 1189, 1189*b*
  lower, abnormalities of, 1153–1154
    macroglossia as, 1153, 1153*b*, 1158*f*
    micrognathia as, 1153–1154, 1158*f*
    retrognathia as, 1153–1154
  midface abnormalities of, 1148–1153
  normal, sonography of, 1134–1135, 1135*f*
  orbital abnormalities in, 1140–1143
  routine sonographic views of, 1021, 1024*f*
  soft tissue tumors of, 1154, 1160*f*
Facial nerve, pediatric, anatomy of, 1630
Falciform ligament, 77, 79*f*
  pediatric, 1731, 1731*f*–1732*f*
Fallopian tube(s), 585–589
  anatomy of, 565, 565*f*
  carcinoma in, 589
  hydrosalpinx of, 585–587, 587*f*
  normal sonographic appearance of, 568
  pediatric, torsion of, 1875–1876
  PID and, 587–589, 588*f*
  torsion of, 589
Falx sign, bright, in osteogenesis imperfecta type II, 1392
Familial hypocalciuric hypercalcemia, primary hyperparathyroidism distinguished from, 734
Familial juvenile nephronophthisis, 359
Familial paraganglioma syndromes, pheochromocytomas with, 1826
Fanconi anemia, 1746
Fanconi pancytopenia, 1400, 1402*f*
Far field, of beam, 8
Fasciitis
  necrotizing, of perineum, 846–847
  planter, injection for, 902, 904*f*
Fascioliasis, 176–178, 177*f*–178*f*
FAST. *See* Focused abdominal sonography for trauma
FASTER. *See* First and Second Trimester Evaluation of Risk
Fastigial point, 1189–1190
Fat, Crohn disease and creeping, 269, 271*f*
Fat necrosis
  injectable steroid complications with, 901
  simulating anterior abdominal wall hernias, 500, 502*f*
Fat-fluid levels, in breast cysts, 775, 778*f*
Fatty liver, 91–92, 92*f*–93*f*
Fecal incontinence, anal endosonography in, 305, 305*f*
Fecaliths, in acute appendicitis, 1857, 1859*f*
Feet. *See* Foot
Feminization, testicular, 1368
  dysplastic gonads and, 1899
  primary amenorrhea in, 1887
Feminizing adrenal tumors, pseudoprecocious puberty and, 1888
Femoral artery
  common, 966
    AVF of, 974*f*
    normal appearance of, 966–967, 967*f*
    pseudoaneurysms of, 973*f*
    stenosis of, 969*f*
  superficial, 966
    bypass graft of, 975*f*
    calcification of, 968, 970*f*
    normal appearance of, 966–967
    occlusion of, 967*f*, 969*f*
    stenosis of, 969*f*, 971*f*
Femoral canal, as landmark for femoral hernias, 482, 485*f*
Femoral hernias, 471, 481–483. *See also* Hernia(s), femoral
Femoral vein
  bifurcation of, 980–981
  common
    as landmark for femoral hernias, 482, 485*f*
    normal anatomy of, 500, 981*f*
    ultrasound examination of, 982–983
  compression of, normal, 982*f*
  DVT in duplicated, detecting, 988, 988*f*
  normal, 989*f*
  phasicity, 459, 459*f*–460*f*
Femur, fetal
  bowing of, 1380*f*
  deficiency of, proximal focal, 1400, 1400*f*
  hypoplasia of, in caudal regression, 1237–1238
  length of
    assessment of, 1378, 1379*t*, 1380*f*
    BPD in heterozygous achondroplasia compared to, 1398, 1398*f*
    in gestational age determination, 1448, 1449*f*, 1449*t*
    in second-trimester, 1023*f*
  short, etiology of, 1381
  subtrochanteric, absence of, 1400
  "telephone receiver", 1380*f*
Femur, head of, pediatric
  avascular necrosis of, 1930
  in DDH assessment, 1923
  position of, in evaluation of infant at risk, 1927
  in sonogram of hip from transverse/flexion view, 1927, 1928*f*
Femur-fibula-ulnar complex, 1400
Femur/foot length ratio, 1379
Femur-tibia-radius complex, 1400
Fertilization, cycle of, 1051, 1051*f*
Fetal akinesia sequence, 1401
Fetal alcohol syndrome, 1194
  rhabdomyosarcoma associated with, 1908
Fetal artery, aberrant, sirenomelia from, 1238
Fetal Echocardiography, indications for, 1270–1273, 1273*b*
Fetal endoscopic tracheal occlusion (FETO), 1264
Fetal fibronectin (FFN), 1501
Fetal growth restriction, echogenic bowel and, 1316
Fetal hemoglobin deficit, immune hydrops and, 1419. *See also* Hemoglobin, fetal
Fetal hydrops. *See* Hydrops, fetal
Fetal lobation, in kidneys, 317, 1781, 1781*f*
Fetal period, 1054
Fetal renal hamartomas, 1818–1820
Fetal therapy, cervical assessment and, 1505
FETO. *See* Fetal endoscopic tracheal occlusion
Fetomaternal transfusion, maternal serum alpha-fetoprotein elevation in, 1228
Fetter syndrome, craniosynostosis in, 1136–1138
Fetus. *See also specific organs*
  adrenal glands of
    masses in, 1353–1354, 1353*f*, 1353*t*
    normal, 1353, 1353*f*
  assessment of, for alloimmunization, 1421–1423, 1421*b*, 1422*f*, 1422*t*
  assessment of well-being of, 1455–1460
    BPP for, 1456–1458, 1457*f*, 1457*t*
    Doppler ultrasound for, 1458–1460, 1459*f*–1460*f*
  "Buddha position" of, 1401
  coexistent hydatidiform molar pregnancy and, 1078–1080, 1081*f*
  death of
    echogenic bowel and, 1316
    maternal serum alpha-fetoprotein elevation in, 1228
  definition of, 1445
  ears of
    abnormalities of, 1148, 1148*f*
    length of, in trisomy 21, 1101
    low-set, 1148
  foot of, deformities of, 1404–1407
  gestational age determination and measurements of, 1016, 1016*b*, 1444–1449
    age assignment and, 1449, 1450*t*
    in first trimester, 1444–1445, 1445*f*–1446*f*, 1445*t*–1446*t*
    in second and third trimesters, 1446–1448, 1447*f*–1450*f*, 1447*t*–1449*t*
  growth of
    abnormalities of, 1453–1455
    assessment of, 1022–1029
    curves depicting, 1453, 1453*f*
    restriction of, 1455
  growth restriction of, echogenic bowel and, 1316
  hand of, deformities of, 1404–1407
  keepsake imaging of, 49*b*, 50
  large-for-gestational age, 1453–1454
    diabetic mothers and, 1454, 1455*t*
    incidence of, 1453–1454
    sonographic criteria for, 1454*t*–1455*t*
  malformations of, diagnostic accuracy of, 1030
  megacystis in, 1360, 1360*b*, 1360*f*
  movements of, musculoskeletal development and, 1378
  MRI of, 1031–1032, 1031*f*
  presentation of, determination of, 1021, 1022*f*
  situs of, determination of, 1021, 1022*f*
  small-for-gestational age, 1454–1455, 1454*b*
  sonographic appearance of, normal, 1018*f*
  weight assessment for, 1450–1453
    in relation to gestational age, 1451–1453, 1452*t*, 1453*f*
  weight estimation for, 1450–1453
    formulas in, 1451, 1451*t*
    gestational age compared to, 1453, 1453*f*
    recommended approach in, 1451, 1452*t*
FFN. *See* Fetal fibronectin
Fibrinous peritonitis, 509*f*
Fibroadenoma, 797, 797*f*
Fibrochondrogenesis, 1396
Fibroelastosis, endocardial, fetal, 1294, 1295*f*
  heart block and, 1425
Fibroglandular tissue, asymmetrical, split-screen imaging and, 769, 769*f*
Fibroids, uterine, 538–540, 539*f*, 540*b*
Fibrolamellar carcinoma, 122–123
Fibrolipomas, coccygeal dimples and, 1679
Fibroma(s)
  cardiac, fetal, 1294
  gastrointestinal, endosonographic identification of, 301
  ovarian, 585, 586*f*

Fibroma(s) *(Continued)*
paratesticular, 1903–1904
simulating anterior abdominal wall hernias, 500–501, 502*f*
Fibromatosis, ovarian edema differentiated from, 1878–1879
Fibromatosis coli, pediatric, inflammatory disease and, 1663–1664, 1663*f*
Fibromuscular dysplasia
carotid flow disturbances in, 928
of internal carotid artery, 944–946, 946*f*
renal artery stenosis and, 447, 447*f*
renovascular disease and, 368
Fibronectin, fetal, 1501
Fibrosarcomas
paratesticular, 1903–1904
simulating anterior abdominal wall tumors, 500–501, 502*f*
Fibroscan, 1764
Fibrosis
retroperitoneal, 464–465, 465*f*
testicular, after orchitis, 846, 849*f*
tubulointerstitial, 359
Fibrothorax, sonographic appearance of, 1702
Fibrous cap thinning, microRNAs and, 920
Fibrous pseudotumors, 838, 840*f*
Field of view (FOV), 105, 505–506
musculoskeletal system and extended, 857
in obstetric sonography, 1036, 1036*f*
Filar cyst, in newborn, 1674–1675, 1678*f*
Filum terminale
formation of, 1673, 1673*f*
lipomas of, 1674
closed spinal dysraphism and, 1684–1685, 1686*f*
normal anatomy of, 1674–1675, 1677*f*
Fine-needle aspiration biopsy
parathyroid adenoma and accuracy of, 746
of thyroid gland, 709–710, 710*t*, 722
Fingers, syndactyly of, 1105*f*
Finite amplitude distortion, in soft tissue heating, 37–38, 37*f*
First and Second Trimester Evaluation of Risk (FASTER), 1090–1091, 1095
Fistula(s). *See also* Arteriovenous fistulas
aortoenteric, 438
bladder, 334, 335*f*
cholecystenteric, 207
choledochoduodenal, 175–176, 177*f*
choledochoenteric, 175–176, 177*f*
Crohn disease and formation of, 276, 279*f*–280*f*
dorsal enteric, pediatric, 1686–1688
enterocutaneous, 612
in imperforate anus, 1847–1848, 1850*f*
neurenteric, 1674
perianal, perianal inflammatory disease in, 305–306
tracheoesophageal, fetal
CHAOS and, 1254–1255
esophageal atresia and, 1305
vesicocolic, 1310–1312
vesicocutaneous, 334
vesicoenteric, 334
vesicoureteral, 334
vesicouterine, 334
vesicovaginal, 334
Fitz-Hugh-Curtis syndrome, PID and, 1887
Flash artifacts, 60–61
Flexor hallucis longus tendon, injection of, 902, 903*f*
Flexor retinaculum, thickening of, 865
Fluid, in neonatal/infant brain imaging, 1512
Fluorescent in situ hybridization, in hydrops diagnosis, 1433–1434
Fluoroscopic guidance, for drainage catheter placement, 610
FNH. *See* Focal nodular hyperplasia
Foam cysts, in breast, 779, 781*f*
Focal depth, in obstetric sonography, 1036, 1036*f*
Focal hypertrichosis, tethered cord and, 1679
Focal nodular hyperplasia (FNH)
adenoma differentiated from, 116–117
CEUS for diagnosis of, 113–115, 115*f*
characterization of, with microbubble contrast agents, 106, 106*f*, 108*t*, 109*f*
Doppler ultrasound characterization of, 113
of liver, 112–115, 114*f*–115*f*
pediatric, 1746
sulfur colloid scanning and, 115
Focal subcortical heterotopia, 1196
Focal therapy, for prostate cancer, 400
Focal zone, 505–506
Focused abdominal sonography for trauma (FAST), 508
Folic acid, in spina bifida prevention, 1224–1225
Follicular adenomas, thyroid, pediatric, 1646–1648, 1647*f*
Follicular carcinoma, of thyroid gland, 701, 701*b*, 706*f*–707*f*
pediatric, 1648
Follicular cysts
menstrual cycle and, 568
pediatric, 1875
Fondaparinux, 598
Fontanelle
mastoid, neonatal/infant brain imaging through, 1512, 1517–1518, 1517*f*, 1519*f*
duplex Doppler, 1574, 1575*f*
posterior, neonatal/infant brain imaging through, 1512, 1517, 1517*f*–1518*f*
duplex Doppler, 1574, 1575*f*
Fontanelle, anterior
cerebral artery, compression of, in hydrocephalus, RI and, 1582, 1584*f*
neonatal/infant brain imaging through, 1512–1513
coronal planes in, 1513*f*
duplex Doppler, 1574, 1575*f*
sagittal planes in, 1516*f*
Foot (Feet). *See also* Clubfoot
fetal
deformities of, 1404–1407
length of, measurement of, 1379, 1381*f*
rocker-bottom, 1406*f*, 1407
in skeletal dysplasia, 1382
injection of, 901
superficial peritendinous and periarticular, 902–904, 903*f*–904*f*
pediatric, congenital deformities of, 1932–1933
club foot as, 1932
vertical talus as, 1932–1933, 1932*f*
Foramen magnum approach
for duplex Doppler ultrasound of neonatal/infant brain, 1574, 1575*f*
for TCD sonography, 1592, 1595*f*
Foramen of Magendie, neonatal/infant, in mastoid fontanelle imaging, 1517–1518
Foramen ovale, 1273–1275, 1275*f*, 1279, 1282*f*
sonographic appearance of, 1280, 1283*f*
Foraminal flap, sonographic appearance of, 1283*f*
Forearm muscle, hernia of, 859*f*
Forearm veins, sonographic evaluation of, 996–998, 998*f*
Foregut, 1304–1305
bronchopulmonary malformations of, pediatric, 1716, 1718*f*
cysts of, 1650
Forehead, fetal, abnormalities of, 1137*f*, 1139–1140, 1139*b*, 1140*f*–1141*f*
Foreign body(ies)
embedded in soft tissue, 872, 873*f*
in gastrointestinal tract, 300
Foreign body(ies) *(Continued)*
interventional sonography, pediatric, for deep removal of, 1961, 1965*f*
in vagina, pediatric, 1887
Fornices
cavum septi pellucidi mistaken for, 1521
fetal, normal sonographic appearance of, 1168
4Kscore, 396
Four-dimensional ultrasound, for fetal heart assessment, 1277
Fournier gangrene, acute scrotal pain from, 846–847
FOV. *See* Field of view
Fracture(s)
fetal, in skeletal dysplasias, 1380*f*, 1381–1382
in osteogenesis imperfecta, 1392, 1393*f*
pediatric, rib, 1727
testicular, 850, 850*f*
Frame rate
in obstetric sonography, 1036
in renal artery duplex Doppler sonography, 449
Frank dislocation, of hip, 1927
Fraser syndrome, 1253
Fraternal twins. *See* Dizygotic twins
Fraunhofer zone, of beam, 8
Free air, pneumoperitoneum and, 525*f*, 526
"Freehand" technique, for percutaneous needle biopsies, 600, 602*f*
Frequency compounding, 7–8
Frequency spectrum bandwidth, 7–8
Frequency(ies)
acoustic, 2
band of, 7
in sound waves, 2, 2*f*
Fresnel zone, of beam, 8
Frontal bossing, 1137*f*, 1139, 1139*b*
in skeletal dysplasia, 1382
Frontal horns, of ventricles
in Chiari II malformation, 1526, 1527*f*–1528*f*
in corpus callosum agenesis, 1528, 1530*f*–1531*f*
neonatal/infant
in coronal imaging, 1514, 1514*f*–1515*f*
cysts of, 1522, 1522*f*, 1566
Frontonasal prominence, 1134
Frontothalamic distance, in trisomy 21, 1101
Fryn syndrome, CDH and, 1263
Fukuyama syndrome, cobblestone lissencephaly in, 1195
Full-thickness rotator cuff tears, 886–887, 887*f*–888*f*
Fundal adenomyomas, 202, 204*f*
Fundamental echo, 58–59
Fundus, uterine, 530
Fungal diseases
genitourinary, 330–331
hepatic, 86–87, 88*f*
Fungus balls
in collecting systems, 330–331, 331*f*
formation of, in neonatal candidiasis, 1794, 1795*f*
Fused vertebrae, pediatric, 1688
Fusiform dilatation, 283

G

G6PD. *See* Glucose-6-phosphate dehydrogenase deficiency
Gadopentetate dimeglumine, as pregnancy category C drug, 1032
Gain settings, 505–506
Galactoceles, 775
Galactography, 799
Galactosemia, inborn errors of metabolism and, 1738
Gallbladder, 188–207. *See also* Cholecystitis
absent or small, in biliary atresia, 1734–1735, 1737, 1738*f*

Gallbladder *(Continued)*
adenomas of, 203–204, 205*f*
adenomyomas of, 202–204, 204*f*–205*f*
adenomyomatosis of, 202, 203*f*–205*f*
agenesis of, 190–194
anatomy of, 188–194, 193*f*
aspiration of, 614, 616*f*
biliary sludge and, 194–195, 196*f*
calcification of, 202, 202*f*
carcinoma of, 206–207, 206*f*
drainage of, 613–614, 616*f*
duplication of, 194
fetal, 1318–1319, 1319*f*
choledochal cysts and, 1319, 1320*f*
enlarged, 1318
gallstones and, 1319, 1320*f*
nonvisualization of, 1318–1319
gallstone disease of, 194, 195*f*
hepatization of, 195
hourglass, 202, 205*f*
intrahepatic, 188–190, 193*f*
malignancies of, 204–206
milk of calcium bile and, 194, 195*f*
pediatric, wall thickening in, 1741
perforation of, 198*f*, 200
polyps of, 203–206, 203*b*
cholesterol, 203, 205*f*
inflammatory, 203–204, 205*f*
porcelain, 202, 202*f*
small, in biliary atresia, 1737, 1738*f*
sonographic nonvisualization of, causes of, 190–194, 194*b*
sonographic technique for, 194
variants of, normal, 188–194
volvulus of, 201
wall thickening in
causes of, 198, 199*f*, 200*b*
in children, 1741
hyperemia in, in acute cholecystitis, 197*f*, 198–199
sympathetic, 199–200, 201*f*
Gallstone disease, 194, 195*f*
Gallstones
acute pancreatitis and, 221
fetal, 1319, 1320*f*
pediatric, 1741, 1743*f*
diseases associated with, 1741*b*
Gamma-glutamyl transpeptidase (GGTP), 1318
Gamna-Gandy bodies, in spleen, 157
Ganglion
cysts
injection for, 907–909, 909*f*
ultrasound techniques for, 869–870, 869*f*
subacromial-subdeltoid bursa thickening with, 889–891, 892*f*
Ganglioneuroblastoma, pediatric, 1825
Ganglioneuromas, adrenal, 427–428
benign, pediatric, 1825
Gangrene, Fournier, 846–847
Gangrenous appendix, pediatric, 1857, 1861*f*
Gangrenous cholecystitis, 198*f*, 200
Gartner cyst, pediatric, 1883–1884
Gas, free intraperitoneal, in acute abdomen, 277–281, 282*f*
Gas bubbles, free, as blood pool contrast agents, 55
Gastric diaphragm, pediatric, 1839, 1840*f*
Gastric ulcers, pediatric, 1839–1840, 1840*f*
Gastric vein, left, pediatric
Doppler studies of, best approach for, 1752
flow direction of, in portal hypertension, 1752, 1757
in intrahepatic portal hypertension, 1761
Gastritis, pediatric, 1839–1840, 1840*f*
Gastrocolic trunk, pancreatic head and, 212
Gastroduodenal artery, pancreatic head and, 211–212, 213*f*
Gastroesophageal reflux, sonographic detection, 1834, 1834*f*
Gastrointestinal tract. *See also* Acute abdomen; Crohn disease
acute abdomen and, 277–290
anatomy of, 257–261
CF and, 300
Crohn disease and, 266–269
endosonography of, 300–307
for anal canal, 302–307, 304*f*–307*f*, 306*b*
for rectum, 301–302, 301*f*–304*f*
for upper gastrointestinal tract, 300–301
gut edema and, 295, 297*f*
gut signature and, 257, 257*f*–259*f*, 257*t*
infections of, 295–300
AIDS patients and, 296
bezoars and, 300
celiac disease and, 300
congenital cysts and, 297, 298*f*
hematomas and, 299
intraluminal foreign bodies and, 300
ischemic bowel disease and, 297
mucocele of appendix and, 299, 299*f*
peptic ulcer and, 299, 300*f*
pneumatosis intestinalis and, 297–299, 299*f*
pseudomembranous colitis and, 296–297, 298*f*
layers of, 257, 257*f*–258*f*
masses of, 592
mechanical bowel obstruction and, 293
neoplasms of, 261–266
adenocarcinoma as, 261–264, 263*f*–264*f*
lymphoma as, 264–266, 266*f*
metastases as, 266, 267*f*
stromal tumors as, 264, 265*f*
paralytic ileus and, 294*f*, 295
pediatric
cysts of, 1860–1862, 1863*f*–1864*f*
duplication cysts of, 1860, 1863*f*, 1875
neoplasms of, 1860–1862, 1864*f*
sonographic technique for, 257–261, 262*f*
Gastrointestinal tract, fetal, 1304–1322. *See also specific organs*
anomalies of, hydrops from, 1427–1428, 1428*f*
Gastroschisis
fetal, 1322–1325
associated conditions of, 1324–1325
epidemiology of, 1322–1323
management of, 1325
pathogenesis of, 1323
prenatal diagnosis of, 1323–1324, 1324*f*
maternal serum alpha-fetoprotein elevation in, 1228
Gastrulation, 1053
disorders of, 1686–1689
in spine embryology, 1672
Gaucher disease, spleen and, 157, 158*f*
Gel cysts, 779, 781*f*
Gender
fetal, identification of, 1367, 1367*f*
in multifetal pregnancy, chorionicity and, 1119
pediatric kidney length according to, 1776–1778, 1778*t*
pediatric kidney volume according to, 1776–1778, 1778*t*
TCD sonography velocity evaluation and, 1595
Genetic amniocentesis, 1108–1109, 1108*f*
Genetic disorders, fetal hydrops from, 1432
Genital tract, fetal, 1366–1369
abnormal, 1367–1368, 1368*f*
hydrocolpos and, 1368
normal, 1366–1367, 1366*f*–1367*f*
ovarian cysts and, 1369, 1369*f*
Genitalia, fetal
abnormal, 1367–1368, 1368*f*
ambiguous, 1365, 1368*f*
normal, 1366–1367, 1366*f*–1367*f*
Genitourinary tract. *See also* Bladder; Kidney(s); Renal artery(ies); Renal cell carcinoma; Renal vein(s); Transitional cell carcinoma; Ureter; Urethra; Urinary tract
abnormalities of, in Miller-Dieker syndrome, 1195
anatomy of, 311–314
bladder diverticula and, 374, 374*f*
congenital anomalies of, 317–323
bladder development and, 322
kidney ascent and, 318
kidney growth and, 317–318
ureteral bud and, 318–321
urethral development and, 323, 323*f*
vascular development and, 321–322
duplex collecting system and, 319, 320*f*
embryology of, 311
infections of, 323–333
AIDS and, 331–333, 332*f*–333*f*
alkaline-encrusted pyelitis as, 324–325
Candida albicans as, 330–331, 331*f*
cystitis as, 333
echinococcal disease as, 331, 332*f*
fungal, 330–331
papillary necrosis as, 328–329, 329*b*, 329*f*
parasitic, 331
pyelonephritis as, 323–328
pyonephrosis as, 325, 326*f*
schistosomiasis as, 331
tuberculosis as, 329–330, 330*f*
medical diseases of, 369–372
acute cortical necrosis as, 370, 372*f*
acute interstitial nephritis as, 370
acute tubular necrosis as, 370
amyloidosis as, 372
diabetes mellitus as, 372
endometriosis as, 372, 372*f*
glomerulonephritis as, 370, 371*f*
interstitial cystitis as, 372, 373*f*
neurogenic bladder and, 372–374, 373*f*
obstruction of
hydronephrosis and, 316, 317*b*
pitfalls in assessment of, 317
postsurgical evaluation of, 374–375
sonographic technique for, 314–315
stones in, 334–340
trauma to, 365–366
tumors of, 340–356
adenocarcinoma as, 348
angiomyolipoma as, 351–352, 351*f*–352*f*
leukemia as, 353–354
lymphoma as, 352–353
metastases as, 354–355
oncocytoma as, 348–351
rare, 355–356
renal cell carcinoma as, 340–344
squamous cell carcinoma as, 348
transitional cell carcinoma as, 346–348
urachal adenocarcinomas as, 355
vascular abnormalities of, 366–369
AVF and malformation as, 366–367, 366*f*
renal vascular Doppler ultrasound and, 366
Germ cell tumors
ovarian, 582–585
pediatric, 1879
testicular, 822–825, 822*b*
mixed, 822–823, 825*f*
nonseminomatous, 823–824, 825*f*
regressed, 824–825, 825*f*–826*f*
thymus, 1723–1724

Germinal epithelium, 565
Germinal matrix hemorrhage, hypoxic-ischemic injury in premature infant and, 1541–1543, 1542*f*, 1543*b*, 1543*t*
Germinal matrix of, neonatal/infant, development of, 1524, 1524*f*
Gerota fascia, 314
Gestational age
  alpha-fetoprotein levels compared to, 1227*f*
  calculation of, 1049
  cervical length and, 1499–1500, 1499*f*
    spontaneous PTB prediction based on, 1500–1501, 1501*t*
  definition of, 1443–1444
  determination of
    accuracy of, 1449, 1450*t*
    composite formulas for, 1448–1449
    routine ultrasound screening in, 1022–1029
  estimation of
    CRL in, 1062
    in first trimester, 1061–1062
    gestational sac size in, 1061, 1061*f*
    MSD in, 1061, 1061*f*, 1444–1445, 1445*t*
    routine ultrasound screening in, 1022–1029
  extremity long-bone lengths and BPD at, 1379*t*
  fetal measurements for determining, 1016, 1016*b*, 1444–1449
    age assignment and, 1449, 1450*t*
    in first trimester, 1444–1445, 1445*f*–1446*f*, 1445*t*–1446*t*
    in second and third trimesters, 1446–1448, 1447*f*–1450*f*, 1447*t*–1449*t*
  fetal weight assessment in relation to, 1451–1453, 1452*t*, 1453*f*
  fetal weight estimation compared to, 1453, 1453*f*
  for heterozygous achondroplasia detection, 1381
  kidney length compared to, 1776–1778, 1780*f*
  PSV blood flow in MCA as function of, 1421, 1422*t*
  thermal effects of ultrasound and, 1037–1038
  thoracic circumference and length correlated with, 1247*t*
  usage of term, 1167
Gestational sac, 1017*f*
  abnormal size of, 1063
  chorionic bump in, 1065
  chorionic sac fluid of, 1054–1055, 1056*f*
  discriminatory level for seeing, 1056
  early pregnancy failure and
    appearance concerns in, 1065, 1066*f*
    no embryo in, 1063–1065, 1065*f*
    small MSD in relationship to CRL in, 1066, 1067*f*
  identification of, in gestational age determination, 1444, 1445*f*, 1446*t*
  mean diameter of
    CRL and, early pregnancy failure and, 1066, 1067*f*
    in gestational age determination, 1444–1445, 1445*t*
  normal sonographic appearance of, 1054–1055, 1055*f*–1056*f*
  size of, in gestational age estimation, 1061, 1061*f*
  threshold level for seeing, 1056
  transvaginal ultrasound for identification of, 1054–1055
  β-hCG levels and, 1056–1057
Gestational trophoblastic disease, 556, 1077–1084, 1479
  hydatidiform molar pregnancy and, 1078–1080
    complete, 1078, 1079*f*
    partial, 1078, 1080*f*
    vaginal bleeding and, 1078
Gestational trophoblastic disease *(Continued)*
  PTN and, 1078, 1080–1084, 1082*f*
    choriocarcinoma and, 1080–1082, 1083*f*
    diagnosis and treatment of, 1083–1084
    Doppler ultrasound for, 1083
    after hydatidiform molar pregnancy, 1080, 1081*f*
    invasive mole, 1080, 1081*f*
    PSTT and, 1082
    sonographic features of, 1082–1083
"Geyser sign", 889–891, 892*f*
GGTP. *See* Gamma-glutamyl transpeptidase
Ghost triad, biliary atresia and, 1737, 1738*f*
Giant pigmented nevi, choroid plexus papillomas in, 1209
Giant-cell tumors, in TSC, 1200*f*
Glenohumeral joint, 878–879, 878*f*
  effusion of, 893–894, 894*f*
Glenohumeral joint, injection of, 901, 901*f*
Glenoid fossa, 878–879, 878*f*
Glial scarring, in PVL, 1552–1553
Glioependymal cysts, cavum veli interpositi cysts differentiated from, 1170
Gliomas, hypothalamic, precocious puberty and, 1887
Glisson capsule, 77
Glomerulonephritis, 370, 371*f*
  CKD and, 1796–1798
Glomus, choroid plexus, neonatal/infant, development of, 1522–1523, 1523*f*
Glomuvenous malformation, in venous malformations of neck, 1657
Glucocorticoid, secretion of, 417
Glucose, plasma levels of, high, NTDs from, 1218
Glucose-6-phosphate dehydrogenase (G6PD) deficiency, 1431
Glutaric aciduria type 1, 1540–1541
Glycogen storage disease (GSD)
  inborn errors of metabolism and, 1738
  liver in, 92
  pediatric
    type I, adenomas in, 1746
    tyrosinemia and, 1740*f*
Goiter(s)
  adenomatous, sonographic appearance of, 727
  fetal, 1159–1163, 1162*f*
  multinodular, 711, 711*f*
    in children, 1648, 1648*f*
    parathyroid adenomas detection and, 746
    sonographic appearance of, 727
  in thyroid gland nodular disease, 695–697, 695*f*–699*f*
Goitrous hypothyroidism, 694
Goldenhar syndrome, clefts of secondary palate in, 1153
Gonadal dysgenesis, primary amenorrhea in, 1887
Gonadal stromal tumors, testicular, 826, 827*f*
Gonadal veins, anatomic variants of, 457
Gonadoblastoma(s), 826, 827*f*
  pediatric, 1880
    in dysplastic gonads, 1899–1901
Gonads
  differentiation of, 1887
  dysplastic, 1899–1901
Gonococcal perihepatitis, PID and, 1887
Gorlin syndrome, 585
Gout, rheumatoid arthritis and, 867–869, 868*f*
Graafian follicle, 1049
Graded compression sonography, 283
Graft infarction, pediatric renal transplantation and, 1807–1809, 1808*f*
Graft-dependent hyperparathyroidism, 742–744, 743*f*
Graft-versus-host disease, pediatric, intestinal wall thickening in, 1853–1854, 1855*f*
Granulocytic sarcomas, pediatric, neck, 1666, 1667*f*
Granuloma(s)
  of liver, pediatric, 1748
  silicone, in extracapsular breast implant rupture, 805–807, 806*f*
  sperm, 841, 843*f*
  splenic, pediatric, 1771*f*
  stitch, after herniorrhaphy, 494–496, 495*f*
Granulomatous cystitis, pediatric, 1908
Granulomatous disease, chronic, gastric mucosa thickening in, 1839–1840
Granulomatous mastitis, 803–804
Granulomatous peritonitis, 514
Granulomatous prostatitis, 390, 390*f*
Granulosa cell tumor, ovarian, 585
  pediatric, 1880
    pseudoprecocious puberty and, 1887
Graves disease
  fetal goiter in, 1159–1163
  thyroid gland and, 727, 727*f*
    pediatric, 1646, 1646*f*
Gray-scale median level, for echolucency of plaque, 922
Great arteries, transposition of, 1289–1290, 1289*f*–1290*f*
Great saphenous vein (GSV)
  acute DVT in, 984, 984*f*
  anatomy of, 981–982, 981*f*
  vein mapping of, 989–990
Great vessels, fetal, short-axis view of, 1275, 1278*f*
Green-tag feature, in color Doppler, 932–933
Groin
  definition of, 471
  hernias of, dynamic ultrasound of
    contents of, 472–473
    entities stimulating, 499–500, 501*f*
    key sonographic landmarks for, 474
    maneuvers for, 473–474, 474*f*–475*f*
    recurrent, 494–496
    report for, 471–472
    technical requirements for, 471
  pain, 470–471
Growth. *See* Fetus, growth of; Intrauterine growth restriction
Growth discordance, in multifetal pregnancy, 1123, 1123*f*
GSD. *See* Glycogen storage disease
GSV. *See* Great saphenous vein
Gubernaculum testis, 851
Guidewire exchange technique, for drainage catheter placement, 610
Gut
  edema, 295, 297*f*
  primitive, 1057
  signature, 257, 257*f*–259*f*, 257*t*
  strictures in, in Crohn disease, 269–274, 275*f*–276*f*
Gut wall
  CEUS and, 261
  Doppler ultrasound evaluation of, 260–261, 262*f*
  elastography and, 261
  layers of, 257, 257*f*–258*f*
  masses in, 258
  pathology of, 257–258, 260*f*
  pseudokidney sign in, 257, 260*f*
  target pattern in, 257, 260*f*
  thickening of
    Crohn disease and, 269, 270*f*–271*f*
    pathology related to, 257
Gynecology. *See also* Fallopian tube(s); Uterus
  anatomy in, 564–570, 565*f*
  nongynecologic pelvic masses and, 591–592
Gynecomastia, in testicular choriocarcinoma, 824
Gyral interdigitation, in Chiari II malformation, 1526, 1528*f*

Gyri
abnormalities of, in lissencephaly, 1195
development of, 1167
normal sonographic appearance of, 1169, 1171*f*

H
HAART. *See* Highly active antiretroviral therapy
Haglund deformity, 903*f*
Hamartoma(s)
biliary, 83, 83*f*–84*f*
dysraphic, 1682
fetal renal, 1818–1820
hypothalamic, precocious puberty and, 1887
pediatric, mesenchymal, 1744
splenic, 153–156, 156*f*
testicular, 829, 829*f*
in TSC, 1200*f*
Hamstring tendon, injection of, 905–907, 907*f*–908*f*
Handedness, obstetric sonography and, 1040
Hand(s). *See also* Clubhand
clenched, in trisomy 18, 1103, 1103*f*
fetal
amputation of, in amniotic band sequence, 1403*f*
deformities of, 1404–1407
in skeletal dysplasia, 1382
injection of, 901
superficial peritendinous and periarticular, 904, 905*f*
persistent clenched, 1404
"trident" configuration of, achondroplasia and, 1407, 1408*f*
Harmonic imaging
of biliary tree, 168, 169*f*
B-mode, 60
contrast agents with, 58–64
spectral and power mode Doppler, 60–61, 60*f*–62*f*
tissue, 13, 13*f*–14*f*, 38, 61–62
Harmonic power angio, 66
Harmonics, generation of, 13, 13*f*
Hartmann pouch, 188
Hashimoto thyroiditis, 724, 725*f*–727*f*
fetal goiter in, 1159–1163
pediatric, 1645, 1646*f*
HCB. *See* Hypertrophied column of Bertin
HCC. *See* Hepatocellular carcinoma
hCG. *See* Human chorionic gonadotropin
Head, fetal
abnormalities of, 1135–1140
craniosynostosis and, 1136–1139, 1137*f*–1138*f*
in shape, 1136–1139, 1137*f*
in size, 1135–1136
wormian bones as, 1139, 1139*b*, 1139*f*
circumference of
in gestational age determination, 1446–1447, 1447*f*–1448*f*, 1448*t*
in second-trimester, 1023*f*
measurements of, in gestational age determination, 1446–1448, 1447*f*–1448*f*, 1447*t*–1448*t*
oblong, 1136–1138
sonographic views of, 1021, 1024*f*
Head, pediatric, lesions of, 1961, 1966*f*
Headaches, pediatric TCD sonography for, 1610–1611, 1612*f*
Healing response, impaired, injectable steroid complications with, 901
Heart. *See also* Congenital heart disease
congenital defects of
thickened NT in, 1095–1097, 1096*f*
in trisomy 18, 1103
in trisomy 21, 1097, 1098*f*
Heart *(Continued)*
disease of
carotid flow waveforms and, 936–937, 936*f*
CDH and, 1263
ischemic, 433
in Miller-Dieker syndrome, 1195
early pregnancy failure and absence of beating, 1063, 1064*f*
echogenic focus in, in trisomy 21, 1100*f*, 1101
embryonic
activity of, normal sonographic appearance of, 1058–1059, 1060*f*
beating of, in gestational age determination, 1445, 1445*f*, 1446*t*
embryos with CRL less than 7mm and no beating, 1064
rate, TCD sonography velocity evaluation and, 1595
Heart, fetal. *See also* Echocardiography, fetal
arrhythmias of, 1295–1297
bradycardia as, 1297, 1297*f*
CHD and, 1270–1273
congenital heart block as, 1297, 1297*f*
hydrops from, 1424, 1425*f*
PACs and PVCs as, 1295–1296
tachycardia as, 1296–1297, 1296*f*
atrioventricular valves of, 1274–1275
axis of, 1245
abnormal, mortality rate with, 1273
dimensions of, 1276*f*
disease of, congenital
recurrence risks in offspring for, 1273*t*
recurrence risks in siblings for, 1273*t*
risk factors associated with, 1271*t*–1272*t*
dysfunction of, from Ebstein anomaly, 1286
failure of, in sacrococcygeal teratoma, 1238–1239
malformations of, with AVSD, 1285–1286
normal anatomy of, 1273–1277
position of, 1245
abnormal, mortality rate with, 1273
routine sonographic views of, 1021, 1025*f*
scanning techniques for, 1273–1277
four-chamber view of, 1273–1275, 1277*f*
situs of, 1245
structural anomalies of, 1277–1295
aortic stenosis as, 1292
APVR as, 1290, 1291*f*
ASD as, 1277–1280, 1282*f*–1283*f*
AVSD as, 1284–1286, 1284*f*–1285*f*
cardiac tumors as, 1293–1294, 1293*f*–1294*f*
cardiomyopathy as, 1295*f*
cardiosplenic syndrome as, 1292–1293, 1293*b*
coarctation of aorta as, 1291, 1292*f*
DORV as, 1288–1289, 1289*f*
Ebstein anomaly as, 1286–1287, 1286*f*
ectopia cordis as, 1295, 1296*f*, 1329
hydrops from, 1423–1424
hypoplastic left heart syndrome as, 1287, 1287*f*
hypoplastic right ventricle as, 1287, 1287*f*
pentalogy of Cantrell and, 1329
pulmonic stenosis as, 1292
TGA as, 1289–1290, 1289*f*–1290*f*
TOF as, 1288, 1288*f*
truncus arteriosus as, 1288, 1289*f*
univentricular heart as, 1287–1288, 1287*f*
VSDs as, 1281–1284, 1283*f*–1284*f*
tumor of, 1293–1294, 1293*f*–1294*f*
hydrops from, 1424
ultrasound assessment of
color Doppler, 1275–1277, 1282*f*
spectral Doppler, 1275, 1281*f*
Heart, fetal *(Continued)*
three-dimensional and four-dimensional, 1277
univentricular, 1287–1288, 1287*f*
valves of, morphology of, 1285*f*
valvular stenosis of, 1275–1277
ventricles of, short-axis view of, 1275, 1278*f*
Heart block, fetal
complete, hydrops from, 1423–1424
congenital, 1297, 1297*f*
hydrops from, 1425
Heating
of bone, 37, 37*f*, 37*t*
of soft tissue, 37–38, 37*f*
Heerfordt disease, chronic pediatric sialadenitis in, 1634–1635
Height, pediatric, kidney length compared to, 1776–1778, 1777*f*
Hemangioblastoma, intracranial, fetal, 1208
Hemangioendothelioma(s)
epithelioid, hepatic, 123–124
infantile, 1319*f*
liver and, 1743–1744, 1745*f*
Hemangioma(s)
cardiac
fetal, 1294
in infants, 1293
cavernous
of bladder, 356
CEUS characterization of, 111, 113*f*
Doppler ultrasound characterization of, 109–110
of liver, 108–112, 112*f*–113*f*
percutaneous needle biopsy of, 603–604, 604*f*
characterization of, with microbubble contrast agents, 106, 106*f*–107*f*, 108*t*
cutaneous rapidly involuting cogenital, 1742–1743
dacryocystocele differentiated from, 1143
fetal
cardiac, 1294
face, 1154, 1160*f*
of liver, 1319*f*
infantile
of neck, 1655, 1656*f*
parotid gland, 1636, 1637*f*
tethered cord and, 1679
intraspinal, pediatric, 1689–1691
paratesticular, 1903–1904
pediatric
gastrointestinal, 1862, 1864*f*
liver and, 1742–1743, 1744*f*
sclerosis of, 112
segmental, tethered cord and, 1679
splenic, 148, 153–157, 156*f*
subcutaneous, spinal canal and, 1697, 1697*f*
umbilical cord, 1483
Hemangiopericytoma
renal, 356
splenic lesions in, 153
Hemangiosarcoma, of liver, 123
Hematoceles, scrotal, 835*f*, 836
pediatric, 1902
Hematoma(s)
in AVF for hemodialysis, 1002–1003, 1005*f*
bladder augmentation and, 1912–1913
bladder flap, cesarean sections and, 556–557, 557*f*
duodenal, pediatric, 1842, 1845*f*
epidural, neonatal/infant, 1557
of gastrointestinal tract, 299
intestinal, small bowel obstruction from, 1843
intraparenchymal, 638
after liver transplantation, 638, 644*f*

Hematoma(s) *(Continued)*
pelvic, 591
perinephric fluid collections and, 1809
preplacental, 1471, 1475*f*
renal, 365–366
after renal transplantation, 665, 671*f*
simulating anterior abdominal wall hernias, 500, 502*f*
splenic, 158, 159*f*
pediatric, 1770, 1771*f*
stitch, after herniorrhaphy, 494–496, 495*f*
subamniotic, 1474
subchorionic, 1474
placental abruption differentiated from, 1471, 1474*f*
subdural, neonatal/infant, 1557, 1558*f*
subfascial, cesarean sections and, 556–557, 557*f*
subplacental, 1471, 1474*f*
in synthetic arteriovenous graft for hemodialysis, 1002–1003
testicular, 848–850, 850*f*
pediatric, 1897–1898
Hematometra
cervical carcinoma and, 546, 547*f*, 549
cornual, 551–552
Hematometrocolpos, 1882*f*
from imperforate hymen, 546–547, 546*f*
Hematopoiesis, in yolk sac, 1057
Hematospermia, prostate and, 394, 394*b*
Hematotrachelos, 546
Hemidiaphragm, eventration of, 1263*f*
Hemihypertrophy
hepatoblastomas and, 1746
Wilms tumor screening with, 1818
Hemimegalencephaly, 1195
Hemithorax, pediatric, radiopaque
in neonatal chylothorax, 1704*f*
partially, 1705*f*
Hemivertebrae
pediatric, 1688–1689
scoliosis and kyphosis from, 1235–1237
Hemobilia, 174, 175*f*
Hemodialysis, 996–1006
AVF and
aneurysms near, 1003, 1005*f*
arm and leg swelling with, 1006, 1009*f*
hematomas near, 1002–1003, 1005*f*
maturation of, evaluating, 1003
occlusion of, 1006
palpable focal masses near, 1002–1003
placement for, 996, 997*f*
pseudoaneurysms near, 1003, 1005*f*
stenoses associated with, 1003–1006, 1007*f*–1008*f*
ultrasound evaluation of, 1000–1006, 1002*f*–1003*f*
for ESRD, 996
sonographic examination technique for, 996
synthetic arteriovenous graft and
aneurysms near, 1003
arm and leg swelling with, 1006, 1009*f*
hematomas near, 1002–1003
occlusion of, 1006, 1010*f*
palpable focal masses near, 1002–1003
placement of, 996, 997*f*
pseudoaneurysms near, 1003, 1006*f*
stenoses associated with, 1006, 1008*f*
ultrasound examination of, 1002, 1004*f*
ultrasound examination and protocol for, 1000
thigh graft and, preoperative mapping for, 1000, 1001*f*
vein mapping before, 996–1000
upper extremity, 996–998, 998*f*–1000*f*
Hemoglobin, fetal deficit in, immune hydrops and, 1419
Hemolysis
fetal, hydrops from, 1431
from obstetric sonography, 1038
Hemolytic anemia, fetal, hepatomegaly, and, 1316
Hemolytic-uremic syndrome (HUS), pediatric
Doppler assessment of, 1805, 1807*f*
intestinal wall thickening in, 1851*f*, 1853–1854
Hemoperitoneum, 507–508, 508*f*
Hemorrhage(s)
adrenal, 422–424, 424*f*
fetal, 1354
after liver transplantation, 638, 645*f*
neonatal, 1824–1825, 1825*f*
arachnoid cysts differentiated from, 1192–1193
cavum veli interpositi cysts differentiated from, 1170
cerebellar, neonatal/infant brain and, 1548–1550, 1549*f*
fetal, hydrops from, 1431
hypoxic-ischemic events and
cerebellar, 1548–1550, 1549*f*
germinal matrix, 1541–1543, 1542*f*, 1543*b*, 1543*t*
intraparenchymal, 1547–1548, 1547*f*–1549*f*
intraventricular, 1544–1545, 1544*f*–1546*f*, 1545*b*
intraventricular, with hydrocephalus, 1545–1547, 1546*f*–1547*f*
subarachnoid, 1550, 1550*f*
subependymal, 1543–1544, 1543*f*–1544*f*
intracranial
fetal, 1206, 1207*f*
neonatal/infant brain and, duplex Doppler sonography of, 1580–1581, 1584*f*
intramural, pediatric, in Henoch-Schönlein purpura, 1853, 1855*f*
intraparenchymal
IUFD and, 1124*f*
neonatal/infant brain and, 1547–1548, 1547*f*–1549*f*
intraplacental, thick placenta in, 1466
intraplaque, in heterogenous plaque, 920–921
intraventricular
from germinal matrix hemorrhage, 1541
with hydrocephalus, 1545–1547, 1546*f*–1547*f*
neonatal/infant brain and, 1544–1545, 1544*f*–1546*f*, 1545*b*
signs of, 1545*b*
pediatric
ovarian cysts and, 1877, 1878*f*–1879*f*
spinal canal, 1695, 1695*f*–1696*f*
thyroid, 1646, 1647*f*
percutaneous needle biopsy complications with, 608, 609*f*
placental, 1474
posterior fossa, 1548–1550
postpartum, in fetal hydrops, 1436
subarachnoid, neonatal/infant brain and, 1550, 1550*f*
subchorionic
early pregnancy failure and, 1069, 1069*f*
fetal echogenic bowel and, 1315*f*
subdural, fetal, bilateral, 1207*f*
subependymal, neonatal/infant brain and, 1543–1544, 1543*f*–1544*f*
Hemorrhagic cholecystitis, 200
Hemorrhagic cystitis, pediatric, 1908, 1910*f*
Hemorrhagic ovarian cysts, 570–571, 571*f*, 575
Hemothorax, sonographic appearance of, 1702, 1707*f*
Henoch-Schönlein purpura, 845–846, 1842
pediatric, 1853, 1855*f*
scrotal and testicular involvement in, 1899
Heparin, 598
Hepatic alveolar echinococcus, 90
Hepatic artery
anastomosis of, for liver transplantation, 624
aneurysms of, after liver transplantation, 1768, 1769*f*–1770*f*
anomalies of, 80–81
liver circulation and, 78
after liver transplantation
normal appearance of, 625
occlusion of, 626–627
pseudoaneurysms of, 634, 636*f*
resistive index elevation in, 634
stenosis of, 631–634, 634*f*–635*f*, 1766
thrombosis of, 627, 628*f*, 631, 633*f*
pediatric, Doppler studies of, best approaches for, 1752–1754, 1755*f*
pseudoaneurysm of, 104
after liver transplantation, 634, 636*f*
Hepatic vein(s)
anatomic variants of, 457
anomalies of, 81–82
fetal liver calcifications and, 1316–1318
liver circulation and, 80
normal, 76, 76*f*, 77*t*
occlusion of, in Budd-Chiari syndrome, 100–102, 100*f*–101*f*
pediatric
anatomy of, 1733–1734, 1734*f*
Doppler studies of, best approaches for, 1752
thrombosis of, suprahepatic portal hypertension and, 1763, 1763*f*
stenosis of, after liver transplantation, 637, 643*f*
strictures of, in cirrhosis, 95, 95*f*
Hepatitis, 1203–1204
A, 83
acute, 84–85, 85*f*–86*f*, 172
gallbladder wall thickening signs in, 201*f*
B, 83–84
maternal hydrops from, 1432
C, 84
chronic, 85
from congenital herpes, hepatitis from, 1739*f*
D, 84
E, 84
neonatal, jaundice and, 1734, 1737–1738, 1739*f*
viral, 83–85
Hepatization, of gallbladder, 195
Hepatoblastomas, pediatric, 1746, 1747*f*
pseudoprecocious puberty and, 1888
Hepatocellular carcinoma (HCC)
CEUS for detection of, 120–122, 123*f*
characterization of, with microbubble contrast agents, 106, 106*f*
in cirrhotic liver, characterization of, 122, 122*t*
fibrolamellar subtype of, 122–123
inborn errors of metabolism and, 1738
of liver, 118–123, 120*f*–121*f*, 122*t*, 123*f*
pediatric, 1746
portal vein thrombosis from, 120, 121*f*
sonographic appearance of, 119–120, 120*f*
Hepatocyte nuclear factor 1β–related (HNF1β) disease, 1350–1351
Hepatoduodenal ligament, 77, 79*f*
Hepatofugal portal venous flow, 1750, 1757
Hepatolithiasis, 179
Hepatomegaly, fetal, 1316, 1317*f*
Hepatopetal portal venous flow, 1750
Hepatosplenomegaly
from CMV, 1204
fetal, 1317*f*
in immune hydrops, 1422
Hereditary hemorrhagic telangiectasia, 104
Hereditary lymphedema, fetal, 1403–1404, 1405*f*
Hereditary nonpolyposis colorectal cancer syndrome, 578
Hermaphroditism, true, pediatric, 1891, 1899

Hernia(s). *See also* Diaphragmatic hernia
Amyand, 472–473, 473*f*
anterior abdominal wall, dynamic ultrasound of
contents of, 472–473
entities stimulating, 500–501, 502*f*
maneuvers for, 473–474, 474*f*–475*f*
technical requirements for, 471
types of, 471, 471*f*
ventral, 488–494
bilateral, 1262
Bochdalek, 1258
complications of, 496–499
congenital diaphragmatic, 1248*t*
direct inguinal
in athletes, 485–486
bilateral, 480–481, 484*f*
characteristics of, 479–481
classification of, 475
conjoined tendon insufficiency and, 479–481, 483*f*–484*f*
incidence of, 479–480, 482*f*
key findings with, 476*t*
location of, 474–475, 476*f*–477*f*
dynamic maneuvers for imaging of, 473–474, 474*f*–475*f*
femoral, 471
characteristics of, 481–483
diagnostic accuracy with, 481
with inguinal hernia, 493–494, 495*f*
key findings with, 476*t*
key sonographic landmarks of, 474–475, 477*f*
locations of, 482, 485*f*
strangulated, 500*f*
Teale, 482, 485*f*
Valsalva maneuver and, 472*f*, 483
forearm muscle, 859*f*
groin, dynamic ultrasound of
contents of, 472–473
entities stimulating, 499–500, 501*f*
key sonographic landmarks for, 474
maneuvers for, 473–474, 474*f*–475*f*
recurrent, 494–496
report for, 471–472
technical requirements for, 471
at Hesselbach triangle, inferior aspect, 476*t*
hiatal, sonographic appearance of, 1834, 1834*f*
incarcerated, 496–497
incisional, 492–493, 494*f*
indirect inguinal
Canal of Nuck delayed closure from, 476–477, 477*f*
characteristics of, 476–479
classification of, 475
inferior epigastric artery relationship to, 476–477, 478*f*
key findings with, 476*t*
location of, 474–475, 476*f*–477*f*
nonsliding, 477–478, 478*f*
pediatric, 1902
round ligaments relationship to, 476–479, 480*f*
into scrotum, 478–479, 482*f*
sliding, 477–478, 478*f*
spermatic cord relationship to, 476–479, 479*f*, 481*f*
inguinal, 471, 475–488
Amyand, 472–473, 473*f*
bowel-containing, 472–473, 473*f*
classification of, 475
dynamic ultrasound of, Valsalva maneuver for, 473, 474*f*, 483
with femoral hernia, 493–494, 495*f*
fluid-containing, 472–473, 473*f*
indirect, 472*f*
Hernia(s) *(Continued)*
key sonographic landmarks of, 474–475, 476*f*–477*f*
pediatric, 1899, 1902, 1902*f*
types of, 476*t*
linea alba, 488–491
diagnosing, 490
diastasis recti abdominis and, 489–490, 489*f*
epigastric, 488–491, 490*f*–491*f*
hypogastric, 488–489, 491, 491*f*
periumbilical, 492, 494*f*
spectrum of appearances of, 489, 489*f*
strangulated, 499*f*
of liver, 80
Morgagni, 1258, 1718*f*
multiple, 493–494, 495*f*
obstructed, 496–497
of omentum, 1902
pantaloon, 493–494, 495*f*
paraumbilical, 492
pericardial, 1258, 1262
periumbilical
linea alba, 492, 494*f*
strangulated, 500*f*
repair of
mesh in, sonography and, 496, 497*f*–498*f*
pain after, 494–496, 495*f*
spiral clips in, pain from, 497, 498*f*
scrotal, 836, 836*f*
pediatric, 1902
shape of, complication potential and, 497, 499*f*
spigelian, 471
characteristics of, 483–484
key findings with, 476*t*
key sonographic landmarks of, 474–475, 476*f*–477*f*
location of, 483, 486*f*
shape in, 483–484, 487*f*
strangulated, 483–484, 488*f*
torn aponeurosis and abdominis tendon in, 483–484, 487*f*
sports, 484–488, 488*f*–489*f*
strangulated
femoral, 500*f*
findings in, 498–499, 499*t*
linea alba, 499*f*
periumbilical, 500*f*
spigelian, 483–484, 488*f*
umbilical, 491–492, 492*f*–493*f*
ventral, 488–494
Herniation
midgut, physiologic, in embryo, 1077, 1077*f*, 1322, 1323*f*
omphalocele confused with, 1325, 1327*f*
of thymus, superior, 1723
Herniorrhaphy, 470–471
Herpes simplex virus
congenital
hepatitis from, 1739*f*
neonatal/infant brain and, 1560
fetal
brain development and, 1204
hydrops from, 1432
Hertz, definition of, 2
Hesselbach triangle, herniation at inferior aspect of, 476*t*
Heterotaxy syndrome, right-sided stomach and, 1307, 1309*f*
Heterotopia, 1196, 1199*f*
Heterotopic gestation, 1070–1071, 1072*f*
Heterozygous achondroplasia, 1396–1398, 1398*f*
detection of, gestational age for, 1381
inheritance pattern for, 1379–1380
Hiatal hernias, sonographic appearance of, 1834, 1834*f*
HIFU. *See* High-intensity focused ultrasound
High pass filters, 29, 30*f*
Higher harmonics, 58–59
High-intensity focused ultrasound (HIFU), 31–33, 33*f*
for prostate cancer, 400
Highly active antiretroviral therapy (HAART), 331–333
High-velocity jets, color Doppler, in carotid stenosis, 926, 926*f*, 933
aliasing, 933
HII. *See* Hypoxic ischemic injury
Hilar cholangiocarcinoma, 185–188
CEUS assessment of, 188, 191*f*
criteria for unresectable, 187*b*
Doppler ultrasound assessment for, 187–188, 189*f*–191*f*
treatment and staging for, 186–187
tumor growth patterns in, 186
Hindgut, 1304–1305
Hip(s)
dislocated, campomelic dysplasia and, 1395
fetal, dislocation of, spina bifida and, 1233
injection of, 900*f*, 901–902
Hip(s), pediatric. *See also* Developmental dislocation and dysplasia of hip
atypical, 1932, 1933*f*
capsule of, echogenic, 1923
DDH and, 1920–1930
dislocation of
definition of, 1923
teratologic, 1932
joint effusion in, 1930–1932, 1931*f*
nondevelopmental dysplasia abnormalities of, 1930–1932
normal, 1923
painful, 1930–1932
sonography of, indications for, 1922*b*
stability of
in evaluation of infant at risk, 1927
tests determining, 1923
subluxation of, 1923
Hirschsprung disease, 1312, 1312*f*
neuroblastoma with, pediatric, 1825
Histiocytosis
Langerhans cell
in infant, 1751*f*
metastasis of, to testes, 1901
sinus, metastasis of, to testes, 1901
Histogenesis, 1524, 1525*b*
Histopathologists, definition of, 600
Histoplasmosis
adrenal glands in, 423
pediatric, lymph nodes and, 1660–1663
Hitchhiker thumb
in diastrophic dwarfism, 1382, 1406
diastrophic dysplasia and, 1398, 1398*f*
HIV. *See* Human immunodeficiency virus
HIV cholangiopathy, 181–182, 181*f*
HIV-associated nephropathy (HIVAN), 332–333, 333*f*
HNF1β. *See* Hepatocyte nuclear factor 1β–related disease
Hodgkin lymphoma, pediatric, neck, 1665, 1665*f*
Hodgkin's disease, splenic lesions in, 152–153, 154*f*
Holoprosencephaly (HPE)
agnathia and, 1154, 1159*f*
alobar, 1187, 1188*f*
ball type of, 1187–1189
classification of, 1187*b*
cup type of, 1187–1189, 1188*f*
hydranencephaly differentiated from, 1208

Holoprosencephaly (HPE) *(Continued)*
neonatal/infant, 1534–1535, 1534*b*, 1536*f*
pancake type of, 1187–1189
classification of, 1187*b*
corpus callosum agenesis and, 1526–1528
factors associated with, 1187*b*
fetal brain and, 1186–1189, 1187*b*, 1188*f*, 1189*b*
fetal facial changes associated with, 1189, 1189*b*
hypotelorism and, 1140
lobar, 1187–1189
classification of, 1187*b*
neonatal/infant, 1535
microforms of, 1187
midline interhemispheric form of, 1187, 1189
classification of, 1187*b*
neonatal/infant, 1535–1536
neonatal/infant, 1532–1536
alobar, 1534–1535, 1534*b*, 1536*f*
classification of, 1534*f*
lobar, 1535
midline interhemispheric form of, 1535–1536
semilobar, 1535
semilobar, 1187–1189, 1188*f*
classification of, 1187*b*
neonatal/infant, 1535
thickened NT and, 1096*f*
in trisomy 13, 1104, 1105*f*
Holosystolic valvular insufficiency, in AVSD, 1285–1286
Holt-Oram syndrome, 1401
Homozygous Achondroplasia, thanatophoric dysplasia differentiated from, 1389, 1389*f*
Hormonal states, decreased, primary amenorrhea in, 1887
Hormone replacement therapy (HRT), 529
endometrium abnormalities after menopause and, 544–545, 544*b*, 545*f*
Hormonogenesis, disorders of, thyroid hyperplasia from, 695
Horseshoe kidneys, 159–160, 318, 319*f*
fetal, 1345–1346, 1345*f*
with megalourethra, 1362
pediatric, 1784, 1785*f*
Hourglass gallbladder, 202, 205*f*
HPE. *See* Holoprosencephaly
HPS. *See* Hypertrophic pyloric stenosis
HRT. *See* Hormone replacement therapy
Human chorionic gonadotropin (β-hCG), 1049, 1884–1885
concentration of, in trisomy 21, 1089–1090
ectopic pregnancy and, 1071
free, 1089–1090
gestational sac and, 1056–1057
normal ultrasound appearance of, 1055–1057, 1057*b*
Human immunodeficiency virus (HIV), 331
chronic parotitis in children with, 1635, 1636*f*
fetal brain and, 1203–1204
nephropathy associated with, 332–333, 333*f*
Humerus length, in trisomy 21, 1101
HUS. *See* Hemolytic-uremic syndrome
Hutch diverticula, 310
Hydatid abscesses, 613
Hydatid cysts
in *Echinococcosis*, 1748
renal, 331, 332*f*
splenic, 147, 150*f*
Hydatid disease, hepatic, 88–90, 89*f*–90*f*
Hydatid sand, 88–89
Hydatidiform molar pregnancy, 1078–1080. *See also* Persistent trophoblastic neoplasia
coexistent normal fetus and, 1078–1080, 1081*f*
complete, 1078, 1079*f*
partial, 1078, 1080*f*
pediatric, 1884, 1884*f*
Hydatidiform molar pregnancy *(Continued)*
PTN after, 1080, 1081*f*
vaginal bleeding and, 1078
Hydranencephaly
fetal, 1208, 1208*f*
neonatal/infant, 1538, 1538*f*
Hydrocele(s), scrotal, 834–836, 835*f*
fetal, 1367
in fetal hydrops, 1413, 1416*f*
pediatric, 1899, 1902, 1902*f*
Hydrocephalus, 1681
communicating, 1177–1178
extraventricular obstructive, 1538
fetal brain and, 1174–1178
from germinal matrix hemorrhage, 1541
HPE differentiated from, 1189
hydranencephaly differentiated from, 1208
intraventricular obstructive, 1538
in neonatal/infant, duplex Doppler sonography and, 1581–1583, 1584*f*
neonatal/infant brain and, 1538–1541
causes of, 1540*b*
cerebrospinal fluid production and circulation and, 1538–1541
intraventricular hemorrhage with, 1545–1547, 1546*f*–1547*f*
obstructive, 1177–1178
in Dandy-Walker malformation, 1529–1530
pediatric, TCD sonography in monitoring of, 1611–1614, 1613*f*
postmeningitis, 1887
in trisomy 18, 1103
VM differentiated from, 1611–1612
X-linked, 1177
Hydrocephalus ex vacuo, 1177–1178
Hydrocolpos
fetal, 1368
pediatric, 1881, 1882*f*
Hydrometra, 546, 547*f*
Hydrometrocolpos, 546–547
cloacal malformation and, 1363
pediatric, 1881
Hydromyelia
in myelocystocele, 1233
pediatric, 1688
Hydronephrosis
causes of, 316, 317*b*
definition of, 1354
fetal
degree of, risk of postnatal pathology by, 1355, 1356*t*
in duplication anomalies, 1359–1360, 1359*f*, 1360*b*
grading system for, 1354, 1355*f*
from UPJ obstruction, 1358, 1358*f*
VUR and, 1360
genitourinary tract obstruction and, 316, 317*b*
pediatric, causes of, 1785–1791
bladder exstrophy and, 1791, 1791*f*
bladder outlet obstruction and, 1788, 1789*f*–1790*f*
MMIHS and, 1788–1791
prune belly syndrome and, 1788
UPJ obstruction and, 1786, 1787*f*
urachal anomalies and, 1791, 1792*f*–1793*f*
ureteral obstruction and, 1786–1788, 1787*f*
VUR and, 1788, 1790*f*
in pregnancy, 316
Hydrops, fetal
adrenal glands and, 1353–1354
AVSD associated with, 1285–1286
in CHD, 1270
chorioangioma management and, 1476
from CMV, 1204
CPAM and development of, 1248–1249, 1426, 1427*f*
Hydrops, fetal *(Continued)*
delivery and, 1436
diagnostic approach to, 1432–1435
fetal investigations in, 1433–1435
history in, 1432
maternal investigations in, 1433
obstetric sonography in, 1432–1433
postnatal investigations in, 1435
workshop for, summary of, 1433*t*
etiology of, 1418–1419, 1421*f*
immune, 1419–1423
definition of, 1413
noninvasive assessment of alloimmunization for, 1421–1423, 1421*b*, 1422*f*, 1422*t*
RhoGAM and, 1418
maternal complications in, 1436
nonimmune, 1423–1432
anemia and, 1431
arrhythmias and, 1424, 1425*f*
cardiac tumors and, 1424
cardiovascular causes of, 1423–1425, 1424*f*
causes and associations of, 1412, 1414*t*
chromosomal abnormalities and, 1429–1430, 1430*f*
definition of, 1413
drugs and, 1432
endocrine disorders and, 1432
fetal welfare assessment in, 1435
gastrointestinal tract anomalies and, 1427–1428, 1428*f*
genetic disorders and, 1432
idiopathic disorders and, 1432
infection and, 1431–1432, 1431*f*
lymphatic dysplasia and, 1428, 1436*f*
metabolic disorders and, 1432
mortality rate in, 1435
neck abnormalities and, 1425, 1426*f*
pathophysiology of, 1423, 1423*f*
skeletal dysplasia and, 1432
thoracic anomalies and, 1425–1427, 1427*f*
tumors and, 1430–1431
twins and, 1429, 1429*f*
urinary tract anomalies and, 1428, 1429*f*
obstetric prognosis in, 1435–1437
postnatal outcome of, 1437
predelivery aspiration procedures in, 1437
in sacrococcygeal teratoma, 1238–1239
sonographic features of, 1413–1418
ascites and, 1413, 1415*f*–1416*f*
pericardial effusion and, 1416, 1418*f*
placentomegaly and, 1418, 1420*f*
pleural effusions and, 1413–1416, 1417*f*, 1425
polyhydramnios and, 1418, 1420*f*, 1432–1433
subcutaneous edema and, 1417, 1419*f*–1420*f*
thick placenta in, 1466, 1467*f*
Hydrops tubae profluens, 589
Hydrosalpinx, 573
of fallopian tubes, 585–587, 587*f*
PID and, 1885
Hydrosonourethrography, 1872
Hydrosonovaginography, 1870–1871, 1871*f*
Hydrostatic reduction, of intussusception, ultrasound-guided, 1844–1845
Hydrothorax, fetal, hydrops from, 1425–1426
Hygromas. *See* Cystic hygroma(s)
Hymen, imperforate, hematometrocolpos form, 546–547, 546*f*
Hypercalcemia
familial hypocalciuric, 734
medullary nephrocalcinosis and, 1798
Hypercalciuria, medullary nephrocalcinosis and, 1798
Hyperechogenic kidneys, 1351–1352, 1352*f*
Hyperechoic caudate nuclei, neonatal/infant brain and, 1557, 1557*f*

Hyperechoic tissue, in breast sonography, 796–797, 796*f*
Hyperemia
  in acute cholecystitis, 197*f*, 198–199
  Crohn disease and, 269, 272*f*–273*f*
  reactive, in testicular detorsion, 1895
  testicular, pediatric, 1896
Hyperoxaluria, primary, CKD and, 1796–1798
Hyperparathyroidism
  graft-dependent, 742–744, 743*f*
  pediatric, 1650
  persistent, 741–744, 744*f*
    imaging importance in, 749, 751*f*–752*f*
  primary, 733–735
    causes of, 734*b*
    diagnosis of, 734
    MAP for, 749
    pathology of, 734
    prevalence of, 733–734
    treatment of, 734–735
  recurrent, 741–744, 743*f*
    ethanol ablation for, 751–754, 754*f*
  secondary, 744–745
    calcimimetics for, 734
    ethanol ablation for, 751–754, 754*f*
  tertiary, 751
Hyperreactio luteinalis, 572
Hyperreflexia, detrusor, 372–374, 373*f*
Hypertelorism
  conditions associated with, 1140, 1141*b*, 1144*f*–1145*f*
  midface hypoplasia with, 1149*f*
  in skeletal dysplasias, 1382
Hypertension. *See also* Portal hypertension
  carotid flow waveforms and, 935*f*, 936–937
  fetal, adrenal glands and, 1353–1354
  maternal, IUGR and, 1455
  pulmonary, with CDH, 1264
  renovascular
    clinical findings suggesting, 446*b*
    renal artery stenosis and, 446–447
  renovascular disease and, 368
Hyperthermia
  NTDs from, 1218
  safety and, 38, 38*f*
  teratogenic effects from, 38
Hyperthyroidism
  fetal goiter in, 1163
  Graves disease and, 727, 727*f*
Hypertrichosis, focal, tethered cord and, 1679
Hypertrophic cardiomyopathy, 1294–1295
Hypertrophic obstructive cardiomyopathy, 1292
Hypertrophic pyloric stenosis (HPS), 1835–1838, 1835*b*, 1837*f*–1838*f*
  pitfalls in diagnosis of, 1838, 1838*b*, 1839*f*
  pylorospasm and minimal muscular, 1836–1838, 1838*f*
Hypertrophied column of Bertin (HCB), 313–314, 314*b*, 315*f*
Hypertrophy
  of adrenal glands, 416–417
  concentric, 1294–1295
  kidney and compensatory, 317–318
Hyperventilation, arterial velocities and, 1595
Hyperventilation therapy, pediatric, TCD sonography and, 1614
Hypoalbuminemia, gallbladder wall thickening and, 199*f*
Hypochondrogenesis, achondrogenesis type 2 differentiated from, 1391
Hypoechogenicity, in breast sonography, 792–793, 794*f*
Hypoechoic metastases, of liver, 125, 127*f*–128*f*
Hypogastric hernias, 488–489, 491, 491*f*
Hypophosphatasia, 1383*f*
  achondrogenesis differentiated from, 1391
  anencephaly differentiated from, 1179
  calvarial compressibility in, 1382
  lethal, 1392–1395, 1395*f*
  sonographic appearance of, 1380*f*
Hypophosphatasia congenita, 1392
Hypopituitarism, primary, pediatric, 1891
Hypoplasia. *See also* Pulmonary hypoplasia, fetal
  cerebellar, 1190
  of femur, fetal, in caudal regression, 1237–1238
  of kidneys, 317
  of middle phalanx in trisomy 21, 1101
  midface, 1148, 1149*f*–1150*f*
  pontocerebellar, 1190
  pulmonary, 1245–1246
  of thyroid gland, 694, 694*f*
  of uterus, 538
  vermis, 1190–1192, 1192*f*
    inferior, arachnoid cysts differentiated from, 1192–1193
Hypoplastic left heart syndrome, 1287, 1287*f*, 1292
Hypoplastic left ventricle, 1292
Hypoplastic right ventricle, 1287, 1287*f*
Hypoplastic scapulae, in campomelic dysplasia, 1381–1382, 1395, 1396*f*
Hypospadias, fetal, 1367
Hypotelorism
  conditions associated with, 1140, 1140*b*, 1142*f*–1144*f*
  craniosynostosis and, 1136–1138
Hypothalamus, in menstrual cycle, 1050*f*
Hypothyroidism
  congenital, 694
    pediatric, 1642–1643
    pediatric ovarian cysts and, 1875
  fetal
    fetal goiter in, 1163
    wormian bones in, 1139
  goitrous, 694
Hypoventilation, arterial velocities and, 1595
Hypoxic ischemic injury (HII), 1580, 1581*f*–1582*f*
Hypoxic-ischemic events, neonatal/infant brain and, 1541–1557
  arterial watershed and, 1541, 1541*t*
  cerebral edema and, 1550–1556
    diffuse, 1553–1555, 1554*f*
  cerebral infarction and, 1550–1556
    focal, 1555–1556, 1556*b*, 1556*f*
  hemorrhage and
    cerebellar, 1548–1550, 1549*f*
    germinal matrix, 1541–1543, 1542*f*, 1543*b*, 1543*t*
    intraparenchymal, 1547–1548, 1547*f*–1549*f*
    intraventricular, 1544–1545, 1544*f*–1546*f*, 1545*b*
    intraventricular, with hydrocephalus, 1545–1547, 1546*f*–1547*f*
    subarachnoid, 1550, 1550*f*
    subependymal, 1543–1544, 1543*f*–1544*f*
  hyperechoic caudate nuclei and, 1557, 1557*f*
  injury patterns from, 1541*t*
  lenticulostriate vasculopathy and, 1556–1557
  PVL and, 1541, 1550–1553, 1551*f*–1553*f*

I

IBD. *See* Inflammatory bowel disease
Identical twins. *See* Monozygotic twins
Idiopathic disorders, fetal hydrops from, 1432
Idiopathic varicocele, 837–838
IEA. *See* Inferior epigastric artery
IgG4. *See* Immunoglobulin G4
IJV. *See* Internal jugular vein
Ileal conduits, evaluation of, 375, 375*f*
Ileal obstruction, fetal, 1310
Ileitis, terminal, 288
Ileus
  meconium, 1310
  paralytic, 294*f*, 295
Iliac, angle of, in trisomy 21, 1101
Iliac artery, 966
  stenosis of, 971*f*
Iliac veins, 455–464
  anatomy of, 456–457
  external, ultrasound examination of, 982
  thrombosis of, 459–460, 459*f*–461*f*
    detection difficulties with, 988, 988*f*
Ilioinguinal nerve entrapment of, after herniorrhaphy, 496
Iliopsoas tendon, injection for, 905, 906*f*
Illicit drugs, fetal gastroschisis and, 1322–1323
Image display, 9–13, 9*f*–11*f*
Image quality
  key determinants of, 16–19
  spatial resolution in, 16–19, 18*f*–19*f*
Image storage, 12–13
Imaging. *See also specific techniques*
  amplitude and phase modulation, 64, 65*f*
  for drainage, ultrasound-guided, 610, 610*f*
  keepsake, 49*b*, 50
  pancreatitis approach of
    acute, 221–222, 221*b*
    chronic, 231
  parathyroid adenomas and accuracy in, 746–749
  percutaneous needle biopsy methods for, 599
  pitfalls in, 19–21
  plane-wave contrast, 64
  pulse inversion, 62–63, 62*f*–63*f*
  renal cell carcinoma approach for, 341, 341*f*
  special modes of, 13–16
    elastography, 15–16, 16*b*, 17*f*–18*f*
    spatial compounding, 13–15, 14*f*–15*f*
    3-D ultrasound, 15, 16*f*
    tissue harmonic imaging, 13, 13*f*–14*f*, 61–62
  split-screen, for breast assessment, 769, 769*f*
  temporal maximum intensity projection, 64, 65*f*
  triggered, 65
  volume, in obstetric sonography, 1030
Immunocompromised patients
  acute typhlitis and, 287–288, 289*f*
  hepatic candidiasis in, 86–87, 88*f*
Immunoglobulin A nephropathy, CKD and, 1796–1798
Immunoglobulin G4 (IgG4)
  associated disease, 1635
  cholangitis related to, 182–184, 185*f*
Immunosuppression, adrenal glands and, 423
Impedance
  high-resistance waveform in brachial artery, 27*f*
  low-resistance waveform in peripheral vascular bed, 27*f*
Imperforate anus, 1310–1311
  block vertebrae with, 1689, 1692*f*
  high, pediatric, risk of spinal dysraphism with, 1689
  pediatric, 1847–1848, 1850*f*
Imperforate hymen, hematometrocolpos form, 546–547, 546*f*
Implantation, 1051, 1052*f*
Implants, breast
  abnormal capsule in, 804
  extracapsular rupture of, 805–807, 806*f*
  fill valve causing palpable abnormalities in, 804, 804*f*
  intracapsular rupture of, 804–805, 805*f*
  radial folds causing palpable abnormalities in, 804, 804*f*

Implants, breast *(Continued)*
shell in, 804
silicon granulomas and, 805–807, 806*f*
ultrasound evaluation of, 804–807, 804*f*–806*f*
in vitro fertilization (IVF), CHD risk with, 1270–1273
Inborn errors of metabolism, fetal hydrops from, 1432
Incarcerated hernias, 496–497
Incisional hernias, 492–493, 494*f*
Inclusion cysts
amnion, 1061
epidermal, 779
peritoneal, 508–509, 509*f*, 573, 573*f*
surface epithelial, 569, 573
vaginal, pediatric, 1883–1884
Incomplete subclavian steal, 952–953, 953*b*, 953*f*
Incontinence, fecal, anal endosonography in, 305, 305*f*
Indirect controls, 48–50, 49*t*
Indistinct margins, in breast sonography, 787, 787*f*
Indomethacin
in fetal hydrops management, 1436
in utero exposure to, fetal hydrops from, 1432
Inertial cavitation, 40, 67–68
Infants. *See* Brain, neonatal/infant, imaging of
Infarction(s)
cerebral, neonatal/infant, 1550–1556
focal, 1555–1556, 1556*b*, 1556*f*
luxury perfusion and, 1580–1581, 1584*f*
epididymitis and, pediatric, 1896
graft, pediatric renal transplantation and, 1807–1809, 1808*f*
hepatic, after liver transplantation, 638–639, 646*f*
maternal floor, 1473–1474, 1476*f*
omental
pediatric, appendicitis differentiated from, 1858–1860, 1858*f*
segmental, right-sided, 288, 289*f*
periventricular hemorrhagic, in infants, 1547
placental, 1466, 1473–1474, 1476*f*–1477*f*
after renal transplantation
global, 653
segmental, 653–655, 657*f*
silent cerebral, SCD and, 1598
splenic, 156–157, 157*f*
pediatric, 1770, 1771*f*
testicular
pediatric, 1895
segmental, 832, 832*f*
Infection(s). *See also* Bacteria, pediatric infections from; Cytomegalovirus infection; Liver, infectious diseases of; Urinary tract, pediatric, infection of; Virus(es), pediatric infections from
of biliary tree, 176–182
in breast cysts, 782–785, 785*f*
breast ultrasound for, 803–804, 803*f*–804*f*
fetal
brain development and, 1203–1204, 1205*f*
dural sinus thrombosis from, 1205–1206
echogenic bowel and, 1316
hydrops and, 1431–1432, 1431*f*
liver calcifications and, 1316–1318
of gastrointestinal tract, 295–300
AIDS patients and, 296
bezoars and, 300
celiac disease and, 300
congenital cysts and, 297, 298*f*
cystic fibrosis and, 300
hematomas and, 299
intraluminal foreign bodies and, 300
ischemic bowel disease and, 297
mucocele of appendix and, 299, 299*f*
peptic ulcer and, 299, 300*f*
Infection(s) *(Continued)*
pneumatosis intestinalis and, 297–299, 299*f*
pseudomembranous colitis and, 296–297, 298*f*
of genitourinary tract, 323–333
AIDS and, 331–333, 332*f*–333*f*
alkaline-encrusted pyelitis as, 324–325
Candida albicans as, 330–331, 331*f*
cystitis as, 333
fungal, 330–331
papillary necrosis as, 328–329, 329*b*, 329*f*
parasitic, 331
pyelonephritis as, 323–328
pyonephrosis as, 325, 326*f*
schistosomiasis as, 331
tuberculosis as, 329–330, 330*f*
of liver, 83–91
of neonatal/infant brain
acquired, 1560, 1561*f*–1563*f*
CMV, 1558–1560, 1559*f*
congenital, 1557–1560, 1559*f*
after pancreas transplantation, 682
percutaneous needle biopsy complications with, 609
renal transplantation complications with, 651–653, 655*f*–657*f*
soft tissue, 872–874, 873*f*–874*f*
of spinal canal, pediatric, 1695
of urinary tract, pediatric
jaundice in, 1738
lower, 1904–1905, 1908, 1910*f*–1911*f*
of uterus, pediatric, 1885–1887
of vagina, pediatric, 1885–1887
Infectious cystitis, 333, 334*f*
Infective peritonitis, 517, 519*f*
Inferior epigastric artery (IEA)
as landmark for inguinal hernias, 474–475, 476*f*
relationship of indirect inguinal hernia to, 476–477, 478*f*
Inferior thyroid artery, 693
Inferior thyroid vein, 693, 694*f*
Inferior vas aberrans of Haller, 820–821
Inferior vena cava (IVC), 75–76, 75*f*, 455–464
anastomosis of, for liver transplantation, 624–625
anatomic variants of, 457, 458*f*
anatomy of, 456–457
azygous continuation of, 457
Budd-Chiari syndrome and, 463
dilation of, 464
duplicated, 457, 458*f*
filters of, 464, 464*f*
left, 457
neoplasms of, 463–464
nutcracker syndrome and, 460–461, 462*f*
pancreatic head and, 211–212, 213*f*
pelvic congestion syndrome and, 461–463, 463*f*
stenosis of, after liver transplantation, 636–637, 641*f*
thrombosis of, 459–460
after liver transplantation, 636–637, 642*f*, 1766, 1769*f*–1770*f*
Inferior vesical artery, 384
Infertility
cryptorchidism of testis and, 851
ectopic pregnancy and, 1070
TRUS for prostate and, 392–394, 393*f*
Infiltrative metastases, of liver, 125–128, 126*f*
Inflammation
in acute pancreatitis, 222–225, 224*f*–228*f*
of appendix, 282–285
in breast cysts, 782–785, 785*f*
in Crohn disease
creeping fat and, 269, 271*f*
masses and, 275–276, 278*f*–279*f*
perianal inflammation and, 276, 281*f*, 305–306
Inflammation *(Continued)*
of epididymis, 846
of musculoskeletal system, pediatric, 1936–1938, 1937*f*–1938*f*
noninfectious, 1938
of prostate, 389, 390*f*
of salivary glands, pediatric, 1632–1635
acute, 1632–1634, 1632*f*–1633*f*
chronic, 1634–1635, 1634*f*–1636*f*
of tendons, 861–862, 862*f*
Inflammatory abdominal aortic aneurysm, 439–440, 443*f*
Inflammatory bowel disease (IBD), 266–269. *See also* Crohn disease
Inflammatory disease
pediatric, neck and, 1658–1664
lymph nodes and, 1658–1663, 1661*f*–1663*f*
pediatric, thyroid gland and, 1643–1646, 1645*f*–1646*f*
perianal, transanal sonography in, 305–307, 306*b*, 307*f*
Inflammatory myofibroblastic tumor, pediatric, 1812
Inflammatory pseudotumors
gastric mucosa thickening in, 1839–1840
pediatric cystitis and, 1794, 1797*f*
splenic, 153–156
Infrahyoid space, pediatric, 1628–1629. *See also* Parathyroid glands, pediatric; Thyroid gland, pediatric
anatomy of, 1640, 1642*f*
cystic lesions of, differential diagnosis of, 1644*b*
cysts of, 1650
laryngoceles of, 1650
visceral space of, 1640–1650
Infraspinatus tendon
anatomy of, normal, 879, 879*f*
ultrasound evaluation of, 883–884, 885*f*
Infundibulopelvic (suspensory) ligament, 564–565
Infundibulum, 565
Inguinal canal, testis in, 851, 851*f*
Inguinal hernias. *See* Hernia(s), inguinal
Inguinal wall insufficiency, posterior, sports hernia and, 486, 488*f*
Inionschisis, definition of, 1225*t*
Injections. *See* Musculoskeletal injection(s)
Inner cell mass, 1051
Innominate artery, 916, 938
Inspissated cysts, 779, 781*f*
Instrumentation. *See also* Transducer(s)
basic components of, 7–12
for Doppler ultrasound, 24–25, 25*b*, 25*f*–26*f*
image display in, 9–11, 9*f*–11*f*
mechanical sector scanners, 11
receiver in, 8–9, 8*f*–9*f*
transducer arrays in, 11–12, 12*f*
transducer in, 7–8
transmitter in, 7
Insula, fetal, normal sonographic appearance of, 1168
Insulin, NTDs from, 1218
Insulinomas, pediatric, 1865
Intellectual functioning, in spina bifida, 1233
Intensity
of sound, 5
of ultrasonic power, 35
Interdigital neuromas, injection for, 904, 904*f*
Interhemispheric fissure, fetal, normal sonographic appearance of, 1168, 1169*f*
Intermittent harmonic power Doppler imaging, 66, 66*f*
Intermittent imaging, with contrast agents, 64–67, 66*f*
Internal echoes, in renal cysts, 357, 357*b*
Internal inguinal ring, as landmark for inguinal hernias, 474–475, 476*f*

Internal jugular vein (IJV)
acute DVT of, 994*f*
anatomy of, 990–991, 990*f*
as cerebral blood vessel, 955–956
monophasic venous waveforms of, stenosis and, 1006, 1009*f*
phlebectasia of, 1658, 1660*f*
sonographic technique for, 955, 955*f*
thrombosis of, 955–956, 956*f*–957*f*
central line placement causing, 1658, 1661*f*
ultrasound examination for, 991, 991*f*
Internal oblique aponeurosis, torn, in spigelian hernia, 483–484, 487*f*
Internal urethral sphincter, 384
International Society for Ultrasound in Obstetrics and Gynecology (ISUOG), 1041
Interphalangeal joint, injection of, short-axis approach to, 901
Intersegmental laminar fusion, pediatric, 1688
Interstitial ectopic pregnancy, 1073, 1074*f*
Interstitial line sign, 1073
Interventional sonography, pediatric
for abscess drainage, 1953
appendiceal, 1956, 1960*f*
transrectal, 1953–1954, 1954*f*
anatomy for, 1950
colon or bowel and, 1950
diaphragm and, 1950, 1950*f*
antibiotics for, 1951
for biopsy
devices for, 1950
mediastinal mass, 1956, 1959*f*
targeted organ lesion, 1961, 1961*f*–1962*f*
central venous access for, 1954
Chiba needle for, 1948
color Doppler ultrasound and, 1945
CT and, 1943, 1943*t*
for deep foreign body removal, 1961, 1965*f*
drainage catheters for, 1948
equipment for, 1943
freehand, 1945–1947
correcting needle angle in, 1947, 1949*f*
correcting off-target needle in, 1947
initial needle placement and localization in, 1945–1946, 1945*f*–1946*f*
locating needle after insertion in, 1946–1947, 1947*f*–1948*f*
mechanical guides compared to, 1945
training aids for, 1947
guidance methods in, 1943, 1943*t*
for head lesions, 1961, 1966*f*
initial puncture device for, 1949–1950
local anesthetic technique for, 1951, 1952*f*
multimodality interventional suites for, 1943, 1944*f*
for musculoskeletal procedures, 1961, 1963*f*–1964*f*
for neck lesions, 1961, 1967*f*
one compared to two operators for, 1943–1945
patient and, 1942–1943
for percutaneous cholangiography and drainage, 1956, 1959*f*
for peritoneal drainage, 1954–1956, 1958*f*
personnel for, 1943
for PICC, 1954, 1955*f*–1957*f*
for pleural drainage, 1954–1956, 1958*f*
principles of, 1942–1943
sedation for, 1950–1951
for steroid injection, 1961, 1964*f*
transducers in, 1943
locating needle after insertion and, 1946–1947, 1947*f*
typical procedures for, 1951–1953
aims and expectations in, 1952–1953
coagulation studies in, 1952
Interventional sonography, pediatric *(Continued)*
difficult catheter fixation for, in infants, 1953
initial ultrasound in, before sedation, 1953
postprocedural care and follow-up in, 1953
prior consultation and studies in, 1951–1952
Interventricular septum, viewed from right ventricle, 1283*f*
Intervillous spaces, 1465–1466
blood flow in, 1467–1468, 1468*f*
Intestinal hematomas, small bowel obstruction from, 1843
Intestinal inflammatory disease, pediatric, 1848–1862. *See also* Appendicitis, pediatric
appendicitis as, 1855–1860, 1857*b*, 1858*f*–1862*f*
ascariasis and, 1853, 1853*f*
Crohn disease and, 1853, 1854*f*
graft-versus-host disease and, 1853–1854, 1855*f*
Henoch-Schönlein purpura and, 1853, 1855*f*
HUS and, 1851*f*, 1853–1854
mucosal, 1851, 1851*f*
NEC and, 1854–1855, 1855*b*, 1856*f*
transmural, 1851, 1852*f*
Intestinal malrotation
with midgut volvulus, 1841–1842, 1843*f*–1844*f*
midline stomach and, 1307
Intestinal wall thickening, pediatric, causes of, 1851, 1851*b*, 1851*f*–1852*f*, 1853–1854, 1855*f*
Intestine(s), acoustic cavitation in, 43. *See also* Bowel; Gastrointestinal tract
Intima-media complex, in carotid wall, 918–919, 919*f*
Intima-media thickness, atherosclerotic disease and, 918–919
Intraamniotic bleeding, fetal echogenic bowel and, 1316
Intraatrial septum, embryologic development of, 1282*f*
Intracardiac focus, echogenic, in trisomy 21, 1100*f*, 1101
Intracranial hemorrhage
fetal, 1206, 1207*f*
neonatal/infant brain and, duplex Doppler sonography of, 1580–1581, 1584*f*
Intracranial pressure, increased, vasospasm differentiated from, 1609–1610
Intracranial tumors, neonatal/infant brain and, duplex Doppler sonography of, 1585, 1587*f*
Intradecidual sac sign, 1054, 1055*f*
Intraductal intrahepatic cholangiocarcinoma, 185, 186*f*–187*f*
Intraductal papillary mucinous neoplasm (IPMN), 245–247, 245*f*–246*f*
Intradural lipomas, pediatric, 1686, 1687*f*
Intrahepatic cholangiocarcinoma, 184–185, 186*f*
intraductal, 185, 186*f*–187*f*
Intrahepatic stones, in biliary tree, 173, 173*f*
Intramedullary lipoma, 1686
Intramural sinus tract, in Crohn disease, 269, 274*f*
Intraoperative ultrasound
for adrenal glands, 429
for liver, 133
Intraparenchymal hematomas, 638
Intraparenchymal hemorrhage
IUFD and, 1124*f*
neonatal/infant brain and, 1547–1548, 1547*f*–1549*f*
Intraperitoneal gas, free, in acute abdomen, 277–281, 282*f*
Intraperitoneal stomach, 218–219, 220*f*
Intrasubstance rotator cuff tears, 888, 890*f*
Intratesticular artery, 821, 821*f*
Intratesticular cysts, 829, 830*f*
Intratesticular variocele, pediatric, 1891–1892
Intratesticular vessels, pediatric, 1888
Intrauterine devices (IUDs), 529
PID and, 587
uterine sonographic techniques and, 552–554, 553*f*
Intrauterine fetal death (IUFD), 1123–1125, 1124*f*
Intrauterine growth restriction (IUGR), 1062
from CMV, 1204
diagnosis of, 1455
fetal monitoring in, 1455
in Miller-Dieker syndrome, 1195
multifetal pregnancy morbidity and mortality and, 1119–1123
ossification delayed in, 1091
risk factors for, 1455–1460
fetal and placental, 1456*b*
maternal, 1456*b*
with spina bifida, 1233
in triploidy, 1105*f*
in trisomy 18, 1077
Intrauterine pregnancy, 1052–1053
Intravaginal torsion, 844, 844*f*
Intravascular ultrasound, in plaque characterization, 943
Intravenous Doppler contrast agents, 1749–1750
Intravenous ultrasound contrast agents, 1746
Intraventricular hemorrhage
from germinal matrix hemorrhage, 1541
neonatal/infant brain and, 1544–1545, 1544*f*–1546*f*, 1545*b*
with hydrocephalus, 1545–1547, 1546*f*–1547*f*
signs of, 1545*b*
Intussusception
MBO from, 293, 296*f*
pediatric, 1843–1847
Doppler ultrasound for, 1849*f*
false-positive, 1843, 1846*f*
Henoch-Schönlein purpura complicated with, 1853
ileocolic, 1847*f*–1848*f*
small bowel, 1844–1845, 1849*f*
sonographic signs of, 1843*b*
Invasive fibrous thyroiditis, 727–728, 728*f*
Invasive mole persistent trophoblastic neoplasia, 1080, 1081*f*
Iodine, deficiency of, thyroid hyperplasia from, 695
IPMN. *See* Intraductal papillary mucinous neoplasm
Irradiation, microcephaly from, 1194
Ischemic bowel disease, 297
Ischemic stricture, renal transplantation and, 1811
Ischemic-thrombotic damage, thick placenta in, 1466
Ischium, in sonogram of hip from transverse/flexion view, 1927, 1928*f*
Isolated ventriculomegaly (IVM), 1176
Isomerism, left atrial, AVSD and, 1284
Isthmus, 565, 692
ISUOG. *See* International Society for Ultrasound in Obstetrics and Gynecology
IUDs. *See* Intrauterine devices
IUFD. *See* Intrauterine fetal death
IUGR. *See* Intrauterine growth restriction
IVC. *See* Inferior vena cava
Ivemark syndrome, 1292
IVF. *See in vitro* fertilization
IVM. *See* Isolated ventriculomegaly

J

Jaundice
neonatal, 1734–1740
Alagille syndrome and, 1737

Jaundice *(Continued)*
bile duct spontaneous rupture and, 1734, 1737
biliary atresia and, 1734–1735, 1737, 1738*f*
causes of, 1734, 1735*b*
choledochal cysts and, 1735–1737, 1735*f*–1736*f*
inborn errors of metabolism and, 1738–1740, 1739*b*, 1740*f*
interlobular bile duct paucity and, 1737
neonatal hepatitis and, 1734, 1737–1738, 1739*f*
urinary tract infection/sepsis and, 1738
in periampullary neoplasms, 236
Jejunal obstruction, fetal, 1310
Jejunoileal atresia, small bowel obstruction with, 1310, 1311*f*
Jeune syndrome, 1395, 1398
Joint assessment, ultrasound techniques for, 866–869, 867*f*–869*f*
Joint effusion, rheumatoid arthritis and, 867, 867*f*
Joint(s)
fetal, multiple contractures of, in arthrogryposis multiplex congenita, 1401, 1405*f*
injections of, 901–902, 901*f*–902*f*
Joubert syndrome, 1182, 1190
Dandy-Walker malformation differentiated from, 1532
vermian hypoplasia with, 1191
Jugular vein, internal. *See* Internal jugular vein
Junctional parenchymal defect, 313, 314*f*
renal, 1781, 1781*f*
Juvenile cystic adenomyoma, 541
Juxtaglomerular tumors, 355–356
Juxtaphrenic paravertebral masses, pediatric, 1723

K

Kaposi sarcoma, liver in, 129
Kasabach-Merritt sequence, fetal hydrops from, 1430–1431
Kasabach-Merritt syndrome, 108
Kawasaki disease
acute, pediatric, 1741
cervical adenopathy in children with, 1660–1663
Keepsake imaging, of fetus, 49*b*, 50
Keyhole sign, from posterior urethral valves in fetus, 1361, 1361*f*
Kidney(s). *See also* End-stage renal disease; Renal artery(ies); Renal vein(s); Ureteral bud
abscesses of
acute pyelonephritis and, 325, 325*f*
drainage of, 617, 618*f*
transplantation complications with, 651, 656*f*
acute cortical necrosis of, 370, 372*f*
acute interstitial nephritis and, 370
acute tubular necrosis of, 370
agenesis of, 318–319
anatomy of, 311–314, 313*f*–315*f*
older child and adult, 1781–1783
angiomyolipoma of, 351–352, 351*f*–352*f*
ascent of, congenital anomalies related to, 318, 318*f*–319*f*
cadaveric, paired, in transplantation, 643–644, 648*f*
calculi in, 334–336, 336*f*–337*f*
entities that mimic, 336, 337*b*, 337*f*
capsule of, 314
carcinoid tumor of, 355–356
compensatory hypertrophy of, 317–318
congenital anomalies of, 1336
cysts of, 356–365
in acquired cystic kidney disease, 340, 364, 364*f*
calcifications of, 358, 358*f*
complex, 357, 357*b*, 358*f*
cortical, 356–359
hydatid, 331, 332*f*
internal echoes in, 357, 357*b*

Kidney(s) *(Continued)*
lithium nephropathy and, 361, 363*f*
in localized cystic disease, 362–364, 363*f*
malignant potential of, 359
medullary, 359
in multicystic dysplastic kidney, 361, 362*f*
in multilocular cystic nephroma, 361–362, 363*f*
parapelvic, 359, 360*f*
percutaneous management of, 617–618, 619*f*
in polycystic kidney disease, 359–361, 361*f*–362*f*
septations in, 357–358, 357*b*, 358*f*
simple, 356–357, 357*f*
in TSC, 364–365, 365*f*
in von Hippel-Lindau disease, 364, 364*f*
development of, 311, 312*f*
disease of
acquired cystic, 340, 364, 364*f*
cystic, 356–365
end-stage, reflux nephropathy and, 327, 327*f*
localized, 362–364, 363*f*
medullary, 359
neoplasm-related, 364–365
polycystic, 359–361, 361*f*–362*f*
renal cell carcinoma and acquired cystic, 340
ectopia and, 318, 318*f*
failure of, chronic, transplantation for, 641
glomerulonephritis of, 370, 371*f*
growth of, congenital anomalies related to, 317–318
hemangiopericytoma of, 356
hematomas of, 365–366
horseshoe, 159–160, 318, 319*f*
fetal, 1345–1346, 1345*f*, 1362
pediatric, 1784, 1785*f*
hypoplasia of, 317
intrathoracic, pediatric, 1716
lacerations of, 365–366, 366*f*
leiomyomas of, 355–356
leukemia involving, 353–354
lymphomas of, 333, 352–353, 353*b*
maternal, IUGR and, 1455
medullary sponge, 339, 340*f*, 359
pediatric, 1799
metastases to, 354, 355*f*
multicystic dysplastic, 361, 362*f*
multilocular cystic nephroma and, 361–362, 363*f*
oncocytoma of, 348–351
parenchyma of, calcification of, 339–340, 340*f*
pelvic, 318, 318*f*
identification of, 592
percutaneous needle biopsy of, 605–606, 606*f*–607*f*
"putty", 330
sarcomas of, 356
shattered, 365–366
sonographic technique for, 314
squamous cell carcinoma of, 348
supernumerary, 319
thoracic, 318
transitional cell carcinoma of, 346–347, 346*f*–349*f*
trauma to, 365–366, 366*f*
tumors of, rare, 355–356
vascular abnormalities of, 366–369
renal vascular Doppler ultrasound and, 366

Kidneys, fetal
agenesis of
bilateral, 1342–1344, 1343*f*–1344*f*, 1344*b*
unilateral, 1344
VUR with, 1360
cystic disease of, 1346–1352
ADPKD and, 1350, 1350*f*
ARPKD and, 1348–1350, 1349*f*

Kidneys, fetal *(Continued)*
bilateral reniform enlargement of, 1348, 1349*f*
HNF1β mutations in, 1350–1351
MCDK as, 1346–1347, 1346*f*–1347*f*
Meckel-Gruber syndrome and, 1351, 1351*f*
obstructive cystic renal dysplasia as, 1347–1348, 1347*f*–1348*f*
syndromes associated with, 1350–1351, 1351*f*
duplex, VUR with, 1360
ectopic, 1344–1345, 1344*f*–1345*f*
embryology of, 1336–1338, 1337*f*
horseshoe, 1345–1346, 1345*f*
megalourethra and, 1362
hyperechogenic, 1351–1352, 1352*f*
length of, at 14-42 weeks' gestation, 1338–1339, 1339*t*
lobation in, 317, 1781, 1781*f*
lobes of, formation of, 1781, 1781*f*
normal sonographic appearance of, 1342*f*
pelvic, 1344–1345, 1344*f*
postnatal function of
fetal urinalysis in prediction of, 1365, 1365*t*
poor, antenatal predictors of, 1364*b*
routine sonographic view of, 1026*f*
sonographic appearance of, 1338–1339, 1338*f*
tumors of, 1352–1353, 1353*f*

Kidneys, pediatric. *See also* Hydronephrosis, pediatric, causes of; Nephrocalcinosis; Urinary tract, pediatric
abscess of, complicating acute pyelonephritis, 1792–1793
absence of, 1784, 1784*f*
biopsies of, Doppler assessment of, 1809, 1810*f*–1811*f*
"cake", 1785
crossed-fused ectopia, 1784–1785, 1785*f*
cystic disease of, 1812–1818
ADPKD and, 1814–1815, 1815*f*
ARPKD and, 1812–1813, 1814*f*
MCDK and, 1815, 1816*f*
medullary cystic kidney disease and, 1816, 1817*f*
nephronophthisis and, 1815–1816, 1816*f*
cysts of, congenital, 1816–1818
dialysis and acquired, 1816–1818, 1817*f*
after liver transplantation, 1816–1818
in TSC, 1816, 1817*f*
in VHL disease, 1816
Doppler ultrasound for, 1778
dysplastic, 1798, 1798*f*
focal scarring of, from acute pyelonephritis, 1792, 1793*f*
horseshoe, 1784, 1785*f*
hydronephrosis and, 1785–1791
length of
age, height, weight compared to, 1776–1778, 1777*f*
by age, with single functioning kidney, 1779*t*
birth weight and gestational age compared to, 1776–1778, 1780*f*
normal measurements of, 1776–1778, 1777*f*
position for visualizing, 1776*f*
reference values for, according to age and gender, 1776–1778, 1778*t*
medical diseases of, 1794–1798
acute kidney injury as, 1795–1796, 1796*b*, 1797*f*
chronic kidney disease as, 1796–1798, 1797*t*, 1798*f*
normal anatomy of, 1781–1783, 1781*f*–1782*f*
normal term, 1781–1783
"pancake", 1785
pelvic, 1908
premature, normal, 1781–1783
renal duplication and, 1783–1784, 1784*f*

Kidneys, pediatric *(Continued)*
sonographic technique for, 1776–1781
patient preparation for, 1776, 1776*t*
transplantation of
Doppler ultrasound in, 1807–1812
parenchymal abnormalities and, 1809–1810, 1812*f*
perinephric fluid collections in, 1809, 1811*f*
tumors of, 1812, 1813*f*
urologic complications and, 1810–1812
vascular complications in, 1807–1809, 1808*f*, 1810*f*–1811*f*
trauma to, 1801, 1802*f*
tumors of, 1818–1820
angiomyolipoma as, 1820, 1822*f*
mesoblastic nephroma as, 1818–1820, 1821*f*
MLCN as, 1820, 1822*f*
RCC as, 1820, 1821*f*
renal lymphoma as, 1820, 1823*f*
Wilms, 1818, 1818*f*–1820*f*
vascular disease of, Doppler assessment of, 1801–1805
acute renal vein thrombosis and, 1804–1805, 1804*b*, 1804*f*
clinical applications of, 1803–1805
HUS and, 1805, 1807*f*
increased resistance to intrarenal flow and, 1802–1803, 1803*b*, 1803*f*
normal anatomy and flow patterns and, 1801–1802, 1803*f*
renal artery stenosis and, 1805, 1805*t*, 1806*f*
in renal transplantation, 1807–1809, 1808*f*, 1810*f*–1811*f*
technique for, 1801
vessel patency and, 1803–1804
volume of
by age, with single functioning kidney, 1779*t*
determination of, 1776, 1776*f*
mean total, 1779*t*
reference values for, according to age and gender, 1776–1778, 1778*t*
Kimura disease, 1635
Klebsiella, 846
Kleihauer-Betke test, 1421
Klinefelter syndrome, 826
pediatric, 1891
testicular microlithiasis and, 1904
Klippel-Trénaunay-Weber syndrome, hemimegalencephaly associated with, 1195
Knee, dislocations of, pediatric, 1933–1934, 1934*f*
Kniest dysplasia, achondrogenesis type 2 differentiated from, 1391
Krukenberg tumor, 585
Küttner tumor, 1635
Kyphoscoliosis
body stalk anomaly and, 1329
fetal, 1404
in skeletal dysplasias, 1382
Kyphosis, fetal, 1235–1237, 1236*f*, 1237*b*
cervical, in campomelic dysplasia, 1381–1382

L

Labor, preterm, 1495–1496. *See also* Preterm birth
Labrum, of acetabulum, 1923
Lacerations
pediatric pregnancy and, 1884
renal, 365–366, 366*f*
Lactobezoars, 1840, 1841*f*
Laminae
in posterior angled transaxial scan plane, 1224*f*
in posterior transaxial scan plane, 1222*f*
in spina bifida, 1228, 1229*f*–1230*f*
Laminectomy, spinal sonography after, 1697
Langerhans cell histiocytosis
in infant, 1751*f*
metastasis of, to teste, 1901
Langer-Saldino form of achondrogenesis, 1391
Laparoscopy, for ectopic pregnancy, 1076
Large bowel, dilated loops of, 1311–1312
Large-for-gestational age (LGA) fetus, 1453–1454
diabetic mothers and, 1454, 1455*t*
incidence of, 1453–1454
sonographic criteria for, 1454*t*–1455*t*
Larsen syndrome
elbow and knee dislocation and, 1933–1934
teratologic hip dislocation and, 1932
Laryngeal webs, fetal, CHAOS and, 1253
Laryngoceles, pediatric, 1650
Laryngotracheomalacia, 1395
Larynx, fetal, CHAOS and, 1253
Lateral nasal prominence, 1134, 1134*f*
Lateral resolution, 19, 19*f*
Lehman syndrome, spina bifida and, 1226
Leiomyoma(s)
adenomyosis coexisting with, 541
bladder, 356
gastric, 265*f*
gastrointestinal, endosonographic identification of, 301
paratesticular, 1903–1904
renal, 355–356
spermatic cord, 840–841, 840*f*
uterine, 538–540, 539*f*, 540*b*
Leiomyomatosis peritonealis disseminata, 523–524, 525*f*
Leiomyosarcoma(s)
bladder, 356
gastric, 265*f*
paratesticular, 1903–1904
uterine, 540, 541*f*
Lemierre syndrome, 1658, 1661*f*
Lemon sign, in Chiari II malformation, 1183–1185, 1184*f*
spina bifida screening and, 1221, 1232–1233
Lemon-shaped skull, 1136, 1137*f*
Lenticulostriate vasculopathy, 1203, 1204*f*, 1585, 1588*f*
neonatal/infant, 1556–1557
Leptomeningeal collaterals, MCA occlusion, 1610
Leriche syndrome, 441–442
Lesser omentum, portal hypertension and thickened, 1756, 1756*f*
Lesser peritoneal sac, 218–219, 220*f*
Leukemia
acute lymphocytic, AKI and, 1796
liver metastases from, pediatric, 1746
lymphadenopathy from, 1724
ovarian infiltration by, pediatric, 1880
in pancreas, pediatric, 1865
renal involvement in, 353–354
salivary gland infiltration by, pediatric, 1639
testicular, 827, 828*f*
pediatric, 1901, 1901*f*
Leukodystrophy, megalencephaly associated with, 1194–1195
Leukomalacia, periventricular. *See* Periventricular leukomalacia
Levocardia, 1273
Levotransposition, of great arteries, 1289–1290
Levovist, 55–56, 107, 111*f*
Leydig cells
testosterone secretion and, 819
tumors of, 826, 827*f*
pediatric, testicular, 1900, 1900*f*
LGA. *See* Large-for-gestational age fetus
LHBT. *See* Long head biceps tendon
LHR. *See* Lung-to-head circumference ratio
Li-Fraumeni syndrome
adrenocortical neoplasms and, 1827
prenatal intracranial tumors in, 1208
Ligament(s)
anatomy of, normal, 862–863, 863*f*
falciform, 77, 79*f*
pediatric, 1731, 1731*f*–1732*f*
injuries to, 862–863, 863*f*–864*f*
diagnosing, 864, 864*f*
of liver, 77, 79*f*–80*f*
ultrasound techniques for, 862–864
Ligamentum teres, 77, 80*f*
Ligamentum venosum, 77
pediatric, 1731, 1731*f*
Limb deformities, congenital
pediatric, 1933
PFFD and, 1933, 1934*f*
tibial hemimelia and, 1933
Limb enlargement, asymmetrical, 1403
Limb pterygium, 1403
Limb reduction defects, 1399–1404
amniotic band sequence as, 1401, 1403*f*
arthrogryposis multiplex congenita as, 1401–1404, 1405*f*
caudal regression syndrome as, 1401, 1404*f*
deformations as, 1399
disruptions as, 1399
isolated, 1400
malformations as, 1399
nomenclature of, 1400*t*
proximal focal femoral deficiency as, 1400, 1400*f*
radial ray, 1400–1401, 1401*f*–1402*f*
sirenomelia as, 1401, 1404*f*
terminal transverse, 1400
Limb shortening, patterns of, 1381, 1381*b*, 1382*f*
Limb-body wall complex, 1182–1183, 1329
OEIS differentiated from, 1328–1329
Limb–body wall complex, 1401
Limey bile, 194, 195*f*
Lindegaard ratio, 1596, 1609–1610
Linea alba, appearance of, 489, 489*f*
Linea alba hernias, 488–491. *See also* Hernia(s), linea alba
Linear array transducers
beam steering in, 10–11, 11*f*
use and operation of, 11–12
Lingual thyroid, pediatric, 1639
Lipid cysts, in breast, 775–779, 779*f*
Lipoadenomas, parathyroid, 735
Lipoleiomyomas, 539*f*, 540
Lipoma(s)
corpus callosum, 1529, 1533*f*
filum terminale, 1674
closed spinal dysraphism and, 1684–1685, 1686*f*
intracranial, fetal, 1209–1210, 1210*f*
intradural, pediatric, 1686, 1687*f*
intramedullary, 1686
intramuscular, simulating anterior abdominal wall hernias, 500, 502*f*
of liver, 117–118, 119*f*
midline, in corpus callosum agenesis, 1201
pancreatic, 249–251, 250*f*
paratesticular, 1903–1904
parotid gland, pediatric, 1639
simulating groin hernias, 500, 501*f*
spermatic cord, 840–841, 840*f*
spina bifida occulta with, 1226
subcutaneous
simulating anterior abdominal wall hernias, 500, 502*f*
tethered cord and, 1679
ultrasound techniques for, 870, 871*f*, 871*t*

Lipomyelocele, closed spinal dysraphism and, pediatric, 1682, 1684*f*
Lipomyelomeningoceles
  closed spinal dysraphism and, pediatric, 1682, 1685*f*
  spine embryology and differentiation of, 1674
Liposarcomas, scrotal, 840*f*, 841
Lips, fetal, normal sonographic appearance of, 1135*f*. *See also* Cleft lip/palate
Lissencephaly
  classical (type 1), 1195, 1196*f*
  cobblestone (type 2), 1195, 1197*f*
  fetal, 1195–1196, 1196*f*–1197*f*
  neonatal/infant, 1537
Lithium nephropathy, 361, 363*f*
Lithium therapy, long-term, primary hyperparathyroidism and, 734
Lithotripters, acoustic cavitation evidence from, 42–43, 42*f*
Littoral cell angioma, splenic, 153–156, 156*f*
Liver
  abscesses of
    drainage of pyogenic, 612–613, 614*f*–615*f*
    after liver transplantation, 638–639, 646*f*
    from pyogenic bacteria, 85–86, 87*f*
  agenesis of, 80
  anatomy of
    Couinaud, 76–77, 77*t*, 78*f*
    echogenicity of, 80, 81*f*
    hepatic venous, 76, 76*f*, 77*t*
    ligaments, 77, 79*f*–80*f*
    normal, 75–80, 75*f*–76*f*, 77*t*
    size of, 80
  anomalies of
    congenital, 82–83
    developmental, 80–82
    vascular, 80–82
  bare area of, 77
  benign neoplasms of, 108–118
    adenoma as, 115–117, 116*f*–118*f*
    angiomyolipomas as, 117–118, 119*f*
    cavernous hemangioma as, 108–112, 112*f*–113*f*, 603–604, 604*f*
    FNH as, 112–115, 114*f*–115*f*
    lipomas as, 117–118, 119*f*
  biopsy of
    percutaneous, 132–133
    percutaneous needle, 603–604, 603*f*–604*f*
  circulation in, 78–80
    hepatic artery and, 78
    hepatic veins and, 80
    portal veins and, 78
  cirrhosis of, 92–96
    Doppler ultrasound characteristics of, 95, 95*f*
    HCC and, 122, 122*t*
    intrahepatic portal hypertension from, 96
    morphologic patterns of, 92–95, 94*f*
    pseudocirrhosis of, 125–128, 129*f*
    sonographic features of, 95*b*
    SWE and, 95–96
  cysts of, 82, 82*f*–83*f*
    autosomal dominant polycystic kidney disease and, 83
    percutaneous management of, 618
    peribiliary, 82–83
  fatty, 91–92, 92*f*–93*f*
  fetal, 1316–1318
    calcifications of, 1316–1318, 1317*f*, 1318*b*
    cysts and, 1318, 1318*f*
    hemangioma of, 1319*f*
    hepatomegaly and, 1316, 1317*f*
  fibrosis of, periportal, Caroli disease with, 171
  fissures of, 75–76
    accessory, 80, 81*f*
  fluid collection in, after transplantation, 638–639, 645*f*–646*f*
Liver *(Continued)*
  glycogen storage disease affecting, 92
  herniation of, 80
  infectious diseases of, 83–91
    bacterial, 85–86, 87*f*
    fungal, 86–87, 88*f*
    parasitic, 87–90, 89*f*–90*f*
    Pneumocystis carinii and opportunistic, 91, 91*f*
    viral hepatitis, 83–85
  intraoperative ultrasound for, 133
  in Kaposi sarcoma, 129
  lobes of, 75–76, 75*f*–76*f*
  lymphoma of, 125, 129*f*
  malignant neoplasms of, 118–124
    EHE as, 123–124
    HCC as, 118–123, 120*f*–121*f*, 122*t*, 123*f*
    hemangiosarcoma as, 123
  masses of, 105–107
    characterization of, 105–106, 106*f*–107*f*, 108*t*, 109*f*–110*f*
    detection of, 106–107, 111*f*
    microbubble contrast agents in characterization of, 105–106, 106*f*–107*f*, 108*t*, 109*f*–110*f*
    neoplasms in, 107–129
  metabolic disorders of, 91–96
  metastatic disease of, 124–129, 126*f*–130*f*
  portosystemic shunts and, 130–132
    transjugular intrahepatic, 131–132, 132*b*, 132*f*–133*f*
  scalloping of, in pseudomyxoma peritonei, 514, 518*f*
  schistosomiasis of, 90
  situs inversus totalis of, 80
  sonographic technique for, 75, 75*f*
  trauma to, 129–132, 131*f*
  vascular abnormalities in, 96–104
    Budd-Chiari syndrome as, 98–103, 100*f*–103*f*
    hepatic artery pseudoaneurysm as, 104
    hereditary hemorrhagic telangiectasia as, 104
    intrahepatic portosystemic venous shunts as, 104
    peliosis hepatis as, 104, 104*f*
    portal hypertension as, 96–98, 96*f*–97*f*
    portal vein aneurysms as, 103–104
    portal vein thrombosis as, 98, 99*f*–100*f*
  veno-occlusive disease of, 103
  volumetric imaging of, 75
  as window to pleural space, 1702, 1707*f*
Liver, pediatric. *See also* Jaundice, neonatal; Liver transplantation, pediatric; Portal hypertension, pediatric
  abscess of, 1746–1748, 1751*f*
    parasitic, 1747–1748
    pyogenic, 1746–1747, 1751*f*
  adenomas of, 1746
    inborn errors of metabolism and, 1738
  anatomy of, 1730–1734
    hepatic vein, 1733–1734, 1734*f*
    portal vein, 1731–1734, 1732*f*
    segmental, external, 1730–1731, 1731*f*
  biliary rhabdomyosarcoma in, 1746, 1749*f*
  biopsy of, targeted, 1962*f*
  cholelithiasis and, 1741, 1741*b*, 1743*f*
  cirrhosis and, 1741, 1742*f*
  congenital fibrosis of, prehepatic portal hypertension from, 1757–1759, 1762*f*
  Doppler assessment of, 1748–1764
    basic principles of, 1748–1750
    of normal flow patterns in splanchnic vessels, 1750
    for portal hypertension, 1752–1754, 1754*f*–1755*f*
    possibilities and pitfalls of, 1750
Liver, pediatric *(Continued)*
    sonographic technique for, 1750–1752
    surgical portosystemic shunts and, 1764
  Echinococcosis in, 1748
  fatty degeneration/infiltration of, 1740, 1740*f*
  FNH and, 1746
  granulomas of, 1748
  HCC of, 1746
  hemangiomas and, 1742–1743, 1744*f*
  hepatoblastomas of, 1746, 1747*f*
  infantile hemangioendotheliomas and, 1743–1744, 1745*f*
  jaundice and, 1734–1740
  left lobe of, 1731–1733
  masses in, 1743*b*
  mesenchymal hamartomas and, 1744
  metastases to, 1746, 1750*f*
  quadrate lobe of, 1731–1733
  right lobe of, 1733, 1733*f*
  schistosomiasis in, 1748
  steatosis and, 1740, 1740*f*, 1741*b*
  SWE and, 1764, 1765*f*
  tumor angiogenesis detection in, 1746
  tumors of, 1741–1746
    benign, 1742–1746
    identification of, 1741–1742
    malignant, 1746
  undifferentiated embryonal sarcoma and, 1746, 1748*f*
Liver flukes, biliary tree and, 176–179, 177*f*–179*f*
Liver transplantation, 624–641
  abscess after, 638–639, 646*f*
  adrenal hemorrhage after, 638, 645*f*
  arterial complications of, 629–635
    celiac artery stenosis as, 634–635, 637*f*
    hepatic artery pseudoaneurysms as, 634, 636*f*
    hepatic artery resistive index elevation as, 634
    hepatic artery stenosis as, 631–634, 634*f*–635*f*
    hepatic artery thrombosis as, 627, 628*f*, 631, 633*f*
  biliary tree complications with, 625–629
    bile leakage as, 627–629, 629*f*
    biliary sludge as, 629, 631*f*
    biliary stones as, 629, 632*f*
    biliary strictures as, 626–627, 627*f*–628*f*
    pneumobilia as, 625, 1767–1768, 1769*f*–1770*f*
    recurrent sclerosing cholangitis as, 629, 630*f*
    sphincter of Oddi dysfunction as, 629
  biloma after, 638
  choledochojejunostomy for, 625
  common bile duct anastomosis for, 625
  contraindications for, 624
  Doppler studies of recipient of, pediatric, 1764–1769
    with multiorgan transplants, 1768–1769
    for posttransplantation evaluation, 1766–1768, 1768*f*–1770*f*
    for pretransplantation evaluation, 1764–1766
    rejection in, 1767
  fluid collection after
    extrahepatic, 638, 644*f*–645*f*
    intrahepatic, 638–639, 645*f*–646*f*
  hematomas after, 638, 644*f*
  hepatic artery anastomosis for, 624
  infarction after, 638–639, 646*f*
  intrahepatic solid masses complicating, 639–641, 646*f*
  IVC anastomosis for, 624–625
  living related donor, 625
  normal appearance of, 625, 626*f*, 1767*f*
  patient selection for, 624
  pediatric
    Doppler studies of recipient of, 1764–1769
    renal cysts after, 1816–1818
  portal vein anastomosis for, 624

Liver transplantation *(Continued)*
PTLD after, 683–688, 687*f*
split liver graft and, from deceased donor, 625
surgical technique for, 624–625, 624*f*
venous complications of
hepatic artery aneurysms as, 1768, 1769*f*–1770*f*
hepatic vein stenosis as, 637, 643*f*
IVC stenosis as, 636–637, 641*f*
IVC thrombosis as, 636–637, 642*f*, 1766, 1769*f*–1770*f*
portal vein aneurysms as, 1768, 1769*f*–1770*f*
portal vein stenosis as, 635–636, 638*f*, 1766, 1768*f*
portal vein thrombosis as, 635–636, 639*f*–640*f*, 1766
Lobar emphysema, congenital, 1251, 1253*f*
"Lobster claw" deformity, 1406–1407, 1406*f*
Localized cystic disease, 362–364, 363*f*
Long head biceps tendon (LHBT), 879, 880*f*–881*f*
longitudinal split tear of, 893, 894*f*
pathology of, 892–893
tenosynovitis and, 892–893, 893*f*
Longitudinal split tear, of long head of biceps, 893, 894*f*
Longitudinal waves, 2–3
Longus colli muscle, parathyroid adenomas confused with, 745
Lower face abnormalities, 1153–1154
macroglossia as, 1153, 1153*b*, 1158*f*
micrognathia as, 1153–1154, 1158*f*
retrognathia as, 1153–1154
Lower limb anomalies, pediatric, 1689
Lower urinary tract symptoms (LUTS), 387–388
Lumbar arteries, 446, 446*f*
Lumbar spine deficiency, in caudal regression, 1237–1238
LUMBAR syndrome, tethered cord and, 1679
Lumbosacral area, spina bifida in, 1228
Lumbosacral hypogenesis, spinal cord embryology and, 1674
Lung(s). *See also* Pulmonary hypoplasia, fetal
acoustic cavitation in, 43
CHAOS and, 1253–1255, 1254*f*
congenital malformations of
BPS as, 1250–1251, 1251*f*
CLO as, 1251–1252, 1253*f*
CPAM as, 1246–1252
pediatric
abscess in, 1711, 1713*f*
atelectatic, 1714, 1716*f*
consolidated, 1711, 1714*f*–1715*f*
disease of, pleural disease differentiated from, sonography in, 1709, 1710*f*
parenchyma, 1711–1716
sequestrations in, 1715–1716, 1717*f*
percutaneous needle biopsy of, 607–608, 609*f*
pleuropulmonary blastoma and, 1252–1253
Lung(s), fetal
development of, 1243
stages of, 1245*b*
hypoplasia of
campomelic dysplasia and, 1384*f*
in lethal skeletal dysplasia, 1386, 1386*b*
lethality of skeletal dysplasia and, 1382, 1384*f*
masses in, hydrops from, 1426
size of, evaluation of, 1244
space-occupying lesions and, 1243
Lung-to-head circumference ratio (LHR), 1262
Luteal phase defect, early pregnancy failure from, 1062–1063
Luteoma of pregnancy, 572
LUTS. *See* Lower urinary tract symptoms
Luxury perfusion, cerebral infarction with, 1580–1581, 1584*f*
"Lying down" adrenal sign
in bilateral renal agenesis, 1342, 1343*f*
in neonate with absence of left kidney, 1784, 1784*f*
Lyme disease, pediatric, 1936
Lymph node(s)
breast cancer and assessment of, 807–810, 808*f*–810*f*
cortex of, 807
eccentric cortical thickening of, 807–808, 809*f*
hilum of, 807
masses of, in carotid region, 948, 949*f*
normal appearance of, 807, 808*f*
pathologic, near carotid bifurcation, 948, 949*f*
pediatric, inflammatory disease of, 1658–1663, 1661*f*–1663*f*
Rotter, 762, 808–810, 810*f*
Lymphadenitis, pediatric, 1658–1663, 1662*f*–1663*f*
Lymphadenopathy
in Crohn disease, 269, 272*f*
Doppler ultrasound assessment of, 771–772, 772*f*
pediatric
age and causes of, 1660, 1662*t*
cervical, 1658, 1660–1663
mediastinal masses and, 1724
site of node and causes of, 1660, 1662*t*
supraclavicular, 1658
retroperitoneal, 464
in tuberculous peritonitis, 521
Lymphangiectasia, appearance of, 1412, 1413*f*
Lymphangioma(s)
abdominal, pediatric, 1862, 1864*f*
fetal, neck, hydrops from, 1425
paratesticular, 1903–1904
pediatric pancreas and, 1865
pelvic, mesenteric cysts in, 509–510, 510*f*
splenic, 148
Lymphatic dysplasia, congenital, hydrops from, 1428, 1436*f*
Lymphatic malformations. *See also* Cystic hygroma(s)
fetal neck abnormalities and, 1159, 1161*f*
macroglossia in, 1153, 1153*b*, 1158*f*
pediatric
of chest, 1723
chest wall, macrocystic, ultrasound-guided sclerotherapy of, 1726, 1727*f*
of neck, 1655–1657, 1657*f*
parotid gland, 1636, 1637*f*
submandibular space, 1639–1640
in Turner syndrome, 1159
Lymphedema, hereditary, fetal, 1403–1404, 1405*f*
Lymphocele(s)
pelvic, 591
after renal transplantation, 665–666, 673*f*–674*f*
pediatric, 1809, 1811*f*
Lymphocytic leukemia, acute, 1796
Lymphoma(s)
adrenal, 426–427, 427*f*
AIDS-related, 266, 266*f*
B-cell, AKI and, 1796
bladder, 353, 354*f*
Burkitt, pediatric, 1860
gastric, endosonographic identification of, 301
gastrointestinal, 264–266, 266*f*
pediatric, 1862
genitourinary tract tumors and, 352–353
Hodgkin, pediatric, neck, 1665, 1665*f*
Lymphoma(s) *(Continued)*
of liver, 125, 129*f*
lymphadenopathy from, 1724
mediastinal, pediatric, biopsy of, 1956
non-Hodgkin, 125, 264–266
pediatric, neck, 1665
splenic lesions in, 152–153, 154*f*
ovarian, 585
pediatric, 1880
pediatric
liver metastases from, 1746
neck, 1665, 1665*f*
paratesticular, 1903–1904
peritoneal, 513, 517*f*
renal, 333, 352–353, 353*b*
pediatric, 1820, 1823*f*
retroperitoneal, 464
salivary gland, pediatric, 1639
of small bowel, 266, 266*f*
splenic lesions in
nodular, 152, 154*f*
solid, 152–153
testicular, 826–827, 828*f*
pediatric, 1901
of thyroid gland, 708–709, 709*f*
pediatric, 1648
ureteral, 353
Lymphoplasmacytic sclerosing pancreatitis, 236
Lymphoproliferative disorder. *See* Posttransplant lymphoproliferative disorder
Lysosomal disorders, fetal hydrops from, 1432

M

Macrocephaly, 1135–1136
fetal brain and, 1194–1195
Macrocranium(ia)
in skeletal dysplasia, 1382
in thanatophoric dysplasia, 1387
Macrocysts, ovarian, pediatric, 1873–1875
Macroglossia, 1153, 1153*b*, 1158*f*
Macronodular cirrhosis, 92–93
Macrosomia, 1453
sonographic criteria for, 1454*t*–1455*t*
Maffucci syndrome, in venous malformations of neck, 1657
Magnetic resonance angiography (MRA), in carotid stenosis diagnosis, 916
Magnetic resonance imaging (MRI), 32–33
breast ultrasound correlation with, 810–811, 811*f*–812*f*
of CNS, 1166–1167
of fetal brain, 1166–1167, 1172*f*
for fetal spine, 1216
for fetal urinary tract abnormalities, 1342, 1342*f*
of fetus, 1031–1032, 1031*f*
musculoskeletal system ultrasound compared to, 856
parathyroid adenomas and accuracy of, 748, 749*f*
in pregnancy, 1031–1032, 1031*f*
shoulder ultrasound compared to, 877–878
in skeletal dysplasia evaluation, 1385
Mainzer-Saldino syndrome, 1395
Majewski syndrome, 1396
Malacoplakia, 333, 333*f*
Male pseudohermaphroditism, dysplastic gonads and, 1899
Malformations, definition of, 1399
Malignancies, childhood, obstetric sonography and, 1041
Malignant melanoma, splenic lesions in, 153, 155*f*
MALToma, pediatric, 1639

Mammary ducts
  normal sonographic appearance of, 762, 764*f*
  subareolar and intranipple, scanning of, 762, 765*f*
Mammary fascia, 761, 762*f*
Mammary zone, of breast, 761, 761*f*, 763*f*
Mandible, fetal, normal sonographic appearance of, 1135*f*
Mandibular nasal prominence, 1134, 1134*f*
MAP (minimal-access parathyroidectomy), 749, 750*f*
Marfan syndrome, 946
Marginal placental cord insertion, 1484–1485, 1487*f*
  multifetal pregnancy and, 1119
Massa intermedia, enlarged, in Chiari II malformation, 1526, 1527*f*
Masseter muscle, pediatric, chloroma of, 1641*f*
Massive splenomegaly, 145, 146*t*
Masticator space, pediatric, pathology of, 1640, 1641*f*
Mastitis
  granulomatous, 803–804
  periductal, 771, 771*f*
  sonography for, 803–804
Maternal age, chromosomal abnormalities risk and, 1088, 1089*f*
Maternal floor infarction, 1473–1474, 1476*f*
Mathias laterality sequence, spina bifida and, 1226
Matrix metalloproteinases (MMPs), 434
Maxilla, fetal, normal sonographic appearance of, 1135*f*
Maxillary nasal prominence, 1134, 1134*f*
Maximum vertical pocket, 1339
Maximum-intensity projection (MIP), 105–106
Mayer-Rokitansky-Küster-Hauser syndrome, 1881–1883, 1882*f*
May-Thurner syndrome, 456–457
MBO. *See* Mechanical bowel obstruction
MCA. *See* Middle cerebral artery
McCune-Albright syndrome, pediatric ovarian cysts and, 1875
MCDA. *See* Monochorionic diamniotic twins
MCDK. *See* Multicystic dysplastic kidney
MCMA. *See* Monochorionic monoamniotic twins
MDCT. *See* Multidetector computed tomography
Mean sac diameter (MSD)
  in gestational age estimation, 1061, 1061*f*, 1444–1445, 1445*t*
  of gestational sac
    for gestational age estimation, 1444–1445, 1445*t*
    small, in relationship to CRL, early pregnancy failure and, 1066, 1067*f*
  yolk sac and, 1057
Mechanical beam steering, 10–11
Mechanical bowel obstruction (MBO)
  afferent loop, 293
  closed-loop, 293, 295*f*
  gastrointestinal tract and, 293
  intussusception causing, 293, 296*f*
  midgut malrotation predisposing to, 293
  sonographic assessment of, 293, 294*f*
Mechanical index (MI)
  for acoustic cavitation, 44–45, 45*f*
  definition of, 58
  microbubbles as contrast agents and, 58, 58*b*, 105
  in obstetric sonography, 1035
Mechanical sector scanners, 11
Mechanical ventilation, in neonatal/infant brain, 1578, 1579*f*
Meckel diverticulum
  intussusception and, 1844–1845, 1849*f*
  pediatric appendicitis differentiated from, 1858–1860, 1862*f*
Meckel-Gruber syndrome
  Dandy-Walker malformation differentiated from, 1532
  fetal brain dorsal induction errors and, 1182
  fetal cystic kidneys and, 1351, 1351*f*
  spina bifida and, 1226
Meconium ileus, 1310
  fetal CF and, 1316
Meconium periorchitis, focal calcifications from, 1904, 1904*f*
Meconium peritonitis
  fetal
    CF and, 1316
    hydrops from, 1428, 1428*f*
    liver calcifications and, 1316–1318
    massive ascites in, 1418–1419, 1421*f*
    small bowel and, 1313, 1313*t*, 1314*f*
  pediatric
    cystic, 1842–1843, 1846*f*
    testicular torsion and, 1892–1893
Medial fibroplasia, renal artery stenosis and, 447
Medial gastrocnemius muscle, tear of, 858, 859*f*
Medial nasal prominence, 1134, 1134*f*
Median arcuate ligament syndrome, 453, 453*f*
Mediastinal shift, in unilateral pulmonary hypoplasia, 1246, 1247*f*
Mediastinum
  fetal, masses in, hydrops from, 1425
  pediatric, assessment of, 1702, 1703*f*–1704*f*
  pediatric, masses of, 1723–1724
    abnormal thymus location mimicking, 1723
    anterior, 1723–1724
    biopsy of, 1956, 1959*f*
    lymphadenopathy and, 1724
    posterior, 1724
    thymic index and, 1723, 1724*t*, 1725*f*, 1726*t*
Mediastinum testis, 819, 820*f*
  pediatric, 1888
Medical renal disease. *See* Kidneys, pediatric, medical diseases of
Medulla
  adrenal, functions of, 417
  cerebral, as foramen magnum approach landmark, 1592, 1595*f*
Medullary carcinoma, of thyroid gland, 701–707, 707*f*–708*f*
  pediatric, 1648
Medullary cystic kidney disease, 359
  pediatric, 1816, 1817*f*
Medullary nephrocalcinosis, 339, 340*f*
  pediatric, 1798–1799, 1799*f*
Medullary sponge kidney, 339, 340*f*, 359
  pediatric, 1799
Megacalices, congenital, 321
Mega-cisterna magna
  fetal, 1189
    arachnoid cysts differentiated from, 1192–1193
    normal sonographic appearance of, 1168–1169
  neonatal/infant, Dandy-Walker malformation differentiated from, 1531, 1534*f*
Megacystis, fetal, 1360, 1360*b*, 1360*f*
  megalourethra and, 1362*f*
Megacystis-microcolon-intestinal hypoperistalsis syndrome (MMIHS), 1362–1363
  pediatric hydronephrosis and, 1788–1791
Megacystitis, fetal, thickened NT and, 1096*f*
Megahertz, definition of, 2
Megalencephaly, 1194–1195
Megalourethra, fetal, urinary tract obstruction in, 1362, 1362*f*
Megaureter(s)
  congenital, 321, 322*f*
  fetal, 1358–1359
  primary, pediatric hydronephrosis and, 1786–1788, 1787*f*
Meigs syndrome, 585
Membranous glomerulonephritis, 369
Membranous VSDs, 1281
MEN. *See* Multiple endocrine neoplasia
Ménétrier disease, gastric mucosa thickening in, 1839–1840
Meningeal layer, in myelocystocele, 1233
Meningitis, neonatal/infant, 1560, 1561*f*–1562*f*
Meningocele
  atretic, tethered cord and, 1679
  fetal
    cranial, 1179
    definition of, 1225*t*
    pathogenesis of, 1226
    sonographic findings in, 1218
    spina bifida occulta and, 1226
  posterior, closed spinal dysraphism and pediatric, 1682–1683
Meningoencephalocele, 1218
Meningomyelocele, fetal cloacal exstrophy and, 1328
Menopause
  endometrial abnormalities after
    bleeding and, 545–546
    fluid and, 546–547, 546*b*, 547*f*
    hormone use and, 544–545, 544*b*, 545*f*
  ovaries after, 569
    cysts in, 569–570, 571*f*
Menstrual age
  definition of, 1443–1444
  usage of term, 1167
Menstrual cycle, interrelationships in, 1050*f*
Menstruating females, ovarian volume in, 1873, 1875*t*
Mesencephalon, formation of, 1077
Mesenchymal dysplasia, of placenta, 1479, 1479*f*
Mesenchymal tumors, intracranial, fetal, 1208
Mesenchyme, formation of, 1053
Mesenteric, adenopathy, in acute abdomen, 282
Mesenteric adenitis
  pediatric, 1858–1860, 1862*f*
  right lower quadrant pain in acute abdomen from, 288
Mesenteric adenopathy, in acute abdomen, 282
Mesenteric artery(ies), 451–455. *See also* Celiac artery
  anatomy of, 451, 452*f*
  celiac artery as, 451
  duplex Doppler sonography of, 453–455, 455*f*
    interpretation of, 454–455, 456*f*–458*f*
  inferior
    anatomy of, 451, 452*f*
    connections of, with superior mesenteric artery, 451
    duplex Doppler sonography of, 454
  ischemia of, 451–453
  in median arcuate ligament syndrome, 453, 453*f*
  stenosis of, turbulence after, 454, 456*f*
  superior
    anatomy of, 451, 452*f*
    connections of, with inferior mesenteric artery, 451
    duplex Doppler sonography of, 454
    occluded, 454–455, 458*f*
    stenosis of, 457*f*
Mesenteric cyst(s)
  fetal, ovarian cysts differentiated from, 1369
  gastrointestinal cysts differentiated from, 1860, 1863*f*
  pediatric, ovarian cysts differentiated from, 1875
  peritoneal, 509–510, 510*f*
Mesenteric vein(s)
  clots in, in acute pancreatitis, 224–225, 227*f*
  pediatric
    Doppler studies of, best approaches for, 1752
    flow direction in, in portal hypertension, 1752

Mesentery, small bowel, 505, 505*f*
Mesoblastic nephroma
  congenital, 1352–1353, 1353*f*
  pediatric, 1818–1820, 1821*f*
Mesocardia, 1273
Mesocolon, transverse, inflammation of, in acute pancreatitis, 224–225, 226*f*
Mesoderm layer, of trilaminar embryonic disc, 1216–1217, 1217*f*
Mesomelia, 1381, 1381*b*, 1382*f*
Mesonephric (wolffian) duct, 820–821
Mesonephros, 311, 312*f*, 1336–1338
Mesorchium, torsion of, pediatric, 1325
Mesosalpinx, 564–565
Mesothelioma(s)
  cardiac, in infants, 1293
  multicystic, 508–509
  pediatric, 1712*f*
  peritoneal, primary, 513, 516*f*
Mesovarium, 564–565
Metabolic disorders
  fetal hydrops from, 1432
  of liver, 91–96
  neonatal jaundice caused by, 1734
  neonatal/infant brain abnormalities from, 1538
Metabolic syndrome, fatty liver in, 91
Metabolism, inborn errors of, jaundice and, 1738–1740, 1739*b*, 1740*f*
Metacarpophalangeal joint, injection of, short-axis approach to, 901
Metanephrogenic blastema, in kidney development, 311, 312*f*
Metanephros, 311, 312*f*, 1053–1054, 1336–1338
Metastasis(es)
  adrenal, 425–426, 426*f*–427*f*
  to biliary tree, 188, 192*f*
  bladder, 354–355, 355*f*
  of breast cancer, lymph node assessment for, 807–810, 808*f*–810*f*
  characterization of, with microbubble contrast agents, 106*f*
  drop, 266, 267*f*
  gastrointestinal, 266, 267*f*
  genitourinary tract tumors and, 354–355
  of liver, 124–129, 126*f*–130*f*
    bulls-eye pattern of, 125, 127*f*
    calcified, 125, 128*f*
    CEUS diagnosis of, 128–129, 130*f*
    cystic, 125, 128*f*
    echogenic, 125, 128*f*
    hypoechoic, 125, 127*f*–128*f*
    infiltrative, 125–128, 126*f*
    pediatric, 1746, 1750*f*
    target pattern of, 125, 127*f*
  neuroblastoma, paratesticular, 1903–1904
  ovarian, 585, 586*f*
  pancreatic, 251, 251*f*
  pediatric, neck, 1666–1667, 1667*f*
  peritoneal, 510
  renal, 354, 355*f*
  retroperitoneal, 464, 465*f*
  salivary gland, pediatric, 1639
  to spleen, cystic, 148
  splenic
    nodular lesions in, 152, 154*f*
    percutaneous needle biopsy of, 608*f*
    solid lesions in, 153, 155*f*
  testicular, 822*b*, 826–829, 826*b*
    hamartomas as, 829, 829*f*
    leukemia as, 827, 828*f*
    lymphoma as, 826–827, 828*f*
    myeloma as, 827–829
    pediatric, 1901
Metastasis(es) *(Continued)*
  of thyroid gland, 709, 710*f*
  ureteral, 354
Metastatic nodal disease, pediatric, neck, 1666–1667, 1667*f*
Metatarsophalangeal joints, injection of, short-axis approach to, 900*f*, 901
Methotrexate, in ectopic pregnancy management, 1076, 1076*f*
Metopic craniosynostosis, 1137*f*
MI. *See* Mechanical index
Micrencephaly, 1194
Microabscesses, splenic, 150–152, 154*f*
Microbubbles
  acoustic behavior of, regimens of, 57*t*, 58–59, 59*f*
  as contrast agents, 53–54, 54*f*
    behavior of, incident pressure and, 56–58, 57*t*
    disruption of, 64–67, 66*f*
    FNH characterization with, 106, 106*f*, 108*t*, 109*f*
    future of technology for, 68–69, 69*f*–70*f*
    HCC characterization with, 106, 106*f*
    hemangioma characterization with, 106, 106*f*–107*f*, 108*t*
    inertial cavitation and, 67–68
    lesional enhancement with, 105, 106*f*–107*f*, 109*f*
    liver mass characterization with, 105–106, 106*f*–107*f*, 108*t*, 109*f*–110*f*
    MI and, 58, 58*b*, 105
    need for, 56–58, 57*f*
    regulation of, 68
    safety of, 67–68
  resonance of, in ultrasound field, 58, 59*f*
Microcalcifications, in thyroid nodules, papillary carcinoma and, 699, 702*f*
Microcephaly, 1135–1136
  fetal brain and, 1194, 1195*f*
  sloped forehead in, 1139, 1141*f*
Microcolon, fetal, in MMIHS, 1362–1363, 1788–1791
Microcysts, in breast, 782, 784*f*
Microemboli, cerebral, in pediatric procedures, 1622
Microembolization, intraoperative, TCD detection of, 950
Microencephaly, temperature increase in utero and, 1037
Microgallbladder, in biliary atresia, 1737, 1738*f*
Micrognathia, 1153–1154, 1158*f*
  campomelic dysplasia and, 1395
Microlithiasis, 194–195
  acute pancreatitis and, 221
  testicular, pediatric, 1904, 1904*f*
Microlithiasis, testicular, 833, 833*b*, 834*f*
Microlobulations, in breast sonography, 789, 791*f*
Micromelia, fetal, 1381, 1381*b*, 1382*f*
  in achondrogenesis, 1391, 1391*f*
  in lethal skeletal dysplasia, 1386
  in osteogenesis imperfecta type II, 1391–1392, 1392*f*
  severe
    with decreased thoracic circumference, 1387*t*
    in hypophosphatasia, 1392
    in thanatophoric dysplasia, 1387
Micromelic dysplasia, features of, 1397*t*
Micronodular cirrhosis, 92–93
Micropenis, fetal, 1367
Microphthalmia
  midface hypoplasia with, 1149*f*
  sonographic evaluation of, 1140, 1145*f*, 1147*b*
  temperature increase in utero and, 1037
microRNAs, fibrous cap thinning and, 920
Microstomia, 1154
Microtia
  hypotelorism and, 1142*f*
  incidence of, 1148
Midaortic syndrome, renal artery stenosis and, 447
Middle cerebral artery (MCA)
  cerebroplacental ratio and, 1458, 1460*f*
  cerebrovascular disease indicators with SCD and, 1600*f*, 1604*f*–1605*f*
  Doppler ultrasound of
    in fetal alloimmunization detection, 1421, 1422*f*
    in fetal assessment, 1458–1460, 1460*f*
  neonatal/infant, in coronal imaging, 1514
  occlusion of, leptomeningeal collaterals and, 1610
  PSV of blood flow in, 1421–1423, 1421*b*, 1422*t*
  as transtemporal approach landmark, 1592, 1593*f*–1594*f*
Midface abnormalities, 1148–1153. *See also* Cleft lip/palate
  absent nasal bone as, 1133–1134, 1150*f*
  cleft lip and palate as, 1151–1153
  hypoplasia as, 1148, 1149*f*–1150*f*
Midface hypoplasia, craniosynostosis and, 1136–1138
Midgut, 1304–1305
  physiologic herniation of, 1077, 1077*f*, 1322, 1323*f*
    omphalocele confused with, 1325, 1327*f*
  volvulus
    intestinal malrotation with, 1841–1842, 1843*f*–1844*f*
    "whirlpool" sign of, 1841–1842, 1843*f*
Midline, in sagittal imaging of neonatal/infant brain, 1515, 1516*f*
Midline falx, fetal, sonographic view of, 1024*f*
Migrational abnormalities, corpus callosum agenesis and, 1526–1528
Mikulicz disease, 1635
Milk allergy, gastric mucosa thickening and, 1839–1840
Milk of calcium
  bile, 194, 195*f*
  breast cysts and, 775, 776*f*–777*f*
  cysts, as renal transplantation complication, 653, 657*f*
  renal, calyceal diverticula and, 1799, 1800*f*
Miller-Dieker syndrome, 1195
Mineralization
  abnormal, in achondrogenesis, 1391, 1391*f*
  decreased
    in hypophosphatasia, 1392, 1395*f*
    in osteogenesis imperfecta type II, 1392, 1393*f*
  of thalamostriate vessels, 1203, 1204*f*
Minimal-access parathyroidectomy (MAP), 749, 750*f*
MIP. *See* Maximum-intensity projection
Mirizzi syndrome, 174, 174*f*
Mirror syndrome, fetal hydrops prognosis and, 1436
Misregistration, of structure, 5, 6*f*
Misregistration artifacts, 3*f*, 420–421
Mitral regurgitation, fetal, hydrops from, 1423–1424
Mitral stenosis, fetal, hydrops from, 1423–1424
MLCN. *See* Multilocular cystic nephroma
MMIHS. *See* Megacystis-microcolon-intestinal hypoperistalsis syndrome
M-mode echocardiography, fetal, 1275, 1280*f*–1281*f*
M-mode ultrasound, 9, 9*f*
MMPs. *See* Matrix metalloproteinases

Molar pregnancy. *See* Hydatidiform molar pregnancy
Molar tooth, Joubert syndrome and, 1182
Mole, Breus, 1471
Mondor disease, 768
Monochorionic diamniotic (MCDA) twins, 1019*f*, 1058*f*, 1115–1116, 1116*f*
  CHD and, 1270–1273
  complications of, 1125–1129
    TAPS and, 1126–1127
    TRAP and, 1127–1129, 1127*f*–1128*f*
    TTTS and, 1125–1126, 1125*t*, 1126*f*
  growth discrepancy in, 1123*f*
  IUFD and, 1124*f*
  sonographic findings of, chorionicity and, 1119, 1121*f*
Monochorionic monoamniotic (MCMA) twins, 1057, 1115–1116, 1116*f*
  complications of, 1125–1129, 1129*f*
    TAPS and, 1126–1127
    TRAP and, 1127–1129, 1127*f*–1128*f*
    TTTS and, 1125–1126, 1125*t*, 1126*f*
  conjoined twins as, 1130*f*
  IUFD and, 1124*f*
  sonographic findings of, chorionicity and, 1119, 1121*f*
Mononucleosis
  of parotid gland, pediatric, 1632*f*
  splenic enlargement and, pediatric, 1769
Monorchidism, 1890
Monosomy X. *See* Turner syndrome
Monozygotic (identical) twins, 1115, 1116*f*
Morgagni hernia, 1258, 1718*f*
Morton neuromas, injection for, 904, 904*f*
Morula, 1051, 1051*f*
Motor function, impaired, in spina bifida, 1233
Moyamoya angiopathy, SCD and, 1598, 1600*f*, 1602*f*, 1608*f*, 1610
mpMRI. *See* Multiparametric magnetic resonance imaging
MRA. *See* Magnetic resonance angiography
MRI. *See* Magnetic resonance imaging
MSD. *See* Mean sac diameter
Mucinous cystadenocarcinoma, ovarian, 580*f*, 581
Mucinous cystadenoma, ovarian, 580*f*–581*f*, 581
Mucinous cystic neoplasm, 247–248, 247*f*
Mucocele, of appendix, 299, 299*f*
Mucoepidermoid carcinoma, salivary gland, pediatric, 1638
Müllerian ducts
  cysts of, pediatric, 1908, 1910*f*
  duplication of, 1881
  uterus and anomalies of, 529, 533–538, 537*f*
    categories of, 534, 536*f*
Multicystic dysplastic kidney (MCDK), 361, 362*f*
  fetal, 1346–1347, 1346*f*–1347*f*
  pediatric, 1815, 1816*f*
Multicystic mesotheliomas, 508–509
Multidetector computed tomography (MDCT), 238, 241, 241*b*
Multifetal pregnancy
  amniocentesis in, 1125–1126
  amnionicity in, 1115–1116, 1116*f*
    determining, 1057, 1058*f*
    sonographic determination of, 1117, 1119*t*
    triplets and, 1122*f*
  aneuploidy screening in, 1091
  birth weight discordance in, 1123
  cervical assessment in, 1504–1505
  chorionicity in, 1115–1116, 1116*f*
    sonographic determination of, 1117–1119, 1118*f*, 1119*t*, 1120*f*–1121*f*
    triplets and, 1122*f*
  congenital malformation in, 1123
  first-trimester scans in, 1017, 1019*f*
  general issues with, 1119–1123
Multifetal pregnancy *(Continued)*
  growth discordance in, 1123, 1123*f*
  hydrops in, 1429, 1429*f*
  identification of, routine ultrasound screening in, 1029
  incidence of, 1115
  maternal serum alpha-fetoprotein elevation in, 1228
  morbidity and mortality in
    IUFD and, 1123–1125, 1124*f*
    IUGR and, 1119–1123
    prematurity and, 1119–1123
  placental cord insertion and, 1119, 1122*f*
  placentation and, 1115–1116, 1116*f*
  zygosity in, 1115–1116, 1116*f*
Multilocular cystic nephroma (MLCN), 361–362, 363*f*
  pediatric, 1820, 1822*f*
Multinodular goiter, 711, 711*f*
  parathyroid adenomas detection and, 746
  sonographic appearance of, 727
Multiparametric magnetic resonance imaging (mpMRI), 381–382
  prostate cancer, TRUS fusion with, 406–407, 410–411
Multipath artifact, 19–21, 21*f*
Multiple endocrine neoplasia (MEN), 421
  pheochromocytomas with, 1826, 1910–1912
  type I, 734
  type II, 701
  type IIA, 734
Multiple gland disease, parathyroid adenomas in, 735, 738*f*
Mumps
  EF from, 1294
  orchitis, 1896
  parotitis from, pediatric, 1632
Mural nodules, PAM causing, 782, 783*f*–784*f*
Murphy sign, 198–199, 199*f*, 201*f*
Muscle-eye-brain disease, cobblestone lissencephaly in, 1195
Muscle(s)
  anatomy of, 857–858, 858*f*
  atrophy, 859, 860*f*
    rotator cuff, 888–889, 891*f*
    ultrasound for, 877–878
  injuries to, 858–859, 858*f*–859*f*
  medial gastrocnemius, tear of, 858, 859*f*
  myofascial defects and, 858–859, 859*f*
  ultrasound techniques for, 857–859
Muscular dystrophy, congenital, cobblestone lissencephaly in, 1195
Muscular VSDs, 1281, 1284*f*
Musculoskeletal injection(s)
  anesthetics for, 901
  of Baker cyst, 907–909, 908*f*
  bursal, 907–909, 908*f*
  for calcific tendinitis, 909, 911*f*
  corticosteroids for, 900
  of deep tendons, 904–907
    abductor, 905–907, 907*f*
    biceps, 904–905, 905*f*–906*f*
    hamstring, 905–907, 907*f*–908*f*
    iliopsoas, 905, 906*f*
  of ganglion cyst, 907–909, 909*f*
  intratendinous, 909–910, 912*f*
  of joints, 901–902, 901*f*–902*f*
  materials for, 900–901
  pain as indication for, 898
  of paralabral cysts, 907–909, 910*f*–911*f*
  perineural, 910–912, 913*f*
  superficial peritendinous and periarticular, 902–904
    for foot and ankle, 902–904, 903*f*–904*f*
    for hand and wrist, 904, 905*f*
Musculoskeletal injection(s) *(Continued)*
  technique for, 899–900
    long-axis approach in, 900–901, 900*f*–901*f*
    short-axis approach in, 900–901, 900*f*
Musculoskeletal system. *See also* Bone(s); Ligament(s); Muscle(s); Tendon(s)
  fetal, development of, movements and, 1378
  interventions for
    contrast agents in, 898
    technical considerations for, 898–899, 899*f*
  pediatric
    congenital deformities of, 1933
    congenital nonhip dislocations of, 1933–1936
    inflammation of, 1936–1938, 1937*f*–1938*f*
    inflammation of, noninfectious, 1938
    interventional sonography for, 1961, 1963*f*–1964*f*
    trauma to, 1938–1939, 1939*f*
  ultrasound techniques for
    Doppler imaging in, 857, 857*f*
    elastography in, 857
    extended field of view in, 857
    general considerations in, 856–857
    MRI compared to, 856
Mycobacterial infections, pediatric, lymphadenitis differentiated from, 1660–1663
Mycobacterium avium-intracellulare, 91
Mycobacterium tuberculosis, 329–330, 1852–1853
Myelination
  development of, 1167
  in organogenesis, 1524–1525
Myelocele, open spinal dysraphism and, pediatric, 1681, 1683*f*
Myelocystocele
  fetal, 1233–1234, 1234*f*–1235*f*
  pediatric, 1683–1684, 1686*f*
Myelodysplasia, 1382
Myelolipomas, adrenal, 420–421, 420*b*, 420*f*
Myeloma, testicular, 827–829
Myelomeningocele(s), 1218
  definition of, 1225*t*
  fetal surgery for, 1233
  no Chiari II malformation and search for, 1526, 1529*f*
  open compared to closed, 1226
  open spinal dysraphism and, pediatric, 1681, 1683*f*
  pathogenesis of, 1226
  pediatric, neurogenic bladder in, 1907
  spine embryology and, 1674
Myeloschisis, 1218, 1226
  definition of, 1225*t*
  sonographic findings in, 1218
Myocardium, fetal, hydrops from decreased function of, 1425
Myofascial defects, 858–859, 859*f*
Myofibroblastic tumor, inflammatory, pediatric, 1812
Myofibromatosis, congenital infantile, 1664, 1665*f*
Myometrium
  abnormalities of, 538–541
    adenomyosis as, 540–541, 540*b*, 542*f*
    leiomyoma as, 538–540, 539*f*, 540*b*
    leiomyosarcomas as, 540, 541*f*
  calcifications of, 531–533, 533*f*–534*f*
  layers of, 531
  veins of, 531–532, 533*f*
Myopathy, congenital, atypical hips and, 1932
Myositis, complicated lymphadenitis with, 1662*f*

N

Nabothian cysts, 533, 535*f*, 1499
Nanodroplets, therapeutic use of, 68
Nasal bone, fetal
  absent, 1133–1134, 1150*f*
  in aneuploidy screening, 1093–1095, 1094*b*, 1094*f*

Nasal bone, fetal *(Continued)*
NT in, 1094
in trisomy 21, 1099–1100, 1099*f*
Nasal placodes, 1134
NASCET. *See* North American Symptomatic Carotid Endarterectomy Trial
Nasolacrimal ducts, obstruction of, dacryocystocele from, 1143, 1147*f*
National Council on Radiation Protection and Measurements (NCRP), 38–39
Near field, of beam, 8
Near-field structures, neonatal/infant brain and, duplex Doppler sonography of, 1585, 1588*f*
NEC. *See* Necrotizing enterocolitis
Neck, fetal. *See also* Face, fetal
abnormalities of, 1154–1163
cervical teratoma as, 1159, 1161*f*
goiter as, 1159–1163, 1162*f*
lymphatic malformations as, 1159, 1161*f*
NT and, thickening of, 1154–1159
thyromegaly as, 1159–1163
embryology and development of, 1134
hydrops from, 1425, 1426*f*
normal, sonography of, 1135, 1136*f*
Neck, pediatric. *See also* Infrahyoid space, pediatric; Suprahyoid space, pediatric
carotid space of, 1650
congenital abnormalities of, 1651–1654
branchial, 1651, 1651*f*–1653*f*
cervical teratomas and, 1654, 1654*f*
dermoid cysts and, 1652–1654, 1654*f*
ectopic thymus and, 1652, 1653*f*
epidermoid cysts and, 1652–1654
danger space of, 1650
deep cervical fascia of, 1628, 1629*f*
iatrogenic lesions and, 1658, 1661*f*
inflammatory disease of, 1658–1664
fibromatosis coli and, 1663–1664, 1663*f*
lymph nodes and, 1658–1663, 1661*f*–1663*f*
lesions of, 1961, 1967*f*
neoplasms of, 1664–1667
congenital infantile myofibromatosis as, 1664, 1665*f*
granulocytic sarcomas as, 1666, 1667*f*
lymphoma as, 1665, 1665*f*
malignant, 1664–1667
metastases and, 1666–1667, 1667*f*
neuroblastoma as, 1665–1666, 1666*f*
pilomatricoma as, 1664, 1664*f*
rhabdomyosarcoma as, 1665, 1666*f*
normal anatomy of, 1628–1629
prevertebral space of, 1650
retropharyngeal space of, 1650
superficial fascia of, 1628, 1629*f*
vascular anomalies of, 1654–1655
malformations, 1655–1658, 1655*b*, 1657*f*, 1659*f*
tumors, 1655, 1655*b*, 1656*f*
Neck masses of, in carotid region, 947–948, 949*f*–950*f*
Necrotizing enterocolitis (NEC), 1854–1855, 1855*b*, 1856*f*
Necrotizing fasciitis, of perineum, 846–847
Needle(s). *See also* Biopsy(ies), percutaneous needle
large-caliber, uses of, 600
for musculoskeletal interventions, technique for, 898–899, 899*f*
for percutaneous needle biopsies
guidance systems for, 600, 601*f*
selection of, 599–600
visualization in, 601–603, 602*f*
small-caliber, uses of, 599–600
Neisseria gonorrhoeae, 846
Neonatal brain sonography. *See* Brain, neonatal/infant, imaging of
Neonatal resuscitation, in fetal hydrops, 1437
Nephrectomy, evaluation after, 374–375
Nephritis, acute interstitial, 370
Nephroblastoma, pediatric, 1818
Nephroblastomatosis, pediatric, 1818
Nephrocalcinosis, 339–340, 340*f*, 359
cortical, 339
pediatric, 1798, 1798*b*, 1798*f*
medullary, 339, 340*f*
pediatric, 1798–1799, 1799*f*
Nephroma
cystic, multilocular, 361–362, 363*f*, 1820, 1822*f*
mesoblastic
congenital, 1352–1353, 1353*f*
pediatric, 1818–1820, 1821*f*
Nephronophthisis
familial juvenile, 359
pediatric, 1815–1816, 1816*f*
Nephropathy
HIV-associated, 332–333, 333*f*
lithium, 361, 363*f*
reflux, 327, 327*f*
Nephrosis, congenital, maternal serum alpha-fetoprotein elevation in, 1228
Nephrotoxic drugs, AKI and, 1796
Nerve sheath tumors, 871, 872*f*
Nerve(s)
anatomy of, normal, 864–865, 865*f*
dysfunction of, 865–866, 866*f*
ilioinguinal, entrapment of, after herniorrhaphy, 496
subluxation of, 865–866
ultrasound techniques for, 864–866
Nesidioblastosis, pediatric pancreatic enlargement and, 1865, 1865*f*
Neural arch, ossification of, 1218
Neural canal, in spine embryology, 1217
Neural crest cells, 1133–1134, 1672–1673
Neural plate, in spine embryology, 1217
Neural process, ossification of, 1218, 1219*f*
Neural tube
closure of, 1524, 1525*b*
abnormalities of, 1218
brain disorders of, neonatal/infant, 1526–1532
Chiari malformations and neonatal/infant disorders of, 1526, 1526*b*, 1527*f*–1529*f*
corpus callosum agenesis and neonatal/infant disorders of, 1526–1528, 1529*b*, 1530*f*–1533*f*
corpus callosum lipoma and neonatal/infant disorders of, 1529, 1533*f*
Dandy-Walker malformation and neonatal/infant disorders of, 1529–1532, 1530*b*, 1533*f*–1534*f*
formation of, 1524, 1672–1673, 1673*f*
in spine embryology, 1217, 1218*t*
Neural tube defects (NTDs), 1183. *See also* Spina bifida
CDH and, 1263
descriptions of, 1218
risk factors for, 1225*b*
spina bifida and, 1223
teratogens inducing, 1218
ultrasound screening of, 1226–1228
X-linked, 1226
Neurenteric cysts
fetal, 1256
pediatric, 1686–1688
Neurenteric fistula, 1674
Neuroblastoma(s)
adrenal, 427–428
fetal, 1353–1354, 1353*f*
pediatric, 1825–1826, 1826*f*
metastatic, paratesticular, 1903–1904
pediatric
intraspinal, 1689–1691, 1693*f*
liver metastases from, 1746, 1750*f*
metastasis of, to teste, 1901
neck, 1665–1666, 1666*f*
ovarian, 1880
presacral, 1914, 1915*f*
Wilms tumor mistaken for, 1818
Neuroepithelial tumors, intracranial, fetal, 1208
Neurofibroma(s)
bladder, 356
paratesticular, 1903–1904
plexiform, in intraoperative procedures, 1621*f*
Neurofibromatosis
hemimegalencephaly associated with, 1195
prenatal intracranial tumors in, 1208
renal artery stenosis and, 447
rhabdomyosarcoma associated with, 1908
type 1
megalencephaly associated with, 1194–1195
neuroblastoma with, pediatric, 1825
pheochromocytomas with, 1826
Neurogenic bladder, 372–374, 373*f*
pediatric, hydronephrosis and, 1788
Neurogenic tumors, pediatric, 1724
Neurologic development, obstetric sonography and, 1040–1041
Neuroma, interdigital, injection for, 904, 904*f*
Neuronal proliferation, in organogenesis, 1524–1525
Neurons
development of, 1167
neonatal/infant, injury to, diffuse, duplex Doppler sonography and, 1580
Neurulation, 1053, 1179
in spine embryology, 1217, 1672, 1673*f*
Nevus, giant pigmented, choroid plexus papillomas in, 1209
Nipple discharge, ultrasound examination for, 798–799, 799*f*–801*f*
Nitric oxide, inhaled, 1578
Nodular lesions. *See also* Thyroid gland, nodular disease of
splenic, 148–152, 151*f*–154*f*
thyroid, 694–723
Nonarthrosclerotic carotid disease, 944–948. *See also* Carotid artery(ies), nonarthrosclerotic diseases of
ultrasound examination of, 916
Noncommunicating rudimentary uterine horn, 546
Non-Hodgkin lymphoma, 125, 264–266
pediatric, neck, 1665
of peritoneum, 513, 517*f*
splenic lesions in, 152–153, 154*f*
Nonlinear echoes, contrast agents and, 58–64
amplitude and phase modulation imaging and, 64, 65*f*
harmonic B-mode imaging and, 60
harmonic spectral and power Doppler and, 60–61, 60*f*–62*f*
plane-wave contrast imaging and, 64
pulse inversion Doppler imaging and, 63–64
pulse inversion imaging and, 62–63, 62*f*–63*f*
temporal maximum intensity projection imaging and, 64, 65*f*
tissue harmonic imaging and, 61–62
Nonne-Milroy lymphedema, 1403–1404, 1405*f*
Nonobstructive cardiomyopathy, 1294–1295

Nonrhizomelic chondrodysplasia punctata, 1399
Nonright-handedness, obstetric sonography and, 1040
Nonseminomatous germ cell tumors (NSGCTs), 822*b*, 823–824, 825*f*
Noonan syndrome
  characteristics of, 1887
  low-set ears in, 1148
  pulmonic stenosis and, 1292
Norepinephrine, secretion of, 417
North American Symptomatic Carotid Endarterectomy Trial (NASCET), 916, 929
Nose, fetal
  abnormalities of, 1151
  bones of
    absent, 1133–1134, 1150*f*
    in aneuploidy screening, 1093–1095, 1094*b*, 1094*f*
    NT in, 1094
    in trisomy 21, 1099–1100, 1099*f*
  normal sonographic appearance of, 1135*f*
  saddle, in skeletal dysplasia, 1382
Notochord
  disorders of midline
    formation, 1689
    integration, 1686–1689
  in spine embryology, 1216–1217, 1217*f*, 1218*t*
Notochordal process, in spine embryology, 1217, 1217*f*, 1218*t*
Notochordal remnants, in spine embryology, 1217, 1217*f*, 1218*t*
NSGCTs. *See* Nonseminomatous germ cell tumors
NT. *See* Nuchal translucency
NTDs. *See* Neural tube defects
Nuchal cord, 1483–1484
Nuchal fold, in trisomy 21, 1097–1099, 1099*f*, 1154–1159
Nuchal translucency (NT)
  in aneuploidy risk assessment, 1018–1019, 1019*f*, 1049
  CRL compared to, 1089, 1090*f*
  echogenic material in yolk sac and, 1067–1068
  in fetal nasal bone assessment, 1094
  HPE and thickened, 1096*f*
  measurement technique for, standardization of, 1091–1093, 1092*b*
  with normal karyotype, 1095–1097, 1096*f*
  screening of, human studies on, 1039–1040
  thickened
    abdominal wall defects and, 1095–1096
    anencephaly and, 1096*f*
    congenital heart defects and, 1095–1097, 1096*f*
    in cystic hygroma, hydrops and, 1425
    cystic hygroma and, 1096*f*
    diaphragmatic hernia and, 1095–1096
    fetal neck conditions and, 1154–1159
    megacystitis and, 1096*f*
    omphalocele and, 1096*f*
  in trisomy 13, 1093
  in trisomy 18, 1093
  in trisomy 21, 1089, 1090*f*
Nutcracker syndrome (nutcracker phenomenon), 460–461, 462*f*, 838, 839*f*
Nutrients, yolk sac in transfer of, 1057
Nyquist limit, 29–30, 32*f*

O

Obesity
  fatty liver in, 91
  renal artery duplex Doppler sonography in, 447
Observed-to-expected lung-to-head ratio (o/e LHR), 1262
Obstetric sonography. *See also* Pregnancy, first trimester of
  auditory response in, 1038
  bioeffects of
    animal research and, 1038–1039
    behavioral changes and, 1040–1041
    birth weight and, 1040
    childhood malignancies and, 1041
    congenital malformations and, 1041
    delayed speech and, 1040
    Doppler ultrasound and, 1041
    dwell time and, 1036
    dyslexia and, 1040
    human studies on, 1039–1041
    instrument outputs and, 1035–1036
    mechanical, 1038
    neurologic development and, 1040–1041
    nonright-handedness and, 1040
    scanning mode and, 1035
    system setup and, 1035–1036, 1035*f*–1037*f*
    thermal, 1036–1038
  cell aggregation in, 1038
  cell membrane alteration from, 1038
  contrast agent avoidance in, 1038
  default output power for, 1035
  Doppler mode, sample volume and velocity range in, 1036
  duration of, as function of TI in, 1035–1036, 1036*f*, 1042*t*
  equipment for, 1015–1016
  field of view in, 1036, 1036*f*
  focal depth in, 1036, 1036*f*
  frame rate in, 1036
  guidelines for, 1016–1022
    in first trimester, 1016–1019, 1016*b*, 1017*f*–1020*f*
    level I examination in, 1019–1020, 1021*f*–1029*f*
    level II examination in, 1019–1022, 1023*b*
    in second and third trimesters, 1019–1022, 1020*b*
  hemolysis from, 1038
  in hydrops diagnosis, 1432–1433
  MI in, 1035
  personnel for, 1015–1016
  receiver gain in, 1036
  for routine screening, 1022–1031
    benefits of, 1030*b*
    for fetal malformations, diagnostic accuracy of, 1030
    in gestational age estimation, 1022–1029
    perinatal outcomes and, 1029–1030
    prudent use of, 1030–1031
    three- and four-dimensional ultrasound in, 1030, 1042, 1043*f*
    in twin/multiple pregnancy identification, 1029
  safety of, 1034–1035
    guidelines for, 1041–1042, 1042*t*, 1043*f*
  tactile sensation in, 1038
  training for, 1015–1016
  transducer heating in, 1038
  transducer selection for, 1035
  volume imaging in, 1030
Obstructed hernias, 496–497
Obstructive cystic renal dysplasia, 1347–1348, 1347*f*–1348*f*
Obstructive uropathy, CKD and, 1796–1798
Occipital fissure, neonatal/infant, development of, 1520–1521
Occipital horn(s)
  atrium of fetal, transverse measurement in, 1178
  neonatal/infant
    in coronal imaging, 1515
    in corpus callosum agenesis, 1528, 1530*f*–1531*f*
Occipital horn(s) *(Continued)*
    in posterior fontanelle imaging, 1517, 1518*f*
Occipital lobe cortex, neonatal/infant, in coronal imaging, 1514*f*, 1515
Occipitofrontal diameter, in gestational age determination, 1446, 1447*f*
Occlusion, 27
o/e LHR. *See* Observed-to-expected lung-to-head ratio
OEIS complex, 1328–1329, 1329*f*, 1365–1366, 1689
OHS. *See* Ovarian hyperstimulation syndrome
Oligodactyly
  definition of, 1399
  fetal, 1406*f*
Oligohydramnios
  definition of, 1340
  diagnostic significance of, 1340–1341
  early, 1066, 1067*f*
  fetal lung size and, 1244
  in sirenomelia, 1238
Oligospermia, prostate and, 393
Omental cakes, 266, 267*f*
Omentum
  cysts of, pediatric ovarian cysts differentiated from, 1875
  greater, 505, 505*f*
  herniated, 1902
  infarction of
    pediatric, appendicitis differentiated from, 1858–1860, 1858*f*
    right-sided segmental, 288, 289*f*, 521, 523*f*
  lesser, 505
Omohyoid muscle, 692*f*, 694
Omphalocele
  detection of, early, 1018–1019, 1020*f*
  fetal, 1325–1326, 1326*f*
    associated conditions with, 1325, 1327*f*
    cloacal exstrophy and, 1328
    epidemiology of, 1325
    management of, 1325–1326
    pentalogy of Cantrell and, 1329
    prenatal diagnosis of, 1325, 1327*f*
  liver herniation in, 80
  maternal serum alpha-fetoprotein elevation in, 1228
  in Miller-Dieker syndrome, 1195
  with spina bifida, 1233
  thickened NT and, 1096*f*
  in triploidy, 1105*f*
  in trisomy 18, 1103, 1103*f*
    fetal, 1325
Omphalomesenteric duct, 1059
Oncocytoma, renal, 348–351
Oncotype DX test, 396
One-Stop Clinic to Assess Risk (OSCAR), 1090
Oocyte, transport of, 1049
Ophthalmic artery
  cerebrovascular disease indicators with SCD and flow in, 1599*f*
  evaluation of, orbital approach to, 1592, 1596*f*
Opisthorchiasis, biliary tree and, 178–179
Opportunistic infection, *Pneumocystis carinii* and, 91, 91*f*
Optison, 56
  harmonic emission from, 58–59, 59*f*
Oral contraceptives, hepatic adenomas and, 1746
Oral-facial-digital syndrome 4, 1395
Orbital window, for TCD sonography, 1592, 1596*f*
Orbits, fetal
  abnormalities of, 1140–1143
    anophthalmia as, 1140, 1145*f*
    coloboma as, 1143, 1146*f*
    congenital cataracts as, 1143, 1147*b*
    dacryocystocele as, 1143, 1147*f*
    exorbitism as, 1140

Orbits, fetal *(Continued)*
hypertelorism as, 1140, 1141*b*, 1144*f*–1145*f*, 1149*f*
hypotelorism as, 1140, 1140*b*, 1142*f*–1144*f*
microphthalmia as, 1140, 1145*f*, 1147*b*
proptosis as, 1140
normal sonographic appearance of, 1135*f*
Orchitis, 845–846
isolated, 1896
pediatric, 1896
sonographic appearance of, 846, 847*f*–849*f*
Organ of Giraldés, 820–821
Organ transplantation, 623–624. *See also* Liver transplantation; Pancreas transplantation; Posttransplant lymphoproliferative disorder; Renal transplantation
Organogenesis
definition of, 1524
stages of, 1524, 1525*b*, 1525*f*
Oriental cholangiohepatitis, 179
Oropharynx, teratomas of, 1159
Ortolani test, for hip stability, 1923
OSCAR. *See* One-Stop Clinic to Assess Risk
Osler-Weber-Rendu disease, 104
Ossification centers
primary, 1091
secondary, 1091, 1378*f*
Osteitis pubis, sports hernia and, 486–487, 489*f*
Osteoarthritis, 869, 869*f*
acromioclavicular joint, 893, 894*f*
Osteogenesis, normal, 1091
Osteogenesis imperfecta, 1391–1392
anencephaly differentiated from, 1179
bowing of long bones in, 1381–1382
classification of, by type, 1394*t*
facial profile in, 1394*f*
fractures in, 1392, 1393*f*
sonographic appearance of, 1380*f*
3-D reconstruction of, 1385*f*
type I, 1391–1392, 1393*f*, 1394*t*, 1399
bowing of femur in, 1380*f*
type II, 1391–1392, 1392*f*–1394*f*, 1394*t*
calvarial compressibility in, 1382, 1392, 1393*f*
diagnosis of, 1376–1377
hypophosphatasia differentiated from, 1392–1395
type III, 1391–1392, 1393*f*, 1394*t*, 1399
type IV, 1391–1392, 1394*t*, 1399
type V, 1391–1392
wormian bones in, 1139
Osteomyelitis, pediatric, 1936–1938, 1938*f*
of costochondral junction, aspiration and drainage of, 1963*f*
Ostium primum, 1279
Ostium primum ASD, 1279–1280, 1283*f*
Ostium secundum, 1279
Ostium secundum ASD, 1279–1280, 1282*f*
Otocephaly, 1148
Outflow tracts, fetal, routine sonographic view of, 1025*f*
Ovarian artery(ies), 565–566, 565*f*
pediatric, 1875
Ovarian crescent sign, 581
Ovarian cycle, 1051, 1051*f*
Ovarian follicles, 1049
Ovarian hyperstimulation syndrome (OHS), 572, 572*f*
Ovarian remnant syndrome, 571
Ovarian vein(s)
thrombophlebitis, 589–590, 589*f*
thrombosis of, 369, 589–590, 589*f*
Ovary(ies)
anatomy of, 564–570, 565*f*
calcification in, 566–568
Ovary(ies) *(Continued)*
cystadenocarcinoma of
mucinous, 580*f*, 581
serous, 580–581, 580*f*
cystadenoma of
mucinous, 580*f*–581*f*, 581
serous, 580–581, 580*f*
cysts in
dermoid, 582–584, 583*f*
fetal, 1369, 1369*f*
functional, 570–571, 571*f*
hemorrhagic, 570–571, 571*f*, 575
menstrual cycle and follicular, 568
neonatal, 1876*f*
paratubal, 573
parovarian, 573
percutaneous management of, 618–619
peritoneal inclusion, 573, 573*f*
postmenopausal, 569–570, 571*f*
surface epithelial inclusion, 569, 573
in triploidy, 1105*f*
edema of, massive, 578
endometriosis in, 574–576, 575*f*–576*f*
fetal, cysts in, 1369, 1369*f*
hyperstimulation of, 572, 572*f*
lymphomas of, 585
in menstrual cycle, 1050*f*
menstrual cycle changes to, 568–569, 569*f*
neoplasms of, 578–585
borderline, 580*f*, 581
clear cell, 581, 582*f*
cystadenocarcinomas as, 580–581, 580*f*
cystadenomas as, 580–581, 580*f*–581*f*
cystic teratomas as, 582–584, 582*b*, 583*f*
dysgerminomas as, 584, 584*f*
endodermal sinus, 585
endometrioid, 581
fibromas as, 585, 586*f*
germ cell, 582–585
granulosa cell, 585
metastatic, 585, 586*f*
ovarian cancer as, 578–579
Sertoli-Leydig cell, 585
sex cord-stromal, 585
surface epithelial-stromal, 579–582, 580*f*–582*f*
thecomas as, 585
transitional cell, 581–582, 582*f*
types of, 579*t*
nonneoplastic lesions of, 570–578
cysts as, functional, 570–571, 571*f*
endometriosis as, 574–576, 575*f*–576*f*
ovarian remnant syndrome as, 571
polycystic ovarian syndrome as, 573–574, 574*f*
pregnancy-associated, 572, 572*f*
polycystic ovarian syndrome and, 573–574, 574*f*
postmenopausal, 569
cysts in, 569–570, 571*f*
pregnancy-associated lesions of, 572, 572*f*
punctate echogenic foci in, 566–568, 568*f*
shape of, 565–566
sonography for
normal appearance in, 566–568, 567*f*
technique in, 566
torsion of, 576–578, 577*f*
volume of, 566
Ovary(ies), pediatric, 1873
abnormalities of, 1875–1881
cysts of, 1873–1877
hemorrhagic, 1877, 1878*f*–1879*f*
in polycystic ovarian disease, 1877–1878, 1879*f*
torsion and, 1875–1876, 1876*b*, 1877*f*
ectopic, 1874*f*
edema of, massive, 1878–1879, 1879*f*
Ovary(ies), pediatric *(Continued)*
macrocysts of, 1873–1875
neoplasms of, 1879–1881, 1880*b*, 1880*f*
normal, 1874*f*
torsion of, 1875–1876, 1876*b*, 1877*f*
volume measurements for, 1873, 1875*t*
Ovotestis, pediatric, 1891, 1891*f*
Ovulation, 1049
Oxygenation, extracorporeal membrane. *See* Extracorporeal membrane oxygenation

P

Pacchionian, 1177
Pachygyria, in lissencephaly, 1195
PACs. *See* Premature atrial contractions
PACS. *See* Picture archiving and communications system
Paget-Schroetter syndrome, pediatric, 1721, 1723*f*
Painless (silent) thyroiditis, 725–727
Palate. *See also* Cleft lip/palate
cleft, 1151–1153
secondary
fetal, 1135, 1135*f*
isolated cleft of, 1153
Palmar arch, 977–978, 980*f*
PAM. *See* Papillary apocrine metaplasia
Pampiniform plexus, 565–566, 565*f*
"Pancake" kidneys, pediatric, 1785
Pancreas
abscesses of, 230
anatomy of, 210–219
surrounding structures and, 218–219, 220*f*
variants of, 218
annular, small bowel obstruction and, 1308
body of, 211, 211*f*–212*f*
carcinoma of, 236–238, 238*b*
color Doppler ultrasound for, 241, 241*b*, 241*f*–243*f*, 241*t*
detection of, 238–241
resectability imaging in, 241
ultrasound findings for, 238–241, 239*f*–240*f*
CEUS for, 251
cystic neoplasms of, 243–248, 243*t*
intraductal papillary mucinous, 245–247, 245*f*–246*f*
mucinous, 247–248, 247*f*
rare, 248, 248*b*
serous, 243, 244*f*–245*f*
solid-pseudopapillary tumor, 248, 248*f*
cysts of, 242–248, 243*f*
congenital, 1865
fetal, 1320
high-risk features of, 243*b*
simple, 243, 244*f*
VHL disease and, 243, 244*f*
embryology of, 215–218, 218*f*
endocrine tumors of, 248–249, 249*f*–250*f*, 249*t*
enlarged, in acute pancreatitis, 222, 223*f*
fatty, 215, 216*f*–217*f*
fetal, 1319–1320
annular, 1320, 1321*f*
cysts of, 1320
head of, 211–213, 213*f*–214*f*
lipoma of, 249–251, 250*f*
metastases of, 251, 251*f*
neoplasms of, 236–241
periampullary, 236
unusual and rare, 249–251
parenchyma of, 213–215, 215*f*–217*f*
pediatric, 1862–1865
neoplasms of, 1865, 1865*f*
normal anatomy of, 1862
pancreatitis and, 1862–1865, 1864*f*–1865*f*
sonographic technique for, 1862

Pancreas *(Continued)*
percutaneous needle biopsy of, 604–605, 605*f*
pseudoaneurysms of, 230, 230*f*
pseudocysts of
acute pancreatitis complications with, 228–229, 229*f*
chronic pancreatitis complications with, 232, 233*f*–234*f*
drainage of, 230, 615–617, 617*f*
pediatric pancreatitis and, 1864–1865, 1865*f*
pseudomass of, 214–215, 217*f*
shape of, 214–215, 217*f*
size of, 214, 216*f*
sonographic technique for, 210–219, 211*f*
tail of, 213, 214*f*
Pancreas divisum, 218, 220*f*
pediatric pancreatitis and, 1862–1864, 1864*f*
Pancreas transplantation, 666–682
abnormal, 676–682
AVF as, 678, 680*f*
fluid collections as, 682, 683*f*
pancreatitis as, 679–682, 681*f*
pseudoaneurysms as, 678, 680*f*
rejection as, 678–679, 681*f*
thrombosis as, 677–678, 678*f*–679*f*
alloimmune arteritis after, 677
bladder drainage in, 668–672, 675*f*
CEUS for, 676
duodenal leaks after, 682
endocrine drainage in, 672, 675*f*
enteric drainage in, 672
infection after, 682
normal appearance after, 676, 676*f*
surgical techniques for, 668–676, 673*t*, 675*f*
venous drainage in, 672–676
Pancreatic duct, 215–218, 219*f*–220*f*
Pancreaticoduodenectomy, 233
Pancreatitis
acute, 219–230
abscess complications of, 230
biliary sludge and, 221
causes of, 221, 221*t*
clinical spectrum of, 220–221
common bile duct stones and, 221
complications of, 225–230, 225*b*
enlarged pancreas from, 222, 223*f*
fluid collection complications in, 228, 228*f*
gallstones and, 221
imaging approach for, 221–222, 221*b*
necrosis complications of, 230
pseudocyst complications in, 228–230, 229*f*
treatment for complications of, 230
ultrasound findings in, 222–225, 222*t*, 223*f*–228*f*
vascular complications of, 230, 230*f*–231*f*
autoimmune, 236, 237*f*
chronic, 230–236
imaging approach for, 231
masses associated with, 233–236, 235*f*–237*f*
portal vein thrombosis in, 232–233, 235*f*
pseudocysts in, 232, 233*f*–234*f*
sclerosing, 236
splenic vein thrombosis in, 232–233, 234*f*–235*f*
tumefactive, 236
ultrasound findings on, 231–233, 231*f*–235*f*
lymphoplasmacytic sclerosing, 236
after pancreas transplantation, 679–682, 681*f*
pediatric, 1862–1865, 1864*f*–1865*f*
Pancreatoblastoma, pediatric, 1865
Pancytopenia, Fanconi, 1400, 1402*f*
Panovarian cysts, 573
Pantaloon hernias, 493–494, 495*f*
Papillary apocrine metaplasia (PAM), 778*f*, 779, 780*f*–781*f*
mural nodules caused by, 782, 783*f*–784*f*
Papillary carcinoma
ethanol ablation of cervical nodal metastasis from, 720, 721*f*
of thyroid gland, 698–701, 701*f*–705*f*
cystic, sonographic features of, 705*f*, 713
pediatric, 1648, 1649*f*
Papillary cystadenomas, of epididymis, 840–841
Papillary microcarcinoma, of thyroid, 701, 706*f*
Papillary necrosis, 328–329, 329*b*, 329*f*
Papillary process, 75–76
Papilloma(s)
breast, 769–771, 770*f*
intracystic, 782, 783*f*
intraductal, 799, 799*f*–800*f*
peripheral, 799, 800*f*
choroid plexus
Aicardi syndrome and giant pigmented nevi in, 1209
neonatal/infant, 1562, 1565*f*
in neonatal/infant brain, duplex Doppler sonography of, 1588*f*
VM with, 1177–1178
transitional cell, lower urinary tract, pediatric, 1910–1912
VM with, 1177–1178
PAPP-A. *See* Pregnancy-associated plasma protein A
Paracentesis, 610, 610*f*
Paracoccidiomycosis, 423
Paradidymis, 820–821
Paragangliomas, carotid body tumors and, 947–948, 949*f*
Paralabral cysts, injection for, 907–909, 910*f*–911*f*
Parallel orientation, in breast sonography
not (taller-than-wide), 789–790, 792*f*
wider-than-tall, 797, 797*f*
Paralytic ileus, 294*f*, 295
Parameniscal cysts, 907–909
Paramesonephric duct cysts, pediatric. *See* Müllerian ducts
Parapelvic cysts, 359, 360*f*
Paraplegia, traumatic, neurogenic bladder in, 1907
Parapneumonic collections, in pediatric chest, 1710–1711
Pararenal spaces, inflammation in, in acute pancreatitis, 224–225, 225*f*
Parasagittal infarction, from hypoxic-ischemic injury in full-term infant, 1541
Parasites, fetal brain and, 1203–1204
Parasitic diseases
of genitourinary tract, 331
of liver, 87–90, 89*f*–90*f*
Paratenon, 859
Parathyroid glands. *See also* Hyperparathyroidism
adenomas of
carcinomas differentiated from, 735–736, 738*f*
carotid sheath/undescended, 740, 742*f*
combined modalities for accuracy with, 748
compression for detection of, 739
CT accuracy for, 748, 748*f*
echogenicity of, 735, 736*f*
ectopic locations of, 739–741
false-negative examination for, 745*b*, 746
false-positive examination for, 745–746, 745*b*
fine-needle aspiration biopsy accuracy for, 746
hypoechoic, 735
imaging accuracy with, 746–749
inferior, 738–739, 739*f*
internal architecture of, 735, 736*f*
intrathyroid, 740, 742*f*
localization of, 736–741
mediastinal, 740, 741*f*, 748
MRI accuracy in, 748, 749*f*
multiple gland disease in, 735, 738*f*
percutaneous needle biopsy of, 750–751, 753*f*
pitfalls in examination of, 745–746, 745*b*
Parathyroid glands *(Continued)*
retrotracheal/retroesophageal, 739–740, 740*f*
scintigraphy accuracy for, 747, 747*f*
shape of, 735, 735*f*
size of, 735, 737*f*
sonographic appearance of, 735–736
sonographic examination and typical locations in, 736–739, 739*f*
superior, 738–739, 739*f*
surgical removal of, 749, 750*f*
ultrasound accuracy for, 746–747, 748*f*
vascularity of, 735, 737*f*
anatomy of, 732–733, 733*f*
autotransplantation of tissue of, recurrent hyperparathyroidism from, 742–744, 743*f*
carcinoma of
adenomas differentiated from, 735–736, 738*f*
primary hyperparathyroidism from, 734
ectopic, 733, 739–741
embryology of, 732–733
enlarged, in secondary hyperparathyroidism, 745
eutopic, 733
inferior, 733
pediatric, 1650, 1650*f*
supernumerary, 733
Parathyroid hormone, chief cells in production of, 733
Parathyroidectomy, minimal-access, for primary hyperparathyroidism, 749, 750*f*
Parathyromatosis, in persistent hyperparathyroidism, 744, 744*f*
Paratubal cysts, 573
Paraumbilical hernias, 492
Paraumbilical veins, pediatric
flow direction in, in portal hypertension, 1752, 1757, 1758*f*
in intrahepatic portal hypertension, 1761
Paraurethral cysts, pediatric, 1883–1884
Parenchymal abscess, pediatric renal transplantation and, 1812
Parenchymal calcification, renal, 339–340, 340*f*
Parenchymal junctional defects, 313, 314*f*
Parietal peritoneal line, 510–511
Parinaud oculoglandular syndrome, 1633–1634
Parotid glands, pediatric
accessory, 1630
acinic cell carcinoma of, 1638, 1639*f*
anatomy of, 1630, 1630*f*
bacterial infections in, 1632–1633, 1632*f*
deep lobe of, 1630
hemangiomas of, 1636, 1637*f*
lipomas of, 1639
lymphatic malformation of, 1636, 1637*f*
nodal enlargement in, 1633–1634
peripheral nerve sheath tumors of, 1639
Parotid space, pediatric, 1629, 1630*f*
cystic lesions of, 1639, 1640*b*
Parotitis
HIV and, 1635, 1636*f*
juvenile, recurrent, 1634, 1634*f*
from mumps, 1632
Parovarian cysts, pediatric, 1875, 1876*f*
Paroxysmal supraventricular tachycardia, fetal, 1296, 1296*f*
Partial molar pregnancy, 1078, 1080*f*
Partial subclavian steal, 952–953, 953*b*, 953*f*
Partial-thickness rotator cuff tears, 887–888, 889*f*–890*f*
Particulate ascites, 507
Parvovirus infection, fetal
hydrops from, 1431–1432, 1431*f*
massive ascites in, 1418–1419
Pascals, 16

Patau syndrome. *See* Trisomy 13
Patellar dislocation, congenital, pediatric, 1934, 1935*f*
Patent ductus arteriosus, intracranial RI and, 1576
Patent urachus, 322
  pediatric, 1791
PCA. *See* Posterior cerebral artery
PCA3 score, 396
PCOS. *See* Polycystic ovarian syndrome
Peak end diastolic ICA/CCA ratio, in assessing degree of carotid stenosis, 930
Peak systolic ICA/CCA ratio
  in assessing degree of carotid stenosis, 930
  in internal carotid artery stenosis evaluation, 937
Peak systolic velocity (PSV), 450
  arterial stenosis and, 969, 971*f*
  bypass graft dysfunction and, 974–975
  in determining carotid stenosis, 929–930
  of MCA blood flow, 1421–1423, 1421*b*, 1422*t*
Pectoralis minor muscle, 878–879
Pediatric patients. *See also* Adrenal gland(s), pediatric; Bladder, pediatric; Hip(s), pediatric; Liver, pediatric; Neck, pediatric; Spinal canal, pediatric; Transcranial Doppler sonography, pediatric; Urinary tract, pediatric
  adrenal sonography for, 1820–1827
  female anatomy in, normal, 1872–1875
  pelvic sonographic technique for, 1870–1872
  renal artery stenosis and, 447
  spleen of, 1769–1772
Pedicles
  in lateral longitudinal scan plane, 1223*f*
  in lateral transaxial scan plane, 1222*f*
  in posterior angled transaxial scan plane, 1224*f*
  spina bifida in, 1228, 1229*f*–1230*f*
Peliosis, splenic, 147
Peliosis hepatis, 104, 104*f*
Pelvic abscesses, 283
  drainage of, 612, 613*f*
Pelvic adnexa. *See* Adnexa
Pelvic congestion syndrome, 461–463, 463*f*
  as adnexal vascular abnormality, 590, 590*f*
Pelvic inflammatory disease (PID), 566
  fallopian tubes and, 587–589, 588*f*
  IUDs and, 587
  pediatric, 1885–1887, 1886*b*, 1886*f*
  sonographic findings of, 587*t*
  tubo-ovarian complex and abscess in, 588–589, 588*f*, 1886–1887, 1886*f*
Pelvic kidney, 318, 318*f*
  fetal, 1344–1345, 1344*f*
  pediatric, 1908
Pelvic masses
  in adult women, sonographic evaluation of, 590–591, 591*t*
  gastrointestinal tract, 592
  nongynecologic, 591–592
  postoperative, 591
  urinary tract, 592
Pelvic sonographic technique, pediatric, 1870–1872. *See also specific organs*
Pelvic varices, pediatric
  hemorrhagic ovarian cyst differentiated from, 1877, 1879*f*
  in portal hypertension, 1760*f*
Pelvis
  fetal, routine sonographic views of, 1021, 1026*f*
  free fluid of, ectopic pregnancy and, 1072, 1073*f*
  pediatric, sonographic technique for, 1870–1872
  TAS for, 564
Pelvoinfundibular atresia, with MCDK, 1346
Penile chordee, fetal, 1367
Pentalogy of Cantrell, 1295
  fetal abdominal wall and, 1329
  OEIS differentiated from, 1328–1329
Peptic ulcer, 299, 300*f*
Percent free PSA (%fPSA), 395
Percutaneous cholangiography and drainage, pediatric, 1956, 1959*f*
Percutaneous needle biopsy. *See* Biopsy(ies), percutaneous needle
Percutaneous umbilical cord blood sampling (PUBS), 1434–1435, 1434*f*–1435*f*
Perfluorocarbons, in contrast agents, 56, 107, 111*f*
Perforation, of bowel, in Crohn disease, 274–275, 277*f*
Perfusion
  disruption-replenishment imaging measuring, 66–67, 67*f*
  luxury, cerebral infarction with, 1580–1581, 1584*f*
Perianal inflammation, in Crohn disease, 276, 281*f*, 305–306
Perianal inflammatory disease, transanal sonography in, 305–307, 306*b*, 307*f*
Periaortitis, chronic, 439–440, 464, 465*f*
Peribiliary cysts, liver and, 82–83
Pericardial effusion, fetal, 1258, 1258*f*
  in hydrops, 1416, 1418*f*
Pericardial hernias, 1258, 1262
Pericholecystic fluid collection, in perforated gallbladder, 200
Pericholecystic hyperechogenicity, NEC and, 1854–1855
Periductal mastitis, of breast, 771, 771*f*
Perienteric soft tissues, in acute abdomen, 281–282
Perihepatitis, gonococcal or chlamydial, PID and, 1887
Perimembranous VSDs, 1281
Perinephric abscesses
  acute pyelonephritis and, 325
  pediatric renal transplantation and, 1812
  after renal transplantation, 664–665
Perinephric fluid collections, pediatric renal transplantation and, 1809, 1811*f*
Perineum, necrotizing fasciitis of, 846–847
Period, of sound wave, 2, 2*f*
Peripheral arteries, 965–978
  aneurysms of, lower extremity, 971–972, 972*f*
  AVF of, 973–974, 974*f*
  lower extremity, 966–975
    aneurysm of, 971–972, 972*f*
    AVF of, 973–974, 974*f*
    AVMs of, 973
    bypass grafts of, 974–975, 975*f*
    normal anatomy of, 966
    occlusion of, 967–968, 967*f*–969*f*
    pseudoaneurysm of, 972–973, 973*f*
    stenosis of, 968–971, 969*f*–971*f*
    ultrasound examination and protocol for, 966–967, 967*f*
  occlusion of, lower extremity, 967–968, 967*f*–969*f*
  pseudoaneurysms of, lower extremity, 972–973, 973*f*
  sonographic examination technique for, 965
  stenosis of
    evaluation of, 965–966, 966*f*
    lower extremity, 968–971, 969*f*–971*f*
    tardus-parvus waveforms in, 965–966
  upper extremity, 975–978
    aneurysm of, 976
    normal anatomy of, 975–976, 976*f*
    occlusion of, 976
    radial artery evaluation for coronary bypass graft and, 977–978, 980*f*
Peripheral arteries *(Continued)*
    stenosis of, 976, 978*f*–979*f*
    thoracic outlet syndrome in, 976–977, 980*f*
    ultrasound examination and protocol for, 976
Peripheral cholangiocarcinoma. *See* Intrahepatic cholangiocarcinoma
Peripheral nerves
  normal anatomy of, 864–865, 865*f*
  sheath tumors, parotid gland, pediatric, 1639
Peripheral sexual precocity, pediatric ovarian cysts and, 1875
Peripheral veins, 978–996. *See also* Deep venous thrombosis
  lower extremity, 980–990
    acute DVT of, 983–984, 983*f*–985*f*
    chronic DVT of, 984, 986*f*–987*f*
    complete venous Doppler for, 989
    deep venous system of, 980–981, 981*f*
    DVT follow-up recommendations for, 989
    normal anatomy of, 980–982
    potential pitfalls with, 984–989, 988*f*
    superficial venous system of, 981–982, 981*f*
    ultrasound examination and protocol for, 982–983, 982*f*
    vein mapping of, 989–990
    venous insufficiency in, deep, 989, 990*f*
  sonographic examination technique for, 979–980
  upper extremity, 990–996
    acute DVT of, 992–994, 994*f*–995*f*
    chronic DVT of, 994–995, 995*f*–996*f*
    hemodialysis and ultrasound examination of, 1000
    normal anatomy of, 990–991, 990*f*
    potential pitfalls with, 995–996
    ultrasound examination and protocol for, 991–992, 991*f*–993*f*
    vein mapping of, before hemodialysis, 996–998, 998*f*–1000*f*
Peripherally inserted central catheter (PICC), 993*f*
  interventional sonography for, pediatric, 1954, 1955*f*–1957*f*
Periportal cuffing, in acute hepatitis, 85, 85*f*–86*f*
Periportal hepatic fibrosis, Caroli disease with, 171
Periprocedural antithrombotics, percutaneous needle biopsy and, 598–599
Perirenal space, inflammation in, in acute pancreatitis, 224–225, 225*f*
Perirenal urinoma, from UPJ obstruction, 1358, 1358*f*
Peristalsis, 257
Peritoneal bands, obstruction from, 1841–1842
Peritoneal cavity, 504
  fluid in, free compared to loculated, 508, 509*f*
  localized inflammatory process of, 521, 523*f*
Peritoneum
  anatomy of, 504
  ascites and, 506–508, 507*f*–509*f*
  carcinomatosis of, 510–511, 510*f*–515*f*
  cysts in
    inclusion, 508–509, 509*f*, 573, 573*f*
    mesenteric, 509–510, 510*f*
  endometriosis and, 521–523, 524*f*
  inflammatory disease of, 514–521
  leiomyomatosis peritonealis disseminata and, 523–524, 525*f*
  metastases of, 510
  Non-Hodgkin lymphoma of, 513, 517*f*
  parietal, 504
  pneumoperitoneum and, 524–526, 525*f*
  pseudomyxoma peritonei and, 513–514, 518*f*
  sonographic technique for, 505–506, 506*f*–507*f*

Peritoneum *(Continued)*
tumors of, 510–514
carcinomatosis as, 510–511, 510*f*–515*f*
primary, 511–513, 515*f*–517*f*
pseudomyxoma peritonei as, 513–514, 518*f*
visceral, 504
Peritonitis
abscesses and, 517, 520*f*
chemical, 514
definition of, 514
fibrinous, 509*f*
granulomatous, 514
Histoplasma, 520*f*
infective, 517, 519*f*
meconium
CF and, 1316
cystic, pediatric, 1842–1843, 1846*f*
hydrops from, 1428, 1428*f*
liver calcifications and, 1316–1318
massive ascites in, 1418–1419, 1421*f*
small bowel and, 1313, 1313*t*, 1314*f*
primary, 517
sclerosing, 514, 521, 523*f*
tuberculous, 517–521, 522*f*
Peritrigonal blush, in sagittal imaging of neonatal/infant brain, 1517
Periumbilical hernias, 492, 494*f*, 500*f*
Perivascular inflammation, in acute pancreatitis, 224–225, 226*f*–227*f*
Periventricular cysts, of neonatal/infant brain, 1566, 1566*f*
Periventricular hemorrhagic infarction, in infants, 1547
Periventricular leukomalacia (PVL)
cystic, 1551–1552, 1552*f*
from hypoxic-ischemic injury in premature infant, 1541, 1550–1553, 1551*f*–1553*f*
IUFD and, 1124*f*
in neonatal/infant brain, 1541, 1550–1553, 1551*f*–1553*f*, 1566
Periventricular leukomalacia, IUFD and, 1124*f*
Periventricular nodular heterotopia, 1196, 1199*f*
Perlman syndrome
CDH and, 1263
hyperechogenic kidneys and, 1351
Peroneal arteries, 966
Peroneal tendons, posterior, injection of, 902, 903*f*
Peroneal veins, 981
Persistent terminal ventricle, pediatric, 1685
Persistent trophoblastic neoplasia (PTN), 1078, 1080–1084, 1082*f*
choriocarcinoma and, 1080–1082, 1083*f*
diagnosis and treatment of, 1083–1084
Doppler ultrasound for, 1083
after hydatidiform molar pregnancy, 1080, 1081*f*
invasive mole, 1080, 1081*f*
PSTT and, 1082
sonographic features of, 1082–1083
Perthes disease, 1930
Peutz-Jeghers syndrome, 544, 826
Pfeiffer syndrome
bilateral complete cleft lip/palate in, 1156*f*
craniosynostosis in, 1136–1138
hypertelorism with exorbitism in, 1145*f*
midface hypoplasia in, 1148
PFFD. *See* Proximal focal femoral deficiency
PHACES syndrome, pediatric, 1655
Phalanx, middle, hypoplasia of, in trisomy 21, 1101
Pharyngeal pouches, 1651
Phase aberration, 13
Phase inversion, 62–63
Phase modulation imaging, 64, 65*f*
Phased array transducers
beam steering in, 10–11, 11*f*
use and operation of, 12
Phenylketonuria, microcephaly from, 1194
Pheochromocytomas
adrenal, 421, 422*f*
pediatric, 1826–1827, 1827*f*
percutaneous needle biopsy of, 607
bladder, 356
definition of, 1826
lower urinary tract, pediatric, 1910–1912
PHI. *See* Prostate Health Index
Phlebectasia, IJV, 1658, 1660*f*
Phleboliths, in venous malformations of neck, 1657
Phlegmonous change, in Crohn's disease, 274–275, 277*f*
Phocomelia, definition of, 1399
Phrygian cap, 194
Physics of ultrasound, 1. *See also* Acoustics; Doppler ultrasound; Instrumentation
acoustics in, 2–7
Doppler ultrasound in, 21–30
HIFU in, 31–33, 33*f*
image display and storage in, 12–13
image quality in, 16–19
imaging pitfalls in, 19–21
instrumentation in, 7–12, 24–25, 25*b*, 25*f*–26*f*
operating modes and clinical implications in, 30–31
special imaging modes in, 13–16
Phytobezoars, 300
PI. *See* Pulsatility index
PICC. *See* Peripherally inserted central catheter
Picture archiving and communications system (PACS), 12–13
PID. *See* Pelvic inflammatory disease
Pierre-Robin sequence
campomelic dysplasia and, 1395
clefts of secondary palate in, 1153
micrognathia with, 1153, 1158*f*
Piezoelectricity, 7
Pilomatricoma, pediatric, neck and, 1664, 1664*f*
Pineal cyst, cavum veli interpositi cysts differentiated from, 1170
Pinworms, 1853
Pituitary gland, in menstrual cycle, 1050*f*
PKD1 gene, mutation in, in ADPKD, 1350
PKD2 gene, mutation in, in ADPKD, 1350
PKHD1 gene, mutation in, in ARPKD, 1348–1350
Placenta
abruption of, 1471–1473, 1474*f*–1475*f*
fetal hydrops and, 1436
pediatric pregnancy and, 1884
accessory lobes of, 1480–1481, 1481*f*
battledore, 1484
bilobed, 1481, 1482*f*
circumvallate, 1479–1480, 1480*f*–1481*f*
cysts of, subchorionic, 1474, 1477*f*
development of, 1465–1469, 1466*f*
hydropic degeneration of, 1078
infarctions of, 1466, 1473–1474, 1476*f*–1477*f*
insertion of umbilical cord into, 1484, 1485*f*
low, 1469, 1470*f*
marginal sinus of, 1466, 1467*f*
masses of, 1474–1476
chorioangioma as, 1476, 1478*f*–1479*f*
malignant, 1476
mesenchymal dysplasia of, 1479, 1479*f*
in molar gestations, 1479, 1480*f*
morphologic abnormalities of, 1479–1481
in multifetal pregnancy, chorionicity and, 1119, 1120*f*
position of, sonographic determination of, 1469, 1470*f*
postpartum, 1487–1489, 1490*f*
RPOC and, 1487–1489, 1490*f*
size of, 1466–1467, 1467*f*–1468*f*
sonographic appearance of, 1466, 1467*f*
subamniotic hematomas of, 1474
subchorionic hematomas of, 1474
Placenta *(Continued)*
succenturiate lobes of, 1480–1481, 1481*f*
thickness of, 1466, 1467*f*
in third stage of labor, 1487
vascularity of, 1468*f*
Doppler ultrasound and, 1467–1469
vascularization of, 1052–1053
volume of
in first trimester, in early pregnancy evaluation, 1466–1467
second trimester, assessment of, 1466, 1468*f*
Placenta accreta, 1470–1471, 1472*f*–1473*f*
Placenta increta, 1470–1471
Placenta percreta, 1470–1471, 1473*f*
Placenta previa, 1469–1470
complete, 1469, 1470*f*
marginal, 1469, 1470*f*
placenta accreta with, 1471
Placental bed, subinvolution of, 556
Placental cord insertion, multifetal pregnancy and, 1119, 1122*f*
Placental lakes, 1466, 1467*f*
Placental shelf, 1479–1480
Placental villi, hydropic degeneration of, 1078, 1080*f*
Placental volume quotient, 1466–1467
Placental-site trophoblastic tumor (PSTT), 530–531, 1082
Placentation, multifetal pregnancy and, 1115–1116, 1116*f*
Placentomegaly, fetal, hydrops and, 1418, 1420*f*
Placodes
nasal, 1134
spinal dysraphism and, pediatric, 1680
Plagiocephalic heads, 1136–1138
Plane-wave contrast imaging, 64
Plantar fasciitis, injection for, 902, 904*f*
Plaque(s)
in atherosclerosis, 433
carotid
atheromatous, 919
atherosclerotic rupture of, 919–920
calcified, 920–921, 921*f*
carotid artery dissection and, 946
characterization of, 919–922, 920*f*–922*f*, 922*b*
heterogenous, 920–921, 922*f*
homogenous, 920–921, 920*f*–921*f*, 936–937, 938*f*
intraplaque hemorrhage and, 920–921
morphology of, ultrasound types of, 921, 922*b*
nonstenotic, 936–937, 938*f*
qualitative assessment of, in carotid stenosis, 924
tandem, in carotid stenosis, 923–924
types 1-4, 921, 922*b*
ulceration of, 923, 923*b*, 923*f*–924*f*
vulnerable, identification of, treatment decisions and, 943
Plasma protein A, pregnancy-associated, 1089–1090
Plasmacytoma, 827–829
Platelet-rich plasma, intratendinous injection of, 909–910
Platyspondyly
in skeletal dysplasias, 1382
in thanatophoric dysplasia, 1388–1389, 1390*f*
Plavix (clopidogrel), 598
PLCO (Prostate, Lung, Colorectal and Ovarian Cancer Screening Trial), 397
Pleomorphic adenomas, salivary gland, pediatric, 1636–1638, 1638*f*
Pleural disease, pediatric, pulmonary disease differentiated from, sonography in, 1709, 1710*f*
Pleural drainage, fetal, hydrops from, 1426–1427

Pleural effusions
fetal, 1256–1258, 1257*f*
hydrops and, 1413–1416, 1417*f*, 1425
lung size and, 1244
primary, 1256
secondary, 1256
pediatric
drainage of, ultrasound-guided, 1724–1725
sonographic signs of, 1702–1711, 1704*f*–1708*f*
Pleural fluid, pediatric
aspiration of, ultrasound-guided, 1724–1725, 1726*f*
through hepatic window, 1707*f*
pneumonia with small amount of, 1706*f*
septated, 1702, 1708*f*
sonogram compared to CT scan for, 1709, 1711*f*
sonographic signs of
bare area sign in, 1709, 1709*f*
color Doppler ultrasound signal in, 1709, 1710*f*
diaphragm sign in, 1709
displaced-crus sign in, 1709
free movement in, with respiration, 1709, 1709*f*
septations in, 1709
sonographic signs of, 1709, 1709*b*
through splenic window, 1707*f*
Pleuropulmonary blastoma, 1252–1253
Plexiform neurofibroma, in intraoperative procedures, 1621*f*
Plicae palmatae, 533, 535*f*
PMPI. *See* Power modulation pulse inversion
Pneumatosis intestinalis
in acute abdomen, 277–281
in gastrointestinal tract, 297–299, 299*f*
pediatric, sonography for, 1854–1855
Pneumobilia
biliary tree and, 175–176, 176*f*
after liver transplantation, 625, 1767–1768, 1769*f*–1770*f*
Pneumocystis carinii, hepatic opportunistic infection by, 91, 91*f*
Pneumonia, pediatric, 1711–1714
air bronchograms from, 1702, 1703*f*, 1708*f*
chest radiograph compared to ultrasound for, 1712–1714, 1715*f*
on chest ultrasound, 1703*f*
empyema from, 1707*f*
round, 1711–1712, 1715*f*
with small amount of pleural fluid, 1706*f*
Pneumoperitoneum, 524–526, 525*f*
Pneumothoraces, sonographic detection of, 1725–1726
Poland syndrome, ribs in, 1382–1384
Polar arteries, 445–446
Polycystic kidney disease, 359–361
autosomal dominant, 83, 243, 361, 362*f*
pediatric, 1814–1815, 1815*f*
autosomal recessive, 359, 361*f*, 1799
pediatric, 1812–1813, 1814*f*
congenital hepatic fibrosis and, 1757–1759, 1762*f*
fetal pancreatic cysts and, 1320
Polycystic ovarian disease, pediatric, 1877–1878, 1879*f*
Polycystic ovarian syndrome (PCOS), 573–574, 574*f*
Polycythemia, dural sinus thrombosis from, 1205–1206
Polydactyly
definition of, 1399
fetal, 1405–1406
postaxial, in trisomy 13, 1104, 1105*f*
Polydactyly *(Continued)*
short-rib, syndromes associated with, 1382, 1383*f*, 1395–1396, 1397*f*
toe, fetal, 1406*f*
Polyhydramnios
anorectal malformations and, 1311–1312
cervical assessment in, 1505
diagnostic significance of, 1340–1341
esophageal atresia and, 1305–1306
fetal hydrops and, 1418, 1420*f*, 1432–1433
jejunoileal atresia and, 1310
in lethal skeletal dysplasias, 1386
meconium peritonitis and, 1313
with mesoblastic nephroma, 1352–1353
in trisomy 18, 1104
Polymicrogyria, 1196, 1198*f*
Polyorchidism, 838–839, 841*f*
pediatric, 1891
Polypoid intraluminal tumors, 261–264, 263*f*
Polyps
endometrial, 544, 548, 549*f*
tamoxifen and, 544–545
intussusception and, 1844–1845
urethral, posterior, pediatric, bladder outlet obstruction from, 1906, 1906*f*
Polysplenia, 159–161
in cardiosplenic syndrome, 1292, 1293*b*
fetal, 1320
univentricular heart with, 1287–1288
Polysplenia syndrome
biliary atresia in, 1737, 1738*f*
Doppler evaluation of liver transplant recipient with, 1764–1766
Polyvinyl chloride, 123
Pontocerebellar hypoplasia, 1190
Pontocerebellar syndrome, vermian dysplasia with, 1191
Popliteal artery, 966
aneurysms of, 972*f*
normal appearance of, 966–967
occlusion of, 968*f*
Popliteal cysts, pediatric, 1939
Popliteal vein
normal anatomy of, 980–981, 981*f*
ultrasound examination of, 982–983
Porcelain gallbladder, 202, 202*f*
Porencephalic cysts, neonatal/infant brain and, 1537, 1565
Porencephaly
from germinal matrix hemorrhage, 1541
HPE differentiated from, 1189
from intraparenchymal hemorrhage, 1547, 1548*f*
Porta hepatis, 77, 79*f*
Portal hypertension
duplex Doppler sonography in, 98
intrahepatic, from cirrhosis, 96
left sided, splenic vein thrombosis from, in chronic pancreatitis, 232–233, 234*f*–235*f*
liver vascular abnormalities and, 96–98, 96*f*–97*f*
portosystemic venous collaterals in, 96–98, 96*f*
presinusoidal, 96
splenomegaly and, 145, 147*f*
Portal hypertension, pediatric, 1756–1757
backward-flow theory of, 1760–1761
Doppler assessment of
abnormal flow patterns in, 1754–1756
abnormal hepatic arterial Doppler patterns in, 1755–1756
absent Doppler signal in, 1754, 1754*b*
arterialized flow patterns in, 1754
hepatofugal flow in, 1757
intrahepatic portal hypertension and, 1759–1762
in liver disease, 1752–1754, 1754*f*–1755*f*
Portal hypertension, pediatric *(Continued)*
of normal flow patterns in splanchnic vessels, 1750
paraumbilical veins flow direction in, 1757, 1758*f*
pelvic varices in, 1760*f*
possibilities and pitfalls of, 1750
in prehepatic portal hypertension, 1757–1759
reversed flow in, 1754–1755
sonographic technique for, 1750–1752
splenorenal shunts in, 1757, 1759*f*
in suprahepatic (posthepatic) portal hypertension, 1762–1764, 1763*f*
surgical portosystemic shunts and, 1764
to-and-fro flow in, 1754–1755, 1755*f*
Doppler ultrasound assessment of, 1748–1764
basic principles of, 1748–1750
forward-flow theory of, 1760–1761
thickened lesser omentum and, 1756, 1756*f*
Portal triad, 78
Portal vein(s)
anastomosis of, for liver transplantation, 624
aneurysms of, 103–104
after liver transplantation, 1768, 1769*f*–1770*f*
anomalies of, 81
cavernous transformation of, 98, 99*f*
clots in, in acute pancreatitis, 224–225, 228*f*
fetal liver calcifications and, 1316–1318
left, Doppler studies of, best approach for, 1752
liver circulation and, 78
main, Doppler studies of, best approach for, 1752
normal, 76, 77*t*, 78*f*
pediatric
anatomy of, 1731–1734, 1732*f*
cavernous transformation of, in prehepatic portal hypertension, 1757, 1761*f*
flow direction through, meals and, 1750
left, branches of, 1734
left, Doppler studies of, 1750
right, branches of, 1733*f*, 1734
thrombosis of, 1757, 1757*b*
pseudostenosis of, 636
stenosis of, after liver transplantation, 635–636, 638*f*, 1766, 1768*f*
thrombosis of, 98, 99*f*–100*f*
chronic pancreatitis and, 232–233, 235*f*
from HCC, 120, 121*f*
after liver transplantation, 635–636, 639*f*–640*f*, 1766
malignant, 98, 99*f*
pediatric, 1757, 1757*b*
Portosystemic shunts
intrahepatic, 104, 1761–1762
liver and, 130–132
in portal hypertension, 1757
portocaval, patency of, Doppler assessment of, 1764
surgical, 1764
total or partial, 1764
transjugular intrahepatic, 131–132, 132*b*, 132*f*–133*f*, 1764
Portosystemic venous collaterals, in portal hypertension, 96–98, 96*f*
spontaneous routes of, 1752, 1754*f*
Port-wine stains, 1679
Postablation tubal sterilization syndrome, 551–552
Postaxial polydactyly, fetal, 1405–1406
Posterior cerebral artery (PCA), as transtemporal approach landmark, 1592, 1593*f*–1594*f*
Posterior fossa. *See also* Cerebellum
abnormalities of, 1192
hemorrhage of, 1548–1550

Posterior fossa *(Continued)*
subarachnoid cysts of, Dandy-Walker malformation differentiated from, 1190, 1531, 1531*b*
ventral induction errors in, 1189–1192
Posterior inguinal wall insufficiency, sports hernia and, 486, 488*f*
Postmeningitis hydrocephalus, 1887
Posttransplant lymphoproliferative disorder (PTLD), 682–688
Epstein-Barr virus and, 682
after liver transplantation, 683–688, 687*f*
patterns of, 688
pediatric, 1812, 1813*f*
after renal transplantation, 683–688, 684*f*–686*f*
treatment options for, 688
Posttraumatic aortic stenosis, 444
Posttraumatic pseudoaneurysms, of common carotid artery, 948, 950*f*
Pouch of Douglas, 566
endometrioma in, 524*f*
Power Doppler ultrasound, 25, 25*b*, 26*f*
amplitude evaluation in, 935
for carotid stenosis evaluation, 935–939, 935*b*
pitfalls and adjustments in, 935*f*–939*f*, 936–939, 937*b*
color streaking in, breast cysts with, 775, 776*f*
harmonic imaging and, 60–61, 60*f*–62*f*
intermittent harmonic, 66, 66*f*
for neonatal/infant brain, 1573–1574
for prostate cancer, 404*f*–405*f*, 406
for prostate examination, 387
Power modulation pulse inversion (PMPI), 64
Power settings, 505–506
Preaxial polydactyly, fetal, 1405–1406
Precocious pseudopuberty, pediatric ovarian cysts and, 1875
Precocious puberty, 1746, 1887–1888
Predelivery aspiration procedure, in fetal hydrops, 1437
Preeclampsia
fetal hydrops prognosis and, 1436
pediatric pregnancy and, 1884
placental infarction in, 1477*f*
Preexisting cavitation nuclei, 41
Pregnancy. *See also* Ectopic pregnancy; Hydatidiform molar pregnancy; Multifetal pregnancy
adnexal cysts in, 1020
"cornual", 1073
early failure of, 1062–1069
hydronephrosis in, 316
iliac vein compression in, 459, 460*f*
keepsake imaging in, 49*b*, 50
luteoma of, 572
MRI in, 1031–1032, 1031*f*
ovarian lesions associated with, 572, 572*f*
pediatric, 1884–1885
second trimester of
indications for ultrasound in, 1015, 1016*b*
ultrasound guidelines for, 1019–1022, 1020*b*
teen, fetal gastroschisis and, 1322–1323
thermal index for bone in late, 1039
thermal index for soft tissue in early, 1039
third trimester of
indications for ultrasound in, 1015, 1016*b*
ultrasound guidelines for, 1019–1022, 1020*b*
of unknown location, 1075
uterus size in, 531
Pregnancy, first trimester of. *See also* Aneuploidy, screening for, first-trimester; Ectopic pregnancy; Gestational trophoblastic disease
aneuploidy screening for, 1089–1097
change during, 1048
early failure of, 1062–1069
Pregnancy, first trimester of *(Continued)*
amnion size in, 1066, 1067*f*–1068*f*
arrhythmia and, 1069
chromosomal anomaly causing, 1062
CRL and no heartbeat in, 1063, 1064*f*
diagnostic findings of, 1063–1064, 1063*b*
embryonic bradycardia and, 1068–1069, 1068*f*
embryos with CRL less than 7mm and no heartbeat in, 1064
gestational sac appearance concerns in, 1065, 1066*f*
gestational sac with no embryo in, 1063–1065, 1065*f*
gestational sac with small MSD in relationship to CRL, 1066, 1067*f*
luteal phase defect causing, 1062–1063
spontaneous abortion rate and, 1062, 1062*t*
subchorionic hemorrhage and, 1069, 1069*f*
worrisome findings of, 1064–1069, 1065*t*
yolk sac size and shape in, 1067–1068, 1068*f*
ectopic, 1069–1076
embryo evaluation during, 1076–1077
embryology in, 1049–1054
gestational age estimation in, 1061–1062
gestational trophoblastic disease and, 1077–1084
indications for ultrasound in, 1015, 1016*b*
maternal physiology in, 1049–1054
normal anatomy in, 1077, 1077*f*
normal sonographic appearance of, 1054–1061
amnion in, 1057, 1059*f*–1060*f*
β-hCG levels and, 1055–1057, 1057*b*
embryo in, 1057, 1059*f*–1060*f*
embryonic cardiac activity in, 1058–1059, 1060*f*
gestational sac in, 1054–1055, 1055*f*–1056*f*
umbilical cord cysts in, 1061, 1061*f*
umbilical cord in, 1059–1061
yolk sac in, 1057, 1058*f*
sonography in
current trends in, 1049
goals of, 1049
transvaginal ultrasound safety in, 1049
ultrasound guidelines for, 1016–1019, 1016*b*, 1017*f*–1020*f*
Pregnancy dating, 1022
Pregnancy of unknown location (PUL), 1075
Pregnancy-associated plasma protein A (PAPP-A), 1089–1090
Premammary zone, of breast, 761, 761*f*
Premature atrial contractions (PACs), 1295–1296
Premature rupture of membranes, pulmonary hypoplasia and, 1246
Premature ventricular contractions (PVCs), 43
fetal arrhythmias and, 1295–1296
Premenarchal girls, ovarian volume in, 1873, 1875*t*
Preplacental hematoma, 1471, 1475*f*
Presacral mass(es)
fetal, 1239, 1239*b*
pediatric, 1913–1915, 1913*b*, 1914*f*–1915*f*
solid, 1914–1915
Presteal waveform, 953*b*, 954, 954*f*
Preterm birth (PTB)
cervical length and, 1499–1500, 1499*f*
short, 1500–1501, 1500*f*, 1501*t*
definition of, 1495
incidence of, 1495
multifetal pregnancy morbidity and mortality and, 1119–1123
prior, cervical assessment in, 1504
spontaneous, prediction of, 1495–1496, 1501–1503
cervical change rate in, 1501
cervical funneling in, 1501, 1502*f*
dynamic cervical change in, 1501–1503, 1503*f*
gestational age at cervical length measurement in, 1500–1501, 1501*t*
Preterm birth (PTB) *(Continued)*
obstetric factors in, 1501
sonographic features in, 1503, 1504*f*
PRF. *See* Pulse repetition frequency
Primary peritoneal mesothelioma, 513, 516*f*
Primary peritoneal serous papillary carcinoma, 511–513, 515*f*
Primary peritonitis, 517
Primary sclerosing cholangitis, biliary tree and, 182, 183*f*, 184
Primitive neuroectodermal tumors, neonatal/infant brain and, 1562
Proboscis
cyclopia with, 1140, 1144*f*
in trisomy 13, 1104, 1105*f*
Probst bundles, in corpus callosum agenesis, 1528
Process vaginalis, relationship of indirect inguinal hernia to, 476–477
Processus vaginalis, 819
pediatric, 1902
Profunda femoris artery, 966
nonocclusive thrombi in, missing, 988
Profunda femoris vein
chronic DVT in, 987*f*
normal anatomy of, 980–981, 981*f*
Prominence, forming fetal face, 1134, 1134*f*
Pronephros, 311, 312*f*, 1336–1338
Propagation speed, of transducer, 7
Propagation velocity
artifact, 3, 3*f*, 420–421
of sound, 2–3, 3*f*
in SWE, 16, 18*f*
Proptosis, 1140
Prosencephalon, formation of, 1077
Prostaglandin-induced antral foveolar hyperplasia, 1839–1840
Prostate
abscesses of, 389, 390*f*, 392
adenocarcinoma of, 395
anatomy of, 382–384
axial, 383*f*, 384
neural structures in, 384
sagittal, 383*f*, 384–386
vascular, 384, 386*f*
zonal, 382–384, 382*f*–383*f*, 385*f*–386*f*
azoospermia and, 393
benign conditions of, 387–392
benign ductal ectasia of, 387, 388*f*
benign hyperplasia of, 384, 385*f*–386*f*, 387–388
biopsy of
PSA-directed, 395
ultrasound-guided, 407–411, 408*f*
calcifications of, 387, 388*f*
cancer of, 394–407
active surveillance for, 401
alternate biomarkers of, 396
brachytherapy for, 401, 402*f*
CEUS for, 406
color Doppler ultrasound for, 404*f*, 406
elastography for, 407
epidemiology of, 395
external beam radiotherapy for, 400–401, 401*f*
focal therapy for, 400
high-intensity focused ultrasound for, 400
histologic grading of, 399–400
key facts of, 395*b*
mortality by age in, 397
mpMRI-TRUS fusion for, 406–407, 410–411
power mode Doppler ultrasound for, 404*f*–405*f*, 406
prostate-specific antigen in, 395–396, 396*b*
radical prostatectomy for, 400, 401*f*
screening for, 396–397
sonographic appearance of, 403–407, 403*f*–405*f*, 406*b*
staging, 397–400, 397*f*, 398*t*, 399*f*

Prostate *(Continued)*
therapy for, 400–402, 401*f*–402*f*
3-D ultrasound for, 406–407
transrectal sonography of, 302, 302*f*, 403–406, 403*f*–405*f*, 406*b*
watchful waiting for, 401
congenital abnormalities in, 392
corpora amylacea of, 387
cysts of, 388, 390–392, 391*f*
hematospermia and, 394, 394*b*
infertility and, 392–394, 393*f*
inflammation of, 389, 390*f*
normal variants of, 387, 388*f*
oligospermia and, 393
pediatric, anatomy of, 1888, 1888*f*
prostatitis and, 389–390, 390*f*
transurethral resection of, 385*f*–386*f*, 388
ultrasound of
appearance in, 383*f*, 384–386, 385*f*–386*f*
equipment and technique for, 386–387, 386*f*
history of, 381–382
power mode Doppler, 387
transrectal, 381–382
volume of, 387
weight of, 387
Prostate, Lung, Colorectal and Ovarian Cancer Screening Trial (PLCO), 397
Prostate Health Index (PHI), 396
Prostatectomy, TRUS-guided biopsy after radical, 411, 411*f*
Prostate-specific antigen (PSA), 381–382
density of, 395–396
in directing biopsy, 395
elevated levels of, 395
free/total ratio of, 395
velocity of, 396
Prostatic artery, 384
Prostatism. *See* Lower urinary tract symptoms
Prostatitis, chronic, 389–390, 390*f*
Proteus syndrome, hemimegalencephaly associated with, 1195
Proximal focal femoral deficiency (PFFD), 1400, 1400*f*
pediatric, 1933, 1934*f*
Prune belly syndrome
fetal
lower urinary tract obstruction from, 1361–1362
megalourethra and, 1362
pediatric
hydronephrosis and, 1788
lower urinary tract obstruction and, 1906
PSA. *See* Prostate-specific antigen
Psammoma bodies, in papillary carcinoma of thyroid gland, 698
Psammomatous calcification, in peritoneal nodule, 510–511, 513*f*
Pseudoacetabulum, in DDH, 1921
Pseudoaneurysm(s)
abdominal aortic dilation from, 441
anastomotic, 438
in AVF for hemodialysis, 1003, 1005*f*
common carotid artery posttraumatic, 948, 950*f*
of common femoral artery, 973*f*
hepatic artery, 104
after liver transplantation, 634, 636*f*
after pancreas transplantation, 678, 680*f*
pancreatic, 230, 230*f*
of peripheral arteries
lower extremity, 972–973, 973*f*
upper extremity, 976, 977*f*
radial artery, 977*f*
renal biopsies and, Doppler assessment of, 1809, 1811*f*
Pseudoaneurysm(s) *(Continued)*
after renal transplantation, 664, 669*f*–670*f*
in synthetic arteriovenous graft for hemodialysis, 1003, 1006*f*
Pseudoascites, 1413, 1415*f*
Pseudocirrhosis, of liver, 125–128, 129*f*
Pseudocyst(s)
gastrointestinal cysts differentiated from, 1860, 1863*f*
meconium, fetal, 1313, 1314*f*
ovarian cysts differentiated from, 1369
pancreatic
acute pancreatitis complications with, 228–229, 229*f*
chronic pancreatitis complications with, 232, 233*f*–234*f*
drainage of, 230, 615–617, 617*f*
pediatric pancreatitis and, 1864–1865, 1865*f*
splenic, 146–147, 149*f*
umbilical cord, 1483, 1484*f*
Pseudoephedrine, fetal gastroschisis and, 1322–1323
Pseudohermaphroditism
female, prenatal diagnosis of, 1368
male, dysplastic gonads and, 1899
Pseudokidney sign, in gut wall, 257, 260*f*
Pseudomembranous colitis, 1850*f*
gastrointestinal tract infections and, 296–297, 298*f*
Pseudomonas, 846
Pseudomyxoma peritonei, 513–514, 518*f*, 581
Pseudopapillary tumor, of pancreas, pediatric, 1865, 1865*f*
Pseudopolyps, cystitis and, 333, 333*f*
Pseudoprecocious puberty, 1887–1888
Pseudopuberty, precocious, pediatric ovarian cysts and, 1875
Pseudospectral broadening, in carotid spectral analysis, 927
Pseudostenosis, of portal vein, 636
Pseudostring of flow, on power Doppler, 935
Pseudosyndactyly, fetal, 1404
Pseudothalidomide syndrome, 1401
Pseudotumor(s)
fibrous, 838, 840*f*
inflammatory
gastric mucosa thickening in, 1839–1840
pediatric cystitis and, 1794, 1797*f*
splenic, 153–156
Pseudoulceration, of carotid artery, 923
Psoriatic arthritis, of hand and wrist, injections for, 904
PSTT. *See* Placental-site trophoblastic tumor
PSV. *See* Peak systolic velocity
PTB. *See* Preterm birth
PTLD. *See* Posttransplant lymphoproliferative disorder
PTN. *See* Persistent trophoblastic neoplasia
Puberty, precocious, 1746, 1887–1888
PUBS. *See* Percutaneous umbilical cord blood sampling
PUL. *See* Pregnancy of unknown location
Pulmonary agenesis, 1245–1246
Pulmonary aplasia, 1245–1246
Pulmonary artery, fetal
continuity of, 1278*f*
diameter of, 1277*f*
dilated, TOF and, 1288
Pulmonary atresia
Ebstein anomaly with, 1286
fetal, hydrops from, 1423–1424
hypoplastic right ventricle secondary to, 1287
TOF and, 1288
Pulmonary development, fetal, 1243
Pulmonary embolism, DVT causing
lower extremity, 979, 981*f*
upper extremity, 994
Pulmonary hypertension, with CDH, 1264
Pulmonary hypoplasia
fetal, 1245–1246
campomelic dysplasia and, 1384*f*
causes of, 1246*t*
hydrops and, 1413
in lethal skeletal dysplasia, 1386, 1386*b*
lethality of skeletal dysplasia and, 1382, 1384*f*
premature rupture of membranes and, 1246
primary, 1245
secondary, 1245, 1246*f*
unilateral, 1246, 1247*f*
pediatric, 1689
Pulmonary lymphangiectasia, 1258, 1259*f*
Pulmonary sequestrations, pediatric, 1715–1716, 1717*f*
Pulmonary veins
anatomy of, normal, 1290, 1291*f*
anomalous, 1290, 1291*f*
Pulmonic stenosis, 1292
in TGA, 1289
Pulsatility index (PI), 27, 27*f*
of intracranial vessels, 1595
Pulse average intensity, 36
Pulse inversion Doppler imaging, 63–64
Pulse inversion imaging, 62–63, 62*f*–63*f*
Pulse length, 8
Pulse repetition frequency (PRF)
in color Doppler, setting of, for low-flow vessel evaluation, 933
in color Doppler ultrasound, 28, 29*f*, 30–31
increasing, to overcome aliasing, 939
output control and, 48–50
transmitter controlling, 7
Pulsed wave Doppler, 24, 25*f*
testicular flow, 1890
testicular hyperemia and, pediatric, 1896
Pulsed wave operating modes, 7
Pulsed wave ultrasound, 36
Pulse-echo principle, 36
Purkinje system, 1297
Pus, 1953
Push-and-pull maneuver, in dynamic examination of hip, 1926*f*, 1927
PVCs. *See* Premature ventricular contractions
PVL. *See* Periventricular leukomalacia
Pyelectasis
definition of, 1354
fetal, significance of, 1355
Pyelitis
alkaline-encrusted, 324–325
emphysematous, 326–327, 327*f*
Pyelonephritis
acute, 323–325
gallbladder wall thickening signs in, 201*f*
pediatric, 1792–1793, 1793*f*–1794*f*
renal and perinephric abscess from, 325, 325*f*
on sonography, 324, 324*b*, 324*f*
chronic, 327, 327*f*–328*f*
pediatric, 1794, 1795*f*
emphysematous, 325–326, 326*f*
renal transplantation complications with, 653, 657*f*
as genitourinary tract infection, 323–328
transplant, 651, 655*f*
xanthogranulomatous, 328, 329*f*
Pyknodysostosis, wormian bones in, 1139
Pyloric atresia, dilated fetal stomach differentiated from, 1307

Pyloric muscle
hypertrophy of
minimal, in pylorospasm, 1836–1838, 1838*f*
in pyloric stenosis, 1835–1838, 1835*b*, 1837*f*–1838*f*
tangential imaging artifacts of, 1834–1835, 1836*f*
Pyloric stenosis
dilated fetal stomach differentiated from, 1307, 1308*f*
hypertrophic, 1835–1838, 1835*b*, 1837*f*–1838*f*
pitfalls in diagnosis of, 1838, 1838*b*, 1839*f*
pylorospasm and minimal muscular, 1836–1838, 1838*f*
Pylorospasm, 1836–1838, 1838*f*
Pyoceles, scrotal, 835*f*, 836
Pyogenic bacteria, liver abscesses from, 85–86, 87*f*
pediatric, 1746–1747, 1751*f*
Pyonephrosis
genitourinary tract infections and, 325, 326*f*
pediatric, complicating acute pyelonephritis, 1793, 1794*f*
renal transplantation complication with, 651, 655*f*
Pyosalpinx, 587–588

Q
Quadrigeminal cistern, 1518

R
Rachischisis, 1218
definition of, 1225*t*
Radial arteries, 531–532
calcification of, evaluation for, 998, 998*f*
for coronary bypass graft, evaluation of, 977–978, 980*f*
pseudoaneurysm of, 977*f*
Radial ray anomalies, 1103*f*
Radial ray defects, 1400–1401, 1401*f*–1402*f*
Radial veins, normal anatomy of, 990–991
Radiation forces, 35
Radical prostatectomy
for prostate cancer, 400, 401*f*
TRUS-guided biopsy after, 411, 411*f*
Radiofrequency ablation, for autonomously functioning thyroid nodules, 720
Radiography, for skeletal dysplasia evaluation, 1384
Radiotherapy, external beam, for prostate cancer, 400–401, 401*f*
Radius, aplastic or hypoplastic, in Fanconi pancytopenia, 1400, 1402*f*
Ranula, pediatric, 1639–1640, 1640*f*
Ranunculi, 313
in kidney development, 1781, 1781*f*
Rapidly involuting congenital hemangiomas, cutaneous, 1742–1743
Rapunzel syndrome, trichobezoars and, 1840
RAR. *See* Renal aortic ratio
Rarefaction, in sound wave, 2, 2*f*
RCC. *See* Renal cell carcinoma
Real-time B-mode ultrasound, 9–10, 10*f*
Receiver, 8–9, 8*f*–9*f*
Receiver gain, in obstetric sonography, 1036
Rectal cleansing, prior to TRUS, 387
Rectouterine recess, 528
Rectum, carcinoma of, 301–302, 301*f*–304*f*
Red blood cell production, decreased, from fetal hydrops, 1431
Red cell alloimmunization, screening fetus with hydrops for risk of, 1421–1423, 1421*b*, 1422*f*, 1422*t*
Reflected sound, 3–4
Reflection, in acoustics, 4, 5*f*
Reflection coefficient, 4
Reflectors
diffuse, 4, 5*f*
specular, 4, 4*b*, 5*f*
Reflux nephropathy, CKD and, 1796–1798
Refraction, 5, 6*f*
Rejection
acute, renal transplantation abnormalities and, 1809–1810
chronic, renal transplantation abnormalities and, 1810, 1812*f*
in liver transplantation, pediatric, 1767
in pancreas transplantation, 678–679, 681*f*
in renal transplantation
acute, 649–651, 653*f*
chronic, 651, 654*f*
Remapping, of amplitudes, 9
Renal agenesis, 318–319
Renal aortic ratio (RAR), 450
Renal artery(ies)
accessory, 445–446
anatomy of, 445–446
aneurysms of, 369, 369*f*, 451
duplex Doppler sonography of, 447–450, 450*f*
false-positive/false-negative results with, 450, 450*f*
interpretation of, 450
fetal
absent, 1344*f*
normal, 1344*f*
infarction of, 366, 367*f*
occlusion of, 366
pediatric
patency, Doppler assessment of, 1803–1804
stenosis of, Doppler assessment of, 1805, 1805*t*, 1806*f*
polar, 445–446
stenosis of, 368–369, 368*f*
causes of, 447
Doppler assessment of, pediatric, 1809
false-positive Doppler diagnosis of, 658, 661*f*
intraparenchymal, 658
pediatric, Doppler assessment of, 1805, 1805*t*, 1806*f*
in pediatric patients, 447
after renal transplantation, 655–658, 656*b*, 658*f*–661*f*
renovascular hypertension and, 446–447, 446*b*
thrombosis of, after renal transplantation, 653–655, 657*f*
Doppler assessment of, pediatric, 1807–1809, 1808*f*
Renal biopsies, pediatric, Doppler assessment of, 1809, 1810*f*–1811*f*
Renal calculi, 334–336, 336*f*–337*f*
entities that mimic, 336, 337*b*, 337*f*
Renal cell carcinoma (RCC)
acquired cystic kidney disease and, 340
biopsy of, 343–344, 345*f*
classic diagnostic triad for, 340
cystic, 343, 343*f*
Doppler ultrasound for detection of, 343, 344*f*
genitourinary tumors and, 340–344
histologic subtypes of, 340
imaging approaches to, 341, 341*f*
interpretation pitfalls with, 344, 345*f*
necrotic, 343
papillary, 342
pediatric, 1820, 1821*f*
prognosis of, 343–344
radiofrequency ablation of, 341, 341*f*
sonographic appearance of, 341–343, 342*f*–344*f*
treatment approaches to, 341
von Hippel-Lindau disease and, 340
Renal collecting system, pediatric. *See also* Hydronephrosis, pediatric, causes of
dilation of, 1785
duplication of, 1783–1784, 1784*f*
urolithiasis and, 1799–1801, 1799*f*
Renal cortex, 313, 313*f*
Renal duplication, pediatric, 1783–1784, 1784*f*
Renal dysgenesis, 361
Renal dysplasia, 361, 1689
obstructive cystic, 1347–1348, 1347*f*–1348*f*
Renal hilum, 311–313
Renal junctional parenchymal defect, 1781, 1781*f*
Renal medullary pyramids, 313, 313*f*
Renal milk of calcium, calyceal diverticula and, 1799, 1800*f*
Renal parenchyma, 313
Renal pelvic diameter (RPD), 1354, 1354*f*
normal, 1355
Renal pelvic echo, 1339
Renal pelvis. *See also* Hydronephrosis
adenocarcinoma of, 348
fetal
diameter of, measurement of, 1354, 1354*f*
dilation of, 1354
pediatric
duplication of, 1784*f*
wall thickening in, from acute pyelonephritis, 1792, 1793*f*
Renal sinus, 311–313
Renal transplantation, 641–666
abnormal, 649
AVMs complicating, 661–664, 667*f*–670*f*
twinkling artifacts mimicking, 662–664, 668*f*
cadaveric kidneys in, paired, 643–644, 648*f*
for chronic renal failure, 641
donor renal vein anastomosis in, 643
fluid collections after, 664–666, 671*f*–674*f*
hematomas after, 665, 671*f*
infarctions after
global, 653
segmental, 653–655, 657*f*
lymphoceles after, 665–666, 673*f*–674*f*
pediatric, 1809, 1811*f*
normal appearance of, 644–648
Doppler ultrasound assessment in, 648, 651*f*–652*f*
gray-scale assessment in, 644–648, 648*f*–650*f*
parenchymal pathology complicating, 649–653
abscesses as, 651, 656*f*
acute rejection as, 649–651, 653*f*
acute tubular necrosis as, 649–651, 653*f*
chronic rejection as, 651, 654*f*
emphysematous pyelonephritis as, 653, 657*f*
hyperacute rejection and, 651
infections as, 651–653, 655*f*–657*f*
milk of calcium cysts as, 653, 657*f*
pediatric, 1809–1810, 1812*f*
pyonephrosis as, 651, 655*f*
pediatric
Doppler ultrasound for, 1807–1812
parenchymal abnormalities and, 1809–1810, 1812*f*
perinephric fluid collections in, 1809, 1811*f*
tumors of, 1812, 1813*f*
urologic complications and, 1810–1812
vascular complications in, 1807–1809, 1808*f*, 1810*f*–1811*f*
perinephric abscesses after, 664–665
postrenal collecting system obstruction complicating, 630*f*–633*f*, 659–661
prerenal vascular complications of, 653–659
arterial thrombosis as, 653–655, 657*f*
renal artery stenosis as, 655–658, 656*b*, 658*f*–661*f*
renal vein stenosis as, 658–659, 663*f*
venous thrombosis as, 658, 662*f*
pseudoaneurysms after, 664, 669*f*–670*f*
PTLD after, 683–688, 684*f*–686*f*
surgical technique for, 641–644, 648*f*
ureter anastomosis of in, 643, 648*f*

Renal transplantation *(Continued)*
ureteral obstruction complicating, 659–660, 663*f*–664*f*
urinomas after, 665, 672*f*
pediatric, 1809
Renal tubular acidosis, medullary nephrocalcinosis and, 1798
Renal tubular disease, inborn errors of metabolism and, 1738
Renal vein(s)
donor, anastomosis, in renal transplantation, 643
left, anatomic variants of, 457
pediatric
acute thrombosis of, Doppler assessment of, 1804–1805, 1804*b*, 1804*f*
patency of, Doppler assessment of, 1803–1804
stenosis of, after renal transplantation, 658–659, 663*f*
thrombosis of, 369, 370*f*
Doppler assessment of, pediatric, 1809
hyperechogenic kidneys and, 1351
pediatric, acute, Doppler assessment of, 1804–1805, 1804*b*, 1804*f*
after renal transplantation, 658, 662*f*
urinary tract calcifications and, 1799, 1800*f*
Renal/abdominal circumference ratio, 1338–1339
Renal-coloboma syndrome, MCDK and, 1815
Renovascular disease, 368
Renovascular hypertension
clinical findings suggesting, 446*b*
renal artery stenosis and, 446–447
Resistive index (RI), 27, 27*f*
in ACA, in infants, 1576, 1577*t*
in hepatic artery, elevation of, after liver transplantation, 634
intracranial, 1595
in asphyxiated infants, 1580
factors changing, 1612*t*
factors modifying, 1576, 1576*f*–1577*f*, 1576*t*
hydrocephalus and, 1582, 1584*f*
intrarenal, pediatric, causes of increased, 1802–1803, 1803*b*, 1803*f*
in monitoring intracranial hemodynamics in infants, 1576, 1577*t*
in renal artery duplex Doppler sonography, 450
in shunt malfunction and hydrocephalus, 1613, 1613*f*
Resolution, spatial, 16–19, 18*f*–19*f*
Resuscitation, neonatal, in fetal hydrops, 1437
Retained products of conception (RPOC), 554–555
pediatric, 1884, 1884*f*
placenta and, 1487–1489, 1490*f*
Rete testis, 819
tubular ectasia of, 829–830, 830*f*
pediatric, 1891–1892, 1892*f*
Retinoblastoma, metastasis of, to teste, 1901
Retinoic acid, NTDs from, 1218
Retrocalcaneal bursal injection, 902, 903*f*
Retrocaval ureter, 322
Retrognathia, 1153–1154
Retrogressive differentiation, in spine embryology, 1672, 1673*f*
Retromammary zone, of breast, 761, 761*f*
Retromandibular vein, pediatric, 1630, 1630*f*
Retroperitoneum, 210. *See also* Abdominal aortic aneurysm
abdominal aortic aneurysm and, 433–439
abdominal aortic dilation and, 439–441
atherosclerosis and, 432–433
fibrosis of, 464–465, 465*f*
fluid collections in, 464
masses in, 464
metastases of, 464, 465*f*
nonvascular diseases of, 464–465
Retroperitoneum *(Continued)*
prepancreatic, inflammation of, in acute pancreatitis, 224–225, 224*f*–225*f*
stenotic disease of abdominal aorta and, 441–445, 445*f*
Retrorenal spleen, 162
Reverberation artifacts, 19, 20*f*
posterior, liver abscess and, 85–86, 87*f*
Rh alloimmunization, screening fetus with hydrops for risk of, 1421–1423
Rh_0(D) immune globulin (RhoGAM), in immune hydrops prevention, 1418
Rhabdoid tumors
intraspinal, pediatric, 1689–1691
neonatal/infant brain and, 1562
Rhabdomyoma(s), cardiac
fetal, 1293–1294, 1293*f*
fetal hydrops from, 1424, 1424*f*
in infants, 1293
tuberous sclerosis, 1424
Rhabdomyosarcoma(s)
bladder, 356
pediatric, 1820, 1823*f*
pediatric
biliary, in liver, 1746, 1749*f*
embryonal, paratesticular, 1903–1904, 1903*f*
hydrosonovaginography and, 1871*f*
lower urinary tract and, 1908–1912, 1912*f*
metastasis of, to teste, 1901
neck, 1665, 1666*f*
presacral, 1914–1915
salivary gland, 1638–1639
vaginal, 1883, 1883*f*
scrotal, 840*f*, 841
in TSC, 1200*f*
Rh(D) antibodies, immune hydrops and, 1419
Rheumatoid arthritis, 866
erosive, 867, 868*f*
gout and, 867–869, 868*f*
of hand and wrist, injections for, 904
joint effusion in, 867, 867*f*
Rheumatoid nodules, in Achilles tendon, 867, 868*f*
Rhizomelia, 1381, 1381*b*, 1382*f*
Rhizomelic chondrodysplasia punctata, 1399
Rhizomelic dysplasia, features of, 1397*t*
RhoGAM. *See* Rh_0(D) immune globulin
Rhombencephalic cavity, 1167
Rhombencephalic neural tube, 1167
Rhombencephalon, formation of, 1077, 1077*f*, 1167
Rhombencephalosynapsis, 1192
RI. *See* Resistive index
Rib shadowing, in pediatric chest sonography, 1710
Rib(s)
fractures of, pediatric, 1727
in skeletal dysplasias, 1382–1384
Riedel lobe, 80
Riedel struma, 727–728, 728*f*
Right atrial isomerism, in total APVR, 1290
"Rim-rent" rotator cuff tears, 888, 890*f*
"Ring of fire" sign, in pediatric ectopic pregnancy, 1884–1885
Ring-down artifacts, 266, 266*f*
Roberts syndrome, 1401
Rocker-bottom foot, 1406*f*, 1407
Rokitansky-Aschoff sinuses, 202, 203*f*
Rolland-Desbuquois, 1399
Rostral neuropore, 1167
Rotator cable, 882, 884*f*
Rotator cuff. *See also* Shoulder
anatomy of, 879, 879*f*
hydroxyapatite crystal deposition in, 891–892
muscle atrophy of, 888–889, 891*f*
musculature evaluation of, 884–886, 885*f*
postsurgical, 888, 891*f*
Rotator cuff *(Continued)*
shoulder dysfunction and pathology of, 877
tears of, 886–892
background on, 886
calcific tendinitis and, 891–892, 892*f*
full-thickness, 886–887, 887*f*–888*f*
partial-thickness, 887–888, 889*f*–890*f*
subacromial-subdeltoid bursa and, 888–889, 892*f*
tendinosis as, 886, 886*f*
Rotator interval, 879, 880*f*
ultrasound evaluation of, 881–882
Rotter lymph nodes, 762, 808–810, 810*f*
Round ligament(s), 528, 564–565
cysts of, simulating groin hernias, 500, 501*f*
relationship of indirect inguinal hernia to, 476–479, 480*f*
thrombosis of, simulating groin hernias, 500, 501*f*
varices of, simulating groin hernias, 500, 501*f*
Round pneumonia, pediatric, 1711–1712, 1715*f*
RPD. *See* Renal pelvic diameter
RPOC. *See* Retained products of conception
Rubella
congenital, neonatal/infant brain and, 1560
fetal hydrops from, 1432
maternal, pulmonic stenosis and, 1292
Rudimentary horn, 538
Rupture of membranes, preterm premature
cervical assessment in, 1505

S

SAAAVE Act. *See* Screening Abdominal Aortic Aneurysms Very Efficiently Act
Sacral agenesis, 1689
fetal, 1237
in caudal regression, 1237–1238
in caudal regression syndrome, 1401
Sacral bone tumors, 1914–1915
Sacrococcygeal teratomas
fetal, 1238–1239, 1238*b*, 1239*f*
hydrops from, 1430–1431
pediatric, 1691, 1694*f*
classification of, 1691*t*
cystic, 1694*f*
intrapelvic, 1694*f*
presacral, 1913, 1914*f*
Saddle nose, in skeletal dysplasia, 1382
Safety. *See also* Bioeffects
AIUM on diagnostic ultrasound and general, 47, 47*b*
hyperthermia and, 38, 38*f*
of microbubble contrast agents, 67–68
of obstetric sonography, 1034–1035
guidelines for, 1041–1042, 1042*t*, 1043*f*
of transvaginal ultrasound in first trimester of pregnancy, 1049
Sagittal sinus, fetal, thrombosis of, 1206*f*
Saldino-Noonan syndrome, 1396
Salivary glands, pediatric, 1629–1639. *See also* Parotid glands, pediatric; Submandibular glands, pediatric
anatomy of, 1630–1631
inflammation of, 1632–1635
acute, 1632–1634, 1632*f*–1633*f*
chronic, 1634–1635, 1634*f*–1636*f*
masses of, 1636–1639
neoplasms of, 1636–1639, 1638*f*–1639*f*
vascular masses of, 1636, 1637*f*
viral infections of, 1632, 1632*f*
Salmon patches, 1679
Salmonella, 1852–1853
Sample volume, in obstetric Doppler ultrasound, 1036

Sample volume size, Doppler ultrasound and, 29*b*, 30
Sandal toes, fetal, 1406*f*, 1407
Saphenofemoral junction, as landmark for femoral hernias, 482, 485*f*
Sappey plexus, 762
Sarcoid, chronic pediatric sialadenitis in, 1634–1635
Sarcoidosis, epididymis and, 841, 843*f*
Sarcoma botryoides, pediatric, 1820, 1883, 1908
Sarcoma(s)
  embryonal, undifferentiated, in pediatric liver, 1746, 1748*f*
  endometrial, 551, 551*f*
  granulocytic, pediatric, neck, 1666, 1667*f*
  Kaposi, liver in, 129
  masticator space, pediatric, 1640, 1641*f*
  renal, 356
  soft tissue, 871–872, 872*f*
  uterine, 551
Sawtooth flow disturbance, from temporal tap, 918, 918*f*
Scanning mode, obstetric sonography and, 1035
Scapulae, 878–879, 878*f*
  hypoplastic, in campomelic dysplasia, 1381–1382
Scars
  from cesarean sections, 557, 558*f*
  exuberant, simulating anterior abdominal wall hernias, 500, 502*f*
SCC. *See* Squamous cell carcinoma
SCD. *See* Sickle cell disease
Schistosomiasis
  bladder, 331, 331*f*
  liver, 90
    pediatric, 1748
  urinary tract, 331
Schizencephalic clefts, hydranencephaly differentiated from, 1208
Schizencephaly
  CMV infection and, 1536–1537, 1558
  fetal, 1196, 1199*f*
  HPE differentiated from, 1189
  hydranencephaly differentiated from, 1208
  neonatal/infant, 1536–1537, 1537*f*
Schneckenbecken dysplasia, 1396
Scintigraphy, in parathyroid adenomas of, 747, 747*f*
Sclerosing cholangitis, recurrent, complicating liver transplantation, 629, 630*f*
Sclerosing peritonitis, 514, 521, 523*f*
Sclerosis of hemangioma, diagnostic challenges with, 112
Sclerotherapy
  ethanol, 719
  ultrasound-guided, of macrocystic lymphatic malformation, pediatric, 1726, 1727*f*
Sclerotome, in spine embryology, 1217–1218, 1217*f*, 1218*t*
Scoliosis
  fetal, 1235–1237, 1237*b*
    campomelic dysplasia and, 1395
  pediatric, 1688
Screening Abdominal Aortic Aneurysms Very Efficiently (SAAAVE) Act, 435
Scrotal pearls, 836–837, 837*f*
Scrotal sac, torsion of, pediatric, 1325
Scrotoliths, 836–837, 837*f*, 1897
Scrotum. *See also* Epididymis; Testis(es)
  anatomy of, 819–822, 819*f*–821*f*
  bifid, fetal, 1367
  calcifications of, 833–834, 833*b*, 834*f*
  calculi in, extratesticular, 836–837, 837*f*
  cysts of, extratesticular, 839, 842*f*
  edema of, idiopathic, 846
  epididymal lesions and, 839–841
Scrotum *(Continued)*
  fibrous pseudotumor and, 838, 840*f*
  hematoceles of, 835*f*, 836
    pediatric, 1902
  hernia and, 836, 836*f*
  hydroceles of, 834–836, 835*f*
    fetal, 1367
    pediatric, 1899, 1902, 1902*f*
  indirect inguinal hernias extending into, 478–479, 482*f*
  liposarcomas of, 840*f*, 841
  masses in, 822–834
  pain in, acute, 841–847
    causes of, 843*b*
    from epididymitis, 846, 847*f*–848*f*, 1895–1896, 1896*f*
    from epididymo-orchitis, 846, 847*f*–849*f*
    from Fournier gangrene, 846–847
    secondary to intraabdominal process, 1899
    from testicular torsion, 844–846, 844*f*–845*f*
    from torsion of testicular appendage, 846
  pathologic lesions of, extratesticular, 834–841, 836*b*
  pediatric
    acute pain or swelling in, 1892–1899, 1892*b*
    anatomy of, 1888
    edema of, acute idiopathic, 1898–1899, 1898*f*
    hematoceles of, 1902
    Henoch-Schönlein purpura and, 1899
    hernia and, 1902
    hydroceles of, 1899, 1902, 1902*f*
    masses of, 1899–1904
    masses of, extratesticular causes of, 1902–1903
    masses of, intratesticular causes of, 1899–1902
    masses of, paratesticular, 1903–1904
    trauma to, 1897–1898, 1898*f*
  polyorchidism and, 838–839, 841*f*
  pyoceles of, 835*f*, 836
  rhabdomyosarcomas of, 840*f*, 841
  sonography of
    current uses of, 819*b*
    technique for, 818–819
  trauma to, 847–851, 850*f*
  tumors of, extratesticular, 840–841, 840*f*
  varicoceles of, 837–838, 838*f*–839*f*
S/D ratio. *See* Systolic-to-diastolic ratio
Sebaceous cysts, 779, 781*f*
Second harmonic, transducers and, 105
Second-generation contrast agents, 56
Secretin injection, 218
Segmental spinal dysgenesis, 1674, 1689, 1691*f*
Segmentation, in organogenesis, 1524, 1525*f*
Seldinger technique, for drainage catheter placement, 611
Selective uptake contrast agents, 56, 57*f*
Seminal vesicles, 382*f*–383*f*, 384
  calcification of, 392
  congenital abnormalities in, 392
  cysts of, 392, 393*f*
    pediatric, 1908, 1910*f*
  pediatric, anatomy of, 1888, 1888*f*
Seminiferous tubules, 819
Seminoma(s), 584
  cryptorchidism and, 851
  pediatric
    in dysplastic gonads, 1899
    sonography of, 1899, 1900*f*
  testicular, 823, 823*f*–824*f*
Sensenbrenner syndrome, 1395
Sepsis, pediatric, jaundice in, 1738
Septate uterus, 534–536, 536*f*–537*f*
Septations, in renal cysts, 357–358, 357*b*, 358*f*
Septi pellucidi, absence of, 1201–1203
Septic arthritis, pediatric, 1936, 1937*f*
Septic shock, AKI and, 1796
Septo-optic dysplasia (SOD)
  fetal brain and, 1201–1203, 1203*f*
  HPE differentiated from, 1187–1189
  neonatal/infant brain and, 1532–1534, 1535*f*
  in rhombencephalosynapsis, 1192
Septula testis, 819, 820*f*
Septum pellucidum
  absent, in rhombencephalosynapsis, 1192
  cavum of, fetal, sonographic view of, 1024*f*
Septum primum, 1279
Septum secundum, 1280
Seroma(s)
  pelvic, 591
  retrosternal, 1726*f*
  spinal canal, pediatric, 1697, 1697*f*
  stitch, after herniorrhaphy, 494–496, 495*f*
Serous cystadenocarcinoma, ovarian, 580–581, 580*f*
Serous cystadenoma, ovarian, 580–581, 580*f*
Serous cystic neoplasm, 243, 244*f*–245*f*
Sertoli cell tumors, 826, 827*f*
  pediatric, 1900
Sertoli-Leydig cell tumor, 585
Serum, Urine and Ultrasound Screening Study (SURUSS), 1090
Sex cord-stromal tumors
  ovarian, 585
  testicular, 825–826, 827*f*
Sex reversal, in campomelic dysplasia, 1395
SGA. *See* Small-for-gestational age fetus
Shadowing
  acoustic, 786
    breast sonography and, 791–792, 793*f*
    carcinoma causing, 791–792, 793*f*
    decreased/absent, in skeletal dysplasias, 1381–1382
    malignant masses causes, differential diagnosis for, 792
    by rib, in pediatric chest sonography, 1710
  as artifacts, 19–21, 22*f*
  in uterine fibroids, 539*f*, 540, 540*b*
Shattered kidney, 365–366
Shear wave elastography (SWE), 16, 17*f*–18*f*, 772
  cirrhosis of liver and, 95–96
  for pediatric liver, 1764, 1765*f*
Shear waves, in bone, 39
Shigella, 1852
Shockwave, 37, 37*f*
Short umbilical cord, 1481
Short-rib polydactyly syndromes, 1382, 1383*f*, 1395–1396, 1397*f*
Shoulder. *See also* Rotator cuff
  anatomy of, 878–879, 878*f*
  arthropathy and, 893–894
    degenerative, 893, 894*f*
    inflammatory, 893–894, 894*f*
  clinical perspective on, 877–878
  injection of, 901, 901*f*
  pediatric, brachial plexus injury and, 1934–1936, 1936*f*–1937*f*
  posterior, 884
  rotator cuff pathology and dysfunction of, 877
  subacromial impingement of, 877–879, 882–883
  ultrasound techniques for
    anisotropy and, 895, 895*f*
    Crass position in, 881, 883*f*
    modified Crass position in, 881, 883*f*–884*f*
    MRI compared to, 877–878
    pitfalls in, 895, 895*f*
    protocol for, 879–886, 880*t*
Shunt(s). *See also* Portosystemic shunts
  for hydrocephalus, in neonatal/infant brain, duplex Doppler sonography of, 1582, 1584*f*
  in hydrocephalus, malfunction of, RI in, 1613, 1613*f*

Shunt(s) *(Continued)*
right-to-left, pediatric, TCD sonography evaluation of, 1614–1618
splenorenal, in portal hypertension, pediatric, 1757, 1759*f*
ventriculoperitoneal, for Dandy-Walker malformation, 1530
vesicoamniotic, for lower urinary tract obstruction, 1363–1365, 1364*f*, 1365*t*
Shwachman-Diamond syndrome, nesidioblastosis and, 1865, 1865*f*
Sialadenitis, pediatric, chronic, 1634–1635, 1635*f*
Sialoblastoma, salivary gland, pediatric, 1638–1639
Sialolithiasis, pediatric, of submandibular gland, 1633, 1633*f*
Sickle cell disease (SCD)
ACA stenosis with, 1607*f*
bone marrow transplantation for, 1598
cerebrovascular disease indicators with, 1598, 1599*b*
MCA and, 1600*f*, 1604*f*–1605*f*
ophthalmic artery flow as, 1599*f*
stroke and, 1601*f*–1603*f*
DICA stenosis and, 1606*f*
moyamoya angiopathy and, 1598, 1600*f*, 1602*f*, 1608*f*, 1610
silent cerebral infarcts and, 1598
sleep-disordered breathing and, 1611
spleen in, 157
stroke and
cerebrovascular disease indicators with, 1601*f*–1603*f*
risk categories for, 1599–1604, 1605*t*, 1606–1607
screening for, 1598
velocity indications of, 1605–1607
TCD sonography for, 1591, 1598–1608, 1599*b*, 1599*f*–1608*f*
Side lobe artifacts, 19, 20*f*
Side lobes, 19, 20*f*
Silent cerebral infarcts, SCD and, 1598
Silent (painless) thyroiditis, 725–727
Silicon granulomas, in extracapsular breast implant rupture, 805–807, 806*f*
Silver-Handmaker, 1399
Simple cysts
of breast, 774, 775*f*
of pediatric testes, solitary, 1901–1902
Simpson-Golabi-Behmel syndrome
CDH and, 1263
hyperechogenic kidneys in, 1351
Single-photon emission computed tomography (SPECT), 747, 747*f*
Sinus bradycardia, fetal, 1297
Sinus venosus ASD, 1280, 1282*f*
Sinus(es)
dorsal dermal, pediatric, 1686, 1688*f*
urachal, 322, 323*f*
Sinusoidal obstruction syndrome, 1762–1763
Sirenomelia, fetal, 1238, 1238*f*, 1401, 1404*f*
Sirenomelia sequence, sacral agenesis in, 1237
Site-specific ovarian cancer syndrome, 578
Situs inversus totalis, of liver, 80
Sjögren syndrome, chronic pediatric sialadenitis in, 1634–1635
Skeletal deformities, fetal lung size and, 1244
Skeletal dysplasia, fetal
categories of, 1377*t*
diagnosis of, 1376–1377, 1377*b*
femur/foot length ratio in, 1379
hydrops from, 1432
lethal, 1386–1396
achondrogenesis as, 1391
campomelic dysplasia as, 1395, 1396*f*
Skeletal dysplasia, fetal *(Continued)*
features of, 1386*b*
hypophosphatasia as, 1392–1395, 1395*f*
osteogenesis imperfecta as, 1391–1392
short-rib polydactyly syndromes as, 1395–1396, 1397*f*
thanatophoric dysplasia as, 1387–1390
lethality of, pulmonary hypoplasia and, 1382, 1384*f*
nonlethal or variable prognosis, 1396–1399
asphyxiating thoracic dysplasia as, 1398
chondrodysplasia punctata as, 1399
diastrophic dysplasia as, 1398, 1398*f*
dyssegmental dysplasia as, 1399
Ellis-van Creveld syndrome as, 1398–1399
heterozygous achondroplasia as, 1396–1398, 1398*f*
micromelic dysplasia as, 1397*t*
osteogenesis imperfecta types I, III, IV as, 1399
rhizomelic dysplasia as, 1397*t*
prevalence of, 1376, 1377*t*
sonographic evaluation of, 1379–1386, 1379*b*
with abnormal bone length or appearance, 1380–1384, 1381*b*, 1382*f*–1384*f*
additional imaging in, 1384–1386
molecular diagnosis in, 1385–1386
MRI in, 1385
with positive family history, 1379–1380
radiography in, 1384
3-D ultrasound in, 1384, 1385*f*
three-dimensional CT in, 1384–1385
Skeletal dysplasia, pediatric, atypical hips and, 1932
Skeletal survey, in fetal hydrops diagnosis, 1435
Skeleton, fetal. *See also* Limb reduction defects
aneuploidy findings in, 1407–1409
limb reduction defects and, 1399–1404
normal, 1089–1097
development of, 1089, 1378*f*
extremity measurements of, 1089, 1379*t*, 1380*f*–1381*f*
triploidy and, 1408–1409
trisomy 13 and, 1408, 1408*b*
trisomy 18 and, 1408, 1408*b*
trisomy 21 and, 1408, 1408*b*
Skin folds, thickened, in lethal skeletal dysplasias, 1386
Skull, fetal
cloverleaf-shaped, 1136
craniosynostosis with, 1137*f*–1138*f*
in skeletal dysplasias, 1382
in thanatophoric dysplasia type 2, 1388–1389, 1389*f*
lemon-shaped, 1136, 1137*f*
strawberry-shaped, 1136, 1137*f*
Sleep apnea, pediatric TCD sonography for, 1611
Sleep-disordered breathing, 1611
"Sliding organ sign", 566
Slipped capital femoral epiphysis, 1931–1932
Sludge
biliary
acute pancreatitis and, 221
gallbladder and, 194–195, 196*f*
gallbladder, pediatric, 1741, 1743*f*
spontaneous PTB and, 1503
tumefactive, 195, 196*f*, 1741
SMA. *See* Superior mesenteric artery
Small bowel. *See also* Bowel; Echogenic bowel
fetal, 1308–1316
anorectal malformations and, 1310–1312, 1311*f*
dilated loops of, 1311–1312
Small bowel *(Continued)*
duodenal atresia and obstruction of, 1308–1309, 1310*f*
echogenic, 1313–1316, 1315*f*
enteric duplication cysts and, 1312–1313, 1313*f*
Hirschsprung disease and, 1312, 1312*f*
jejunoileal atresia obstructing, 1310, 1311*f*
meconium ileus and, 1310
meconium peritonitis and, 1313, 1313*t*, 1314*f*
meconium pseudocyst and, 1313, 1314*f*
lymphoma of, 266, 266*f*
pediatric, 1841–1847
anatomy of, 1841, 1842*f*
intussusception and, 1844–1845, 1849*f*
obstruction of, 1842–1843, 1846*f*
sonographic technique for, 1841
Small bowel mesentery, 505, 505*f*
Small saphenous vein, 981–982, 981*f*
Small-for-gestational age (SGA) fetus, 1454–1455, 1454*b*
SMI. *See* Superb microvascular imaging
Smith-Lemli-Opitz syndrome
ambiguous genitalia and, 1367
microcephaly in, 1194
SMV. *See* Superior mesenteric vein
Snell law, 5
Society for Fetal Urology, grading system of, for hydronephrosis, 1354, 1355*f*
SOD. *See* Septo-optic dysplasia
Soft tissue(s)
foreign bodies embedded in, 872, 873*f*
ganglia, compression and, 865
heating of, 37–38, 37*f*
infection of, 872–874, 873*f*–874*f*
masses of, 869–872, 869*f*–872*f*, 871*t*
perienteric, in acute abdomen, 281–282
sarcomas, 871–872, 872*f*
thermal index for, in early, 1039
tumors of, fetal face and, 1154, 1160*f*
Soft Tissue Thermal Index (TIS), 39
Solid-pseudopapillary tumor, 248, 248*f*
Soluble form, of injectable steroids, 900
Somites, in spine embryology, 1216–1217, 1217*f*, 1218*t*
Sonazoid, 56
Sonochemistry, acoustic cavitation and, 42, 42*f*
Sonographic air bronchograms. *See* Air bronchograms, sonographic
Sonohysterography, uterine, 529
Sonoluminescence, 42
SonoVue, 56
Sotos syndrome, megalencephaly associated with, 1194–1195
Sound
attenuation of sound energy, 5–7, 7*f*, 35
intensity of, 5
physical effects of, 35
propagation of, 2–3, 3*f*
propagation velocity of, 2–3, 3*f*
reflected, 3–4
theoretical understanding of, 58–59
Sound waves, 2, 2*f*
Spatial compounding, 13–15, 14*f*–15*f*
Spatial focusing, tissue heating and, 35
Spatial peak temporal average (SPTA), 32
Spatial resolution, 16–19, 18*f*–19*f*
Speckle, 4, 5*f*
contrast effect of, 13–15, 14*f*
spatial compounding and, 13–15
SPECT. *See* Single-photon emission computed tomography

Spectral broadening, in Doppler ultrasound, 24, 24*f*, 29, 29*b*, 31*f*
in carotid artery stenosis, 927, 927*f*
in peripheral arterial stenosis, 968, 969*f*
Spectral window, 925, 925*f*
Specular reflectors, 4, 4*b*, 5*f*
Speech, delayed, obstetric sonography and, 1040
Sperm, transport of, 1049–1051
Sperm granuloma, epididymis and, 841, 843*f*
Spermatic cord
anatomy of, 821–822, 821*f*
leiomyomas of, 840–841, 840*f*
lipomas of, 840–841, 840*f*
pediatric
cysts of, 1902–1903
torsion of, 1324–1325, 1369
relationship of indirect inguinal hernia to, 476–479, 479*f*, 481*f*
torsion of, 841–843, 845*f*
Spermatoceles, 839, 842*f*
paratesticular, 1904
pediatric, 1902–1903
Sphincter, internal urethral, 384
Sphincter of Oddi, dysfunction of, complicating liver transplantation, 629
Spiculated breast carcinoma, 786
Spiculation, in breast sonography, 787–788, 788*f*
Spigelian fascia
anatomy of, 483–484
spigelian hernia location and, 483, 486*f*
Spigelian hernias, 471, 483–484. *See also* Hernia(s), spigelian
Spina bifida, 1218, 1223–1233. *See also* Neural tube defects
abnormalities associated with
caudal regression as, 1237–1238, 1237*f*
cranial, 1228–1233
noncranial, 1233
sacral agenesis as, 1237
anatomic landmarks establishing, 1228*b*
closed, cranial changes in, 1183–1186, 1185*f*, 1185*t*–1186*t*
definition of, 1225*t*
evaluation protocol for, with 3-D volume data, 1223*b*
NTDs and, 1223
open, cranial changes in, 1183–1186, 1184*f*, 1185*t*–1186*t*
pathogenesis and pathology in, 1226
prevention of, folic acid in, 1224–1225
prognosis of, 1228*b*
screening for
alpha-fetoprotein in, 1221, 1226–1228, 1226*b*, 1227*f*
Chiari II malformation in, 1221, 1228, 1230–1233
ultrasound in, 1226–1228
sonographic findings in, 1228, 1229*f*–1232*f*
sonographic signs of, 1233*b*
terminology of, 1680
Spina bifida occulta
definition of, 1225*t*
pathology of, 1226
Spinal canal, pediatric. *See also* Spinal dysraphism, pediatric
acoustic window for, 1672, 1673*f*, 1674, 1675*f*
anomalies of, 1678–1679
arachnoid cysts of, 1695–1697, 1696*f*
embryology of, 1672–1674, 1673*f*
hemorrhage and, 1695, 1695*f*–1696*f*
infection of, 1695
normal anatomy of, 1674–1678, 1675*f*–1680*f*
seromas and, 1697, 1697*f*
sonographic technique for, 1674–1678
intraoperative uses of, 1697
subcutaneous hemangioma and, 1697, 1697*f*
Spinal canal, pediatric *(Continued)*
tethered cord and, 1678–1679, 1681*f*
tumors of, 1689–1691, 1691*t*, 1693*f*–1694*f*
Spinal column agenesis, 1689
Spinal cord
fetal, normal position of, 1218–1221, 1221*f*
pediatric, abnormally long, 1685
tumor of, pediatric, neurogenic bladder in, 1907
Spinal dysgenesis, segmental, 1674, 1689, 1691*f*
Spinal dysraphism, fetal, 1218
cephalocele as, 1139–1140
definition of, 1225*t*
Spinal dysraphism, pediatric
classification of, 1680–1681, 1682*t*
closed, with subcutaneous mass, 1682–1684, 1682*t*
lipomyelocele and, 1682, 1684*f*
lipomyelomeningocele and, 1682, 1685*f*
meningocele and, 1682–1683
myelocystocele and, 1683–1684, 1686*f*
closed, without subcutaneous mass, 1684–1689
abnormally long spinal cord and, 1685
anomalies at risk for, 1689, 1689*b*
caudal agenesis and, 1689, 1690*f*
complex states of, 1686–1689
diastematomyelia and, 1688–1689, 1688*f*
dorsal dermal sinus and, 1686, 1688*f*
dorsal enteric fistulas and, 1686–1688
filum terminale lipomas and, 1684–1685, 1686*f*
intradural lipomas and, 1686, 1687*f*
midline notochordal formation disorders, 1689
midline notochordal integration disorders, 1686–1689
persistent terminal ventricle and, 1685
segmental spinal dysgenesis and, 1689, 1691*f*
simple states of, 1684–1686
definition of, 1679–1680
open, 1681–1682, 1682*t*
Chiari II malformation with, 1681–1682
myelomeningocele and, 1681, 1683*f*
placodes and, 1680
terminology of, 1680
Spine, fetal. *See also* Spina bifida
abnormalities of
definition of terms for, 1225*t*
diastematomyelia as, 1234–1235, 1236*f*
kyphosis as, 1235–1237, 1236*f*, 1237*b*
myelocystocele as, 1233–1234, 1234*f*–1235*f*
presacral masses as, 1239, 1239*b*
sacrococcygeal teratomas as, 1238–1239, 1238*b*, 1239*f*
scoliosis as, 1235–1237, 1237*b*
sirenomelia as, 1238, 1238*f*
spina bifida as, 1223–1233
assessment of, in skeletal dysplasia, 1382
developmental anatomy of, 1216–1221
embryology of, 1216–1218, 1217*f*, 1218*t*
lower, cloacal exstrophy and, 1328
normal position of, 1218–1221, 1221*f*
ossification of, 1218, 1219*f*–1220*f*
in lateral longitudinal scan plane, 1223*f*
in posterior angled transaxial scan plane, 1224*f*
in posterior longitudinal scan plane, 1224*f*
timing and pattern of, 1220*t*
routine sonographic views of, 1021, 1027*f*
scanning techniques for, 1221–1223
MRI for, 1216
scan planes in, 1221, 1222*f*–1224*f*
3-D ultrasound in, 1216, 1221–1223
Spiral arteries, 531–532
Spiral clips, pain from, after herniorrhaphy, 497, 498*f*
Spleen
abscesses of, 148, 151*f*
drainage of, 617
absence of, 142
accessory, 158–159, 160*f*, 1771*f*
anatomy of, 139–142
bare area of, 139–141, 141*f*
biopsy of
percutaneous needle, 607, 608*f*
ultrasound-guided, 161
congenital anomalies of, 158–161
cysts of, 146–148, 146*b*, 148*f*–151*f*
fetal, 1320–1322, 1322*f*
embryology of, 139–142, 140*f*
fetal, 1320–1322, 1321*f*
cysts of, 1320–1322, 1322*f*
splenomegaly and, 1320
focal abnormalities of, 146–157
cysts as, 146–148, 146*b*, 148*f*–151*f*
nodular lesions as, 148–152, 151*f*–154*f*
solid lesions as, 152–157
focal solid lesions of, 152–157
benign, 153–157, 155*b*, 156*f*–157*f*
malignant, 152–153, 154*f*–155*f*, 155*b*
functions of, 141
Gamna-Gandy bodies in, 157
Gaucher disease in, 157, 158*f*
hamartomas of, 153–156, 156*f*
hemangiomas of, 148, 153–157, 156*f*
hematomas of, 158, 159*f*
infarctions of, 156–157, 157*f*
interventional procedures for, 161
lymphangiomas of, 148
measurement of, sonographic approach to, 143–145, 145*f*
metastases to, cystic, 148
nodular lesions of, 148–152
calcified, 150, 153*f*
in candidiasis, 150–152, 154*f*
causes of, 152*b*
in lymphoma, 152, 154*f*
metastatic, 152, 154*f*
microabscesses as, 150–152, 154*f*
in tuberculosis, 150, 151*f*–152*f*
pathologic conditions of, 145–158
pediatric, 1769–1772
abscesses of, 1769
calcifications in, 1769
contusion to, 1771*f*
cysts of, 1769
enlargement of, 1769, 1770*b*, 1771*f*
granulomas of, 1771*f*
hematomas of, 1770, 1771*f*
infarcts of, 1770, 1771*f*
spontaneous rupture of, 1770
wandering, 1770–1772
peliosis of, 147
pitfalls in interpretation of, 161–162, 161*f*
retrorenal, 162
rupture of, 158
in SCD, 157
sonographic appearance of, 142–158, 144*f*–145*f*
sonographic technique for, 142, 142*f*–143*f*
trauma to, 158, 159*f*–160*f*
tuberculosis and, 150, 151*f*–152*f*
wandering, 159, 161*f*
weight of, 141
as window to pleural space, 1702, 1707*f*
Splenic varices, in portal hypertension, 1759*f*
Splenic vein
pancreatic body and, 211, 211*f*
pediatric
Doppler studies of, best approach for, 1752
flow direction in, in portal hypertension, 1752

Splenic vein *(Continued)*
thrombosis of
acute pancreatitis complicated by, 230, 231*f*
chronic pancreatitis and, 232–233, 234*f*–235*f*
Splenogonadal fusion, 833
paratesticular, 1904
Splenomegaly
causes of, 145, 146*t*
complications of, 146
diagnosis of, 145–146
fetal, 1320
massive, 145, 146*t*
portal hypertension as cause of, 145, 147*f*
in sickle cell disease, 157
sonographic appearance of, 143*f*–144*f*
Splenorenal ligament, 139–141, 140*f*
Splenorenal shunts, in portal hypertension, pediatric, 1757, 1759*f*
Splenosis, posttraumatic, 160–161
Splenunculi, 158–159, 160*f*
Split cord malformation
fetal, 1234–1235
pediatric, 1688–1689, 1688*f*
Split liver graft, from deceased donor, 625
Split-screen imaging, for breast assessment, 769, 769*f*
Sports hernias, 484–488, 488*f*–489*f*
SPTA. *See* Spatial peak temporal average
Squamous cell carcinoma (SCC), 348
Staghorn calculus
tyrosinemia and, 1799, 1800*f*
in xanthogranulomatous pyelonephritis, 328, 329*f*
Standard sonographic examination, 1019
Standoff pad, in breast tumor imaging, 767, 767*f*
Steatosis
diffuse, 91, 92*f*
in inborn errors of metabolism, 1738
pediatric, 1740, 1740*f*, 1741*b*
Stein-Leventhal syndrome, 573
pediatric, 1877–1878, 1879*f*
Stener lesion, 864, 864*f*
Stenotic disease, of abdominal aorta, 441–445, 445*f*
Stensen duct, pediatric, 1630
Stent graft, 438
Stepladder sign, in intracapsular breast implant rupture, 804–805, 805*f*
Sternocleidomastoid muscle, 692*f*, 694
Sternohyoid muscle, 692*f*, 694
Sternum, defect of, pentalogy of Cantrell and, 1329
Steroids
anabolic, therapy with, hepatic adenomas and, 1746
injectable, for musculoskeletal interventions, 900–901
injection of, interventional sonography for, pediatric, 1961, 1964*f*
Stickler syndrome, clefts of secondary palate in, 1153
Stippled epiphyses, 1399
Stitch abscess, after herniorrhaphy, 494–496, 495*f*
Stomach, fetal, 1306–1308
absent or small, 1306, 1306*b*
esophageal atresia and, 1305–1306, 1305*f*
dilated, 1307, 1308*f*
intraluminal gastric masses in, 1308, 1309*f*
midline, 1307, 1308*f*–1309*f*
normal, 1307*f*
right-sided, 1307, 1308*f*–1309*f*
Stomach, pediatric, 1833–1840
anatomy of, 1834–1835, 1835*f*–1836*f*
antrum distention in, HPS pitfalls and, 1838, 1839*f*
Stomach, pediatric *(Continued)*
artifact of empty, 1838, 1839*f*
bezoars and, 1840, 1841*f*
gastric diaphragm and, 1839, 1840*f*
gastric ulcers and, 1839–1840, 1840*f*
gastritis and, 1839–1840, 1840*f*
HPS and, 1835–1838, 1835*b*, 1837*f*–1838*f*
pitfalls in diagnosis of, 1838, 1838*b*, 1839*f*
pylorospasm and minimal muscular, 1836–1838, 1838*f*
optimal measurements of, 1834*b*
sonographic technique for, 1833–1835
Stomodeum, 1133–1134
Strain elastography, 16, 17*f*, 772
Strain modulus, 15–16
Strangulated hernias. *See* Hernia(s), strangulated
Strawberry-shaped skull, 1136, 1137*f*
Streaming, 35
Streptococcal meningitis, group B, neonatal/infant, 1560, 1561*f*–1562*f*
Stress maneuvers, for hip stability determination, 1923
Strictures in, in Crohn disease, 269–274, 275*f*–276*f*
String sign, occluded carotid artery distinguished from, 939
Stroke
cardioembolic, 915–916
from carotid artery stenosis, 915–916
in neonatal/infant brain, duplex Doppler sonography and, 1580–1581, 1584*f*
SCD and
cerebrovascular disease indicators with, 1601*f*–1603*f*
risk categories for, 1599–1604, 1605*t*, 1606–1607
screening for, 1598
velocity indications of, 1605–1607
Stromal cell tumors, ovarian, pediatric, 1879
Stromal tumors, gastrointestinal, 264, 265*f*
pediatric, 1862
Struma ovarii, 584
Sturge-Weber syndrome
facial hemangiomas in, 1154
pheochromocytomas with, 1910–1912
TCD sonography assessing, 1614
Subacromial impingement, of shoulder, 877–879, 882–883
Subacromial spurs, 878–879
Subacromial-subdeltoid bursa, 879
appearance of, normal, 889, 891*f*
rotator cuff tears and, 888–889, 892*f*
thickening of, 889–891, 892*f*
with ganglion, 889–891, 892*f*
Subacute granulomatous thyroiditis, 724, 724*f*
Subamniotic hematomas, of placenta, 1474
Subarachnoid hemorrhages, neonatal/infant brain and, 1550, 1550*f*
Subarachnoid spaces, neonatal/infant
development of, 1520–1521
fluid collections in, duplex Doppler sonography of, 1585, 1588*f*
Subchorionic cysts
maternal floor infarction with, 1474, 1476*f*
placental, 1474, 1477*f*
Subchorionic hematoma, 1474
placental abruption differentiated from, 1471, 1474*f*
Subchorionic hemorrhage
early pregnancy failure and, 1069, 1069*f*
fetal echogenic bowel and, 1315*f*
Subclavian artery, 975
stenosis of, 976, 978*f*–979*f*
Subclavian steal phenomenon, 952–954, 953*b*, 953*f*–954*f*, 976, 979*f*
Subclavian vein
anatomy of, 990–991, 990*f*
stenosis of, sever, 1006, 1009*f*
ultrasound examination for, 991, 991*f*
Subcutaneous edema, fetal, in hydrops, 1417, 1419*f*–1420*f*
Subdural effusions, neonatal/infant, duplex Doppler imaging of, 1585, 1588*f*
Subdural hematomas, neonatal/infant, 1557, 1558*f*
Subdural hemorrhage, fetal, bilateral, 1207*f*
Subependymal cysts, 1543–1544
of neonatal/infant brain, 1566, 1567*f*
Subependymal hemorrhage, neonatal/infant brain and, 1543–1544, 1543*f*–1544*f*
Subfascial hematomas, cesarean sections and, 556–557, 557*f*
Subglottic stenosis or atresia, CHAOS and, 1253
Sublingual gland, pediatric, anatomy of, 1631, 1631*f*
Subluxation, 1923, 1927
Submandibular glands, pediatric
anatomy of, 1630–1631, 1631*f*
pleomorphic adenoma of, 1638*f*
sialolithiasis of, 1633, 1633*f*
Submandibular space, pediatric, 1630–1631, 1631*f*
cystic lesions of, 1639–1640, 1640*b*
Submandibular window, for TCD sonography, 1592–1593
Subphrenic abscess, 1716
Subplacental hematoma, 1471, 1474*f*
Subscapular fossa, 878–879
Subscapularis tendon
anatomy of, normal, 878–879, 879*f*
ultrasound evaluation of, 880, 882*f*
Subtrochanteric femur, absence of, 1400
Subvalvular aortic stenosis, 1292
Succenturiate lobes, of placenta, 1480–1481, 1481*f*
"Sugar icing", 868*f*
Sulcation disorders, of neonatal/infant brain, 1536–1537
Sulcus(i), of brain
development of, 1167
neonatal/infant
development of, 1520–1521, 1520*f*–1521*f*
effacement of, in diffuse cerebral edema, 1553, 1554*f*
normal sonographic appearance of, 1169, 1171*f*
radial arrangement of, in corpus callosum agenesis, 1528, 1532*f*
Sulfur colloid scanning, FNH and, 115
"Sunburst sign," in corpus callosum agenesis, 1528, 1532*f*
Superb microvascular imaging (SMI), 1746
basic technique of, 1749–1750, 1752*f*
Superficial fascia, pediatric, 1628, 1629*f*
Superficial peritendinous and periarticular injections, 902–904
for foot and ankle, 902–904, 903*f*–904*f*
for hand and wrist, 904, 905*f*
Superficial venous insufficiency, 981–982
Superior mesenteric artery (SMA)
pancreatic body and, 211, 211*f*
small bowel obstruction and, 1308
Superior mesenteric vein (SMV), 211, 211*f*
Superior vena cava (SVC)
anatomy of, 991
catheter position for, pediatric, 1716–1721, 1722*f*
stenosis, with PICC line, 993*f*
thrombosis of, pediatric, 1721, 1721*b*, 1722*f*
ultrasound examination of, 991–992, 992*f*
Supernumerary glands, 733
Supernumerary kidneys, 319
Supernumerary testes, 838–839, 841*f*

Superoanteromedial ridge, 416–417
Supraclavicular lymphadenopathy, pediatric, 1658
Suprahyoid space, pediatric
  anatomy of, 1628–1640, 1629*f*
  cystic lesions of, 1639–1640, 1640*b*, 1640*f*–1641*f*
  masticator space of, pathology of, 1640, 1641*f*
  salivary glands in, 1629–1639
    anatomy of, 1630–1631
Supraspinatus fossa, 878–879
Supraspinatus tendon
  anatomy of, 878–879
  calcific tendinitis of, 891–892, 892*f*
  postoperative, 888, 891*f*
  tendinosis of, 886*f*
  ultrasound evaluation of, 881–883, 883*f*–884*f*
Supratentorial tumors, neonatal/infant brain and, 1562
Supraventricular tachycardia (SVTs)
  with Ebstein anomaly, 1286–1287
  fetal, 1296–1297, 1296*f*
    hydrops from, 1424, 1425*f*
Surface epithelial inclusion cysts, 569, 573
Surface epithelial-stromal tumors, 579–582, 580*f*–582*f*
SURUSS. *See* Serum, Urine and Ultrasound Screening Study
Surveillance
  of AAA, 435–437
    CT in, 437
    sonographic technique for, 436–437, 436*f*–437*f*
  active, for prostate cancer, 401
Suspensory (infundibulopelvic) ligament, 564–565
Sutures, cranial, premature fusion of, 1136–1139, 1138*b*, 1138*f*–1139*f*
SVC. *See* Superior vena cava
SVTs. *See* Supraventricular tachycardia
SWE. *See* Shear wave elastography
Swyer syndrome, 1887
Sylvian fissure, neonatal/infant, development of, 1514*f*–1515*f*, 1520–1521
Syncytiotrophoblast, 1049, 1051–1052, 1052*f*, 1466*f*
Syndactyly
  fetal, 1406, 1406*f*
  of fingers, in triploidy, 1105*f*, 1406
Synechia, amniotic band sequence and, 1401
Synovitis, 867, 869
  hip joint, pediatric, 1931*f*
Syntelencephaly, 1187, 1189, 1535–1536
Synthetic arteriovenous graft. *See* Arteriovenous graft, synthetic
Syphilis, 1203–1204
  fetal hydrops from, 1431–1432
Syringocele, 1683–1684
Syrinx, 1681
System setup, obstetric sonography and, 1035–1036, 1035*f*–1037*f*
Systemic lupus erythematosus, maternal, fetal AVB from, 1297
Systolic velocity, cerebral, factors changing, 1612*t*
Systolic-to-diastolic ratio (S/D ratio), 27, 27*f*

T

"T" sign, in monochorionicity, 1119, 1119*t*, 1121*f*
Tachyarrhythmias, fetal, hydrops from, 1424
Tachycardia
  fetal, 1296–1297, 1296*f*
  neonatal/infant, intracranial RI and, 1576
  supraventricular
    with Ebstein anomaly, 1286–1287
    fetal, 1296–1297, 1296*f*
    fetal, hydrops from, 1424, 1425*f*
  ventricular, 1296
Tactile sensation, in obstetric sonography, 1038
Tailgut cysts, 297, 298*f*
Takayasu arteritis
  aortic stenosis in, 444
  of common carotid artery, 944–946, 947*f*
Talipes equinovarus, fetal, 1406*f*, 1407
  campomelic dysplasia and, 1395
Talipomanus, fetal, 1407
TAMM. *See* Time-averaged mean of maximum velocity
Tamoxifen, 544–545, 545*f*
Tandem plaques, in carotid stenosis, 923–924
TAPS. *See* Twin anemia polycythemia sequence
Tardus-parvus waveform(s)
  arterial stenosis and, 969, 971*f*
  in hepatic artery thrombosis after liver transplantation, 631, 633*f*
  in internal carotid artery stenosis, 934*f*, 938
  pediatric renal artery stenosis and, 1809
  in peripheral artery stenosis, 965–966
  in popliteal artery occlusion, 968*f*
  in renal artery duplex Doppler sonography, 450, 450*f*
  in renal artery stenosis, 368, 368*f*
  in subclavian steal phenomenon, 953*b*, 954
Target pattern, in gut wall, 257, 260*f*
Targeted organ lesion biopsy, 1961, 1961*f*–1962*f*
TAS. *See* Transabdominal sonography
TASC. *See* Trans-Atlantic Inter-Society Consensus
TCC. *See* Transitional cell carcinoma
TCD. *See* Transcranial Doppler sonography
TDLUs. *See* Terminal ductolobular units
Teale femoral hernia, 482, 485*f*
Teen mothers, fetal gastroschisis and, 1322–1323
Tegmento-vermian angle, 1189–1190
Telangiectasia, hereditary hemorrhagic, 104
Telencephalon, formation of, 1077
"Telephone receiver" femur, 1380*f*
Temporal average intensity, 36
Temporal bone approach, for duplex Doppler ultrasound of neonatal/infant brain, 1574, 1575*f*
Temporal horns, of lateral ventricles, neonatal/infant, in coronal imaging, 1514–1515
Temporal maximum intensity projection imaging, 64, 65*f*
Temporal peak intensity, 36, 36*f*
Temporal tap, in external carotid artery identification, 918, 918*f*
Tendinitis, calcific
  injections for, 909, 911*f*
  of supraspinatus tendon, 891–892, 892*f*
Tendinosis, 859–861, 861*f*
  de Quervain, injection for, 904, 905*f*
  rotator cuff, 886, 886*f*
  in sports hernia, 486
  of supraspinatus tendon, 886*f*
Tendon(s)
  anatomy of, normal, 859, 860*f*
  anisotropy of, 859, 860*f*, 899
  calcification of, 859–861
  conjoined
    direct inguinal hernia and, 479–481, 483*f*–484*f*
    weakness/tear of, sports hernia and, 485–486, 489*f*
  inflammation of, 861–862, 862*f*
  injections of deep, 904–907
  injuries to, 859–861, 861*f*
  tears to, 861, 861*b*, 862*f*
  ultrasound techniques for, 859–862
Tenosynovitis, 861–862, 862*f*
  long head of biceps, 892–893, 893*f*
  stenosing, injections for, 902
Tenotomy, percutaneous, 909–910, 913*f*
Teratocarcinomas, pediatric, testicular, 1899
Teratogenic effects, from hyperthermia, 38
Teratogens, thermal effects of ultrasound and, 1037
Teratologic hip dislocation, pediatric, 1932
Teratoma(s). *See also* Sacrococcygeal teratomas
  cystic, ovarian, 582–584, 582*b*, 583*f*
  dacryocystocele differentiated from, 1143
  fetal
    cardiac, 1294
    cervical, 1159, 1161*f*
    intracranial, 1208–1209, 1209*f*
    intrapericardial, hydrops from, 1424
    neck, hydrops from, 1425, 1426*f*
    sacrococcygeal, 1238–1239, 1238*b*, 1239*f*, 1430–1431
  immature, 584
  neonatal/infant
    brain, 1562
    cardiac, 1293
  pediatric
    benign, ovarian, 1880, 1880*f*
    cervical, 1654, 1654*f*
    hemorrhagic ovarian cyst differentiated from, 1877
    pseudoprecocious puberty and, 1887
    sacrococcygeal, 1691, 1691*t*, 1694*f*
    testicular, 1899
    thymic, 1723–1724
  testicular, 823–824, 825*f*
  thyroid gland, 1648
Teres minor tendon
  anatomy of, 878–879
  ultrasound evaluation of, 884
Terminal ductolobular units (TDLUs), of breast, 760–761
  carcinoma in, 789–790, 792*f*
  sonographic appearance of, 762, 766*f*
Terminal ileitis, 288
Terminal myelocystocele, 1234
Terminal transverse limb defects, amniotic band sequence and, 1400
Terminal ventricle, persistent, pediatric, 1685
Tessier clefts, classification of, 1152–1153, 1153*f*
Testicular appendage, pediatric, torsion of, 1897, 1897*f*
Testicular artery(ies), 820*f*–821*f*, 821
Testicular duplication, pediatric, 1891
Testicular feminization, fetal, 1368
Testicular microlithiasis, pediatric, 1904, 1904*f*
Testicular torsion, 844–846, 844*f*–845*f*
  pediatric
    acute, 1893–1894, 1894*f*
    acute scrotal pain from, 1892
    chronic, 1895
    color Doppler sonography in, 1895–1899, 1896*b*
    detorsion of, 1895–1896
    extravaginal, 1892–1893, 1893*f*
    incomplete, 1896
    intravaginal, 1893–1894, 1893*f*
    late, 1895
    "missed", 1895, 1895*f*
    within scrotal sac, 1893–1894
    sonographic signs of, 1894*b*
    spontaneous detorsion of, 1896
    types of, 1893–1894, 1893*f*
Testis(es). *See also* Scrotum
  abscess of, 831–832, 831*f*
  adrenal rests and, 832–833, 833*f*, 1824
  anatomy of, 819, 819*f*–820*f*
  appendix, 820–821, 820*f*
    pediatric, 1897
  arterial supply of, 820*f*–821*f*, 821
  cryptorchid, seminomas in, 823
  cryptorchidism and, 851, 851*f*
    pediatric, 826
  cystic dysplasia of, 830

Testis(es) *(Continued)*
cysts of, 829, 829*b*
cystic dysplasia and, 830
epidermoid, 830*f*, 831
intratesticular, 829, 830*f*
tubular ectasia of rete testis and, 829–830, 830*f*
ectopia of, transverse, 1890
feminization of, 826
dysplastic gonads and, 1899
primary amenorrhea in, 1887
fetal
descent of, 1367
undescended, 1367
fibrosis of, after orchitis, 846, 849*f*
fracture of, 850, 850*f*
gubernaculum, 851
hematoma of, 848–850, 850*f*
heterogeneous "striped", 846, 849*f*
infarction of
after herniorrhaphy, 494–496, 495*f*
segmental, 832, 832*f*
in inguinal canal, 851, 851*f*
malpositioned, 851
mediastinum, 819, 820*f*
pediatric, 1888
metastases to, 822*b*, 826–829, 826*b*
hamartomas as, 829, 829*f*
leukemia as, 827, 828*f*
lymphoma as, 826–827, 828*f*
myeloma as, 827–829
microlithiasis of, 833, 833*b*, 834*f*
pediatric
accessory, 1891
anatomy of, 1888–1890, 1889*f*
appendix, 1897
bilobed, 1891
congenital abnormalities of, 1890–1892, 1890*f*
cystic dysplasia of, 1891–1892, 1891*f*
cysts of, solitary simple, 1901–1902
detorsion of, 1895
hematomas of, 1897–1898
Henoch-Schönlein purpura and, 1899
hyperemia of, 1896
infarction of, 1895
newborn, 1888, 1889*f*
ovotestis and, 1891, 1891*f*
postpubertal, 1888–1890, 1889*f*
rete, tubular ectasia of, 1891–1892, 1892*f*
rupture of, 1897–1898, 1898*f*
smaller than normal, 1891
torsion of, 1870, 1892–1899, 1893*f*–1894*f*, 1894*b*, 1896*b*
undescended, right, 1890, 1890*f*
rete, 819
tubular ectasia of, 829–830, 830*f*, 1891–1892, 1892*f*
rupture of, 848, 850*f*
seminomas in, 823, 823*f*–824*f*
septula, 819, 820*f*
splenogonadal fusion and, 833
supernumerary, 838–839, 841*f*
torsion knot and, 844, 845*f*
trauma to, 847–851, 850*f*
tumors of, 822–834
choriocarcinoma as, 824, 825*f*, 1899
classification of, 822*b*
embryonal carcinoma as, 823, 825*f*, 1899
endodermal sinus, 823–824, 825*f*, 1899
germ cell, 822–825, 822*b*, 825*f*–826*f*
gonadal stromal, 826, 827*f*
Leydig cell, 826, 827*f*
malignant, 822–826
markers of, 822
Testis(es) *(Continued)*
metastatic, 822*b*
mixed germ cell, 822–823, 822*b*, 825*f*
non-germ cell, 825–826
nonseminomatous germ cell, 822*b*, 823–824, 825*f*
pediatric, 1899–1902
regressed germ cell, 824–825, 825*f*–826*f*
Sertoli cell, 826, 827*f*
sex cord-stromal, 825–826, 827*f*
stromal, 822, 822*b*
teratocarcinomas as, 1899
teratomas as, 823–824, 825*f*, 1899
yolk sac, 823–824, 825*f*
undescended, 851, 851*f*
dysplastic gonads and, 1899
in prune belly syndrome, 1361–1362
right, pediatric, 1890, 1890*f*
Testosterone, Leydig cells and secretion of, 819
Tethered cord, 1674
in diastematomyelia, 1236*f*
fetal cloacal exstrophy and, 1328
pediatric, 1678–1679, 1681*f*
spina bifida occulta and, 1226
Tetralogy of Fallot (TOF), 1288, 1288*f*
Tetraphocomelia, Roberts syndrome and, 1401
TGA. *See* Transposition of great arteries
TGC. *See* Time gain compensation
Thalamostriate vessels, mineralization of, 1203, 1204*f*
Thalamus
fetal, normal sonographic appearance of, 1168
neonatal/infant, sagittal imaging of, 1515, 1517*f*
vasculopathy of, neonatal/infant brain and, 1556–1557
α-Thalassemia, nonimmune hydrops from, 1423, 1431
Thanatophoric dysplasia
bowing of long bones in, 1381–1382
campomelic dysplasia differentiated from, 1388–1389
cloverleaf-shaped skull and, 1136, 1137*f*, 1389*f*
craniosynostosis in, 1136–1138, 1137*f*
diagnosis of, 1376–1377
homozygous achondroplasia differentiated from, 1389, 1389*f*
lethal skeletal dysplasia and, 1387–1390
megalencephaly associated with, 1194–1195
platyspondyly in, 1388–1389, 1390*f*
sonographic appearance of, 1380*f*
type 1, 1388–1389
type 2, 1388–1389, 1389*f*
Thanatophoric skeletal dysplasia, cortical malformations and, 1193–1194
Theca externa, 1049
Theca lutein cysts, 570, 572
pediatric, 1875
Thecomas, ovarian, 585
Thelarche, pseudoprecocious puberty and, 1888
Thermal effects, in ultrasound, 31. *See also* Bioeffects, thermal
obstetric, 1036–1038
Thermal index (TI), 38–40, 38*b*
for bone, in late pregnancy, 1039
obstetric sonography duration as function of, 1035–1036, 1036*f*, 1042*t*
for soft tissue, in early pregnancy, 1039
tissue model of
with bone at focus, 39
with bone at surface, 39–40
homogeneous, 39
Thigh graft, hemodialysis and, preoperative mapping for, 1000, 1001*f*
Thoracentesis, pediatric, ultrasound-guided, 1725–1726
Thoracic ectopia cordis, 1295, 1296*f*
Thoracic kidney, 318
Thoracic outlet syndrome, in upper extremity peripheral arteries, 976–977, 980*f*
Thoracoabdominal ectopia cordis, 1295
Thoracoabdominal schisis, 1401
Thorax, fetal
anomalies of, hydrops from, 1425–1427, 1427*f*
circumference and length of
gestational age correlated with, 1247*t*
pulmonary hypoplasia and, 1382, 1384*f*
circumference of, decreased
in hypophosphatasia, 1392
severe micromelia with, 1387*t*
echogenic lesions of, differential diagnosis of, 1248*t*
Thorotrast, 123
Three-dimensional (3-D) ultrasound, 15, 16*f*
for breast lesions, 773
for fetal heart assessment, 1277
for fetal spine, 1216, 1221–1223
for neonatal/infant brain imaging, 1518
in placental volume assessment, 1466, 1468*f*
for prostate cancer, 406–407
for skeletal dysplasia evaluation, 1384, 1385*f*
for uterus, 529
Threshold level, for seeing gestational sac, 1056
Thrill, from carotid stenosis, color Doppler, 933
Thrombocytopenia, alloimmune, intracranial hemorrhage and, 1206
Thrombocytopenia–absent radius syndrome, 1401, 1402*f*
Thrombophlebitis, ovarian vein, 589–590, 589*f*
Thrombosis. *See also* Deep venous thrombosis
cerebral sinovenous, 1547–1548
dural sinus
fetal, 1205–1206, 1206*f*
neonatal/infant, 1585
hepatic artery, after liver transplantation, 627, 628*f*, 631, 633*f*
hepatic vein, pediatric, suprahepatic portal hypertension and, 1763, 1763*f*
IJV, 955–956, 956*f*–957*f*
central line placement causing, 1658, 1661*f*
of iliac veins, 459–460, 459*f*–461*f*
detection difficulties with, 988, 988*f*
of IVC, 459–460
after liver transplantation, 636–637, 642*f*, 1766, 1769*f*–1770*f*
ovarian vein, 369, 589–590, 589*f*
after pancreas transplantation, 677–678, 678*f*–679*f*
portal vein, 98, 99*f*–100*f*
chronic pancreatitis and, 232–233, 235*f*
from HCC, 120, 121*f*
after liver transplantation, 635–636, 639*f*–640*f*, 1766
malignant, 98, 99*f*
pediatric, 1757, 1757*b*
renal artery, after renal transplantation, 653–655, 657*f*
Doppler assessment of, pediatric, 1807–1809, 1808*f*
renal vein, 369, 370*f*
Doppler assessment of, pediatric, 1809
hyperechogenic kidneys and, 1351
pediatric, acute, Doppler assessment of, 1804–1805, 1804*b*, 1804*f*
after renal transplantation, 658, 662*f*
round ligament, simulating groin hernia, 500, 501*f*

Thrombosis *(Continued)*
of splenic vein
acute pancreatitis complicated by, 230, 231*f*
chronic pancreatitis and, 232–233, 234*f*–235*f*
SVC, pediatric, 1721, 1721*b*, 1722*f*
vascular, pediatric chest and, 1716–1721, 1721*f*–1723*f*
Thumb
aplastic or hypoplastic, in Fanconi pancytopenia, 1400, 1402*f*
hitchhiker
in diastrophic dwarfism, 1382, 1406
diastrophic dysplasia and, 1398, 1398*f*
triphalangeal, in Aase syndrome, 1401
Thump artifacts, 60
Thymic cyst, 1652, 1653*f*, 1723–1724
Thymic index, 1723, 1725*f*
formula for calculation of, 1724*t*
normal, for children under 2, 1726*t*
Thymopharyngeal ducts, formation of, 1652
Thymus
fetal, normal appearance of, 1244*f*
pediatric
benign abnormalities of, 1723–1724
cervical ectopic, 1723
ectopic, 1652, 1653*f*
mediastinal masses and abnormal location of, 1723
normal, blood vessels of chest and, 1716–1721, 1721*f*
superior herniation of, 1723
Thyroglossal duct cysts, pediatric, 1640, 1643, 1644*f*–1645*f*
Thyroid artery, superior, 918
Thyroid gland. *See also* Thyroiditis
adenomas of, 697, 700*f*
anatomy of, 692–694, 692*f*
aplasia of, 694, 694*f*
carcinoma of, 695, 698–708
anaplastic, 707–708, 708*b*, 709*f*
follicular, 701, 701*b*, 706*f*–707*f*, 1648
incidence of, 722, 722*f*–723*f*
medullary, 701–707, 707*f*–708*f*, 1648
papillary, 698–701, 701*f*–705*f*, 713, 1648, 1649*f*
papillary microcarcinoma, 701, 706*f*
CEUS for assessment of, 692, 714–715
congenital abnormalities of, 694, 694*f*
cysts, calcifications of, 695
diffuse disease of, 723–728, 723*b*
adenomatous goiter as, 727
Graves disease and, 727, 727*f*, 1646, 1646*f*
ectopic, 694
elastography for assessment of, 692, 714–715, 715*f*–716*f*
ethanol injection for nodular disease of
for autonomously functioning nodules, 719–720
for benign cystic lesions, 719, 719*f*
for solitary solid benign "cold" nodules, 720
fetal, normal sonographic appearance of, 1136*f*
hypoplasia of, 694, 694*f*
incidentally detected nodule and, 720–723, 722*f*–723*f*, 723*b*
instrumentation for, 691–692, 692*f*
lingual, pediatric, 1639
lobes of, 692
lymphoma of, 708–709, 709*f*
metastases to, 709, 710*f*
nodular disease of, 694–723
adenomas in, 697, 700*f*
carcinoma in, 698–708
fine-needle aspiration biopsy in, 709–710, 710*t*, 722
hyperplasia and goiter in, 695–697, 695*f*–699*f*
Thyroid gland *(Continued)*
lymphoma in, 708–709, 709*f*, 1648
metastases in, 709, 710*f*
parathyroid adenomas confused with, 745–746
pathologic features of, 695–709
sonographic correlates of, 695–709
sonographic evaluation of, 695*b*
pediatric
cancer of, 1648, 1648*b*, 1649*f*
congenital lesions of, 1642–1643
cysts of, 1646, 1647*f*
dimensions of, normal, 1642*t*
dysgenesis of, 1642–1643
ectopic, 1642–1643, 1644*f*
follicular adenoma of, 1646–1648, 1647*f*
hemiagenesis of, 1642–1643, 1643*f*
hemorrhage in, 1646, 1647*f*
inflammatory disease of, 1643–1646, 1645*f*–1646*f*
isthmus of, 1640–1642
lobes of, normal thickness of, 1643*t*
masses of, 1646–1648, 1647*f*–1649*f*, 1648*b*
normal anatomy of, 1640–1642, 1642*f*, 1642*t*–1643*t*
pseudonodule of, 1646
pyramidal lobe of, 1640–1642
retrosternal, 1723
volume of, normal, 1643*t*
sonographic applications in, 710–720
for benign and malignant nodule differentiation, 696*f*–699*f*, 712–714, 712*t*
CEUS for, 692, 714–715
elastography for, 692, 714–715, 715*f*–716*f*
incidentally detected nodule and, 720–723, 722*f*–723*f*, 723*b*
needle biopsy guidance for, 715–720, 718*f*–719*f*, 721*f*
for thyroid mass detection, 710–712, 711*f*–712*f*
TIRADS for, 714
sonographic technique for, 691–692, 692*f*
vascularity of, 693, 694*f*
volume of, measuring, 692–693, 693*f*
Thyroid Imaging Reporting and Data System (TIRADS), 714
Thyroid inferno, in Graves disease, 727, 727*f*
Thyroiditis, 723*b*
acute suppurative, 723–724
chronic autoimmune lymphocytic, 724, 725*f*–727*f*
de Quervain, 1645
focal, pediatric, 1645
Hashimoto, 724, 725*f*–727*f*
fetal goiter and, 1159–1163
pediatric, 1645, 1646*f*
invasive fibrous, 727–728, 728*f*
painless (silent), 725–727
subacute granulomatous, 724, 724*f*
Thyromegaly, fetal, 1159–1163
TI. *See* Thermal index
TIA. *See* Transient ischemic attack
TIB. *See* Thermal index for bone
Tibia, dislocation of, pediatric, 1934*f*
Tibial artery
anterior, 966
normal appearance of, 966–967
posterior, 966
sonographic technique for, 967
Tibial hemimelia, pediatric, 1933
Tibial tendons, posterior, injection of, 902, 903*f*
Tibial veins
anterior, 981, 981*f*
posterior, 981, 981*f*
Tibioperoneal trunk, 966, 981
Time gain compensation (TGC)
artifacts and settings of, 19–21
control of, 8–9, 8*f*
output control and, 50
Time-averaged mean of maximum (TAMM) velocity, 1593, 1605–1606
Time-averaged peak velocity, 1593
"Tip of the iceberg" sign, 582–583
TIPS. *See* Transjugular intrahepatic portosystemic shunts
TIRADS. *See* Thyroid Imaging Reporting and Data System
TIS. *See* Thermal index for soft tissue
Tissue harmonic imaging, 13, 13*f*–14*f*, 38, 61–62
Tissue heating
spatial focusing and, 35
temporal considerations in, 36, 36*f*
tissue type and, 36, 36*f*
Tissue plasminogen activator (TPA), 1622
Tissue vibration artifact, 973–974, 974*f*
T-lymphotropic virus, 1203–1204
TMPRSS2:ERG test, 396
Tobacco, fetal gastroschisis and, 1322–1323
Toe polydactyly, fetal, 1406*f*
Toes, sandal, 1406*f*, 1407
TOF. *See* Tetralogy of Fallot
Tongue, fetal, abnormally enlarged, 1153, 1153*b*, 1158*f*
TORCH infections, 1203–1204
neonatal/infant brain and, 1511, 1558
Torsion, testicular. *See* Testicular torsion
Torsion knot, 844, 845*f*
Toxemia, pediatric pregnancy and, 1884
Toxoplasmosis
fetal brain and, 1204
fetal hydrops from, 1432
prenatal, neonatal/infant brain and, 1558–1560
TPA. *See* Tissue plasminogen activator
Trabecula septomarginalis, moderator band of, 1274–1275
Trachea, fetal, CHAOS and, 1253
Tracheal webs, fetal, CHAOS and, 1253
Tracheoesophageal fistula, fetal
CHAOS and, 1254–1255
esophageal atresia and, 1305
Transabdominal scanning, for placenta previa, 1469
Transabdominal sonography (TAS), for pelvis, 564
Trans-Atlantic Inter-Society Consensus (TASC), 970
Transcranial Doppler (TCD) sonography
adult
functional, 1622
indications for, 1598–1623, 1598*b*
vasospasm and, 1608–1610, 1610*t*
for carotid artery examination, 948–950, 950*f*
pediatric
ACA collateral flow evaluation and, 1610, 1611*f*
angle correction for, 1607
asphyxia and, 1614, 1616*f*
AVM detection with, 1614, 1615*f*
brain death and, 1618–1620, 1618*b*, 1619*f*–1620*f*
in cardiopulmonary bypass, 1621–1622
in CEA, 1621
cerebral edema and, 1614, 1617*f*
contrast enhancement for, 1597
ECMO monitoring with, 1622
equipment types for, 1591–1592
factors changing indices in, 1612*t*
foramen magnum approach for, 1592, 1595*f*
functional, 1622
headaches and, 1610–1611, 1612*f*
hydrocephalus and, 1611–1614, 1613*f*
hyperventilation therapy and, 1614

Transcranial Doppler (TCD) sonography *(Continued)*
indications for, 1598–1623, 1598*b*
in intraoperative neuroradiologic procedures, 1620–1622, 1621*f*–1622*f*
limitations for, 1597, 1597*t*
orbital approach for, 1592, 1596*f*
pitfalls in, 1597, 1597*t*
power settings for, 1597
right-to-left shunt evaluation with, 1614–1618
for SCD, 1591, 1598–1608, 1599*b*, 1599*f*–1608*f*
sleep apnea and, 1611
submandibular approach for, 1592–1593
technique for, 1592–1596
TPA and, 1622
transtemporal approach for, 1592, 1593*f*–1594*f*
vascular malformations and, 1614, 1615*f*
vasospasm and, 1608–1610, 1609*f*, 1610*t*
velocity evaluation in, 1593, 1595–1596
Transducer(s), 7–8
arrays, 11–12, 12*f*
hand-held, for breast sonography, 788, 789*f*–790*f*
heating, in obstetric sonography, 1038
heeling and toeing of, 768
in interventional sonography, pediatric, 1943
locating needle after insertion and, 1946–1947, 1947*f*
for neonatal/infant brain imaging, 1512
output control and, 50
percutaneous needle biopsies and sterilization of, 600
second harmonic and, 105
selection of, 12
for obstetric sonography, 1035
Transfundal pressure, dynamic cervical change and, 1501–1503
Transfusion, fetomaternal, maternal serum alpha-fetoprotein elevation in, 1228. *See also* Twin-twin transfusion syndrome
Transhepatic cholangiography, 614–615
Transient double-bubble sign, 1309
Transient elastography, 1764
Transient ischemic attack (TIA), 916
carotid artery embolism causing, 919
Transitional cell carcinoma (TCC)
bladder, 347–348, 350*f*
genitourinary tract tumors and, 346–348
nonpapillary, 346
ovarian, 581–582, 582*f*
papillary, 346
renal, 346–347, 346*f*–349*f*
synchronous, 346
ureteral, 347
Transitional cell papilloma, lower urinary tract, pediatric, 1910–1912
Transjugular intrahepatic portosystemic shunts (TIPS), 131–132, 132*b*, 132*f*–133*f*, 463, 1764
Translabial ultrasound
of cervix, 1497
of female urethra, 315, 316*f*
Transmediastinal artery, 820*f*, 821
Transmitter, 7
Transorbital approach, for duplex Doppler ultrasound of neonatal/infant brain, 1574, 1575*f*
Transperineal biopsy, TRUS-guided, 411
Transperineal scanning, in Crohn disease, 276
Transperineal ultrasound
cervix in, 1497, 1497*f*
in ureteral calculi detection, 337
Transplantation, organ, 623–624. *See also* Liver transplantation; Pancreas transplantation; Posttransplant lymphoproliferative disorder; Renal transplantation
Transposition of great arteries (TGA), 1289–1290, 1289*f*–1290*f*
Transrectal ultrasound (TRUS)
biopsy guided by, 407–411, 408*f*
analgesia and, 407
antibiotic prophylaxis and, 407, 408*f*
anticoagulation and, 407–408
bowel preparation and, 407
indications and sampling for, 409, 409*b*, 410*f*
in men with absent anus, 411
mpMRI-TRUS fusion, 410–411
other applications of, 411–412
preparation for, 407–408
after radical prostatectomy, 411, 411*f*
side effects and complications in, 409
technique for, 408–409, 408*f*
transperineal, 411
brachytherapy guided by, 401, 402*f*
for drainage of pelvic abscesses, 612
for hematospermia, 394
infertility and, 392–394, 393*f*
of male urethra, 315, 316*f*
probes for, 386–387, 386*f*
of prostate, 381–382
prostate cancer, mpMRI fusion with, 406–407, 410–411
prostate cancer and, 302, 302*f*, 403–406, 403*f*–405*f*, 406*b*
in rectal carcinoma staging, 301
rectal cleansing prior to, 387
Transtemporal window
for TCD sonography, 1592, 1593*f*–1594*f*
for transcranial Doppler sonography, 948
Transurethral resection of ejaculatory ducts, 393
Transurethral resection of prostate (TURP), 385*f*–386*f*, 388
Transvaginal sonography, in peritoneal disease evaluation, 506, 506*f*–507*f*
Transvaginal ultrasound
for acute appendicitis diagnosis, 283, 285*f*
for adnexa assessment, 566
cervical abnormal findings on, 1503*b*
for cervix, 1497–1498, 1497*f*–1498*f*
diagnostic value of, 258
for drainage of pelvic abscesses, 612, 613*f*
endometrial thickness assessment with, 545–546
in gestational sac identification, 1054–1055
for pediatric pelvis, 1870–1871
for placenta previa, 1469
in pregnancy, safety of, 1049
thermal effects of, 38
in ureteral calculi detection, 337, 338*f*
for uterus, 529, 529*b*
in yolk sac identification, 1057
Transventricular valvotomy, 1292
Transverse abdominis tendon, torn, in spigelian hernia, 483–484, 487*f*
Transverse mesocolon, 219, 220*f*
Transverse myelitis, pediatric, neurogenic bladder in, 1907
Transverse testicular ectopia, 1890
Transverse waves, 2–3
TRAP. *See* Twin reversed arterial perfusion
Trauma
biliary, hemobilia from, 174, 175*f*
bladder, 366
cervical, carotid artery damage from, 946, 948*f*
dural sinus thrombosis from, 1205–1206
focused abdominal sonography for, 508
to genitourinary tract, 365–366
Trauma *(Continued)*
to liver, 129–132, 131*f*
to lower urinary tract, pediatric, 1912
to musculoskeletal system pediatric, 1938–1939, 1939*f*
pediatric
epididymitis following, 1897
scrotum and, 1897–1898, 1898*f*
renal, 365–366, 366*f*
scrotal, 847–851, 850*f*
splenic, 158, 159*f*–160*f*
testicular, 847–851, 850*f*
ureteral, 366
Treacher Collins syndrome
clefts of secondary palate in, 1153
midface hypoplasia in, 1148
Triangular cord sign, in biliary atresia, 1734–1735, 1737, 1738*f*
Trichobezoars, 300, 1840, 1841*f*
Tricuspid atresia
fetal, hydrops from, 1423–1424
hypoplastic right ventricle with, 1287
Tricuspid insufficiency, fetal, spectral Doppler assessment of, 1281*f*
Tricuspid regurgitation
in aneuploidy screening, 1095
in Ebstein anomaly, 1286
neonatal/infant, cardiac pulsations in veins and, 1578, 1578*f*
"Trident hand" configuration, achondroplasia and, 1407, 1408*f*
Triggered imaging, 65
Trigone, 314
neonatal/infant, in coronal imaging, 1515
pediatric, identification of, 1871, 1872*f*
Triorchidism, 1891
Triphalangeal thumb, in Aase syndrome, 1401
Triphasic waveform, 966–967
Triplets, amnionicity and chorionicity and, 1122*f*
Triploid karyotype, partial molar pregnancy and, 1078
Triploidy, 1078
common sonographic findings in, 1104–1106, 1104*b*, 1105*f*
Dandy-Walker malformation in, 1105*f*
fetal hydrops from, 1429–1430
IUGR in, 1105*f*
omphalocele in, 1105*f*
ovarian cysts in, 1105*f*
skeletal findings in, 1408–1409
syndactyly of fingers in, 1105*f*, 1406
Triradiate cartilage
of hip, 1923
in sonogram of hip from transverse/neutral view, 1927
Trisomy 9, horseshoe kidney in, 1345–1346
Trisomy 13 (Patau syndrome)
common sonographic findings in, 1104, 1104*b*, 1105*f*
facial clefts in, 1151
fetal hydrops from, 1429–1430
fetal omphalocele and, 1325
fetal pentalogy of Cantrell and, 1329
HPE in, 1104, 1105*f*
hyperechogenic kidneys in, 1351
NT in, 1093
polydactyly in, 1104, 1105*f*
proboscis in, 1104, 1105*f*
skeletal findings with, 1408, 1408*b*
umbilical cord cysts in, 1483
Trisomy 17, biliary atresia and, 1737
Trisomy 18 (Edwards syndrome)
biliary atresia and, 1737
CDH and, 1263

Trisomy 18 (Edwards syndrome) *(Continued)*
choroid plexus cyst in, 1103*f*, 1104
clenched hands in, 1103, 1103*f*
common sonographic findings in, 1103–1104, 1103*b*, 1103*f*
congenital heart defects in, 1103
ectopia cordis and, fetal, 1329
facial clefts in, 1151
fetal hydrops from, 1429–1430
fetal pentalogy of Cantrell and, 1329
horseshoe kidney in, 1345–1346
hydrocephalus in, 1103
IUGR and, 1104
mega-cisterna magna and, 1168–1169
NT in, 1093
omphalocele in, 1103, 1103*f*
fetal, 1325
polyhydramnios in, 1104
skeletal findings with, 1408, 1408*b*
umbilical cord cysts in, 1103*f*, 1483
Trisomy 21 (Down syndrome)
absent nasal bone in, 1150
adjunct features of, 1101
A-V canal, 1098*f*
AVSD and, 1101, 1284
β-hCG concentration in, 1089–1090
choroid plexus cysts and, 1101
congenital heart defects in, 1097, 1098*f*
duodenal atresia in, 1097, 1098*f*
ear length in, 1101
echogenic bowel in, 1100*f*, 1101
echogenic intracardiac focus in, 1100*f*, 1101
femur length in, 1100–1101
fetal hepatomegaly and, 1316
fetal hydrops from, 1429–1430
frontothalamic distance in, 1101
genetic sonography in, 1102–1103
humerus length in, 1101
hypoplasia of middle phalanx in, 1101
iliac angle measurements in, 1101
macroglossia in, 1153
markers in, 1097
cluster of, likelihood ratios of, 1098*t*
combined, 1100*t*, 1101–1103
common second-trimester, 1099*b*
isolated, likelihood ratios of, 1097*t*
midface hypoplasia in, 1148
nasal bone in, 1099–1100, 1099*f*
NT in, 1089, 1090*f*
nuchal fold in, 1097–1099, 1099*f*, 1154–1159
prevalence of, 1088–1089
risk for, short femur indicating, 1381
risk ratio for, revised, 1102*b*
screening for, second-trimester, 1097–1103, 1098*f*
skeletal findings with, 1408, 1408*b*
structural anomalies in, 1101
urinary tract dilation in, 1100*f*, 1101
VM in, 1098*f*
VSDs in, 1098*f*, 1101
wormian bones in, 1139
Trocar technique, for drainage catheter placement, 611, 611*f*
Trophoblastic blood flow, 1083
Trophoblastic tumor, placental-site, 1082
True hermaphroditism, pediatric, 1891, 1899
Truncal artery, 1288
Truncal valve, 1288
Truncus arteriosus, 1288, 1289*f*
Trunk, length of, shortened, in achondrogenesis, 1391
TRUS. *See* Transrectal ultrasound
TSC. *See* Tuberous sclerosis
T-shaped uterus, 1881
TTT. *See* Twin-twin transfusion syndrome
Tubal occlusion devices, 553*f*, 554
Tubal ring, ectopic, 1072, 1073*f*
Tuberculosis
of adrenal glands, 423
epididymitis associated with, 841, 843*f*
spleen and, 150, 151*f*–152*f*
urinary tract, 329–330, 330*f*
Tuberculosis colitis, 287–288
Tuberculous peritonitis, 517–521, 522*f*
Tuberous sclerosis (TSC)
angiomyolipoma and, 351
cardiac rhabdomyomas and, 1293, 1424
fetal brain and, 1198, 1200*f*
hemimegalencephaly associated with, 1195
pediatric, renal cysts in, 1816, 1817*f*
pheochromocytomas with, 1826, 1910–1912
prenatal intracranial tumors in, 1208
renal cysts in, 364–365, 365*f*
Tubo-ovarian abscess, in pelvic inflammatory disease, 588–589, 588*f*, 1886–1887, 1886*f*
Tubo-ovarian complex, in pelvic inflammatory disease, 588–589, 588*f*, 1886–1887, 1886*f*
Tubular ectasia, 359
of rete testis, 829–830, 830*f*
pediatric, 1891–1892, 1892*f*
Tubular necrosis, acute, 370
acute kidney injury and, 1795–1796, 1797*f*
renal transplantation complication with, 649–651, 653*f*, 1809
Tubuli recti, 819
Tubulointerstitial fibrosis, 359
Tumefactive chronic pancreatitis, 236
Tumefactive sludge, 195, 196*f*, 1741
Tunica albuginea
ovarian, 565
testicular, 819, 819*f*–820*f*
cysts of, 829, 830*f*
pediatric, 1888
Tunica vaginalis, 819, 819*f*
cysts of, 829, 830*f*
pediatric, 1902–1903
pathologic lesions of, 834–836, 835*f*
pediatric, 1902
Tunica var, 819
Tunica vasculosa, 821
Turner syndrome (monosomy X)
anasarca in fetus with, 1417, 1420*f*
cystic hygromas in, 1106–1107, 1106*f*
fetal hydrops from, 1429–1430, 1430*f*
horseshoe kidney in, 1345–1346
lymphatic malformation in, 1159
midface hypoplasia in, 1148
primary amenorrhea in, 1887
small aorta in, 1106*f*, 1107
sonographic findings in, 1106–1107, 1106*f*
TURP. *See* Transurethral resection of prostate
Turribrachycephaly, 1138*f*
Twin anemia polycythemia sequence (TAPS), 1126–1127
"Twin peak" sign, 1119, 1119*t*, 1120*f*
Twin pregnancies, skeletal abnormalities in, 1384
Twin reversed arterial perfusion (TRAP), 1127–1129, 1127*f*–1128*f*, 1429
Twinkling artifacts
bezoars and, 1840
mimicking AVMs after renal transplantation, 662–664, 668*f*
renal calculi indicated by, 336, 337*f*
urolithiasis and, 1799–1801, 1799*f*
Twin(s)
acardiac, hydrops and, 1429
aneuploidy screening for, 1091
congenital malformation of, 1123
conjoined, 1115–1116
complications with, 1129–1130, 1130*f*
Twin(s) *(Continued)*
dichorionic diamniotic, 1019*f*, 1115–1116, 1116*f*
growth discrepancy in, 1123*f*
placental findings in, 1119
sonographic findings of, chorionicity and, 1119, 1120*f*
dizygotic, 1115–1116, 1116*f*
growth discrepancy in, 1123, 1123*f*
hydrops in, 1429, 1429*f*
IUFD and, 1123–1125, 1124*f*
monochorionic diamniotic, 1019*f*, 1058*f*, 1115–1116, 1116*f*
CHD risk with, 1270–1273
complications of, 1125–1129
growth discrepancy in, 1123*f*
IUFD and, 1124*f*
sonographic findings of, chorionicity and, 1119, 1121*f*
TAPS complications with, 1126–1127
TRAP and, 1127–1129, 1127*f*–1128*f*
TTTS complications and, 1125–1126, 1125*t*, 1126*f*
monochorionic monoamniotic, 1057, 1115–1116, 1116*f*
complications of, 1125–1129, 1129*f*
conjoined twins as, 1130*f*
IUFD and, 1124*f*
sonographic findings of, chorionicity and, 1119, 1121*f*
TAPS complications with, 1126–1127
TRAP and, 1127–1129, 1127*f*–1128*f*
TTTS complications and, 1125–1126, 1125*t*, 1126*f*
at 12 weeks, 1129*f*
at 28 weeks, 1129*f*
monozygotic, 1115, 1116*f*
vanishing, 1117
Twin-twin transfusion syndrome (TTTS), 1203
advanced, 1125–1126, 1126*f*
complications of, 1125–1126, 1125*t*, 1126*f*
early identification of, 1125, 1126*f*
hydrops from, 1429, 1429*f*
pulmonic stenosis and, 1292
staging system for, 1125*t*
2-D echocardiography, 10
Two-dimensional array transducers, 12, 12*f*
Typhlitis, acute, 287–288, 289*f*
Tyrosinemia
GSD and, 1740*f*
management of, 1738
staghorn calculus and, 1799, 1800*f*

U

Uhl anomaly, 1286
UKCTOCS. *See* United Kingdom Collaborative Trial of Ovarian Cancer Screening
Ulcer craters, in plaque ulceration, 923, 924*f*
Ulcerative colitis, 266–267
Ulcer(s)
duodenal, perforated, gallbladder wall thickening signs in, 201*f*
gastric, pediatric, 1839–1840, 1840*f*
penetrating, in abdominal aorta, 441, 444*f*
peptic, 299, 300*f*
Ulnar nerve, dislocation of, at elbow, 865–866, 866*f*
Ulnar ray defects, 1399
Ulnar veins, normal anatomy of, 990–991
Ultrasound speckle, 4, 5*f*
Umbilical artery(ies), 1059
aneurysms of, 1483
fetal assessment of, Doppler ultrasound for, 1458, 1459*f*
fetal cloacal exstrophy and single, 1328
single, 1484, 1484*f*
spontaneous rupture of, 1483
Umbilical coiling index, twisting of, 1482, 1482*f*

Umbilical cord, 1481–1487
abnormalities of, in monochorionic twins, 1119
appearance of, 1481–1484
cysts of, 1483, 1483*f*
sonographic appearance of, 1061, 1061*f*
in trisomy 18, 1103*f*
diameter of, 1482
edematous, 1484*f*
entangled, chorionicity and, 1119, 1121*f*
excessive length of, 1481
fetal, amniotic band syndrome and, 1330
funic presentation of, 1485–1487, 1489*f*
hemangiomas of, 1483
insertion of
marginal, 1484–1485, 1487*f*
into placenta, 1484, 1485*f*
velamentous, 1119, 1122*f*, 1484–1485, 1486*f*
knots of, true, 1482–1483
normal sonographic appearance of, 1059–1061
nuchal, 1483–1484
prolapse of, fetal hydrops and, 1436
pseudocysts of, 1483, 1484*f*
routine sonographic views of, 1021, 1029*f*
short, 1481
size of, 1481–1484
tumors of, 1483
twisting of, 1482
absent, 1482, 1482*f*
vasa previa and, 1485–1487, 1488*f*–1489*f*
Umbilical hernias, 491–492, 492*f*–493*f*
Umbilical veins, 1059
pediatric, recanalized, in portal hypertension, 1758*f*
Uncinate process, pancreatic head and, 212, 213*f*
Undescended testis, 851, 851*f*
right, pediatric, 1890, 1890*f*
Unfused amnion, 1057
Unicornuate uterus, 536*f*–537*f*, 538, 1881
United Kingdom Collaborative Trial of Ovarian Cancer Screening (UKCTOCS), 578
Univentricular heart, 1287–1288, 1287*f*
UPJ obstruction. *See* Ureteropelvic junction obstruction
Upright positioning, for dynamic ultrasound of hernias, 474
Urachal sinus, pediatric, 1907–1908, 1909*f*
Urachus, 1337*f*, 1338
adenocarcinomas of, 355
in bladder development, 311, 312*f*
cysts of, 322, 323*f*
ovarian cysts differentiated from, 1369
pediatric, 1907–1908, 1909*f*
pediatric hydronephrosis and, 1791, 1792*f*–1793*f*
pediatric ovarian cysts differentiated from, 1875
diverticula of, 322, 323*f*
pediatric, 1907–1908, 1909*f*
patent, 322
pediatric, 1791
pediatric
cysts of, 1907–1908, 1909*f*
diverticula of, 1907–1908, 1909*f*
patent, 1907–1908, 1909*f*
remnant of, normal, 1871
sinus of, 1791
sinus of, 322, 323*f*
pediatric, 1791
Ureteral bud
congenital anomalies related to, 318–321
congenital megacalices and, 321
congenital megaureter and, 321, 322*f*
duplex collecting system and, 319, 320*f*
Ureteral bud *(Continued)*
renal agenesis and, 318–319
supernumerary kidneys and, 319
UPJ obstruction and, 321, 321*f*
ureteroceles and, 310, 319, 321*f*
in kidney development, 311, 312*f*
Ureteral jets, color Doppler ultrasound for, 1781*f*
Ureteral reflux, bladder augmentation and, 1912–1913
Ureteral reimplantation, pediatric, 1912, 1913*f*
Ureteric bud, 1336–1338
Ureteric jets, pediatric, 1781*f*, 1906–1907
Ureterocele(s)
congenital anomalies related to, 310, 319, 321*f*
fetal, in duplication anomalies, 1359–1360, 1359*f*, 1360*b*
pediatric
in duplication anomalies, 1783–1784, 1784*f*
ectopic, 1904–1905, 1905*f*
Ureteropelvic junction (UPJ) obstruction, 318
congenital anomalies related to, 321, 321*f*
fetal
hydronephrosis from, 1358, 1358*f*
perirenal urinomas from, 1358, 1358*f*
pediatric, hydronephrosis and, 1786, 1787*f*
VUR with, 1360
Ureterovesical junction obstruction, pediatric, 1906–1907, 1907*f*
Ureter(s)
adenocarcinoma of, 348
anastomosis of, in renal transplantation, 643, 648*f*
anatomy of, 313*f*, 314
atretic, with MCDK, 1346
calculi in, 325, 325*f*, 337–338, 338*f*–339*f*
bladder augmentation and, 1912–1913
complicating renal transplantation, 659–660, 663*f*–664*f*
congenital megaureter and, 321, 322*f*
development of, 311, 312*f*
distal, dilated, 592
lymphomas of, 353
metastases to, 354
obstruction of, renal transplantation complications from, 659–660, 663*f*–664*f*
pediatric, 1906–1907, 1907*f*–1908*f*
duplication of, 1783–1784, 1784*f*, 1904–1905
ectopic, 1904–1905
ectopic insertion of, hydronephrosis and, 1788
obstruction of, hydronephrosis and, 1786–1788, 1787*f*
reimplantation of, 1912, 1913*f*
retrocaval, 322
sonographic technique for, 314
squamous cell carcinoma of, 348
transitional cell carcinoma of, 347
trauma to, 366
Urethra
development of, 311
congenital anomalies of, 323, 323*f*
diverticula of, 323, 323*f*
fetal
atresia, lower urinary tract obstruction from, 1361, 1361*f*
megalourethra and atresia of, 1362
obstruction of, renal pelvic dilation and, 1355–1356
pediatric
diverticulum of, anterior, bladder outlet obstruction from, 1906
duplication of, bladder outlet obstruction from, 1906
normal, 1872*f*
Urethra *(Continued)*
polyp of, posterior, bladder outlet obstruction from, 1906, 1906*f*
sonographic technique for, 315, 316*f*
Urethral valve(s)
anterior, pediatric, bladder outlet obstruction from, 1906
fetal
lower urinary tract obstruction from, 1361, 1361*f*
megalourethra and, 1362
pediatric
hydronephrosis and, 1788, 1789*f*
posterior, 1905–1906, 1906*f*
Urinary diversion, evaluation after, 375, 375*f*
Urinary stasis, pediatric, 1799, 1800*f*
Urinary tract
congenital anomalies of, 1336
dilation of, in trisomy 21, 1100*f*, 1101
echinococcal disease of, 331, 332*f*
LUTS and, 387–388
masses of, 592
obstruction of, 387–388
schistosomiasis of, 331
tuberculosis of, 329–330, 330*f*
Urinary tract, fetal. *See also* Hydronephrosis
abnormalities of, 1340–1366
bilateral renal agenesis as, 1342–1344, 1343*f*–1344*f*, 1344*b*
characterizing, 1341
evaluation of, 1342*b*
horseshoe kidney as, 1345–1346, 1345*f*
MRI for diagnosing, 1342, 1342*f*
prenatal diagnosis of, 1340, 1340*b*
prevalence of, 1340
renal cystic disease as, 1346–1352 (*See also* Kidneys, fetal, cystic disease of)
renal ectopia as, 1344–1345, 1344*f*–1345*f*
unilateral renal agenesis as, 1344
embryology of, 1336–1338, 1337*f*
lower, obstruction of, 1360–1363
cloacal malformation and, 1363, 1363*f*
cystoscopy for, 1363–1365
hydrops from, 1428, 1429*f*
from megacystis, 1360, 1360*b*, 1360*f*
from megalourethra, 1362, 1362*f*
MMIHS and, 1362–1363
from posterior urethral valves, 1361, 1361*f*
from prune belly syndrome, 1361–1362
from urethral atresia, 1361, 1361*f*
in utero intervention for, 1363–1365, 1364*f*, 1365*t*
vesicoamniotic shunts for, 1363–1365, 1364*f*, 1365*t*
normal, 1336–1340
sonographic appearance of, 1338–1339, 1338*f*
upper, dilation of, 1354–1360, 1354*f*–1355*f*, 1356*t*, 1357*f*
duplication anomalies and, 1359–1360, 1359*f*, 1360*b*
management of, 1356–1358
UPJ obstruction and, 1358, 1358*f*
vesicoureteral junction obstruction and, 1358–1359
VUR and, 1360
Urinary tract, pediatric. *See also* Bladder, pediatric; Kidneys, pediatric
calcification of, 1798–1801
cortical nephrocalcinosis and, 1798, 1798*b*, 1798*f*
dystrophic, 1799
medullary nephrocalcinosis of, 1798–1799, 1799*f*

Urinary tract, pediatric *(Continued)*
renal vein thrombosis and, 1799, 1800*f*
urinary stasis and, 1799, 1800*f*
urolithiasis and, 1799–1801, 1799*f*
congenital anomalies of, 1783–1785
renal duplication as, 1783–1784, 1784*f*
dilation of, classification of, 1785–1786, 1786*f*
infection of, 1791–1794
cystitis and, 1794, 1796*f*–1797*f*, 1908, 1910*f*–1911*f*
jaundice in, 1738
neonatal candidiasis and, 1794, 1795*f*
pyelonephritis, acute, and, 1792–1793, 1793*f*–1794*f*
pyelonephritis, chronic, and, 1794, 1795*f*
lower, 1904–1913
congenital anomalies of, 1904–1906, 1905*f*–1907*f*
infection of, 1904–1905, 1908, 1910*f*–1911*f*
neoplasms of, 1908–1912, 1912*f*
trauma to, 1912
obstruction of, renal transplantation and, 1811
sonography of, 1776–1783
patient preparation for, 1776, 1776*t*
technique for, 1776–1781
Urinary tract dilation (UTD), 1785–1786, 1786*f*
Urine leak, renal transplantation and, 1810–1811
Urinoma(s)
bladder augmentation and, 1912–1913
pelvic, 591
perirenal, from UPJ obstruction, 1358, 1358*f*
after renal transplantation, 665, 672*f*
pediatric, 1809
Urogenital sinus, in bladder development, 311, 312*f*
Urolithiasis, pediatric calcification and, 1799–1801, 1799*f*
Uropathy
pediatric, obstructive, CKD and, 1796–1798
postnatal, pyelectasis as marker for, 1355
U.S. Preventive Services Task Force (USPSTF), 397, 434–435
U-shaped configuration, 1927, 1928*f*
UTD. *See* Urinary tract dilation
Uterine artery(ies), 528–529, 565–566, 565*f*
embolization of, for uterine fibroids, 540
pediatric, 1875
Uterine septum, circumvallate placenta confused with, 1479–1480, 1481*f*
Uterine synechia, circumvallate placenta confused with, 1479–1480, 1481*f*
Uterine veins, 531–532, 533*f*
Uterocervical anomalies, cervical assessment in, 1505
Utero-ovarian ligament, 565
Uterus. *See also* Cervix; Endometrium; Myometrium
accessory and cavitated mass of, 541
anatomy of, 528–530, 529*f*
sections in, 530
arcuate, 534, 536–538, 536*f*–537*f*
bicornuate, 534, 536*f*–537*f*, 538, 1881, 1881*f*
cervical abnormalities and, 541–544, 543*f*
DES exposure of, 534, 536*f*, 1881
didelphys, 534, 536*f*–537*f*, 1881
endometrial abnormalities and, 544–552
enlargement of, 538*b*
hypoplasia of, 538
isolated, primary amenorrhea in, 1887
leiomyomas of, 538–540, 539*f*, 540*b*
leiomyosarcomas of, 540, 541*f*
müllerian duct anomalies and, 529, 533–538, 537*f*
categories of, 534, 536*f*

Uterus *(Continued)*
myometrial abnormalities of, 538–541
neonatal, 1872–1873, 1873*f*
obstruction of, 546–547, 546*f*–547*f*
pediatric, 1872–1873
abnormalities of, 1881–1887
agenesis of, primary amenorrhea in, 1887
congenital anomalies of, 1881–1883
endocrine abnormalities and, 1887–1888
infection and, 1885–1887
neoplasms of, 1883–1884
PID and, 1885–1887, 1886*b*, 1886*f*
postpubertal, 1872–1873, 1873*t*
precocious puberty and, 1887–1888
pregnancy and, 1884–1885
prepubertal, 1872–1873, 1873*f*, 1873*t*
postpartum findings in, 554–557
AVMs and, 556, 556*f*
bleeding and, 554
after cesarean section, 556–557, 557*f*–558*f*
endometritis and, 555–556
normal, 554, 554*f*
placental site trophoblastic tumor and, 530–531
RPOC and, 554–555, 555*f*
pregnant
dehiscence or rupture of, assessing risk for, 1020
second-trimester scan of, 1020, 1021*f*
sarcomas of, 551
septate, 534–536, 536*f*–537*f*
size of, 531
sonographic techniques for, 528–530, 529*b*
IUDs and, 552–554, 553*f*
normal findings in, 530–533
positioning in, 530–531, 530*f*
tubal occlusion devices and, 553*f*, 554
sonohysterography for, 529
three-dimensional ultrasound for, 529
transvaginal ultrasound for, 529, 529*b*
T-shaped, 1881
unicornuate, 536*f*–537*f*, 538, 1881
Utricle cysts, prostatic, 391*f*, 392

V

VACTERL association, 1689
duodenal atresia and, 1308
fetal renal anomalies for, 1341
ribs in, 1382–1384
sacral agenesis in, 1237
VACTERL sequence, 1306, 1311
Vagina, 528–529
bleeding in, hydatidiform molar pregnancy and, 1078
pediatric, 1873
abnormalities of, 1881–1887
atretic, vaginal obstruction from, 1881
congenital anomalies of, 1881–1883
endocrine abnormalities and, 1887–1888
foreign bodies in, 1887
infection and, 1885–1887
neoplasms of, 1883–1884, 1883*f*
precocious puberty and, 1887–1888
pregnancy and, 1884–1885
stenotic, vaginal obstruction from, 1881
Peutz-Jeghers syndrome and watery discharge of, 544
Vaginal fornix, 528–529
Vaginal pessary, cervical incompetence and, 1507
Vaginal progesterone, 17α-OHPC compared to, 1507
Vaginal septum, 538
transverse, vaginal obstruction from, 1881
Vaginitis, pediatric, 1887

Vallecula
cysts, pediatric, 1640, 1641*f*
neonatal/infant, in mastoid fontanelle imaging, 1517–1518, 1519*f*
Valproic acid, NTDs from, 1218
Valsalva maneuver, 471, 992
for dynamic ultrasound of hernias
femoral, 472*f*, 483
inguinal, 473, 474*f*
Valve leaflet morphology, 1285*f*
Valvular aortic stenosis, 1292
Varicella
fetal brain and, 1203–1204
fetal hydrops from, 1432
Varices
gallbladder wall, in chronic pancreatitis, 233, 235*f*
gastric mural, in chronic pancreatitis, 233, 235*f*
gastrointestinal, endosonographic identification of, 301
round ligament, simulating groin hernias, 500, 501*f*
Varicocele(s)
idiopathic, 837–838
pediatric, 1902–1903, 1903*f*
scrotal, 837–838, 838*f*–839*f*
Vas aberrans of Haller, 1897*f*
inferior, 820–821
Vas deferens, 819–820
absence of, 394
calcification of, 392
cysts of, 842*f*
Vasa aberrantia, 820–821
Vasa previa, 1480, 1485–1487, 1488*f*–1489*f*
Vascular abnormalities, in liver. *See* Liver, vascular abnormalities in
Vascular anomalies, of neck, pediatric, 1654–1655, 1655*b*
malformations, 1655–1658, 1655*b*, 1657*f*, 1659*f*
tumors, 1655, 1655*b*, 1656*f*
Vascular malformations
fetal, 1204–1208, 1206*f*
dural sinus thrombosis as, 1205–1206, 1206*f*
hydranencephaly as, 1208, 1208*f*
intracranial hemorrhage as, 1206, 1207*f*
pediatric
in masticator space, 1640, 1641*f*
in neck, 1655–1658, 1655*b*, 1657*f*, 1659*f*
Vasculitis
acute, gut edema and, 295, 297*f*
autoimmune, Henoch-Schönlein purpura and, 1853
mesenteric ischemia from, 453
renal artery stenosis and, 447
Vasectomy, epididymis changes following, 841, 843*f*
Vasodilation, 27
Vasospasm, 950
pediatric, TCD sonography for, 1608–1610, 1609*f*, 1610*t*
VATER syndrome
fetal renal anomalies in, 1341
spina bifida and, 1226
Vein mapping
before hemodialysis, 996–1000
upper extremity, 996–998, 998*f*–1000*f*
of lower extremity peripheral veins, 989–990
Vein of Galen
aneurysms of, 1204, 1206*f*
arachnoid cysts differentiated from, 1192–1193
in neonatal/infant brain, duplex Doppler sonography of, 1583–1584, 1585*f*–1586*f*
cavum veli interpositi cysts differentiated from aneurysm of, 1170

Vein of Galen *(Continued)*
malformations of, neonatal/infant brain and, 1566, 1567*f*
Vein of Markowski, 1180
fetal brain and, 1204
Velamentous umbilical cord insertion, 1484–1485, 1486*f*
multifetal pregnancy and, 1119, 1122*f*
Velocardiofacial syndrome, clefts of secondary palate in, 1153
Velocity
arterial stenosis and, 969, 970*f*
diastolic, end, in assessing degree of carotid stenosis, 930
in Doppler spectral analysis of carotid artery, 925
stroke and SCD indications with, 1605–1607
systolic
cerebral, factors changing, 1612*t*
peak, in determining carotid stenosis, 929–930
TCD sonography evaluation of, 1593, 1595–1596
time-averaged mean of maximum, 1593, 1605–1606
time-averaged peak, 1593
Velocity range, in obstetric Doppler sonography, 1036
Velocity ratios, in carotid artery stenosis evaluation, 937
Venography
in IJV, 955–956
wedge hepatic, 1764
Veno-occlusive disease, hepatic, 103
Venous drainage, in pancreas transplantation, 672
Venous insufficiency
deep, causes of, 989, 990*f*
superficial, 981–982
Venous malformations, pediatric
of neck, 1657
of salivary gland, 1636
Venous occlusive disease, hepatic, small-vessel, 1762–1763
Venous venous (VV) anastomoses, 1125, 1125*f*
Ventilation, mechanical, in neonatal/infant brain, 1578, 1579*f*
Ventral hernias, 488–494
Ventral induction errors, fetal brain and, 1186–1203
arachnoid cysts as, 1192–1193, 1193*f*
in cerebellum, 1189–1192
Dandy-Walker malformation as, 1190, 1190*f*
HPE as, 1186–1189, 1187*b*, 1188*f*, 1189*b*
mega-cisterna magna as, 1192, 1193*f*
in posterior fossa, 1189–1192
rhombencephalosynapsis as, 1192
vermis hypoplasia or dysplasia as, 1190–1192, 1192*f*
Ventricle(s)
cardiac
double-outlet right, fetal, 1288–1289, 1289*f*
echogenic foci, significance of, 1294, 1294*f*
hypoplastic left, fetal, 1292
hypoplastic right, fetal, 1287, 1287*f*
neonatal/infant, left, dysfunction of, intracranial RI and, 1576
cerebral, fetal, sonographic view of, 1024*f*
fourth
cisterna magna clot of, 1546*f*
trapped, in intraventricular hemorrhage, 1545–1547
Ventricle(s) *(Continued)*
lateral, neonatal/infant
coarctation of, 1566
in coronal imaging, 1513–1515, 1514*f*–1515*f*
in sagittal imaging, 1515–1517, 1517*f*
measurement technique for, 1174–1176, 1175*f*
medial wall of, separation of choroid from, in VM evaluation, 1176, 1176*f*
persistent terminal, pediatric, 1685
third
in corpus callosum agenesis, 1528, 1531*f*
fetal, normal sonographic appearance of, 1168
Ventricular aneurysms, congenital, 1294
Ventricular diverticula, 1294
Ventricular septal defects (VSDs), 1270, 1281–1284, 1283*f*–1284*f*
with spina bifida, 1233
in trisomy 21, 1098*f*, 1101
Ventricular tachycardia, fetal, 1296
Ventriculitis
chemical, 1206
in intraventricular hemorrhage, 1545–1547
neonatal/infant brain and, 1560, 1563*f*
Ventriculoarterial discordance, in TGA, 1289
Ventriculomegaly (VM)
CDH and, 1263
conditions associated with, 1178*b*
fetal brain and, 1174–1178
hydrocephalus differentiated from, 1611–1612
isolated, 1176
IUFD and, 1124*f*
marked, 1176, 1177*f*
measurement technique for, 1174–1176, 1175*f*
mild, 1176, 1177*f*
neonatal/infant hydranencephaly compared to, 1538*f*
pathogenesis of, 1177–1178
in rhombencephalosynapsis, 1192
in spina bifida, 1184*f*, 1230–1232
in trisomy 21, 1098*f*
ultrasound evaluation of, 1177*f*, 1178
Ventriculus terminalis
formation of, 1673, 1673*f*
normal anatomy of, 1674, 1677*f*
Verma-Naumoff syndrome, 1396
Vermian agenesis, 1190
Vermian dysplasia, Dandy-Walker malformation differentiated from, 1190
Vermis
abnormalities of, 1192
cerebellar, 1167, 1515, 1516*f*, 1524
dysplasia of, 1190–1192, 1192*f*
embryology of, 1167
hypoplasia of, 1190–1192, 1192*f*
inferior, arachnoid cysts differentiated from, 1192–1193
hypoplasia/dysgenesis/agenesis of, 1190–1191
keyhole-shaped defect in, 1191–1192
neonatal/infant
in coronal imaging, 1514–1515, 1514*f*
development of, 1524
trapezoidal vermian defect in, 1191–1192
Vertebral artery, 950–955
anatomy of, 951, 951*f*
occlusion of, 954–955
stenosis of, 954–955, 955*f*
subclavian steal phenomenon and, 952–954, 953*b*, 953*f*–954*f*
subclavian steal with transient flow reversal in, 979*f*
technique and normal examination of, 951–952, 951*f*–952*f*
Vertebral vein, 951*f*, 952
Vertebrobasilar insufficiency, symptoms of, 950–951
Vertical talus, congenital, 1932–1933, 1932*f*
Verumontanum, 382*f*–383*f*, 384
Vesicoamniotic shunts, for lower urinary tract obstruction, 1363–1365, 1364*f*, 1365*t*
Vesicocentesis, 1363–1364
Vesicocolic fistulas, 1310–1312
Vesicocutaneous fistulas, 334
Vesicoenteric fistulas, 334
Vesicourachal diverticulum, pediatric, 1775, 1791
Vesicoureteral fistulas, 334
Vesicoureteral junction obstruction, fetal, megaureters from, 1358–1359
Vesicoureteral reflux (VUR), 1906–1907
fetal, 1360
nephropathy associated with, 327
pediatric, 1905
hydronephrosis and, 1788, 1790*f*
renal transplantation and, 1811
unilateral renal agenesis and, 1344
Vesicouterine fistulas, 334
Vesicouterine pouch, 528
Vesicovaginal fistulas, 334
Vessel stenosis, 25
VHL disease. *See* von Hippel-Lindau disease
Villi, in placental development, 1465–1466, 1466*f*
Villitis, thick placenta and, 1467*f*
Virus(es)
fetal, IUGR and, 1455
hepatitis, 83–85
pediatric infections from
cervical lymphadenopathy in, 1660
salivary gland, 1632, 1632*f*
Visceral heterotaxy, splenic abnormalities in, 159–160
Vitelline arteries and veins, 1057, 1059
Vitelline duct, 1057, 1059
VM. *See* Ventriculomegaly
VMCs. *See* Von Meyenburg complexes
Voltage, 7
Volume imaging, in obstetric sonography, 1030
Volumetric imaging, of liver, 75
Volvulus
of gallbladder, 201
midgut
intestinal malrotation with, 1841–1842, 1843*f*–1844*f*
"whirlpool" sign of, 1841–1842, 1843*f*
small bowel obstruction and, 1308
Vomer, deviation of, in cleft palate, 1151
von Gierke disease, 1740*f*
von Hippel-Lindau (VHL) disease
epididymal cystadenomas and, 1904
pancreatic cysts and, 243, 244*f*
fetal, 1320
papillary cystadenoma with, 840–841
pediatric, renal cysts in, 1816
pheochromocytomas with, 1826, 1910–1912
renal cell carcinoma and, 340
renal cysts in, 364, 364*f*
von Hippel-Lindau syndrome, prenatal intracranial tumors in, 1208
Von Meyenburg complexes (VMCs), 83, 83*f*–84*f*
VSDs. *See* Ventricular septal defects
VUR. *See* Vesicoureteral reflux
VV anastomoses. *See* Venous venous anastomoses

W

WAGR syndrome, pediatric, 1818
"Waist sign", 587–588
Waldeyer fossa, 566, 567*f*

Walker-Warburg syndrome
cobblestone lissencephaly in, 1195
Dandy-Walker malformation differentiated from, 1190
diagnosis of, 1195
vermian hypoplasia with, 1191
Wall filters
in Doppler ultrasound, 29, 30*f*
in renal artery duplex Doppler sonography, 449
Wall-echo-shadow complex, 194, 195*f*
Wandering spleen, 159, 161*f*
pediatric, 1770–1772
Warfarin, 598
Warthin tumor, 1638
Watchful waiting, for prostate cancer, 401
Water enema technique, contrast agents in, 1870–1871, 1871*f*
Waterhouse-Friderichsen syndrome, 422
Waveform(s). *See also* Tardus-parvus waveform(s)
of carotid arteries, 925–926, 925*f*
intrarenal, in renal artery duplex Doppler sonography, 450, 450*f*
Wavelength, in sound waves, 2, 2*f*
Weaver syndrome, megalencephaly associated with, 1194–1195
Wedge hepatic venography, 1764
Weigert-Meyer rule, 1359, 1783
Weight, fetal
assessment of, 1450–1453
in relation to gestational age, 1451–1453, 1452*t*, 1453*f*
estimation for, 1450–1453
formulas in, 1451, 1451*t*
gestational age compared to, 1453, 1453*f*
recommended approach in, 1451, 1452*t*
Weight, pediatric, kidney length compared to, 1777*f*
at birth, 1776–1778, 1780*f*
Weighted mean frequency, in color Doppler ultrasound, 28
Wells score, 979
Weyers acrodental dysostosis, 1395
WFUMB. *See* World Federation for Ultrasound in Medicine and Biology
Wharton duct, pediatric, 1630–1631, 1631*f*
Wharton jelly, 1059, 1482
Whipple resection, 233
"Whirlpool" sign, of midgut volvulus, 1841–1842, 1843*f*
White matter injury of prematurity (WMIP), 1512, 1550–1553. *See also* Periventricular leukomalacia
Wilms tumor, 1352–1353, 1804
neuroblastomas mistaken for, 1818
pediatric
kidneys and, 1818, 1818*f*–1820*f*
liver metastases from, 1746
metastasis of, to teste, 1901
Windsock configuration, duodenal diaphragm in, 1842, 1844*f*
WMIP. *See* White matter injury of prematurity
Wolffian (mesonephric) duct, 820–821
Wolf-Hirschhorn syndrome ($4p^-$), 1139, 1140*f*
midface hypoplasia in, 1148
World Federation for Ultrasound in Medicine and Biology (WFUMB), 1041
Wormian bones, 1139, 1139*b*, 1139*f*
Wrist, injection of, 901
superficial peritendinous and periarticular, 904, 905*f*

X

Xanthogranulomatous cholecystitis, 202
Xanthogranulomatous pyelonephritis (XGP), 328, 329*f*, 348
X-linked hydrocephalus, 1177
X-linked NTDs, 1226

Y

Yersinia, 1852–1853, 1852*f*
"Yin-yang" pattern, in renal biopsy pseudoaneurysms, 1809, 1811*f*
Yolk sac tumors, 585, 823–824, 825*f*
Yolk sac(s)
angiogenesis wall of, 1057
assessment of, 1016, 1016*b*
calcification of, 1067, 1068*f*
diameter of, measurement, 1017*f*
echogenic material in, 1067–1068
embryo in, 1058*f*
hematopoiesis in, 1057
identification of, in gestational age determination, 1445, 1445*f*, 1446*t*
MSD and, 1057
normal sonographic appearance of, 1057, 1058*f*
number of, amnionicity and, 1117
in nutrient transfer, 1057
primary, formation of, 1051, 1052*f*
secondary, formation of, 1051, 1053*f*
size and shape of, in early pregnancy failure, 1067–1068, 1068*f*
transvaginal ultrasound for identification of, 1057
Yolk stalk, 1059

Z

Zellweger syndrome, 1196, 1399
subependymal cysts from, 1566
Zero baseline, shifting, to overcome aliasing, 939
Zika virus, 1194, 1203–1204
congenital, neonatal/infant brain and, 1560
Zona fasciculata, 417
Zona glomerulosa, 417
Zona reticularis, 417
Zuckerkandl fascia, 314
Zygosity, in multifetal pregnancy, 1115–1116, 1116*f*
Zygote, formation of, 1051, 1051*f*

This page intentionally left blank

This page intentionally left blank

ClinicalKey®

Fast answers and trusted evidence

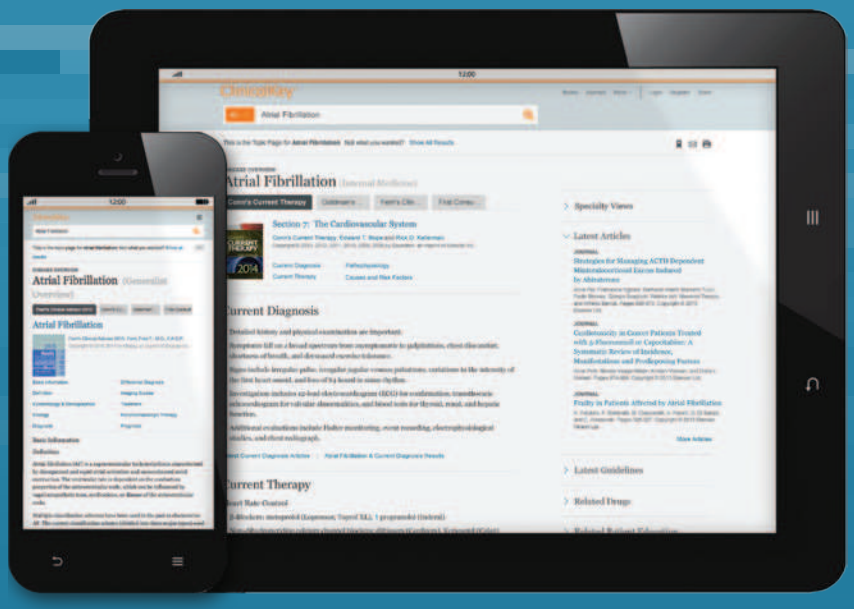

Drive better outcomes with a clinical search engine that makes it easier to find and apply relevant knowledge.

Fast
Anticipates your query, recognizing concepts and offering shortcuts

Complete
Draws relevant answers from a wide range of current, comprehensive content across 30+ medical and surgical specialties

Convenient
Accessible at the patient's bedside or on the go, making it easy to discover, share, and apply content anywhere

Trusted
Content from Elsevier, the name healthcare professionals worldwide rely on

ckey.co/books

ELSEVIER

DIAGNOSTIC ULTRASOUND

5TH EDITION

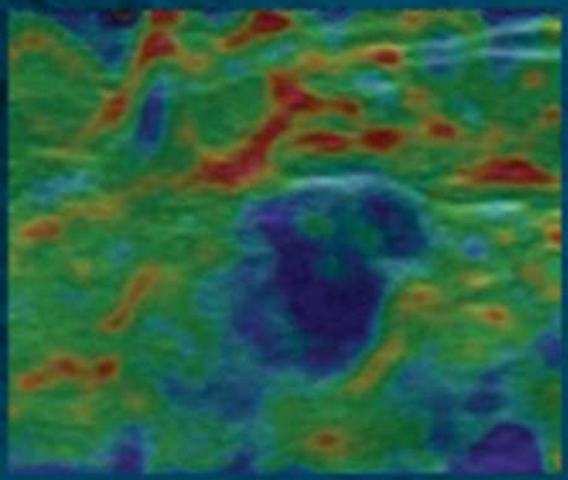
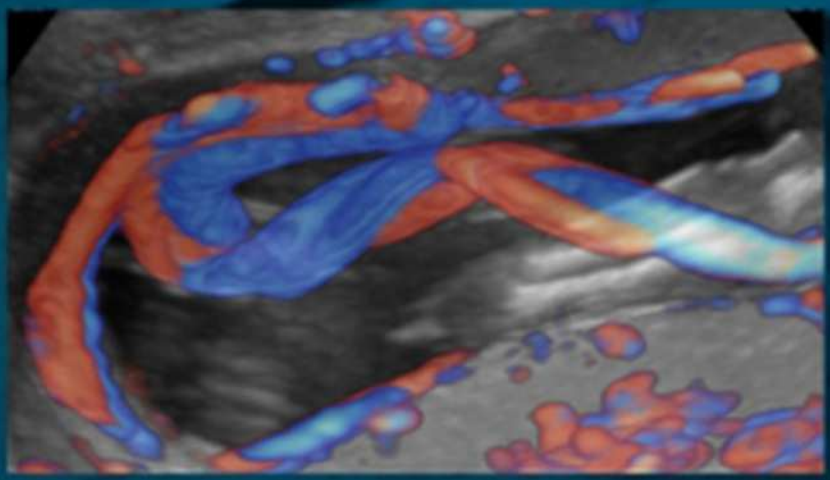

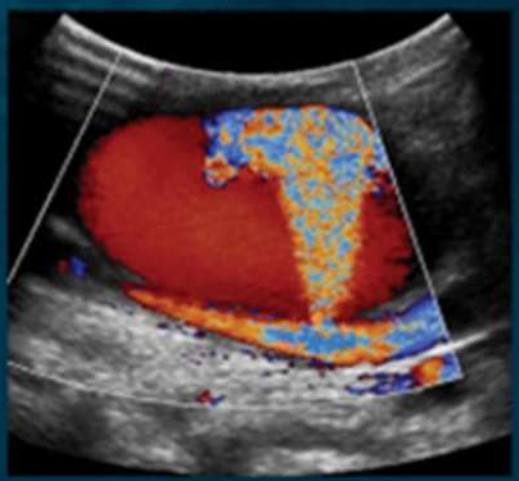

CAROL M. RUMACK

DEBORAH LEVINE

ELSEVIER

DIAGNOSTIC ULTRASOUND

This page intentionally left blank

DIAGNOSTIC ULTRASOUND

5TH EDITION

CAROL M. RUMACK, MD, FACR
Vice Chair of Education and Professional Development
Professor of Radiology and Pediatrics
Associate Dean for GME
University of Colorado School of Medicine
Denver, Colorado

DEBORAH LEVINE, MD, FACR
Co-Chief of Ultrasound
Director of OB/Gyn Ultrasound
Vice Chair of Academic Affairs
Department of Radiology
Beth Israel Deaconess Medical Center
Professor of Radiology
Harvard Medical School
Boston, Massachusetts

ELSEVIER

ELSEVIER

1600 John F. Kennedy Blvd.
Ste 1800
Philadelphia, PA 19103-2899

DIAGNOSTIC ULTRASOUND, FIFTH EDITION ISBN: 978-0-323-40171-5

Copyright © 2018 by Elsevier, Inc. All rights reserved.

Chapter 32: Mary C. Frates retains copyright for the original figures appearing in the chapter.
Chapter 42: Carol B. Benson and Peter M. Doubilet retain copyright for their original figures appearing in the chapter.

No part of this publication may be reproduced or transmitted in any form or by any means, electronic or mechanical, including photocopying, recording, or any information storage and retrieval system, without permission in writing from the publisher. Details on how to seek permission, further information about the Publisher's permissions policies and our arrangements with organizations such as the Copyright Clearance Center and the Copyright Licensing Agency, can be found at our website: www.elsevier.com/permissions.

This book and the individual contributions contained in it are protected under copyright by the Publisher (other than as may be noted herein).

Notices

Knowledge and best practice in this field are constantly changing. As new research and experience broaden our understanding, changes in research methods, professional practices, or medical treatment may become necessary.

Practitioners and researchers must always rely on their own experience and knowledge in evaluating and using any information, methods, compounds, or experiments described herein. In using such information or methods they should be mindful of their own safety and the safety of others, including parties for whom they have a professional responsibility.

With respect to any drug or pharmaceutical products identified, readers are advised to check the most current information provided (i) on procedures featured or (ii) by the manufacturer of each product to be administered, to verify the recommended dose or formula, the method and duration of administration, and contraindications. It is the responsibility of practitioners, relying on their own experience and knowledge of their patients, to make diagnoses, to determine dosages and the best treatment for each individual patient, and to take all appropriate safety precautions.

To the fullest extent of the law, neither the Publisher nor the authors, contributors, or editors, assume any liability for any injury and/or damage to persons or property as a matter of products liability, negligence or otherwise, or from any use or operation of any methods, products, instructions, or ideas contained in the material herein.

Previous editions copyrighted 2011, 2005, 1998, and 1993.

Library of Congress Cataloging-in-Publication Data

Names: Rumack, Carol M., editor. | Levine, Deborah, 1962- editor.
Title: Diagnostic ultrasound / [edited by] Carol M. Rumack, Deborah Levine.
Other titles: Diagnostic ultrasound (Rumack)
Description: 5th edition. | Philadelphia, PA : Elsevier, [2018] | Includes bibliographical references and index.
Identifiers: LCCN 2017019887 | ISBN 9780323401715 (hardcover : alk. paper)
Subjects: | MESH: Ultrasonography
Classification: LCC RC78.7.U4 | NLM WN 208 | DDC 616.07/543–dc23
LC record available at https://lccn.loc.gov/2017019887

Executive Content Strategist: Robin Carter
Senior Content Development: Manager: Taylor Ball
Publishing Services Manager: Catherine Jackson
Senior Project Manager: Daniel Fitzgerald
Design Manager: Amy Buxton
Illustrations Manager: Nichole Beard

Printed in China.

Last digit is the print number: 9 8 7 6 5 4 3 2 1

ELSEVIER Book Aid International Working together to grow libraries in developing countries
www.elsevier.com • www.bookaid.org

ABOUT THE EDITORS

Carol M. Rumack, MD, FACR, is Professor of Radiology and Pediatrics at the University of Colorado School of Medicine in Denver, Colorado. Her clinical practice is based at the University of Colorado Hospital. Her primary research has been in neonatal sonography of high-risk infants, particularly the brain, on which she has published and lectured widely. She is a Fellow, previous Chair of the Ultrasound Commission, past president of the American College of Radiology, and American Association for Women Radiologists, and a Fellow of both the American Institute of Ultrasound in Medicine and the Society of Radiologists in Ultrasound. She and her husband, Barry, have two children, Becky and Marc, and five grandchildren.

Deborah Levine, MD, FACR, is Professor of Radiology at Beth Israel Deaconess Medical Center, Boston, and Harvard Medical School. At Beth Israel Deaconess Medical Center she is Vice Chair of Academic Affairs of the Department of Radiology, Co-Chief of Ultrasound, and Director of Ob/Gyn Ultrasound. Her main areas of clinical and research interest are obstetric and gynecologic imaging. She is a Fellow and past Vice President of the American College of Radiology and a Fellow (and 2016-2017 President) of the Society of Radiologists in Ultrasound. She and her husband, Alex, have two children, Becky and Julie.

This page intentionally left blank

CONTRIBUTORS

Jacques S. Abramowicz, MD, FACOG, FAIUM
Professor and Director
Ultrasound Services Department of Obstetrics and Gynecology University of Chicago
Chicago, Illinois
United States

Ronald S. Adler, MD, PhD
Professor of Radiology
New York University School of Medicine
Department of Radiology
NYU Langone Medical Center
New York, New York
United States

Allison Aguado, MD
Assistant Professor
Department of Radiology
Cincinnati Children's Hospital Medical Center
Cincinnati, Ohio
United States

Rochelle Filker Andreotti, MD
Professor of Clinical Radiology
Associate Professor of Clinical Obstetrics and Gynecology
Department of Radiology and Radiological Sciences
Vanderbilt University
Nashville, Tennessee
United States

Elizabeth Asch, MD
Instructor in Radiology
Harvard Medical School
Brigham and Women's Hospital
Boston, Massachusetts
United States

Thomas D. Atwell, MD
Professor of Radiology
Department of Radiology
Mayo Clinic
Rochester, Minnesota
United States

Amanda K. Auckland, BS, RT(R), RDMS, RVT, RDCS
Diagnostic Medical Sonographer
Division of Ultrasound/Prenatal Diagnosis and Genetics
University of Colorado Hospital
Aurora, Colorado
United States

Diane S. Babcock, MD
Professor Emerita of Radiology and Pediatrics
University of Cincinnati College of Medicine
Cincinnati Children's Hospital Medical Center
Cincinnati, Ohio
United States

Beryl Benacerraf, MD
Clinical Professor of Obstetrics and Gynecology and Radiology
Brigham and Women's Hospital
Clinical Professor of Obstetrics and Gynecology
Massachusetts General Hospital
Harvard Medical School
Boston, Massachusetts
United States

Carol B. Benson, MD
Professor of Radiology
Harvard Medical School
Director of Ultrasound and Co-Director of High Risk Obstetrical Ultrasound
Department of Radiology
Brigham and Women's Hospital
Boston, Massachusetts
United States

Raymond E. Bertino, MD, FACR, FSRU
Medical Director of Vascular and General Ultrasound
OSF Saint Francis Medical Center
Clinical Professor of Radiology and Surgery
University of Illinois College of Medicine
Peoria, Illinois
United States

Edward I. Bluth, MD, FACR, FSRU
Chairman Emeritus
Ochsner Clinic Foundation
Professor
Ochsner Clinical School
University of Queensland, School of Medicine
New Orleans, Louisiana
United States

Bryann Bromley, MD
Professor of Obstetrics, Gynecology and Reproductive Biology, part time
Harvard Medical School
Department of Obstetrics and Gynecology
Massachusetts General Hospital
Brigham and Women's Hospital
Boston, Massachusetts
United States

Olga R. Brook, **MD**
Assistant Professor
Harvard Medical School
Associate Director of CT
Department of Radiology
Beth Israel Deaconess Medical Center
Boston, Massachusetts
United States

Douglas Brown, **MD**
Professor of Radiology
Department of Radiology
Mayo Clinic College of Medicine and Science
Rochester, Minnesota
United States

Dorothy Bulas, **MD**
Professor of Pediatrics and Radiology
George Washington University Medical Center
Pediatric Radiologist
Children's National Health Systems
Washington DC
United States

Peter N. Burns, **PhD**
Professor and Chairman
Department of Medical Biophysics
University of Toronto
Senior Scientist, Imaging Research
Sunnybrook Research Institute
Toronto, Ontario
Canada

Vito Cantisani, **MD, PhD**
Department of Radiologic, Oncologic and Pathologic Sciences
Policlinic Umberto I
Sapienza University
Rome
Italy

Ilse Castro-Aragon, **MD**
Assistant Professor of Radiology
Boston University School of Medicine
Section Head, Pediatric Radiology
Boston Medical Center
Boston, Massachusetts
United States

J. William Charboneau, **MD**
Emeritus Professor of Radiology
Department of Radiology
Mayo Clinic
Rochester, Minnesota
United States

Humaira Chaudhry, **MD**
Section Chief, Abdominal Imaging
Assistant Professor
Department of Radiology
Rutgers-New Jersey Medical School
Newark, NJ
United States

Tanya Punita Chawla, **MBBS, FRCR, MRCP, FRCPC**
Assistant Professor and Staff Radiologist
Joint Department of Medical Imaging
University of Toronto
Toronto, Ontario
Canada

Christina Marie Chingkoe, **MD**
Department of Radiology
Beth Israel Deaconess Medical Center
Boston, Massachusetts
United States

David Chitayat, **MD**
Professor
Department of Pediatrics, Obstetrics and Gynecology, Molecular Genetics and Laboratory Medicine and Pathobiology
Medical Director
The MSc program in Genetic Counselling, Department of Molecular Genetics
University of Toronto
Head
The Prenatal Diagnosis and Medical Genetics Program
Mount Sinai Hospital
Staff
Pediatrics, Division of Clinical and Metabolic Genetics
Hospital for Sickkids
Toronto, Ontario
Canada

Peter L. Cooperberg, **OBC, MDCM, FRCP(C), FACR**
Professor Emeritus
Department of Radiology
University of British Columbia
Vancouver, British Columbia
Canada

Lori A. Deitte, **MD, FACR**
Vice Chair of Education and Professor
Department of Radiology and Radiological Sciences
Vanderbilt University
Nashville, Tennessee
United States

Peter M. Doubilet, MD, PhD
Professor of Radiology
Harvard Medical School
Senior Vice Chair
Department of Radiology
Brigham and Women's Hospital
Boston, Massachusetts
United States

Julia A. Drose, RDMS, RDCS, RVT
Associate Professor
Department of Radiology
University of Colorado Hospital
Aurora, Colorado
United States

Alexia Egloff, MD
Diagnostic Imaging and Radiology
Children's National Health Systems
Washington DC
United States

Judy A. Estroff, MD
Instructor
Boston University School of Medicine
Department of Radiology
Boston Children's Hospital
Boston, Massachusetts
United States

Katherine W. Fong, MBBS, FRCPC
Associate Professor
Medical Imaging and Obstetrics and Gynecology
University of Toronto
Co-director, Centre of Excellence in Obstetric Ultrasound
Mount Sinai Hospital
Toronto, Ontario
Canada

J. Brian Fowlkes, PhD
Professor
Department of Radiology
University of Michigan
Ann Arbor, Michigan
United States

Mary C. Frates, MD
Associate Professor of Radiology
Department of Radiology
Harvard Medical School
Brigham and Women's Hospital
Boston, Massachusetts
United States

Hournaz Ghandehari, MD, FRCPC
Department of Medical Imaging
Abdominal Division
University of Toronto
Sunnybrook Health Sciences Centre
Toronto, Ontario
Canada

Phyllis Glanc, MDCM
Associate Professor
University of Toronto
Department Medical Imaging, Obstetric & Gynecology
Sunnybrook Health Sciences Centre
Toronto, Ontario
Canada

S. Bruce Greenberg, MD
Professor of Radiology and Pediatrics
Department of Radiology
University of Arkansas for Medical Sciences
Little Rock, Arkansas
United States

Leslie E. Grissom, MD
Clinical Professor of Radiology and Pediatrics
Department of Radiology
Sidney Kimmel Medical College at Thomas Jefferson University
Philadelphia, Pennsylvania
Attending Radiologist
Department of Medical Imaging
Nemours Alfred I. duPont Hospital for Children
Wilmington, Delaware
United States

Anthony E. Hanbidge, MB, BCh, FRCPC
Associate Professor
Department of Medical Imaging
University of Toronto
Site Director, Abdominal Imaging
Toronto Western Hospital
Joint Department of Medical Imaging
University Health Network, Mount Sinai Hospital and Women's College Hospital
Toronto, Ontario
Canada

H. Theodore Harcke, MD, FACR, FAIUM
Sidney Kimmel Medical College at Thomas Jefferson University
Chairman, Emeritus
Department of Medical Imaging
Nemours/A I duPont Hospital for Children
Wilmington, Delaware
United States

Christy K. Holland, **PhD**
Scientific Director of the Heart, Lung, and Vascular Institute
Professor
Department of Internal Medicine
Division of Cardiovascular Health and Disease
University of Cincinnati
Cincinnati, Ohio
United States

Thierry A.G.M. Huisman, **MD**
Professor of Radiology, Pediatrics, Neurology, and Neurosurgery
Director Pediatric Radiology and Pediatric Neuroradiology
Russell H. Morgan Department of Radiology and Radiological Science
The Johns Hopkins University School of Medicine
Baltimore, Maryland
United States

Bonnie J. Huppert, **MD**
Assistant Professor of Radiology
Consultant in Radiology
Department of Radiology
Mayo Clinic
Rochester, Minnesota
United States

Alexander Jesurum, PhD
Weston, Massachusetts
United States

Susan D. John, **MD**
Professor and Chair
Department of Diagnostic and Interventional Imaging
University of Texas Medical School Houston
Houston, Texas
United States

Neil Johnson, **MBBS, FRANZCR, MMed**
Professor
Department of Radiology and Pediatrics
Cincinnati Children's Hospital Medical Center
Cincinnati, Ohio
United States

Stephen I. Johnson, **MD**
Staff Radiologist
Department of Radiology
Ochsner Clinic Foundation
New Orleans, Louisiana
United States

Anne Kennedy, **MB, BCh**
Vice Chair Clinical Operations
Department of Radiology
University of Utah
Salt Lake City, Utah
United States

Julia Eva Kfouri, **BSc, MD, FRCSC-MFM**
Clinical Associate
Division of Maternal Fetal Medicine
Department of Obstetrics and Gynecology
Mount Sinai Hospital
Toronto, Ontario
Canada

Korosh Khalili, **MD, FRCPC**
Associate Professor
Department of Medical Imaging
University of Toronto
University Health Network
Princess Margaret Hospital
Toronto, Ontario
Canada

Beth M. Kline-Fath, **MD**
Professor of Radiology
Department of Radiology
Cincinnati Children's Hospital Medical Center
Cincinnati, Ohio
United States

Elizabeth Lazarus, **MD**
Associate Professor
Department of Diagnostic Imaging
Warren Alpert Medical School of Brown University
Providence, Rhode Island
United States

Deborah Levine, **MD, FACR**
Co-Chief of Ultrasound
Director of OB/Gyn Ultrasound
Vice Chair of Academic Affairs
Department of Radiology
Beth Israel Deaconess Medical Center
Professor of Radiology
Harvard Medical School
Boston, Massachusetts
United States

Mark E. Lockhart, **MD, MPH**
Professor of Radiology and Chief, Body Imaging
Department of Radiology
University of Alabama at Birmingham
Birmingham, Alabama
United States

Ana P. Lourenco, **MD**
Associate Professor of Diagnostic Imaging
Diagnostic Imaging
Alpert Medical School of Brown University
Providence, Rhode Island
United States

Martha Mappus Munden, **MD**
Associate Professor of Radiology
Department of Pediatric Radiology
Texas Children's Hospital
Houston, Texas
United States

John R. Mathieson, **MD**
Clinical Associate Professor
University of British Columbia
Vancouver, British Columbia
Medical Director and Department Head
Vancouver Island Health Authority
Victoria, British Columbia
Canada

Giovanni Mauri, **MD**
Division of Interventional Radiology
European Institute of Oncology
Milan
Italy

Colm McMahon, **MB, BAO, BCh, MRCPI, FFR(RCSI)**
Assistant Professor
Department of Radiology
Harvard Medical School
Beth Israel Deaconess Medical Center
Brookline, Massachusetts
United States

Rashmi J. Mehta, **MD, MBA**
Clinical Radiology Fellow
Department of Radiology
Beth Israel Deaconess Medical Center
Boston, Massachusetts
United States

Nir Melamed, **MD, MSc**
Associate Professor
Department of Obstetrics and Gynecology
University of Toronto
Sunnybrook Health Sciences Center
Toronto, Ontario
Canada

Christopher R.B. Merritt, **MD**
New Orleans, Louisiana
United States

Derek Muradali, **MD, FRCPC**
Associate Professor and Staff Radiologist
Department of Medical Imaging
St Michaels Hospital
University of Toronto
Toronto, Ontario
Canada

Elton Mustafaraj, **DO**
Resident, Department of Radiology
University of Illinois College of Medicine
Peoria, Illinois
United States

Lisa Napolitano, **RDMS**
Department of Radiology
Beth Israel Deaconess Medical Center
Boston, Massachusetts
United States

Sara M. O'Hara, **MD**
Professor of Radiology & Pediatrics
Department of Radiology
Cincinnati Children's Hospital
Cincinnati, Ohio
United States

Harriet J. Paltiel, **MDCM**
Associate Professor of Radiology
Harvard Medical School
Department of Radiology
Boston Children's Hospital
Boston, Massachusetts
United States

Jordana Phillips, **MD**
Department of Radiology
Beth Israel Deaconess Medical Center
Boston, Massachusetts
United States

Andrea Poretti, **MD**
Assistant Professor of Radiology
Section of Pediatric Neuroradiology
Division of Pediatric Radiology
Russell H. Morgan Department of Radiology and Radiological Science
The Johns Hopkins University School of Medicine
Baltimore, Maryland
United States

Theodora A. Potretzke, **MD**
Assistant Professor
Department of Radiology
Mayo Clinic
Rochester, Minnesota
United States

Rupa Radhakrishnan, **MBBS**
Assistant Professor
Department of Radiology
Cincinnati Children's Hospital Medical Center
Cincinnati, Ohio
United States

Carl Reading, **MD**
Professor of Radiology
Department of Radiology
Mayo Clinic
Rochester, Minnesota
United States

Michelle L. Robbin, **MD, MS**
Professor of Radiology and Biomedical Engineering
Department of Radiology
University of Alabama at Birmingham
Birmingham, Alabama
United States

Henrietta Kotlus Rosenberg, **MD**
Radiologist-in-Chief
Kravis Children's Hospital at Mount Sinai
Director of Pediatric Radiology
Department of Radiology
Mount Sinai Hospital
Professor of Radiology and Pediatrics
Icahn School of Medicine at Mount Sinai
New York, New York
United States

Carol M. Rumack, **MD, FACR**
Vice Chair of Education and Professional Development
Professor of Radiology and Pediatrics
Associate Dean for GME
University of Colorado School of Medicine
Denver, Colorado
United States

Eric Sauerbrei, **BSc, MSc, MD, FRCPC**
Professor of Radiology
Diagnostic Imaging
Queens University
Kingston, Ontario
Canada

Chetan Chandulal Shah, **MD, MBA**
Faculty, Department of Radiology
Mayo Clinic
Pediatric Radiologist
Department of Pediatric Radiology
Nemours
Wolfson Children's Hospital
Jacksonville, Florida
United States

Thomas D. Shipp, **MD**
Associate Professor of Obstetrics, Gynecology & Reproductive Biology
Harvard Medical School
Department of Obstetrics & Gynecology
Brigham & Women's Hospital
Boston, Massachusetts
United States

William L. Simpson, **Jr.**, **MD**
Associate Professor
Department of Radiology
Icahn School of Medicine at Mount Sinai
New York, New York
United States

Luigi Solbiati, **MD**
Professor of Radiology
Department of Radiology
Humanitas University and Research Hospital
Rozzano (Milan)
Italy

Daniel Sommers, **MD**
Associate Professor
Department of Radiology
University of Utah
Salt Lake City, Utah
United States

Elizabeth R. Stamm, **MD**
Associate Professor
Department of Radiology
University of Colorado Hospital
Aurora, Colorado
United States

A. Thomas Stavros, **MD, FACR**
Medical Director
Ultrasound Invision
Sally Jobe Breast Center
Englewood, Colorado
United States

Maryellen R.M. Sun, **MD**
Department of Radiology
Lowell General Hospital
Lowell, Massachusetts
United States

Wendy Thurston, MD
Assistant Professor
Department of Medical Imaging
University of Toronto
Chief, Diagnostic Imaging
Department of Diagnostic Imaging
St. Joseph's Health Centre
Courtesy Staff
Department of Medical Imaging
University Health Network
Toronto, Ontario
Canada

Ants Toi, MD, FRCPC, FAIUM
Professor of Radiology and of Obstetrics and Gynecology
University of Toronto
Radiologist
Medical Imaging
Mt. Sinai Hospital
Toronto, Ontario
Canada

Laurie Troxclair, BS, RDMS, RVT
Ochsner Clinic Foundation
New Orleans, Louisiana
United States

Mitchell Tublin, MD
Professor and Vice Chair
Department of Radiology
University of Pittsburgh School of Medicine
Pittsburgh, Pennsylvania
United States

Heidi R. Umphrey, MD, MS
Associate Professor of Radiology
Department of Radiology
University of Alabama at Birmingham
Birmingham, Alabama
United States

Sheila Unger, MD
University of Lausanne
Lausanne
Switzerland

Patrick M. Vos, MD
Clinical Assistant Professor
Department of Radiology
University of British Columbia
Vancouver, British Columbia
Canada

Therese M. Weber, MD, MS
Professor of Radiology
Department of Radiology
University of Alabama at Birmingham
Birmingham, Alabama
United States

Kirsten L. Weind Matthews, PhD, MBBS, FRCPC
Lecturer, Medical Imaging
University of Toronto
Department of Medical Imaging
Mount Sinai Hospital
Toronto, Ontario
Canada

Stephanie R. Wilson, MD
Clinical Professor
Department of Radiology
Department of Medicine, Division of Gastroenterology
University of Calgary
Calgary, Alberta
Canada

Thomas Winter, MD
Professor and Chief of Abdominal Imaging
Department of Radiology
University of Utah
Salt Lake City, Utah
United States

Cynthia E. Withers, MD
Radiologist (retired)
Sansum Clinic and Santa Barbara Cottage Hospital
Santa Barbara, California
United States

Corrie Yablon, MD
Assistant Professor
Department of Radiology
University of Michigan
Ann Arbor, Michigan
United States

Hojun Yu, MD
Radiologist
Department of Diagnostic Imaging
Queen Elizabeth II Hospital
Grande Prairie, Alberta
Canada

This page intentionally left blank

In memory of my parents, Drs. Ruth and Raymond Masters, who encouraged me to enjoy the intellectual challenge of medicine and the love of making a difference in patients' lives.
Carol M. Rumack

To Alex, Becky, and Julie—your love and support made this work possible.
Debbie Levine

This page intentionally left blank

PREFACE

The fifth edition of *Diagnostic Ultrasound* is a major revision. Previous editions have been very well accepted as reference textbooks and have been the most commonly used reference in ultrasound education and practices worldwide. The text and references have all been updated and are now all available online. We are pleased to provide over 2500 new/revised images (with over 5800 images total) and over 380 new videos (with 480 total videos). The display of real-time ultrasound has helped to capture those abnormalities that require a sweep through the pathology to truly appreciate the lesion as well. Daily we find that cine or video clips show important areas between still images that help to make certain a diagnosis or relationships between lesions. Now we rarely need to go back to reevaluate a lesion with another scan, making patient imaging more efficient. Another new offering in this textbook is a completely online "virtual" chapter on artifacts. PowerPoint videos explain many of the artifacts that are linked to images and videos in the text.

The fifth edition was a major change for our editorial team, as we said a fond farewell to Stephanie Wilson and Bill Charboneau. Their expertise is still felt in this edition, as they have contributed chapters on gastrointestinal ultrasound (liver, biliary tree, and gastrointestinal tract, which are all some of Stephanie's passions) and thyroid and interventional ultrasound (just some of Bill's areas of expertise).

Nearly 100 outstanding new and continuing authors have contributed to this edition, and all are recognized experts in the field of ultrasound. As in prior editions, we have emphasized the use of collages to show many examples of similar anatomy and pathology. These images reflect the spectrum of sonographic changes that may occur in a given disease, instead of the most common manifestation only.

The book's format has been redesigned with key points in addition to the outline at the beginning of each chapter. There are again colored boxes to highlight the important or critical features of sonographic diagnoses. Key terms and concepts are emphasized in boldface type. To direct the readers to other research and literature of interest, comprehensive reference lists are provided.

Diagnostic Ultrasound is again divided into two volumes. Volume I consists of Parts I to III. Part I contains chapters on physics and biologic effects of ultrasound and includes descriptions of elastography and contrast agents. Part II covers abdominal sonography and includes two completely revised chapters on pelvic sonography, along with chapters on interventional procedures (including those in the thorax) and organ transplantation. Part III presents small parts imaging, including thyroid, breast, scrotum, carotid, a completely revised chapter on imaging of the extracranial vessels, and two completely revised musculoskeletal imaging chapters, as well as an updated chapter on musculoskeletal intervention.

Volume II begins with Part IV, with obstetric ultrasound, which has important updates in first-trimester scanning and screening for aneuploidy including cell-free DNA. Part V comprehensively covers pediatric sonography, including pediatric interventional sonography. Completely revised chapters on the pediatric spinal canal and pediatric kidney are replete with new images and scanning techniques.

Diagnostic Ultrasound is for practicing physicians, residents, medical students, sonographers, and others interested in understanding the vast applications of diagnostic sonography in patient care. Our goal is for *Diagnostic Ultrasound* to continue to be the most comprehensive reference book available in the sonographic literature, with a highly readable style and superb images.

Carol M. Rumack, MD, FACR
Deborah Levine, MD, FACR

This page intentionally left blank

ACKNOWLEDGMENTS

We wish to express our deepest appreciation and sincerest gratitude:

To all of our outstanding authors, who have contributed extensive, newly updated, and authoritative text and images and videos. We cannot thank them enough for their efforts on this project.

To Alexander Jesurum, PhD, whose outstanding efforts kept the references updated for all of our authors and who helped in author contact and communication.

To Lisa Napolitano, RDMS, who spent hours finding and cropping videos to supplement our online edition.

To Robin Carter, Executive Content Strategist at Elsevier, who has worked closely with us on this project from the very beginning of the fifth edition.

To Taylor Ball and Dan Fitzgerald at Elsevier, who kept us on track for the process of updating and copyediting the entire manuscript.

It has been an intense year for everyone, and we are very proud of this superb edition of *Diagnostic Ultrasound.*

This page intentionally left blank

CONTENTS

VOLUME I

PART I Physics

1 **Physics of Ultrasound,** 1
Christopher R.B. Merritt

2 **Biologic Effects and Safety,** 34
J. Brian Fowlkes and Christy K. Holland

3 **Contrast Agents for Ultrasound,** 53
Peter N. Burns

PART II Abdominal and Pelvic Sonography

4 **The Liver,** 74
Stephanie R. Wilson and Cynthia E. Withers

5 **The Spleen,** 139
Patrick M. Vos, John R. Mathieson, and Peter L. Cooperberg

6 **The Biliary Tree and Gallbladder,** 165
Korosh Khalili and Stephanie R. Wilson

7 **The Pancreas,** 210
Thomas Winter and Maryellen R.M. Sun

8 **The Gastrointestinal Tract,** 256
Stephanie R. Wilson

9 **The Kidney and Urinary Tract,** 310
Mitchell Tublin, Deborah Levine, Wendy Thurston, and Stephanie R. Wilson

10 **The Prostate and Transrectal Ultrasound,** 381
Ants Toi

11 **The Adrenal Glands,** 416
Christina Marie Chingkoe, Olga R. Brook, and Deborah Levine

12 **The Retroperitoneum,** 432
Raymond E. Bertino and Elton Mustafaraj

13 **Dynamic Ultrasound of Hernias of the Groin and Anterior Abdominal Wall,** 470
Deborah Levine, Lisa Napolitano, and A. Thomas Stavros

14 **The Peritoneum,** 504
Anthony E. Hanbidge, Korosh Khalili, and Stephanie R. Wilson

15 **The Uterus,** 528
Douglas Brown and Deborah Levine

16 **The Adnexa,** 564
Rochelle Filker Andreotti and Lori A. Deitte

17 **Ultrasound-Guided Biopsy of Chest, Abdomen, and Pelvis,** 597
Theodora A. Potretzke, Thomas D. Atwell, J. William Charboneau, and Carl Reading

18 **Organ Transplantation,** 623
Derek Muradali and Tanya Punita Chawla

PART III Small Parts, Carotid Artery, and Peripheral Vessel Sonography

19 **The Thyroid Gland,** 691
Luigi Solbiati, J. William Charboneau, Vito Cantisani, Carl Reading, and Giovanni Mauri

20 **The Parathyroid Glands,** 732
Bonnie J. Huppert and Carl Reading

21 **The Breast,** 759
Jordana Phillips, Rashmi J. Mehta, and A. Thomas Stavros

22 **The Scrotum,** 818
Daniel Sommers and Thomas Winter

23 **Overview of Musculoskeletal Ultrasound Techniques and Applications,** 856
Colm McMahon and Corrie Yablon

24 **The Shoulder,** 877
Colm McMahon and Corrie Yablon

25 **Musculoskeletal Interventions,** 898
Ronald S. Adler

26 **The Extracranial Cerebral Vessels,** 915
Edward I. Bluth, Stephen I. Johnson, and Laurie Troxclair

27 **Peripheral Vessels,** 964
Mark E. Lockhart, Heidi R. Umphrey, Therese M. Weber, and Michelle L. Robbin

VOLUME II

PART IV Obstetric and Fetal Sonography

28 **Overview of Obstetric Imaging,** 1015
Deborah Levine

29 **Bioeffects and Safety of Ultrasound in Obstetrics,** 1034
Jacques S. Abramowicz

30 **The First Trimester,** 1048
Elizabeth Lazarus and Deborah Levine

31 **Chromosomal Abnormalities,** 1088
Bryann Bromley and Beryl Benacerraf

32 **Multifetal Pregnancy,** 1115
Mary C. Frates

33 **The Fetal Face and Neck,** 1133
Ana P. Lourenco and Judy A. Estroff

34 **The Fetal Brain,** 1166
Ants Toi and Deborah Levine

35 **The Fetal Spine,** 1216
Elizabeth Asch and Eric Sauerbrei

36 **The Fetal Chest,** 1243
Dorothy Bulas

37 **The Fetal Heart,** 1270
Elizabeth R. Stamm and Julia A. Drose

38 **The Fetal Gastrointestinal Tract and Abdominal Wall,** 1304
Nir Melamed, Anne Kennedy, and Phyllis Glanc

39 **The Fetal Urogenital Tract,** 1336
Katherine W. Fong, Julia Eva Kfouri, and Kirsten L. Weind Matthews

40 **The Fetal Musculoskeletal System,** 1376
Phyllis Glanc, David Chitayat, and Sheila Unger

41 **Fetal Hydrops,** 1412
Deborah Levine

42 **Fetal Measurements: Normal and Abnormal Fetal Growth and Assessment of Fetal Well-Being,** 1443
Carol B. Benson and Peter M. Doubilet

43 **Sonographic Evaluation of the Placenta,** 1465
Thomas D. Shipp

44 **Cervical Ultrasound and Preterm Birth,** 1495
Hournaz Ghandehari and Phyllis Glanc

PART V Pediatric Sonography

45 **Neonatal and Infant Brain Imaging,** 1511
Carol M. Rumack and Amanda K. Auckland

46 **Duplex Sonography of the Neonatal and Infant Brain,** 1573
Thierry A.G.M. Huisman and Andrea Poretti

47 **Doppler Sonography of the Brain in Children,** 1591
Dorothy Bulas and Alexia Egloff

48 **The Pediatric Head and Neck,** 1628
Rupa Radhakrishnan and Beth M. Kline-Fath

49 **The Pediatric Spinal Canal,** 1672
Ilse Castro-Aragon, Deborah Levine, and Carol M. Rumack

50 **The Pediatric Chest,** 1701
Chetan Chandulal Shah and S. Bruce Greenberg

51 **The Pediatric Liver and Spleen,** 1730
Sara M. O'Hara

52 **The Pediatric Urinary Tract and Adrenal Glands,** 1775
Harriet J. Paltiel and Diane S. Babcock

53 **The Pediatric Gastrointestinal Tract,** 1833
Susan D. John and Martha Mappus Munden

54 **Pediatric Pelvic Sonography,** 1870
William L. Simpson, Jr., Humaira Chaudhry, and Henrietta Kotlus Rosenberg

55 **The Pediatric Hip and Other Musculoskeletal Ultrasound Applications,** 1920
Leslie E. Grissom and H. Theodore Harcke

56 **Pediatric Interventional Sonography,** 1942
Neil Johnson and Allison Aguado

Appendix: Ultrasound Artifacts: A Virtual Chapter
Korosh Khalili, Hojun Yu, Alexander Jesurum, and Deborah Levine
Index, I-1

VIDEO CONTENTS

4 The Liver
Stephanie R. Wilson and Cynthia E. Withers

Video 4.1 **Normal liver, sagittal sweep**
Video 4.2 **Normal liver, subcostal sweep**
Video 4.3 **Focal fat in the liver**
Video 4.4 **Geographic fatty infiltration of the liver**
Video 4.5 **CEUS of FNH with classic enhancement features**
Video 4.6 **CEUS of the flash-filling hemangioma shown in Fig. 4.47**
Video 4.7 **CEUS of focal nodular hyperplasia**
Video 4.8 **CEUS of focal nodular hyperplasia**
Video 4.9 **CEUS of hepatic adenoma in a young woman**
Video 4.10 **CEUS of small hepatocellular carcinoma**
Video 4.11 **CEUS of hepatocellular carcinoma**
Video 4.12 **Classic colorectal metastasis**
Video 4.13 **CEUS of liver metastasis**
Video 4.14 **CEUS of liver metastasis**

5 The Spleen
Patrick M. Vos, John R. Mathieson, and Peter L. Cooperberg

Video 5.1 **Normal spleen in sagittal plane**
Video 5.2 **Normal spleen in transverse plane**
Video 5.3 **Contrast study of lymphoma manifesting as a hypoechoic solitary splenic lesion**

6 The Biliary Tree and Gallbladder
Korosh Khalili and Stephanie R. Wilson

Video 6.1 **Distal common bile duct and ampulla of Vater**
Video 6.2 **Intrahepatic bile duct stones**
Video 6.3 **Distal common bile duct stone**
Video 6.4 **Choledochoduodenal fistula**
Video 6.5 **Primary sclerosing cholangitis**
Video 6.6 **Primary sclerosing cholangitis**
Video 6.7 **Cholangiocarcinoma complicating primary sclerosing cholangitis**
Video 6.8 **Cholangiocarcinoma complicating primary sclerosing cholangitis**
Video 6.9 **Cholelithiasis**
Video 6.10 **Acute cholecystitis**
Video 6.11 **Perforated cholecystitis with liver abscess**

7 The Pancreas
Thomas Winter and Maryellen R.M. Sun

Video 7.1 **Normal pancreas**
Video 7.2 **Acute pancreatitis**
Video 7.3 **Acute pancreatitis**
Video 7.4 **Chronic pancreatitis**
Video 7.5 **Chronic pancreatitis**
Video 7.6 **Pancreatic pseudocyst**
Video 7.7 **Pancreatic carcinoma**
Video 7.8 **Pancreatic carcinoma**
Video 7.9 **Intraductal papillary mucinous neoplasm**
Video 7.10 **Mucinous cystic neoplasm**

8 The Gastrointestinal Tract
Stephanie R. Wilson

Video 8.1 **An incidentally detected neuroendocrine tumor (carcinoid) of the small bowel**
Video 8.2 **Classic features of Crohn disease on a sweep through the terminal ileum**
Video 8.3 **Loss of stratification of the bowel wall layers in severe subacute inflammation of the sigmoid colon in a patient with Crohn disease**
Video 8.4 **Stricture in Crohn disease**
Video 8.5 **Color Doppler shows hyperemia in thickened bowel wall in Crohn disease**
Video 8.6 **Contrast-enhanced longitudinal image of Crohn disease**
Video 8.7 **Contrast-enhanced cross-sectional image of Crohn disease**
Video 8.8 **Severe fixation and acute angulation of the ileum with stricture and enteroenteric fistula**
Video 8.9 **Incomplete small bowel obstruction in patient with Crohn disease**
Video 8.10 **Dysfunctional and excess peristalsis**
Video 8.11 **Localized perforation with a phlegmonous inflammatory mass**
Video 8.12 **Enteroenteric fistula**
Video 8.13 **Normal appendix**
Video 8.14 **Perforated appendix**
Video 8.15 **Acute diverticulitis in second trimester of pregnancy**
Video 8.16 **Paralytic ileus**
Video 8.17 **Incomplete bowel obstruction due to an inflammatory stricture from Crohn disease seen only on endovaginal scan**

9 The Kidney and Urinary Tract
Mitchell Tublin, Deborah Levine, Wendy Thurston, and Stephanie R. Wilson

Video 9.1 **Doppler jet**
Video 9.2 **Renal cell carcinoma**
Video 9.3 **Transitional cell carcinoma of the bladder**
Video 9.4 **Bladder diverticula**

11 The Adrenal Glands
Christina Marie Chingkoe, Olga R. Brook, and Deborah Levine

Video 11.1 **Normal adrenal gland**
Video 11.2 **Adrenal adenoma**
Video 11.3 **Adrenal adenoma**
Video 11.4 **Adrenal gland with calcification**

12 The Retroperitoneum
Raymond E. Bertino and Elton Mustafaraj

Video 12.1 **Type 2 endoleak from inferior mesenteric artery–aorta**
Video 12.2 **Type 2 endoleak on enhanced computed tomography scan**
Video 12.3 **Type 3 endoleak, transverse image**
Video 12.4 **Type 3 endoleak, longitudinal image**
Video 12.5 **Aortic pseudoaneurysm (contained rupture), longitudinal image**
Video 12.6 **Restenosis of stented accessory left renal artery**
Video 12.7 **Angiogram of restenosis of stented accessory left renal artery**

Video 12.8 **Angiogram of stented accessory left renal artery restenosis after restenting**
Video 12.9 **Normal right renal artery**
Video 12.10 **Left renal artery stenosis with color bruit and aliasing throughout cardiac cycle**
Video 12.11 **Nutcracker syndrome**
Video 12.12 **Nutcracker syndrome after stent placement**
Video 12.13 **Prominent arcuate veins**
Video 12.14 **Mildly prominent arcuate veins**
Video 12.15 **Angiogram of left ovarian vein during coil placement**

13 Dynamic Ultrasound of Hernias of the Groin and Anterior Abdominal Wall
Deborah Levine, Lisa Napolitano, and A. Thomas Stavros

Video 13.1 **Fat-containing indirect inguinal hernia**
Video 13.2 **Direct inguinal hernia with intraperitoneal and preperitoneal fat**
Video 13.3 **Note bowel peristalsis in this inguinal hernia**
Video 13.4 **Large fat-containing direct inguinal hernia**
Video 13.5 **Change in hernia contents during Valsalva maneuver**
Video 13.6 **Completely reducible large wide-necked fat-containing ventral hernia**
Video 13.7 **Partially reducible indirect inguinal hernia containing fat and bowel**
Video 13.8 **Nonreducible fat-containing epigastric linea alba hernia**
Video 13.9 **Large bowel-containing indirect inguinal hernia extending into scrotum**
Video 13.10 **Fat-containing femoral hernia**
Video 13.11 **Moderate-sized fat-containing nonreducible left spigelian hernia**
Video 13.12 **Large fat- and bowel-containing incompletely reducible spigelian hernia**
Video 13.13 **Diastasis recti abdominis**
Video 13.14 **Fat-containing ventral hernia**
Video 13.15 **Small fat-containing nonreducible epigastric linea alba hernia**
Video 13.16 **Two adjacent moderate-sized fat-containing incompletely reducible epigastric linea alba hernias**
Video 13.17 **Mesh with strong shadow makes evaluation for recurrent hernia difficult**
Video 13.18 **Two adjacent moderate-sized fat-containing incisional hernias in patient after transverse rectus abdominis myocutaneous (TRAM) flap breast reconstruction**
Video 13.19 **Fat-containing incisional hernia**
Video 13.20 **Moderate-sized fat-containing reducible incisional hernia**
Video 13.21 **Moderate-sized fat-containing reducible recurrent inguinal hernia at the edge of mesh**
Video 13.22 **Pantaloon hernias**
Video 13.23 **Strangulated right femoral hernia**
Video 13.24 **Round ligament and inguinal canal (canal of Nuck) in a female with hydrocele**

14 The Peritoneum
Anthony E. Hanbidge, Korosh Khalili, and Stephanie R. Wilson

Video 14.1 **Tumor infiltration of the omentum**
Video 14.2 **Tumor implant in the pouch of Douglas**
Video 14.3 **Tumor implant in the pouch of Douglas**
Video 14.4 **Peritoneal carcinomatosis—parietal peritoneum**
Video 14.5 **Peritoneal carcinomatosis—visceral peritoneum**
Video 14.6 **Peritoneal carcinomatosis—visceral peritoneum**
Video 14.7 **Peritoneal mesothelioma**
Video 14.8 **Endometrioma in the pouch of Douglas**
Video 14.9 **Endometriotic plaque**
Video 14.10 **Endometriotic plaque**

15 The Uterus
Douglas Brown and Deborah Levine

Video 15.1 **Unicornuate uterus**
Video 15.2 **Bicornuate uterus**
Video 15.3 **Fibroid with cystic necrotic change**
Video 15.4 **Adenomyosis**
Video 15.5 **Prolapsing polyp**
Video 15.6 **Endometrial polyp**
Video 15.7 **Endometrial polyp**
Video 15.8 **Endometrial carcinoma**
Video 15.9 **Endometrial carcinoma with hematometra**
Video 15.10 **Synechia**
Video 15.11 **Low position of intrauterine device (IUD)**
Video 15.12 **Vascularized retained products of conception**
Video 15.13 **Bladder flap hematoma and sutures after cesarean section**

16 The Adnexa
Rochelle Filker Andreotti and Lori A. Deitte

Video 16.1 **Bowel peristalsis**
Video 16.2 **Hemorrhagic cyst**
Video 16.3 **Endometrioma**
Video 16.4 **Atypical endometrioma**
Video 16.5 **Deep infiltrating endometriosis**
Video 16.6 **Ovarian torsion**
Video 16.7 **Clear cell carcinoma in endometrioma**
Video 16.8 **Yolk sac tumor**
Video 16.9 **Hydrosalpinx in 70-year-old woman with adnexal cyst**
Video 16.10 **Hydrosalpinx in 35-year-old with complex left adnexal cyst**
Video 16.11 **Pelvic inflammatory disease caused by *Neisseria Gonorrhoeae***

17 Ultrasound-Guided Biopsy of Chest, Abdomen, and Pelvis
Theodora A. Potretzke, Thomas D. Atwell, J. William Charboneau, and Carl Reading

Video 17.1 **Ultrasound-guided omental core biopsy**
Video 17.2 **Ultrasound-guided liver core biopsy**
Video 17.3 **Ultrasound-guided liver mass biopsy using "freehand" technique**
Video 17.4 **Ultrasound-guided liver mass biopsy using "freehand" technique**
Video 17.5 **Power Doppler imaging improving drain conspicuity**
Video 17.6 **Transvaginal adnexal cyst local anesthesia**
Video 17.7 **Transvaginal adnexal cyst aspiration**

18 Organ Transplantation
Derek Muradali and Tanya Punita Chawla

Video 18.1 **Normal renal transplant, sagittal**
Video 18.2 **Normal renal transplant, transverse**
Video 18.3 **Arteriovenous malformation renal transplant**
Video 18.4 **Partially thrombosed pseudoaneurysm in hilum of renal transplant**
Video 18.5 **Normal pancreas transplant, sagittal**
Video 18.6 **Normal pancreas transplant, transverse**

19 The Thyroid Gland
Luigi Solbiati, J. William Charboneau, Vito Cantisani, Carl Reading, and Giovanni Mauri

Video 19.1 **Colloid cysts**
Video 19.2 **Honeycomb pattern of benign nodule**
Video 19.3 **Adenoma**
Video 19.4 **Papillary carcinoma: fine calcifications**
Video 19.5 **Papillary carcinoma: coarse and fine calcifications**
Video 19.6 **Fine-needle aspiration (FNA)**
Video 19.7 **Hashimoto thyroiditis**

20 The Parathyroid Glands
Bonnie J. Huppert and Carl Reading

Video 20.1 **Cystic and solid parathyroid adenoma**
Video 20.2 **Small parathyroid adenoma**
Video 20.3 **Multiple gland parathyroid hyperplasia**
Video 20.4 **Multiple gland parathyroid hyperplasia**
Video 20.5 **Superior parathyroid adenoma**
Video 20.6 **Superior parathyroid adenoma**
Video 20.7 **Inferior parathyroid adenoma**
Video 20.8 **Inferior parathyroid adenoma**
Video 20.9 **Ectopic superior parathyroid adenoma**
Video 20.10 **Intrathyroid parathyroid adenoma**
Video 20.11 **Intrathyroid parathyroid adenoma**
Video 20.12 **Ectopic parathyroid adenoma**
Video 20.13 **Parathyromatosis in the postoperative neck**
Video 20.14 **Parathyroid adenoma**
Video 20.15 **Small inferior parathyroid adenoma and multinodular goiter**
Video 20.16 **Small inferior parathyroid adenoma and multinodular thyroid**
Video 20.17 **Ectopic intrathyroid parathyroid adenoma biopsy**
Video 20.18 **Ectopic parathyroid adenoma biopsy**
Video 20.19 **Ethanol ablation of recurrent graft-dependent hyperparathyroidism**

21 The Breast
Jordana Phillips, Rashmi J. Mehta, and A. Thomas Stavros

Video 21.1 **Importance of light pressure for color Doppler examination**
Video 21.2 **Importance of light pressure for color Doppler examination**
Video 21.3 **Normal cyst**
Video 21.4 **Intraductal papilloma**
Video 21.5 **Percutaneous biopsy using spring-loaded biopsy device**

22 The Scrotum
Daniel Sommers and Thomas Winter

Video 22.1 **Atrophic testis with seminoma**
Video 22.2 **Epidermoid cyst**
Video 22.3 **Varicocele in patient performing a Valsalva maneuver, with gray-scale and color Doppler sonography**
Video 22.4 **Postvasectomy appearance of epididymis and vas deferens**
Video 22.5 **"Dancing sperm" postvasectomy image of scrotum**
Video 22.6 **Acute orchitis**
Video 22.7 **Inferior traumatic tunica albuginea rupture, hematoma in testis, and extrusion of seminiferous tubules**

23 Overview of Musculoskeletal Ultrasound Techniques and Applications
Colm McMahon and Corrie Yablon

Video 23.1 **Normal biceps muscle and distal tendon**
Video 23.2 **Normal Achilles tendon**
Video 23.3 **Normal finger flexor tendons—dynamic imaging**
Video 23.4 **Dynamic ulnar nerve subluxation**
Video 23.5 **Short-axis imaging of a Baker cyst**

24 The Shoulder
Colm McMahon and Corrie Yablon

Video 24.1 **Dynamic assessment for subcoracoid impingement**
Video 24.2 **Illustration of imaging the supraspinatus in long axis and the transition to infraspinatus posteriorly**
Video 24.3 **Dynamic assessment for subacromial impingement**
Video 24.4 **Dynamic imaging showing increased prominence of glenohumeral effusion on external rotation**
Video 24.5 **Short-axis imaging of the supraspinatus tendon**

25 Musculoskeletal Interventions
Ronald S. Adler

Video 25.1 **Intraarticular injection of a hip under ultrasound guidance**
Video 25.2 **Biceps tendon sheath injection using a rotator interval approach**
Video 25.3 **Aspiration of a spinoglenoid notch cyst**
Video 25.4 **Injection of calcific tendinosis**
Video 25.5 **Autologous blood injection of 50-year-old woman with lateral epicondylitis**
Video 25.6 **Depiction of Tenex procedure**
Video 25.7 **Posthydrodissection of sural nerve in a 59-year-old female patient**

26 The Extracranial Cerebral Vessels
Edward I. Bluth, Stephen I. Johnson, and Laurie Troxclair

Video 26.1 **Minimal homogeneous plaque at carotid bulb (gray-scale)**
Video 26.2 **Considerable homogenous plaque at ICA (gray-scale)**
Video 26.3 **Type 3 homogeneous plaque with less than 50% sonolucency (gray-scale)**
Video 26.4 **Type 3 homogeneous plaque with low-grade stenosis of the ICA (gray-scale)**
Video 26.5 **Calcified plaque in the CCA (gray-scale)**
Video 26.6 **Heterogeneous plaque in the left ICA (type 1) (gray-scale)**
Video 26.7 **Heterogeneous plaque (type 1) with greater than 50% sonolucency within the plaque of the left ICA (gray-scale)**
Video 26.8 **Heterogeneous plaque (type 2) in the ICA (gray-scale)**
Video 26.9 **High-grade stenosis in the proximal right ICA (color Doppler)**
Video 26.10 **Heterogeneous plaque in the ICA (color Doppler)**
Video 26.11 **Heterogeneous plaque in the left ICA (power Doppler)**
Video 26.12 **High-grade stenosis in the ICA (power Doppler)**
Video 26.13 **High-grade stenosis of the ICA (power Doppler)**
Video 26.14 **Low-grade stenosis in the ICA (color Doppler)**
Video 26.15 **Normal spectral waveform of the proximal ICA**
Video 26.16 **Normal spectral waveform of the mid ICA**
Video 26.17 **Normal spectral waveform of the distal ICA**
Video 26.18 **Normal spectral waveform of the right distal CCA**
Video 26.19 **High-grade stenosis in the ICA (power Doppler)**

Video 26.20 **High-grade stenosis in the ICA (color Doppler)**
Video 26.21 **High-grade stenosis with spectral broadening (color and spectral Doppler)**
Video 26.22 **Color and spectral Doppler of low-grade stenosis in the ICA**

27 Peripheral Vessels
Mark E. Lockhart, Heidi R. Umphrey, Therese M. Weber, and Michelle L. Robbin

Video 27.1 **Acute thrombus in the superficial femoral artery**
Video 27.2 **Occlusion of the superficial femoral artery with a large collateral exiting proximal to the occlusion**
Video 27.3 **Severe calcification of the superficial femoral artery limits ability to see within the artery lumen with gray-scale imaging**
Video 27.4 **Common femoral artery pseudoaneurysm**
Video 27.5 **Common femoral artery to common femoral vein arteriovenous fistula (AVF)**
Video 27.6 **Arterial bypass graft stenosis on grayscale and color Doppler**
Video 27.7 **Large radial artery pseudoaneurysm with rent in arterial wall**
Video 27.8 **Large radial artery pseudoaneurysm**
Video 27.9 **Subclavian steal**
Video 27.10 **Normal femoral vein compression during study to assess for deep venous thrombosis**
Video 27.11 **Acute common femoral vein (CFV) thrombus**
Video 27.12 **Nonocclusive slightly mobile thrombus within the great saphenous vein (GSV) with extension into the common femoral vein (CFV)**
Video 27.13 **Acute deep venous thrombosis in right lower extremity**
Video 27.14 **Chronic vein occlusion with collaterals**
Video 27.15 **Chronic common femoral vein (CFV) occlusion with normal antegrade flow in the femoral vein, and flow reversal in the profunda femoral vein**
Video 27.16 **Slow flow in patent, compressible vein without deep venous thrombosis, longitudinal cine clip**
Video 27.17 **Slow flow in patent, compressible vein without deep venous thrombosis, transverse cine clip**
Video 27.18 **Thrombus in one of paired femoral veins**
Video 27.19 **Normal femoral vein valve**
Video 27.20 **Normal internal jugular vein (IJV) on gray scale compression cine clip**
Video 27.21 **Acute internal jugular thrombus**
Video 27.22 **Nonocclusive thrombus in one brachial vein in the paired brachial veins**
Video 27.23 **Acute thrombus around peripherally inserted central catheter (PICC) line in the basilic vein**
Video 27.24 **Acute thrombus around peripherally inserted central catheter (PICC) line in the basilic vein**
Video 27.25 **Thick-walled cephalic vein with chronic thrombus**
Video 27.26 **Large hematoma adjacent to arteriovenous fistula (AVF)**
Video 27.27 **Small AVF basilic vein pseudoaneurysm**
Video 27.28 **Graft wall irregularity and degeneration from repeated punctures**
Video 27.29 **Graft venous anastomosis stenosis with peak systolic velocity measuring 6.1 m/sec in highest velocity portion of jet**

28 Overview of Obstetric Imaging
Deborah Levine

Video 28.1 **Normal 6-week embryo with cardiac activity**
Video 28.2 **Normal first-trimester embryo with rhombencephalon appearing as a fluid collection in the region of the head**
Video 28.3 **Sagittal view of uterus with 17-week gestational age fetus in cephalic presentation and anterior placenta**
Video 28.4 **Normal intracranial anatomy at 19 weeks' gestation**
Video 28.5 **Four-chamber view of beating fetal heart**
Video 28.6 **Scan through the heart**
Video 28.7 **Normal kidneys and lumbosacral spine**
Video 28.8 **Transverse fetal spine**
Video 28.9 **Bladder and umbilical arteries**

30 The First Trimester
Elizabeth Lazarus and Deborah Levine

Video 30.1 **Early embryonic cardiac activity**
Video 30.2 **Early pregnancy failure at 7 weeks**
Video 30.3 **Expanded amnion in nonviable pregnancy**
Video 30.4 **Ten-week demise with calcified yolk sac**
Video 30.5 **Small subchorionic hemorrhage**
Video 30.6 **Right ectopic pregnancy with adnexal mass separating from the ovary with manual pressure**
Video 30.7 **Ruptured ectopic pregnancy**
Video 30.8 **Cesarean section implantation in retroflexed uterus**
Video 30.9 **Normal rhombencephalon**
Video 30.10 **Persistent trophoblastic neoplasia**
Video 30.11 **Choriocarcinoma**

31 Chromosomal Abnormalities
Bryann Bromley and Beryl Benacerraf

Video 31.1 **Nuchal translucency**
Video 31.2 **Cystic hygroma**
Video 31.3 **Nasal bone in first trimester**
Video 31.4 **Echogenic bowel**
Video 31.5 **Amniocentesis needle being withdrawn from amniotic fluid cavity**

32 Multifetal Pregnancy
Mary C. Frates

Video 32.1 **Quintuplets, 9 weeks' gestational age**
Video 32.2 **Conjoined embryos, 7 weeks' gestational age**
Video 32.3 **Monochorionic monoamniotic twins, 26 weeks' gestational age**
Video 32.4 **Three separate placentas in a trichorionic triplet pregnancy at 13 weeks' gestational age**
Video 32.5 **Velamentous cord insertion in a twin, 34 weeks' gestational age**
Video 32.6 **Growth and fluid discrepancies in dichorionic twins, 24 weeks' gestational age**
Video 32.7 **Twin-twin transfusion syndrome, 22 weeks' gestational age**
Video 32.8 **Twin reversed arterial perfusion sequence, 16 weeks' gestational age**
Video 32.9 **Monochorionic monoamniotic twins, 12 weeks' gestational age**
Video 32.10 **Monochorionic monoamniotic twins, 28 weeks' gestational age**
Video 32.11 **Monochorionic monoamniotic conjoined twins, 35 weeks' gestational age**

33 The Fetal Face and Neck
Ana P. Lourenco and Judy A. Estroff

Video 33.1 **Left 2 complete cleft lip, cleft alveolus, and cleft palate in sagittal plane in 20-week gestational age fetus**
Video 33.2 **Left unilateral complete cleft lip, cleft alveolus, and cleft palate in axial plane in 20-week gestational age fetus**
Video 33.3 **Left unilateral complete cleft lip, cleft alveolus, and cleft palate in coronal plane in 20-week gestational age fetus**
Video 33.4 **Micrognathia at gestational age 20 weeks**

34 The Fetal Brain
Ants Toi and Deborah Levine

Video 34.1 **Normal brain, axial**
Video 34.2 **Normal brain, coronal**
Video 34.3 **Normal brain, sagittal**
Video 34.4 **Choroid plexus cysts**
Video 34.5 **Bilateral ventriculomegaly**
Video 34.6 **Chiari malformation in fetus with spinal neural tube defect**
Video 34.7 **Holoprosencephaly**
Video 34.8 **Second trimester agenesis of corpus callosum**
Video 34.9 **Agenesis of corpus callosum in coronal plane**
Video 34.10 **Agenesis of corpus callosum in sagittal plane**
Video 34.11 **Agenesis of corpus callosum in axial plane with midline cyst**
Video 34.12 **Absence of septal leaflets**

35 The Fetal Spine
Elizabeth Asch and Eric Sauerbrei

Video 35.1 **Normal transaxial spine**
Video 35.2 **Normal longitudinal spine**
Video 35.3 **Myelomeningocele**
Video 35.4 **Closed neural tube defect: transaxial**
Video 35.5 **Closed neural tube defect: longitudinal**
Video 35.6 **Sacrococcygeal teratoma**

36 The Fetal Chest
Dorothy Bulas

Video 36.1 **Congenital pulmonary adenomatoid malformation**
Video 36.2 **Small pleural effusion at 16 weeks' gestational age**
Video 36.3 **Left-sided congenital diaphragmatic hernia at 32 weeks' gestational age (transverse view)**
Video 36.4 **Left-sided congenital diaphragmatic hernia at 32 weeks' gestational age (sagittal view)**
Video 36.5 **Large left-sided congenital diaphragmatic hernia with large amount of liver in chest**
Video 36.6 **Right-sided congenital diaphragmatic hernia**

37 The Fetal Heart
Elizabeth R. Stamm and Julia A. Drose

Video 37.1 **Normal apical four-chamber view**
Video 37.2 **Normal sub-costal four-chamber view**
Video 37.3 **Normal appearance of the aorta and pulmonary artery**
Video 37.4 **Color Doppler of the aorta and pulmonary artery**
Video 37.5 **Short-axis view of the color Doppler of the ventricles and great arteries**
Video 37.6 **Three-vessel and trachea view**
Video 37.7 **Aortic arch**
Video 37.8 **Aortic arch**
Video 37.9 **Atrioventricular septal defect**
Video 37.10 **Hypoplastic left heart syndrome**
Video 37.11 **Hypoplastic right heart**
Video 37.12 **Ebstein anomaly**
Video 37.13 **Tetralogy of Fallot**

38 The Fetal Gastrointestinal Tract and Abdominal Wall
Nir Melamed, Anne Kennedy, and Phyllis Glanc

Video 38.1 **Esophageal atresia**
Video 38.2 **Gastric debris**
Video 38.3 **Gastric debris**
Video 38.4 **Duodenal atresia**
Video 38.5 **Jejunal atresia**
Video 38.6 **Duplication cyst**
Video 38.7 **Meconium peritonitis**
Video 38.8 **Echogenic bowel**
Video 38.9 **Normal gallbladder**
Video 38.10 **Annular pancreas**
Video 38.11 **Splenic cyst**
Video 38.12 **Gastroschisis**
Video 38.13 **Omphalocele**
Video 38.14 **Bladder exstrophy**
Video 38.15 **Cloacal exstrophy**

39 The Fetal Urogenital Tract
Katherine W. Fong, Julia Eva Kfouri, and Kirsten L. Weind Matthews

Video 39.1 **"Lying down" adrenal sign due to unilateral renal agenesis**
Video 39.2 **Bilateral renal agenesis**
Video 39.3 **Pelvic kidney**
Video 39.4 **Cross-fused renal ectopia**
Video 39.5 **Horseshoe kidney**
Video 39.6 **Autosomal recessive polycystic kidney disease**
Video 39.7 **Perinephric urinoma**
Video 39.8 **Primary megaureter**
Video 39.9 **Megalourethra**
Video 39.10 **Cloacal dysgenesis**
Video 39.11 **Ovarian cyst**

40 The Fetal Musculoskeletal System
Phyllis Glanc, David Chitayat, and Sheila Unger

Video 40.1 **Thanatophoric dysplasia**
Video 40.2 **Clubfeet at 21 weeks**

41 Fetal Hydrops
Deborah Levine

Video 41.1 **Fetal abdomen at 30 weeks gestational age in fetus with a small amount of ascites and polyhydramnios**
Video 41.2 **Bilateral pleural effusions, left greater than right**
Video 41.3 **Large unilateral pleural effusion inverts the hemidiaphragm and is associated with ascites**
Video 41.4 **Small pericardial effusion in fetus with poorly contractile and echogenic heart**
Video 41.5 **Anasarca in fetus with congenital pulmonary airway malformation**
Video 41.6 **Middle cerebral artery Doppler**
Video 41.7 **Poorly contractile heart abnormal appearing heart, bilateral pleural effusions, and marked anasarca**

42 Fetal Measurements: Normal and Abnormal Fetal Growth and Assessment of Fetal Well-Being
Carol B. Benson and Peter M. Doubilet

Video 42.1 **Early embryonic heartbeat**
Video 42.2 **Fetal movement**
Video 42.3 **Fetal breathing movements**

43 Sonographic Evaluation of the Placenta
Thomas D. Shipp

Video 43.1 **Placental lake**
Video 43.2 **Thick placenta**
Video 43.3 **Placenta accreta**
Video 43.4 **Placenta increta**
Video 43.5 **Placenta percreta**
Video 43.6 **Abruption**
Video 43.7 **Abruption**
Video 43.8 **Preplacental hematoma**
Video 43.9 **Preplacental hematoma**
Video 43.10 **Placental infarction**
Video 43.11 **Placental infarction**
Video 43.12 **Circumvallate placenta**
Video 43.13 **Circumvallate placenta**
Video 43.14 **Bilobed placenta**
Video 43.15 **Velamentous cord insertion and two-vessel cord**
Video 43.16 **Umbilical cord insertion into placenta**
Video 43.17 **Vasa previa**

44 Cervical Ultrasound and Preterm Birth
Hournaz Ghandehari and Phyllis Glanc

Video 44.1 **Open cervix with large funnel and bulging membranes**
Video 44.2 **Closed cervix with mobile debris at the internal os**
Video 44.3 **Open cervix with mobile debris in the dilated cervical canal and adjacent to the external os**

45 Neonatal and Infant Brain Imaging
Carol M. Rumack and Amanda K. Auckland

Video 45.1 **Normal coronal sweep**
Video 45.2 **Normal sagittal sweep**
Video 45.3 **Normal mastoid sweep**
Video 45.4 **Chiari II malformation**
Video 45.5 **Ventriculomegaly in association with Chiari II malformation (seen in Video 45.4)**
Video 45.6 **Chiari II malformation, pointed frontal and large occipital horn; partial absence of corpus callosum (same neonate as in Videos 45.4 and 45.5)**
Video 45.7 **Tethered cord in patient with Chiari II malformation, sagittal scan**
Video 45.8 **Absence of cavum septi pellucidi, coronal scan**
Video 45.9 **Right subacute subependymal, intraventricular, and right frontal intraparenchymal hemorrhages, coronal scan**
Video 45.10 **Right subependymal, caudothalamic groove, and hemorrhage and intraventricular hemorrhage, sagittal scan**
Video 45.11 **Cisterna magna clot**
Video 45.12 **Acute intraventricular echogenic blood**
Video 45.13 **Bilateral intraventricular hemorrhage and intraparenchymal hemorrhage**
Video 45.14 **Acute highly echogenic hemorrhage**
Video 45.15 **Intraventricular hemorrhage**
Video 45.16 **Cystic periventricular leukomalacia**
Video 45.17 **Cytomegalovirus with punctate calcifications**
Video 45.18 **Multiple focal calcifications**
Video 45.19 **Ventricular septation**

47 Doppler Sonography of the Brain in Children
Dorothy Bulas and Alexia Egloff

Video 47.1 **Normal color Doppler of circle of Willis in 6-year-old**
Video 47.2 **Spectral wave form of the right middle cerebral artery**
Video 47.3 **Normal spectral Doppler of right bifurcation**
Video 47.4 **Four-year-old pending brain death after fall from second story**
Video 47.5 **Eight-year-old pending brain death after motor vehicle accident postcraniectomy for hematoma**

48 The Pediatric Head and Neck
Rupa Radhakrishnan and Beth M. Kline-Fath

Video 48.1 **Wharton duct stone**
Video 48.2 **Multinodular goiter**
Video 48.3 **Infantile hemangioma**
Video 48.4 **Lymphatic malformation**

49 The Pediatric Spinal Canal
Ilse Castro-Aragon, Deborah Levine, and Carol M. Rumack

Video 49.1 **Normal cauda equina**
Video 49.2 **Normal filum terminale**
Video 49.3 **Skin dimple and hypoechoic tract in subcutaneous tissues extending to normal coccyx**
Video 49.4 **Lipomyelocele in sagittal view**
Video 49.5 **Sagittal lipomyelocele**
Video 49.6 **Lipomyelocele in transverse view**
Video 49.7 **Lipomyelomeningocele**
Video 49.8 **Segmental spinal dysgenesis in sagittal view**
Video 49.9 **Segmental spinal dysgenesis patient with fatty filum**

50 The Pediatric Chest
Chetan Chandulal Shah and S. Bruce Greenberg

Video 50.1 **Moving septations within pleural fluid**
Video 50.2 **Hemidiaphragmatic motion in an infant**
Video 50.3 **Hemidiaphragmatic movement in healthy 31-month-old child**
Video 50.4 **Hemidiaphragmatic paralysis in an infant after cardiac surgery**

51 The Pediatric Liver and Spleen
Sara M. O'Hara

Video 51.1 **Normal porta hepatis showing portal vein, hepatic artery, and common bile duct**
Video 51.2 **Neonatal hepatitis**
Video 51.3 **Steatosis from obesity**
Video 51.4 **Multiple cutaneous hemangiomas in a 1-month-old infant**
Video 51.5 **Multiple cutaneous hemangiomas in a 1-month-old infant**
Video 51.6 **Hepatic abscess**
Video 51.7 **Normal flow in the main portal vein**
Video 51.8 **Normal branching vessels in the liver**
Video 51.9 **Normal third- and fourth-order branches in the liver**
Video 51.10 **Cavernous transformation of the portal vein**
Video 51.11 **Pneumobilia, an expected finding following portoenterostomy**

52 The Pediatric Urinary Tract and Adrenal Glands
Harriet J. Paltiel and Diane S. Babcock

Video 52.1 **Crossed renal ectopia**
Video 52.2 **Contrast-enhanced urosonography depicts a normal bladder**
Video 52.3 **Contrast-enhanced urosonography demonstrates vesicoureteral reflux**
Video 52.4 **Contrast-enhanced urosonography shows a normal male urethra**
Video 52.5 **Inflammatory pseudotumor**
Video 52.6 **Laceration of the mid-lateral aspect of the left kidney and perirenal hematoma**
Video 52.7 **Multicystic dysplastic kidney**
Video 52.8 **Burkitt lymphoma involving kidney**
Video 52.9 **Neuroblastoma**

54 Pediatric Pelvic Sonography
William L. Simpson, Jr., Humaira Chaudhry, and Henrietta Kotlus Rosenberg

Video 54.1 **Water vaginogram**
Video 54.2 **Normal postpubertal ovary**
Video 54.3 **Polycystic ovarian morphology**
Video 54.4 **Normal postpubertal testis**
Video 54.5 **Testicular microlithiasis**

55 The Pediatric Hip and Other Musculoskeletal Ultrasound Applications
Leslie E. Grissom and H. Theodore Harcke

Video 55.1 **Normal coronal/flexion view, midacetabulum**
Video 55.2 **Normal coronal/flexion view, posterior lip**
Video 55.3 **Subluxation, coronal/flexion view, midacetabulum**
Video 55.4 **Dislocatable hip, coronal/flexion view, midacetabulum**
Video 55.5 **Dislocatable hip, coronal/flexion view, posterior lip**
Video 55.6 **Normal transverse/flexion view**
Video 55.7 **Subluxation, transverse/flexion view**
Video 55.8 **Dislocation, transverse/flexion view**

56 Pediatric Interventional Sonography
Neil Johnson and Allison Aguado

Video 56.1 **Peripherally inserted central catheter (PICC) line placement**
Video 56.2 **Video loops showing debris attached to and obstructing the drainage catheter during diagnostic and therapeutic aspiration of heavily bloodstained abdominal fluid with floating debris**
Video 56.3 **Video loops showing debris attached to and obstructing the drainage catheter during diagnostic and therapeutic aspiration of heavily bloodstained abdominal fluid with floating debris**
Video 56.4 **Appendiceal abscess with catheter touching fecalith**
Video 56.5 **Gaucher disease patient rib biopsy**
Video 56.6 **Gaucher rib osteomyelitis drain catheter being advanced**
Video 56.7 **Gaucher rib prebiopsy showing pus and displaceable rib**
Video 56.8 **Juvenile rheumatoid arthritis tendon sheath steroid injection**

Appendix: Ultrasound Artifacts: A Virtual Chapter
Korosh Khalili, Hojun Yu, Alexander Jesurum, and Deborah Levine

Video A.1 **Propagation velocity artifact**
Video A.2 **Attenuation-related artifacts**
Video A.3 **Shadowing**
Video A.4 **Showing in region of cauda equina**
Video A.5 **Increased through transmission**
Video A.6 **Path of sound assumption**
Video A.7 **Mirror image artifact**
Video A.8 **Comet-tail artifact**
Video A.9 **Comet-tail artifact in adenomyomatosis**
Video A.10 **Refraction from the anterior abdominal wall**
Video A.11 **Anisotropy**
Video A.12 **Anisotropy at supraspinatus tendon insertion**
Video A.13 **Reverberation artifact from free intraperitoneal gas**
Video A.14 **Ring-down artifact**
Video A.15 **Ring-down artifact from air in bile ducts**
Video A.16 **Dirty shadowing**
Video A.17 **Side lobe artifact**
Video A.18 **Partial volume averaging explanation**
Video A.19 **Tissue vibration artifact**
Video A.20 **Tissue vibration artifact from left renal artery stenosis with color bruit and aliasing**
Video A.21 **Aliasing seen in common femoral artery to common femoral vein arteriovenous fistula**
Video A.22 **Twinkle explanation**
Video A.23 **Twinkle**

This page intentionally left blank

DIAGNOSTIC ULTRASOUND

This page intentionally left blank

CHAPTER 28

Overview of Obstetric Imaging

Deborah Levine

SUMMARY OF KEY POINTS

- Ultrasound allows for accurate prediction of gestational age.
- The appropriate training and skills are necessary for safely performing and accurately interpreting obstetric ultrasound
- There are many options for screening pregnant women, most of which include ultrasound.
- Routine obstetric ultrasound has specific recommended views that allow for depiction of many, but not all, fetal anomalies.
- Three-dimensional ultrasound, fetal Doppler examinations, and fetal magnetic resonance imaging may be used when additional information is needed beyond that available with routine gray-scale ultrasound.

CHAPTER OUTLINE

TRAINING, PERSONNEL, AND EQUIPMENT
ULTRASOUND GUIDELINES
First Trimester
Second and Third Trimesters
ROUTINE ULTRASOUND SCREENING
Estimation of Gestational Age
Identification of Twin/Multiple Pregnancies
Screening and Perinatal Outcomes
Fetal Malformations: Diagnostic Accuracy
Three-Dimensional Ultrasound
Prudent Use of Ultrasound
MAGNETIC RESONANCE IMAGING
CONCLUSION

There were more than 3.9 million live births in the United States in 2013.[1] Ultrasound is the most frequently used imaging modality for assessment of pregnancy. With care being taken to keep exposure to ultrasound limited to medically needed information, and with imaging performed at the appropriate power settings, ultrasound is safe for use in pregnancy.

Indications for ultrasound during the **first trimester** include pregnancy dating, assessment of women with bleeding or pain, and assessment of nuchal translucency in screening for aneuploidy. In the **second trimester,** ultrasound is used for pregnancy dating, assessment of interval growth, assessment of patients with abnormal pain or bleeding, assessment of size-to-dates discrepancy, routine survey of fetal anatomy, and assessment of maternal complications due to conditions such as age, drug use, or history of previous abnormalities.

In cases of multiple gestations, ultrasound is used to assess growth and complications of twinning. In women with history of cervical incompetence, ultrasound is used to screen for cervical changes that put a patient at risk for preterm delivery. In the **third trimester,** ultrasound is predominantly used to assess fetal growth and well-being. Ultrasound is increasingly used for fetal procedures such as testing for aneuploidy, drainage of abnormal fetal fluid collections, and guidance for fetal surgery. Ultrasound is well recognized as the screening modality of choice, but additional information may be needed beyond that available with ultrasound. In many of these cases, especially those with fetal central nervous system abnormalities, fetal magnetic resonance imaging (MRI) can help clarify the diagnosis.

Part IV of this textbook focuses on obstetric ultrasound and reviews specific fetal organ system anatomy and pathology, with chapters also on safety of ultrasound in pregnancy, assessment of twins, and growth. Fetal magnetic resonance (MR) and three-dimensional (3D) ultrasound images are added throughout to illustrate the benefit of these techniques in select cases.

TRAINING, PERSONNEL, AND EQUIPMENT

Obstetric ultrasound diagnosis is critically dependent on examiner training and experience.[2,3] Physicians and sonographers performing obstetric ultrasound examinations should have completed appropriate training and should be appropriately credentialed and/or boarded. Accreditation of ultrasound laboratories improves compliance with published minimum standards and guidelines.[4] Ultrasound practitioners should be knowledgeable regarding the basic physical principles of ultrasound, equipment, record-keeping requirements, indications, and safety of using ultrasound in pregnancy. Studies should be conducted with real-time scanners

Indications for First-Trimester Ultrasound

- Confirmation of the presence of an intrauterine pregnancy
- Suspected ectopic pregnancy
- Vaginal bleeding
- Pelvic pain
- Estimation of gestational age
- Diagnosis or evaluation of multiple gestations
- Confirmation of cardiac activity
- Adjunct to chorionic villus sampling, embryo transfer, and localization, and removal of an intrauterine device
- Assessment for certain fetal anomalies, such as anencephaly, in high-risk patients
- Measurement of nuchal translucency when part of a screening program for fetal aneuploidy
- Suspected ectopic pregnancy
- Suspected hydatidiform mole
- Maternal pelvic masses and/or uterine abnormalities

Modified from Collaborative Subcommittee. ACR–ACOG–AIUM–SRU practice parameter for the performance of obstetrical ultrasound. American College of Radiology; 2014.[5]

using a transabdominal and/or transvaginal approach, depending on the gestational age and the region of interest. The choice of transducer frequency is a trade-off between beam penetration and resolution. In general, a 3- to 5-MHz transducer frequency provides sufficient resolution with adequate depth penetration in all but the extremely obese patient. During early pregnancy, a 4- to 7-MHz abdominal transducer or a 5- to 10-MHz vaginal transducer can provide superior resolution while still allowing adequate penetration. Higher-frequency transducers are most useful in achieving high-resolution scans of anatomy close to the probe, and lower-frequency transducers are useful when increased penetration of the sound beam is necessary and when a wider field of view is needed. Use of Doppler ultrasound and 3D imaging depends on the specific indication. As in all imaging studies, complete documentation of the images and a formal written interpretation are essential for quality assurance, accreditation, and medicolegal issues.

ULTRASOUND GUIDELINES

First Trimester

The current guidelines of the American College of Radiology (ACR) and American Institute of Ultrasound in Medicine (AIUM) for the performance of first-trimester obstetric ultrasound examination include documentation of the location of the pregnancy (intrauterine vs. extrauterine), documentation of the appearance of the maternal uterus and ovaries (Fig. 28.1), and assessment of **gestational age,** either by measurement of mean sac diameter (before visualization of embryonic pole; Fig. 28.2) or by embryonic/fetal pole crown-rump length[5] (Fig. 28.3). Another important structure to assess is the **yolk sac.** An image of the heart rate is taken using M-mode ultrasound. It is important to use M-mode rather than spectral Doppler ultrasound on the embryo to limit power deposition. Late in the first trimester,

Indications for Second- and Third-Trimester Ultrasound

- Estimation of gestational (menstrual) age
- Evaluation of fetal growth
- Evaluation of fetal anatomy and fetal well-being
- Vaginal bleeding
- Abdominal or pelvic pain
- Cervical insufficiency
- Determination of fetal presentation
- Suspected multiple gestation
- Adjunct to amniocentesis or other procedure
- Evaluation of discrepancy between uterine size (as measured by fundal height) and clinical dates
- Pelvic mass
- Suspected hydatidiform mole
- Adjunct to cervical cerclage placement
- Suspected ectopic pregnancy
- Suspected fetal death
- Suspected uterine abnormality
- Suspected amniotic fluid abnormalities
- Suspected placental abruption
- Adjunct to external cephalic version
- Premature rupture of membranes and/or premature labor
- Previous abnormal screening exams
- Follow-up evaluation of placental location for suspected placenta previa or accreta
- Previous congenital anomaly
- Screening for or follow-up of fetal anomalies

Modified from Collaborative Subcommittee. ACR–ACOG–AIUM–SRU practice parameter for the performance of obstetrical ultrasound. American College of Radiology; 2014.[5]

dating can be performed with measurement of the biparietal diameter and head circumference rather than crown-rump length.

Videos 28.1 and 28.2 show normal first-trimester findings of an early embryo with cardiac activity (Video 28.1) and normal findings of rhombencephalon (Video 28.2).

In the first trimester it is important to not only establish the location of the pregnancy (intrauterine versus extrauteruine) but when intrauterine, to carefully determine if it is a potentially viable pregnancy or if it is a nonviable pregnancy.[6-9] Due to the

General Survey Guidelines for First-Trimester Ultrasound

- Gestational sac
  - Location of pregnancy: intrauterine vs. extrauterine
- Gestational age (as appropriate)
  - Mean sac diameter
  - Embryonic pole length or crown rump length
- Yolk sac
- Cardiac activity on M-mode ultrasound
- Embryo/fetal number (amnionicity/chorionicity)
- Maternal anatomy: uterus and adnexa

Modified from Collaborative Subcommittee. ACR–ACOG–AIUM–SRU practice parameter for the performance of obstetrical ultrasound. American College of Radiology; 2014.[5]

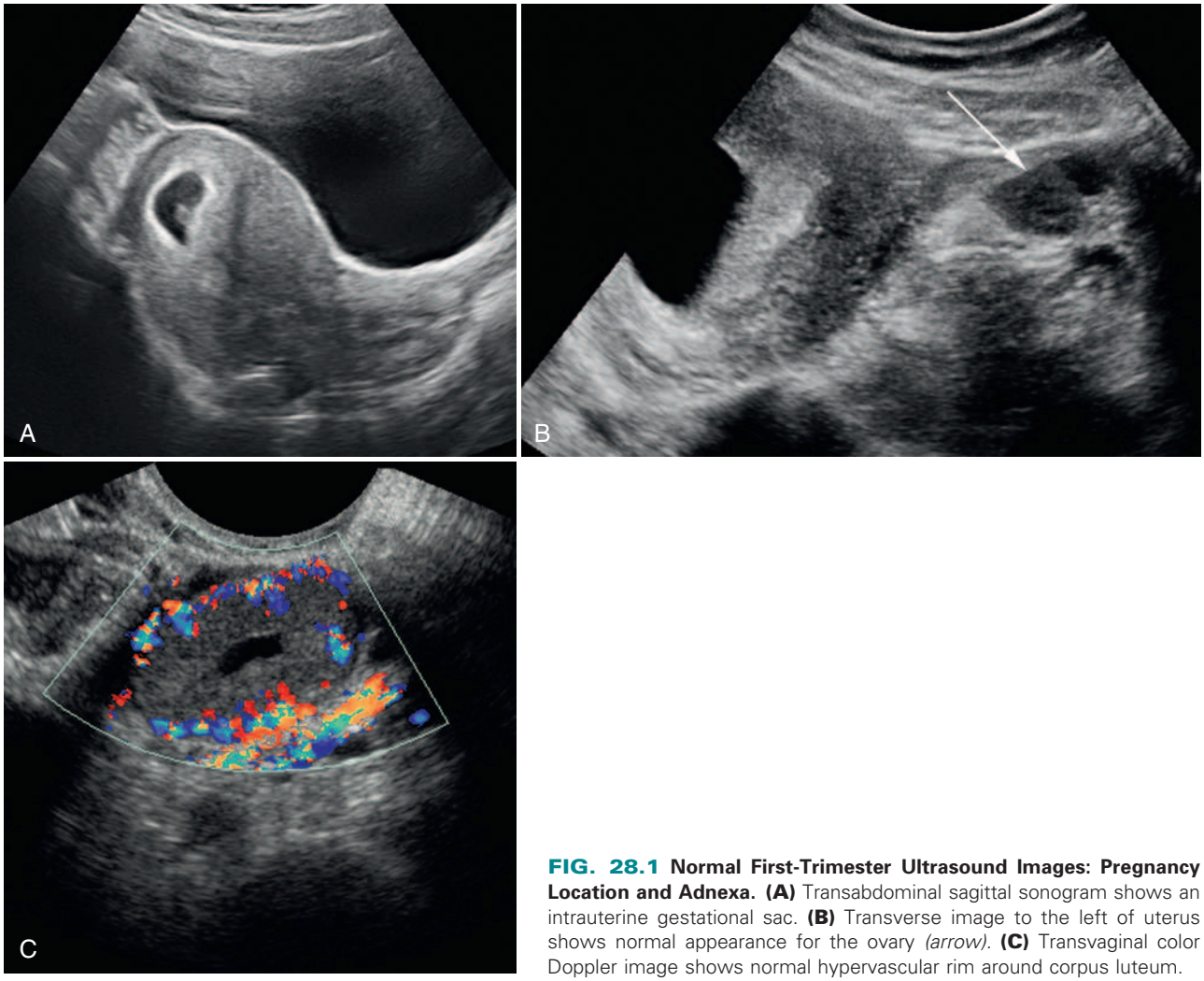

FIG. 28.1 Normal First-Trimester Ultrasound Images: Pregnancy Location and Adnexa. (A) Transabdominal sagittal sonogram shows an intrauterine gestational sac. **(B)** Transverse image to the left of uterus shows normal appearance for the ovary *(arrow)*. **(C)** Transvaginal color Doppler image shows normal hypervascular rim around corpus luteum.

FIG. 28.2 Normal First-Trimester Measurement of Sac Diameter. Transvaginal sagittal image shows sagittal measurement of sac diameter *(calipers)*. Measurements in three orthogonal planes are averaged to calculate the mean sac diameter. Note yolk sac within the gestational sac.

variety of medical professionals performing and interpreting ultrasound in a variety of clinical settings, thresholds for the diagnosis of a failed pregnancy have been increased in order to not misdiagnose a potentially viable pregnancy. These issues are discussed in detail in Chapter 30.

In cases of multiple gestation, first-trimester scans should document the fetal number as well as the amnionicity and chorionicity (Fig. 28.4). Chapter 32 discusses the assessment of multifetal pregnancies.

In addition, the American College of Obstetricians and Gynecologists (ACOG) recommends that prenatal testing for aneuploidy be offered to all pregnant women.[10] Clinicians must understand current screening options (and the tradeoffs between them), including traditional serum analysis (with or without nuchal translucency ultrasonography) or cell-free DNA so that they can discuss these options appropriately with the patient. Cell-free DNA testing uses DNA from the placenta to assess the risk of the fetus having a chromosomal abnormality; it does not assess risk for fetal anomalies such as neural tube defects or ventral wall defects. Management decisions, including termination of the pregnancy, should not be based on the results of the cell-free

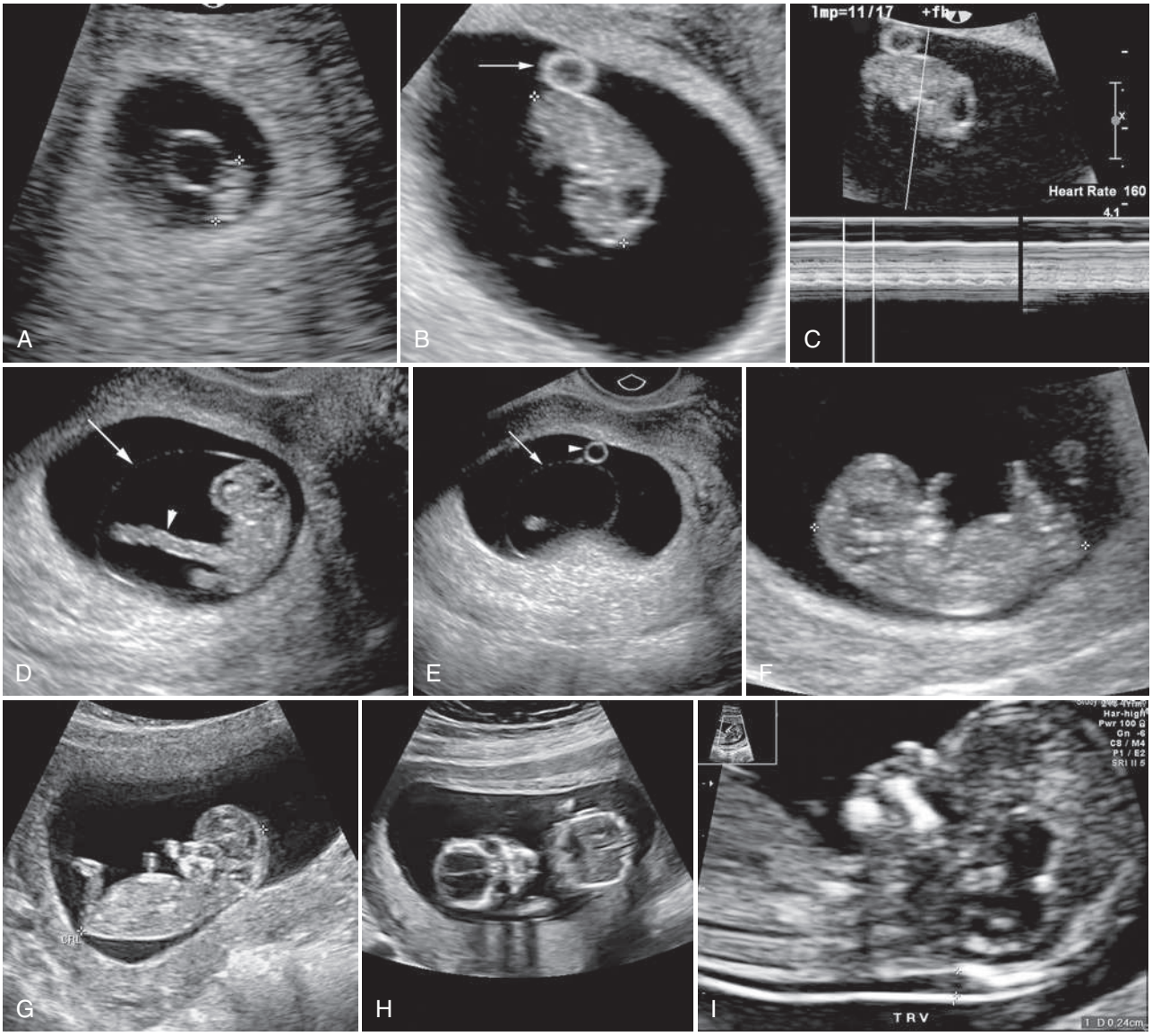

FIG. 28.3 First-Trimester Ultrasound Images: Embryo and Fetus. **(A)** Normal embryo at 6.5 weeks' gestation. Note embryonic pole *(calipers)* adjacent to yolk sac. **(B)** Normal embryo at 8 weeks' gestation. Note embryo *(calipers)* and adjacent yolk sac *(arrow)*. **(C)** M-mode ultrasound from same embryo as in **B.** Note normal heart rate of 160 beats/min. **(D)** Normal embryo at 9 weeks' gestational age. Note embryo within amnion *(arrow)* and umbilical cord *(arrowhead)*. **(E)** Just lateral to image in **D,** note yolk sac *(arrowhead)* is located outside the amnion *(arrow)*. **(F)** Sagittal ultrasound at 10.5 weeks' gestation. **(G)** Sagittal ultrasound at 11.5 weeks' gestation. **(H)** Coronal view of face at 13 weeks' gestation. **(I)** Sagittal ultrasound of nuchal translucency *(calipers)* at 13 weeks' gestation. See also Videos 28.1 and 28.2.

DNA screening alone.[10] Patients should be counseled that a negative cell-free DNA test result does not ensure an unaffected pregnancy. According to a 2015 ACOG committee opinion, "Given the performance of conventional screening methods, the limitations of cell-free DNA screening performance, and the limited data on cost-effectiveness in the low-risk obstetric population, conventional screening methods remain the most appropriate choice for first-line screening for most women in the general obstetric population."[10]

Thus despite increased use of cell-free DNA testing, ultrasound screening is still being performed by measuring **nuchal translucency** between 11 and 14 weeks of gestation (see Fig. 28.3I). This measurement, in conjunction with maternal age and serology, can be used to determine an individualized risk of fetal aneuploidy (see Chapter 31). Increased use of maternal serum screening, as well as first- and second-trimester ultrasound have reduced the number of interventional procedures to detect aneuploidy while increasing the number of prenatal diagnoses of aneuploidy.[11] Given the increased scanning late in the first trimester, it is also increasingly common for a limited anatomic survey to be conducted in the late first trimester. Anomalies that should be detected this early include **anencephaly** (Fig. 28.5) and **omphalocele** (Fig. 28.6). Although substantial information can be obtained at this time, the first-trimester anatomic survey is unlikely to replace the second-trimester anatomic survey, since many structures are difficult

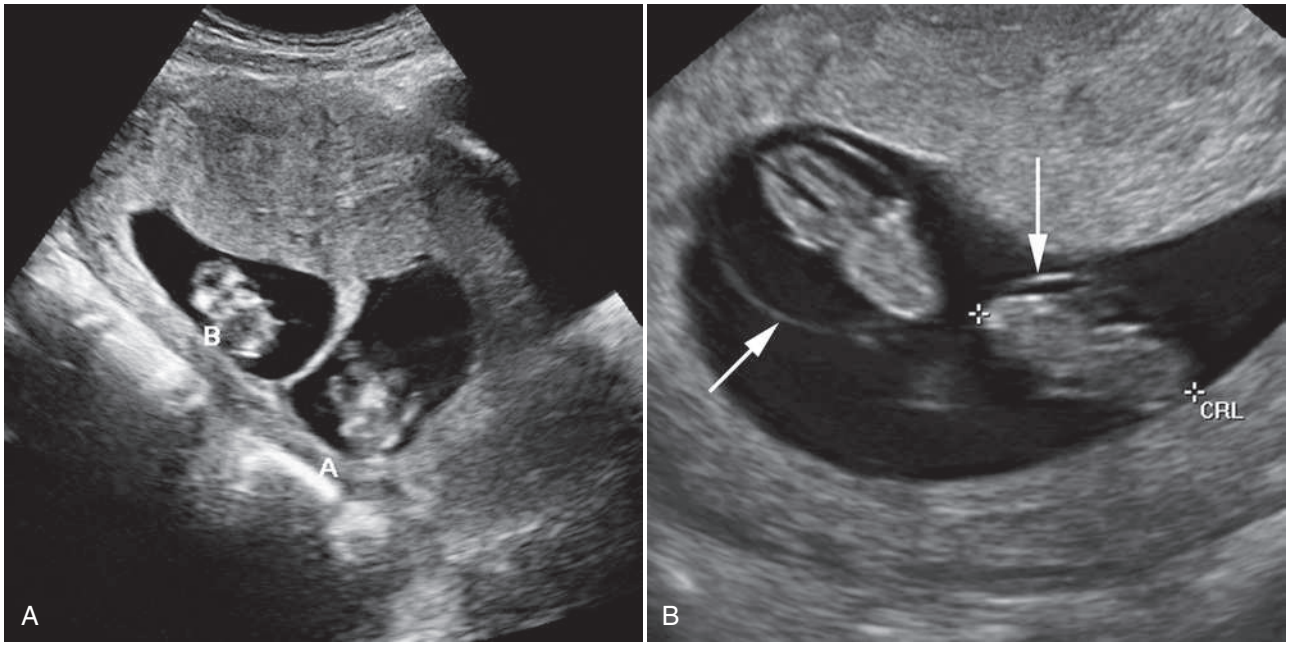

FIG. 28.4 Multiple Gestations. The entire gestational sac should be examined to identify multiple gestations. **(A)** Transabdominal image of **diamniotic dichorionic twins.** Note the thick, dividing membrane that separates twin A *(A)*, the presenting twin, from twin B *(B)*. **(B)** Transvaginal image of **diamniotic monochorionic twins** at 8 weeks' gestational age (*calipers* denote crown rump length *[CRL]*) with two thin membranes (*arrows,* amnion) still close to embryonic poles.

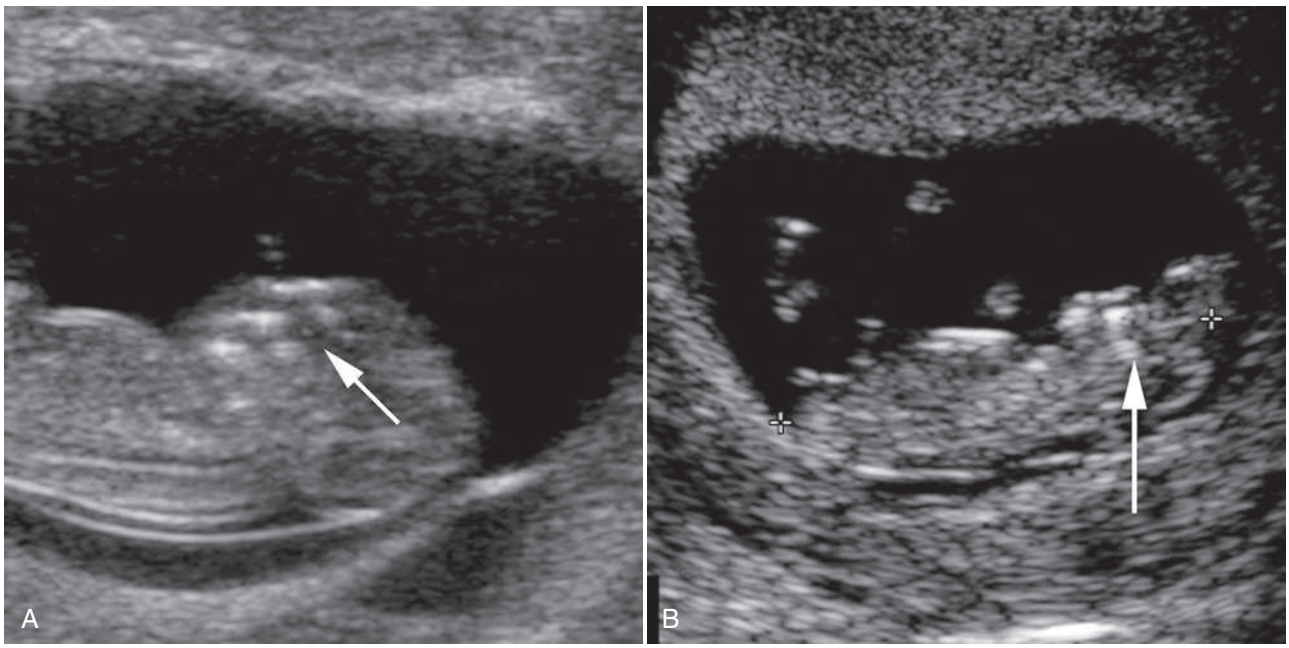

FIG. 28.5 Anencephaly. (A) Sagittal ultrasound at 10 weeks' gestation. **(B)** Sagittal ultrasound in a different fetus at 12 weeks' gestation. Note the orbits *(arrow)* with absent ossified cranium above this level with angiomatous stroma. The *calipers* mark the estimate of the crown rump length, made difficult due to angiomatous stroma above the orbits.

to visualize completely early in the second trimester, particularly the heart, cardiac outflow tracts, posterior fossa, and distal spine.

Second and Third Trimesters

The current ACR/AIUM guidelines for the performance of the second- and third-trimester obstetric ultrasound examinations describe the **standard sonographic examination.**[5] It is important to understand that the guidelines were written to maximize detection of many fetal abnormalities but are not expected to allow for detection of all structural abnormalities.

The terminology **level I** and **level II** examinations refer to "standard" or "routine" (level I) and "high risk," "specialized," or "detailed" (level II) obstetric ultrasound. The concept of these

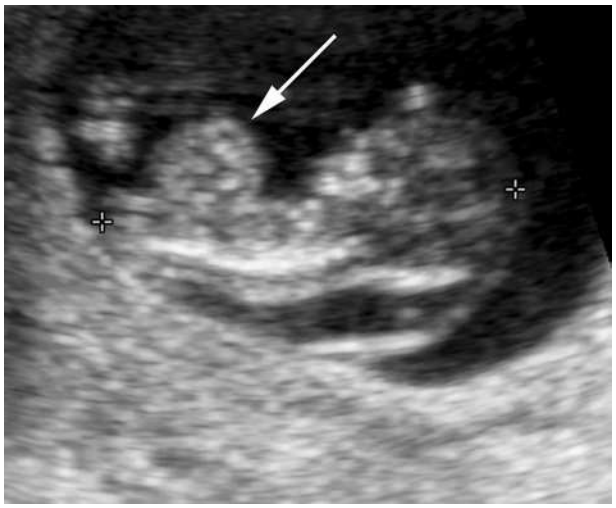

FIG. 28.6 Omphalocele at 11 Weeks' Gestational Age. Sagittal view of fetus *(calipers)* shows a large, abdominal wall defect *(arrow).*

two levels of scanning is that the standard, basic, routine, or level I examination is performed routinely on pregnant patients (Figs. 28.7 to 28.15, Videos 28.3) to 28.9. The methods to obtain all the required images are described in detail in subsequent chapters. This chapter provides a collage of figures as a guide for the anatomic survey and common additional views obtained during a fetal survey.

In general, the "standard fetal anatomic survey" refers to the **second-trimester scan,** typically performed between 16 and 22 weeks of gestation. When anatomic surveys are performed at 20 to 22 weeks' gestational age, there is less need for repeat scans to document normal anatomy compared to studies performed earlier in pregnancy.[12] However, there are practical considerations when determining the optimal timing of studies. In well-dated pregnancies in women who are unlikely to want amniocentesis, a survey at 20 to 22 weeks' gestation is optimal. However, if a pregnancy is not well-dated, an earlier scan may be needed both to establish accurate dates for the pregnancy and to assess the anatomy. Some centers offer the scan at 16 weeks' gestation to coincide with performance of genetic amniocentesis and/or midtrimester quadruple serum screening.

The level I examination consists of investigation of the maternal uterus and ovaries, the cervix, and placenta (Fig. 28.7, Video 28.3), as well as a systematic review of fetal anatomy. **Adnexal cysts** are common in pregnant women. In early pregnancy a cyst is most likely the corpus luteum. If a cyst appears atypical or enlarges beyond the middle second trimester, it should be further assessed. Leiomyoma position and size should be documented. If the myometrium appears thin in the lower uterine segment (e.g., <3 mm in a woman with prior cesarean section), the myometrium should be measured with transvaginal sonography and should be followed later in pregnancy because the thin myometrium puts the woman at risk for **uterine dehiscence** and/or **rupture.** It is helpful to begin the examination with a sagittal midline view to assess the cervix. If the cervix appears abnormally short or if placenta previa is suspected, a vaginal scan can then be performed.

Survey Guidelines for Second- and Third-Trimester Ultrasound

GENERAL SURVEY
Cardiac activity: document with M-mode
Presentation: cephalic, breech, transverse, variable
Fetal number: for multiples, amnionicity/chorionicity, concordance with size, amniotic fluid
Maternal anatomy: uterus, adnexa, and cervix
Gestational age and fetal weight assessment
- Biparietal diameter
- Head circumference
- Abdominal circumference
- Femur length

Amniotic fluid
- Estimate as normal
- If abnormal, quantify if high or low

Placenta: position

FETAL ANATOMIC SURVEY

Head, Face, and Neck
Cerebellum
Choroid plexus
Cisterna magna
Lateral cerebral ventricles
Midline falx
Cavum septi pellucidi
Upper lip

Chest
Four-chamber view
Outflow tracts

Abdomen
Stomach (presence, size, and situs)
Kidneys, bladder
Umbilical cord insertion site into fetal abdomen
Umbilical cord vessel number

Spine
Cervical, thoracic, lumbar, and sacral

Extremities
Legs and arms

Genitalia (Sex)
In multiple gestations and when medically indicated

Modified from Collaborative Subcommittee. ACR–ACOG–AIUM–SRU practice parameter for the performance of obstetrical ultrasound. American College of Radiology; 2014.[5]

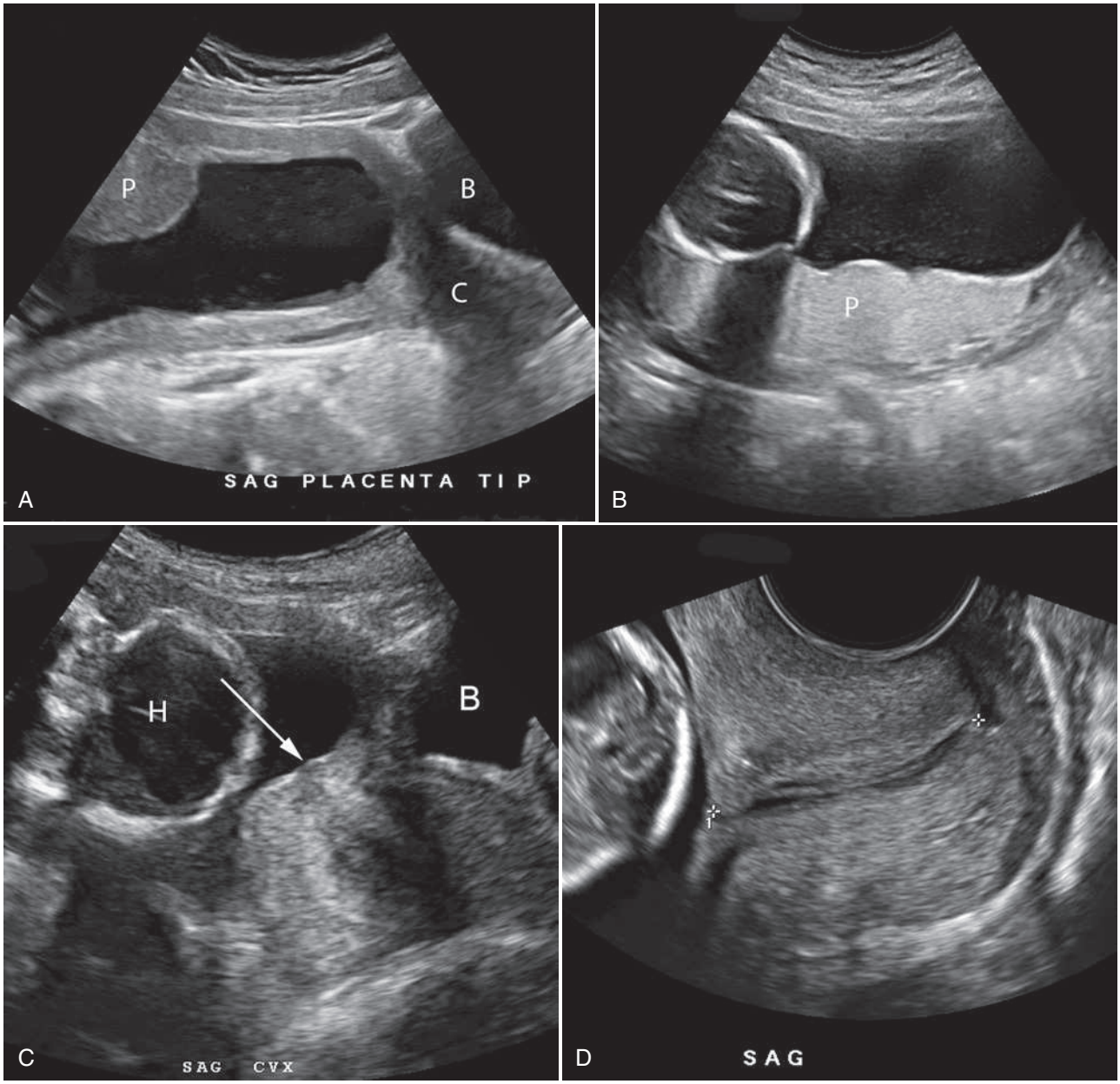

FIG. 28.7 Overview of Uterus, Cervix, and Fetal Position. (A) Sagittal sonogram of uterus shows a normal-appearing cervix *(C)* and an anterior placenta *(P),* with the placental tip far away from the internal cervical os. *B,* Bladder. **(B)** Transverse sonogram of posterior placenta *(P).* **(C)** Transabdominal image of normal-appearing cervix (*arrow* on internal os). Note bladder *(B)* and fetal head *(H).* With the head as the presenting part, the fetus is in cephalic position. **(D)** Transvaginal sonogram of normal-appearing cervix *(calipers).* See also Video 28.3.

Transverse and longitudinal scans of the entire uterine cavity are then performed for assessment of **fetal cardiac activity,** amniotic fluid volume, localization of the placenta, and determination of **fetal presentation** and **situs** (Fig. 28.8). Knowledge of the plane of section across the maternal abdomen, combined with the position of the fetal spine and right-sided and left-sided structures within the fetal body, allows accurate determination of fetal position and identification of normal and pathologic anatomy. Some congenital anomalies, such as dextrocardia, will be recognized only if a structure is identified as "abnormal" by virtue of its atypical position related to the position of the fetus.

Biometry is performed to estimate gestational age and fetal weight (Fig. 28.9). Assessment of gestational age in the second and third trimesters is discussed in more detail in Chapter 42. Additional views in routine obstetric sonography include the head and face (Fig. 28.10, Video 28.4), heart (Fig. 28.11, Videos 28.5 and 28.6), abdomen and pelvis (Fig. 28.12, Video 28.7), spine (Fig. 28.13, Video 28.8), extremities (Fig. 28.14), and umbilical cord (Fig. 28.15, Video 28.9).

Other specialized sonographic examinations include fetal Doppler sonography, biophysical profile, fetal echocardiography, and additional biometric measurements.

The high-risk, targeted, detailed, or level II scan should have a specific indication that requires a detailed fetal sonogram, performed by a clinician with expertise in obstetric imaging.[13,14] This high-risk scan is performed when an anomaly is suspected

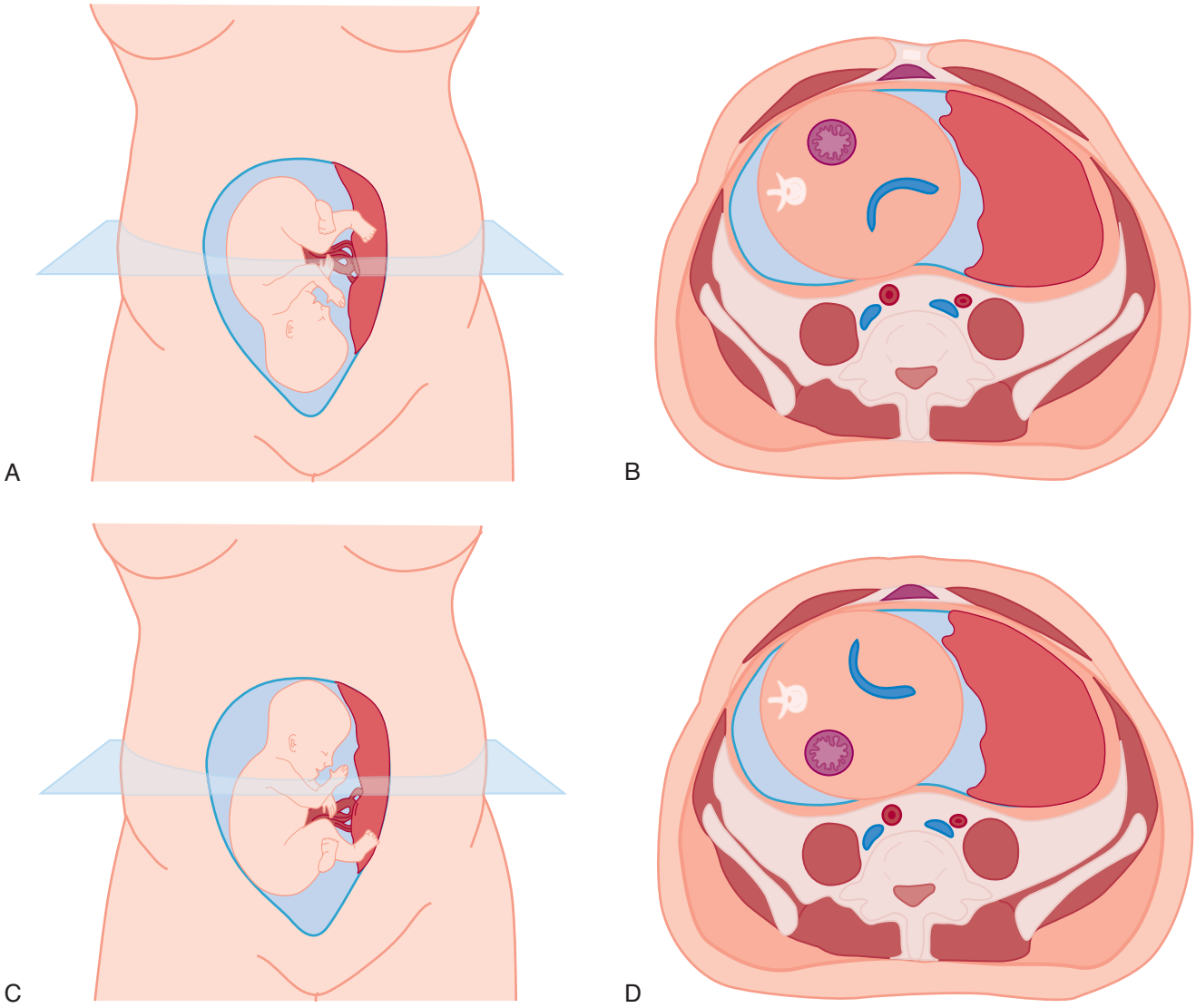

FIG. 28.8 Determination of Situs. (A) Scan plane and **(B)** transverse scan diagram. With fetus in cephalic position and spine on the maternal right side, the left-sided stomach is "up" on the side closest to the transducer. **(C)** Scan plane and **(D)** with the fetus in breech position and spine on the maternal right side, the left-sided stomach is "down" on the side farthest away from the transducer.

because of maternal medical or family history, or if abnormal results are suspected on a routine scan. These high-risk scans include detailed views of fetal anatomy beyond those obtained in the routine exam. Wax et al.[14] provide a more complete description of these anomalies.

ROUTINE ULTRASOUND SCREENING

Estimation of Gestational Age

Determination of the **expected date of delivery** (EDD) is especially important in obstetric practice because it is used to intervene in pregnancies considered to be "growth restricted" and in postterm pregnancies. Multiple studies have demonstrated that routine use of ultrasound results in more accurate assessment of the EDD than does last menstrual period (LMP) dating or physical examination, even in women with regular and certain menstrual dates.[15-18] **Pregnancy dating** is most accurately performed in the first half of pregnancy. **Fetal growth** should be assessed by comparison to earlier scans in pregnancy whenever possible. In a Cochrane review of nine trials of routine ultrasound in early pregnancy, routine use of early ultrasound and the subsequent adjustment of the EDD led to a significant reduction in the number of postterm pregnancies.[19]

A rule of thumb is that in the first trimester, LMP dating should be maintained unless ultrasound yields an EDD more than 7 days off; in the second trimester, ultrasound should be used to change EDD if it is off by more than 2 weeks (and follow-up is then needed to ensure appropriate interval growth); and in the third trimester, a 3-week discrepancy between LMP and ultrasound dating is allowed but needs to be taken into the clinical context, with assessment for growth restriction or

Text continued on p. 1029.

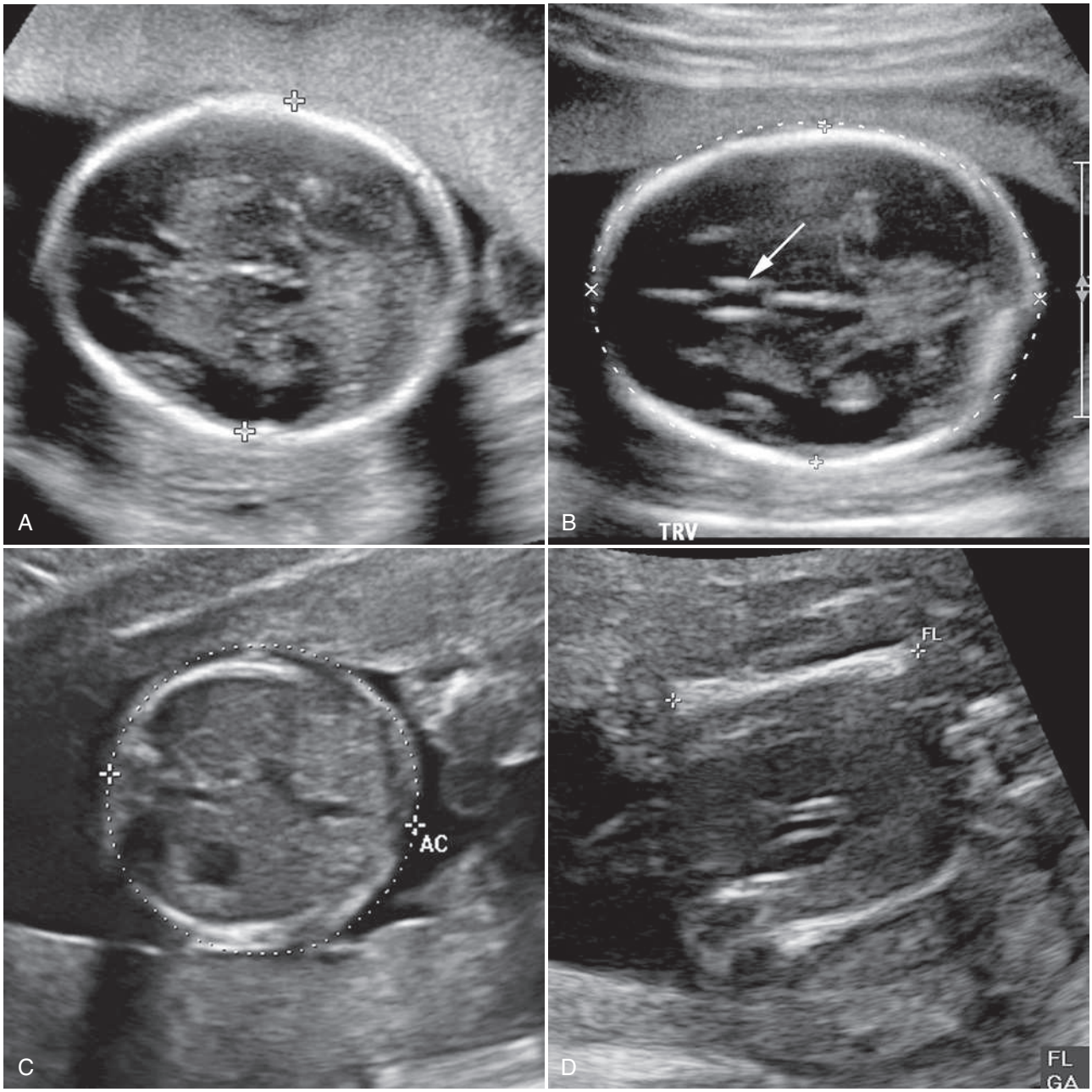

FIG. 28.9 Second-Trimester Biometry. (A) Biparietal diameter. Note the level of this ultrasound image at the thalamus and third ventricle. The calipers are placed from the outer skull in the near field to the inner skull in the far field. **(B) Head circumference.** Note how circumference is measured around the outside of the skull. Arrow depicts cavum of the septum pellucidum. **(C) Abdominal circumference** *(AC).* Note the curve of the portal vein and stomach on this transverse image, with circumference drawn around the outside of the skin. **(D) Femur length** *(FL).* Note that the "upside" femur should be measured, with the shaft of the bone as near to perpendicular to the scan plane as possible, excluding the distal femoral epiphysis.

Indications for Detailed Fetal Anatomic Survey

- Previous fetus or child with a congenital, genetic, or chromosomal abnormality
- Known or suspected fetal anomaly or known growth disorder in the current pregnancy
- Fetus at increased risk for a congenital anomaly, such as maternal diabetes, pregnancy conceived via assisted reproductive technology, high maternal body mass index (≥35 kg/m^2), multiple gestation, abnormal screening results, teratogen exposure
- Fetus at increased risk for a genetic or chromosomal abnormality, such as parental carrier of a chromosomal or genetic abnormality, maternal age 35 years or older at delivery, abnormal screening results
- Other conditions affecting the fetus, including congenital infections, maternal drug dependence, isoimmunization, abnormalities of amniotic fluid

Modified from Wax J, Minkoff H, Johnson A, et al. Consensus report on the detailed fetal anatomic ultrasound examination: indications, components, and qualifications. J Ultrasound Med. 2014;33(2):189-195.[14]

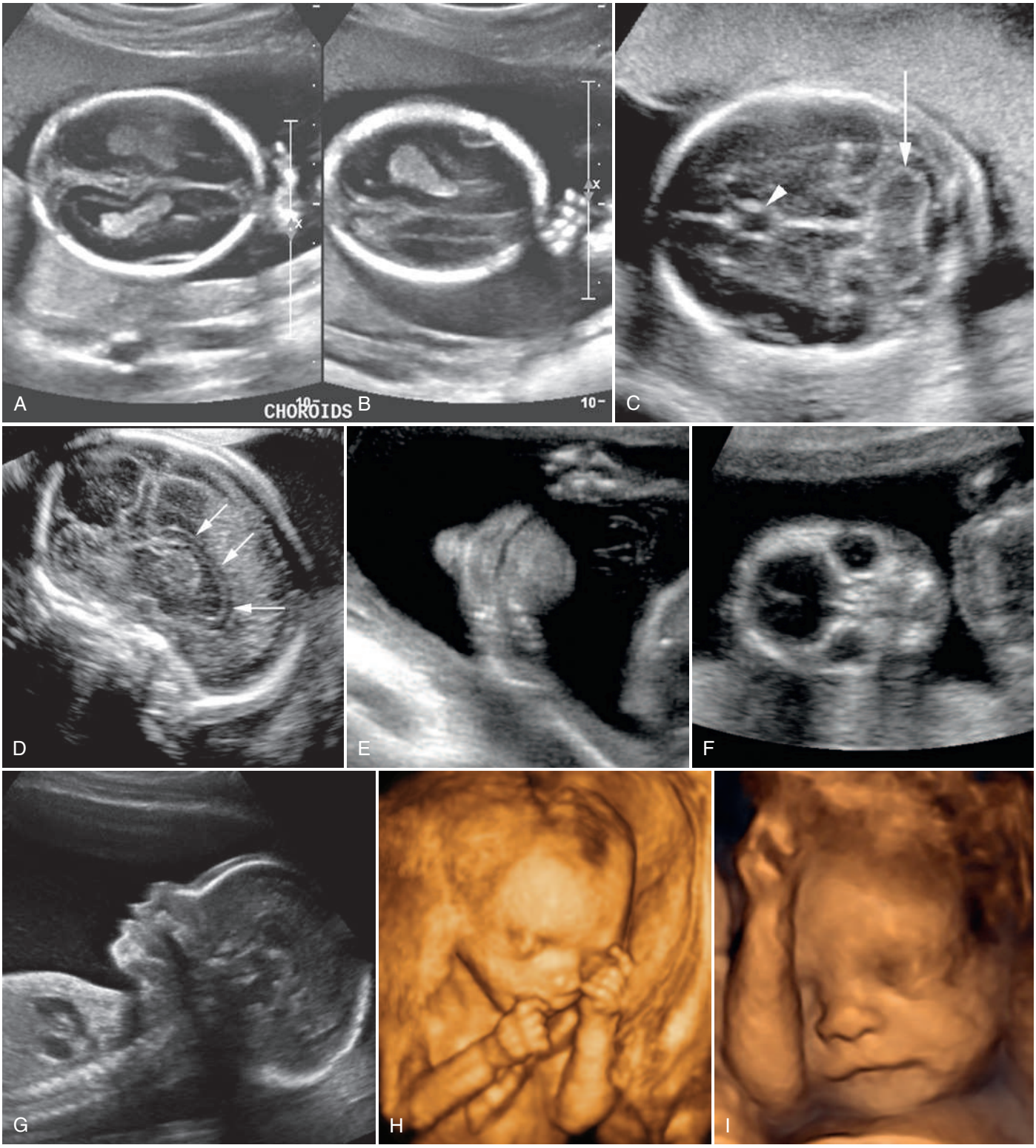

FIG. 28.10 Sonographic Views of Fetal Head and Face. In addition to the biparietal diameter and head circumference, required views of the head include images of the **cerebral ventricles, cerebellum, cavum of the septum pellucidum, midline falx, and nose and lips.** Additional views that can be obtained are angled views to demonstrate both sides of the choroid plexus and views through the anterior fontanelle or midline sutures to demonstrate the corpus callosum as well as views of the orbits and profile. **(A)** Axial and **(B)** oblique axial images show cerebral ventricles filled with **choroid plexus. (C)** Axial image shows cerebellum *(arrow)* and cavum of the septum pellucidum *(arrowhead).* **(D)** Transvaginal sagittal view of the corpus callosum *(arrows).* Required view of the face is of the nose and lips. Additional views include orbits and profile. **(E)** Coronal view of nose and lips. **(F)** Coronal view of orbits. **(G)** Sagittal view of facial profile. **(H)** and **(I)** Three-dimensional images of fetal face. See also Video 28.4. (**A** and **B** courtesy of Dr. A. Toi.)

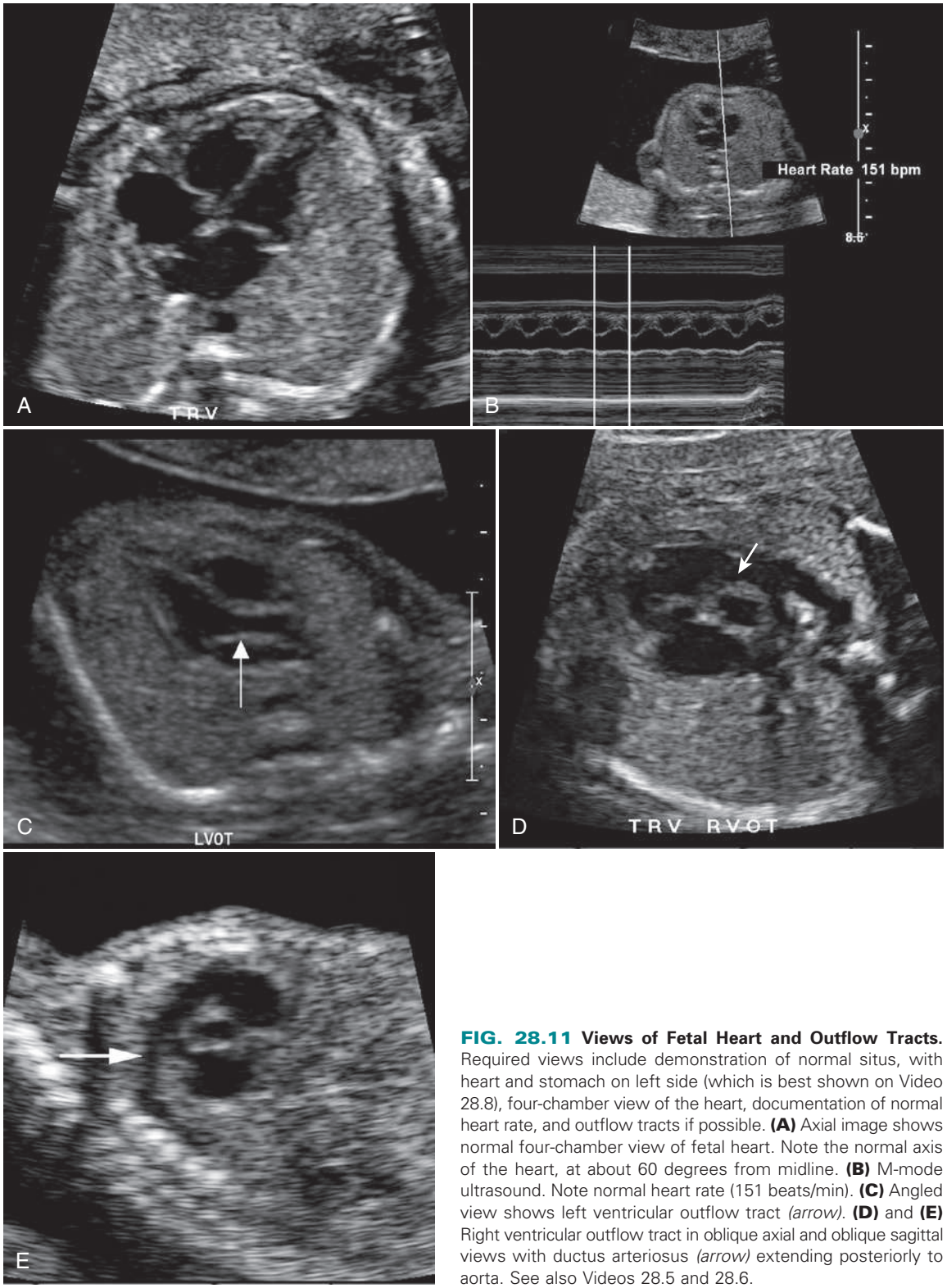

FIG. 28.11 Views of Fetal Heart and Outflow Tracts. Required views include demonstration of normal situs, with heart and stomach on left side (which is best shown on Video 28.8), four-chamber view of the heart, documentation of normal heart rate, and outflow tracts if possible. **(A)** Axial image shows normal four-chamber view of fetal heart. Note the normal axis of the heart, at about 60 degrees from midline. **(B)** M-mode ultrasound. Note normal heart rate (151 beats/min). **(C)** Angled view shows left ventricular outflow tract *(arrow)*. **(D)** and **(E)** Right ventricular outflow tract in oblique axial and oblique sagittal views with ductus arteriosus *(arrow)* extending posteriorly to aorta. See also Videos 28.5 and 28.6.

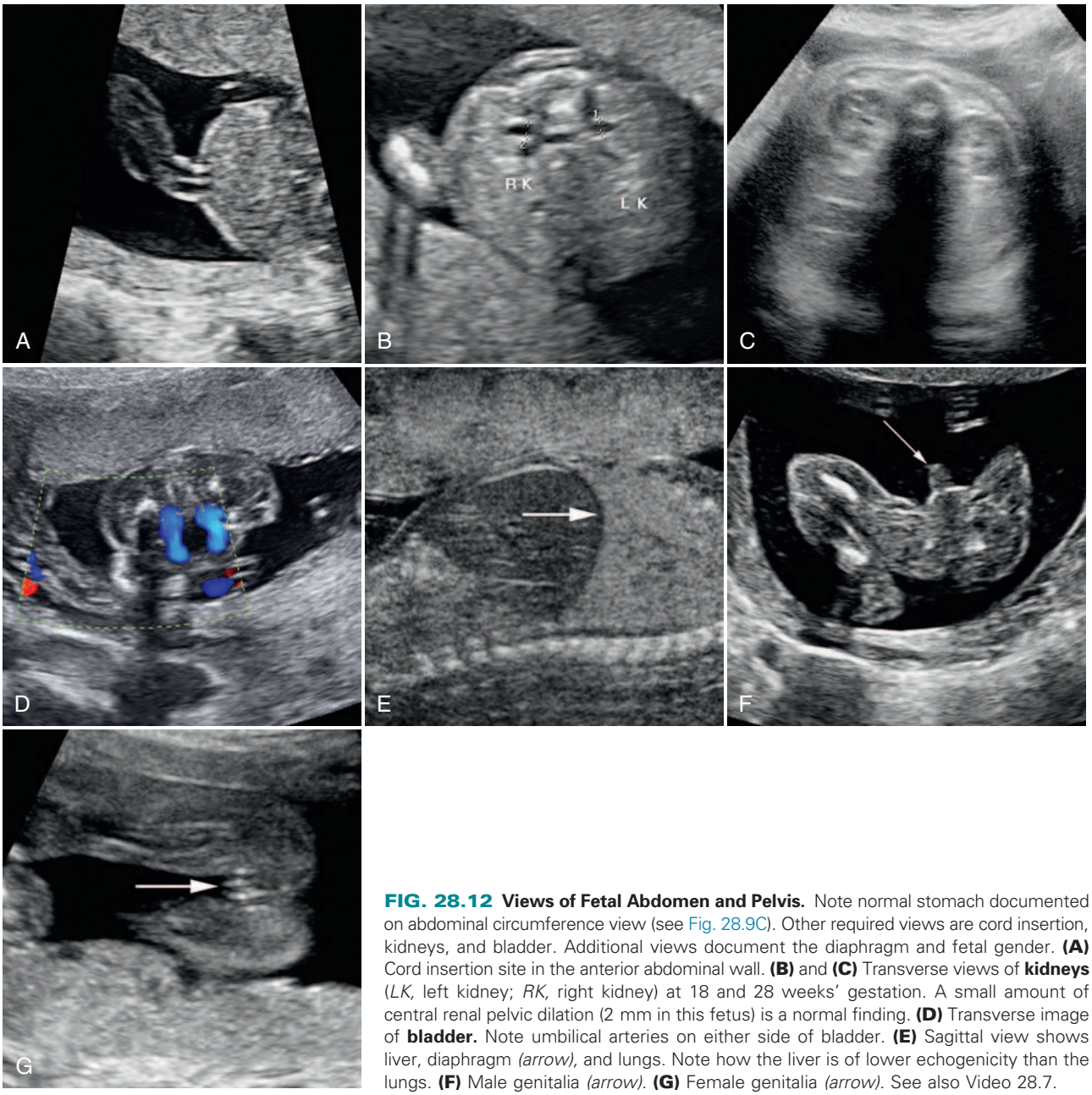

FIG. 28.12 Views of Fetal Abdomen and Pelvis. Note normal stomach documented on abdominal circumference view (see Fig. 28.9C). Other required views are cord insertion, kidneys, and bladder. Additional views document the diaphragm and fetal gender. **(A)** Cord insertion site in the anterior abdominal wall. **(B)** and **(C)** Transverse views of **kidneys** (*LK,* left kidney; *RK,* right kidney) at 18 and 28 weeks' gestation. A small amount of central renal pelvic dilation (2 mm in this fetus) is a normal finding. **(D)** Transverse image of **bladder.** Note umbilical arteries on either side of bladder. **(E)** Sagittal view shows liver, diaphragm *(arrow),* and lungs. Note how the liver is of lower echogenicity than the lungs. **(F)** Male genitalia *(arrow).* **(G)** Female genitalia *(arrow).* See also Video 28.7.

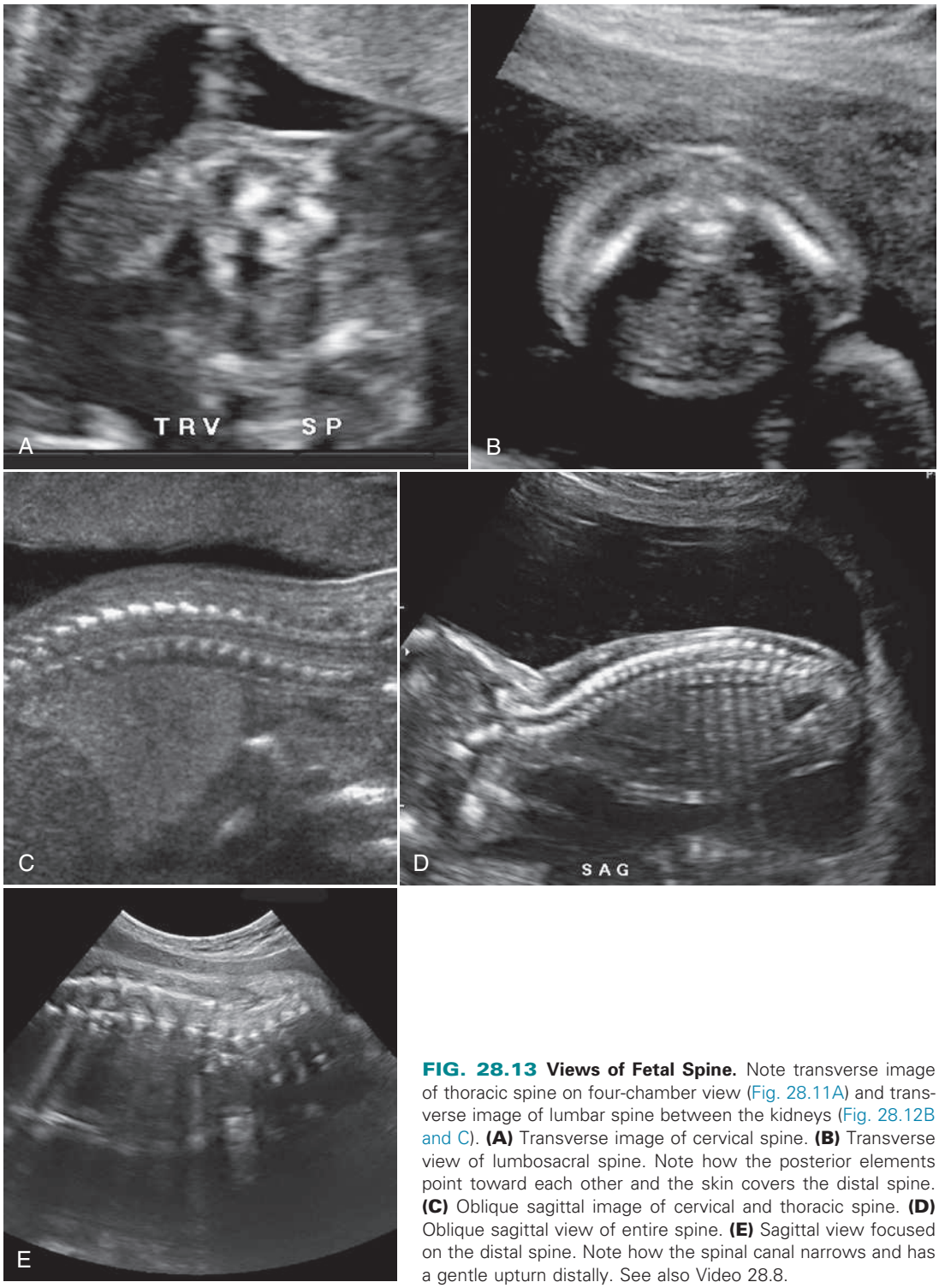

FIG. 28.13 Views of Fetal Spine. Note transverse image of thoracic spine on four-chamber view (Fig. 28.11A) and transverse image of lumbar spine between the kidneys (Fig. 28.12B and C). **(A)** Transverse image of cervical spine. **(B)** Transverse view of lumbosacral spine. Note how the posterior elements point toward each other and the skin covers the distal spine. **(C)** Oblique sagittal image of cervical and thoracic spine. **(D)** Oblique sagittal view of entire spine. **(E)** Sagittal view focused on the distal spine. Note how the spinal canal narrows and has a gentle upturn distally. See also Video 28.8.

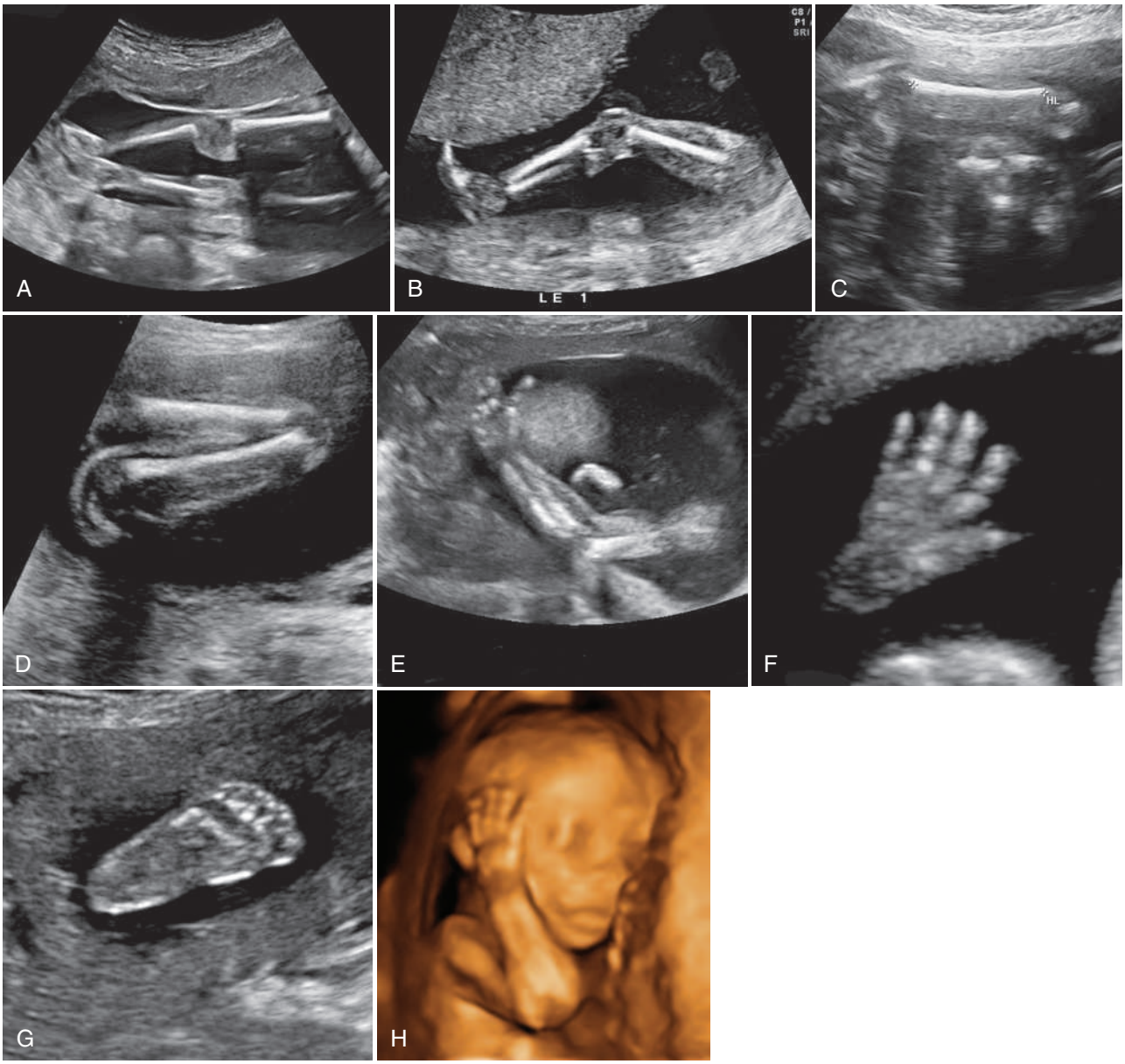

FIG. 28.14 View of Fetal Extremities. Required views include documentation of all four extremities. Additional views include measurements of all the long bones and demonstration of the fingers and toes. **(A)** and **(B)** Lower extremities. **(C)**-**(E)** Upper extremities. **(F)** Hand. Note four fingers with thumb partially out of the field of view. **(G)** Foot. **(H)** Three-dimensional view of upper extremity. (See also Fig. 28.10H for 3D view of hands.)

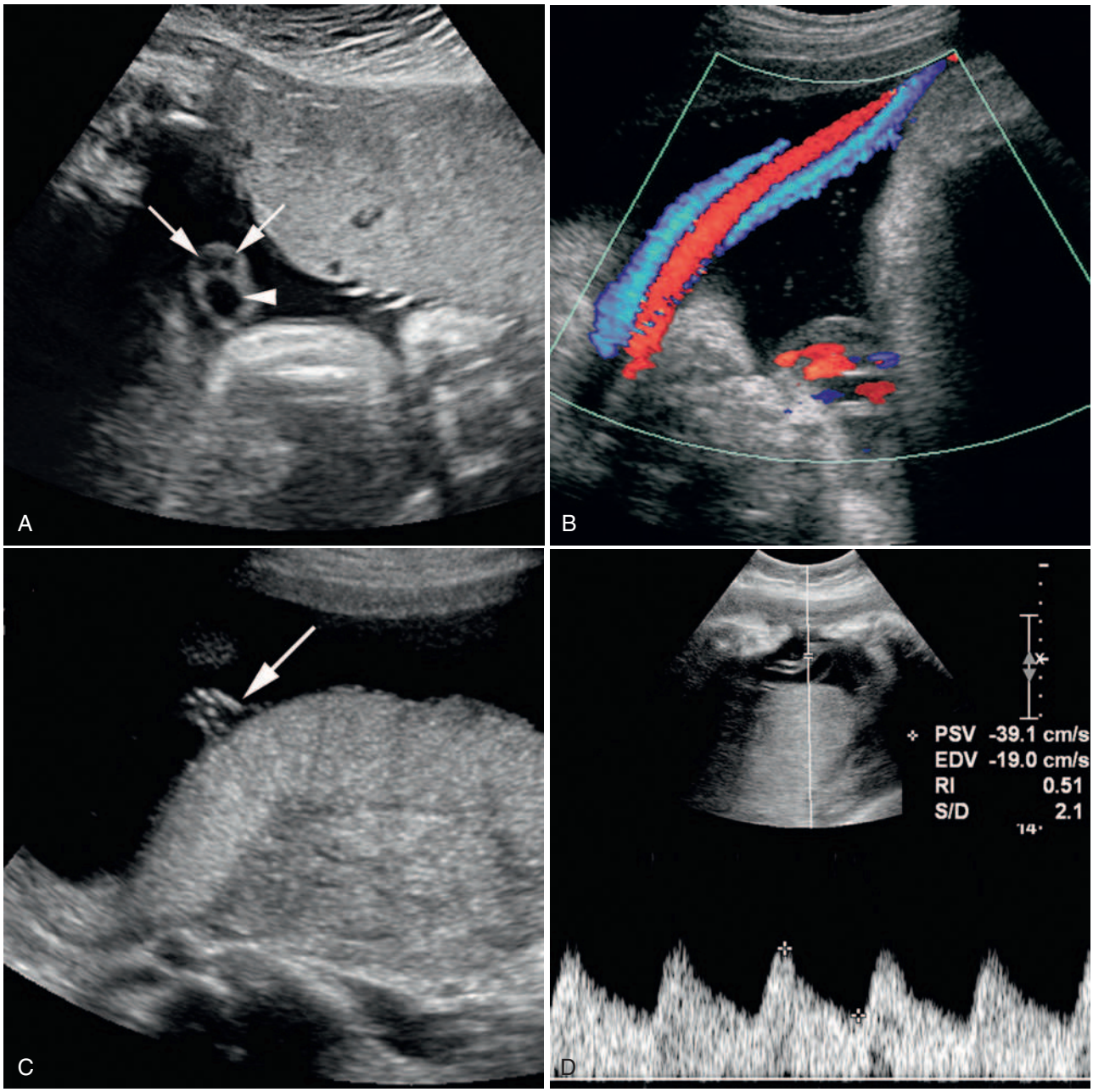

FIG. 28.15 Views of Umbilical Cord. Required views include cord insertion site into the anterior abdominal wall (see Fig. 28.12A) and documentation of number of vessels in the umbilical cord. Additional views include cord insertion site into the placenta and Doppler examination of the cord. **(A)** Transverse image of **three-vessel umbilical cord.** Note two arteries *(arrows)* that are smaller than the single vein *(arrowhead)*. See also Video 28.9 and Fig. 28.12D. **(B)** Color Doppler longitudinal image of three-vessel cord. **(C) Cord insertion site** *(arrow)* into the placenta. **(D)** Spectral Doppler image documents normal umbilical arterial systolic-to-diastolic ratio in third-trimester fetus.

macrosomia if appropriate. It is important to recognize that if a pregnancy is redated after the first trimester, follow-up is needed to assess for appropriate interval growth (see Chapter 42).

Identification of Twin/Multiple Pregnancies

A major benefit of routine ultrasound screening is early identification of multiple gestations.[3,16,20-22] Randomized clinical trials comparing routine second-trimester ultrasound examination with sonography performed for clinical indications have shown that a substantial number of twin pregnancies are not recognized until the third trimester or delivery in women who do not undergo routine ultrasound. The improved diagnosis of twins leads to improved perinatal outcome because of a reduced incidence of low birth weight, smallness for gestational age, prematurity, low Apgar scores, and stillbirths.[20]

Screening and Perinatal Outcomes

The value of a routine second-trimester scan in apparently normal pregnancies to identify those at high risk for unsuspected problems is controversial. Many countries perform one, two, or even three sonograms as part of routine obstetric care.[21,23,24]

Benefits of Routine Second-Trimester Ultrasound Screening

- More accurate gestational age
- Detection of major malformations before birth
- Earlier detection of multiple pregnancy
- Fewer low-birth-weight singleton births
- Lower incidence of induction for postterm pregnancy
- Early detection of placenta previa
- Reassurance of a normal pregnancy

It can be difficult to interpret the results of studies designed to assess the impact of routine screening.[3,16,21] Not only do anomalies need to be detected by ultrasound, but to show the benefit of ultrasound there must be a documented difference in outcome, either in termination of pregnancies (potentially leading to decreased perinatal mortality from loss of anomalous fetuses) or in improved perinatal care. Because these studies do not necessarily control for these outcomes, the benefits of screening—in particular the importance of parental understanding of fetal anomalies when pregnancies with fetal anomalies are continued—are difficult to demonstrate.

The Helsinki Ultrasound Trial reported a significant decrease in perinatal mortality among the ultrasound-screened group, from 9 to 4.6 per 1000.[21] This was attributed to the relatively high rate of detection of fetal anomalies in that study (58% of major malformations were detected before 24 weeks) with subsequent termination of fetuses with anomalies.

In the Routine Antenatal Diagnostic Imaging with Ultrasound (RADIUS) trial, the investigators did not find a significant difference in "adverse perinatal outcome" (defined as fetal death, neonatal death, or neonatal morbidity) in the screened versus control groups. The explanation for the lack of improved outcome was the limited sensitivity of routine sonography in the detection of congenital abnormalities (16.6% before 24 weeks and 34.8% before 40 weeks) coupled with a low rate of pregnancy termination once the diagnosis had been made.[3] A subsequent meta-analysis based on four randomized clinical trials with data on 15,935 women (7992 were allocated to routine sonography vs. 7943 to selective scanning) found the perinatal mortality rate was significantly lower in patients allocated to routine scanning, again because of the early detection of fetal abnormalities that led to induced abortions.[25] The authors concluded that routine ultrasound scanning is effective and useful as a screening test for malformations.

Fetal Malformations: Diagnostic Accuracy

The incidence of major congenital abnormalities at birth in the general population is 2% to 3%, yet these abnormalities are responsible for 20% to 25% of perinatal deaths and an even higher percentage of perinatal morbidity. Prenatal detection of an anomaly increases the options for pregnancy management, and in select cases the disorder may be amenable to intrauterine treatment. For these reasons, offering routine ultrasound as a screening test for congenital abnormalities is an attractive concept. However, the performance of screening ultrasound in detecting abnormalities in the low-risk population is variable, with sensitivity and specificity ranging from 14% to 85% and 93% to 99%, respectively.[3,24,26-32] The wide range in sensitivity can be partially explained by what authors used as the definition of an "anomaly" and the experience of the individuals performing and interpreting the studies.[24,31] Another factor is the type of anomaly. In the Eurofetus study,[33] the best detected abnormalities were of the urinary system (88.5%) and central nervous system (88.3%). Cardiac abnormalities were not well detected, whether major (38.8%) or minor (20.8%), and the lowest rates of detection were for minor abnormalities of the musculoskeletal system (18% vs. 73.6% for major defects) and cleft lip and palate (18%).[33] Another important issue is the gestational age when the study is performed. In the Eurofetus Study, for example, 38.5% of the anomalies were diagnosed after 29 weeks' gestation. Other factors influencing sensitivity of prenatal sonography include the quality of equipment, prevalence of a particular defect, maternal body habitus, and examination protocol.[24,33,34]

Many of the benefits of ultrasound are nonquantifiable. Having time to adjust prenatally to information about an anomaly can improve both the clinician's and the parents' approach to the pregnancy and birth, as well as their abilities to make decisions about prenatal and postnatal treatment.[35] It is important for patients and their physicians to understand the limitations of ultrasound. Not all abnormalities can be detected. The accuracy of prenatal ultrasound is variable and often depends on where and by whom it is being performed.

Three-Dimensional Ultrasound

In addition to two-dimensional (2D) images, 3D imaging allows for reconstructed images in planes that were not previously available. This allows for improved visualization of facial anomalies[36] and anomalies of the hands, feet, and spine.[37] In addition, 3D images may be more comprehensible to the patient, promoting better understanding of the abnormality.[36,37] 4-dimensional imaging is just viewing the 3D images over time and rarely adds additional diagnostic value. Cervical assessment is also thought to be more complete with volume imaging.[38] **Volume imaging** can be used to assess the lungs,[39,40] which is used in fetuses with suspected pulmonary hypoplasia. Reconstructed images can be helpful to image portions of the brain.[41] Subsequent chapters integrate 3D images as appropriate.

Prudent Use of Ultrasound

The AIUM, ACR, and ACOG collaborative guidelines on performance of obstetric ultrasound state, "This diagnostic procedure should be performed only when there is a valid medical indication, and the lowest possible ultrasonic exposure setting should be used to gain the necessary diagnostic information under the 'as low as reasonably achievable' (ALARA) principle."[5] Although there is no reliable evidence of physical harm to human fetuses from diagnostic ultrasound imaging using current technology, public health experts, clinicians, and industry representatives agree that casual use of sonography, especially during pregnancy, should be avoided. The U.S. Food and Drug Administration (FDA) views the promotion, sale, or lease of ultrasound equipment for making "keepsake" fetal videos as an unapproved use of a

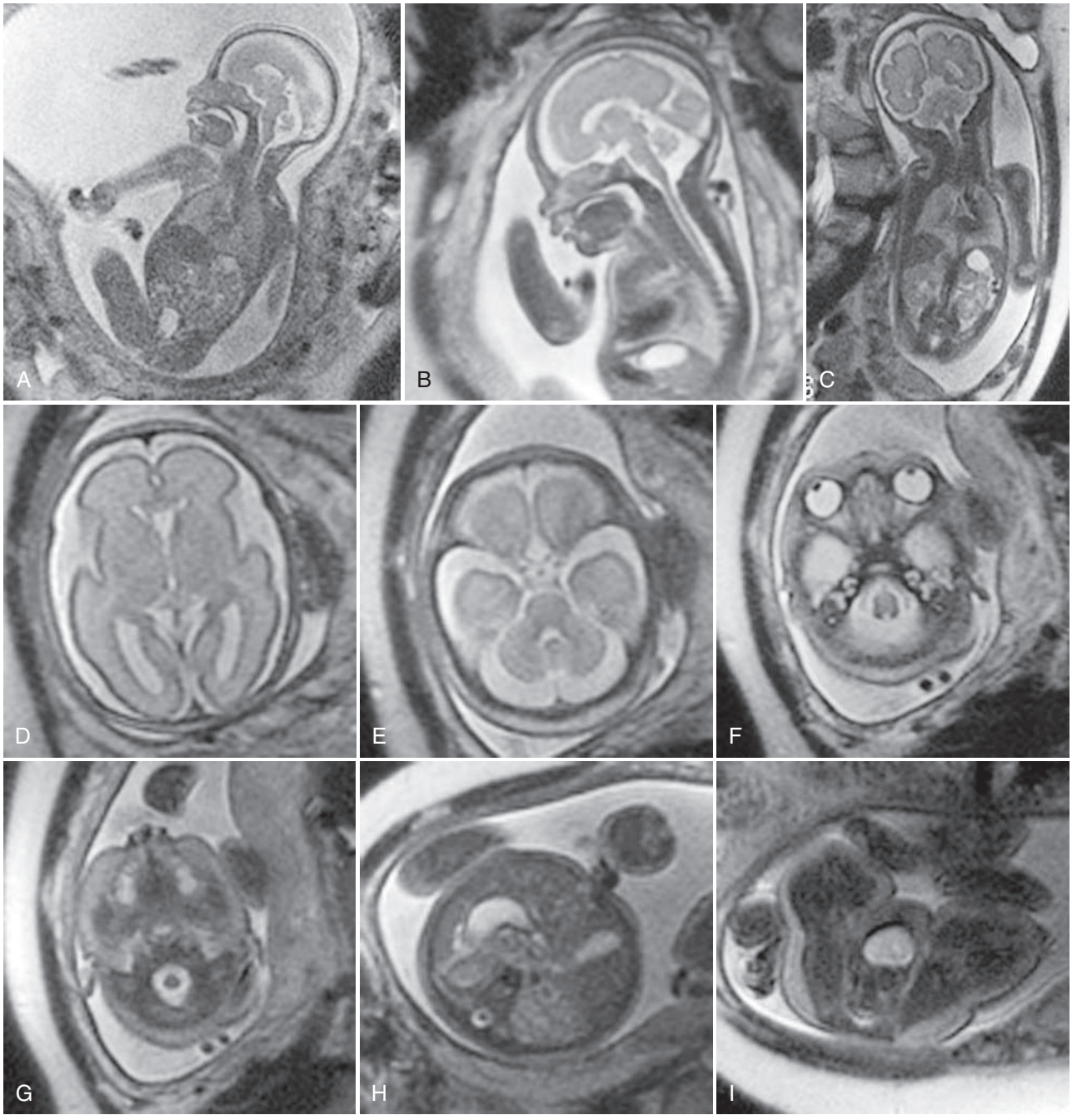

FIG. 28.16 Normal Fetal MRI: Representative T2-Weighted Images. (A) Sagittal view of fetal head with fetal body in coronal plane. **(B)** Sagittal view of fetal head. Note normal appearance of corpus callosum and soft palate, with fluid outlining the soft palate above the tongue. **(C)** Coronal view of the brain, chest, and abdomen. Note normal appearance to the lungs, diaphragm, stomach, and kidneys. **(D)** Axial view of brain with normal-appearing lateral ventricles. **(E)** Oblique axial view of brain shows normal cerebellar hemispheres and vermis. **(F)** Axial view at level of globes. Note the dark lens in each globe. **(G)** Axial view at level of palate. Note that majority of the alveolar tooth-bearing ridge is well depicted. **(H)** Axial view at level of stomach and gallbladder. Note spinal cord outlined by fluid in thecal sac. **(I)** Axial view at level of bladder.

medical device.[42] Medically indicated obstetric imaging can easily integrate making copies of key images for parents who want an early view of their baby.

MAGNETIC RESONANCE IMAGING

Ultrasound is the screening modality of choice for fetal imaging. However, when additional information regarding fetal anatomy or pathology is needed, fast MRI is increasingly being used as a correlative imaging modality in select cases (Fig. 28.16). MRI is useful in these cases because it has no ionizing radiation, provides excellent soft tissue contrast, has multiple planes for reconstruction, and has a large field of view, allowing for improved depiction of many complex fetal abnormalities.

It is important to tailor the examination to answer specific questions raised either by patient history or by previous

sonographic examination. In the past decade, software and hardware have allowed for fetal MR images to be obtained in about 400 milliseconds. This allows for fetal imaging to be performed without maternal or fetal sedation. The ease of performing these examinations and the superb contrast resolution afforded by T2-weighted MRI have popularized the use of this imaging tool to improve prenatal diagnosis.

There are no known biologic risks from MRI. The MR procedure is not believed to be hazardous to the fetus.[43-55] No delayed sequelae from MR examination have been encountered, and it is expected that the potential risk for any delayed sequelae is extremely small or nonexistent.

However, most studies on fetal risk have been performed at 1.5 Tesla. Heating has been shown in animal studies at 3.0 Tesla.[56] Therefore when possible fetal studies should be done at 1.5T.

Gadolinium is the contrast typically used for MRI, but it is not recommended for fetal examination. Gadolinium crosses the placenta and appears within the fetal bladder soon after intravenous administration. The contrast is excreted from the fetal bladder into the amniotic fluid, where it is then swallowed and potentially reabsorbed from the gastrointestinal tract. Because of this reabsorption, the half-life of gadolinium in the fetal circulation is not known.[57] This drug has been shown to have adverse effects on the fetus in animal models. **Gadopentetate dimeglumine** has been shown to impair development slightly in rats (at 2.5 times the human dose, 0.1 mmol/kg), and in rabbits (at 7.5 times the human dose).[58,59] It is considered a **pregnancy category C** drug, meaning that it should be given only if potential benefit outweighs the risk; animal studies have revealed adverse effects, but no controlled studies have been performed in humans.[58] Therefore we do not use contrast for fetal examinations at our institution.

CONCLUSION

Ultrasound is a readily available, noninvasive, and safe means of evaluating fetal well-being, determining gestational age, and assessing the intrauterine environment. It is an indispensable tool for the practice of obstetrics. Ultrasound is also a screening test, yielding results that must be interpreted and integrated in a knowledgeable manner. As with physical examination, the ultrasound study is most helpful when performed in a consistent and reproducible fashion, carefully documenting positive and negative findings important in clinical decision making. The information gained from routine obstetric ultrasound may provide reassurance, guide therapy, or identify a pathologic condition that merits further investigation.

REFERENCES

1. Martin J, Hamilton B, Osterman M. Births in the United States, 2013. Hyattsville, MD: National Center for Health Statistics; 2014.
2. Levi S. Ultrasound in prenatal diagnosis: polemics around routine ultrasound screening for second trimester fetal malformations. Prenat Diagn. 2002;22(4):285-295.
3. Ewigman BG, Crane JP, Frigoletto FD, et al. Effect of prenatal ultrasound screening on perinatal outcome. RADIUS Study Group. N Engl J Med. 1993;329(12):821-827.
4. Abuhamad AZ, Benacerraf BR, Woletz P, Burke BL. The accreditation of ultrasound practices: impact on compliance with minimum performance guidelines. J Ultrasound Med. 2004;23(8):1023-1029.
5. Collaborative Subcommittee. ACR–ACOG–AIUM–SRU practice parameter for the performance of obstetrical ultrasound. American College of Radiology; 2014.
6. Barnhart K, van Mello NM, Bourne T, et al. Pregnancy of unknown location: a consensus statement of nomenclature, definitions, and outcome. Fertil Steril. 2011;95(3):857-866.
7. Chambers SE, Muir BB, Haddad NG. Ultrasound evaluation of ectopic pregnancy including correlation with human chorionic gonadotrophin levels. Br J Radiol. 1990;63(748):246-250.
8. Jeve Y, Rana R, Bhide A, Thangaratinam S. Accuracy of first-trimester ultrasound in the diagnosis of early embryonic demise: a systematic review. Ultrasound Obstet Gynecol. 2011;38(5):489-496.
9. Thilaganathan B. The evidence base for miscarriage diagnosis: better late than never. Ultrasound Obstet Gynecol. 2011;38(5):487-488.
10. American College of Obstetricians and Gynecologists. Cell-free DNA screening for fetal aneuploidy. Practice Bulletin. 2015;No. 640.
11. Benn PA, Egan JF, Fang M, Smith-Bindman R. Changes in the utilization of prenatal diagnosis. Obstet Gynecol. 2004;103(6):1255-1260.
12. Schwarzler P, Senat MV, Holden D, et al. Feasibility of the second-trimester fetal ultrasound examination in an unselected population at 18, 20 or 22 weeks of pregnancy: a randomized trial. Ultrasound Obstet Gynecol. 1999;14(2):92-97.
13. Filly RA. Level 1, level 2, level 3 obstetric sonography: I'll see your level and raise you one. Radiology. 1989;172(2):312.
14. Wax J, Minkoff H, Johnson A, et al. Consensus report on the detailed fetal anatomic ultrasound examination: indications, components, and qualifications. J Ultrasound Med. 2014;33(2):189-195.
15. Mongelli M, Wilcox M, Gardosi J. Estimating the date of confinement: ultrasonographic biometry versus certain menstrual dates. Am J Obstet Gynecol. 1996;174(1 Pt 1):278-281.
16. Eik-Nes SH, Salvesen KA, Okland O, Vatten LJ. Routine ultrasound fetal examination in pregnancy: the 'Alesund' randomized controlled trial. Ultrasound Obstet Gynecol. 2000;15(6):473-478.
17. Bennett MJ, Little G, Dewhurst J, Chamberlain G. Predictive value of ultrasound measurement in early pregnancy: a randomized controlled trial. Br J Obstet Gynaecol. 1982;89(5):338-341.
18. Waldenstrom U, Axelsson O, Nilsson S, et al. Effects of routine one-stage ultrasound screening in pregnancy: a randomised controlled trial. Lancet. 1988;2(8611):585-588.
19. Neilson JP. Ultrasound for fetal assessment in early pregnancy. Cochrane Database Syst Rev. 2000;(2):CD000182.
20. Hughey MJ, Olive DL. Routine ultrasound scanning for the detection and management of twin pregnancies. J Reprod Med. 1985;30(5):427-430.
21. Saari-Kemppainen A, Karjalainen O, Ylostalo P, Heinonen OP. Ultrasound screening and perinatal mortality: controlled trial of systematic one-stage screening in pregnancy. The Helsinki Ultrasound Trial. Lancet. 1990; 336(8712):387-391.
22. Bakketeig LS, Eik-Nes SH, Jacobsen G, et al. Randomised controlled trial of ultrasonographic screening in pregnancy. Lancet. 1984;2(8396): 207-211.
23. Blondel B, Ringa V, Breart G. The use of ultrasound examinations, intrapartum fetal heart rate monitoring and beta-mimetic drugs in France. Br J Obstet Gynaecol. 1989;96(1):44-51.
24. Levi S, Hyjazi Y, Schaapst JP, et al. Sensitivity and specificity of routine antenatal screening for congenital anomalies by ultrasound: the Belgian Multicentric Study. Ultrasound Obstet Gynecol. 1991;1(2): 102-110.
25. Bucher HC, Schmidt JG. Does routine ultrasound scanning improve outcome in pregnancy? Meta-analysis of various outcome measures. BMJ. 1993; 307(6895):13-17.
26. Lys F, De Wals P, Borlee-Grimee I, et al. Evaluation of routine ultrasound examination for the prenatal diagnosis of malformation. Eur J Obstet Gynecol Reprod Biol. 1989;30(2):101-109.
27. Rosendahl H, Kivenen S. Antenatal detection of congenital malformations by routine ultrasonography. Obstet Gynecol. 1989;73(6):947-951.

28. Shirley IM, Bottomley F, Robinson VP. Routine radiographer screening for fetal abnormalities by ultrasound in an unselected low risk population. Br J Radiol. 1992;65(775):564-569.
29. Luck CA. Value of routine ultrasound scanning at 19 weeks: a four year study of 8849 deliveries. BMJ. 1992;304(6840):1474-1478.
30. Chitty LS, Hunt GH, Moore J, Lobb MO. Effectiveness of routine ultrasonography in detecting fetal structural abnormalities in a low risk population. BMJ. 1991;303(6811):1165-1169.
31. Levi S, Montenegro NA. Eurofetus: an evaluation of routine ultrasound screening for the detection of fetal defects. Aims and method. Ann N Y Acad Sci. 1998;847:103-117.
32. Fadda GM, Capobianco G, Balata A, et al. Routine second trimester ultrasound screening for prenatal detection of fetal malformations in Sassari University Hospital, Italy: 23 years of experience in 42,256 pregnancies. Eur J Obstet Gynecol Reprod Biol. 2009;144(2):110-114.
33. Grandjean H, Larroque D, Levi S. The performance of routine ultrasonographic screening of pregnancies in the Eurofetus Study. Am J Obstet Gynecol. 1999;181(2):446-454.
34. Crane JP, LeFevre ML, Winborn RC, et al. A randomized trial of prenatal ultrasonographic screening: impact on the detection, management, and outcome of anomalous fetuses. The RADIUS Study Group. Am J Obstet Gynecol. 1994;171(2):392-399.
35. Berwick DM, Weinstein MC. What do patients value? Willingness to pay for ultrasound in normal pregnancy. Med Care. 1985;23(7):881-893.
36. Johnson DD, Pretorius DH, Budorick NE, et al. Fetal lip and primary palate: three-dimensional versus two-dimensional US. Radiology. 2000;217(1):236-239.
37. Dyson RL, Pretorius DH, Budorick NE, et al. Three-dimensional ultrasound in the evaluation of fetal anomalies. Ultrasound Obstet Gynecol. 2000;16(4):321-328.
38. Bega G, Lev-Toaff A, Kuhlman K, et al. Three-dimensional multiplanar transvaginal ultrasound of the cervix in pregnancy. Ultrasound Obstet Gynecol. 2000;16(4):351-358.
39. Gerards FA, Engels MA, Twisk JW, van Vugt JM. Normal fetal lung volume measured with three-dimensional ultrasound. Ultrasound Obstet Gynecol. 2006;27(2):134-144.
40. Jani J, Cannie M, Sonigo P, et al. Value of prenatal magnetic resonance imaging in the prediction of postnatal outcome in fetuses with diaphragmatic hernia. Ultrasound Obstet Gynecol. 2008;32(6):793-799.
41. Zalel Y, Yagel S, Achiron R, et al. Three-dimensional ultrasonography of the fetal vermis at 18 to 26 weeks' gestation: time of appearance of the primary fissure. J Ultrasound Med. 2009;28(1):1-8.
42. U.S. Food and Drug Administration. Fetal keepsake videos. Washington DC. Updated 2015. Available from: www.fda.gov/MedicalDevices/Safety/AlertsandNotices/PatientAlerts/ucm064756.htm. Accessed 1 July 2017.
43. Wolff S, Crooks LE, Brown P, et al. Tests for DNA and chromosomal damage induced by nuclear magnetic resonance imaging. Radiology. 1980;136(3):707-710.
44. Kanal E, Gillen J, Evans JA, et al. Survey of reproductive health among female MR workers. Radiology. 1993;187(2):395-399.
45. Baker PN, Johnson IR, Harvey PR, et al. A three-year follow-up of children imaged in utero with echo-planar magnetic resonance. Am J Obstet Gynecol. 1994;170(1 Pt 1):32-33.
46. Chew S, Ahmadi A, Goh PS, Foong LC. The effects of 1.5T magnetic resonance imaging on early murine in-vitro embryo development. J Magn Reson Imaging. 2001;13(3):417-420.
47. Clements H, Duncan KR, Fielding K, et al. Infants exposed to MRI in utero have a normal paediatric assessment at 9 months of age. Br J Radiol. 2000;73(866):190-194.
48. Glover P, Hykin J, Gowland P, et al. An assessment of the intrauterine sound intensity level during obstetric echo-planar magnetic resonance imaging. Br J Radiol. 1995;68(814):1090-1094.
49. Kok RD, de Vries MM, Heerschap A, van den Berg PP. Absence of harmful effects of magnetic resonance exposure at 1.5 T in utero during the third trimester of pregnancy: a follow-up study. Magn Reson Imaging. 2004;22(6):851-854.
50. Levine D, Zuo C, Faro CB, Chen Q. Potential heating effect in the gravid uterus during MR HASTE imaging. J Magn Reson Imaging. 2001;13(6):856-861.
51. Merkle EM, Dale BM, Paulson EK. Abdominal MR imaging at 3T. Magn Reson Imaging Clin N Am. 2006;14(1):17-26.
52. Myers C, Duncan KR, Gowland PA, et al. Failure to detect intrauterine growth restriction following in utero exposure to MRI. Br J Radiol. 1998;71(845):549-551.
53. Schwartz JL, Crooks LE. NMR imaging produces no observable mutations or cytotoxicity in mammalian cells. AJR Am J Roentgenol. 1982;139(3):583-585.
54. Shellock FG, Crues JV. MR procedures: biologic effects, safety, and patient care. Radiology. 2004;232(3):635-652.
55. U.S. Food and Drug Administration. Guidance for content and review of a magnetic resonance diagnostic device 510 (k) application. Washington, DC: FDA; 1988.
56. Cannie M, De Keyser F, Van Laere S, et al. Potential heating effect in the gravid uterus by using 3T MR imaging protocols: experimental study in miniature pigs. Radiology. 2016;754-761.
57. Shellock FG, Kanal E. Bioeffects and safety of MR procedures. In: Edelman RR, Hesselink JR, Zlatkin MB, editors. Clinical magnetic resonance imaging. 2nd ed. Philadelphia: Saunders; 1996. p. 429.
58. Laboratories B. Magnevist product information. Wayne, NJ: Berlex Laboratories; 1994.
59. Runge VM. Safety of approved MR contrast media for intravenous injection. J Magn Reson Imaging. 2000;12(2):205-213.

CHAPTER 29

Bioeffects and Safety of Ultrasound in Obstetrics

Jacques S. Abramowicz

SUMMARY OF KEY POINTS

- Obstetric ultrasound should only be performed with a clear indication, with calibrated machines, and by proficient professionals.
- Know the specific machine being used (what causes increase in output power).
- Keep the examination as short as possible and use the lowest possible output power but compatible with arriving at the correct diagnosis (as low as reasonably achievable [ALARA] principle).
- Keep track of the onscreen thermal index (TI) and mechanical index (MI).
- Keep the TI under 1.
- Keep the MI under 1.
- Start the scan at low power output and increase power only if necessary.
- It is preferable to use gain compensation over increasing output power.
- Be very cautious when using Doppler in the first trimester or in the immediate vicinity of bone.

CHAPTER OUTLINE

INSTRUMENT OUTPUTS
Scanning Mode
System Setup
Dwell Time
THERMAL EFFECTS
MECHANICAL EFFECTS
BIOEFFECTS OF ULTRASOUND
Animal Research
Human Studies
Birth Weight
Delayed Speech
Dyslexia
Nonright-Handedness
Neurologic Development and Behavioral Issues
Congenital Malformations
Childhood Malignancies
IS DOPPLER DIFFERENT?
SAFETY GUIDELINES
CONCLUSION

More than half a century of extensive use in clinical obstetric and radiologic practice has shown that diagnostic ultrasound does not cause major abnormalities in the fetus. Ultrasound, however, is a form of energy and clinicians must consider whether subtle effects are possible when such energy penetrates living tissues. Although some effects have been described in animals, no immediate human correlation can be made. Conversely, "no effects detected so far" does not necessarily means "no effect." Only large, epidemiologic studies can solve this problem. In the United States, most women who receive prenatal care are referred for at least one ultrasound scan; in many other countries, almost 100% of these women are exposed to ultrasound. In reproductive endocrinology, numerous scans are performed on the ovaries (and the follicles) and the very early developing embryo or fetus.[1] Furthermore, multiple examinations are often performed during pregnancy, with or without clear indication. Because of this near-universal exposure of pregnant women and their unborn children to ultrasound, given its tremendous diagnostic value,[2] the issues of possible effects and safety need to be addressed. The issue of whether short-term or long-term adverse bioeffects to the fetus may result from exposure to ultrasound has been raised since the beginning of the clinical use of this modality.[3,4]

It is well established that under certain conditions, ultrasound can have undesirable side effects. This and the issue of safety have been discussed extensively in the literature.[3,5-24] Two conflicting points need clarification: (1) to date, no evidence has been found of harmful effects of ultrasound in humans at clinical exposure levels, but (2) all available published epidemiologic data are from before 1992. Since then, acoustic output of diagnostic systems for fetal use was increased by a factor of almost 8, from 94 mW/cm^2 to 720 mW/cm^2, and, in reality, a factor of 16 (from 46 mW/cm^2) based on earlier regulations.[25] Additional concerns follow:

- An increasing number of fetuses in the first trimester, a time of maximal susceptibility to external insults, are exposed to ultrasound, particularly spectral Doppler.[26]
- "Entertainment" ultrasound, scanning to obtain pictures or videos of the fetus (fetal "keepsake" videos) without a medical indication has burgeoned[27] despite calls for avoidance of unnecessary exposure.[10,28,29]
- Clinical users of obstetric ultrasound appear to have limited knowledge and awareness of bioeffects and safety.[30]

Thus the main goals of this chapter are as follows:

1. Summarize the literature on bioeffects in experimental settings as well as the available knowledge on bioeffects in the human fetus.
2. Analyze changes that occurred over time in energy levels of ultrasound machines and the regulations involved.
3. Describe how manipulation of many instrument controls alters acoustic energy and thus exposure.
4. Educate sonographers and physicians on how best to minimize fetal exposure without sacrificing diagnostic quality.

INSTRUMENT OUTPUTS

Over the years, output of ultrasound instruments has increased.[31,32] Furthermore, many machine controls can alter the output, and various machines can behave differently when manipulating similar controls. For example, keeping in mind that the degree of temperature elevation is proportional to the product of the amplitude of the sound wave times the pulse length and the pulse repetition frequency, it becomes immediately evident why any change (augmentation) in these characteristics can add to the risk of elevating the temperature, a potential mechanism for bioeffects. Three important parameters under end-user control are the (1) scanning/operating mode (including transducer choice), (2) system setup and output control, and (3) dwell time.

Scanning Mode

When comparing modes, the spatial peak temporal average intensity (ISPTA) increases from B-mode (average, 34 mW/cm^2) to M-mode to color Doppler to spectral Doppler (average, 1180 mW/cm^2).[33] Average ISPTA values are 1 W/cm^2 in Doppler mode but can reach 10 W/cm^2. Caution is therefore recommended when applying this mode. Color Doppler has higher intensities than B-mode but is still much lower than spectral Doppler, mainly because of the mode of operation: sequences of pulses, scanned through the area of interest ("box"). High pulse repetition frequencies are used in pulsed Doppler techniques, generating greater temporal average intensities and power than B-mode or M-mode and thus greater heating potential. Also, because the beam needs to be held in relatively constant position over the vessel of interest in spectral Doppler ultrasound, temporal average intensity may further increase. This is particularly concerning in first-trimester applications. In addition, **transducer choice** is important because it will determine frequency, penetration, resolution, and field of view.

System Setup

Starting or **default output power** is another important ultrasound parameter. Some manufacturers "boot" their machines with high power, which supposedly produces a better image, and the sonographer must act to decrease that power. Other systems boot up with low power and, only if judged necessary, the sonographer will increase that power. In, For example, the Doppler signal in Fig. 29.1A was obtained with a high power, as reflected by an elevated TI of 2.9, whereas in Fig. 29.1B the power was greatly reduced (TI = 0.6), and the image is still diagnostic. Also, the examiner fine-tunes to optimize the image, influencing output but with no visible effect, except to change **thermal index** (TI) and **mechanical index** (MI), as discussed in Chapter 2.

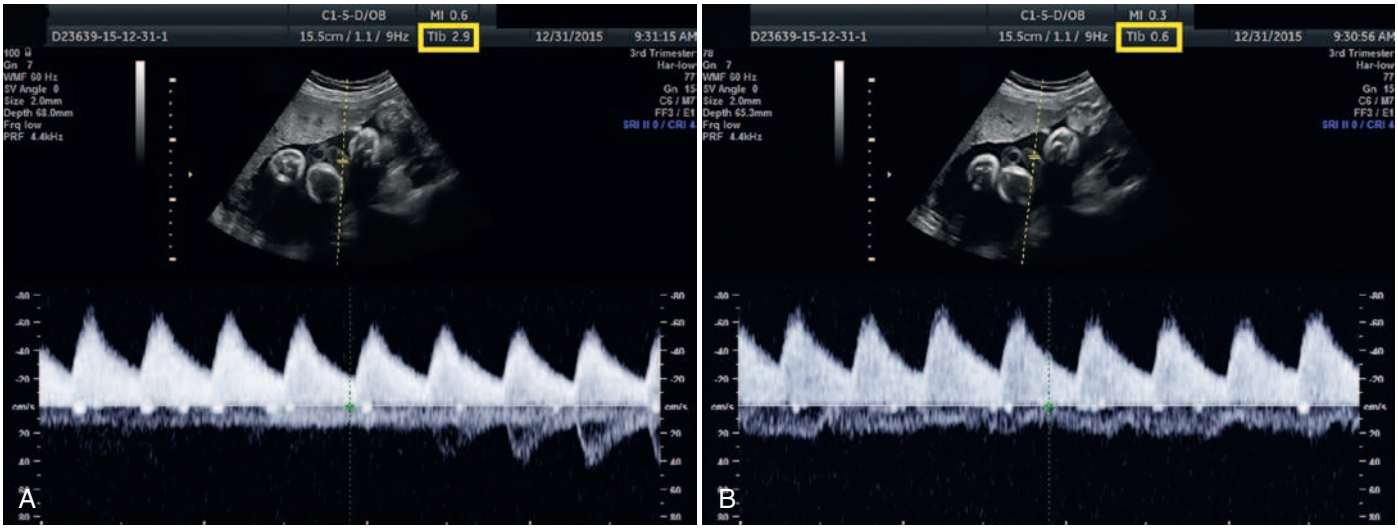

FIG. 29.1 Effect of Changing Power Setting on Thermal Index of Bone (TIB) During Spectral Doppler Velocity Measurements of Umbilical Artery. (A) The output power is high, and the thermal index (TI) is 2.9 *(yellow box)*. **(B)** The power has been lowered; the TI is now 0.6, and the tracing is still diagnostic.

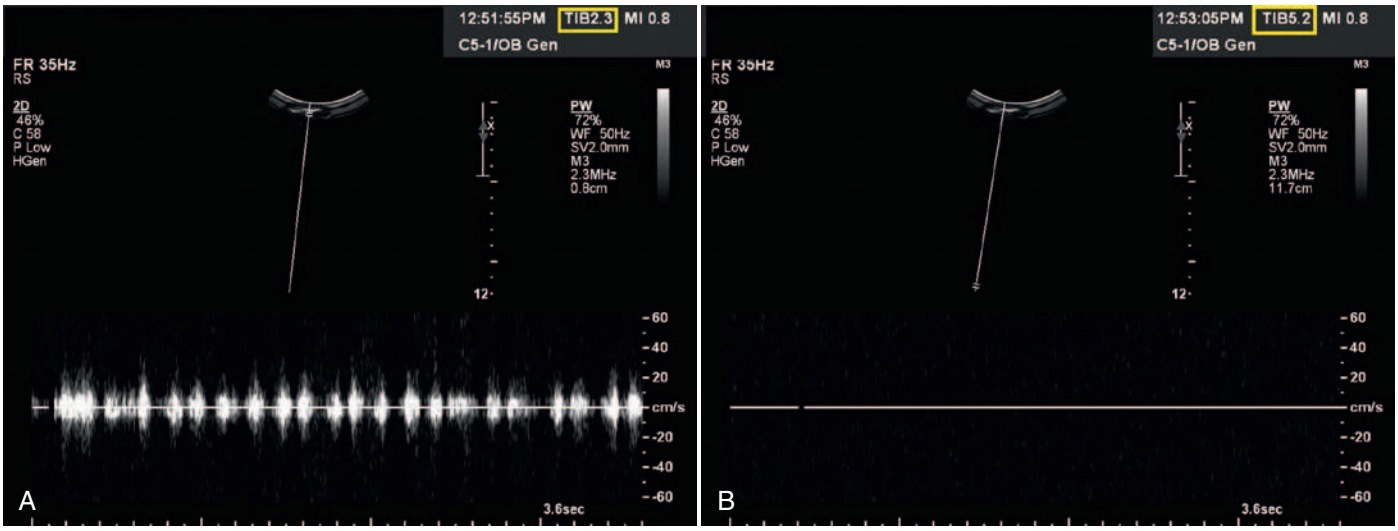

FIG. 29.2 Effect of Changing Focal Area on Thermal Index of Bone (TIB) During Spectral (Pulsed) Doppler Examination. Changing the focal area from **(A)** near field to **(B)** far field changes the thermal index *(yellow box)* from 2.3 to 5.2.

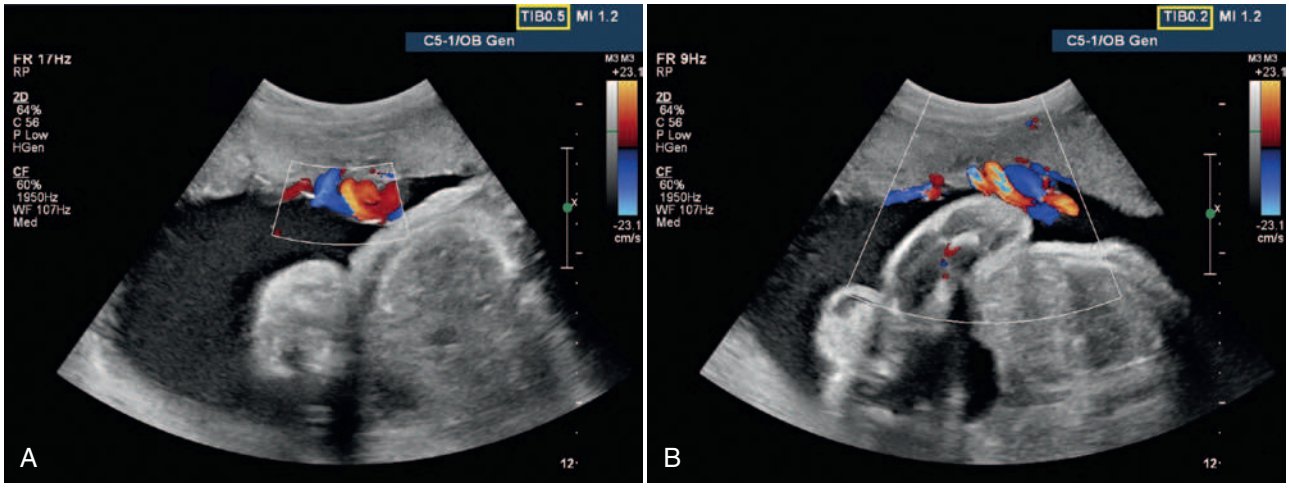

FIG. 29.3 Effect of Changing Size of Color Box on Thermal Index of Bone (TIB) During Color Doppler Examination of Umbilical Cord. Changing the size of the box from **(A)** large to **(B)** small changes the thermal index *(yellow box)* from 0.2 to 0.5.

Controls that regulate output include **focal depth,** usually with greatest power at deeper focus (Fig. 29.2) but occasionally with highest power in the near field; **increasing frame rate;** and **limiting the field of view,** as by high-resolution magnification or certain zooms. In Doppler mode, changing **sample volume** and **velocity range** (to optimize received signals) will change output. In Fig. 29.3, only the size of the color box is smaller, which caused increased TI on the output. It should be remembered that **receiver gain** often has similar effects as these controls on the recorded image (postprocessing), but no effect on the output of the outgoing beam (preprocessing), and therefore it is completely safe to manipulate. In Fig. 29.4A, the output power is high. In Fig. 29.4B, the output power has been greatly reduced (as reflected by a very low TI) and the image is much less diagnostic. In Fig. 29.4C, the receiver gain has been greatly increased, resulting in an image that looks identical to that in Fig. 29.4A but there were no changes in acoustic power, as reflected by unchanged TI and MI or power percentage. In other words, the receiver gain should be maximized before output is increased, which will rarely, if ever, be necessary.

Dwell Time

Dwell time is the **actual scanning time** and thus directly under control of the examiner. Dwell time is not taken into account in the calculation of the safety indices and generally is not reported in clinical or experimental studies. However, it takes only one pulse to induce cavitation and about a minute to raise temperature to its peak. Directly correlated with dwell time is **examiner experience,** that is, the examiner's knowledge of anatomy, bioeffects, instrument controls, and scanning techniques.

THERMAL EFFECTS

That diagnostic ultrasound can induce thermal changes in various animals has been demonstrated.[34] In addition, hyperthermia has clearly been shown to be teratologic to many species.[35-43] Elevated

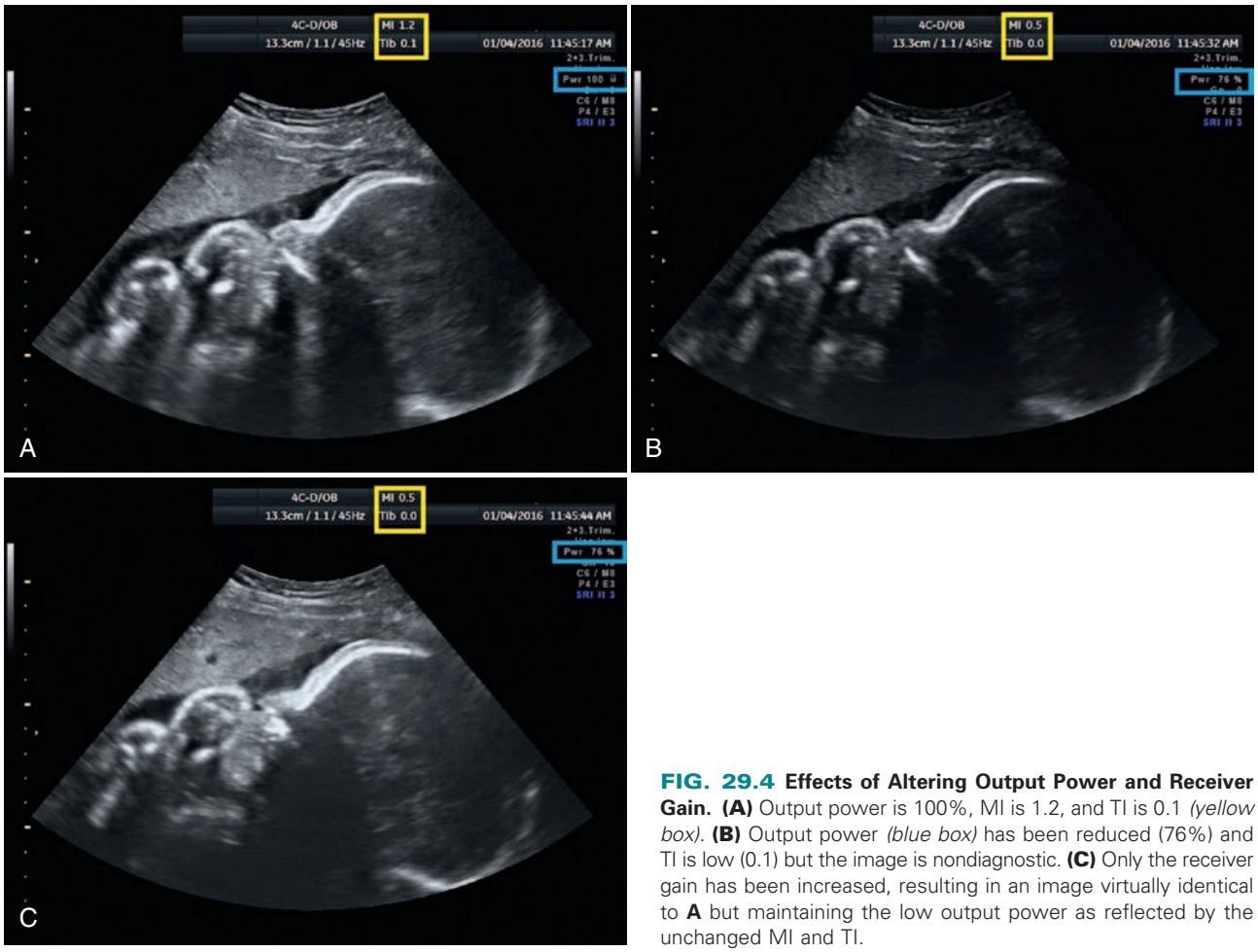

FIG. 29.4 Effects of Altering Output Power and Receiver Gain. (A) Output power is 100%, MI is 1.2, and TI is 0.1 *(yellow box).* **(B)** Output power *(blue box)* has been reduced (76%) and TI is low (0.1) but the image is nondiagnostic. **(C)** Only the receiver gain has been increased, resulting in an image virtually identical to **A** but maintaining the low output power as reflected by the unchanged MI and TI.

maternal temperature, whether from illness or exposure to heat, can produce teratogenic effects.[20,37,38,41-56] A rise less than 2°C is thought to be safe,[57] although any temperature increase for any amount of time may have some effect,[46,58] and a rise of 2.5°C may be considered significant.[59] A major question is whether diagnostic ultrasound can induce a rise in temperature in the fetus that could reach dangerous levels.[13,57,60] Temperature elevation in the human fetus cannot be exactly measured but can be estimated fairly accurately.[61,62] For prolonged ultrasound exposures, temperature elevations of up to 5°C have been obtained.[57] Thus *any* temperature increment for *any* period of time has *some* effect; the higher the temperature differential or the longer the temperature increment, the greater is the likelihood of producing an effect. Although these assumptions cannot be demonstrated in diagnostic ultrasound and no human data exist, clinicians should keep these facts in mind when performing obstetric ultrasound. This also forms part of the argument against nonmedical or nonindicated ultrasound examinations.

As with any external influence on the pregnancy, **gestational age** is a vital factor. **Milder** (in time or intensity) exposures during the preimplantation period (very early gestational age) could have similar or worse consequences than **more severe** exposures during embryonic and fetal development and could result in fetal demise and abortion or structural and functional defects. Such a dose analysis is not available. As for many other **teratogens,** the central nervous system (CNS) is most at risk because of a lack of compensatory growth by undamaged neuroblasts. In experimental animals the most common defects associated with temperature increase are of the neural tube **(anencephaly, microencephaly)** and the eyes **(microphthalmia, cataract).** Associated with CNS defects are functional and behavioral problems.[45] Other organ defects secondary to hyperthermia include defects of craniofacial development (e.g., clefts) and anomalies of the axial and appendicular skeleton,[63] the body wall, teeth, and heart.

Gestational age is critical when considering heat dispersion. In midterm, there was no significant difference when guinea pig fetal brains were exposed, alive (perfused) or postmortem (nonperfused), in the focal region of the ultrasound beam. However, a significant cooling effect of vascular perfusion was observed when the fetuses reached the stage of late gestation near term, when the cerebral vessels were well developed.[64] In early human pregnancy, less than 6 weeks, the minimal fetal perfusion may reduce heat dispersion.[65] The increased sensitivity of Doppler devices suggests evidence of blood flow within embryonic vesicles after heart formation, with the simultaneous development of a uterine circulatory pathway in the developing placenta. The flow is often referred to as "nonpulsatile" or

"percolating"[66,67] with near-minimal Doppler-measured velocities, as opposed to later in pregnancy. At about week 12 of gestation, the plugs of the spiral arteries are "loosened" and allow for freer blood circulation.[68,69]

Thus perfusion status is far from approaching that for normal tissue levels (as assumed in the TI algorithm) for much of the first trimester. Only later, when "free circulation" is established (about week 11 or 12 of gestation), does the tissue become normally perfused, when the embryonic circulation actually links up with the maternal circulation.[69] This absence of perfusion may result in underestimation of the actual ultrasound-induced temperature in early gestation. This warrants extreme caution in first-trimester scanning, particularly with the recent increase in utilization of Doppler in the first trimester.[70-73]

Also, the issue of **transducer heating** may be particularly relevant in the first trimester, if performing endovaginal scanning.[72,74] A mitigating factor is motion (even very small) of the examiner's hand, as well as the patient's breathing and body movements (in obstetric ultrasound, both mother and fetus), which tend to spread the region being heated. However, for spectral (pulsed) Doppler studies, it is necessary to have the transducer as steady as possible. Because the intensity and acoustic power associated with Doppler ultrasound are the highest of all the general-use categories, time spent scanning with Doppler ultrasound mode is crucial. Ziskin[75] reported that average duration of 15,973 Doppler ultrasound examinations was 27 minutes (longest, 4 hours!). It is clear that temperature increases of 1°C are easily reached in routine scanning.[76] Elevation of up to 1.5°C were obtained in the first trimester and up to 4°C in the second and third trimesters, particularly with the use of pulsed Doppler.[77] In many clinical machines, TI values of 5 or 6 can be obtained in Doppler mode.

MECHANICAL EFFECTS

Although effects have been described in neonates or adult animals, because gas bubbles are not present in fetal lung or bowel, it is assumed that the risk from mechanical effect secondary to cavitation is minimal.[78] Several other mechanical effects do not appear to involve cavitation, such as **tactile sensation** of the ultrasound wave, **auditory response, cell aggregation,** and **cell membrane alteration. Hemolysis** has also been reported,[79] although some cavitation nuclei must be present for hemolysis to occur. Such microbubbles would be provided by the introduction of ultrasound **contrast agents** to the area under ultrasound examination. However, there is currently no clear clinical indication for the use of these agents in fetal ultrasound.[80,81] In addition, fetal stimulation caused by pulsed ultrasound insonation has been described, with no apparent relation to cavitation.[82] This effect may be secondary to radiation forces associated with ultrasound exposures. No harmful effects of diagnostic ultrasound secondary to nonthermal mechanisms have been reported in human fetuses. However, because of these known mechanical effects of ultrasound in living tissues, and because pressures in Doppler propagation are much higher than in B-mode imaging, further caution is recommended in the use of ultrasound, particularly in the first trimester.[83]

BIOEFFECTS OF ULTRASOUND

Animal Research

Multiple studies have shown effects of ultrasound in a wide variety of species.[84-87] Studies of gross effects on the brain and liver of cats showed well-defined lesions and demyelination in the brain[88] and tissue damage in the liver[89] resulting from ultrasound exposure of a few seconds at 1 and 3 MHz, respectively. Other observed effects include limb paralysis, as a result of spinal cord injury in the rat,[90,91] as well as lesions in the liver, kidney, and testes of rabbits.[92] Changes in fertility were demonstrated in male mice after in utero ultrasound exposure of the testes.[93] Although some effects are likely caused by mechanical processes, very high temperature elevations (much higher than with diagnostic ultrasound) may be more directly involved with the tissue damage. It took acoustic pressures generated by lithotripsy to obtain effects in muscles,[94] as well as hemorrhage in bowel[95] and lungs.[96] These intensities are much higher than in diagnostic ultrasound but are helpful in understanding the mechanisms involved with possible bioeffects of ultrasound.

Several major clinical end points for bioeffects in animals that could have direct relevance to human studies include fetal growth and birth weight, effects on brain and CNS function, and change in hematologic function. High-level exposures were associated with decreased body weight at birth in exposed monkeys compared with controls, but all showed catch-up growth when examined at 3 months of age.[97] Decreased birth weight after prenatal exposure to ultrasound has also been reported in mice[98,99] but not convincingly in rats.[100] Clear species differences therefore seem to exist,[101] making it difficult to extrapolate to the human. In a report of 30 pregnancies in monkeys, half were exposed to ultrasound.[97] The scanned fetuses had lower birth weights and were shorter than the control group. No significant differences were noted in rate of abortions, major malformations, or stillbirths. Moreover, all showed catch-up growth when examined at 3 months of age. In situ intensities were higher than routinely used in clinical obstetric imaging in the human. Studies in mice have shown increased mortality and decreased body weight after in utero exposure to diagnostic ultrasound.[102,103] Gross lesions have been described in the CNS[104] and the spine[91] in mammals.

Neurologic or behavioral findings may be sensitive markers of teratogenic effect.[84,105] Pregnant Swiss albino mice were exposed to diagnostic ultrasound for 10, 20, or 30 minutes on day 14.5 (fetal period) of gestation and compared with sham-exposed controls.[106] Significant behavioral alterations in the exposed groups included decreased locomotor and exploratory activity and more trials needed for learning. No changes were observed in physiologic reflexes or postnatal survival. The authors concluded that ultrasound exposure during the early fetal period can impair brain function in the adult mouse.[106] In another study, the same authors found increased anxiolytic activity and learning latency in ultrasound-treated animals.[107] Pregnant Swiss albino mice were exposed to similar diagnostic levels of ultrasound for 10 minutes on day 11.5 or 14.5. Behavioral tests at 3 and 6 months post partum showed more pronounced effects in the 14.5-day than in the 11.5-day group. The authors concluded that exposure

to diagnostic ultrasound during the late organogenesis period or early fetal period in mice may cause changes in postnatal behavior.[107]

An intriguing paper was published on memory changes in chicks after being insonated in ovo with various levels of Doppler ultrasound.[108] Exposure was to 5 or 10 minutes of B-mode, or to 1, 2, 3, 4, or 5 minutes of pulsed Doppler ultrasound. Two hours after hatching, chicks were trained to recognize certain colors in relation to some feeding procedures. B-mode exposure on day 19 (of a 21-day gestation) did not affect memory. However, significant memory impairment occurred after 4 and 5 minutes of pulsed Doppler exposure, as expressed by the inability to discern the colors. Short-, intermediate- and long-term memory was equally impaired, suggesting an inability to learn. The chicks were still unable to learn with a second training session. Although there are major differences in terms of length of gestation, amount of "energy received," and other technical issues when compared with human fetal exposure, these findings raise important questions on the potential effect of pulsed Doppler ultrasound in utero exposure on cognitive function.

As mentioned previously, ultrasound induces thermal changes in various animals, and hyperthermia clearly is teratogenic to many species.[35-43,64,109] In guinea pigs, mean temperature increases of 4.9°C close to parietal bone and 1.2°C in the midbrain were recorded after 2-minute ultrasound exposures, although at exposure conditions higher than usually employed in clinical examinations.[64] After only 2 minutes of insonation with an ISPTA of 2.9 W/cm^2 (about four times higher than the current U.S. Food and Drug Administration allowance for diagnostic use), mean maximum temperature increases varied from 1.2°C at 30 days to 5.2°C at 60 days. Importantly, 80% of the mean maximum temperature increase occurred within 40 seconds. This rapid rate of heating is relevant to the safety of clinical examinations in which the dwell time may be an important factor. Because maximal ultrasound-induced temperature increase occurs in the fetal brain near bone, worst-case heating will occur later in pregnancy, when the ultrasound beam impinges on bone, and less will occur earlier in pregnancy, when bone is less mineralized. This is one of the justifications to utilize **thermal index for bone** (TIB) late in pregnancy and **thermal index for soft tissue** (TIS) earlier.

In 2006 Ang et al.[110] evaluated the effect of ultrasound insonation in pregnant mice on neuronal position within the embryonic cerebral cortex of the fetuses. Neurons generated at embryonic day 16 that normally migrate to the superficial cortical layers were chemically labeled. A small but statistically significant number of neurons remained scattered within inappropriate cortical layers and in the subjacent white matter, failing to acquire their proper position when exposed to ultrasound for a total of 30 minutes or longer during their migration. However, several major differences exist between this experimental setup and clinical ultrasound in humans,[111] most notably the length of exposure (up to 7 hours). No real mechanistic explanation was given for the findings, there was no real dose-response effect, and scans were performed over a short period of several days. The experimental setup was such that embryos received whole-brain exposure to the beam, which is rare in humans (although possible very early in pregnancy), and the small brains of mice develop over days. Thus, although the study merits repeating, the applicability to human embryology is questionable.[111]

These animal studies suggest precaution with obstetric ultrasound. However, the animal studies to date do not implicate ultrasound used at daily clinical exposure levels with major adverse fetal effects.

Human Studies

Among the published epidemiologic studies on obstetric ultrasound exposure,[14,49,112-115] some have serious limitations, such as lack of a testable hypothesis for causation of the studied effect, small samples, poorly matched controls, and, most often, lack of information on acoustic output and exact quantification of exposure (number of episodes, duration of exposure, and inability to calculate "dose"). These limitations are a major problem in the analysis of published data,[116] particularly with new imaging modalities that have potentially high energy levels and new applications of existing modalities. Typical examples are spectral Doppler ultrasound analysis of the tricuspid artery at 11 to 14 weeks' gestation in screening for Down syndrome[26] and studies of the fetal heart anatomy and function during the first trimester.[71,117-120] There is no epidemiologic or other information on levels of exposure or possible effects at these early, particularly susceptible gestational ages. Several "epidemiologic" reports are actually case-control studies and require caution in their interpretation. The effects being studied (e.g., low estimated fetal weight) may be the same as the clinical indication for performing the ultrasound examination ("suspected intrauterine growth delay"). Thus an association, but not a causal relationship, may exist between the ultrasound and the growth delay.

A further crucial confounding factor is that major congenital anomalies occur in 3% to 5% of the general human population. An increment of 1% to 2% over this "background" incidence would be a major clinical effect but might go undetected as an individual finding in routine clinical practice and would be detectable only after prolonged observation in large populations. Also, some underreporting occurs; for example, a certain number of birth defects is expected in any ultrasound study in relatively large (>1000) populations. Often, however, these studies describe no anomalies in the study group or in the control population; in a survey of more than 121,000 patients among 68 examiners, combining 292 institute-years of experience, 3000 to 5000 anomalies would be expected as background rate, but none were reported.[121]

In fact, rigorous epidemiologic studies of the adverse bioeffects of ultrasound are scarce. Several biologic end points have been analyzed in the human fetus or neonate to determine whether prenatal exposure to diagnostic ultrasound had observable effects: intrauterine growth restriction and low birth weight,[122] delayed speech,[123] vision and hearing,[124] dyslexia,[125] neurologic and mental development or behavioral issues,[126,127] malignancies,[128] and nonright-handedness.[129,130] Most findings have never been duplicated, and the majority of studies have been negative for any association, with the possible exception of low birth weight.

There are no epidemiologic studies related to the output display standard (thermal and mechanical indices) and clinical

outcomes. Only a few clinical studies describe routine scan,[131] first-trimester scan,[132] particularly, **nuchal translucency** screening,[133] as well as Doppler[132] and three-dimensional (3D)/four-dimensional (4D) ultrasound.[134] Furthermore, although some studies address the issue of repeat scans,[135,136] it was not as an analysis of potential cumulative effects for which no information is available.

Birth Weight

In one often-quoted study of more than 2000 infants, a small (116 g at term) but statistically significant lower mean birth weight was found in the half exposed to ultrasound compared with the nonexposed group.[137] However, information was collected several years after exposure, with no indications known and no exposure information available. Moreover, in a later study, the authors concluded that the relationship of ultrasound exposure to reduced birth weight may be caused by shared common risk factors, which lead to both exposure and a reduction in birth weight,[138] an association but not a causal relationship.

A twice-greater risk of low birth weight was reported in another retrospective study after four or more exposures to diagnostic ultrasound.[14] These results were not reproduced in another retrospective study with a large population, originally of 10,000 pregnancies exposed to ultrasound matched with 500 controls and with 6-year follow-up.[139] No increased congenital malformations, chromosomal abnormalities, infant neoplasms, speech or hearing impairment, or developmental problems were observed in this latter study.

In a randomized controlled trial of more than 2800 pregnant women, about half received five ultrasound imaging and Doppler flow studies at 18, 24, 28, 34, and 38 weeks of gestation, and half received a single ultrasound imaging at 18 weeks.[122] An increased risk of intrauterine growth restriction was detected in those exposed to frequent Doppler ultrasound examinations, possibly through effects on bone growth. However, when children were examined at 1 year of age, there were no differences between the study and control groups. In addition, after examining their original subjects after 8 years, the investigators found no evidence of adverse neurologic outcome.[136] Similarly, other randomized studies found no harmful effect of one or two prenatal scans on growth.[140,141] Curiously, in some studies, birth weight was slightly higher in the scanned group, but not significantly, except in one group of newborns exposed to ultrasound in utero who weighed on average 42 g (75 g in reported smokers) more than the control group.[141] Thus ultrasound exposure in utero does not appear to be associated with reduced birth weight, although Doppler ultrasound exposure may have some risks.[114]

Delayed Speech

To determine if an association exists between prenatal ultrasound exposure and delayed speech in children, Campbell et al.[123] studied 72 children with delayed speech and found a higher rate of ultrasound exposure in utero compared with the 144 control subjects. However, this retrospective study used records more than 5 years old, with neither a dose-response effect nor any relationship to time of exposure. A much larger study of more than 1100 children exposed in utero and 1000 controls found no significant differences in delayed speech, limited vocabulary, or stuttering.[142]

Dyslexia

Dyslexia has been extensively studied. Stark et al.[125] compared more than 4000 children (ages 7-12 years) exposed to ultrasound in utero to matched controls, analyzing outcome measures at birth (Apgar scores, gestational age, head circumference, birth weight, length, congenital abnormalities, neonatal/congenital infection) or in early infancy (hearing, visual acuity/color vision, cognitive function, behavior). No significant differences were found, except for a significantly greater proportion of dyslexia in children exposed to ultrasound. Given the design of the study and the presence of several possible confounding factors, the authors indicated that dyslexia could be incidental.

Subsequently, long-term follow-up studies of more than 600 children with various tests for dyslexia (e.g., spelling, reading) were performed.[143-147] End points included evaluation for dyslexia along with examination of nonright-handedness, said to be associated with dyslexia. No statistically significant differences were found between ultrasound-exposed children and controls for reading, spelling, arithmetic, or overall performance, as reported by teachers. Specific dyslexia tests showed similar incidence rates among scanned children and controls in reading, spelling, and intelligence scores and no discrepancy between intelligence and reading or spelling. Therefore the original finding of dyslexia was not confirmed in subsequent randomized controlled trials. It is considered unlikely that routine ultrasound screening can cause dyslexia.

Nonright-Handedness

A possible link between prenatal exposure to ultrasound and subsequent nonright-handedness at age 8 to 9 years in children exposed to ultrasound in utero was first reported in 1993 from Norway.[146] According to the authors, however, the difference was "only barely significant at the 5% level" and was restricted to boys.[148] A second group of researchers (including Salvesen, main author of the first study), studying a new population of more than 3000 children from Sweden, reported similar findings of a statistically significant association between ultrasound exposure in utero and nonright-handedness in males.[129] An intriguing recent study showed that fetuses self-touched their faces more often with the left hand than the right, as observed by ultrasound, in correlation to stress levels of the mother.[149] Furthermore, laterality is, mostly, genetically determined[150] but could, naturally, be modified by external factors. Evidence is insufficient to infer a direct effect on brain structure or function, or even that nonright-handedness is an adverse effect.

Neurologic Development and Behavioral Issues

Neurons of the cerebral neocortex in mammals, including humans, are generated during fetal life in the brain proliferative zones and then migrate to their final destination by following an inside-to-outside sequence. This neuronal migration occurs in the human fetal brain mainly from 6 to 11 weeks of gestation[151] but continues until 32 weeks. It has long been theorized that

external factors such as ultrasound could affect this process.[152] In another study, only 2 of 123 variables were found to be disturbed at birth, but not at 1 year of age, in children exposed in utero; these variables are **grasp reflex** and **tonic neck reflex.**[153] The significance was not elaborated, and some doubts exist regarding statistical validity. Stark et al.[125] reported that vision and intelligence scores were identical among 425 exposed infants and 381 controls. A large report found no association between routine exposure to prenatal ultrasound and school performance (deficits in attention, motor control, perception, vision, and hearing).[154] In more than 4900 children age 15 to 16 years, no differences were found in school performance between exposed and nonexposed children, except for a lower score for exposed boys in physical education.[155]

Behavioral changes may be a more sensitive marker of subtle brain damage than obvious structural alterations.[156] Such changes have been described in animals,[84,105] although often transient.[97] An interesting study in mice was recently published.[157] As detailed earlier, there may be male preponderance of nonright-handedness after in utero ultrasound exposure. Furthermore, an increased prevalence of autism exists in males and there are reports of excess nonright-handedness in this population. Pregnant mice were exposed to 30 minutes of diagnostic ultrasound at embryonic day 14.5. Social behavior of their male pups was analyzed 3 weeks after birth. Ultrasound-exposed pups were significantly ($P < .01$) less interested in social interaction than sham-exposed pups and demonstrated significantly ($P < .05$) more activity relative to the sham-exposed pups (only in the presence of an unfamiliar mouse). These results suggest that social behavior in young mice was altered by in utero exposure to diagnostic ultrasound. The authors' conclusions are that this may be relevant for autism but that major differences between the exposure of diagnostic ultrasound of mice and humans preclude conclusions regarding human exposure and require further studies. Indeed, no such changes have been reported in humans. In particular, schizophrenia and other psychoses have not been found to be associated with prenatal ultrasound exposure.[158] The question has been raised about the increased rate of autism observed over the past few years and its relation to the greatly increased use of ultrasound in obstetrics. Although a major upsurge in both have occurred, there is no cause and effect demonstrable between the two.[159]

Congenital Malformations

In humans, prenatal ultrasound has not been shown to result in an increased incidence of congenital anomalies, as found in animals.

Childhood Malignancies

No association has been found between ultrasound exposure in utero and the later development of leukemia[160,161] or solid tumors in children.[128,162-166]

Again, although some of these studies were published in 2007 or 2008, the populations studied were exposed to ultrasound in utero 20 to 30 years ago, that is, with instruments generating lower outputs and with minimal or no information available on exposure conditions.

IS DOPPLER DIFFERENT?

Spectral (pulsed) Doppler uses high pulse repetition frequencies, generating greater temporal average intensities and powers than B- or M-mode, and hence greater heating potential (see "Thermal Effects").[75] Adequate diagnostic information may be obtained with low output levels (as documented by values of the TI), as demonstrated in Fig. 29.1. This has been reported in the literature, specifically for Doppler, the mode with the highest output, both in early and later pregnancy.[167,168] In fact, under pressure from bioeffects and safety committees of various professional organizations (American Institute of Ultrasound in Medicine [AIUM], European Federation of Societies of Ultrasound in Medicine and Biology [EFSUMB], International Society for Ultrasound in Obstetrics and Gynecology [ISUOG], and World Federation for Ultrasound in Medicine and Biology [WFUMB]), several manufacturers have changed their default settings, specifically for pulsed Doppler in fetal mode, from very high (as it was originally, presumably in an attempt to obtain better images) to very low, with the end user capable of raising the output, if desired. Because acoustic output is high in Doppler, special precaution is recommended, particularly in early gestation.[169]

SAFETY GUIDELINES

It is difficult to issue precise safety recommendations because of the multitude of ultrasound instruments, each with a selection of transducers and used in a variety of applications. Patient characteristics further complicate the task.[170] Safety guidelines are very important, however, given the very low level of knowledge about bioeffects and safety of ultrasound among clinical end users. In a questionnaire distributed to ultrasound active end users (of which 82% were obstetricians), only 17.7% gave the correct answer of the definition of the TI. Approximately 96% did not know the proper definition for MI. Almost 80% of respondents did not know the correct answer to the multiple choice question of where to find the acoustic indices; answer options were the machine documentation, a textbook, a complicated calculation or in real time on the ultrasound monitor (the correct answer).[171] Similar results were recorded in surveys abroad, performed in Europe, Asia, or the Middle East,[172-174] indicating that clinical end users worldwide show poor knowledge regarding safety issues of ultrasound during pregnancy.[30] More recently, knowledge among residents in obstetrics and gynecology was also found to be grossly lacking.[175] Similar results were obtained in a survey of sonographers, and years of experience made no difference.[176]

In another study, compliance with the **ALARA** (as low as reasonably achievable) principle by practitioners seeking credentialing for nuchal translucency (NT) measurement between 11 and 14 weeks' gestation was evaluated. Only 5% of the providers used the correct TI type (TIB) at lower than 0.5 for all submitted images, 6% at lower than 0.7, and 12% at 1.0 or lower. A TI (TIB or TIS) higher than 1.0 was used by almost 20% of the providers. Proficiency in NT measurement and educational background (physician or sonographer) did not influence compliance with ALARA. The authors concluded that clinicians seeking

credentialing in NT do not demonstrate compliance with the recommended use of the TI in monitoring acoustic output.[177] An easy way to reduce exposure is to reduce the TI and MI, using the appropriate controls, and/or reduce the dwell time. The 1999 statement of the British Medical Ultrasound Society, reconfirmed in 2009, declares[178]:

> *For equipment for which the safety indices are displayed over their full range of values, the TI should always be less than 0.5 and the MI should always be less than 0.3. When the safety indices are not displayed, T_{max} should be less than 1°C and MI_{max} should be less than 0.3. Frequent exposure of the same subject is to be avoided.*

The British Medical Ultrasound Society has strict recommendations for maximum allowed exposure time (T_{max}), depending on the TI (Table 29.1).

Miller and Ziskin[57] demonstrated a logarithmic relationship between exposure duration and temperature elevation in producing harmful bioeffects in animal fetuses. For temperatures below 43°C, the exposure time necessary for every 1°C increase in temperature was decreased by a factor of 4. Using a maximum "safe" exposure time of 4 minutes for a temperature elevation of 4°C, based on these calculations, the following maximal exposure times are allowable with no apparent obvious risks: 128 minutes at 1°C, 64 at 2°C, 16 at 3°C, and only 4 minutes at 4°C. Precautions are, naturally, of particular importance in early gestation[179,180] and for Doppler exposure.[181]

General recommendations from major professional organizations follow. It is strongly recommended to consult various safety statements published on these organizations' websites.[182-192]

1. A diagnostic ultrasound exposure that produces a maximum in situ temperature rise of no more than 1.5°C above normal physiologic levels (37°C) may be used clinically without reservation on thermal grounds.[193]
2. A diagnostic ultrasound exposure that elevates embryonic and fetal in situ temperature above 41°C (4°C above normal temperature) for 5 minutes or more should be considered potentially hazardous.[193,194] In this regard, maternal temperature elevation (e.g., from viral disease) should be considered because body temperature of the fetus will also be increased above normal.[48]
3. The risk of adverse effects is increased with the duration of exposure (dwell time).[195]
4. Based on available information, there is no reason to withhold scanning in B-mode for medical indications. The risk of thermal damage secondary to heating appears to be negligible.[193]
5. M-mode ultrasound appears to be safe and not to cause thermal damage (Fig. 29.5).[48]
6. Spectral Doppler ultrasound may produce high intensities, and routine Doppler examination during the embryonic period is rarely indicated.[196]
7. Three-dimensional (3D) and four-dimensional (4D) ultrasound are based on two-dimensional (2D) B-mode imaging with multiple 2D planes obtained and assembled (reconstructed) into a volume. Hence the exposure is really to B-mode and is, most likely, safe. Time of exposure has to be watched to avoid long episodes of scanning to obtain the "ideal" 3D volume (Fig. 29.6).
8. Education of ultrasound operators is crucial; the responsibility for the safe use of ultrasound devices is shared between the users and the manufacturers, who should ensure the accuracy of the output display.[196]
9. The AIUM advocates the responsible use of diagnostic ultrasound and strongly discourages the nonmedical use of ultrasound for "entertainment" purposes. The use of ultrasound without a medical indication to view the fetus, obtain a picture of the fetus, or determine the fetal gender is inappropriate and contrary to responsible medical practice. Ultrasound should be used by qualified health professionals to provide medical benefit to the patient.[28]
10. Examinations should be kept as short as possible and with as low MI and TI outputs as possible, but without sacrificing diagnostic accuracy. Follow the **as low as reasonably achievable** (ALARA) principle.[197]

TABLE 29.1 Duration of Obstetric Ultrasound as a Function of Thermal Index

Thermal Index (TI)	Recommended Upper Limit
0.7	60 min
1	30 min
1.5	15 min
2	4 min
2.5	1 min

Modified from British Medical Ultrasound Society (BMUS) Safety Group. Guidelines for the safe use of diagnostic ultrasound equipment. Ultrasound. 2010;18:52-59.[178]

CONCLUSION

Diagnostic ultrasound has been used in medicine in general and obstetrics and gynecology in particular for more than half a century. No confirmed biologic effects have been described in patients as a result of exposure to diagnostic ultrasound. Such effects, however, have been described in animals, often at exposure levels higher than, but also occasionally equivalent to, those used in clinical practice. Epidemiologic information available is from studies performed on instruments with acoustic output much lower than current machines. Often, exposure data are insufficient and number of subjects too small. Furthermore, "no reported effects" does not mean "no effects," and such biologic effects may be identified in the future. Prudent use of ultrasound in fetal scanning, following the ALARA principle, is therefore recommended. Based on known mechanisms, there is no contraindication to the use of B-mode, M-mode, 3D/4D, and color Doppler ultrasound, when clinically indicated. However, special precaution is necessary when applying pulsed Doppler ultrasound, particularly in the first trimester.

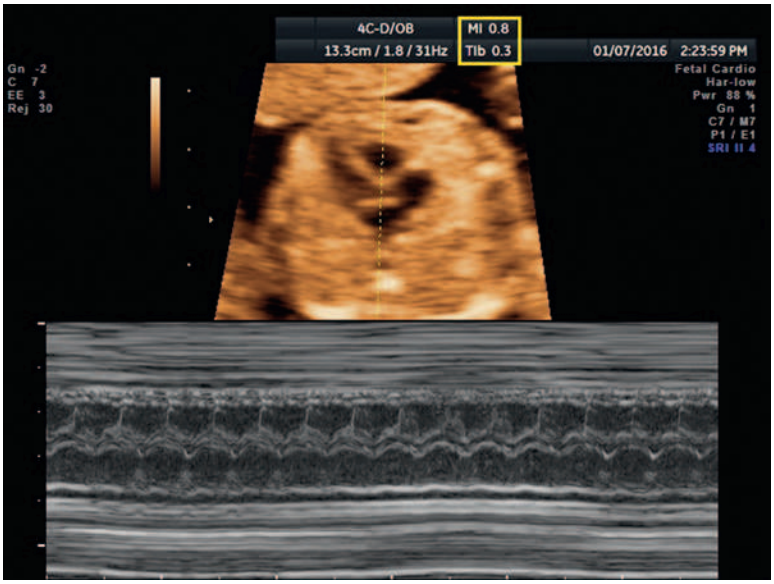

FIG. 29.5 **M-Mode Tracing, Obtained With Low TI (0.3) and MI (0.8).**

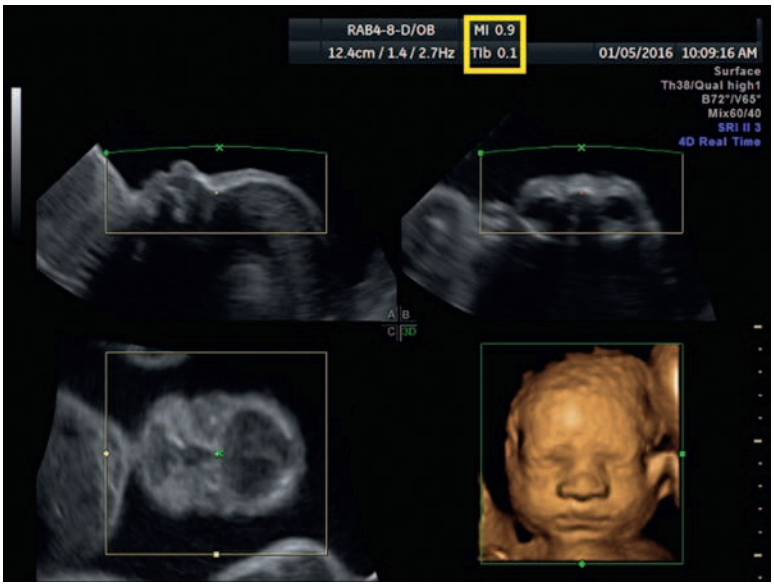

FIG. 29.6 **Multiplanar Images and Three-Dimensional Reconstructed Volume With Low TI (0.1) and MI (0.9).**

REFERENCES

1. Abramowicz JS. Ultrasound in reproductive medicine: is it safe? In: Stadtmauer LA, Tur-Kaspa I, editors. Ultrasound imaging in reproductive medicine. New York: Springer; 2014. p. 3-16.
2. Abramowicz JS. Benefits and risks of ultrasound in pregnancy. Semin Perinatol. 2013;37(5):295-300.
3. Dewhurst CJ. The safety of ultrasound. Proc R Soc Med. 1971;64(9): 996-997.
4. Donald I. The safety of using sonar. Dev Med Child Neurol. 1974;16(1): 90-92.
5. Hellman LM, Duffus GM, Donald I, Sunden B. Safety of diagnostic ultrasound in obstetrics. Lancet. 1970;1(7657):1133-1134.
6. Lele PP. Safety and potential hazards in the current applications of ultrasound in obstetrics and gynecology. Ultrasound Med Biol. 1979;5(4):307-320.
7. Meyer RA. Diagnostic ultrasound: hazardous or safe? Appl Radiol. 1982;11(5):71-74.
8. Kremkau FW. Biological effects and possible hazards. Clin Obstet Gynaecol. 1983;10(3):395-405.
9. Brown BS. How safe is diagnostic ultrasonography? Can Med Assoc J. 1984;131(4):307-311.
10. Wells PN. The prudent use of diagnostic ultrasound. British Institute of Radiology presidential address 1986. Br J Radiol. 1986;59(708): 1143-1151.
11. Reece EA, Assimakopoulos E, Zheng XZ, et al. The safety of obstetric ultrasonography: concern for the fetus. Obstet Gynecol. 1990;76(1): 139-146.
12. Salvesen KA, Eik-Nes SH. Is ultrasound unsound? A review of epidemiological studies of human exposure to ultrasound. Ultrasound Obstet Gynecol. 1995;6(4):293-298.
13. Abramowicz JS. Ultrasound in obstetrics and gynecology: is this hot technology too hot? J Ultrasound Med. 2002;21(12):1327-1333.
14. Marinac-Dabic D, Krulewitch CJ, Moore Jr RM. The safety of prenatal ultrasound exposure in human studies. Epidemiology. 2002;13(Suppl. 3):S19-S22.
15. Church CC, Miller MW. Quantification of risk from fetal exposure to diagnostic ultrasound. Prog Biophys Mol Biol. 2007;93(1-3):331-353.

16. Toms DA. Safety issues in fetal ultrasound. Jan 2007. Available from: http://www.fetalultrasoundsafety.net/Downloads/fetalultrasoundsafety.pdf. Accessed 26 December 2015.
17. ter Haar G. Ultrasound bio-effects and safety considerations. Front Neurol Neurosci. 2015;36:23-30.
18. Nyborg WL. Safety of ultrasound diagnosis. Science. 1974;186(4169):1074.
19. Stratmeyer ME, Christman CL. Biological effects of ultrasound. Women Health. 1982;7(3-4):65-81.
20. Barnett SB, Rott HD, ter Haar GR, et al. The sensitivity of biological tissue to ultrasound. Ultrasound Med Biol. 1997;23(6):805-812.
21. Miller MW, Brayman AA. Biological effects of ultrasound. The perceived safety of diagnostic ultrasound within the context of ultrasound biophysics: a personal perspective. Echocardiography. 1997;14(6 Pt 1):615-628.
22. Kieler H, Cnattingius S, Haglund B, et al. Ultrasound and adverse effects. Ultrasound Obstet Gynecol. 2002;20(1):102-103.
23. Bly S, Van den Hof MC. Obstetric ultrasound biological effects and safety. J Obstet Gynaecol Can. 2005;27(6):572-580.
24. Duck FA. Hazards, risks and safety of diagnostic ultrasound. Med Eng Phys. 2008;30(10):1338-1348.
25. Miller MW, Brayman AA, Abramowicz JS. Obstetric ultrasonography: a biophysical consideration of patient safety—the "rules" have changed. Am J Obstet Gynecol. 1998;179(1):241-254.
26. Ndumbe FM, Navti O, Chilaka VN, Konje JC. Prenatal diagnosis in the first trimester of pregnancy. Obstet Gynecol Surv. 2008;63(5):317-328.
27. Simonsen SE, Branch DW, Rose NC. The complexity of fetal imaging: reconciling clinical care with patient entertainment. Obstet Gynecol. 2008;112(6):1351-1354.
28. American Institute of Ultrasound in Medicine. AIUM official statement: prudent use in obstetrics. 2007.
29. Ziskin MC. The prudent use of diagnostic ultrasound. J Ultrasound Med. 1987;6(8):415-416.
30. Sheiner E, Abramowicz JS. Clinical end users worldwide show poor knowledge regarding safety issues of ultrasound during pregnancy. J Ultrasound Med. 2008;27(4):499-501.
31. Duck FA, Martin K. Trends in diagnostic ultrasound exposure. Phys Med Biol. 1991;36(11):1423-1432.
32. Cibull SL, Harris GR, Nell DM. Trends in diagnostic ultrasound acoustic output from data reported to the US Food and Drug Administration for device indications that include fetal applications. J Ultrasound Med. 2013;32(11):1921-1932.
33. Duck FA, Henderson J. Acoustic output of modern instruments: is it increasing? In: Barnett SB, Kossoff G, editors. Safety of diagnostic ultrasound. New York: Parthenon; 1998. p. 147.
34. Abramowicz JS, Barnett SB, Duck FA, et al. Fetal thermal effects of diagnostic ultrasound. J Ultrasound Med. 2008;27(4):541-559.
35. Chance PF, Smith DW. Hyperthermia and meningomyelocele and anencephaly. Lancet. 1978;1(8067):769-770.
36. Edwards MJ. Congenital defects in guinea pigs. Following induced hyperthermia during gestation. Arch Pathol. 1967;84(1):42-48.
37. Halperin LR, Wilroy Jr RS. Maternal hyperthermia and neural-tube defects. Lancet. 1978;2(8082):212-213.
38. Shiota K. Induction of neural tube defects and skeletal malformations in mice following brief hyperthermia in utero. Biol Neonate. 1988;53(2):86-97.
39. Graham Jr JM, Edwards MJ, Edwards MJ. Teratogen update: gestational effects of maternal hyperthermia due to febrile illnesses and resultant patterns of defects in humans. Teratology. 1998;58(5):209-221.
40. Li Z, Ren A, Liu J, et al. Maternal flu or fever, medication use, and neural tube defects: a population-based case-control study in Northern China. Birth Defects Res A Clin Mol Teratol. 2007;79(4):295-300.
41. Lipson AH, Edwards MJ. Maternal sauna and hyperthermia during pregnancy and cardiovascular and other malformations in offspring. Eur J Epidemiol. 1993;9(6):676-678.
42. Little BB, Ghali FE, Snell LM, et al. Is hyperthermia teratogenic in the human? Am J Perinatol. 1991;8(3):185-189.
43. Shaw GM, Todoroff K, Velie EM, Lammer EJ. Maternal illness, including fever and medication use as risk factors for neural tube defects. Teratology. 1998;57(1):1-7.
44. Dombrowski SC, Martin RP, Huttunen MO. Association between maternal fever and psychological/behavior outcomes: a hypothesis. Birth Defects Res A Clin Mol Teratol. 2003;67(11):905-910.
45. Edwards MJ, Saunders RD, Shiota K. Effects of heat on embryos and foetuses. Int J Hyperthermia. 2003;19(3):295-324.
46. Miller MW, Nyborg WL, Dewey WC, et al. Hyperthermic teratogenicity, thermal dose and diagnostic ultrasound during pregnancy: implications of new standards on tissue heating. Int J Hyperthermia. 2002;18(5):361-384.
47. Moretti ME, Bar-Oz B, Fried S, Koren G. Maternal hyperthermia and the risk for neural tube defects in offspring: systematic review and meta-analysis. Epidemiology. 2005;16(2):216-219.
48. European Committee for Medical Ultrasound Safety (ECMUS). Thermal teratology. Eur J Ultrasound. 1999;9(3):281-283.
49. National Council on Radiation Protection and Measurements. Exposure criteria for medical diagnostic ultrasound. II. Criteria based on all known mechanisms. NCRP Report No. 140. Bethesda, Md: NCRP; 2002.
50. Acs N, Banhidy F, Puho E, Czeizel AE. Maternal influenza during pregnancy and risk of congenital abnormalities in offspring. Birth Defects Res A Clin Mol Teratol. 2005;73(12):989-996.
51. Cleves MA, Malik S, Yang S, et al. Maternal urinary tract infections and selected cardiovascular malformations. Birth Defects Res A Clin Mol Teratol. 2008;82(6):464-473.
52. Miller MW, Church CC, Miller RK, Edwards MJ. Fetal thermal dose considerations during the obstetrician's watch: implications for the pediatrician's observations. Birth Defects Res C Embryo Today. 2007;81(3):135-143.
53. Peterka M, Tvrdek M, Likovsky Z, et al. Maternal hyperthermia and infection as one of possible causes of orofacial clefts. Acta Chir Plast. 1994;36(4):114-118.
54. Superneau DW, Wertelecki W. Similarity of effects—experimental hyperthermia as a teratogen and maternal febrile illness associated with oromandibular and limb defects. Am J Med Genet. 1985;21(3):575-580.
55. Dreier JW, Andersen AM, Berg-Beckhoff G. Systematic review and meta-analyses: fever in pregnancy and health impacts in the offspring. Pediatrics. 2014;133(3):e674-e688.
56. Luteijn JM, Brown MJ, Dolk H. Influenza and congenital anomalies: a systematic review and meta-analysis. Hum Reprod. 2014;29(4):809-823.
57. Miller MW, Ziskin MC. Biological consequences of hyperthermia. Ultrasound Med Biol. 1989;15(8):707-722.
58. Miller MW, Miller HE, Church CC. A new perspective on hyperthermia-induced birth defects: the role of activation energy and its relation to obstetric ultrasound. J Therm Biol. 2005;30:400-409.
59. Brent RL. Is hyperthermia a direct or indirect teratogen? Teratology. 1986;33(3):373-374.
60. Barnett SB. Can diagnostic ultrasound heat tissue and cause biological effects? In: Barnett SB, Kossoff G, editors. Safety of diagnostic ultrasound. New York: Parthenon; 1998. p. 30.
61. Nyborg WL, Steele RB. Temperature elevation in a beam of ultrasound. Ultrasound Med Biol. 1983;9(6):611-620.
62. Nyborg WL, O'Brien Jr WD. An alternative simple formula for temperature estimates. J Ultrasound Med. 1989;8(11):653-654.
63. Martínez-Frías ML, García Mazario MJ, Caldas CF, et al. High maternal fever during gestation and severe congenital limb disruptions. Am J Med Genet. 2001;98(2):201-203.
64. Horder MM, Barnett SB, Vella GJ, et al. Ultrasound-induced temperature increase in guinea-pig fetal brain in utero: third-trimester gestation. Ultrasound Med Biol. 1998;24(9):1501-1510.
65. Jauniaux E, Gulbis B, Burton GJ. The human first trimester gestational sac limits rather than facilitates oxygen transfer to the foetus—a review. Placenta. 2003;24(Suppl. A):S86-S93.
66. Carbillon L, Perrot N, Uzan M, Uzan S. Doppler ultrasonography and implantation: a critical review. Fetal Diagn Ther. 2001;16(6):327-332.
67. Kurjak A, Kupesic S. Doppler proof of the presence of intervillous circulation. Ultrasound Obstet Gynecol. 1996;7(6):463-464.
68. Jauniaux E. Intervillous circulation in the first trimester: the phantom of the color Doppler obstetric opera. Ultrasound Obstet Gynecol. 1996;8(2):73-76.

69. Makikallio K, Tekay A, Jouppila P. Uteroplacental hemodynamics during early human pregnancy: a longitudinal study. Gynecol Obstet Invest. 2004;58(1):49-54.
70. Wloch A, Rozmus-Warcholinska W, Czuba B, et al. Doppler study of the embryonic heart in normal pregnant women. J Matern Fetal Neonatal Med. 2007;20(7):533-539.
71. Russell NE, McAuliffe FM. First-trimester fetal cardiac function. J Ultrasound Med. 2008;27(3):379-383.
72. Duck FA. Is it safe to use diagnostic ultrasound during the first trimester? Ultrasound Obstet Gynecol. 1999;13(6):385-388.
73. Smythe GE, MacRae DJ. Letter: doppler ultrasound and fetal hazard. Lancet. 1975;2(7925):134.
74. Calvert J, Duck F, Clift S, Azaime H. Surface heating by transvaginal transducers. Ultrasound Obstet Gynecol. 2007;29(4):427-432.
75. Ziskin MC. Intrauterine effects of ultrasound: human epidemiology. Teratology. 1999;59(4):252-260.
76. O'Brien WD, Siddiqi TA. Obstetric sonography: the output display standard and ultrasound bioeffects. In: Fleischer AC, Manning FA, Jeanty P, Romero R, editors. Sonography in obstetrics and gynecology: principles and practice. 6th ed. New York: McGraw-Hill; 2001. p. 29-48.
77. Bly SH, Vlahovich S, Mabee PR, Hussey RG. Computed estimates of maximum temperature elevations in fetal tissues during transabdominal pulsed Doppler examinations. Ultrasound Med Biol. 1992;18(4):389-397.
78. Carstensen EL, Gates AH. The effects of pulsed ultrasound on the fetus. J Ultrasound Med. 1984;3(4):145-147.
79. Dalecki D, Raeman CH, Child SZ, et al. Hemolysis in vivo from exposure to pulsed ultrasound. Ultrasound Med Biol. 1997;23(2):307-313.
80. Abramowicz JS. Ultrasonographic contrast media: has the time come in obstetrics and gynecology? J Ultrasound Med. 2005;24(4):517-531.
81. Miller MW, Brayman AA, Sherman TA, et al. Comparative sensitivity of human fetal and adult erythrocytes to hemolysis by pulsed 1 MHz ultrasound. Ultrasound Med Biol. 2001;27(3):419-425.
82. Fatemi M, Ogburn Jr PL, Greenleaf JF. Fetal stimulation by pulsed diagnostic ultrasound. J Ultrasound Med. 2001;20(8):883-889.
83. Duck FA. Acoustic streaming and radiation pressure in diagnostic applications: what are the implications? In: Barnett SB, Kossoff G, editors. Safety of diagnostic ultrasound. New York: Parthenon; 1998. p. 87-98.
84. Jensh RP, Brent RL. Intrauterine effects of ultrasound: animal studies. Teratology. 1999;59(4):240-251.
85. Harvey EN, Loomis AL. High-frequency sound waves of small intensity and their biological effects. Nature. 1928;121:622-624.
86. Sikov MR. Effect of ultrasound on development. Part 1: introduction and studies in inframammalian species. Report of the Bioeffects Committee of the American Institute of Ultrasound in Medicine. J Ultrasound Med. 1986;5(10):577-583.
87. Sikov MR. Effect of ultrasound on development. Part 2: studies in mammalian species and overview. J Ultrasound Med. 1986;5(11):651-661.
88. Fry FJ, Kossoff G, Eggleton RC, Dunn F. Threshold ultrasonic dosages for structural changes in the mammalian brain. J Acoust Soc Am. 1970;48(6):Suppl 2:1413.
89. Frizzell LA, Carstensen EL, Davis JD. Ultrasonic absorption in liver tissue. J Acoust Soc Am. 1979;65(5):1309-1312.
90. Frizzell LA, Lee CS, Aschenbach PD, et al. Involvement of ultrasonically induced cavitation in the production of hind limb paralysis of the mouse neonate. J Acoust Soc Am. 1983;74(3):1062-1065.
91. Borrelli MJ, Frizzell LA, Dunn F. Ultrasonically induced morphological changes in the mammalian neonatal spinal cord. Ultrasound Med Biol. 1986;12(4):285-295.
92. Frizzell LA, Linke CA, Carstensen EL, Fridd CW. Thresholds for focal ultrasonic lesions in rabbit kidney, liver, and testicle. IEEE Trans Biomed Eng. 1977;24(4):393-396.
93. Carnes KI, Hess RA, Dunn F. The effect of ultrasound exposure in utero on the development of the fetal mouse testis: adult consequences. Ultrasound Med Biol. 1995;21(9):1247-1257.
94. Hynynen K. The threshold for thermally significant cavitation in dog's thigh muscle in vivo. Ultrasound Med Biol. 1991;17(2):157-169.
95. Dalecki D, Raeman CH, Child SZ, Carstensen EL. Intestinal hemorrhage from exposure to pulsed ultrasound. Ultrasound Med Biol. 1995;21(8):1067-1072.
96. Dalecki D, Child SZ, Raeman CH, et al. Ultrasonically induced lung hemorrhage in young swine. Ultrasound Med Biol. 1997;23(5):777-781.
97. Tarantal AF, Hendrickx AG. Evaluation of the bioeffects of prenatal ultrasound exposure in the cynomolgus macaque (Macaca fascicularis): II. Growth and behavior during the first year. Teratology. 1989;39(2):149-162.
98. Hande MP, Devi PU. Effect of in utero exposure to diagnostic ultrasound on the postnatal survival and growth of mouse. Teratology. 1993;48(5):405-411.
99. O'Brien WD. Dose-dependent effects of ultrasound on fetal weight in mice. J Ultrasound Med. 1983;2:1-8.
100. Vorhees CV, Acuff-Smith KD, Schilling MA, et al. Behavioral teratologic effects of prenatal exposure to continuous-wave ultrasound in unanesthetized rats. Teratology. 1994;50(3):238-249.
101. O'Brien Jr WD, Januzik SJ, Dunn F. Ultrasound biologic effects: a suggestion of strain specificity. J Ultrasound Med. 1982;1(9):367-370.
102. Hande MP, Devi PU. Effect of prenatal exposure to diagnostic ultrasound on the development of mice. Radiat Res. 1992;130(1):125-128.
103. Rao S, Ovchinnikov N, McRae A. Gestational stage sensitivity to ultrasound effect on postnatal growth and development of mice. Birth Defects Res A Clin Mol Teratol. 2006;76(8):602-608.
104. Borrelli MJ, Bailey KI, Dunn F. Early ultrasonic effects upon mammalian CNS structures (chemical synapses). J Acoust Soc Am. 1981;69(5):1514-1516.
105. Norton S, Kimler BF, Cytacki EP, Rosenthal SJ. Prenatal and postnatal consequences in the brain and behavior of rats exposed to ultrasound in utero. J Ultrasound Med. 1991;10(2):69-75.
106. Devi PU, Suresh R, Hande MP. Effect of fetal exposure to ultrasound on the behavior of the adult mouse. Radiat Res. 1995;141(3):314-317.
107. Hande MP, Devi PU, Karanth KS. Effect of prenatal ultrasound exposure on adult behavior in mice. Neurotoxicol Teratol. 1993;15(6):433-438.
108. Schneider-Kolsky ME, Ayobi Z, Lombardo P, et al. Ultrasound exposure of the foetal chick brain: effects on learning and memory. Int J Dev Neurosci. 2009;27(7):677-683.
109. Milunsky A, Ulcickas M, Rothman KJ, et al. Maternal heat exposure and neural tube defects. JAMA. 1992;268(7):882-885.
110. Ang Jr ES, Gluncic V, Duque A, et al. Prenatal exposure to ultrasound waves impacts neuronal migration in mice. Proc Natl Acad Sci USA. 2006;103(34):12903-12910.
111. Abramowicz JS. Prenatal exposure to ultrasound waves: is there a risk? Ultrasound Obstet Gynecol. 2007;29(4):363-367.
112. Kieler H. Epidemiological studies on adverse effects of prenatal ultrasound—which are the challenges? Prog Biophys Mol Biol. 2007;93(1-3):301-308.
113. Newman PG. Studies of ultrasound safety in humans: clinical benefit vs. risk. In: Barnett SB, Kossoff G, editors. Safety of diagnostic ultrasound. New York: Parthenon; 1998.
114. Salvesen KA. Epidemiological prenatal ultrasound studies. Prog Biophys Mol Biol. 2007;93(1-3):295-300.
115. Ziskin MC, Petitti DB. Epidemiology of human exposure to ultrasound: a critical review. Ultrasound Med Biol. 1988;14(2):91-96.
116. Edmonds PD, Abramowicz JS, Carson PL, et al. Guidelines for Journal of Ultrasound in Medicine authors and reviewers on measurement and reporting of acoustic output and exposure. J Ultrasound Med. 2005;24:1171-1179.
117. Carvalho JS. Fetal heart scanning in the first trimester. Prenat Diagn. 2004;24(13):1060-1067.
118. Makikallio K, Jouppila P, Rasanen J. Human fetal cardiac function during the first trimester of pregnancy. Heart. 2005;91(3):334-338.
119. Becker R, Wegner RD. Detailed screening for fetal anomalies and cardiac defects at the 11-13-week scan. Ultrasound Obstet Gynecol. 2006;27(6):613-618.
120. Vinals F, Ascenzo R, Naveas R, et al. Fetal echocardiography at 11 + 0 to 13 + 6 weeks using four-dimensional spatiotemporal image correlation telemedicine via an Internet link: a pilot study. Ultrasound Obstet Gynecol. 2008;31(6):633-638.
121. Ziskin MC. Survey of patients exposed to diagnostic ultrasound. In: Reid JM, Sikov MR, editors. Interactions of ultrasound and biological tissues.

Proceedings of a workshop, Battelle Seattle Research Center, Seattle, 1971. Rockville, Md: Bureau of Radiological Health, U.S. Department of Health, Education and Welfare; 1973. pp. 203-206.
122. Newnham JP, Evans SF, Michael CA, et al. Effects of frequent ultrasound during pregnancy: a randomised controlled trial. Lancet. 1993;342(8876): 887-891.
123. Campbell JD, Elford RW, Brant RF. Case-control study of prenatal ultrasonography exposure in children with delayed speech. CMAJ. 1993;149(10): 1435-1440.
124. Kieler H, Haglund B, Waldenstrom U, Axelsson O. Routine ultrasound screening in pregnancy and the children's subsequent growth, vision and hearing. Br J Obstet Gynaecol. 1997;104(11):1267-1272.
125. Stark CR, Orleans M, Haverkamp AD, Murphy J. Short- and long-term risks after exposure to diagnostic ultrasound in utero. Obstet Gynecol. 1984;63(2):194-200.
126. Bricker L, Neilson JP, Dowswell T. Routine ultrasound in late pregnancy (after 24 weeks' gestation). Cochrane Database Syst Rev. 2008;(4): CD001451.
127. Kieler H, Haglund B, Cnattingius S, et al. Does prenatal sonography affect intellectual performance? Epidemiology. 2005;16(3):304-310.
128. Cartwright RA, McKinney PA, Hopton PA, et al. Ultrasound examinations in pregnancy and childhood cancer. Lancet. 1984;2(8410):999-1000.
129. Kieler H, Axelsson O, Haglund B, et al. Routine ultrasound screening in pregnancy and the children's subsequent handedness. Early Hum Dev. 1998;50(2):233-245.
130. Salvesen KA. Ultrasound and left-handedness: a sinister association? Ultrasound Obstet Gynecol. 2002;19(3):217-221.
131. Sheiner E, Freeman J, Abramowicz JS. Acoustic output as measured by mechanical and thermal indices during routine obstetric ultrasound examinations. J Ultrasound Med. 2005;24(12):1665-1670.
132. Sheiner E, Shoham-Vardi I, Pombar X, et al. An increased thermal index can be achieved when performing Doppler studies in obstetric sonography. J Ultrasound Med. 2007;26(1):71-76.
133. Sheiner E, Abramowicz JS. Acoustic output as measured by thermal and mechanical indices during fetal nuchal translucency ultrasound examinations. Fetal Diagn Ther. 2009;25(1):8-10.
134. Sheiner E, Hackmon R, Shoham-Vardi I, et al. A comparison between acoustic output indices in 2D and 3D/4D ultrasound in obstetrics. Ultrasound Obstet Gynecol. 2007;29(3):326-328.
135. Bellieni CV, Buonocore G, Bagnoli F, et al. Is an excessive number of prenatal echographies a risk for fetal growth? Early Hum Dev. 2005;81(8): 689-693.
136. Newnham JP, Doherty DA, Kendall GE, et al. Effects of repeated prenatal ultrasound examinations on childhood outcome up to 8 years of age: follow-up of a randomised controlled trial. Lancet. 2004;364(9450): 2038-2044.
137. Moore Jr RM, Barrick MK, Hamilton TM. Effect of sonic radiation on growth and development. Am J Epidemiol. 1982;116:571.
138. Moore Jr RM, Diamond EL, Cavalieri RL. The relationship of birth weight and intrauterine diagnostic ultrasound exposure. Obstet Gynecol. 1988;71(4): 513-517.
139. Lyons EA, Dyke C, Toms M, Cheang M. In utero exposure to diagnostic ultrasound: a 6-year follow-up. Radiology. 1988;166(3):687-690.
140. Saari-Kemppainen A, Karjalainen O, Ylostalo P, Heinonen OP. Ultrasound screening and perinatal mortality: controlled trial of systematic one-stage screening in pregnancy. The Helsinki Ultrasound Trial. Lancet. 1990; 336(8712):387-391.
141. Waldenstrom U, Axelsson O, Nilsson S, et al. Effects of routine one-stage ultrasound screening in pregnancy: a randomised controlled trial. Lancet. 1988;2(8611):585-588.
142. Salvesen KA, Vatten LJ, Bakketeig LS, Eik-Nes SH. Routine ultrasonography in utero and speech development. Ultrasound Obstet Gynecol. 1994;4(2): 101-103.
143. Bakketeig LS, Eik-Nes SH, Jacobsen G, et al. Randomised controlled trial of ultrasonographic screening in pregnancy. Lancet. 1984;2(8396): 207-211.
144. Eik-Nes SH, Okland O, Aure JC, Ulstein M. Ultrasound screening in pregnancy: a randomised controlled trial. Lancet. 1984;1(8390):1347.
145. Salvesen KA, Bakketeig LS, Eik-nes SH, et al. Routine ultrasonography in utero and school performance at age 8-9 years. Lancet. 1992;339(8785): 85-89.
146. Salvesen KA, Vatten LJ, Eik-Nes SH, et al. Routine ultrasonography in utero and subsequent handedness and neurological development. BMJ. 1993;307(6897):159-164.
147. Salvesen KA, Vatten LJ, Jacobsen G, et al. Routine ultrasonography in utero and subsequent vision and hearing at primary school age. Ultrasound Obstet Gynecol. 1992;2(4):243-244, 245-247.
148. Salvesen KA, Eik-Ness SH, Vatten LJ, et al. Routine ultrasound scanning in pregnancy [authors' reply]. BMJ. 1993;307:1562.
149. Reissland N, Aydin E, Francis B, Exley K. Laterality of foetal self-touch in relation to maternal stress. Laterality. 2015;20(1):82-94.
150. Hepper PG. The developmental origins of laterality: fetal handedness. Dev Psychobiol. 2013;55(6):588-595.
151. Sidman RL, Rakic P. Neuronal migration, with special reference to developing human brain: a review. Brain Res. 1973;62(1):1-35.
152. Mole R. Possible hazards of imaging and Doppler ultrasound in obstetrics. Birth. 1986;13:Suppl:23-33 suppl.
153. Scheidt PC, Stanley F, Bryla DA. One-year follow-up of infants exposed to ultrasound in utero. Am J Obstet Gynecol. 1978;131(7): 743-748.
154. Salvesen K. Routine ultrasonography in utero and development in childhood. In: Tejani N, editor. Obstetrical events and developmental sequelae. 2nd ed. Boca Raton, Fla: CRC Press; 1994.
155. Stalberg K. Prenatal ultrasound and x-ray-potentially adverse effects on the CNS. Upsalla, Sweden: Upsalla Universitet; 2008.
156. Coyle I, Wayner MJ, Singer G. Behavioral teratogenesis: a critical evaluation. Pharmacol Biochem Behav. 1976;4(2):191-200.
157. McClintic AM, King BH, Webb SJ, Mourad PD. Mice exposed to diagnostic ultrasound in utero are less social and more active in social situations relative to controls. Autism Res. 2014;7(3):295-304.
158. Stalberg K, Haglund B, Axelsson O, et al. Prenatal ultrasound scanning and the risk of schizophrenia and other psychoses. Epidemiology. 2007;18(5):577-582.
159. Abramowicz JS. Ultrasound and autism: association, link, or coincidence? J Ultrasound Med. 2012;31(8):1261-1269.
160. Shu XO, Potter JD, Linet MS, et al. Diagnostic X-rays and ultrasound exposure and risk of childhood acute lymphoblastic leukemia by immunophenotype. Cancer Epidemiol Biomarkers Prev. 2002;11(2):177-185.
161. Naumburg E, Bellocco R, Cnattingius S, et al. Prenatal ultrasound examinations and risk of childhood leukaemia: case-control study. BMJ. 2000;320(7230):282-283.
162. Kinnier Wilson LM, Waterhouse JA. Obstetric ultrasound and childhood malignancies. Lancet. 1984;2(8410):997-999.
163. Bunin GR, Buckley JD, Boesel CP, et al. Risk factors for astrocytic glioma and primitive neuroectodermal tumor of the brain in young children: a report from the Children's Cancer Group. Cancer Epidemiol Biomarkers Prev. 1994;3(3):197-204.
164. Sorahan T, Lancashire R, Stewart A, Peck I. Pregnancy ultrasound and childhood cancer: a second report from the Oxford Survey of Childhood Cancers. Br J Obstet Gynaecol. 1995;102(10):831-832.
165. Salvesen KA, Eik-Nes SH. Ultrasound during pregnancy and birthweight, childhood malignancies and neurological development. Ultrasound Med Biol. 1999;25(7):1025-1031.
166. Stalberg K, Haglund B, Axelsson O, et al. Prenatal ultrasound and the risk of childhood brain tumour and its subtypes. Br J Cancer. 2008;98(7): 1285-1287.
167. Sande RK, Matre K, Eide GE, Kiserud T. Ultrasound safety in early pregnancy: reduced energy setting does not compromise obstetric Doppler measurements. Ultrasound Obstet Gynecol. 2012;39(4):438-443.
168. Sande RK, Matre K, Eide GE, Kiserud T. The effects of reducing the thermal index for bone from 1.0 to 0.5 and 0.1 on common obstetric pulsed wave Doppler measurements in the second half of pregnancy. Acta Obstet Gynecol Scand. 2013;92(7):790-796.
169. ter Haar GR, Abramowicz JS, Akiyama I, et al. Do we need to restrict the use of Doppler ultrasound in the first trimester of pregnancy? Ultrasound Med Biol. 2013;39(3):374-380.

170. Kossoff G, Griffiths KA, Garrett WJ, et al. Thickness of tissues intervening between the transducer and fetus and models for fetal exposure calculations in transvaginal sonography. Ultrasound Med Biol. 1993;19(1):59-65.
171. Sheiner E, Shoham-Vardi I, Abramowicz JS. What do clinical users know regarding safety of ultrasound during pregnancy? J Ultrasound Med. 2007;26(3):319-325.
172. Marsal K. The output display standard: has it missed its target? Ultrasound Obstet Gynecol. 2005;25(3):211-214.
173. Piscaglia F, Tewelde AG, Righini R, et al. Knowledge of the bio-effects of ultrasound among physicians performing clinical ultrasonography: results of a survey conducted by the Italian Society for Ultrasound in Medicine and Biology (SIUMB). J Ultrasound. 2009;12:6-11.
174. Akhtar W, Arain MA, Ali A, et al. Ultrasound biosafety during pregnancy: what do operators know in the developing world? National survey findings from Pakistan. J Ultrasound Med. 2011;30(7):981-985.
175. Houston LE, Allsworth J, Macones GA. Ultrasound is safe… right? Resident and maternal-fetal medicine fellow knowledge regarding obstetric ultrasound safety. J Ultrasound Med. 2011;30(1):21-27.
176. Bagley J, Thomas K, DiGiacinto D. Safety practices of sonographers and their knowledge of the biologic effects of sonography. J Diag Med Sonography. 2011;27:252-261.
177. Bromley B, Spitz J, Fuchs K, Thornburg LL. Do clinical practitioners seeking credentialing for nuchal translucency measurement demonstrate compliance with biosafety recommendations? Experience of the Nuchal Translucency Quality Review Program. J Ultrasound Med. 2014;33(7):1209-1214.
178. British Medical Ultrasound Society (BMUS) Safety Group. Guidelines for the safe use of diagnostic ultrasound equipment. Ultrasound. 2010;18: 52-59.
179. Lees C, Abramowicz JS, Brezinka C, et al. Ultrasound from conception to 10+0 weeks of gestation. London: Royal College of Obstetricians and Gynaecologists; 2015. Scientific Impact Paper No. 49.
180. Abramowicz JS. Ultrasound in the first trimester and earlier: how to keep it safe. In: Abramowicz JS, editor. First trimester ultrasound: a comprehensive guide. Cham. Switzerland: Springer; 2015. p. 1-19.
181. Abramowicz JS. Fetal Doppler: how to keep it safe? Clin Obstet Gynecol. 2010;53(4):842-850.
182. American Institute of Ultrasound in Medicine. AIUM official statement: Prudent use in pregnancy. 2012. Available from: http://www.aium.org/officialStatements/33. Accessed 26 December 2015.
183. American Institute of Ultrasound in Medicine. AIUM official statement: Keepsake fetal imaging. 2012. Available from: http://www.aium.org/officialStatements/31. Accessed 26 December 2015.
184. American Institute of Ultrasound in Medicine. AIUM official statement: As low as reasonably achievable (ALARA) principle. 2014. Available from: http://www.aium.org/officialStatements/39. Accessed 26 December 2015.
185. American Institute of Ultrasound in Medicine. AIUM Statement on mammalian biological effects of heat. 2015. Available from: http://www.aium.org/officialStatements/17. Accessed 26 December 2015.
186. British Medical Ultrasound Society. BMUS Statement on the safe use and potential hazards of diagnostic ultrasound. 2000, reconfirmed 2012. Available from: https://www.bmus.org/static/uploads/resources/statement_on_the_safe_use_and_potential_hazards_of_diagnostic_ultrasound.pdf. Accessed 26 December 2015.
187. BMUS. Guidelines for the safe use of diagnostic ultrasound equipment. Ultrasound. 2010;18:52-59.
188. British Medical Ultrasound Society Safety Group. BMUS Statement for the general public on the safety of medical ultrasound imaging. 2012. Available from: https://www.bmus.org/static/uploads/resources/Statement_for_the_General_Public_on_the_Safety_of_Medical_Ultrasound_Imaging.pdf. Accessed 26 December 2015.
189. European Committee for Medical Ultrasound Safety of the European Federation of Societies for Ultrasound in Medicine and Biology. ECMUS Statement on the use of diagnostic ultrasound for producing souvenir images or recordings in pregnancy. 2012. Available from: https://www.bmus.org/static/uploads/resources/ECMUS_Souvenir_Scanning.pdf. Accessed 26 December 2015.
190. European Committee for Medical Ultrasound Safety of the European Federation of Societies for Ultrasound in Medicine and Biology. ECMUS Guidelines for the safe use of Doppler ultrasound for clinical application. 2013. Available from: http://www.efsumb-portal.org/ep/article.php?id=50. Accessed 26 December 2015.
191. International Society for Ultrasound in Obstetrics and Gynecology. ISUOG safety statements, 2000-2015. Available from: http://www.isuog.org/StandardsAndGuidelines/Statements+and+Guidelines/Safety+Statements/. Accessed 26 December 2015.
192. World Federation of Ultrasound in Medicine and Biology. WFUMB/ISUOG Statement on the safe use of Doppler ultrasound during 11-14 week scans (or earlier in pregnancy). 2011, reaffirmed 2015. Available from: http://www.wfumb.org/safety-statements/. Accessed 26 December 2015.
193. World Federation for Ultrasound in Medicine and Biology. WFUMB Symposium on Safety and Standardisation in Medical Ultrasound. Issues and recommendations regarding thermal mechanisms for biological effects of ultrasound. Hornbaek, Denmark, 30 August-1 September 1991. Ultrasound Med Biol. 1992;18(9):731-810.
194. Barnett SB. WFUMB Symposium on Safety of Ultrasound in Medicine. Conclusions and recommendations on thermal and non-thermal mechanisms for biological effects of ultrasound. Kloster-Banz, Germany, 14-19 April 1996. World Federation for Ultrasound in Medicine and Biology. Ultrasound Med Biol. 1998;24(Suppl. 1):i-xvi, S1-S58.
195. Health Canada. Guidelines for the safe use of diagnostic ultrasound: Canada Minister of Public Works and Government Services; 2001.
196. Abramowicz JS, Kossoff G, Marsal K, Ter Haar G. Safety statement, 2000 (reconfirmed 2003). International Society of Ultrasound in Obstetrics and Gynecology (ISUOG). Ultrasound Obstet Gynecol. 2003;21(1):100.
197. Barnett SB, Ter Haar GR, Ziskin MC, et al. International recommendations and guidelines for the safe use of diagnostic ultrasound in medicine. Ultrasound Med Biol. 2000;26(3):355-366.

CHAPTER 30

The First Trimester

Elizabeth Lazarus and Deborah Levine

SUMMARY OF KEY POINTS

- First-trimester development follows a predictable pattern on first-trimester ultrasound.
- Some ultrasound findings are definitive for early pregnancy failure, whereas others are suggestive and require follow-up.
- Ultrasound is vital in the diagnosis of ectopic pregnancy in typical and atypical locations.
- Gestational trophoblastic disease is composed of four entities, and ultrasound is helpful in their diagnosis and management.

CHAPTER OUTLINE

MATERNAL PHYSIOLOGY AND EMBRYOLOGY
SONOGRAPHIC APPEARANCE OF NORMAL INTRAUTERINE PREGNANCY
Gestational Sac
β-hCG and Early Pregnancy Ultrasound
Yolk Sac
Embryo and Amnion
Embryonic Cardiac Activity
Umbilical Cord and Cord Cyst
ESTIMATION OF GESTATIONAL AGE
Gestational Sac Size
Crown-Rump Length
EARLY PREGNANCY FAILURE
Diagnostic Findings of Early Pregnancy Failure
Crown-Rump Length 7 mm or Greater and No Heartbeat
Gestational Sac Mean Sac Diameter 25 mm or Greater and No Embryo
Worrisome Findings of Early Pregnancy Failure
Embryos With Crown-Rump Length Less Than 7 mm and No Heartbeat
Gestational Sac With Mean Sac Diameter 16 to 24 mm and No Embryo
Gestational Sac Appearance
Small Mean Sac Diameter in Relationship to Crown-Rump Length
Abnormally Large Amnion With Respect to Embryo Size
Yolk Sac Size and Shape
Embryonic Bradycardia
Subchorionic Hemorrhage
ECTOPIC PREGNANCY
Clinical Presentation
Sonographic Diagnosis
Heterotopic Gestation
Serum β-hCG Levels
Specific Sonographic Findings
Nonspecific Sonographic Findings
Adnexal Mass
Free Fluid
Endometrium
Implantation Sites
Pregnancy of Unknown Location
Management
EVALUATION OF THE EMBRYO
Normal Embryologic Findings
Mimicking Pathology
Rhombencephalon
Physiologic Anterior Abdominal Wall Herniation
Abnormal Embryos
GESTATIONAL TROPHOBLASTIC DISEASE
Hydatidiform Molar Pregnancy
Complete Molar Pregnancy
Partial Molar Pregnancy
Coexistent Hydatidiform Mole and Normal Fetus
Persistent Trophoblastic Neoplasia
Invasive Mole
Choriocarcinoma
Placental-Site Trophoblastic Tumor
Sonographic Features of Persistent Trophoblastic Neoplasia
Diagnosis and Treatment
CONCLUSION

The first trimester of pregnancy is a period of rapid change that spans fertilization, formation of the blastocyst, implantation, gastrulation, neurulation, the embryonic period (weeks 6-10), and early fetal life.[1] First-trimester sonographic diagnosis traditionally focused on evaluation of growth by serial examination to differentiate normal from abnormal gestations. This has changed since the advent of transvaginal sonography (TVS), which affords enhanced resolution over transabdominal sonography (TAS), with earlier visualization of the gestational sac and its contents,[2] earlier identification of embryonic cardiac activity,[3] and improved visualization of embryonic and fetal structures.

Despite these technologic improvements, it is important to set clinically relevant and realistic goals for first-trimester sonographic diagnosis. Most examinations are requested because the patient has vaginal bleeding or pain, or a palpable mass has been identified on physical examination. Ultrasound in the first trimester is often requested to diagnose early pregnancy failure or an ectopic pregnancy.

The goals of first-trimester sonography include (1) visualization and localization of the gestational sac (intrauterine or ectopic pregnancy) and (2) early identification of embryonic demise and other forms of nonviable gestation. It also seeks to identify those pregnancies that are at increased risk for early pregnancy failure. First-trimester ultrasound accurately dates the duration or menstrual/gestational age of the pregnancy and assists in early diagnosis of fetal abnormalities, including identification of embryos more likely to be abnormal, based on secondary criteria (e.g., abnormal yolk sac). In multifetal pregnancies, first-trimester ultrasound can be used to determine the number of embryos and the chorionicity and amnionicity.

Current trends in ultrasound late in the first trimester focus on **nuchal translucency** screening combined with maternal age and maternal serum screening to determine the risk of chromosomal abnormalities and structural anomalies. Associated with the increased emphasis on late first-trimester ultrasound and first-trimester screening, there is an opportunity to visualize fetal anomalies earlier than at the time of the standard 18- to 20-week scan. First-trimester diagnosis of specific anomalies is discussed in the chapters covering those organ systems.

As experience with early first-trimester ultrasound evolves, reliable sonographic indicators of ectopic pregnancy and embryonic demise have been established.[4-6] The accuracy of some sonographic signs used as indicators of the presence of a live embryo or of embryonic demise depends on the use of modern, high-resolution ultrasound equipment and the operator's expertise. Published values in the literature based on data using high-frequency transducers cannot be applied to lower-resolution 5.0-MHz transducers.[7,8] The TVS signs listed in this chapter assume the use of modern equipment with a transducer frequency of at least 7 to 8 MHz, with meticulous scanning technique. Transducers with frequencies of 10 MHz or higher can provide improved spatial resolution, identifying abnormal and normal features at even earlier points in pregnancy.[9] Nyberg and Filly[6] emphasize that experienced physicians who interpret ultrasound rarely rely on a single parameter and simultaneously consider multiple variables to create a diagnostic impression.

MATERNAL PHYSIOLOGY AND EMBRYOLOGY

All dates presented in this chapter are in **menstrual age** or **gestational age,** in keeping with the radiologic and obstetric literature, rather than in embryologic age, as used by embryologists. This can be counted as follows:

$$\text{Gestational age} = \text{Conceptual age} + 2 \text{ weeks}$$

Early in the menstrual cycle, the pituitary secretes rising levels of follicle-stimulating hormone (FSH) and luteinizing hormone (LH), which cause the growth of 4 to 12 primordial follicles into **primary ovarian follicles**[10] (Fig. 30.1). When a fluid-filled cavity or antrum forms in the follicle, it is referred to as a **secondary follicle.** The primary oocyte is off to one side of the follicle and surrounded by follicular cells or the **cumulus oophorus.** One follicle becomes dominant, bulges on the surface of the ovary, and becomes a "mature follicle" or **graafian follicle.** It continues to enlarge until ovulation, with the remainder of the follicles becoming atretic. The developing follicles produce estrogen. The estrogen level remains relatively low until 4 days before ovulation, when the dominant or active follicle produces an estrogen surge, after which an LH and prostaglandin surge results in ovulation. Ovulation follows the LH peak within 12 to 24 hours. Actual expulsion of the oocyte from the mature follicle is aided by several factors, including the intrafollicular pressure, possibly contraction of the smooth muscle in the **theca externa** stimulated by prostaglandins, and enzymatic digestion of the follicular wall.[11]

Ovulation occurs on approximately day 14 of the menstrual cycle with expulsion of the secondary oocyte from the surface of the ovary. In women with a menstrual cycle longer than 28 days, this ovulation occurs later, so that the secretory phase of the menstrual cycle remains at about 14 days. After ovulation, the follicle collapses to form the **corpus luteum,** which secretes progesterone and, to a lesser degree, estrogen. If a pregnancy does not occur, the corpus luteum involutes. In pregnancy, involution of the corpus luteum is prevented by **human chorionic gonadotropin** (hCG), which is produced by the outer layer of cells of the gestational or chorionic sac **(syncytiotrophoblast).**

Before ovulation, **endometrial proliferation** occurs in response to estrogen secretion (Fig. 30.1). After ovulation, the endometrium becomes thickened, soft, and edematous under the influence of progesterone.[12] The glandular epithelium secretes a glycogen-rich fluid. If pregnancy occurs, continued production of progesterone results in more marked hypertrophic changes in the endometrial cells and glands to provide nourishment to the **blastocyst.** These hypertrophic changes are referred to as the **decidual reaction** and occur as a hormonal response regardless of the site of implantation, intrauterine or ectopic.

Oocyte transport into the fimbriated end of the fallopian tube occurs at ovulation as the secondary oocyte is expelled with the follicular fluid and is "picked up" by the fimbria. The sweeping movement of the fimbria, the currents produced by the action of the cilia of the mucosal cells, and the gentle peristaltic waves from contractions of the fallopian musculature all draw the oocyte into the tube.[13]

The mechanism of **sperm transport** is regulated to maximize the chance of fertilization and ensure the most rigorous sperm will be available.[14] From 200 to 600 million sperm and the ejaculate fluid are deposited in the vaginal fornix during intercourse. Sperm must move through the cervical canal and its mucous plug, up the endometrial cavity, and down the fallopian tube to meet the awaiting oocyte within the distal third or ampullary portion of the fallopian tube. Sperm were thought to move primarily using their tails, although they travel at 2 to 3 mm per minute, which would take about 50 minutes to travel the 20 cm to their destination. Settlage et al.[13] found motile sperm within the ampulla between 5 and 10 minutes after deposition near the external cervical os. If inert particles such as radioactive macroaggregates or carbon particles are placed near the external os, they too will be picked up and transported up the uterus and down the tubes. Contractions of the inner layer of myometrium are believed to create a negative pressure strong enough to suck up particles and move them up the endometrial canal. These contractions

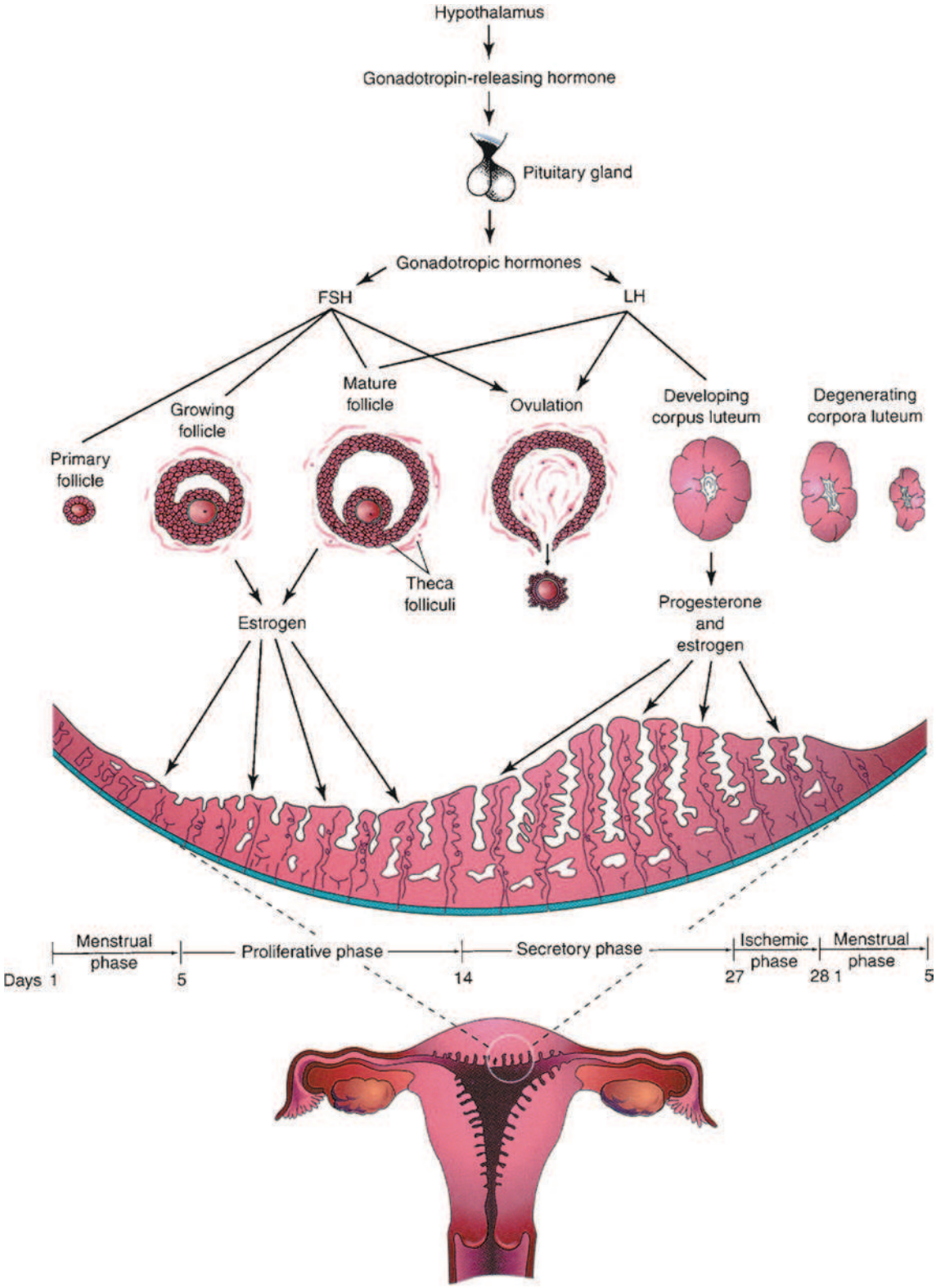

FIG. 30.1 Schematic Drawing of Interrelationships Among the Hypothalamus, Pituitary Gland, Ovaries, and Endometrial Lining. *FSH,* Follicle-stimulating hormone; *LH,* luteinizing hormone. (With permission from Moore KL. The developing human: clinically oriented embryology. 10th ed. Philadelphia: Elsevier; 2016.[1])

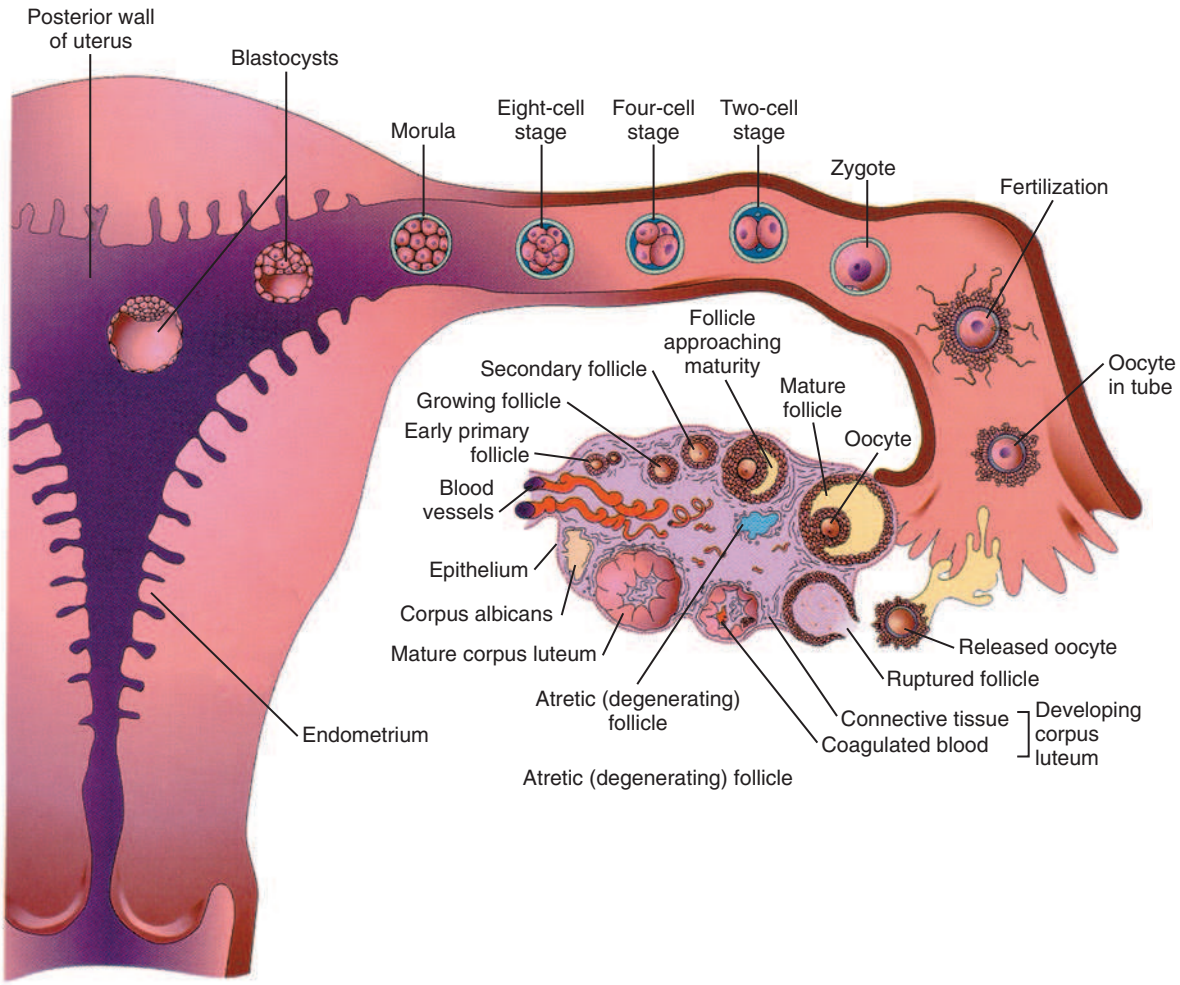

FIG. 30.2 Diagram of Ovarian Cycle, Fertilization, and Human Development to the Blastocyst Stage. (With permission from Moore KL. The developing human: clinically oriented embryology. 10th ed. Philadelphia: Elsevier; 2016.[1])

have been demonstrated in nonpregnant women and increase in strength and frequency to peak at 3.5 contractions per minute at ovulation.[15]

Fertilization occurs on or about day 14 as the mature ovum and sperm unite to form the **zygote** in the outer third of the fallopian tube (Fig. 30.2). Cellular division of the zygote occurs during transit through the fallopian tube. By the time the conceptus enters the uterus, about day 17, it is at the 12- to 15-cell stage **(morula).** By day 20, the conceptus has matured to the **blastocyst stage.** The blastocyst is a fluid-filled cyst lined with trophoblastic cells that contain a cluster of cells at one side called the **inner cell mass.** On day 20, the blastocyst at the site of the inner cell mass burrows through the endometrial membrane into the hyperplastic endometrium, and implantation begins[16] (Fig. 30.3A).

Implantation is completed by day 23 as the endometrial membrane re-forms over the blastocyst (Fig. 30.3B). During implantation, the **amniotic cavity** forms in the inner cell mass. A bilaminar embryonic disk separates the amniotic cavity from the exocoelomic cavity. The **primary (primitive) yolk sac** forms at about 23 days of gestational age as the blastocyst cavity becomes lined by the exocoelomic membrane and hypoblast. As the extraembryonic coelom forms, the primary yolk sac is pinched off and extruded, resulting in the formation of the **secondary yolk sac** (Fig. 30.4). Standard embryology texts indicate that the secondary yolk sac forms at approximately 27 to 28 days of menstrual age, when the mean diameter of the gestational sac is approximately 3 mm. It is the secondary yolk sac, rather than the primary yolk sac, that is visible with ultrasound. For the remainder of this chapter, the term **yolk sac** is used to refer to the *secondary* yolk sac. The extraembryonic coelom becomes the **chorionic cavity.**

Later, because of differential growth, the yolk sac comes to lie between the amnion and chorion. During week 4, there is rapid proliferation and differentiation of the **syncytiotrophoblast,** forming primary **chorionic villi.** Traditional thinking that the syncytiotrophoblastic cells invade the maternal endometrial vessels, leaving maternal blood to bathe the trophoblastic ring, has been challenged. Hustin[16] compared TVS to hysteroscopy of the placenta, chorionic villous sampling tissue, and

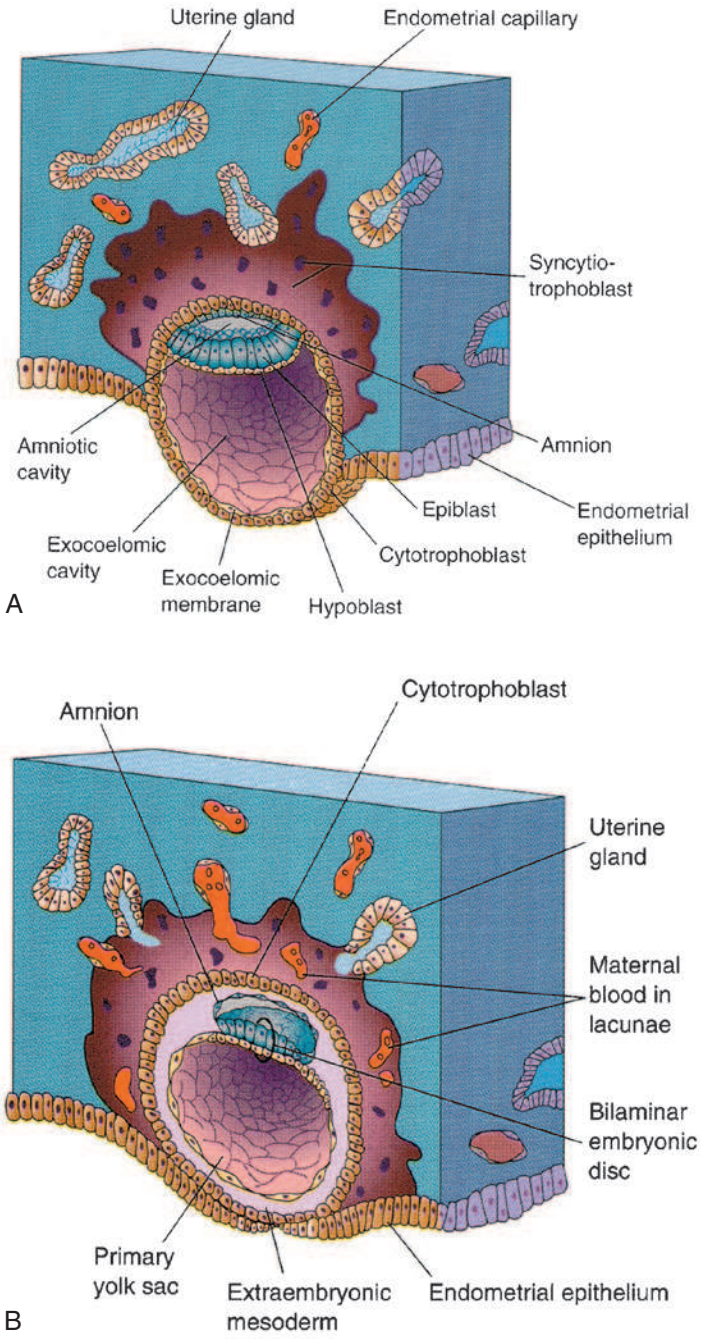

FIG. 30.3 Implantation of the Blastocyst Into Endometrium. Entire conceptus is approximately 0.1 mm at this stage. **(A)** Partially implanted blastocyst at approximately 22 days. **(B)** Almost completely implanted blastocyst at about 23 days. (With permission from Moore KL. The developing human: clinically oriented embryology. 10th ed. Philadelphia: Elsevier; 2016.[1])

hysterectomy specimens with an early pregnancy in situ. Before 12 weeks, the intervillous space contains no blood, only clear fluid, and on histologic examination, the villous tissue is separated from the maternal circulation by a continuous layer of trophoblastic cells. Only after the third month does the trophoblastic shell become broken and the maternal circulation become continuous with the intervillous space. Furthermore, at weeks 8 and 9 of gestation, the trophoblastic shell forms plugs within the spiral arteries, allowing only filtered plasma to permeate the placenta.[17] In two-thirds of abnormal pregnancies, the trophoblastic shell is thinner and fragmented, and the trophoblastic invasion of the spiral arteries is reduced or absent.[18]

Vascularization of the placenta occurs at the beginning of the fifth week. Oh et al.[19] showed significant increases in sac size from 5 weeks onward in normal **intrauterine pregnancy** (IUP) versus pregnancy failure. The rationale for placental vascularization was based on early work by Folkman,[20] who showed that tumors can grow to a size of 3 mm being nourished only by diffusion. To exceed this size, cells must recruit host blood vessels, or the cells at the center will receive inadequate nutrition.

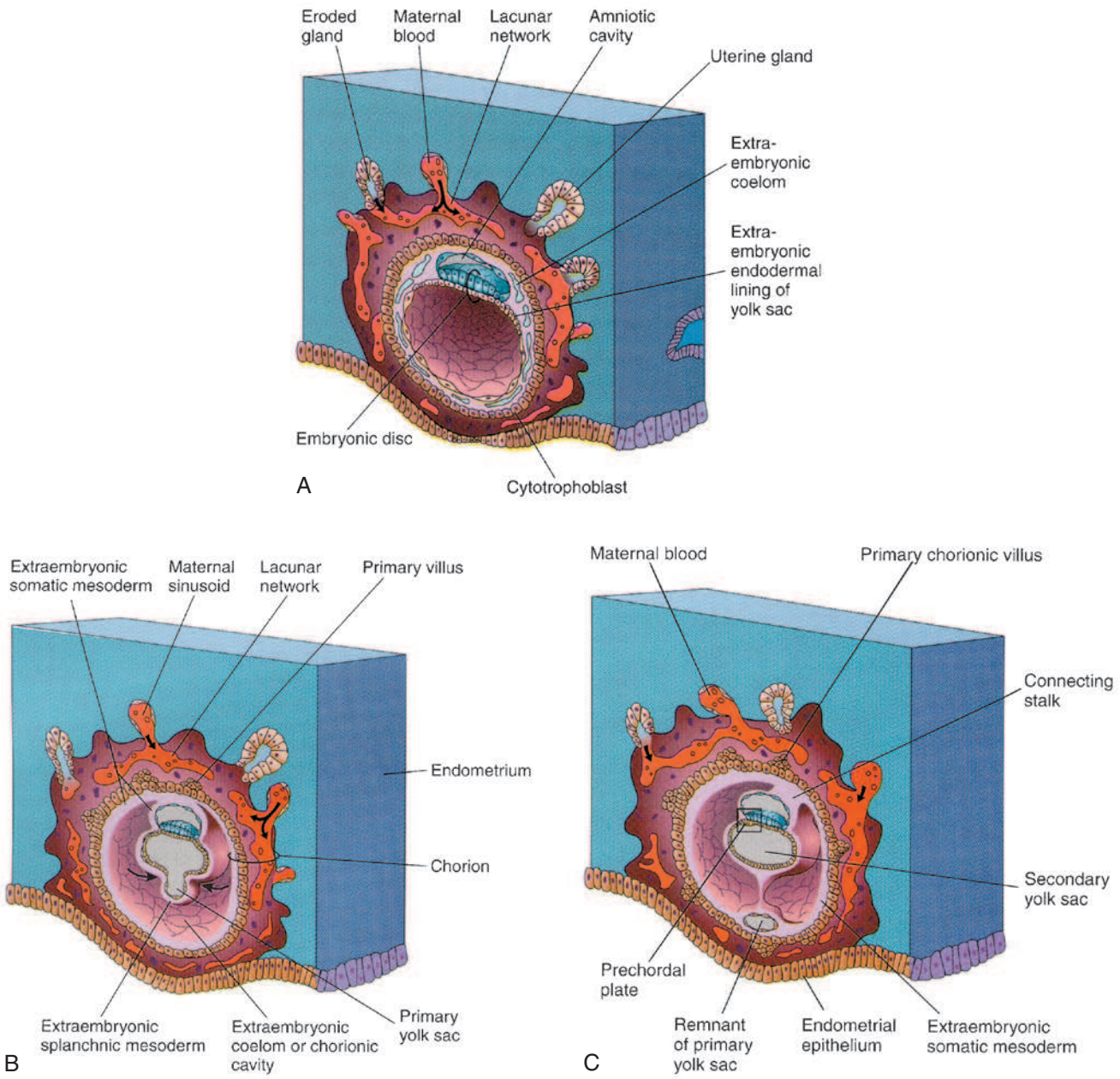

FIG. 30.4 Formation of Secondary Yolk Sac. (A) Approximately 26 days: formation of cavities within extraembryonic mesoderm. These cavities will enlarge to form extraembryonic coelom. **(B)** About 27 days and **(C)** 28 days: formation of secondary yolk sac with extrusion of primary yolk sac. Extraembryonic coelom will become chorionic cavity. (With permission from Moore KL. The developing human: clinically oriented embryology. 10th ed. Philadelphia: Elsevier; 2016.[1])

Similarly, the rapidly growing embryonic implantation must be vascularized by the 3-mm stage that occurs at 5 weeks' gestation.

During the fifth week, the embryo is converted by the process of **gastrulation** from a bilaminar disk to a trilaminar disk with the three primary germ cell layers: ectoderm, mesoderm, and endoderm. During gastrulation, the primitive streak and notochord form. The primitive streak gives rise to the **mesenchyme,** which forms the connective tissue of the embryo and stromal components of all glands.

The formation of the neural plate and its closure to form the neural tube is referred to as **neurulation.** This process begins in the fifth week in the thoracic region and extends caudally and cranially, resulting in complete closure by the end of the sixth week (day 42). Failure of closure of the neural tube results in neural tube defects.

During the fifth week, two cardiac tubes (the primitive heart) develop from splanchnic mesodermal cells. By the end of the fifth week, these tubes begin to pump into a primitive paired vascular system. By the end of the fifth week, a vascular network develops in the chorionic villi that connect through the umbilical arteries and vein to the primitive embryonic vascular network.

Essentially all internal and external structures appear in the adult form during the **embryonic period,** which ends at 10

menstrual weeks. By the end of the sixth week, blood flow is unidirectional, and by the end of the eighth week, the heart attains its definitive form. The peripheral vascular system develops slightly later and is completed by the end of the tenth week. The primitive gut forms during week 6. The midgut herniates into the umbilical cord from week 8 through the end of week 12. The rectum separates from the urogenital sinus by the end of week 8, and the anal membrane perforates by the end of week 10. The **metanephros,** or primitive kidneys, ascend from the pelvis, starting at approximately week 8, but do not reach their adult position until week 11. Limbs are formed with separate fingers and toes. Almost all congenital malformations except abnormalities of the genitalia originate before or during the embryonic period. External genitalia are still in a sexless state at the end of week 10 and do not reach mature fetal form until the end of week 14.

Early in the **fetal period,** body growth is rapid and head growth relatively slower, with the **crown-rump length (CRL)** doubling between weeks 11 and 14.

SONOGRAPHIC APPEARANCE OF NORMAL INTRAUTERINE PREGNANCY

Gestational Sac

Implantation usually occurs in the fundal region of the uterus between day 20 and day 23.[21] In a study of early implantation sites in 21 patients, it was found that implantation occurs most frequently on the uterine wall ipsilateral to the ovulating ovary and least often on the contralateral wall.[21] In addition, in a study of predominant sleeping positions in the peri-implantation period, Magann et al.[22] found that the 33% of women who slept prone were most likely to have a high or fundal implantation than those who slept on their back or side. The latter groups predominantly had implantations corresponding to their resting posture.

At 23 days, the entire conceptus measures approximately 0.1 mm in diameter and cannot be imaged by TAS or TVS techniques. The earliest sonographic sign of an IUP was described by Yeh et al.,[23] who identified a focal echogenic zone of decidual thickening at the site of implantation at about 3½ to 4 weeks of gestational age. This sign is nonspecific and of limited diagnostic value.

The first reliable gray-scale evidence of an IUP is visualization of a small (1-2 mm fluid collection surrounded by an echogenic rim) **gestational sac** within the thickened decidua. Yeh et al.[23] originally identified this sign, referred to as the **intradecidual sign,** which is seen at about 4.5 weeks' gestation. An intradecidual gestational sac should be eccentrically located within the endometrium. It is important to ensure that the sac abuts the endometrial canal to distinguish an intrauterine gestational sac from a **decidual cyst.**

The intradecidual sign was originally described on TAS,[23] with a sensitivity of 92%, specificity 100%, and overall accuracy of 93% for distinguishing between early IUP and ectopic pregnancy. Chiang et al.[24] looked at this sign using TVS and found overall sensitivity of 60% to 68%, specificity of 97% to 100%, and overall accuracy of 67% to 73%, indicating that the sign, when present, is useful for diagnosing an IUP. When absent, it does not reliably exclude an IUP. It is usually possible to demonstrate an early IUP as a small intradecidual sac between 4½ and 5 weeks' gestational age using TVS (Figs. 30.5 and 30.6). Using a high-frequency (7.5-10 MHz) TVS, Oh et al.[19] were able to identify a gestational sac in all 67 patients scanned between 28 and 42 days' gestational age (**mean sac diameter** [MSD] between 28 and 35 days was 2.6 mm).

The **double-decidual sign** (also called double decidual sac sign) was described by Bradley et al.[25] and Nyberg et al.[26] as a method for distinguishing between an early IUP and an endometrial fluid collection of other origin, such as the pseudosac of an ectopic pregnancy. A well-defined double-decidual sign is an accurate predictor of the presence of an IUP. A vague or absent double-decidual sign should be considered nondiagnostic because it does not reliably exclude an IUP.[27]

The endometrium in the pregnant state is called the **decidua capsularis, decidua vera,** and **decidua basalis.** The double-decidual sign is based on visualization of the gestational sac as an echogenic ring formed by the decidua capsularis and chorion laeve eccentrically located within the decidua vera (Fig. 30.6), forming two echogenic rings. The outer ring is formed by the echogenic endometrium of the lining of the uterus. The **decidua basalis–chorion frondosum** (future placenta) may also be visualized as an area of eccentric echogenic thickening. The double-decidual sign was initially described, and is considered most useful, on TAS. It can usually be identified by about 5.5 to 6 weeks' gestational age and is useful in establishing an intrauterine gestation prior to TAS ability to visualize the yolk sac. It is almost always resolvable by the time the gestational sac reaches 10 mm, at which point the yolk sac is typically visible by TVS, thus diminishing the usefulness of this finding.[28]

Parvey et al.[29] found a double-decidual sign in only 53% of early pregnancies with no yolk sac or embryo present. They also assessed visualization of the echogenic chorionic rim alone as a sign of IUP and found its presence in 64% of cases. It was more clearly defined in later pregnancies with a higher β-hCG level (mean, 16,082 mIU/mL) and thin, less clearly defined, or even absent in the earliest pregnancies. Using a higher-frequency 10-MHz transvaginal transducer to scan patients who had a positive pregnancy test and only a small (<1 cm) intrauterine "fluid collection" seen with a 6- to 7-MHz transducer, Benacerraf et al.[9] were able to improve their diagnostic confidence in eight patients with an IUP. This demonstrates the need to scan TVS with a high-frequency transducer when an early pregnancy is in question. Even with use of modern TVS equipment, the double-decidual sign is absent in at least 35% of intrauterine gestational sacs.[30]

The **normal gestational sac** is round in the very early stages and implants immediately beneath the thin, echogenic endometrial stripe (see Fig. 30.5). As it enlarges, the sac often has a somewhat oval shape because of the pressure exerted by the muscular uterine walls (Fig. 30.7). It can be distorted during TVS by compressing the uterus with the vaginal probe. The gestational (or chorionic) sac is filled with extracoelomic or **chorionic sac fluid,** which is normally weakly reflective and more echogenic than the amniotic

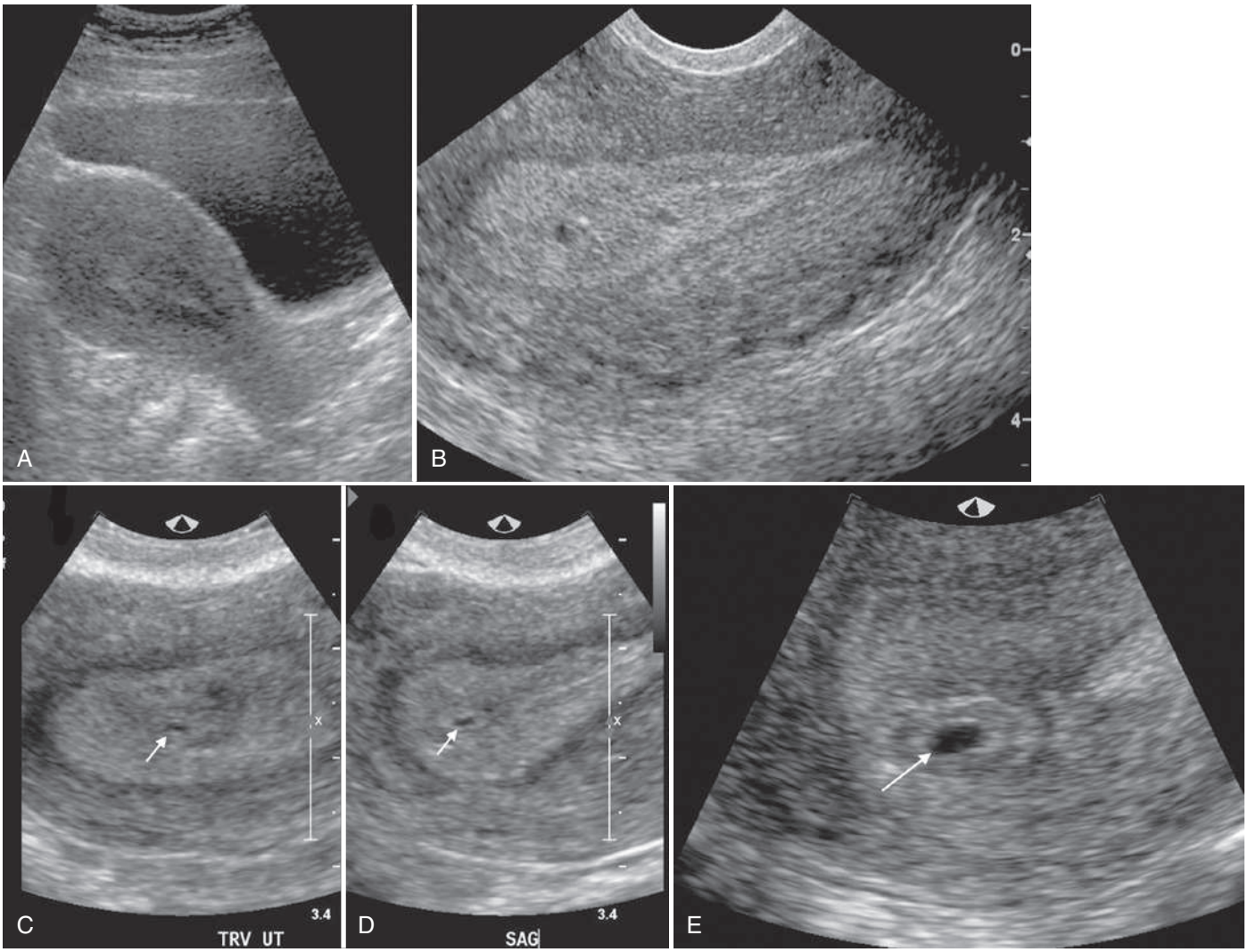

FIG. 30.5 Intradecidual Sac Sign at 32 Days. (A) TAS fails to show the gestational sac. **(B)** TVS shows the echogenic ring of the sac implanted just below the endometrial stripe. In another woman **(C)** transverse and **(D)** sagittal TVS show an early gestational sac *(arrow)*. The sac *(arrow)* slightly displaces the endometrial stripe posteriorly and has a slightly echogenic rim, seen best on **(E)** high-resolution image.

fluid. This difference is best appreciated if the system gain is increased. The low-level echoes within the chorionic fluid are accentuated, and yet the amniotic fluid remains echo free[31] (Fig. 30.8). The low-level echoes are likely caused by the relatively thick proteinaceous material in chorionic fluid.[32]

Some researchers have investigated using **color flow Doppler sonography** to help identify the presence of an early IUP. Emerson et al.[33] found that the detection of peritrophoblastic flow of high velocity and low impedance increased the sensitivity of detection of IUP from 90% to 99%. Parvey et al.[29] found this flow pattern in only 15% of IUPs without a visible yolk sac or embryo. They considered that combining the Doppler findings with the sonographic identification of inner chorionic rim would yield a high sensitivity and specificity of over 90%. However, this exposes the early **IUP** to the increased power deposition of Doppler scanning (see Chapter 29). Therefore Doppler should not be routinely performed when assessing the early IUP.[34] However, when scanning in the adnexal region, use of Doppler and associated power deposition is not a concern, because the first-trimester pregnancy (if ectopic) is nonviable (and because any IUP would be out of the field of insonation).

β-hCG and Early Pregnancy Ultrasound

Serum hCG levels perform an important complementary role with ultrasound in the evaluation of early pregnancy. Levels using the serum beta subunit of human chorionic gonadotropin **(β-hCG)** provide a reproducible value that can help guide management in clinical practice.

A negative serum β-hCG level excludes pregnancy in a young woman with pain or bleeding. The serum β-hCG test yields positive results at approximately 23 days of gestational age,[35] before a normal intrauterine gestational sac may be imaged with TVS. A disproportionately lower than expected β-hCG level is an indicator of a poor prognosis.[36] The World Health Organization (WHO) has issued several sets of standards for β-hCG, calibrated in International Units (IU). Over the years, β-hCG levels have

been measured using the first International Reference Preparation (IRP), the Second International Standard (IS), the Third IS, and the Fourth IS. The Second IS produces values that are approximately half that of the First IRP and Third and Fourth IS. The WHO recommends that the Third and Fourth IS should be used for calibration of immunoassays.[37]

In a literature review, Nyberg and Filly[6] noted the importance of the appropriate use of a threshold level and a discriminatory level of β-hCG for the appearance of a gestational sac. The **threshold level** identifies the earliest one can expect to see a sac, and the **discriminatory level** identifies when one should always see the sac. Although the menstrual history provides useful information early in a woman's obstetric care, because of the variability in the timing of ovulation and the unreliability of menstrual history, discriminatory levels based on history are of limited clinical use.

A gestational sac can often be visualized sonographically at low serum β-hCG levels. As TVS has improved, threshold values

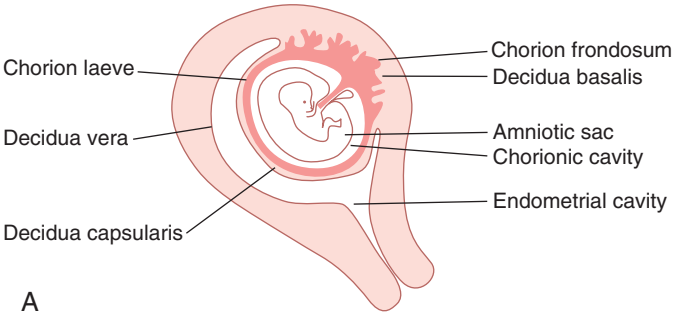

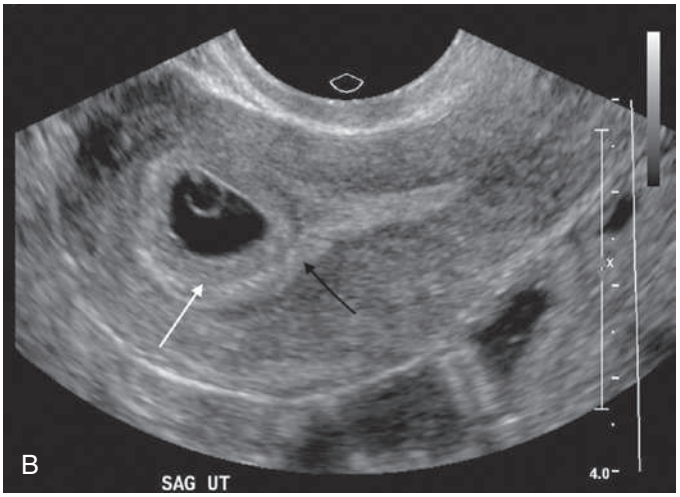

FIG. 30.6 Double-Decidual Sign. (A) Diagram of anatomic basis showing three layers of decidua and endometrial cavity. **(B)** Sagittal TVS at 5 weeks 6 days shows the decidua capsularis around the gestational sac *(white arrow)* and the maternal decidua vera *(black arrow)* as separate echogenic bands.

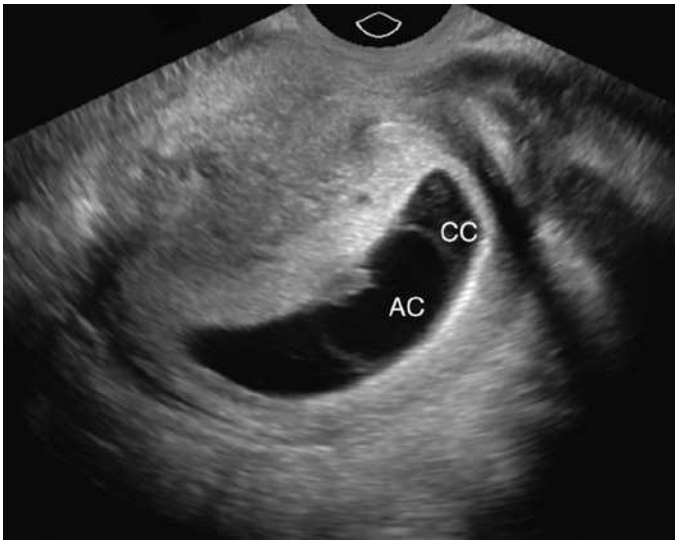

FIG. 30.8 Echogenicity of Fluids. TVS of a 9-week sac with the relatively echo-free in appearance of the amniotic cavity *(AC)* and mild echogenicity in the chorionic cavity *(CC)*.

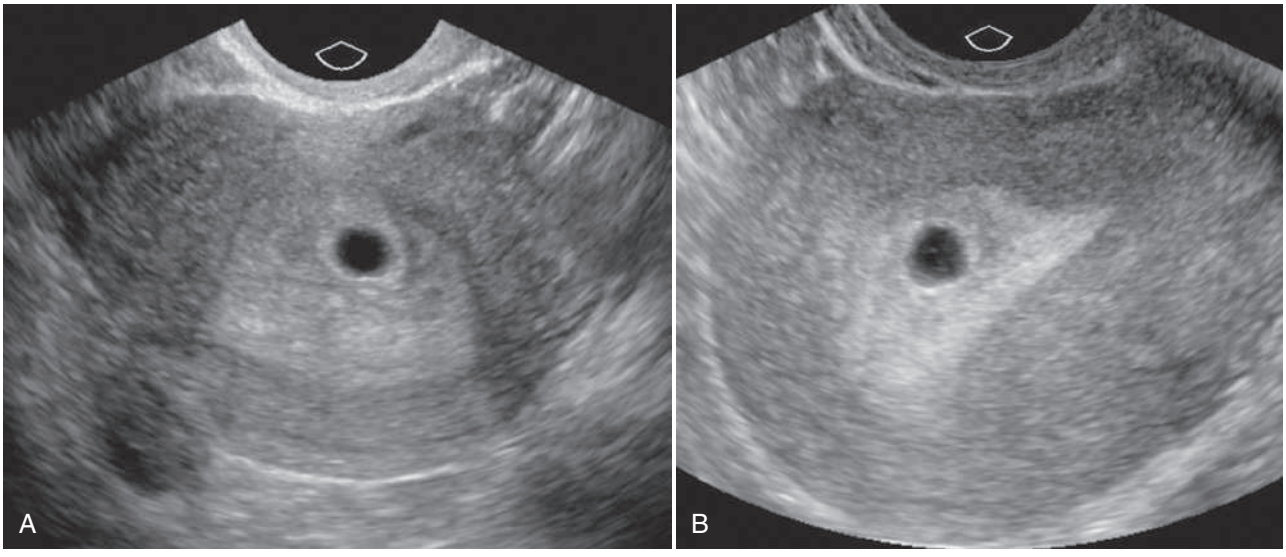

FIG. 30.7 Early Gestational Sac. (A) Transverse and **(B)** sagittal TVS scan at 5 weeks 1 day. The sac is seen as a well-defined, smooth, rounded fluid collection with a thin surrounding echogenic chorion.

have dropped to as low as 390 mIU/mL.[38] Extensive efforts have been made to identify a discriminatory level for the serum β-hCG, defined as the level of serum β-hCG above which sonographers should always visualize an intrauterine sac on ultrasound to be considered normal. Work by Barnhart indicated that this level, using TVS, should be set at 1000 to 2000 mIU/mL.[38-40] However, additional studies have shown that a single value of β-hCG is of limited value. Mehta at el.[41] showed that although the absence of a visible sac at a β-hCG level of 2000 mIU/mL is suggestive of an abnormal outcome, it is not diagnostic, as 33% (17 of 51 in her series) of such early pregnancies went on to have normal outcomes.

Discriminatory levels can be used to guide management but cannot be used as absolute indicators that the absence of a sonographically demonstrable gestation sac is abnormal. Serial β-hCG measurements are usually more helpful than a single measurement in identifying abnormal from normal pregnancy, and ultrasound can document important diagnostic features regardless of the exact β-hCG value.[5]

Barriers to Use of Strict β-hCG Thresholds in Determination of Pregnancy

Resolution of the ultrasound scanner
Patient body habitus
Position of the uterus
Type of hormonal assay
Experience of the sonographer
Masses such as fibroids
Multiple gestations

Yolk Sac

At 4 weeks' menstrual age, the primary yolk sac begins to regress and the secondary yolk sac develops. The secondary yolk sac is the first structure to be seen normally within the gestational sac. Using TAS, it is often seen when the MSD is 10 to 15 mm and should typically be visualized by an MSD of 20 mm.[42] TVS allows earlier and more detailed visualization of the yolk sac (Figs. 30.6 and 30.9), which is typically visualized by an MSD of 8 mm.[28] However, the visualization of a yolk sac without an embryonic pole occurs only for a brief period of time. In patients being scanned for pregnancy of unknown viability, the MSD of 25 is used as the threshold, with need to visualize an embryo at this time.

The demonstration of a yolk sac may be critical in differentiating an early intrauterine gestational sac from a pseudosac.[28] Although the double-decidual sign is not 100% specific for presence of an IUP, the identification of a yolk sac within the early gestational sac is diagnostic of IUP. The yolk sac plays an important role in human embryonic development.[10] While the placental circulation is developing, the yolk sac plays a role in **transfer of nutrients** to the developing embryo in the third and fourth weeks. **Angiogenesis** occurs in the wall of the yolk sac in the fifth week. The mesenchymal cells or angioblasts aggregate to form "blood islands"; a cavity forms within these islands, which fuse with others to form networks of endothelial channels. Vessels extend into adjacent areas by endothelial budding and fusion with other vessels. This vascular network in the wall of the yolk sac eventually joins the embryonic circulation via the paired **vitelline arteries and veins** through a stalk called the **vitelline duct. Hematopoiesis** occurs first in the well-vascularized extraembryonic mesoderm covering the yolk sac wall in the fifth week, in the liver in the eighth week, and later in the spleen, bone marrow, and lymph nodes. The dorsal part of the yolk sac is incorporated into the embryo as **primitive gut** (foregut, midgut, and hindgut) in the sixth week. The yolk sac remains connected to the midgut by the vitelline duct (Fig. 30.10).

Lindsay et al.[43] reported that the yolk sac grows at a rate of 0.1 mm per millimeter of MSD growth when the MSD is less than 15 mm, then slows to 0.03 mm. The upper limit of normal for yolk sac diameter between 5 and 10 weeks of gestational age is 5.6 mm.

The number of yolk sacs present can be helpful in determining **amnionicity** of a multifetal pregnancy (Fig. 30.11). In general, the number of yolk sacs and the number of amniotic sacs are the same. In a **monochorionic monoamniotic** (MCMA) twin gestation, there will be two embryos, one chorionic sac, one amniotic sac, and one yolk sac. Levi et al.[44] examined four MCMA twin pregnancies, all with a single yolk sac. One was a conjoined twin and one a twin ectopic, with both pregnancies terminated. The other two pregnancies delivered normally at 34 weeks. Of the four cases, two had a larger-than-normal yolk sac (>5.6 mm), and one yolk sac was irregular in contour. Therefore in MCMA twins, a single, large, or normal-sized yolk sac with two live embryos can result in a normal twin delivery.

Embryo and Amnion

Visualization of the amnion in the absence of an embryo usually occurs in intrauterine embryonic death as a result of resorption of the embryo[45] (Fig. 30.12).

Amniotic fluid is a colorless, fetal dermal transudate; as the skin cornifies and the kidneys begin to function, at about 11 weeks, it becomes pale yellow. The amnion becomes visible when the embryo has a CRL of 2 mm at 6 weeks. The cavity becomes almost spherical by about 7 weeks, likely a result of the more rapid increase in fluid volume relative to the growth of the sac membrane to accommodate it. The actual rate of fluid increase is more rapid after about 9 weeks (Fig. 30.13), when urine is produced. Fluid accumulates at about 5 mL per day at 12 weeks. The amniotic cavity expands to fill the chorionic cavity completely by week 16. It is therefore normal to identify the amnion as a separate membrane or sac within the chorionic cavity before 16 weeks (Fig. 30.14). Occasionally, the amnion and chorionic membranes may fail to be juxtaposed at week 16 (so-called **unfused amnion**), and separation of these membranes may persist for a short time.[46]

Iatrogenic or spontaneous rupture of the amniotic membrane in the first trimester is a rare occurrence and even more rarely results in the **amniotic band sequence.** This rupture may result in retraction of the amnion in part or in whole, up to the base of the umbilical cord where the amnion and chorion are adherent. More often, the floating amniotic membranes do not adhere to the fetus, and no fetal anomalies occur.

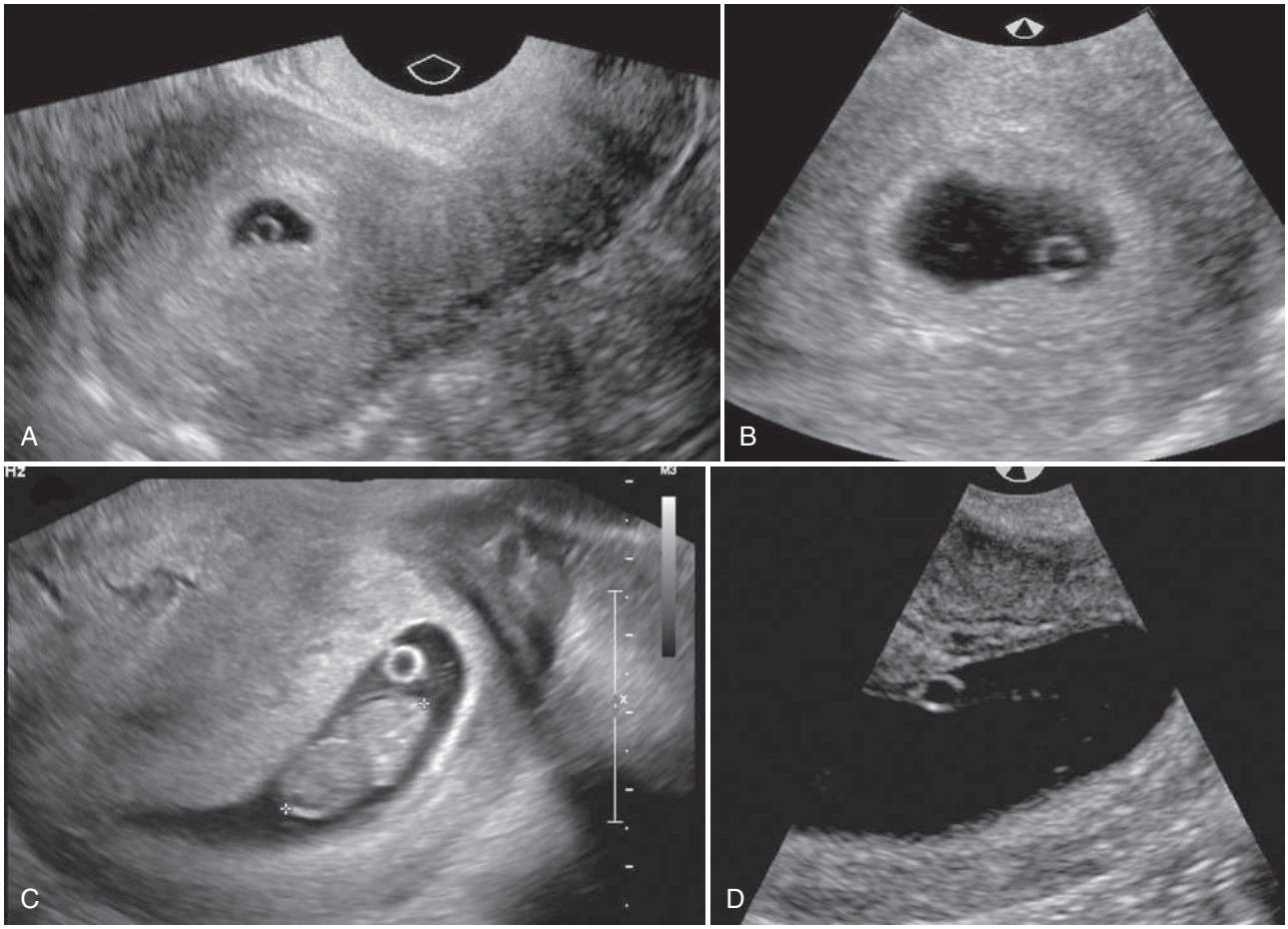

FIG. 30.9 Normal Yolk Sac. (A) Sagittal and **(B)** transverse TVS of the early IUP demonstrates the yolk sac at 5 weeks 5 days. **(C)** Yolk sac is seen separate from embryo *(calipers)* at 9 weeks. **(D)** At 11 weeks, yolk sac lies at edge of chorionic sac outside of early amnion.

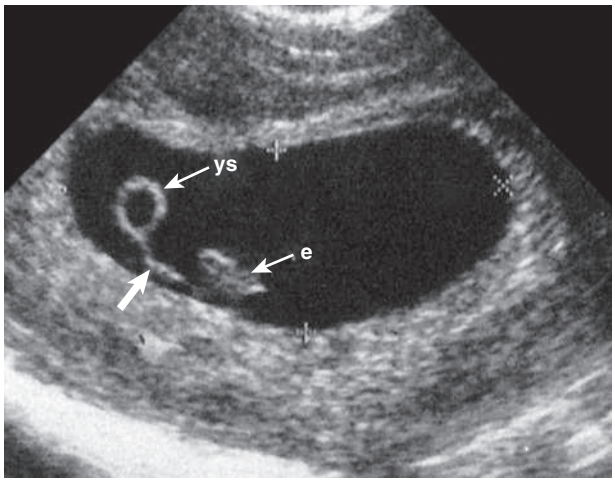

FIG. 30.10 Normal Embryo at 8 Weeks. TVS shows vitelline duct *(thick arrow),* yolk sac *(ys),* and embryo *(e).*

FIG. 30.11 Early Monochorionic Diamniotic (MCDA) Twins. Two separate yolk sacs are seen within a single chorion at 5 weeks 5 days. It is too early to visualize the two amnions.

Embryonic Cardiac Activity

Using TVS, an embryo with a CRL as small as 1 to 2 mm may be identified immediately adjacent to the yolk sac (Fig. 30.15). In normal pregnancies the embryo can be identified in gestational sacs as small as 10 mm and should always be identified when the MSD is equal to or greater than 25 mm with optimal scanning parameters and high-resolution TVS.[4,5]

Embryologic data suggest the tubular heart begins to beat at 36 to 37 days' gestational age.[10] Cadkin and McAlpin[47] described cardiac activity adjacent to the yolk sac before the embryo can

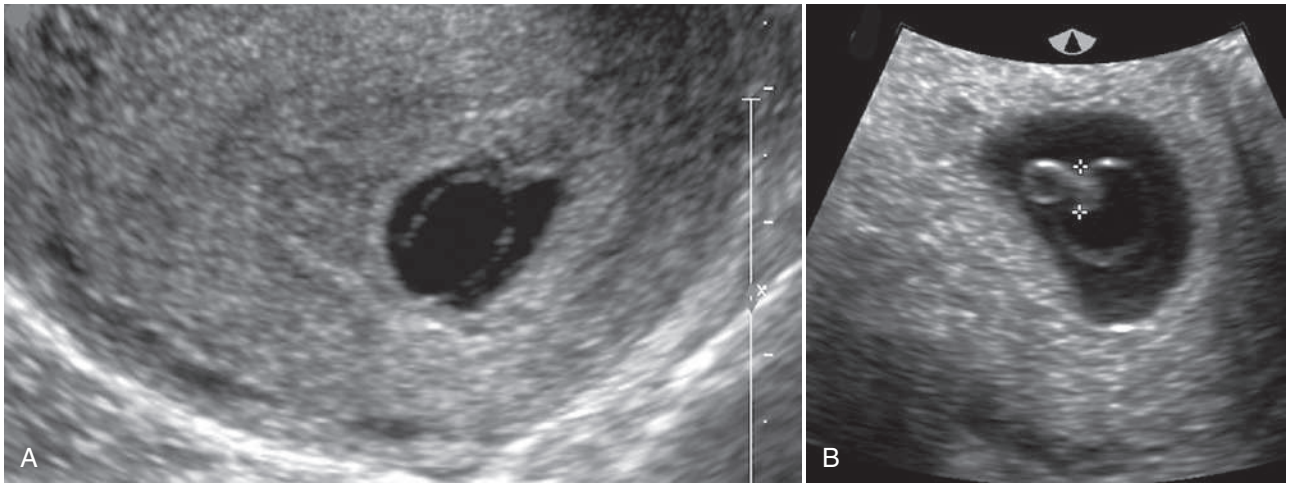

FIG. 30.12 Abnormal Amnion. (A) TVS at 9 weeks demonstrates an **empty amnion** within the gestational sac. This pregnancy eventually failed. **(B) Expanded amnion** at 7 weeks. Note how the amnion is much larger than would be expected for an embryo *(calipers)* of this size. This pregnancy did not progress.

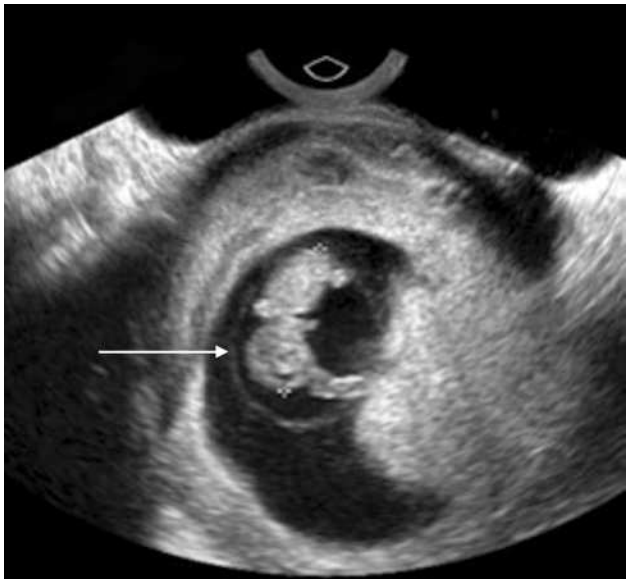

FIG. 30.13 Normal 9-Week 4-Day Gestation. TVS shows the embryo *(calipers)* and the amnion *(arrow)* separate from the surrounding chorion.

be fully visualized at the end of the fifth week. Ragavendra et al.[48] placed a 12.5-MHz endoluminal catheter transducer into the endometrial canal adjacent to the gestational sac. They identified cardiac activity in an embryo with a CRL of 1.5 mm and resolved the two walls of the heart, seen only as a tube. Using TVS, cardiac activity is typically seen by the time an embryo is 2 mm in size, and is almost always seen by 5-mm CRL. However, for strict diagnosis of nonviable pregnancy the threshold is set at 7 mm CRL.[4,5] Normal embryonic cardiac activity is greater than 100 beats per minute (bpm) (Video 30.1) when the embryo is less than 6.3 weeks and 120 bpm at or beyond 6.3 weeks.[49] When embryonic cardiac activity is visualized and the rate is less than 100 bpm, then follow-up should be obtained. We have seen pregnancies with small embryos of 1–2 mm in size with heart rates of 80–99 bpm with normal follow-up (see Fig. 30.15).

Umbilical Cord and Cord Cyst

The umbilical cord is formed at the end of the sixth week (CRL = 4.0 mm) as the amnion expands and envelops the connecting stalk, the yolk stalk, and the allantois. The cord contains two umbilical arteries, a single umbilical vein, the allantois, and yolk stalk (also called the **omphalomesenteric duct** or **vitelline duct**), all of which are embedded in **Wharton jelly.** The **umbilical arteries** arise from the internal iliac arteries and in the newborn become the superior vesical arteries and the medial umbilical ligaments. The **umbilical vein** carries oxygenated blood from the placenta to the fetus. The oxygenated blood is shunted through the ductus venosus into the inferior vena cava and the heart. The single left umbilical vein in the newborn becomes the ligamentum teres, which attaches to the left branch of the portal vein. The ductus venosus becomes the ligamentum venosum.

The **allantois** is associated with bladder development and becomes the urachus and the median umbilical ligament. It extends into the proximal portion of the umbilical cord. The **yolk stalk** connects the primitive gut to the yolk sac. The paired **vitelline arteries and veins** accompany the stalk to provide blood supply to the yolk sac. The arteries arise from the dorsal aorta to supply initially the yolk sac, then the primitive gut. The arteries remain as the celiac axis, superior and inferior mesenteric arteries supplying the foregut, midgut, and hindgut, respectively. The vitelline veins drain directly into the sinus venosus of the heart. The right vein is later incorporated into the right hepatic vein. The portal vein is also formed by an anastomotic network of vitelline veins.

The length of the umbilical cord has a close linear relationship with gestational age in normal pregnancies. Hill et al.[50] found they could reliably measure the cord lengths in 53 embryos at 6 to 11 weeks' gestational age. Also, the cord lengths in 60% of dead embryos were more than two standard deviations (2 SD) below the value for that expected gestational age.

The width of the umbilical cord has also been measured sonographically, and Ghezzi et al.[51] found a steady increase from 8 to 15 weeks. There was a significant correlation between cord

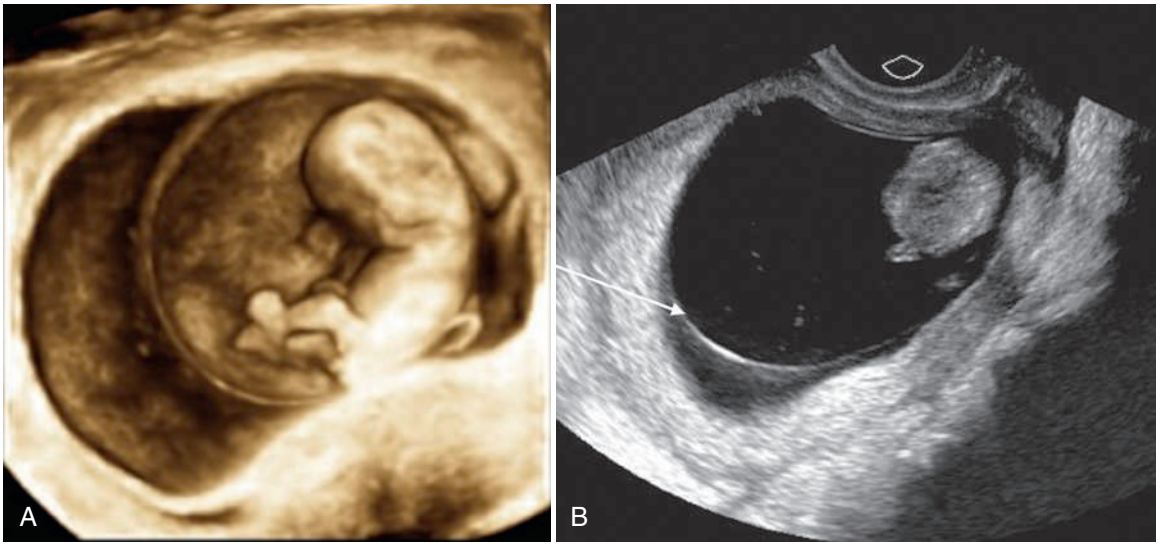

FIG. 30.14 Normal 12-Week Gestation. (A) Surface rendering image from three-dimensional TVS shows the embryo within the amnion. **(B)** Two-dimensional TVS shows the amnion *(arrow)* approaching, but not fused with, the chorionic sac.

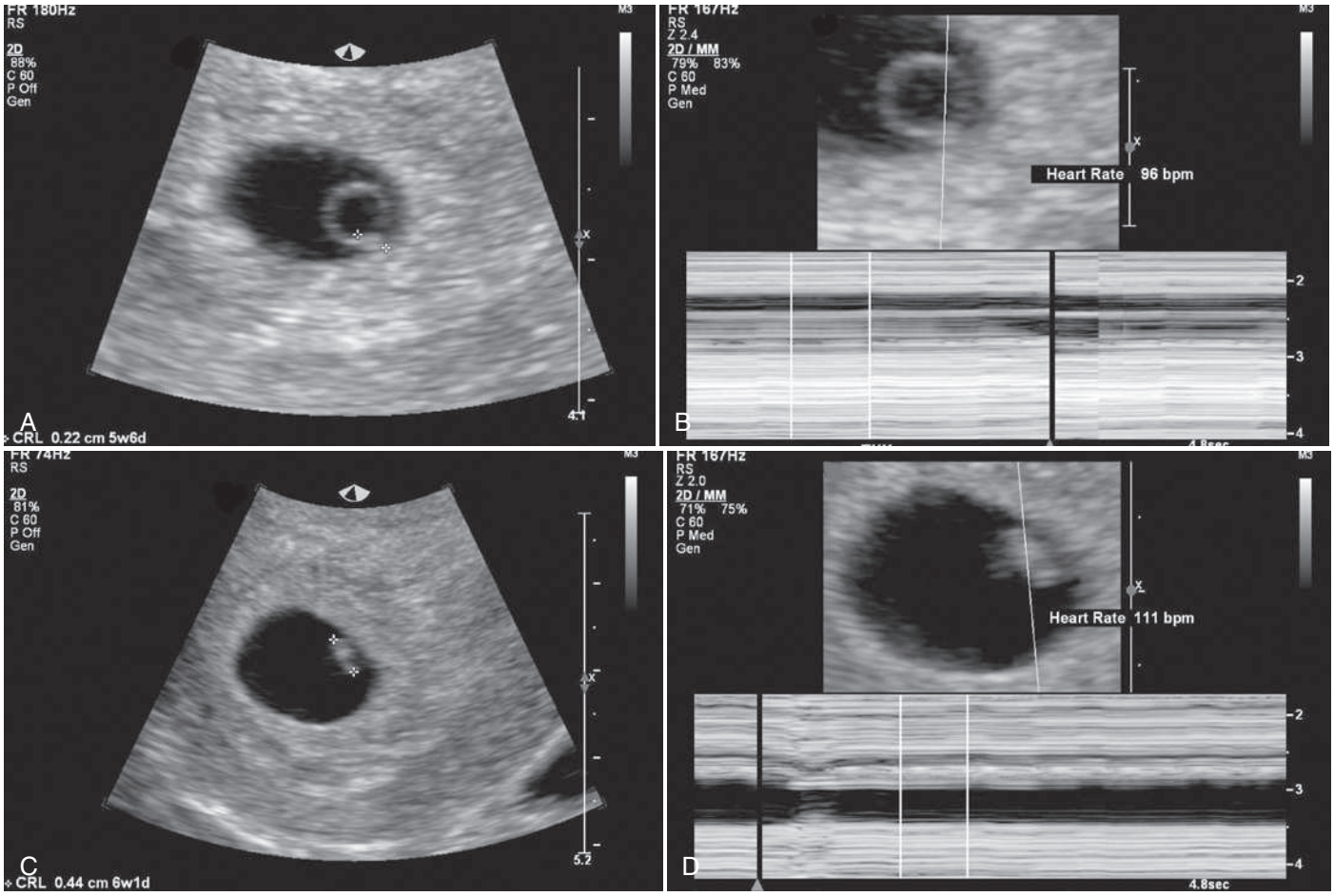

FIG. 30.15 Normal Embryo With Early Cardiac Activity. (A) Image shows 5-week 6-day embryo *(calipers)* adjacent to the yolk sac. **(B)** M-mode ultrasound shows a heart rate of 96 beats/min. **(C)** Two days later, the embryonic pole *(calipers)* has grown and **(D)** the heart rate has increased to 111 beats/min. See also Video 30.1.

diameter and gestational age ($r = 0.78$; $P < .001$), CRL ($r = 0.75$; $P < .001$), and biparietal diameter ($r = 0.81$; $P < .001$) but no correlation with birth weight or placental weight. The cord diameter was significantly smaller by at least 2 SD in patients who developed preeclampsia or had a miscarriage.

Cysts and pseudocysts within the cord have been described in the first trimester.[52] Cysts are usually seen in the eighth week and usually resolve by the 12th week. They are singular, closer to the embryo/fetus than the placenta, with a mean size of 5.2 mm (Fig. 30.16). Cysts may originate from remnants of the allantois or omphalomesenteric duct and characteristically have an epithelial lining.[53] It is hypothesized that the cyst is an **amnion inclusion cyst** that occurs as the amnion was enveloping the umbilical cord. In a series of 1159 consecutive patients scanned between 7 and 14 weeks, Ghezzi et al.[54] found 24 cord cysts at a prevalence of 2.1%. Single cysts in the first trimester were associated with a normal outcome and a healthy infant, whereas multiple or complex cysts were associated with an increased risk of miscarriage or aneuploidy. Thus although umbilical cord cysts have been associated with chromosomal abnormalities if seen in the second and third trimesters, those seen in the first trimester typically resolve and are not associated with poor outcome.

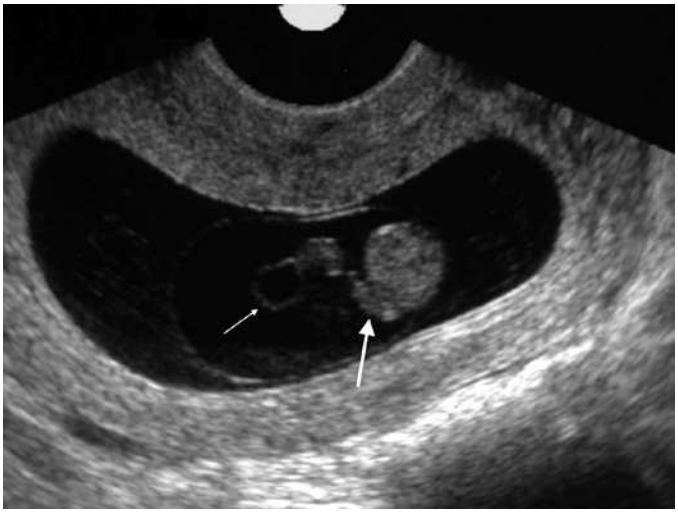

FIG. 30.16 Umbilical Cord Cyst at 10 Weeks. TVS shows a cyst *(small arrow)* arising from the cord *(large arrow)*. On subsequent examination (not shown) the cyst was no longer seen.

ESTIMATION OF GESTATIONAL AGE

During the first trimester, gestational age can be estimated sonographically with greater accuracy than at any other stage of pregnancy. As pregnancy progresses, biologic variation results in wider variation around the mean for all sonographic parameters at a given gestational age.

Gestational Sac Size

The MSD offers an opportunity to date an early pregnancy before the embryo can be visualized. The MSD is an average of the diameter of the sac, obtained by adding the anteroposterior and craniocaudad diameters on the sagittal view of the uterus to the transverse diameter obtained on the transverse view and dividing by three (Fig. 30.17). The gestational age can be predicted by MSD using the following formula: menstrual age in days = MSD in mm + 30.[55] The MSD increases in size at a rate of 1.1 mm per day.[56] If MSD is very small, about 2 mm, gestational age is 4 to 4½ weeks, and MSD of about 5 mm is 5 weeks. At 5½ weeks, a yolk sac appears (see Fig. 30.9A and B). At 6 weeks, an embryo first appears adjacent to the yolk sac (see Fig. 30.15A). When the embryo is first seen, cardiac activity is appreciated as a consistent flicker[40] (Fig. 30.15B and Video 30.1).

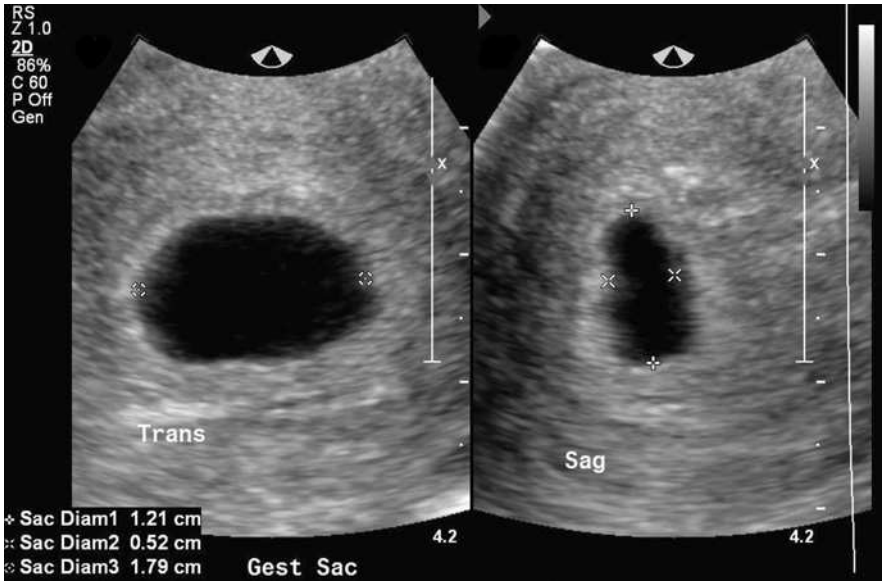

FIG. 30.17 Gestational Age Established by Mean Sac Diameter (MSD). Gestational age can be estimated measuring the sac in three dimensions. Average of three measurements is used to correlate with gestational age prior to visualization of the embryonic pole. MSD of 12 mm is consistent with gestational age of 6 weeks 0 days. However, these data are not used to formally establish pregnancy dating. Sonographic dating of the pregnancy is done with the crown-rump length when cardiac activity is present.

Crown-Rump Length

Once the embryonic pole is visualized (just before 6 weeks), measurement of the CRL of the embryo is considered the most accurate method to date the pregnancy.[57,58]

EARLY PREGNANCY FAILURE

One of the most important roles of ultrasound in the first trimester is to identify early pregnancies that have failed or that are more likely to fail. Studies have demonstrated a 20% to 31% rate of early pregnancy loss after implantation in normal healthy volunteers.[59,60] Many pregnancies abort before the pregnancy is confirmed by either ultrasound or a chemical pregnancy test. Approximately 50% of miscarriage is caused by chromosomal abnormalities.[61] Early pathologic studies of Hertig and Rock,[60] also showed a high frequency of morphologic abnormalities in preimplantation embryos. Loss rates are increased with increased maternal age and prior history of early pregnancy failure.[62]

Although the etiology of first-trimester pregnancy loss is still not fully understood, there are many known and suspected causes. In a study of 232 first-trimester patients (normal, healthy women, positive urinary pregnancy test, and no vaginal bleeding) with TVS at the first visit, Goldstein[57] determined the incidence of subsequent pregnancy loss by following all to delivery or spontaneous abortion. This group had an overall pregnancy loss rate of 11.5% in the embryonic period, (i.e., <70 days from last menstrual period). The loss rate diminished as the pregnancy progressed. The loss rate was 8.5% when a yolk sac was seen, 7.2% with an embryo of CRL less than 5 mm, 3.3% with CRL 6 to 10 mm, and 0.5% with CRL greater than 10 mm. The loss rate leveled off at 2% from 14 to 20 weeks. Therefore under the best circumstances, the pregnancy loss rate will be 11.5% overall, from 5 weeks onward. Once the embryo reaches a CRL of 10 mm, there is about a 98% chance of a successful outcome. Westin et al. confirmed that after 12 weeks menstrual age, the miscarriage rate decreases to 0.5% in low-risk women.[63]

A patient who is in the process of a spontaneous abortion will often present with brownish spotting, a decrease in the symptoms of pregnancy (breast tenderness, nausea), and on examination, a uterus smaller than expected. The latter sign is subjective and not reliable in early gestation. Bleeding is a common complication in early pregnancy, affecting approximately 25% of women with documented pregnancies.[42] Women who present with bleeding have a much higher incidence of pregnancy loss. In women who present with a closed cervical os and uterine bleeding in the first trimester, 50% will eventually abort. Using TVS, Falco et al.[64] studied 270 patients with first-trimester bleeding at 5 to 12 weeks' gestation; 45% were diagnosed initially as a nonviable pregnancy or empty gestational sac. Of the remaining singletons with demonstrable fetal cardiac activity, 15% (23/149) subsequently aborted. In a later prospective study of 50 patients with MSD of 16 mm or less, no embryo, and first-trimester bleeding, Falco et al.[65] found that 64% eventually miscarried; 13/18 (72%) of those who continued to delivery had a yolk sac seen; and 13/32 (40%) went on to fail even though a yolk sac was present. Advanced maternal age (>35) and low serum β-hCG (<1200 mIU/mL IRP) were associated with increased risk of pregnancy failure.

Table 30.1 summarizes the rate of spontaneous abortion in women with and without bleeding in early pregnancy.[57,64,66,67]

One theorized cause of early pregnancy failure is chromosomal anomaly in the early embryo. Sorokin et al.[68] performed chorionic villous sampling in 795 first-trimester pregnancies and found that 35 had a nonviable pregnancy before the procedure; 19 of the 35 women had subsequent chorionic villous sampling, and all were aneuploid. Ten cases had chromosomal abnormalities, virtually always lethal in the embryonic period, and nine had defects with moderate potential for viability. Gestations with low viability potential had a larger discrepancy (23.4 ± 8.3 days) in estimated minus observed gestational age, which was significantly greater than that of gestations with moderate viability potential (8.9 ± 4.3 days; $P < .001$). The absence of an embryonic pole was more common in the first group. This demonstrates that the more severe the anomaly is, the more likely that very early embryonic demise or **intrauterine growth restriction** will occur.

Another cause of early pregnancy failure is **luteal phase defect,** thought to be failure of the corpus luteum to support the conceptus adequately once implantation has occurred. This may result from a shortened luteal phase in cases of ovulation induction and *in vitro* fertilization (IVF), or from luteal dysfunction, more frequently seen in obese women or women older than 37 years of age.[69] Luteal phase defect has been defined as a delay of more than 2 days in histologic development of the endometrium relative to the day of the cycle. The underlying cause may be decreased hormone production by the corpus luteum, decreased levels of

TABLE 30.1 Rate of Spontaneous Abortion in Early Pregnancy

Study	Age (Wk)	Number	Indication	Abortion Rate (%)
Goldstein[57]	5-10	232	Routine	11.5
Pandya et al.[66]	10-13	17,870	Routine	2.8
Stabile et al.[67]	5-16	624	Bleeding	45
Falco et al.[64]	5-12	270	Bleeding	51.5
Falco et al.[64]	5-12	149	Bleeding + live embryo/fetus	15
Pandya et al.[66]	10-13	17,870	Bleeding	15.6

FSH or LH or abnormal patterns of secretion, or a decreased response of the endometrium to progesterone.

Angiogenesis of the corpus luteum may be needed for the regulation of progesterone production. Kupesic et al.[70] found that the resistive index (RI) in intraovarian arteries in normal nongravid women dropped below 0.47 in the luteal phase compared to a group with luteal phase defect who had a high resistance throughout the menstrual cycle, with RI always above 0.50. They suggest that Doppler sonography may predict functional capacity of the corpus luteum, at least in the nongravid state. Blumenfeld and Ruach[69] were successful in treating luteal phase defect in a group undergoing ovulation induction and in patients with previous abortions, using hCG administration twice weekly in the sixth and tenth weeks. This reduced the rate of miscarriage from 49% to 17.8% ($P < .01$).

Currently, as medical management for a failed pregnancy may include intervention with misoprostol that may harm a potentially viable pregnancy, a false positive diagnosis of early pregnancy failure can lead to negative consequences. This has led to a philosophy espoused by the Society of Radiologists in Ultrasound of using conservative criteria on ultrasound for early pregnancy failure that would eliminate a false positive result.[5,27] Early pregnancy failure may not always be able to be diagnosed or excluded on the basis of a single ultrasound, and follow-up studies may be necessary for conclusive diagnosis.

Diagnostic Findings of Early Pregnancy Failure

Diagnostic Findings of Early Pregnancy Failure

CRL of 7 mm without a heartbeat
MSD of 25 mm without an embryonic pole

Crown-Rump Length 7 mm or Greater and No Heartbeat

In patients with a sonographically demonstrable embryo, no cardiac activity is one of the most important factors in predicting pregnancy outcome. The absence of cardiac activity does not necessarily indicate embryonic demise, however, because TVS can identify a normal, very early embryo without cardiac activity.

Many studies have demonstrated that cardiac activity is expected when CRL is greater than 5 mm. Levi et al.[3] reviewed a series of 96 patients with CRL of less than 5 mm to assess the predictive value of the presence or absence of cardiac activity using TVS. Of 71 patients available for follow-up, 46 embryos had cardiac activity, 35 progressed to at least the late second trimester, and 11 ended as first-trimester demise. Of the 25 embryos without demonstrable cardiac activity, 5 (20%) were normal and 20 (80%) ended as first-trimester embryonic deaths. Of the five normal embryos without demonstrable cardiac activity on initial TVS, three had initial CRL of less than 1.9 mm. Standard embryology texts indicate that the embryonic heart begins to beat at the beginning of the sixth week, when the CRL is 1.5 to 3 mm. Thus it is not surprising that cardiac activity may or may not be identified in normal embryos with CRL less than 2 mm. In the study by Levi et al., initial TVS assessment failed to identify cardiac activity in 2 of 25 normal embryos with CRL of 2 to 4 mm. TVS enabled correct identification of cardiac activity in 100% of normal embryos with CRL of 4 to 4.9 mm.[3] Pennell et al.[71] found that 16 of 18 embryos with CRL less than 5 mm had no cardiac activity on initial TVS assessment but demonstrated cardiac activity on follow-up TVS. Cardiac motion was seen on TVS in all pregnancies with CRL greater than 5 mm.

The combination of vaginal bleeding and absent cardiac activity in embryos of CRL less than 5 mm on TVS is associated with a very poor prognosis. Aziz et al.[72] reviewed outcomes in embryos of CRL of 5 mm or less with absent cardiac activity on TVS, in women presenting with vaginal bleeding; all resulted in pregnancy failure.

Before making a diagnosis of embryonic demise, it is critical to ensure that the examination is of high quality, performed with modern equipment and an appropriate transducer frequency, and that the entire embryo is visualized. A high frame rate must be used, and the frame-averaging mode must be turned off. If there is any doubt in the diagnosis, follow-up examination should be performed. There is interobserver variability in measurement, even by experienced sonographers. In a prospective cross-sectional study on 1060 women, Abdullah et al. demonstrated that changing the CRL cutoff to greater than 7 mm would minimize the risk of a false positive diagnosis of miscarriage. A generous cutoff ensures that a desired pregnancy would not be mistakenly terminated by the administration of medication for chemical miscarriage or dilation and curettage to remove products of conception[4,5] (Fig. 30.18, Video 30.2). It is also imperative that transmitted maternal pulsations are not mistaken for embryonic cardiac pulsations, especially when evaluating a static M-mode image to verify embryonic cardiac activity (Figs. 30.18B and 30.19).

Gestational Sac Mean Sac Diameter 25 mm or Greater and No Embryo

In many patients the embryo is not visualized on the initial sonogram, and the diagnosis of pregnancy failure cannot be made on the basis of lack of cardiac activity. In these patients the diagnosis of pregnancy failure may be made based on gestational sac characteristics. The most reliable indicator of abnormal outcome based on gestational sac features is **abnormal size.**[2,42]

Using TVS, an MSD of 8 mm or more without a demonstrable yolk sac, or 16 mm with no demonstrable embryo, are not typical and are suggestive of pregnancy failure.[5,43] However, recent studies have documented gestational sacs up to 21 mm with initially no visible embryos that went on to be viable pregnancies.[4] Most authors allow a few millimeters of leeway in MSD measurements as a margin of error, and many do not use the absent yolk sac as a sign of pregnancy failure. This is partly due to interobserver variability in measurements. Given these variables, the Society of Radiologists in Ultrasound recently advocated diagnosing early pregnancy failure by gestational sac size only for sacs with MSD of 25 mm or greater with no embryo[5] (Fig. 30.20).

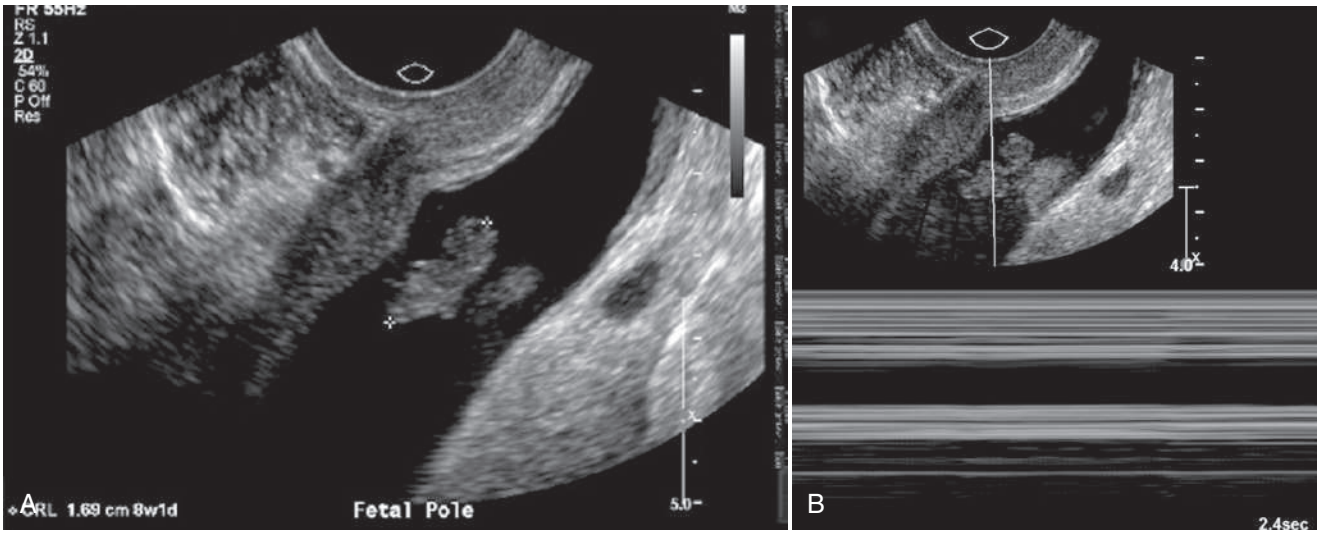

FIG. 30.18 Ultrasound Findings Diagnostic of Early Pregnancy Failure. (A) TVS shows an embryo *(calipers)* measuring larger than 7 mm without cardiac activity. **(B)** M-Mode confirms no fetal cardiac activity. See also Video 30.2.

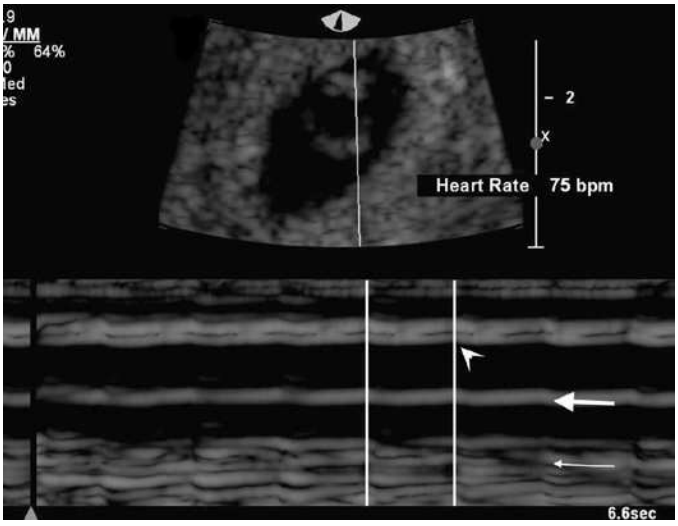

FIG. 30.19 M-Mode Documenting Transmitted Maternal Uterine Arterial Pulsations Mistaken for Fetal Cardiac Pulsations. Maternal uterine pulsations *(small arrow)* are transmitted to the inferior portion of the yolk sac *(large arrow)* and embryo *(arrowhead)* and mistakenly measured as a slow embryonic cardiac activity at 75 beats/min. Key to transmitted pulsation is noting the same rate throughout the different depths of tissue insonated.

Furthermore, these parameters only apply to high-resolution TVS and cannot be used for examinations performed with a 5-MHz TVS probe. Rowling et al.[73] studied early pregnancies with lower-frequency TVS probes (5 MHz) as well as higher-frequency probes (9-5 MHz broadband). The gestational sac was first seen at 6.4 mm in size with the lower frequency but at 4.6 mm with higher frequencies. A yolk sac was always seen in normal pregnancies with a gestational sac greater than 5 mm, and an embryo was always seen with a sac of 13 mm, using frequencies above 5 MHz.

Worrisome Findings of Early Pregnancy Failure

Additional sonographic features may suggest an abnormal outcome but lack the specificity in isolation to diagnose early pregnancy failure. These include findings involving the gestational sac, yolk sac, amnion, yolk sac, and embryo (Table 30.2).

Embryos With Crown-Rump Length Less Than 7 mm and No Heartbeat

If on initial imaging, an embryo is seen measuring less than 7 mm and lacking cardiac activity, the findings are worrisome but not entirely diagnostic of early pregnancy failure. As previously stated, findings on ultrasound follow a typical pattern with an embryo with a heartbeat demonstrable at 6 weeks.[40] Small embryos usually demonstrate measurable cardiac activity, but lack of a heartbeat in a small embryo of less than 7 mm may still result in a normal pregnancy. Follow-up sonography should be performed in these cases. Given the reliable pattern of growth, early pregnancy failure can also be verified on ultrasound by lack of visualization of an embryo with cardiac activity on follow-up scans. Embryonic cardiac activity should be documented by 11 days after a scan demonstrating a gestational sac with a yolk sac or by 14 days after a scan demonstrating a gestational sac without a yolk sac. If the pregnancy does not meet these milestones in this time interval, early pregnancy failure can be reliably diagnosed.[5]

Gestational Sac With Mean Sac Diameter 16 to 24 mm and No Embryo

As mentioned earlier, using TVS findings of either an MSD of 8 mm or more without a demonstrable yolk sac, or 16 mm with no demonstrable embryo, is not typical and is suggestive of pregnancy failure. Normal gestational sac growth is 1.1 mm/day. Nyberg et al.[56] found that patients with early pregnancy failure had MSD growth rates of less than 0.7 mm/day. This growth rate is

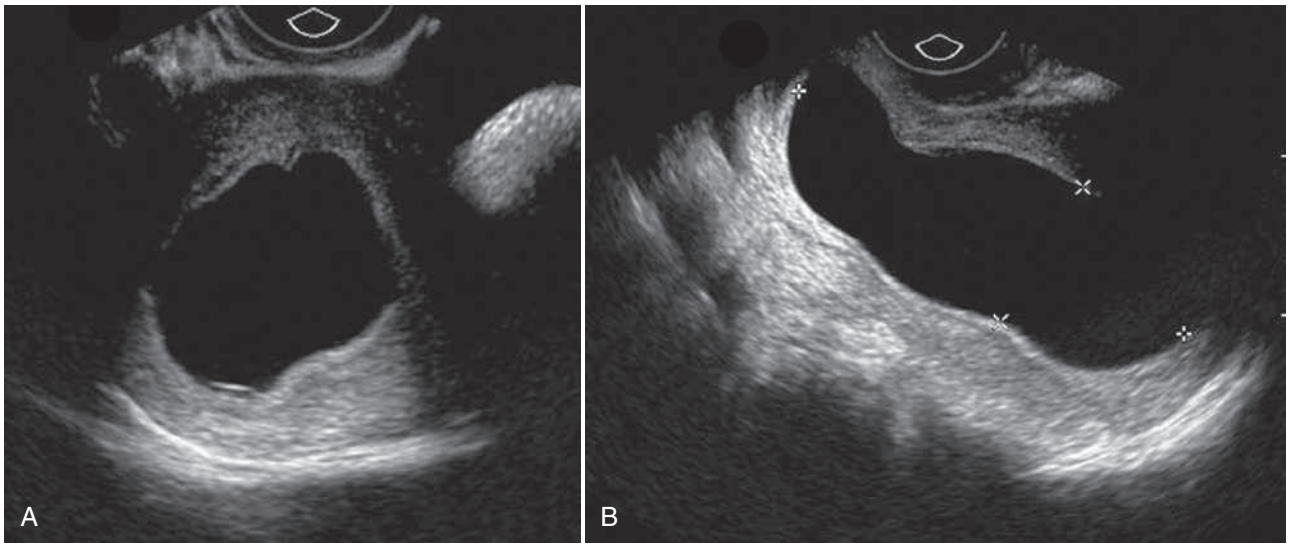

FIG. 30.20 TVS Findings Diagnostic of Early Pregnancy Failure With Large, Empty Sac. (A) Transverse and **(B)** sagittal images of an empty gestational sac with MSD *(calipers)* greater than 25 mm. No yolk sac or embryonic pole is visualized.

TABLE 30.2 Worrisome Findings for Early Pregnancy Failure

Finding	Comment
Embryo with CRL < 7 mm and no heartbeat	Embryo 2-6 mm without cardiac activity is a worrisome finding. Follow-up is needed to assess for cardiac activity in 1 week to ensure 100% specificity in diagnosis of miscarriage.
Gestational sac with MSD 16-24 mm and no embryo	Embryo is typically seen by the time the MSD is 16 mm. Follow-up in 10-14 days is needed to ensure 100% specificity in diagnosis of miscarriage.
Gestational sac appearance	Irregular shape of sac, low position of sac, and weak decidual reaction are associated with miscarriage, but the size of the embryo and presence or absence of cardiac activity guides the diagnosis of miscarriage.
Small MSD in relationship to CRL	Low fluid is associated with poor outcome. If MSD-CRL < 5, follow-up is recommended.
Abnormal amnion size	Expanded amnion or empty amnion as evaluated by an experienced sonologist is diagnostic of miscarriage. If any uncertainty is present, then follow-up should be obtained.
Yolk sac > 6 mm Calcified yolk sac	Findings are associated with miscarriage, but the size of the embryo and presence or absence of cardiac activity guides the diagnosis.
Embryonic bradycardia	Heart rate (HR) < 100 may be seen with 1- to 2-mm embryo and be a normal finding. In general, when HR is <100, follow-up is recommended.
Large subchorionic hemorrhage	Large hemorrhage is associated with miscarriage, but the size of the embryo and presence or absence of cardiac activity guides the diagnosis of miscarriage.

useful information in assessing the normal development in serial examinations. With an expected growth rate of 1.1 mm/day, one should see an appropriate increase in sac size and, if normal, the appearance of a yolk sac or an embryo. If the growth is less than expected, it becomes more suggestive of early pregnancy failure. On follow-up imaging, absence of an embryo with a heartbeat 7 to 13 days after a scan showing a gestational sac without a yolk sac or 7 to 10 days after a scan showing a gestational sac with a yolk sac remains suspicious. Given the remaining small chance that such pregnancies may still progress, longer time intervals between examinations are necessary for confident diagnosis.[5]

Gestational Sac Appearance

The following gestational sac criteria are not reliable in isolation but indicate a pregnancy at increased risk for early failure: distorted gestational sac **shape,** thin **trophoblastic reaction** (<2 mm), weakly echogenic **trophoblast,** and **abnormally low position** of the gestational sac within the endometrial cavity[42] (Fig. 30.21).

A **"chorionic bump,"** a focal irregular convexity or bulge in the surrounding choriodecidual reaction into the gestational sac, is associated with a guarded prognosis with a live birth rate for these pregnancies of less than 50%. The bulge likely represents a small hematoma.[74]

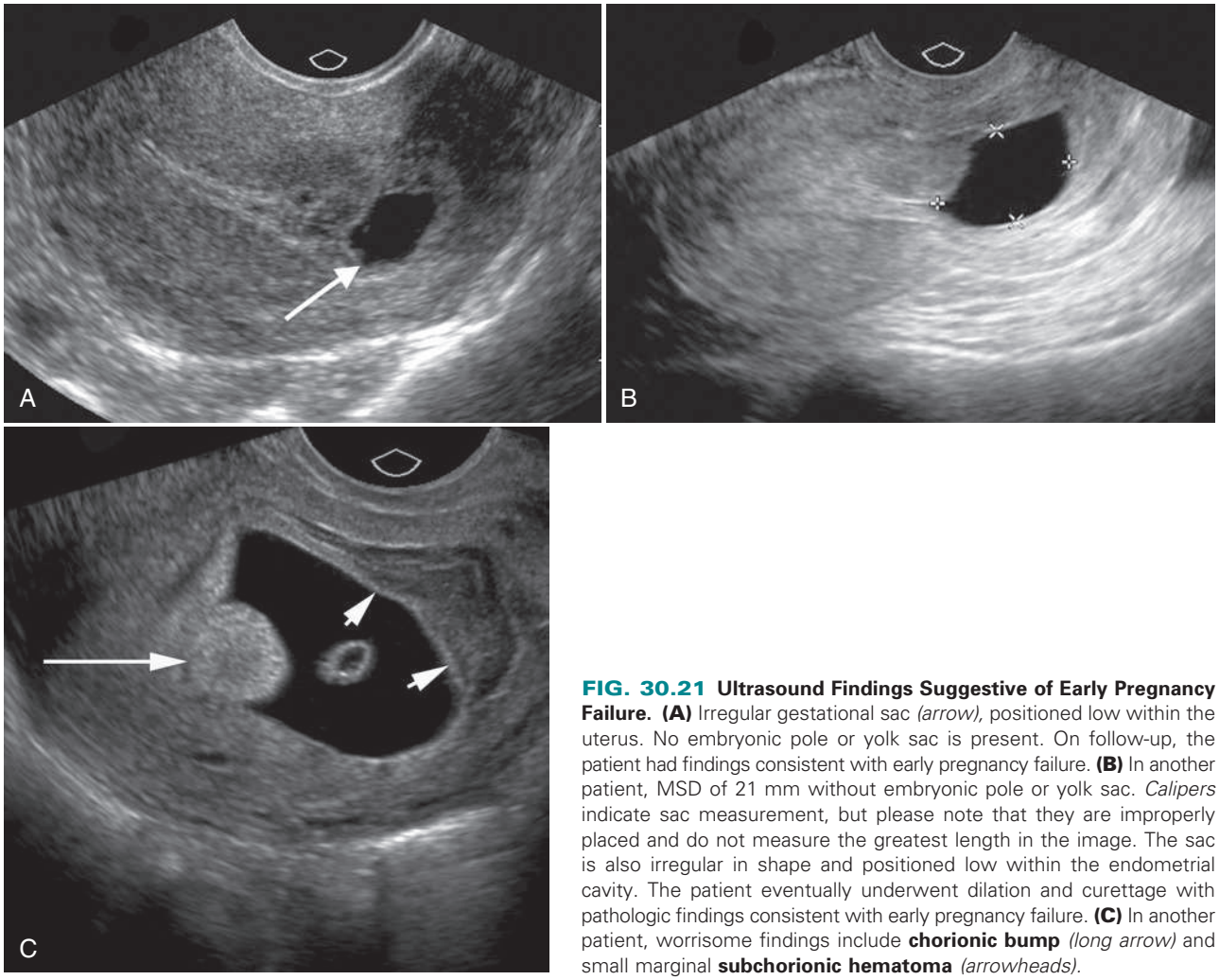

FIG. 30.21 Ultrasound Findings Suggestive of Early Pregnancy Failure. (A) Irregular gestational sac *(arrow),* positioned low within the uterus. No embryonic pole or yolk sac is present. On follow-up, the patient had findings consistent with early pregnancy failure. **(B)** In another patient, MSD of 21 mm without embryonic pole or yolk sac. *Calipers* indicate sac measurement, but please note that they are improperly placed and do not measure the greatest length in the image. The sac is also irregular in shape and positioned low within the endometrial cavity. The patient eventually underwent dilation and curettage with pathologic findings consistent with early pregnancy failure. **(C)** In another patient, worrisome findings include **chorionic bump** *(long arrow)* and small marginal **subchorionic hematoma** *(arrowheads).*

Small Mean Sac Diameter in Relationship to Crown-Rump Length

An additional feature that portends a higher likelihood of early pregnancy failure is a small sac size in relationship to CRL. Bromley et al.[75] found that in 16 patients at 5½ to 9 weeks' gestational age with an MSD less than 5 mm greater than the CRL (i.e., MSD − CRL = <5 mm), sometimes termed **early oligohydramnios,** 15 (94%) had spontaneous first-trimester abortion despite a normal heart rate for age (Fig. 30.22). As noted by Giacomello, this is not truly "oligohydramnios" as the small sac size is due to reduction of chorionic fluid, outside of the amnion.[76] A later study by Rowling demonstrated that this finding may not be as ominous as originally thought, with at least 35% of such cases progressing to the second trimester or to a normal delivery.[73]

Abnormally Large Amnion With Respect to Embryo Size

The amnion is usually visualized *after* the embryo, so it should not be visualized in the absence of an embryo.[45] In normal pregnancies, the amnion is not usually visible until the CRL of the embryo is greater than approximately 7 mm.[77,78] A large visible amniotic sac compared to the CRL is suggestive of abnormal outcome.[45,79] Horrow[77] demonstrated that the difference between the CRL and the amniotic sac diameter is 1.1 ± 2.0 mm in normal embryos but 8.6 ± 3.8 mm in abnormal pregnancies. In abnormal early pregnancies, the chorionic cavity remained appropriate in size relative to the embryonic CRL, indicating that the increased difference in CRL compared to amnion diameter is caused by enlargement of the amnion rather than a small embryo. This finding is especially useful in early embryos before visualization of cardiac activity. As with other predictors of abnormal outcome, patients with abnormal amnion appearance, either the "empty amnion"[45] (Fig. 30.23) or "expanded amnion"[78,79] (Fig. 30.24, Video 30.3) where the amnion is too large for an embryo of a particular size, should be considered to have a nonviable pregnancy. However, the expertise of the individual interpreting the exam is important. If any question remains about viability of the pregnancy, a follow-up ultrasound examination is prudent.[78] At times the clinician may see two sacs within the gestational sac. Although it may be a monochorionic diamniotic pregnancy (see Fig. 30.11), it may also be a failed pregnancy with an empty amnion (or very small embryo with respect to the size of the amnion) and a yolk sac (see Figs. 30.12B and 30.25).

Yolk Sac Size and Shape

Studies have attempted to characterize the normal sonographic appearance of the yolk sac and to identify abnormal morphologic features that may predict poor fetal outcome.[80] In general, a yolk sac diameter greater than 5.6 mm between 5 and 10 weeks is associated with an abnormal outcome in singleton pregnancies.[43] However, a yolk sac greater than 5.6 mm may be seen normally in MCMA twins.[44] Kucuk et al.[80] found that yolk sac shape alone had a sensitivity of 29% and specificity of 95% in predicting an abnormal outcome. An abnormally **large yolk sac** is often the first sonographic indicator of pathology and is often associated with subsequent embryonic demise. Even if the pregnancy survives the first trimester, the fetus may still be abnormal. Although the number of cases is small, large yolk sacs have been associated with abnormalities such as trisomy 21, partial molar pregnancy,[81] and omphalocele; thus follow-up anatomic surveys for the finding of an abnormal appearing yolk sac are recommended.

A **calcified yolk sac** appears as a shadowing echogenic mass in the absence of any other identifiable yolk sac. A calcified yolk sac will usually be seen with a dead embryo and may calcify within 36 hours after demise (Fig. 30.26, Video 30.4).

The yolk sac can be filled with **echogenic material** and is not the same as one that is calcified. This can be seen in live pregnancies. Szabo et al.[82] followed such cases alone and in conjunction with **nuchal lucency** in 3620 first-trimester pregnancies. They found 39 cases (1.0%) of echogenic yolk sacs 1.8 to 4.0 mm in diameter in pregnancies at 9 to 11 weeks' menstrual age; 19 of the 39 (49%) had both a nuchal lucency greater than 3 mm and

FIG. 30.22 Small Sac Size in Relationship to Embryo (MSD – CRL = <5 mm). The gestational sac containing a yolk sac and embryonic pole is smaller than expected. This pregnancy eventually failed.

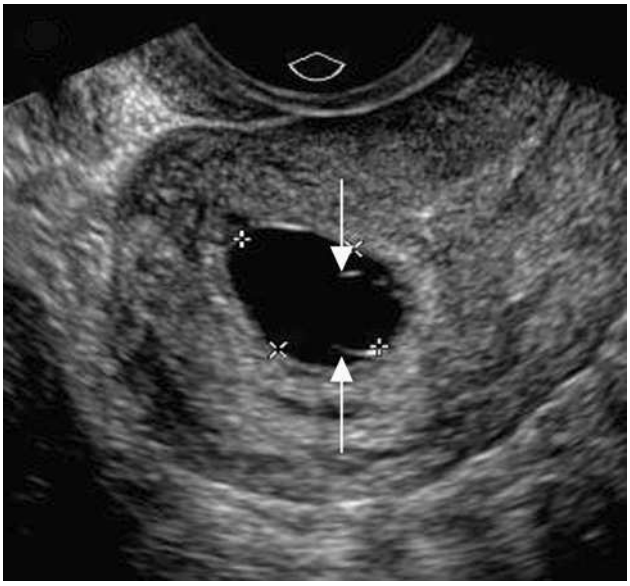

FIG. 30.23 Empty Amnion. TVS at 6 weeks by dates shows gestational sac *(calipers)* with an abnormally large empty amnion *(arrows)*. Early pregnancy failure was later confirmed.

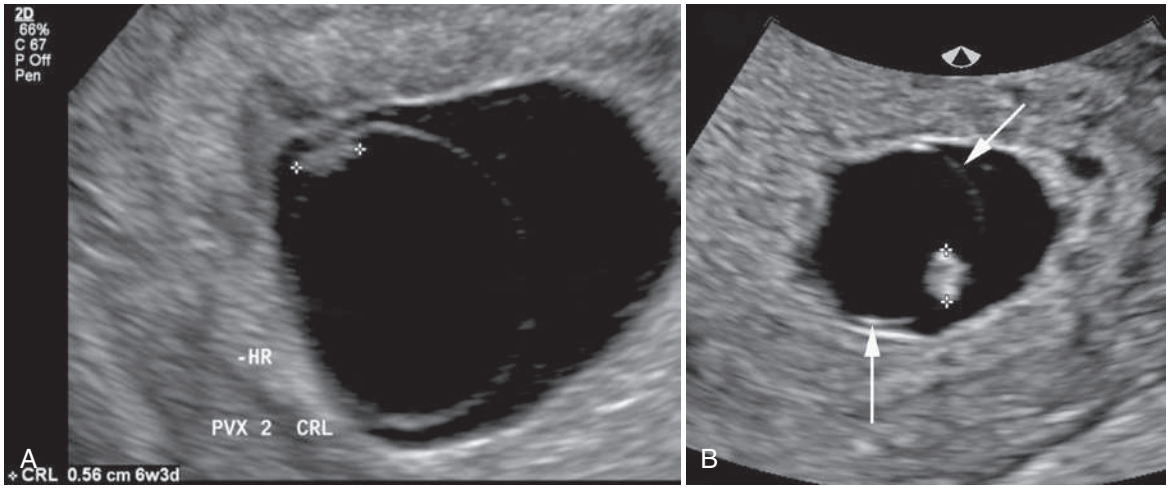

FIG. 30.24 Expanded Amnion in Nonviable Pregnancy. Two different examples **(A)** and **(B)** show a small embryo *(calipers)* with amnion (*arrows* in Figure **B**) that is too large for an embryo of this size. No cardiac activity was documented in either embryo. See also Video 30.3.

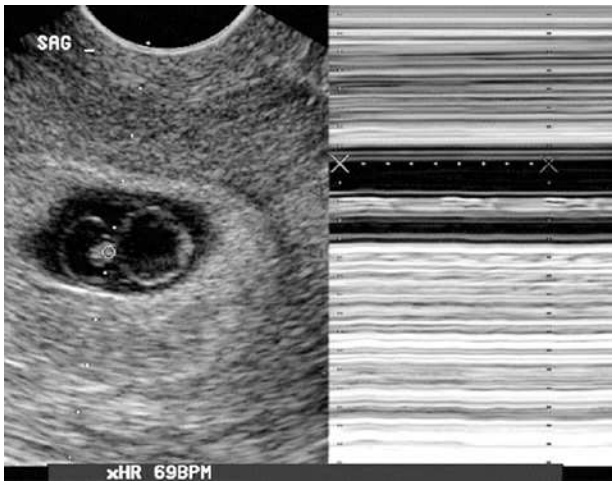

FIG. 30.25 Embryonic Bradycardia. A small embryo in a 10-week by dates pregnancy with a heart rate of 69 beats/min. This embryo later was found to not have cardiac activity. A round amniotic sac is seen on the left and the large yolk sac is seen to the right of the embryo.

an echogenic yolk sac, with all 19 chromosomally abnormal, and the other 20 (51%) had an echogenic yolk sac as the only unusual finding, with all delivered normally.

Embryonic Bradycardia

Although embryonic cardiac activity indicates that the embryo is alive at examination, an abnormally slow heart rate may predict impending demise. The embryonic heart rate increases between 6 and 9 weeks' gestation. At 6 weeks' menstrual age, the mean embryonic heart rate ranges from 90 to 133 bpm, and at 9 weeks' gestation it ranges from 144 to 170 bpm. The lower the heart rate is, the greater the chance is of miscarriage. Doubilet and Benson[49] found that a heart rate less than 80 bpm in embryos with a CRL less than 5 mm was universally associated with subsequent embryonic demise. A rate of 80 to 90, 90 to 99, and 100 bpm were associated with risk of demise of 64%, 32%, and 11%, respectively. Rates below 100 bpm before 6.3 weeks' gestation and below 120 bpm between 6.3 and 7 weeks' gestation are associated with a high risk of miscarriage.[49,83] Additionally, even

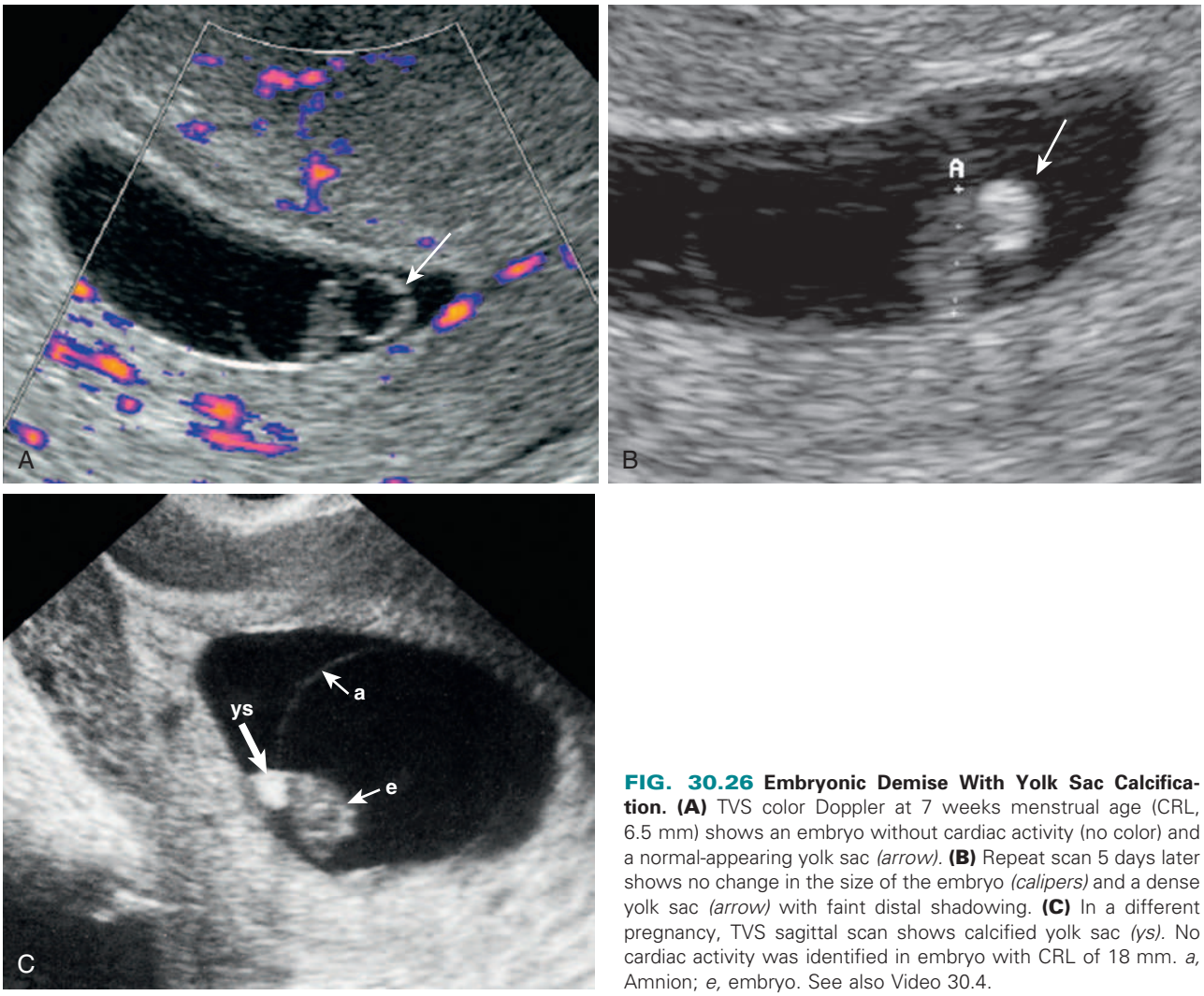

FIG. 30.26 Embryonic Demise With Yolk Sac Calcification. (A) TVS color Doppler at 7 weeks menstrual age (CRL, 6.5 mm) shows an embryo without cardiac activity (no color) and a normal-appearing yolk sac *(arrow)*. **(B)** Repeat scan 5 days later shows no change in the size of the embryo *(calipers)* and a dense yolk sac *(arrow)* with faint distal shadowing. **(C)** In a different pregnancy, TVS sagittal scan shows calcified yolk sac *(ys)*. No cardiac activity was identified in embryo with CRL of 18 mm. *a,* Amnion; *e,* embryo. See also Video 30.4.

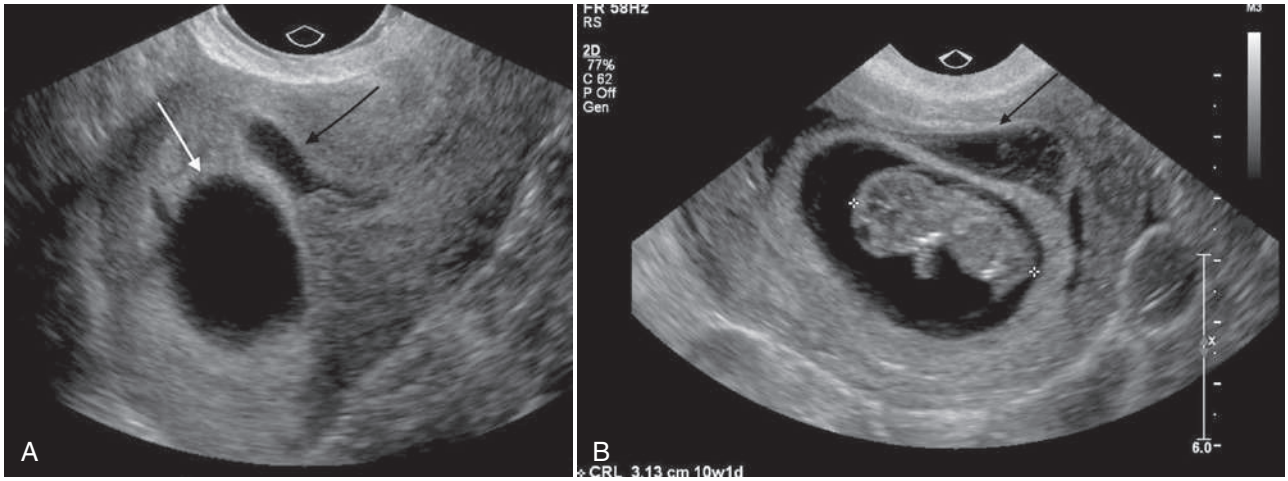

FIG. 30.27 Subchorionic Hematoma. (A) Sagittal TVS at 7 weeks' gestation shows a small hypoechoic collection *(black arrow)* adjacent to the gestational sac *(white arrow)*. The live embryo was not in the field of view. The bleed resolved and pregnancy continued uneventfully. **(B)** In another patient, sagittal transverse TVS at 10 weeks' gestation shows a large subacute hemorrhage *(black arrow)* with a lacy appearance to the clot. A live embryo *(calipers)* is present. See also Video 30.5.

if normal cardiac activity is documented on a follow-up study after 8 weeks, the rate of subsequent first-trimester demise remains elevated if a slow embryonic heart rate is detected at 6 to 7 weeks.[83] Embryos with slow heart rates documented before 7.0 weeks of gestation may also be associated with an increase in cardiac, chromosomal, and other structural anomalies.[84]

Arrhythmia is also an indicator of first-trimester loss.[85] In a group of 950 patients, Vaccaro et al.[85] found four arrhythmias, with three having ventricular bradycardia, all of which were dead on follow-up scan within 2 weeks.

Embryos with abnormally rapid heart rates, above 135 bpm before 6.3 weeks or at least 155 bpm at 6.3 to 7.0 weeks have a good prognosis, with a high likelihood of normal outcome.[86]

Subchorionic Hemorrhage

Subchorionic hemorrhage, or a hematoma resulting from elevation of the placental margin or marginal sinus rupture,[87] causes elevation of the chorionic membrane (Fig. 30.27, Video 30.5). **Acute hemorrhage** is usually hyperechoic or isoechoic relative to the decidua. The hemorrhage gradually becomes sonolucent in 1 to 2 weeks.

This finding may be associated with vaginal bleeding. The incidence of subchorionic hematomas early in pregnancy ranges from 1.3% to 18%.[88] The association of subchorionic hematomas with early pregnancy failure is variable, but most studies support that worse outcomes are seen in "large" hematomas extending 50% or more of the circumference of the gestational sac and in hematomas diagnosed earlier in the first trimester (Fig. 30.27B).

Pedersen and Mantoni[89] studied 342 pregnant women from 9 to 20 weeks' gestation presenting with vaginal bleeding and found subchorionic hematomas in 18%, averaging 20 mL (range, 2-150) in size. This study found no difference in the rate of miscarriage (10%) or premature delivery (11%) between the patients with and without subchorionic hematomas.

In a retrospective study of 516 patients with first-trimester bleeding, Bennett et al.[90] found an overall pregnancy loss rate of 9.3%. Pregnancy loss increased with increasing maternal age and decreasing gestational age. For women over age 35, the rate is 13.8% (vs. 7.3 for those younger than 35 years), and for those presenting at or before 8 weeks, it is 13.7% (vs. only 5.9% for those later in gestation). The most important predictor for pregnancy loss was the presence of a large subchorionic hemorrhage.[90] The small or medium-sized hemorrhages (i.e., ≤50% the sac circumference) had a miscarriage rate of 9%, versus 18.8% for the larger subchorionic hemorrhages. In a study involving patients from 5 to 14 weeks' gestation, Leite et al. found that patients with very large hematomas were associated with adverse outcome in 46% of pregnancies. In their study, vaginal bleeding was not associated with a poor prognosis, but diagnosis at early gestational age was associated with a worse outcome.[91]

ECTOPIC PREGNANCY

Ectopic pregnancy remains one of the leading causes of maternal death in the United States. It accounts for 1.4% of all pregnancies and approximately 15% of maternal deaths. Although the incidence of ectopic pregnancy is increasing, the mortality rate has declined to less than 1 in 1000 cases compared with 3.5 in 1000 in 1970.[92,93] The increased incidence is likely caused by increased prevalence of the risk factors as well as earlier diagnosis, whereas heightened awareness and improved diagnostic capabilities have led to a decrease in the mortality rate.

Clinical Presentation

The classic clinical triad of pain, abnormal vaginal bleeding, and a palpable adnexal mass is present in approximately 45% of patients with ectopic pregnancy.[94] In addition, the positive predictive value of this triad is only 14%. Other presenting signs and symptoms include any combination of the classic triad, as well as amenorrhea, adnexal tenderness, and cervical motion tenderness. Schwartz and Di Pietro[94] found that only 9% of patients with clinically suspected ectopic pregnancy actually had an ectopic pregnancy, whereas 17% had symptomatic ovarian cysts, 13% had pelvic inflammatory disease, 8% had dysfunctional uterine

bleeding, and 7% had spontaneous abortions. The clinical presentation is thus nonspecific. In addition, even in retrospect, 8.7% of proven ectopic pregnancies are sonographically normal at the time of initial evaluation.[95]

The **prevalence** of ectopic pregnancy varies according to the patient population and their inherent risk factors. Nevertheless, all patients in the reproductive age group are at risk. Factors that increase the **risk** of ectopic pregnancy include tubal abnormality preventing passage of the zygote or resulting in delayed transit; previous ectopic pregnancy,[96,97] cesarean section, or tubal reconstructive surgery; pelvic inflammatory disease; chlamydial salpingitis[98]; intrauterine contraceptive devices; and increased age or parity.

There is an association between **infertility** and ectopic pregnancy, likely because of the shared tubal abnormalities in both conditions. The risk factors for ectopic pregnancy are therefore present in patients who undergo ovulation induction or IVF and embryo transfer. The increased incidence of multiple pregnancies with ovulation induction and IVF further increases the risk for both ectopic and **heterotopic** (coexistent intrauterine and ectopic) gestation. The hydrostatic forces generated during **embryo transfer** may also contribute to the increased risk.[99] The frequency of heterotopic pregnancy was originally estimated on a theoretic basis to be 1 in 30,000 pregnancies. More recent data indicate that the rate is approximately 1 in 7000 pregnancies.[100,101]

Risk of Ectopic Pregnancy

Any tubal abnormality that may prevent passage of zygote or result in delayed transit
Previous tubal pregnancy
History of tubal reconstructive surgery
Pelvic inflammatory disease
Intrauterine contraceptive device
Increased maternal age
Increased parity
Previous cesarean section

Sonographic Diagnosis

Because any woman of child-bearing age is at risk for ectopic pregnancy, determining the location of a pregnancy is required for any pregnant woman who has a pelvic ultrasound. The differential diagnosis for pelvic pain in early pregnancy is vast, including ectopic pregnancy, early pregnancy failure, tubo-ovarian torsion, degenerating fibroids, and ovarian cysts.

A limited TAS is recommended in all cases of suspected ectopic pregnancy in which the TVS does not provide a clear diagnosis, looking for findings that may be outside the range of the transvaginal probe. Although a full bladder is preferred, in the emergent setting patients should not be required to fill their bladder prior to imaging.[102] The TAS exam should include views of the uterus and adnexa in the sagittal and transverse orientations. When fluid is seen in the pelvis, it is helpful to look higher in the abdomen for the extent of fluid to provide a sense of the degree of blood loss. With a large volume of blood loss, the patient could decompensate rapidly. Fluid seen in the upper abdomen should impart a greater sense of urgency to the clinical setting (Figs. 30.28 and 30.29).

TVS assessment of the uterus, ovaries, and adnexal regions should almost always be performed, as it is superior to TAS in evaluating the endometrial contents and adnexa, providing a diagnosis more often and earlier. Views of the uterus in the sagittal and transverse planes should be performed to assess for a small gestational sac. The adnexa should be imaged with documentation of the ovaries as well as the space between the ovaries and uterus as this is the most common location of an ectopic adnexal mass.[103] During the TVS, it may be helpful to perform a gentle bimanual examination with the probe and a hand providing gentle pressure to move a questionable mass away from the ovary. If the mass moves separately from the ovary (Video 30.6), it is more likely to be an ectopic mass rather than an ovarian mass, most commonly a corpus luteal cyst. A suspected ectopic mass should be assessed during the TVS for local tenderness. The probe is used to apply light pressure on the mass. This pressure almost always elicits pain similar to the

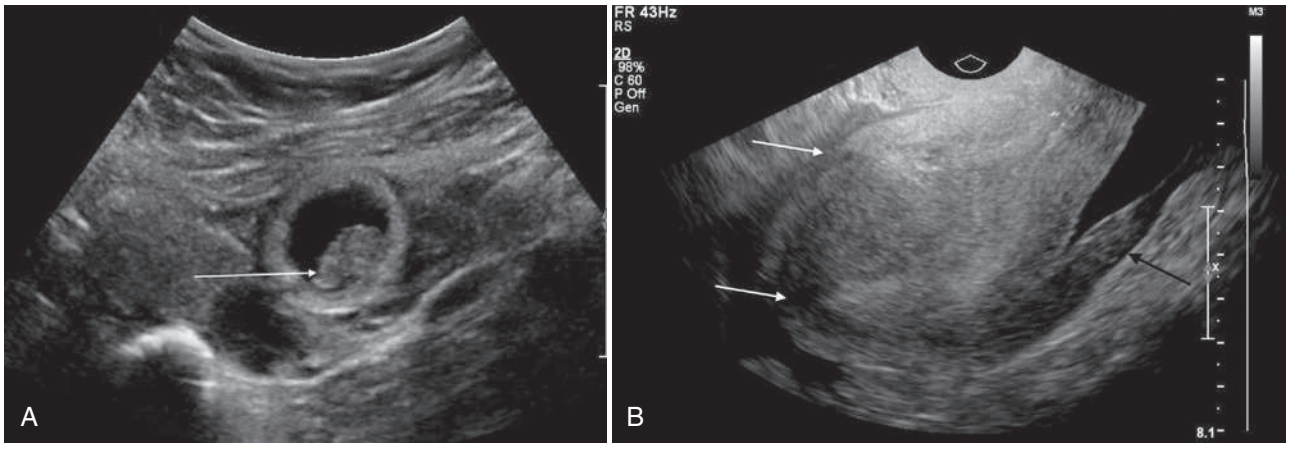

FIG. 30.28 Live Ectopic Pregnancy. A 33-year-old woman with left lower quadrant pain at 9 weeks' gestation. **(A)** Transverse TAS of the right adnexa shows a gestational sac with an embryo. Cardiac activity was seen at real-time imaging. **(B)** TVS shows the uterus *(white arrows)* and some clot in the cul-de-sac *(black arrow)*. However, the ectopic pregnancy was only seen on the TAS.

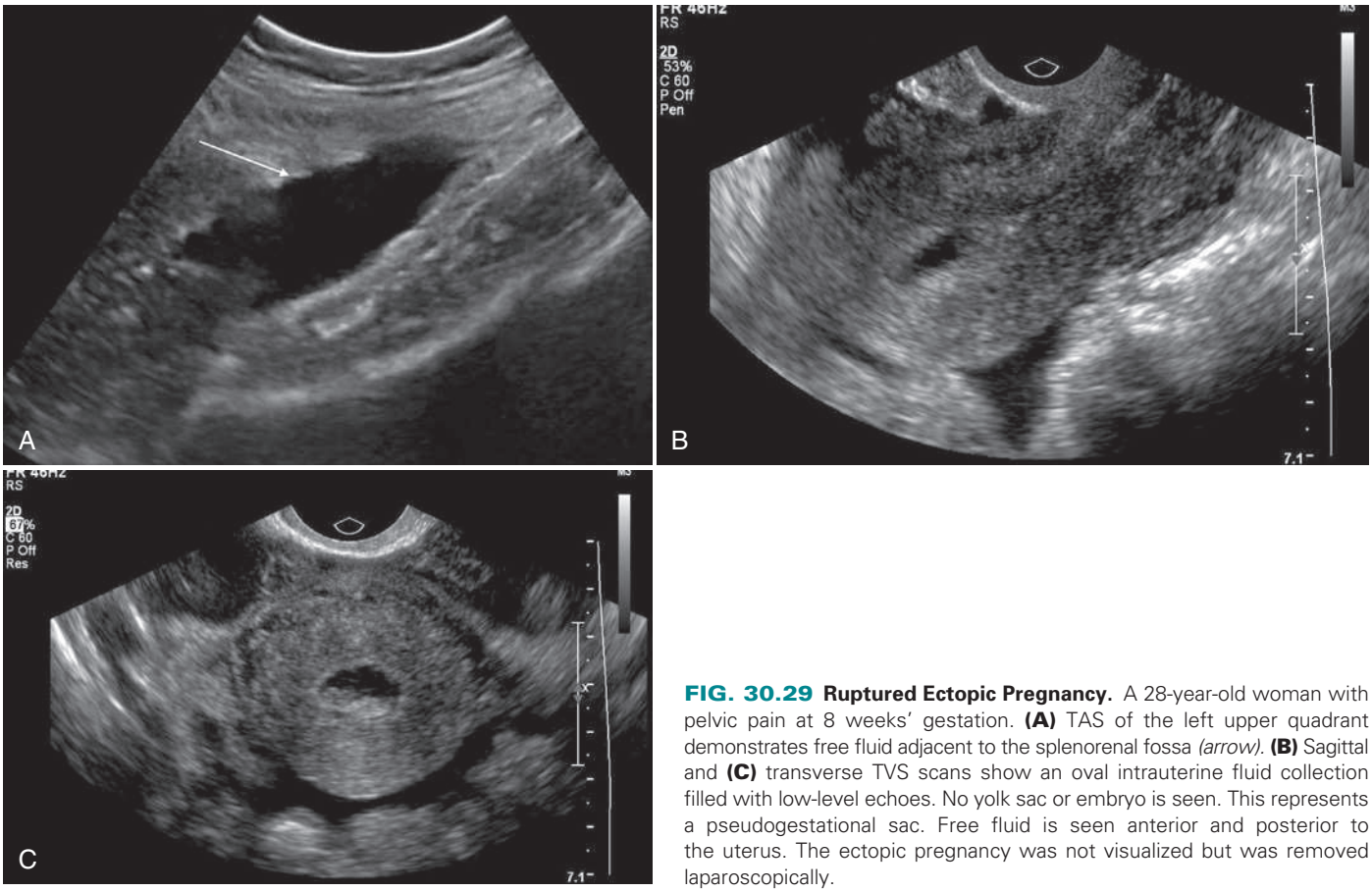

FIG. 30.29 Ruptured Ectopic Pregnancy. A 28-year-old woman with pelvic pain at 8 weeks' gestation. **(A)** TAS of the left upper quadrant demonstrates free fluid adjacent to the splenorenal fossa *(arrow)*. **(B)** Sagittal and **(C)** transverse TVS scans show an oval intrauterine fluid collection filled with low-level echoes. No yolk sac or embryo is seen. This represents a pseudogestational sac. Free fluid is seen anterior and posterior to the uterus. The ectopic pregnancy was not visualized but was removed laparoscopically.

sensation that brought the patient to hospital initially. Pain can also be felt with other inflammatory or expanding masses, such as a hemorrhagic corpus luteum. The pelvis and cul-de-sac should be examined for fluid.

TVS ultrasound may miss an ectopic pregnancy located high out of the field of view of the probe or when a pelvic mass such as a fibroid or bowel gas is located between the vagina and the adnexa.[104-106] In 5% of cases, findings may be present that only TAS can identify[107] (see Fig. 30.28).

Heterotopic Gestation

If a normal IUP is identified, the likelihood of ectopic pregnancy is drastically reduced. In the presence of an IUP, the risk of coexistent ectopic pregnancy **(heterotopic gestation)** lies between 1 in 4000 and 1 in 7000.[100,108] However, even in the presence of an IUP, evaluation of the adnexa should be performed to screen for a possible coexistent ectopic pregnancy, especially in women who present with adnexal pain and women with a history of assisted reproduction techniques such as IVF.[109] The risk for heterotopic pregnancy may be as high as 1% to 3% in women undergoing ovulation induction[110] (Fig. 30.30).

Serum β-hCG Levels

Serum β-hCG levels play an important adjunctive role in the early diagnosis of ectopic pregnancy. A negative β-hCG level excludes the possibility of live pregnancy in a woman presenting with pain whereas a negative ultrasound does not. As previously stated, the WHO recommends that the Third IS and the identical Fourth IS should be used for calibration of immunoassays.[37] In general, we expect to visualize a gestational sac when the β-hCG level is greater than 2000 mIU/mL (IRP). Discriminatory levels such as this can be used to guide management but cannot be used as absolute indicators that the absence of a sonographically demonstrable gestation sac with this level of β-hCG is abnormal. A 2013 study by Connolly found that of 366 patients with first-trimester pain and bleeding, whose pregnancies ultimately were shown to be viable, a hCG level of 3510 mIU/mL was needed for a gestational sac to be seen 99% of the time.[111] Serial β-hCG measurements are usually more helpful than a single measurement in identifying abnormal from normal pregnancy, and ultrasound may document important diagnostic features regardless of the β-hCG value.[5] The β-hCG level in a normal pregnancy has a doubling time of approximately 2 days, whereas patients with a failed or failing gestation have a falling β-hCG level. Patients with ectopic pregnancy usually have a slower increase in β-hCG levels, although they occasionally show patterns similar to a normal pregnancy or spontaneous abortion.

Specific Sonographic Findings

The most specific sonographic sign of ectopic pregnancy is documentation of a live embryo in an extrauterine location (Fig.

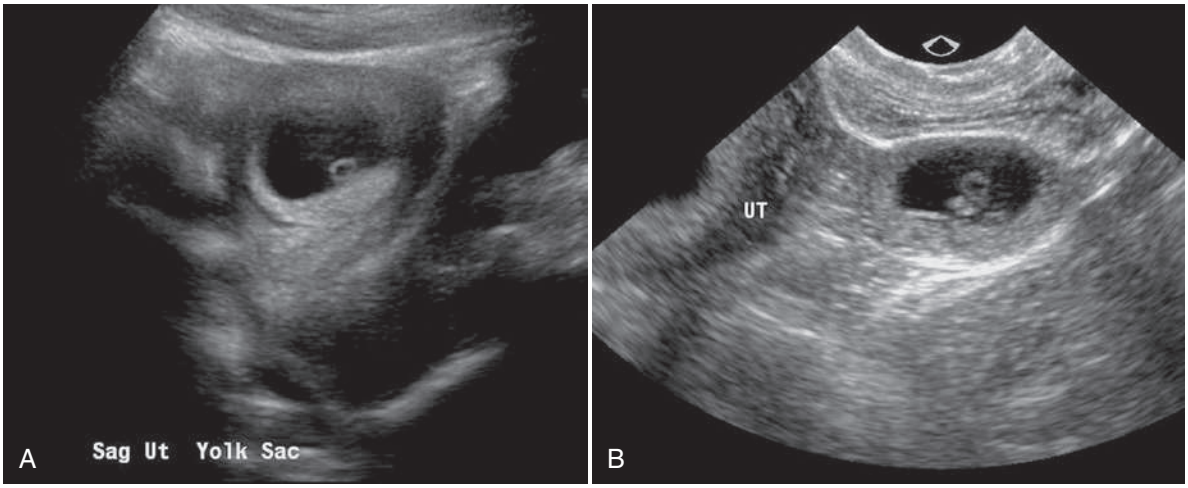

FIG. 30.30 Heterotopic Pregnancy at 6 Weeks. (A) Sagittal TAS demonstrates an intrauterine gestational sac containing a yolk sac. **(B)** Transverse TVS shows an extrauterine gestational sac in the left adnexa. The left ectopic pregnancy was treated surgically and the patient went on to have an otherwise uneventful pregnancy. *UT,* Uterus.

30.30). This finding is 100% specific but a has a low sensitivity of 15% to 20%.[104,112]

Nonspecific Sonographic Findings

Adnexal Mass

The most common location for ectopic pregnancy to occur is in the fallopian tube, with 75% to 80% in the ampullary portion, 10% in the infundibular, 5% in the fimbria, and 2% to 4% in the interstitial segment. Ectopic pregnancies in a tubal location often produce a mass in the adnexa, which is the most common ultrasonographic finding.[107,113] The mass may be solid or heterogeneous and is comprised mostly of blood products from bleeding into the wall and lumen of the fallopian tube. Adnexal masses containing a tubal ring with or without central identifying features such as yolk sac or embryo increases the specificity of the finding.[103]

Using TVS Fleischer et al.[114] found an **ectopic tubal ring** in 49% of patients with ectopic pregnancy and in 68% of unruptured tubal pregnancies. The tubal ring can usually be differentiated from a corpus luteum cyst because the cyst is eccentrically located with a rim of ovarian tissue. A tubal ring is a concentric ring created by the trophoblast of the ectopic pregnancy surrounding the chorionic sac. This ring is often within a hematoma that may be confined to the fallopian tube or that may extend outside it (Fig. 30.31). Frates et al.[115] found that an ectopic tubal ring was more echogenic than ovarian parenchyma, in contrast to the corpus luteum, which typically is as echogenic or less echogenic than ovarian parenchyma. The wall of the corpus luteum is usually less echogenic than the endometrium, whereas Stein et al.[116] found that the tubal ring of an ectopic pregnancy was more echogenic than the endometrium in 32% of cases, a finding that can be helpful in distinguishing between a tubal ring and a corpus luteum cyst.

The ectopic tubal ring may be obscured or replaced by a mass that is often echogenic (Fig. 30.31) but may be of mixed echogenicity. Easily overlooked or mistaken for fat or bowel, these masses will be found only with a high index of suspicion and careful TVS of the adnexa, looking for the tubal ring or mass that is focally tender. Color Doppler can be helpful in finding the mass, which may be hyperemic (Fig. 30.31B). However, the corpus luteum also is hyperemic and is much more common than ectopic pregnancy, so merely seeing a "ring of fire" around an adnexal lesion is not sufficient for diagnosis of ectopic pregnancy. Other entities can cause an adnexal mass such as hemorrhagic corpus luteum cyst, endometriosis, and abscess and is therefore not diagnostic.[114]

Free Fluid

TVS is extremely sensitive in detecting **free pelvic fluid.** Small amounts of free fluid can be seen in both ectopic and intrauterine pregnancies. The presence of echogenic free fluid (Figs. 30.28B and 30.31B, Video 30.7) or blood clots in the posterior cul-de-sac in pregnant patients, without sonographic evidence of an IUP and especially when found in high quantities or in association with an adnexal mass, indicates a high risk of ectopic pregnancy but can also be seen in cases of ruptured corpus luteum cyst. Echogenic fluid correlates with hemoperitoneum at surgery.[117] Thus if there is a large amount of blood in the pelvis and an ectopic pregnancy is not visualized, whether the diagnosis is ruptured ectopic pregnancy or ruptured ovarian cyst is not as important as the hemodynamic stability of the patient. Unstable patients are treated surgically with either diagnosis.

Endometrium

There is no specific endometrial appearance or thickness that can be used to distinguish a patient with ectopic pregnancy from those with an early IUP.[118] The most common appearance of the endometrium in ectopic pregnancy is normal or a generalized increased echogenicity due to decidual reaction. Pseudogestational sacs are endometrial fluid collections surrounded by echogenic endometrium from a prominent decidual reaction. These fluid collections are present in 5% to 10% of ectopic pregnancies. They tend to be lenticular in shape (Fig. 30.29B) with internal

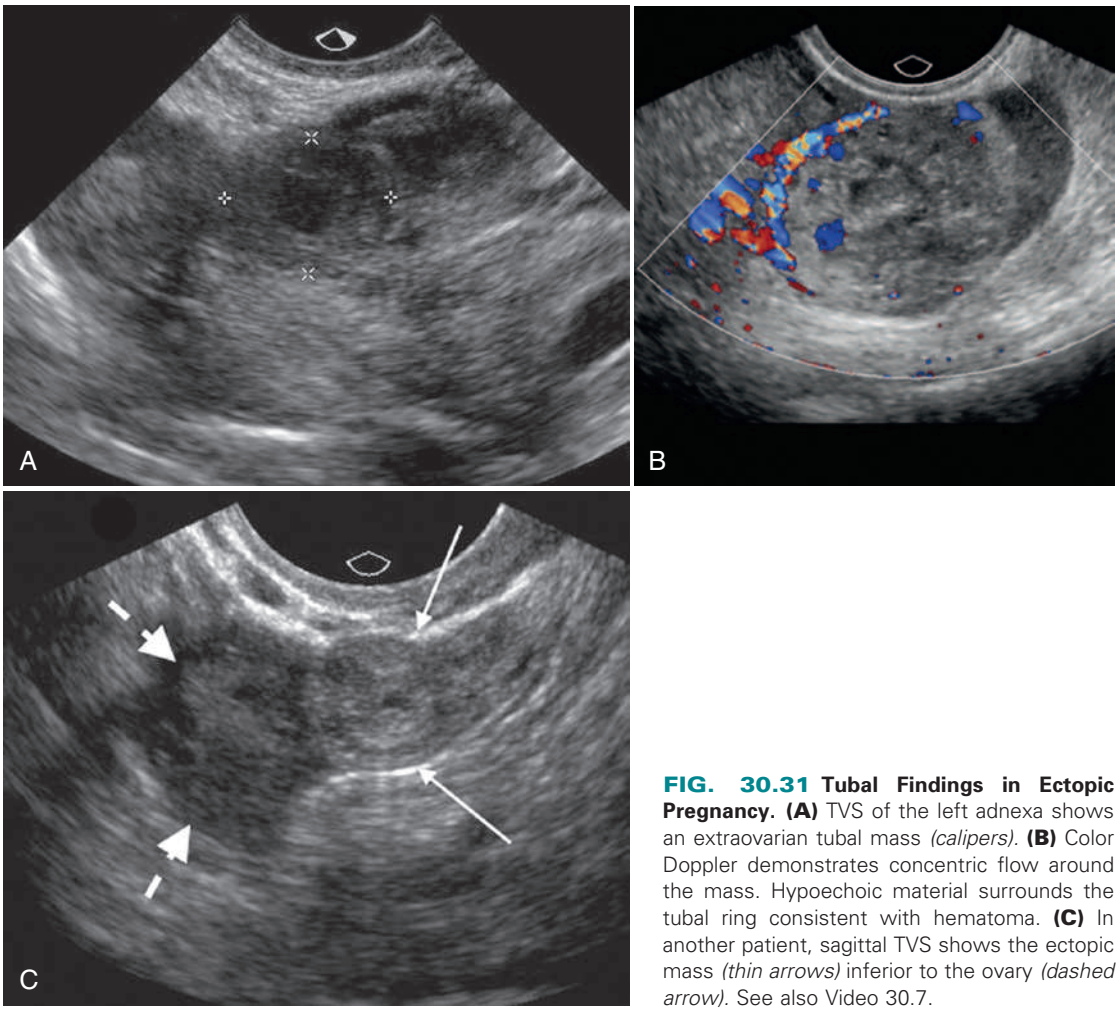

FIG. 30.31 Tubal Findings in Ectopic Pregnancy. (A) TVS of the left adnexa shows an extraovarian tubal mass *(calipers).* **(B)** Color Doppler demonstrates concentric flow around the mass. Hypoechoic material surrounds the tubal ring consistent with hematoma. **(C)** In another patient, sagittal TVS shows the ectopic mass *(thin arrows)* inferior to the ovary *(dashed arrow).* See also Video 30.7.

echoes due to blood, but they can be smooth and rounded with debris that could be mistaken for products of conception.[104,109]

Implantation Sites

Ectopic pregnancy may occur in several sites. Approximately 95% of ectopic pregnancies occur in the ampullary or isthmic portions of the fallopian tube. The second most common site, about 2% to 4% of all ectopic pregnancies, is an interstitial pregnancy occurring in the intramural portion of the tube, where it traverses the wall of the uterus to enter the endometrial canal[103] (Fig. 30.32).

Implantation in the superior lateral portion of the endometrial canal but not within the intramural portion of the tube is normal and is not an ectopic pregnancy. This is often mistaken for an ectopic pregnancy, but echogenic endometrium can be seen around the sac (double-decidual sign), and if followed even for 1 week, the sac grows and attains a more typical appearance in the endometrial canal. Three-dimensional ultrasound can add in the confidence of the diagnosis of both interstitial ectopic and eccentric intrauterine pregnancy.[119]

Because of the distensibility of this portion of the fallopian tube, **interstitial ectopic pregnancies** may present and rupture later than other tubal gestations, often causing massive intraperitoneal hemorrhage from the dilated arcuate arteries and veins, which lie in the outer third of the myometrium between the thin outer myometrium and the thick intermediate layer.[119] The mortality of interstitial pregnancy is twice that of other ectopic pregnancies. Ackerman et al.[120] found that the two currently used sonographic signs of myometrial thinning and sac eccentricity are unreliable and described the more useful **interstitial line sign.** The interstitial line is a thin, echogenic line extending from the endometrial canal up to the center of the interstitial sac or hemorrhagic mass. It was seen in 92% of interstitial ectopic pregnancies. The line is the nondistended, empty endometrial canal. The interstitial ectopic pregnancy is usually surrounded by trophoblast but should not have a double-decidual sign. Treatment historically was surgical with cornual resection, but now less invasive therapy with local injection of potassium chloride or with local or intramuscular injection of methotrexate is performed to avoid uterine surgery. Occasionally this type of ectopic pregnancy is mistakenly called a **"cornual pregnancy."** However this term should be reserved for a gestational sac lying within a rudimentary horn or within one horn of a bicornuate uterus.[119]

Cervical ectopic pregnancies are to the result of implantation in the endocervical canal (Fig. 30.33). They are rare, accounting

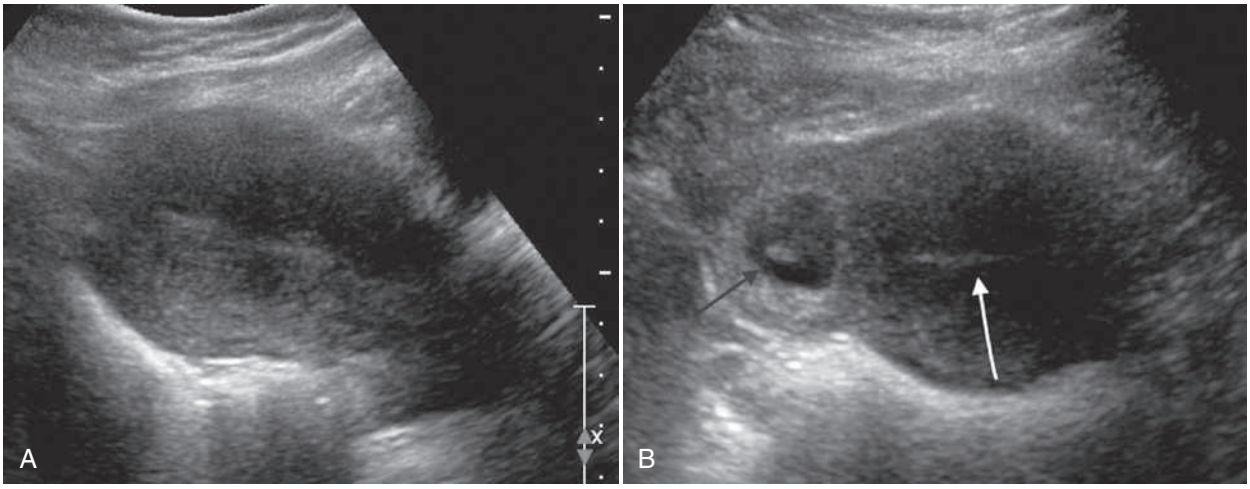

FIG. 30.32 Interstitial Ectopic Pregnancy. (A) Sagittal TAS demonstrates an unremarkable endometrial stripe. **(B)** Transverse TAS shows a gestational sac containing an embryo *(black arrow)* eccentrically positioned within the uterus, separate from the endometrial stripe *(white arrow)*. The pregnancy was terminated with direct injection of methotrexate within the gestational sac, avoiding uterine surgery.

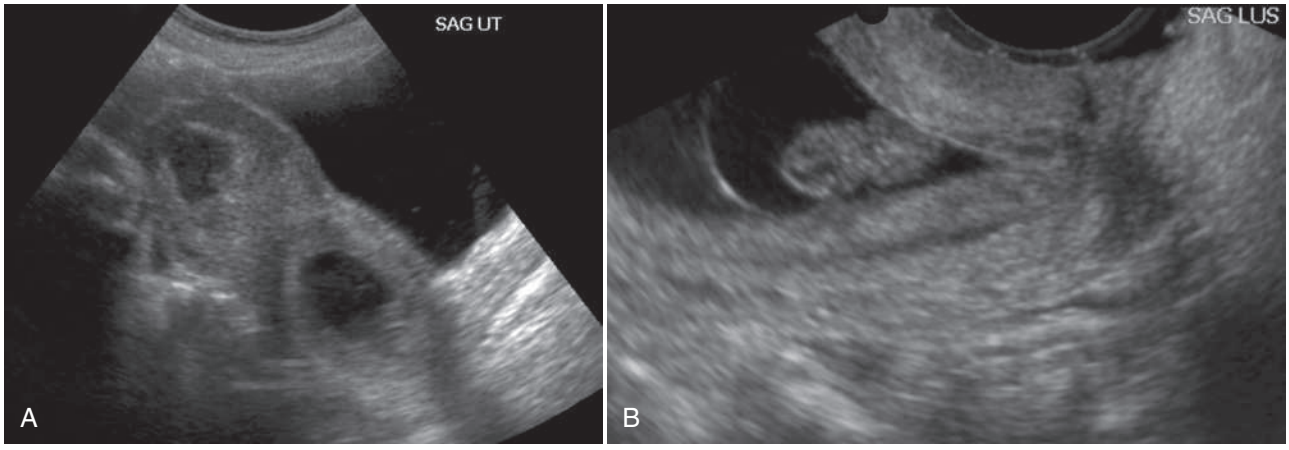

FIG. 30.33 Cervical Ectopic Pregnancy. (A) TAS sagittal view of the uterus shows a pseudogestational sac in the endometrium. A second fluid collection is seen in the cervix secondary to the gestational sac. **(B)** Sagittal TVS of the cervix shows a gestational sac containing an embryo.

for less than 1% of all ectopic pregnancies, and can be confused with abortion in progress. Ultrasound can help to distinguish an intracervical ectopic pregnancy by documenting an embryo with a heartbeat or color Doppler–documented peritrophoblastic flow. Remember that an aborting gestational sac may present in the lower uterine segment and cervix on its way out of the uterus. Sonographically in an aborting gestation, the sac will be oblong, the embryo (if present) will not have a heartbeat, and there will be no trophoblastic vascularity because it has detached from the uterine wall. Clinically, both situations are associated with vaginal bleeding, but the abortion will more likely produce crampy pain as well. Occasionally an abortion in progress will still show flow when being scanned, but follow-up imaging will show lack of flow. Therefore before any interventional procedure for a cervical ectopic is performed, we always check to see if cardiac activity is still present.

Cesarean scar implantation appears to be increasing, with more cases appearing in the literature.[121] The patient may present with painless vaginal bleeding and a history of one or more cesarean sections. An early sonogram will show a sac implanted in the lower uterine segment, with local thinning of the myometrium (Fig. 30.34, Video 30.8). There is usually prominent vascularity at the implantation site. Catastrophic hemorrhage may result, with the need for complete hysterectomy. Treatment of a scar implantation is often protracted. A dilation and curettage procedure is seldom advised because the thin lower segment may be perforated. Medical therapy is more common, with methotrexate taken systemically and often injected locally as well. Presence of a live embryo may require careful injection of potassium chloride into the embryo to stop cardiac activity.

Abdominal pregnancies are also rare. These pregnancies often result from uterine rupture from an interstitial ectopic pregnancy (Fig. 30.35) but may also more rarely occur from direct implantation. When diagnosed in the first trimester, these pregnancies are typically treated in a similar way to tubal ectopic pregnancies. When diagnosed in the third trimester, abdominal pregnancies may result in a viable neonate.

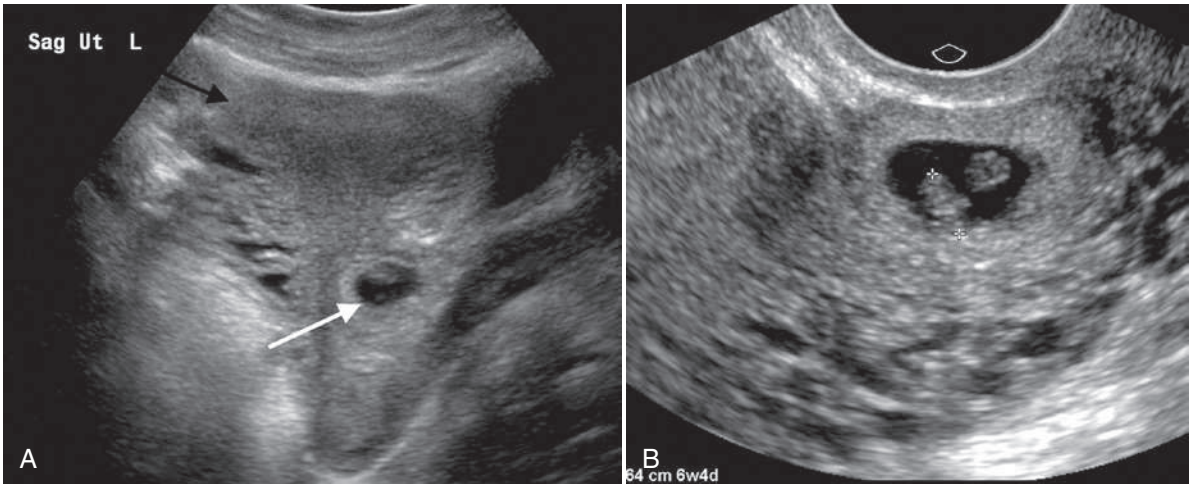

FIG. 30.34 Cesarean Scar Implantation. (A) TAS at 7 weeks' gestation shows a sac *(white arrow)* in the anterior lower uterine segment, far from the uterine fundus *(black arrow).* **(B)** TVS shows the sac in the region of the c-section scar with an embryo *(calipers)* and yolk sac. No myometrium is visualized anterior to the sac. See also Video 30.8.

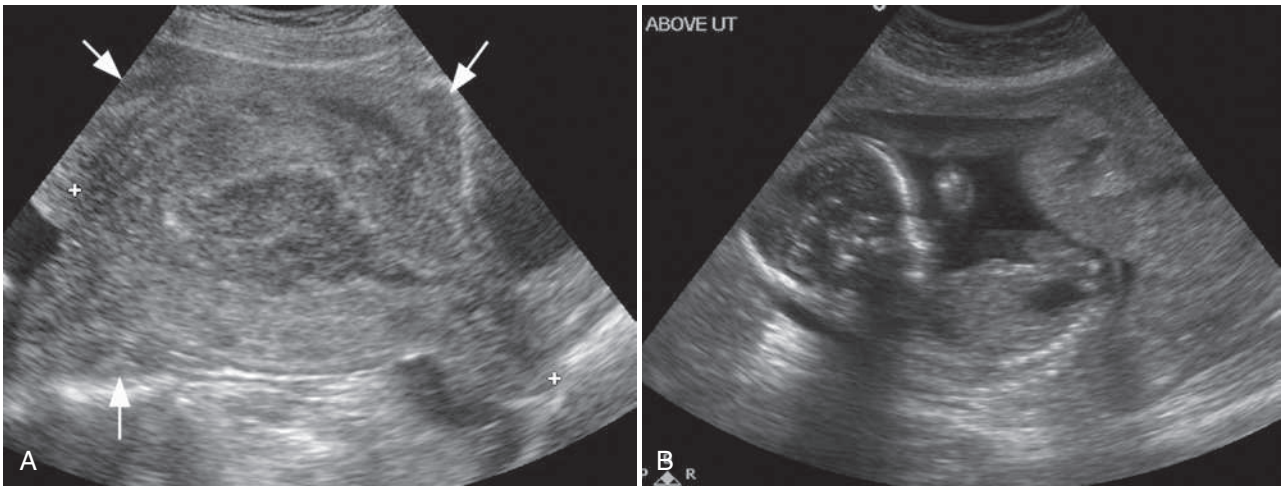

FIG. 30.35 Abdominal Ectopic Pregnancy. A 19-year-old woman with acute abdominal pain and syncope. **(A)** Sagittal TAS demonstrates a mildly enlarged uterus with an endometrial cavity distended with blood. Blood is also seen surrounding the uterus *(arrows).* **(B)** TAS superior to the uterine fundus demonstrates a 15-week abdominal ectopic pregnancy. Surgical treatment confirmed abdominal ectopic secondary to uterine rupture caused by an interstitial ectopic pregnancy.

Pregnancy of Unknown Location

In first-trimester patients, the initial TVS correctly identifies the site of in over 90% of patients.[106] In the absence of a well-defined IUP, or in the absence of an ectopic pregnancy, other findings can suggest the location of the implantation but are nonspecific and can result in diagnostic error. Recently, women with a positive pregnancy test who have no evidence of either an IUP or ectopic pregnancy on TVS have been categorized as having **pregnancy of unknown location** (PUL).[122,123] The differential diagnosis for PUL includes a very early IUP, an abnormal IUP, spontaneous miscarriage, and ectopic pregnancy.[124] The proportion of patients categorized as PUL depends on gestational age at examination (and of course depends on the quality of the scan and expertise of the imager).

In a series of 5318 unselected women in the first trimester, 456 (8.7%) were classified as PUL.[106] Of the 456 patients classified as PUL, 31 (6.8%) had ectopic pregnancies. The PUL group benefits from close follow-up because of their high incidence of ectopic pregnancy. Kirk et al.[106] showed that a single TVS examination correctly diagnosed ectopic pregnancy in 96.1% of patients undergoing surgical management. Therefore 3.9% of patients diagnosed with ectopic pregnancy and treated nonsurgically could have normal or abnormal IUPs. Thus it is important to consider the clinical history and presentation before using nonspecific parameters in the management of patients with ectopic pregnancy.

Management

The conventional management of ectopic pregnancy has been surgical, with resection of the diseased tube. Improved diagnostic capabilities, including TVS, allow for earlier diagnosis and the potential for a more conservative approach to treatment. The

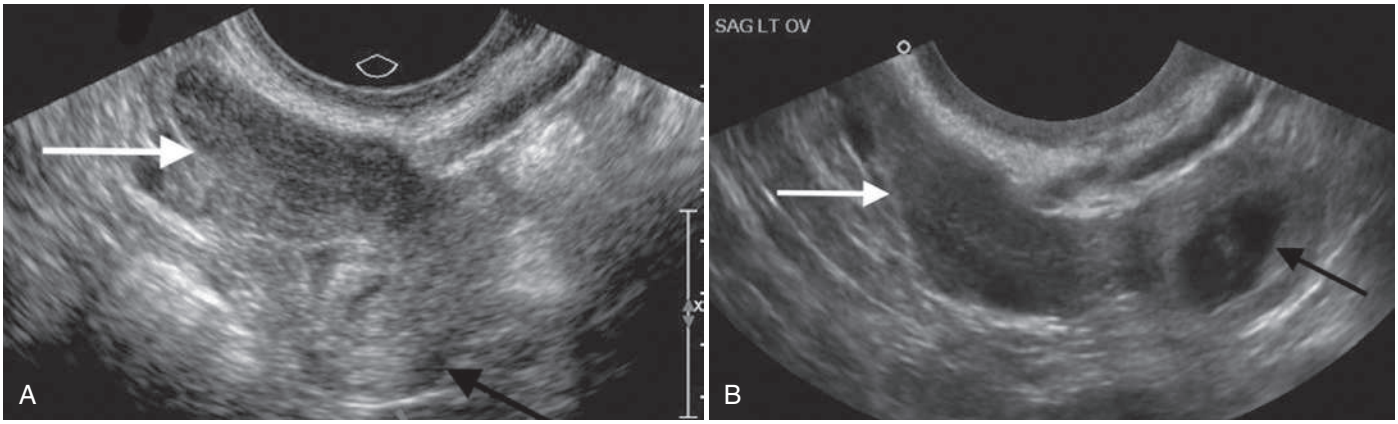

FIG. 30.36 Left Ectopic Pregnancy Failed Medical Management. A 38-year-old woman with pain and bleeding from left ectopic pregnancy treated with methotrexate. **(A)** At initial diagnosis, left extraovarian ectopic mass *(black arrow)* was found adjacent to the left ovary *(white arrows).* HCG levels continued to rise. **(B)** Repeat scan 2 weeks later shows growth of adnexal mass now containing a gestational sac with embryonic pole. The ectopic pregnancy was then treated successfully with salpingectomy.

ultimate goal is to diagnose the ectopic pregnancy before tubal rupture and to treat it so as to minimize tubal scarring while maintaining tubal patency.

Laparoscopy is often used for definitive diagnosis in ectopic pregnancy and for the more conservative surgical procedures such as salpingotomy.[125] The diseased tube is incised and microdissection used to remove the gestational sac. The incision is then left to heal by secondary intention. The rate of subsequent IUP in these surgical patients is 61.4%, with a 15% rate of recurrent ectopic pregnancy.[126]

Medical management has also been successful in the treatment of early ectopic pregnancy. Cell growth inhibitors such as methotrexate are injected systemically (intravenous, intramuscular, or oral administration) and the serum β-hCG levels followed closely. The methotrexate kills the rapidly dividing trophoblastic cells, which are then reabsorbed, resulting in falling β-hCG levels and, ideally, preservation of the tubal lumen.[127] Success rates range from 61% to 93% for local injection[128] and from 65% to 94% for intramuscular treatment.[129] The rate of side effects is 21% with parenteral administration and 2% with local injection under ultrasonic guidance.

Medical treatment is most successful in tubal pregnancies (vs. interstitial ectopic pregnancy or cervical ectopic pregnancy), those cases with smaller ectopic masses, less free fluid, and those without embryonic cardiac activity.

Barnhart et al.[130] reviewed studies of multidose and single-dose regimens of methotrexate and found an overall success rate of 89% (1181 of 1327 women). The single dose was used more often but was associated with a significantly greater chance of failure than multidose therapy, although it had fewer side effects. Hajenius et al.[128] compared treatment options of laparoscopy, laparotomy, methotrexate (local vs. systemic, single vs. multiple dose), and expectant management (where patients are monitored without treatment). Multidose intramuscular methotrexate is most cost-effective in patients with low serum β-hCG than laparoscopic salpingostomy. In all cases, both therapies had similar results, with laparoscopy having a higher cost and longer hospital stay.

Nazac et al.[129] studied 137 women with an unruptured ectopic pregnancy and hematosalpinx seen on TVS. They found that in cases with an hCG level less than 1000 mIU/mL, local injection of methotrexate (1 mg/kg) directly into the sac after first aspirating the contents had a 92.5% success rate compared with 67% for intramuscular administration. The local injection was performed vaginally using the same technique as for follicle aspiration during oocyte retrieval in IVF.

A common complication of methotrexate therapy is a rupture of the ectopic pregnancy, with increased pelvic pain and tenderness and the appearance of a hemorrhagic mass. Usually these will resolve with conservative management but occasionally will require surgical intervention. Even with successful treatment of an ectopic pregnancy, an adnexal mass may increase in size as a result of edema and hemorrhage. However, any evidence of further continuation of growth of the ectopic pregnancy is evidence of failure of the therapy (Fig. 30.36).

Conservative management is becoming more common for the stable patient with low or declining levels of β-hCG. Success rates of up to 69.2% have been reported.[126]

EVALUATION OF THE EMBRYO

The diagnosis of specific fetal anomalies in the first trimester is discussed in the chapters pertaining to the involved organ system. Nuchal translucency screening is discussed in the Chapter 31. This discussion is limited to general principles of assessment of the embryo in the first trimester. Current trends in first-trimester diagnosis, including widespread acceptance of TVS, nuchal translucency screening, maternal serum markers, and cell free DNA testing, combined with improved sonographic resolution, have resulted in the potential diagnosis of a wide range of defects in the first trimester. As the resolution of ultrasound equipment improves, visualization of embryologic structures becomes possible. It is critical that incorrect decisions are not made on the basis of incomplete understanding of normal and abnormal embryonic and fetal anatomy in the first trimester. Therefore if any uncertainty surrounds the findings in an early scan,

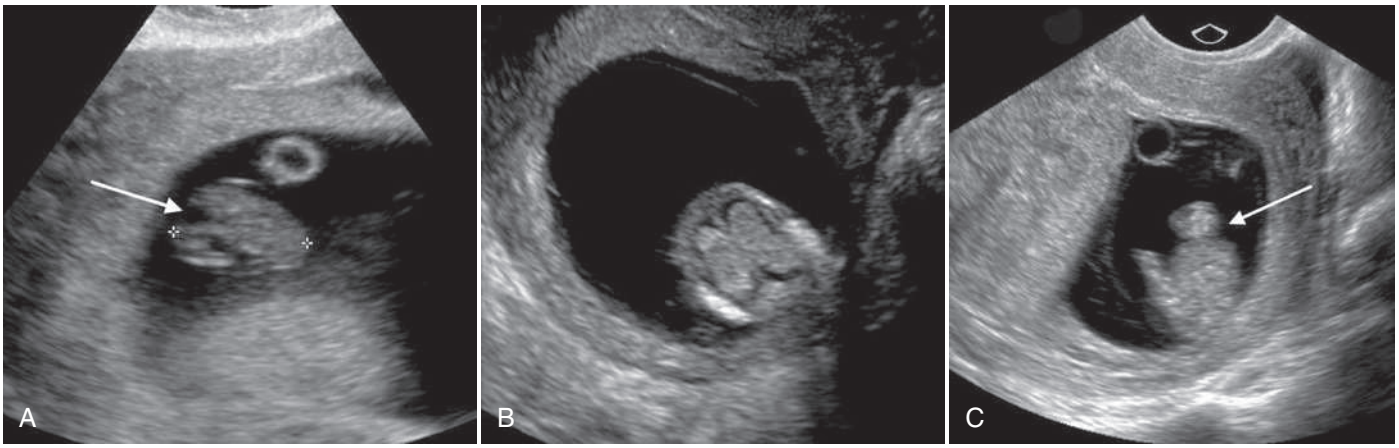

FIG. 30.37 Normal First-Trimester Anatomy. (A) Embryo *(calipers)* at 7 weeks 6 days demonstrates a cystic appearance in the cranial region *(arrow)* representing the normal **rhombencephalon.** See also Video 30.9. **(B)** Transverse scan of a 12-week fetus shows normal **lateral ventricles with choroid plexus** filling most of the lateral ventricles. **(C)** Ten-week embryo has the typical echogenic bowel herniated into the base of the umbilical cord *(arrows)* due to **physiologic midgut herniation.**

a follow-up sonographic examination may be indicated for evaluation of fetal morphologic characteristics in the second trimester.

Three major points should be considered: (1) normal embryologic/fetal development may mimic pathology, (2) abnormal embryos/fetuses may appear normal early in pregnancy, and (3) discrepancies between dates and embryo size may be the only visible manifestation of pathology in some first-trimester examinations.

Normal Embryologic Findings Mimicking Pathology

Normal embryologic development in the first trimester may mimic pathologic changes more often seen in the second and third trimesters.

Rhombencephalon

During the sixth week, three primary brain vesicles form: the **prosencephalon** (forebrain), the **mesencephalon** (midbrain), and the **rhombencephalon** (hindbrain).[10] Small cystic structures can be seen normally in the posterior aspect of the embryonic head. The earliest cystic structure seen at 6 to 8 weeks' gestation represents the normal embryonic **cystic rhombencephalon,** which later forms the normal fourth ventricle and should not be mistaken for a posterior fossa cyst of pathologic importance[131] (Fig. 30.37A, Video 30.9). The prosencephalon divides into an anterior portion known as the **telencephalon** and a posterior **diencephalon.** The telencephalic vesicles later form the lateral ventricles, and the diencephalon (and to a lesser degree the telencephalon) forms the third ventricle. After approximately 9 weeks, the lateral ventricles can be identified sonographically as two small cystic spaces in the embryonic head at 11 weeks and are more evident with the large choroid plexus almost filling them at 13 weeks (Fig. 30.37B). By 12 weeks the lateral ventricles extend almost to the inner table of the skull, and on sonography, only a small rim of cerebral cortex can be demonstrated to surround them. The choroid plexus is echogenic and fills the lateral ventricles completely except for the frontal horns.

Physiologic Anterior Abdominal Wall Herniation

During embryogenesis, the midgut normally herniates into the umbilical cord at the beginning of the eighth week of gestation. The midgut rotates 90 degrees counterclockwise and then returns to the abdomen during the 12th week. As the midgut returns to the abdomen, further rotation occurs, completing the normal rotation of the midgut.

Schmidt et al.[132] describe the normal physiologic appearance of the anterior abdominal wall during this period. The herniated bowel appears as a small, echogenic mass (6-9 mm) protruding into the cord at approximately 8 weeks (CRL, 17-20 mm). The echogenic mass decreases to 5 to 6 mm at 9 weeks (CRL, 23-26 mm). The size of the mass of herniated bowel varies. Follow-up examinations reveal reduction of the hernia between 10 and 12 weeks. In up to 20% of normal pregnancies, the herniated bowel may still be found outside the fetal abdomen at 12 weeks (Fig. 30.37C).

Abnormal Embryos

Many embryonic abnormalities may not be sonographically visible in the first trimester. In the first trimester, abnormal embryos may appear normal. Ultrasound in the first trimester is best at detecting abnormalities of the neurologic system, such as anencephaly; abdominal wall defects, such as omphalocele; and severe abnormalities of the urologic system, such as megacystis. These are illustrated in the chapter on chromosome abnormalities (Chapter 31, see Fig. 31.6) where first trimester screening for chromosome abnormalities is described. Individual first-trimester anomalies are discussed in the chapters regarding their specific organ systems.

GESTATIONAL TROPHOBLASTIC DISEASE

Gestational trophoblastic disease is a spectrum of cellular proliferations stemming from the placental villous trophoblast encompassing four main types: hydatidiform mole (complete

and partial), invasive mole, choriocarcinoma, and placental trophoblastic tumor.[133]

Hydatidiform Molar Pregnancy

Hydatidiform molar pregnancy is the most common and benign form of gestational trophoblastic disease, with an incidence of 1 in 1000 pregnancies in North America.[134] The incidence is much higher in the Asian population. There is an increased risk in teenagers, in women older than 35 years of age, and in women with a previous molar pregnancy. The risk also increases with the number of previous spontaneous abortions.[135] Molar pregnancy is characterized histologically by cystic (hydatidiform) degeneration of chorionic villi, with absent or inadequate vascularization and abnormal trophoblastic proliferation. Embryos or fetuses are either absent or abnormal.

The most frequent presenting symptom is **vaginal bleeding,** which occurs in more than 90% of cases. Passage of vesicles (hydropic villi) through the vagina occurs frequently and is considered specific for the diagnosis of molar pregnancy.[136] The uterus may be enlarged for dates, and there may also be rapid uterine enlargement. Medical complications include pregnancy-induced hypertension, hyperemesis gravidarum, preeclampsia, and hyperthyroidism. The routine use of ultrasound for any woman with bleeding in pregnancy allows for early diagnosis, and few women in current practice show the classic features of hyperemesis and preeclampsia.[137]

Serum β-hCG levels in molar pregnancy are abnormally elevated, usually greater than 100,000 mIU/mL. The ovaries may be greatly enlarged in complete molar pregnancy by multiple, bilateral theca lutein cysts. These are large, usually multilocular, and may undergo hemorrhage or torsion and can be a source of pelvic pain. Theca lutein cysts are most marked when trophoblastic proliferation is severe, and when hCG is elevated. They are seen much less often in the first trimester.[138,139]

Molar pregnancy is treated by uterine evacuation, which is adequate in most patients. Approximately 80% of complete moles and 95% of partial moles will subsequently follow a benign course.[136,140] However, accurate diagnosis and classification of molar pregnancy are important because of the risk of persistent trophoblastic neoplasia (PTN). The American College of Obstetrics and Gynecology currently recommends follow-up testing for hCG for 6 months after levels become undetectable.[141]

Hydatidiform molar pregnancy is classified as either complete molar pregnancy or partial molar pregnancy on the basis of cytogenetic and pathologic features.

Complete Molar Pregnancy

Complete molar pregnancy is characterized by a **diploid karyotype** of 46,XX in 80% to 90% of cases, with the chromosomal DNA being exclusively paternal in origin.[142] This occurs when an ovum with absent or inactive maternal chromosomes is fertilized by a normal haploid sperm. Occasionally, fertilization of an empty ovum by two haploid sperm results in a 46,XY pattern.[135] As the embryo dies at an early stage, no fetal parts are seen.[142] The placenta is entirely replaced by abnormal, hydropic chorionic villi with excessive trophoblastic proliferation.

The classic sonographic features of complete molar pregnancy include an enlarged uterus with a central heterogeneous echogenic mass that expands the endometrial canal. The mass contains multiple cystic spaces of varying size, representing the hydropic villi (Fig. 30.38). These cystic spaces may vary in size from a few millimeters to 2 to 3 cm. In the second trimester, TAS diagnosis is highly accurate. The second trimester appearance typically presents as an echogenic mass containing multiple tiny cysts due to the hydropic villi in what used to be termed a "snowstorm" pattern. However, with the higher frequencies now used the "snowstorm" has become a "bunch of grapes."

In the first trimester, molar pregnancies have a variable appearance on ultrasound, sometimes appearing as a predominantly solid, echogenic mass or even as an intrauterine fluid collection because tiny hydropic villi may not be adequately resolved (Fig. 30.39). In these cases, a molar pregnancy may not be able to be differentiated from a miscarriage.

Partial Molar Pregnancy

Partial molar pregnancy has a **triploid karyotype** of 69,XXX, 69,XXY, or 69,XYY and is also referred to as "triploidy." Most partial moles have one set of maternal chromosomes and two sets of paternal chromosomes, resulting from fertilization of a normal ovum by two haploid sperm. Triploidy of maternal origin is not associated with gestational trophoblastic disease.[143] Pathologically, partial molar pregnancy has well-developed but generally **anomalous (triploid) fetal tissues. Hydropic degeneration of placental villi** is focal, interspersed with normal placental villi (Fig. 30.40).

Triploidy is discussed in more detail in Chapter 31.

Placental **hydropic degeneration** (unrelated to trophoblastic neoplasia) may also show similar sonographic features. Hydropic degeneration occurs frequently in first-trimester abortion of any cause. The associated cystic spaces may be difficult or impossible to differentiate from an early mole. Therefore in cases with equivocal ultrasound features, the products of conception should be carefully evaluated to avoid missing a hydatidiform mole.

Recent studies have shown that **sonography is much more accurate in diagnosing complete molar pregnancy than partial molar pregnancy.** Kirk et al.[144] evaluated sonography in the first trimester and found an accuracy of 95% for the diagnosis of complete mole and 20% for partial mole, with an overall accuracy for hydatidiform mole of 44%. In 859 pathologically diagnosed hydatidiform moles, Fowler et al.[145] found that sonography performed in the first and early second trimester had a similar 44% overall accuracy and an accuracy of 79% and 29% for complete and partial moles, respectively. Also, the sonographic detection rate improved after 14 weeks' gestation.

Coexistent Hydatidiform Mole and Normal Fetus

In complete moles, an embryo or fetus is absent except in the rare event of a coexistent twin pregnancy. These twin pregnancies with an apparently normal fetus and a hydatidiform mole are uncommon, with an estimated incidence of 1 in 20,000 to 100,000 pregnancies.[146,147] It is differentiated from a partial molar pregnancy by identifying a normal-appearing fetus with a corresponding normal placenta adjacent to a mass of placental tissue that

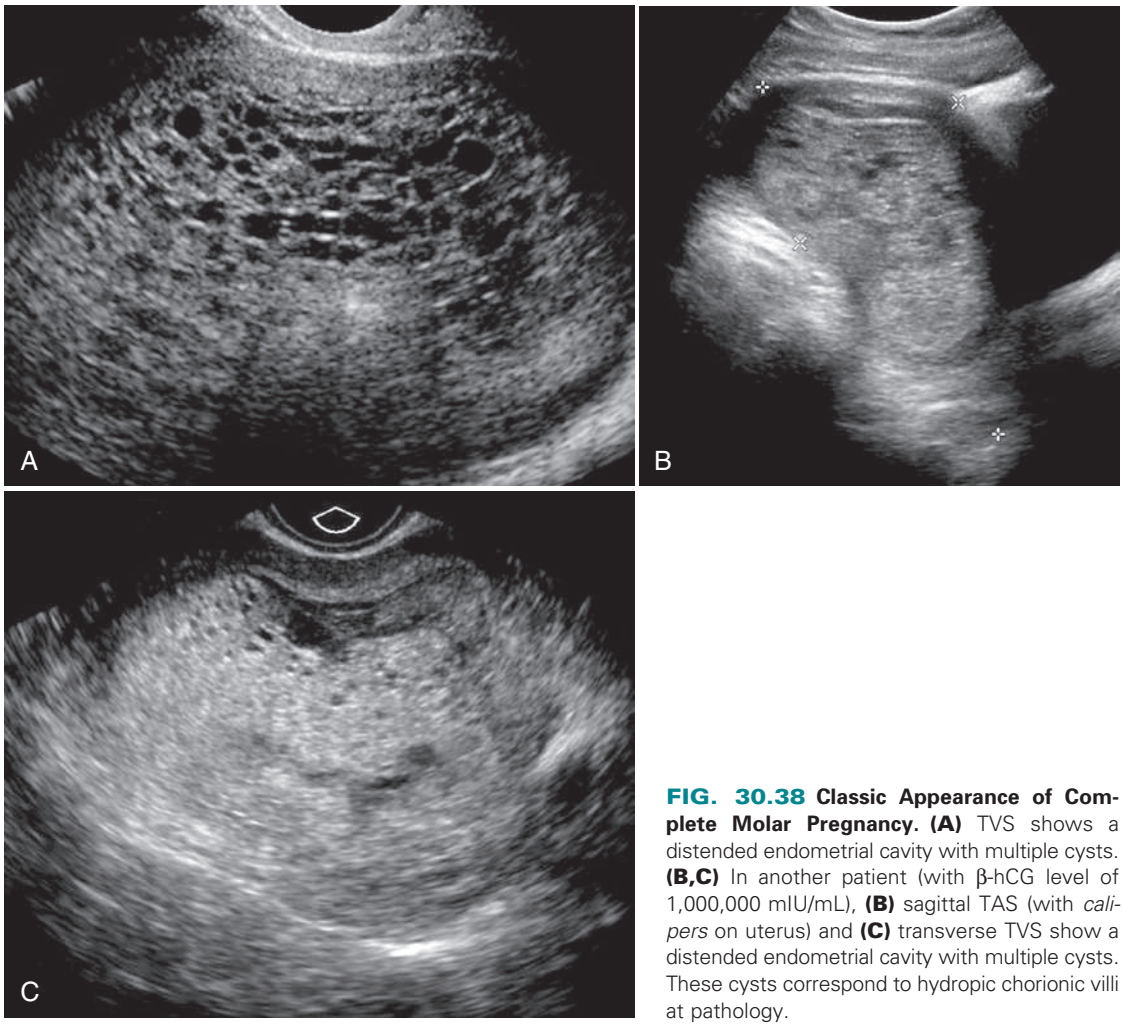

FIG. 30.38 Classic Appearance of Complete Molar Pregnancy. (A) TVS shows a distended endometrial cavity with multiple cysts. **(B,C)** In another patient (with β-hCG level of 1,000,000 mIU/mL), **(B)** sagittal TAS (with *calipers* on uterus) and **(C)** transverse TVS show a distended endometrial cavity with multiple cysts. These cysts correspond to hydropic chorionic villi at pathology.

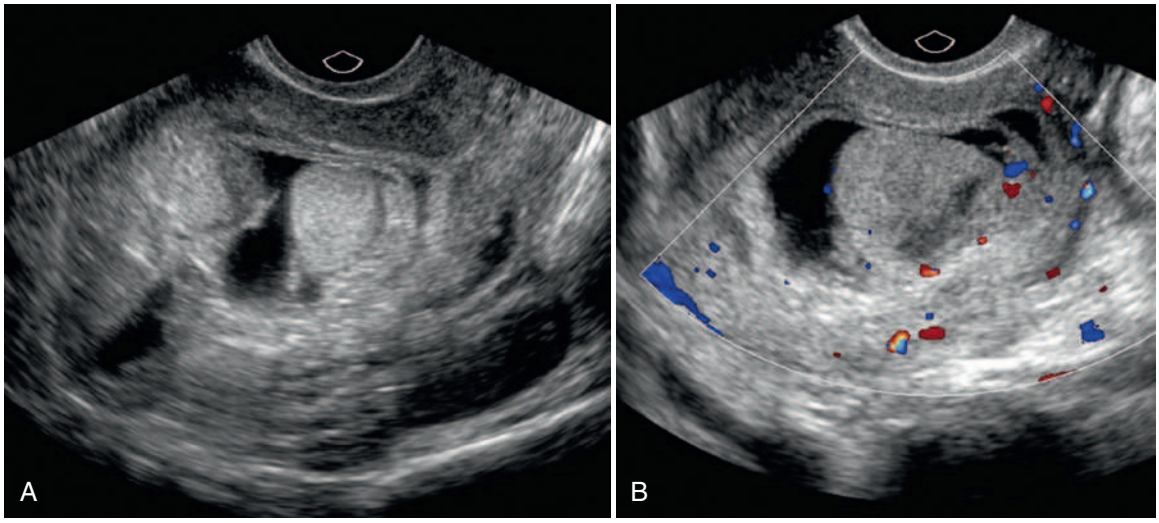

FIG. 30.39 Atypical Appearance Complete Molar Pregnancy. A 33-year-old at 8 weeks' gestation with β-hCG level of 73,000 mIU/mL. Sagittal TVS **(A)** without and **(B)** with color Doppler demonstrate irregular soft tissue masses protruding into the gestational sac.

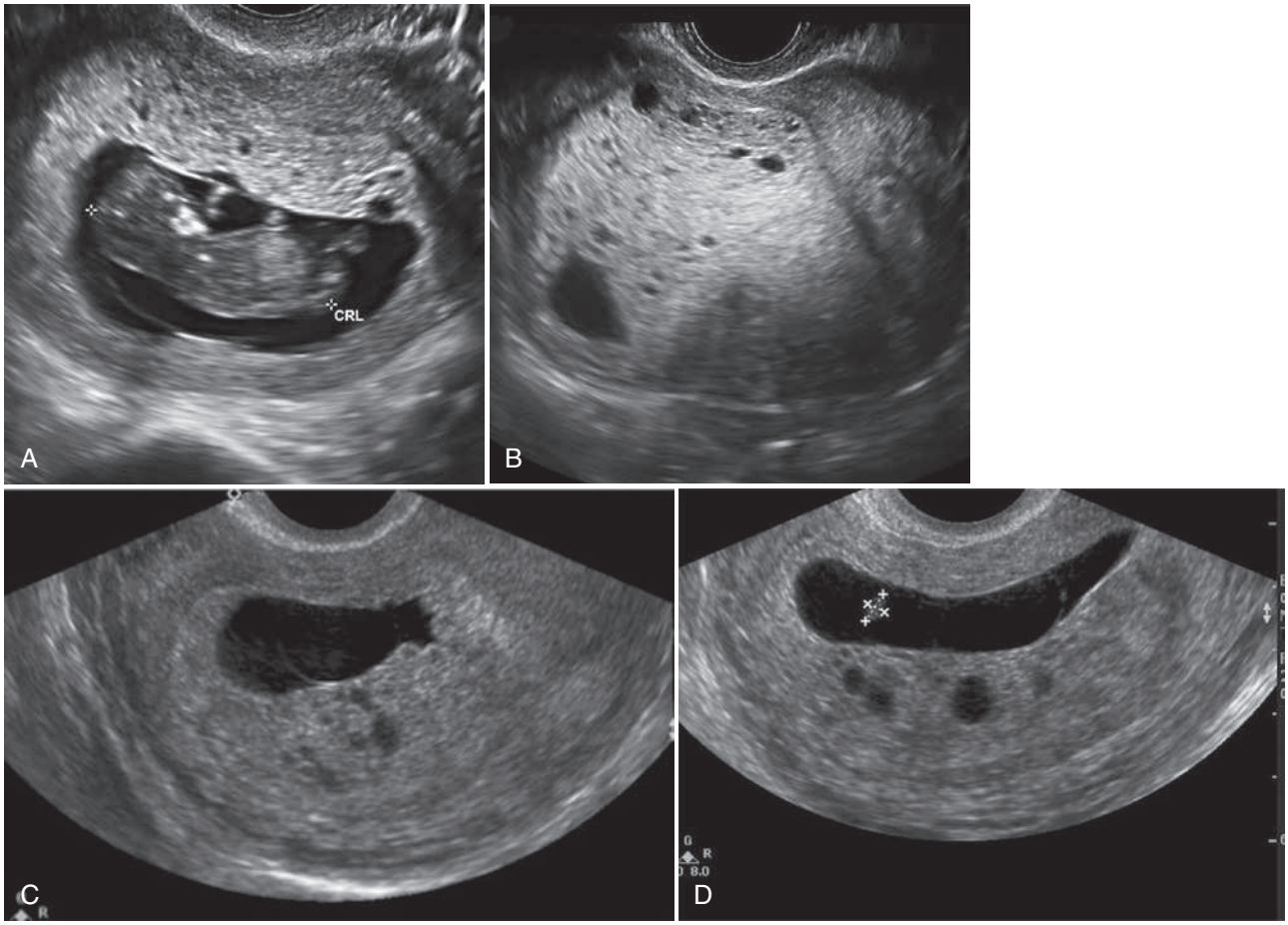

FIG. 30.40 Partial Molar Pregnancy. (A) and **(B)** TVS images show a fetus with a large thick cystic placenta. *CRL,* Crown-rump length. In another patient at 14 weeks' menstrual age (history of bleeding and β-hCG of 32,117 mIU/mL), **(C)** transverse and **(D)** sagittal TVS scans demonstrate an intrauterine gestational sac containing a smaller than expected embryonic pole *(calipers)* without a heartbeat. Multiple small cystic spaces are seen in the placenta.

demonstrates molar changes (Fig. 30.41). Initial studies suggested that these patients were at high risk for developing PTN.[146] However, a larger study of 77 cases showed that the risk of PTN was similar to that after a singleton complete mole and was not increased by continuing the pregnancy.[147] The 53 women who decided to continue the pregnancy had an increased risk of pregnancy complications, but 20 (38%) delivered a live baby, usually after 32 weeks.

Persistent Trophoblastic Neoplasia

PTN is a life-threatening complication of pregnancy that includes invasive mole, choriocarcinoma, and the extremely rare placental-site trophoblastic tumor. PTN occurs most often after molar pregnancy (Figs. 30.42 and 30.43, Video 30.10); up to 20% of complete moles develop persistent disease requiring additional therapy.[134,136] Complete moles with severe degrees of trophoblastic proliferation are at the highest risk, with persistent disease developing in 50% or more of these patients.[140] The risk is also increased in patients older than 40 years of age and in women who have had multiple molar pregnancies.[142] The risk of persistent disease after partial molar pregnancy is much lower, occurring in approximately 5%.[136,142] Less often, PTN develops after a normal term delivery, spontaneous abortion, or, in rare cases, an ectopic pregnancy.[134]

Invasive Mole

Invasive mole is the **most common form of PTN,** accounting for 80% to 95% of cases.[148] Patients usually present with vaginal bleeding and persistent elevation of serum hCG within 1 to 3 months after molar evacuation.[149] Histologically, invasive mole is characterized by the presence of formed chorionic villi and trophoblastic proliferation deep in the myometrium (see Fig. 30.42). It is considered biologically benign and is usually confined to the uterus; in rare cases, molar tissue can penetrate the whole thickness of the myometrium, leading to uterine perforation, which may cause severe hemorrhage.[150] Lesions can invade beyond the uterus to parametrial tissues, adjacent organs, and blood vessels. Rarely, invasive molar villi may embolize to distant sites, including the lungs and brain.

Choriocarcinoma

Choriocarcinoma is an extremely rare malignancy with an incidence of 1 in 30,000 pregnancies. Although it may occur after any pregnancy, the most important risk factor for

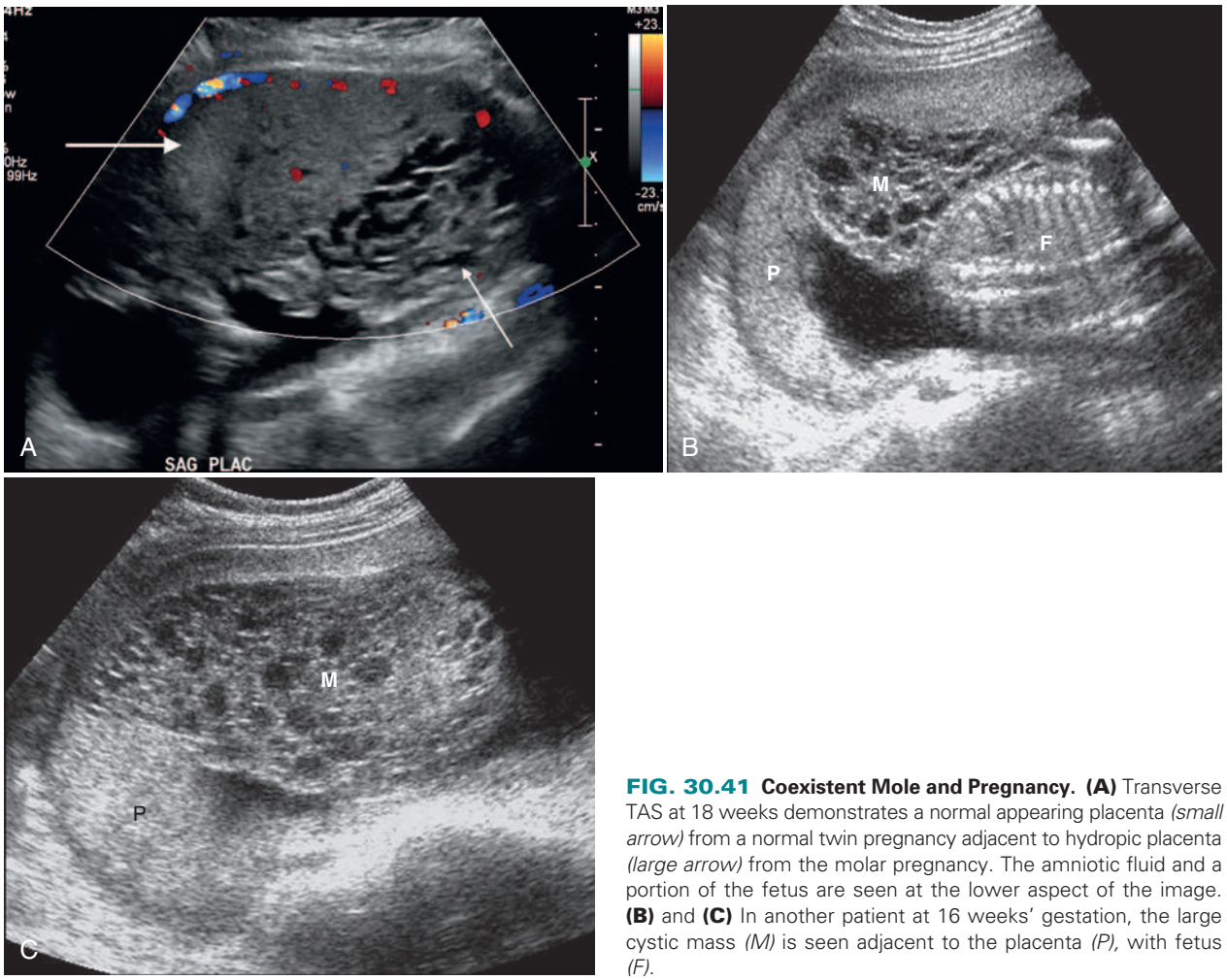

FIG. 30.41 Coexistent Mole and Pregnancy. (A) Transverse TAS at 18 weeks demonstrates a normal appearing placenta *(small arrow)* from a normal twin pregnancy adjacent to hydropic placenta *(large arrow)* from the molar pregnancy. The amniotic fluid and a portion of the fetus are seen at the lower aspect of the image. **(B)** and **(C)** In another patient at 16 weeks' gestation, the large cystic mass *(M)* is seen adjacent to the placenta *(P),* with fetus *(F).*

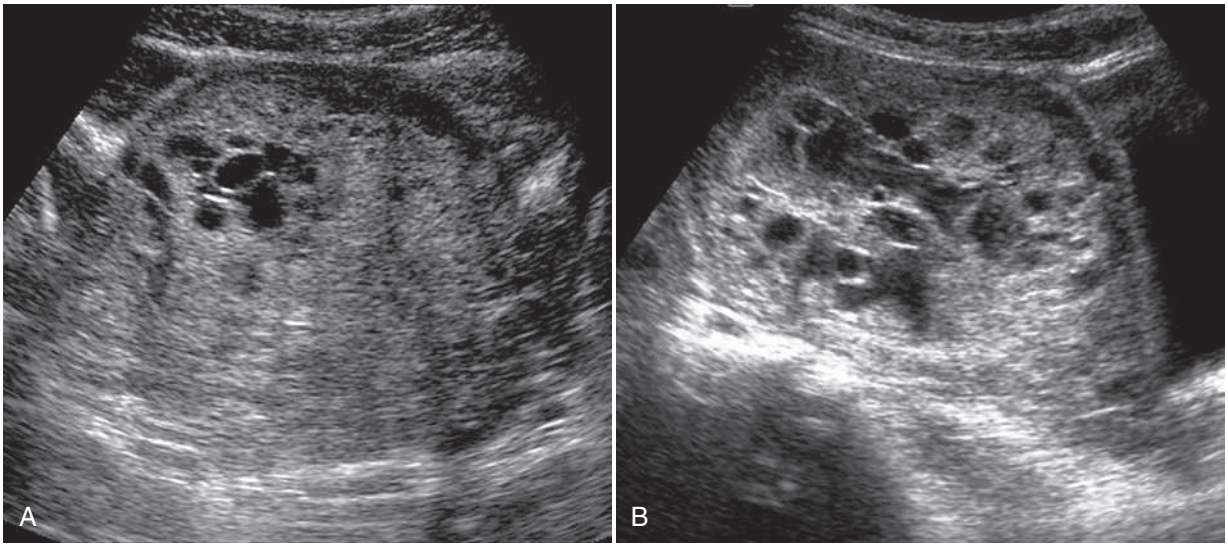

FIG. 30.42 Invasive Mole 6 Weeks After Evacuation of Complete Mole. (A) Transverse and **(B)** sagittal TAS images show large mass filled with multiple cystic spaces extending deep into the myometrium on the right side.

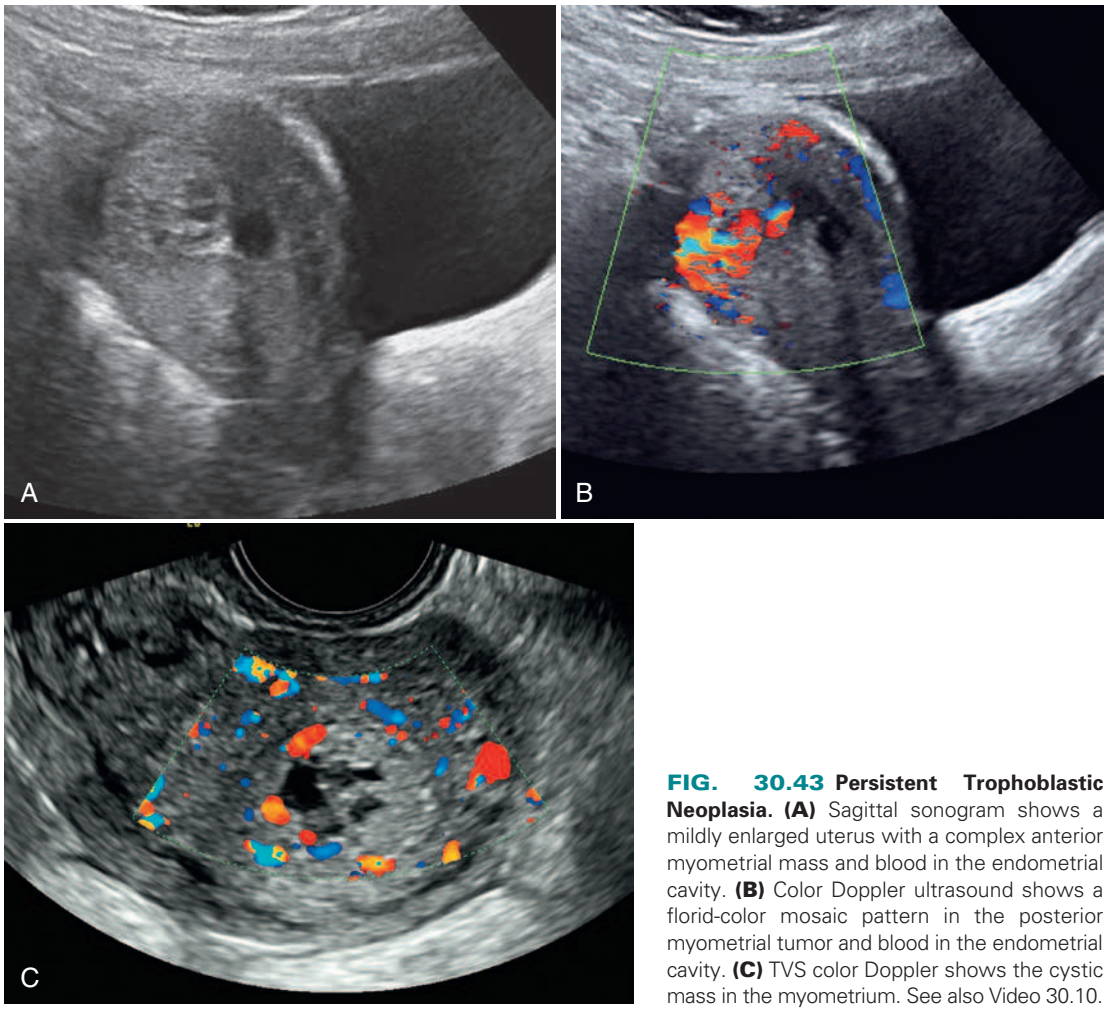

FIG. 30.43 Persistent Trophoblastic Neoplasia. (A) Sagittal sonogram shows a mildly enlarged uterus with a complex anterior myometrial mass and blood in the endometrial cavity. **(B)** Color Doppler ultrasound shows a florid-color mosaic pattern in the posterior myometrial tumor and blood in the endometrial cavity. **(C)** TVS color Doppler shows the cystic mass in the myometrium. See also Video 30.10.

choriocarcinoma is molar pregnancy (Fig. 30.44, Video 30.11). Molar gestations precede 50% to 80% of cases, and 1 in 40 molar pregnancies gives rise to choriocarcinoma. Choriocarcinoma is a purely cellular lesion characterized histologically by the invasion of the myometrium by abnormal, proliferating trophoblast and the absence of formed villi. Hemorrhage and necrosis are prominent features.[135] Early vascular invasion is common, resulting in distant metastases, most frequently affecting the lungs, followed by the liver, brain, gastrointestinal tract, and kidney. Respiratory compromise may be the initial presentation.[151] Venous invasion and retrograde metastases to the vagina and pelvic structures are also common.[151]

Placental-Site Trophoblastic Tumor

Placental-site trophoblastic tumor (PSTT) is the **rarest and most fatal form of PTN.**[152] As with choriocarcinoma and invasive mole, PSTT can follow any type of gestation, but in more than 90% of cases it develops after a normal term delivery.[150] The tumor may occur from as early as 1 week to many years after pregnancy. Vaginal bleeding is the most common symptom, although some women may present with amenorrhea. Histologically, PSTT is distinct from other forms of trophoblastic neoplasia. It arises from nonvillous "intermediate" trophoblast that infiltrates the decidua, spiral arteries, and myometrium at the placental bed. PSTT may be confined to the uterus, may be locally invasive in the pelvis, or may metastasize to the lungs, lymph nodes, peritoneum, liver, pancreas, or brain. Serum hCG is not a reliable marker for PSTT; it is usually negative or only mildly elevated. Histochemical staining of intermediate trophoblast for hCG is weak or absent, whereas staining for human placental lactogen is strongly positive. Unfortunately, serum human placental lactogen is not a reliable predictor of tumor behavior.[152] Surgical therapy is recommended because these lesions tend to resist chemotherapy and have a high risk of metastasis.

Sonographic Features of Persistent Trophoblastic Neoplasia

Sonography plays an important role in detecting and staging PTN and in monitoring response to therapy. The small, myometrial lesions typical of this condition may not be apparent on TAS.[153] Invasive mole, choriocarcinoma, and PSTT may appear similar sonographically.[154,155] The most frequently described sonographic abnormality in PTN is a focal, echogenic myometrial nodule.[151,153-155] The lesion usually lies close to the endometrial cavity, but it may be found deep in the myometrium. Lesions may appear solid and uniformly echogenic, hypoechoic, or

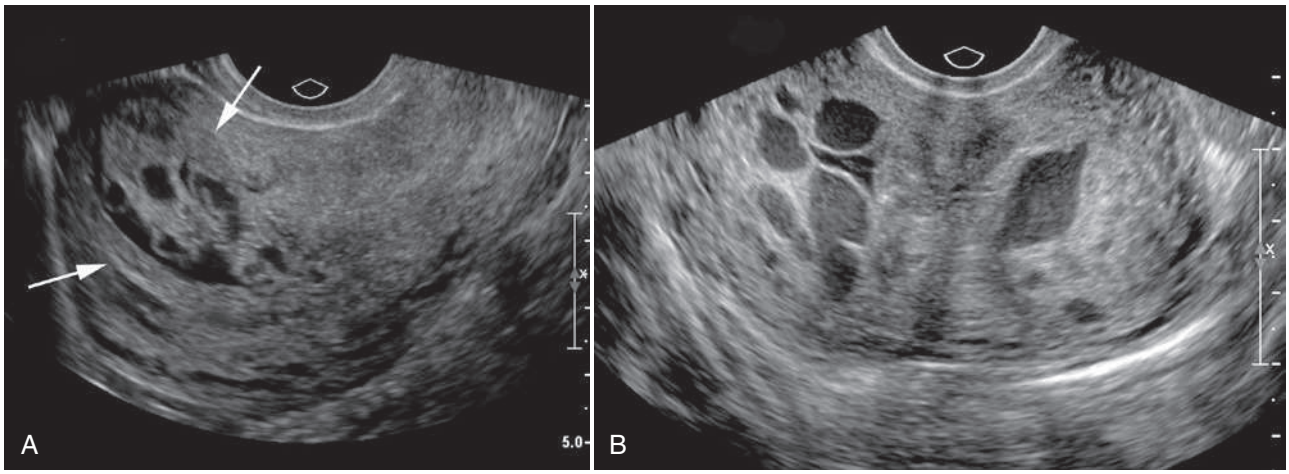

FIG. 30.44 Choriocarcinoma After Normal Pregnancy. (A) Sagittal and **(B)** transverse TVS images show an ill-defined endometrium *(arrows)* with multiple large cystic spaces. See also Video 30.11.

complex and multicystic, similar to molar tissue. Thick-walled, irregular anechoic areas may be seen, resulting from tissue necrosis and hemorrhage.[153-155] In other cases, anechoic areas within lesions represent vascular spaces. When tumor replaces the entire myometrium, the uterus is enlarged, with the myometrium appearing heterogeneous and lobulated. The tumor may extend beyond the uterus to the parametrium, pelvic side wall, and adjacent organs. In extreme cases, PTN appears as a large, undifferentiated pelvic mass. Sonography can be diagnostic in the correct setting (e.g., recent molar pregnancy, rising serum hCG, previously documented normal sonogram).

After effective therapy, sonographic lesions become progressively more hypoechoic and smaller in size. Eventually, no residual abnormality is apparent in many cases. However, up to 50% of patients will have persistent abnormalities after therapy that may be difficult to distinguish from active lesions sonographically.

Duplex and color Doppler ultrasound features of PTN reflect the marked hypervascularity of invasive trophoblast.[156,157] Uterine spiral arteries feed directly into prominent vascular spaces, which then communicate with draining veins. These **functional arteriovenous shunts** produce abnormal uterine hypervascularity and high-velocity, low-impedance blood flow on duplex interrogation.[156] **Trophoblastic blood flow** has characteristic, high PSV and low RI. PSV is usually greater than 50 cm/sec and is often over 100 cm/sec. RI is usually less than 0.5 and is often well below 0.4. In contrast, normal myometrial blood flow usually has a PSV of less than 50 cm/sec and an RI in the range of 0.7. Color Doppler sonographic features typical of PTN include extensive color aliasing, admixture of color signals, loss of discreteness of vessels, and chaotic vascular arrangement. Regions of abnormal color Doppler ultrasound frequently appear larger than corresponding sonographic abnormalities.

Trophoblastic signals on spectral Doppler ultrasound are not unique to PTN. They are seen in all conditions with functioning trophoblast, including failed pregnancy, retained products of conception, and ectopic pregnancy. These potential pitfalls are distinguished from PTN by clinical findings, sonographic morphology, and pathology. However, PSTT should remain a consideration even with a normal hCG level. In most patients the diagnosis of PTN is fairly straightforward, and additional information provided by Doppler ultrasound is supportive but not critical. However, when PTN is not suspected clinically, duplex and color Doppler sonography may provide the first indication of trophoblastic disease by showing marked hypervascularity and typical trophoblastic blood flow within lesions. Doppler ultrasound also improves diagnostic specificity by showing normal uterine waveforms when PTN is absent and sonography is abnormal, as when other uterine lesions mimic the appearance of PTN, or persistent nonspecific abnormalities remain after effective therapy.[157]

Diagnosis and Treatment

Because PTN arises most often after a molar pregnancy, the diagnosis is usually based on abnormal regression of hCG after uterine evacuation. A histologic diagnosis is not considered mandatory because curettage risks uterine perforation and does not significantly alter management or outcome.[151,158] Patients are treated on the basis of clinical staging that includes computed tomography of the brain, chest, abdomen, and pelvis.

With the exception of PSTT, hCG level is a sensitive and specific marker for detecting and monitoring PTN. Normal mean disappearance time of hCG in benign moles ranges from 7 to 14 weeks (median, 11 weeks) but can be as long as a year. Contraception is recommended for 6 months after a normal hCG has been attained in order to distinguish a rising hCG resulting from persistent or recurrent disease from that due to pregnancy.[133]

PTN is broadly classified as **nonmetastatic** or **metastatic** on the basis of staging computed tomography of the brain, chest, abdomen, and pelvis.[151,158] Nonmetastatic PTN has an excellent prognosis. Single-agent therapy with methotrexate achieves sustained remission in virtually 100% of cases.[158] Metastatic PTN is subdivided into **low-risk** and **high-risk** groups. Virtually all patients with low-risk metastatic disease are cured with simple chemotherapy.[151] In contrast, patients with high-risk disease have a substantially worse prognosis and a high likelihood of failure

with single-agent therapy. High-risk, poor-prognosis disease is indicated by duration of disease for more than 4 months, pretreatment hCG levels greater than 40,000 mIU/mL, presence of brain or liver metastases, antecedent term pregnancy, and prior history of failed chemotherapy. These patients are treated aggressively with appropriate combinations of intense multiagent chemotherapy, adjuvant radiotherapy, and surgery. By tailoring therapy in this way, even high-risk patients have cure rates of 80% to 90%.[151,159]

CONCLUSION

First-trimester sonography plays an important role in establishing the location of a pregnancy and determining if the pregnancy is potentially viable (cardiac activity seen). Knowledge of the landmarks with respect to the appearance of the gestational sac, yolk sac, and embryo are important in the appropriate triage of patients who present with pain and bleeding in the first trimester.

REFERENCES

1. Moore KL. The developing human: clinically oriented embryology. 10th ed. Philadelphia: Elsevier; 2016.
2. Levi CS, Lyons EA, Lindsay DJ. Early diagnosis of nonviable pregnancy with endovaginal US. Radiology. 1988;167(2):383-385.
3. Levi CS, Lyons EA, Zheng XH, et al. Endovaginal US: demonstration of cardiac activity in embryos of less than 5.0 mm in crown-rump length. Radiology. 1990;176(1):71-74.
4. Abdallah Y, Daemen A, Kirk E, et al. Limitations of current definitions of miscarriage using mean gestational sac diameter and crown-rump length measurements: a multicenter observational study. Ultrasound Obstet Gynecol. 2011;38(5):497-502.
5. Doubilet PM, Benson CB, Bourne T, et al. Diagnostic criteria for nonviable pregnancy early in the first trimester. N Engl J Med. 2013;369(15):1443-1451.
6. Nyberg DA, Filly RA. Predicting pregnancy failure in 'empty' gestational sacs. Ultrasound Obstet Gynecol. 2003;21(1):9-12.
7. Levi CS. Prediction of early pregnancy failure on the basis of mean gestational sac size and absence of a sonographically demonstrable yolk sac. Radiology. 1995;195(3):873.
8. Rowling SE, Langer JE, Coleman BG, et al. Sonography during early pregnancy: dependence of threshold and discriminatory values on transvaginal transducer frequency. AJR Am J Roentgenol. 1999;172(4):983-988.
9. Benacerraf BR, Shipp TD, Bromley B. Does the 10-MHz transvaginal transducer improve the diagnostic certainty that an intrauterine fluid collection is a true gestational sac? J Clin Ultrasound. 1999;27(7):374-377.
10. Moore KL, Persaud TVN, editors. The developing human: clinically oriented embryology. 6th ed. Philadelphia: Saunders; 1998.
11. Oehninger S, Hodgen GD. Hypothalamic-pituitary-ovarian uterine axis. In: Copeland LJ, editor. Textbook of gynecology. Philadelphia: Saunders; 1993.
12. Jones GS, Jones HW. Cyclical cytology and histology. In: Jones GS, Jones HW, editors. Gynecology. 3rd ed. Baltimore: Williams & Wilkins; 1982. p. 46-68.
13. Settlage DS, Motoshima M, Tredway DR. Sperm transport from the external cervical os to the fallopian tubes in women: a time and quantitation study. Fertil Steril. 1973;24(9):655-661.
14. Suarez SS, Pacey AA. Sperm transport in the female reproductive tract. Hum Reprod Update. 2006;12(1):23-37.
15. Lyons EA, Taylor PJ, Zheng XH, et al. Characterization of subendometrial myometrial contractions throughout the menstrual cycle in normal fertile women. Fertil Steril. 1991;55(4):771-774.
16. Hustin J. Vascular physiology and pathophysiology of early pregnancy. In: Bourne T, Jauniaux E, Jurkovic D, editors. Transvaginal color Doppler. Heidelberg: Springer-Verlag; 1995. p. 47-56.
17. Jauniaux E. Intervillous circulation in the first trimester: the phantom of the color Doppler obstetric opera. Ultrasound Obstet Gynecol. 1996;8(2):73-76.
18. Hustin J, Jauniaux E, Schaaps JP. Histological study of the materno-embryonic interface in spontaneous abortion. Placenta. 1990;11(6):477-486.
19. Oh JS, Wright G, Coulam CB. Gestational sac diameter in very early pregnancy as a predictor of fetal outcome. Ultrasound Obstet Gynecol. 2002;20(3):267-269.
20. Folkman J. Tumor angiogenesis: therapeutic implications. N Engl J Med. 1971;285(21):1182-1186.
21. Kawakami Y, Andoh K, Mizunuma H, et al. Assessment of the implantation site by transvaginal ultrasonography. Fertil Steril. 1993;59(5):1003-1006.
22. Magann EF, Roberts WE, McCurley S, et al. Dominant maternal sleep position influences site of placental implantation. Mil Med. 2002;167(1):67-69.
23. Yeh HC, Goodman JD, Carr L, Rabinowitz JG. Intradecidual sign: a US criterion of early intrauterine pregnancy. Radiology. 1986;161(2):463-467.
24. Chiang G, Levine D, Swire M, et al. The intradecidual sign: is it reliable for diagnosis of early intrauterine pregnancy? AJR Am J Roentgenol. 2004;183(3):725-731.
25. Bradley WG, Fiske CE, Filly RA. The double sac sign of early intrauterine pregnancy: use in exclusion of ectopic pregnancy. Radiology. 1982;143(1):223-226.
26. Nyberg DA, Laing FC, Filly RA, et al. Ultrasonographic differentiation of the gestational sac of early intrauterine pregnancy from the pseudogestational sac of ectopic pregnancy. Radiology. 1983;146(3):755-759.
27. Doubilet PM, Benson CB. First, do no harm… To early pregnancies. J Ultrasound Med. 2010;29(5):685-689.
28. Nyberg DA, Mack LA, Harvey D, Wang K. Value of the yolk sac in evaluating early pregnancies. J Ultrasound Med. 1988;7(3):129-135.
29. Parvey HR, Dubinsky TJ, Johnston DA, Maklad NF. The chorionic rim and low-impedance intrauterine arterial flow in the diagnosis of early intrauterine pregnancy: evaluation of efficacy. AJR Am J Roentgenol. 1996;167(6):1479-1485.
30. Doubilet PM, Benson CB. Double sac sign and intradecidual sign in early pregnancy: interobserver reliability and frequency of occurrence. J Ultrasound Med. 2013;32(7):1207-1214.
31. Birnholz JC, Madanes AE. Amniotic fluid accumulation in the first trimester. J Ultrasound Med. 1995;14(8):597-602.
32. Campbell J, Wathen N, Macintosh M, et al. Biochemical composition of amniotic fluid and extraembryonic coelomic fluid in the first trimester of pregnancy. Br J Obstet Gynaecol. 1992;99(7):563-565.
33. Emerson DS, Cartier MS, Altieri LA, et al. Diagnostic efficacy of endovaginal color Doppler flow imaging in an ectopic pregnancy screening program. Radiology. 1992;183(2):413-420.
34. Laing FC, Brown DL, Price JF. Intradecidual sign: is it effective in diagnosis of an early intrauterine pregnancy? Radiology. 1997;204(3):655-660.
35. Golstein DP, Koaca TS. The subunit radioimmunoassay for hCG: clinical application. In: Taymar M, Green TH, editors. Progress in gynecology. New York: Grune & Stratton; 1975. p. 145-184.
36. Nyberg DA, Filly RA, Filho DL, et al. Abnormal pregnancy: early diagnosis by US and serum chorionic gonadotropin levels. Radiology. 1986;158(2):393-396.
37. Stenman UH, Tiitinen A, Alfthan H, Valmu L. The classification, functions, and clinical use of different isoforms of HCG. Hum Reprod Update. 2006;12(6):769-784.
38. Connolly A, Ryan DH, Stuebe AM, Wolfe HM. Reevaluation of discriminatory and threshold levels of serum β-hCG in early pregnancy. Obstet Gynecol. 2013;121(1):65-70.
39. Barnhart K, Mennuti MT, Benjamin I, et al. Prompt diagnosis of ectopic pregnancy in an emergency department setting. Obstet Gynecol. 1994;84(6):1010-1015.
40. Bree RL, Edwards M, Bohm-Velez M, et al. Transvaginal sonography in the evaluation of normal early pregnancy: correlation with HCG level. AJR Am J Roentgenol. 1989;153(1):75-79.

41. Mehta TS, Levine D, Beckwith B. Treatment of ectopic pregnancy: is a human chorionic gonadotropin level of 2,000 mIU/mL a reasonable threshold? Radiology. 1997;205(2):569-573.
42. Nyberg DA, Laing FC, Filly RA. Threatened abortion: sonographic distinction of normal and abnormal gestation sacs. Radiology. 1986;158(2):397-400.
43. Lindsay DJ, Lovett IS, Lyons EA, et al. Yolk sac diameter and shape at endovaginal US: predictors of pregnancy outcome in the first trimester. Radiology. 1992;183(1):115-118.
44. Levi CS, Lyons EA, Dashefsky SM, et al. Yolk sac number, size and morphologic features in monochorionic monoamniotic twin pregnancy. Can Assoc Radiol J. 1996;47(2):98-100.
45. McKenna KM, Feldstein VA, Goldstein RB, Filly RA. The empty amnion: a sign of early pregnancy failure. J Ultrasound Med. 1995;14(2):117-121.
46. Kaufman AJ, Fleischer AC, Thieme GA, et al. Separated chorioamnion and elevated chorion: sonographic features and clinical significance. J Ultrasound Med. 1985;4(3):119-125.
47. Cadkin AV, McAlpin J. Detection of fetal cardiac activity between 41 and 43 days of gestation. J Ultrasound Med. 1984;3(11):499-503.
48. Ragavendra N, McMahon JT, Perrella RR, et al. Endoluminal catheter-assisted transcervical US of the human embryo. Work in progress. Radiology. 1991;181(3):779-783.
49. Doubilet PM, Benson CB. Embryonic heart rate in the early first trimester: what rate is normal? J Ultrasound Med. 1995;14(6):431-434.
50. Hill LM, DiNofrio DM, Guzick D. Sonographic determination of first trimester umbilical cord length. J Clin Ultrasound. 1994;22(7):435-438.
51. Ghezzi F, Raio L, Di Naro E, et al. First-trimester sonographic umbilical cord diameter and the growth of the human embryo. Ultrasound Obstet Gynecol. 2001;18(4):348-351.
52. Skibo LK, Lyons EA, Levi CS. First-trimester umbilical cord cysts. Radiology. 1992;182(3):719-722.
53. Sepulveda W. Beware of the umbilical cord 'cyst. Ultrasound Obstet Gynecol. 2003;21(3):213-214.
54. Ghezzi F, Raio L, Di Naro E, et al. Single and multiple umbilical cord cysts in early gestation: two different entities. Ultrasound Obstet Gynecol. 2003;21(3):215-219.
55. Nyberg DA, Filly RA, Mahony BS, et al. Early gestation: correlation of HCG levels and sonographic identification. AJR Am J Roentgenol. 1985;144(5):951-954.
56. Nyberg DA, Mack LA, Laing FC, Patten RM. Distinguishing normal from abnormal gestational sac growth in early pregnancy. J Ultrasound Med. 1987;6(1):23-27.
57. Goldstein SR. Embryonic death in early pregnancy: a new look at the first trimester. Obstet Gynecol. 1994;84(2):294-297.
58. American Institute of Ultrasound in Medicine. AIUM practice guideline for the performance of obstetric ultrasound examinations. J Ultrasound Med. 2013;32(6):1083-1101.
59. Wilcox AJ, Weinberg CR, O'Connor JF, et al. Incidence of early loss of pregnancy. N Engl J Med. 1988;319(4):189-194.
60. Hertig AT, Rock J. A series of potentially abortive ova recovered from fertile women prior to the first missed menstrual period. Am J Obstet Gynecol. 1949;58(5):968-993.
61. Stephenson MD, Awartani KA, Robinson WP. Cytogenetic analysis of miscarriages from couples with recurrent miscarriage: a case-control study. Hum Reprod. 2002;17(2):446-451.
62. Practice Committee of the American Society for Reproductive Medicine. Evaluation and treatment of recurrent pregnancy loss: a committee opinion. Fertil Steril. 2012;98(5):1103-1111.
63. Westin M, Kälén K, Saltvedt S, et al. Miscarriage after a normal scan at 12-14 gestational weeks in women at low risk of carrying a fetus with chromosomal anomaly according to nuchal translucency screening. Ultrasound Obstet Gynecol. 2007;30(5):728-736.
64. Falco P, Milano V, Pilu G, et al. Sonography of pregnancies with first-t rimester bleeding and a viable embryo: a study of prognostic indicators by logistic regression analysis. Ultrasound Obstet Gynecol. 1996;7(3):165-169.
65. Falco P, Zagonari S, Gabrielli S, et al. Sonography of pregnancies with first-trimester bleeding and a small intrauterine gestational sac without a demonstrable embryo. Ultrasound Obstet Gynecol. 2003;21(1):62-65.
66. Pandya PP, Snijders RJ, Psara N, et al. The prevalence of non-viable pregnancy at 10-13 weeks of gestation. Ultrasound Obstet Gynecol. 1996;7(3):170-173.
67. Stabile I, Campbell S, Grudzinskas JG. Ultrasonic assessment of complications during first trimester of pregnancy. Lancet. 1987;2(8570):1237-1240.
68. Sorokin Y, Johnson MP, Uhlmann WR, et al. Postmortem chorionic villus sampling: correlation of cytogenetic and ultrasound findings. Am J Med Genet. 1991;39(3):314-316.
69. Blumenfeld Z, Ruach M. Early pregnancy wastage: the role of repetitive human chorionic gonadotropin supplementation during the first 8 weeks of gestation. Fertil Steril. 1992;58(1):19-23.
70. Kupesic S, Kurjak A, Vujisic S, Petrovic Z. Luteal phase defect: comparison between Doppler velocimetry, histological and hormonal markers. Ultrasound Obstet Gynecol. 1997;9(2):105-112.
71. Pennell RG, Needleman L, Pajak T, et al. Prospective comparison of vaginal and abdominal sonography in normal early pregnancy. J Ultrasound Med. 1991;10(2):63-67.
72. Aziz S, Cho RC, Baker DB, et al. Five-millimeter and smaller embryos without embryonic cardiac activity: outcomes in women with vaginal bleeding. J Ultrasound Med. 2008;27(11):1559-1561.
73. Rowling SE, Coleman BG, Langer JE, et al. First-trimester US parameters of failed pregnancy. Radiology. 1997;203(1):211-217.
74. Harris RD, Couto C, Karpovsky C, et al. The chorionic bump: a first-trimester pregnancy sonographic finding associated with a guarded prognosis. J Ultrasound Med. 2006;25(6):757-763.
75. Bromley B, Harlow BL, Laboda LA, Benacerraf BR. Small sac size in the first trimester: a predictor of poor fetal outcome. Radiology. 1991;178(2):375-377.
76. Giacomello F. Small size as a predictor of poor fetal outcome [letter]. Radiology. 1992;184(2):578.
77. Horrow MM. Enlarged amniotic cavity: a new sonographic sign of early embryonic death. AJR Am J Roentgenol. 1992;158(2):359-362.
78. Yegul NT, Filly RA. The expanded amnion sign: evidence of early embryonic death. J Ultrasound Med. 2009;28(10):1331-1335.
79. Filly RA. The expanded amnion sign: evidence of early embryonic death [author response]. J Ultrasound Med. 2010;29(2):323-324.
80. Kucuk T, Duru NK, Yenen MC, et al. Yolk sac size and shape as predictors of poor pregnancy outcome. J Perinat Med. 1999;27(4):316-320.
81. Gürel SA, Gürel H. A large yolk sac may be important in the early diagnosis of gestational trophoblastic disease: a case report. Eur J Obstet Gynecol Reprod Biol. 2000;91(1):91-93.
82. Szabo J, Gellen J, Szemere G, Farago M. Significance of hyper-echogenic yolk sac in first-trimester screening for chromosome aneuploidy]. Orv Hetil. 1996;137(42):2313-2315.
83. Doubilet P, Benson C. Outcome of first-trimester pregnancies with slow embryonic heart rate at 6-7 weeks gestation and normal heart rate by 8 weeks at US. Radiology. 2005;2005(236):643-646.
84. Doubilet PM, Benson CB, Chow JS. Long-term prognosis of pregnancies complicated by slow embryonic heart rates in the early first trimester. J Ultrasound Med. 1999;18(8):537-541.
85. Vaccaro H, Amor F, Leyton M, Sepulveda W. Arrhythmia in early pregnancy: a predictor of first-trimester pregnancy loss. Ultrasound Obstet Gynecol. 1998;12(4):248-251.
86. Doubilet PM, Benson CB, Chow JS. Outcome of pregnancies with rapid embryonic heart rates in the early first trimester. AJR Am J Roentgenol. 2000;175(1):67-69.
87. Sauerbrei EE, Pham DH. Placental abruption and subchorionic hemorrhage in the first half of pregnancy: US appearance and clinical outcome. Radiology. 1986;160(1):109-112.
88. Ball RH, Ade CM, Schoenborn JA, Crane JP. The clinical significance of ultrasonographically detected subchorionic hemorrhages. Am J Obstet Gynecol. 1996;174(3):996-1002.
89. Pedersen JF, Mantoni M. Prevalence and significance of subchorionic hemorrhage in threatened abortion: a sonographic study. AJR Am J Roentgenol. 1990;154(3):535-537.
90. Bennett GL, Bromley B, Lieberman E, Benacerraf BR. Subchorionic hemorrhage in first-trimester pregnancies: prediction of pregnancy outcome with sonography. Radiology. 1996;200(3):803-806.

91. Leite J, Ross P, Rossi AC, Jeanty P. Prognosis of very large first-trimester hematomas. J Ultrasound Med. 2006;25:1441-1445.
92. Atrash HK, Friede A, Hogue CJ. Ectopic pregnancy mortality in the United States, 1970-1983. Obstet Gynecol. 1987;70(6):817-822.
93. Lawson HW, Atrash HK, Saftlas AF, et al. Ectopic pregnancy surveillance, United States, 1970-1985. MMWR CDC Surveill Summ. 1988;37(5): 9-18.
94. Schwartz RO, Di Pietro DL. beta-hCG as a diagnostic aid for suspected ectopic pregnancy. Obstet Gynecol. 1980;56(2):197-203.
95. Ackerman TE, Levi CS, Lyons EA, et al. Decidual cyst: endovaginal sonographic sign of ectopic pregnancy. Radiology. 1993;189(3):727-731.
96. Nagamani M, London S, Amand PS. Factors influencing fertility after ectopic pregnancy. Am J Obstet Gynecol. 1984;149(5):533-535.
97. Schoen JA, Nowak RJ. Repeat ectopic pregnancy: a 16-year clinical survey. Obstet Gynecol. 1975;45(5):542-546.
98. Coupet E. Ectopic pregnancy: the surgical epidemic. J Natl Med Assoc. 1989;81(5):567-572.
99. Rein MS, Di Salvo DN, Friedman AJ. Heterotopic pregnancy associated with in vitro fertilization and embryo transfer: a possible role for routine vaginal ultrasound. Fertil Steril. 1989;51(6):1057-1058.
100. Hann LE, Bachman DM, McArdle CR. Coexistent intrauterine and ectopic pregnancy: a re-evaluation. Radiology. 1984;152(1):151-154.
101. Wong WS, Mao K. Combined intrauterine and tubal ectopic pregnancy. Aust N Z J Obstet Gynaecol. 1989;29(1):76-77.
102. Herztberg BS, Kliewer MA, Bowie JD. Sonographic evaluation for ectopic pregnancy: transabdominal scanning of patients with nondistended urinary bladders as a complement to transvaginal sonography. AJR Am J Roentgenol. 1999;173(3):773-775.
103. Levine D. Ectopic pregnancy. Radiology. 2007;245(2):385-397.
104. Thorsen MK, Lawson TL, Aiman EJ, et al. Diagnosis of ectopic pregnancy: endovaginal vs transabdominal sonography. AJR Am J Roentgenol. 1990;155(2):307-310.
105. Zinn HL, Cohen HL, Zinn DL. Ultrasonographic diagnosis of ectopic pregnancy: importance of transabdominal imaging. J Ultrasound Med. 1997;16(9):603-607.
106. Kirk E, Papageorghiou AT, Condous G, et al. The diagnostic effectiveness of an initial transvaginal scan in detecting ectopic pregnancy. Hum Reprod. 2007;22(11):2824-2828.
107. Brown DL, Doubilet PM. Transvaginal sonography for diagnosing ectopic pregnancy. J Ultrasound Med. 1994;13:259-266.
108. Rizk B, Tan SL, Morcos S, et al. Heterotopic pregnancies after in vitro fertilization and embryo transfer. Am J Obstet Gynecol. 1991;164(1 Pt 1): 161-164.
109. Frates MC, Laing FC. Sonographic evaluation of ectopic pregnancy: an update. AJR Am J Roentgenol. 1995;165(2):251-259.
110. Fernandez H, Gervaise A. Ectopic pregnancies after infertility treatment: modern diagnosis and therapeutic strategy. Hum Reprod Update. 2004;10(6):503-513.
111. Connolly A, Ryan DH, Stuebe AM, Wolfe HM. Reevaluation of discriminatory and threshold levels for serum beta-hCG in early pregnancy. Obstet Gynecol. 2013;121(1):65-70.
112. Cacciatore B, Stenman UH, Ylostalo P. Comparison of abdominal and vaginal sonography in suspected ectopic pregnancy. Obstet Gynecol. 1989;73(5 Pt 1):770-774.
113. Nyberg DA, Filly RA, Laing FC, et al. Ectopic pregnancy. Diagnosis by sonography correlated with quantitative HCG levels. J Ultrasound Med. 1987;6(3):145-150.
114. Fleischer AC, Pennell RG, McKee MS, et al. Ectopic pregnancy: features at transvaginal sonography. Radiology. 1990;174(2):375-378.
115. Frates MC, Visweswaran A, Laing FC. Comparison of tubal ring and corpus luteum echogenicities: a useful differentiating characteristic. J Ultrasound Med. 2001;20(1):27-31.
116. Stein MW, Ricci ZJ, Novak L, et al. Sonographic comparison of the tubal ring of ectopic pregnancy with the corpus luteum. J Ultrasound Med. 2004;23(1):57-62.
117. Chen PC, Sickler GK, Dubinsky TJ, et al. Sonographic detection of echogenic fluid and correlation with culdocentesis in the evaluation of ectopic pregnancy. AJR Am J Roentgenol. 1998;170(5):1299-1302.
118. Mehta TS, Levine D, McArdle CR. Lack of sensitivity of endometrial thickness in predicting presence of an ectopic pregnancy. J Ultrasound Med. 1999;18(2):117-122.
119. Malinowski A, Bates SK. Semantics and pitfalls in the diagnosis of cornual/interstitial pregnancy. Fertil Steril. 2006;86(6):1764.e11-1764.e14.
120. Ackerman TE, Levi CS, Dashefsky SM, et al. Interstitial line: sonographic finding in interstitial (cornual) ectopic pregnancy. Radiology. 1993;189(1): 83-87.
121. Wang W, Long W, Yu Q. Complication of cesarean section: pregnancy on the cicatrix of a previous cesarean section. Chin Med J. 2002;115(2): 242-246.
122. Barnhart K, van Mello NM, Bourne T, et al. Pregnancy of unknown location: a consensus statement of nomenclature, definitions and outcome. Fertil Steril. 2011;95(3):857-866.
123. Bottomley C, Van Belle V, Mukri F, et al. The optimal timing of an ultrasound scan to assess the location and viability of an early pregnancy. Hum Reprod. 2009;24(8):1811-1817.
124. Moschos E, Twickler DM. Endometrial thickness predicts intrauterine pregnancy in patients with pregnancy of unknown location. Ultrasound Obstet Gynecol. 2008;32(7):929-934.
125. Stangel JJ. Recent techniques for the conservative management of tubal pregnancy. Surgery, laparoscopy and medicine. J Reprod Med. 1986;31(2): 98-101.
126. Yao M, Tulandi T. Current status of surgical and nonsurgical management of ectopic pregnancy. Fertil Steril. 1997;67(3):421-433.
127. Ory SJ, Villanueva AL, Sand PK, Tamura RK. Conservative treatment of ectopic pregnancy with methotrexate. Am J Obstet Gynecol. 1986;154(6): 1299-1306.
128. Hajenius PJ, Mol BW, Bossuyt PM, et al. Interventions for tubal ectopic pregnancy. Cochrane Database Syst Rev. 2000;(2):CD000324.
129. Nazac A, Gervaise A, Bouyer J, et al. Predictors of success in methotrexate treatment of women with unruptured tubal pregnancies. Ultrasound Obstet Gynecol. 2003;21(2):181-185.
130. Barnhart KT, Gosman G, Ashby R, Sammel M. The medical management of ectopic pregnancy: a meta-analysis comparing "single dose" and "multidose" regimens. Obstet Gynecol. 2003;101(4):778-784.
131. Cyr DR, Mack LA, Nyberg DA, et al. Fetal rhombencephalon: normal US findings. Radiology. 1988;166(3):691-692.
132. Schmidt W, Yarkoni S, Crelin ES, Hobbins JC. Sonographic visualization of physiologic anterior abdominal wall hernia in the first trimester. Obstet Gynecol. 1987;69(6):911-915.
133. Lurain JR. Gestational trophoblastic disease 1: epidemiology, pathology, clinical presentation and diagnosis of gestational trophoblastic disease, and management of hydatidiform mole. Am J Obstet Gynecol. 2010;203(6): 531-539.
134. Semer DA, Macfee MS. Gestational trophoblastic disease: epidemiology. Semin Oncol. 1995;22(2):109-112.
135. Wagner BJ, Woodward PJ, Dickey GE. From the archives of the AFIP. Gestational trophoblastic disease: radiologic-pathologic correlation. Radiographics. 1996;16(1):131-148.
136. Rose PG. Hydatidiform mole: diagnosis and management. Semin Oncol. 1995;22(2):149-156.
137. Sebire NJ, Rees H, Paradinas F, et al. The diagnostic implications of routine ultrasound examination in histologically confirmed early molar pregnancies. Ultrasound Obstet Gynecol. 2001;18(6):662-665.
138. Lazarus E, Hulka C, Siewert B, Levine D. Sonographic appearance of early complete molar pregnancies. J Ultrasound Med. 1999;18(9): 589-594.
139. Benson CB, Genest DR, Bernstein MR, et al. Sonographic appearance of first trimester complete hydatidiform moles. Ultrasound Obstet Gynecol. 2000;16(2):188-191.
140. Goldstein DP, Berkowitz RS. Current management of complete and partial molar pregnancy. J Reprod Med. 1994;39(3):139-146.
141. Berkowitz RS, Goldstein DP. Clinical practice. Molar pregnancy. N Engl J Med. 2009;360(16):1639-1645.
142. Berkowitz RS, Goldstein DP. Chorionic tumors. N Engl J Med. 1996;335(23):1740-1748.

143. Green CL, Angtuaco TL, Shah HR, Parmley TH. Gestational trophoblastic disease: a spectrum of radiologic diagnosis. Radiographics. 1996;16(6): 1371-1384.
144. Kirk E, Papageorghiou AT, Condous G, et al. The accuracy of first trimester ultrasound in the diagnosis of hydatidiform mole. Ultrasound Obstet Gynecol. 2007;29(1):70-75.
145. Fowler DJ, Lindsay I, Seckl MJ, Sebire NJ. Routine pre-evacuation ultrasound diagnosis of hydatidiform mole: experience of more than 1000 cases from a regional referral center. Ultrasound Obstet Gynecol. 2006;27(1):56-60.
146. Steller MA, Genest DR, Bernstein MR, et al. Natural history of twin pregnancy with complete hydatidiform mole and coexisting fetus. Obstet Gynecol. 1994;83(1):35-42.
147. Sebire NJ, Foskett M, Paradinas FJ, et al. Outcome of twin pregnancies with complete hydatidiform mole and healthy co-twin. Lancet. 2002;359(9324): 2165-2166.
148. Greenfield AW. Gestational trophoblastic disease: prognostic variables and staging. Semin Oncol. 1995;22(2):142-148.
149. Jain KA. Gestational trophoblastic disease: pictorial review. Ultrasound Q. 2005;21(4):245-253.
150. Jauniaux E. Ultrasound diagnosis and follow-up of gestational trophoblastic disease. Ultrasound Obstet Gynecol. 1998;11(5):367-377.
151. Soper JT. Identification and management of high-risk gestational trophoblastic disease. Semin Oncol. 1995;22(2):172-184.
152. Finkler NJ. Placental site trophoblastic tumor. Diagnosis, clinical behavior and treatment. J Reprod Med. 1991;36(1):27-30.
153. Mangili G, Spagnolo D, Valsecchi L, Maggi R. Transvaginal ultrasonography in persistent trophoblastic tumor. Am J Obstet Gynecol. 1993;169(5): 1218-1223.
154. Caspi B, Elchalal U, Dgani R, et al. Invasive mole and placental site trophoblastic tumor. Two entities of gestational trophoblastic disease with a common ultrasonographic appearance. J Ultrasound Med. 1991;10(9): 517-519.
155. Sakamoto C, Oikawa K, Kashimura M, Egashira K. Sonographic appearance of placental site trophoblastic tumor. J Ultrasound Med. 1990;9(9): 533-535.
156. Desai RK, Desberg AL. Diagnosis of gestational trophoblastic disease: value of endovaginal color flow Doppler sonography. AJR Am J Roentgenol. 1991;157(4):787-788.
157. Chan FY, Chau MT, Pun TC, et al. A comparison of colour Doppler sonography and the pelvic arteriogram in assessment of patients with gestational trophoblastic disease. Br J Obstet Gynaecol. 1995;102(9): 720-725.
158. Kennedy AW. Persistent nonmetastatic gestational trophoblastic disease. Semin Oncol. 1995;22(2):161-165.
159. Lurain JR. High-risk metastatic gestational trophoblastic tumors. Current management. J Reprod Med. 1994;39(3):217-222.

CHAPTER 31

Chromosomal Abnormalities

Bryann Bromley and Beryl Benacerraf

SUMMARY OF KEY POINTS

- Screening for aneuploidy using the nuchal translucency (NT) measurement should be performed by a credentialed provider participating in an ongoing quality-monitoring program.
- In chromosomally normal fetuses with an increased NT, normal anatomy and no identifiable genetic syndromes, there does not appear to be a higher risk of developmental delay than in the general population.
- A "marker" identified during a second-trimester sonogram should prompt a detailed evaluation of the fetus and correlation with a priori risk estimates for aneuploidy.
- The constellation of sonographic findings seen in the second trimester may lead physicians to suspect a specific chromosomal abnormality.
- Cell-free DNA screening with reportable results has superior test performance metrics compared with traditional screening for targeted aneuploidies; however, false-positive and false-negative results occur. Positive results should be confirmed by a diagnostic test. Negative results do not ensure a normal outcome.

CHAPTER OUTLINE

FIRST-TRIMESTER SCREENING FOR ANEUPLOIDY
Nuchal Translucency and Trisomy 21
Serum Biochemical Markers
Combined First-Trimester Screening
Integrated and Sequential Screening
Standardization of Nuchal Translucency Measurement Technique
Nuchal Translucency and Other Aneuploidies
Cystic Hygroma
Nasal Bone
Other Markers for Aneuploidy
Reversed Flow in Ductus Venosus
Tricuspid Regurgitation
Thickened Nuchal Translucency With Normal Karyotype
SECOND-TRIMESTER SCREENING FOR TRISOMY 21
Nuchal Fold
Facial Profile (Nasal Bone)
Femur Length
Humerus Length
Urinary Tract Dilation
Echogenic Bowel
Echogenic Intracardiac Focus
Structural Anomalies
Adjunct Features of Trisomy 21
Combined Markers
TRISOMY 18 (EDWARDS SYNDROME)
Choroid Plexus Cysts
TRISOMY 13 (PATAU SYNDROME)
TRIPLOIDY
MONOSOMY X (TURNER SYNDROME)
PRENATAL SCREENING FOR ANEUPLOIDY WITH CELL-FREE DNA
DIAGNOSTIC TESTING
CONCLUSION

The current standard of obstetric care in the United States is to offer prenatal screening for aneuploidy to all women who present for care before 20 weeks' gestation.[1] If a woman chooses to have a prenatal risk assessment for aneuploidy, multiple sonographic markers and biochemical parameters are available in both the first and the second trimester. Recently, the paradigm for prenatal screening has included the evaluation of **cell-free DNA** in the maternal plasma and diagnostic testing has expanded beyond the basic karyotype to include microarray analysis that can detect small deletions and duplications in the genome, known as "copy number variants" (CNVs).[2,3] The choices available depend on the gestational age of the fetus at presentation for obstetric care and the availability of resources within the local demographic area. Screening algorithms are becoming progressively more diverse with varying trade-offs.[4] Counseling by an experienced provider is recommended.[5]

Background risk for **aneuploidy** (deviation from exact multiple of haploid number of chromosomes) depends on maternal age, fetal age, family history, and previously affected pregnancy. Whereas trisomies 21, 18, and 13 increase in frequency as maternal age increases, monosomy X and triploidy remain at a constant rate[6] (Fig. 31.1).

Trisomy 21 (Down syndrome) is the most common aneuploidy to result in a live birth and is the most frequently identifiable genetic cause of mental retardation. The estimated prevalence has increased over the past 20 years because of trends in advancing maternal age and is estimated to be 1 in 504 in the second trimester.[7] Trisomies 18 and 13 are rarer, with a prevalence of 1 in

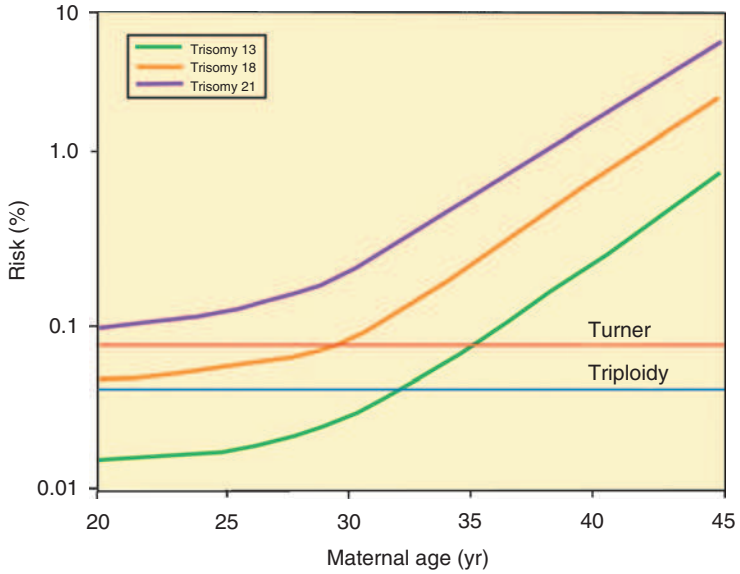

FIG. 31.1 Maternal Age–Related Risk for Chromosomal Abnormalities.

5000 and 1 in 10,000, respectively.[8] The frequency of aneuploidy is higher earlier in gestation because of the fetal loss rate associated with chromosomal abnormalities as gestation progresses. Fetal death with trisomy 21 between the first or second trimester and birth is 30% and 20%, respectively. Fetal death between the first trimester and birth with trisomies 18 and 13 is approximately 80%.[6,9]

FIRST-TRIMESTER SCREENING FOR ANEUPLOIDY

First-trimester screening for aneuploidy that incorporates ultrasound provides a patient-specific numeric risk estimate of trisomy 21, 18 and 13. It may also be a clue for other chromosomal conditions.[10] Most pregnancies are normal, so most women can be reassured early in gestation that their risk of aneuploidy is low. Others may find that the risk estimate is high enough that to undergo a secondary **screening with cell-free DNA** or diagnostic testing (chorionic villous sampling) to obtain a karyotype or microarray analysis. If the results are abnormal, the patient has time to obtain additional information and explore resources that are available before making a decision about continuing or terminating a pregnancy. The decision to terminate can be made with privacy and at a time in pregnancy when safe methods of pregnancy interruption are available.[11]

Nuchal Translucency and Trisomy 21

In 1866, Dr. Langdon Down reported a classification of individuals with developmental delay who had similar physical characteristics. He described the skin as "deficient in elasticity, giving the appearance of being too large of the body."[12] Fetuses with trisomy 21 as well as other aneuploidies often have excess fluid in the subcutaneous tissue behind the fetal neck (Fig. 31.2A, Video 31.1). Sonographically, this appears as an echolucent fluid collection between the soft tissue over the cervical spine and an echogenic line representing the skin edge. This fluid space is called the **nuchal translucency** (NT)[13] (Fig. 31.2B). The lucency is thought to represent mesenchymal edema and is often associated with distended jugular lymphatics (Fig. 31. 2C). The prevailing theory suggests an alteration in lymphangiogenesis and delayed lymphatic development. Other possible causes include cardiac failure and abnormal extracellular matrix, but these do not explain the localized and transient nature of the NT. Most likely, the cause is a complex interaction of factors.[14] NT normally increases with advancing gestational age, and therefore the measurement is compared to **crown-rump length** (CRL, Fig. 31.2D). An NT greater than 95% for CRL is considered thickened. An NT greater than 99% does not change significantly with CRL and is approximately 3.5 mm[15] (Fig. 31.2E).

In 1992, Nicolaides et al.[13] reported that an NT of 3 mm or greater in the first trimester was associated with a 35% risk of chromosomal abnormality. The association between chromosome anomalies and a thickened NT was subsequently confirmed in a large, prospective multicenter trial of 20,804 pregnancies. The risk of trisomy 21 can be calculated by multiplying the a priori (presumptive) risk by a **likelihood ratio** derived from the degree of deviation in NT from the expected NT. This methodology, in conjunction with a risk cutoff of 1 in 300, resulted in the identification of 80% of fetuses with trisomy 21, with a **false-positive rate** (FPR) of 5%.[16] Snijders et al.[17] evaluated the use of NT and maternal age to detect trisomy 21 in a multicenter trial that included 22 different sites and 306 trained sonographers. Using a threshold of 1 in 300, the sensitivity for the detection of trisomy 21 was 82% for an FPR of 8%. If the FPR was set at 5%, the sensitivity for the detection of trisomy 21 was 77%.

Serum Biochemical Markers

A variety of serum biochemical markers have different concentrations in pregnancies with trisomy 21 compared with euploid

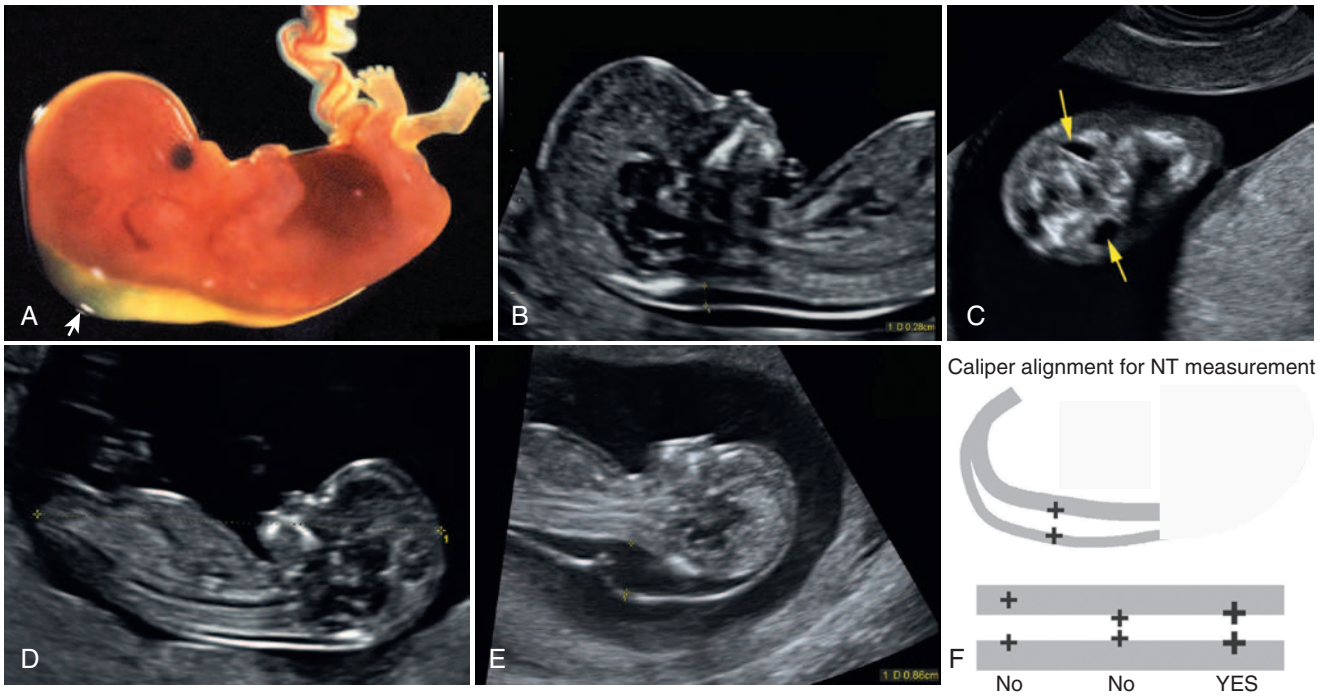

FIG. 31.2 Nuchal Translucency. (A) Gross pathology image of a fetus with trisomy 21 demonstrating the fluid collection at the back of the neck known as the "nuchal translucency" (NT; *arrow*). (Courtesy of Dr. Eva Pajkrt, University of Amsterdam.) **(B)** Midsagittal view of a euploid fetus demonstrating the correct method of measuring the NT. See also Video 31.1. **(C)** Axial view through the fetal neck showing distended jugular lymphatic sacs *(arrows)*. **(D)** Midsagittal view of a first-trimester fetus showing the correct method of measuring the crown-rump length. **(E)** Midsagittal view of a first-trimester fetus showing a thick NT (8.6 mm). **(F)** Schematic illustrating the correct method of caliper placement. (Courtesy of Dr. Bernard Benoit, Princess Grace Hospital, Monaco.)

pregnancies. The maternal serum of women carrying fetuses with trisomy 21 has a higher concentration of **free beta human chorionic gonadotropin** (free β-hCG) and lower concentration of **pregnancy-associated plasma protein A** (PAPP-A) compared with the serum of women carrying euploid fetuses. The use of these serum markers, in conjunction with maternal age, results in identification of 62% of fetuses with trisomy 21 at an FPR of 5%.[18]

Combined First-Trimester Screening

There is no association between NT measurement and serum levels of free β-hCG or PAPP-A in euploid fetuses or in those with trisomy 21. This independence allows the combination of NT screening and biochemical screening, resulting in a more effective method of risk assessment than either method individually.[19,20] Wald et al.[21] demonstrated that the combination of NT measurement with maternal serum PAPP-A and free β-hCG, known as the **combined first-trimester screening** test, results in the detection of 85% of trisomy 21 fetuses at an FPR of 5%.

First-trimester screening using NT measurement and serum biochemical measurement has been further validated in four large studies. The One-Stop Clinic to Assess Risk (OSCAR) screening trial in the United Kingdom studied 12,339 women with singleton pregnancies between 10 and 14 weeks' gestation. First-trimester screening was accepted by 97.5% of the women, and if they screened positive (risk ≥ 1:300), 77% underwent invasive diagnostic testing. There were 25 cases of trisomy 21, of which 23 (92%) were detected, with an FPR of 5%. The detection rates of both trisomy 13 and 18 were 100%.[22]

A multicenter trial in North America (BUN study) similarly evaluated 8514 patients with singleton pregnancies between 74 and 97 days' gestation. A screening result was considered positive if the risk of trisomy 21 was 1 in 270 or higher or the risk of trisomy 18 was 1 in 150 or higher. There were 61 cases of trisomy 21; detection rate was 79% with a 5% FPR. The detection rate of trisomy 18 was 90% with a 2% FPR.[23]

The Serum, Urine and Ultrasound Screening Study (SURUSS) evaluated the efficacy, safety, and cost-effectiveness of first- and second-trimester screening for trisomy 21. This prospective study was conducted primarily in the United Kingdom on 47,053 pregnancies between 9 and 13 weeks' gestation. In the first trimester the combined test had a sensitivity of 85% for the detection of trisomy 21 with an FPR of 6%.[24]

The First and Second Trimester Evaluation of Risk (FASTER) was the largest trial based in the United States and was designed to determine how best to screen pregnant women for trisomy 21. This multicenter trial included 36,120 patients with complete first-trimester data, of whom 92 fetuses had trisomy 21. The trial included NT measurements as well as serum biochemistry in both the first and the second trimester, revealing the results to patients only in the second trimester, after both serum screens.

The detection rate of trisomy 21 was 87%, 85%, and 82% at 11, 12, and 13 weeks' gestation, respectively, at a 5% FPR. For a detection rate of 85%, NT alone (without biochemical data) had an unacceptably high FPR of 20%. If the FPR was set at the more acceptable level of 5%, the sensitivity for detection of trisomy 21 fell to 68%.[25]

Screening for aneuploidy in twin gestations is less robust than in singleton gestations and is hampered by nuances of placentation. Determination of amnionicity and chorionicity is crucial. Sebire et al.[26] studied a series of 448 twin pregnancies and identified 88% of trisomy 21 fetuses (FPR 7%) using an NT less than 95%. The prevalence of a thickened NT is higher in euploid monochorionic twins than in euploid dichorionic twins, which may relate to placental structure or fetal anomalies. Discordance of NT measurements in monochorionic twins may predict twin-to-twin transfusion syndrome.[27,28] Additionally, the contribution of biochemical markers increases the complexity of risk assessment in twin gestations because the concentration of markers relates to the pregnancy (as opposed to the individual fetus). Spencer and Nicolaides[29] identified 75% of trisomy 21 fetuses (FPR of 7%) using biochemical markers and NT measurement. Wald and Rish[30] reported that at a set FPR of 5%, the estimated detection rate of trisomy 21 was 84% in monochorionic twins and 70% in dichorionic twins. This compares to an 85% estimated detection rate in singletons. Recently, it has been reported that the risk of trisomy 21 in twins may not be as high as previously thought, especially in monozygotic twins; these data add to the complexity of risk assessment. In a large population study based in Europe examining the prevalence of Down syndrome among monozygotic and dizygotic twins, the adjusted risk ratio (RR) of Down syndrome was 0.58 (95% CI, 0.53-0.62) for twins compared with singletons. This was most pronounced in monozygotic twins where the adjusted RR was 0.34 (95% CI, 0.25-0.44). In dizygotic twins the adjusted RR was 1.34 (95% CI, 1.23-1.46).[31]

A major question is whether an NT measurement exists above which there is no benefit to additional biochemical screening. Results of the FASTER trial were evaluated with specific attention to this question. An NT of 4 mm or greater was identified in 32 patients (0.09 %). In this group the lowest combined risk assessment for trisomy 21 in euploid fetuses was 1 in 8 and for aneuploid fetuses was 7 in 8. There were 128 patients with NT of 3 mm or greater. The lowest risk of trisomy 21 among euploid fetuses using combined screening was 1 in 1479, and the lowest risk among those with aneuploidy was 1 in 2. Only 10 patients (8%) had the risk lowered below 1 in 200, all of whom had normal outcome. These authors concluded that there is minimal benefit in waiting for combined screening results in fetuses with NT of 3 mm or larger and no benefit for those with NT of 4 mm or larger.[32]

Integrated and Sequential Screening

Wald et al.[33] introduced the concept of **integrated screening,** in which first- and second-trimester evaluation is used to provide a *single* risk estimate for trisomy 21.

The FASTER trial compared screening strategies across the first and second trimesters. There were 33,546 patients with complete first- and second-trimester data available, including 87 fetuses with trisomy 21. The fully integrated screen that included first-trimester NT measurement along with PAPP-A and a second-trimester quad screen resulted in the detection of 95% of fetuses with trisomy 21 at a 5% FPR or 87% if the FPR was set at 1%.[25] A disadvantage of integrated screening is that the patient does not have any screening results in the first trimester, and fetuses at high risk of trisomy 21 are not identified until the midtrimester.[34] Compounding this, as many as 20% of patients may not comply with the second-trimester screen.[24,35]

Two alternative approaches have been proposed in response to the criticism of late notification of patients at "high risk" of aneuploidy. Each of these sequential protocols discloses first-trimester results to patients above a specific "high-risk" threshold.[35,36] Women above the threshold and therefore considered at highest risk can be referred for genetic counseling and diagnostic testing early in gestation. In the *step-wise protocol,* those not identified in the high-risk group undergo second-trimester biochemical screen. In the *contingent protocol,* only those women at intermediate risk (≥1:50 and <1:1500) go on to the second-trimester biochemical screening while those at low risk (<1:1500) are not offered additional screening. In each protocol the results of first- and second-trimester screening are **integrated** and reported as a single number because if they are independently interpreted, the FPR is unacceptably high.[1,37] Those with a risk of 1 in 270 or higher were offered genetic counseling and diagnostic testing.

Cuckle et al.[35] retrospectively calculated the midtrimester risks of trisomy 21 from the FASTER trial data. In this study, patients were categorized as "high risk" (>1:30), "borderline risk" (1:30-1:1500), and "low risk" (<1:1500) based on the results of the first-trimester evaluation. Only patients in the borderline category underwent recalculation of risk based on second-trimester biochemical screening. The initial detection of trisomy 21 (>1:30) after first-trimester screening was 60% with an FPR of 1.2%. Of the remaining population, 23% were at borderline risk and calculated as having additional screening. Contingent screening identified 91% of fetuses with trisomy 21, with a 4.5% FPR. Stepwise screening, in which all women other than those at highest risk had calculated first- and second-trimester testing, had a detection rate of 92% with an FPR of 5.1%. Integrated screening, in which all women had both first-semester and second-trimester testing, had a detection rate of 88% with an FPR of 4.9%. This study showed that **contingent screening,** in which only 23% of the population went on to the second-trimester biochemical serum screen, had a similar detection rate of trisomy 21 as the protocols in which most if not all patients had recalculation of risk with second-trimester biochemistry.

Standardization of Nuchal Translucency Measurement Technique

For NT screening to be accurate, standardization of technique, training, and ongoing monitoring are crucial. This education, validation, and ongoing quality assurance has been

supported by two organizations: the Nuchal Translucency Quality Review program based in the United States and the Fetal Medicine Foundation based in the United Kingdom. The criteria and caliper placement for measuring the NT are illustrated in Fig. 31.2 (see also Video 31.1 for real time scanning without measurement). The specific details for credentialing can be found at www.ntqr.org or www.fetalmedicine.org.

The fetal CRL must be between 45 and 84 mm although variations exist among laboratories that perform the biochemical component. The accuracy of the NT measurement and the CRL is critical because the NT measurement is converted into multiples of the median (MoM) based on the CRL. An adequate sonographic image to measure the CRL requires the fetus to occupy a majority of the image space and be in a neutral position. The longest straight line between the fetal crown and rump is measured at least three times and the average of three good measurements is used.

Haddow et al.[38] showed that accuracy is critical when obtaining an NT measurement. They studied 4412 women who underwent first-trimester screening with biochemistry and NT in which no specific training in NT measurement was required although the method for measuring NT was a standard protocol. Measurement of the NT varied considerably between centers and could not be reliably incorporated into risk calculations. Furthermore, the center with the highest success rate in obtaining an NT measurement (100%) had the lowest sensitivity (0%) for identifying trisomy 21. Results from the BUN trial revealed that after training, measurements were initially smaller than expected compared with normative values developed by Fetal Medicine Foundation. With increasing experience, the measurements of the BUN trial were in concordance with published norms.[23,39]

Criteria for an Accurate Crown-Rump Length

ALARA: Thermal Index BONE < 0.7[40]

MAGNIFICATION
The fetus fills the majority of the image space available

MIDSAGITTAL VIEW
Fetal spine midsagittal
Profile, spine, and rump are visible

NEUTRAL POSITION
The spine is in line with the head
Fluid is visible between the fetal chin and chest

MEASUREMENT
Angle of insonation perpendicular to fetus
Fetus horizontal on image
Calipers are placed on the outer border of the skin at crown and rump

Fetal Nuchal Translucency (NT) Measurement Technique

ALARA: Thermal Index BONE < 0.7[40]

CLEAR NT MARGINS
Thin NT line
Angle of insonation perpendicular to NT space
Fetus horizontal on image
TIPS for optimal imaging:
1. Optimize your focal zone
2. Reduce your dynamic range
3. Reduce the gain
4. Review harmonics. Possible edge enhancement optimized with harmonics off
5. Avoid post freeze zoom
6. Narrow your sector

FETUS IN MIDSAGITTAL PLANE
Fetal spine midsagittal in thoracic and cervical region
Tip of nose in profile
Third and fourth ventricles in brain demonstrated

FETUS OCCUPIES MAJORITY OF IMAGE
Head, neck, and upper thorax fill image
Fetus occupies more than 50% of image space; a second fetus of the same size would not fit in the image space

HEAD IN A NEUTRAL POSITION
Head in line with the spine, angle of neck and chest is less than 90 degrees
Pocket of fluid should be visible between chin and neck

AMNION SEEN SEPARATELY FROM NT LINE
Fetus is seen away from uterine wall and separate from the amnion

MEASUREMENT
Calipers (cursors) must be + (plus/positive)
Crossbar of caliper is on the NT line at the inner border adjacent to the lucency
Measurement is perpendicular to long axis of fetus
Measurement is taken at the WIDEST part of the lucency (If nuchal cord, measure above and below the cord and average)

A poorly done NT measurement has a negative impact on detection of aneuploidy, and inaccuracy of 0.5 mm decreases sensitivity by 18%.[41] Training an inexperienced examiner to obtain reliable reproducible NT measurements takes 80 to 100 scans.[42]

Screening using an NT measurement is not always possible because of limited availability of this specialized ultrasound in certain areas and a variety of maternal conditions, including large myomas and high maternal body mass index, which may hamper the ability to obtain a reliable measurement. Initial studies suggested that an NT value was obtainable in 99% of cases, but clinical studies report an 80% initial success rate.[43,44]

If an accurate NT measurement is not possible, a serum-only version of the integrated test should be offered. The performance of the serum integrated test with no ultrasound component has

approximately an 85% detection rate for Down syndrome at a 5% FPR.[22,25,33]

Nuchal Translucency and Other Aneuploidies

A thickened NT has been used to detect fetuses with trisomy 18. These fetuses have an abnormal biochemical pattern with very low β-hCG and very low PAPP-A. The BUN trial of 8514 screened pregnancies, using a risk cutoff of 1 in 150, identified 91% of fetuses with trisomy 18 with a 2% FPR. Additionally, four in five fetuses with trisomy 13 were identified.[23] These trisomies result in fetuses that have multiple congenital malformations and rarely survive beyond the first year of life. The FASTER trial reported a detection rate of 78% for all nontrisomy 21 aneuploidies at FPR of 6% when first-trimester screening included those cystic hygroma or combined screening.[45] Spencer and Nicolaides[46] developed an algorithm for the detection of trisomy 18 and 13 that included maternal age, NT, free β-hCG, and PAPP-A. Using a risk cutoff of 1 in 150, they predicted a 95% detection rate for these chromosomal defects with FPR of 0.3%. In a population-based study of 452,901 women with singleton gestations, the detection rates of aneuploidy based on first-trimester and sequential screening was 81.6% at a FPR of 4.5%. The detection rates of trisomy 21, 18, and 13 were 92.9%, 93.2%, and 80.4% respectively. The detection of monosomy X and triploidy were 80.1% and 91.0%.[47] In a recent prospective validation study the first-trimester combined test detected 90%, 97%, and 92% of trisomies 21, 18, and 13, respectively, as well as >90% of cases of monosomy X, >85% of triploidies, and >30% of other chromosomal abnormalities, at FPR of 4%.[48]

Cystic Hygroma

The distinction between a first-trimester cystic hygroma and a thick NT is controversial. Historically, a cystic hygroma has been diagnosed when the hypoechoic space at the back of the neck extends down the fetal back and contains septations (Fig. 31.3, Video 31.2). Malone et al.[49] reported on 134 cases of cystic hygroma identified in the FASTER trial from 38,167 screened pregnancies. Chromosomal abnormalities were present in 51% of these patients and major structural anomalies were identified in 34% of those without karyotypic anomaly. Survival with normal outcome was confirmed in 17% of cases. These investigators reported an increased risk of aneuploidy, cardiac malformations, and fetal death in fetuses with cystic hygroma compared with those who had a simple, thickened NT.[49] Other investigators have reported that septations are seen in all thickened NTs if examined in the transverse suboccipitobregmatic plane and that the incidence of adverse outcome is related to NT thickness rather than appearance.[50,51]

Nasal Bone

Dr. Down, in his original essay describing the physical features of a category of developmentally delayed individuals, identified the nose as being small.[12] Not surprisingly, many fetuses with trisomy 21 have a small or absent nasal bone. The fetal nasal bone can be seen by ultrasound starting at approximately 11 weeks' gestation. The first-trimester nasal bone evaluation is technically challenging, and competency in assessing nasal bone reportedly takes an average of 80 scans.[52] The criteria for a nasal bone evaluation are shown in Fig. 31.4 and Video 31.3. Initial first-trimester screening studies report that the nasal bone is absent in 73% of fetuses with trisomy 21 and 0.5% of euploid fetuses.[53] Cicero et al.[54] studied 5918 fetuses between 11 and 14 weeks and obtained a fetal profile in 99%. An absent fetal nasal bone in euploid fetuses varied by ethnicity. A nasal bone was not identified in 2.2% of Caucasian fetuses, 9% of African Caribbean fetuses, and 5% of Asian fetuses. Younger fetuses also have a higher incidence of nonvisualization of the nasal bone. Absence of the nasal bone was seen in 4.7%, 3.4%, 1.4%, and 1% of euploid fetuses with CRL of 45 to 54 mm, 55 to 64 mm, 65 to 74 mm, and 75 to 84 mm, respectively.

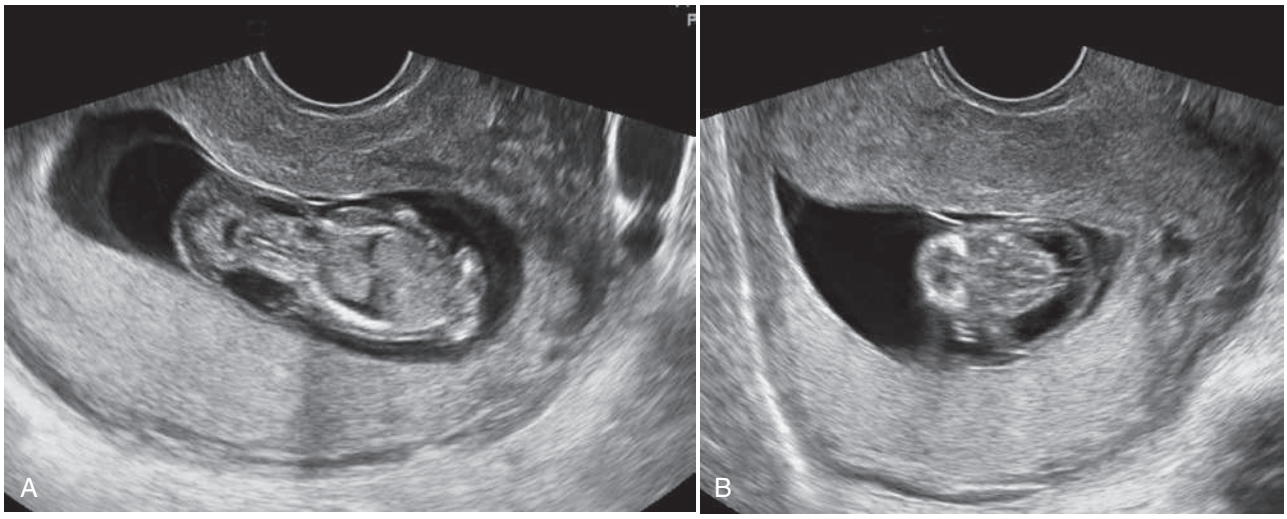

FIG. 31.3 Cystic Hygroma. (A) First-trimester fetus with skin thickening that extends around the entire body, consistent with cystic hygroma, and bilateral distended jugular lymphatic sacs. Note the bilateral **pleural effusions,** indicating **hydrops. (B)** Axial scan through the head of the same fetus shows septations within the nuchal thickening. See also Video 31.2.

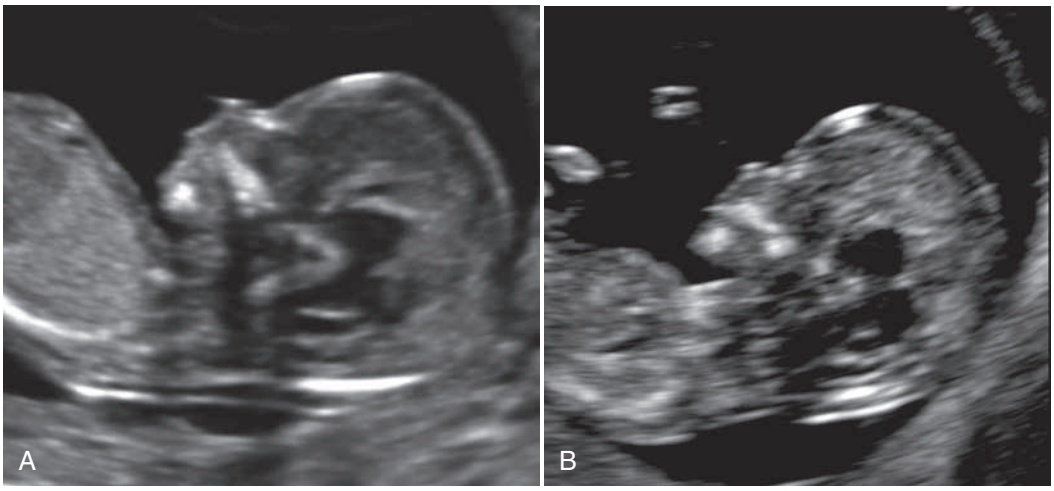

FIG. 31.4 First-Trimester Nasal Bone Assessment. (A) Midsagittal profile of a fetus shows the correct method of assessing the nasal bone. Note that the nasal bone is more echogenic than the overlying skin and they form an equal (=) sign. **(B)** Midsagittal profile of a fetus with trisomy 21 shows the echogenic overlying skin but **absent nasal bone.** See also Video 31.3.

Criteria for Nasal Bone (NB) Evaluation

ALARA: Thermal Index BONE < 0.7[40]
Margins of fetal anatomy clear without ambiguity in nasal anatomy
Fetus in midsagittal plane
- Fetal spine midsagittal in thoracic and cervical region
- Tip of nose clearly seen in profile and the skin edge over the nasal bridge is identified
- Care must be taken to demonstrate the skin edge separately from the NB so that an equal (=) sign is apparent
- Third and fourth ventricle are identified in the brain

Fetus occupies majority of image
- Head, neck, and upper thorax fill image
- Fetus occupies more than 50% of width and length of image

Angle of insonation 45 degrees to fetal profile, perpendicular to NB
Echogenicity of NB is comparable to other bony structures and similar or brighter than the overlying skin.

Nonvisualization of the nasal bone increases with thickened NT measurements. In fetuses with an NT below the 95th percentile, 1.6% had a nonvisualized nasal bone, compared with 2.7% for NT above the 95th percentile of 3.4 mm, 5.4% for NT 3.5 to 4.4 mm, 6% for NT 4.5 to 5.4 mm, and 15% for NT of 5.5 mm or greater. In this same study, an absent nasal bone was seen in 69% of trisomy 21 fetuses and in 32% of fetuses with other chromosomal defects.[54]

No significant association exists between the biochemical markers free β-hCG and PAPP-A and the fetal nasal bone; therefore these can be combined to refine the first-trimester risk assessment for trisomy 21.[55] Cicero et al.[56] prospectively evaluated 20,418 singleton fetuses between 11 and 14 weeks. The fetal nasal bone was absent in 238 (1.2%), was present in 19,937 (97.6%), and could not be evaluated in 243 (1.2%). A fetal nasal bone was absent in 113 in 20,165 (0.6%) of chromosomally normal fetuses and in 87 in 140 (62.1%) of fetuses with trisomy 21. The combination of NT and biochemical markers in the first trimester (combined first-trimester screening) resulted in the identification of 90% of fetuses with trisomy 21 at an FPR of 5%. Inclusion of the nasal bone resulted in the same rate of detection of trisomy 21 but with the FPR decreasing to 2.5%. These statistics held true if all fetuses underwent screening with a nasal bone evaluation performed at the time the NT was measured or if the nasal bone was evaluated in a two-stage approach in which only those at intermediate risk based on combined screening results underwent nasal bone evaluation. Orlandi et al.[57] used a simplified method for assessing the presence or absence of the nasal bone in which the nasal bone was considered absent only if there was no line below the nasal bridge at all. They found that using this strategy resulted in fewer cases being classified as absent while maintaining a high detection rate for aneuploidy.

Not all investigators have been as successful using the fetal nasal bone to assess for aneuploidy. Sepulveda et al.[58] reported on 1287 consecutive fetuses being evaluated for NT and presence or absence of a nasal bone. Overall, 110 fetuses (8.5%) had an NT at or above 95% and 25 (1.9%) had an absent nasal bone. Of the 31 trisomy 21 fetuses, 28 had an NT above 95% and 13 had an absent nasal bone. The detection rate of trisomy 21 was 90.3% using NT and 41.9% using an absent nasal bone. All but one fetus with an absent nasal bone had a thickened NT, and only two normal fetuses had an absent nasal bone. These authors concluded that although an absent nasal bone is highly predictive of trisomy 21, it is less useful as a sonographic marker than the NT. Malone et al.[59] reported that the nasal bone evaluation was not a useful test for population screening.

It is evident that the issues surrounding nasal bone screening in the first trimester are complex. The identification of the nasal bone as present or absent is a specialized skill that is attained

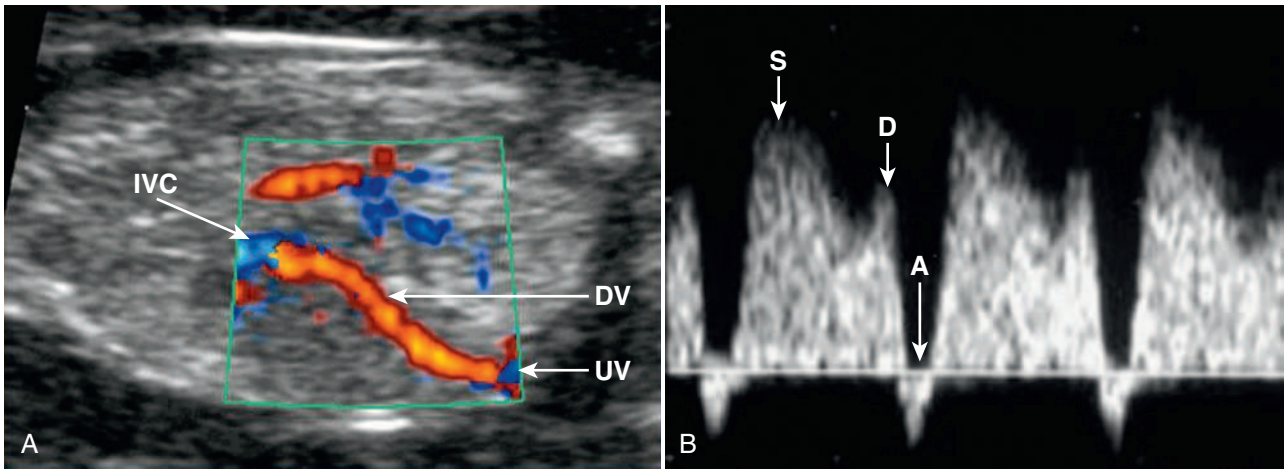

FIG. 31.5 Reversed Flow in Ductus Venosus. (A) Color Doppler anatomy of vessels at oblique sagittal view of fetal trunk. *DV,* Ductus venosus; *IVC,* inferior vena cava; *UV,* umbilical vein. **(B)** Abnormal ductus venosus sonogram shows a **reversed *a* wave.** Absent or reversed a-wave flow can occur in cardiac failure, with or without cardiac defects, and in chromosomally abnormal fetuses. *D,* Diastole; *S,* systole.

with experience, even for competent imagers. It has been recommended that the nasal bone be considered a contingency marker in patients whose first-trimester risk based on NT and biochemistry is in an intermediate-risk category between 1 in 101 and 1 in 1000.[56,60,61]

Other Markers for Aneuploidy

Reversed Flow in Ductus Venosus

The ductus venosus directs well-oxygenated blood from the umbilical vein to the coronary and cerebral circulation. Abnormal blood flow demonstrated as a reversed *a* wave in the ductus venosus is seen in 80% of fetuses with trisomy 21 and in 5% of euploid fetuses[9,62] (Fig. 31.5).

Tricuspid Regurgitation

Tricuspid regurgitation has also been proposed as a method of risk assessment. Falcon et al.[63] compared 77 fetuses with trisomy 21 and 232 chromosomally normal fetuses from singleton pregnancies at 11 to 14 weeks of gestation. Tricuspid regurgitation was identified in 57 (74%) of trisomy 21 fetuses and in 16 (7%) of euploid fetuses. No relationship between tricuspid regurgitation and the levels of maternal serum free β-hCG and PAPP-A was identified. The authors concluded that an integrated sonographic and biochemical test can identify about 90% of trisomy 21 fetuses for a 2% to 3% FPR.

First-trimester sonographic screening using NT and maternal age (without biochemistry) is enhanced by using additional ultrasound markers of nasal bone, tricuspid and ductus venosus flow. Detection rates of Down syndrome of 80%, 87%, and 94% are reported when using one, two, or three additional ultrasound markers while maintaining the FPR at 3%.[64]

Thickened Nuchal Translucency With Normal Karyotype

A thickened NT is associated with an increased risk of structural fetal anomalies including **congenital heart defects** (CHDs). In a study of 29,154 euploid fetuses between 10 to 14 weeks' gestation, Hyett et al.[65] identified 50 with CHDs; 56% of the fetuses were from a group of 1822 with an NT thickness greater than 95%. In a meta-analysis evaluating the screening performance of increased first-trimester NT for the detection of major CHDs, eight independent studies with 58,492 patients were reviewed. An NT greater than 99% had a sensitivity of 30% for the detection of CHDs. If an NT greater than 99% is used as an indication for a fetal echocardiogram, 1 in 16 referred cases would have CHDs. If the threshold was lowered to fetuses with an NT greater than 95%, 1 in 33 referred cases would have a major CHD.[66] Data from the FASTER trial confirmed that the incidence of major CHD increased with increasing NT, although the sensitivity for CHD detection was only 9.6%. These investigators concluded that NT lacked the qualities of a good screening test for heart disease; however, an NT of 2.5 MoM (99%) or greater is considered an indication for fetal echocardiography.[67] A population-based study evaluating the performance of a first-trimester thickened NT in the detection of critical CHDs in euploid liveborn infants demonstrated that an NT of greater than 99% had a 5-fold increased risk while an NT of 3.5 mm or larger had a 12-fold increased risk compared with fetuses whose NT measured less than 90% for CRL.[68]

Fetuses with a thick NT are at increased risk for a variety of major congenital abnormalities in addition to CHDs (Fig. 31.6). In combined data from 28 studies of 6153 euploid fetuses with thick NT, the prevalence of major anomalies was 7.3% (range, 3%-50%). The prevalence of major anomalies increased from 1.6% in those with an NT less than 95% to 2.5% in those with an NT 95% to 99%, 10% in those with an NT of 3.5 to 4.4 mm, and increasing dramatically thereafter to 46% in those with an NT greater than 6.5 mm.[15] Anomalies demonstrated included facial clefts, diaphragmatic hernia, abdominal wall defects as well as a multitude of other structural abnormalities. Timmerman et al. demonstrated an increased risk of oral facial cleft in chromosomally normal fetuses with a thick NT.[69] In a large population-based study of euploid infants examining the relation

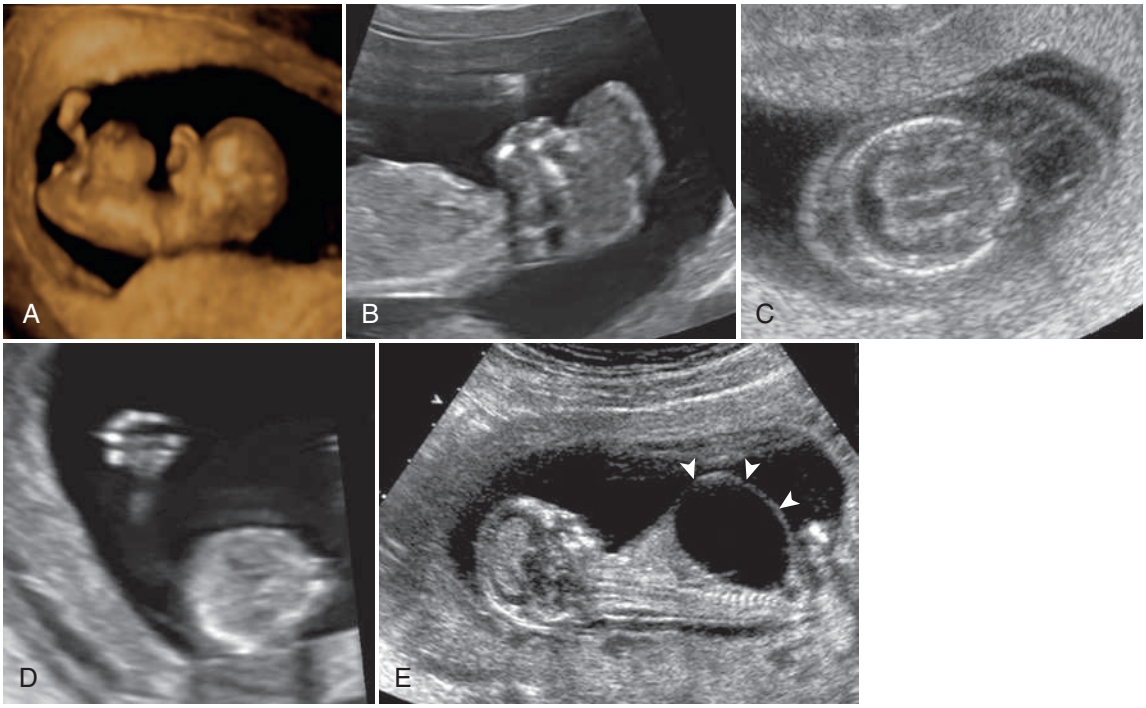

FIG. 31.6 Structural Abnormalities Seen at the 11- to 14-Week Ultrasound Performed for NT Assessment. (A) Three-dimensional image of fetus demonstrating an **omphalocele. (B)** Sagittal scan of a fetus demonstrating an irregular cephalic contour characteristic of **anencephaly. (C)** Transverse view of the fetal head demonstrating a monoventricle of **alobar holoprosencephaly.** Note the septated **cystic hygroma. (D)** View of the fetal hand demonstrating polydactyly. **(E)** Sagittal view of a fetus with a large cystic structure *(arrowheads)* in the fetal pelvis characteristic of **megacystis.** Note that the amniotic fluid volume is still normal because of gestational age.

of an increased NT and major noncardiac structural defects, an NT measurement of 95% or greater or NT of 3.5 mm or larger was associated with an increased risk compared with those having an NT less than 90% for CRL. The most commonly identified anomalies were hydrocephalus, agenesis/hypoplasia/dysgenesis of the lung, atresia or stenosis of the small intestine, osteodystrophies, and diaphragmatic anomalies. In this study, the association with orofacial clefts seen by Timmerman was not noted; however, the populations studied were quite different.[47] A fetus with a thickened NT should be evaluated for other structural abnormalities as extensively as possible at the time of the first-trimester scan.[70-72] In ongoing pregnancies, a detailed structural evaluation with meticulous attention to fetal cardiac imaging in the second trimester is warranted.

In chromosomally normal fetuses, the risk of intrauterine demise increases with increasing NT. In a study of 6650 pregnancies undergoing NT screening, the prevalence of miscarriage, fetal death, or termination for an anomaly was 1.5% in euploid fetuses with an NT below the 95th percentile compared with 18% in those with an NT above the 99th percentile.[73] Westin et al.[74] reported on 16,260 euploid fetuses from an unselected population to determine how well NT measurements predicted adverse outcome. The overall rate of adverse outcome was 2.7%. The risk of adverse outcome increased with higher NT measurements. An NT of 3 mm or greater was associated with a 6-fold increase in adverse outcome, 3.5 mm or greater with a 15-fold increased risk, and 4.5 mm or greater with a 30-fold increased risk. These authors concluded that likelihood ratios could be used to calculate an individual's risk of adverse outcome but could not reliably distinguish between normal and adverse outcome.

Not all fetuses with a thick NT have an abnormal outcome. In 2001, Souka et al.[75] reported on 1320 euploid singleton pregnancies with an NT of 3.5 mm or greater. These fetuses underwent sonographic evaluation at 14 to 16 weeks and 20 to 22 weeks. The chance of a live birth with no defect was 86% in the group with an NT of 3.5 to 4.4 mm, 77% for NT of 4.5 to 5.4 mm, and 67% for NT of 5.5 to 6.4 mm. In fetuses with an NT of 6.5 mm or greater, the chance of normal outcome was 31%. In total, there were 200 fetuses (15.5%) with abnormalities, 80% of which were diagnosed prenatally. There were 1080 (82%) survivors, 60 (6%) of whom had abnormalities requiring medical or surgical care or were developmentally delayed. In a group of 82 fetuses with persistent nuchal thickening but an otherwise normal scan, 19% had an adverse outcome. In the group of 980 euploid fetuses with a normal second-trimester scan, there were 22 (2%) with adverse outcome. Severe developmental delay was seen in 1 in 82 (1%) with isolated persistent nuchal thickening, compared with 4 in 980 (0.4%) with a normal scan.[75]

Bilardo et al.[76] reviewed the outcome of 675 pregnancies with an increased NT, known karyotype, and known pregnancy outcome. Of the study group, 451 (67%) had a normal karyotype, and 19% of these euploid pregnancies had an adverse outcome. The range of abnormal outcome varied with the degree of NT thickening, from 8% with NT between the 95% and 3.4 mm to 80% with NT of 6.5 mm or greater. Second-trimester sonography

was performed on 425 euploid fetuses, and an abnormality was identified in 50 fetuses (12%). Of fetuses with a suspicious or abnormal scan, 86% had an adverse outcome. A normal second-trimester ultrasound was reported on 375 (88%) of fetuses, and 96% of those were alive and well. Of fetuses with a thickened NT in the first trimester, normal karyotype, and normal second-trimester scan, 4% had an adverse outcome, which included intrauterine demise, structural defects, and genetic syndromes. The most frequently missed anomalies on ultrasound were cardiac defects, underscoring the need for detailed fetal echocardiography in fetuses with a thick NT.

Senat et al.[77] prospectively evaluated long-term outcome in children with a normal karyotype and a NT at or greater than 99%. The study population consisted of 179 fetuses that underwent midtrimester sonography as well as fetal echocardiography. There were 17 fetal losses, including 10 malformations, 5 intrauterine demises, 1 miscarriage, and 1 termination. At 2 years of age, 89% (of 162 liveborns evaluated) of children had no malformations and normal developmental testing. Eleven percent of children had a structural abnormality noted after birth. Two children (1.2%) had neurologic delay. In one child, the delay was isolated, and in the other it was associated with an unidentified syndrome. These authors concluded that when the karyotype is normal and the sonogram is normal with resolution of the NT, the outcome is not adversely affected at 2 years of age. This was supported by Miltoft et al. in a prospective study of chromosomally normal fetuses with NT of at least 99% and normal ultrasound findings who were evaluated by an Ages and Stages Questionnaire and found no increased risk of developmental delay at 2 years of age when compared with a control group.[78] Sotiriadis et al. in a review of the literature concluded that there does not appear to be a higher risk of developmental delay than the general population in chromosomally normal fetuses with an increased NT, normal anatomy, and no identifiable genetic syndromes.[79]

The finding of a thickened NT should prompt a comprehensive conversation concerning genetic associations by an experienced provider. Advances in diagnostic testing include chromosomal microarray analysis (CMA), which can detect chromosomal abnormalities that are too small to be detected by standard karyotype. The benefit of CMA in fetuses with a thickened NT is controversial. Schou et al. did not detect any chromosomal aberrations of clinical importance in 100 fetuses with an NT of 99th percentile or greater.[80] Similarly, Huang et al. did not find additional pathogenic CNVs in fetuses with an NT between 3 and 4 mm without other detectable abnormalities.[81] Leung et al. reported that 8.3% of fetuses with an NT greater than 3.5 mm and a normal karyotype had a pathologic submicroscopic chromosomal abnormality. In those fetuses with additional sonographic findings, pathogenic CNVs were identified in 20% compared with 5.3% in those without additional sonographic findings.[82] In a prospective series of patients with an NT of at least 3.5 mm and normal quantitative fluorescence–polymerase chain reaction for aneuploidy, CMA identified pathogenic CNVs in 12.8% of fetuses and variants of uncertain significance in 3.2 %.[83] In a recent meta-analysis, Grande et al. reported that genomic microarray provides incremental yield in 5% of fetuses with an increased NT and normal karyotype. The pooled prevalence of variants of uncertain significance was 1%.[84] A thickened NT has been associated with myriad genetic disorders, the most common being Noonan syndrome.[9,15,85]

SECOND-TRIMESTER SCREENING FOR TRISOMY 21

Although first-trimester risk assessment allows a patient the benefit of time in using the information to make decisions regarding pregnancy, not all women present for prenatal care early enough in gestation to take advantage of this benefit.

Ultrasound is an integral part of risk assessment for aneuploidy in the second trimester.[86-94] Approximately 25% of fetuses with trisomy 21 have a major congenital anomaly, such as cardiac defect or duodenal atresia[90,91] (Fig. 31.7). The cornerstone to identifying fetuses with trisomy 21 has been the recognition of sonographic **"markers,"** which are variations in anatomy that are usually associated with normal outcome but carry a statistically increased risk of aneuploidy. Some of these markers are well-known physical entities such as the thickened nuchal fold and the small nasal bone.[12] Others are findings specific to prenatal sonography, such as an echogenic intracardiac focus, urinary tract dilation, slightly short femoral and humeral length, and echogenic bowel. The identification of a marker should prompt a comprehensive fetal sonographic examination to look for other markers and structural abnormalities. The presence or absence of a marker and the associated clinical significance must be interpreted in the setting of the patient's a priori risk for aneuploidy (Figs. 31.8-31.10 and Tables 31.1-31.3).

Nuchal Fold

Early studies showed that the presence of a thickened nuchal fold identified 40% of fetuses with trisomy 21 with FPR of 0.1%.[95-98] This measurement is obtained using an axial view through the

TABLE 31.1 Likelihood Ratios (LRs) of Isolated Markers for Trisomy 21

Marker	LR[90]	LR[91]	LR[94]	LR[109a]
Nuchal fold	11.0	—	17	3.79
Short humerus	5.1	5.8	7.5	.78
Short femur	1.5	1.2	2.7	.61
Echogenic bowel	6.7	—	6.1	1.65
Echogenic intracardiac focus	1.8	1.4	2.8	.95
Urinary tract dilation	1.5	1.5	1.9	1.08
Ventriculomegaly	—	—	—	3.81
Absent or hypoplastic nasal bone	—	—	—	6.58
Aberrant right subclavian artery	—	—	—	3.94
Structural anomaly	—	3.3	—	—

[a]Derived by multiplying positive LR for the given marker by the negative LR for each of the other markers excluding short humerus but including absent or hypoplastic nasal bone, mild ventriculomegaly, and aberrant right subclavian artery.

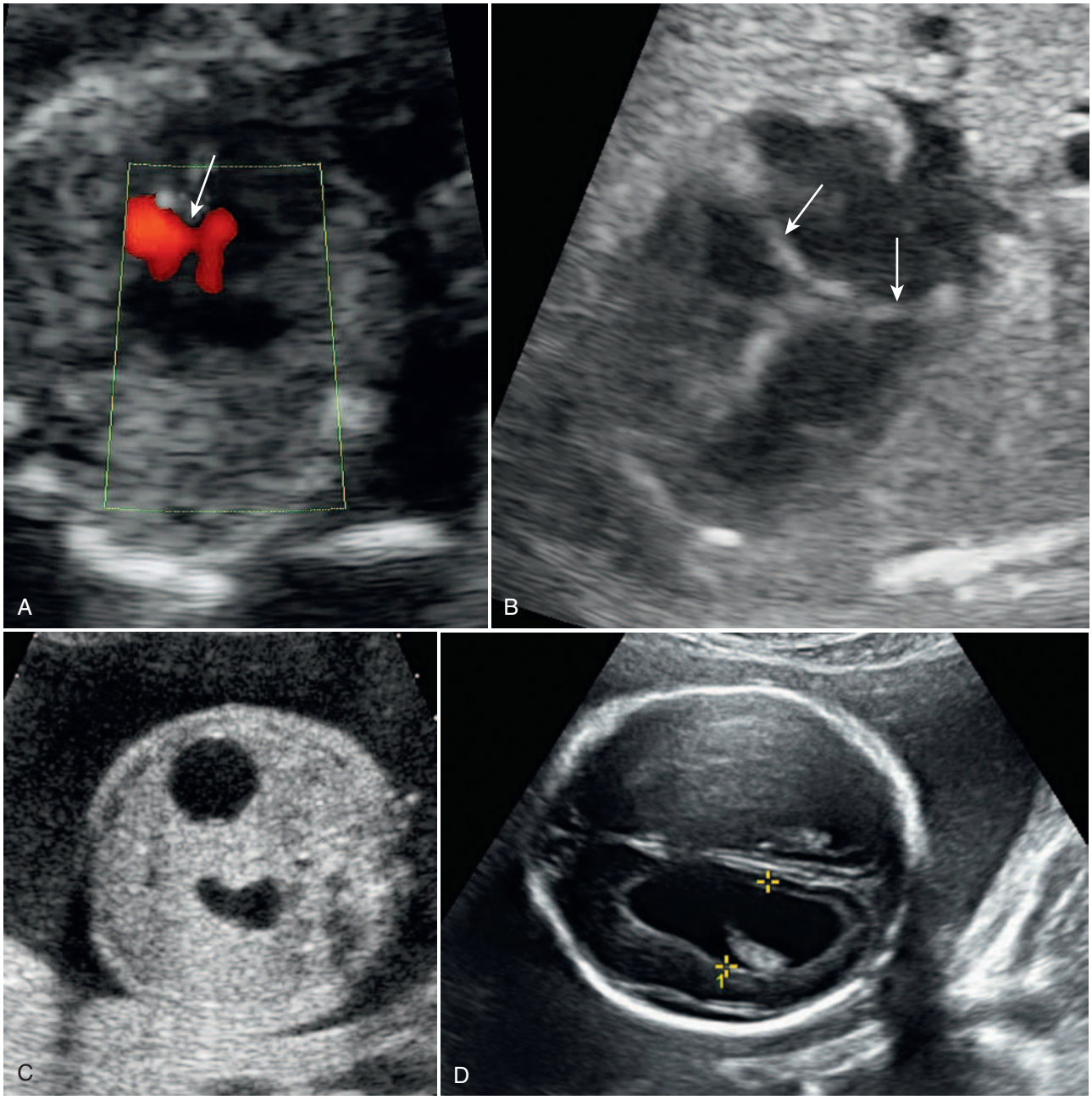

FIG. 31.7 Major Congenital Anomalies in Trisomy 21 Detected in the Second Trimester. (A) Ventriculoseptal defect (VSD). Four-chamber view of the heart with a ventriculoseptal defect *(arrow)* demonstrated with color flow Doppler. **(B) Atrioventricular (A-V) canal.** Four-chamber view of the fetal heart demonstrates a complete **A-V canal.** Note the abnormal "flattening" of the mitral and tricuspid valves into a **common A-V valve** *(arrows).* **(C) Duodenal atresia.** Axial scan through the fetal abdomen shows a double bubble. **(D) Ventriculomegaly.** Axial scan through the cranium of a fetus with trisomy 21 shows dangling choroid in fetus with ventriculomegaly. Note that *calipers* were placed on the ventricles during scanning but are not in the appropriate location or scanning plane for measuring the ventricles.

TABLE 31.2 Trisomy 21: Likelihood Ratios (LRs) of Cluster of Markers

Markers (#)	LR[90]	LR[91]
0	0.36	0.2
1	2	1.9
2	9.7	6.2
3	115.2	80

fetal head, across the thalami and angled posteriorly to include the cerebral peduncles, cerebellar hemispheres, and cisterna magna as well as the occipital bone. The measurement is made from the surface of the occipital bone to the surface of the skin edge (Fig. 31.8). Care must be taken not to angle below the occiput because this will lead to spuriously large measurements. Initially, a measurement of 6 mm or greater was considered abnormal; however, 5 mm was later determined to be a more sensitive threshold, with little change in the specificity.[99] Interobserver variability for this measurement is small (1 mm), establishing

the nuchal fold as a highly reproducible measurement.[100] More recently, some have suggested that because the nuchal fold measurement fits a log gaussian distribution, it should be evaluated as a continuous variable and interpreted in the context of gestation-specific norms, to allow a more refined method of risk analysis.[101,102] Numerous investigators have confirmed that a thickened nuchal skin fold is an important marker for detecting trisomy 21, and after more than 30 years, it remains one of the most important second-trimester markers.[103-109]

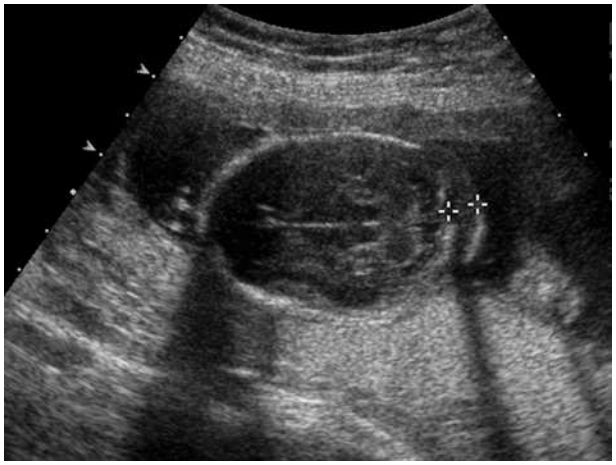

FIG. 31.8 Nuchal Fold. Axial scan through the fetal head of a second-trimester fetus demonstrating a thickened nuchal fold *(calipers),* measuring 6 mm.

Trisomy 21: Common Second-Trimester Sonographic Markers

Nuchal fold
Absent or hypoplastic nasal bone
Short femur
Short humerus
Echogenic bowel
Echogenic intracardiac focus
Urinary tract dilation
Mild ventriculomegaly

Facial Profile (Nasal Bone)

The appearance of the fetal nasal bone is an important sonographic marker utilized for identifying fetuses at increased risk for trisomy 21[110] (Fig. 31.9). The fetal nasal bone is evaluated on a midsagittal view of the fetal profile. The angle of insonation should be 90 degrees to the longitudinal axis of nasal bone although a slightly oblique angle (45 or 135 degrees) helps to define the edges of the nasal bone more sharply. If the nasal bone is viewed "on end" (0 or 180 degrees), it will appear erroneously as absent.[111] In 239 fetuses referred for amniocentesis because of a risk of trisomy 21 of 1 in 270 or greater, Bromley et al.[112] reported that 6 in 16 (37%) fetuses with trisomy 21 did not have a detectable nasal bone. Of the fetuses with a detectable nasal bone, the mean length was shorter in those with trisomy 21 than in euploid

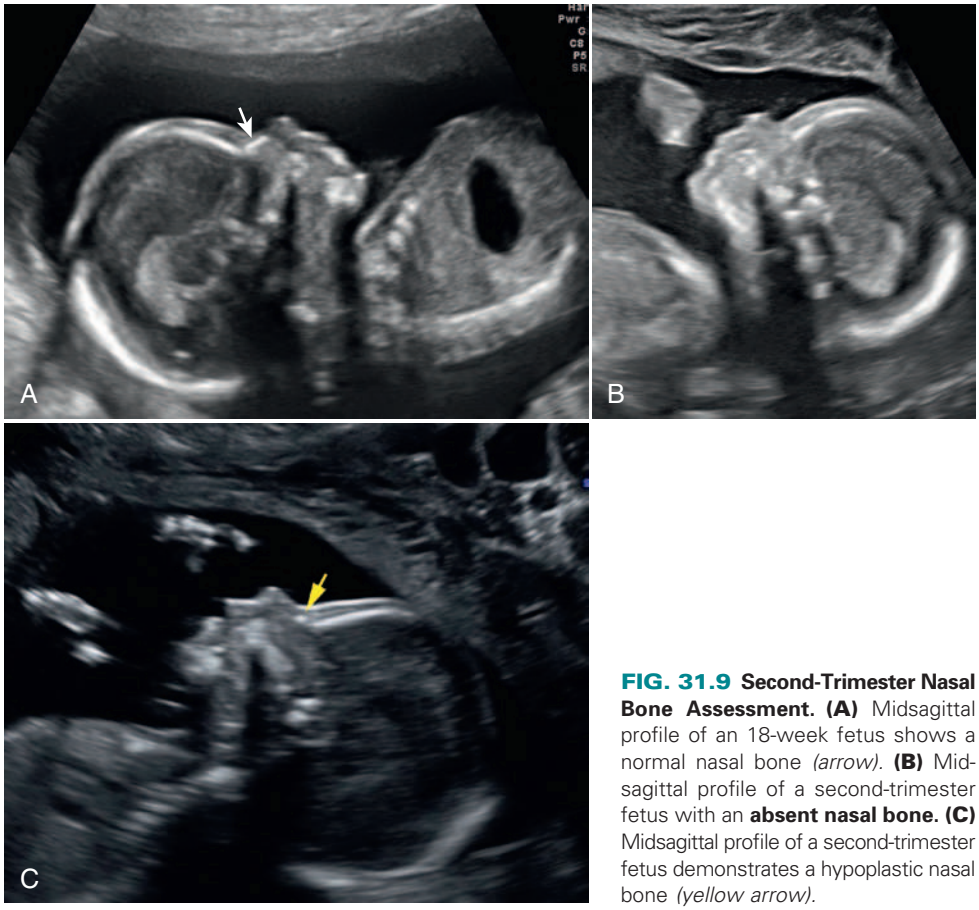

FIG. 31.9 Second-Trimester Nasal Bone Assessment. (A) Midsagittal profile of an 18-week fetus shows a normal nasal bone *(arrow).* **(B)** Midsagittal profile of a second-trimester fetus with an **absent nasal bone. (C)** Midsagittal profile of a second-trimester fetus demonstrates a hypoplastic nasal bone *(yellow arrow).*

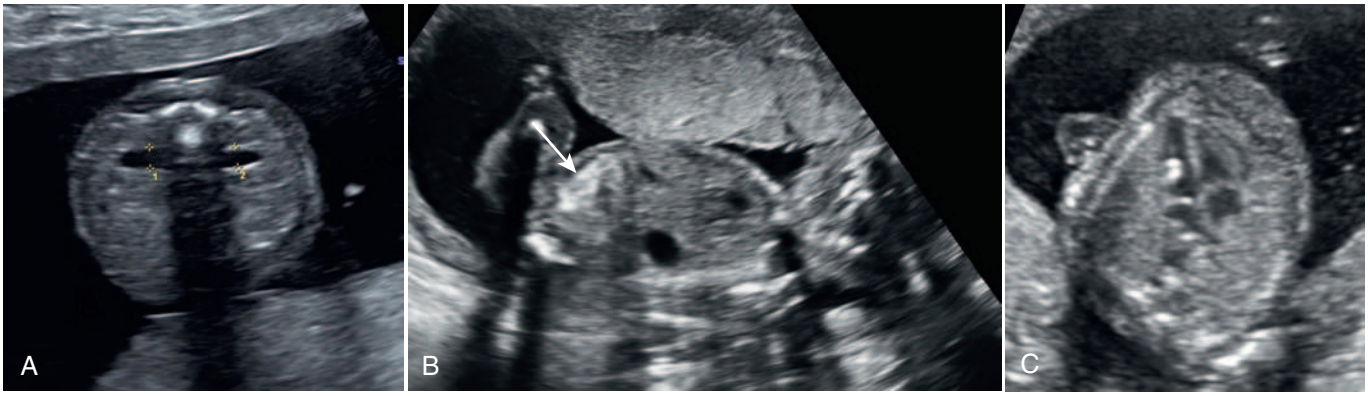

FIG. 31.10 Second-Trimester Markers for Trisomy 21. (A) Urinary tract dilation. Transverse scan through the fetal abdomen at 18 weeks shows urinary tract dilation. The maximal diameter of the intrarenal renal pelvis measures 4 mm *(calipers)*. Measurements are optimally performed with the fetal spine at 12 or 6 o'clock. **(B) Echogenic bowel.** Sagittal scan through the fetal abdomen in the second trimester reveals a focus of echogenic bowel *(arrow)*. Note that the bowel is as bright as bone. See also Video 31.4. **(C) Echogenic intracardiac focus** (EIF). Axial scan through the fetal chest showing the four-chamber view of the heart with a "double" EIF in the left ventricle.

TABLE 31.3 Pooled Estimates of Detection Rates (DRs), False-Positive Rate (FPR), Positive and Negative Likelihood Ratios (LR^+ and LR^-)

Marker	DR	FPR	LR^+	LR^-
Nuchal fold	26.0	1.0	23.30	0.80
Short femur	27.7	6.4	3.72	0.80
Short humerus	30.3	4.6	4.81	0.74
Echogenic bowel	16.7	1.1	11.44	0.90
Echogenic intracardiac focus	24.4	3.9	5.83	0.80
Urinary tract dilation	13.9	1.7	7.63	0.92
Ventriculomegaly	7.5	0.2	27.52	0.94
Absent or hypoplastic nasal bone	59.8	2.8	23.27	0.46
Aberrant right subclavian artery	30.7	1.5	21.48	0.71

Modified from Agathokleous M, Chaveeva P, Poon LC, et al. Meta-analysis of second-trimester markers for trisomy 21. Ultrasound Obstet Gynecol. 2013;41(3):247-261.[109]

fetuses. A receiver-operator characteristic curve for the prediction of trisomy 21 based on biparietal diameter (BPD)/nasal bone length (NBL) reveals that a cutoff of 11 or greater identifies 69% of trisomy 21 fetuses with a 5% FPR. Other authors recommend measurement of less than 5th percentile or an absolute measurement of less than 2.5 mm as thresholds to predict aneuploidy.[113-116]

Vintzileos et al.[117] retrospectively evaluated the significance of the nasal bone ossification in fetuses referred for genetic sonogram; 29 fetuses with trisomy 21 were compared to 102 euploid fetuses. Absence of the nasal bone was seen in 41% of fetuses with trisomy 21 and none of the euploid fetuses. The absence of the fetal nasal bone is as powerful a marker for trisomy 21 as the thickened nuchal fold.[118]

Odibo et al.[119] suggested that evaluating the NBL as a multiple of the median is the optimal method of using this marker. These investigators examined 3634 women at increased risk for aneuploidy and nasal bone assessment was possible in 3197 women (88%), 23 of whom had fetuses with trisomy 21. An NBL of less than 0.75 MoM provided the best definition of nasal bone hypoplasia and had a sensitivity and specificity of 49% and 92%, respectively, compared with 61% and 84% for BPD/NBL greater than 11. These investigators favor the incorporation of absent nasal bone as a major marker for trisomy 21 in the second-trimester genetic sonographic screening because of its ease of identification and better specificity compared with MoM of less than 0.75.

There is variation in the prevalence of a hypoplastic or absent nasal bone depending on ethnicity. Cicero et al.[115] reported that 8.8% of patients of African Caribbean ancestry had an absent or hypoplastic nasal bone, compared with 0.5% of Caucasian fetuses, thus limiting the utility of this marker in patients of African Caribbean heritage.

Three-dimensional ultrasound has been used to evaluate the presence or absence of the fetal nasal bone. In 20 fetuses with trisomy 21, Benoit and Chaoui[120] found 9 had either an absent or a hypoplastic nasal bone on two-dimensional ultrasound. The three-dimensional evaluation showed bilateral nasal bone absence in six fetuses and unilateral nasal bone absence in three. Prenasal thickness (PT) has recently been reported as a useful marker for the detection of trisomy 21 in the second and third trimester. In a retrospective evaluation of 159 fetuses with trisomy 21, Vos et al. reported on the NBL and PT as well as ratios of NBL/PT and prefrontal space ratios to identify fetuses with trisomy 21.[121] These ratios were not gestational age related and at least one of these four findings was identified on 95.3% of fetuses with trisomy 21. The NBL/PT and prefrontal space ratios individually identified 86% and 80% of fetuses with trisomy 21. In the setting of a normal karyotype and otherwise normal detailed imaging, the outcome for an isolated absent nasal bone is favorable.[122]

Femur Length

A short femur was one of the earliest recognized features in the sonographic detection of trisomy 21.[123] The expected femoral length (FL = –9.645 + 0.9338 × BPD) accounts for 94% of variation in normal length.[124] Based on BPD, a measured-to-expected

femur length ratio of 0.91 or less identifies 40% of fetuses with trisomy 21, with a 5% FPR.[125] Although all agree that fetuses with trisomy 21 have shorter femurs than euploid fetuses, the difference is quite small, and the clinical utility of this finding remains controversial.[126] Additionally, femur length varies among fetuses of different ethnicity. Asian fetuses tend to have shorter femurs and black fetuses longer femurs compared with white fetuses.[127] Such differences may be sufficient to question the usefulness of the femur as a marker in many populations.

Humerus Length

The length of the humerus is a more sensitive and specific marker for trisomy 21 than the femoral length.[128] Benacerraf et al.[129] found that the measured humeral length was shorter than the expected humeral length in fetuses with trisomy 21, with a measured-to-expected humeral length ratio of less than 0.90 the optimal criterion for detecting affected fetuses (expected humeral length = −7.9404 + 0.8492 × BPD). The use of this ratio identified 50% of the fetuses with trisomy 21, with a 6.2% FPR.[129]

Urinary Tract Dilation

In the second trimester, mild urinary tract dilation is considered present if the maximal anteroposterior diameter of the intrarenal pelvis measures 4 mm or more[130] (Fig. 31.10A). Among fetuses with trisomy 21, 17% to 25% have urinary tract dilation, compared with 2% to 3% of euploid fetuses.[130,131]

Echogenic Bowel

Echogenic bowel is seen in 0.2% to 0.8% of fetuses in the second trimester.[132-134] To be considered echogenic, the bowel must appear as a well-delineated homogeneous area that is as bright as the adjacent bone when the operator is using a transducer with a frequency of 5 MHz or less (Fig. 31.10B, Video 31.4). The incidence of chromosomal abnormalities in the setting of echogenic bowel ranges from 3% to 27%.[132-137] The cause of echogenic bowel seen in association with aneuploidy may be related to poor bowel motility and decreased water content of meconium.[137] In addition to aneuploidy, echogenic bowel is associated with cystic fibrosis, infectious causes such as cytomegalovirus, primary bowel abnormalities, and severe growth restriction. It has also been associated with fetal ingestion of blood and impending fetal demise.[132-137]

Echogenic Intracardiac Focus

An echogenic intracardiac focus (EIF) is a discrete, bright white dot that appears as bright as bone in the region of the papillary muscle of the heart (Fig. 31.10C). An EIF is usually located within the left ventricle but can be seen in either or both cardiac ventricles. Most are seen as a single focus, but they may occur as multiple foci. This sonographic finding is caused by mineralization of the papillary muscle and is seen in 16% of fetuses with trisomy 21 as well as 5% of euploid fetuses.[138,139]

An EIF is the most common marker to occur as an isolated entity both in fetuses with trisomy 21 and in euploid fetuses.[90,91] An EIF carries a twofold to fourfold increased risk of trisomy 21.[90,91,94,139,140] This marker cannot be used reliably in patients of Asian ancestry because of the high prevalence of the EIF in the euploid Asian population.[141]

The identification of an EIF is confounded by technical considerations such as cardiac position.[142] When the interventricular septum is pointing directly toward or away from the transducer beam in an apical or basal view, an EIF is detected more often than when the septum is imaged perpendicular to the transducer beam in a lateral view. To be convinced that an EIF is present, it must be as bright as bone and seen in several planes. Other normal specular reflectors in the fetal heart, such as the moderator band in the right ventricle, can be mistaken for an EIF. Winn et al.[143] evaluated 200 patients scanned between 18 and 22 weeks' gestation. The rate of "true" echogenic intracardiac foci was 11 in 200 (5.5%). The rate of "false" echogenic foci was 34 in 200 (17%). The most common locations for a false EIF were the moderator band, endocardial cushion, and tricuspid valve annulus.

Recently, an aberrant right subclavian artery has been reported as a useful prenatal ultrasound marker for the detection of trisomy 21.[144] A recent meta-analysis reported the prevalence of aberrant right subclavian artery in fetuses with trisomy 21 is 23.6% compared with 1.02% in euploid fetuses. The identification of an aberrant right subclavian artery should prompt genetic sonography including fetal echocardiography and correlation with a priori risk estimates.[145]

Structural Anomalies

Approximately 25% of fetuses with trisomy 21 are identified as having a structural anomaly, including cardiac defects, duodenal atresia, ventriculomegaly, and hydrops[90,91,132,146] (see Fig. 31.7). Cardiac defects are seen in approximately 50% of newborns with trisomy 21 and include atrioventricular septal defects and ventriculoseptal defects. With meticulous technique, these can be found prenatally in 80% to 90% of fetuses with trisomy 21.[147]

Adjunct Features of Trisomy 21

Adjunctive features that may be seen on occasion in fetuses with trisomy 21 but are not robust enough to adjust the risk of aneuploidy include iliac angle measurements, ear length, clinodactyly, hypoplasia of the middle phalanx of the fifth digit, sandal gap toe, and frontothalamic distance. These features are difficult to standardize, and there is substantial overlap between those with and without trisomy 21. The identification of an adjunctive feature should prompt a genetic sonogram in which markers with established likelihood ratios are evaluated and correlated with a priori risk estimates.[148-154]

Cases of trisomy 21 have been reported in fetuses with choroid plexus cysts.[155] However, this is believed to result from the population incidence of choroid plexus cysts rather than from trisomy 21.[156]

Combined Markers

The finding of individual sonographic markers can be used to estimate a risk of aneuploidy.[156-163] In the early years of genetic sonography, a scoring index was utilized that rated the markers as "major" (score of 2 for thickened nuchal fold or major anomaly) and "minor" (score of 1 for each finding, such as short femur, short humerus, pyelectasis, echogenic bowel, and EIF).[157,158] A cumulative score of 2 or more identified 73% of fetuses with trisomy 21, with an FPR of 4%. Nyberg et al.[90,162] suggested integrating these markers into risk assessment by using Bayes

theorem and likelihood ratios. They showed that likelihood ratios could be calculated for each isolated marker, then applied to the patient's a priori (presumptive) risk using Bayes theorem. This resulted in a revised risk of aneuploidy based on the presence or absence of specific markers. Table 31.1 shows a comparison of four studies that computed likelihood ratios for trisomy 21 using isolated markers.

Clusters of markers, even minor ones, confer more risk than individual markers alone[90,91] (Table 31.2). Winter et al.[89] demonstrated that the genetic sonogram scoring index and the method of ultrasound risk assessment using likelihood ratios were essentially equivalent in the detection rate of trisomy 21. The advantage of using likelihood ratios is that a patient's specific risk of aneuploidy can be calculated and balanced against the risk of pregnancy loss associated with an invasive procedure. Even in the largest studies, the number of fetuses with an isolated marker is small, leading some to recommend that a revised risk estimate for aneuploidy is statistically more robust if the overall likelihood ratio is calculated by the product of the positive and negative likelihood ratios for each marker.[109,164]

Trisomy 21: Revised Risk Ratio Calculations

Revised risk = a priori risk × likelihood ratio (LR)

EXAMPLE 1: METHOD USING ISOLATED LR

A 25-year-old woman with a priori risk of trisomy 21 of 1:500 based on quad screen.

Detailed ultrasound shows an isolated echogenic intracardiac focus (EIF) (LR ≈ 2).

Revised risk = 1:500 × 2 = 1:250

EXAMPLE 2: METHOD USING "CLUSTER OF MARKER" LR

A 39-year-old woman with a priori risk of trisomy 21 of 1:1000 based combined screen.

Detailed ultrasound shows EIF and urinary tract dilation (LR ≈ 6 from two markers).

Revised risk = 1:1000 × 6 = 1:166

EXAMPLE 3: METHOD USING POSITIVE AND NEGATIVE LRS FOR EACH MARKER

Short humerus not used in calculation

A 28-year-old woman with a priori risk of trisomy 21 of 1:1000 based combined screen.

Detailed ultrasound shows EIF and short femur. Negative for nuchal fold, urinary tract dilation, echogenic bowel, nasal bone, and ventriculomegaly.

Revised Risk: 1:1000 × LR for combination of positive/negative = 4.41 (5.83 × 3.72 × 0.92 × 0.90 × 0.80 × 0.46 × 0.94) = 1/226

Likelihood ratios in examples 1 and 2 are with permission from Bromley B, Lieberman E, Shipp TD, Benacerraf BR. The genetic sonogram: a method of risk assessment for Down syndrome in the second trimester. J Ultrasound Med. 2002;21(10):1087-1096.[91]
Likelihood ratios in example 3 are with permission from Agathokleous M, Chaveeva P, Poon LC, et al. Meta-analysis of second-trimester markers for trisomy 21. Ultrasound Obstet Gynecol. 2013;41(3):247-261.[109]

Agathokleous et al. performed a meta-analysis of second-trimester markers for Down syndrome using data published after 1995. Weighted independent estimates of detection rates, FPRs, and positive and negative likelihood ratios for each marker was calculated.[109]

Genetic sonography is best used in conjunction with a priori risk estimates based on an accepted screening protocol.[163,165-169] Souter et al.[167] demonstrated that serum biochemical marker analytes and sonography are independent and therefore can be used in conjunction with each other to modify the risk of aneuploidy. Several investigators have shown that patients of advanced maternal age who had a normal genetic sonogram and reassuring serum screen are at a lower risk for trisomy 21.[90,91,166,169] The absence of markers has been shown to reduce the risk of trisomy 21 by (60%-90%).[90,91,109,164] This may be even more dramatic as many studies were published before the nasal bone was recognized as an important marker in second-trimester risk assessment. In a recent meta-analysis, the absence of markers conferred a 7.7-fold reduction in risk of Down syndrome[109] (Table 31.3).

Most studies on genetic sonography were performed in the time period prior to the use of first-trimester risk assessment, whether by combined screening or integrated screening. The clinical utility of the genetic sonogram after first-trimester risk assessment for Down syndrome is controversial. Rozenberg et al.[170] performed a multicenter interventional study in an unselected population to evaluate the performance of first-trimester combined screening followed by second-trimester ultrasound. First-trimester combined screening identified 80% of fetuses with trisomy 21 at a screen-positive rate of 2.7%. Using a thickened nuchal fold or the presence of a major anomaly on a second-trimester ultrasound increased the detection rate to 90%, with a screen-positive rate of 4.2%.

Krantz et al.[171] performed a simulation study to assess genetic sonography as a sequential screen for trisomy 21 after first-trimester risk assessment. First-trimester combined screening resulted in a detection rate of 88.5% with a 4.2% FPR. A follow-up with genetic sonography using individual marker likelihood ratios to modify the first-trimester risk for screen-negative patients detected an additional 6.1% of trisomy 21 cases for an additional 1.2% FPR, giving a total detection rate of 94.6% and a total FPR of 5.4%. If a contingent protocol were adopted in which only patients with a first-trimester risk between 1 in 300 and 1 in 2500 were evaluated, the additional detection rate would be 4.8% with FPR of 0.7%, giving a total detection rate of 93% and a total FPR of 4.9%. These authors concluded that second-trimester genetic sonography, if used properly, can be an effective sequential screen after first-trimester risk assessment.

The clinical utility of genetic sonography after prior screening for Down syndrome was studied on 7842 pregnancies, including 59 with Down syndrome, who participated in the FASTER trial.[164] At a set FPR of 5%, adding genetic sonography to the combined screen or the integrated test increased the detection rate of Down syndrome from 81% to 90% and 93% to 98% respectively. A smaller increase in detection rate was noted for the stepwise or contingent protocols, from 97% to 98% and 95% to 97%, respectively. Other studies have suggested that genetic sonography after combined screening or sequential screening may decrease the

FPR with no significant change in detection rate of Down syndrome.[172,173] It has been cautioned that the use of genetic sonography after first-trimester risk assessment may result in increased patient anxiety without increasing the detection rate of trisomy or false reassurance.[173,174] While historically the finding of an isolated marker would potentially result in a diagnostic test that came with an associated risk of fetal loss, the recent incorporation of cell-free DNA provides a secondary level of screening that does not carry a risk of pregnancy loss. A negative cell-free DNA analysis makes the identification of a marker of unlikely clinical importance with respect to aneuploidy screening.[175] Certain markers such as short femur, echogenic bowel, or urinary tract dilation may be associated with other concerning clinical situations.

TRISOMY 18 (EDWARDS SYNDROME)

Trisomy 18 is the second most common autosomal trisomy, with a prevalence of 4.8 per 10,000 total births.[176] With improving prenatal diagnosis and associated high termination rates, the live birth prevalence has decreased to 0.1 in 1000.[177] Individuals with this disorder have a limited capacity for survival, with 44% of those identified in utero dying before birth.[178] About 50% of affected newborns die within the first week, and only 5% to 10% survive beyond the first year of life. Those who survive are severely intellectually disabled and physically handicapped.[179]

Fetuses with trisomy 18 have a plethora of anomalies. Sonographically, 77% to 97% of fetuses with trisomy 18 can be identified by the presence of these structural malformations.[180-184] The more common structural anomalies in fetuses with trisomy 18 include **congenital heart defects, central nervous system anomalies, hydrocephalus, diaphragmatic hernia, omphalocele** (70% of which only contain bowel), and **abnormally clenched hands** (with overlapping index fingers)[180-184] (Fig. 31.11). In our experience, cases of trisomy 18 not identified by prenatal ultrasound have been scanned early in the second trimester, when a complete structural survey was not feasible or when other factors such as surgical scarring or maternal body habitus precluded optimal visualization of the fetus.[157,158]

Trisomy 18: Common Sonographic Findings

Choroid plexus cyst
Strawberry-shaped skull
Abnormal cerebellum, cisterna magna
Neural tube defects
Cardiac defects
Omphalocele
Esophageal atresia
Diaphragmatic hernia
Clenched hands, overlapping index fingers
Radial ray anomalies, limb reduction defects
Clubfeet, rocker-bottom feet
Intrauterine growth restriction (especially with polyhydramnios)

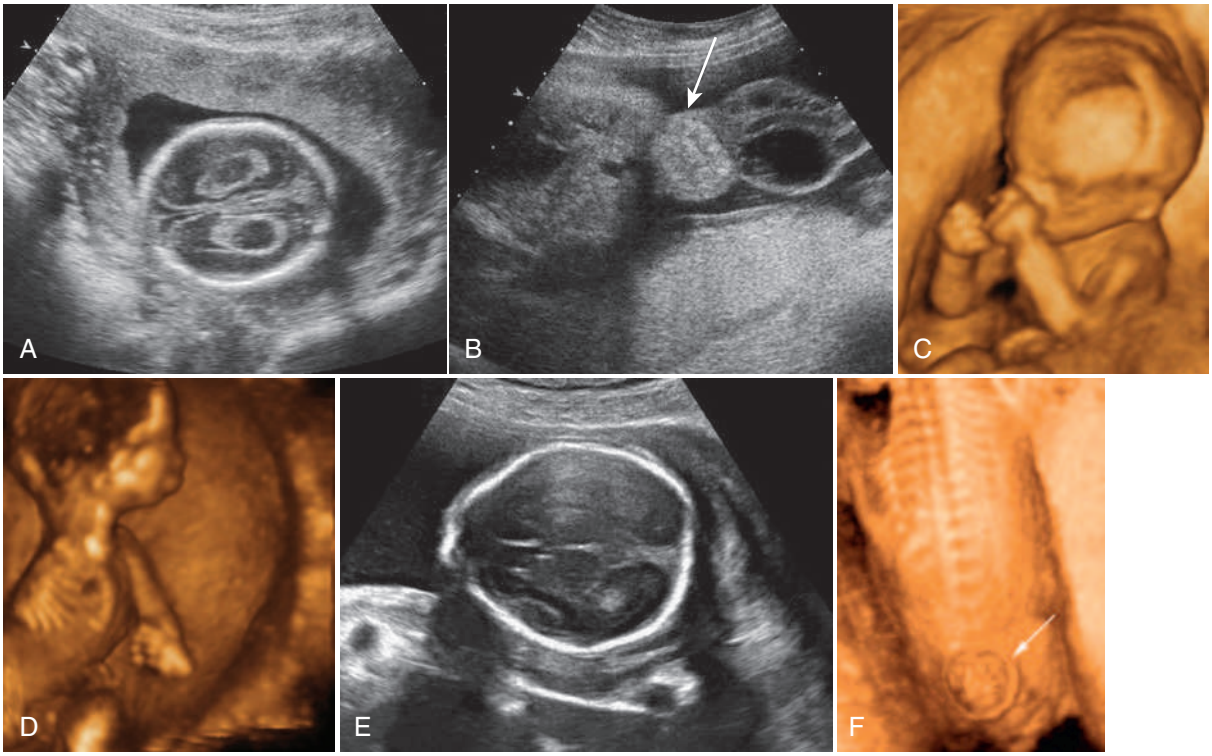

FIG. 31.11 Second-Trimester Sonographic Findings in Trisomy 18. (A) Choroid plexus cyst. Scan through the fetal head at 18 weeks shows bilateral choroid plexus cysts. **(B) Omphalocele.** Scan of the fetal lower abdomen shows a bowel-containing omphalocele *(arrow)* as well as an **umbilical cord cyst. (C) Clenched fists.** Three-dimensional scan of a midtrimester fetus shows characteristic clenching of the hands and overlapping fingers. **(D) Radial ray anomaly.** Three-dimensional scan demonstrates a radial ray anomaly. Note the **micrognathia** as well. **(E) Strawberry-shaped skull. (F)** Three-dimensional scan of the fetal spine at 18 weeks demonstrating a **neural tube defect** *(arrow)*.

The sonographic findings observed in fetuses with trisomy 18 vary with gestational age. As expected, anomalies such as cystic hygromas are seen more frequently in the late first and early second trimester, whereas cardiac defects and growth restriction tend to be later findings. In a review of 47 fetuses with trisomy 18, Nyberg et al.[183] identified cardiac defects in 14% before 24 weeks' gestation and in 78% scanned after 24 weeks. **Intrauterine growth restriction** (IUGR) was seen in 28% of affected fetuses scanned at less than 24 weeks and in 89% of those evaluated in the third trimester. IUGR, in combination with **polyhydramnios,** is an ominous observation highly predictive of trisomy 18.[183,185] In addition to those mentioned earlier, other findings, such as radial ray defects, rocker-bottom feet, clubfeet, strawberry-shaped skull (flattening of occiput with pointing of frontal bones), and abnormal-appearing cerebellum and cisterna magna, have been reported.[179-190]

Choroid Plexus Cysts

Choroid plexus cysts (CPCs) are discrete echolucencies within the choroid plexus that result from the folding of the neuroepithelium, trapping secretory products and desquamated cells[191] (Fig. 31.11A). CPCs are seen in 1% to 2% of the normal fetuses and are most common in the second trimester, usually resolving by 28 weeks' gestation.[180-182] About 30% of fetuses with trisomy 18 have CPCs.[182,183] The majority of fetuses with trisomy 18 also have other structural anomalies to suggest aneuploidy.[180-183] Cyst number, size, and laterality are not useful in distinguishing affected fetuses from normal fetuses.[192-194] Additionally, resolution of CPCs does not necessarily reflect a normal karyotype.[195]

The predictive value of isolated CPCs for aneuploidy is low when no other abnormalities are seen.[155,182] Therefore after a CPC is seen, a detailed ultrasound assessment of the fetus should be performed. In the setting of an isolated CPC, correlation with a priori risk of trisomy 18 based on an accepted screening protocol is recommended.[155,196] Cheng et al.[197] reported on the significance of isolated CPCs in a population previously screened with NT and found that the likelihood ratio for trisomy 18 was not increased in those with normal NT measurements. Noninvasive prenatal screening with cell-free DNA can be considered. Invasive testing is not warranted in the setting of an isolated CPC.[185,193,194,198-202]

TRISOMY 13 (PATAU SYNDROME)

Trisomy 13 is the third most common autosomal trisomy with a prevalence of 1.9 in 10,000 total births.[176] With improving prenatal diagnosis and associated high termination rates, the live birth prevalence has decreased to 0.03 in 1000.[177] Individuals with trisomy 13 have numerous structural abnormalities and are severely intellectually disabled. Anomalies often seen include forebrain defects, ocular malformations, facial clefts, heart defects, and abnormal extremities. In fetuses that are not terminated, there is a 46% intrauterine fetal death rate and 93% early neonatal mortality rate.[203] Rarely, survival is more long term.[204] Sonographic detection of fetuses with trisomy 13 is 90% to 100% (Fig. 31.12).[157,158,205-209]

Trisomy 13: Common Sonographic Findings

- Holoprosencephaly
- Microcephaly
- Neural tube defects
- Facial clefts, ocular anomalies
- Cardiac defects
- Echogenic intracardiac focus
- Congenital diaphragmatic hernia
- Omphalocele
- Echogenic kidneys
- Postaxial polydactyly
- Intrauterine growth restriction

Cardiac and central nervous system defects are the most frequently identified anomalies. The most common central nervous system malformations identified in trisomy 13 are **holoprosencephaly, ventriculomegaly, microcephaly,** and posterior fossa malformations. **Alobar holoprosencephaly** is often associated with severe midline facial defects, including **hypotelorism, microphthalmia, anophthalmia, cyclopia,** and **proboscis.** In addition, fetuses with trisomy 13 often have postaxial **polydactyly,** abnormal hand configuration, **echogenic kidneys,** atypical calcifications, and **IUGR.**[205-209]

TRIPLOIDY

Triploidy is the result of a complete extra set of chromosomes (69 chromosomes) and is not related to maternal age.[210] The extra set of chromosomes may be paternally derived (diandric), usually from a double fertilization, or maternally derived (digynic) from fertilization of a diploid egg.[211] The frequency of the parental origin has been widely disparate with diandric cases in 20% to 85%.[212] Triploidy occurs in 1% to 3% of conceptions, and most are spontaneously aborted.[213,214] The prevalence of triploidy at 11 to 14 weeks is 1 in 6614 and survival of a fetus with triploidy beyond 20 weeks' gestation is unusual.[48,210] Paternal triploid origin is often associated with a large placenta filled with cystic spaces and moderate growth restriction. Triploidy on the basis of an extra maternal chromosomal complement is usually associated with a small placenta and asymmetric IUGR.[211,213] Fetuses with triploidy have a multitude of structural malformations, most often involving the central nervous system, heart, and hands[214,215] (Fig. 31.13).

Triploidy: Common Sonographic Findings

- Neural tube defects
- Ventriculomegaly
- Posterior fossa anomalies
- Micrognathia
- Cardiac anomalies
- Omphalocele
- Renal anomalies
- Talipes equinovarus
- 3-4 Syndactyly
- Asymmetric growth restriction
- Abnormal placenta (hydropic changes or small)
- Oligohydramnios

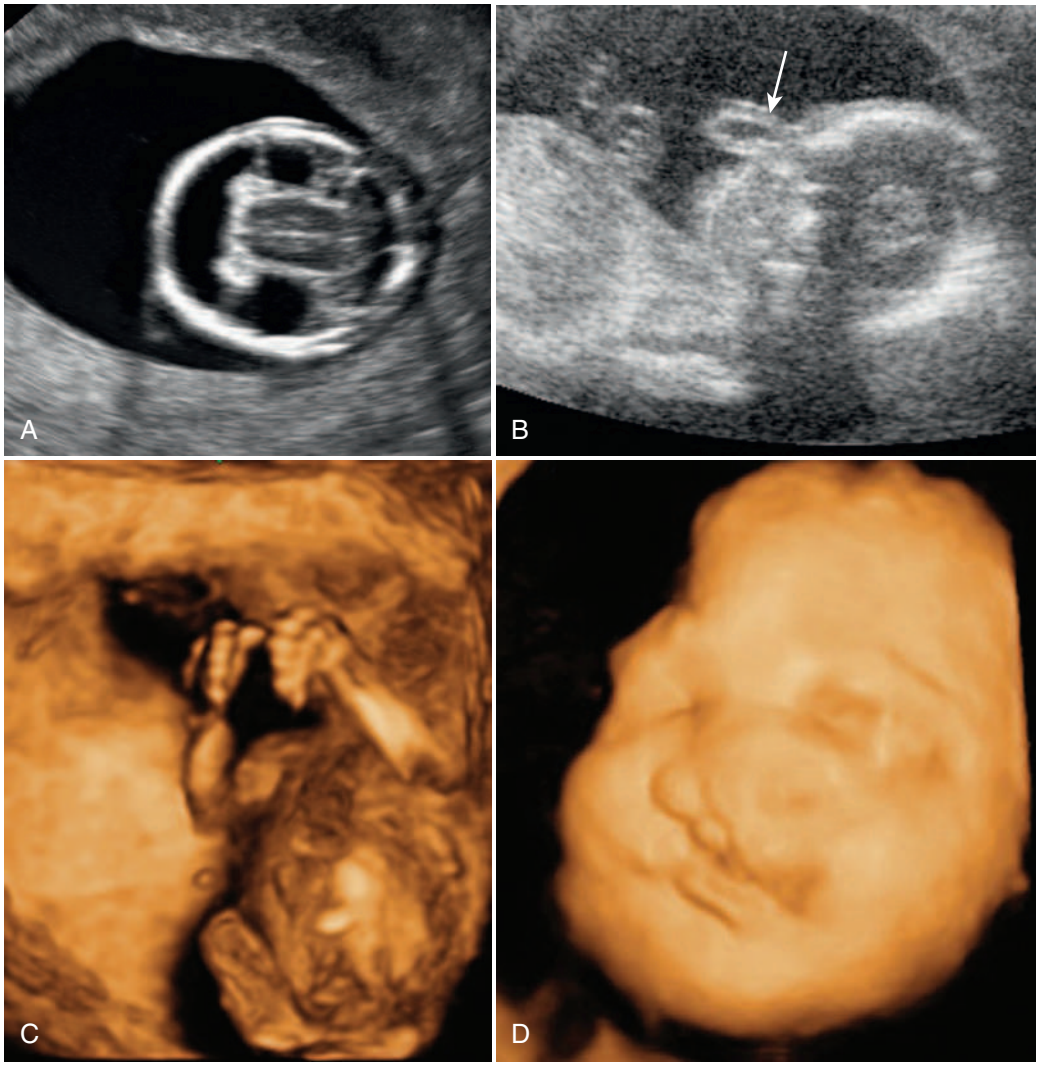

FIG. 31.12 Sonographic Findings in Trisomy 13. (A) Alobar holoprosencephaly at 11 weeks. **(B) Proboscis** *(arrow)*. **(C)** Postaxial **polydactyly** on three-dimensional image at 14 weeks. **(D)** Three-dimensional scan of a third-trimester fetus shows a large, midline **facial cleft.**

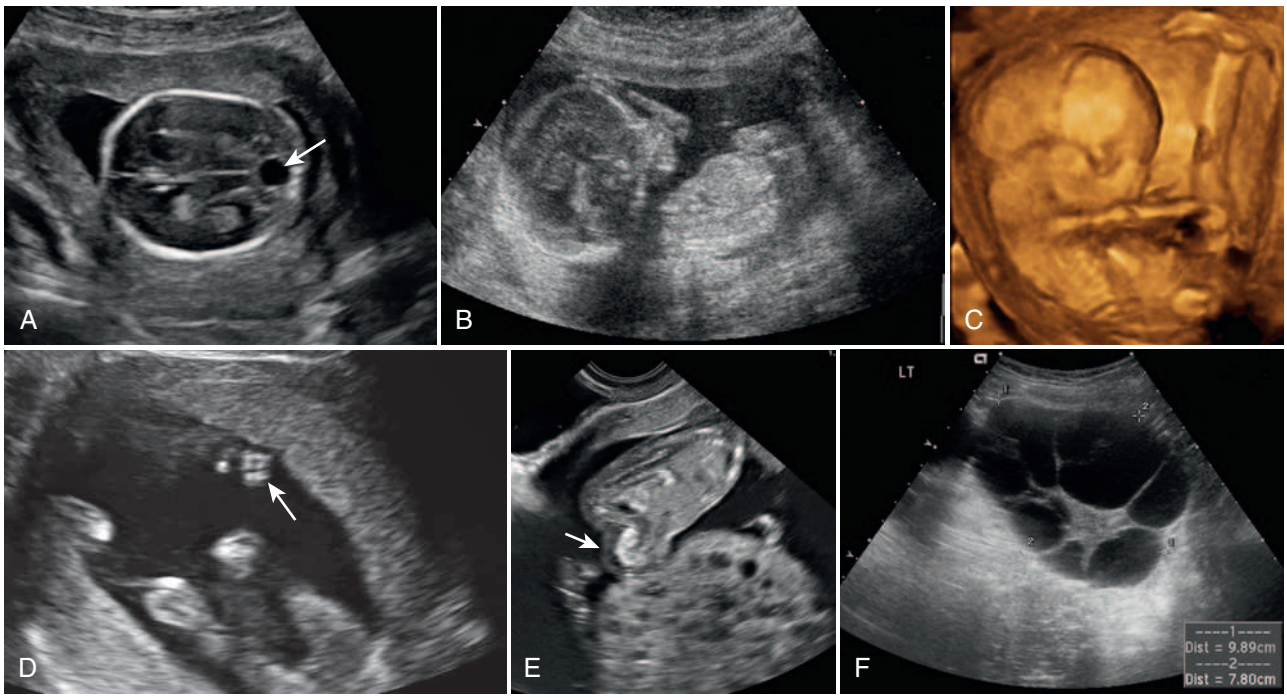

FIG. 31.13 Second-Trimester Sonographic Findings in Triploidy. (A) Dandy-Walker malformation *(arrow)*. **(B)** and **(C)** Asymmetrical IUGR. Note the discrepancy in size of the head and body. **(D) Syndactyly** of the fingers *(arrow)*. **(E)** Scan through the placenta showing multiple lucencies as well as an omphalocele *(arrow)*. **(F)** Maternal ovaries with multiple cysts characteristic of theca lutein cysts.

Triploidy can be associated with maternal complications, including early-onset preeclampsia, bilateral multicystic ovaries, hyperemesis gravidarum, and persistent trophoblastic disease.[216,217]

Jauniaux et al.[214] described 70 cases of triploidy scanned between 13 and 29 weeks' gestation. Anatomic defects were found in 93% of cases, with abnormalities of the hands (predominantly 3-4 syndactyly) the most frequent finding (52%). Cerebral ventriculomegaly was identified in 37%. Cardiac defects, primarily atrioventricular septal defects, were detected in 34% of fetuses. Micrognathia affected 26% of fetuses. Placental molar changes were seen in 29%, and amniotic fluid volume was decreased in 44%. Asymmetrical growth restriction was noted in 72% of cases, and each of these fetuses had a sonographically normal–appearing placenta.[214]

MONOSOMY X (TURNER SYNDROME)

Turner syndrome is the result of a 45,X chromosomal complement, usually caused by loss of the paternal X chromosome, and is unrelated to maternal age. About 95% of conceptuses are spontaneously aborted. Turner syndrome occurs in 1 in 2000 to 1 in 5000 live births.[218-221] The lethal type of Turner syndrome seen in the midtrimester of pregnancy generally presents with large septated cystic hygromas, total body **lymphedema, pleural effusions, ascites,** and cardiac defects[218,219] (Fig. 31.14).

Cystic hygromas are malformations of the lymphatic system and appear as saccular septated fluid collections, most often surrounding the back of the fetal head and neck. Azar et al.[220] reported that 75% of fetuses with bilateral dorsal septated nuchal

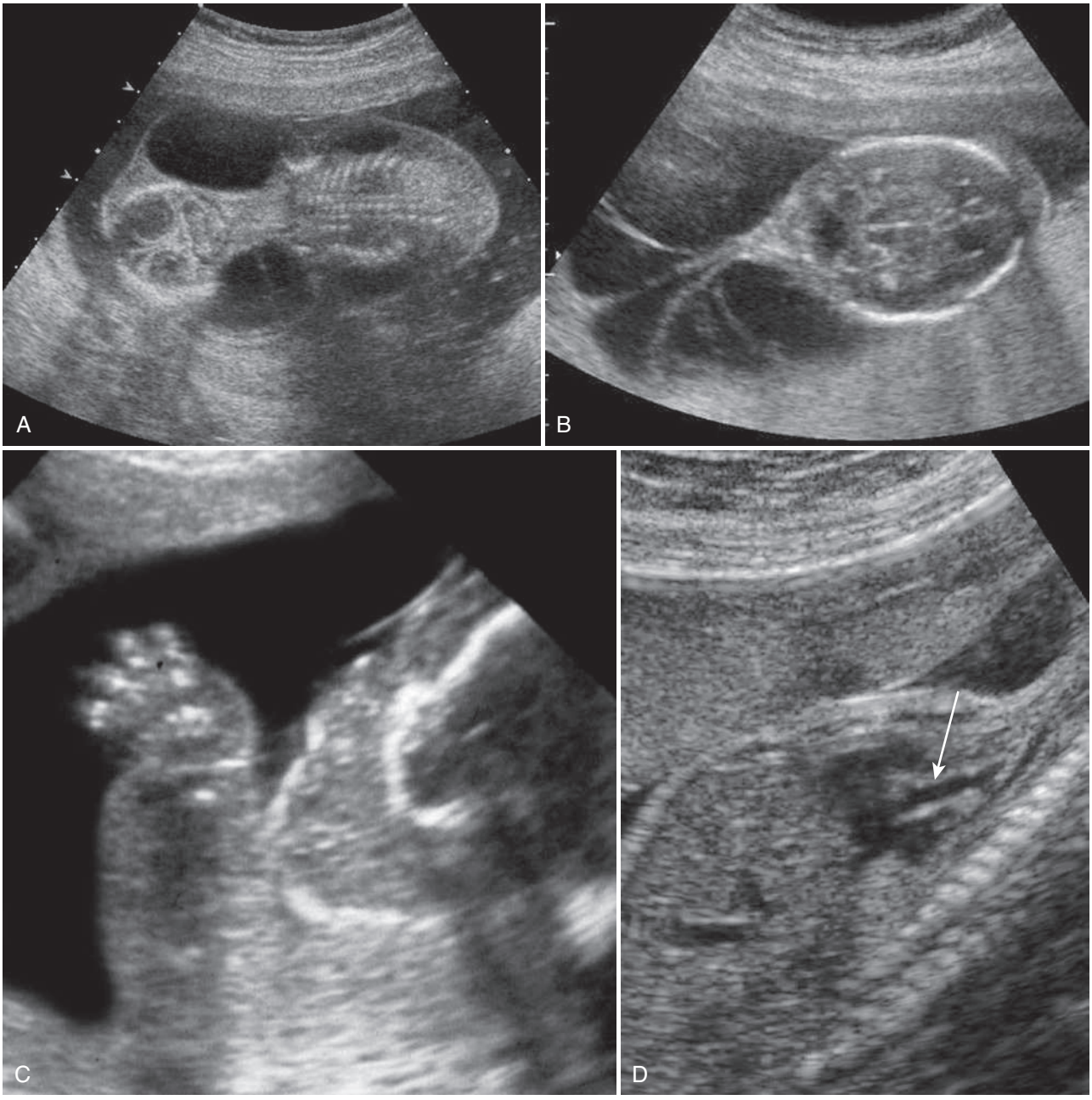

FIG. 31.14 Second-Trimester Sonographic Findings in Monosomy X (Turner Syndrome). (A) and **(B)** Large septated **cystic hygromas. (C)** Hydropic fetal arm in a fetus with severe lymphangiectasia. **(D)** Small aorta *(arrow)* in fetus with **interrupted aortic arch.**

cervical cystic hygromas had chromosomal anomalies, the most common being Turner syndrome (94%). Although many second-trimester fetuses with cystic hygromas have Turner syndrome, other karyotypic abnormalities, including trisomies 21, 18, and 13 and triploidy, have also been reported. In general, cystic hygromas in fetuses with Turner syndrome are larger than those seen with other karyotypic abnormalities, and fetuses with Turner syndrome may also have generalized lymphedema extending down the torso and extremities.

Cardiac abnormalities, most often left-sided defects such as coarctation of the aorta, may be identified in 10% to 48% of fetuses with Turner syndrome. However, this may be an underestimation because many fetuses are identified late in the first semester or early in the second trimester, when optimal cardiac evaluation is not likely.[218-221] Baena et al.[218] reported on 125 cases of Turner syndrome from an unselected population and noted that 67% were identified prenatally. The most common sonographic findings were cystic hygromas (59%) and hydrops (19%).

PRENATAL SCREENING FOR ANEUPLOIDY WITH CELL-FREE DNA

Recently the incorporation of **cell-free DNA** analysis into screening for aneuploidy has revolutionized the paradigm of risk assessment. The option for aneuploidy screening by cell-free DNA has been supported by the American College of Obstetricians and Gynecologists (ACOG) for women at increased risk for this condition.[222] Cell-free DNA from placental origin makes up 10% to 15% of circulating cell-free DNA in maternal plasma and is used to screen for trisomy 21, 18, and 13 as early as 10 weeks' gestation. Sex chromosome analysis may be requested. The relative proportion of fetal to maternal origin of circulating cell-free DNA is termed the fetal fraction and is essential for an accurate test result. Three different methods of cell-free DNA analysis have been described—massively parallel shotgun sequencing, chromosome-selective sequencing, and single nucleotide polymorphism–based analysis—each with high sensitivity and specificity for trisomy 21 and 18.[223-225] Sensitivity for trisomy 13 and monosomy X is somewhat lower although specificity remains high. Gil et al. in a recent meta-analysis reported weighted pool detection rates and FPRs of 99.2% and 0.09% for trisomy 21, 96.3 and .13% for trisomy 18, and 91% and .13% for trisomy 13.[226] For monosomy X, the weighted pool detection rate was 90.3% with a FPR of .23%. Accuracy for sex determination generally exceeds 98%.[222] Although cell-free DNA with reportable results has excellent performance metrics for the detection of common chromosomal trisomies, it remains a screening test. False-positive results may occur as a result of confined placental mosaicism, true fetal mosaicism, maternal chromosomal abnormality, a demised second twin, or maternal malignancy.[222,227] False-negative results may occur with low-level fetal mosaicism, low fetal fraction of circulating cell-free DNA, insufficient depth of sequencing, or sample error. Of note, between 1% and 8% of the population may have unreportable findings or a "no call" result. This situation is most likely to occur when there is a lower fetal fraction of cell-free DNA or results that are "too close" to call.[228,229] A low fetal fraction is associated with early gestational age, aneuploidy, and high maternal body mass index.[229,230] Patients with unreportable results should be referred for genetic counseling and offered detailed ultrasound evaluation and diagnostic testing.[222] Performance of cell-free DNA screening on living twin gestations is feasible, but early data suggest that the detection rate for trisomy 21 and 18 is slightly lower and that test failure is higher compared with singletons.[231] Recommendations for the use of cell-free DNA are regularly updated, and cell-free DNA screening currently is not recommended by ACOG in women with multiple gestations.[222]

Performance metrics on the general population are excellent although the positive predictive value of the test is lower than in a high-risk population. There is no argument when a result is reported, that cell-free DNA screening has a higher sensitivity and specificity, lower FPR, and higher PPV for the detection of trisomy 21 and 18 than combined screening, but it does not detect other conditions that are important to the health and well-being of the fetus.[228,232] It must be kept in mind that although cell-free DNA is an excellent screening test for targeted chromosomal abnormalities, both appropriate pretest counseling and confirmation of positive results before any irreversible decisions concerning the pregnancy are undertaken is critical.[222] Patients should be counseled that a negative result does not ensure an unaffected pregnancy as there is a residual risk of a targeted trisomy as well as other chromosomal abnormalities or genetic conditions. Cell-free DNA may not detect 16.9% to 23.4% of chromosomal abnormalities that may be identified by traditional screening algorithms.[233,234] Cell-free DNA screening is of limited utility in patients with sonographic abnormalities and they should be offered diagnostic testing. Benachi et al. report that in women with fetal abnormalities detected through use of ultrasonography, the rate of pathogenic chromosome abnormalities missed by cell-free DNA is at least 8%.[235] Shani et al., in a retrospective cohort study of 3140 invasive diagnostic procedures in singletons, reported clinically significant chromosomal abnormalities were present in 220 (7%).[236] Based on current published detection rates for cell-free DNA, including "nonreportable" results, these authors calculated that cell-free DNA would not have detected 99 in 220 (45%) of chromosomal abnormalities.

DIAGNOSTIC TESTING

Diagnostic testing can be performed by chorionic villus sampling in the late first trimester or by amniocentesis in the second trimester. Diagnostic testing options are rapidly expanding beyond conventional karyotype and may include CMA, which identifies microalterations known as CNVs on a genomic scale. These CNVs may be pathogenic, benign, or of unknown significance.[237] In 4% to 10% of fetuses with a structural anomaly and a normal karyotype, CMA may detect abnormal CNVs.[237,238] Whole exome sequencing may provide further insight into prenatal diagnosis.[239]

Chorionic villus sampling is performed between 10 and 13 weeks' gestation. Placental villi are obtained either through a transabdominal or transvaginal approach under ultrasound guidance depending on placental location. For transabdominal approach an 18- or 20-gauge needle is advanced into the placenta

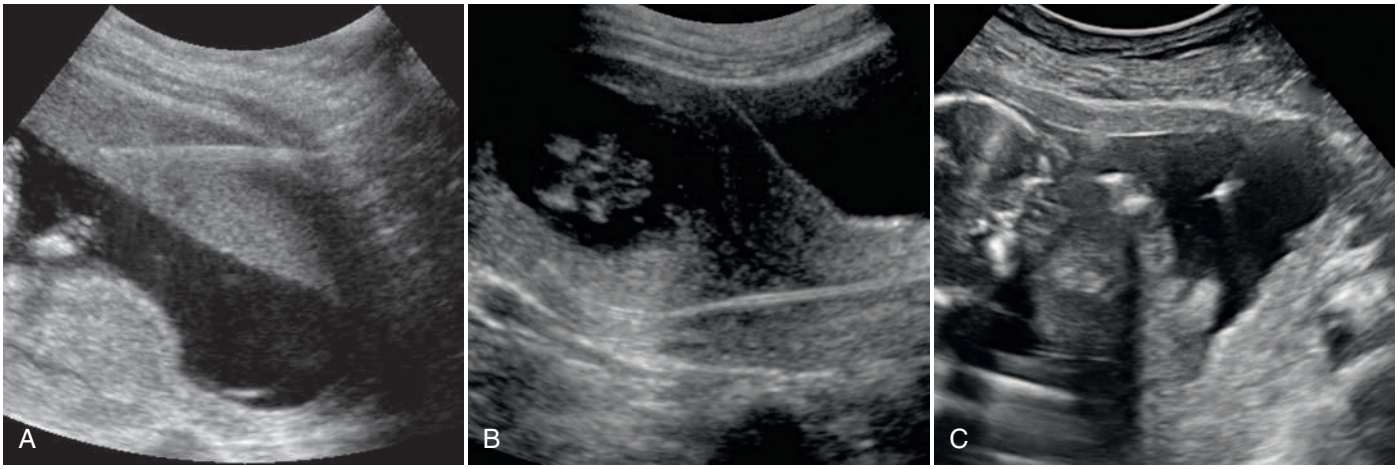

FIG. 31.15 Diagnostic Procedures. (A) Transabdominal **chorionic villus sampling.** Transverse image of needle entering the placenta. **(B)** Transcervical chorionic villus sampling. Sagittal image shows a catheter passing through the cervix and into the placenta. Note the full bladder and amniotic cavity. **(C) Amniocentesis.** Transverse ultrasound image shows needle entering the amniotic fluid. See also Video 31.5.

and the stylet removed (Fig. 31.15A). A 20-mL syringe with about 2 mL of cell-transport medium is connected to the needle. The needle is then guided back and forth through the placenta while suction is intermittently applied to the syringe. The needle is withdrawn and the cell-transport medium is drawn though the needle to clear any remaining villi. The specimen is examined under a dissecting microscope for adequacy. For transcervical CVS (Fig. 31.15B), a 5.7-Fr flexible CVS cannula with a rigid metal introducer is guided into the cervix under direction visualization, and then into the placenta under sonographic guidance (Fig. 31.15B). The introducer is withdrawn and a 20-mL syringe with about 2 mL of transport medium is connected to the cannula. Suction is intermittently applied to the cannula as it is slowly withdrawn from the placenta. As with all fetal procedures, the fetal heart rate is documented after the procedure. Women who are Rh negative and who have an Rh-positive partner are given RhoGAM.

The CVS specimen can then be tested with fluorescent in situ hybridization (FISH), direct cytogenetic analysis, or cultured villi for numerous conditions.[240,241] One concern with CVS is that there is a discrepancy between the prenatal cytogenetic diagnosis from placental source and the fetal karyotype. The U.S. Collaborative Study on CVS and other large registries have found that a successful genetic diagnosis can be obtained in 99.7% of cases, with an FPR of 11 per 10,000 pregnancies.[242,243] There were no diagnostic errors involving trisomy 13, 18, or 21 in these studies.[242] Maternal cell contamination occurs in 0.8% to 2.2% of cases.[242,244] Approximately 0.5% of CVS samples will have an ambiguous finding that needs confirmation by amniocentesis.[245] **Confined placental mosaicism** is seen in 0.7% to 1.6% of cases[242-244] and may be caused by meiotic errors with subsequent "trisomy rescue" or by mitotic errors in the developing morula.[246] Confined placental mosaicism can also cause a false-positive cell-free DNA result and, in some cases, diagnostic testing by amniocentesis is suggested.[247]

A recent meta-analysis reports a weighted pooled procedure–related miscarriage at less than 24 weeks for CVS as 0.22% (95% CI, −0.71%-1.16%).[248] The Canadian Collaborative CVS-Amniocentesis Clinical Trial group recruited women at less than 12 weeks' gestational age and randomized them to CVS in the first trimester or amniocentesis at 15 to 17 weeks' gestational age. No significant differences were seen in fetal loss rates.[249] Caughey et al.[250] compared CVS, amniocentesis, and control groups of women at similar gestational ages who declined intervention and found no significant differences in the adjusted loss rates between the CVS and amniocentesis groups in the most recent study period reported. Early concerns about an increased risk of oromandibular-limb hypogenesis syndrome[251] have been not been upheld.[252] A report by the World Health Organization on the safety of CVS found that the risk of limb reduction defects by week was comparable to that of the general population, except at 8 weeks' gestational age, when it was elevated with CVS.[253]

Genetic amniocentesis is typically performed between 15 and 20 weeks' gestation (Fig. 31.15C). Sonographic guidance is used for location of a fluid pocket. Most often a 22-gauge 3.5-inch long spinal needle is used (Fig. 31.15C, Video 31.5). For larger patients a longer needle may be required. The placenta is avoided if possible, but performing the procedure through the placenta is thought to be safe. Typically 15 to 20 mL of fluid is removed (with a rule of thumb being 1 mL per week of gestation). When amniocentesis is performed in multiple gestations, care is taken to approach each sac separately. The reported procedure-related loss rate before 24 weeks' gestation in a recent meta-analysis was 0.11% (95% CI, −0.04%-0.26%).[248] The heterogeneity of studies on diagnostic testing limits a precise estimation of procedure-related loss for CVS or amniocentesis; however, the added procedure-related risk following is quite low (0.2% and 0.1%).[254] The commonly quoted procedure loss rate is "less than 1 in 300 to 500 procedures."[254] Leakage of amniotic fluid may occur after a genetic amniocentesis, although favorable pregnancy outcomes are seen in more than 90% of women with expectant management.[255,256] Amniocentesis between 11 and 13 weeks' gestation has been associated with increased pregnancy loss rates,

membrane rupture, and talipes equinovarus as well as higher amniotic fluid culture failures and therefore is not recommended.[254] As with all fetal procedures, the fetal heart rate is documented after the procedure. Women who are Rh negative and have an Rh-positive partner are given RhoGAM.

CONCLUSION

Over the past three decades, risk assessment for aneuploidy has progressed to the point that maternal age alone or NT width alone is no longer considered adequate for determining the risk of having a chromosomally abnormal offspring. Obstetric sonography, in conjunction with maternal serum analytes, has become a powerful tool in the assessment aneuploidy risk in both the first and the second trimester. In the second trimester the diverse sonographic patterns seen with the different aneuploidies allow clinicians to guide patients to a presumptive diagnosis. Recent advances in cell-free DNA analysis provide exceptional screening performance targeted specifically for trisomies 21 and 18 and, to a slightly lesser degree, for trisomy 13; however, other chromosomal abnormalities that are potentially detected by combined screening or diagnostic testing are not identified. Karyotype has been the standard for fetuses with structural anomalies; however, microarray analysis to determine CNV abnormalities will augment the detection of clinically significant disorders, most notably in fetuses with structural abnormalities. When considering all detectable chromosome problems, multiple marker screening including NT, with the option of diagnostic testing for screen positive results, is the optimal strategy for most women. For pregnant women aged 40 years or older, cell-free DNA as a primary screening tool is optimal.[4]

REFERENCES

1. ACOG Committee on Practice Bulletins. ACOG Practice Bulletin No. 77: Screening for fetal chromosomal abnormalities. Obstet Gynecol. 2007;109(1):217-227.
2. Martin CL, Kirkpatrick BE, Ledbetter DH. Copy number variants, aneuploidies, and human disease. Clin Perinatol. 2015;42(2):227-242, vii.
3. American College of Obstetricians and Gynecologists. The use of chromosomal microarray analysis in prenatal diagnosis. Practice Bulletin. 2013;No. 581.
4. Kaimal AJ, Norton ME, Kuppermann M. Prenatal testing in the genomic age: clinical outcomes, quality of life, and costs. Obstet Gynecol. 2015;126(4):737-746.
5. Sachs A, Blanchard L, Buchanan A, et al. Recommended pre-test counseling points for noninvasive prenatal testing using cell-free DNA: a 2015 perspective. Prenat Diagn. 2015;35(10):968-971.
6. Snijders RJ, Sebire NJ, Nicolaides KH. Maternal age and gestational age-specific risk for chromosomal defects. Fetal Diagn Ther. 1995;10(6):356-367.
7. Egan JF, Benn P, Borgida AF, et al. Efficacy of screening for fetal Down syndrome in the United States from 1974 to 1997. Obstet Gynecol. 2000;96(6):979-985.
8. Schreinemachers DM, Cross PK, Hook EB. Rates of trisomies 21, 18, 13 and other chromosome abnormalities in about 20,000 prenatal studies compared with estimated rates in live births. Hum Genet. 1982;61(4):318-324.
9. Nicolaides KH. Nuchal translucency and other first-trimester sonographic markers of chromosomal abnormalities. Am J Obstet Gynecol. 2004;191(1):45-67.
10. Baer RJ, Norton ME, Shaw GM, et al. Risk of selected structural abnormalities in infants after increased nuchal translucency measurement. Am J Obstet Gynecol. 2014;211(6):675 e1-675 e19.
11. Hume H, Chasen ST. Trends in timing of prenatal diagnosis and abortion for fetal chromosomal abnormalities. Am J Obstet Gynecol. 2015;213(4):545 e1-545 e4.
12. Down JLH. Observations on an ethnic classification of idiots. Clinical Lecture Reports. 3. London: London Hospital; 1866. p. 259-262.
13. Nicolaides KH, Azar G, Byrne D, et al. Fetal nuchal translucency: ultrasound screening for chromosomal defects in first trimester of pregnancy. BMJ. 1992;304(6831):867-869.
14. Bekker MN, Haak MC, Rekoert-Hollander M, et al. Increased nuchal translucency and distended jugular lymphatic sacs on first-trimester ultrasound. Ultrasound Obstet Gynecol. 2005;25(3):239-245.
15. Souka AP, Von Kaisenberg CS, Hyett JA, et al. Increased nuchal translucency with normal karyotype. Am J Obstet Gynecol. 2005;192(4):1005-1021.
16. Pandya PP, Snijders RJ, Johnson SP, et al. Screening for fetal trisomies by maternal age and fetal nuchal translucency thickness at 10 to 14 weeks of gestation. Br J Obstet Gynaecol. 1995;102(12):957-962.
17. Snijders RJ, Noble P, Sebire N, et al. UK multicentre project on assessment of risk of trisomy 21 by maternal age and fetal nuchal-translucency thickness at 10-14 weeks of gestation. Fetal Medicine Foundation First Trimester Screening Group. Lancet. 1998;352(9125):343-346.
18. Wald NJ, Kennard A, Hackshaw AK. First trimester serum screening for Down's syndrome. Prenat Diagn. 1995;15(13):1227-1240.
19. Brizot ML, Snijders RJ, Bersinger NA, et al. Maternal serum pregnancy-associated plasma protein A and fetal nuchal translucency thickness for the prediction of fetal trisomies in early pregnancy. Obstet Gynecol. 1994;84(6):918-922.
20. Brizot ML, Snijders RJ, Butler J, et al. Maternal serum hCG and fetal nuchal translucency thickness for the prediction of fetal trisomies in the first trimester of pregnancy. Br J Obstet Gynaecol. 1995;102(2):127-132.
21. Wald NJ, Kennard A, Hackshaw A, McGuire A. Antenatal screening for Down's syndrome. J Med Screen. 1997;4(4):181-246.
22. Spencer K, Spencer CE, Power M, et al. Screening for chromosomal abnormalities in the first trimester using ultrasound and maternal serum biochemistry in a one-stop clinic: a review of three years prospective experience. BJOG. 2003;110(3):281-286.
23. Wapner R, Thom E, Simpson JL, et al. First-trimester screening for trisomies 21 and 18. N Engl J Med. 2003;349(15):1405-1413.
24. Wald NJ, Rodeck C, Hackshaw AK, et al. First and second trimester antenatal screening for Down's syndrome: the results of the Serum, Urine and Ultrasound Screening Study (SURUSS). J Med Screen. 2003;10(2):56-104.
25. Malone FD, Canick JA, Ball RH, et al. First-trimester or second-trimester screening, or both, for Down's syndrome. N Engl J Med. 2005;353(19):2001-2011.
26. Sebire NJ, Snijders RJ, Hughes K, et al. Screening for trisomy 21 in twin pregnancies by maternal age and fetal nuchal translucency thickness at 10-14 weeks of gestation. Br J Obstet Gynaecol. 1996;103(10):999-1003.
27. Kagan KO, Gazzoni A, Sepulveda-Gonzalez G, et al. Discordance in nuchal translucency thickness in the prediction of severe twin-to-twin transfusion syndrome. Ultrasound Obstet Gynecol. 2007;29(5):527-532.
28. Monni G, Iuculano A, Zoppi MA. Screening and invasive testing in twins. J Clin Med. 2014;3(3):865-882.
29. Spencer K, Nicolaides KH. Screening for trisomy 21 in twins using first trimester ultrasound and maternal serum biochemistry in a one-stop clinic: a review of three years experience. BJOG. 2003;110(3):276-280.
30. Wald NJ, Rish S. Prenatal screening for Down syndrome and neural tube defects in twin pregnancies. Prenat Diagn. 2005;25(9):740-745.
31. Boyle B, Morris JK, McConkey R, et al. Prevalence and risk of Down syndrome in monozygotic and dizygotic multiple pregnancies in Europe: implications for prenatal screening. BJOG. 2014;121(7):809-819.
32. Comstock CH, Malone FD, Ball RH, et al. Is there a nuchal translucency millimeter measurement above which there is no added benefit from first trimester serum screening? Am J Obstet Gynecol. 2006;195(3):843-847.

33. Wald NJ, Watt HC, Hackshaw AK. Integrated screening for Down's syndrome on the basis of tests performed during the first and second trimesters. N Engl J Med. 1999;341(7):461-467.
34. Palomaki GE, Steinort K, Knight GJ, Haddow JE. Comparing three screening strategies for combining first- and second-trimester Down syndrome markers. Obstet Gynecol. 2006;107(2 Pt 1):367-375.
35. Cuckle HS, Malone FD, Wright D, et al. Contingent screening for Down syndrome—results from the FaSTER trial. Prenat Diagn. 2008;28(2): 89-94.
36. Ball RH, Caughey AB, Malone FD, et al. First- and second-trimester evaluation of risk for Down syndrome. Obstet Gynecol. 2007;110(1):10-17.
37. Platt LD, Greene N, Johnson A, et al. Sequential pathways of testing after first-trimester screening for trisomy 21. Obstet Gynecol. 2004;104(4): 661-666.
38. Haddow JE, Palomaki GE, Knight GJ, et al. Screening of maternal serum for fetal Down's syndrome in the first trimester. N Engl J Med. 1998;338(14):955-961.
39. Snijders RJ, Thom EA, Zachary JM, et al. First-trimester trisomy screening: nuchal translucency measurement training and quality assurance to correct and unify technique. Ultrasound Obstet Gynecol. 2002; 19(4):353-359.
40. Safety Group of the British Medical Ultrasound Society. Guidelines for the safe use of diagnostic ultrasound equipment 2009. Available from: https://www.bmus.org/static/uploads/resources/BMUS-Safety-Guidelines-2009-revision-FINAL-Nov-2009.pdf. Accessed 18 January 2016.
41. Evans MI, Van Decruyes H, Nicolaides KH. Nuchal translucency measurements for first-trimester screening: the 'price' of inaccuracy. Fetal Diagn Ther. 2007;22(6):401-404.
42. Braithwaite JM, Kadir RA, Pepera TA, et al. Nuchal translucency measurement: training of potential examiners. Ultrasound Obstet Gynecol. 1996;8(3):192-195.
43. Nicolaides KH. The 11-13+6 weeks scan. London: Fetal Medicine Foundation; 2004.
44. Wax JR, Pinette MG, Cartin A, Blackstone J. The value of repeated evaluation after initial failed nuchal translucency measurement. J Ultrasound Med. 2007;26(6):825-828.
45. Breathnach FM, Malone FD, Lambert-Messerlian G, et al. First- and second-trimester screening: detection of aneuploidies other than Down syndrome. Obstet Gynecol. 2007;110(3):651-657.
46. Spencer K, Nicolaides KH. A first trimester trisomy 13/trisomy 18 risk algorithm combining fetal nuchal translucency thickness, maternal serum free beta-hCG and PAPP-A. Prenat Diagn. 2002;22(10):877-879.
47. Baer RJ, Flessel MC, Jelliffe-Pawlowski LL, et al. Detection rates for aneuploidy by first-trimester and sequential screening. Obstet Gynecol. 2015;126(4): 753-759.
48. Santorum M, Wright D, Syngelaki A, et al. Accuracy of first trimester combined test in screening for trisomies 21, 18 and 13. Ultrasound Obstet Gynecol. 2016. Aug 23. [Epub ahead of print.]
49. Malone FD, Ball RH, Nyberg DA, et al. First-trimester septated cystic hygroma: prevalence, natural history, and pediatric outcome. Obstet Gynecol. 2005;106(2):288-294.
50. Molina FS, Avgidou K, Kagan KO, et al. Cystic hygromas, nuchal edema, and nuchal translucency at 11-14 weeks of gestation. Obstet Gynecol. 2006;107(3):678-683.
51. Sonek J, Croom C, McKenna D, Neiger R. First-trimester septated cystic hygroma: prevalence, natural history, and pediatric outcome. Obstet Gynecol. 2006;107(2 Pt 1):424.
52. Cicero S, Dezerega V, Andrade E, et al. Learning curve for sonographic examination of the fetal nasal bone at 11-14 weeks. Ultrasound Obstet Gynecol. 2003;22(2):135-137.
53. Cicero S, Curcio P, Papageorghiou A, et al. Absence of nasal bone in fetuses with trisomy 21 at 11-14 weeks of gestation: an observational study. Lancet. 2001;358(9294):1665-1667.
54. Cicero S, Rembouskos G, Vandecruys H, et al. Likelihood ratio for trisomy 21 in fetuses with absent nasal bone at the 11-14-week scan. Ultrasound Obstet Gynecol. 2004;23(3):218-223.
55. Cicero S, Bindra R, Rembouskos G, et al. Integrated ultrasound and biochemical screening for trisomy 21 using fetal nuchal translucency, absent fetal nasal bone, free beta-hCG and PAPP-A at 11 to 14 weeks. Prenat Diagn. 2003;23(4):306-310.
56. Cicero S, Avgidou K, Rembouskos G, et al. Nasal bone in first-trimester screening for trisomy 21. Am J Obstet Gynecol. 2006;195(1):109-114.
57. Orlandi F, Rossi C, Orlandi E, et al. First-trimester screening for trisomy-21 using a simplified method to assess the presence or absence of the fetal nasal bone. Am J Obstet Gynecol. 2005;192(4):1107-1111.
58. Sepulveda W, Wong AE, Dezerega V. First-trimester ultrasonographic screening for trisomy 21 using fetal nuchal translucency and nasal bone. Obstet Gynecol. 2007;109(5):1040-1045.
59. Malone FD, Ball RH, Nyberg DA, et al. First-trimester nasal bone evaluation for aneuploidy in the general population. Obstet Gynecol. 2004;104(6): 1222-1228.
60. Rosen T, D'Alton ME, Platt LD, Wapner R. First-trimester ultrasound assessment of the nasal bone to screen for aneuploidy. Obstet Gynecol. 2007;110(2 Pt 1):399-404.
61. Ville Y. What is the role of fetal nasal bone examination in the assessment of risk for trisomy 21 in clinical practice? Am J Obstet Gynecol. 2006;195(1):1-3.
62. Borrell A, Gonce A, Martinez JM, et al. First-trimester screening for Down syndrome with ductus venosus Doppler studies in addition to nuchal translucency and serum markers. Prenat Diagn. 2005;25(10):901-905.
63. Falcon O, Auer M, Gerovassili A, et al. Screening for trisomy 21 by fetal tricuspid regurgitation, nuchal translucency and maternal serum free beta-hCG and PAPP-A at 11 + 0 to 13 + 6 weeks. Ultrasound Obstet Gynecol. 2006;27(2):151-155.
64. Abele H, Wagner P, Sonek J, et al. First trimester ultrasound screening for Down syndrome based on maternal age, fetal nuchal translucency and different combinations of the additional markers nasal bone, tricuspid and ductus venosus flow. Prenat Diagn. 2015;35(12):1182-1186.
65. Hyett J, Perdu M, Sharland G, et al. Using fetal nuchal translucency to screen for major congenital cardiac defects at 10-14 weeks of gestation: population based cohort study. BMJ. 1999;318(7176):81-85.
66. Makrydimas G, Sotiriadis A, Ioannidis JP. Screening performance of first-trimester nuchal translucency for major cardiac defects: a meta-analysis. Am J Obstet Gynecol. 2003;189(5):1330-1335.
67. Simpson LL, Malone FD, Bianchi DW, et al. Nuchal translucency and the risk of congenital heart disease. Obstet Gynecol. 2007;109(2 Pt 1): 376-383.
68. Jelliffe-Pawlowski LL, Norton ME, Shaw GM, et al. Risk of critical congenital heart defects by nuchal translucency norms. Am J Obstet Gynecol. 2015;212(4):518 e1-518 e10.
69. Timmerman E, Pajkrt E, Maas SM, Bilardo CM. Enlarged nuchal translucency in chromosomally normal fetuses: strong association with orofacial clefts. Ultrasound Obstet Gynecol. 2010;36(4):427-432.
70. Salomon LJ, Alfirevic Z, Bilardo CM, et al. ISUOG practice guidelines: performance of first-trimester fetal ultrasound scan. Ultrasound Obstet Gynecol. 2013;41(1):102-113.
71. Bromley B, Shipp TD, Lyons J, et al. Detection of fetal structural anomalies in a basic first-trimester screening program for aneuploidy. J Ultrasound Med. 2014;33(10):1737-1745.
72. Wagner P, Sonek J, Hoopmann M, et al. First-trimester screening for trisomy 18, 13, triploidy and Turner syndrome by a detailed early anomaly scan. Ultrasound Obstet Gynecol. 2016;48(4):446-451.
73. Michailidis GD, Economides DL. Nuchal translucency measurement and pregnancy outcome in karyotypically normal fetuses. Ultrasound Obstet Gynecol. 2001;17(2):102-105.
74. Westin M, Saltvedt S, Almstrom H, et al. By how much does increased nuchal translucency increase the risk of adverse pregnancy outcome in chromosomally normal fetuses? A study of 16,260 fetuses derived from an unselected pregnant population. Ultrasound Obstet Gynecol. 2007;29(2): 150-158.
75. Souka AP, Krampl E, Bakalis S, et al. Outcome of pregnancy in chromosomally normal fetuses with increased nuchal translucency in the first trimester. Ultrasound Obstet Gynecol. 2001;18(1):9-17.
76. Bilardo CM, Muller MA, Pajkrt E, et al. Increased nuchal translucency thickness and normal karyotype: time for parental reassurance. Ultrasound Obstet Gynecol. 2007;30(1):11-18.

77. Senat MV, Bussieres L, Couderc S, et al. Long-term outcome of children born after a first-trimester measurement of nuchal translucency at the 99th percentile or greater with normal karyotype: a prospective study. Am J Obstet Gynecol. 2007;196(1):53.e1-53.e6.
78. Miltoft CB, Ekelund CK, Hansen BM, et al. Increased nuchal translucency, normal karyotype and infant development. Ultrasound Obstet Gynecol. 2012;39(1):28-33.
79. Sotiriadis A, Papatheodorou S, Makrydimas G. Neurodevelopmental outcome of fetuses with increased nuchal translucency and apparently normal prenatal and/or postnatal assessment: a systematic review. Ultrasound Obstet Gynecol. 2012;39(1):10-19.
80. Schou KV, Kirchhoff M, Nygaard U, et al. Increased nuchal translucency with normal karyotype: a follow-up study of 100 cases supplemented with CGH and MLPA analyses. Ultrasound Obstet Gynecol. 2009;34(6):618-622.
81. Huang J, Poon LC, Akolekar R, et al. Is high fetal nuchal translucency associated with submicroscopic chromosomal abnormalities on array CGH? Ultrasound Obstet Gynecol. 2014;43(6):620-624.
82. Leung TY, Vogel I, Lau TK, et al. Identification of submicroscopic chromosomal aberrations in fetuses with increased nuchal translucency and apparently normal karyotype. Ultrasound Obstet Gynecol. 2011;38(3):314-319.
83. Lund IC, Christensen R, Petersen OB, et al. Chromosomal microarray in fetuses with increased nuchal translucency. Ultrasound Obstet Gynecol. 2015;45(1):95-100.
84. Grande M, Jansen FA, Blumenfeld YJ, et al. Genomic microarray in fetuses with increased nuchal translucency and normal karyotype: a systematic review and meta-analysis. Ultrasound Obstet Gynecol. 2015;46(6):650-658.
85. Pergament E, Alamillo C, Sak K, Fiddler M. Genetic assessment following increased nuchal translucency and normal karyotype. Prenat Diagn. 2011;31(3):307-310.
86. Vintzileos AM, Egan JF. Adjusting the risk for trisomy 21 on the basis of second-trimester ultrasonography. Am J Obstet Gynecol. 1995;172(3):837-844.
87. Bromley B, Lieberman E, Benacerraf BR. The incorporation of maternal age into the sonographic scoring index for the detection at 14-20 weeks of fetuses with Down's syndrome. Ultrasound Obstet Gynecol. 1997;10(5):321-324.
88. Bromley B, Shipp T, Benacerraf BR. Genetic sonogram scoring index: accuracy and clinical utility. J Ultrasound Med. 1999;18(8):523-528.
89. Winter TC, Uhrich SB, Souter VL, Nyberg DA. The "genetic sonogram": comparison of the index scoring system with the age-adjusted US risk assessment. Radiology. 2000;215(3):775-782.
90. Nyberg DA, Souter VL, El-Bastawissi A, et al. Isolated sonographic markers for detection of fetal Down syndrome in the second trimester of pregnancy. J Ultrasound Med. 2001;20(10):1053-1063.
91. Bromley B, Lieberman E, Shipp TD, Benacerraf BR. The genetic sonogram: a method of risk assessment for Down syndrome in the second trimester. J Ultrasound Med. 2002;21(10):1087-1096.
92. Vintzileos AM, Guzman ER, Smulian JC, et al. Second-trimester genetic sonography in patients with advanced maternal age and normal triple screen. Obstet Gynecol. 2002;99(6):993-995.
93. Hobbins JC, Lezotte DC, Persutte WH, et al. An 8-center study to evaluate the utility of mid-term genetic sonograms among high-risk pregnancies. J Ultrasound Med. 2003;22(1):33-38.
94. Smith-Bindman R, Hosmer W, Feldstein VA, et al. Second-trimester ultrasound to detect fetuses with Down syndrome: a meta-analysis. JAMA. 2001;285(8):1044-1055.
95. Benacerraf BR, Barss VA, Laboda LA. A sonographic sign for the detection in the second trimester of the fetus with Down's syndrome. Am J Obstet Gynecol. 1985;151(8):1078-1079.
96. Benacerraf BR, Frigoletto Jr FD. Soft tissue nuchal fold in the second-trimester fetus: standards for normal measurements compared with those in Down syndrome. Am J Obstet Gynecol. 1987;157(5):1146-1149.
97. Benacerraf BR, Laboda LA, Frigoletto FD. Thickened nuchal fold in fetuses not at risk for aneuploidy. Radiology. 1992;184:239-242.
98. Benacerraf BR, Frigoletto Jr FD, Cramer DW. Down syndrome: sonographic sign for diagnosis in the second-trimester fetus. Radiology. 1987;163(3):811-813.
99. Crane JP, Gray DL. Sonographically measured nuchal skinfold thickness as a screening tool for Down syndrome: results of a prospective clinical trial. Obstet Gynecol. 1991;77(4):533-536.
100. Donnenfeld AE, Meister D, Allison J, et al. Interobserver variability of sonographically determined second-trimester nuchal skinfold thickness measurements. Ultrasound Obstet Gynecol. 1995;5(2):119-122.
101. Borrell A, Costa D, Martinez JM, et al. Criteria for fetal nuchal thickness cut-off: a re-evaluation. Prenat Diagn. 1997;17(1):23-29.
102. Wapner RJ. Nuchal fold and nasal bone: how should we use them in Down syndrome screening? Am J Obstet Gynecol. 2008;199(3):213-214.
103. Gray DL, Crane JP. Optimal nuchal skin-fold thresholds based on gestational age for prenatal detection of Down syndrome. Am J Obstet Gynecol. 1994;171(5):1282-1286.
104. Grandjean H, Sarramon MF. Sonographic measurement of nuchal skinfold thickness for detection of Down syndrome in the second-trimester fetus: a multicenter prospective study. The AFDPHE Study Group. Association Française pour le Dépistage et la Prévention des Handicaps de l'Enfant. Obstet Gynecol. 1995;85(1):103-106.
105. Watson WJ, Miller RC, Menard MK, et al. Ultrasonographic measurement of fetal nuchal skin to screen for chromosomal abnormalities. Am J Obstet Gynecol. 1994;170(2):583-586.
106. Landwehr Jr JB, Johnson MP, Hume RF, et al. Abnormal nuchal findings on screening ultrasonography: aneuploidy stratification on the basis of ultrasonographic anomaly and gestational age at detection. Am J Obstet Gynecol. 1996;175(4 Pt 1):995-999.
107. Lynch L, Berkowitz GS, Chitkara U, et al. Ultrasound detection of Down syndrome: is it really possible? Obstet Gynecol. 1989;73(2):267-270.
108. Smith-Bindman R, Chu P, Goldberg JD. Second trimester prenatal ultrasound for the detection of pregnancies at increased risk of Down syndrome. Prenat Diagn. 2007;27(6):535-544.
109. Agathokleous M, Chaveeva P, Poon LC, et al. Meta-analysis of second-trimester markers for trisomy 21. Ultrasound Obstet Gynecol. 2013;41(3):247-261.
110. Sonek JD, Nicolaides KH. Prenatal ultrasonographic diagnosis of nasal bone abnormalities in three fetuses with Down syndrome. Am J Obstet Gynecol. 2002;186(1):139-141.
111. Sonek JD, Cicero S, Neiger R, Nicolaides KH. Nasal bone assessment in prenatal screening for trisomy 21. Am J Obstet Gynecol. 2006;195(5):1219-1230.
112. Bromley B, Lieberman E, Shipp TD, Benacerraf BR. Fetal nose bone length: a marker for Down syndrome in the second trimester. J Ultrasound Med. 2002;21(12):1387-1394.
113. Odibo AO, Sehdev HM, Dunn L, et al. The association between fetal nasal bone hypoplasia and aneuploidy. Obstet Gynecol. 2004;104(6):1229-1233.
114. Bunduki V, Ruano R, Miguelez J, et al. Fetal nasal bone length: reference range and clinical application in ultrasound screening for trisomy 21. Ultrasound Obstet Gynecol. 2003;21(2):156-160.
115. Cicero S, Sonek JD, McKenna DS, et al. Nasal bone hypoplasia in trisomy 21 at 15-22 weeks' gestation. Ultrasound Obstet Gynecol. 2003;21(1):15-18.
116. Cusick W, Provenzano J, Sullivan CA, et al. Fetal nasal bone length in euploid and aneuploid fetuses between 11 and 20 weeks' gestation: a prospective study. J Ultrasound Med. 2004;23(10):1327-1333.
117. Vintzileos A, Walters C, Yeo L. Absent nasal bone in the prenatal detection of fetuses with trisomy 21 in a high-risk population. Obstet Gynecol. 2003;101(5 Pt 1):905-908.
118. Odibo AO, Sehdev HM, Gerkowicz S, et al. Comparison of the efficiency of second-trimester nasal bone hypoplasia and increased nuchal fold in Down syndrome screening. Am J Obstet Gynecol. 2008;199(3):281.e1-281.e5.
119. Odibo AO, Sehdev HM, Stamilio DM, et al. Defining nasal bone hypoplasia in second-trimester Down syndrome screening: does the use of multiples of the median improve screening efficacy? Am J Obstet Gynecol. 2007;197(4):361.e1-361.e4.

120. Benoit B, Chaoui R. Three-dimensional ultrasound with maximal mode rendering: a novel technique for the diagnosis of bilateral or unilateral absence or hypoplasia of nasal bones in second-trimester screening for Down syndrome. Ultrasound Obstet Gynecol. 2005;25(1):19-24.
121. Vos FI, De Jong-Pleij EA, Bakker M, et al. Nasal bone length, prenasal thickness, prenasal thickness-to-nasal bone length ratio and prefrontal space ratio in second- and third-trimester fetuses with Down syndrome. Ultrasound Obstet Gynecol. 2015;45(2):211-216.
122. Dukhovny S, Wilkins-Haug L, Shipp TD, et al. Absent fetal nasal bone: what does it mean for the euploid fetus? J Ultrasound Med. 2013; 32(12):2131-2134.
123. Lockwood C, Benacerraf B, Krinsky A, et al. A sonographic screening method for Down syndrome. Am J Obstet Gynecol. 1987;157(4 Pt 1): 803-808.
124. Benacerraf BR, Gelman R, Frigoletto Jr FD. Sonographic identification of second-trimester fetuses with Down's syndrome. N Engl J Med. 1987;317(22): 1371-1376.
125. Benacerraf BR, Cnann A, Gelman R, et al. Can sonographers reliably identify anatomic features associated with Down syndrome in fetuses? Radiology. 1989;173(2):377-380.
126. Nyberg DA, Resta RG, Hickok DE, et al. Femur length shortening in the detection of Down syndrome: is prenatal screening feasible? Am J Obstet Gynecol. 1990;162(5):1247-1252.
127. Shipp TD, Bromley B, Mascola M, Benacerraf B. Variation in fetal femur length with respect to maternal race. J Ultrasound Med. 2001;20(2): 141-144.
128. FitzSimmons J, Droste S, Shepard TH, et al. Long-bone growth in fetuses with Down syndrome. Am J Obstet Gynecol. 1989;161(5):1174-1177.
129. Benacerraf BR, Neuberg D, Frigoletto Jr FD. Humeral shortening in second-trimester fetuses with Down syndrome. Obstet Gynecol. 1991;77(2): 223-227.
130. Benacerraf BR, Mandell J, Estroff JA, et al. Fetal pyelectasis: a possible association with Down syndrome. Obstet Gynecol. 1990;76(1):58-60.
131. Corteville JE, Dicke JM, Crane JP. Fetal pyelectasis and Down syndrome: is genetic amniocentesis warranted? Obstet Gynecol. 1992;79(5 Pt 1):770-772.
132. Nyberg DA, Resta RG, Luthy DA, et al. Prenatal sonographic findings of Down syndrome: review of 94 cases. Obstet Gynecol. 1990;76(3 Pt 1):370-377.
133. Bromley B, Doubilet P, Frigoletto Jr FD, et al. Is fetal hyperechoic bowel on second-trimester sonogram an indication for amniocentesis? Obstet Gynecol. 1994;83(5 Pt 1):647-651.
134. Dicke JM, Crane JP. Sonographically detected hyperechoic fetal bowel: significance and implications for pregnancy management. Obstet Gynecol. 1992;80(5):778-782.
135. Nyberg DA, Resta RG, Mahony BS, et al. Fetal hyperechogenic bowel and Down's syndrome. Ultrasound Obstet Gynecol. 1993;3(5):330-333.
136. Scioscia AL, Pretorius DH, Budorick NE, et al. Second-trimester echogenic bowel and chromosomal abnormalities. Am J Obstet Gynecol. 1992;167(4 Pt 1):889-894.
137. Sepulveda W, Sebire NJ. Fetal echogenic bowel: a complex scenario. Ultrasound Obstet Gynecol. 2000;16(6):510-514.
138. Roberts DJ, Genest D. Cardiac histologic pathology characteristic of trisomies 13 and 21. Hum Pathol. 1992;23(10):1130-1140.
139. Bromley B, Lieberman E, Laboda L, Benacerraf BR. Echogenic intracardiac focus: a sonographic sign for fetal Down syndrome. Obstet Gynecol. 1995;86(6):998-1001.
140. Winter TC, Anderson AM, Cheng EY, et al. Echogenic intracardiac focus in 2nd-trimester fetuses with trisomy 21: usefulness as a US marker. Radiology. 2000;216(2):450-456.
141. Shipp TD, Bromley B, Lieberman E, Benacerraf BR. The frequency of the detection of fetal echogenic intracardiac foci with respect to maternal race. Ultrasound Obstet Gynecol. 2000;15(6):460-462.
142. Levine D, Mehta TS, Min KK, et al. Technical factors influencing sonographic visualization of fetal echogenic intracardiac foci. J Clin Ultrasound. 2000;28(9):479-484.
143. Winn VD, Sonson J, Filly RA. Echogenic intracardiac focus: potential for misdiagnosis. J Ultrasound Med. 2003;22(11):1207-1214.
144. Paladini D, Sglavo G, Pastore G, et al. Aberrant right subclavian artery: incidence and correlation with other markers of Down syndrome in second-trimester fetuses. Ultrasound Obstet Gynecol. 2012;39(2):191-195.
145. Scala C, Leone Roberti Maggiore U, Candiani M, et al. Aberrant right subclavian artery in fetuses with Down syndrome: a systematic review and meta-analysis. Ultrasound Obstet Gynecol. 2015;46(3):266-276.
146. Rotmensch S, Liberati M, Bronshtein M, et al. Prenatal sonographic findings in 187 fetuses with Down syndrome. Prenat Diagn. 1997;17(11): 1001-1009.
147. DeVore GR, Alfi O. The use of color Doppler ultrasound to identify fetuses at increased risk for trisomy 21: an alternative for high-risk patients who decline genetic amniocentesis. Obstet Gynecol. 1995;85(3):378-386.
148. Abuhamad AZ, Kolm P, Mari G, et al. Ultrasonographic fetal iliac length measurement in the screening for Down syndrome. Am J Obstet Gynecol. 1994;171(4):1063-1067.
149. Shipp TD, Bromley B, Lieberman E, Benacerraf BR. The iliac angle as a sonographic marker for Down syndrome in second-trimester fetuses. Obstet Gynecol. 1997;89(3):446-450.
150. Bahado-Singh RO, Wyse L, Dorr MA, et al. Fetuses with Down syndrome have disproportionately shortened frontal lobe dimensions on ultrasonographic examination. Am J Obstet Gynecol. 1992;167(4 Pt 1):1009-1014.
151. Benacerraf BR, Harlow BL, Frigoletto Jr FD. Hypoplasia of the middle phalanx of the fifth digit. A feature of the second trimester fetus with Down's syndrome. J Ultrasound Med. 1990;9(7):389-394.
152. Shimizu T, Salvador L, Hughes-Benzie R, et al. The role of reduced ear size in the prenatal detection of chromosomal abnormalities. Prenat Diagn. 1997;17(6):545-549.
153. Lettieri L, Rodis JF, Vintzileos AM, et al. Ear length in second-trimester aneuploid fetuses. Obstet Gynecol. 1993;81(1):57-60.
154. Gill P, Vanhook J, Fitzsimmons J, et al. Fetal ear measurements in the prenatal detection of trisomy 21. Prenat Diagn. 1994;14(8):739-743.
155. Gupta JK, Cave M, Lilford RJ, et al. Clinical significance of fetal choroid plexus cysts. Lancet. 1995;346(8977):724-729.
156. Bromley B, Lieberman R, Benacerraf BR. Choroid plexus cysts: not associated with Down syndrome. Ultrasound Obstet Gynecol. 1996;8(4):232-235.
157. Benacerraf BR, Neuberg D, Bromley B, Frigoletto Jr FD. Sonographic scoring index for prenatal detection of chromosomal abnormalities. J Ultrasound Med. 1992;11(9):449-458.
158. Benacerraf BR, Nadel A, Bromley B. Identification of second-trimester fetuses with autosomal trisomy by use of a sonographic scoring index. Radiology. 1994;193(1):135-140.
159. Vintzileos AM, Campbell WA, Guzman ER, et al. Second-trimester ultrasound markers for detection of trisomy 21: which markers are best? Obstet Gynecol. 1997;89(6):941-944.
160. Bahado-Singh RO, Oz AU, Kovanci E, et al. New Down syndrome screening algorithm: ultrasonographic biometry and multiple serum markers combined with maternal age. Am J Obstet Gynecol. 1998;179(6 Pt 1):1627-1631.
161. Bahado-Singh RO, Deren O, Tan A, et al. Ultrasonographically adjusted midtrimester risk of trisomy 21 and significant chromosomal defects in advanced maternal age. Am J Obstet Gynecol. 1996;175(6):1563-1568.
162. Nyberg DA, Luthy DA, Resta RG, et al. Age-adjusted ultrasound risk assessment for fetal Down's syndrome during the second trimester: description of the method and analysis of 142 cases. Ultrasound Obstet Gynecol. 1998;12(1):8-14.
163. Vintzileos AM, Campbell WA, Rodis JF, et al. The use of second-trimester genetic sonogram in guiding clinical management of patients at increased risk for fetal trisomy 21. Obstet Gynecol. 1996;87(6):948-952.
164. Aagaard-Tillery KM, Malone FD, Nyberg DA, et al. Role of second-trimester genetic sonography after Down syndrome screening. Obstet Gynecol. 2009;114(6):1189-1196.
165. Nyberg DA, Luthy DA, Cheng EY, et al. Role of prenatal ultrasonography in women with positive screen for Down syndrome on the basis of maternal serum markers. Am J Obstet Gynecol. 1995;173(4):1030-1035.
166. Vintzileos AM, Guzman ER, Smulian JC, et al. Choice of second-trimester genetic sonogram for detection of trisomy 21. Obstet Gynecol. 1997;90(2):187-190.

167. Souter VL, Nyberg DA, Benn PA, et al. Correlation of second-trimester sonographic and biochemical markers. J Ultrasound Med. 2004;23(4):505-511.
168. Pinette MG, Egan JF, Wax JR, et al. Combined sonographic and biochemical markers for Down syndrome screening. J Ultrasound Med. 2003;22(11):1185-1190.
169. DeVore GR, Romero R. Genetic sonography: an option for women of advanced maternal age with negative triple-marker maternal serum screening results. J Ultrasound Med. 2003;22(11):1191-1199.
170. Rozenberg P, Bussieres L, Chevret S, et al. Screening for Down syndrome using first-trimester combined screening followed by second-trimester ultrasound examination in an unselected population. Am J Obstet Gynecol. 2006;195(5):1379-1387.
171. Krantz DA, Hallahan TW, Macri VJ, Macri JN. Genetic sonography after first-trimester Down syndrome screening. Ultrasound Obstet Gynecol. 2007;29(6):666-670.
172. Sood M, Rochelson B, Krantz D, et al. Are second-trimester minor sonographic markers for Down syndrome useful in patients who have undergone first-trimester combined screening? Am J Obstet Gynecol. 2010;203(4):408 e1-408 e4.
173. Shamshirsaz AA, Ravangard SF, Turner G, et al. Efficacy of the genetic sonogram in a stepwise sequential protocol for down syndrome screening. J Ultrasound Med. 2013;32(9):1607-1613.
174. Caughey AB, Lyell DJ, Washington AE, et al. Ultrasound screening of fetuses at increased risk for Down syndrome: how many missed diagnoses? Prenat Diagn. 2006;26(1):22-27.
175. Reddy UM, Abuhamad AZ, Levine D, et al. Fetal imaging: executive summary of a joint Eunice Kennedy Shriver National Institute of Child Health and Human Development, Society for Maternal-Fetal Medicine, American Institute of Ultrasound in Medicine, American College of Obstetricians and Gynecologists, American College of Radiology, Society for Pediatric Radiology, and Society of Radiologists in Ultrasound Fetal Imaging Workshop. J Ultrasound Med. 2014;33(5):745-757.
176. Springett A, Wellesley D, Greenlees R, et al. Congenital anomalies associated with trisomy 18 or trisomy 13: a registry-based study in 16 European countries, 2000-2011. Am J Med Genet A. 2015;167A(12):3062-3069.
177. Irving C, Richmond S, Wren C, et al. Changes in fetal prevalence and outcome for trisomies 13 and 18: a population-based study over 23 years. J Matern Fetal Neonatal Med. 2011;24(1):137-141.
178. Yamanaka M, Setoyama T, Igarashi Y, et al. Pregnancy outcome of fetuses with trisomy 18 identified by prenatal sonography and chromosomal analysis in a perinatal center. Am J Med Genet A. 2006;140(11):1177-1182.
179. Jones KL, Smith DW. Smith's recognizable patterns of human malformation. 5th ed. Philadelphia: Saunders; 1997.
180. Papp C, Ban Z, Szigeti Z, et al. Role of second trimester sonography in detecting trisomy 18: a review of 70 cases. J Clin Ultrasound. 2007;35(2):68-72.
181. Watson WJ, Miller RC, Wax JR, et al. Sonographic findings of trisomy 18 in the second trimester of pregnancy. J Ultrasound Med. 2008;27(7):1033-1038.
182. Benacerraf BR, Harlow B, Frigoletto Jr FD. Are choroid plexus cysts an indication for second-trimester amniocentesis? Am J Obstet Gynecol. 1990;162(4):1001-1006.
183. Nyberg DA, Kramer D, Resta RG, et al. Prenatal sonographic findings of trisomy 18: review of 47 cases. J Ultrasound Med. 1993;12(2):103-113.
184. Goetzinger KR, Stamilio DM, Dicke JM, et al. Evaluating the incidence and likelihood ratios for chromosomal abnormalities in fetuses with common central nervous system malformations. Am J Obstet Gynecol. 2008;199(3):285.e1-285.e6.
185. Carlson DE, Platt LD, Medearis AL. The ultrasound triad of fetal hydramnios, abnormal hand posturing, and any other anomaly predicts autosomal trisomy. Obstet Gynecol. 1992;79(5 Pt 1):731-734.
186. Benacerraf BR, Saltzman DH, Estroff JA, Frigoletto Jr FD. Abnormal karyotype of fetuses with omphalocele: prediction based on omphalocele contents. Obstet Gynecol. 1990;75(3 Pt 1):317-319.
187. Nicolaides KH, Salvesen DR, Snijders RJ, Gosden CM. Strawberry-shaped skull in fetal trisomy 18. Fetal Diagn Ther. 1992;7(2):132-137.
188. Nyberg DA, Mahony BS, Hegge FN, et al. Enlarged cisterna magna and the Dandy-Walker malformation: factors associated with chromosome abnormalities. Obstet Gynecol. 1991;77(3):436-442.
189. Hill LM, Marchese S, Peterson C, Fries J. The effect of trisomy 18 on transverse cerebellar diameter. Am J Obstet Gynecol. 1991;165(1):72-75.
190. Thurmond AS, Nelson DW, Lowensohn RI, et al. Enlarged cisterna magna in trisomy 18: prenatal ultrasonographic diagnosis. Am J Obstet Gynecol. 1989;161(1):83-85.
191. Shuangshoti S, Roberts MP, Netsky MG. Neuroepithelial (colloid) cysts: Pathogenesis and relation to choroid plexus and ependyma. Arch Pathol. 1965;80:214-224.
192. Achiron R, Barkai G, Katznelson MB, Mashiach S. Fetal lateral ventricle choroid plexus cysts: the dilemma of amniocentesis. Obstet Gynecol. 1991;78(5 Pt 1):815-818.
193. Benacerraf BR, Laboda LA. Cyst of the fetal choroid plexus: a normal variant? Am J Obstet Gynecol. 1989;160(2):319-321.
194. Nadel AS, Bromley BS, Frigoletto Jr FD, et al. Isolated choroid plexus cysts in the second-trimester fetus: is amniocentesis really indicated? Radiology. 1992;185(2):545-548.
195. Platt LD, Carlson DE, Medearis AL, Walla CA. Fetal choroid plexus cysts in the second trimester of pregnancy: a cause for concern. Am J Obstet Gynecol. 1991;164(6 Pt 1):1652-1655.
196. Leonardi MR, Wolfe HM, Lanouette JM, et al. The apparently isolated choroid plexus cyst: importance of minor abnormalities in predicting the risk for aneuploidy. Fetal Diagn Ther. 1998;13(1):49-52.
197. Cheng PJ, Shaw SW, Soong YK. Association of fetal choroid plexus cysts with trisomy 18 in a population previously screened by nuchal translucency thickness measurement. J Soc Gynecol Investig. 2006;13(4):280-284.
198. Reinsch RC. Choroid plexus cysts—association with trisomy: prospective review of 16,059 patients. Am J Obstet Gynecol. 1997;176(6):1381-1383.
199. Coco C, Jeanty P. Karyotyping of fetuses with isolated choroid plexus cysts is not justified in an unselected population. J Ultrasound Med. 2004;23(7):899-906.
200. Bronsteen R, Lee W, Vettraino IM, et al. Second-trimester sonography and trisomy 18: the significance of isolated choroid plexus cysts after an examination that includes the fetal hands. J Ultrasound Med. 2004;23(2):241-245.
201. Bethune M. Time to reconsider our approach to echogenic intracardiac focus and choroid plexus cysts. Aust N Z J Obstet Gynaecol. 2008;48(2):137-141.
202. Ouzounian JG, Ludington C, Chan S. Isolated choroid plexus cyst or echogenic cardiac focus on prenatal ultrasound: is genetic amniocentesis indicated? Am J Obstet Gynecol. 2007;196(6):595.e1-595.e3.
203. Barry SC, Walsh CA, Burke AL, et al. Natural history of fetal trisomy 13 after prenatal diagnosis. Am J Med Genet A. 2015;167A(1):147-150.
204. Redheendran R, Neu RL, Bannerman RM. Long survival in trisomy-13-syndrome: 21 cases including prolonged survival in two patients 11 and 19 years old. Am J Med Genet. 1981;8(2):167-172.
205. Benacerraf BR, Frigoletto Jr FD, Greene MF. Abnormal facial features and extremities in human trisomy syndromes: prenatal US appearance. Radiology. 1986;159(1):243-246.
206. Benacerraf BR, Miller WA, Frigoletto Jr FD. Sonographic detection of fetuses with trisomies 13 and 18: accuracy and limitations. Am J Obstet Gynecol. 1988;158(2):404-409.
207. Watson WJ, Miller RC, Wax JR, et al. Sonographic detection of trisomy 13 in the first and second trimesters of pregnancy. J Ultrasound Med. 2007;26(9):1209-1214.
208. Papp C, Beke A, Ban Z, et al. Prenatal diagnosis of trisomy 13: analysis of 28 cases. J Ultrasound Med. 2006;25(4):429-435.
209. Lehman CD, Nyberg DA, Winter 3rd TC, et al. Trisomy 13 syndrome: prenatal US findings in a review of 33 cases. Radiology. 1995;194(1):217-222.
210. Ferguson-Smith MA, Yates JR. Maternal age specific rates for chromosome aberrations and factors influencing them: report of a collaborative European study on 52,965 amniocenteses. Prenat Diagn. 1984;4(Spec No):5-44.
211. Jacobs PA, Szulman AE, Funkhouser J, et al. Human triploidy: relationship between parental origin of the additional haploid complement and development of partial hydatidiform mole. Ann Hum Genet. 1982;46(Pt 3):223-231.

212. Joergensen MW, Niemann I, Rasmussen AA, et al. Triploid pregnancies: genetic and clinical features of 158 cases. Am J Obstet Gynecol. 2014;211(4):370 e1-370 e19.
213. McFadden DE, Robinson WP. Phenotype of triploid embryos. J Med Genet. 2006;43(7):609-612.
214. Jauniaux E, Brown R, Rodeck C, Nicolaides KH. Prenatal diagnosis of triploidy during the second trimester of pregnancy. Obstet Gynecol. 1996;88(6):983-989.
215. Jauniaux E, Brown R, Snijders RJ, et al. Early prenatal diagnosis of triploidy. Am J Obstet Gynecol. 1997;176(3):550-554.
216. Rijhsinghani A, Yankowitz J, Strauss RA, et al. Risk of preeclampsia in second-trimester triploid pregnancies. Obstet Gynecol. 1997;90(6): 884-888.
217. Goldstein DP, Berkowitz RS. Current management of complete and partial molar pregnancy. J Reprod Med. 1994;39(3):139-146.
218. Baena N, De Vigan C, Cariati E, et al. Turner syndrome: evaluation of prenatal diagnosis in 19 European registries. Am J Med Genet A. 2004;129A(1):16-20.
219. Wax JR, Blakemore KJ, Baser I, Stetten G. Isolated fetal ascites detected by sonography: an unusual presentation of Turner syndrome. Obstet Gynecol. 1992;79(5 Pt 2):862-863.
220. Azar GB, Snijders RJ, Gosden C, Nicolaides KH. Fetal nuchal cystic hygromata: associated malformations and chromosomal defects. Fetal Diagn Ther. 1991;6(1-2):46-57.
221. Papp C, Beke A, Mezei G, et al. Prenatal diagnosis of Turner syndrome: report on 69 cases. J Ultrasound Med. 2006;25(6):711-717.
222. American College of Obstetricians and Gynecologists. Cell-free DNA screening for fetal aneuploidy. Practice Bulletin. 2015;No. 640.
223. Bianchi DW, Platt LD, Goldberg JD, et al. Genome-wide fetal aneuploidy detection by maternal plasma DNA sequencing. Obstet Gynecol. 2012;119(5):890-901.
224. Zimmermann B, Hill M, Gemelos G, et al. Noninvasive prenatal aneuploidy testing of chromosomes 13, 18, 21, X, and Y, using targeted sequencing of polymorphic loci. Prenat Diagn. 2012;32(13):1233-1241.
225. Sparks AB, Struble CA, Wang ET, et al. Noninvasive prenatal detection and selective analysis of cell-free DNA obtained from maternal blood: evaluation for trisomy 21 and trisomy 18. Am J Obstet Gynecol. 2012;206(4):319.e1-319.e9.
226. Gil MM, Quezada MS, Revello R, et al. Analysis of cell-free DNA in maternal blood in screening for fetal aneuploidies: updated meta-analysis. Ultrasound Obstet Gynecol. 2015;45(3):249-266.
227. Cuckle H, Benn P, Pergament E. Cell-free DNA screening for fetal aneuploidy as a clinical service. Clin Biochem. 2015;48(15):932-941.
228. Bianchi DW, Parker RL, Wentworth J, et al. DNA sequencing versus standard prenatal aneuploidy screening. N Engl J Med. 2014;370(9):799-808.
229. Pergament E, Cuckle H, Zimmermann B, et al. Single-nucleotide polymorphism-based noninvasive prenatal screening in a high-risk and low-risk cohort. Obstet Gynecol. 2014;124(2 Pt 1):210-218.
230. Ashoor G, Syngelaki A, Poon LC, et al. Fetal fraction in maternal plasma cell-free DNA at 11-13 weeks' gestation: relation to maternal and fetal characteristics. Ultrasound Obstet Gynecol. 2013;41(1):26-32.
231. Bevilacqua E, Gil MM, Nicolaides KH, et al. Performance of screening for aneuploidies by cell-free DNA analysis of maternal blood in twin pregnancies. Ultrasound Obstet Gynecol. 2015;45(1):61-66.
232. Norton ME, Jacobsson B, Swamy GK, et al. Cell-free DNA analysis for noninvasive examination of trisomy. N Engl J Med. 2015;372(17): 1589-1597.
233. Petersen OB, Vogel I, Ekelund C, et al. Potential diagnostic consequences of applying non-invasive prenatal testing: population-based study from a country with existing first-trimester screening. Ultrasound Obstet Gynecol. 2014;43(3):265-271.
234. Norton ME, Jelliffe-Pawlowski LL, Currier RJ. Chromosome abnormalities detected by current prenatal screening and noninvasive prenatal testing. Obstet Gynecol. 2014;124(5):979-986.
235. Benachi A, Letourneau A, Kleinfinger P, et al. Cell-free DNA analysis in maternal plasma in cases of fetal abnormalities detected on ultrasound examination. Obstet Gynecol. 2015;125(6):1330-1337.
236. Shani H, Goldwaser T, Keating J, Klugman S. Chromosomal abnormalities not currently detected by cell-free fetal DNA: a retrospective analysis at a single center. Am J Obstet Gynecol. 2016;214(6):729.e1-3729.e11.
237. Hillman SC, McMullan DJ, Hall G, et al. Use of prenatal chromosomal microarray: prospective cohort study and systematic review and meta-analysis. Ultrasound Obstet Gynecol. 2013;41(6):610-620.
238. Wapner RJ, Martin CL, Levy B, et al. Chromosomal microarray versus karyotyping for prenatal diagnosis. N Engl J Med. 2012;367(23): 2175-2184.
239. Drury S, Williams H, Trump N, et al. Exome sequencing for prenatal diagnosis of fetuses with sonographic abnormalities. Prenat Diagn. 2015;35(10): 1010-1017.
240. van den Berg C, Van Opstal D, Brandenburg H, et al. Accuracy of abnormal karyotypes after the analysis of both short- and long-term culture of chorionic villi. Prenat Diagn. 2000;20(12):956-969.
241. Aina-Mumuney A, Wood ED, Corson VL, et al. Clinical consequences of an increasing trend of preferential use of cultured villi for molecular diagnosis by CVS. Prenat Diagn. 2008;28(4):332-334.
242. Ledbetter DH, Zachary JM, Simpson JL, et al. Cytogenetic results from the U.S. Collaborative Study on CVS. Prenat Diagn. 1992;12(5):317-345.
243. Hahnemann JM, Vejerslev LO. Accuracy of cytogenetic findings on chorionic villus sampling (CVS)—diagnostic consequences of CVS mosaicism and non-mosaic discrepancy in centres contributing to EUCROMIC 1986-1992. Prenat Diagn. 1997;17(9):801-820.
244. Brun JL, Mangione R, Gangbo F, et al. Feasibility, accuracy and safety of chorionic villus sampling: a report of 10741 cases. Prenat Diagn. 2003;23(4):295-301.
245. Evans MI, Andriole S, Evans SM. Genetics: update on prenatal screening and diagnosis. Obstet Gynecol Clin North Am. 2015;42(2):193-208.
246. Wolstenholme J. Confined placental mosaicism for trisomies 2, 3, 7, 8, 9, 16, and 22: their incidence, likely origins, and mechanisms for cell lineage compartmentalization. Prenat Diagn. 1996;16(6):511-524.
247. Grati FR, Bajaj K, Malvestiti F, et al. The type of feto-placental aneuploidy detected by cfDNA testing may influence the choice of confirmatory diagnostic procedure. Prenat Diagn. 2015;35(10):994-998.
248. Akolekar R, Beta J, Picciarelli G, et al. Procedure-related risk of miscarriage following amniocentesis and chorionic villus sampling: a systematic review and meta-analysis. Ultrasound Obstet Gynecol. 2015;45(1):16-26.
249. Lippman A, Tomkins DJ, Shime J, Hamerton JL. Canadian multicentre randomized clinical trial of chorion villus sampling and amniocentesis. Final report. Prenat Diagn. 1992;12(5):385-408.
250. Caughey AB, Hopkins LM, Norton ME. Chorionic villus sampling compared with amniocentesis and the difference in the rate of pregnancy loss. Obstet Gynecol. 2006;108(3 Pt 1):612-616.
251. Firth HV, Boyd PA, Chamberlain P, et al. Severe limb abnormalities after chorion villus sampling at 56-66 days' gestation. Lancet. 1991;337(8744): 762-763.
252. Froster UG, Jackson L. Limb defects and chorionic villus sampling: results from an international registry, 1992-94. Lancet. 1996;347(9000): 489-494.
253. World Health Organization WHO/PAHO consultation on CVS. Evaluation of chorionic villus sampling safety. Prenat Diagn. 1999;19(2):97-99.
254. American College of Obstetricians and Gynecologists. ACOG Practice Bulletin No. 88, December 2007. Invasive prenatal testing for aneuploidy. Obstet Gynecol. 2007;110(6):1459-1467.
255. Borgida AF, Mills AA, Feldman DM, et al. Outcome of pregnancies complicated by ruptured membranes after genetic amniocentesis. Am J Obstet Gynecol. 2000;183(4):937-939.
256. Devlieger R, Millar LK, Bryant-Greenwood G, et al. Fetal membrane healing after spontaneous and iatrogenic membrane rupture: a review of current evidence. Am J Obstet Gynecol. 2006;195(6):1512-1520.

CHAPTER 32

Multifetal Pregnancy

Mary C. Frates

SUMMARY OF KEY POINTS

- Multifetal pregnancies have higher rates of perinatal morbidity and mortality than singletons.
- Chorionicity is the major determining feature for the inherent unique complications faced by multiple gestations.
- Fetal growth differences and congenital malformations are increased in all types of multiple gestations.
- In monochorionic twins with a single demise, there is a high risk of severe cerebral and other injuries in the survivor.
- Sonography permits the diagnosis of syndromes unique to monochorionic twins, including twin-twin transfusion syndrome, twin anemia polycythemia sequence, twin reversed arterial perfusion sequence, and conjoined twins.

CHAPTER OUTLINE

ZYGOSITY/CHORIONICITY
DETERMINATION OF CHORIONICITY
GENERAL ISSUES
LOSS OF A TWIN
COMPLICATIONS OF MONOCHORIONICITY
Twin-Twin Transfusion Syndrome
Twin Anemia Polycythemia Sequence
Twin Reversed Arterial Perfusion Sequence
MONOAMNIOTIC TWINS
CONJOINED TWINS

Pregnancies with more than one fetus have become an increasingly common obstetric occurrence, primarily as a result of assisted reproductive technologies. Most **multifetal** pregnancies are **twins,** with higher-order multiples also possible. The rate of twins occurring naturally is 1 in 80 births,[1] yet the rate of twin births continues to rise. According to the Center for Disease Control Vital Statistics,[2] whereas the number of overall births in the United States was stable to slightly decreased in 2013 compared with 2012, the rate of twins reached a new high of 33.7 per 1000 births. The rate of triplet or higher births has been dropping since 1998, with a 2013 rate of 119.5 per 100,000 births. Modifications of assisted reproductive techniques are in part responsible for the declining rate of triplet and higher-order multiple gestations since the peak in 1998.[3] Multifetal pregnancies are subject to all the same considerations of singleton pregnancies but are also at particular risk for premature delivery and growth restriction. In 2013, more than one of every two twins and more than 9 of every 10 triplets was born preterm or with low birth weight.[2] In addition, there are unique issues that arise in multiple gestations, and it is critical for imagers to have a full understanding of these possible complications.

ZYGOSITY/CHORIONICITY

Twins are either **dizygotic** (fraternal) or **monozygotic** (identical). Among spontaneous twins, approximately two-thirds are dizygotic and one-third are monozygotic. Dizygotic twins occur when two separate ova are fertilized by two separate sperm. The rate of dizygotic twinning varies with maternal age (increased with older mothers), race, and family history. Monozygotic twins occur when a single ovum is fertilized by a single sperm and the embryo then divides from 2 to 14 days after fertilization. The timing of the division will dictate the type of twin. Spontaneous monozygotic twinning is uniform across the world (3.5/1000), and historically is not affected by maternal age, race, or other known factor.[1] However, there is currently an increased incidence of monozygotic twins from 2 to 12 times the expected rate following *in vitro* fertilization.[4-6] It has been reported that in patients undergoing assisted reproduction, the timing of single embryo transfer can affect the rate of monozygotic twins, with a higher rate seen following a 5- to 6-day transfer as compared to a 2- to 3-day transfer and a higher rate in patients who have undergone assisted hatching.[7,8] Higher-order multiples may have any combination of zygosity.

For management of a twin pregnancy, the type of twin is characterized by chorionicity rather than zygosity. Chorionicity is the major determining feature for the inherent unique complications faced by multiple gestations, with monochorionic pregnancies at the highest risk.[9] Therefore accurate determination of chorionicity is critical to ensure appropriate obstetric management of a twin pregnancy.[10]

Dizygotic twins are always **dichorionic diamniotic,** meaning that each twin has its own placenta (chorion), amnion, and amniotic fluid. Each twin exists in a separate intrauterine

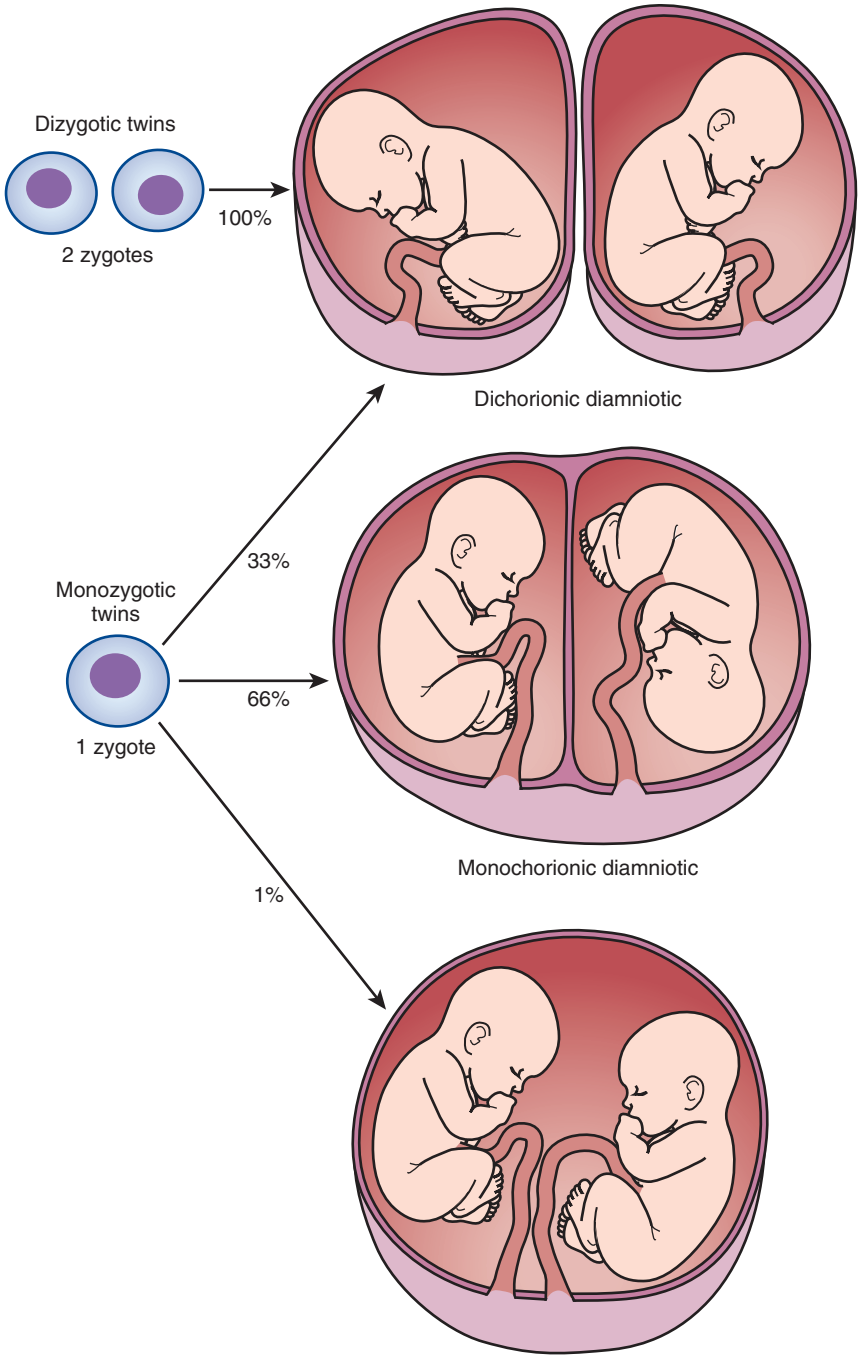

FIG. 32.1 Diagram Illustrating Zygosity and Placentation in Twins. Of twin gestations, two-thirds are dizygotic and one-third are monozygotic. All dizygotic twins result in diamniotic dichorionic pregnancies. Monozygotic twins can be dichorionic (33%), monochorionic diamniotic (66%), or monoamniotic monochorionic (approximately 1%).

environment, and the twins are genetically different. In contrast, there are three possible variations of chorionicity for monozygotic twins, who are genetically identical. Twins that occur when a single zygote divides within the first 4 days after fertilization have their own placenta (chorion), amnion, and amniotic fluid (dichorionic diamniotic, seen in one-third of cases). Monozygotic twins that occur from a later division share a placenta (chorion), but each has its own amnion (**monochorionic diamniotic,** seen in two-thirds). When the division occurs between days 7 and 14, the twins will share a placenta (chorion), amnion, and amniotic fluid (**monochorionic, monoamniotic,** seen in approximately 1%) (Fig. 32.1). Any later time of division will result in **conjoined** twins.[11] The increased risks associated with multiple gestations are related to chorionicity rather than zygosity, and ultrasound plays a critical role in the determination of twin type. Chorionicity is most easily and accurately determined via sonography in the first trimester. Both chorionicity and amnionicity must be established for each embryo.

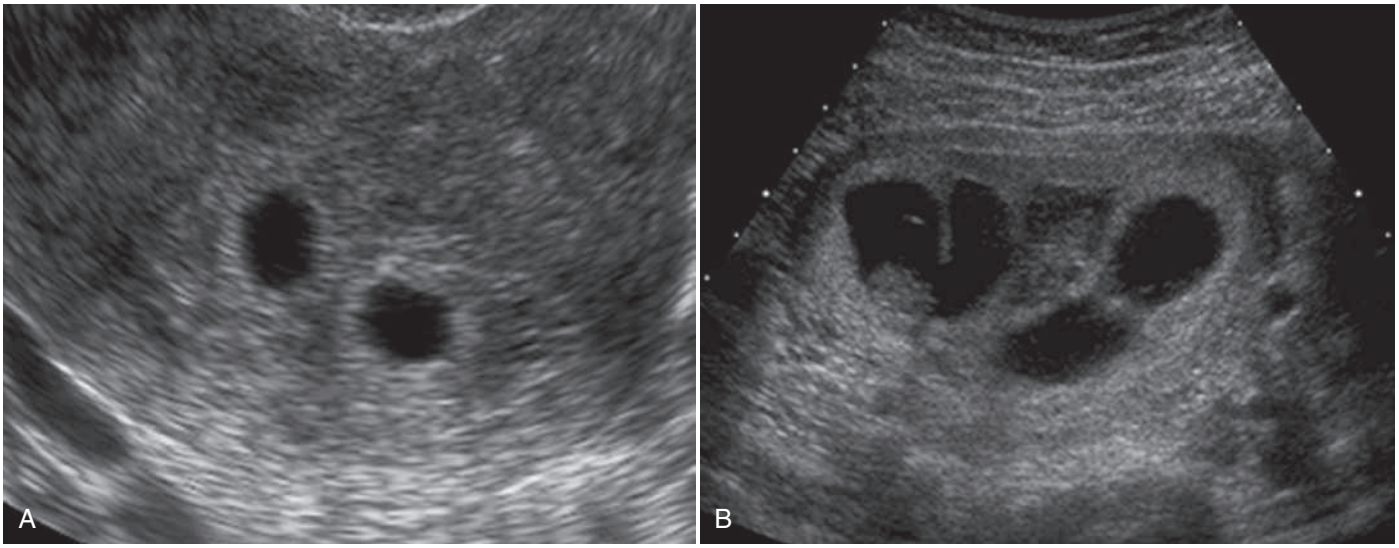

FIG. 32.2 The Number of Gestational Sacs Corresponds to Chorionicity. (A) Early dichorionic twins. Two separate gestational sacs are seen. **(B)** Quintuplets following assisted reproduction. Five separate gestational sacs are visible, with a single live embryo within each sac. See also Video 32.1.

DETERMINATION OF CHORIONICITY

Ultrasonography plays a vital role in the evaluation of multiple gestations, beginning with the first-trimester study. It is at this examination that the possibility of a twin or higher-order gestation will first be raised. A transvaginal approach is standard for early pregnancy (<8 weeks' gestational age) and may be useful later in the first trimester if transabdominal imaging is not definitive.[12] Determination of chorionicity is best performed very early in gestation, when the gestation sac size is small and the number of distinct sacs can be clearly established. The number of sacs will determine the number of chorions (Fig. 32.2, Video 32.1). Each sac should be evaluated for the presence of a yolk sac, embryo, and cardiac activity. To successfully identify monochorionic twins or higher-order multiples, careful evaluation of the contents of each sac is critical, to search for more than one yolk sac or embryo. In addition to accurately determining chorionicity, first-trimester ultrasound is also highly accurate at dating pregnancy,[13] which is particularly important for multiple gestations. The initial ultrasound report must clearly define the type of gestation, including chorionicity for each embryo, and should provide a single gestational age, as the first sonogram will be used for dating and for directing management of the pregnancy. In patients who have conceived via *in vitro* fertilization, the embryo transfer date should be used to establish the gestational age. For spontaneous multiples, if the size of the embryos is similar, an average of crown-rump lengths will provide an accurate gestational age. If the embryos are significantly different in size, the pregnancy should be dated based on the crown-rump length of the largest embryo, as any size discrepancy in the first trimester is likely related to an abnormality of the smaller embryo.

A potential pitfall in the early assessment of multiple gestations is the "appearing twin." At very early gestational ages (<7 weeks), the number of gestational sacs in the uterus may be undercounted, and the content of each sac is indeterminate.[14] A second or third gestational sac may appear, or a second embryo may be seen within a single sac. In contrast, because of the high background loss rate in the first trimester, twins may also "vanish."[15,16] Loss of a twin before 8 weeks' gestational age has minimal, if any, effect on the surviving twin, regardless of the chorionicity.[17,18]

Two distinct gestational sacs within the endometrial cavity indicates dichorionic twins. A single gestational sac containing two yolk sacs is a monochorionic pregnancy, and amnionicity then needs to be determined. The number of yolk sacs within a sac was historically thought to accurately predict the number of amnions[19]; that is, two yolk sacs in a single gestational sac corresponds with monochorionic diamniotic twins while one yolk sac with two embryos indicates monochorionic monoamniotic twins. However, more recently there have been reports of two yolk sacs leading to two embryos within a single amnion, as well as a single yolk sac leading to two embryos and two separate amniotic sacs.[20,21] It is clear that early multiples require close follow-up before assigning the amnionicity. The amnion can first be appreciated around the embryo just after 7 weeks' gestation; however, it may be very subtle, and scanning at 8 or 9 weeks' gestation or later may be more straightforward. Ultrasound has been shown to be highly accurate in assigning chorionicity during the first trimester,[22] in particular with the high resolution provided with a transvaginal transducer (Fig. 32.3, Video 32.2). In one large multicenter study, assignment of chorionicity with ultrasound was correct in 93.6% of twin gestations when performed before 20 weeks, with the most accurate classification occurring in pregnancies less than 14 weeks.[10] In this cohort, the likelihood of misclassification rose with each week of gestational age.

As the gestational sacs begin to grow and fill the endometrial cavity, the sacs begin to impress on each other, and it may be less obvious whether there are two separate sacs. At this time in the late first trimester and beyond, other methods can be used to determine chorionicity with sonography[23] (Table 32.1).

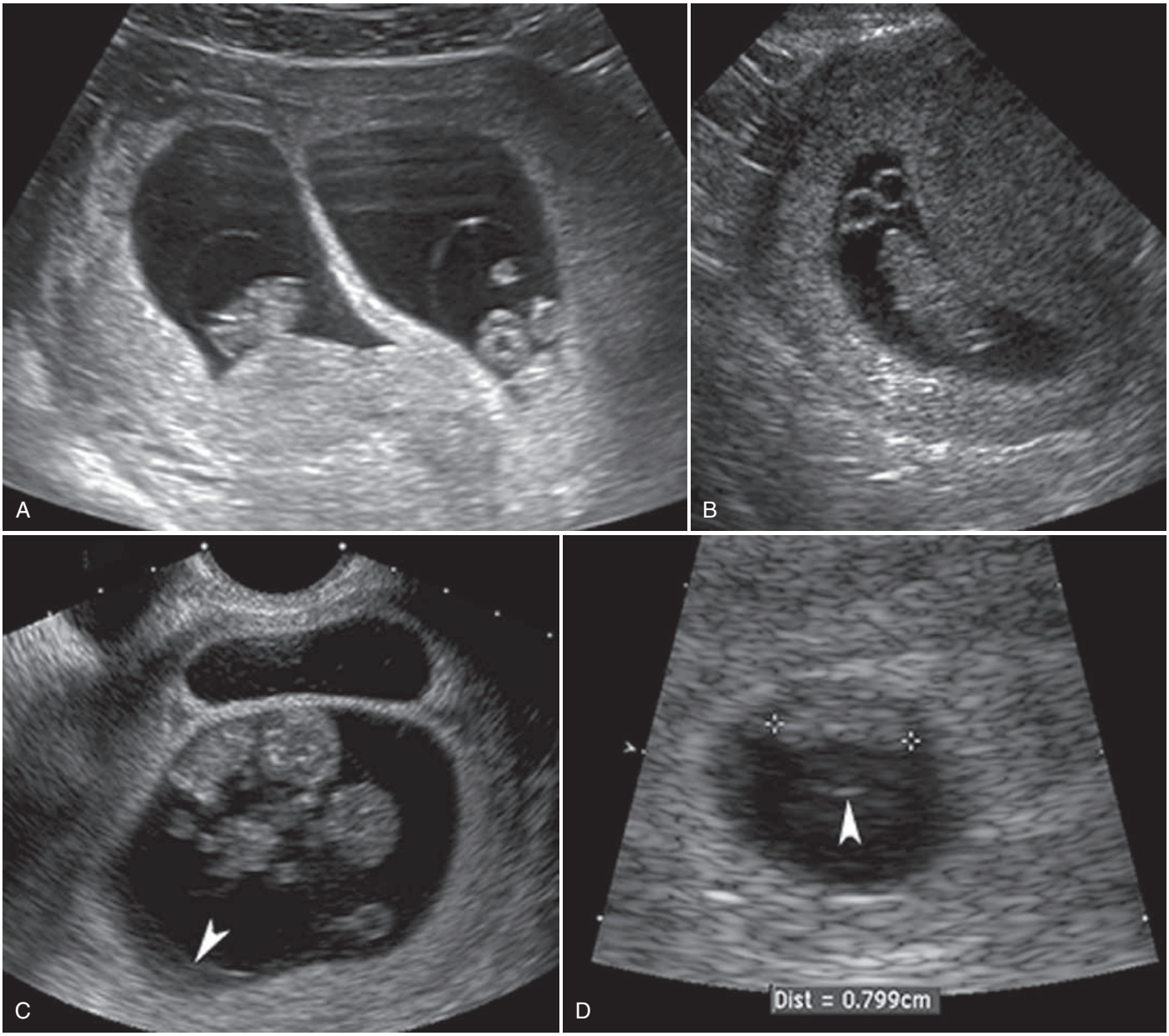

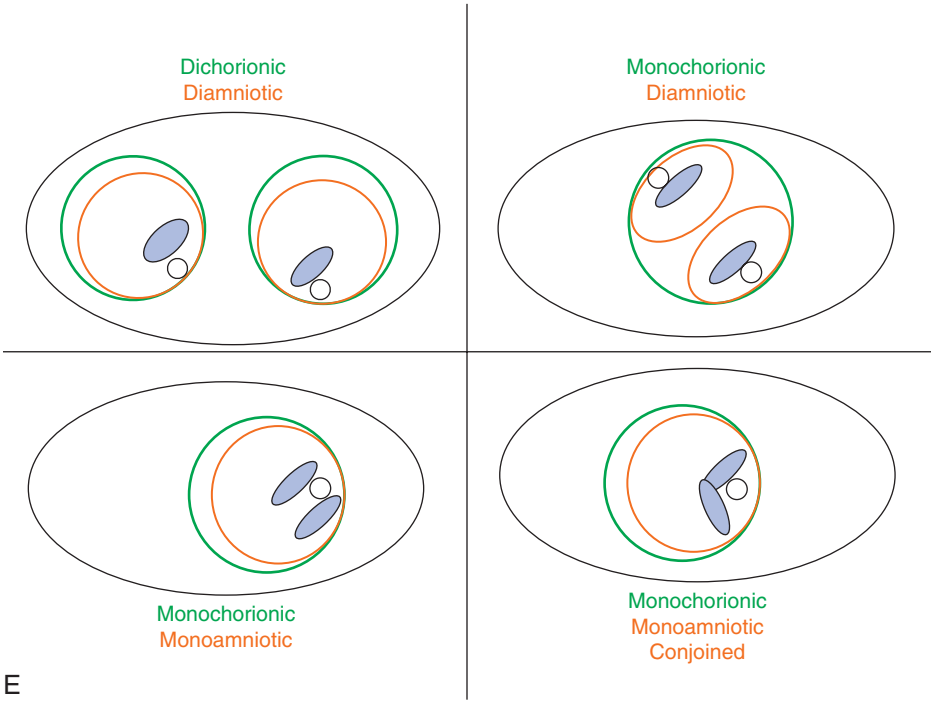

FIG. 32.3 First-Trimester Twins. (A) Dichorionic diamniotic twins. Two separate gestational sacs, each with embryo and yolk sac. Note the thin amnion separated from the chorion in each sac. **(B)** Monochorionic diamniotic twins. Single gestational sac with two yolk sacs and two embryos (only one is shown). **(C)** Monochorionic monoamniotic twins. Single gestational sac with two separate embryos and a single surrounding amnion *(white arrowhead).* **(D)** Monochorionic monoamniotic **conjoined twins.** Single gestational sac with a single amnion *(white arrowhead),* and a single large embryo that contains two heart beats. See also Video 32.2. **(E)** Corresponding line diagram of first-trimester pregnancies. *Blue,* Embryo; *brown,* amnion; *green,* chorion; *small black,* yolk sac.

TABLE 32.1 Sonographic Findings Used to Assign Chorionicity and Amnionicity in the Second and Third Trimesters

Dichorionic	Monochorionic Diamniotic	Monochorionic Monoamniotic
Two separate placentas or can merge to appear as a single placenta	Single placenta	Single placenta
Twin peak sign	T sign	—
Different or same fetal sex	Same sex	Same sex
Thick membrane	Thin membrane	No membrane
—	—	Entangled cords

As a first step, the placental locations should be determined. Two separate placentas indicate a dichorionic pregnancy.[1] However, approximately 50% of dichorionic placentas can appear fused at sonography.[24] If only a single placenta is seen, the fetal surface of the placenta should be searched for a twin peak or delta sign,[25-27] indicating a dichorionic gestation. This sign is a triangular extension of placenta into the intertwin membrane. Two layers of amnion and two layers of chorion form the intertwin membrane of a dichorionic gestation, and proliferating chorion frequently extends between the two chorionic membranes and separates the amnions, thus forming the peak or triangle (Fig. 32.4). This appearance is not continuous across the entire membrane, but rather occurs in patches that can be difficult to identify as the gestational age increases.

In a monochorionic gestation, the separating membrane is composed of two layers of amnion only, without chorion. The two-amnion membrane meets the placenta/single chorion in a T-shaped manner (Fig. 32.5). Because of the presence of four layers (in dichorionic twins with the two thicker chorions and two thin amnions) versus two layers of membranes (in monochorionic twins with two thin amnions) between sacs, the membrane is subjectively thicker in dichorionic gestations than in monochorionic gestations, but this method is less reliable for chorionicity determination than the others described earlier. When the fetus is large enough to assess anatomy, fetal sex can assist in differentiating twin types. Two different sexes are obviously dichorionic, whereas same-sex twins can be either dichorionic or monochorionic. Monoamniotic twins can be accurately identified when there is entanglement of either fetal parts or the cord (Fig. 32.6, Video 32.3). For higher-order multiples, any combination of chorionicity and amnionicity is possible, and more than one means of determining the type of gestation may be needed (Fig. 32.7, Video 32.4).

GENERAL ISSUES

Multiple gestations require the full sonographic evaluation appropriate for singleton pregnancies but have additional unique issues. One important role of the ultrasonologist is to establish which fetus is which, in a way that will allow continuous identification of each fetus until delivery. This determination is made on the first ultrasound in the second trimester or in the late first trimester at the time of nuchal translucency measurement. The fetus whose anatomic part is presenting (i.e., is closest to the cervix) is termed fetus 1 (or A). This fetus should remain fetus 1 for the rest of the pregnancy, even if it moves out of the presenting position at some point. Although a change in position is unlikely to happen if the initial determination was correct, it might occasionally occur, particularly when the intertwin membrane inserts near the cervix. The nonpresenting fetus is labeled twin 2 (or B). In larger-order multiples, the location in the uterus is used as an identifying characteristic—triplet 2 is upper right, triplet 3 is upper left, or vice versa. There is no standard method of labeling higher-order births beyond the presenter as number 1. Whichever method is chosen needs to be clearly reported and reproducible for all follow-up studies. In addition to proximity to the cervix, other clues for identifying which fetus is which are placental location, sex, discordant growth, and any potential anomaly. For higher-order multiples, the placentation/chorionicity should be reported at every exam, and this will help the sonographer with labeling—for example, dichorionic triamniotic triplets: triplet 1 is presenting with an anterior placenta, triplets 2 (upper right) and 3 (upper left) share a posterior placenta.

Good visualization of the intertwin membrane is essential and can be challenging at later gestational ages and in monochorionic gestations. The majority of monochorionic pregnancies are diamniotic, and lack of membrane visualization is typically due to oligohydramnios or overlapping fetal parts. Assessment of the amniotic fluid volume is performed for each fetus individually. Fluid volume is assessed either subjectively by an experienced examiner or using the deepest vertical pocket (see Chapter 42). Cutoffs of greater than 8 cm and less than 2 cm within one sac are generally accepted values to define polyhydramnios and oligohydramnios, respectively.[28] Occasionally, separation of the intertwin membrane can be appreciated, with amniotic fluid tracking between the membranes. This appearance has not been shown to be associated with an adverse outcome.[29]

The umbilical cord of each fetus should be evaluated for the presence of three vessels, as both monochorionic and dichorionic pregnancies have a higher incidence of single umbilical artery than do singletons.[30] In multiple gestations 17% to 22% have an abnormal placental cord insertion with its associated adverse outcomes as compared with 8% of singletons.[31,32] The abnormal cord insertions include both **marginal** (11% of twins) and **velamentous** (6%) insertions[31] and the placental cord insertion of each fetus should be documented (Fig. 32.8, Video 32.5). A velamentous cord insertion in one or both twins is more common in pregnancies conceived with assisted reproductive technology, as well as in twins with intrauterine growth restriction.[33-35]

Twin pregnancies are known to have higher rates of perinatal morbidity and mortality than singletons,[36-38] and the risk is closely related to chorionicity.[39,40] Greater-order multiples have still higher risks. The primary complications are premature delivery, intrauterine growth restriction, and intrauterine demise of one or

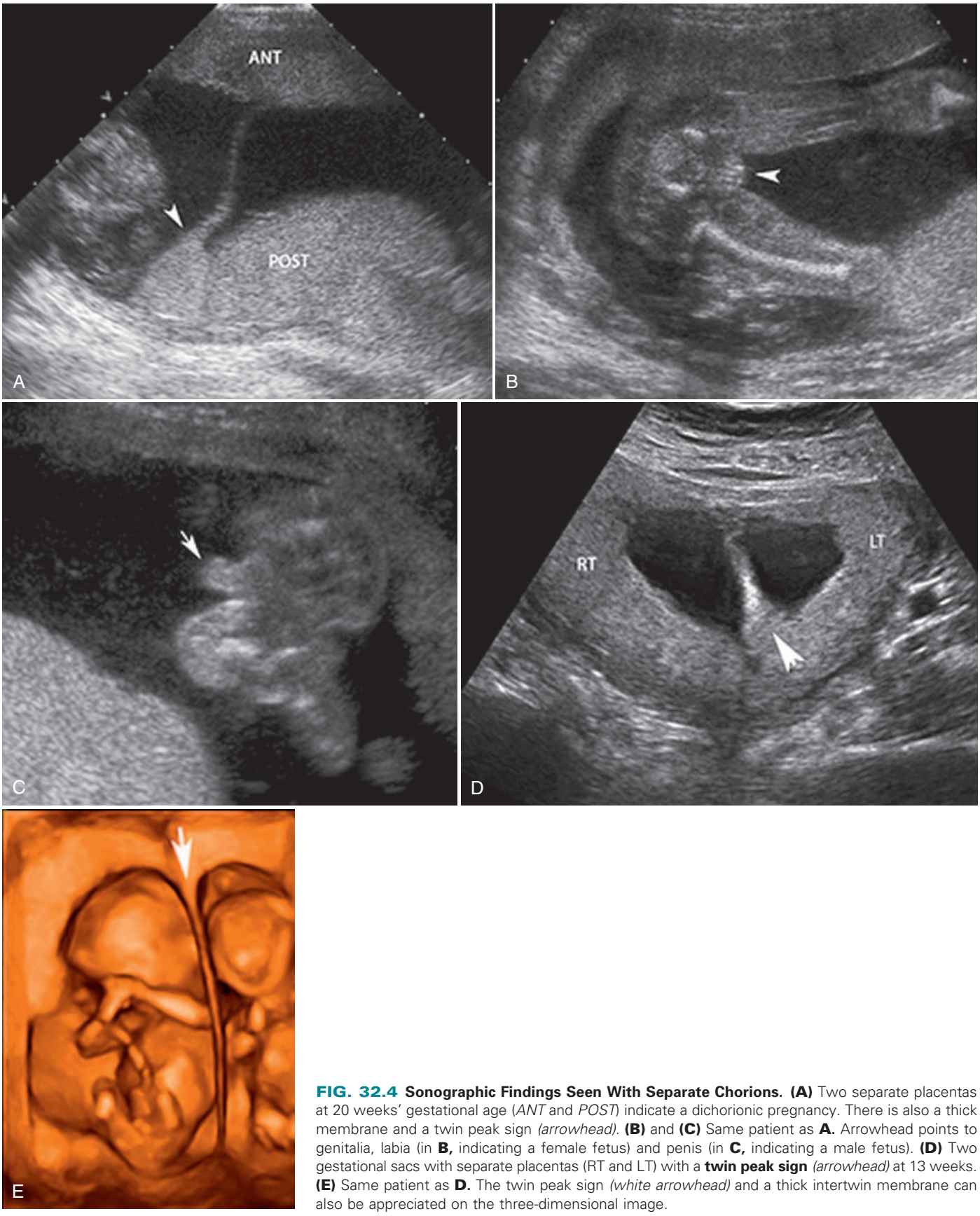

FIG. 32.4 Sonographic Findings Seen With Separate Chorions. (A) Two separate placentas at 20 weeks' gestational age (*ANT* and *POST*) indicate a dichorionic pregnancy. There is also a thick membrane and a twin peak sign *(arrowhead).* **(B)** and **(C)** Same patient as **A.** Arrowhead points to genitalia, labia (in **B,** indicating a female fetus) and penis (in **C,** indicating a male fetus). **(D)** Two gestational sacs with separate placentas (RT and LT) with a **twin peak sign** *(arrowhead)* at 13 weeks. **(E)** Same patient as **D.** The twin peak sign *(white arrowhead)* and a thick intertwin membrane can also be appreciated on the three-dimensional image.

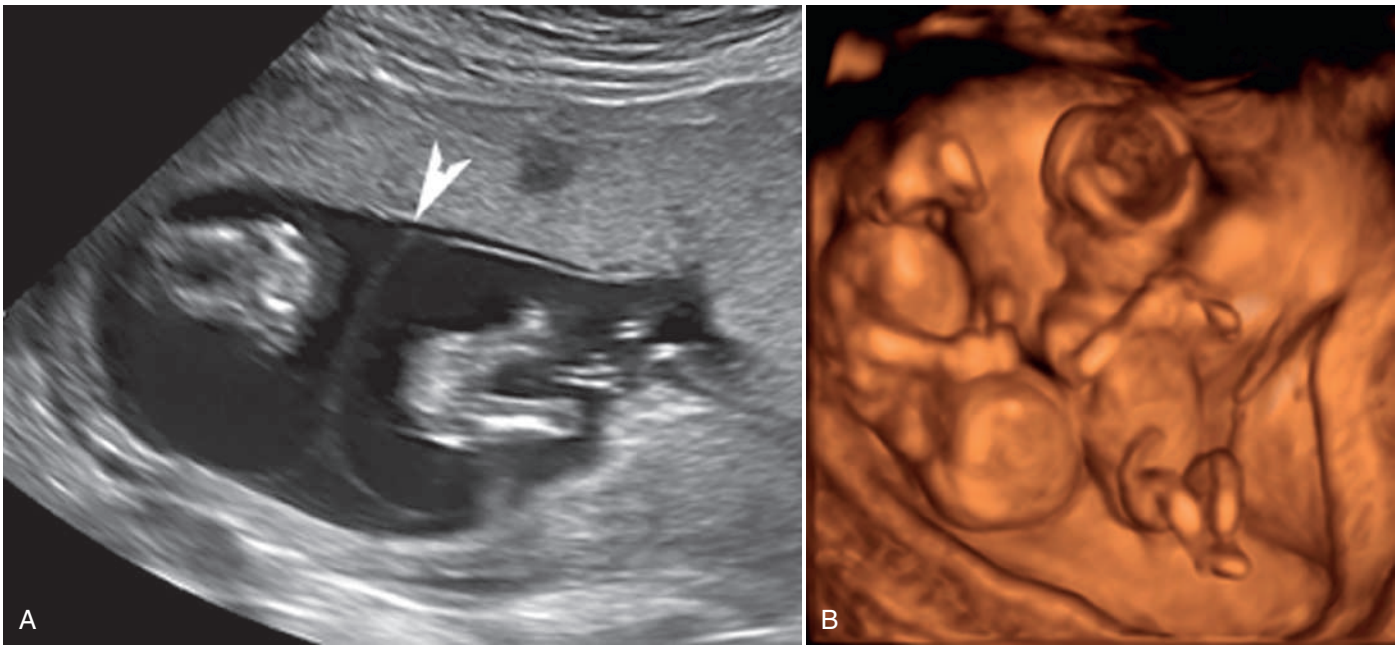

FIG. 32.5 Sonographic Findings Seen With Monochorionic Twins. (A) Monochorionic diamniotic twin gestation at 12.5 weeks' gestational age. There is an amnion visible around each fetus, which meets the anterior placenta in a T configuration *(white arrowhead)*. **(B)** Same patient as **A.** The thin membrane is not visible on the three-dimensional image of the twins.

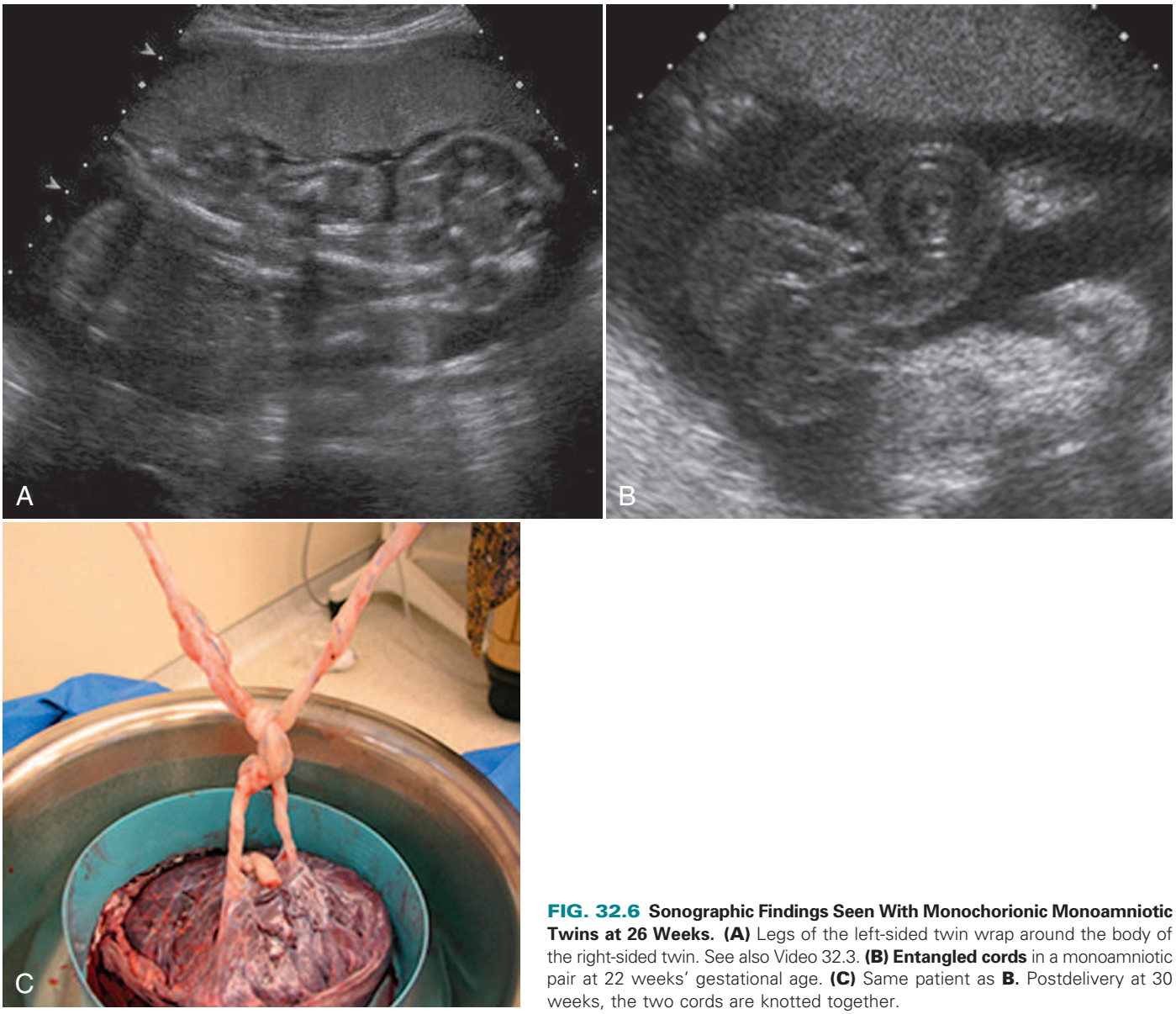

FIG. 32.6 Sonographic Findings Seen With Monochorionic Monoamniotic Twins at 26 Weeks. (A) Legs of the left-sided twin wrap around the body of the right-sided twin. See also Video 32.3. **(B) Entangled cords** in a monoamniotic pair at 22 weeks' gestational age. **(C)** Same patient as **B.** Postdelivery at 30 weeks, the two cords are knotted together.

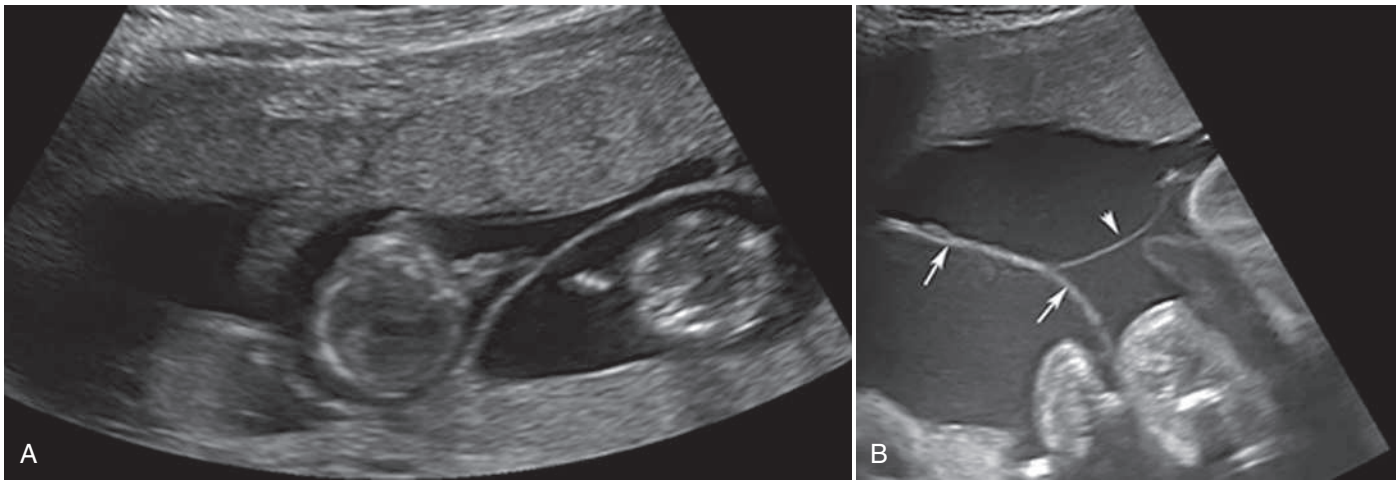

FIG. 32.7 Triplet Pregnancy Categorization. Each triplet needs amnionicity and chorionicity assigned accurately; analysis of more than one characteristic might be needed. **(A)** Three separate placentas in a trichorionic triplet pregnancy at 13 weeks. There is a posterior placenta on the left. The two anterior placentas appear merged, but a **twin peak sign** is present. See also Video 32.4. **(B) Triplet pregnancy** at 26 weeks' gestational age. There is both a thin *(white arrowhead)* and a thick *(white arrows)* membrane, consistent with triamniotic dichorionic twins.

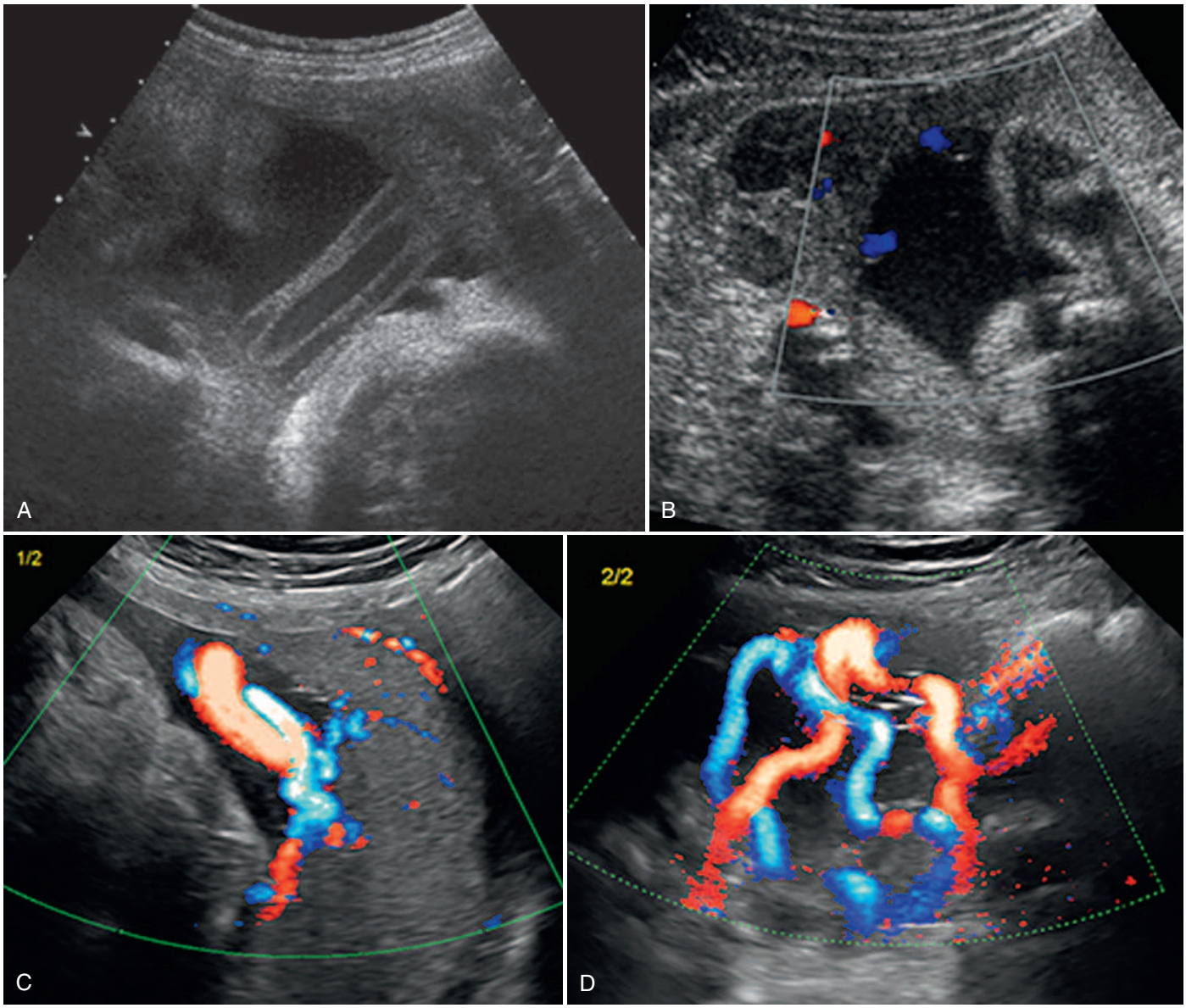

FIG. 32.8 Velamentous Cord Insertion. Up to one-quarter of twin gestations have an abnormal placental cord insertion. **(A)** Straight separate vessels are seen approaching the placenta in a 34-week twin. See also Video 32.5. **(B)** Same patient as **A.** Separate vessels *(blue)* can be seen on the surface of the placenta with color Doppler. **(C)** Power Doppler image of a normal placental cord insertion in twin 1 of a monochorionic gestation at 29 weeks' gestational age. **(D)** Same patient as **C.** Power Doppler image of a velamentous placental cord insertion in twin 2.

more fetuses. In a study of more than 3600 twin pregnancies, 2 liveborn infants occurred in 96% of dichorionic pregnancies, 86% of monochorionic diamniotic twins, and 67% of monochorionic monoamniotic twins. Before 22 weeks' gestation, the risk of spontaneous loss of both fetuses is significantly higher in monochorionic twins than dichorionic twins, and in monochorionic monoamniotic twins than in monochorionic diamniotic twins.[39,41,42] It is interesting to note that another large study of multiples found that when anomalous fetuses and intrauterine losses are excluded, the neonatal outcome for multiple gestation infants is similar to that of singletons who are born at similar gestational ages.[43] It is clear that premature delivery is an important influencing factor on the poor outcomes of multiple gestations.

Fetal growth differences in multiple gestations are well recognized. Twin fetuses are smaller than singletons, and monochorionic twins are more affected.[44] The growth differences are most profound after 30 weeks' gestation. Altered growth patterns in monochorionic twins are related to unequal placental sharing, whereas a discrepancy in dichorionic twin growth may potentially be due to a more or less favorable uterine implantation site[33] (Fig. 32.9, Video 32.6). Ultrasound estimation of fetal weight in twins and triplets has been shown to be accurate, and it is an important means of monitoring multiple gestations, as there is an increased risk of fetal loss with discordant fetal weights.[45-48] Fetal weights are considered discordant when there is a 15% to 25% weight difference, as determined by the following formula: (Larger twin estimated weight – smaller twin estimated weight)/larger twin estimated weight × 100.[49,50] The North American Fetal Therapy Network recommends ultrasound measurements to assess fetal growth every 4 weeks.[51] Others agree with a 4-week interval for dichorionic twins but suggest a 2-week interval for monochorionic twins from 16 weeks until delivery, because of the higher intrinsic risk associated with monochorionicity.[13,52,53] There is evidence to suggest that ultrasound surveillance, including measurements every 2 weeks, is appropriate for both monochorionic and dichorionic twins,[54] and more frequent monitoring is appropriate in any multiple gestation when there is weight discordance or other complication.[13,51] In general, umbilical artery Doppler is not recommended without an indication, such as growth restriction, unexplained oligohydramnios, or maternal hypertension.[13] When Doppler studies are performed without a definitive indication, abnormal results may lead to unnecessary interventions such as antenatal hospitalization and increased surveillance, which do not improve outcome.[55,56]

All types of twins have an increased risk of a congenital malformation.[57-59] A congenital anomaly occurs in singleton pregnancies at a rate of 2% to 3%, and this rate is doubled in all types of twins, with monochorionic twins twice as likely as dichorionic twins to have an anomaly.[60] This increased risk includes all types of congenital anomalies except for chromosomal abnormalities. A complete fetal anatomic survey is therefore recommended for all twin gestations at 18 to 22 weeks' gestational age.[13,61] Monochorionic twins are at increased risk in particular for congenital heart disease, with a rate as high as 7.5%,[62-64] and the rate is highest in twins affected with twin-twin transfusion syndrome. A monochorionic gestation is considered an indication for fetal echocardiography.[51,65]

LOSS OF A TWIN

Single intrauterine fetal death (IUFD) occurs in approximately 4% to 7% of twin pregnancies.[17,42] In a recent large study of twin outcomes with two live fetuses after 12 weeks' gestation, the rate of intrauterine fetal demise of one twin after 22 weeks was twice as high for monochorionic diamniotic as compared to dichorionic twins.[39] Higher losses are also seen with higher degrees of weight discordance between fetuses.[66] Loss of a single twin is therefore not uncommon and typically occurs in the third trimester. In a small number of these pregnancies, there is subsequent demise

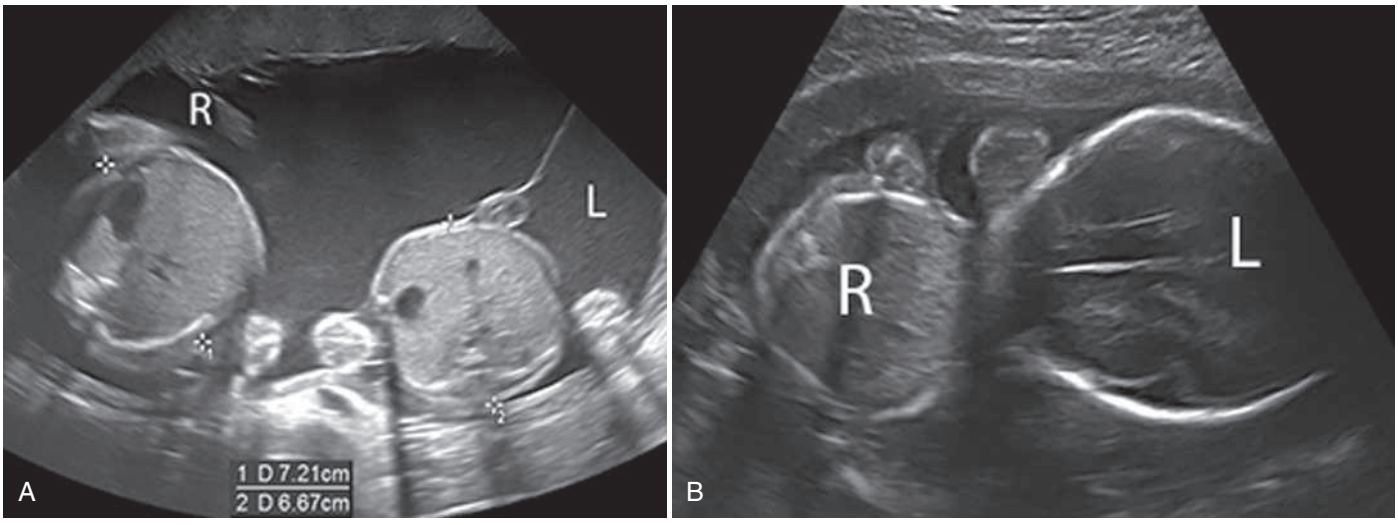

FIG. 32.9 Growth Discrepancy in Twins. (A) Monochorionic diamniotic twins at 28 weeks' gestational age. The twin on the maternal right *(R)* is larger with more amniotic fluid. The left-sided twin *(L)* is smaller and has less fluid. **(B)** Diamniotic dichorionic twins at 24 weeks. The abdomen of the twin on the right *(R)* is markedly smaller in comparison to the head of the twin on the left *(L),* and there is oligohydramnios. The right-sided twin measures approximately 19 weeks; the left-sided twin is normally grown. See also Video 32.6.

of the second twin,[42,67,68] which is also more likely in monochorionic twins, and the risk is particularly high for monoamniotic twins.[39] After loss of one twin, the surviving twin is at increased risk for adverse outcome, and the risk is again associated with chorionicity, as a result of the vascular anastomoses in a shared placenta.

In a dichorionic gestation with a single IUFD, there is no significant risk of injury to the surviving fetus, but there is an increased rate of preterm delivery.[67] However, in monochorionic twins with a single demise, risk of severe cerebral injury in the survivor may be as high as 25% to 34%.[68,69] In these cases, fetofetal hemorrhage is thought to be responsible. When the first fetus expires, there is a sudden drop in vascular resistance across the placental anastomoses and blood is shunted away from the survivor, with subsequent anemia, hypotension, and hypoperfusion of vital organs. This mechanism has been confirmed with in utero documentation of anemia in surviving fetuses.[17,70,71] The developing central nervous system is at highest risk for significant injury, and the consequences of the insult may not be apparent immediately. The sonographic manifestations of cerebral ischemia are similar to those seen in premature infants, namely, intracranial hemorrhage, middle cerebral artery infarction, and periventricular white matter injury with subsequent leukomalacia (Fig. 32.10). Renal injury can result in cortical necrosis, and limb reduction

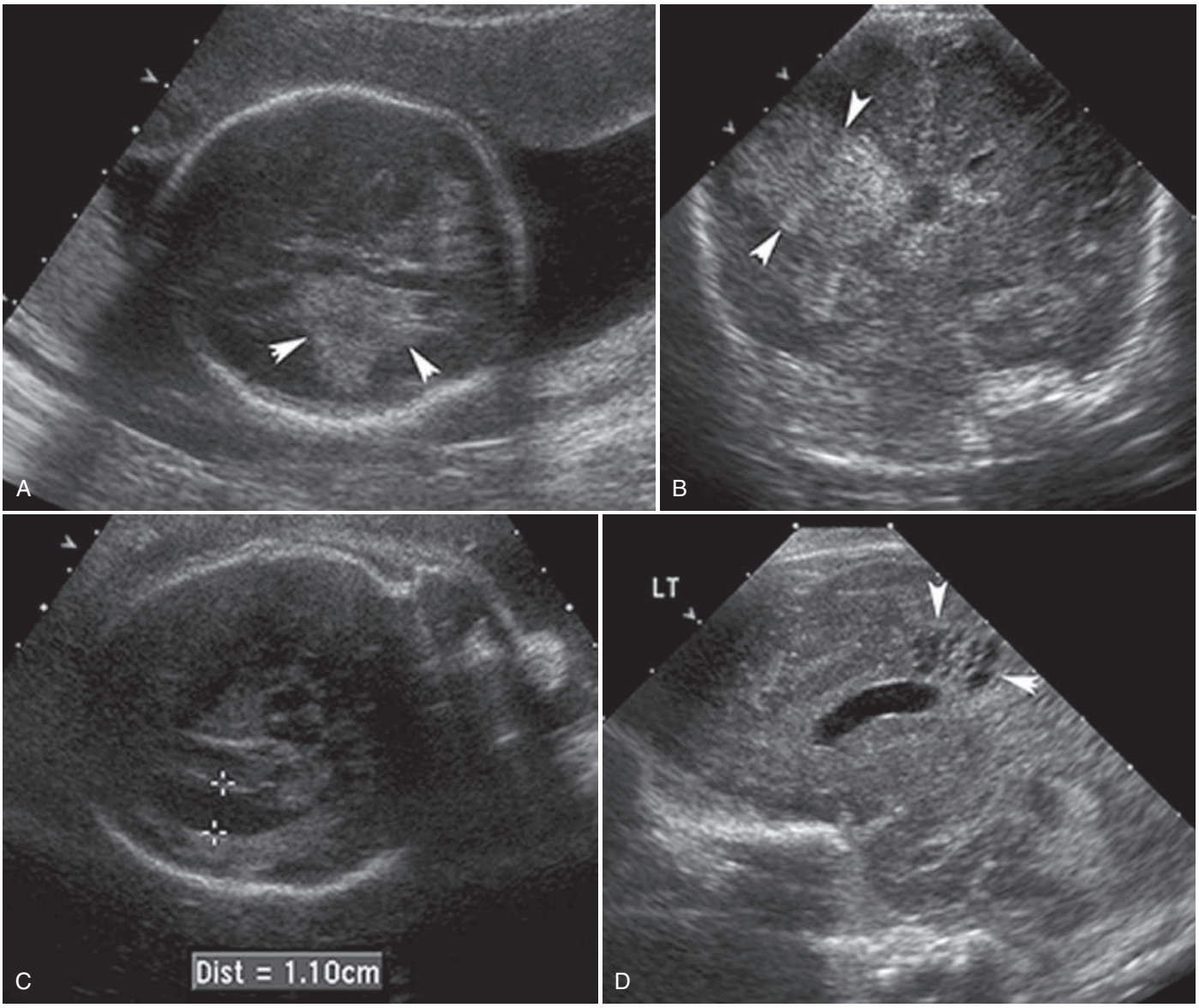

FIG. 32.10 Sequelae of Intrauterine Fetal Demise in Monochorionic Twin Gestations. (A) Axial image of the fetal head 24 hours after **amnioreduction** of 1800 mL from the gestational sac of this fetus. There is an echogenic lesion inseparable from the dependent lateral ventricle consistent with intraparenchymal hemorrhage *(arrowheads).* **(B)** Same patient as **A.** Postnatal head ultrasound of the same twin, day of life 1, 48 hours after amnioreduction. There is a large **intraparenchymal hemorrhage** on the right *(arrowheads).* **(C)** Monochorionic twin at 30 weeks' gestational age, following an IUFD of its twin 3 weeks ago. There is new **ventriculomegaly** of the survivor. **(D)** Same patient as **C,** 1 week later. Postnatal head ultrasound on day of life 3 shows cystic changes *(arrowheads)* in a parietal periventricular location consistent with **periventricular leukomalacia,** the result of the intrauterine fetal demise 4 weeks earlier.

injuries are possible.[69] The combination of twin-twin transfusion syndrome and single IUFD places the survivor at increased risk for cerebral injury.[69]

COMPLICATIONS OF MONOCHORIONICITY

The increased risks of abnormal growth, prematurity, and intrauterine demise seen in monochorionic gestations are all related to the single placental mass that is shared between the two fetuses. The majority of monochorionic placentas have vascular connections that cross back and forth between the two fetal-placental circulations, allowing minute amounts of blood exchange between twins. The anastomoses can be superficial or deep, and there are three distinct types: arterial/arterial (AA), arterial venous (AV), and venous venous (VV)[33] (Fig. 32.11). AA anastomoses are usually bidirectional and small and are found in 87% of placentas. AV anastomoses are unidirectional, deep, and found in 94% of monochorionic placentas. VV anastomoses are bidirectional, superficial, and found in a minority of placentas.[33,72,73] Within a monochorionic placenta, the degree and direction of flow across a combination of the three types of anastomoses are responsible for the unique complications of monochorionicity described in this section, as well as the general issues of growth and survival.[74,75]

Twin-Twin Transfusion Syndrome

This common complication (Table 32.2) affects between 10% and 23% of monochorionic twins. It is defined by oligohydramnios (deepest vertical pocket < 2 cm) with a small or empty bladder in the donor and polyhydramnios (deepest vertical pocket > 8 cm) with a distended bladder in the recipient in a monochorionic pregnancy.[52,57,72,76] Twin-twin transfusion syndrome (TTTS) was initially thought to include both amniotic fluid and fetal hematocrit differentials; however, it is now known that no in utero transfusion occurs with this syndrome, as hematocrits are often similar in both fetuses,[77] and the process could therefore be termed "twin oligohydramnios/polyhydramnios syndrome." Fetuses with TTTS have the same number of AV as, and more VV anastomoses than, fetuses without TTTS; however, it is the presence of more AA anastomoses that appears to be protective.[74,78,79] The unequal anastomoses allow a net transfer of volume from one fetal circulation to the other, creating a volume overloaded fetus (the recipient) and a hypovolemic fetus with poor renal perfusion and decreased urine output (the donor).[80]

The syndrome is usually first identified between 16 and 26 weeks' gestation (Fig. 32.12, Video 32.7). Serial ultrasounds of all monochorionic gestations are recommended to monitor for the development of TTTS, with fluid and bladder checks every 2 weeks.[52,53,81] A useful staging system proposed in 1999 (Table 32.3) can help diagnose the syndrome early in its progression.[76]

The syndrome begins with unequal amniotic fluid and bladder volumes and can advance to severe oligohydramnios (stuck twin), hydrops of either twin, and potential fetal demise. A stuck twin occurs when there is such a tiny amount of amniotic fluid around the donor fetus that the intertwin membrane cannot be identified because it is so closely applied to that fetus. The fetus in the sac with low fluid is restricted in movement and seems adherent to the wall of the uterus, often appearing suspended or "stuck" in comparison with the freely moving co-twin with its surrounding

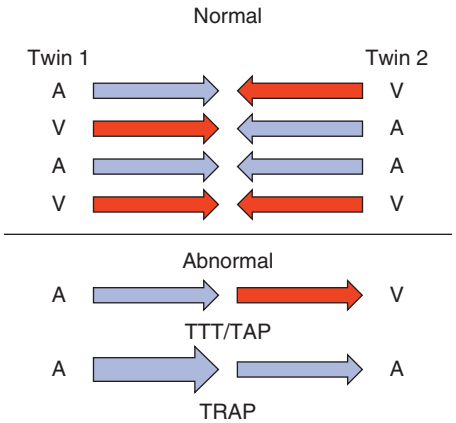

FIG. 32.11 Patterns of Vascular Anastomoses in Monochorionic Placentas. Monochorionic placentas contain arterial/arterial (AA), arterial venous (AV), and venous venous (VV) anastomoses. Unequal flow can lead to the unique complications of TTTS, TAPS, and TRAP. *Blue,* Arterial/deoxygenated flow; *red,* venous/oxygenated flow.

TABLE 32.2 Complications of Twin-Twin Transfusion Syndrome

Donor	Recipient
Oligohydramnios, may be "stuck"	Polyhydramnios
IUGR, small size	Possible hydrops
Small/nonvisualized bladder	Dilated bladder ± dilated renal pelves
	Large size
	Cardiomegaly
If live born, has better outcome	Struggles postnatally

IUGR, Intrauterine growth restriction.

TABLE 32.3 Quintero Staging of Twin-Twin Transfusion Syndrome

Stage	Findings
I	Amniotic fluid differential (oligohydramnios in donor and polyhydramnios in recipient)
II	Nonvisualized bladder in donor
III	Absent or reversed umbilical artery diastolic flow in donor
IV	Hydrops in either fetus
V	IUFD of one fetus

IUFD, Intrauterine fetal death.
Modified from Quintero R, Morales W, Allen M, et al. Staging of twin-twin transfusion syndrome. J Perinatol. 1999;19(8):550-555.[76]

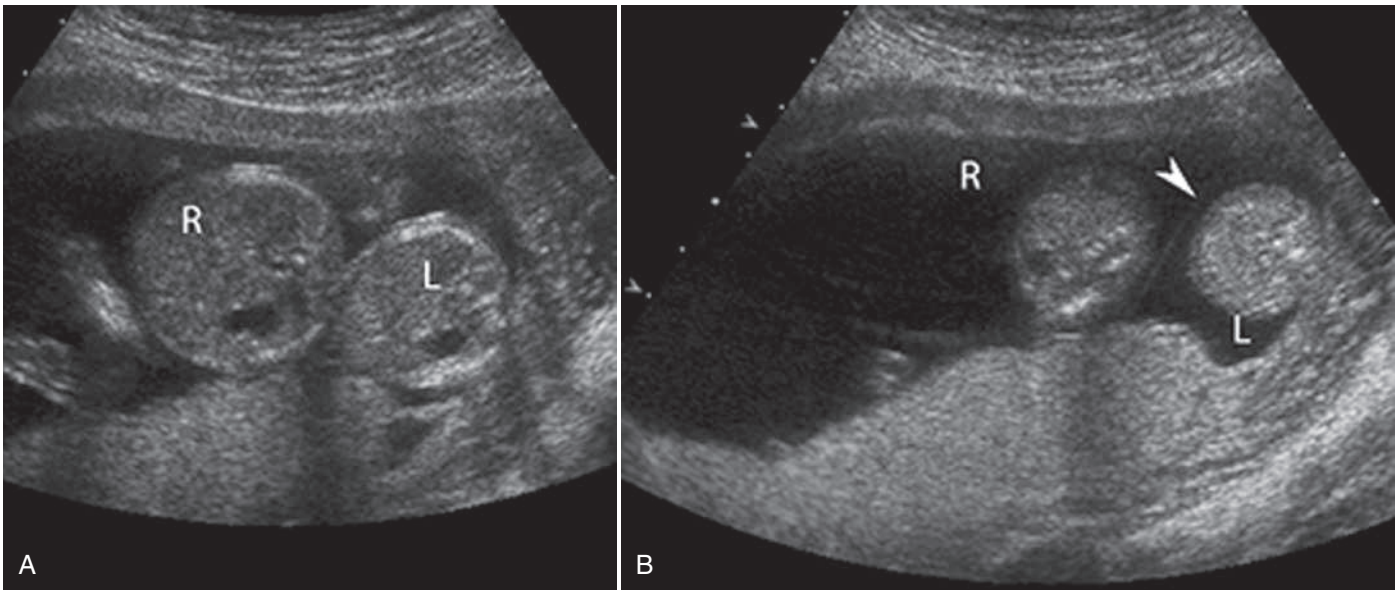

FIG. 32.12 Early Twin-Twin Transfusion Syndrome; Stage I. (A) and **(B)** Monochorionic twins at 16 weeks' gestational age. A discrepancy in abdominal diameters is apparent. The smaller twin on the maternal left *(L)* has much less amniotic fluid than the larger twin on the maternal right *(R)*. The very thin separating amnion is visible between the twins *(arrowhead)*. See also Video 32.7.

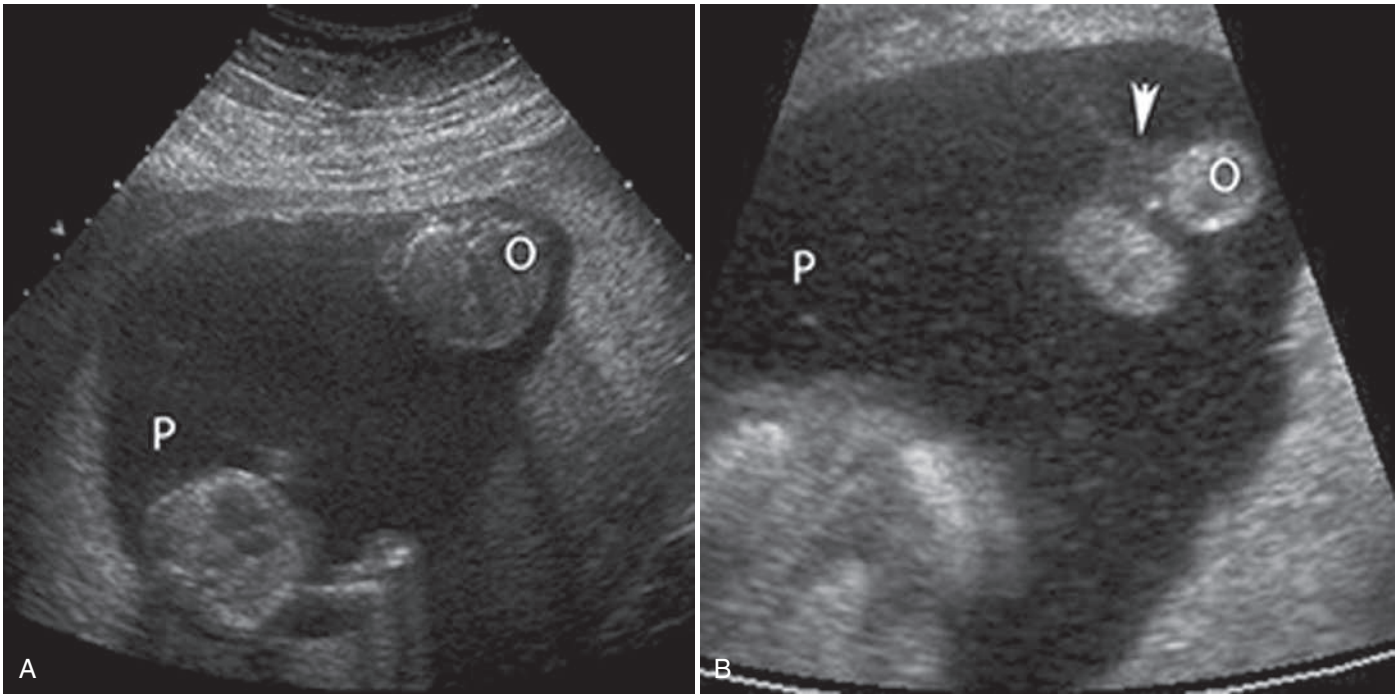

FIG. 32.13 Twin-Twin Transfusion; Stuck Twin. (A) and **(B)** Monochorionic twins at 16 weeks' gestational age. One twin *(O)* is "stuck" to the anterior uterine wall as a result of severe oligohydramnios. Its twin *(P)* is far posterior, freely moving in a large amount of amniotic fluid. The membrane *(arrowhead)* is barely visible surrounding a tiny amount of echogenic amniotic fluid between the legs of the "stuck" twin.

polyhydramnios (Fig. 32.13). In addition to fluid discrepancies, findings can include growth discordance (>20% difference in estimated fetal weight, with the donor smaller than the recipient), growth restriction of the donor, and cardiomegaly caused by volume overload in the recipient.[80] Untreated, approximately three-quarters of stage I fetuses remain stable or regress, whereas the perinatal loss rate for stage III or higher is between 70% and 100%.[52] A treatment option for TTTS is fetoscopic laser surgery performed at specialized centers worldwide; a less invasive alternative is serial amniocentesis to equalize fluid volumes and decrease the risk of preterm labor.[82,83]

Twin Anemia Polycythemia Sequence

The twin anemia polycythemia sequence (TAPS) was first described in 2007 by Lopriore et al., who presented two cases of presumed TTTS without associated amniotic fluid

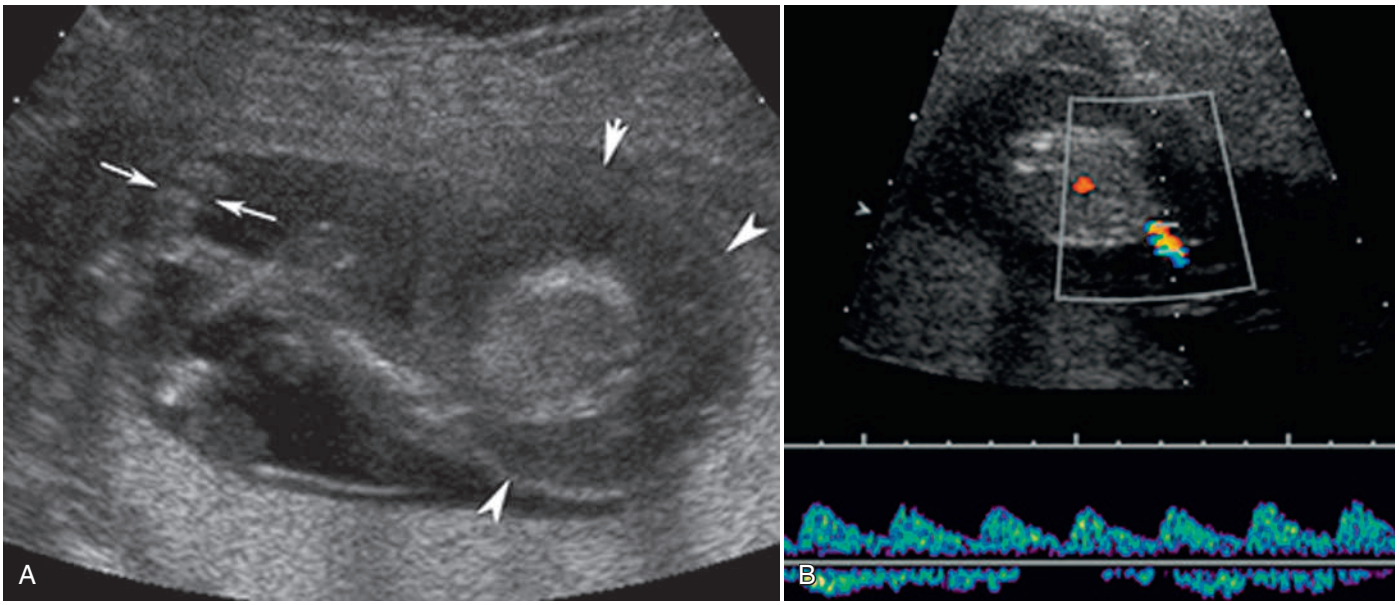

FIG. 32.14 Twin Reversed Arterial Perfusion Sequence. (A) Acardiac twin at 16 weeks. There is marked soft tissue edema around the trunk of the twin *(arrowheads)* and a club foot *(arrows)*. Despite the absence of a heart or upper body, there is active movement of the fetus. See also Video 32.8. **(B)** Same patient as **A.** Reversed flow in the acardiac twin umbilical artery, with pulsatile arterial flow entering at the umbilicus.

discordance.[84] TAPS occurs when there is sufficient unequal passage of red cells via the placental anastomoses such that one twin becomes anemic (the donor) and one becomes polycythemic (the recipient). The transfusion occurs extremely slowly via tiny unidirectional AV anastomoses, over a long period of time.[33,72] TAPS occurs in approximately 5% of monochorionic twins,[85] although this rate is higher following laser treatment for TTTS when all of the anastomoses have not been ablated.[86] Although amniotic fluid discordance is often seen as part of the TAPS sequence, the discordance is not as great as seen in TTTS. The diagnosis of TAPS is made prenatally with Doppler interrogation of the middle cerebral artery in each fetus. Doppler imaging of the middle cerebral artery has been shown to be an accurate noninvasive method for determining the presence of anemia in utero, nearly replacing percutaneous umbilical blood sampling in many centers.[87] Optimal technique is critical because incorrect technique can lead to false-positive diagnoses of anemia.[88] The anemic fetus will demonstrate elevated peak systolic velocity in the middle cerebral artery (>1.5 multiples of the median), while the polycythemic fetus demonstrates decreased velocities (<1.0 multiples of the median)[72,89] (see Chapter 41, Table 41.2). An additional sonographic finding occasionally seen in TAPS is two different placental echogenicities, with each region corresponding to a different fetal circulation.[90,91] Because TAPS typically occurs at a later gestational age than TTTS, the morbidity and mortality rates are much lower than those for TTTS.[92] However, late-onset TAPS can be associated with growth discordance and even intrauterine demise, and assessments of middle cerebral artery velocities are recommended every 2 weeks in the third trimester in monochorionic twins.[72,90]

Twin Reversed Arterial Perfusion Sequence

The twin reversed arterial perfusion (TRAP) sequence is a rare condition that occurs when one twin has an absent or severely malfunctioning heart and there is a large unbalanced AA anastomosis within a monochorionic placenta.[72] Blood flow is directed from the umbilical artery of one twin (pump twin with a normal heart) through the placenta and into the umbilical artery in the second twin, thus reversing flow in that umbilical artery. Flow is then directed inferiorly down the iliac arteries to the lower extremities of the second fetus and then out of the umbilical vein in a reversed direction back to the placenta. VV anastomoses allow that blood to then return to the pump twin. Flow in the recipient twin is deoxygenated, and its circulation exists only inferior to the diaphragm. The recipient is often grossly malformed above the diaphragm with an absent or malformed heart, head, and upper extremities, but can be remarkably intact inferior to the diaphragm, and has been termed an "acardiac twin" or "acardiac monster." This fetus retains the ability to move independently, as the spinal cord and lower extremities can be normally developed (Fig. 32.14, Video 32.8). The exact mechanism that creates the TRAP process is unclear, but it may be related to demise of the recipient twin with continued growth and development in the absence of a beating heart from the reversed circulation. Alternatively, the recipient fetus could be anomalous from conception. The TRAP sequence can be missed at first- or early second-trimester sonography when it is mistaken for a fetal demise because of the lack of cardiac activity. Color and pulsed Doppler interrogation will identify reversal of flow in the umbilical arteries and vein of the acardiac twin (Fig. 32.15). There is a high risk of IUFD of the donor twin related to high

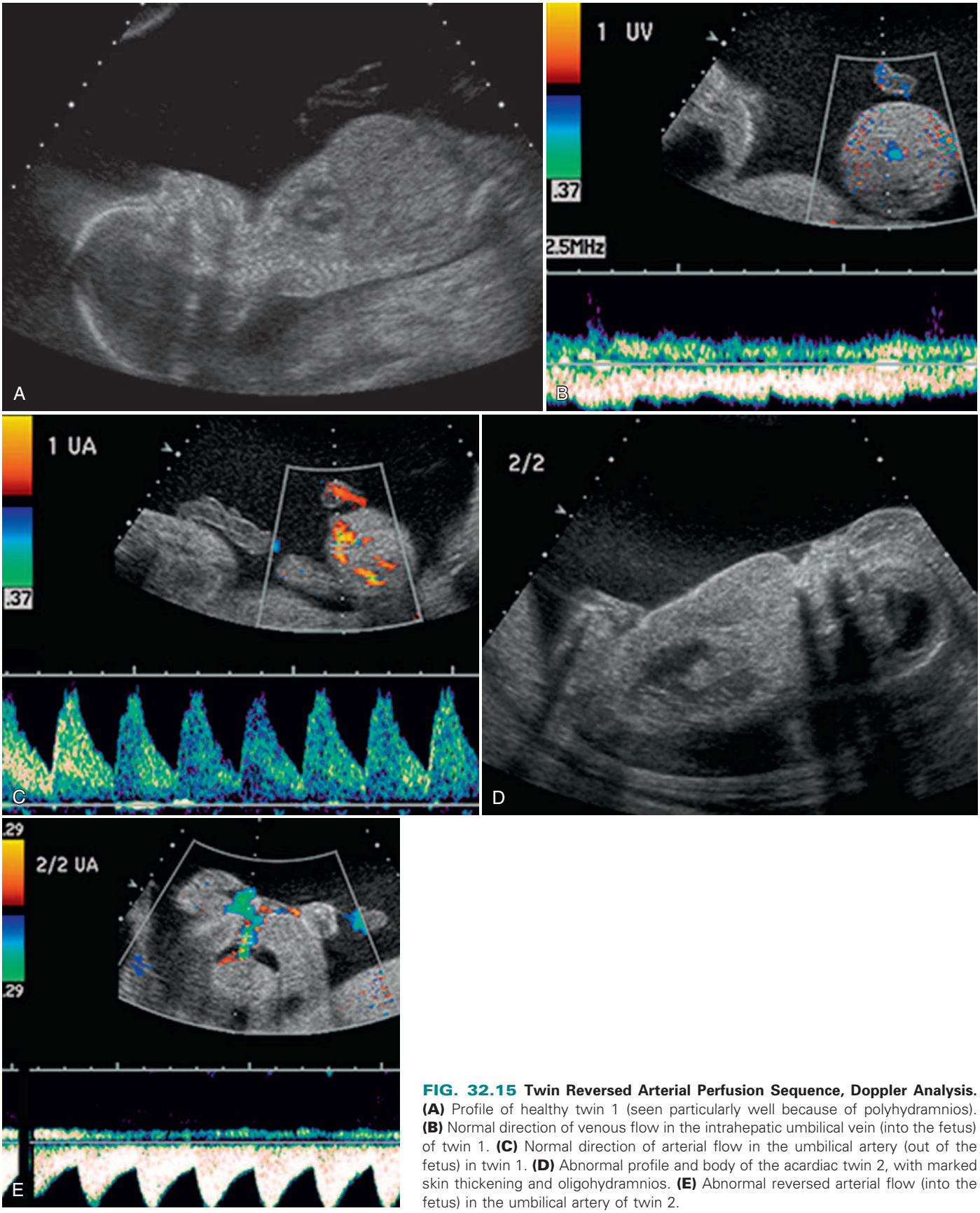

FIG. 32.15 Twin Reversed Arterial Perfusion Sequence, Doppler Analysis. **(A)** Profile of healthy twin 1 (seen particularly well because of polyhydramnios). **(B)** Normal direction of venous flow in the intrahepatic umbilical vein (into the fetus) of twin 1. **(C)** Normal direction of arterial flow in the umbilical artery (out of the fetus) in twin 1. **(D)** Abnormal profile and body of the acardiac twin 2, with marked skin thickening and oligohydramnios. **(E)** Abnormal reversed arterial flow (into the fetus) in the umbilical artery of twin 2.

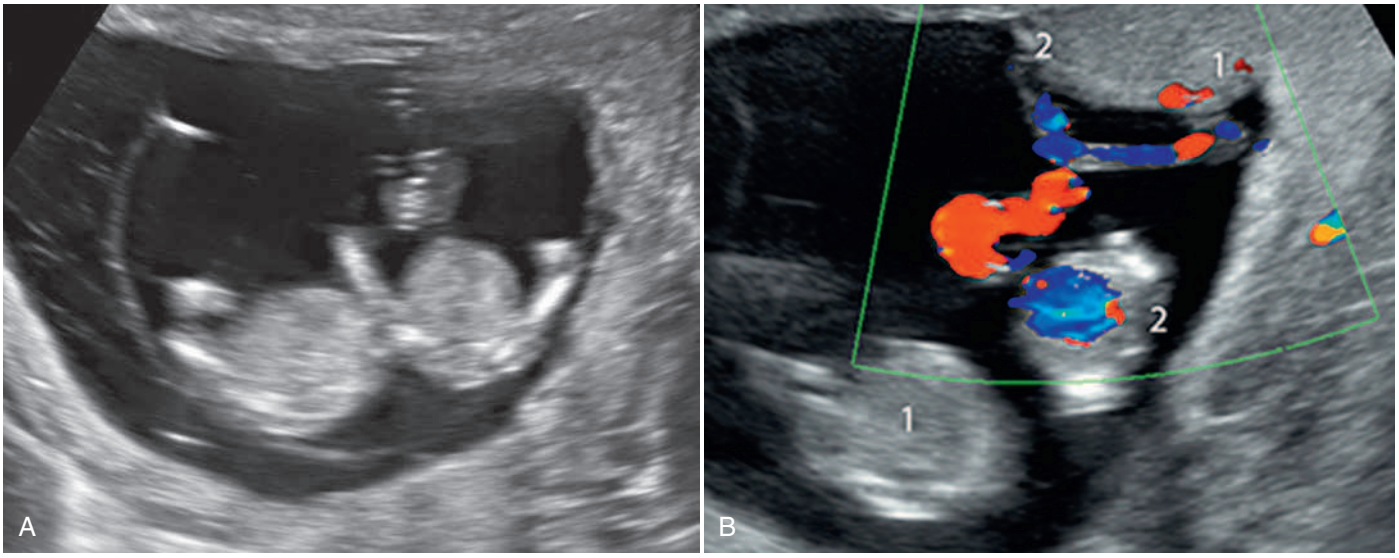

FIG. 32.16 Monochorionic Monoamniotic Twins, 12 Weeks' Gestational Age. (A) Transverse image of the fetal chests in a single gestational sac. The umbilical cords are entwined anteriorly. **(B)** Corresponding color Doppler image demonstrates the cords twisting together and then separating to insert into the anterior placenta. See also Video 32.9.

output cardiac failure and polyhydramnios,[93] particularly if the weight of the acardiac twin is more than 70% of the donor twin. In this situation, intervention to interrupt the abnormal circulation to the acardiac twin may be beneficial.[94-96]

MONOAMNIOTIC TWINS

In a monoamniotic pregnancy, both fetuses are located within a single amnion and therefore a single chorion. This rare type of twinning has the highest morbidity and mortality rate of any type of twin.[33] Monoamniotic twins should be suspected when no intertwin membrane is identified by 10 to 12 weeks' gestational age and can be confirmed at any age when the umbilical cords are seen to twist together or become entangled (Figs. 32.16 and 32.17, Videos 32.9 and 32.10). In the late first trimester, transvaginal imaging may provide better resolution to confirm the absence of a membrane. The monoamniotic placenta has the same three types of vascular anastomoses as found with diamniotic twins; however, there are more AA anastomoses, fewer AV anastomoses, and a similar number of VV anastomoses in monoamniotic twins when compared with diamniotic monochorionic twins. In addition to all of the potential complications of a monochorionic gestation, monoamniotic twins are at risk for cord knotting or entanglement at any gestational age, although the clinical significance of cord entanglement is unclear, as several studies have shown no improvement in outcome following ultrasound diagnosis of an entangled cord.[97,98] Discordant fetal anomalies can affect as high as 20% of monoamniotic pregnancies.[99] Monoamniotic twins are at high risk of unexpected and usually double intrauterine fetal demise, thought to be related to fetofetal hemorrhage via large AA anastomoses following cord compression.[72,100] Survival of monoamniotic twins may be as high as 80% with intensive surveillance and early delivery.[101,102]

FIG. 32.17 Monochorionic Monoamniotic Twins, 28 Weeks' Gestational Age. The umbilical cord of one fetus wraps loosely around a transverse section of the other cord *(arrows)*. See also Video 32.10.

CONJOINED TWINS

Conjoined twins are a rare type of monoamniotic twins that occur with late division of the embryo. The twins can be conjoined at any skin site and are diagnosed by demonstrating contiguous skin covering between two fetuses. The in utero rate of conjoined twins is estimated at 1 in 50,000 gestations, with an IUFD rate of 60% and an additional high loss rate after birth.[103] Conjoined twins are generally classified by the site of joining,[104] although the anatomy of each pair is unique. Careful sonographic evaluation of each fetus is imperative for a full assessment of the degree of sharing that exists, which will help with an accurate prognosis

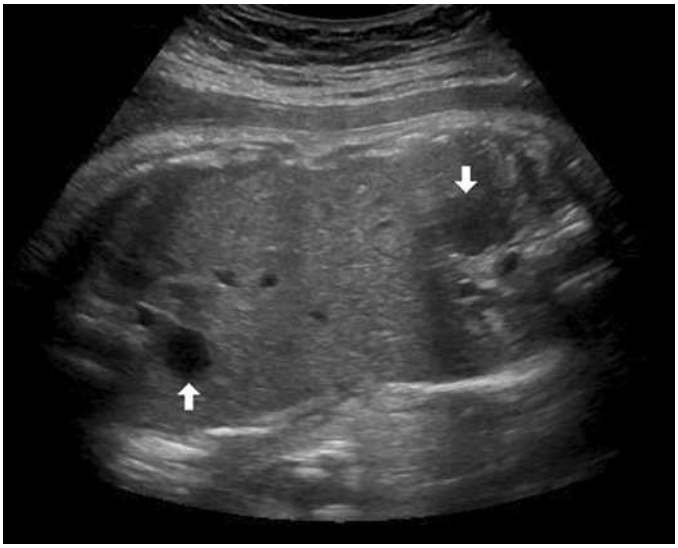

FIG. 32.18 Monochorionic Monoamniotic Conjoined Twins, 35 Weeks' Gestational Age. The twins share a liver (*arrows* mark the stomach of each twin) and the hearts are merged. See also Video 32.11.

for surgical separation.[105,106] Conjoined twins can be diagnosed in the late first trimester (see Fig. 32.3D); however, a detailed survey will be required by 18 to 20 weeks' gestation for the most accurate evaluation of the degree of visceral and vascular sharing (Fig. 32.18, Video 32.11). The umbilical cord may also be fused, with more than three vessels seen within a single cord.[106] Formal fetal echocardiography is indicated, as cardiac anomalies are highly related to outcome.[106]

REFERENCES

1. Benirschke K, Kim C. Multiple pregnancy. NEJM. 1973;288(24):1276-1284.
2. Martin JA, Hamilton BE, Osterman MJ, et al. Births: final data for 2013. Natl Vital Stat Rep. 2015;64(1):1-65.
3. The Practice Committee of the American Society for Reproductive Medicine and the Practice Committee of the Society for Assisted Reproductive Technology. Criteria for number of embryos to transfer: a committee opinion. Fertil Steril. 2013;99(1):44-46.
4. Rao A, Sairam S, Shehata H. Obstetric complications of twin pregnancies. Best Pract Res Clin Obstet Gynaecol. 2004;18(4):557-576.
5. Aston KI, Peterson CM, Carrell DT. Monozygotic twinning associated with assisted reproductive technologies: a review. Reproduction. 2008;136(4):377-386.
6. Vitthala S, Gelbaya TA, Brison DR, et al. The risk of monozygotic twins after assisted reproductive technology: a systematic review and meta-analysis. Hum Reprod Update. 2008;15(1):45-55.
7. Kanter JR, Boulet SL, Kawwass JF, et al. Trends and correlates of monozygotic twinning after single embryo transfer. Obstet Gynecol. 2015;125(1):111-117.
8. Chow JS, Benson CB, Racowsky C, et al. Frequency of a monochorionic pair in multiple gestations: relationship to mode of conception. J Ultrasound Med. 2001;20(7):757-760.
9. Lopes Perdigao J, Straub H, Zhou Y, et al. Perinatal and obstetric outcomes of dichorionic vs trichorionic triplet pregnancies. Am J Obstet Gynecol. 2016;214(5):659.e1-659.e5.
10. Blumenfeld YJ, Momirova V, Rouse DJ, et al. Accuracy of sonographic chorionicity classification in twin gestations. J Ultrasound Med. 2014;33(12):2187-2192.
11. Fox H, Elston CW. Pathology of the placenta. Major Probl Pathol. 1978;7:1-491.
12. American Institute of Ultrasound in Medicine. AIUM practice guideline for the performance of obstetric ultrasound examinations. J Ultrasound Med. 2013;32(6):1083-1101.
13. Reddy UM, Abuhamad AZ, Levine D, et al. Fetal imaging: executive summary of a joint Eunice Kennedy Shriver National Institute of Child Health and Human Development, Society for Maternal-Fetal Medicine, American Institute of Ultrasound in Medicine, American College of Obstetricians and Gynecologists, American College of Radiology, Society for Pediatric Radiology, and Society of Radiologists in Ultrasound Fetal Imaging workshop. Obstet Gynecol. 2014;123(5):1070-1082.
14. Doubilet PM, Benson CB. "Appearing twin": undercounting of multiple gestations on early first trimester sonograms. J Ultrasound Med. 1998;17(4):199-203.
15. Landy H, Weiner S, Corson S, et al. The "vanishing twin": ultrasonographic assessment of fetal disappearance in the first trimester. Am J Obstet Gynecol. 1986;155(1):14-19.
16. Benson CB, Doubilet PM, Laks MP. Outcome of twin gestations following sonographic demonstration of two heart beats in the first trimester. Ultrasound Obstet Gynecol. 1993;3(5):343-345.
17. Blickstein I, Perlman S. Single fetal death in twin gestations. J Perinat Med. 2013;41(1):65-69.
18. Pinborg A. Consequences of vanishing twins in IVF/ICSI pregnancies. Hum Reprod. 2005;20(10):2821-2829.
19. Bromley B, Benacerraf B. Using the number of yolk sacs to determine amnionicity in early first trimester monochorionic twins. J Ultrasound Med. 1995;14(6):415-419.
20. Corbett SL, Shmorgun D. Yolk sac number does not predict reliably amnionicity in monochorionic twin pregnancies: a case of a monochorionic monoamniotic twin pregnancy with two distinct yolk sacs on early first-trimester ultrasound. Ultrasound Obstet Gynecol. 2012;39(5):607-608.
21. Shen O, Samueloff A, Beller U, Rabinowitz R. Number of yolk sacs does not predict amnionicity in early first-trimester monochorionic multiple gestations. Ultrasound Obstet Gynecol. 2005;27(1):53-55.
22. Stenhouse E, Hardwick C, Maharaj S, et al. Chorionicity determination in twin pregnancies: how accurate are we? Ultrasound Obstet Gynecol. 2002;19(4):350-352.
23. Wan J, Schrimmer D, Taché V, et al. Current practices in determining amnionicity and chorionicity in multiple gestations. Prenat Diagn. 2011;31(1):125-130.
24. Filly RA, Goldstein RB, Callen PW. Monochorionic twinning: sonographic assessment. AJR Am J Roentgenol. 1990;154(3):459-469.
25. Bessis R, Papiernik E. Echographic imagery of amniotic membranes in twin pregnancies. Prog Clin Biol Res. 1981;69A:183-187.
26. Finberg HJ. The "twin peak" sign: reliable evidence of dichorionic twinning. J Ultrasound Med. 1992;11(11):571-577.
27. Sepulveda W, Sebire NJ, Hughes K, et al. The lambda sign at 10-14 weeks of gestation as a predictor of chorionicity in twin pregnancies. Ultrasound Obstet Gynecol. 1996;7(6):421-423.
28. Magann E, Doherty D, Ennen C, et al. The ultrasound estimation of amniotic fluid volume in diamniotic twin pregnancies and prediction of peripartum outcomes. Am J Obstet Gynecol. 2007;196(6):570.e1-570.e6.
29. Bibbo C, Clapp M, Rosenthal E, et al. The relationship between intertwin membrane separation and pregnancy outcome. Obstet Gynecol. 2015;126(5):994-998.
30. Klatt J, Kuhn A, Baumann M, Raio L. Single umbilical artery in twin pregnancies. Ultrasound Obstet Gynecol. 2012;39(5):505-509.
31. Ebbing C, Kiserud T, Johnsen S, et al. Prevalence, risk factors and outcomes of velamentous and marginal cord insertions: a population-based study of 634,741 pregnancies. PLoS ONE. 2013;8(7):e70380.
32. Yonetani N, Ishii K, Kawamura H, et al. Significance of velamentous cord insertion for twin-twin transfusion syndrome. Fetal Diagn Ther. 2015;38(4):276-281.
33. Hubinont C, Lewi L, Bernard P, et al. Anomalies of the placenta and umbilical cord in twin gestations. Am J Obstet Gynecol. 2015;213(4):S91-S102.

34. Jauniaux E, Ben-Ami I, Maymon R. Do assisted-reproduction twin pregnancies require additional antenatal care? Reprod Biomed Online. 2013;26(2):107-119.
35. De Paepe ME, Shapiro S, Hanley LC, et al. Correlation between cord insertion type and superficial choriovasculature in diamniotic-monochorionic twin placentas. Placenta. 2011;32(11):901-905.
36. Gezer A, Rashidova M, Güralp O, Öçer F. Perinatal mortality and morbidity in twin pregnancies: the relation between chorionicity and gestational age at birth. Arch Gynecol Obstet. 2011;285(2):353-360.
37. Smith N, Wilkins-Haug L, Santolaya-Forgas J, et al. Contemporary management of monochorionic diamniotic twins: outcomes and delivery recommendations revisited. Am J Obstet Gynecol. 2010;203(2):133.e1-133.e6.
38. Roqué H, Gillen-Goldstein J, Funai E, et al. Perinatal outcomes in monoamniotic gestations. J Matern Fetal Neonatal Med. 2003;13(6):414-421.
39. Kristiansen MK, Joensen BS, Ekelund CK, et al. Perinatal outcome after first-trimester risk assessment in monochorionic and dichorionic twin pregnancies: a population-based register study. BJOG. 2015;122(10):1362-1369.
40. Glinianaia SV, Obeysekera MA, Sturgiss S, Bell R. Stillbirth and neonatal mortality in monochorionic and dichorionic twins: a population-based study. Hum Reprod. 2011;26(9):2549-2557.
41. D'Antonio F, Khalil A, Dias T, Thilaganathan B. Early fetal loss in monochorionic and dichorionic twin pregnancies: analysis of the Southwest Thames Obstetric Research Collaborative (STORK) multiple pregnancy cohort. Ultrasound Obstet Gynecol. 2013;41(6):632-636.
42. McPherson J, Odibo A, Shanks A, et al. Impact of chorionicity on risk and timing of intrauterine fetal demise in twin pregnancies. Am J Obstet Gynecol. 2012;207(3):190.e1-190.e6.
43. Garite T, Clark R, Elliott J, Thorp J. Twins and triplets: the effect of plurality and growth on neonatal outcome compared with singleton infants. Am J Obstet Gynecol. 2004;191(3):700-707.
44. Stirrup OT, Khalil A, D'Antonio F, Thilaganathan B. Fetal growth reference ranges in twin pregnancy: analysis of the Southwest Thames Obstetric Research Collaborative (STORK) multiple pregnancy cohort. Ultrasound Obstet Gynecol. 2014;45(3):301-307.
45. Weissman A, Matanes E, Drugan A. Accuracy of ultrasound in estimating fetal weight and growth discordancy in triplet pregnancies. J Perinat Med. 2016;44(2):223-227.
46. Harper L, Weis M, Odibo A, et al. Significance of growth discordance in appropriately grown twins. Am J Obstet Gynecol. 2013;208(5):393.e1-393.e5.
47. Khalil A, Khan N, Bowe S, et al. Discordance in fetal biometry and Doppler are independent predictors of the risk of perinatal loss in twin pregnancies. Am J Obstet Gynecol. 2015;213(2):222.e1-222.e10.
48. Blickstein I, Kalish R. Birthweight discordance in multiple pregnancy. Twin Res. 2003;6(06):526-531.
49. American College of Obstetricians and Gynecologists and Society for Maternal-Fetal Medicine. ACOG Practice Bulletin No. 144: Multifetal gestations: twin, triplet, and higher-order multifetal pregnancies. Obstet Gynecol. 2014;123(5):1118-1132.
50. Morin L, Lim K. Ultrasound in twin pregnancies. J Obstet Gynaecol Can. 2011;33(6):643-656.
51. Emery S, Bahtiyar M, Dashe J, et al. The North American Fetal Therapy Network consensus statement. Obstet Gynecol. 2015;125(5):1236-1243.
52. Society for Maternal-Fetal Medicine, Simpson LL. Twin-twin transfusion syndrome. Am J Obstet Gynecol. 2013;208(1):3-18.
53. Thorson H, Ramaeker D, Emery S. Optimal interval for ultrasound surveillance in monochorionic twin gestations. Obstet Gynecol. 2011;117(1):131-135.
54. Corcoran S, Breathnach F, Burke G, et al. Dichorionic twin ultrasound surveillance: sonography every 4 weeks significantly underperforms sonography every 2 weeks: results of the Prospective Multicenter ESPRiT Study. Am J Obstet Gynecol. 2015;213(4):551.e1-551.e5.
55. Pessel C, Merriam A, Vani K, et al. Do Doppler studies enhance surveillance of uncomplicated monochorionic diamniotic twins? J Ultrasound Med. 2015;34(4):569-575.
56. DeJesus Allison S, Javitt M, et al. ACR Appropriateness Criteria® Multiple gestations. Ultrasound Q. 2012;28(2):149-155.
57. Sperling L, Kiil C, Larsen LU, et al. Detection of chromosomal abnormalities, congenital abnormalities and transfusion syndrome in twins. Ultrasound Obstet Gynecol. 2007;29(5):517-526.
58. Rustico MA, Baietti MG, Coviello D, et al. Managing twins discordant for fetal anomaly. Prenat Diagn. 2005;25(9):766-771.
59. Chauhan S, Scardo J, Hayes E, et al. Twins: prevalence, problems, and preterm births. Am J Obstet Gynecol. 2010;203(4):305-315.
60. Glinianaia SV, Rankin J, Wright C. Congenital anomalies in twins: a register-based study. Hum Reprod. 2008;23(6):1306-1311.
61. Vink J, Wapner R, D'Alton ME. Prenatal diagnosis in twin gestations. Semin Perinatol. 2012;36(3):169-174.
62. Pettit KE, Merchant M, Machin GA, et al. Congenital heart defects in a large, unselected cohort of monochorionic twins. J Perinatol. 2012;33(6):457-461.
63. Campbell KH, Copel JA, Ozan Bahtiyar M. Congenital heart defects in twin gestations. Minerva Ginecol. 2009;61(3):239-244.
64. Bahtiyar MO, Dulay AT, Weeks BP, et al. Prevalence of congenital heart defects in monochorionic/diamniotic twin gestations: a systematic literature review. J Ultrasound Med. 2007;26(11):1491-1498.
65. American Institute of Ultrasound in Medicine. AIUM practice guideline for the performance of fetal echocardiography. J Ultrasound Med. 2013;32(6):1067-1082.
66. D'Antonio F, Khalil A, Morlando M, Thilaganathan B. Accuracy of predicting fetal loss in twin pregnancies using gestational age-dependent weight discordance cut-offs: analysis of the STORK multiple pregnancy cohort. Fetal Diagn Ther. 2015;38(1):22-28.
67. Ong SSC, Zamora J, Khan KS, Kilby MD. Prognosis for the co-twin following single-twin death: a systematic review. BJOG. 2006;113(9):992-998.
68. Hillman S, Morris R, Kilby M. Co-twin prognosis after single fetal death. Obstet Gynecol. 2011;118(4):928-940.
69. van Klink JM, van Steenis A, Steggerda SJ, et al. Single fetal demise in monochorionic pregnancies: incidence and patterns of cerebral injury. Ultrasound Obstet Gynecol. 2015;45(3):294-300.
70. Nicolini U, Pisoni M, Cela E, Roberts A. Fetal blood sampling immediately before and within 24 hours of death in monochorionic twin pregnancies complicated by single intrauterine death. Am J Obstet Gynecol. 1998;179(3):800-803.
71. Okamura K, Murotsuki J, Tanigawara S, et al. Funipuncture for evaluation of hematologic and coagulation indices in the surviving twin following co-twin's death. Obstet Gynecol. 1994;83(6):975-978.
72. Lewi L, Deprest J, Hecher K. The vascular anastomoses in monochorionic twin pregnancies and their clinical consequences. Am J Obstet Gynecol. 2013;208(1):19-30.
73. Lewi L, Cannie M, Blickstein I, et al. Placental sharing, birthweight discordance, and vascular anastomoses in monochorionic diamniotic twin placentas. Am J Obstet Gynecol. 2007;197(6):587.e1-587.e8.
74. Denbow M, Cox P, Taylor M, et al. Placental angioarchitecture in monochorionic twin pregnancies: relationship to fetal growth, fetofetal transfusion syndrome, and pregnancy outcome. Am J Obstet Gynecol. 2000;182(2):417-426.
75. Fick A, Feldstein V, Norton M, et al. Unequal placental sharing and birth weight discordance in monochorionic diamniotic twins. Am J Obstet Gynecol. 2006;195(1):178-183.
76. Quintero R, Morales W, Allen M, et al. Staging of twin-twin transfusion syndrome. J Perinatol. 1999;19(8):550-555.
77. Saunders NJ, Snijders RJM, Nicolaides KH. Twin-twin transfusion syndrome during the 2nd trimester is associated with small intertwin hemoglobin differences. Fetal Diagn Ther. 1991;6(1-2):34-36.
78. de Villiers SF, Zhao DP, Cohen D, et al. Correlation between veno-venous anastomoses, TTTS and perinatal mortality in monochorionic twin pregnancies. Placenta. 2015;36(5):603-606.
79. de Villiers SF, Slaghekke F, Middeldorp JM, et al. Arterio-arterial vascular anastomoses in monochorionic placentas with and without twin-twin transfusion syndrome. Placenta. 2012;33(8):652-654.
80. Mosquera C, Miller R, Simpson L. Twin-twin transfusion syndrome. Semin Perinatol. 2012;36(3):182-189.
81. Carver A, Haeri S, Moldenhauer J, et al. Monochorionic diamniotic twin pregnancy: timing and duration of sonographic surveillance for detection

of twin-twin transfusion syndrome. J Ultrasound Med. 2011;30(3): 297-301.
82. Senat M-V, Deprest J, Boulvain M, et al. Endoscopic laser surgery versus serial amnioreduction for severe twin-to-twin transfusion syndrome. N Engl J Med. 2004;351(2):136-144.
83. Gebb J, Dar P, Rosner M, Evans M. Long-term neurologic outcomes after common fetal interventions. Am J Obstet Gynecol. 2015;212(4):527.e1-527.e9.
84. Lopriore E, Middeldorp JM, Oepkes D, et al. Twin anemia-polycythemia sequence in two monochorionic twin pairs without oligo-polyhydramnios sequence. Placenta. 2007;28(1):47-51.
85. Lewi L, Jani J, Blickstein I, et al. The outcome of monochorionic diamniotic twin gestations in the era of invasive fetal therapy: a prospective cohort study. Am J Obstet Gynecol. 2008;199(5):514.e1-514.e8.
86. Robyr R, Lewi L, Salomon L, et al. Prevalence and management of late fetal complications following successful selective laser coagulation of chorionic plate anastomoses in twin-to-twin transfusion syndrome. Am J Obstet Gynecol. 2006;194(3):796-803.
87. Mari G, Deter RL, Carpenter RL, et al. Noninvasive diagnosis by Doppler ultrasonography of fetal anemia due to maternal red-cell alloimmunization. Collaborative Group for Doppler Assessment of the Blood Velocity in Anemic Fetuses. N Engl J Med. 2000;342(1):9-14.
88. Mari G. Middle cerebral artery peak systolic velocity for the diagnosis of fetal anemia: the untold story. Ultrasound Obstet Gynecol. 2005;25(4): 323-330.
89. Slaghekke F, Pasman S, Veujoz M, et al. Middle cerebral artery peak systolic velocity to predict fetal hemoglobin levels in twin anemia-polycythemia sequence. Ultrasound Obstet Gynecol. 2015;46(4):432-436.
90. Slaghekke F, Kist WJ, Oepkes D, et al. Twin anemia-polycythemia sequence: diagnostic criteria, classification, perinatal management and outcome. Fetal Diagn Ther. 2010;27(4):181-190.
91. Stritzke A, Thomas S, Somerset D. Placental dichotomy: a hint in twin anemia polycythemia sequence. J Obstet Gynaecol Can. 2014;36(12): 1097-1100.
92. Rossi AC, Prefumo F. Perinatal outcomes of twin anemia-polycythemia sequence: a systematic review. J Obstet Gynaecol Can. 2014;36(8): 701-707.
93. Moore T, Gale S, Benirschke K. Perinatal outcome of forty-nine pregnancies complicated by acardiac twinning. Am J Obstet Gynecol. 1990;163(3): 907-912.
94. Peeters S, Devlieger R, Middeldorp J, et al. Fetal surgery in complicated monoamniotic pregnancies: case series and systematic review of the literature. Prenat Diagn. 2014;34(6):586-591.
95. Tan TYT, Sepulveda W. Acardiac twin: a systematic review of minimally invasive treatment modalities. Ultrasound Obstet Gynecol. 2003;22(4): 409-419.
96. Rodeck C, Deans A, Jauniaux E. Thermocoagulation for the early treatment of pregnancy with an acardiac twin. N Engl J Med. 1998;339(18): 1293-1295.
97. Rossi AC, Prefumo F. Impact of cord entanglement on perinatal outcome of monoamniotic twins: a systematic review of the literature. Ultrasound Obstet Gynecol. 2013;41(2):131-135.
98. Aurioles-Garibay A, Hernandez-Andrade E, Romero R, et al. Presence of an umbilical artery notch in monochorionic/monoamniotic twins. Fetal Diagn Ther. 2014;36(4):305-311.
99. Baxi L, Walsh C. Monoamniotic twins in contemporary practice: a single-center study of perinatal outcomes. J Matern Fetal Neonatal Med. 2010;23(6):506-510.
100. Hack K, Derks J, Schaap A, et al. Perinatal outcome of monoamniotic twin pregnancies. Obstet Gynecol. 2009;113(2 Pt 1):353-360.
101. Heyborne K, Porreco R, Garite T, et al. Improved perinatal survival of monoamniotic twins with intensive inpatient monitoring. Am J Obstet Gynecol. 2005;192(1):96-101.
102. Van Mieghem T, De Heus R, Lewi L, et al. Prenatal management of monoamniotic twin pregnancies. Obstet Gynecol. 2014;124(3):498-506.
103. Spitz L. Conjoined twins. Prenat Diagn. 2005;25(9):814-819.
104. Spencer R. Anatomic description of conjoined twins: a plea for standardized terminology. J Pediatr Surg. 1996;31(7):941-944.
105. Winkler N, Kennedy A, Byrne J, Woodward P. The imaging spectrum of conjoined twins. Ultrasound Q. 2008;24(4):249-255.
106. Kingston C, McHugh K, Kumaradevan J, et al. Imaging in the preoperative assessment of conjoined twins. Radiographics. 2001;21(5):1187-1208.

CHAPTER 33

The Fetal Face and Neck

Ana P. Lourenco and Judy A. Estroff

SUMMARY KEY POINTS

- Ear and eye anomalies often accompany abnormalities of the skull and face.
- Abnormalities of fetal head size and shape may be associated with various syndromes and chromosomal anomalies.
- Hypoplastic or absent nasal bone may be seen in fetuses with trisomy 21.
- Cleft lip may be associated with cleft palate, and detailed description of the cleft is important to accurately counsel parents, predict postnatal outcome, and anticipate type of treatment.
- Isolated cleft palate is rarely diagnosed on prenatal ultrasound and is often associated with micrognathia and a variety of syndromes.
- Micrognathia is best assessed on sagittal midline views, can be associated with a variety of syndromes, and may lead to difficulties with feeding and airway management.
- Fetal neck masses are uncommon, and include lymphatic malformations, teratomas, hemangiomas, and thyromegaly. Evaluation of the fetal airway in relation to the mass is critical for delivery planning.

CHAPTER OUTLINE

EMBRYOLOGY AND DEVELOPMENT
Face
Neck
SONOGRAPHY OF THE NORMAL FETAL FACE
ABNORMALITIES OF THE HEAD
Abnormal Size
Abnormal Shape
Craniosynostosis
Wormian Bones
Forehead Abnormalities
Encephaloceles
ORBIT ABNORMALITIES
Hypotelorism
Hypertelorism
Microphthalmia and Anophthalmia
Coloboma
Dacryocystocele
Congenital Cataracts
EAR ABNORMALITIES
MIDFACE ABNORMALITIES
Hypoplasia
Absent Nasal Bone
Other Nasal Abnormalities
Cleft Lip and Palate
Unilateral Cleft Lip or Palate
Bilateral Cleft Lip or Palate
Median Cleft Lip or Palate
Unusual Facial (Tessier) Clefts
Isolated Cleft of Secondary Palate
LOWER FACE ABNORMALITIES
Macroglossia and Oral Masses
Micrognathia and Retrognathia
SOFT TISSUE TUMORS
NECK ABNORMALITIES
Nuchal Translucency and Thickening
Lymphatic Malformation (Cystic Hygroma)
Cervical Teratoma
Thyromegaly and Goiter
CONCLUSION
Acknowledgments

With technical advances in gray-scale and three-dimensional (3-D) imaging, sonographic evaluation of the fetal face and neck has become a routine part of the second-trimester fetal anatomic survey.[1] An increasing number of craniofacial anomalies are detectable in the first trimester. Abnormalities of the fetal face are particularly important because they are frequently associated with syndromes and chromosomal anomalies. This chapter reviews the embryology and normal development of the fetal face and neck and describes anomalies that can be detected sonographically.

EMBRYOLOGY AND DEVELOPMENT

Face

Fetal face development begins at approximately 4 weeks' gestation and rapidly progresses, with the completion of major events by 8 weeks' gestation (Fig. 33.1). In this complex process, ectoderm, mesoderm, endoderm, and neural crest cells all interact to develop the classic human facial features. Ectoderm surrounds the **stomodeum** (primitive mouth). The paired pharyngeal arches, or **branchial arches,** composed of central mesenchyme with outer

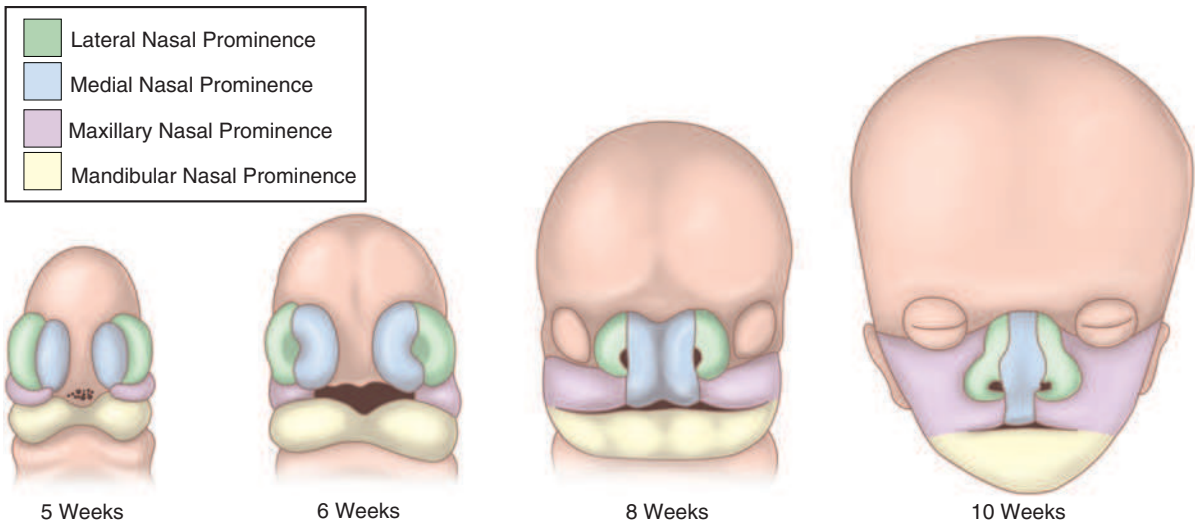

FIG. 33.1 Embryology of the Fetal Face at Gestational Ages 5 Through 10 Weeks. (Courtesy of Andrew S. Phelps, MD.)

ectoderm and inner endoderm coverings, progress to fuse in the midline. **Neural crest cells** give rise to connective tissues of the face (cartilage, bone, ligaments).

Five main tissue buds (called **prominences**) form the fetal face. The **frontonasal** prominence forms the forehead and dorsum apex of the nose. The **lateral nasal** prominences form the nasal ala. The **medial nasal** prominences form the nasal septum. **Maxillary** prominences form the upper cheeks and most of the upper lip. **Mandibular** prominences form the lower cheeks, lower lip, and chin. The maxillary and mandibular processes are derived from the first branchial arch. The remaining branchial arches go on to form the oropharynx.

During the fourth week of gestation, the frontal prominence forms at the cephalic end of the embryo. The two nasal **placodes** are present on the frontal prominence, and the optic discs are present posterolaterally. In the stomodeum, the buccopharyngeal membrane becomes fenestrated.

The fifth week brings development of nasal pits in the nasal placodes and differentiation of medial and lateral nasal prominences. The lens vesicles invaginate within the optic discs, and the caudal end of the medial nasal prominences begins to fuse with the maxillary prominences.

During the sixth week, six **auricular hillocks** (mesenchymal swellings) form and will become the pinna of the ears. Auricular pits may arise when these nodules do not fuse completely. Medial and lateral nasal prominences fuse, and the maxillary prominences begin to form the upper jaw. The nasal septum forms as the medial nasal prominences join in the midline. The edges of the optic fissures fuse, and the hyaloid vessels are present in the center of the optic stalk. These vessels will eventually form the retinal artery and vein.

By the seventh week, the tip of the nose is visible in profile, and the pinna of the ears is taking shape. The central axis of the nose and philtrum are formed as fusion of the medial nasal prominences is completed. Eyelids become prominent.[2-5] By the end of the eighth week, the developing eye is up to 2 mm in diameter.[6]

Neck

Development of the fetal neck is similarly complex, with extensive embryologic events contributing to development of vascular, neurologic, musculoskeletal, lymphatic, and endocrine systems. The laryngotracheal groove forms during the fourth week of gestation along the floor of the primitive mouth. After evagination of this groove, the laryngotracheal diverticulum forms. The distal end forms the lung bud. The endoderm of this diverticulum forms the epithelium of the larynx and trachea. The endothelium of the larynx proliferates and temporarily occludes its lumen. Recanalization occurs by the tenth gestational week, with formation of the laryngeal ventricle, vocal folds, and vestibular folds. The fourth and sixth pharyngeal arches form the surrounding cartilage and muscles.[2-4]

At 4 to 6 weeks' gestation, right and left jugular lymph sacs develop as diverticula of the subclavian veins. Lymphatic capillaries permeate the body and drain into these sacs. Abnormal connections between the lymphatic sacs and venous system are thought to contribute to lymphatic malformation and thickened nuchal translucency (NT) in the first trimester, as well as a thickened nuchal fold in the second trimester.[7]

SONOGRAPHY OF THE NORMAL FETAL FACE

Sonographic evaluation of the fetal face is part of the routine anatomic survey in midpregnancy, but little is actually required. According to the American Institute of Ultrasound in Medicine 2013 practice guidelines, only visualization of the fetal upper lip is mandatory during an anatomic survey.[1] Although not required, it is possible to obtain exquisite multiplanar two-dimensional (2-D), 3-D, and four-dimensional (4-D) views of the fetal face with state-of-the-art equipment.[8] Profile and 3-D[9] views (Fig. 33.2A) are helpful, especially when a true coronal view cannot be obtained because of fetal position. Sagittal 3-D volumes of the fetal face can often be obtained in these situations, and the

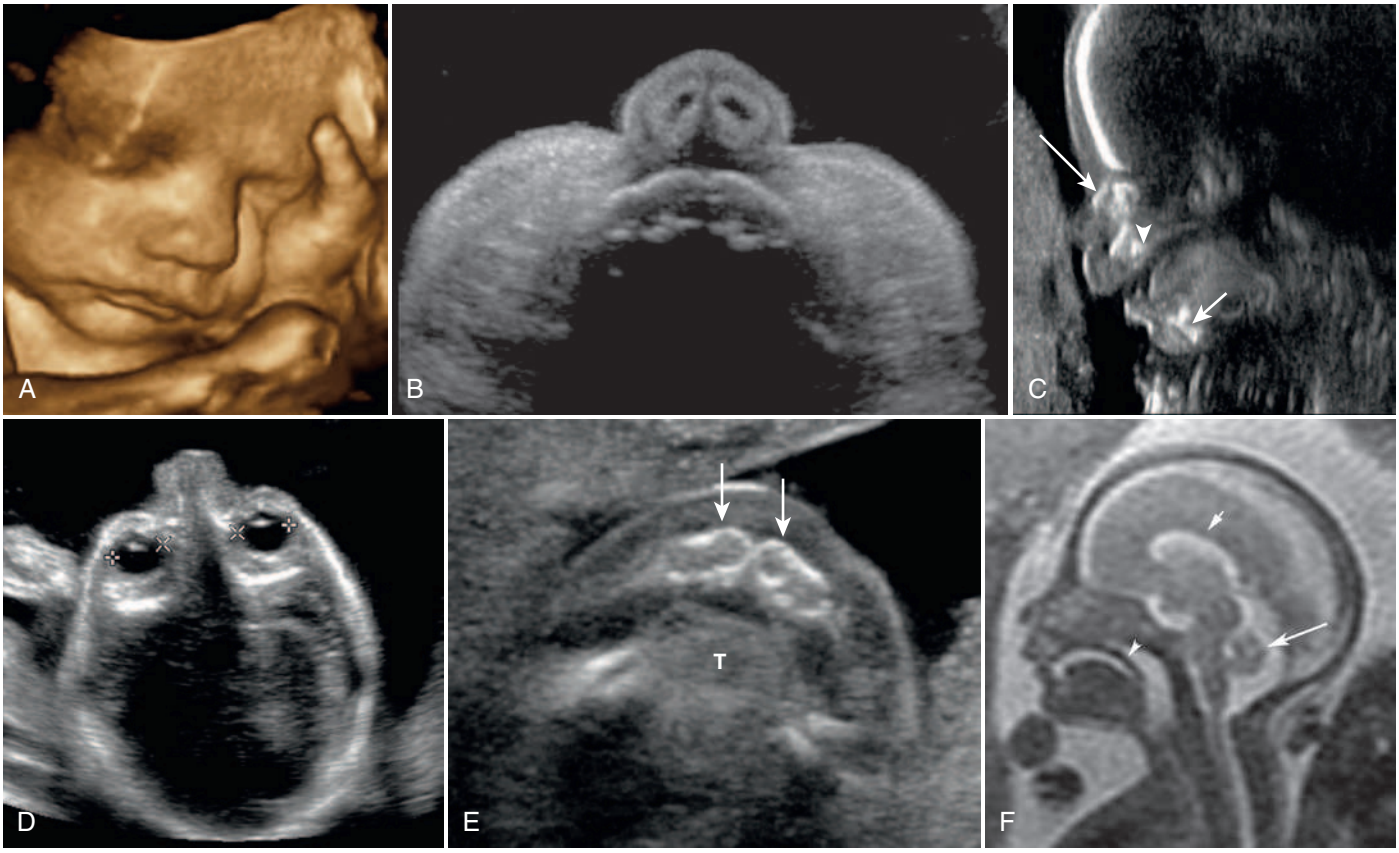

FIG. 33.2 Normal Fetal Face. (A) Three-dimensional (3-D) sonogram of a normal 30-week fetus. **(B)** Nose and lips. Coronal sonogram of normal nostrils and maxillary teeth of a different fetus at 33 weeks' gestation. **(C)** Profile of the face of a 17-week fetus shows a normal nasal bone *(long arrow),* maxilla *(arrowhead),* and mandible *(short arrow).* **(D)** Normal orbits in axial view (*cursors:* +, outer orbital distance; x, inner orbital distance). **(E)** Normal maxilla. Axial view of anterior aspect of the maxilla in a 17-week fetus shows the tongue *(T)* and tooth buds in the alveolus *(arrows).* **(F)** Sagittal T2-weighted magnetic resonance image of a normal fetal face at 27 weeks' gestation shows normal midline structures, such as corpus callosum *(short arrow),* cerebellar vermis *(long arrow),* and secondary palate *(arrowhead).*

image can then be rotated to show the upper lip and palate clearly. Coronal (see Fig. 33.2B) and axial views of the fetal nose and lips are obligatory in screening for fetal cleft lip.

The sagittal **facial profile** view is acquired whenever possible and should demonstrate the presence and normal configuration of the nasal bone, lips, chin, and forehead (see Fig. 33.2C). Three-dimensional volumes[10-13] can frequently be obtained and can be helpful for characterizing abnormalities. Axial views of the orbits can be obtained to verify that both globes are present, of normal size, and at a normal distance apart (see Fig. 33.2D). Axial images of the maxilla and alveolar ridge can be obtained to determine if a cleft primary palate is present (see Fig. 33.2E). The palate separates the nasal cavity from the oral cavity. The **secondary palate** is difficult to visualize on 2-D sonography but may be evaluated with special 3-D sonographic views[14-16] and is often readily visible on midline sagittal and coronal fetal magnetic resonance imaging (MRI; see Fig. 33.2F).

Images of the **fetal neck** are obtained in sagittal, axial, and coronal planes to evaluate the cervical spine and airway and to assess for masses (Fig. 33.3). The neck should also be evaluated for abnormal positioning, such as hyperextension, which can be present with anterior neck masses such as an enlarged thyroid or cervical teratoma. Thickening of the nuchal fold is evaluated at the second-trimester survey and is measured in the suboccipital bregmatic plane, where notable landmarks include the cavum septum pellucidum, cerebral peduncles, cerebellar hemispheres, and cisterna magna.

ABNORMALITIES OF THE HEAD

Abnormal Size

The fetal head is typically oval in configuration, and in this case, measurements of biparietal diameter (BPD) and head circumference will give similar estimates of gestational age. If sonographic head measurements are three standard deviations (SDs) below the mean, microcephaly is diagnosed.[17] If the measurements are greater than 3 SDs above the mean, macrocephaly is suggested.[5] Abnormalities of head size are important. **Microcephaly** may be associated with abnormalities of brain development and often leads to poor neurologic outcome. **Macrocephaly** may have a benign cause, such as a family history of a large head, or pathologic

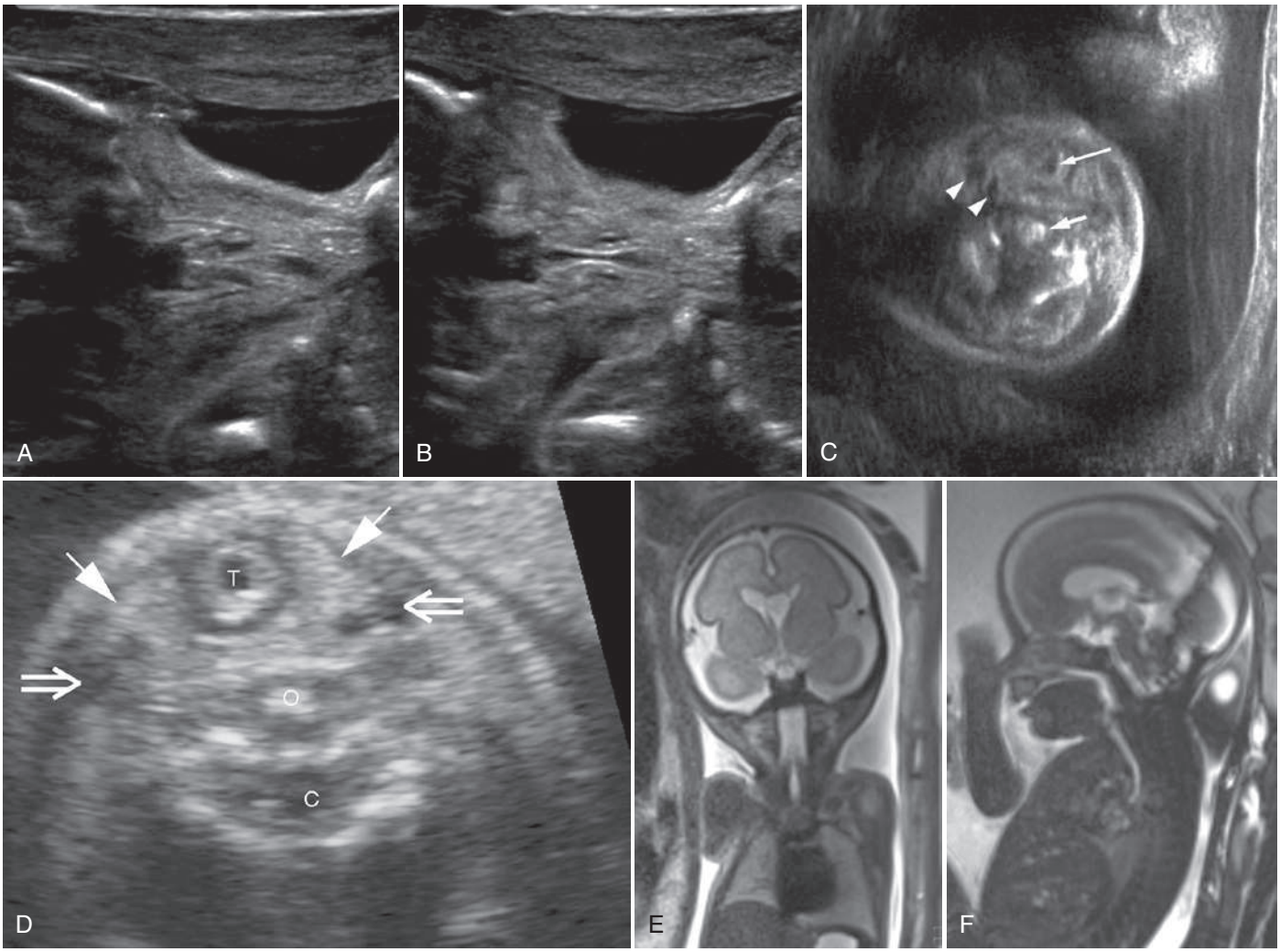

FIG. 33.3 Normal Neck. (A) Coronal sonogram of 21-week fetus showing pyriform sinuses, closed glottis, and subglottic trachea. **(B)** Coronal view showing open glottis. **(C)** Axial view of the neck showing carotid and jugular vessels *(arrowheads),* trachea *(long arrow),* and vertebral body *(short arrow).* **(D)** Axial view of neck shows thyroid *(arrows).* The carotids medially and the jugular veins laterally *(open arrows)* are posterior to the thyroid. The trachea *(T)* is in the midline, and behind it a vertebral body with a small central developing ossification center *(O).* The spinal cord *(C)* is in the vertebral arch. **(E)** and **(F)** Magnetic resonance imaging coronal **(E)** and sagittal **(F)** views of normal glottis, vocal cords, and subglottic trachea in a different, 27-week fetus.

causes such as underlying brain maldevelopment or injury or, rarely, a space-occupying lesion. If the fetal head is sufficiently large, cephalopelvic disproportion can occur at delivery, leading to failure of labor to progress and the need for cesarean delivery.

Abnormal Shape

Abnormal head shape takes many forms. An abnormally long and narrow (oblong) cranium is described as **dolichocephaly** and is more frequently seen in fetuses in breech position and in the setting of oligohydramnios. An abnormally round head is termed **brachycephaly,** which may be caused by premature fusion of the coronal sutures. A **lemon-shaped skull,** with indentation of the frontal bones, is often seen in association with open neural tube defects and the Chiari II malformation of the hindbrain, but it may also be seen in normal fetuses[18,19] (Fig. 33.4). A **strawberry-shaped skull**—flattening of the occiput and narrowing of the bifrontal portion of the cranium—may be seen in association with trisomy 18.[20] A **cloverleaf-shaped skull** is seen with some dwarfs, especially **thanatophoric dysplasia,** and in some fetuses with craniosynostosis.

Craniosynostosis

Craniosynostosis describes a heterogeneous group of disorders in which there is premature fusion of one or several of the cranial sutures. Although abnormal head shape may be diagnosed in utero, this diagnosis often does not become evident until after birth. It occurs in about 1 per 2500 births. Recent research suggests that the pathophysiology of craniosynostosis is related to abnormal molecular signaling by fibroblast growth factors,[21-23] leading to

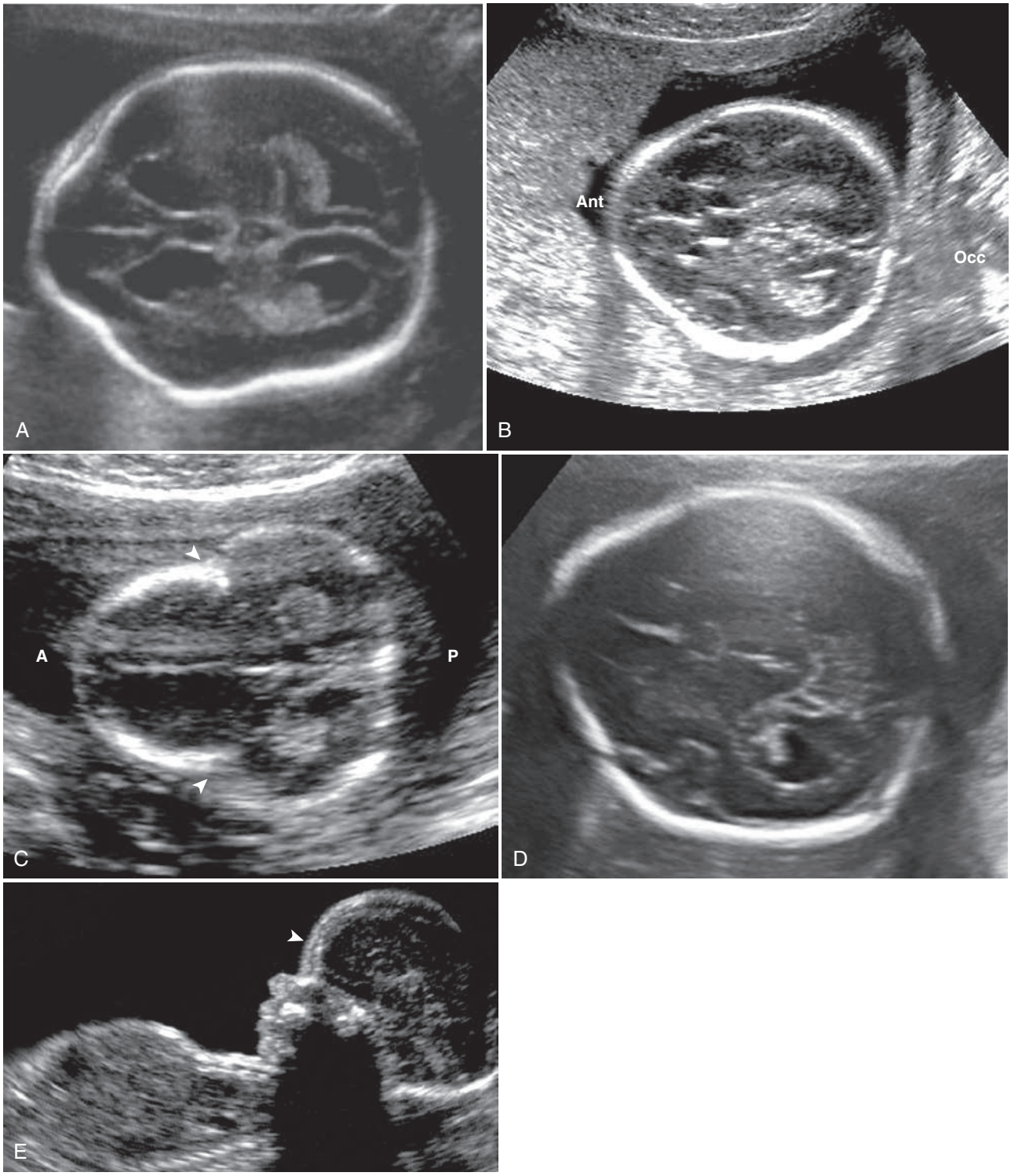

FIG. 33.4 Variety of Abnormal Head Shapes. (A) Lemon-shaped skull in association with neural tube defect. Axial sonogram shows concave deformity of the frontal bone as well as ventriculomegaly at 23 weeks' gestation. **(B) Brachycephaly and strawberry shape** (pointing anteriorly, flat occiput) at 20 weeks in a fetus with trisomy 18. Cephalic index is 96% (normal, 80%). *Ant,* Forehead; *Occ,* occiput. **(C) Craniosynostosis with cloverleaf skull.** Note the trilobite shape seen with craniosynostosis of the coronal *(arrowheads)* and other sutures except the squamosal in this fetus with **thanatophoric dysplasia.** *A,* Anterior; *P,* posterior. **(D) Metopic craniosynostosis.** Axial sonogram of a 27-week fetus with a pointed anterior skull secondary to metopic synostosis. **(E) Frontal bossing** *(arrowhead)* in a fetus with hypochondroplasia. Also note a "saddle nose," with the nasal bone meeting the frontal bone at an abnormal 90 degrees. A small thorax and a protuberant abdomen are present. (**B** and **C** courtesy of Ants Toi, MD.)

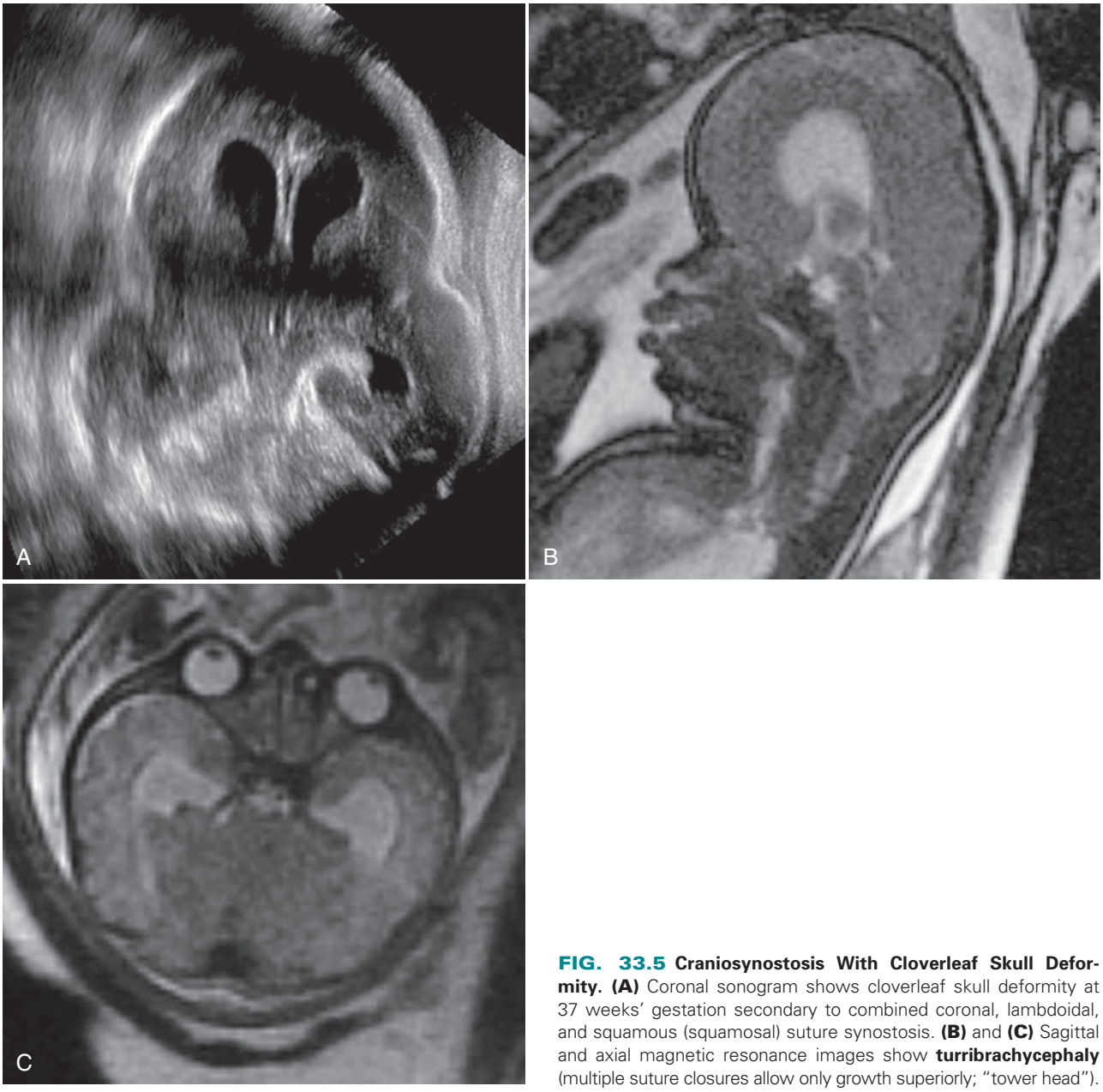

FIG. 33.5 Craniosynostosis With Cloverleaf Skull Deformity. (A) Coronal sonogram shows cloverleaf skull deformity at 37 weeks' gestation secondary to combined coronal, lambdoidal, and squamous (squamosal) suture synostosis. **(B)** and **(C)** Sagittal and axial magnetic resonance images show **turribrachycephaly** (multiple suture closures allow only growth superiorly; "tower head").

premature closure of cranial sutures (Fig. 33.5). About 85% of cases are isolated and about 15% syndromic. Craniosynostosis is associated with multiple syndromes, including **Apert, Crouzon, Pfeiffer, Antley-Bixler, Beare-Stevenson, Fetter,** and **Carpenter,** as well as **thanatophoric dysplasia.** The abnormal head shapes resulting from craniosynostosis can lead to facial abnormalities, including **hypertelorism, hypotelorism, exorbitism,** and **midface hypoplasia.** Dolichocephaly **(oblong head)** is the most common craniosynostosis condition and results from premature fusion of the sagittal suture. Asymmetrical heads are termed **plagiocephalic.**[24]

When fetal position is favorable, it is possible to trace the sutures sonographically and to evaluate their patency using high-frequency linear array probes.

Classification of Skull Deformities Based on Sutures Involved

Dolichocephaly/scaphocephaly: sagittal suture; most common synostosis
Anterior plagiocephaly: one coronal suture
Posterior plagiocephaly: one lambdoid suture
Brachycephaly: bilateral coronal suture; second most common synostosis
Trigonocephaly: metopic suture
Oxycephaly/turricephaly: all skull sutures and sutures at base of skull
Cloverleaf (kleeblattschädel): all but squamous (squamosal) suture

Prenatal diagnosis can be difficult; fetuses can appear normal in midtrimester but show changes in late pregnancy, when normal physiologic molding can be a confounder. In at-risk cases, head shape changes have been seen as early as 12 weeks. The fused sutures can be detected as absence of the sonolucent space normally seen between skull bones. The loss of hypoechoic suture appearance lags shape changes by 4 to 16 weeks. Three-dimensional multiplanar and surface rendering are helpful. Associated anomalies can allow differentiation among types.[25-27]

Additional problems can arise from the cranial deformity, including intracranial hypertension, obstructive apnea, proptosis, visual loss, dental malocclusion, and intellectual impairment. Learning disorders have been observed in 47% of school-age children.[26]

Fetuses prenatally suspected to have craniosynostosis should undergo detailed neurologic and anatomic sonography. MRI may be helpful. Postnatally, computed tomography (CT) surface rendering helps confirm the diagnosis and is needed for surgical treatment planning. Family history and molecular analysis for *FGFR* and *TWIST* mutations can help. Multidisciplinary counseling including craniofacial and neurosurgical specialists is important because therapy can involve molding helmets and surgery.[26,28,29]

Wormian Bones

Wormian bones are ossicles located in the sutures or fontanelles and may be associated with multiple conditions, such as **pyknodysostosis, osteogenesis imperfecta, cleidocranial dysplasia, hypothyroidism,** and **trisomy 21.** Three-dimensional views are particularly useful in the assessment of wormian bones (Fig. 33.6).

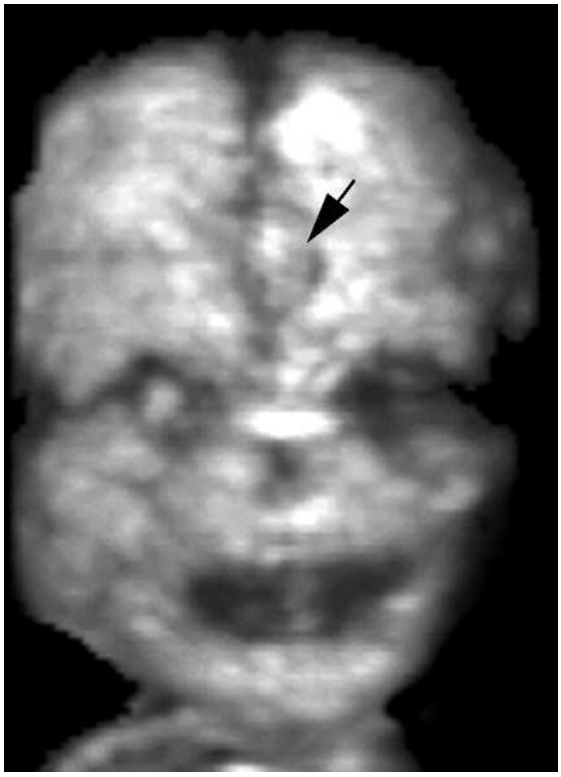

FIG. 33.6 Wormian Bone. An extra ossification center *(arrow)* is identified between the frontal bones of a fetus with trisomy 18.

Differential Diagnosis of Wormian Bones

Cleidocranial dysplasia
Congenital hypothyroidism
Hypophosphatasia
Osteogenesis imperfecta
Trisomy 21
Menkes kinky-hair syndrome
Progeria
Pyknodysostosis

Forehead Abnormalities

The forehead is best evaluated in the sagittal profile view, where the angle between the frontal and nasal bone can be assessed. **Frontal bossing** is abnormal prominence of the frontal bones and is a rare finding on fetal sonography. However, it has been reported in a variety of bony dysplasias and syndromes, including achondroplasia and thanatophoric dysplasia, and in syndromes with associated craniosynostosis.

Wolf-Hirschhorn ($4p^-$) syndrome has an abnormally sloped forehead, the "Greek warrior facies" (Fig. 33.7). The forehead can also be sloped in the settings of **microcephaly** and **encephalocele,** in which the forebrain is underdeveloped (Fig. 33.8).

Differential Diagnosis of Frontal Bossing

Achondroplasia
Acromegaly
Basal cell nevus
Cleidocranial dysostosis
Congenital syphilis
Crouzon syndrome
Fetal trimethadione
Pfeiffer syndrome
Russell-Silver syndrome
Thanatophoric dysplasia

Encephaloceles

An encephalocele or **cephalocele** is an abnormal protrusion of the brain and/or meninges through a defect in the skull and is considered a form of **spinal dysraphism.** In the United States and Western Europe, the occiput is the most common location for encephaloceles. Frontoethmoidal encephaloceles are more often found in Southeast Asia. Many encephaloceles are diagnosed during fetal sonography; they appear as abnormal defects in the calvaria with herniation of brain tissue or meninges. Fetal MRI is excellent for evaluating contents of the encephalocele and in assessing the appearance of the intracranial brain parenchyma.

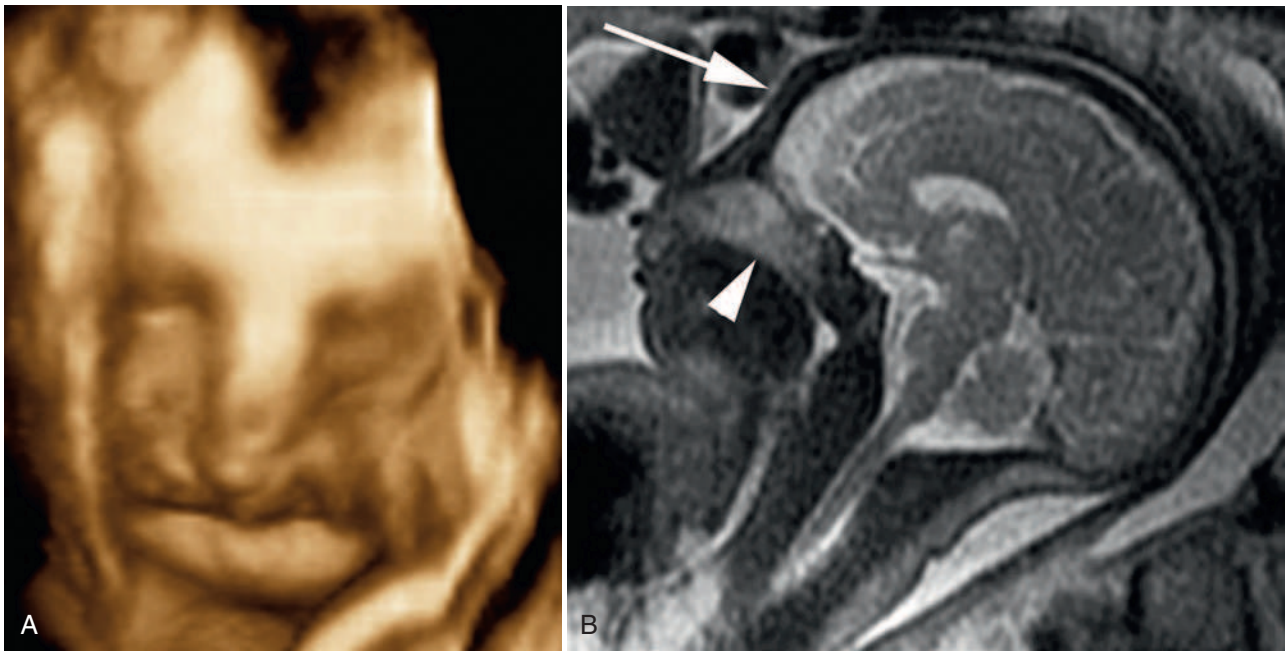

FIG. 33.7 Sloped Forehead in Fetus With Wolf-Hirschhorn Syndrome and Cleft Palate. (A) Coronal three-dimensional and **(B)** sagittal magnetic resonance images show a broad, flat nasal bridge and forehead at 34 weeks' gestation, the so-called "Greek warrior helmet" facies. Note sloped forehead (*arrow* in **[B]**) and absence of the secondary palate (*arrowhead* in **[B]** showing nasopharynx communicating with oropharynx).

Frontal encephaloceles can be seen during sonographic evaluation of the fetal face and are often associated with hypertelorism and midline facial clefting[30] (see Chapter 34).

ORBIT ABNORMALITIES

Sonographic evaluation of the fetal orbits is best obtained in axial or coronal views, in which one can confirm the presence of both orbits, evaluating their sizes and shapes and the distance between them. The sagittal view may help to evaluate abnormal anterior displacement of the globes (**proptosis** or **exorbitism**). The orbits should be symmetrical in size and the outer and inner interorbital distances within a normal range. Detailed nomograms are available for reference[31,32] (Table 33.1).

Hypotelorism

Hypotelorism is defined as an abnormally small distance between the orbits and is often associated with other anomalies[33,34] (Fig. 33.9). **Holoprosencephaly** (Fig. 33.10) can be associated with **cyclopia** (single midline eye with failed development of nose with or without a proboscis [Fig. 33.11]); **ethmocephaly** (hypotelorism with failed development of nose and a proboscis); or **cebocephaly** (hypotelorism and poorly developed nose with a single nostril).

Hypertelorism

Hypertelorism is defined as widely spaced eyes (Figs. 33.12 and 33.13). Given the embryologic development of the eyes and their migration from a lateral position to midline, hypertelorism may result from abnormalities that interfere with this normal migration. Large orbits can result in abnormal orbital measurements; Table 33.1 provides normal diameter of the globes.[35]

Conditions Associated With Hypotelorism

- Abnormalities of the brain
  - Holoprosencephaly
  - Microcephaly
- Chromosomal abnormalities
  - Trisomies 13, 18, and 21
  - Chromosome 5p deletion
- Head shape abnormalities
  - Trigonocephaly
- Syndromes
  - Langer-Giedion syndrome
  - Oculodentodigital dysplasia
  - Nasal maxillary dysostosis (Binder syndrome)
  - Myotonic dystrophy
  - Meckel-Gruber syndrome
  - Williams syndrome

Microphthalmia and Anophthalmia

Abnormally small orbits (microphthalmia) or absent orbits (anophthalmia) are rarely diagnosed on fetal sonography, but, when present, are frequently associated with chromosomal abnormalities or syndromes[36,37] (Fig. 33.14). Fetal karyotype analysis should be considered and a careful search for additional fetal abnormalities undertaken.

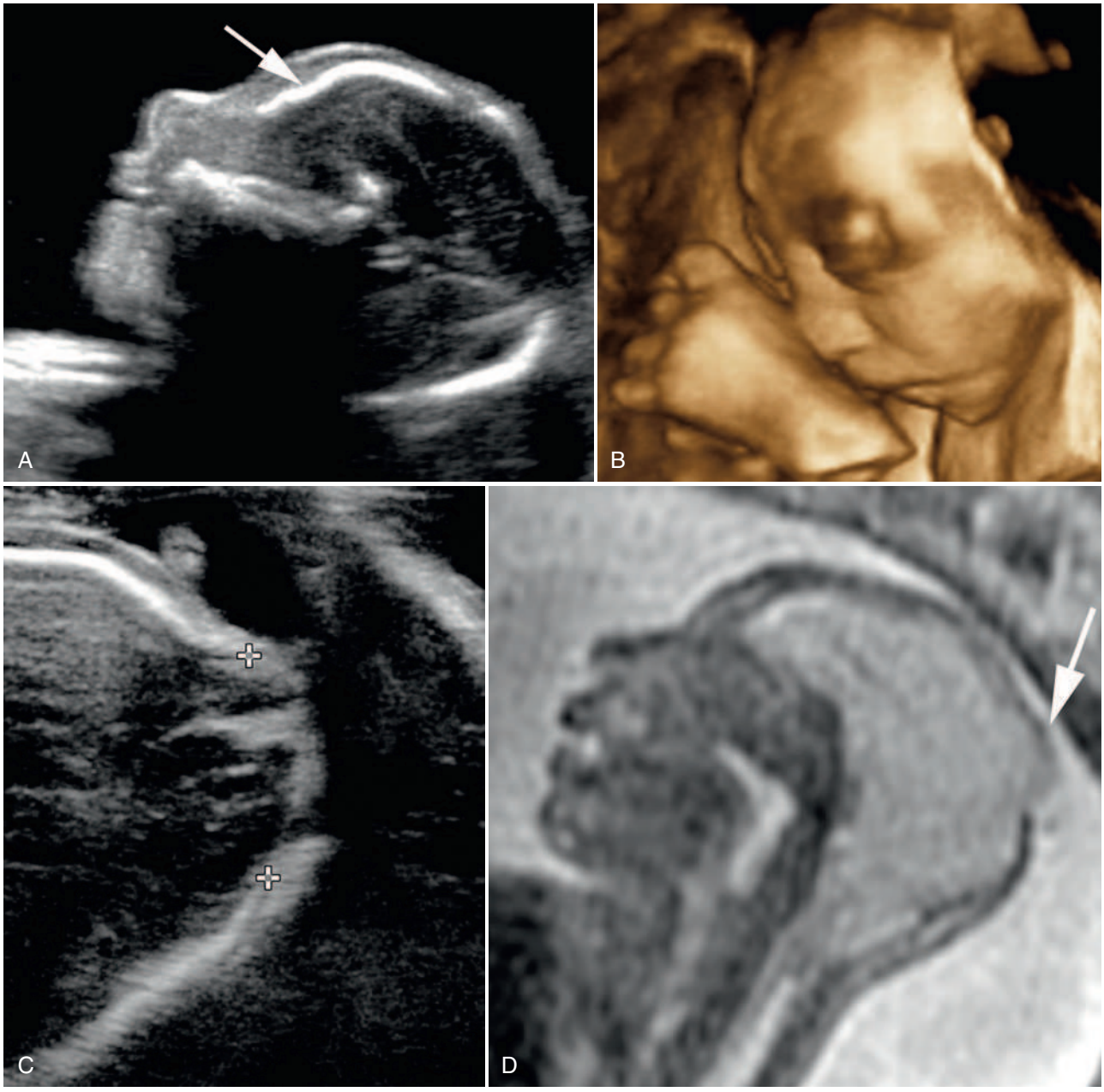

FIG. 33.8 Sloped Forehead in Fetus With Posterior Encephalocele. **(A)** and **(B)** Two-dimensional and three-dimensional sonographic profiles of a 28-week fetus with microcephaly and a small posterior encephalocele. The sloping forehead *(arrow)* is caused by a lack of forebrain development. **(C)** Axial sonogram shows high occipital defect *(calipers)* through which a small amount of dysplastic brain protrudes. **(D)** Sagittal magnetic resonance image shows microcephaly and the high occipital defect in the skull *(arrow)*.

Conditions Associated With Hypertelorism

- Chromosomal abnormalities
  - Trisomy 9p
  - 45,XO
- Single-gene disorders
  - Apert syndrome
  - Crouzon syndrome
  - Noonan syndrome
- Developmental abnormalities
  - Craniosynostosis
  - Anterior encephalocele
  - Median facial cleft
  - Megalencephaly
  - Agenesis of the corpus callosum
  - Orbital teratoma
  - Cleft lip
- Teratogens
  - Dilantin
  - Valproate

TABLE 33.1 Normal Orbital Diameters in the Fetus

Gestational Age (wk)	INNER DIAMETERS (mm)			OUTER DIAMETERS (mm)		
	5th Percentile	50th Percentile	95th Percentile	5th Percentile	50th Percentile	95th Percentile
13	4	7	10	12	16	20
14	5	8	11	14	18	22
15	5	8	11	17	21	25
16	6	9	12	19	23	27
17	7	10	13	21	25	29
18	8	11	14	24	27	31
19	8	11	14	26	30	34
20	9	12	15	28	32	36
21	10	13	16	30	34	38
22	10	13	16	32	36	40
23	11	14	17	33	37	41
24	12	14	17	35	39	43
25	12	15	18	37	41	45
26	13	16	19	39	43	47
27	13	16	19	40	44	48
28	14	17	20	42	46	50
29	14	17	20	43	47	51
30	15	18	21	45	49	52
31	15	18	21	46	50	54
32	16	19	22	47	51	55
33	17	20	23	48	52	56
34	17	20	23	49	53	57
35	18	21	24	50	54	58

Table generated from raw data using two separate quadratic regression models:
Outer diameter = –2.17 + 3.36(Age) – 0.03 (Age^2)
$R^2 = 0.96$, $p < .001$
Inner diameter = –4.14 + 0.94(Age) – 0.007 (Age^2)
$R^2 = 0.84$; $p < .001$
With permission from Trout T, Budorick NE, Pretorius DH, McGahan JP. Significance of orbital measurements in the fetus. J Ultrasound Med. 1994;13(12):937-943.[32]

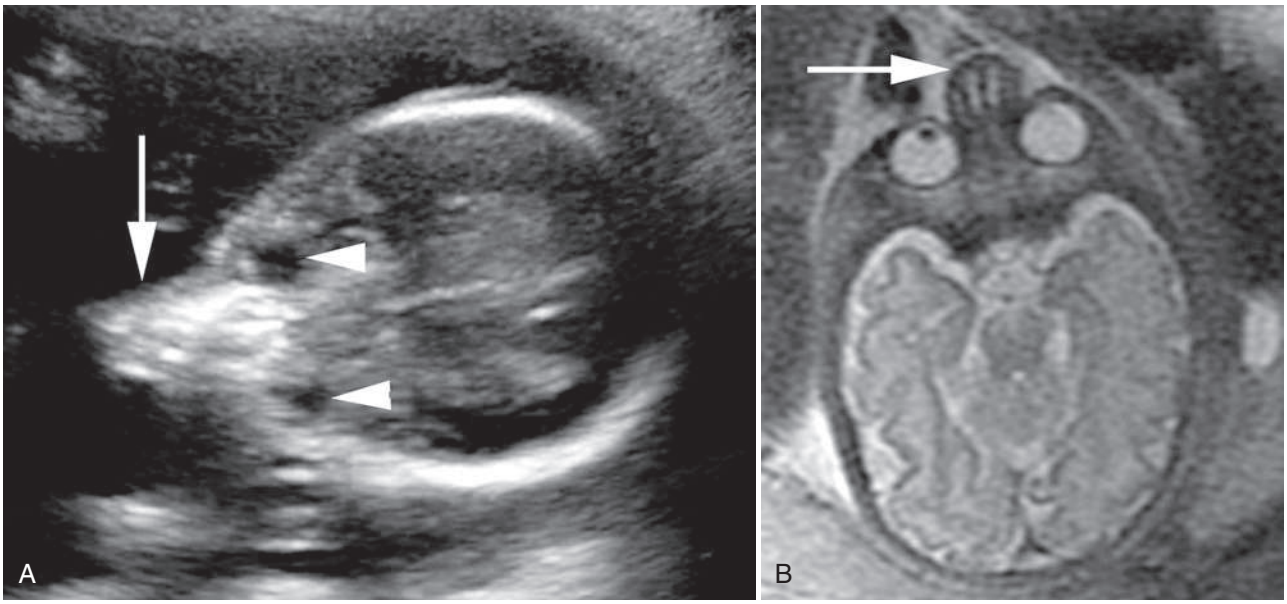

FIG. 33.9 Hypotelorism. (A) Microtia and **hypotelorism.** Axial sonogram shows small orbits *(arrowheads),* close together in the face, and the protuberant maxilla *(arrow).* The fetus also had agnathia and low-set ears (see Fig. 33.29). **(B) Hypotelorism** and abnormal nose *(arrow)* at 35 weeks' gestation. Axial magnetic resonance image of a 35-week fetus shows the relatively small intraorbital distance and an abnormal nose. The fetus was in deep vertex prone position, and the face could not be seen on fetal sonography before magnetic resonance imaging. This fetus was diagnosed postnatally with a complex Tessier cleft.

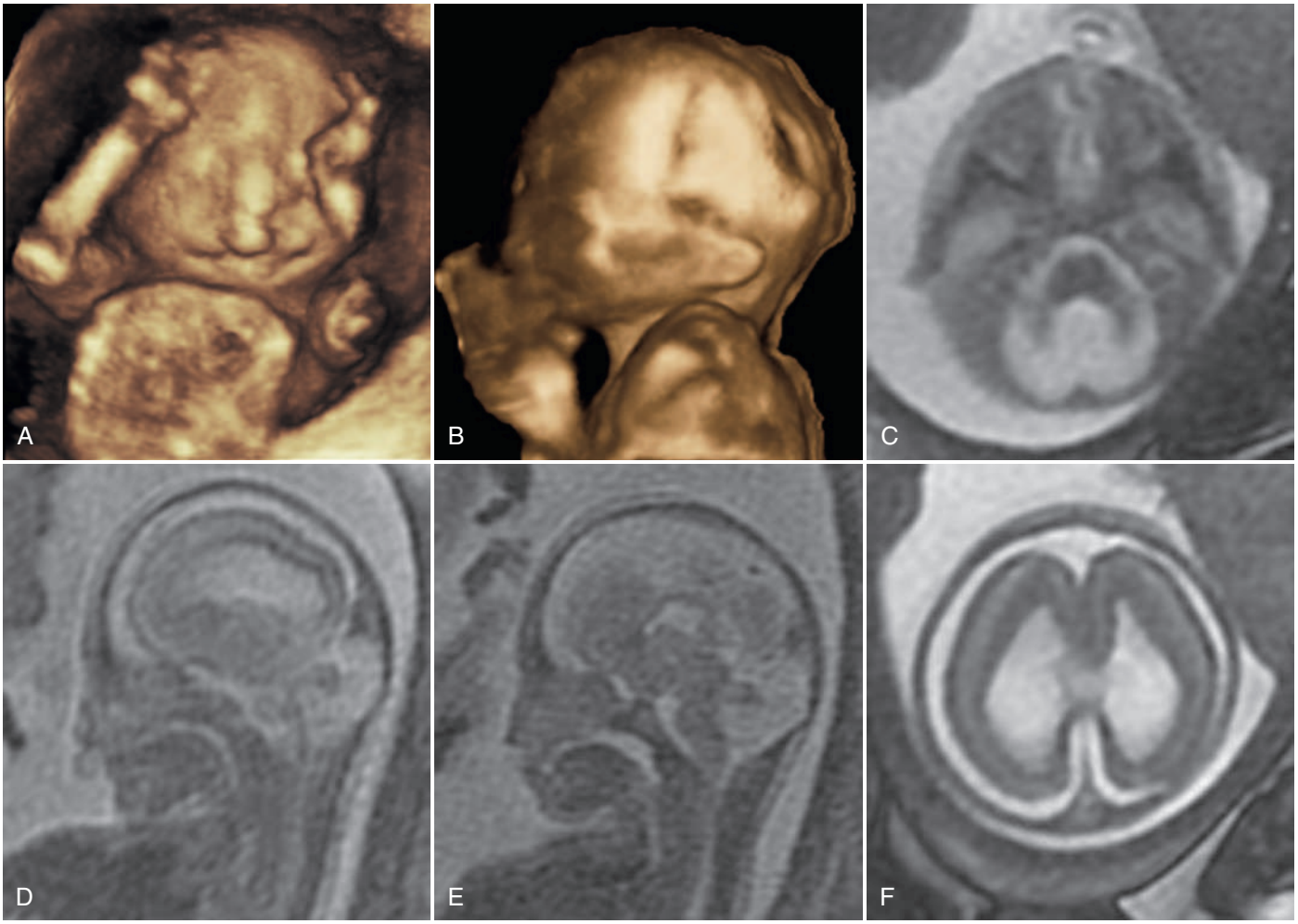

FIG. 33.10 Holoprosencephaly. Nineteen-week fetus with trisomy 13 including multiple anomalies. **(A)** Bilateral cleft lip and palate. **(B)** Low-set ears. **(C)** and **(D)** Proboscis and inferior vermian hypoplasia. **(E)** and **(F)** Semilobar holoprosencephaly.

Coloboma

Coloboma results from incomplete closure of the optic fissure and most often affects the **iris** inferiorly[6] (Fig. 33.15). However, it can affect any structure from the eyelid to the optic nerve or retina. Vision may or may not be affected, depending on the structures affected and the severity of the abnormality. Diagnosis in utero depends on visualization of a focal bulge in the posterior aspect of the globe. In cases where bones cause artifacts in this region and this assessment is crucial, 3-D ultrasound[38] or MRI[39] can be helpful. Coloboma is a rare diagnosis (0.2 per 1000)[40] and may be associated with other anomalies and syndromes, such as **CHARGE syndrome** (*c*oloboma, *h*eart defects, choanal *a*tresia, *r*estriction of growth and development, *g*enital and *e*ar anomalies).

Dacryocystocele

Dacryocystoceles result from obstruction of the **nasolacrimal ducts** (Fig. 33.16). These appear as cystic masses that may contain low-level internal echoes, located inferomedially to the orbit in the expected location of the nasolacrimal duct. There is usually no mass effect on the globe, and there is no increased vascular flow in or around these masses. Diagnosis is usually made after 30 weeks' gestation; the nasolacrimal ducts do not complete canalization until the third trimester.[41] The characteristic appearance and location of dacryocystoceles should allow differentiation from other facial masses, such as **teratomas** (often solid or mixed cystic and solid, and may contain calcifications) or **hemangiomas** (solid, echogenic sonographic appearance, with increased vascular flow). The natural history of dacryocystoceles is variable, with some resolving in utero, or postnatally with conservative measures such as massage and application of warm compresses, and others requiring probing or surgical intervention after birth.[42]

Congenital Cataracts

Congenital cataracts may be diagnosed on prenatal sonography, which will show a rounded echogenic mass in the anterior portion of the globe. Causes of congenital cataracts include genetic disorders, infection, syndromes, and microphthalmia.[5] Some cases are inherited by either autosomal dominant or autosomal recessive transmission. This is a rare disorder, with a reported incidence of approximately 3 per 10,000 births.[43]

Text continued on p. 1148.

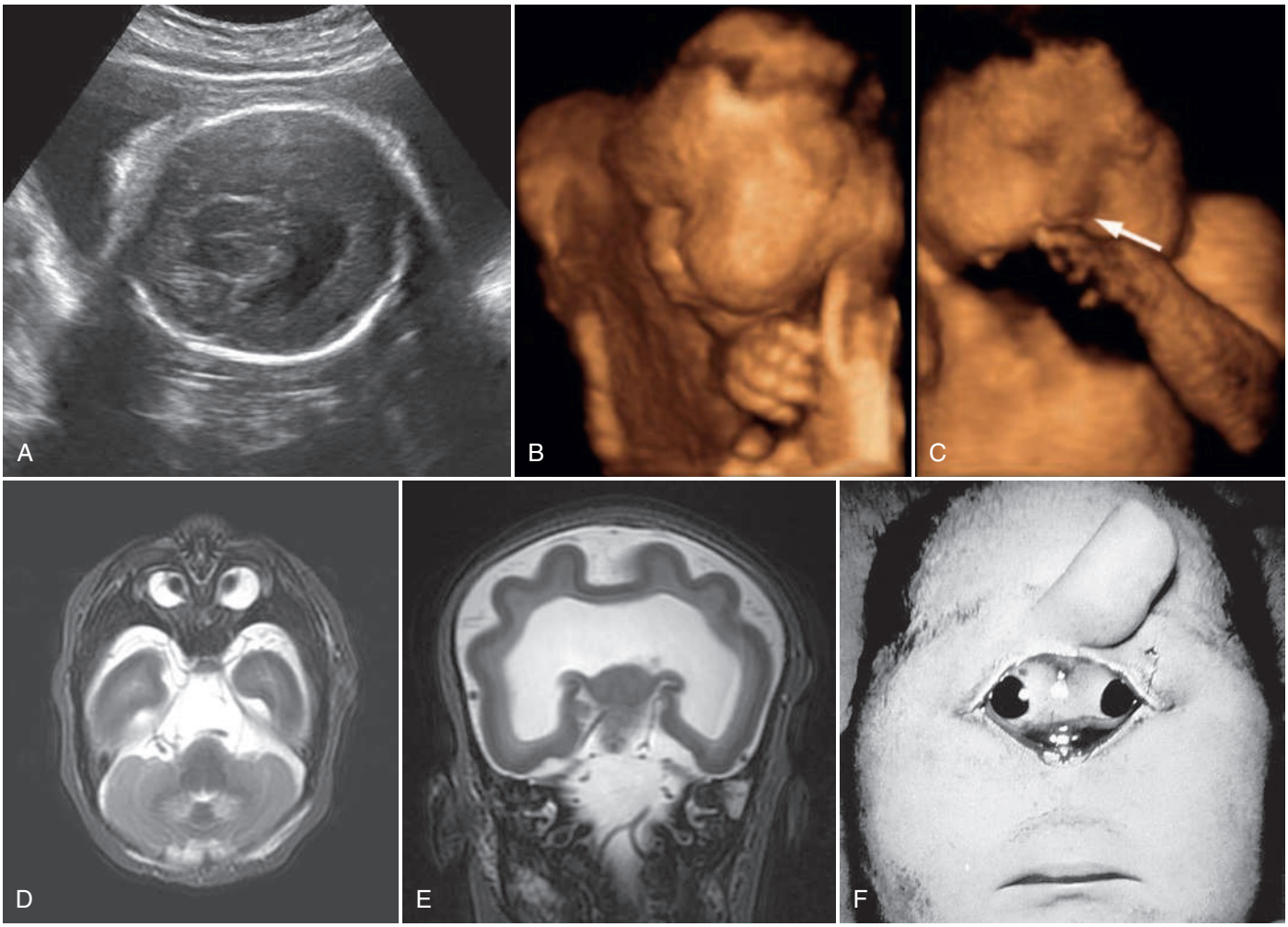

FIG. 33.11 Hypotelorism. Fetal sonography at 33 weeks showing fused thalami and holoprosencephaly on two-dimensional ultrasound **(A)** and hypotelorism, flat midface, and single nostril *(arrow)* on three-dimensional sonography (**B** and **C**). **(D)** and **(E)** Postnatal magnetic resonance imaging shows cyclopia **(D)**, and alobar holoprosencephaly **(E)**. **(F)** Postnatal photograph of a different infant, demonstrating cyclopia with fused globes, supraorbital proboscis, and absent nose. (**A-C** courtesy of Diana Rodrigues, MD, Boston Maternal Fetal Medicine. **F** courtesy of Margot Van Allan, MD, Hospital for Sick Children, Toronto.)

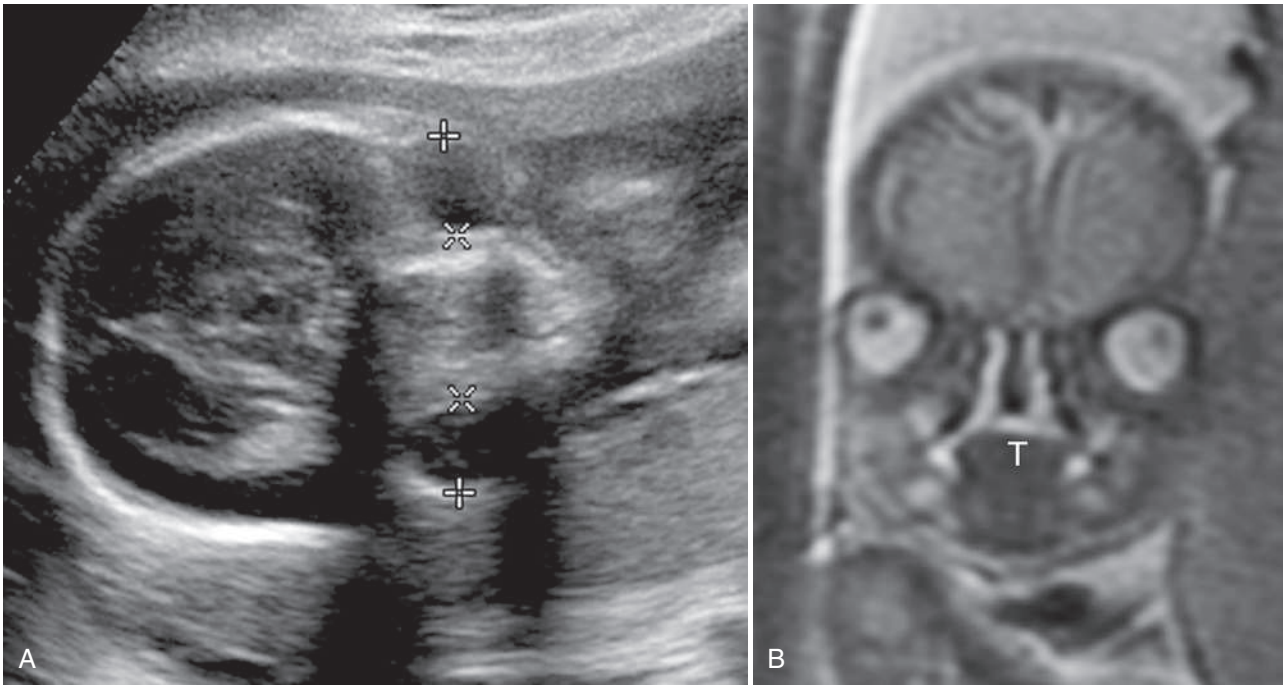

FIG. 33.12 Hypertelorism in Fetus at 25 Weeks With Bilateral Cleft Lip and Palate. (A) Axial sonogram shows hypertelorism (*cursors:* +, outer orbital diameter; x, inner orbital diameter). **(B)** Coronal magnetic resonance image shows hypertelorism and bilaterally absent palatal shelves. Note the absent secondary palate above the tongue *(T)* with communication of the amniotic fluid between the oropharynx and nasopharynx.

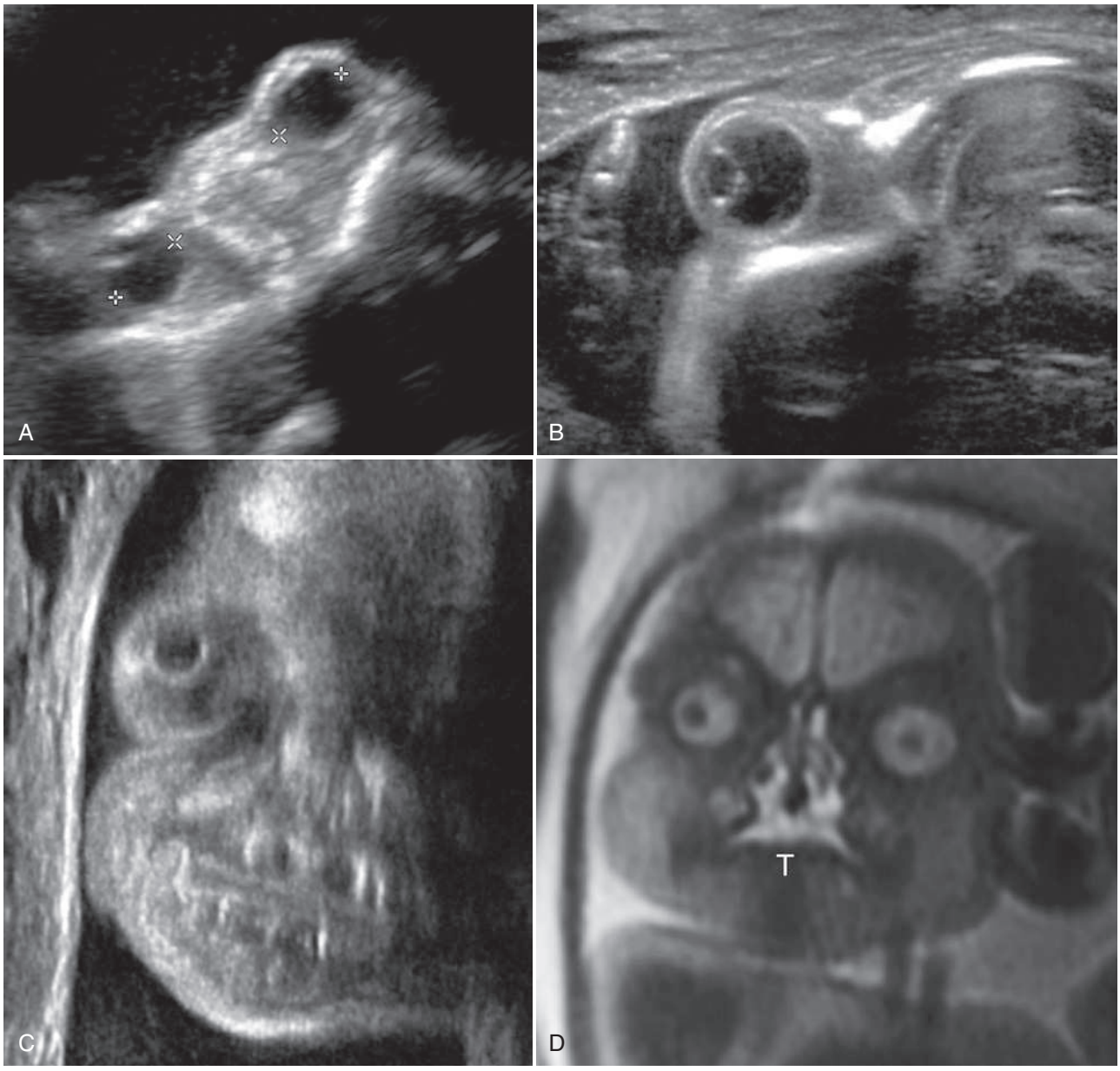

FIG. 33.13 Hypertelorism With Exorbitism in Fetus With Pfeiffer Syndrome. (A) Axial sonogram demonstrates hypertelorism (*cursors:* +, outer orbital diameter; x, inner orbital diameter) at 22 weeks' gestation. The outer orbital diameter was consistent with 25 weeks and 3 days (3 weeks greater than age by dates). **(B)** and **(C)** Axial and coronal sonograms show abnormally protuberant globe (exorbitism). **(D)** Coronal magnetic resonance image shows hypertelorism and bilateral cleft palate. Note the communication of the oropharynx with the nasopharynx, caused by defect in the palate above the tongue *(T).*

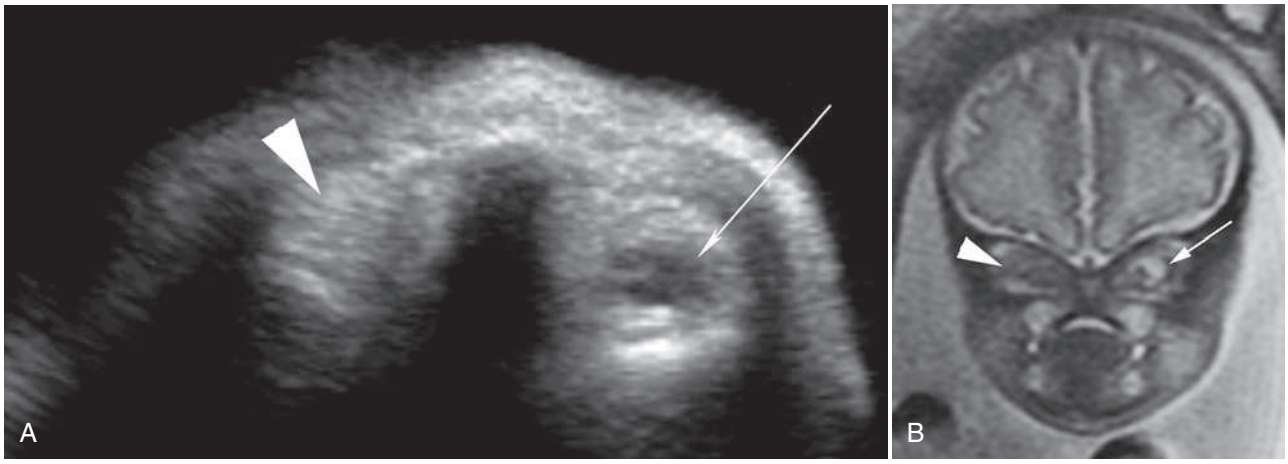

FIG. 33.14 Microphthalmia and Anophthalmia at 34 Weeks' Gestation. (A) Axial sonogram and **(B)** coronal magnetic resonance image show right anophthalmia *(arrowhead)* and left microphthalmia *(arrow).*

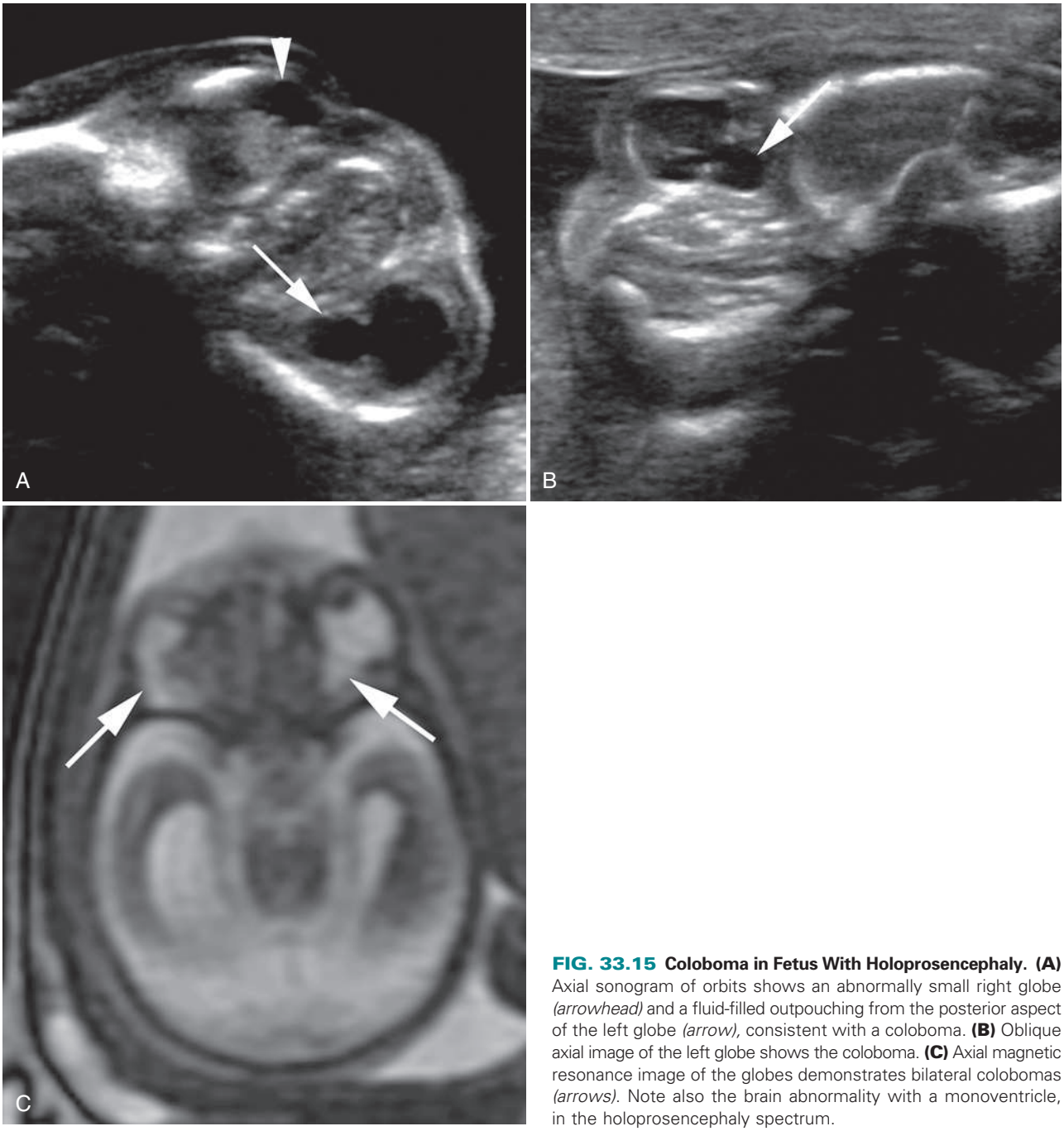

FIG. 33.15 Coloboma in Fetus With Holoprosencephaly. (A) Axial sonogram of orbits shows an abnormally small right globe *(arrowhead)* and a fluid-filled outpouching from the posterior aspect of the left globe *(arrow),* consistent with a coloboma. **(B)** Oblique axial image of the left globe shows the coloboma. **(C)** Axial magnetic resonance image of the globes demonstrates bilateral colobomas *(arrows)*. Note also the brain abnormality with a monoventricle, in the holoprosencephaly spectrum.

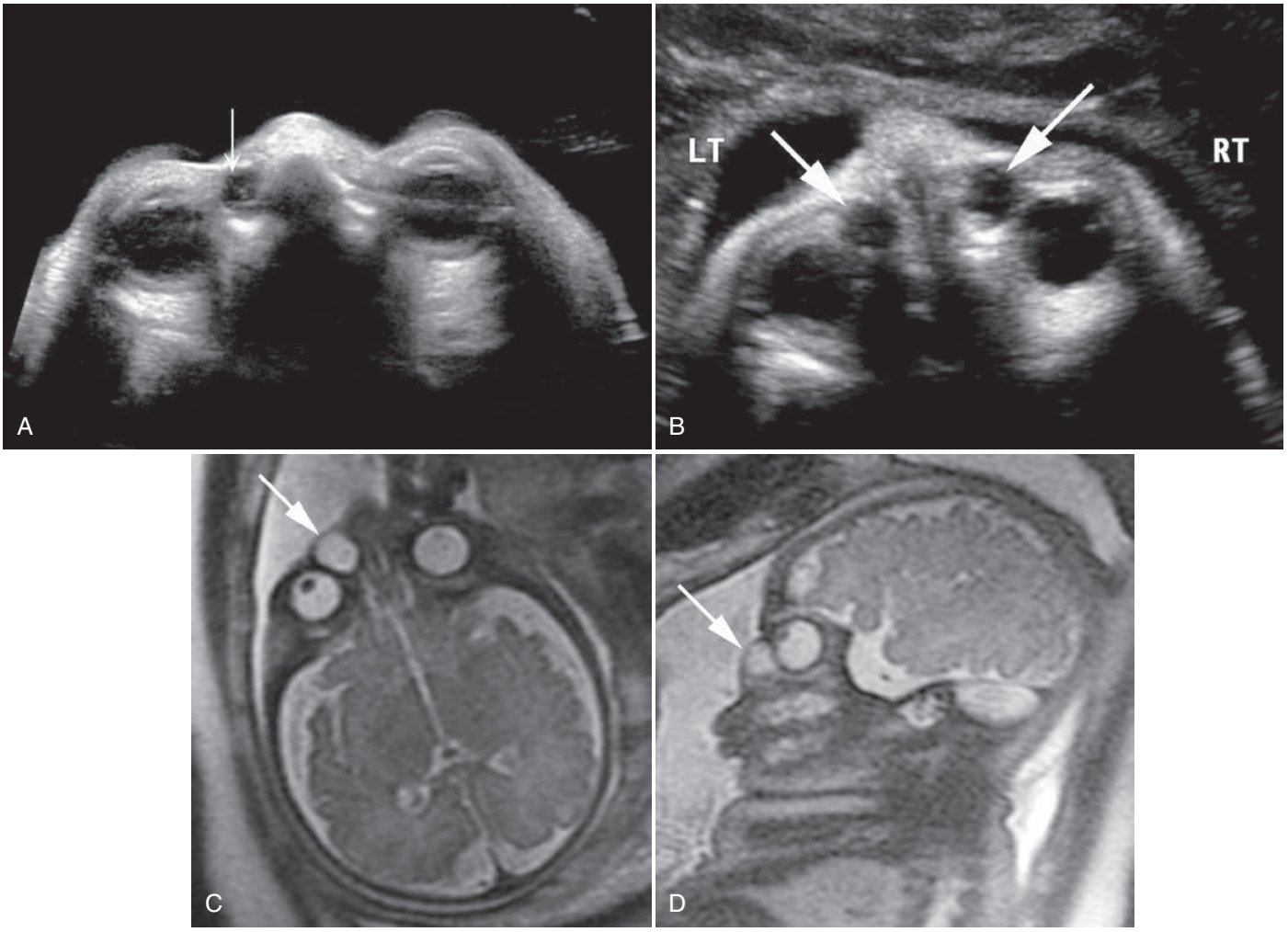

FIG. 33.16 Dacryocystocele. (A) Sonogram at 33 weeks shows unilateral dacryocystocele *(arrow)*. **(B)** Axial sonogram at 35 weeks shows fluid collections anteromedial to each orbit, consistent with bilateral dacryocystoceles *(arrows)*. **(C)** and **(D)** Axial and sagittal magnetic resonance images of a different 35-week fetus with a right dacryocystocele *(arrow)*.

Associations With Microphthalmos

- Single-gene disorders
  - Walker-Warburg syndrome
  - Fraser (cryptophthalmos) syndrome
  - Meckel Gruber syndrome
- Chromosomal abnormalities
  - Trisomy 13
  - Trisomy 18
- Drugs or irradiation
  - Ionizing radiation (4-11 weeks)
  - Ethanol
  - Thalidomide
  - Isotretinoin (retinoic acid)
- Maternal disease
  - Diabetes
  - Cytomegalovirus
  - Rubella
  - Toxoplasmosis
- Other
  - Encephalocele
  - Orbital tumors
  - CHARGE syndrome
  - VATER association

CHARGE, Coloboma, heart defects, choanal atresia, growth/development restriction, genital/ear anomalies; *VATER,* vertebral defect, imperforate anus, tracheoesophageal fistula, radial and renal dysplasia.

Differential Diagnosis of Congenital Cataracts

- Arthrogryposis
- Chondrodysplasia punctata
- Congenital aniridia
- Congenital ichthyosis
- Chromosomal abnormalities (21, 18, 13)
- G6PD deficiency
- Homocystinuria
- Hypochondroplasia
- Microphthalmia
- Infection
  - Rubella
  - Toxoplasmosis
- Syndromes
  - Marfan
  - Neu-Laxova
  - Smith-Lemli-Opitz
  - Walker-Warburg
- X-linked cataract (Hutterite)

G6PD, Glucose-6-phosphate dehydrogenase.

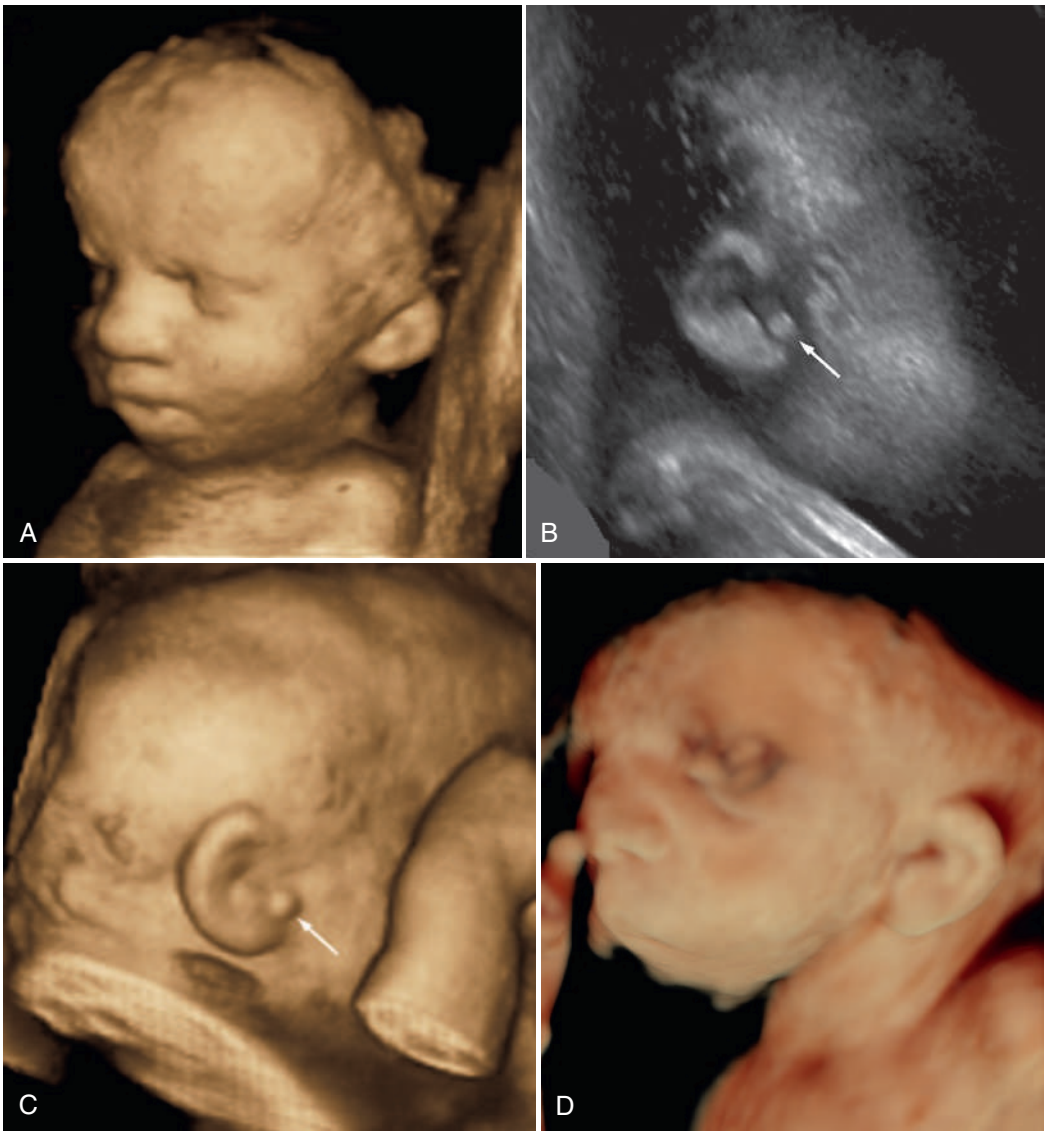

FIG. 33.17 Abnormal Ears. (A) Week 28 fetal sonography showing low-set ears and skin tag *(arrows)* on two-dimensional **(B)** and three-dimensional **(C)** images. **(D)** A different 27-week fetus with agnathia, microstomia, and low-set, abnormally turned ears.

EAR ABNORMALITIES

Abnormalities of the ears can be very difficult to diagnose on fetal sonography, but **low-set ears** are associated with multiple syndromes, including **Noonan syndrome** and certain trisomies. Low-set ears are described as the helix joining the cranium at a level below a horizontal plane through the inner canthi of the eyes. Ear anomalies may be more easily detected on 3-D sonography than on 2-D studies[44,45] (Fig. 33.17).

Microtia, or small ears, is a rare anomaly with an incidence of approximately 1 per 10,000 live births[46] and is often associated with syndromes and aneuploidy. Of 96 aneuploid fetuses, Yeo and colleagues[47] reported that 66% had small (<10th percentile) ears on sonography.

Otocephaly is a condition with union of the ears on the front of the neck and is caused by failure of ascent of the auricles during embryologic development. This is usually a fatal anomaly, often associated with agnathia or micrognathia, as well as holoprosencephaly. The most severe form of otocephaly may be associated with absence of the eyes, forebrain, and mouth.

MIDFACE ABNORMALITIES

Hypoplasia

The midface is the area between the upper lip and forehead. Midface hypoplasia can arise from a variety of causes, including syndromes such as **Apert, Crouzon, Treacher Collins,**[48] **Wolf-Hirschhorn,**[49] **Pfeiffer** (see Fig. 33.13), **Turner,** and **trisomy 21.** Midface hypoplasia may also result from facial clefts, craniosynostosis, and skeletal dysplasias. Midface hypoplasia is best demonstrated on sagittal midline views of the face, where one can see abnormal concavity of the midface, between the lower margin of the orbits and the upper jaw (Figs. 33.18 and 33.19).

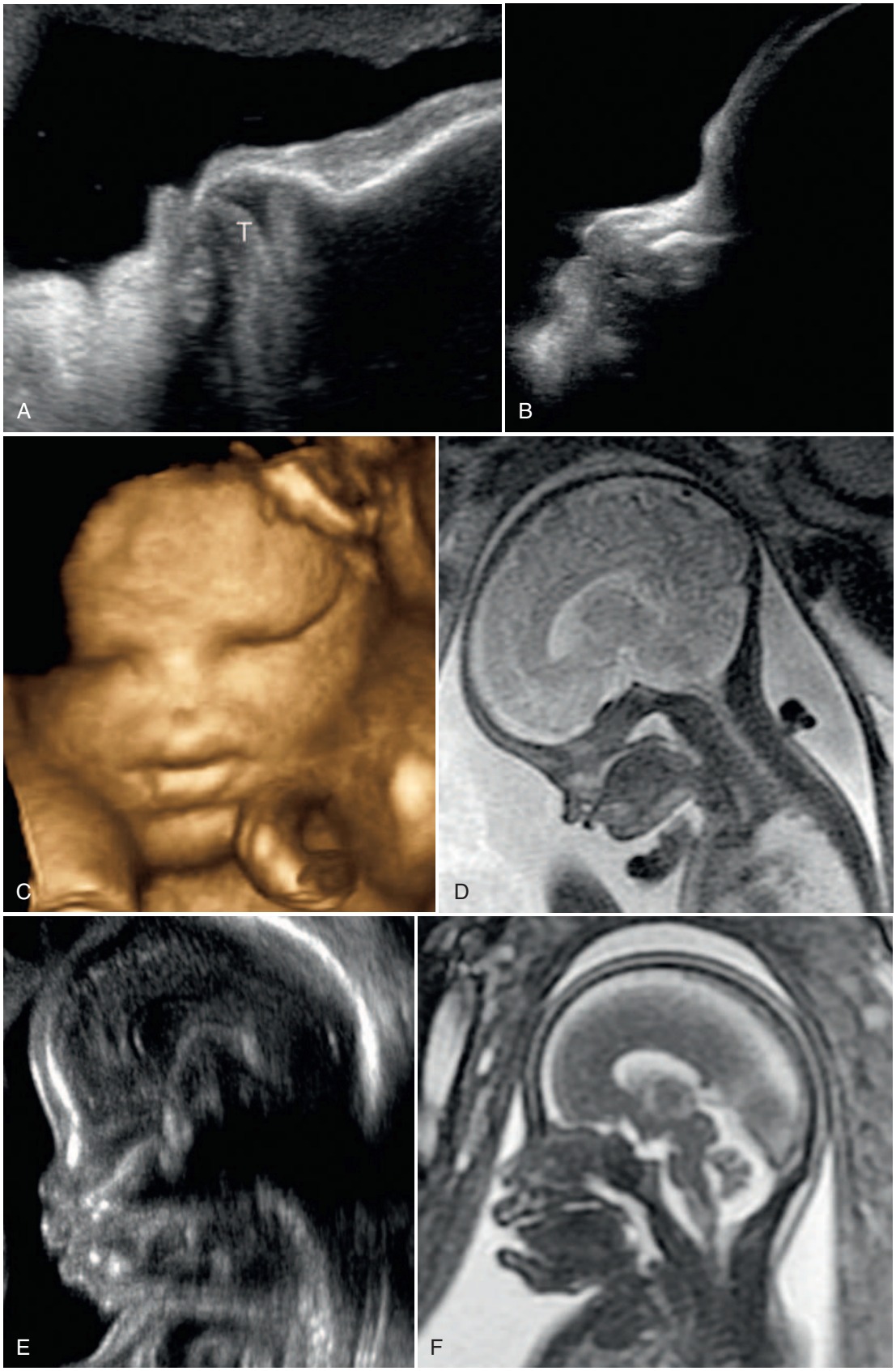

FIG. 33.18 Midface Hypoplasia. (A) Midface hypoplasia in association with **cleft lip and palate.** Sagittal view of the face shows midface retrusion in a 34-week fetus with unilateral complete left cleft lip and palate. Note the absent palate above the tongue *(T)*. **(B)**-**(D)** Midface hypoplasia in association with **microphthalmia** seen with sagittal ultrasound, three-dimensional ultrasound, and magnetic resonance imaging, respectively. **(E)** and **(F)** Midface hypoplasia in a fetus with **hypertelorism** (seen in same fetus as in Fig. 33.13). **(E)** Sagittal sonogram and **(F)** magnetic resonance image show an abnormally shaped skull and midface hypoplasia.

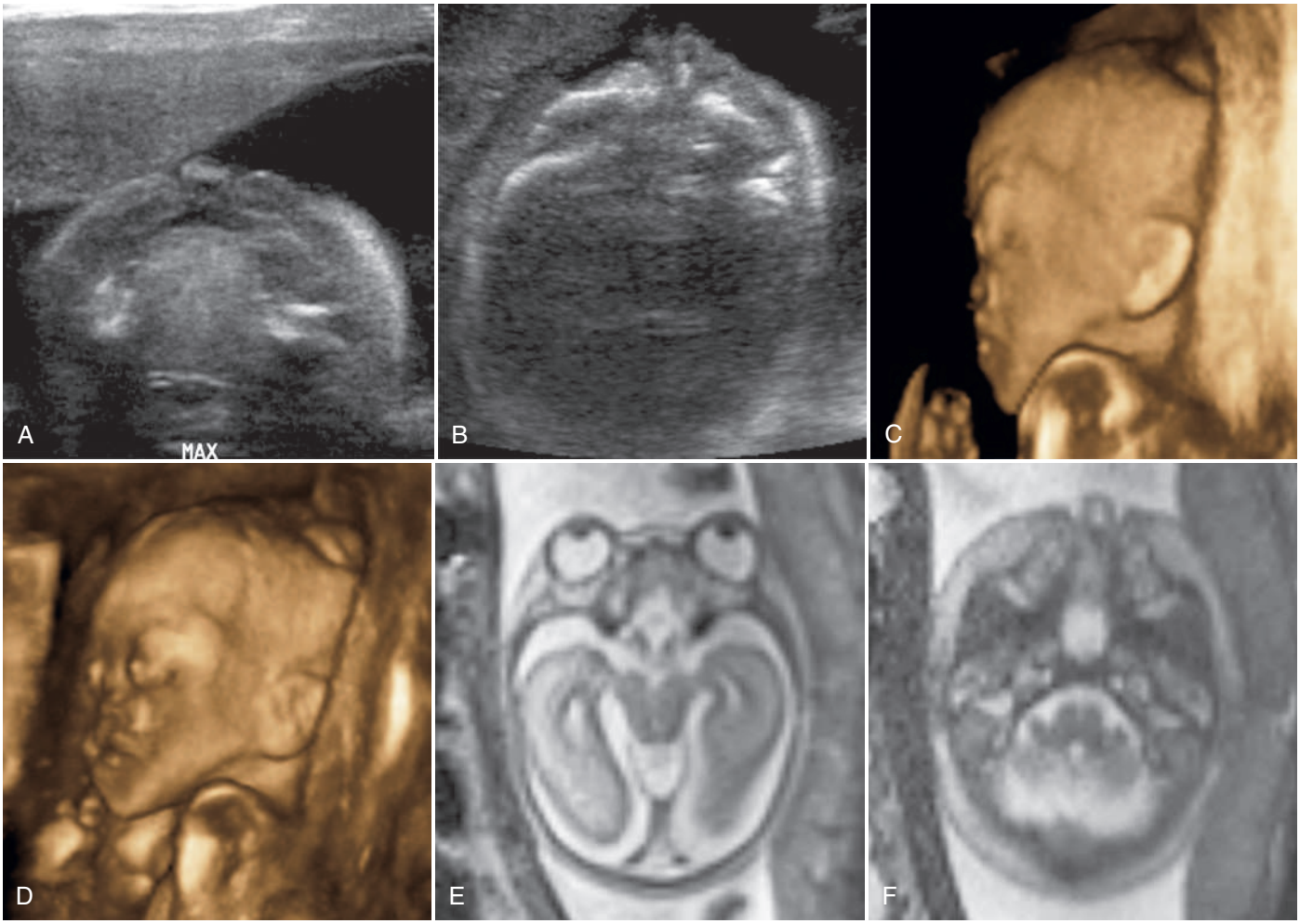

FIG. 33.19 Midface Hypoplasia. A 21-week fetal sonogram **(A-D)** and magnetic resonance images (**E** and **F**) show bilateral cleft lip and midline incisor. The flat profile of the fetus can be well appreciated on the three-dimensional views (**C** and **D**). Proptosis is evident in **(D)** and **(E)**.

Absent Nasal Bone

Hypoplastic or absent nasal bone is seen with increased incidence in fetuses with **trisomy 21** and can be evaluated sonographically in the first trimester as part of early risk assessment. The fetal nasal bone is best evaluated in a midsagittal plane at sonography (Fig. 33.20). Some have found that combining data regarding the presence or absence of the fetal nasal bone with NT measurements improves the accuracy of detection of trisomy 21 at first-trimester screening.[50] Cicero's initial study on evaluation of the nasal bone in first-trimester examinations found that 73% of fetuses with trisomy 21 had an absent nasal bone.[50] Other studies have reported absent nasal bone in 50% to 67% of fetuses with trisomy 21.[51,52] The absence of a nasal bone at second-trimester sonography, or abnormally short nasal bone measurements in combination with other markers of aneuploidy, increases detection of aneuploidy.[53,54]

It is important to note, however, that accurate sonographic evaluation of the fetal nasal bone can be technically challenging. There are specific guidelines for nasal bone imaging.[55] Studies have shown that even experienced sonographers need to perform at least 80 supervised examinations that conform to specified

FIG. 33.20 Absent Nasal Bone. Profile of third-trimester fetus with trisomy 13 and absent nasal bone.

standards before they are proficient in sonographic nasal bone evaluation.[56]

Other Nasal Abnormalities

Fetal nasal masses are rare but can be identified with ultrasound. Differential considerations include glioma, dermoid, hemangioma, and encephalocele. Fetal MRI is often helpful in assessing for intracranial extension, which is seen with encephalocele and may be present with nasal gliomas. Nasal gliomas are composed of heterotopic neuroglial tissue, usually located on the bridge or side of the nose, and may be extranasal (60%), intranasal (30%), or both (10%).[57-60] Nasal gliomas, in contrast to hemangiomas, usually do not demonstrate significant vascular blood flow on Doppler. Dermoids are often solid and cystic, heterogeneous masses. Hemangiomas are frequently echogenic and demonstrate vascular flow on Doppler. Encephaloceles may contain only meninges and cerebrospinal fluid and thus appear cystic, or may contain brain tissue and appear heterogeneous.

Frontonasal dysplasia is a rare anomaly[61,62] involving abnormalities of the eyes, forehead, and nose and is defined by the presence of two or more of the following: hypertelorism, skin-covered gap in the bones of the forehead (anterior cranium bifidum occultum), broad nasal root, median facial cleft, nasal ala cleft, lack of formation of nasal tip, and V-shaped frontal hairline (widow's peak).[63]

Cleft Lip and Palate

Worldwide incidence of cleft lip, with or without cleft palate, is approximately 1 per 700 live births,[64] with an incidence in Caucasians of approximately 1 per 1000 live births. The incidence of facial clefting is lower in the African American population (0.3 per 1000), higher among Asians (2 per 1000), and highest in Native Americans (3.6 per 1000 live births). It is more common in males than females.[65] These abnormalities usually result from failure of fusion of the medial nasal prominences and maxillary prominences. Although facial clefts may occur as an isolated finding, they are present with increased frequency in chromosomal anomalies, including **trisomies 13 and 18,** and in other structural anomalies, especially those involving the heart and central nervous system.[66-68] Reports vary, with aneuploidy rates of 5% to 30% in association with facial clefts.[69-71] Thus identification of a facial cleft should prompt a detailed and complete evaluation of the fetus for additional anomalies. Some isolated facial clefts are familial, with the recurrence risk dependent on number of affected parents and siblings.[72]

Reported accuracy in the sonographic detection of fetal cleft lip and palate ranges from 16% to 93%.[73-78] Robinson and colleagues[77] found that sonography performed after 20 weeks' gestation had a significantly higher detection rate for cleft lip than did studies performed before 20 weeks, and they subsequently recommended that fetuses at high risk for cleft lip be evaluated after 20 weeks' gestation (Video 33.1, Video 33.2, Video 33.3). Using state-of-the-art equipment, high-frequency probes, and endovaginal sonography, detection is possible at earlier gestational ages. Some question the efficiency and usefulness of 3-D sonography in evaluating clefts,[79] but many have found 3-D applications to be extremely helpful.[8,80,81] Recent studies have described 3-D techniques for evaluating the primary and secondary palate during the first trimester.[82-84] Sommerlad and colleagues[85] found the 3-D reverse face view could be obtained in 90% of patients at 20 to 34 weeks' gestational age and correctly classified clefts of the lip, alveolar ridge, and palate in nearly 90% of patients. However, evaluation of the secondary palate remains challenging, even with 3-D flipped face techniques[86] and modifications[87] of this technique, with adequate views obtained in just over a third of patients imaged.

Differential Diagnosis of Cleft Lip and Palate

- Teratogens
  - Diphenylhydantoin (phenytoin)
  - Valproic acid
  - Retinoic acid
  - Carbamazepine
  - Diazepam
- Amniotic band syndrome
- Holoprosencephaly
- Ectodermal dysplasia
- Frontonasal dysplasia
- Robert syndrome
- Miller syndrome
- Trisomies 13, 18, and 21
- Triploidy

Fetal facial clefts should be described as completely as possible, using standard craniofacial terminology and including accurate description and classification of the cleft in relation to the lip, nostril, alveolus (maxillary tooth bearing arc), and secondary palate (Fig. 33.21). The secondary palate has an anterior, bony segment and a posterior, soft tissue segment. Both cleft lip and cleft palate may be unilateral or bilateral.

Information important to the surgeons for accurate parental counseling, postnatal repair planning, and prognosis includes whether the cleft is unilateral or bilateral and complete or incomplete (Fig. 33.22). A **complete cleft lip** is defined as a cleft that fully divides the lip and extends completely through the base of the ala of the nose and that usually is associated with a cleft of the underlying tooth-bearing alveolus as well. An **incomplete cleft lip** involves a portion of the lip, but at least a band of soft tissue spans the cleft. Incomplete cleft lip does not involve the ipsilateral underlying bony tooth-bearing alveolus (Fig. 33.23).

Associated sonographic signs of a cleft palate include an abnormally high position of the fetal tongue, hypertelorism, deviation of the **vomer** (a triangular bone in the nasal septum forming the posterior and inferior portion of the septum), and micrognathia.[71,88,89] To describe the type of cleft, two embryonic structures are considered: (1) the primary palate, formed by the prolabium, premaxilla, and columella, which includes the lip, nares, and alveolus, and (2) the secondary palate, which begins at the incisive foramen and is formed by a horizontal portion of the maxilla, the horizontal portion of the palatine bones, and the soft palate.

Cleft palate may interfere with fetal swallowing and result in polyhydramnios. Infants with cleft palate have difficulty with feeding, are at increased risk of otitis media, and may have difficulty with hearing and speech.[65]

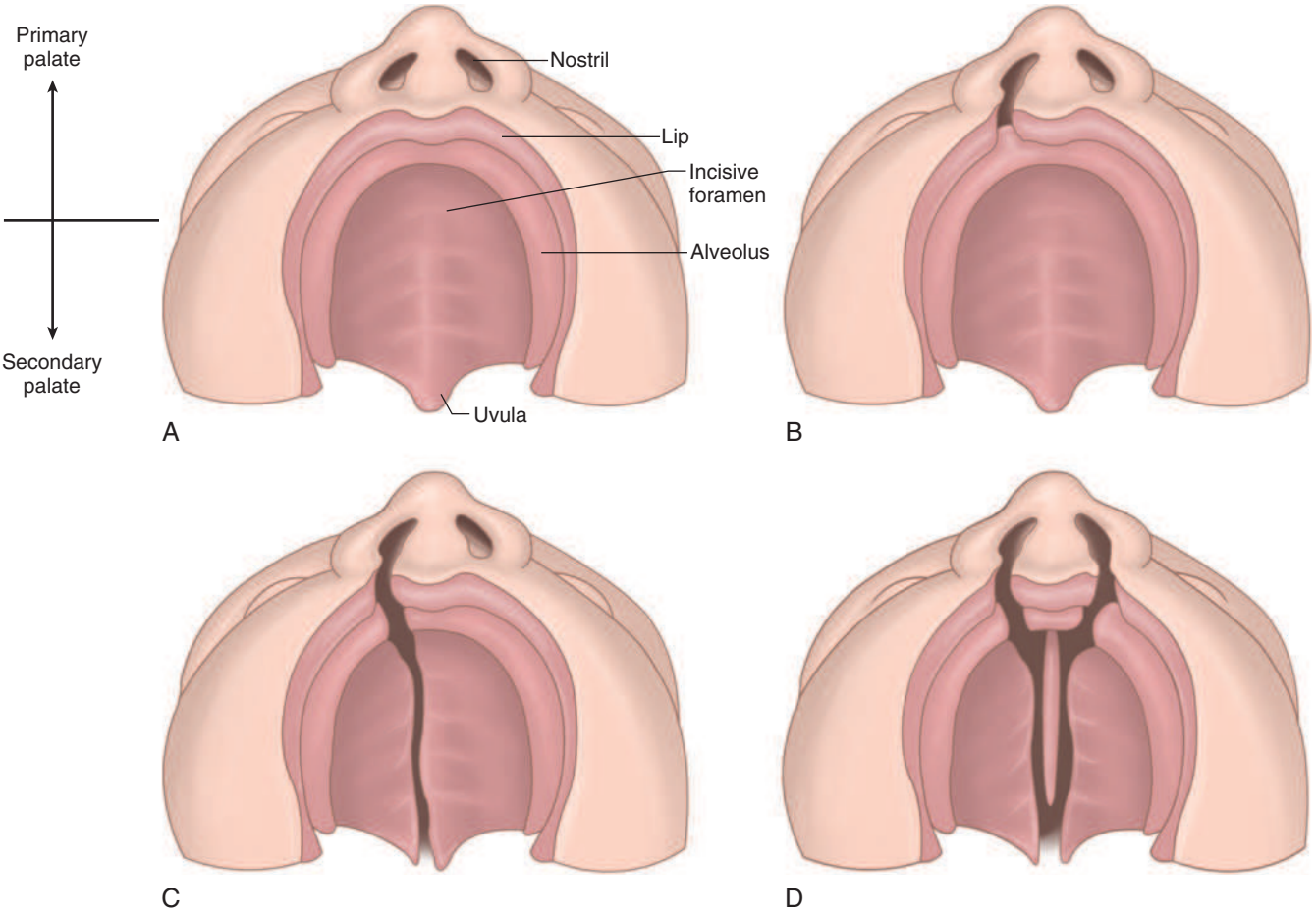

FIG. 33.21 Patterns of Clefting of Lip and Palate. (A) Normal anatomy of lip, primary palate, and secondary palate. The primary palate encompasses features anterior to the horizontal line, and the secondary palate is posterior to the blue line. **(B)** Isolated unilateral cleft lip involving the lip and nose. **(C)** Complete unilateral cleft lip and palate. The cleft lip extends through the primary palate, through the incisive foramen, and through the secondary palate. **(D)** Bilateral cleft lip and palate. This cleft extends on both sides through the nose, lip, primary and secondary palate (Courtesy of Andrew S. Phelps, MD.)

Associated Signs of Cleft Palate With Cleft Lip

AXIAL AND CORONAL VIEWS
Lips: cleft
Nares: flattened or deformed
Vomer: deviated away from side of cleft; often midline if bilateral cleft lip and palate
Maxilla: interrupted alveolus, wide gap
Orbits: hypertelorism

SAGITTAL VIEWS
Profile: midface retrusion
Tongue: high position in oropharynx

Unilateral Cleft Lip or Palate

Unilateral clefts occur more often on the left side. In a unilateral cleft lip or palate, there is often an offset between the two sides of the cleft, which are described as the "greater segment" on the side opposite the cleft, and the "lesser segment" on the side of the cleft (Fig. 33.24).

Bilateral Cleft Lip or Palate

Only about 10% of facial clefts are bilateral. In bilateral cleft lip or palate, the midsagittal view will often show an abnormal premaxillary protrusion of soft tissue anterior to and above the normal position of the upper lip (Fig. 33.25). Bilateral cleft lip and palate may be symmetrical or asymmetrical (Fig. 33.26).

Median Cleft Lip or Palate

Median cleft lip is a classic finding in **alobar holoprosencephaly.** In these cases, head size is small for menstrual dates and there is hypotelorism.[90] However, median cleft lip and palate can also be seen without holoprosencephaly. In these cases, head size and ocular diameters are normal.[90]

Unusual Facial (Tessier) Clefts

Asymmetrical clefts in unusual locations may be the result of **amniotic band syndrome** or may fall into the **Tessier cleft** category (see Fig. 33.22). Tessier clefts are rare, occurring in 1 to 5 per 100,000 live births.[91] These clefts are classified by the relationship of the cleft to the mouth, nose, and eye sockets and are numbered from 1 to 14, with the midline designated as 0.

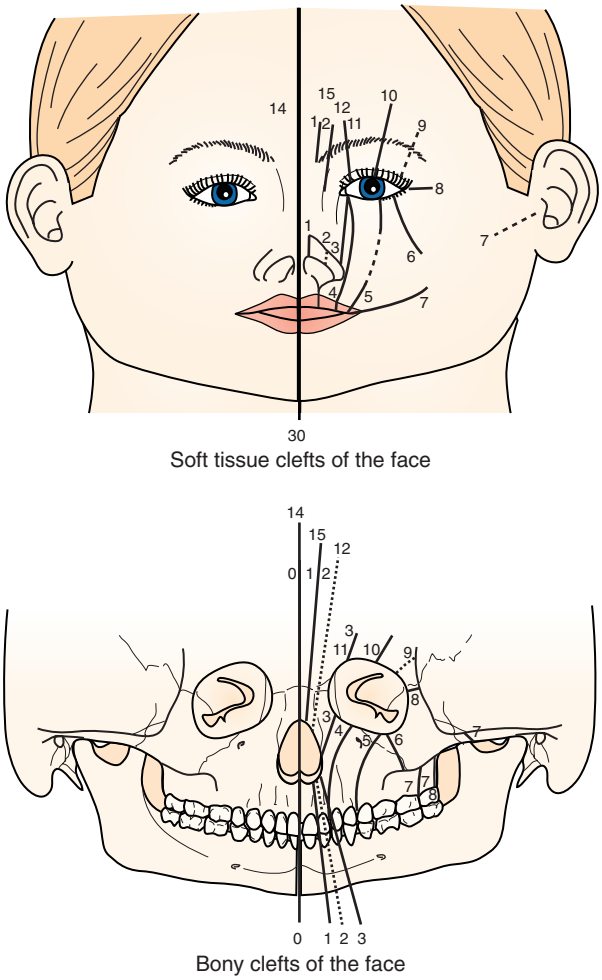

FIG. 33.22 Classification of Tessier Clefts. These clefts are classified by the relationship of the cleft to the mouth, nose, and eye sockets and are numbered from 1 to 14 with the midline designated as 0. Knowledge of these types of clefts is important for prenatal imaging, so that when unusual clefts are seen, they can be recognized as part of this spectrum. (Modified from Tessier P. Anatomical classification: facial, cranio-facial and latero-facial clefts. J Maxillofac Surg 1976;4:69-92.[92])

Tessier clefts can involve either the soft tissues (e.g., hairline, eyebrows, eyelids, nostrils, lips, ears) or the skeleton.[92] In some cases 3-D ultrasound has identified facial clefts not detectable on 2-D images.[93]

Isolated Cleft of Secondary Palate

Isolated clefts of the secondary palate are embryologically distinct from cleft lip or palate and are less common, occurring in approximately 1 per 2500 live births.[64] This abnormality is rarely[94] identified on prenatal sonography because of shadowing from overlying bony structures. Sonographic diagnosis is based on secondary signs, such as abnormal oropharyngeal fluid flow with color Doppler imaging[71] and high position of the tongue.[74,76,95] Cleft soft palate without cleft lip is more strongly associated with syndromes and chromosomal anomalies than cleft palate in concert with cleft lip.[76]

Syndromes associated with clefts of the secondary palate (without cleft lip) include **Goldenhar syndrome, Pierre-Robin sequence, Treacher Collins syndrome, Stickler syndrome,** and **velocardiofacial syndrome.** Three-dimensional sonography is often helpful in assessing the secondary palate, given a favorable fetal position and gestational age and adequate amniotic fluid.[14-16,96-99] Sagittal fetal MRI is helpful in delineating the normal soft tissues of the palate and in accurately characterizing palatal clefting, even when isolated to the posterior secondary (soft) palate.[88,89,100]

LOWER FACE ABNORMALITIES

Macroglossia and Oral Masses

Macroglossia, an abnormally enlarged tongue, has a variety of causes and can, at times, be identified on fetal sonography, visualized as the tongue protruding outside the oral cavity, typically on sagittal or axial views (Fig. 33.27). The etiology of macroglossia includes Beckwith-Wiedemann syndrome, trisomy 21, and vascular malformations such as lymphatic malformation or hemangioma.[101] If macroglossia is identified, a careful evaluation for the associated findings of **Beckwith-Wiedemann syndrome** and for markers of **trisomy 21** should follow.

Conditions Associated With Macroglossia

Beckwith-Wiedemann syndrome
Trisomy 21
Congenital hypothyroidism
Lymphangioma
Hemangioma
Inborn error of metabolism
Isolated autosomal dominant trait
Lingual thyroid
Neurofibroma
Epignathus

Micrognathia and Retrognathia

Micrognathia is a small chin, and retrognathia (retrognathism) is a posteriorly displaced chin. These are distinct abnormalities that frequently occur together. **Pierre-Robin sequence** is the clinical triad of micrognathia, glossoptosis (downward displacement of the tongue), and subsequent airway obstruction, often associated with cleft soft palate (Fig. 33.28). This finding is associated with syndromes (e.g., Stickler, velocardiofacial, Miller-Diecker, Beckwith-Wiedemann, Treacher Collins, Pfeiffer, femoral-facial); chromosomal anomalies (typically trisomy 18 or 13); and skeletal dysplasias (e.g., diastrophic, spondyloepiphyseal, congenital, camptomelic). If the abnormality is severe enough to interfere with fetal swallowing in utero, polyhydramnios may result. Micrognathia can lead to substantial feeding difficulties and problems with airway management after birth. Prenatal diagnosis is thus critical to delivery planning.

Micrognathia is best seen on midsagittal views of the fetal face and is identified by subjective assessment by the sonologist (Video 33.4). Although there have been attempts to standardize

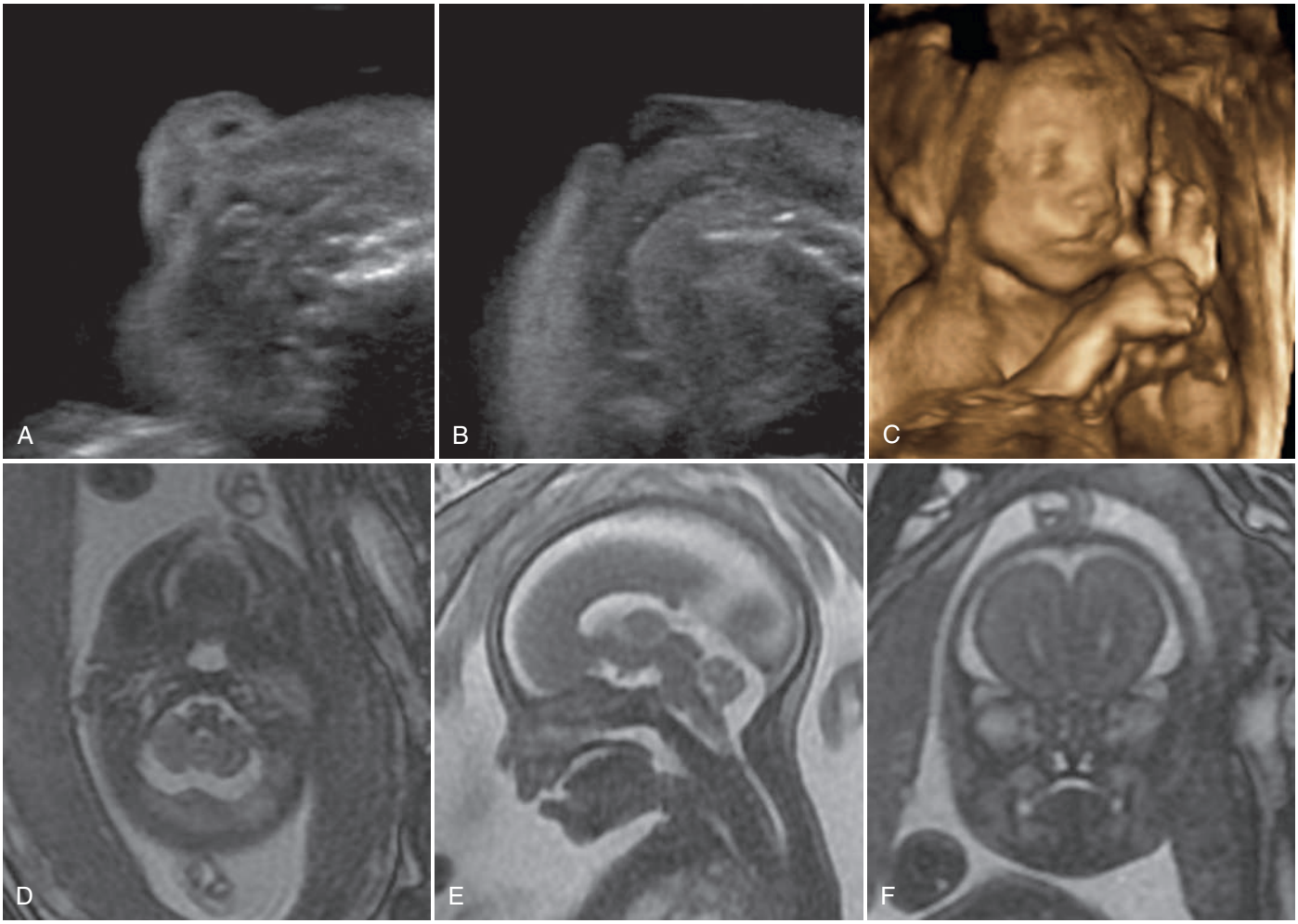

FIG. 33.23 Incomplete Cleft Lip. Two-dimensional (**A** and **B**) and three-dimensional **(C)** sonography of a 22-week fetus with unilateral incomplete left cleft lip. **(D)-(F)** Fetal magnetic resonance images showing intact alveolus **(D)** and intact secondary palate (**E** and **F**).

fetal jaw measurements[102-104] to identify micrognathia more objectively, there is no consensus on methodology. Three-dimensional sonography offers an additional method for the evaluation of micrognathia, because data can be manipulated to obtain a true sagittal view of the fetal face, which might otherwise not be possible.[105] Many fetuses with micrognathia have additional abnormalities,[106-108] so the physician should carefully search for associated anomalies, and fetal karyotyping is recommended. Fetal MRI may also be helpful. A recent study[107] showed that nearly all fetuses with moderate or severe micrognathia on prenatal MRI had Robin sequence. Although micrognathia is generally diagnosed in the second trimester and beyond, some[82] have reported findings of micrognathia identified in the first trimester.

Agnathia is total or partial absence of the lower jaw and is often associated with holoprosencephaly (Fig. 33.29). **Microstomia** is a small mouth, often associated with agnathia and otocephaly.[5]

SOFT TISSUE TUMORS

Soft tissue or bony tumors can cause alterations in head size or shape. A relatively common soft tissue lesion involving the face is a **hemangioma** (Fig. 33.30). Vascular anomalies such as hemangiomas are the most common tumors of infancy, and most are medically insignificant. On fetal sonography, hemangiomas often appear as echogenic, predominantly solid masses. These masses may contain detectable vascular channels with flow on Doppler ultrasound evaluation. Hemangiomas often increase in size during fetal life and can be infiltrative, affecting large areas. Classically, hemangiomas do not infiltrate bony structures. Hemangiomas can occur in any location and can involve the fetal face[109] or neck. With larger lesions, the risk of high-output cardiac failure increases owing to vascular shunting in the lesion. There may also be platelet trapping in the hemangioma, leading to thrombocytopenia (also referred to as "Kasabach-Merritt syndrome"). The adjacent skull may be thinner and may be associated with brain anomalies as in **Sturge-Weber syndrome.**[110-113]

NECK ABNORMALITIES

Nuchal Translucency and Thickening

The **nuchal translucency** (NT) is the fluid collection that forms posterior to the fetal neck during early development. Studies

Text continued on p. 1159.

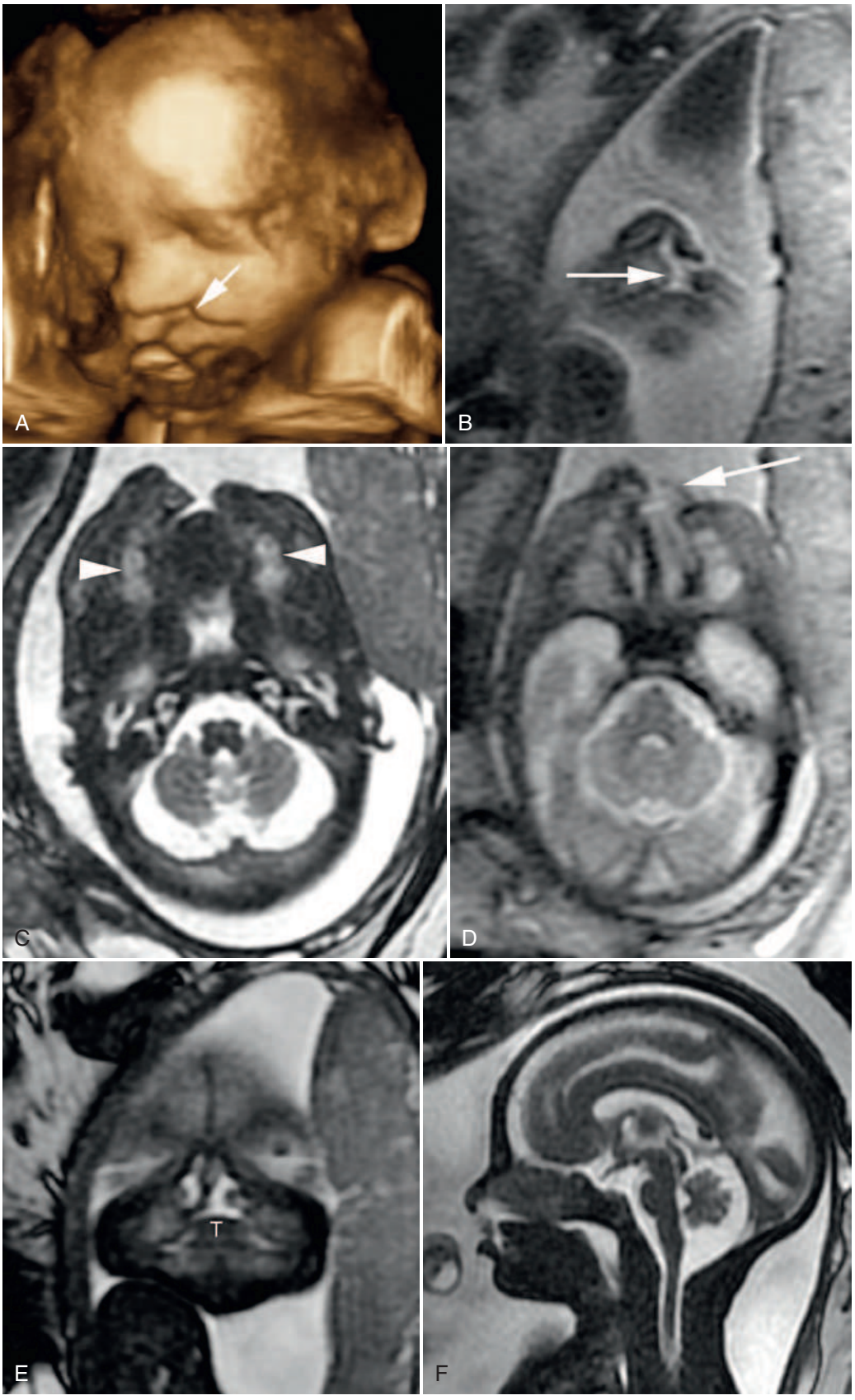

FIG. 33.24 Unilateral Complete Cleft Lip and Palate. (A) Coronal three-dimensional sonogram of the fetal lip and nose shows a normal right nostril and lip, cleft left lip *(arrow),* and a downward-sloping left nostril at 29 weeks' gestation. **(B)** Coronal magnetic resonance imaging (MRI) shows complete left cleft lip, with deformation of left nostril *(arrow).* **(C)** Axial MRI shows complete cleft left alveolus and lip (*arrowheads* indicate lateral margins of bony tooth-bearing alveolus), with greater segment on the right and lesser segment on the left. **(D)** Axial MRI shows deviation of the tip of the bony nasal septum (vomer) away from the side of the cleft *(arrow).* **(E)** Coronal MRI shows an intact right horizontal palatal shelf and absence of the left palatal shelf above the tongue *(T).* Note how a small amount of amniotic fluid in the oral cavity is helpful in making this determination. **(F)** Sagittal MRI shows an abnormally high position of the tongue, in keeping with a complete left cleft lip and palate. See also Videos 33.1, 33.2, and 33.3.

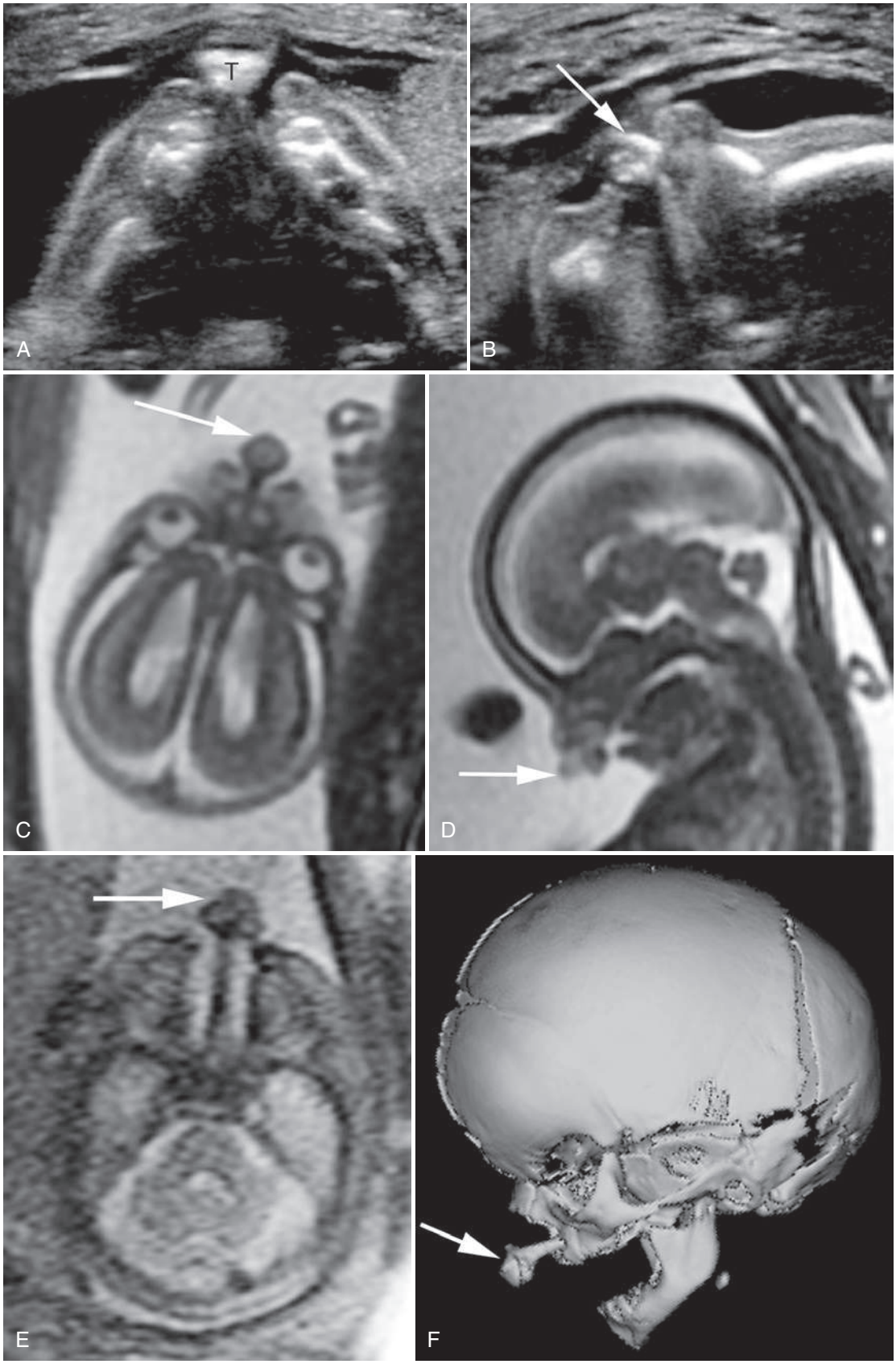

FIG. 33.25 Bilateral Complete Cleft Lip and Palate. (A) Axial sonogram of 18-week fetus with bilateral complete cleft lip and palate shows bilateral clefts in the tooth-bearing alveolus of the maxilla, with two tooth buds *(T)* displaced anteriorly in the intermaxillary segment. **(B)** Sagittal sonogram shows protrusion of the intermaxillary segment of the maxilla *(arrow)*. **(C)** and **(D)** Oblique axial and sagittal MR images show bilateral cleft lip and the anteriorly displaced intermaxillary segment of the maxilla *(arrow)*. **(E)** In a different fetus at 22 weeks with **Pfeiffer syndrome,** axial magnetic resonance imaging shows bilateral cleft palate with displaced intermaxillary segment of the maxilla *(arrow)* (see also Fig. 33.13). **(F)** Postnatal three-dimensional computed tomography reconstruction shows coronal craniosynostosis and the marked anterior position of the intermaxillary segment *(arrow)*.

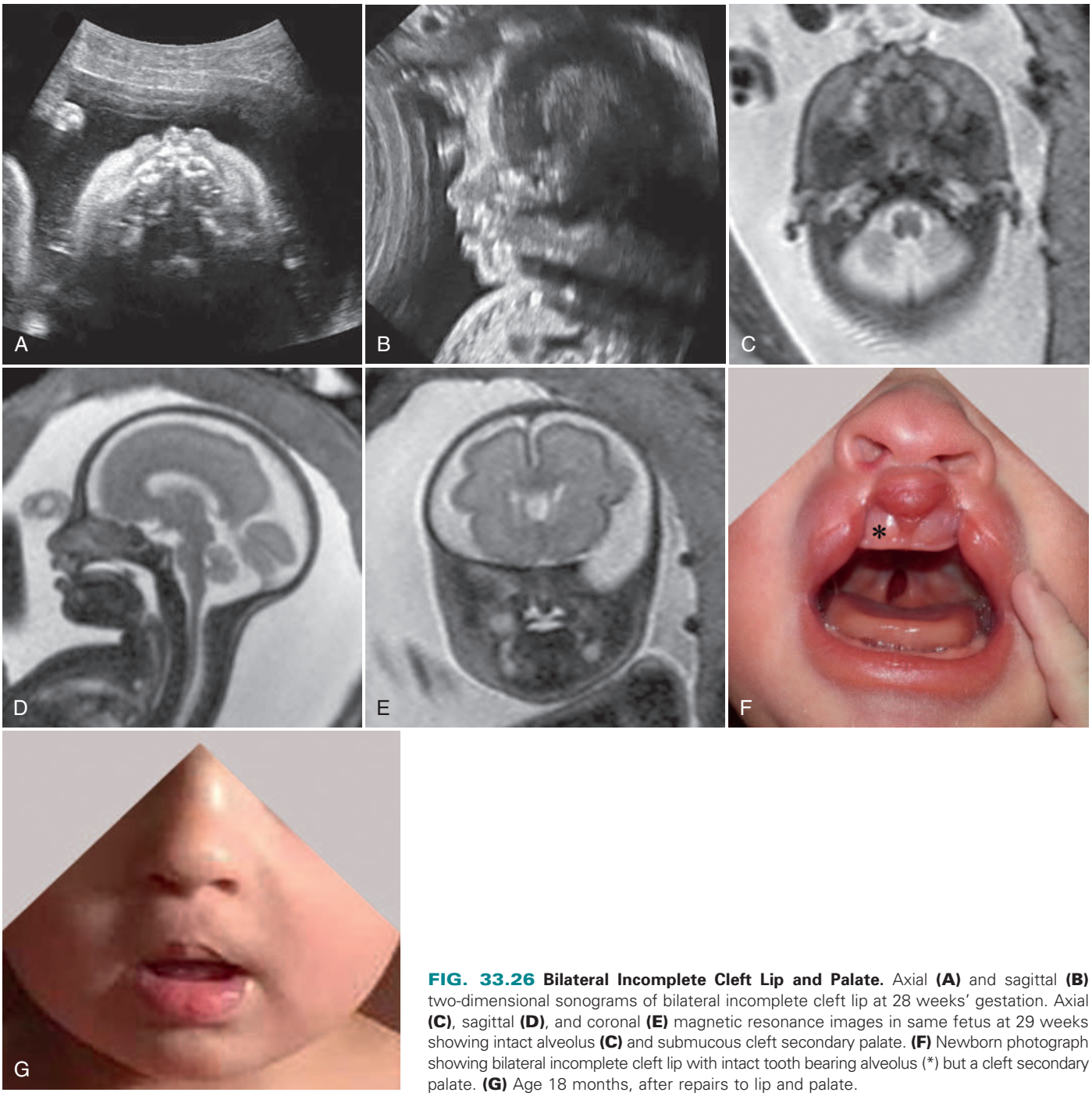

FIG. 33.26 Bilateral Incomplete Cleft Lip and Palate. Axial **(A)** and sagittal **(B)** two-dimensional sonograms of bilateral incomplete cleft lip at 28 weeks' gestation. Axial **(C)**, sagittal **(D)**, and coronal **(E)** magnetic resonance images in same fetus at 29 weeks showing intact alveolus **(C)** and submucous cleft secondary palate. **(F)** Newborn photograph showing bilateral incomplete cleft lip with intact tooth bearing alveolus (*) but a cleft secondary palate. **(G)** Age 18 months, after repairs to lip and palate.

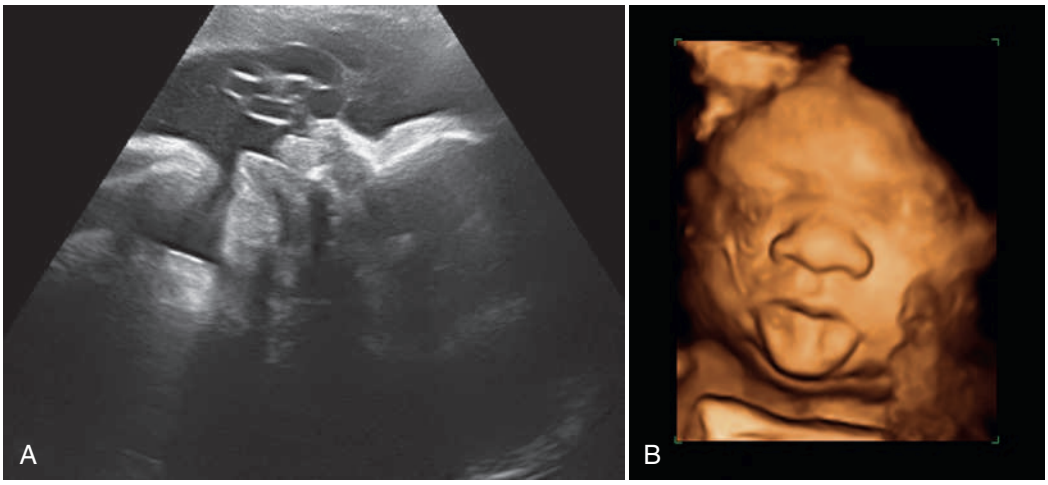

FIG. 33.27 Abnormal Tongue. Sagittal sonogram **(A)** and 3D ultrasound **(B)** showing macroglossia in a 33-week fetus with Beckwith-Wiedemann syndrome.

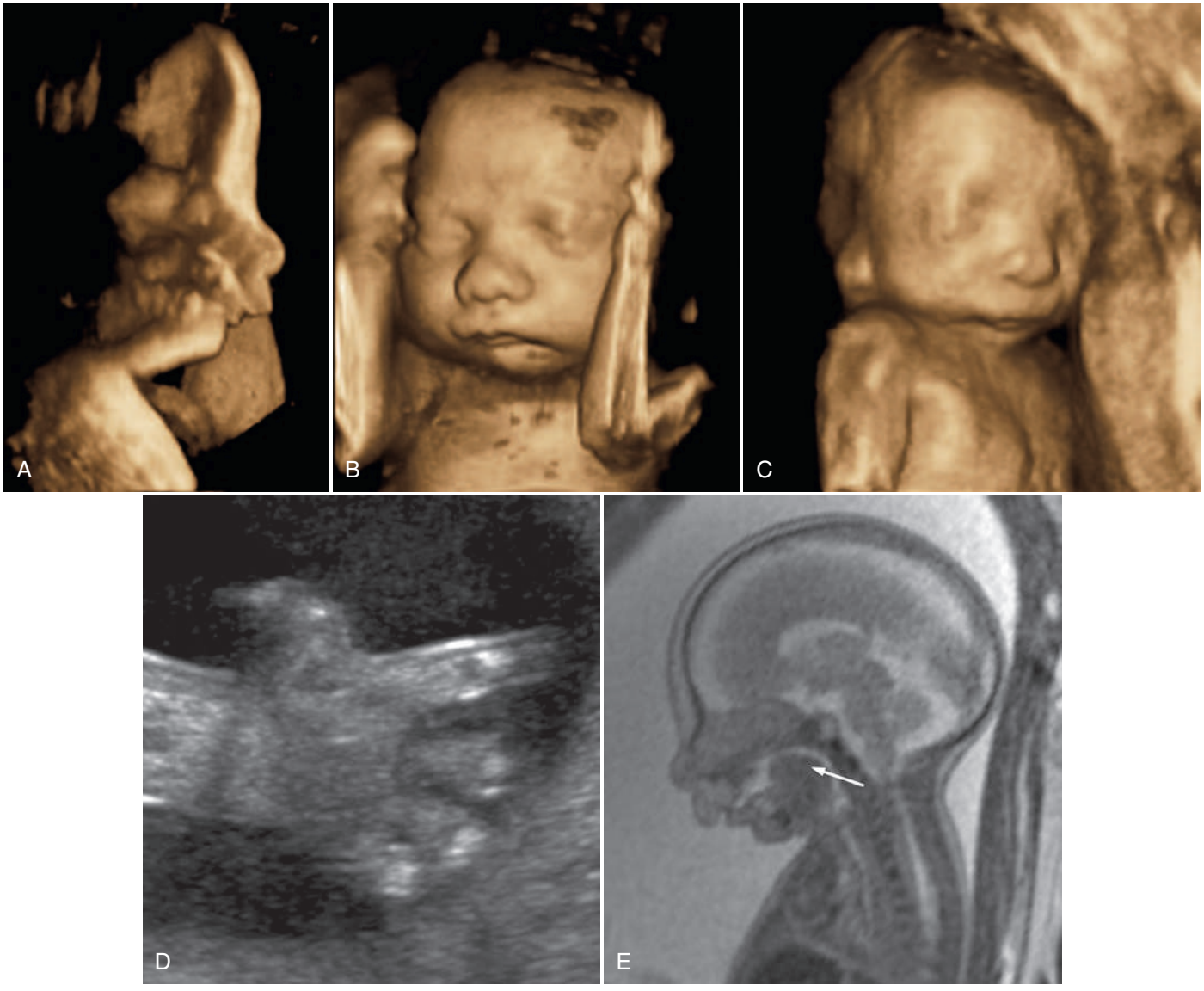

FIG. 33.28 Micrognathia. (A) and **(B)** Three-dimensional fetal sonogram at 33 weeks shows micrognathia; fetus also had high-riding posterior tongue, secondary palatal defect, left nasolacrimal duct cyst, and ventriculomegaly. **(C)-(E)** In a different fetus at 24 weeks. **(C)** Three-dimensional sonogram shows micrognathia. **(D)** Two-dimensional sonogram shows a hyperextended thumb, and **(E)** magnetic resonance imaging shows micrognathia and cleft secondary palate. Note high position of the tongue *(arrow)*. See also Video 33.4.

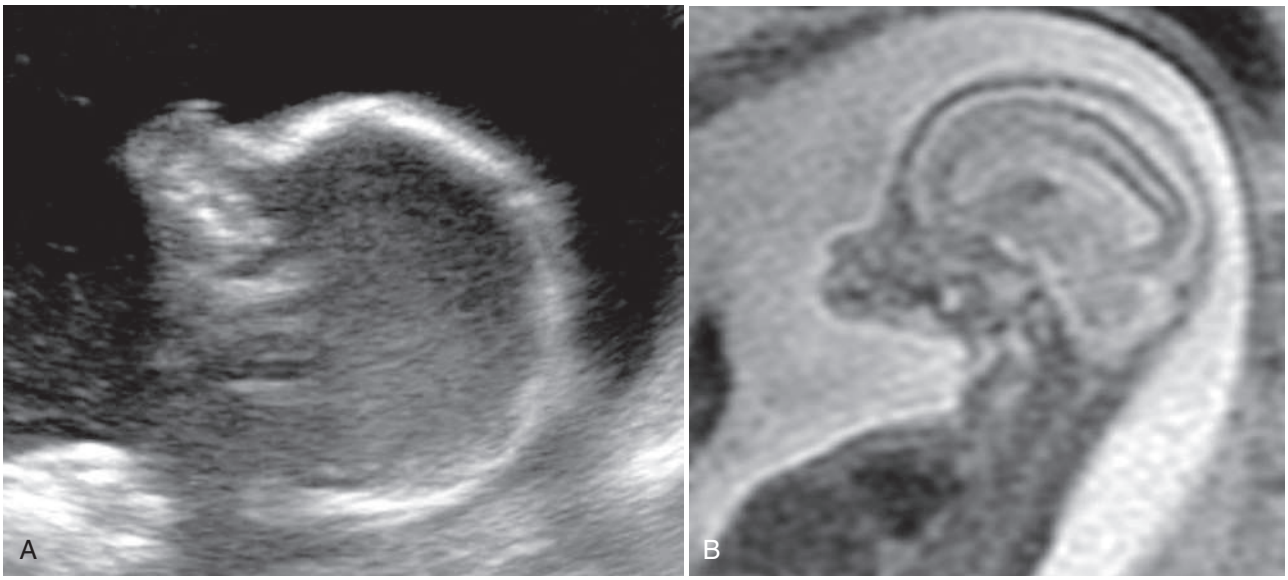

FIG. 33.29 Agnathia Microstomia. (A) Sagittal sonogram, and **(B)** magnetic resonance image show the absent mandible.

have shown that thickened NT measurements in the first trimester are associated with fetal aneuploidy, cardiac defects, other major malformations, and adverse pregnancy outcome.[114-118] Images must be obtained in midsagittal plane[119] by trained sonographers, and measurements are combined with patient age, gestational age, and serum testing to give a risk for aneuploidy (see Chapter 31). In the second trimester, the **nuchal fold thickness** is measured in the suboccipital bregmatic plane. A measurement of 6 mm or greater from 15 to 22 weeks is associated with an increased risk of trisomy 21.[120,121] The measurement is taken in the midline from the outer edge of the occipital bone to the outer edge of the skin.

Lymphatic Malformation (Cystic Hygroma)

Lymphatic malformation, known historically as "cystic hygroma," is a septated fluid collection behind the fetal neck, thought to result from early maldevelopment of the lymphatic system. This abnormality is highly associated with **Turner syndrome** (XO), other chromosomal anomalies, and cardiac structural abnormalities. When associated with hydrops, fetal mortality is very high. As with an increased NT, if a lymphatic malformation is diagnosed and chromosomes are found to be normal, the fetus should still be carefully evaluated for cardiac abnormalities.

Lymphatic malformations can occur elsewhere in the head and neck and may be microcystic or macrocystic. They are presumed to result from obstructed lymphatic sacs that do not communicate with main lymphatic channels. Although benign, morbidity is associated with mass effect on the fetal airway when such masses arise in the face and neck (Fig. 33.31). In this setting, fetal MRI is often useful for evaluation of the fetal airway and for delivery planning. Fluid-filled lymphatic malformations, even when large, are much more malleable than solid teratomas of the head and neck and are less likely to compromise the airway. When these malformations involve the tongue, cystic hygromas may interfere with swallowing and feeding after birth.

Cervical Teratoma

Teratoma is the most common tumor in neonates, with the majority located at the sacrum and coccyx. Approximately 5% of teratomas arise in the neck or oropharynx. Cervical teratomas occur equally in males and females.[122] Sonographically, teratomas are usually complex masses composed of both cystic and solid elements and are often associated with regions of calcification. There is usually vascular flow within the solid portions of the mass. In the neck, they are usually anterolateral in location and can become quite large, often involving the thyroid gland. When they arise in the neck, teratomas may impinge on the airway, interfere with fetal swallowing, and result in polyhydramnios. Evaluation of the fetal airway is particularly important to delivery planning and is often best accomplished with fetal MRI (Fig. 33.32).

When teratomas arise in the neck, there can be hyperextension of the fetal neck, best seen in sagittal views. Teratomas of the oropharynx **(epignathus)** often protrude from the mouth. Although most teratomas are histologically benign, prognosis depends on the degree of mass effect on the trachea and the ability to secure the infant's airway at delivery. If there is substantial mass effect on the airway, the **ex utero intrapartum treatment (EXIT) procedure** may be necessary. This complex procedure requires a team of specialists for the mother and fetus and involves cesarean delivery, with preservation of the maternal-fetal circulation through the placenta until the neonatal airway can be secured.[123-127]

Thyromegaly and Goiter

Fetal goiter is rare (1 per 30,000 to 50,000 live births)[128] and most often related to maternal thyroid disease, such as **Graves disease**[129] or **Hashimoto thyroiditis,** with antibodies that cross the placenta and lead to fetal thyroid dysfunction. Maternal use of **thyroid blocking agents** (e.g., propylthiouracil) may also result

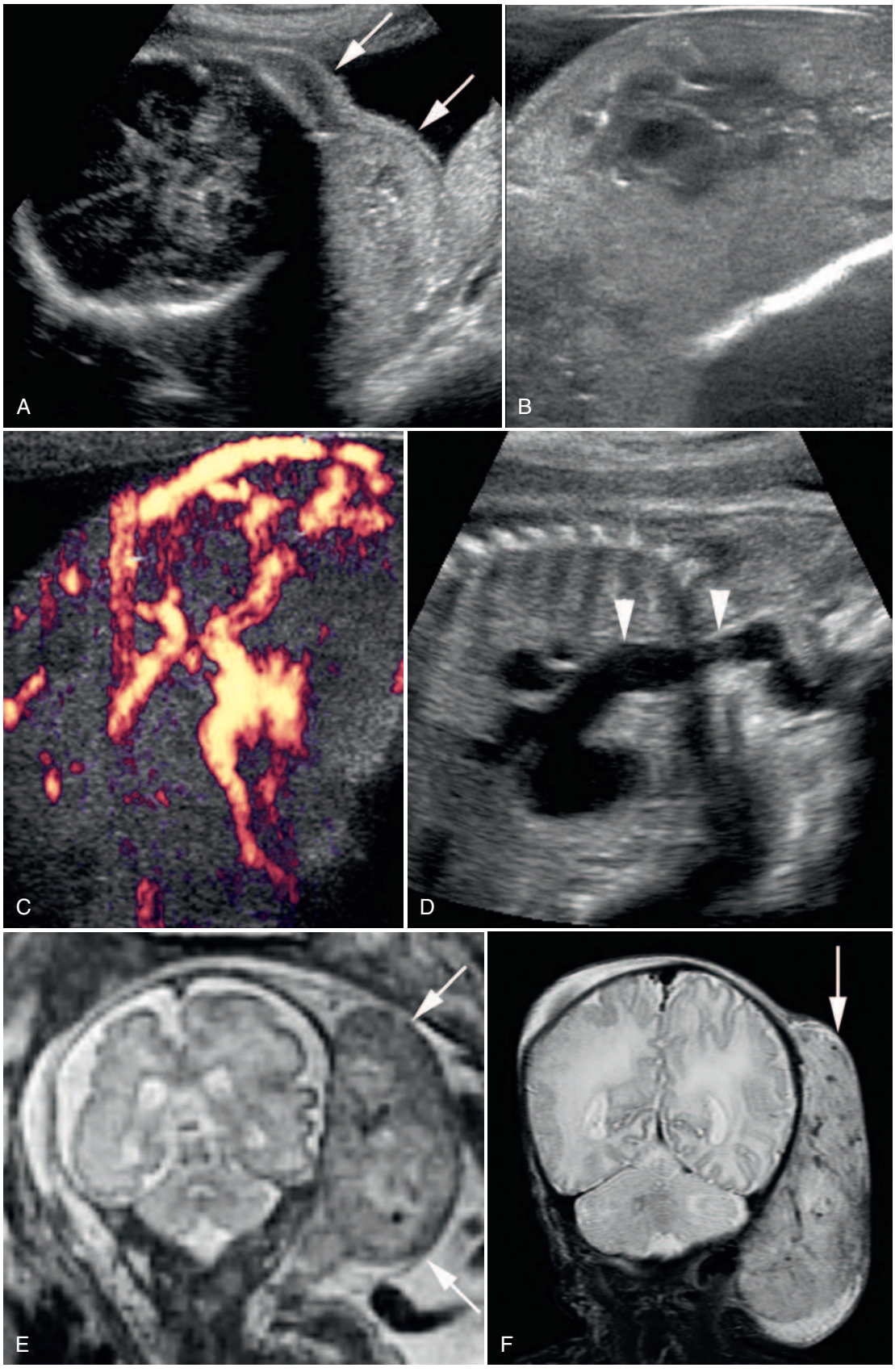

FIG. 33.30 Hemangioma at 30 Weeks' Gestation. (A) Axial sonogram shows a large, lateral and posterior soft tissue scalp mass *(arrows).* **(B)** High-frequency coned-down view illustrates the heterogeneous echogenicity of the mass. **(C)** Power Doppler view demonstrates the vascularity of the mass. **(D)** Oblique sonogram of the fetal chest and neck show a greatly enlarged superior vena cava *(arrowheads).* The heart was also enlarged, and the fetus was in heart failure from the volume of blood circulating through the scalp mass. **(E)** Coronal prenatal and **(F)** postnatal magnetic resonance images show the left scalp mass *(arrows).*

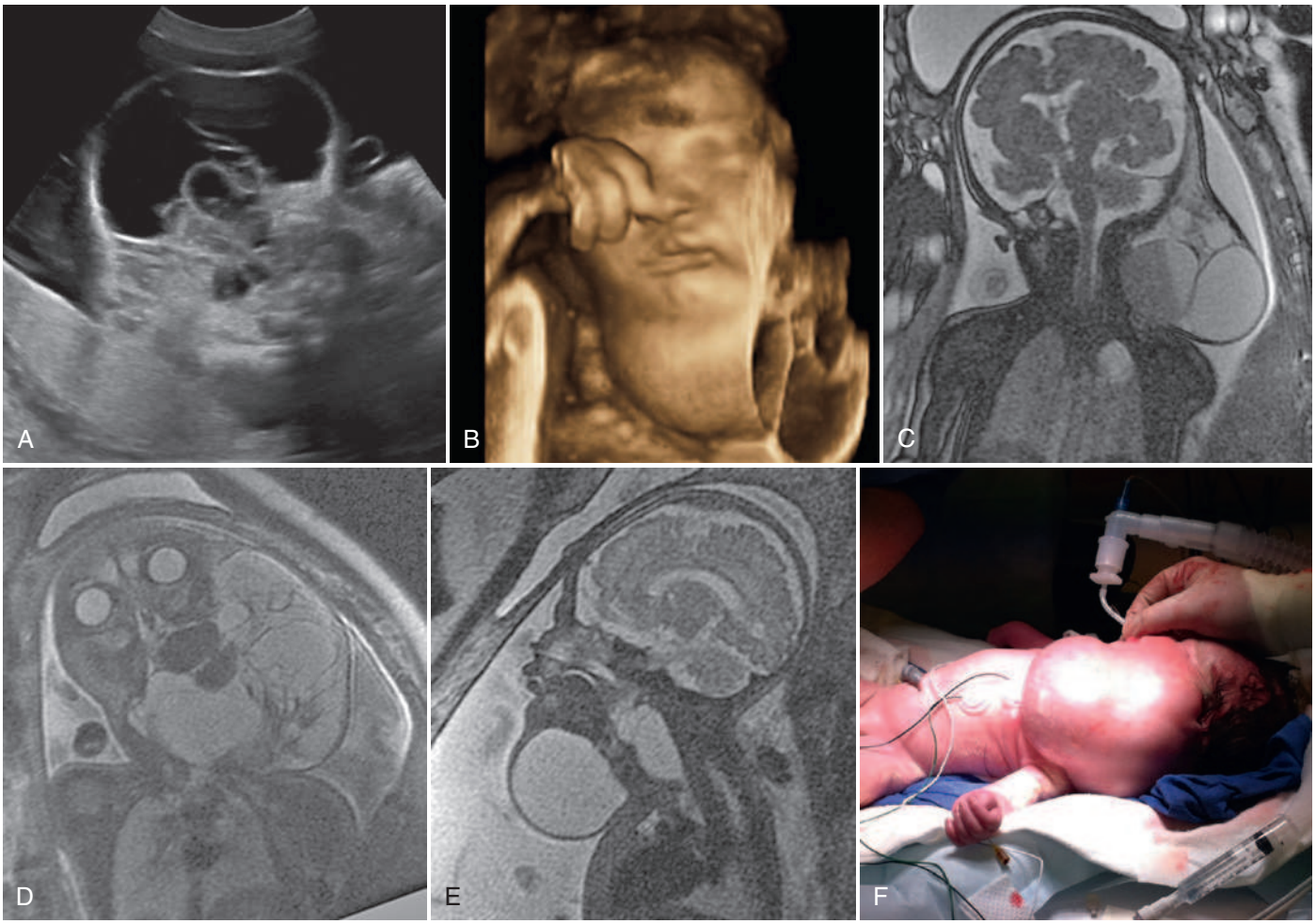

FIG. 33.31 Lymphatic Malformation. (A) Two-dimensional sonogram of left neck mass at 35 weeks showing complex cystic and solid appearance. **(B)** Three-dimensional sonogram showing left-sided mass. Coronal (**C** and **D**) and sagittal **(E)** fetal magnetic resonance images show the complex mass, potentially blocking the airway. **(F)** The newborn, with large left-sided neck mass, was successfully intubated during delivery by EXIT (ex utero intrapartum treatment) procedure.

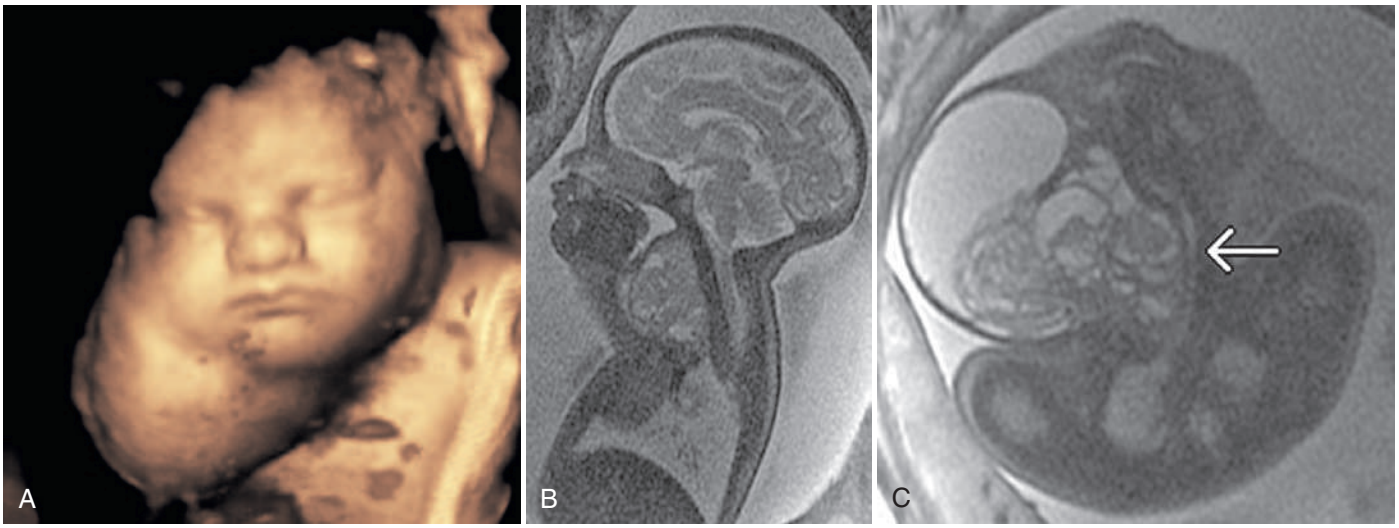

FIG. 33.32 Teratoma. (A) Three-dimensional sonogram at 34 weeks shows a right-sided cervical teratoma. Sagittal **(B)** and axial **(C)** T2-weighted fetal magnetic resonance images. Note visualization of the trachea *(arrow),* suggesting that the airway would likely be patent at birth.

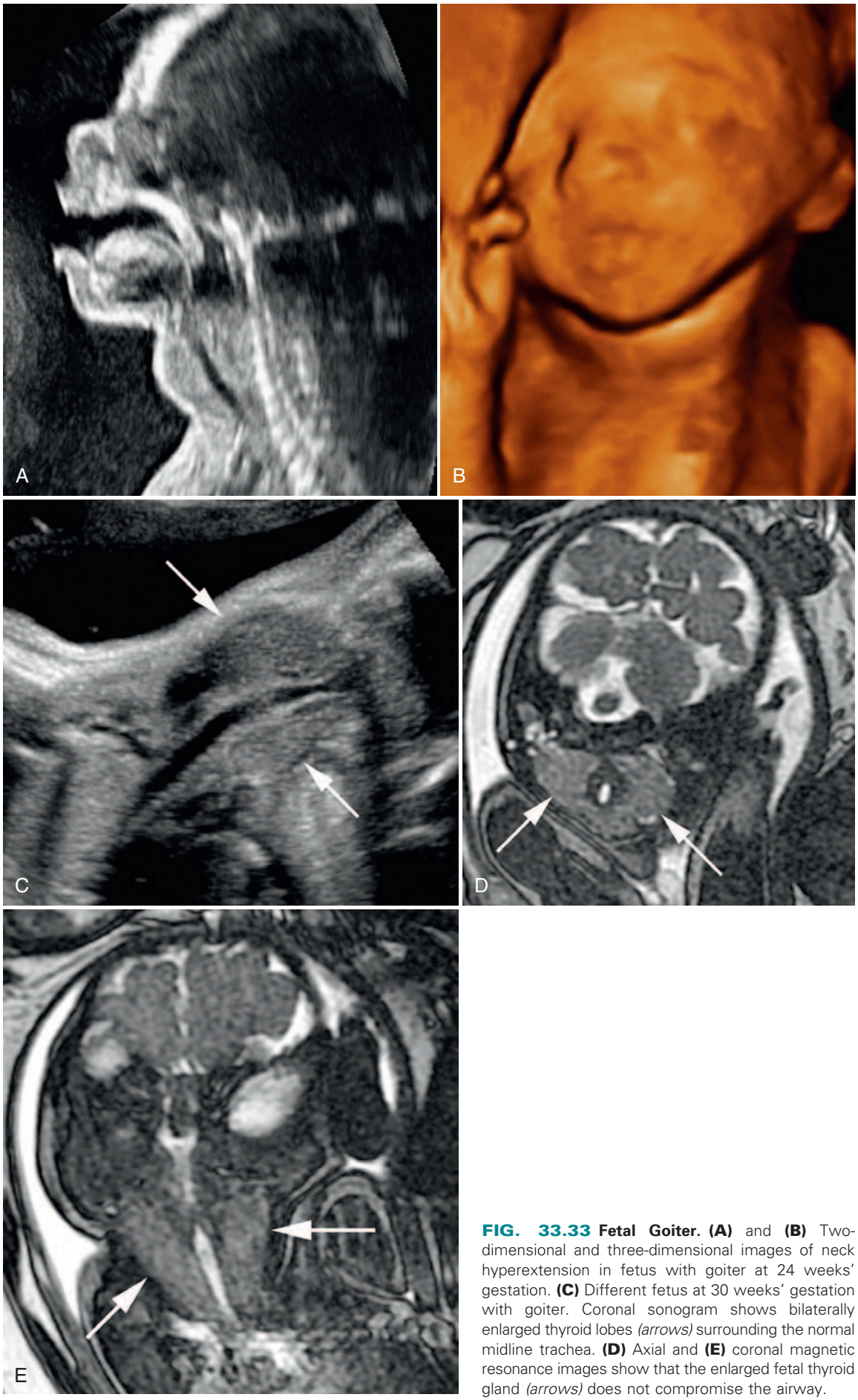

FIG. 33.33 Fetal Goiter. (A) and **(B)** Two-dimensional and three-dimensional images of neck hyperextension in fetus with goiter at 24 weeks' gestation. **(C)** Different fetus at 30 weeks' gestation with goiter. Coronal sonogram shows bilaterally enlarged thyroid lobes *(arrows)* surrounding the normal midline trachea. **(D)** Axial and **(E)** coronal magnetic resonance images show that the enlarged fetal thyroid gland *(arrows)* does not compromise the airway.

in fetal goiter. Primary fetal thyroid dysfunction may also cause goiter.

Fetal goiter appears as a midline homogeneous solid mass in the anterior neck surrounding the trachea (Fig. 33.33). There may be increased blood flow to the goiter. When large, fetal goiters cause hyperextension of the neck, leading to interference with fetal swallowing and resultant polyhydramnios. Neck hyperextension can lead to fetal malpresentation and can cause difficulties at delivery. Cordocentesis may be necessary to determine if there is fetal hypothyroidism or hyperthyroidism. In the setting of fetal **hypothyroidism,** treatment with intraamniotic thyroid hormone will often lead to a decrease in size of the fetal goiter.[130] After treatment with intrauterine thyroxine, fetal goiter may decrease in size, and hyperextension of the fetal neck may resolve. In cases of fetal **hyperthyroidism,** it is important to evaluate for fetal tachycardia and high-output cardiac failure.

CONCLUSION

Prenatal sonographic evaluation of the fetal face and neck offers an opportunity to identify many abnormalities. These observations are often essential to prenatal counseling and prognosis because of the association of many of these abnormalities with syndromes and chromosomal anomalies. Appropriate diagnosis of abnormalities allows for planning of the appropriate mode of delivery and therapy when the fetal airway is potentially compromised.

Acknowledgments

We would like to acknowledge with gratitude the assistance of librarians Alison Clapp and Miriam Geller and the administrative assistance of Susan Ivey, Department of Radiology, at Children's Hospital Boston. Special thanks also to Ants Toi, MD, for the discussion on craniosynostosis.

REFERENCES

1. American Institute of Ultrasound in Medicine. AIUM practice guidelines for the performance of obstetric ultrasound examinations 2013 [updated 2013]. Available from: www.aium.org/resources/guidelines/obstetric.pdf.
2. Moore KL, Persaud TVN, Torchia MG. The developing human: clinically oriented embryology. 10th ed. Philadelphia: Saunders; 2015.
3. Van de Water TR, Staecker H. Otolaryngology: basic science and clinical review. New York: Thieme; 2006.
4. Brookes M, Zietman A. Clinical embryology: a color atlas and text. Boca Raton, FL: CRC Press; 1998.
5. Nyberg DA, McGahan JP, Pretorius DH, Pilu G. Diagnostic imaging of fetal anomalies. Philadelphia: Lippincott Williams & Williams; 2002.
6. Forrester JV, Dick AD, McMenamin PG, et al. The eye: basic sciences in practice. 4th ed. New York: Saunders; 2015.
7. Haak MC, Bartelings MM, Jackson DG, et al. Increased nuchal translucency is associated with jugular lymphatic distension. Hum Reprod. 2002;17(4):1086-1092.
8. Kurjak A, Azumendi G, Andonotopo W, Salihagic-Kadic A. Three- and four-dimensional ultrasonography for the structural and functional evaluation of the fetal face. Am J Obstet Gynecol. 2007;196(1):16-28.
9. Johnson DD, Pretorius DH, Budorick NE, et al. Fetal lip and primary palate: three-dimensional versus two-dimensional US. Radiology. 2000;217(1):236-239.
10. De Jong-Pleij EA, Ribbert LS, Tromp E, Bilardo CM. Three-dimensional multiplanar ultrasound is a valuable tool in the study of the fetal profile in the second trimester of pregnancy. Ultrasound Obstet Gynecol. 2010;35(2):195-200.
11. Ocal DF, Nas T, Guler I. The place of four-dimensional ultrasound in evaluating fetal anomalies. Ir J Med Sci. 2015;184(3):607-612.
12. Tonni G, Martins WP, Guimaraes Filho H, Araujo Junior E. Role of 3-D ultrasound in clinical obstetric practice: evolution over 20 years. Ultrasound Med Biol. 2015;41(5):1180-1211.
13. Merz E, Abramovicz J, Baba K, et al. 3D imaging of the fetal face—recommendations from the International 3D Focus Group. Ultraschall Med. 2012;33(2):175-182.
14. Campbell S, Lees C, Moscoso G, Hall P. Ultrasound antenatal diagnosis of cleft palate by a new technique: the 3D "reverse face" view. Ultrasound Obstet Gynecol. 2005;25(1):12-18.
15. Chen ML, Chang CH, Yu CH, et al. Prenatal diagnosis of cleft palate by three-dimensional ultrasound. Ultrasound Med Biol. 2001;27(8):1017-1023.
16. Lee W, Kirk JS, Shaheen KW, et al. Fetal cleft lip and palate detection by three-dimensional ultrasonography. Ultrasound Obstet Gynecol. 2000;16(4):314-320.
17. Chervenak FA, Jeanty P, Cantraine F, et al. The diagnosis of fetal microcephaly. Am J Obstet Gynecol. 1984;149(5):512-517.
18. Thomas M. The lemon sign. Radiology. 2003;228(1):206-207.
19. Nyberg DA, Mack LA, Hirsch J, Mahony BS. Abnormalities of fetal cranial contour in sonographic detection of spina bifida: evaluation of the "lemon" sign. Radiology. 1988;167(2):387-392.
20. Nicolaides KH, Salvesen DR, Snijders RJ, Gosden CM. Strawberry-shaped skull in fetal trisomy 18. Fetal Diagn Ther. 1992;7(2):132-137.
21. Slater BJ, Lenton KA, Kwan MD, et al. Cranial sutures: a brief review. Plast Reconstr Surg. 2008;121(4):170e-178e.
22. Hajihosseini MK. Fibroblast growth factor signaling in cranial suture development and pathogenesis. Front Oral Biol. 2008;12:160-177.
23. Rawlins JT, Opperman LA. TGF-beta regulation of suture morphogenesis and growth. Front Oral Biol. 2008;12:178-196.
24. Hukki J, Saarinen P, Kangasniemi M. Single suture craniosynostosis: diagnosis and imaging. Front Oral Biol. 2008;12:79-90.
25. Delahaye S, Bernard JP, Renier D, Ville Y. Prenatal ultrasound diagnosis of fetal craniosynostosis. Ultrasound Obstet Gynecol. 2003;21(4):347-353.
26. Flores-Sarnat L. New insights into craniosynostosis. Semin Pediatr Neurol. 2002;9(4):274-291.
27. Gorincour G, Rypens F, Grignon A, et al. Prenatal diagnosis of cloverleaf skull: watch the hands! Fetal Diagn Ther. 2005;20(4):296-300.
28. Dover MS. Abnormal skull shape: clinical management. Pediatr Radiol. 2008;38(Suppl. 3):S484-S487.
29. Renier D, Lajeunie E, Arnaud E, Marchac D. Management of craniosynostoses. Childs Nerv Syst. 2000;16(10-11):645-658.
30. Brunelle F, Baraton J, Renier D, et al. Intracranial venous anomalies associated with atretic cephalocoeles. Pediatr Radiol. 2000;30(11):743-747.
31. Robinson AJ, Blaser S, Toi A, et al. MRI of the fetal eyes: morphologic and biometric assessment for abnormal development with ultrasonographic and clinicopathologic correlation. Pediatr Radiol. 2008;38(9):971-981.
32. Trout T, Budorick NE, Pretorius DH, McGahan JP. Significance of orbital measurements in the fetus. J Ultrasound Med. 1994;13(12):937-943.
33. Tan ST, Mulliken JB. Hypertelorism: nosologic analysis of 90 patients. Plast Reconstr Surg. 1997;99(2):317-327.
34. Bianchi D, Crombleholme T, D'Alton M, Malone F. Fetology: diagnosis and management of the fetal patient. 2nd ed. New York: McGraw-Hill Professional; 2010.
35. Dilmen G, Koktener A, Turhan NO, Tez S. Growth of the fetal lens and orbit. Int J Gynaecol Obstet. 2002;76(3):267-271.
36. Verma AS, Fitzpatrick DR. Anophthalmia and microphthalmia. Orphanet J Rare Dis. 2007;2:47.
37. Warburg M. Classification of microphthalmos and coloboma. J Med Genet. 1993;30(8):664-669.
38. Bault JP, Quarello E. Retinal coloboma: prenatal diagnosis using a new technique, the 'virtual fetal eyeground'. Ultrasound Obstet Gynecol. 2009;33(4):495-496.

39. Righini A, Avagliano L, Doneda C, et al. Prenatal magnetic resonance imaging of optic nerve head coloboma. Prenat Diagn. 2008;28(3):242-246.
40. Bateman JB. Microphthalmos. Int Ophthalmol Clin. 1984;24(1):87-107.
41. Cohen AJ, Mercandetti M, Brazzo BG. The lacrimal system: diagnosis, management and surgery. 2nd ed. New York: Springer; 2015.
42. Wong HS, Tait J, Pringle KC. Viewing of the soft and the hard palate on routine 3-D ultrasound sweep of the fetal face—a feasibility study. Fetal Diagn Ther. 2008;24(2):146-154.
43. Rahi JS, Dezateux C. Measuring and interpreting the incidence of congenital ocular anomalies: lessons from a national study of congenital cataract in the UK. Invest Ophthalmol Vis Sci. 2001;42(7):1444-1448.
44. Shih JC, Shyu MK, Lee CN, et al. Antenatal depiction of the fetal ear with three-dimensional ultrasonography. Obstet Gynecol. 1998;91(4):500-505.
45. Ginsberg NA, Cohen L, Dungan JS, et al. 3-D ultrasound of the fetal ear and fetal autosomal trisomies: a pilot study of a new screening protocol. Prenat Diagn. 2011;31(3):311-314.
46. Eavey RD. Microtia and significant auricular malformation. Ninety-two pediatric patients. Arch Otolaryngol Head Neck Surg. 1995;121(1):57-62.
47. Yeo L, Guzman ER, Ananth CV, et al. Prenatal detection of fetal aneuploidy by sonographic ear length. J Ultrasound Med. 2003;22(6):565-576.
48. Lowe LH, Booth TN, Joglar JM, Rollins NK. Midface anomalies in children. Radiographics. 2000;20(4):907-922.
49. Dietze I, Fritz B, Huhle D, et al. Clinical, cytogenetic and molecular investigation in a fetus with Wolf-Hirschhorn syndrome with paternally derived 4p deletion. Case report and review of the literature. Fetal Diagn Ther. 2004;19(3):251-260.
50. Cicero S, Curcio P, Papageorghiou A, et al. Absence of nasal bone in fetuses with trisomy 21 at 11-14 weeks of gestation: an observational study. Lancet. 2001;358(9294):1665-1667.
51. Orlandi F, Bilardo CM, Campogrande M, et al. Measurement of nasal bone length at 11-14 weeks of pregnancy and its potential role in Down syndrome risk assessment. Ultrasound Obstet Gynecol. 2003;22(1):36-39.
52. Otano L, Aiello H, Igarzabal L, et al. Association between first trimester absence of fetal nasal bone on ultrasound and Down syndrome. Prenat Diagn. 2002;22(10):930-932.
53. Vintzileos A, Walters C, Yeo L. Absent nasal bone in the prenatal detection of fetuses with trisomy 21 in a high-risk population. Obstet Gynecol. 2003;101(5 Pt 1):905-908.
54. Cusick W, Provenzano J, Sullivan CA, et al. Fetal nasal bone length in euploid and aneuploid fetuses between 11 and 20 weeks' gestation: a prospective study. J Ultrasound Med. 2004;23(10):1327-1333.
55. Rosen T, D'Alton ME, Platt LD, Wapner R. First-trimester ultrasound assessment of the nasal bone to screen for aneuploidy. Obstet Gynecol. 2007;110(2 Pt 1):399-404.
56. Cicero S, Dezerega V, Andrade E, et al. Learning curve for sonographic examination of the fetal nasal bone at 11-14 weeks. Ultrasound Obstet Gynecol. 2003;22(2):135-137.
57. Okumura M, Francisco RP, Lucato LT, et al. Prenatal detection and postnatal management of an intranasal glioma. J Pediatr Surg. 2012;47(10):1951-1954.
58. Chmait RH, Pretorius DH, Hull AD. Nasal glioma. Ultrasound Obstet Gynecol. 2002;20(4):417-418.
59. Huisman MA, Timmer A, Zeinstra M, et al. Matrix-metalloproteinase activity in first trimester placental bed biopsies in further complicated and uncomplicated pregnancies. Placenta. 2004;25(4):253-258.
60. Tonni G, Lituania M, Bonasoni MP, De Felice C. Prenatal ultrasound and histological diagnosis of fetal nasal glioma (heterotopic central nervous system tissue): report of a new case and review of the literature. Arch Gynecol Obstet. 2011;283(Suppl. 1):55-59.
61. Recio-Rodriguez M, Fernandez-Mayoralas DM, Fernandez-Jaen A, et al. Prenatal diagnosis of frontonasal dysplasia associated with bilateral periventricular nodular heterotopia. J Child Neurol. 2014;29(10):NP122-NP126.
62. Esmer AC, Kalelioglu I, Kayserili H, et al. Prenatal diagnosis of frontonasal dysplasia with anterior encephalocele. J Turk Ger Gynecol Assoc. 2013;14(1):50-52.
63. Wu E, Vargevik K, Slavotinek AM. Subtypes of frontonasal dysplasia are useful in determining clinical prognosis. Am J Med Genet A. 2007;143A(24):3069-3078.
64. Sadler TW. Langman's medical embryology. 14th ed. Philadelphia: Lippincott Williams & Wilkins; 2014.
65. Kirschner RE, LaRossa D. Cleft lip and palate. Otolaryngol Clin North Am. 2000;33(6):1191-1215, v-vi.
66. Berge SJ, Plath H, van de Vondel PT, et al. Fetal cleft lip and palate: sonographic diagnosis, chromosomal abnormalities, associated anomalies and postnatal outcome in 70 fetuses. Ultrasound Obstet Gynecol. 2001;18:422-431.
67. Chmait R, Pretorius D, Moore T, et al. Prenatal detection of associated anomalies in fetuses diagnosed with cleft lip with or without cleft palate in utero. Ultrasound Obstet Gynecol. 2006;27(2):173-176.
68. Calzolari E, Pierini A, Astolfi G, et al. Associated anomalies in multimalformed infants with cleft lip and palate: an epidemiologic study of nearly 6 million births in 23 EUROCAT registries. Am J Med Genet A. 2007;143a(6):528-537.
69. Nyberg DA, Sickler GK, Hegge FN, et al. Fetal cleft lip with and without cleft palate: US classification and correlation with outcome. Radiology. 1995;195(3):677-684.
70. Walker SJ, Ball RH, Babcook CJ, Feldkamp MM. Prevalence of aneuploidy and additional anatomic abnormalities in fetuses and neonates with cleft lip with or without cleft palate: a population-based study in Utah. J Ultrasound Med. 2001;20(11):1175-1180.
71. Perrotin F, de Poncheville LM, Marret H, et al. Chromosomal defects and associated malformations in fetal cleft lip with or without cleft palate. Eur J Obstet Gynecol Reprod Biol. 2001;99:19-24.
72. Benacerraf BR. Ultrasound of fetal syndromes. 2nd ed. St. Louis: Elsevier Health Sciences; 2007.
73. Stoll C, Clementi M. Prenatal diagnosis of dysmorphic syndromes by routine fetal ultrasound examination across Europe. Ultrasound Obstet Gynecol. 2003;21(6):543-551.
74. Shaikh D, Mercer NS, Sohan K, et al. Prenatal diagnosis of cleft lip and palate. Br J Plast Surg. 2001;54(4):288-289.
75. Cash C, Set P, Coleman N. The accuracy of antenatal ultrasound in the detection of facial clefts in a low-risk screening population. Ultrasound Obstet Gynecol. 2001;18(5):432-436.
76. Clementi M, Tenconi R, Bianchi F, Stoll C. Evaluation of prenatal diagnosis of cleft lip with or without cleft palate and cleft palate by ultrasound: experience from 20 European registries. EUROSCAN study group. Prenat Diagn. 2000;20(11):870-875.
77. Robinson JN, McElrath TF, Benson CB, et al. Prenatal ultrasonography and the diagnosis of fetal cleft lip. J Ultrasound Med. 2001;20(11):1165-1170.
78. Hanikeri M, Savundra J, Gillett D, et al. Antenatal transabdominal ultrasound detection of cleft lip and palate in Western Australia from 1996 to 2003. Cleft Palate Craniofac J. 2006;43(1):61-66.
79. Ghi T, Perolo A, Banzi C, et al. Two-dimensional ultrasound is accurate in the diagnosis of fetal craniofacial malformation. Ultrasound Obstet Gynecol. 2002;19(6):543-551.
80. Wang LM, Leung KY, Tang M. Prenatal evaluation of facial clefts by three-dimensional extended imaging. Prenat Diagn. 2007;27(8):722-729.
81. McGahan MC, Ramos GA, Landry C, et al. Multislice display of the fetal face using 3-dimensional ultrasonography. J Ultrasound Med. 2008;27(11):1573-1581.
82. Sepulveda W, Cafici D, Bartholomew J, et al. First-trimester assessment of the fetal palate: a novel application of the Volume NT algorithm. J Ultrasound Med. 2012;31(9):1443-1448.
83. Martinez-Ten P, Adiego B, Illescas T, et al. First-trimester diagnosis of cleft lip and palate using three-dimensional ultrasound. Ultrasound Obstet Gynecol. 2012;40(1):40-46.
84. Zajicek M, Achiron R, Weisz B, et al. Sonographic assessment of fetal secondary palate between 12 and 16 weeks of gestation using three-dimensional ultrasound. Prenat Diagn. 2013;33(13):1256-1259.
85. Sommerlad M, Patel N, Vijayalakshmi B, et al. Detection of lip, alveolar ridge and hard palate abnormalities using two-dimensional ultrasound enhanced with the three-dimensional reverse-face view. Ultrasound Obstet Gynecol. 2010;36(5):596-600.

86. Sepulveda W, Wong AE, Castro F, et al. Feasibility of 3-dimensional sonographic examination of the fetal secondary palate during the second-trimester anatomy scan. J Ultrasound Med. 2011;30(12):1619-1624.
87. Ramos GA, Romine LE, Gindes L, et al. Evaluation of the fetal secondary palate by 3-dimensional ultrasonography. J Ultrasound Med. 2010;29(3):357-364.
88. Ghi T, Tani G, Savelli L, et al. Prenatal imaging of facial clefts by magnetic resonance imaging with emphasis on the posterior palate. Prenat Diagn. 2003;23(12):970-975.
89. Stroustrup Smith A, Estroff JA, Barnewolt CE, et al. Prenatal diagnosis of cleft lip and cleft palate using MRI. AJR Am J Roentgenol. 2004;183(1):229-235.
90. Cohen Jr MM. Holoprosencephaly: clinical, anatomic, and molecular dimensions. Birth Defects Res A Clin Mol Teratol. 2006;76(9):658-673.
91. Longaker MT, Lipshutz GS, Kawamoto Jr HK. Reconstruction of Tessier no. 4 clefts revisited. Plast Reconstr Surg. 1997;99(6):1501-1507.
92. Tessier P. Anatomical classification facial, cranio-facial and latero-facial clefts. J Maxillofac Surg. 1976;4(2):69-92.
93. Chang YL, Lien R, Chang SD, Chao AS. Prenatal 3D sonographic diagnosis of an isolated lateral facial cleft. J Clin Ultrasound. 2012;40(4):219-221.
94. Maarse W, Pistorius LR, Van Eeten WK, et al. Prenatal ultrasound screening for orofacial clefts. Ultrasound Obstet Gynecol. 2011;38(4):434-439.
95. Benacerraf BR, Sadow PM, Barnewolt CE, et al. Cleft of the secondary palate without cleft lip diagnosed with three-dimensional ultrasound and magnetic resonance imaging in a fetus with Fryns' syndrome. Ultrasound Obstet Gynecol. 2006;27(5):566-570.
96. Pilu G, Segata M. A novel technique for visualization of the normal and cleft fetal secondary palate: angled insonation and three-dimensional ultrasound. Ultrasound Obstet Gynecol. 2007;29(2):166-169.
97. Faure JM, Baumler M, Boulot P, et al. Prenatal assessment of the normal fetal soft palate by three-dimensional ultrasound examination: is there an objective technique? Ultrasound Obstet Gynecol. 2008;31(6):652-656.
98. Faure JM, Captier G, Baumler M, Boulot P. Sonographic assessment of normal fetal palate using three-dimensional imaging: a new technique. Ultrasound Obstet Gynecol. 2007;29(2):159-165.
99. Wong RK, VanderVeen DK. Presentation and management of congenital dacryocystocele. Pediatrics. 2008;122(5):e1108-e1112.
100. Levine D, Cavazos C, Kazan-Tannus JF, et al. Evaluation of real-time single-shot fast spin-echo MRI for visualization of the fetal midline corpus callosum and secondary palate. AJR Am J Roentgenol. 2006;187(6):1505-1511.
101. Neville BW, Damm DD, Allen CM, Chi AC. Oral and maxillofacial pathology. 4th ed. St. Louis, MO: Saunders; 2015 May 2015.
102. Otto C, Platt LD. The fetal mandible measurement: an objective determination of fetal jaw size. Ultrasound Obstet Gynecol. 1991;1(1):12-17.
103. Chitty LS, Campbell S, Altman DG. Measurement of the fetal mandible—feasibility and construction of a centile chart. Prenat Diagn. 1993;13(8):749-756.
104. Paladini D, Morra T, Teodoro A, et al. Objective diagnosis of micrognathia in the fetus: the jaw index. Obstet Gynecol. 1999;93(3):382-386.
105. Lee W, McNie B, Chaiworapongsa T, et al. Three-dimensional ultrasonographic presentation of micrognathia. J Ultrasound Med. 2002;21(7):775-781.
106. Vettraino IM, Lee W, Bronsteen RA, et al. Clinical outcome of fetuses with sonographic diagnosis of isolated micrognathia. Obstet Gynecol. 2003;102(4):801-805.
107. Rogers-Vizena CR, Mulliken JB, Daniels KM, Estroff JA. Prenatal features predictive of Robin sequence identified by fetal magnetic resonance imaging. Plast Reconstr Surg. 2016;137(6):999e-1006e.
108. Lind K, Aubry MC, Belarbi N, et al. Prenatal diagnosis of Pierre Robin sequence: accuracy and ability to predict phenotype and functional severity. Prenat Diagn. 2015;35(9):853-858.
109. Ocaranza M, Rompel SM, Gutierrez J, Sepulveda W. Forehead hemangioma: a rare location for a large vascular tumor in a fetus. J Ultrasound Med. 2011;30(8):1158-1161.
110. Mulliken JB, Glowacki J. Hemangiomas and vascular malformations in infants and children: a classification based on endothelial characteristics. Plast Reconstr Surg. 1982;69(3):412-422.
111. Enjolras O, Mulliken JB. Vascular tumors and vascular malformations (new issues). Adv Dermatol. 1997;13:375-423.
112. Mulliken JB, Anupindi S, Ezekowitz RA, Mihm Jr MC. Case records of the Massachusetts General Hospital. Weekly clinicopathological exercises. Case 13-2004. A newborn girl with a large cutaneous lesion, thrombocytopenia, and anemia. N Engl J Med. 2004;350(17):1764-1775.
113. Legiehn GM, Heran MK. Venous malformations: classification, development, diagnosis, and interventional radiologic management. Radiol Clin North Am. 2008;46(3):545-597, vi.
114. Hyett J, Perdu M, Sharland G, et al. Using fetal nuchal translucency to screen for major congenital cardiac defects at 10-14 weeks of gestation: population based cohort study. BMJ. 1999;318(7176):81-85.
115. Souka AP, Krampl E, Bakalis S, et al. Outcome of pregnancy in chromosomally normal fetuses with increased nuchal translucency in the first trimester. Ultrasound Obstet Gynecol. 2001;18(1):9-17.
116. Michailidis GD, Economides DL. Nuchal translucency measurement and pregnancy outcome in karyotypically normal fetuses. Ultrasound Obstet Gynecol. 2001;17(2):102-105.
117. Makrydimas G, Sotiriadis A, Ioannidis JP. Screening performance of first-trimester nuchal translucency for major cardiac defects: a meta-analysis. Am J Obstet Gynecol. 2003;189(5):1330-1335.
118. Tanriverdi HA, Ertan AK, Hendrik HJ, et al. Outcome of cystic hygroma in fetuses with normal karyotypes depends on associated findings. Eur J Obstet Gynecol Reprod Biol. 2005;118(1):40-46.
119. Luchi C, Persico N, Rembouskos G, Nicolaides KH. Practical approach to obtain the mid-sagittal plane of the fetal face at 11-13 weeks' gestation by two-dimensional ultrasound. Ultrasound Obstet Gynecol. 2014;44(5):617-618.
120. Benacerraf BR, Frigoletto Jr FD. Soft tissue nuchal fold in the second-trimester fetus: standards for normal measurements compared with those in Down syndrome. Am J Obstet Gynecol. 1987;157(5):1146-1149.
121. Benacerraf BR, Gelman R, Frigoletto Jr FD. Sonographic identification of second-trimester fetuses with Down's syndrome. N Engl J Med. 1987;317(22):1371-1376.
122. Woodward PJ, Sohaey R, Kennedy A, Koeller KK. From the archives of the AFIP: a comprehensive review of fetal tumors with pathologic correlation. Radiographics. 2005;25(1):215-242.
123. Hirose S, Farmer DL, Lee H, et al. The ex utero intrapartum treatment procedure: looking back at the EXIT. J Pediatr Surg. 2004;39(3):375-380.
124. Otteson TD, Hackam DJ, Mandell DL. The ex utero intrapartum treatment (EXIT) procedure: new challenges. Arch Otolaryngol Head Neck Surg. 2006;132(6):686-689.
125. Bouchard S, Johnson MP, Flake AW, et al. The EXIT procedure: experience and outcome in 31 cases. J Pediatr Surg. 2002;37(3):418-426.
126. Wagner W, Harrison MR. Fetal operations in the head and neck area: current state. Head Neck. 2002;24(5):482-490.
127. Leva E, Pansini L, Fava G, et al. The role of the surgeon in the case of a giant neck mass in the EXIT procedure. J Pediatr Surg. 2005;40(4):748-750.
128. Fisher DA, Klein AH. Thyroid development and disorders of thyroid function in the newborn. N Engl J Med. 1981;304(12):702-712.
129. Bisschop PH, van Trotsenburg AS. Images in clinical medicine. Neonatal thyrotoxicosis. N Engl J Med. 2014;370(13):1237.
130. Morine M, Takeda T, Minekawa R, et al. Antenatal diagnosis and treatment of a case of fetal goitrous hypothyroidism associated with high-output cardiac failure. Ultrasound Obstet Gynecol. 2002;19(5):506-509.

CHAPTER 34

The Fetal Brain

Ants Toi and Deborah Levine

SUMMARY OF KEY POINTS

- Protocol-based ultrasound carefully performed by a knowledgeable and experienced examiner following established guidelines is very sensitive in evaluating the central nervous system (CNS).
- Ventriculomegaly can be due to many underlying conditions, including obstruction, destruction, and dysmorphism, or a combination.
- In cases of brain abnormalities in which additional morphologic or functional information is needed beyond that available with ultrasound, magnetic resonance imaging can be helpful.
- Best results in assessment of complex CNS abnormalities are obtained when there is a multidisciplinary consultation and collaboration among specialists in imaging, genetics, and prenatal and postnatal care.

CHAPTER OUTLINE

DEVELOPMENTAL ANATOMY
Embryology
Sonographic Anatomy
Variants (Usually Normal)
Choroid Plexus Cysts
Blake Pouch Cyst
Cavum Veli Interpositi
VENTRICULOMEGALY AND HYDROCEPHALUS
Pathogenesis of Ventriculomegaly
Ultrasound Evaluation of Ventriculomegaly
SPECIFIC ABNORMALITIES
ERRORS OF DORSAL INDUCTION
Anencephaly and Exencephaly
Cephalocele and Encephalocele
Ciliopathies
Joubert Syndrome
Meckel-Gruber Syndrome
Amniotic Band Sequence/Limb–Body Wall Complex
Cranial Changes in Spina Bifida
ERRORS OF VENTRAL INDUCTION
Holoprosencephaly
Posterior Fossa and Cerebellum
Dandy-Walker Malformation
Vermis Hypoplasia or Dysplasia
Mega–Cisterna Magna
Rhombencephalosynapsis
Other Posterior Fossa Abnormalities
Arachnoid Cysts
Malformations of Cortical Development
Microcephaly
Macrocephaly and Megalencephaly
Hemimegalencephaly
Lissencephaly
Focal Cortical Changes
Other Malformations of Cortical Development
Tuberous Sclerosis
Agenesis and Dysgenesis of Corpus Callosum
Absence of Septi Pellucidi and Septo-Optic Dysplasia
INTRACRANIAL CALCIFICATIONS
INFECTIONS
VASCULAR MALFORMATIONS
Thrombosis of Dural Sinuses
Hemorrhagic Lesions
Hydranencephaly
TUMORS
CONCLUSION
Acknowledgments

Anomalies of the central nervous system (CNS) are the most common cause of referral for prenatal diagnosis and result in great anxiety for parents. CNS anomalies occur with a frequency of about 1.4 to 1.6 per 1000 live births but are seen in about 3% to 6% of stillbirths.[1] The increased use of maternal serum alpha-fetoprotein (MS-AFP) screening and first-trimester nuchal translucency (NT) screening has resulted in increased numbers of pregnancies being referred for evaluation of the CNS and suspected anomalies. Fortunately, protocol-based ultrasound carefully performed by a knowledgeable and experienced examiner following established guidelines is very sensitive in evaluating the CNS.[2-6] Routine scanning is currently recommended at 18 to 20 weeks of gestation. Although many cerebral anomalies are detectable in the first trimester and early second trimester, others develop or become apparent only later in pregnancy.[7-11]

Magnetic resonance imaging (MRI) has become an important supplement after initial ultrasound evaluation. Multiparametric MRI using special sequences allows evaluation of areas that are difficult to assess with ultrasound, can be used to evaluate tissue properties beyond morphology, and provides new insights into ischemia, tumor characteristics, bleeding, brain metabolism, and neural tracts, which can allow unprecedented clarification of suspected disorders.[12-15] Debate continues regarding the role of ultrasound versus MRI in evaluating the fetal CNS.[16,17] We believe that ultrasound will continue to be the initial screening modality and that MRI will increasingly be used to clarify findings. The

important issues for the examiner are familiarity with the strengths and limitations of all imaging modalities, expertise in their use, and collaboration with specialists in other disciplines.[15,18-20]

DEVELOPMENTAL ANATOMY

Embryology

Knowledge of fetal gestational age is particularly important when evaluating anatomy in early pregnancy. In this chapter we use **menstrual age** and **gestational age** as typically used clinically and with ultrasound studies to mean "age from last menses" or "postmenstrual weeks." For consistency will convert "fertilization age" or "conception age" used in publications to menstrual age by adding 2 weeks.

CNS development is controlled by numerous genes with functions not only in the CNS but also in the rest of the body, and the understanding of the molecular basis of development and malformations is occurring at an explosive rate.[21] Morphologic changes start at about the fifth menstrual week when cells destined to form the notochord infiltrate into the embryonic disc and induce the overlying embryonic tissue to thicken, fold over, and fuse as the neural tube. Zipperlike fusion starts in the midtrunk of the embryo and then extends to the cranial and caudal ends (Table 34.1). Final anterior closure, at the **rostral neuropore,** occurs by about 5½ menstrual weeks, and a few days later at the **caudal neuropore.** By the sixth week, the cephalic end enlarges and flexes to become the brain.[22,23] Transvaginal ultrasound and *in vitro* MRI can demonstrate many of the stages.[8,9,24] By 12 to 15 menstrual weeks, almost all structures and processes are in their final form except for the **corpus callosum, cerebellar vermis, neuronal migration** (from the periventricular germinal matrix), development of the **sulci** and **gyri,** and **myelination.** These latter structures and processes develop from about 15 weeks onward. The corpus callosum starts developing at about 12 weeks. Its development induces the formation of the two septi pellucidi and the intervening space, the **cavum septi pellucidi** (CSP) and **cavum Vergae** (after Andrea Verga in 1851).[8,25]

TABLE 34.1 Differentiation of Brain Regions From Primary Vesicles

Primary Vesicle	Secondary Vesicle	Mature Structure
Forebrain	Telencephalon	Cerebral hemispheres Basal ganglia Olfactory system
	Diencephalon	Thalamus Hypothalamus
Midbrain	Mesencephalon	Midbrain
Hindbrain	Metencephalon	Pons Cerebellum
	Myelencephalon	Medulla

Modified from Moore K. Essentials of human embryology. Toronto, Ontario: BC Decker; 1988.[26]

The dorsal aspect of the neural tube at the hindbrain **(rhombencephalon)** is very thin and membranous (**membranous area** or **area membranosa**). In the first trimester, the enclosed central neural canal, the rhombencephalic cavity, is very large and forms a conspicuous cystic cavity that should not be mistaken for an abnormality.[8] This space eventually becomes the fourth ventricle. The membrane is divided into an anterior rostral area (anterior membranous area or area membranosa rostralis) and posterior caudal area (posterior membranous area or area membranosa caudalis) by a fold, the plica choroidea, which will become the choroid of the fourth ventricle. The **cerebellum** and **vermis** develop as lateral and rostral proliferations into the anterior membranous area. The posterior membranous area eventually fenestrates to form the foramina of Magendie and Luschka. The posterior membranous area can bulge into the cisterna magna to a variable extent, forming the **Blake pouch.** With high-resolution equipment, the Blake pouch can be seen in most fetuses, where it is often mistaken for arachnoid strands.[27-29] The cerebellum and vermis are essentially formed by 22 weeks. Care must be taken before 22 weeks to avoid mistaking the incompletely developed early vermis for vermian dysplasia or hypoplasia.[30]

Cortex and neuron development starts at about 5 weeks and is complete by 28 weeks. There are three complex overlapping stages: proliferation, migration, and organization. Neurons proliferate and develop from glial stem cells at the surface of the ventricles and ganglionic eminence. Migration occurs via two pathways, projectional and tangential. In projectional migration, neurons follow a radially oriented glial scaffold directly to the cortical surface, with later-forming neurons passing through the earlier layers to the pial surface. From 17 to 34 weeks, this migration can be seen as bands or laminations that are visible on MRI and ultrasound as the ventricular zone, intermediate zone, subplate zone, and cortical plate. This regular pattern is disturbed with migrational disorders, malformations, and infections such as cytomegalovirus (CMV).[31-33] In tangential migration, GABAergic cells from the ganglionic eminence take a tangential route through the cortex and provide neurons with controlling functions. The ganglionic eminence overlying the thalamus is more evident on MRI than ultrasound.[34,35] The cortex undergoes folding into gyri to accommodate the extra cells. Finally, neurons in the cortex organize local connections and send axons remotely as large tracts such as the corpus callosum to connect the hemispheres. Development requires normally functioning genes and is easily disrupted by intrinsic and extrinsic insults such as fetal and maternal metabolic disorders, hypoxia, infections, and teratogens. Note that with teratogens, the final morphologic appearance reflects the gestational age and stage at which disruption occurred, rather than the specific agent.[21,36]

Sonographic Anatomy

The early embryo is best examined transvaginally. The cephalic end is identifiable by about 8 weeks. By 10 or 11 weeks, bones of the vault show mineralization. At this age, the brain mantle is very thin. The ventricles are large and filled with choroid, which provides nourishment for the developing brain.[37] A large, echo-free space behind the hindbrain represents the **rhombencephalic cavity,** which decreases in size as the cerebellum forms

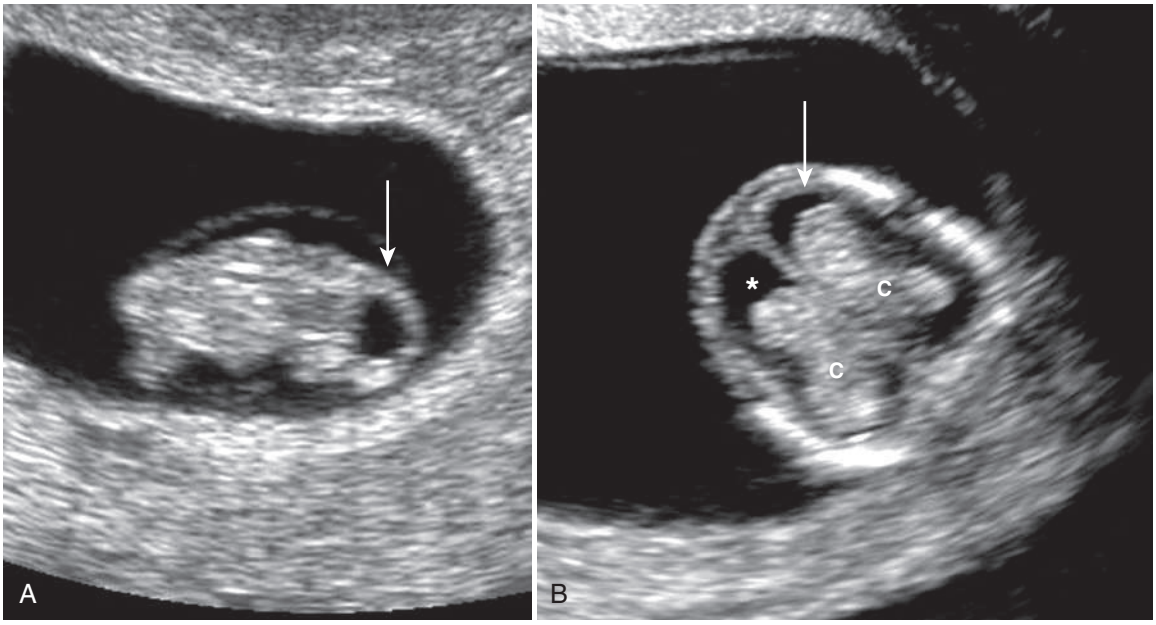

FIG. 34.1 Early Normal Fetal Head Images Obtained With Transvaginal Probe. (A) At 8 menstrual weeks the head is clearly differentiated from the trunk and limb buds. The intracranial cystic structure is the fetal rhombencephalic cavity *(arrow),* a normal space that eventually becomes the fourth ventricle. **(B) Scan at 12½ weeks.** Note that the cerebral cortex is very thin *(at tip of arrow).* The choroid plexuses *(C)* are very large and fill the ventricles (*) from side to side. Ossification is already visible in the skull bones.

and is destined to become the fourth ventricle. In the first trimester the normal rhombencephalic cavity appears especially large and prominent and should not be mistaken for an abnormality[8,38] (Fig. 34.1A).

After 13 or 14 weeks, most cerebral structures can be identified ultrasonographically (see Fig. 34.1B). In the second trimester, three standard transaxial planes or views (thalamic, ventricular, and cerebellar) can lead to the detection of more than 95% of sonographically detectable cerebral anomalies.[2,3,5,39] These three views (thalamic view, ventricular view, and cerebellar view) form the starting point for routine scanning. If abnormality is suspected, then additional views including transvaginal scan and the midline view to assess the corpus callosum and vermis are useful to clarify problems[5,20,40] (Fig. 34.2, Video 34.1, Video 34.2, and Video 34.3).

Cranial Structures to Note at Routine Anatomic Scan

Measurement of biparietal diameter and head circumference
Head shape
Bone density
Falx and interhemispheric fissure
Ventricle size and appearance
Cavum of the septi pellucidi (CSP)
Thalamus
Cerebellum and vermis
Cisterna magna
Nuchal fold
(Median view for corpus callosum and vermis—not part of routine scanning, but increasingly being done)

The **thalamic view** displays the **thalamus, third ventricle, fornices, basal ganglia, insula,** and **ambient cistern** and is used to measure the biparietal diameter (BPD), occipitofrontal diameter (OFD), and head circumference (HC) (see Fig. 34.2A). The smooth straight interhemispheric fissure is visible on this and the ventricular view. If the fissure appears irregular, then abnormalities of the corpus callosum and other cerebral structures should be suspected.[41,42] The **ventricular view** is slightly higher than the thalamic view and shows the bodies and, more important, the **atria of the lateral ventricles** as well as the **interhemispheric fissure** (see Fig. 34.2B).

Atrial width (occipital horn width) is the most useful and accepted measurement of ventricular size.[3,5,6] The atrium of the lateral ventricles is the site of confluence of the bodies, occipital horns, and temporal horns. Fortuitously, with abnormalities this is the part of the ventricle that undergoes the earliest and most marked enlargement. Ventricular measurement is a required element of routine scans and is easily performed during routine obstetric scanning. Usually only the distal ventricle is measured because the closer ventricle is obscured by artifact; it is assumed that the ventricles are symmetrical, but mild asymmetry is common (Fig. 34.3). Measurements should be performed in a very standardized manner on true axial views. Calipers should be placed touching the inner walls of the ventricles opposite the deepest part of the parieto-occipital fissure; a normal value is taken as below 10 mm.[39] Ventricular abnormality, especially enlargement, is a key finding in the initial detection of CNS abnormalities and is seen in about 88% of fetuses with cerebral abnormalities.[39,43]

The **cerebellar view** is obtained by rotating the transducer into a suboccipitobregmatic plane centered on the thalamus to show the **cerebellar hemispheres.** This view shows the cerebellum,

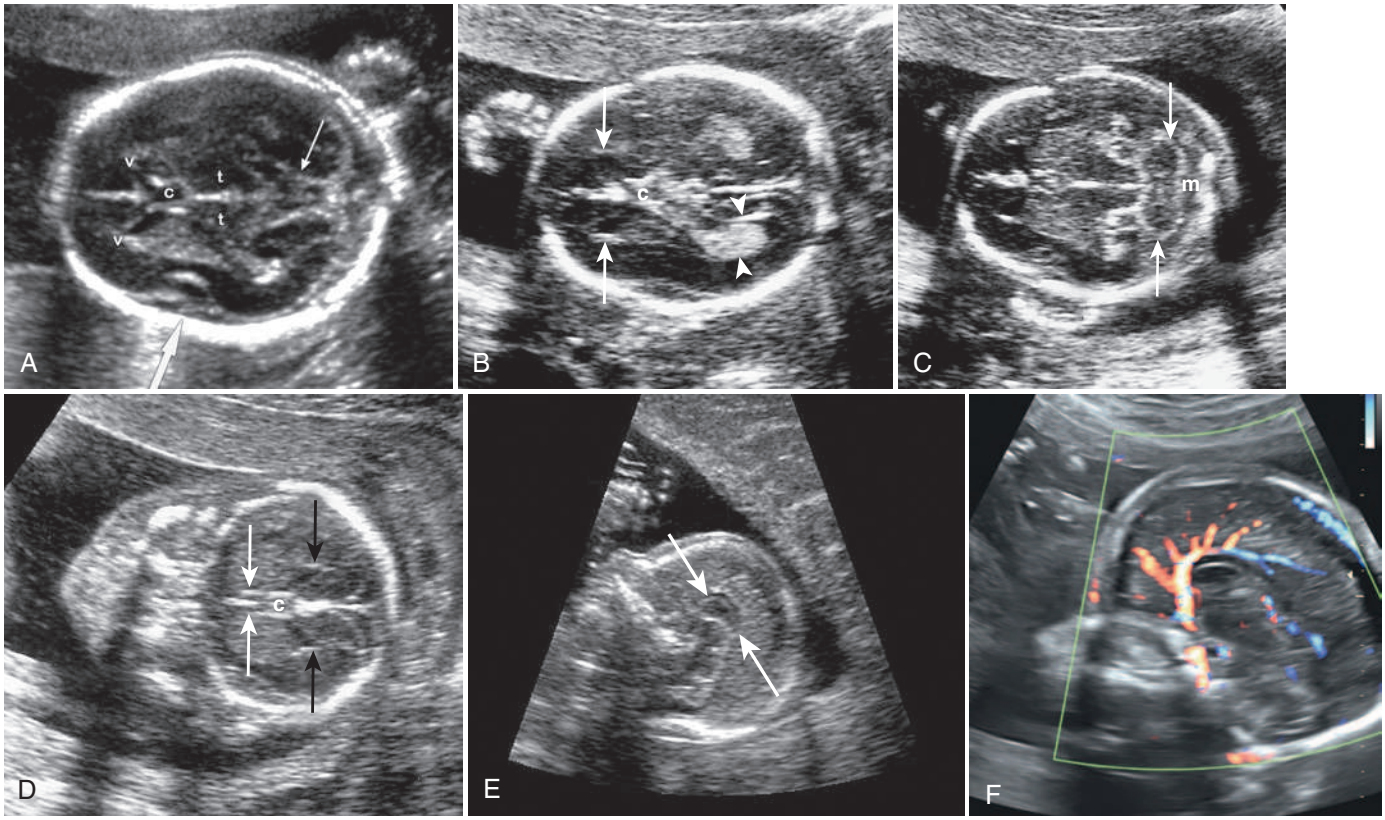

FIG. 34.2 Standard and Additional Planes for Viewing Cerebral Structures. (A) Thalamic view at 20 menstrual weeks. This transverse view at the level of the diamond-shaped thalamus-hypothalamus complex *(t)* contains the slitlike midline third ventricle. The echogenic triangular area behind the thalamus and between the occipital lobes is the ambient cistern *(arrow),* which contains cerebrospinal fluid (CSF) but is rendered echogenic because of strands of meninges supporting the brain structures. The insula is a short, brightly echogenic line *(thick arrow)* containing the pulsating middle cerebral artery branches. It is surrounded by normal white matter that is very hypoechoic and should not be mistaken for fluid. The echogenic band between thalamus and insula is the basal ganglia. Anteriorly are the tips of the anterior frontal horns of the lateral ventricles *(v),* and between them is the boxlike cavum septi pellucidi *(c).* **(B) Ventricular view at 18 weeks.** The atrium of the occipital horn is filled with echogenic choroid, and the ventricle measurement is indicated *(arrowheads).* Note that the choroid fills more than 60% of atrium width. The measurement between the medial ventricle wall and the choroid is less than 3 mm. The tips of the anterior frontal horns are visible *(arrows). c,* Cavum septi pellucidi. **(C) Cerebellar view at 18 menstrual weeks** is obtained by rotating the transducer from the thalamic view so that the cerebellar hemispheres *(arrows)* in the posterior fossa come into view, connected in the midline by the slightly more echogenic and narrower vermis. The cisterna magna *(m)* is visible between the cerebellum and the occipital bone. Also visible in this view are the thalamus, third ventricle, anterior horns, and cavum septi pellucidi. **(D) Coronal view at 19 weeks through the coronal suture** shows anterior frontal horns *(black arrows)* and large nerve trunks; the fornices *(white arrows)* are clearly visible below the cavum septi pellucidi *(c).* **(E) Midsagittal view through metopic suture at 19 weeks** shows normal corpus callosum *(arrows)* containing the cavum septi pellucidi in its arc below the corpus callosum. The echogenic cerebellar vermis is visible posteriorly. **(F) Sagittal color Doppler image shows the pericallosal artery.** Coronal and median views such as **(E)** and **(F)** are invaluable when there are concerns regarding midline structures.

cisterna magna, **cavum septi pellucidi** (CSP), and frequently the anterior horns of the lateral ventricles. Up to about 24 weeks, the transverse cerebellar diameter corresponds to gestational weeks. The **cisterna magna** is the cerebrospinal fluid (CSF) space behind the cerebellum and is measured between the cerebellar vermis and inner occipital bone on an axial plane that includes the anterior end of the CSP and the midplane of the cerebellum. It is normally 2 to 10 mm[5,44] (see Fig. 34.2C). Cisterna magna obliteration suggests **Chiari II malformation** and spina bifida. Excessive enlargement may be seen with **mega–cisterna magna, Blake pouch cyst, vermian dysplasia, Dandy-Walker syndrome,** and **arachnoid cysts.**[45-47]

Additional sonographic views and projections using the windows provided by the fontanelles and sutures can help to clarify brain anatomy and development. The **median (midsagittal) view** through the metopic suture–anterior fontanelle–sagittal suture shows midline structures such as the corpus callosum and occasionally the cerebellar vermis and brainstem[5] (see Fig. 34.2E-F). The posterolateral mastoid fontanelles can provide access to the cerebellum and occipital lobes and ventricles.

The **sulci** and **gyri** undergo predictable development patterns that can be assessed as early as 18 weeks. Special views to evaluate development of sulci and insula can be helpful in detecting abnormal development such as lissencephaly[48-50] (Fig. 34.4).

Multiplanar three-dimensional (3-D) imaging can be used to reconstruct axial and median views to assess the brain in any orientation. Midsagittal reconstructions are especially helpful in evaluating abnormalities of the corpus callosum and cerebellum.[40,51-53] Head shape and ossification should be noted with all these views (see Chapter 33). Although ultrasound is the mainstay

FIG. 34.3 Ventricular Measurement. Image at 20 weeks showing the appropriate position of calipers to measure the lateral ventricle.

of a prenatal examination, MRI has been proven to be valuable to further assess problems found with ultrasound. MRI provides excellent anatomic images after about 22 weeks' gestation and is superior in evaluating the character of brain tissue and the periphery of the brain, where ultrasound visibility is limited (Fig. 34.5). However, MRI has limitations in showing cerebral calcifications and small cysts.[18,54,55]

Variants (Usually Normal)

Choroid Plexus Cysts

Choroid plexus cysts (CPCs) are cystlike spaces in the choroid plexus and are due to entrapment of CSF within an infolding of neuroepithelium (Fig. 34.6, Video 34.4). It is suggested that only CPCs over 3 mm should be considered substantial enough to be termed "choroid plexus cyst." They are common and seen in 1% to 6% of fetuses between 14 and 24 weeks' gestation. Most are small and disappear without consequence by about 28 weeks. Rarely, large cysts may transiently dilate the lateral ventricles. They do not affect neurological development.[56]

The great majority of CPCs are found incidentally in normal fetuses, but they can be associated with trisomy 18. About 50% of trisomy 18 fetuses have CPC, and they are the only obvious initial finding in about 10% of trisomy 18 cases. Likelihood ratios of trisomy 18 with isolated CPC are about 7 (range 4-12) times the mother's background risk. Size and bilaterality of the cysts do not affect incidence of aneuploidy. Fetuses with trisomy 18 almost always have other detectable abnormalities. When CPCs are found, there should be a detailed search for features of trisomy 18, especially the hands, heart, and CNS. Other tests of aneuploidy risk should be reviewed, including maternal age, serum screening, and cell free fetal DNA testing (noninvasive prenatal testing [NIPT]) to ensure low aneuploidy risk. Many feel that patients with isolated CPC and low aneuploidy risk, especially with normal NIPT findings, do not warrant further counseling or testing.[20,57,58]

Blake Pouch Cyst

Blake pouch cyst, described by Robert Blake over 100 years ago, is a thin-walled cystic structure commonly seen in the midline of the posterior fossa behind the lower portion of the cerebellar vermis and brainstem. Because it contains CSF, this cyst is echo free, unlike the adjacent subarachnoid fluid, which is slightly echogenic owing to fine strands in the subarachnoid space (Fig. 34.7). Of note, this difference in appearance of the fluid and Blake cyst walls are not visible on MRI. With careful scanning, we have found that a Blake pouch cyst is visible in almost every fetus varying in size from tiny to large and conspicuous. A large Blake pouch can be associated with vermian rotation to 40 to 50 degrees with an intact vermis. Some feel this rotation results from delayed fenestration of the foramina of Magendie and Luschka and secondary cystic dilation of the inferior membranous area, which is the pouch and elevates the vermis. If isolated, the rotation typically decreases in later pregnancy and outcome is good.[28,59] When isolated, it should not be mistaken for abnormality. Three-dimensional ultrasound with midline reconstruction is especially helpful in this regard and can confirm vermian normality, as can MRI. We agree with those who feel that the mega–cisterna magna (MCM) is simply a large Blake pouch cyst, possibly resulting from delayed fenestration of the foramina; however, a few with isolated MCM may show developmental delay.[27,29,60]

Cavum Veli Interpositi

Cavum veli interpositi (CVI) is a small cystic collection in the midline, seen below the splenium of the corpus callosum, behind the upper brainstem and above the region of the pineal gland (Fig. 34.8). It represents fluid in the potential space in the telea choroidea above the third ventricle. Most CVIs are seen just below the splenium, but they can extend anteriorly above the third ventricle to the foramina of Monroe. Coronal, midsagittal, and 3-D scans to help to confirm the diagnosis and MRI and color Doppler exclude vascular abnormality such as vein of Galen aneurysm[61] (see Fig. 34.8C). Although infrequently described in the prenatal ultrasound literature, we have found small CVIs, with maximal diameter less than 8 mm, to be very common on axial scans at 18 to 20 weeks. The pediatric literature reports a CVI incidence of 5% to 34%.[62] Most CVIs are of no clinical consequence, and many recede spontaneously with normal long-term neurologic outcome.[62-65] Occasionally, however, large cysts can distort the brainstem and adjacent brain, causing obstructive hydrocephalus (HC), and need treatment by unroofing.

The physiologic CVI cysts tend to be isolated, unilocular, and small (<10 mm) and remain stable or recede over time. There is no known genetic association. The differential diagnosis includes cysts and cystlike conditions that occur in the midline, such as **dilated cavum Vergae, glioependymal cysts, arachnoid cysts, cystic tumors** (mainly cystic teratomas), **vein of Galen aneurysm, pineal cyst,** and **hemorrhage.** Pathologic cystic collections are generally larger, enlarge over time, and have associated abnormalities such as corpus callosum dysgenesis, ventriculomegaly (VM), or solid masses.[61,62,64,65]

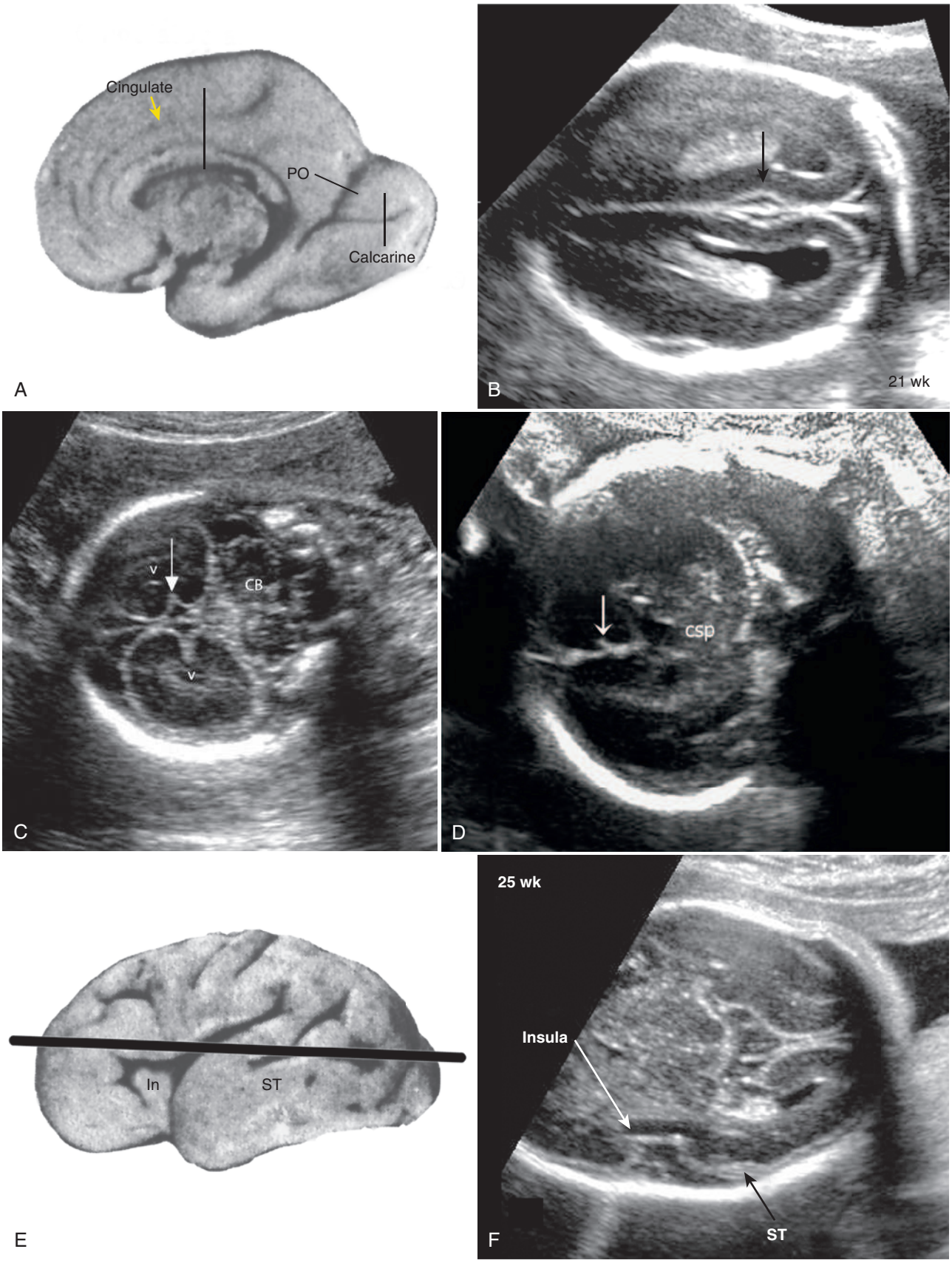

FIG. 34.4 Scan Planes *(Dark Lines)* Used to Assess Early-Appearing Sulci. Note that the scan planes are perpendicular to the direction of the sulcus being evaluated. **(A) Medial hemispheric surface at 26 weeks.** Coronal scan plane is best for cingulate sulcus *(yellow arrow)* and calcarine sulcus. Axial plane is best for parieto-occipital sulcus *(PO).* **(B) Axial view at 21 weeks** shows the diamond shape formed by the normal parieto-occipital sulci *(arrow).* **(C) Coronal view through the occipital lobes at 24 weeks** shows the calcarine sulcus *(arrow)* on the medial surface of the occipital lobe. Mild left-right asymmetry is normal. *CB,* Cerebellum; *V,* ventricles. **(D) Coronal view through parietal brain** shows the notch of the cingulate sulcus *(arrow)* above the bodies of the lateral ventricles and cavum septi pellucidi *(csp).* This is an excellent view to confirm normal cavum septi pellucidi. **(E) Lateral view of brain surface at 26 weeks** shows the scan plane used to evaluate the insula *(In)* and superior temporal sulcus *(ST)* behind it. **(F) Angular plateau of the insula** on axial view, and behind it the subtle indentation of the **superior temporal sulcus** *(arrow with ST).* (Anatomic images modified from Dorovini-Zis K, Dolman C. Gestational development of the brain. Arch Pathol Lab Med. 1977;101:192-195. Ultrasound images from Toi A, Chitayat D, Blaser S. Abnormalities of the foetal cerebral cortex. Prenat Diagn. 2009;29[4]:355-371.[188])

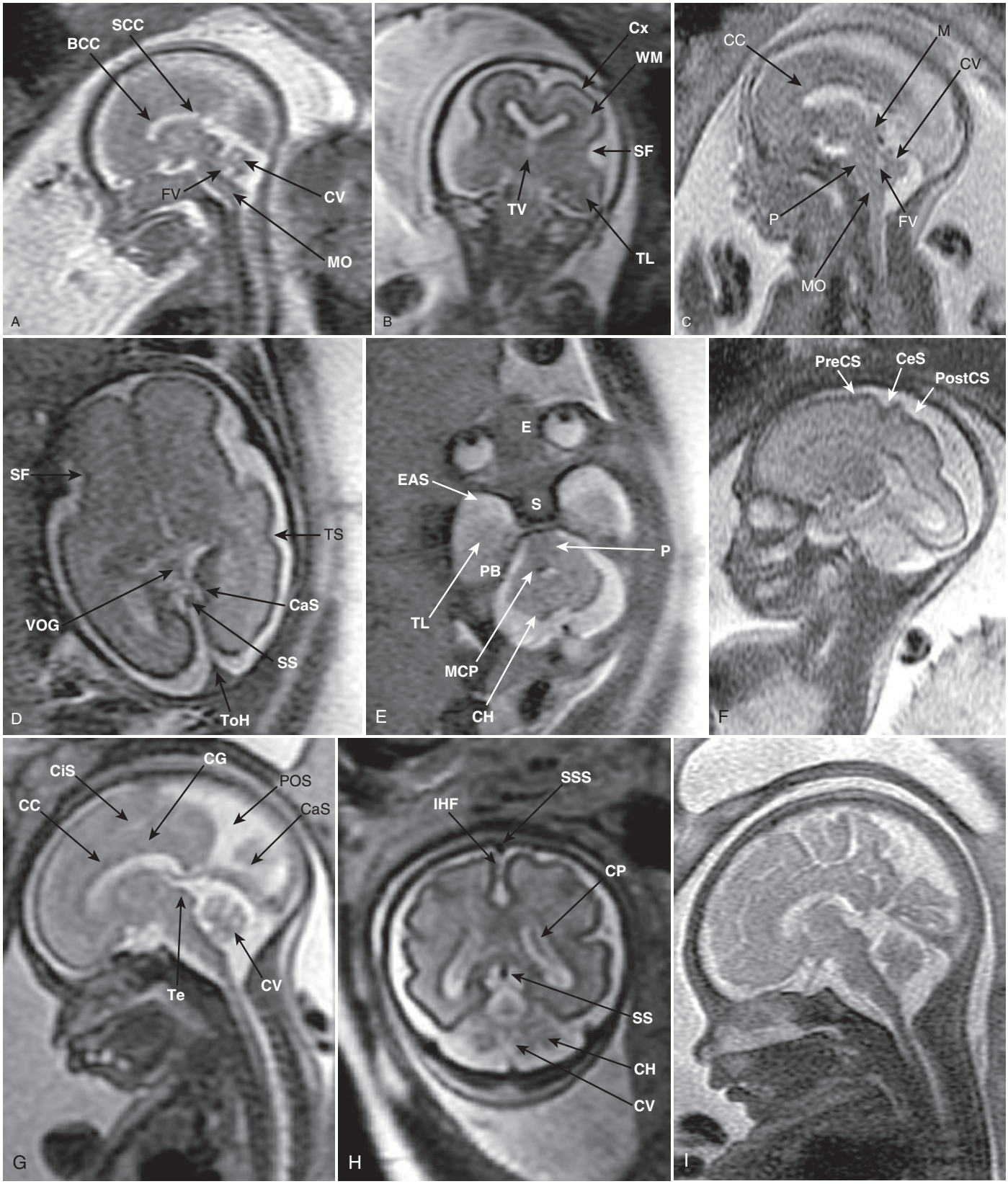

FIG. 34.5 Normal Brain Appearance on Magnetic Resonance Imaging (MRI). T2-weighted images at 20 weeks (**[A]** and **[B]**), 22 weeks **(C),** 26 weeks (**[D]** and **[E]**), 27 weeks (**[F]-[H]**), and 34 weeks **(I);** in sagittal midline **([A], [C], [G], [I]),** parasagittal **(F),** coronal (**[B]** and **[H]**), and axial (**[D]** and **[E]**) planes. *BCC,* Developing body of the corpus callosum; *CaS,* calcarine sulcus; *CC,* corpus callosum; *CeS,* central sulcus; *CG,* cingulate gyrus; *CH,* cerebellar hemispheres; *CiS,* cingulate sulcus; *CP,* choroid plexus; *CV,* cerebellar vermis; *Cx,* cerebral cortex; *E,* ethmoid bone; *EAS,* extraaxial space; *FV,* fourth ventricle; *IHF,* interhemispheric fissure; *M,* midbrain; *MCP,* middle cerebellar peduncle; *MO,* medulla oblongata; *P,* pons; *POS,* parieto-occipital sulcus; *PostCS,* postcentral sulcus; *PreCS,* precentral sulcus; *S,* sphenoid bone; *SCC,* splenium of the corpus callosum; *SF,* sylvian fissure; *SS,* straight sinus; *SSS,* superior sagittal sinus; *Te,* tectum; *TL,* temporal lobe; *ToH,* torcular Herophili; *TS,* temporal sulcus; *TV,* third ventricle; *VOG,* vein of Galen; *WM,* white matter. (With permission from Levine D, Robson C. MR imaging of normal brain in the second and third trimesters. In: Levine D, editor. Atlas of fetal MRI. Bristol, PA: Taylor & Francis; 2005.[256])

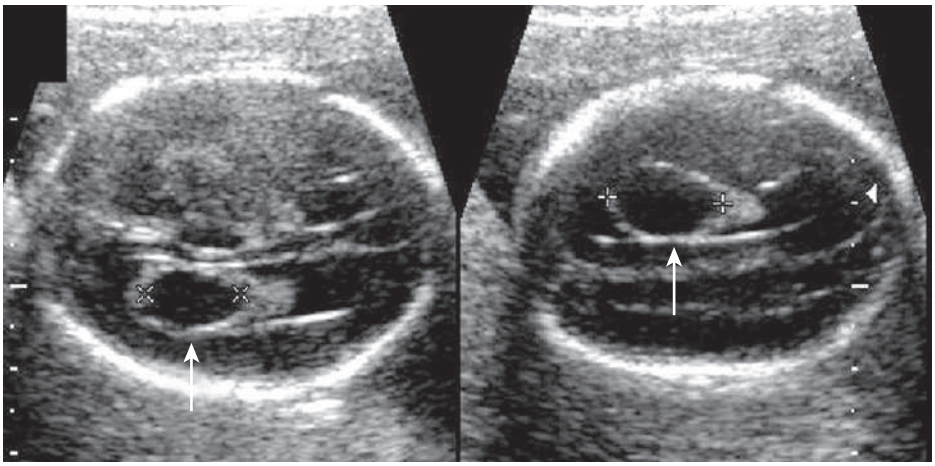

FIG. 34.6 Bilateral Choroid Plexus Cysts *(Arrows).* Note that on the right, an oblique scan plane has been used to view the upper hemisphere through the squamosal suture. See also Video 34.4.

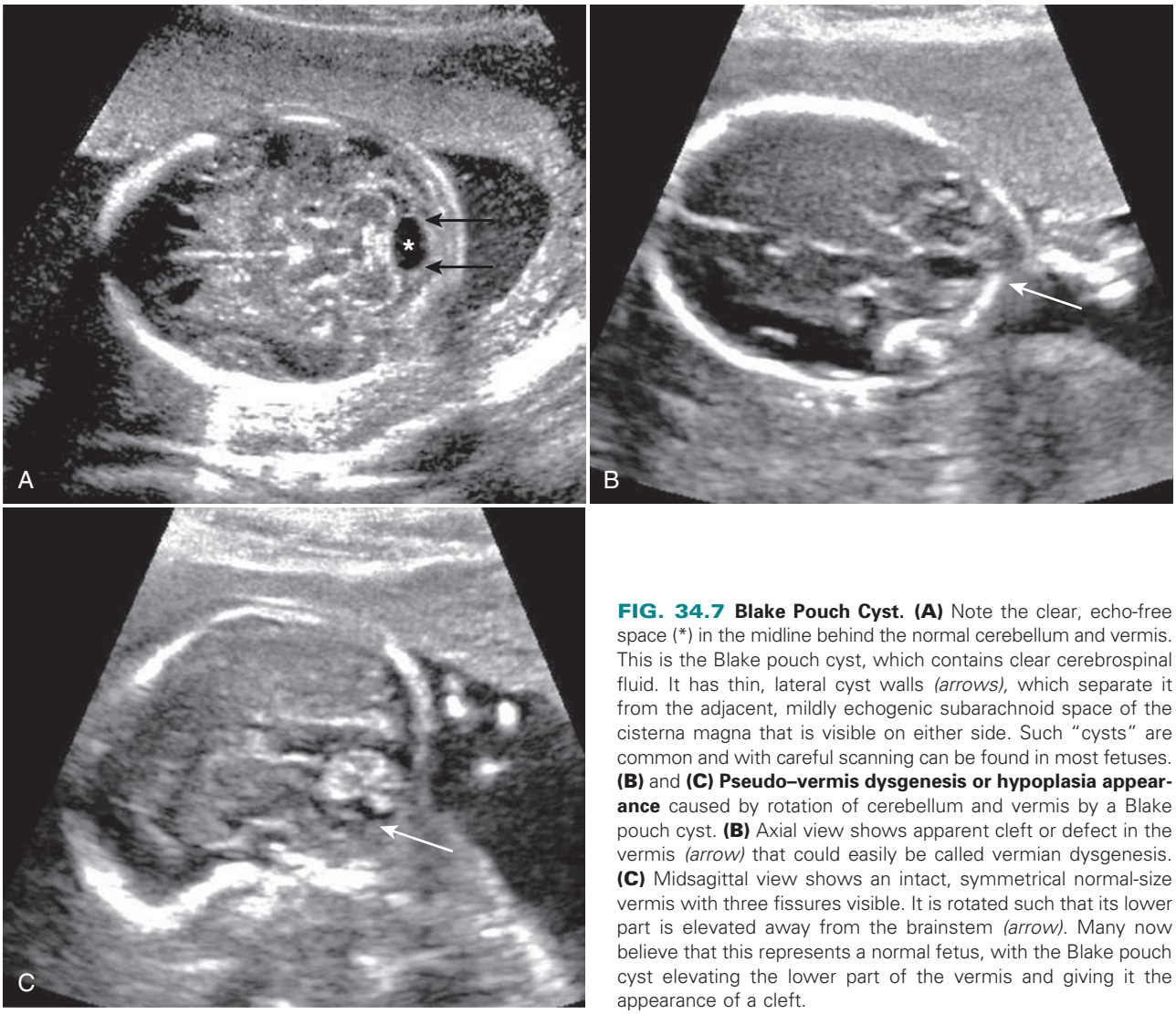

FIG. 34.7 Blake Pouch Cyst. (A) Note the clear, echo-free space (*) in the midline behind the normal cerebellum and vermis. This is the Blake pouch cyst, which contains clear cerebrospinal fluid. It has thin, lateral cyst walls *(arrows),* which separate it from the adjacent, mildly echogenic subarachnoid space of the cisterna magna that is visible on either side. Such "cysts" are common and with careful scanning can be found in most fetuses. **(B)** and **(C) Pseudo–vermis dysgenesis or hypoplasia appearance** caused by rotation of cerebellum and vermis by a Blake pouch cyst. **(B)** Axial view shows apparent cleft or defect in the vermis *(arrow)* that could easily be called vermian dysgenesis. **(C)** Midsagittal view shows an intact, symmetrical normal-size vermis with three fissures visible. It is rotated such that its lower part is elevated away from the brainstem *(arrow).* Many now believe that this represents a normal fetus, with the Blake pouch cyst elevating the lower part of the vermis and giving it the appearance of a cleft.

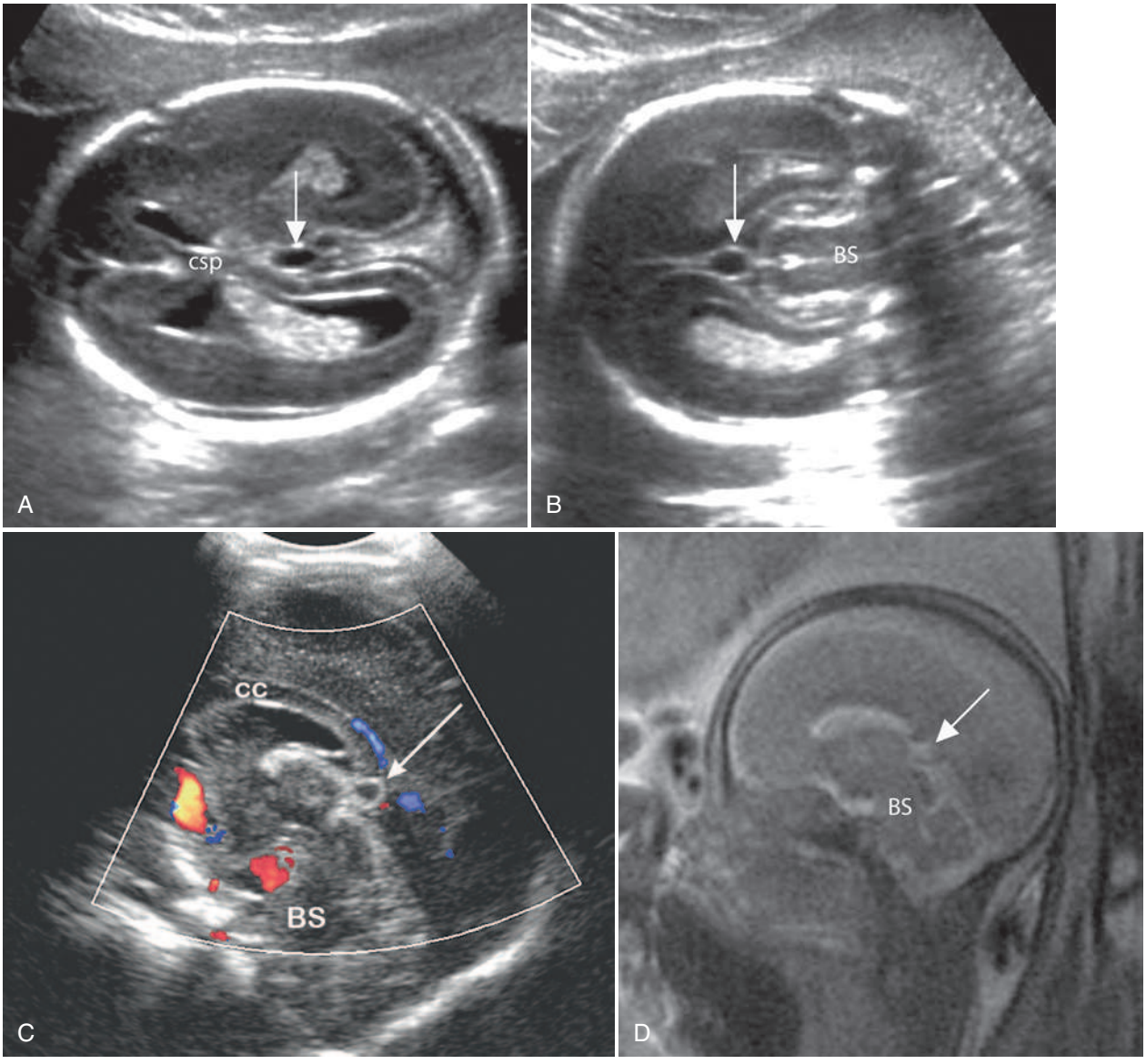

FIG. 34.8 Cavum Veli Interpositi (CVI). (A) CVI on axial view at 19 weeks *(arrow). csp,* Cavum septi pellucidi. CVIs of this size are frequent but are commonly overlooked. **(B)** CVI on coronal view *(arrow). BS,* Brainstem. **(C)** CVI on color Doppler sagittal view *(arrow)* lying just below the splenium of the corpus callosum *(cc). BS,* Brainstem. There is no flow on color Doppler. **(D)** T2-weighted magnetic resonance image of 21-week fetus showing CVI *(arrow).*

Fetuses with suspected CVI cysts should undergo detailed neurosonography and anatomic scan including Doppler to exclude vein of Galen aneurysm. If there are any atypical features or associated findings, then MRI can be helpful in further investigation. We no longer monitor incidentally discovered small (<8 mm) isolated cysts but perform follow-up scans if the cysts are especially conspicuous or if there is parental concern.

VENTRICULOMEGALY AND HYDROCEPHALUS

The term **ventriculomegaly** (VM) describes ventricles 10 mm or larger at the atrium. Care should be taken to measure the ventricles in the appropriate plane; an oblique plane will lead to an apparently enlarged ventricle if the trigone is measured. The head itself may be normal, large, or even smaller than expected for menstrual age. "Hydrocephalus" refers to enlarged ventricles associated with increased intracranial pressure and thus is typically associated with head enlargement.[66] Ventricular abnormality, especially enlargement, is the most commonly encountered cranial abnormality at prenatal ultrasound, with prenatal incidence of 10 to 80 per 10,000 pregnancies. It is often the key finding in the initial detection of CNS abnormalities and is found in about 88% of fetuses with cerebral abnormalities[39,43,67,68] (Fig. 34.9).

Ventricle measurement technique is important and details should be remembered. With the head in a true axial view, measurements are generally taken only of the distal ventricle since the near ventricle is obscured by skull bone artifact and ventricles are presumed to be symmetrical. Calipers are placed

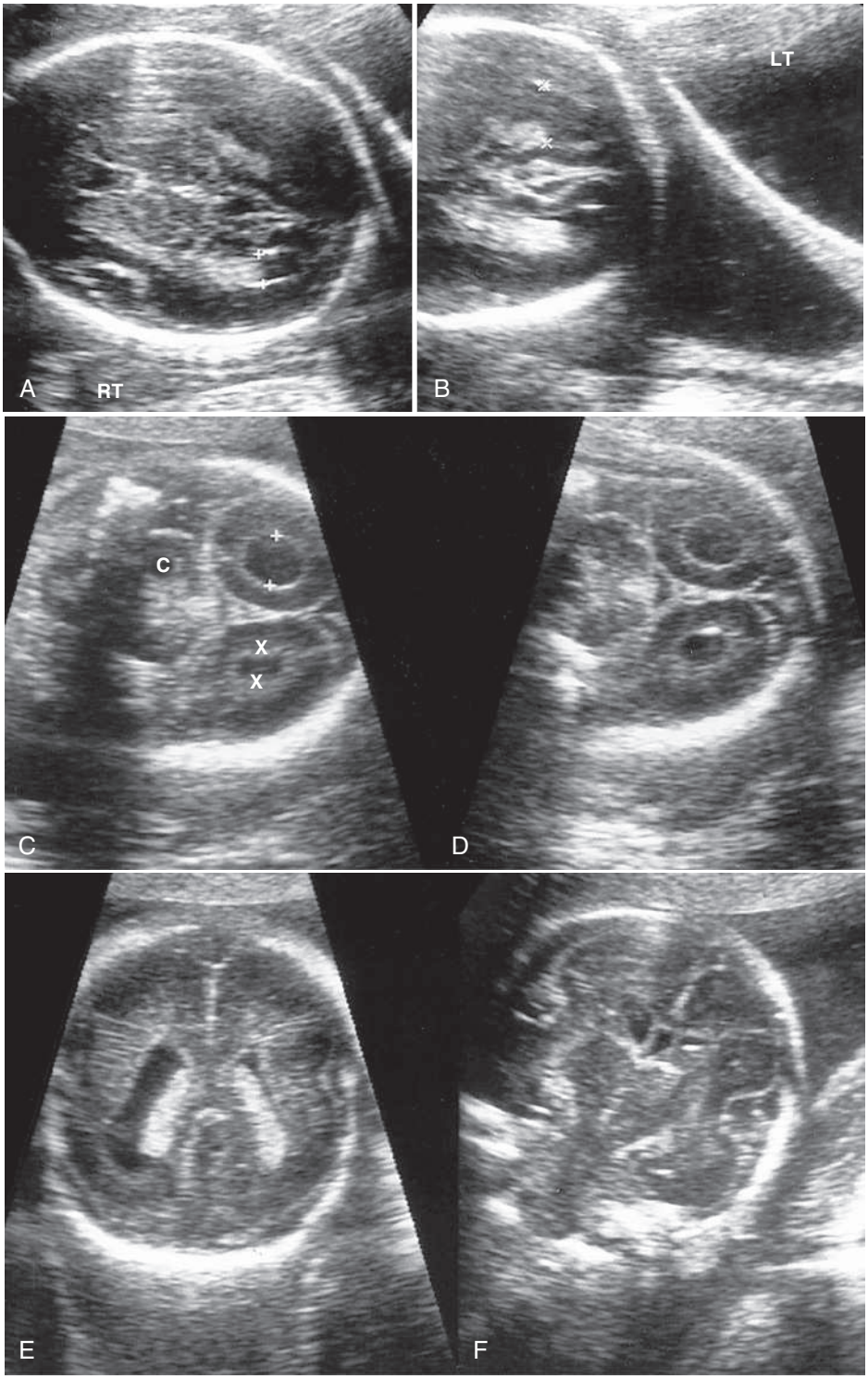

FIG. 34.9 Assessment of Ventricles at 23 Weeks Shows Normal, Mild Asymmetry. (A) Axial view shows the usually measured lower ventricle *(calipers).* **(B)** By viewing through the posterior squamosal suture, one can visualize the upper ventricle in the oblique axial plane *(calipers).* Oblique image planes can increase the ventricular measurement; thus it is important to obtain a true axial view that shows both ventricles for measurement if the upper ventricle appears enlarged. **(C)** and **(D)** Coronal "owl's eye" view through the lambdoid suture shows asymmetry of the occipital horns *(calipers).* Mild asymmetry less than 2 to 3 mm is common and normal. *c,* Cerebellum. **(E)** and **(F)** Views taken through the anterior fontanelle analogous to neonatal head ultrasound are an alternate approach to assessing both ventricles. **(E)** shows the occipital horns and **(F)** shows the anterior horns and confirms slight ventricular asymmetry.

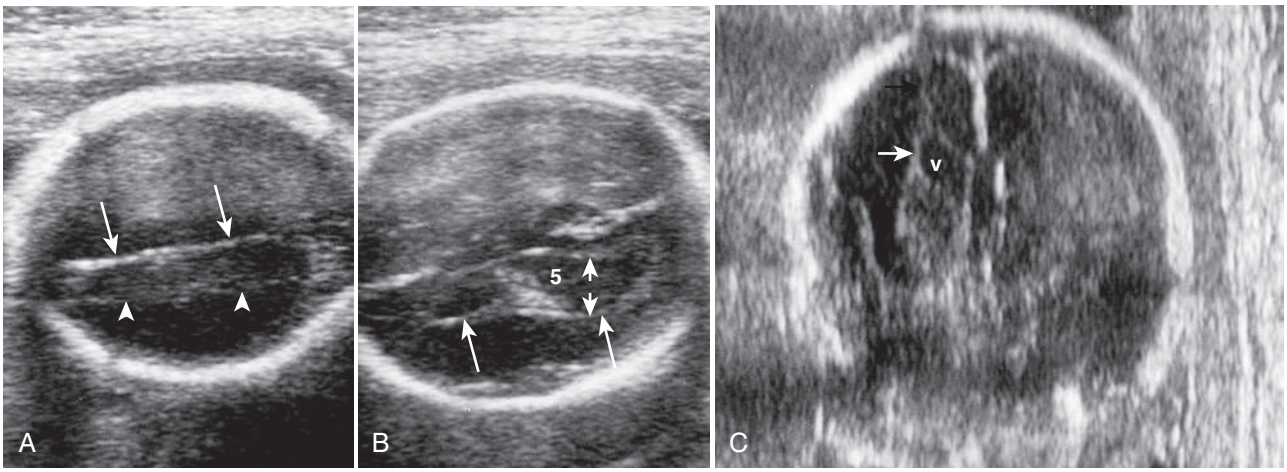

FIG. 34.10 Supraventricular Marginal Venous Echoes at 26 Menstrual Weeks Versus Ventricular Walls. (A) Transverse view above the level of the ventricles shows echoes from the marginal veins, which form a finely dotted line *(arrowheads)* parallel to the interhemispheric fissure *(long arrows)* that should not be mistaken for ventricular margins. **(B)** Transverse view at the ventricular plane shows mild ventricular enlargement, with the occipital horn measuring over 10 mm *(short arrows)* and the choroid separated from the medial wall of the occipital horn by 5 mm *(5)*. The margin of the lateral ventricle *(long arrows)* is curved and diverges from the midline, unlike the venous "line," which is straight and parallels the midline. **(C)** Coronal view through the region of the thalamus. The lateral ventricle wall echo *(arrow)* is lateral to the supraventricular venous echo, which goes from the top of the ventricle *(v)* to the surface of the hemisphere.

at the widest part in the fluid space touching the inner ventricle wall perpendicular to the ventricle axis.[6] For consistency measurements should be taken opposite the parieto-occipital fissure.[69] It is possible, however, to measure the near ventricle directly by waiting for the head to turn or exploiting access provided by the squamosal and lambdoid sutures and the posterolateral (mastoid) fontanelles and on 3-D multiplanar reconstructions and even on coronal views using the "owl's eye" view. But it is important to ensure that all measurements are made in the true axial plane[5,39] (see Figs. 34.3 and 34.9). Visualization of the near ventricle and hemisphere should be performed whenever VM is suspected.

There are pitfalls to ventricular measurement. Errors arise if the plane of view is not axial or if there is an improper choice of ventricle boundary.[70] The insula, the extreme capsule of the basal ganglia, the supraventricular veins, the medial wall of the occipital lobe (see Fig. 34.2A-B and Fig. 34.10), and reverberation echoes of the proximal skull all can appear as lines, which should not be mistaken for ventricular walls.

Between 14 and 38 weeks, the transverse atrial measurement is reported constant at 7.5 mm (standard deviation [SD], 0.7 mm).[2] Measurements of 10 mm or larger suggest VM with a low false-positive rate. A finding of 10 mm is not a clear criterion of abnormality, but rather it is generally accepted that at 10 mm or more the ventricle is sufficiently different to warrant additional attention and investigation.[6,43,71-73] Note that the 10-mm limit was initially proposed by Dr. Filly as the upper limit not because it definitively distinguished normal from abnormal, but rather because it was an easy number to remember at all gestational ages and identified most fetuses with findings that were felt to be different enough to warrant counseling and further investigation. It was understood that some fetuses with ventricles larger than 10 mm may be entirely normal.[43,73]

In general, 10 to 12 mm is termed **mild** or **borderline;** 12 to 15 mm is **moderate** (although some authors consider up to 15 mm in the mild range); and greater than 15 mm is **marked** VM.[66,71] Although 10.0 mm has been considered the upper limit of normal, there are reports of normal outcomes with ventricles larger than 10 mm,[72] and some have suggested raising the upper limit of normal to 11 or 12 mm. Ten millimeters is already about 4 SDs above the mean, and we agree with others that 10 mm should remain the criterion above which counseling and investigation should occur[5,43,72] (Fig. 34.11).

As an alternative approach to detection of mild VM, Mahony and colleagues suggested using choroid separation from the medial ventricle wall and reported that normally this distance is 1 to 2 mm after 15 weeks. Measurements of 3 mm or more were associated with abnormal outcomes when combined with other fetal abnormalities, even if the ventricle measurement was normal.[74] Hertzberg and colleagues found that 20% of such fetuses had abnormal outcomes.[75] However, many believe that this approach is too sensitive and unnecessarily creates anxiety in parents.

Ventricular enlargement is termed **isolated ventriculomegaly** (IVM) if there are no associated cerebral or somatic findings and the karyotype is normal. At time of diagnosis of VM, about 60% will have additional abnormalities, and 40% will not. Unfortunately, at birth, even after detailed ultrasound and prenatal MRI, about 7% to 16% of infants with apparent IVM are found to have additional abnormalities.[71,76,77]

Enlargement of the lateral cerebral ventricles is not the primary problem. Although VM may be an isolated finding, it is often the sonographically conspicuous finding of numerous disorders and syndromes.[43,78,79] It is the underlying changes in the brain that are clinically important, not only the size and appearance of the ventricles. Cerebral functional alterations are only variably

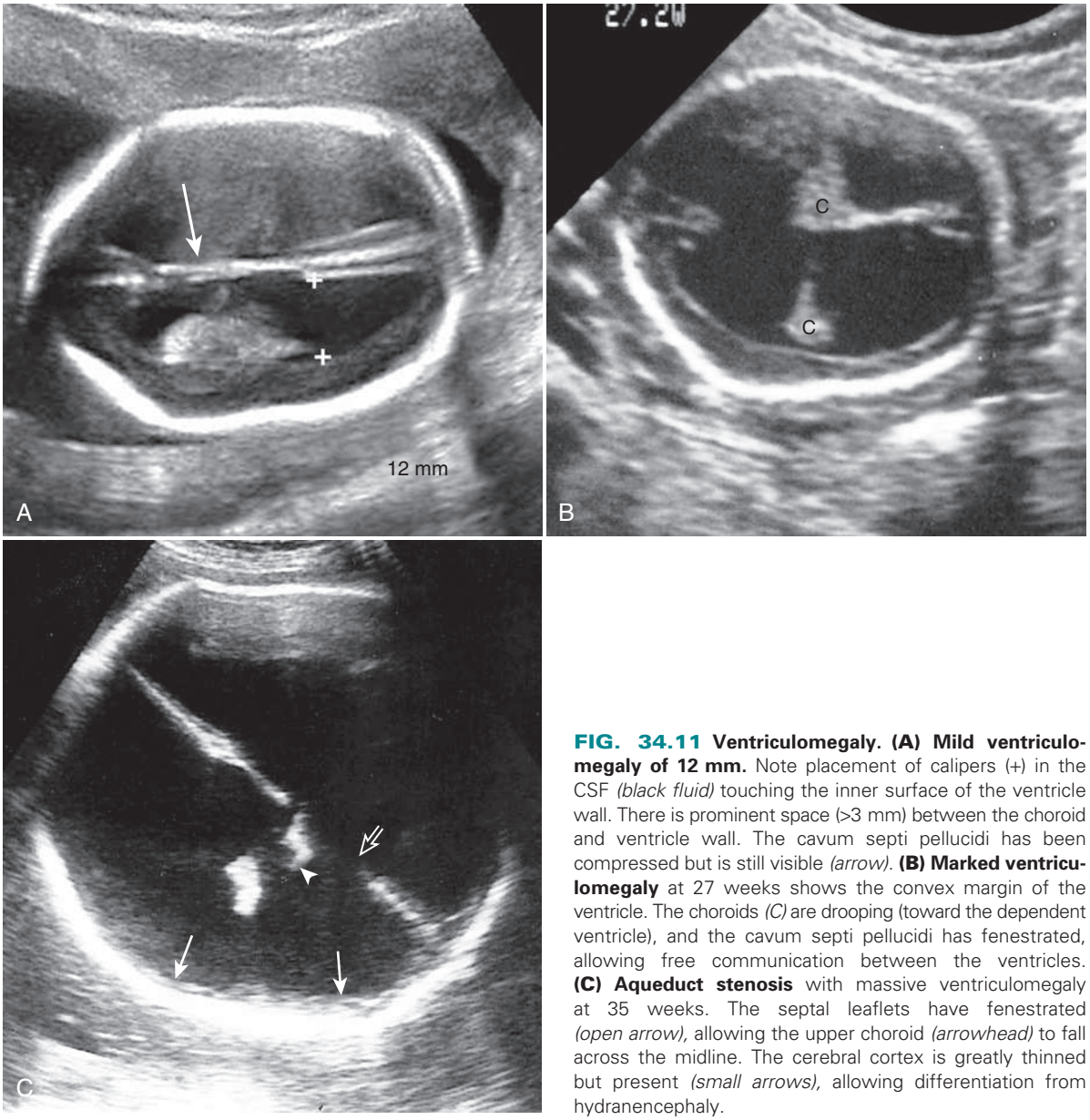

FIG. 34.11 Ventriculomegaly. (A) Mild ventriculomegaly of 12 mm. Note placement of calipers (+) in the CSF *(black fluid)* touching the inner surface of the ventricle wall. There is prominent space (>3 mm) between the choroid and ventricle wall. The cavum septi pellucidi has been compressed but is still visible *(arrow).* **(B) Marked ventriculomegaly** at 27 weeks shows the convex margin of the ventricle. The choroids *(C)* are drooping (toward the dependent ventricle), and the cavum septi pellucidi has fenestrated, allowing free communication between the ventricles. **(C) Aqueduct stenosis** with massive ventriculomegaly at 35 weeks. The septal leaflets have fenestrated *(open arrow),* allowing the upper choroid *(arrowhead)* to fall across the midline. The cerebral cortex is greatly thinned but present *(small arrows),* allowing differentiation from hydranencephaly.

predicted by ventricular size, cortical thinning, and appearance.[66] A single institution study of 29,000 pregnancies found VM in 0.38% of fetuses (1 in 265). Of these, 57% were not isolated and had other abnormalities. In the 43% with IVM, VM was mild in 40% (10-15 mm) and marked in 60% (>15 mm). Abnormal neurodevelopmental outcome was poorest with nonisolated (91%) and marked IVM cases (68%) but was seen in only 19% of mild VM cases.[77]

The approximate frequencies of cerebral abnormalities seen with VM are **aqueduct stenosis,** 30% to 40%; **Chiari II malformation** with spina bifida, 25% to 30%; **Dandy-Walker complex,** 7% to 10%; and less common conditions including **agenesis of the corpus callosum**. In general, associated CNS and somatic malformations are common. Chromosomal and genetic abnormalities are more common with nonisolated (25%-36%) than isolated (3%-6%) VM and include the **trisomies** and **X-linked hydrocephalus** in males and numerous other conditions.[67,71,78,79]

Pathogenesis of Ventriculomegaly

CSF is secreted by the choroid plexus of the lateral, third, and fourth ventricles, as well as by the cerebral capillaries.[80] CSF flows from the lateral ventricles with assistance of ciliary activity of ependymal cells through the foramina of Monro, third ventricle, aqueduct of Sylvius, and fourth ventricle and out the **foramina of Magendie and Luschka** into the subarachnoid space of the posterior fossa, from where it courses over the surface of the brain to be absorbed by the **pacchionian** or **arachnoid granulations** and lymphatics.[66,81]

Ventricular enlargement generally occurs in one of four scenarios. First and most commonly, there is obstruction of CSF flow in the brain, usually at the aqueduct **(intraventricular**

obstructive hydrocephalus). Alternatively, the site of blockage may be outside the ventricular system, or there may be failure of absorption (**extraventricular obstructive hydrocephalus** or **communicating hydrocephalus**). Second and less often, VM results from excess CSF secretion with **choroid plexus papillomas.** Third, VM can follow cerebral destruction and brain shrinkage as a result of abnormal brain development or diverse insults **(hydrocephalus ex vacuo)**. Fourth, it may be a feature of generalized cerebral malformation. Apart from the effects of the basic underlying disorder, the degree of brain injury with HC varies with age of onset and magnitude and duration of the dilation, all of which affect periventricular axons, myelin, and microvasculature, resulting in cerebrovascular injury, gliosis, and inflammation and compensation by neuroplasticity.[66,82]

Examples of Conditions Associated With Ventriculomegaly

Obstructive hydrocephalus
Aqueduct stenosis (idiopathic, infections, bleeding, X-linked, obstructing masses)
Spina bifida with Chiari II malformation
Large choroid plexus cyst
Excess cerebrospinal fluid (CSF) production
Choroid plexus papillomas
Destructive processes (encephaloclasis)
Vascular insult
Infection
Ischemia
Schizencephaly
Hydranencephaly
Cerebral malformations
Aneuploidy (trisomies 21, 18, 13)
Agenesis of corpus callosum
Vermian dysgenesis and Dandy-Walker malformation
Holoprosencephaly
Neuronal migration abnormalities (lissencephaly, schizencephaly)
Microcephaly

Ultrasound Evaluation of Ventriculomegaly

The detection of VM is generally straightforward, but the determination of its etiology can be difficult. Several approaches to measuring ventricular size have been described: atrial width, choroid separation, ventricle-to-hemisphere ratio, combined anterior horn width, and visual anatomic appearance. Of these, the universally accepted method is the **transverse measurement of the atrium of the occipital horn** (see Figs. 34.3, 34.9A, and 34.11A). Methodological scanning can often determine specific causes.[39] The size of the head is not helpful in detecting VM, and frequently the BPD remains normal even with severe ventricular enlargement. Nomograms of other parts of the ventricles are available but not in common use.[83]

In the first trimester the choroid plexus should fill the prominent-appearing lateral ventricle, except for the conspicuous fluid containing anterior frontal horn of the lateral ventricle, which should not be mistaken for abnormality (see Fig. 34.1B). VM manifests as a small-appearing choroid plexus with excess surrounding fluid.[8]

Qualitative appearances suggesting ventricular enlargement include convexity (outward bulge) to the lateral wall of the lateral ventricle and asymmetrical position of the left and right choroids, which fall with gravity when unsupported by ventricular walls because the choroids are denser than CSF ("droopy" or "dangling" choroids) (Fig. 34.11B, Video 34.5). With massive ventricular enlargement, the interhemispheric structures, particularly the septum pellucidum, undulate with maternal pulse and movements and can become disrupted (fenestrate), allowing the left and right lateral ventricles to communicate. The upper choroid can fall across the midline through this hole and into the lower ventricle (Fig. 34.11C).

Once ventricular enlargement is suspected, attention turns to etiology and a detailed search for associated cerebral and somatic abnormalities that may suggest specific causes or syndromes. Both left and right ventricles should be measured, and both hemispheres evaluated.[5,39,67,68] Associated brain abnormalities may be subtle and not readily appreciated on standard axial scanning. Coronal and sagittal views both transabdominally and transvaginally and use of 3-D multiplanar scans can be especially helpful to detect abnormalities of the cerebellar vermis and corpus callosum.[5,79] MRI adds additional information in 5% to 50% of cases, especially with respect to parenchymal injury, migrational disorders, ischemia, hemorrhage, and brainstem abnormalities.[17,71,76,84-86]

Fetuses with suspected VM should be evaluated by a knowledgeable team with experience in the investigation, counseling, management, and follow-up of prenatally discovered abnormalities. Additional testing can be offered including karyotype and molecular analysis, testing for infection (especially CMV, *Toxoplasma,* and rubella), platelet antibodies, and follow-up examinations to follow ventricle growth and to detect additional late-appearing findings that may relate to prognosis (porencephaly, malformation of cortical development, hemorrhage). Postpartum evaluation is important to evaluate for additional prenatally unsuspected abnormalities and to plan treatments.[39,66,68,71,82]

Prognosis relates to the degree of VM, progression of VM, and especially the presence of associated abnormalities. In cases of VM associated with chromosomal or other CNS and somatic abnormalities, the prognosis and recurrence risk relate to underlying conditions.[71,87] When VM is truly isolated, neurodevelopmental outcome relates to the degree of enlargement. Normal functional outcome is reported in about 85% to 96% of mild (10-12 mm), 76% of moderate (12-15 mm), and 28% of severe (>15 mm) cases. Outcome is better if VM is stable or decreases, and worse with enlarging ventricles. Unilateral cases behave similarly.[71,78,88,89]

Counseling of parents remains difficult, and long-term outcome remains guarded. Laskin and colleagues[88] reported that initially 85% of children had a favorable outcome, but this decreased to 79% by 20 months. Remember also that 2% to 3% or more of entirely normal-appearing fetuses and children can also have developmental disability, and it is not clear how this rate compares with those with IVM.[71,76]

SPECIFIC ABNORMALITIES

Congenital CNS abnormalities often reflect the *time* of insult in prenatal life rather than the specific cause. Increasingly, CNS abnormalities are being associated with gene mutations at the molecular level. Genes control cortical development and neuron migration, and the same genes also have roles in somatic development. The understanding of these complex and interrelated molecular mechanisms of disease and maldevelopment is changing rapidly. Increasingly, malformations are starting to be categorized based on their underlying genetic and molecular abnormalities rather than on morphologic appearances.[21,90-92] Even if the genes are normal, their functions can be variably disturbed by external influences, such as anoxia, infections, and teratogens, and the final outcomes will typically reflect the timing and intensity of the insults more than their specific nature.[36]

To reach an accurate diagnosis and help with investigation, counseling, and treatment, evaluation should include not only CNS changes, but also additional, subtle cerebral and somatic findings. Additional clues can be found in pregnancy history, family history, course of current pregnancy (including maternal conditions such as diabetes), medications, illnesses, occupations and exposures, and evaluation of parents and close relatives. If there is a known risk of specific conditions, online resources such as Online Mendelian Inheritance in Man (OMIM, http://www.ncbi.nlm.nih.gov/omim) and consultation with experts in other specialties can be helpful in providing a list of findings to target on ultrasound examination and MRI.

ERRORS OF DORSAL INDUCTION

CNS development begins with development of the notochord, which subsequently induces the dorsal development of the neural plate, which closes to form the neural tube, which becomes the spinal cord and part of the brain. Errors of **dorsal induction** can result from many different genetic and teratogenic factors and affect development of the dorsal neural plate and closure of the neural canal **(neurulation).**[93,94]

Anencephaly and Exencephaly

Anencephaly follows failure of closure of the rostral neuropore leading to failed cranial vault development and unprotected exposed brain tissue **(exencephaly),** the subsequent destruction of which leaves a flattened, amorphous vascular-neural mass (area cerebrovasculosa) characteristic of anencephaly (Fig. 34.12). Facial structures and orbits are present. Associated spinal and non-CNS abnormalities and polyhydramnios are common. On occasion, the dysraphic abnormality involves the head and entire spine **(craniorachischisis).**[95,96] **Acrania** is sometimes defined as a normal brain with absent skull, and therefore this term should not typically be used in cases of anencephaly or exencephaly, even though the cranial vault is absent.

Prevalence of anencephaly is about 1 per 1000 births. Risk is increased in families with neural tube defects (NTDs), young or old mothers, or diabetes and with antiepileptic drugs. Folate appears protective. Chromosomal abnormality is seen in 2%, and additional abnormalities are common including cleft lip, cardiac defects, club feet, and abdominal wall defects.[96,97]

Detection of anencephaly before 14 weeks can be difficult because a relatively normal-appearing brain structure can be present, but the diagnosis has been suggested as early as 10½ weeks.[10,38] The diagnosis can be missed unless the examiner specifically looks for ossified cranial bones. Ultrasonically visible ossification of frontal bones may not be apparent until 10 weeks, and anencephaly should not be diagnosed before this gestational age. Commonly, however, the cerebral mass is deformed, often looking like "Mickey Mouse ears." An additional clue to diagnosis is the identification of amniotic fluid that is more echogenic than the extraamniotic subchorionic fluid owing to intraamniotic debris shed from the uncovered brain.[98] The introduction of the NT scan and increasing familiarity with first-trimester appearances has shown that most anencephalic fetuses can be detected in the late first trimester.[10,99]

Differential diagnosis includes other conditions in which the cranial bones are absent or lack mineralization, such as **amniotic band sequence,** large **encephaloceles, osteogenesis imperfecta,** and **hypophosphatasia.** With amniotic band sequence **(early amnion rupture sequence)** the fetuses typically have an asymmetrical defect accompanied by body wall defects and/or amputation of body parts and occasional oligohydramnios, and membranes may be visible in amniotic fluid, or the fetus may be stuck to the side of the uterus or placenta. Unlike anencephaly and open spina bifida, early amnion rupture sequence is sporadic and without increased recurrence risk. In general, large encephaloceles have more calvarial development than seen with anencephaly, but occasionally the two can appear similar. In either case, the prognosis remains hopeless.[96,100]

The outcome of anencephaly is invariably fatal, and pregnancy termination is offered at any gestational age.

Cephalocele and Encephalocele

A **cephalocele** is a herniation of intracranial structures through a defect in the cranium or skull base. It is termed **cranial meningocele** when it contains only meninges and CSF and **encephalocele** when it contains brain tissue. Among live births the incidence is about 1 to 5 per 10,000, but this underestimates the true incidence because many die at or before birth.[101,102] Most encephaloceles occur in the midline in the occipital (75%), frontal (13%), or parietal (12%) regions (Fig. 34.13). Anteriorly they can extend into the mouth, nasal, and sphenoid areas, where their identification can be difficult.[103-106] Off-midline lesions are commonly associated with amniotic band syndrome.[101] Cephaloceles can occur as isolated lesions, but most (20%-60%) are associated with other anomalies or syndromes involving the head, spine, face, skeleton, or kidneys. Chromosomal abnormality is seen in 14% to 60%, especially trisomies 18 and 13.[97,102] Interestingly, in the Western world the occipital location is more common, whereas in Asia frontonasal location predominates.[102,105,106]

Although at first glance cephaloceles resemble spina bifida, there are some differences. Spina bifida is a failure of primary closure (neurulation), whereas many cephaloceles are skin covered and likely are a secondary abnormality after neurulation, possibly

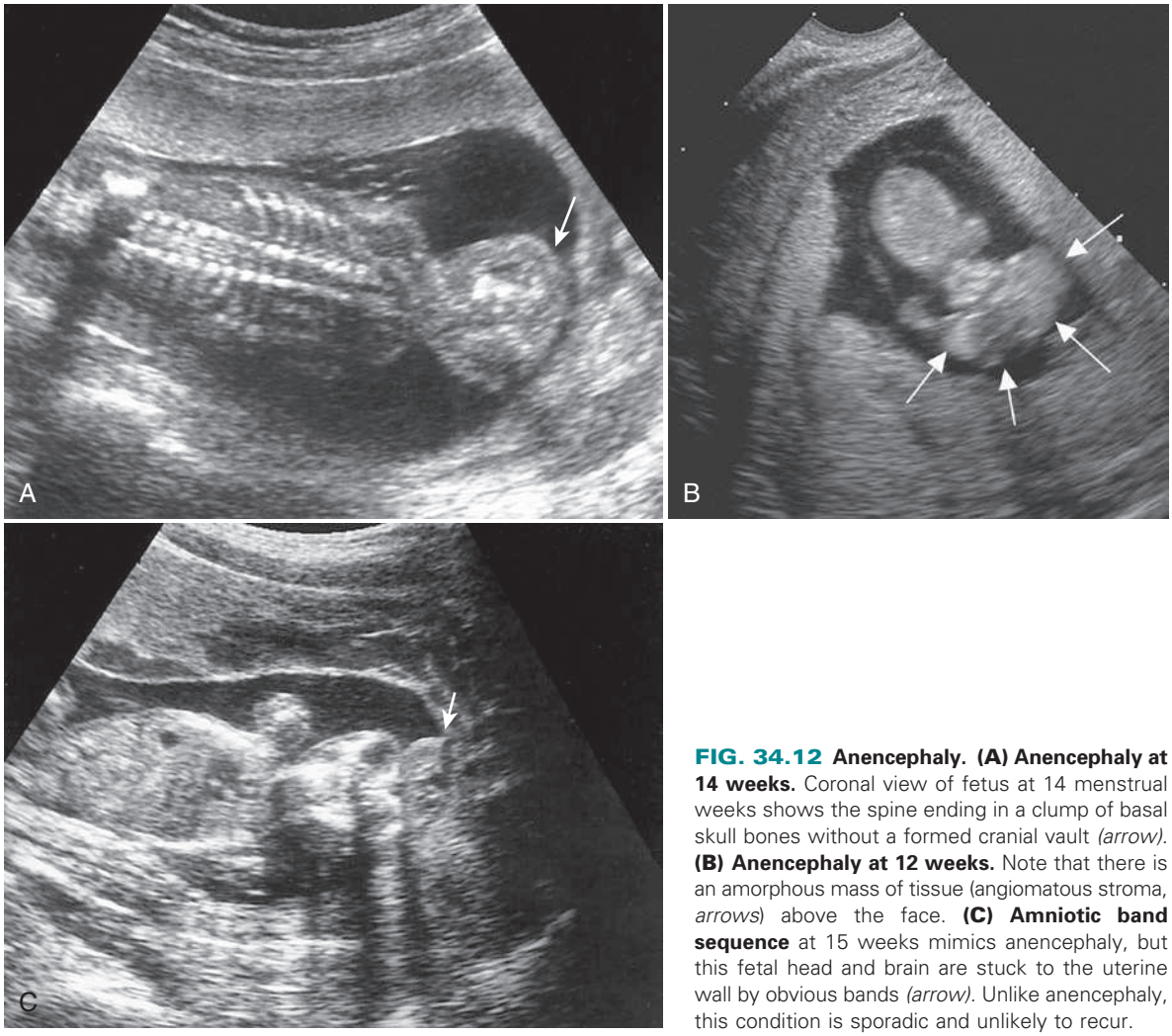

FIG. 34.12 Anencephaly. (A) Anencephaly at 14 weeks. Coronal view of fetus at 14 menstrual weeks shows the spine ending in a clump of basal skull bones without a formed cranial vault *(arrow)*. **(B) Anencephaly at 12 weeks.** Note that there is an amorphous mass of tissue (angiomatous stroma, *arrows*) above the face. **(C) Amniotic band sequence** at 15 weeks mimics anencephaly, but this fetal head and brain are stuck to the uterine wall by obvious bands *(arrow)*. Unlike anencephaly, this condition is sporadic and unlikely to recur.

representing abnormal mesenchymal migration or, in the case of frontonasal cephaloceles, a failure of closure of normal diverticulation. Because many are skin covered, MS-AFP is elevated in only 33% compared with spina bifida (62%) and anencephaly (92%). This makes ultrasound the primary diagnostic tool. Cephaloceles are more likely to be associated with additional cerebral and somatic abnormalities and syndromes. Common associated cerebral abnormalities involve the midline structures such as the corpus callosum, cerebellum, and brainstem and include venous abnormalities, holoprosencephaly (HPE), HC, and facial clefting (Table 34.2). Over 30 syndromes include cephaloceles; many are related to gene dysfunctions that affect both CNS and somatic development. These additional abnormalities strongly affect prognosis, so whenever a cephalocele is found, there should be a detailed search for other anomalies, and MRI and genetic evaluation should be considered.[102-105,107,108]

Ultrasonographically, an encephalocele manifests as a cystic mass at the surface of the skull, typically in the midline (see Fig. 34.13). Contained brain with a visible bony defect confirms the diagnosis, but it may be difficult to see the contained, often abnormal, brain tissue, and the bony defect may also be small and difficult to detect. Encephaloceles can be seen during first-trimester ultrasound and are often preceded by an enlarged rhombencephalic cavity.[99] MRI is helpful to confirm the diagnosis and, more important, to search for additional features that can affect prognosis and counseling.[18,101,102]

Other lesions that should be considered in the differential diagnosis when a scalp lesion is seen include cystic hygroma, hemangioma, scalp edema or cephalohematoma, epidermal scalp cyst, branchial cleft cyst, dermoid cyst, dacryocystocele, epignathus, and cervical teratoma.[104,110,111]

The **atretic cephalocele** is a variant that is infrequently recognized prenatally, manifesting as a small, blisterlike subcutaneous collection in the skin in the midline near the vertex at the surface of a seemingly intact skull (see Fig. 34.13E). Diagnostic clues are abnormalities of the superior sagittal sinus, which may have multiple channels, and the persistence of the prosencephalic **vein of Markowski,** which runs in the falx (falcine sinus) from the region of the start of the vein of Galen to the sagittal sinus underlying the encephalocele. As with other cephaloceles, there may be other cerebral abnormalities, especially involving the midline, which can affect outcomes. However, if the cephalocele is isolated, the children in general do well.[104,110,111]

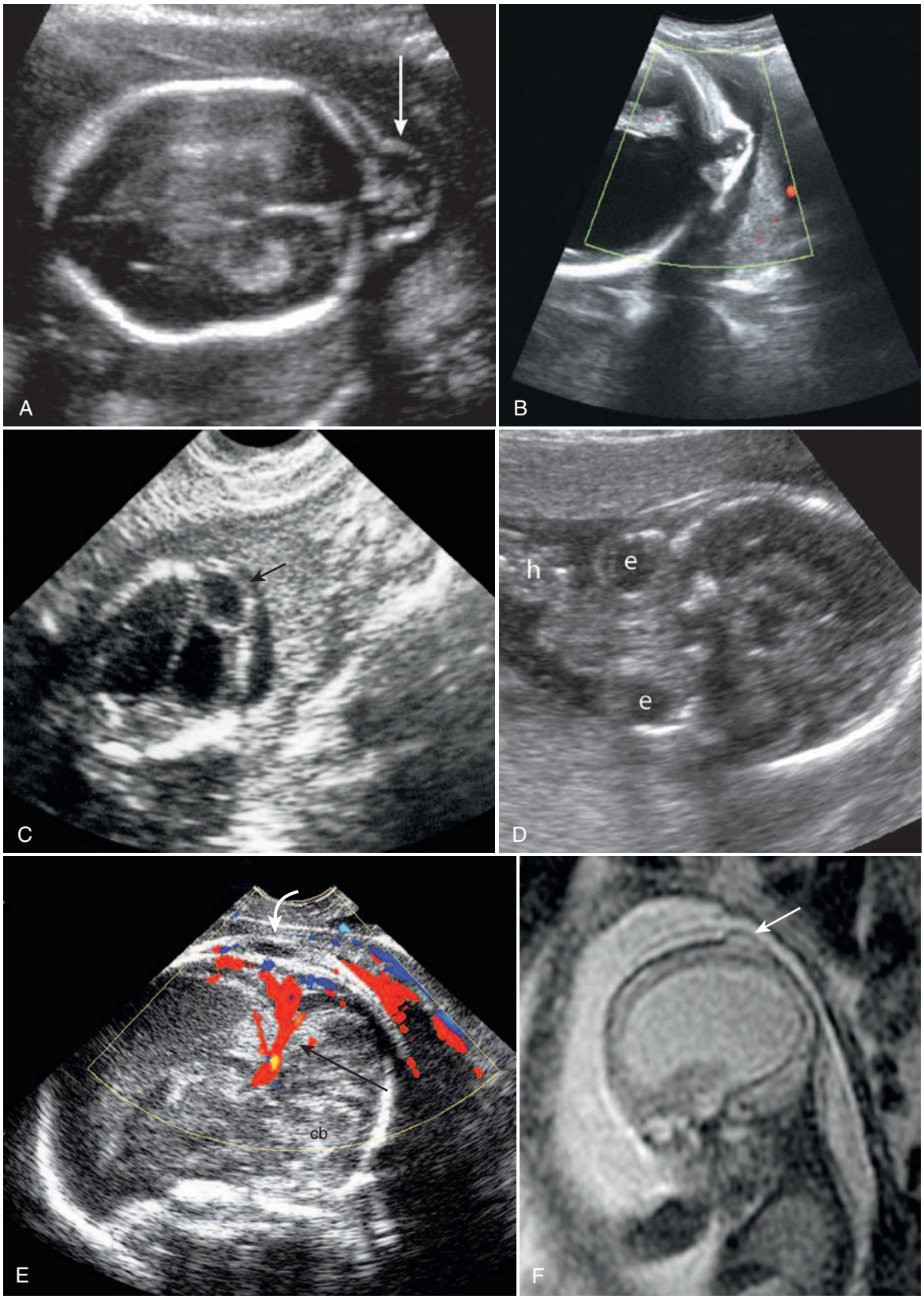

FIG. 34.13 Encephalocele. (A) Occipital encephalocele on axial view at 22 menstrual weeks shows brain tissue *(arrow)* herniating through the occipital bony skull defect. **(B)** In another fetus, a small skull defect is seen with only meninges and no brain tissue in this fetus with ventriculomegaly and **meningocele. (C) Asymmetrical parietal encephalocele** *(arrow).* Coronal view at 21 menstrual weeks shows asymmetrical encephalocele. **(D) Anterior encephalocele** *(arrow)* at 18 weeks containing brain herniated through a defect between the orbits where it appears as a mass in the expected area of the nose. Also, slight hypertelorism is present. *e,* Eyes; *h,* hand. **(E) Atretic encephalocele** seen as a small subtle blister *(curved arrow)* in the scalp on midsagittal color Doppler image. Typically, these do not contain brain tissue but are associated with an abnormal falcine venous sinus of Markowski *(arrow),* which courses from the cerebral vein to the superior sagittal sinus. The vein of Galen can be absent. *cb,* Cerebellum. **(F)** Small encephalocele *(arrow)* associated with severe ventriculomegaly on magnetic resonance image.

TABLE 34.2 Features of Some Autosomal Recessive Syndromes Associated With Encephalocele[a]

Meckel-Gruber	Cystic renal dysplasia, polydactyly, other central nervous system abnormalities, microphthalmia, cleft lip and palate, micrognathia, ciliopathy
Walker-Warburg	Hydrocephalus, agyria (lissencephaly type 2), retinal dysplasia, vermis hypoplasia, kinked brainstem, muscular dystrophy
Joubert and related	Vermian hypoplasia, deep interpeduncular fossa (molar tooth), hydrocephalus, ciliopathy
Hydrolethalus	Hydrocephalus, cerebral abnormality, polyhydramnios, micrognathia, polydactyly, heart defects
Fraser	Cryptophthalmos, syndactyly, genital abnormality, renal abnormality, laryngeal stenosis
Robert	Phocomelia (pseudo-thalidomide), cleft lip and palate, intrauterine growth restriction

[a]Note that all have many other additional findings.[109]

The prognosis of cephaloceles depends on the location of the lesion, the amount of herniated brain, the formation of the underlying brain, associated anomalies, and genetic abnormalities. Prenatal and perinatal mortality rates are high, and intellectual impairment is common. If discovered before viability, pregnancy termination is considered. Later in pregnancy, management depends on the size and location of the encephalocele and associated anomalies.[102,112,113]

Ciliopathies

Ciliopathies are a group of disorders resulting from abnormal structure or function of cell surface cilia due to mutations in ciliary genes. Cilia are found on the surface of almost all cells of vertebrates, and their functions are very much more complex than providing simple transport as seen in bronchi and various anatomic ducts. Normally functioning cilia are required for the normal development and function of seemingly unrelated sites including brain, kidneys, eyes, liver, and skeleton. In the brain, cell surface cilia are involved with brain patterning and neuronal migration and help direct CSF flow. Abnormal ciliary function may result in HC and other cerebral malformations including encephaloceles.[114] Over 40 mutations of ciliary genes have been found, resulting in over 1000 polypeptide abnormalities. As result, the expression of ciliary gene mutation is variable. A single gene mutation may cause different phenotypes, and mutations of different genes may result in the same phenotype. Commonly encountered ciliopathies have overlapping features such as encephaloceles and include **Meckel-Gruber syndrome, Joubert syndrome, orofaciodigital syndrome, Bardet-Biedl syndrome, autosomal recessive polycystic kidneys, autosomal dominant polycystic kidneys, Jeune asphyxiating thoracic dystrophy, Ellis-van Creveld syndrome,** and others.[115]

Joubert Syndrome

Joubert syndrome and related disorders (JSRD) have the key feature of molar tooth sign visible on MRI. The molar tooth appearance results from hypoplasia of the cerebellar vermis, horizontal thick elongated cerebral peduncles, and deep interpeduncular fossa at upper pons; on axial MRI of the brainstem, these features look like a **molar tooth.** This sign is used as the diagnostic test in children. JSRD is clinically characterized by hypotonia, ataxia, psychomotor delay, irregular breathing, and abnormal eye movements and has an incidence of about 1 per 80,000 pregnancies. Different combinations of ciliary gene mutations can result in primary Joubert syndrome, and related disorders have variable abnormalities of the neurons, eye, renal tubules, and bile ducts and polydactyly.[116]

On ultrasound the molar tooth sign findings of vermian hypoplasia, thickened cerebral peduncles, and interpeduncular notch may be visible by 20 weeks and confirmed by MRI if needed.[117] Additional cerebral imaging findings can include abnormalities of the corpus callosum and neuronal migrational abnormalities, Dandy-Walker malformation (DWM), and encephalocele as well as abnormalities in somatic structures. If the mutation is known (about 50%), early diagnosis is possible with chorionic villus sampling (CVS).

Prognosis is generally poor and related to extent of breathing and feeding problems in the short term and renal and hepatic complications in the long term.

Meckel-Gruber Syndrome

Meckel-Gruber syndrome is likely the most common syndromic abnormality of the CNS and is characterized by occipital encephalocele, enlarged dysplastic kidneys, hepatic duct proliferation, polydactyly, posterior fossa abnormalities, and craniofacial and heart defects and has features that overlap with JSRS. Incidence is 1 per 13,000 to 140,000 live births. It is a lethal autosomal recessive disorder associated with mutations in several ciliary genes. The detection of its classic triad of large echogenic kidneys, encephalocele, and postaxial polydactyly can allow diagnosis as early as 14 weeks, but oligohydramnios in later pregnancy may hinder detection of some of these features. Autosomal recessive polycystic disease and trisomy 13 should be considered in the differential diagnosis. Genetic testing may be possible in at-risk families.[118]

Amniotic Band Sequence/Limb–Body Wall Complex

Amniotic band sequence/limb–body wall complex describes a variable collection of disruptive abnormalities and is associated with adherence of the fetus to bands in the amnion.

Cases are sporadic, occurring in about 1 to 10 per 10,000 pregnancies, and typically have normal karyotype. Fetuses with these conditions have a very variable range of complex, generally

asymmetrical abnormalities that range from minor to massively disruptive. Cranial manifestations may initially mimic anencephaly, encephalocele, and other cerebral abnormalities and are often associated with asymmetrical facial disruptions. The literature on the etiology and pathogenesis of these sporadic conditions is confusing and controversial and includes amniotic rupture, vascular disruption, and abnormal development of embryonic body folds. There is a common theme of combinations of amniotic abnormality and asymmetrical fetal disruptions. Bands may be seen attached to abnormal body parts, or the fetus is partly fixed to the uterine wall. **Limb–body wall complex** terminology is often used if there is a more severe malformation consisting of encephalocele with facial clefts, thoracoschisis or abdominoschisis, short umbilical cord, and limb defects. Often there are internal abnormalities that cannot be explained by amniotic bands such as congenital heart disease, renal agenesis, and intestinal atresias. Minor variants may have only **constrictive amniotic bands** resulting in annular constrictions or focal malformations of limb parts.

The findings at ultrasound vary with affected areas. Clues to diagnosis are asymmetrical abnormalities and amniotic bands attaching to the fetus or fetal parts that are stuck to the uterine wall (as with limb–body wall complex). The bands can be hard to see, and technique needs to be optimized and gain increased to demonstrate them. In some cases fetal anatomy is so disrupted that parts become unrecognizable and this massive disruption is the clue to the diagnosis. The condition can mimic anencephaly or encephalocele, and often additional intracranial abnormities are present (see Fig. 34.12C).

The major disruptions are lethal. Three-dimensional ultrasound and MRI can be helpful in clarifying the extent of the lesions. Prognosis, counseling, and management depend on the nature and degree of disruptions. Fortunately, these anomalies are sporadic, with negligible recurrence risk.[96,119-121]

Cranial Changes in Spina Bifida

Spina bifida or **neural tube defect** (NTD) is the second most common birth defect after congenital heart disease. Two general groups are recognized: open (not skin covered) and closed (skin covered). Both result from abnormalities associated with neural tube closure. Open lesions result from failure of closure of the neural tube, leaving a defect that leaks CSF and exposes neural tissue to the damaging effects of amniotic fluid. About 80% to 90% are open, appearing as dorsal cyst (myelocele or meningomyelocele depending on neural content) or rachischisis (uncovered open defect). Open lesions are commonly associated with elevated MS-AFP above 2.50 multiples of the median (MoM). The remaining 10% to 20% are closed (occult) lesions that are skin covered and do not leak AFP and in which MS-AFP levels are normal. Closed defects result from failure of separation of the neural tube from the skin and abnormal adjacent mesenchymal tissue development. These cause variable spinal, vertebral, and cutaneous lesions including lipoma, lipomeningocele, hypertrichosis, tags, dorsal pits, and others.[122]

The incidence is about 0.2 to 10 per 1000 pregnancies and has decreased by about 70% following folate supplementation. The etiology is multifactorial and includes syndromes, genetic abnormalities, and maternal and fetal factors including diabetes and teratogens such as anticonvulsants.[108,123,124]

Open spina bifida is virtually always associated with the **Chiari II** malformation which is a complex deformity involving calvaria, dura, cerebrum, and hindbrain. In Chiari II malformation the striking abnormalities are evident in the small posterior fossa and include herniations of the vermis, pons, and medulla; **brainstem kinking; small fourth ventricle; aqueduct stenosis;** and **tectal beaking.** There are, however, additional pancranial changes that involve the skull bones (beaten silver appearance or **Lükenschädel**), small posterior fossa, falx (interdigitation of sulci, low-lying tentorium and transverse sinuses), large massa intermedia, cerebral hemispheres (hydrocephalus, dysgenesis of corpus callosum, heterotopias, malformations of cortical development, and distortion of the limbic system).[125-127] It is believed that leakage of CSF through the spinal defect leads to a cascade of events resulting in a small underdeveloped posterior fossa followed by hindbrain compression and obstruction to CSF flow, which leads to additional cerebral and calvarial abnormalities.[126] Some believe that failure of neural tube closure is not just a single event, but rather is only part of a spectrum of developmental abnormalities not yet fully defined but that result in multiple additional cerebral and somatic abnormalities.[125]

Of newborns with spinal NTDs, it was found that 80% had isolated NTDs. The remaining 20% had additional anomalies including chromosomal abnormalities or sporadic abnormalities involving virtually all systems.[123,128] An autopsy study found that 68% of cases with spina bifida had non-CNS anomalies, most commonly skeletal (club feet), but also involving kidneys, gastrointestinal tract, abdominal wall, and other structures.[129] A recent multicenter prenatal ultrasound study found chromosome abnormalities in 6.2% of cases (most commonly, trisomy 18 and triploidy) and structural abnormalities in 4.6% (most commonly heart defects).[130]

The actual spinal abnormality of open NTD can be very difficult to see at screening ultrasound, but the defect leaks CSF containing alpha-fetoprotein (AFP), which may become detectable in maternal serum (MS-AFP). This was the basis of earlier serum AFP screening for open defects. Maternal serum levels greater than 2.5 MoM at 16 to 18 weeks detected 88% of anencephalic fetuses and 79% of fetuses with open NTDs but were also found in 3% of normal fetuses. However, all closed, skin-covered NTDs were missed by MS-AFP screening.[131]

In the 1980s it was found that open NTDs are virtually always associated with readily detected ultrasonographic cranial changes of **Chiari II malformation** in the second trimester (Fig. 34.14, Video 34.6). This is unlike closed spina bifida, in which the brain and posterior fossa are normal and the spinal abnormality can be detected only with careful direct examination of the spine (Fig. 34.15).[132] Improvements and standardization and use of these cerebral signs now allow second-trimester detection of open spina bifida in 88% to 96% of cases, and even 100% in some expert hands. Many believe that second-trimester ultrasound has replaced MS-AFP screening for open lesions (anencephaly, encephalocele, open spina bifida).[130]

Many second-trimester cranial signs of spina bifida have been suggested (Table 34.3). The most commonly used are obliteration

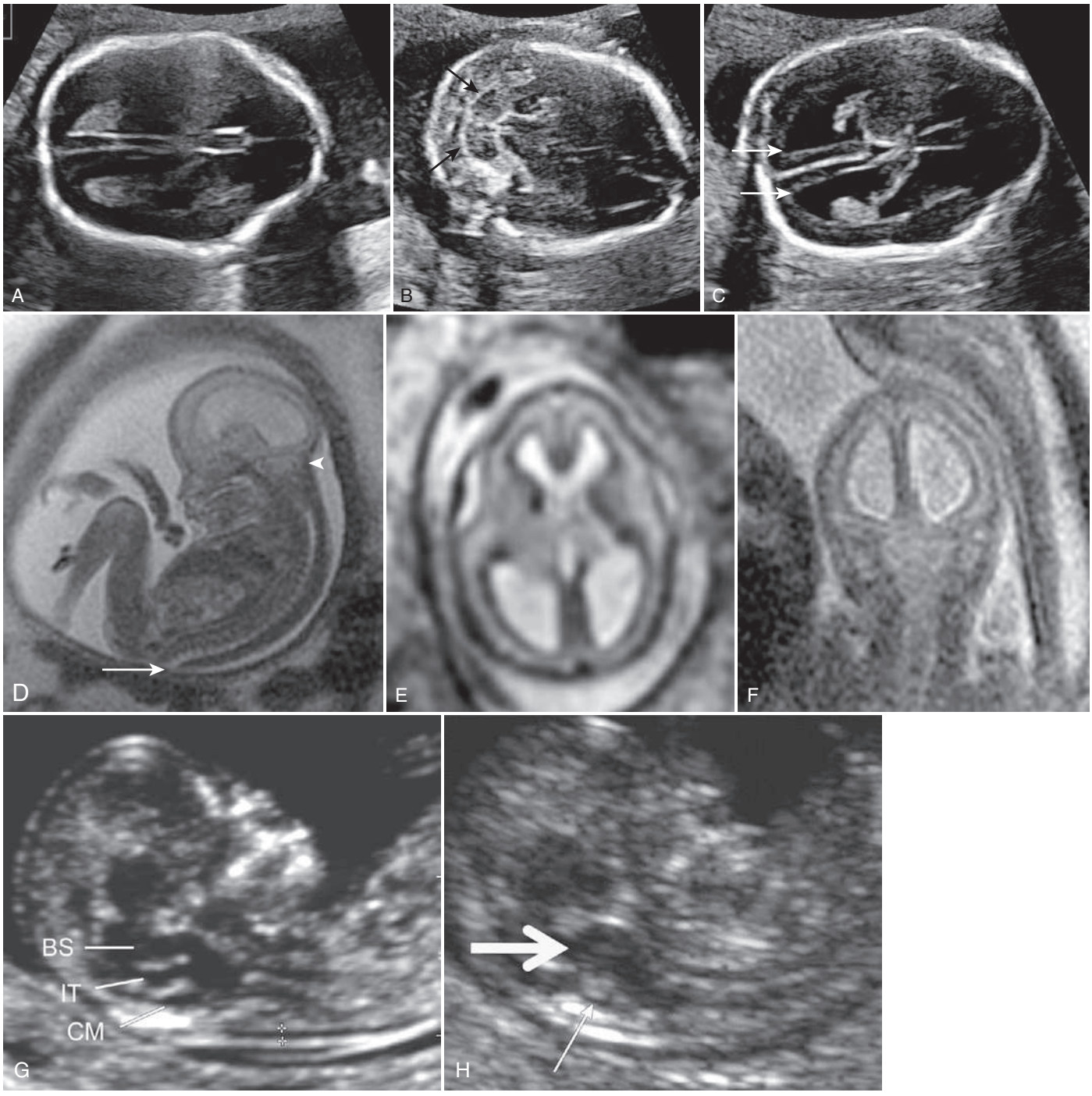

FIG. 34.14 Cranial Findings of Chiari II Malformation With Open Spina Bifida. (A) "Lemon sign" with indentation of frontal bones. **(B) "Banana sign"** of compressed cerebellum *(arrows).* The cerebellum is tightly compressed against the occipital bone and curves around the brainstem, and there is no fluid in the cisterna magna (effacement of cisterna magna). **(C)** Axial ultrasound shows the pointed appearance of the posterior tips of the ventricles *(arrows).* **(D)** Sagittal T2-weighted magnetic resonance image shows inferior displacement of the cerebellum typical of the Chiari II malformation *(arrowhead)* and inferiorly, the spinal defect *(arrow).* **(E)** Axial magnetic resonance image shows the pointed appearance of the ventricles. **(F)** Coronal magnetic resonance image shows ventriculomegaly and obliteration of the cisterna magna. **(G) Normal intracranial translucency** *(IT)* at 12 weeks. Note three dark bands and four white lines. Intracranial translucency is really the forming fourth ventricle. *BS,* Brainstem; *CM,* cisterna magna. **(H) Abnormal IT with spina bifida.** The brainstem *(thick arrow)* is thickened. The IT and CM are absent (do not contain fluid) *(small arrow).* (Courtesy of Dr. K. Fong, Mt. Sinai Hospital, Toronto, Ontario.)

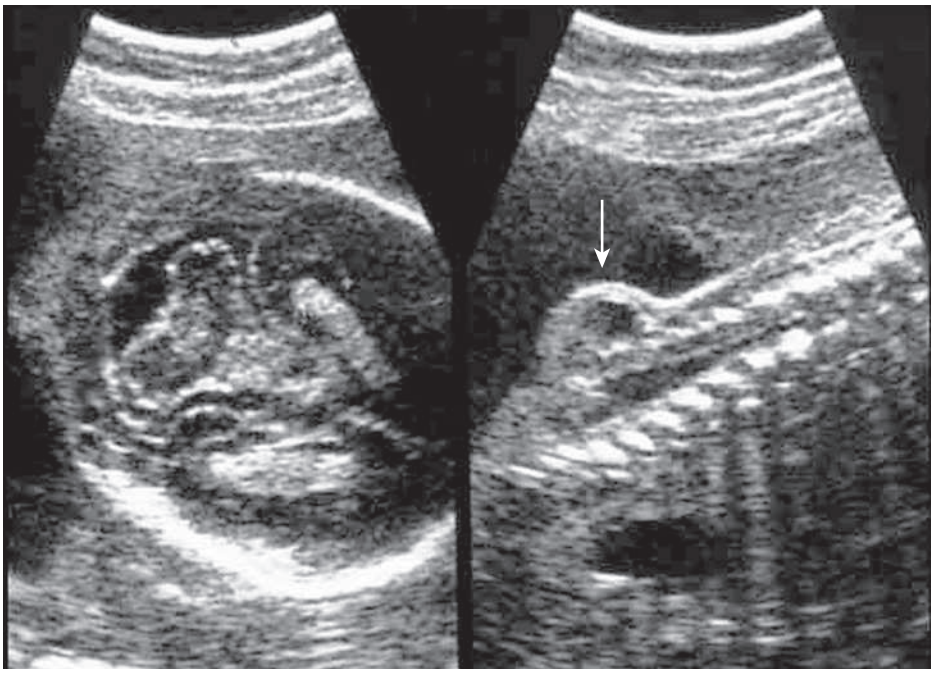

FIG. 34.15 Closed, Skin-Covered Spina Bifida at 21 Weeks. The right image shows an obvious meningomyelocele *(arrow)*. On the left image, note the normal ventricles, cerebellum, and cisterna magna. Fetuses with closed, skin-covered spina bifida do not have a Chiari II malformation and lack the typical intracranial signs. The maternal serum alpha-fetoprotein (MS-AFP) is normal because the skin covers the defect.

TABLE 34.3 Second-Trimester Cranial Signs Associated With Open Spina Bifida[122,130,133,135]

Finding	Frequency	Comments
Effacement of cisterna magna	95%-100%	From about 14 weeks onward
Bifrontal indentation ("lemon sign")	53%-100%	14-24 weeks, disappears later. Also seen in 1% of normal fetuses and in other conditions such as skeletal dysplasia
Cerebellar "banana" sign	62%-97%	Cerebellum wrapped around brainstem
Ventriculomegaly > 10 mm	46%-86%	More common after 24 weeks
Small BPD < 5th percentile	26%-70%	
Small head circumference < 5%	26%-70%	
Small cerebellum < 10%	96%	
Funneling of posterior fossa	96%	Clivus-supraocciput angle < 72 degrees
Pointed dilated occipital horns	70%	Seen on axial view

or effacement of the cisterna magna, the **"lemon sign"** (bifrontal indentation), the **"banana sign"** (cerebellum wrapped around brainstem) and VM exceeding 10 mm. Less frequently used second-trimester signs include small BPD and head circumference (even if VM is present), funneling of the posterior fossa as measured by a small clivus-supraocciput angle, and pointing of the occipital horn. Some caveats to these signs bear attention. The level or extent of the spina bifida does not relate to the cranial signs. The lemon sign is seen more commonly before 24 weeks (5%-100%) but in only 13% after 24 weeks. It is less pronounced in fetuses with abnormal chromosomes and can also be seen in about 1% of normal fetuses.[133-135] The banana sign and VM can worsen over the course of gestation.

There are increasing efforts to screen for spina bifida with ultrasound at time of NT scan.[99,136-145] Interestingly, the spinal defect has been detected as a dorsal abnormality as early as 9 weeks before head changes become apparent.[38,137] After about 12 weeks, cranial changes may begin to be observed (see Fig. 34.14G-H, Table 34.4). These include decrease in head size, altered head shape, and alterations in the posterior fossa including posterior displacement of the midbrain and cerebral peduncles, thickening of the brainstem, and loss of fluid spaces in the cisterna magna and fourth ventricle. A recent prospective study of markers in the first trimester by highly trained operators using IT and cisterna magna appearances found positive or suspicious findings in 11 of 11 cases (100%).[140] Management in first-trimester cases

TABLE 34.4 First-Trimester Signs of Open Spina Bifida

Sign	Sensitivity	Comments
DIRECT SIGN		
Spinal abnormality (meningocele, kyphoscoliosis)[38,140]	50%-60%	9 weeks onward Dorsal mass or irregularity apparent before cranial changes
INDIRECT SIGNS		
BPD plus biomarkers[131,136]	70%	BPD small, AFP elevated
BPD/abdominal diameter ratio ≤1[145]	69%	
BPD below 5th percentile[145]	50%-56%	
Frontomaxillary angle below 5% for CRL[144]	90%	Sloping forehead appearance
"Lemon sign" or "acorn sign"[146]	?	Similar to "lemon sign" in midtrimester
Brainstem/occipital bone ratio[143]	87%-100%	Decreased with spina bifida
Brainstem diameter above 95th percentile[143]	96.7%	Brainstem diameter is increased
Four-line view observed[142]	67	The normal four lines demarcating the anterior and posterior brainstem, fourth ventricle, and occipital bone are not seen
Parallel cerebral peduncles or posterior position of brainstem[137,138]	?	Seen on axial view below BPD level
Absent IT[140]	18%	
Absent cisterna magna[140]	64%	Fluid not seen in cisterna magna
Prospective studies using IT, four-line view, BPD, IT/CM ratio, brainstem diameter, BSOB[140]	50%-100%	

BPD, Biparietal diameter; *BSOB,* brainstem/occipital bone ratio; *CM,* cisterna magna; *CRL,* crown-rump length; *IT,* intracranial translucency.
References 38, 99, 131, 136-138, 140-142, 144-146.

differs from management during the second trimester because the indirect cranial findings are only suggestive, and direct confirmation of the spinal defect in the first trimester is difficult. The sensitivity, specificity, and false-positive rate of these signs have not been established. It is prudent to reassess suspected cases at 15 to 16 weeks when spinal abnormalities and more specific cranial findings become more confidently detectable.[99]

The investigation of fetuses suspected of having spinal abnormalities includes detailed evaluation for associated cranial and somatic abnormalities. Determination of the spinal level of the defect is important for functional prognosis regarding bowel and bladder function and ambulation. MRI may help demonstrate additional brain abnormalities including cerebral hypoplasia and migrational and callosal abnormalities. Karyotype testing should be performed because 7% to 16% have chromosomal abnormality even with apparently isolated NTDs.[97,147]

Prognosis varies and depends on associated abnormalities. Overall survival is about 66% at 20 years. Prenatal surgery in selected cases is associated with additional maternal and prematurity risks related to the procedure. However, fetuses that undergo surgery have reduced hindbrain herniation, reduced need for ventricular shunting (40% vs. 82%), and improvement in neuromotor functions such as walking (42% vs. 21%), but no improvement in urinary function.[148] Prognosis and quality of life in children with open NTDs relates to manifestations of Chiari II malformation including apnea, swallowing, lower cranial nerve function, and foramen magnum impaction. Other issues include spinal deformities, tethered cord, and progressive orthopedic problems. About 70% have an IQ above 80, half can live independently, and 25% to 38% are capable of active employment.[124]

ERRORS OF VENTRAL INDUCTION

Errors of **ventral induction** occur in the rostral end of the embryo and result in brain abnormalities of the prosencephalon, mesencephalon, and rhombencephalon and usually also affect facial development.[93] The prosencephalon is induced to develop through a process of ventral induction consisting of formation, cleavage, and development of midline structures and facial structures. Several developmental abnormalities can occur. Absence of prosencephalic formation is rare and includes **aprosencephaly** (absence of the prosencephalon) and **atelencephaly** (absence of the telencephalon). More common is failure of prosencephalic and adjacent facial patterning and cleavage resulting in incomplete separation of prosencephalon into two distinct hemispheres, associated with abnormalities of midline and facial structures manifesting as the different degrees of HPE.[149,150]

Holoprosencephaly

Holoprosencephaly (HPE) is a complex brain malformation resulting from incomplete separation of the prosencephalic diverticulum into right and left cerebral hemispheres. It is often associated with facial abnormalities. It is the most common abnormality of brain development and is seen in about 1 per 250 conceptuses but only 1 per 16,000 live births because only 3% survive to delivery.[149,151-153]

Cerebral hemisphere development starts at about 5 weeks with prechordal mesoderm migration into the area anterior to the notochord where under genetic control it induces midface and forebrain development. Normally apoptosis of midline areas results in separation of facial and prosencephalic structures into left and right sides by 5 weeks. The failure to separate by apoptosis results in the fused cerebral and facial appearances of HPE. The severity of facial dysmorphism correlates with cerebral abnormalities in about 80% of cases ("the face predicts the brain"). Not surprisingly, additional abnormalities involving any part of the brain and body are found in about 50% to 65% of cases.[149-153]

HPE etiology and phenotype are heterogeneous and result from multiple varied genetic and environmental "hits" to the development process. HPE is part of different syndromes and about 40% have chromosomal abnormalities, but many cases are sporadic and without etiologic explanation.[150-152,154]

Factors Associated With Holoprosencephaly

Environmental teratogens: alcohol, smoking, retinoic acid, salicylates, anticonvulsants
Metabolic: insulin-dependent diabetes (1% risk)
Infections: cytomegalovirus, toxoplasmosis, rubella
Syndromes with normal karyotype (about 25% of holoprosencephaly)
- Smith-Lemli-Opitz
- Pallister-Hall
- Velocardiofacial
- Meckle

Chromosomal abnormalities
- Trisomy 13 (70% have holoprosencephaly)
- Trisomy 18
- Triploidy

Gene mutations
- *SHH* (Sonic Hedgehog; expressed in notochord and floor plate of neural tube)
- *ZIC2* (has role in neurulation in dorsal midline)
- Unexplained/sporadic (50%-65%)

Isolated HPE can have autosomal dominant inheritance with incomplete penetrance and variable expression. Parents of affected children should be examined for mild manifestations such as single central incisor and absent nasal cartilage.[153-155]

HPE is a continuous malformation that is classically divided by DeMyer[156] into three overlapping phenotypic types depending on severity: **alobar** (75% of cases, monoventricular, face typically abnormal), **semilobar** (10% of cases, anterior hemispheres fail to separate but there are two posterior lobes), and **lobar** (10% of cases, two hemispheres form, but the anterior forebrain is incompletely separated). About 5% are atypical forms, including a **midline interhemispheric form (syntelencephaly).** Severe cases often have a dorsal cyst, the dilated suprapineal recess of the third ventricle dilation secondary to obstruction of CSF flow by thalamic fusion[149,151-154] (Fig. 34.16, Video 34.7). The range of abnormalities is much larger than these simple categorizations suggest, involving not only the cerebrum but also basal ganglia and other lower areas. Furthermore, there are **microforms of HPE** with mild manifestations such as single midline incisor tooth, hypotelorism, or absence of olfactory lobes.[149,151-154]

General Anatomic Classification of Holoprosencephaly

ALOBAR
Single forebrain ventricle
No interhemispheric division
Absent olfactory tracts
Absent corpus callosum
Nonseparation (fusion) of deep gray nuclei
Dorsal cyst
Facial abnormality common

SEMILOBAR
Rudimentary cerebral lobes
Incomplete anterior hemisphere division
Absent or small olfactory tracts
Absent anterior corpus callosum (posterior part may develop)
Variable nonseparation of deep gray nuclei

LOBAR
Fully developed cerebral lobes
Distinct interhemispheric division
Midline continuous frontal neocortex
Corpus callosum absent, hypoplastic, or normal
Separation of deep gray nuclei
Fused fornices
Azygous (wandering) anterior cerebral artery

MIDLINE INTERHEMISPHERIC FORM (SYNTELENCEPHALY)
Failed separation of parietal hemispheres
Vertical sylvian fissure appearing to connect across the midline at the vertex
Anterior and posterior corpus callosum formed
Absent or abnormal central corpus callosum
Normal separation of hypothalamus and lentiform nuclei
Gray matter heterotopia

Prenatal diagnosis is based mainly on imaging findings.[149,154] HPE has been diagnosed as early as 9 weeks through demonstration of a single ventricle, single orbit, and proboscis.[152,153] In such early cases, it is important not to mistake the normal rhombencephalic cavity for HPE.

In later pregnancy, typically there is absence of the CSP, variable absence of the falx, and fused appearance of midline structures. **Alobar holoprosencephaly** has three variants—pancake, cup, and ball—depending on the size and configuration of the dorsal cyst. The **pancake** type has a small, flattened plate of cerebrum anteriorly, with a large dorsal cyst posteriorly. The **cup** type has more anterior cerebrum, forming an anterior cuplike mantle and a dorsal cyst. The **ball** type has a single, featureless, monoventricle surrounded by a mantle of ventricle of varying thickness. With **semilobar holoprosencephaly** there is a rudimentary attempt at cleavage of occipital horns (see Fig. 34.16D). Because

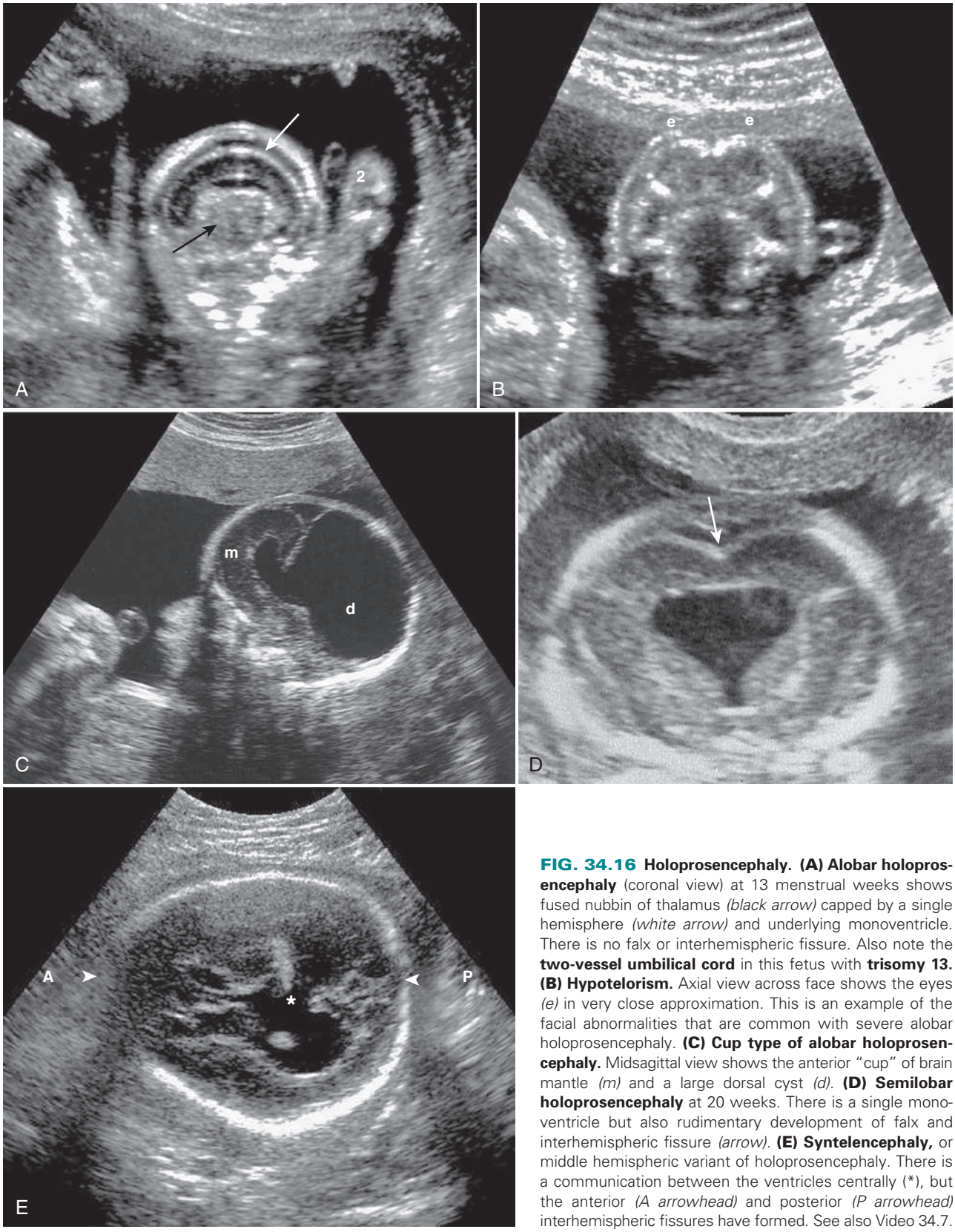

FIG. 34.16 Holoprosencephaly. (A) Alobar holoprosencephaly (coronal view) at 13 menstrual weeks shows fused nubbin of thalamus *(black arrow)* capped by a single hemisphere *(white arrow)* and underlying monoventricle. There is no falx or interhemispheric fissure. Also note the **two-vessel umbilical cord** in this fetus with **trisomy 13. (B) Hypotelorism.** Axial view across face shows the eyes *(e)* in very close approximation. This is an example of the facial abnormalities that are common with severe alobar holoprosencephaly. **(C) Cup type of alobar holoprosencephaly.** Midsagittal view shows the anterior "cup" of brain mantle *(m)* and a large dorsal cyst *(d)*. **(D) Semilobar holoprosencephaly** at 20 weeks. There is a single monoventricle but also rudimentary development of falx and interhemispheric fissure *(arrow)*. **(E) Syntelencephaly,** or middle hemispheric variant of holoprosencephaly. There is a communication between the ventricles centrally (*), but the anterior *(A arrowhead)* and posterior *(P arrowhead)* interhemispheric fissures have formed. See also Video 34.7.

lobar holoprosencephaly forms cerebral hemispheres, it may be difficult if not impossible to diagnose prenatally. Features that suggest lobar HPE include absence of septi pellucidi, fusion and squaring of the frontal horns, and an abnormal appearance of two large nerve trunks, the **fornices,** which are rudimentary and appear fused into a single tract above the third ventricle. With color Doppler sonography, the anterior cerebral artery may have an azygous (wandering) course, "crawling" under the skull. Fusion of the fornices in HPE may help differentiate HPE from **septo-optic dysplasia** (SOD).[157]

Many authors emphasize detection of associated facial abnormalities in diagnosing HPE (see Fig. 34.16B). Facial changes are seen more frequently with more severe HPE and have been categorized into four main groups, with severity approximating degree of brain abnormality.[151-155]

Facial Changes Associated With Holoprosencephaly[151]

Cyclopia with single eye, with or without proboscis
Ethmocephaly (hypotelorism and proboscis between the eyes)
Cebocephaly (hypotelorism, nose with single nostril)
Median cleft lip and palate and hypotelorism
Single central incisor

The differential diagnosis includes severe **hydrocephalus, septo-optic dysplasia** (SOD), **absence of septi pellucidi, schizencephaly, hydranencephaly,** and **porencephaly.**[153,158] Milder forms can be difficult to diagnose even after delivery and may need specialized experienced neuroradiologic consultation.[153] For counseling purposes, it is important to determine the degree of cerebral malformation and whether it is isolated or part of a syndrome or associated with additional abnormalities. MRI and chromosome and genetic analysis can be helpful.[151,154]

Prognosis is variable and depends on severity of HPE, associated abnormalities, and medical and neurologic complications. Severely affected fetuses do poorly or die in utero. Mildly affected children may exhibit few symptoms and may live a normal life. About 75% need shunting.[151] In general, the severity of clinical problems and neurologic dysfunction correlates with the degree of hemispheric and hypothalamic failure of separation and can include endocrinopathy (especially diabetes insipidus), temperature dysregulation, motor and movement abnormalities, and developmental delay.[154,159] Pregnancy termination is generally considered after prenatal diagnosis. Survivors are managed symptomatically.

The fourth variant of HPE, the **middle interhemispheric form** of HPE, also called **syntelencephaly,** has a separation of the anterior and posterior parts of the hemispheres, but fusion is present in the central region of the brain between parietal hemispheres, and the face is typically normal. In general, cases involve mild VM, absence of parts of the septi pellucidi, abnormality of the midpart of the corpus callosum, and dorsal cysts. The condition can resemble mild VM with septal fenestration. Coronal scanning may show fusion of the central parts of the hemisphere. MRI helps confirm this appearance and typically shows sylvian fissures connecting abnormally across the midline[153,154,158,160] (see Fig. 34.16E).

The middle interhemispheric form tends to have better outcomes with functional disabilities similar to those with lobar HPE, but endocrine functions are normal because the hypothalamus tends to be spared.

Posterior Fossa and Cerebellum

Cerebellar development starts at about 6 to 7 weeks' gestation, and the final gross form is achieved by about 18 to 20 weeks. It develops as thickenings of lateral rhombic lips, which enlarge posteriorly and are joined in the midline by the vermis, which develops from the rostral aspect. These thickenings grow into the thin membranous dorsal aspect of the neural tube, the **area membranacea,** which is the rhombencephalic "cyst" that is prominent in early pregnancy and later becomes the fourth ventricle and fenestrates, forming the foramina of Magendie and Luschka.[27,29] There is a rapid acceleration of growth starting about 24 weeks, after which the rule that "cerebellar diameter = weeks gestation" no longer holds. Cerebellar components continue to develop to about 7 months after birth, and final neuronal organization continues to about 20 months after delivery. As the posterior fossa develops, the brainstem initially becomes flexed or kinked (mesencephalic, pontine, and cervical flexures) but again straightens out by about 14 to 16 weeks as the spinal cord expands with developing spinal nerve tracts.[161] There are many genetic and molecular mechanisms involved in cerebellar development, and these have additional roles in CNS and somatic development. Consequently, abnormal cerebellar development is often accompanied by developmental and functional changes in the cerebral cortex and other parts of the body. Specific malformations may suggest genetic syndromes, but any malformation can also result from disruptive processes including infection or teratogenic, metabolic, or traumatic insults.[162,163] Functionally, the cerebellum not only controls voluntary movements but is also involved in nonmotor and cognitive functions. Many children with cerebellar malformations come to medical attention because of developmental and behavioral issues.[162,164-166]

The cerebellum is routinely examined with standard axial views, focusing on transverse diameter, the intactness and size of the vermis, and the depth of the cisterna magna, which should measure less than 10 mm.[5] When an abnormality is suspected, midsagittal views are important to evaluate the integrity, size, rotation, and fissures of the vermis as well as the appearance of the fourth ventricle and brainstem. Transvaginal scanning, 3-D ultrasound, and MRI including sagittal views are especially useful (Fig. 34.17). Care should be taken before 18 weeks to not mistake the incompletely formed vermis for a defect.[30,86,167-171]

With careful technique, as discussed earlier, a small physiologic **Blake pouch** is visible in over 80% of fetuses, as a small cyst in the midline just below the valleculae at the lower border of the cerebellum that does not affect the cerebellum in the midline (see Fig. 34.7A). When this structure enlarges, it can rotate the vermis or it may expand behind the cerebellum as a **mega–cisterna magna.**[29]

Additional anatomic features of the vermis are visible on midsagittal views (see Fig. 34.17). The fourth ventricle is a small

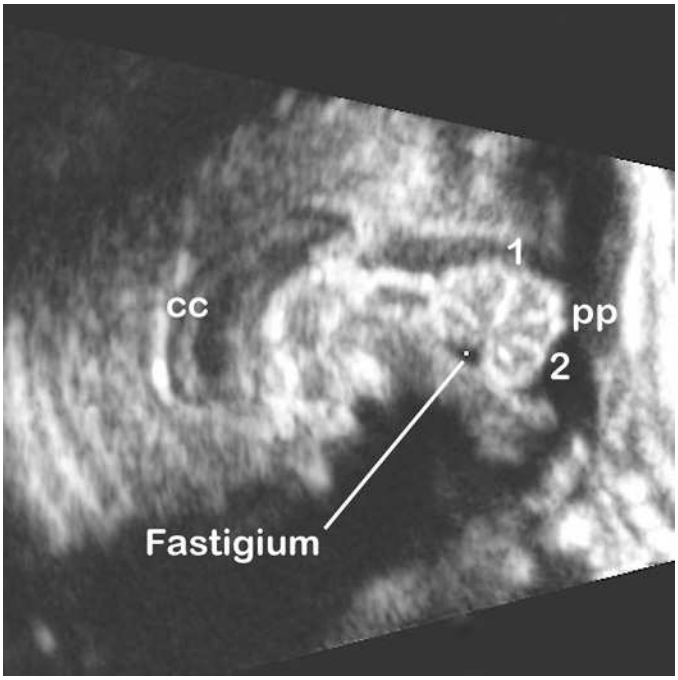

FIG. 34.17 Three-Dimensional (3-D) Midsagittal View of Normal Brain. Three-dimensional midsagittal view of normal brain at 21 weeks using volume contrast imaging (VCI). This is basically a thick-slice scan that increases contrast and decreases noise. Note the triangular shape of the cerebellar vermis behind the brainstem. This is the best view to evaluate the corpus callosum *(cc)* and vermis. Line indicates apex of the fourth ventricle and fastigial point. Normally as here, the upper and lower parts of the cerebellum touch the brainstem. A line connecting the fastigium and declive (the most posterior bulging part of the vermis) normally divides the vermis into approximately equal upper and lower portions. After about 20 weeks, three vermian fissures can usually be identified as white septa invaginating into the darker cerebellum. They are the primary *(1),* the prepyramidal *(pp),* and the secondary *(2)* fissures. More fissures become visible with advancing age as are seen in this fetus.

triangular space that normally has a pointed apex, the **fastigial point.** The upper and lower parts usually touch the brainstem, but the lower part may rotate outward **(tegmento-vermian angle)** to about 10 degrees. A line drawn between the fastigial point and the most posterior bulge of the vermis bisects the vermis into approximately equal halves. Nomograms are available for vermian dimensions. Vermian fissures become visible after about 18 weeks and can be used to help determine normal vermis development. The primary fissure between the culmen and declive is seen at about the 2 o'clock position by 24 weeks, and the secondary between the pyramis and uvula at the 5 o'clock position by 30 weeks. Commonly a third fissure is visible horizontally between these two.

Practically, it is easiest to approach posterior fossa abnormalities anatomically and consider three elements as suggested by Guibaud: fluid space in the posterior fossa, cerebellar size, and cerebellar morphology.[169,170] Suspected abnormalities should be further evaluated with detailed examination of the brain and body including midsagittal views and 3-D ultrasound along with MRI to evaluate the brainstem and cerebellar vermis.[30,59,169-171]

Increased fluid and torcular elevation suggest **Dandy-Walker malformation,** whereas normally sited torcular position and normal cerebellar morphology suggest **mega–cisterna magna, Blake pouch cyst,** or **arachnoid cyst.** If the cerebellum is globally small, then the brainstem should be evaluated. A normal brainstem suggests **cerebellar hypoplasia,** and a small brainstem suggests **pontocerebellar hypoplasia.** Focal reductions suggest ischemia or hemorrhage. Global reductions suggest syndromes, aneuploidy, and infections. If there is anatomic abnormality, then considerations include **vermian agenesis** as with **Joubert syndrome** and spina bifida with **Chiari II.**

Counseling regarding posterior fossa abnormalities is difficult because fetuses with different conditions are variously grouped together.[172,173] Frustratingly, prenatal appearances often do not correlate with findings at pathology.[174] Genetic abnormalities have been described with many posterior fossa disorders, and many have autosomal recessive inheritance.[162,175] If posterior abnormalities are suspected, expert imaging opinion and interdisciplinary consultation should be considered.[30]

Dandy-Walker Malformation

Classic DWM is a triad of partial or complete vermian agenesis, cystic enlargement of the fourth ventricle, and elevated torcular or tentorium (Fig. 34.18). It occurs in about 1 per 30,000 pregnancies and is felt to arise from abnormal development of the membranous roof of the fourth ventricle at about 7 to 10 weeks. Midsagittal imaging is important because prognosis is associated with the degree of vermian abnormality as well as the presence of associated abnormalities. Additional CNS anomalies are common, especially **hydrocephalus** (70%-90%), **dysgenesis of the corpus callosum** (30%), **encephalocele** (16%), **migrational disorders, brainstem dysgenesis,** and **spina bifida.** Somatic abnormalities occur in 20% to 30%, including cystic kidneys, congenital heart disease, and facial clefts. DWM has a multifactorial etiology, and most cases are seen in association with genetic and nongenetic syndromes. At the 11- to 14-week scan, a large posterior fossa may be the first sign of DWM but can also be seen with chromosomal abnormality and other malformations and should be reassessed later in the pregnancy.[99,176]

The differential diagnosis includes **vermian dysplasia, Blake pouch cyst,** and **posterior fossa subarachnoid cysts.** Investigations include fetal MRI, assessment for maternal TORCH infection, chromosome analysis, microarray analysis, and consideration of syndromic forms, including **Walker-Warburg syndrome.**

The prognosis of DWM depends on associated abnormalities. Those with isolated DWM and relatively normal vermis do better, but those with associated CNS or somatic abnormalities do poorly. Neonatal mortality ranges from 12% to 55%. In live-born children, intelligence is normal in about 40%, borderline in 20%, and subnormal in 40%.[170,177]

Vermis Hypoplasia or Dysplasia

Vermis hypoplasia or dysplasia describes a conspicuous cleft between the inferior parts of the cerebellar hemispheres due to deficiency or absence of the lower part of the vermis. Controversy surrounds this appearance, which has been variously termed

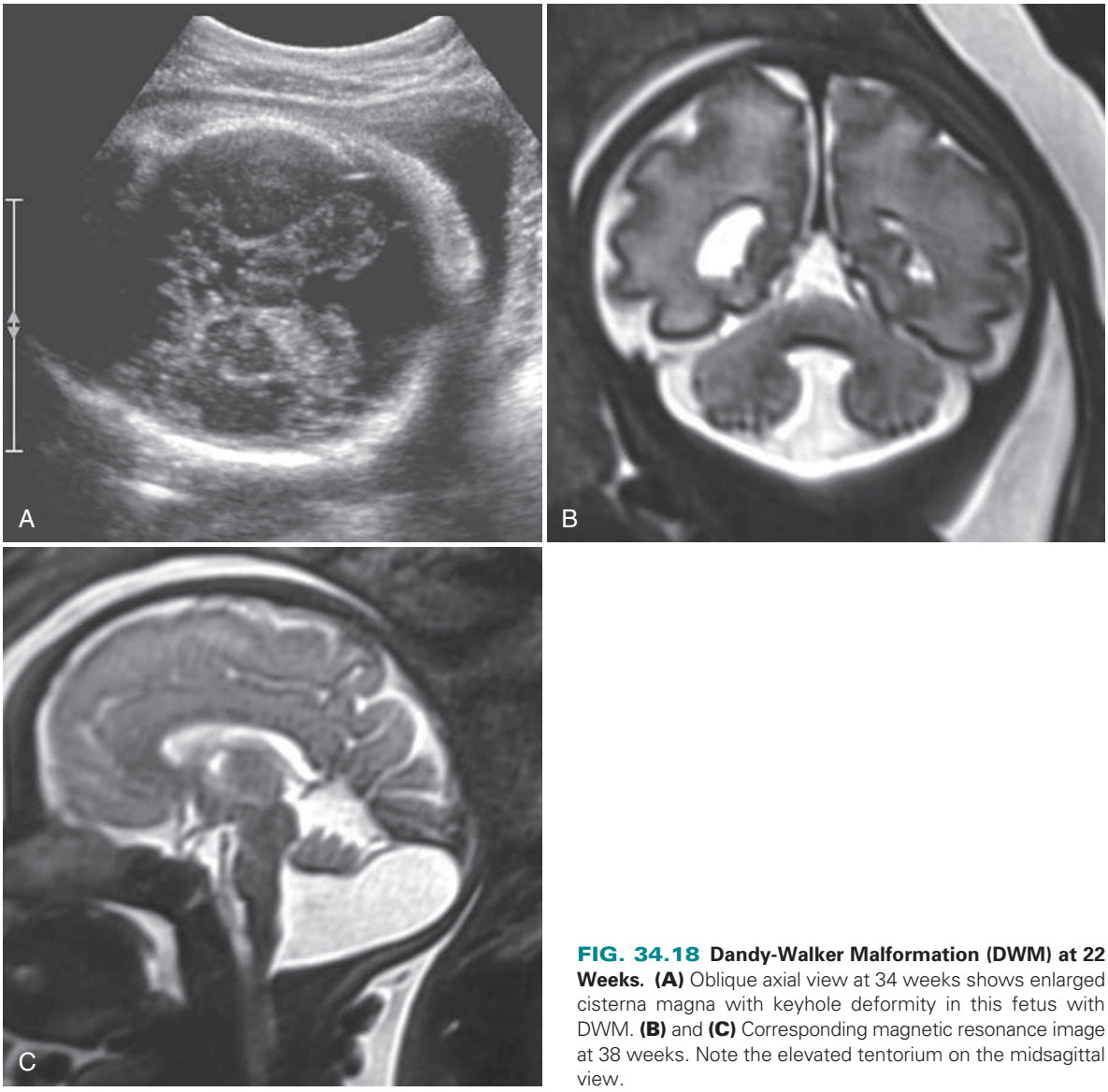

FIG. 34.18 Dandy-Walker Malformation (DWM) at 22 Weeks. (A) Oblique axial view at 34 weeks shows enlarged cisterna magna with keyhole deformity in this fetus with DWM. **(B)** and **(C)** Corresponding magnetic resonance image at 38 weeks. Note the elevated tentorium on the midsagittal view.

Dandy-Walker variant; Dandy-Walker continuum; (inferior) vermian hypoplasia, dysgenesis, or agenesis; and **Blake pouch cyst.**[30] The currently accepted term is **vermian hypoplasia or dysplasia.** Problems have arisen because on standard axial cerebellar views the Blake pouch can mimic this appearance.[28]

The vermis develops superiorly to inferiorly. Hypoplasia or developmental arrest results in varying-size deficits of the inferior portion, leaving a relatively square defect that communicates with the fourth ventricle and separates the lower cerebellar hemispheres. In general, the posterior fossa is not enlarged. Midsagittal scans, 3-D imaging, and MRI are important to evaluate the size and shape of the vermis and the shape of the fourth ventricle and to determine if normal early fissures have developed.[30,59,169,171]

There are diagnostic pitfalls. Hypoplasia or dysplasia should not be diagnosed earlier than 18 weeks, before vermian development is complete. On routine axial scans an excessively steep scanning angle may give the appearance of a prominent cleft between the lower portions of the cerebellar hemispheres that mimics vermian hypoplasia[30,178] (see Fig. 34.7B-C).

True cases of vermian hypoplasia are usually associated with additional abnormalities similar to those seen with DWM, and these help confirm the diagnosis (Fig. 34.19). Vermian hypoplasia can be associated with several syndromes, including **Joubert and related syndromes, Walker-Warburg syndrome, cerebro-oculo-muscular syndrome,** and **pontocerebellar syndrome.**[30,175]

Counseling is difficult. In one series, up to 50% of fetuses with the characteristic ultrasound findings of vermian dysplasia were functionally normal after delivery.[179] Ultrasound findings more likely to predict true abnormality were **trapezoidal vermian defect,** cisterna magna larger than 10 mm, and complete aplasia of the vermis. In contrast, normal cases tended to have a **keyhole-shaped defect.**[174] Prenatal MRI is helpful but also has limitations.

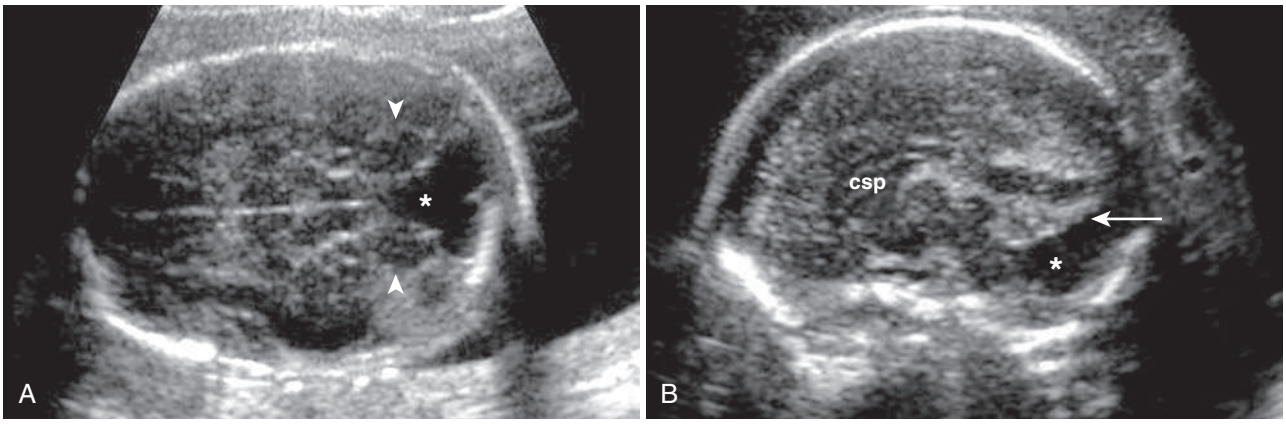

FIG. 34.19 Vermis Dysplasia or Hypoplasia. (A) Axial view shows fetus at 20 weeks with cleft (*) separating the cerebellar hemispheres *(arrowheads).* **(B)** Sagittal view shows the cerebellar vermis to be deficient in its inferior portion *(arrow),* with a fluid space in the expected region of the lower vermis (*). *csp,* Corpus callosum and cavum septi pellucidi.

In studies from Children's Hospital in Boston, postnatal MRI failed to confirm prenatal MRI findings in 6 of 42 cases (5 vermian hypoplasia, 1 mega–cisterna magna) but found additional, mainly cerebral abnormalities in 10 of 42 cases (heterotopias, brainstem hypoplasia, lissencephaly, hemorrhage).[164,180] Because of the diagnostic uncertainties, when vermian abnormality is suspected, additional anomalies should be sought. Additional investigation includes history, assessment for maternal TORCH infection, MRI, chromosome analysis, and molecular DNA analysis if the chromosomes are normal.[30]

Mega–Cisterna Magna

Mega–cisterna magna (MCM) refers to an enlargement of the cisterna magna beyond 10 mm with intact vermis (Fig. 34.20). On careful scanning, it can be noted that the contained fluid is anechoic and cyst walls can be seen in the far periphery, similar to a large Blake cyst. Many believe that MCM is just enlargement of a Blake cyst behind the cerebellum and without vermis rotation. When the condition is isolated, most children are normal. However, if not isolated, only 11% have normal outcome. The majority of nonisolated cases have VM, congenital infection, or karyotype abnormalities, especially trisomy 18. Differential diagnosis includes arachnoid cyst compressing the posterior fossa and DWM. Arachnoid cysts displace an otherwise normally formed cerebellum and frequently lie behind or above the cerebellum, may be asymmetrical, and do not communicate with the fourth ventricle.[46,177]

Rhombencephalosynapsis

Rhombencephalosynapsis is a rare hypoplasia of the cerebellum characterized by complete or partial absence of the vermis and fusion of the cerebellar hemispheres and dentate nuclei. Most cases are sporadic, although familial cases have been described.

Rhombencephalosynapsis may manifest with VM as early as 14 weeks. Cerebellar findings may not be initially conspicuous on the usual axial views. The defining findings at ultrasound are a small, bean-shaped cerebellum that lacks the typical echogenic waistlike narrowing at the vermis and cerebellar hemispheric fissures that are continuous from side to side without midline interruption. Midsagittal views show absence of the typical vermian fissures and may show an abnormally shaped fourth ventricle. These findings are more readily seen on MRI.[181,182]

Additional cerebral and somatic abnormalities are common. Cerebral findings primarily involve midline structures and include aqueduct stenosis, agenesis of the corpus callosum, absent septum pellucidum, and SOD. Somatic abnormalities include segmentation errors of the spine, phalangeal and radial ray defects, and occasional defects of the cardiovascular, respiratory, and urinary tract.

Prognosis is poor and most children die in childhood, but some may survive into adulthood. Most survivors are neurologically delayed and have movement disorders.[182]

Other Posterior Fossa Abnormalities

The vermis receives a disproportionate degree of discussion because vermian abnormalities are relatively conspicuous on routine second-trimester ultrasound. Numerous other, difficult-to-detect or late-appearing abnormalities also involve the posterior fossa. These include hypoplasia, clefts, changes related to ischemia, hemorrhage and infarct, cortical migration disorders (type 2 cobblestone lissencephaly), metabolic disorders, and other neurodegenerative disorders.

When abnormalities of the cerebellum and posterior fossa are suspected, then detailed neurosonography and somatic sonography should be performed and consideration given to further investigations including MRI and karyotype, assessment for infections, and expert counseling.[30,166,172,175,183]

Arachnoid Cysts

Arachnoid cysts are benign, noncommunicating fluid collections within arachnoid membranes. Most appear stable and require no surgical treatment. They can occur intracranially and in the spinal canal and on occasion they can be detected in the first trimester. Locations by order of frequency are the sylvian fissure or temporal fossa, posterior fossa, over the cerebral convexity, and midline supratentorial, including suprasellar (Fig. 34.21). Even if very large, arachnoid cysts rarely cause symptoms. Occasionally they interfere with CSF

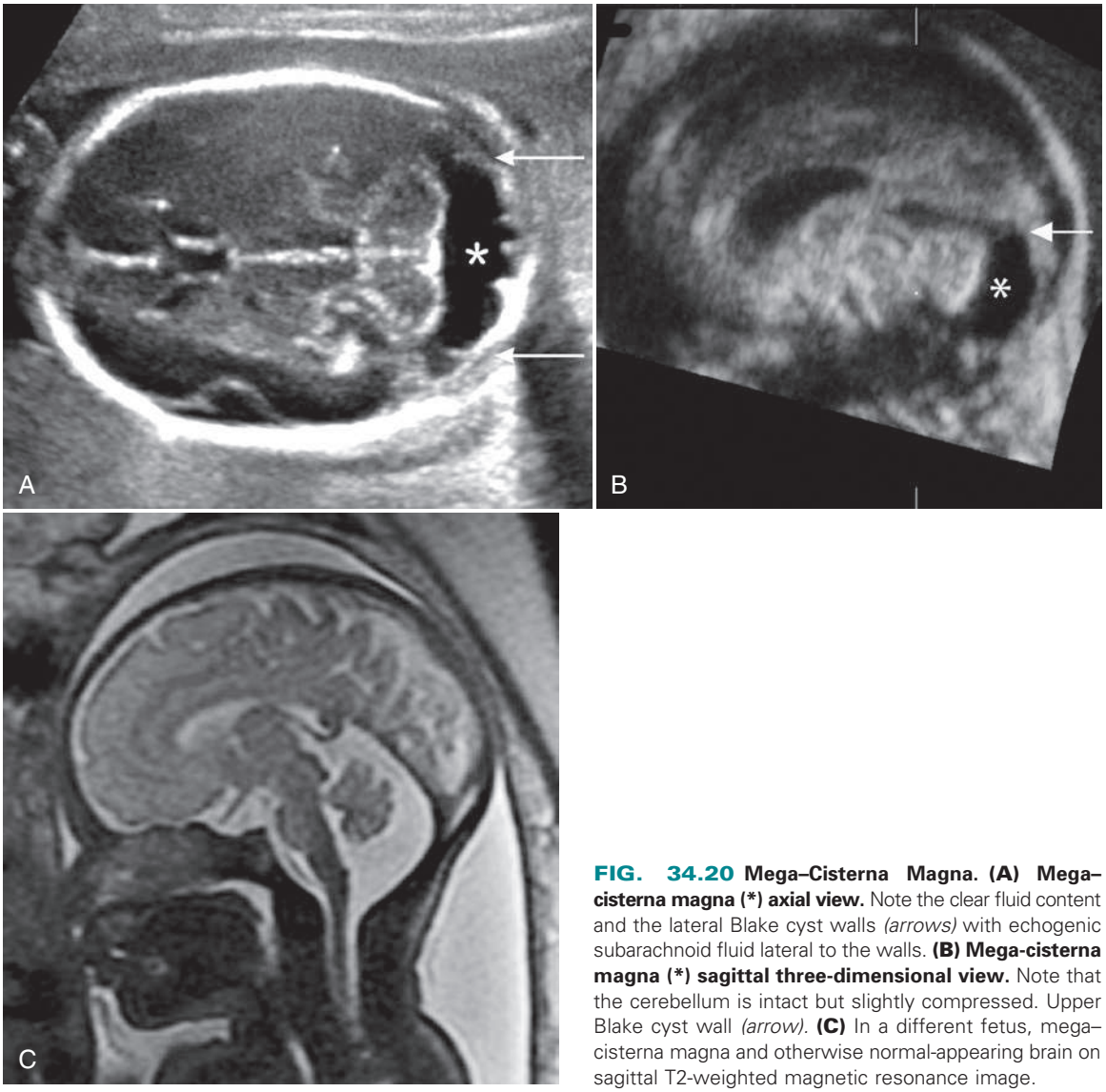

FIG. 34.20 Mega–Cisterna Magna. (A) Mega–cisterna magna (*) axial view. Note the clear fluid content and the lateral Blake cyst walls *(arrows)* with echogenic subarachnoid fluid lateral to the walls. **(B) Mega-cisterna magna (*) sagittal three-dimensional view.** Note that the cerebellum is intact but slightly compressed. Upper Blake cyst wall *(arrow)*. **(C)** In a different fetus, mega–cisterna magna and otherwise normal-appearing brain on sagittal T2-weighted magnetic resonance image.

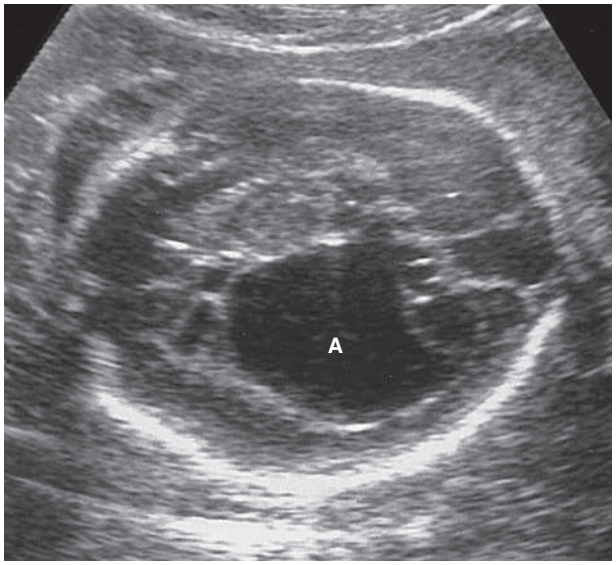

FIG. 34.21 Arachnoid Cyst. Arachnoid cyst *(A)* in the supratentorial, interhemispheric position at 25 weeks.

circulation and require decompression. Midline cysts can accompany dysgenesis of the corpus callosum, so when a supratentorial cyst is seen, it is important to evaluate the entire corpus callosum. In the suprasellar region these cysts may be associated with pituitary dysfunction. The differential diagnosis depends on the location. Arachnoid cysts in the posterior fossa can be confused with **DWM, inferior vermian hypoplasia, mega–cisterna magna,** and **Blake pouch cysts.** The differential diagnosis of supratentorial cysts includes **cavum veli interpositi** (CVI), **aneurysm of vein of Galen, hemorrhage,** and **cystic tumors.** Pediatric neurosurgical opinion is important in evaluating and counseling these patients, many of whom require no treatment.[27,65,184,185]

Malformations of Cortical Development

Malformations of cortical development comprise a broad and heterogeneous collection of conditions resulting from disturbances in the major steps of cortical development including neuronal proliferation in germinal zone and apoptosis, migration, and cortical organization. Cortical changes may be focal or global

and can result from intrinsic factors, as mutations in genes controlling brain development, or extrinsic insults including syndromes, maternal diseases (phenylketonuria), teratogens (anoxia, drugs, x-rays), metabolic abnormalities, and fetal infections, but often a cause cannot be found. Changes often reflect time of insult rather than its specific nature.[91,186-188] The responsible genes often function at many developmental stages and in many different body structures apart from the brain. Different mutations of the same gene may result in different syndromes. Abnormalities may be found in seemingly unrelated organs, as in **thanatophoric skeletal dysplasia,** in which abnormal function of the *FGFR3* gene causes both cortical brain malformations and skeletal abnormalities.[189]

Cerebral changes with malformations of cortical development are heterogeneous. VM is common. They generally share variable degrees of thickened, disorganized cortical neuronal layers and alterations in sulcal, gyral, and white matter patterns and abnormal corpus callosum or posterior fossa. Cortical abnormalities may be difficult to detect until sulcal development becomes visible at about 24 weeks. Some may not be detectable in utero and may become evident only as symptoms (and abnormalities) develop in later life. Detailed classification of these disorders is complex and based variously on genetics, biologic pathways, neuroimaging features, and first-affected developmental stage. The past few years have shown a dramatic increase in the understanding of the genetic and molecular basis of these malformations. The current classification is acknowledged to be neither perfect nor complete and is subject to updating with new genetic discoveries. In practice they are described by the general conspicuous patterns they present, including **microcephaly, macrocephaly, lissencephaly, polymicrogyria** (PMG), **periventricular nodular heterotopia,** and **schizencephaly.**[91,190-192]

For all these conditions, investigation requires detailed examination including MRI, which can help focus further directions for more targeted testing. Multidisciplinary consultation is important for optimal prenatal assessment and counseling. Additional investigations depend on individual situations and can include detailed family and pregnancy history, infection screening, amniocentesis for karyotype and array-comparative genomic hybridization (CGH), commonly called microarray, other testing for specific gene mutations, and other specific testing as suggested by clinical and imaging appearances. Prognosis varies depending on the severity of the condition and associated abnormalities, and epilepsy and developmental delay are common.[193-195]

Classification of Malformations of Cortical Development

ABNORMAL NEURONAL PROLIFERATION OR APOPTOSIS

Abnormal Brain Size
Microcephaly
Megalencephaly (macrocephaly)
Hemimegalencephaly

Abnormal Proliferation
Nonneoplastic or neoplastic

ABNORMAL NEURONAL MIGRATION
Classical lissencephaly and subcortical band heterotopia
Cobblestone lissencephaly and complex or congenital muscular dystrophy
Heterotopia

ABNORMAL CORTICAL ORGANIZATION
Polymicrogyria
Schizencephaly

NOT OTHERWISE CLASSIFIED
Secondary to inborn errors of metabolism (mitochondrial, pyruvate)
Peroxisomal disorders

Modified from Raybaud[191] and Barkovich.[196]

Microcephaly

Microcephaly describes a disproportionately small head for fetal age and body size. Precise diagnostic definition is difficult, but in general, microcephaly is diagnosed if the head circumference less than 3 SDs below the expected mean and intrauterine growth restriction (IUGR) has been excluded. Some suggest using 2 SDs, but this would include many normal individuals. Incidence at birth ranges from 1 per 1360 to 10,000. The diagnosis implies failure of brain development **(micrencephaly).** Etiology is heterogeneous and can be related to a great variety of prenatal causes including genetic factors, environmental issues, asphyxia, infections **(Zika virus),**[197] maternal conditions **(phenylketonuria),** drugs (e.g., **fetal alcohol syndrome**), diverse syndromes (e.g., **Smith-Lemli-Opitz, Cornelia de Lange**), and **irradiation.** On pathologic examination, the brain may be small but normal in appearance, or it may have diverse findings, including simplified gyri, porencephaly, absent corpus callosum, and VM. Associated CNS and non-CNS abnormalities are common.[91,188,198]

Microcephaly should be suspected if the head size is smaller than expected. Measurements alone have only a limited ability to diagnose microcephaly. In one study, only 4 of 24 fetuses with small measurements had the diagnosis confirmed at delivery. Other findings include brain abnormality, abnormal head-to-abdomen circumference ratio, sloping forehead, and small frontal lobe size (Fig. 34.22).

Microcephaly is usually is not evident until late in pregnancy when the head size fails to grow normally, but it has been seen as early as 15 weeks. When a smaller-than-expected fetal head is encountered, there should be a careful search for cerebral and other anomalies that would help to confirm clinical importance. Ultrasonography of the brain can be difficult because the cranial bones become closely approximated and hinder visibility. MRI is helpful in evaluation of the cerebral parenchyma and associated abnormalities.[7,199] Small head size can be associated with subnormal mental ability; the smaller the head circumference, the lower the performance level. Prognosis varies with CNS and associated abnormalities.

Macrocephaly and Megalencephaly

Macrocephaly implies a large head with circumference of 2 SDs or greater or at the 98th percentile for gestational age. It excludes

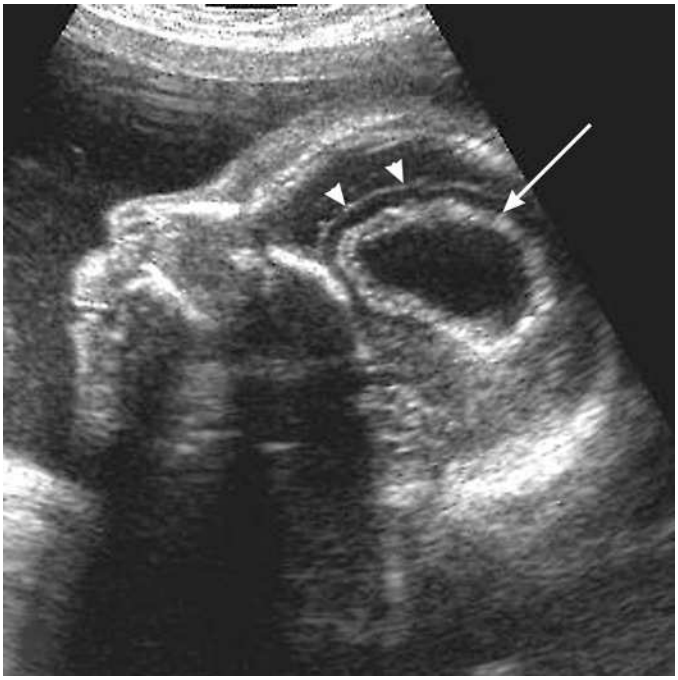

FIG. 34.22 Microcephaly and micrencephaly at 25 weeks with **periventricular calcification** *(arrow)* in fetus with **pseudo-TORCH.** Note the underdeveloped brain parenchyma *(arrowheads).*

conditions with relative head enlargement such as asymmetrical IUGR, HC, tumors, and triploidy. **Megalencephaly** refers to cerebral gigantism (i.e., enlarged brain). It is typically categorized as genetic (nonsyndromic or syndromic) or nongenetic (HC following hemorrhage or infection, posttraumatic, arachnoid cysts). Nonsyndromic implies isolated head or brain enlargement without other significant abnormality. Syndromic implies association with other abnormalities or syndromes such as overgrowth syndromes **(Beckwith-Wiedemann, Sotos, Weaver),** skeletal dysplasias **(thanatophoric dysplasia, achondroplasia),** neurocutaneous syndromes **(neurofibromatosis type 1),** and metabolic conditions such as **leukodystrophy** and organic acidurias. Head enlargement can appear early by 20 weeks but typically does not manifest until the third trimester or in early childhood.[200-203]

Benign familial macrocephaly (external HC) accounts for about 50% of cases of macrocephaly. It is an autosomal dominant condition with increased subarachnoid fluid. It typically manifests late in pregnancy or even after delivery but has been seen as early as 18 weeks when there is a history of other family members who had large heads. Most children are functionally normal.[201,202]

When the head measurements are larger than expected (macrocephaly), there should be a careful search for intracranial abnormalities and non-CNS abnormalities. Family history of large headedness can help. Multidisciplinary counseling and investigation are important. Prognosis can be favorable to poor depending on etiology.

Hemimegalencephaly

Hemimegalencephaly is a malformation of cortical development with hamartomatous enlargement of one hemisphere with defects in all aspects of neuronal migration. Most cases are sporadic and of unknown cause. Typically there is macrocephaly at birth. It may be isolated or associated with neurocutaneous and somatic hemihypertrophy syndromes including **neurofibromatosis, tuberous sclerosis** (TSC), **epidermal nevus syndrome, Proteus syndrome, Klippel-Trénaunay-Weber** syndrome, and others. On the affected side the hemisphere and ventricle are enlarged and the brain has abnormal texture and sulcation. The unaffected hemisphere is generally normal but can be distorted owing to compression and may also show less severe migrational abnormalities. Functional deficiency and seizures are common, the latter on occasion requiring hemispherectomy.[204-207]

Lissencephaly

Lissencephaly describes a brain that has a smooth surface lacking normal gyration. It is due to a global disturbance in neuronal migration. The most severe manifestation is a completely smooth cortex lacking gyri **(agyria),** but some cases show large, malformed gyri **(pachygyria).** There are two general types that have fundamentally different developmental mechanisms. In **type 1 lissencephaly (classical lissencephaly),** neurons fail to migrate to the cortex. In **type 2 lissencephaly (cobblestone lissencephaly),** the neurons migrate but do not stop at the cortical surface and overmigrate into the subarachnoid membranes overgrowing surface vessels, resulting in "cobblestone cortex." Both types are etiologically heterogeneous and related to many gene mutations and are commonly associated with additional CNS and somatic abnormalities.[21,91,192,208] Previously it was thought that lissencephaly could not be diagnosed before 28 weeks, but familiarity with the normal early sulcal development has allowed diagnosis of type 1 **(Miller-Dieker syndrome)** by 23 weeks,[48] and type 2 **(Walker-Warburg syndrome)** at 14 weeks.[209]

Type 1 or **classical lissencephaly** manifests as a smooth cortex and hourglass shape on axial views associated with mild VM, a primitive insula, delayed or absent sulcation, and abnormal cortical vascularity but sparing of the cerebellar vermis (Fig. 34.23). There are several variants. The more common Miller-Dieker syndrome has gene abnormality at 17p13.3 *(LIS1)* and is associated with **congenital heart disease, omphalocele, genitourinary abnormalities, IUGR,** and **dystrophic facies.** Girls with **X-linked** type 1 lissencephaly may function normally despite "double cortex" cerebral changes that can be seen with MRI, but boys do poorly.[48]

Type 2 or **cobblestone lissencephaly** is associated with malfunction of genes that also function in muscle development (e.g., *POMT1/2, FKRP, FKTN*). These conditions are grouped as **congenital muscular dystrophy.** These infants typically have additional CNS and somatic abnormalities and lack muscle tone at birth (floppy baby). The most severe phenotype, **Walker-Warburg syndrome,** is also called **HARD-E** for ***h*ydrocephalus, *a*gyria, *r*etinal *d*ysplasia, and/or *e*ncephalocele** and includes a **kinked brainstem.** Less severe phenotypes include **Fukuyama syndrome** and **muscle-eye-brain disease.** Ultrasound changes may be evident by 20 weeks and include VM and absent, delayed, or abnormal sulcal development; cerebellar vermian dysplasia; eye abnormalities; small encephalocele; and abnormal kinked brainstem (Fig. 34.24).[48,208,209]

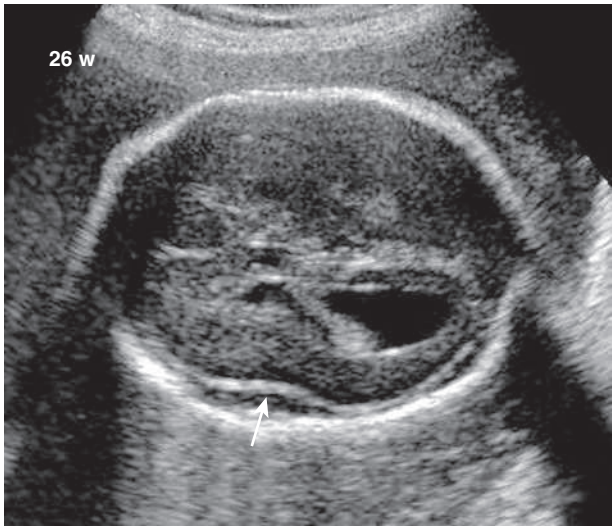

FIG. 34.23 Type 1 Lissencephaly (Miller-Dieker Syndrome) in 26-Week Fetus. Note the mild ventriculomegaly and lack of sulcal formation. The insula is very smooth and shallow *(arrow)* and lacks the angular plateau appearance expected at this age. Brain shows increased echogenicity associated with migrational disturbance.

Fetal MRI and gene mutation analysis can help confirm the diagnosis. Postnatal outcome is poor but varies with the specific condition.[192,208]

Focal Cortical Changes

Polymicrogyria (PMG) is probably the most common malformation of cortical development. It is a heterogeneous malformation characterized by excessive numbers of small shallow, abnormal gyri and irregularity of the cortex/white matter interface. The distribution may be focal or global. PMG may be isolated or associated with many genetic and acquired conditions; however, in most cases the cause cannot be found. Mutations have been found in over 30 genes including the tubulin family and include metabolic conditions such as **peroxisomal disorders** and **DiGeorge syndrome** (22q11.2). Nongenetic conditions include infection with **CMV** and hypoxia and ischemia.

Focal cortical changes typically manifest in mid to late pregnancy and are difficult to detect with ultrasound, where the cortical contour can have a **sawtooth** appearance. They are typically found at MRI in fetuses referred for evaluation of other abnormalities initially detected by ultrasound. PMG is the most common cortical malformation in children with epilepsy and can manifest with developmental delay. The heterogeneity of causes and manifestations makes counseling difficult[192,195,205,210] (Fig. 34.25).

Heterotopia describes localized nodules of disorganized neurons in abnormal locations anywhere in the brain. On MRI three types are described: **periventricular nodular heterotopia, focal subcortical heterotopia,** and **band heterotopia.** Only the periventricular nodules are readily detectable on prenatal ultrasound and visible as irregular lining of the ventricular surface (Fig. 34.26). The nodules are more conspicuous on MRI, which can also depict the intraparenchymal and cortical nodules, which are difficult to recognize by ultrasound. Etiology is heterogeneous. Cases can be isolated but other CNS and somatic abnormalities are common, especially involving the corpus callosum. The differential diagnosis includes ventricular irregularity associated with **CMV, hemorrhage,** and **tuberous sclerosis.** Prognosis varies depending on underlying syndromes and associated abnormalities and ranges from essentially normal to having variable deficits and epilepsy, which are common; in some the disorder is lethal.[192,195,205,211]

Schizencephaly (split brain) is a rare structural malformation of the cerebrum characterized by congenital clefts or defects that extend through the hemisphere from ventricle to outer cortex. The clefts are usually symmetrical and involve the parietal or temporal regions. They are lined by cortical gray matter often with PMG, unlike clastic injury resulting in porencephaly in which white matter lines the clefts. The tracts may be open **(open lip),** allowing CSF communication between the ventricle and subarachnoid space, or solid (**closed lip,** consisting of an abnormal, solid gray matter tract between the ventricle and brain surface). Etiology can be destructive **(encephaloclastic)** or developmental. Destructive etiologies include **vascular injury, ischemia,** teratogen exposure (e.g., **cocaine**), infections (especially **CMV**), and trauma, and appearances can be similar to **porencephaly** or **hydranencephaly.** Developmental cases are considered to be related to PMG arising from disordered neuronal migration and organization. Most cases are found in late pregnancy during investigation of VM, but they have been seen in the middle trimester. The diagnosis rests on detection of the cerebral clefts or abnormal gray matter traversing from ventricle to cortex (Fig. 34.27). There may be associated midline defects including SOD, dysgenesis of the corpus callosum, absence of the septi pellucidi, other malformations of cortical development, and optic nerve abnormalities. Fetal MRI allows superior characterization of cortical and gray matter changes.

Neurodevelopmental delay and seizures are common. Suspected cases benefit from multidisciplinary consultation and counseling. Prognosis relates to the size of the defect and associated abnormalities.[19,195,205,212,213]

Other Malformations of Cortical Development

Cortical malformations can accompany infections, inborn errors of metabolism (e.g., **peroxisomal disorders**), **mitochondrial disease,** and conditions with unknown etiology.[91,188] **Metabolic** and **neurodegenerative disorders** can be associated with abnormal brain development but are typically not detectable prenatally by ultrasound. However, some are associated with diverse changes such as IUGR, microcephaly or macrocephaly, abnormal corpus callosum, migrational and cerebellar abnormality, cerebral calcifications, cerebral cysts, renal and hepatic changes, congenital heart disease, and hydrops.[214,215] The most common is **Zellweger (cerebrohepatorenal) syndrome,** a lethal peroxisomal disorder. Affected fetuses can have increased NT in the first trimester and later show VM, subependymal germinolytic cysts, migrational abnormality, hepatomegaly, cortical renal cysts, and **chondrodysplasia punctata.** The diagnosis can be confirmed by DNA and biochemical testing of fetal cells obtained by CVS.[214-216]

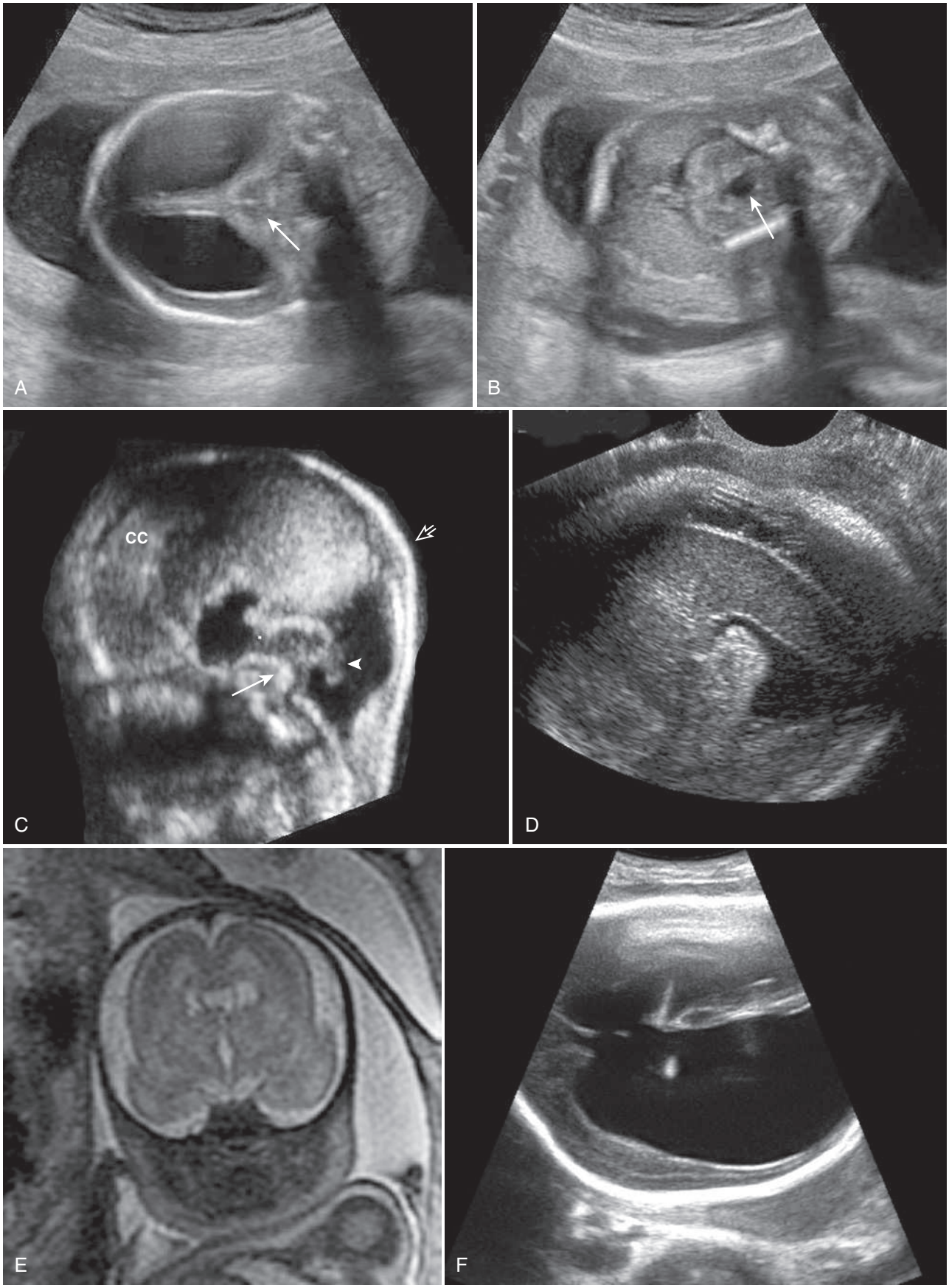

FIG. 34.24 Type 2 Lissencephaly (Cobblestone Cortex, Walker-Warburg Phenotype) at 21 Weeks. (A) Coronal view shows the large, smooth ventricles and the very small brainstem *(arrow).* **(B)** Defect in vermis (vermian hypoplasia; *arrow*). **(C)** Midsagittal view shows the Z-shaped kink in the brainstem *(arrow),* which represents failure of the brainstem to straighten and lose the early embryologic flexures, a process that normally occurs after 12 to 13 weeks. Also, the cerebellar vermis is very small *(arrowhead).* The third ventricle is malformed. The corpus callosum *(cc)* is malformed and extremely elevated. There is a minute occipital encephalocele *(open arrowhead).* This fetus also had eye abnormalities. **(D)** In a different fetus at 36 weeks, transvaginal scan shows smooth cortex (agyria), abnormal for this gestational age. **(E)** Coronal T2-weighted magnetic resonance image shows the smooth cortex and abnormal bands of high signal intensity in the parenchyma. Note the prominent extraaxial CSF spaces. **(F)** Another fetus with severe VM and lissencephaly caused by Walker-Warburg syndrome. Note that this is the same fetus shown in Fig. 34.13B with a small cephalocele.

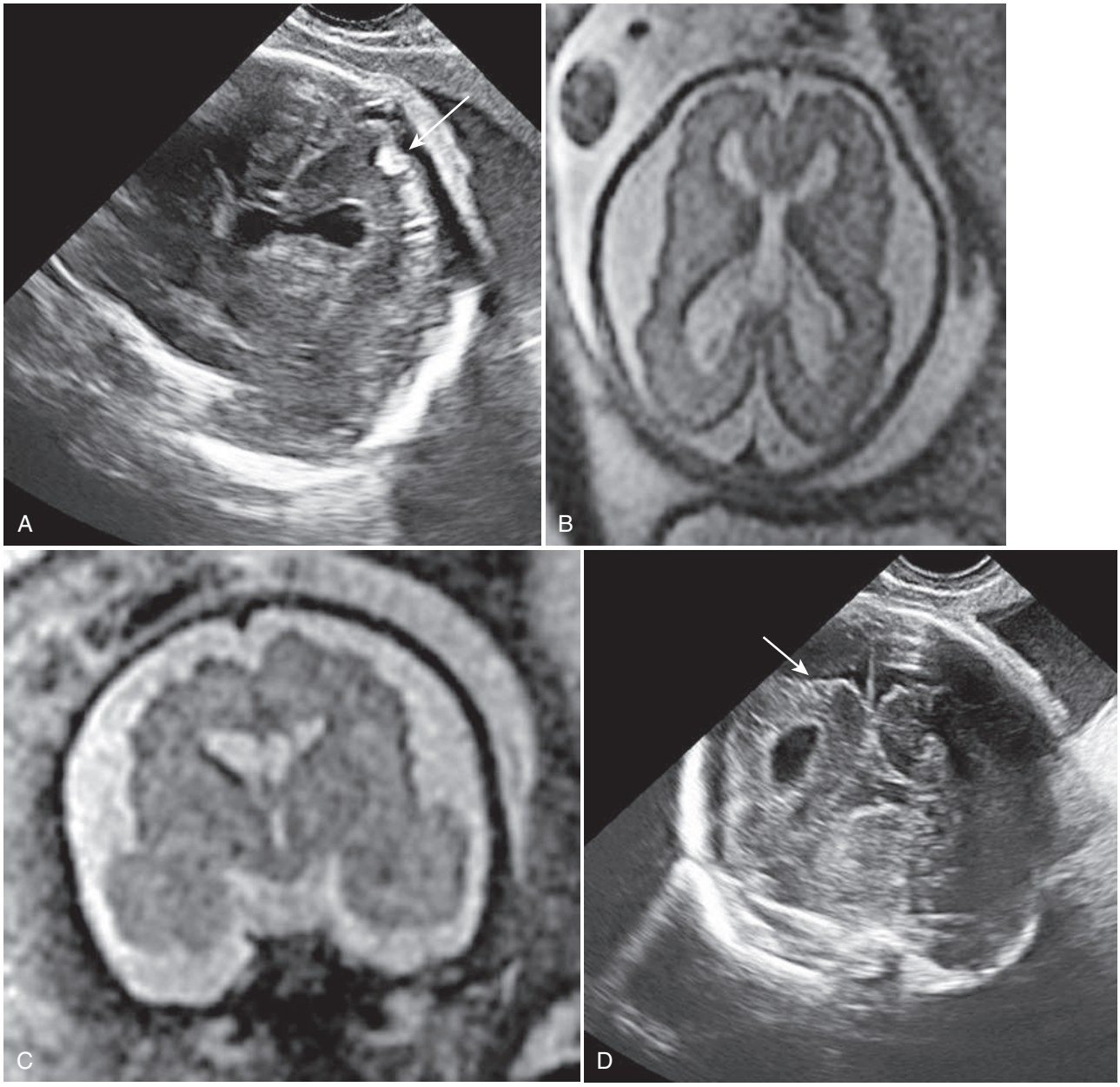

FIG. 34.25 Polymicrogyria. (A) Irregular appearance to the cortex and cortical calcification *(arrow)* on coronal transvaginal sonogram at 25 weeks. **(B)** and **(C)** Axial **(B)** and coronal **(C)** T2-weighted magnetic resonance imaging (MRI) scans show **sawtooth** appearance of the cortex at 25 weeks. Note how the calcifications were better visualized on the sonogram than on MRI. **(D)** Polymicrogyria at 30 weeks' gestational age. Note ventriculomegaly and prominent extraaxial cerebrospinal fluid (CSF). The shrunken brain has fallen away from the skull, leaving a wide, CSF-filled subarachnoid space **(hydrocephalus ex vacuo).** Note also the fine nodularity of the surface of the brain *(arrow).*

Tuberous Sclerosis

Tuberous sclerosis (TSC) is a multisystem, hamartomatous condition involving abnormalities of the brain, skin, heart, eyes, and kidneys. It is autosomal dominant related to abnormal *TSC1* and *TSC2* genes; however, about 70% of cases are a de novo mutation. Clinical diagnosis is made using a combination of major and minor findings including cranial findings of cortical tubers and white matter migration lines, subependymal nodules, subependymal giant cell astrocytomas, cardiac rhabdomyomas, renal angiomyolipomas, and skin lesions.[217,218]

Prenatal diagnosis usually is made in late pregnancy after discovery of echogenic cardiac rhabdomyomas and demonstration of subependymal nodules or cortical tubers on neurosonography or MRI (Fig. 34.28). MRI has shown lesions as early as 21 weeks in fetuses known to be at risk.[219] If the gene abnormality is known, prenatal diagnosis is possible using CVS or amniocentesis as well as neurosonography and fetal MRI. Diagnosis in other suspected cases may be aided by looking for subtle manifestations of TSC in the parents. Epilepsy and neurologic impairment are common. Morbidity and mortality predominantly relate to CNS and renal disease.[218]

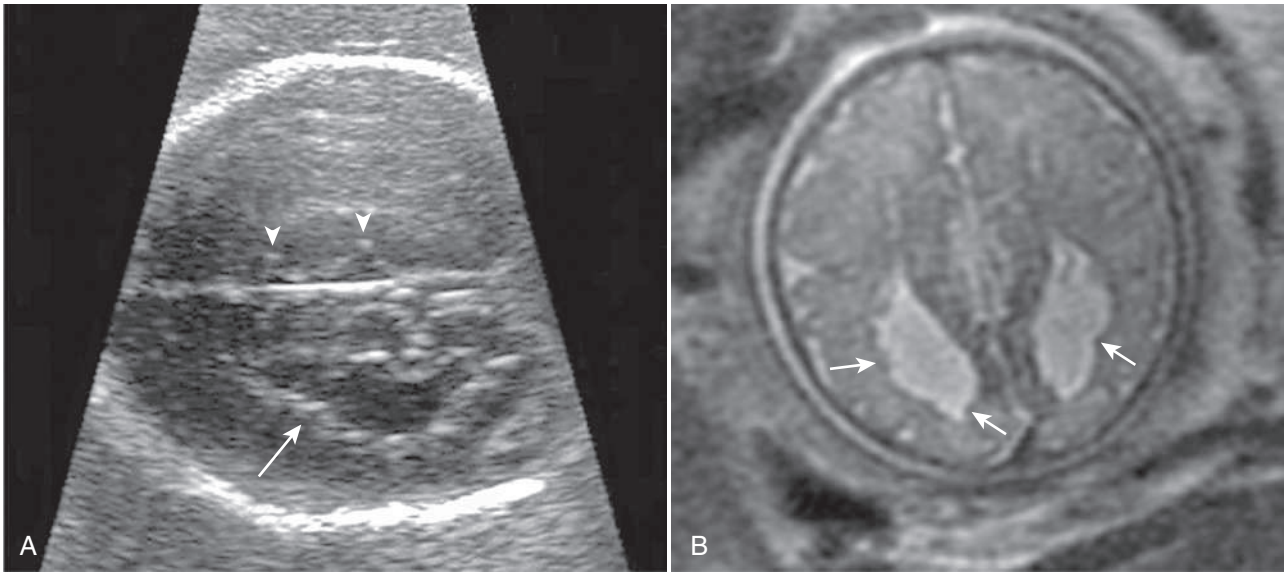

FIG. 34.26 Periventricular Nodular Heterotopia and Agenesis of the Corpus Callosum (ACC). (A) In fetus with ACC at 31 weeks, note the very nodular lining of the ventricle wall *(arrow)*. This represents accumulations of neurons that have failed to migrate to the cortex. Note the separation of the hemispheres and abnormal orientation of interhemispheric sulci (hairy midline; *arrowheads*). **(B)** Transverse T2-weighted magnetic resonance image in a different fetus at 35 weeks shows ACC and nodular heterotopias *(arrows)*.

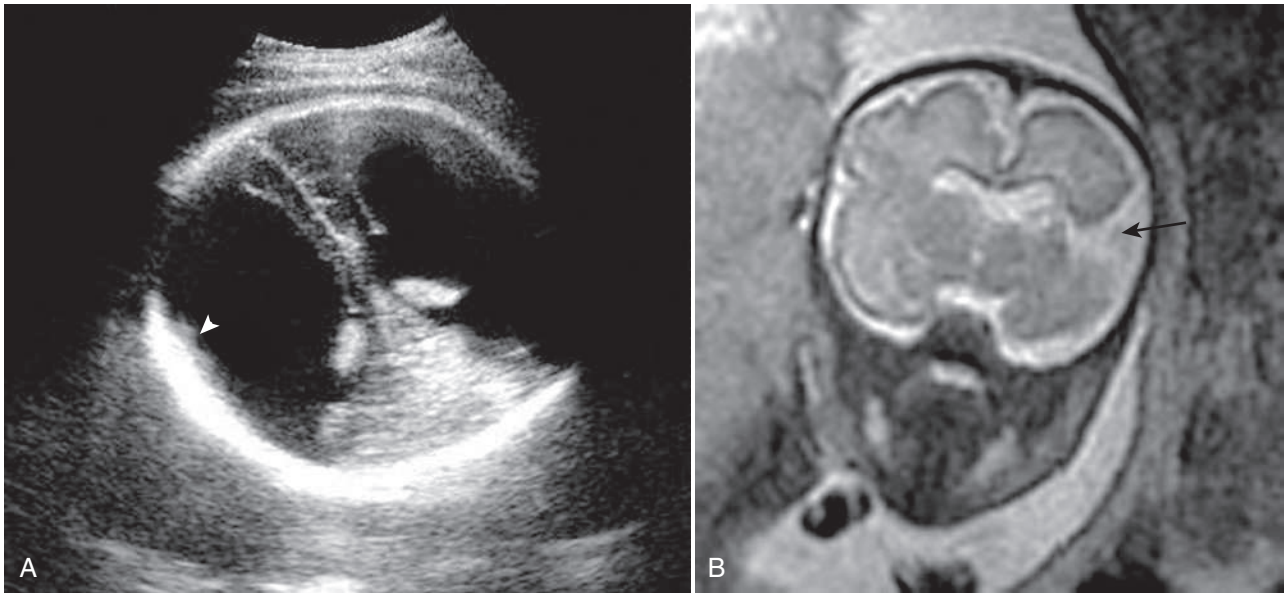

FIG. 34.27 Open-Lip Schizencephaly. (A) There are large gaps in the parietal regions with no brain tissue at the periphery *(arrowhead)*. There is partial sparing of the frontal and occipital regions. **(B)** Coronal T2-weighted magnetic resonance image in a different fetus with absent septal leaflets (absent septum pellucidum) shows region of schizencephaly *(arrow)*.

Agenesis and Dysgenesis of Corpus Callosum

Agenesis of the corpus callosum (ACC) is failure of normal development of the corpus callosum and other commissures that connect the left and right hemisphere. The prevalence of ACC in neonates is about 1.4 per 10,000 live births but is higher in developmentally disabled individuals. This likely is an underestimate of the prenatal incidence because many affected fetuses die in utero, and not all cases are postnatally diagnosed.[154,220]

The corpus callosum is the largest of three commissures that connect and allow communication between the cerebral hemispheres, the other two being the anterior commissure and the posterior hippocampal commissure. Any of these three commissures may be absent singularly or in combination. Development of the corpus callosum starts at about 12 weeks from the lamina terminalis near the anterior end of the third ventricle; it becomes detectable by about 15 weeks and is complete by about

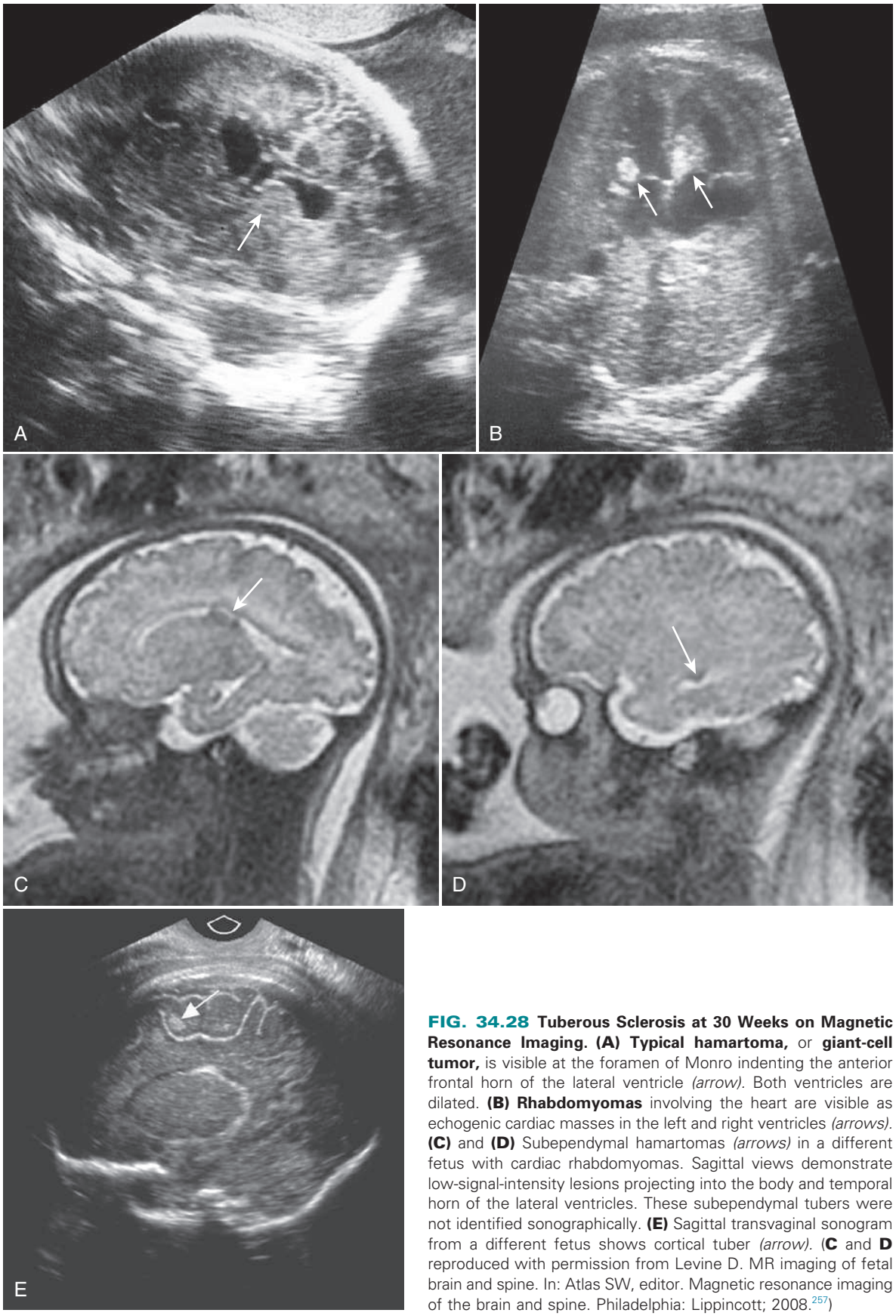

FIG. 34.28 Tuberous Sclerosis at 30 Weeks on Magnetic Resonance Imaging. (A) Typical hamartoma, or **giant-cell tumor,** is visible at the foramen of Monro indenting the anterior frontal horn of the lateral ventricle *(arrow)*. Both ventricles are dilated. **(B) Rhabdomyomas** involving the heart are visible as echogenic cardiac masses in the left and right ventricles *(arrows)*. **(C)** and **(D)** Subependymal hamartomas *(arrows)* in a different fetus with cardiac rhabdomyomas. Sagittal views demonstrate low-signal-intensity lesions projecting into the body and temporal horn of the lateral ventricles. These subependymal tubers were not identified sonographically. **(E)** Sagittal transvaginal sonogram from a different fetus shows cortical tuber *(arrow)*. (**C** and **D** reproduced with permission from Levine D. MR imaging of fetal brain and spine. In: Atlas SW, editor. Magnetic resonance imaging of the brain and spine. Philadelphia: Lippincott; 2008.[257])

20 weeks. Development proceeds in an anteroposterior manner, beginning anteriorly with the genu, then body and splenium posteriorly, and finally the anterior tip, the rostrum.[8,25,154] The corpus callosum measures 4 mm at 16 weeks and grows to 45 mm by term. There is no gender difference in length, but it is thicker in girls.[221] Callosal development is associated with the development of the septal leaflets and the CSP. When septal leaflets are present, at least the anterior portion of the corpus callosum has formed.[25,40]

ACC may be complete or partial, developmental or acquired. ACC has a high incidence of associated malformations, suggesting that it is part of a generalized widespread developmental disturbance. Additional CNS abnormalities are reported in 45% to 80% of fetuses, especially involving the posterior fossa, including **DWM, inferior vermian hypoplasia, Chiari II,** and abnormal neuronal migration. Somatic and metabolic abnormalities are seen in up to 60% and include facial abnormalities, congenital heart disease, and skeletal and genitourinary abnormalities. ACC is part of numerous syndromes including **Aicardi** and **Joubert** syndrome and acquired conditions such as **fetal alcohol syndrome** and infections.[25,154,220]

Developmental disturbances after the corpus callosum has started to form usually interrupt the formation of the more posterior parts of the corpus callosum, but insults after callosal development is complete can cause secondary atrophy of previously developed central portions. Because callosal development is not complete until 20 weeks, early diagnosis of ACC may be difficult.[154,222] Diagnosis of abnormalities of the corpus callosum requires it to be directly imaged in the midsagittal plane; this view is not currently included in the recommended views for the routine anatomy scan (see Figs. 34.2E and 34.17) but should be used with detailed neurosonography whenever a fetal morphologic abnormality is detected.

On routine scans reliance for screening for callosal and other midline abnormalities is placed on indirect findings on the standard views, especially the CSP, which should be sought on all axial scans after about 16 to 17 weeks. These indirect findings include absent or deformed CSP, VM with colpocephaly (teardrop ventricles), ventricles parallel to the midline, interhemispheric widening, and on occasion associated findings such as interhemispheric cysts and lipomas (Fig. 34.29; see also Fig. 34.26; Video 34.8, Video 34.9, Video 34.10, and Video 34.11). If the CSP is not seen with certainty on standard scans, then additional coronal and sagittal views should be taken to evaluate it and, more important, the corpus callosum and to evaluate for other midline conditions such as HPE.[2,25,223,224] Unless care is taken, it is possible to overlook CSP abnormality because with partial ACC a small CSP may be present and with complete ACC there may be a high-riding third ventricle or an interhemispheric cyst that mimics the CSP. Unfortunately, the indirect signs such as VM, colpocephaly, and hemispheric separation are not always present.[222]

Once the diagnosis is suspected, coronal and median views, especially with transvaginal scanning and 3-D ultrasound, help to confirm the diagnosis. The diagnosis is made on midsagittal views that show that the corpus callosum is absent or deficient and can show corroborating findings. On coronal views the third ventricle may be elevated and the crossing corpus callosum tracts are absent. The medial walls of the anterior horns of the lateral ventricles are commonly indented from their superomedial aspect by the **bundles of Probst** (buildup of callosal fibers that fail to cross midline) and change the ventricular configuration from a V to a U (**Viking** or **steer horn** appearance). Color flow Doppler scans can be used to demonstrate an abnormal course of the pericallosal and cingulate arteries, which normally follow the contour of the callosomarginal sulcus, but with ACC they assume a more radial course. This vascular change may already be seen in the first trimester.[99] Occasionally, fetuses with callosal abnormalities develop **interhemispheric cysts** or a **midline lipoma.** The cysts may be herniations from the third ventricle or separated from the ventricles when they are commonly associated with migrational abnormality. In the third trimester the medial hemispheric sulci assume a "sunburst" orientation radiating from the thalamus instead of the normal arc of the cingulate sulcus. On axial views this gives the appearance of a **"hairy midline"** with sulci radiating out from the interhemispheric fissure.[154] MRI is helpful to confirm the diagnosis and especially to search for additional, subtle abnormalities such as migrational disorders.[154,220]

Pitfalls in sonographic interpretation include mistaking the high position of the third ventricle, other fluid spaces, and the fornices for the CSP. On 3-D scans, care must be taken to avoid mistaking the pericallosal sulcus for the corpus callosum.[225,226] Other conditions may also show CSP abnormality including HC with septal fenestrations, SOD, HPE, and schizencephaly. Marked HC may fenestrate the septal leaves, raising the suspicion of ACC, but midsagittal scanning can show the displaced stretched corpus callosum in its expected location.

Investigation of suspected cases includes detailed CNS and somatic ultrasound, karyotype (chromosomal abnormalities occur in about 18%), microarray, screening for TORCH infections, and MRI. If pregnancy continues, follow-up examinations may detect late-appearing abnormalities. Prognosis relates to the associated anomalies, but unfortunately about 15% of associated problems are not evident prenatally. The prognosis for truly isolated ACC can be good in 65% to 75% of cases but guarded, because unfortunately in some cases functional deficits do not become apparent until later life.[220]

Absence of Septi Pellucidi and Septo-Optic Dysplasia

Absence of the septi pellucidi is rare and occurs in about 2 to 3 per 100,000 pregnancies. It can be primary, resulting from developmental disturbances including HPE, SOD, schizencephaly, ACC, and malformations of cortical development, or secondary after disruption as with HC or porencephaly.[25,154] Absence is virtually always associated with other abnormalities, and absence of the CSP warrants detailed neurosonography assessment. Rarely it can be isolated with good outcome.

Septo-optic dysplasia (SOD, **de Morsier syndrome**) manifests as heterogeneous triad of absence of septi pellucidi and CSP, hypoplasia of optic nerves and chiasm, and pituitary dysfunction (Fig. 34.30, Video 34.12). It is heterogeneous in etiology and appearance. Most cases are sporadic, but some are familial. On ultrasound, there is absence of the septi pellucidi. On coronal

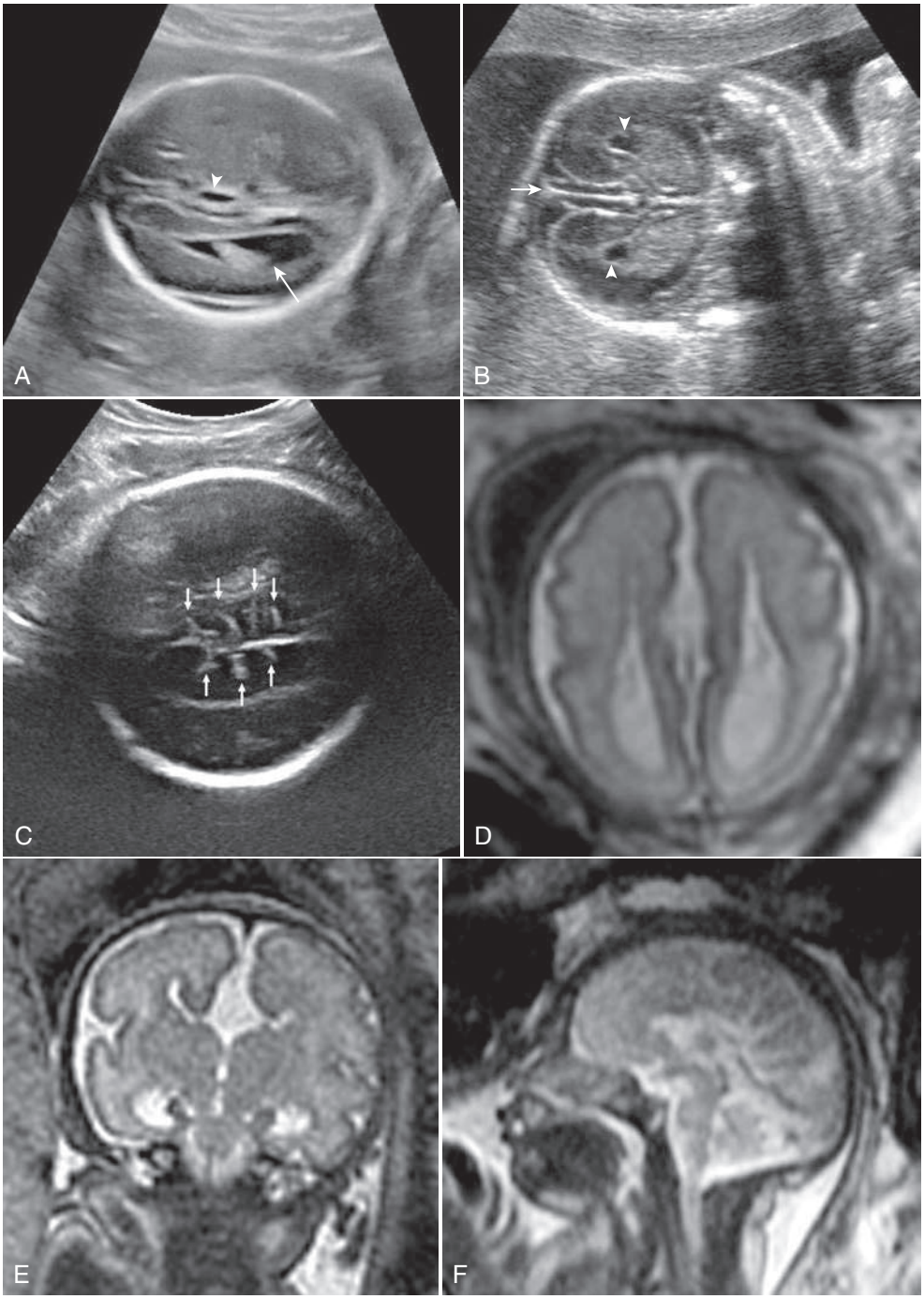

FIG. 34.29 Agenesis of Corpus Callosum (ACC). (A) Ventricular view at 21 menstrual weeks shows characteristic borderline dilation of occipital ventricle *(arrow)* and pointed, slightly spread anterior horns. This "teardrop" ventricle configuration is called **colpocephaly.** The midline fluid space *(arrowhead)* is the elevated dilated third ventricle, which should not be mistaken for the cavum septi pellucidi (CSP), which should be more rectangular and is absent in fetuses with ACC. **(B)** Coronal view through the anterior ventricles *(arrowheads)* shows that the frontal horns have a U or "Viking horn" configuration instead of the normal V orientation. The hemispheres are excessively separated from the falx *(arrow),* and the septal leaflets and CSP are absent. **(C)** Axial supraventricular view at 38 weeks shows the "hairy midline" with many sulci perpendicular to the interhemispheric fissure *(arrows),* the axial correlate of the "sunburst" sign caused by the abnormal radial orientation of interhemispheric sulci. **(D)** Transverse T2-weighted magnetic resonance image at 29 weeks shows colpocephaly with teardrop-shaped ventricles, parallel orientation of the frontal horns, and hemispheric separation. **(E)** Coronal magnetic resonance image in a different fetus at 30 weeks shows the vertical orientation of the frontal horns and lack of crossing fibers of the corpus callosum. **(F)** Sagittal view from fetus at 31 weeks with **partial ACC** shows the sunburst radial orientation of sulci posteriorly, where interhemispheric sulci extend farther inferiorly than normal owing to lack of corpus callosum. See also Videos 34.8, 34.9, and 34.10.

Ultrasound Findings of Agenesis or Dysgenesis of Corpus Callosum

SECOND TRIMESTER

Axial Views

Cavum septi pellucidi (CSP) is absent or appears atypical (consider also holoprosencephaly, septo-optic dysplasia, hydrocephalus, schizencephaly)

Mild ventriculomegaly with pointed anterior horns (teardrop shape = colpocephaly)

Ventricles are parallel

Widening of interhemispheric space (the normal single line becomes 3 lines = falx + medial surface of each hemisphere)

Coronal Views

Anterior horns have a U configuration (Viking helmet or steer horn)

CSP is not visible above the fornices

Possible high-riding third ventricle in 50%-60% (which may mimic CSP)

Midsagittal Views

Corpus callosum absent, short, or deformed

Circular loop of pericallosal artery is not present

THIRD TRIMESTER

On axial view, many sulci perpendicular to the interhemispheric fissure (hairy midline)

Midsagittal view shows radial orientation of sulci from the thalamus (sunburst appearance)

OTHER

Interhemispheric cyst or lipoma

Additional anomalies, especially of midline and posterior fossa structures

FIG. 34.30 Septo-Optic Dysplasia. Coronal image shows absence of the cavum of the septum pellucidum. See also Video 34.11.

views the frontal horns are squared with inferior pointing astride the fornices. The interhemispheric fissure and anterior cerebral arteries are normal. Differentiation from mild degrees of HPE can be difficult, and some believe that SOD is a mild variant of lobar HPE. MRI is helpful to assess the brain for other abnormalities such as migrational disorders and also to assess the optic nerves and chiasm. Tests of maternal urine and blood and fetal blood may be helpful to evaluate for the associated fetal endocrine deficiencies. Counseling is difficult because the prognosis is variable and includes disturbed vision and hypothalamic-pituitary insufficiency, including growth deficit and diabetes insipidus.[154,223]

INTRACRANIAL CALCIFICATIONS

Brain calcifications may be found in any part of the brain including white matter, periventricular regions, brain surface, and vessels. Calcification patterns may suggest underlying etiology. They usually occur in late gestation (see Figs. 34.22, 34.31, and 34.32). There are numerous associated conditions including **microcephaly,** intrauterine infections **(CMV, toxoplasmosis, herpes, parvovirus, HIV, Zika),** hemorrhagic and hypoxic or ischemic conditions including **twin-twin transfusion,** tumors **(teratoma),** neurocutaneous syndromes **(tuberous sclerosis, neurofibromatosis, Sturge-Weber syndrome),** other syndromes **(Aicardi, pseudo-TORCH), aneuploidy** (especially trisomy 13 and 21), and vascular abnormalities **(venous thrombosis, arteriovenous malformations).** When calcifications are found, detailed examination and multidisciplinary consultation are suggested. Prognosis depends on the underlying condition.[227-229]

Lenticulostriate vasculopathy (also called **thalamostriate vasculopathy**) is seen as branching linear densities in the thalami and basal ganglia caused by mineralization around the vessels in the basal ganglia (Fig. 34.31). Lenticulostriate vasculopathy appears because of perivascular deposition of iron rather than calcium. Etiology is undetermined. It may be seen in normal fetuses with good outcome but also occurs in association with many diverse conditions, including infection (CMV, rubella, varicella, syphilis, HIV, Zika), aneuploidy (mainly trisomy 13 and 21), fetal alcohol syndrome, asphyxia, twin-twin transfusion, dysmorphism, and congenital disorders. Parenchymal calcifications are more likely to be associated with infection than isolated lenticulostriate vasculopathy. When associated with other conditions, the prognosis depends on the underlying condition.[230,231]

INFECTIONS

A variety of infections that involve the fetal CNS caused by viruses, bacteria, or parasites are vertically transmitted from mother to fetus or baby during pregnancy or delivery. These are included in the TORCH complex, an acronym that is changing over time. **TORCH infections** include ***t*oxoplasmosis,** *o*ther, ***r*ubella, *C*MV,** and ***h*erpes simplex virus.** The "other" group includes variable pathogens such as **Coxsackie virus, varicella zoster (chickenpox), HIV, human T-lymphotropic virus, parvovirus, hepatitis, syphilis,** and **Zika.** They have differing

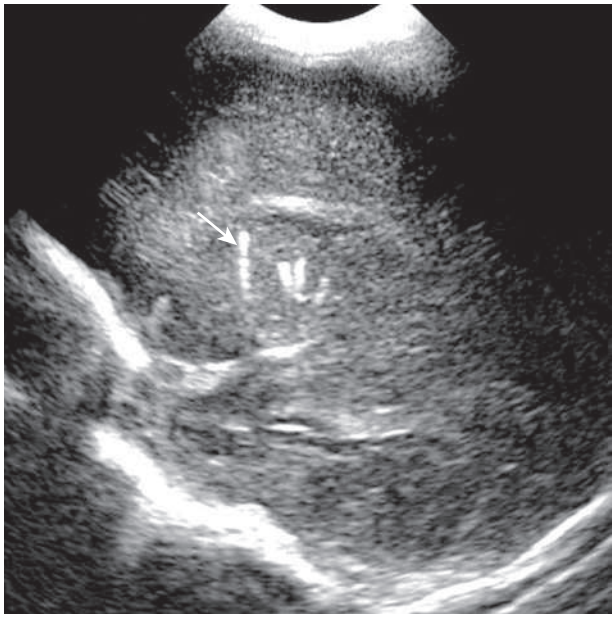

FIG. 34.31 Echogenic Mineralized Thalamostriate Vessels *(Arrow).* These vessels form an echogenic arborizing (branching) pattern in the thalamus, which may be seen in normal fetuses but can be associated with many fetal conditions.

effects depending on the individual pathogens and time of maternal infection. Immunization, prenatal screening, and case management protocols have been proposed.[232] The Zika infection (particularly in the first trimester) tends to be very severe with micrencephaly, microcephaly, cortical abnormalities, dysgenesis of the corpus callosum, and calcifications, which are often at the gray-white junction.[197]

In North America, **CMV** is most common intrauterine infection, affecting about 0.2% to 2.0% of live births, and is a common cause of mental retardation and sensorineural hearing loss. The next most common infections in North America are **toxoplasmosis** and **herpes simplex.** The severity of injury often relates more to the age when infection first occurs and affects brain development than to the specific organism. Cerebral and noncerebral ultrasound findings as noted below for CMV are shared by many of the infections, so detection of any of these findings should include general assessment for infections. Unfortunately, several findings can appear or evolve in late pregnancy, so surveillance with ultrasound should continue throughout pregnancy, with MRI employed as appropriate.[11,233-235]

Most mothers acquire primary CMV infection through contact with infected persons, but reinfection can also occur. CMV affects 1% to 2% of pregnancies, and vertical transmission to the fetus occurs in 30% to 40%. About 10% to 15% of these have symptoms at birth, and of these about 20% to 30% die and 90% of survivors have neurodevelopmental handicap. Of the 85% to 90% of infants who appear normal at birth, 5% to 15% will develop late complications including hearing loss or developmental delays.

Diagnosis of fetal infection can be made via amniocentesis. Ultrasound and MRI are used to help determine prognosis but are imperfect at predicting outcomes. The odds ratio of poor outcome with noncerebral abnormality is 7.2 and with cerebral abnormality is 25.5; although the absence of findings is reassuring, it does not guarantee a good outcome. Cerebral and posterior fossa findings include VM, increased periventricular echogenicity, calcifications, ventricular synechiae, microcephaly, periventricular pseudocysts or other cysts, malformations of cortical development, and cerebellar abnormality (Fig. 34.32). Noncerebral findings include **echogenic bowel, hepatomegaly, IUGR, oligohydramnios** or **polyhydramnios, ascites** or **pleural effusion, liver calcifications,** and **placental enlargement.**[233-237]

Congenital **toxoplasmosis** is caused by the transplacental passage of the parasite *Toxoplasma gondii* from an infected mother who is typically asymptomatic and acquires infection through contact with raw or undercooked meat, cat litter, or exposure to infected water or soil (gardening). In the United States, 15% of childbearing-age women are infected, and incidence of congenital toxoplasmosis is about 400 to 4000 per year. Interestingly, transmission to the fetus increases with gestational age and is estimated at about only 6% to 15% in the first trimester but increases to 60% to 81% in the third trimester. If untreated, about 20% to 50% develop infection. Fetal disease severity, however, decreases with age and is highest in the first trimester. Prenatal cerebral findings may appear late after 24 weeks and suggest a poor prognosis and can include **VM, cerebral calcifications, echogenic parenchymal nodules, diffuse periventricular echogenicity, callosal dysgenesis, microcephaly, IUGR,** and **hydrops.** Most fetuses (70%-90%) are infected in later pregnancy and are asymptomatic at birth, but some manifest the diagnostic triad **(chorioretinitis, hydrocephalus, intracranial calcifications)** and **hepatosplenomegaly.** Asymptomatic infants remain at high risk of developing late chorioretinitis and neurologic deficits. Maternal serum testing and amniocentesis can confirm infection. Prenatal and postnatal therapy can improve outcomes.[232,238-240]

VASCULAR MALFORMATIONS

A variety of vascular malformations are described prenatally, including the **vein of Galen aneurysmal malformation, dural sinus malformation, and pial arteriovenous malformation.**[241] The most common is the vein of Galen aneurysmal malformation, which is a congenital anomaly of midline choroidal and mural vessels that drain into and dilate the embryonic precursor of the vein of Galen, the median prosencephalic **vein of Markowski,** which in turn drains through an aberrant falcine sinus that can be mistaken for the vein of Galen. In general, this anomaly becomes detectable in the third trimester as a cystlike midline space behind the thalamus with turbulent follow on Doppler (Fig. 34.33). In prenatal cases 81% are associated other abnormalities that predict a poor outcome, including heart failure and cerebral abnormalities such as VM, malformations of cortical development, and ischemic and hemorrhagic changes. It is not associated with chromosomal abnormality. Postnatal treatment is with embolization, which is delayed to about 6 months unless there is heart failure. Outcome can be good in the few who have isolated lesions and no heart failure.[11,241-243]

Pial arteriovenous malformations are abnormal, usually supratentorial, superficial arteriovenous communications eventually draining into and dilating the vein of Galen. They may result

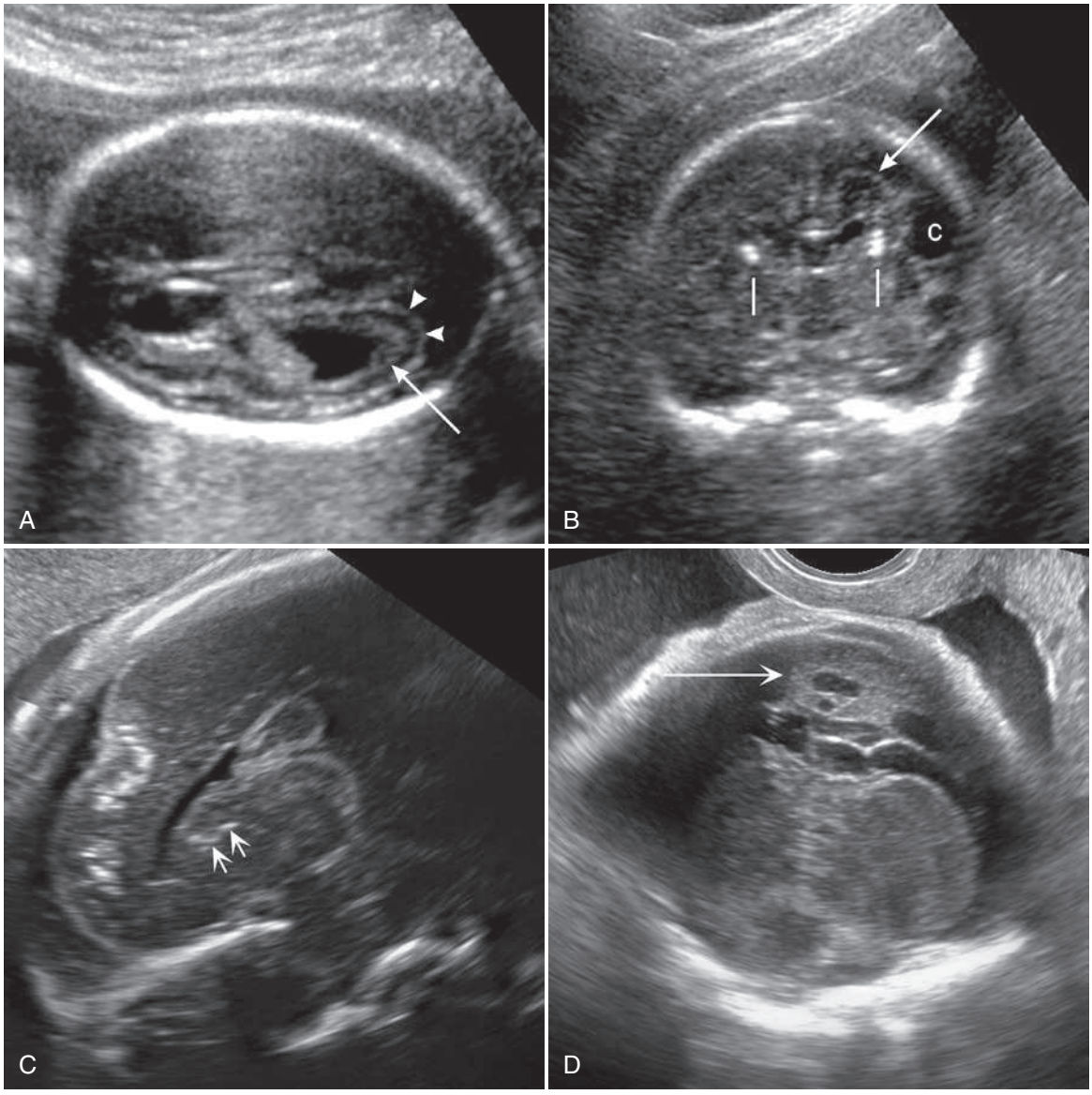

FIG. 34.32 Fetal Infection. (A) and **(B) CMV infection** shows enlarged ventricles with marked periventricular echogenicity *(arrow)* and small smooth brain (lissencephaly) *(arrowheads)*. **(B)** Note calcification in the basal ganglia *(lines),* small smooth brain *(arrow),* and cortical cyst *(c)*. **(C)** and **(D)** Zika infection. **(C)** Parasagittal transvaginal view of the fetal brain shows calcifications at the gray-white interface and in the basal ganglia *(arrows)*. **(D)** Oblique coronal view shows blood *(arrow)* posterior to the cerebellum in the region of the confluence of sinuses. (**A** and **B** courtesy of Dr. K. Fong, Mt. Sinai Hospital, Toronto, Ontario. **C** and **D** Reproduced with permission from Soares de Oliveira-Szejnfeld P, Levine D, Melo AS et al. Congenital brain abnormalities and Zika virus: what the radiologist can expect to see prenatally and postnally. Radiology. 2016;281[1]:203-218.[197])

in heart failure. Treatment is with embolization early after delivery.[241]

Dural sinus malformations are congenital vascular malformations, characterized by massive dilation of one or more dural sinuses, which usually appear postnatally but can occur prenatally as early as 19 weeks. There may be associated thrombus or arteriovenous fistula. Color Doppler may be helpful, but in some the flow is too slow to create a signal. These malformations can regress prenatally or progress to cause brain damage, hemorrhage, or heart failure. Evaluation includes detailed ultrasound and MRI. Treatment is with embolization, but only 10% have normal outcomes.[241,242,244]

Thrombosis of Dural Sinuses

Dural sinus thrombosis can be idiopathic (40%), but cases can be seen with hypercoagulable states such as trauma, infection, **polycythemia,** and deficiency of physiologic anticoagulants (e.g., **antithrombin protein C, protein S, factor V Leiden**). Ultrasound typically reveals an echogenic mass (the thrombus) surrounded by a hypoechogenic area in the region of the venous sinuses, generally near the torcula and associated with absence of flow (Fig. 34.34). The more proximal sinuses may be dilated and the brain compressed. Many dural thromboses are initially misdiagnosed as tumors or subdural bleed. Most cases are found in

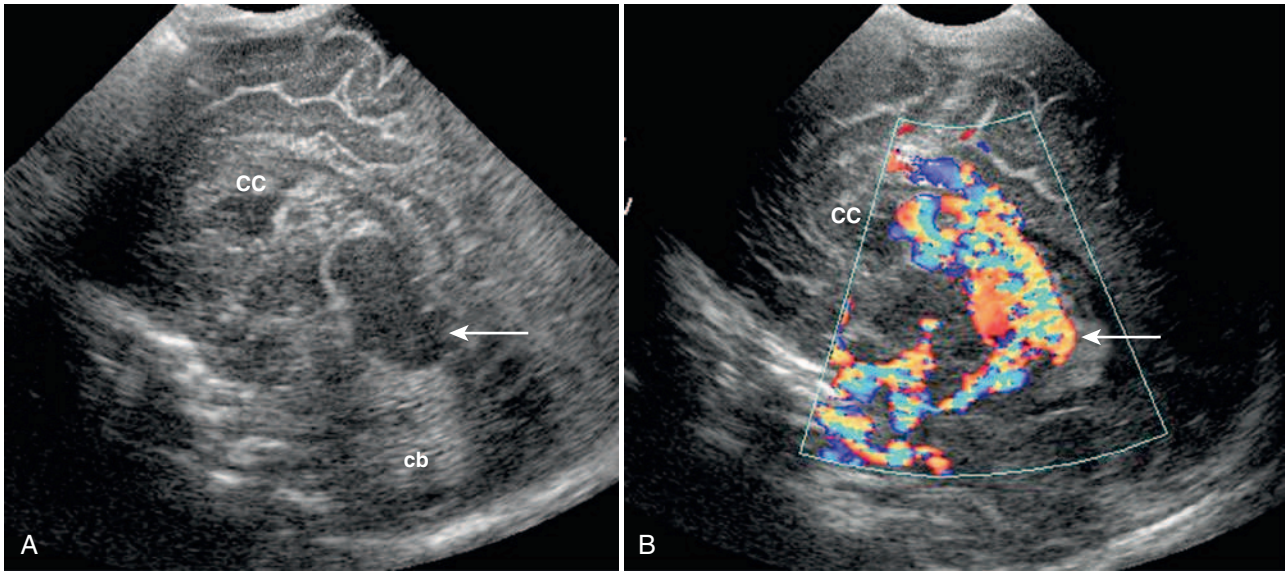

FIG. 34.33 Vein of Galen Aneurysm. (A) Midsagittal view shows a hypoechoic "cyst" *(arrow)* behind the brainstem and under the splenium of the corpus callosum *(cc). cb,* Cerebellum. At first glance it could be mistaken to be a large cavum veli interpositi. **(B)** Color Doppler examination shows the prominent vascularity characteristic of this malformation.

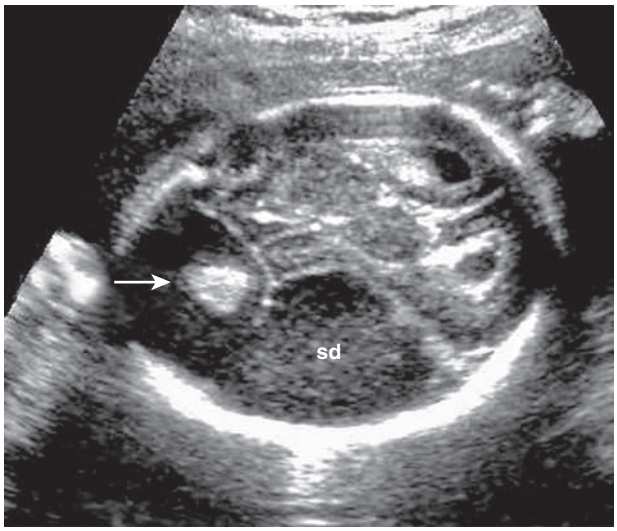

FIG. 34.34 Sagittal Sinus Thrombosis. There is an echogenic mass *(arrow)* in a fluidlike space in the midline anteriorly. This represents thrombus in a dilated sagittal sinus. There is also a subdural collection *(sd).* (Courtesy of Dr. K. Fong, Mt. Sinai Hospital, Toronto, Ontario).

the second and third trimesters and can be confirmed with MRI, which also helps to evaluate the brain for other abnormalities and areas of hemorrhage. Differential diagnosis includes tumors, intracranial bleeding, and dural sinus malformations. A substantial proportion resolve spontaneously over 3 to 11 weeks. The prognosis appears good if no other abnormalities are found and the brain appears normal.[11,245]

Hemorrhagic Lesions

Intracranial hemorrhage describes bleeding in and around the brain. The incidence is about 1 per 10,000 live births.[246] The most common sites are similar to those seen in premature neonates. In a series of 109 antenatal intracranial bleeds, 89 were intracerebral (79 intraventricular, 10 infratentorial), and 20 were subdural.[247] As in neonates, cerebral bleeds are graded from 1 to 4 and may be followed by **chemical ventriculitis** (thick echogenic ventricular lining), **hydrocephalus, porencephalic cysts, white matter injury,** and **periventricular leukomalacia.** About half are idiopathic. Predisposing factors include hypoxia, fetal coagulation disorders (including **alloimmune thrombocytopenia** and maternal anticoagulation), **death of a monochromic co-twin,** seizures, viral or bacterial **infection,** febrile disease, drugs **(cocaine), maternal-fetal hemorrhage,** and trauma.[11,246-248]

On ultrasound, the bleed appears as an echogenic collection in the ventricles and surrounding brain (Fig. 34.35). This hemorrhage later organizes and condenses into clots and may be associated with VM and echogenic thickening of ventricular walls (chemical ventriculitis). The findings may resolve or progress to HC, porencephaly, cerebral clefts, and cortical malformations. Those with ischemia may also develop cystic leukomalacia. Subdural hemorrhages appear as an echogenic collection underlying the skull and compressing the adjacent brain.[246,247]

The prognosis varies greatly and depends largely on fetal age, extent of injury, and underlying factors. About 50% die in utero or shortly after birth, and about half the survivors have deficits. As expected, some with mild changes may resolve completely, and more severe (grade 3-4) changes and cerebral changes predict a poor outcome. Ultrasound can accurately diagnose bleeds, but MRI can more accurately define the extent of the lesion and may demonstrate additional ischemic changes in white matter[246,247] (see Fig. 34.35). Investigation of suspected cases includes trauma and drug history, as well as maternal screening for antiplatelet antibodies and thrombophilia.[246,248]

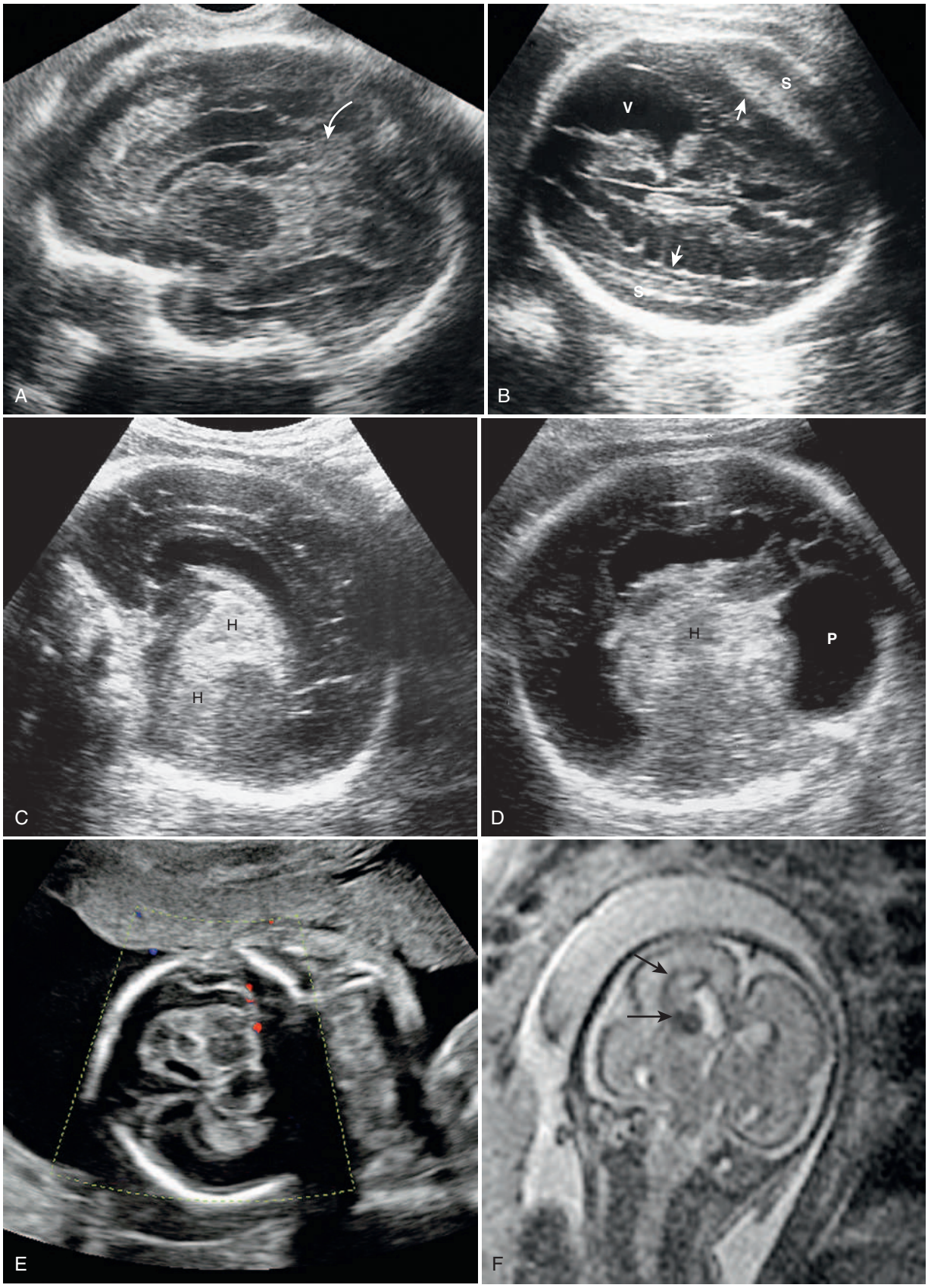

FIG. 34.35 Intracranial Hemorrhage. (A) Grade 4 intracerebral hemorrhage with clot *(arrow)* extending into the occipital cortex on parasagittal view. **(B) Bilateral subdural hemorrhages** *(S)* compressing the brain *(arrows)* and associated with slight asymmetrical ventricular enlargement *(V)*. These hemorrhages resolved spontaneously in this case, and the child did well. No cause was found. Most children with this finding do poorly. **(C)** Parasagittal and **(D)** coronal views of **thalamic and brainstem hemorrhage** *(H)* at 38 weeks. The posthemorrhagic porencephalic cyst *(P)* helps to differentiate this from tumor such as teratoma. Hypoxia was the likely cause. This fetus died shortly after the examination. **(E)** Coronal view at 23 weeks shows a grade 4 hemorrhage with clot extending into the parenchyma. **(F)** T2-weighted magnetic resonance image shows the low signal intensity of blood products in the parenchyma *(arrows)*. The relatively high signal intensity in the surrounding parenchyma suggests edema and venous infarction.

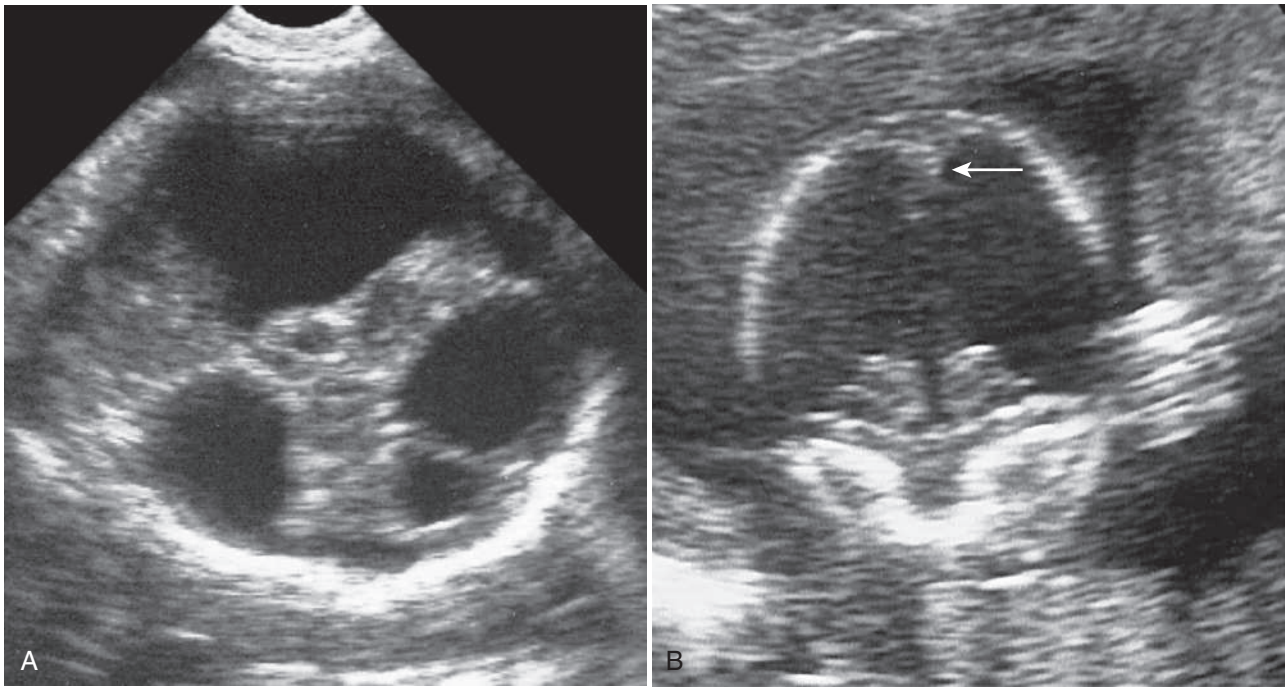

FIG. 34.36 Hydranencephaly. (A) Transverse thalamic view at 38 weeks shows asymmetrical cerebral destruction with preserved interhemispheric fissure. **(B)** Hydranencephaly at 17 weeks shows cranium filled with fluid. At first, the appearance suggests alobar holoprosencephaly, but the presence of the falx *(arrow)* and lack of thalamic fusion as indicated by the large third ventricle help confirm hydranencephaly.

Hydranencephaly

Hydranencephaly is a rare disorder in which almost all the cerebral hemispheres in the approximate distribution of the supraclinoid middle cerebral artery are absent and replaced by CSF and debris covered by a thin, membranous sac. Commonly there is partial sparing in the distribution of the anterior and posterior cerebral arteries, including portions of the frontal, temporal, and occipital lobes. The basal ganglia and thalami are hypoplastic, but the brainstem and cerebellum are intact. Cases are sporadic, with an incidence of about 1 per 5000 pregnancies. Many consider hydranencephaly to be the most severe form of porencephaly following occlusion of the internal carotid artery or middle cerebral artery. It may be associated with infections, toxins, hypoxic conditions, and trauma and may occur as a complication of twin-twin transfusion syndrome.

On ultrasound, the cerebral cortex is absent and the cerebrum is replaced initially by mildly echogenic fluid that becomes clear over time (Fig. 34.36). The falx is present but may be hypoplastic. Posterior fossa structures appear normal. Most cases are found in late pregnancy, but cases have been described as early as 11 weeks. Findings start with cerebral echogenicity, thought to result from ischemia or hemorrhage, followed by characteristic fluid replacement of the cerebrum. The differential diagnosis includes other conditions causing large, fluid-filled cranial spaces, such as severe **hydrocephalus, alobar holoprosencephaly,** bilateral subdural collections, **schizencephaly,** and **atelencephaly.** With **hydrocephalus,** there is generally uniform VM and a peripheral thin cerebral mantle, and color Doppler ultrasound shows flow in the middle cerebral arteries. In **holoprosencephaly** there is thalamic fusion and absence of the falx. **Subdural collections** compress the brain into the midline. Large **schizencephalic clefts** can appear similar to hydranencephaly, but in schizencephaly the lips of the clefts are lined by gray matter, which may be identifiable on MRI.

Most affected fetuses die in utero. At birth, diagnosis can be readily made clinically by cerebral transillumination. Most die in the first year, but survival in a vegetative state to 32 years has been described.[96,249,250]

TUMORS

Prenatal intracranial solid tumors are rare, occurring in about 1.4 to 3.6 per 100,000 pregnancies, and account for about 10% of all perinatal tumors. About 45% are **teratomas,** followed by **neuroepithelial tumors (astrocytomas, medulloblastoma, choroid plexus papilloma, gliomas)** (43%), **craniopharyngioma** (7%), **mesenchymal tumors (meningioma, sarcoma)** (5%), and **hemangioblastoma** (0.4%). Most are sporadic. A few are associated with familial syndromes that have genetic abnormalities, such as **neurofibromatosis, tuberous sclerosis, von Hippel–Lindau,** and **Li-Fraumeni syndrome.** Fetal brain tumors tend to be supratentorial in location, unlike tumors in older children, which are more likely to involve posterior fossa structures.[251-253]

The prenatal sonographic finding is an enlarged head containing a complex intracranial mass, occasionally with calcifications, macrocephaly, and HC (Fig. 34.37). The tumors grow quickly and can erode into the orbit, oral cavity, or neck. Associated

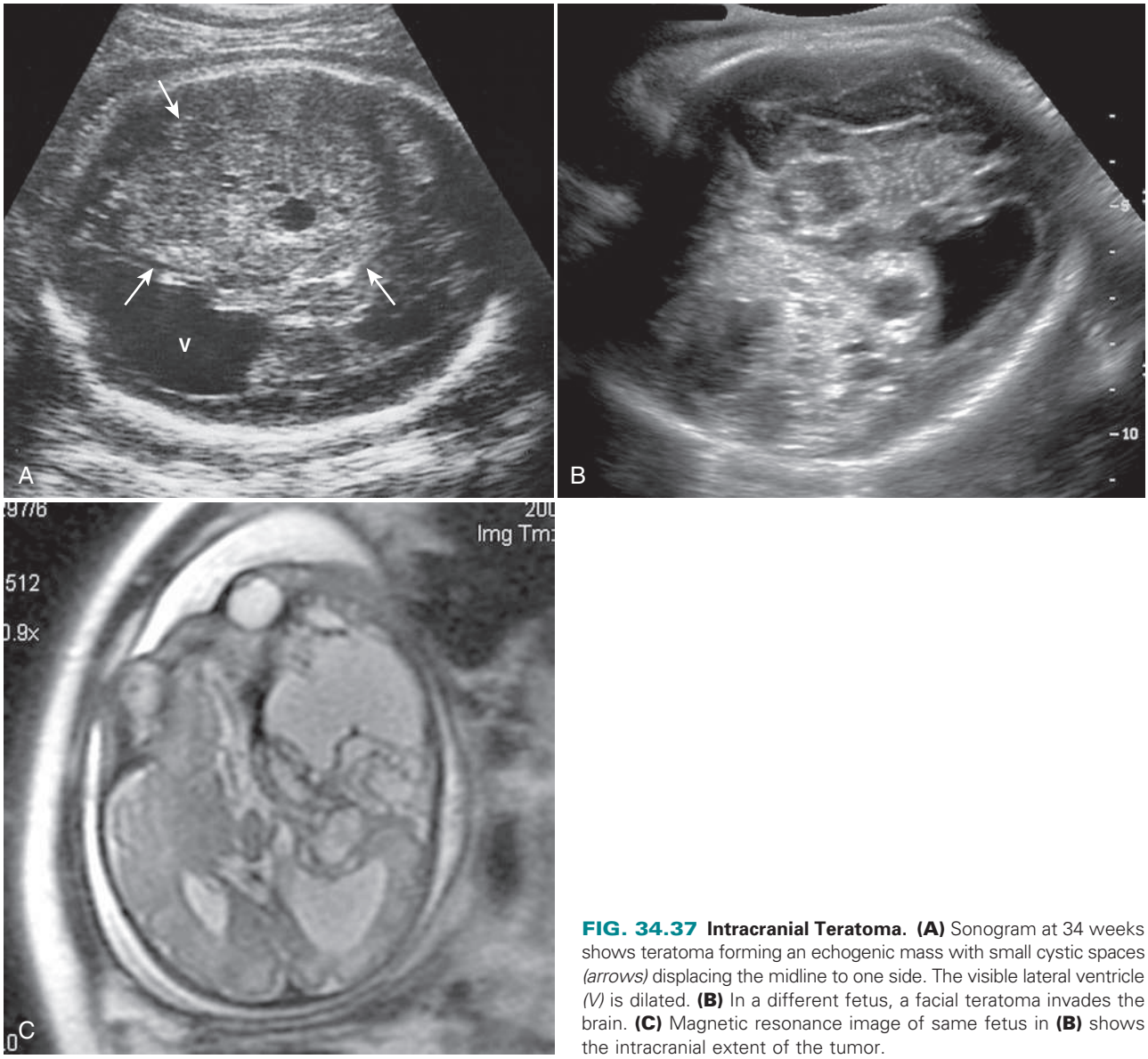

FIG. 34.37 Intracranial Teratoma. (A) Sonogram at 34 weeks shows teratoma forming an echogenic mass with small cystic spaces *(arrows)* displacing the midline to one side. The visible lateral ventricle *(V)* is dilated. **(B)** In a different fetus, a facial teratoma invades the brain. **(C)** Magnetic resonance image of same fetus in **(B)** shows the intracranial extent of the tumor.

findings include polyhydramnios and intracranial hemorrhage. Diagnosis is typically made in the third trimester on ultrasound triggered by excessive uterine growth due to polyhydramnios, although teratomas have been discovered as early as 17 weeks. Fetuses suspected to have brain tumors should undergo detailed ultrasound examination to look for associated abnormalities, which can occur in about 12% of cases, especially involving the face. Most have normal karyotype. MRI is helpful in characterizing the mass, evaluating tumor extension, and differentiating tumors from other conditions such as hemorrhage, sinus thrombosis, and vascular malformations.[251,252]

Outcomes are poor, especially if tumors appear early. Overall survival is about 28% and relates to size and location of tumor, its histology, surgical resectability, response to chemotherapy, and condition of the fetus at diagnosis. The large head size can interfere with delivery and require cephalocentesis to allow vaginal delivery. Of the few survivors, almost all have long-term neurologic deficits. Slightly better survival is seen with choroid plexus papilloma (73%) and meningeal tumors (36%).[251-253]

Choroid plexus papillomas are large, finely nodular masses that grow into the lateral ventricle and produce excessive CSF, resulting in severe dilation of the entire ventricular system and macrocephaly. Most are sporadic, but a few are associated with **Aicardi syndrome** and **giant pigmented nevi.** Surgical resection can be curative but is technically difficult because the vascular nature of choroid plexus papillomas can result in fatal hemorrhage. Overall survival is about 73%.[251]

Intracranial lipomas are not "neoplasms" but rather a malformation of meninx primitiva development. Instead of resorbing at 8 to 10 weeks, the meninx persists and develops into a mass of mature adipose tissue. The incidence is 4 to 40 per 100,000 autopsies. Most are near the corpus callosum, but they can arise in any cistern. They can interfere with callosal development, and associated dysgenesis of the corpus callosum

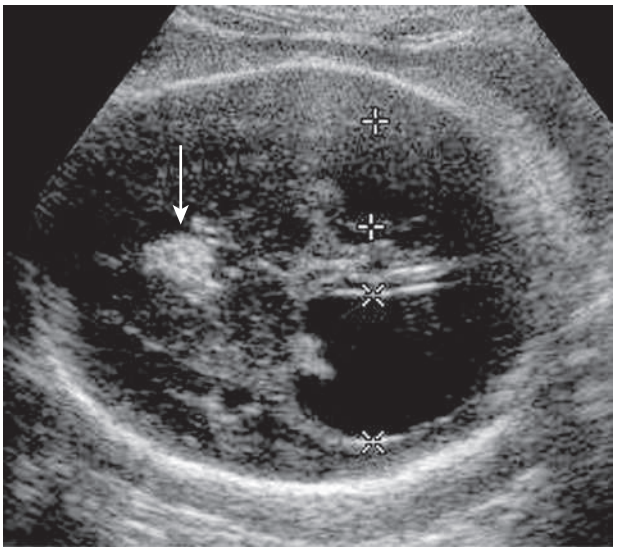

FIG. 34.38 Lipoma. Midline lipoma forming an echogenic mass near the foramina of Monro at the expected anterior end of the corpus callosum *(arrow)*. These are not neoplasms and represent abnormal differentiation of meningeal anlagen (precursors) into fat. Midline lipomas are often associated with dysgenesis of the corpus callosum, as in this fetus, in which the cavum septi pellucidi is absent and the ventricles *(calipers)* are dilated.

is common. Additional associations include aneurysms and other midline brain and facial malformations. At ultrasound, intracranial lipomas appear as early as 23 weeks as an echogenic mass or plaque in the midline in the region of the corpus callosum with occasional calcification and even ossification. (Fig. 34.38). MRI is helpful to confirm the fatty nature of the mass and to further evaluate changes in the corpus callosum and remaining brain. Most do not grow. Many patients are asymptomatic, but the associated abnormalities may cause symptoms including seizures and developmental delays. Surgical treatment of the lipoma is generally not indicated and can be dangerous because of the strong attachment of the lipoma to surrounding structures and the nerves and vessels within the mass.[254,255]

CONCLUSION

Assessment of the fetal CNS, more than any other organ system, is frequently enhanced by the addition of fetal MRI. The combination of ultrasound and MRI allows for many other experts to aid in the investigation, diagnosis, and management of fetal conditions, including pediatric neuroradiologists, neurologists, neurosurgeons, geneticists, pathologists, and other specialists. The understanding of the genetic basis, pathophysiology, natural history, and prognosis of many conditions and syndromes is increasing explosively as a result of this cross-fertilization and collaboration. Those performing ultrasound are discovering the complexities and large spectrum of neonatal diseases. Those providing postnatal care are discovering that prenatal conditions affecting the fetus are often very different from conditions that affect neonates who survive pregnancy. Best results are obtained when there is multidisciplinary consultation and collaboration.

Acknowledgments

The advice and support of our colleagues Drs. Susan Blaser, David Chitayat, Katherine Fong, Charles Raybaud, and Patrick Shannon are acknowledged and appreciated.

REFERENCES

1. Chitty LS, Pilu G. The challenge of imaging the fetal central nervous system: an aid to prenatal diagnosis, management and prognosis. Prenat Diagn. 2009;29(4):301-302.
2. Filly RA, Cardoza JD, Goldstein RB, Barkovich AJ. Detection of fetal central nervous system anomalies: a practical level of effort for a routine sonogram. Radiology. 1989;172(2):403-408.
3. American Institute of Ultrasound in Medicine (AIUM). AIUM practice guideline for the performance of obstetric ultrasound examinations. J Ultrasound Med. 2013;32(6):1083-1101.
4. Grandjean H, Larroque D, Levi S. The performance of routine ultrasonographic screening of pregnancies in the Eurofetus Study. Am J Obstet Gynecol. 1999;181(2):446-454.
5. Malinger G, Monteagudo A, Pilu G, et al. Sonographic examination of the fetal central nervous system: guidelines for performing the 'basic examination' and the 'fetal neurosonogram. Ultrasound Obstet Gynecol. 2007;29(1):109-116.
6. Salomon LJ, Alfirevic Z, Berghella V, et al. Practice guidelines for performance of the routine mid-trimester fetal ultrasound scan. Ultrasound Obstet Gynecol. 2011;37(1):116-126.
7. Malinger G, Lerman-Sagie T, Watemberg N, et al. A normal second-trimester ultrasound does not exclude intracranial structural pathology. Ultrasound Obstet Gynecol. 2002;20(1):51-56.
8. Blaas HG, Eik-Nes SH. Sonoembryology and early prenatal diagnosis of neural anomalies. Prenat Diagn. 2009;29(4):312-325.
9. Pooh RK, Kurjak A. 3D/4D sonography moved prenatal diagnosis of fetal anomalies from the second to the first trimester of pregnancy. J Matern Fetal Neonatal Med. 2012;25(5):433-455.
10. Saltvedt S, Almstrom H, Kublickas M, et al. Detection of malformations in chromosomally normal fetuses by routine ultrasound at 12 or 18 weeks of gestation—a randomised controlled trial in 39,572 pregnancies. BJOG. 2006;113(6):664-674.
11. Carletti A, Colleoni GG, Perolo A, et al. Prenatal diagnosis of cerebral lesions acquired in utero and with a late appearance. Prenat Diagn. 2009;29(4):389-395.
12. Jakab A, Pogledic I, Schwartz E, et al. Fetal cerebral magnetic resonance imaging beyond morphology. Semin Ultrasound CT MR. 2015;36(6):465-475.
13. Lyons K, Cassady C, Jones J, et al. Current role of fetal magnetic resonance imaging in neurologic anomalies. Semin Ultrasound CT MR. 2015;36(4):298-309.
14. Plunk MR, Chapman T. The fundamentals of fetal MR imaging: Part 1. Curr Probl Diagn Radiol. 2014;43(6):331-346.
15. Pistorius LR, Hellmann PM, Visser GH, et al. Fetal neuroimaging: ultrasound, MRI, or both? Obstet Gynecol Surv. 2008;63(11):733-745.
16. Malinger G, Lerman-Sagie T. Re: additional value of fetal magnetic resonance imaging in the prenatal diagnosis of central nervous system anomalies: a systematic review of the literature. Ultrasound Obstet Gynecol. 2015;45(2):236-237.
17. Rossi AC, Prefumo F. Additional value of fetal magnetic resonance imaging in the prenatal diagnosis of central nervous system anomalies: a systematic review of the literature. Ultrasound Obstet Gynecol. 2014;44(4):388-393.
18. Guibaud L. Contribution of fetal cerebral MRI for diagnosis of structural anomalies. Prenat Diagn. 2009;29(4):420-433.
19. Hagmann CF, Robertson NJ, Leung WC, et al. Foetal brain imaging: ultrasound or MRI. A comparison between magnetic resonance imaging and a dedicated multidisciplinary neurosonographic opinion. Acta Paediatr. 2008;97(4):414-419.
20. Reddy UM, Abuhamad AZ, Levine D, et al. Fetal imaging: executive summary of a joint Eunice Kennedy Shriver National Institute of Child Health and

Human Development, Society for Maternal-Fetal Medicine, American Institute of Ultrasound in Medicine, American College of Obstetricians and Gynecologists, American College of Radiology, Society for Pediatric Radiology, and Society of Radiologists in Ultrasound Fetal imaging workshop. J Ultrasound Med. 2014;33(5):745-757.
21. Dyment DA, Sawyer SL, Chardon JW, Boycott KM. Recent advances in the genetic etiology of brain malformations. Curr Neurol Neurosci Rep. 2013;13(8):364.
22. Greene ND, Copp AJ. Development of the vertebrate central nervous system: formation of the neural tube. Prenat Diagn. 2009;29(4):303-311.
23. O'Rahilly R, Müller R, editors. Human embryology and teratology. 2nd ed. New York: Wiley-Liss; 1996.
24. Hansen PE, Ballesteros MC, Soila K, et al. MR imaging of the developing human brain. Part 1. Prenatal development. Radiographics. 1993;13(1): 21-36.
25. Sundarakumar DK, Farley SA, Smith CM, et al. Absent cavum septum pellucidum: a review with emphasis on associated commissural abnormalities. Pediatr Radiol. 2015;45(7):950-964.
26. Moore K. Essentials of human embryology. Toronto, Ontario: BC Decker; 1988.
27. Nelson Jr MD, Maher K, Gilles FH. A different approach to cysts of the posterior fossa. Pediatr Radiol. 2004;34(9):720-732.
28. Paladini D, Quarantelli M, Pastore G, et al. Abnormal or delayed development of the posterior membranous area of the brain: anatomy, ultrasound diagnosis, natural history and outcome of Blake's pouch cyst in the fetus. Ultrasound Obstet Gynecol. 2012;39(3):279-287.
29. Robinson AJ, Goldstein R. The cisterna magna septa: vestigial remnants of Blake's pouch and a potential new marker for normal development of the rhombencephalon. J Ultrasound Med. 2007;26(1):83-95.
30. Malinger G, Lev D, Lerman-Sagie T. The fetal cerebellum. Pitfalls in diagnosis and management. Prenat Diagn. 2009;29(4):372-380.
31. Kostovic I, Judas M, Rados M, Hrabac P. Laminar organization of the human fetal cerebrum revealed by histochemical markers and magnetic resonance imaging. Cereb Cortex. 2002;12(5):536-544.
32. Pugash D, Hendson G, Dunham CP, et al. Sonographic assessment of normal and abnormal patterns of fetal cerebral lamination. Ultrasound Obstet Gynecol. 2012;40(6):642-651.
33. Rados M, Judas M, Kostovic I. In vitro MRI of brain development. Eur J Radiol. 2006;57(2):187-198.
34. Boitor-Borza D, Kovacs T, Stamatian F. Ganglionic eminence within the early developing brain visualized by 3D transvaginal ultrasound. Med Ultrason. 2015;17(3):289-294.
35. Righini A, Cesaretti C, Conte G, et al. Expanding the spectrum of human ganglionic eminence region anomalies on fetal magnetic resonance imaging. Neuroradiology. 2016;58(3):293-300.
36. Itabashi HH. Forensic neuropathology a practical review of the fundamentals. Boston: Elsevier Academic Press; 2007.
37. Crade M, Patel J, McQuown D. Sonographic imaging of the glycogen stage of the fetal choroid plexus. AJR Am J Roentgenol. 1981;137(3): 489-491.
38. Blaas HG. Detection of structural abnormalities in the first trimester using ultrasound. Best Pract Res Clin Obstet Gynaecol. 2014;28(3):341-353.
39. Guibaud L, Lacalm A. Etiological diagnostic tools to elucidate 'isolated' ventriculomegaly. Ultrasound Obstet Gynecol. 2015;46(1):1-11.
40. Monteagudo A, Timor-Tritsch IE. Normal sonographic development of the central nervous system from the second trimester onwards using 2D, 3D and transvaginal sonography. Prenat Diagn. 2009;29(4):326-339.
41. Vinals F, Correa F, Goncalves-Pereira PM. Anterior and posterior complexes: a step towards improving neurosonographic screening of midline and cortical anomalies. Ultrasound Obstet Gynecol. 2015;46(5):585-594.
42. Vinurel N, Van Nieuwenhuyse A, Cagneaux M, et al. Distortion of the anterior part of the interhemispheric fissure: significance and implications for prenatal diagnosis. Ultrasound Obstet Gynecol. 2014;43(3):346-352.
43. Filly RA, Goldstein RB, Callen PW. Fetal ventricle: importance in routine obstetric sonography. Radiology. 1991;181(1):1-7.
44. Araujo Júnior E, Martins WP, Rolo LC, et al. Normative data for fetal cisterna magna length measurement between 18 and 24 weeks of pregnancy. Childs Nerv Syst. 2014;30(1):9-12.
45. Zimmer EZ, Lowenstein L, Bronshtein M, et al. Clinical significance of isolated mega cisterna magna. Arch Gynecol Obstet. 2007;276(5): 487-490.
46. Dror R, Malinger G, Ben-Sira L, et al. Developmental outcome of children with enlargement of the cisterna magna identified in utero. J Child Neurol. 2009;24(12):1486-1492.
47. Haimovici JA, Doubilet PM, Benson CB, Frates MC. Clinical significance of isolated enlargement of the cisterna magna (>10 mm) on prenatal sonography. J Ultrasound Med. 1997;16(11):731-734.
48. Ghai S, Fong KW, Toi A, et al. Prenatal US and MR imaging findings of lissencephaly: review of fetal cerebral sulcal development. Radiographics. 2006;26(2):389-405.
49. Quarello E, Stirnemann J, Ville Y, Guibaud L. Assessment of fetal sylvian fissure operculization between 22 and 32 weeks: a subjective approach. Ultrasound Obstet Gynecol. 2008;32(1):44-49.
50. Toi A, Lister WS, Fong KW. How early are fetal cerebral sulci visible at prenatal ultrasound and what is the normal pattern of early fetal sulcal development? Ultrasound Obstet Gynecol. 2004;24(7):706-715.
51. Pashaj S, Merz E, Wellek S. Biometry of the fetal corpus callosum by three-dimensional ultrasound. Ultrasound Obstet Gynecol. 2013;42(6): 691-698.
52. Rizzo G, Capponi A, Pietrolucci ME, et al. An algorithm based on OmniView technology to reconstruct sagittal and coronal planes of the fetal brain from volume datasets acquired by three-dimensional ultrasound. Ultrasound Obstet Gynecol. 2011;38(2):158-164.
53. Tonni G, Grisolia G, Sepulveda W. Second trimester fetal neurosonography: reconstructing cerebral midline anatomy and anomalies using a novel three-dimensional ultrasound technique. Prenat Diagn. 2014;34(1): 75-83.
54. Levine D, Barnes PD, Madsen JR, et al. Central nervous system abnormalities assessed with prenatal magnetic resonance imaging. Obstet Gynecol. 1999;94(6):1011-1019.
55. Pooh RK, Nagao Y, Pooh K. Fetal neuroimaging by transvaginal 3D ultrasound and MRI. Ultrasound Rev Obstet Gynecol. 2006;6:123-134.
56. Fong K, Chong K, Toi A, et al. Fetal ventriculomegaly secondary to isolated large choroid plexus cysts: prenatal findings and postnatal outcome. Prenat Diagn. 2011;31(4):395-400.
57. Van den Hof MC, Wilson RD. Fetal soft markers in obstetric ultrasound. J Obstet Gynaecol Can. 2005;27(6):592-636.
58. Ebrashy A, Kurjak A, Adra A, et al. Controversial ultrasound findings in mid trimester pregnancy. Evidence based approach. J Perinat Med. 2016;44(2):131-137.
59. Chapman T, Mahalingam S, Ishak GE, et al. Diagnostic imaging of posterior fossa anomalies in the fetus and neonate: part 1, normal anatomy and classification of anomalies. Clin Imaging. 2015;39(1):1-8.
60. Gandolfi Colleoni G, Contro E, et al. Prenatal diagnosis and outcome of fetal posterior fossa fluid collections. Ultrasound Obstet Gynecol. 2012;39(6): 625-631.
61. Chen CY, Chen FH, Lee CC, et al. Sonographic characteristics of the cavum velum interpositum. AJNR Am J Neuroradiol. 1998;19(9):1631-1635.
62. Shah PS, Blaser S, Toi A, et al. Cavum veli interpositi: prenatal diagnosis and postnatal outcome. Prenat Diagn. 2005;25(7):539-542.
63. Eisenberg VH, Zalel Y, Hoffmann C, et al. Prenatal diagnosis of cavum velum interpositum cysts: significance and outcome. Prenat Diagn. 2003; 23(10):779-783.
64. Saba L, Anzidei M, Raz E, et al. MR and CT of brain's cava. J Neuroimaging. 2013;23(3):326-335.
65. Vergani P, Locatelli A, Piccoli MG, et al. Ultrasonographic differential diagnosis of fetal intracranial interhemispheric cysts. Am J Obstet Gynecol. 1999;180(2 Pt 1):423-428.
66. Gaglioti P, Oberto M, Todros T. The significance of fetal ventriculomegaly: etiology, short- and long-term outcomes. Prenat Diagn. 2009;29(4): 381-388.
67. Tully HM, Dobyns WB. Infantile hydrocephalus: a review of epidemiology, classification and causes. Eur J Med Genet. 2014;57(8):359-368.
68. Verhagen JM, Schrander-Stumpel CT, Krapels IP, et al. Congenital hydrocephalus in clinical practice: a genetic diagnostic approach. Eur J Med Genet. 2011;54(6):e542-e547.

69. Guibaud L. Fetal cerebral ventricular measurement and ventriculomegaly: time for procedure standardization. Ultrasound Obstet Gynecol. 2009; 34(2):127-130.
70. Heiserman J, Filly RA, Goldstein RB. Effect of measurement errors on sonographic evaluation of ventriculomegaly. J Ultrasound Med. 1991; 10(3):121-124.
71. Melchiorre K, Bhide A, Gika AD, et al. Counseling in isolated mild fetal ventriculomegaly. Ultrasound Obstet Gynecol. 2009;34(2):212-224.
72. Farrell TA, Hertzberg BS, Kliewer MA, et al. Fetal lateral ventricles: reassessment of normal values for atrial diameter at US. Radiology. 1994; 193(2):409-411.
73. Filly RA, Goldstein RB. The fetal ventricular atrium: fourth down and 10 mm to go. Radiology. 1994;193(2):315-317.
74. Mahony BS, Nyberg DA, Hirsch JH, et al. Mild idiopathic lateral cerebral ventricular dilatation in utero: sonographic evaluation. Radiology. 1988;169(3):715-721.
75. Hertzberg BS, Lile R, Foosaner DE, et al. Choroid plexus–ventricular wall separation in fetuses with normal-sized cerebral ventricles at sonography: postnatal outcome. AJR Am J Roentgenol. 1994;163(2):405-410.
76. Pagani G, Thilaganathan B, Prefumo F. Neurodevelopmental outcome in isolated mild fetal ventriculomegaly: systematic review and meta-analysis. Ultrasound Obstet Gynecol. 2014;44(3):254-260.
77. Weichert J, Hartge D, Krapp M, et al. Prevalence, characteristics and perinatal outcome of fetal ventriculomegaly in 29,000 pregnancies followed at a single institution. Fetal Diagn Ther. 2010;27(3):142-148.
78. Gaglioti P, Danelon D, Bontempo S, et al. Fetal cerebral ventriculomegaly: outcome in 176 cases. Ultrasound Obstet Gynecol. 2005;25(4):372-377.
79. D'Addario V, Pinto V, Di Cagno L, Pintucci A. Sonographic diagnosis of fetal cerebral ventriculomegaly: an update. J Matern Fetal Neonatal Med. 2007;20(1):7-14.
80. Vintzileos AM, Ingardia CJ, Nochimson DJ. Congenital hydrocephalus: a review and protocol for perinatal management. Obstet Gynecol. 1983;62(5): 539-549.
81. Lee JE, Gleeson JG. Cilia in the nervous system: linking cilia function and neurodevelopmental disorders. Curr Opin Neurol. 2011;24(2): 98-105.
82. McAllister JP 2nd. Pathophysiology of congenital and neonatal hydrocephalus. Semin Fetal Neonatal Med. 2012;17(5):285-294.
83. Monteagudo A, Timor-Tritsch IE. Moomjy M. Nomograms of the fetal lateral ventricles using transvaginal sonography. J Ultrasound Med. 1993;12(5):265-269.
84. Garel C, Fetal MRI. what is the future? Ultrasound Obstet Gynecol. 2008;31(2):123-128.
85. Morris JE, Rickard S, Paley MN, et al. The value of in-utero magnetic resonance imaging in ultrasound diagnosed foetal isolated cerebral ventriculomegaly. Clin Radiol. 2007;62(2):140-144.
86. Stroustrup Smith A, Levine D, et al. Magnetic resonance imaging of the kinked fetal brain stem: a sign of severe dysgenesis. J Ultrasound Med. 2005;24(12):1697-1709.
87. Baffero GM, Crovetto F, Fabietti I, et al. Prenatal ultrasound predictors of postnatal major cerebral abnormalities in fetuses with apparently isolated mild ventriculomegaly. Prenat Diagn. 2015;35(8):783-788.
88. Laskin MD, Kingdom J, Toi A, et al. Perinatal and neurodevelopmental outcome with isolated fetal ventriculomegaly: a systematic review. J Matern Fetal Neonatal Med. 2005;18(5):289-298.
89. Sadan S, Malinger G, Schweiger A, et al. Neuropsychological outcome of children with asymmetric ventricles or unilateral mild ventriculomegaly identified in utero. BJOG. 2007;114(5):596-602.
90. Uher BF, Golden JA. Neuronal migration defects of the cerebral cortex: a destination debacle. Clin Genet. 2000;58(1):16-24.
91. Barkovich AJ, Guerrini R, Kuzniecky RI, et al. A developmental and genetic classification for malformations of cortical development: update 2012. Brain. 2012;135(Pt 5):1348-1369.
92. Sarnat HB, Flores-Sarnat L. Integrative classification of morphology and molecular genetics in central nervous system malformations. Am J Med Genet A. 2004;126a(4):386-392.
93. van der Knaap MS, Valk J. Classification of congenital abnormalities of the CNS. AJNR Am J Neuroradiol. 1988;9(2):315-326.
94. Greene ND, Copp AJ. Neural tube defects. Annu Rev Neurosci. 2014;37:221-242.
95. Goldstein RB, Filly RA. Prenatal diagnosis of anencephaly: spectrum of sonographic appearances and distinction from the amniotic band syndromex. AJR Am J Roentgenol. 1988;151:547-550.
96. Naidich TP, Griffiths PD, Rosenbloom L. Central nervous system injury in utero: selected entities. Pediatr Radiol. 2015;45(Suppl. 3):S454-S462.
97. Sepulveda W, Corral E, Ayala C, et al. Chromosomal abnormalities in fetuses with open neural tube defects: prenatal identification with ultrasound. Ultrasound Obstet Gynecol. 2004;23(4):352-356.
98. Cafici D, Sepulveda W. First-trimester echogenic amniotic fluid in the acrania-anencephaly sequence. J Ultrasound Med. 2003;22(10): 1075-1079.
99. Engels AC, Joyeux L, Brantner C, et al. Sonographic detection of central nervous system defects in the first trimester of pregnancy. Prenat Diagn. 2016;36(3):266-273.
100. Chen CP, Chang TY, Lin YH, Wang W. Prenatal sonographic diagnosis of acrania associated with amniotic bands. J Clin Ultrasound. 2004;32(5): 256-260.
101. Goldstein RB, LaPidus AS, Filly RA. Fetal cephaloceles: diagnosis with US. Radiology. 1991;180(3):803-808.
102. Kasprian GJ, Paldino MJ, Mehollin-Ray AR, et al. Prenatal imaging of occipital encephaloceles. Fetal Diagn Ther. 2015;37(3):241-248.
103. Hoving EW. Nasal encephaloceles. Childs Nerv Syst. 2000;16(10-11): 702-706.
104. Moron FE, Morriss MC, Jones JJ, Hunter JV. Lumps and bumps on the head in children: use of CT and MR imaging in solving the clinical diagnostic dilemma. Radiographics. 2004;24(6):1655-1674.
105. Hunt JA, Hobar PC. Common craniofacial anomalies: facial clefts and encephaloceles. Plast Reconstr Surg. 2003;112(2):606-615.
106. Tirumandas M, Sharma A, Gbenimacho I, et al. Nasal encephaloceles: a review of etiology, pathophysiology, clinical presentations, diagnosis, treatment, and complications. Childs Nerv Syst. 2013;29(5):739-744.
107. Chen CP. Syndromes, disorders and maternal risk factors associated with neural tube defects (I). Taiwan J Obstet Gynecol. 2008;47(1):1-9.
108. Copp AJ, Stanier P, Greene ND. Neural tube defects: recent advances, unsolved questions, and controversies. Lancet Neurol. 2013;12(8): 799-810.
109. Chen CP. Syndromes, disorders and maternal risk factors associated with neural tube defects (V). Taiwan J Obstet Gynecol. 2008;47(3): 259-266.
110. Brunelle F, Baraton J, Renier D, et al. Intracranial venous anomalies associated with atretic cephalocoeles. Pediatr Radiol. 2000;30(11):743-747.
111. Siverino RO, Guarrera V, Attina G, et al. Parietal atretic cephalocele: associated cerebral anomalies identified by CT and MR imaging. Neuroradiol J. 2015;28(2):217-221.
112. Bannister CM, Russell SA, Rimmer S, et al. Can prognostic indicators be identified in a fetus with an encephalocele? Eur J Pediatr Surg. 2000;10(Suppl. 1):20-23.
113. Bui CJ, Tubbs RS, Shannon CN, et al. Institutional experience with cranial vault encephaloceles. J Neurosurg. 2007;107(1 Suppl.):22-25.
114. Tissir F, Qu Y, Montcouquiol M, et al. Lack of cadherins Celsr2 and Celsr3 impairs ependymal ciliogenesis, leading to fatal hydrocephalus. Nat Neurosci. 2010;13(6):700-707.
115. Waters AM, Beales PL. Ciliopathies: an expanding disease spectrum. Pediatr Nephrol. 2011;26(7):1039-1056.
116. Brancati F, Dallapiccola B, Valente EM. Joubert syndrome and related disorders. Orphanet J Rare Dis. 2010;5:20.
117. Pugash D, Oh T, Godwin K, et al. Sonographic 'molar tooth' sign in the diagnosis of Joubert syndrome. Ultrasound Obstet Gynecol. 2011;38(5): 598-602.
118. Chen CP. Meckel syndrome: genetics, perinatal findings, and differential diagnosis. Taiwan J Obstet Gynecol. 2007;46(1):9-14.
119. Aguirre-Pascual E, Epelman M, Johnson AM, et al. Prenatal MRI evaluation of limb-body wall complex. Pediatr Radiol. 2014;44(11):1412-1420.
120. Daltro P, Fricke BL, Kline-Fath BM, et al. Prenatal MRI of congenital abdominal and chest wall defects. AJR Am J Roentgenol. 2005;184(3): 1010-1016.

121. Iqbal CW, Derderian SC, Cheng Y, et al. Amniotic band syndrome: a single-institutional experience. Fetal Diagn Ther. 2015;37(1):1-5.
122. D'Addario V, Rossi AC, Pinto V, et al. Comparison of six sonographic signs in the prenatal diagnosis of spina bifida. J Perinat Med. 2008;36(4): 330-334.
123. Chen CP. Syndromes, disorders and maternal risk factors associated with neural tube defects (III). Taiwan J Obstet Gynecol. 2008;47(2):131-140.
124. Thompson DN. Postnatal management and outcome for neural tube defects including spina bifida and encephalocoeles. Prenat Diagn. 2009;29(4): 412-419.
125. Kawamura T, Morioka T, Nishio S, et al. Cerebral abnormalities in lumbosacral neural tube closure defect: MR imaging evaluation. Childs Nerv Syst. 2001;17(7):405-410.
126. McLone DG, Dias MS. The Chiari II malformation: cause and impact. Childs Nerv Syst. 2003;19(7-8):540-550.
127. Miller E, Widjaja E, Blaser S, et al. The old and the new: supratentorial MR findings in Chiari II malformation. Childs Nerv Syst. 2008;24(5): 563-575.
128. Stoll C, Dott B, Alembik Y, Roth MP. Associated malformations among infants with neural tube defects. Am J Med Genet A. 2011;155A(3): 565-568.
129. Nielsen LA, Maroun LL, Broholm H, et al. Neural tube defects and associated anomalies in a fetal and perinatal autopsy series. APMIS. 2006;114(4): 239-246.
130. Bahlmann F, Reinhard I, Schramm T, et al. Cranial and cerebral signs in the diagnosis of spina bifida between 18 and 22 weeks of gestation: a German multicentre study. Prenat Diagn. 2015;35(3):228-235.
131. Bredaki FE, Poon LC, Birdir C, et al. First-trimester screening for neural tube defects using alpha-fetoprotein. Fetal Diagn Ther. 2012;31(2): 109-114.
132. Campbell J, Gilbert WM, Nicolaides KH, Campbell S. Ultrasound screening for spina bifida: cranial and cerebellar signs in a high-risk population. Obstet Gynecol. 1987;70(2):247-250.
133. Ball RH, Filly RA, Goldstein RB, Callen PW. The lemon sign: not a specific indicator of meningomyelocele. J Ultrasound Med. 1993;12(3):131-134.
134. Barkovich AJ, Gressens P, Evrard P. Formation, maturation, and disorders of brain neocortex. AJNR Am J Neuroradiol. 1992;13(2):423-446.
135. Callen AL, Filly RA. Supratentorial abnormalities in the Chiari II malformation, I: the ventricular "point.". J Ultrasound Med. 2008;27(1):33-38.
136. Bernard JP, Cuckle HS, Stirnemann JJ, et al. Screening for fetal spina bifida by ultrasound examination in the first trimester of pregnancy using fetal biparietal diameter. Am J Obstet Gynecol. 2012;207(4):306 e1-306 e5.
137. Buisson O, De Keersmaecker B, Senat MV, et al. Sonographic diagnosis of spina bifida at 12 weeks: heading towards indirect signs. Ultrasound Obstet Gynecol. 2002;19(3):290-292.
138. Chaoui R, Benoit B, Heling KS, et al. Prospective detection of open spina bifida at 11-13 weeks by assessing intracranial translucency and posterior brain. Ultrasound Obstet Gynecol. 2011;38(6):722-726.
139. Chaoui R, Nicolaides KH. From nuchal translucency to intracranial translucency: towards the early detection of spina bifida. Ultrasound Obstet Gynecol. 2010;35(2):133-138.
140. Chen FC, Gerhardt J, Entezami M, et al. Detection of spina bifida by first trimester screening—results of the prospective multicenter Berlin IT-Study. Ultraschall Med. 2017;38(2):151-157.
141. Finn M, Sutton D, Atkinson S, et al. The aqueduct of Sylvius: a sonographic landmark for neural tube defects in the first trimester. Ultrasound Obstet Gynecol. 2011;38(6):640-645.
142. Kappou D, Papastefanou I, Pilalis A, et al. Towards detecting open spina bifida in the first trimester: the examination of the posterior brain. Fetal Diagn Ther. 2015;37(4):294-300.
143. Lachmann R, Chaoui R, Moratalla J, et al. Posterior brain in fetuses with open spina bifida at 11 to 13 weeks. Prenat Diagn. 2011;31(1):103-106.
144. Lachmann R, Picciarelli G, Moratalla J, et al. Frontomaxillary facial angle in fetuses with spina bifida at 11-13 weeks' gestation. Ultrasound Obstet Gynecol. 2010;36(3):268-271.
145. Simon EG, Arthuis CJ, Haddad G, et al. Biparietal/transverse abdominal diameter ratio </= 1: potential marker for open spina bifida at 11-13-week scan. Ultrasound Obstet Gynecol. 2015;45(3):267-272.
146. Sebire NJ, Noble PL, Thorpe-Beeston JG, et al. Presence of the 'lemon' sign in fetuses with spina bifida at the 10-14-week scan. Ultrasound Obstet Gynecol. 1997;10(6):403-405.
147. Kennedy D, Chitayat D, Winsor EJ, et al. Prenatally diagnosed neural tube defects: ultrasound, chromosome, and autopsy or postnatal findings in 212 cases. Am J Med Genet. 1998;77(4):317-321.
148. Danzer E, Johnson MP. Fetal surgery for neural tube defects. Semin Fetal Neonatal Med. 2014;19(1):2-8.
149. Winter TC, Kennedy AM, Woodward PJ. Holoprosencephaly: a survey of the entity, with embryology and fetal imaging. Radiographics. 2015;35(1):275-290.
150. Fernandes M, Hebert JM. The ups and downs of holoprosencephaly: dorsal versus ventral patterning forces. Clin Genet. 2008;73(5): 413-423.
151. Dubourg C, Bendavid C, Pasquier L, et al. Holoprosencephaly. Orphanet J Rare Dis. 2007;2:8.
152. Blaas HG, Eriksson AG, Salvesen KA, et al. Brains and faces in holoprosencephaly: pre- and postnatal description of 30 cases. Ultrasound Obstet Gynecol. 2002;19(1):24-38.
153. Hahn JS, Barnes PD. Neuroimaging advances in holoprosencephaly: refining the spectrum of the midline malformation. Am J Med Genet C Semin Med Genet. 2010;154C(1):120-132.
154. Volpe P, Campobasso G, De Robertis V, Rembouskos G. Disorders of prosencephalic development. Prenat Diagn. 2009;29(4):340-354.
155. Ming JE, Muenke M. Holoprosencephaly: from Homer to Hedgehog. Clin Genet. 1998;53(3):155-163.
156. Demyer W, Zeman W, Palmer CD. Familial alobar holoprosencephaly (arhinencephaly) with median cleft lip and palate. Report of patient with 46 chromosomes. Neurology. 1963;13:913-918.
157. Bernard JP, Drummond CL, Zaarour P, et al. A new clue to the prenatal diagnosis of lobar holoprosencephaly: the abnormal pathway of the anterior cerebral artery crawling under the skull. Ultrasound Obstet Gynecol. 2002;19(6):605-607.
158. Malinger G, Lev D, Kidron D, et al. Differential diagnosis in fetuses with absent septum pellucidum. Ultrasound Obstet Gynecol. 2005;25(1): 42-49.
159. Plawner LL, Delgado MR, Miller VS, et al. Neuroanatomy of holoprosencephaly as predictor of function: beyond the face predicting the brain. Neurology. 2002;59(7):1058-1066.
160. Lewis AJ, Simon EM, Barkovich AJ, et al. Middle interhemispheric variant of holoprosencephaly: a distinct cliniconeuroradiologic subtype. Neurology. 2002;59(12):1860-1865.
161. Nakayama T, Yamada R. MR imaging of the posterior fossa structures of human embryos and fetuses. Radiat Med. 1999;17(2):105-114.
162. Doherty D, Millen KJ, Barkovich AJ. Midbrain and hindbrain malformations: advances in clinical diagnosis, imaging, and genetics. Lancet Neurol. 2013;12(4):381-393.
163. Jissendi-Tchofo P, Severino M, Nguema-Edzang B, et al. Update on neuroimaging phenotypes of mid-hindbrain malformations. Neuroradiology. 2015;57(2):113-138.
164. Limperopoulos C, Robertson RL, Estroff JA, et al. Diagnosis of inferior vermian hypoplasia by fetal magnetic resonance imaging: potential pitfalls and neurodevelopmental outcome. Am J Obstet Gynecol. 2006;194(4): 1070-1076.
165. Aletebi FA, Fung KF. Neurodevelopmental outcome after antenatal diagnosis of posterior fossa abnormalities. J Ultrasound Med. 1999;18(10):683-689.
166. Boltshauser E. Cerebellar imaging—an important signpost in paediatric neurology. Childs Nerv Syst. 2001;17(4-5):211-216.
167. Paladini D, Volpe P. Posterior fossa and vermian morphometry in the characterization of fetal cerebellar abnormalities: a prospective three-dimensional ultrasound study. Ultrasound Obstet Gynecol. 2006;27(5): 482-489.
168. Vinals F, Munoz M, Naveas R, et al. The fetal cerebellar vermis: anatomy and biometric assessment using volume contrast imaging in the C-plane (VCI-C). Ultrasound Obstet Gynecol. 2005;26(6):622-627.
169. Guibaud L. Practical approach to prenatal posterior fossa abnormalities using MRI. Pediatr Radiol. 2004;34(9):700-711.

170. Guibaud L, des Portes V. Plea for an anatomical approach to abnormalities of the posterior fossa in prenatal diagnosis. Ultrasound Obstet Gynecol. 2006;27(5):477-481.
171. Robinson AJ, Blaser S, Toi A, et al. The fetal cerebellar vermis: assessment for abnormal development by ultrasonography and magnetic resonance imaging. Ultrasound Q. 2007;23(3):211-223.
172. Adamsbaum C, Moutard ML, Andre C, et al. MRI of the fetal posterior fossa. Pediatr Radiol. 2005;35(2):124-140.
173. Patel S, Barkovich AJ. Analysis and classification of cerebellar malformations. AJNR Am J Neuroradiol. 2002;23(7):1074-1087.
174. Phillips JJ, Mahony BS, Siebert JR, et al. Dandy-Walker malformation complex: correlation between ultrasonographic diagnosis and postmortem neuropathology. Obstet Gynecol. 2006;107(3):685-693.
175. Parisi MA, Dobyns WB. Human malformations of the midbrain and hindbrain: review and proposed classification scheme. Mol Genet Metab. 2003;80(1-2):36-53.
176. Volpe P, Muto B, Passamonti U, et al. Abnormal sonographic appearance of posterior brain at 11-14 weeks and fetal outcome. Prenat Diagn. 2015;35(7):717-723.
177. Chapman T, Mahalingam S, Ishak GE, et al. Diagnostic imaging of posterior fossa anomalies in the fetus and neonate: part 2, Posterior fossa disorders. Clin Imaging. 2015;39(2):167-175.
178. Babcook CJ, Chong BW, Salamat MS, et al. Sonographic anatomy of the developing cerebellum: normal embryology can resemble pathology. AJR Am J Roentgenol. 1996;166(2):427-433.
179. Pilu G, Hobbins JC. Sonography of fetal cerebrospinal anomalies. Prenat Diagn. 2002;22(4):321-330.
180. Limperopoulos C, Robertson Jr RL, Khwaja OS, et al. How accurately does current fetal imaging identify posterior fossa anomalies? AJR Am J Roentgenol. 2008;190(6):1637-1643.
181. Malinger G, Ginath S, Lerman-Sagie T, et al. The fetal cerebellar vermis: normal development as shown by transvaginal ultrasound. Prenat Diagn. 2001;21(8):6876-6892.
182. Pasquier L, Marcorelles P, Loget P, et al. Rhombencephalosynapsis and related anomalies: a neuropathological study of 40 fetal cases. Acta Neuropathol. 2009;117(2):185-200.
183. Poretti A, Leventer RJ, Cowan FM, et al. Cerebellar cleft: a form of prenatal cerebellar disruption. Neuropediatrics. 2008;39(2):106-112.
184. Boltshauser E, Martin F, Altermatt S. Outcome in children with space-occupying posterior fossa arachnoid cysts. Neuropediatrics. 2002;33(3):118-121.
185. Hayward R. Postnatal management and outcome for fetal-diagnosed intracerebral cystic masses and tumours. Prenat Diagn. 2009;29(4):396-401.
186. de Wit MC, Lequin MH, de Coo IF, et al. Cortical brain malformations: effect of clinical, neuroradiological, and modern genetic classification. Arch Neurol. 2008;65(3):358-366.
187. Montenegro MA, Guerreiro MM, Lopes-Cendes I, et al. Interrelationship of genetics and prenatal injury in the genesis of malformations of cortical development. Arch Neurol. 2002;59(7):1147-1153.
188. Toi A, Chitayat D, Blaser S. Abnormalities of the foetal cerebral cortex. Prenat Diagn. 2009;29(4):355-371.
189. Wang DC, Shannon P, Toi A, et al. Temporal lobe dysplasia: a characteristic sonographic finding in thanatophoric dysplasia. Ultrasound Obstet Gynecol. 2014;44(5):588-594.
190. Mirzaa GM, Paciorkowski AR. Introduction: brain malformations. Am J Med Genet C Semin Med Genet. 2014;166C(2):117-123.
191. Raybaud C, Widjaja E. Development and dysgenesis of the cerebral cortex: malformations of cortical development. Neuroimaging Clin N Am. 2011;21(3):483-543, vii.
192. Malinger G, Kidron D, Schreiber L, et al. Prenatal diagnosis of malformations of cortical development by dedicated neurosonography. Ultrasound Obstet Gynecol. 2007;29(2):178-191.
193. Malinger G, Lev D, Lerman-Sagie T. Assessment of fetal intracranial pathologies first demonstrated late in pregnancy: cell proliferation disorders. Reprod Biol Endocrinol. 2003;1:110.
194. De Catte L, De Keersmaeker B, Claus F. Prenatal neurologic anomalies: sonographic diagnosis and treatment. Paediatr Drugs. 2012;14(3):143-155.
195. Guerrini R, Dobyns WB. Malformations of cortical development: clinical features and genetic causes. Lancet Neurol. 2014;13(7):710-726.
196. Barkovich AJ, Kuzniecky RI, Jackson GD, et al. A developmental and genetic classification for malformations of cortical development. Neurology. 2005;65(12):1873-1887.
197. Soares de Olivera-Szejnfeld P, Levine D, Melo AS, et al. Congenital brain abnormalities and Zika virus: what the radiologist can expect to see prenatally and postnatally. Radiology. 2016;281(1):203-218.
198. Abuelo D. Microcephaly syndromes. Semin Pediatr Neurol. 2007;14(3):118-127.
199. Schwarzler P, Homfray T, Bernard JP, et al. Late onset microcephaly: failure of prenatal diagnosis. Ultrasound Obstet Gynecol. 2003;22(6):640-642.
200. Almgren M, Schalling M, Lavebratt C. Idiopathic megalencephaly—possible cause and treatment opportunities: from patient to lab. Eur J Paediatr Neurol. 2008;12(6):438-445.
201. Malinger G, Lev D, Ben-Sira L, et al. Can syndromic macrocephaly be diagnosed in utero? Ultrasound Obstet Gynecol. 2011;37(1):72-81.
202. Williams CA, Dagli A, Battaglia A. Genetic disorders associated with macrocephaly. Am J Med Genet A. 2008;146A(15):2023-2037.
203. Olney AH. Macrocephaly syndromes. Semin Pediatr Neurol. 2007;14(3):128-135.
204. Flores-Sarnat L. Hemimegalencephaly: part 1. Genetic, clinical, and imaging aspects. J Child Neurol. 2002;17(5):373-384.
205. Andrade CS, Leite Cda C. Malformations of cortical development: current concepts and advanced neuroimaging review. Arq Neuropsiquiatr. 2011;69(1):130-138.
206. Flores-Sarnat L. Hemimegalencephaly syndrome. Handb Clin Neurol. 2008;87:153-176.
207. Tinkle BT, Schorry EK, Franz DN, et al. Epidemiology of hemimegalencephaly: a case series and review. Am J Med Genet A. 2005;139(3):204-211.
208. Fry AE, Cushion TD, Pilz DT. The genetics of lissencephaly. Am J Med Genet C Semin Med Genet. 2014;166C(2):198-210.
209. Lacalm A, Nadaud B, Massoud M, et al. Prenatal diagnosis of cobblestone lissencephaly associated with Walker-Warburg syndrome based on a specific sonographic pattern. Ultrasound Obstet Gynecol. 2016;47(1):117-122.
210. Stutterd CA, Leventer RJ. Polymicrogyria: a common and heterogeneous malformation of cortical development. Am J Med Genet C Semin Med Genet. 2014;166C(2):227-239.
211. Blondiaux E, Sileo C, Nahama-Allouche C, et al. Periventricular nodular heterotopia on prenatal ultrasound and magnetic resonance imaging. Ultrasound Obstet Gynecol. 2013;42(2):149-155.
212. Denis D, Chateil JF, Brun M, et al. Schizencephaly: clinical and imaging features in 30 infantile cases. Brain Dev. 2000;22(8):475-483.
213. Denis D, Maugey-Laulom B, Carles D, et al. Prenatal diagnosis of schizencephaly by fetal magnetic resonance imaging. Fetal Diagn Ther. 2001;16(6):354-359.
214. Nissenkorn A, Michelson M, Ben-Zeev B, Lerman-Sagie T. Inborn errors of metabolism: a cause of abnormal brain development. Neurology. 2001;56(10):1265-1272.
215. Spronsen FJ, Smit GP, Erwich JJ. Inherited metabolic diseases and pregnancy. BJOG. 2005;112(1):2-11.
216. Strenge S, Froster UG, Wanders RJ, et al. First-trimester increased nuchal translucency as a prenatal sign of Zellweger syndrome. Prenat Diagn. 2004;24(2):151-153.
217. Wortmann SB, Reimer A, Creemers JW, Mullaart RA. Prenatal diagnosis of cerebral lesions in tuberous sclerosis complex (TSC). Case report and review of the literature. Eur J Paediatr Neurol. 2008;12(2):123-126.
218. Northrup H, Koening M, Pearson D, Au K. Tuberous sclerosis complex. GeneReviews. 2015. Available from: http://www.ncbi.nlm.nih.gov/books/NBK1220/. Updated Sept. 3, 2015; accessed Feb. 13, 2016.
219. Levine D, Barnes P, Korf B, Edelman R. Tuberous sclerosis in the fetus: second-trimester diagnosis of subependymal tubers with ultrafast MR imaging. AJR Am J Roentgenol. 2000;175(4):1067-1069.
220. Santo S, D'Antonio F, Homfray T, et al. Counseling in fetal medicine: agenesis of the corpus callosum. Ultrasound Obstet Gynecol. 2012;40(5):513-521.

221. Achiron R, Lipitz S, Achiron A. Sex-related differences in the development of the human fetal corpus callosum: in utero ultrasonographic study. Prenat Diagn. 2001;21(2):116-120.
222. Paladini D, Pastore G, Cavallaro A, et al. Agenesis of the fetal corpus callosum: sonographic signs change with advancing gestational age. Ultrasound Obstet Gynecol. 2013;42(6):687-690.
223. Winter TC, Kennedy AM, Byrne J, Woodward PJ. The cavum septi pellucidi: why is it important? J Ultrasound Med. 2010;29(3):427-444.
224. Hosseinzadeh K, Luo J, Borhani A, Hill L. Non-visualisation of cavum septi pellucidi: implication in prenatal diagnosis? Insights Imaging. 2013;4(3): 357-367.
225. Malinger G, Lerman-Sagie T, Vinals F. Three-dimensional sagittal reconstruction of the corpus callosum: fact or artifact? Ultrasound Obstet Gynecol. 2006;28(5):742-743.
226. Malinger G, Lev D, Lerman-Sagie T. The fetal corpus callosum. 'The truth is out there'. Ultrasound Obstet Gynecol. 2007;30(2):140-141.
227. Livingston JH, Stivaros S, Warren D, Crow YJ. Intracranial calcification in childhood: a review of aetiologies and recognizable phenotypes. Dev Med Child Neurol. 2014;56(7):612-626.
228. McCartney E, Squier W. Patterns and pathways of calcification in the developing brain. Dev Med Child Neurol. 2014;56(10):1009-1015.
229. Melo AS, Malinger G, Ximenes R, et al. Zika virus intrauterine infection causes abnormality and microcephaly: tip of the iceberg? Ultrasound Obstet Gynecol. 2016;47:6-7.
230. Mittendorf R, Covert R, Pryde PG, et al. Association between lenticulostriate vasculopathy (LSV) and neonatal intraventricular hemorrhage (IVH). J Perinatol. 2004;24(11):700-705.
231. El Ayoubi M, de Bethmann O, Monset-Couchard M. Lenticulostriate echogenic vessels: clinical and sonographic study of 70 neonatal cases. Pediatr Radiol. 2003;33(10):697-703.
232. Neu N, Duchon J, Zachariah P. TORCH infections. Clin Perinatol. 2015;42(1):77-103, viii.
233. Malinger G, Lev D, Lerman-Sagie T. Imaging of fetal cytomegalovirus infection. Fetal Diagn Ther. 2011;29(2):117-126.
234. Benoist G, Salomon LJ, Mohlo M, et al. Cytomegalovirus-related fetal brain lesions: comparison between targeted ultrasound examination and magnetic resonance imaging. Ultrasound Obstet Gynecol. 2008;32(7):900-905.
235. Yinon Y, Farine D, Yudin MH. Screening, diagnosis, and management of cytomegalovirus infection in pregnancy. Obstet Gynecol Surv. 2010;65(11): 736-743.
236. Benoist G, Salomon LJ, Jacquemard F, et al. The prognostic value of ultrasound abnormalities and biological parameters in blood of fetuses infected with cytomegalovirus. BJOG. 2008;115(7):823-829.
237. Farkas N, Hoffmann C, Ben-Sira L, et al. Does normal fetal brain ultrasound predict normal neurodevelopmental outcome in congenital cytomegalovirus infection? Prenat Diagn. 2011;31(4):360-366.
238. Kieffer F, Wallon M. Congenital toxoplasmosis. Handb Clin Neurol. 2013;112:1099-1101.
239. Malinger G, Werner H, Rodriguez Leonel JC, et al. Prenatal brain imaging in congenital toxoplasmosis. Prenat Diagn. 2011;31(9):881-886.
240. Paquet C, Yudin MH, Society of Obstetricians and Gynaecologists of Canada. Toxoplasmosis in pregnancy: prevention, screening, and treatment. J Obstet Gynaecol Can. 2013;35(1):78-81.
241. Garel C, Azarian M, Lasjaunias P, Luton D. Pial arteriovenous fistulas: dilemmas in prenatal diagnosis, counseling and postnatal treatment. Report of three cases. Ultrasound Obstet Gynecol. 2005;26(3):293-296.
242. Toulgoat F, Lasjaunias P. Vascular malformations of the brain. Handb Clin Neurol. 2013;112:1043-1051.
243. Deloison B, Chaloughi G, Sonigo P, et al. Hidden mortality of prenatally diagnosed vein of Galen aneurysmal malformation: retrospective study and review of the literature. Ultrasound Obstet Gynecol. 2012;40: 652-658.
244. McInnes M, Fong K, Grin A, et al. Malformations of the fetal dural sinuses. Can J Neurol Sci. 2009;36(1):72-77.
245. Corral E, Stecher X, Malinger G, et al. Thrombosis of the torcular Herophili in the fetus: a series of eight cases. Prenat Diagn. 2014;34(12):1176-1181.
246. Elchalal U, Yagel S, Gomori JM, et al. Fetal intracranial hemorrhage (fetal stroke): does grade matter? Ultrasound Obstet Gynecol. 2005;26(3): 233-243.
247. Ghi T, Simonazzi G, Perolo A, et al. Outcome of antenatally diagnosed intracranial hemorrhage: case series and review of the literature. Ultrasound Obstet Gynecol. 2003;22(2):121-130.
248. Kutuk MS, Yikilmaz A, Ozgun MT, et al. Prenatal diagnosis and postnatal outcome of fetal intracranial hemorrhage. Childs Nerv Syst. 2014;30(3): 411-418.
249. Pavone P, Pratico AD, Vitaliti G, et al. Hydranencephaly: cerebral spinal fluid instead of cerebral mantles. Ital J Pediatr. 2014;40:79.
250. Sepulveda W, Cortes-Yepes H, Wong AE, et al. Prenatal sonography in hydranencephaly: findings during the early stages of disease. J Ultrasound Med. 2012;31(5):799-804.
251. Isaacs Jr H. II. Perinatal brain tumors: a review of 250 cases. Pediatr Neurol. 2002;27(5):333-342.
252. Cassart M, Bosson N, Garel C, et al. Fetal intracranial tumors: a review of 27 cases. Eur Radiol. 2008;18(10):2060-2066.
253. Isaacs Jr H. I. Perinatal brain tumors: a review of 250 cases. Pediatr Neurol. 2002;27(4):249-261.
254. Yildiz H, Hakyemez B, Koroglu M, et al. Intracranial lipomas: importance of localization. Neuroradiology. 2006;48(1):1-7.
255. Ickowitz V, Eurin D, Rypens F, et al. Prenatal diagnosis and postnatal follow-up of pericallosal lipoma: report of seven new cases. AJNR Am J Neuroradiol. 2001;22(4):767-772.
256. Levine D, Robson C. MR imaging of normal brain in the second and third trimesters. In: Levine D, editor. Atlas of fetal MRI. Briston, PA: Taylor & Francis; 2005.
257. Levine D. MR imaging of fetal brain and spine. In: Atlas SW, editor. Magnetic resonance imaging of the brain and spine. Philadelphia: Lippincott; 2008.

CHAPTER 35

The Fetal Spine

Elizabeth Asch and Eric Sauerbrei

SUMMARY OF KEY POINTS

- Neural tube defects (NTDs) are a common congenital anomaly with clinically important associated morbidity and mortality rates.
- Most open NTDs will have associated intracranial abnormalities, most commonly Chiari II malformation, detected by sonography.
- Although much less common, closed NTDs are less likely to have associated intracranial abnormalities and require careful examination of the spine for detection.
- Other spinal abnormalities such as scoliosis, sacral agenesis, caudal regression, sirenomelia, and sacrococcygeal teratoma have distinct sonographic appearances that aid in prenatal diagnosis.

CHAPTER OUTLINE

DEVELOPMENTAL ANATOMY
Embryology of the Spine
Ossification of the Fetal Spine
Normal Position of the Spinal Cord
SCANNING TECHNIQUES
Three-Dimensional Ultrasound
SPINA BIFIDA
Folic Acid Fortification
Pathogenesis and Pathology
Alpha-Fetoprotein and Ultrasound Screening
Sonographic Findings in the Spine
Associated Cranial Abnormalities
Associated Noncranial Abnormalities
Prognosis
Fetal Surgery for Myelomeningocele
MYELOCYSTOCELE
DIASTEMATOMYELIA
SCOLIOSIS AND KYPHOSIS
SACRAL AGENESIS
CAUDAL REGRESSION
SIRENOMELIA
SACROCOCCYGEAL TERATOMA
PRESACRAL FETAL MASS

Abnormalities of the spine are some of the most common congenital abnormalities. In the United States, overall incidence of neural tube defects (NTDs) was approximately 1 to 2 in 1000 births[1] before 2000, but by 2007 it was less than 0.5 in 1000 pregnancies primarily as a result of the widespread use of folic acid before conception[2,3] and the addition of folic acid to enriched grain products.[4] Since the institution of folic acid supplementation, an estimated 1300 cases of NTDs each year have been prevented in the United States.[5] At least 42 nations practice mandatory folic acid fortification to combat NTDs.[6-10]

NTDs are associated with substantial morbidity and mortality rates. Many survivors have severe long-term morbidity that has a profound emotional, physical, and financial impact on their families. Fortunately, the birth incidence of spina bifida and anencephaly is decreasing in many areas of the world as a result of maternal screening programs (maternal serum tests and antenatal ultrasound) and, more recently, the administration of folic acid to women of child-bearing age.

In prenatal imaging, **three-dimensional** (3D) **ultrasound** and **fetal magnetic resonance imaging** (MRI) are making a positive impact, especially for precise localization of spina bifida and complete delineation of associated abnormalities. This precise information is useful for prognosis and possibly for prenatal surgery. Prenatal surgery for closure of myelomeningoceles is practiced in only a few centers at this time.

DEVELOPMENTAL ANATOMY

Embryology of the Spine

The precursors of the spinal cord and surrounding spinal column develop in the third and fourth weeks after conception (fifth and sixth menstrual weeks). During the third conceptual week, the bilaminar germ disc evolves into the trilaminar germ disc, which consists of the **ectoderm** layer (part of the amniotic cavity), the middle **mesoderm** layer, and the **endoderm** layer (part of the yolk sac cavity) (Fig. 35.1A). The mesoderm layer develops a midline central tube, the **notochordal process,** which runs along the long axis of the embryonic disc. The mesoderm lateral to the notochordal process has three components: paraxial mesoderm, intermediate mesoderm, and lateral plate mesoderm. By day 21 conceptual age, the hollow-tube notochordal process

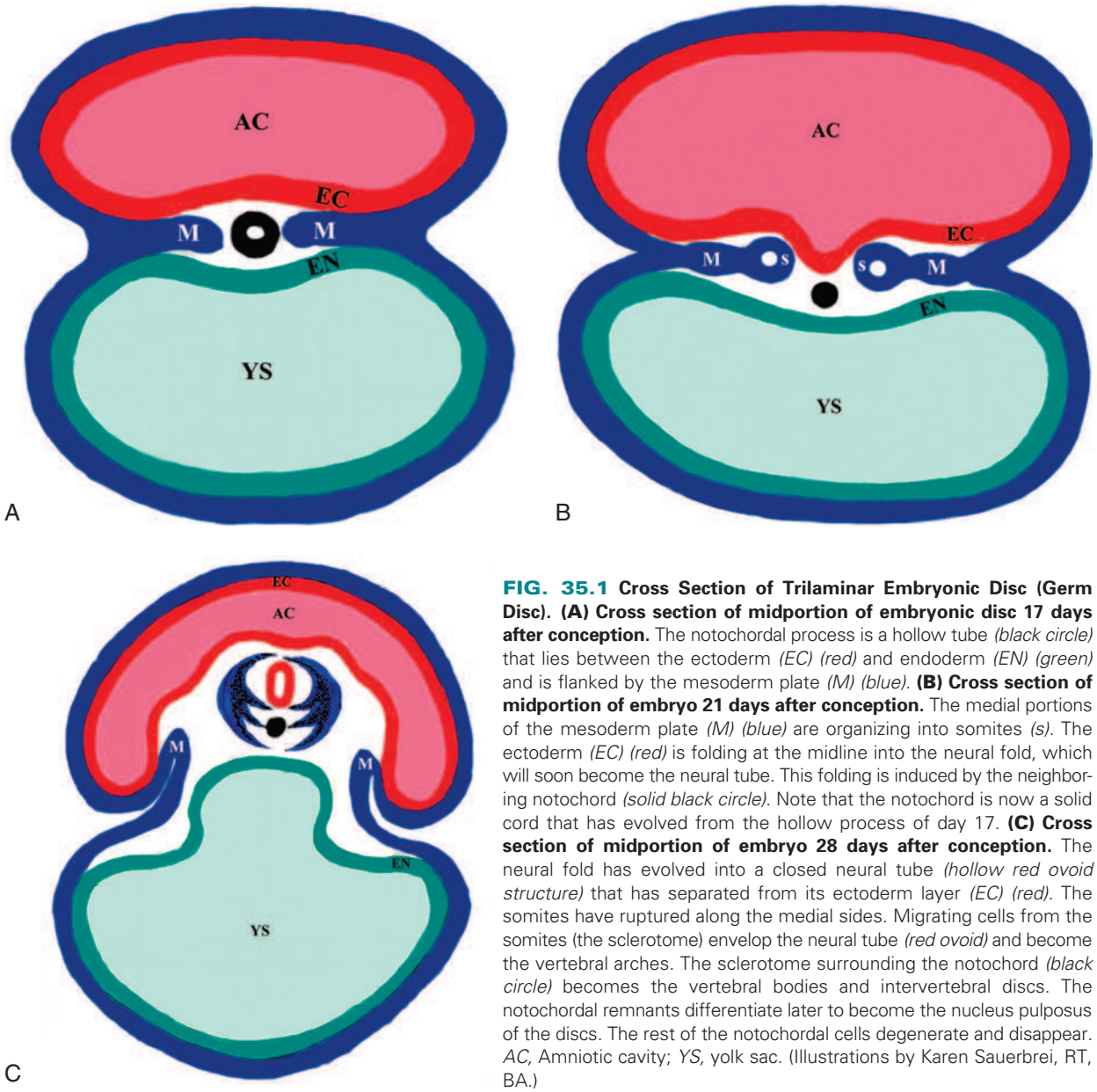

FIG. 35.1 Cross Section of Trilaminar Embryonic Disc (Germ Disc). (A) Cross section of midportion of embryonic disc 17 days after conception. The notochordal process is a hollow tube *(black circle)* that lies between the ectoderm *(EC) (red)* and endoderm *(EN) (green)* and is flanked by the mesoderm plate *(M) (blue).* **(B) Cross section of midportion of embryo 21 days after conception.** The medial portions of the mesoderm plate *(M) (blue)* are organizing into somites *(s).* The ectoderm *(EC) (red)* is folding at the midline into the neural fold, which will soon become the neural tube. This folding is induced by the neighboring notochord *(solid black circle).* Note that the notochord is now a solid cord that has evolved from the hollow process of day 17. **(C) Cross section of midportion of embryo 28 days after conception.** The neural fold has evolved into a closed neural tube *(hollow red ovoid structure)* that has separated from its ectoderm layer *(EC) (red).* The somites have ruptured along the medial sides. Migrating cells from the somites (the sclerotome) envelop the neural tube *(red ovoid)* and become the vertebral arches. The sclerotome surrounding the notochord *(black circle)* becomes the vertebral bodies and intervertebral discs. The notochordal remnants differentiate later to become the nucleus pulposus of the discs. The rest of the notochordal cells degenerate and disappear. *AC,* Amniotic cavity; *YS,* yolk sac. (Illustrations by Karen Sauerbrei, RT, BA.)

has evolved into a solid cord called the **notochord,** and the paraxial mesoderm has developed multiple discrete bumps called **somites,** of which there are 37 pairs when fully developed (Fig. 35.1B).

The notochord and the rest of the intraembryonic mesoderm induce the development of the **neural plate** in the ectoderm layer (amniotic cavity side of the germ disc), starting on conceptual day 18. The neural plate grows in length and breadth until conceptual day 21, when neurulation begins. **Neurulation** is the process of folding of the neural plate into the **neural tube,** probably induced by the adjacent notochord. The lateral edges of the neural folds begin to fuse dorsally into a closed neural tube in the occipitocervical region, leaving an opening at the cranial end **(cranial neuropore)** and the caudal end **(caudal neuropore).** The hollow center of the neural tube is called the **neural canal,** which will become the central canal of the spinal cord and ventricular system of the brain. By day 24 conceptual age, the cranial neuropore closes, and by day 25 the caudal neuropore closes (Table 35.1).

The cranial end of the neural tube becomes the brain, and the caudal end becomes the spinal cord. In week 4 conceptual age, after the neural tube has formed, the adjacent 37 pairs of somites in the intraembryonic mesoderm give rise to the vertebral bodies and vertebral arches that will surround the spinal cord. A group of cells, the **sclerotome,** migrates from the somites and surrounds the adjacent neural tube and notochord. The ventral portion of the sclerotome surrounds the notochord and forms the rudiment of the vertebral body. The dorsal portion of the sclerotome surrounds the neural tube and forms the precursors to the vertebral arch (Fig. 35.1C). In the fetus, the **notochordal**

TABLE 35.1 Spine Embryology During Third and Fourth Weeks After Conception

Menstrual Age (Days)	Conceptual Age (Days)	Embryo Length (mm)	Sac Diameter (mm)	Landmarks
31	17	0.5	2	Trilaminar disc Notochordal process Paraxial mesoderm (Fig. 35.1A)
35	21	2	4	Notochord Neural plate Somites (Fig. 35.1B)
42	28	5	10	Neural tube Notochord Sclerotome (Fig. 35.1C)

remnant corresponds to the nucleus pulposus of the intervertebral discs.[11]

Abnormalities of neural tube closure not only affect the spinal cord and brain but also interfere with normal development of surrounding vertebral arches, which are derived from adjacent mesodermal somites. Disturbances of neural tube closure underlie **spina bifida** and **anencephaly** defects.

Caudal regression defects may be related to defective development of the mesoderm layer in week 3 conceptual age, during transformation of the germ disc from two layers (bilaminar) to three layers (trilaminar). Various degrees of abnormal mesoderm development account for the wide spectrum of abnormalities found in caudal regression.

A failure of part of the neural tube to close, called **spinal dysraphism,** disrupts development of the nervous system and disrupts the induction of the overlying vertebral arches. The resulting open vertebral canal is called **spina bifida.** If dura and arachnoid protrude from the spinal canal, the result is a **meningocele.** If neural tissue and meninges protrude, the result is a **myelomeningocele.** In the most severe NTDs, the neural tube fails to form and fails to separate from the overlying ectoderm. In the spine, this condition is called **rachischisis** or **myeloschisis;** the open spinal cord is exposed along the dorsal surface of the fetus. If the defect involves the cranial neural tube, the brain is represented by an exposed dorsal mass of undifferentiated neural tissue, called **exencephaly, anencephaly,** or **craniorachischisis.** Differentiated brain and meninges may bulge from a nonossified gap in the skull **(meningoencephalocele),** but this is not related to failure of neural tube closure.

In animals, certain teratogens can induce NTDs: **retinoic acid, insulin,** and **high plasma glucose levels.** In humans, implicated factors include **valproic acid** (antiepileptic), **maternal diabetes,** and **hyperthermia.** Valproic acid may interfere with folate metabolism.

Ossification of the Fetal Spine

Prenatal sonography readily portrays the ossified portions of the fetal spine, whereas the nonossified cartilage is more difficult to delineate. It is therefore important for sonographers and sonologists to understand the temporal and spatial ossification patterns during fetal development in order to optimize spinal evaluation.

Each vertebra will develop three ossification centers: the centrum, right neural process, and left neural process.[12] The **centrum** will form the central part of the vertebral body, and the **neural process** will form the posterolateral parts of the vertebral body and pedicles, the transverse processes, the laminae, and the articular processes.

Ossification begins in the lower thoracic fetal spine at approximately 10 weeks' gestation (menstrual age).[13] Ossification of the **centra** progresses in cranial and caudal directions simultaneously. **Neural arch** ossification proceeds caudally from the lower thoracic (T) spine to the lumbar (L) spine. It proceeds sequentially from L1 through L5 and then into the sacral (S) spine. By 13 weeks' menstrual age, there are three ossification centers in vertebrae C1 through L3[14] (Fig. 35.2). Neural arch ossification begins as a small focus at the base of the transverse process and extends simultaneously into the pedicle anteriorly and into the lamina posteriorly (Fig. 35.3).

Ultrasound evaluation for spina bifida usually occurs between 16 and 22 weeks' gestation. By 16 weeks, there is enough ossification in the neural arches to assess for spina bifida to level L5,[15] by 19 weeks to level S1, and by 22 weeks to level S2 (Figs. 35.4 and 35.5). In some fetuses, there may be enough neural arch ossification to assess for spina bifida before these gestational ages. Braithwaite et al.[16] assessed the fetal anatomy at 12 to 13 weeks' gestation by a combination of transabdominal and transvaginal sonography and reported successful examination of the vertebrae and overlying skin in both the transverse and the coronal plane in all cases. Others have reported successful prenatal diagnosis of spina bifida at 12 to 14 weeks' gestation on the basis of abnormal cranial findings.[17-19] They caution that although the characteristic cranial findings may be present at 11 to 14 weeks, the prevalence of these findings in the first trimester remains to be determined (Table 35.2). Furthermore, closed NTDs are less likely to be associated with abnormal cranial findings and therefore are more difficult to detect in the first trimester.

Normal Position of the Spinal Cord

For fetuses at 19 to 33 weeks' gestation, the **conus medullaris** is normally situated at level L2-L3 or higher (Fig. 35.6). Level L3 is taken to be *indeterminate* and L3-L4 or lower as *abnormal.*[20] For those fetuses with tethered cord, the position of the conus

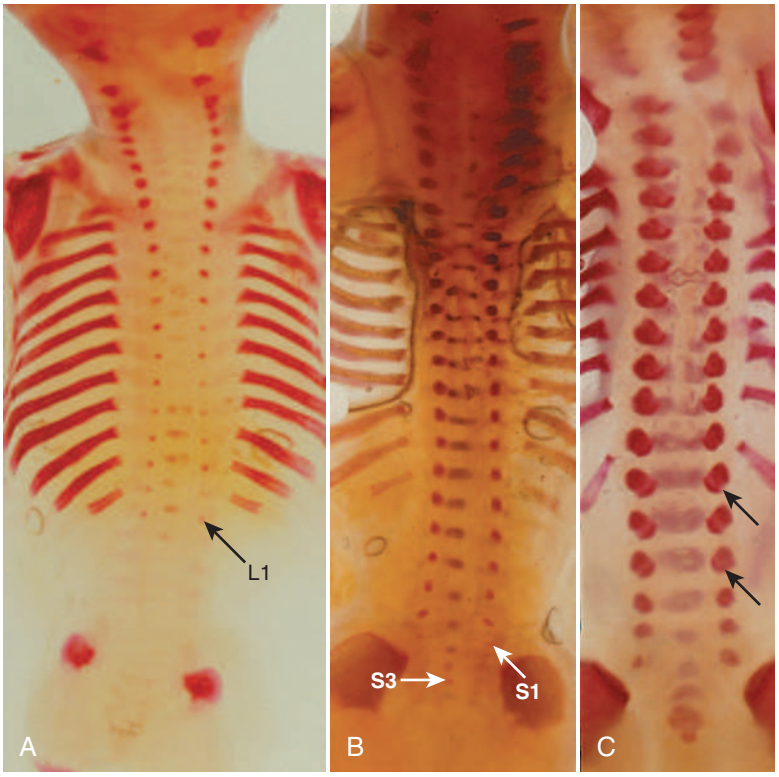

FIG. 35.2 Spine Ossification at 11 Weeks + 4 Days' Menstrual Age. (A) Ossification of neural processes extends from C1 to L1 *(arrow).* The neural process ossification starts at the base of the transverse process, which lies at the junction of the pedicle and the lamina. **(B) Spine ossification at 13 weeks' menstrual age.** Ossification extends to level S1 neural process *(S1 arrow)* and S3 vertebral body *(S3 arrow).* **(C) Spine ossification at 15 weeks + 2 days' menstrual age.** Ossification now extends into the laminae of the vertebral arches in the thoracic and lumbar spine. Arrows demonstrate ossification of the laminae at levels L1 and L3. Ossification of the laminae is minimal at S1.

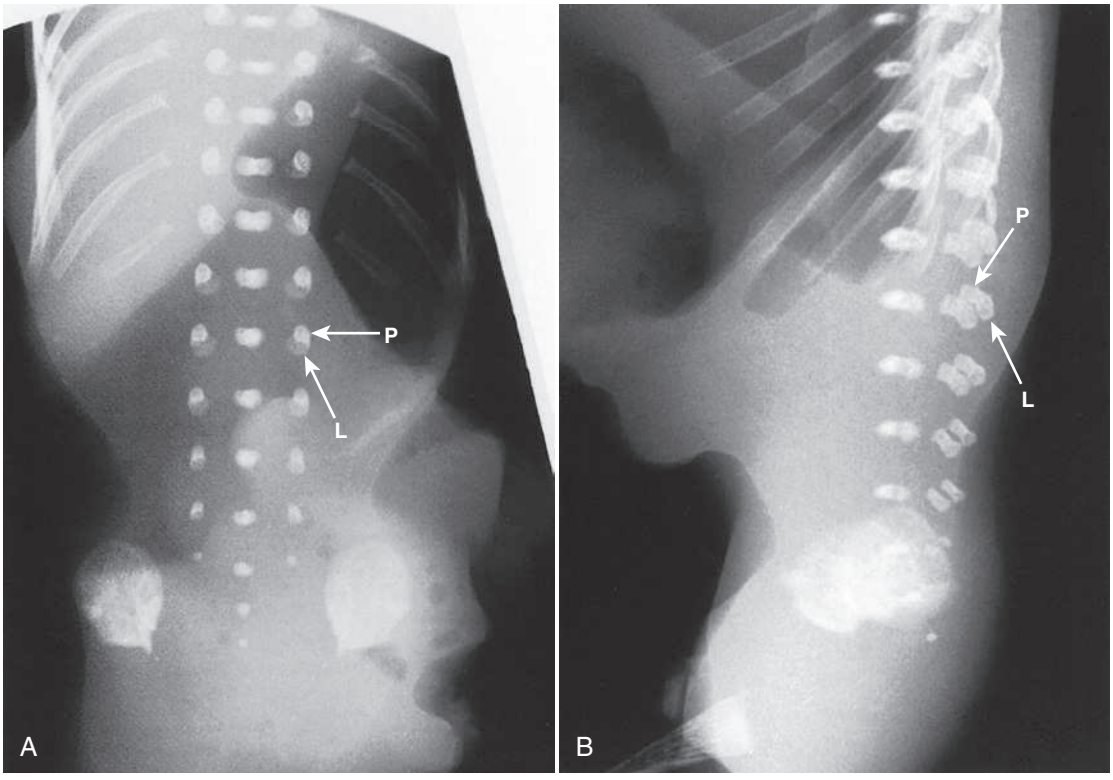

FIG. 35.3 Spine Ossification on Radiographs at 14 Weeks' Gestation. (A) Anteroposterior and **(B)** lateral radiographs. Well-developed ossification in the centra now extends down to level S3. Ossification in the lumbar neural processes extends into the lamina *(L)* and pedicles *(P).* The neural process ossification starts to resemble the shape of the cartilaginous neural process rather than the focal dotlike ossification at 13 weeks' gestation.

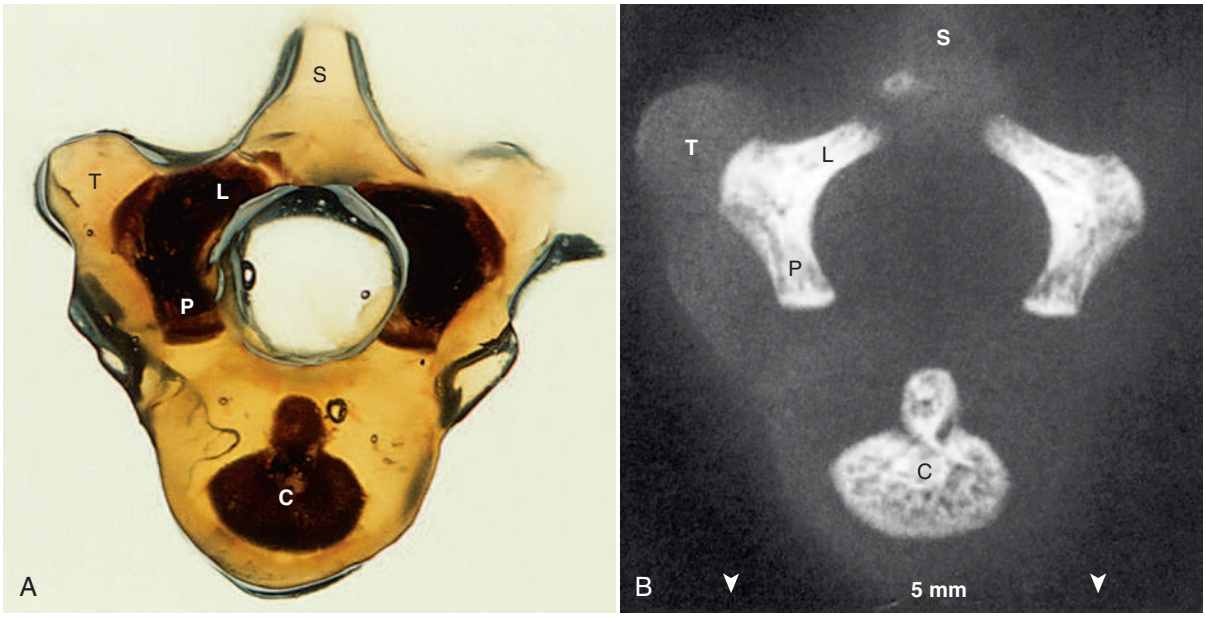

FIG. 35.4 Vertebral Ossification of T9 at 16 Weeks' Gestation. (A) Specimen. **(B)** Radiograph. Ossification extends quite far into the pedicles *(P)* and laminae *(L)*. Note the early ossification in the base of the transverse processes *(T)*. The width of the vertebra is about 5 mm. There is ossification within the centrum *(C)*. *S,* Spinous process (cartilage); *T,* transverse process (cartilage). The distance between the *arrowheads* is 5 mm.

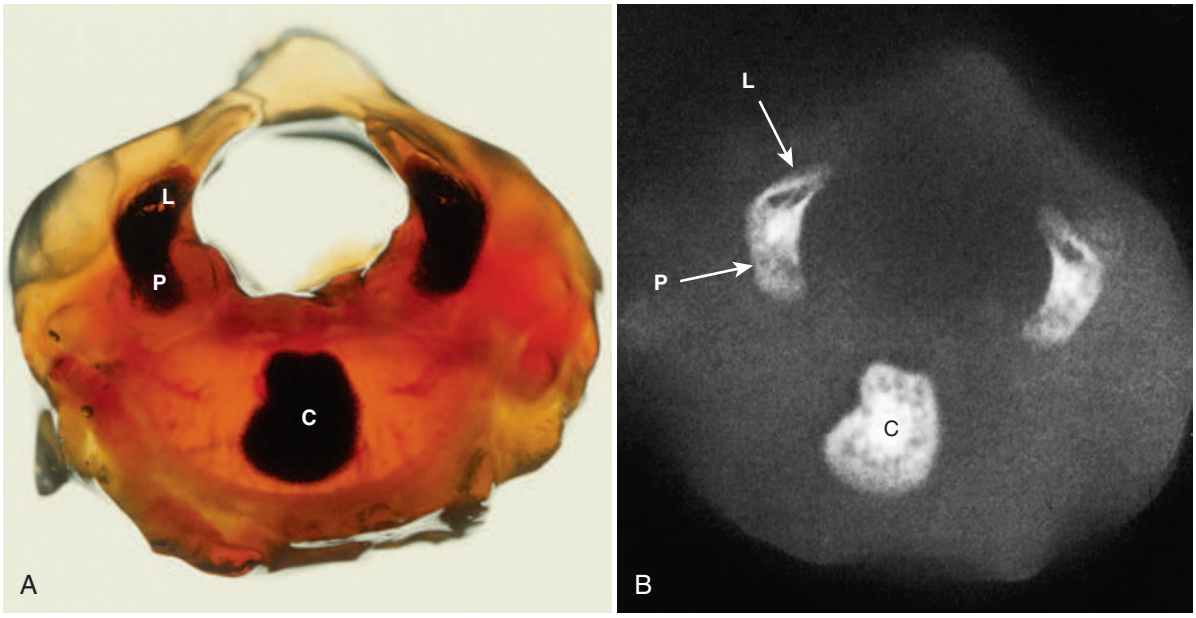

FIG. 35.5 Vertebral Ossification of L5 at 17 Weeks' Gestation. (A) Specimen. **(B)** Radiograph. There is usually enough ossification at this gestation in the pedicles *(P)* and laminae *(L)* to determine the true course of these structures in radiographs and sonograms. The width of the vertebra is about 5 mm. There is ossification within the centrum *(C)*.

TABLE 35.2 Timing and Pattern of Fetal Spine Ossification (10-22 Weeks' Menstrual/Gestational Age)

Age (Wk)	Events
10	Ossification appears in lower thoracic spine vertebral bodies.
13	Some ossification is present from C1 to L5 vertebral bodies and arches.
13-22	Neural arch ossification simultaneously extends anteriorly into the pedicles and posteriorly into the laminae.
16	Enough neural arch ossification appears to assess for spina bifida to level L5.
19	Enough neural arch ossification appears to assess for spina bifida to level S1.
22	Enough neural arch ossification appears to assess for spina bifida to level S2.

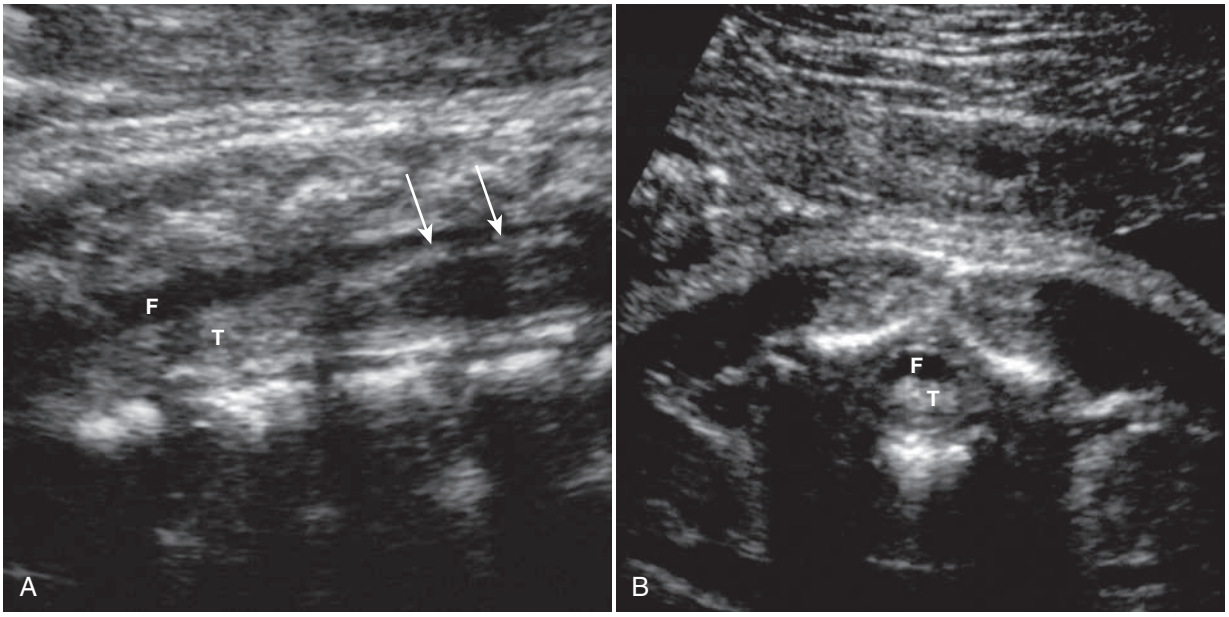

FIG. 35.6 Normal Spinal Cord. (A) Posterior longitudinal and **(B)** posterior transaxial (transverse) sonograms of a normal spinal cord. Note the normal position of the cord *(arrows)* and filum terminale *(T)* in the dependent portion of the spinal canal. Cerebrospinal fluid *(F)* is seen between the anterior aspect of the spinal cord and the anterior wall of the spinal canal.

medullaris is usually lower than normal. For earlier pregnancy (13-18 weeks' gestation), the conus medullaris may be normally as low as L4. At term, the conus is normally at or above L2.[21]

SCANNING TECHNIQUES

In clinical practice, the most useful scan planes to assess the posterior neural arches are posterior transaxial (Fig. 35.7), lateral transaxial (Fig. 35.8), lateral longitudinal (coronal) (Fig. 35.9), posterior longitudinal (sagittal) (Fig. 35.10), and posterior angled transaxial (Fig. 35.11). The posterior angled transaxial scan plane is useful to visualize the pedicles and laminae simultaneously. Because the laminae course caudal to the transaxial plane, which contains the centrum and pedicles, only the angled scan plane can depict the pedicles and laminae simultaneously in their entirety.

The detection rate of spina bifida at 18 to 20 weeks' gestation may be 80% or less during routine screening ultrasound,[22] because the accuracy of ultrasound depends on the skill and experience of the operator. The accuracy of referral centers performing detailed targeted imaging because of a suspected NTD or high **maternal serum alpha-fetoprotein** (MS-AFP) level is close to 100%.

A detailed sonogram of the fetal spine may be requested for several reasons: previous suspicious ultrasound, family history of NTD, or raised serum or amniotic fluid AFP. To enhance detection of spina bifida, a detailed protocol should be consistently followed. The first step in assessing for spina bifida is scanning the head, because most fetuses with open spina bifida have signs of a **Chiari II malformation** in the brain at 16 to 22 weeks' gestation. These signs include obliterated cisterna magna **(banana sign),** concave frontal bones **(lemon sign),** and dilated lateral cerebral ventricles.[23,24] The sensitivity of the banana sign for open spina bifida is close to 99%, and false-positive diagnoses are rare, although the lemon sign may occur in 1% to 2% of normal fetuses.

The next step is to determine the position of the fetal spine. The scan plane is placed perpendicular to the long axis of the fetal spine, either posterior transaxial or lateral transaxial (see Figs. 35.7 and 35.8). The sonographer should scan from one end of the spine to the other while maintaining the scan plane perpendicular to the spine (Video 35.1). This is repeated several times. In the process, the sonographer builds up an impression of the 3D structures of the spine. The scan plane should then be repositioned parallel to the long axis of the fetal spine to obtain posterior longitudinal and lateral longitudinal views. The sonographer then examines all levels of the spine in posterior transaxial, lateral transaxial, lateral longitudinal, and posterior longitudinal scan planes (Video 35.2). This may not be possible in a short time because of fetal position, but this usually changes enough in 30 to 45 minutes at 16 to 22 weeks to obtain all scan planes. If the spine cannot be visualized optimally, a repeat scan can be performed at a later gestational age. In both axial and longitudinal scan plans, it is important to visualize the skin covering the fetal back by ensuring that amniotic fluid is interposed between the fetus and the uterine wall.

Three-Dimensional Ultrasound

Three-dimensional ultrasound imaging has shown promise in evaluating normal fetal structures and in providing additional information in abnormalities of many fetal structures, including the spine, hand, foot, and face.[25-34] Bony structures can be visualized with maximum-intensity projection methods (see Fig. 35.9D). In evaluation of spinal abnormalities, 3D ultrasound is most

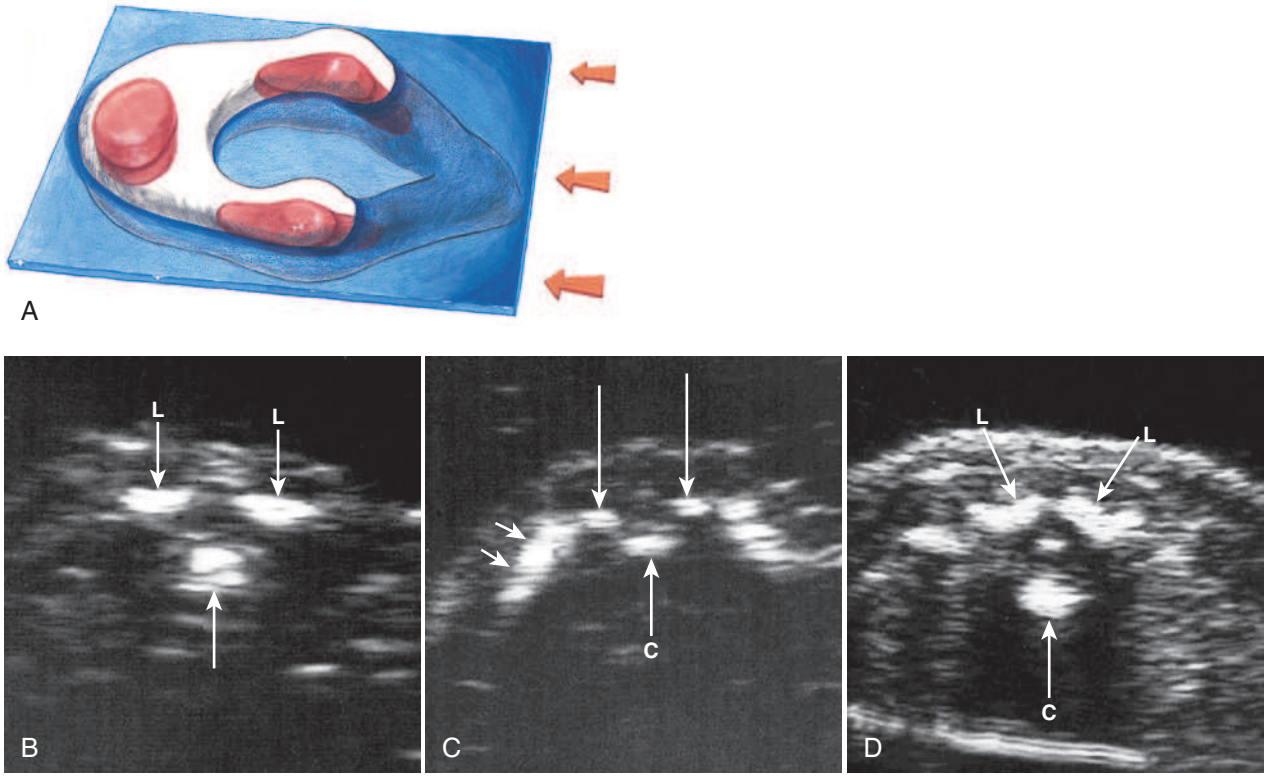

FIG. 35.7 Posterior Transaxial Scan Plane. (A) Diagram shows the incident sound beam *(arrows)* reflecting off the posterior surfaces, clearly demonstrating the **laminae** and **centrum** but not the pedicles. The red structures represent the ossified portions of the vertebra. **(B)** The L3 vertebra at 17 weeks' gestation demonstrates the ossified laminae *(L)* and the ossified centrum *(bottom arrow)* but not the pedicles. **(C)** Scan of S1 vertebra at 17 weeks shows early ossification at the lamina-pedicle junction on each side *(long thin arrows).* With this amount of ossification, determining the course of the laminae is not possible, and thus excluding spina bifida is difficult. *C,* Ossified centrum; *short arrows,* iliac wing. **(D)** Scan of T10 at 24 weeks' gestation shows advanced ossification in the laminae *(L, arrows)* almost reaching midline. Despite their advanced ossification, the pedicles are not visualized in this scan plane. *C,* Ossified centrum.

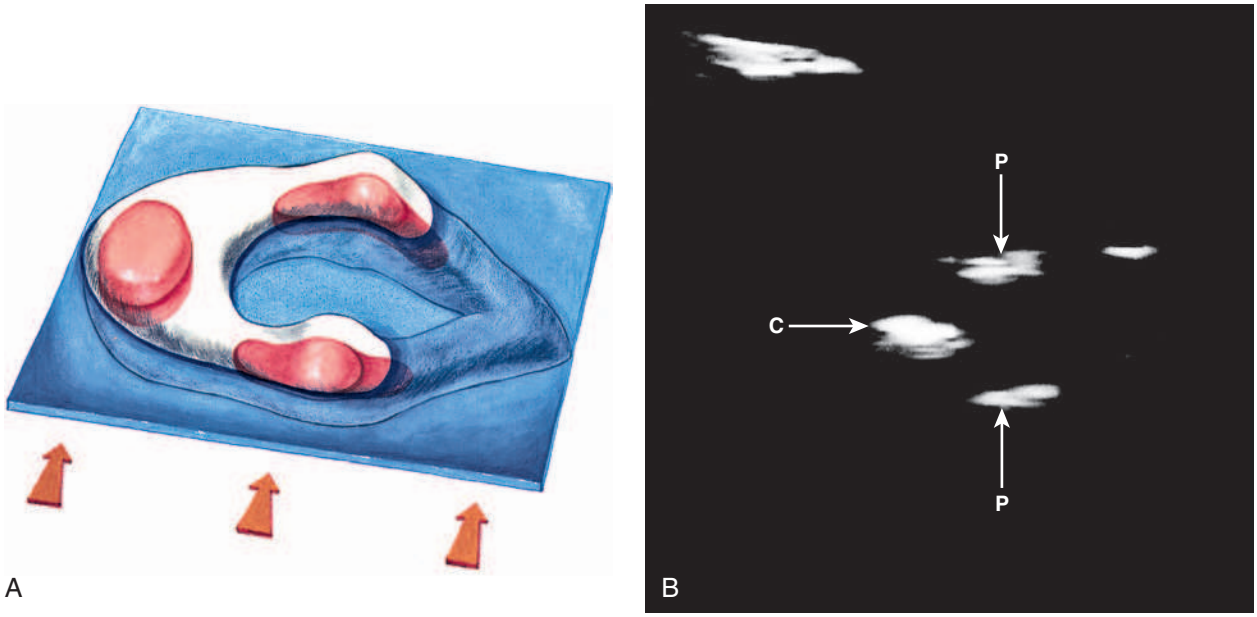

FIG. 35.8 Lateral Transaxial (Transverse) Scan Plane. (A) Diagram shows the incident sound beam *(arrows)* reflecting off the lateral surfaces of the centrum and the near pedicle and off the medial surface of the far pedicle, demonstrating the **centrum** and **pedicles,** but not the laminae. The laminae course toward midline (thus sound beam is not perpendicular to laminar surface) and caudally (thus out of the plane of sound beam). The red structures are ossified portions of the vertebra. **(B)** Scan of vertebra L3 at 17 weeks' gestation shows the ossified pedicles *(P)* and the ossified centrum *(C)* but not the laminae.

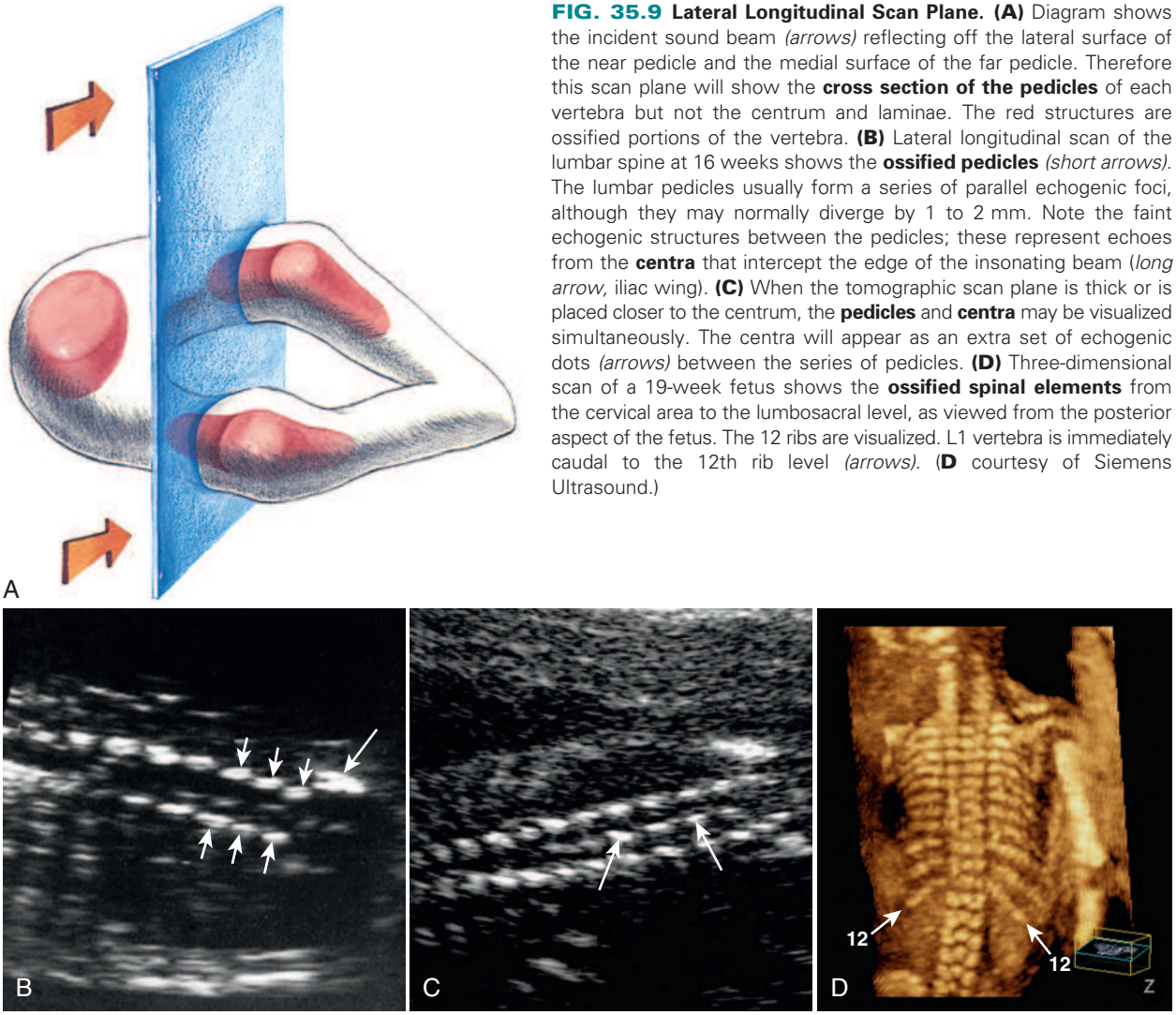

FIG. 35.9 Lateral Longitudinal Scan Plane. (A) Diagram shows the incident sound beam *(arrows)* reflecting off the lateral surface of the near pedicle and the medial surface of the far pedicle. Therefore this scan plane will show the **cross section of the pedicles** of each vertebra but not the centrum and laminae. The red structures are ossified portions of the vertebra. **(B)** Lateral longitudinal scan of the lumbar spine at 16 weeks shows the **ossified pedicles** *(short arrows).* The lumbar pedicles usually form a series of parallel echogenic foci, although they may normally diverge by 1 to 2 mm. Note the faint echogenic structures between the pedicles; these represent echoes from the **centra** that intercept the edge of the insonating beam (*long arrow,* iliac wing). **(C)** When the tomographic scan plane is thick or is placed closer to the centrum, the **pedicles** and **centra** may be visualized simultaneously. The centra will appear as an extra set of echogenic dots *(arrows)* between the series of pedicles. **(D)** Three-dimensional scan of a 19-week fetus shows the **ossified spinal elements** from the cervical area to the lumbosacral level, as viewed from the posterior aspect of the fetus. The 12 ribs are visualized. L1 vertebra is immediately caudal to the 12th rib level *(arrows).* (**D** courtesy of Siemens Ultrasound.)

helpful in localizing spinal defects accurately by using simultaneous multiplanar imaging and referencing to the volume-rendered image.[25,28] For determination of spinal level, T12 is taken to be the most caudal vertebra with a corresponding rib. Three-dimensional ultrasound may also show concomitant rib deformities in the setting of spinal abnormalities and is useful for counseling prospective parents by providing a more understandable visual demonstration of the skeletal abnormality.

SPINA BIFIDA

Spina bifida implies a physical defect in the structure of the spinal canal that may result in a protrusion of its contents (meninges, cerebrospinal fluid, and neural tissue) (Table 35.3). These defects usually occur along the dorsal midline (most often in the lumbosacral area) but in rare cases may occur anteriorly.

Open NTDs occur in less than 0.5 per 1000 births in North America and with higher frequencies in other geographic areas. Hispanic women in the United States have a higher incidence of births affected by NTDs, possibly because of a higher prevalence of a mutation in the methylenetetrahydrofolate reductase deficiency gene.[35] In one area of China, the overall prevalence of NTDs in 2003 was 13.9 per 1000 live births.[36] In recent years, however, there has been a decline in the incidence of NTDs. Some of this decline may be attributed to screening programs, which include measurement of MS-AFP and performance of second-trimester ultrasound.[37,38]

Protocol to Evaluate Spina Bifida With Three-Dimensional Volume Data

- Volume data are acquired from sagittal and transverse sweeps through the spine.
- Volume data are reformatted to display standardized multiplanar views of the fetal spine.
- Three-dimensional reconstruction of the fetal spine (with maximum-intensity projection filter) visualizes the ossified spinal elements.
- To determine spinal level, the 12th thoracic (T12) is taken to be the most caudal vertebra with a corresponding rib.

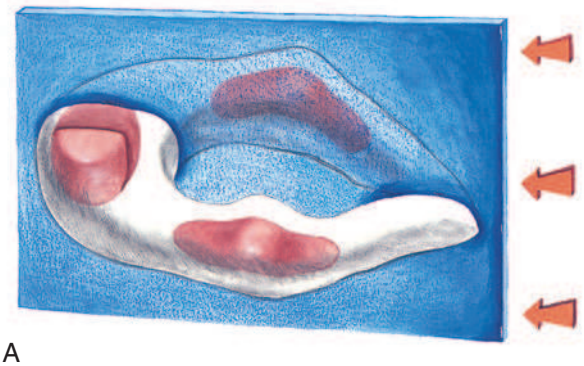

A

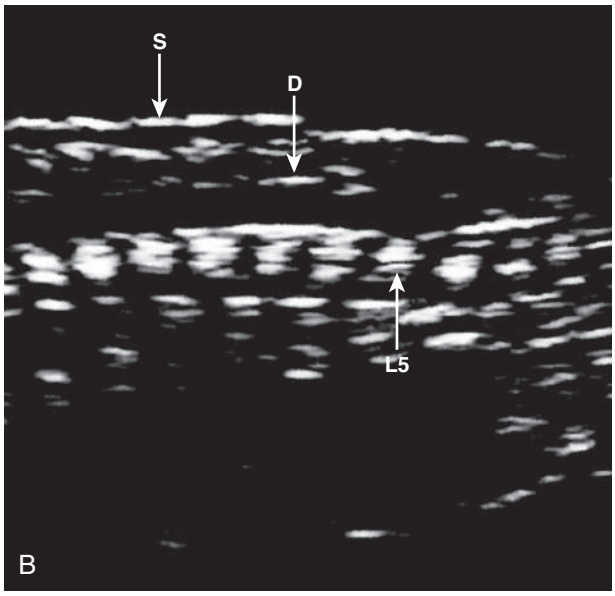

FIG. 35.10 Posterior Longitudinal Scan Plane. (A) Diagram shows the incident sound beam *(arrows)* reflecting off the posterior surface of the **centrum.** If there is no ossification in the laminae near the midline, the laminae will not be visible on the scan; only the centra will be seen. If the laminar ossification is present near the midline, the centra and laminae will be seen as echogenic foci. The red structures are ossified portions of the vertebra. **(B)** Posterior longitudinal scan of the lumbosacral spine at 15 weeks shows **ossification in the centra** of the lower thoracic, lumbar, and sacral spine (*L5,* centrum of vertebra). In this midline scan, no ossification is present posterior to the posterior surface of the dural sac *(D). S,* Skin surface.

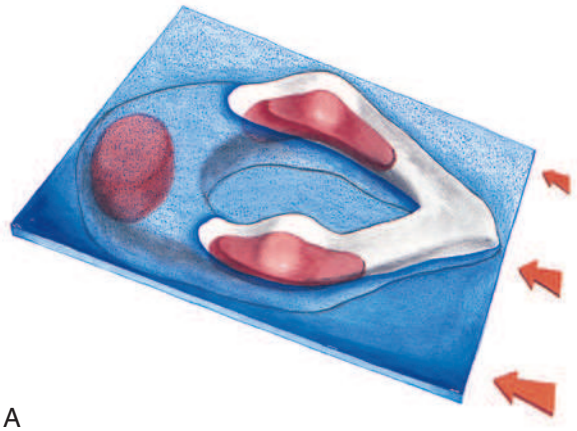

A

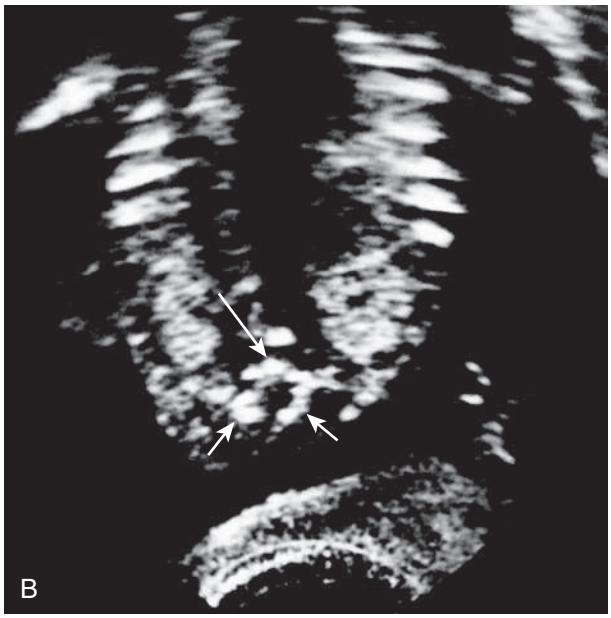

FIG. 35.11 Posterior Angled Transaxial (Transverse) Scan Plane. (A) Diagram shows the incident sound beam *(arrows)* reflecting off the posterior aspects of the **laminae** and portions of the **pedicles.** The beam may also reflect off the ossified centrum. This scan plane can depict the **entire ring of ossification** of the spinal canal. The red structures are ossified portions of the vertebra. **(B)** Endovaginal scan at 18 weeks in the midlumbar spine outlines the curvilinear structure of each neural arch (*short arrows,* lamina plus pedicle) and the ossified centrum *(long arrow).* Together these structures form the **ossified ring of the spinal canal.**

Folic Acid Fortification

Another major factor in the decline of the incidence of NTDs is the use of folic acid to prevent NTDs. Several clinical trials have demonstrated a decreased risk of NTDs by at least 60% with the maternal use of periconceptual folic acid supplements.[39-43] The reduction occurs in mothers with previously affected pregnancies and in mothers without this risk. In 1992 the U.S. Department of Health and Human Services[44] and the Expert Advisory Group in the United Kingdom[45] recommended supplementation of 0.4 mg of folic acid for women in the general population trying to conceive. Women who are at high risk because of a previously affected fetus should take 4 mg of folic acid daily.[1] Routine folic acid supplementation around the time of conception confers a 72% to 87% decrease in probability of NTDs.[3,40] However, this knowledge and these recommendations have not translated into a reduction of the incidence of NTDs in the general population,[46,47] largely because only a minority take folic acid routinely in the reproductive years, and in those who do, supplementation may not be taken at the proper time. Studies in the 1990s demonstrated that less than 45% of pregnant women took folic acid before conception.[48-50] In 2007, 40% of all U.S. women of reproductive age (15-45 years) took daily supplements of folic acid. Daily supplements could be one serving of breakfast cereal fortified with 100% of the recommended daily value of folic acid or a supplement with 0.4 mg of folic acid daily.[4]

Another strategy to increase folic acid levels is the systematic fortification of food stuffs with folic acid. In March 1996 the

TABLE 35.3 Definition of Terms for Spinal Abnormalities

Term	Definition	Comment
Spinal dysraphism (neural tube defect)	Failure of part of neural tube to close.	This disrupts both differentiation of central nervous system and induction of vertebral arches.
Spina bifida	Defect in posterior midline neural arch.	Arches fail to fuse along dorsal midline and fail to enclose vertebral canal.
Spina bifida occulta	Vertebral arches of a single vertebra fail to fuse.	Underlying neural tube differentiates normally; does not protrude from vertebral canal.
Meningocele	Dura and arachnoid protrude from vertebral canal through spina bifida defect in posterior midline neural arches.	
Myelomeningocele	Dura, arachnoid, and neural tissue protrude from vertebral canal through spina bifida defect in posterior midline neural arches.	
Rachischisis (e.g., myeloschisis)	Neural folds corresponding to future spinal cord fail to fuse and fail to differentiate (myeloschisis), invaginate, and separate from surface ectoderm.	The deformed underdeveloped spinal cord is exposed dorsally. This is the most severe form of spinal neural tube defect.
Cranioschisis (e.g., exencephaly, anencephaly)	Neural folds corresponding to future brain fail to fuse and fail to differentiate, invaginate (exencephaly, anencephaly), and separate from surface ectoderm.	The brain is represented by an exposed dorsal mass of undifferentiated neural tissue.
Inionschisis	Failure of neural tube to differentiate properly and close in occipital and upper spinal region.	

U.S. Food and Drug Administration ordered that fortification with folate of all enriched grain products be started no later than January 1, 1998 (0.14 mg per 100 g of grain). Honein et al.[51] demonstrated a 19% reduction in NTDs in the United States as an effect of folic acid fortification of grains. This study did not take into account the large percentage of NTDs that are prenatally diagnosed and electively terminated. A study in Nova Scotia demonstrated a decrease of annual incidence of NTDs by 54% after implementation of folic acid fortification, from 2.58 in 1000 births from 1991 to 1997 to 1.17 in 1000 births from 1998 to 2000.[52] This study included terminated pregnancies, which is important because more than 50% of all pregnancies affected with NTDs in Nova Scotia resulted in elective termination. A failure to include these terminated pregnancies may underestimate the benefit of folic acid–fortified grains. In Canada, folic acid fortification of grain products was legislated to begin in November 1998, at levels similar to U.S. levels. Since then in Canada, the prevalence of NTDs nationally has decreased from 1.58 in 1000 births before fortification to 0.86 in 1000 births during the full-fortification period, a 46% reduction.[7] Geographic differences almost disappeared after fortification began. The observed reduction rate was greater for spina bifida (53%) than for anencephaly and encephalocele (38% and 31%, respectively).

Lipomyelomeningocele (LMMC) is a type of NTD similar to myelomeningocele, with a prevalence of about 0.5 in 10,000 births. Studies in Hawaii and Canada have shown that LMMC rates are not affected by folic acid fortification, unlike the significant rate reduction in myelomeningoceles. LMMC seems to be pathogenetically distinct from myelomengocele.[53,54]

The risk of NTD rises to 20 to 30 per 1000 live births for women with a previous infant with an NTD. This constitutes about a 10-fold increase in risk over the general population.[55] A meta-analysis of randomized trials of folic acid for the prevention of recurrent NTDs demonstrated an 87% reduction in NTDs in women who took supplements before the start of pregnancy.[3] Other factors that increase the risk of NTD include anticonvulsant therapy with valproic acid or carbamazepine (10-20:1000), warfarin and vitamin A use, pregestational diabetes, obesity, parent with spina bifida (11:1000), and sibling of fetus with multiple vertebral defects and scoliosis (15-30:1000).[56] Low maternal vitamin B12 status may also be a risk factor for NTDs. In Ontario, Ray et al.[57] demonstrated a tripling of the risk for NTD in the presence of low maternal B12 status, as measured by serum holotranscobalamin at 15 to 20 weeks' gestation.

Risk Factors for Neural Tube Defect (NTD)

- Folic acid deficiency
- Previous sibling with NTD
- Maternal anticonvulsants
  - Valproic acid
  - Carbamazepine
- Maternal warfarin
- Maternal vitamin A
- Pregestational diabetes
- Obesity
- Parent with spina bifida
- Low maternal vitamin B12

Pathogenesis and Pathology

Most cases of spina bifida result from failure of closure of the embryologic neural tube, although some may be caused by rupture of the neural tube after primary closure. Most NTDs occur as isolated malformations in chromosomally normal individuals, although 9% to 17% of fetuses with spina bifida have chromosomal abnormalities (mostly trisomy 18 and trisomy 13).[58,59] Typically, chromosomally abnormal fetuses have other abnormalities detected by sonography in addition to the spinal abnormality. Some NTDs are part of a genetic condition. Autosomal dominant conditions include **Lehman syndrome.** Autosomal recessive conditions include **Meckel-Gruber syndrome** and **VATER syndrome** (vertebral defect, imperforate anus, tracheoesophageal fistula, radial and renal dysplasia). Two X-linked conditions are the **Mathias laterality sequence** and **X-linked neural tube defects.**[2]

A number of studies have found the incidence of NTD to be about 10 times higher in spontaneously aborted pregnancies than in term births, indicating an in utero selection against embryos with such defects.[60]

In the most severe form of NTD, the embryologic neural tube (the precursor to the spinal cord) remains open in addition to the overlying mesodermal structures, which include the neural arch, muscles, and skin. The resultant pathology is **myeloschisis;** the open, flattened spinal cord is exposed posteriorly through a wide defect in the posterior neural arch and associated musculature and skin.

In less severe cases of NTD, the major anatomic defect is in the structures derived from the mesodermal tissues overlying the embryologic neural tube. Although the spinal cord often is anatomically intact, the embryologic neural tube has failed to induce closure of the overlying neural arches, muscles, and skin. The result is a **myelomeningocele,** a cystic mass protruding from the spinal canal. The cystic mass wall is composed of thin arachnoid membrane without skin covering, and the contents are cerebrospinal fluid and neural elements. Occasionally, a myelomeningocele is covered with skin. A skin-covered myelomeningocele is considered a **closed defect,** and a myelomeningocele without skin covering is considered an **open defect.** An open defect allows AFP to escape into the surrounding amniotic fluid; a closed defect does not. Thus a closed or skin-covered defect is not usually associated with raised levels of AFP in the amniotic fluid or maternal serum. Infrequently, the protruding cystic mass contains only cerebrospinal fluid and no neural elements, a **meningocele.**

Spina bifida occulta is restricted to involvement of the mesoderm of the posterior vertebral arch and rarely exhibits intrinsic maldevelopment of the spinal cord. This may result from an insult occurring at the end of the fourth embryologic week (sixth menstrual week), causing failure of complete formation of the posterior midline structures. The prevalence of spina bifida occulta, excluding cases that later disappear (i.e., delayed ossification of preexisting intact cartilage), is approximately 17%.[61] The lumbosacral spine is most often involved. About 66% of spina bifida occulta cases have skin manifestations: nevi, lumbosacral lipomas, dermal sinus, hypertrichosis (tuft of hair, "horse's tail or fawn's tail"), or scarred area. A sacral pit or dimple is not highly correlated with spina bifida occulta. Although infrequently associated with other abnormalities, spina bifida occulta may be associated with urologic dysfunction and tethered cord syndrome, foot deformity, increased incidence of spondylolisthesis, and intervertebral disc herniation. Spina bifida occulta is difficult to detect with prenatal ultrasound unless it is associated with a **lipoma,** a simple **meningocele,** or **tethered cord.** A history of familial spina bifida occulta is not known to be a risk factor for an open NTD.[2]

Alpha-Fetoprotein and Ultrasound Screening

Because most NTDs occur in families with no history of such abnormalities, prenatal detection relies on routine screening measures, including ultrasound and MS-AFP measurement.

Alpha-fetoprotein is a glycoprotein (molecular weight 70,000) produced by fetal liver. Some of it enters the amniotic fluid through fetal urine, and a small amount crosses the placenta to maternal serum. Normal AFP levels in amniotic fluid and maternal serum vary with gestational age. MS-AFP and amniotic fluid AFP are elevated in NTDs that are not skin covered. If the upper limit of normal MS-AFP is taken to be 2.5 multiples of the median (MOM) for a given gestational age, MS-AFP will be elevated in approximately 90% of open NTDs. About 2% of normal pregnancies have an elevated MS-AFP; that is, of all the elevated test results for MS-AFP, most fetuses will be normal (Fig. 35.12). At this stage, a detailed ultrasound examination is required to determine which fetuses actually have an NTD.

Causes of Elevated Maternal Serum Alpha-Fetoprotein

- Multifetal pregnancy
- Fetal death
- Fetomaternal transfusion
- Omphalocele and gastroschisis
- Congenital nephrosis
- Esophageal or duodenal atresia
- Polycystic kidney disease
- Renal agenesis
- Urinary obstruction
- Epidermolysis bullosa
- Sacrococcygeal teratoma
- Cystic hygroma
- Osteogenesis imperfect
- Cloacal exstrophy
- Cyclopia
- Normal (2% of pregnancies)

Norem at al.[62] found that MS-AFP testing was normal in 25% of NTDs (25 of 102 cases). These included 15 of the 40 (38%) spina bifida cases screened, 6 of the 9 (67%) encephalocele cases screened, and 4 of the 53 (8%) anencephaly cases screened. Of the 186 NTD cases diagnosed prenatally, 115 (62%) were initially

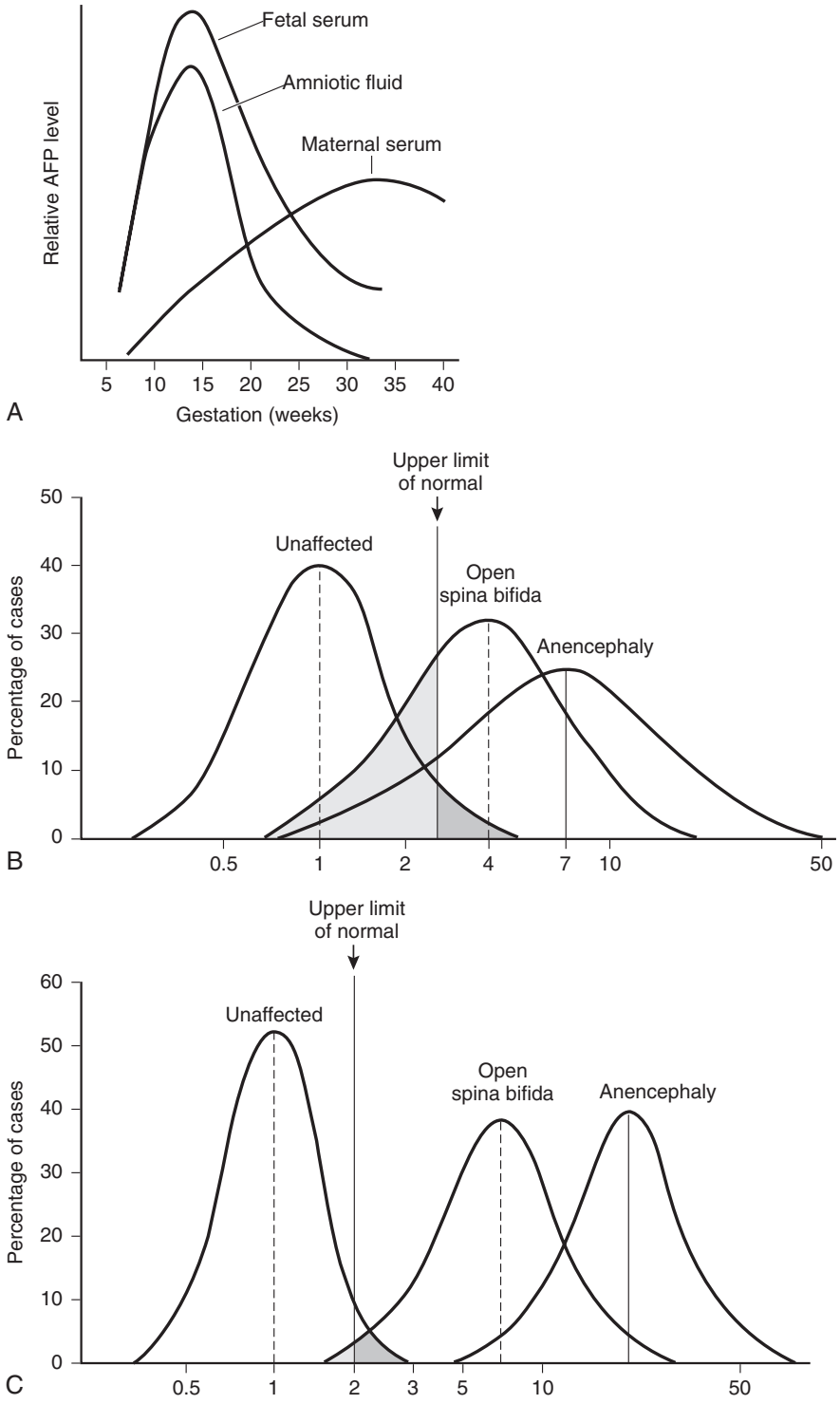

FIG. 35.12 Alpha-Fetoprotein Levels Versus Gestational (Menstrual) Age. (A) Normal alpha-fetoprotein (AFP) levels in fetal serum, amniotic fluid, and maternal serum (MS) vary with gestational age. It is imperative to have accurate dating to evaluate AFP results properly. **(B)** MS-AFP at 16 to 18 weeks' gestation. (Percentage of cases vs. AFP levels, expressed as multiples of the median [MOM] along horizontal axis.) There is considerable overlap in the values of MS-AFP between normal pregnancies and those with fetuses affected with open spina bifida and anencephaly. This illustration demonstrates the overlap (*shaded areas* under the curves) when 2.5 MOM are taken to be upper normal. A cutoff of 2.0 MOM would detect more affected pregnancies but increase the rate of false positives and possible amniocentesis in normal pregnancies. *Lighter-shaded area,* False negatives (i.e., test negative, but NTD present); *darker-shaded area,* false positives (i.e., test positive, but fetus normal). **(C)** Amniotic fluid AFP at 16 to 18 weeks' gestation. (Percentage of cases vs. AFP levels, expressed as MOM along horizontal axis.) There is significantly less overlap between normal pregnancies and pregnancies with open NTDs. The shaded area under the curves to the left of 2 represents the false negatives, and the shaded area to the right of 2 represents the false positives. In practice, the false positives can be largely excluded by normal acetylcholinesterase levels in the amniotic fluid.

detected by routine sonography during the second trimester without knowledge of MS-AFP values. Sixty-nine (37%) were diagnosed by targeted sonography after MS-AFP screening indicated a higher risk for NTD. Two (1%) were diagnosed by pathology examination after miscarriage.

MS-AFP is also elevated in **multifetal pregnancy, fetal death, fetomaternal transfusion,** and in other fetal anomalies associated with a defect in the skin, such as **omphalocele** and **gastroschisis** (50%-60% of cases), **congenital nephrosis** (Finnish type, 100% of cases), and infrequently in esophageal or duodenal atresia, polycystic kidney disease, renal agenesis, urinary obstruction, epidermolysis bullosa, sacrococcygeal teratoma, cystic hygroma, osteogenesis imperfecta, cloacal exstrophy, and cyclopia.

Because of the high sensitivity of the cerebellar signs associated with open spina bifida, some centers rely almost exclusively on ultrasound to diagnose NTDs. For women with elevated MS-AFP and no sonographic explanation for the abnormal test result (e.g., wrong dates, multiple fetuses, dead fetus, anencephaly, spina bifida, abdominal wall defect, other fetal abnormality causing elevated AFP), or when there is poor visualization of the spine, **amniocentesis** may be offered. If the amniotic fluid AFP is normal and there is no **acetylcholinesterase** (AChE) present, the likelihood of an open NTD is very low. If the amniotic fluid AFP is elevated and AChE is present, an open NTD or abdominal wall defect may be present but undetected by sonography.

Between 1989 and 1990, 1.1 million women in California had MS-AFP tests in early pregnancy.[63] From these tests, 1390 fetal abnormalities were found (1.3 fetal anomalies per 1000 pregnancies), consisting of 710 NTDs (417 cases of anencephaly, 247 cases of spina bifida, and 46 cases of encephalocele) and 680 nonneural abnormalities (286 anterior abdominal wall defects, 163 cases of trisomy 21, and 231 other chromosomal abnormalities). With the declining use of MS-AFP testing in favor of genetic screening, sonography is increasingly important in screening for NTDs.

Sonographic Findings in the Spine

Spina bifida may occur anywhere in the fetal spine but is most common in the **lumbosacral** area.[64] Ultrasound findings in the spine consist of abnormalities of the ossified posterior elements and related soft tissues.

In spina bifida the **laminae** fail to converge toward midline, and this is best visualized with the posterior transaxial scan plane (Fig. 35.13A and B, Video 35.3). If the **pedicles** are normally positioned and there is no myelomeningocele, the posterior transaxial scan plane is the only view that will depict the abnormality with reliability. When the pedicles are displaced more laterally than usual, the lateral transaxial and lateral longitudinal scan planes will also demonstrate the bony abnormalities of spina bifida (Fig. 35.13C and D). All these scan planes will usually demonstrate the meningocele or myelomeningocele if it is present (Figs. 35.14, 35.15, and 35.16; Videos 35.4 and 35.5). The posterior longitudinal scan best demonstrates a myelomeningocele and the soft tissue defect when no cystic mass is present.

In most cases of spina bifida, there is abnormal divergence or splaying of the pedicles over several vertebral levels. This is best appreciated in 3D images and in lateral longitudinal views, where multiple interpedicular distances can be evaluated simultaneously (see Fig. 35.13). However, there is normally mild divergence of the pedicles in the cervical spine compared with the thoracic spine, and there may be slight divergence (by 1 to 2 mm) in the lumbar spine compared with the thoracic spine in normal fetuses (see Fig. 35.2).

Sonography can also be used to determine the level and extent of the spinal abnormality. The level of the defect is taken to be the top or most cephalic end of the bone malformation.[65] Fetal MRI and fetal ultrasound are equally effective in determining the lesion level in a fetus with myelomeningocele,[66] although each modality may misdiagnose the upper level by two or more segments in 20% of cases. Fetal MRI is more sensitive in evaluation of the spinal cord itself, yielding additional information in about 10% of cases.[67]

The prognosis is influenced by the defect level, the NTD type, the presence or absence of associated anomalies, the presence or absence of chromosomal abnormalities, and the presence or absence of cranial abnormalities, such as Chiari II malformation and ventriculomegaly. Biggio et al.[68] described the outcome in 33 infants with isolated open spina bifida. Lower lesion levels and smaller ventricular size were associated with ambulatory status. All infants with L4-sacral NTD were ambulatory. Of patients with L1-L3 NTD, 50% were ambulatory. No infant with thoracic NTD was ambulatory. No infant with myeloschisis was ambulatory.

Associated Cranial Abnormalities

The biparietal diameter may be less than expected (even when the lateral ventricles are enlarged).[69,70] Four other cranial findings are particularly useful in raising suspicion of an NTD: nonvisualization of the cisterna magna, deformation of the cerebellar shape (banana sign), concave frontal bones (lemon sign), and dilation of the lateral cerebral ventricles.

Chiari II malformation is highly associated with open spina bifida (>97% of cases). This cranial lesion consists of variable degrees of displacement of the cerebellar vermis, fourth ventricle, and medulla oblongata through the foramen magnum into the upper cervical canal and is usually easier to identify than the spinal lesion between 16 and 24 weeks' gestation. In transaxial scans through the posterior fossa, Chiari II malformation is manifest as a deformation of the cerebellar shape (banana sign) and nonvisualization of the cisterna magna. Cranial malformations may signal the sonographer that a detailed study of the spine is required to search for spina bifida.

Anatomic Landmarks Used to Establish Level of Bony Defect

- T12 corresponds to the medial ends of the most caudal ribs.
- L5-S1 lies at the superior margin of the iliac wing.[28]
- S4 is the most caudal vertebral body ossification center in the second trimester.[65]
- S5 is the most caudal vertebral body ossification center in the third trimester.[65]

Thoracic *(T),* lumbar *(L),* and sacral *(S)* vertebrae.

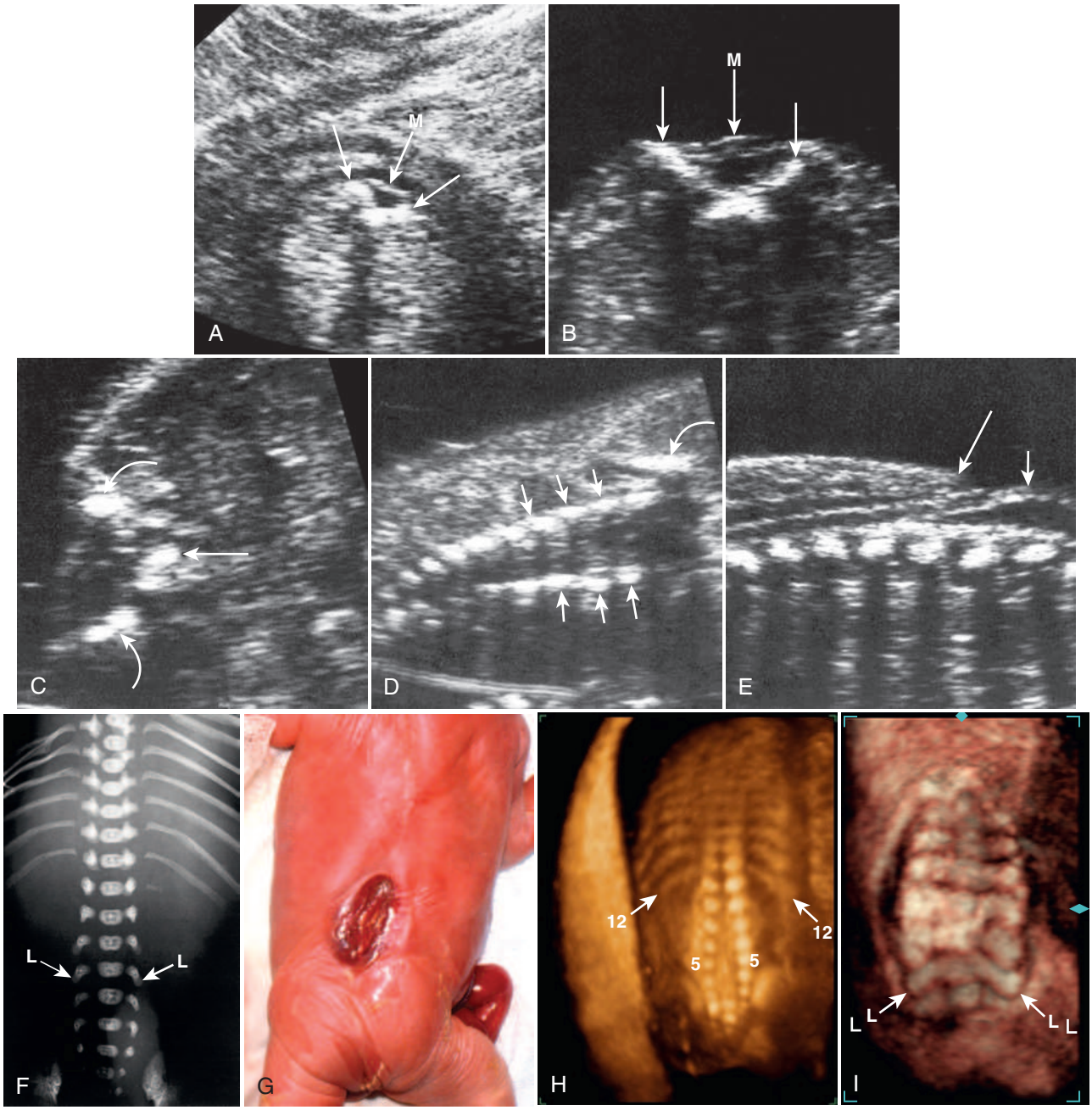

FIG. 35.13 Myeloschisis. (A) Posterior transaxial scan shows splaying of the lumbar laminae *(arrows)* away from midline. Only a thin membrane *(M)* overlies the spinal defect posteriorly. **(B)** Posterior transaxial scan of the specimen after delivery shows in more detail the splaying of the laminae *(arrows)* away from midline and the membrane *(M)* covering the defect. **(C)** Lateral transaxial scan of specimen shows increased distance between the pedicles *(curved arrows)* and mild lateral angulation of the pedicles away from their expected positions (*straight arrow,* ossified centrum). **(D)** Lateral longitudinal scan of specimen shows the progressive enlargement of the interpedicular distances in the lumbar spine, indicative of spina bifida. Ossified pedicles *(straight arrows);* iliac wing *(curved arrow).* **(E)** Posterior longitudinal scan of specimen shows abrupt truncation of the soft tissues of the fetal back *(long arrow)* at the site of the open neural tube defect; *short arrow,* spinal cord. **(F)** Radiograph of specimen shows divergence of the laminae *(L)* away from midline instead of the normal course, which is toward midline. **(G)** Photograph of myeloschisis defect of the thoracolumbar spine shows exposed, disorganized neural tissue within the defect. **(H)** Three-dimensional scan of another fetus at 19 weeks, as viewed from the posterior aspect of the fetus. Note the abnormal divergence of the pedicles in the lumbar spine (*arrows,* 12th rib level; *5,* level L5). **(I)** Three-dimensional scan of a different fetus at 21 weeks, as viewed from the posterior aspect of the fetus. Note the divergence of the lumbar pedicles and the splaying of the laminae *(L)* away from the midline. (**I** courtesy of Siemens Ultrasound.)

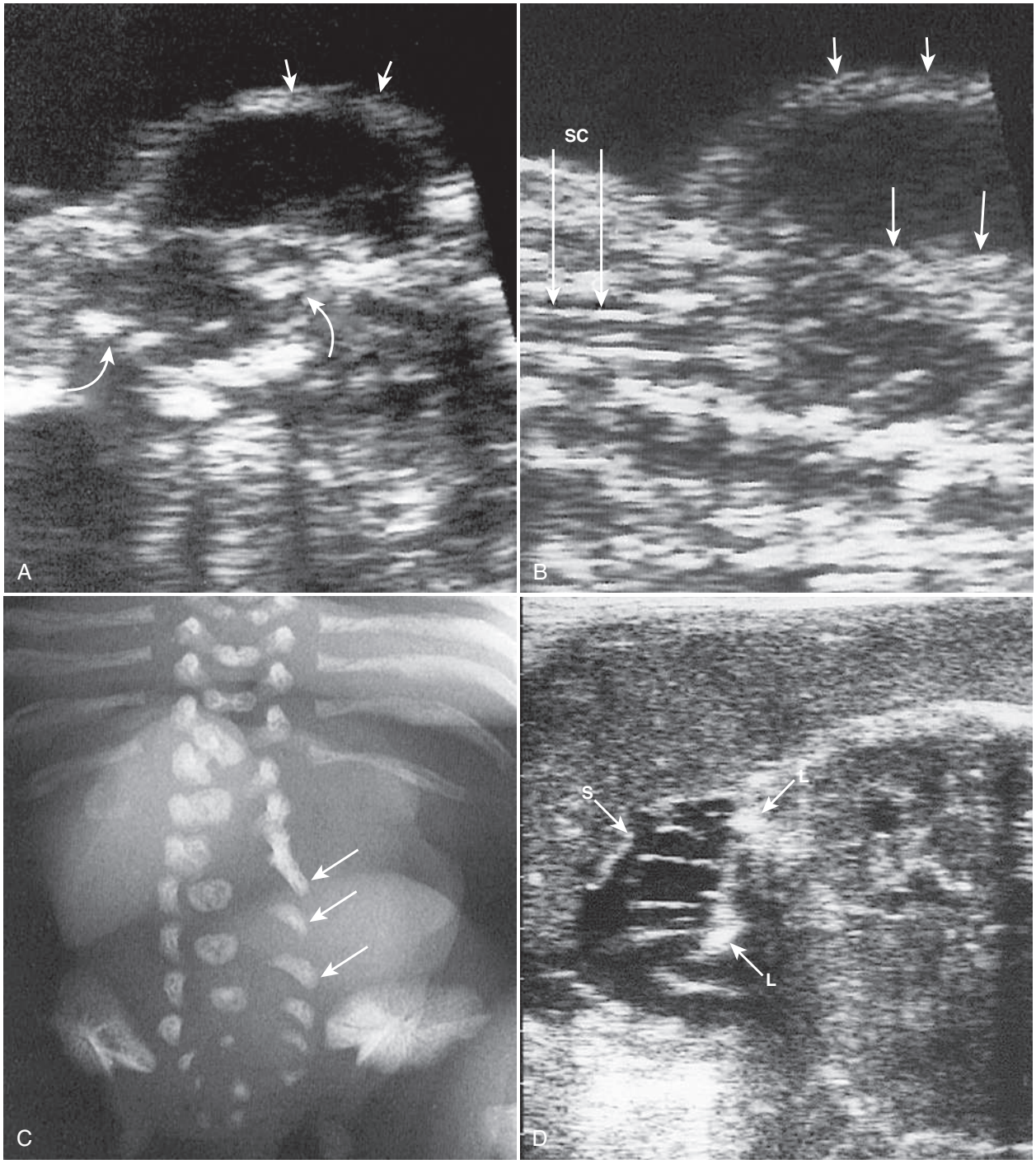

FIG. 35.14 Spina Bifida With Myelomeningocele, 17 Weeks' Gestation Specimen. (A) Posterior transaxial scan of the midlumbar spine shows the splaying of the laminae *(curved arrows)* and the myelomeningocele sac *(short arrows)*. **(B)** Posterior longitudinal scan of the thoracolumbar area shows the myelomeningocele sac *(short arrows)* and disorganized neural tissue *(long arrows)* within it; *SC,* spinal cord. **(C)** Radiograph shows the interpedicular distances in the lumbar spine are widened and the laminae are splayed laterally *(arrows)*. **(D)** Lateral transaxial scan in a different fetus shows the myelomeningocele sac *(S)* containing linear echoes representing neural tissue and the splayed laminae/pedicles complex *(L, arrows)*.

Spinal dysraphism allows a leak of cerebrospinal fluid from the spinal canal into the amniotic fluid, which causes low intracranial pressure early in pregnancy. Low intracranial pressure induces a smaller-than-normal posterior fossa compartment. The cerebellum then grows into this abnormally small space, which leads to obliteration of the cisterna magna, compression of the cerebellar hemispheres, herniation of the cerebellar tonsils into the cervical spinal canal, and related abnormalities such as **ventriculomegaly.** Ventriculomegaly is usually mild in the second trimester and worsens postpartum after repair of the spinal defect. Ventriculomegaly is seen in 44% to 86% of fetuses with spina bifida.[71,72] The most common single cause of ventriculomegaly is

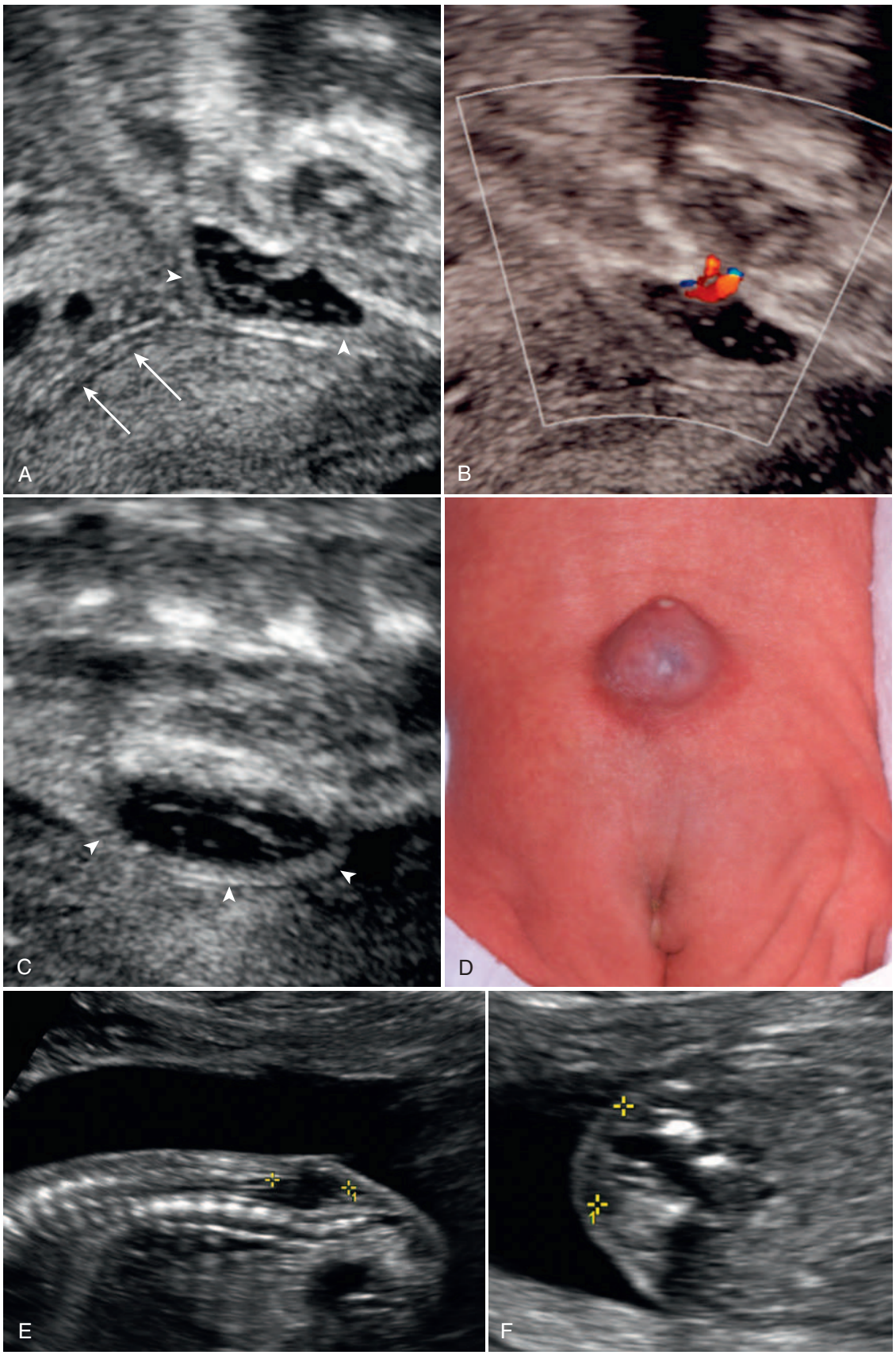

FIG. 35.15 Skin-Covered Myelomeningocele. (A) Endovaginal posterior transaxial scan shows a myelomeningocele sac covered by a thick wall *(arrowheads).* Echogenic material passes through the spina bifida defect into the myelomeningocele sac. Endocervical canal *(arrows).* **(B)** Endovaginal color Doppler posterior transaxial scan demonstrates a blood vessel protruding from the spinal canal into the myelomeningocele sac. **(C)** Endovaginal posterior longitudinal scan shows the myelomeningocele sac covered by a thick wall *(arrowheads).* **(D)** Neonatal picture shows the focal skin-covered lumbar myelomeningocele. The bluish tinge within the sac is a blood vessel detected by endovaginal color Doppler in **B. (E)** and **(F)** Longitudinal and posterior transaxial scans of a different fetus at 19 weeks' gestational age demonstrate a small posterior cyst containing neural elements *(calipers)* covered by skin protruding through the splayed laminae. No intracranial abnormalities were demonstrated.

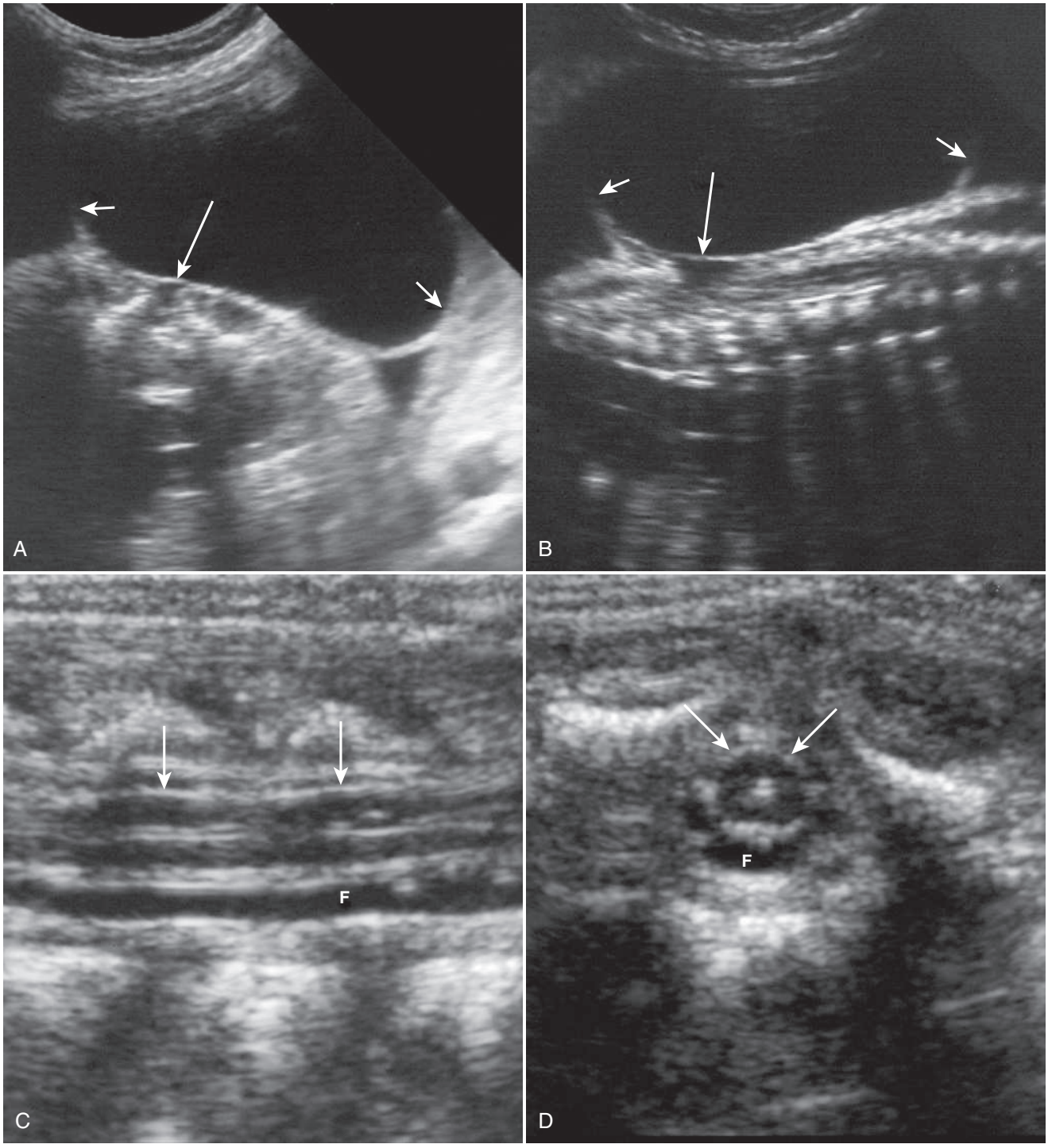

FIG. 35.16 Lumbar Meningocele, 34 Weeks' Gestation. (A) Posterior transaxial sonogram demonstrates a fluid-filled sac *(short arrows)* along the fetal back. There is a small defect in the neural arch *(long arrow)*. **(B)** Posterior longitudinal sonogram shows the wall of the meningocele *(short arrows)* and the focal spina bifida defect in the posterior neural arch *(long arrow)*. **(C)** Posterior longitudinal and **(D)** posterior transaxial sonograms demonstrate abnormally posterior thoracic spinal cord *(arrows)* in the nondependent portion of the spinal canal. Cerebrospinal fluid *(F)* is between the anterior aspect of the spinal cord and the anterior wall of the spinal canal.

spina bifida, although only 30% to 40% of fetuses with enlarged ventricles actually have spina bifida. On ultrasound, the Chiari II malformation manifests as obliteration of the cisterna magna.[73,74] The compression of the cerebellum changes its shape, giving the **banana sign.**[71,75] In two different series, obliteration of the cisterna magna was noted in 22 of 23 cases with spina bifida at 16 to 27 weeks' gestation[74] and in 18 of 20 cases at 24 weeks and earlier.[74]

Concave deformity of the fetal frontal bones in the second trimester is called the **lemon sign.**[76] Various authors have shown that 85% of fetuses with spina bifida before 24 weeks' gestation have the lemon sign.[72,77-79] In practice, the lemon sign can be

difficult to portray unequivocally. The lemon sign spontaneously resolves in the third trimester.[78] In addition, it is seen in 1% of normal fetuses.[77,78] The lemon sign should prompt detailed examination of the posterior fossa, to search for obliteration of the cisterna magna and for the banana sign, and the fetal spine, for direct evidence of spina bifida.

Associated Noncranial Abnormalities

Foot deformities, primarily **clubfoot,** and **dislocation of the hips** are frequently associated with spina bifida.[80] These abnormalities are caused by imbalanced muscular actions resulting from peripheral nerve involvement with the NTD. In fetuses with open spina bifida, 24% demonstrate additional morphologic abnormalities on second-trimester sonography, such as renal abnormalities, **choroid plexus cysts, cardiac ventricular septal defect, omphalocele,** and **intrauterine growth restriction.**[58]

Sonographic Signs of Spina Bifida

Nonvisualization of cisterna magna
Deformation of cerebellum (banana sign)
Concave frontal bones (lemon sign)
Dilation of the lateral ventricles
Chiari II malformation (97%)
Biparietal diameter lower than expected

Prognosis

It is difficult to predict the long-term prognosis in a fetus with an identified myelomeningocele. However, the outcome is better for low lesions (lower lumbar or sacral), closed defects, and those with minimal or no hydrocephalus and no compression of the hindbrain from Chiari II malformation.[55,66,75,81] In more than 880 patients[82] of live deliveries with spina bifida, about 85% survived past age 10, and 2% died in the neonatal period. Of the survivors, about 50% had some type of learning disability. About 25% of survivors had an intelligence quotient (IQ) above 100, with about 75% above 80. About 33% of survivors developed symptoms and signs related to pressure on the hindbrain and brainstem (e.g., pain, weakness, and spasticity in arms), and some required cervical laminectomy to relieve the pressure. Wong and Paulozzi[83] found 5-year survival rates of 82.7% for 1979-1983, 88.5% for 1984-1988, and 91.0% for 1989-1994. Determining prognosis for survival for current newborns is more difficult because of medical and surgical advances since studies describing patients born in the 1960s, 1970s, and 1980s.[2]

Beyond survival, multiple impairments may affect the individual, including **motor dysfunction, bladder and bowel dysfunction,** and **intellectual impairment.**[2] Degree of muscle dysfunction is defined by the highest level of the open NTD, not by the number of involved vertebrae or the size of the overlying sac. When the lesion is thoracic, the **legs** are without muscle function, and when it is upper lumbar (L1-L2), useful leg function is minimal. When the upper level is L3-L5, the prognosis for long-term walking and the need for assistive devices are difficult to predict. Those with sacral defects will usually be able to walk well but with imperfect gait. Almost all people with spina bifida, including those with sacral defects, will have some degree of bowel and bladder dysfunction.

It is very difficult to predict the ultimate level of **intellectual functioning.** In general, those who do not require ventricular shunting have much better outcomes for intellectual functioning. In those requiring shunts, the average IQ is approximately 80, which is low-normal range.[84] The rate of profound intellectual impairment (IQ < 20) in those with shunts is 5%, usually related to medical complications such as shunt infections and Chiari II effects (e.g., apnea, hypoxia).

Fetal Surgery for Myelomeningocele

The first fetal surgery for repair of myelomeningocele was performed in 1997. A formal clinical trial was performed from 2003 to 2010, with early termination of the study due to positive fetal results (decreased hindbrain herniation/need for shunt and improved spinal level of function). However, families and clinicians must evaluate the potential for improved function for the child against the risks of fetal/maternal surgical morbidity, most commonly preterm delivery and uterine dehiscence.[85] Fetal myelomeningocele is a nonlethal entity; in utero surgery for repair of myelomeningocele is potentially lethal.[86]

Although myelomeningocele is a primary embryologic disorder, neurologic damage is also secondary to progressive in utero damage to the exposed spinal cord. The development of techniques to close open NTDs before birth has generated great interest and hope for fetal interventions and outcomes. Prior to the 2003 trial, preliminary observations from two centers suggested that improvements may occur not in spinal cord function as originally postulated[87] but in the extent of the hindbrain herniation and the frequency that shunting is required to control hydrocephalus. In a report of 25 patients who underwent intrauterine myelomeningocele repair at Vanderbilt University, no improvement in leg function resulted from the surgery, but there was a substantially reduced incidence of moderate to severe hindbrain herniation (4% vs. 50%) and a moderate reduction in the incidence of shunt-dependent hydrocephalus (58% vs. 92%).[88] The number of U.S. centers is limited to prevent the uncontrolled proliferation of new centers offering this complex multidisciplinary procedure.[89] Prospective parents electing surgery[90] should weigh the potential benefits against the potential risks.[90-93]

MYELOCYSTOCELE

Myelocystocele is an uncommon form of spinal dysraphism. There is dilation of the central canal of the spinal cord. The central canal herniates posteriorly through the spinal cord and through the posterior neural arch to form an exterior sac. There may be no associated spina bifida lesion.

The sac is composed of three layers, from inner to outer: the **hydromyelia sac,** which is lined by spinal canal ependyma; the **meningeal layer,** which is contiguous with the meninges around the spinal cord; and the **skin.** The fluid within the inner sac is continuous with the fluid of the central canal of the spinal cord; the fluid between the hydromyelia sac and the meningeal layer is continuous with the subarachnoid fluid.

Myelocystocele may occur at any level of the spine and is often associated with Chiari II malformation.[94-96] Prenatal and postnatal sonography demonstrates a "cyst within a cyst" appearance (Fig. 35.17). Splaying of the laminae and pedicles may or may not be present. The prognosis for a myelocystocele is worse than for a simple meningocele; infants with a simple meningocele may remain normal neurologically after surgical repair. The prognosis with myelocystocele is worse because there is usually some degree of associated myelodysplasia (i.e., dysplasia of spinal cord). Although neurologic function is normal in the immediate postoperative period, neurologic deficits often become apparent later in life.

A **terminal myelocystocele** occurs at the spinal cord termination. The central canal of the spinal cord herniates with overlying arachnoid and cerebrospinal fluid through a defect in posterior spinal elements and presents as a skin-covered mass along the posterior aspect of the lumbosacral area. There may be associated maldevelopment of the lower spine, pelvis, genitalia, bowel, bladder, kidneys, and abdominal wall. MRI provides the best imaging evaluation of the morphologic abnormalities after birth.[97-99]

DIASTEMATOMYELIA

Diastematomyelia, also termed **split-cord malformation,** is a partial or complete sagittal cleft in the spinal cord, the distal conus of the cord, or filum terminale. Diastematomyelia is characterized by a sagittal osseous or fibrous septum in the spinal

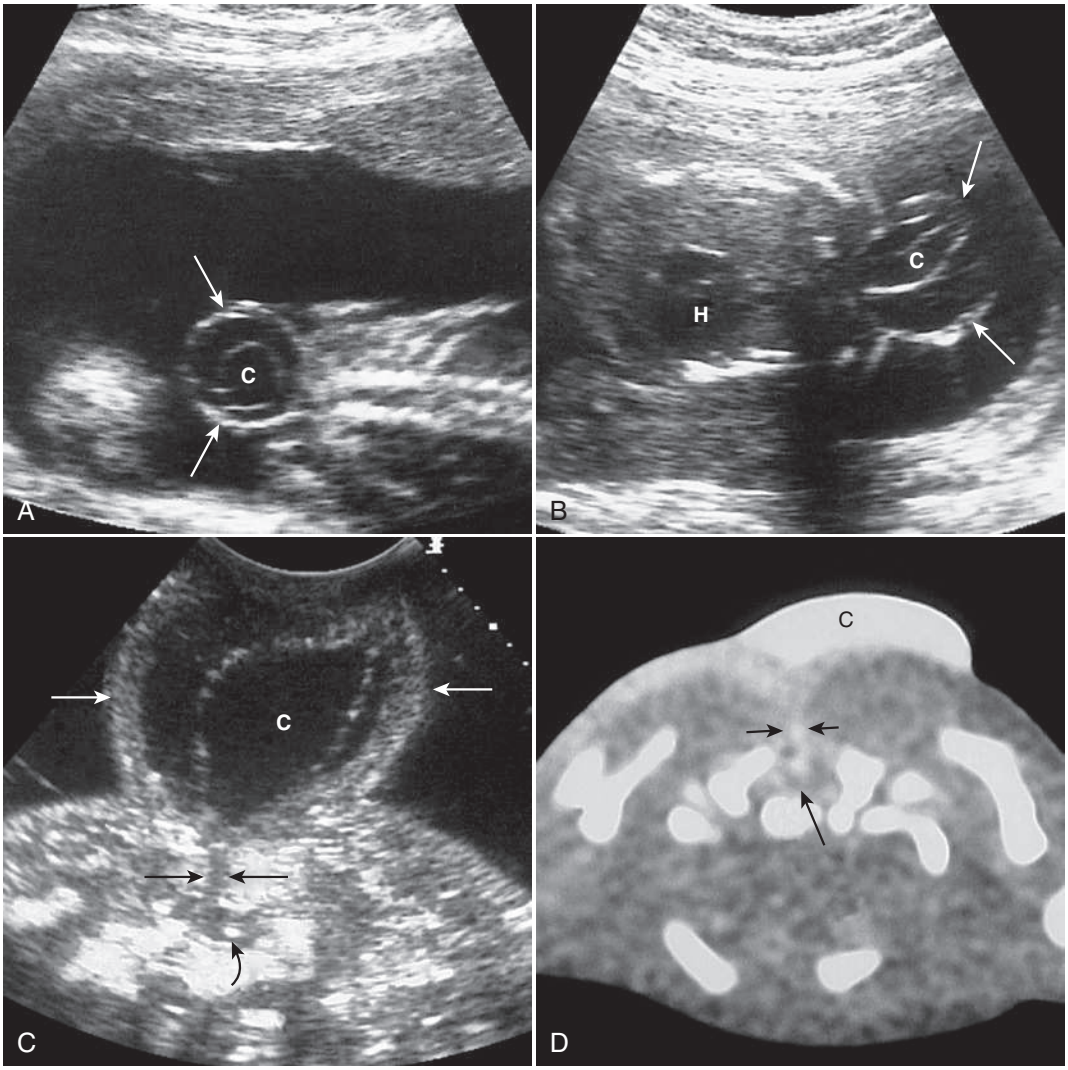

FIG. 35.17 Myelocystocele. (A) Coronal sonogram of thoracic spine at 18 weeks' gestation demonstrates a double-walled cystic mass *(arrows)* with inner cystic component *(C)* arising from the upper thoracic area. **(B)** Axial sonogram of the fetal chest 1 week later demonstrates a double-walled cystic mass *(arrows)* arising along the posterior aspect of the fetal chest; *H,* fetal heart. The inner cystic component *(C)* is slightly smaller and flattened compared to the first scan. No abnormality was noted in the ossified neural arch. **(C)** Sonogram of the specimen demonstrates the double-walled cystic mass *(white arrows)* arising from the posterior thorax with a hypoechoic tract *(black arrows)* extending from the posterior aspect of the spinal cord *(curved arrow)* toward the central cystic component *(C)* of the posterior mass. **(D)** CT scan of the specimen after injection of water-soluble contrast material into the cyst demonstrates contrast within the cyst *(C)* and within a sinus tract *(short arrows),* leading to the spinal cord *(long arrow).*

Continued

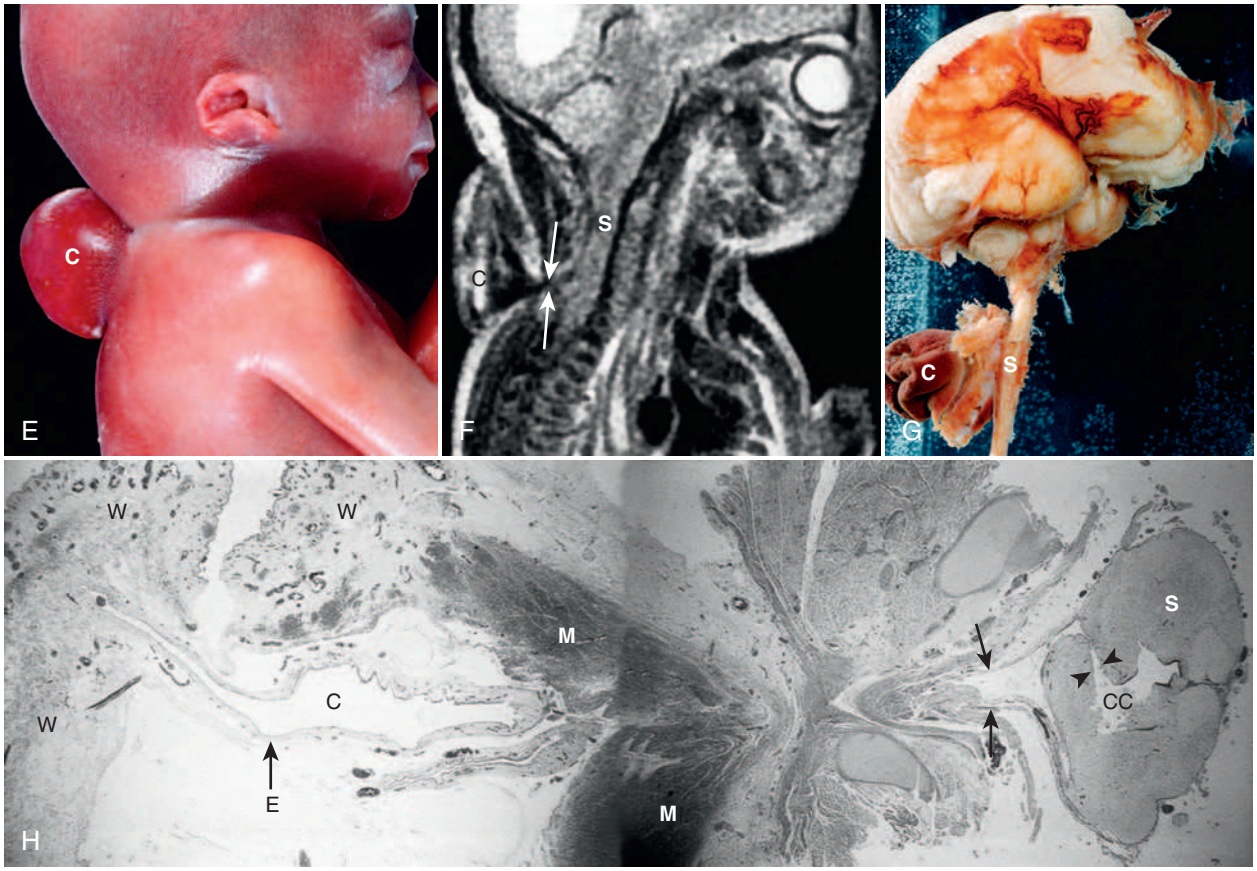

FIG. 35.17, cont'd **(E)** Lateral view of the posterior cystic thoracic mass *(C).* **(F)** Sagittal magnetic resonance scan demonstrates the cystic mass along the upper thoracic area, with the small sinus tract *(arrows)* extending from the posterior aspect of the spinal cord *(S)* toward the cystic mass *(C).* **(G)** Gross pathologic specimen demonstrates the collapsed cyst *(C)* in contiguity with the cervical portion of the spinal cord *(S).* **(H)** Histologic section shows abnormal channel *(arrows)* communicating with the posterior aspect of the spinal cord *(S),* as well as defect in the posterior spinal cord *(arrowheads)* communicating with the central canal *(CC)* of the spinal cord. *C,* Central cystic component of posterior mass *(M); E,* ependymal lining of central cyst, which communicates with central canal of spinal cord; *W,* outer wall of cystic mass.

cord.[100,101] This may be associated with a spina bifida defect and hydromyelia (dilation of central canal of spinal cord) but may occur in the absence of overt spina bifida.[102] Diastematomyelia may also be associated with segmental anomalies of the vertebral bodies or visceral malformations such as horseshoe or ectopic kidney, utero-ovarian malformation, and anorectal malformation. If the spinal canal is traversed by a **bony septum** or **spur,** the septum will appear as an abnormal hyperechoic focus,[103-105] which is best demonstrated in the posterior transaxial and lateral longitudinal scan planes (Fig. 35.18). When diastematomyelia is not associated with other spinal anomalies, the prognosis is favorable. In seven of eight cases reported by Has et al.,[106] the defects had normal amniotic AFP and AChE levels and were considered isolated. Their review of the literature showed 26 cases diagnosed prenatally, 12 of which had no associated abnormality and had a favorable prognosis.

SCOLIOSIS AND KYPHOSIS

Kyphosis is exaggerated curvature of the spine in the sagittal plane. **Scoliosis** is lateral curvature of the spine in the coronal plane. Kyphosis and scoliosis may be positional and nonpathologic or permanent based on an underlying structural abnormality, such as **hemivertebrae, butterfly vertebrae,** and **block vertebrae.** Pathologic kyphosis and scoliosis are often associated with **spina bifida** or **ventral abdominal wall defects.**[107] Less common associations include limb–body wall complex, amniotic band syndrome, arthrogryposis, skeletal dysplasias, VACTERL association (vertebral abnormalities, anal atresia, cardiac abnormalities, tracheoesophageal fistula, renal agenesis, and limb defects),[108,109] and caudal regression syndrome. Mild scoliosis may be caused by a **hemivertebra** (Fig. 35.19).[106,109]

The posterior longitudinal scan is the best view to assess for kyphosis; the lateral longitudinal plane is the best to assess for scoliosis (Fig. 35.19). Because oligohydramnios can cause positional curvature in the fetal spine, a confident diagnosis of pathologic kyphosis or scoliosis should be made only if the curvature is severe. Possible associated anomalies must then be sought because prognosis depends on the coexistent anomalies.

A **hemivertebra** represents underdevelopment or nondevelopment of one-half of a vertebral body; that is, one of the two early

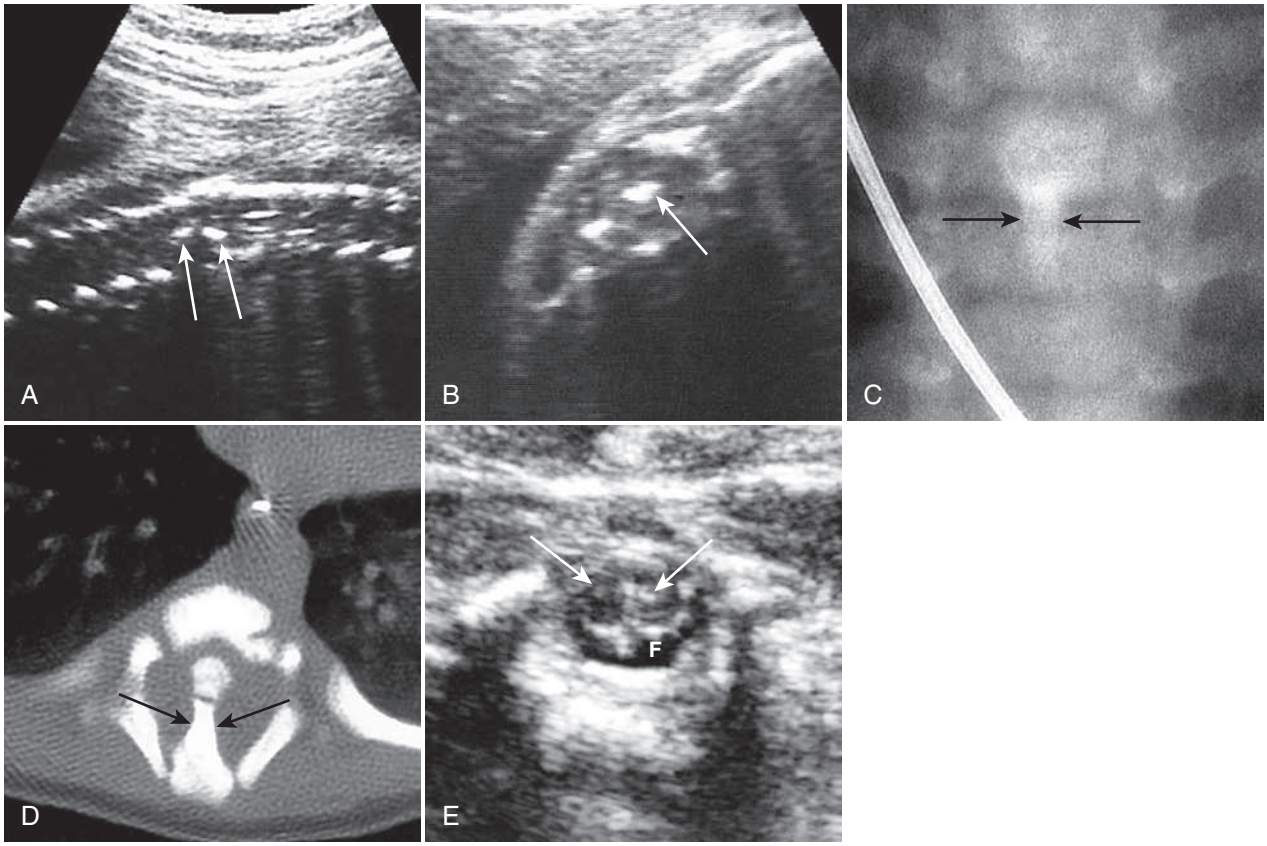

FIG. 35.18 Diastematomyelia. (A) Coronal and **(B)** axial sonograms of the spine demonstrate two hyperechoic foci *(arrows)* caused by the bony septum within the spinal canal with intact skin along the fetal back. **(C)** Anteroposterior radiograph and **(D)** CT scan demonstrate a bony septum *(arrows)* within the central portion of the spinal canal. **(E) Diplomyelia** and **tethered cord.** Posterior transaxial sonogram of another fetus shows cord in the nondependent portion of the spinal canal with fluid *(F)* interposed between the cord and anterior margin of the spinal canal. The anterior aspect of the cord has a bilobed shape instead of a smooth, circular arc with bilateral central canal echoes *(arrows)*.

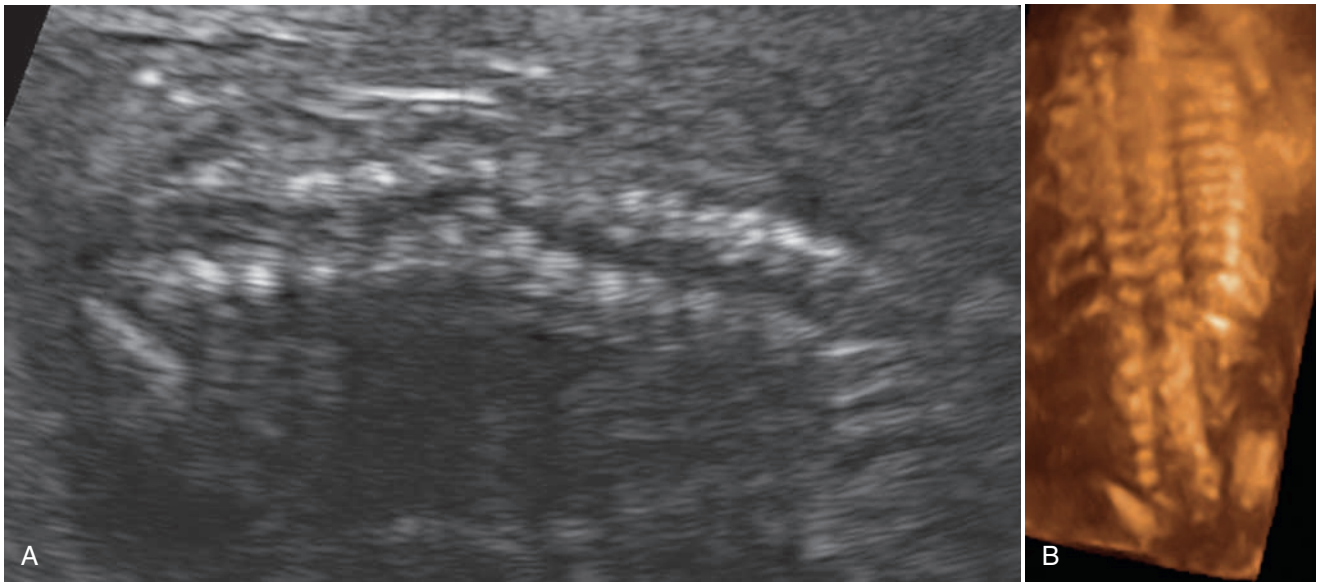

FIG. 35.19 Kyphosis. (A) Sagittal scan of the spine demonstrates a focal kyphosis at the thoracolumbar junction. **(B)** Three-dimensional image of the same patient demonstrates a left upper lumbar hemivertebra as the cause of the kyphosis.

chondrification centers is deficient. The remaining ossification center is displaced laterally with respect to the vertebrae above and below it, leading to a short-segment mild scoliosis. The abnormalities can be detected prenatally and may be best portrayed with 3D ultrasound.[31-34] Fetuses with an isolated hemivertebra have an excellent prognosis, whereas those with other fetal anomalies (e.g., Potter syndrome; cardiac, intestinal, intracranial, and limb anomalies) have a poor prognosis.[110] The presence of associated anomalies reduces the survival rate to approximately 50%. If oligohydramnios is also present, the mortality rate approaches 100%.[111]

Causes of Scoliosis or Kyphosis

Hemivertebrae
Butterfly vertebrae
Block vertebrae
Spina bifida
Ventral abdominal wall defects
Limb–body wall complex
Amniotic band syndrome
Arthrogryposis
Skeletal dysplasias
VACTERL[a] association
Caudal regression syndrome

[a]Vertebral abnormalities, anal atresia, cardiac abnormalities, tracheoesophageal fistula, renal agenesis, and limb defects.

SACRAL AGENESIS

Sacral agenesis is an uncommon fetal abnormality that may be present in conditions such as **caudal regression sequence, sirenomelia sequence, cloacal exstrophy sequence,** and the **VACTERL association.** The caudal regression sequence (caudal regression syndrome) and the sirenomelia sequence are thought to be separate pathologic entities.[112,113]

CAUDAL REGRESSION

In caudal regression or dysplasia, abnormalities of the lower spine and limbs occur, including **sacral agenesis, lumbar spine deficiency,** and leg anomalies such as **femoral hypoplasia** (Fig. 35.20). Defects of the neural tube and the genitourinary,

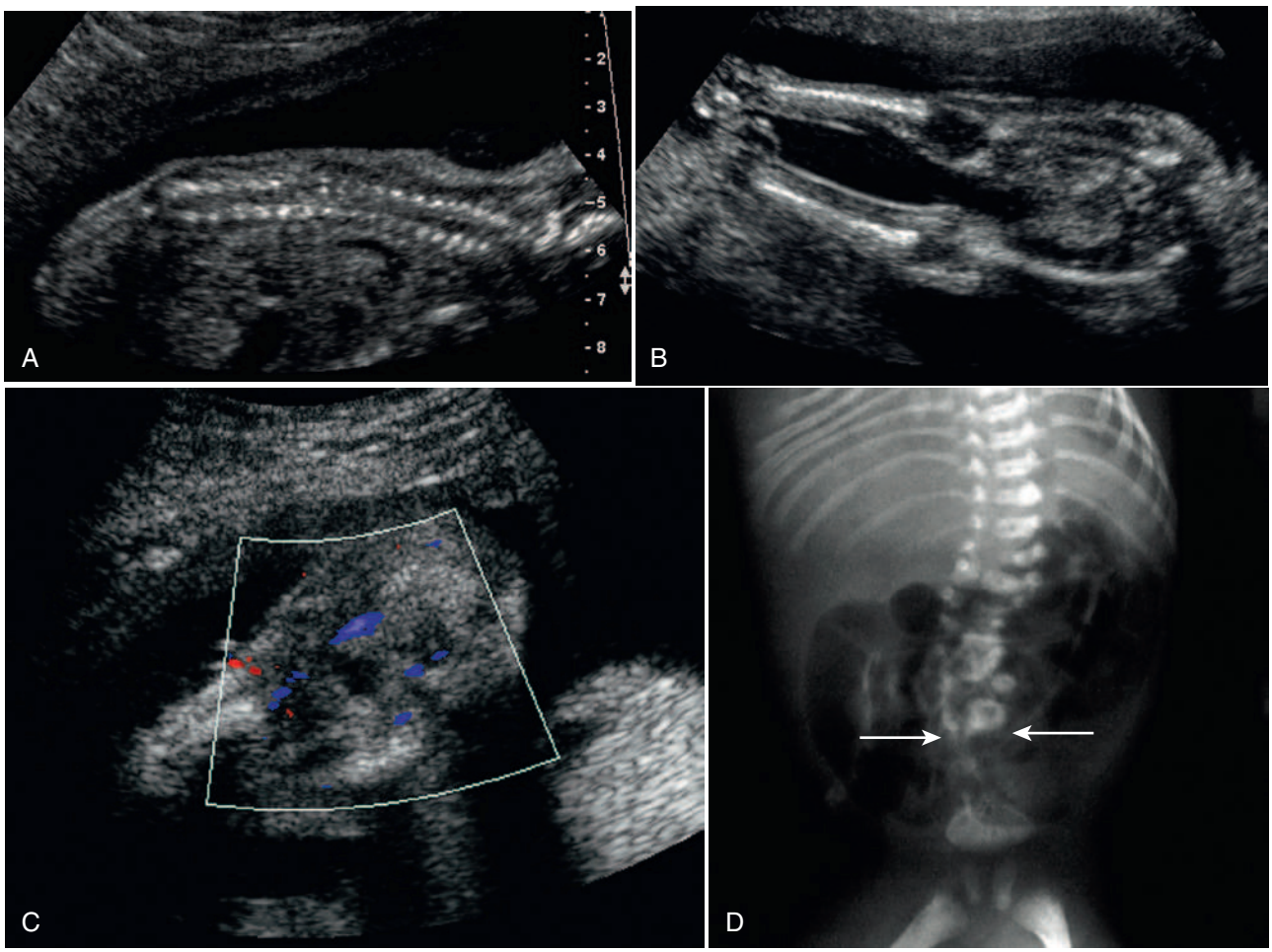

FIG. 35.20 Caudal Regression. (A) Sagittal sonogram of spine at 21 weeks shows abrupt termination of ossified vertebral bodies. **(B)** Transverse view of pelvis with legs in long axis shows lack of ossified pelvic bones and atrophic musculature about the lower extremities. **(C)** Transverse color Doppler image at level of bladder shows lack of ossified pelvic bones. **(D)** In a different fetal specimen, radiograph shows abrupt termination *(arrows)* of the lumbar spine and absence of the sacrum. The pelvic bones are small and deformed.

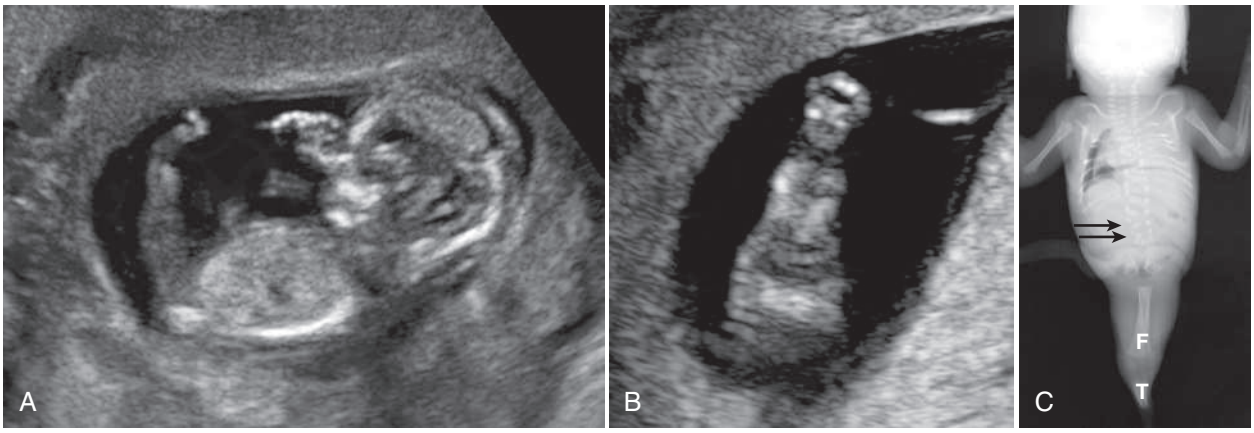

FIG. 35.21 Sirenomelia. (A) Sagittal view of fetus at 12 weeks' gestation shows unusual angulation of lower extremity. **(B)** Long-axis view of a single lower extremity. **(C)** In a different fetus, radiograph shows single femur *(F)* and single tibia *(T)*. Note the segmented defects in the vertebrae of the thoracic and lumbar spine *(arrows)*.

gastrointestinal, and cardiac systems are common. Occurrence is sporadic; caudal regression is more common in infants of mothers with diabetes mellitus. The cause has not been established. Sonography can demonstrate absence of the sacrum and shortened femurs. The legs can be flexed and abducted at the hips, and there may be clubfoot. Sonography may detect associated urinary anomalies (renal agenesis, cystic dysplasia, caliectasis) and gastrointestinal abnormalities (e.g., duodenal atresia).[114] The prognosis depends on the severity and extent of the skeletal abnormalities and associated anomalies. In sacral agenesis with no internal organ involvement, there are usually deficits in the legs and deficient control of bladder and bowel functions. In infants with internal organ involvement, the prognosis is related to these defects.

SIRENOMELIA

Sirenomelia sequence is a rare disorder in which the legs are fused and the feet are deformed or absent[115] (Fig. 35.21). The cause is probably an **aberrant fetal artery** that branches from the upper abdominal aorta and passes into the umbilical cord to the placenta.[116] Arterial blood flow bypasses the lower fetal body. The distal abdominal aorta, the aorta's distal branches, and subtended structures are small and underdeveloped. This leads to malformations of spine, legs, kidneys, gut, and genitalia. Normally the umbilical arteries, which arise from the fetal iliac arteries, carry blood from the fetus into the umbilical cord and then into the placenta.

At sonography, there is advanced **oligohydramnios** because of reduced or absent renal function. The legs are fused, or there is a single leg. The feet are absent, or there may be a single foot. There may be sacral agenesis, deficiency of the lower lumbar spine, and thoracic anomalies. These findings may be difficult to appreciate because of the advanced oligohydramnios or anhydramnios.[112] The prolonged anhydramnios causes pulmonary hypoplasia, which is usually fatal. The risk of recurrence is the same as in the general population.

SACROCOCCYGEAL TERATOMA

Fetal teratomas may arise from the sacrum or coccyx, from other midline structures from the level of the brain to the coccyx, or from the gonads.[117] Sacrococcygeal teratomas arise from the pluripotent cells of Hensen node located anterior to the coccyx. Sacrococcygeal teratomas contain all three germ layers (ectoderm, mesoderm, and endoderm) and thus may contain elements of many tissues, including neural, respiratory, and gastrointestinal. Sacrococcygeal tumor is rare (1:35,000 births)[118] but is the most common tumor among neonates. Females are affected four times more frequently than males. Sacrococcygeal teratomas are classified into four types[118]: **type I,** tumor predominantly external with only minimal presacral involvement; **type II,** tumor presenting externally but with significant intrapelvic extension; **type III,** tumor apparent externally but with predominant pelvic mass and extension into the abdomen; **type IV,** tumor presacral with no external presentation (Fig. 35.22).[117]

Types of Sacrococcygeal Teratomas

Type I (47%): external mass predominant
Type II (34%): external mass with significant internal component
Type III (9%): internal mass predominant, with smaller external component
Type IV (10%): presacral mass only

At birth, 75% of sacrococcygeal teratomas are benign, 12% are immature, and 13% are malignant. Because malignant potential increases with the age of the infant, surgery must be performed shortly after birth.

Sonography usually demonstrates a mass in the rump or buttocks area adjacent to the spine[119] (Video 35.6). Most teratomas (85%) are either solid or mixed (solid and cystic); 15% are mostly cystic, which is a benign sign. Calcifications are frequently present.

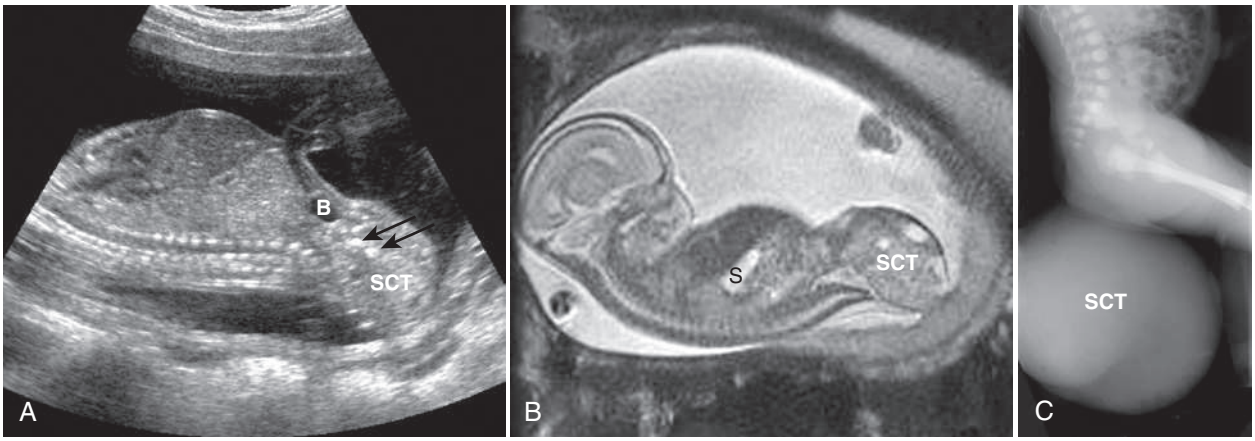

FIG. 35.22 Sacrococcygeal Teratoma. (A) Sagittal sonogram shows type II sacrococcygeal teratoma *(SCT)* that is predominantly external but has a substantial intrapelvic component. The tumor extends up to level L5 and displaces the fetal urinary bladder *(B)* anteriorly. Note the calcifications *(arrows)* within the tumor. **(B)** T2-weighted sagittal magnetic resonance image demonstrates the extent and internal structure of the sacrococcygeal tumor *(SCT); S,* stomach. **(C)** Lateral radiograph in a different neonate. (**A** and **B** courtesy of Drs. Fong, Pantazi, and Toi, Mt. Sinai Hospital, Toronto.)

Large masses may displace and distort neighboring structures, such as the rectum and urinary bladder (see Fig. 35.22). Compression of the distal ureters may cause hydronephrosis. Larger solid tumors may develop substantial **arteriovenous shunting,** causing **fetal cardiac failure** and **hydrops.**[120] The development of hydrops in the presence of a sacrococcygeal teratoma carries a poor prognosis.[120-124]

PRESACRAL FETAL MASS

The differential diagnosis of a presacral fetal mass also includes chordoma, anterior myelomeningocele, neurenteric cyst, neuroblastoma, sarcoma, lipoma, bone tumor, lymphoma, and rectal duplication. Amniotic fluid AFP is often elevated in sacrococcygeal tumor, and AChE is often present in the amniotic fluid. These results exclude most other causes, except a myelomeningocele.

Presacral Masses

Sacrococcygeal teratoma
Chordoma
Anterior myelomeningocele
Neurenteric cyst
Neuroblastoma
Sarcoma
Lipoma
Bone tumor
Lymphoma
Rectal duplication

If a fetal sacrococcygeal teratoma is suspected from prenatal sonograms, serial sonograms should be arranged to monitor the pregnancy to assess for complications, especially signs of fetal cardiac failure. Complete fetal assessment should also include the internal characteristics of the tumor, the size of the tumor, and associated fetal anomalies.

For masses less than 4.5 cm in diameter, without associated abnormalities, vaginal delivery is considered. For masses greater than 4.5 cm diameter, cesarean section may be considered because of the risk of dystocia and hemorrhage during vaginal delivery. In utero surgery for arteriovenous shunting has been described for treatment of fetal hydrops from congestive heart failure in early pregnancy (<30 weeks), but this should be considered only in experienced hands.[120,121]

REFERENCES

1. Fishman MA. Birth defects and supplemental vitamins. Curr Treat Options Neurol. 2000;2(2):117-122.
2. Shaer CM, Chescheir N, Schulkin J. Myelomeningocele: a review of the epidemiology, genetics, risk factors for conception, prenatal diagnosis, and prognosis for affected individuals. Obstet Gynecol Surv. 2007;62(7):471-479.
3. Grosse SD, Collins JS. Folic acid supplementation and neural tube defect recurrence prevention. Birth Defects Res A Clin Mol Teratol. 2007;79(11):737-742.
4. Trends in folic acid supplement intake among women of reproductive age—California, 2002-2006. MMWR Morb Mortal Wkly Rep. 2007;56(42):1106-1109.
5. Williams J, Mai CT, Mulinare J, et al. Updated estimates of neural tube defects prevented by mandatory folic acid fortification—United States, 1995-2011. MMWR Morb Mortal Wkly Rep. 2015;64(1):1-5.
6. Solomons NW. Food fortification with folic acid: has the other shoe dropped? Nutr Rev. 2007;65(11):512-515.
7. De Wals P, Tairou F, Van Allen MI, et al. Reduction in neural-tube defects after folic acid fortification in Canada. N Engl J Med. 2007;357(2):135-142.
8. Safdar OY, Al-Dabbagh AA, Abuelieneen WA, Kari JA. Decline in the incidence of neural tube defects after the national fortification of flour (1997-2005). Saudi Med J. 2007;28(8):1227-1229.
9. Sayed AR, Bourne D, Pattinson R, et al. Decline in the prevalence of neural tube defects following folic acid fortification and its cost-benefit in South Africa. Birth Defects Res A Clin Mol Teratol. 2008;82(4):211-216.
10. Jentink J, van de Vrie-Hoekstra NW, de Jong-van den Berg LT, Postma MJ. Economic evaluation of folic acid food fortification in The Netherlands. Eur J Public Health. 2008;18(3):270-274.
11. Larsen WJ. Human embryology. 2nd ed. New York: Churchill Livingstone; 1997.
12. O'Rahilly R, Muller F, Meyer DB. The human vertebral column at the end of the embryonic period proper. 1. The column as a whole. J Anat. 1980;131(Pt 3):565-575.

13. Bagnall KM, Harris PF, Jones PR. A radiographic study of the human fetal spine. 2. The sequence of development of ossification centres in the vertebral column. J Anat. 1977;124(Pt 3):791-802.
14. Ford DM, McFadden KD, Bagnall KM. Sequence of ossification in human vertebral neural arch centers. Anat Rec. 1982;203(1):175-178.
15. Budorick NE, Pretorius DH, Grafe MR, Lou KV. Ossification of the fetal spine. Radiology. 1991;181(2):561-565.
16. Braithwaite JM, Armstrong MA, Economides DL. Assessment of fetal anatomy at 12 to 13 weeks of gestation by transabdominal and transvaginal sonography. Br J Obstet Gynaecol. 1996;103(1):82-85.
17. Blumenfeld Z, Siegler E, Bronshtein M. The early diagnosis of neural tube defects. Prenat Diagn. 1993;13(9):863-871.
18. Sebire NJ, Noble PL, Thorpe-Beeston JG, et al. Presence of the 'lemon' sign in fetuses with spina bifida at the 10-14-week scan. Ultrasound Obstet Gynecol. 1997;10(6):403-405.
19. Bernard JP, Suarez B, Rambaud C, et al. Prenatal diagnosis of neural tube defect before 12 weeks' gestation: direct and indirect ultrasonographic semeiology. Ultrasound Obstet Gynecol. 1997;10(6):406-409.
20. Robbin ML, Filly RA, Goldstein RB. The normal location of the fetal conus medullaris. J Ultrasound Med. 1994;13(7):541-546.
21. Zalel Y, Lehavi O, Aizenstein O, Achiron R. Development of the fetal spinal cord: time of ascendance of the normal conus medullaris as detected by sonography. J Ultrasound Med. 2006;25(11):1397-1401.
22. Thiagarajah S, Henke J, Hogge WA, et al. Early diagnosis of spina bifida: the value of cranial ultrasound markers. Obstet Gynecol. 1990;76(1): 54-57.
23. Babcook CJ, Goldstein RB, Barth RA, et al. Prevalence of ventriculomegaly in association with myelomeningocele: correlation with gestational age and severity of posterior fossa deformity. Radiology. 1994;190(3): 703-707.
24. Watson WJ, Chescheir NC, Katz VL, Seeds JW. The role of ultrasound in evaluation of patients with elevated maternal serum alpha-fetoprotein: a review. Obstet Gynecol. 1991;78(1):123-128.
25. Dyson RL, Pretorius DH, Budorick NE, et al. Three-dimensional ultrasound in the evaluation of fetal anomalies. Ultrasound Obstet Gynecol. 2000;16(4):321-328.
26. Riccabona M, Johnson D, Pretorius DH, Nelson TR. Three dimensional ultrasound: display modalities in the fetal spine and thorax. Eur J Radiol. 1996;22(2):141-145.
27. Bonilla-Musoles F, Machado LE, Osborne NG, et al. Two- and three-dimensional ultrasound in malformations of the medullary canal: report of four cases. Prenat Diagn. 2001;21(8):622-626.
28. Lee W, Chaiworapongsa T, Romero R, et al. A diagnostic approach for the evaluation of spina bifida by three-dimensional ultrasonography. J Ultrasound Med. 2002;21(6):619-626.
29. Schild RL, Wallny T, Fimmers R, Hansmann M. The size of the fetal thoracolumbar spine: a three-dimensional ultrasound study. Ultrasound Obstet Gynecol. 2000;16(5):468-472.
30. Johnson DD, Pretorius DH, Riccabona M, et al. Three-dimensional ultrasound of the fetal spine. Obstet Gynecol. 1997;89(3):434-438.
31. Wax JR, Watson WJ, Miller RC, et al. Prenatal sonographic diagnosis of hemivertebrae: associations and outcomes. J Ultrasound Med. 2008;27(7):1023-1027.
32. Kalache KD, Bamberg C, Proquitte H, et al. Three-dimensional multi-slice view: new prospects for evaluation of congenital anomalies in the fetus. J Ultrasound Med. 2006;25(8):1041-1049.
33. Merce LT, Barco MJ, Bau S. Three-dimensional volume sonographic study of fetal anatomy: intraobserver reproducibility and effect of examiner experience. J Ultrasound Med. 2008;27(7):1053-1063.
34. Gindes L, Benoit B, Pretorius DH, Achiron R. Abnormal number of fetal ribs on 3-dimensional ultrasonography: associated anomalies and outcomes in 75 fetuses. J Ultrasound Med. 2008;27(9):1263-1271.
35. Volcik KA, Blanton SH, Tyerman GH, et al. Methylenetetrahydrofolate reductase and spina bifida: evaluation of level of defect and maternal genotypic risk in Hispanics. Am J Med Genet. 2000;95(1):21-27.
36. Li Z, Ren A, Zhang L, et al. Extremely high prevalence of neural tube defects in a 4-county area in Shanxi Province, China. Birth Defects Res A Clin Mol Teratol. 2006;76(4):237-240.
37. Cragan JD, Roberts HE, Edmonds LD, et al. Surveillance for anencephaly and spina bifida and the impact of prenatal diagnosis—United States, 1985-1994. MMWR CDC Surveill Summ. 1995;44(4):1-13.
38. EUROCAT Working Group. Prevalence of neural tube defects in 20 regions of Europe and the impact of prenatal diagnosis, 1980-1986. EUROCAT Working Group. J Epidemiol Community Health. 1991;45(1):52-58.
39. Laurence KM, James N, Miller MH, et al. Double-blind randomised controlled trial of folate treatment before conception to prevent recurrence of neural-tube defects. Br Med J (Clin Res Ed). 1981;282(6275):1509-1511.
40. MRC Vitamin Study Research Group. Prevention of neural tube defects: results of the Medical Research Council Vitamin Study. MRC Vitamin Study Research Group. Lancet. 1991;338(8760):131-137.
41. Werler MM, Shapiro S, Mitchell AA. Periconceptional folic acid exposure and risk of occurrent neural tube defects. JAMA. 1993;269(10): 1257-1261.
42. Czeizel AE. Prevention of congenital abnormalities by periconceptional multivitamin supplementation. BMJ. 1993;306(6893):1645-1648.
43. Lumley J, Watson L, Watson M, Bower C. Periconceptional supplementation with folate and/or multivitamins for preventing neural tube defects. Cochrane Database Syst Rev. 2000;(2):CD001056.
44. Recommendations for the use of folic acid to reduce the number of cases of spina bifida and other neural tube defects. MMWR Recomm Rep. 1992;41(RR-14):1-7.
45. Great Britain, Department of Health, et al. Folic acid and the prevention of neural tube defects: report from an expert advisory group. London: Department of Health; 1992.
46. Kadir RA, Sabin C, Whitlow B, et al. Neural tube defects and periconceptional folic acid in England and Wales: retrospective study. BMJ. 1999;319(7202): 92-93.
47. Rosano A, Smithells D, Cacciani L, et al. Time trends in neural tube defects prevalence in relation to preventive strategies: an international study. J Epidemiol Community Health. 1999;53(10):630-635.
48. Sharpe G, Young G. Folic acid and the prevention of neural tube defects. Most pregnant women do not take folic acid. BMJ. 1995;311(6999):256.
49. Wild J, Sutcliffe M, Schorah CJ, Levene MI. Prevention of neural-tube defects. Lancet. 1997;350(9070):30-31.
50. Huttly WJ, Wald NJ, Walters JC. Folic acid supplementation before pregnancy remains inadequate. BMJ. 1999;319(7223):1499.
51. Honein MA, Paulozzi LJ, Mathews TJ, et al. Impact of folic acid fortification of the US food supply on the occurrence of neural tube defects. JAMA. 2001;285(23):2981-2986.
52. Persad VL, Van den Hof MC, Dubé JM, Zimmer P. Incidence of open neural tube defects in Nova Scotia after folic acid fortification. CMAJ. 2002;167(3):241-245.
53. Forrester MB, Merz RD. Descriptive epidemiology of lipomyelomeningocele, Hawaii, 1986-2001. Birth Defects Res A Clin Mol Teratol. 2004;70(12): 953-956.
54. De Wals P, Van Allen MI, Lowry RB, et al. Impact of folic acid food fortification on the birth prevalence of lipomyelomeningocele in Canada. Birth Defects Res A Clin Mol Teratol. 2008;82(2):106-109.
55. Main DM, Mennuti MT. Neural tube defects: issues in prenatal diagnosis and counselling. Obstet Gynecol. 1986;67(1):1-16.
56. Lescale KB, Eddleman KA, Chervenak FA. The fetal neck and spine. In: McGahan JP, Porto M, editors. Diagnostic obstetrical ultrasound. Philadelphia: Lippincott; 1994. p. 195.
57. Ray JG, Wyatt PR, Thompson MD, et al. Vitamin B12 and the risk of neural tube defects in a folic-acid-fortified population. Epidemiology. 2007;18(3): 362-366.
58. Babcook CJ, Goldstein RB, Filly RA. Prenatally detected fetal myelomeningocele: is karyotype analysis warranted? Radiology. 1995;194(2): 491-494.
59. Sepulveda W, Corral E, Ayala C, et al. Chromosomal abnormalities in fetuses with open neural tube defects: prenatal identification with ultrasound. Ultrasound Obstet Gynecol. 2004;23(4):352-356.
60. Byrne J, Warburton D. Neural tube defects in spontaneous abortions. Am J Med Genet. 1986;25(2):327-333.
61. Gregerson DM. Clinical consequences of spina bifida occulta. J Manipulative Physiol Ther. 1997;20(8):546-550.

62. Norem CT, Schoen EJ, Walton DL, et al. Routine ultrasonography compared with maternal serum alpha-fetoprotein for neural tube defect screening. Obstet Gynecol. 2005;106(4):747-752.
63. Filly RA, Callen PW, Goldstein RB. Alpha-fetoprotein screening programs: what every obstetric sonologist should know. Radiology. 1993;188(1):1-9.
64. Ames MD, Schut L. Results of treatment of 171 consecutive myelomeningoceles, 1963 to 1968. Pediatrics. 1972;50(3):466-470.
65. Kollias SS, Goldstein RB, Cogen PH, Filly RA. Prenatally detected myelomeningoceles: sonographic accuracy in estimation of the spinal level. Radiology. 1992;185(1):109-112.
66. Aaronson OS, Hernanz-Schulman M, Bruner JP, et al. Myelomeningocele: prenatal evaluation—comparison between transabdominal US and MR imaging. Radiology. 2003;227(3):839-843.
67. von Koch CS, Glenn OA, Goldstein RB, Barkovich AJ. Fetal magnetic resonance imaging enhances detection of spinal cord anomalies in patients with sonographically detected bony anomalies of the spine. J Ultrasound Med. 2005;24(6):781-789.
68. Biggio Jr JR, Owen J, Wenstrom KD, Oakes WJ. Can prenatal ultrasound findings predict ambulatory status in fetuses with open spina bifida? Am J Obstet Gynecol. 2001;185(5):1016-1020.
69. Roberts AB, Campbell S. Small biparietal diameter of fetuses with spina bifida: implications for antenatal screening. Br J Obstet Gynaecol. 1980;87(10):927-928.
70. Wald N, Cuckle H, Boreham J, Stirrat G. Small biparietal diameter of fetuses with spina bifida: implications for antenatal screening. Br J Obstet Gynaecol. 1980;87(3):219-221.
71. Nyberg DA, Mack LA, Hirsch J, et al. Fetal hydrocephalus: sonographic detection and clinical significance of associated anomalies. Radiology. 1987;163(1):187-191.
72. Nicolaides KH, Campbell S, Gabbe SG, Guidetti R. Ultrasound screening for spina bifida: cranial and cerebellar signs. Lancet. 1986;2(8498):72-74.
73. Pilu G, Romero R, Reece EA, et al. Subnormal cerebellum in fetuses with spina bifida. Am J Obstet Gynecol. 1988;158(5):1052-1056.
74. Goldstein RB, Podrasky AE, Filly RA, Callen PW. Effacement of the fetal cisterna magna in association with myelomeningocele. Radiology. 1989;172(2):409-413.
75. Benacerraf BR, Stryker J, Frigoletto Jr FD. Abnormal US appearance of the cerebellum (banana sign): indirect sign of spina bifida. Radiology. 1989;171(1):151-153.
76. Furness ME, Barbary JE, Verco PW. A pointer to spina bifida: fetal head shape in the second trimester. In: Gill RW, Dadd MJ, editors. WFUMB (World Federation of Ultrasound in Medicine and Biology). Sidney: Pergamon Press; 1985. p. 296.
77. Campbell J, Gilbert WM, Nicolaides KH, Campbell S. Ultrasound screening for spina bifida: cranial and cerebellar signs in a high-risk population. Obstet Gynecol. 1987;70(2):247-250.
78. Nyberg DA, Mack LA, Hirsch J, Mahony BS. Abnormalities of fetal cranial contour in sonographic detection of spina bifida: evaluation of the "lemon" sign. Radiology. 1988;167(2):387-392.
79. Penso C, Redline RW, Benacerraf BR. A sonographic sign which predicts which fetuses with hydrocephalus have an associated neural tube defect. J Ultrasound Med. 1987;6(6):307-311.
80. Sharrard WJ. The mechanism of paralytic deformity in spina bifida. Dev Med Child Neurol. 1962;4:310-313.
81. Lorber J. Results of treatment of myelomeningocele. An analysis of 524 unselected cases, with special reference to possible selection for treatment. Dev Med Child Neurol. 1971;13(3):279-303.
82. Nelson Jr MD, Bracchi M, Naidich TP, McLone DG. The natural history of repaired myelomeningocele. Radiographics. 1988;8(4):695-706.
83. Wong LY, Paulozzi LJ. Survival of infants with spina bifida: a population study, 1979-94. Paediatr Perinat Epidemiol. 2001;15(4):374-378.
84. Oakeshott P, Hunt GM. Long-term outcome in open spina bifida. Br J Gen Pract. 2003;53(493):632-636.
85. Adzick NS, Thom EA, Spong CY, et al. A randomized trial of prenatal versus postnatal repair of myelomeningocele. N Engl J Med. 2011;364(11):993-1004.
86. Bliton MJ, Zaner RM. Over the cutting edge: how ethics consultation illuminates the moral complexity of open-uterine fetal repair of spina bifida and patients' decision making. J Clin Ethics. 2001;12(4):346-360.
87. Walsh DS, Adzick NS, Sutton LN, Johnson MP. The rationale for in utero repair of myelomeningocele. Fetal Diagn Ther. 2001;16(5):312-322.
88. Tulipan N, Bruner JP, Hernanz-Schulman M, et al. Effect of intrauterine myelomeningocele repair on central nervous system structure and function. Pediatr Neurosurg. 1999;31(4):183-188.
89. Fichter MA, Dornseifer U, Henke J, et al. Fetal spina bifida repair—current trends and prospects of intrauterine neurosurgery. Fetal Diagn Ther. 2008;23(4):271-286.
90. Bruner JP, Tulipan N, Paschall RL, et al. Fetal surgery for myelomeningocele and the incidence of shunt-dependent hydrocephalus. JAMA. 1999;282(19):1819-1825.
91. Holmes NM, Nguyen HT, Harrison MR, et al. Fetal intervention for myelomeningocele: effect on postnatal bladder function. J Urol. 2001;166(6):2383-2386.
92. Holzbeierlein J, Pope JI, Adams MC, et al. The urodynamic profile of myelodysplasia in childhood with spinal closure during gestation. J Urol. 2000;164(4):1336-1339.
93. Sutton LN, Adzick NS, Bilaniuk LT, et al. Improvement in hindbrain herniation demonstrated by serial fetal magnetic resonance imaging following fetal surgery for myelomeningocele. JAMA. 1999;282(19):1826-1831.
94. Steinbok P, Cochrane DD. The nature of congenital posterior cervical or cervicothoracic midline cutaneous mass lesions. Report of eight cases. J Neurosurg. 1991;75(2):206-212.
95. Bhargava R, Hammond DI, Benzie RJ, et al. Prenatal demonstration of a cervical myelocystocele. Prenat Diagn. 1992;12(8):653-659.
96. Steinbok P. Dysraphic lesions of the cervical spinal cord. Neurosurg Clin N Am. 1995;6(2):367-376.
97. Byrd SE, Harvey C, McLone DG, Darling CF. Imaging of terminal myelocystoceles. J Natl Med Assoc. 1996;88(8):510-516.
98. Choi S, McComb JG. Long-term outcome of terminal myelocystocele patients. Pediatr Neurosurg. 2000;32(2):86-91.
99. Muthukumar N. Terminal and nonterminal myelocystoceles. J Neurosurg. 2007;107(2 Suppl.):87-97.
100. Allen LM, Silverman RK. Prenatal ultrasound evaluation of fetal diastematomyelia: two cases of type I split cord malformation. Ultrasound Obstet Gynecol. 2000;15(1):78-82.
101. Sonigo-Cohen P, Schmit P, Zerah M, et al. Prenatal diagnosis of diastematomyelia. Childs Nerv Syst. 2003;19(7-8):555-560.
102. Dabra A, Gupta R, Sidhu R, et al. Sonographic diagnosis of diastematomyelia in utero: a case report and literature review. Australas Radiol. 2001;45(2):222-224.
103. Raghavendra BN, Epstein FJ, Pinto RS, et al. Sonographic diagnosis of diastematomyelia. J Ultrasound Med. 1988;7(2):111-113.
104. Anderson NG, Jordan S, MacFarlane MR, Lovell-Smith M. Diastematomyelia: diagnosis by prenatal sonography. AJR Am J Roentgenol. 1994;163(4):911-914.
105. Korsvik HE, Keller MS. Sonography of occult dysraphism in neonates and infants with MR imaging correlation. Radiographics. 1992;12(2):297-306.
106. Has R, Yuksel A, Buyukkurt S, et al. Prenatal diagnosis of diastematomyelia: presentation of eight cases and review of the literature. Ultrasound Obstet Gynecol. 2007;30(6):845-849.
107. Harrison LA, Pretorius DH, Budorick NE. Abnormal spinal curvature in the fetus. J Ultrasound Med. 1992;11(9):473-479.
108. Patten RM, Van Allen M, Mack LA, et al. Limb-body wall complex: in utero sonographic diagnosis of a complicated fetal malformation. AJR Am J Roentgenol. 1986;146(5):1019-1024.
109. Van Allen MI, Curry C, Walden CE, et al. Limb-body wall complex: II. Limb and spine defects. Am J Med Genet. 1987;28(3):549-565.
110. Benacerraf BR, Greene MF, Barss VA. Prenatal sonographic diagnosis of congenital hemivertebra. J Ultrasound Med. 1986;5(5):257-259.
111. Zelop CM, Pretorius DH, Benacerraf BR. Fetal hemivertebrae: associated anomalies, significance, and outcome. Obstet Gynecol. 1993;81(3):412-416.

112. Twickler D, Budorick N, Pretorius D, et al. Caudal regression versus sirenomelia: sonographic clues. J Ultrasound Med. 1993;12(6):323-330.
113. Sepulveda W, Corral E, Sanchez J, et al. Sirenomelia sequence versus renal agenesis: prenatal differentiation with power Doppler ultrasound. Ultrasound Obstet Gynecol. 1998;11(6):445-449.
114. Baxi L, Warren W, Collins MH, Timor-Tritsch IE. Early detection of caudal regression syndrome with transvaginal scanning. Obstet Gynecol. 1990;75 (3 Pt 2):486-489.
115. Stocker JT, Heifetz SA. Sirenomelia. A morphological study of 33 cases and review of the literature. Perspect Pediatr Pathol. 1987;10:7-50.
116. Stevenson RE, Jones KL, Phelan MC, et al. Vascular steal: the pathogenetic mechanism producing sirenomelia and associated defects of the viscera and soft tissues. Pediatrics. 1986;78(3):451-457.
117. Bloechle M, Bollmann R, Zienert A, et al. [Fetal teratoma—diagnosis and management]. Zentralbl Gynakol. 1992;114(4):175-180.
118. Altman RP, Randolph JG, Lilly JR. Sacrococcygeal teratoma: American Academy of Pediatrics Surgical Section Survey-1973. J Pediatr Surg. 1974;9(3):389-398.
119. Sheth S, Nussbaum AR, Sanders RC, et al. Prenatal diagnosis of sacrococcygeal teratoma: sonographic-pathologic correlation. Radiology. 1988;169(1): 131-136.
120. Bond SJ, Harrison MR, Schmidt KG, et al. Death due to high-output cardiac failure in fetal sacrococcygeal teratoma. J Pediatr Surg. 1990;25(12): 1287-1291.
121. Langer JC, Harrison MR, Schmidt KG, et al. Fetal hydrops and death from sacrococcygeal teratoma: rationale for fetal surgery. Am J Obstet Gynecol. 1989;160(5 Pt 1):1145-1150.
122. Gross SJ, Benzie RJ, Sermer M, et al. Sacrococcygeal teratoma: prenatal diagnosis and management. Am J Obstet Gynecol. 1987;156(2):393-396.
123. Teal LN, Angtuaco TL, Jimenez JF, Quirk Jr JG. Fetal teratomas: antenatal diagnosis and clinical management. J Clin Ultrasound. 1988;16(5): 329-336.
124. Robertson FM, Crombleholme TM, Frantz 3rd ID, et al. Devascularization and staged resection of giant sacrococcygeal teratoma in the premature infant. J Pediatr Surg. 1995;30(2):309-311.

CHAPTER 36

The Fetal Chest

Dorothy Bulas

SUMMARY OF KEY POINTS

- Normal fetal lungs appear homogeneously echogenic on ultrasound surrounding the heart with a cardiothoracic ratio that remains constant through the second and third trimesters.
- Pulmonary hypoplasia can be primary or secondary and unilateral or bilateral.
- Congenital pulmonary airway malformations (CPAMs) are a spectrum of disorders that include bronchopulmonary malformation, hybrid lesions (CPAM and sequestration), and congenital lobar overinflation/bronchial atresia.
- A large fetal lung mass can compress and shift the heart and vena cava, resulting in fetal hydrops.
- Congenital pulmonary airway malformation volume ratio (CVR) is the CPAM volume divided by the head circumference. A CVR of 1.6 or less without a dominant cyst is considered low risk for the development of hydrops.
- Congenital lobar overinflation (CLO) appears echogenic on ultrasound and can involve a segment or subsegment of lung. CLO accounts for up to 20% of prenatally diagnosed fetal lung malformations.
- Congenital diaphragmatic hernias have a variable outcome dependent on severity of lung hypoplasia, liver herniation, and the presence of additional anomalies.

CHAPTER OUTLINE

DEVELOPMENT OF STRUCTURES IN THE CHEST
Pulmonary Development
Normal Sonographic Features of the Fetal Chest
Normal Diaphragm
Normal Thymus
PULMONARY HYPOPLASIA, APLASIA, AND AGENESIS
CONGENITAL PULMONARY AIRWAY MALFORMATION SPECTRUM
Congenital Pulmonary Airway Malformation
Bronchopulmonary Sequestration
Congenital Lobar Overinflation
PLEUROPULMONARY BLASTOMA
CONGENITAL HIGH AIRWAY OBSTRUCTION
BRONCHOGENIC CYST
NEURENTERIC CYST
PLEURAL EFFUSION
PERICARDIAL EFFUSION
PULMONARY LYMPHANGIECTASIA
CONGENITAL DIAPHRAGMATIC HERNIA
Other Hernias and Eventration
Associated Anomalies
Morbidity and Mortality
In Utero Therapy
CONCLUSION

Familiarity with the normal development of the fetal chest is critical both for recognizing chest anomalies and for understanding the consequences of these anomalies. Accurate prenatal diagnosis of thoracic lesions is important in providing appropriate recommendations for counseling, planning potential in utero interventions, and determining the optimal mode of delivery and postnatal care. Prenatal imaging can identify thoracic lesions and assess their impact on mediastinal structures and potential development of hydrops. Although chest abnormalities may be associated with lethal pulmonary hypoplasia, fatal chromosomal abnormalities, and lethal structural anomalies, many chest lesions resolve in utero with minimal sequelae. Fetal magnetic resonance imaging (MRI) can be a useful adjunct in cases with unclear sonographic diagnosis or potential need for in utero interventions.

DEVELOPMENT OF STRUCTURES IN THE CHEST

Pulmonary Development

In the human lung, there are five distinct stages of development, during which the lung matures and the number of alveoli increases.[1,2] At birth, the lungs are functional but structurally immature; the greatest increase in number of alveoli occurs postnatally. During the first 3 years of life, the alveoli are formed through a septation process that increases the gas exchange surface area. It is important to understand that this lung development process is ongoing, and that **space-occupying lesions,** or extrinsic abnormalities that do not allow for normal lung growth, can lead to improper lung development.

Normal Sonographic Features of the Fetal Chest

The fetal lungs are identified by ultrasound as homogeneously echogenic tissue surrounding the heart, separated by the hypoechoic, dome-shaped diaphragm from the abdominal organs (Fig. 36.1A and B). The fetal ribs are highly echogenic, curved bony structures arising near the spine and extending anteriorly to encompass more than half the thoracic circumference. Lung echogenicity varies during gestation, in general increasing in echogenicity as lung development progresses.

Assessment of lung volume is important for evaluation of fetuses at risk for pulmonary hypoplasia, particularly in cases of **congenital diaphragmatic hernia** (CDH), **pleural effusions,** prolonged **oligohydramnios,** and **skeletal deformities.** Methods to assess pulmonary size include measurement of the thoracic circumference,[3] lung area (defined as internal thoracic area minus cardiac area in diastole on a transverse four-chamber view[4]), and three-dimensional lung volumetry with ultrasound or MRI.[5-7]

The fetal lungs, thorax, and heart grow at similar rates, such that the normal cardiothoracic ratio remains constant in the

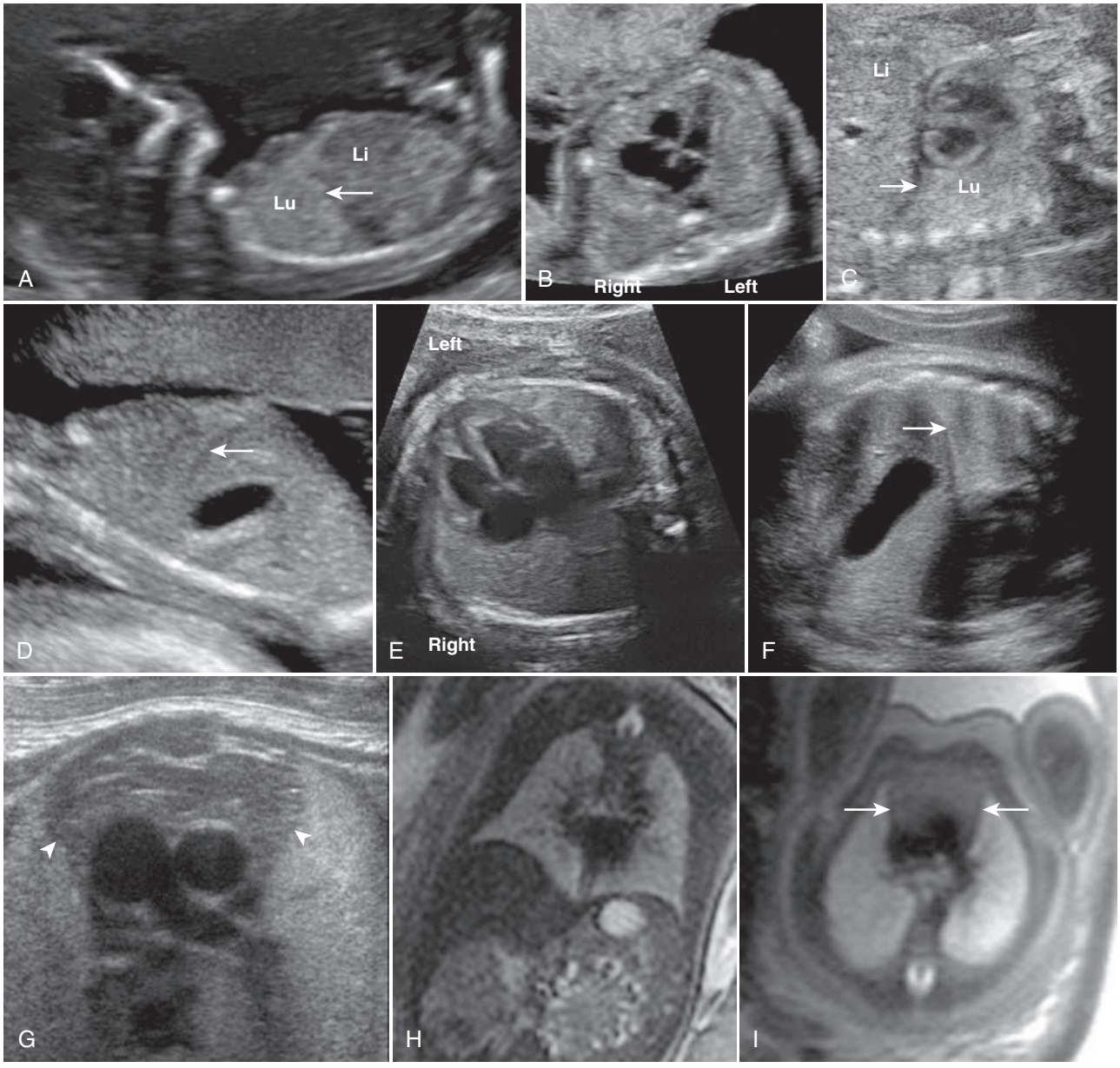

FIG. 36.1 Normal Fetal Chest. (A) Sagittal view of torso at 13 weeks. Note liver *(Li),* lungs *(Lu),* and diaphragm *(arrow).* **(B)** Four-chamber view of the heart surrounded by the homogeneous echogenic lungs at 18 weeks. **(C)** Coronal and **(D)** sagittal views of chest at 18 weeks show the dome-shaped hemidiaphragms *(arrow)* separating the lungs *(Lu)* from intraabdominal organs and the relative hypoechoic appearance of the liver *(Li).* **(E)** and **(F)** Axial and sagittal views of fetal chest *(arrow)* at 37 weeks. **(G)** Normal appearance of fetal **thymus** *(arrowheads)* at 37 weeks' gestation. **(H)** Coronal T2-weighted MRI shows normal lungs and diaphragm at 37 weeks. **(I)** Axial T2-weighted MRI of thymus *(arrows)* anterior to heart. The thymus is relatively hypoechoic to the surrounding lungs on ultrasound and intermediate signal on MRI.

second and third trimesters. On a normal four-chamber transverse view of the heart, the heart should occupy one-third to one-half the sonographic diameter of the thorax.

Stages of Human Lung Development

1. **Embryonic stage.** Extends to about 7 weeks
2. **Pseudoglandular stage.** Extends from 6 to 16 weeks; the lungs resemble tubuloacinar glands, with epithelial tubes sprouting and branching into the surrounding mesenchyme
3. **Canalicular stage.** Extends from 16 to 28 weeks; the cuboid epithelium differentiates into type I and type II cells, with production of surfactant and formation of the first, thin, air-blood barriers
4. **Saccular stage.** Extends from 28 to 36 weeks; the pulmonary parenchyma forms, the surrounding connective tissues thins, and the surfactant system matures
5. **Alveolar stage.** Extends from the 36th week of gestation to the first 3 years of life

The cardiac position and axis are constant in normal fetuses. The apex of the heart points left and touches the anterior chest wall. The posterior aspect of the right atrium lies to the right of midline[8] (Fig. 36.1E).

Familiarity with the normal anatomy and position of the fetal heart is crucial, along with in utero establishment of the right and left sides of the fetus. The reference to cardiac position and **situs** is identified by noting that the left atrium lies posteriorly, closest to the spine, and the right ventricle lies anteriorly, closest to the chest wall. Any deviation in the position of the heart should prompt a search for cardiac or pulmonary abnormalities. Anatomy of the fetal heart, including size and position, can be easily influenced by extracardiac thoracic anomalies.

Normal Diaphragm

Early in embryogenesis, the narrow pleuroperitoneal duct connects the **pleural and peritoneal cavities.** The development of the **diaphragm,** at 9 weeks' gestation, divides the two cavities. The normal diaphragm can be visualized as early as 10 weeks of gestation.[9,10] The diaphragm appears as a thin, hypoechoic, arched line separating the chest from intraabdominal contents (Fig. 36.1C-F). It is best recognized as a dome on each side on sagittal and coronal views, with no difference in the height of the diaphragm on either side.[11] The intact left hemidiaphragm is more easily verified by the presence of the fluid-filled stomach in the abdomen. On the right side, however, meticulous effort is required to identify the hypoechoic linear muscular diaphragm between the liver and lung.

Normal Thymus

The fetal thymus can be identified as early as 14 weeks' gestation in the anterior mediastinum. By the third trimester, the thymus is visualized as an ovoid, relatively hypoechoic structure[12,13] (Fig. 36.1G and I). The thymus contains spindle-shaped echogenicities that differentiate it from the surrounding echogenic lungs.[14] Thymus size varies greatly during gestation. Thymic imaging and measurements are not performed routinely on prenatal scans. However, prenatal identification and measurement of the fetal thymus is important when **DiGeorge syndrome** (with thymic aplasia or hypoplasia) is suspected. At times a large thymus will be confused with a mediastinal mass. Homogeneity and lack of mediastinal deviation can help differentiate normal thymus from a mediastinal teratoma or thymic cyst. The normal thymic average transverse measurement is 12 mm at 19 weeks' gestation and 33 mm at 33 weeks.[14] The normal thymic average perimeter is 128 mm at 38 weeks.[12] Acute fetal thymic involution has been reported in association with chorioamnionitis.[15]

Mediastinal teratomas[16,17] are rare anterior mediastinal complex masses. By ultrasound, the mass is heterogeneous and calcifications may be noted. MRI is a useful adjunct in the assessment of the mass for potential in utero and postnatal surgical treatment. The mass can cause polyhydramnios secondary to esophageal compression, and hydrops due to impaired venous return with resultant fetal demise.[16] Fetal intervention with aspiration of the tumor cyst has been described with a resultant decrease in intrathoracic pressure, which may stop the progression to hydrops and prevent lung hypoplasia. The ex utero intrapartum treatment (EXIT) procedure may be recommended to establish a proper airway at delivery.[16]

PULMONARY HYPOPLASIA, APLASIA, AND AGENESIS

Pulmonary hypoplasia is defined as a reduction in the number of cells, airways, and alveoli that results in an absolute decrease in the size and weight of the fetal lungs relative to gestational age.[18] Aplasia is the presence of rudimentary bronchi with no associated lung parenchyma. Agenesis is the complete absence of bronchi, vessels, and lung parenchyma. The earlier the insult to the fetal lungs occurs, the more severe is the degree of pulmonary hypoplasia, aplasia, or agenesis.[19] Pulmonary hypoplasia can result in postnatal respiratory distress and associated high neonatal mortality.[20] Pulmonary hypoplasia can be primary or secondary and can be unilateral or bilateral depending on the cause and time of insult to the lungs. **Primary** pulmonary hypoplasia is rare and is caused by a primary process in which the lung does not form normally. **Unilateral pulmonary agenesis** has an incidence of 1 in 15,000 births and is associated with other congenital anomalies.[21] **Bilateral pulmonary agenesis** is incompatible with postnatal life.

Secondary causes of pulmonary hypoplasia include masses that compress the lungs (e.g., CDH), skeletal malformations that do not allow the lungs to grow (e.g., thanatophoric dysplasia) (Fig. 36.2), and severe prolonged oligohydramnios (e.g., bilateral renal agenesis). Other factors that contribute to pulmonary hypoplasia include hormonal influences, pulmonary fluid dynamics, and abnormal fetal breathing movements.[22] The majority of cases of pulmonary hypoplasia are associated with major structural or chromosomal abnormalities (Table 36.1).

FIG. 36.2 Secondary Pulmonary Hypoplasia in Fetus With Thanatophoric Dysplasia. Transverse sonogram of the fetal chest at 20 weeks' gestation demonstrates a small chest circumference secondary to abnormally **short ribs** in this fetus with thanatophoric dysplasia.

TABLE 36.1 Causes of Pulmonary Hypoplasia

Main Category	Examples
Primary pulmonary hypoplasia or aplasia	Developmental abnormality
Thoracic space-occupying process	Congenital diaphragmatic hernia Lung masses Mediastinal mass Large pleural effusions
Oligohydramnios	Bilateral renal agenesis Prolonged preterm rupture of membranes
Skeletal anomalies	Skeletal dysplasias Chest wall tumors
Abnormal breathing	Phrenic nerve abnormalities, neuromuscular and central nervous system abnormalities
Chromosomal anomalies and syndromes	Trisomy 13, 18, and 21

Prenatal prediction of pulmonary hypoplasia and the degree of severity are important for parental counseling as well as for postnatal management planning, particularly if intensive respiratory care is required immediately after birth.[23] Proposed methods for prediction of prenatal pulmonary hypoplasia[24] include estimation of lung volumes by three-dimensional ultrasound[25,26] or by MRI,[27] thoracic circumference[28,29] (Table 36.2),[30] lung-to-head ratio,[9,31] lung-to-body weight ratio,[23] and Doppler studies of pulmonary arteries.[32]

Prognosis and management are variable and depend on the severity of the hypoplasia, age at delivery, and nature of the associated conditions. Absence of fetal breathing movements in the setting of oligohydramnios in pregnancies resulting from **premature rupture of membranes** is a predictor for pulmonary hypoplasia.[4] The spectrum of clinical outcomes ranges from mild respiratory insufficiency to neonatal death.

In cases of **unilateral** pulmonary hypoplasia or aplasia, there is mediastinal shift to the side of the hypoplastic lung, with no associated mass in the contralateral lung to explain the degree of mediastinal shift[33] (Fig. 36.3). The contralateral lung may be enlarged and echogenic.[21] Pulmonary hypoplasia can also be secondary to space-occupying lesions, such as congenital pulmonary airway malformations (CPAMs), diaphragmatic hernia (CDH), or pleural effusion.

CONGENITAL PULMONARY AIRWAY MALFORMATION SPECTRUM

An echogenic lesion in the fetal thorax (Table 36.3) or a cystic lesion in the fetal thorax can be part of the **CPAM** spectrum. This spectrum includes lesions that have been historically called **congenital cystic adenomatoid malformation** (CCAM), **bronchopulmonary sequestration** (BPS), and **congenital lobar emphysema.** CPAM is a congenital hamartomatous lung lesion that communicates with the bronchial tree through an abnormal communication and has normal pulmonary blood supply and venous drainage into the pulmonary veins.[34] BPS is normally developed lung tissue with systemic circulation. However, CPAM and BPS lesions often occur together and are then call hybrid lesions or part of the CPAM spectrum.[35-37] For clarity, we will describe these lesions separately, but the reader should be aware that careful histologic inspection will often find regions of CPAM in what appears to be a sequestration, as well as lesions that resemble a CPAM that have both pulmonic and systemic feeding vessels. Both of these types of lesions can have air trapping postnatally and therefore may have elements of congenital lobar overinflation (CLO; previously known as **congenital lobar emphysema**).

Congenital Pulmonary Airway Malformation

CPAM accounts for about 25% of congenital lung masses,[38] with an incidence of 1 in 25,000 live births.[39] It is comprised of pulmonary tissue with abnormal bronchial proliferation that may involve either lung or any lobe. In 85% to 95% of cases, CPAM is limited to one lobe or segment, with 2% to 3% of CPAMs occurring bilaterally and with the right and left lungs equally affected.[40]

CPAM results from a pulmonary insult during embryologic development of the bronchial tree before the seventh week of gestation, resulting in failure of bronchial maturation and lack of normal alveoli. Histologically, CPAM is differentiated from other lung masses by the absence of bronchial cartilage and bronchial tubular glands, with overproduction of terminal

TABLE 36.2 Normal Thoracic Circumference Correlated With Gestational Age

	PREDICTIVE PERCENTILES								
Age (Wk)	**2.5**	**5**	**10**	**25**	**50**	**75**	**90**	**95**	**97.5**
16	5.9	6.4	7.0	8.0	9.1	10.3	11.3	11.9	12.4
17	6.8	7.3	7.9	8.9	10.1	11.2	12.2	12.8	13.3
18	7.7	8.2	8.8	9.8	11.0	12.1	13.1	13.7	14.2
19	8.6	9.1	9.7	10.7	11.9	13.0	14.0	14.6	15.1
20	9.5	10.0	10.6	11.7	12.9	13.9	15.0	15.5	16.0
21	10.4	11.0	11.6	12.6	13.7	14.8	15.8	16.4	16.9
22	11.3	11.9	12.5	13.5	14.6	15.7	16.7	17.3	17.8
23	12.2	12.8	13.4	14.4	15.5	16.6	17.6	18.2	18.8
24	13.2	13.7	14.3	15.3	16.4	17.5	18.5	19.1	19.7
25	14.1	14.6	15.2	16.2	17.3	18.4	19.4	20.0	20.6
26	15.0	15.5	16.1	17.1	18.2	19.3	20.3	21.0	21.5
27	15.9	16.4	17.0	18.0	19.1	20.2	21.3	21.9	22.4
28	16.8	17.3	17.9	18.9	20.0	21.2	22.2	22.8	23.3
29	17.7	18.2	18.8	19.8	21.0	22.1	23.1	23.7	24.2
30	18.6	19.1	19.7	20.7	21.9	23.0	24.0	24.6	25.1
31	19.5	20.0	20.6	21.6	22.8	23.9	24.9	25.5	26.0
32	20.4	20.9	21.5	22.6	23.7	24.8	25.8	26.4	26.9
33	21.3	21.8	22.5	23.5	24.6	25.7	26.7	27.3	27.8
34	22.2	22.8	23.4	24.4	25.5	26.6	27.6	28.2	28.7
35	23.1	23.7	24.3	25.3	26.4	27.5	28.5	29.1	29.6
36	24.0	24.6	25.2	26.2	27.3	28.4	29.4	30.0	30.6
37	24.9	25.5	26.1	27.1	28.2	29.3	30.3	30.9	31.5
38	25.9	26.4	27.0	28.0	29.1	30.2	31.2	31.9	32.4
39	26.8	27.3	27.9	28.9	30.0	31.1	32.2	32.8	33.3
40	27.7	28.2	28.8	29.8	30.9	32.1	33.1	33.7	34.2

With permission from Chitkara U, Rosenberg J, Chevanak FA, et al. Prenatal sonographic assessment of thorax: normal values. Am J Obstet Gynecol. 1987;156(5):1069-1074.[30]

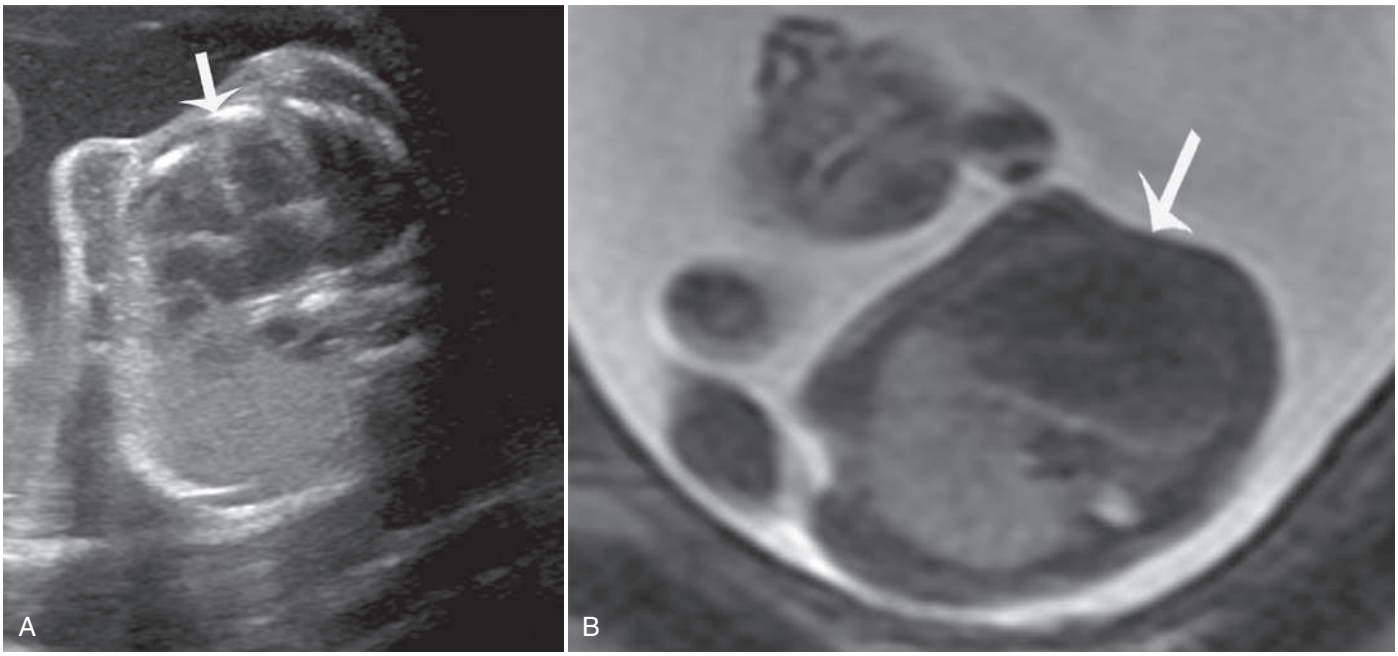

FIG. 36.3 Unilateral Pulmonary Hypoplasia. (A) Axial sonogram of the fetal chest at 33 weeks' gestation demonstrates mediastinal shift to the left *(arrow)*. No lung mass is present. **(B)** Axial MRI of the chest confirms the mediastinal shift and lack of a lung mass.

TABLE 36.3 Differential Diagnosis of Echogenic Lesion in Fetal Thorax

Abnormality	Location	Distinguishing Features
Congenital pulmonary airway malformation (CPAM)	Unilateral (2%-3% bilateral)	Multiple cysts may be seen in association with echogenic lesion
Sequestration	Unilateral; left lower lobe most often	Systemic blood supply
Congenital lobar overinflation	Unilateral; upper lobe most often	Similar to microcystic CPAM; enlarged echogenic lung with mediastinal shift
Congenital diaphragmatic hernia (CDH)	Typically unilateral; left sided most often	Peristalsis of bowel in chest Stomach above diaphragm Absence of part of the diaphragm
Congenital high airway obstruction (CHAOS)	Bilateral	Distended trachea and main central airways Symmetrical bilateral enlarged lungs with eversion of hemidiaphragms

bronchiolar structures without alveolar differentiation, except in the subpleural areas.[41-43] The resulting cystic lesions result in enlargement of the affected lobe (or segment). If sufficiently large, CPAM will result in mediastinal shift and interfere with normal alveolar development in the adjacent lung. Communication with the tracheobronchial tree usually is retained, with vascular supply and venous drainage to the pulmonary circulation, unless CPAM is associated with sequestration. In these cases this is called a "hybrid lesion."

There are different classification schemes for CPAMs depending on histology[44] or on prenatal sonographic appearance.[44,45] The three main types described sonographically are **type I** (large cysts measuring 2-10 cm), **type II** (multiple small cysts), and **type III** (microcystic, appearing as echogenic lesions).

Sonographic diagnosis can be made as early as 16 weeks. CPAM may appear as a solid echogenic lung mass (microcystic) or as a mixed, cystic and solid mass (Fig. 36.4, Video 36.1). Color Doppler ultrasound may demonstrate vascular flow to the lesion from branches of the pulmonary artery. Typically, there is no systemic feeding vessel, although as mentioned, CPAM can occur in concert with sequestration. The lesions with microcysts appear solid and echogenic, whereas the macrocystic CPAMs have demonstrable cysts. Occasionally, only a single large cyst is visualized.

As with any chest mass, it is important to assess for associated mediastinal shift, polyhydramnios, and hydrops because these factors impact prognosis and management.[45,46] It is the size of the CPAM rather than the size of the cysts that determines whether or not the fetus develops **hydrops.** Macrocystic lesions usually have a more favorable prognosis. Large CPAMs can result in cardiac and vena cava compression, leading to altered hemodynamics and hydrops as a result of elevated central venous pressure that may require in utero intervention.[47]

The CPAM volume ratio (CVR), a measurement initially described by ultrasound, should be measured to assess prognosis and risk of hydrops. It is obtained by calculating the volume of the lung mass (height × anteroposterior diameter × transverse diameter × 0.52) and dividing it by the head circumference. A CVR less than 1.6 indicates a 14% risk of developing hydrops for fetuses with macrocystic lesions and 3% for those with microcystic lesions. If the CVR is greater than 1.6, the risk increased to 75%.[48] In the absence of hydrops, the prognosis is good, with reported live birth rates of 95% and higher.[49-51] Untreated hydrops as a result of CPAM, however, has an anticipated mortality rate of up to 100%.[52-61] Hydrops is therefore an indication for in utero fetal therapy, and close follow-up in the second and early third trimesters is important when a high CVR is encountered. However, if there is fluid, such as ascites, in only a single body cavity, spontaneous regression of the lesion and improvement in fluid status is still possible.[62] Steroids have been used in an attempt to prevent the development of hydrops or help speed the regression of the lesion, particularly with microcystic CPAM. In uncontrolled studies, maternal steroid administration appeared to reverse hydrops and improve outcome.[55-59] However, it is possible that fetal thoracic growth and/or CPAM regression rather than steroids account for the resolution of hydrops.

With macrocystic CPAM, steroid therapy appears to be less helpful, with in utero therapy generally consisting of either draining the largest cyst with a single stick procedure[48] (Fig. 36.4G) or, if fluid reaccumulates, placing a shunt.[60,61] Rarely is open fetal surgery indicated. A meta-analysis showed that shunting of CPAMs improved survival in fetuses with hydrops compared with no effect on survival in fetuses with chest masses without hydrops.[63] The success with open fetal surgery in cases of CPAM ranges between 29% and 62% but has the limitation of expected preterm delivery.[64]

Associated anomalies, most often renal, intestinal, and cardiac, are present in up to 26% of cases,[35,44-46,65] more frequently when CPAM is bilateral.[40] Therefore a complete fetal anatomic survey is indicated. The differential diagnosis includes BPS, CLO, bronchogenic cyst, CDH, laryngeal or tracheal occlusion, neurenteric/enteric cysts, and mediastinal teratomas.

MRI has become a useful adjunct in the evaluation and management of CPAM[66] (Fig. 36.4H and I). Macrocysts have a high T2-weighted signal intensity, whereas microcysts have moderately high signal intensity and are relatively homogeneous. As the lesions regress, they develop lower signal intensity on T2-weighted imaging.[67]

Longitudinal studies of CPAM have demonstrated that most CPAMs demonstrate rapid progressive growth from about weeks

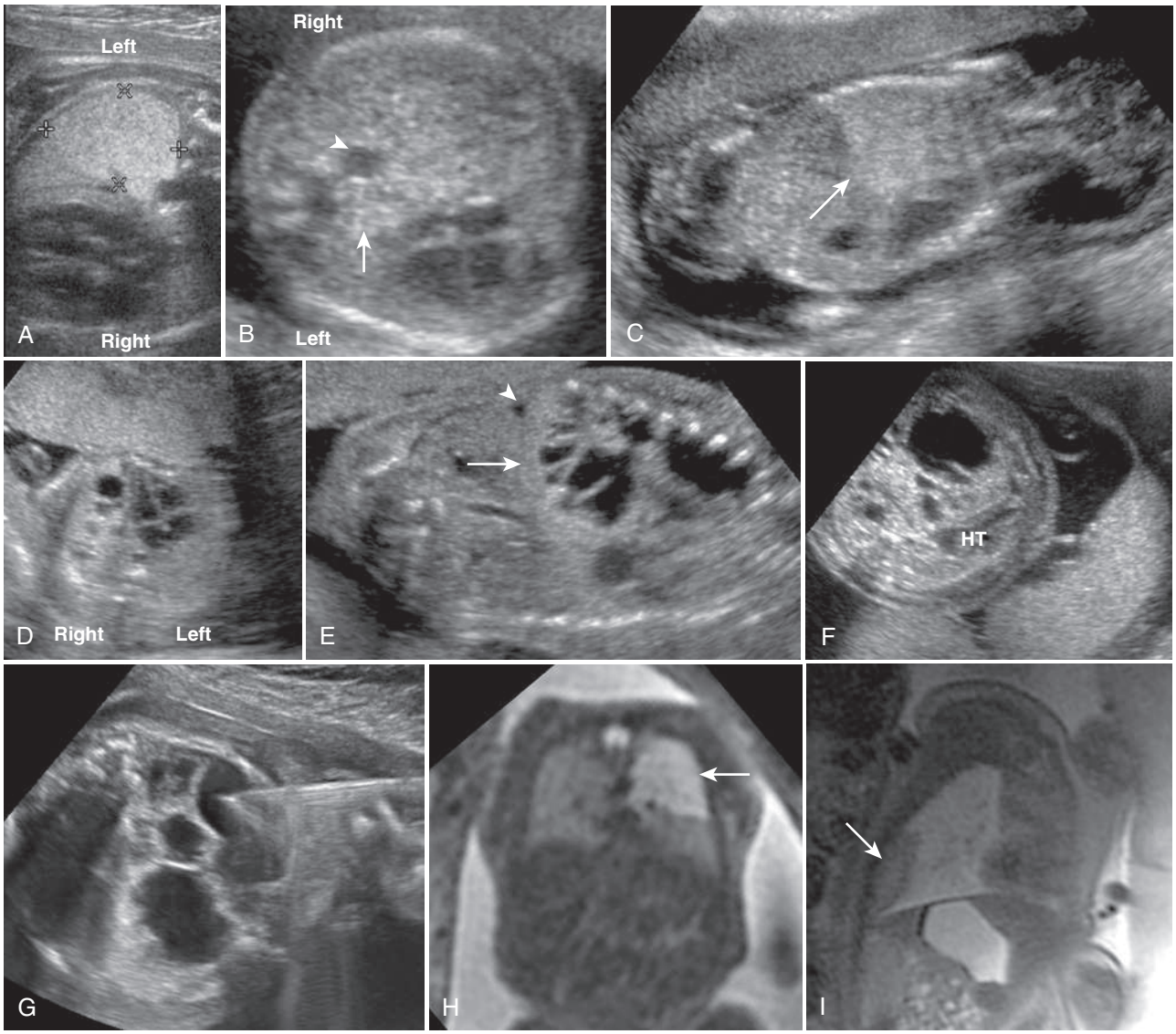

FIG. 36.4 Congenital Pulmonary Airway Malformation (CPAM). (A) Axial sonogram at 28 weeks shows a homogeneously echogenic mass *(calipers)* in the mid–left hemithorax with no large cysts or feeding vessels. There is mild mediastinal shift to the right. **(B)** Axial sonogram of right-sided CPAM *(arrow)* at 20 weeks with small cysts, the largest of which is 8 mm *(arrowhead).* There is moderate mediastinal shift to the left. **(C)** Sagittal oblique sonogram shows CPAM everting the hemidiaphragm *(arrow).* **(D)** Transverse view of chest with CPAM containing small cysts and mild mediastinal shift. **(E)** and **(F)** Axial and oblique coronal images at 25 weeks in a macrocystic CPAM *(arrow)* with eversion of the hemidiaphragm, trace ascites *(arrowhead),* and severe mediastinal shift with compression of the heart *(HT).* **(G)** Ultrasound-guided percutaneous drainage of CPAM. A 20-gauge needle was inserted into the largest cyst with relief of cardiac compression. **(H)** Coronal T2-weighted MRI shows a well-circumscribed area of T2 hyperintensity *(arrow)* in the left upper lobe. **(I)** Oblique coronal T2-weighted MRI shows a well-circumscribed area of low T2 signal *(arrow)* in a fetus with a typical, resolving CPAM. See also Video 36.1.

20 to 26 of gestation, peaking at about 25 weeks,[48,62] and then growth plateaus and often regresses.[68] There are no reliable criteria for determining which lesions will continue to grow versus those that will stabilize or regress. About 50% of masses persist to delivery.[49] Fifteen percent of these masses decrease in size during the late second and the third trimesters; the majority have a relative decrease in size as a result of normal fetal thoracic growth, but a few increase in size.[46,62] As masses decrease in size, their echogenicity can become similar to that of surrounding normal lung because of an increase in normal lung echogenicity and decrease in echogenicity of the CPAM. Thus they may become difficult to visualize late in gestation, with residual mass effect being the main finding on ultrasound.

If the fetus does not develop hydrops before 26 weeks, the prognosis is generally good.[49,69] Close surveillance of the growth of these lesions is recommended throughout the second trimester particularly if the CVR is higher than 1.6. Delivery planning should be made in conjunction with the neonatology and/or pediatric surgery teams. If the lung mass has resolved or is small with no mediastinal shift or hydrops, the presence of a CPAM itself is not an indication for early delivery or cesarean delivery[69] as neonatal respiratory issues are unlikely.

CVR may help predict the risk of neonatal respiratory problems.[49,70] In a retrospective study a final CVR of greater than 1.0 in nonhydropic fetuses was predictive of respiratory symptoms at birth (sensitivity, specificity, positive and negative predictive values: 75%, 98%, 75%, and 98%, respectively) and perinatal resection (sensitivity, specificity, positive and negative predictive values: 100%, 98%, 75%, and 100%, respectively).[49]

For fetuses with large masses that cause mediastinal shift and/or hydrops, delivery should be planned for a tertiary care center with an neonatal intensive care unit (NICU) capable of providing extracorporeal membrane oxygenation (ECMO), and with pediatric surgeons experienced in care of these infants.[50,71] If hydrops develops after 32 weeks of gestation, early delivery is recommended, possibly with the use of the EXIT procedure.[71] In EXIT, the fetus is partially delivered and intubated without clamping the umbilical cord. Uteroplacental blood flow and gas exchange are maintained to provide uterine relaxation, and amnioinfusion is performed to maintain uterine volume. This provides time for resection of the lung mass prior to complete delivery of the infant in rare instances or, more often, cannulation for ECMO, thus creating a controlled situation for delayed removal of the CPAM. Overall neonatal survival of 90% has been reported.[72]

Although regression of CPAM on prenatal ultrasound is common, the lesion does not completely disappear.[73] In asymptomatic neonates, the lesion may not be seen on chest radiography after birth. In these cases, postnatal computed tomography (CT) is recommended. Postnatal removal of asymptomatic masses is recommended because of potential secondary infection, and risk of carcinomas arising in CPAM.[74] The timing of surgical resection of CPAM remains controversial, but most centers favor elective surgical resection in the first year of life.[75]

Bronchopulmonary Sequestration

BPS is an anomaly in which nonfunctioning pulmonary tissue is not in normal continuity with the native tracheobronchial tree[76] and has a blood supply from the systemic circulation. Sequestrations account for up to 6% of congenital lung malformations.[77,78] Concomitant anomalies associated with sequestration include CDH, **diaphragmatic eventration and paralysis, bronchogenic cyst, ectopic pancreas, vertebral anomalies,** and **foregut duplication.** Hybrid combinations of CPAM and BPS are relatively common, having connection with both the pulmonary and the systemic arterial supply.

There are two main types of sequestration: intralobar and extralobar. A third variant is suggested when communicating bronchopulmonary foregut malformation is present.[79]

Extralobar sequestration (also known as **extrapulmonary sequestration**) accounts for 25% of BPS postnatally. This lesion is a supernumerary lung bud invested by its own pleura, typically deriving its blood supply from the splanchnic vessels surrounding the foregut, which results in the systemic blood supply.[80] The venous drainage is usually through a single vessel into the azygous, hemiazygos, and/or the vena cava system. In up to 25% of cases, however, the extralobar sequestration is partially drained through pulmonary veins. Extralobar sequestration is typically found in the left posterior costodiaphragmatic sulcus between the lower lobe and the hemidiaphragm (80%).[81] Extralobar sequestrations occur below the diaphragm in suprarenal locations in 10% to 15% of cases (with a differential diagnosis of **neuroblastoma and adrenal hemorrhage**).[82] In rare cases, sequestration may present as a mediastinal or pericardial mass.[83]

Intralobar sequestration comprises abnormal lung tissue with systemic arterial supply within the normal lung, sharing the visceral pleura and draining to pulmonary veins although connections to the vena cava, azygous vein, or right atrium can also occur.[81] It occurs more often in the lower lobes and slightly more often on the left. Postnatally it accounts for 75% of cases of BPS.[84]

Sequestration can be detected on prenatal sonogram as early as 16 weeks' gestation.[85] Typically, a sequestration appears as a well-defined, homogeneous, echogenic wedge-shaped pulmonary mass in the lower lobe adjacent to the hemidiaphragm (Fig. 36.5). Classically, these lesions do not have cysts. However, cysts can result from dilated bronchioles or hybrid lesions of concomitant CPAM. Sequestration can be distinguished from other congenital lung masses by identifying on Doppler interrogation a systemic artery arising from the thoracic or abdominal aorta feeding the mass. Determination of where the vessel arises is important for counseling parents about the approach that will be needed for postnatal surgical removal of the mass. The differential diagnosis includes CPAM, CLO, CDH, neuroblastoma, and adrenal hemorrhage.

MRI can help confirm the diagnosis and location of the mass (above, within, or below the diaphragm). The mass is high signal on T2-weighted images. A feeding vessel may be noted as a low signal line coursing from the aorta to the mass.[61,86] Small sequestrations with minimal mediastinal shift have a benign clinical course.[37] As with other chest masses, a large sequestration may result in mediastinal shift. However, most prenatally detected sequestrations are of small or medium size. These lesions usually regress in size during gestation.[37,45] Large sequestrations can be complicated by pleural effusions and with hydrops can lead to increased prenatal mortality (Fig. 36.6). Effusions can be secondary to a large mass compressing the heart and vena cava or due to torsion around the vascular pedicle.[89] Hydrops is rare but can occur secondary to shunting of the systemic arterial feeder or mass effect from the sequestration itself with associated mediastinal shift and compression of the heart or inferior vena cava. For such complicated cases, the pleural effusion can be treated with pleuroamniotic shunting and drainage.[87-89] Laser surgery has also been attempted with some success.[90,91]

Prognosis is excellent in the absence of hydrops.[92] Mortality rate is as high as 80% if hydrops is present.[61] Masses that appear to resolve in utero are typically still present on postnatal CT scans.

Apparent resolution of masses can be the result of outgrowth of the systemic circulation or torsion around the vascular pedicle. As they regress, they are more difficult to see on ultrasound and can produce low signal intensity on MRI.[52,93]

Delivery planning should include input from the neonatologist and pediatric surgeon. If the mass is small, there is no indication for early delivery or cesarean section. For fetuses with large masses with hydrops, delivery should be at a tertiary care center. If

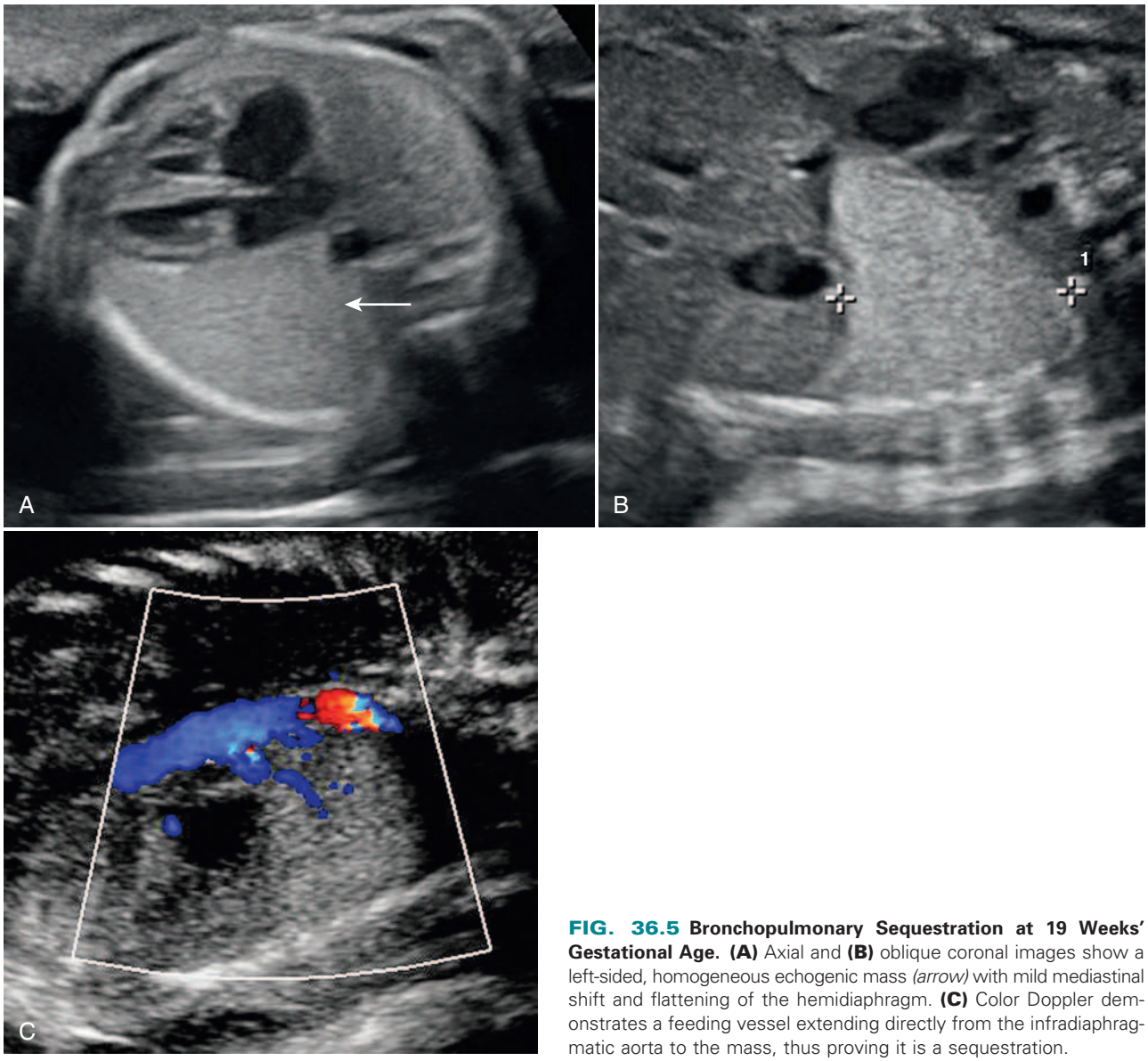

FIG. 36.5 Bronchopulmonary Sequestration at 19 Weeks' Gestational Age. (A) Axial and **(B)** oblique coronal images show a left-sided, homogeneous echogenic mass *(arrow)* with mild mediastinal shift and flattening of the hemidiaphragm. **(C)** Color Doppler demonstrates a feeding vessel extending directly from the infradiaphragmatic aorta to the mass, thus proving it is a sequestration.

hydrops develops after 32 weeks' gestation, early delivery is recommended, possibly with use of the EXIT procedure.

Congenital Lobar Overinflation

CLO is overinflation of a lung lobe without destruction of alveolar septa. Pathologically there are two subgroups. One is associated with an overinflated lung secondary to an intrinsic cartilage abnormality of the airway, absent bronchial cartilage, or extrinsic compression by a dilated pulmonary artery or bronchogenic cyst. The collapsed airway acts as a one-way valve resulting in trapping of fluid prenatally and air postnatally. This form, previously known as **congenital lobar emphysema,** occurs more frequently in the left upper lobe. A second subgroup is characterized by lobar, segmental, or subsegmental overinflation with an association with bronchial atresia. This subgroup can be seen in the lower lobes and has fewer symptoms. In up to 50% of cases CLO is idiopathic.[94,95]

On prenatal ultrasound, CLO is similar in appearance to microcystic CPAM, manifesting as a homogeneous echogenic mass. A central dilated bronchus helps confirm the diagnosis of an associated bronchial anomaly. Mass effect with mediastinal shift may occur with herniation of the overinflated lung to the contralateral side[96-98] (Fig. 36.7).

On color Doppler, CLO has a blood supply from the pulmonary artery and drains to the pulmonary vein.[94] Echocardiogram should be performed to exclude congenital heart disease.[99]

On MRI, CLO is characterized by increased T2-weighted signal intensity with a lobar distribution. It is more homogeneous than CPAM and less high in signal than BPS. The lung anatomy is intact with stretched hilar vessels.[100]

As with CPAM, the lesion can regress in utero.[101] Hydrops has been described; thus follow-up examination should be performed prenatally to document stability.[102,103] Because of the nonspecific appearance, even if the mass regresses in size, postnatal

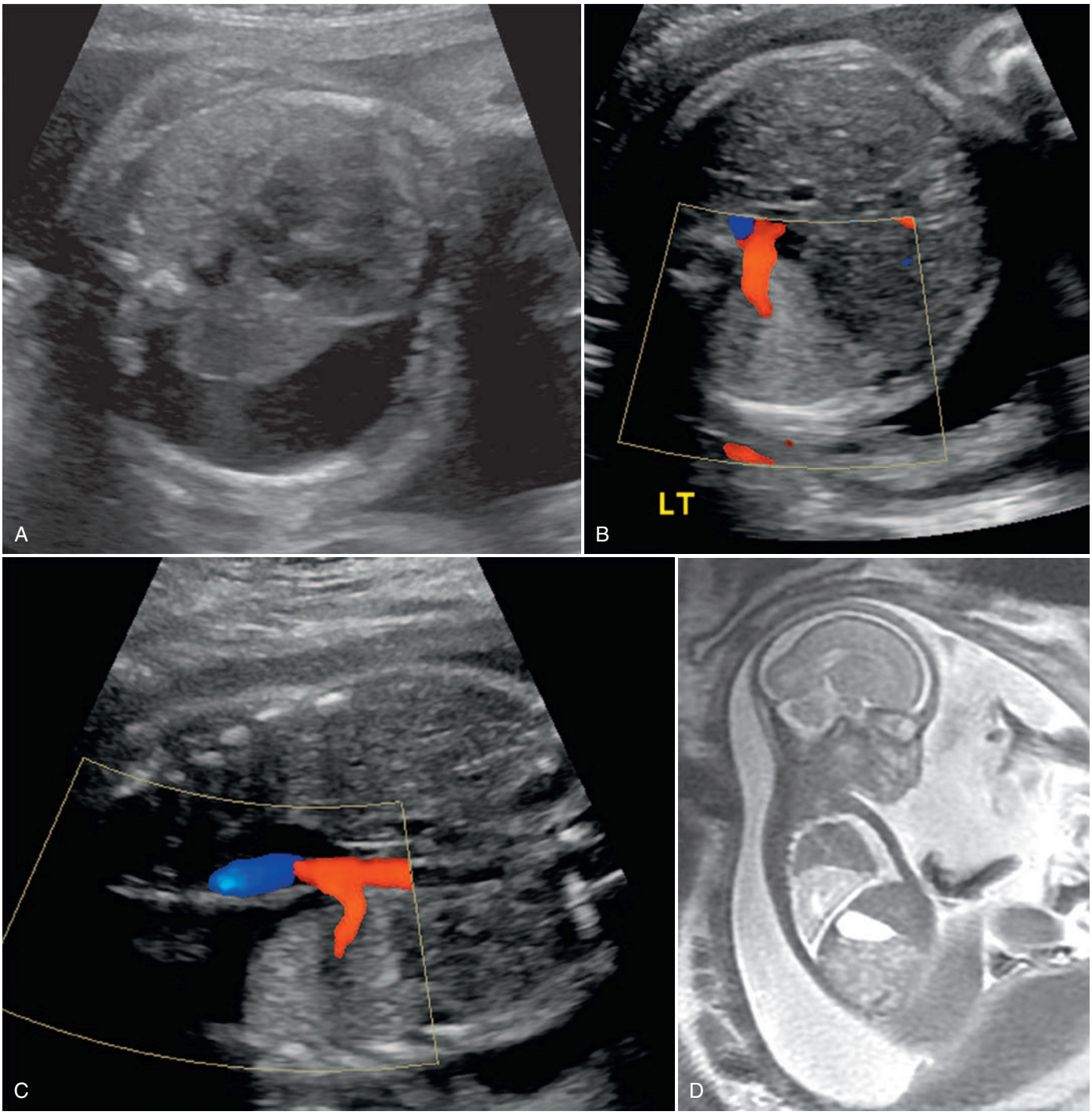

FIG. 36.6 Bronchopulmonary Sequestration With Effusion. (A) Axial image of the fetal chest demonstrates a left pleural effusion with moderate mediastinal shift to the right. **(B)** Axial and **(C)** coronal color Doppler images show a systemic feeding vessel coursing into the echogenic left lower lobe. **(D)** Sagittal T2-weighted MRI shows the high signal intensity left lower lobe mass with a moderate surrounding effusion.

follow-up is required because air trapping and respiratory distress may necessitate lobar resection.[102]

PLEUROPULMONARY BLASTOMA

Pleuropulmonary blastoma is a rare primary neoplasm originating from the pleuropulmonary mesenchyme (previously called **pulmonary blastoma** or **malignant mesenchymoma**).[104] Three pleuropulmonary blastoma types have been described: type I (exclusively cystic), type II (mixed cystic and solid lesion), and type III (predominantly solid mass).[105]

Seen on ultrasound, pleuropulmonary blastoma appears as a complex macrocystic lesion in the chest, indistinguishable from a CPAM. Features that help differentiate pleuropulmonary blastoma from CPAM include a positive family history, presence of multifocal lesions, and association with pleural effusion.[106]

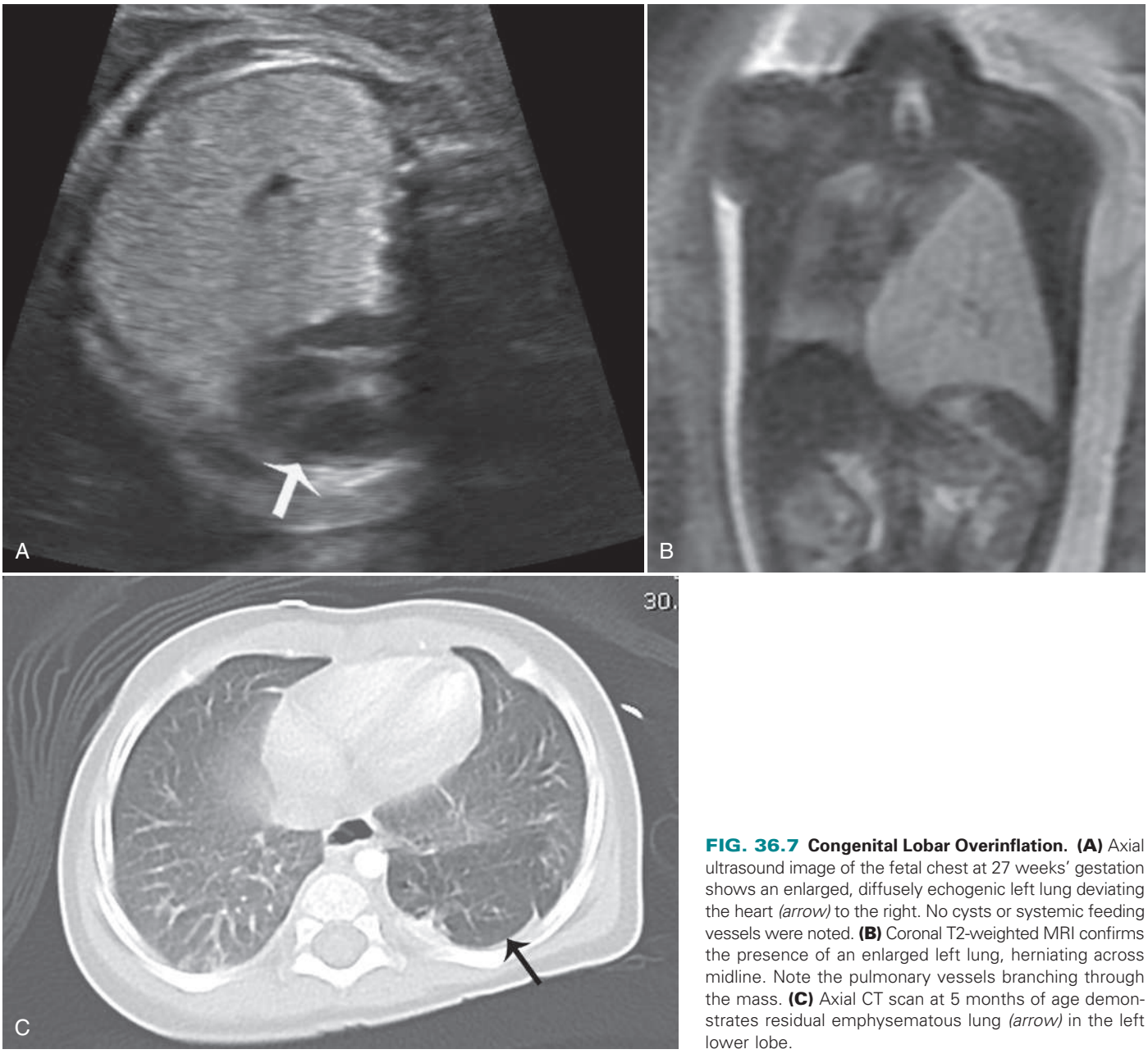

FIG. 36.7 Congenital Lobar Overinflation. (A) Axial ultrasound image of the fetal chest at 27 weeks' gestation shows an enlarged, diffusely echogenic left lung deviating the heart *(arrow)* to the right. No cysts or systemic feeding vessels were noted. **(B)** Coronal T2-weighted MRI confirms the presence of an enlarged left lung, herniating across midline. Note the pulmonary vessels branching through the mass. **(C)** Axial CT scan at 5 months of age demonstrates residual emphysematous lung *(arrow)* in the left lower lobe.

There are no definitive imaging findings to distinguish type I pleuropulmonary blastoma from type I CPAM.[107] Progressive enlargement in the third trimester or postnatally is suggestive of a pleuropulmonary blastoma in contradistinction of a CPAM, which should get smaller over time. Early diagnosis and complete resection are key to a good outcome.[106]

CONGENITAL HIGH AIRWAY OBSTRUCTION

Congenital high airway obstruction syndrome (CHAOS) is a spectrum of conditions characterized by incomplete or complete obstruction of the high fetal airway.[108,109] Any fetal abnormality that obstructs the larynx or trachea, causing intrinsic atresia or extrinsic compression can result in CHAOS. **Laryngeal atresia** is the most frequent cause. Other causes include **laryngeal** or **tracheal webs, laryngeal cysts, tracheal atresia, subglottic stenosis** or **atresia,** and **laryngeal *or* tracheal agenesis.**[110] If untreated, CHAOS is almost always lethal.[109]

Although sporadic with unknown incidence, CHAOS can be part of various chromosomal disorders.[111,112] It can be familial with autosomal dominant inheritance and variable expression.[113] Laryngeal atresia can occur as part of **Fraser syndrome** (tracheal or laryngeal atresia, renal agenesis, microphthalmia, and syndactyly or polydactyly) with autosomal recessive inheritance.[112-114]

Prenatal ultrasound findings can be visualized as early as 16 weeks' gestation.[115] Findings include bilateral symmetrically enlarged echogenic lungs, dilated fluid-filled trachea and central bronchi, and flattened or everted diaphragms[116-119] (Fig. 36.8).

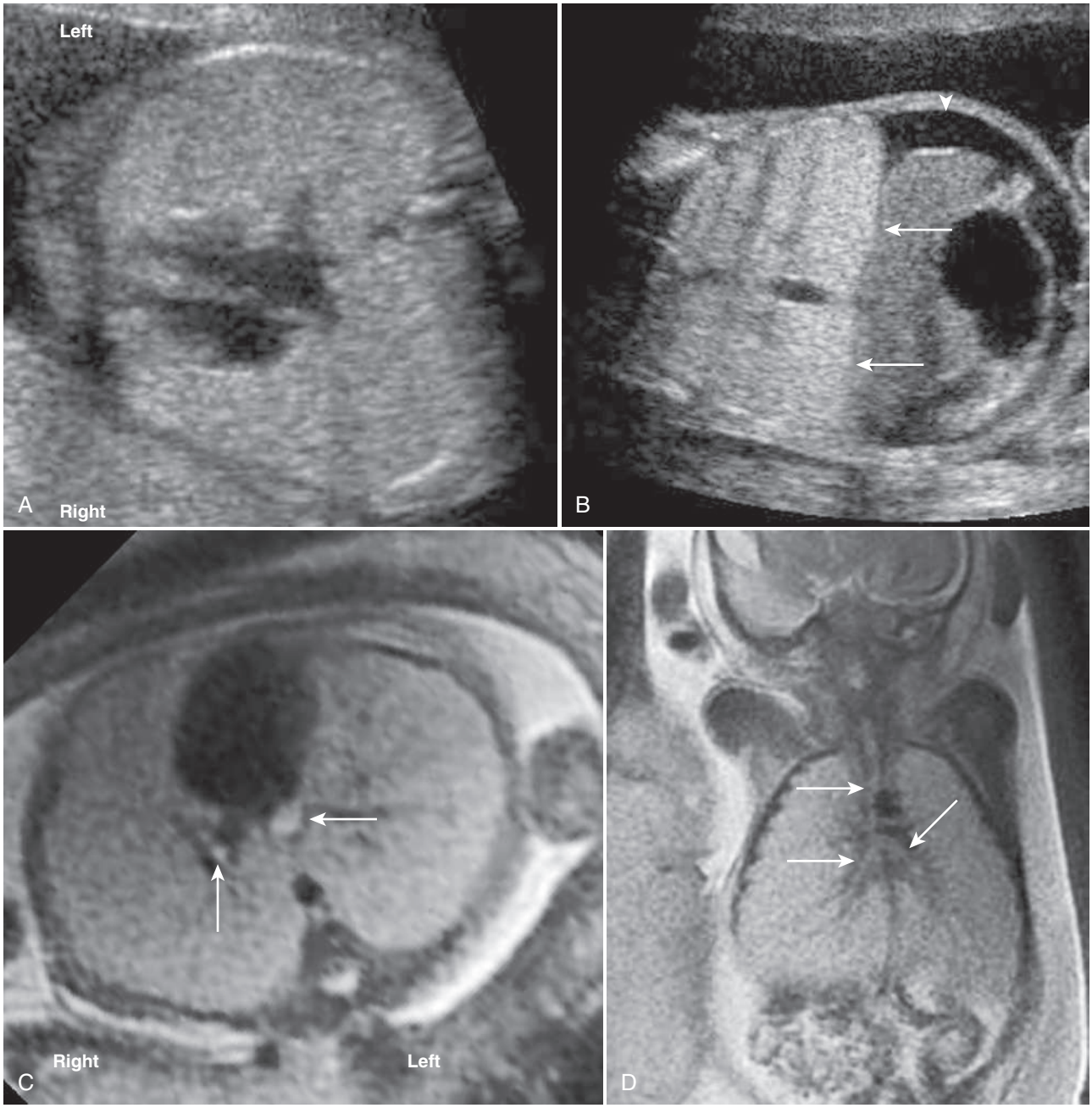

FIG. 36.8 Congenital High Airway Obstruction Syndrome (CHAOS) at 19 Weeks. (A) Axial and **(B)** and coronal views of the chest show diffusely enlarged, echogenic lungs bilaterally with eversion of the hemidiaphragms *(arrows)* and ascites *(arrowhead)*. **(C)** and **(D)** Axial and coronal T2-weighted MR images show increased lung volume and fluid-filled airways *(arrows)*. (Courtesy of Katherine Fong, MD, University of Toronto.)

The heart usually assumes a more central and anterior position than normal and is often compressed as the size of the lungs increases.[110] Frequently, there are associated findings of ascites and other signs of hydrops. The mechanism of ascites may be from compression of the heart and great vessels by the enlarged lungs.[120] Either polyhydramnios or oligohydramnios may be present.

The lungs are distended and appear homogeneously echogenic because of increased fluid and increased lung growth induced by the upper airway obstruction.[110] The increased number of tissue-fluid interfaces produces the hyperechoic appearance of the lungs. Lung volume can increase up to 15 times the expected size. The hyperplastic lungs are edematous but otherwise histologically normal.[110]

MRI can be used to identify the region of obstruction and assist in decisions regarding in utero intervention and intrapartum procedures. Characteristic findings include increased lung volume, diffuse increase in lung intensity on T2-weighted images, and a dilated fluid-filled trachea and bronchi.[116] Extrinsic causes of tracheal compression can be evaluated.[118]

More than 50% of fetuses with laryngeal obstruction have associated abnormalities, most often in the renal system and

central nervous system. At times, CHAOS is in association with a **tracheoesophageal fistula.** This fistula acts as an alternative pathway for the accumulated fluid, leading to a decrease in lung volume, reversal of diaphragmatic eversion, and resolution of ascites and polyhydramnios.[108]

If untreated, laryngeal and tracheal atresia can lead to death either in utero from hydrops or within minutes after birth from respiratory compromise. Neonatal survival is possible if the delivery is performed with the **ex utero intrapartum treatment** (EXIT) procedure.[121-124] The EXIT procedure involves tracheostomy placement below the level of the obstruction while maternal placental circulation is maintained.

BRONCHOGENIC CYST

Bronchogenic cysts (Table 36.4) are rare anomalies that result from abnormal budding or branching of the tracheobronchial tree. They are most often located in the mediastinum in the subcarinal region.[125] However, 15% of bronchogenic cysts occur in the lungs, pleura, and diaphragm. They account for 11% to 18% of mediastinal masses in infants and children.[126,127] The cyst is lined by ciliated mucus-secreting bronchial epithelium and may be mucus-filled. Although the mediastinal cysts do not communicate with the bronchopulmonary tree, intrapulmonary cysts usually do.

Bronchogenic cysts range in size from a few millimeters to more than 5 cm. On prenatal ultrasound, they usually appear as anechoic unilocular intrathoracic cysts (Fig. 36.9), at times with layering echogenic material.[128,129] If the cyst does not cause mass effect, it typically will not cause a problem in utero. However, if the cyst compresses the airway, it can lead to airway obstruction at birth.[130] The main differential diagnosis is CPAM. However, CPAM usually has more than one cyst and an associated echogenic mass with mass effect. If a bronchogenic cyst causes obstruction, it may lead to the distal lung accumulating fluid, masquerading as an echogenic lung lesion such as CPAM or sequestration.

The cyst can be mediastinal or parenchymal. Mediastinal lesions are typically unilocular, located midline in the subcarinal region (75%). Parenchymal lesions are usually simple unilocular cysts located along the tracheobronchial tree. Septations may be seen. At times the cyst can cause bronchial compression and result in distal overinflation.

Fetal MRI can be helpful in cases with an unclear diagnosis. The cyst exhibits high signal intensity on T2-weighted imaging. When the cyst causes obstruction, there will be distal lung overinflation, and the lung will become hyperintense as well.[130] Surgical resection for bronchogenic cysts is performed postnatally

TABLE 36.4 Differential Diagnosis of Fetal Thoracic Cystic Lesion

	Distinguishing Features
Congenital pulmonary airway malformation (CPAM)	Associated with echogenic lung mass, typically multiple cysts
Congenital diaphragmatic hernia (CDH)	Peristalsis of bowel in chest Stomach above diaphragm Absence of part of the diaphragm
Teratoma	Mass does not obey lobar boundaries; may have calcifications
Neurenteric cyst	Adjacent to spine
Bronchogenic cyst	Typically single cyst, may obstruct and have distal hyperinflated lung
Esophageal duplication	Adjacent to esophagus
Lymphangioma	Crosses anatomic boundaries

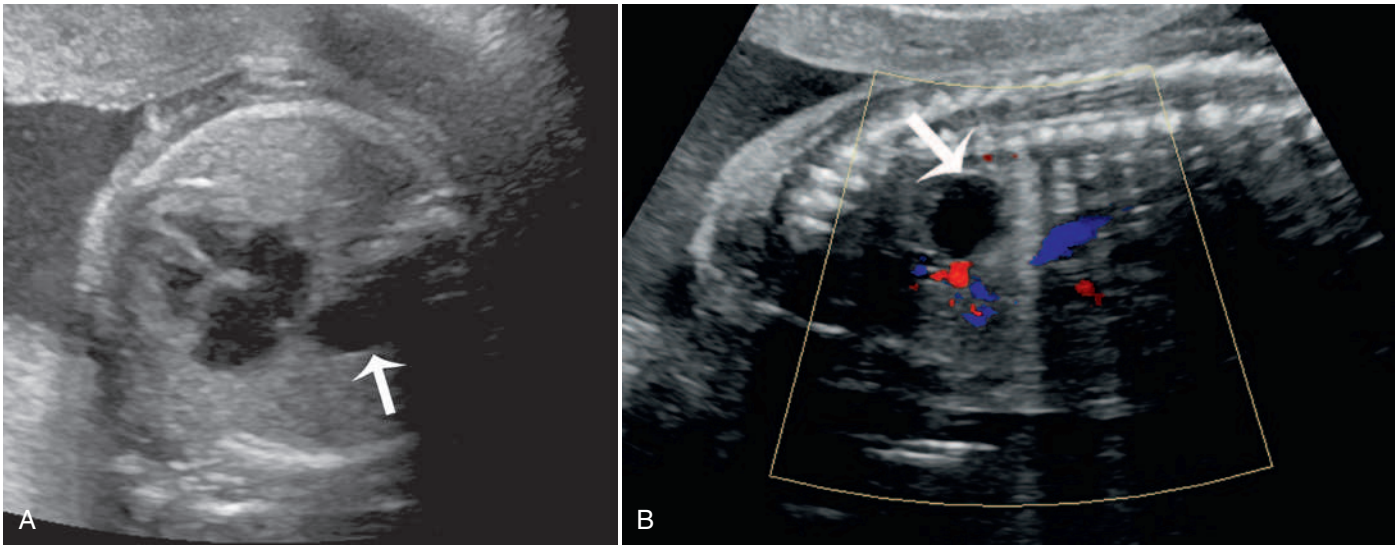

FIG. 36.9 Bronchogenic Cyst at 23 Weeks. (A) Axial gray-scale and **(B)** sagittal color Doppler ultrasound images of the chest demonstrate a simple cyst *(arrow)* posterior to the heart.

because of the associated increased risk for hemorrhage, infection, or malignancy.[131]

NEURENTERIC CYST

Neurenteric cysts represent a posterior enteric remnant caused by incomplete separation of the notochord from the foregut during embryogenesis. They typically occur in the posterior mediastinum or in the spinal canal midline. The cysts can have a septated or bilobed appearance. Associated spinal abnormalities are typically present but difficult to identify prenatally.[132-135] MRI is a useful adjunct in the further evaluation of the spine. **Esophageal duplication cysts** should be considered in the differential of midline chest cysts.

PLEURAL EFFUSION

Any fluid in the pleural space is abnormal. If sufficiently large, pleural effusion may result in mass effect, leading to compression of the heart and hydrops as well as compression of the lungs, resulting in pulmonary hypoplasia.[136]

Primary pleural effusion is rare, with an incidence of up to 1 in 15,000 pregnancies.[137,138] It is most often caused by chylothorax,[139] which results from defective development of the lymphatic system. Any insult to the course of the **thoracic duct** in the posterior mediastinum in the fetal chest can result in chylous fetal pleural effusion.[140] This can be on either the right or the left side, because the thoracic duct in the posterior mediastinum crosses from right to left at the fifth thoracic level. Primary pleural effusion is suspected when the effusion is unilateral or is much larger on one side than the other and when no other signs of hydrops are present. Primary effusions are characterized by having high pressures, resolving rapidly after thoracentesis and developing hydrops restricted to the upper fetal body.[141]

Primary chylothorax is associated with aneuploidy in 2% to 6% of cases.[142,143] By definition, chylothorax in neonates is identified when fluid contains more than 1.1 mmol/L triglycerides with oral fat intake, with lymphocyte proportion exceeding 80%.[144] However, the fetus is fasting in utero, and the mean percentage of lymphocytes in the blood of normal fetuses is normally greater than 80%.[145] Therefore these parameters do not apply in utero.

Secondary pleural effusion occurs in association with aneuploidy **(Turner syndrome or trisomy 21), infection** (**TORCH** [toxoplasmosis, rubella, cytomegalovirus, herpes simplex, HIV]), genetic syndromes, and other structural malformations (**CPAM, BPS, lymphangiectasia,** cardiac anomalies).[142-145] These syndromes typically present with bilateral pleural effusions (particularly in fetuses with hydrops)[140] but occasionally with unilateral effusion.

Pleural effusions appear on prenatal ultrasound as anechoic fluid collections in the pleural space, leading to the appearance of the lung floating in the fluid, surrounded by the chest wall and diaphragm[146] (Fig. 36.10, Video 36.2). Small effusions appear as an anechoic thin rim outlining the lungs and the mediastinum. Larger unilateral effusions result in mass effect, causing mediastinal shift and flattening or eversion of the diaphragm. If isolated and small, pleural effusions have a benign course. If large with mass effect, untreated fetal pleural effusion has a mortality rate of 22% to 53%.[137,140,147-149]

Small pleural effusions do not shift the mediastinum. Pleural effusions associated with hydrops may be unilateral or bilateral, often beginning as unilateral collections that progress bilaterally. Once hydrops develops (cardiac compression from unilateral effusion), distinguishing between primary and secondary effusion can be difficult. If mediastinal shift is visualized in association with a small pleural effusion, a chest mass such as a CDH, CPAM, or BPS should be sought. MRI may help identify associated abnormalities not seen by ultrasound, such as an inconspicuous CPAM or BPS. Depending on the content of the pleural fluid (lipid, protein, or blood products), different signal intensities might be seen with MRI in both T1- and T2-weighted images that may help establish the causal diagnosis.[150]

Prenatal pleural effusion has a variable natural course ranging from spontaneous resolution to progressive development of hydrops and polyhydramnios with high risk for perinatal morbidity and mortality.[140] An effusion ratio can be obtained by ultrasound (area of effusion divided by area of thorax) and followed with serial examinations. If it elevates, it increases the risk of evolution to hydrops,[141] but no cutoff ratio has demonstrated usefulness as a prognostic tool.[151]

A fetal assessment for associated anomalies, including echocardiography, maternal serology for infections, and fetal karyotyping, should be performed.[141,152] Prognosis depends on the presence of associated abnormalities, whether it is unilateral or bilateral, the size of hydrothorax, and severity of mediastinal shift. A small primary hydrothorax can have spontaneous resolution in 22% of cases.[142] Unilateral effusions, spontaneously resolved effusions, and those without mediastinal shift or hydrops have a 73% to 100% survival rate.[140,141]

Progression from unilateral to bilateral effusions is associated with impending hydrops. When large, bilateral, and with mediastinal shift, the mortality rate increases to 52%.[140] With progression to hydrops, the mortality rate increases to 62%.[140] Secondary hydrothorax has a worse outcome. The mortality rate in these cases can be up to 98% depending on size, progression to hydrops, and underlying cause.[140]

Pleural effusions are treated by drainage if the effusion is isolated (or asymmetrical) without additional anomalies, typically in fetuses at risk for developing hydrops (i.e., those with severe mediastinal shift or with other signs of hydrops already present).[63] Typically, a pleural effusion is drained with a single stick procedure.[153] If it recurs, placement of a thoracoamniotic shunt is an option.[154] A series of 65 fetuses showed thoracoamniotic shunts to have a high survival rate in nonhydropic fetuses of 93%, with survival of 86% in the hydropic group.[4] Risks of prenatal thoracoamniotic shunts include fetal hemorrhage, blockage or migration of the shunt, and placental abruption or preterm labor. In cases of large effusions, drainage immediately before delivery can assist in airway management at birth. A 2007 systematic review of prenatal intervention for isolated primary pleural effusion without hydrops suggested that survival rates after prenatal intervention are as high as 60%.[138]

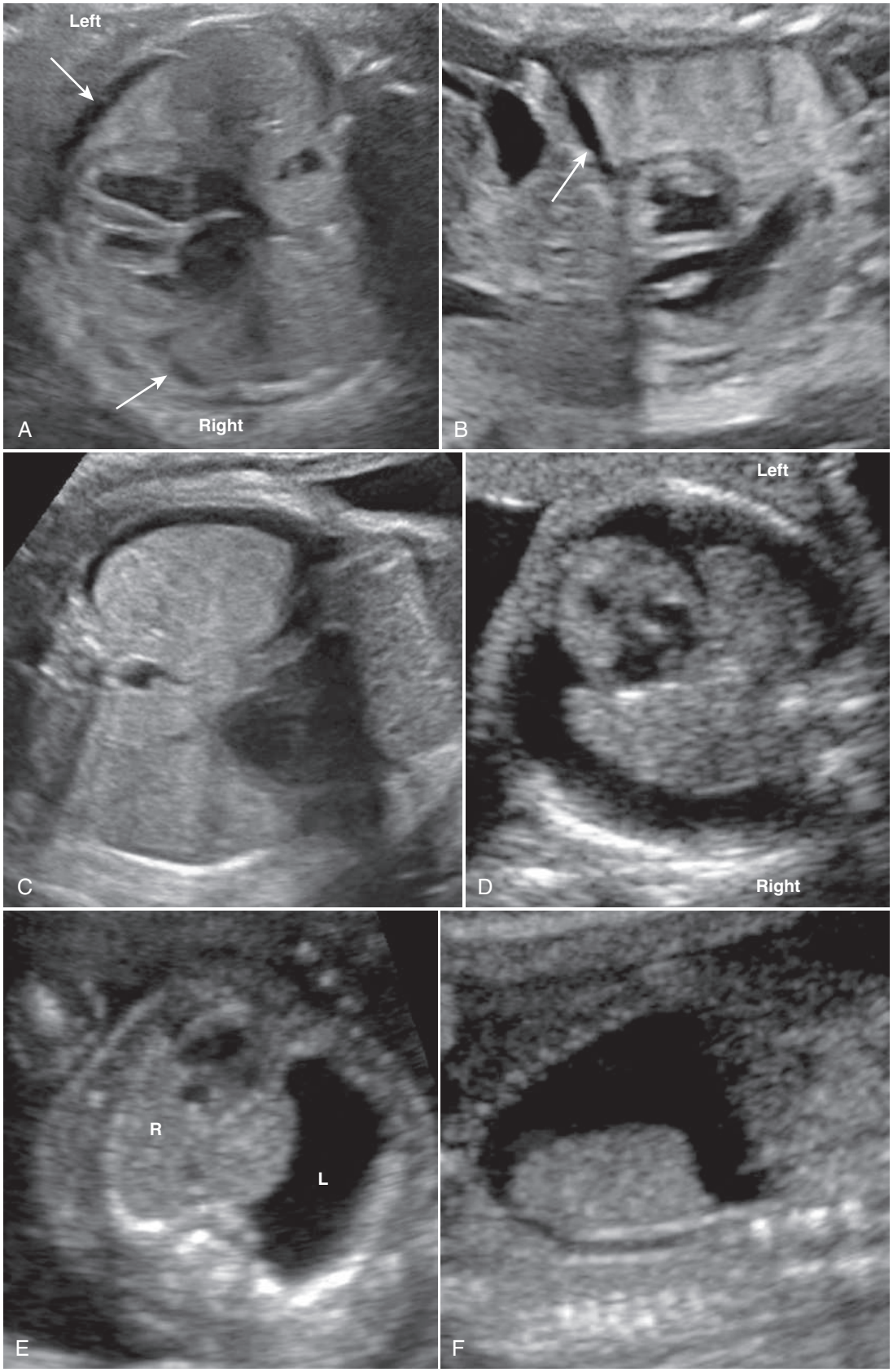

FIG. 36.10 Pleural Effusion. (A) Axial and **(B)** coronal views of small pleural effusions at 25 weeks *(arrows).* **(C)** Axial view of effusion at 28 weeks with mild mediastinal shift. **(D)** Axial view shows moderate bilateral effusions outlining the lungs. The effusions are about the same size, so there is no mediastinal shift. **(E)** Axial and **(F)** oblique sagittal views at 17 weeks show a large left effusion *(L)* with severe mediastinal shift to the right *(R).* See also Video 36.2.

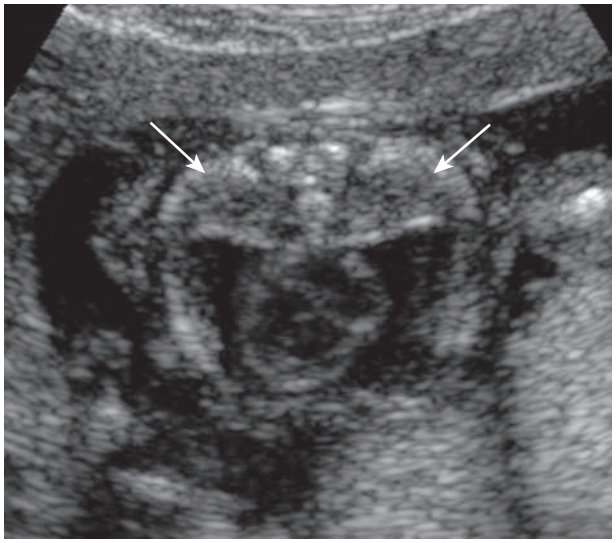

FIG. 36.11 Pericardial Effusion. Note how the lungs *(arrows)* are compressed posteriorly in the fetal chest by the effusion surrounding the heart.

Case reports of other treatment options include pleurodesis and intrapleural injection of autologous blood, which yield a survival rate of 80%.[155,156]

PERICARDIAL EFFUSION

In contrast to pleural effusions that surround the lungs and compress the tissue medially, pericardial effusions are antero-medial fluid collections. Fluid collections of up to 2 mm in thickness are common, and a small amount of pericardial fluid (up to 7 mm, in isolation) can be a normal finding.[157] A large pericardial effusion compresses the lungs against the posterior chest wall (Fig. 36.11). The heart is visualized as "floating" within the anterior thoracic fluid collection.

PULMONARY LYMPHANGIECTASIA

Pulmonary lymphangiectasia is a congenital obstruction and dilation of the pulmonary lymphatic system. The lungs become enlarged and stiff, with development of effusions that can result in respiratory failure. There are primary and secondary forms of pulmonary lymphangiectasia. The secondary form is caused by congenital heart diseases that result in poor venolymphatic return.[158-160] Ultrasound findings can be subtle with pleural effusions and heterogeneous lung parenchyma (Fig. 36.12). The use of echocardiography is important to exclude cardiac anomalies.

Fetal MRI demonstrates pleural effusions and lung heterogeneity. Tubular T2-hyperintense branches may be present radiating from the hila. A heterogeneous pattern referred to as the "nutmeg lung" (Fig. 36.12C) provides a more specific diagnosis.[161]

Postnatal management includes restriction of dietary fats, pleural effusion drainage, pleurodesis, and thoracic duct ligation. Recent experimental treatment using ethiodized oil to embolize the patulous pulmonary lymphatics has shown some success.[162]

CONGENITAL DIAPHRAGMATIC HERNIA

CDH results from failure of the pleuroperitoneal canal to close at the end of organogenesis.[163] A "dual hit" hypothesis suggests that the defect arises in the embryologic period (first hit), and during further gestation, lung development is impaired (second hit).[164] The defect in the diaphragm allows herniation of viscera into the chest. Mass effect from visceral organs in the chest has an adverse impact on the normal development of the fetal cardiac and pulmonary systems. Thus CDH is associated with substantial morbidity and mortality.[165-168] The incidence of CDH is about 1 in 3000 births.

CDHs can be classified based on location; types include posterolateral Bochdalek hernia (70%-75%), anterior Morgagni hernia (23%-28%), and central defects (2%-7%). Most CDHs (85%-90%) are left sided, 10% to 15% are right sided, and only 2% are bilateral.[169-173] Complete **agenesis of the diaphragm,** herniation of the central tendinous part, **pericardial hernia,** membrane-covered hernias, and **eventration of the diaphragm** are rarer manifestations.[173]

Ultrasound findings of CDH include presence of stomach bubble, gallbladder or bowel within the thoracic cavity, deviation of the heart and mediastinum, herniated liver, abnormal position of the umbilical and hepatic veins, pleural effusion, and polyhydramnios.[170,174,175] The abdominal circumference is often small, with a scaphoid shape of the abdomen secondary to displacement of viscera into the chest.[176]

Left-sided CDH is most often diagnosed when the stomach is in the chest near the left atrium, with absence of the normal stomach below the diaphragm (Fig. 36.13, Videos 36.3 and 36.4). Small and large bowel as well as the liver, spleen, and kidney can herniate into the thorax. As the abdominal contents herniate into the chest, mediastinal shift occurs with the heart deviating to the right.[9,172,177] In large hernias, mediastinal shift is severe, leading to vascular compromise. Compression of the heart, impaired swallowing, and partial obstruction of the gastrointestinal tract lead to polyhydramnios, which is present in up to 69% of cases, particularly late in gestation (by the third trimester).[165,178,179]

Prenatal sonographic diagnosis of CDH can be made as early as the first trimester.[180-182] Detection rate sonographically in centers with screening programs is as high as 74%, with an increased detection rate when CDH is associated with other anomalies.[183]

At times, a left-sided hernia will be present with the stomach in the abdomen and only small bowel loops in the chest. Real-time ultrasound can demonstrate peristalsis of the bowel in the chest. Paradoxical movement of abdominal contents during fetal inspiration on real-time sonogram may help to confirm CDH, along with traditional sonographic findings.[166]

In most left-sided hernias the left lobe of the liver herniates into the chest. The diagnosis of liver in the chest is made by direct visualization of the liver (Video 36.5). At times, sonographic detection of intrathoracic liver is difficult because of the liver's isoechoic appearance with the fetal lung. In these cases,

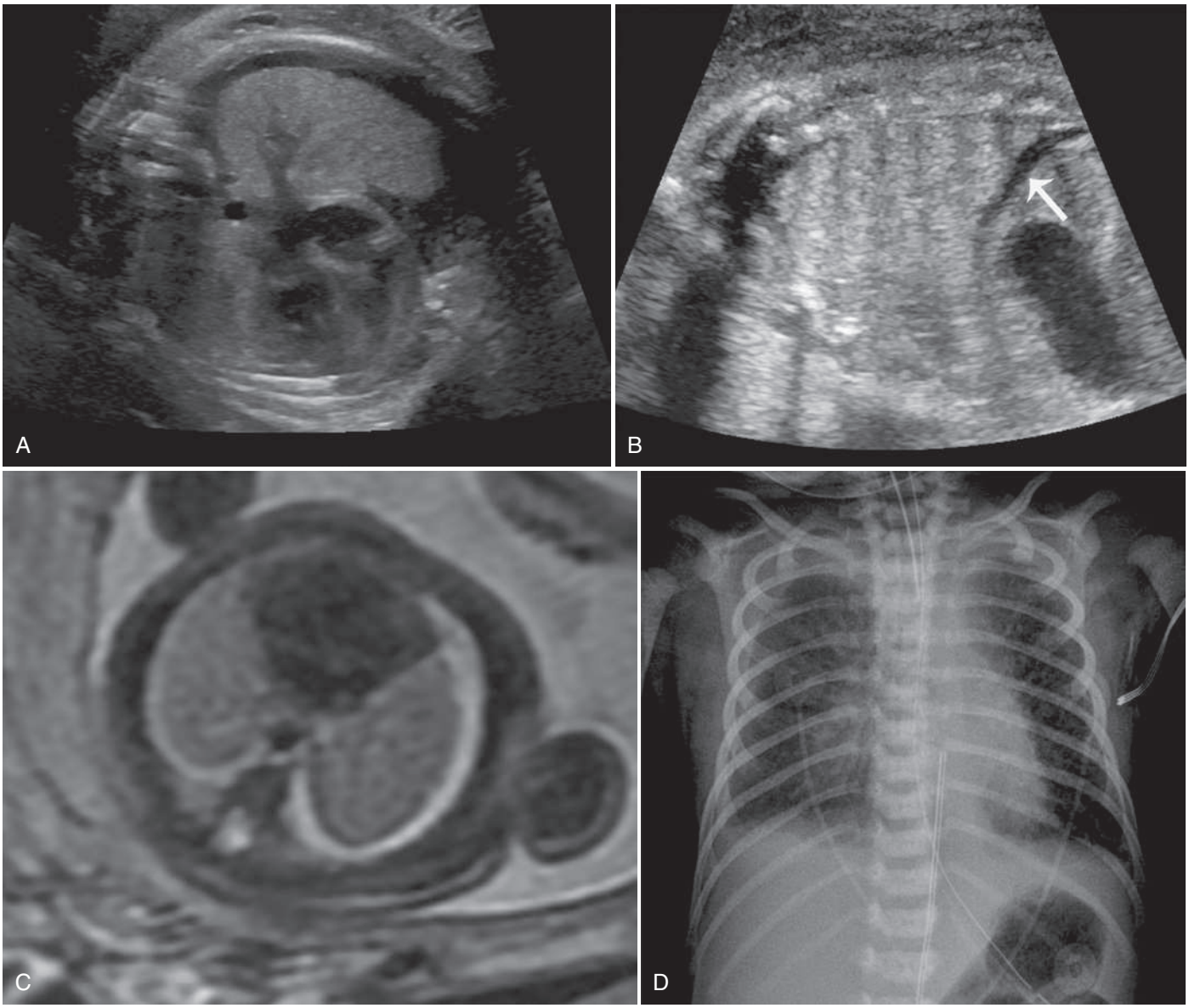

FIG. 36.12 Congenital Primary Pulmonary Lymphangiectasia. (A) Axial and **(B)** sagittal sonograms of the fetal chest at 28 weeks' gestation demonstrate pleural effusions *(arrow)*. The underlying lungs are heterogeneous. **(C)** Axial T2-weighted image confirms the presence of small effusions and heterogenous lung parenchyma "nutmeg" in appearance. **(D)** Chest radiograph at 2 days of age demonstrates course interstitial markings and small effusions, right greater than left.

examination of the course of the portal and hepatic veins is helpful to demonstrate hepatic vessels extending into the chest.[177] The intraabdominal hepatic vein takes a curved course (Fig. 36.13E), and the left portal vein branches will be seen at or above the diaphragm.[174]

In a right-sided hernia, the liver herniates into the chest, and mediastinal shift is to the left (Fig. 36.14, Video 36.6). Liver echogenicity can appear similar to the lung, so visualization of gallbladder and hepatic vessels in the thorax is helpful in confirming the diagnosis. Bowel can also herniate, but the stomach is located below the diaphragm. Because of kinking of the intrahepatic inferior vena cava, ascites (with fluid extending into the chest) and hydrops can develop. Absence of the hypoechoic muscular diaphragm on the right helps in differentiating CDH from other fetal chest masses.

Complete anatomic examination should be performed to assess for presence of associated anomalies (25%-75%). Echocardiography is indicated because congenital cardiac defects occur in 10% to 35% of cases and decrease survival from 73% to 67% if it is a minor defect or to 36% if it is a major complex cardiac defect.[184]

MRI is a useful adjuvant for confirming the diagnosis of a CDH and assessing for additional abnormalities. MRI better demonstrates the position of the liver and the amount of herniation due to differentiation of the hepatic lobe (bright on T1-weighted imaging) from the compressed lung or a solid type

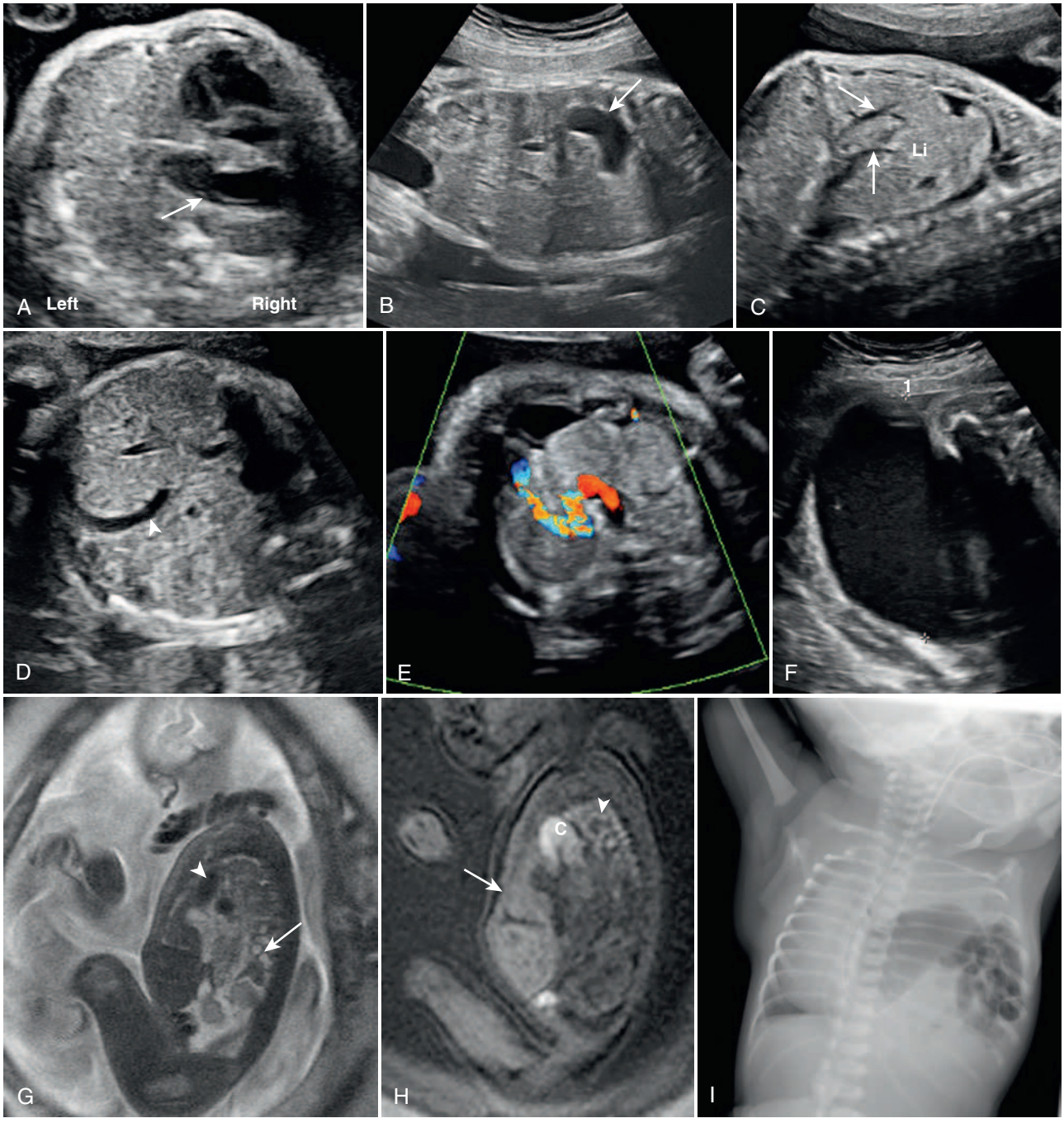

FIG. 36.13 Left-Sided Congenital Diaphragmatic Hernia. (A) Axial view of chest at 28 weeks' gestation shows the stomach *(arrow)* in the chest with mediastinal shift to the right. **(B)** Coronal image in a different fetus at 28 weeks shows a slightly distended stomach *(arrow)* in the chest. **(C)** Oblique sagittal image shows a large amount of liver *(Li)* in the chest. Note the hepatic vessels *(arrows).* **(D)** Axial view of abdomen shows abnormal course of umbilical vein *(arrowhead)* resulting from the liver herniation into the chest. **(E)** Oblique axial view of chest shows kinked hepatic vessels. **(F)** Axial view in the right lower quadrant shows the associated polyhydramnios complicating the pregnancy in the same fetus. **(G)** Sagittal T2-weighted fetal MRI shows the small bowel *(arrow)* and colon *(arrowhead)* in chest with small pleural effusion. **(H)** Sagittal T1-weighted fetal MRI shows liver *(arrow)* in chest. Note bright signal of meconium in colon *(C)* in chest, as well as small bowel loops *(arrowhead)* in chest. **(I)** Postnatal radiograph shows the bowel in the left chest, nasogastric tube in the left chest, and a tiny, hypoplastic right lung. See also Videos 36.3, 36.4, and 36.5.

of CPAM.[185-187] MRI can reveal the location of bowel because of the bright T1 signal of meconium. If the superior aspect of herniated bowel is rounded with trapped fluid below, a hernia sac can be suggested. These membrane-covered hernias are associated with a better prognosis.[185] MRI is also useful for the visualization of the normal ipsilateral and contralateral lung, allowing for the measurement of lung volumes useful for predicting outcome.[188] MRI measurements include total lung volume, observed-to-expected total fetal lung volume (o/e TFLV), percent predicted lung volume (PPLV), fetal

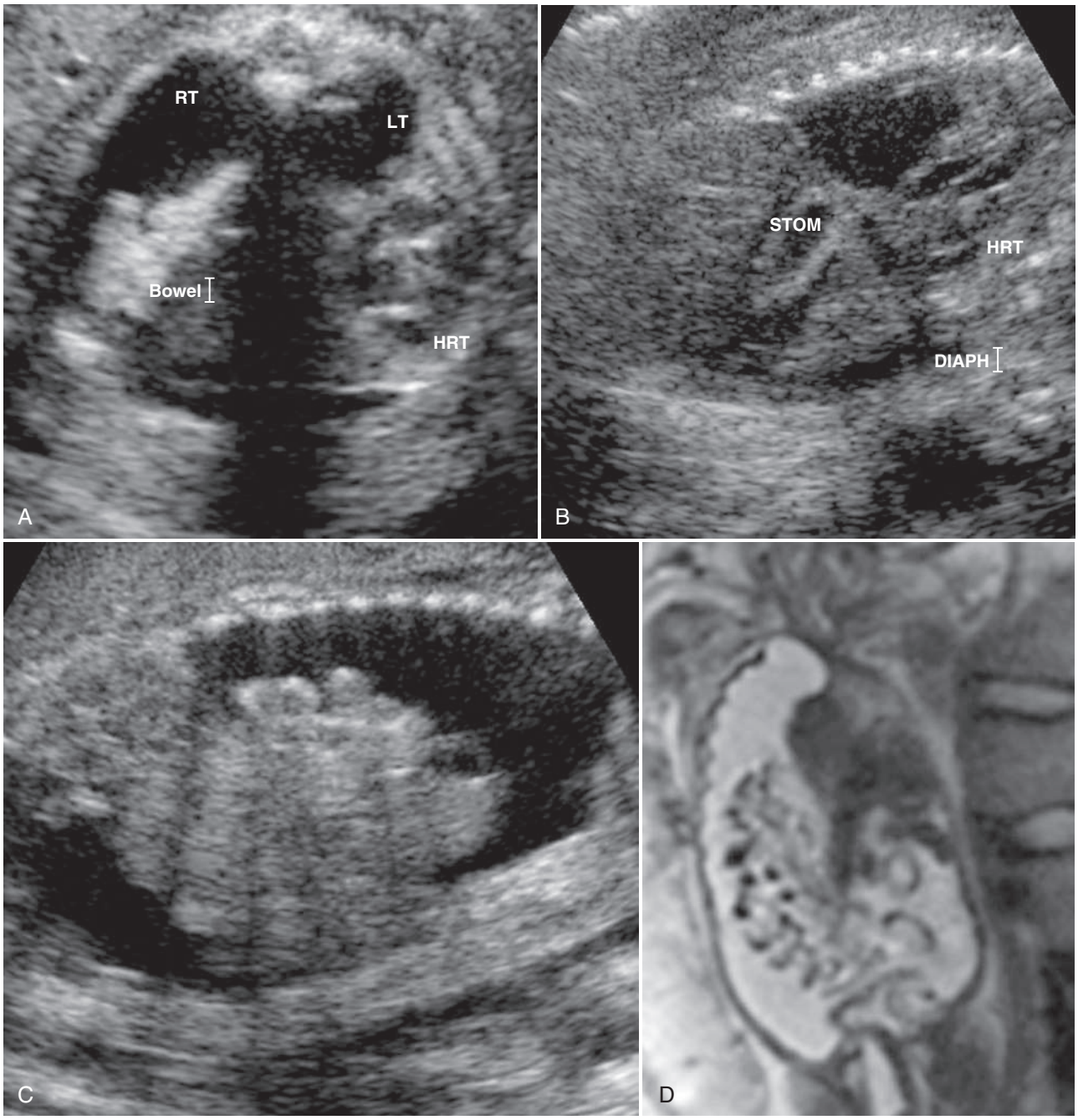

FIG. 36.14 Right-Sided Congenital Diaphragmatic Hernia at 30 Weeks. (A) Axial and **(B)** and **(C)** oblique sagittal images show bilateral pleural effusions *(RT, LT)* and bowel loops in the right hemithorax with mediastinal shift with heart *(HRT)* displaced to the left. The left hemidiaphragm *(DIAPH)* is intact, with the stomach *(STOM)* below the diaphragm. **(D)** Coronal T2-weighted MRI shows fluid extending from the abdomen into the chest with mediastinal shift to left. Note the lack of a right hemidiaphragm, as well as bowel in the right chest. See also Video 36.6.

lung volume to fetal body volume (FLV/FBV) ratio, percent liver herniation (%LH), and herniated liver to fetal thoracic volume ratio (LiTR).[186,188] MRI can also measure the diameter of the aorta and pulmonary arteries used to obtain the modified McGoon index as a prognostic indicator of pulmonary hypertension.[189]

Prognosis varies depending on the side of the herniation, the position of the liver, associated abnormalities, and gestation age at diagnosis.[190-196] The presence of a large amount of herniated liver decreases survival substantially.[197] The severity of lung hypoplasia and lung hypertension are major determinants in mortality and morbidity rates.[31,198,199] A large hernia diagnosed early in gestation results in relatively worse pulmonary hypoplasia with a resulting higher mortality rate than does a small hernia diagnosed late in gestation without associated findings. Bilateral hernias are typically fatal. Familial and syndromic hernias usually have a worse prognosis compared to isolated hernias.[184,191-195]

Poor Prognostic Factors in Congenital Diaphragmatic Hernia

Right-sided or bilateral hernia
Early gestational age at diagnosis
Small lung size (measured by lung-to-head ratio or volumetry)
Associated abnormalities (structural or chromosomal)
Hydrops
Polyhydramnios
Degree of mediastinal shift
Intrauterine growth restriction
Liver in chest

Predictors of Decreased Survival in Congenital Diaphragmatic Hernia

Ultrasound LHR < 1
Ultrasound o/e LHR < 25%
Three-dimensional ultrasound TFLV < 35%
Low o/e pulmonary artery ratios
MRI o/e TFLV < 25%
MRI PPLV < 15%
MRI LiTR > 20%

LHR, Lung-to-head ratio; *LiTR,* liver to fetal thoracic volume ratio; *MRI,* magnetic resonance imaging; *o/e,* observed-to-expected; *PPLV,* percent predicted lung volume; *TFLV,* total fetal lung volume.

With the use of ultrasound and MRI various measurements have been taken to estimate the severity of lung hypoplasia and probable outcome of the fetus. By ultrasound, the **lung-to-head circumference ratio** (LHR) has been used as a predictor of outcome for left-sided CDH. To obtain this ratio the right lung is measured at the level of the four-chamber view and that number is divided by the head circumference to standardize for gestational age. Metkus et al. first described the LHR, noting those with an LHR less than 0.6 did not survive.[31] Laudy et al. found that an LHR less than 1 had 100% mortality whereas an LHR greater than 1.4 predicted a 100% survival.[200] The LHR appears to be most reliable between 24 and 34 weeks' gestation.[201]

Three techniques to calculate the LHR using ultrasound have been described:

1. At the four-chamber heart, the largest transverse dimension of the right lung is drawn parallel to the sternum and the largest anteroposterior measurement is obtained at a perpendicular angle. These are multiplied and then divided by the head circumference in millimeters.
2. At the four-chamber heart, the maximum transverse measurement is multiplied by the longest perpendicular anteroposterior measurement. These are multiplied, and then the total is divided by the head circumference in millimeters.
3. At the four-chamber heart, the outline of the right lung is traced in millimeters and then divided by the head circumference.

The tracing method has been shown to be the most accurate in predicting survival in some centers.[202] Generally an LHR less than 1 suggests a poor outcome, with a survival rate of 45%.[203,204] The variability of LHR's prognostic value is due to differences in methodology and dependence on gestational age resulting in a controversial association with mortality.[204,205]

To improve outcome assessment, another ultrasound measure, **the observed-to-expected lung-to-head ratio (o/e LHR)** has been used. This ratio appears to have a better predictive value compared with LHR.[206-209] A ratio of less than 25% is associated with lower survival rates.[207,210]

Three-dimensional ultrasound has been utilized in patients with CDH to assess lung volume. An o/e TFLV less than 35% shown to predict survival. However, in up to 45% of cases, the measures are suboptimal with sonographic measurements typically 25% lower than MRI values.[206]

Prenatal pulmonary artery measurements at the hila at the level of the four-chamber view have been performed.[211-214] Measuring the main right and left pulmonary artery and comparing with normals via an observed-to-expected ratio shows a reduction in values in fetuses with CDH and pulmonary hypoplasia. Doppler wave forms have been useful in defining the most severe CDH cases. Increased pulmonary artery pulsatility index (>1) and peak early diastolic reversed flow in the main pulmonary artery (>3.5) reflect high resistance in pulmonary vascular bed with preferential flow through the ductus arteriosus and are correlated with poor lung growth.[215,216]

Other tests utilized in CDH include a hyperoxygenation test for pulmonary vascular reactivity at 31 to 36 weeks' gestation, in which reactivity (20% reduction in pulmonary artery pretest pulsatility index) suggests a good outcome,[217,218] and assessment of fractional moving blood volume because a decrease in this fraction is correlated with decreased lung growth and an increased intrapulmonary artery impedance in CDH.[219-223]

Patients with fetuses with CDH generally undergo extensive prenatal imaging and counseling. Follow-up ultrasound examinations should be performed to assess fetal well-being, amniotic fluid levels, lung volume, and changes in mediastinal shift that could result in hemodynamic changes.

Other Hernias and Eventration

In **bilateral hernias** the falciform ligament is drawn into the hernia.[224,225] Mediastinal shift is variable, but typically the heart is displaced anteriorly and superiorly. Features of both right- and left-sided CDH are present.

Pericardial hernias result from failure of the retrosternal portion of the septum transversum to close the communication between the pericardial and peritoneal cavities.[226] The liver may herniate into the pericardial sac.[171,225] Pericardial effusion results from mass effect on the heart and obstruction of venous return or from mechanical irritation of membranes.[227] Because the differential diagnosis of a pericardial mass includes pericardial tumors such as teratoma, it is important to recognize the liver as part of the hernial sac contents by identifying the hepatic vessels in the mass.[219,228]

In **diaphragmatic eventration** the intact diaphragm is displaced cephalad at the weakened muscular portion, without communication between the abdominal and thoracic cavities[229] (Fig. 36.15). Diaphragmatic eventration is associated with a lower

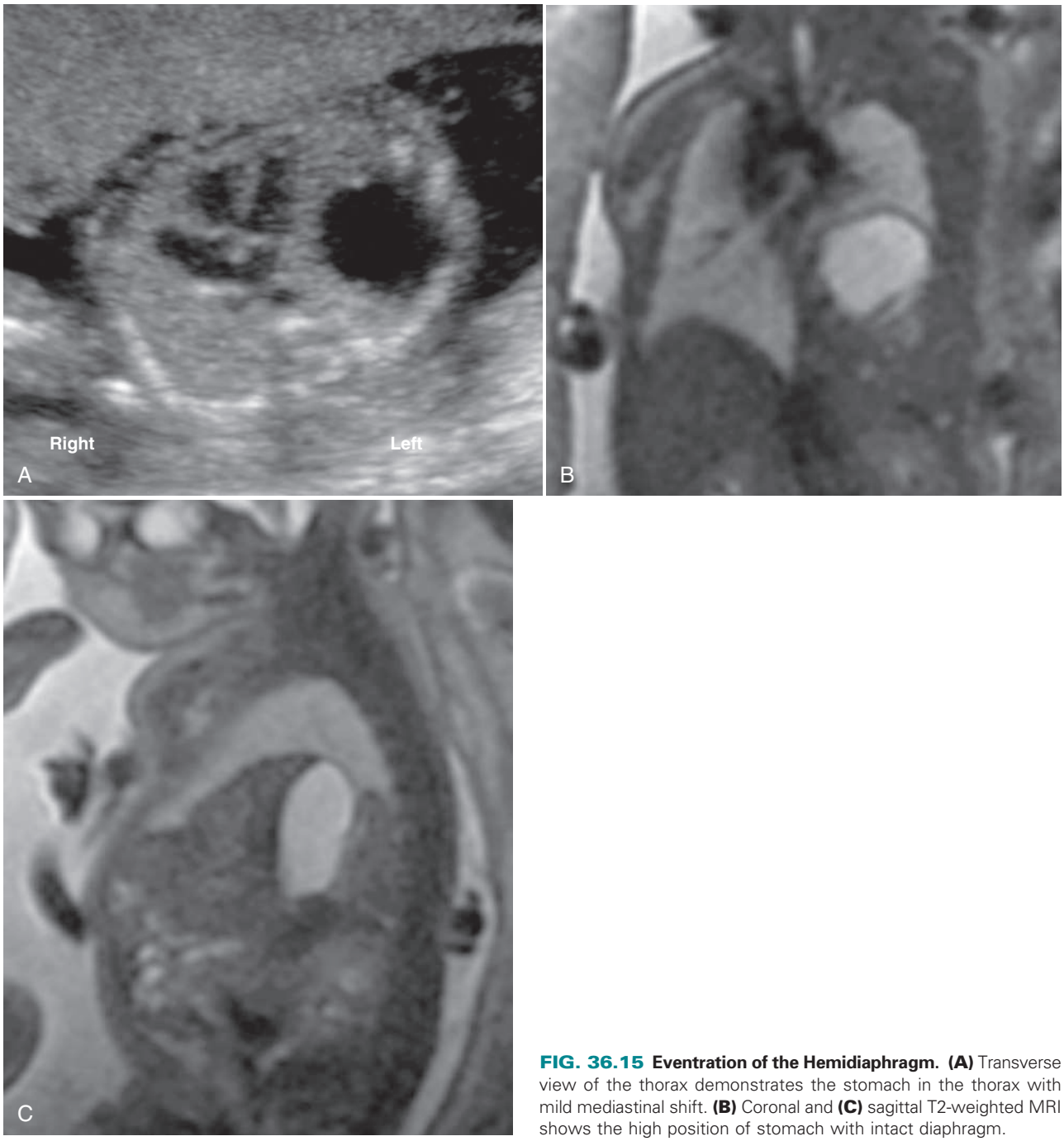

FIG. 36.15 Eventration of the Hemidiaphragm. (A) Transverse view of the thorax demonstrates the stomach in the thorax with mild mediastinal shift. **(B)** Coronal and **(C)** sagittal T2-weighted MRI shows the high position of stomach with intact diaphragm.

perinatal mortality rate compared to CDH and may not require surgical repair. Thus it is crucial to make the distinction between the two diagnoses to provide appropriate counseling.

Associated Anomalies

CDH may be an isolated defect or may be associated with other structural, chromosomal, or syndromal anomalies. Associated anomalies are present in 25% to 55% of cases. **Congenital heart disease** is the most common association (20%), with hemodynamically significant heart disease in 11% of cases.[230-232] Because of the high rate of associated cardiac abnormalities, formal fetal echocardiography is indicated in fetuses with CDH.

Associated central nervous system anomalies are second in frequency of associated structural abnormalities in fetuses with CDH; these anomalies include **anencephaly, ventriculomegaly,** and **neural tube defects.**[191] Chromosomal abnormalities occur in 10% to 20% of antenatally detected CDH, the most common being **trisomy 18.**[192,193] Chromosomal abnormalities are most common when CDH is present in association with other structural abnormalities. Given the high association with aneuploidy, chromosomal assessment is typically performed. Associated syndromes include **Fryn, Beckwith-Wiedemann, Simpson-Golabi-Behmel, Brachmann–de Lange,** and **Perlman.**[195]

TABLE 36.5 Sample Studies of Predictors of Survival in Left-Sided Congenital Diaphragmatic Hernia

Imaging Findings	Sign/ Value	Outcome (% Survival)
Liver position[208]	Liver up	45%
	Liver down	93%
LHR ratio[208]	<1	35%
	>1	75%
o/e LHR[210]	<25%	poor
o/e TLV MRI[184,207]	<25%	poor (13%)

LHR, Lung to head ratio; *o/e*, observed to expected; *TLV*, total lung volume.

Morbidity and Mortality

Mortality varies widely depending on gestational age at diagnosis, side of the hernia (right-sided hernias have poorer survival than left-sided hernias,[195] and bilateral hernias have worse prognosis than do unilateral hernias), associated abnormalities, hernia size, liver position,[183] presence of hydrops, degree of mediastinal shift, polyhydramnios, and size of the residual lung.[31] Table 36.5 provides examples of using imaging findings to predict prognosis (survival predictors).

Mortality from CDH can be high because of termination of pregnancy and in utero demise (secondary to associated abnormalities and hydrops). After birth, CDH results in high rates of morbidity and mortality because of pulmonary hypoplasia, pulmonary hypertension, and iatrogenic trauma to the airways from mechanical ventilation. Pulmonary hypertension in newborns in association with CDH is thought to be caused by the wall thickening of the small pulmonary arteries. Severity of pulmonary hypoplasia and pulmonary hypertension is related to the volume and timing of herniation of abdominal viscera into the hemithorax.[233,234] In a 2000 meta-analysis[234] of studies from 1975 to 1998, of 676 prenatally diagnosed fetuses, 142 (21%) were terminated, 36 (5%) died in utero, 333 (49%) died postnatally, and only 165 (24%) survived. More recent studies show improved survival rates. In a 1999-2001 trial, survival of fetuses (without in utero intervention) with an LHR of less than 1.4 and liver in the chest (i.e., fetuses presumed to have poor survival rates) was 77%.[235] Impro`ved overall survival rates in recent years have been attributed to alterations in clinical care for CDH, including minimization of iatrogenic lung injury by gentle ventilation and nutritional support.[232,236-238] Outcome is improved if delivery is at a center with health care professionals experienced in caring for infants with CDH.

In Utero Therapy

Options for treatment of CDH focus on lung development. Small hernias with a large amount of visualized lung or hernias diagnosed late in pregnancy can be delivered at a tertiary care center where NICU services (including ECMO) are available. EXIT to ECMO has been offered in some centers but has not demonstrated significant survival benefit.[197]

Fetal surgery can be performed at specialized centers for fetuses least likely to survive with conventional postnatal therapies.[180] Surgery is performed to aid in lung growth and typically is not directed at repair of the diaphragmatic defect, because open fetal surgery is associated with premature rupture of membranes and premature labor. In addition, repair of CDH is associated with intraoperative death caused by kinking of the umbilical vein and ductus venosus as the liver is reduced into the abdomen.[239]

Current in utero therapy is aimed at **fetal endoscopic tracheal occlusion** (FETO), by balloon or clips, which stimulates lung growth.[240-242] The procedure is performed under combined spinal and epidural anesthesia and fetal analgesia. A 1.2-mm endoscope within a 3.0-mm sheath is introduced into the trachea to place a detachable balloon between the carina and vocal cords.[243] FETO has improved prognosis of severe CDH, with its effect dependent on the preexisting lung size. Other treatment options, such as combining FETO with other modalities (e.g., surfactant, corticosteroids), are being investigated.[244,245]

New nonsurgical prenatal options are being evaluated, including pharmacologic treatments and stem cell–based strategies, and could be promising in treating pulmonary hypertension and hypoplasia.

CONCLUSION

When an abnormality of the fetal thorax is visualized, it is important to have a thorough approach to the fetal evaluation. The echogenicity of the lesion, whether it is cystic or solid, location and appearance of the heart, size of normal-appearing lung, evidence of hydrops, and associated abnormalities are important at initial diagnosis. Follow-up to assess interval change in appearance and development of hydrops is important for prognosis. The specific diagnosis is important in determining potential in utero therapy, guiding the appropriate mode of delivery, and explaining to the parents the types of postnatal therapy that may be needed.

REFERENCES

1. Wayne ER, Campbell JB, Burrington JD, Davis WS. Eventration of the diaphragm. J Pediatr Surg. 1974;9(5):643-651.
2. Wigglesworth JS, Desai R, Hislop AA. Fetal lung growth in congenital laryngeal atresia. Pediatr Pathol. 1987;7(5-6):515-525.
3. Abu Musa AA, Hata T, Hata K, et al. Ultrasonographic measurement of fetal lung. Gynecol Obstet Invest. 1990;30(3):139-142.
4. Blott M, Greenough A, Nicolaides KH, Campbell S. The ultrasonographic assessment of the fetal thorax and fetal breathing movements in the prediction of pulmonary hypoplasia. Early Hum Dev. 1990;21(3):143-151.
5. Cannie M, Jani J, Meersschaert J, et al. Prenatal prediction of survival in isolated diaphragmatic hernia using observed to expected total fetal lung volume determined by magnetic resonance imaging based on either gestational age or fetal body volume. Ultrasound Obstet Gynecol. 2008; 32(5):633-639.
6. Osada H, Iitsuka Y, Masuda K, et al. Application of lung volume measurement by three-dimensional ultrasonography for clinical assessment of fetal lung development. J Ultrasound Med. 2002;21(8):841-847.
7. Osada H, Kaku K, Masuda K, et al. Quantitative and qualitative evaluations of fetal lung with MR imaging. Radiology. 2004;231(3):887-892.
8. Tegnander E, Eik-Nes SH, Linker DT. Incorporating the four-chamber view of the fetal heart into the second-trimester routine fetal examination. Ultrasound Obstet Gynecol. 1994;4(1):24-28.

9. Blaas HG, Eik-Nes SH. Sonographic development of the normal foetal thorax and abdomen across gestation. Prenat Diagn. 2008;28(7):568-580.
10. de Vries JI, Visser GH, Prechtl HF. The emergence of fetal behaviour. I. Qualitative aspects. Early Hum Dev. 1982;7(4):301-322.
11. Malas MA, Evcil EH, Desdicioglu K. Size and location of the fetal diaphragm during the fetal period in human fetuses. Surg Radiol Anat. 2007; 29(2):155-164.
12. Zalel Y, Gamzu R, Mashiach S, Achiron R. The development of the fetal thymus: an in utero sonographic evaluation. Prenat Diagn. 2002;22(2): 114-117.
13. Felker RE, Cartier MS, Emerson DS, Brown DL. Ultrasound of the fetal thymus. J Ultrasound Med. 1989;8(12):669-673.
14. Cho JY, Min JY, Lee YH, et al. Diameter of the normal fetal thymus on ultrasound. Ultrasound Obstet Gynecol. 2007;29(6):634-638.
15. Toti P, De Felice C, Stumpo M, et al. Acute thymic involution in fetuses and neonates with chorioamnionitis. Hum Pathol. 2000;31(9):1121-1128.
16. Takayasu H, Kitano Y, Juroda T, et al. Successful management of a large fetal mediastinal teratoma complicated by hydrops fetalis. J Pediatr Surg. 2010;45:E21-E24.
17. Hubbard AM, Adzick NS, Crombleholme TM, et al. Congenital chest lesions: diagnosis and characterization with Prenatal MR imaging. Radiology. 1999;212:43.
18. Lauria MR, Gonik B, Romero R. Pulmonary hypoplasia: pathogenesis, diagnosis, and antenatal prediction. Obstet Gynecol. 1995;86(3):466-475.
19. Rotschild A, Ling EW, Puterman ML, Farquharson D. Neonatal outcome after prolonged preterm rupture of the membranes. Am J Obstet Gynecol. 1990;162(1):46-52.
20. Laudy JA, Wladimiroff JW. The fetal lung. 2: Pulmonary hypoplasia. Ultrasound Obstet Gynecol. 2000;16(5):482-494.
21. Yancey MK, Richards DS. Antenatal sonographic findings associated with unilateral pulmonary agenesis. Obstet Gynecol. 1993;81(5 Pt 2):847-849.
22. Hislop A, Hey E, Reid L. The lungs in congenital bilateral renal agenesis and dysplasia. Arch Dis Child. 1979;54(1):32-38.
23. Ruano R, Martinovic J, Aubry MC, et al. Predicting pulmonary hypoplasia using the sonographic fetal lung volume to body weight ratio—how precise and accurate is it? Ultrasound Obstet Gynecol. 2006;28(7):958-962.
24. Harstad TW, Twickler DM, Leveno KJ, Brown CE. Antepartum prediction of pulmonary hypoplasia: an elusive goal? Am J Perinatol. 1993;10(1): 8-11.
25. Jani JC, Cannie M, Peralta CF, et al. Lung volumes in fetuses with congenital diaphragmatic hernia: comparison of 3D US and MR imaging assessments. Radiology. 2007;244(2):575-582.
26. Ruano R, Aubry MC, Barthe B, et al. Three-dimensional sonographic measurement of contralateral lung volume in fetuses with isolated congenital diaphragmatic hernia. J Clin Ultrasound. 2008;36(5):273-278.
27. Rypens F, Metens T, Rocourt N, et al. Fetal lung volume: estimation at MR imaging initial results. Radiology. 2001;219:236-241.
28. Tanigaki S, Miyakoshi K, Tanaka M, et al. Pulmonary hypoplasia: prediction with use of ratio of MR imaging-measured fetal lung volume to US-estimated fetal body weight. Radiology. 2004;232(3):767-772.
29. Fong K, Ohlsson A, Zalev A. Fetal thoracic circumference: a prospective cross-sectional study with real-time ultrasound. Am J Obstet Gynecol. 1988;158(5):1154-1160.
30. Chitkara U, Rosenberg J, Chervenak FA, et al. Prenatal sonographic assessment of the fetal thorax: normal values. Am J Obstet Gynecol. 1987;156(5): 1069-1074.
31. Metkus AP, Filly RA, Stringer MD, et al. Sonographic predictors of survival in fetal diaphragmatic hernia. J Pediatr Surg. 1996;31(1):148-151.
32. Laudy JA, Gaillard JL, vd Anker JN, et al. Doppler ultrasound imaging: a new technique to detect lung hypoplasia before birth? Ultrasound Obstet Gynecol. 1996;7(3):189-192.
33. Bromley B, Benacerraf BR. Unilateral lung hypoplasia: report of three cases. J Ultrasound Med. 1997;16(9):599-601.
34. Ch'In KY, Tang MY. Congenital adenomatoid malformation of one lobe of a lung with general anasarca. Arch Pathol (Chic). 1949;48(3):221-229.
35. Stocker JT, Kagan-Hallet K. Extralobar pulmonary sequestration: analysis of 15 cases. Am J Clin Pathol. 1979;72(6):917-925.
36. Bratu I, Flageole H, Chen MF, et al. The multiple facets of pulmonary sequestration. J Pediatr Surg. 2001;36(5):784-790.
37. Lopoo JB, Goldstein RB, Lipshutz GS, et al. Fetal pulmonary sequestration: a favorable congenital lung lesion. Obstet Gynecol. 1999;94(4):567-571.
38. Rosado-de-Christenson ML, Stocker JT. Congenital cystic adenomatoid malformation. Radiographics. 1991;11(5):865-886.
39. Laberge JM, Flageole H, Pugash D, et al. Outcome of the prenatally diagnosed congenital cystic adenomatoid lung malformation: a Canadian experience. Fetal Diagn Ther. 2001;16(3):178-186.
40. Thorpe-Beeston JG, Nicolaides KH. Cystic adenomatoid malformation of the lung: prenatal diagnosis and outcome. Prenat Diagn. 1994;14(8): 677-688.
41. Adzick NS, Harrison MR, Glick PL, et al. Fetal cystic adenomatoid malformation: prenatal diagnosis and natural history. J Pediatr Surg. 1985;20(5): 483-488.
42. Bunduki V, Ruano R, da Silva MM, et al. Prognostic factors associated with congenital cystic adenomatoid malformation of the lung. Prenat Diagn. 2000;20(6):459-464.
43. Fine C, Adzick NS, Doubilet PM. Decreasing size of a congenital cystic adenomatoid malformation in utero. J Ultrasound Med. 1988;7(7): 405-408.
44. Stocker JT, Madewell JE, Drake RM. Congenital cystic adenomatoid malformation of the lung. Classification and morphologic spectrum. Hum Pathol. 1977;8(2):155-171.
45. Adzick NS, Harrison MR, Crombleholme TM, et al. Fetal lung lesions: management and outcome. Am J Obstet Gynecol. 1998;179(4):884-889.
46. Bromley B, Parad R, Estroff JA, Benacerraf BR. Fetal lung masses: prenatal course and outcome. J Ultrasound Med. 1995;14(12):927-936.
47. Mahle WT, Rychik J, Tian ZY, et al. Echocardiographic evaluation of the fetus with congenital cystic adenomatoid malformation. Ultrasound Obstet Gynecol. 2000;16(7):620-624.
48. Crombleholme TM, Coleman B, Hedrick H, et al. Cystic adenomatoid malformation volume ratio predicts outcome in prenatally diagnosed cystic adenomatoid malformation of the lung. J Pediatr Surg. 2002;37(3): 331-338.
49. Cavoretto P, Molina F, Poggi S, et al. Prenatal diagnosis and outcome of echogenic fetal lung lesions. Ultrasound Obstet Gynecol. 2008;32(6): 769-783.
50. Mann S, Wilson RD, Bebbington MW, et al. Antenatal diagnosis and management of congenital cystic adenomatoid malformation. Semin Fetal Neonatal Med. 2007;12(6):477-481.
51. Raychaudhuri P, Pasupati A, James A, et al. Prospective study of antenatally diagnosed congenital cystic adenomatoid malformations. Pediatr Surg Int. 2011;27(11):1159-1164.
52. Lecomte B, Hadden H, Coste K, et al. Hyperechoic congenital lung lesions in a non-selected population: from prenatal detection till perinatal management. Prenat Diagn. 2009;29(13):1222-1230.
53. Schott S, Mackensen-Haen S, Wallwiener M, et al. Cystic adenomatoid malformation of the lung causing hydrops fetalis: case report and review of the literature. Arch Gynecol Obstet. 2009;280(2):293-296.
54. Grethel EJ, Wagner AJ, Clifton MS, et al. Fetal intervention for mass lesions and hydrops improves outcome: a 15-year experience. J Pediatr Surg. 2007;42(1):117-123.
55. Curran PF, Jelin EB, Rand L, et al. Prenatal steroids for microcystic congenital cystic adenomatoid malformations. J Pediatr Surg. 2010;45(1):145-150.
56. Morris LM, Lim FY, Livingston JC, et al. High-risk fetal congenital pulmonary airway malformations have a variable response to steroids. J Pediatr Surg. 2009;44(1):60-65.
57. Loh KC, Jelin E, Hirose S, et al. Microcystic congenital pulmonary airway malformation with hydrops fetalis: steroids vs open fetal resection. J Pediatr Surg. 2012;47(1):36-39.
58. Derderian SC, Coleman AM, Jeanty C, et al. Favorable outcomes in high-risk congenital pulmonary airway malformations treated with multiple courses of maternal betamethasone. J Pediatr Surg. 2015;50(4): 515-518.
59. Peranteau WH, Boelig MM, Khalek N, et al. Effect of single and multiple courses of maternal betamethasone on prenatal congenital lung lesion growth and fetal survival. J Pediatr Surg. 2016;51(1):28-32.

60. Peranteau WH, Adzick NS, Boelig MM, et al. Thoracoamniotic shunts for the management of fetal lung lesions and pleural effusions: a single-institution review and predictors of survival in 75 cases. J Pediatr Surg. 2015;50(2):301-305.
61. Azizkhan RG, Crombleholme TM. Congenital cystic lung disease: contemporary antenatal and postnatal management. Pediatr Surg Int. 2008;24(6):643-657.
62. Kunisaki SM, Barnewolt CE, Estroff JA, et al. Large fetal congenital cystic adenomatoid malformations: growth trends and patient survival. J Pediatr Surg. 2007;42(2):404-410.
63. Knox EM, Kilby MD, Martin WL, Khan KS. In-utero pulmonary drainage in the management of primary hydrothorax and congenital cystic lung lesion: a systematic review. Ultrasound Obstet Gynecol. 2006;28(5):726-734.
64. Harrison MR, Adzick NS, Jennings RW, et al. Antenatal intervention for congenital cystic adenomatoid malformation. Lancet. 1990;336(8721):965-967.
65. Harmath A, Csaba A, Hauzman E, et al. Congenital lung malformations in the second trimester: prenatal ultrasound diagnosis and pathologic findings. J Clin Ultrasound. 2007;35(5):250-255.
66. Hubbard AM, States LJ. Fetal magnetic resonance imaging. Top Magn Reson Imaging. 2001;12(2):93-103.
67. Levine D, Barnewolt CE, Mehta TS, et al. Fetal thoracic abnormalities: MR imaging. Radiology. 2003;228(2):379-388.
68. Kunisaki SM, Fauza DO, Barnewolt CE, et al. Ex utero intrapartum treatment with placement on extracorporeal membrane oxygenation for fetal thoracic masses. J Pediatr Surg. 2007;42(2):420-425.
69. van Leeuwen K, Teitelbaum DH, Hirschl RB, et al. Prenatal diagnosis of congenital cystic adenomatoid malformation and its postnatal presentation, surgical indications, and natural history. J Pediatr Surg. 1999;34(5):794-798.
70. Ehrenberg-Buchner S, Stapf AM, Berman DR, et al. Fetal lung lesions: can we start to breathe easier? Am J Obstet Gynecol. 2013;208(2):151.e1-151.e7.
71. Adzick NS. Open fetal surgery for life-threatening fetal anomalies. Semin Fetal Neonatal Med. 2010;15(1):1-8.
72. Wilson RD. In utero therapy for fetal thoracic abnormalities. Prenat Diagn. 2008;28(7):619-625.
73. van Leeuwen K, Teitelbaum DH, Hirschl RB, et al. Prenatal diagnosis of congenital cystic adenomatoid malformation and its postnatal presentation, surgical indications, and natural history. J Pediatr Surg. 1999;34(5):794-798.
74. Stacher E, Ullmann R, Halbwedl I, et al. Atypical goblet cell hyperplasia in congenital cystic adenomatoid malformation as a possible preneoplasia for pulmonary adenocarcinoma in childhood: a genetic analysis. Hum Pathol. 2004;35(5):565-570.
75. Marshall KW, Blane CE, Teitelbaum DH, van Leeuwen K. Congenital cystic adenomatoid malformation: impact of prenatal diagnosis and changing strategies in the treatment of the asymptomatic patient. AJR Am J Roentgenol. 2000;175(6):1551-1554.
76. Rosado-de-Christenson ML, Frazier AA, Stocker JT, Templeton PA. From the archives of the AFIP. Extralobar sequestration: radiologic-pathologic correlation. Radiographics. 1993;13(2):425-441.
77. Halkic N, Cuenoud PF, Corthesy ME, et al. Pulmonary sequestration: a review of 26 cases. Eur J Cardiothorac Surg. 1998;14(2):127-133.
78. Savic B, Birtel FJ, Tholen W, et al. Lung sequestration: report of seven cases and review of 540 published cases. Thorax. 1979;34(1):96-101.
79. Corbett HJ, Humphrey GM. Pulmonary sequestration. Paediatr Respir Rev. 2004;5(1):59-68.
80. Sade RM, Clouse M, Ellis Jr FH. The spectrum of pulmonary sequestration. Ann Thorac Surg. 1974;18(6):644-658.
81. Frazier AA, Rosado de Christenson ML, Stocker JT, Templeton PA. Intralobar sequestration: radiologic-pathologic correlation. Radiographics. 1997;17(3):725-745.
82. Chan YF, Oldfield R, Vogel S, Ferguson S. Pulmonary sequestration presenting as a prenatally detected suprarenal lesion in a neonate. J Pediatr Surg. 2000;35(9):1367-1369.
83. Levi A, Findler M, Dolfin T, et al. Intrapericardial extralobar pulmonary sequestration in a neonate. Chest. 1990;98(4):1014-1015.
84. Abbey P, Das CJ, Pangtey GS, et al. Imaging in bronchopulmonary sequestration. J Med Imaging Radiat Oncol. 2009;53(1):22-31.
85. Langer B, Donato L, Riethmuller C, et al. Spontaneous regression of fetal pulmonary sequestration. Ultrasound Obstet Gynecol. 1995;6(1):33-39.
86. Sepulveda W. Perinatal imaging in bronchopulmonary sequestration. J Ultrasound Med. 2009;28(1):89-94.
87. Yildirim G, Gungorduk K, Aslan H, Ceylan Y. Prenatal diagnosis of an extralobar pulmonary sequestration. Arch Gynecol Obstet. 2008;278(2):181-186.
88. Hayashi S, Sago H, Kitano Y, et al. Fetal pleuroamniotic shunting for bronchopulmonary sequestration with hydrops. Ultrasound Obstet Gynecol. 2006;28(7):963-967.
89. Coleman AM, Merrow AC, Crombleholme TM, et al. Fetal MRI of torsed bronchopulmonary sequestration with tension hydrothorax and hydrops in a twin gestation. Fetal Diagn Ther. 2016;40(2):156-160.
90. Cruz-Martinez R, Méndez A, Dueñas-Riaño J, et al. Fetal laser surgery prevents fetal death and avoids the need for neonatal sequestrectomy in cases with bronchopulmonary sequestration. Ultrasound Obstet Gynecol. 2015;46(5):627-628.
91. Mallmann MR, Geipel A, Bludau M, et al. Bronchopulmonary sequestration with massive pleural effusion: pleuroamniotic shunting vs intrafetal vascular laser ablation. Ultrasound Obstet Gynecol. 2014;44(4):441-446.
92. Pinto RM, Araujo Júnior E, Augusto LC, et al. Spontaneous regression of intralobar pulmonary sequestration during the pregnancy: report of two cases through relationships between mass and fetal biometry and review of the literature. J Matern Fetal Neonatal Med. 2016;29(11):1720-1724.
93. Breysem L, Bosmans H, Dymarkowski S, et al. The value of fast MR imaging as an adjunct to ultrasound in prenatal diagnosis. Eur Radiol. 2003;13(7):1538-1548.
94. Olutoye OO, Coleman BG, Hubbard AM, Adzick NS. Prenatal diagnosis and management of congenital lobar emphysema. J Pediatr Surg. 2000;35(5):792-795.
95. Barth R. Congenital lobar overinflation (CLO)/congenital lobar emphysema (CLE)—not an uncommon cause for a fetal chest mass. Pediatr Radiol. 2009;39(Suppl. 2):S83-S109.
96. Ankermann T, Oppermann HC, Engler S, et al. Congenital masses of the lung, cystic adenomatoid malformation versus congenital lobar emphysema: prenatal diagnosis and implications for postnatal treatment. J Ultrasound Med. 2004;23(10):1379-1384.
97. Babu R, Kyle P, Spicer RD. Prenatal sonographic features of congenital lobar emphysema. Fetal Diagn Ther. 2001;16(4):200-202.
98. Pariente G, Aviram M, Landau D, Hershkovitz R. Prenatal diagnosis of congenital lobar emphysema: case report and review of the literature. J Ultrasound Med. 2009;28(8):1081-1084.
99. Moideen I, Nair SG, Cherian A, Rao SG. Congenital lobar emphysema associated with congenital heart disease. J Cardiothorac Vasc Anesth. 2006;20(2):239-241.
100. Liu YP, Shih SL. Congenital lobar emphysema: appearance on fetal MRI. Pediatr Radiol. 2008;38(11):1264.
101. Quinton AE, Smoleniec JS. Congenital lobar emphysema—the disappearing chest mass: antenatal ultrasound appearance. Ultrasound Obstet Gynecol. 2001;17(2):169-171.
102. Nazem M, Hosseinpour M. Evaluation of early and late complications in patients with congenital lobar emphysema: a 12 year experience. Afr J Paediatr Surg. 2010;7(3):144-146.
103. Kunisaki SM, Fauza DO, Nemes LP, et al. Bronchial atresia: the hidden pathology within a spectrum of prenatally diagnosed lung masses. J Pediatr Surg. 2006;41(1):61-65.
104. Priest JR, McDermott MB, Bhatia S, et al. Pleuropulmonary blastoma: a clinicopathologic study of 50 cases. Cancer. 1997;80(1):147-161.
105. Hill DA, Ivanovich J, Priest JR, et al. DICER1 mutations in familial pleuropulmonary blastoma. Science. 2009;325(5943):965.
106. Miniati DN, Chintagumpala M, Langston C, et al. Prenatal presentation and outcome of children with pleuropulmonary blastoma. J Pediatr Surg. 2006;41(1):66-71.

107. Naffaa LN, Donnelly LF. Imaging findings in pleuropulmonary blastoma. Pediatr Radiol. 2005;35(4):387-391.
108. Lim FY, Crombleholme TM, Hedrick HL, et al. Congenital high airway obstruction syndrome: natural history and management. J Pediatr Surg. 2003;38(6):940-945.
109. Hedrick MH, Ferro MM, Filly RA, et al. Congenital high airway obstruction syndrome (CHAOS): a potential for perinatal intervention. J Pediatr Surg. 1994;29(2):271-274.
110. Vidaeff AC, Szmuk P, Mastrobattista JM, et al. More or less CHAOS: case report and literature review suggesting the existence of a distinct subtype of congenital high airway obstruction syndrome. Ultrasound Obstet Gynecol. 2007;30(1):114-117.
111. Kanamori Y, Kitano Y, Hashizume K, et al. A case of laryngeal atresia (congenital high airway obstruction syndrome) with chromosome 5p deletion syndrome rescued by ex utero intrapartum treatment. J Pediatr Surg. 2004;39(1):E25-E28.
112. King SJ, Pilling DW, Walkinshaw S. Fetal echogenic lung lesions: prenatal ultrasound diagnosis and outcome. Pediatr Radiol. 1995;25(3):208-210.
113. Vanhaesebrouck P, De Coen K, Defoort P, et al. Evidence for autosomal dominant inheritance in prenatally diagnosed CHAOS. Eur J Pediatr. 2006;165(10):706-708.
114. Witters I, Moerman P, Fryns JP. Prenatal echographic diagnosis of laryngeal atresia as part of a multiple congenital anomalies (MCA) syndrome. Genet Couns. 2000;11(3):215-219.
115. Morrison PJ, Macphail S, Williams D, et al. Laryngeal atresia or stenosis presenting as second-trimester fetal ascites—diagnosis and pathology in three independent cases. Prenat Diagn. 1998;18(9):963-967.
116. Mong A, Johnson AM, Kramer SS, et al. Congenital high airway obstruction syndrome: MR/US findings, effect on management, and outcome. Pediatr Radiol. 2008;38(11):1171-1179.
117. Langer JE, Coleman BG. Case 2: Diagnosis: congenital high airway obstruction syndrome. Ultrasound Q. 2007;23(1):67-70.
118. Courtier J, Poder L, Wang ZJ, et al. Fetal tracheolaryngeal airway obstruction: prenatal evaluation by sonography and MRI. Pediatr Radiol. 2010;40(11):1800-1805.
119. Joshi P, Satija L, George R, et al. Congenital high airway obstruction syndrome-antenatal diagnosis of a rare case of airway obstruction using multimodality imaging. Med J Armed Forces India. 2012;68(1):78-80.
120. Kalache KD, Chaoui R, Tennstedt C, Bollmann R. Prenatal diagnosis of laryngeal atresia in two cases of congenital high airway obstruction syndrome (CHAOS). Prenat Diagn. 1997;17(6):577-581.
121. Crombleholme TM, Sylvester K, Flake AW, Adzick NS. Salvage of a fetus with congenital high airway obstruction syndrome by ex utero intrapartum treatment (EXIT) procedure. Fetal Diagn Ther. 2000;15(5):280-282.
122. Bui TH, Grunewald C, Frenckner B, et al. Successful EXIT (ex utero intrapartum treatment) procedure in a fetus diagnosed prenatally with congenital high-airway obstruction syndrome due to laryngeal atresia. Eur J Pediatr Surg. 2000;10(5):328-333.
123. Martinez JM, Castanon M, Gomez O, et al. Evaluation of fetal vocal cords to select candidates for successful fetoscopic treatment of congenital high airway obstruction syndrome: preliminary case series. Fetal Diagn Ther. 2013;34(2):77-84.
124. Roybal JL, Liechty KW, Hedrick HL, et al. Predicting the severity of congenital high airway obstruction syndrome. J Pediatr Surg. 2010;45(8):1633-1639.
125. Rogers LF, Osmer JC. Bronchogenic cyst. A review of 46 cases. Am J Roentgenol Radium Ther Nucl Med. 1964;91:273-290.
126. Snyder ME, Luck SR, Hernandez R, et al. Diagnostic dilemmas of mediastinal cysts. J Pediatr Surg. 1985;20(6):810-815.
127. Parikh D, Samuel M. Congenital cystic lung lesions: is surgical resection essential? Pediatr Pulmonol. 2005;40(6):533-537.
128. Albright EB, Crane JP, Shackelford GD. Prenatal diagnosis of a bronchogenic cyst. J Ultrasound Med. 1988;7(2):90-95.
129. Levine D, Jennings R, Barnewolt C, et al. Progressive fetal bronchial obstruction caused by a bronchogenic cyst diagnosed using prenatal MR imaging. AJR Am J Roentgenol. 2001;176(1):49-52.
130. Reece EA, Lockwood CJ, Rizzo N, et al. Intrinsic intrathoracic malformations of the fetus: sonographic detection and clinical presentation. Obstet Gynecol. 1987;70:627-632.
131. Eber E. Antenatal diagnosis of congenital thoracic malformations: early surgery, late surgery, or no surgery? Semin Respir Crit Care Med. 2007;28(3):355-366.
132. Uludag S, Madazli R, Erdogan E, et al. A case of prenatally diagnosed fetal neurenteric cyst. Ultrasound Obstet Gynecol. 2001;18(3):277-279.
133. Macaulay KE, Winter 3rd TC, Shields LE. Neurenteric cyst shown by prenatal sonography. AJR Am J Roentgenol. 1997;169(2):563-565.
134. Perera GB, Milne M. Neurenteric cyst: antenatal diagnosis by ultrasound. Australas Radiol. 1997;41(3):300-302.
135. Wilkinson CC, Albanese CT, Jennings RW, et al. Fetal neurenteric cyst causing hydrops: case report and review of the literature. Prenat Diagn. 1999;19(2):118-121.
136. Castillo RA, Devoe LD, Hadi HA, et al. Nonimmune hydrops fetalis: clinical experience and factors related to a poor outcome. Am J Obstet Gynecol. 1986;155(4):812-816.
137. Longaker MT, Laberge JM, Dansereau J, et al. Primary fetal hydrothorax: natural history and management. J Pediatr Surg. 1989;24(6):573-576.
138. Deurloo KL, Devlieger R, Lopriore E, et al. Isolated fetal hydrothorax with hydrops: a systematic review of prenatal treatment options. Prenat Diagn. 2007;27(10):893-899.
139. Lange IR, Manning FA. Antenatal diagnosis of congenital pleural effusions. Am J Obstet Gynecol. 1981;140(7):839-840.
140. Aubard Y, Derouineau I, Aubard V, et al. Primary fetal hydrothorax: a literature review and proposed antenatal clinical strategy. Fetal Diagn Ther. 1998;13(6):325-333.
141. Derderian SC, Trivedi S, Farrell J, et al. Outcomes of fetal intervention for primary hydrothorax. J Pediatr Surg. 2014;49(6):900-903.
142. Achiron R, Weissman A, Lipitz S, et al. Fetal pleural effusion: the risk of fetal trisomy. Gynecol Obstet Invest. 1995;39(3):153-156.
143. Nicolaides KH, Rodeck CH, Gosden CM. Rapid karyotyping in non-lethal fetal malformations. Lancet. 1986;1(8476):283-287.
144. Buttiker V, Fanconi S, Burger R. Chylothorax in children: guidelines for diagnosis and management. Chest. 1999;116(3):682-687.
145. Poblete A, Roberts A, Trespidi L, et al. Fetal and maternal white cells and B- and T-lymphocyte subpopulations in pregnant women with recent infection. Fetal Diagn Ther. 2001;16(6):378-383.
146. Carroll B. Pulmonary hypoplasia and pleural effusions associated with fetal death in utero: ultrasonic findings. AJR Am J Roentgenol. 1977;129(4):749-750.
147. Weber AM, Philipson EH. Fetal pleural effusion: a review and meta-analysis for prognostic indicators. Obstet Gynecol. 1992;79(2):281-286.
148. Klam S, Bigras JL, Hudon L. Predicting outcome in primary fetal hydrothorax. Fetal Diagn Ther. 2005;20(5):366-370.
149. Hagay Z, Reece A, Roberts A, Hobbins JC. Isolated fetal pleural effusion: a prenatal management dilemma. Obstet Gynecol. 1993;81(1):147-152.
150. Cannie M, Jani J, De Keyzer F, et al. Magnetic resonance imaging of the fetal lung: a pictorial essay. Eur Radiol. 2008;18(7):1364-1374.
151. Pellegrinelli JM, Kohler A, Kohler M, et al. Prenatal management and thoracoamniotic shunting in primary fetal pleural effusions: a single centre experience. Prenat Diagn. 2012;32(5):467-471.
152. Bigras JL, Ryan G, Suda K, et al. Echocardiographic evaluation of fetal hydrothorax: the effusion ratio as a diagnostic tool. Ultrasound Obstet Gynecol. 2003;21(1):37-40.
153. Petres RE, Redwine FO, Cruikshank DP. Congenital bilateral chylothorax. Antepartum diagnosis and successful intrauterine surgical management. JAMA. 1982;248(11):1360-1361.
154. Roberts AB, Clarkson PM, Pattison NS, et al. Fetal hydrothorax in the second trimester of pregnancy: successful intra-uterine treatment at 24 weeks gestation. Fetal Ther. 1986;1(4):203-209.
155. Okawa T, Takano Y, Fujimori K, et al. A new fetal therapy for chylothorax: pleurodesis with OK-432. Ultrasound Obstet Gynecol. 2001;18(4):376-377.

156. Tanemura M, Nishikawa N, Kojima K, et al. A case of successful fetal therapy for congenital chylothorax by intrapleural injection of OK-432. Ultrasound Obstet Gynecol. 2001;18(4):371-375.
157. Di Salvo DN, Brown DL, Doubilet PM, et al. Clinical significance of isolated fetal pericardial effusion. J Ultrasound Med. 1994;13(4):291-293.
158. Raman SP, Pipavath SN, Raghu G, et al. Imaging of thoracic lymphatic diseases. AJR Am J Roentgenol. 2009;193(6):1504-1513.
159. Seed M, Bradley T, Bourgeois J, et al. Antenatal MR imaging of pulmonary lymphangiectasia secondary to hypoplastic left heart syndrome. Pediatr Radiol. 2009;39:747-749.
160. Saul D, Degenhardt K, Iyoob S, et al. Hypoplastic left heart syndrome and the nutmeg lung pattern in utero: a cause and effect relationship or prognostic indicator? Pediatr Radiol. 2015.
161. Victoria T, Andronikou S. The fetal MR appearance of 'nutmeg lung': findings in 8 cases linked to pulmonary lymphangiectasia. Pediatr Radiol. 2014; 44(10):1237-1242.
162. Gray M, Kovatis KZ, Stuart T, et al. Treatment of congenital pulmonary lymphangiectasia using ethiodized oil lymphangiography. J Perinatol. 2014;34(9):720-722.
163. Chinn DH, Filly RA, Callen PW, et al. Congenital diaphragmatic hernia diagnosed prenatally by ultrasound. Radiology. 1983;148(1):119-123.
164. Keijzer R, Liu J, Deimling J, et al. Dual-hit hypothesis explains pulmonary hypoplasia in the nitrofen model of congenital diaphragmatic hernia. Am J Pathol. 2000;156(4):1299-1306.
165. Albanese C, Lopoo J, Goldstein R, et al. Fetal liver position and perinatal outcome for congenital diaphragmatic hernia. Prenat Diagn. 1998;18(11): 1138-1142.
166. Sista AK, Filly RA. Paradoxical movement of abdominal contents: a real-time sonographic finding indicating a congenital diaphragmatic hernia. J Ultrasound Med. 2007;26(11):1617-1619.
167. Harrison MR, Adzick NS, Estes JM, Howell LJ. A prospective study of the outcome for fetuses with diaphragmatic hernia. JAMA. 1994;271(5): 382-384.
168. Conforti A, Losty P. Perinatal management of congenital diaphragmatic hernia. Early Hum Dev. 2006;82(5):283-287.
169. Leeuwen L, Fitzgerald D. Congenital diaphragmatic hernia. J Paediatr Child Health. 2014;50(9):667-673.
170. Graham G, Devine P. Antenatal diagnosis of congenital diaphragmatic hernia. Semin Perinatol. 2005;29(2):69-76.
171. Jain K, Sen J, Rathee S, Saini J. Antenatal diagnosis of a Morgagni hernia in the second trimester. J Clin Ultrasound. 2008;36(2):116-118.
172. Robnett-Filly B, Goldstein RB, Sampior D, Hom M. Morgagni hernia: a rare form of congenital diaphragmatic hernia. J Ultrasound Med. 2003;22(5):537-539.
173. Gucciardo L, Deprest J, Done E, et al. Prediction of outcome in isolated congenital diaphragmatic hernia and its consequences for fetal therapy. Best Pract Res Clin Obstet Gynaecol. 2008;22(1):123-138.
174. Bootstaylor BS, Filly RA, Harrison MR, Adzick NS. Prenatal sonographic predictors of liver herniation in congenital diaphragmatic hernia. J Ultrasound Med. 1995;14(7):515-520.
175. Claus F, Sandaite I, DeKoninck P, et al. Prenatal anatomical imaging in fetuses with congenital diaphragmatic hernia. Fetal Diagn Ther. 2011;29(1): 88-100.
176. Benacerraf BR, Greene MF. Congenital diaphragmatic hernia: US diagnosis prior to 22 weeks gestation. Radiology. 1986;158(3):809-810.
177. Deprest J, Jani J, Van Schoubroeck D, et al. Current consequences of prenatal diagnosis of congenital diaphragmatic hernia. J Pediatr Surg. 2006;41(2): 423-430.
178. Doné E, Gucciardo L, Van Mieghem T, et al. Prenatal diagnosis, prediction of outcome and in utero therapy of isolated congenital diaphragmatic hernia. Prenat Diagn. 2008;28(7):581-591.
179. Harrison MR, Adzick NS, Nakayama DK, deLorimier AA. Fetal diaphragmatic hernia: fetal but fixable. Semin Perinatol. 1985;9(2):103-112.
180. Conforti AF, Losty PD. Perinatal management of congenital diaphragmatic hernia. Early Hum Dev. 2006;82(5):283-287.
181. Adzick N, Vacanti J, Lillehei C, et al. Fetal diaphragmatic hernia: ultrasound diagnosis and clinical outcome in 38 cases. J Pediatr Surg. 1989;24(7): 654-658.
182. Daskalakis G, Anastasakis E, Souka A, et al. First trimester ultrasound diagnosis of congenital diaphragmatic hernia. J Obstet Gynaecol Res. 2007;33(6):870-872.
183. Garne E, Haeusler M, Barisic I, et al. Congenital diaphragmatic hernia: evaluation of prenatal diagnosis in 20 European regions. Ultrasound Obstet Gynecol. 2002;19(4):329-333.
184. Danzer E, Hedrick H. Controversies in the management of severe congenital diaphragmatic hernia. Semin Fetal Neonatal Med. 2014;19(6):376-384.
185. Plunk MR, Chapman T. The fundamentals of fetal magnetic resonance imaging: Part 2. Curr Probl Diagn Radiol. 2014;43(6):347-355.
186. Benachi A, Cordier A, Cannie M, Jani J. Advances in prenatal diagnosis of congenital diaphragmatic hernia. Semin Fetal Neonatal Med. 2014;19(6): 331-337.
187. Levine D. Ultrasound versus magnetic resonance imaging in fetal evaluation. Top Magn Reson Imaging. 2001;12(1):25-38.
188. Barnewolt CE, Kunisaki SM, Fauza DO, et al. Percent predicted lung volumes as measured on fetal MRI; a useful biometric parameter for risk stratification in congenital diaphragmetic hernia. J Pediatr Surg. 2007;42: 193-197.
189. Vuletin J, Lim F, Cnota J, et al. Prenatal pulmonary hypertension index: novel prenatal predictor of severe postnatal pulmonary artery hypertension in antenatally diagnosed congenital diaphragmatic hernia. J Pediatr Surg. 2010;45(4):703-708.
190. Hidaka N, Ishii K, Mabuchi A, et al. Associated anomalies in congenital diaphragmatic hernia: perinatal characteristics and impact on postnatal survival. J Perinat Med. 2015;43(2):245-252.
191. Graziano J. Cardiac anomalies in patients with congenital diaphragmatic hernia and their prognosis: a report from the Congenital Diaphragmatic Hernia Study Group. J Pediatr Surg. 2005;40(6):1045-1050.
192. Bollmann R, Kalache K, Mau H, et al. Associated malformations and chromosomal defects in congenital diaphragmatic hernia. Fetal Diagn Ther. 1995;10(1):52-59.
193. Sabharwal A, Davis C, Howatson A. Post-mortem findings in fetal and neonatal congenital diaphragmatic hernia. Eur J Pediatr Surg. 2000; 10(2):96-99.
194. Geary MP, Chitty LS, Morrison JJ, et al. Perinatal outcome and prognostic factors in prenatally diagnosed congenital diaphragmatic hernia. Ultrasound Obstet Gynecol. 1998;12(2):107-111.
195. Enns GM, Cox VA, Goldstein RB, et al. Congenital diaphragmatic defects and associated syndromes, malformations, and chromosome anomalies: a retrospective study of 60 patients and literature review. Am J Med Genet. 1998;79(3):215-225.
196. Jani J, Nicolaides KH, Benachi A, et al. Timing of lung size assessment in the prediction of survival in fetuses with diaphragmatic hernia. Ultrasound Obstet Gynecol. 2008;31(1):37-40.
197. Losty P. Congenital diaphragmatic hernia: where and what is the evidence? Semin Pediatr Surg. 2014;23(5):278-282.
198. Madenci A, Sjogren A, Treadwell M, et al. Another dimension to survival: predicting outcomes with fetal MRI versus prenatal ultrasound in patients with congenital diaphragmatic hernia. J Pediatr Surg. 2013;48(6): 1190-1197.
199. Jeanty C, Kunisaki S, MacKenzie T. Novel non-surgical prenatal approaches to treating congenital diaphragmatic hernia. Semin Fetal Neonatal Med. 2014;19(6):349-356.
200. Laudy JAM, Van Gucht M, Van Dooren MF, et al. Congenital diaphragmatic hernia: an evaluation of the prognostic value of the lung-to-head ratio and other prenatal parameters. Prenat Diagn. 2003;23(8):634-639.
201. Yang S, Nobuhara K, Keller R, et al. Reliability of the lung-to-head ratio as a predictor of outcome in fetuses with isolated left congenital diaphragmatic hernia at gestation outside 24-26 weeks. Am J Obstet Gynecol. 2007;197(1): 30.e1-30.e7.
202. Peralta CFA, Cavoretto P, Csapo B, et al. Assessment of lung area in normal fetuses at 12-32 weeks. Ultrasound Obstet Gynecol. 2005;26(7): 718-724.
203. Van Mieghem T, Cruz-Martinez R, Allegaert K, et al. Outcome of fetuses with congenital diaphragmatic hernia and associated intrafetal fluid effusions managed in the era of fetal surgery. Ultrasound Obstet Gynecol. 2012; 39(1):50-55.

204. Cruz-Martinez R, Figueras F, Moreno-Alvarez O, et al. Learning curve for lung area to head circumference ratio measurement in fetuses with congenital diaphragmatic hernia. Ultrasound Obstet Gynecol. 2010;36(1):32-36.
205. Arkovitz M, Russo M, Devine P, et al. Fetal lung-head ratio is not related to outcome for antenatal diagnosed congenital diaphragmatic hernia. J Pediatr Surg. 2007;42(1):107-111.
206. Jani JC, Peralta CFA, Ruano R, et al. Comparison of fetal lung area to head circumference ratio with lung volume in the prediction of postnatal outcome in diaphragmatic hernia. Ultrasound Obstet Gynecol. 2007;30(6):850-854.
207. Gorincour G, Bouvenot J, Mourot MG, et al. Prenatal prognosis of congenital diaphragmatic hernia using magnetic resonance imaging measurement of fetal lung volume. Ultrasound Obstet Gynecol. 2005;26(7):738-744.
208. Hedrick HL, Danzer E, Merchant A, et al. Liver position and lung-to-head ratio for prediction of extracorporeal membrane oxygenation and survival in isolated left congenital diaphragmatic hernia. Am J Obstet Gynecol. 2007;197:422.e1-422.e4.
209. McHoney M. Congenital diaphragmatic hernia. Early Hum Dev. 2014;90(12):941-946.
210. Jani J, Nicolaides KH, Keller RL, et al. Observed to expected lung area to head circumference ratio in the prediction of survival in fetuses with isolated diaphragmatic hernia. Ultrasound Obstet Gynecol. 2007;30(1):67-71.
211. Ruano R, Takashi E, da Silva MM, et al. Prediction and probability of neonatal outcome in isolated congenital diaphragmatic hernia using multiple ultrasound parameters. Ultrasound Obstet Gynecol. 2011;39(1):42-49.
212. Sokol J, Bohn D, Lacro R, et al. Fetal pulmonary artery diameters and their association with lung hypoplasia and postnatal outcome in congenital diaphragmatic hernia. Am J Obstet Gynecol. 2002;186(5):1085-1090.
213. Ruano R, de Fátima Yukie Maeda M, Niigaki JI, Zugaib M. Pulmonary artery diameters in healthy fetuses from 19 to 40 weeks' gestation. J Ultrasound Med. 2007;26(3):309-316.
214. Ruano R, Aubry M, Barthe B, et al. Predicting perinatal outcome in isolated congenital diaphragmatic hernia using fetal pulmonary artery diameters. J Pediatr Surg. 2008;43(4):606-611.
215. Moreno-Alvarez O, Hernandez-Andrade E, Oros D, et al. Association between intrapulmonary arterial Doppler parameters and degree of lung growth as measured by lung-to-head ratio in fetuses with congenital diaphragmatic hernia. Ultrasound Obstet Gynecol. 2008;31(2):164-170.
216. Cruz-Martinez R, Moreno-Alvarez O, Hernandez-Andrade E, et al. Contribution of intrapulmonary artery Doppler to improve prediction of survival in fetuses with congenital diaphragmatic hernia treated with fetal endoscopic tracheal occlusion. Ultrasound Obstet Gynecol. 2010;35(5):572-577.
217. Broth R, Wood D, Rasanen J, et al. Prenatal prediction of lethal pulmonary hypoplasia: the hyperoxygenation test for pulmonary artery reactivity. Am J Obstet Gynecol. 2002;187(4):940-945.
218. Cruz-Martinez R, Hernandez-Andrade E, Moreno-Alvarez O, et al. Prognostic value of pulmonary Doppler to predict response to tracheal occlusion in fetuses with congenital diaphragmatic hernia. Fetal Diagn Ther. 2011;29(1):18-24.
219. Ruano R, Aubry M, Barthe B, et al. Quantitative analysis of fetal pulmonary vasculature by 3-dimensional power Doppler ultrasonography in isolated congenital diaphragmatic hernia. Am J Obstet Gynecol. 2006;195(6):1720-1728.
220. Mahieu-Caputo D, Aubry MC, El Sayed M, et al. Evaluation of fetal pulmonary vasculature by power Doppler imaging in congenital diaphragmatic hernia. J Ultrasound Med. 2004;23(8):1011-1017.
221. Hernandez-Andrade E, Thuring-Jönsson A, Jansson T, et al. Fractional moving blood volume estimation in the fetal lung using power Doppler ultrasound: a reproducibility study. Ultrasound Obstet Gynecol. 2004;23(4):369-373.
222. Moreno-Alvarez O, Cruz-Martinez R, Hernandez-Andrade E, et al. Lung tissue perfusion in congenital diaphragmatic hernia and association with the lung-to-head ratio and intrapulmonary artery pulsed Doppler. Ultrasound Obstet Gynecol. 2010;35(5):578-582.
223. Cruz-Martinez R, Moreno-Alvarez O, Hernandez-Andrade E, et al. Changes in lung tissue perfusion in the prediction of survival in fetuses with congenital diaphragmatic hernia treated with fetal endoscopic tracheal occlusion. Fetal Diagn Ther. 2011;29(1):101-107.
224. Bingham JAW. Herniation through congenital diaphragmatic defects. Br J Surg. 1959;47(201):1-15.
225. Lanteri R, Santangelo M, Rapisarda C, et al. Bilateral Morgagni-Larrey hernia: a rare cause of intestinal occlusion. Arch Surg. 2004;139(12):1299-1300.
226. Einzig S, Munson DP, Singh S, et al. Intrapericardial herniation of the liver: uncommon cause of massive pericardial effusion in neonates. AJR Am J Roentgenol. 1981;137(5):1075-1077.
227. Iliff PJ, Eyre JA, Westaby S, et al. Neonatal pericardial effusion associated with central eventration of the diaphragm. Arch Dis Child. 1983;58(2):147-149.
228. Jain KK, Sen J, Rathee SK, Saini J. Antenatal diagnosis of a Morgagni hernia in the second trimester. J Clin Ultrasound. 2008;36(2):116-118.
229. Jeanty C, Nien JK, Espinoza J, et al. Pleural and pericardial effusion: a potential ultrasonographic marker for the prenatal differential diagnosis between congenital diaphragmatic eventration and congenital diaphragmatic hernia. Ultrasound Obstet Gynecol. 2007;29(4):378-387.
230. Stringer M, Goldstein R, Filly R, et al. Fetal diaphragmatic hernia without visceral herniation. J Pediatr Surg. 1995;30(9):1264-1266.
231. Wynn J, Yu L, Chung W. Genetic causes of congenital diaphragmatic hernia. Semin Fetal Neonatal Med. 2014;19(6):324-330.
232. Harrison M, Mychaliska G, Albanese C, et al. Correction of congenital diaphragmatic hernia in utero IX: fetuses with poor prognosis (liver herniation and low lung-to-head ratio) can be saved by fetoscopic temporary tracheal occlusion. J Pediatr Surg. 1998;33(7):1017-1023.
233. Walsh D, Hubbard A, Olutoye O, et al. Assessment of fetal lung volumes and liver herniation with magnetic resonance imaging in congenital diaphragmatic hernia. Am J Obstet Gynecol. 2000;183(5):1067-1069.
234. Skari H, Bjornland K, Haugen G, et al. Congenital diaphragmatic hernia: a meta-analysis of mortality factors. J Pediatr Surg. 2000;35:1187-1197.
235. Harrison MR, Keller RL, Hawgood SB, et al. A randomized trial of fetal endoscopic tracheal occlusion for severe fetal congenital diaphragmatic hernia. N Engl J Med. 2003;349(20):1916-1924.
236. Javid P, Jaksic T, Skarsgard E, Lee S. Survival rate in congenital diaphragmatic hernia: the experience of the Canadian Neonatal Network. J Pediatr Surg. 2004;39(5):657-660.
237. Stege G, Fenton A, Jaffray B. Nihilism in the 1990s: the true mortality of congenital diaphragmatic hernia. Pediatrics. 2003;112(3):532-535.
238. Kitano Y. Prenatal intervention for congenital diaphragmatic hernia. Semin Pediatr Surg. 2007;16(2):101-108.
239. Harrison MR, Adzick NS, Flake AW, et al. Correction of congenital diaphragmatic hernia in utero: VI. Hard-earned lessons. J Pediatr Surg. 1993;28(10):1411-1417.
240. Deprest J, Flemmer A, Gratacos E, Nicolaides K. Antenatal prediction of lung volume and in-utero treatment by fetal endoscopic tracheal occlusion in severe isolated congenital diaphragmatic hernia. Semin Fetal Neonatal Med. 2009;14(1):8-13.
241. Rollins M. Recent advances in the management of congenital diaphragmatic hernia. Curr Opin Pediatr. 2012;24(3):379-385.
242. Hedrick H. Management of prenatally diagnosed congenital diaphragmatic hernia. Semin Pediatr Surg. 2013;22(1):37-43.
243. Jani J, Keller RL, Benachi A, et al. Prenatal prediction of survival in isolated left-sided diaphragmatic hernia. Ultrasound Obstet Gynecol. 2006;27(1):18-22.
244. David AL, Weisz B, Gregory L, et al. Ultrasound-guided injection and occlusion of the trachea in fetal sheep. Ultrasound Obstet Gynecol. 2006;28(1):82-88.
245. Davey M, Danzer E, Schwarz U, et al. Prenatal glucocorticoids and exogenous surfactant therapy improve respiratory function in lambs with severe diaphragmatic hernia following fetal tracheal occlusion. Pediatr Res. 2006;60(2):131-135.

CHAPTER 37

The Fetal Heart

Elizabeth R. Stamm and Julia A. Drose

SUMMARY OF KEY POINTS

- Moderate to severe congenital heart disease (CHD) occurs in approximately 6 per 1000 live births.
- The incidence of CHD is much higher in the fetal population, estimated to be at least 15 per 1000.
- The incidence of CHD is higher with positive family history, monochorionic twins, and *in vitro* fertilization.
- Most fetuses with CHD have no known risk factors.
- Fetal echocardiography is a safe and effective method of detecting CHD.
- Early detection of CHD may have a substantial impact on care and prognosis, allowing intrauterine therapy, carefully planned delivery, and parental counseling.
- Advancements in surgical techniques and perioperative management have significantly improved prognosis in many cases.

CHAPTER OUTLINE

NORMAL FETAL CARDIAC ANATOMY AND SCANNING TECHNIQUES
STRUCTURAL ANOMALIES
Atrial Septal Defect
Ventricular Septal Defect
Atrioventricular Septal Defect
Ebstein Anomaly
Hypoplastic Right Ventricle
Hypoplastic Left Heart Syndrome
Univentricular Heart
Tetralogy of Fallot
Truncus Arteriosus
Double-Outlet Right Ventricle
Transposition of Great Arteries
Anomalous Pulmonary Venous Return
Coarctation of Aorta
Aortic Stenosis
Pulmonic Stenosis
Cardiosplenic Syndromes
Cardiac Tumors
Cardiomyopathy
Ectopia Cordis
ARRHYTHMIAS
Premature Atrial and Ventricular Contractions
Tachycardia
Bradycardia
Congenital Heart Block

Sonographic evaluation of the fetal heart can identify cardiac abnormalities that affect obstetric care in a variety of ways, including mode of delivery, location of delivery, intrauterine therapy, parental reassurance, and opportunity for termination. **Congenital heart disease** (CHD) is a significant problem, with an incidence of moderate and severe CHD of approximately 6 per 1000 live births. If trivial lesions such as tiny muscular **ventricular septal defects** (VSDs) are included, the incidence is as high as 75 per 1000 live births.[1] It is more difficult to determine the exact incidence of CHD in the fetal population. One large study suggested that CHD occurs in at least 15 per 1000 fetuses.[2] More than 20% of perinatal deaths caused by congenital malformations are the result of a congenital heart defect.[3] In 85% of CHD cases, both environmental and genetic factors are involved (Table 37.1).[4-7] The remaining 15% of cardiac anomalies are associated with a single gene or chromosomal abnormality.[5] The risk of CHD increases to 2% to 3% with an affected sibling and to approximately 10% with two affected siblings or an affected mother—although the incidence is variable depending on the type of CHD in the affected relative.[5,8] The risk to offspring of affected mothers is substantially higher than for those with affected fathers, suggesting that cytoplasmic inheritance may play a role in the genetics of CHD (Tables 37.2 and 37.3). Only 50% of recurrent heart lesions are of the same type as the previously diagnosed defect.[9]

Extracardiac malformations occur in 25%,[10] and **chromosomal anomalies** occur in 13% of live-born neonates with CHD.[11-13] About 50% of fetuses with nonimmune hydrops and cardiac anomalies have a chromosomal anomaly, and 10% will have extracardiac anomalies.[14] **Hydrops** in the setting of CHD is predictive of a very poor prognosis.

Although the most common indications for formal **fetal echocardiography** are family history of CHD and **fetal arrhythmia,** the majority of these fetuses will have normal hearts. The highest incidence of CHD occurs in patients referred because of an abnormal four-chamber view, fetal hydrops, or significant polyhydramnios on a routine obstetric ultrasound.[15,16] A routine ultrasound examination with a suspected fetal cardiac anomaly is associated with a 50% to 69% risk of CHD in live-born infants.[17,18] Monochorionic twins are at a higher risk for CHD,

TABLE 37.1 Congenital Heart Disease and Associated Risk Factors

Factor	Frequency	Most Common Lesions
MATERNAL CONDITIONS		
Diabetes	3%-5%	TGA, VSD, coarctation
Lupus erythematosus	(1%-5%)	Heart block
Phenylketonuria	(12%-14%)	TOF, VSD, ASD, coarctation
Infection		Cardiomyopathy
Rubella	(1%-2%)	TOF, PS, VSD, ASD, PDA, cardiomegaly
DRUGS		
Accutane (retinoic acid)	8%-20%	Truncus, TGA, TOF, DORV, VSD, AO arch interruption, or hypoplasia
Alcohol	25%-30%	VSD, ASD, PDA, DORV, PA, TOF, dextrocardia
Amantadine		Single vent with PA
Amphetamines	5%-10%	VSD, TGA, PDA
Azathioprine		PS
Carbamazepine		ASD, PDA
Chlordiazepoxide		Unspecified CHD
Codeine		Unspecified CHD
Cortisone		VSD, coarctation
Coumadin		Unspecified CHD
Cyclophosphamide		TOF
Cytarabine		TOF
Daunorubicin		TOF
Dextroamphetamine		ASD
Diazepam		Unspecified CHD
Dilantin (hydantoin)		AS, VSD, ASD, coarctation
Lithium	<2%	Ebstein anomaly, TA, ASD, dextrocardia, MA
Methotrexate		Dextrocardia
Oral contraceptives		Unspecified CHD
Paramethadione		TOF
Penicillamine		VSD
Primidone		VSD
Progesterone		TOF, truncus, VSD
Quinine		Unspecified CHD
Thalidomide	5%-10%	TOF, VSD, ASD, truncus
Trifluoperazine		TGA
Trimethadione	15%-30%	ASD, VSD, TGA, TOF, HLHS, AS, PS
Valproic acid		TOF, coarctation, HLHS, AS, ASD, VSD, interrupted AO arch, PA without VSD
Warfarin (Coumadin)		Unspecified CHD
SYNDROMES		
Apert		VSD, coarctation, TOF
Arthrogryposis multiplex congenita		VSD, coarctation, AS, PDA
Atrial myxoma, familial		Myxoma
Beckwith-Wiedemann		Cardiomegaly
C syndrome (Opitz trigonocephaly)		PDA
Carpenter		VSD, PS, TGA, PDA
Cat's eye (22 partial trisomy)	40%	TAPVR, VSD, ASD
CHARGE		VSD, ASD
CHILD		VSD, ASD
Conradi-Hünermann (chondrodysplasia punctata)		VSD, PDA
de Lange	29%	VSD, TOF, DORV, PDA
DiGeorge		VSD, coarctation, truncus
Ellis–van Creveld (chondroectodermal dysplasia)	50%	ASD, single atrium
Fanconi pancytopenia		ASD, PDA
Goldenhar		TOF, VSD, ASD
Holt-Oram		ASD, VSD

Continued

TABLE 37.1 Congenital Heart Disease and Associated Risk Factors—cont'd

Factor	Frequency	Most Common Lesions
Kartagener		Dextrocardia
Klippel-Feil		VSD, TGA, TAPVR
Laurence-Moon (Bardet-Biedl)		VSD
Leopard		PS
Meckel-Gruber		VSD, ASD, coarctation, PS, PDA
Noonan		PS, VSD, ASD, PDA
Pallister-Hall		Unspecified CHD
Pierre Robin		ASD
Poland		TOF, ASD, PDA, VSD
Refsum		A-V conduction defects
Seckel		VSD, PDA
Smith-Lemli-Opitz		VSD, PDA
Treacher Collins		VSD, ASD, PDA
Rubinstein-Taybi		ASD, VSD, PDA
Silver		TOF, VSD
Short rib polydactyly (non-Majewski type)		TGA, DOLV, DORV, HRH, AVSD
Thrombocytopenia absent radius (TAR)		ASD, TOF, dextrocardia
VACTERL		Unspecified CHD
Waardenburg		VSD
Weill-Marchesani		PS, VSD
Williams		Supravalvular AS, PS, VSD, ASD
Zellweger		VSD, ASD, PDA
CHROMOSOMAL		
Trisomy 13 (Patau)	90%	VSD, ASD, dextroposition, PDA
Trisomy 18 (Edward)	99%	Bicuspid AV, PS, VSD, ASD, PDA
Trisomy 21 (Down)	50%	A-V canal, VSD, ASD, PDA
Triploidy		ASD, VSD
5p– (cri du chat)	30%	Unspecified CHD
9p–		VSD, PS, PDA
Partial trisomy 10q	50%	Unspecified CHD
13q–		Unspecified CHD
T 20p syndromes		VSD, TOF
Turner (45,X)	20%	Bicuspid AV, AS, coarctation, VSD, ASD, AVSD
8 trisomy (mosaic)	50%	VSD, ASD, PDA
9 trisomy (mosaic)	50%	VSD, coarctation, DORV
13 q	25%	VSD
+14q	50%	ASD, TOF, PDA
18q	50%	VSD
XXXXY	14%	ASD, ARCA, PDA
DISEASES AND CONDITIONS		
Crouzon		Coarctation, PDA
Neurofibromatosis		PS, coarctation
Tuberous sclerosis		Rhabdomyoma, angioma
Thalassemia major		Cardiomyopathy

AO, Aorta; *ARCA,* anomalous right coronary artery; *AS,* aortic stenosis; *ASD,* atrial septal defect; *AV,* aortic valve; *A-V,* atrioventricular; *AVSD,* atrioventricular septal defect; *CHD,* congenital heart disease; *DOLV,* double-outlet left ventricle; *DORV,* double-outlet right ventricle; *HLHS,* hypoplastic left heart syndrome; *HRH,* hypoplastic right heart; *MA,* mitral atresia; *PA,* pulmonary atresia; *PDA,* patent ductus arteriosus; *PS,* pulmonary stenosis; *TA,* tricuspid atresia; *TAPVR,* total anomalous pulmonary venous return; *TGA,* transposition of great arteries; *TOF,* tetralogy of Fallot; *truncus,* truncus arteriosus; *VSD,* ventricular septal defect.
Data from Lachman RS and Donofrio MT.[45,251]

TABLE 37.2 Recurrence Risks in Siblings for Any Congenital Heart Defect[a]

Defect	SUGGESTED RISK (%)	
	If One Sibling	If Two Siblings
Fibroelastosis	4	12
Ventricular septal defect	3	10
Patent ductus arteriosus	3	10
Atrioventricular septal defect	3	10
Atrial septal defect	2.5	8
Tetralogy of Fallot	2.5	8
Pulmonary stenosis	2	6
Coarctation of aorta	2	6
Aortic stenosis	2	6
Hypoplastic left heart	2	6
Transposition	1.5	5
Tricuspid atresia	1	3
Ebstein anomaly	1	3
Truncus	1	3
Pulmonary atresia	1	3

[a]Combined data published during two decades from European and North American populations.
With permission from Nora J.[252]

TABLE 37.3 Suggested Offspring Recurrence Risk (%) for Congenital Heart Defects Given One Affected Parent

Defect	AFFECTED PARENT	
	Father	Mother
Aortic stenosis	3	13-18
Atrial septal defect	1.5	4-4.5
Atrioventricular septal defect	1	14
Coarctation of aorta	2	4
Pulmonary stenosis	2	4-6.5
Tetralogy of Fallot	1.5	2.5
Ventricular septal defect	2	6-10

With permission from Nora J.[252]

with literature suggesting a ninefold increase in the incidence of CHD in **monochorionic-diamniotic twin** gestations.[19] Lastly, there appears to be a slightly increased risk of CHD with ***in vitro* fertilization** (IVF), although at least some of this increased risk appears to be related to the increased incidence of twin pregnancies associated with IVF.[20] Most fetuses with CHD have no known risk factors, which underscores the importance of a meticulous evaluation of the four-chamber heart views and outflow tracts on all routine obstetric ultrasound examinations. When severe structural cardiac anomalies are identified before viability, termination may be offered. Certainly, one of the most important aspects of fetal echocardiography is the psychological relief it affords parents whenever normal cardiac anatomy and function are documented in a fetus at risk.

NORMAL FETAL CARDIAC ANATOMY AND SCANNING TECHNIQUES

The fetal heart is similar to that of the adult, with several anatomic and physiologic differences. The long axis of the fetal heart is perpendicular to the long axis of the body, such that a transverse section through the fetal thorax demonstrates the four cardiac chambers in a single view. The adult heart, in contrast, is obliquely oriented with its long axis along a line between the left hip and the right shoulder. The **four-chamber view** is important because 10% to 96% of structural anomalies are detectable on this view.[21-26]

Common Indications for Fetal Echocardiography

- Abnormal heart on routine ultrasound
- Hydrops
- Polyhydramnios
- Fetal arrhythmia
- Fetal chromosomal anomalies
- Fetal extracardiac anomalies
- Family history (congenital heart disease [CHD], syndromes associated with CHD)
- Maternal disease (diabetes, collagen vascular, phenylketonuria)
- Maternal infection (rubella)
- Teratogen exposure
- Increased nuchal translucency on first-trimester screening
- *In vitro* fertilization
- Monochorionic twins
- Monitoring response to intrauterine therapy
- Monitoring fetus at risk for decompensation (persistent tachyarrhythmia, hydrops)

Cardiac axis and position are normally such that the apex of the heart points to the left and the bulk of the heart is in the left side of the chest (Fig. 37.1A). This is **levocardia.** In **mesocardia** the heart is central with the apex pointing anteriorly. In **dextrocardia** the apex is directed rightward, and the heart is primarily in the right side of the chest. This abnormality must be distinguished from **dextroposition** (Fig. 37.1B), in which the heart maintains a normal axis but is displaced to the right by an external process, such as a left chest mass or pleural effusion. **Abnormal cardiac axis** is associated with a 50% mortality and **abnormal cardiac position** with an 81% mortality.[27]

The fetal cardiovascular system contains several unique shunts: the **ductus venosus, foramen ovale,** and **ductus arteriosus** (Fig. 37.2). Antenatally, the placenta rather than the lungs is the fetus's sole source of oxygen. Oxygenated blood leaves the placenta through the umbilical vein and travels through the hepatic vasculature and ductus venosus to the inferior vena cava (IVC) and then into the fetal right atrium. As a result of increased velocity, blood entering the IVC via the ductus venosus is shunted

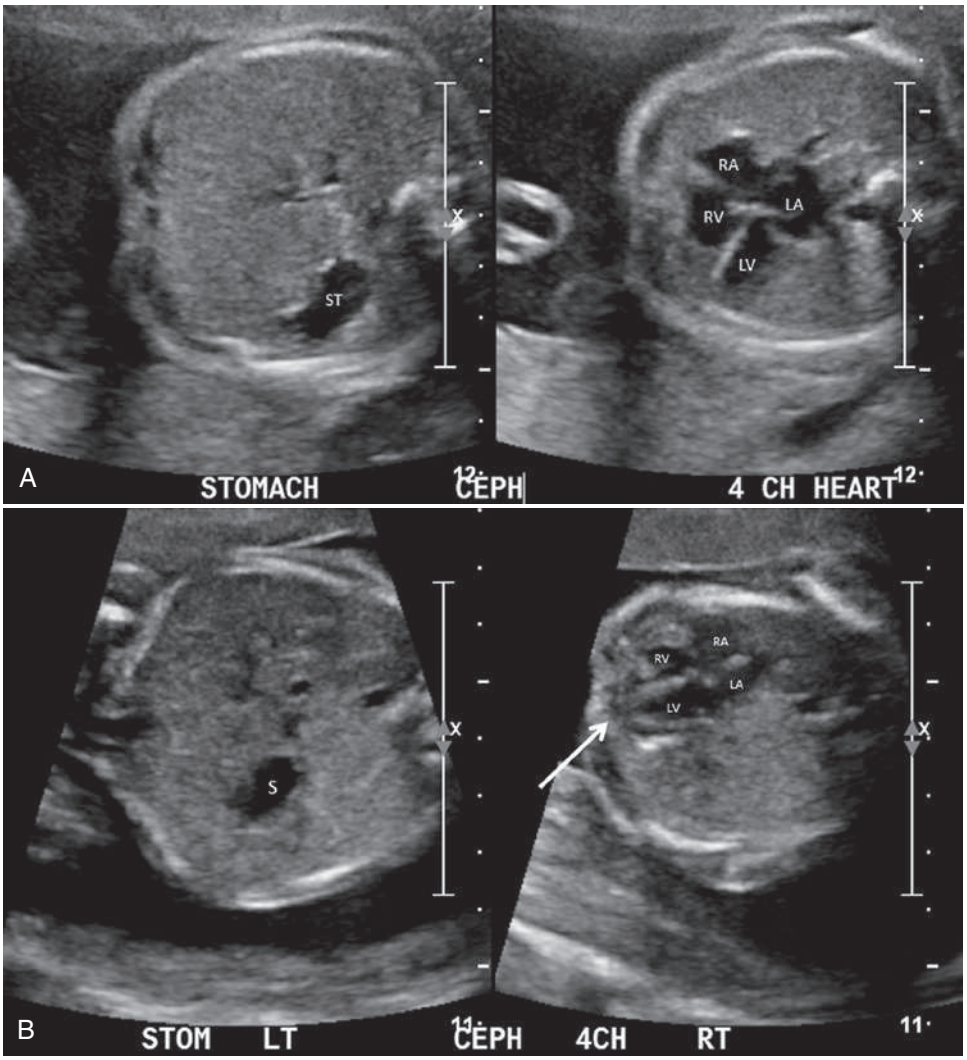

FIG. 37.1 Heart Position and Axis. (A) Normal position and axis of the heart. The heart is predominantly in the left side of the chest, with the apex of the heart pointing leftward. Dual-screen image shows the stomach also on the left side. **(B) Dextroposition** of fetal heart caused by a large, **congenital pulmonary airway malformation.** Transverse image through the fetal chest shows the heart displaced to the right, but the apex *(arrow)* remaining leftward. *LA,* Left atrium; *LV,* left ventricle; *RA,* right atrium; *RV,* right ventricle; *S,* stomach. Dual-screen image shows the stomach on the correct left side.

across the foramen ovale to the left atrium and then into the left ventricle, the aorta, and the fetal brain. Poorly oxygenated blood from the superior vena cava (SVC) also enters the right atrium, and mixes with the blood entering from the IVC, but continues to the right ventricle and pulmonary artery. Most of this blood is directed through the ductus arteriosus into the descending aorta. Thus these shunts function so that the majority of output from both ventricles enters the systemic circulation, rather than a substantial portion entering the pulmonary circulation, as in the adult. Blood that enters the pulmonary vasculature via the pulmonary artery is returned to the left atrium by the four pulmonary veins. From the left atrium it enters the left ventricle and ultimately the descending aorta, returning to the placenta via the iliac and umbilical arteries. Normal values for measurements of the fetal heart and great vessels are shown in Figs. 37.3 and 37.4.

Fetal echocardiography is best accomplished at 18 to 22 weeks of gestation.[28] Before 18 weeks, resolution is frequently limited by the small size of the fetal heart. After 22 weeks the examination may be compromised by progressive ossification of the fetal skull, spine, and long bones; the relatively smaller amniotic fluid volume; and unaccommodating fetal position. Importantly, some congenital cardiac abnormalities progress in utero and may be subtle or unrecognizable at or before 22 weeks but more obvious closer to term.[29,30] Tachyarrhythmias may not become apparent until the third trimester.[31] In some cases, first-trimester evaluation of the fetal heart may be accomplished with transvaginal ultrasound as early as 11 to 14 weeks.[32-34] More recently, diagnostic results have been possible with a transabdominal approach at 11 to 13 weeks.[34] However, first-trimester fetal echocardiography is limited and should be considered an adjunct to second-trimester evaluation, not a replacement.

Scanning the fetal heart requires a systematic approach, beginning with determination of the position of the fetus within the uterus and the heart within the fetal chest. A transverse view through the fetal thorax above the level of the diaphragm

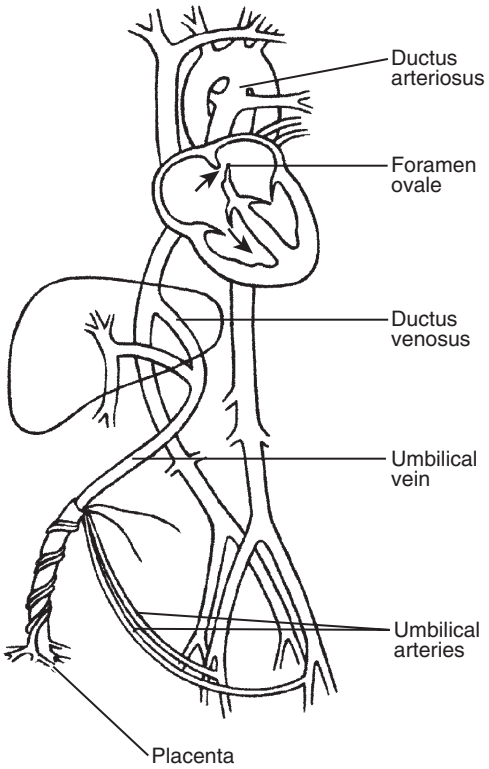

FIG. 37.2 Diagram of Fetal Shunts. Blood from the umbilical vein is shunted through the ductus venosus to the right atrium and then across the foramen ovale to the left atrium. Fetal cardiac output from the right side of the heart is shunted to the descending aorta through the ductus arteriosus.

demonstrates four cardiac chambers. **Four-chamber views** can be obtained with the angle of insonation parallel to the interventricular septum (**apical four-chamber view;** Fig. 37.5A, Video 37.1) or perpendicular to the septum (**subcostal four-chamber view;** Fig. 37.5B, Video 37.2). In a four-chamber view the echogenic foraminal flap of the **foramen ovale** can be observed moving into the left atrium. The two superior pulmonary veins may be seen entering the spherical left atrium. The **atrioventricular valves** are visible in the four-chamber view. The septal leaflet of the tricuspid valve inserts slightly more apically on the interventricular septum than the anterior leaflet of the mitral valve. The left ventricle has a relatively smooth inner wall, and a more elongated shape than the right ventricle. In the normal heart, the left ventricle is the apex forming ventricle. The internal surface of the right ventricle is coarse, particularly near the apex, where the **moderator band** of the **trabecula septomarginalis** is frequently recognized as a small, brightly echogenic focus. This helps identify the morphologic right ventricle.

From the subcostal four-chamber view, angling the transducer toward the fetus's right shoulder permits evaluation of the continuity of the left ventricle with the ascending aorta (Fig. 37.6). Further angulation in the same direction shows the right ventricle in continuity with the pulmonary artery (Fig. 37.7, Videos 37.3 and 37.4). The diameter of the pulmonary artery is approximately 9% larger than that of the aorta between 14 and 42 weeks. The measured differences in these vessels and with M-mode versus two-dimensional (2-D) imaging are negligible (2%-5%) for both the pulmonary artery and the aorta.[35] Further rightward rotation produces a sagittal view of the fetal thorax and a short-axis view of the ventricles (Fig. 37.8, Video 37.5). Angulation toward the left fetal shoulder from this view shows the aorta as a central circle, with the pulmonary artery draping anteriorly and to the left (Fig. 37.9).

The **apical four-chamber view** may also be used as a starting point when evaluating normal cardiac anatomy. Yagel and colleagues[36] described a series of planes arising from the apical four-chamber view, all accomplished by moving the transducer in a cephalad direction. A slight cephalad advancement will show an **apical five-chamber view,** which is useful in assessing continuity of the ascending aorta with the left ventricle (Fig. 37.10). Continued cephalad movement should result in visualization of the bifurcating pulmonary artery and its relationship to the right ventricle. A **three-vessel and trachea view** should be visualized next (Fig. 37.11, Video 37.6). This view allows evaluation of the main pulmonary artery–ductus arteriosus confluence, the transverse aortic arch, and the SVC. Comparison of vessel size, confirmation of vessel presence, and determination of blood flow direction with color Doppler can all be accomplished at this level. In addition, appropriate location of both great vessels to the left of the trachea can be confirmed.[36] Returning to a sagittal plane of the fetus, directing the transducer from the fetal left shoulder to the right hemithorax demonstrates the distinctive candy-cane shape of the **aortic arch** (Fig. 37.12, Videos 37.7 and 37.8). The three major vessels to the head and neck and the **ductus arteriosus** may be seen. The aortic arch should not be confused with the **ductal arch** (Fig. 37.13), which is formed by the right ventricular outflow tract, pulmonary artery, and ductus arteriosus. The ductal arch is broader and flatter than the aortic arch. Lastly, sliding the transducer to the right while maintaining a sagittal plane on the fetus should allow visualization of the IVC and SVC entering the right atrium.

M-mode echocardiography provides a 2-D image of motion over time. It is useful in evaluating heart rate, chamber size, wall thickness, and wall motion (Fig. 37.14). Simultaneous M-mode imaging through an atrium and ventricle is helpful in analyzing arrhythmias (Fig. 37.15). Chamber size and function should be evaluated at the level of the atrioventricular (A-V) valves.[37]

Spectral Doppler ultrasound evaluation of the fetal heart can be used to determine the velocity of flow through the vessels or valves (Fig. 37.16) and to evaluate regurgitant flow through the valves of the heart (Fig. 37.17). Variation in flow velocity may reflect structural or functional cardiac abnormalities. For example, a stenotic A-V valve will be associated with an abnormal flow pattern through the affected valve. Spectral Doppler ultrasound is useful in assessing the functional significance of structural abnormalities and arrhythmias.

Color Doppler ultrasound permits a rapid interrogation of flow patterns within the heart and great vessels (Fig. 37.18), allowing functional and structural abnormalities to be more rapidly characterized. For example, **valvular stenosis** is clearly demonstrated with color Doppler ultrasound, as is reversed flow through insufficient valves or in the great vessels. Color Doppler ultrasound often reduces the amount of time required for spectral

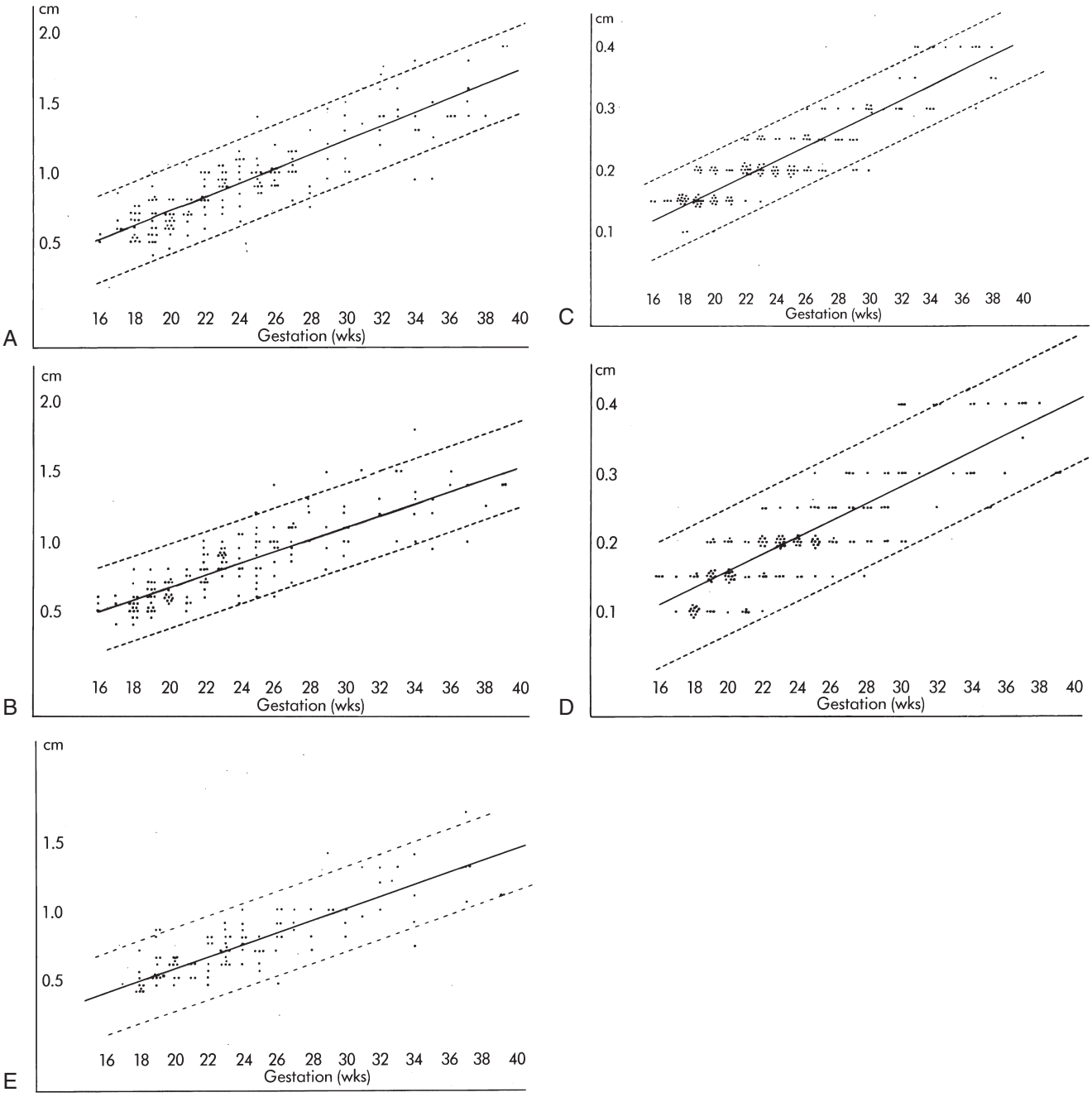

FIG. 37.3 Cardiac Dimensions. (A) Left ventricular internal dimension versus gestational age. $y = 0.049x - 0.262$. **(B)** Right ventricular internal dimension versus gestational age. $y = 0.045x - 0.228$. **(C)** Posterior left ventricular wall thickness versus gestational age. $y = 0.012x - 0.063$. **(D)** Septal thickness versus gestational age. $y = 0.012x - 0.088$. **(E)** Left atrial internal dimension versus gestational age. $y = 0.040x - 0.214$. In each graph, the 95% confidence limits represent twice the standard error of the mean. (With permission from Allan LD, Joseph MC, Boyd EG, Campbell S, Tynan M. M-mode echocardiography in the developing human fetus. Br Heart J. 1982;47[6]:573-583.[250])

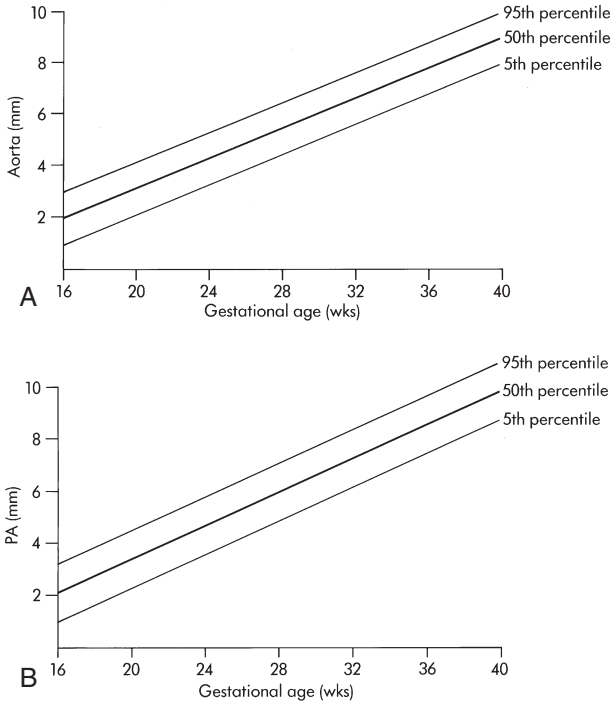

FIG. 37.4 Diameter of Aortic Root and Pulmonary Artery. (A) Diameter of aortic root versus gestational age. **(B)** Diameter of pulmonary artery *(PA)* versus gestational age. Norms and confidence limits for echocardiographic measurements. (With permission from Cartier MS, Davidoff A, Warneke LA, et al. The normal diameter of the fetal aorta and pulmonary artery: echocardiographic evaluation in utero. Am J Roentgenol. 1987;149[5]:1003-1007.[35])

Doppler ultrasound evaluation of the heart, particularly in the setting of complex cardiac anomalies.[38-41] Subtle lesions such as small VSDs may be more reliably and easily identified with the use of color flow Doppler ultrasound.

The utility of several advanced technologies has been reported in the evaluation of the fetal heart, including three-dimensional (3-D) and four-dimensional (4-D) ultrasound, **tissue Doppler imaging, strain** and **strain rate imaging,** as well as **fetal magnetocardiography** and **cardiovascular magnetic resonance imaging** (MRI).[42-44] However, many of these require specialized transducers or other equipment, sophisticated algorithms and specialized technical expertise. Additionally, limited resolution and cardiac motion are still considered major disadvantages in some settings.[45]

STRUCTURAL ANOMALIES

Atrial Septal Defect

An **atrial septal defect** (ASD) results from an error in the amount of tissue resorbed or deposited in the interatrial septum. It is the fifth most common form of CHD and is the most common form in adult patients.[46,47] ASDs occur in 1 per 1500 live births[48,49] and comprise 6.7% of CHD in live-born infants.[46] ASDs occur twice as often in females as males.[50,51] ASDs are associated with a variety of cardiac, extracardiac, and chromosomal abnormalities. ASDs can be classified by embryogenesis, size, or relationship to the fossa ovalis.

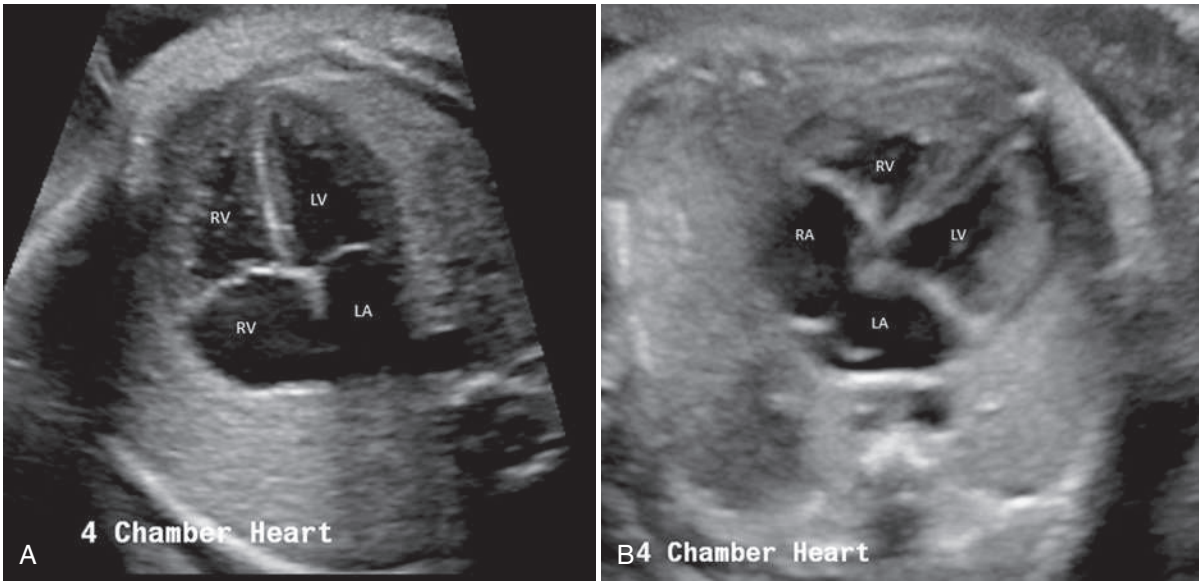

FIG. 37.5 Four-Chamber View of Heart. (A) Apical four-chamber view shows the interatrial and interventricular septa parallel to the angle of insonation. See also Video 37.1. **(B)** Subcostal four-chamber view shows the interatrial and interventricular septa perpendicular to the angle of insonation. See also Video 37.2. *LA,* Left ventricle; *LV,* left ventricle; *RA,* right atrium; *RV,* right ventricle.

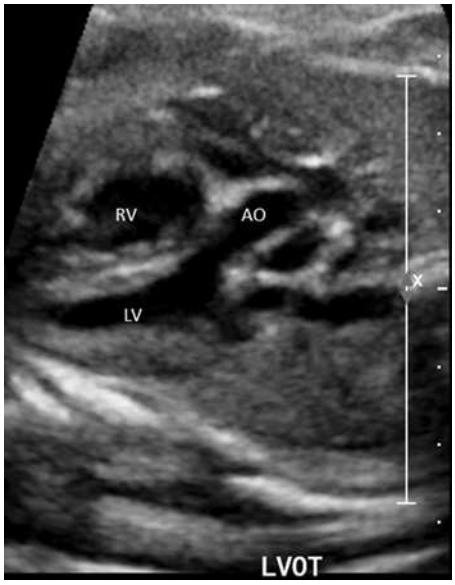

FIG. 37.6 Continuity of aorta *(AO)* with left ventricle *(LV). RV,* right ventricle. See also Videos 37.3 and 37.4.

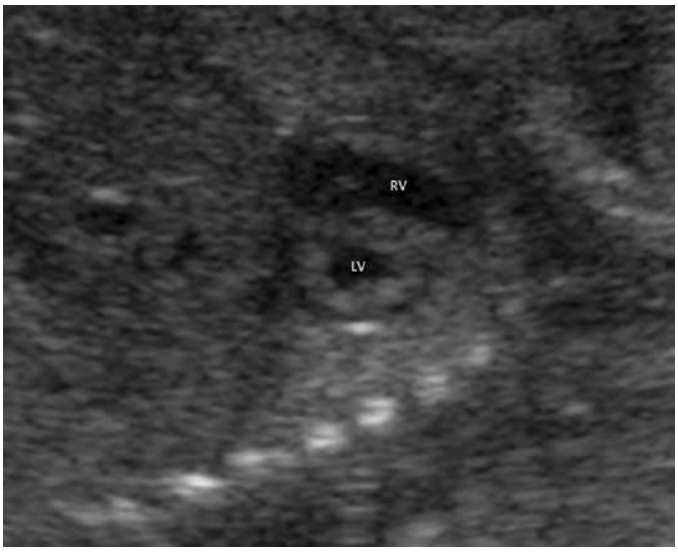

FIG. 37.8 Short-Axis View of Ventricles. Anterior right ventricle *(RV)* is normally slightly larger than the left ventricle *(LV).* See also Video 37.5.

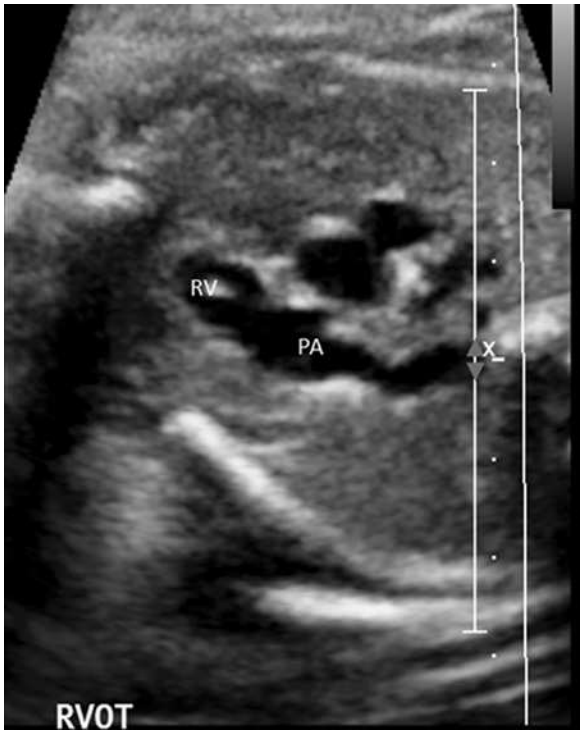

FIG. 37.7 Continuity of pulmonary artery *(PA)* with right ventricle (RV). See also Video 37.3 and Video 37.4.

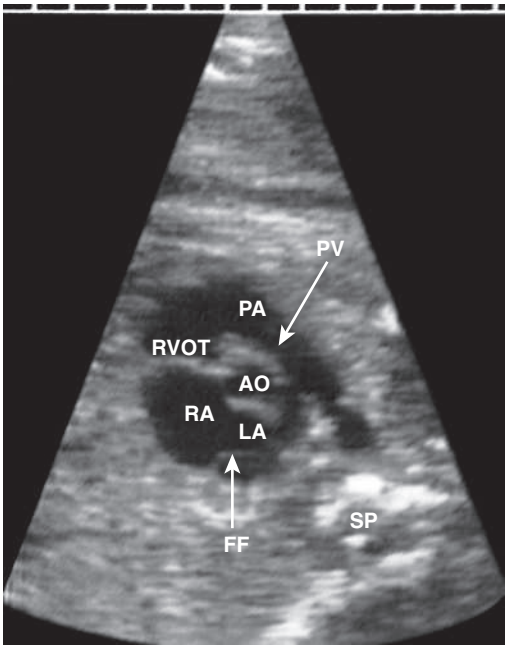

FIG. 37.9 Short-Axis View of Great Vessels. Aorta *(AO)* in center with pulmonary artery *(PA)* draping anteriorly. *FF,* Foraminal flap; *LA,* left atrium; *PV,* pulmonic valve; *RA,* right atrium; *RVOT,* right ventricular outflow tract; *SP,* spine.

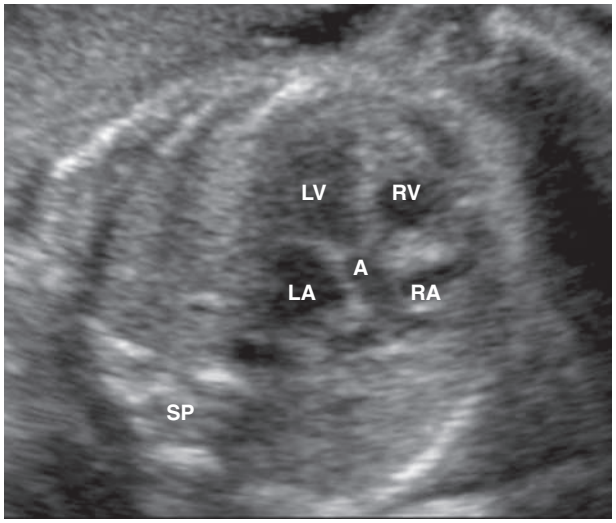

FIG. 37.10 Apical five-chamber view shows continuity of the aorta *(A)* with the left ventricle *(LV). LA,* Left atrium; *RA,* right atrium; *RV,* right ventricle; *SP,* spine.

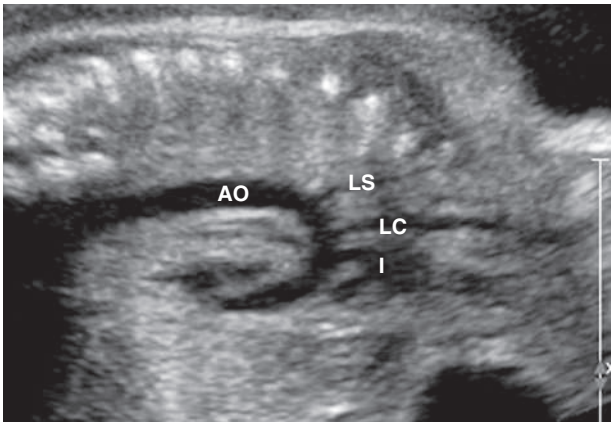

FIG. 37.12 Normal Aortic Arch. Sagittal view shows the rounded, "candy-cane" appearance of aortic arch and the head and neck vessels arising from it. See also Video 37.7 and Video 37.8. *AO,* Descending aorta; *I,* innominate artery; *LC,* left carotid artery; *LS,* left subclavian artery.

FIG. 37.11 Three-vessel and trachea view shows the correct orientation of the main pulmonary artery–ductus arteriosus confluence *(P),* the transverse aortic arch *(A),* and the superior vena cava *(S).* This view also shows the two great vessels correctly positioned on the left side of the trachea *(T).* See also Video 37.6. *SP,* Spine.

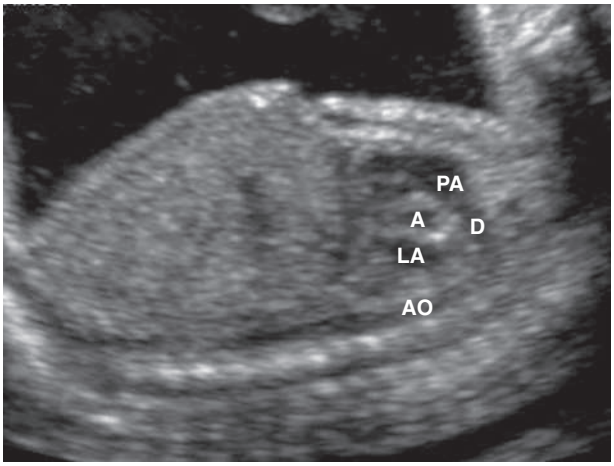

FIG. 37.13 Normal Ductal Arch. Sagittal view shows pulmonary artery *(PA)* draping over the aorta *(A)* and joining the ductus arteriosus *(D),* which then joins the descending aorta *(AO). LA,* Left atrium.

Embryologically, between the fourth and sixth weeks of gestation the primitive atrium is divided into right and left halves. The **septum primum,** a crescent-shaped membrane, develops along the cephalad portion of the atrium and grows caudally toward the **endocardial cushions.** The space between these two structures, termed the **ostium primum,** disappears when the septum primum fuses with the endocardial cushion. Before complete fusion, however, multiple small fenestrations develop in the septum primum, coalescing to form the **ostium secundum.**

A second crescent-shaped membrane subsequently develops just to the right of the septum primum. As this membrane grows toward the endocardial cushion, it partially covers the ostium secundum. Its crescent-shaped lower border never entirely fuses with the endocardial cushion, leaving an opening, the **foramen ovale** (Fig. 37.19).

Ostium secundum ASDs make up more than 80% of all ASDs and generally occur in isolation. This ASD is caused by excessive resorption of the septum primum (foraminal flap) or by inadequate growth of the septum secundum (Fig. 37.20A). The **ostium primum ASD** is the second most common type and is located low in the atrial septum, near the atrioventricular (A-V) valves. Although the ostium primum ASD may occur alone, it is more frequently associated with a more complex congenital cardiac anomaly, the **atrioventricular septal defect** (AVSD) (Fig. 37.20B).

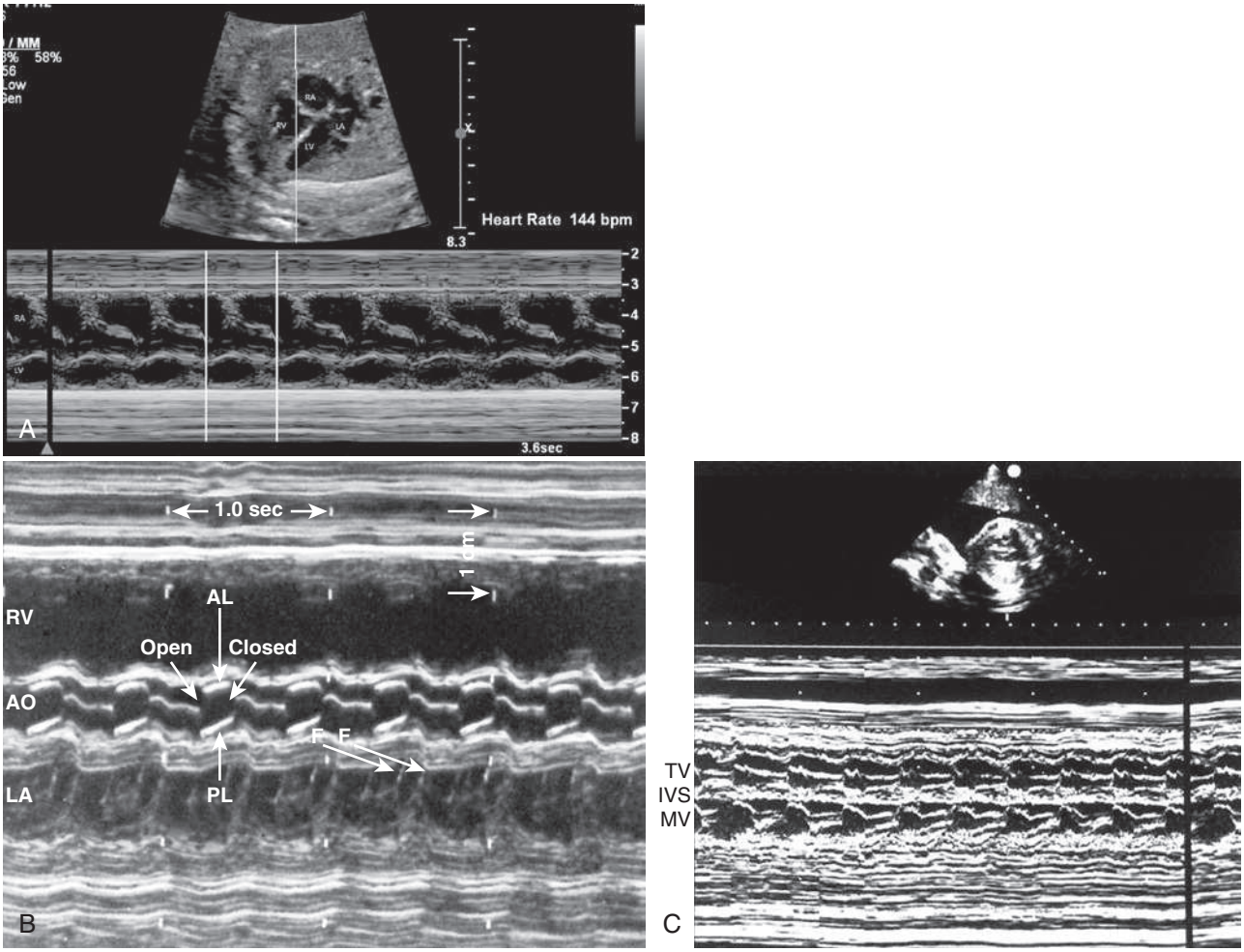

FIG. 37.14 M-Mode Echocardiography. (A) M-mode tracing through the right atrium *(RA)* and the left ventricle *(LV)* showing normal atrial contractions followed by normal ventricular contractions. *LA,* Left atrium; *RV,* right ventricle. **(B)** M-mode tracing through the aortic root shows the aortic valve opening and closing. The foraminal flap *(F)* can be seen opening into the left atrium *(LA). AL,* Anterior leaflet of aortic valve; *AO, aorta; PL,* posterior leaflet of aortic valve; *RV,* right ventricle. **(C)** M-mode tracing shows opening and closing of the mitral valve *(MV)* and tricuspid valve *(TV). IVS,* Interventricular septum.

The **sinus venosus ASD** is a rare defect that can be divided into two types: (1) **sinus venosus ASD of the SVC,** with the defect adjacent to the SVC, and (2) **sinus venosus ASD of the IVC,** with the defect adjacent to the IVC. The first type is often associated with **anomalous pulmonary venous return** (APVR) (Fig. 37.20C). **Coronary sinus ASDs,** located at the ostium of the coronary sinus in the right atrium, may also occur but are exceedingly rare.

The prenatal sonographic diagnosis of ASD is difficult because the normal patent foramen ovale, which allows blood to flow from the right to the left atrium in utero, itself represents an ASD. It can be difficult to distinguish a small, pathologic ASD from the normal patent foramen ovale. The foraminal flap, or septum primum, is clearly visualized on the four-chamber view. It has a "loose pocket" configuration, appearing either circular or linear in shape as it opens into the left atrium[52,53] (Fig. 37.21).

The **septum secundum,** which is thick and relatively stationary, makes up the majority of the atrial septum. The foramen ovale is an opening in the septum secundum. The septum secundum and foramen ovale are well visualized in the four-chamber views. The maximal size of the normal foramen ovale differs by 1 mm or less from the aortic root diameter at all gestational ages.[54] An **ostium secundum ASD** appears as a larger than expected defect in the central portion of the atrial septum near the foramen ovale. Alternatively, it can appear as a deficient foraminal flap.

If the lowest portion of the atrial septum (just adjacent to the A-V valves) is deficient, an **ostium primum** defect should be suspected (Fig. 37.22). Color Doppler ultrasound may be helpful in the diagnosis of larger ASDs. However, small ASDs are commonly obscured by the normal flow through the patent foramen ovale.[55,56]

A large right-to-left shunt is physiologic in utero, and thus an ASD usually does not compromise the fetus hemodynamically. After birth, the shunt may cause right ventricular overload and pulmonary hypertension. Spontaneous closure of an ASD will occur in approximately two-thirds of patients.[57] Patients with small ASDs may remain asymptomatic into their 50s.[58]

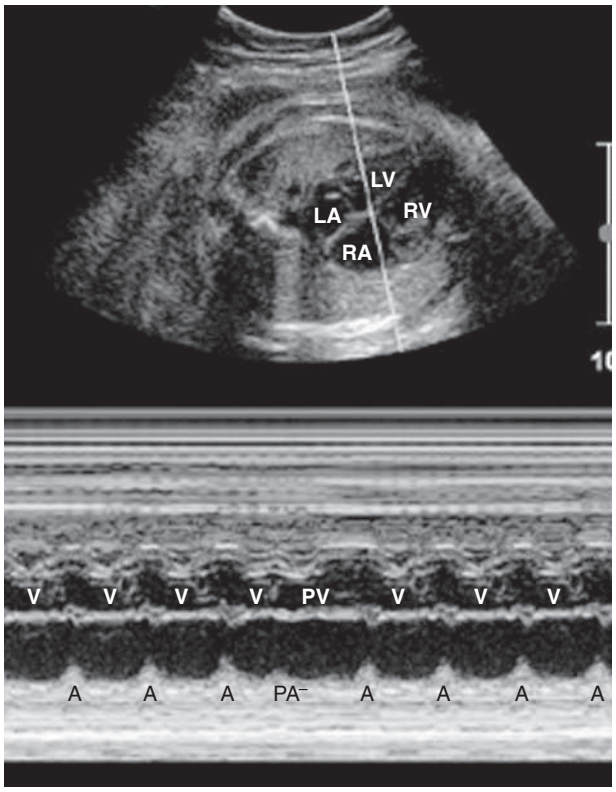

FIG. 37.15 Using M-Mode Echocardiography to Analyze an Arrhythmia: Conducted Premature Atrial Contractions. The cursor is placed simultaneously through the left ventricle *(LV)* and right atrium *(RA)*. The M-mode tracing shows normal atrial beats *(A)* followed by a premature atrial contraction *(PA)*. The ventricles show normal ventricular contraction *(V)* following each atrial beat and a premature beat *(PV)* following the premature atrial contraction. *LA,* Left atrium; *RV,* right ventricle.

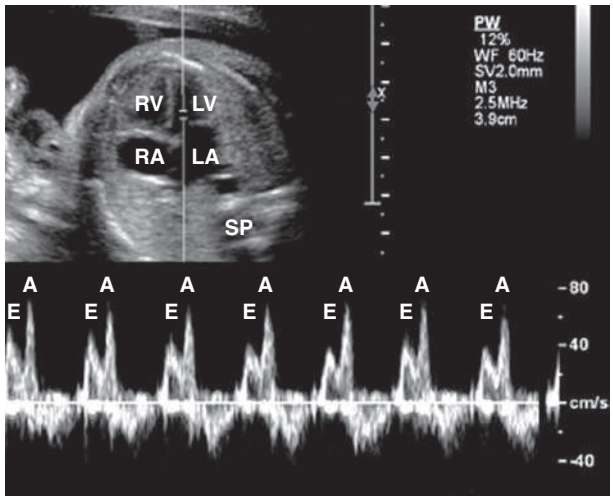

FIG. 37.16 Spectral Doppler Ultrasound Used to Interrogate a Normal Mitral Valve. Spectral Doppler sample volume is placed distal to the mitral valve in the left ventricle *(LV)*. A normal mitral valve waveform is appreciated above the baseline, showing the normal early diastolic *(E)* and atrial contraction *(A)* wave points. *LA,* Left atrium; *RA,* right atrium; *RV,* right ventricle; *SP,* spine.

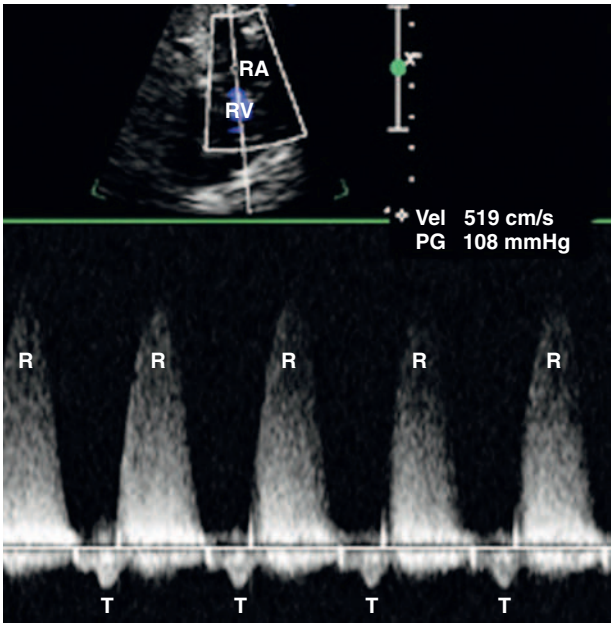

FIG. 37.17 Tricuspid Insufficiency. Spectral Doppler sample volume is placed proximal to the tricuspid valve in the right atrium *(RA)*. The regurgitant flow *(R)* can be seen above the baseline. This implies that the valve has not closed completely during systole, and therefore blood flow is retrograde into the right atrium. *RV,* Right ventricle; *T,* tricuspid valve.

Ventricular Septal Defect

Isolated VSD is the most common cardiac anomaly, accounting for 30% of heart defects diagnosed in live-born infants and 9.7% diagnosed in utero.[46,47,59] VSDs are associated with other cardiac anomalies in 50% of cases.[60] Of the structural cardiac defects, VSDs have the highest recurrence rate and the highest association with teratogen exposure. They are classified according to their position in the interventricular septum (Fig. 37.23) as **membranous** or **muscular VSD** (inlet, trabecular, outlet).[60]

About 80% of VSDs occur in the membranous portion of the septum.[61] However, because most membranous defects also involve a portion of the muscular septum, they are usually referred to as **perimembranous** defects. The subcostal four-chamber view provides optimal evaluation of the interventricular septum. At sonography, a VSD appears as an area of discontinuity in the interventricular septum. When the defect is small, this diagnosis is problematic, and at least one-third of VSDs are missed on the four-chamber view.[21,55,62-66] Color Doppler imaging may improve the diagnostic accuracy for VSD. However, most are missed on fetal echocardiography.[55,66,67] Small VSDs not detectable on gray-scale echocardiography may be documented with color Doppler ultrasound in some cases[39] (Fig. 37.24). In the setting of an isolated VSD, color Doppler ultrasound imaging typically shows bidirectional interventricular shunting, with a systolic right-to-left shunt and a late diastolic left-to-right shunt.

The prognosis for an infant with an isolated VSD is excellent, and many such defects go undetected. The rate of spontaneous closure of isolated muscular VSDs by 5 years of life is much higher (65%) than that for isolated perimembranous VSDs (20%).[68] Overall about 40% of VSDs spontaneously close in the first year

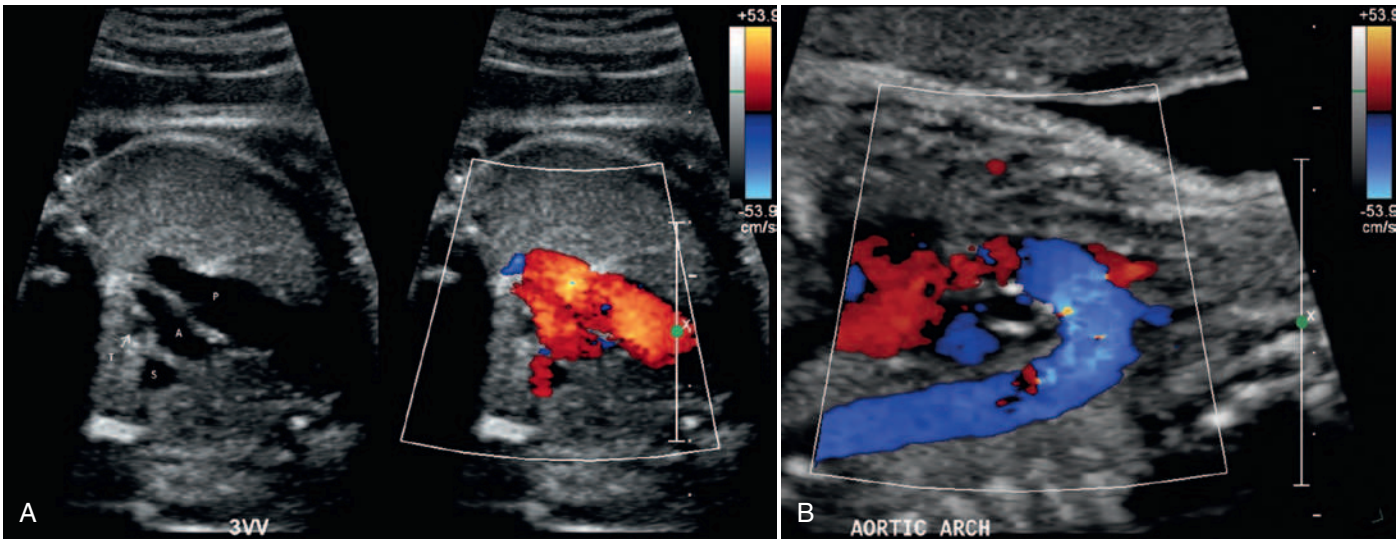

FIG. 37.18 Using Color Doppler Ultrasound to Access Normal Blood Flow. (A) Dual screen three-vessel view (3VV) image with color Doppler ultrasound shows normal flow through the pulmonary artery *(P),* the aorta *(A),* and the superior vena cava *(S).* **(B)** Color Doppler ultrasound shows normal blood flow through the aortic arch.

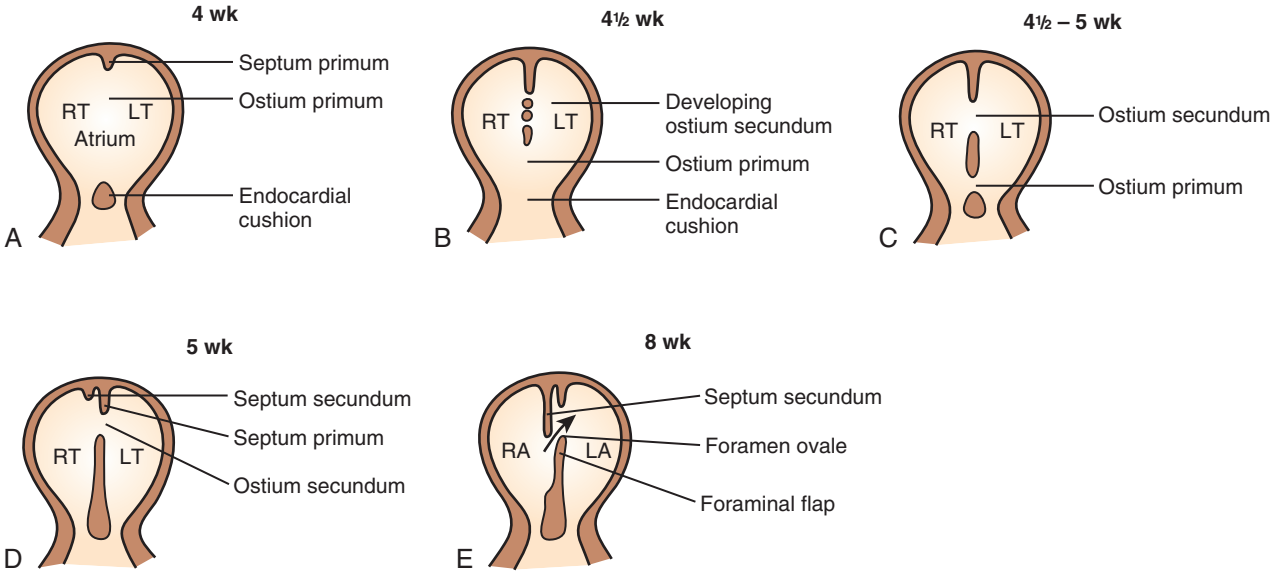

FIG. 37.19 Development of Intraatrial Septum (Viewed Facing Patient). (A) At 4 weeks' gestation the septum primum is small. A large ostium primum is present. **(B)** At 4½ weeks, enlargement of the septum primum results in reduction in size of the ostium primum. Perforations in the septum primum develop. **(C)** Perforations in the septum primum coalesce to form the ostium secundum. **(D)** At 5 weeks the septum primum has fused to the endocardial cushions, and the septum secundum begins to develop to the right of the septum primum. **(E)** At 8 weeks the septum secundum has enlarged, now covering the ostium secundum. Blood flows from the right atrium through the valve mechanism (foraminal flap) of the foramen ovale.

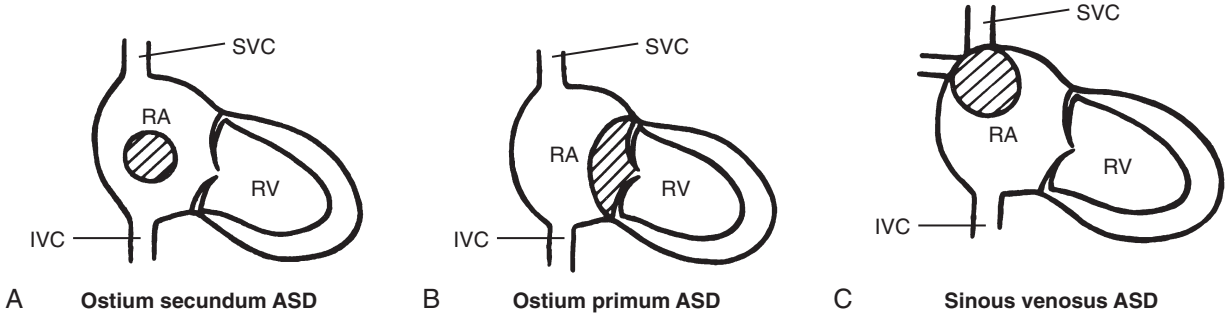

FIG. 37.20 Types of Atrial Septal Defect (ASD). Schema of the atrial septum viewed from the right atrium *(RA).* **(A)** Ostium secundum ASD. **(B)** Ostium primum ASD. **(C)** Sinus venosus ASD. *IVC,* Inferior vena cava; *RV,* right ventricle; *SVC,* superior vena cava.

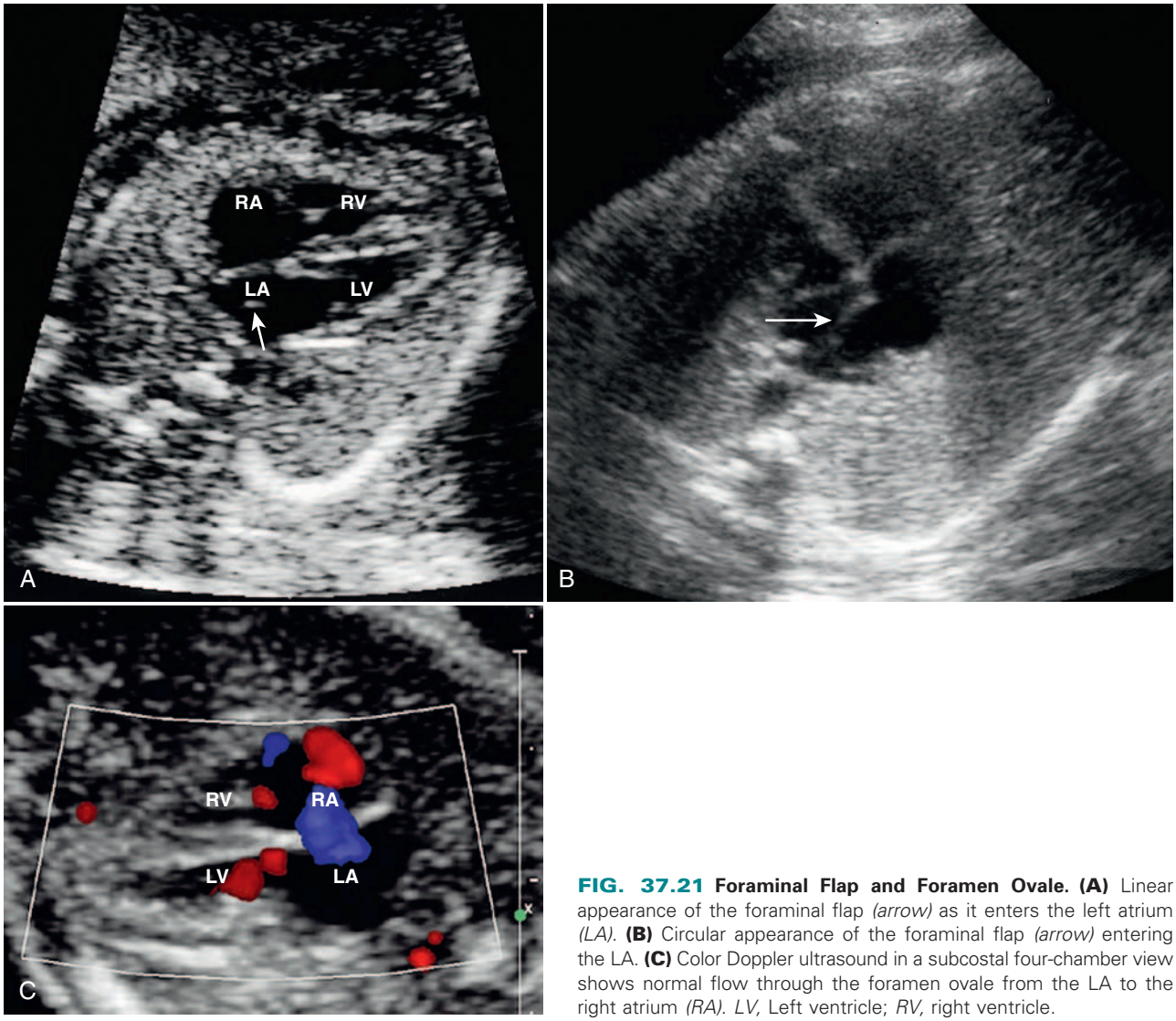

FIG. 37.21 Foraminal Flap and Foramen Ovale. (A) Linear appearance of the foraminal flap *(arrow)* as it enters the left atrium *(LA).* **(B)** Circular appearance of the foraminal flap *(arrow)* entering the LA. **(C)** Color Doppler ultrasound in a subcostal four-chamber view shows normal flow through the foramen ovale from the LA to the right atrium *(RA). LV,* Left ventricle; *RV,* right ventricle.

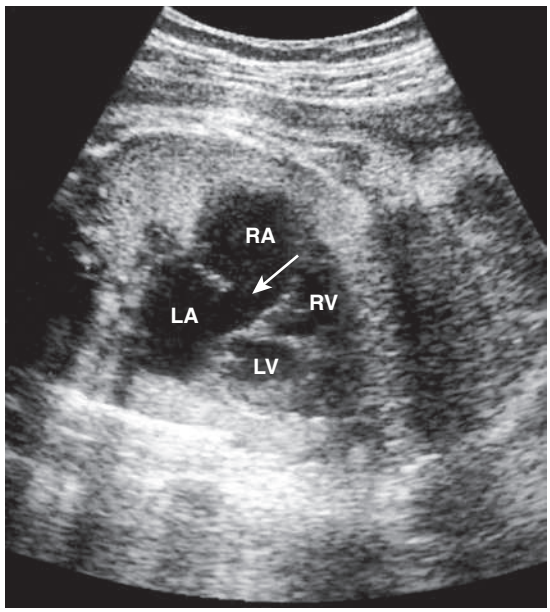

FIG. 37.22 Four-chamber view shows an **ostium primum atrial septal defect** *(arrow)* in a fetus with an atrioventricular septal defect. *LA,* Left atrium; *LV,* left ventricle; *RA,* right atrium; *RV,* right ventricle.

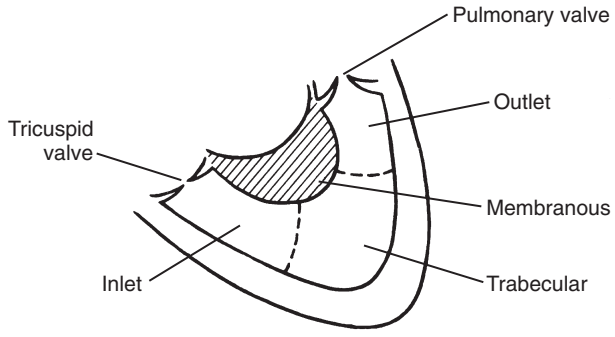

FIG. 37.23 Interventricular Septum Viewed From Right Ventricle. The membranous septum and the three portions of the muscular septum (inlet, outlet, and trabecular) are demonstrated. Ventricular septal defects may occur in any of these locations.

of life, and 60% resolve by 5 years of age.[69-71] However, large defects detected in the fetus are associated with an 84% mortality.[72] Concurrent cardiac, extracardiac, and chromosomal anomalies (trisomy 13, 18, 21, and 22) are associated with a worse prognosis.

VSDs may be extremely difficult to diagnose in utero, particularly when small in size. In addition, many small VSDs will close in utero or shortly after birth. A "pseudo" VSD in the membranous portion of the septum may be appreciated when evaluating the interventricular septum from an apical four-chamber view. This occurs when the angle of insonation is parallel to the septum, causing an artifactual dropout of the thin, membranous septum.

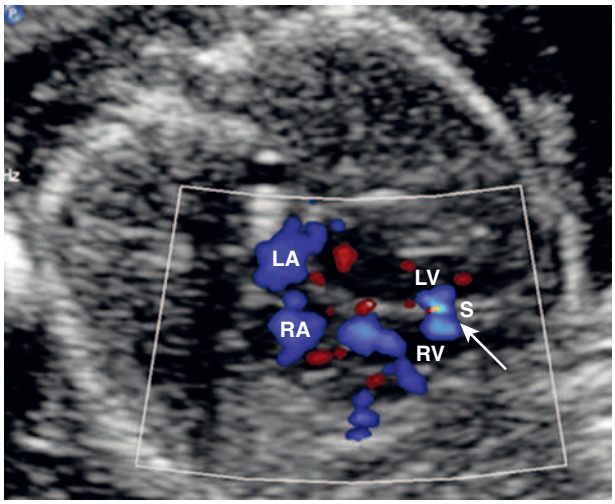

FIG. 37.24 Muscular Ventricular Septal Defect (VSD). Subcostal four-chamber view using color Doppler ultrasound shows a muscular VSD *(arrow)* across the interventricular septum *(S). LA,* Left atrium; *LV,* left ventricle; *RA,* right atrium; *RV,* right ventricle.

Atrioventricular Septal Defect

AVSD refers to a spectrum of cardiac abnormalities involving various degrees of deficiency of the interatrial and interventricular septa and of the mitral and tricuspid valves. These defects arise when the endocardial cushions fail to fuse properly and were previously called **endocardial cushion defects** or **A-V canal defects.** Almost two-thirds of fetuses with AVSD have additional cardiac anomalies.[73-75] About one-third are associated with **left atrial isomerism** (both atria anatomically resemble the left), and of these the majority of affected fetuses have **complete heart block.**[72,73] Chromosomal (especially **trisomy 21**) or extracardiac anomalies are associated in 78% of AVSDs.[72]

Embryologically, in the primitive heart, the common atrium and ventricle communicate through the A-V canal. Development of the endocardial cushion results in division of the single, large A-V canal into two separate orifices, separating the atria from the ventricles (Fig. 37.25). The interatrial and interventricular septa develop concurrently, eventually dividing the single atrium and ventricle into right and left portions. When the endocardial cushions fail to fuse properly, normal development of the mitral and tricuspid valves cannot occur, and an AVSD results (Fig. 37.26).

AVSDs are divided into complete and partial or incomplete forms.[76] In both, the A-V valves are abnormal. In **complete AVSD** a single, multileaflet valve is present, whereas in **incomplete AVSD** two of the leaflets (bridging leaflets) are connected by a narrow strip of tissue, resulting in the appearance of two valve

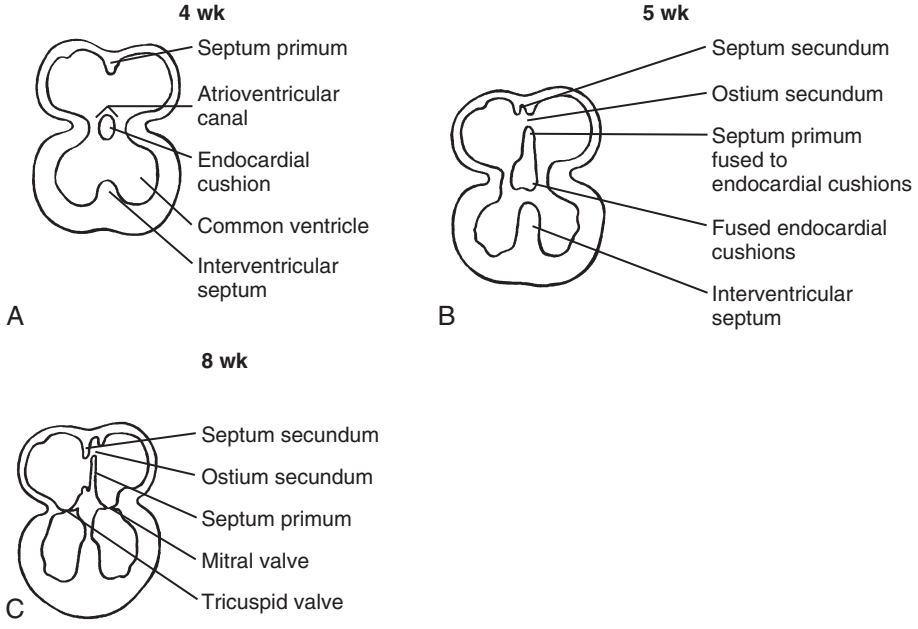

FIG. 37.25 Normal Development of Endocardial Cushions. (A) In the fourth week the endocardial cushions divide the atrioventricular canal into two orifices. **(B)** By the fifth week the communication between the atria, the ostium secundum, is smaller. The ventricular septum has grown, almost obliterating the communication between the ventricles. **(C)** At 8 weeks, complete development of the endocardial cushions and atrioventricular valves results in four distinct cardiac chambers.

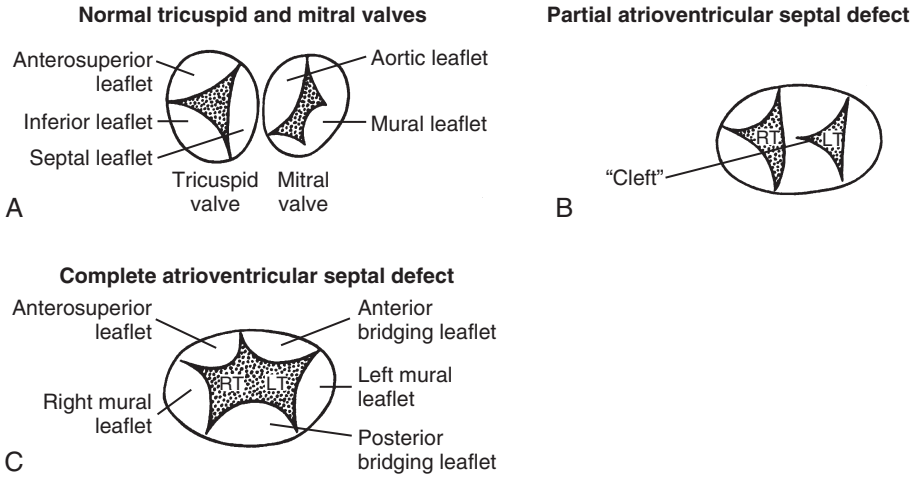

FIG. 37.26 Valve Leaflet Morphology. (A) Normal heart. **(B)** Partial atrioventricular septal defect (AVSD). **(C)** Complete AVSD. *LT,* Left abnormal valve; *RT,* right abnormal valve.

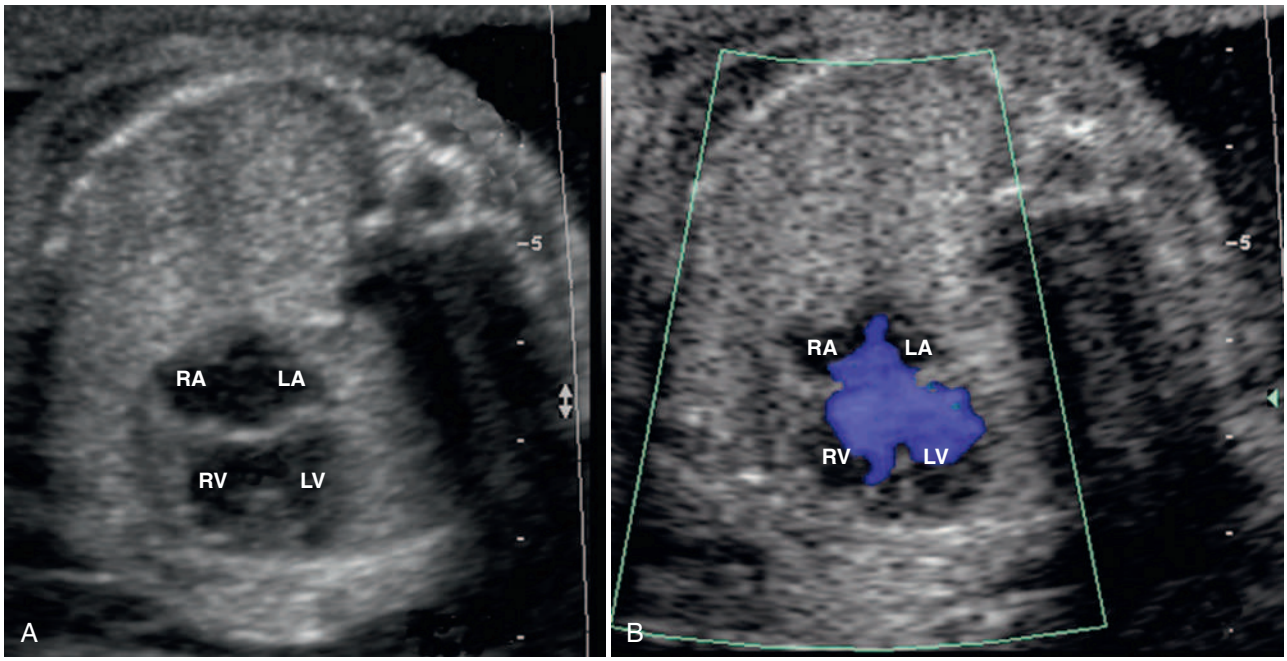

FIG. 37.27 Atrioventricular Septal Defect (AVSD). (A) Apical four-chamber view shows absent atrial septum, resulting in a single large atrium (RA-LA). A ventricular septal defect is visible between the left ventricle *(LV)* and right ventricle *(RV).* A single, multileaflet atrioventricular valve is also appreciated. **(B)** Apical four-chamber view shows color Doppler ultrasound filling the **atrioventricular septal defect.** See also Video 37.9. *LA,* Left atrium; *RA,* right atrium.

orifices. Complete AVSD has variable amounts of deficient tissue in the atrial and ventricular septa. The incomplete form is associated with an ostium primum ASD. At fetal echocardiography, 97% of AVSDs are complete, although after birth only 69% are complete.[67,72] The fetal incidence of AVSD is four times greater than that in the live-born population, indicating a high incidence of in utero demise.[46,47,77]

AVSDs are considered **balanced** when the A-V junction is connected to both the right and the left ventricle, such that blood flow is relatively evenly distributed. If this connection exists with primarily one ventricle, such as in the setting of a hypoplastic left ventricle, it is termed an **unbalanced AVSD.**

Sonographically, a defect in the atrial or ventricular septum with an associated single abnormal A-V valve is visible in a four-chamber view (Fig. 37.27, Video 37.9). The abnormal valve should be suspected when the normal offset of the A-V valves is not visualized or when only a single A-V valve is appreciated in a short-axis view. Demonstration of two A-V valve orifices allows for differentiation between complete and incomplete forms of AVSD.[62]

Color Doppler ultrasound demonstrates an open area of flow across the AVSD and the abnormal A-V valve. Color Doppler ultrasound imaging is particularly useful in the detection of valvular insufficiency.[78] **Holosystolic valvular insufficiency** is

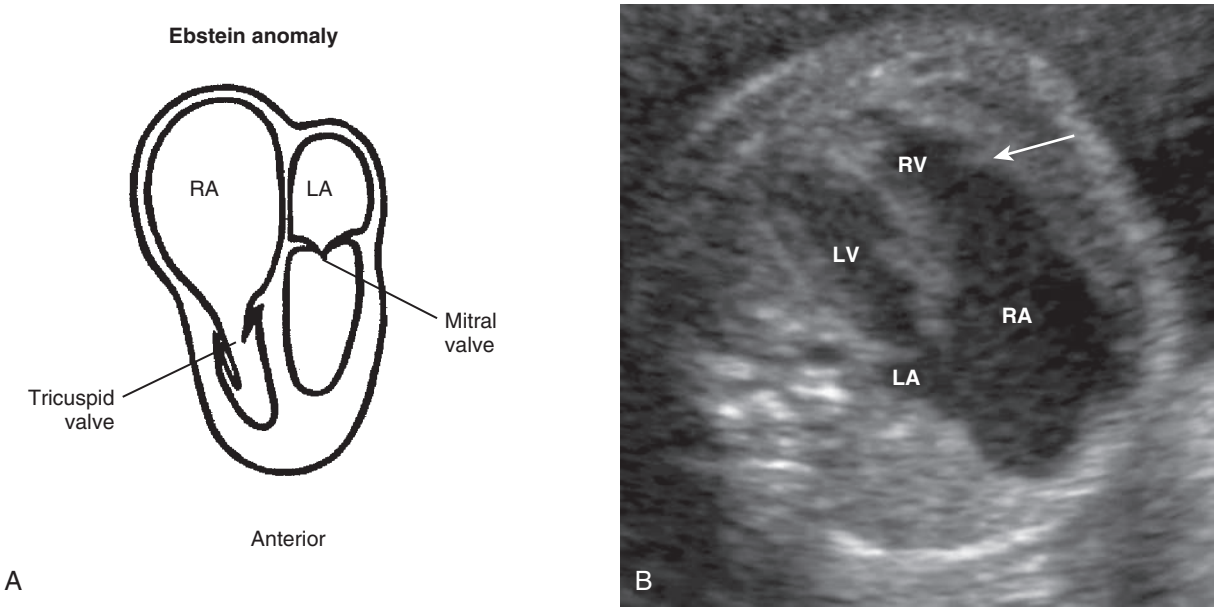

FIG. 37.28 Ebstein Anomaly. (A) Diagram showing the tricuspid valve apically displaced, resulting in an enlarged right atrium *(RA)* and a small, functional right ventricle *(RV)*. **(B)** Gray-scale image shows tricuspid valve *(arrow)* displaced inferiorly, resulting in an "atrialized" RV and enlarged RA. See also Video 37.12. *LA,* Left atrium; *LV,* left ventricle.

closely associated with **fetal hydrops** and a worsening prognosis.[79] Frequently, a left ventricular–to–right atrial jet can be identified across the ostium primum defect before the onset of holosystolic valvular insufficiency.[38] **Cardiac malformations** associated with AVSD include septum secundum ASD, hypoplastic left heart syndrome (HLHS), valvular pulmonary stenosis, coarctation of the aorta, and tetralogy of Fallot (TOF). A meta-analysis of published cases of AVSD diagnosed prenatally confirmed that chromosomal anomalies are common, occurring in 25% to 58% of affected fetuses.[80] Therefore karyotyping is indicated. Associated **extracardiac anomalies** are common, including **omphalocele, duodenal atresia, tracheoesophageal atresia, facial clefts, cystic hygroma, neural tube defects,** and **multicystic kidneys.**[80]

The fetus with an AVSD and associated defects has a poor prognosis. When hydrops is present, few survive the neonatal period.[81] Despite advances in pediatric cardiothoracic surgery, the overall outcome for antenatally diagnosed AVSD remains variable, with many studies reporting 5-year to 15-year survival rates below 50%.[80,82] Others have reported excellent long-term results with newer surgical techniques such as the two-patch technique with early complete cleft closure for complete AVSD repair.[83]

Ebstein Anomaly

Ebstein anomaly is characterized by inferior displacement of the tricuspid valve, frequently with **tethered attachments** of the leaflets, **tricuspid dysplasia,** and right ventricular dysplasia[84-88] (Fig. 37.28, Video 37.12). Ebstein anomaly makes up approximately 7% of cardiac anomalies in the fetal population and has an incidence of 0.5% to 1% in high-risk populations.[64,89,90] It occurs in approximately 1 per 20,000 live births.[91]

Early data from biased retrospective studies suggested that **lithium** use during pregnancy was associated with an estimated 500-fold increase in the incidence of Ebstein anomaly in exposed fetuses.[91-96] It is now clear that the increased risk is less than 2%.[45,97] Ebstein anomaly may be associated with a variety of structural cardiovascular defects, particularly **pulmonary atresia or stenosis,**[98] **arrhythmias,** and **chromosomal anomalies.**[86,99-102]

Ebstein anomaly is readily detected in utero.[99,103] The sonographic diagnosis rests on recognition of apical displacement of the tricuspid valve into the right ventricle, an enlarged right atrium containing a portion of the **"atrialized" right ventricle,** and a reduction in size of the functional right ventricle. Differential diagnosis includes tricuspid valvular dysplasia, **Uhl anomaly,** and idiopathic right atrial enlargement, but none of these has an inferiorly displaced tricuspid valve, the most reliable sign of Ebstein anomaly. Ebstein anomaly is one of the few structural defects that may cause substantial **cardiac dysfunction** in utero, frequently with cardiomegaly, hydrops, and tachyarrhythmias.[86] Examination with spectral and color Doppler ultrasound is helpful in demonstrating **tricuspid valve regurgitation,** which causes further enlargement of the right atrium and ventricle.[104] Tethered distal attachments of the tricuspid valve, marked right atrial enlargement, and left ventricular compression with narrowing of the pulmonary outflow tract are all associated with a poor prognosis.[86] Fetuses diagnosed with Ebstein anomaly and tricuspid dysplasia have a poor prognosis, with an overall perinatal mortality (fetal demise or death before neonatal discharge) of 45%.[105]

Arrhythmias, particularly **supraventricular tachycardias** (SVTs), are common with Ebstein anomaly and can further compromise the fetus. Overall, the 3-month mortality rate for patients diagnosed in utero is 80%.[86,103] Surgical correction of Ebstein anomaly in young children is associated with a low mortality rate and an excellent quality of life.[106-108] Because clinical

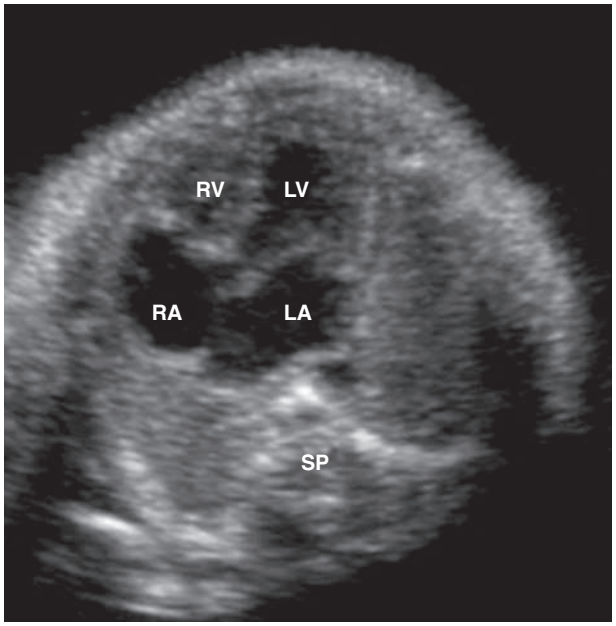

FIG. 37.29 Hypoplastic Right Ventricle. Apical four-chamber view shows small, right ventricular chamber *(RV)*. See also Video 37.11. *LA,* Left atrium; *LV,* left ventricle; *RA,* right atrium; *SP,* spine.

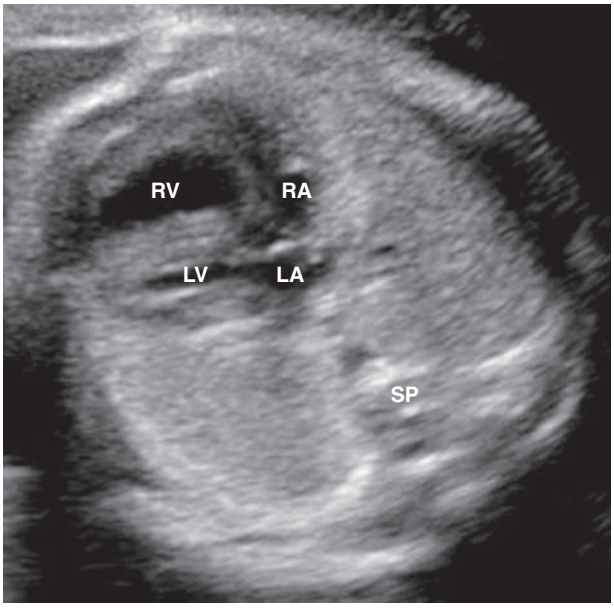

FIG. 37.30 Hypoplastic Left Heart Syndrome. The left atrium *(LA)* and left ventricle *(LV)* are small. See also Video 37.10. *RA,* Right atrium; *RV,* right ventricle; *SP,* spine.

presentation, treatment options, and prognosis are inconsistent, case-by-case management is variable.[109]

Hypoplastic Right Ventricle

In general, hypoplastic right ventricle occurs secondary to **pulmonary atresia with intact interventricular septum.** It has an incidence of 1.1% among stillbirths.[46] **Tricuspid atresia** may be associated with a hypoplastic right ventricle, but this is not as common.[110] Pathophysiologically, hypoplasia of the right ventricle develops because of a reduction in blood flow secondary to inflow impedance from tricuspid atresia or outflow impedance from pulmonary arterial atresia. Typical sonographic findings include a small, hypertrophic right ventricle and a small or absent pulmonary artery[110] (Fig. 37.29, Video 37.11). Spectral Doppler ultrasound may be helpful in demonstrating decreased flow through the tricuspid valve or pulmonary artery. Congestive heart failure and hydrops may develop from tricuspid regurgitation. After birth, closure of the ductus arteriosus frequently results in neonatal death. Prognosis improves with preoperative prostaglandin infusion to maintain the patency of the ductus.[111]

Hypoplastic Left Heart Syndrome

In **hypoplastic left heart syndrome,** the left ventricular cavity is pathologically reduced in size. HLHS constitutes approximately 7% to 9% of all congenital cardiac lesions.[112] It has a 2:1 male predominance and a recurrence risk of 0.5%.[112,113] The small left ventricle results from decreased blood flow into or out of the left ventricle. The primary abnormalities include **aortic atresia, aortic stenosis,** and **mitral valve atresia.** It is associated with **coarctation of the aorta** in 80% of cases.[114] The primary sonographic feature of HLHS is a small left ventricle (Fig. 37.30, Video 37.10). The mitral valve is typically hypoplastic or atretic, as is the aorta.[115] Color Doppler ultrasound is extremely helpful in the setting of HLHS, usually demonstrating the absence of flow through the mitral and aortic valves.[39]

Three decades ago this syndrome had an extremely poor prognosis, with 25% mortality in the first week of life and most untreated infants dying within 6 weeks.[116] Comfort care was provided, but little could be done to prolong survival. Currently it is expected that up to 70% of newborns with HLHS may reach adulthood owing to advancements in surgical techniques, perioperative management, and postoperative care.[117] Prenatal diagnosis of HLHS is beneficial for preventing ductal shock and keeping affected infants stable in the preoperative stage.[118-120] Monophasic blood flow across the mitral valve, restricted or absent flow through the foramen ovale, and retrograde flow through the aorta are all considered poor prognostic signs in utero. Despite significant advancements in medical and surgical management over the past 30 years, follow-up studies indicate that children with HLHS often experience major developmental delays[121] and decreased exercise performance, even after heart transplantation.[122] A recent meta-analysis found that although deficits remain, substantial improvement in neurodevelopment has occurred over the past 20 years in patients with surgically corrected HLHS.[123]

Univentricular Heart

In univentricular heart, two atria empty into a single ventricle, via two A-V valves or a common A-V valve. Univentricular heart is rare, accounting for approximately 2% of CHD.[47] It results from a failure of the interventricular septum to develop. The single chamber has a left ventricular morphology in 85% of cases.[124] Associated cardiac anomalies are common,[125] with **asplenia** or **polysplenia** occurring in 13%.[126] Sonographically,

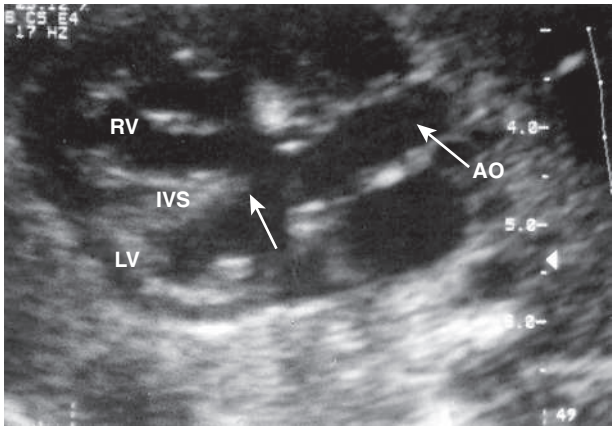

FIG. 37.31 Tetralogy of Fallot. The aorta *(AO)* overrides both the right ventricle *(RV)* and the left ventricle *(LV)*. A ventricular septal defect *(arrows)* is also appreciated. See also Video 37.13. *IVS,* Interventricular septum.

a single ventricle with absence of the interventricular septum is seen. Doppler ultrasound examination is helpful in determining if a normal outflow tract is present. A nonfunctioning, rudimentary accessory ventricle may be present in some cases. Differential diagnosis includes a large VSD and hypoplastic right or left ventricle.

Patients with outflow tract stenosis have a poor prognosis.[127] Death is typically caused by congestive heart failure or arrhythmia.[77] Pulmonary artery banding and shunts yield a 70% 5-year survival rate. Ventricular septation has a postoperative survival rate of approximately 56%.[125,128] More recent literature indicates that there continues to be a high mortality rate for univentricular heart after surgical correction, with an 8-year survival after **modified Blalock-Taussig shunt** of only 68%.[129] After a **Glenn bidirectional cavopulmonary connection,** 8-year survival is slightly higher at 74%.[130]

Tetralogy of Fallot

Tetralogy of Fallot consists of (1) VSD, (2) overriding aorta, (3) hypertrophy of the right ventricle, and (4) stenosis of the right ventricular outflow tract (Fig. 37.31, Video 37.13). It accounts for 5% to 10% of CHD in live births[46] and is associated with a variety of cardiac, extracardiac, and chromosomal anomalies.[72] A study of 129 fetuses diagnosed in utero with TOF reported additional cardiac anomalies in 57%, extracardiac anomalies in 50%, and chromosomal anomalies in 49%. The first trimester nuchal translucency was above the 95th percentile in 47% of fetuses.[131]

TOF occurs when the **conus septum** is located too far anteriorly, thus dividing the conus into a smaller, anterior right ventricular portion and a larger posterior part. Closure of the interventricular septum is incomplete, causing the aorta to override both ventricles.[132] The VSD typically occurs in the perimembranous portion of the septum. Right ventricular hypertrophy rarely occurs in utero, but the overriding aorta is reliably seen.[133,134] **Pulmonary atresia or stenosis,** or a **dilated pulmonary artery** secondary to absence of the valve, may be appreciated. The diagnosis of TOF has been made before 15 weeks' gestation using transvaginal ultrasound.[33] Color Doppler imaging is helpful in making the diagnosis of TOF.[135]

The newborn with the classic form of TOF who has pulmonary stenosis rather than pulmonary atresia is typically asymptomatic at birth but develops cyanosis and a murmur in the first weeks of life. Early primary repair of TOF is routinely performed with a low surgical mortality and postoperative morbidity.[136] Typical cases of TOF are repaired at 4 to 6 months of age, with close to 90% survival at 1 year.[137] Patients surviving early surgery (before 5 years old) have a 32-year survival of 90%.[138] The presence of congestive heart failure in the fetus or newborn with TOF is associated with 17% to 41% mortality.[139,140]

Truncus Arteriosus

Truncus arteriosus accounts for 1.3% of fetal cardiac anomalies and is characterized by a single large vessel arising from the base of the heart. This vessel supplies the coronary arteries and the pulmonary and systemic circulations. Aortic anomalies occur in 20% and noncardiac anomalies in 48% of patients with truncus arteriosus.[141] In almost all patients a VSD is present. The **truncal valve** may have two to six cusps and in general overrides the ventricular septum. Four types of truncus arteriosus have been identified by **Collett and Edwards,**[142] as follows:

- **Type I** has a pulmonary artery that bifurcates into right and left branches after it arises from the ascending portion of the truncal vessel.
- **Type II** has right and left pulmonary arteries arising separately from the posterior truncus.
- **Type III** has pulmonary arteries that arise from the sides of the proximal truncus.
- **Type IV** has systemic collateral vessels from the descending aorta as the source of flow.

The single, large **truncal artery** with overriding ventricular septum and an associated VSD is identified on four-chamber and outflow tract views (Fig. 37.32). This anomaly has been diagnosed as early as 13 weeks.[34] Color Doppler imaging is particularly helpful in the setting of truncus arteriosus because it facilitates accurate localization of the pulmonary arteries and rapidly detects truncal valvular insufficiency. In the 1980s, prognosis was poor, with an overall mortality of 70%.[141] More recent studies have indicated that 10-year to 20-year survival is excellent for infants undergoing complete repair of truncus arteriosus.[143] However, these patients continue to experience significant comorbidities throughout childhood, with significant deficits in exercise tolerance and overall functional status.[144]

Double-Outlet Right Ventricle

Double-outlet right ventricle (DORV) represents less than 1% of all CHD and occurs when more than 50% of both the aorta and the pulmonary artery arise from the right ventricle.[145,146] DORV is classified into the following three types:

- Aorta posterior and to the right of the pulmonary artery
- Aorta and pulmonary artery parallel, with the aorta to the right **(Taussig-Bing type)**
- Aorta and pulmonary artery parallel, with the aorta anterior and to the left

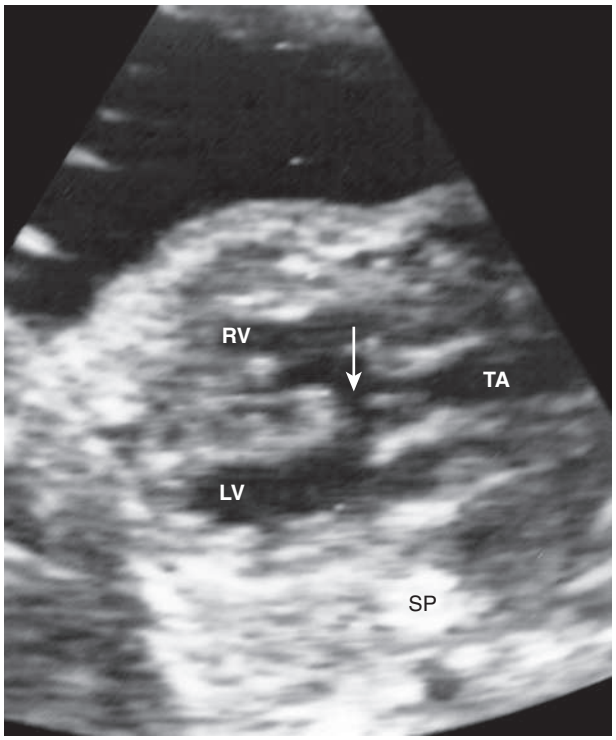

FIG. 37.32 Truncus Arteriosus. The single truncal artery *(TA)* overrides both the right ventricle *(RV)* and left ventricle *(LV)*. A ventricular septal defect *(arrow)* is present. No pulmonary artery was seen, helping to differentiate from tetralogy of Fallot. *SP,* Spine.

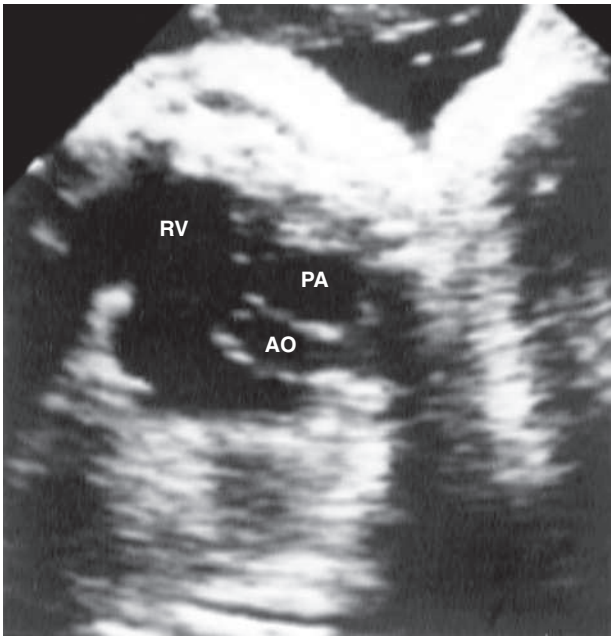

FIG. 37.33 Double-Outlet Right Ventricle. The aorta *(AO)* and pulmonary artery *(PA)* both arise from the right ventricle *(RV)* in a parallel fashion.

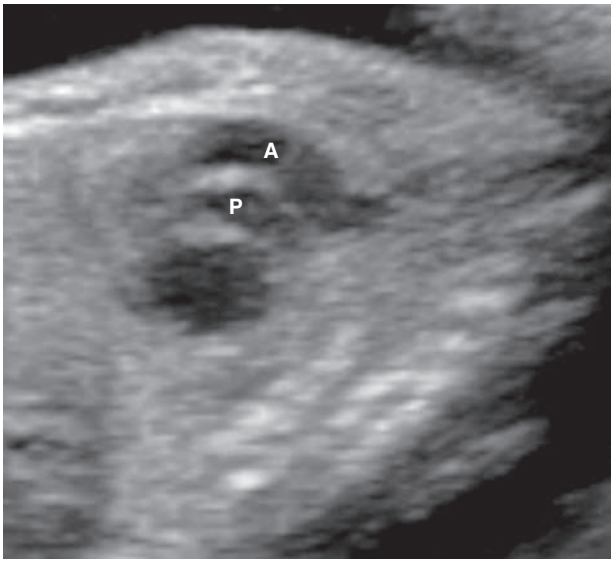

FIG. 37.34 Complete Transposition of Great Arteries. The aorta *(A)* is anterior to the pulmonary artery *(P)*. This abnormal arrangement results in both vessels running parallel to each other in this short-axis view.

DORV is associated with other cardiac defects (particularly VSD), various extracardiac defects, fetal chromosomal anomalies, maternal diabetes, and maternal alcohol consumption.[5,146,147] With surgical intervention, 10-year survival as high as 97% has been reported.[145] A more recent study reported near 94% overall 5-year survival after surgical correction.[148] When extracardiac or chromosomal anomalies are present, prognosis is poor, with 69% mortality when the diagnosis of DORV is made in utero.[147] Sonographically, the aorta and pulmonary artery arise predominantly from the right ventricle (Fig. 37.33). Differential diagnosis includes transposition of the great vessels and TOF.

Transposition of Great Arteries

Transposition of the great arteries (TGA) is subdivided into two types: (1) complete or **dextrotransposition** (D-TGA) in 80% and (2) congenitally corrected or **levotransposition** (L-TGA) in 20% of fetuses with transposition. In both types, **ventriculoarterial discordance** is present. (The aorta arises from the right ventricle, and the pulmonary artery arises from the left ventricle.) **Complete transposition** (D-TGA) is defined as **atrioventricular concordance** (atria and ventricles are correctly paired) with ventriculoarterial (V-A) discordance (Fig. 37.34). It comprises 5.5% of heart disease in the fetal population.[47] D-TGA is also classified into two types, depending on the absence (70%) or presence of a VSD. A variety of cardiac anomalies are associated with D-TGA, including **pulmonic stenosis,** which rarely occurs in the absence of a VSD. In 8% of cases, other organ systems are involved. Chromosomal anomalies are not commonly associated with TGA.

In D-TGA, the aorta arises from the right ventricle, receives systemic blood, and returns it to the systemic circulation. The pulmonary artery arises from the left ventricle, receives pulmonary venous blood, and returns it to the lungs. In general, the aortic root lies anterior and slightly to the right of the pulmonary outflow tract. With closure of the ductus arteriosus and foramen ovale after birth, this condition is incompatible with life unless an associated shunt allows mixing of the separate right and left circulations.

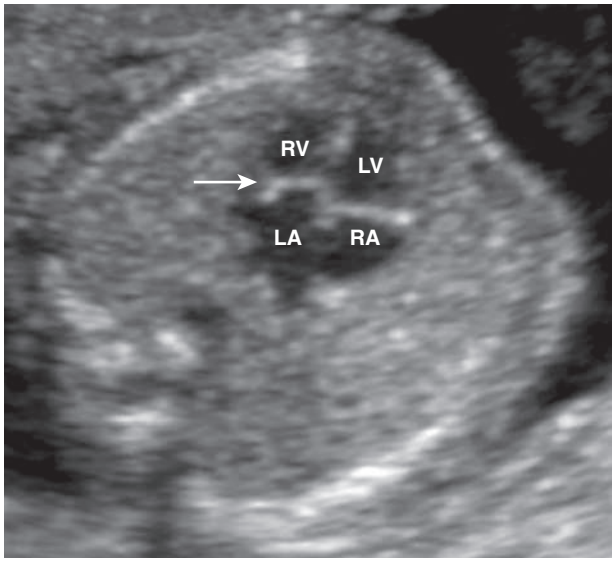

FIG. 37.35 Congenitally Corrected Transposition of Great Arteries. An apical four-chamber view shows the morphologic right ventricle *(RV)* and morphologic left ventricle *(LV)* located on the incorrect sides of the heart. This is evidenced by identifying the atrioventricular valve leaflets inserting *(arrow)* on the left side of the heart in a more apical location than the right-sided atrioventricular valve leaflet insertion. *LA,* Left atrium; *RA,* right atrium.

Sonographic diagnosis depends on demonstrating that the great vessels exit the heart in parallel, rather than crossing in the normal fashion. This is optimally seen in a long-axis or short-axis view of the great vessels. A three-vessel view is also useful because only one great vessel (aorta) is usually visualized at this level, in this setting.

Most neonates with D-TGA require immediate treatment. Initially, a temporizing shunt may be created before definitive treatment, frequently with the arterial switch procedure. With surgical intervention, 12-month survival can be expected in 80%.[149] Early intervention (within 3 days of life) when using the **arterial switch operation** is optimal and is associated with an operative mortality below 2%. Major morbidity and cost increase daily thereafter.[150]

Corrected transposition (L-TGA) is characterized by A-V discordance with V-A discordance (Fig. 37.35). It comprises 1% of CHD and 20% of cases of fetal TGA.[47] The aorta, which arises from the left-sided, morphologic right ventricle, is anterior and to the left of the pulmonary artery. The pulmonary artery arises from the right-sided, morphologic left ventricle. VSD and pulmonic stenosis occur in approximately half the cases.[124,151] Malformation and inferior displacement of the morphologic tricuspid valve may be present. Pathophysiologically, the flow of blood through the heart to the pulmonic and systemic circulations is normal, even though the morphologic right ventricle is on the left and the morphologic left ventricle is on the right.

The antenatal sonographic diagnosis rests on demonstrating a parallel arrangement to the great vessels, similar to D-TGA. Differentiating D-TGA from L-TGA entails identification of the morphologic right and left ventricles. The **moderator band** will be seen on the anatomic left side. In addition, the tricuspid valve will be situated on the anatomic left side, so its more apical septal leaflet should be identified. Associated cardiac defects are common and diverse, including VSD, pulmonary stenosis or atresia, ASD, DORV, tricuspid valve anomalies, dextrocardia, mesocardia, and situs inversus. Fetal **A-V block** is common with TGA.[152]

In the absence of associated cardiac anomalies, patients with corrected TGA may remain asymptomatic throughout their lives.

Anomalous Pulmonary Venous Return

APVR can be divided into two subgroups: **total anomalous pulmonary venous return** (TAPVR), in which none of the pulmonary veins drains into the left atrium, and **partial anomalous pulmonary venous return** (PAPVR), in which at least one of the pulmonary veins has an anomalous connection. TAPVR constitutes 2.3% of cases of CHD.[153,154] The four types of anomalous pathways are as follows:

1. The pulmonary veins drain into a vertical vein that empties into the innominate vein and then into the SVC.
2. The pulmonary veins drain into the coronary sinus and then into the right atrium.
3. The pulmonary veins drain directly into the right atrium.
4. The pulmonary vein drains into the portal vein and into the IVC via the ductus venosus.

Embryologically, TAPVR is thought to result from failure of obliteration of the normal connections between the primitive pulmonary vein and the splanchnic, umbilical, vitelline, and cardinal veins. TAPVR is associated with AVSDs and **polysplenia** and **asplenia** syndromes.

The antenatal sonographic diagnosis of TAPVR is difficult because the anomalous veins are generally extremely small and variable in their course. Often the first sign of APVR is mild right ventricular and pulmonary artery prominence, in which case a careful search for the four normal pulmonary veins should be undertaken.[155] This can be difficult because the two inferior pulmonary veins are usually more difficult to visualize than the two superior veins, even in a normal fetal heart. Color and spectral Doppler ultrasound are helpful in documenting the normal pulmonary venous anatomy and in detecting and following the anomalous connections (Fig. 37.36).

The diagnosis of TAPVR is suspected when no pulmonary veins are seen entering the left atrium (Fig. 37.37). A small left atrium resulting from decreased blood return and lack of normal incorporation of the common pulmonary vein into the left atrium is also suggestive of TAPVR. Approximately one-third of patients with TAPVR have associated cardiac anomalies.[156] **Right atrial isomerism** is common. Associated extracardiac anomalies include gut malrotation and midline liver and stomach.[157,158] TAPVR causes minimal hemodynamic disturbance in utero, although hydrops occasionally results. Left untreated, the majority of infants die before 1 year of age.[133] Although PAPVR has also been diagnosed in utero, the diagnosis is more difficult and can be made only when pulmonary veins are seen entering the left atrium as well as the right atrium or an accessory pathway to the right atrium.[159] APVR is associated with high morbidity and mortality, largely because of the high incidence of additional cardiac anomalies.[157,159] Surgical correction of TAPVR is associated with an operative mortality of nearly 20%.[160]

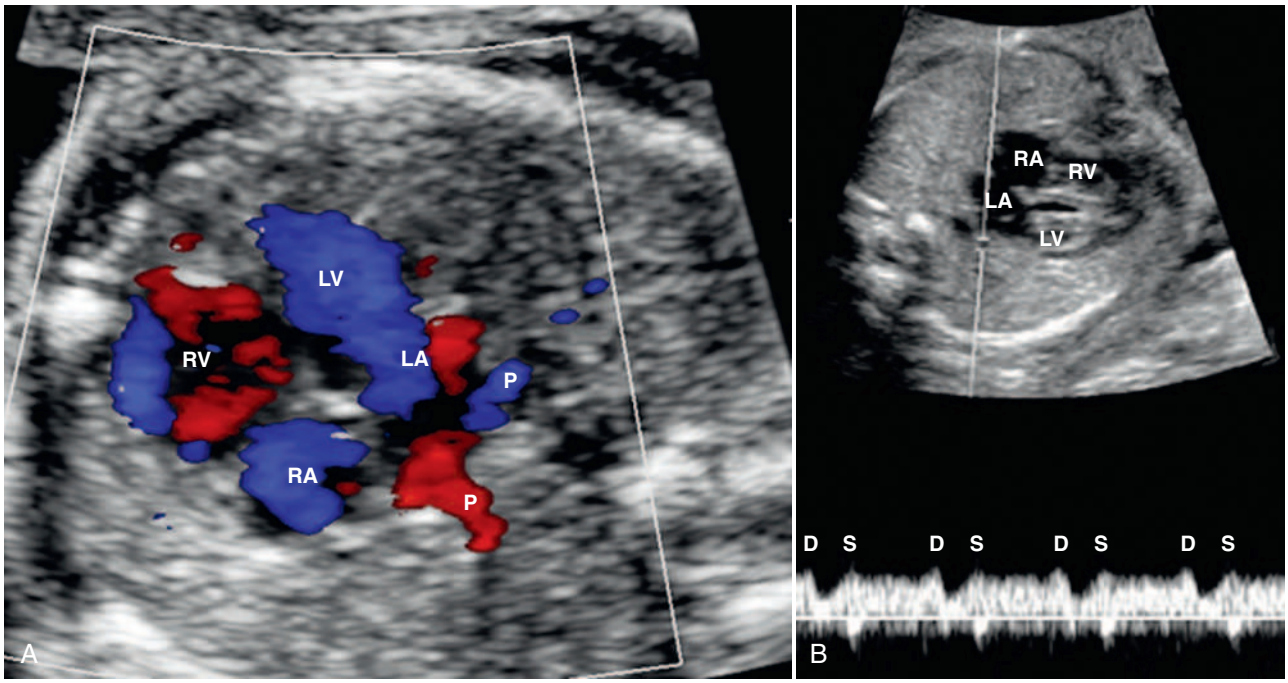

FIG. 37.36 Normal Pulmonary Venous Anatomy. (A) Four-chamber view using color Doppler ultrasound shows two superior pulmonary veins *(P)* entering the left atrium *(LA)*. **(B)** Subcostal four-chamber view using pulsed Doppler ultrasound shows normal waveform and direction of pulmonary venous flow into the LA. *D,* Diastolic peak; *LV,* left ventricle; *RA,* right ventricle; *RV,* right ventricle; *S,* systolic peak.

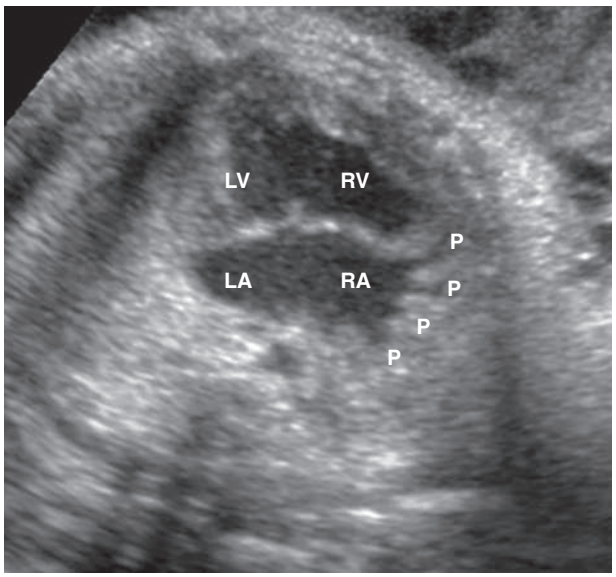

FIG. 37.37 Total Anomalous Pulmonary Venous Return. Apical four-chamber view shows anomalous insertion of all four pulmonary veins *(P)* into the right atrium *(RA). LA,* Left atrium; *LV,* left ventricle; *RV,* right ventricle.

Coarctation of Aorta

Aortic coarctation is a narrowing of the aortic lumen, usually occurring between the insertion of the ductus arteriosus and the left subclavian artery. Its severity ranges from a slight narrowing at the distal end of the arch to severe hypoplasia of the entire arch. Of fetuses with CHD, coarctation has an incidence of 6.8%.[47] Almost 80% of the cases are associated with other cardiac anomalies, including abnormal aortic valve (bicuspid or stenotic), VSD, DORV, and AVSD. Chromosomal abnormalities occur in 5%, and almost 5% of coarctations are associated with maternal diabetes.[59,161] Coarctations are present in approximately 20% of individuals with Turner syndrome (45X).[5]

Three embryologic theories have been proposed to explain the origin of coarctation of the aorta: (1) a primary developmental defect with failure of connection of the fourth and sixth aortic arches with the descending aorta[162]; (2) aberrant ductal tissue at the level of the aortic arch[163,164]; and (3) decreased blood flow through the aortic isthmus.[165]

Sonographic detection of coarctation is difficult.[25] Ventricular size discrepancy with a prominent right ventricle and relatively small left ventricle,[55,165] with a right-to-left ventricle diameter ratio greater than 2 standard deviations (SDs) above the norm,[166,167] suggests coarctation of the aorta. Likewise, a discrepancy in pulmonary artery–to–ascending aorta diameter that falls greater than 2 SDs above the normal ratio of 1.18 to 0.06[167] is suggestive of coarctation.[166] Color Doppler ultrasound is useful in identifying the area of narrowing. Spectral Doppler ultrasound may detect increased velocity distal to the narrowed segment (Fig. 37.38). Many coarctations do not become evident until closure of the ductus arteriosus at birth. In addition, infants with coarctation of the aorta may not develop clinical or echocardiographic signs of coarctation until 6 to 12 weeks after closure of the ductus arteriosus. If coarctation of the aorta is suspected on fetal echocardiogram, the infant should be followed to at least 1 year of age.[168] Although isolated coarctation has a good prognosis, 39% mortality is reported when associated anomalies are present.[169] Treatment is usually accomplished with angioplasty or stenting with good results.[170]

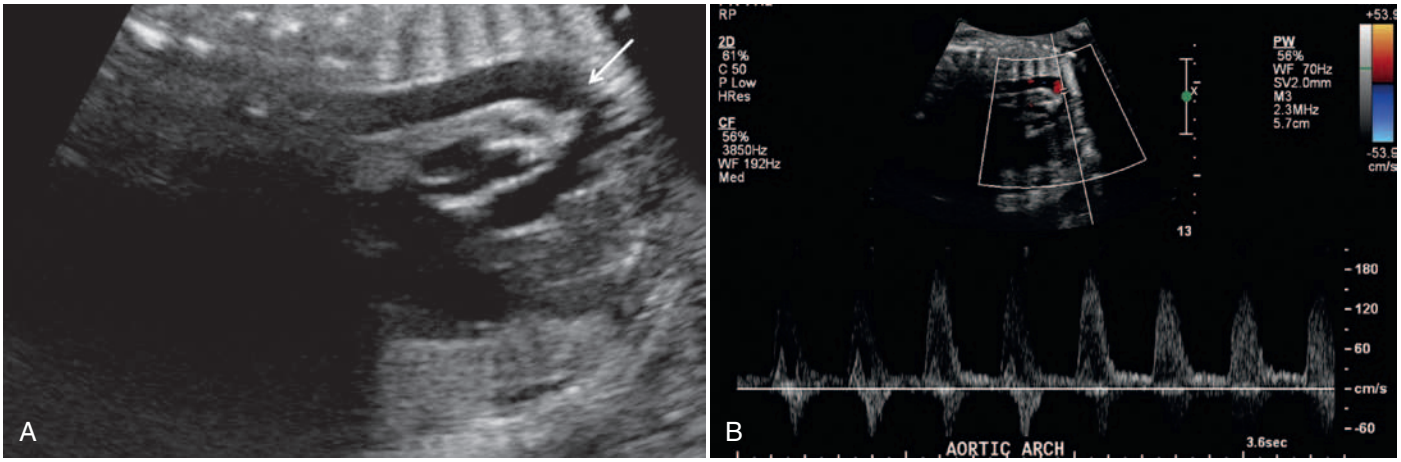

FIG. 37.38 Coarctation of Aorta. (A) Gray-scale image showing narrowing of the aortic arch *(arrow)* at the level of the isthmus. **(B)** Spectral Doppler tracing shows increased velocity and bidirectional blood flow through the aortic arch.

Aortic Stenosis

Aortic stenosis is a stricture or obstruction of the ventricular outflow tract occurring in 5.2% of newborns.[46] Aortic stenosis is divided into supravalvular, valvular, and subvalvular types. The supravalvular type of aortic stenosis has not been reported in utero. **Valvular** aortic stenosis is more frequent in males and is associated with a bicuspid aortic valve and chromosomal abnormalities.[171] **Subvalvular** aortic stenosis is associated with inherited disorders, **asymmetrical septal hypertrophy** (ASH), and **hypertrophic obstructive cardiomyopathy.** Infants of diabetic mothers may have a transient form of left ventricular outflow tract obstruction secondary to ASH.

Thickening of the aortic valve, poststenotic dilation of the aorta, and ventricular enlargement are clues to valvular aortic stenosis. In addition, real-time evaluation of the aortic valve may show it persisting, as opposed to moving normally in and out of the field of view. Thickening of the interventricular septum may be seen in subvalvular aortic stenosis. In all cases, increased velocity through the aortic valve will be identified on pulsed Doppler ultrasound. Early-onset aortic stenosis results in **endocardial fibroelastosis** (EF) and **hypoplastic left ventricle.**[172]

Aortic stenosis progresses in utero and may not be apparent on early (<16 weeks) fetal echocardiograms. In some cases these defects may not be apparent until after birth.[29] A mortality rate of 23% in the first year of life is reported with aortic stenosis.[173] Prognosis has improved with appropriate surgery, with mortality of 1.9% to 9%.[174,175] In some cases, severe aortic stenosis in midgestation may progress in utero to **hypoplastic left heart syndrome.** In cases of critical aortic valvular stenosis, in utero balloon valvuloplasty has been performed with good results.[176]

Pulmonic Stenosis

Pulmonic stenosis may occur at the valve level or at the infundibulum. It occurs in 7.4% of live-born infants with CHD.[46] Dysplastic and stenotic pulmonic valves are seen in **Noonan syndrome** and with **maternal rubella.** Pulmonic stenosis is associated with TAPVR, ASD, supravalvular aortic stenosis, and TOF. The incidence of pulmonic stenosis is higher in monochorionic pregnancies and is 10 times more frequent in the recipient twin of a pregnancy affected with **twin-twin transfusion syndrome.**[177] In this setting the recipient's heart becomes hypertrophic secondary to increased preload. This is similar to the ASH present in fetuses of diabetic mothers and results in anatomic obstruction of the outflow tract.[172]

Increased velocity through the pulmonic valve and hypertrophy of the right ventricle suggest pulmonic stenosis. Similar to aortic stenosis, a real-time image of the stenotic pulmonic valve will show it persisting in the field of view. As with aortic stenosis, pulmonic stenosis tends to progress in utero. Pulmonic stenosis has a variable outcome and can be managed with closed **transventricular valvotomy** or percutaneous balloon valvuloplasty.[178,179] In utero pulmonary balloon valvuloplasty has also been successful but is still in its early phase.[180]

Cardiosplenic Syndromes

Cardiosplenic syndromes are syndromes associated with **asplenia (right isomerism)** and **polysplenia (left isomerism).** Both are defects of lateralization in which symmetrical development of normally asymmetrical organs or organ systems occurs.[180] Asplenia **(Ivemark syndrome)** and polysplenia syndromes are usually considered separate clinical entities. However, they have many characteristics in common, including **situs inversus** or **situs ambiguus** of various visceral organs, complex congenital heart defects,[181] and increased incidence of chronic arrhythmias.[182]

Pathologically, in asplenia or bilateral right-sidedness, left-sided organs are a mirror image of normally right-sided organs. This results in right atrial isomerism, bilateral trilobed lungs, bilateral right bronchi and pulmonary arteries, ipsilateral location of the aorta and IVC (either left or right side), absence of the spleen, a midline horizontal liver, and bilateral SVC.[183] In polysplenia or bilateral left-sidedness, the right lung and bronchial tree morphologically mirror those of the left. In many cases, intrahepatic interruption of the IVC with azygous continuation is present, as are multiple spleens and left atrial isomerism.[184]

Cardiac anomalies associated with these syndromes include TAPVR or PAPVR, ASD, VSD, univentricular heart, TGA, DORV, and pulmonic/aortic stenosis or atresia. Coarctation, hypoplastic

Asplenia and Polysplenia: Associated Findings

ASPLENIA
Absence of spleen
Bilateral right-sidedness
Right atrial isomerism
Bilateral trilobed lungs
Bilateral right bronchi and pulmonary arteries
Ipsilateral location of the aorta and IVC
Bilateral SVC
Situs ambiguous
Midline horizontal liver

POLYSPLENIA
Multiple spleens
Bilateral left-sidedness
Left atrial isomerism
Bilateral bilobed lungs
Bilateral left bronchi and pulmonary arteries
Interruption of IVC
Azygous continuation of IVC
Situs ambiguous
Midline horizontal liver
Congenital heart disease
Complete atrioventricular block

IVC, Inferior vena cava; *SVC,* superior vena cava.

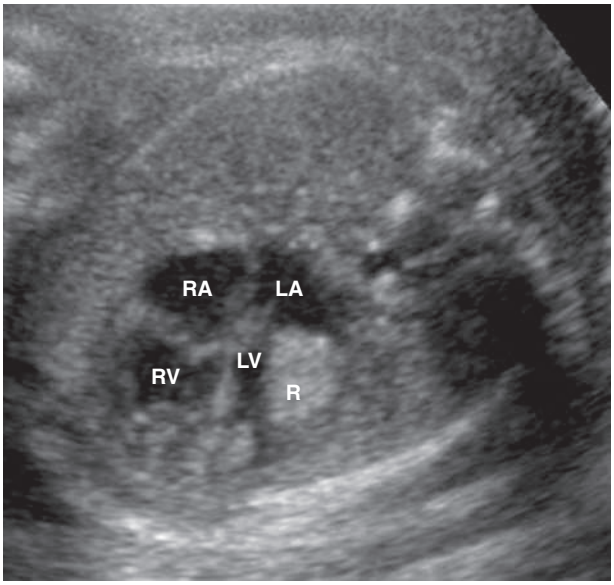

FIG. 37.39 Rhabdomyoma. Apical four-chamber view shows an echogenic mass in the left ventricle *(LV),* consistent with a rhabdomyoma *(R). LA,* Left atrium; *RA,* right atrium; *RV,* right ventricle.

left ventricle, mitral stenosis, cor triatriatum, dextrocardia, right atrial hypoplasia, AVSD, truncus arteriosus, and TOF have also been observed.[184-188] Complete A-V block with an AVSD is associated with polysplenia. Polysplenia syndrome is the second most common disease associated with fetal heart block (after L-TGA).[186]

Cardiosplenic syndromes should be considered when CHD occurs with an arrhythmia. If these syndromes are suspected, a careful search is made for the fetal spleen, which has been visualized at 20 weeks' gestation, with careful consideration of the location of the fetal stomach.[186,189] Other abnormal relationships, such as ipsilateral aorta and IVC (associated with asplenia) or interruption of the IVC with continuation of the azygous vein (associated with polysplenia), may be documented prenatally.

The mortality rate with cardiosplenic syndromes is extremely high. Treatment depends largely on the type and number of associated anomalies. Because cardiac malformations associated with polysplenia are often less severe, they are more amenable to surgical correction than lesions associated with asplenia.[189,190] Neonates with asplenia have a higher mortality and postoperative morbidity because of the high frequency of associated complex cardiac malformations. In polysplenia the greatest attrition occurs in the prenatal period and is often related to heart block with resultant hydrops.[188]

Cardiac Tumors

Fetal cardiac tumors are rare. Approximately 10% are malignant.[191,192] Until the infant is 1 year of age, the majority of cardiac and pericardial masses are **rhabdomyomas** (58%) and **teratomas** (19%). Cardiac **fibromas** account for approximately 12% of the tumors in this age group. Other, less frequent tumors include **mesothelioma** of the A-V node and cardiac **hemangioma** (approximately 2% each).

Sonographically, fetal cardiac **rhabdomyomas** appear as solid, echogenic masses. Rhabdomyomas **(cardiac hamartomas)** are usually multiple, typically arising from the interventricular septum[193-199] (Fig. 37.39). Rhabdomyomas may develop in utero after an initially normal fetal echocardiogram and may increase in size and number over time.[29,196,200-202] This finding underscores the importance of serial fetal echocardiograms in fetuses at risk for rhabdomyomas.

Of patients with cardiac rhabdomyomas, 30% to 78% have **tuberous sclerosis.**[193-195] Other signs of tuberous sclerosis are rarely found in fetal life, with the exception of subependymal tubers in the brain, which can be detected with fetal MRI or by mass effect leading to hydrocephalus.[193] Unfortunately, the absence of cardiac neoplasms in a fetus at risk for tuberous sclerosis does not exclude this diagnosis.[196]

Cardiac tumors become hemodynamically significant by causing obstruction to the outflow tracts or A-V valves, resulting in congestive heart failure, hydrops, pericardial effusion, and arrhythmias.[193] Prognosis depends on the size, number, and location of the tumor as well as associated arrhythmias and anomalies. A meta-analysis of 138 published cases of fetal cardiac rhabdomyomas found that size greater than 20 mm, presence of arrhythmia, and hydrops were significantly associated with increased morbidity.[200] Infants with cardiac rhabdomyomas have a guarded prognosis. Rhabdomyomas are hormone-sensitive neoplasms, which explains their tendency to spontaneously regress.[203] Clinical manifestations associated with fetal cardiac rhabdomyomas are diverse, ranging from spontaneous regression of the tumor to sudden death.[192] After birth, the cells lose the

ability to divide, rhabdomyomas can be expected to shrink or completely resolve, and patients can often be treated conservatively.[204] However, because of the association of rhabdomyomas with tuberous sclerosis and arrhythmias, prognosis remains guarded.[205]

Teratomas may appear as cystic, complex, or solid masses. These are intrapericardial in origin, with attachment to the aortic root or pulmonary artery, and are virtually always associated with a large pericardial effusion. Although teratomas are generally considered to be benign, they can recur after surgical excision and may undergo malignant degeneration.[204] Fetal teratomas are weakly associated with tuberous sclerosis.[196]

Rare cardiac tumors include fibromas and hemangiomas. **Fibromas** are almost always single and typically have central necrosis and calcification.[201] Fibromas are usually located in the ventricular septum, making resection problematic. **Hemangiomas** are even rarer and are usually associated with the right atrium or interventricular septum, often with an intracavitary component. Cardiac hemangiomas are heterogeneous with cystic and solid components, often with calcifications. They are frequently associated with a pericardial effusion.[201]

Echogenic foci within a ventricle should not be mistaken for a cardiac tumor. These are thought to represent areas of mineralization of papillary muscle or chordae tendineae. These usually occur in the left ventricle (93%) but may occur in the right ventricle (5%) or both ventricles (2%) and are generally clinically insignificant[206-208] (Fig. 37.40). Echogenic foci have been associated with chromosomal anomalies such as trisomy 21 and 13. However, more recent literature suggests that in isolation, in an otherwise low-risk pregnancy, an increased risk of aneuploidy does not exist.[208]

Congenital ventricular aneurysms or **diverticula** may be appreciated in utero. Both are usually isolated findings. Ventricular aneurysms appear sonographically as an outpouching of the ventricular myocardium that usually does not contract with the ventricle. A diverticulum of the ventricle appears as a cystic structure connected to the ventricle by a narrow channel. These often do contract with the associated ventricle during systole.[209]

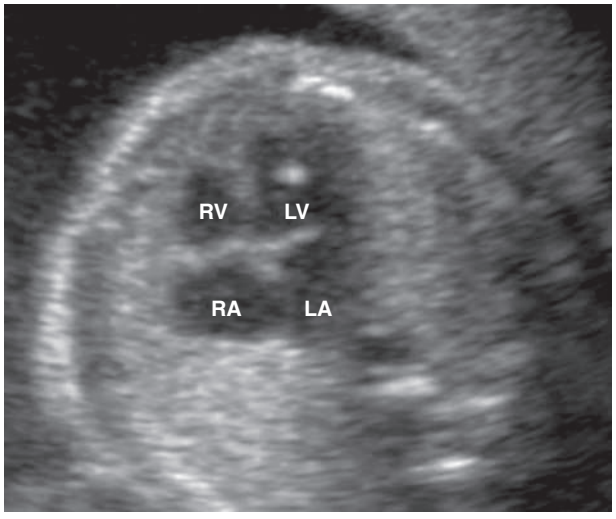

FIG. 37.40 Echogenic Intracardiac Focus. Apical four-chamber view of a fetal heart with an echogenic focus in the left ventricle *(LV). LA,* Left atrium; *RA,* right atrium; *RV,* right ventricle.

Cardiomyopathy

Cardiomyopathy encompasses a diverse group of cardiac disorders with variable etiologies and anatomic and functional characteristics, and all result in an alteration in cardiac function. Cardiomyopathies account for 8% to 11% of fetal cardiovascular disease,[210] but only 1.8% of CHD in live-born infants.[154] Approximately one-third of fetuses with cardiomyopathy die in utero, which accounts for the difference in these numbers.[211]

A variety of conditions can cause fetal cardiomyopathy (Fig. 37.41), including viral and bacterial infections, inborn errors of metabolism, **endocardial fibroelastosis, familial cardiomyopathy,** and **maternal diabetes.** Infectious agents act by damaging the myocardium and producing a myocarditis with resultant cardiomyopathy.[212] In the setting of storage diseases, the myocardium becomes hypertrophic secondary to the accumulation of various products within the myocardial cells. Many cases are idiopathic.[213]

Endocardial fibroelastosis (EF) is a poorly understood process in which diffuse endocardial thickening develops in one or more cardiac chambers. EF is divided into two broad categories, primary and secondary. Primary or isolated EF occurs in the absence of other structural cardiac anomalies. In primary EF the affected ventricle may be dilated or constricted.[214] Viral myocarditis is thought to be the cause of primary fetal EF, with **mumps** and **coxsackievirus B** the most common infections.[213,214] Secondary EF occurs in the setting of a structural cardiac anomaly and usually results in dilation of the affected chambers. The dilated form occurs with **coarctation of the aorta, aortic valvular disease, mitral valvular disease,** and other lesions. The less common constricted form is associated with aortic stenosis or atresia. In both types of EF the mural endocardium is largely replaced by collagen and elastic tissue, giving it a glistening-white appearance grossly[213] and a striking echogenic appearance at echocardiography (Fig. 37.42).

An increased incidence of **asymmetrical septal hypertrophy** (ASH) or **concentric hypertrophy** has long been recognized in **infants of diabetic mothers.**[215] The characteristics of these types of cardiomyopathy have been well documented echocardiographically.[215-218] Overall cardiac size in fetuses of diabetic mothers can be increased as a result of the hypertrophy.[219] Fetal **hypertrophic cardiomyopathy** can be expected in about 20% of pregnancies with pregestational diabetes and appears to be associated with an elevated third-trimester maternal hemoglobin A_{1c} and with an elevated neonatal insulinlike growth factor-1 (IGF-1) level.[220] Regardless of the cause, severe cardiomyopathy results in decreased cardiac function and a tendency to develop congestive heart failure. This may be secondary to obstruction of ventricular emptying in obstructive forms of cardiomyopathy or to pump failure in nonobstructive forms. The sonographic diagnosis of obstructive cardiomyopathy depends on the demonstration of hypertrophy of the ventricular wall or septum. **Nonobstructive cardiomyopathy** can be diagnosed by demonstrating dilation of one or more cardiac chambers along with poor ventricular contractility. About 37% of live-born infants with cardiomyopathy

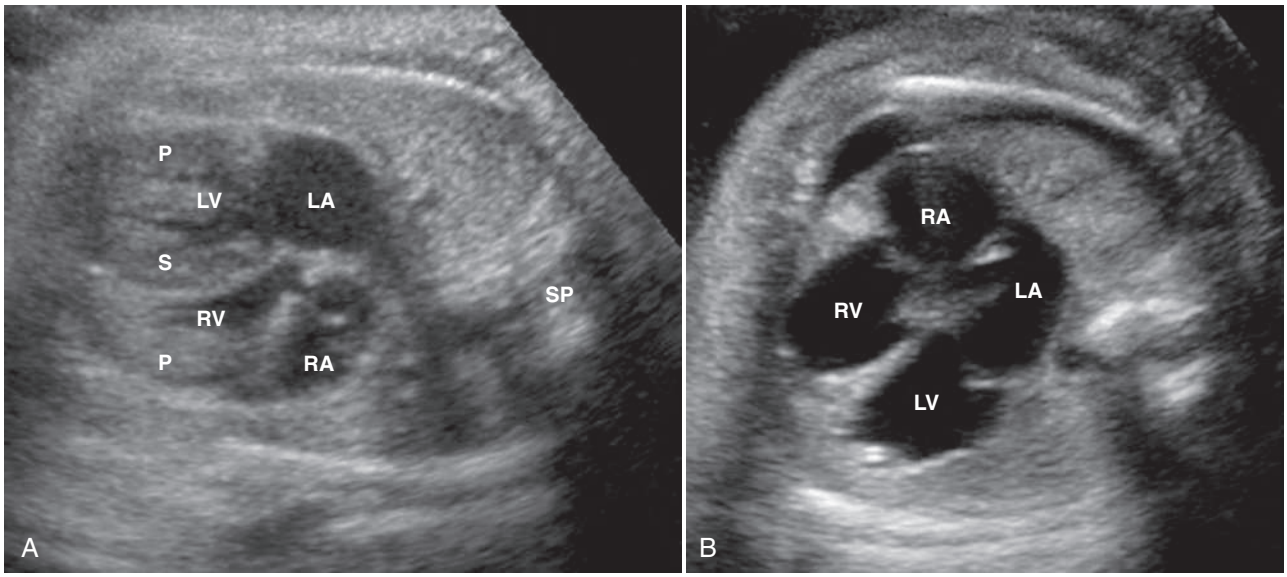

FIG. 37.41 Cardiomyopathy. (A) Concentric hypertrophy of the ventricular heart walls *(P)* and the interventricular septum *(S)* in fetus with **hypertrophic cardiomyopathy. (B)** All four cardiac chambers are enlarged, occupying more than half the fetal chest in this fetus with **dilated cardiomyopathy.** A pleural effusion is also seen. *LA,* Left atrium; *LV,* left ventricle; *RA,* right atrium; *RV,* right ventricle; *SP,* spine.

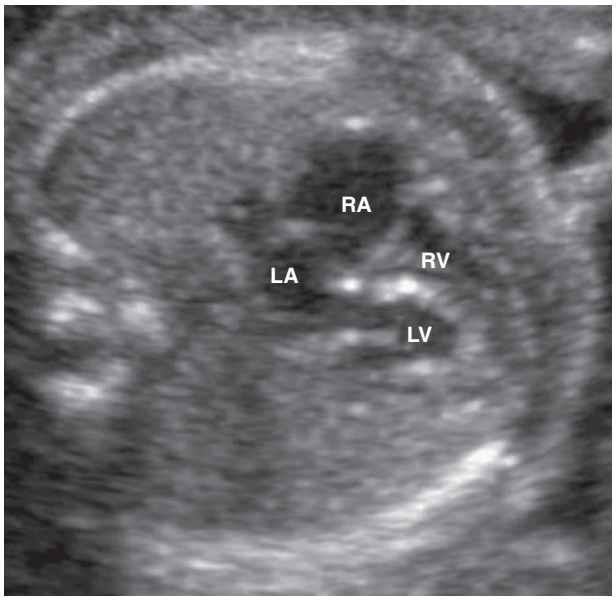

FIG. 37.42 Endocardial Fibroelastosis. Subcostal four-chamber view shows echogenic walls of the left ventricle *(LV). LA,* Left atrium; *RA,* right atrium; *RV,* right ventricle.

have associated anomalies.[154] The prognosis for fetal cardiomyopathy is variable, depending on the severity of the cardiac lesion, the underlying cause, and associated anomalies. When hydrops accompanies cardiomyopathy, the prognosis is poor.

Ectopia Cordis

Ectopia cordis is a rare malformation in which the heart is located outside the thoracic cavity. It results from failure of fusion of the lateral body fold in the thoracic region. Ectopia cordis is classified by the following four types[221]:

1. **Thoracic** (60%). The heart is displaced from the thoracic cavity through a sternal defect.
2. **Abdominal** (30%). The heart is displaced into the abdomen through a diaphragmatic defect.
3. **Thoracoabdominal** (7%). The heart is displaced from the chest through a defect in the lower sternum, with an associated diaphragmatic or ventral abdominal wall defect (pentalogy of Cantrell).
4. **Cervical** (3%). The heart is displaced into the neck area.

Although most cases are isolated, ectopia cordis may be associated with **pentalogy of Cantrell,** a condition characterized by a sternal cleft, ventral diaphragmatic hernia, omphalocele, intracardiac anomalies, and ectopia cordis.[222] A variety of cardiac and chromosomal anomalies are associated with ectopia cordis. The sonographic diagnosis is generally not difficult and has been made as early as 9 weeks' gestation,[223] although the abdominal and cervical types have not been reported in utero (Fig. 37.43). The prognosis is poor, with most infants dying within a few days of birth.[224]

ARRHYTHMIAS

Premature Atrial and Ventricular Contractions

Premature atrial contractions (PACs) and **premature ventricular contractions** (PVCs) are abnormal atrial or ventricular contractions originating from locations other than the sinus node. PACs account for almost 75% and PVCs for 8% of fetal arrhythmias.[40,225] PACs are associated with redundancy of the foraminal flap **(atrial septal aneurysm),** maternal caffeine ingestion, and smoking.[226,227] In 1% to 2% of PACs, a structural cardiac anomaly is present.[37]

PACs may be **conducted** or **nonconducted.** In either case, the **atrial pacemaker** is "reset" so that the next normal atrial

beat is also early. PVCs have an early ventricular contraction that is not preceded by an atrial contraction. The atrial pacemaker is not reset, and the next normal beat occurs when expected, as if the rhythm were regular. Thus PVCs are **compensatory,** allowing the preexisting rhythm to continue, whereas PACs are generally **less than compensatory.** PACs and PVCs may be distinguished by M-mode or spectral Doppler sonography (see Fig. 37.15) by placing the M-mode cursor or spectral Doppler sample volume simultaneously through an atrial and ventricular structure. PACs followed by ventricular contraction are described as **"conducted,"** whereas a PAC that is not followed by a ventricular contraction is **"nonconducted"** or "blocked." These must be differentiated from A-V block, in which a PAC does not occur. Conducted PACs can be distinguished from PVCs by noting that a PAC precedes the early ventricular beat and that, in the majority of cases, PACs are less than compensatory whereas PVCs are generally compensatory.

Premature contractions are benign arrhythmias in most cases. Most disappear in utero or in the early neonatal period. From 1% to 2% of PACs may evolve into sustained tachyarrhythmia.[228]

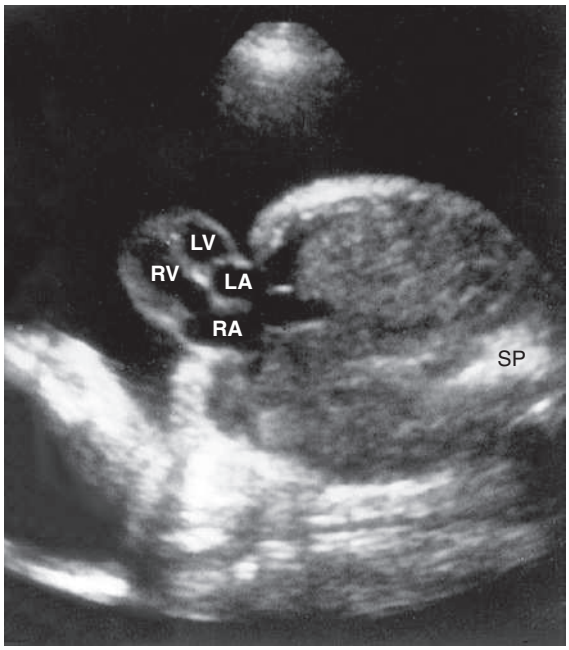

FIG. 37.43 Thoracic Ectopia Cordis. The heart is located outside the thorax. *LA,* Left atrium; *LV,* left ventricle; *RA,* right ventricle; *RV,* right ventricle; *SP,* spine.

Tachycardia

Fetal tachycardia is a heart rate greater than 180 beats/min. **Supraventricular tachycardias** (SVTs) are more common in the fetus than ventricular tachycardias. Of cases of SVT, 5% to 10% are associated with CHD.[229]

SVTs are classified as follows:

- **Paroxysmal supraventricular tachycardia:** atrial rate of 180 to 300 beats/min and a conduction rate of 1:1 (Fig. 37.44).
- **Atrial flutter:** atrial rate of 300 to 400 beats/min, frequently associated with heart block, and a conduction rate of 2:1 to 4:1, yielding a ventricular rate of 60 to 200 beats/min.
- **Atrial fibrillation:** atrial rate of greater than 400 beats/min and an irregular ventricular response at a rate of 120 to 160 beats/min.

Ventricular tachycardia is defined as a rapid heart rate associated with three or more consecutive premature ventricular systoles.

Fetal cardiac rhythm disturbances are usually first suspected on the basis of auscultatory findings. M-mode and pulsed Doppler echocardiography are useful in identifying and characterizing tachycardias by observing the atrial and ventricular rates. The M-mode tracing is obtained through the heart to allow independent assessment of atrial and ventricular wall motion. Further information is obtained from simultaneous recordings of the atrial and ventricular walls or A-V and semilunar valve motion. Spectral Doppler ultrasound evaluation can demonstrate

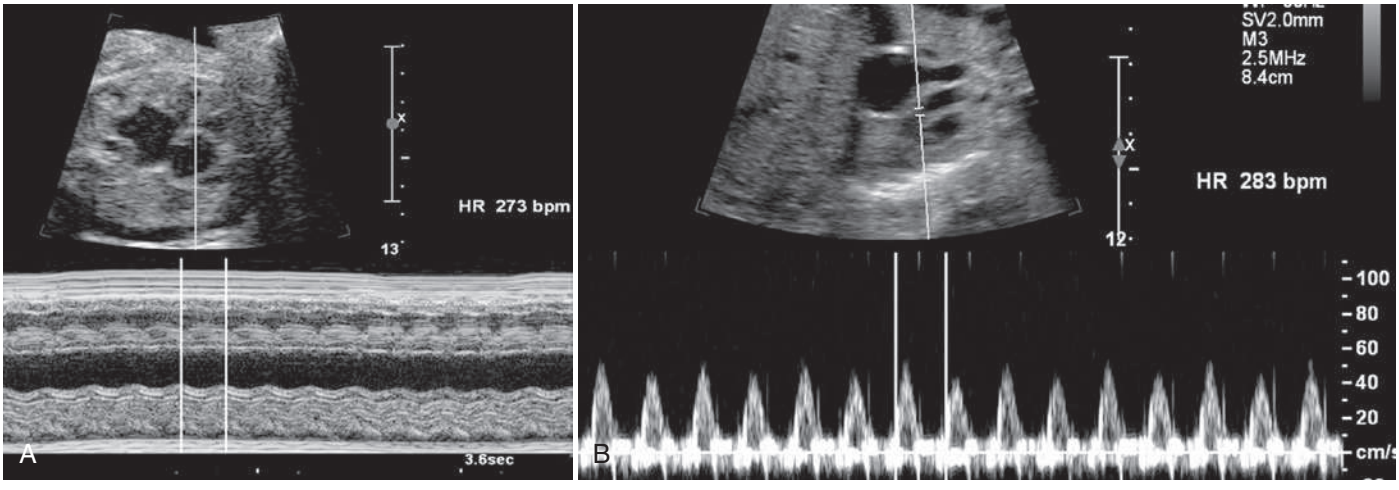

FIG. 37.44 Supraventricular Tachycardia. (A) M-mode tracing through the left ventricle and the right atrium shows a fetal heart rate of 273 beats/min and a 1:1 conduction. **(B)** Spectral Doppler ultrasound through the aortic valve in the same fetus shows a heart rate of 283 beats/min.

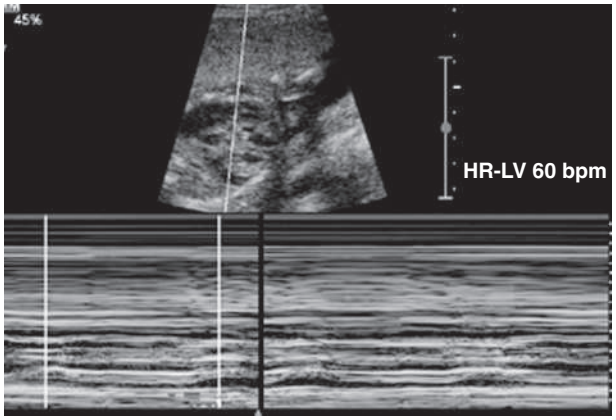

FIG. 37.45 Fetal Bradycardia. M-mode tracing shows ventricular rate of 60 beats/min.

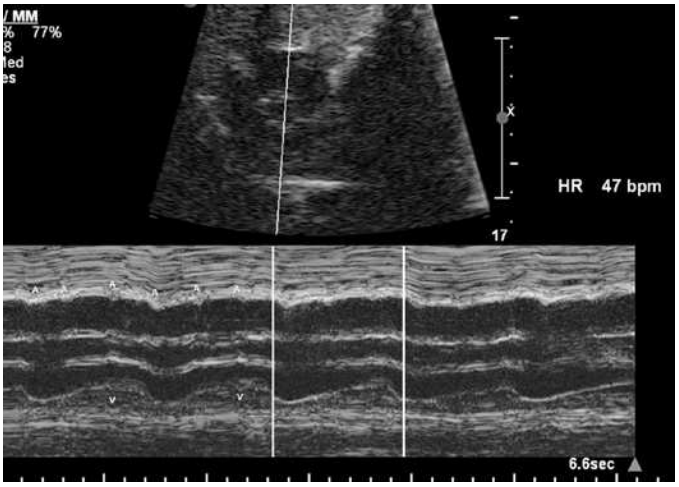

FIG. 37.46 Complete Heart Block. M-mode tracing shows a slow ventricular rate *(V)* of 47 beats/min, with an irregular disassociated atrial rate *(A)*.

decreased flow velocities and cardiac output during SVT.[230] Fetal SVT can lead to fetal cardiovascular compromise, hydrops, and death.

Most fetal tachycardias have a relatively good prognosis and can be treated in utero with various pharmacologic agents. Careful interrogation of the tricuspid valve with color and spectral Doppler ultrasound imaging is warranted in the setting of fetal tachycardia because tricuspid valvular dysfunction with tricuspid regurgitation can be the first indication of imminent congestive failure and hydrops.[231,232] In the presence of hydrops, immediate and aggressive therapy is warranted.[225,228,233-238] Several antiarrhythmic drugs are available to attempt to cardiovert SVTs in utero. Prognosis in the setting of fetal tachyarrhythmia depends on a number of factors, including type and duration of arrhythmia, presence of structural cardiac anomalies, gestational age, and response to intrauterine therapy.[231]

Bradycardia

Fetal bradycardia is a "prolonged" heart rate of 100 beats/min or less (Fig. 37.45). Approximately 5% of fetal arrhythmias are classified as bradycardia.[37] Transient bradycardia can be related to an increase in intrauterine pressure, occasionally secondary to the pressure of an ultrasound transducer or fetal compression of the umbilical cord.[239,240] This is often seen during fetal sonograms and is of no clinical consequence, unless the bradyarrhythmia is sustained.

Sinus bradycardia without fetal hypoxia is rare.[240] If less than 80 beats/min, sinus bradycardia may be associated with fetal asphyxia. A fetal heart rate below 80 beats/min lasting longer than 13 minutes is associated with acidemia-induced cerebral palsy.[241] Heart rates lower than 100 beats/min during the first trimester are associated with an increased risk of fetal demise.[242] When bradycardia is associated with an increased nuchal translucency, risk for CHD is increased, and early transvaginal fetal echocardiography should be considered. Complex CHD has been detected in the first trimester in this clinical setting.[242] The fetus with sustained bradycardia should have careful follow-up and monitoring for signs of cardiac failure. Persistent bradycardia may warrant early delivery. In utero treatment has had limited success.[243]

Congenital Heart Block

Failure of transmission of impulses from the atrium to the ventricles results in **atrioventricular block** (AVB). AVB is classified into the following three types:

- **First-degree block:** a prolonged PR interval results in a conduction delay, but without markedly abnormal rate or rhythm. This may only be appreciated in utero by measuring the PR interval on spectral Doppler tracing.
- **Second-degree block:** with blockage of a single atrial beat **(Mobitz type I)** or with intermittent conduction abnormalities, such that the ventricular rate is a fraction of the atrial rate **(Mobitz type II).**
- **Third-degree** or **complete heart block:** the ventricular and atrial rates are entirely dissociated (Fig. 37.46).

In the normal heart, an electrical impulse originates from the sinoatrial (SA) node and travels to the A-V node and through the **Purkinje system** to the ventricles. AVB results from immaturity or complete absence of the conducting system or from abnormalities at the level of the A-V node. This rare disorder is associated with **maternal collagen vascular disease (systemic lupus erythematosus).**[244] After one affected child, further pregnancies carry a 17% to 30% risk for AVB.[245,246] Serial fetal echocardiograms are useful in the fetus at risk for congenital complete heart block related to maternal lupus. This monitoring allows early detection and treatment of the immune-mediated fetal myocarditis and congenital complete heart block.[247-249]

In the absence of associated structural abnormalities, the prognosis for a fetus with congenital heart block is good. However, at least 40% of fetuses with complete heart block have structural cardiac abnormalities.[37] When associated cardiac anomalies exist, the prognosis is poor. Fetuses with AVB are at risk for heart failure and should be monitored closely. Overall, the vast majority of fetuses with arrhythmias have a good outcome. The incidence of associated structural cardiac disease is as low as 0.3%, similar to that in the general population, and the incidence of significant arrhythmia is only 1.6%.[249]

REFERENCES

1. Hoffman JI, Kaplan S. The incidence of congenital heart disease. J Am Coll Cardiol. 2002;39(12):1890-1900.
2. Tegnander E, Williams W, Johansen OJ, et al. Prenatal detection of heart defects in a non-selected population of 30,149 fetuses—detection rates and outcome. Ultrasound Obstet Gynecol. 2006;27(3):252-265.
3. Young ID, Clarke M. Lethal malformations and perinatal mortality: a 10 year review with comparison of ethnic differences. Br Med J (Clin Res Ed). 1987;295(6590):89-91.
4. Jones KL, Smith DW. Smith's recognizable patterns of human malformation. 6th ed. Philadelphia: Saunders-Elsevier; 2006.
5. Nora JJ. Medical genetics: principles and practice. 4th ed. Philadelphia: Lea & Febiger; 1994.
6. Nyberg DA, Mahony BS, Pretorius D. Diagnostic ultrasound of fetal anomalies: text and atlas. Chicago: Year Book Medical Publishers; 1990.
7. Romero R. Prenatal diagnosis of congenital anomalies. Norwalk, CT: Appleton & Lange; 1988.
8. Nora JJ, Nora AH. Maternal transmission of congenital heart diseases: new recurrence risk figures and the questions of cytoplasmic inheritance and vulnerability to teratogens. Am J Cardiol. 1987;59(5):459-463.
9. Reed KL. Fetal echocardiography. Semin Ultrasound CT MR. 1991; 12(1):2-10.
10. Greenwood RD, Rosenthal A, Parisi L, et al. Extracardiac abnormalities in infants with congenital heart disease. Pediatrics. 1975;55(4):485-492.
11. Berg KA, Boughman JA, Astemborski JA, et al. Implications for prenatal cytogenetic analysis from Baltimore-Washington study of liveborn infants with confirmed congenital heart defects (CHD). Am J Hum Genet. 1986;39:A50.
12. Berg KA, Clark EB, Astemborski JA, Boughman JA. Prenatal detection of cardiovascular malformations by echocardiography: an indication for cytogenetic evaluation. Am J Obstet Gynecol. 1988;159(2):477-481.
13. Wladimiroff JW, Stewart PA, Sachs ES, Niermeijer MF. Prenatal diagnosis and management of congenital heart defect: significance of associated fetal anomalies and prenatal chromosome studies. Am J Med Genet. 1985;21(2): 285-290.
14. Allan LD. Fetal echocardiography. Clin Obstet Gynecol. 1988;31(1): 61-79.
15. Callan NA, Maggio M, Steger S, Kan JS. Fetal echocardiography: indications for referral, prenatal diagnoses, and outcomes. Am J Perinatol. 1991;8(6): 390-394.
16. Bromley B, Estroff JA, Sanders SP, et al. Fetal echocardiography: accuracy and limitations in a population at high and low risk for heart defects. Am J Obstet Gynecol. 1992;166(5):1473-1481.
17. Copel JA, Kleinman CS. The impact of fetal echocardiography on perinatal outcome. Ultrasound Med Biol. 1986;12(4):327-335.
18. Simpson LL. Indications for fetal echocardiography from a tertiary-care obstetric sonography practice. J Clin Ultrasound. 2004;32(3):123-128.
19. Bahtiyar MO, Dulay AT, Weeks BP, et al. Prevalence of congenital heart defects in monochorionic/diamniotic twin gestations: a systematic literature review. J Ultrasound Med. 2007;26(11):1491-1498.
20. Bahtiyar MO, Campbell K, Dulay AT, et al. Is the rate of congenital heart defects detected by fetal echocardiography among pregnancies conceived by in vitro fertilization really increased? A case-historical control study. J Ultrasound Med. 2010;29(6):917-922.
21. Vergani P, Mariani S, Ghidini A, et al. Screening for congenital heart disease with the four-chamber view of the fetal heart. Am J Obstet Gynecol. 1992;167(4 Pt 1):1000-1003.
22. Copel JA, Pilu G, Green J, et al. Fetal echocardiographic screening for congenital heart disease: the importance of the four-chamber view. Am J Obstet Gynecol. 1987;157(3):648-655.
23. Kirk JS, Riggs TW, Comstock CH, et al. The prospective evaluation of fetal cardiac anatomy: a comparison of 4 and 5 chamber views in 5967 patients. Am J Obstet Gynecol. 1993;168:291.
24. Wyllie J, Wren C, Hunter S. Screening for fetal cardiac malformations. Br Heart J. 1994;71(4 Suppl.):20-27.
25. Sharland GK, Allan LD. Screening for congenital heart disease prenatally. Results of a 2 1/2-year study in the South East Thames Region. Br J Obstet Gynaecol. 1992;99(3):220-225.
26. Tegnander E, Eik-Nes SH, Johansen OJ, Linker DT. Prenatal detection of heart defects at the routine fetal examination at 18 weeks in a non-selected population. Ultrasound Obstet Gynecol. 1995;5(6):372-380.
27. Comstock CH. Normal fetal heart axis and position. Obstet Gynecol. 1987;70(2):255-259.
28. AIUM practice guideline for the performance of fetal echocardiography. J Ultrasound Med. 2013;32(6):1067–1082.
29. Yagel S, Weissman A, Rotstein Z, et al. Congenital heart defects: natural course and in utero development. Circulation. 1997;96(2):550-555.
30. Trines J, Hornberger LK. Evolution of heart disease in utero. Pediatr Cardiol. 2004;25(3):287-298.
31. Simpson JM, Sharland GK. Fetal tachycardias: management and outcome of 127 consecutive cases. Heart. 1998;79(6):576-581.
32. Dolkart LA, Reimers FT. Transvaginal fetal echocardiography in early pregnancy: normative data. Am J Obstet Gynecol. 1991;165(3):688-691.
33. Achiron R, Weissman A, Rotstein Z, et al. Transvaginal echocardiographic examination of the fetal heart between 13 and 15 weeks' gestation in a low-risk population. J Ultrasound Med. 1994;13(10):783-789.
34. Weiner Z, Lorber A, Shalev E. Diagnosis of congenital cardiac defects between 11 and 14 weeks' gestation in high-risk patients. J Ultrasound Med. 2002;21(1):23-29.
35. Cartier MS, Davidoff A, Warneke LA, et al. The normal diameter of the fetal aorta and pulmonary artery: echocardiographic evaluation in utero. Am J Roentgenol. 1987;149(5):1003-1007.
36. Yagel S, Cohen SM, Achiron R. Examination of the fetal heart by five short-axis views: a proposed screening method for comprehensive cardiac evaluation. Ultrasound Obstet Gynecol. 2001;17(5):367-369.
37. Reed KL. Fetal arrhythmias: etiology, diagnosis, pathophysiology, and treatment. Semin Perinatol. 1989;13(4):294-304.
38. Gembruch U, Chatterjee MS, Bald R, et al. Color Doppler flow mapping of fetal heart. J Perinat Med. 1991;19(1-2):27-32.
39. Chiba Y, Kanzaki T, Kobayashi H, et al. Evaluation of fetal structural heart disease using color flow mapping. Ultrasound Med Biol. 1990;16(3): 221-229.
40. Benacerraf BR, Sanders SP. Fetal echocardiography. Radiol Clin North Am. 1990;28(1):131-147.
41. Sharland GK, Chita SK, Allan LD. The use of colour Doppler in fetal echocardiography. Int J Cardiol. 1990;28(2):229-236.
42. Yagel S, Cohen SM, Shapiro I, Valsky DV. 3D and 4D ultrasound in fetal cardiac scanning: a new look at the fetal heart. Ultrasound Obstet Gynecol. 2007;29(1):81-95.
43. Acar P, Dulac Y, Taktak A, Abadir S. Real-time three-dimensional fetal echocardiography using matrix probe. Prenat Diagn. 2005;25(5):370-375.
44. Brekke S, Tegnander E, Torp HG, Eik-Nes SH. Tissue Doppler gated (TDOG) dynamic three-dimensional ultrasound imaging of the fetal heart. Ultrasound Obstet Gynecol. 2004;24(2):192-198.
45. Donofrio MT, Moon-Grady AJ, Hornberger LK, et al. Diagnosis and treatment of fetal cardiac disease: a scientific statement from the American Heart Association. Circulation. 2014;129(21):2183-2242.
46. Hoffman JI, Christianson R. Congenital heart disease in a cohort of 19,502 births with long-term follow-up. Am J Cardiol. 1978;42(4): 641-647.
47. Allan LD, Crawford DC, Anderson RH, Tynan M. Spectrum of congenital heart disease detected echocardiographically in prenatal life. Br Heart J. 1985;54(5):523-526.
48. Keith JD. Atrial septal defect: ostium secundum, ostium primum, and atrioventricularis communis (common AV canal). In: Keith JD, Rowe RD, Vlad P, editors. Heart disease in infancy and childhood. 3rd ed. New York: Macmillan; 1978. p. 330-404.
49. Samanek M. Children with congenital heart disease: probability of natural survival. Pediatr Cardiol. 1992;13(3):152-158.
50. Fyler DC. Atrial septal defect secundum. In: Fyler DC, editor. Nadas' pediatric cardiology. Philadelphia: Hanley and Belfus; 1992. p. 513-524.

51. Feldt RH, Avasthey P, Yoshimasu F, et al. Incidence of congenital heart disease in children born to residents of Olmsted County, Minnesota, 1950-1969. Mayo Clin Proc. 1971;46(12):794-799.
52. Crelin ES. Anatomy of the newborn; an atlas. Philadelphia: Lea & Febiger; 1969.
53. Kachalia P, Bowie JD, Adams DB, Carroll BA. In utero sonographic appearance of the atrial septum primum and septum secundum. J Ultrasound Med. 1991;10(8):423-426.
54. Wilson AD, Rao PS, Aeschlimann S. Normal fetal foramen flap and transatrial Doppler velocity pattern. J Am Soc Echocardiogr. 1990;3(6):491-494.
55. Benacerraf BR, Pober BR, Sanders SP. Accuracy of fetal echocardiography. Radiology. 1987;165(3):847-849.
56. DeVore GR, Horenstein J, Siassi B, Platt LD. Fetal echocardiography. VII. Doppler color flow mapping: a new technique for the diagnosis of congenital heart disease. Am J Obstet Gynecol. 1987;156(5):1054-1064.
57. Cockerham JT, Martin TC, Gutierrez FR, et al. Spontaneous closure of secundum atrial septal defect in infants and young children. Am J Cardiol. 1983;52(10):1267-1271.
58. Steele PM, Fuster V, Cohen M, et al. Isolated atrial septal defect with pulmonary vascular obstructive disease—long-term follow-up and prediction of outcome after surgical correction. Circulation. 1987;76(5):1037-1042.
59. Ferencz C, Rubin JD, McCarter RJ, et al. Cardiac and noncardiac malformations: observations in a population-based study. Teratology. 1987;35(3):367-378.
60. Goor DA, Lillehei CW. Congenital malformations of the heart: embryology, anatomy, and operative considerations. New York: Grune & Stratton; 1975.
61. Grahm TP, Bender HW, Spach M. Ventricular septal defects. In: Moss AJ, Adams FH, Emmanouilides GC, editors. Heart disease in infancy, childhood, and adolescence. 2nd ed. Baltimore: Williams & Wilkins; 1977.
62. Allan LD, Crawford DC, Anderson RH, Tynan MJ. Echocardiographic and anatomical correlations in fetal congenital heart disease. Br Heart J. 1984;52(5):542-548.
63. Allan LD, Tynan M, Campbell S, Anderson RH. Identification of congenital cardiac malformations by echocardiography in midtrimester fetus. Br Heart J. 1981;46(4):358-362.
64. Parness IA, Yeager SB, Sanders SP, et al. Echocardiographic diagnosis of fetal heart defects in mid trimester. Arch Dis Child. 1988;63(10 Spec No):1137-1145.
65. Yagel S, Sherer D, Hurwitz A. Significance of ultrasonic prenatal diagnosis of ventricular septal defect. J Clin Ultrasound. 1985;13(8):588-590.
66. Brown DL, Emerson DS, Cartier MS, et al. Congenital cardiac anomalies: prenatal sonographic diagnosis. Am J Roentgenol. 1989;153(1):109-114.
67. Sutherland GR, Smyllie JH, Ogilvie BC, Keeton BR. Colour flow imaging in the diagnosis of multiple ventricular septal defects. Br Heart J. 1989;62(1):43-49.
68. Garne E. Atrial and ventricular septal defects—epidemiology and spontaneous closure. J Matern Fetal Neonatal Med. 2006;19(5):271-276.
69. Hoffman JI. Natural history of congenital heart disease. Problems in its assessment with special reference to ventricular septal defects. Circulation. 1968;37(1):97-125.
70. Hoffman JI, Rudolph AM. The natural history of isolated ventricular septal defect with special reference to selection of patients for surgery. Adv Pediatr. 1970;17:57-79.
71. Hoffman JI, Rudolph AM. The natural history of ventricular septal defects in infancy. Am J Cardiol. 1965;16(5):634-653.
72. Crawford DC, Chita SK, Allan LD. Prenatal detection of congenital heart disease: factors affecting obstetric management and survival. Am J Obstet Gynecol. 1988;159(2):352-356.
73. Machado MV, Crawford DC, Anderson RH, Allan LD. Atrioventricular septal defect in prenatal life. Br Heart J. 1988;59(3):352-355.
74. Carvalho JS, Rigby ML, Shinebourne EA, Anderson RH. Cross sectional echocardiography for recognition of ventricular topology in atrioventricular septal defect. Br Heart J. 1989;61(3):285-288.
75. Freedom RM, Culham JAG, Moes CAF. Angiocardiography of congenital heart disease. New York: Macmillan; 1984.
76. Becker AE, Anderson RH. Atrioventricular septal defects: What's in a name? J Thorac Cardiovasc Surg. 1982;83(3):461-469.
77. Fontana RS, Edwards JE. Congenital cardiac disease. Philadelphia: Saunders; 1962.
78. Shenker L, Reed KL, Marx GR, et al. Fetal cardiac Doppler flow studies in prenatal diagnosis of heart disease. Am J Obstet Gynecol. 1988;158(6 Pt 1):1267-1273.
79. Gembruch U, Knopfle G, Chatterjee M, et al. Prenatal diagnosis of atrioventricular canal malformations with up-to-date echocardiographic technology: report of 14 cases. Am Heart J. 1991;121(5):1489-1497.
80. Rasiah SV, Ewer AK, Miller P, et al. Outcome following prenatal diagnosis of complete atrioventricular septal defect. Prenat Diagn. 2008;28(2):95-101.
81. Allan LD, Crawford DC, Sheridan R, Chapman MG. Aetiology of non-immune hydrops: the value of echocardiography. Br J Obstet Gynaecol. 1986;93(3):223-225.
82. Bader RS, Punn R, Silverman NH. Evaluation of risk factors for prediction of outcome in fetal spectrum of atrioventricular septal defects. Congenit Heart Dis. 2014;9(4):286-293.
83. Bakhtiary F, Takacs J, Cho MY, et al. Long-term results after repair of complete atrioventricular septal defect with two-patch technique. Ann Thorac Surg. 2010;89(4):1239-1243.
84. Genton E, Blount Jr SG. The spectrum of Ebstein's anomaly. Am Heart J. 1967;73(3):395-425.
85. Lev M, Liberthson RR, Joseph RH, et al. The pathologic anatomy of Ebstein's disease. Arch Pathol. 1970;90(4):334-343.
86. Roberson DA, Silverman NH. Ebstein's anomaly: echocardiographic and clinical features in the fetus and neonate. J Am Coll Cardiol. 1989;14(5):1300-1307.
87. Zuberbuhler JR, Becker AE, Anderson RH, Lenox CC. Ebstein's malformation and the embryological development of the tricuspid valve. With a note on the nature of "clefts" in the atrioventricular valves. Pediatr Cardiol. 1984;5(4):289-295.
88. Anderson KR, Zuberbuhler JR, Anderson RH, et al. Morphologic spectrum of Ebstein's anomaly of the heart: a review. Mayo Clin Proc. 1979;54(3):174-180.
89. Stewart PA, Wladimiroff JW, Reuss A, Sachs ES. Fetal echocardiography: a review of six years experience. Fetal Ther. 1987;2(4):222-231.
90. Sharland GK, Chita SK, Allan LD. Tricuspid valve dysplasia or displacement in intrauterine life. J Am Coll Cardiol. 1991;17(4):944-949.
91. Nora JJ, Nora AH, Toews WH. Letter: Lithium, Ebstein's anomaly, and other congenital heart defects. Lancet. 1974;2(7880):594-595.
92. Nora JJ, Nora AH. The evolution of specific genetic and environmental counseling in congenital heart diseases. Circulation. 1978;57(2):205-213.
93. Schou M, Goldfield MD, Weinstein MR, Villeneuve A. Lithium and pregnancy. I. Report from the Register of Lithium Babies. Br Med J. 1973;2(5859):135-136.
94. Weinstein MR, Goldfield M. Cardiovascular malformations with lithium use during pregnancy. Am J Psychiatry. 1975;132(5):529-531.
95. Park JM, Sridaromont S, Ledbetter EO, Terry WM. Ebstein's anomaly of the tricuspid valve associated with prenatal exposure to lithium carbonate. Am J Dis Child. 1980;134(7):703-704.
96. Kallen B, Tandberg A. Lithium and pregnancy. A cohort study on manic-depressive women. Acta Psychiatr Scand. 1983;68(2):134-139.
97. Jacobson SJ, Jones K, Johnson K, et al. Prospective multicentre study of pregnancy outcome after lithium exposure during first trimester. Lancet. 1992;339(8792):530-533.
98. Anderson RH, Silverman NH, Zuberbuhler JR. Congenitally unguarded tricuspid orifice: its differentiation from Ebstein's malformation in association with pulmonary atresia and intact ventricular septum. Pediatr Cardiol. 1990;11(2):86-90.
99. Oberhoffer R, Cook AC, Lang D, et al. Correlation between echocardiographic and morphological investigations of lesions of the tricuspid valve diagnosed during fetal life. Br Heart J. 1992;68(6):580-585.
100. Handler JB, Berger TJ, Miller RH, et al. Partial atrioventricular canal in association with Ebstein's anomaly. Echocardiographic diagnosis and surgical correction. Chest. 1981;80(4):515-517.

101. Fink BW. Congenital heart disease: a deductive approach to its diagnosis. 2nd ed. Chicago: Year Book Medical Publishers; 1985.
102. Copel JA, Cullen M, Green JJ, et al. The frequency of aneuploidy in prenatally diagnosed congenital heart disease: an indication for fetal karyotyping. Am J Obstet Gynecol. 1988;158(2):409-413.
103. Hornberger LK, Sahn DJ, Kleinman CS, et al. Tricuspid valve disease with significant tricuspid insufficiency in the fetus: diagnosis and outcome. J Am Coll Cardiol. 1991;17(1):167-173.
104. Gembruch U, Hansmann M, Redel DA, Bald R. Fetal two-dimensional Doppler echocardiography (colour flow mapping) and its place in prenatal diagnosis. Prenat Diagn. 1989;9(8):535-547.
105. Freud LR, Escobar-Diaz MC, Kalish BT, et al. Outcomes and predictors of perinatal mortality in fetuses with Ebstein anomaly or tricuspid valve dysplasia in the current era: a multicenter study. Circulation. 2015;132(6): 481-489.
106. Boston US, Dearani JA, O'Leary PW, et al. Tricuspid valve repair for Ebstein's anomaly in young children: a 30-year experience. Ann Thorac Surg. 2006;81(2):690-695.
107. Brown ML, Dearani JA, Danielson GK, et al. The outcomes of operations for 539 patients with Ebstein anomaly. J Thorac Cardiovasc Surg. 2008;135(5):1120-1136, 36.e1-e7.
108. Palmen M, de Jong PL, Klieverik LM, et al. Long-term follow-up after repair of Ebstein's anomaly. Eur J Cardiothorac Surg. 2008;34(1):48-54.
109. Paranon S, Acar P. Ebstein's anomaly of the tricuspid valve: from fetus to adult: congenital heart disease. Heart. 2008;94(2):237-243.
110. Grundy H, Burlbaw J, Gowdamarajan R, et al. Antenatal detection of hypoplastic right ventricle with fetal M-mode echocardiography. A report of two cases. J Reprod Med. 1987;32(4):301-304.
111. de Leval M, Bull C, Stark J, et al. Pulmonary atresia and intact ventricular septum: surgical management based on a revised classification. Circulation. 1982;66(2):272-280.
112. Schaffer RM, Corio FJ. Sonographic diagnosis of hypoplastic left heart syndrome in utero. J Diag Med Sonogr. 1988;6:319-320.
113. Yagel S, Mandelberg A, Hurwitz A, Jlaser Y. Prenatal diagnosis of hypoplastic left ventricle. Am J Perinatol. 1986;3(1):6-8.
114. Hawkins JA, Doty DB. Aortic atresia: morphologic characteristics affecting survival and operative palliation. J Thorac Cardiovasc Surg. 1984; 88(4):620-626.
115. Saied A, Folger Jr GM. Hypoplastic left heart syndrome. Clinicopathologic and hemodynamic correlation. Am J Cardiol. 1972;29(2):190-198.
116. Doty DB. Aortic atresia. J Thorac Cardiovasc Surg. 1980;79(3):462-463.
117. Feinstein JA, Benson DW, Dubin AM, et al. Hypoplastic left heart syndrome: current considerations and expectations. J Am Coll Cardiol. 2012;59 (1 Suppl.):S1-S42.
118. Satomi G, Yasukochi S, Shimizu T, et al. Has fetal echocardiography improved the prognosis of congenital heart disease? Comparison of patients with hypoplastic left heart syndrome with and without prenatal diagnosis. Pediatr Int. 1999;41(6):728-732.
119. Mahle WT, Clancy RR, McGaurn SP, et al. Impact of prenatal diagnosis on survival and early neurologic morbidity in neonates with the hypoplastic left heart syndrome. Pediatrics. 2001;107(6):1277-1282.
120. Tworetzky W, McElhinney DB, Reddy VM, et al. Improved surgical outcome after fetal diagnosis of hypoplastic left heart syndrome. Circulation. 2001;103(9):1269-1273.
121. Mahle WT, Wernovsky G. Neurodevelopmental outcomes in hypoplastic left heart syndrome. Semin Thorac Cardiovasc Surg Pediatr Card Surg Annu. 2004;7:39-47.
122. Jenkins PC, Chinnock RE, Jenkins KJ, et al. Decreased exercise performance with age in children with hypoplastic left heart syndrome. J Pediatr. 2008;152(4):507-512.
123. Sistino JJ, Bonilha HS. Improvements in survival and neurodevelopmental outcomes in surgical treatment of hypoplastic left heart syndrome: a meta-analytic review. J Extra Corpor Technol. 2012;44(4):216-223.
124. Becker AE, Anderson RH. Pathology of congenital heart disease. Boston: Butterworths; 1981.
125. Moodie DS, Ritter DG, Tajik AH, et al. Long-term follow-up after palliative operation for univentricular heart. Am J Cardiol. 1984;53(11):1648-1651.
126. Moodie DS, Ritter DG, Tajik AJ, O'Fallon WM. Long-term follow-up in the unoperated univentricular heart. Am J Cardiol. 1984;53(8): 1124-1128.
127. Hallermann FJ, Davis GD, Ritter DG, Kincaid OW. Roentgenographic features of common ventricle. Radiology. 1966;87(3):409-423.
128. McKay R, Pacifico AD, Blackstone EH, et al. Septation of the univentricular heart with left anterior subaortic outlet chamber. J Thorac Cardiovasc Surg. 1982;84(1):77-87.
129. Alsoufi B, Gillespie S, Kogon B, et al. Results of palliation with an initial modified Blalock-Taussig shunt in neonates with single ventricle anomalies associated with restrictive pulmonary blood flow. Ann Thorac Surg. 2015;99(5):1639-1646.
130. Alsoufi B, Manlhiot C, Awan A, et al. Current outcomes of the Glenn bidirectional cavopulmonary connection for single ventricle palliation. Eur J Cardiothorac Surg. 2012;42(1):42-48.
131. Poon LC, Huggon IC, Zidere V, Allan LD. Tetralogy of Fallot in the fetus in the current era. Ultrasound Obstet Gynecol. 2007;29(6):625-627.
132. Netter F. The Ciba Collection of medical illustrations. V. Heart. New Jersey: CIBA; 1978.
133. Lev M, Rimoldi JA, Rowlatt UF. The quantitative anatomy of cyanotic tetralogy of Fallot. Circulation. 1964;30:531-538.
134. DeVore GR, Siassi B, Platt LD. Fetal echocardiography. VIII. Aortic root dilatation—a marker for tetralogy of Fallot. Am J Obstet Gynecol. 1988;159(1):129-136.
135. Anderson CF, McCurdy Jr CM, McNamara MF, Reed KL. Case of the day. 8. Diagnosis: color Doppler aided diagnosis of tetralogy of Fallot. J Ultrasound Med. 1994;13(4):341-342.
136. Egbe AC, Uppu SC, Mittnacht AJ, et al. Primary tetralogy of Fallot repair: predictors of intensive care unit morbidity. Asian Cardiovasc Thorac Ann. 2014;22(7):794-799.
137. Gibbs JL, Monro JL, Cunningham D, Rickards A. Survival after surgery or therapeutic catheterisation for congenital heart disease in children in the United Kingdom: analysis of the central cardiac audit database for 2000-1. BMJ. 2004;328(7440):611.
138. Murphy JG, Gersh BJ, Mair DD, et al. Long-term outcome in patients undergoing surgical repair of tetralogy of Fallot. N Engl J Med. 1993;329(9):593-599.
139. Kleinman CS, Donnerstein RL, DeVore GR, et al. Fetal echocardiography for evaluation of in utero congestive heart failure. N Engl J Med. 1982; 306(10):568-575.
140. Lakier JB, Stanger P, Heymann MA, et al. Tetralogy of Fallot with absent pulmonary valve. Natural history and hemodynamic considerations. Circulation. 1974;50(1):167-175.
141. Fyler DC. Report of the New England Regional Infant Cardiac Program. Pediatrics. 1980;65(2 Pt 2):375-461.
142. Collett RW, Edwards JE. Persistent truncus arteriosus; a classification according to anatomic types. Surg Clin North Am. 1949;29(4): 1245-1270.
143. Rajasinghe HA, McElhinney DB, Reddy VM, et al. Long-term follow-up of truncus arteriosus repaired in infancy: a twenty-year experience. J Thorac Cardiovasc Surg. 1997;113(5):869-878.
144. O'Byrne ML, Mercer-Rosa L, Zhao H, et al. Morbidity in children and adolescents after surgical correction of truncus arteriosus communis. Am Heart J. 2013;166(3):512-518.
145. Kirklin JW, Pacifico AD, Blackstone EH, et al. Current risks and protocols for operations for double-outlet right ventricle. Derivation from an 18 year experience. J Thorac Cardiovasc Surg. 1986;92(5):913-930.
146. Stewart PA, Wladimiroff JW, Becker AE. Early prenatal detection of double outlet right ventricle by echocardiography. Br Heart J. 1985;54(3): 340-342.
147. Kim N, Friedberg MK, Silverman NH. Diagnosis and prognosis of fetuses with double outlet right ventricle. Prenat Diagn. 2006;26(8): 740-745.
148. Li S, Ma K, Hu S, et al. Surgical outcomes of 380 patients with double outlet right ventricle who underwent biventricular repair. J Thorac Cardiovasc Surg. 2014;148(3):817-824.

149. Trusler GA, Castaneda AR, Rosenthal A, et al. Current results of management in transposition of the great arteries, with special emphasis on patients with associated ventricular septal defect. J Am Coll Cardiol. 1987;10(5):1061-1071.
150. Anderson BR, Ciarleglio AJ, Hayes DA, et al. Earlier arterial switch operation improves outcomes and reduces costs for neonates with transposition of the great arteries. J Am Coll Cardiol. 2014;63(5):481-487.
151. Allwork SP, Bentall HH, Becker AE, et al. Congenitally corrected transposition of the great arteries: morphologic study of 32 cases. Am J Cardiol. 1976;38(7):910-923.
152. Rutledge JM, Nihill MR, Fraser CD, et al. Outcome of 121 patients with congenitally corrected transposition of the great arteries. Pediatr Cardiol. 2002;23(2):137-145.
153. DiSessa TG, Emerson DS, Felker RE, et al. Anomalous systemic and pulmonary venous pathways diagnosed in utero by ultrasound. J Ultrasound Med. 1990;9(6):311-317.
154. Ferencz C, Rubin JD, McCarter RJ, et al. Congenital heart disease: prevalence at livebirth. The Baltimore-Washington Infant Study. Am J Epidemiol. 1985;121(1):31-36.
155. Allan LD, Sharland GK. The echocardiographic diagnosis of totally anomalous pulmonary venous connection in the fetus. Heart. 2001;85(4):433-437.
156. Carter RE, Capriles M, Noe Y. Total anomalous pulmonary venous drainage. A clinical and anatomical study of 75 children. Br Heart J. 1969;31(1):45-51.
157. Patel CR, Lane JR, Spector ML, et al. Totally anomalous pulmonary venous connection and complex congenital heart disease: prenatal echocardiographic diagnosis and prognosis. J Ultrasound Med. 2005;24(9):1191-1198.
158. Hashmi A, Abu-Sulaiman R, McCrindle BW, et al. Management and outcomes of right atrial isomerism: a 26-year experience. J Am Coll Cardiol. 1998;31(5):1120-1126.
159. Valsangiacomo ER, Hornberger LK, Barrea C, et al. Partial and total anomalous pulmonary venous connection in the fetus: two-dimensional and Doppler echocardiographic findings. Ultrasound Obstet Gynecol. 2003;22(3):257-263.
160. Padalino MA, Cavalli G, De Franceschi M, et al. Surgical outcomes of total anomalous pulmonary venous connection repair: a 22-year experience. J Card Surg. 2014;29(5):678-685.
161. Allan LD, Crawford DC, Tynan M. Evolution of coarctation of the aorta in intrauterine life. Br Heart J. 1984;52(4):471-473.
162. Rosenberg H. Coarctation of the aorta: morphology and pathogenesis considerations. In: Rosenberg HS, Bolande RP, editors. Perspectives in pediatric pathology, vol. I. Chicago: Year Book Medical Publishers; 1973.
163. Bruins C. Twelfth Edgar Mannheimer lecture. Competition between aortic isthmus and ductus arteriosus; reciprocal influence of structure and flow. Eur J Cardiol. 1978;8(1):87-97.
164. Hutchins GM. Coarctation of the aorta explained as a branch-point of the ductus arteriosus. Am J Pathol. 1971;63(2):203-214.
165. Benacerraf BR, Saltzman DH, Sanders SP. Sonographic sign suggesting the prenatal diagnosis of coarctation of the aorta. J Ultrasound Med. 1989;8(2):65-69.
166. Hornberger LK, Sahn DJ, Kleinman CS, et al. Antenatal diagnosis of coarctation of the aorta: a multicenter experience. J Am Coll Cardiol. 1994;23(2):417-423.
167. Sahn DJ, Lange LW, Allen HD, et al. Quantitative real-time cross-sectional echocardiography in the developing normal human fetus and newborn. Circulation. 1980;62(3):588-597.
168. Head CE, Jowett VC, Sharland GK, Simpson JM. Timing of presentation and postnatal outcome of infants suspected of having coarctation of the aorta during fetal life. Heart. 2005;91(8):1070-1074.
169. Hesslein PS, Gutgesell HP, McNamara DG. Prognosis of symptomatic coarctation of the aorta in infancy. Am J Cardiol. 1983;51(2):299-303.
170. Moore JW, Vincent RN, Beekman 3rd RH, et al. Procedural results and safety of common interventional procedures in congenital heart disease: initial report from the National Cardiovascular Data Registry. J Am Coll Cardiol. 2014;64(23):2439-2451.
171. Clark CE, Henry WL, Epstein SE. Familial prevalence and genetic transmission of idiopathic hypertrophic subaortic stenosis. N Engl J Med. 1973;289(14):709-714.
172. Barrea C, Alkazaleh F, Ryan G, et al. Prenatal cardiovascular manifestations in the twin-to-twin transfusion syndrome recipients and the impact of therapeutic amnioreduction. Am J Obstet Gynecol. 2005;192(3):892-902.
173. Campbell M. The natural history of congenital aortic stenosis. Br Heart J. 1968;30(4):514-526.
174. Messina LM, Turley K, Stanger P, et al. Successful aortic valvotomy for severe congenital valvular aortic stenosis in the newborn infant. J Thorac Cardiovasc Surg. 1984;88(1):92-96.
175. Jones M, Barnhart GR, Morrow AG. Late results after operations for left ventricular outflow tract obstruction. Am J Cardiol. 1982;50(3):569-579.
176. Freud LR, McElhinney DB, Marshall AC, et al. Fetal aortic valvuloplasty for evolving hypoplastic left heart syndrome: postnatal outcomes of the first 100 patients. Circulation. 2014;130(8):638-645.
177. Stagnati V, Chalouhi GE, Essaoui M, et al. Pulmonary stenosis in complicated monochorionic twin pregnancies: prevalence, management and outcome. Prenat Diagn. 2015;35(11):1085-1092.
178. Merrill WH, Shuman TA, Graham Jr TP, et al. Surgical intervention in neonates with critical pulmonary stenosis. Ann Surg. 1987;205(6):712-718.
179. Marantz PM, Huhta JC, Mullins CE, et al. Results of balloon valvuloplasty in typical and dysplastic pulmonary valve stenosis: Doppler echocardiographic follow-up. J Am Coll Cardiol. 1988;12(2):476-479.
180. Galindo A, Gutierrez-Larraya F, Velasco JM, de la Fuente P. Pulmonary balloon valvuloplasty in a fetus with critical pulmonary stenosis/atresia with intact ventricular septum and heart failure. Fetal Diagn Ther. 2006;21(1):100-104.
181. Niikawa N, Kohsaka S, Mizumoto M, et al. Familial clustering of situs inversus totalis, and asplenia and polysplenia syndromes. Am J Med Genet. 1983;16(1):43-47.
182. Loomba RS, Willes RJ, Kovach JR, Anderson RH. Chronic arrhythmias in the setting of heterotaxy: differences between right and left isomerism. Congenit Heart Dis. 2016;11(1):7-18.
183. Rose V, Izukawa T, Moes CA. Syndromes of asplenia and polysplenia. A review of cardiac and non-cardiac malformations in 60 cases with special reference to diagnosis and prognosis. Br Heart J. 1975;37(8):840-852.
184. Peoples WM, Moller JH, Edwards JE. Polysplenia: a review of 146 cases. Pediatr Cardiol. 1983;4(2):129-137.
185. Zlotogora J, Elian E. Asplenia and polysplenia syndromes with abnormalities of lateralisation in a sibship. J Med Genet. 1981;18(4):301-302.
186. Stewart PA, Becker AE, Wladimiroff JW, Essed CE. Left atrial isomerism associated with asplenia: prenatal echocardiographic detection of complex congenital cardiac malformations. J Am Coll Cardiol. 1984;4(5):1015-1020.
187. Garcia OL, Metha AV, Pickoff AS, et al. Left isomerism and complete atrioventricular block: a report of six cases. Am J Cardiol. 1981;48(6):1103-1107.
188. Berg C, Geipel A, Smrcek J, et al. Prenatal diagnosis of cardiosplenic syndromes: a 10-year experience. Ultrasound Obstet Gynecol. 2003;22(5):451-459.
189. Schmidt W, Yarkoni S, Jeanty P, et al. Sonographic measurements of the fetal spleen: clinical implications. J Ultrasound Med. 1985;4(12):667-672.
190. de Araujo LM, Silverman NH, Filly RA, et al. Prenatal detection of left atrial isomerism by ultrasound. J Ultrasound Med. 1987;6(11):667-670.
191. McAllister Jr HA. Primary tumors of the heart and pericardium. Pathol Annu. 1979;14(Pt 2):325-355.
192. Dennis MA, Appareti K, Manco-Johnson ML, et al. The echocardiographic diagnosis of multiple fetal cardiac tumors. J Ultrasound Med. 1985;4(6):327-329.
193. Smythe JF, Dyck JD, Smallhorn JF, Freedom RM. Natural history of cardiac rhabdomyoma in infancy and childhood. Am J Cardiol. 1990;66(17):1247-1249.
194. Simcha A, Wells BG, Tynan MJ, Waterston DJ. Primary cardiac tumours in childhood. Arch Dis Child. 1971;46(248):508-514.
195. Crawford DC, Garrett C, Tynan M, et al. Cardiac rhabdomyomata as a marker for the antenatal detection of tuberous sclerosis. J Med Genet. 1983;20(4):303-304.
196. Groves AM, Fagg NL, Cook AC, Allan LD. Cardiac tumours in intrauterine life. Arch Dis Child. 1992;67(10 Spec No):1189-1192.

197. Bender BL, Yunis EJ. The pathology of tuberous sclerosis. Pathol Annu. 1982;17(Pt 1):339-382.
198. Journel H, Roussey M, Plais MH, et al. Prenatal diagnosis of familial tuberous sclerosis following detection of cardiac rhabdomyoma by ultrasound. Prenat Diagn. 1986;6(4):283-289.
199. DeVore GR, Hakim S, Kleinman CS, Hobbins JC. The in utero diagnosis of an interventricular septal cardiac rhabdomyoma by means of real-time-directed, M-mode echocardiography. Am J Obstet Gynecol. 1982;143(8):967-969.
200. Chao AS, Chao A, Wang TH, et al. Outcome of antenatally diagnosed cardiac rhabdomyoma: case series and a meta-analysis. Ultrasound Obstet Gynecol. 2008;31(3):289-295.
201. Holley DG, Martin GR, Brenner JI, et al. Diagnosis and management of fetal cardiac tumors: a multicenter experience and review of published reports. J Am Coll Cardiol. 1995;26(2):516-520.
202. Gava G, Buoso G, Beltrame GL, et al. Cardiac rhabdomyoma as a marker for the prenatal detection of tuberous sclerosis. Case report. Br J Obstet Gynaecol. 1990;97(12):1154-1157.
203. Wacker-Gussmann A, Strasburger JF, Cuneo BF, et al. Fetal arrhythmias associated with cardiac rhabdomyomas. Heart Rhythm. 2014;11(4):677-683.
204. Uzun O, Wilson DG, Vujanic GM, et al. Cardiac tumours in children. Orphanet J Rare Dis. 2007;2:11.
205. Pipitone S, Mongiovi M, Grillo R, et al. Cardiac rhabdomyoma in intrauterine life: clinical features and natural history. A case series and review of published reports. Ital Heart J. 2002;3(1):48-52.
206. Levy DW, Mintz MC. The left ventricular echogenic focus: a normal finding. Am J Roentgenol. 1988;150(1):85-86.
207. Petrikovsky BM, Challenger M, Wyse LJ. Natural history of echogenic foci within ventricles of the fetal heart. Ultrasound Obstet Gynecol. 1995;5(2):92-94.
208. Arda S, Sayin NC, Varol FG, Sut N. Isolated fetal intracardiac hyperechogenic focus associated with neonatal outcome and triple test results. Arch Gynecol Obstet. 2007;276(5):481-485.
209. Ohlow MA, von Korn H, Lauer B. Characteristics and outcome of congenital left ventricular aneurysm and diverticulum: analysis of 809 cases published since 1816. Int J Cardiol. 2015;185:34-45.
210. Pedra SR, Smallhorn JF, Ryan G, et al. Fetal cardiomyopathies: pathogenic mechanisms, hemodynamic findings, and clinical outcome. Circulation. 2002;106(5):585-591.
211. Yinon Y, Yagel S, Hegesh J, et al. Fetal cardiomyopathy—in utero evaluation and clinical significance. Prenat Diagn. 2007;27(1):23-28.
212. Drose JA, Dennis MA, Thickman D. Infection in utero: US findings in 19 cases. Radiology. 1991;178(2):369-374.
213. Schryer MJ, Karnauchow PN. Endocardial fibroelastosis; etiologic and pathogenetic considerations in children. Am Heart J. 1974;88(5):557-565.
214. Griffin LD, Kearney D, Ni J, et al. Analysis of formalin-fixed and frozen myocardial autopsy samples for viral genome in childhood myocarditis and dilated cardiomyopathy with endocardial fibroelastosis using polymerase chain reaction (PCR). Cardiovasc Pathol. 1995;4(1):3-11.
215. Sheehan PQ, Rowland TW, Shah BL, et al. Maternal diabetic control and hypertrophic cardiomyopathy in infants of diabetic mothers. Clin Pediatr (Phila). 1986;25(5):266-271.
216. Lendrum B, Pildes RS, Serratto M, et al. The spectrum of myocardial abnormality in infants of diabetic mothers. Pediatr Cardiol. 1979;1:172.
217. Gutgesell HP, Speer ME, Rosenberg HS. Characterization of the cardiomyopathy in infants of diabetic mothers. Circulation. 1980;61(2):441-450.
218. Halliday HL. Hypertrophic cardiomyopathy in infants of poorly-controlled diabetic mothers. Arch Dis Child. 1981;56(4):258-263.
219. Veille JC, Hanson R, Sivakoff M, et al. Fetal cardiac size in normal, intrauterine growth retarded, and diabetic pregnancies. Am J Perinatol. 1993;10(4):275-279.
220. Gonzalez AB, Young L, Doll JA, et al. Elevated neonatal insulin-like growth factor I is associated with fetal hypertrophic cardiomyopathy in diabetic women. Am J Obstet Gynecol. 2014;211(3):290.e1-290.e7.
221. Kanagasuntheram R, Verzin JA. Ectopia cordis in man. Thorax. 1962;17:159-167.
222. Cantrell JR, Haller JA, Ravitch MM. A syndrome of congenital defects involving the abdominal wall, sternum, diaphragm, pericardium, and heart. Surg Gynecol Obstet. 1958;107(5):602-614.
223. Chang Y, Yang MJ, Wang PH, Chen CY. Three-dimensional HDlive image of ectopia cordis in a twin fetus at 9 gestational weeks. Taiwan J Obstet Gynecol. 2015;54(4):463-464.
224. Ghidini A, Sirtori M, Romero R, Hobbins JC. Prenatal diagnosis of pentalogy of Cantrell. J Ultrasound Med. 1988;7(10):567-572.
225. Lingman G, Lundstrom NR, Marsal K, Ohrlander S. Fetal cardiac arrhythmia. Clinical outcome in 113 cases. Acta Obstet Gynecol Scand. 1986;65(3):263-267.
226. Stewart PA, Wladimiroff JW. Fetal atrial arrhythmias associated with redundancy/aneurysm of the foramen ovale. J Clin Ultrasound. 1988;16(9):643-650.
227. Rice MJ, McDonald RW, Reller MD. Fetal atrial septal aneurysm: a cause of fetal atrial arrhythmias. J Am Coll Cardiol. 1988;12(5):1292-1297.
228. Kleinman CS. Prenatal diagnosis and management of intrauterine arrhythmias. Fetal Ther. 1986;1(2-3):92-95.
229. Shenker L. Fetal cardiac arrhythmias. Obstet Gynecol Surv. 1979;34(8):561-572.
230. Reed KL, Sahn DJ, Marx GR, et al. Cardiac Doppler flows during fetal arrhythmias: physiologic consequences. Obstet Gynecol. 1987;70(1):1-6.
231. Chao RC, Ho ES, Hsieh KS. Fetal atrial flutter and fibrillation: prenatal echocardiographic detection and management. Am Heart J. 1992;124(4):1095-1098.
232. Silverman NH, Kleinman CS, Rudolph AM, et al. Fetal atrioventricular valve insufficiency associated with nonimmune hydrops: a two-dimensional echocardiographic and pulsed Doppler ultrasound study. Circulation. 1985;72(4):825-832.
233. Cameron A, Nicholson S, Nimrod C, et al. Evaluation of fetal cardiac dysrhythmias with two-dimensional, M-mode, and pulsed Doppler ultrasonography. Am J Obstet Gynecol. 1988;158(2):286-290.
234. Kleinman CS, Copel JA, Weinstein EM, et al. Treatment of fetal supraventricular tachyarrhythmias. J Clin Ultrasound. 1985;13(4):265-273.
235. Kleinman CS, Donnerstein RL, Jaffe CC, et al. Fetal echocardiography. A tool for evaluation of in utero cardiac arrhythmias and monitoring of in utero therapy: analysis of 71 patients. Am J Cardiol. 1983;51(2):237-243.
236. Wiggins Jr JW, Bowes W, Clewell W, et al. Echocardiographic diagnosis and intravenous digoxin management of fetal tachyarrhythmias and congestive heart failure. Am J Dis Child. 1986;140(3):202-204.
237. Komaromy B, Gaal J, Lampe L. Fetal arrhythmia during pregnancy and labour. Br J Obstet Gynaecol. 1977;84(7):492-496.
238. Mendoza GJ, Almeida O, Steinfeld L. Intermittent fetal bradycardia induced by midpregnancy fetal ultrasonographic study. Am J Obstet Gynecol. 1989;160(5 Pt 1):1038-1040.
239. Minagawa Y, Akaiwa A, Hidaka T, et al. Severe fetal supraventricular bradyarrhythmia without fetal hypoxia. Obstet Gynecol. 1987;70(3 Pt 2):454-456.
240. Laboda LA, Estroff JA, Benacerraf BR. First trimester bradycardia. A sign of impending fetal loss. J Ultrasound Med. 1989;8(10):561-563.
241. Kodama Y, Sameshima H, Yamashita R, et al. Intrapartum fetal heart rate patterns preceding terminal bradycardia in infants (>34 weeks) with poor neurological outcome: a regional population-based study in Japan. J Obstet Gynaecol Res. 2015;41(11):1738-1743.
242. Sciarrone A, Masturzo B, Botta G, et al. First-trimester fetal heart block and increased nuchal translucency: an indication for early fetal echocardiography. Prenat Diagn. 2005;25(12):1129-1132.
243. Carpenter Jr RJ, Strasburger JF, Garson Jr A, et al. Fetal ventricular pacing for hydrops secondary to complete atrioventricular block. J Am Coll Cardiol. 1986;8(6):1434-1436.
244. McCue CM, Mantakas ME, Tingelstad JB, Ruddy S. Congenital heart block in newborns of mothers with connective tissue disease. Circulation. 1977;56(1):82-90.
245. Crawford D, Chapman M, Allan L. The assessment of persistent bradycardia in prenatal life. Br J Obstet Gynaecol. 1985;92(9):941-944.
246. Julkunen H, Eronen M. The rate of recurrence of isolated congenital heart block: a population-based study. Arthritis Rheum. 2001;44(2):487-488.

247. Friedman DM. Fetal echocardiography in the assessment of lupus pregnancies. Am J Reprod Immunol. 1992;28(3-4):164-167.
248. Buyon J, Roubey R, Swersky S, et al. Complete congenital heart block: risk of occurrence and therapeutic approach to prevention. J Rheumatol. 1988;15(7):1104-1108.
249. Copel JA, Liang RI, Demasio K, et al. The clinical significance of the irregular fetal heart rhythm. Am J Obstet Gynecol. 2000;182(4):813-817.
250. Allan LD, Joseph MC, Boyd EG, et al. M-mode echocardiography in the developing human fetus. Br Heart J. 1982;47(6):573-583.
251. Lachman R, Taybi H. Taybi and Lachman's radiology of syndromes, metabolic disorders, and skeletal dysplasias. 5th ed. Philadelphia: Mosby-Elsevier.; 2007.
252. Nora J. Medical genetics: principles and practice. 4th ed. Philadelphia: Lea & Febiger; 1994.

CHAPTER 38

The Fetal Gastrointestinal Tract and Abdominal Wall

Nir Melamed, Anne Kennedy, and Phyllis Glanc

SUMMARY OF KEY POINTS

- The gastrointestinal (GI) tract and abdominal wall anomalies are diverse. Although they may occur in isolation, many are associated with syndromic or karyotype abnormalities; thus it is important to search for associated anomalies.
- Familiarity with normal development is needed to recognize the varying appearances during gestation of structures such as the abdominal wall with physiologic midgut herniation, the identification of the gallbladder in the latter half of pregnancy, or the appearance of meconium at different stages of gestation.
- The prognosis and presentation of a GI tract or abdominal wall anomaly may vary with the stage of gestation.
- Anomalies of the GI tract may be diagnosed as part of the evaluation of indirect clues such as polyhydramnios.
- Early prenatal diagnosis, in particular of abdominal wall anomalies, may be performed by late first trimester, in conjunction with a nuchal translucency evaluation.
- Abnormalities of the GI tract may not be clinically apparent in the newborn; thus prenatal diagnosis facilitates appropriate triage to a center that can provide treatment.

CHAPTER OUTLINE

THE GASTROINTESTINAL TRACT
Embryology of the Digestive Tube
Esophagus
Esophageal Atresia
Stomach
Small or Absent Fetal Stomach
Dilated Fetal Stomach
Midline or Right-Sided Stomach
Intraluminal Gastric Masses
Small Bowel and Colon
Bowel Obstruction
Meconium Ileus
Anorectal Malformations
Hirschsprung Disease
Enteric Duplication Cysts
Meconium Peritonitis and Pseudocyst
Echogenic Bowel
Liver
Hepatomegaly
Hepatic Calcifications
Hepatic Cysts and Masses
Gallbladder and Biliary System
Nonvisualization of the Gallbladder
Fetal Gallstones
Choledochal Cyst
Pancreas
Annular Pancreas
Pancreatic Cysts
Spleen
Splenomegaly
Splenic Cysts
ABDOMINAL WALL
Embryology
Gastroschisis
Epidemiology
Pathogenesis
Prenatal Diagnosis
Associated Conditions
Management
Omphalocele
Epidemiology
Prenatal Diagnosis
Associated Conditions
Management
Bladder Exstrophy
Cloacal Exstrophy
Ectopia Cordis
Other Complex Body Wall Defects
Pentalogy of Cantrell
Body Stalk Anomaly
Amniotic Band Syndrome

Systematic and thorough evaluation of the fetal gastrointestinal (GI) tract and abdominal wall is critical to ascertain the risk of isolated and multiple fetal abnormalities. Anomalies of the fetal abdomen may be the only sonographic evidence of multisystem organ derangement secondary to conditions such as genetic disorders or fetal infection. Furthermore, detection of fetal intraabdominal masses or abnormalities is important because these conditions may not be detected on the routine newborn examination. In some cases, anomalies of the GI tract may be diagnosed as part of the evaluation of indirect clues such as polyhydramnios.

THE GASTROINTESTINAL TRACT

Embryology of the Digestive Tube

The GI tract begins to develop in the third and fourth weeks of life. The primitive gut tube is formed by incorporation of the

dorsal part of the yolk sac into the embryo following the longitudinal and lateral folding of the embryonic disc. The gut tube is lined by the embryonic endoderm and is closed at its cranial and caudal ends by the oropharyngeal membrane and the cloacal membrane, respectively.[1] Subsequently, the gut tube undergoes regionalization into three portions. The **foregut,** the most cranial portion, gives rise to the esophagus, stomach, duodenum, liver and bile ducts, and pancreas. The **hindgut,** the most caudal portion, differentiates into the distal part of the colon (beyond the splenic flexure), which is partially supplied by the inferior mesenteric artery. In between, the **midgut** gives rise to the largest part of the intestine, which is supplied by the superior mesenteric artery, and includes the second half of the duodenum (distal to the ampulla of Vater), jejunum, ileum, ascending colon, and the proximal two-thirds of the transverse colon. The midgut remains in connection with the yolk sac via the yolk stalk (omphalomesenteric duct or vitelline duct).[2-6]

Esophagus

Esophageal Atresia

The normal fetal esophagus, extending from the pharynx to the stomach, is collapsed and may therefore be difficult to visualize, or it may be demonstrated as two or four echogenic lines representing the esophageal walls.

Developmentally, the trachea and esophagus differentiate inferiorly from the posterior pharynx. Incomplete differentiation of the respiratory and GI tracts can lead to **esophageal atresia** with or without **tracheoesophageal fistulas.** The incidence of all types of tracheoesophageal fistulas is 2.8 per 10,000 pregnancies.[7,8] There are five types of esophageal atresia,[9] with the most common having a fistula to the distal esophagus. Because most types of esophageal atresia (90%)[10] are associated with tracheoesophageal fistulas, in many cases the stomach (although often small) will be visualized on ultrasound, and polyhydramnios may be absent or mild or present only later in gestation (Table 38.1).

The main sonographic signs of esophageal atresia include **absent or small stomach** (Fig. 38.1), **polyhydramnios,** and the **esophageal pouch sign** (fluid collection in the blind end of the esophagus)[11] (Fig. 38.2A). At times a distended oropharynx will be seen (Fig. 38.2B, Video 38.1). However, the demonstration of esophageal pouch can be difficult because of variation in the location and periodic emptying of the pouch. The antenatal diagnosis of esophageal atresia is challenging, and in many cases the diagnosis is only made during the neonatal period. One

TABLE 38.1 Types of Esophageal Atresia

Type	Description	Proportion of Esophageal Atresia (EA) Cases
A	EA without tracheoesophageal (TE) fistula	10%
B	EA with TE fistula to the proximal esophageal segment	<1%
C	EA with TE fistula to the distal esophageal segment	85%
D	EA with TE fistula to both proximal and distal esophageal segments	<1%
E	TE fistula without esophageal atresia	5%

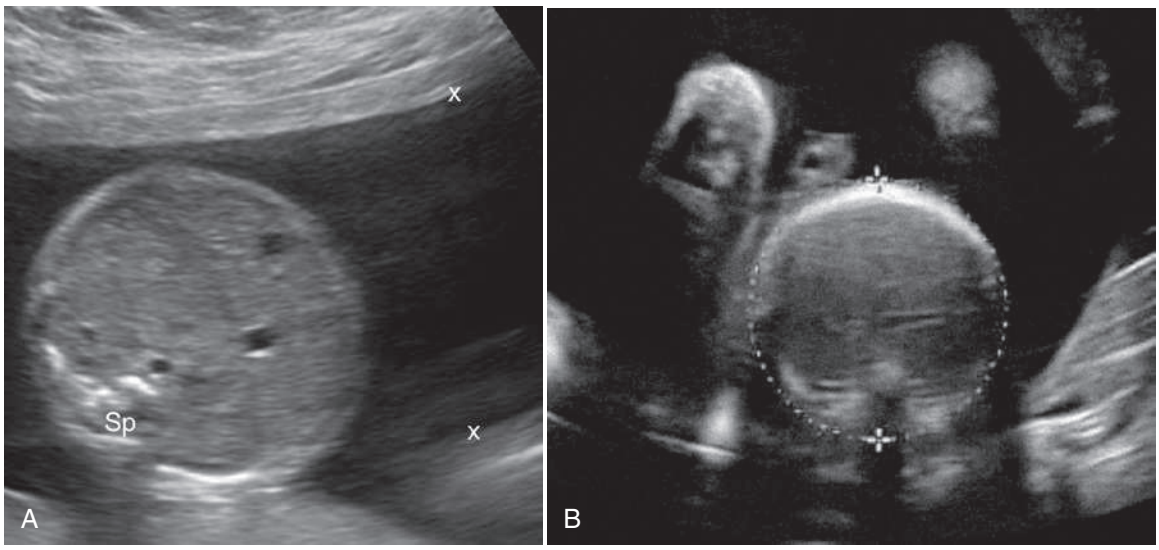

FIG. 38.1 Esophageal Atresia and Absent Stomach. (A) Transverse ultrasound through the abdomen in a 25-week fetus shows no visible stomach. Polyhydramnios is present; vertical pocket of amniotic fluid *(X marks)* measured >8 cm. *Sp,* Spine. **(B)** Third-trimester fetus with absent stomach and polyhydramnios.

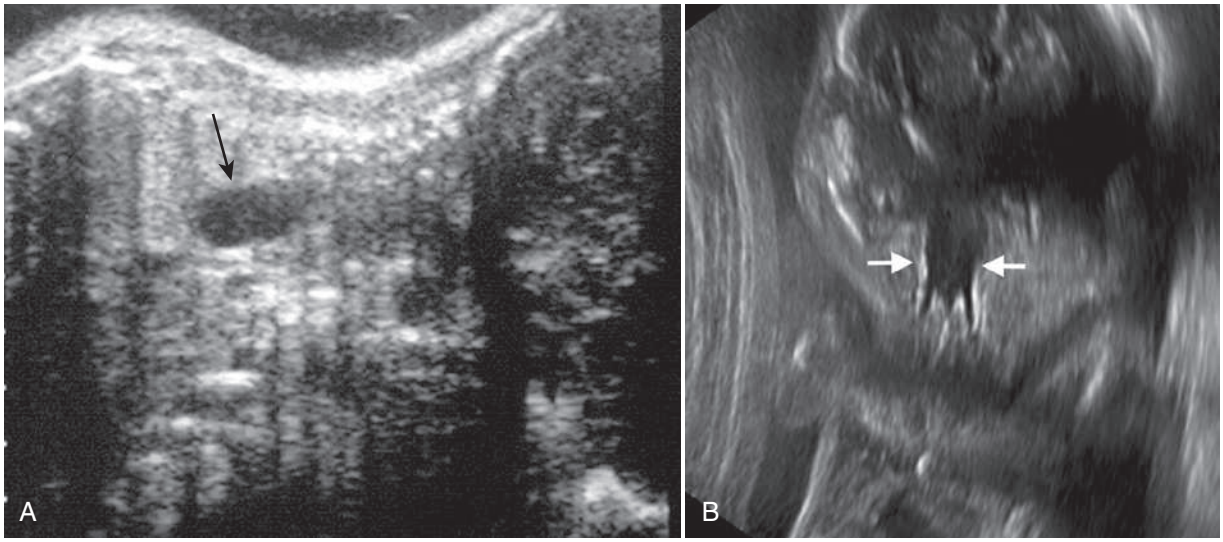

FIG. 38.2 Esophageal Atresia. (A) Coronal view of upper thorax shows a distended **esophageal pouch** *(arrow).* **(B)** Coronal image through the neck in a 25-week fetus shows distended oropharynx *(arrows)* secondary to esophageal atresia. See also Video 38.1.

study reported the antenatal detection rate of esophageal atresia to be 42%.[12] The combination of inability to see the stomach on ultrasound and the presence of polyhydramnios is more suggestive of esophageal atresia than absent stomach alone, but the positive predictive value of this combination is still relatively modest (56%).[12]

Esophageal atresia is associated with additional anomalies in more than 50% of cases,[8,13] and a detailed anatomic evaluation, including echocardiography, should be performed in a fetus with this suspected diagnosis. It has been reported that as many as half of tracheoesophageal fistulas are part of the **VACTERL sequence,**[7] a sporadic nonrandom group of coexisting defects (*v*ertebral defects, *a*nal atresia, *c*ardiac anomalies, *t*racheoesophageal fistula with *e*sophageal atresia, *r*enal and *l*imb defects such as radial dysplasia). Amniocentesis should be considered because the risk of aneuploidy ranges from 5% to 10%.[7] Corrective surgery for esophageal atresia has a success rate of 90% and is influenced by the presence of associated anomalies.[10]

Stomach

The fetal stomach can be seen as early as 7 weeks and should be noted routinely by 13 to 14 weeks' gestation[14] (Fig. 38.3). The stomach should be seen as a cystic structure in the left upper abdomen. It is important to confirm the location of the stomach because a midline or right-sided stomach is associated with heterotaxy syndrome.

Small or Absent Fetal Stomach

Fluid in the stomach should be reliably visualized on first-trimester screening or fetal anatomic survey and all subsequent fetal evaluations. Nonvisualization of the stomach on an anatomic survey (see Fig. 38.1), although potentially a normal finding following recent emptying of the stomach, is associated with an increased risk of fetal abnormalities and may be the result of esophageal obstruction or atresia, disorders affecting the mechanism of swallowing, severe oligohydramnios (which limits the amount of amniotic fluid swallowed by the fetus), or abnormal location of the stomach.

Absent Stomach

ESOPHAGEAL OBSTRUCTION
Esophageal atresia
Esophageal compression (e.g., goiter, tumor or masses in the pharynx, lungs, or mediastinum)

DISORDERS AFFECTING SWALLOWING
Anatomic factors (e.g., cleft palate)
Neurologic disorders

SEVERE OLIGOHYDRAMNIOS OR ANHYDRAMNIOS
DISPLACEMENT OF THE STOMACH
Congenital diaphragmatic hernia
Abdominal wall defects
Heterotaxy syndromes

When the stomach appears small or absent, it is important to allow sufficient time for it to fill, in case it has recently emptied. Generally, the stomach will fill during a 30-minute examination.[15] Careful attention must be paid to the amniotic fluid volume (oligohydramnios or polyhydramnios), general tone and presence of swallowing movements, the appearance of the thorax and diaphragm (masses, diaphragmatic hernia), and abdominal situs.

In one retrospective study, an abnormal outcome (structural abnormalities, antenatal or postnatal death) occurred in 23 (85%) of 27 fetuses with an absent stomach and 27 (52%) of 52 fetuses with a small stomach (combined, 63%). Karyotype was abnormal in 8 (38%) of 21 fetuses with an absent stomach and 2 (4%) of 46 fetuses with a small stomach.[16] For these reasons, the finding of a persistently absent stomach on serial ultrasound scans should trigger a detailed anatomic assessment, genetic counseling, and consideration of chromosomal testing.

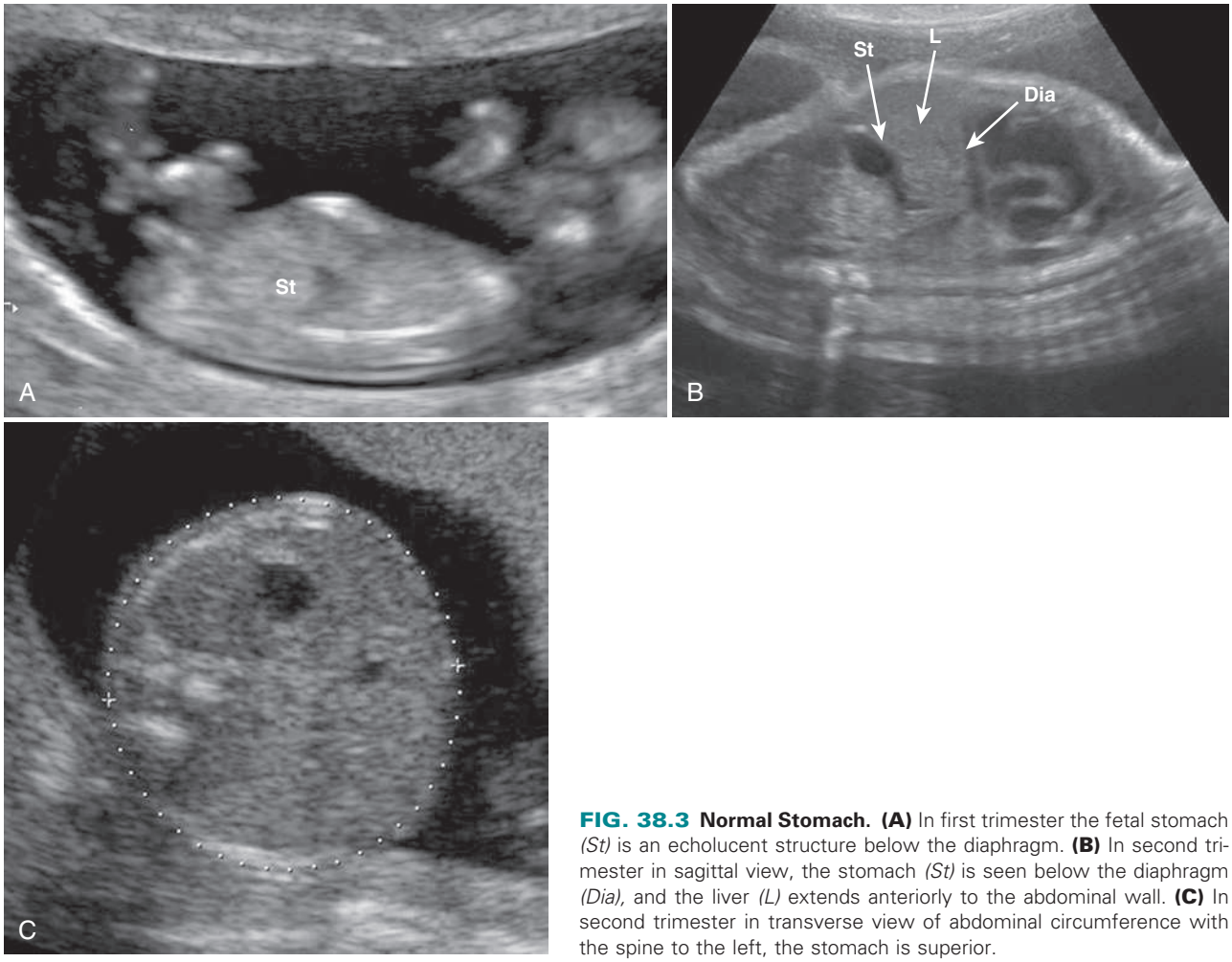

FIG. 38.3 Normal Stomach. (A) In first trimester the fetal stomach *(St)* is an echolucent structure below the diaphragm. **(B)** In second trimester in sagittal view, the stomach *(St)* is seen below the diaphragm *(Dia),* and the liver *(L)* extends anteriorly to the abdominal wall. **(C)** In second trimester in transverse view of abdominal circumference with the spine to the left, the stomach is superior.

Dilated Fetal Stomach

In the second or third trimester a prominent or transiently dilated fetal stomach may be seen on ultrasound. Use of a nomogram can aid in identifying true outliers.[17] However, there is a considerable variation in the normal size of the stomach, and given the asymmetrical shape of the stomach, standardization of the measurement of the stomach dimensions is difficult.[15] In addition, because of the considerable normal fluctuations in stomach size, the diagnosis of a dilated fetal stomach requires that the stomach be persistently dilated throughout a 30-minute assessment as well as on successive examinations. The differential diagnosis of a dilated fetal stomach includes normal variation in stomach size and GI atresia (e.g., **duodenal atresia, pyloric atresia**) as well as pyloric stenosis (Fig. 38.4).

Pyloric atresia is a rare form of intestinal atresia.[18-20] The underlying cause is thought to be different than that of atresia of other parts of the GI tract, and a familial form with an autosomal recessive transmission is well documented.[21] A unique aspect of pyloric atresia is the association with **epidermolysis bullosa,** an often fatal skin disorder characterized by blisters in the skin and mucosal membranes which is inherited in an autosomal recessive pattern. The main sonographic findings in cases of pyloric atresia include gastric dilatation (which can be massive), esophageal dilatation caused by gastroesophageal reflux, and severe polyhydramnios. The co-presence of epidermolysis bullosa may be suggested by elevated levels of maternal serum alpha-fetoprotein and snowflake appearance of the amniotic fluid[22] and can be confirmed by molecular analysis of fetal skin biopsy.[21,23]

Midline or Right-Sided Stomach

An abnormal position of the stomach is an important clue for the presence of a severe abnormality and therefore requires detailed anatomic assessment. A right-sided stomach (Fig. 38.5B) should raise the possibility of **heterotaxy syndrome,** which is characterized by an abnormal symmetry of the viscera and veins and is associated with complex cardiac anomalies, intestinal malrotation, and splenic (asplenia or polysplenia) (Fig. 38.6) and hepatic abnormalities.[24,25] The incidence of heterotaxy syndrome with asplenia or polysplenia is 0.45 per 10,000 pregnancies.[26] Because of the combined cardiovascular and GI abnormalities, infant mortality is high, with the 1-year mortality rate reaching 32%.[27] A midline stomach can represent i**ntestinal malrotation.**[28]

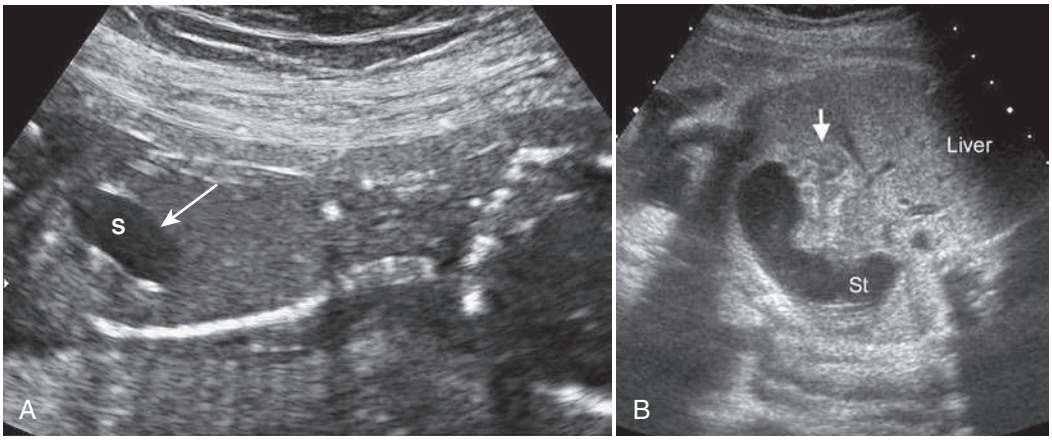

FIG. 38.4 Dilated Stomach. (A) Dilated fetal stomach *(S)* in the second trimester. In sagittal view the stomach is visible extending inferiorly into the pelvis. Although this fetus had a persistently dilated stomach during an anatomic survey, it resolved by the next ultrasound, and the fetus had a normal outcome. **(B) Pyloric stenosis.** Transverse ultrasound in 32-week fetus shows a dilated stomach *(St)* with prominent sustained contraction of the pylorus *(arrow).*

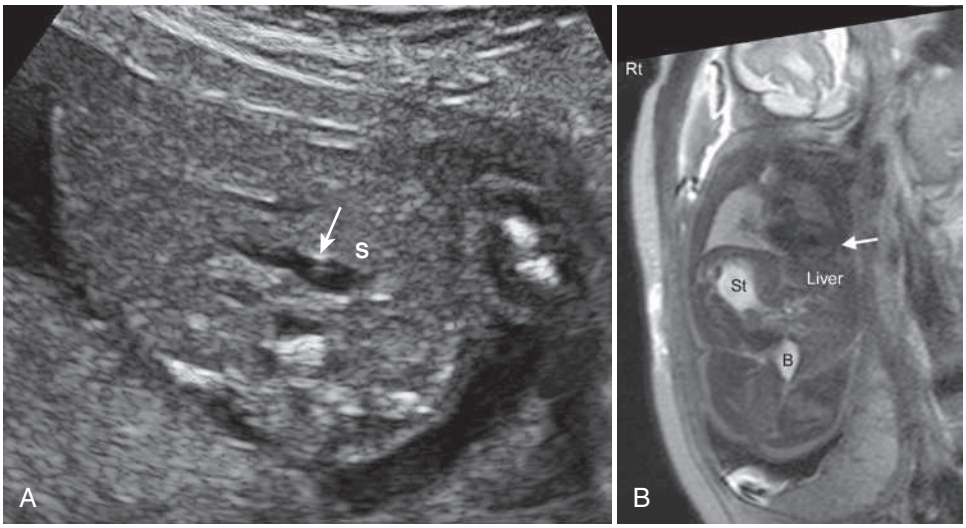

FIG. 38.5 Stomach in Abnormal Location. (A) Midline stomach in fetus with **heterotaxy.** Transverse view of the abdomen shows a midline stomach *(arrow).* This was the only abnormality seen at time of fetal survey; fetal echocardiogram revealed anomalous pulmonary venous return, and the diagnosis of heterotaxy was confirmed postnatally. **(B)** Heterotaxy syndrome with **right-sided stomach.** Coronal T2-weighted fetal magnetic resonance image (MRI) at 34 weeks shows left-sided liver and right-sided stomach *(St).* The cardiac apex *(arrow)* is directed left. *B,* Bladder.

Intraluminal Gastric Masses

The presence of irregular **echogenic content** or **debris** within the fetal stomach can often be seen on routine ultrasound exams (Fig. 38.7, Videos 38.2 and 38.3). This finding is nonspecific and when found in isolation it is most likely to be a normal finding. Such debris most often represents blood, skin cells, or meconium swallowed by the fetus.[29-32]

Small Bowel and Colon

In the first trimester and early in the second trimester, the small and large bowel appear somewhat heterogeneous, with an echogenicity similar to that of the liver. Later in pregnancy, fluid can be seen in the small bowel loops, and meconium can be seen in the colon. Most cases of GI atresia are thought to represent a failure of recanalization of the bowel lumen, which is a solid tube early in fetal life.

Bowel Obstruction

Duodenal Obstruction. Dilatation of the duodenum resulting from **duodenal stenosis** or **duodenal atresia** is the most common type of bowel obstruction in the fetus, occurring in 1 or 2 per 10,000 live births.[33-35] Duodenal atresia may result from failure of recanalization of the duodenal lumen, periampullary obstruction, complete absence of a duodenal segment, or vascular ischemia.[36-39] Less commonly, duodenal obstruction may be secondary to mechanical factors such as **annular pancreas, superior mesenteric artery syndrome,** or **volvulus.**[40,41]

Associated anomalies are common and are present in more than half of cases[42]; most notably, 30% to 44% of cases of duodenal atresia are associated with trisomy 21.[33,43] Familial cases of duodenal atresia have also been reported.[44] Duodenal atresia is also associated with anomalies of the **VACTERL** spectrum.[45,46]

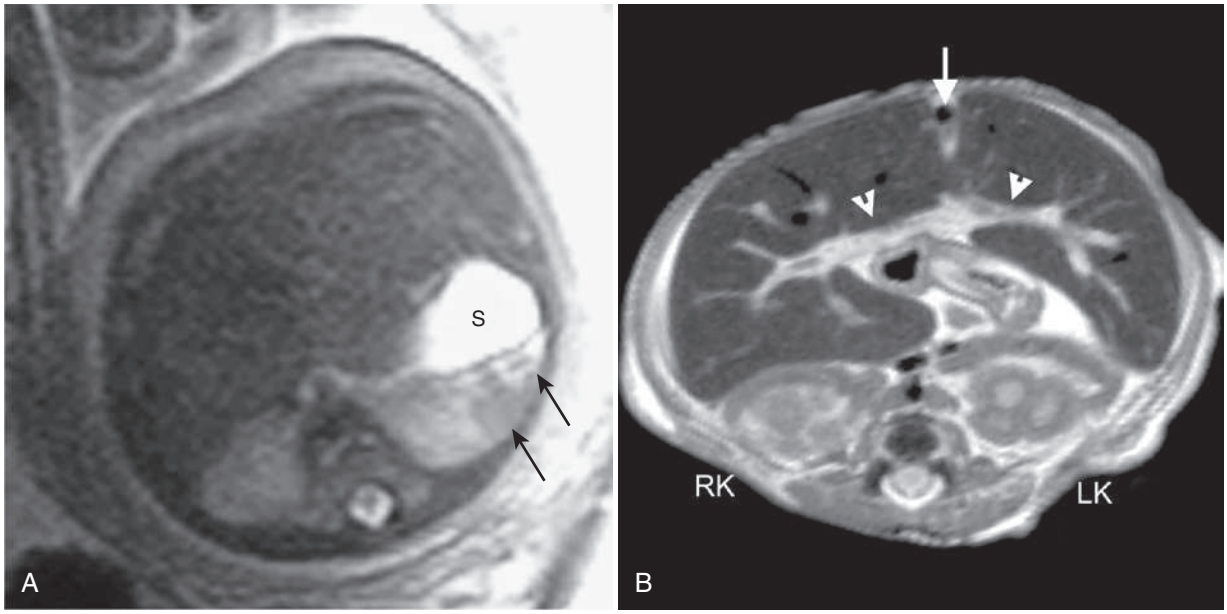

FIG. 38.6 Heterotaxy With Asplenia or Polysplenia. (A) Polysplenia. Transverse MRI of fetus with complex congenital heart disease (not shown) with multiple splenules *(arrows)* in the left upper quadrant. *S,* Stomach. **(B) Asplenia** in a transverse image from an autopsy MRI in a term infant with nonreparable, complex congenital heart disease as part of a heterotaxy syndrome shows asplenia with central liver placement. The portal vein *(arrowheads)* bifurcates centrally. The arrow denotes the umbilical vein. *LK,* Left kidney; *RK,* right kidney.

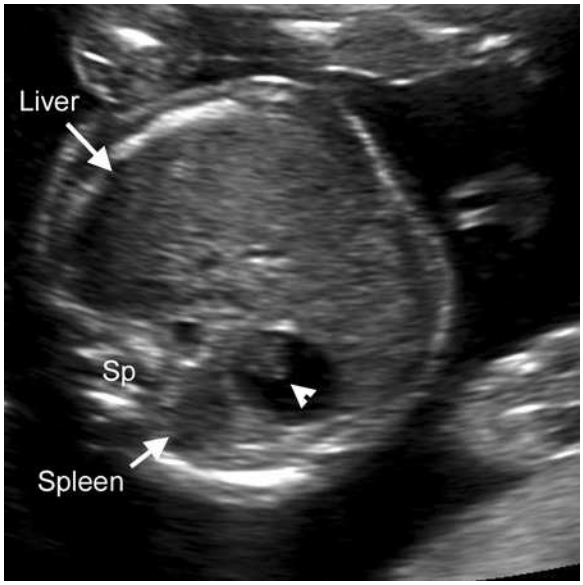

FIG. 38.7 Gastric Debris. Transverse image through the abdomen in a 25-week fetus shows a masslike structure in the stomach *(arrowhead).* This is a benign finding thought to represent swallowed debris or vernix. *Sp,* Spine. See also Videos 38.2 and 38.3.

The sonographic hallmarks in cases of duodenal atresia are the presence of severe polyhydramnios (which may not be present until the late second or third trimester) and the **"double-bubble" sign,** in which a second echolucent mass is seen medial to the stomach bubble in a transverse view of fetal abdomen (Fig. 38.8, Video 38.4). This sign is the result of the dilated segment of the duodenum proximal to the atretic area and is highly suggestive of duodenal obstruction. It is important to demonstrate continuity between the fluid-filled structures to prove that the diagnosis is duodenal stenosis/atresia.

A prominent incisura angularis of the stomach may be mistaken for a "double bubble" if these are in different planes, but a careful real-time longitudinal examination of the stomach can eliminate this possibility. Other, less common reasons for an apparent double-bubble sign include **choledochal cyst** and **duodenal duplication cyst.**[43,47] In addition, several cases of **transient double-bubble sign** during the second trimester have been reported, with normal outcomes.[48,49]

As in all cases of proximal bowel obstruction, polyhydramnios is frequently present by the late second trimester[50-52] but is often absent in the early second trimester at the time of routine fetal survey. This is in part related to the relative difference in the amount of amniotic fluid swallowed per day at different times of gestation. The fetus swallows a relatively small amount of amniotic fluid (2-7 mL of fluid per day) during early second trimester, compared to 450 mL at term.[53] In a European study of 138 cases of postnatally confirmed duodenal atresia, polyhydramnios was present in only 33% of cases.[54] For these reasons, duodenal atresia is commonly diagnosed during the third trimester, whereas in the early second trimester both false-negative and false-positive diagnoses have been reported.[48,49] Thus the proportion of cases diagnosed prenatally ranges widely between 34% and 87%.[43,50,55-57]

It has been suggested that prenatal diagnosis of duodenal atresia has the potential to decrease neonatal morbidity.[50] Finding the double-bubble sign should trigger detailed anatomic survey, fetal echocardiography, as well as genetic counseling and consideration of amniocentesis given the high association with trisomy 21.

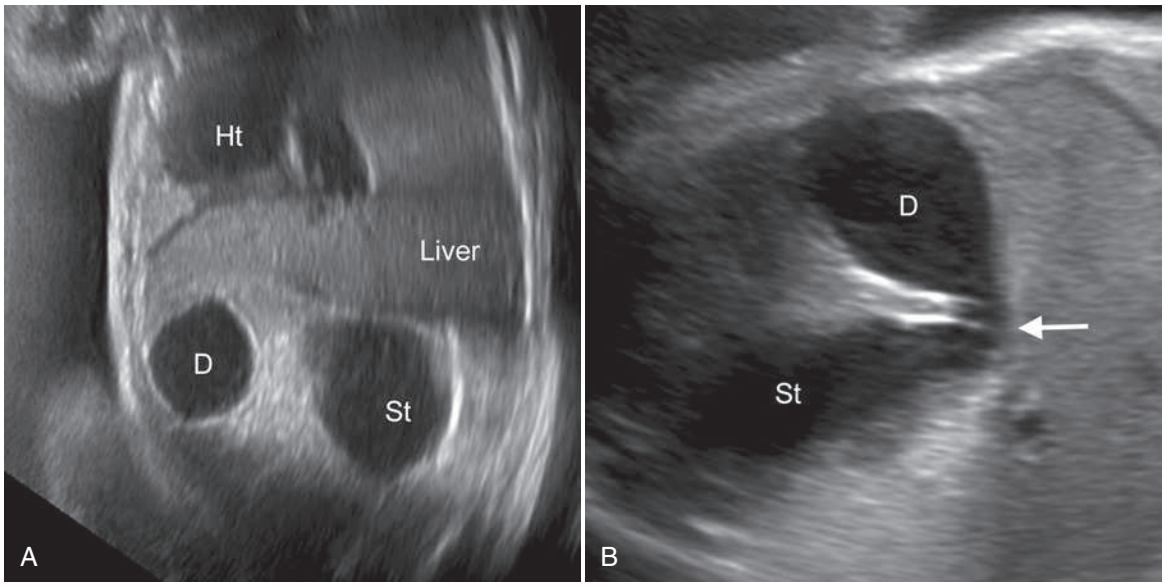

FIG. 38.8 Duodenal Atresia. (A) Oblique sagittal view through the fetal abdomen at 33 weeks shows the "double-bubble" sign of duodenal atresia with the fluid-filled stomach *(St)* and duodenum *(D). Ht,* Heart. **(B)** Oblique coronal view shows continuity *(arrow)* between the stomach and duodenum. See also Video 38.4.

Jejunal and Ileal Obstruction. The prevalence of **jejunoileal atresia** ranges from 0.5 to 1.1 cases per 10,000 live births.[58,59] Jejunal atresias are slightly more common (51%) than ileal.[60] The most common hypothesis with respect to the etiology for jejunoileal atresia is early vascular compromise of the developing midgut.[57] In animals, induced vascular compromise leads to isolated bowel atresias.[61] This hypothesis is also supported by the association of intestinal atresia with placental complications and other abnormalities of vascular origin such as gastroschisis.[62] **"Apple peel" jejunal atresia** is a subtype that involves agenesis of the mesentery, is more often familial,[54,63,64] and is likely of a different etiology. **Cystic fibrosis** is a common underlying cause of ileal obstruction; the thick meconium associated with cystic fibrosis can lead to ileal obstruction **(meconium ileus)** with or without echogenic bowel.[65,66]

Although jejunal and ileal atresia are often discussed as a single entity, there are major differences between these two conditions. Jejunal atresia is more likely to involve multiple sites and is less often associated with in utero perforation than is ileal atresia, likely because of the lower compliance of the ileum. In addition, the risk of associated anomalies depends on the site of obstruction. Whereas jejunal atresias have been associated with extra-GI anomalies and chromosomal disorders in up to 42% of cases, the rate of associated anomalies in cases of ileal atresia is only about 2%.[54,67] Both conditions are associated with other GI abnormalities, including malrotation, meconium peritonitis, and duplication cysts.[68]

The prenatal diagnosis of jejunoileal obstruction is based on **dilated loops of bowel** (Fig. 38.9, Video 38.5), most frequently without a dilated stomach and sometimes with hyperperistalsis. If peristalsis is not observed, dilated small bowel can be difficult to distinguish from dilated colon. The cutoff used to define dilated small bowel is greater than 7 mm for loop diameter or greater than 13 mm for loop length.[65] The diagnosis of jejunoileal atresia is typically not made until late in the second trimester, as dilatation of the bowel is often not seen before that stage. The rate of **polyhydramnios** decreases as the site of bowel obstruction becomes more distal. Thus polyhydramnios in cases of jejunoileal atresia is less common than in cases of duodenal or esophageal atresia; it has been reported in about one-third of cases of jejunal atresia and is even less common in cases of ileal atresia.[69] It is often not possible to confidently differentiate between jejunal and ileal atresia in utero; the more dilated loops visible, the more likely it is to be a distal or ileal obstruction. Another sonographic sign associated with jejunoileal obstruction is **echogenic bowel,** reflecting thickened meconium due to the intestinal stasis. **Ascites** and **abdominal calcifications** can be seen in cases of obstruction complicated by perforation, a complication seen more commonly in cases of ileal obstruction. In a recent systematic review on the accuracy of sonographic diagnosis of small bowel obstruction, a large variation in the detection rate of small bowel obstruction was noted (10%-100%), with the detection rate being considerably higher for jejunal atresia (66%) than for ileal atresia (26%).[70]

Meconium Ileus

Meconium ileus relates to obstruction of the ileum by thickened meconium. Some cases are associated with **cystic fibrosis,** but only a minority (up to 20%) of cases of cystic fibrosis will present with meconium ileus during pregnancy.[71,72] The presence of **echogenic bowel** in addition to the general sonographic signs of bowel obstruction increases the likelihood of meconium ileus. The differential diagnosis and diagnostic approach in cases of echogenic bowel and meconium peritonitis are discussed later in this chapter.

Anorectal Malformations

The incidence of **anorectal malformation** is in the range of 0.8 to 4 per 10,000 live births.[73] The spectrum of anorectal

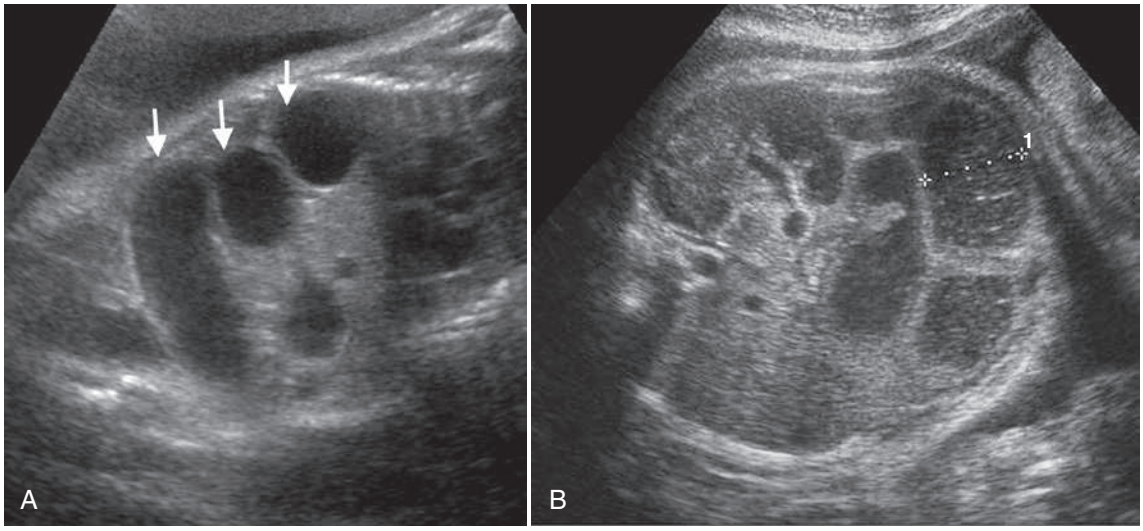

FIG. 38.9 Jejunal and Ileal Atresia. (A) Jejunal atresia. Coronal image through the abdomen of a 30-week fetus shows several dilated loops of small bowel *(arrows).* **(B)** Ileal atresia. Transverse fetal abdomen with multiple dilated loops of bowel. The bowel lumen is measured in the largest transverse diameter *(calipers).* See also Video 38.5.

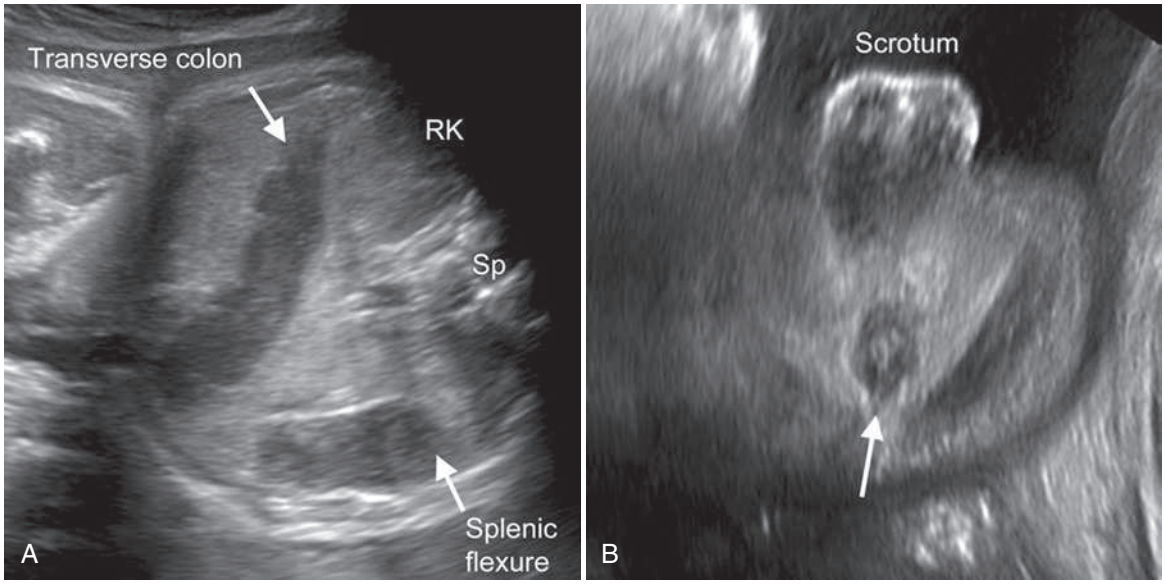

FIG. 38.10 Normal Colon and Anal Dimple. (A) Normal third-trimester large bowel. Transverse image through the abdomen at 37 weeks shows prominent meconium-filled loops of colon. This is normal in the third trimester and should not be taken to indicate bowel obstruction. *RK,* Right kidney; *Sp,* spine. **(B)** Although not part of standard scan guidelines, the anal dimple *(arrow)* can easily be demonstrated on a transverse plan through the perineum. Visualization of the dimple excludes anal atresia.

malformations ranges from isolated **imperforate anus** to more complex **cloacal malformations.** They are classified as **low, intermediate,** and **high** based on whether the bowel ends below, at the same level, or above the level of the levator ani muscle, respectively. The majority of cases (>90%) are **low malformations.**[74] **High malformations** are less common and are often associated with vesicocolic **fistulas.**

Anorectal malformations are frequently associated with chromosomal and structural anomalies, in 48% to 98% of cases.[75-77] **Anal atresia** is also part of the **VACTERL sequence**[76-78] and is associated with a large number of genetic syndromes. Given the high rate of associated abnormalities, a detailed fetal survey, fetal echocardiogram, genetic counseling, and discussion of aneuploidy risk should be included in the management of cases with suspected anorectal malformations.

The prenatal detection rate of anorectal malformations is lower than that of more proximal types of bowel obstruction and ranges from 7% to 24%.[55,79,80] The main sonographic sign is **dilated loops of small or large bowel,** although this should be distinguished from normal prominent colon loops during the third trimester (Fig. 38.10A). **Polyhydramnios** is absent in the majority of cases.[81,82] Sonographic assessment would commonly reveal signs of associated anomalies such as in the case of VACTERL association and associated chromosomal abnormalities.[83] In cases

complicated by **vesicocolic fistula,** intraluminal calcifications may be seen and have been attributed to mixing of meconium with urine.[84] More recently, inability to visualize the anal mucosa on transverse transperineal view (known as the **anal dimple,** which is the result of the echogenic mucosa surrounded by the hypoechoic muscle of the anal sphincter) has been suggested as an important sonographic marker in cases of imperforated anus (Fig. 38.10B).[85]

Hirschsprung Disease

Hirschsprung disease is a congenital disorder of the colon caused by absence of ganglia in the distal colon, thereby leading to functional colonic obstruction. It affects about 1 of 5000 live births.[86] The diseased segment usually involves the most distal part of the colon, including the internal anal sphincter, and extends proximally to involve variable portions of the colon, with the most severe forms involving the whole colon. Hirschsprung disease is associated with chromosomal and structural abnormalities in about 10% to 20% of cases, and up to 10% of cases are associated with trisomy 21.[87]

Prenatal diagnosis of Hirschsprung disease is uncommon and is usually made in severe forms involving the entire length of colon. The sonographic signs in these cases are nonspecific and include bowel dilatation, polyhydramnios, and echogenic bowel (Fig. 38.11).[87] Thus the majority of cases are diagnosed within the early neonatal period, with the most common sign being failure to pass meconium.[88-90]

Enteric Duplication Cysts

Enteric duplication cysts are classified by the anatomic region involved rather than by the histology of the mucosal lining.[91] The incidence is estimated at 1 per 10,000 infants.[92,93] They result from abnormal recanalization of the GI tract and may or may not communicate with the lumen of the GI tract. Enteric duplication cysts can be associated with any area of the GI tract, but they are most common in the terminal ileum.[94] They may present

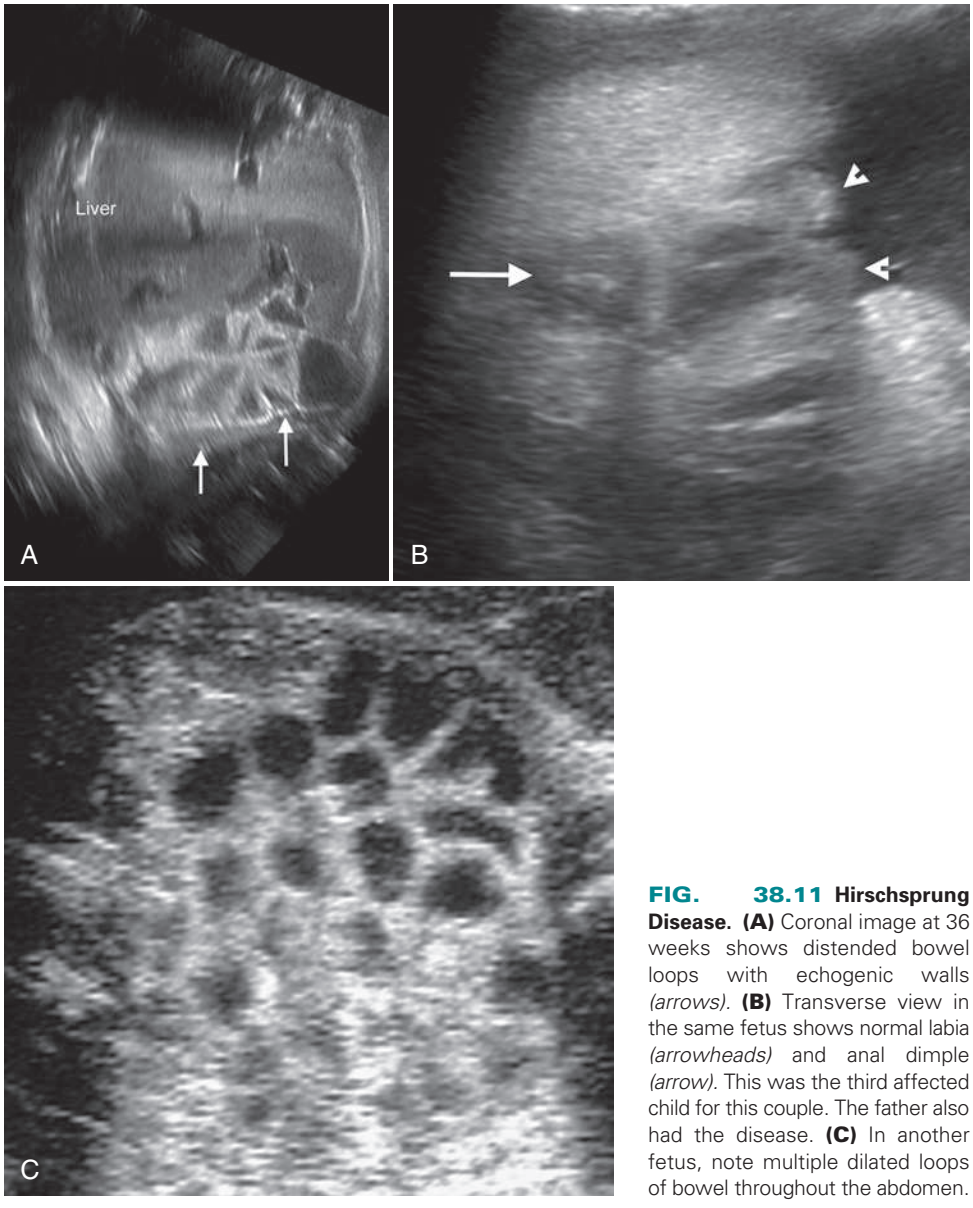

FIG. 38.11 Hirschsprung Disease. (A) Coronal image at 36 weeks shows distended bowel loops with echogenic walls *(arrows).* **(B)** Transverse view in the same fetus shows normal labia *(arrowheads)* and anal dimple *(arrow).* This was the third affected child for this couple. The father also had the disease. **(C)** In another fetus, note multiple dilated loops of bowel throughout the abdomen.

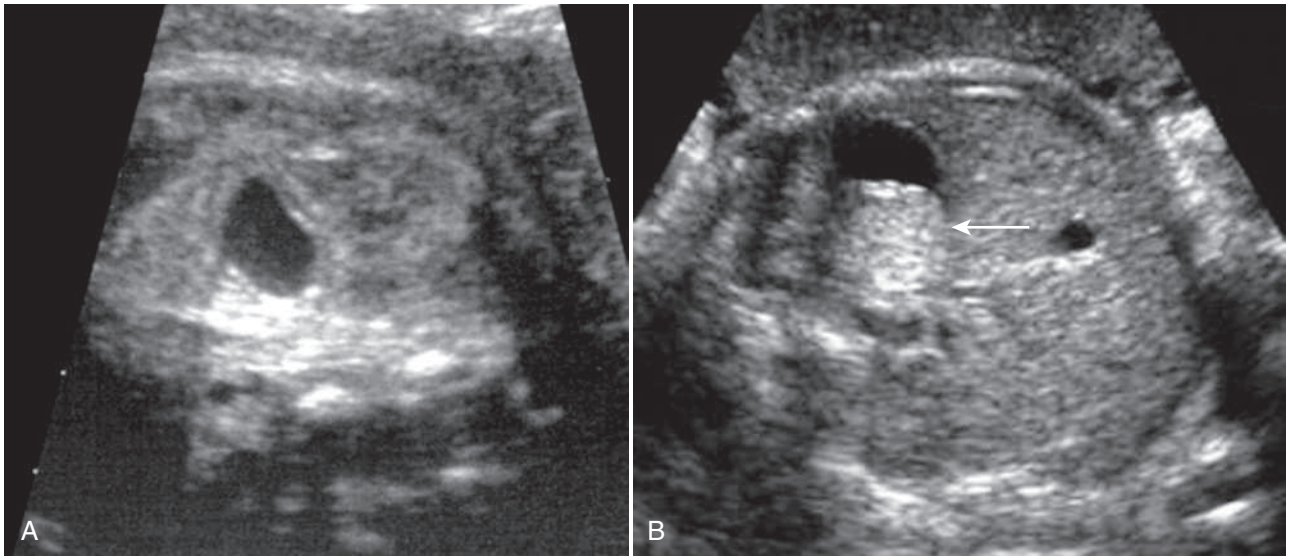

FIG. 38.12 Enteric Duplication Cyst. (A) Note the characteristic double line around the wall, which distinguishes a gut duplication from other abdominal cysts. **(B)** Atypical appearance of gastric duplication cyst with echogenic material *(arrow)*. Note how cyst impinges on stomach. See also Video 38.6. (With permission from McNamara A, Levine D. Intraabdominal fetal echogenic masses: a practical guide to diagnosis and management. Radiographics. 2005;25[3]:633-645.[32])

in utero or postnatally either as an incidental finding or in association with bowel obstruction.[92,94] Associated anomalies occur in up to 30% of cases, most often of the GI tract.[94]

Enteric duplication cysts present at ultrasound as **cystic or echogenic tubular structures** with well-defined borders.[95] They are classically anechoic and cystic but at times are filled with echogenic material. The borders typically have a **double layer ("gut signature"),** although this may be hard to demonstrate and may require high-resolution linear transducers[94,96] (Fig. 38.12, Video 38.6). Depending on the site of presentation, the differential diagnosis includes **hepatic cysts, choledochal cysts, bowel atresias,** and **ovarian cysts.** Peristalsis of the cysts can help differentiate these masses from those of non-GI origin.[97] Postnatally, the standard treatment is surgical because of the associated risk of bowel obstruction.[92]

Meconium Peritonitis and Pseudocyst

Meconium peritonitis is the result of in utero bowel perforation that is followed by leakage of meconium into the peritoneal cavity, which subsequently leads to chemical irritation and inflammatory response. The sonographic hallmark of meconium peritonitis is the finding of **abdominal calcifications** representing calcification of the peritoneum outlining bowel or liver (Figs. 38.13 and 38.14A). Additional findings may include **ascites** (Video 38.7), **echogenic bowel, dilated bowel,** and **polyhydramnios.**[98,99] In some cases, the extruded meconium becomes walled off in the peritoneum and develops a heterogeneous cystic appearance, a finding known as **meconium pseudocyst** (Fig. 38.14). Meconium pseudocyst is characterized by a cyst encircled by an echogenic rim.

Both meconium ileus and meconium peritonitis are associated with cystic fibrosis in 8% to 40% of cases.[98,100] The need for postnatal surgery in cases of meconium peritonitis can be predicted based on the combination of findings observed (Table 38.2).[101] Once meconium peritonitis or meconium ileus has been diagnosed, serial fetal sonography is recommended. Because of the association with additional fetal anomalies, delivery at a center with a neonatal intensive care unit and pediatric surgery is recommended.

TABLE 38.2 Meconium Peritonitis Findings and Likelihood of Need for Surgery

Findings	Likelihood of Need for Postnatal Surgery (%)[101]
Isolated calcifications	0%
Calcifications and pseudocyst, ascites, or bowel dilatation	52%
Calcifications and two of the following: pseudocyst, ascites, or bowel dilatation	80%
Calcifications, pseudocyst, ascites, and bowel dilatation	100%
Polyhydramnios and any of above findings	69%

Modified from Zangheri G, Andreani M, Ciriello E, et al. Fetal intra-abdominal calcifications from meconium peritonitis: sonographic predictors of postnatal surgery. Prenat Diagn. 2007;27(10):960-963.[101]

Echogenic Bowel

Echogenic bowel, which refers to increased brightness of the fetal bowel at the time of ultrasound examination, is a marker for several fetal disorders.[102-105] The most commonly used criterion for the diagnosis of echogenic bowel is echogenicity that is similar

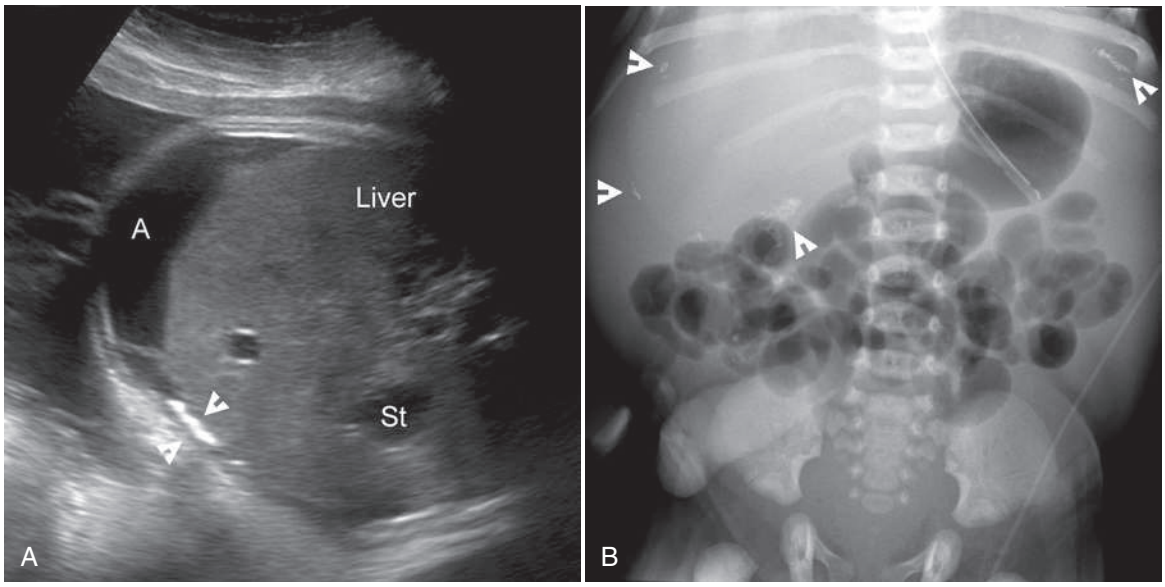

FIG. 38.13 Meconium Peritonitis. (A) Transverse image at 34 weeks shows ascites *(A)* surrounding the liver with associated calcifications *(arrowheads)* on the liver surface; a finding typical of meconium peritonitis. *St,* Stomach. **(B)** Abdominal radiograph in the neonate confirms peritoneal calcifications *(arrowheads).* See also Video 38.7.

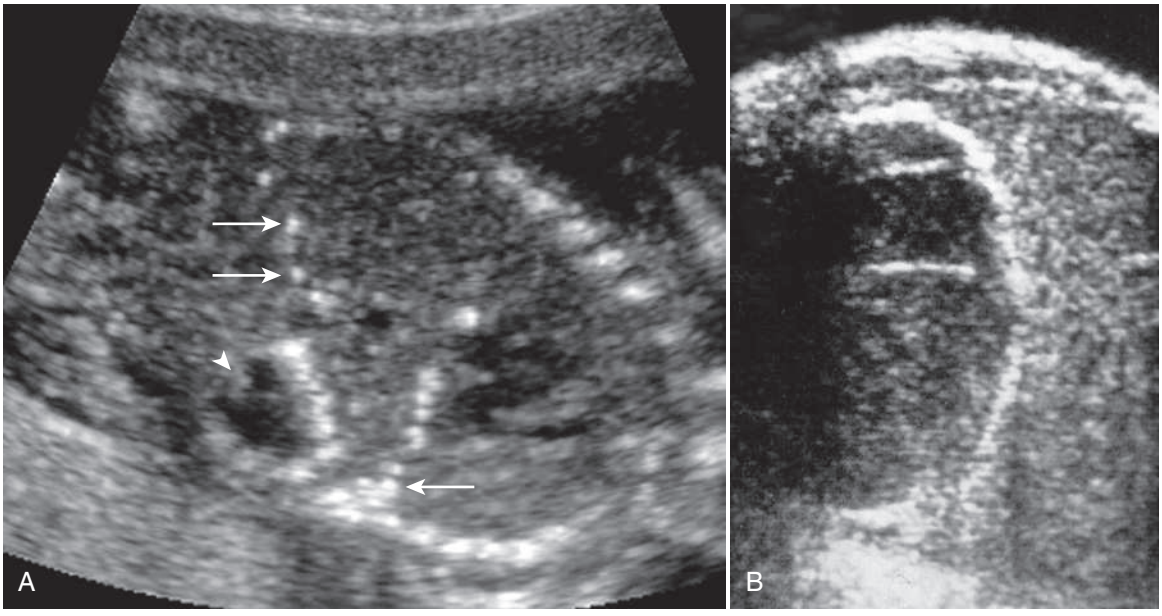

FIG. 38.14 Meconium Pseudocyst. (A) Oblique sagittal view of the torso shows multiple calcifications on the peritoneal surface of the liver in a fetus with a meconium pseudocyst *(arrowhead),* with an irregularly calcified wall. **(B)** Meconium pseudocyst in another fetus. Note cyst with debris with calcified rim *(arrows).* (With permission from McNamara A, Levine D. Intraabdominal fetal echogenic masses: a practical guide to diagnosis and management. Radiographics. 2005;25[3]:633-645.[32])

or greater than that of adjacent bone, such as the iliac bone.[106] To avoid a false-positive diagnosis due to artifacts and image processing, the diagnosis of echogenic bowel requires that the lowest level of ultrasound gain at which bones still appear white be used and that all image enhancement algorithms be disabled (Fig. 38.15, Video 38.8). The use of a high-frequency probe (8 MHz) can lead to overdiagnosis of echogenic bowel[107]; therefore the diagnosis of echogenic bowel should always be confirmed using a low-frequency (≤5 MHz) probe. Despite these attempts to standardize the diagnosis of echogenic bowel, it should be recognized that there is a significant subjective component in the diagnosis of echogenic bowel, which can lead to significant interobserver variability.[108]

When strict diagnostic criteria are used, the incidence of echogenic bowel in the general obstetric population is 0.2% to 0.7%.[79,106] Because the echogenicity of normal bowel increases throughout pregnancy, the finding of echogenic bowel becomes normal in the third trimester. In particular, meconium in the colon can be seen normally as echogenic material in the third trimester.

Aneuploidy. The confirmation of hyperechogenic bowel on second-trimester ultrasound requires careful evaluation of the fetus because of the association with chromosomal abnormalities (Fig. 38.16A). In most series, fetuses with chromosomal abnormalities are likely to have other abnormal sonographic findings.[109]

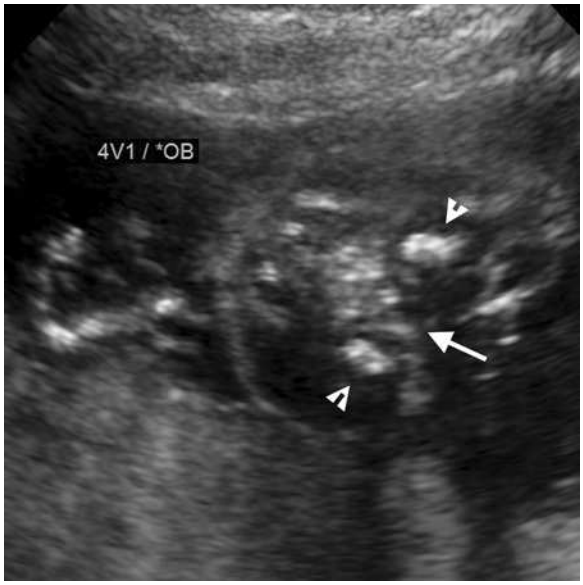

FIG. 38.15 Echogenic Bowel. Transverse image through fetal pelvis shows bowel loops *(arrow)* that are as echogenic as bone (*arrowheads* on ischial tuberosities). The image was obtained with the 4-MHz vector transducer and harmonics turned off. See also Video 38.8.

The risk of aneuploidy in fetuses with echogenic bowel as an isolated finding is 1.4% to 6.7%.[109-111] In a study of 281 fetuses with echogenic bowel, the rate of chromosomal abnormalities was 6.7% in cases of isolated echogenic bowel compared with 17.4% in cases of echogenic bowel accompanied by major anomalies.

The most common chromosomal disorder associated with echogenic bowel is trisomy 21[110,111]; in a recent meta-analysis of second-trimester markers for trisomy 21, echogenic bowel was associated with a positive likelihood ratio of 11.4 for trisomy 21.[112] The reason for the association between trisomy 21 and

Conditions Associated With Echogenic Bowel

Aneuploidy—mainly trisomy 21; less commonly trisomies 13 and 18, 45,X0, triploidy
Cystic fibrosis
Intraamniotic bleeding—swallowed blood (placental hemorrhage, postprocedural)
Fetal infection—CMV, parvovirus B19, varicella, herpes simplex, toxoplasmosis
Gastrointestinal tract atresias, obstructions, dysmotility or stasis
Fetal growth restriction
Fetal anemia
Fetal demise

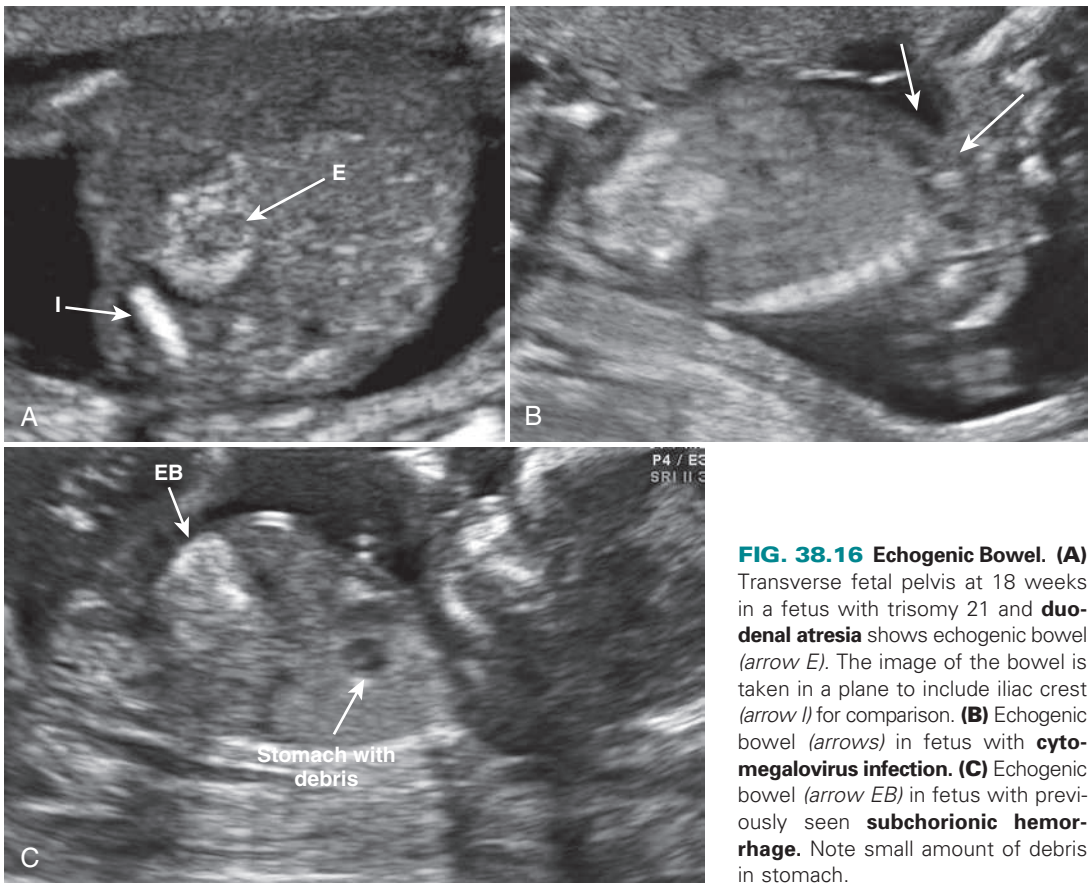

FIG. 38.16 Echogenic Bowel. (A) Transverse fetal pelvis at 18 weeks in a fetus with trisomy 21 and **duodenal atresia** shows echogenic bowel *(arrow E)*. The image of the bowel is taken in a plane to include iliac crest *(arrow I)* for comparison. **(B)** Echogenic bowel *(arrows)* in fetus with **cytomegalovirus infection. (C)** Echogenic bowel *(arrow EB)* in fetus with previously seen **subchorionic hemorrhage.** Note small amount of debris in stomach.

echogenic bowel is unclear, but it has been attributed to the presence of GI dysfunction and dysmotility.[113] Intestinal stasis, for any reason, can lead to increased absorption of fluid from the bowel lumen, which can result in thick meconium and therefore increased echogenicity of the bowel content.[114] Other chromosomal abnormalities that have been associated with echogenic bowel include trisomies 13 and 18, 45,X0, and triploidies.[110,111,115]

Cystic Fibrosis. Echogenic bowel, meconium ileus, and **meconium peritonitis** are possible sonographic findings in fetuses with cystic fibrosis.[116] The echogenic appearance of the bowel in fetuses with cystic fibrosis is the result of the biochemical alterations in the secretory-digestive-absorptive function of the small intestinal mucosa, which can result in the meconium being more viscous than normal and therefore more echogenic.[117] The incidence of cystic fibrosis in fetuses with isolated echogenic bowel varies from 1.3% to 5%.[106,118,119]

Intraamniotic Bleeding. Echogenic bowel has been noted in pregnancies complicated by vaginal bleeding, in those with asymptomatic subchorionic hemorrhage, and following invasive procedures such as chorionic villous sampling and amniocentesis. Each of these conditions may result in intraamniotic bleeding, and the blood-containing amniotic fluid swallowed by the fetus can be visible as echogenic debris in the fetal stomach or as increased echogenicity of the bowel content (Fig. 38.16C).[114,120] In a case series of pregnant women undergoing amniocentesis, there was evidence of blood in the amniotic fluid on spectrophotometry of 8 in 40 (20%) of those with echogenic bowel compared to 3 in 64 (5%) of those without.[121] In one series, 19% of fetuses with isolated echogenic bowel had sonographic evidence of intrauterine bleeding, of which 70% were confirmed to have intraamniotic bleeding on amniocentesis.[122] History of bleeding during pregnancy, history of invasive procedure earlier in pregnancy, sonographic evidence of retroplacental or subchorionic hemorrhage, or evidence of debris in the fetal stomach provides support for intraamniotic bleeding as the cause of echogenic bowel.

Fetal Infection. Echogenic bowel is one of the manifestations of fetal infection, including cytomegalovirus (CMV), parvovirus B19, varicella, herpes simplex, and toxoplasmosis (Fig. 38.16B).[123] The incidence of infection in fetuses with echogenic bowel is in the range of 0.5% to 6.3%.[122,124,125] The cause of the echogenic bowel in fetuses with infection is not known but may be related to inflammation and edema of the bowel wall as well as the associated decreased peristalsis of the infected bowel.

Bowel Obstruction. As previously noted, bowel of obstruction or stasis for any reason, including GI atresia or Hirschsprung disease,[89] can result in thickening of the meconium and therefore increase in the echogenicity of bowel content.

Fetal Growth Restriction and Fetal Demise. The risk of both **fetal growth restriction** and **fetal demise** increases in the second and third trimesters in fetuses with echogenic bowel. The reported incidence is 10% to 20% for fetal growth restriction[102,118] and 6% to 15% for fetal demise.[73,118,126] In a recent study of 188 fetuses with isolated echogenic bowel (i.e., after the exclusion of chromosomal abnormalities, major malformation, and fetal infection), the rate of fetal growth restriction and fetal demise were 19.5% and 7.3%, respectively (compared with 12.9% and 0.9% in the control group, respectively). Possible explanation for these findings is the association between subchorionic bleeding (which can result in echogenic bowel) with fetal growth restriction and fetal demise.[127] In addition, in cases of severe fetal growth restriction, it is believed that redistribution of cardiac output in the compromised fetus to vital organs (i.e., brain, heart, and adrenal gland) results in decreased splanchnic blood flow, including perfusion to the bowel, which can result in impaired peristalsis.[128] The association of echogenic bowel with fetal anemia, which can also result in bowel hypoxia, provides support to this hypothesis.[129]

Summary. Given the associations described previously, the finding of echogenic bowel requires careful investigation and appropriate monitoring. The evaluation of pregnancies with echogenic bowel typically includes (1) genetic counseling and consideration of amniocentesis or cell-free fetal DNA testing; (2) parental screening for cystic fibrosis; (3) maternal serology for viral infections, including CMV and parvovirus B19; (4) detailed sonographic assessment for associated structural anomalies or soft markers, signs of bowel obstruction, assessment of fetal biometry, placental morphology, and amniotic fluid; and (5) follow-up for growth. Information regarding episodes of vaginal bleeding or invasive testing earlier in pregnancy should be recorded. In cases where the investigation is negative, the finding of "isolated" echogenic bowel may represent a normal variant or a false-positive finding, and fetal outcome may be normal.

Liver

The fetal liver is clearly visualized in the upper abdomen in the second half of gestation, although earlier in gestation it has an echogenicity similar to renal echoes.

Hepatomegaly

Given the asymmetrical shape of the liver, accurate determination of its size is difficult and is associated with high interobserver variability. Therefore in many cases the diagnosis of **hepatomegaly** is made subjectively. Hepatomegaly is associated with a variety of conditions including **fetal hemolytic anemia** which results in a compensatory increase in hematopoiesis within the liver,[130] **metabolic and storage diseases, fetal infections**[131] (Fig. 38.17), **liver masses, hepatic congestion secondary to cardiac failure,** and overgrowth syndromes such as **Beckwith-Wiedemann syndrome.**[132,133] Hepatomegaly has also been associated with **trisomy 21,** possibly because of the abnormal myelopoiesis in these fetuses.[134]

Hepatic Calcifications

Hepatic calcifications can be single or multiple (Fig. 38.18). In one series, hepatic calcifications were identified in 14 of 24,600 consecutive pregnancies scanned between 15 and 26 weeks, representing an incidence of 1 in 1750 pregnancies.[135] The pathophysiology of hepatic calcifications in otherwise normal fetuses is unknown, and in the **majority of cases, such calcifications represent an isolated finding** and have no clinical consequence.[136] However, hepatic calcifications are associated with

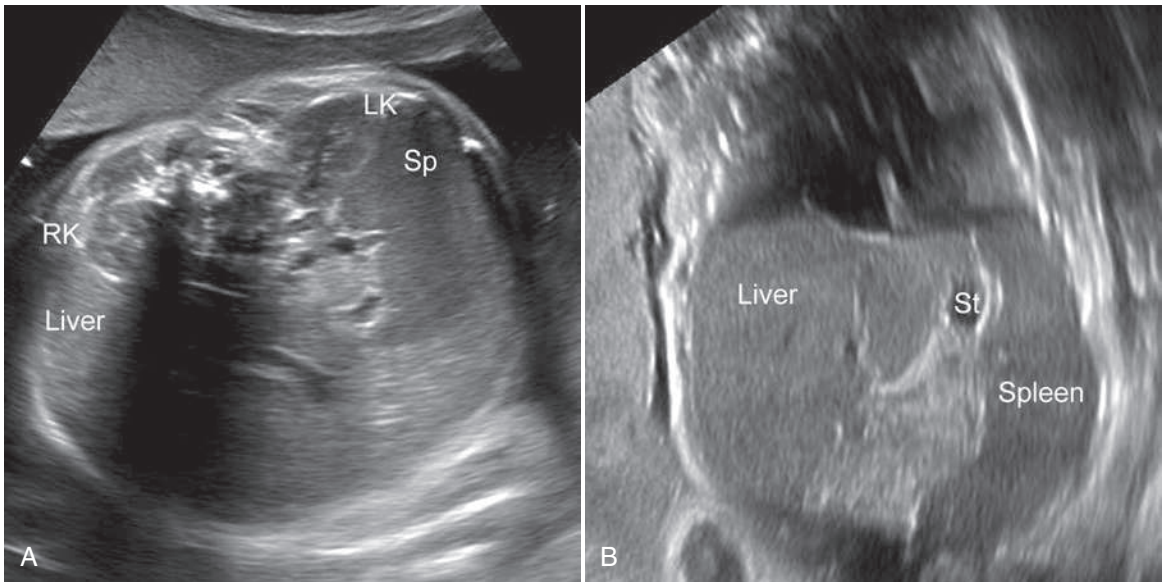

FIG. 38.17 Hepatosplenomegaly. (A) Transverse and **(B)** reconstructed coronal images at 33 weeks show marked hepatosplenomegaly in a fetus with congenital **cytomegalovirus infection.** *LK,* Left kidney; *RK,* right kidney; *Sp,* spleen; *St,* stomach.

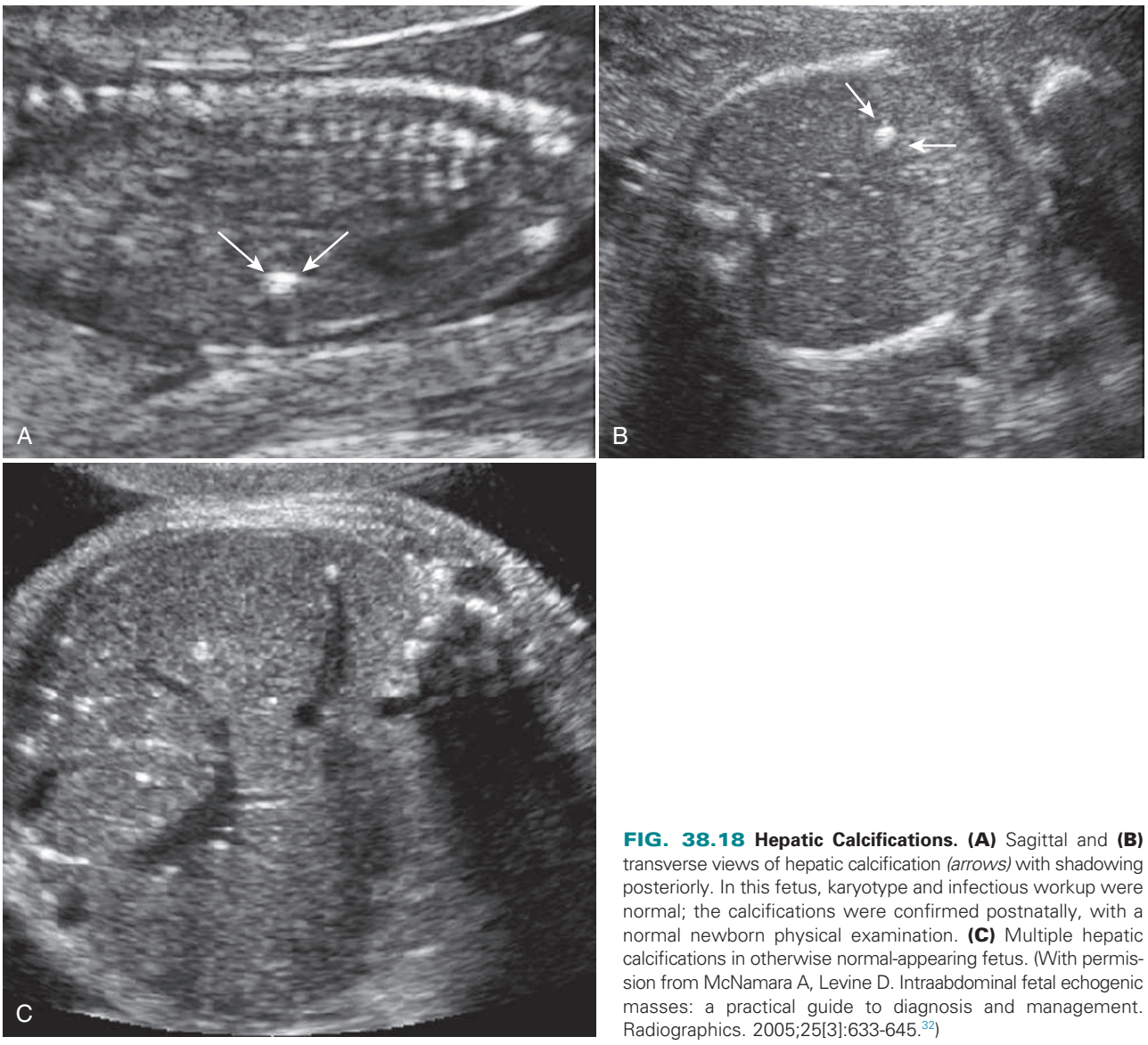

FIG. 38.18 Hepatic Calcifications. (A) Sagittal and **(B)** transverse views of hepatic calcification *(arrows)* with shadowing posteriorly. In this fetus, karyotype and infectious workup were normal; the calcifications were confirmed postnatally, with a normal newborn physical examination. **(C)** Multiple hepatic calcifications in otherwise normal-appearing fetus. (With permission from McNamara A, Levine D. Intraabdominal fetal echogenic masses: a practical guide to diagnosis and management. Radiographics. 2005;25[3]:633-645.[32])

aneuploidy and **fetal infections** (e.g., CMV,[137] parvovirus B19,[138] and varicella[139]). Calcifications of the liver parenchyma should be distinguished from peritoneal calcifications that outline the liver surface and peritoneal cavity, which can be secondary to **meconium peritonitis** and may therefore be associated with **cystic fibrosis.** Calcifications associated with **vascular insult** have also been reported, including **thromboembolism of the hepatic and portal veins.**[140] Hepatic calcifications may occur with **hepatic masses** (discussed later). In a series of 21 pregnancies with isolated hepatic calcifications, there was one case of trisomy 21 and one case of parvovirus B19 infection; the rest of the fetuses had normal outcomes.[138]

Conditions Associated With Hepatic Calcifications

Normal variant—majority of cases when isolated or few
Aneuploidy
Fetal infection—CMV, parvovirus B19, varicella, herpes simplex, toxoplasmosis
Hepatic vascular insult/ischemia
Hepatic mass

When hepatic calcifications are visualized, it is important to assess the number, size, and distribution of the calcifications; determine whether associated hepatic masses are present; document normal flow in the liver to rule out thrombosis; search for other signs of fetal infection; and assess for any structural or growth abnormalities. Genetic counseling and screening for cystic fibrosis and fetal infections should be included in the investigation of these cases.

Hepatic Cysts and Masses

The majority of hepatic masses are hypoechoic or cystic and may include **hepatic cysts** (Fig. 38.19), **hemangiomas** (Fig. 38.20), and **abnormal myelopoiesis** in fetuses with trisomy 21.[134] Less commonly, **solid echogenic masses** may be identified, which may represent benign lesions such as **hamartoma** (which may have a cystic or mixed cystic-solid appearance) and **adenoma,** as well as malignant lesions as **hepatoblastoma.** Color flow Doppler ultrasound should be used to determine the vascularity of the lesions. Vascular hepatic lesions include **congenital hemangiomas** and **hepatoblastomas,** although it should be emphasized that most hemangiomas are small and appear avascular on color Doppler ultrasound. Such vascular lesions, especially when of large size, may lead to **high-output cardiac failure and hydrops,** and **fetal anemia and thrombocytopenia (Kasabach-Merritt sequence).**[141-143] Therefore these fetuses should be followed for signs of hydrops and fetal anemia using middle cerebral artery Doppler.[144-147]

Gallbladder and Biliary System

The normal fetal gallbladder is an oblong, echolucent structure in the anterior liver (Fig. 38.21, Video 38.9), generally located 45 degrees to the right of midline and inferior to the umbilical vein. The gallbladder increases in size with gestation.[148] In multiple series, visualization of the gallbladder was most common from

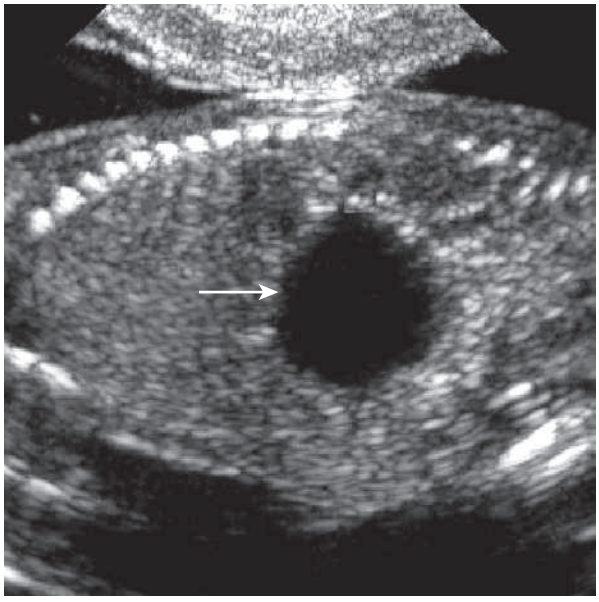

FIG. 38.19 Hepatic Cyst. Hepatic cyst *(arrow)* in sagittal view of the abdomen.

20 to 32 weeks.[149,150] **Enlarged gallbladder** is associated with fetal aneuploidy, but all reported fetuses also had other prenatally visualized anomalies.[114]

Nonvisualization of the Gallbladder

Nonvisualization of the gallbladder is associated with gallbladder agenesis/atresia, cystic fibrosis,[151,152] aneuploidy,[151] and biliary atresia.[149,153,154] Extrahepatic biliary atresia is a rare congenital disorder, with an incidence of 0.6 in 10,000 live births according to a population-based study.[155] It is the single leading cause for liver transplantation during childhood and is commonly associated with additional anomalies.[155,156] The diagnosis of extrahepatic biliary atresia should be considered whenever the gallbladder cannot be visualized. Additional findings may include a cyst in the region of the hepatic hilum.[153] Bardin et al., in a study of 32 fetuses in which the gallbladder could not be visualized, reported that amniotic levels of gamma-glutamyl transpeptidase (GGTP) can assist in the prediction of pregnancy outcome. Of the 27 (84%) fetuses with normal GGTP levels, only 1 had an abnormal karyotype, whereas 3 of the 5 fetuses with low GGTP were diagnosed with extrahepatic biliary atresia.[154]

In a series of 578 fetuses, Hertzberg et al.[149] demonstrated the gallbladder between 12 and 40 weeks in 82.5% of cases, but none of the fetuses with isolated nonvisualization of the gallbladder had any adverse neonatal outcome. Blazer et al.[150] reported on 29,749 consecutive women whose fetuses were imaged by both transabdominal and transvaginal sonography at 14 to 16 weeks. The gallbladder could not be visualized in 34 (0.1%) fetuses, and investigation that included amniocentesis and screening for cystic fibrosis was offered in all of these cases. Additional abnormalities were identified in 14 (41%) of these fetuses. All 20 fetuses in which nonvisualization of the gallbladder was an isolated finding had a normal karyotype and appeared normal after birth. In another series of 37 fetuses with nonvisualization of the gallbladder, 5 (13.5%) were found to have

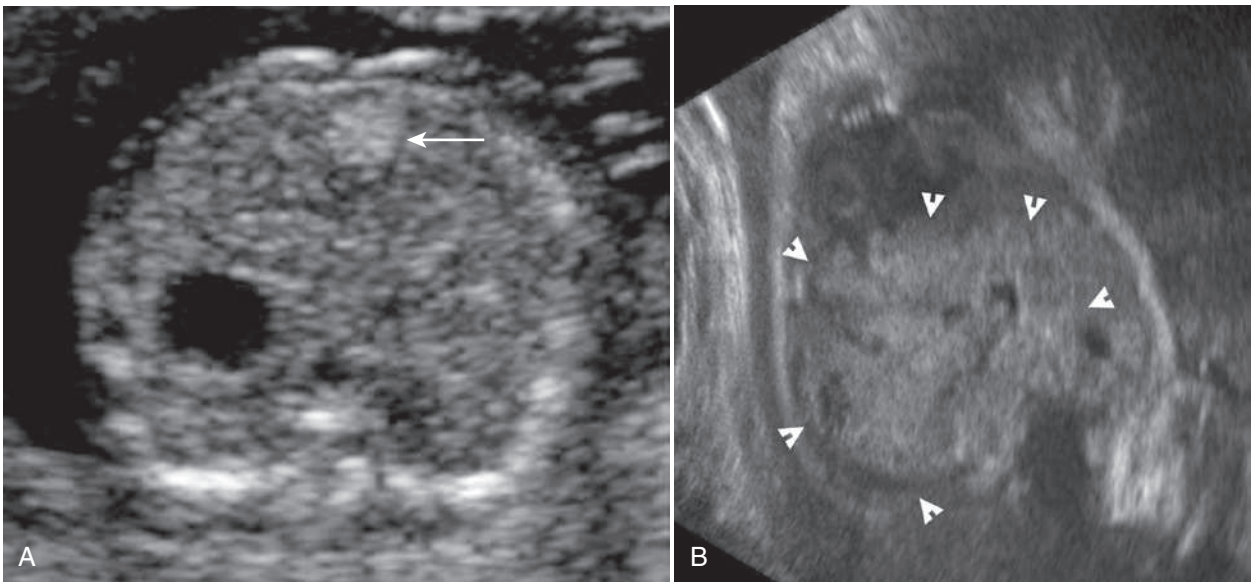

FIG. 38.20 Hepatic Mass. (A) Hepatic hemangioma *(arrow)* in 18-week fetus. **(B)** Coronal ultrasound at 34 weeks shows a large, heterogenous echogenic mass *(arrowheads)* replacing the entire right lobe of the liver, thought to be an **infantile hemangioendothelioma.** The infant was delivered at 38 weeks because of signs of cardiac decompensation but did well with spontaneous tumor involution over several months. (**A** with permission from McNamara A, Levine D. Intraabdominal fetal echogenic masses: a practical guide to diagnosis and management. Radiographics. 2005;25[3]:633-645.[32])

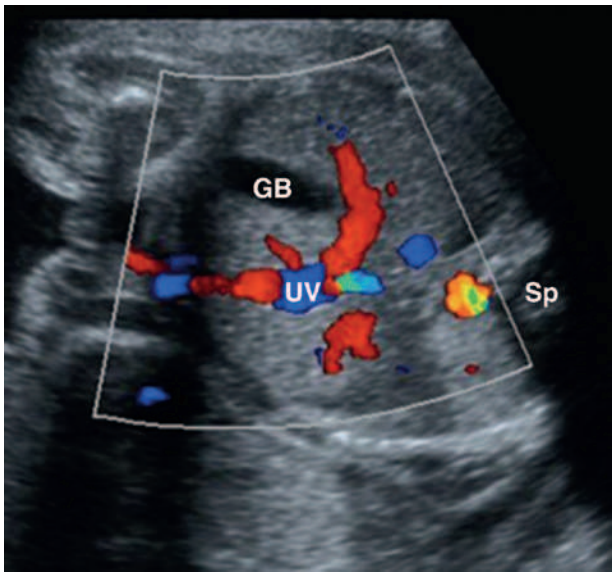

FIG. 38.21 Normal Gallbladder. Transverse color Doppler image at 35 weeks shows the normal gallbladder *(GB)* as an oval, anechoic structure in the right upper quadrant. The umbilical vein *(UV)* enters the portal venous system anterior to the aorta and inferior vena cava, which are seen anterior to the spine *(Sp)*. See also Video 38.9.

cystic fibrosis, but in all of these cases echogenic bowel was present as well.[152]

Thus nonvisualization of the gallbladder should be followed by a detailed scan for additional structural abnormalities, soft markers for aneuploidy, and other markers of cystic fibrosis such as echogenic bowel. Screening for cystic fibrosis and amniocentesis for karyotype and assessment of the level of liver enzymes in the amniotic fluid may be offered as well. When these investigations are negative, fetal outcome is expected to be normal in the majority of cases. In many of these cases, the gallbladder will become apparent later in pregnancy or after delivery.[154] In the remainder of cases, the underlying cause may be agenesis of the gallbladder, which may be considered as an anatomic variant.

Fetal Gallstones

Echodensities in the fetal gallbladder can represent either **sludge** or **gallstones** and are most commonly seen in the third trimester.[157-159] **Gallstones** may produce acoustic shadowing (Fig. 38.22). In most cases, postnatal resolution occurs, and children are asymptomatic.

Choledochal Cyst

Choledochal cysts are rare congenital cystic dilatations of the biliary tree and are associated with biliary atresia and hepatic fibrosis[160] (Fig. 38.23). The most common form involves a segment or all of the extrahepatic common bile duct; however, they may also present as diverticular outpouching of the extrahepatic duct or involve the intrahepatic ducts (Caroli disease). Cystic lesions of the biliary tree in utero may be anechoic or may contain echogenic debris. Although these lesions can be due to choledochal cyst, a cyst in the right upper quadrant can also be due to a rare bilobed gallbladder. The main differential diagnosis is **extrahepatic biliary atresia.** In most cases choledochal cysts are resected after birth, given the risk of cholangitis, fibrosis, and potential malignancy.

Pancreas

Visualization of the pancreas is often not possible at the time of the second-trimester anatomy scan. The pancreas may be seen

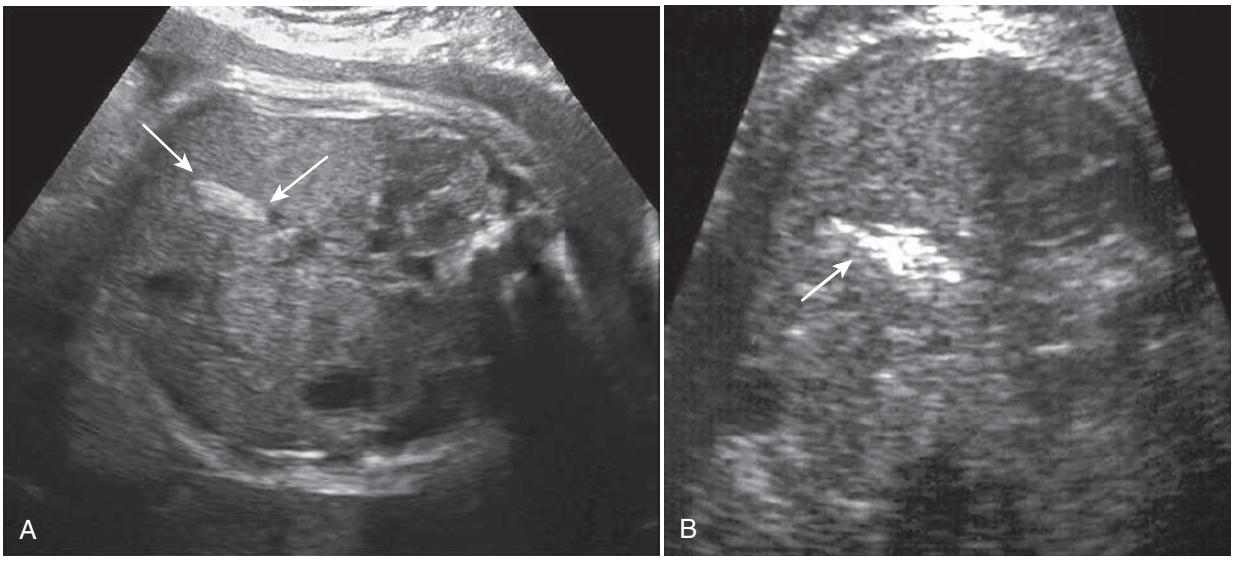

FIG. 38.22 Gallbladder Sludge and Stones. (A) Transverse third-trimester abdomen shows the lumen of the gallbladder surrounding echogenic material *(arrows)* consistent with sludge. This fetus had a normal newborn course. **(B)** Fetus with gallstones *(arrow)*.

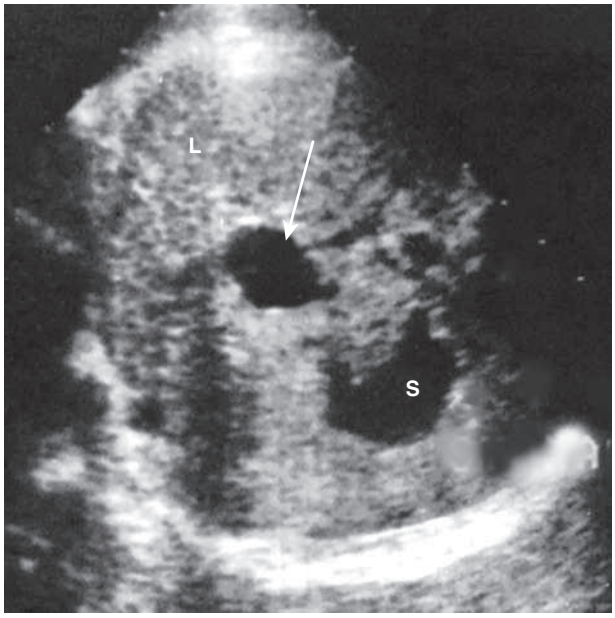

FIG. 38.23 Choledochal Cyst. Transverse view of abdomen shows a cyst *(arrow)* with stomach *(S)* on the left and liver *(L)* on the right.

as elongated structure in a transverse plane at the level of the kidneys and behind the stomach.

Annular Pancreas

Annular pancreas is a rare developmental anomaly that accounts for 1% of neonatal intestinal obstructions.[161,162] The annular tissue in these cases has been suggested to originate from the ventral pancreatic bud.[163] Annular pancreas is considered in the differential diagnosis of a dilated duodenum or the double-bubble sign[54,164] (Fig. 38.24, Video 38.10). A case report demonstrated an echogenic mass surrounding the distal part of the dilated duodenum. Three-dimensional ultrasound was suggested to be helpful in making this diagnosis.[162] Annular pancreas has been associated with trisomy 21 and malrotation.

Pancreatic Cysts

Pancreatic cyst is a rare congenital abnormality of the pancreas that originates from the pancreatic duct and may appear as a single cystic or multicystic mass.[165-168] Pancreatic cysts may be idiopathic but also have been associated with **Beckwith-Wiedemann syndrome,**[169] **polycystic kidney disease,** and **von Hippel–Lindau disease.** In many cases, the pancreatic origin of the cysts cannot be determined prenatally.

Spleen

The fetal spleen is visualized in the left upper abdomen, lateral to the spine and superior to the left kidney. The relationship to the fetal stomach can vary (Fig. 38.25). Nomograms are available for splenic size from 18 weeks until term.[170,171] **Asplenia** or **polysplenia** (see Fig. 38.5) are associated with heterotaxy syndromes and warrant a detailed fetal cardiac examination.

Splenomegaly

Splenomegaly is associated with conditions similar to those associated with **hepatomegaly** (see Fig. 38.17), **hemolytic fetal anemia** when it correlates with the severity of fetal anemia,[172,173] **fetal infections,**[174] **metabolic and storage disorders, trisomy 21,**[175] and overgrowth syndromes such as **Beckwith-Wiedemann syndrome.**

Splenic Cysts

Fetal **splenic cysts** are rare, usually benign, and are associated with overall good prognosis[176,177] (Fig. 38.26, Video 38.11). The natural history of splenic cysts is variable. Although these cysts may regress spontaneously,[178] in some cases they are complicated by infection, rapid growth, rupture, and/or bleeding.[179] Therefore

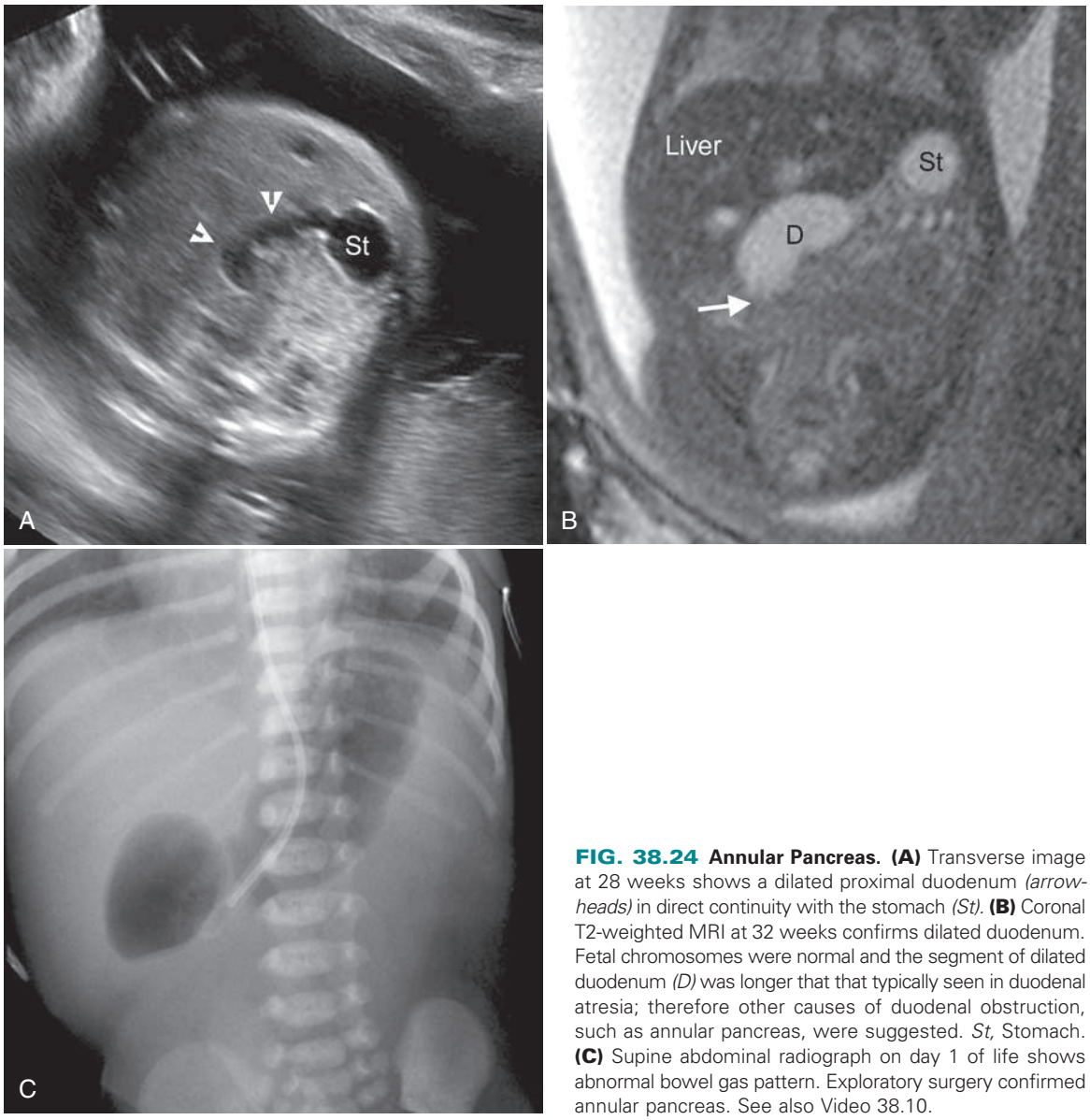

FIG. 38.24 Annular Pancreas. (A) Transverse image at 28 weeks shows a dilated proximal duodenum *(arrowheads)* in direct continuity with the stomach *(St)*. **(B)** Coronal T2-weighted MRI at 32 weeks confirms dilated duodenum. Fetal chromosomes were normal and the segment of dilated duodenum *(D)* was longer that that typically seen in duodenal atresia; therefore other causes of duodenal obstruction, such as annular pancreas, were suggested. *St,* Stomach. **(C)** Supine abdominal radiograph on day 1 of life shows abnormal bowel gas pattern. Exploratory surgery confirmed annular pancreas. See also Video 38.10.

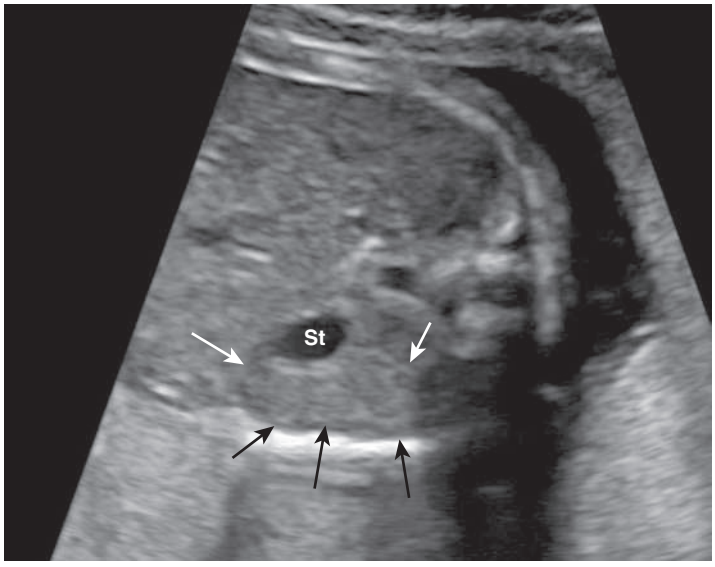

FIG. 38.25 Normal Spleen. Normal spleen *(arrows)* in the transverse view of second-trimester abdomen. *St,* Stomach.

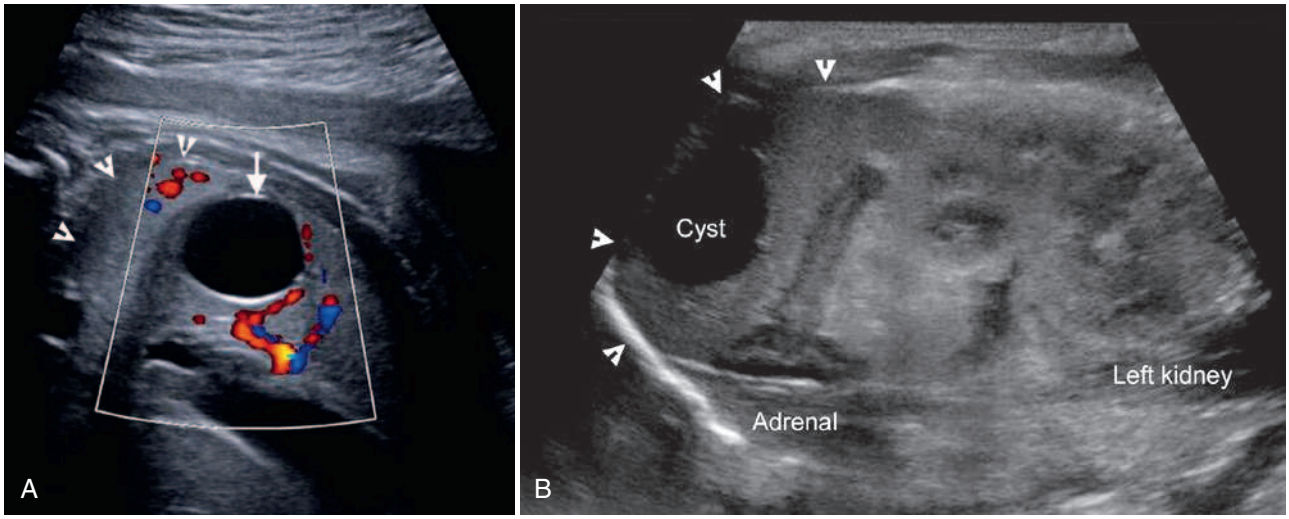

FIG. 38.26 Splenic Cyst. (A) Oblique transverse color Doppler image through the fetal abdomen at 34 weeks shows a simple cyst *(arrow)* in the left upper quadrant. The arrowheads outline the diaphragmatic surface of the spleen. The kidney was clearly separate from the mass. **(B)** Coronal image of the neonatal abdomen confirms that the cyst is in the spleen *(arrowheads)* and separate from the left adrenal and left kidney. See also Video 38.11.

these cysts, when detected antenatally, should be followed by serial ultrasound. Detailed anatomic assessment is indicated for the presence of associated anomalies or cysts involving other organs such as kidneys and liver.

ABDOMINAL WALL

The most common types of abdominal wall defects are **gastroschisis** and **omphalocele.** Other, less common types include **bladder exstrophy, cloacal exstrophy, ectopia cordis,** and more severe ventral body wall defects including **pentalogy of Cantrell, body stalk anomaly,** and **abdominoschisis in amniotic band syndrome.** The overall incidence of abdominal wall defects is 6.3 per 10,000 pregnancies.[180] Because of the loss of integrity in the epidermal covering, abdominal wall defects are associated with elevated levels of **maternal serum alpha-fetoprotein (MS-AFP).** In the past 3 decades, with both maternal serum screening and fetal anatomic surveys becoming routine, the majority of abdominal wall defects are diagnosed by the second trimester. Centers that practice universal first-trimester screening have documented confirmation of diagnoses earlier than 14 weeks.[14,181] With increased access to early scanning, earlier diagnosis is expected to become more common.

Embryology

The embryonic abdominal wall develops from the lateral plate mesoderm and ectoderm between day 16 and day 26 of embryonic life. Each lateral plate of mesoderm splits into parietal and visceral layers, the space between which becomes the body cavity (**coelom** or **celum**), which later differentiates into the peritoneal, pericardial, and pleural cavities.[182-184] The lateral folds (consisting of the parietal layer of the lateral plate mesoderm and the overlying ectoderm) then fold around the coelom caudally, cephalad, and laterally. In the normal enfolding process, the lateral folds come together and fuse to form the ventral body wall. Failure of this process to be completed because of teratogenic or vascular factors lead to a defect in the ventral body wall. Depending on the location of the defect in the ventral abdominal wall, the result can be **gastroschisis** (abdominal region), **ectopia cordis** (thoracic region), or **bladder exstrophy** (pelvic region).

In parallel to the development of the ventral body wall, rapid growth and elongation of the bowel takes place, and the abdominal cavity is temporarily too small to accommodate all of its contents. This results in transient protrusion of the intestine into the extraembryonic coelom at the base of the umbilical cord, a process termed **physiologic midgut herniation**[185] (Figs. 38.27 and 38.28). This herniation is usually visible on ultrasound from 9 to 11 weeks and resolves (or undergoes reduction) by 12 weeks of gestation.[181,186] Therefore if prominent material is seen at the cord insertion site, and it is unclear whether this finding represents an abdominal wall defect or physiologic bowel herniation, a follow-up scan in 1 to 2 weeks will resolve the issue. Failure of the gut loops to return to the body cavity beyond that point has been suggested as the underlying cause in cases of omphalocele.[184] Thus persistence of the midgut herniation beyond 12 weeks or the presence of content other than intestine (e.g., liver) in the herniation should be considered as evidence of true abdominal wall defect (i.e., **omphalocele**).

Gastroschisis

Gastroschisis is a relatively small (<4 cm in most cases), full-thickness paraumbilical defect of the abdominal wall, most often located to the right of the umbilicus. Free-floating loops of bowel in the amniotic fluid are the key finding on ultrasound.

Epidemiology

In population-based studies in Europe, Australia, and Japan, the incidence of gastroschisis has increased from 0.4 to 1.6

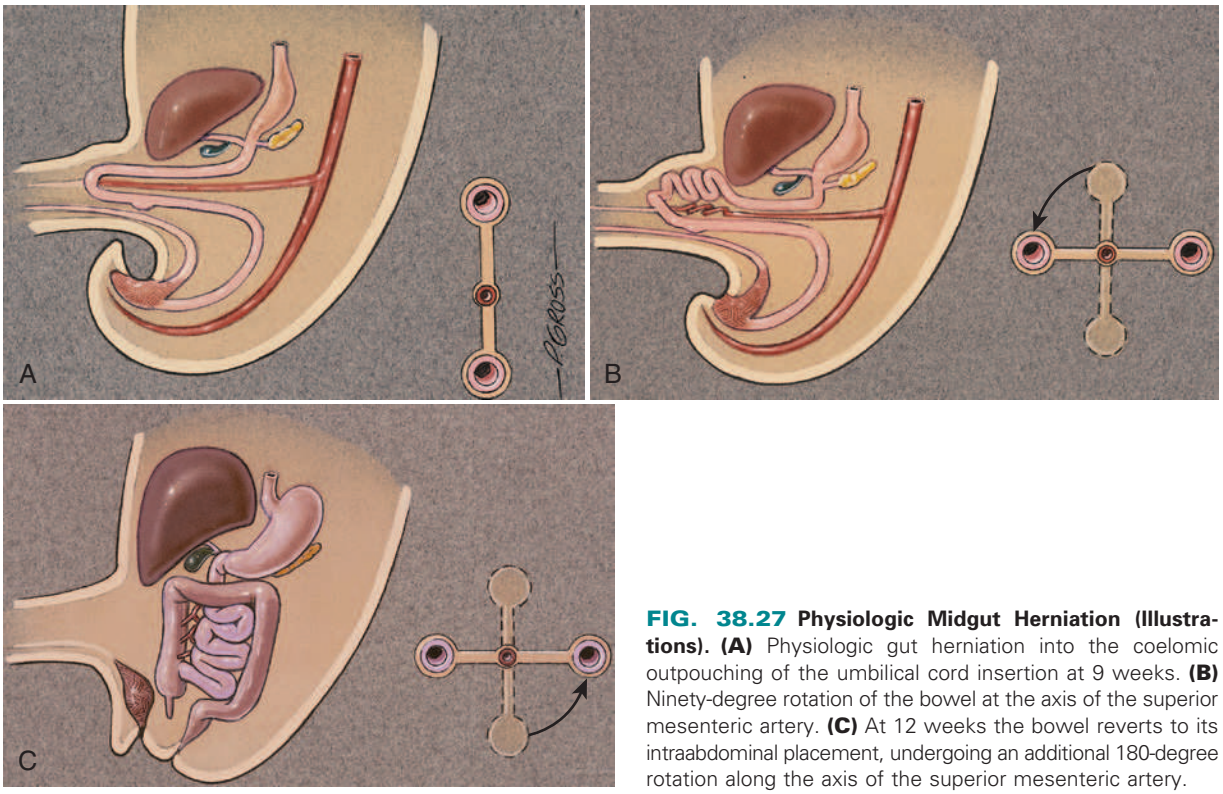

FIG. 38.27 Physiologic Midgut Herniation (Illustrations). (A) Physiologic gut herniation into the coelomic outpouching of the umbilical cord insertion at 9 weeks. **(B)** Ninety-degree rotation of the bowel at the axis of the superior mesenteric artery. **(C)** At 12 weeks the bowel reverts to its intraabdominal placement, undergoing an additional 180-degree rotation along the axis of the superior mesenteric artery.

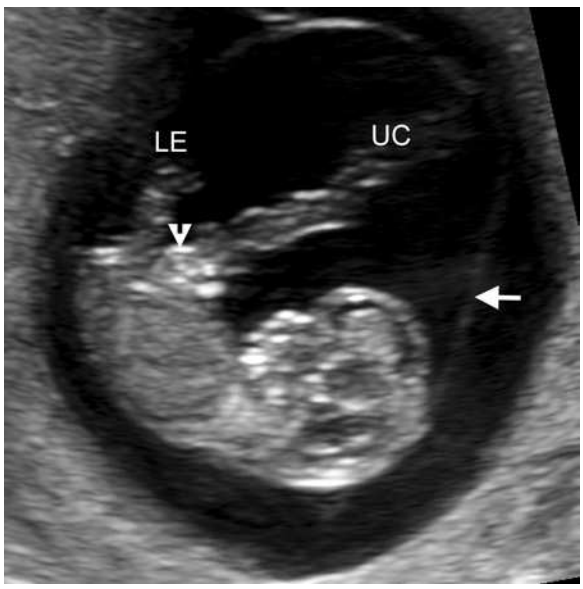

FIG. 38.28 Physiologic Midgut Herniation. Sagittal image at 10 weeks shows echogenic loops of bowel *(arrowhead)* in the base of the normal umbilical cord *(UC)*. The lower extremities *(LE)* are visible and the amnion *(arrow)* has not yet expanded sufficiently to fill the chorionic cavity. These are all normal observations at this gestational age.

per 10,000 up to 1.4 to 4 per 10,000 live births during the past 35 years.[187-191] There is no gender predilection in the affected fetuses. The incidence is higher in **teenage mothers,** with the largest population-based study showing a 10-fold higher incidence in 15- to 19-year-old women compared with 20- to 25-year-old women.[188] Other factors associated with gastroschisis include use of **tobacco, illicit drugs,** and **pseudoephedrine.**[187,188,191-196] More recently, a possible association of gastroschisis with agricultural chemicals such as **atrazine** has been suggested.[197-199]

Pathogenesis

The pathogenesis of gastroschisis is unclear. One hypothesis is that the abdominal wall defect is the result of an isolated vascular compromise of the abdominal wall in the first trimester. This hypothesis is supported by the risk factors for gastroschisis listed in the previous paragraph, as well as by the association of gastroschisis with other fetal abnormalities that are thought to have an underlying vascular cause. Other proposed causes include failed development of the mesoderm and the lateral mesodermal enfolding,[200] rupture of the amniotic membrane at the base of the umbilical cord, disruption of the right vitelline artery with subsequent body wall damage, and abnormal extension of apoptosis patterns during regression of the right umbilical vein.[184]

Prenatal Diagnosis

The diagnosis of gastroschisis is relatively straightforward when the defect is limited, and free-floating loops of bowel are identified intraamniotically; in these cases the diagnosis can already be made as early as the first trimester.[188,201] Most often the defect is located at the right paraumbilical region (Fig. 38.29, Video 38.12). The free-floating bowel has a characteristic **cauliflower-like appearance.** The bowel may appear echogenic due to edema and inflammation of the wall secondary to long-standing exposure

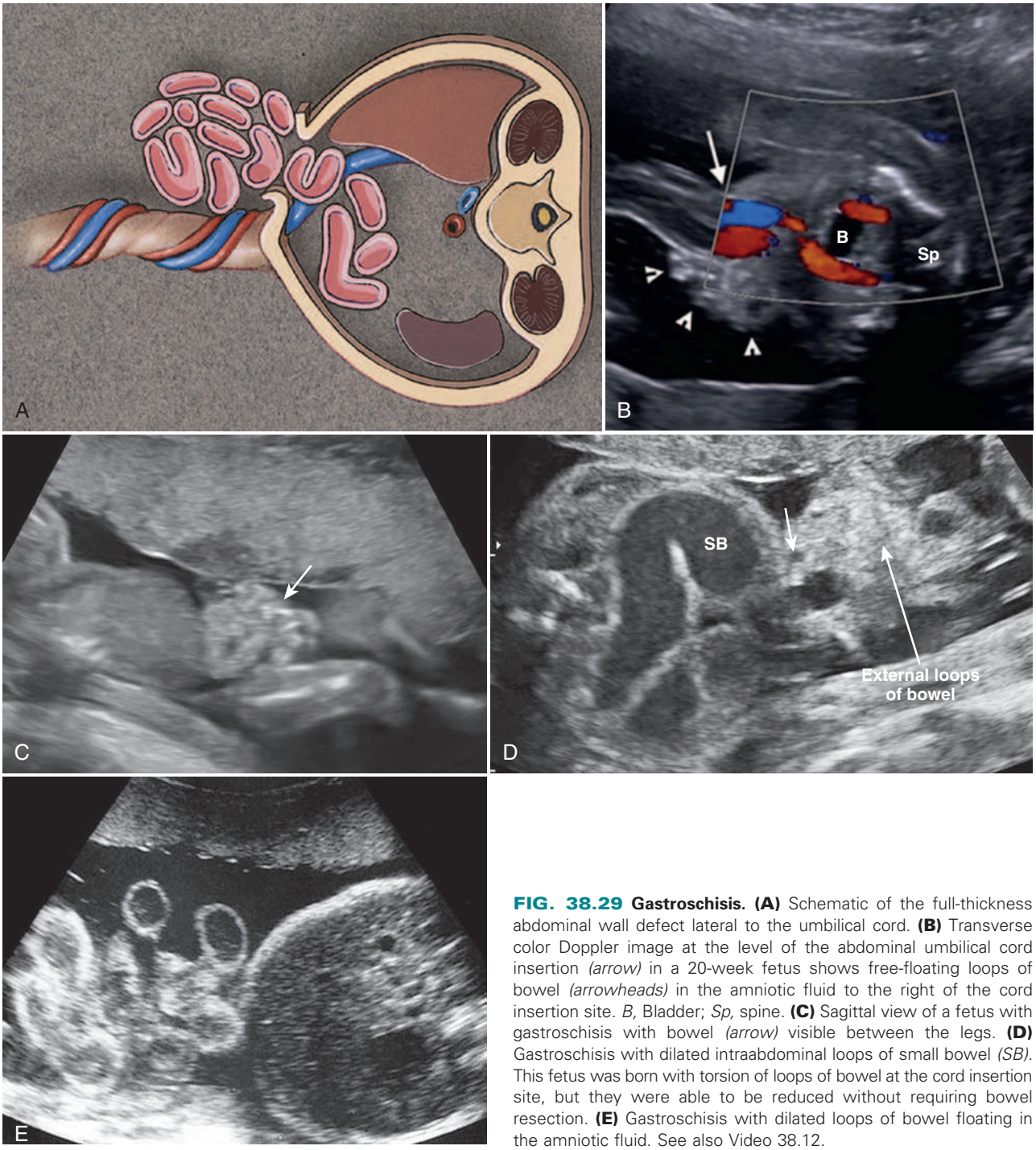

FIG. 38.29 Gastroschisis. (A) Schematic of the full-thickness abdominal wall defect lateral to the umbilical cord. **(B)** Transverse color Doppler image at the level of the abdominal umbilical cord insertion *(arrow)* in a 20-week fetus shows free-floating loops of bowel *(arrowheads)* in the amniotic fluid to the right of the cord insertion site. *B,* Bladder; *Sp,* spine. **(C)** Sagittal view of a fetus with gastroschisis with bowel *(arrow)* visible between the legs. **(D)** Gastroschisis with dilated intraabdominal loops of small bowel *(SB).* This fetus was born with torsion of loops of bowel at the cord insertion site, but they were able to be reduced without requiring bowel resection. **(E)** Gastroschisis with dilated loops of bowel floating in the amniotic fluid. See also Video 38.12.

to amniotic fluid. **Dilated loops of bowel** may be seen either within or outside the abdomen due to associated bowel obstruction secondary to the small abdominal opening or associated volvulus. The stomach is often displaced downward within the abdominal cavity. The umbilical cord inserts normally into the abdomen, adjacent to but separate from the defect. Less often the defect extends upward or laterally and may include structures other than the intestine, such as liver and stomach.

Associated Conditions

Associated GI abnormalities such as atresias, stenosis, perforations, or volvulus are reported in 11% to 31% of cases.[180,202,203] Many of these associated GI conditions are believed to be the result of gastroschisis.[204,205] Additional non-GI anomalies are less common.[202-204,206-208] The risk of **aneuploidy** in cases of isolated gastroschisis is similar to that of the general population.[191,202,206,207] An increased risk of preterm birth, fetal growth restriction (up

to 60% of cases) and stillbirth (4.5%-12%) have been reported in fetuses with gastroschisis. In a recent meta-analysis, the incidence of stillbirth after 36 weeks was only 1.3%.[209] The mechanism responsible for the increased risk of fetal growth restriction and stillbirth remains unclear.[190,206,210]

Management

Initial management of gastroschisis involves detailed sonographic assessment to confirm the diagnosis and assess the extent of the abdominal wall defect and involved organs. The presence of associated anomalies on ultrasound should be documented. Close monitoring with ultrasound and nonstress test are indicated during the third trimester given the increased risk of fetal growth restriction, fetal demise, and GI complications (e.g., obstruction and perforation), although clear guidelines regarding the onset and frequency of monitoring are lacking. The presence of dilated stomach and/or dilated loops of bowel, either within the fetal abdomen or within the amniotic cavity, should be documented. Fetal weight estimation should be done using formulas that are based on indices of fetal head and femur length but not abdominal circumference to avoid underestimation of fetal weight.[211]

The optimal timing of delivery is debated. Given the increased risk of stillbirth and the concern that prolonged in utero exposure of the bowel to amniotic fluid may worsen outcomes, two trials compared the outcome of fetuses that were born preterm (average, 35 weeks) versus those delivered at term or for abnormal fetal testing.[212,213] Neither trial showed an improved outcome in the preterm group. Thus delivery prior to 37 weeks should be considered only in cases of fetal growth restriction or abnormal fetal testing. There is no evidence supporting early delivery in cases of bowel dilatation. In a recent study of 296 pregnancies complicated by gastroschisis, it was found that induction of labor at 37 weeks of gestation was associated with reduced risks of sepsis, bowel damage, and neonatal death compared with pregnancies managed expectantly beyond 37 weeks of gestation.[214] These data may support a practice of routine delivery in the early term period (37-38 weeks). With respect to mode of delivery, there is no evidence that cesarean delivery improves neonatal outcome, and therefore cesarean delivery should be reserved for the usual obstetric indications.[215] Neonatal outcome in cases of gastroschisis is associated with an overall survival rate of over 90%, although outcome is less favorable in cases of complex gastroschisis.[216,217]

Omphalocele

Omphalocele refers to herniation of the intestine and other abdominal organs into the base of the umbilical cord through an enlarged umbilical ring, with the umbilical cord inserting at the apex of the herniated sac. The herniated content is covered by amnion and peritoneum (Fig. 38.30, Video 38.13).

Epidemiology

The incidence of omphalocele varies geographically, from 0.6 per 10,000 births in Japan[191] to 6 per 10,000 births in the British Isles.[202,206] In a registry-based study from the United States, the incidence of omphalocele was 1.92 per 10,000 live births.[218] Omphalocele has been reported to be more common in women 35 to 40 years old[191] and also among women younger than 20 years.[218] Other associations include male sex and multiple gestations.[218]

Prenatal Diagnosis

In the first trimester, **physiologic midgut herniation** can be mistaken for an omphalocele. This normal finding is limited to herniation of bowel loops and should resolve by 12 weeks. It should never include the liver, and the herniation should not be more than 1 cm into the cord. The presence of even small herniation into the base of the umbilical cord beyond 12 weeks is therefore diagnostic of omphalocele (Fig. 38.30B).

Most cases of omphalocele are readily detected at the time of the second-trimester scan as a protrusion of abdominal content, mainly small bowel loops, into the base of the umbilical cord, contained within a sac consisting of peritoneum and amniotic membrane. In cases of large defects, the omphalocele may contain other organs such as liver and stomach (Fig. 38.31). The umbilical cord can be seen inserted on the herniated sac rather than directly to the abdominal wall.

Associated Conditions

In contrast to gastroschisis, omphalocele is commonly associated with chromosomal abnormalities (10%-30%)[191,202] and additional structural abnormalities (55%-58%).[202,208,219] The most common aneuploidies are **trisomies 13 and 18.**[220,221] The risk of genetic abnormalities is higher in the presence of additional structural abnormalities as well as in cases with a small defect when the herniated content is limited to small bowel (see Fig. 38.30B). Thus cases where the liver is found in the omphalocele are less likely to be associated with chromosomal abnormalities. Omphalocele is associated with several single gene mutation syndromes (including autosomal dominant, autosomal recessive, and X-linked recessive disorders),[222] and Beckwith-Weidemann syndrome. **Beckwith-Weidemann syndrome** involves a mutation or deletion of imprinted genes within the chromosome 11p15.5 region and is associated with omphalocele, macroglossia, and overgrowth (Fig. 38.32).

Associated structural abnormalities are common and include midline defects (cardiac, cleft lip and palate, and spinal/vertebral anomalies), clubfoot, and central nervous system anomalies.[219] Because of the common association with aneuploidies and multisystem anomalies, many of these pregnancies are terminated, potentially biasing outcome data.

Management

The finding of fetal omphalocele should trigger a detailed evaluation for the presence of associated structural anomalies, including fetal echocardiography.[223] Genetic counseling is recommended and amniocentesis should be offered to assess for karyotype or microarray, as well as for screening for specific genetic syndromes, including Beckwith-Wiedemann syndrome.

Fetal monitoring with serial ultrasound examinations is recommended given an increased risk for polyhydramnios, ascites, fetal growth restriction, and stillbirth. As in the case of

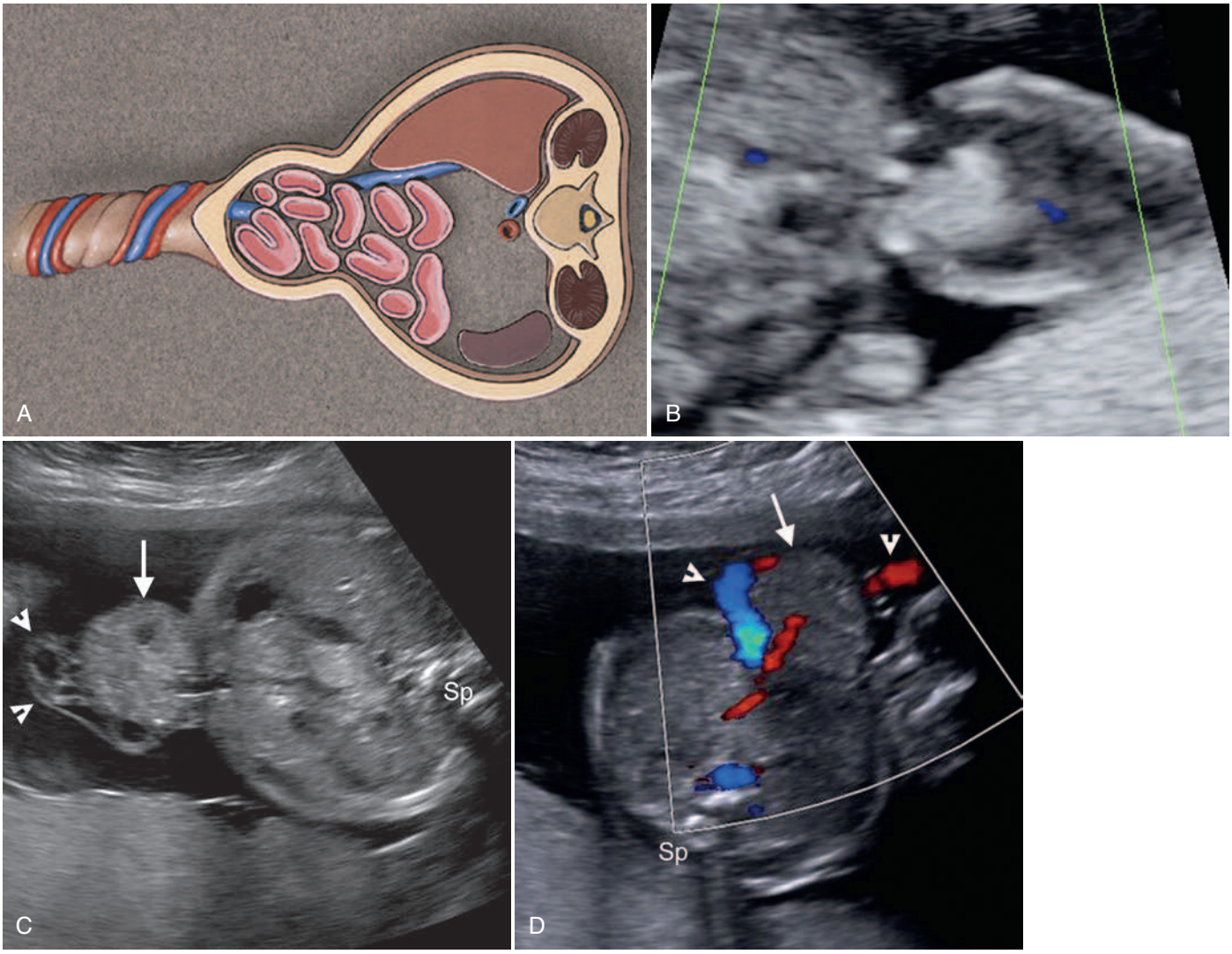

FIG. 38.30 Small Omphalocele. (A) Schematic of membrane covered omphalocele containing only bowel. **(B)** Transverse image of abdomen with loop of bowel herniated into base of umbilical cord. The fetus had trisomy 18. **(C)** Transverse image of abdomen at 26 weeks shows a bowel-only omphalocele *(arrow).* The umbilical cord *(arrowheads)* inserts onto the membrane, which covers the defect. *Sp,* Spine. **(D)** Transverse color Doppler image at 26 weeks shows a bowel-only omphalocele *(arrow).* The umbilical vessels *(arrowheads)* course around the bowel, in the membrane that covers the defect. *Sp,* Spine. See also Video 38.13.

gastroschisis, fetal weight estimation should be done using formulas that are based on indices of fetal head and femur length but not abdominal circumference to avoid underestimation of fetal weight.[224]

There is no evidence that early delivery or cesarean delivery are associated with improved outcomes.[225] Therefore vaginal delivery following spontaneous onset of labor should be preferred unless other indications are present for induction of labor or cesarean delivery. Neonatal outcome is mainly determined by the presence of associated genetic and/or structural anomalies.[191,218]

Bladder Exstrophy

Bladder exstrophy refers to infraumbilical abdominal wall defect that results from incomplete closure of the lower abdominal wall and the anterior wall of the bladder.[226] It is a rare abdominal wall defect with an incidence of about 1 of 30,000 births.[227]

The prenatal diagnosis of bladder exstrophy is mainly based on the inability to visualize the bladder. The exposed bladder mucosa may become inflamed and thickened and may therefore appear as an irregular contour of the lower anterior abdominal wall (Video 38.14).[228] Another clue for the diagnosis is caudal displacement of the umbilical cord insertion site (Fig. 38.33). Associated anomalies include genital abnormalities such as **epispadias,** a combination known as **bladder exstrophy–epispadias complex.**[226]

Neonatal survival is overall good, although the repair of these defects is complex, often requiring staged procedures, to maintain continence and functional genital tissue.[229,230]

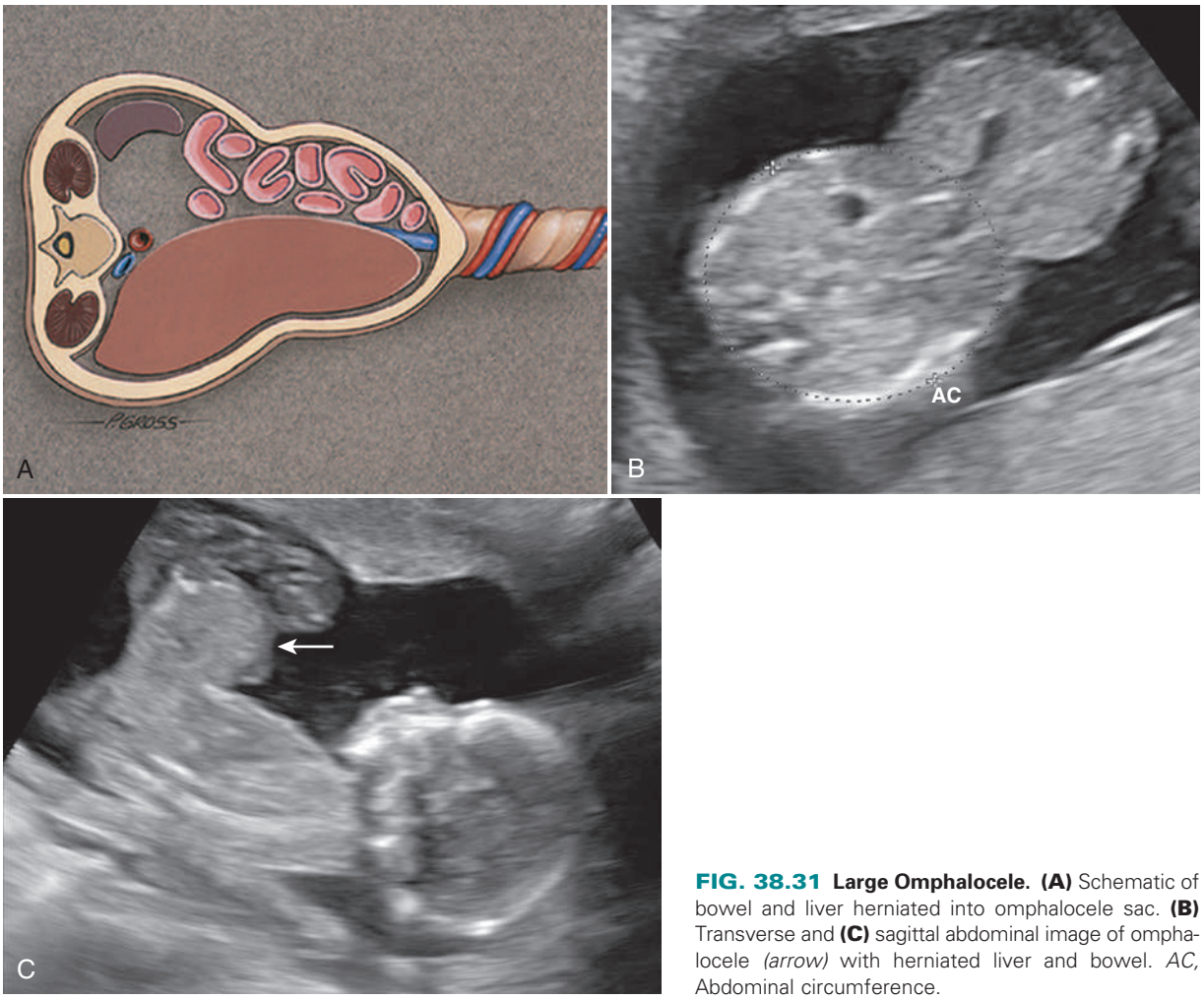

FIG. 38.31 Large Omphalocele. (A) Schematic of bowel and liver herniated into omphalocele sac. **(B)** Transverse and **(C)** sagittal abdominal image of omphalocele *(arrow)* with herniated liver and bowel. *AC,* Abdominal circumference.

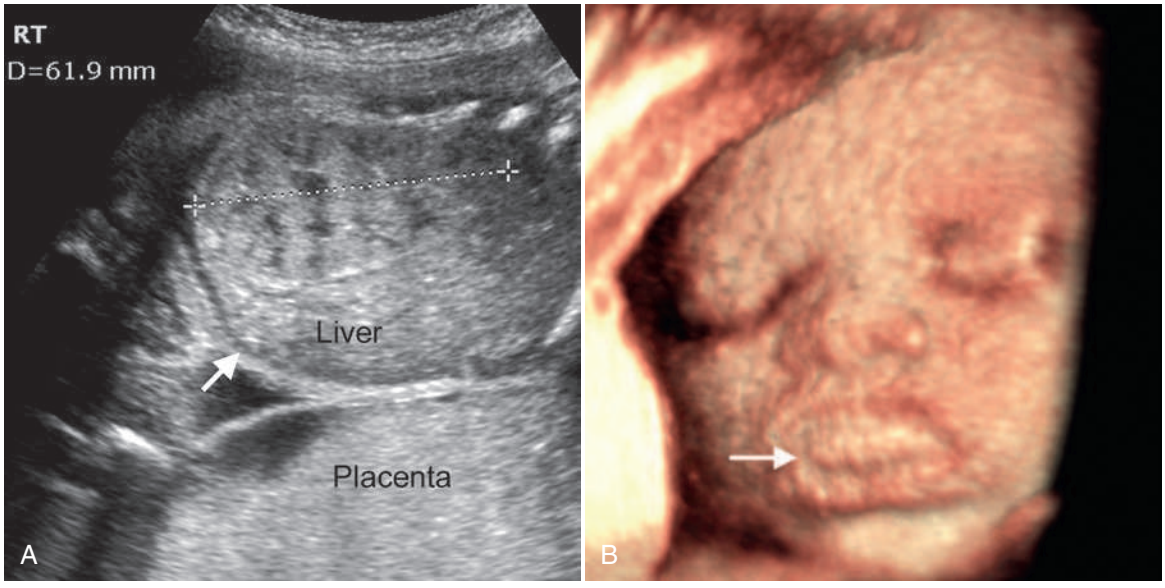

FIG. 38.32 Beckwith-Wiedemann Syndrome. (A) Coronal oblique ultrasound at 28 weeks shows the right kidney measuring 6.9 cm, well above the 95th percentile. The adjacent liver *(arrows)* extends beyond the renal margins indicating that it is enlarged as well. Visceromegaly is part of Beckwith-Wiedemann syndrome. **(B)** Three-dimensional surface rendered view of the fetal face in the same case shows macroglossia *(arrow).*

FIG. 38.33 Bladder Exstrophy. (A) Transvaginal sonogram at 16 weeks shows an abdominal wall defect *(arrows),* located low in the abdomen. The bladder was not visualized. *Sp,* Spine. **(B)** Postmortem photograph shows bladder exstrophy. *UC,* Umbilical cord. **(C)** Bladder exstrophy *(arrow)* in a different fetus. See also Video 38.14.

Cloacal Exstrophy

Cloacal exstrophy is a more complex multisystem abdominal wall defect that affects all the components of the **cloaca** (bladder and urethra, genitalia and rectum), as well as **lower spine.** Cloacal exstrophy is often termed **OEIS complex** (*o*mphalocele-*e*xstrophy–*i*mperforate anus–*s*pinal dysraphism) (Fig. 38.34, Video 38.15). **Genital abnormalities** are also common.[231] The pathogenesis of cloacal exstrophy is unclear but has been attributed to premature rupture of the cloacal membrane or to very early defect in the closure of the ventral body wall.[228] It occurs at a higher rate in monozygous than in dizygous twins,[129] suggesting a vascular component.

The prenatal diagnosis is based on the combination of **omphalocele, inability to visualize the bladder** and **anal dimple,** and the presence of spine anomalies such as **meningomyelocele** or **tethered cord.** Additional findings may include genital abnormalities (e.g., **epispadias**), **single umbilical artery, renal abnormalities** and **ascites.**[232,233] A unique sonographic sign is the **"elephant trunk,"** which is the result of a prolapsed loop of bowel between the two halves of the open bladder.[234]

Diagnosis of OEIS has been reported as early as 13 weeks.[69] Diagnostic difficulties can occur in differentiating this disorder from other complex abdominal wall defects including **limb–body wall complex** and **pentalogy of Cantrell.**[129,231,235] Although the features of OEIS (when seen) are specific, the detection rate is

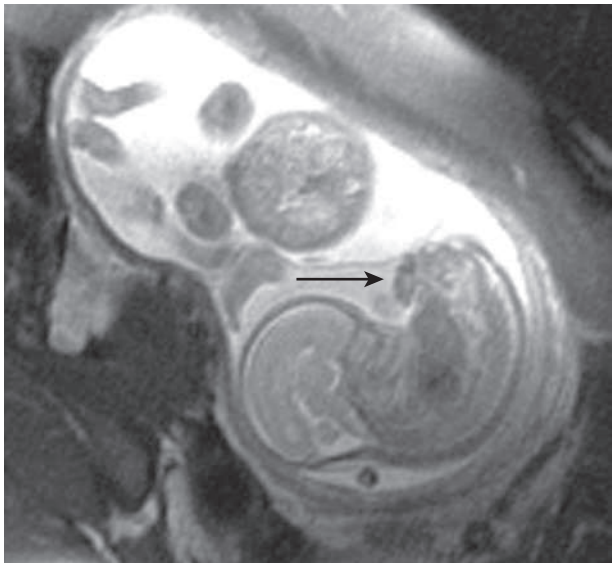

FIG. 38.34 Omphalocele-Exstrophy–Imperforate Anus–Spinal Defects (Cloacal Exstrophy). T2-weighted MRI of twins. The upper twin was normal with normal amniotic fluid. The lower twin had oligohydramnios with a lower anterior abdominal wall defect *(arrow)*. See also Video 38.15.

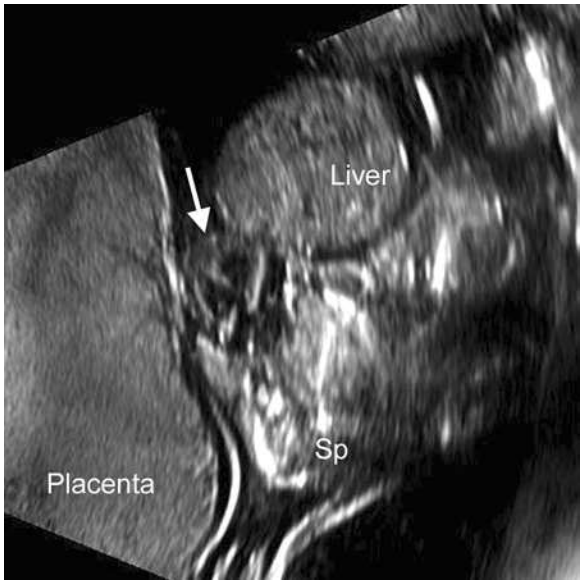

FIG. 38.35 Ectopia Cordis. Transverse image through the chest on one of a dichorionic twin pair shows that the liver and heart *(arrow)* are external to the thorax. *Sp,* Spine. This is a lethal malformation, in this case, caused by amniotic bands, which were visible in real time. The co-twin was normal and was delivered at term.

probably low and it is likely that many cases of OEIS are misdiagnosed. Once this diagnosis has been made, genetic counseling is recommended, and amniocentesis may be considered to identify gender prior to birth.

Ectopia Cordis

Ectopia cordis is a midline defect of the upper fetal ventral body wall through which all or part of the heart extrudes, with or without a membrane (Fig. 38.35). Most commonly the heart protrudes at the level of the chest through a defect involving the sternum, but the heart can be located at the cervical or abdominal region. Association with **structural cardiac anomalies** or other **abdominal wall defects** is common.[236] Prognosis is poor, although survivors have been reported.[237] **Trisomy 18** has been associated with this diagnosis, especially in the presence of additional abnormalities.[238,239]

Other Complex Body Wall Defects

In cases when the insult during the formation of the ventral abdominal wall is severe and takes place at an early embryonic developmental stage, the result is large and/or multiple defects of the ventral body wall, with evisceration of multiple organs of the abdomen, chest, and pelvis. These disorders are often associated with other anomalies involving the limbs, urinary system, external genitalia, and spine. Several syndromes and associations have been suggested to describe these conditions, each including different combinations of the previously listed defects. However, given the considerable overlap between these syndromes, it remains unclear whether they represent distinct pathogenetic entities or different manifestations of a single basic disorder. This overlap often results in a significant confusion in the terminology used to describe these conditions.

Pentalogy of Cantrell

Pentalogy of Cantrell is a rare complex disorder of the ventral body wall that refers to a combination of **defect of the sternum, ectopia cordis, cardiac anomalies** (e.g., septal defects, tetralogy of Fallot, transposition of great arteries), **defect of the anterior diaphragm and diaphragmatic pericardium,** and **supraumbilical abdominal wall defect** (most commonly **omphalocele**).[240,241] Other associated anomalies include midline abnormalities such as **facial cleft** and **encephalocele.** Given the association with **trisomies 18 and 13,** genetic consultation is recommended. Most of these cases are sporadic, and the risk of recurrence is low. The prognosis of this disorder is poor.[242]

Body Stalk Anomaly

Body stalk anomaly (also known as **limb–body wall complex**) is a rare and lethal disorder of the anterior abdominal wall. There are three hallmarks of this disorder: (1) There is a severe disruption of the abdominal and thoracic walls. (2) The abdominal and thoracic organs (e.g., heart, lungs, liver, bowel, bladder) are located outside the body cavity and are contained within a sac that is closely attached to the placenta, leading to a relatively fixed position of the fetus. (3) The umbilical cord is very short or absent, possibly because of a failure of the body stalk to develop properly. Associated musculoskeletal abnormalities are common and include severe **kyphoscoliosis** and **limb defects** such as **club foot** and absent or malformed limbs.[243-245]

The pathogenesis of this disorder is unclear, and several hypotheses have been suggested, including early vascular disruption, disruption due to amniotic bands following early amniotic rupture, or complete failure of the folding process of the embryonic disc.[246] This disorder is always lethal.

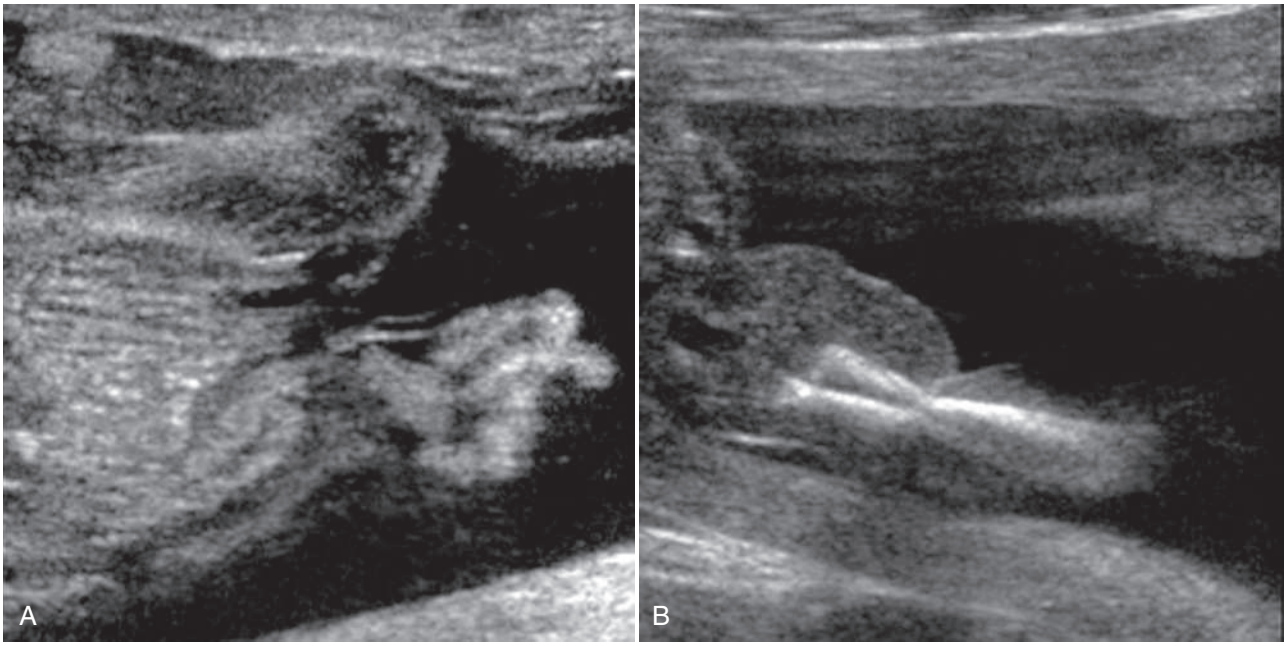

FIG. 38.36 Amniotic Band Syndrome. (A) Transverse view of abdomen shows anterior abdominal wall defect. **(B)** View of lower extremity shows constriction ring caused by amniotic bands. The constellation of findings is consistent with amniotic band syndrome.

Amniotic Band Syndrome

Amniotic band syndrome can affect any part of the fetus, and in a small proportion of cases it can affect the fetal abdominal or thoracic walls.[247] In these cases, the defect can appear similar to that of gastroschisis, with the **abdominal and/or thoracic organs floating freely within the amniotic cavity** with no sac around them (Fig. 38.36). The diagnosis of amniotic band syndrome is suggested by the demonstration of the **amniotic bands** and the presence of additional findings that are associated with disruption due to amniotic bands including **limb defects** (constriction or amputation of a limb), **encephalocele,** and **facial clefts.**[248] Unlike body stalk anomaly, the **umbilical cord can be demonstrated** in these cases.

REFERENCES

1. Moore KL, Persaud TVN. The developing human: clinically oriented embryology. 6th ed. Philadelphia: Saunders; 1998.
2. Wells JM, Melton DA. Vertebrate endoderm development. Annu Rev Cell Dev Biol. 1999;15:393-410.
3. Gilbert S. Developmental biology. 6th ed. Sunderland, Mass: Sinauer; 2000.
4. Fong GH, Rossant J, Gertsenstein M, Breitman ML. Role of the Flt-1 receptor tyrosine kinase in regulating the assembly of vascular endothelium. Nature. 1995;376(6535):66-70.
5. Fukamachi H, Takayama S. Epithelial-mesenchymal interaction in differentiation of duodenal epithelium of fetal rats in organ culture. Experientia. 1980;36(3):335-336.
6. Gannon M, Wright C. Endodermal patterning and organogenesis. In: Moody SA, editor. Cell lineage and fate determination. San Diego: Academic Press; 1999. p. 583-615.
7. Shaw-Smith C. Oesophageal atresia, tracheo-oesophageal fistula, and the VACTERL association: review of genetics and epidemiology. J Med Genet. 2006;43(7):545-554.
8. Torfs CP, Curry CJ, Bateson TF. Population-based study of tracheoesophageal fistula and esophageal atresia. Teratology. 1995;52(4):220-232.
9. Holder TM, Cloud DT, Lewis Jr JE, Pilling GP 4th. Esophageal atresia and tracheoesophageal fistula. A survey of its members by the Surgical Section of the American Academy of Pediatrics. Pediatrics. 1964;34:542-549.
10. Houben CH, Curry JI. Current status of prenatal diagnosis, operative management and outcome of esophageal atresia/tracheo-esophageal fistula. Prenat Diagn. 2008;28(7):667-675.
11. Shulman A, Mazkereth R, Zalel Y, et al. Prenatal identification of esophageal atresia: the role of ultrasonography for evaluation of functional anatomy. Prenat Diagn. 2002;22(8):669-674.
12. Stringer MD, McKenna KM, Goldstein RB, et al. Prenatal diagnosis of esophageal atresia. J Pediatr Surg. 1995;30(9):1258-1263.
13. Sparey C, Jawaheer G, Barrett AM, Robson SC. Esophageal atresia in the Northern Region Congenital Anomaly Survey, 1985-1997: prenatal diagnosis and outcome. Am J Obstet Gynecol. 2000;182(2):427-431.
14. Blaas HG, Eik-Nes SH, Kiserud T, Hellevik LR. Early development of the abdominal wall, stomach and heart from 7 to 12 weeks of gestation: a longitudinal ultrasound study. Ultrasound Obstet Gynecol. 1995;6(4):240-249.
15. Zimmer EZ, Chao CR, Abramovich G, Timor-Tritsch IE. Fetal stomach measurements: not reproducible by the same observer. J Ultrasound Med. 1992;11(12):663-665.
16. McKenna KM, Goldstein RB, Stringer MD. Small or absent fetal stomach: prognostic significance. Radiology. 1995;197(3):729-733.
17. Goldstein I, Reece EA, Yarkoni S, et al. Growth of the fetal stomach in normal pregnancies. Obstet Gynecol. 1987;70(4):641-644.
18. Mithwani AA, Hashmi A, Adil S. Epidermolysis bullosa and congenital pyloric atresia. BMJ Case Rep. 2013;2013:doi:10.1136/bcr-2013-201207.
19. Farmakis SG, Herman TE, Siegel MJ. Congenital pyloric atresia, type B; with junctional epidermolysis bullosa. J Perinatol. 2014;34(7):572-573.
20. Short SS, Grant CN, Merianos D, et al. A case of congenital pyloric atresia with dystrophic epidermolysis bullosa. Pediatr Surg Int. 2014;30(6):681-684.
21. Moore CC. Congenital gastric outlet obstruction. J Pediatr Surg. 1989;24(12):1241-1246.
22. Meizner I, Carmi R. The snowflake sign. A sonographic marker for prenatal detection of fetal skin denudation. J Ultrasound Med. 1990;9(10):607- 609.
23. Seubert DE, Feldman B, Krivchenia EL, et al. Molecular and fetal tissue biopsy capabilities are needed to maximize prenatal diagnosis of junctional epidermolysis bullosa: fetal skin biopsy using a 1-mm microendoscope. Fetal Diagn Ther. 2000;15(2):89-92.

24. Bartram U, Wirbelauer J, Speer CP. Heterotaxy syndrome—asplenia and polysplenia as indicators of visceral malposition and complex congenital heart disease. Biol Neonate. 2005;88(4):278-290.
25. Lin JH, Chang CI, Wang JK, et al. Intrauterine diagnosis of heterotaxy syndrome. Am Heart J. 2002;143(6):1002-1008.
26. Webber SA, Sandor GGS, Patterson MWH, et al. Prognosis in asplenia syndrome: a population-based review. Cardiol Young. 1992;2:129-135.
27. Gilljam T, McCrindle BW, Smallhorn JF, et al. Outcomes of left atrial isomerism over a 28-year period at a single institution. J Am Coll Cardiol. 2000;36(3):908-916.
28. Cassart M, Massez A, Lingier P, et al. Sonographic prenatal diagnosis of malpositioned stomach as a feature of uncomplicated intestinal malrotation. Pediatr Radiol. 2006;36(4):358-360.
29. Fakhry J, Shapiro LR, Schechter A, et al. Fetal gastric pseudomasses. J Ultrasound Med. 1987;6(4):177-180.
30. Nyberg DA, Mack LA, Patten RM, Cyr DR. Fetal bowel. Normal sonographic findings. J Ultrasound Med. 1987;6(1):3-6.
31. Walker JM, Ferguson DD. The sonographic appearance of blood in the fetal stomach and its association with placental abruption. J Ultrasound Med. 1988;7(3):155-161.
32. McNamara A, Levine D. Intraabdominal fetal echogenic masses: a practical guide to diagnosis and management. Radiographics. 2005;25(3):633-645.
33. Murshed R, Nicholls G, Spitz L. Intrinsic duodenal obstruction: trends in management and outcome over 45 years (1951-1995) with relevance to prenatal counselling. Br J Obstet Gynaecol. 1999;106(11):1197-1199.
34. Bittencourt DG, Barini R, Marba S, Sbragia L. Congenital duodenal obstruction: does prenatal diagnosis improve the outcome? Pediatr Surg Int. 2004;20(8):582-585.
35. Fonkalsrud EW, DeLorimier AA, Hays DM. Congenital atresia and stenosis of the duodenum. A review compiled from the members of the Surgical Section of the American Academy of Pediatrics. Pediatrics. 1969;43(1):79-83.
36. Calisti A, Oriolo L, Cozzi DA, et al. Prenatal diagnosis of duodenal obstruction selects cases with a higher risk of maternal-foetal complications and demands in utero transfer to a tertiary centre. Fetal Diagn Ther. 2008;24(4):478-482.
37. de Silva NT, Young JA, Wales PW. Understanding neonatal bowel obstruction: building knowledge to advance practice. Neonatal Netw. 2006;25(5):303-318.
38. Grosfeld JL, Rescorla FJ. Duodenal atresia and stenosis: reassessment of treatment and outcome based on antenatal diagnosis, pathologic variance, and long-term follow-up. World J Surg. 1993;17(3):301-309.
39. Touloukian R. Diagnosis and treatment of jejunoileal atresia. World J Surg. 1993;17:1422-1423.
40. Caspi B, Deutsch H, Grunshpan M, et al. Prenatal manifestation of superior mesenteric artery syndrome. Prenat Diagn. 2003;23(11):932-934.
41. Mustafawi AR, Hassan ME. Congenital duodenal obstruction in children: a decade's experience. Eur J Pediatr Surg. 2008;18(2):93-97.
42. Mirza B, Sheikh A. Multiple associated anomalies in patients of duodenal atresia: a case series. J Neonatal Surg. 2012;1(2):23.
43. Romero R, Ghidini A, Costigan K, et al. Prenatal diagnosis of duodenal atresia: does it make any difference? Obstet Gynecol. 1988;71(5):739-741.
44. Poki HO, Holland AJ, Pitkin J. Double bubble, double trouble. Pediatr Surg Int. 2005;21(6):428-431.
45. Quan L, Smith DW. The VATER association. Vertebral defects, Anal atresia, T-E fistula with esophageal atresia, Radial and Renal dysplasia: a spectrum of associated defects. J Pediatr. 1973;82(1):104-107.
46. Traubici J. The double bubble sign. Radiology. 2001;220(2):463-464.
47. Malone FD, Crombleholme TM, Nores JA, et al. Pitfalls of the 'double bubble' sign: a case of congenital duodenal duplication. Fetal Diagn Ther. 1997;12(5):298-300.
48. Zimmer EZ, Bronshtein M. Early diagnosis of duodenal atresia and possible sonographic pitfalls. Prenat Diagn. 1996;16(6):564-566.
49. Petrikovsky BM. First-trimester diagnosis of duodenal atresia. Am J Obstet Gynecol. 1994;171(2):569-570.
50. Cohen-Overbeek TE, Grijseels EW, Niemeijer ND, et al. Isolated or non-isolated duodenal obstruction: perinatal outcome following prenatal or postnatal diagnosis. Ultrasound Obstet Gynecol. 2008;32(6):784-792.
51. Kimble RM, Harding JE, Kolbe A. Does gut atresia cause polyhydramnios? Pediatr Surg Int. 1998;13(2-3):115-117.
52. Filkins K, Russo J, Flowers 3rd WK. Third trimester ultrasound diagnosis of intestinal atresia following clinical evidence of polyhydramnios. Prenat Diagn. 1985;5(3):215-220.
53. Grand RJ, Watkins JB, Torti FM. Development of the human gastrointestinal tract. A review. Gastroenterology. 1976;70(5 Pt 1):790-810.
54. Dalla Vecchia LK, Grosfeld JL, West KW, et al. Intestinal atresia and stenosis: a 25-year experience with 277 cases. Arch Surg. 1998;133(5):490-496.
55. Stoll C, Alembik Y, Dott B, Roth MP. Evaluation of prenatal diagnosis of congenital gastro-intestinal atresias. Eur J Epidemiol. 1996;12(6):611-616.
56. Haeusler MC, Berghold A, Stoll C, et al. Prenatal ultrasonographic detection of gastrointestinal obstruction: results from 18 European congenital anomaly registries. Prenat Diagn. 2002;22(7):616-623.
57. Komuro H, Amagai T, Hori T, et al. Placental vascular compromise in jejunoileal atresia. J Pediatr Surg. 2004;39(11):1701-1705.
58. Hemming V, Rankin J. Small intestinal atresia in a defined population: occurrence, prenatal diagnosis and survival. Prenat Diagn. 2007;27(13):1205-1211.
59. Baglaj M, Carachi R, Lawther S. Multiple atresia of the small intestine: a 20-year review. Eur J Pediatr Surg. 2008;18(1):13-18.
60. Prasad TR, Bajpai M. Intestinal atresia. Indian J Pediatr. 2000;67(9):671-678.
61. Patricolo M, Noia G, Rossi L, et al. An experimental animal model of intestinal obstruction to simulate in utero therapy for jejunoileal atresia. Fetal Diagn Ther. 1998;13(5):298-301.
62. Komuro H, Hori T, Amagai T, et al. The etiologic role of intrauterine volvulus and intussusception in jejunoileal atresia. J Pediatr Surg. 2004;39(12):1812-1814.
63. Blyth H, Dickson JA. Apple peel syndrome (congenital intestinal atresia): a family study of seven index patients. J Med Genet. 1969;6(3):275-277.
64. Seashore JH, Collins FS, Markowitz RI, Seashore MR. Familial apple peel jejunal atresia: surgical, genetic, and radiographic aspects. Pediatrics. 1987;80(4):540-544.
65. Font GE, Solari M. Prenatal diagnosis of bowel obstruction initially manifested as isolated hyperechoic bowel. J Ultrasound Med. 1998;17(11):721-723.
66. Irish MS, Ragi JM, Karamanoukian H, et al. Prenatal diagnosis of the fetus with cystic fibrosis and meconium ileus. Pediatr Surg Int. 1997;12(5-6):434-436.
67. Piper HG, Alesbury J, Waterford SD, et al. Intestinal atresias: factors affecting clinical outcomes. J Pediatr Surg. 2008;43(7):1244-1248.
68. Raherison R, Grosos C, Lemale J, et al. Prenatal intestinal volvulus: a life-threatening event with good long-term outcome. Arch Pediatr. 2012;19(4):361-367.
69. Wax JR, Hamilton T, Cartin A, et al. Congenital jejunal and ileal atresia: natural prenatal sonographic history and association with neonatal outcome. J Ultrasound Med. 2006;25(3):337-342.
70. Virgone C, D'Antonio F, Khalil A, et al. Accuracy of prenatal ultrasound in detecting jejunal and ileal atresia: systematic review and meta-analysis. Ultrasound Obstet Gynecol. 2015;45(5):523-529.
71. Dupuis A, Keenan K, Ooi CY, et al. Prevalence of meconium ileus marks the severity of mutations of the Cystic Fibrosis Transmembrane Conductance Regulator (CFTR) gene. Genet Med. 2015.
72. Muller F, Simon-Bouy B, Girodon E, et al. Predicting the risk of cystic fibrosis with abnormal ultrasound signs of fetal bowel: results of a French molecular collaborative study based on 641 prospective cases. Am J Med Genet. 2002;110(2):109-115.
73. Al-Kouatly HB, Chasen ST, Karam AK, et al. Factors associated with fetal demise in fetal echogenic bowel. Am J Obstet Gynecol. 2001;185(5):1039-1043.
74. Cuschieri A, Group EW. Descriptive epidemiology of isolated anal anomalies: a survey of 4.6 million births in Europe. Am J Med Genet. 2001;103(3):207-215.
75. Cho S, Moore SP, Fangman T. One hundred three consecutive patients with anorectal malformations and their associated anomalies. Arch Pediatr Adolesc Med. 2001;155(5):587-591.

76. Jenetzky E. Prevalence estimation of anorectal malformations using German diagnosis related groups system. Pediatr Surg Int. 2007;23(12): 1161-1165.
77. Rich M, Brock W, Peña A. Spectrum of genitourinary malformations in patients with imperforate anus. Pediatr Surg Int. 1988;3:120-123.
78. Martínez-Frías ML, Bermejo E, Rodríguez-Pinilla E. Anal atresia, vertebral, genital, and urinary tract anomalies: a primary polytopic developmental field defect identified through an epidemiological analysis of associations. Am J Med Genet. 2000;95(2):169-173.
79. Corteville JE, Gray DL, Langer JC. Bowel abnormalities in the fetus—correlation of prenatal ultrasonographic findings with outcome. Am J Obstet Gynecol. 1996;175(3 Pt 1):724-729.
80. Brantberg A, Blaas HG, Haugen SE, et al. Imperforate anus: a relatively common anomaly rarely diagnosed prenatally. Ultrasound Obstet Gynecol. 2006;28(7):904-910.
81. Harris RD, Nyberg DA, Mack LA, Weinberger E. Anorectal atresia: prenatal sonographic diagnosis. AJR Am J Roentgenol. 1987;149(2):395-400.
82. Taipale P, Rovamo L, Hiilesmaa V. First-trimester diagnosis of imperforate anus. Ultrasound Obstet Gynecol. 2005;25(2):187-188.
83. Tongsong T, Wanapirak C, Piyamongkol W, Sudasana J. Prenatal sonographic diagnosis of VATER association. J Clin Ultrasound. 1999;27(7):378-384.
84. Mandell J, Lillehei CW, Greene M, Benacerraf BR. The prenatal diagnosis of imperforate anus with rectourinary fistula: dilated fetal colon with enterolithiasis. J Pediatr Surg. 1992;27(1):82-84.
85. Perlman S, Bilik R, Leibovitch L, et al. More than a gut feeling—sonographic prenatal diagnosis of imperforate anus in a high-risk population. Prenat Diagn. 2014;34(13):1307-1311.
86. Vermesh M, Mayden KL, Confino E, et al. Prenatal sonographic diagnosis of Hirschsprung's disease. J Ultrasound Med. 1986;5(1):37-39.
87. Jakobson-Setton A, Weissmann-Brenner A, Achiron R, et al. Retrospective analysis of prenatal ultrasound of children with Hirschsprung disease. Prenat Diagn. 2015;35(7):699-702.
88. Eliyahu S, Yanai N, Blondheim O, et al. Sonographic presentation of Hirschsprung's disease. A case of an entirely aganglionic colon and ileum. Prenat Diagn. 1994;14(12):1170-1172.
89. Bashiri A, Burstein E, Hershkowitz R, et al. Fetal echogenic bowel at 17 weeks' gestational age as the early and only sign of a very long segment of Hirschsprung disease. J Ultrasound Med. 2008;27(7):1125-1126.
90. Szylberg L, Marszalek A. Diagnosis of Hirschsprung's disease with particular emphasis on histopathology. A systematic review of current literature. Prz Gastroenterol. 2014;9(5):264-269.
91. Gross RE. Duplications of the alimentary tract. The surgery of infancy and childhood. Philadelphia: Saunders; 1953. p. 221-245.
92. O'Neil J, Rowe M, editors. Duplications of the gastrointestinal tract. St Louis: Mosby; 1995.
93. Ben-Ishay O, Connolly SA, Buchmiller TL. Multiple duplication cysts diagnosed prenatally: case report and review of the literature. Pediatr Surg Int. 2013;29(4):397-400.
94. Richards DS, Langham MR, Anderson CD. The prenatal sonographic appearance of enteric duplication cysts. Ultrasound Obstet Gynecol. 1996;7(1):17-20.
95. Cheng G, Soboleski D, Daneman A, et al. Sonographic pitfalls in the diagnosis of enteric duplication cysts. AJR Am J Roentgenol. 2005;184(2):521-525.
96. Palacios A, De Vera M, Martínez-Escoriza JC. Prenatal sonographic findings of duodenal duplication: case report. J Clin Ultrasound. 2013;41(Suppl. 1):1-5.
97. Spottswood SE. Peristalsis in duplication cyst: a new diagnostic sonographic finding. Pediatr Radiol. 1994;24(5):344-345.
98. Konje JC, de Chazal R, MacFadyen U, Taylor DJ. Antenatal diagnosis and management of meconium peritonitis: a case report and review of the literature. Ultrasound Obstet Gynecol. 1995;6(1):66-69.
99. Foster MA, Nyberg DA, Mahony BS, et al. Meconium peritonitis: prenatal sonographic findings and their clinical significance. Radiology. 1987;165(3): 661-665.
100. Dirkes K, Crombleholme TM, Craigo SD, et al. The natural history of meconium peritonitis diagnosed in utero. J Pediatr Surg. 1995;30(7): 979-982.
101. Zangheri G, Andreani M, Ciriello E, et al. Fetal intra-abdominal calcifications from meconium peritonitis: sonographic predictors of postnatal surgery. Prenat Diagn. 2007;27(10):960-963.
102. Goetzinger KR, Cahill AG, Macones GA, Odibo AO. Echogenic bowel on second-trimester ultrasonography: evaluating the risk of adverse pregnancy outcome. Obstet Gynecol. 2011;117(6):1341-1348.
103. Mailath-Pokorny M, Klein K, Klebermass-Schrehof K, et al. Are fetuses with isolated echogenic bowel at higher risk for an adverse pregnancy outcome? Experiences from a tertiary referral center. Prenat Diagn. 2012;32(13):1295-1299.
104. Saha E, Mullins EW, Paramasivam G, et al. Perinatal outcomes of fetal echogenic bowel. Prenat Diagn. 2012;32(8):758-764.
105. Buiter HD, Holswilder-Olde Scholtenhuis MA, Bouman K, et al. Outcome of infants presenting with echogenic bowel in the second trimester of pregnancy. Arch Dis Child Fetal Neonatal Ed. 2013;98(3):F256-F259.
106. Al-Kouatly HB, Chasen ST, Streltzoff J, Chervenak FA. The clinical significance of fetal echogenic bowel. Am J Obstet Gynecol. 2001;185(5):1035-1038.
107. Vincoff NS, Callen PW, Smith-Bindman R, Goldstein RB. Effect of ultrasound transducer frequency on the appearance of the fetal bowel. J Ultrasound Med. 1999;18(12):799-803.
108. Harrison KL, Martinez D, Mason G. The subjective assessment of echogenic fetal bowel. Ultrasound Obstet Gynecol. 2000;16(6):524-529.
109. Ekin A, Gezer C, Taner CE, Ozeren M. The effect of associated structural malformations in the prediction of chromosomal abnormality risk of fetuses with echogenic bowel. J Matern Fetal Neonatal Med. 2016;29(1):41-45.
110. Goetzinger KR, Stamilio DM, Dicke JM, et al. Evaluating the incidence and likelihood ratios for chromosomal abnormalities in fetuses with common central nervous system malformations. Am J Obstet Gynecol. 2008;199(3): 285.e1-285.e6.
111. Leung WC, Waters JJ, Chitty L. Prenatal diagnosis by rapid aneuploidy detection and karyotyping: a prospective study of the role of ultrasound in 1589 second-trimester amniocenteses. Prenat Diagn. 2004;24(10): 790-795.
112. Agathokleous M, Chaveeva P, Poon LC, et al. Meta-analysis of second-trimester markers for trisomy 21. Ultrasound Obstet Gynecol. 2013; 41(3):247-261.
113. Antonarakis SE, Epstein CJ. The challenge of Down syndrome. Trends Mol Med. 2006;12(10):473-479.
114. Sepulveda W, Hollingsworth J, Bower S, et al. Fetal hyperechogenic bowel following intra-amniotic bleeding. Obstet Gynecol. 1994;83(6):947-950.
115. Strocker AM, Snijders RJ, Carlson DE, et al. Fetal echogenic bowel: parameters to be considered in differential diagnosis. Ultrasound Obstet Gynecol. 2000;16(6):519-523.
116. Scotet V, Dugueperoux I, Audrezet MP, et al. Focus on cystic fibrosis and other disorders evidenced in fetuses with sonographic finding of echogenic bowel: 16-year report from Brittany, France. Am J Obstet Gynecol. 2010; 203(6):592.e1-592.e6.
117. Eggermont E. Gastrointestinal manifestations in cystic fibrosis. Eur J Gastroenterol Hepatol. 1996;8(8):731-738.
118. Ghose I, Mason GC, Martinez D, et al. Hyperechogenic fetal bowel: a prospective analysis of sixty consecutive cases. BJOG. 2000;107(3): 426-429.
119. Monaghan KG, Feldman GL. The risk of cystic fibrosis with prenatally detected echogenic bowel in an ethnically and racially diverse North American population. Prenat Diagn. 1999;19(7):604-609.
120. Petrikovsky B, Smith-Levitin M, Holsten N. Intra-amniotic bleeding and fetal echogenic bowel. Obstet Gynecol. 1999;93(5 Pt 1):684-686.
121. Sepulveda W, Reid R, Nicolaidis P, et al. Second-trimester echogenic bowel and intraamniotic bleeding: association between fetal bowel echogenicity and amniotic fluid spectrophotometry at 410 nm. Am J Obstet Gynecol. 1996;174(3):839-842.
122. Yaron Y, Hassan S, Geva E, et al. Evaluation of fetal echogenic bowel in the second trimester. Fetal Diagn Ther. 1999;14(3):176-180.
123. Degani S. Sonographic findings in fetal viral infections: a systematic review. Obstet Gynecol Surv. 2006;61(5):329-336.
124. Simon-Bouy B, Satre V, Ferec C, et al. Hyperechogenic fetal bowel: a large French collaborative study of 682 cases. Am J Med Genet A. 2003; 121A(3):209-213.

125. Muller F, Dommergues M, Aubry MC, et al. Hyperechogenic fetal bowel: an ultrasonographic marker for adverse fetal and neonatal outcome. Am J Obstet Gynecol. 1995;173(2):508-513.
126. Sepulveda W, Nicolaidis P, Mai AM, et al. Is isolated second-trimester hyperechogenic bowel a predictor of suboptimal fetal growth? Ultrasound Obstet Gynecol. 1996;7(2):104-107.
127. Ball RH, Ade CM, Schoenborn JA, Crane JP. The clinical significance of ultransonographically detected subchorionic hemorrhages. Am J Obstet Gynecol. 1996;174(3):996-1002.
128. Zhu MY, Milligan N, Keating S, et al. The hemodynamics of late onset intrauterine growth restriction by MRI. Am J Obstet Gynecol. 2016;214(3):367.
129. Lam YH, Tang MH, Lee CP, Tse HY. Echogenic bowel in fetuses with homozygous alpha-thalassemia-1 in the first and second trimesters. Ultrasound Obstet Gynecol. 1999;14(3):180-182.
130. Stiller RJ, Herzlinger R, Siegel S, Whetham JC. Fetal ascites associated with ABO incompatibility: case report and review of the literature. Am J Obstet Gynecol. 1996;175(5):1371-1372.
131. Ceola AF, Angtuaco TL. US case of the day. Congenital cytomegalovirus infection. Radiographics. 1999;19(5):1385-1387.
132. Ranzini AC, Day-Salvatore D, Turner T, et al. Intrauterine growth and ultrasound findings in fetuses with Beckwith-Wiedemann syndrome. Obstet Gynecol. 1997;89(4):538-542.
133. Mulik V, Wellesley D, Sawdy R, Howe DT. Unusual prenatal presentation of Beckwith-Wiedemann syndrome. Prenat Diagn. 2004;24(7):501-503.
134. Hamada H, Yamada N, Watanabe H, et al. Hypoechoic hepatomegaly associated with transient abnormal myelopoiesis provides clues to trisomy 21 in the third-trimester fetus. Ultrasound Obstet Gynecol. 2001;17(5):442-444.
135. Bronshtein M, Blazer S. Prenatal diagnosis of liver calcifications. Obstet Gynecol. 1995;86(5):739-743.
136. Stein B, Bromley B, Michlewitz H, et al. Fetal liver calcifications: sonographic appearance and postnatal outcome. Radiology. 1995;197(2):489-492.
137. Zalel Y, Gilboa Y, Berkenshtat M, et al. Secondary cytomegalovirus infection can cause severe fetal sequelae despite maternal preconceptional immunity. Ultrasound Obstet Gynecol. 2008;31(4):417-420.
138. Simchen MJ, Toi A, Bona M, et al. Fetal hepatic calcifications: prenatal diagnosis and outcome. Am J Obstet Gynecol. 2002;187(6):1617-1622.
139. Tongsong T, Srisupundit K, Traisrisilp K. Prenatal sonographic diagnosis of congenital varicella syndrome. J Clin Ultrasound. 2012;40(3):176-178.
140. Achiron R, Seidman DS, Afek A, et al. Prenatal ultrasonographic diagnosis of fetal hepatic hyperechogenicities: clinical significance and implications for management. Ultrasound Obstet Gynecol. 1996;7(4):251-255.
141. Pott Bartsch EM, Paek BW, Yoshizawa J, et al. Giant fetal hepatic hemangioma. Case report and literature review. Fetal Diagn Ther. 2003;18(1):59-64.
142. Morris J, Abbott J, Burrows P, Levine D. Antenatal diagnosis of fetal hepatic hemangioma treated with maternal corticosteroids. Obstet Gynecol. 1999;94(5 Pt 2):813-815.
143. Gembruch U, Baschat AA, Gloeckner-Hoffmann K, et al. Prenatal diagnosis and management of fetuses with liver hemangiomata. Ultrasound Obstet Gynecol. 2002;19(5):454-460.
144. Dukler D, Oepkes D, Seaward G, et al. Noninvasive tests to predict fetal anemia: a study comparing Doppler and ultrasound parameters. Am J Obstet Gynecol. 2003;188(5):1310-1314.
145. Detti L, Mari G, Akiyama M, et al. Longitudinal assessment of the middle cerebral artery peak systolic velocity in healthy fetuses and in fetuses at risk for anemia. Am J Obstet Gynecol. 2002;187(4):937-939.
146. Scheier M, Hernandez-Andrade E, Carmo A, et al. Prediction of fetal anemia in rhesus disease by measurement of fetal middle cerebral artery peak systolic velocity. Ultrasound Obstet Gynecol. 2004;23(5):432-436.
147. Moise Jr KJ. The usefulness of middle cerebral artery Doppler assessment in the treatment of the fetus at risk for anemia. Am J Obstet Gynecol. 2008;198(2):161.e1-161.e4.
148. Goldstein I, Tamir A, Weisman A, et al. Growth of the fetal gall bladder in normal pregnancies. Ultrasound Obstet Gynecol. 1994;4(4):289-293.
149. Hertzberg BS, Kliewer MA, Maynor C, et al. Nonvisualization of the fetal gallbladder: frequency and prognostic importance. Radiology. 1996;199(3):679-682.
150. Blazer S, Zimmer EZ, Bronshtein M. Nonvisualization of the fetal gallbladder in early pregnancy: comparison with clinical outcome. Radiology. 2002;224(2):379-382.
151. Shen O, Rabinowitz R, Yagel S, Gal M. Absent gallbladder on fetal ultrasound: prenatal findings and postnatal outcome. Ultrasound Obstet Gynecol. 2011;37(6):673-677.
152. Dugueperoux I, Scotet V, Audrezet MP, et al. Nonvisualization of fetal gallbladder increases the risk of cystic fibrosis. Prenat Diagn. 2012;32(1):21-28.
153. Chalouhi GE, Muller F, Dreux S, et al. Prenatal non-visualization of fetal gallbladder: beware of biliary atresia! Ultrasound Obstet Gynecol. 2011;38(2):237-238, author reply 238-240.
154. Bardin R, Ashwal E, Davidov B, et al. Nonvisualization of the fetal gallbladder: can levels of gamma-glutamyl transpeptidase in amniotic fluid predict fetal prognosis? Fetal Diagn Ther. 2016;39(1):50-55.
155. Livesey E, Cortina Borja M, Sharif K, et al. Epidemiology of biliary atresia in England and Wales (1999-2006). Arch Dis Child Fetal Neonatal Ed. 2009;94(6):F451-F455.
156. Yoon PW, Bresee JS, Olney RS, et al. Epidemiology of biliary atresia: a population-based study. Pediatrics. 1997;99(3):376-382.
157. Brown DL, Teele RL, Doubilet PM, et al. Echogenic material in the fetal gallbladder: sonographic and clinical observations. Radiology. 1992;182(1):73-76.
158. Suma V, Marini A, Bucci N, et al. Fetal gallstones: sonographic and clinical observations. Ultrasound Obstet Gynecol. 1998;12(6):439-441.
159. Kiserud T, Gjelland K, Bogno H, et al. Echogenic material in the fetal gallbladder and fetal disease. Ultrasound Obstet Gynecol. 1997;10(2):103-106.
160. Gallivan EK, Crombleholme TM, D'Alton ME. Early prenatal diagnosis of choledochal cyst. Prenat Diagn. 1996;16(10):934-937.
161. Pachi A, Maggi E, Giancotti A, et al. Ultrasound diagnosis of fetal annular pancreas. J Perinat Med. 1989;17(5):361-364.
162. Dankovcik R, Muranska S, Kucera E, et al. Prenatal three-dimensional sonographic findings associated with annular pancreas. Fetal Diagn Ther. 2010;27(1):57-60.
163. Etienne D, John A, Menias CO, et al. Annular pancreas: a review of its molecular embryology, genetic basis and clinical considerations. Ann Anat. 2012;194(5):422-428.
164. Pansini M, Magerkurth O, Haecker FM, Sesia SB. Annular pancreas associated with duodenal obstruction. BMJ Case Rep. 2012;2012.
165. Bronstein M, Reichler A, Borochowitz Z, et al. Early prenatal diagnosis of polycystic pancreas with narrow thorax and short limb dwarfism. Am J Med Genet. 1994;49(1):6-9.
166. Sepulveda W, Carstens E, Sanchez J, Gutierrez J. Prenatal diagnosis of congenital pancreatic cyst: case report and review of the literature. J Ultrasound Med. 2000;19(5):349-352.
167. Choi SJ, Kang MC, Kim YH, et al. Prenatal detection of a congenital pancreatic cyst by ultrasound. J Korean Med Sci. 2007;22(1):156-158.
168. Chung JH, Lim GY, Song YT. Congenital true pancreatic cyst detected prenatally in neonate: a case report. J Pediatr Surg. 2007;42(9):E27-E29.
169. Fremond B, Poulain P, Odent S, et al. Prenatal detection of a congenital pancreatic cyst and Beckwith-Wiedemann syndrome. Prenat Diagn. 1997;17(3):276-280.
170. Schmidt W, Yarkoni S, Jeanty P, et al. Sonographic measurements of the fetal spleen: clinical implications. J Ultrasound Med. 1985;4(12):667-672.
171. Hata T, Kuno A, Dai SY, et al. Three-dimensional sonographic volume measurement of the fetal spleen. J Obstet Gynaecol Res. 2007;33(5):600-605.
172. Oepkes D, Meerman RH, Vandenbussche FP, et al. Ultrasonographic fetal spleen measurements in red blood cell-alloimmunized pregnancies. Am J Obstet Gynecol. 1993;169(1):121-128.
173. Bahado-Singh R, Oz U, Mari G, et al. Fetal splenic size in anemia due to Rh-alloimmunization. Obstet Gynecol. 1998;92(5):828-832.
174. Chaoui R, Zodan-Marin T, Wisser J. Marked splenomegaly in fetal cytomegalovirus infection: detection supported by three-dimensional power Doppler ultrasound. Ultrasound Obstet Gynecol. 2002;20(3):299-302.

175. Mancuso A, Rijhsinghani A. Elevated delta OD 450 due to transient abnormal myelopoiesis in a Down syndrome fetus with hepatosplenomegaly on ultrasound. Prenat Diagn. 2014;34(3):299-301.
176. Venkataraman D. Fetal splenic cyst: antenatal diagnosis and outcome. BMJ Case Rep. 2009;2009.
177. Dankovcik R, Urdzik P, Lazar I, et al. Conservative management in three cases of prenatally recognized splenic cyst using 2D, 3D, multi-slice and Doppler ultrasonography. Fetal Diagn Ther. 2009;26(3):177-180.
178. Kabra NS, Bowen JR. Congenital splenic cyst: a case report and review of the literature. J Paediatr Child Health. 2001;37(4):400-402.
179. Shukla RM, Mukhopadhyay M, Mandal KC, Mukhopadhyay B. Giant congenital infected splenic cyst: an interesting case report and review of the literature. Indian J Surg. 2010;72(3):260-262.
180. Molik KA, Gingalewski CA, West KW, et al. Gastroschisis: a plea for risk categorization. J Pediatr Surg. 2001;36(1):51-55.
181. Carvalho MH, Brizot ML, Lopes LM, et al. Detection of fetal structural abnormalities at the 11-14 week ultrasound scan. Prenat Diagn. 2002; 22(1):1-4.
182. Gilbert SF. Developmental biology. 6th ed. Sunderland, Mass.: Sinauer Associates; 2000.
183. Duhamel B. Embryology of exomphalos and allied malformations. Arch Dis Child. 1963;38(198):142-147.
184. Sadler TW. The embryologic origin of ventral body wall defects. Semin Pediatr Surg. 2010;19(3):209-214.
185. Hutchin P. Somatic anomalies of the umbilicus and anterior abdominal wall. Surg Gynecol Obstet. 1965;120:1075-1090.
186. Timor-Tritsch IE, Warren WB, Peisner DB, Pirrone E. First-trimester midgut herniation: a high-frequency transvaginal sonographic study. Am J Obstet Gynecol. 1989;161(3):831-833.
187. Penman DG, Fisher RM, Noblett HR, Soothill PW. Increase in incidence of gastroschisis in the south west of England in 1995. Br J Obstet Gynaecol. 1998;105(3):328-331.
188. Nichols CR, Dickinson JE, Pemberton PJ. Rising incidence of gastroschisis in teenage pregnancies. J Matern Fetal Med. 1997;6(4):225-229.
189. Tan KH, Kilby MD, Whittle MJ, et al. Congenital anterior abdominal wall defects in England and Wales 1987-93: retrospective analysis of OPCS data. BMJ. 1996;313(7062):903-906.
190. Reid KP, Dickinson JE, Doherty DA. The epidemiologic incidence of congenital gastroschisis in Western Australia. Am J Obstet Gynecol. 2003;189(3):764-768.
191. Suita S, Okamatsu T, Yamamoto T, et al. Changing profile of abdominal wall defects in Japan: results of a national survey. J Pediatr Surg. 2000; 35(1):66-71.
192. Mastroiacovo P. Risk factors for gastroschisis. BMJ. 2008;336(7658): 1386-1387.
193. Kirby RS, Marshall J, Tanner JP, et al. Prevalence and correlates of gastroschisis in 15 states, 1995 to 2005. Obstet Gynecol. 2013;122(2 Pt 1):275-281.
194. Skarsgard ED, Meaney C, Bassil K, et al. Maternal risk factors for gastroschisis in Canada. Birth Defects Res A Clin Mol Teratol. 2015;103(2):111-118.
195. Hume Jr RF, Gingras JL, Martin LS, et al. Ultrasound diagnosis of fetal anomalies associated with in utero cocaine exposure: further support for cocaine-induced vascular disruption teratogenesis. Fetal Diagn Ther. 1994; 9(4):239-245.
196. Haddow JE, Palomaki GE, Holman MS. Young maternal age and smoking during pregnancy as risk factors for gastroschisis. Teratology. 1993;47(3):225-228.
197. Waller SA, Paul K, Peterson SE, Hitti JE. Agricultural-related chemical exposures, season of conception, and risk of gastroschisis in Washington State. Am J Obstet Gynecol. 2010;202(3):241.e1-241.e6.
198. Goodman M, Mandel JS, DeSesso JM, Scialli AR. Atrazine and pregnancy outcomes: a systematic review of epidemiologic evidence. Birth Defects Res B Dev Reprod Toxicol. 2014;101(3):215-236.
199. Mac Bird T, Robbins JM, Druschel C, et al. Demographic and environmental risk factors for gastroschisis and omphalocele in the National Birth Defects Prevention Study. J Pediatr Surg. 2009;44(8):1546-1551.
200. Feldkamp ML, Carey JC, Sadler TW. Development of gastroschisis: review of hypotheses, a novel hypothesis, and implications for research. Am J Med Genet A. 2007;143A(7):639-652.
201. Economides DL, Braithwaite JM. First trimester ultrasonographic diagnosis of fetal structural abnormalities in a low risk population. Br J Obstet Gynaecol. 1998;105(1):53-57.
202. Rankin J, Dillon E, Wright C. Congenital anterior abdominal wall defects in the north of England, 1986-1996: occurrence and outcome. Prenat Diagn. 1999;19(7):662-668.
203. Snyder CL. Outcome analysis for gastroschisis. J Pediatr Surg. 1999;34(8):1253-1256.
204. Feldkamp ML, Botto LD, Byrne JL, et al. Clinical presentation and survival in a population-based cohort of infants with gastroschisis in Utah, 1997-2011. Am J Med Genet A. 2015.
205. Hunter AG, Stevenson RE. Gastroschisis: clinical presentation and associations. Am J Med Genet C Semin Med Genet. 2008;148C(3): 219-230.
206. Barisic I, Clementi M, Hausler M, et al. Evaluation of prenatal ultrasound diagnosis of fetal abdominal wall defects by 19 European registries. Ultrasound Obstet Gynecol. 2001;18(4):309-316.
207. Mastroiacovo P, Lisi A, Castilla EE, et al. Gastroschisis and associated defects: an international study. Am J Med Genet A. 2007;143A(7):660-671.
208. Corey KM, Hornik CP, Laughon MM, et al. Frequency of anomalies and hospital outcomes in infants with gastroschisis and omphalocele. Early Hum Dev. 2014;90(8):421-424.
209. South AP, Stutey KM, Meinzen-Derr J. Metaanalysis of the prevalence of intrauterine fetal death in gastroschisis. Am J Obstet Gynecol. 2013;209(2): 114.e1-114.e13.
210. Santiago-Munoz PC, McIntire DD, Barber RG, et al. Outcomes of pregnancies with fetal gastroschisis. Obstet Gynecol. 2007;110(3):663-668.
211. Chaudhury P, Haeri S, Horton AL, et al. Ultrasound prediction of birthweight and growth restriction in fetal gastroschisis. Am J Obstet Gynecol. 2010;203(4):395.e1-395.e5.
212. Logghe HL, Mason GC, Thornton JG, Stringer MD. A randomized controlled trial of elective preterm delivery of fetuses with gastroschisis. J Pediatr Surg. 2005;40(11):1726-1731.
213. Puligandla PS, Janvier A, Flageole H, et al. The significance of intrauterine growth restriction is different from prematurity for the outcome of infants with gastroschisis. J Pediatr Surg. 2004;39(8):1200-1204.
214. Baud D, Lausman A, Alfaraj MA, et al. Expectant management compared with elective delivery at 37 weeks for gastroschisis. Obstet Gynecol. 2013;121(5):990-998.
215. Salihu HM, Emusu D, Aliyu ZY, et al. Mode of delivery and neonatal survival of infants with isolated gastroschisis. Obstet Gynecol. 2004;104(4): 678-683.
216. Bradnock TJ, Marven S, Owen A, et al. Gastroschisis: one year outcomes from national cohort study. BMJ. 2011;343:d6749.
217. Sinkey RG, Habli MA, South AP, et al. Sonographic markers associated with adverse neonatal outcomes among fetuses with gastroschisis: an 11-year, single-center review. Am J Obstet Gynecol. 2016;214(2):275.e1-275.e7.
218. Marshall J, Salemi JL, Tanner JP, et al. Prevalence, correlates, and outcomes of omphalocele in the United States, 1995-2005. Obstet Gynecol. 2015;126(2): 284-293.
219. Blazer S, Zimmer EZ, Gover A, Bronshtein M. Fetal omphalocele detected early in pregnancy: associated anomalies and outcomes. Radiology. 2004;232(1):191-195.
220. Brantberg A, Blaas HG, Haugen SE, Eik-Nes SH. Characteristics and outcome of 90 cases of fetal omphalocele. Ultrasound Obstet Gynecol. 2005;26(5):527-537.
221. Henrich K, Huemmer HP, Reingruber B, Weber PG. Gastroschisis and omphalocele: treatments and long-term outcomes. Pediatr Surg Int. 2008;24(2):167-173.
222. DiLiberti JH. Familial omphalocele: analysis of risk factors and case report. Am J Med Genet. 1982;13(3):263-268.
223. Calzolari E, Bianchi F, Dolk H, Milan M. Omphalocele and gastroschisis in Europe: a survey of 3 million births 1980-1990. EUROCAT Working Group. Am J Med Genet. 1995;58(2):187-194.
224. Nicholas S, Tuuli MG, Dicke J, et al. Estimation of fetal weight in fetuses with abdominal wall defects: comparison of 2 recent sonographic formulas to the Hadlock formula. J Ultrasound Med. 2010;29(7):1069-1074.

225. Segel SY, Marder SJ, Parry S, Macones GA. Fetal abdominal wall defects and mode of delivery: a systematic review. Obstet Gynecol. 2001;98(5 Pt 1):867-873.
226. Gearhart JJ. Exstrophy-epispadias complex and bladder anomalies. In: Walsh PC, Vaughan ED, Wein AJ, editors. Campbell's urology. 7th ed. Philadelphia: Saunders; 1998.
227. Boyd PA, Haeusler M, Barisic I. EUROCAT Report 9: Surveillance of congenital anomalies in Europe 1980-2008. Birth Defects Res A Clin Mol Teratol. 2011;91(Suppl. 1):S1.
228. Pakdaman R, Woodward PJ, Kennedy A. Complex abdominal wall defects: appearances at prenatal imaging. Radiographics. 2015;35(2):636-649.
229. Baird AD, Mathews RI, Gearhart JP. The use of combined bladder and epispadias repair in boys with classic bladder exstrophy: outcomes, complications and consequences. J Urol. 2005;174(4 Pt 1):1421-1424.
230. Borer JG, Gargollo PC, Hendren WH, et al. Early outcome following complete primary repair of bladder exstrophy in the newborn. J Urol. 2005;174(4 Pt 2):1674-1678.
231. Keppler-Noreuil K, Gorton S, Foo F, et al. Prenatal ascertainment of OEIS complex/cloacal exstrophy—15 new cases and literature review. Am J Med Genet A. 2007;143A(18):2122-2128.
232. Hamosh A, Amberger J, Bocchini C, et al. Omphalocele. Online Mendelian Inheritance in Man: National Center for Biotechnical Information; 2002.
233. Pajkrt E, Petersen OB, Chitty LS. Fetal genital anomalies: an aid to diagnosis. Prenat Diagn. 2008;28(5):389-398.
234. Hamada H, Takano K, Shiina H, et al. New ultrasonographic criterion for the prenatal diagnosis of cloacal exstrophy: elephant trunk-like image. J Urol. 1999;162(6):2123-2124.
235. Kallen K, Castilla EE, Robert E, et al. OEIS complex—a population study. Am J Med Genet. 2000;92(1):62-68.
236. Sepulveda W, Wong AE, Simonetti L, et al. Ectopia cordis in a first-trimester sonographic screening program for aneuploidy. J Ultrasound Med. 2013;32(5):865-871.
237. Falkensammer CB, Ayres NA, Altman CA, et al. Fetal cardiac malposition: incidence and outcome of associated cardiac and extracardiac malformations. Am J Perinatol. 2008;25(5):277-281.
238. Fox JE, Gloster ES, Mirchandani R. Trisomy 18 with Cantrell pentalogy in a stillborn infant. Am J Med Genet. 1988;31(2):391-394.
239. Bick D, Markowitz RI, Horwich A. Trisomy 18 associated with ectopia cordis and occipital meningocele. Am J Med Genet. 1988;30(3):805-810.
240. Cantrell JR, Haller JA, Ravitch MM. A syndrome of congenital defects involving the abdominal wall, sternum, diaphragm, pericardium, and heart. Surg Gynecol Obstet. 1958;107(5):602-614.
241. Martin RA, Cunniff C, Erickson L, Jones KL. Pentalogy of Cantrell and ectopia cordis, a familial developmental field complex. Am J Med Genet. 1992;42(6):839-841.
242. Chandran S, Ari D. Pentalogy of Cantrell: an extremely rare congenital anomaly. J Clin Neonatol. 2013;2(2):95-97.
243. Daskalakis G, Pilalis A, Papadopoulos D, Antsaklis A. Body stalk anomaly diagnosed in the 2nd trimester. Fetal Diagn Ther. 2003;18(5):342-344.
244. Bugge M. Body stalk anomaly in Denmark during 20 years (1970-1989). Am J Med Genet A. 2012;158A(7):1702-1708.
245. Ginsberg NE, Cadkin A, Strom C. Prenatal diagnosis of body stalk anomaly in the first trimester of pregnancy. Ultrasound Obstet Gynecol. 1997;10(6):419-421.
246. Murphy A, Platt LD. First-trimester diagnosis of body stalk anomaly using 2- and 3-dimensional sonography. J Ultrasound Med. 2011;30(12):1739-1743.
247. Barzilay E, Harel Y, Haas J, et al. Prenatal diagnosis of amniotic band syndrome—risk factors and ultrasonic signs. J Matern Fetal Neonatal Med. 2015;28(3):281-283.
248. Barros M, Gorgal G, Machado AP, et al. Revisiting amniotic band sequence: a wide spectrum of manifestations. Fetal Diagn Ther. 2014;35(1):51-56.

CHAPTER 39

The Fetal Urogenital Tract

Katherine W. Fong, Julia Eva Kfouri, and Kirsten L. Weind Matthews

SUMMARY OF KEY POINTS

- Evaluation of amniotic fluid volume (subjective assessment combined with semiquantitative methods such as maximum vertical pocket or amniotic fluid index) provides important information about some maternal and fetal conditions, as well as placental function.
- Sonographic findings suspicious of renal cystic disease include cysts, renal hyperechogenicity, and/or large kidneys. Whenever renal cystic disease is suspected, it is useful to perform a renal ultrasound of the parents to check for unknown familial disease.
- Evaluation of urinary tract dilation should include measurement of the anteroposterior renal pelvic diameter; identification of calyceal dilation and renal parenchymal, ureteral, or bladder abnormalities; and assessment of amniotic fluid volume.
- In fetuses with lower urinary tract obstruction, a fetal urinary function profile (combining sonographic and biochemical predictors) is most useful clinically in selecting the fetus that will benefit from in utero intervention.
- Examination of fetal genitalia plays a key role in the diagnostic workup of many structural abnormalities and genetic disorders, as well as in the assessment of multiple pregnancies.

CHAPTER OUTLINE

THE NORMAL URINARY TRACT
Embryology
Sonographic Appearance
Amniotic Fluid Volume
URINARY TRACT ABNORMALITIES
Bilateral Renal Agenesis
Unilateral Renal Agenesis
Renal Ectopia
Horseshoe Kidney
Renal Cystic Disease
Multicystic Dysplastic Kidney
Obstructive Cystic Renal Dysplasia
Autosomal Recessive Polycystic Kidney Disease
Autosomal Dominant Polycystic Kidney Disease
Syndromes Associated With Renal Cystic Disease
Hyperechogenic Kidneys
Renal Neoplasm
Adrenal Mass
Upper Urinary Tract Dilation
Ureteropelvic Junction Obstruction
Vesicoureteral Junction Obstruction and Primary Megaureter
Duplication Anomalies
Vesicoureteral Reflux
Lower Urinary Tract Obstruction
In Utero Intervention: Fetal Vesicoamniotic Shunting and Cystoscopy
Nonvisualized Bladder
Bladder Exstrophy
THE GENITAL TRACT
Normal Genitalia
Abnormal Genitalia
Hydrocolpos
Ovarian Cysts
CONCLUSION
Acknowledgments

Evaluation of the fetal urogenital tract is an integral part of the obstetric ultrasound examination. Sonography depicts normal developmental anatomy and allows detection and characterization of many genitourinary abnormalities. In addition, assessment of the amniotic fluid volume (AFV) often provides important prognostic information regarding fetal renal function. Accurate and early prenatal diagnosis is important because this may influence obstetric and neonatal management.

Congenital anomalies of the kidney and urinary tract (CAKUT) account for approximately 30% of all malformations detected on routine prenatal sonography.[1,2] A systematic sonographic approach is proposed, which includes a search for associated anomalies and detailed evaluation of renal structure and function.

THE NORMAL URINARY TRACT

Embryology

The **permanent kidney (metanephros)** is the third in a series of excretory organs in the human embryo, forming after the **pronephros** and **mesonephros.**[3] In the seventh menstrual week, the metanephros begins to develop from two sources: the metanephric diverticulum (ureteric bud) and the metanephric mass of intermediate mesoderm (Fig. 39.1). The **ureteric bud** is an outgrowth from the mesonephric duct, near its entrance into the cloaca. It elongates and branches in a dichotomous pattern, giving rise to the ureter, renal pelvis, calyces, and

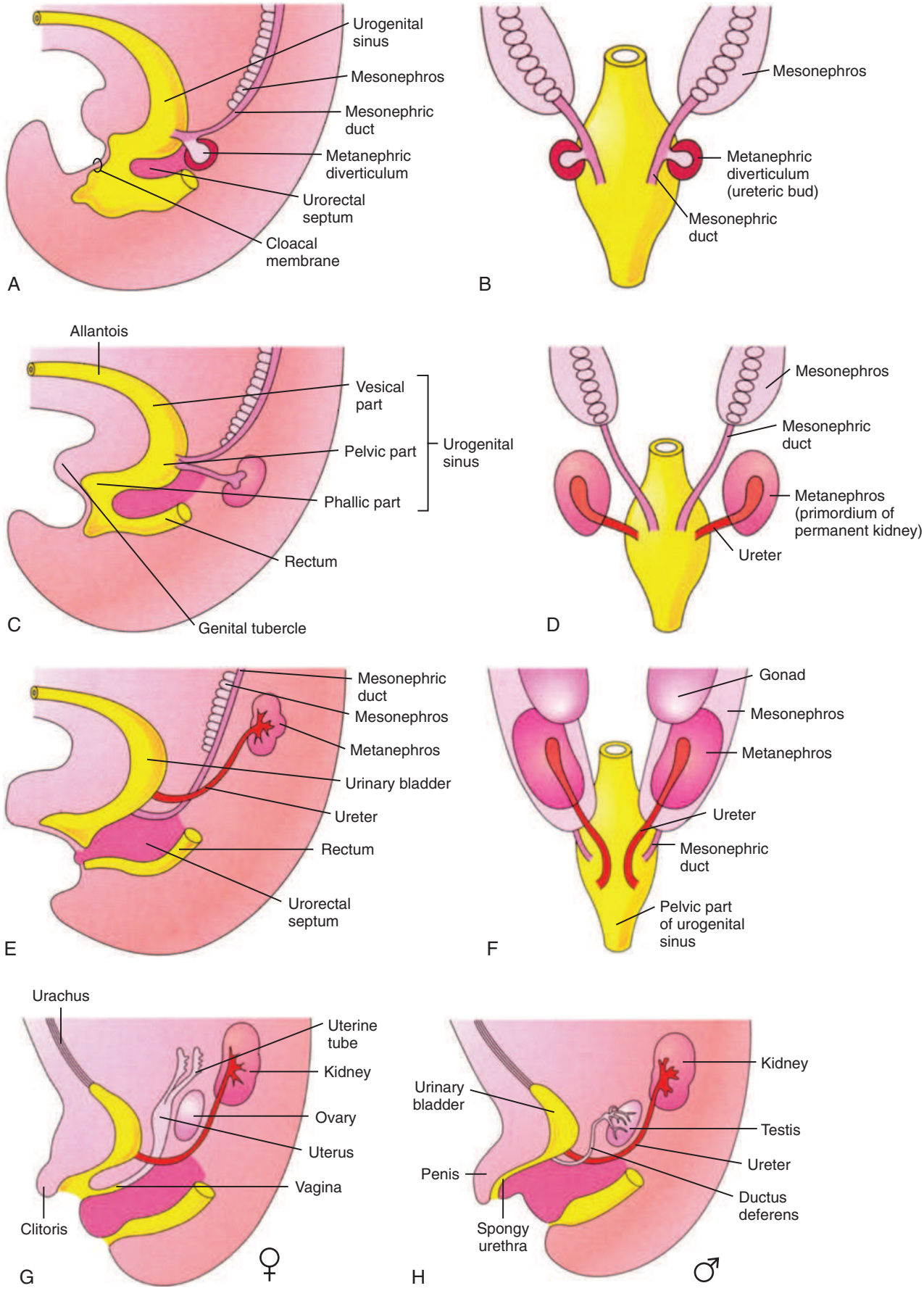

FIG. 39.1 Embryology of the Urinary Tract. Diagrams show division of the cloaca into the urogenital sinus and rectum; absorption of the mesonephric ducts; development of the permanent kidneys (metanephroi), urinary bladder, urethra, and urachus; and changes in the location of the ureters. **(A)** Lateral view of the caudal half of a 5-week-old embryo. **(B), (D),** and **(F)** Dorsal views. **(C), (E), (G),** and **(H)** Lateral views. The stages shown in **(G)** and **(H)** are reached by the 12th week. (With permission from Moore KL, Persaud TVN, editors. The developing human: clinically oriented embryology. 7th ed. Philadelphia: Saunders; 2003.[3])

collecting tubules. Through interaction with the metanephric mesoderm, the ureteric bud induces the formation of nephrons. In early embryonic life, the kidneys are located in the pelvis, but they "ascend" to their adult position by the 11th menstrual week. At this gestation, the kidneys start to produce urine.

By the ninth menstrual week, the **cloaca** (caudal part of hindgut) is divided by the urorectal septum into the rectum posteriorly and the urogenital sinus anteriorly (see Fig. 39.1). The urinary bladder, the female urethra, and most of the male urethra develop from the urogenital sinus and the surrounding splanchnic mesenchyme. Initially, the bladder is continuous with the allantois, but this structure soon constricts and becomes a fibrous cord, the urachus, which extends from the apex of the bladder to the umbilicus.

Sonographic Appearance

In the **first trimester** the fetal kidneys are best examined by transvaginal sonography. The kidneys are seen as oval, hyperechoic structures in the paravertebral regions, with a small, central sonolucent area caused by fluid in the renal pelvis[4] (Fig. 39.2A). By 12 to 13 weeks of gestation, the kidneys can be visualized in 99% of cases with combined transabdominal and transvaginal sonography.[5] In the **second trimester** the kidneys often appear as isoechoic structures adjacent to the fetal spine on transabdominal sonography (Fig. 39.2B). As the fetus matures, corticomedullary differentiation becomes more obvious, especially in the third trimester (Figs. 39.2C-D). The renal pyramids orient in anterior and posterior rows and are hypoechoic relative to the renal cortex. In the **third trimester** the renal cortex is isoechoic or slightly hyperechoic to liver and spleen. With fat deposition in the perinephric region, an echogenic border develops, and the kidney becomes better delineated. Normal fetal lobations are often visible and give the kidneys an undulating contour.

The kidneys grow throughout pregnancy. Table 39.1 provides a **nomogram of renal lengths** at 14 to 42 weeks of gestation.[6] The often-quoted rule of thumb that "renal length in millimeters approximates gestational age in weeks" applies only to a narrow gestational age range of 18 to 21 weeks. There are also published

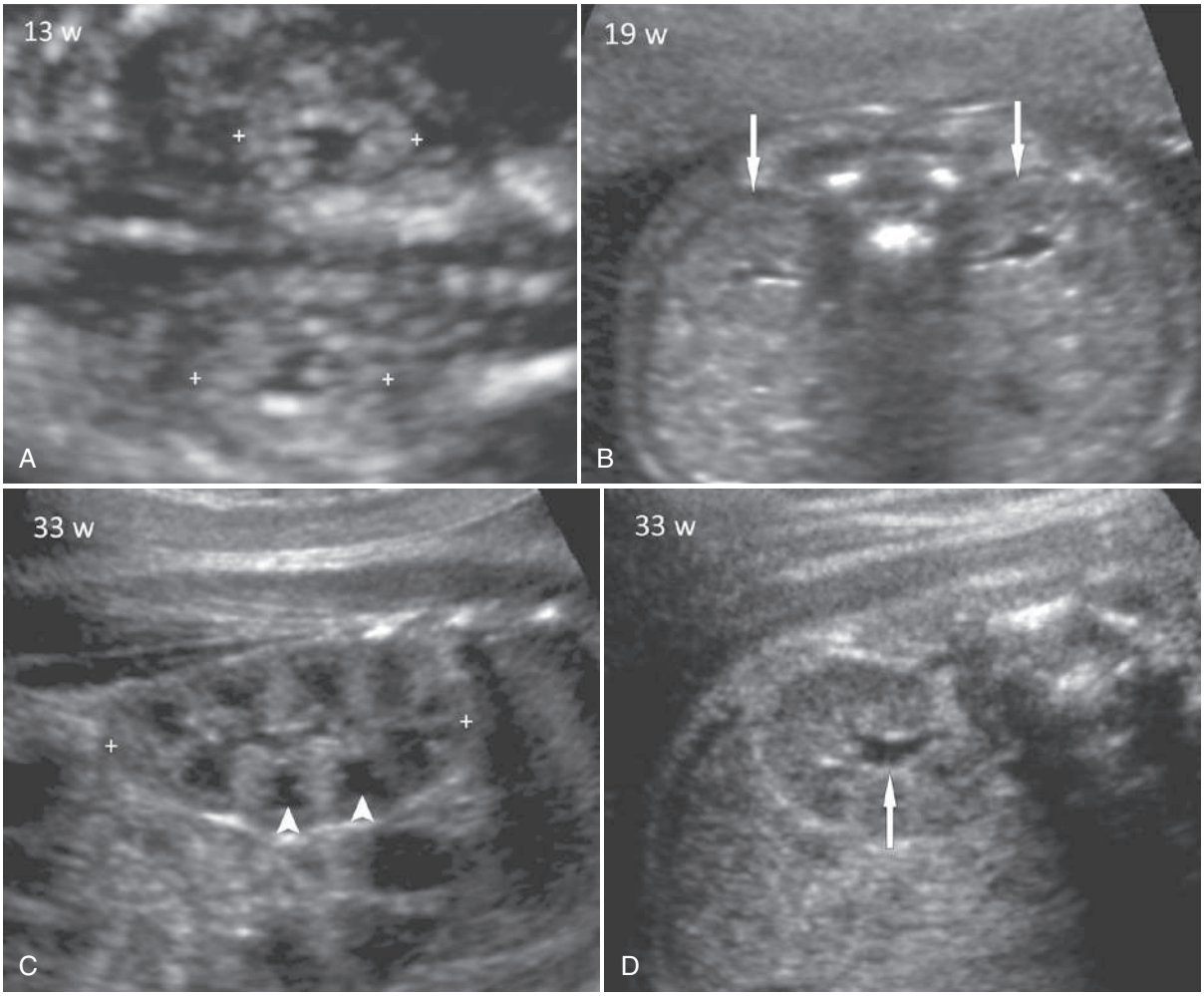

FIG. 39.2 Normal Sonographic Appearance of Kidneys at Different Gestational Ages. (A) Transvaginal scan at **13 weeks** of gestation in the coronal plane shows normal kidneys *(calipers),* which appear hyperechoic, with small central sonolucent area caused by fluid in the renal pelvis. **(B)** Transabdominal scan at **19 weeks** in the transverse plane shows the kidneys *(arrows)* as paired isoechoic structures adjacent to the fetal spine, with a small amount of fluid in the renal pelvis. **(C)** and **(D)** Longitudinal and transverse scans at **33 weeks** show the kidney well outlined by perinephric fat, with normal corticomedullary differentiation. The pyramids *(arrowheads)* are hypoechoic. There is a small amount of fluid in the renal pelvis *(arrow).*

TABLE 39.1 Renal Lengths at 14-42 Weeks' Gestation

		FITTED CENTILES				
Week	***N***	**3rd**	**10th**	**50th**	**90th**	**97th**
14	3	7.5	8.0	9.3	10.8	11.6
15	3	8.8	9.5	11.0	12.8	13.7
16	2	10.2	11.0	12.7	14.8	15.8
17	12	11.6	12.5	14.5	16.8	18.1
18	10	13.1	14.1	16.3	18.9	20.3
19	15	14.6	15.6	18.2	21.1	22.6
20	15	16.1	17.2	20.0	23.2	24.9
21	15	17.5	18.8	21.8	25.4	27.2
22	14	19.0	20.4	23.6	27.4	29.4
23	16	20.4	21.9	25.4	29.5	31.6
24	17	21.8	23.4	27.1	31.5	33.8
25	18	23.1	24.8	28.8	33.4	35.8
26	20	24.4	26.2	30.4	35.3	37.8
27	24	25.6	27.5	31.9	37.1	39.7
28	18	26.8	28.7	33.4	38.7	41.5
29	19	27.9	29.9	34.7	40.3	43.2
30	19	28.9	31.0	36.0	41.8	44.8
31	23	29.9	32.1	37.2	43.2	46.3
32	23	30.8	33.0	38.3	44.5	47.7
33	22	31.6	33.9	39.4	45.7	49.0
34	19	32.4	34.7	40.3	46.8	50.2
35	20	33.1	35.4	41.1	47.8	51.2
36	23	33.7	36.1	41.9	48.7	52.2
37	14	34.2	36.7	42.6	49.4	53.0
38	17	34.7	37.2	43.2	50.1	53.8
39	13	35.1	37.6	43.7	50.7	54.4
40	14	35.4	38.0	44.1	51.2	54.9
41	26	35.7	38.3	44.5	51.6	55.4
42	17	36.0	38.6	44.8	52.0	55.7

N, Number of fetuses for each week of gestation.
With permission from Chitty LS, Altman DG. Charts of fetal size: kidney and renal pelvis measurements. Prenat Diagn. 2003;23(11): 891-897.[6]

charts of renal anteroposterior diameter, transverse diameter, and volume.[6] Sometimes, it is difficult to define the exact renal borders, especially at the upper pole, because of shadowing from ribs or poor distinction from the adrenal gland. Fetal breathing can aid in renal visualization. It is also important to avoid using an oblique section through the kidney for measurement. The **renal/abdominal circumference** ratio remains constant at 0.27 to 0.30 throughout pregnancy.[7]

The calyces are not normally visualized, but some fluid is typically seen in the renal pelvis. The highly characteristic **renal pelvic echo** is often the key to finding the kidneys in the second trimester. Measurements of the renal pelvis are discussed in the section on upper urinary tract (UT) dilation. The normal ureter is 1 to 2 mm in diameter and is not normally visible.

By using transvaginal sonography, the **bladder** can be seen as early as 11 weeks of gestation.[4] By 12 to 13 weeks, the bladder is visualized in 98% of cases using both transabdominal and transvaginal sonography.[5] The bladder is thin walled and situated anteriorly in the pelvis. The **umbilical** (superior vesical) **arteries** run lateral to the bladder as they course toward the umbilicus (Fig. 39.3). The hourly fetal urine production increases with advancing gestation, from a mean value of 4 to 5 mL/hr at 20 weeks to 52 to 56 mL/hr at 40 weeks.[8,9] Three-dimensional (3-D) ultrasound measurements demonstrate reproducible urine production rates based on bladder volumes, but tend to estimate higher rates in the third trimester compared with the standard two-dimensional (2-D) technique.[10] The **maximum bladder volume** increases from a mean value of 1 mL at 20 weeks to 36 mL at 41 weeks.[8] The normal bladder fills and empties (either partially or completely) approximately every 25 minutes (range, 7-43 min). Therefore changes in bladder volume should be observed during the course of the obstetric sonogram.

Amniotic Fluid Volume

Evaluation of amniotic fluid volume (AFV) provides important information about some maternal and fetal conditions, as well as placental function. Evaluation of AFV is a key component of fetal biophysical assessment. After 16 weeks, fetal urine production becomes the major source of amniotic fluid.[11] Fetal lung secretions, fetal swallowing, and intramembranous resorption of water into the fetal circulation via fetal vessels on the placental surface also contribute to AFV homeostasis.[12]

Several methods are used to assess AFV. Subjective assessment can be combined with semiquantitative techniques, such as measurement of the **maximum vertical pocket** (or **single deepest vertical pocket**) and **amniotic fluid index** (AFI). Significant oligohydramnios results in compression of the fetus, marked crowding of fetal parts, and poor visualization of fetal anatomy. With polyhydramnios, one gets the impression of a "swimming" fetus. The subjective assessment of AFV by experienced sonographers has been shown to be reliable.[13] However, there are conflicting data regarding the reliability of both the maximum vertical pocket technique and the AFI.[13-15] The technique for measuring the deepest amniotic fluid pockets should follow these guidelines:

- The maximum depth of the fluid pocket should be measured in a perpendicular direction.
- The pocket should have a width of at least 1 cm (avoid measuring narrow, slitlike pockets).
- The pocket should be free of fetal small parts and umbilical cord.

The following classification has been proposed for the maximum vertical pocket method: vertical depth of the pocket less than 2 cm indicates moderate to severe oligohydramnios, 2 to 8 cm is normal, and greater than 8 cm indicates polyhydramnios.[16]

Amniotic Fluid Assessment

Vertical Depth	
<2 cm	Oligohydramnios
2-8 cm	Normal
>8 cm	Polyhydramnios

[a]Maximum vertical pocket method.

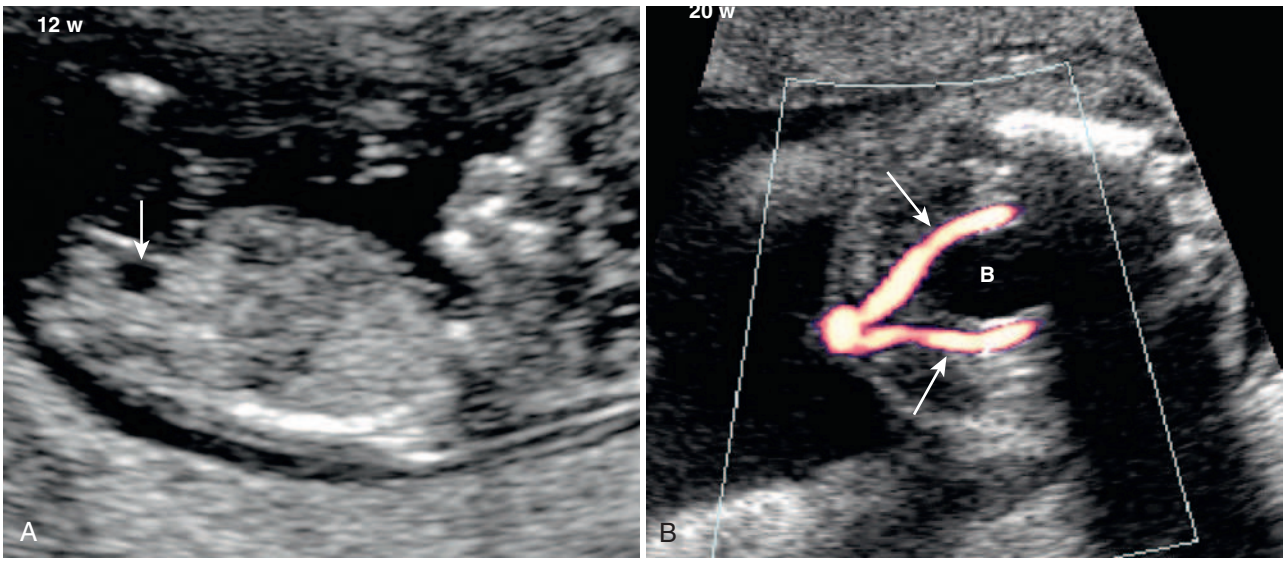

FIG. 39.3 Normal Urinary Bladder. (A) Sagittal image of a 12-week fetus. Note normal urinary bladder *(arrow)*. **(B)** Power Doppler image of the umbilical arteries *(arrows)* at 20 weeks' gestation helps in the identification of any questionable fluid-filled structure in the pelvis as the urinary bladder *(B)*.

The AFI is obtained by measuring the deepest amniotic fluid pocket in each of the four quadrants of the uterus, and the sum of the four measurements is the index.[14,17] AFI varies with gestational age (Table 39.2).[18] In the late second trimester and in the third trimester, an AFI of 5 cm to 24 cm has been considered as normal.[19] It is recommended that when AFI is less than 10 cm, three measurements should be averaged.[14] The semiquantitative methods are useful for following AFV on serial examinations, particularly by multiple examiners of varying experience.

Oligohydramnios is typically defined as either a single maximum vertical pocket of amniotic fluid of less than 2 cm or alternatively, an AFI of less than 5 cm.[20] Recently, a meta-analysis of four randomized controlled trials comparing the use of AFI (<5 cm) versus the single deepest vertical pocket (<2 cm) during antepartum fetal surveillance did not show any evidence that one method is superior to the other in predicting poor perinatal outcomes.[21] However, the use of AFI increased the rate of diagnosis of oligohydramnios and subsequent induction of labor. It was concluded that the single deepest vertical pocket measurement is the method of choice for amniotic fluid assessment during fetal surveillance.[21] This approach is supported by the American College of Obstetricians and Gynecologists (ACOG), as well as the findings of the recently completed SAFE trial.[20,22]

In multiple pregnancies, the maximum vertical pocket technique is commonly used for assessment of amniotic fluid, with similar cutoffs for abnormal as for singletons.[12,19,23] A systematic review of studies on amniotic fluid assessment and adverse outcomes in twin pregnancies has cautioned that sonographic evaluation of AFV has high specificity but poor sensitivity for the detection of abnormal AFV, and more rigorous studies in this area are required.[24]

URINARY TRACT ABNORMALITIES

The prevalence of UT malformations varies among studies, likely because of differences in study population and methods of surveillance. In a recent analysis of 709,030 births in 12 European countries, the prevalence of congenital malformations of the UT was 1.6 per 1000 births.[25] The overall prenatal detection rate was high: 82% and 88.5% in two studies.[1,25] However, it varied from 36% to 100% in different centers.[25] Many factors could account for the variation of prenatal detection rates, including the study population (high risk vs. unselected), timing of the ultrasound scan, expertise of the operator, quality of the ultrasound equipment, extent of follow-up, and ascertainment of congenital anomalies. For major UT anomalies, 57% were detected before 24 weeks.[1] Lethal UT anomalies account for 10% of pregnancy terminations.[26]

Prenatal Diagnosis of Urinary Tract Abnormalities

Assessment of amniotic fluid volume
Localization and characterization of urinary tract abnormalities
Search for associated abnormalities

A systematic approach to the prenatal diagnosis of UT abnormalities includes assessment of AFV, localization and characterization of UT abnormalities, assessment of fetal gender, and search for associated abnormalities.

Normal AFV in the second half of pregnancy implies at least one functioning kidney and a patent urinary conduit to the amniotic cavity. If **oligohydramnios** is present without a history

TABLE 39.2 Amniotic Fluid Index Values in Normal Pregnancy

	AMNIOTIC FLUID INDEX (cm)						
Gestational Age (wk)	No.	5th Percentile	10th Percentile	50th Percentile	Mean	90th Percentile	95th Percentile
14	50	2.8	3.1	5	5.4	8	8.6
15	50	3.2	3.6	5.4	5.7	8.2	9.1
16	50	3.6	4.1	5.8	6.1	8.5	9.6
17	50	4.1	4	6.3	6.6	9	10.3
18	50	4.6	5.1	6.8	7.1	9.7	11.1
19	50	5.1	5.6	7.4	7.7	10.4	12
20	50	5.5	6.1	8	8.3	11.3	12.9
21	50	5.9	6.6	8.7	8.9	12.2	13.9
22	50	6.3	7.1	9.3	9.6	13.2	14.9
23	50	6.7	7.5	10	10.3	14.2	15.9
24	50	7	7.9	10.7	11	15.2	16.9
25	50	7.3	8.2	11.4	11.7	16.1	17.8
26	50	7.5	8.4	12	12.3	17	18.7
27	50	7.6	8.6	12.6	12.8	17.8	19.4
28	50	7.6	8.6	13	13.3	18.4	19.9
29	50	7.6	8.6	13.4	13.6	18.8	20.4
30	50	7.5	8.5	13.6	13.8	18.9	20.6
31	50	7.3	8.4	13.6	13.8	18.9	20.6
32	50	7.1	8.1	13.6	13.7	18.7	20.4
33	50	6.8	7.8	13.3	13.4	18.2	20
34	50	6.4	7.4	12.9	13	17.7	19.4
35	50	6	7	12.4	12.5	16.9	18.7
36	50	5.6	6.5	11.8	11.8	16.2	17.9
37	50	5.1	6	11.1	11.1	15.3	16.9
38	50	4.7	5.5	10.3	10.3	14.4	15.9
39	50	4.2	5	9.4	9.4	13.7	14.9
40	50	3.7	4.5	8.6	8.6	12.9	13.9
41	50	3.3	4	7.8	7.7	12.3	12.9

With permission from Magann EF, Sanderson M, Martin JN, Chauhan S. The amniotic fluid index, single deepest pocket, and two-diameter pocket in normal human pregnancy. Am J Obstet Gynecol. 2000;182(6):1581-1588.[18]

of ruptured membranes, maternal drug intake (e.g., angiotensin-converting enzyme [ACE] inhibitors,[27] angiotensin II receptor antagonists,[28] cyclooxygenase-2 [COX-2] selective and nonselective inhibitors,[29] nonsteroidal antiinflammatory drugs,[30] cocaine[31]), or evidence of intrauterine growth restriction (IUGR), UT anomalies must be strongly suspected. In the setting of a UT abnormality, normal AFV indicates a good prognosis. Oligohydramnios in the early second trimester carries a very poor prognosis because of the associated pulmonary hypoplasia. Occasionally and paradoxically, **polyhydramnios** may occur, especially with unilateral obstructive uropathy, with **mesoblastic nephroma,** or when there are concomitant abnormalities of the central nervous system (CNS) or gastrointestinal (GI) tract.

The following questions are helpful in defining and characterizing the UT abnormality:

- Is the bladder identified and normal in appearance?
- Are kidneys present? Are they normal in position, size, and echogenicity? Are renal cysts identified?
- Is the UT dilated? If so, to what degree, at which level, and what is the cause?
- Is the involvement unilateral or bilateral, symmetrical or asymmetrical?
- What is the fetal gender?

It is important to perform a detailed anatomic scan to search for associated abnormalities, which may indicate the presence of a syndrome or chromosomal abnormality. Renal anomalies may be part of the **VATER association** (vertebral defects, anal atresia, tracheoesophageal fistula, radial defects, and renal anomalies). An expansion of this syndrome, **VACTERL,** includes cardiac and nonradial limb defects. Associated nonurinary anomalies have been reported in 34% of infants with CAKUT, most common in the musculoskeletal, digestive, cardiovascular, and central nervous systems.[32] When there are additional malformations, the risk for fetal chromosomal abnormalities is substantially increased compared with the maternal age–related risk: 30 times higher for multiple defects versus 3 times higher for isolated renal defect.[33]

In addition, **renal ultrasound** is recommended for **parents** (and siblings) of fetuses suspected to have certain renal

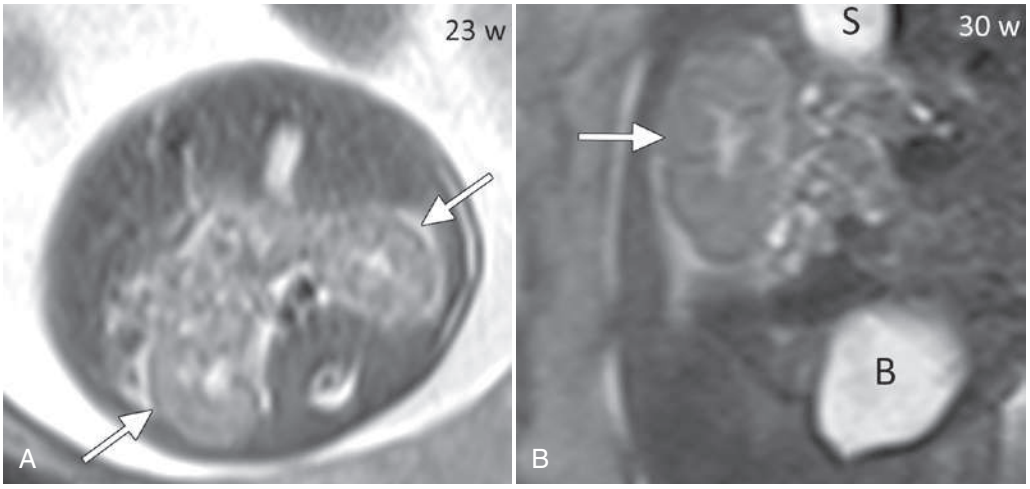

FIG. 39.4 Magnetic Resonance Images of Normal Kidneys. T2-weighted magnetic resonance images at **(A)** 23 weeks' gestation and **(B)** 30 weeks' gestation. The renal parenchyma *(arrows)* shows low to intermediate signal intensity. The renal collecting system and bladder *(B)* shows high signal intensity. *S,* Stomach.

abnormalities (polycystic kidney disease, renal agenesis or adysplasia), because it may help to diagnose the type of polycystic kidney disease in the fetus, detect asymptomatic renal pathology in parents (and siblings), and counsel parents regarding the recurrence risk.[34-36]

Fetal magnetic resonance imaging (MRI) may be used as an adjunctive imaging modality for improving diagnostic accuracy of UT abnormalities.[37,38] It may help to identify the kidneys when sonographic visualization is limited by anhydramnios (or severe oligohydramnios) and large maternal body habitus (Fig. 39.4).[39,40] Finally, with the advent of diffusion-weighted imaging, the measurement of water apparent diffusion coefficient has shown promise in differentiating between normal and abnormal renal parenchyma, which could serve as a noninvasive method of assessing fetal renal function.[41,42]

Evaluation of the Fetal Urinary Tract

BLADDER
- Presence
- Appearance and size

KIDNEYS
- Presence
- Number
- Position
- Appearance (echogenicity, cysts)
- Unilateral or bilateral

COLLECTING SYSTEM
- Dilation
- Level of obstruction
- Cause of obstruction
- Unilateral or bilateral

FETAL GENDER

Bilateral Renal Agenesis

Bilateral renal agenesis is a lethal congenital anomaly with an incidence of approximately 1 in 4000 births and a 2.5:1 male preponderance.[43,44] The ureteric buds fail to develop; thus the kidneys are absent. Because no urine is produced, severe oligohydramnios or anhydramnios results. Pulmonary hypoplasia is the major cause of neonatal death. Other features of "Potter's sequence" include typical facies (beaked nose, low-set ears, prominent epicanthic folds, hypertelorism), limb deformities, and IUGR.

The ultrasound findings include severe oligohydramnios or anhydramnios and nonvisualization of the kidneys and bladder. Before 16 weeks' gestation, AFV is not dependent on urine production and may be normal despite absent renal function. The absence of fetal kidneys should be the most specific finding, but this may be difficult to document because of poor image quality associated with oligohydramnios. In addition, bowel or adrenal glands in the renal fossae may be mistaken for kidneys.[45] However, recognition of the distinctive, flattened appearance of the adrenal gland on longitudinal sonogram **("lying down" adrenal sign)** helps to confirm that the kidney did not develop in the flank[46] (Fig. 39.5, Video 39.1).

Repeated and consistent nonvisualization of the urinary bladder (over 1 hour) is a secondary sign of bilateral renal agenesis (Fig. 39.6). Conversely, identification of a normal bladder excludes this diagnosis. A small **urachal diverticulum** may mimic the bladder, but its lack of filling and emptying distinguishes it from the bladder. A major challenge is to reliably distinguish between fetuses with bilateral renal agenesis and those with impaired renal function from severe uteroplacental insufficiency or IUGR.

Several techniques have been proposed to improve visualization of fetal structures: intraamniotic and intraperitoneal infusion of isotonic saline,[47] transvaginal ultrasound,[48] and color Doppler ultrasound imaging.[49,50] The transvaginal probe is particularly useful in the second trimester and with breech presentation (Fig. 39.6, Video 39.2). Color Doppler imaging can be used to diagnose

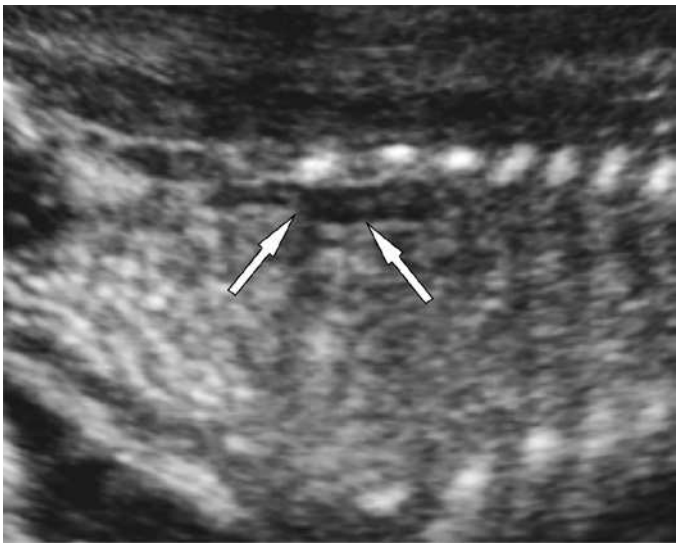

FIG. 39.5 "Lying Down" Adrenal Sign. Longitudinal scan through the renal fossa shows absence of the kidney and the flattened adrenal gland *(arrows)*. The lying-down adrenal sign is an indication of renal agenesis or ectopia. See also Video 39.1.

absent renal arteries, providing further evidence for the diagnosis of bilateral renal agenesis (Fig. 39.7). More important, it helps to map out the renal arteries in difficult cases of oligohydramnios, thereby confirming the presence of kidneys and avoiding confusion (Fig. 39.8).

Fetal MRI may help to identify the kidneys when sonographic visualization is limited. However, the kidneys can be difficult to visualize early in gestation. Therefore it may be difficult for MRI to exclude renal agenesis before 24 weeks' gestation, if the kidneys are not seen.

Bilateral renal agenesis is usually an isolated and sporadic abnormality. However, in a small percentage of cases it may be secondary to a chromosomal abnormality or part of a genetic syndrome (such as Fraser syndrome), or a developmental defect (such as VACTERL association).[51,52] There is conflicting evidence with regard to associations between bilateral renal agenesis and maternal factors such as prepregnancy obesity, periconception smoking, and alcohol consumption.[53] In nonsyndromic cases, the recurrence risk of having another child with bilateral renal agenesis is approximately 4%.[34,54] However, up to 15% of the

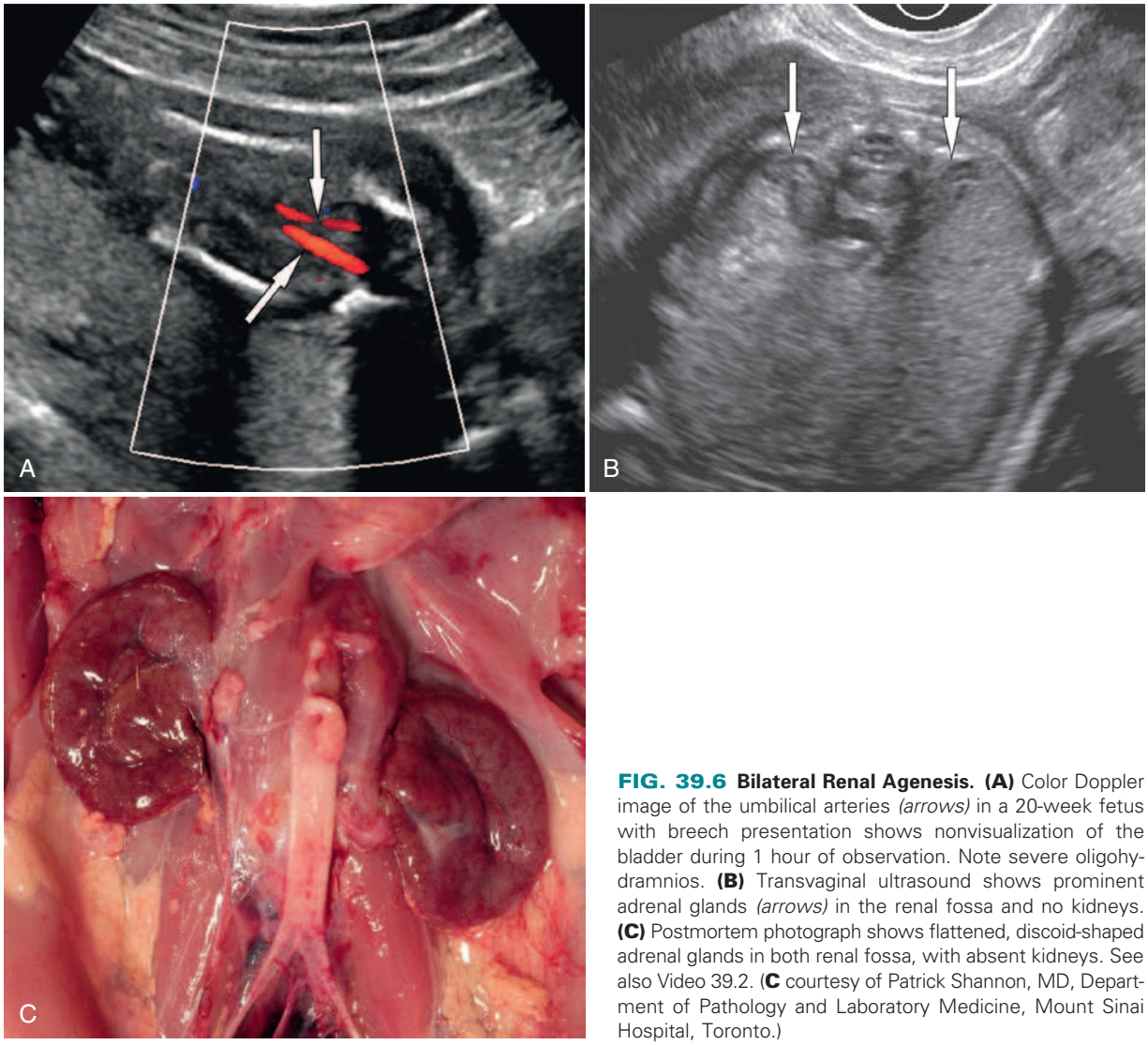

FIG. 39.6 Bilateral Renal Agenesis. (A) Color Doppler image of the umbilical arteries *(arrows)* in a 20-week fetus with breech presentation shows nonvisualization of the bladder during 1 hour of observation. Note severe oligohydramnios. **(B)** Transvaginal ultrasound shows prominent adrenal glands *(arrows)* in the renal fossa and no kidneys. **(C)** Postmortem photograph shows flattened, discoid-shaped adrenal glands in both renal fossa, with absent kidneys. See also Video 39.2. (**C** courtesy of Patrick Shannon, MD, Department of Pathology and Laboratory Medicine, Mount Sinai Hospital, Toronto.)

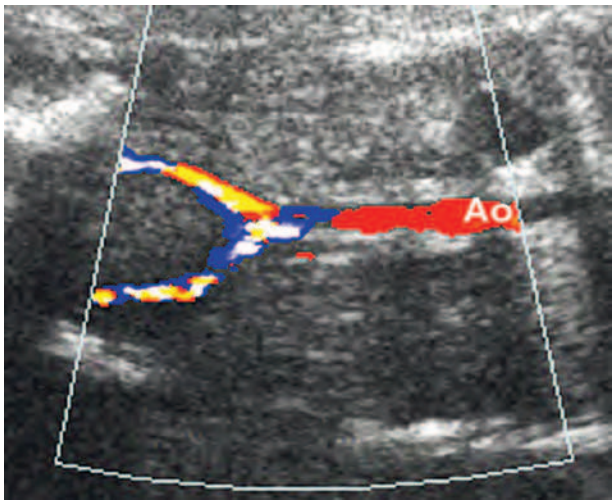

FIG. 39.7 Absent Renal Arteries. Color Doppler ultrasound shows no renal artery arising from the aorta *(Ao)* in a fetus with bilateral renal agenesis.

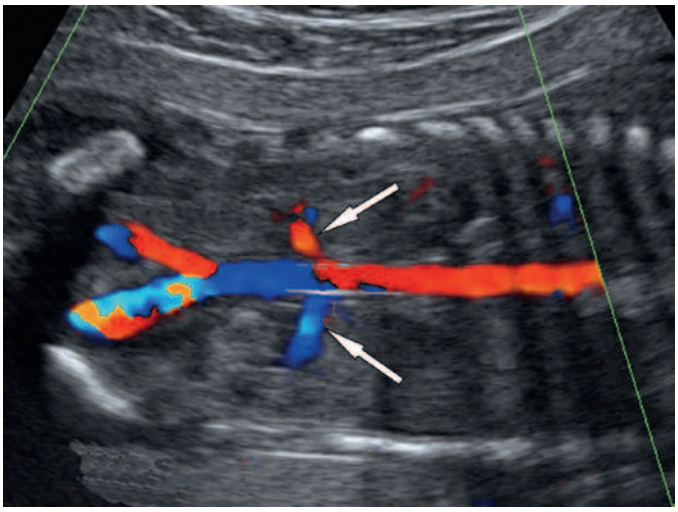

FIG. 39.8 Normal Renal Arteries. Color Doppler ultrasound maps out the renal arteries bilaterally *(arrows)* in a 19-week fetus, confirming the presence of kidneys.

Bilateral Renal Agenesis

SONOGRAPHIC FINDINGS
Severe oligohydramnios
Absent kidneys
"Lying down" adrenal sign
Absent renal arteries on color Doppler imaging
Nonvisualization of bladder (over 1 hour)

TECHNICAL LIMITATIONS
Poor image quality caused by oligohydramnios
Fetal position (breech presentation)

PITFALLS IN INTERPRETATION
Amniotic fluid volume may be normal before 16 weeks' gestation
Bowel or adrenal glands can be mistaken for kidneys
Urachal diverticulum may mimic the bladder
Empty bladder may be caused by impaired renal function from other causes (e.g., intrauterine growth restriction)

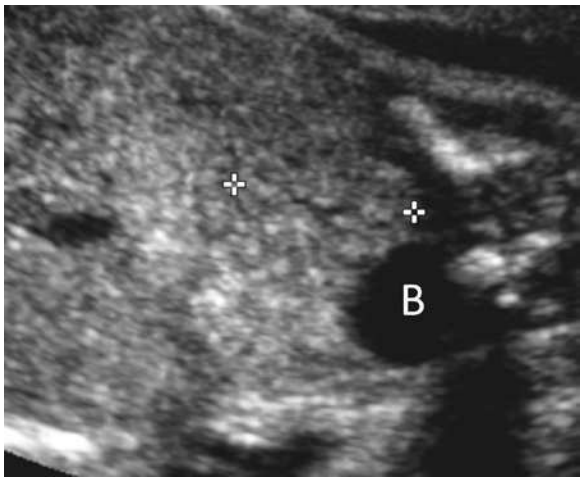

FIG. 39.9 Pelvic Kidney. Coronal image in a 23-week fetus shows the ectopic kidney *(calipers)* adjacent to the iliac wing and bladder *(B)*. See also Video 39.3.

first- and second-degree relatives of affected fetuses have been found to have congenital renal anomalies, most often unilateral renal agenesis; and in these families the recurrence risk may be higher.[34,36] Screening parents and siblings with renal ultrasound is recommended.[34]

Unilateral Renal Agenesis

Unilateral renal agenesis is three to four times more common than bilateral renal agenesis, occurring 1 in 1000 births.[3] It can be difficult to diagnose prenatally because AFV is normal and the bladder appears normal. A common pitfall is failure to image the renal fossa in the far field because of acoustic shadowing from the spine, especially in the transverse plane. Meticulous attention to technique is necessary (rotating the transducer, changing the maternal position, or repeated observations). If a kidney is not found in the renal fossa, most are either congenitally absent or ectopic.[55,56] The contralateral kidney may be enlarged because of compensatory hypertrophy.[57] There is a high incidence of contralateral renal abnormalities, the most common being **vesicoureteral reflux** (VUR).[58] Unilateral renal agenesis is associated with genital, cardiac, skeletal, and GI abnormalities, as well as with multiorgan syndromes.[59] Isolated unilateral renal agenesis has a good prognosis. Neonatal urologic workup is necessary, including a voiding cystourethrogram (VCUG).

The recurrence risk to parents of a baby with isolated unilateral renal agenesis is about 1% if the parents have normal renal ultrasound. However, if one parent has a congenital solitary kidney, the risks to offspring are 7% for congenital solitary kidney and 1% for bilateral renal agenesis.[60]

Renal Ectopia

One or both kidneys may be in an abnormal position. The incidence of renal ectopia varies between 1:500 and 1:1200 births, with **pelvic kidney** being the most common form.[61] When the renal fossa is empty, careful scanning may demonstrate the ectopic kidney adjacent to the bladder or iliac wing (Fig. 39.9, Video 39.3). However, prenatal detection is often difficult because

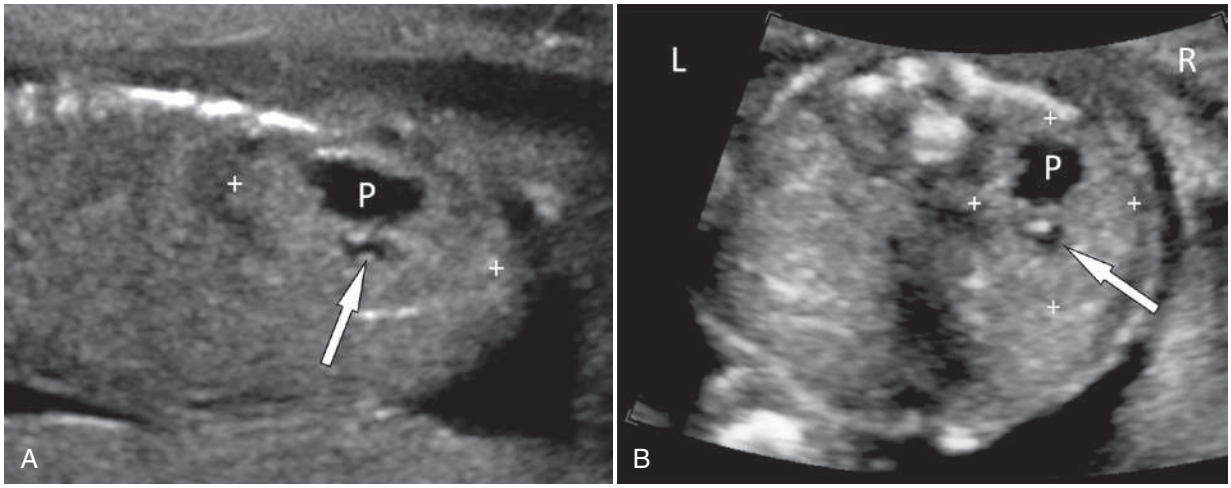

FIG. 39.10 Cross-Fused Renal Ectopia. Sagittal **(A)** and axial **(B)** images show an enlarged bilobed kidney in the right renal fossa *(calipers).* No kidney was seen in the left renal fossa. The normally located right (posterior) kidney has a dilated renal pelvis *(P).* It is fused with the left (anterior) kidney with a normal renal pelvis *(arrow)* to form a "lump kidney." See also Video 39.4.

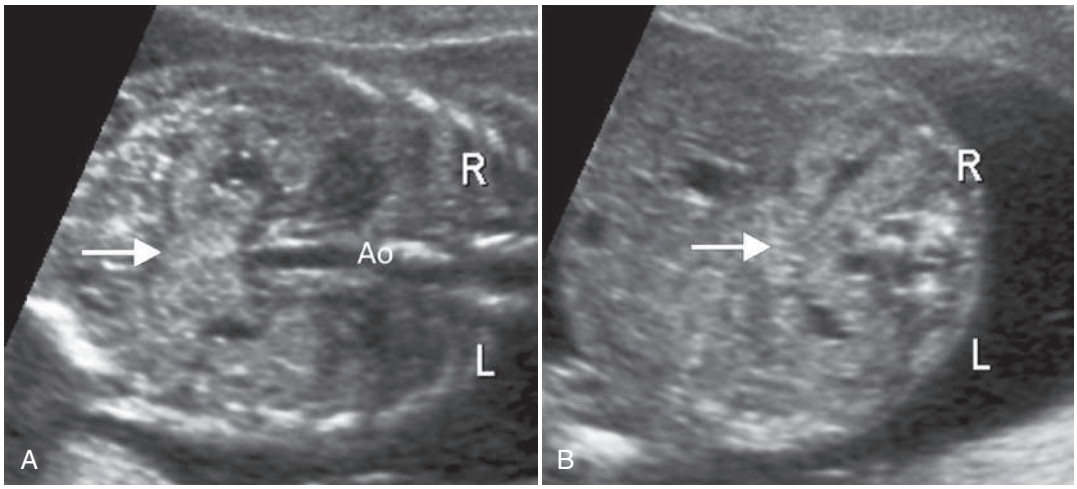

FIG. 39.11 Horseshoe Kidney. (A) Coronal image in a 19-week fetus shows the bridge of renal parenchyma *(arrow)* connecting the lower poles of the kidneys, anterior to the aorta *(Ao).* **(B)** Axial image shows, in addition to the fused isthmus *(arrow),* the abnormal anterior orientation of the renal pelvis bilaterally.

pelvic kidneys may be indistinguishable from bowel loops and are frequently smaller than normally positioned kidneys. Pelvic kidneys may be hypoplastic or dysplastic. Postnatally impaired renal function has been found in 33% of pelvic kidneys, although the overall renal function remained normal at a median follow-up of 8 years.[62]

When the ectopic kidney is located on the opposite side of the abdomen relative to its ureteral insertion into the bladder, it is defined as **crossed renal ectopia.** In most cases, the crossed ectopic kidney fuses with the normally located kidney **(crossed fused renal ectopia),** and an enlarged bilobed kidney is seen (Fig. 39.10, Video 39.4). Crossed renal ectopia is divided into six subgroups based on the degree of fusion and location and rotation of the fused renal mass.[63] Most commonly, the crossed ectopic kidney is inferior to the normally positioned kidney, and the upper pole of the ectopic kidney is fused to the lower pole of the normal kidney.

Renal ectopia is associated with a high incidence of urologic abnormalities (most often VUR), as well as nonurinary malformations.[64] Neonatal renal ultrasound is necessary. A VCUG is indicated if there is hydronephrosis in the ectopic or contralateral kidney.

Horseshoe Kidney

Horseshoe kidney is the most common fusion anomaly of the kidney, occurring in 1:400 to 1:500 births.[3,61] Prenatal sonographic findings include abnormal longitudinal axis of both kidneys and a bridge of renal tissue connecting the lower poles (Fig. 39.11, Video 39.5). Despite its relative frequency, this disorder is seldom diagnosed prenatally because the findings are subtle, and surrounding bowel can obscure the fused isthmus. The majority of horseshoe kidneys have an abnormal anterior orientation of the renal pelvis bilaterally. Measurement of the renal pelvic angle on a true axial image of both kidneys is useful for

diagnosis, and angles less than 140 degrees are highly suggestive of horseshoe kidney.[65] A horseshoe kidney is frequently associated with other anomalies (e.g., urogenital, cardiac, skeletal, CNS) and chromosomal abnormalities such as **Turner syndrome, trisomy 18,** and **trisomy 9.** Isolated horseshoe kidney is a relatively benign disorder that requires postnatal urologic follow-up because of higher prevalence of VUR, renal calculi, UT infections, and hydronephrosis.

Renal Cystic Disease

Renal cystic disease consists of a heterogeneous group of disorders with inherited and acquired causes. Because of their diverse etiology, histology, and clinical presentation, a widely accepted classification does not exist. The Potter classification is based on histology and does not take into account recent advances in molecular genetics.[66] A more recent classification based on the genetic or nongenetic origin of fetal renal cystic diseases has been proposed.[67] Among the **nongenetic cystic diseases,** multicystic dysplastic kidney (MCDK) and obstructive dysplasia are the most common. **Genetic diseases** include **autosomal recessive** and **autosomal dominant polycystic kidney disease** (ADPKD), and a growing number of cilia-related disorders **(ciliopathies)** associated with cystic kidneys as well as other abnormalities.[68,69] Many of these diseases have been associated with one or several genetic mutations, and an accurate genetic diagnosis is crucial for genetic counseling, prenatal diagnosis, and clinical management.

Multicystic Dysplastic Kidney

MCDK is the most common form of renal cystic disease in childhood and represents one of the most common abdominal masses in the neonate. The majority of cases are associated with an **atretic ureter** and **pelvoinfundibular atresia.** The kidney is replaced by multiple cysts of varying sizes. Between the cysts is a dense stroma, and there is usually no normal renal parenchyma. Kidneys affected with multicystic dysplasia are almost always nonfunctional. Thus the prognosis depends entirely on the function of the contralateral kidney. Multicystic renal dysplasia usually affects the whole kidney. However, it can be segmental and can occur in the portion of the duplex kidney supplied by the atretic ureter.

The sonographic findings correlate with the gross pathologic appearance. The malformed kidney is usually enlarged but may be normal in size or small. There are multiple cysts of varying sizes that do not communicate with one another and are randomly distributed (Fig. 39.12). Large peripheral cysts distort the reniform contour. The renal pelvis and ureter are usually atretic and not visible. On color Doppler evaluation, the renal artery is either absent or very small. Occasionally an MCDK with a large central cyst and small peripheral cysts can mimic hydronephrosis from ureteropelvic junction (UPJ) obstruction (see later discussion). In hydronephrosis, however, the dilated calyces are of uniform size and anatomically aligned and communicate with the dilated renal pelvis. The kidney usually maintains the reniform contour, with renal parenchyma present peripherally.

The appearance and size of the MCDK may change markedly during gestation and after birth (see Fig. 39.12). On serial examinations, the kidney and its cysts may increase or decrease in size or may initially enlarge and later involute.[70] This variable appearance may result from residual renal function and/or progressive fibrosis.

Assessment of the contralateral kidney is very important. In 19% to 24% of cases, multicystic renal dysplasia is bilateral[71,72] (Fig. 39.13). In unilateral multicystic renal dysplasia, contralateral renal abnormalities are present in 13% to 26%, including renal agenesis and UPJ obstruction.[71,73] In fetuses with MCDK, severe oligohydramnios and nonvisualization of the urinary bladder imply lethal renal disease, either bilateral MCDK or contralateral severe renal dysfunction or agenesis. Normal AFV is reassuring. If there is contralateral hydronephrosis, follow-up ultrasound is necessary to monitor any progressive dilation or oligohydramnios that may affect obstetric management. Unilateral MCDK, without associated renal or nonrenal abnormalities, is associated with a favorable outcome.[74] A postnatal ultrasound is performed after 48 hours of age. Prophylactic antibiotic therapy is usually initiated soon after birth, pending the results of postnatal ultrasound and

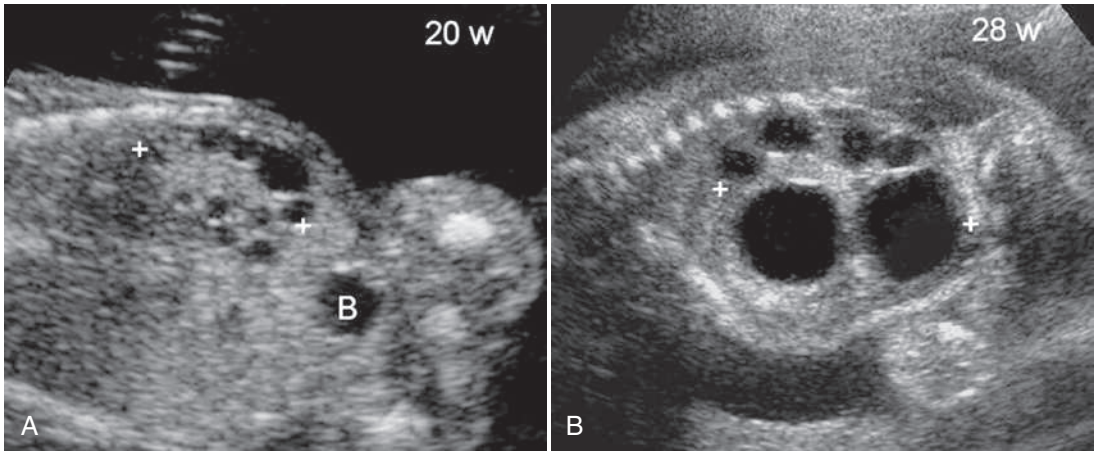

FIG. 39.12 Unilateral Multicystic Dysplastic Kidney. (A) Image of the fetus at 20 weeks' gestation demonstrates multiple small cysts in a slightly enlarged kidney *(calipers); B,* bladder. **(B)** Follow-up image at 28 weeks' gestation demonstrates a greatly enlarged kidney *(calipers).* Cysts have increased in size, do not communicate, and are randomly distributed.

nephrology consultation. A VCUG is indicated if there is contralateral hydronephrosis or a history of UT infection.[75]

The natural history of MCDK is toward spontaneous **involution.** This has been well documented both before and after birth.[70,72] The longer the duration of follow-up, the higher is the likelihood that the dysplastic kidney will become so small as to not be evident sonographically. The risk of hypertension associated with MCDKs does not appear to be greater than that of the general population,[76] and the rates of malignant transformation of MCDK are small.[77] Although there are some proponents for routine laparoscopic nephrectomy, conservative management (with clinical and ultrasound surveillance) is favored in most centers.[78] Most cases of MCDK are sporadic, with a low recurrence risk. However, some cases have been associated with mutations in hepatocyte nuclear factor 1β (HNF1β), which carries an autosomal dominant mode of inheritance with both interfamilial and intrafamilial variability in the clinical manifestations.[79]

FIG. 39.13 Bilateral Multicystic Dysplastic Kidneys. Transvaginal image in a 16-week fetus demonstrates numerous small bilateral cysts *(arrows)* and no normal renal parenchyma. Note anhydramnios due to nonfunctioning kidneys.

Obstructive Cystic Renal Dysplasia

The effect of urinary obstruction on subsequent renal development depends on the time of onset and severity of the obstruction. Experimental work in lambs has shown that urinary obstruction starting in the last half of gestation causes simple hydronephrosis and, when severe, parenchymal atrophy.[80] However, if the urinary obstruction starts during the first half of gestation, **renal dysplasia** and sometimes cyst formation will occur[80-82] (Fig. 39.14). The fetal UT responds differently to chronic obstruction than the adult UT. In adults with chronic urethral obstruction, the pelvicalyceal system is usually greatly dilated; in the fetus there may be a relative lack of pelvicalyceal dilation and possible development of macroscopic renal cysts.

Unilateral renal dysplasia can be caused by UPJ obstruction or ureterovesical junction (UVJ) obstruction. Bilateral disease is caused by severe **bladder outlet obstruction,** usually due to urethral atresia or posterior urethral valves. The severity of renal dysplasia is related to the timing and severity of obstruction to

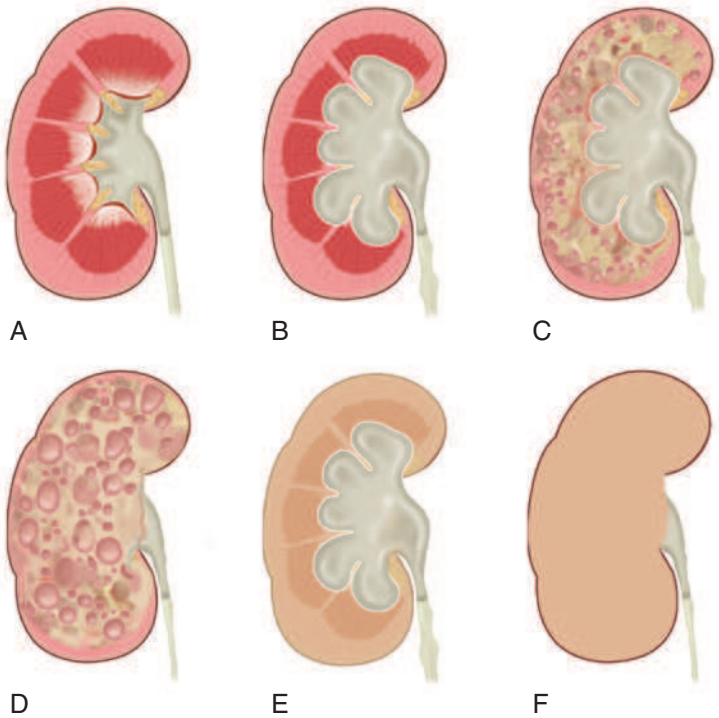

FIG. 39.14 Urinary Tract Obstruction Produces a Varied Response From the Kidneys. (A) Normal kidney. **(B) Pelvicaliectasis,** with or without parenchymal atrophy. **(C) Renal cystic dysplasia,** with parenchymal cysts. **(D)** The dysplastic kidney may cease to function (lack of pelvicaliectasis). **(E)** and **(F)** Alternatively, the kidney may show increased echogenicity, with no visible cysts but with pelvicaliectasis **(E)** or without pelvicaliectasis **(F).** In these cases, dysplasia is probably, but not invariably, present.

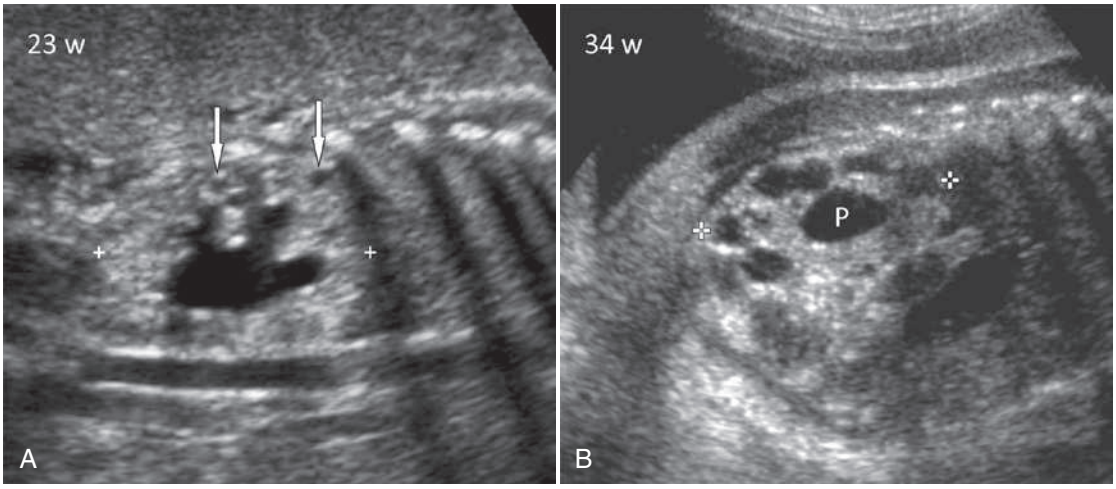

FIG. 39.15 Obstructive Cystic Dysplasia. (A) Coronal image of fetus at 23 weeks with ureteropelvic junction obstruction shows increased echogenicity of the kidney *(calipers)* with small cortical cysts *(arrows),* indicative of irreversible renal damage. **(B)** Sagittal image at 34 weeks shows the cysts have increased in size and the kidney is large. There is some functioning renal tissue, as fluid is seen in the slightly dilated renal pelvis *(P).*

urine flow.[83] The size of the kidneys varies from small to normal to markedly enlarged. In some cases the enlargement is caused partly by the presence of cysts and partly by hydronephrosis. Cysts are usually present in the subcapsular area of the cortex. In a fetus with obstructive uropathy, the sonographic identification of **cortical cysts** is indicative of renal dysplasia (i.e., irreversible renal damage)[84] (Fig. 39.15). Dysplastic kidneys may also demonstrate cortical thinning and increased echogenicity relative to the surrounding fetal structures, with loss of corticomedullary differentiation. However, **increased cortical echogenicity is not a specific finding,**[85] and a diagnosis of renal dysplasia cannot be made on the basis of increased parenchymal echogenicity alone. Furthermore, it is important to recognize that not all dysplastic kidneys have sonographically visible cysts or increased cortical echogenicity, so one cannot accurately predict the absence of renal dysplasia. Renal function relates directly to the degree of dysplasia, which determines the prognosis of patients surviving the perinatal period.

In general, if the obstruction is early and complete, the renal parenchymal findings will be predominantly macroscopic cysts and will simulate multicystic renal dysplasia. Sonographic distinction between MCDK and obstructive cystic renal dysplasia may be difficult, especially in the absence of hydronephrosis. In obstructive cystic renal dysplasia, recognizable parenchyma surrounds the relatively small cysts, whereas in MCDK, no normal renal parenchyma can be identified between cysts, and the cysts can be of varying size and can be quite large. Obstructive cystic renal dysplasia most often occurs with urethral obstruction. Therefore sonographic evidence of urethral obstruction is helpful in suggesting the diagnosis. In addition, renal dysplasia from lower UT obstruction frequently involves both kidneys, whereas bilateral MCDK occurs in only 19% to 24% of cases.[71,72]

Autosomal Recessive Polycystic Kidney Disease

The incidence of autosomal recessive polycystic kidney disease (ARPKD) is 1 in 20,000 live births. In the past this was termed "infantile polycystic kidney disease," but the presentation can be after the neonatal period; thus the preferred term is "autosomal recessive polycystic kidney disease." It primarily involves the kidneys and biliary tract. The clinical spectrum is wide and varies from the **perinatal form,** with severe renal disease, minimal hepatic fibrosis, and early death from pulmonary hypoplasia, to the **juvenile form,** with minimal renal disease, marked hepatic fibrosis, and longer survival. Diffuse dilation of the renal collecting tubules produces numerous cysts smaller than 2 mm, predominantly in the medulla. Both kidneys are enlarged, but a smooth contour is maintained. The cut surface has a spongelike appearance, with small cysts that tend to be arranged perpendicular to the renal capsule (Fig. 39.16).

Sonography reveals **bilateral reniform enlargement** of the kidneys (see Fig. 39.16). There is poor delineation of the intrarenal structures. The numerous tiny cysts are usually smaller than the limit of sonographic resolution, but they create multiple acoustic interfaces, accounting for the characteristic increased renal echogenicity.[86] In a fetus, the finding of bilateral, very large (>4 standard deviations), diffusely hyperechoic kidneys with poor corticomedullary differentiation, with or without visible cysts, is most likely due to ARPKD.[67,87] Another typical pattern is very large kidneys with a peripheral hypoechoic rim surrounding the centrally increased echogenicity or **hyperechoic pyramids (reversed corticomedullary differentiation)** (Fig. 39.17, Video 39.6).[67] When renal function is abnormal, there is oligohydramnios, and the bladder is small or absent.

Usually, but not always, ultrasound shows evidence of ARPKD by 24 to 26 weeks' gestation.[88,89] Autosomal recessive PKD may be diagnosed by ultrasound in the second trimester based on the characteristic renal abnormalities, especially if the fetus is at risk.[88] However, because of the variability in phenotypic expression and gestational age at onset, the kidneys may appear normal initially, only becoming abnormal later.[88] Thus a normal sonogram in a fetus at risk for ARPKD does not exclude this disease, and prenatal diagnosis using sonography can be unreliable, especially in early pregnancy. ARPKD is inherited in an autosomal recessive manner, and thus the recurrence risk is 25%.

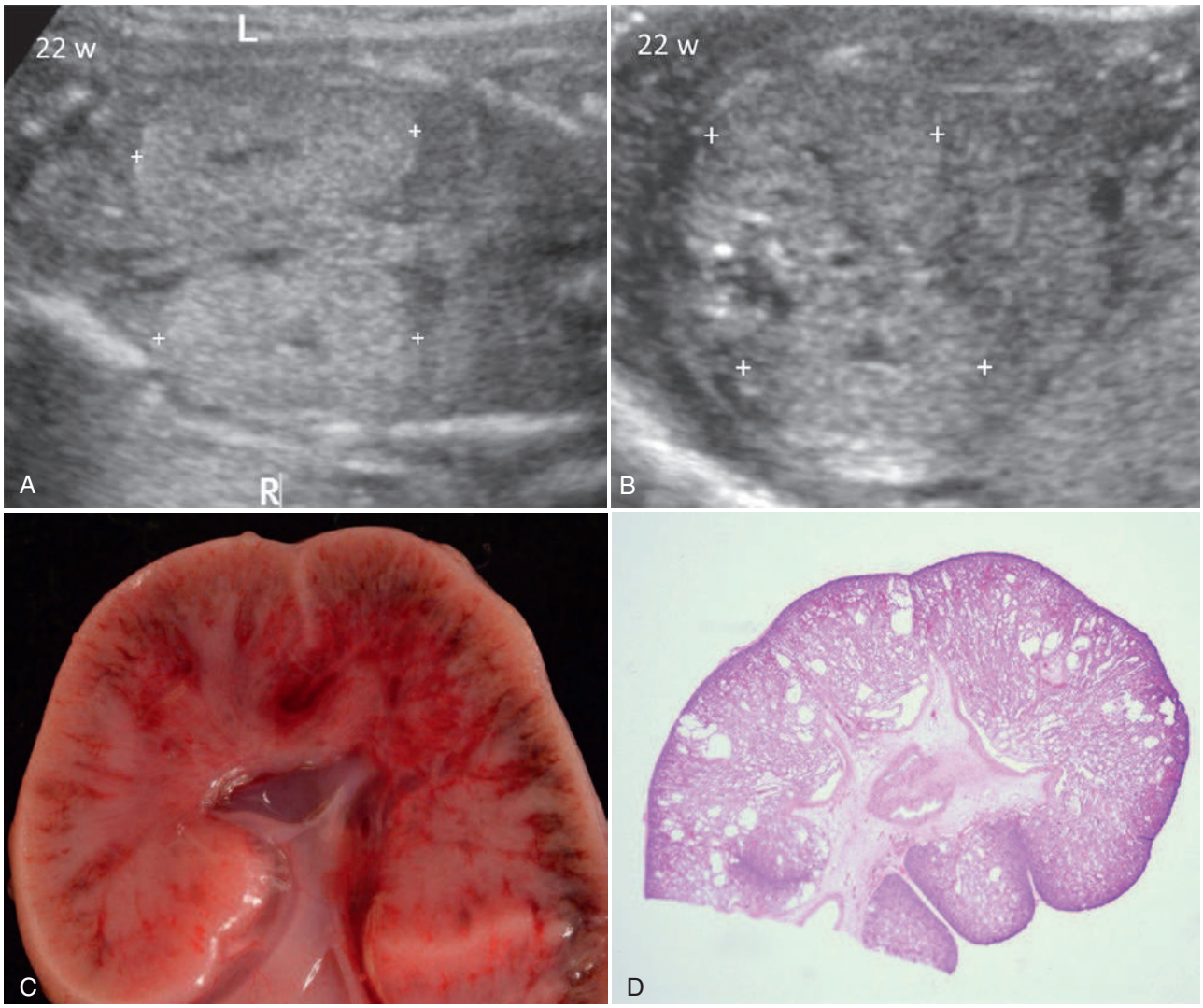

FIG. 39.16 Autosomal Recessive Polycystic Kidney Disease (Early Presentation). (A) and **(B)** Coronal and transverse scans of a 22-week fetus show bilateral large, diffusely hyperechoic kidneys *(calipers)* with loss of corticomedullary differentiation. **(C)** Photograph of cut surface of kidney shows a spongelike appearance. The small cysts are difficult to see. **(D)** Photograph of whole-mount section shows small cysts that tend to be arranged perpendicular to the renal capsule (hematoxylin-eosin stain). (**C** and **D** courtesy of Sarah Keating, MD, Department of Pathology and Laboratory Medicine, Mount Sinai Hospital, Toronto.)

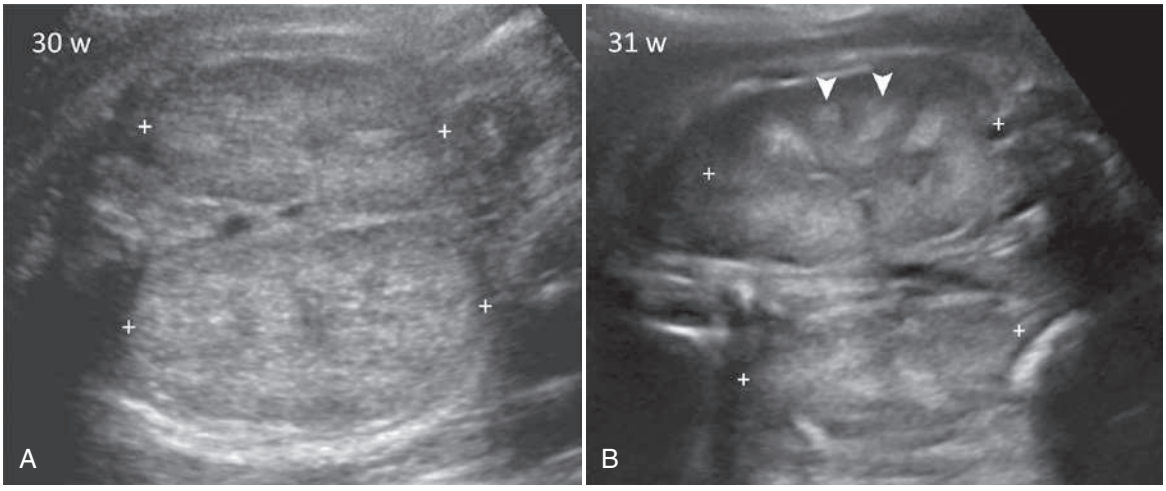

FIG. 39.17 Autosomal Recessive Polycystic Kidney Disease (Third-Trimester Presentation). (A) Coronal scan of a 30-week fetus shows markedly enlarged kidneys *(calipers),* with a hypoechoic peripheral rim surrounding the centrally increased echogenicity. Right kidney measures 7.5 cm in length and left kidney 8 cm. **(B)** Coronal scan of a different fetus at 31 weeks' gestation shows markedly enlarged kidneys *(calipers),* with hyperechoic pyramids *(arrowheads),* resulting in "reversed corticomedullary differentiation."

ARPKD is caused by mutation in the ***PKHD1* gene,** which has been mapped to chromosome 6p12, allowing prenatal genetic diagnosis in at-risk families.[90,91]

Autosomal Dominant Polycystic Kidney Disease

ADPKD is the most common of the hereditary renal cystic diseases, with an incidence of 1 : 1000 in the general population. Although this was previously termed "adult polycystic kidney disease," the presentation can be in the prenatal period or in childhood; thus the preferred term is "autosomal dominant polycystic kidney disease." It is characterized by cyst formation in the kidneys and liver. Cysts may also be present in the pancreas and spleen, and the disorder is associated with CNS aneurysms. In the early stage of the disease, only a small percentage of nephrons show cystic dilation. In the established adult disease, the kidneys are enlarged and contain multiple cysts of varying sizes.

ADPKD is usually not detected prenatally because the fetal kidneys typically appear normal. In **rare** cases, ADPKD can manifest during the **fetal or neonatal** period with symmetrical moderately enlarged hyperechoic kidneys, within which small cysts (<7 mm) may be identified (Fig. 39.18).[92,93] The bladder is usually present, and AFV is often normal. In contrast to ARPKD, in which corticomedullary differentiation is absent,[86] increased corticomedullary differentiation has been reported in ADPKD. In a series of 27 cases of abnormal-appearing kidneys on prenatal ultrasound and final diagnosis of ADPKD (note that this is a biased population because the kidneys appeared abnormal prenatally), 20 had increased corticomedullary differentiation, six had absent or decreased corticomedullary differentiation; and 1 had normal corticomedullary differentiation.[93] Because the kidneys may appear normal in the second trimester, follow-up scans are necessary in fetuses at risk for ADPKD.

A **family history** of ADPKD is critical in making the diagnosis of ADPKD in the fetus. Because the disease is autosomal dominant, the recurrence risk is 50%. However, it has been reported that over 50% of the affected parents were not aware of their disease at the time of obstetric ultrasound.[92,93] Therefore ultrasound of the parents' kidneys is helpful in establishing the cause. Two ADPKD causative genes have been identified: ***PKD1*** (located on chromosome 16p13) and ***PKD2*** (located on chromosome 4q21).[94] Hence, prenatal genetic diagnosis is possible. Affected families with early-onset disease in their offspring have a high recurrence risk for fetal presentation in subsequent affected pregnancies.[69]

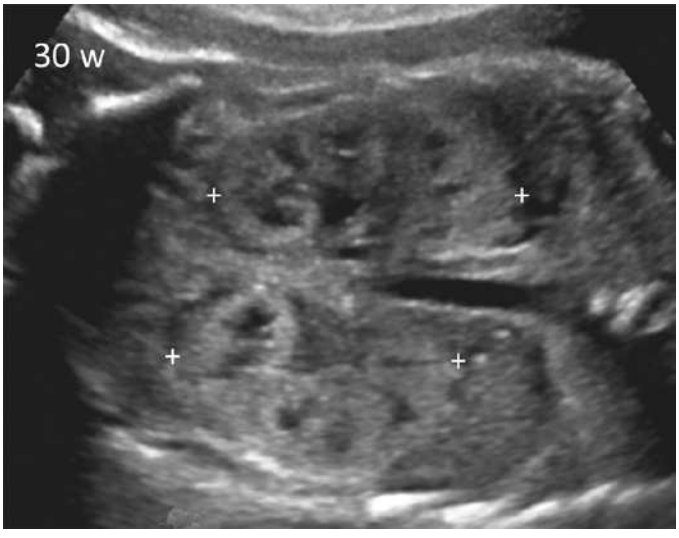

FIG. 39.18 Autosomal Dominant Polycystic Kidney Disease. Coronal scan of 30-week fetus shows enlarged kidneys *(calipers),* measuring 5 cm in length (>3 SD), with increased corticomedullary differentiation due to increased echogenicity of the cortex.

The long-term prognosis for the fetus with ADPKD diagnosed by ultrasound is still not well known because of limited data on postnatal renal evolution and short duration of follow-up. Initial reports suggested that although the majority of ADPKD infants survive, they tend to have earlier onset and more significant hypertension and a more rapid decline in renal function than their affected adult relatives.[90,95,96] More recent studies reported a favorable prognosis in most children with prenatally diagnosed ADPKD.[97,98] In a study of 26 consecutive children with prenatal ADPKD (excluding three terminations of pregnancy with very large kidneys and anhydramnios), Boyer and colleagues reported favorable prognosis in infancy and childhood, with 19 (73%) children asymptomatic, 5 (19%) with hypertension, and 2 (8%) with chronic renal insufficiency (mean duration of follow-up, 76 months; range, 0.5-262 months).[97] In another study of 42 patients with prenatal ADPKD, there were four terminations of pregnancy, and among 35 patients with known serum creatinine (age of patients at last follow-up ranged from 1 month to 20 years), renal function was abnormal in only 2.[98]

Syndromes Associated With Renal Cystic Disease

Approximately 30% of fetuses with trisomy 13 have echogenic/cystic kidneys. Other genetic conditions associated with renal cystic disease include single-gene disorders categorized as **ciliopathies** (disorders caused by mutations in genes with products that localize to the cilium-centrosome complex). These include **Bardet-Biedl syndrome, hepatocyte nuclear factor 1β–related disease, Joubert syndrome,** and **Meckel syndrome.** The phenotypes due to the altered proteins vary from cystic kidney disease and blindness to neurologic phenotypes, obesity, and diabetes.

HNF1β is a transcription factor that is critical for the development of kidney and pancreas. Mutations in the *HNF1β/TCF2* gene result in various phenotypes that include renal cysts and diabetes. *HNF1β* mutations are often found in fetuses with severe renal anomalies.[79,99,100] In a retrospective study of 377 patients with various congenital renal anomalies, the prevalence of *HNF1β* mutation was (20%).[79] Among 56 patients who carried *HNF1β* mutation and who had prenatal sonography, various renal phenotypes were observed. The most common (seen in 34 of 56 fetuses) was isolated bilateral hyperechogenic kidneys, normal in size or slightly enlarged (size ≤ +3 SD).[79] Other, less frequent renal abnormalities were bilateral MCDK (in 2), unilateral MCDK (in 8), and unilateral renal agenesis or hypoplasia (in 5).

HNF1β mutations follow an autosomal dominant mode of inheritance. However, when the family history is evaluated, one has to keep in mind incomplete penetrance and considerable interfamilial and intrafamilial phenotypic variability, as well as

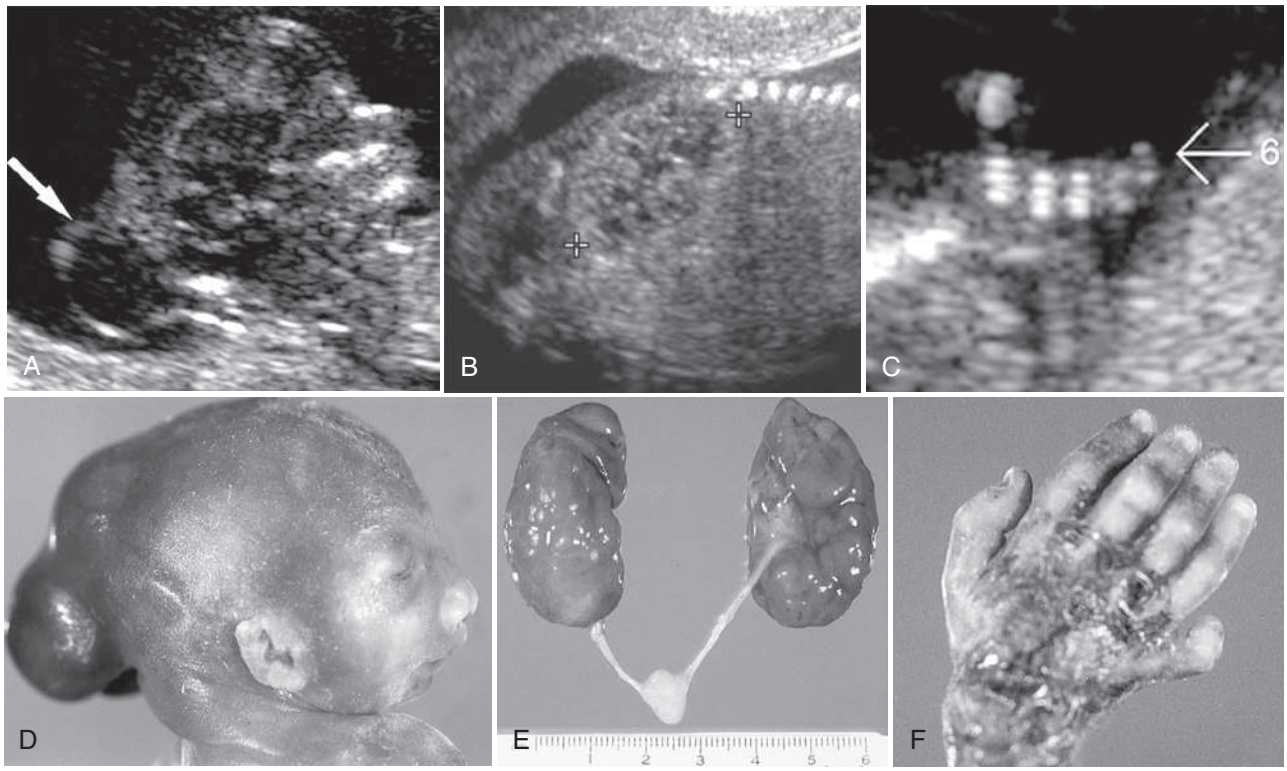

FIG. 39.19 Meckel-Gruber Syndrome. (A)-(C) Ultrasound images of a 14-week fetus show classic features of Meckel-Gruber syndrome: an occipital encephalocele *(thick arrow),* large kidneys (only one shown *[calipers]*) with a mottled cystic appearance, and postaxial polydactyly *(thin arrow).* **(D)-(F)** Postmortem photographs of the fetus (at 18 weeks' gestation) demonstrate occipital encephalocele, large kidneys, and postaxial polydactyly.

new dominant mutation and gene deletion. The severity of the renal disease can be extremely variable (from prenatal oligohydramnios or anhydramnios to normal renal function in adulthood) and is not correlated with the genotype.[79]

Meckel syndrome, also known as **Meckel-Gruber syndrome,** is a lethal autosomal recessive ciliopathy that carries a 25% risk of recurrence. It can be detected by sonography at 11 to 14 weeks' gestation, particularly in families with prior affected pregnancies.[101] Sonographic diagnosis requires identification of at least two features of the classic triad: **enlarged echogenic, cystic kidneys** (present in almost 100% of cases); **occipital encephalocele** (60%-85%); and **postaxial polydactyly** (55%)[102] (Fig. 39.19). During second-trimester sonography, it can be difficult to detect the encephalocele and polydactyly because of oligohydramnios. Microcephaly can be a useful clue to the presence of an encephalocele. The kidneys are markedly enlarged (+4 SD), with a mottled cystic appearance of the medulla surrounded by the hyperechoic cortex.[103] Numerous small cysts are present, most smaller than 5 mm. The diagnosis of Meckel syndrome is particularly important for counseling regarding the recurrence risk and possible prenatal and preimplantation genetic diagnosis in future pregnancies. Meckel syndrome can be caused by mutations in 1 of at least 13 genes. The proteins coded by these genes are known to have a major role in cilia formation.

Hyperechogenic Kidneys

Fetal kidneys are considered hyperechogenic or "bright" when they appear more echogenic than expected, compared with the adjacent liver or spleen (Fig. 39.20).[67] Hyperechogenic kidneys seen on prenatal ultrasound represent a diagnostic and prognostic dilemma, particularly in the presence of normal AFV. There is a wide differential diagnosis, including genetically inherited renal diseases **(ARPKD, ADPKD, HNF1β mutations, Bardet-Biedl syndrome, Perlman syndrome, Simpson-Golabi-Behmel), obstructive dysplasia, aneuploidy,** infections (especially **cytomegalovirus**), **nephroblastomatosis, renal vein thrombosis,** toxic injury, ischemia, and in some cases normal variant.[104]

The proposed algorithm is useful for the evaluation of hyperechogenic kidneys (Fig. 39.21). If there is sonographic evidence of UT obstruction, renal dysplasia is a possibility, especially when the kidneys are small or normal in size and there are peripheral cortical cysts.[85] When extrarenal malformations are detected, assessment of karyotype is indicated to exclude aneuploidy (especially **trisomy 13**). If the kidneys and the biometric measurements are above the 95th percentile, an overgrowth syndrome (Perlman syndrome, Simpson-Golabi-Behmel syndrome) should be considered. In both conditions, there is generalized organomegaly and the AFV may be increased. In **Perlman syndrome** there may be micrognathia and depressed nasal bridge. In **Simpson-Golabi-Behmel syndrome,** there may be congenital diaphragmatic hernia, cleft lip or palate, and polydactyly. In **Bardet-Biedl syndrome,** in addition to enlarged hyperechogenic kidneys, postaxial polydactyly can be detected.

In several prospective and retrospective series of prenatally diagnosed, isolated, bilaterally enlarged hyperechogenic kidneys, the most common underlying diagnosis was ARPKD, followed

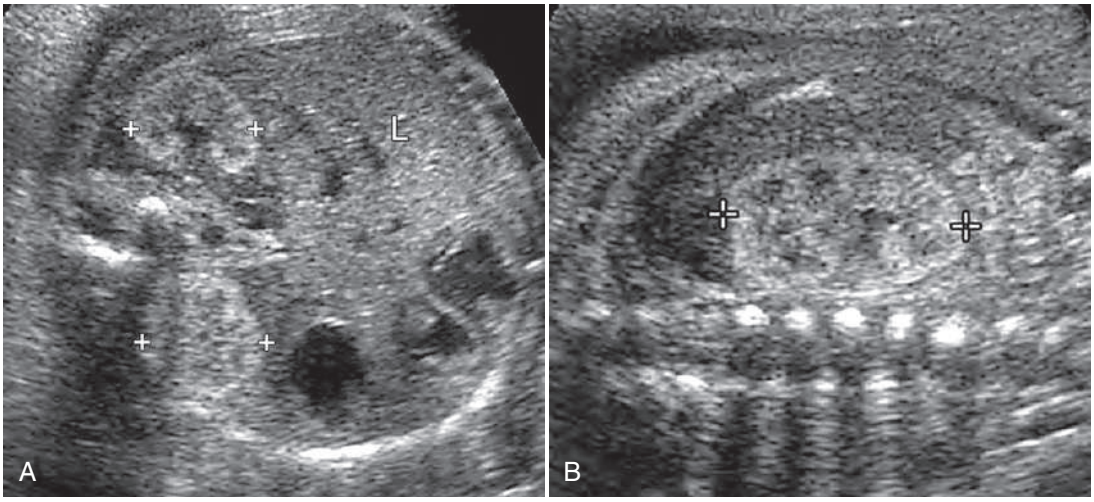

FIG. 39.20 Hyperechogenic Kidneys. Transverse **(A)** and longitudinal **(B)** scans of a 24-week fetus show increased cortical echogenicity of both kidneys *(calipers),* more than expected when compared with liver *(L)* and increased corticomedullary differentiation. The kidneys were normal in size, and AFV was normal. Ultrasound at 32 weeks *(not shown)* showed similar findings. Postnatal ultrasound *(not shown)* on day 8 confirmed normal-sized kidneys with increased cortical echogenicity, and there were several tiny cortical cysts. Parents had normal kidneys. Genetic testing for autosomal recessive polycystic kidney disease (ARPKD) and hepatocyte nuclear factor 1β (HNF1β) was negative. The child, at age 9 years, has normal renal function. Ultrasound *(not shown)* showed multiple 1- to 3-mm cysts in the medulla and cortex bilaterally. No definitive cause for the bilateral cystic kidneys has been identified.

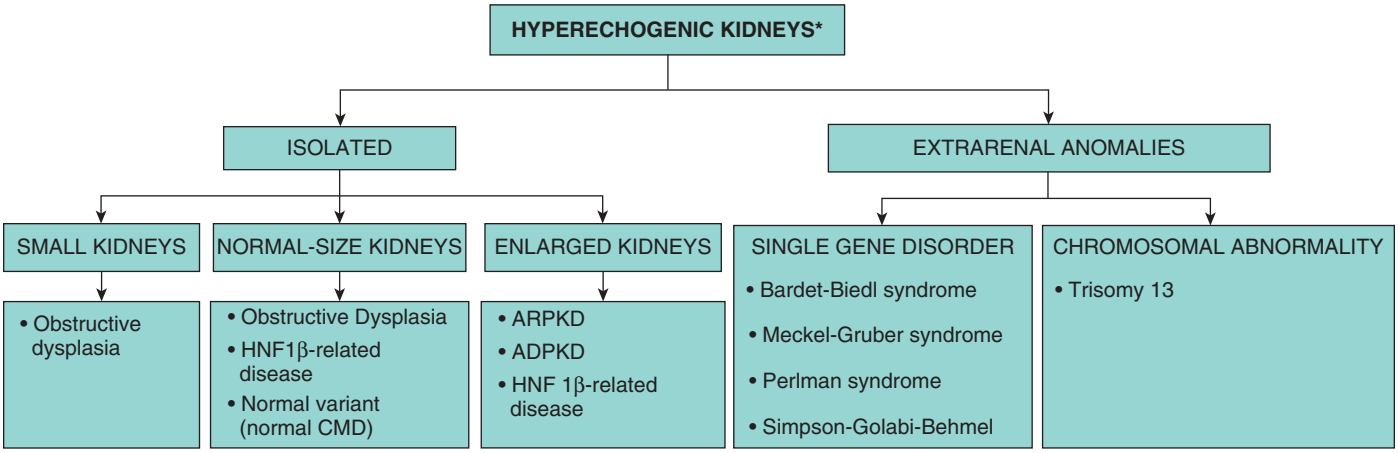

FIG. 39.21 Algorithm for Sonographic Evaluation of Hyperechogenic Kidneys. *No family history. Otherwise, a positive family history suggests recurrence of the known disorder. *ADPKD,* Autosomal dominant polycystic kidney disease; *ARPKD,* autosomal recessive polycystic kidney disease; *CMD,* corticomedullary differentiation; *HNF1β,* hepatocyte nuclear factor 1β–related disease.

by ADPKD.[87,105,106] A detailed family history and an ultrasound examination of the parents' kidneys are important. In ADPKD, usually one parent has the disease, and sonography usually establishes the diagnosis. However, new mutations associated with ADPKD can occur. Normal AFV favors ADPKD. In ARPKD there is usually oligohydramnios, and there may be a previously affected sibling.

Only some of the underlying causes of hyperechogenic kidneys can be diagnosed during the prenatal period on the basis of family history, AFV, associated abnormalities, and genetic analysis.[107] In many cases a definitive diagnosis will require postnatal investigations, including histology and DNA analysis. The kidney size and AFV are the best predictors of perinatal outcome.[105,106] Bilateral hyperechogenic kidneys that are normal in size with preservation of medullary pyramids, and that are associated with normal AFV, have a favorable outcome and may represent a normal variant.[85,108] Although further studies are necessary to determine specific prognostic factors, in cases of prenatal hyperechogenic kidneys, the parents should be counselled that parenchymal renal disease cannot be ruled out and there is a possibility of renal failure after birth or in early childhood.[109]

Renal Neoplasm

Congenital mesoblastic nephroma is the most common renal neoplasm in the fetus and newborn.[110] It is a benign hamartoma composed of mesenchymal tissue (spindle cells), as opposed to the epithelial tissue of **Wilms tumor.** Wilms tumor is a malignant lesion that is extremely rare in the fetus. Sonographically, mesoblastic nephroma is indistinguishable from Wilms tumor.

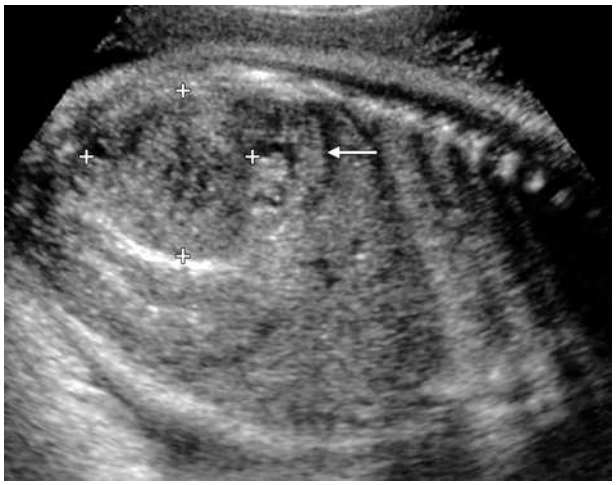

FIG. 39.22 Congenital Mesoblastic Nephroma. Longitudinal scan of a 35-week fetus shows a large, heterogeneous solid mass *(calipers)* replacing most of the right kidney, except for the upper pole *(arrow)*.

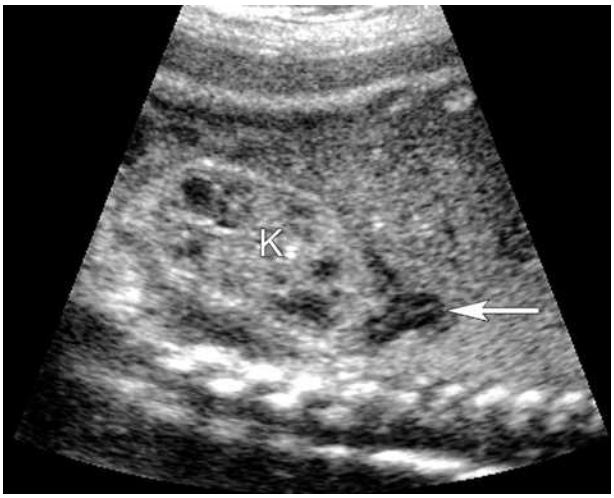

FIG. 39.23 Normal Adrenal Gland. Longitudinal scan of a 31-week fetus demonstrates the Y- or V-shaped adrenal gland *(arrow)* at the superior border of the kidney *(K)*.

Mesoblastic nephroma is usually seen as a moderately echogenic, solid mass completely replacing the kidney or localized to part of the kidney[111] (Fig. 39.22). The mass may demonstrate increased vascularity and cystic components. **Polyhydramnios** is a frequent association[110,112] and may lead to preterm labor and preterm birth. Perinatal complications are likely, including acute fetal distress, neonatal hypertension, and hypercalcemia.[110] Other reported fetal renal tumors include an intrarenal **neuroblastoma,** a tumor much more frequently associated with the adrenal gland.[113]

Adrenal Mass

At the end of the first trimester, the normal adrenal glands appear as pyramid-shaped hypoechoic structures at the superior aspect of the kidneys. They are quite prominent, approximately half the size of the kidney. The size of the adrenal gland increases with gestation, but relatively less than the kidney. During the second and third trimesters, corticomedullary differentiation is apparent, with a hyperechoic medulla and a hypoechoic cortex. On longitudinal sonogram, the adrenals are seen as V- or Y-shaped structures superior to the kidneys (Fig. 39.23).

Abnormalities of the adrenal gland include hemorrhage, cyst, hypertrophy, and tumor. The differential diagnosis for fetal suprarenal masses includes those of adrenal origin (including adrenal **neuroblastoma, adrenal hemorrhage, adrenal cyst,** and **rarely adrenal cortical adenoma or carcinoma**) and those of extraadrenal origin (including those of renal origin [such as **mesoblastic nephroma, duplication anomaly with hydronephrosis, upper-pole cystic dysplasia, urinoma**], intraabdominal **pulmonary sequestration, enteric duplication cysts, splenic cysts,** and **lymphangioma**) (Table 39.3).[114-116]

Neuroblastoma may occur anywhere along the sympathetic chain, but 90% are located in the adrenal gland. The prenatal sonographic appearance is variable and ranges from a complex cystic mass with thick septations (the most common presentation), to a uniformly echogenic solid mass (Fig. 39.24), to rarely calcified.[116-118] Importantly, a complex cystic neuroblastoma is

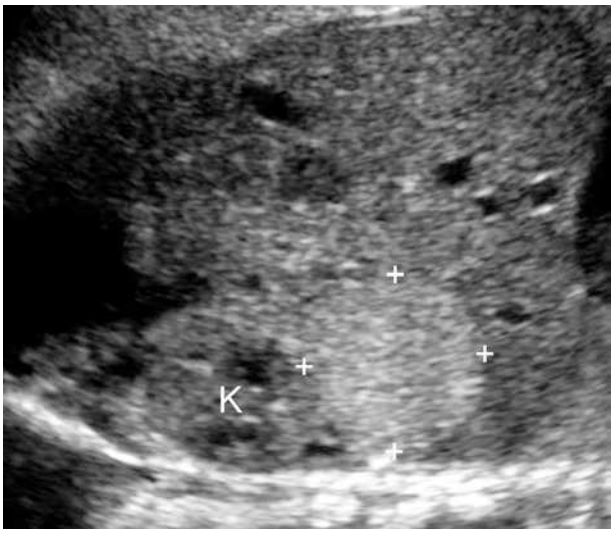

FIG. 39.24 Adrenal Neuroblastoma. Longitudinal scan shows a large echogenic solid mass *(calipers)* adjacent to the upper pole of the left kidney *(K)*. (Courtesy of John R Mernagh, MD, McMaster University Medical Center, Hamilton, Ontario.)

TABLE 39.3 Suprarenal Masses

Adrenal Origin	Nonadrenal Origin
Neuroblastoma	Renal origin: tumor (e.g., mesoblastic nephroma), duplication anomaly, upper-pole cystic dysplasia, urinoma
Hemorrhage	Intraabdominal pulmonary sequestration
Cyst	Enteric duplication cyst
Adenoma or carcinoma	Splenic cyst
	Lymphangioma

more likely to regress, whereas those with an echogenic appearance are more likely to grow.[116] The adrenal gland is not identified on the ipsilateral side. Most reported cases of neuroblastoma have been identified in the third trimester. Metastases (liver, placenta) and **hydrops** are rare but have been reported.[119,120] **Fetal hypertension** with secondary **cardiomyopathy** diagnosed on fetal echocardiography has also been reported, due to either elevation in circulating catecholamines produced by the tumor versus compression of the renal artery by the bulk of the tumor causing renovascular hypertension.[121] MRI may be useful for detailed anatomic characterization of the tumor and extent of disease.[116] Associated fetal anomalies have been reported, particularly cardiac defects, in addition to certain syndromes.[120] There may be maternal symptoms of hypertension, tachycardia, or preeclampsia, which result from elevated catecholamines and correlate with a more advanced stage of disease.[122]

Prenatally detected neuroblastomas generally have a favorable outcome, and surgical resection is usually curative.[120,123] A recent prospective study evaluating expectant observation versus surgical management confirmed the safety and effectiveness of expectant observation as a primary management strategy in infants younger than 6 months with small adrenal masses (solid tumors < 3.1 cm or cystic tumors < 5 cm with at least 25% cystic component) that were shown to be stage 1 according to the International Neuroblastoma Staging System.[124] This approach allows for avoidance of surgery in a large majority of infants whose tumors regress spontaneously.[124]

Adrenal hemorrhage, which is much more common in the neonate than in the fetus, can have a prenatal sonographic appearance similar to that of an adrenal or renal neoplasm. Color Doppler shows no flow within the mass and may be helpful in differentiation.[125] The key to the diagnosis of adrenal hemorrhage is evolution of the lesion over time; serial sonograms demonstrate a change in echogenicity (from solid appearing to cystic) and a decrease in size of the mass.[126,127] However, because neuroblastomas may also regress, it is important to obtain postnatal follow-up in fetuses with presumed adrenal hemorrhage.

Upper Urinary Tract Dilation

Dilation of the upper UT accounts for approximately 50% of all prenatally detected renal abnormalities.[128] It may be unilateral or bilateral and is more common in males than females.[129] Prospective studies in unselected populations have reported a prevalence of 0.7% to 3.9% in the second trimester.[129-131] In the majority of cases (50%-70%), the UT dilation is **transient or physiologic** and has no clinical significance.[132,133] In other cases, the dilation is due to an obstructive or nonobstructive etiology, including **ureteropelvic junction obstruction** (10%-30%), **vesicoureteral reflux** (10%-40%), **ureterovesical junction obstruction/megureter** (5%-15%), **posterior urethral valves** (1%-5%), and uncommon causes (duplex system, ectopic ureter, ureterocele, urethral atresia).[133]

"Hydronephrosis" refers to abnormal dilation of the renal pelvis and calyces. The term "pyelectasis" implies a milder form of hydronephrosis, with dilation of the renal pelvis only. Measurement of the anteroposterior **renal pelvic diameter** (RPD) is the simplest and the most common technique used to evaluate renal pelvic dilation. For optimal technique, a transverse image of the kidneys is obtained with the spine at the 12 or 6 o'clock position, and the measurement should be taken at the maximal diameter of the **intrarenal** pelvis (Fig. 39.25). The size of the renal pelvis increases throughout gestation, and there are published nomograms for RPD.[6,134,135] Controversy surrounds the definition and clinical importance of mild renal pelvic dilation, and different threshold values of RPD have been used for the antenatal diagnosis of renal pelvic dilation. In general, the cutoff values for RPD vary between 4 mm and 5 mm in the second trimester and between 7 and 10 mm in the third trimester.[130,131,136-142] Although using a cutoff value of 4 mm in midgestation can increase the sensitivity for the detection of renal pathology, it is important to realize that it can lead to a high false-positive rate, perhaps generating unnecessary parental anxiety.[143] Factors such as maternal hydration status, maternal pyelectasis, and size of the fetal bladder may affect the RPD measurement.[144-147] These findings suggest caution when considering the implications of renal pelvic dilation based on a single RPD measurement. **Calyceal dilation** is an important finding and is always pathologic, independent of the pelvic size.[131,143] The **Society for Fetal Urology** (SFU) proposed a classification system in 1993, based on the degree of renal pelvic dilation (mild, moderate, marked), while also including parameters of calyceal dilation and the appearance of the renal parenchyma.[132,148] The classification system consists of five grades: grade 0 representing no dilation, and grades 1 to 4 representing dilation of increasing severity (Fig. 39.26).

A consensus conference in March 2014 proposed a standardized classification system for UT dilation based on seven ultrasound parameters: (1) anteroposterior RPD; (2) calyceal dilation—central (major calyces) or peripheral (minor calyces); (3) renal parenchymal thickness (subjective assessment); (4) renal parenchymal appearance (echogenicity, corticomedullary

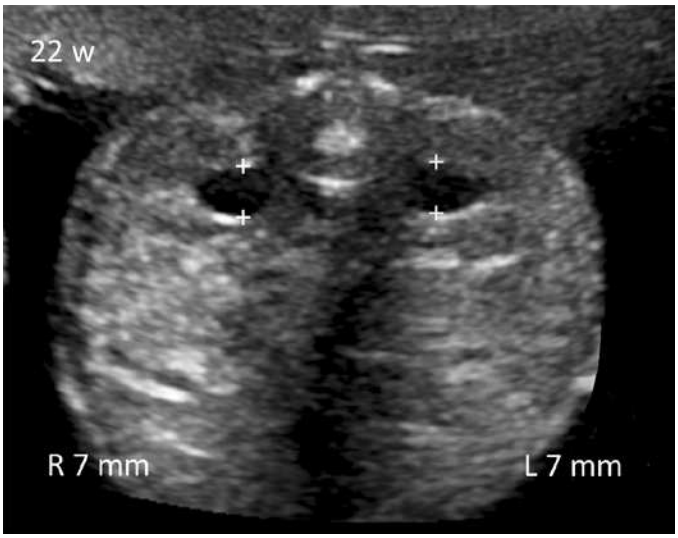

FIG. 39.25 Measurement of Anterior-Posterior Renal Pelvic Diameter (RPD). Transverse scan of the abdomen in a 22-week fetus, obtained with the fetus in a prone position, shows dilated renal pelvis bilaterally. The calipers are placed at the widest part of the intrarenal fluid.

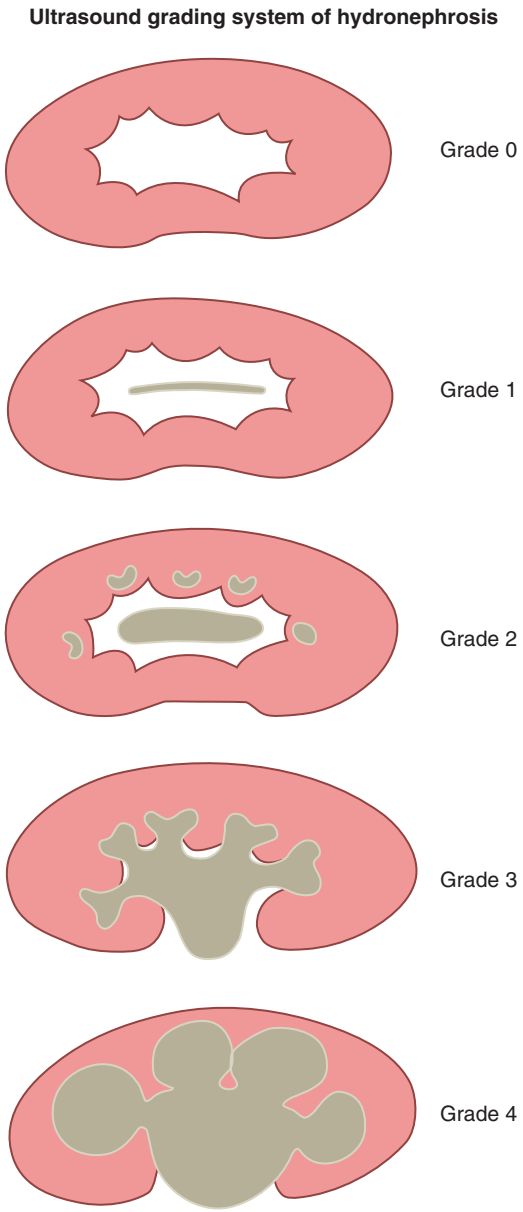

FIG. 39.26 Society for Fetal Urology Grading System. This classification is based on the appearance of the renal pelvis, calyces, and renal parenchyma. **Grade 0:** no hydronephrosis; intact central renal complex. **Grade 1:** only dilated renal pelvis; there is some fluid in the renal pelvis. **Grade 2:** dilated renal pelvis and a few calyces are visible. **Grade 3:** all the calyces are dilated. **Grade 4:** further dilation of renal pelvis and calyces, with thin renal parenchyma. (Modified from Baskin LS. Prenatal hydronephrosis. In: Baskin LS, Kogan B, Duckett J, editors. Handbook of pediatric urology. Philadelphia: Lippincott-Raven; 1997. p. 15.[281])

differentiation, cortical cysts); (5) ureteral abnormalities; (6) bladder abnormalities; and (7) oligohydramnios.[133]

The classification is based on the presence of the most concerning feature. The proposed thresholds for **normal RPD are less than 4 mm at 16 to 27 weeks and less than 7 mm at 28 weeks or more** (Table 39.4).

The detection of UT dilation (pyelectasis) is important for two reasons: **aneuploidy** and **postnatal uropathy.** The significance of UT dilation as a marker for aneuploidy is discussed in Chapter 31. UT dilation is usually an isolated finding, but a detailed ultrasound examination should be performed to detect other UT pathologic processes and nonrenal anomalies. UT dilation may be the first manifestation of obstructive uropathy. Studies that have correlated outcome with UT dilation varied widely in methodology, using different RPD cut-offs and different outcome measures. In a meta-analysis of 17 studies (104,572 patients screened), Lee and colleagues examined antenatal hydronephrosis (1308 subjects) as a predictor of postnatal outcome.[149] The risk of any postnatal pathology was 12% for mild, 45% for moderate, and 88% for severe hydronephrosis (Table 39.5). There was a significant increase in the risk of postnatal pathology with increasing degree of hydronephrosis. A prospective study by Sairam and colleagues[131] reported on the natural history of hydronephrosis diagnosed in 227 fetuses on midtrimester ultrasound in an unselected population. They demonstrated that 96% of the fetuses with mild hydronephrosis (RPD > 4 mm and < 7 mm at 18-23 weeks) experienced resolution in either the third trimester or the early neonatal period; none required postnatal surgery. However, approximately one in three fetuses with moderate to severe hydronephrosis (RPD > 7 mm or presence of caliectasis at 18-23 weeks) required postnatal surgery. A meta-analysis by Sidhu and colleagues combined data from seven studies and reported on the findings of serial postnatal renal sonography in children with isolated antenatal hydronephrosis.[150] There was resolution, improvement, or stabilization of hydronephrosis in 98% of patients with SFU grades 1 and 2 and stabilization of hydronephrosis in 51% of those with SFU grades 3 and 4. These results suggest that mild hydronephrosis is a relatively benign condition.

In utero progression also increases the likelihood of postnatal uropathy and urologic surgery.[141,151-153] An abnormal RPD in the third trimester is the best ultrasound criterion to predict postnatal uropathy.[128,141] In cases of mild isolated UT dilation, serial follow-up scans every 3 to 4 weeks are not necessary, but a repeat ultrasound in the third trimester is recommended. As prenatal resolution has been shown to be frequent,[131,142] this will also identify a group in which postnatal follow-up may not even be necessary.[133] In general, the larger the RPD, the lower the spontaneous resolution rate, the more likely it is associated with postnatal pathology, and the greater the need for postnatal surgery.[131,150,154-156]

A risk stratification of prenatal UT dilation into a low-risk group and an increased-risk group has been proposed.[133] Fetuses with isolated mild UT dilation are classified in the low-risk group (Fig. 39.27) if the RPD is 4 to less than 7 mm at less than 28 weeks, and 7 to less than 10 mm at 28 weeks or more. Fetuses with greater degrees of UT dilation (RPD ≥ 7 mm at <28 weeks and ≥ 10 mm at ≥28 weeks) or any one of several findings—peripheral calyceal dilation, abnormal renal parenchymal thickness or appearance, dilated ureter, abnormal bladder, or oligohydramnios—are considered at increased risk for postnatal uropathy (Fig. 39.28).

The majority of infants identified prenatally as having UT dilation are asymptomatic at birth. Pediatric nephrologists and urologists vary greatly in their management of antenatally diagnosed UT dilation, because an evidence-based protocol

TABLE 39.4 Urinary Tract Classification System and Follow-Up

	Low Risk	Increased Risk
DIAGNOSIS		
Renal pelvic diameter 16-27 weeks	4-<7 mm	≥7 mm
Renal pelvic diameter ≥ 28 weeks	7-<10 mm	≥10 mm
Calyceal dilation	Central only	Peripheral
Parenchymal thickness	Normal	Abnormal
Parenchymal appearance	Normal	Abnormal
Ureters	Normal	Abnormal
Bladder	Normal	Abnormal
Amniotic fluid[a]	Normal or increased	Oligohydramnios
FOLLOW-UP		
During pregnancy	One additional ultrasound ≥32 weeks	Initial follow-up ultrasound in 4-6 weeks[b]
Postnatal to 1 month of age	Two additional ultrasounds at >48 hours 1-6 months later	Consider antibiotic prophylaxis Ultrasound at >48 hours to 1 month[b]
Other	Aneuploidy risk modification if indicated	Aneuploidy risk modification if indicated Specialist consultation (e.g., nephrology, urology)

[a]Amniotic fluid can be abnormal in low-risk fetuses if due to a nonrenal cause (such as intrauterine growth restriction or premature rupture of membranes).
[b]Certain situations (severe abnormalities such as posterior urethral valves or bilateral severe hydronphrosis) may require more expedient follow-up.
Modified from Nguyen HT, Benson CB, Bromley B, et al. Multidisciplinary consensus on the classification of prenatal and postnatal urinary tract dilation (UTD classification system). J Pediatr Urol. 2014;10(6):982-998.[133]

TABLE 39.5 Risk of Postnatal Pathology by Degree of Antenatal Hydronephrosis

	DEGREE OF ANTENATAL HYDRONEPHROSIS, % (95% CONFIDENCE INTERVAL)			
Pathology	**Mild**	**Moderate**	**Severe**	***P* Value**
Any pathology	11.9 (4.5-28.0)	45.1 (25.3-66.6)	88.3 (53.7-98.0)	<.001
Ureteropelvic junction	4.9 (2.0-11.9)	17.0 (7.6-33.9)	54.3 (21.7-83.6)	<.001
Vesicoureteral reflux	4.4 (1.5-12.1)	14.0 (7.1-25.9)	8.5 (4.7-15.0)	.10
Posterior urethral valves	0.2 (0.0-1.4)	0.9 (0.2-2.9)	5.3 (1.2-21.0)	<.001
Ureteral obstruction	1.2 (0.2-8.0)	9.8 (6.3-14.9)	5.3 (1.4-18.2)	.025
Other[a]	1.2 (0.3-4.0)	3.4 (0.5-19.4)	14.9 (3.6-44.9)	.002

[a]Includes prune belly syndrome, VATER syndrome, and unclassified.
Hydronephrosis was classified based on anteroposterior diameter of renal pelvis:
Second trimester: mild 4-<7 mm, moderate 7-10 mm, severe >10 mm.
Third trimester: mild 7-<9 mm, moderate 9-15 mm, severe >15 mm.
Modified from Lee RS, Cendron M, Kinnamon DD, Nguyen HT. Antenatal hydronephrosis as a predictor of postnatal outcome: a meta-analysis. Pediatrics. 2006;118(2):586-593.[149]

is lacking.[132,157,158] There are no uniformly accepted guidelines regarding antibiotic prophylaxis, postnatal workup, and surgery. However, a **postnatal renal ultrasound** is the first examination of choice. In the neonate, the relative state of dehydration and physiologic oliguria in the first 24 to 48 hours of life can result in underestimation of the degree of dilation and a false-negative renal ultrasound.[159] Therefore ultrasound should not be performed before 48 hours after birth, except for cases of oligohydramnios, urethral obstruction, and bilateral high-grade dilation. It is important to recognize that hydration status can cause a transient increase in renal pelvic size and also has an effect on the bladder volume. In the presence of UT dilation, ultrasound should be repeated after bladder emptying in order to assess accurately the severity of UT dilation. Many authors would perform voiding cystourethrography only when postnatal renal ultrasound findings are abnormal.[160,161] The indication for functional renal imaging by renal scintigraphy depends on the particular clinical situation. Recently, magnetic resonance urography has shown promise as a method to assess renal function without the use of radiation.[162,163]

In summary, we propose the following management protocol for UT dilation detected in the second trimester with regard to

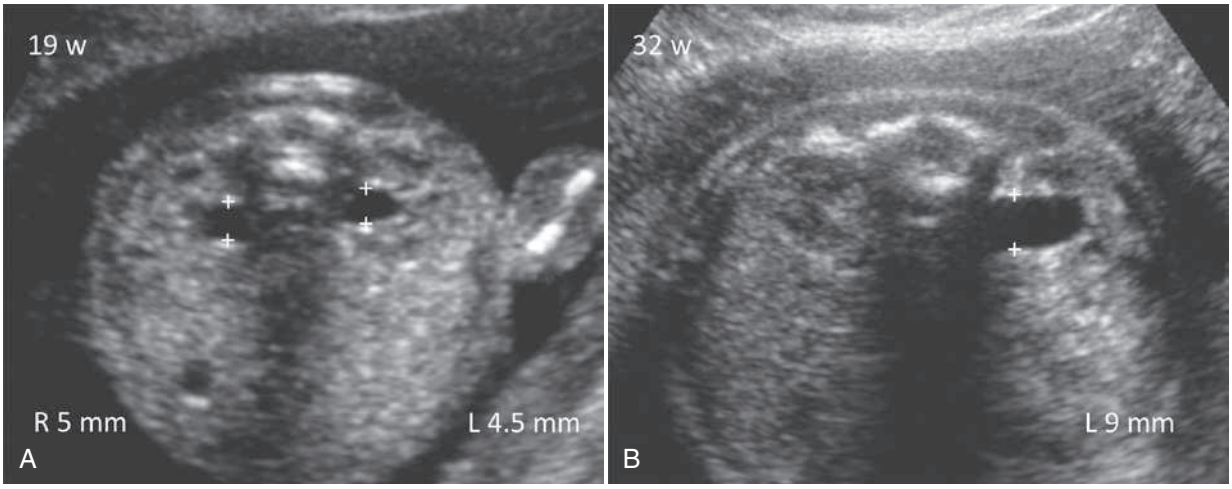

FIG. 39.27 Urinary Tract Dilation—Low Risk. (A) Fetal kidneys at 19 weeks gestation. Transverse image demonstrates an anteroposterior renal pelvic diameter (RPD) measuring 5 mm bilaterally. **(B)** Fetal kidneys at 32 weeks' gestation (different case). Transverse image demonstrates an anteroposterior RPD measuring 9 mm in the left kidney.

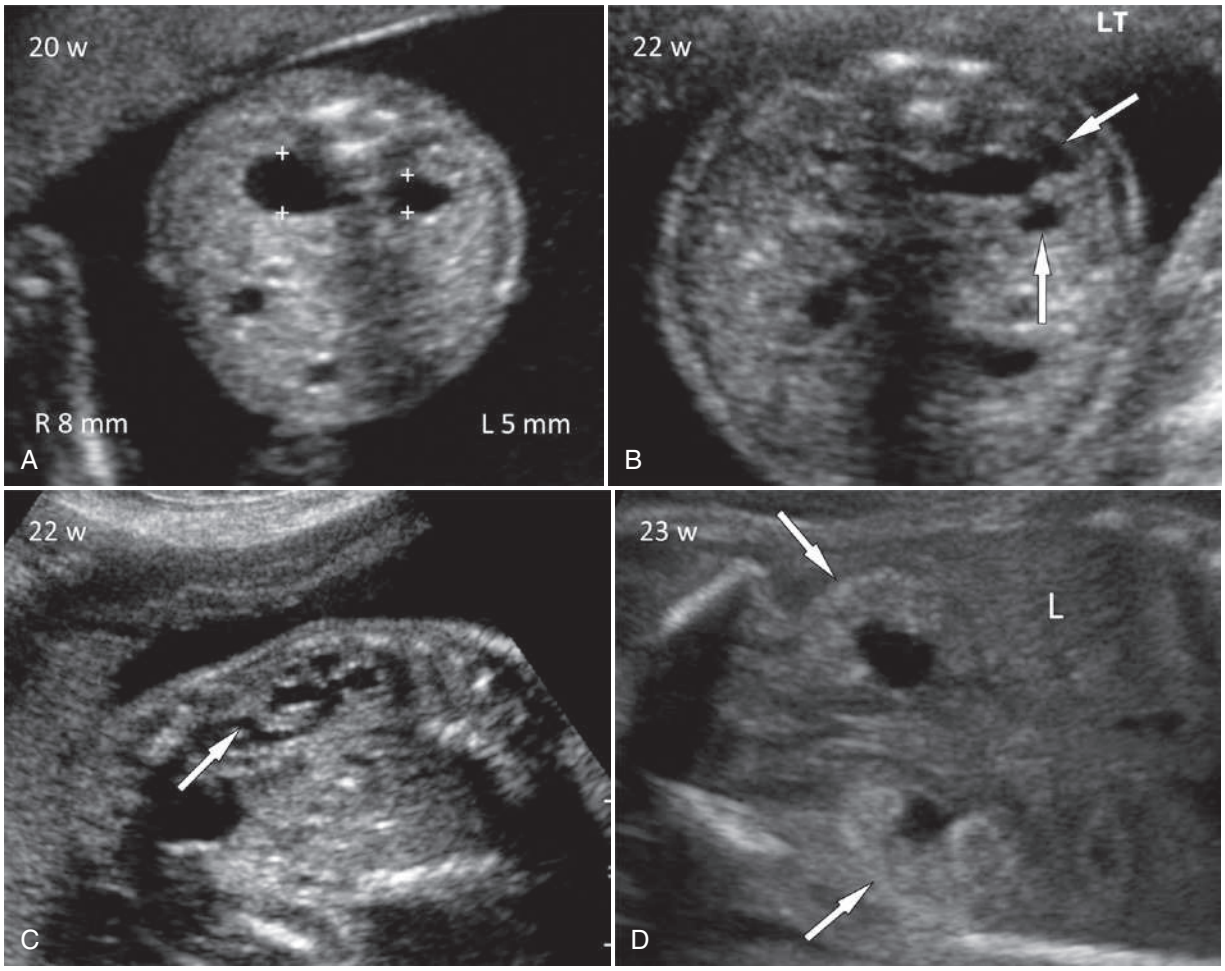

FIG. 39.28 Urinary Tract Dilation—Increased Risk. (A) Fetal kidneys at 20 weeks' gestation. Transverse image demonstrates an anteroposterior renal pelvic diameter (RPD) measuring 8 mm *(calipers)* in the right kidney. **(B)** Transverse image in a different fetus at 22 weeks demonstrates an anteroposterior RPD measuring 6 mm in the left kidney, but there is peripheral calyceal dilation *(arrows)*. **(C)** In the same fetus as **(B),** sagittal view demonstrates peripheral calyceal dilation and a dilated ureter *(arrow)*. The bladder is not dilated. **(D)** In a different fetus at 23 weeks' gestation, coronal image shows abnormal renal parenchyma bilaterally *(arrows),* which is more echogenic than the liver *(L)*. The RPD (measured on transverse view, *not shown*) was 6 mm.

repeating antenatal ultrasound, postnatal ultrasound, and antibiotic prophylaxis after delivery based on the recently published consensus guidelines[133]:

1. **Low-risk group:** If isolated mild UT dilation is detected at 16 to 27 weeks' gestational age, a repeat ultrasound is recommended at 32 weeks or later to reassess the RPD, kidneys, bladder, and AFV. Parents are counseled that it is a common finding and may be physiologic or transient, and that the risk of postnatal uropathy is small. If the ultrasound at 32 weeks' gestational age or later shows resolution (RPD < 7 mm) and no other findings, no further prenatal or postnatal follow-up is necessary. If UT dilation persists (RPD 7 to <10 mm), two postnatal renal ultrasound scans should be performed: the first at more than 48 hours but less than 1 month after birth, and the second exam 1 to 6 months later.
2. **Increased-risk group:** For fetuses in this category, a repeat ultrasound in 4 to 6 weeks is recommended, but the frequency of sonographic monitoring is at the discretion of the health care provider, depending on the findings. Prenatal consultation with pediatric specialists (nephrology, urology) is also recommended, especially in situations that may result in marked renal dysfunction or possible surgical intervention. For fetuses with RPD of 10 mm or greater at the third-trimester ultrasound, our approach is to initiate antibiotic prophylaxis after delivery, pending the results of the postnatal renal ultrasound.

Ureteropelvic Junction Obstruction

Obstruction at the UPJ is the most common cause of nonphysiologic neonatal hydronephrosis,[164-166] with an incidence of 1 in 2000 live births.[167] It is also one of the most common reasons for postnatal surgery of the UT.[128,164] Most cases of UPJ obstruction are functional (caused by a muscular abnormality) rather than the result of fixed anatomic lesions such as fibrous adhesions, kinks, valves, or aberrant vessels.[168] However, the etiology of functional obstruction is multifactorial and likely polygenic, with no known cause in most cases.[165] UPJ obstruction is more common in males, more frequently unilateral, and more often on the left side.[169]

On sonography, a dilated renal pelvis with or without caliectasis is identified. The ureter and the bladder are not dilated. Severe chronic obstruction leads to effacement of the calyces and thinning of the renal cortex (SFU grade 4) (Fig. 39.29). Rarely, the renal pelvis may be extremely dilated, appearing as a large, unilocular cystic mass. Rupture of the collecting system results in the development of a perirenal urinoma (Fig. 39.30, Video 39.7). This "pop-off" mechanism may protect the obstructed kidney from further prenatal damage and may diminish the degree of hydronephrosis. The affected kidney should be carefully assessed for renal dysplasia, however, because the probability of a nonfunctional dysplastic ipsilateral kidney is about 80%.[170]

The AFV is usually normal. When unilateral hydronephrosis is accompanied by oligohydramnios, a search for contralateral renal pathology is warranted (e.g., renal agenesis, multicystic renal dysplasia). UPJ obstruction may be associated with VUR and extrarenal abnormalities. When the contralateral kidney is normal, the prenatal detection of unilateral UPJ obstruction should not alter obstetric management. In cases of unilateral UPJ obstruction diagnosed before 24 weeks, severe dilation (RPD > 15 mm) is predictive of impaired postnatal renal function in the affected kidney.[171] When there is bilateral UPJ obstruction, the prognosis depends on the severity and duration of obstruction and on the AFV. Serial ultrasound evaluations are necessary to assess the AFV, progression of hydronephrosis, and development of renal dysplasia. Early delivery is rarely indicated, except when there is progressive bilateral obstruction with severe oligohydramnios. Treatment algorithms for hydronephrosis due to UPJ obstruction include both conservative and surgical approaches depending on the severity of the hydronephrosis.

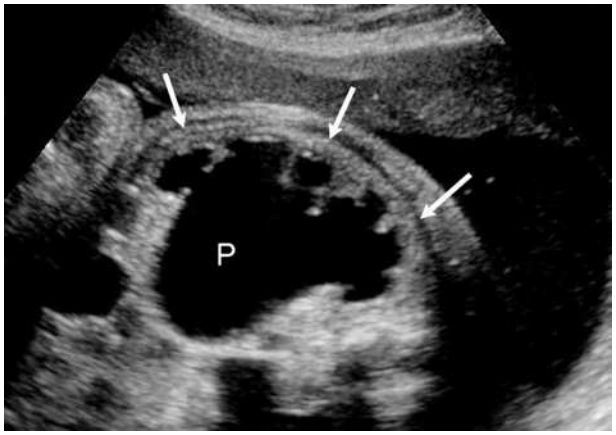

FIG. 39.29 Ureteropelvic Junction Obstruction. Longitudinal scan shows moderate caliectasis and extremely dilated renal pelvis *(P)*, with thinning of the cortex *(arrows)*.

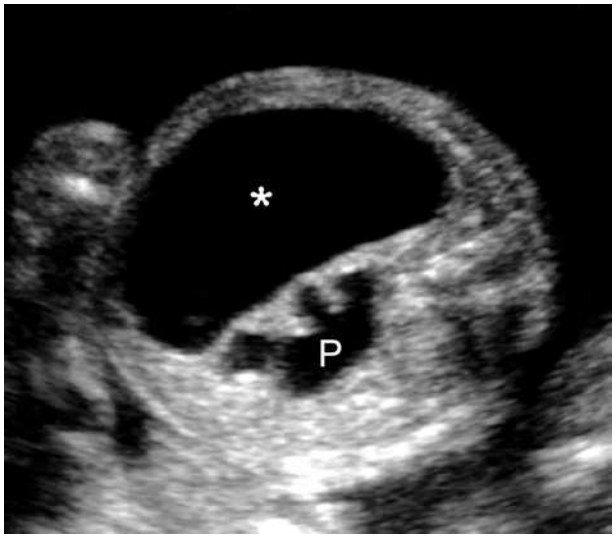

FIG. 39.30 Perirenal Urinoma. Transverse scan of fetal abdomen at 22 weeks' gestation shows a large perirenal urinoma (*) displacing and compressing the kidney, which demonstrates dilated calyces and pelvis *(P)* caused by ureteropelvic junction obstruction. See also Video 39.7.

Vesicoureteral Junction Obstruction and Primary Megaureter

Vesicoureteral junction obstruction is more common in males and is bilateral in up to 25% of cases.[172] Coexisting anomalies

of the UT (VUR, UPJ obstruction, multicystic dysplasia) are frequently present. Primary **megaureters** are classified into three types. In type I or primary obstructed megaureter, there is proximal dilation due to relative obstruction by a short aperisaltic segment of the ureter near the vesicoureteral junction. The transvesical course and insertion of the ureter are normal. It is thought to be due to muscular derangement with increased connective tissue in the affected segment of the ureter. Type II or refluxing primary megaureter is usually the result of an abnormality involving or closely associated with the vesicoureteral junction including a short or absent intravesical ureter, a congenital paraureteric diverticulum, or another abnormality of the vesicoureteral junction. Type III, or nonrefluxing, nonobstructed primary megaureter, is the most common of the three types. As the name suggests, neither reflux nor apparent obstruction of the distal ureter is found. The dilation starts just above the bladder, and the cause is unknown.[173]

On sonography, the affected kidney demonstrates dilation of the ureter with or without dilation of the renal pelvis (Video 39.8). A slightly dilated ureter may be difficult to recognize or may be mistaken for bowel, although bowel contents are usually more echogenic than urine. Identification of peristalsis in a fluid-filled tubular structure does not confirm bowel because it can occur with hydroureter as well. To be certain, the serpiginous cystic segments must be traced to either the renal pelvis or bladder. In addition, the ureter generally comes into close contact with the spine, but the small bowel does not. The ureteral dilation can be severe, so size alone does not preclude megaureter as a possible diagnosis.

In cases diagnosed prenatally as megaureter, prophylactic antibiotic therapy is commenced soon after birth because of the high risk of UT infections. Postnatal investigations including ultrasound and voiding cystourethrography are necessary to exclude VUR and bladder outlet obstruction. In the absence of urethral obstruction or VUR, a diuretic renogram is performed to evaluate for vesicoureteral junction obstruction. Most cases of primary megaureter either resolve spontaneously or improve when managed conservatively.[174,175] The degree of UT dilation and megaureter type are significant predictors of the spontaneous resolution rate.[174,176]

Duplication Anomalies

Embryologically, the duplex kidney results from two ureteral buds arising from the mesonephric duct to grow into the metanephric blastema. Duplication of the collecting system may be partial or complete. Many cases are found incidentally in the general population with no clinical significance.[177] In **complete duplication,** two pelvicalyceal systems and two separate ureters drain the kidney. The lower-pole ureter usually inserts into the bladder at the normal site, although the intramural portion may be shorter than usual. The upper-pole ureter often inserts ectopically, inferior and medial to the orifice of the lower-pole ureter **(Weigert-Meyer rule).**[173,177] Its orifice may be stenotic and obstructed, and there is often a ureterocele. The upper-pole ureter may have an insertion entirely outside the bladder (e.g., into the urethra or vagina). Classically, the upper-pole moiety obstructs, whereas the lower-pole moiety refluxes. Sonographic findings useful for prenatal diagnosis include unilateral renal enlargement, identification of two separate noncommunicating renal pelves, hydronephrosis in the upper and/or lower pole, ipsilateral dilated ureter(s), and ureterocele.[178-181] The finding of dilation of the upper-pole collecting system and ureterocele is the best diagnostic clue[178,179] (Fig. 39.31). The lower-pole moiety may also appear hydronephrotic because of VUR. In some instances, identification of two separate collecting systems, or the nondilated lower pole of a duplex kidney, may be difficult because of its small size and displacement by the dilated upper renal pelvis and ureter. Renal pelvic dilation has been shown to progress with increasing gestational age, and in many cases the diagnosis of a duplex kidney becomes apparent only in the third trimester.[180,181]

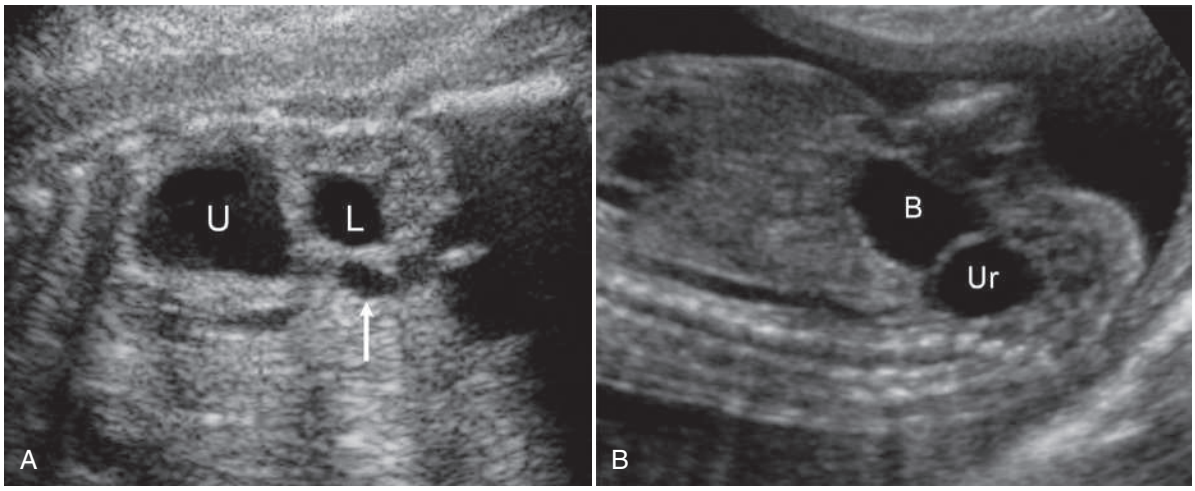

FIG. 39.31 Duplication Anomalies. (A) Longitudinal scan shows two separate collecting systems. The hydronephrotic, upper-pole renal pelvis *(U)* is continuous with the dilated ureter *(arrow)*. The lower-pole collecting system *(L)* is dilated because of reflux. **(B)** Longitudinal scan of the pelvis shows the ureterocele *(Ur)* separated from the lumen of the bladder *(B)* by a thin, curvilinear wall of the ureterocele.

Duplex Kidney Findings

Unilateral renal enlargement
Two separate noncommunicating renal pelves
Hydronephrosis of the upper and/or lower pole
Ipsilateral dilated ureter(s)
Ureterocele

Ureteroceles are cystic dilations of the intravesical submucosal ureter. A careful evaluation of the urinary bladder is necessary to detect the **ureterocele,** which is seen as a well-defined, thin-walled cyst within the bladder (see Fig. 39.31B). The diagnosis is easy when the bladder is partially full but can be overlooked if the bladder is empty or only minimally distended. A full bladder can compress the ureterocele, resulting in nonvisualization. A small nonobstructive ureterocele may be an incidental finding. However, most ureteroceles are detected prenatally during the evaluation of hydronephrosis.[182] A large ureterocele may cross the midline and obstruct the contralateral ureter or the bladder outlet and cause bilateral hydronephrosis. Ureteroceles that are large or prolapsed into the urethra may cause bladder outlet obstruction. Fetal therapy, such as fetoscopic laser surgery to decompress the distal urethral obstruction, can be helpful in cases with progressive bladder outlet obstruction, oligohydramnios, or concerns for permanent damage to the renal parenchyma.[183]

Complicated duplex collecting systems are associated with substantial morbidity. The prognosis depends on the degree of renal damage from reflux and obstruction. The outcome is improved with prenatal diagnosis, because it allows planning of postnatal care, including the administration of prophylactic antibiotics from birth, reducing the incidence of UT infections and renal function impairment.[181,184]

Vesicoureteral Reflux

VUR can be **primary** (incompetent valve mechanism at the UVJ) or **secondary** (due to an obstruction in the UT and high detrusor pressures). The main prenatal sonographic finding is hydronephrosis, which may be unilateral or bilateral. The ureter may be dilated. Intermittent dilation of the collecting system favors VUR. Fluctuation or variation in the RPD (changing by more than 3 mm) during the course of an obstetric sonogram is strongly associated with high-grade VUR (grade IV or V).[185] VUR may be associated with other renal abnormalities, including **UPJ obstruction, duplex kidney, MCDK,** and **unilateral renal agenesis.**[177,186]

The reported prevalence of VUR in children with prenatally detected hydronephrosis varies widely because different RPD cutoff values are used for inclusion and different protocols for postnatal investigations (voiding cystourethrography either in all cases or only after an abnormal postnatal renal ultrasound examination). A systematic review of 18 studies showed a mean prevalence of 15% for postnatal primary VUR after prenatally detected hydronephrosis.[187]

A normal postnatal ultrasound study does not exclude VUR. However, if two successive renal ultrasound examinations (at day 5 and at 1 month) were normal, voiding cystourethrography showed abnormalities in only 6.7% of patients.[188] Neonatal reflux is more common in male infants. It is often of low grade, with a high rate of spontaneous resolution by 2 years of age.[189] However, in those children with high-grade VUR, spontaneous resolution is rare. There is a significant correlation between high-grade VUR and findings of either renal dysplasia on ultrasound or renal damage scars on DMSA renal scan.[189,190] Most neonates with VUR are managed conservatively with antibiotic prophylaxis.

Lower Urinary Tract Obstruction

Fetal **megacystis** has been reported as early as 10 to 14 weeks' gestation when the longitudinal bladder diameter is 7 mm or more[191] (Fig. 39.32). In the second or third trimester, the definition of megacystis is more subjective but includes an enlarged bladder that fails to empty over 45 minutes of observation.[192,193] At 10 to 14 weeks' gestation, the incidence is 1:1600.[191] In a series of 145 fetuses with early megacystis, when the bladder diameter measured 7 to 15 mm, chromosomal abnormalities were detected in approximately 25% of cases.[194] In those with normal karyotype, there was spontaneous resolution of the megacystis by 20 weeks' gestation in 90% of cases. In contrast, with severe megacystis, defined as bladder length greater than 15 mm, the risk of chromosomal defects was 11%; and in the chromosomally normal group, it was invariably associated with progressive, obstructive uropathy.[194] Therefore follow-up ultrasound and assessment of karyotype in cases of identified first-trimester megacystis are necessary to provide prognostic information and identify the role, if any, of a diagnostic or therapeutic fetal procedure.

Causes of Fetal Megacystis

Posterior urethral valves
Urethral atresia or stricture
Ureterocele
Prune belly syndrome
Megalourethra
Cloacal malformation
Megacystis-microcolon–intestinal hypoperistalsis syndrome

FIG. 39.32 Megacystis in First Trimester. Transabdominal sagittal image of a 12-week fetus shows a distended thick-walled bladder *(arrow),* measuring 13 mm in length. There is no hydronephrosis.

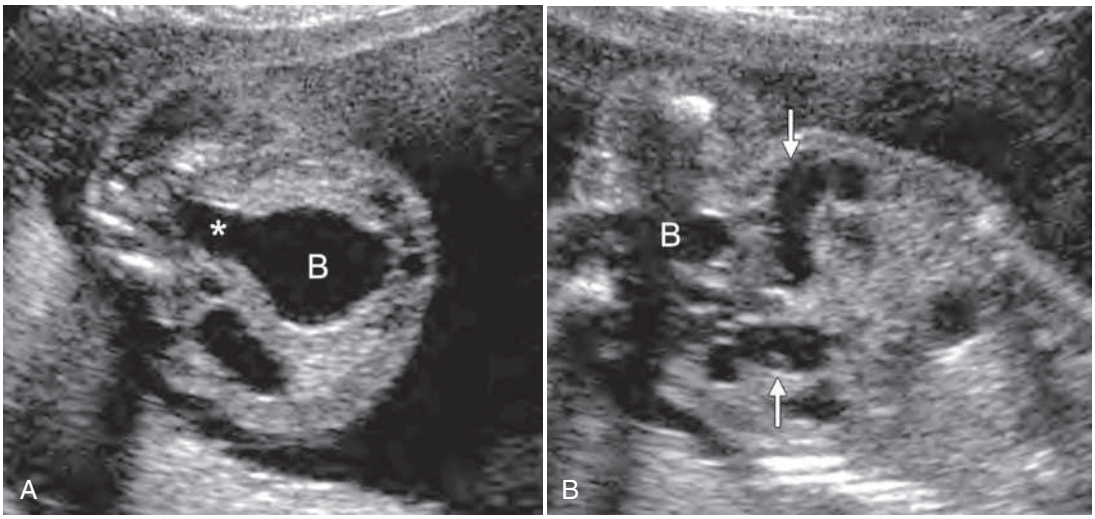

FIG. 39.33 Posterior Urethral Valves Causing Urethral Level Obstruction. (A) Dilated urinary bladder *(B)* and proximal urethra (*) give the appearance of a keyhole, characteristic of urethral obstruction in a 21-week fetus. **(B)** Coronal scan shows dilated tortuous ureters *(arrows)*.

Posterior urethral valves are the most common cause of lower urinary tract obstruction (LUTO), followed by urethral atresia or stricture. Posterior urethral valves are seen exclusively in males and may cause total, intermittent, or partial obstruction, with variable prognosis. Most cases are sporadic, occurring in 1:5000 male births; and the recurrence risk is small.[195] Intravesical pressure generated secondary to the obstruction results in a persistently dilated urinary bladder, with a dilated proximal urethra **(keyhole sign)** (Fig. 39.33). However, the keyhole sign is not a reliable indicator of posterior urethral valves because it can also be seen in fetuses with other pathologies, including VUR and primary megaureter.[196] There may be **thickening of the bladder wall** (>3 mm), bilateral tortuous hydroureters, and hydronephrosis. If the obstruction is severe and long-standing, progressive renal parenchymal fibrosis and dysplasia develop, resulting in severe oligohydramnios, pulmonary hypoplasia, and compression deformities (Potter syndrome). There may be spontaneous bladder rupture with urinary ascites (Fig. 39.34) or a calyceal rupture with perirenal urinoma.[197] If spontaneous decompression occurs, this "safety valve" may protect the kidneys from further prenatal damage and may diminish the degree of hydronephrosis.

Urethral atresia causes the most severe, and earliest detected, form of obstructive uropathy. The sonographic features include a greatly distended bladder that may fill the whole abdomen, and anhydramnios after the first trimester (Fig. 39.35). Urethral atresia is almost always fatal, because of associated renal dysplasia and pulmonary hypoplasia, and only case reports of survivors following antenatal treatment have been described.[195,198]

Prune belly syndrome is a rare congenital disorder characterized by megacystis, deficiency of abdominal musculature, and cryptorchidism. It is rarely reported in females. Several mechanisms for the pathogenesis of prune belly syndrome have been suggested. Some authors believe that it results from a primary mesodermal defect, but the more prevailing theory is that in utero urethral obstruction leads to a distended urinary system with secondary defective abdominal musculature.[199] The abdominal wall has a flaccid, wrinkled appearance; hence the name

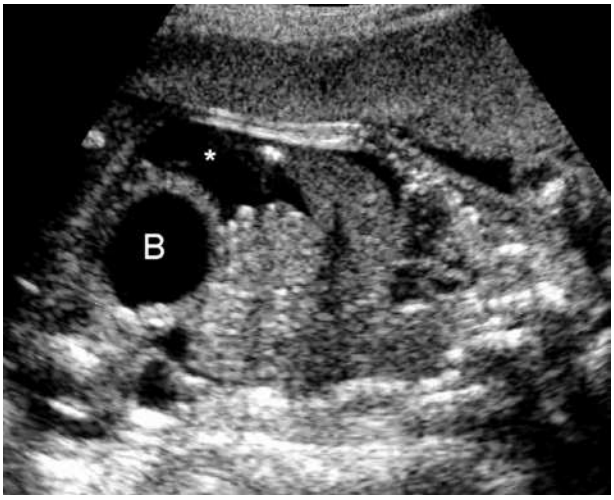

FIG. 39.34 Urinary Ascites. Longitudinal scan of a 22-week fetus shows a thick-walled bladder *(B)* and urinary ascites (*) caused by spontaneous rupture of severe megacystis.

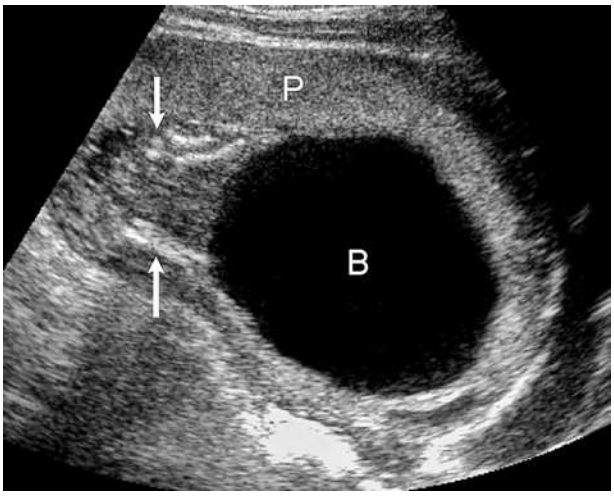

FIG. 39.35 Urethral Atresia. Coronal scan of a 17-week fetus shows a greatly distended bladder *(B)* that occupies the entire abdomen. The thorax *(arrows)* is compressed and bell shaped because of **pulmonary hypoplasia.** There is **anhydramnios.** *P,* Placenta.

"prune belly" syndrome. Typically, the **bladder** is **very large and thin walled.** The posterior urethra is usually not dilated, and there is no keyhole sign.[200] It is very difficult to differentiate this condition from posterior urethral valves, although the appearance of the bladder and urethra may be helpful. The ureters are tortuous and dilated, with bilateral hydronephrosis. If oligohydramnios is present, it is difficult to demonstrate undescended testes. Other abnormalities may be present, including congenital heart disease, intestinal malrotation, and musculoskeletal deformities.

Megalourethra is characterized by a congenital deficiency of the mesodermal tissues of the phallus, with **dilation of the penile urethra and enlargement of the penis.** This condition has been classified into two types, fusiform and scaphoid urethra, but it is preferable to consider it as a spectrum. Urinary stasis in the dilated penile urethra results in functional obstruction of the UT. The prenatal sonographic findings include those of LUTO, with dilation and elongation of the penile urethra[201,202] (Fig. 39.36, Video 39.9). Associated malformations of the UT include urethral atresia, posterior urethral valves, prune belly syndrome, and horseshoe kidney. Abnormalities involving the GI tract and spine and VACTERL association have been reported. The prognosis depends on the degree of renal dysfunction and the severity of associated anomalies. Survivors are at risk of renal insufficiency, impotence, and infertility.

Megacystis-microcolon–intestinal hypoperistalsis syndrome (MMIHS) is a rare, nonobstructive cause of megacystis with a 4:1 female predominance. The syndrome is characterized by the presence of **nonobstructive bladder distention,** intestinal

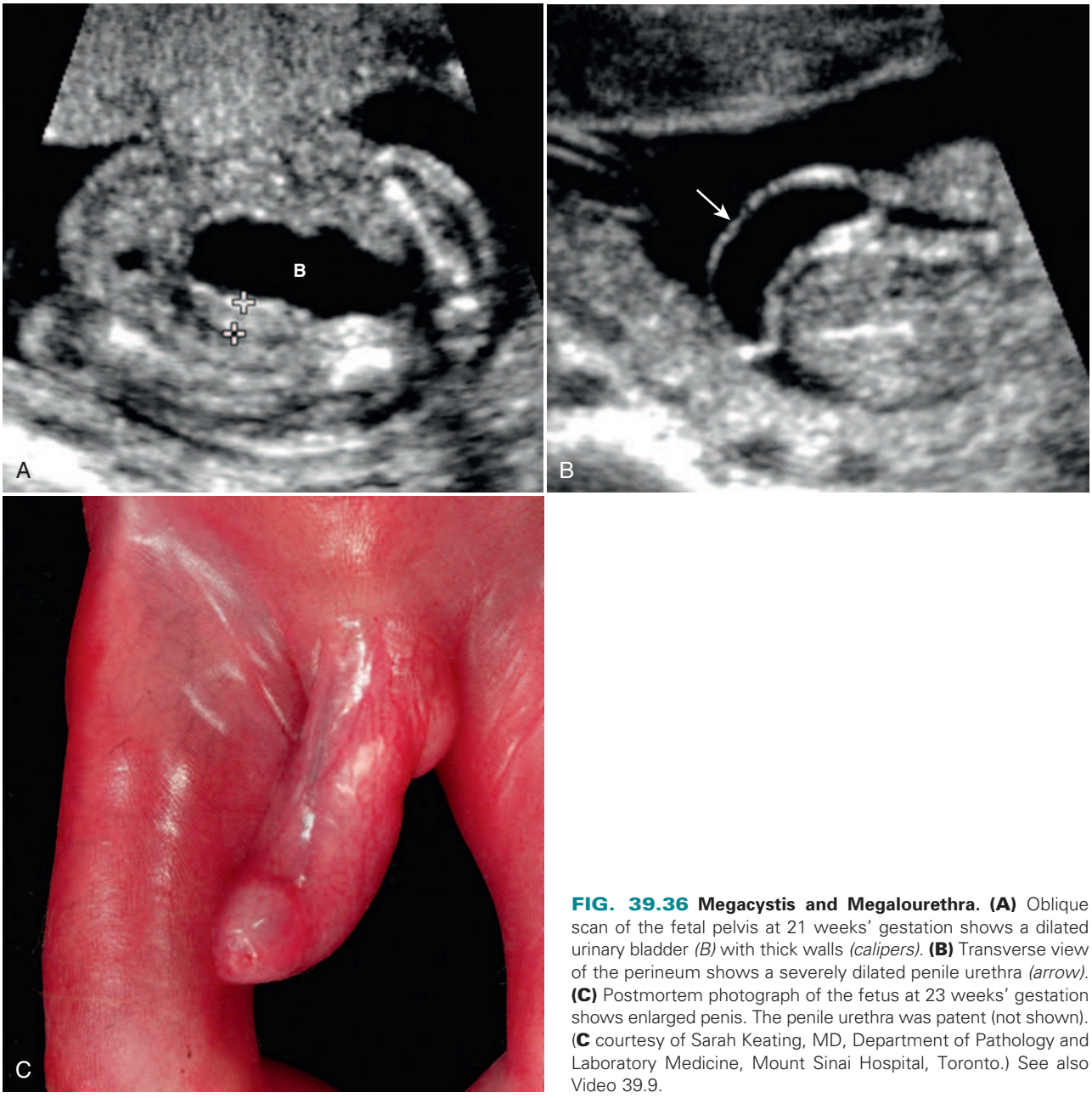

FIG. 39.36 Megacystis and Megalourethra. (A) Oblique scan of the fetal pelvis at 21 weeks' gestation shows a dilated urinary bladder *(B)* with thick walls *(calipers).* **(B)** Transverse view of the perineum shows a severely dilated penile urethra *(arrow).* **(C)** Postmortem photograph of the fetus at 23 weeks' gestation shows enlarged penis. The penile urethra was patent (not shown). (**C** courtesy of Sarah Keating, MD, Department of Pathology and Laboratory Medicine, Mount Sinai Hospital, Toronto.) See also Video 39.9.

hypoperistalsis, and **microcolon.** Differentiating this condition from the more common posterior urethral valves is important because MMIHS carries a dismal prognosis and fetal bladder shunting is not indicated. The key distinguishing features are (1) the amniotic fluid is normal or increased; (2) the fetus is usually female; and (3) very rarely, a dilated small bowel may be present.[203] MRI is a useful adjunct for diagnosis; it can confirm the presence of microcolon when an enlarged bladder is visualized on ultrasound.[204] In fetuses with LUTO, an abnormal amniotic fluid digestive enzyme profile has shown a sensitivity of 80% and a specificity of 89% for MMIHS.[205] The precise genetic etiology of this syndrome remains unclear. Most occurrences are sporadic, and case reports of familial consanguineous cases have been described, suggesting an autosomal recessive inheritance model.[206,207] Recently, genetic advances in whole-exome sequencing have allowed the identification of mutations, such as *ACTG2,* encoding smooth-muscle actin, which may be implicated in the etiology of the disease.[208,209]

Cloacal malformation is very rare, with an incidence of 1:50,000 births. It results from failure of migration and/or fusion of the urorectal septum with the cloacal membrane.[210] This in turn causes persistence of the cloaca and cloacal membrane and failure of normal differentiation of external genitalia. There is a wide spectrum of abnormalities, with the most severe being cloacal dysgenesis (in which there is no perineal opening). In some cases, there is a single perineal opening that serves as the outlet for urine, genital secretions, and meconium. Lower UT abnormalities (reflux, ureteral ectopia, duplication of bladder) and genital abnormalities (duplication or atresia of uterus and vagina) are common, as are abnormalities of the kidneys and spine. Additional complications are related to **obstruction of the urinary, genital, and gastrointestinal tracts.** The usual sonographic presentation is that of LUTO in a female fetus (Fig. 39.37, Video 39.10). One or more cystic structures are seen arising from the pelvis, and their appearance depends on the anatomy involved. There may be a dilated bladder, with associated bilateral hydroureter and hydronephrosis. A septate cystic mass may be seen due to hydrocolpos and associated müllerian duct anomalies. The distal bowel may be dilated. If there is a communication between the distal bowel and the urinary system, a cystic mass containing calcifications (meconium mixed with urine) may be seen[211] (see Fig. 39.37B). Oligohydramnios, and in some cases, anhydramnios, may be present. Other sonographic findings include ascites, ambiguous genitalia, and vertebral anomalies.[212] Prenatal sonographic diagnosis of cloacal malformation is challenging. Fetal MRI is useful for assessment of the anorectal and pelvic anatomy. It can clarify cloacal malformations with high position of the distal bowel and a long common cloacal channel.[213]

In Utero Intervention: Fetal Vesicoamniotic Shunting and Cystoscopy

For a carefully selected group of fetuses with severe LUTO, permanent in utero bladder drainage may be a therapeutic option. The objective of vesicoamniotic shunting is to allow free drainage of urine from the bladder into the amniotic cavity. This decompresses the UT and should correct oligohydramnios, may theoretically prevent or stabilize renal dysplastic change, and allows unimpeded lung development. This approach assumes that renal function has not already been destroyed. Careful selection of suitable cases is critical, and the goal is often the identification and rigorous evaluation of reliable predictors of postnatal renal function.[33,214-221]

A detailed sonographic evaluation of the fetus is a prerequisite, to define the probable cause and evaluate prognosis. Intervention is not indicated if the ultrasound examination suggests either MMIHS or cloacal dysgenesis or if the fetus is female, because of their uniformly dismal prognosis.

Fine-needle aspiration under ultrasound guidance **(vesicocentesis)** allows for fetal renal function, karyotype, and microarray to be evaluated.[33,216-218] If the urine reaccumulates rapidly (which itself may indicate function) and the other prognostic factors

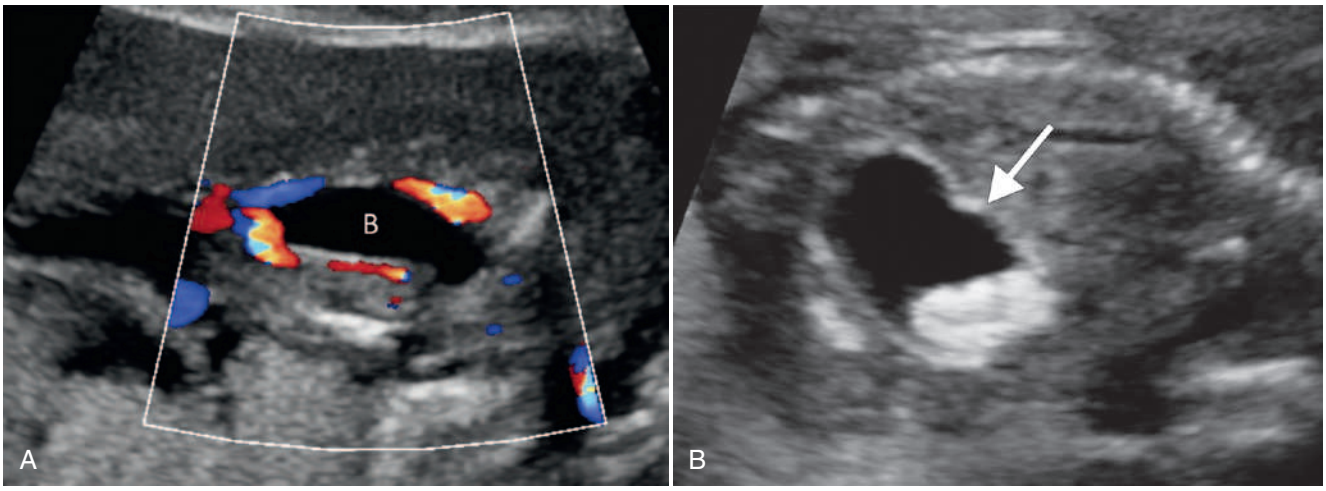

FIG. 39.37 Cloacal Dysgenesis. (A) Transverse view of the pelvis in a 17-week fetus shows a large bladder *(B)* and **(B)** sagittal view of the left side of the abdomen shows a cystic mass *(arrow)* superior to the bladder, representing a dilated bowel loop with intraluminal calcifications (meconium mixed with urine), indicating a urinary-bowel fistula. See also Video 39.10.

are favorable, placement of a permanent vesicoamniotic shunt may be considered. Fetal urinary sodium (Na^+), calcium (Ca^{++}), and β_2-microglobulin (in combination) are the best predictors of postnatal renal function.[215-220,222]

Antenatal Predictors of Poor Postnatal Renal Function

ULTRASOUND
Severe oligohydramnios, especially if early onset
Increased renal echogenicity
Renal cortical cysts
Slow bladder refilling after vesicocentesis

FETAL URINE
↑ Sodium level (Na^+)
↑ Calcium level (Ca^{++})
↑ β_2-Microglobulin level

FETAL BLOOD
↑ β_2-Microglobulin level

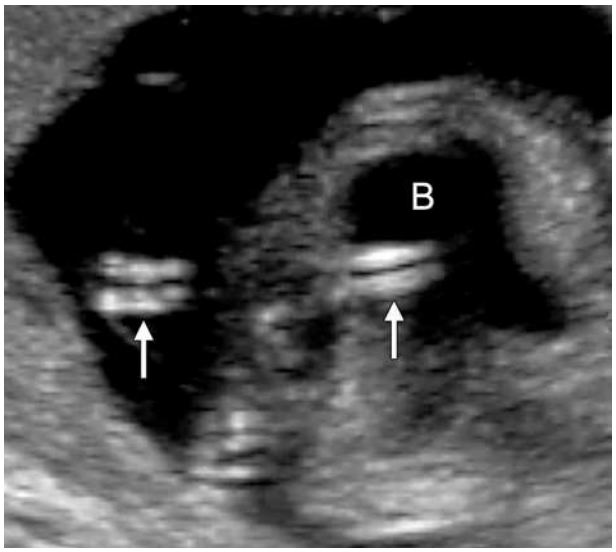

FIG. 39.38 Vesicoamniotic Shunt. Arrows indicate catheter in the decompressed bladder *(B)* and amniotic fluid. Note normal amniotic fluid volume.

Initially, fixed cutoff values were suggested for each variable as prognostic predictors.[82] However, the normal levels of most parameters vary with gestational age and must be interpreted accordingly. Specifically, sodium and β_2-microglobulin levels decrease throughout gestation, whereas calcium and creatinine values rise.[215,216,221] In general, more hypotonic fetal urine correlates with a more favorable outcome. Some groups advocate that sequential urine sampling over 48 to 72 hours is most reflective of true renal function because an initial bladder tap will obtain urine that has been present for an extended period of time.[215,223,224] A systematic review of 23 papers and 572 pregnancies reported that the two most accurate tests of fetal renal function were calcium and sodium above the 95th percentile for gestation, while β_2-microglobulin was slightly less accurate.[225] A recent retrospective study of fetal urine biochemistry in 72 cases of megacystis diagnosed before 23 weeks gestation supported the usefulness of β_2-microglobulin, sodium, chloride, and calcium in defining a poor renal prognosis.[226]

It has been suggested that fetal blood levels of β_2-microglobulin may better assess glomerular filtration rate than urinary markers, which generally reflect tubular function.[227] Blood sampling for electrolytes and β_2-microglobulin may also be useful when no urine can be collected by vesicocentesis.[224] Recently, advances in proteomics have allowed the identification of 26 fetal urinary peptides that show promise in predicting renal function after birth, although they are not yet integrated into clinical practice.[228] To date, a **urinary function profile,** which combines a number of biochemical and sonographic predictors, appears to be of greatest clinical value. We use the reference values published by Muller and colleagues for fetal urinary sodium, calcium, and β_2-microglobulin.[221] Only carefully selected fetuses with "favorable" fetal urinary analysis, despite significant oligohydramnios, are likely to benefit from in utero intervention; and in our center, only a handful of the fetuses who are referred with LUTO go on to such treatment.

Our approach is to counsel the parents extensively beforehand, with input from a multidisciplinary team of fetal medicine, pediatrics, urology, nephrology, and social work specialists. Parents are also given the opportunity to speak to others who have faced similar dilemmas. Before any decision is made, we try to ensure that they have an unbiased and complete account of the situation and are fully aware that, despite successful shunt placement, renal failure or pulmonary hypoplasia may still ensue.[227,229-231]

Vesicoamniotic shunting is performed by the percutaneous insertion of a small, plastic, double-coiled Silastic pigtail catheter into the bladder under continuous ultrasound guidance. To facilitate insertion, amnioinfusion is undertaken beforehand. Antibiotic prophylaxis and tocolysis (rectal indomethacin and oral calcium channel blockers) are used. We strive to place the shunt anteriorly in the midline, ideally below the umbilical cord insertion[224] (Fig. 39.38). Color Doppler is used to help avoid maternal and fetal blood vessels. **Early intervention** is probably necessary for this procedure to successfully prevent pulmonary hypoplasia and preserve renal function.[195] Typically AFV is low before intervention. Occasionally, intervention may be considered in light of documented worsening of renal function on urinalysis or progressively abnormal renal appearance on ultrasound, despite a normal AFV. Rarely, it may be warranted to place the shunt directly into a dilated renal pelvis rather than the bladder. Shunts may become blocked or dislodged and will require replacement in some cases.

Recently, fetal cystoscopy and laser ablation of the posterior urethral valves have been introduced as an alternative diagnostic and therapeutic approach to the management of obstructive uropathy.[232,233] Theoretical advantages include more physiologic drainage by allowing "cyclic voiding," determining the cause of LUTO by differentiating posterior urethral valves (PUV) from urethral atresia, avoiding the need for amnioinfusion, and avoiding shunt complications, such as migration and blockage.

TABLE 39.6 Long-Term Outcomes After Prenatal Vesicoamniotic Shunting for Obstructive Uropathies

Study	Follow-Up	Alive (%)	Renal Failure[a] (%)	Renal Insufficiency	Normal[b]
Freedman et al[231]	14/21	62	36	21	43
Holmes et al[227]	14/14	57	63		37
McLorie et al[230]	9/9	67	50		50
Biard et al[234]	20/31	91	33	22	45
Müller Brochut[235]	13/13	70[c]	29	71	0

[a]Renal Failure: transplant or dialysis.
[b]Glomerular filtration rate > 70 mL/min.
[c]Excluding three terminations of pregnancies.
Courtesy of Greg Ryan, MB, Fetal Medicine Unit, Mount Sinai Hospital, University of Toronto.

Antenatal management of LUTO is challenging because the natural history of the condition is highly variable and depends on the cause, severity, duration, and gestational age of onset of the obstruction. Studies that have reported on the long-term outcomes in children with in utero vesicoamniotic shunting are observational in nature and based on small and heterogeneous populations.[227,230,231,234,235] As seen in Table 39.6, these retrospective series report 57% to 91% survival in those treated, with normal postnatal renal function in 0% to 50% of survivors. In two of the series, one-third of patients were lost to follow-up. A systematic review of 20 observational studies involving 369 fetuses in which a bladder drainage procedure was attempted concluded that prenatal bladder drainage improved perinatal survival, especially in fetuses with poor predicted prognosis based on fetal urinalysis, but the effects on long-term renal function were uncertain.[236] Recently, a multicenter randomized controlled trial, PLUTO (Percutaneous vesicoamniotic shunting for fetal LUTO), comparing fetal shunting versus conservative management, was stopped early because of poor recruitment (only 31 of the planned 150 pregnancies were randomly assigned during a 4-year period), and its results should be interpreted with caution.[237] The as-treated analysis showed that fetuses that underwent bladder shunting had a three-times-higher chance of postnatal survival (to 28 days) than nonshunted fetuses. However, only two of the seven shunted survivors had normal renal function at age 2 years. The PLUTO results emphasize the need for further research, given that the goal is to improve not only survival, but also long-term renal function. However, the inability to complete the trial does not bode well for future trials of fetal intervention for LUTO. Strategies to assess fetal renal function more reliably and to offer timely therapeutic interventions in appropriate cases are lacking. Furthermore, long-term follow-up data about neurodevelopment, morbidity, and quality of life are necessary to inform parents about the risks and benefits of intervention.

Nonvisualized Bladder

Visualization of the bladder is part of the routine anatomic survey. Visualization of the umbilical arteries on either side of the bladder can aid in detection of a bladder that is difficult to visualize. Because bladder emptying leads to a small or nonvisualized bladder, if the bladder is not initially visualized then additional images should be taken later in the examination. Absent bladder may be due to failure of urine production (e.g., as a result of some combination of severe bilateral abnormalities such as agenesis, dysplasia, or obstruction, severe IUGR or placental insufficiency); failure to store urine (e.g., as a result of cloacal exstrophy, cloacal malformation, or bladder exstrophy or ureters that insert ectopically below the bladder).

Nonvisualization of Fetal Bladder: Etiology

FAILURE OF URINE PRODUCTION
Bilateral severe renal abnormality (renal agenesis, MCDK, ARPKD, UPJ obstruction, renal dysplasia)
Severe intrauterine growth restriction or placental insufficiency

FAILURE TO STORE URINE
Bladder exstrophy
Cloacal exstrophy
Cloacal malformation
Bilateral ectopic ureter with drainage outside of bladder

ARPKD, Autosomal recessive polycystic kidney disease; *MCDK,* multicystic dysplastic kidney; *UPJ,* ureteropelvic junction.

Bladder Exstrophy

Bladder exstrophy occurs once in 10,000 to 40,000 births, more often in males.[3] It is caused by incomplete median closure of the inferior part of the anterior abdominal wall and anterior wall of the urinary bladder. There is exposure and protrusion of the posterior wall of the bladder. Sonographically, AFV and kidneys are normal, but a fluid-filled bladder is not identified.[238,239] An irregular mass may be seen arising from the anterior abdominal wall, inferior to the umbilicus, formed by the exstrophied bladder with heaped-up mucosa (Fig. 39.39). Other findings include a low umbilical cord insertion site into the abdomen, widening of the pubic bones, and abnormal genitalia, such as a small penis.[238,240] Prenatal sonographic diagnosis is challenging because all the findings may not be present, and a urachal cyst may be confused for a bladder.[239] Fetal MRI may be considered to clarify the anatomic defect and confirm the diagnosis.[241] Bladder exstrophy is usually a sporadic and isolated defect. Rarely, it has been reported with the **OEIS complex: omphalocele, exstrophy**

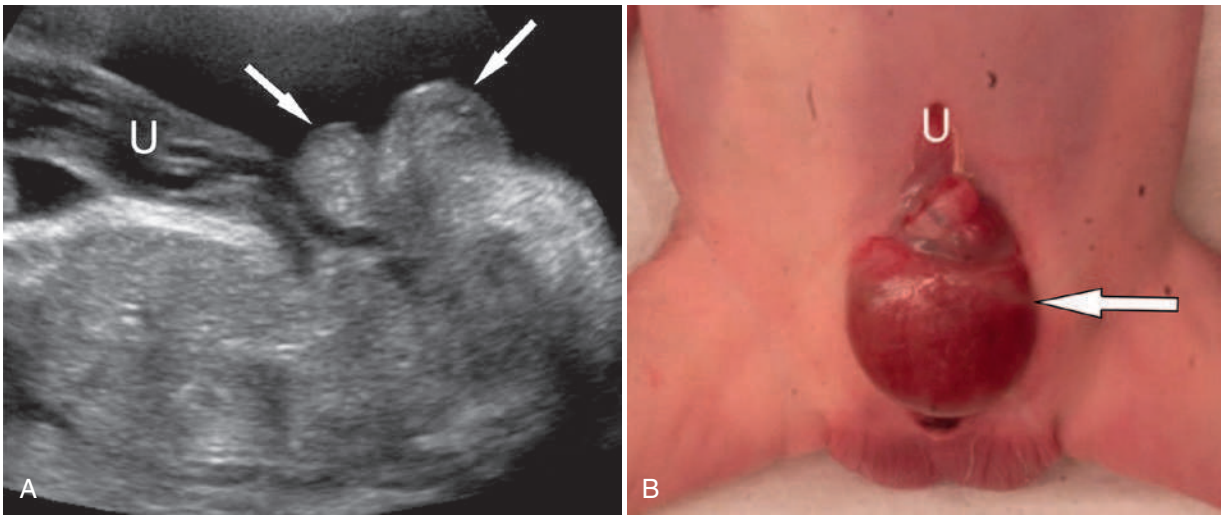

FIG. 39.39 Bladder Exstrophy. (A) Longitudinal scan of the lower fetal abdomen in a 29-week fetus shows an irregular mass on the anterior abdominal wall *(arrows),* below the umbilical cord insertion *(U).* A fluid-filled bladder was not identified. Note normal amniotic fluid volume. **(B)** Corresponding photograph shows the exposed bladder *(arrows)* below the umbilical cord *(U).*

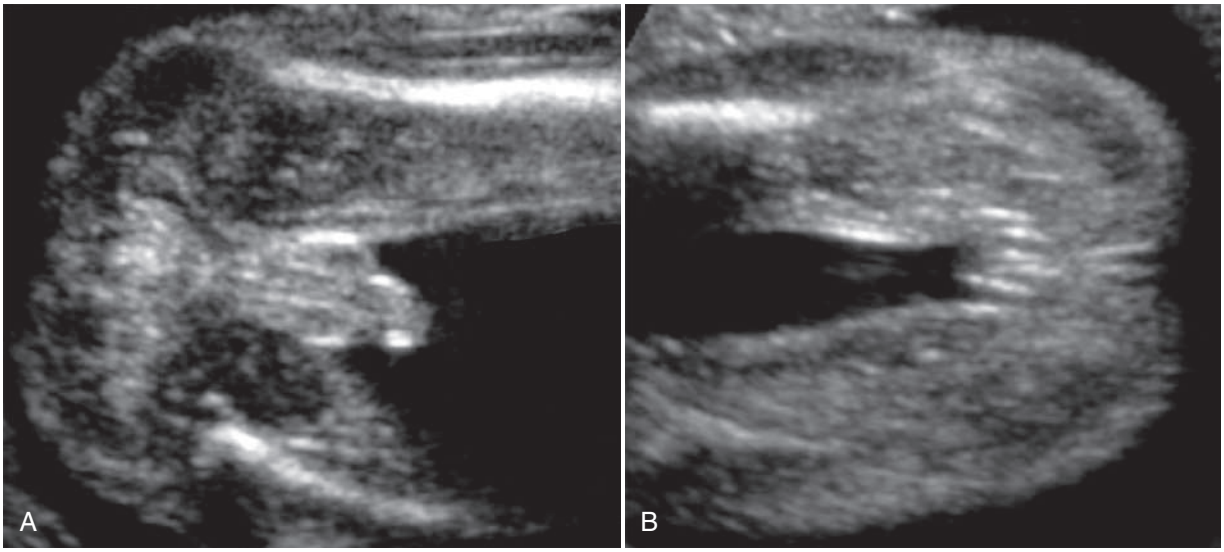

FIG. 39.40 Normal Genitalia. (A) Normal 19-week male fetus. Transverse scan of the perineum shows the penis and scrotum. **(B)** Normal 19-week female fetus. Transverse scan of the perineum shows the labial folds.

of bladder, imperforate anus, and spinal defects. Renal anomalies and abnormalities of the lower limbs are often present.[242,243]

THE GENITAL TRACT

Normal Genitalia

Fetal sex determination has medical as well as social implications. These include (1) history of X-linked disorders, (2) assignment of dizygosity in twin pregnancies, (3) exclusion of maternal cell contamination during amniocentesis or chorionic villous sampling, (4) need to confirm fetal gender to diagnose certain structural abnormalities (e.g., posterior urethral valves, ovarian cysts), and (5) familial syndromes in which genital abnormalities are common.

In the second trimester, fetal sex determination is based on direct visualization of the **external genitalia:** the penis and scrotum in males, and the labia majora and minora, represented by two or four parallel lines, respectively, in females (Fig. 39.40). Inopportune fetal position, oligohydramnios, maternal obesity, and operator inexperience represent the major limitations in fetal gender assessment. Errors may occur when the rounded, apposed labia are mistaken for a small, empty scrotum or when the umbilical cord is mistaken for the penis. The accuracy of fetal sex determination ranges from 92% to 100%.[244] When conventional methods fail or in the setting of ambiguous genitalia, fetal sex can be assigned by sonographic evaluation of the pelvic organs in the second and third trimesters of pregnancy.[245] It has been reported that measurement of the distance between the posterior wall of the fetal bladder and the anterior wall of the

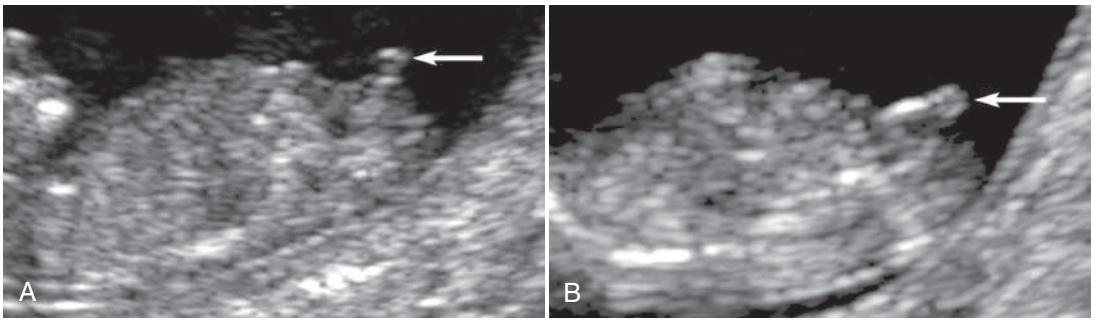

FIG. 39.41 First-Trimester Gender Identification. (A) Sagittal scan of a 12-week male fetus shows the vertical and relatively cranially directed phallus *(arrow).* **(B)** Sagittal scan of a 12-week female fetus shows the horizontal/caudally directed phallus *(arrow).*

rectum, when performed on an axial image of the pelvis, can be used to distinguish between male and female internal genitalia.[245] However, further studies are required to refine the discriminatory values.

In the late first trimester, fetal sex determination is possible, based on the direction of the genital tubercle in the midsagittal plane. In males the genital tubercle (penis) points cranially or vertically; in females the genital tubercle (clitoris) points caudally or horizontally (Fig. 39.41). By measuring the angle of the genital tubercle to a horizontal line through the lumbosacral skin surface (genital angle), gender assignment was possible in 93% of fetuses at 12 to 14 weeks of gestation (male when the angle was greater than 30 degrees and female when the angle was less than 10 degrees).[246] At all ages, male gender was correctly assigned in 99% to 100%. However, the accuracy of female gender assignment improved with gestational age, from 91.5% at 12 to 12 + 3 weeks, to 100% at 13 to 13 + 6 weeks. The use of 3-D multiplanar ultrasound allows the midsagittal plane to be obtained and the genitalia to be visualized more easily.[247] As a result the genital angle can be measured accurately, and this technique has been found to be accurate and reproducible for fetal gender assignment before 14 weeks of gestation.[248]

Testicular descent into the scrotum occurs after 25 weeks' gestation.[249] After 32 weeks, both testes have descended in 97% of the fetuses. Small hydroceles are common in third-trimester male fetuses (15%) and are usually of no clinical importance (Fig. 39.42).[250] However, large hydroceles, especially if they increase in size over time, suggest an open communication between the processus vaginalis and peritoneal cavity. In such cases, postnatal evaluation for inguinal hernia should be performed.[251]

FIG. 39.42 Hydroceles. Scan of the scrotal sac in a 38-week male fetus demonstrates testes and bilateral hydroceles.

Abnormal Genitalia

An abnormality of the genitalia may be an isolated finding or associated with other major malformations. In a male fetus, abnormal ultrasound findings include **micropenis, penile chordee** (abnormal curvature of penis), a shawl or **bifid scrotum,** and **undescended testes** (in third trimester).[252-254] Confirmation of **hypospadias** can be achieved by demonstrating the origin of the urine jet from either the midshaft or the base of the penis. In the female an enlarged clitoris is the most common finding. It can be difficult to define **ambiguous genitalia** accurately (Fig. 39.43). A male fetus with micropenis, bifid scrotum, and undescended testes may not be distinguished from the virilized female with clitoral enlargement (and labial fusion). If ambiguous genitalia are suspected, a karyotype is obtained to determine the genetic makeup of the fetus. Ambiguous genitalia, syndactyly, and multiple other anomalies raise suspicion for **Smith-Lemli-Opitz syndrome,** an autosomal recessive disorder due to mutations in the gene encoding 7-dehydrocholesterol reductase *(DHCR7);* thus elevation of 7-dehydrocholesterol in amniotic fluid is a reliable marker for prenatal diagnosis of Smith-Lemli-Opitz syndrome.[255] This condition is also suggested by low maternal serum estriol (uE3) in the second trimester.[256] DNA analysis can also be performed.[257]

When ultrasound suggests male genitalia and the fetus is genetically female, **congenital adrenal hyperplasia** (CAH) is the most common cause. The condition is autosomal recessive, so there may be a previously affected sibling. More than 90% of cases result from mutations of the *CYP21A2* gene, leading to 21-hydroxylase deficiency. When a proband exists, prenatal diagnosis is possible with chorionic villous sampling.[258] Recent advances in the use of cell-free fetal DNA have shown potential for the noninvasive prenatal diagnosis of CAH as well.[259] In the

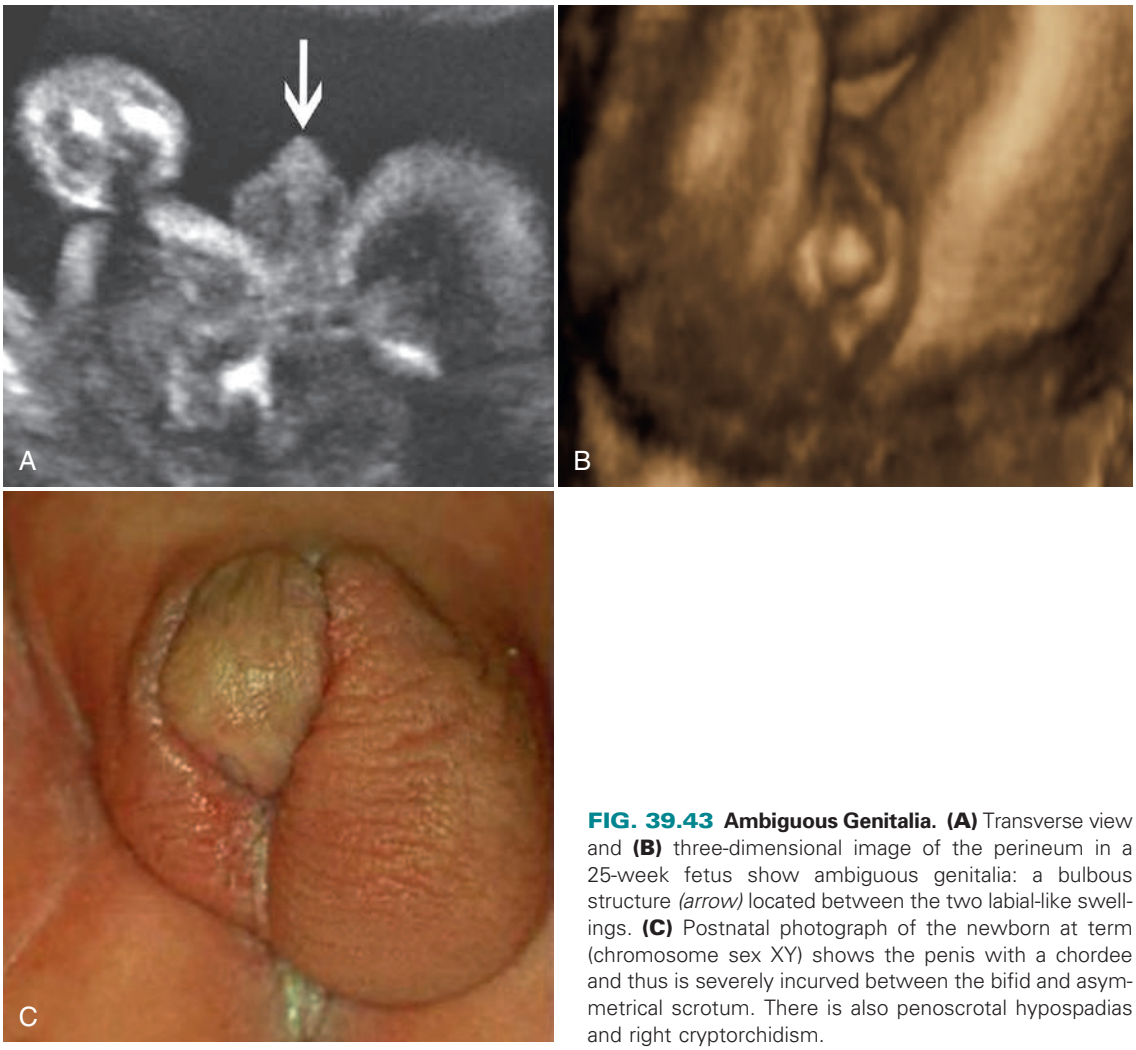

FIG. 39.43 Ambiguous Genitalia. (A) Transverse view and **(B)** three-dimensional image of the perineum in a 25-week fetus show ambiguous genitalia: a bulbous structure *(arrow)* located between the two labial-like swellings. **(C)** Postnatal photograph of the newborn at term (chromosome sex XY) shows the penis with a chordee and thus is severely incurved between the bifid and asymmetrical scrotum. There is also penoscrotal hypospadias and right cryptorchidism.

absence of a family history, the ultrasound findings of enlarged fetal adrenal glands and ambiguous genitalia are suggestive of CAH.[260,261] Prenatal maternal administration of dexamethasone can prevent or reduce virilization in affected female fetuses, but it must be initiated on or before the ninth week of pregnancy (before prenatal diagnosis of CAH can be made currently).[259] Because the offspring of carrier parents have a 1 in 4 chance of having CAH, and therefore only 1 in 8 will be a CAH-affected female, mothers who want to undergo prenatal dexamethasone treatment will be unnecessarily treating seven of eight fetuses, who would be exposed to the risks of several weeks of steroid therapy. A systematic review of the safety of prenatal steroid therapy in CAH concluded that the available literature is uncertain and inconclusive regarding the benefits or harms of dexamethasone use in this setting, and this medication should be prescribed only after the parents have received detailed and informed counseling.[262-264]

Prenatal diagnosis of female **pseudohermaphroditism** with bilateral luteoma of pregnancy has been reported.[265] In a genetic male with female external genitalia, **testicular feminization** is likely. Intersex states may be divided into hormonally and nonhormonally mediated abnormalities. The latter often have associated cloacal anomalies or chromosomal aberrations or may conform to one of numerous multimalformation syndromes. In many cases, an accurate diagnosis and final gender assignment can be made only postnatally.

Hydrocolpos

Hydrocolpos is dilation of the vagina caused by fluid accumulation. It is associated with uterine dilation in hydrometrocolpos. It occurs as a result of vaginal hypoplasia or agenesis, transverse septum, or imperforate hymen. Hydrocolpos appears as a **midline pelvic mass, posterior to the bladder.** It is generally anechoic but may contain echogenic fluid with a fluid-debris level. When associated with müllerian duct anomalies, it may appear as a septate mass.[266] The enlarged vagina and uterus may compress the UT and cause hydronephrosis or hydroureter. Hydrocolpos may be associated with a wide spectrum of urorectal septum malformations. Therefore a detailed sonographic examination including identification of a normal anal canal and rectum provides important information for prenatal counseling.[267] MRI may be useful as an adjunct to ultrasound when pelvic anatomy is not well identified or to aid in diagnosis of cloacal malformation or other associated GI abnormalities.[213,267,268]

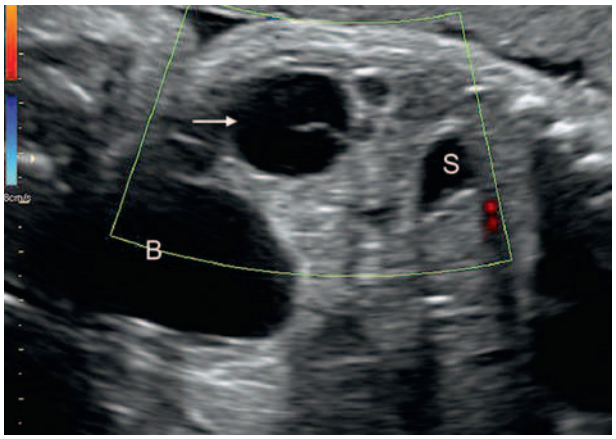

FIG. 39.44 Ovarian Cyst. Coronal scan demonstrates a cyst *(arrow)* in the lower abdomen of a 35-week female fetus, separate from the kidneys *(not shown),* bladder *(B),* and stomach *(S).* (Courtesy of John R. Mernagh, MD, McMaster University Medical Center, Hamilton, Ontario.)

Ovarian Cysts

The vast majority of fetal ovarian cysts are benign functional cysts.[269] They result from excessive stimulation of the fetal ovary by placental and maternal hormones. They are usually diagnosed in the third trimester. The main criteria for diagnosis are the presence of a cystic mass, usually located in one side of the pelvis or lower abdomen; normal urinary and GI tracts; and female gender. The diagnosis is presumptive because other lesions, such as **enteric duplication cysts, mesenteric cysts, meconium pseudocysts,** or **urachal cysts,** cannot be ruled out with certainty. Most ovarian cysts are small and hypoechoic (Fig. 39.44). The "daughter cyst" sign (describing a smaller cyst within a larger ovarian cyst) is considered pathognomonic.[270] When complicated by torsion or hemorrhage, ovarian cysts may appear complex (Video 39.11). A fluid-debris level, a retracting clot, or internal septa may be demonstrated.[271] The wall may be echogenic from dystrophic calcification.

The outcome depends on the cyst size and complications such as torsion. The natural course for most ovarian cysts (>50%) is spontaneous resolution, either prenatally or postnatally (usually within 6 months of birth).[272-274] With simple cysts larger than 4 to 5 cm, there is an increased risk of complications, such as torsion, hemorrhage, and rupture.[275] Because torsion could result in necrosis, adhesion formation, and potential loss of the ovary with impaired fertility, some authors advocate prenatal aspiration of large simple cysts to prevent torsion.[276,277] However, the value of fetal cyst aspiration is controversial.[278,279] Cyst recurrence is common[277] and there are procedure-related complications (infection, premature labor, rupture of membranes).[278] In most cases, identification of an ovarian cyst does not alter obstetric care. Our approach is conservative; we do not aspirate cysts. Serial ultrasound is performed to monitor for change in size or internal echogenicity. Extremely large cysts may cause intestinal obstruction, polyhydramnios, and dystocia.

Postnatal management options include observation, percutaneous cyst aspiration, and surgery. Asymptomatic infants are managed conservatively with serial ultrasound until the cyst resolves.[273,280] Symptomatic cysts and cysts that persist or increase in size are indications for surgery.

CONCLUSION

UT anomalies are among the most common antenatally detected fetal anomalies. A thorough sonographic evaluation of renal structure, function, and associated anomalies will improve the accuracy of antenatal diagnosis, thus enabling optimal obstetric and neonatal management.

Acknowledgments

Special thanks to Dr. David Chitayat for reviewing the section on renal cystic disease; Dr. Greg Ryan for reviewing the sections on lower urinary tract obstruction and in utero intervention; and Dr. Ants Toi and the sonographers of the Joint Department of Medical Imaging at Mount Sinai Hospital and Women's College Hospital in Toronto for providing many wonderful images.

REFERENCES

1. Grandjean H, Larroque D, Levi S. The performance of routine ultrasonographic screening of pregnancies in the Eurofetus Study. Am J Obstet Gynecol. 1999;181(2):446-454.
2. Toka HR, Toka O, Hariri A, Nguyen HT. Congenital anomalies of kidney and urinary tract. Semin Nephrol. 2010;30(4):374-386.
3. Moore KL, Persaud TVN, editors. The developing human: clinically oriented embryology. 7th ed. Philadelphia: Saunders; 2003.
4. Bronshtein M, Yoffe N, Brandes JM, Blumenfeld Z. First and early second-trimester diagnosis of fetal urinary tract anomalies using transvaginal sonography. Prenat Diagn. 1990;10(10):653-666.
5. Braithwaite JM, Armstrong MA, Economides DL. Assessment of fetal anatomy at 12 to 13 weeks of gestation by transabdominal and transvaginal sonography. Br J Obstet Gynaecol. 1996;103(1):82-85.
6. Chitty LS, Altman DG. Charts of fetal size: kidney and renal pelvis measurements. Prenat Diagn. 2003;23(11):891-897.
7. Grannum P, Bracken M, Silverman R, Hobbins JC. Assessment of fetal kidney size in normal gestation by comparison of ratio of kidney circumference to abdominal circumference. Am J Obstet Gynecol. 1980;136(2):249-254.
8. Rabinowitz R, Peters MT, Vyas S, et al. Measurement of fetal urine production in normal pregnancy by real-time ultrasonography. Am J Obstet Gynecol. 1989;161(5):1264-1266.
9. Fagerquist M, Fagerquist U, Oden A, Blomberg SG. Fetal urine production and accuracy when estimating fetal urinary bladder volume. Ultrasound Obstet Gynecol. 2001;17(2):132-139.
10. Lee SM, Park SK, Shim SS, et al. Measurement of fetal urine production by three-dimensional ultrasonography in normal pregnancy. Ultrasound Obstet Gynecol. 2007;30(3):281-286.
11. Abramovich D. The volume of amniotic fluid and its regulating factors. In: Fairweather D, Eskers T, editors. Amniotic fluid research and clinical application. 2nd ed. Amsterdam: Excerpta Medica; 1978. p. 31-49.
12. Moore TR. Amniotic fluid dynamics reflect fetal and maternal health and disease. Obstet Gynecol. 2010;116(3):759-765.
13. Goldstein RB, Filly RA. Sonographic estimation of amniotic fluid volume. Subjective assessment versus pocket measurements. J Ultrasound Med. 1988;7(7):363-369.
14. Moore TR, Cayle JE. The amniotic fluid index in normal human pregnancy. Am J Obstet Gynecol. 1990;162(5):1168-1173.
15. Williams K, Wittmann B, Dansereau J. Intraobserver reliability of amniotic fluid volume estimation by two techniques: amniotic fluid index vs. maximum vertical pocket. Ultrasound Obstet Gynecol. 1993;3(5):346-349.
16. Chamberlain PF, Manning FA, Morrison I, et al. Ultrasound evaluation of amniotic fluid volume. I. The relationship of marginal and decreased amniotic

fluid volumes to perinatal outcome. Am J Obstet Gynecol. 1984; 150(3):245-249.
17. Phelan JP, Ahn MO, Smith CV, et al. Amniotic fluid index measurements during pregnancy. J Reprod Med. 1987;32(8):601-604.
18. Magann EF, Sanderson M, Martin JN, Chauhan S. The amniotic fluid index, single deepest pocket, and two-diameter pocket in normal human pregnancy. Am J Obstet Gynecol. 2000;182(6):1581-1588.
19. Moise Jr KJ. Toward consistent terminology: assessment and reporting of amniotic fluid volume. Semin Perinatol. 2013;37(5):370-374.
20. ACOG Committee on Practice Bulletins—Obstetrics. Practice Bulletin No. 145: antepartum fetal surveillance. Obstet Gynecol. 2014;124(1):182-192.
21. Nabhan AF, Abdelmoula YA. Amniotic fluid index versus single deepest vertical pocket: a meta-analysis of randomized controlled trials. Int J Gynaecol Obstet. 2009;104(3):184-188.
22. Kehl S, Schelkle A, Thomas A, et al. Single deepest vertical pocket or amniotic fluid index as evaluation test for preventing adverse pregnancy outcome (SAFE trial): a multicenter, open-label, randomized controlled trial. Ultrasound Obstet Gynecol. 2016;47(6):674-979.
23. Magann EF, Doherty DA, Ennen CS, et al. The ultrasound estimation of amniotic fluid volume in diamniotic twin pregnancies and prediction of peripartum outcomes. Am J Obstet Gynecol. 2007;196(6):570.e1-570.e6.
24. Ippolito DL, Bergstrom JE, Lutgendorf MA, et al. A systematic review of amniotic fluid assessments in twin pregnancies. J Ultrasound Med. 2014;33(8):1353-1364.
25. Wiesel A, Queisser-Luft A, Clementi M, et al. Prenatal detection of congenital renal malformations by fetal ultrasonographic examination: an analysis of 709,030 births in 12 European countries. Eur J Med Genet. 2005;48(2): 131-144.
26. Thomas DF. Prenatally detected uropathy: epidemiological considerations. Br J Urol. 1998;81(Suppl. 2):8-12.
27. Murki S, Kumar P, Dutta S, Narang A. Fatal neonatal renal failure due to maternal enalapril ingestion. J Matern Fetal Neonatal Med. 2005;17(3): 235-237.
28. Saji H, Yamanaka M, Hagiwara A, Ijiri R. Losartan and fetal toxic effects. Lancet. 2001;357(9253):363.
29. Locatelli A, Vergani P, Bellini P, et al. Can a cyclo-oxygenase type-2 selective tocolytic agent avoid the fetal side effects of indomethacin? BJOG. 2001;108(3):325-326.
30. Kaplan BS, Restaino I, Raval DS, et al. Renal failure in the neonate associated with in utero exposure to non-steroidal anti-inflammatory agents. Pediatr Nephrol. 1994;8(6):700-704.
31. Mitra SC. Effect of cocaine on fetal kidney and bladder function. J Matern Fetal Med. 1999;8(6):262-269.
32. Stoll C, Dott B, Alembik Y, Roth MP. Associated nonurinary congenital anomalies among infants with congenital anomalies of kidney and urinary tract (CAKUT). Eur J Med Genet. 2014;57(7):322-328.
33. Nicolaides KH, Cheng HH, Abbas A, et al. Fetal renal defects: associated malformations and chromosomal defects. Fetal Diagn Ther. 1992;7(1): 1-11.
34. Roodhooft AM, Birnholz JC, Holmes LB. Familial nature of congenital absence and severe dysgenesis of both kidneys. N Engl J Med. 1984;310(21):1341-1345.
35. Deshpande C, Hennekam RC. Genetic syndromes and prenatally detected renal anomalies. Semin Fetal Neonatal Med. 2008;13(3):171-180.
36. Schwaderer AL, Bates CM, McHugh KM, McBride KL. Renal anomalies in family members of infants with bilateral renal agenesis/adysplasia. Pediatr Nephrol. 2007;22(1):52-56.
37. Kajbafzadeh AM, Payabvash S, Sadeghi Z, et al. Comparison of magnetic resonance urography with ultrasound studies in detection of fetal urogenital anomalies. J Pediatr Urol. 2008;4:32-39.
38. Chauvin NA, Epelman M, Victoria T, Johnson AM. Complex genitourinary abnormalities on fetal MRI: imaging findings and approach to diagnosis. Am J Roentgenol. 2012;199(2):W222-W231.
39. Martin C, Darnell A, Duran C, et al. Magnetic resonance imaging of the intrauterine fetal genitourinary tract: normal anatomy and pathology. Abdom Imaging. 2004;29(3):286-302.
40. Gupta P, Kumar S, Sharma R, et al. The role of magnetic resonance imaging in fetal renal anomalies. Int J Gynaecol Obstet. 2010;111:209-212.
41. Manganaro L, Francioso A, Savelli S, et al. Fetal MRI with diffusion-weighted imaging (DWI) and apparent diffusion coefficient (ADC) assessment in the evaluation of renal development: preliminary experience in normal kidneys. Radiol Med. 2009;114(3):403-413.
42. Savelli S, Di Maurizio M, Perrone A, et al. MRI with diffusion-weighted imaging (DWI) and apparent diffusion coefficient (ADC) assessment in the evaluation of normal and abnormal fetal kidneys: preliminary experience. Prenat Diagn. 2007;27(12):1104-1111.
43. Potter EL. Bilateral absence of ureters and kidneys: a report of 50 cases. Obstet Gynecol. 1965;25:3-12.
44. Spiro JE, Konrad M, Rieger-Fackeldey E, et al. Renal oligo- and anhydramnios: cause, course and outcome—a single-center study. Arch Gynecol Obstet. 2015;292(2):327-336.
45. Bronshtein M, Amit A, Achiron R, et al. The early prenatal sonographic diagnosis of renal agenesis: techniques and possible pitfalls. Prenat Diagn. 1994;14(4):291-297.
46. Hoffman CK, Filly RA, Callen PW. The "lying down" adrenal sign: a sonographic indicator of renal agenesis or ectopia in fetuses and neonates. J Ultrasound Med. 1992;11(10):533-536.
47. Haeusler MC, Ryan G, Robson SC, et al. The use of saline solution as a contrast medium in suspected diaphragmatic hernia and renal agenesis. Am J Obstet Gynecol. 1993;168(5):1486-1492.
48. Benacerraf BR. Examination of the second-trimester fetus with severe oligohydramnios using transvaginal scanning. Obstet Gynecol. 1990;75(3 Pt 2):491-493.
49. DeVore GR. The value of color Doppler sonography in the diagnosis of renal agenesis. J Ultrasound Med. 1995;14(6):443-449.
50. Sepulveda W, Stagiannis KD, Flack NJ, Fisk NM. Accuracy of prenatal diagnosis of renal agenesis with color flow imaging in severe second-trimester oligohydramnios. Am J Obstet Gynecol. 1995;173(6):1788-1792.
51. Martinez-Frias ML, Bermejo E, Rodriguez-Pinilla E, Prieto D. Does single umbilical artery (SUA) predict any type of congenital defect? Clinical-epidemiological analysis of a large consecutive series of malformed infants. Am J Med Genet A. 2008;146a(1):15-25.
52. Boyd PA, Tonks AM, Rankin J, et al. Monitoring the prenatal detection of structural fetal congenital anomalies in England and Wales: register-based study. J Med Screen. 2011;18(1):2-7.
53. Slickers JE, Olshan AF, Siega-Riz AM, et al. Maternal body mass index and lifestyle exposures and the risk of bilateral renal agenesis or hypoplasia: the National Birth Defects Prevention Study. Am J Epidemiol. 2008;168(11): 1259-1267.
54. Carter CO, Evans K, Pescia G. A family study of renal agenesis. J Med Genet. 1979;16(3):176-188.
55. Chow JS, Benson CB, Lebowitz RL. The clinical significance of an empty renal fossa on prenatal sonography. J Ultrasound Med. 2005;24(8): 1049-1054.
56. Yuksel A, Batukan C. Sonographic findings of fetuses with an empty renal fossa and normal amniotic fluid volume. Fetal Diagn Ther. 2004;19(6): 525-532.
57. Cho JY, Moon MH, Lee YH, et al. Measurement of compensatory hyperplasia of the contralateral kidney: usefulness for differential diagnosis of fetal unilateral empty renal fossa. Ultrasound Obstet Gynecol. 2009;34(5): 515-520.
58. Cascio S, Paran S, Puri P. Associated urological anomalies in children with unilateral renal agenesis. J Urol. 1999;162(3 Pt 2):1081-1083.
59. Woolf AS, Hillman KA. Unilateral renal agenesis and the congenital solitary functioning kidney: developmental, genetic and clinical perspectives. BJU Int. 2007;99(1):17-21.
60. McPherson E. Renal anomalies in families of individuals with congenital solitary kidney. Genet Med. 2007;9(5):298-302.
61. Dunnick NR, Sandler CM, Newhouse JH, Amis Jr ES, editors. Textbook of uroradiology. 4th ed. Philadelphia: Lippincott Williams & Wilkins; 2008.
62. Batukan C, Yuksel A. Prenatal diagnosis and postnatal outcome of pelvic kidneys. Prenat Diagn. 2011;31:356-359.
63. Solanki S, Bhatnagar V, Gupta AK, Kumar R. Crossed fused renal ectopia: challenges in diagnosis and management. J Indian Assoc Pediatr Surg. 2013;18(1):7-10.

64. Arena F, Arena S, Paolata A, et al. Is a complete urological evaluation necessary in all newborns with asymptomatic renal ectopia? Int J Urol. 2007;14(6):491-495.
65. Cho JY, Lee YH, Toi A, Macdonald B. Prenatal diagnosis of horseshoe kidney by measurement of the renal pelvic angle. Ultrasound Obstet Gynecol. 2005;25(6):554-558.
66. Osathanondh V, Potter EL. Pathogenesis of polycystic kidneys. Historical survey. Arch Pathol. 1964;77:459-465.
67. Avni FE, Garel C, Cassart M, et al. Imaging and classification of congenital cystic renal diseases. Am J Roentgenol. 2012;198:1004-1013.
68. Hildebrandt F, Benzing T, Katsanis N. Ciliopathies. N Engl J Med. 2011;364(16):1533-1543.
69. Bergmann C. ARPKD and early manifestations of ADPKD: the original polycystic kidney disease and phenocopies. Pediatr Nephrol. 2015;30(1): 15-30.
70. Dungan JS, Fernandez MT, Abbitt PL, et al. Multicystic dysplastic kidney: natural history of prenatally detected cases. Prenat Diagn. 1990;10(3): 175-182.
71. Kleiner B, Filly RA, Mack L, Callen PW. Multicystic dysplastic kidney: observations of contralateral disease in the fetal population. Radiology. 1986;161(1):27-29.
72. Lazebnik N, Bellinger MF, Ferguson JE 2nd, et al. Insights into the pathogenesis and natural history of fetuses with multicystic dysplastic kidney disease. Prenat Diagn. 1999;19(5):418-423.
73. van Eijk L, Cohen-Overbeek TE, den Hollander NS, et al. Unilateral multicystic dysplastic kidney: a combined pre- and postnatal assessment. Ultrasound Obstet Gynecol. 2002;19(2):180-183.
74. Eckoldt F, Woderich R, Smith RD, Heling KS. Antenatal diagnostic aspects of unilateral multicystic kidney dysplasia—sensitivity, specificity, predictive values, differential diagnoses, associated malformations and consequences. Fetal Diagn Ther. 2004;19(2):163-169.
75. Aslam M, Watson AR, Trent, Anglia MSG. Unilateral multicystic dysplastic kidney: long term outcomes. Arch Dis Child. 2006;91(10): 820-823.
76. Narchi H. Risk of hypertension with multicystic kidney disease: a systematic review. Arch Dis Child. 2005;90(9):921-924.
77. Narchi H. Risk of Wilms tumour with multicystic kidney disease: a systematic review. Arch Dis Child. 2005;90(2):147-149.
78. Hains DS, Bates CM, Ingraham S, Schwaderer AL. Management and etiology of the unilateral multicystic dysplastic kidney: a review. Pediatr Nephrol. 2009;24:233-241.
79. Heidet L, Decramer S, Pawtowski A, et al. Spectrum of HNF1B mutations in a large cohort of patients who harbor renal diseases. Clin J Am Soc Nephrol. 2010;5(6):1079-1090.
80. Beck AD. The effect of intra-uterine urinary obstruction upon the development of the fetal kidney. J Urol. 1971;105(6):784-789.
81. Glazer GM, Filly RA, Callen PW. The varied sonographic appearance of the urinary tract in the fetus and newborn with urethral obstruction. Radiology. 1982;144(3):563-568.
82. Harrison MR, Filly RA. The fetus with obstructive uropathy: pathophysiology, natural history, selection and treatment. In: Harrison MR, Golbus MS, Filly RA, editors. The unborn patient: prenatal diagnosis and treatment. 2nd ed. Philadelphia: Saunders; 1991. p. 328-393.
83. Ingraham SE, Saha M, Carpenter AR, et al. Pathogenesis of renal injury in the megabladder mouse: a genetic model of congenital obstructive nephropathy. Pediatr Res. 2010;68(6):500-507.
84. Mahony BS, Filly RA, Callen PW, et al. Fetal renal dysplasia: sonographic evaluation. Radiology. 1984;152(1):143-146.
85. Estroff JA, Mandell J, Benacerraf BR. Increased renal parenchymal echogenicity in the fetus: importance and clinical outcome. Radiology. 1991;181(1):135-139.
86. Avni FE, Garel L, Cassart M, et al. Perinatal assessment of hereditary cystic renal diseases: the contribution of sonography. Pediatr Radiol. 2006;36(5):405-414.
87. Chaumoitre K, Brun M, Cassart M, et al. Differential diagnosis of fetal hyperechogenic cystic kidneys unrelated to renal tract anomalies: a multicenter study. Ultrasound Obstet Gynecol. 2006;28(7):911-917.
88. Reuss A, Wladimiroff JW, Stewart PA, Niermeijer MF. Prenatal diagnosis by ultrasound in pregnancies at risk for autosomal recessive polycystic kidney disease. Ultrasound Med Biol. 1990;16(4):355-359.
89. Barth RA, Guillot AP, Capeless EL, Clemmons JJ. Prenatal diagnosis of autosomal recessive polycystic kidney disease: variable outcome within one family. Am J Obstet Gynecol. 1992;166(2):560-561.
90. Zerres K, Mucher G, Becker J, et al. Prenatal diagnosis of autosomal recessive polycystic kidney disease (ARPKD): molecular genetics, clinical experience, and fetal morphology. Am J Med Genet. 1998;76(2):137-144.
91. Guay-Woodford LM, Bissler JJ, Braun MC, et al. Consensus expert recommendations for the diagnosis and management of autosomal recessive polycystic kidney disease: report of an international conference. J Pediatr. 2014;165(3):611-617.
92. Pretorius DH, Lee ME, Manco-Johnson ML, et al. Diagnosis of autosomal dominant polycystic kidney disease in utero and in the young infant. J Ultrasound Med. 1987;6(5):249-255.
93. Brun M, Maugey-Laulom B, Eurin D, et al. Prenatal sonographic patterns in autosomal dominant polycystic kidney disease: a multicenter study. Ultrasound Obstet Gynecol. 2004;24(1):55-61.
94. Cornec-Le Gall E, Audrezet MP, Le Meur Y, et al. Genetics and pathogenesis of autosomal dominant polycystic kidney disease: 20 years on. Hum Mutat. 2014;35(12):1393-1406.
95. Fick GM, Johnson AM, Strain JD, et al. Characteristics of very early onset autosomal dominant polycystic kidney disease. J Am Soc Nephrol. 1993;3(12):1863-1870.
96. MacDermot KD, Saggar-Malik AK, Economides DL, Jeffery S. Prenatal diagnosis of autosomal dominant polycystic kidney disease (PKD1) presenting in utero and prognosis for very early onset disease. J Med Genet. 1998;35(1):13-16.
97. Boyer O, Gagnadoux MF, Guest G, et al. Prognosis of autosomal dominant polycystic kidney disease diagnosed in utero or at birth. Pediatr Nephrol. 2007;22(3):380-388.
98. Audrézet MP, Corbiere C, Lebbah S, et al. Comprehensive *PKD1* and *PKD2* mutation analysis in prenatal autosomal dominant polycystic kidney disease. J Am Soc Nephrol. 2016;27(3):722-729.
99. Decramer S, Parant O, Beaufils S, et al. Anomalies of the *TCF2* gene are the main cause of fetal bilateral hyperechogenic kidneys. J Am Soc Nephrol. 2007;18(3):923-933.
100. Madariaga L, Morinière V, Jeanpierre C, et al. Severe prenatal renal anomalies associated with mutations in *HNF1B* or *PAX2* genes. Clin J Am Soc Nephrol. 2013;8(7):1179-1187.
101. Sepulveda W, Sebire NJ, Souka A, et al. Diagnosis of the Meckel-Gruber syndrome at eleven to fourteen weeks' gestation. Am J Obstet Gynecol. 1997;176(2):316-319.
102. Nyberg DA, Hallesy D, Mahony BS, et al. Meckel-Gruber syndrome. Importance of prenatal diagnosis. J Ultrasound Med. 1990;9(12): 691-696.
103. Ickowicz V, Eurin D, Maugey-Laulom B, et al. Meckel-Gruber syndrome: sonography and pathology. Ultrasound Obstet Gynecol. 2006;27: 296-300.
104. Avni FE, Hall M. Renal cystic diseases in children: new concepts. Pediatr Radiol. 2010;40(6):939-946.
105. Tsatsaris V, Gagnadoux MF, Aubry MC, et al. Prenatal diagnosis of bilateral isolated fetal hyperechogenic kidneys. Is it possible to predict long term outcome? BJOG. 2002;109(12):1388-1393.
106. Emmanuelli V, Lahoche-Manucci A, Holder-Espinasse M, et al. Prenatal diagnosis of hyperechogenic kidneys: a study of 17 cases. J Gynecol Obstet Biol Reprod (Paris). 2010;39(8):637-646.
107. Al-Hamed MH, Kurdi W, Alsahan N, et al. Genetic spectrum of Saudi Arabian patients with antenatal cystic kidney disease and ciliopathy phenotypes using a targeted renal gene panel. J Med Genet. 2016;53(5): 338-347.
108. Carr MC, Benacerraf BR, Estroff JA, Mandell J. Prenatally diagnosed bilateral hyperechoic kidneys with normal amniotic fluid: postnatal outcome. J Urol. 1995;153(2):442-444.
109. Mashiach R, Davidovits M, Eisenstein B, et al. Fetal hyperechogenic kidney with normal amniotic fluid volume: a diagnostic dilemma. Prenat Diagn. 2005;25:553-558.

110. Leclair MD, El-Ghoneimi A, Audry G, et al. The outcome of prenatally diagnosed renal tumors. J Urol. 2005;173(1):186-189.
111. Chen WY, Lin CN, Chao CS, et al. Prenatal diagnosis of congenital mesoblastic nephroma in mid-second trimester by sonography and magnetic resonance imaging. Prenat Diagn. 2003;23(11):927-931.
112. Linam LE, Yu X, Calvo-Garcia MA, et al. Contribution of magnetic resonance imaging to prenatal differential diagnosis of renal tumors: report of two cases and review of the literature. Fetal Diagn Ther. 2010;28(2):100-108.
113. Garnier S, Maillet O, Haouy S, et al. Prenatal intrarenal neuroblastoma mimicking a mesoblastic nephroma: a case report. J Pediatr Surg. 2012;47(8):e21-e23.
114. Rubenstein SC, Benacerraf BR, Retik AB, Mandell J. Fetal suprarenal masses: sonographic appearance and differential diagnosis. Ultrasound Obstet Gynecol. 1995;5(3):164-167.
115. Avni FE, Massez A, Cassart M. Tumours of the fetal body: a review. Pediatr Radiol. 2009;39(11):114711-114757.
116. Maki E, Oh K, Rogers S, Sohaey R. Imaging and differential diagnosis of suprarenal masses in the fetus. J Ultrasound Med. 2014;33:895-904.
117. Heling KS, Chaoui R, Hartung J, et al. Prenatal diagnosis of congenital neuroblastoma. Analysis of 4 cases and review of the literature. Fetal Diagn Ther. 1999;14(1):47-52.
118. Sauvat F, Sarnacki S, Brisse H, et al. Outcome of suprarenal localized masses diagnosed during the perinatal period: a retrospective multicenter study. Cancer. 2002;94(9):2474-2480.
119. Toma P, Lucigrai G, Marzoli A, Lituania M. Prenatal diagnosis of metastatic adrenal neuroblastoma with sonography and MR imaging. Am J Roentgenol. 1994;162(5):1183-1184.
120. Isaacs Jr H. Fetal and neonatal neuroblastoma: retrospective review of 271 cases. Fetal Pediatr Pathol. 2007;26(4):177-184.
121. Cun L, Zhe M, Xinfeng Z, et al. Fetal neuroblastoma with fetal hypertension. Ultrasound Obstet Gynecol. 2008;31(1):106-107.
122. Jennings RW, LaQuaglia MP, Leong K, et al. Fetal neuroblastoma: prenatal diagnosis and natural history. J Pediatr Surg. 1993;28(9):1168-1174.
123. Ho PT, Estroff JA, Kozakewich H, et al. Prenatal detection of neuroblastoma: a ten-year experience from the Dana-Farber Cancer Institute and Children's Hospital. Pediatrics. 1993;92(3):358-364.
124. Nuchtern JG, London WB, Barnewolt CE, et al. A prospective study of expectant observation as primary therapy for neuroblastoma in young infants: a Children's Oncology Group study. Ann Surg. 2012;256(4):573-580.
125. Schwarzler P, Bernard JP, Senat MV, Ville Y. Prenatal diagnosis of fetal adrenal masses: differentiation between hemorrhage and solid tumor by color Doppler sonography. Ultrasound Obstet Gynecol. 1999;13(5):351-355.
126. Rahman S, Ohlsson A, Fong KW, Glanc P. Fetal adrenal hemorrhage in a diamniotic, dichorionic twin: case report and review of controversies in diagnosis and management. J Ultrasound Med. 1997;16(4):297-300.
127. Schrauder MG, Hammersen G, Siemer J, et al. Fetal adrenal haemorrhage—two-dimensional and three-dimensional imaging. Fetal Diagn Ther. 2008;23(1):72-75.
128. Policiano C, Djokovic D, Carvalho R, et al. Ultrasound antenatal detection of urinary tract anomalies in the last decade: outcome and prognosis. J Matern Fetal Neonatal Med. 2015;28(8):959-963.
129. Chudleigh PM, Chitty LS, Pembrey M, Campbell S. The association of aneuploidy and mild fetal pyelectasis in an unselected population: the results of a multicenter study. Ultrasound Obstet Gynecol. 2001;17(3):197-202.
130. Thompson MO, Thilaganathan B. Effect of routine screening for Down's syndrome on the significance of isolated fetal hydronephrosis. Br J Obstet Gynaecol. 1998;105(8):860-864.
131. Sairam S, Al-Habib A, Sasson S, Thilaganathan B. Natural history of fetal hydronephrosis diagnosed on mid-trimester ultrasound. Ultrasound Obstet Gynecol. 2001;17(3):191-196.
132. Nguyen HT, Herndon CD, Cooper C, et al. The Society for Fetal Urology consensus statement on the evaluation and management of antenatal hydronephrosis. J Pediatr Urol. 2010;6(3):212-231.
133. Nguyen HT, Benson CB, Bromley B, et al. Multidisciplinary consensus on the classification of prenatal and postnatal urinary tract dilation (UTD classification system). J Pediatr Urol. 2014;10(6):982-998.
134. van Vuuren SH, Damen-Elias HA, Stigter RH, et al. Size and volume charts of fetal kidney, renal pelvis and adrenal gland. Ultrasound Obstet Gynecol. 2012;40(6):659-664.
135. Odibo AO, Marchiano D, Quinones JN, et al. Mild pyelectasis: evaluating the relationship between gestational age and renal pelvic anterior-posterior diameter. Prenat Diagn. 2003;23(10):824-827.
136. Chudleigh T. Mild pyelectasis. Prenat Diagn. 2001;21(11):936-941.
137. Livera LN, Brookfield DS, Egginton JA, Hawnaur JM. Antenatal ultrasonography to detect fetal renal abnormalities: a prospective screening programme. BMJ. 1989;298(6685):1421-1423.
138. Benacerraf BR, Mandell J, Estroff JA, et al. Fetal pyelectasis: a possible association with Down syndrome. Obstet Gynecol. 1990;76(1):58-60.
139. Corteville JE, Dicke JM, Crane JP. Fetal pyelectasis and Down syndrome: is genetic amniocentesis warranted? Obstet Gynecol. 1992;79(5 [Pt 1]):770-772.
140. Anderson NG, Abbott GD, Mogridge N, et al. Vesicoureteric reflux in the newborn: relationship to fetal renal pelvic diameter. Pediatr Nephrol. 1997;11(5):610-616.
141. Ismaili K, Hall M, Donner C, et al. Results of systematic screening for minor degrees of fetal renal pelvis dilatation in an unselected population. Am J Obstet Gynecol. 2003;188(1):242-246.
142. Scarborough PL, Ferrara E, Storm DW. Should prenatal hydronephrosis that resolves before birth be followed postnatally? Analysis and comparison to persistent prenatal hydronephrosis. Pediatr Nephrol. 2015;30(9):1485-1491.
143. Corteville JE, Gray DL, Crane JP. Congenital hydronephrosis: correlation of fetal ultrasonographic findings with infant outcome. Am J Obstet Gynecol. 1991;165(2):384-388.
144. Babcook CJ, Silvera M, Drake C, Levine D. Effect of maternal hydration on mild fetal pyelectasis. J Ultrasound Med. 1998;17(9):539-544.
145. Graif M, Kessler A, Hart S, et al. Renal pyelectasis in pregnancy: correlative evaluation of fetal and maternal collecting systems. Am J Obstet Gynecol. 1992;167(5):1304-1306.
146. Petrikovsky BM, Cuomo MI, Schneider EP, et al. Isolated fetal hydronephrosis: beware the effect of bladder filling. Prenat Diagn. 1995;15(9):827-829.
147. Damen-Elias HA, Stigter RH, De Jong TP, Visser GH. Variability in dilatation of the fetal renal pelvis during a bladder filling cycle. Ultrasound Obstet Gynecol. 2004;24(7):750-755.
148. Fernbach SK, Maizels M, Conway JJ. Ultrasound grading of hydronephrosis: introduction to the system used by the Society for Fetal Urology. Pediatr Radiol. 1993;23(6):478-480.
149. Lee RS, Cendron M, Kinnamon DD, Nguyen HT. Antenatal hydronephrosis as a predictor of postnatal outcome: a meta-analysis. Pediatrics. 2006;118(2):586-593.
150. Sidhu G, Beyene J, Rosenblum ND. Outcome of isolated antenatal hydronephrosis: a systematic review and meta-analysis. Pediatr Nephrol. 2006;21(2):218-224.
151. Ek S, Lidefeldt KJ, Varricio L. Fetal hydronephrosis; prevalence, natural history and postnatal consequences in an unselected population. Acta Obstet Gynecol Scand. 2007;86(12):1463-1466.
152. Wickstrom E, Maizels M, Sabbagha RE, et al. Isolated fetal pyelectasis: assessment of risk for postnatal uropathy and Down syndrome. Ultrasound Obstet Gynecol. 1996;8(4):236-240.
153. Hothi DK, Wade AS, Gilbert R, Winyard PJ. Mild fetal renal pelvis dilatation: much ado about nothing? Clin J Am Soc Nephrol. 2009;4(1):168-177.
154. Coplen DE, Austin PF, Yan Y, et al. The magnitude of fetal renal pelvic dilatation can identify obstructive postnatal hydronephrosis, and direct postnatal evaluation and management. J Urol. 2006;176(2):724-727.
155. Barbosa JA, Chow JS, Benson CB, et al. Postnatal longitudinal evaluation of children diagnosed with prenatal hydronephrosis: insights in natural history and referral pattern. Prenat Diagn. 2012;32(13):1242-1249.
156. Dos Santos J, Parekh RS, Piscione TD, et al. A new grading system for the management of antenatal hydronephrosis. Clin J Am Soc Nephrol. 2015;10(10):1783-1790.
157. Ismaili K, Avni FE, Piepsz A, et al. Current management of infants with fetal renal pelvis dilation: a survey by French-speaking pediatric nephrologists and urologists. Pediatr Nephrol. 2004;19(9):966-971.

158. Epelman M, Daneman A, Donnelly LF, et al. Neonatal imaging evaluation of common prenatally diagnosed genitourinary abnormalities. Semin Ultrasound CT MR. 2014;35(6):528-554.
159. Laing FC, Burke VD, Wing VW, et al. Postpartum evaluation of fetal hydronephrosis: optimal timing for follow-up sonography. Radiology. 1984;152(2):423-424.
160. de Bruyn R, Gordon I. Postnatal investigation of fetal renal disease. Prenat Diagn. 2001;21(11):984-991.
161. Lidefelt KJ, Ek S, Mihocsa L. Is screening for vesicoureteral reflux mandatory in infants with antenatal renal pelvis dilatation? Acta Paediatr. 2006; 95(12):1653-1656.
162. Vivier PH, Dolores M, Taylor M, et al. MR urography in children. Part 1: how we do the F0 technique. Pediatr Radiol. 2010;40(5):732-738.
163. Vivier PH, Dolores M, Taylor M, Dacher JN. MR urography in children. Part 2: how to use ImageJ MR urography processing software. Pediatr Radiol. 2010;40(5):739-746.
164. Quirino IG, Diniz JS, Bouzada MC, et al. Clinical course of 822 children with prenatally detected nephrouropathies. Clin J Am Soc Nephrol. 2012;7(3):444-451.
165. Chevalier RL, Thornhill BA, Forbes MS, Kiley SC. Mechanisms of renal injury and progression of renal disease in congenital obstructive nephropathy. Pediatr Nephrol. 2010;25(4):687-697.
166. Gokce I, Biyikli N, Tugtepe H, et al. Clinical spectrum of antenatally detected urinary tract abnormalities with respect to hydronephrosis at postnatal ultrasound scan. Pediatr Surg Int. 2012;28(5):543-552.
167. Pates JA, Dashe JS. Prenatal diagnosis and management of hydronephrosis. Early Hum Dev. 2006;82(1):3-8.
168. Alberti C. Congenital ureteropelvic junction obstruction: physiopathology, decoupling of tout court pelvic dilatation-obstruction semantic connection, biomarkers to predict renal damage evolution. Eur Rev Med Pharmacol Sci. 2012;16(2):213-219.
169. Karnak I, Woo LL, Shah SN, et al. Results of a practical protocol for management of prenatally detected hydronephrosis due to ureteropelvic junction obstruction. Pediatr Surg Int. 2009;25(1):61-67.
170. Gorincour G, Rypens F, Toiviainen-Salo S, et al. Fetal urinoma: two new cases and a review of the literature. Ultrasound Obstet Gynecol. 2006;28(6): 848-852.
171. Barker AP, Cave MM, Thomas DF, et al. Fetal pelvi-ureteric junction obstruction: predictors of outcome. Br J Urol. 1995;76(5):649-652.
172. Liu HY, Dhillon HK, Yeung CK, et al. Clinical outcome and management of prenatally diagnosed primary megaureters. J Urol. 1994;152(2 Pt 2):614-617.
173. Berrocal T, Lopez-Pereira P, Arjonilla A, Gutierrez J. Anomalies of the distal ureter, bladder, and urethra in children: embryologic, radiologic, and pathologic features. Radiographics. 2002;22(5):1139-1164.
174. McLellan DL, Retik AB, Bauer SB, et al. Rate and predictors of spontaneous resolution of prenatally diagnosed primary nonrefluxing megaureter. J Urol. 2002;168(5):2177-2180.
175. Shukla AR, Cooper J, Patel RP, et al. Prenatally detected primary megaureter: a role for extended followup. J Urol. 2005;173(4):1353-1356.
176. Calisti A, Oriolo L, Perrotta ML, et al. The fate of prenatally diagnosed primary nonrefluxing megaureter: do we have reliable predictors for spontaneous resolution? Urology. 2008;72(2):309-312.
177. Whitten SM, Wilcox DT. Duplex systems. Prenat Diagn. 2001;21(11):952-957.
178. Abuhamad AZ, Horton Jr CE, Horton SH, Evans AT. Renal duplication anomalies in the fetus: clues for prenatal diagnosis. Ultrasound Obstet Gynecol. 1996;7(3):174-177.
179. Vergani P, Ceruti P, Locatelli A, et al. Accuracy of prenatal ultrasonographic diagnosis of duplex renal system. J Ultrasound Med. 1999;18(7):463-467.
180. Whitten SM, McHoney M, Wilcox DT, et al. Accuracy of antenatal fetal ultrasound in the diagnosis of duplex kidneys. Ultrasound Obstet Gynecol. 2003;21(4):342-346.
181. Adiego B, Martinez-Ten P, Perez-Pedregosa J, et al. Antenatally diagnosed renal duplex anomalies: sonographic features and long-term postnatal outcome. J Ultrasound Med. 2011;30(6):809-815.
182. Godinho AB, Nunes C, Janeiro M, et al. Ureterocele: antenatal diagnosis and management. Fetal Diagn Ther. 2013;34(3):188-191.
183. Torres Montebruno X, Martinez JM, Eixarch E, et al. Fetoscopic laser surgery to decompress distal urethral obstruction caused by prolapsed ureterocele. Ultrasound Obstet Gynecol. 2015;46(5):623-626.
184. Upadhyay J, Bolduc S, Braga L, et al. Impact of prenatal diagnosis on the morbidity associated with ureterocele management. J Urol. 2002;167(6): 2560-2565.
185. Anderson NG, Allan RB, Abbott GD. Fluctuating fetal or neonatal renal pelvis: marker of high-grade vesicoureteral reflux. Pediatr Nephrol. 2004;19(7):749-753.
186. Zerin JM, Ritchey ML, Chang AC. Incidental vesicoureteral reflux in neonates with antenatally detected hydronephrosis and other renal abnormalities. Radiology. 1993;187(1):157-160.
187. van Eerde AM, Meutgeert MH, de Jong TP, Giltay JC. Vesico-ureteral reflux in children with prenatally detected hydronephrosis: a systematic review. Ultrasound Obstet Gynecol. 2007;29(4):463-469.
188. Ismaili K, Avni FE, Hall M. Results of systematic voiding cystourethrography in infants with antenatally diagnosed renal pelvis dilation. J Pediatr. 2002;141(1):21-24.
189. Ismaili K, Hall M, Piepsz A, et al. Primary vesicoureteral reflux detected in neonates with a history of fetal renal pelvis dilatation: a prospective clinical and imaging study. J Pediatr. 2006;148(2):222-227.
190. Penido Silva JM, Oliveira EA, Diniz JS, et al. Clinical course of prenatally detected primary vesicoureteral reflux. Pediatr Nephrol. 2006;21(1): 86-91.
191. Sebire NJ, Von Kaisenberg C, Rubio C, et al. Fetal megacystis at 10-14 weeks of gestation. Ultrasound Obstet Gynecol. 1996;8(6):387-390.
192. Yiee J, Wilcox D. Abnormalities of the fetal bladder. Semin Fetal Neonatal Med. 2008;13(3):164-170.
193. Montemarano H, Bulas DI, Rushton HG, Selby D. Bladder distention and pyelectasis in the male fetus: causes, comparisons, and contrasts. J Ultrasound Med. 1998;17(12):743-749.
194. Liao AW, Sebire NJ, Geerts L, et al. Megacystis at 10-14 weeks of gestation: chromosomal defects and outcome according to bladder length. Ultrasound Obstet Gynecol. 2003;21(4):338-341.
195. Carroll SG, Soothill PW, Tizard J, Kyle PM. Vesicocentesis at 10-14 weeks of gestation for treatment of fetal megacystis. Ultrasound Obstet Gynecol. 2001;18(4):366-370.
196. Bernardes LS, Aksnes G, Saada J, et al. Keyhole sign: how specific is it for the diagnosis of posterior urethral valves? Ultrasound Obstet Gynecol. 2009;34(4):419-423.
197. Perks AE, MacNeily AE, Blair GK. Posterior urethral valves. J Pediatr Surg. 2002;37(7):1105-1107.
198. Gonzalez R, De Filippo R, Jednak R, Barthold JS. Urethral atresia: long-term outcome in 6 children who survived the neonatal period. J Urol. 2001;165(6 Pt 2):2241-2244.
199. Papantoniou N, Papoutsis D, Daskalakis G, et al. Prenatal diagnosis of prune-belly syndrome at 13 weeks of gestation: case report and review of literature. J Matern Fetal Neonatal Med. 2010;23(10):1263-1267.
200. Osborne NG, Bonilla-Musoles F, Machado LE, et al. Fetal megacystis: differential diagnosis. J Ultrasound Med. 2011;30(6):833-841.
201. Sepulveda W, Elorza C, Gutierrez J, et al. Congenital megalourethra: outcome after prenatal diagnosis in a series of 4 cases. J Ultrasound Med. 2005;24(9): 1303-1308.
202. Amsalem H, Fitzgerald B, Keating S, et al. Congenital megalourethra: prenatal diagnosis and postnatal/autopsy findings in 10 cases. Ultrasound Obstet Gynecol. 2011;37(6):678-683.
203. Fitzsimons RB, Keohane C, Galvin J. Prune belly syndrome with ultrasound demonstration of reduction of megacystis in utero. Br J Radiol. 1985;58(688):374-376.
204. Garel C, Dreux S, Philippe-Chomette P, et al. Contribution of fetal magnetic resonance imaging and amniotic fluid digestive enzyme assays to the evaluation of gastrointestinal tract abnormalities. Ultrasound Obstet Gynecol. 2006;28(3):282-291.
205. Muller F, Dreux S, Vaast P, et al. Prenatal diagnosis of megacystis-microcolon–intestinal hypoperistalsis syndrome: contribution of amniotic fluid digestive enzyme assay and fetal urinalysis. Prenat Diagn. 2005;25(3):203-209.
206. Anneren G, Meurling S, Olsen L. Megacystis-microcolon–intestinal hypoperistalsis syndrome (MMIHS), an autosomal recessive disorder: clinical

reports and review of the literature. Am J Med Genet. 1991;41(2): 251-254.
207. Tuzovic L, Anyane-Yeboa K, Mills A, et al. Megacystis-microcolon–intestinal hypoperistalsis syndrome: case report and review of prenatal ultrasonographic findings. Fetal Diagn Ther. 2014;36(1):74-80.
208. Tuzovic L, Tang S, Miller RS, et al. New insights into the genetics of fetal megacystis: *ACTG2* mutations, encoding gamma-2 smooth muscle actin in megacystis microcolon intestinal hypoperistalsis syndrome (Berdon syndrome). Fetal Diagn Ther. 2015;38(4):296-306.
209. Wangler MF, Gonzaga-Jauregui C, Gambin T, et al. Heterozygous de novo and inherited mutations in the smooth muscle actin *(ACTG2)* gene underlie megacystis-microcolon–intestinal hypoperistalsis syndrome. PLoS Genet. 2014;10(3):e1004258.
210. Escobar LF, Heiman M, Zimmer D, Careskey H. Urorectal septum malformation sequence: prenatal progression, clinical report, and embryology review. Am J Med Genet A. 2007;143A(22):2722-2726.
211. Chaubal N, Dighe M, Shah M, et al. Calcified meconium: an important sign in the prenatal sonographic diagnosis of cloacal malformation. J Ultrasound Med. 2003;22(7):727-730.
212. Jaramillo D, Lebowitz RL, Hendren WH. The cloacal malformation: radiologic findings and imaging recommendations. Radiology. 1990;177(2): 441-448.
213. Calvo-Garcia MA, Kline-Fath BM, Levitt MA, et al. Fetal MRI clues to diagnose cloacal malformations. Pediatr Radiol. 2011;41(9):1117-1128.
214. Favre R, Kohler M, Gasser B, et al. Early fetal megacystis between 11 and 15 weeks of gestation. Ultrasound Obstet Gynecol. 1999;14(6):402-406.
215. Johnson MP, Corsi P, Bradfield W, et al. Sequential urinalysis improves evaluation of fetal renal function in obstructive uropathy. Am J Obstet Gynecol. 1995;173(1):59-65.
216. Nicolini U, Fisk NM, Rodeck CH, Beacham J. Fetal urine biochemistry: an index of renal maturation and dysfunction. Br J Obstet Gynaecol. 1992;99(1):46-50.
217. Lipitz S, Ryan G, Samuell C, et al. Fetal urine analysis for the assessment of renal function in obstructive uropathy. Am J Obstet Gynecol. 1993;168(1 Pt 1):174-179.
218. Muller F, Dommergues M, Mandelbrot L, et al. Fetal urinary biochemistry predicts postnatal renal function in children with bilateral obstructive uropathies. Obstet Gynecol. 1993;82(5):813-820.
219. Crombleholme TM, Harrison MR, Golbus MS, et al. Fetal intervention in obstructive uropathy: prognostic indicators and efficacy of intervention. Am J Obstet Gynecol. 1990;162(5):1239-1244.
220. Qureshi F, Jacques SM, Seifman B, et al. In utero fetal urine analysis and renal histology correlate with the outcome in fetal obstructive uropathies. Fetal Diagn Ther. 1996;11(5):306-312.
221. Muller F, Dommergues M, Bussieres L, et al. Development of human renal function: reference intervals for 10 biochemical markers in fetal urine. Clin Chem. 1996;42(11):1855-1860.
222. Nicolaides KH, Cheng HH, Snijders RJ, Moniz CF. Fetal urine biochemistry in the assessment of obstructive uropathy. Am J Obstet Gynecol. 1992;166(3):932-937.
223. Berry SM, Lecolier B, Smith RS, et al. Predictive value of fetal serum beta 2-microglobulin for neonatal renal function. Lancet. 1995;345(8960): 1277-1278.
224. Nicolini U, Spelzini F. Invasive assessment of fetal renal abnormalities: urinalysis, fetal blood sampling and biopsy. Prenat Diagn. 2001;21(11): 964-969.
225. Morris RK, Quinlan-Jones E, Kilby MD, Khan KS. Systematic review of accuracy of fetal urine analysis to predict poor postnatal renal function in cases of congenital urinary tract obstruction. Prenat Diagn. 2007;27(10): 900-911.
226. Abdennadher W, Chalouhi G, Dreux S, et al. Fetal urine biochemistry at 13-23 weeks of gestation in lower urinary tract obstruction: criteria for in-utero treatment. Ultrasound Obstet Gynecol. 2015;46(3):306-311.
227. Holmes N, Harrison MR, Baskin LS. Fetal surgery for posterior urethral valves: long-term postnatal outcomes. Pediatrics. 2001;108(1):E7.
228. Klein J, Lacroix C, Caubet C, et al. Fetal urinary peptides to predict postnatal outcome of renal disease in fetuses with posterior urethral valves (PUV). Sci Transl Med. 2013;5(198):198ra06.
229. Makino Y, Kobayashi H, Kyono K, et al. Clinical results of fetal obstructive uropathy treated by vesicoamniotic shunting. Urology. 2000;55(1): 118-122.
230. McLorie G, Farhat W, Khoury A, et al. Outcome analysis of vesicoamniotic shunting in a comprehensive population. J Urol. 2001;166(3):1036-1040.
231. Freedman AL, Johnson MP, Smith CA, et al. Long-term outcome in children after antenatal intervention for obstructive uropathies. Lancet. 1999; 354(9176):374-377.
232. Morris RK, Ruano R, Kilby MD. Effectiveness of fetal cystoscopy as a diagnostic and therapeutic intervention for lower urinary tract obstruction: a systematic review. Ultrasound Obstet Gynecol. 2011;37(6):629-637.
233. Ruano R, Sananes N, Sangi-Haghpeykar H, et al. Fetal intervention for severe lower urinary tract obstruction: a multicenter case-control study comparing fetal cystoscopy with vesicoamniotic shunting. Ultrasound Obstet Gynecol. 2015;45(4):452-458.
234. Biard JM, Johnson MP, Carr MC, et al. Long-term outcomes in children treated by prenatal vesicoamniotic shunting for lower urinary tract obstruction. Obstet Gynecol. 2005;106(3):503-508.
235. Müller Brochut AC, Thomann D, Kluwe W, et al. Fetal megacystis: experience of a single tertiary center in Switzerland over 20 years. Fetal Diagn Ther. 2014;36(3):215-222.
236. Morris RK, Malin GL, Khan KS, Kilby MD. Systematic review of the effectiveness of antenatal intervention for the treatment of congenital lower urinary tract obstruction. BJOG. 2010;117(4):382-390.
237. Morris RK, Malin GL, Quinlan-Jones E, et al. Percutaneous vesicoamniotic shunting versus conservative management for fetal lower urinary tract obstruction (PLUTO): a randomised trial. Lancet. 2013;382(9903): 1496-1506.
238. Gearhart JP, Ben-Chaim J, Jeffs RD, Sanders RC. Criteria for the prenatal diagnosis of classic bladder exstrophy. Obstet Gynecol. 1995;85(6): 961-964.
239. Goldstein I, Shalev E, Nisman D. The dilemma of prenatal diagnosis of bladder exstrophy: a case report and a review of the literature. Ultrasound Obstet Gynecol. 2001;17(4):357-359.
240. Prefumo F, Izzi C. Fetal abdominal wall defects. Best Pract Res Clin Obstet Gynaecol. 2014;28(3):391-402.
241. Goyal A, Fishwick J, Hurrell R, et al. Antenatal diagnosis of bladder/cloacal exstrophy: challenges and possible solutions. J Pediatr Urol. 2012;8(2): 140-144.
242. Ben-Neriah Z, Withers S, Thomas M, et al. OEIS complex: prenatal ultrasound and autopsy findings. Ultrasound Obstet Gynecol. 2007;29(2):170-177.
243. Tiblad E, Wilson RD, Carr M, et al. OEIS sequence—a rare congenital anomaly with prenatal evaluation and postnatal outcome in six cases. Prenat Diagn. 2008;28(2):141-147.
244. Odeh M, Granin V, Kais M, et al. Sonographic fetal sex determination. Obstet Gynecol Surv. 2009;64(1):50-57.
245. Glanc P, Umranikar S, Koff D, et al. Fetal sex assignment by sonographic evaluation of the pelvic organs in the second and third trimesters of pregnancy. J Ultrasound Med. 2007;26(5):563-569.
246. Efrat Z, Perri T, Ramati E, et al. Fetal gender assignment by first-trimester ultrasound. Ultrasound Obstet Gynecol. 2006;27(6):619-621.
247. Lev-Toaff AS, Ozhan S, Pretorius D, et al. Three-dimensional multiplanar ultrasound for fetal gender assignment: value of the mid-sagittal plane. Ultrasound Obstet Gynecol. 2000;16(4):345-350.
248. Youssef A, Arcangeli T, Radico D, et al. Accuracy of fetal gender determination in the first trimester using three-dimensional ultrasound. Ultrasound Obstet Gynecol. 2011;37(5):557-561.
249. Achiron R, Pinhas-Hamiel O, Zalel Y, et al. Development of fetal male gender: prenatal sonographic measurement of the scrotum and evaluation of testicular descent. Ultrasound Obstet Gynecol. 1998;11(4):242-245.
250. Pretorius DH, Halsted MJ, Abels W, et al. Hydroceles identified prenatally: common physiologic phenomenon? J Ultrasound Med. 1998;17(1):49-52.
251. Khatib N, Goldstein I, Vitner D, et al. Prenatal diagnosis of scrotal-inguinal hernia: two case reports and review of the English literature. Eur J Obstet Gynecol Reprod Biol. 2013;171(1):9-11.
252. Shapiro E. The sonographic appearance of normal and abnormal fetal genitalia. J Urol. 1999;162(2):530-533.

253. Cheikhelard A, Luton D, Philippe-Chomette P, et al. How accurate is the prenatal diagnosis of abnormal genitalia? J Urol. 2000;164(3 Pt 2): 984-987.
254. Meizner I. The 'tulip sign': a sonographic clue for in-utero diagnosis of severe hypospadias. Ultrasound Obstet Gynecol. 2002;19(3):317.
255. Shinawi M, Szabo S, Popek E, et al. Recognition of Smith-Lemli-Opitz syndrome (RSH) in the fetus: utility of ultrasonography and biochemical analysis in pregnancies with low maternal serum estriol. Am J Med Genet A. 2005;138(1):56-60.
256. Kratz LE, Kelley RI. Prenatal diagnosis of the RSH/Smith-Lemli-Opitz syndrome. Am J Med Genet. 1999;82(5):376-381.
257. Cross JL, Iben J, Simpson CL, et al. Determination of the allelic frequency in Smith-Lemli-Opitz syndrome by analysis of massively parallel sequencing data sets. Clin Genet. 2015;87(6):570-575.
258. Shapiro E, Santiago JV, Crane JP. Prenatal fetal adrenal suppression following in utero diagnosis of congenital adrenal hyperplasia. J Urol. 1989;142(2 Pt 2):663-666.
259. New MI, Tong YK, Yuen T, et al. Noninvasive prenatal diagnosis of congenital adrenal hyperplasia using cell-free fetal DNA in maternal plasma. J Clin Endocrinol Metab. 2014;99(6):E1022-E1030.
260. Saada J, Grebille AG, Aubry MC, et al. Sonography in prenatal diagnosis of congenital adrenal hyperplasia. Prenat Diagn. 2004;24(8):627-630.
261. Pajkrt E, Petersen OB, Chitty LS. Fetal genital anomalies: an aid to diagnosis. Prenat Diagn. 2008;28(5):389-398.
262. Merce Fernandez-Balsells M, Muthusamy K, Smushkin G, et al. Prenatal dexamethasone use for the prevention of virilization in pregnancies at risk for classical congenital adrenal hyperplasia because of 21-hydroxylase (CYP21A2) deficiency: a systematic review and meta-analyses. Clin Endocrinol (Oxf). 2010;73(4):436-444.
263. Miller WL. Fetal endocrine therapy for congenital adrenal hyperplasia should not be done. Best Pract Res Clin Endocrinol Metab. 2015;29(3):469-483.
264. Miller WL, Witchel SF. Prenatal treatment of congenital adrenal hyperplasia: risks outweigh benefits. Am J Obstet Gynecol. 2013;208(5):354-359.
265. Mazza V, Di Monte I, Ceccarelli PL, et al. Prenatal diagnosis of female pseudohermaphroditism associated with bilateral luteoma of pregnancy: case report. Hum Reprod. 2002;17(3):821-824.
266. Manzella A, Filho PB. Hydrocolpos, uterus didelphys and septate vagina in association with ascites: antenatal sonographic detection. J Ultrasound Med. 1998;17(7):465-468.
267. Dhombres F, Jouannic JM, Brodaty G, et al. Contribution of prenatal imaging to the anatomical assessment of fetal hydrocolpos. Ultrasound Obstet Gynecol. 2007;30(1):101-104.
268. Picone O, Laperelle J, Sonigo P, et al. Fetal magnetic resonance imaging in the antenatal diagnosis and management of hydrocolpos. Ultrasound Obstet Gynecol. 2007;30(1):105-109.
269. Garel L, Filiatrault D, Brandt M, et al. Antenatal diagnosis of ovarian cysts: natural history and therapeutic implications. Pediatr Radiol. 1991;21(3): 182-184.
270. Quarello E, Gorincour G, Merrot T, et al. The 'daughter cyst sign': a sonographic clue to the diagnosis of fetal ovarian cyst. Ultrasound Obstet Gynecol. 2003;22(4):433-434.
271. Nussbaum AR, Sanders RC, Hartman DS, et al. Neonatal ovarian cysts: sonographic-pathologic correlation. Radiology. 1988;168(3):817-821.
272. Galinier P, Carfagna L, Juricic M, et al. Fetal ovarian cysts management and ovarian prognosis: a report of 82 cases. J Pediatr Surg. 2008;43(11): 2004-2009.
273. Cesca E, Midrio P, Boscolo-Berto R, et al. Conservative treatment for complex neonatal ovarian cysts: a long-term follow-up analysis. J Pediatr Surg. 2013; 48(3):510-515.
274. Trinh TW, Kennedy AM. Fetal ovarian cysts: review of imaging spectrum, differential diagnosis, management, and outcome. Radiographics. 2015;35(2): 621-635.
275. Giorlandino C, Bilancioni E, Bagolan P, et al. Antenatal ultrasonographic diagnosis and management of fetal ovarian cysts. Int J Gynaecol Obstet. 1994;44(1):27-31.
276. Bagolan P, Giorlandino C, Nahom A, et al. The management of fetal ovarian cysts. J Pediatr Surg. 2002;37(1):25-30.
277. Noia G, Riccardi M, Visconti D, et al. Invasive fetal therapies: approach and results in treating fetal ovarian cysts. J Matern Fetal Neonatal Med. 2012;25(3):299-303.
278. Heling KS, Chaoui R, Kirchmair F, et al. Fetal ovarian cysts: prenatal diagnosis, management and postnatal outcome. Ultrasound Obstet Gynecol. 2002;20(1):47-50.
279. Nakamura M, Ishii K, Murata M, et al. Postnatal outcome in cases of prenatally diagnosed fetal ovarian cysts under conservative prenatal management. Fetal Diagn Ther. 2014;37(2):129-134.
280. Papic JC, Billmire DF, Rescorla FJ, et al. Management of neonatal ovarian cysts and its effect on ovarian preservation. J Pediatr Surg. 2014;49(6): 990-993.
281. Baskin LS. Prenatal hydronephrosis. In: Baskin LS, Kogan B, Duckett J, editors. Handbook of pediatric urology. Philadelphia: Lippincott-Raven; 1997. p. 15.

CHAPTER 40

The Fetal Musculoskeletal System

Phyllis Glanc, David Chitayat, and Sheila Unger

SUMMARY OF KEY POINTS

- Two-dimensional ultrasound is the primary imaging modality for the majority of musculoskeletal disorders.
- When a fetal musculoskeletal dysplasia is suspected on ultrasound, referral to a center with expertise may be helpful.
- A main role of ultrasound is to determine if the condition is likely lethal; it is important to use multiple parameters to make this determination.
- After delivery or pregnancy termination, a diagnosis should be established by a combination of clinical examination, imaging, and molecular studies. Cell culture and DNA banking are essential for molecular investigations. The results should be reviewed with the parents to help in their future reproductive plans.

CHAPTER OUTLINE

NORMAL FETAL SKELETON
Development
Extremity Measurements
SONOGRAPHIC EVALUATION OF FETUS WITH SKELETAL DYSPLASIA
Positive Family History
Abnormal Bone Length or Appearance
Additional Diagnostic Techniques
Three-Dimensional Ultrasound
Radiography
Three-Dimensional Computed Tomography
Magnetic Resonance Imaging
Molecular Diagnosis
LETHAL SKELETAL DYSPLASIAS
Thanatophoric Dysplasia
Achondrogenesis
Osteogenesis Imperfecta
Hypophosphatasia
Campomelic Dysplasia
Short-Rib Polydactyly Syndromes
Other Dysplasias
NONLETHAL OR VARIABLE-PROGNOSIS SKELETAL DYSPLASIAS
Heterozygous Achondroplasia
Diastrophic Dysplasia
Asphyxiating Thoracic Dysplasia
Ellis–van Creveld Syndrome
Chondrodysplasia Punctata
Dyssegmental Dysplasia
Osteogenesis Imperfecta Types I, III, IV—Nonlethal Types
LIMB REDUCTION DEFECTS AND ASSOCIATED CONDITIONS
Proximal Focal Femoral Deficiency
Radial Ray Defects
Amniotic Band Sequence
Caudal Regression Syndrome and Sirenomelia
Arthrogryposis Multiplex Congenita
HAND AND FOOT MALFORMATIONS
SKELETAL FINDINGS ASSOCIATED WITH ANEUPLOIDY
SUMMARY
Acknowledgments

Congenital bone disorders of the skeleton comprise a large and heterogeneous group of disorders primarily affecting the growth and development of the musculoskeletal system. The prevalence of skeletal dysplasias, also called "osteochondrodysplasias," diagnosed prenatally or during the neonatal period, excluding limb amputations, is 2.4 to 4.5 per 10,000 births.[1]

There are three major categories: skeletal dysplasias, dysostoses, and disruptions (Table 40.1). The number of recognized genetic disorders with a substantial skeletal component is increasing, and the distinction among dysplasias, metabolic bone disorders, dysostoses, and malformation syndromes is constantly evolving. The Nosology and Classification of Genetic Skeletal Disorders 2015 revision recognizes 436 genetic bone disorders with a substantial skeletal component[3-6] (Table 40.2).

Despite increased knowledge about the genetic origins of many of these conditions and the improved ability to diagnose and categorize these disorders correctly, the clinical and imaging features remain a fundamental tool for diagnosing and directing the molecular investigation.[3,7] Although many fetal skeletal dysplasias can be accurately identified by prenatal ultrasound, this remains a challenging task because of the low incidence, phenotypic variability, and wide range of appearances.[8] The majority of cases have no family history of a similar condition. Nonetheless, the majority of **lethal skeletal dysplasias,** and in particular the most common—**thanatophoric dysplasia, achondrogenesis,** and **osteogenesis imperfecta** type II—can be diagnosed solely on the basis of prenatal ultrasound.[9] Tretter et al.[10] determined that 26 of 27 lethal skeletal dysplasias were

TABLE 40.1 Major Categories of Skeletal Dysplasias[2]

Skeletal dysplasias	Developmental disorders of chondro-osseous tissue caused by single-gene disorders with prenatal and postnatal manifestations
Dysostoses	Single-gene disorders resulting in malformations of individual bones caused by transient abnormalities of signaling factors
Disruptions	Morphologic defects of an organ or of larger region resulting from extrinsic breakdown or interference with an originally normal developmental process

Modified from Spranger JW, Brill PW, Poznanski AK. Bone dysplasias: an atlas of genetic disorders of skeletal development. 2nd ed. New York: Oxford University Press; 2002.[2]

TABLE 40.2 Birth Prevalence of Skeletal Dysplasias

Skeletal Dysplasia	Prevalence per 100,000 Births
LETHAL DYSPLASIAS	
Thanatophoric dysplasia	2.4 to 6.9
Achondrogenesis	0.9 to 2.3
Osteogenesis imperfecta type IIA	1.8
Hypophosphatasia congenita	1.0
VARIABLE-PROGNOSIS DYSPLASIAS	
Rhizomelic chondrodysplasia punctata	0.5 to 0.9
Campomelic dysplasia	1.0 to 1.5
Asphyxiating thoracic dystrophy	0.8 to 1.4
Ellis–van Creveld syndrome	0.7
Osteogenesis imperfecta (other types)	1.8
NONLETHAL DYSPLASIAS	
Heterozygous achondroplasia	3.3 to 3.8
OVERALL	24.4 to 75.0

identified correctly by prenatal ultrasound; however, only 13 of 27 (48%) received an accurate specific antenatal diagnosis.[10] Eight of 14 (57%) underwent a substantial change in genetic counseling when cytogenetic (including microarray), molecular, pathologic, and imaging findings were combined. Thus although the ultrasound diagnosis of a lethal skeletal dysplasia is highly accurate (85%-95%), a correct specific diagnosis is obtained in only 40% to 55% of cases.[8-10] The addition of correlative radiographs, cytogenetic analysis (including microarray and whole genome sequencing techniques), and pathologic examination can provide a correct specific diagnosis in up 86%.[11]

Nonetheless, an accurate prenatal determination of the lethality of a given skeletal dysplasia is crucial in helping couples with decision making. Typically, a combination of ultrasound, radiologic, and genetic investigation is required to classify a specific congenital musculoskeletal disorder.[11] A prenatal diagnosis of a musculoskeletal anomaly will provide an opportunity for genetic counseling, resulting in pregnancy termination or tertiary-level care depending on the parental decision. A multidisciplinary approach involving the medical imaging team, obstetrician, medical geneticist, and perinatologist is important in optimizing the accuracy of prognosis and determining recurrence risk.[11] If local expertise is unavailable and/or the diagnosis is unknown, consultation with experts in the field should be considered. Detailed and up-to-date information regarding the molecular tests available for the diagnosis of skeletal dysplasias is available at various organizations.

Resources for Molecular Tests for Diagnosis of Skeletal Dysplasias

European Skeletal Dysplasia Network (http://www.esdn.org)
Gene test (https://www.genetest.org)
International Skeletal Dysplasia Society (www.isds.ch)

This information is crucial to the family and to medical personnel involved in planning the management of both current and future pregnancies. This chapter uses a "key features" approach to the sonographic diagnosis of the common skeletal dysplasias to aid in the classification and differential diagnosis.

NORMAL FETAL SKELETON

Development

The high level of intrinsic contrast of the fetal extremities places them among the earliest structures that can be evaluated by ultrasound. By the end of the embryonic period, the differentiation of bones, joints, and musculature is similar to that of an adult and is associated with increased fetal movements.[12,13] Transvaginal ultrasound can demonstrate the limb buds by 7 weeks' gestation, and the foot and hand plates are visible by 8 weeks.[14] Osteogenesis begins in the clavicle and mandible by 8 weeks as well. By 11 or 12 weeks, the **primary ossification centers** of the long bones (e.g., scapula, ileum), as well as the limb articulations and phalanges, can be identified. The ischium, metacarpals, and metatarsals ossify during the fourth month of gestation. The pubis, calcaneus, and talus ossify during the fifth and sixth months. Ossification of the other tarsal and carpal bones occurs postnatally.[15] The direction of growth in the long bones is from proximal to distal, and the lower extremities lag slightly behind the upper extremities.[13]

Of the **secondary ossification centers** in the long bones, only the distal femoral epiphysis, the proximal tibial epiphysis, and occasionally the proximal humeral epiphysis ossify prenatally (Fig. 40.1). The unossified epiphysis appears hypoechoic, with a variably, mildly echogenic center. Ossification begins centrally. The distal femoral epiphysis can ossify as early as 29 weeks' menstrual age and as late as 34 weeks. When it measures greater than 7 mm, the menstrual age is generally later than 37 weeks.[16,17] The proximal tibial epiphysis begins to ossify by 35 menstrual

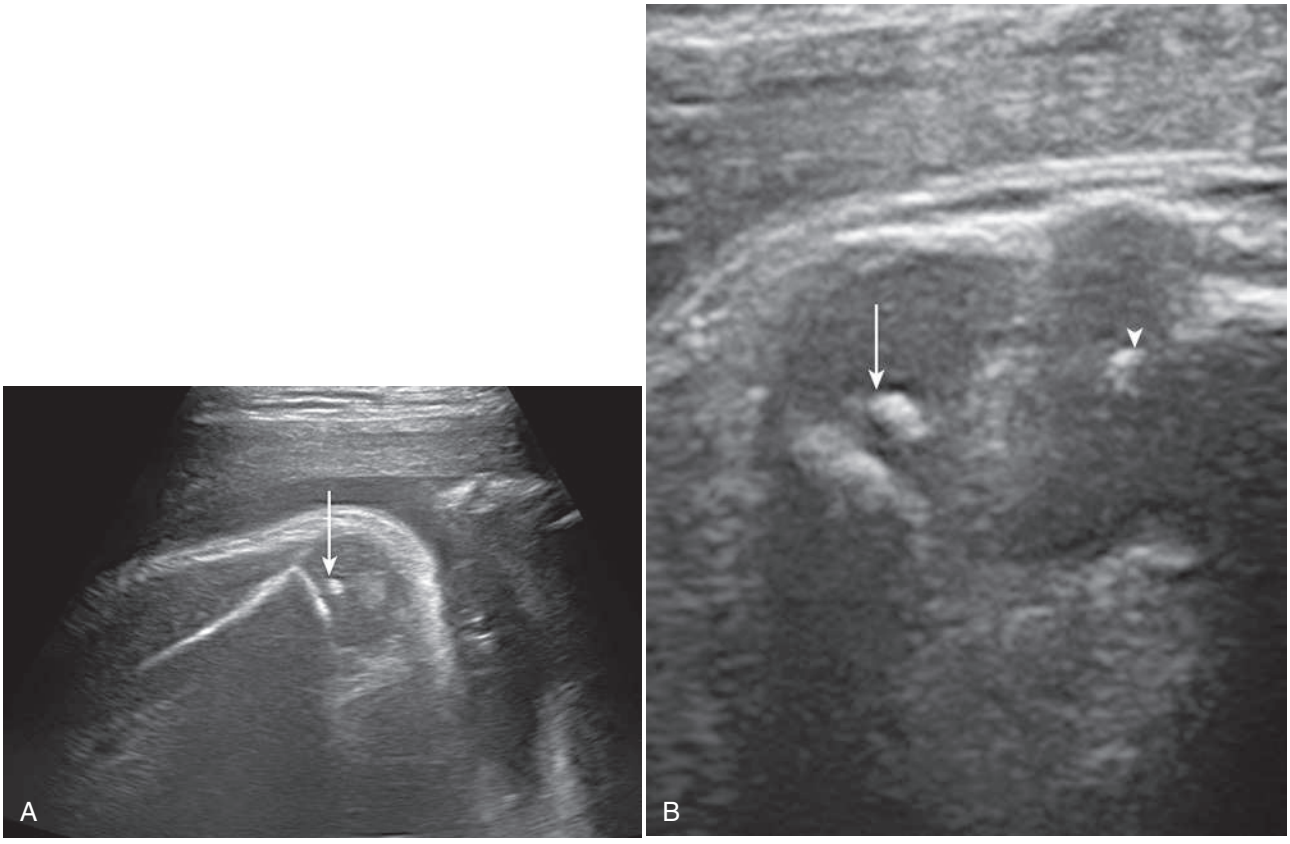

FIG. 40.1 Secondary Ossification Centers in Fetus at 38 Weeks' Gestational Age. (A) View of the femur and distal femoral ossification center *(arrow).* **(B)** View of distal femur and proximal tibia with distal femoral ossification center *(arrow)* and proximal tibial ossification center *(arrowhead).*

weeks.[17] In uncomplicated pregnancies the combination of a distal femoral epiphysis of 3 mm or greater and the presence of a proximal tibial epiphysis is considered a reliable marker of pulmonary maturity.[18] **Intrauterine growth restriction** (IUGR) is associated with a delay in ossification of the distal femoral epiphysis and proximal tibial epiphysis. The earliest secondary epiphysis to ossify is the **calcaneus,** at approximately 20 weeks' gestation, thus marking the earliest point that assessment of delayed ossification of the secondary epiphyseal centers can be attempted.

The fascia within the muscle is highly echogenic compared with the relatively hypoechoic cartilage. The fetal musculature is slightly more echogenic than the relatively hypoechoic cartilage. The fetal joint spaces, in particular the knee, appear echogenic because of the combination of synovium, fat, and microvasculature.[13] The normal development and ultimate function of the fetal musculoskeletal system depend on **fetal movements,** which start by the second half of the first trimester. In the absence of normal fetal motion, the bones and muscles will be underdeveloped, the chest will be narrow, and joint contractures and postural deformities can occur.

Extremity Measurements

It is a standard practice to assess **femur length** (FL) as part of the evaluation of fetal size and morphology. Although measurement of all the long bones is not required in a routine obstetric ultrasound, an overall evaluation of the fetal skeleton should be performed to ensure the presence and bilateral symmetry of the tubular bones. Available charts provide guidance for correlating the length of the extremities with the gestational age (Table 40.3).

The longest femur measurement, excluding both proximal and distal epiphyses, is usually chosen. The inclusion of the **distal femur point,** or the specular reflection of the lateral aspect of the distal femoral epiphysis cartilage, is the most common reason for overestimating FL[19] (Fig. 40.2A). An oblique FL measurement will result in underestimate of length. The lateral border of the femur in the near field of the transducer appears straight, whereas the medial border of the femur in the far field has a curved appearance[20] (Fig. 40.2B).

In the **lower extremity** the lateral bone is the fibula and the medial bone is the tibia. The tibia and fibula end at the same level distally. In the **upper extremity,** pronation may cause the radius and ulna to cross, so it can be difficult to distinguish the ulna from the radius using lateral and medial positions. The ulna is distinguished from the radius by its longer proximal extent and its relationship to the fifth digit distally. The radius and ulna end at the same level distally. Demonstration of this relationship will effectively exclude the majority of radial ray defects.

The **clavicles** grow in a linear fashion, approximately 1 mm per week, and the gestational age in weeks is approximately the length of the clavicle in millimeters from 14 weeks to term. By 40 weeks' gestation, the clavicles measure approximately 40 mm.[21]

TABLE 40.3 Normal Extremity Long-Bone Lengths and Biparietal Diameters at Different Menstrual Ages[a]

Menstrual Age (Weeks)	Biparietal Diameter	BONE					
		Femur	Tibia	Fibula	Humerus	Radius	Ulna
13	2.3 (0.3)	1.1 (0.2)	0.9 (0.2)	0.8 (0.2)	1.0 (0.2)	0.6 (0.2)	0.8 (0.3)
14	2.7 (0.3)	1.3 (0.2)	1.0 (0.2)	0.9 (0.3)	1.2 (0.2)	0.8 (0.2)	1.0 (0.2)
15	3.0 (0.1)	1.5 (0.2)	1.3 (0.2)	1.2 (0.2)	1.4 (0.2)	1.1 (0.1)	1.2 (0.1)
16	3.3 (0.2)	1.9 (0.3)	1.6 (0.3)	1.5 (0.3)	1.7 (0.2)	1.4 (0.3)	1.6 (0.3)
17	3.7 (0.3)	2.2 (0.3)	1.8 (0.3)	1.7 (0.2)	2.0 (0.4)	1.5 (0.3)	1.7 (0.3)
18	4.2 (0.5)	2.5 (0.3)	2.2 (0.3)	2.1 (0.3)	2.3 (0.3)	1.9 (0.2)	2.2 (0.3)
19	4.4 (0.4)	2.8 (0.3)	2.5 (0.3)	2.3 (0.3)	2.6 (0.3)	2.1 (0.3)	2.4 (0.3)
20	4.7 (0.4)	3.1 (0.3)	2.7 (0.2)	2.6 (0.2)	2.9 (0.3)	2.4 (0.2)	2.7 (0.4)
21	5.0 (0.5)	3.5 (0.4)	3.0 (0.4)	2.9 (0.4)	3.2 (0.4)	2.7 (0.4)	3.0 (0.4)
22	5.5 (0.5)	3.6 (0.3)	3.2 (0.3)	3.1 (0.3)	3.3 (0.3)	2.8 (0.5)	3.1 (0.4)
23	5.8 (0.5)	4.0 (0.4)	3.6 (0.2)	3.4 (0.2)	3.7 (0.3)	3.1 (0.4)	3.5 (0.2)
24	6.1 (0.5)	4.2 (0.3)	3.7 (0.3)	3.6 (0.3)	3.8 (0.4)	3.3 (0.4)	3.6 (0.4)
25	6.4 (0.5)	4.6 (0.3)	4.0 (0.3)	3.9 (0.4)	4.2 (0.4)	3.5 (0.3)	3.9 (0.4)
26	6.8 (0.5)	4.8 (0.4)	4.2 (0.3)	4.0 (0.3)	4.3 (0.3)	3.6 (0.4)	4.0 (0.3)
27	7.0 (0.3)	4.9 (0.3)	4.4 (0.3)	4.2 (0.3)	4.5 (0.2)	3.7 (0.3)	4.1 (0.2)
28	7.3 (0.5)	5.3 (0.5)	4.5 (0.4)	4.4 (0.3)	4.7 (0.4)	3.9 (0.4)	4.4 (0.5)
29	7.6 (0.5)	5.3 (0.5)	4.6 (0.3)	4.5 (0.3)	4.8 (0.4)	4.0 (0.5)	4.5 (0.4)
30	7.7 (0.6)	5.6 (0.3)	4.8 (0.5)	4.7 (0.3)	5.0 (0.5)	4.1 (0.6)	4.7 (0.3)
31	8.2 (0.7)	6.0 (0.6)	5.1 (0.3)	4.9 (0.5)	5.3 (0.4)	4.2 (0.3)	4.9 (0.4)
32	8.5 (0.6)	6.1 (0.6)	5.2 (0.4)	5.1 (0.4)	5.4 (0.4)	4.4 (0.6)	5.0 (0.6)
33	8.6 (0.4)	6.4 (0.5)	5.4 (0.5)	5.3 (0.3)	5.6 (0.5)	4.5 (0.5)	5.2 (0.3)
34	8.9 (0.5)	6.6 (0.6)	5.7 (0.5)	5.5 (0.4)	5.8 (0.5)	4.7 (0.5)	5.4 (0.5)
35	8.9 (0.7)	6.7 (0.6)	5.8 (0.4)	5.6 (0.4)	5.9 (0.6)	4.8 (0.6)	5.4 (0.4)
36	9.1 (0.7)	7.0 (0.7)	6.0 (0.6)	5.6 (0.5)	6.0 (0.6)	4.9 (0.5)	5.5 (0.3)
37	9.3 (0.9)	7.2 (0.4)	6.1 (0.4)	6.0 (0.4)	6.1 (0.4)	5.1 (0.3)	5.6 (0.4)
38	9.5 (0.6)	7.4 (0.6)	6.2 (0.3)	6.0 (0.4)	6.4 (0.3)	5.1 (0.5)	5.8 (0.6)
39	9.5 (0.6)	7.6 (0.8)	6.4 (0.7)	6.1 (0.6)	6.5 (0.6)	5.3 (0.5)	6.0 (0.6)
40	9.9 (0.8)	7.7 (0.4)	6.5 (0.3)	6.2 (0.1)	6.6 (0.4)	5.3 (0.3)	6.0 (0.5)
41	9.7 (0.6)	7.7 (0.4)	6.6 (0.4)	6.3 (0.5)	6.6 (0.4)	5.6 (0.4)	6.3 (0.5)
42	10.0 (0.5)	7.8 (0.7)	6.8 (0.5)	6.7 (0.7)	6.8 (0.7)	5.7 (0.5)	6.5 (0.5)

[a]Mean values (cm); value of 2 SD in parentheses.
With permission from Merz E, Kim-Kern MS, Pehl S. Ultrasonic mensuration of fetal limb bones in the second and third trimesters. J Clin Ultrasound. 1987;5(3):175-183.[12]

Foot length is measured from the skin edge overlying the calcaneus to the distal end of the longest toe (the first or second toe) on either the plantar or the sagittal view[22-24] (Fig. 40.3). The ossified FL is almost equivalent to the foot length, resulting in a normal **femur-to-foot length ratio** of approximately 1.0. This ratio remains relatively constant from the 14th week of gestation onward. If the fetus is constitutionally small or there is symmetrical IUGR, the ratio is generally 0.9 or greater. In most skeletal **dysplasias** characterized by short limbs, the ratio is generally less than 0.9 because of the relative sparing of the hands and feet. The greater the deviation is from the lower limits of the norm, the greater is the disproportion and usually also the severity.

SONOGRAPHIC EVALUATION OF FETUS WITH SKELETAL DYSPLASIA

A prenatal evaluation of a skeletal dysplasia is indicated if there is a positive family history or an abnormal length or appearance of the bones at ultrasound.

Assessment of Skeletal Dysplasias: Key Features

Family history
Serial measurements
Degree of limb shortening
Pattern of limb shortening
Presence of bowing, fractures, and angulations
Spine
Thoracic measurements
Hands and feet
Calvarium and facial features

Positive Family History

A positive family history of a sibling or parents affected by a skeletal dysplasia or consanguineous parents should prompt an intensive ultrasound investigation with a focus on targeted

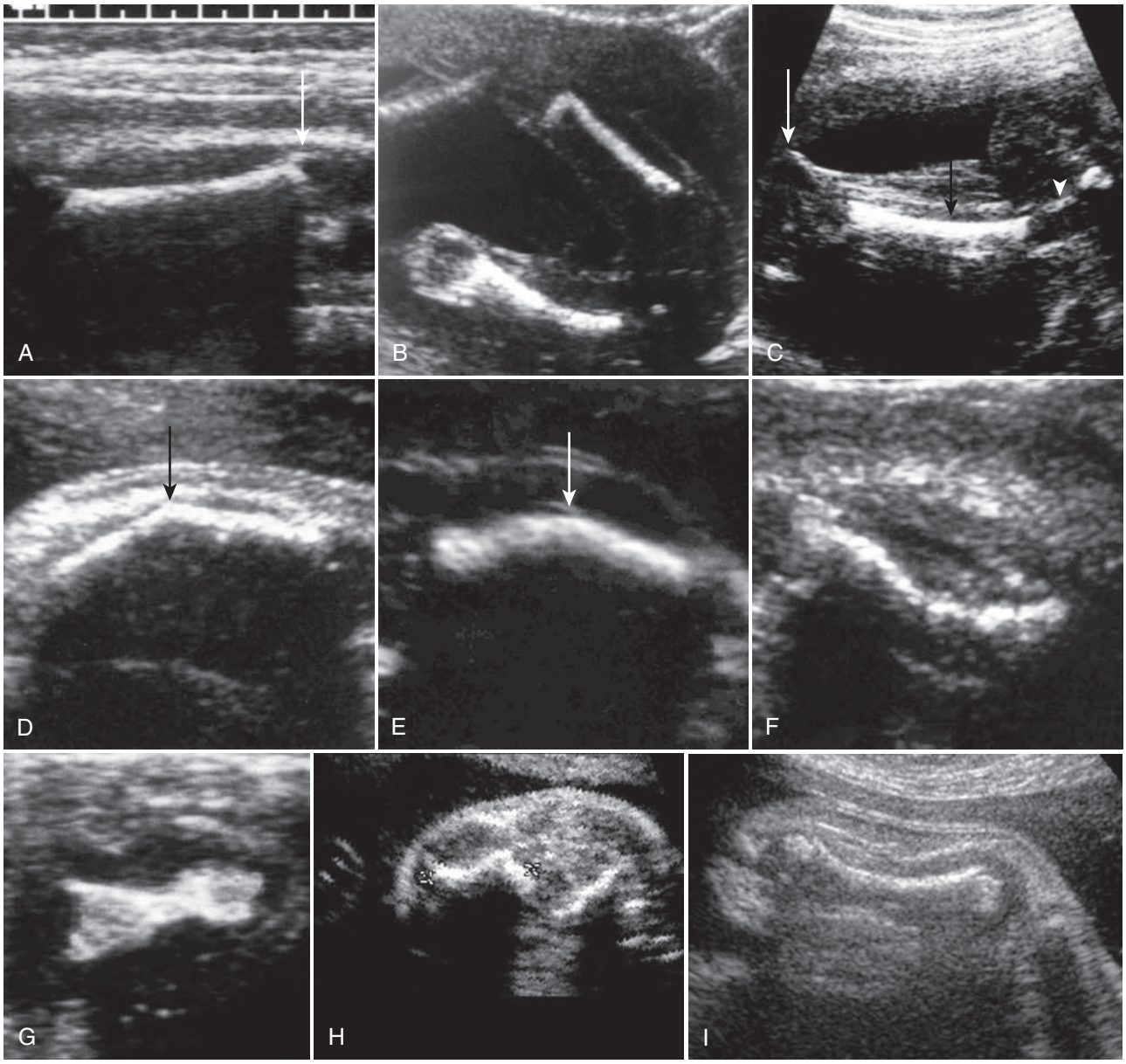

FIG. 40.2 Normal Femur and Spectrum of Abnormal Appearances. (A) Normal femur: measure the longest length, excluding the proximal and distal epiphyses and the specular reflection of the lateral aspect of the distal femoral epiphysis *(arrow).* **(B)** Normal femur in the near field, with straight lateral border versus the curved medial border in the far field of the transducer. **(C)** Isolated **hypoplastic left femur** *(arrowhead),* with normal tibia *(black arrow)* and foot *(white arrow).* **(D) Osteogenesis imperfecta type I.** Isolated femoral fracture with acute angulation *(arrow).* **(E) Campomelic dysplasia.** Mild shortening and a gently curved ventral femoral bowing *(arrow).* **(F) Osteogenesis imperfecta type IIA.** Bowed femur with multiple discontinuities representing fractures. **(G) Hypophosphatasia.** Severe micromelia (relatively broad metaphysis, short diaphysis). **(H) Thanatophoric dysplasia.** Curved, **"telephone receiver"** femur. **(I) Chondrodysplasia punctata.** Third-trimester appearance of a **stippled epiphysis.** (**C** courtesy of Ants Toi, MD, University of Toronto; **D** and **E** courtesy of Shia Salem, MD, University of Toronto.)

abnormalities and serial measurements. A history of consanguinity is important because many of the skeletal dysplasias have an autosomal recessive mode of inheritance. **Heterozygous achondroplasia,** the most common nonlethal skeletal dysplasia, has an autosomal dominant pattern of inheritance. Family history may not be helpful because 80% of cases are caused by a new mutation.

Abnormal Bone Length or Appearance

The fetal femur is often the only long bone routinely measured at the second-trimester ultrasound evaluation. An abnormal FL is traditionally defined as below 2 standard deviations (SD) for gestational age.[25,26] Using this cutoff, 2.5% of all fetuses would be classified as having short limbs. This exceeds the expected frequency of skeletal dysplasias, and thus additional investigations are needed to separate fetuses with a skeletal dysplasia from those with no underlying pathology and those with other diagnoses associated with growth restriction.

When one or all of the long bones measure less than 2 SD for gestational age, a follow-up ultrasound should be done in 3 or 4 weeks to evaluate the interval growth. If the interval femur growth is normal, there is a high likelihood that the fetus does

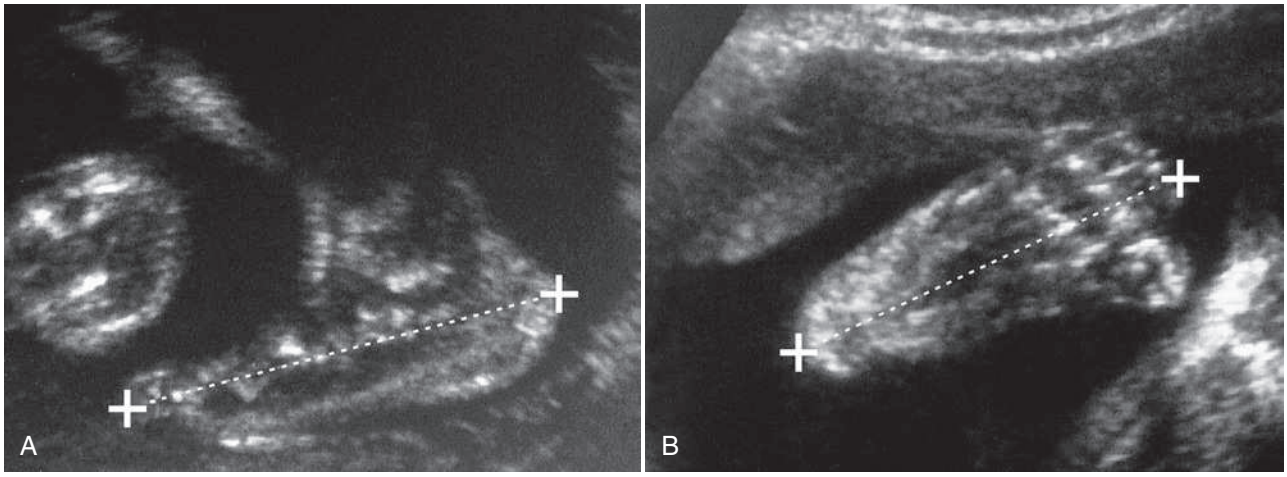

FIG. 40.3 Foot Length Measurement. From the skin edge overlying the calcaneus to the distal end of the longest toe. **(A)** Sagittal measurement; note the normal squared appearance of the heel. **(B)** Plantar measurement.

not have skeletal dysplasia. However, further deviation from the mean by at least 1 SD suggests the presence of a skeletal dysplasia or severe IUGR. When FL measures below 4 SD for gestational age, there is a high likelihood of a skeletal dysplasia. Kurtz et al.[25] have shown that the number of millimeters below the −2 SD line is a simple screening tool to evaluate femoral shortening with the following guidelines:

- If FL is 1 to 4 mm below the −2 SD point, further serial measurements are required to determine if a skeletal dysplasia is present.
- If FL is more than 5 mm below the −2 SD point, there is a high likelihood of a skeletal dysplasia.

The most common cause of a so-called **short femur** is either inaccurate dating or a normal variant in a constitutionally small fetus, which may be associated with a parental or family history of less-than-average stature. In about 13% of cases, a remeasurement will bring the FL into a normal range, likely representing a false-positive diagnosis rather than a growth spurt.[27] Isolated, symmetrical short femurs identified at the second midtrimester ultrasound evaluation are helpful in identifying a group of fetuses at increased risk for low birth weight, small for gestational age, or severe IUGR.[27-29] Typically, these fetuses will also have small abdominal circumference measurements.

Occasionally, fetuses with severe IUGR will have greatly shortened long bones.[30] Associated findings of normal or decreased skin fold measurements, oligohydramnios, abnormal placental morphology, and abnormal Doppler waveforms suggest the diagnosis of IUGR,[31] whereas redundant, thickened skin folds and polyhydramnios typically accompany short-limb dysplasias.

Nonlethal skeletal dysplasias such as **heterozygous achondroplasia** are often not evident before 20 weeks' gestation. The findings of short long bones before 20 weeks indicate a more serious and usually fatal skeletal dysplasia. As a rule, the earlier the detection of limb shortening, the worse is the prognosis. Virtually all cases diagnosed in first trimester are considered severe skeletal dysplasias, with the large majority representing lethal conditions.[32] First-trimester skeletal biometry tables are available.[33] Although mild, isolated shortening of the femur indicates increased risk for **trisomy 21** by 1.5-fold, other factors are more important for assessing this risk.[34]

The **pattern of limb shortening** should be assessed to determine which long-bone segments are most severely affected[9,35] (Fig. 40.4). Rather than millimeters, we find it useful to standardize measurements to "weeks of size" to determine disproportion. There are four main patterns of shortening of the long bones: **rhizomelia,** shortening of the proximal segment; **mesomelia,** shortening of the middle segment; **acromelia,** shortening of the distal segment; and **micromelia,** shortening of the entire limb (mild, mild/bowed, or severe).

Patterns of Limb Shortening

Rhizomelia: shortening of proximal segment (femur, humerus)
Mesomelia: shortening of middle segment (radius, ulna/tibia, fibula)
Acromelia: shortening of distal segment (hands, feet)
Micromelia: shortening of entire limb (mild, mild/bowed, or severe)

The shape, contour, and density of the bones should be assessed for the presence of bowing, angulation, fracture, or thickening. **Bowing** is a nonspecific finding, typically caused by underlying osseous fragility. Although more than 40 distinct disorders are associated with bowed, bent, or angulated femurs, most cases can be accounted for by three relatively frequent disorders: **campomelic dysplasia, thanatophoric dysplasia,** and **osteogenesis imperfecta** (OI).[36] Patients with OI types I and IV can present with apparently isolated in utero bowing of the long bones (especially the femur) without frank fractures (see Fig. 40.2D). Anterior bowing of the tibia, femur, and humerus may suggest the diagnosis of campomelic dysplasia; other more specific findings such as **hypoplastic scapulae** and **cervical kyphosis** are typically present and help distinguish campomelic dysplasia

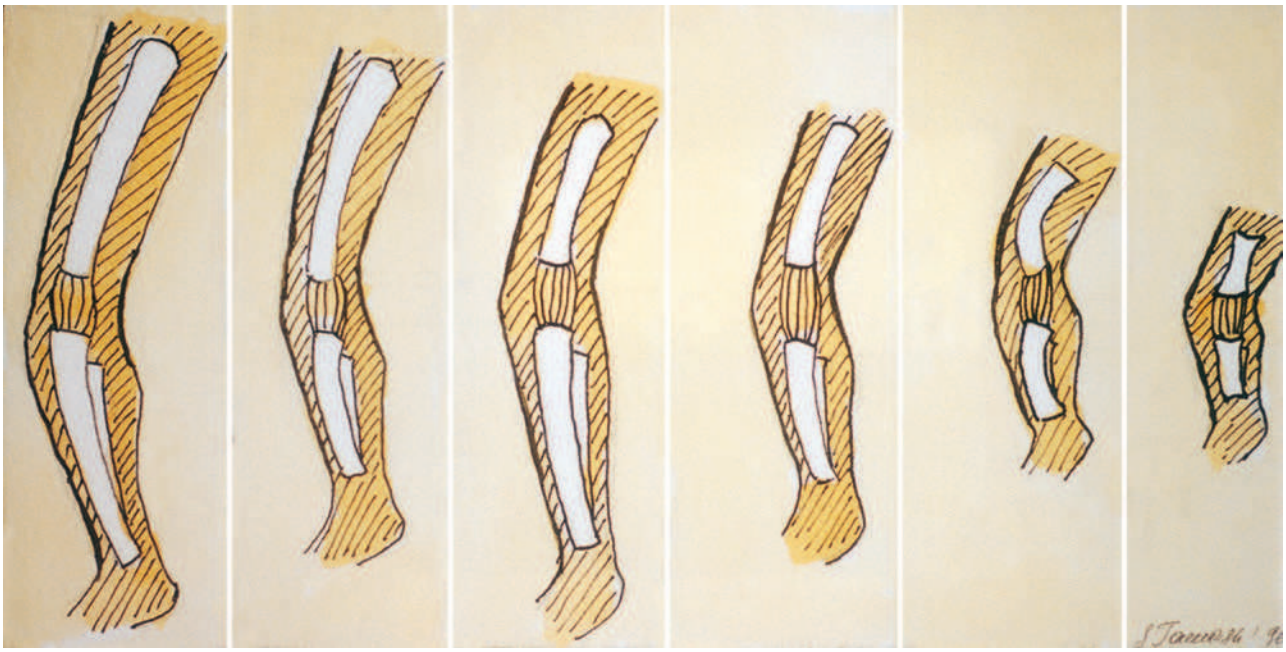

FIG. 40.4 Patterns of Limb Shortening. *Left to right,* Normal, mesomelia, rhizomelia, mild micromelia, mild and curved micromelia, and severe micromelia. (Courtesy of J. Tomash, MD, University of Toronto.)

from OI and thanatophoric dysplasia, which are both more common. Bone **fractures** may appear as angulations or interruptions in the bone contour or as thick, wrinkled contours corresponding to repetitive cycles of fracture and callus formation (see Fig. 40.2F). **Decreased or absent acoustic shadowing** is a marker for decreased mineralization of the long bones. When evident, this is helpful in narrowing the differential diagnosis, but in its absence the bone mineralization may still be abnormal.

The **spine** is assessed for **segmentation anomalies, kyphoscoliosis, platyspondyly** (flattened vertebral bodies), **demineralization, myelodysplasia,** and **caudal regression syndromes.** Although platyspondyly is the most common spine abnormality, it is a challenging prenatal diagnosis.[37] Demineralization of the spine can result in the appearance of ghost vertebrae or nonvisualization of one or all of the three ossification centers (Fig. 40.5). A progressively narrowed lumbar interpedicular distance is associated with homozygous **achondroplasia;** a widened interpedicular distance is associated with **myelodysplasia.** Three-dimensional imaging may provide a large field of view and additional details that may be helpful in achieving a diagnosis (Fig. 40.6).

The most reliable prognostic indicator of the lethality of a given skeletal dysplasia is **pulmonary hypoplasia.** Ultrasound is 85% to 95% accurate in the diagnosis of a lethal skeletal dysplasia on the basis of pulmonary hypoplasia.[8,9] The **thoracic circumference** is measured at the level of the four-chamber heart and compared to nomograms (see Chapter 36, Table 36.2). A thoracic-to-abdominal circumference ratio of less than 0.8 is considered abnormal. The **thoracic length** (from the neck to the diaphragm) is also measured, and the ribs are assessed to determine if they are short. At the level of the four-chamber cardiac view, the ribs should normally encircle at least 70% of the thoracic circumference.[38] The ribs remain in a relatively horizontal plane, as does the cardiac axis, facilitating this evaluation. In a sagittal view, a markedly narrowed anteroposterior diameter of the thorax is associated with pulmonary hypoplasia. In the coronal view, a concave or bell-shaped contour is associated with pulmonary hypoplasia (Fig. 40.7).

The **hands and feet** are examined for deformities such as **clubfoot** or **clubhand.** A **hitchhiker thumb,** or abducted thumb, is associated with **diastrophic dwarfism.** Fixed postural deformities may suggest the diagnosis of **arthrogryposis multiplex congenita. Polydactyly** is associated with **short-rib polydactyly syndromes, Ellis–van Creveld syndrome, asphyxiating thoracic dystrophy,** and some chromosomal abnormalities.

The fetal **cranium** is assessed for the presence of **macrocranium, frontal bossing, cloverleaf skull deformity,** underlying brain abnormalities, and facial abnormalities, such as **saddle nose, hypertelorism,** and **cleft lip and palate.** An abnormal cranial contour may indicate **craniosynostosis** or premature fusion of the sutures. The most reliable sonographic sign of demineralization is increased compressibility of the calvarium. This finding is typically present in fetuses with **osteogenesis imperfecta type II** and **hypophosphatasia.** The falx may appear abnormally bright or echogenic compared to the demineralized calvarium.

The **ribs** are assessed to ensure an adequate length, thus minimizing the risk of pulmonary hypoplasia, and are examined for abnormal number or appearance.[39] The finding of an abnormal number of fetal ribs is an isolated finding of no clinical importance in the majority of cases,[39] associated with minor anomalies in a smaller group (29%) and only occasionally associated with severe malformations. Associated syndromes include **Poland syndrome, VACTERL** association (vertebral abnormalities, anal atresia, cardiac abnormalities, tracheoesophageal fistula, renal agenesis

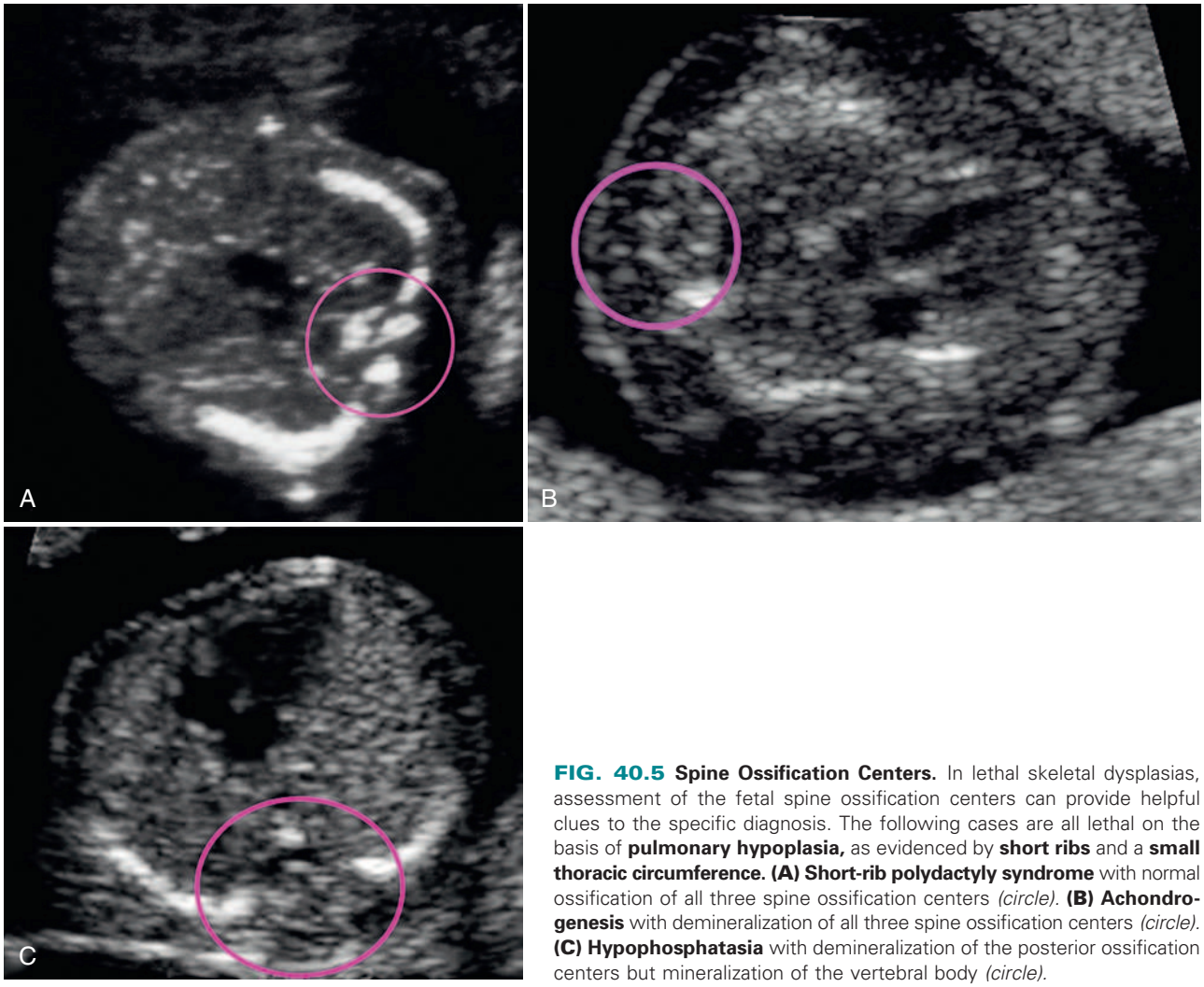

FIG. 40.5 Spine Ossification Centers. In lethal skeletal dysplasias, assessment of the fetal spine ossification centers can provide helpful clues to the specific diagnosis. The following cases are all lethal on the basis of **pulmonary hypoplasia,** as evidenced by **short ribs** and a **small thoracic circumference. (A) Short-rib polydactyly syndrome** with normal ossification of all three spine ossification centers *(circle).* **(B) Achondrogenesis** with demineralization of all three spine ossification centers *(circle).* **(C) Hypophosphatasia** with demineralization of the posterior ossification centers but mineralization of the vertebral body *(circle).*

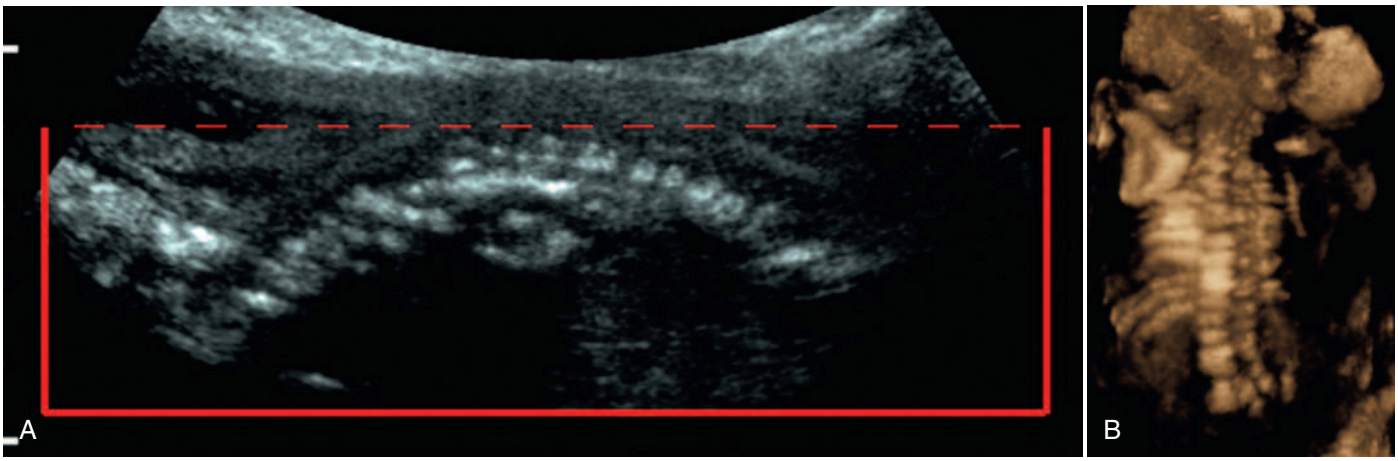

FIG. 40.6 Spondylocostal Dysostosis at 22 Weeks. (A) Sagittal image demonstrates abnormal spine segmentation. **(B)** Three-dimensional rendering of the spine further clarifies the abnormal development of the spine and ribs with abnormal misshapen and abnormally fused vertebrae leading to scoliosis, short trunk length, and widely variant rib spacing.

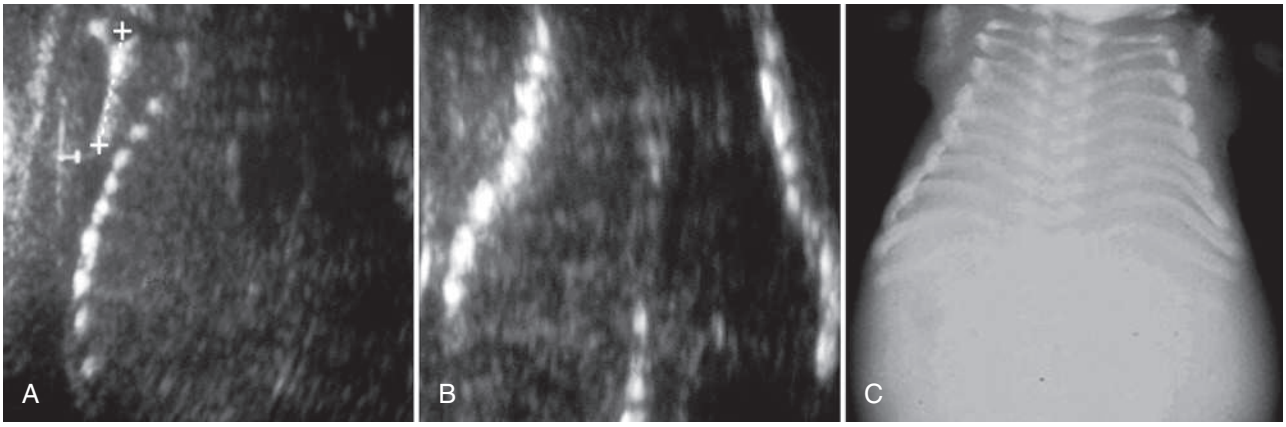

FIG. 40.7 Campomelic Dysplasia and Pulmonary Hypoplasia. Coronal ultrasound images of the thorax in triplet pregnancy at 27 weeks' gestation. **(A)** Normal triplet A shows normal convex contour of the thorax. Calipers measure the scapula. **(B)** Triplet B shows a **bell-shaped thorax. (C)** Radiograph of triplet B confirms a bell-shaped thorax consistent with pulmonary hypoplasia.

FIG. 40.8 Normal Ribs: Three-Dimensional Ultrasound.

and dysplasia, limb defects), **campomelic dysplasia,** and chromosome abnormalities. Three-dimensional ultrasound volume images aid in accurately counting the number of ribs (Fig. 40.8).

Ultimately, a detailed examination of each bone may be required to determine the fetal condition. Specific dysmorphic features of bones (e.g., clavicular or scapular hypoplasia; aplasia of fibula, tibia, or radius; platyspondyly) can be helpful to further define a specific skeletal dysplasia. A detailed evaluation of the cardiovascular, genitourinary, gastrointestinal, and central nervous system should be done concurrently with the musculoskeletal evaluation.

Dizygotic **twin pregnancies** are at similar risk for skeletal abnormalities as singleton pregnancies, and the frequency is increased two to three times in monozygotic twins. Both monozygotic and dizygotic twins can be discordant for genetic and nongenetic skeletal abnormalities. Twin pregnancies are generally discordant and overall, about 15% of twins are concordant for the same anomaly.[40,41]

Additional Diagnostic Techniques

Three-Dimensional Ultrasound

Three-dimensional ultrasound is becoming an increasingly useful complement to two-dimensional ultrasound in diagnosis of skeletal dysplasia and pulmonary hypoplasia. High-contrast structures such as the fetal skeleton are especially amenable to three-dimensional ultrasound-rendering software and post-processing techniques.[42] Surface-rendering capabilities are particularly useful for visualizing subtle facial dysmorphism (such as low-set or deformed ears, micrognathia, or flattening of the facial profile associated with midface hypoplasia), evaluating cranial distortion due to craniosynostosis, or assessing hand and foot abnormalities.[43] However, there are insufficient published data to gauge the diagnostic performance of this modality[44-46] (Fig. 40.9).

Radiography

The role of **prenatal radiography** is limited. Typically, two films might be performed: an anteroposterior view, placing the fetus over the hollow of the pelvis, and an angulated view, with the fetus projected down, away from the maternal sacrum. The appearance of short limbs of normal shape and the presence of growth recovery lines can be useful in distinguishing severe IUGR from a skeletal dysplasia.[31] In contrast, **postnatal radiography** plays an extremely important role in defining the characteristic radiologic features found in many skeletal anomalies.

Three-Dimensional Computed Tomography

Three-dimensional low-dose **computed tomography** (CT) may have a better diagnostic yield than two-dimensional ultrasound

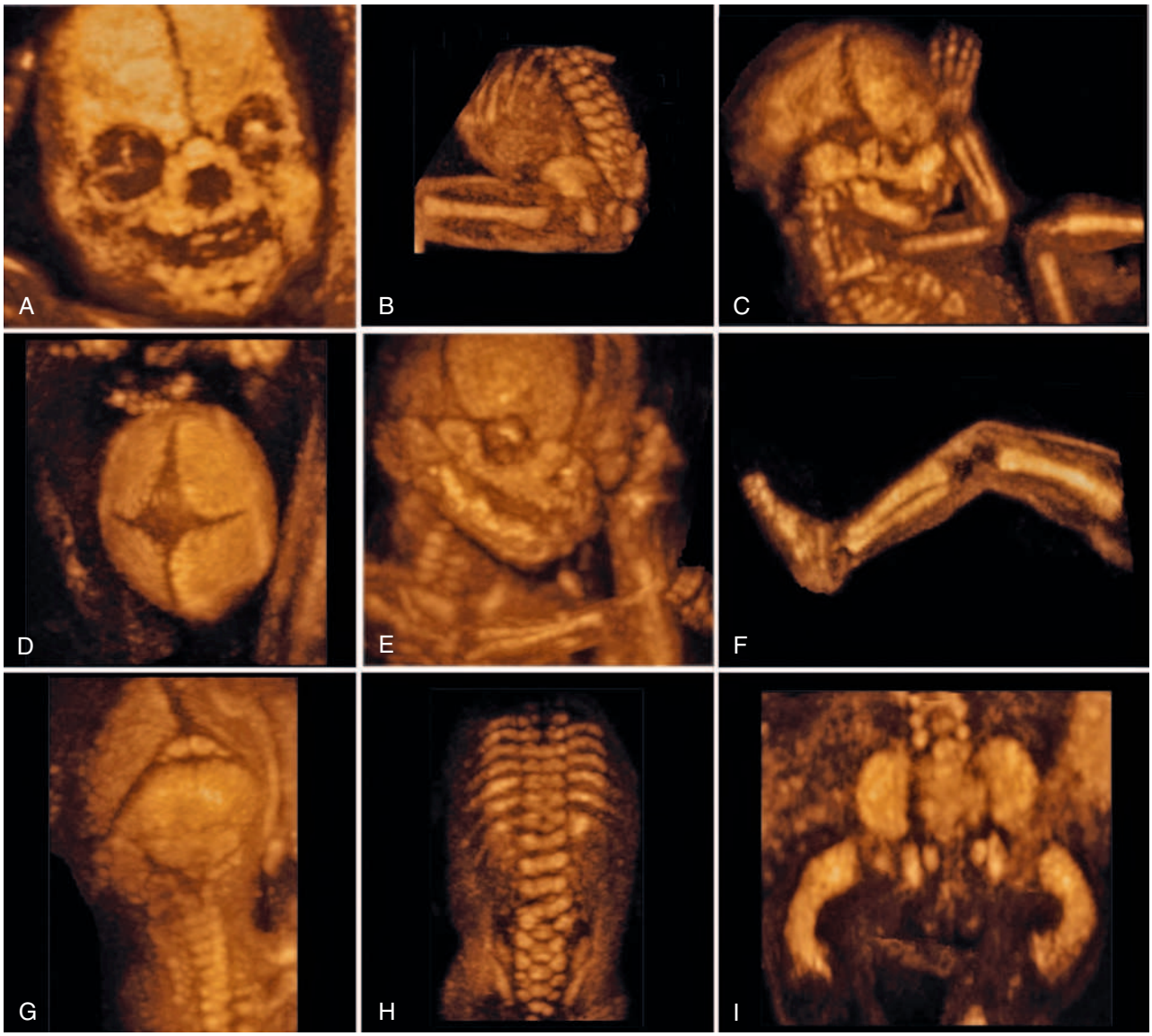

FIG. 40.9 Collage of Three-Dimensional Images. (A) Normal skull at 22 weeks, frontal aspect. **(B)** Femur and iliac bone at 22 weeks. **(C)** Upper extremity at 22 weeks. **(D)** Normal skull at 22 weeks, superior aspect. **(E)** Face and skull at 22 weeks. **(F)** Normal lower limb at 22 weeks, profile. **(G) Wormian bones,** posterior fontanelle. **(H) Hemivertebrae** at 23 weeks. **(I) Osteogenesis imperfecta;** note abnormally shortened, curved, and thickened femurs. (Courtesy of Dr. Bernard Benoit.)

and may provide a valuable complementary diagnostic tool in the appropriate clinical situation.[43,47] It is important to take into consideration the fetal radiation dose, which has been estimated to be in the 3-mGy range. However, new dose reduction techniques such as iterative reconstruction are estimated to reduce the dose by as much as 80%. Postmortem three-dimensional CT scan[48] may provide a "virtual autopsy," particularly when autopsy has been declined.

Magnetic Resonance Imaging

Magnetic resonance imaging (MRI) plays a relatively limited role in the assessment of the fetal skeletal dysplasia. However, in cases with inconclusive ultrasound findings and for cases in which MRI is expected to provide important additional information, MRI may be useful.[49] MRI can also be helpful in the context of "virtual autopsy" for families who have declined autopsy.[50]

Molecular Diagnosis

Molecular confirmation of suspected skeletal dysplasia during pregnancy has traditionally been of limited usefulness because of the length of time needed to obtain a result, especially if the differential diagnosis required sequencing of several genes. The advent of next-generation sequencing technologies is now enabling the simultaneous examination of multiple genes in a reasonable time frame. It should be noted, however, that negative molecular testing does not exclude the diagnosis of a skeletal dysplasia and the prognosis must be based on the imaging findings.

Prenatal diagnosis of monogenic disorders presenting with ultrasound abnormalities traditionally required invasive procedures such as chorionic villus sampling or amniocentesis for obtaining fetal cells and DNA. More recently the noninvasive approach of genetic analysis using circulating cell-free fetal DNA has been utilized as an aid to sonographic prenatal diagnosis of fetal skeletal dysplasia, thus eliminating the risk of fetal loss associated with invasive testing.

Genetic defects have been identified in approximately 70% of the more than 436 skeletal dysplasias.[6] Cell-free fetal DNA testing allows for testing an early point in the pregnancy, prior to ultrasound diagnosis, and thus may be appropriate for a fetus known to be at risk for having skeletal dysplasia because of an affected parent (for autosomal dominant conditions), a carrier mother (for an X-linked condition), or parents identified as being carriers of an autosomal recessive skeletal dysplasia (due to a personal or family history of an affected child or fetus). Finding the diagnosis is important not only for providing early prenatal diagnosis (before diagnostic findings are seen on ultrasound) but also for preimplantation diagnosis in at-risk families.

If both parents are affected (either with the same or a differing autosomal dominant skeletal disorder), the fetus is at 25% risk of inheriting both conditions and this generally causes a more severe skeletal dysplasia and is frequently lethal. In cases where the mutation status of the parents is known, a molecular diagnosis can distinguish between a fetus that has inherited neither dysplasia, one dysplasia, or both.

If the risk of an affected fetus is relatively low, as when only one parent has an autosomal recessive skeletal dysplasia or each of the parents is affected with a different type of autosomal recessive skeletal dysplasia, the appropriateness of molecular diagnosis is less clear. For couples with a previously affected fetus with a de novo dominant disorder, the recurrence risk is probably less than 1% (due to gonadal mosaicism). Nevertheless, prenatal diagnosis should be discussed and performed if the woman or couple requests it.

When the diagnosis remains unknown, the involvement of specialists in skeletal dysplasias may be helpful in determining the diagnosis. It is crucial to obtain postnatal radiographs, fetal or newborn DNA, and fibroblast culture to try and delineate the diagnosis, the causative gene, and gene mutation. This may help in preimplantation or prenatal diagnosis in future pregnancies.

LETHAL SKELETAL DYSPLASIAS

The lethal skeletal dysplasias are characterized by severe **micromelia** and small thoracic circumference with **pulmonary hypoplasia.**[51] The most important determinant of lethality is the presence and degree of pulmonary hypoplasia.[11] In a prospective series by Krakow et al., lethality was accurately predicted in 96.8% of cases.[8] It is important to use multiple parameters to obtain the most accurate prediction of lethality, typically related to the pulmonary hypoplasia associated with a small chest. This extremely high accuracy of the designation of a lethal skeletal dysplasia is important for the management of the pregnancy, delivery, and the newborn, if alive.

Features Suggestive of Pulmonary Hypoplasia

- Thoracic circumference < fifth percentile, measured at the level of the four-chamber view (axial view)
- Thoracic-to-abdominal circumference ratio < 0.6
- Short thoracic length (measured from the neck to the diaphragm) as compared to nomograms
- Markedly narrowed anteroposterior diameter (sagittal view)
- Concave or bell-shaped contour of the thorax (coronal view)
- Femur length–to-abdominal circumference < 0.16

With permission from Krakow D, Lachman RS, Rimoin DL. Guidelines for the prenatal diagnosis of fetal skeletal dysplasias. Genet Med. 2009;11(2):127-133[52]; Nelson DB, Dashe JS, McIntire DD, Twickler DM. Fetal skeletal dysplasias: sonographic indices associated with adverse outcomes. J Ultrasound Med. 2014;33(6):1085-1090.[53]

A comparative study of eight methods for the prediction of fetal lung hypoplasia determined that the lung volumes and the thoracic circumference to abdominal circumference ratios performed best. However, the majority of these studies were performed in fetuses with congenital diaphragmatic hernia and may not be generalizable to the skeletal dysplasia population.[6,54] Other studies showed that the femur-to-abdomen ratio (<0.16) is more accurate in establishing lethality.[53]

Is There a Lethal Skeletal Dysplasia?

CHARACTERISTIC FEATURES
Severe micromelia
Pulmonary hypoplasia

KEY DISTINGUISHING FEATURES
Abnormal mineralization
Fractures
Presence or absence of macrocranium
Thoracic length

In many fetal skeletal dysplasias, the skin and subcutaneous layers continue to grow at a rate proportionately greater than the long bones, resulting in **relatively thickened skin folds,** on occasion mistaken for hydrops fetalis. **Polyhydramnios** is common and may be related to a variable combination of esophageal compression by the small chest, gastrointestinal abnormalities, micrognathia, and/or hypotonia.

The more common lethal skeletal dysplasias occur in less than 1 in 10,000 births and the rare types occur in less than 1 in 100,000 births. The three most common lethal skeletal dysplasias are thanatophoric dysplasia, achondrogenesis, and OI type II, overall accounting for 40% to 60% of all lethal skeletal dysplasias.[5,8,55] There may be variations depending on location and referral patterns; for example, in our tertiary referral care center, the two most common groups were the OI and the fibroblast growth factor receptor type 3 (FGFR3) chondrodysplasia group, which includes thanatophoric dysplasia.[11]

TABLE 40.4 Severe Micromelia With Decreased Thoracic Circumference

	Mineralization	Fractures	Macrocrania	Short Trunk
Thanatophoric dysplasia[ab]	Normal	No	Yes	No
Achondrogenesis	Patchy demineralization	Occasional	Yes	Yes
Osteogenesis imperfecta type II	Generalized demineralization	Innumerable	No	Yes
Hypophosphatasia congenita	Patchy or generalized demineralization	No	No	No

[a]Homozygous achondroplasia is similar to thanatophoric dysplasia but distinguishable because both parents are affected with the heterozygous form of achondroplasia.
[b]Short-rib polydactyly dysplasias are similar to thanatophoric dysplasia, but no macrocrania or polydactyly is present.

FIG. 40.10 Thanatophoric Dysplasia at 33 Weeks. (A) Anteroposterior (AP) radiograph shows normal mineralization, short curved extremity bones, severe platyspondyly with U-shaped vertebral bodies, and narrow thorax with short ribs. **(B)** AP specimen photograph shows severe micromelia with relative sparing of the feet, telescoping of the redundant skin folds, and small, bell-shaped thorax. **(C)** Profile specimen photograph shows macrocranium, frontal bossing, and flattened nasal bridge.

We recommend using a "key features" approach in assessing degree of micromelia, mineralization, presence of macrocranium, and evaluation of thoracic length and circumference to improve the specificity and ease of diagnosis of lethal skeletal dysplasias (Table 40.4).

Thanatophoric Dysplasia

Thanatophoric dysplasia is the most common lethal skeletal dysplasia, with a prevalence of between 0.24 and 0.69 per 10,000 births. The key ultrasound features are early severe micromelia with rhizomelic predominance and **macrocrania** (disproportionately large head) in association with decreased thoracic circumference but a normal trunk length. Mineralization is normal, without bony fractures. In late gestation (third trimester) the extremities are so foreshortened that they protrude at right angles to the body. The skin folds are thickened and redundant secondary to a relatively greater rate of growth of the skin and subcutaneous layers than the bones (Figs. 40.10 and 40.11, Video 40.1).

Sonographic Assessment of Bones

LONG BONES
Degree of limb shortening
Pattern of limb shortening
Degree of mineralization
Presence of fractures, bowing, or angulation
Abnormal shape or contour
Limb reduction anomalies
Hypoplastic or absent bones

SPINE
Degree and pattern of demineralization
Platyspondyly
Segmentation or curvature anomalies
Caudal regression syndrome
Myelodysplasia

THORAX
Thoracic length and circumference
Hypoplastic ribs

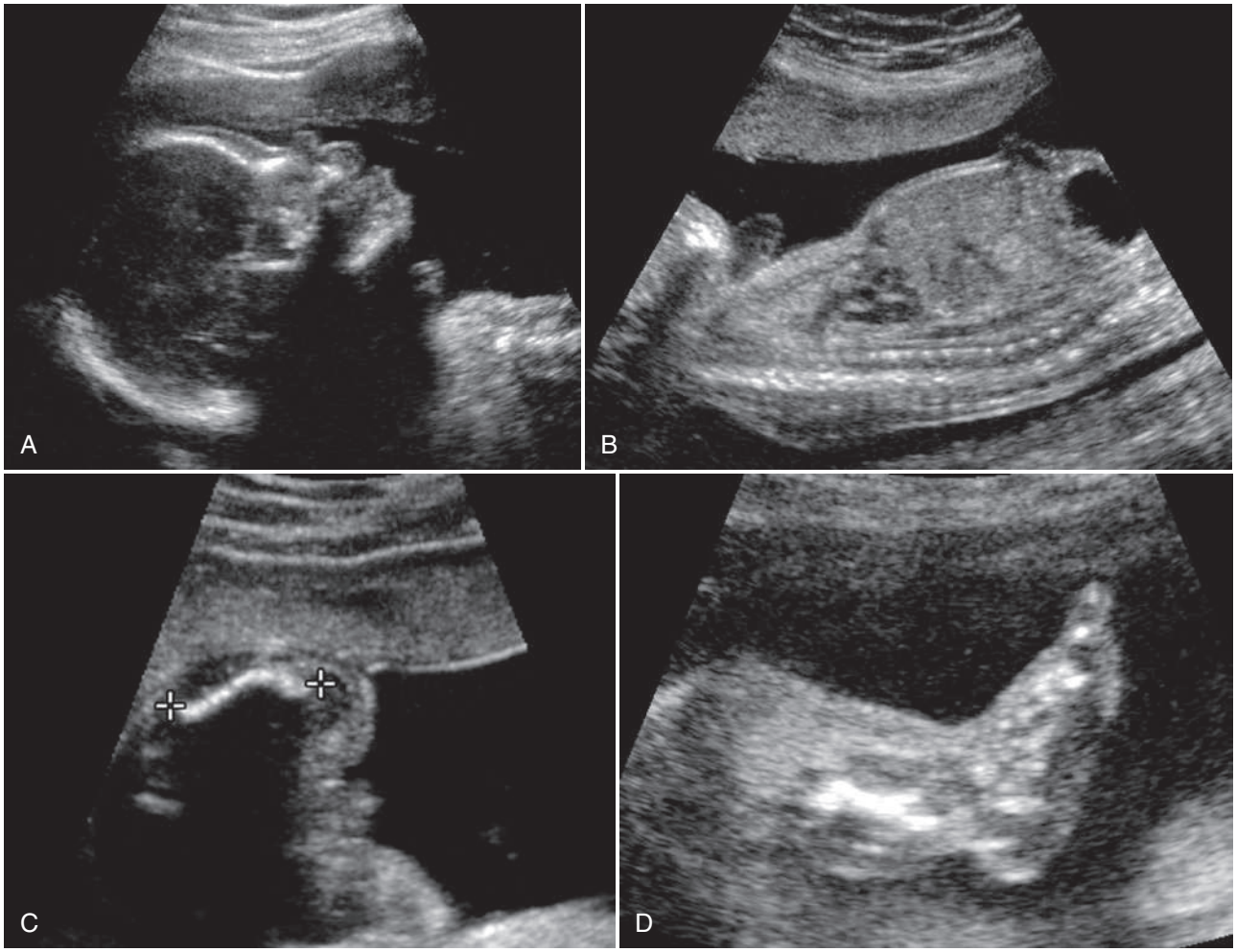

FIG. 40.11 Thanatophoric Dysplasia at 22 Weeks. (A) Profile; midface hypoplasia with flat nasal bridge. **(B)** Sagittal sonogram shows disproportionately narrow thorax and relatively protuberant abdomen, signifying lethal condition on the basis of pulmonary hypoplasia. **(C)** Short curved femur *(calipers)*. **(D)** Sparing of foot length versus extreme shortening of tibia. (Courtesy of Fetal Assessment Unit, University Health Network.)

Sonographic Assessment of Bones—cont'd

Bell-shaped thorax of pulmonary hypoplasia
Convex contour in cross section

HANDS AND FEET
Postural deformities
Abnormal number of digits
Syndactyly

CALVARIUM
Macrocranium
Frontal bossing
Craniosynostosis
Compressibility/abnormal degree of mineralization

FACIAL FEATURES
Cleft lip and palate
Hypertelorism and hypotelorism
Midface hypoplasia/flat nasal bridge

Langer et al.[56] distinguished two types of thanatophoric dysplasia. The more common **type 1** (TD1), usually caused by the R248C and Y373C mutations in the *FGFR3* gene, displays the typical "telephone receiver" shape of the femurs[57,58] (see Fig. 40.2H). This bowed or curved appearance is secondary to the broadened metaphyses at the ends of the severely shortened tubular bones. TD1 is associated with **frontal bossing** and a flattened nasal bridge with **midface hypoplasia.** Occasionally, **craniosynostosis** results in a mild variant of **cloverleaf skull** deformity. **Platyspondyly** is present. In **type 2** (TD2), usually caused by the K650E mutation in the *FGFR3* gene, the femurs are typically straight with flared metaphyses and the skull has a **cloverleaf** or trilobed appearance in the coronal plane that results from premature craniosynostosis of the lambdoid and coronal sutures (Fig. 40.12). Other conditions that may be associated with this unusual skull deformity are **homozygous achondroplasia, campomelic dysplasia,** and **trisomy 13.** Both TD1 and TD2 are autosomal dominant conditions, with all cases caused by new mutations in the *FGFR3* gene. *FGFR* gene mutations are

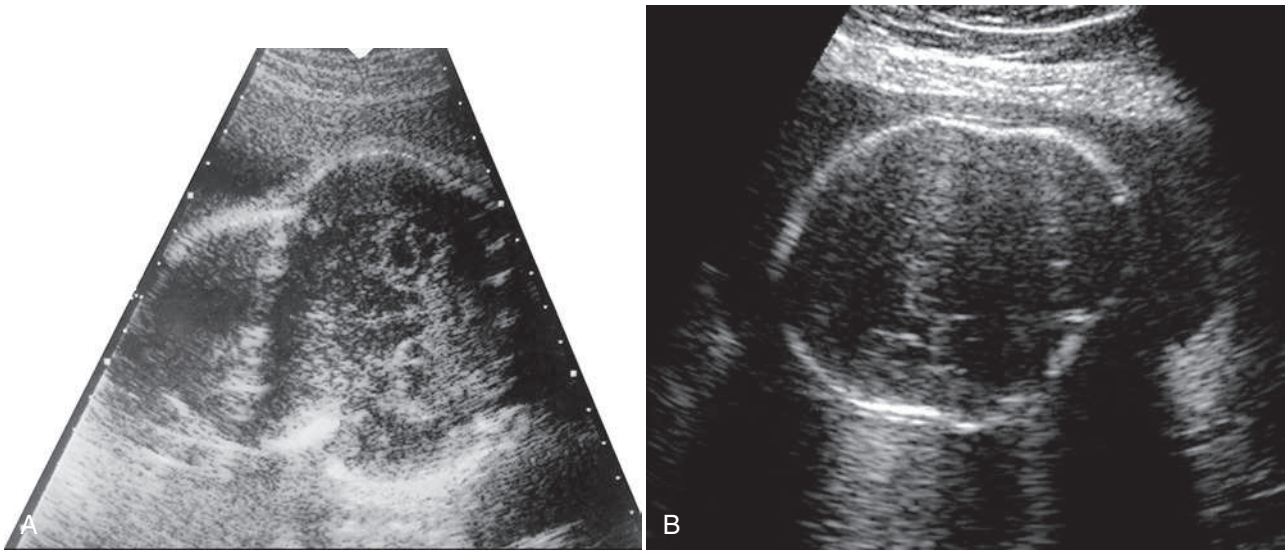

FIG. 40.12 Cloverleaf Deformity of Thanatophoric Dysplasia. (A) Severe variant. **(B)** Mild variant. (Courtesy of Greg Ryan, MD, University of Toronto.)

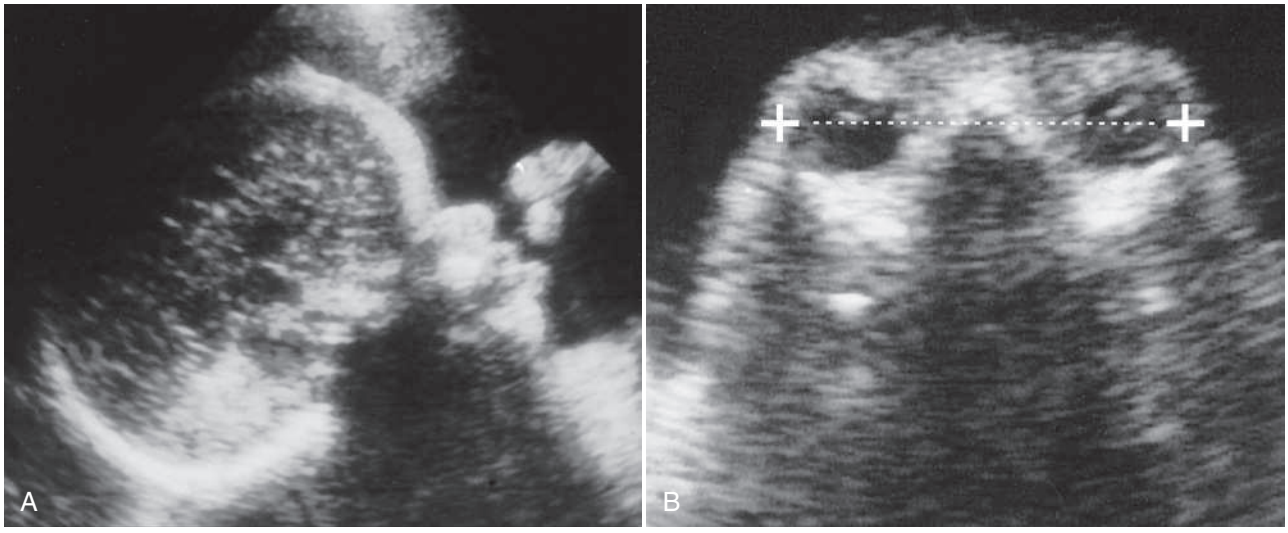

FIG. 40.13 Homozygous Achondroplasia at 34 Weeks. (A) Lateral profile with **macrocranium, frontal bossing,** and **flat nasal bridge. (B)** Axial image through the orbits (*calipers* denote outer orbital diameter) and nasal bones confirms a flat nasal bridge.

also associated with **hypochondroplasia, achondroplasia,** and **acanthosis nigricans (SADDAN syndrome),**[59] as well as a variety of craniosynostoses, including **Crouzon, Apert, and Pfeiffer syndromes.**[58,60]

Thanatophoric dysplasia has many phenotypic similarities to **homozygous achondroplasia.** Both conditions may appear identical from ultrasound and radiographic perspectives. They can be distinguished by the positive family history,[51] in which both parents are affected with the heterozygous form of achondroplasia (Fig. 40.13). Another condition presenting with bowed tubular bones is **campomelic dysplasia,** which can be distinguished from thanatophoric dysplasia by presence or combination of other more specific anomalies such as **hypoplasia of the scapulae** and **micrognathia.**

Platyspondyly, or flattened vertebral bodies, is one of the most characteristic features on anteroposterior radiographs of a thanatophoric dwarf (see Fig. 40.10A). There is a U or H configuration of the vertebral bodies and a relatively increased height of the disc spaces. Platyspondyly appears on ultrasound as a thin vertebral body with a relatively larger, hypoechoic disc space on either side of the vertebral body (Fig. 40.14). The ratio of vertebral body height to vertebral interspace (disc and body) in thanatophoric dysplasia is lower than in normal fetuses. Platyspondyly may also occur in cases of **achondrogenesis** and **OI type II.**[31,51]

Associated central nervous system findings include **holoprosencephaly, agenesis of the corpus callosum, polymicrogyria, heterotopia,** and **ventriculomegaly.** The abnormal deep transverse sulci in the inferior temporal lobes can be visualized on fetal ultrasound routinely at 20 weeks of gestation, thus helping in confirming a specific diagnosis (Fig. 40.15).[61,62] These distinctive features have been identified as early as late first trimester. Prenatal

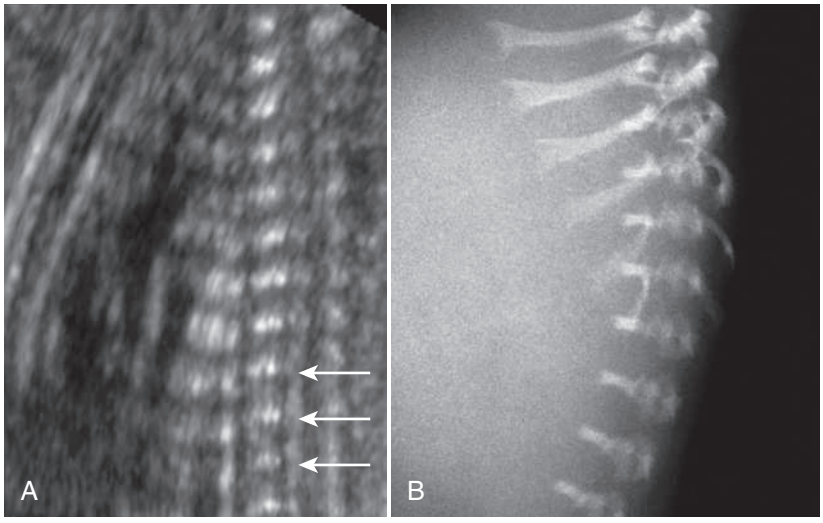

FIG. 40.14 Thanatophoric Dysplasia at 33 Weeks. (A) Platyspondyly appears on ultrasound as a thin vertebral body *(arrows)* with relatively larger hypoechoic intervertebral disc space on either side of the vertebral body. **(B)** Correlative lateral spine radiograph. Note the short ribs with wide-cupped metaphyseal ends.

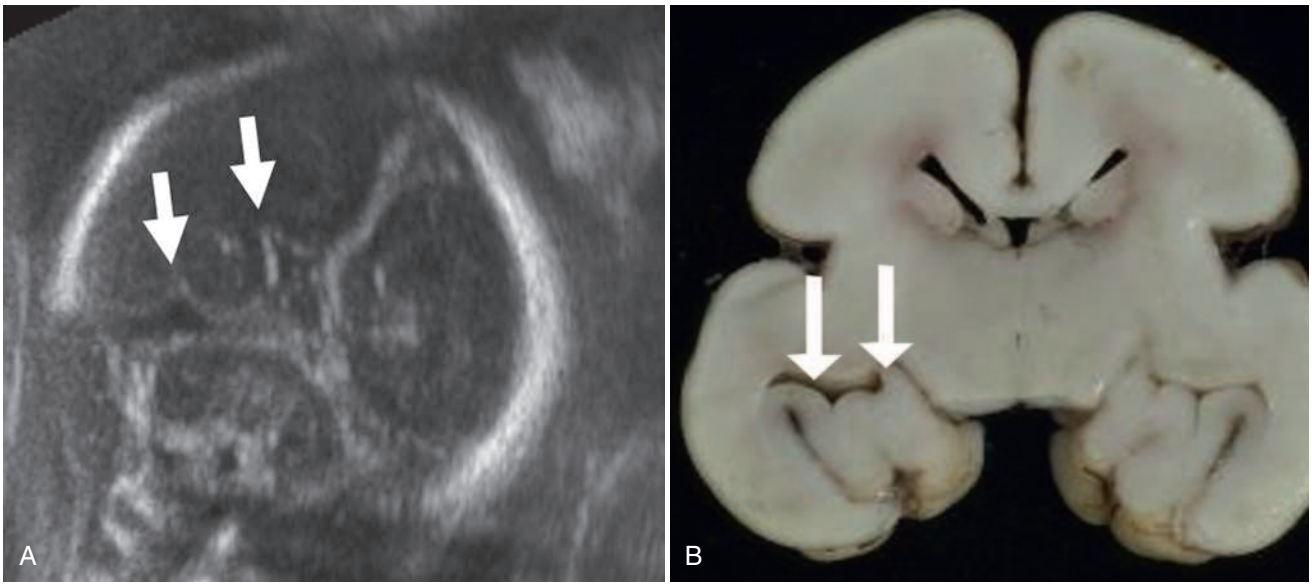

FIG. 40.15 Temporal Lobe Dysplasia in Thanatophoric Dysplasia at 19 Weeks. (A) Modified coronal oblique image demonstrates abnormal temporal lobe gyration with multiple deep sulcation *(arrows).* **(B)** Photograph demonstrates correlation with evidence of deep temporal lobe sulcation *(arrows).*

demonstration of **temporal lobe dysplasia** is variable, likely due to a combination of factors including other striking findings that distract from the diagnosis, lack of dedicated views, and lack of awareness of this feature. Wang et al. demonstrated that 79% of the cases (11/14) had temporal lobe dysplasia detected antenatally even without routine dedicated views.[61] We suggest that in fetuses with severe skeletal dysplasia, specific search for temporal lobe dysplasia using a low axial plane below the level of the biparietal diameter (BPD) image and a coronal oblique plane that includes the cerebellum of midline be added to the institutional protocol to better visualize the temporal lobe in order to improve specificity of diagnosis. Three-dimensional imaging with multiplanar reformats may also demonstrate these findings.

Thanatophoric dysplasia, achondroplasia, and **hypochondroplasia** are all related to the *FGFR3* gene mutation.[51] Temporal lobe dysplasia has been described in children with the latter two conditions; however, the site differs with thanatophoric dysplasia typically showing the abnormal sulcation in the inferior aspect of the temporal lobes versus primarily the medial aspect of the temporal lobes in hypochondroplasia. There is one report of prenatal identification of medial temporal lobe dysplasia on MRI in a case of hypochondroplasia.[63]

Other anomalies may include **horseshoe kidneys, hydronephrosis, congenital heart disease (atrial septal defect and tricuspid insufficiency), radioulnar synostosis,** and **imperforate anus.**[64]

Achondrogenesis

Achondrogenesis is the second most common lethal skeletal dysplasia, with a prevalence of 0.09 to 0.23 per 10,000 births. It is a phenotypically and genetically diverse group of chondrodysplasias characterized by severe **micromelia, macrocranium, decreased thoracic circumference and trunk length,** and **decreased mineralization.**[64,65] The pattern of abnormal mineralization is most marked in the vertebral bodies, ischium, and pubic bones, leading to a greatly shortened trunk length, decreased thoracic circumference, and occasional fractures.[66] Classically, because of abnormal skeletogenesis of the vertebral body, only the two echogenic posterior elements or neural arches appear in a transverse image of the spine. This is in contrast to **hypophosphatasia,** which predominantly involves the posterior elements in the spine with only patchy involvement of the vertebral bodies. Polyhydramnios and thick, redundant skin folds are a common accompaniment of achondrogenesis.[67]

Type 1 achondrogenesis accounts for about 20% of cases and is divided into A and B subtypes (ACG1A and ACG1B).[7,65] ACG1A includes rib fractures, which are not present in ACG1B. Both have autosomal recessive mode of inheritance and thus have a 25% recurrence risk. ACG1A is caused by mutations in *TRIP11,* while ACG1B is caused by mutations in the diastrophic dysplasia sulfate transporter gene. Both ACG1A and ACG1B have a severe form of **micromelia,** evidenced by short, cuboid bones and metaphyseal scalloping with bone spurs at the periphery. Other findings include partial or complete lack of ossification of the calvarium, vertebral bodies, and sacral and pubic bones. Because of the extremely limited skeletal frame, the subcutaneous tissues can appear grotesquely redundant, with multiple telescoped skin folds that may be mistaken prenatally for hydrops fetalis.

Type 2 (AGH2), or the **Langer-Saldino** form, accounts for 80% of achondrogenesis cases. It is caused by a new dominant mutation in the *COL2A1* gene that encodes type II collagen and carries a low recurrence risk. It is characterized by normal calvarial ossification and by absent ossification in the vertebral column and sacral and pubic bones (Fig. 40.16). ACG2 has the least ossification of the vertebral column of all the skeletal dysplasias. The type 2 collagen disorders represent a continuous spectrum from lethal to mild. It may be difficult to come to a firm conclusion about lethality. In general, relatively longer tubular bones and body length are associated with increased survival. **Hypochondrogenesis** is phenotypically similar to ACGE and usually lethal but radiologically less severe with better ossification of the spine, pelvis, and long bones. Another condition to differentiate is **Kniest dysplasia,** characterized by vertebral coronal clefts and metaphyseal expansion (most prominent in the proximal femurs).[2]

These two key features of achondrogenesis—abnormal mineralization and shortened trunk length—distinguish it from thanatophoric dysplasia, which has normal mineralization and a normal trunk length. Both display macrocrania and severe micromelia.

Osteogenesis Imperfecta

OI is a clinically and genetically heterogeneous group of collagen disorders characterized by brittle bones resulting in fractures (Figs. 40.17 and 40.18). The incidence is 1 in 60,000 births. Until recently there were four clinical types of OI, all with an autosomal dominant mode of inheritance and associated with mutations in the *COL1A1* or *COL1A2* genes. Type II OI is lethal, whereas the other types are milder. In the past several years, many new causative genes have been identified.[68,69] Most are involved in the complicated process of maturation, processing, and transport

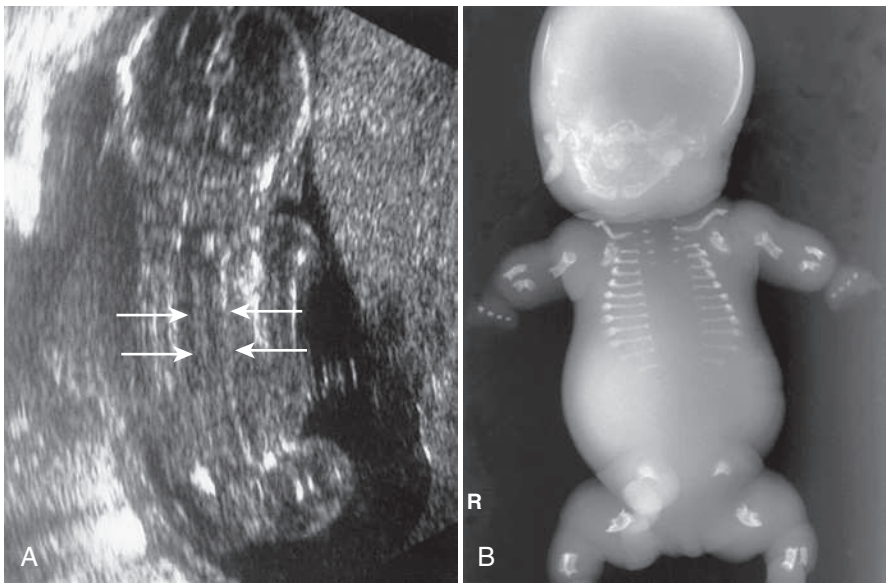

FIG. 40.16 Achondrogenesis at 18 Weeks. (A) Coronal sonogram shows small thorax, redundant subcutaneous tissues, absent spine ossification *(arrows),* and decreased calvarial ossification. **(B)** Postmortem radiograph demonstrates macrocranium, decreased calvarial ossification, virtually absent spine ossification (only some posterior elements are ossified in the cervical region). There is severe **micromelia** with strikingly short wide bones with **metaphyseal spurs.** The ribs are short and horizontal with splayed ends. (Courtesy of Shia Salem, MD, University of Toronto.)

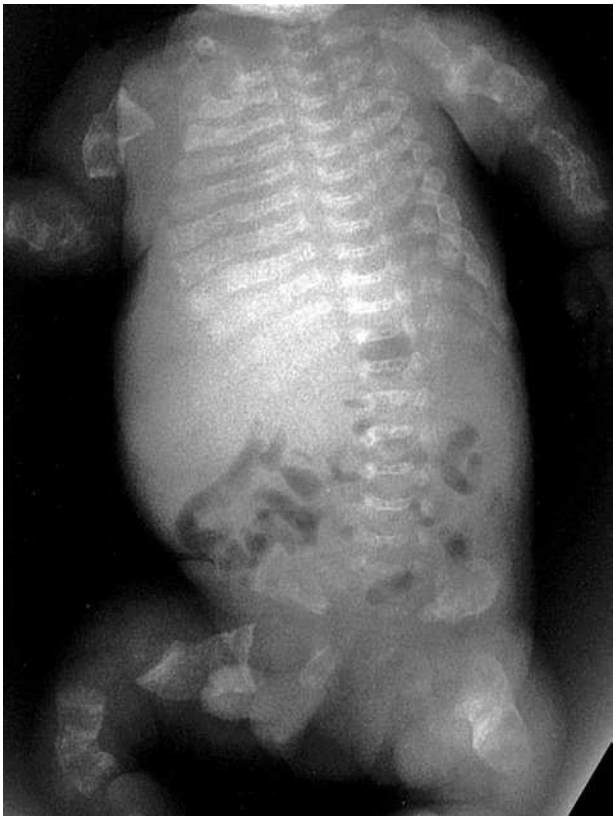

FIG. 40.17 Osteogenesis Imperfecta Type IIA at 32 Weeks. Postmortem radiograph shows severe **micromelia,** thickened bones with wavy contours caused by innumerable fractures and exuberant callus formation, **shortened ribs** with multiple fractures, and **platyspondyly.**

of type 1 collagen (Table 40.5). Most of these forms fit within the Sillence OI phenotypic classification and can still be categorized as OI type I, II, III, or IV despite several having a recessive mode of inheritance. Type V OI is phenotypically distinguishable with hyperplastic callus formation dense metaphyseal bands and ossification of the interosseous membranes of the forearm, and has an autosomal dominant form of inheritance.[70,71] A modification of the Sillence classification, based on skeletal radiographic findings, is still used most often to distinguish the subtypes of OI.[71,72]

Prenatal diagnosis is possible based on DNA obtained from chorionic villus sampling[70] or amniocentesis. Osteogenesis types I, III, and IV are further described in the section on nonlethal skeletal dysplasias.

OI type II is the classic neonatal lethal form and usually results from a new, dominant null mutation in the *COL1A1* gene.[72] The empiric recurrence risk is 6%, most of which are caused by parental germline and somatic mosaicism but can also be the result of one of the autosomal recessive forms of OI. Multiple repetitive in utero fractures occur secondary to defective collagen formation, which results in osseous fragility. Prevalence of OI type II is 0.18 in 10,000 births. The key ultrasound features are severe micromelia, decreased thoracic circumference and trunk length, decreased mineralization, and multiple bone fractures. The cranial vault remains normal in size, but as a result of decreased mineralization there is increased visibility of the intracranial contents and the skull is compressible by the ultrasound transducer (Fig. 40.19). The falx may appear bright or more echogenic than the demineralized cranial vault, with unusual clarity of detail in the near field cerebral hemisphere. Large fontanelles and wormian bones may be noted. Micrognathia is commonly present (Fig. 40.20).

The generalized demineralization results in innumerable fractures. The tubular bones exhibit a classic "accordion" or wrinkled contour caused by multiple in utero fractures with repetitive callus formation. Angulation and bowing are common in association with severe micromelia. On ultrasound, the bones may appear thickened because demineralized bone reflects sound waves less than a normally ossified bone. Acoustic shadowing may be present, absent, or diminished and thus is an unreliable sign. Multiple rib fractures cause the lateral chest contour to be concave rather than convex. The concavity is often most evident at the lateral thorax, and it is speculated that the elbows "bash" in the fragile rib cage. The ribs are hypoplastic, thus appearing shortened. The ribs may have a continuous, beaded, or wavy appearance secondary to repetitive fractures and callus formation. Platyspondyly secondary to multiple compression fractures may be present.

The three criteria for a specific diagnosis of OI type II are (1) FL greater than 3 SD below the mean, (2) demineralization of the calvarium, and (3) multiple fractures within a single bone.[72] The diagnosis may be made as early as 13 to 15 weeks' gestational age. A normal ultrasound examination after 17 weeks excludes this diagnosis.

Hypophosphatasia

Hypophosphatasia congenita, the lethal neonatal form of hypophosphatasia, is an autosomal recessive skeletal dysplasia caused by a deficiency of tissue-nonspecific alkaline phosphatase.[73] Frequency of hypophosphatasia congenita is 1 in 100,000 births. The key features are **severe micromelia, decreased thoracic circumference** with normal trunk length, and **decreased mineralization** with occasional fractures. Cranial vault size remains normal.

The demineralized long bones may be bowed with occasional angulations caused by fractures. The bones appear thin and delicate and may be difficult to visualize. The cranial vault fails to mineralize and may be compressible under locally applied transducer pressure. In contrast to OI, the demineralization in hypophosphatasia congenita varies from a patchy distribution to a diffuse form with severe involvement of the spine and calvarium. The ribs are short, resulting in a decreased thoracic circumference, but the trunk length is normal. Polyhydramnios is a common finding.

The main differential diagnosis is OI type II. Both hypophosphatasia and OI type II display a severe form of micromelia, demineralization, decreased thoracic circumference, and a normal-sized cranial vault that is compressible due to demineralization. In OI type II, the greater degree of osseous fragility results in innumerable fractures and a thickened, wavy appearance of the bones, in contrast to the thin, delicate appearance of the

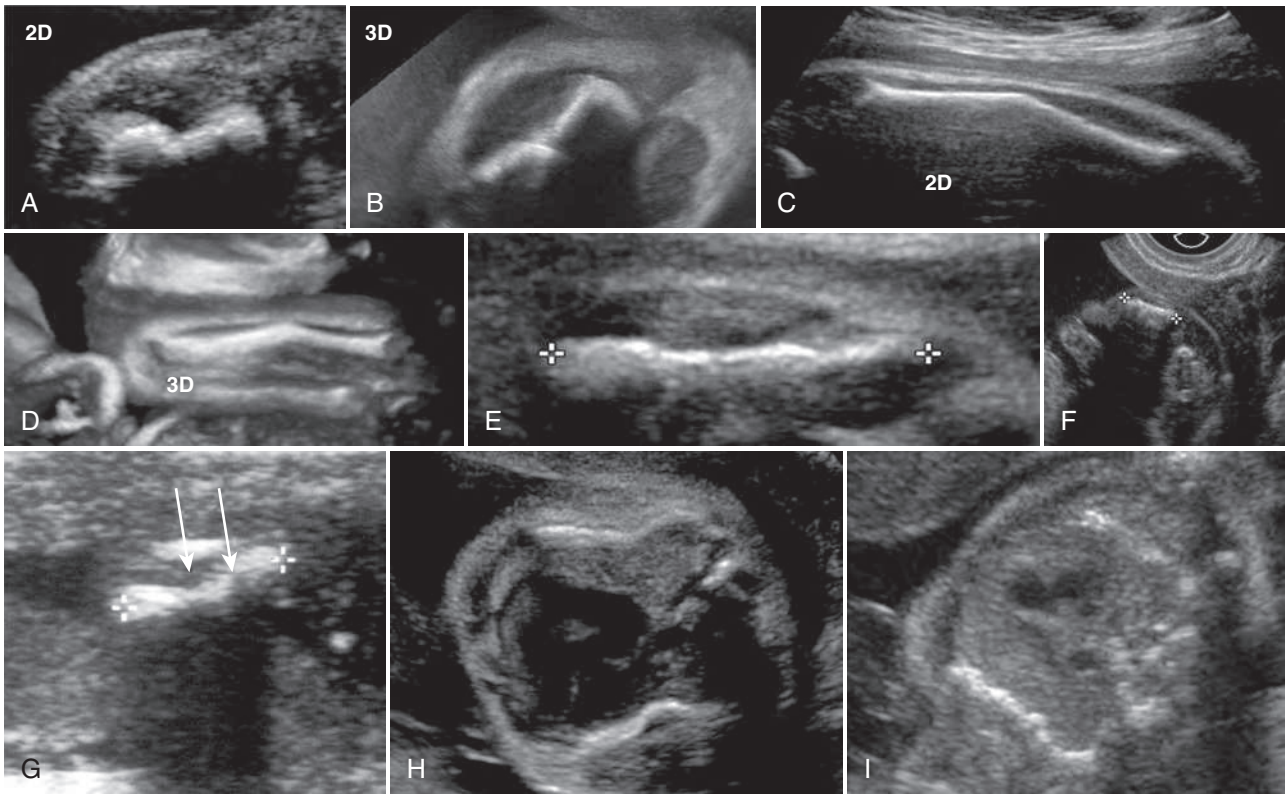

FIG. 40.18 Osteogenesis Imperfecta (OI): Spectrum of Appearances of Fractures. (A) Type IIA. Two-dimensional ultrasound image of extremely shortened femur with at least two bone deformities, consistent with fractures. Note redundant overlying soft tissues. **(B)** Correlative three-dimensional ultrasound image demonstrates a midshaft fracture with callus formation. **(C) Type I.** Nonlethal variant of OI with a mildly angulated femur of normal length. **(D)** Correlative three-dimensional ultrasound image demonstrates the angulated healed fracture. **(E) Type III.** Multiple fractures in the mildly to moderately shortened femur are evidenced by multiple discontinuities in the cortex. The demineralized shaft permits visualization of the thickened cortex. Femur bone length is measured between the *calipers*. **(F) Type II.** Extremely short and thickened femur resulting from repetitive callus formation. Acoustic shadowing is still present in this demineralized fragile bone, and thus its presence is not a reliable sign of normal mineralization. Femur length is measured between the *calipers*. **(G) Type II.** At least two discontinuities are present in the shortened tibia *(arrows),* consistent with fractures. Note acoustic shadowing present despite generalized demineralization. Femur length is measured between the *calipers*. **(H) Type II.** Cross section of the thorax demonstrates a typical concavity noted at the lateral aspect of the thorax. This may be caused by repetitive in utero fractures as the elbows "hit" the fragile rib cage. **(I) Type II.** Cross section of the thorax demonstrates normal-length ribs with multiple fractures within each rib, resulting in a wavy contour.

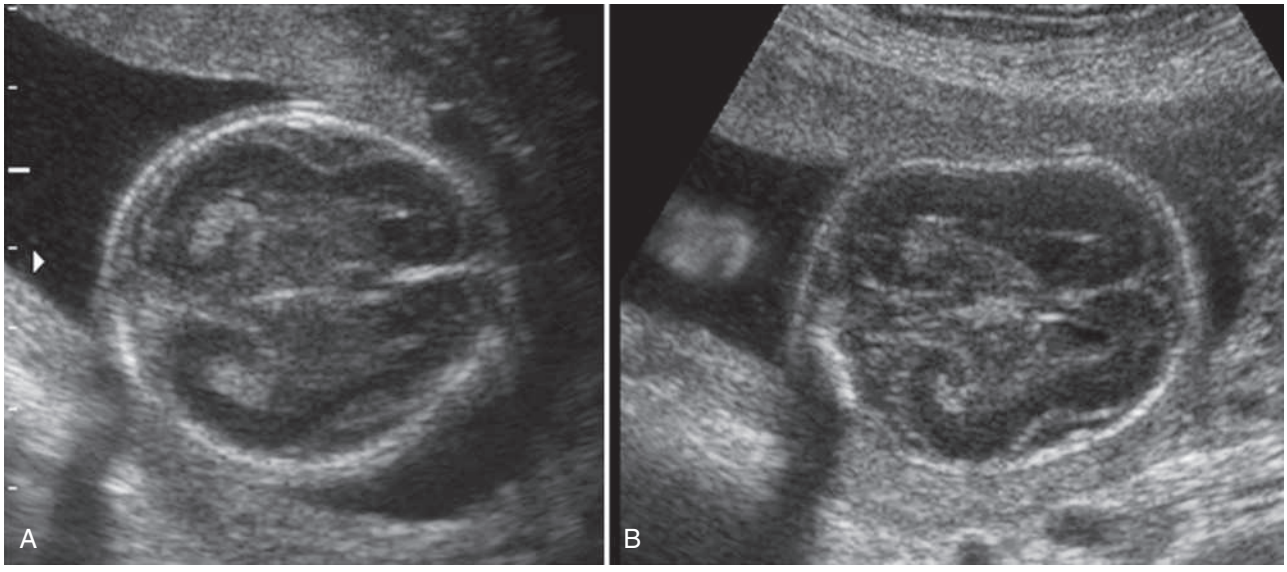

FIG. 40.19 Osteogenesis Imperfecta Type IIA at 17 Weeks. (A) Rounded head contour. **(B)** Gentle transducer compression on the demineralized calvarium results in flattening of the cranial contour. Note widened fontanelles and sutures, as well as ease of visualization of intracranial contents in the near field (which would usually have artifacts caused by shadowing from the ossified skull).

TABLE 40.5 Classification of Osteogenesis Imperfecta by Type

Type	Clinical Features	Prenatal Findings	Prognosis	Inheritance	Molecular Abnormalities
I	Normal stature, little or no deformity, blue sclera, hearing loss in 50% of cases Type IA: normal teeth Type IB: opalescent teeth	Occasionally, short and bowed long bones and fractures	Fair	Autosomal dominant	Nonsense or frameshift mutations in *COL1A1* gene
II	Lethal; hypomineralization of the skull, beaded ribs, compressed femurs, marked long-bone deformity, blue sclera, triangular face, platyspondyly	Severe micromelia Rib and long-bone fractures Hypomineralization of skull	Lethal	Autosomal dominant (new mutations) Parental gonadal mosaicism responsible for recurrence	Glycine missense mutation in *COL1A1* or *COL1A2* genes
III	Usually with long-bone fractures; moderate deformity at birth but progressively deforming bones; triangular face, blue sclera, opalescent teeth, hearing loss, short stature	Occasionally, short and bowed long bones and fractures	Wheelchair bound, nonambulatory	Autosomal dominant Parental gonadal mosaicism responsible for recurrence Autosomal recessive (rare)	Glycine missense mutation in *COL1A1* or *COL1A2* genes
IV	Mild to moderate bone deformity and variable short stature; opalescent teeth in type IVB; hearing loss occurs in some families; white sclera	Occasionally, short and bowed long bones and fractures	Fair	Autosomal dominant Parental gonadal mosaicism responsible for recurrence	Glycine missense mutation in *COL1A1* or *COL1A2* genes

Modified from Sillence DO, Senn A, Danks DM. Genetic heterogeneity in osteogenesis imperfecta. J Med Genet. 1979;16:101-116.[70]

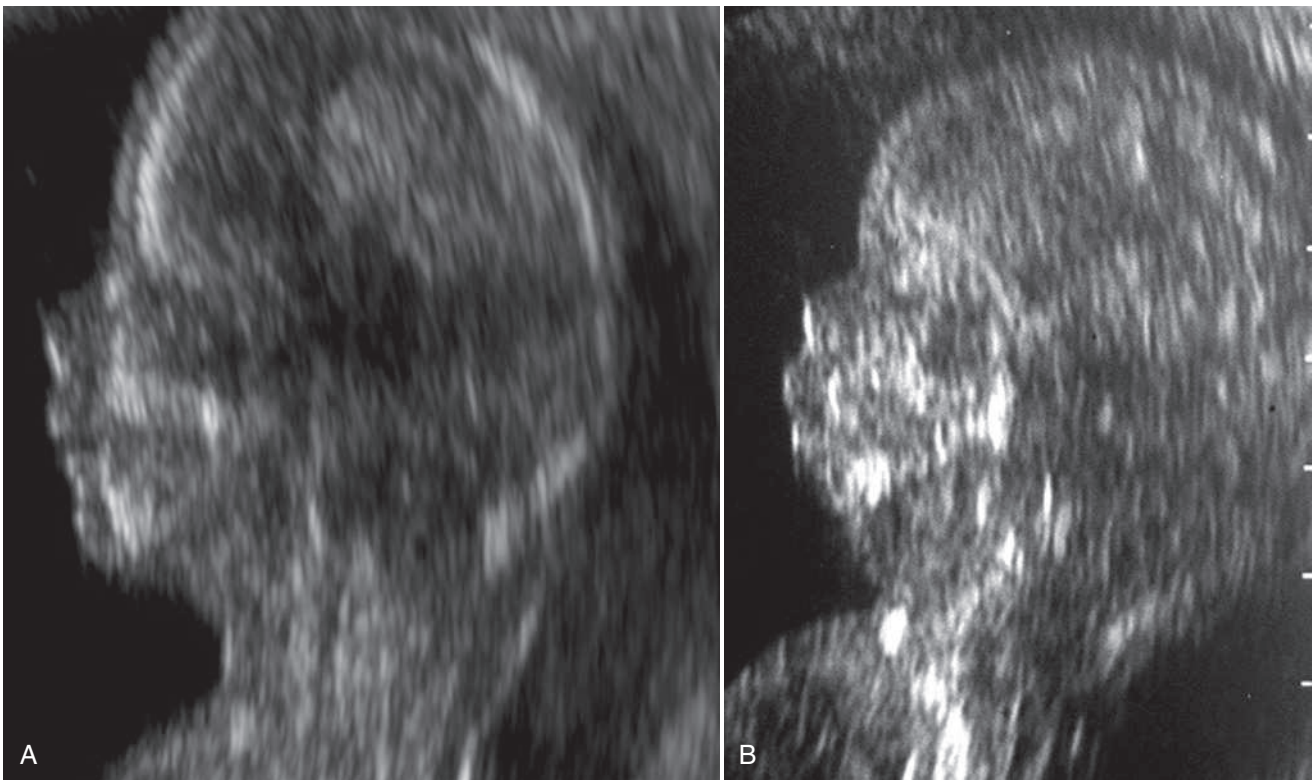

FIG. 40.20 Facial Profile: Normal Versus Osteogenesis Imperfecta (OI). (A) Normal profile of a 14-week fetus. **(B)** Facial profile of a 14-week fetus affected by OI. Note the **absent calvarial and nasal ossification** and **micrognathia.**

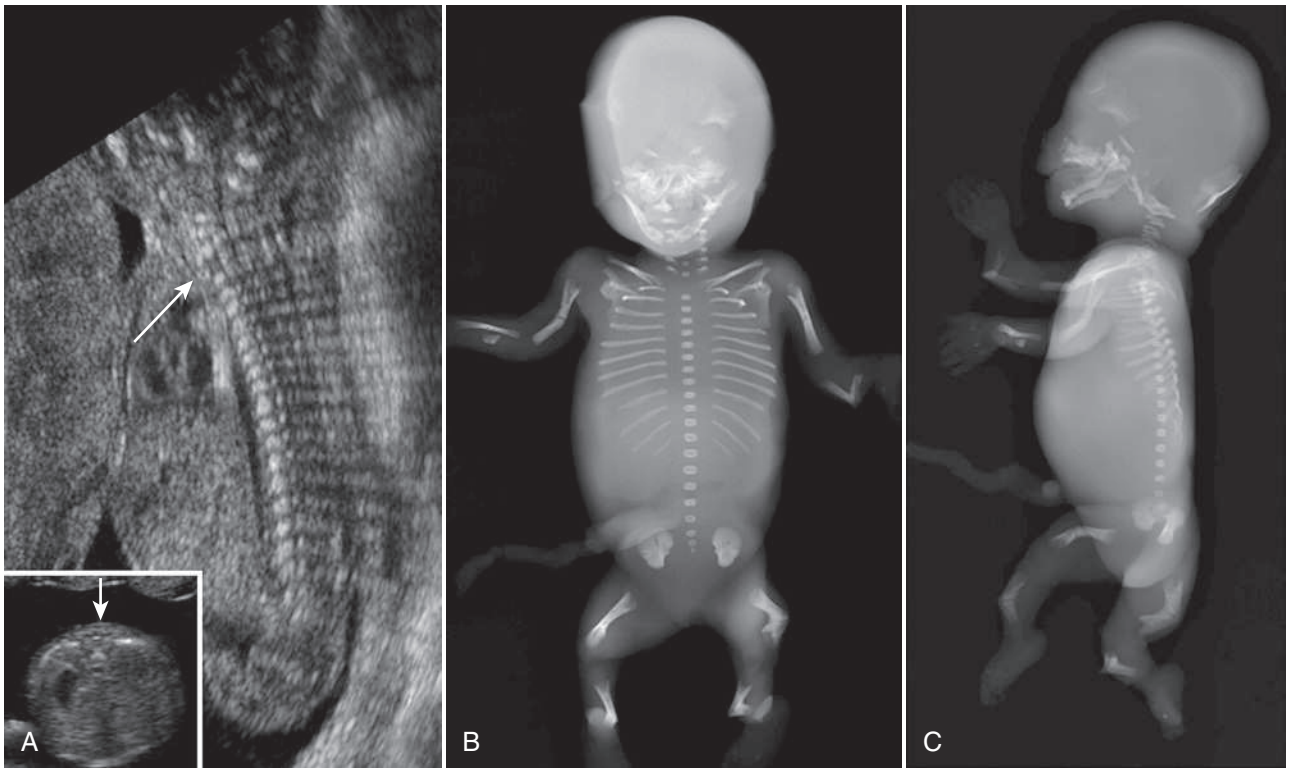

FIG. 40.21 Hypophosphatasia at 18 Weeks. (A) Sagittal image of the spine demonstrates absent ossification of posterior elements of the vertebrae. Patchy form of spine demineralization with absent ossification of a cervical vertebral body *(arrow)*. Note narrow anteroposterior (AP) diameter of thorax. *Inset,* Cross-sectional image of the upper abdomen with absent ossification of posterior elements of the spine *(arrow)* and vertebral body maintaining ossification. **(B)** AP radiograph confirms absent mineralization of a cervical vertebral body, with absent ossification of posterior elements of the vertebrae. Additional findings include **hypoplastic ribs,** occasional fractures, **micromelia,** and decreased cranial vault mineralization. **(C)** Lateral radiograph confirms absent mineralization of posterior elements of the spine.

bones in hypophosphatasia congenita. The normal trunk length and cranial vault size can aid in distinguishing hypophosphatasia from achondrogenesis. Typically, in hypophosphatasia congenita, the posterior elements are poorly ossified, whereas in achondrogenesis, the vertebral bodies are maximally affected by demineralization with relative sparing of the posterior elements[74] (Fig. 40.21). The cartilage is normally formed in hypophosphatasia; thus the fetus has a more normal gross appearance, despite severe bony abnormalities helping to distinguish it from the other lethal skeletal dysplasias.

Campomelic Dysplasia

Campomelic dysplasia, or **bent-limb dysplasia,** is a rare autosomal dominant condition that usually results from a new dominant mutation in *SOX9* (sex-determining region Y-Box 9). The incidence is 0.5 to 1.0 per 100,000 births. Most cases are lethal because of respiratory insufficiency from **laryngotracheomalacia** in combination with a mildly narrowed thorax.

The characteristic skeletal features of campomelic dysplasia are a short and ventrally bowed tibia and femur, a hypoplastic or absent fibula, **talipes equinovarus (clubfoot),** and **hypoplastic scapulae** (Fig. 40.22). Bowing may also occur in the upper extremities. Additional skeletal features may include **scoliosis; hypoplastic or poorly ossified cervicothoracic vertebrae; dislocated hips;** 11 rib pairs; and facial abnormalities, including **micrognathia** and **cleft palate (Pierre Robin sequence).** Approximately 33% of fetuses have congenital heart disease (CHD) and brain (e.g., ventriculomegaly) and renal (e.g., pyelectasis) abnormalities.

Sex reversal is found in about 75% of the affected 46,XY cases, with a gradation of defects ranging from ambiguous genitalia to normal female genitalia phenotype. The gene responsible for campomelic dysplasia is expressed in the fetal brain, the testes, and the perichondrium and chondrocytes of the long bones and ribs.[75]

Short-Rib Polydactyly Syndromes

Short-rib polydactyly dysplasias are a heterogeneous group of rare and lethal skeletal dysplasias with an autosomal recessive mode of inheritance which belongs to a group of conditions called "ciliary chondrodysplasias." Other conditions included in this entity are **Jeune asphyxiating thoracic dystrophy (Jeune syndrome), Mainzer-Saldino syndrome, Sensenbrenner syndrome, cranioectodermal dysplasia, oral-facial-digital syndrome 4 (OFD4, Mohr-Majewski)** and **Ellis–van Creveld syndrome** (EVC). The only exception from this mode of inheritance is **Weyers acrodental dysostosis,** which is caused by heterozygous mutations in the *EVC* genes. All forms are characterized by severe micromelia and decreased thoracic circumference. The cranial vault measurements and bone mineralization are normal. Polydactyly, cardiac, and genitourinary abnormalities are found in most cases.

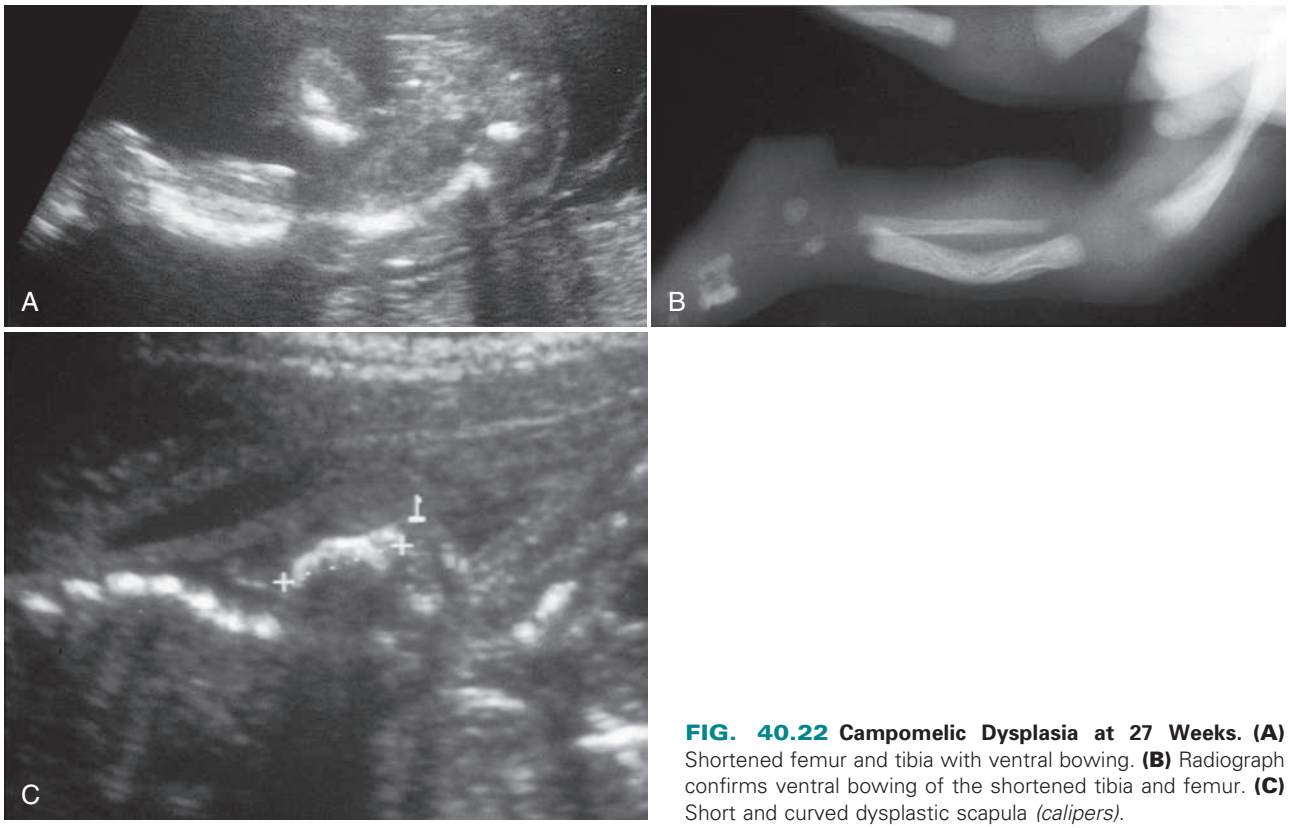

FIG. 40.22 Campomelic Dysplasia at 27 Weeks. (A) Shortened femur and tibia with ventral bowing. **(B)** Radiograph confirms ventral bowing of the shortened tibia and femur. **(C)** Short and curved dysplastic scapula *(calipers)*.

Ellis–van Creveld syndrome (Fig. 40.23A, B, and E) and **asphyxiating thoracic dystrophy** have similar features, but the shortening of the limbs and the narrowing of the thorax are less severe.

The short-rib polydactyly syndromes or short-rib thoracic dysplasia with or without polydactyly consists of multiple types:

Type 1 **(Saldino-Noonan)** and type 3 **(Verma-Naumoff)** syndromes are caused by mutations in the *DYNC2H1* gene (dynein, cytoplasmic 2, heavy chain 1) and *IFT80* gene (intraflagellar transport 80). Type 2 (**Majewski** or **SRTD6**) is caused by mutation in the *DYNC2H1* and *NEK1* genes. Type 4 **(Beemer-Langer)** can occur without polydactyly.[73,76] Type 5 is caused by homozygous or compound heterozygous mutations in the *WDR35* gene. Radiographic and clinical features can distinguish them.[73,76]

Fibrochondrogenesis is a rare, usually fatal condition and survivors suffer from severe physical and neurologic impairment. It is autosomal recessive rhizomelic chondrodysplasia caused by a homozygous mutation or compound heterozygous mutations in the *COL11A1* and *COL11A2* genes. The typical features include narrow chest (short ribs with cupping), short long bones with irregular metaphyses with peripheral spurs, and extraarticular calcifications giving the appearance of stippling, platyspondyly with decreased ossification (particularly cervical vertebrae), and vertebral midline clefts. Other features include flat facies and cleft palate.[77,78]

Other Dysplasias

Other lethal skeletal dysplasias include **atelosteogenesis, boomerang dysplasia, de la Chapelle dysplasia,** and **Schneckenbecken dysplasia.** These dysplasias are rare and difficult to diagnose prenatally.

NONLETHAL OR VARIABLE-PROGNOSIS SKELETAL DYSPLASIAS

The nonlethal or variable-prognosis skeletal dysplasias form a larger group typically presenting with milder and later onset of skeletal abnormalities. Select nonlethal or variable-prognosis skeletal dysplasias with characteristic ultrasound findings are described in Tables 40.6, 40.7, and 40.8.

Heterozygous Achondroplasia

Heterozygous achondroplasia is known to be associated with the c.1138G>A (p.Gly380Arg) gene in about 98% of the cases and the c.1138G>C (p.Gly380Arg) mutation in about 1% of the cases. The *FGFR3* gene is also associated with isolated **craniosynostosis, thanatophoric dysplasia,** and some cases of **hypochondroplasia.**[58,60] The identification of the gene and gene mutations associated with achondroplasia has allowed preimplantation genetic diagnosis as well as prenatal diagnosis, using DNA analysis, when the parents are heterozygous for achondroplasia.[60]

Heterozygous achondroplasia is the most common nonlethal skeletal dysplasia.[5] About 80% of cases are the result of a spontaneous autosomal dominant mutation associated with advanced paternal age, and the remainder are inherited from parental heterozygous achondroplasia. The incidence is 1 in 26,000 births.

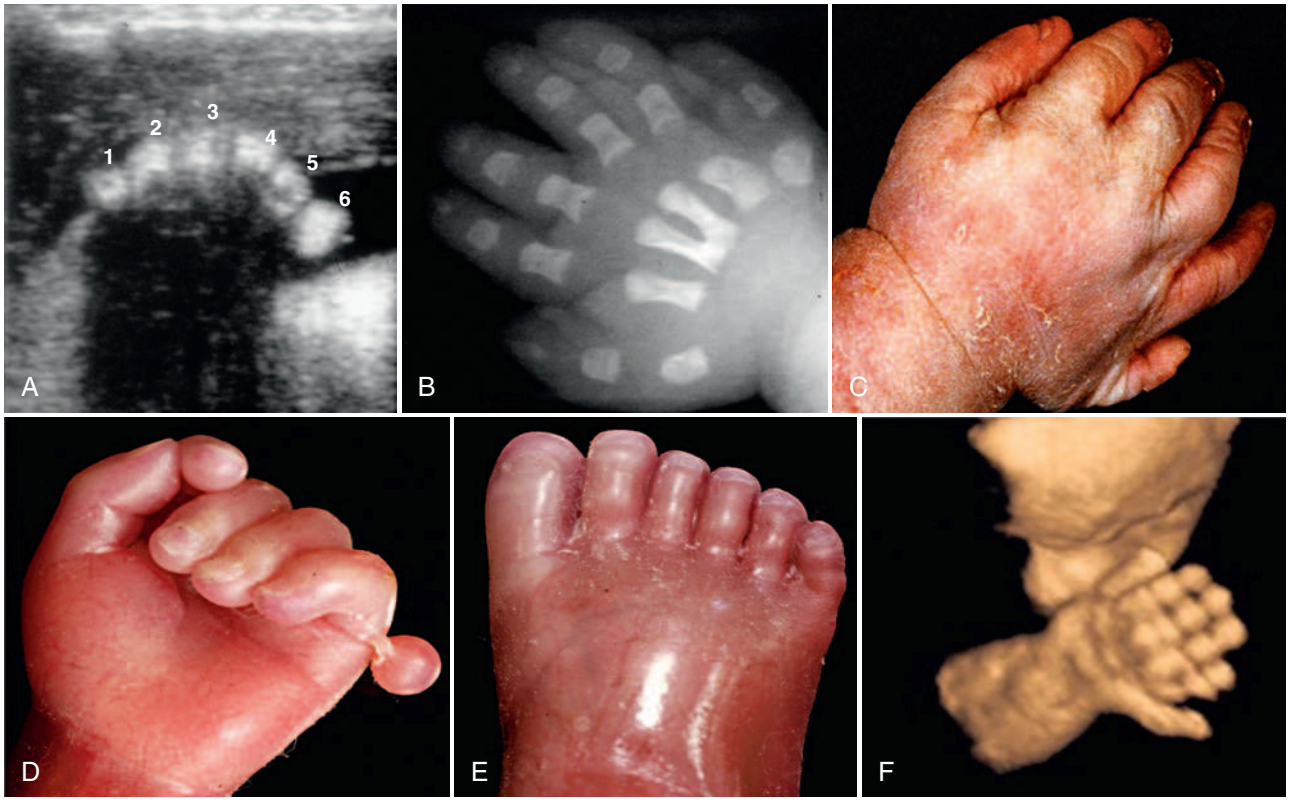

FIG. 40.23 Polydactyly. (A) Ellis–van Creveld syndrome. Postaxial polydactyly on cross section through six digits. **(B)** Corresponding radiograph shows postaxial polydactyly. Note **hypoplastic distal phalanges** and fusion of the third and fourth metacarpals. **(C)** Corresponding pathology specimen. **(D)** Polydactyly may present as a soft tissue nubbin with no bony elements. **(E)** Ellis–van Creveld with toe polydactyly. **(F)** Three-dimensional ultrasound image shows **isolated familial polydactyly.**

TABLE 40.6 Rhizomelic Dysplasia: Key Features

Dysplasia	Prognosis	Degree of Limb Shortening	Key Sonographic Features
Heterozygous achondroplasia	Nonlethal	Mild	Progressive discrepancy in femur length and biparietal diameter
Chondrodysplasia punctata, rhizomelic form	Lethal	Moderate-severe	Stippled epiphysis in third trimester
Diastrophic dysplasia	Variably lethal	Mild-moderate	Hitchhiker thumb, postural deformities, dislocations, joint contractures, clubfoot

TABLE 40.7 Micromelic Dysplasia, Mild: Key Features

Dysplasia	Prognosis	Key Sonographic Features
Asphyxiating thoracic dystrophy	May be lethal	Long narrow thorax, renal anomalies (cystic dysplasia), polydactyly (14%)
Ellis–van Creveld syndrome	May be lethal	Long narrow thorax, congenital heart disease (50% atrial septal defect), polydactyly (100%)

TABLE 40.8 Micromelic Dysplasia, Mild and Bowed: Key Features

Dysplasia	Prognosis	Key Sonographic Features
Osteogenesis imperfecta type III	Nonlethal, progressively deforming	Lower extremities demonstrate greater degree of shortening and fractures/bowing
Campomelic dysplasia	Variably lethal	Ventral-bowing femur and tibia, hypoplastic or absent fibula, hypoplastic scapulas

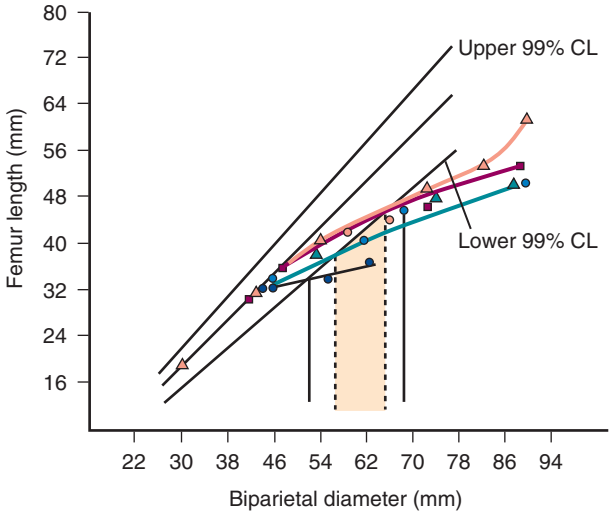

FIG. 40.24 Femur Length (FL) Versus Biparietal Diameter (BPD). Seven cases of recurrent **heterozygous achondroplasia.** The FL falls below the 99% confidence limit (CL) by the time the BPD corresponds to 27 weeks' gestational age (≈69 mm). (With permission from Kurtz AB, Filly RA, Wapner RJ, et al. In utero analysis of heterozygous achondroplasia: variable time of onset as detected by femur length measurements. J Ultrasound Med. 1986;5[3]:137-140.[79])

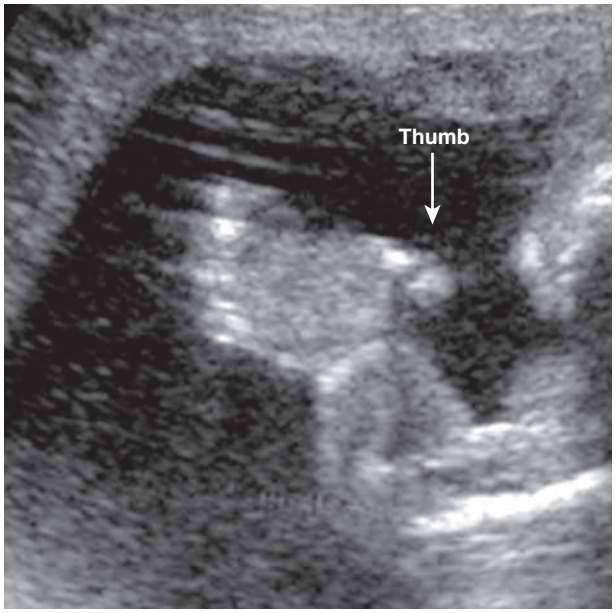

FIG. 40.25 Diastrophic Dysplasia With "Hitchhiker Thumb." (Courtesy of Fetal Assessment Unit, University Health Network.)

The key features are mild to moderate forms of rhizomelic limb shortening (more prominent in upper limbs), **macrocranium, frontal bossing, depressed nasal bridge, midface hypoplasia,** and **brachydactyly,** with a **trident** configuration of the hand. The BPD typically is above the 97th percentile at term. The interpedicular distances progressively narrow from the upper to the lower lumbar spine. There is a progressive discrepancy between FL and BPD during the third trimester, with FL falling below the first percentile compared to BPD[79] (Fig. 40.24). This may occur as early as 21 weeks or as late as 27 weeks' gestational age. Previously considered a diagnosis of the third trimester, recent studies have shown that a second-trimester diagnosis is possible.[79,80]

It is important to recognize that the pattern of BPD greater than expected with FL less than expected for gestational age, in combination with average abdominal circumference measurements, suggests heterozygous achondroplasia. A reliance on the mean of the three values for assessment of gestational age may result in an average value for gestational age, thus masking the BPD/FL discrepancy.

In cases where both parents are heterozygous achondroplasia, fetal ultrasound can differentiate among normal, heterozygous, and homozygous achondroplasia. Patel and Filly[80] report that fetuses with heterozygous achondroplasia have FL that exceeds 34 mm at 26 weeks' BPD age, whereas those with homozygous achondroplasia do not. Fetuses with FL below the third percentile compared with the BPD at 17 weeks' BPD age, with progressive shortening over the following 6 weeks, have homozygous achondroplasia, whereas those with decreasing FL between 17 and 23 weeks' BPD age have heterozygous achondroplasia.[80]

Diastrophic Dysplasia

Diastrophic dysplasia is an autosomal recessive disorder with variable expression and a predominantly rhizomelic form of micromelia. The term *diastrophic* implies "twisted," which reflects the multiple **postural deformities, dislocations, joint contractures,** and **kyphoscoliosis** present.[2] The most characteristic feature is the **"hitchhiker thumb,"** caused by a lateral positioning of the thumb in association with a hypoplastic first metacarpal (Fig. 40.25). The first toe may have similar positioning. There is a severe **talipes equinovarus (clubfoot),** which may be refractory to surgical treatment. Other features include **micrognathia, cleft palate** (50%), and **laryngotracheomalacia.** The life span may be normal if the progressive kyphoscoliosis does not compromise cardiopulmonary function. The diastrophic dysplasia gene was mapped to the long arm of chromosome 5 and found to encode a novel sulfate transporter. Mutations in the same gene are reported in **achondroplasia** type 1B and **atelosteogenesis** type II.[81,82]

Asphyxiating Thoracic Dysplasia

Asphyxiating thoracic dysplasia, or **Jeune syndrome,** is an autosomal recessive disorder with variable expressivity. The incidence is about 1 in 100,000 births. The perinatal mortality rate is high as a result of pulmonary hypoplasia. Those who survive may develop **renal** and **hepatic fibrosis**[2,81] (see Table 40.8). Key features are a mild to moderate form of **micromelia** (60%) with rhizomelic predominance, a long narrow thorax with short **horizontal ribs, inverted "handlebar" appearance of the clavicles, renal dysplasia and cysts,** and **postaxial polydactyly** in 14%.

Ellis–van Creveld Syndrome

Ellis–van Creveld syndrome, or **chondroectodermal dysplasia,** is an autosomal recessive disorder with an incidence of 1 in

150,000 births. The condition has a high prevalence among inbred populations, such as the Amish and the Arabs of the Gaza Strip.[73] It is generally a nonlethal disorder, but death can result from pulmonary hypoplasia.[35,73] The condition is caused by homozygous or compound heterozygous mutation in the *EVC* gene on chromosome 4p16. Ellis–van Creveld syndrome can also be caused by mutation in a nonhomologous gene, *EVC2,* located close to the *EVC* gene. Mutations in the *EVC* and *EVC2* genes also cause **Weyers acrofacial dysostosis,** an allelic disorder showing autosomal dominant mode of inheritance.

Key features include mild to moderate form of **micromelia** with a mesomelic predominance, **short horizontal ribs, postaxial or ulnar polydactyly**[2] (see Fig. 40.23A, B, and E) that is almost 100% in the hands and 25% in the feet,[64] and CHD (50%), most often **atrial septal defect.** Additional findings include a progressive distalward shortening of the extremities with **hypoplastic distal phalanges.** Fusion of the metacarpals and phalanges is common. The presence of polydactyly, CHD, and the absence of renal cysts help to distinguish this condition from **asphyxiating thoracic dystrophy.**

Chondrodysplasia Punctata

Chondrodysplasia punctata, or **stippled epiphyses,** is a heterogeneous group of disorders with many small calcifications **(ossification centers)** in the cartilage, in the ends of bones, and around the spine. Known associated conditions include single-gene disorders such as rhizomelic chondrodysplasia punctata, **Conradi-Hünermann syndrome,** and **Zellweger syndrome (cerebrohepatorenal syndrome);** chromosomal abnormalities such as trisomy 21 and 18; maternal autoimmune diseases; and teratogen exposure (e.g., warfarin, alcohol).[83,84]

Rhizomelic chondrodysplasia punctata is an autosomal recessive condition caused by a peroxisomal disorder that appears as severe, symmetrical, predominantly rhizomelic limb shortening.[73,85] The incidence is 1 in 110,000 births, and it is generally lethal before the second year of life. The condition is the result of peroxisomal dysfunction caused by homozygous or compound heterozygous mutations in the *PEX7* gene. It can be associated with low unconjugated estriol concentration on second-trimester screening for Down syndrome.

The humeri tend to be relatively shorter than the femurs and have **metaphyseal cupping.** The enlarged epiphyses with characteristic stippling may be identified on ultrasound in the third trimester (see Fig. 40.2I). Other abnormalities include dysmorphic facial features, **joint contractures, coronal clefting of the vertebral bodies,** brain abnormalities, and severe mental retardation.

Conradi-Hünermann syndrome, or **the nonrhizomelic** form of chondrodysplasia punctata (CDPX2), is an X-linked dominant condition with extreme phenotypic variations, rendering the antenatal diagnosis difficult in the absence of known family history. The widely variable phenotypic presentation may be related to random X inactivation.[86,87] CDPX2 is uncommon, with X-linked dominant inheritance and possible lethality in the hemizygous male (Xp11).[86] The characteristic skeletal abnormalities are asymmetrical shortening of the extremities with punctate calcifications primarily affecting the ends of long bones, the carpal and tarsal regions, paravertebral region, and pelvic bones. Stature is usually reduced; kyphoscoliosis with shortening of the long bones (particularly femur and humerus) and dysmorphic facial features are common.[84]

Dyssegmental Dysplasia

Dyssegmental dysplasia is a rare autosomal recessive skeletal dysplasia characterized by gross vertebral disorganization. The findings typically include micromelia, short narrow thorax, joint rigidity, **anisospondyly** (gross irregularity of the size and shape of the vertebral bodies) which may include malsegmentation, clefting or "oversize" bodies, kyphoscoliosis, and multiple ossification centers. The gross spine disorganization may be recognized as early as the first trimester. The more severe form is referred to as **Silverman-Handmaker** and the milder form as **Rolland-Desbuquois,** although some think that dyssegmental dysplasia may represent a spectrum of findings caused by different mutations in the heparin sulphate perlecan gene 2 *(HSPG2).*[88]

Osteogenesis Imperfecta Types I, III, IV—Nonlethal Types

OI type I is a mild, "tarda" variant inherited in an autosomal dominant manner as a result of mutation in the *COL1A1* (on chromosome 17) or *COL1A2* (on chromosome 7) and possibly in other collagen genes. OI **type I** is a generalized connective tissue disorder characterized by bone fragility and blue sclerae. The bones are of normal length, and only 5% have fractures at birth. Most fractures occur from childhood to puberty. There is progressive hearing loss in approximately 50% of type I cases. OI **type III** has a heterogeneous mode of inheritance. This is a nonlethal, progressively deforming variety of OI that often spares the humeri, vertebrae, and pelvis. Rib involvement is variable. The blue sclerae will normalize, and there is no associated hearing impairment. **Type IV** is an autosomal dominant form of OI. It is the mildest form, involving isolated fractures. The sclerae are blue at birth but normalize over time. There is no associated hearing impairment.

LIMB REDUCTION DEFECTS AND ASSOCIATED CONDITIONS

These heterogeneous disorders are associated with a spectrum of limb defects caused by chromosomal abnormalities, single-gene disorders, and maternal exposures and diseases. There are three major categories of limb reduction defects. A **malformation** is a defect resulting from an abnormal developmental process. A **deformation** is an abnormality of form, shape, or position caused by mechanical forces. A **disruption** is a defect caused by the extrinsic breakdown or interference with an originally normal developmental process. The defect can consist of the absence of an entire limb **(amelia),** of part of a limb **(phocomelia),** or of digits **(oligodactyly),** or it can involve an increased number of digits **(polydactyly).**[89] It can also affect only the **radial ray** or **ulnar ray,** with or without involvement of the corresponding fingers (Table 40.9).

The overall incidence of congenital limb reduction deformities is estimated at 4 in 100,000 births. An isolated amputation may be caused by **amniotic band sequence, teratogen exposure,** or a vascular accident. The prenatal detection rate of isolated limb reduction defect is estimated at 14.6%, compared to 49.1% when associated anomalies are detected.[90] **Terminal transverse limb defects** are associated with amniotic bands only in some cases, and thus other causes (e.g., vascular disruption, fetal hypoxemia, errors in embryologic development) are suspected in other cases.

TABLE 40.9 Nomenclature of Limb Anomalies

Anomaly	Description
LIMB REDUCTION ANOMALIES	
Amelia	Absent limb
Adactyly	Absent digits
Acheiria	Absent hand
Apodia	Absent foot
Hemimelia	Absent extremity distal to knee or elbow
Phocomelia	Absent middle segment of limb
Ectrodactyly	Split hand
Ulnar or radial hemimelia	Absent ulnar and ulnar digits paraxial or radius and thumb
HAND AND FOOT ANOMALIES	
Clinodactyly	Incurvature of a digit
Camptodactyly	Flexion of a digit
Syndactyly	Fusion of digits
Polydactyly	Extra digits
Oligodactyly	Decreased number of digits

Proximal Focal Femoral Deficiency

Proximal focal femoral deficiency is a rare, sporadic condition, and 35% of those affected are infants of diabetic mothers[64] (see Figs. 40.2C and 40.26). There is an asymmetrical degree of absence of the **subtrochanteric femur,** which may extend to the femoral head and acetabulum.[73] The femoral hypoplasia is often associated with ipsilateral fibular hemimelia, which may result in a bowed appearance of the tibia, similar to that of campomelic dysplasia; however, proximal focal femoral deficiency is generally unilateral. Hypoplasia or aplasia of other long bones, vertebral anomalies, microcephaly, and facial dysmorphism can also occur. If the defect is unilateral, it may represent the **femur-fibula-ulnar complex,** which is nonfamilial, versus the **femur-tibia-radius complex,** which has a strong genetic association.[91] When associated with the unusual facies syndrome, the femoral hypoplasia is usually bilateral.

Radial Ray Defects

Radial ray defects are associated with a wide variety of syndromes. The diagnosis is based on the absence of a visualized distal radius at the same level as the ulna, in association with a radial deviation or clubhand (Fig. 40.27). There may be bowing or hypoplasia of the ulna and a hypoplastic or absent thumb. Ulnar ray defects are rare.

Fanconi pancytopenia (syndrome) is an autosomal recessive blood dyscrasia in which 50% of cases have an associated unilateral or bilateral aplastic or hypoplastic thumb and radius. Identification of the **thumb hypoplasia or aplasia** in association with a **radial ray defect** suggests this diagnosis, initiating discussion of prenatal diagnosis and potential cesarean section to avoid excessive bleeding (Fig. 40.28). Prenatal diagnosis is based on increased chromosome breakage and sister chromatid exchange in cultured amniotic fluid cells, both before and after exposure to diepoxybutane.[92]

FIG. 40.26 Isolated Femoral Hypoplasia at 20 Weeks. Note the downside left femur is short and curved.

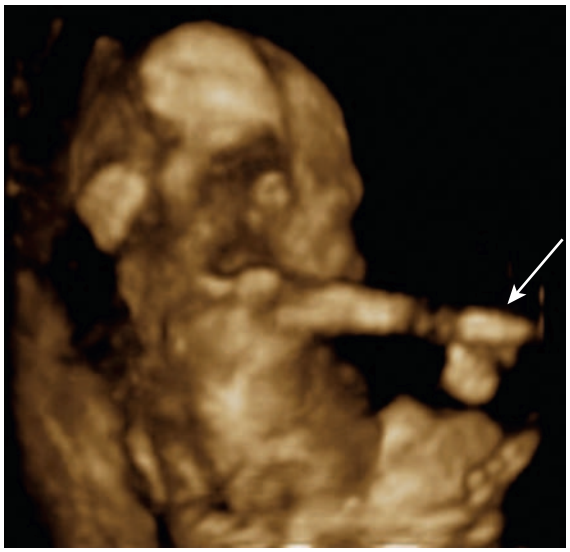

FIG. 40.27 Radial Ray Anomaly Diagnosed at 13 Weeks' Gestation. Three-dimensional ultrasound surface display demonstrates the **hypoplastic radius and ulna** in association with **talipomanus (clubhand)** *(arrow).*

Diamond-Blackfan (Aase syndrome) is genetically a heterogeneous condition with an autosomal dominant mode of inheritance. It is associated with hypoplastic anemia, a hypoplastic distal radius with radial **clubhand,** and a **triphalangeal thumb.** Associated cardiac defects (ventricular septal defect, coarctation of aorta) may be present. Triphalangeal thumb may also be found in **Holt-Oram syndrome,** chromosomal abnormalities, and fetal **hydantoin exposure.**

Thrombocytopenia–absent radius syndrome is an autosomal recessive blood dyscrasia characterized by hypomegakaryocytic thrombocytopenia and bilateral absence of the radii.[93] The thumb is present. The humerus and lower extremities are variably involved. One-third of such patients have CHD, typically tetralogy of Fallot or septal defects. Fetuses are at risk of intracranial hemorrhage, so delivery by cesarean section is recommended (Fig. 40.29). The causative gene is *TBX5.*

Holt-Oram syndrome is an autosomal dominant disorder consisting of a congenital heart defect (atrial or ventricular septal defect) in combination with a variety of upper limb anomalies. The limbs are asymmetrically affected, with the left limb usually showing more effects than the right. The lower extremities are not involved. The causative gene is *TBX5.*

Roberts syndrome, or **pseudothalidomide syndrome,** is an autosomal recessive disorder characterized by **tetraphocomelia** and **bilateral cleft lip and/or palate.** The limb reductions are most prominent in the upper extremities. Typically it is associated with premature separation of the centromere and homozygous or compound heterozygous mutation in the *ESCO2* gene.

Other conditions associated with radial ray abnormalities include **trisomies 18 and 13, the VACTERL association, acrorenal syndrome, Cornelia de Lange syndrome, Goldenhar syndrome, Nager acrofacial dysostosis,** and **Klippel-Feil syndrome.**

Amniotic Band Sequence

Amniotic band sequence is suspected to be secondary to first-trimester rupture of the amnion, resulting in **amniotic bands** that extend from the chorionic surface of the amnion to the fetal tissue.[94,95] The incidence is approximately 1 in 1200 live births but is much higher in spontaneous abortions. Depending on the timing and orientation of the bands, the resultant disruption of fetal organs includes **amputations** of limbs or digits (Figs. 40.30 and 40.31), bizarre facial or cranial clefting, and **thoracoabdominal schisis.** The distribution is asymmetrical. Constriction ring defects are the most common finding. Fibrous bands of tissue with a constricting ring and distal elephantiasis or protrusion of uncovered bone distally are pathognomonic for this anomaly (Fig. 40.32). Antenatally, an aberrant band attached to the fetus, with characteristic deformities and restriction of motion, permits the diagnosis. An amniotic sheet is a **synechia,** or scar in the uterus, and is distinguished from an amniotic band by a thickened base and a free edge.[96] Synechiae are not associated with amniotic band sequence.

The **limb–body wall complex** is a sporadic disorder that occurs in approximately 1 in 4000 births with a similar, but more severe and lethal, complex of fetal malformations.[97] Additional findings include evisceration of internal organs, **myelomeningocele,** marked **scoliosis,** and **short straight umbilical cord.**

Caudal Regression Syndrome and Sirenomelia

Caudal regression syndrome consists of partial to complete **sacral agenesis** and abnormalities of the lumbar spine, pelvis, and lower limbs.[98-100] The majority of cases are associated with maternal **diabetes,** but familial cases have been reported. **Sirenomelia** is characterized by an absent sacrum, fusion of the lower extremities, anorectal atresia, and renal dysgenesis or agenesis (Fig. 40.33). Severe oligohydramnios and single umbilical artery are typically present. Prevalence is approximately 1 in 60,000 births.

Arthrogryposis Multiplex Congenita

Arthrogryposis multiplex congenita is etiologically a heterogeneous group of disorders with **multiple joint contractures** of prenatal onset[101] (Fig. 40.34). Normal fetal motion by approximately 7 or 8 weeks onward is required for development of the musculoskeletal system, and the lack of movement results in joint contractures. Some cases result from extrinsic causes, such as oligohydramnios, twinning, or uterine masses, and most of these have a good prognosis. Intrinsic causes include neuromuscular disorders (most cases) and skeletal and connective tissue disorders. Typically, the severity of the deformity increases distally, with maximal deformity in the hands and feet. This may result in the **"Buddha position"** of the fetus, with arms and legs crossed and ending in clubhand or clubfoot (Fig. 40.34D). The **fetal akinesia sequence** refers to the combination of decreased or no fetal movements, multiple joint contractures, in most cases IUGR, underdevelopment of the bones, pulmonary hypoplasia, typical craniofacial abnormalities, and a short umbilical cord.

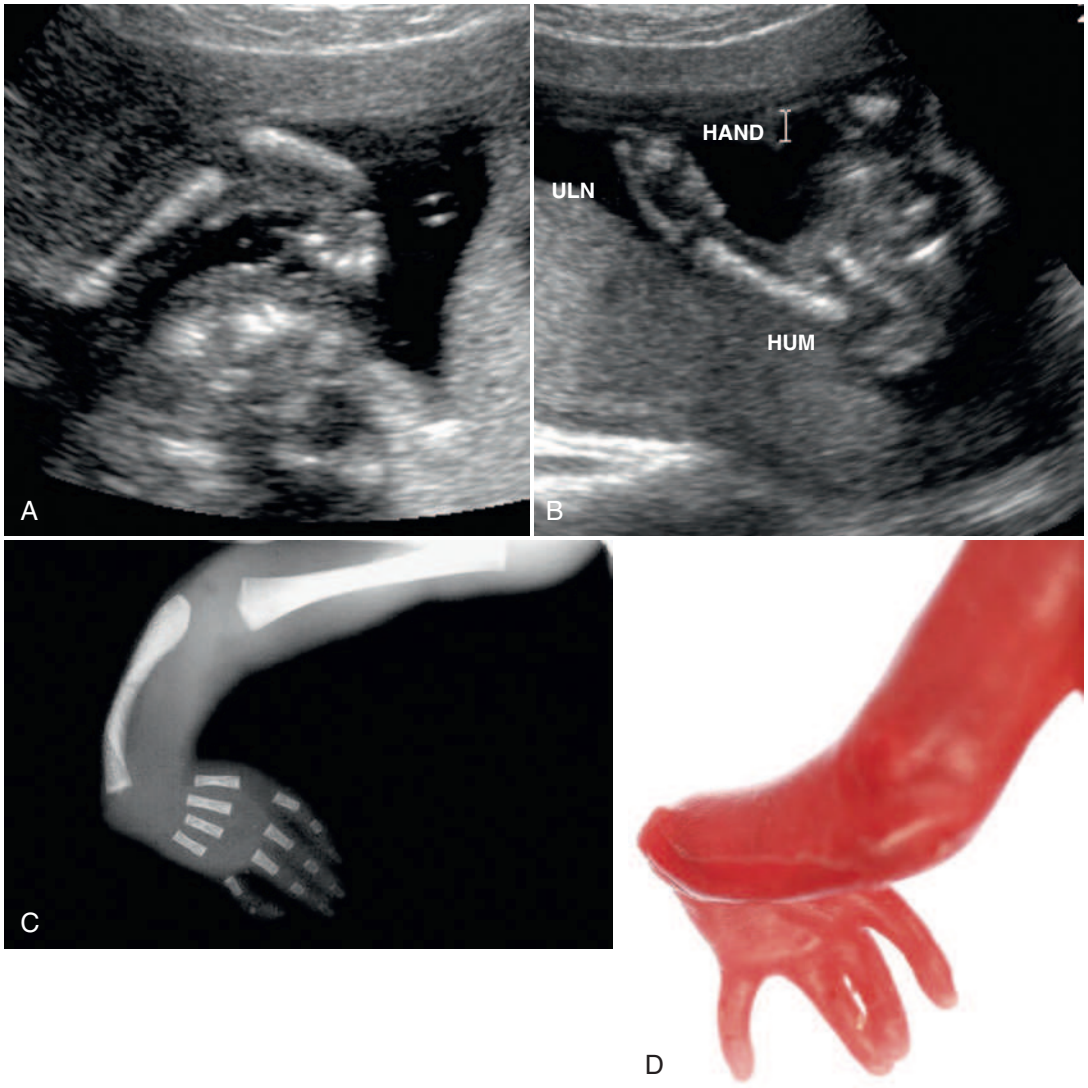

FIG. 40.28 Fanconi Pancytopenia. Radial ray aplasia with talipomanus and bilateral absence of thumbs. (A) Radial deviation left hand, or clubhand, secondary to radial ray aplasia and ulnar hypoplasia. Note absent thumb. **(B)** More extreme example of radial deviation hand or clubhand secondary to radial ray aplasia and ulnar hypoplasia. *HUM,* Humerus; *ULN,* ulna. **(C)** Correlative radiograph (of **A**) of left arm. Note absent thumb. **(D)** Correlative specimen photograph of **A.** Note absent thumb. (Courtesy of Shia Salem, MD, University of Toronto.)

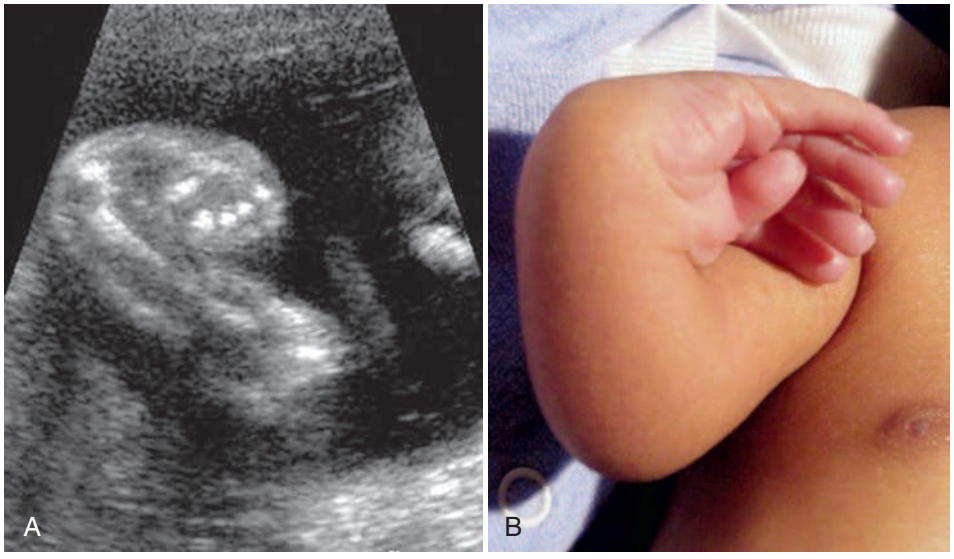

FIG. 40.29 Thrombocytopenia–Absent Radius Syndrome. (A) Absent radius in association with hypoplastic ulna results in talipomanus. Note that thumb is present. **(B)** Correlative specimen photograph.

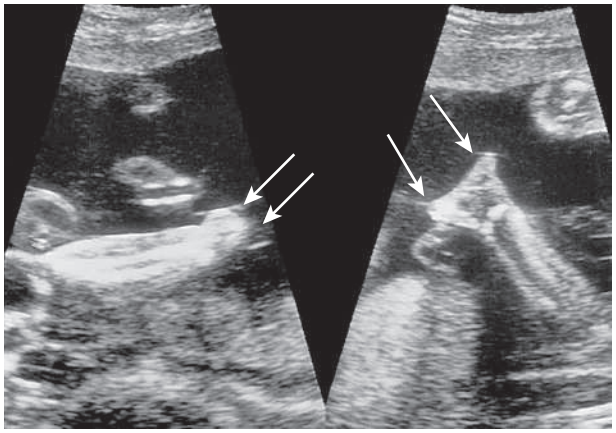

FIG. 40.30 Amputation of the Hand. Upper extremity ends abruptly distal to the wrist, in the midcarpal region *(arrows)*. (Courtesy of Ants Toi, MD, University of Toronto.)

Limb pterygium, or webbing of the skin across a joint, can involve a single joint or several joints[102] and etiologically is a heterogeneous disorder. Popliteal pterygium is the most common dominantly inherited pterygium syndrome and is associated with mutations in the *IRF6* gene.[103]

Asymmetrical **limb enlargement** may be caused by **hemihypertrophy, cutaneous hemangioma** or **lymphangioma, elephantiasis** secondary to a constricting band, **arteriovenous malformations, neurofibromatosis,** or **Beckwith-Wiedemann syndrome.**

Hereditary lymphedema type 1 (Nonne-Milroy lymphedema) is a rare autosomal dominant condition secondary to deficient lymphatic drainage, typically affecting the lower extremities. The subcutaneous tissues of the affected extremity appear diffusely thickened. Associated ascites and pleural effusions may be seen. There is variable expressivity and age of onset[104] (Fig. 40.35).

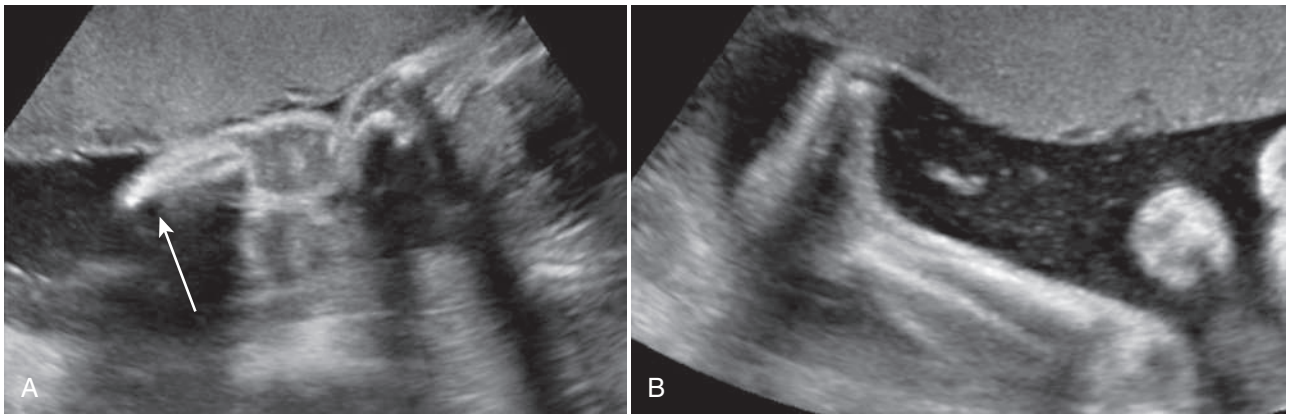

FIG. 40.31 Amputation of Right Lower Extremity. (A) Ultrasound image demonstrates abrupt ending of the right lower limb *(arrow)*. **(B)** Comparison ultrasound image shows normal left lower limb.

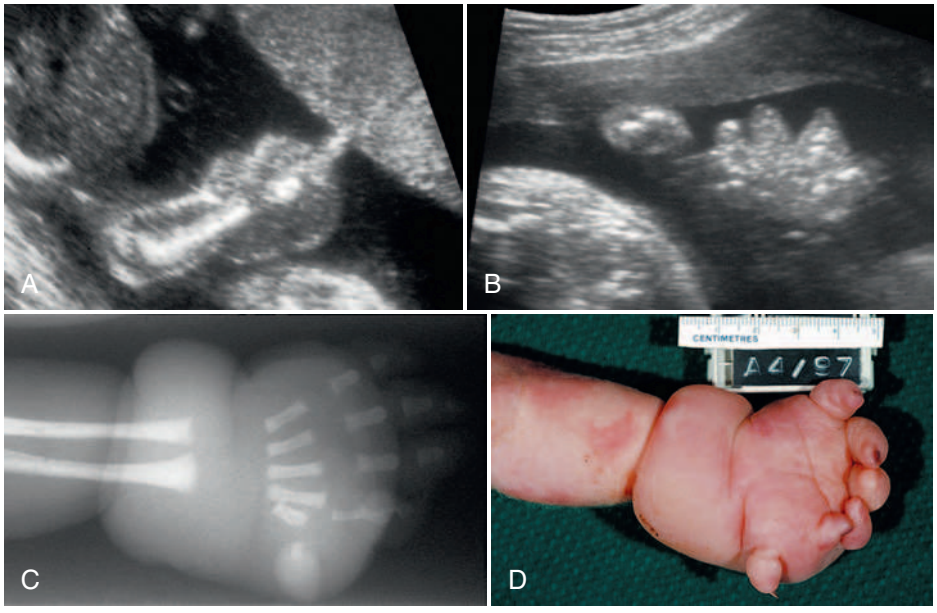

FIG. 40.32 Amniotic Band Sequence. Constriction rings with distal elephantiasis. **(A)** Ultrasound lateral image of the distal forearm and hand demonstrates the two constriction rings with elephantiasis. **(B)** Ultrasound of the digits demonstrates the distal tapering of the digits. **(C)** Radiograph demonstrates the two constriction rings in the distal forearm and hand. **(D)** Correlative specimen photograph.

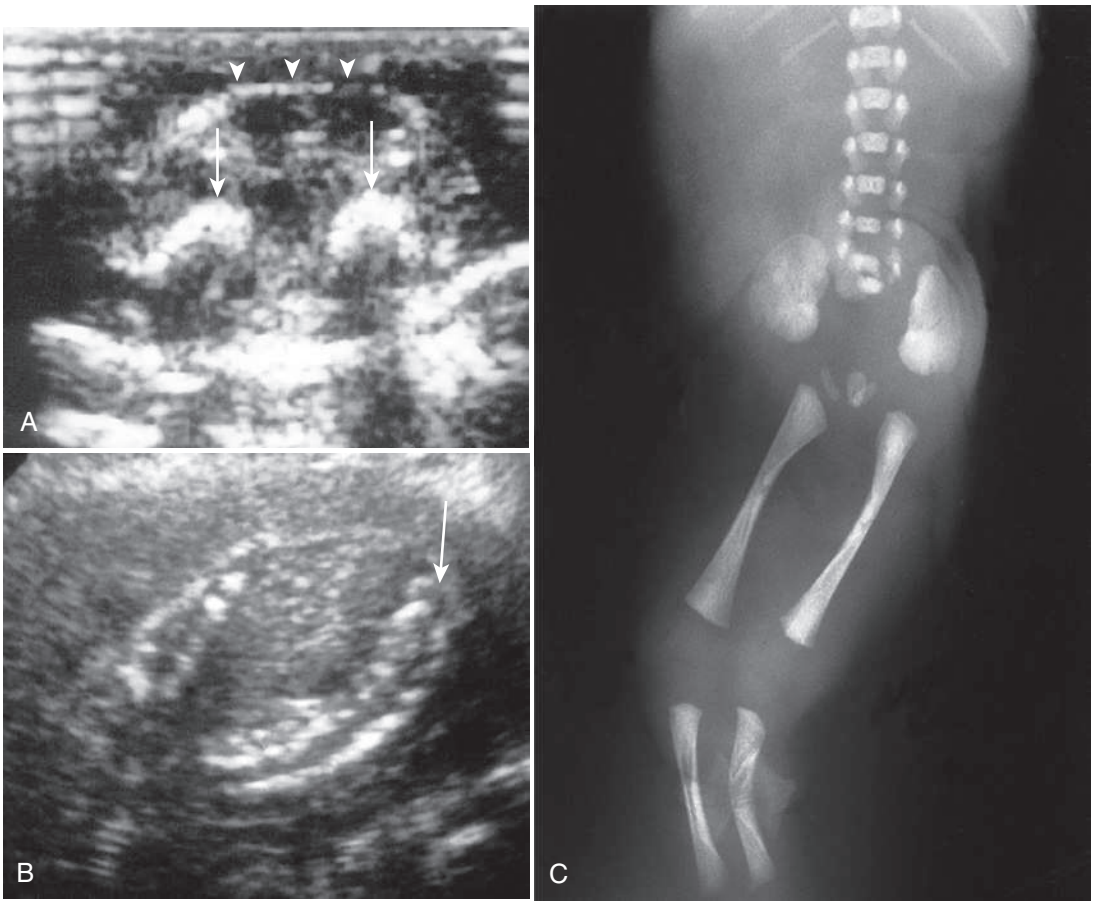

FIG. 40.33 Sirenomelia. (A) Cross section of lower extremities. Femurs *(arrows)* are closer than expected because of fusion of the overlying soft tissues with a continuous layer of overlying skin *(arrowheads).* **(B) Sacral agenesis** with abrupt termination of the lower spine *(arrow).* **(C)** Single, fused lower extremity and sacral agenesis.

Extremity enlargement may also be related to thickened subcutaneous tissues, as in hydrops or large-for-gestational-age infants.

Kyphoscoliosis may be a manifestation of an isolated vertebral defect or may be associated with **myelomeningocele** or with complex syndromes, such as **VACTERL, limb–body wall complex, neurofibromatosis, arthrogryposis, diastrophic dysplasia,** and other skeletal dysplasias.

HAND AND FOOT MALFORMATIONS

A complete digit evaluation can be performed by 12 to 13 weeks' gestation.[105] The fetus typically maintains open hands with digit extension in the first half of gestation, whereas in the second half of gestation the fetus may maintain hand closure for relatively prolonged periods, up to 30 minutes, limiting detailed evaluation. The incidence of finger abnormalities is approximately 1 in 1000 fetuses, of which 60% will have either an associated malformation sequence or karyotypic malformation. The optimal time for evaluation of the hands and feet is during the second trimester.[14,106-108]

Transient findings represent a potential pitfall in the analysis of the distal extremities. During the second half of gestation, the fetus may appear to have **pseudosyndactyly** by maintaining a closed hand for prolonged periods. The diagnosis of an isolated clubfoot can be risky because the fetus can hold the foot in a position to suggest the diagnosis in the absence of a structural defect. An apparent clubfoot may be secondary to positioning against the maternal uterine wall or in the setting of oligohydramnios, which subsequently resolves with a change in fetal position or amniotic fluid volume.

Aneuploidy is associated with an increased risk of hand and foot anomalies, including persistent **clenched hand, overlapping digits, clinodactyly, polydactyly, syndactyly, simian creases, talipes equinovarus, rocker-bottom foot,** and **sandal toes** (Fig. 40.36).

Persistent clenched hand with overlapping of digits occurs in more than 50% of trisomy 18 fetuses and is generally bilateral. This characteristic hand appearance is highly suggestive of trisomy 18 but can also occur in other conditions, such as **fetal akinesia syndrome** and **triploidy.**

Clinodactyly is the permanent incurvature of a finger. Clinodactyly, caused by asymmetrical hypoplasia of the middle phalanx (medial shorter than lateral aspect), most often involves the fifth finger and is associated with trisomies 13, 15, 18, and 21 (Fig. 40.36G). Clinodactyly occurs in 60% of fetuses with trisomy 21; however, up to 18% of normal fetuses may have a

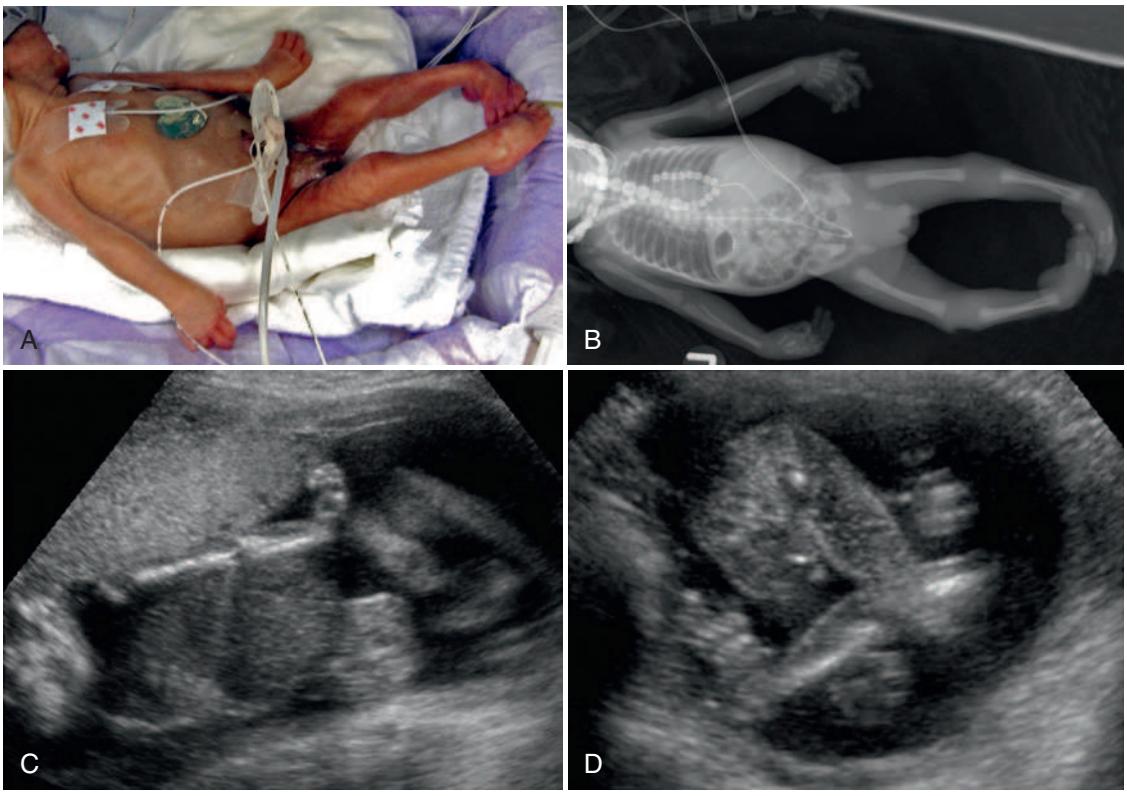

FIG. 40.34 Arthrogryposis Multiplex Congenita. Decreased muscle bulk is replaced by a mixture of fat and adipose tissue, resulting in multiple congenital joint contractures, including fixed internal rotation of shoulders, hyperextension of elbows, flexion of wrists, and talipes equinovarus (clubfoot). Note that severity of deformity increases distally. The knees and hips at birth were demonstrated to be nonrigid contractures amenable to conservative postural therapy. **(A)** Photograph demonstrates fixed contractures of the elbows, wrists, digits, and ankles. **(B)** Radiograph demonstrates similar contractures. **(C)** Ultrasound of upper extremity demonstrates fixed extension of the elbow and fixed flexion of the wrist and digits with talipomanus. **(D)** "Buddha position" with flexed hips, knees, and ankles and clubfoot distally.

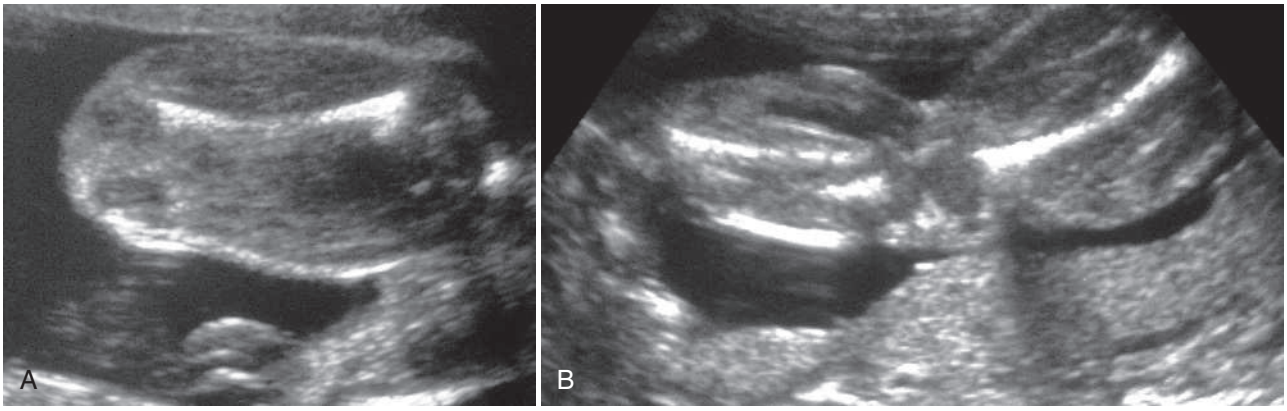

FIG. 40.35 Hereditary Lymphedema at 21 Weeks. (A) Femur surrounded by marked thickening of the subcutaneous tissues. **(B)** Lower extremity with marked thickening of subcutaneous tissues.

mild degree of clinodactyly.[106] **Camptodactyly** is the permanent flexion of a finger caused by flexion contracture of an interphalangeal joint.

Polydactyly is the presence of extra digits on the foot or hand. Most cases are isolated, but extra digits can be associated with syndromes and chromosomal abnormalities. Polydactyly may be diagnosed toward the end of the first trimester. The extra digit may consist of a small, soft tissue projection or a complete digit. **Postaxial polydactyly** (ulnar or fibular) is more common and is found in conditions such as **Ellis–van Creveld syndrome, asphyxiating thoracic dystrophy, short-rib polydactyly syndrome,** and **trisomy 13.**

Polydactyly may be an isolated finding and can be hereditary and familial. Because this form is associated with a good prognosis, it is important to review the pertinent family history. **Preaxial** (radial or tibial) **polydactyly** is found in familial conditions,

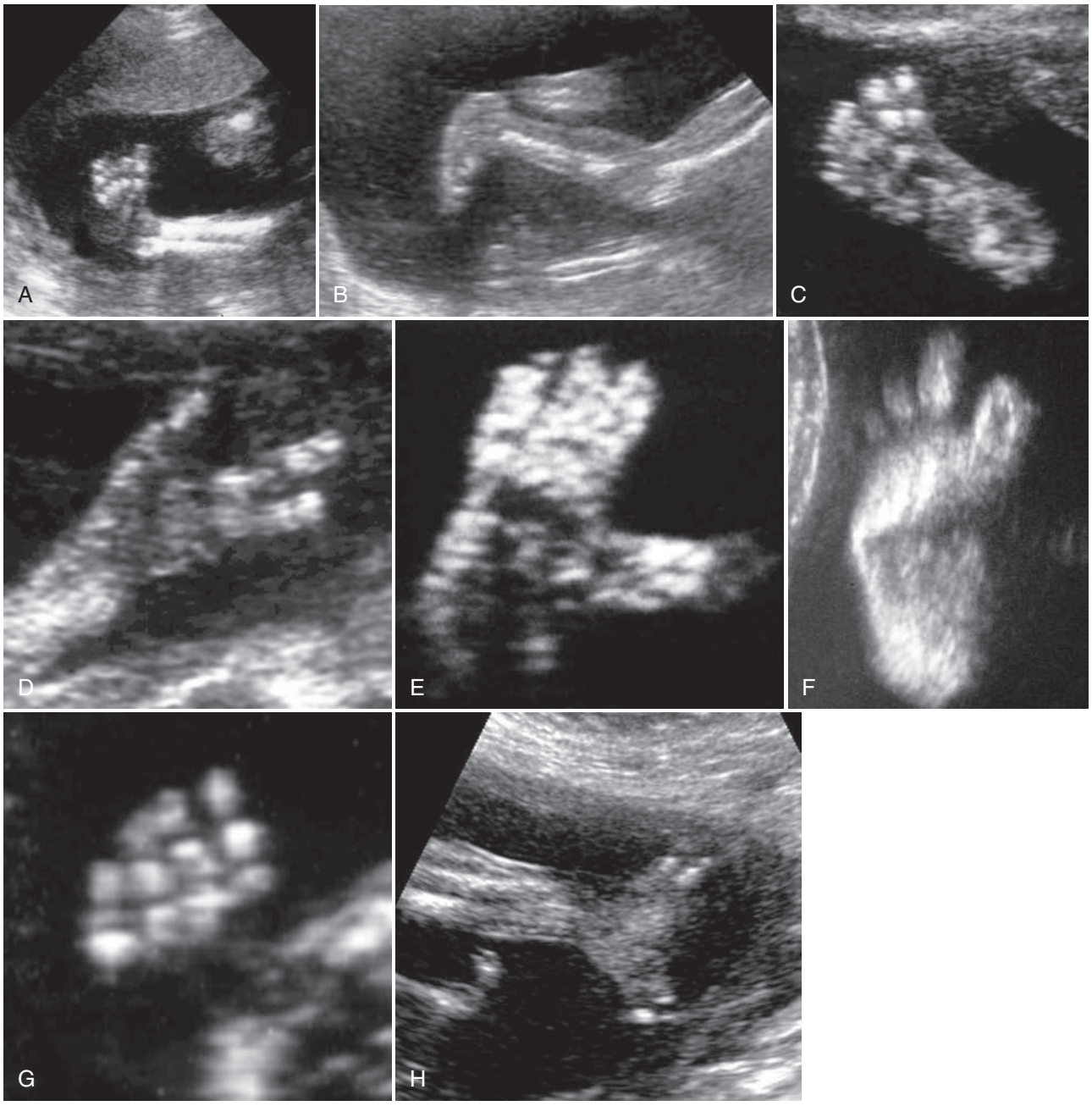

FIG. 40.36 Collage of Hand and Foot Anomalies. (A) Talipes equinovarus (clubfoot). Inverted plantar flexion with medial deviation of the foot results in visualization of the long axis of the foot (metatarsals) and lower leg in the same plane. Note the rounded angle between the foot and lower leg. **(B) Rocker-bottom foot.** Convex sole contour and rounded soft tissue protrusion posterior to the calf soft tissues. **(C) Toe polydactyly,** six digits. **(D) Oligodactyly,** three digits. **(E) Syndactyly.** Soft tissue fusion of the first and second digits. **(F) Sandal toes** in a 37-week fetus with Nager syndrome demonstrates an exaggerated gap between the first and second toes and a plantar skin furrow. **(G) Clinodactyly.** Hypoplastic middle phalanx of fifth digit. **(H) Ectrodactyly,** or split hand or foot deformity. (**C** and **E** courtesy of Ants Toi, MD, University of Toronto; **D** and **H** courtesy of Shia Salem, MD, University of Toronto.)

such as **Fanconi syndrome, Holt-Oram syndrome, acrocephalosyndactyly,** and conditions associated with **triphalangeal thumb.**[73] Central polydactyly can also occur.

Syndactyly refers to soft tissue and/or osseous fusion of digits (Fig. 40.36E). Syndactyly of the third and fourth fingers in association with IUGR in the second trimester suggests the diagnosis of **triploidy.**

An abducted, low-set thumb, or **hitchhiker thumb** (see Fig. 40.25), is associated with **diastrophic dwarfism.** An adducted thumb may be associated with **aqueductal stenosis.**

Ectrodactyly, or the split hand or foot **"lobster claw"** deformity, is a deficiency of the central digits resulting in a cleft. It can occur as an isolated abnormality or in association with other findings, such as **cleft lip and/or palate,** as in

ectrodactyly–ectodermal dysplasia clefting syndrome, Cornelia de Lange syndrome, and **limb-mammary syndrome**[109] (Fig. 40.36H). Many isolated cases are the result of a new dominant mutation or are inherited from parents with minimal manifestations. Thus a careful examination of the parents is needed before counseling low recurrence risk.[109,110]

Talipomanus, or **clubhand,** can be radial or ulnar. Radial clubhand is more common and is generally associated with the syndromes or karyotype abnormalities previously described with radial ray variants. Trisomies 18 and 21, long arm deletion of chromosome 13, and ring formation of chromosome 4 can be associated with radial clubhand. Other conditions associated with talipomanus include the **VACTERL association, Goldenhar syndrome,** and **Klippel-Feil** syndrome. Another abnormality includes a sporadic group of syndromes associated with craniofacial abnormalities, most often cleft lip and palate. Ulnar clubhand, associated with ulnar ray defects, is uncommon and may be an isolated finding.

Talipes equinovarus, or **clubfoot,** occurs in 0.1% to 0.2% of the population. The recurrence risk after the birth of one child with isolated clubfoot is 2% to 3%, and if one of the parents is affected, the recurrence risk is 3% to 4%. It is more common in males than females, and the prenatal diagnosis is based on the recognition of an inverted and plantar-flexed foot in which the metatarsal long axis is in the same plane as the tibia and fibula, in association with a rounded angle of junction between the foot and the lower leg (Fig. 40.37, Video 40.2). The majority are isolated malformations; however, MRI and fetal karyotyping should be considered when clubfoot is found in association with other structural abnormalities.[111-116] The outcome of antenatally detected talipes is primarily dependent on whether it is isolated or associated with other anomalies. Early amniocentesis (<14 weeks) is associated with an increased risk of clubfoot.[117] Hindfoot equinus (plantar flexion), hindfoot varus (inward rotation), forefoot adduction, and variable forefoot cavus (plantar flexion) can also occur.

Congenital talipes equinovarus represents a spectrum ranging from "postural" talipes or nonrigid deformity requiring little active management, to a severe, rigid deformity requiring extensive surgery. The foot is fixed in adduction, supination, and varus position, thus appearing to be turned inward. Tillett et al.[115] found that up to 26% of cases of clubfoot required no active postnatal management, presumably in the postural group. It is difficult to determine if this group is positional or a false-positive diagnosis. False-positive results are most often found in the group with an isolated diagnosis of talipes equinovarus made in late pregnancy, although they can occur at the 18- to 22-week evaluation, at a reported rate of 2.3%.[118] The normal foot may achieve extreme dorsiflexion or plantar flexion, and caution is advised when making the initial diagnosis of isolated clubfoot in the third trimester.[114,116] In the setting of isolated clubfoot (unilateral or bilateral), the likelihood of requiring surgery is approximately 40%.[118]

Rocker-bottom foot is the result of a vertical position of the talus and equinus or vertical position of the calcaneus secondary to a short Achilles tendon (Fig. 40.37B). The tarsal bones are dislocated dorsally, so there is a convex plantar surface with posterior bulging of the calcaneus. It carries a high risk for fetal chromosomal abnormalities such as **trisomies 18 and 13** when associated with other abnormalities, as well as for other syndromes such as **fetal akinesia sequence.**

Brachydactyly is the abnormal shortening of the digits. There is relative sparing of foot length in many skeletal dysplasias, but the hands may be affected. **Achondroplasia** has a characteristic configuration with the digits ending at the same level and unable to approximate the second, third, or fourth digits, leading to the appearance of the "trident hand" (Fig. 40.38).

Sandal toes, or an exaggerated gap between the first and second digits, is often visualized in the normal fetus but has a higher prevalence in trisomy 21 fetuses[14] (see Fig. 40.36F). An elevated first digit or toe may cause a false or transient abnormality that mimics sandal toes.

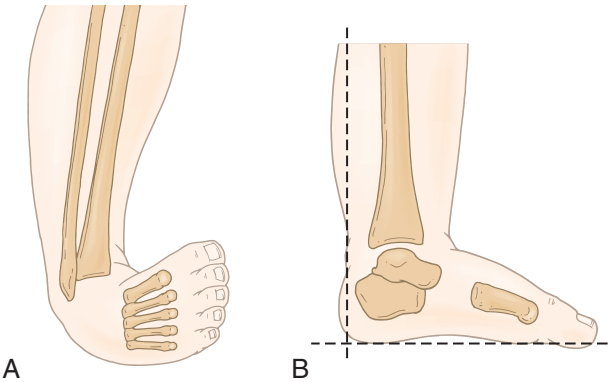

FIG. 40.37 Clubfoot. (A) Inverted, plantar-flexed, and medially deviated foot results in visualization of the long axis of the foot and tibia/fibula in the same plane. Note the rounded angle of junction between the lower leg and foot. **(B) Normal foot.** Note the normal relationship of tibia and fibula to the metatarsals and the normal squared angle of the lower leg to the foot. (With permission from Jeanty P, Romero R, d'Alton M, et al. In utero sonographic detection of hand and foot deformities. J Ultrasound Med. 1985;4[11]:595-601.[108])

SKELETAL FINDINGS ASSOCIATED WITH ANEUPLOIDY

When an abnormality in the musculoskeletal system is detected during routine ultrasound examination, a systematic search is performed to detect other defects that may lead to the diagnosis of a specific genetic or chromosomal defect.[119,120] During the second trimester, an expected-to-measured FL ratio below 0.9, based on BPD, should prompt a detailed examination to assess for other possible features of aneuploidy. However, in the third trimester, a mildly shortened femur is generally associated with asymmetrical IUGR or a constitutional small fetus rather than with aneuploidy. A femur-to-foot ratio greater than 0.9 suggests IUGR rather than a bone dysplasia, whereas a femur-to-foot ratio of less than 0.9 suggests a skeletal dysplasia.[14,121] In general, chromosomal anomalies are associated with a symmetrical form of IUGR versus asymmetrical IUGR often associated with

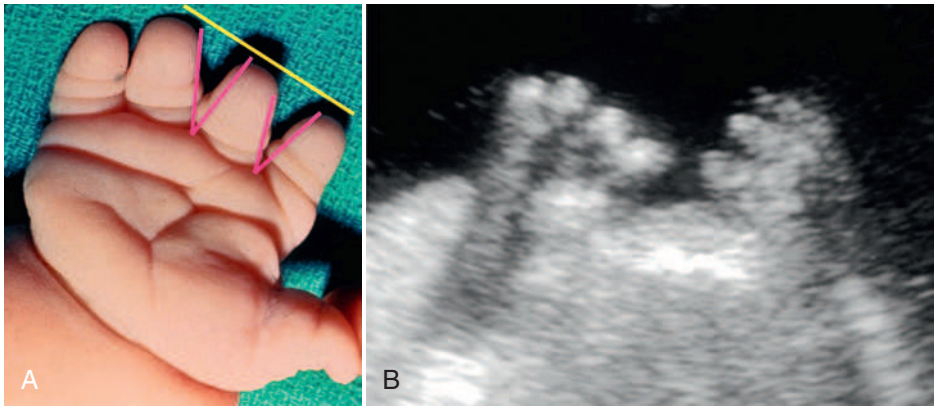

FIG. 40.38 Achondroplasia and the "Trident Hand" Configuration. (A) Homozygous achondroplasia with trident configuration with the digits ending at the same level *(yellow line),* with inability to approximate the second, third, and fourth digits *(pink lines).* **(B)** Homozygous achondroplasia with ultrasound appearance of severe brachydactyly with trident configuration.

uteroplacental insufficiency. Triploidy is an exception, occurring with a severe asymmetrical form of IUGR.

Trisomy 21 (Down syndrome) is the most common chromosome abnormality in newborns, with an incidence of 1 in 600 to 1 in 800. About 95% of such cases result from an additional chromosome 21, 3% result from translocation, and 2% are mosaic. Most cases are sporadic and there is an association with advanced maternal age. Characteristic skeletal findings include mild shortening of the femur and humerus, clinodactyly of the fifth finger, sandal gap toes, flat nasal bridge, frontal bossing, and brachycephaly.

Trisomy 21: Musculoskeletal Features

Mild shortening of femur and humerus
Clinodactyly of fifth finger
Sandal toes
Flat nasal bridge
Frontal bossing
Brachycephaly

Trisomy 18 (Edwards syndrome) is a sporadic condition, in most cases associated with advanced maternal age and with an incidence of 1 in 5000 live births. The classic appearance is a persistently clenched hand with overlapping of the second and third digits and the fourth and fifth digits, often in association with clinodactyly of the fifth digit. The findings are usually bilateral and occur in more than 50% of trisomy 18 cases. Other musculoskeletal findings include radial ray defect in 10% to 50%, syndactyly of the second and third toes, single palmar creases, clubfoot or rocker-bottom foot, incomplete clavicle ossification, and vertebral and rib anomalies. The prognosis is poor; 90% of neonates succumb in the first year of life, and all survivors have profound mental retardation.

Trisomy 18: Musculoskeletal Features

Persistent clenched hand with overlapping digits
Radial ray aplasia variants
Syndactyly
Talipes equinovarus (clubfoot)
Rocker-bottom foot
Vertebral and rib anomalies

Trisomy 13 (Patau syndrome) is in most cases a sporadic disorder with an incidence of 1 in 10,000 live births. The musculoskeletal anomalies include postaxial polydactyly of hands and feet, possible clenched hand (with or without overlapping digits), clinodactyly, and possibly associated hypoplastic ribs and pelvic bones.

Trisomy 13: Musculoskeletal Features

Polydactyly
Persistent clenched hand with or without overlapping digits
Clinodactyly
Hypoplastic ribs and pelvic bones
Microcephaly
Hypotelorism
Facial clefts

Triploidy (69,XXX, 69,XXY, or 69,XXY) occurs in 18% of all early miscarriages, but the incidence is only 1 in 2500 births. In 60% of cases, triploidy results from dispermy, and in 40%, from diploid sperm or diploid egg. Early severe asymmetrical IUGR and oligohydramnios suggest the diagnosis. The placenta may be either small or enlarged and hydropic. Associated musculoskeletal findings include **syndactyly** of the third and fourth fingers, **simian crease, talipes equinovarus,** and **hitchhiker toe** deformity.

Other findings may include **micrognathia, ventriculomegaly, myelomeningocele,** and cardiac abnormalities.

SUMMARY

The finding of a skeletal dysplasia and the subsequent communication of the findings are challenging tasks requiring empathy and support. In some cases, it may not be possible to establish a specific diagnosis and counseling will have to be based on prognosis estimated from ultrasound findings. The implications should be discussed in simple terms permitting the parents to make an informed decision about the management of the pregnancy, the delivery, and postnatal care. This discussion typically involves a multidisciplinary team who provide the most up-to-date information to the parents about options, possible outcomes, and implications for a future pregnancy. The team will usually involve an imaging specialist, maternal-fetal medicine experts, medical geneticists, and the neonatology team. Additional consultation with orthopedic surgeons, palliative treatment groups, social workers, and supportive organizations may be helpful for the family. The mode of delivery should be discussed in advance, especially in conditions associated with fetal macrocrania, in which vaginal delivery at term may not be possible. After delivery or pregnancy termination, the diagnosis should be confirmed by radiographic, photographic, and histomorphic analysis. Cell culture and DNA should be banked and used for further molecular investigation. The parents should be seen at a later time to discuss the results and the implications these results may have on their future reproductive plans.

Acknowledgments

Special thanks to all the staff at Medical Imaging and Maternal Fetal Medicine Departments at Sunnybrook Health Science Center and the Mount Sinai Hospital in Toronto who have provided many wonderful images and generously shared their knowledge and work.

REFERENCES

1. Stevenson DA, Carey JC, Byrne JL, et al. Analysis of skeletal dysplasias in the Utah population. Am J Med Genet A. 2012;158A(5):1046-1054.
2. Spranger JW, Brill PW, Poznanski AK. Bone dysplasias: an atlas of genetic disorders of skeletal development. 2nd ed. New York: Oxford University Press; 2002.
3. Superti-Furga A, Unger S. Nosology and classification of genetic skeletal disorders: 2006 revision. Am J Med Genet A. 2007;143A(1):1-18.
4. Lachman RS, Rappaport V. Fetal imaging in the skeletal dysplasias. Clin Perinatol. 1990;17(3):703-722.
5. Camera G, Mastroiacovo P. Birth prevalence of skeletal dysplasias in the Italian Multicentric Monitoring System for Birth Defects. Prog Clin Biol Res. 1982;104:441-449.
6. Bonafe L, Cormier-Daire V, Hall C, et al. Nosology and classification of genetic skeletal disorders: 2015 revision. Am J Med Genet A. 2015;167(12):2869-2892.
7. Superti-Furga A, Hastbacka J, Wilcox WR, et al. Achondrogenesis type IB is caused by mutations in the diastrophic dysplasia sulphate transporter gene. Nat Genet. 1996;12(1):100-102.
8. Krakow D, Alanay Y, Rimoin LP, et al. Evaluation of prenatal-onset osteochondrodysplasias by ultrasonography: a retrospective and prospective analysis. Am J Med Genet A. 2008;146A(15):1917-1924.
9. Pretorius DH, Rumack CM, Manco-Johnson ML, et al. Specific skeletal dysplasias in utero: sonographic diagnosis. Radiology. 1986;159(1):237-242.
10. Tretter AE, Saunders RC, Meyers CM, et al. Antenatal diagnosis of lethal skeletal dysplasias. Am J Med Genet. 1998;75(5):518-522.
11. Barkova E, Mohan U, Chitayat D, et al. Fetal skeletal dysplasias in a tertiary care center: radiology, pathology, and molecular analysis of 112 cases. Clin Genet. 2015;87(4):330-337.
12. Merz E, Kim-Kern MS, Pehl S. Ultrasonic mensuration of fetal limb bones in the second and third trimesters. J Clin Ultrasound. 1987;15(3):175-183.
13. Mahony BS, Filly RA. High-resolution sonographic assessment of the fetal extremities. J Ultrasound Med. 1984;3(11):489-498.
14. Bromley B, Benacerraf B. Abnormalities of the hands and feet in the fetus: sonographic findings. AJR Am J Roentgenol. 1995;165(5):1239-1243.
15. Greulich WW, Pyle SI. Radiographic atlas of skeletal development of the hand and wrist. 2nd ed. Stanford, Calif: Stanford University Press; 1959.
16. Mahony BS, Callen PW, Filly RA. The distal femoral epiphyseal ossification center in the assessment of third-trimester menstrual age: sonographic identification and measurement. Radiology. 1985;155(1):201-204.
17. Chinn DH, Bolding DB, Callen PW, et al. Ultrasonographic identification of fetal lower extremity epiphyseal ossification centers. Radiology. 1983;147(3):815-818.
18. Goldstein I, Lockwood CJ, Reece EA, Hobbins JC. Sonographic assessment of the distal femoral and proximal tibial ossification centers in the prediction of pulmonic maturity in normal women and women with diabetes. Am J Obstet Gynecol. 1988;159(1):72-76.
19. Goldstein RB, Filly RA, Simpson G. Pitfalls in femur length measurements. J Ultrasound Med. 1987;6(4):203-207.
20. Abrams SL, Filly RA. Curvature of the fetal femur: a normal sonographic finding. Radiology. 1985;156(2):490.
21. Yarkoni S, Schmidt W, Jeanty P, et al. Clavicular measurement: a new biometric parameter for fetal evaluation. J Ultrasound Med. 1985;4(9):467-470.
22. Campbell J, Henderson A, Campbell S. The fetal femur/foot length ratio: a new parameter to assess dysplastic limb reduction. Obstet Gynecol. 1988;72(2):181-184.
23. Platt LD, Medearis AL, DeVore GR, et al. Fetal foot length: relationship to menstrual age and fetal measurements in the second trimester. Obstet Gynecol. 1988;71(4):526-531.
24. Chitkara U, Rosenberg J, Chervenak FA, et al. Prenatal sonographic assessment of the fetal thorax: normal values. Am J Obstet Gynecol. 1987;156(5):1069-1074.
25. Kurtz AB, Needleman L, Wapner RJ, et al. Usefulness of a short femur in the in utero detection of skeletal dysplasias. Radiology. 1990;177(1):197-200.
26. Goncalves L, Jeanty P. Fetal biometry of skeletal dysplasias: a multicentric study. J Ultrasound Med. 1994;13(10):767-775.
27. Papageorghiou AT, Fratelli N, Leslie K, et al. Outcome of fetuses with antenatally diagnosed short femur. Ultrasound Obstet Gynecol. 2008;31(5):507-511.
28. Nelson TR, Ji EK, Lee JH, et al. Stereoscopic evaluation of fetal bony structures. J Ultrasound Med. 2008;27(1):15-24.
29. Weisz B, David AL, Chitty L, et al. Association of isolated short femur in the mid-trimester fetus with perinatal outcome. Ultrasound Obstet Gynecol. 2008;31(5):512-516.
30. Zalel Y, Lehavi O, Schiff E, et al. Shortened fetal long bones: a possible in utero manifestation of placental function. Prenat Diagn. 2002;22(7):553-557.
31. Pattarelli P, Pretorius DH, Edwards DK. Intrauterine growth retardation mimicking skeletal dysplasia on antenatal sonography. J Ultrasound Med. 1990;9(12):737-739.
32. Ngo C, Viot G, Aubry MC, et al. First-trimester ultrasound diagnosis of skeletal dysplasia associated with increased nuchal translucency thickness. Ultrasound Obstet Gynecol. 2007;30(2):221-226.
33. De Biasio P, Prefumo F, Lantieri PB, Venturini PL. Reference values for fetal limb biometry at 10-14 weeks of gestation. Ultrasound Obstet Gynecol. 2002;19(6):588-591.

34. Nyberg DA, Souter VL, El-Bastawissi A, et al. Isolated sonographic markers for detection of fetal Down syndrome in the second trimester of pregnancy. J Ultrasound Med. 2001;20(10):1053-1063.
35. Spirt BA, Oliphant M, Gottlieb RH, Gordon LP. Prenatal sonographic evaluation of short-limbed dwarfism: an algorithmic approach. Radiographics. 1990;10(2):217-236.
36. Alanay Y, Krakow D, Rimoin DL, Lachman RS. Angulated femurs and the skeletal dysplasias: experience of the International Skeletal Dysplasia Registry (1988-2006). Am J Med Genet A. 2007;143A(11):1159-1168.
37. Rouse GA, Filly RA, Toomey F, Grube GL. Short-limb skeletal dysplasias: evaluation of the fetal spine with sonography and radiography. Radiology. 1990;174(1):177-180.
38. Dugoff L, Coffin CT, Hobbins JC. Sonographic measurement of the fetal rib cage perimeter to thoracic circumference ratio: application to prenatal diagnosis of skeletal dysplasias. Ultrasound Obstet Gynecol. 1997;10(4): 269-271.
39. Gindes L, Benoit B, Pretorius DH, Achiron R. Abnormal number of fetal ribs on 3-dimensional ultrasonography: associated anomalies and outcomes in 75 fetuses. J Ultrasound Med. 2008;27(9):1263-1271.
40. Quarello E, Roume J, Molho M, et al. Twins discordant for fetal skeletal abnormalities: a natural confrontation between the two siblings. Prenat Diagn. 2008;28(1):21-27.
41. Rustico MA, Baietti MG, Coviello D, et al. Managing twins discordant for fetal anomaly. Prenat Diagn. 2005;25(9):766-771.
42. Dall'Asta A, Paramasivam G, Lees CC. Crystal Vue technique for imaging of the fetal spine and ribs. Ultrasound Obstet Gynecol. 2015.
43. Ruano R, Molho M, Roume J, Ville Y. Prenatal diagnosis of fetal skeletal dysplasias by combining two-dimensional and three-dimensional ultrasound and intrauterine three-dimensional helical computer tomography. Ultrasound Obstet Gynecol. 2004;24(2):134-140.
44. Xu HX, Zhang QP, Lu MD, Xiao XT. Comparison of two-dimensional and three-dimensional sonography in evaluating fetal malformations. J Clin Ultrasound. 2002;30(9):515-525.
45. Benoit B, Hafner T, Kurjak A, et al. Three-dimensional sonoembryology. J Perinat Med. 2002;30(1):63-73.
46. Benacerraf BR. Three-dimensional fetal sonography: use and misuse. J Ultrasound Med. 2002;21(10):1063-1067.
47. Cassart M, Massez A, Cos T, et al. Contribution of three-dimensional computed tomography in the assessment of fetal skeletal dysplasia. Ultrasound Obstet Gynecol. 2007;29(5):537-543.
48. Tani C, Funama Y, Fujioka C, et al. Radiation dose reduction at MDCT with iterative reconstruction for prenatal diagnosis of skeletal dysplasia: preliminary study using normal fetal specimens. Am J Roentgenol. 2014;203(6):1249-1256.
49. Nagayama M, Watanabe Y, Okumura A, et al. Fast MR imaging in obstetrics. Radiographics. 2002;22(3):563-580.
50. Arthurs OJ, Thayyil S, Addison S, et al. Diagnostic accuracy of postmortem MRI for musculoskeletal abnormalities in fetuses and children. Prenat Diagn. 2014;34(13):1254-1261.
51. Lemyre E, Azouz EM, Teebi AS, et al. Bone dysplasia series. Achondroplasia, hypochondroplasia and thanatophoric dysplasia: review and update. Can Assoc Radiol J. 1999;50(3):185-197.
52. Krakow D, Lachman RS, Rimoin DL. Guidelines for the prenatal diagnosis of fetal skeletal dysplasias. Genet Med. 2009;11(2):127-133.
53. Nelson DB, Dashe JS, McIntire DD, Twickler DM. Fetal skeletal dysplasias: sonographic indices associated with adverse outcomes. J Ultrasound Med. 2014;33(6):1085-1090.
54. Yoshimura S, Masuzaki H, Gotoh H, et al. Ultrasonographic prediction of lethal pulmonary hypoplasia: comparison of eight different ultrasonographic parameters. Am J Obstet Gynecol. 1996;175(2):477-483.
55. Kallen B, Knudsen LB, Mutchinick O, et al. Monitoring dominant germ cell mutations using skeletal dysplasias registered in malformation registries: an international feasibility study. Int J Epidemiol. 1993;22(1):107-115.
56. Langer Jr LO, Yang SS, Hall JG, et al. Thanatophoric dysplasia and cloverleaf skull. Am J Med Genet Suppl. 1987;3:167-179.
57. Chen CP, Chern SR, Shih JC, et al. Prenatal diagnosis and genetic analysis of type I and type II thanatophoric dysplasia. Prenat Diagn. 2001;21(2): 89-95.
58. Vajo Z, Francomano CA, Wilkin DJ. The molecular and genetic basis of fibroblast growth factor receptor 3 disorders: the achondroplasia family of skeletal dysplasias, Muenke craniosynostosis, and Crouzon syndrome with acanthosis nigricans. Endocr Rev. 2000;21(1):23-39.
59. Bellus GA, Bamshad MJ, Przylepa KA, et al. Severe achondroplasia with developmental delay and acanthosis nigricans (SADDAN): phenotypic analysis of a new skeletal dysplasia caused by a Lys650Met mutation in fibroblast growth factor receptor 3. Am J Med Genet. 1999;85(1):53-65.
60. Tavormina PL, Shiang R, Thompson LM, et al. Thanatophoric dysplasia (types I and II) caused by distinct mutations in fibroblast growth factor receptor 3. Nat Genet. 1995;9(3):321-328.
61. Wang DC, Shannon P, Toi A, et al. Temporal lobe dysplasia: a characteristic sonographic finding in thanatophoric dysplasia. Ultrasound Obstet Gynecol. 2014;44(5):588-594.
62. Blaas HG, Vogt C, Eik-Nes SH. Abnormal gyration of the temporal lobe and megalencephaly are typical features of thanatophoric dysplasia and can be visualized prenatally by ultrasound. Ultrasound Obstet Gynecol. 2012;40(2):230-234.
63. Pugash D, Lehman AM, Langlois S. Prenatal ultrasound and MRI findings of temporal and occipital lobe dysplasia in a twin with achondroplasia. Ultrasound Obstet Gynecol. 2014;44(3):365-368.
64. Taybi H, Lachman RS, Taybi H. Radiology of syndromes, metabolic disorders, and skeletal dysplasias. 3rd ed. Chicago: Year Book Medical Publishers; 1990.
65. Hall CM. International nosology and classification of constitutional disorders of bone (2001). Am J Med Genet. 2002;113(1):65-77.
66. DiMaio MS, Barth R, Koprivnikar KE, et al. First-trimester prenatal diagnosis of osteogenesis imperfecta type II by DNA analysis and sonography. Prenat Diagn. 1993;13(7):589-596.
67. Latini G, De Felice C, Parrini S, et al. Polyhydramnios: a predictor of severe growth impairment in achondroplasia. J Pediatr. 2002;141(2):274-276.
68. Minillo RM, Sobreira N, de Faria Soares Mde F, et al. Novel deletion of SERPINF1 causes autosomal recessive osteogenesis imperfecta type VI in two Brazilian families. Mol Syndromol. 2014;5(6):268-275.
69. Marini JC, Blissett AR. New genes in bone development: what's new in osteogenesis imperfecta. J Clin Endocrinol Metab. 2013;98(8):3095-3103.
70. Sillence DO, Senn A, Danks DM. Genetic heterogeneity in osteogenesis imperfecta. J Med Genet. 1979;16(2):101-116.
71. Sillence DO, Barlow KK, Garber AP, et al. Osteogenesis imperfecta type II delineation of the phenotype with reference to genetic heterogeneity. Am J Med Genet. 1984;17(2):407-423.
72. Munoz C, Filly RA, Golbus MS. Osteogenesis imperfecta type II: prenatal sonographic diagnosis. Radiology. 1990;174(1):181-185.
73. Meizner I, Bar-Ziv J. In utero diagnosis of skeletal disorders: an atlas of prenatal sonographic and postnatal radiologic correlation. Boca Raton, Fla: CRC Press; 1993.
74. Bowerman RA. Anomalies of the fetal skeleton: sonographic findings. Am J Roentgenol. 1995;164(4):973-979.
75. Kwok C, Weller PA, Guioli S, et al. Mutations in SOX9, the gene responsible for Campomelic dysplasia and autosomal sex reversal. Am J Hum Genet. 1995;57(5):1028-1036.
76. Wu MH, Kuo PL, Lin SJ. Prenatal diagnosis of recurrence of short rib-polydactyly syndrome. Am J Med Genet. 1995;55(3):279-284.
77. Whitley CB, Langer Jr LO, Ophoven J, et al. Fibrochondrogenesis: lethal, autosomal recessive chondrodysplasia with distinctive cartilage histopathology. Am J Med Genet. 1984;19(2):265-275.
78. Kulkarni ML, Matadh PS, Praveen Prabhu SP, Kulkarni PM. Fibrochondrogenesis. Indian J Pediatr. 2005;72(4):355-357.
79. Kurtz AB, Filly RA, Wapner RJ, et al. In utero analysis of heterozygous achondroplasia: variable time of onset as detected by femur length measurements. J Ultrasound Med. 1986;5(3):137-140.
80. Patel MD, Filly RA. Homozygous achondroplasia: US distinction between homozygous, heterozygous, and unaffected fetuses in the second trimester. Radiology. 1995;196(2):541-545.
81. Hastbacka J, Superti-Furga A, Wilcox WR, et al. Atelosteogenesis type II is caused by mutations in the diastrophic dysplasia sulfate-transporter gene (DTDST): evidence for a phenotypic series involving three chondrodysplasias. Am J Hum Genet. 1996;58(2):255-262.

82. Kaitila I, Ammala P, Karjalainen O, et al. Early prenatal detection of diastrophic dysplasia. Prenat Diagn. 1983;3(3):237-244.
83. Chitayat D, Keating S, Zand DJ, et al. Chondrodysplasia punctata associated with maternal autoimmune diseases: expanding the spectrum from systemic lupus erythematosus (SLE) to mixed connective tissue disease (MCTD) and scleroderma report of eight cases. Am J Med Genet A. 2008;146A(23): 3038-3053.
84. Patel MS, Callahan JW, Zhang S, et al. Early-infantile galactosialidosis: prenatal presentation and postnatal follow-up. Am J Med Genet. 1999;85(1):38-47.
85. Duff P, Harlass FE, Milligan DA. Prenatal diagnosis of chondrodysplasia punctata by sonography. Obstet Gynecol. 1990;76(3 Pt 2):497-500.
86. Umranikar S, Glanc P, Unger S, et al. X-Linked dominant chondrodysplasia punctata: prenatal diagnosis and autopsy findings. Prenat Diagn. 2006;26(13):1235-1240.
87. Pryde PG, Bawle E, Brandt F, et al. Prenatal diagnosis of nonrhizomelic chondrodysplasia punctata (Conradi-Hünermann syndrome). Am J Med Genet. 1993;47(3):426-431.
88. Winship WS, Beighton P. Dyssegmental dysplasia in a South African neonate. Clin Dysmorphol. 2008;17(2):95-98.
89. Koifman A, Nevo O, Toi A, Chitayat D. Diagnostic approach to prenatally diagnosed limb abnormalities. Ultrasound Clin. 2008;3:595-608.
90. Stoll C, Wiesel A, Queisser-Luft A, et al. Evaluation of the prenatal diagnosis of limb reduction deficiencies. EUROSCAN Study Group. Prenat Diagn. 2000;20(10):811-818.
91. Sen Gupta DK, Gupta SK. Familial bilateral proximal femoral focal deficiency. Report of a kindred. J Bone Joint Surg Am. 1984;66(9):1470-1472.
92. Auerbach AD. Fanconi anemia. Dermatol Clin. 1995;13(1):41-49.
93. Hall JG. Thrombocytopenia and absent radius (TAR) syndrome. J Med Genet. 1987;24(2):79-83.
94. Mahony BS, Filly RA, Callen PW, Golbus MS. The amniotic band syndrome: antenatal sonographic diagnosis and potential pitfalls. Am J Obstet Gynecol. 1985;152(1):63-68.
95. Patten RM, Van Allen M, Mack LA, et al. Limb-body wall complex: in utero sonographic diagnosis of a complicated fetal malformation. Am J Roentgenol. 1986;146(5):1019-1024.
96. Randel SB, Filly RA, Callen PW, et al. Amniotic sheets. Radiology. 1988;166(3):633-636.
97. Van Allen MI, Curry C, Gallagher L. Limb body wall complex: I. Pathogenesis. Am J Med Genet. 1987;28(3):529-548.
98. Sonek JD, Gabbe SG, Landon MB, et al. Antenatal diagnosis of sacral agenesis syndrome in a pregnancy complicated by diabetes mellitus. Am J Obstet Gynecol. 1990;162(3):806-808.
99. Twickler D, Budorick N, Pretorius D, et al. Caudal regression versus sirenomelia: sonographic clues. J Ultrasound Med. 1993;12(6):323-330.
100. Valenzano M, Paoletti R, Rossi A, et al. Sirenomelia. Pathological features, antenatal ultrasonographic clues, and a review of current embryogenic theories. Hum Reprod Update. 1999;5(1):82-86.
101. Ohlsson A, Fong KW, Rose TH, Moore DC. Prenatal sonographic diagnosis of Pena-Shokeir syndrome type I, or fetal akinesia deformation sequence. Am J Med Genet. 1988;29(1):59-65.
102. Hall JG, Reed SD, Rosenbaum KN, et al. Limb pterygium syndromes: a review and report of eleven patients. Am J Med Genet. 1982;12(4): 377-409.
103. Kondo S, Schutte BC, Richardson RJ, et al. Mutations in IRF6 cause Van der Woude and popliteal pterygium syndromes. Nat Genet. 2002;32(2): 285-289.
104. Souka AP, Krampl E, Geerts L, Nicolaides KH. Congenital lymphedema presenting with increased nuchal translucency at 13 weeks of gestation. Prenat Diagn. 2002;22(2):91-92.
105. Bronshtein M, Stahl S, Zimmer EZ. Transvaginal sonographic diagnosis of fetal finger abnormalities in early gestation. J Ultrasound Med. 1995;14(8): 591-595.
106. Benacerraf BR, Osathanondh R, Frigoletto FD. Sonographic demonstration of hypoplasia of the middle phalanx of the fifth digit: a finding associated with Down syndrome. Am J Obstet Gynecol. 1988;159(1):181-183.
107. Hegge FN, Prescott GH, Watson PT. Utility of a screening examination of the fetal extremities during obstetrical sonography. J Ultrasound Med. 1986;5(11):639-645.
108. Jeanty P, Romero R, d'Alton M, et al. In utero sonographic detection of hand and foot deformities. J Ultrasound Med. 1985;4(11):595-601.
109. Anneren G, Andersson T, Lindgren PG, Kjartansson S. Ectrodactyly-ectodermal dysplasia-clefting syndrome (EEC): the clinical variation and prenatal diagnosis. Clin Genet. 1991;40(4):257-262.
110. Ianakiev P, Kilpatrick MW, Toudjarska I, et al. Split-hand/split-foot malformation is caused by mutations in the p63 gene on 3q27. Am J Hum Genet. 2000;67(1):59-66.
111. Bakalis S, Sairam S, Homfray T, et al. Outcome of antenatally diagnosed talipes equinovarus in an unselected obstetric population. Ultrasound Obstet Gynecol. 2002;20(3):226-229.
112. Chesney D. Clinical outcome of congenital talipes equinovarus diagnosed antenatally by ultrasound. J Bone Joint Surg Br. 2001;83(3):462-463.
113. Keret D, Bollini G, Dungl P, et al. The fibula in congenital pseudoarthrosis of the tibia: the EPOS multicenter study. European Paediatric Orthopaedic Society (EPOS). J Pediatr Orthop B. 2000;9(2):69-74.
114. Maffulli N. Prenatal ultrasonographic diagnosis of talipes equinovarus: does it give the full picture? Ultrasound Obstet Gynecol. 2002;20(3): 217-218.
115. Tillett RL, Fisk NM, Murphy K, Hunt DM. Clinical outcome of congenital talipes equinovarus diagnosed antenatally by ultrasound. J Bone Joint Surg Br. 2000;82(6):876-880.
116. Treadwell MC, Stanitski CL, King M. Prenatal sonographic diagnosis of clubfoot: implications for patient counseling. J Pediatr Orthop. 1999;19(1): 8-10.
117. Farrell SA, Summers AM, Dallaire L, et al. Club foot, an adverse outcome of early amniocentesis: disruption or deformation? CEMAT. Canadian Early and Mid-Trimester Amniocentesis Trial. J Med Genet. 1999;36(11): 843-846.
118. Canto MJ, Cano S, Palau J, Ojeda F. Prenatal diagnosis of clubfoot in low-risk population: associated anomalies and long-term outcome. Prenat Diagn. 2008;28(4):343-346.
119. Avni EF, Rypens F, Zappa M, et al. Antenatal diagnosis of short-limb dwarfism: sonographic approach. Pediatr Radiol. 1996;26(3):171-178.
120. Snijders RJM, Nicolaides KH. Ultrasound markers for fetal chromosomal defects. New York: Parthenon Publishing Group; 1996.
121. Benacerraf BR, Frigoletto Jr FD, Greene MF. Abnormal facial features and extremities in human trisomy syndromes: prenatal US appearance. Radiology. 1986;159(1):243-246.

CHAPTER 41

Fetal Hydrops

Deborah Levine

SUMMARY OF KEY POINTS

- Hydrops is defined as an abnormal accumulation of interstitial fluid in at least two body cavities (pleural, peritoneal, or pericardial) or one body cavity in association with anasarca (generalized massive edema). Placentomegaly and polyhydramnios are common findings in cases of hydrops but are not needed for the diagnosis.
- Hydrops represents a terminal stage for many conditions, the vast majority of which are fetal in origin.
- The onset of hydrops signifies fetal decompensation.
- Immune causes can be successfully treated in utero, as can an increasing number of nonimmune causes.
- Middle cerebral artery Doppler ultrasound can be used to assess fetuses at risk for anemia.
- A team approach using obstetric imagers, maternal fetal medicine specialists, neonatologists, and geneticists can help to decide which cases are suitable for therapeutic intervention.

CHAPTER OUTLINE

SONOGRAPHIC FEATURES
Ascites
Pleural Effusions
Pericardial Effusions
Subcutaneous Edema
Placentomegaly
Polyhydramnios
ETIOLOGY
IMMUNE HYDROPS
Noninvasive Assessment of Alloimmunization
NONIMMUNE HYDROPS
Pathophysiology
Causes and Associations
Cardiovascular Abnormalities
Neck Abnormalities
Thoracic Anomalies
Gastrointestinal Anomalies
Urinary Tract Anomalies
Lymphatic Dysplasia
Monochorionic Twins
Chromosomal Anomalies
Tumors
Anemia
Infection
Genetic Disorders
Metabolic Disorders
Skeletal Disorders
Endocrine Disorders
Drugs
Idiopathic Disorders
DIAGNOSTIC APPROACH TO HYDROPS
History
Complete Obstetric Ultrasound
Maternal Investigations
Fetal Investigations
Performing PUBS
Fetal Transfusion
Cavity Aspiration
Postnatal Investigations
FETAL WELFARE ASSESSMENT IN NONIMMUNE HYDROPS
OBSTETRIC PROGNOSIS
Maternal Complications (Mirror Syndrome)
Delivery
Predelivery Aspiration Procedures
Postnatal Outcome
CONCLUSION

Hydrops fetalis is an end-stage process for a number of different diseases. It is defined as an abnormal accumulation of interstitial fluid in at least two body cavities (pleural, peritoneal, or pericardial) or one body cavity in association with anasarca (generalized massive edema). Placentomegaly and polyhydramnios are common findings in cases of hydrops but are not needed for the diagnosis.

Lymphangiectasia, which is abnormal dilatation of the lymphatic vessels, should not be mistaken for hydrops. In the first trimester, general body wall lymphangiectasia can have a "space suit" appearance (Fig. 41.1) due to the fluid in the skin and/or subcutaneous tissues. The finding has a poor prognosis, with 26 in 30 prospectively identified cases in the first trimester having abnormal karyotype.[1] However, because there is not typically fluid in other body cavities, this is not hydrops.

Hydrops is the late stage of many processes that lead to redistribution of body fluids among the intravascular and interstitial compartments. This imbalance of fluid can have many causes (Table 41.1). There are at more than 150 different causes of fetal hydrops. Many of the causes and associations with hydrops overlap. The basic etiology of hydrops is an imbalance of interstitial fluid, which may be caused by myocardial failure, high-output cardiac failure, decreased colloid oncotic plasma pressure (anemia), increased capillary permeability, and/or obstruction of venous and lymphatic flow.

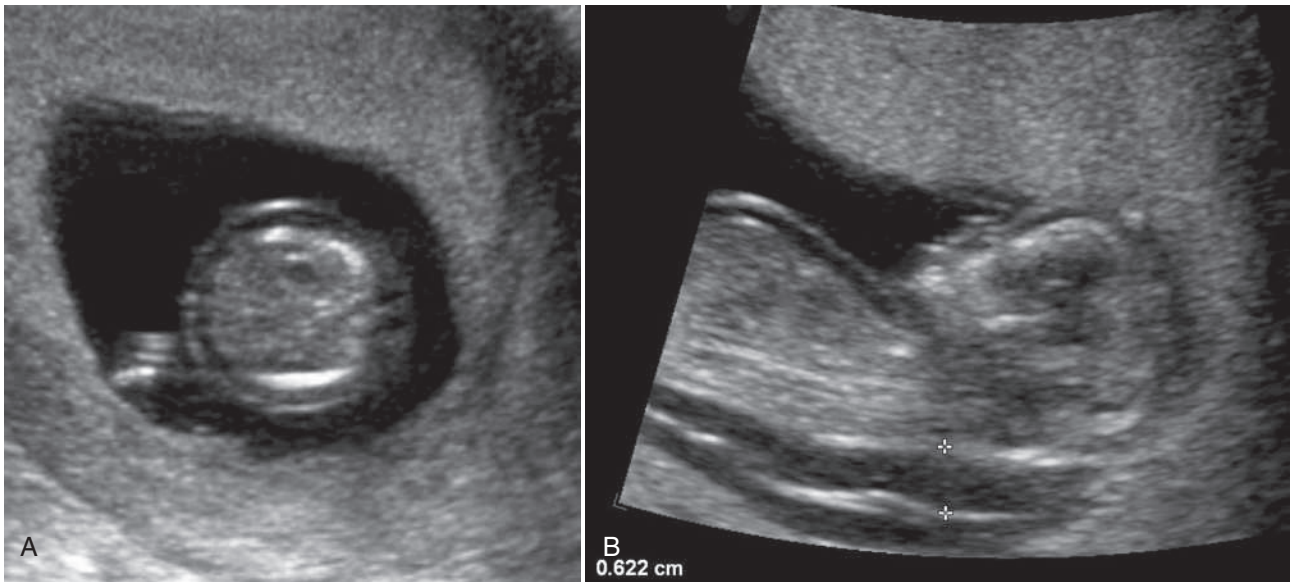

FIG. 41.1 Lymphangiectasia in Fetus With Abnormal Nuchal Translucency. (A) Transverse abdomen shows edema of the skin, but no ascites. **(B)** Sagittal image shows abnormal nuchal translucency of 6 mm *(calipers)* and skin thickening that extends anteriorly around the torso and fetal skull, a "space suit" appearance.

Hydrops can be **immune** or **nonimmune** in origin. Immune hydrops is defined by a circulating antibody against red blood cells (RBCs) in the mother, whereas in nonimmune hydrops no such antibody is found. Before the widespread introduction of rhesus (Rh) anti-D immune globulin in the 1970s, most cases of hydrops were immune,[2,3] whereas currently, about 85% are nonimmune.[4] This chapter reviews the findings of fluid in different body cavities and the causes, diagnosis, and treatment of hydrops. Recent series have reported fetal hydrops mortality rates ranging from 58% to 61%.[4-7] This improved survival compared to older series is thought to be due to fetal medical and interventional techniques that allow for reversal of hydrops in nonaneuploid cases.[4,5] Although hydrops is a relatively common indication for tertiary-level fetal evaluation, because of the many causes, each specific etiology is relatively rare.

SONOGRAPHIC FEATURES

It is important for clinicians to understand the sonographic appearance of fluid in the different interstitial compartments of the fetus. These fluid collections can occur in isolation, as in isolated **ascites** or isolated **pleural** or **pericardial** effusion. When one collection is seen, it is important to assess for a second collection to make the diagnosis of hydrops; the fluid collection must be in at least two body cavities to qualify as hydrops. Other findings in hydrops can include **subcutaneous edema, polyhydramnios,** and **placentomegaly.**

Ascites

Fetal ascites is diagnosed when fluid is seen between **bowel loops,** along the abdominal flanks, around the liver, and outlining the umbilical vessels (Fig. 41.2). In normal fetuses, a small hypoechoic band (<2 mm in thickness) extending along the anterior and lateral fetal abdomen may be present. This "pseudoascites" represents normal abdominal wall muscles or abdominal wall fat and should not be mistaken for an abnormal fluid collection[8] (Fig. 41.3). The distinction between the pseudoascites appearance and true ascites can be made when the transducer angle is changed and the appearance resolves. Pseudoascites does not surround the liver but rather stops at the insertion of the ribs. Note that true ascites will extend around bowel loops (Fig. 41.4, Video 41.1), whereas pseudoascites is always a subcutaneous finding.

Isolated ascites can be an early sign of hydrops. If truly isolated, it can be caused by a urinary or gastrointestinal obstruction. Isolated fetal ascites has a more favorable prognosis than hydrops but requires follow-up to ensure that hydrops does not ensue.

Small collections of ascitic fluid may outline abdominal viscera, including bowel loops or bladder, and may cause an apparent increase in their echogenicity. Larger accumulations outline the liver and spleen (see Fig. 41.2A and D). The umbilical vessels will be seen as parallel echogenic lines traversing the fluid space (see Fig. 41.2C). Bowel loops may be free floating or, when meconium peritonitis is present, may appear as a matted, echogenic posterior mass. In male fetuses, ascitic fluid may track through the patent processus vaginalis into the scrotum, leading to **hydroceles** (Fig. 41.5). Chronic chest compression from massive ascites may result in **pulmonary hypoplasia.**

Pleural Effusions

Pleural effusions typically occur later in hydrops than does ascites. If isolated and small, pleural effusions tend to have a benign course (Fig. 41.6A, Video 41.2). A small effusion is seen as a thin, echolucent rim surrounding lung tissue and may also outline mediastinal structures. Small pleural effusions do not shift the mediastinum. Pleural effusions associated with hydrops may be **unilateral** or **bilateral,** often beginning as unilateral collections that progress to bilateral involvement (Fig. 41.6D). If mediastinal shift is visualized in association with a small pleural effusion, a

TABLE 41.1 Nonimmune Hydrops: Common Causes and Associations[a]

Cause (Percentage of Nonimmune Hydrops)	Mechanism	Examples
Cardiovascular (20%)	Increased central venous pressure	Structural heart disease (hypoplastic left or right heart syndrome, atrioventricular canal) Myocardial or pericardial tumors (rhabdomyoma in tuberous sclerosis) Tachyarrhythmia Bradyarrhythmia (congenital heart block [anti-Rho] or other maternal autoimmune disease)
Monochorionic twins (4%)	Anemia and/or high-output cardiac failure	Twin-to-twin transfusion syndrome (usually the recipient but can occur in the donor), twin anemia polycythemia sequence Acardiac twin (donor)
Lymphatic dysplasia (15%)	Abnormal lymphatic drainage	Congenital lymphatic dysplasia
Neck/chest (2%)	Vena caval obstruction or increased intrathoracic pressure with impaired venous return	Cystic hygroma Congenital high airway obstruction Pleural effusion (chylothorax) Chest mass (congenital pulmonary airway malformation, sequestration, congenital diaphragmatic hernia)
Gastrointestinal (1%)	Obstruction of venous return, gastrointestinal obstruction and infarction with protein loss and decreased colloid osmotic pressure	Portal vein thrombosis Volvulus Obstruction Meconium peritonitis
Urinary tract (1%)	Urinary ascites; nephrotic syndrome with hypoproteinemia	Finnish nephrosis, urinary tract obstruction
Aneuploidy (13%)	Cardiac anomalies, lymphatic dysplasia, anemia, abnormal myelopoiesis	45,XO, trisomy 21, trisomy 18, triploidy
Hematologic (9%[b])	Anemia, high-output cardiac failure; hypoxia (α-thalassemia)	α-Thalassemia (homozygous) Fetomaternal transfusion
Infection (7%)	Anemia, anoxia, endothelial cell damage, increased capillary permeability, myocarditis	Parvovirus, cytomegalovirus, adenovirus, syphilis, toxoplasmosis
Inborn errors of metabolism (1%)	Anemia Hemolysis	Lysosomal storage disease, mucopolysaccharidoses, Gaucher disease, Niemann-Pick disease G6PD deficiency
Other syndromes (5.5%)	Visceromegaly, obstruction of venous return, decreased erythropoiesis, anemia, hypoproteinemia	Noonan syndrome Skeletal dysplasias such as achondroplasia, osteogenesis imperfecta, thanatophoric dysplasia arthrogryposis, congenital myotonic dystrophy
Extrathoracic tumors (1%)	Anemia, high-output cardiac failure, hypoproteinemia	Vascular/lymphatic tumors Teratoma, neuroblastoma, arteriovenous malformation
Maternal		Severe diabetes mellitus, severe anemia, severe hypoproteinemia, thyrotoxicosis Indomethacin use (premature closure of ductus arteriosus)
Placental/cord		Placental or umbilical vein thrombosis, cord knot, chorioangioma
Idiopathic 20%		

[a]Adapted from references 4, 23, 36, 43, 226, and 230-237.
[b]Much higher percentage of hydrops in regions with α-thalassemia, such as Southeast Asia.

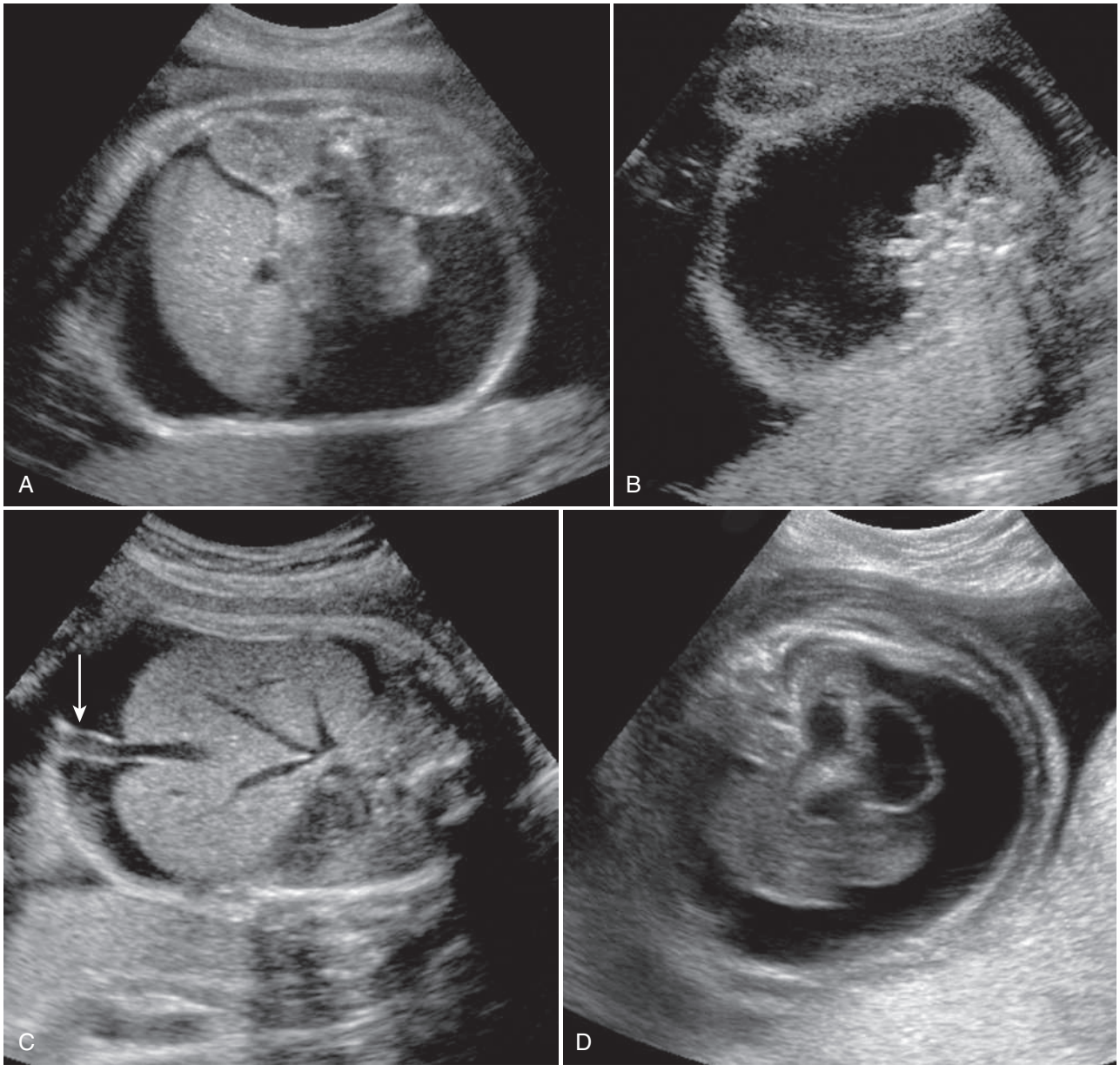

FIG. 41.2 Ascites. (A) Fluid outlines the liver. **(B)** Fluid outlines the bowel, compressing it posteriorly. **(C)** Ascites outlines the umbilical vein *(arrow)*. **(D)** Fluid outlines the liver and stomach. Note associated skin thickening.

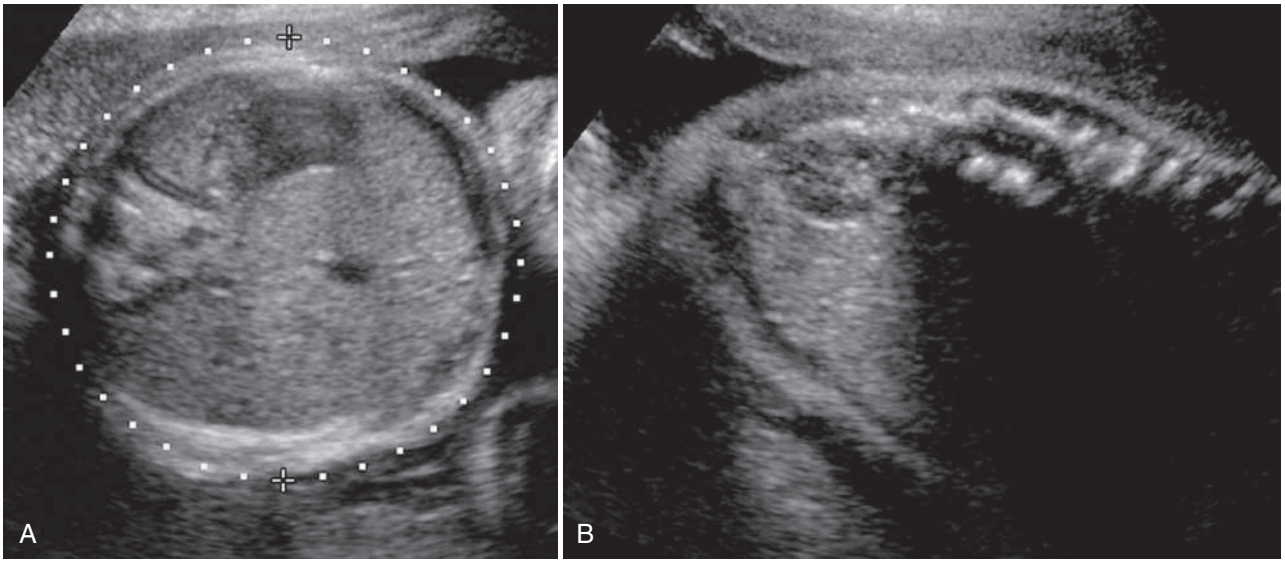

FIG. 41.3 Pseudoascites. (A) Transverse and **(B)** parasagittal ultrasound views show hypoechoic abdominal musculature and fat mimicking ascites. Note that this appearance will change with transducer angle, and the hypoechoic material will always be visualized in the subcutaneous regions, not surrounding bowel.

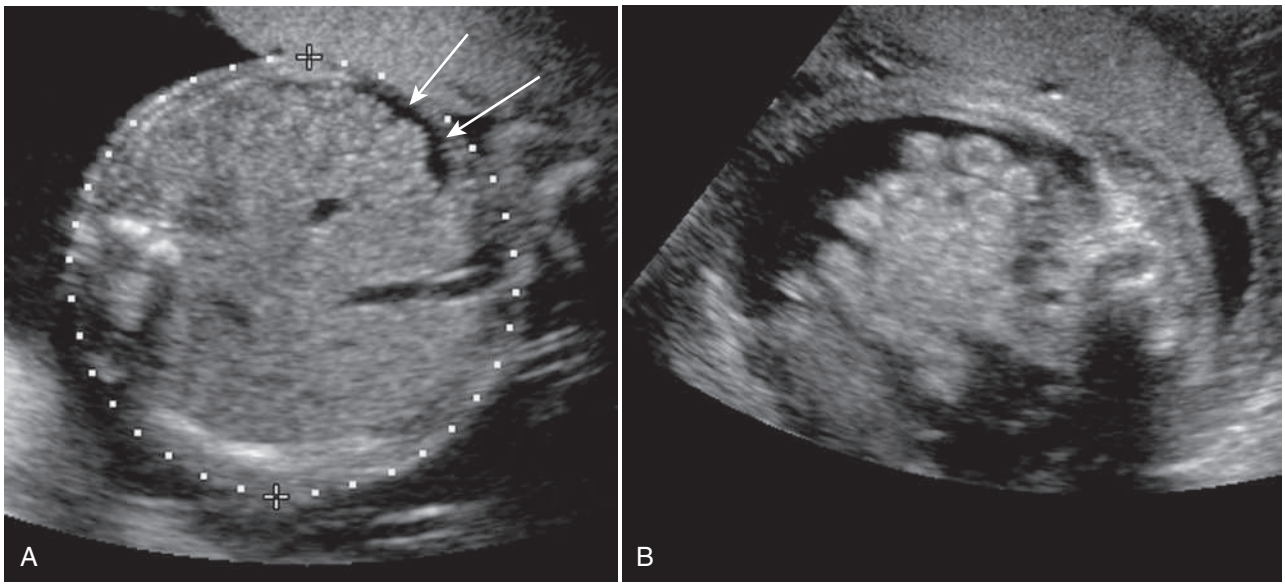

FIG. 41.4 Ascites. (A) Small amount of ascites *(arrows)*. **(B)** Moderate amount of ascites. Note how the ascites surrounds loops of bowel. The bowel can appear echogenic because of through transmission from the fluid. See also Video 41.1.

FIG. 41.5 Hydrocele. Ultrasound of male fetus with hydrops with fluid extending into the scrotum.

chest mass such as a hernia or congenital pulmonary airway malformation (CPAM) should be sought (Fig. 41.7). Larger effusions will lead to flattening and eversion of the hemidiaphragms (Video 41.3) and, when sufficiently large, mediastinal shift. A large, unilateral effusion suggests a local cause, such as **chylothorax.** Although chylothorax begins as a unilateral effusion, it can progress to cause mediastinal shift, obstructing venous return and leading to hydrops. In large, bilateral pleural effusions the lungs appear as free-floating "bat wings" beside the heart (see Fig. 41.6D). When chronic, large effusions can lead to pulmonary hypoplasia. As pleural effusions enlarge, compression or kinking of mediastinal vascular structures causes upper body edema and functional esophageal obstruction, leading to secondary polyhydramnios.

Chylothorax is the most common cause of pleural effusion leading to respiratory distress in the newborn. This is an important diagnosis to suggest when associated with hydrops because drainage can be curative. Drainage of the effusion can lead to reversal of hydrops and can prevent pulmonary hypoplasia. Drainage immediately before delivery can assist in peripartum care. When drained, the fluid has a large number of lymphocytes in clear, yellow fluid. The fluid will not be "milky" until after the infant feeds.

In a recent review of 31 fetuses with primary hydrothorax, 24 had hydrops. Hydropic fetuses were more likely to present with bilateral effusions. Of all fetuses with primary hydrothorax, 21 had fetal interventions. Survival without hydrops was 7/7 (100%), whereas survival with hydrops depended on whether or not the patient had fetal intervention: 12/19 (63%) with intervention and 1/5 (20%) without intervention. Premature delivery was common (44%) among those who had fetal intervention.[9]

Pericardial Effusions

In contrast to pleural effusions that surround the lungs and compress the tissue medially, pericardial effusions are anteromedial fluid collections. Fluid collections of up to 2 mm in thickness are common, and a small amount of pericardial fluid (up to 7 mm, in isolation) can be a normal finding[10] (Fig. 41.8, Video 41.4). A large pericardial effusion compresses the lungs against the posterior chest wall (Fig. 41.9). The heart is visualized as "floating" within the anterior thoracic fluid collection.

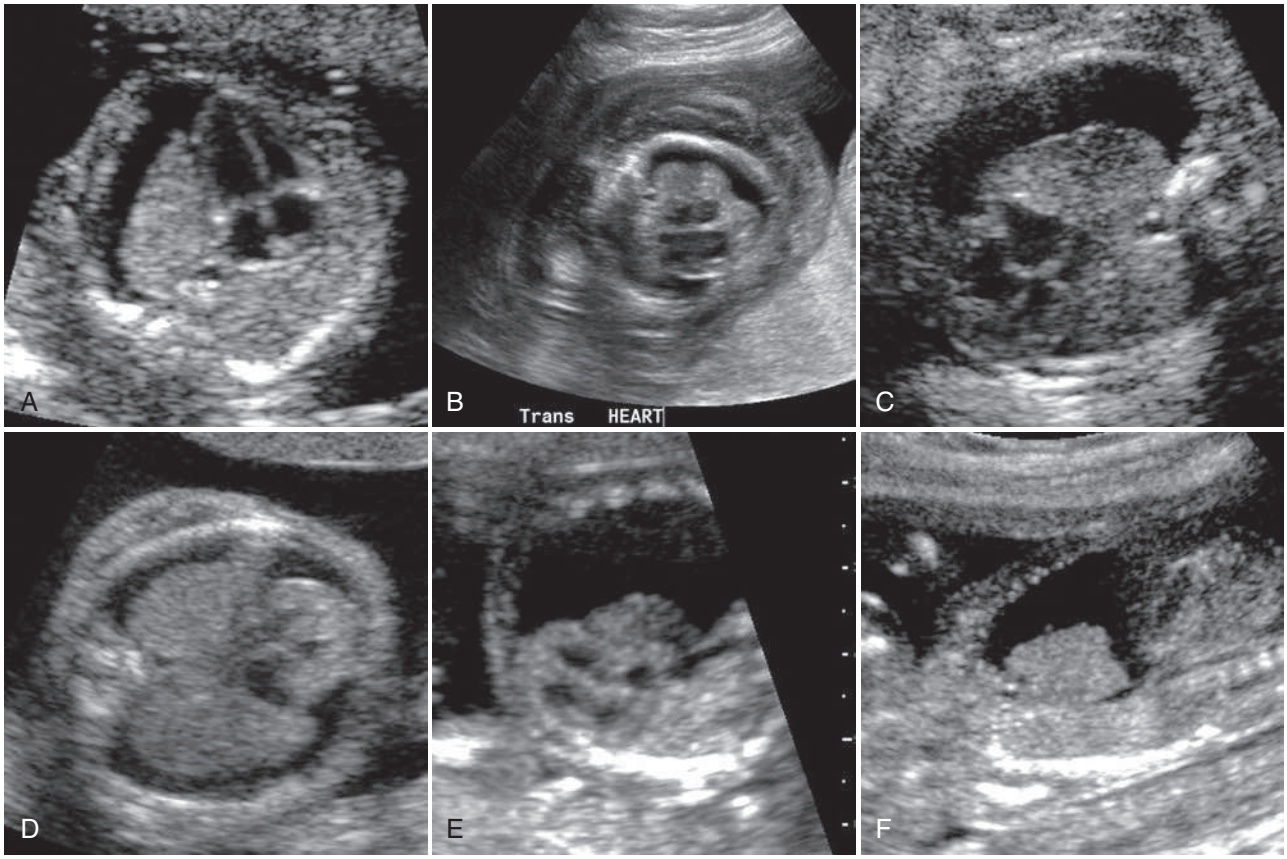

FIG. 41.6 Fetal Pleural Effusions. (A) Unilateral small right pleural effusions. **(B)** Bilateral pleural effusions in fetus with abnormal heart and severe skin thickening. **(C)** Moderate right effusion. Note moderate mediastinal shift to the left. **(D)** Bilateral moderate effusions. Note how the partially compressed lungs appear as free-floating "bat wings." **(E)** Axial and **(F)** oblique coronal views of large right pleural effusion. Note the severe mediastinal shift in **E.** See also Video 41.2.

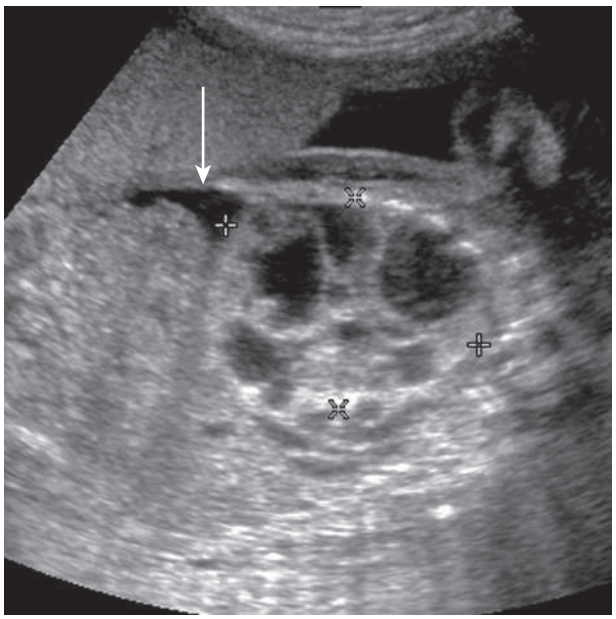

FIG. 41.7 Small Pleural Effusion in Association With Congenital Pulmonary Airway Malformation. Note the large cystic mass *(calipers)* and small pleural effusion *(arrow)*.

Subcutaneous Edema

Subcutaneous edema may be localized or generalized (Fig. 41.10), depending on the cause. A thickness of 5 mm has been suggested as the cutoff value.[11] Edema is most easily seen over the fetal scalp or face, where thickening of skin overlying bone is visualized (Figs. 41.10A and 41.11A). It is important to realize that the **biparietal diameter** and **head circumference** measurements are taken around the skull bone, excluding the skin. Subcutaneous edema may also be seen over the limbs and abdominal wall. Care should be taken not to mistake prominent fat in a macrosomic fetus as anasarca in a hydropic fetus. Subcutaneous edema will increase the abdominal circumference measurement, beyond that which is expected for gestational age (Fig. 41.11B). It is important when measuring the fetus to include the entirety of the skin in the abdominal circumference measurement, because this affects the weight calculation of the fetus. Thus, when biometric assessment of the hydropic fetus is performed, the abdominal circumference measurement is included in the weight calculation, but it should be excluded from the gestational age assessment so that the thickened skin does not falsely elevate estimated fetal age. When generalized subcutaneous edema is present, the appearances may be referred to as "anasarca" (Fig. 41.12, Video 41.5).

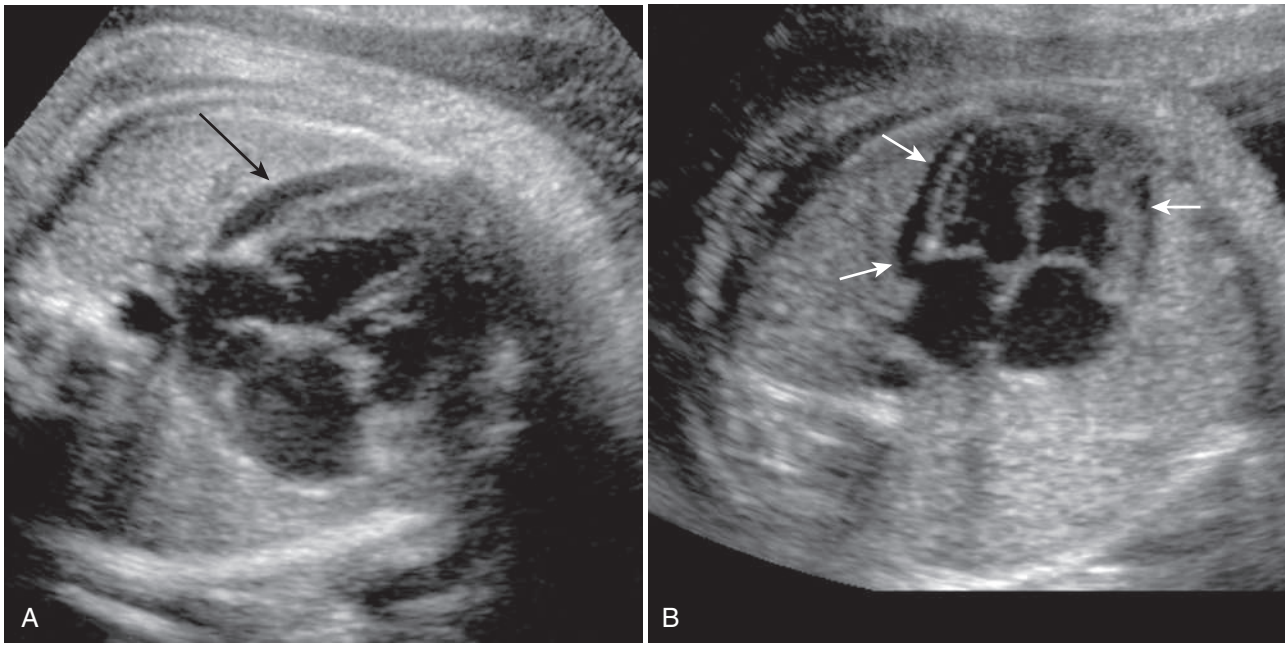

FIG. 41.8 Normal Finding of Small Amount of Pericardial Fluid. (A) and **(B)** Note the small rim of anechoic fluid *(arrows)* in two different fetuses. See also Video 41.4.

FIG. 41.9 Large Pericardial Effusion. Lungs are compressed posteriorly, and the heart appears to be "floating" in the fluid.

Placentomegaly

Placental edema is a variable and usually late sign in hydrops (Fig. 41.13). The sonographic texture of the placenta may be altered, and its appearance may be described as **thickened, echogenic, spongy,** or **ground glass.** Placental dimensions, especially thickness, are increased above the normal of 4 cm thickness in the second trimester and 6 cm in the third trimester.[11-15] When placental edema is secondary to a fetal abnormality, the entire placenta is usually affected. This finding may be used to exclude the very rare primary placental causes of hydrops (e.g., chorioangioma).

Polyhydramnios

The assessment of amniotic fluid is described in Chapters 39 and 42. Polyhydramnios occurs frequently in conjunction with hydrops (Fig. 41.14, see Video 41.1). A single amniotic fluid pocket of 8 cm or more, regardless of gestational age, is a useful threshold for polyhydramnios. Polyhydramnios increases the risk of prematurity, which adds to the morbidity associated with hydrops.

ETIOLOGY

Before the availability of Rho (D) immune globulin (RhoGAM), immune hydrops represented more than 80% of all cases of hydrops. Now, **nonimmune hydrops** represents more than 85% of cases. The **distribution, timing,** and **size** of fluid collections and edema as detected by ultrasound provide clues as to the etiology of hydrops. For example, in **immune hydrops,** ascites appears first, with subcutaneous edema appearing only with more advanced anemia. Intrathoracic collections generally do not occur or occur late in the process.

Generally, pleural and pericardial effusions appear earlier and more prominently with thoracic pathologies, whereas ascites appears earlier and predominates with anemia and primary abdominal pathologies. Massive ascites with associated bowel hyperechogenicity is typical of either **parvovirus** infection (when the ascites is very tense) or a bowel perforation that may be secondary to **meconium peritonitis** (Fig. 41.15). Localized fluid collections may progress to hydrops because of pressure or

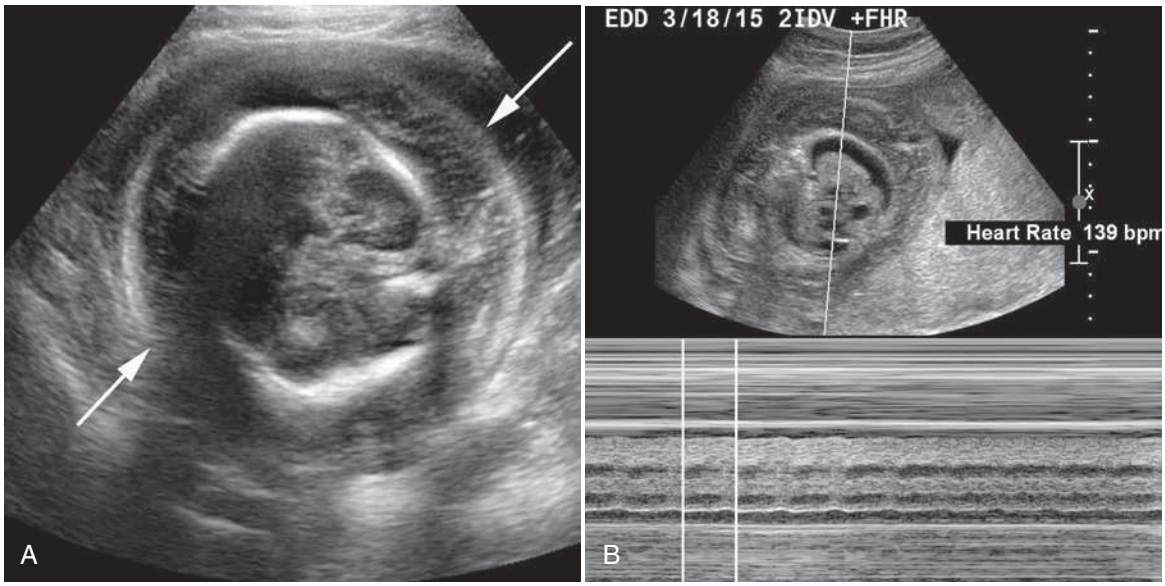

FIG. 41.10 Skin Thickening in Fetus With Hydrops. (A) Transverse view of skull shows marked edematous appearance of the skin *(arrows).* **(B)** In the same fetus, transverse M-mode image of fetal thorax shows normal cardiac rhythm, bilateral pleural effusions, and marked skin thickening.

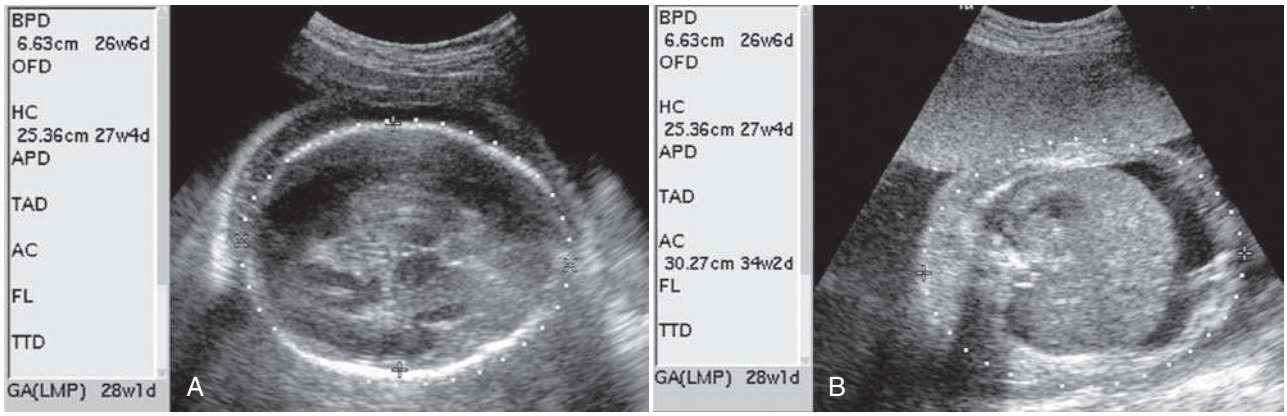

FIG. 41.11 Scalp and Body Wall Edema Are Measured Differently. (A) Fetal scalp edema. Head measurements *(cursors)* are obtained around the bone, not the skin. **(B) Abdominal wall thickening.** Abdominal wall measurements are obtained around the abdomen, including the skin thickening. Note that gestational age is 27 weeks by head circumference *(HC)* but 34 weeks if only abdominal circumference *(AC)* is used. *BPD,* Biparietal diameter.

metabolic effects, and thus the pattern of hydrops may evolve over time.

IMMUNE HYDROPS

Immune hydrops, or **erythroblastosis fetalis,** occurs when a sensitized mother develops antibodies to fetal RBCs that lead to hemolysis. Circulating maternal immunoglobulin G (IgG) antibodies cross the placenta and attack antigen-positive fetal RBCs. The majority of cases still occur in the presence of Rh(D) antibodies. Other antibodies such as Kell, Rh(C), and Rh(E) develop in 1% to 2% of individuals after blood transfusion and cause 2% of hemolytic disease of the fetus. The result is anemia, extramedullary erythropoiesis, hepatosplenomegaly, hypoalbuminemia, and congestive heart failure. Hydrops develops when the **fetal hemoglobin** (HbF) **deficit** exceeds 7 g/dL,[16] probably because of reduced oncotic pressure secondary to hypoalbuminemia, combined with high-output cardiac failure. Eventually, the fetus develops both metabolic and lactic acidosis,[17,18] and once this decompensation occurs, progression of hydrops is rapid, leading to fetal demise within 48 hours.

Causes of maternal sensitivity include fetal maternal hemorrhage and transplacental hemorrhage. In women with incompatible blood types with respect to the fetus (Rh alloimmunization or other RBC antigen), antibodies can be made. This typically occurs after delivery of the first pregnancy and therefore will affect the second pregnancy. Other times of blood sharing include miscarriage, therapeutic abortion, amniocentesis, placental

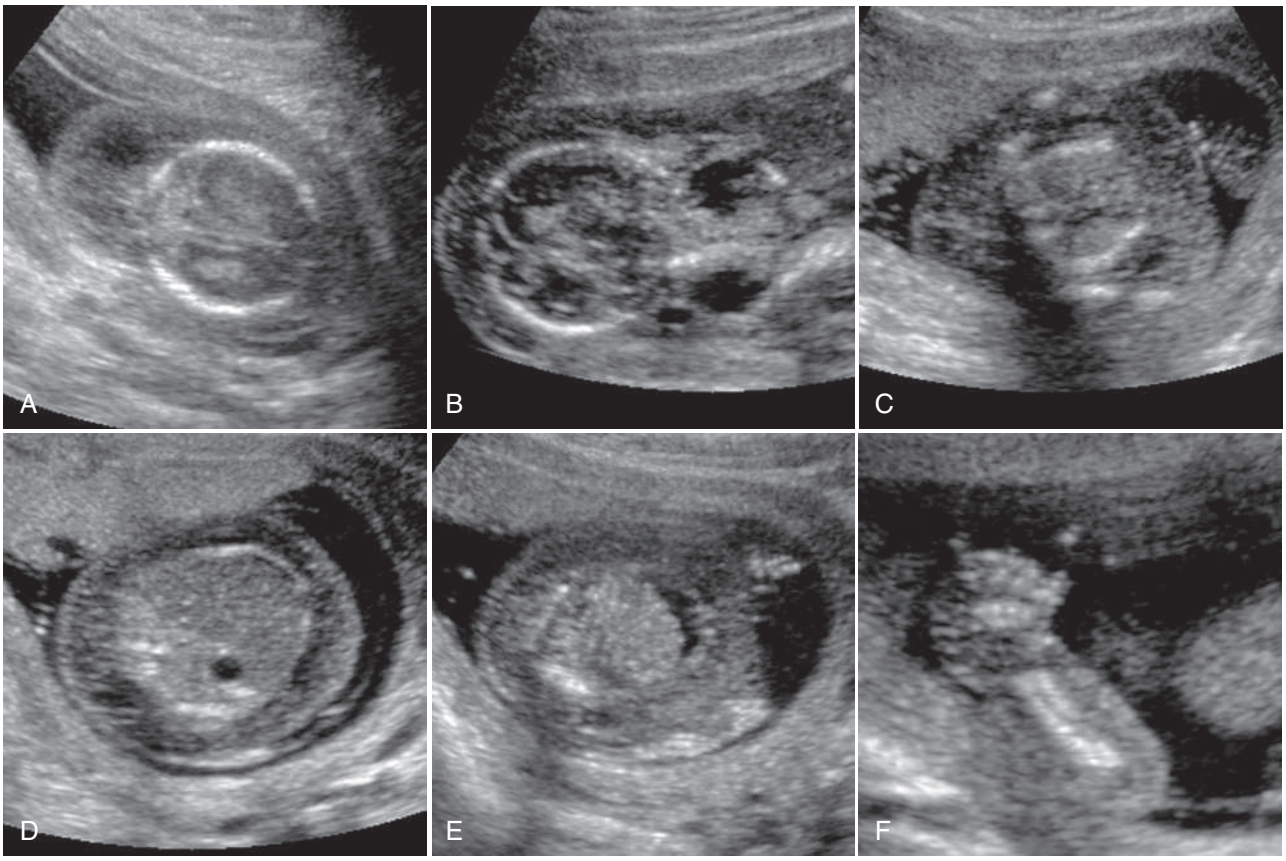

FIG. 41.12 Anasarca in Fetus With Turner Syndrome. (A) Axial view of cystic hygroma behind the neck. **(B)** Coronal view of diffuse scalp edema and cystic hygroma. **(C)** Axial view of thoracic wall edema. **(D)** and **(E)** Axial views of abdomen show body wall edema and ascites. **(F)** Arm with anasarca as well. See also Video 41.5 for example of anasarca associated with congenital pulmonary airway malformation.

FIG. 41.13 Placental Edema. Placental thickness is normally about 1 mm of thickness per week gestational age, and it should not exceed 5 cm in the third trimester.

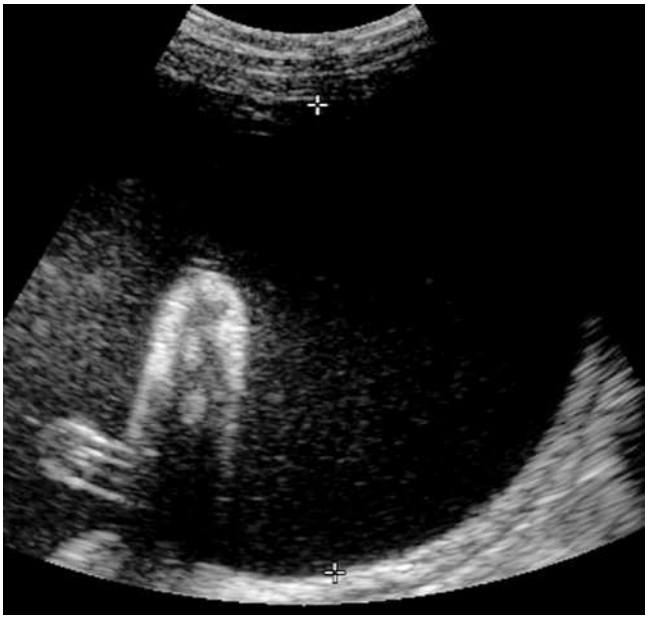

FIG. 41.14 Polyhydramnios. A 12-cm pocket of fluid *(cursors)* in pregnancy complicated by fetus with hydrops.

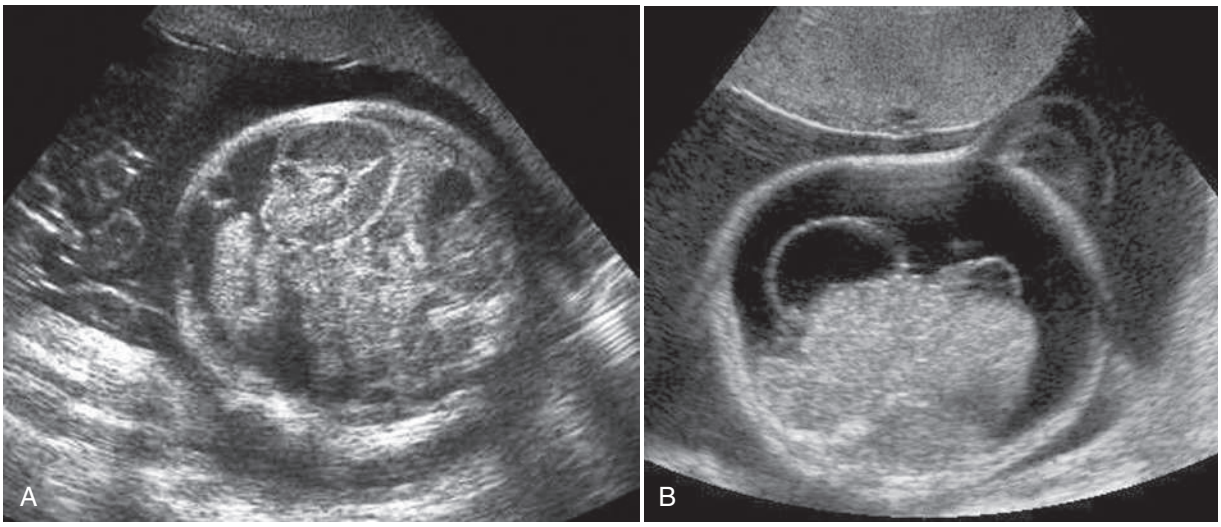

FIG. 41.15 Meconium Peritonitis. (A) Matted and dilated echogenic bowel with ascites, typical of meconium peritonitis. **(B)** Tense ascites in meconium peritonitis.

abruption, incompatible blood transfusions, and transplacental hemorrhage. An additional blood incompatibility issue is fetal **alloimmune thrombocytopenia.**

To avoid maternal sensitization, 300 mg of RhoGAM is given at 28 weeks' gestation in sensitized individuals. This protects against 30 mL of fetal blood. If a greater degree of fetomaternal hemorrhage is suspected, a **Kleihauer-Betke test** can be done to quantify fetal blood in maternal circulation to determine the necessary dose. As a prophylactic measure, RhoGAM is given to Rh-negative women within 48 hours after invasive fetal procedures such as amniocentesis and chorionic villus sampling.

Noninvasive Assessment of Alloimmunization

Fetuses are screened for risk of alloimmunization by determining the Rh status of the parents. If the pregnant woman is Rh negative, the father is screened. If the father of the baby is also Rh negative, no further screening is needed. If the mother is Rh negative and the father is Rh positive, maternal antibody titers are monitored. If they rise above 1:8, further testing is warranted. In the past, this was done with amniocentesis assessing for optical density (OD_{50}) of amniotic fluid (hemolysis increases OD of amniotic fluid), and serial percutaneous umbilical cord blood sampling (PUBS) procedures were performed as indicated to determine hematocrit (Hct). Currently, Hct is indirectly inferred from middle cerebral artery (MCA) Doppler studies, in which **peak systolic velocity** (PSV) is elevated in cases of anemia.

In response to severe anemia, the **fetal circulation becomes hyperdynamic** with increased blood flow velocities, which are thought to result from increased cardiac output and decreased viscosity of fetal blood. In addition, blood flow in the MCA may be increased further because the brain circulation responds quickly to hypoxemia.[19] Although flow velocities in all fetal vessels will be increased, the MCA is particularly suitable for assessment because of its easy visualization with color Doppler imaging (Video 41.6) as it courses directly above the greater wing of the sphenoid bone, carrying more than 80% of cerebral blood flow. The MCA has a high-impedance circulation with continuous forward flow. The method for MCA Doppler includes finding the circle of Willis, measuring a pulsed Doppler waveform of the proximal MCA at the base of the brain soon after its origin from the internal carotid artery (ICA) and obtaining a PSV measurement with the angle of insonation close to 0 degrees (Fig. 41.16B). Intraobserver and interobserver variability is low. Technique is important for obtaining accurate results. In most cases the examination can be performed in less than 5 minutes.

Measurement of Middle Cerebral Artery (MCA) Peak Systolic Velocity (PSV)

1. Obtain an axial section of the head at the level of the sphenoid bones during a period of fetal rest.
2. Use color Doppler ultrasound to identify circle of Willis with MCA at angle close to 0 degrees.
3. Enlarge image of MCA such that it occupies more than 50% of the image.
4. Interrogate MCA soon after its origin from the ICA at angle close to 0 degrees using a 1- to 2-mm sample volume. (If an angle close to 0 degrees cannot be obtained, then angle correction can be utilized.)[20]
5. Measure PSV.
6. Repeat the collection of MCA Doppler ultrasound three times.
7. Repeated waveforms should be similar.

The measured PSV is compared to median measures with respect to gestational age. A measurement of 1.5 multiples of the median (MoM) suggests severe anemia (Table 41.2). In a study of 111 fetuses at risk for anemia and 265 nonanemic fetuses, Mari et al. reported a sensitivity of a single value of MCA-PSV of nearly 100% for moderate or severe anemia with a false-positive rate of 12%.[19]

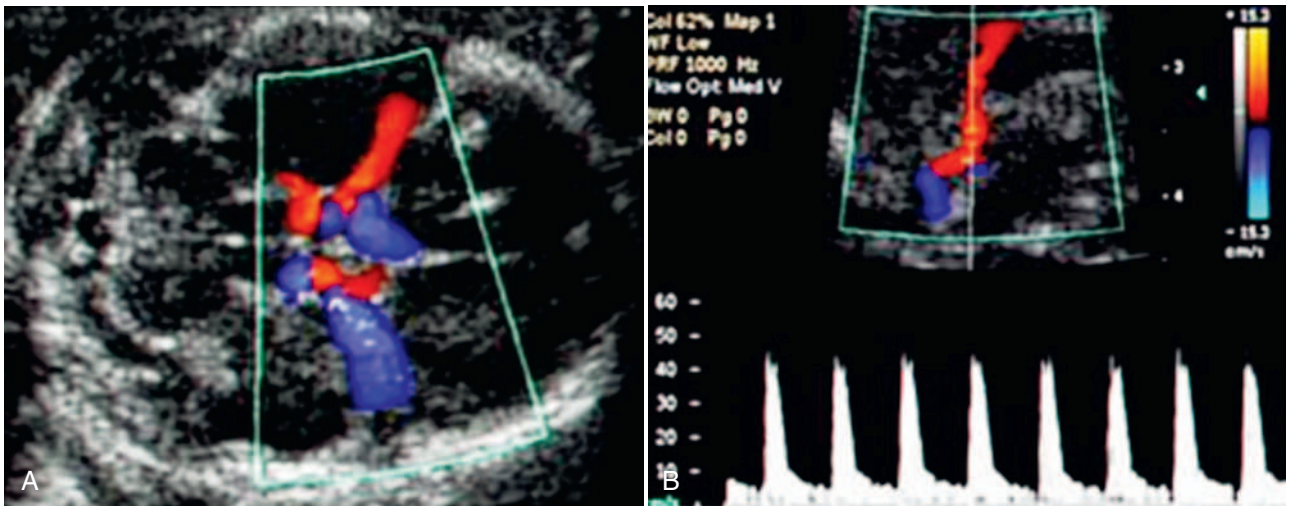

FIG. 41.16 Middle Cerebral Artery (MCA) on Color Doppler Ultrasound. (A) Circle of Willis. **(B)** Spectral Doppler tracing. Note how Doppler gate is on the MCA just after the origin from the internal carotid artery. Note that the MCA is studied with an angle close to 0 degrees; therefore, the velocity is close to the real velocity of the blood flow. See also Video 41.6. (With permission from Mari G, Abuhamad AZ, Cosmi E, et al. Middle cerebral artery peak systolic velocity: technique and variability. J Ultrasound Med. 2005;24:425-430.[229])

TABLE 41.2 Expected Peak Velocity of Systolic Blood Flow in the Middle Cerebral Artery as a Function of Gestational Age

Week of Gestation	MULTIPLES OF THE MEDIAN (cm/sec)			
	1.00 (Median)	1.29	1.50	1.55
18	23.2	29.9	34.8	36.0
20	25.5	32.8	38.12	39.5
22	27.9	36.0	41.9	43.3
24	30.7	39.5	46.0	47.5
26	33.6	43.3	50.4	52.1
28	36.9	47.6	55.4	57.2
30	40.5	52.2	60.7	62.8
32	44.4	57.3	66.6	68.9
34	48.7	62.9	73.1	75.6
36	53.5	69.0	80.2	82.9
38	58.7	75.7	88.0	91.0
40	64.4	83.0	96.6	99.8

With permission from Mari G, Deter RL, Carpenter RL, et al. Noninvasive diagnosis by Doppler ultrasonography of fetal anemia due to maternal red-cell alloimmunization. N Engl J Med. 2000;342(1):9-14.[19]

In 2009, Pretlove et al.[21] published a meta-analysis (that included pooled data from nine studies) on the diagnostic value of MCA Doppler flow studies for fetal anemia. Severe anemia was detected with sensitivity and specificity of 75% and 91%, respectively. The use of the MCA-PSV trends (as opposed to a single measurement) may decrease the false-positive rate to less than 5%.[22]

The timing of MCA-PSV examination surveillance depends on prior history, gestational age, and measured MCA-PSV MoM level. Surveillance should begin when the pregnancy is advanced enough such that a fetal blood sampling procedure or intrauterine transfusion can technically be completed, typically after 18 weeks of gestation. After 24 weeks of gestation, routine testing is usually done on a weekly basis but may be done more frequently with higher MoM levels or other abnormal ultrasound findings that are suggestive of developing anemia.[23]

The **middle cerebral artery peak systolic velocity** (MCA-PSV) **is increased in intrauterine growth-restricted fetuses,** and therefore not all fetuses with elevated MCA-PSV will have anemia. A variable sign of anemia in the fetus is that of **hepatosplenomegaly.** The fetal liver and spleen increase in size because of their increased production of RBCs. However, the fetus may be able to compensate for the breakdown of RBCs and, in such cases, may have a large liver and spleen but would not necessarily be severely anemic. Conversely, more rapid breakdown of RBCs may prevent the fetus from adapting to hemolysis. Therefore, anemia may develop without hepatosplenomegaly.[24,25]

MCA Doppler ultrasound can help time a second fetal transfusion procedure,[26] but need for subsequent transfusions are better predicted by estimating the decrease in fetal hematocrit over time.[27]

Immune hydrops is an indication for urgent **fetal blood sampling** and transfusion. Use of MCA-PSV data allows for PUBS procedures to be timed to the need for in utero transfusions.[19,28,29] In a study of 80 fetuses with hydrops secondary to anemia, when hydrops was mild before treatment (only a thin rim of ascites, with or without pericardial effusion), hydrops was reversed in 88%; when hydrops was severe before treatment, hydrops reversed in only 65%. This stresses the importance of early treatment in cases of suspected anemia. After reversal of hydrops, survival rate was 98%.[30]

It should be recognized that immune hydrops, even untreated, is not uniformly lethal, and can spontaneous reverse, particularly if hydrops is mild, and an infection, such as parvovirus, is self-limited. Complications of transfusion for fetal anemia are detailed

later in this chapter and include in utero demise, preterm delivery, intracranial hemorrhage, and postnatal developmental delays.

NONIMMUNE HYDROPS

Nonimmune hydrops occurs in 1 in 1500 to 1 in 4000 pregnancies. It is a common pathologic finding in first- and second-trimester spontaneous abortions. The cause varies geographically and with gestational age. In North America and Europe, most cases are cardiovascular (20%), hematologic (9%), infective (7%), or chromosomal (13%; usually Turner syndrome; trisomy 21 and 18) in origin (see Table 41.1).[4] In Southeast Asia, however, homozygous **α-thalassemia** is a common cause[31]; in this region, carrier status for α-thalassemia occurs in 5% to 15% of the population. Nonimmune hydrops in homozygous α-thalassemia accounts for 25% of perinatal deaths in Southeast Asia.

Pathophysiology

Nonimmune hydrops represents the terminal stage for many conditions and is frequently multifactorial. Pathophysiology of hydrops may involve increased hydrostatic pressure, high-output cardiac failure, decreased plasma oncotic pressure, increased capillary permeability, obstruction of lymph flow, or a combination of these factors (Fig. 41.17). Fluid collections result from redistribution of fetal body fluids among the intravascular, intracellular, and interstitial compartments, secondary to an imbalance in capillary ultrafiltration and interstitial fluid return.[32] Hypoxia and circulatory failure may result in capillary damage that leads to plasma protein and fluid loss from the intravascular compartment.

Several factors predispose to edema in the fetus versus after birth. Both total body and extracellular fluid compartments are proportionately greater in the fetus, particularly at earlier gestational ages. Colloid osmotic pressure is lower because of lower albumin concentrations. High compliance of the interstitial space facilitates the accumulation of large volumes of fluid. Many causes of hydrops, especially those with a cardiac component, result from an increase in systemic venous pressure, to which the fetus is particularly sensitive. In the fetus, there is a net movement of fluid from the intravascular to the extravascular space. Fivefold larger volumes of fluid are removed by the lymphatics in fetal models than in adult animal models. Thus small elevations in systemic venous pressure (2-3 mm Hg) in the fetus can substantially reduce lymphatic flow and can drive large amounts of fluid into the extracellular space. This process is further enhanced by the relatively greater permeability of fetal capillaries to protein. The fetus is therefore particularly susceptible to small elevations in venous pressure from a number of causes, all of which can result in hydrops.[16,17,33]

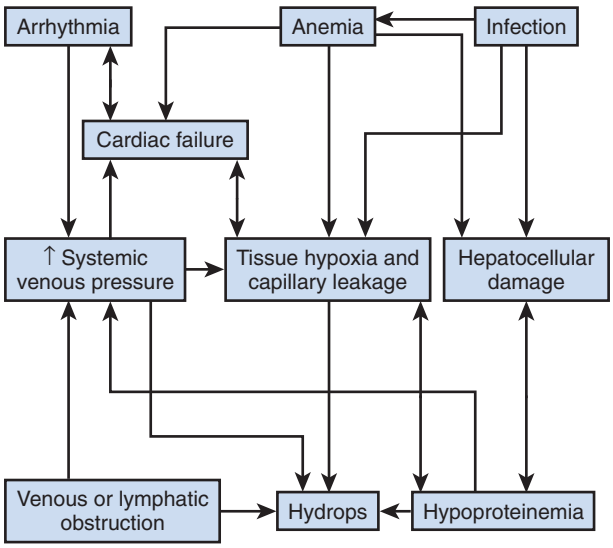

FIG. 41.17 Pathogenesis of Hydrops.

Causes and Associations

Nonimmune hydrops most commonly has a **fetal** etiology but also may be caused by maternal or placental factors. **Maternal** causes (such as poorly controlled diabetes mellitus) are rare and should be differentiated from maternal complications, which are secondary to fetal hydrops (termed **mirror syndrome** because edema develops in the mother of an hydropic fetus, "mirroring" the condition in the fetus).[34,35] Maternal thyrotoxicosis can cause fetal hyperthyroidism and fetal hydrops, with potential for resolution of hydrops after treatment with antithyroid drugs.[36] **Placental** causes, such as **chorioangioma** and other vascular shunts, are relatively rare and are usually associated with high-output failure states and, in some cases, fetal anemia.[37,38] Chorioangiomas need to be large (>4-5 cm) before they lead to hemodynamic compromise. They can be treated by laser, radiofrequency ablation, and/or surgical clip application.[39] Fetal metabolic causes are rare but important, because diagnosis can lead to appropriate neonatal treatment and appropriate counseling of the patients regarding recurrence risks.

A classification scheme for fetal causes is shown in Table 41.1 and has some overlap in the groupings, some of which represent associations rather than causations.

Cardiovascular Abnormalities

Structural cardiovascular abnormalities (Fig. 41.18) are the cause of hydrops in about 20% of cases.[4] However, hydrops is a rare complication of *isolated* cardiac abnormality because the fetus has a parallel flow circulation. In chromosomal abnormalities, for example, other factors with or without cardiac abnormality lead to hydrops.

Right-sided lesions, whether obstructive, such as **pulmonary or tricuspid atresia,** or structural lesions that result in right atrial volume or pressure overload, such as **mitral regurgitation,** can result in congestive heart failure and hydrops.[40,41] Left-sided obstructive lesions, such as **aortic stenosis, mitral stenosis,** and **coarctation of the aorta,** can result in a hypoplastic left heart, causing increased blood flow through the fetal right ventricle, which may result in hydrops.[42] The prognosis of nonimmune hydrops fetalis caused by cardiac structural abnormalities is poor, with a combined fetal and infant mortality rate of 92%, largely because of the severity of the heart defects that cause in utero congestive heart failure.[43] Some fetuses with structural cardiac anomalies also have rhythm disturbances, which contribute to the poor prognosis. In a series of 301 fetuses with atrioventricular

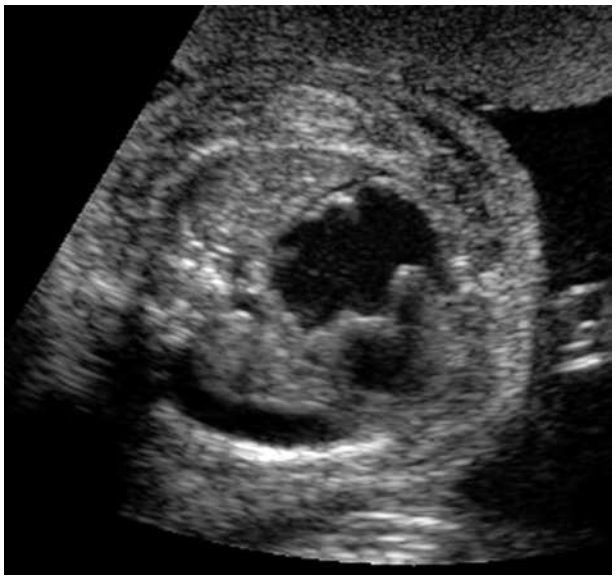

FIG. 41.18 Hydrops Secondary to Structural Cardiac Abnormality. Note the enlarged abnormal heart, pleural effusions, and skin thickening.

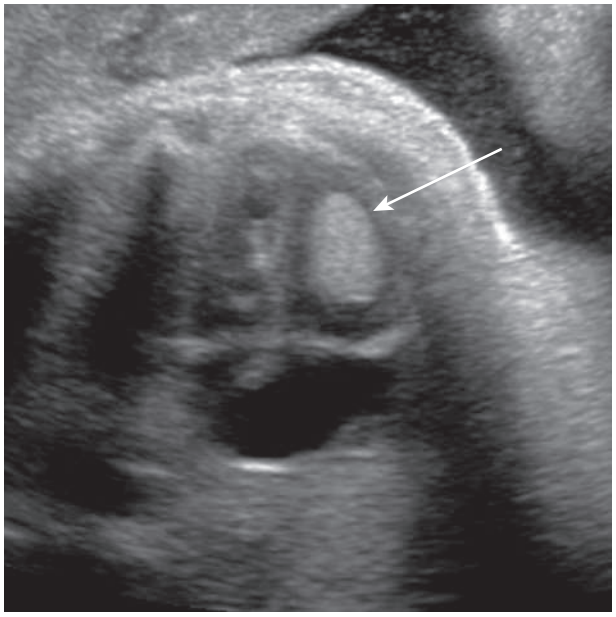

FIG. 41.19 Cardiac Rhabdomyoma. Note the echogenic lesion *(arrow)* adjacent to the myocardium.

(AV) septal defects, the presence of fetal hydrops, together with **bradycardia** from sinus node dysfunction or **complete heart block,** was associated with a poor outcome.[44]

Cardiac Tumors. Cardiac tumors are a rare cause of hydrops.[45-50] Hydrops in the context of cardiac tumors may be caused by several mechanisms, depending on the tumor location, size, and number. Cardiac lesions may cause obstruction to blood flow and alteration of AV valve function and may lead to arrhythmia, cardiac tamponade, pericardial effusion, and hydrops.[47-49]

Rhabdomyomas are the most common fetal cardiac tumor and are seen in association with **tuberous sclerosis** in more than 80% of cases.[50] Rhabdomyomas are also the most common cardiac tumors to cause hydrops. Usually, these tumors are multiple, well-circumscribed, hyperechoic, and homogeneous and mainly involve the ventricular myocardium[48] (Fig. 41.19). Rhabdomyomas tend to grow during the second half of pregnancy,[51] so most are diagnosed during the second and third trimesters.

Intrapericardial teratomas are rare, usually appearing as cystic and solid masses outside the cardiac cavities, arising from the pericardium. Teratomas may be larger than the heart, and rapid growth of the tumor within the small, confined space can result in pericardial effusion and hydrops as a result of cardiac compression.[52,53] Drainage of pericardial fluid associated with an intrapericardial teratoma has been reported, with resolution of associated hydrops.[54,55] Frequently, more than one drainage procedure is necessary.[56] At times, a shunt is placed if fluid rapidly reaccumulates after drainage.[57] Drainage of pericardial effusion secondary to intrapericardial teratoma usually results in a live birth after 32 weeks' gestational age.

Arrhythmias. Arrhythmias associated with hydrops are most often **tachyarrhythmias** (≥200 beats/min) and, less frequently, bradyarrhythmias. The diagnosis is important because treatment can reverse the hydrops. It is important to avoid premature delivery; treatment of a hydropic preterm fetus is difficult. Fetal tachyarrhythmias are most often **supraventricular tachycardia** (SVT, which includes **atrial fibrillation/flutter**)[58] (Fig. 41.20). The prognosis for a fetus with an isolated arrhythmia is favorable, with a 95% likelihood of survival.[59] However, when hydrops is present (41% in this series) with an otherwise isolated arrhythmia, the survival decreases to 73%.[58] When studying neonates who had fetal SVT, most cases are the result of reentry circuits.[60] If the SVT is of limited duration, there are typically no fetal consequences. However, with sustained SVT, hydrops may develop. The presence of hydrops in these cases is associated with more difficult prenatal antiarrhythmic control of the tachycardia and higher mortality. Prenatal control of the tachycardia was achieved in 83% of treated nonhydropic fetuses, compared with 66% of the treated hydropic fetuses.[58]

Tachyarrhythmia treatment is almost always given transplacentally; the pregnant woman is given an antiarrhythmic drug, which crosses the placenta and enters the fetal circulation. Rarely is direct fetal administration required.[31] At present, there is no consensus on first-line treatment of SVT. In one report flecainide and digoxin were slightly more effective than sotalol.[61] Combination therapies (amiodarone/digoxin, amiodarone/flecainide, sotalol/digoxin, and sotalol/flecainide) have been reported to be effective when single agents have failed.[62] Treatment for SVT has been described as early as 13 weeks' gestational age.[63] Prognosis in the setting of fetal tachyarrhythmia depends on a number of factors, including type and duration of arrhythmia, presence of structural cardiac anomalies, gestational age, and response to intrauterine therapy.[64]

In rare cases of SVT and hydrops, preterm delivery (if at sufficient gestational age) may be the best option, allowing for direct treatment of the tachyarrhythmia. Again, however, treatment of a hydropic preterm infant is difficult, and therefore preterm delivery is usually not indicated.

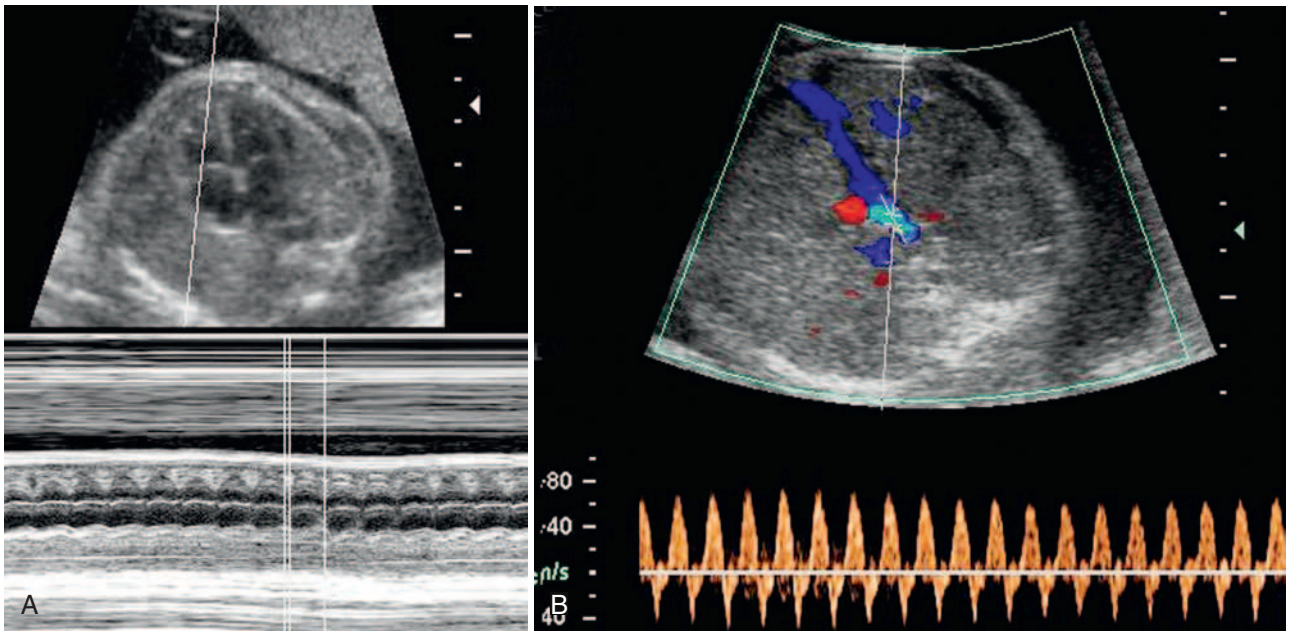

FIG. 41.20 Supraventricular Tachycardia (SVT). (A) Atrial rate of 250 beats/min. **(B)** Color Doppler ultrasound shows ductus venosus waveform with SVT.

Heart Block. Congenital heart block (CHB) is a rare cardiac conduction defect, occurring in 1 in 15,000 to 1 in 20,000 live births. In fetuses with CHB, hydrops results from a combination of low cardiac output, a slow heart rate, and a structural lesion, if present. The increased venous pressure in association with low colloid oncotic pressure leads to edema. Because approximately one-third of fetuses with CHB have associated structural heart defects, a detailed fetal echocardiographic assessment is always warranted.

In isolated heart block, maternal rheumatologic disease is common. Maternal serologic testing for anti-Ro/La antibodies is warranted because transplacental passage of maternal anti-Ro and anti-La autoantibodies is seen in 95% of cases of fetal CHB.[65] These antibodies cross the placenta from as early as 16 weeks' gestational age and initiate inflammatory damage to the fetal conduction system and myocardium.[66,67] Hydrops develops with ventricular rates less than 60 beats/min (about 40% of cases with isolated heart block)[68,69] and has a mortality rate of 25% to 100%.[68,70] Treatment can be given with steroids and plasmapheresis,[71-75] but the efficacy of these is not well established. Epicardial pacemaker can be placed at birth.[76] Although 95% of mothers tested positive for anti-Ro/La antibodies, fewer than 5% of these pregnant patients had signs and symptoms of connective tissue disease at diagnosis of fetal AV block.[65]

When structural abnormalities accompany heart block, hydropic fetuses have a combined fetal and neonatal mortality rate of 83% to 100%.[65,69] Jaeggi et al.[65] reported 29 cases of prenatally diagnosed isolated congenital AV block; six fetuses presented with hydrops: two died antenatally, and four died in the neonatal period.[65] In these cases, corticosteroid use during pregnancy did not reverse hydrops or reduce the severity of AV block. In addition to hydrops, other poor prognostic factors include **endocardial fibroelastosis** with ventricular dysfunction and coexistent structural heart disease.[68]

Decreased Myocardial Function. Cardiomyopathies can be classified as primary or secondary or by an echocardiographic evaluation as **dilated** or **hypertrophic. Primary** fetal cardiomyopathies may have intrinsic causes (e.g., single-gene disorders, mitochondrial disorders, chromosomal abnormalities, α-thalassemia) or extrinsic causes such as infection, maternal disease (autoantibodies or insulin-dependent diabetes), and twin-twin transfusion syndrome. **Secondary** fetal cardiomyopathies are associated with structural or functional cardiac disorders (Video 41.7) and high-output states.[77]

Neck Abnormalities

Neck masses, such as **teratomas** and **lymphangiomas,** cause fetal hydrops from compression or high-output cardiac failure (Fig. 41.21). A **cystic hygroma** (fluid in posterior neck) may indicate a chromosomal (e.g., 45,XO) or other abnormality. Of 42 fetuses with first-trimester cystic hygroma, 14 developed hydrops later in pregnancy. Each of these had a **nuchal translucency** measurement of 3 mm or more at diagnosis of cystic hygroma.[78] For fetuses presenting with hydrops in the first trimester, all have increased nuchal translucency.[79]

Thoracic Anomalies

Hydrops can result from obstruction of venous or lymphatic return due to maldevelopment, compression, kinking, or cardiac tamponade. **Mediastinal masses, pleural effusions,** and **diaphragmatic hernias** may cause nonimmune hydrops by similar mechanisms.[80]

The incidence of **fetal hydrothorax** is estimated at 1 in 15,000 pregnancies. Isolated hydrothorax is most often caused

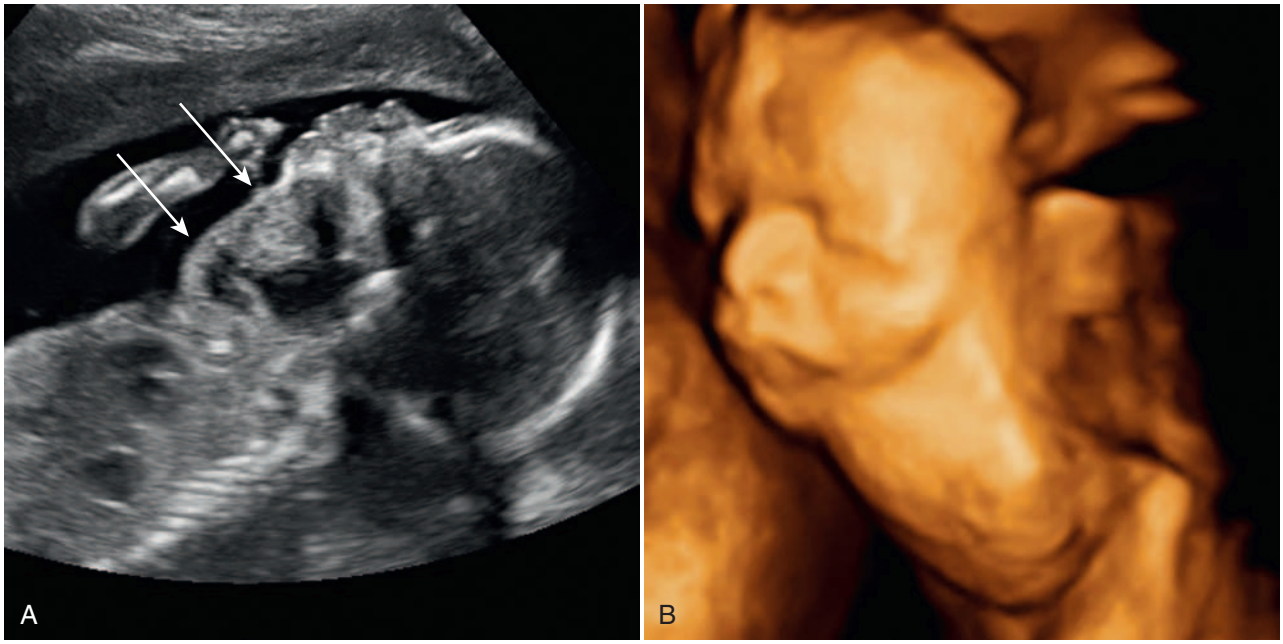

FIG. 41.21 Neck Teratoma. (A) Sagittal ultrasound with face up; mass *(arrows)* elevates chin. **(B)** Three-dimensional ultrasound shows the relation of the mass with the face.

by **congenital chylothorax,** a primary lymphatic abnormality. Accumulation of fluid in the pleural space may lead to pulmonary hypoplasia, compression of the heart, and obstruction of venous return, with subsequent development of hydrops and compression of the esophagus leading to polyhydramnios. Untreated, the perinatal mortality is 22% to 53%.[81-85] Associated malformations (≈25% of cases) and aneuploidy (≈7%) worsen the outcome.[84-87]

In the absence of hydrops, fetuses with isolated hydrothorax have such a good prognosis that invasive prenatal treatment is not indicated.[82,88] However, when hydrops develops, the outcome without intervention is very poor. In a large review, perinatal mortality in the hydropic group was 69% despite prenatal interventions in a number of cases.[84]

An echogenic lung mass is usually a **congenital pulmonary airway malformation** (CPAM), including the previously termed "congenital cystic adenomatoid malformation"; a **bronchopulmonary sequestration** (BPS); congenital lobar emphysema; or, in rare cases, **congenital high airway obstruction syndrome.** Most cases of CPAM, regardless of their size, regress spontaneously at least partially during the third trimester, and only a minority of fetuses become hydropic. Focal lung masses can lead to ipsilateral pleural effusion (Fig. 41.22; see also Fig. 41.7), mediastinal shift, and, ultimately, hydrops. However, the hydrops may not be caused only by the mediastinal shift but also by high-output cardiac failure because of shunting that may occur in an anomalous systemic artery and venous drainage through pulmonary or systemic veins.[89]

In a report of 67 cases of lung masses, only 7% developed hydrops.[90] Of 134 fetuses with CPAM referred to two fetal surgical centers in the United States, 101 were followed expectantly, and all 25 hydropic fetuses died, whereas all 76 nonhydropic fetuses survived,[91] suggesting that fetal surgery might be considered for hydropic cases. In the absence of hydrops, and provided there are no other anomalies, survival in these cases is virtually 100%.[92,93]

When a fetus with CPAM develops hydrops, the prognosis is poor, and antenatal intervention is often advisable. Intervention may be in the form of decompression by cyst aspiration (see Fig. 41.22), shunt, or open fetal surgery. A 2006 meta-analysis showed that shunting of CPAMs improved survival in fetuses with hydrops, as opposed to no effect on survival in fetuses with chest masses without hydrops.[94] Antenatal predictors of progression to hydrops include a combination of microcystic and macrocystic components and a large volume ratio of the mass to the normal lung (>1.6).[95] For fetuses with no dominant cyst and CPAM volume ratio less than 1.6, 97% did not progress to hydrops, whereas in the group with volume ratio greater than 1.6, 75% progressed to hydrops.[95] The success with open fetal surgery in cases of CPAM is variable, 29% to 62%. Antenatal aspiration of a macrocystic CCAM at times may be an effective treatment,[95] but frequently it is ineffective because of rapid reaccumulation of the cyst fluid. In cases with rapid reaccumulation of fluid, thoracoamniotic shunting may be a better approach.[96] Survival after shunting is correlated to gestational age at birth, percent reduction in lesion size, and resolution of hydrops.[97] Maternal administration of steroids also may be helpful.[98]

Although nonimmune hydrops fetalis rarely occurs in BPS cases, it is associated with a high rate of perinatal mortality and severe respiratory insufficiency in the neonate.[99,100] However, neonates with BPS and hydrops can survive.[101] Different strategies of in utero treatment have been proposed, such as thoracoamniotic shunting of pleural effusion,[102-105] thoracentesis and intravascular furosemide and digoxin,[106] alcohol ablation of the vascular pedicle with placement of a shunt,[107] ablation of the abnormal systemic artery from the aorta,[108,109] and open fetal surgery.[99]

In CHAOS the mechanism of hydrops is secondary to cardiac and great vessel compression by the enlarged fetal lungs.[110]

Chest Drainage Procedures. Aneuploidy is present in about 6% of cases of chylothorax and should be excluded.[111] Isolated

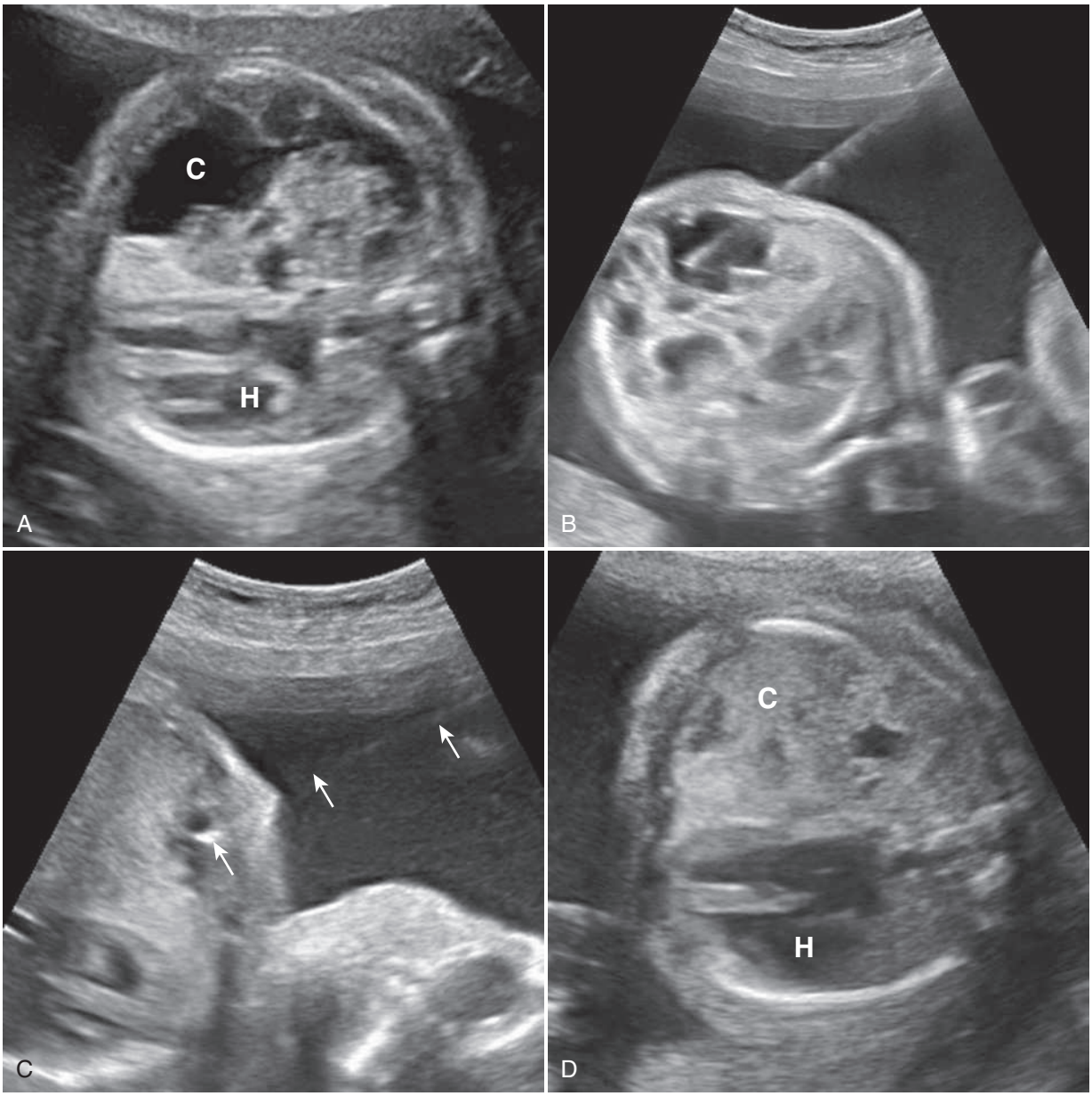

FIG. 41.22 Drainaging of macrocystic congenital pulmonary airway malformation with mediastinal shift and incipient hydrops. **(A)** shows a cyst in the cyst *(c)* with mediastinal shift of the heart *(H)*. **(B)** shows needle in the largest cyst. **(C)** shows decreased size of the cyst. Needle can be seen *(arrows)*. **(D)** At the completion of the procedure, the heart *(H)* is less compressed, and the echogenic chest mass *(c)* can still be seen, but the large cyst is no longer present.

large effusions may be drained initially using a fine needle and the fluid sent for lymphocyte count (>80% lymphocytes in the absence of infection is diagnostic of chylothorax),[112] rapid karyotyping, protein, inclusion bodies, and infection studies. This maneuver also evaluates the ability of the lungs to reexpand and may occasionally be therapeutic. Effusions that recollect rapidly can have multiple drainage procedures or may have shunt placement.[82,113] With treatment, survival is greater than 60%.[114] For large effusions occurring late in pregnancy, therapeutic drainage immediately before delivery facilitates neonatal resuscitation.[115] In a 2015 retrospective review of fetuses with congenital lung lesion or pleural effusion who underwent shunt placement, 97 shunts were placed in 75 fetuses. Average gestational age at shunt placement and birth was 25 and 35 weeks, respectively. Shunt placement resulted in a 55% ± 21% decrease in macrocystic lung lesion volume and complete or partial drainage of the pleural effusion in 29% and 71% of fetuses. Sixty-nine percent of fetuses presented with hydrops, which resolved following shunt placement in 83%. Survival was 68%, which correlated with gestational age at birth, percent reduction in lesion size, unilateral pleural effusions, and hydrops resolution.[97]

Gastrointestinal Anomalies

Anomalies of the gastrointestinal tract typically cause isolated ascites rather than hydrops. If there is local obstruction of lymphatic and venous drainage, as from intestinal obstruction, volvulus, or omphalocele, hydrops may result in rare cases. Abdominal masses presumably act by compression of venous

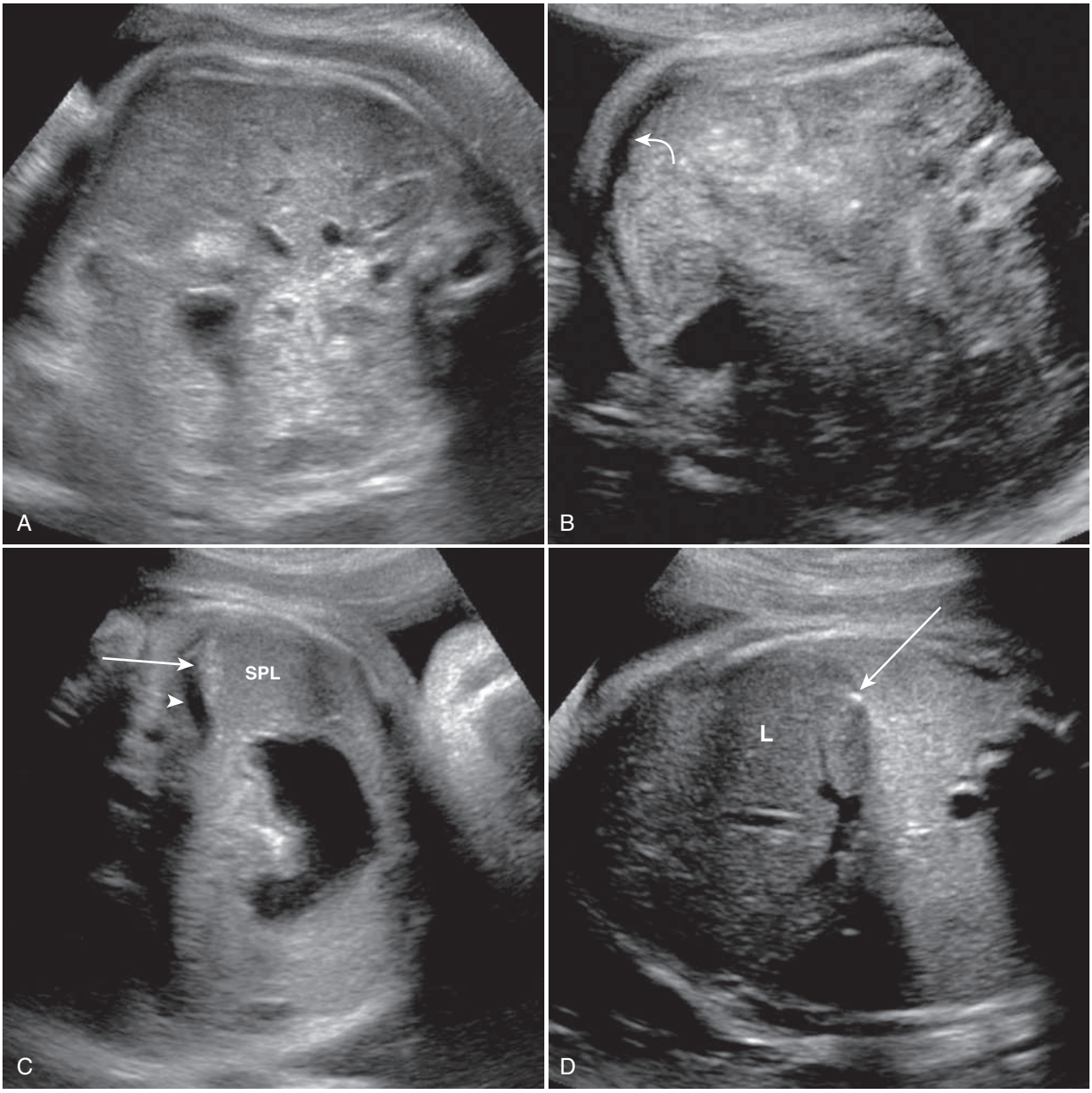

FIG. 41.23 Meconium Peritonitis. (A)-(D) Transverse views of the fetal abdomen demonstrate echogenic bowel and punctate echogenicities *(arrows)* around the spleen *(SPL)* and liver *(L)*. Note associated ascites (*curved arrow* in **B**) and pleural effusion (*arrowhead* in **C**).

return, although hypoproteinemia and/or AV shunting can also play a role.

Meconium peritonitis is associated with fetal **cystic fibrosis** in 70% of cases. Bowel rupture results in a sterile chemical peritonitis, often with ascites[116] (Fig. 41.23; see also Fig. 41.15). The ascites may be clear or particulate on ultrasound, and its appearance may change over time. The bowel will usually have a bunched or matted appearance, and areas of calcification may be visible. If this diagnosis is suspected, the parents should be offered carrier testing for the common cystic fibrosis mutations.

Urinary Tract Anomalies

Urinary tract anomalies are rare causes of hydrops. Congenital nephrosis can lead to severe proteinuria and hypoalbuminemia as the cause of hydrops.[117] Bladder rupture can lead to urinary ascites but rarely hydrops (Fig. 41.24).

Lymphatic Dysplasia

Congenital lymphatic dysplasia may be the source of many cases of hydrops that do not have an obvious cause. Bellini et al.[118] found that six newborns presenting at birth with hydrops of unidentified cause all had lymphatic dysplasia.

Monochorionic Twins

Twins have an increased incidence of hydrops secondary to a higher incidence of congenital anomalies and secondary to complications associated with the monochorionic placenta: **twin-twin transfusion syndrome** (TTTS) and **acardiac twinning.** These are described in detail in Chapter 32. The Quintero classification of TTTS has, as stage IV, hydrops of one or both twins.[119] The **recipient twin** experiences an elevation in cardiac output and blood pressure as a result of shunting of blood through the AV anastomoses. Initially, the increase in right ventricular workload is compensated for by ventricular hypertrophy, with minimal hemodynamic dysfunction. With ongoing volume and pressure overload, the right ventricle stretches and the tricuspid regurgitation begins, probably associated with increase in right ventricular end-diastolic pressure, reflected in the end-diastolic pressure of the right atrium. Atrial contractions against an elevated pressure produce retrograde flow during atrial systole in the ductus venosus, hepatic veins, and inferior vena cava. Eventually, metabolic acidosis and congestive heart failure develop.[120]

Conservative management of early-onset severe TTTS is associated with a survival rate of less than 10%.[121] Death is caused by extreme prematurity, in association with growth restriction in the donor and cardiac failure and hydrops in the recipient (Fig. 41.25). Current series suggest improved survival and decreased neurologic sequelae if severe TTTS before 26 weeks is treated with endoscopic selective laser ablation of the placental vascular anastomoses.[122-124]

For this procedure, a laser is introduced endoscopically into the uterus and used to ablate surface placental vessel anastomoses under ultrasound guidance.

In acardiac twins (**twin reversed arterial perfusion** [TRAP] **sequence**) a monochorionic pair has a pump twin and an acardiac twin. The **pump twin** perfuses the acardiac twin and develops high-output cardiac failure (particularly if the weight of the acardiac twin is >70% of the donor twin) and polyhydramnios.[125] The **acardiac twin** has anasarca but not true hydrops. Treatment involves interruption of the blood flow to the acardiac twin, typically by radiofrequency ablation, laser ablation, or cord ligation.[126-132] Radiofrequency ablation can result in survival of 80%.[133]

FIG. 41.24 Lower Urinary Tract Obstruction. Urinary ascites in obstructive uropathy with bladder rupture. Note the thickened bladder wall.

Chromosomal Anomalies

The incidence of aneuploidy is higher in hydrops cases presenting before 24 weeks than those later in pregnancy. Before 24 weeks, the incidence of aneuploidy in cases of hydrops ranges from 33% to 78%.[134-136] After 24 weeks the incidence of aneuploidy in hydrops is as low as 2%.[135]

Turner syndrome (45,XO) is classically associated with a cystic hygroma in the first and early second trimesters (Fig. 41.26; see also Fig. 41.12). Many of these disorders result in early spontaneous abortion. **Trisomies 21, 18, and 13** and **triploidy** have been associated with nonimmune hydrops, although it is

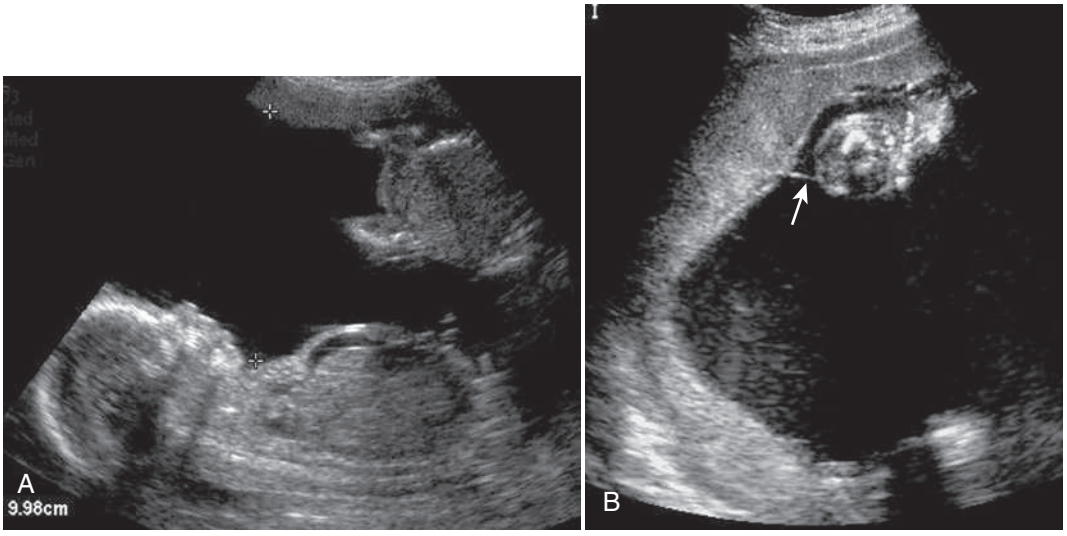

FIG. 41.25 Twin-Twin Transfusion Syndrome at 20 Weeks' Gestation. (A) Polyhydramnios and hydropic recipient twin. **(B)** Note membrane *(arrow)* closely adjacent to the stuck (donor) twin.

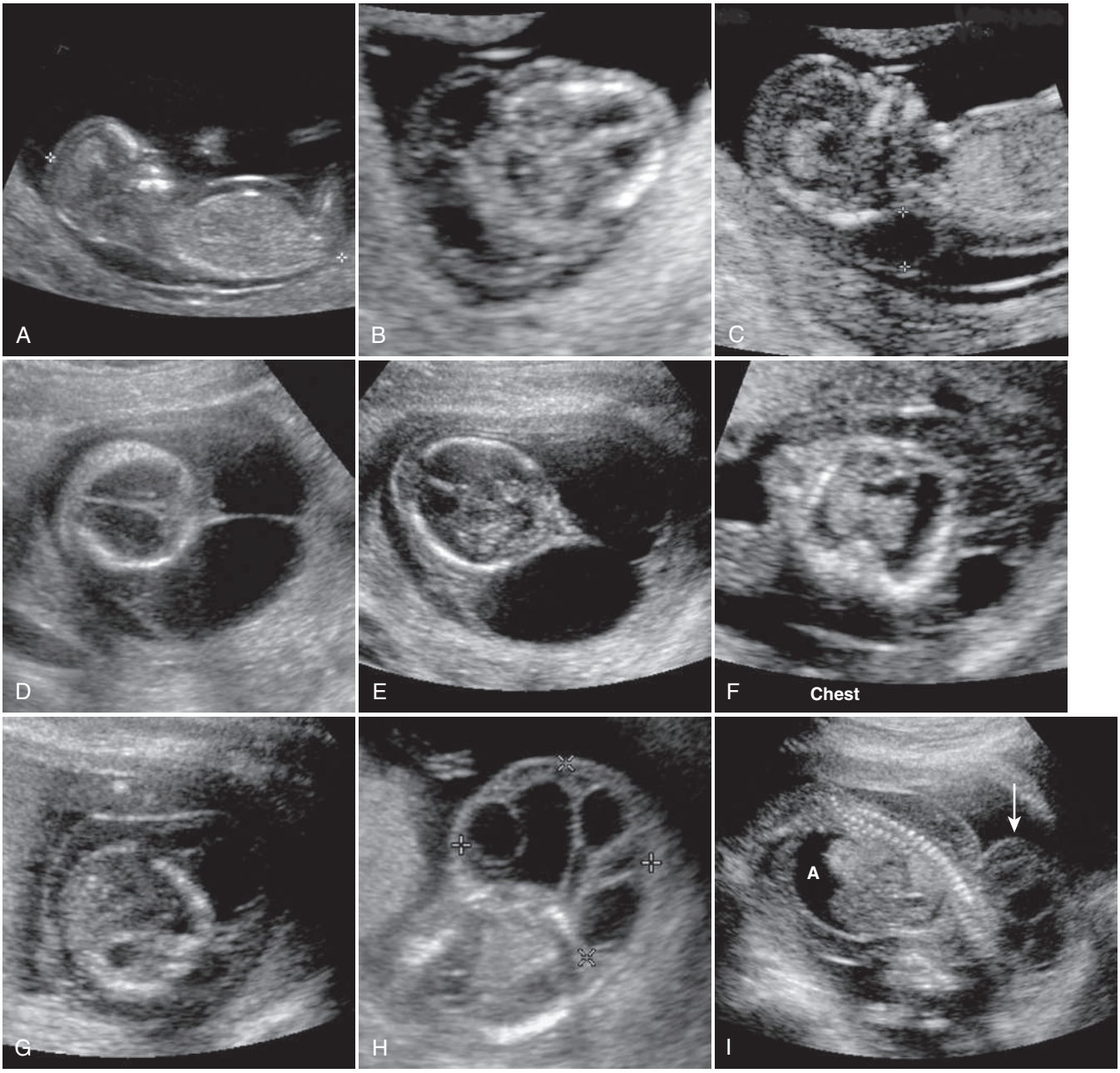

FIG. 41.26 Turner Syndrome in First and Second Trimesters. (A) Fetus at 12 weeks with diffuse skin thickening and lymphangiectasia. **(B)** and **(C)** Fetus at 13 weeks with nuchal thickening and diffuse body wall edema. **(D)-(G)** Fetus at 18 weeks with cystic hygroma and pleural effusion and diffuse body wall edema. **(H)** and **(I)** Fetus at 19 weeks with cystic hygroma *(arrow)* and ascites *(A)*.

often unclear why hydrops develops. There are a few reports of transient abnormal myelopoiesis with trisomy 21 as a cause of hepatomegaly and nonimmune hydrops.[137,138] In these cases, PUBS demonstrates fetal anemia and hypoalbuminemia. A hydropic fetus with multiple structural anomalies, prominent cystic hygromas, or increased nuchal translucency likely has a chromosomal abnormality. The physiologic basis for increased nuchal translucency is incompletely understood, but it may be caused by delayed lymphatic development and/or related to cardiovascular malformations,[139] especially in cases with aneuploidy.[140]

Tumors

Arteriovenous malformations and arteriovenous shunting in large tumors with a high proportion of solid tissue lead to hydrops by causing high-output cardiac failure and leading to **Kasabach-Merritt sequence** (consumptive coagulopathy). Selected fetuses with tumors, such as large **sacrococcygeal teratoma** associated with hydrops, have undergone in utero procedures, including cyst aspiration and open fetal surgical resection. However, these procedures are complicated by preterm delivery and other obstetric complications.[141] More recent reports suggest improved outcomes with laser ablation or alcohol sclerosis targeting the

feeding vessel(s) of the tumor.[142] In utero treatment for sacrococcygeal teratoma has a survival rate of 30% to 55%.[143]

Anemia

Fetal anemia is caused by decreased RBC production, increased hemolysis, or hemorrhage. If the process is gradual, the fetus mounts a compensatory erythropoietic response, and nonimmune hydrops develops only when the anemia exceeds its ability to keep pace, which is typically when the hemoglobin concentration deficit is 7 g/dL or greater.[17] Hydrops results from a combination of high-output cardiac failure and hypoxic capillary damage, causing protein leakage, as well as infiltration of the liver by erythropoietic tissue, leading to portal hypertension.[17]

Decreased Red Blood Cell Production. Homozygotes with **α-thalassemia** cannot manufacture HbF in utero or hemoglobin A (HbA) after birth.[144] Instead, Hb Bart is formed in utero, which has such a high affinity for oxygen that tissue hypoxia results, leading to capillary damage, protein leakage, cardiac failure, and hydrops. Other causes of decreased RBC production in utero include generalized marrow aplasia, as found in parvovirus infection[32,145] and fetal leukemia.[138]

Hemolysis. Glucose-6-phosphate dehydrogenase (G6PD) deficiency has been reported as a rare cause of nonimmune hydrops resulting from increased hemolysis.[146] Hemolysis may also contribute to anemia caused by in utero infection.

Hemorrhage. Blood loss may occur either into another fetus in TTTS, into the fetus itself (e.g., intracranial), into a tumor (e.g., sacrococcygeal teratoma), or transplacental.

Infection

Intrauterine infections account for up to 16% of cases of nonimmune hydrops.[147] An autopsy series of fetuses with in utero demise and nonimmune hydrops showed that 33% had infection.[148] Hydrops may result from effects on the bone marrow (**parvovirus, cytomegalovirus** [CMV], **toxoplasmosis**), myocardium (**adenovirus, coxsackievirus, CMV,** leading to congestive heart failure), vascular endothelium (hypoxic capillary damage causing protein leakage), or overwhelming sepsis with hepatitis and decreased protein production **(syphilis).**[149-154] In addition to hydrops, signs of infection include calcifications in the pericardium or brain, as well as ventriculomegaly.

Parvovirus B19. Parvovirus B19 is responsible for up to 27% of cases of nonimmune hydrops.[155] Myocarditis and fetal anemia secondary to bone marrow aplasia are thought to be the mechanisms of hydrops (Fig. 41.27). The marrow is particularly sensitive to parvovirus infection from 16 to 24 weeks' gestation.[149] The impact on RBC aplasia is further pronounced by the shortened life span of RBCs (45-70 days).[156]

Fetal infection occurs in up to 10% of pregnancies with maternal infection. This leads to an excess fetal loss rate of 9% of fetuses infected between 9 and 20 weeks' gestation.[157] In the first trimester, fetal infection can cause miscarriage, whereas in the second trimester, the fetus is at risk for hydrops. In contrast to most other congenital infections, adverse long-term sequelae are rarely associated with parvovirus.[152] Although hydrops associated with parvovirus B19 can spontaneously resolve without transfusion,[158-161] most cases benefit from intrauterine transfusion. Parvovirus infection is suspected when maternal blood shows positive immunoglobulin M (IgM, indicating a recent infection) and high or increasing IgG. Cordocentesis will show aplastic anemia with few reticulocytes, although at times the hydrops is caused by myocarditis.[158] Fetal parvovirus infection is diagnosed by polymerase chain reaction (PCR) testing of amniotic fluid or fetal blood.[162] PCR results can be available within a few hours.

When maternal parvovirus infection is discovered, serial monitoring of the pregnancy is indicated, with weekly sonograms

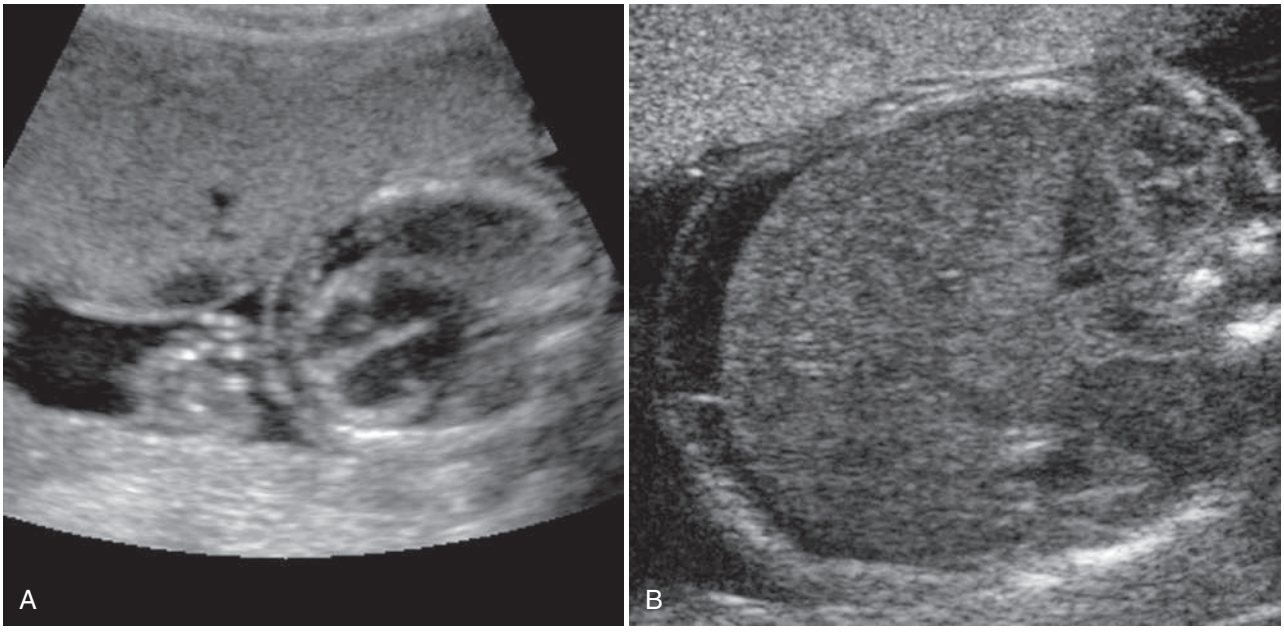

FIG. 41.27 Hydrops in Fetus With Parvovirus Infection and Anemia at 19 Weeks. (A) Transverse view of the fetal thorax shows a slightly enlarged heart with echogenic myocardium and small pericardial effusion. **(B)** Transverse view of abdomen shows ascites. Middle cerebral artery Doppler studies (not shown) showed peak systolic velocity of 55 cm/sec, indicating severe anemia.

for 8 to 12 weeks after maternal infection. Sonograms are performed to assess for signs of hydrops and include Doppler analysis to assess for elevated MCA velocity, as an indication of fetal anemia.

In cases of infection with parvovirus treated with intrauterine transfusion, survival is 43% to 84%.[157,163-165] However, there are also reports of abnormal developmental outcome in up to 31% of cases.[163]

Toxoplasmosis. Congenital infection with *Toxoplasma gondii* can cause anemia, intracerebral or intrahepatic calcifications, ventriculomegaly, and chorioretinitis and can present with hydrops, particularly ascites.[166-168] Most pregnant women with congenital toxoplasmosis are asymptomatic or only mildly symptomatic during pregnancy. The rate of fetal infection varies according to the gestational age at the time of vertical transmission, ranging from 26% to 40%.[166] Prenatal diagnosis of toxoplasmosis can be difficult and depends on the demonstration of maternal seroconversion and/or the parasite in amniotic fluid by PCR or isolation techniques.[166] Diagnosis is important because infected mothers are treated with spiramycin throughout pregnancy; if fetal infection was demonstrated, pyrimethamine and sulfadoxine or sulfadiazine are added to the regimen.[167]

Other Infections. Congenital **CMV** infection is responsible for 1% to 2% of cases of nonimmune hydrops and can occur even with recurrent maternal infection.[169] Fetal treatment can be attempted with umbilical vein injection of ganciclovir[170] or intraperitoneal injection of hyperimmunoglobulin.[171] **Rubella, syphilis,** and **varicella** are less common causes of nonimmune hydrops.[172,173] Diagnosis is important; in cases of syphilis, if the fetus is in the third trimester and the lungs are mature, delivery and treatment with penicillin can lead to resolution of the hydrops. Rare infectious causes of nonimmune hydrops include **herpes simplex virus,**[174,175] **adenovirus,**[176] and acute maternal **hepatitis B** infection.[177]

Genetic Disorders

Multiple nonchromosomal genetic conditions can cause nonimmune hydrops[178] (see Table 41.1). The mechanisms are poorly understood and are multifactorial. In storage diseases, the most likely mechanism is hepatic infiltration resulting in hypoproteinemia or vascular obstruction.

Metabolic Disorders

Inborn errors of metabolism are rare, and these are a rare cause of hydrops. However, diagnosis is important because early treatment of some disorders can lead to improved outcome. Diagnosis is also important for genetic counseling regarding recurrence risk. Lysosomal disorders associated with hydrops fetalis include GM1 gangliosidosis, galactosialidosis, infantile free–sialic acid storage disease, mucopolysaccharidosis types IV and VII, mucolipidosis types I and II, Gaucher disease type II, Farber disease, Niemann-Pick disease, Wolman disease, and multiple sulfatase deficiency.[179] Hydrops fetalis has been associated with deficiencies of G6PD[146] or pyruvate kinase,[180,181] Pearson syndrome[182] and other mitochondrial disorders,[182,183] congenital defects of N-glycosylation,[184] glycogen storage disease type IV,[185] and neonatal hemochromatosis.[186]

Skeletal Disorders

Skeletal dysplasia is a rare cause of hydrops.[178] Examples include achondroplasia, achondrogenesis, osteogenesis imperfecta, hypophosphatasia, and arthrogryposis.

Endocrine Disorders

Fetal endocrine disorders are rare causes of nonimmune hydrops. Fetal hypothyroidism and hyperthyroidism can cause hydrops.[182,187] Hydrops can develop from maternal antibodies crossing the placenta, even if the pregnant patient has already been treated for Graves disease.[188]

Drugs

In utero exposure to **indomethacin** can result in ductus arteriosus constriction and, rarely, hydrops. Because of this, ultrasound evaluation of the ductus arteriosus should be performed within 48 hours of starting indomethacin therapy.[189]

Idiopathic Disorders

The number of idiopathic cases of nonimmune hydrops (for which we still cannot identify a cause) is about 10%[31,147] and will continue to decrease as our investigative abilities improve.

DIAGNOSTIC APPROACH TO HYDROPS

Systematic prenatal evaluation can establish a cause for nonimmune hydrops in up to 90% of cases.[147] This is important not only for the management of the current pregnancy but also for future genetic counseling.[148] A summary of the workup of hydrops is given in Table 41.3.

History

A detailed history may provide the first clues to the cause and may suggest appropriate investigations. For example, a maternal history of systemic lupus erythematosus or diabetes may be relevant, and homozygous α-thalassemia is particularly prevalent in patients of Southeast Asian origin. Blood type can supply a clue to isoimmunization. Maternal diseases with anemia or infection are important. Previous pregnancy losses may be related to one of the inborn errors of metabolism or chromosome rearrangements, and the family history or presence of consanguinity may suggest other genetic conditions. Parvovirus infection is more likely to occur in teachers or day-care workers.[190] Medication use can at times establish a cause.

Complete Obstetric Ultrasound

A comprehensive sonographic evaluation should be the initial step. However, no cause is found through use of sonography in 15% to 30% of cases. **Polyhydramnios** is a common association. A common indication for ultrasound is the clinical suspicion of being large for gestational dates. Collections of fluid in the pleural, peritoneal, and pericardial spaces are diagnostic, and their relative distribution and the timing of their development may give a clue to the cause.[191] Ultrasound markers of aneuploidy suggest

TABLE 41.3 Workup of Hydrops After Fetal Echocardiogram, Maternal History Including Family History, Medications, Exposures

Anatomic Survey		Maternal Tests	Additional Fetal Tests	Invasive Tests/ Treatment	Tests of Amniotic Fluid/ Fetal Blood
Structurally normal		Blood type Rh(D) antigen status Indirect Coombs test (antibody screen) Kleihauer-Betke test Parvovirus serology (other infections to consider: syphilis, CMV, toxoplasmosis)	MCA Doppler		
	Cardiac arrhythmia	Check Ro/La if bradyarrhythmia		Treat if tachyarrhythmia	
	No arrhythmia, MCA Doppler normal			Amniocentesis	Karyotype and/or chromosomal microarray; PCR for CMV and toxo AFAFP Lysosomal enzyme testing
	Anemia (MCA-PSV > 1.5 MoM)	MCV of parents to check for thalassemia (<80 suggests carrier status)		Amnio (at time of PUBS), transfuse if needed	Karyotype and/or chromosomal microarray PCR for CMV and toxo and parvovirus Consider G6PD, pyruvate kinase deficiency, lysosomal enzyme testing if no other cause
Structurally abnormal				Amniocentesis	Karyotype and/or chromosomal microarray, ± PCR for CMV, toxo, DNA testing for specific anomalies as indicated

AFAFP, Amniotic fluid α-fetoprotein; *CMV,* cytomegalovirus; *MCA,* middle cerebral artery; *MCV,* mean corpuscular volume; *MoM,* multiples of the median; *PCR,* polymerase chain reaction; *PSV,* peak systolic velocity; *PUBS,* percutaneous umbilical cord blood sampling.
Adapted from Society for Maternal-Fetal Medicine, Norton ME, Chauhan SP, Dashe JS. Society for Maternal-Fetal Medicine (SMFM) clinical guideline #7: nonimmune hydrops fetalis. Am J Obstet Gynecol. 2015;212(2):127-139.[23]

a chromosomal cause. The degree of polyhydramnios should be assessed because this may pose an imminent threat of premature rupture of the membranes or preterm labor, and the cervix should be imaged to ensure there is no funneling or shortening.

A systematic detailed survey of fetal anatomy should be performed, searching for other clues to the cause of the hydrops. The fetal bladder should be visualized to exclude urinary ascites caused by bladder rupture. Bone length, curvature, density, and presence or absence of fractures should be evaluated to exclude skeletal dysplasias. Stigmata of congenital infection should be assessed, such as microcephaly or calcifications within the fetal brain or liver. A dedicated fetal echocardiographic structural and functional assessment is warranted to evaluate fetal heart structure, rhythm, and function in hydrops.

Maternal Investigations

Maternal blood type, indirect Coombs test (antiglobulin titer), and presence or absence of RBC antibodies should be checked to exclude immune hydrops. Other baseline tests include a complete blood count (CBC) and indices, Kleihauer-Betke test, infection screen (TORCH, parvovirus IgM/IgG), and glucose.

Fetal Investigations

Amniocentesis for fetal karyotype (if at an appropriate gestational age), antigen tests by PCR, and culture for syphilis, CMV, and toxoplasmosis are often indicated. MCA Doppler should be performed, with PUBS when the Doppler indicates anemia. Fluid aspirated from one of the fetal body cavities can also be used for fetal testing. The most appropriate choice depends on gestational age, accessibility, and urgency of results. A rapid karyotype can be obtained successfully from most collections of fetal body fluid.[192] **Fluorescent in situ hybridization** (FISH) can be used to identify common **aneuploidies** (trisomies 13, 18, and 21; monosomy X or Turner syndrome) and other specific deletions and chromosome rearrangements. This technique can provide a result from amniotic fluid in 24 to 48 hours.[193] In practice, the

confirmation or exclusion of the most common aneuploidies is often adequate to guide pregnancy management. Amniotic fluid is preferable for both viral culture and PCR for toxoplasmosis[167] and CMV, and it can be used to assess fetal lung maturity at later gestations. Chorionic villous sampling is an alternative at any gestation for obtaining a rapid karyotype or DNA testing.

Fetal blood sampling is a key investigation in many cases when the chromosomes do not provide a diagnosis. Basic fetal blood work should include a direct Coombs test, CBC and indices, karyotype, protein, albumin, and viral-specific IgM. Other tests are done selectively,[194,195] and samples can be stored for subsequent evaluation. With this approach, the cause of hydrops can be determined in most cases.

Performing PUBS

Cordocentesis has a 1% to 1.6% risk of fetal loss.[196-200] The fetal risks need to be interpreted knowing that these fetuses are at particularly high background risk for fetal loss and adverse outcomes. Ghidini et al.[200] performed a meta-analysis that excluded cases with pathologic fetal conditions and determined that the loss rate in a "low-risk" population undergoing fetal blood sampling was approximately 1.4%. A more recent study found that procedure-related complications of 3.1% and procedure-related loss rates of 1.6%.[196] Other complications of cordocentesis include fetal bradycardia (4%-12%), bleeding at puncture site (20%-40%), hematomas (17%), infection (1%), abruption (rare), fetomaternal hemorrhage (40%), and preterm contractions (7%).[196,198,200,201] Complications are more common with arterial than venous puncture.[199] In a recent report from Belgium, summarizing 14 years' experience,[202] 135 intrauterine transfusions were performed in 56 fetuses. There were no fetal or neonatal deaths. Mild adverse events were noted in 10% and severe events in 1.5%. Hydrops and transfusion in a free loop were associated with an increased risk of adverse events whereas gestational age at transfusion after 34 weeks was not. Besides phototherapy, 65% required additional neonatal treatment for alloimmune anemia. Nonhematologic complications occurred in 24% and were mainly related to preterm birth.

PUBS is recommended when the fetus is at substantial risk for severe fetal anemia (MCA-PSV > 1.5 MoM or hydropic), unless the pregnancy is at a gestational age when risks associated with delivery are considered to be less than those associated with the procedure.[203]

If it is anticipated that the fetus may require transfusion (e.g., parvovirus infection with elevated MCA Doppler velocity), it is prudent to have crossmatched blood and platelets ready to avoid the risks with a second procedure.

PUBS is usually performed in a setting that allows maternal sedation and intervention for fetal distress after 24 weeks, most often an operating room for labor and delivery. The patient is prepped and sterilely draped and the uterus displaced slightly to the left with appropriate maternal wedging. The ultrasound transducer is draped with a sterile sheath to allow guidance on the sterile field. The patient is often given conscious sedation for comfort and to minimize maternal movement during the procedure. Local anesthetic with lidocaine may be used for patient comfort. Ultrasound guidance may be provided by a second provider or by the operator using a freehand technique. A 20- to 22-gauge needle is typically used, and most often the umbilical vein is targeted at the **placental cord insertion** (Fig. 41.28). Other approaches include the **umbilical vein at the fetal cord insertion** or a **free loop of cord.** The needle position is confirmed by obtaining a blood specimen, ultrasound observation of the needle in the vein, and sonographic streaming within the umbilical vein after injection of saline. Heparinized syringes are used for fetal blood sampling, and values for hemoglobin/hematocrit, platelets, and mean corpuscular volume (MCV) are obtained. The fetal MCV (which should be >100 μm^3) is higher than the maternal value and can help confirm fetal origin of the blood sample.

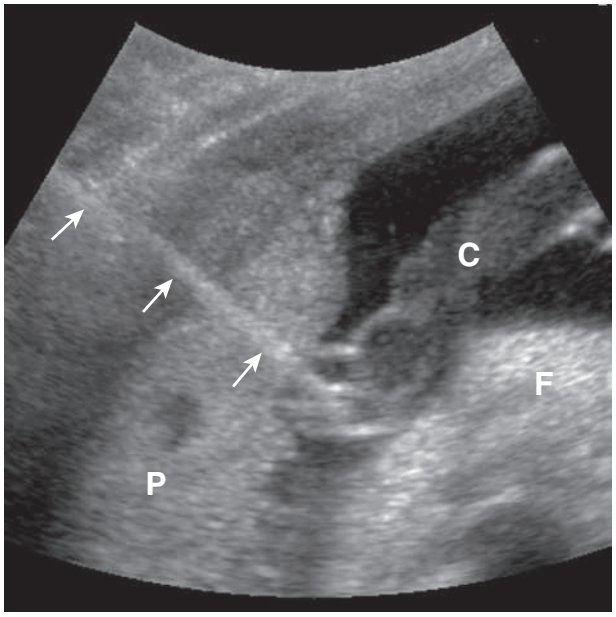

FIG. 41.28 Cordocentesis. Transverse ultrasound image shows needle *(arrows)* traversing placenta *(P)* and entering placental cord insertion. Note loop of umbilical cord *(C)* and fetus *(F)*.

Depending on the insertion site and indication for cordocentesis, fetal paralysis can be considered with vecuronium (0.1 mg/kg estimated fetal weight)[204] or atracurium besylate (0.4 mg/kg estimated fetal weight).[205] Fetal cardiac activity is documented throughout the procedure.

The fetal hematocrit is checked to determine the amount of transfusion needed (Hct < 30% is 2.5th centile >20 weeks). To limit the amount of fluid being transfused into the relatively small circulatory capacity of the fetus, packed RBCs (type O negative; Hct > 90%) are given. The goal is to transfuse to Hct of 40 mL/dL. Successful treatment of anemia with intravascular blood transfusion has been reported as early as 13 weeks' gestation.[145] When performing PUBS it is important to have a team involved that includes genetic counselors (regarding the underlying cause of anemia), laboratory medicine professionals (to check the MCV and have packed RBCs available), and maternal fetal medicine specialists as well as individuals familiar with guidance for procedures with ultrasound.

When PUBS is not possible, particularly at early gestational age when the umbilical cord is small and difficult to safely

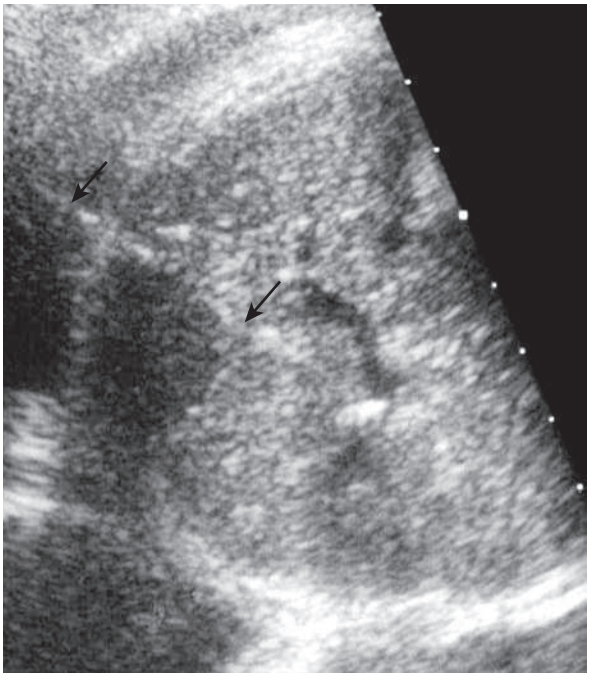

FIG. 41.29 Fetal Blood Sampling in Intrahepatic Portion of Umbilical Vein. Arrows point to the position of the 20-gauge needle in the intrahepatic portion of the umbilical vein.

instrument, intraperitoneal, intrahepatic (Fig. 41.29), or intracardiac transfusion can be performed.[206]

Fetal Transfusion

If fetal transfusion is required, T-connector tubing is often employed for ease of transfusion. The volume to be transfused can be calculated by using the following formula[207]:

$$\text{Volume}_{\text{transfused}}\ (\text{mL}) = \text{Volume}_{\text{fetoplacental unit}}\ (\text{mL}) \times \left[\frac{\text{Hematocrit}_{\text{final}} - \text{Hematocrit}_{\text{initial}}}{\text{Hematocrit}_{\text{transfused blood}}}\right]$$

The fetoplacental volume can be estimated as 1.046 + fetal weight in grams × 0.14.[207] Either maternal cells or donated O-negative, washed, leukocyte-reduced blood is used for transfusion. Maternal cells may be consumed less rapidly than anonymous donation, but timing and pregnancy-associated anemia limit its use.[208] A posttransfusion sample is obtained to evaluate the effects of the procedure. Future transfusions are scheduled based on fetal Doppler assessment[26] or by estimating a 0.7% decrease in the hematocrit per day and scheduling transfusion for estimated hematocrits of 20 to 22 mL/dL.[209]

If the cordocentesis or transfusion is being performed for reasons other than Rh(D) isoimmunization, in a Rh(D)-negative mother, RhoGAM should be administered after the procedure.

Cavity Aspiration

The clinician can usually advance the needle easily into the fetal chest, abdomen, or amniotic fluid at the time of fetal blood sampling or amniocentesis (Fig. 41.30). This can be both diagnostic (e.g., lymphocyte count in chylothorax or for rapid karyotype) and occasionally therapeutic. Simultaneous sampling does not increase the overall procedure risk.

Postnatal Investigations

After birth, the **placenta** should be sent for pathologic analysis, and a **skeletal survey** may be helpful. A geneticist may see the neonate to provide additional input. In cases of death, detailed **autopsy** and placental examination, correlated with antenatal findings, is the best way to determine the cause of nonimmune hydrops.[210,211] Further investigations may be prompted by additional physical findings at autopsy.[212] If a metabolic condition is suspected as the cause of hydrops, inclusion bodies can be sought on microscopy. In some series the cause of hydrops was identified in only 40% to 50% of patients without autopsy,[135] versus 80% to 90% after postmortem examination.[210,213]

FETAL WELFARE ASSESSMENT IN NONIMMUNE HYDROPS

Noninvasive ultrasound techniques for fetal well-being assessment in pregnancies complicated by nonimmune hydrops include biophysical assessment, pulsed Doppler velocimetry of umbilical and regional fetal vessels, and functional cardiac assessment. Fetal Doppler evaluation may give some indication of anemia, cardiac failure, and well-being.[25] Umbilical vein and intrahepatic vein pulsations, or ductus venosus *a*-wave reversal, represent cardiac diastolic dysfunction and have been correlated with poor perinatal outcomes.[214]

OBSTETRIC PROGNOSIS

The overall **mortality** rate among fetuses with nonimmune hydrops is approximately 70%,[31] with mortality in cases of structural abnormalities not amenable to therapy as high as 100%. In a series of 100 cases of nonimmune hydrops, 74 were thought to have a nontreatable cause, and none of these resulted in a live birth; of 26 with a treatable cause, 18 resulted in a live birth and were alive at 1 year of age.[31] Gestational age at diagnosis of hydrops has been used to predict outcome. A 10-year review of 82 cases presenting after 20 weeks[135] reported an overall mortality rate of 87%, and those diagnosed after 24 weeks were more likely to be idiopathic or related to cardiothoracic abnormalities. Spontaneous resolution of hydrops has been reported in fetuses with normal chromosomes diagnosed before 24 weeks.

Although the overall prognosis for fetal hydrops has improved in recent years, most series are small with a mixture of causes and thus are difficult to compare. Some improvement in outcome over earlier reports is attributable to the growing number of cases that are amenable to in utero therapy. Unfortunately, many cases still represent a terminal process. Earlier identification and referral, thorough evaluation, and fetal therapy in appropriate cases are the cornerstone to further improvements in prognosis. Obtaining the best diagnosis is helpful in counseling about recurrence risks.

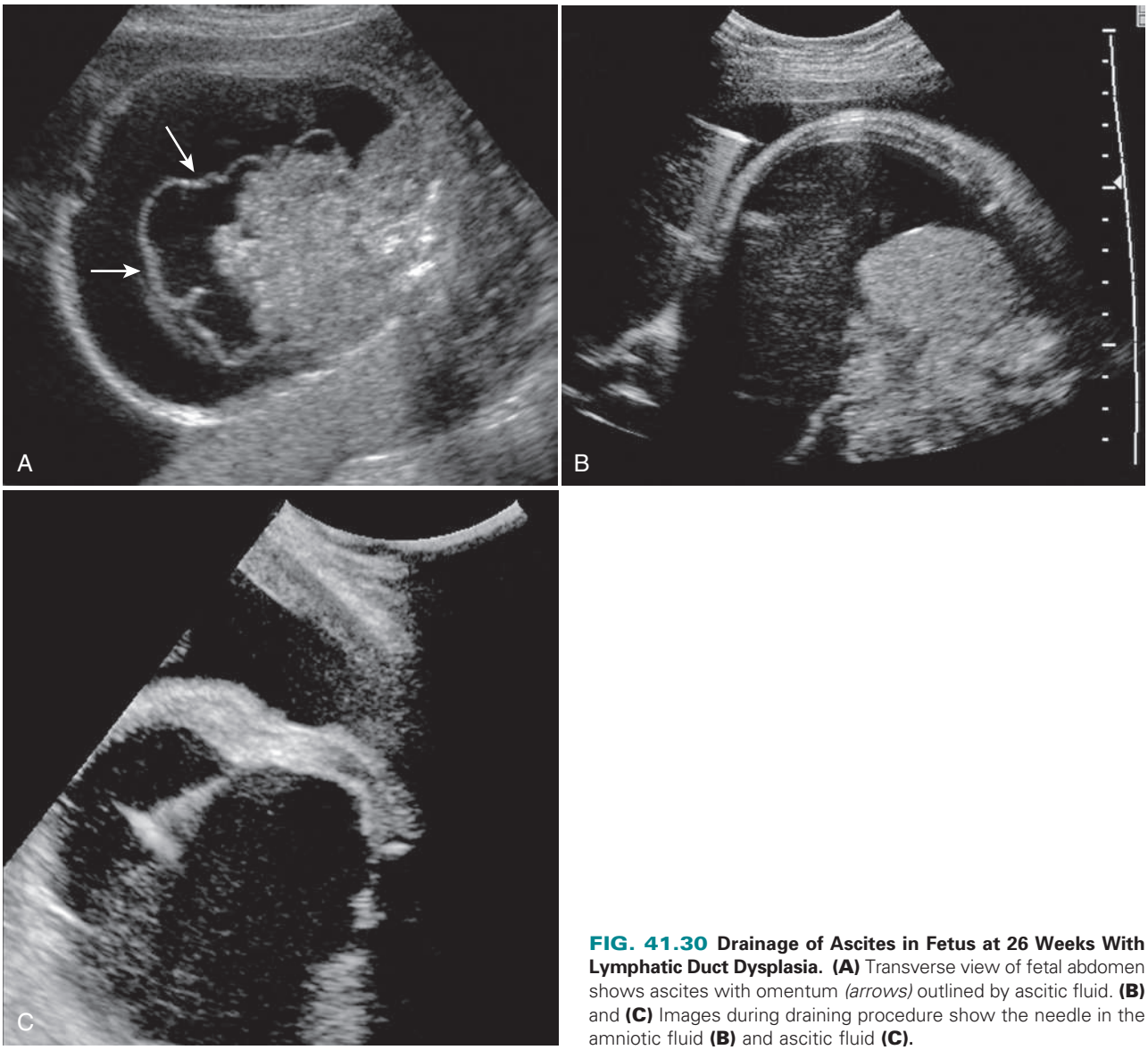

FIG. 41.30 Drainage of Ascites in Fetus at 26 Weeks With Lymphatic Duct Dysplasia. (A) Transverse view of fetal abdomen shows ascites with omentum *(arrows)* outlined by ascitic fluid. **(B)** and **(C)** Images during draining procedure show the needle in the amniotic fluid **(B)** and ascitic fluid **(C)**.

Maternal Complications (Mirror Syndrome)

Maternal complications may occur in association with fetal hydrops. Hypoproteinemia, edema, weight gain, hypertension, oliguria, and **preeclampsia** may develop.[215] This association has been termed **mirror syndrome** because edema in the pregnant patient mirrors that of the hydropic fetus.[34,216,217] The syndrome has been described in conjunction with hydrops of various causes.[215,218,219] Perinatal mortality and morbidity rates are high. Maternal outcome can be improved by delivery of the fetus and placenta or by fetal intervention to treat the cause of the hydrops.[217,220-222] If hydrops cannot be cured, delivery may limit the risk of maternal complications.[35,222]

Espinoza et al.[223] recently suggested the high plasma concentrations of soluble vascular endothelial growth factor receptor 1 (sVEGFR-1) is implicated in the pathophysiology of mirror syndrome. Hypoxia of the villous trophoblast in cases of villous edema leads to increased production and release of sVEGFR-1 and other antiangiogenic factors into the maternal circulation. Excessive concentrations of these products may be responsible for maternal edema in mirror syndrome.

Delivery

Mode and location of delivery are based on obstetric factors, taking into account the underlying prognosis.[224] Uterine overdistention in severe polyhydramnios carries the risks of **placental abruption** and **cord prolapse** after membrane rupture and **postpartum hemorrhage** from uterine atony. Prematurity secondary to polyhydramnios is a major contributing factor to the poor outcome of some neonates. **Therapeutic amniocentesis** before induction of labor may be considered in cases with massive polyhydramnios to decrease the risk of malpresentation or cord prolapse. **Indomethacin** has also been used to decrease the amniotic fluid volume.[225] This drug should be used with caution after 32 weeks' gestation because of the potential for ductal constriction.

Predelivery Aspiration Procedures

Fetal fluid collections may be drained under ultrasound guidance just before delivery to assist with **neonatal resuscitation.** This is particularly relevant if large fetal pleural effusions are present.[115] Massive ascites may also be drained to prevent abdominal dystocia (when vaginal birth is planned) and aid in fetal breathing when ascites has caused elevation of the diaphragms.

Postnatal Outcome

Because of the high incidence of in utero demise, the cause of hydrops in utero is different from that with a live neonate. In a review of 30 cases of hydrops diagnosed between 10 and 14 weeks of pregnancy, all pregnancies with nonimmune hydrops resulted in abortion, intrauterine fetal death, or pregnancy termination.[136] A 2007 national database review of live-born neonates with hydrops found heart problems (13.7%), abnormalities in heart rate (10.4%), TTTS (9%), congenital anomalies (8.7%), chromosomal abnormalities (7.5%), congenital viral infections (6.7%), isoimmunization (4.5%), and congenital chylothorax (3.2%).[226] Mortality rates were highest among neonates with congenital anomalies (57.7%) and lowest among those with congenital chylothorax (5.9%), and a cause could not be determined in 26%. Factors associated independently with death were younger gestational age, low 5-minute Apgar score, and high levels of support needed the first day after birth.[226] This study reported a 36% death rate before discharge or transfer to another hospital. The severity of hydrops and birth gestational age of the infant are the key determinants for survival. This is important because delivering a fetus early to treat worsening hydrops may not improve survival.

Data are limited regarding long-term outcome of children surviving after hydrops. In one series, 13 in 19 (68%) children surviving beyond 1 year of age were normal; two had mild developmental delay at 1 year of age; one 8-year-old child was mentally retarded; and three (16%) had severe psychomotor impairment with marked growth failure.[227] Haverkamp et al.[228] found that 86% of patients had normal psychomotor development, 86% showed normal neurologic status, 7% had minor neurologic dysfunction, and 4% had spastic cerebral paresis.

CONCLUSION

Hydrops represents a terminal stage for many conditions, the vast majority of which are fetal in origin. The onset of hydrops signifies fetal decompensation. Immune causes can be successfully treated in utero, as can an increasing number of nonimmune causes. Whereas in the past, nonimmune hydrops carried virtually 100% mortality, this is no longer the case. A team approach using obstetric imagers, maternal fetal medicine specialists, neonatologists, and geneticists can help to decide which cases are suitable for therapeutic intervention. A comprehensive approach must be taken to the investigation of hydrops, both for the management of the index case and for future counseling. Cornerstones of this investigation are detailed ultrasound, including echocardiography, fetal karyotyping, and other diagnostic interventions as appropriate, and pathologic examination of the fetus and placenta.

REFERENCES

1. Shulman LP, Phillips OP, Emerson DS, et al. Fetal 'space-suit' hydrops in the first trimester: differentiating risk for chromosome abnormalities by delineating characteristics of nuchal translucency. Prenat Diagn. 2000;20(1):30-32.
2. Freda VJ, Gorman JG, Pollack W, et al. Prevention of Rh isoimmunization. Progress report of the clinical trial in mothers. JAMA. 1967;199(6):390-394.
3. Macafee CA, Fortune DW, Beischer NA. Non-immunological hydrops fetalis. J Obstet Gynaecol Br Commonw. 1970;77(3):226-237.
4. Bellini C, Donarini G, Paladini D, et al. Etiology of non-immune hydrops fetalis: an update. Am J Med Genet A. 2015;167a(5):1082-1088.
5. Derderian SC, Jeanty C, Fleck SR, et al. The many faces of hydrops. J Pediatr Surg. 2015;50(1):50-54.
6. Ng ZM, Seet MJ, Erng MN, et al. Nonimmune hydrops fetalis in a children's hospital: a six-year series. Singapore Med J. 2013;54(9):487-490.
7. Yeom W, Paik ES, An JJ, et al. Clinical characteristics and perinatal outcome of fetal hydrops. Obstet Gynecol Sci. 2015;58(2):90-97.
8. Hashimoto BE, Filly RA, Callen PW. Fetal pseudoascites: further anatomic observations. J Ultrasound Med. 1986;5(3):151-152.
9. Derderian SC, Trivedi S, Farrell J, et al. Outcomes of fetal intervention for primary hydrothorax. J Pediatr Surg. 2014;49(6):900-903.
10. Di Salvo DN, Brown DL, Doubilet PM, et al. Clinical significance of isolated fetal pericardial effusion. J Ultrasound Med. 1994;13(4):291-293.
11. Bukowski R, Saade GR. Hydrops fetalis. Clin Perinatol. 2000;27(4):1007-1031.
12. Nicolaides KH, Fontanarosa M, Gabbe SG, Rodeck CH. Failure of ultrasonographic parameters to predict the severity of fetal anemia in rhesus isoimmunization. Am J Obstet Gynecol. 1988;158(4):920-926.
13. Fleischer AC, Killam AP, Boehm FH, et al. Hydrops fetalis: sonographic evaluation and clinical implications. Radiology. 1981;141(1):163-168.
14. Hoddick WK, Mahony BS, Callen PW, Filly RA. Placental thickness. J Ultrasound Med. 1985;4(9):479-482.
15. Lee AJ, Bethune M, Hiscock RJ. Placental thickness in the second trimester: a pilot study to determine the normal range. J Ultrasound Med. 2012;31(2):213-218.
16. Nicolaides KH, Warenski JC, Rodeck CH. The relationship of fetal plasma protein concentration and hemoglobin level to the development of hydrops in rhesus isoimmunization. Am J Obstet Gynecol. 1985;152(3):341-344.
17. Nicolaides KH. Studies on fetal physiology and pathophysiology in rhesus disease. Semin Perinatol. 1989;13(4):328-337.
18. Soothill PW, Nicolaides KH, Rodeck CH. Effect of anaemia on fetal acid-base status. Br J Obstet Gynaecol. 1987;94(9):880-883.
19. Mari G, Deter RL, Carpenter RL, et al. Noninvasive diagnosis by Doppler ultrasonography of fetal anemia due to maternal red-cell alloimmunization. Collaborative Group for Doppler Assessment of the Blood Velocity in Anemic Fetuses. N Engl J Med. 2000;342(1):9-14.
20. Ruma MS, Swartz AE, Kim E, et al. Angle correction can be used to measure peak systolic velocity in the fetal middle cerebral artery. Am J Obstet Gynecol. 2009;200(4):397.e1-397.e3.
21. Pretlove SJ, Fox CE, Khan KS, Kilby MD. Noninvasive methods of detecting fetal anaemia: a systematic review and meta-analysis. BJOG. 2009;116(12):1558-1567.
22. Zimmerman R, Carpenter Jr RJ, Durig P, Mari G. Longitudinal measurement of peak systolic velocity in the fetal middle cerebral artery for monitoring pregnancies complicated by red cell alloimmunisation: a prospective multicentre trial with intention-to-treat. BJOG. 2002;109(7):746-752.
23. Society for Maternal-Fetal Medicine, Norton ME, Chauhan SP, Dashe JS. Society for Maternal-Fetal Medicine (SMFM) clinical guideline #7: nonimmune hydrops fetalis. Am J Obstet Gynecol. 2015;212(2):127-139.
24. Oepkes D, Brand R, Vandenbussche FP, et al. The use of ultrasonography and Doppler in the prediction of fetal haemolytic anaemia: a multivariate analysis. Br J Obstet Gynaecol. 1994;101(8):680-684.

25. Dukler D, Oepkes D, Seaward G, et al. Noninvasive tests to predict fetal anemia: a study comparing Doppler and ultrasound parameters. Am J Obstet Gynecol. 2003;188(5):1310-1314.
26. Detti L, Oz U, Guney I, et al. Doppler ultrasound velocimetry for timing the second intrauterine transfusion in fetuses with anemia from red cell alloimmunization. Am J Obstet Gynecol. 2001;185(5):1048-1051.
27. Scheier M, Hernandez-Andrade E, Fonseca EB, Nicolaides KH. Prediction of severe fetal anemia in red blood cell alloimmunization after previous intrauterine transfusions. Am J Obstet Gynecol. 2006;195(6):1550-1556.
28. Mari G, Adrignolo A, Abuhamad AZ, et al. Diagnosis of fetal anemia with Doppler ultrasound in the pregnancy complicated by maternal blood group immunization. Ultrasound Obstet Gynecol. 1995;5(6):400-405.
29. Daffos F, Capella-Pavlovsky M, Forestier F. Fetal blood sampling during pregnancy with use of a needle guided by ultrasound: a study of 606 consecutive cases. Am J Obstet Gynecol. 1985;153(6):655-660.
30. van Kamp IL, Klumper FJ, Bakkum RS, et al. The severity of immune fetal hydrops is predictive of fetal outcome after intrauterine treatment. Am J Obstet Gynecol. 2001;185(3):668-673.
31. Anandakumar C, Biswas A, Wong YC, et al. Management of non-immune hydrops: 8 years' experience. Ultrasound Obstet Gynecol. 1996;8(3):196-200.
32. Apkon M. Pathophysiology of hydrops fetalis. Semin Perinatol. 1995;19(6):437-446.
33. Allan LD, Crawford DC, Sheridan R, Chapman MG. Aetiology of non-immune hydrops: the value of echocardiography. Br J Obstet Gynaecol. 1986;93(3):223-225.
34. van Selm M, Kanhai HH, Gravenhorst JB. Maternal hydrops syndrome: a review. Obstet Gynecol Surv. 1991;46(12):785-788.
35. Carbillon L, Oury JF, Guerin JM, et al. Clinical biological features of Ballantyne syndrome and the role of placental hydrops. Obstet Gynecol Surv. 1997;52(5):310-314.
36. Treadwell MC, Sherer DM, Sacks AJ, et al. Successful treatment of recurrent non-immune hydrops secondary to fetal hyperthyroidism. Obstet Gynecol. 1996;87(5 Pt 2):838-840.
37. Makino Y, Horiuchi S, Sonoda M, et al. A case of large placental chorioangioma with non-immunological hydrops fetalis. J Perinat Med. 1999;27(2):128-131.
38. Haak MC, Oosterhof H, Mouw RJ, et al. Pathophysiology and treatment of fetal anemia due to placental chorioangioma. Ultrasound Obstet Gynecol. 1999;14(1):68-70.
39. Lim FY, Coleman A, Polzin W, et al. Giant chorioangiomas: perinatal outcomes and techniques in fetoscopic devascularization. Fetal Diagn Ther. 2015;37(1):18-23.
40. Poeschmann RP, Verheijen RH, Van Dongen PW. Differential diagnosis and causes of nonimmunological hydrops fetalis: a review. Obstet Gynecol Surv. 1991;46(4):223-231.
41. Groves AM, Fagg NL, Cook AC, Allan LD. Cardiac tumours in intrauterine life. Arch Dis Child. 1992;67(10 Spec No):1189-1192.
42. Schmider A, Henrich W, Dahnert I, Dudenhausen JW. Prenatal therapy of non-immunologic hydrops fetalis caused by severe aortic stenosis. Ultrasound Obstet Gynecol. 2000;16(3):275-278.
43. Randenberg AL. Nonimmune hydrops fetalis part II: does etiology influence mortality? Neonatal Netw. 2010;29(6):367-380.
44. Huggon IC, Cook AC, Smeeton NC, et al. Atrioventricular septal defects diagnosed in fetal life: associated cardiac and extra-cardiac abnormalities and outcome. J Am Coll Cardiol. 2000;36(2):593-601.
45. Guereta LG, Burgueros M, Elorza MD, et al. Cardiac rhabdomyoma presenting as fetal hydrops. Pediatr Cardiol. 1986;7(3):171-174.
46. Rheuban KS, McDaniel NL, Feldman PS, et al. Intrapericardial teratoma causing nonimmune hydrops fetalis and pericardial tamponade: a case report. Pediatr Cardiol. 1991;12(1):54-56.
47. Tollens T, Casselman F, Devlieger H, et al. Fetal cardiac tamponade due to an intrapericardial teratoma. Ann Thorac Surg. 1998;66(2):559-560.
48. Geipel A, Krapp M, Germer U, et al. Perinatal diagnosis of cardiac tumors. Ultrasound Obstet Gynecol. 2001;17(1):17-21.
49. Scurry J, Watkins A, Acton C, Drew J. Tachyarrhythmia, cardiac rhabdomyomata and fetal hydrops in a premature infant with tuberous sclerosis. J Paediatr Child Health. 1992;28(3):260-262.
50. Bader RS, Chitayat D, Kelly E, et al. Fetal rhabdomyoma: prenatal diagnosis, clinical outcome, and incidence of associated tuberous sclerosis complex. J Pediatr. 2003;143(5):620-624.
51. Paladini D, Palmieri S, Russo MG, Pacileo G. Cardiac multiple rhabdomyomatosis: prenatal diagnosis and natural history. Ultrasound Obstet Gynecol. 1996;7(1):84-85.
52. Perez-Aytes A, Sanchis N, Barbal A, et al. Non-immunological hydrops fetalis and intrapericardial teratoma: case report and review. Prenat Diagn. 1995;15(9):859-863.
53. Catanzarite V, Mehalek K, Maida C, Mendoza A. Early sonographic diagnosis of intrapericardial teratoma. Ultrasound Obstet Gynecol. 1994;4(6):505-507.
54. Czernik C, Stiller B, Hubler M, et al. Hydrops fetalis caused by a large intrapericardial teratoma. Ultrasound Obstet Gynecol. 2006;28(7):973-976.
55. Benatar A, Vaughan J, Nicolini U, et al. Prenatal pericardiocentesis: its role in the management of intrapericardial teratoma. Obstet Gynecol. 1992;79(5 Pt 2):856-859.
56. Paw PT, Jamieson SW. Surgical management of intrapericardial teratoma diagnosed in utero. Ann Thorac Surg. 1997;64(2):552-554.
57. Bader R, Hornberger LK, Nijmeh LJ, et al. Fetal pericardial teratoma: presentation of two cases and review of literature. Am J Perinatol. 2006;23(1):53-58.
58. Simpson JM, Sharland GK. Fetal tachycardias: management and outcome of 127 consecutive cases. Heart. 1998;79(6):576-581.
59. Eronen M. Outcome of fetuses with heart disease diagnosed in utero. Arch Dis Child Fetal Neonatal Ed. 1997;77(1):F41-F46.
60. Naheed ZJ, Strasburger JF, Deal BJ, et al. Fetal tachycardia: mechanisms and predictors of hydrops fetalis. J Am Coll Cardiol. 1996;27(7):1736-1740.
61. Jaeggi ET, Carvalho JS, De Groot E, et al. Comparison of transplacental treatment of fetal supraventricular tachyarrhythmias with digoxin, flecainide, and sotalol: results of a nonrandomized multicenter study. Circulation. 2011;124(16):1747-1754.
62. Wacker-Gussmann A, Strasburger JF, Cuneo BF, Wakai RT. Diagnosis and treatment of fetal arrhythmia. Am J Perinatol. 2014;31(7):617-628.
63. Porat S, Anteby EY, Hamani Y, Yagel S. Fetal supraventricular tachycardia diagnosed and treated at 13 weeks of gestation: a case report. Ultrasound Obstet Gynecol. 2003;21(3):302-305.
64. Chao RC, Ho ES, Hsieh KS. Fetal atrial flutter and fibrillation: prenatal echocardiographic detection and management. Am Heart J. 1992;124(4):1095-1098.
65. Jaeggi ET, Hamilton RM, Silverman ED, et al. Outcome of children with fetal, neonatal or childhood diagnosis of isolated congenital atrioventricular block. A single institution's experience of 30 years. J Am Coll Cardiol. 2002;39(1):130-137.
66. McCue CM, Mantakas ME, Tingelstad JB, Ruddy S. Congenital heart block in newborns of mothers with connective tissue disease. Circulation. 1977;56(1):82-90.
67. Litsey SE, Noonan JA, O'Connor WN, et al. Maternal connective tissue disease and congenital heart block. Demonstration of immunoglobulin in cardiac tissue. N Engl J Med. 1985;312(2):98-100.
68. Schmidt KG, Ulmer HE, Silverman NH, et al. Perinatal outcome of fetal complete atrioventricular block: a multicenter experience. J Am Coll Cardiol. 1991;17(6):1360-1366.
69. Groves AM, Allan LD, Rosenthal E. Outcome of isolated congenital complete heart block diagnosed in utero. Heart. 1996;75(2):190-194.
70. Eronen M, Siren MK, Ekblad H, et al. Short- and long-term outcome of children with congenital complete heart block diagnosed in utero or as a newborn. Pediatrics. 2000;106(1 Pt 1):86-91.
71. Carpenter Jr RJ, Strasburger JF, Garson Jr A, et al. Fetal ventricular pacing for hydrops secondary to complete atrioventricular block. J Am Coll Cardiol. 1986;8(6):1434-1436.
72. Buyon JP, Hiebert R, Copel J, et al. Autoimmune-associated congenital heart block: demographics, mortality, morbidity and recurrence rates obtained from a national neonatal lupus registry. J Am Coll Cardiol. 1998;31(7):1658-1666.

73. Martin TC, Arias F, Olander DS, et al. Successful management of congenital atrioventricular block associated with hydrops fetalis. J Pediatr. 1988; 112(6):984-986.
74. Bierman FZ, Baxi L, Jaffe I, Driscoll J. Fetal hydrops and congenital complete heart block: response to maternal steroid therapy. J Pediatr. 1988;112(4): 646-648.
75. Barclay CS, French MA, Ross LD, Sokol RJ. Successful pregnancy following steroid therapy and plasma exchange in a woman with anti-Ro (SS-A) antibodies. Case report. Br J Obstet Gynaecol. 1987;94(4):369-371.
76. Doti PI, Escoda O, Cesar-Díaz S, et al. Congenital heart block related to maternal autoantibodies: descriptive analysis of a series of 18 cases from a single center. Clin Rheumatol. 2016;35(2):351-356.
77. Pedra SR, Smallhorn JF, Ryan G, et al. Fetal cardiomyopathies: pathogenic mechanisms, hemodynamic findings, and clinical outcome. Circulation. 2002;106(5):585-591.
78. Kharrat R, Yamamoto M, Roume J, et al. Karyotype and outcome of fetuses diagnosed with cystic hygroma in the first trimester in relation to nuchal translucency thickness. Prenat Diagn. 2006;26(4):369-372.
79. Jauniaux E. Diagnosis and management of early non-immune hydrops fetalis. Prenat Diagn. 1997;17(13):1261-1268.
80. Giacoia GP. Right-sided diaphragmatic hernia associated with superior vena cava syndrome. Am J Perinatol. 1994;11(2):129-131.
81. Estoff JA, Parad RB, Frigoletto Jr FD, Benacerraf BR. The natural history of isolated fetal hydrothorax. Ultrasound Obstet Gynecol. 1992;2(3): 162-165.
82. Hagay Z, Reece A, Roberts A, Hobbins JC. Isolated fetal pleural effusion: a prenatal management dilemma. Obstet Gynecol. 1993;81(1):147-152.
83. Longaker MT, Laberge JM, Dansereau J, et al. Primary fetal hydrothorax: natural history and management. J Pediatr Surg. 1989;24(6):573-576.
84. Weber AM, Philipson EH. Fetal pleural effusion: a review and meta-analysis for prognostic indicators. Obstet Gynecol. 1992;79(2):281-286.
85. Aubard Y, Derouineau I, Aubard V, et al. Primary fetal hydrothorax: a literature review and proposed antenatal clinical strategy. Fetal Diagn Ther. 1998;13(6):325-333.
86. Nicolaides KH, Azar GB. Thoraco-amniotic shunting. Fetal Diagn Ther. 1990;5(3-4):153-164.
87. Mussat P, Dommergues M, Parat S, et al. Congenital chylothorax with hydrops: postnatal care and outcome following antenatal diagnosis. Acta Paediatr. 1995;84(7):749-755.
88. Klam S, Bigras JL, Hudon L. Predicting outcome in primary fetal hydrothorax. Fetal Diagn Ther. 2005;20(5):366-370.
89. Morin L, Crombleholme TM, D'Alton ME. Prenatal diagnosis and management of fetal thoracic lesions. Semin Perinatol. 1994;18(3):228-253.
90. Davenport M, Warne SA, Cacciaguerra S, et al. Current outcome of antenatally diagnosed cystic lung disease. J Pediatr Surg. 2004;39(4):549-556.
91. Adzick NS, Harrison MR, Crombleholme TM, et al. Fetal lung lesions: management and outcome. Am J Obstet Gynecol. 1998;179(4):884-889.
92. Barret J, Chitayat D, Sermer M, et al. The prognostic factors in the prenatal diagnosis of the echogenic fetal lung. Prenat Diagn. 1995;15(9): 849-853.
93. Adzick NS, Flake AW, Crombleholme TM. Management of congenital lung lesions. Semin Pediatr Surg. 2003;12(1):10-16.
94. Knox EM, Kilby MD, Martin WL, Khan KS. In-utero pulmonary drainage in the management of primary hydrothorax and congenital cystic lung lesion: a systematic review. Ultrasound Obstet Gynecol. 2006;28(5): 726-734.
95. Crombleholme TM, Coleman B, Hedrick H, et al. Cystic adenomatoid malformation volume ratio predicts outcome in prenatally diagnosed cystic adenomatoid malformation of the lung. J Pediatr Surg. 2002;37(3): 331-338.
96. Ryo E, Okai T, Namba S, et al. Successful thoracoamniotic shunting using a double-flower catheter in a case of fetal cystic adenomatoid malformation associated with hydrops and polyhydramnios. Ultrasound Obstet Gynecol. 1997;10(4):293-296.
97. Peranteau WH, Adzick NS, Boelig MM, et al. Thoracoamniotic shunts for the management of fetal lung lesions and pleural effusions: a single-institution review and predictors of survival in 75 cases. J Pediatr Surg. 2015;50(2): 301-305.
98. Peranteau WH, Wilson RD, Liechty KW, et al. Effect of maternal betamethasone administration on prenatal congenital cystic adenomatoid malformation growth and fetal survival. Fetal Diagn Ther. 2007;22(5): 365-371.
99. Adzick NS. Management of fetal lung lesions. Clin Perinatol. 2003;30(3): 481-492.
100. Dolkart LA, Reimers FT, Helmuth WV, et al. Antenatal diagnosis of pulmonary sequestration: a review. Obstet Gynecol Surv. 1992;47(8): 515-520.
101. da Silva OP, Ramanan R, Romano W, et al. Nonimmune hydrops fetalis, pulmonary sequestration, and favorable neonatal outcome. Obstet Gynecol. 1996;88(4 Pt 2):681-683.
102. Slotnick RN, McGahan J, Milio L, et al. Antenatal diagnosis and treatment of fetal bronchopulmonary sequestration. Fetal Diagn Ther. 1990;5(1): 33-39.
103. Salomon LJ, Audibert F, Dommergues M, et al. Fetal thoracoamniotic shunting as the only treatment for pulmonary sequestration with hydrops: favorable long-term outcome without postnatal surgery. Ultrasound Obstet Gynecol. 2003;21(3):299-301.
104. Becmeur F, Horta-Geraud P, Donato L, Sauvage P. Pulmonary sequestrations: prenatal ultrasound diagnosis, treatment, and outcome. J Pediatr Surg. 1998;33(3):492-496.
105. Chan V, Greenough A, Nicolaides KN. Antenatal and postnatal treatment of pleural effusion and extra-lobar pulmonary sequestration. J Perinat Med. 1996;24(4):335-338.
106. Anandakumar C, Biswas A, Chua TM, et al. Direct intrauterine fetal therapy in a case of bronchopulmonary sequestration associated with non-immune hydrops fetalis. Ultrasound Obstet Gynecol. 1999;13(4): 263-265.
107. Nicolini U, Cerri V, Groli C, et al. A new approach to prenatal treatment of extralobar pulmonary sequestration. Prenat Diagn. 2000;20(9):758-760.
108. Ruano R, de A Pimenta EJ, Marques da Silva M, et al. Percutaneous intrauterine laser ablation of the abnormal vessel in pulmonary sequestration with hydrops at 29 weeks' gestation. J Ultrasound Med. 2007;26(9):1235-1241.
109. Oepkes D, Devlieger R, Lopriore E, Klumper FJ. Successful ultrasound-guided laser treatment of fetal hydrops caused by pulmonary sequestration. Ultrasound Obstet Gynecol. 2007;29(4):457-459.
110. Kalache KD, Chaoui R, Tennstedt C, Bollmann R. Prenatal diagnosis of laryngeal atresia in two cases of congenital high airway obstruction syndrome (CHAOS). Prenat Diagn. 1997;17(6):577-581.
111. Achiron R, Weissman A, Lipitz S, et al. Fetal pleural effusion: the risk of fetal trisomy. Gynecol Obstet Invest. 1995;39(3):153-156.
112. Eddleman KA, Levine AB, Chitkara U, Berkowitz RL. Reliability of pleural fluid lymphocyte counts in the antenatal diagnosis of congenital chylothorax. Obstet Gynecol. 1991;78(3 Pt 2):530-532.
113. Rodeck CH, Fisk NM, Fraser DI, Nicolini U. Long-term in utero drainage of fetal hydrothorax. N Engl J Med. 1988;319(17):1135-1138.
114. Deurloo KL, Devlieger R, Lopriore E, et al. Isolated fetal hydrothorax with hydrops: a systematic review of prenatal treatment options. Prenat Diagn. 2007;27(10):893-899.
115. Cardwell MS. Aspiration of fetal pleural effusions or ascites may improve neonatal resuscitation. South Med J. 1996;89(2):177-178.
116. Mayock DE, Hickok DE, Guthrie RD. Cystic meconium peritonitis associated with hydrops fetalis. Am J Obstet Gynecol. 1982;142(6 Pt 1):704-705.
117. Mark K, Reis A, Zenker M. Prenatal findings in four consecutive pregnancies with fetal Pierson syndrome, a newly defined congenital nephrosis syndrome. Prenat Diagn. 2006;26(3):262-266.
118. Bellini C, Hennekam RC, Boccardo F, et al. Nonimmune idiopathic hydrops fetalis and congenital lymphatic dysplasia. Am J Med Genet A. 2006;140(7): 678-684.
119. Quintero RA, Morales WJ, Allen MH, et al. Staging of twin-twin transfusion syndrome. J Perinatol. 1999;19(8 Pt 1):550-555.
120. Huhta JC. Right ventricular function in the human fetus. J Perinat Med. 2001;29(5):381-389.
121. Berghella V, Kaufmann M. Natural history of twin-twin transfusion syndrome. J Reprod Med. 2001;46(5):480-484.

122. Senat MV, Deprest J, Boulvain M, et al. Endoscopic laser surgery versus serial amnioreduction for severe twin-to-twin transfusion syndrome. N Engl J Med. 2004;351(2):136-144.
123. Quintero RA, Dickinson JE, Morales WJ, et al. Stage-based treatment of twin-twin transfusion syndrome. Am J Obstet Gynecol. 2003;188(5):1333-1340.
124. Gebb J, Dar P, Rosner M, Evans MI. Long-term neurologic outcomes after common fetal interventions. Am J Obstet Gynecol. 2015;212(4):527.e1-527.e9.
125. Moore T, Gale S, Benirschke K. Perinatal outcome of forty-nine pregnancies complicated by acardiac twinning. Am J Obstet Gynecol. 1990;163(3):907-912.
126. Quintero RA, Reich H, Puder KS, et al. Brief report: umbilical-cord ligation of an acardiac twin by fetoscopy at 19 weeks of gestation. N Engl J Med. 1994;330(7):469-471.
127. Peeters S, Devlieger R, Middeldorp J, et al. Fetal surgery in complicated monoamniotic pregnancies: case series and systematic review of the literature. Prenat Diagn. 2014;34(6):586-591.
128. Tan TYT, Sepulveda W. Acardiac twin: a systematic review of minimally invasive treatment modalities. Ultrasound Obstet Gynecol. 2003;22(4):409-419.
129. Hirose M, Murata A, Kita N, et al. Successful intrauterine treatment with radiofrequency ablation in a case of acardiac twin pregnancy complicated with a hydropic pump twin. Ultrasound Obstet Gynecol. 2004;23(5):509-512.
130. Tsao K, Feldstein VA, Albanese CT, et al. Selective reduction of acardiac twin by radiofrequency ablation. Am J Obstet Gynecol. 2002;187(3):635-640.
131. Ville Y, Hyett JA, Vandenbussche FP, Nicolaides KH. Endoscopic laser coagulation of umbilical cord vessels in twin reversed arterial perfusion sequence. Ultrasound Obstet Gynecol. 1994;4(5):396-398.
132. Rodeck C, Deans A, Jauniaux E. Thermocoagulation for the early treatment of pregnancy with an acardiac twin. N Engl J Med. 1998;339(18):1293-1295.
133. Lee H, Bebbington M, Crombleholme TM. North American Fetal Therapy Network. The North American Fetal Therapy Network Registry data on outcomes of radiofrequency ablation for twin-reversed arterial perfusion sequence. Fetal Diagn Ther. 2013;33(4):224-229.
134. Iskaros J, Jauniaux E, Rodeck C. Outcome of nonimmune hydrops fetalis diagnosed during the first half of pregnancy. Obstet Gynecol. 1997;90(3):321-325.
135. McCoy MC, Katz VL, Gould N, Kuller JA. Non-immune hydrops after 20 weeks' gestation: review of 10 years' experience with suggestions for management. Obstet Gynecol. 1995;85(4):578-582.
136. Has R. Non-immune hydrops fetalis in the first trimester: a review of 30 cases. Clin Exp Obstet Gynecol. 2001;28(3):187-190.
137. Hojo S, Tsukimori K, Kitade S, et al. Prenatal sonographic findings and hematological abnormalities in fetuses with transient abnormal myelopoiesis with Down syndrome. Prenat Diagn. 2007;27(6):507-511.
138. Zerres K, Schwanitz G, Niesen M, et al. Prenatal diagnosis of acute non-lymphoblastic leukaemia in Down syndrome. Lancet. 1990;335(8681):117.
139. Hyett JA, Perdu M, Sharland GK, et al. Increased nuchal translucency at 10-14 weeks of gestation as a marker for major cardiac defects. Ultrasound Obstet Gynecol. 1997;10(4):242-246.
140. Jenderny J, Schmidt W, Hecher K, et al. Increased nuchal translucency, hydrops fetalis or hygroma colli. A new test strategy for early fetal aneuploidy detection. Fetal Diagn Ther. 2001;16(4):211-214.
141. Hedrick HL, Flake AW, Crombleholme TM, et al. Sacrococcygeal teratoma: prenatal assessment, fetal intervention, and outcome. J Pediatr Surg. 2004;39(3):430-438.
142. Sananes N, Javadian P, Britto IS, et al. Technical aspects and effectiveness of percutaneous fetal therapies for large sacrococcygeal teratomas—a cohort study and a literature review. Ultrasound Obstet Gynecol. 2015.
143. Van Mieghem T, Al-Ibrahim A, Deprest J, et al. Minimally invasive therapy for fetal sacrococcygeal teratoma: case series and systematic review of the literature. Ultrasound Obstet Gynecol. 2014;43(6):611-619.
144. Dame C, Albers N, Hasan C, et al. Homozygous alpha-thalassaemia and hypospadias—common aetiology or incidental association? Long-term survival of Hb Bart's hydrops syndrome leads to new aspects for counselling of alpha-thalassaemic traits. Eur J Pediatr. 1999;158(3):217-220.
145. Kempe A, Rosing B, Berg C, et al. First-trimester treatment of fetal anemia secondary to parvovirus B19 infection. Ultrasound Obstet Gynecol. 2007;29(2):226-228.
146. Perkins RP. Hydrops fetalis and stillbirth in a male glucose-6-phosphate dehydrogenase-deficient fetus possibly due to maternal ingestion of sulfisoxazole; a case report. Am J Obstet Gynecol. 1971;111(3):379-381.
147. Lallemand AV, Doco-Fenzy M, Gaillard DA. Investigation of nonimmune hydrops fetalis: multidisciplinary studies are necessary for diagnosis—review of 94 cases. Pediatr Dev Pathol. 1999;2(5):432-439.
148. Rodriguez MM, Chaves F, Romaguera RL, et al. Value of autopsy in nonimmune hydrops fetalis: series of 51 stillborn fetuses. Pediatr Dev Pathol. 2002;5(4):365-374.
149. Barron SD, Pass RF. Infectious causes of hydrops fetalis. Semin Perinatol. 1995;19(6):493-501.
150. Porter HJ, Quantrill AM, Fleming KA. B19 parvovirus infection of myocardial cells. Lancet. 1988;1(8584):535-536.
151. Naides SJ, Weiner CP. Antenatal diagnosis and palliative treatment of non-immune hydrops fetalis secondary to fetal parvovirus B19 infection. Prenat Diagn. 1989;9(2):105-114.
152. Morey AL, Keeling JW, Porter HJ, Fleming KA. Clinical and histopathological features of parvovirus B19 infection in the human fetus. Br J Obstet Gynaecol. 1992;99(7):566-574.
153. Oyer CE, Ongcapin EH, Ni J, et al. Fatal intrauterine adenoviral endomyocarditis with aortic and pulmonary valve stenosis: diagnosis by polymerase chain reaction. Hum Pathol. 2000;31(11):1433-1435.
154. Bates Jr HR. Coxsackie virus B3 calcific pancarditis and hydrops fetalis. Am J Obstet Gynecol. 1970;106(4):629-630.
155. von Kaisenberg CS, Jonat W. Fetal parvovirus B19 infection. Ultrasound Obstet Gynecol. 2001;18(3):280-288.
156. Gray ES, Davidson RJ, Anand A. Human parvovirus and fetal anaemia. Lancet. 1987;1(8542):1144.
157. Miller E, Fairley CK, Cohen BJ, Seng C. Immediate and long term outcome of human parvovirus B19 infection in pregnancy. Br J Obstet Gynaecol. 1998;105(2):174-178.
158. Bhal PS, Davies NJ, Westmoreland D, Jones A. Spontaneous resolution of non-immune hydrops fetalis secondary to transplacental parvovirus B19 infection. Ultrasound Obstet Gynecol. 1996;7(1):55-57.
159. Pryde PG, Nugent CE, Pridjian G, et al. Spontaneous resolution of nonimmune hydrops fetalis secondary to human parvovirus B19 infection. Obstet Gynecol. 1992;79(5 Pt 2):859-861.
160. Humphrey W, Magoon M, O'Shaughnessy R. Severe nonimmune hydrops secondary to parvovirus B-19 infection: spontaneous reversal in utero and survival of a term infant. Obstet Gynecol. 1991;78(5 Pt 2):900-902.
161. Cossart YE, Field AM, Cant B, Widdows D. Parvovirus-like particles in human sera. Lancet. 1975;1(7898):72-73.
162. Kovacs BW, Carlson DE, Shahbahrami B, Platt LD. Prenatal diagnosis of human parvovirus B19 in nonimmune hydrops fetalis by polymerase chain reaction. Am J Obstet Gynecol. 1992;167(2):461-466.
163. Nagel HT, de Haan TR, Vandenbussche FP, et al. Long-term outcome after fetal transfusion for hydrops associated with parvovirus B19 infection. Obstet Gynecol. 2007;109(1):42-47.
164. Dembinski J, Haverkamp F, Maara H, et al. Neurodevelopmental outcome after intrauterine red cell transfusion for parvovirus B19-induced fetal hydrops. BJOG. 2002;109(11):1232-1234.
165. De Jong EP, Lindenburg IT, van Klink JM, et al. Intrauterine transfusion for parvovirus B19 infection: long-term neurodevelopmental outcome. Am J Obstet Gynecol. 2012;206(3):204.e1-204.e5.
166. Daffos F, Forestier F, Capella-Pavlovsky M, et al. Prenatal management of 746 pregnancies at risk for congenital toxoplasmosis. N Engl J Med. 1988;318(5):271-275.
167. Friedman S, Ford-Jones LE, Toi A, et al. Congenital toxoplasmosis: prenatal diagnosis, treatment and postnatal outcome. Prenat Diagn. 1999;19(4):330-333.
168. Zornes SL, Anderson PG, Lott RL. Congenital toxoplasmosis in an infant with hydrops fetalis. South Med J. 1988;81(3):391-393.

169. Inoue T, Matsumura N, Fukuoka M, et al. Severe congenital cytomegalovirus infection with fetal hydrops in a cytomegalovirus-seropositive healthy woman. Eur J Obstet Gynecol Reprod Biol. 2001;95(2):184-186.
170. Revello MG, Gerna G. Diagnosis and management of human cytomegalovirus infection in the mother, fetus, and newborn infant. Clin Microbiol Rev. 2002;15(4):680-715.
171. Negishi H, Yamada H, Hirayama E, et al. Intraperitoneal administration of cytomegalovirus hyperimmunoglobulin to the cytomegalovirus-infected fetus. J Perinatol. 1998;18(6 Pt 1):466-469.
172. Barton JR, Thorpe Jr EM, Shaver DC, et al. Nonimmune hydrops fetalis associated with maternal infection with syphilis. Am J Obstet Gynecol. 1992;167(1):56-58.
173. Harger JH, Ernest JM, Thurnau GR, et al. Frequency of congenital varicella syndrome in a prospective cohort of 347 pregnant women. Obstet Gynecol. 2002;100(2):260-265.
174. Anderson MS, Abzug MJ. Hydrops fetalis: an unusual presentation of intrauterine herpes simplex virus infection. Pediatr Infect Dis J. 1999; 18(9):837-839.
175. Ashshi AM, Cooper RJ, Klapper PE, et al. Detection of human herpes virus 6 DNA in fetal hydrops. Lancet. 2000;355(9214):1519-1520.
176. Ranucci-Weiss D, Uerpairojkit B, Bowles N, et al. Intrauterine adenoviral infection associated with fetal non-immune hydrops. Prenat Diagn. 1998; 18(2):182-185.
177. Schroter B, Chaoui R, Meisel H, Bollmann R. [Maternal hepatitis B infection as the cause of nonimmunologic hydrops fetalis]. Z Geburtshilfe Neonatol. 1999;203(1):36-38.
178. Jauniaux E, Van Maldergem L, De Munter C, et al. Nonimmune hydrops fetalis associated with genetic abnormalities. Obstet Gynecol. 1990;75(3 Pt 2):568-572.
179. Wraith JE. Lysosomal disorders. Semin Neonatol. 2002;7(1):75-83.
180. Ravindranath Y, Paglia DE, Warrier I, et al. Glucose phosphate isomerase deficiency as a cause of hydrops fetalis. N Engl J Med. 1987;316(5): 258-561.
181. Gilsanz F, Vega MA, Gomez-Castillo E, et al. Fetal anaemia due to pyruvate kinase deficiency. Arch Dis Child. 1993;69(5 Spec No):523-524.
182. Rotig A, Cormier V, Blanche S, et al. Pearson's marrow-pancreas syndrome. A multisystem mitochondrial disorder in infancy. J Clin Invest. 1990;86(5): 1601-1608.
183. Fayon M, Lamireau T, Bioulac-Sage P, et al. Fatal neonatal liver failure and mitochondrial cytopathy: an observation with antenatal ascites. Gastroenterology. 1992;103(4):1332-1335.
184. de Koning TJ, Toet M, Dorland L, et al. Recurrent nonimmune hydrops fetalis associated with carbohydrate-deficient glycoprotein syndrome. J Inherit Metab Dis. 1998;21(6):681-682.
185. Alegria A, Martins E, Dias M, et al. Glycogen storage disease type IV presenting as hydrops fetalis. J Inherit Metab Dis. 1999;22(3):330-332.
186. Knisely AS, Mieli-Vergani G, Whitington PF. Neonatal hemochromatosis. Gastroenterol Clin North Am. 2003;32(3):877-889, vi-vii.
187. Kessel I, Makhoul IR, Sujov P. Congenital hypothyroidism and nonimmune hydrops fetalis: associated? Pediatrics. 1999;103(1):E9.
188. Stulberg RA, Davies GA. Maternal thyrotoxicosis and fetal nonimmune hydrops. Obstet Gynecol. 2000;95(6 Pt 2):1036.
189. Pratt L, Digiosia J, Swenson JN, et al. Reversible fetal hydrops associated with indomethacin use. Obstet Gynecol. 1997;90(4 Pt 2):676-678.
190. Adler SP, Manganello AM, Koch WC, et al. Risk of human parvovirus B19 infections among school and hospital employees during endemic periods. J Infect Dis. 1993;168(2):361-368.
191. Saltzman DH, Frigoletto FD, Harlow BL, et al. Sonographic evaluation of hydrops fetalis. Obstet Gynecol. 1989;74(1):106-111.
192. Teoh TG, Ryan G, Johnson J, Winsor EJ. The role of fetal karyotyping from unconventional sources. Am J Obstet Gynecol. 1996;175(4 Pt 1): 873-877.
193. Cheong Leung W, Chitayat D, Seaward G, et al. Role of amniotic fluid interphase fluorescence in situ hybridization (FISH) analysis in patient management. Prenat Diagn. 2001;21(4):327-332.
194. Soma H, Yamada K, Osawa H, et al. Identification of Gaucher cells in the chorionic villi associated with recurrent hydrops fetalis. Placenta. 2000;21(4): 412-416.
195. Galjaard H. Fetal diagnosis of inborn errors of metabolism. Baillieres Clin Obstet Gynaecol. 1987;1(3):547-567.
196. Van Kamp IL, Klumper FJ, Oepkes D, et al. Complications of intrauterine intravascular transfusion for fetal anemia due to maternal red-cell alloimmunization. Am J Obstet Gynecol. 2005;192(1):171-177.
197. Tongsong T, Wanapirak C, Kunavikatikul C, et al. Fetal loss rate associated with cordocentesis at midgestation. Am J Obstet Gynecol. 2001;184(4): 719-723.
198. Tongsong T, Wanapirak C, Kunavikatikul C, et al. Cordocentesis at 16-24 weeks of gestation: experience of 1,320 cases. Prenat Diagn. 2000;20(3): 224-228.
199. Weiner CP, Okamura K. Diagnostic fetal blood sampling-technique related losses. Fetal Diagn Ther. 1996;11(3):169-175.
200. Ghidini A, Sepulveda W, Lockwood CJ, Romero R. Complications of fetal blood sampling. Am J Obstet Gynecol. 1993;168(5):1339-1344.
201. Liao C, Wei J, Li Q, et al. Efficacy and safety of cordocentesis for prenatal diagnosis. Int J Gynaecol Obstet. 2006;93(1):13-17.
202. Pasman SA, Claes L, Lewi L, et al. Intrauterine transfusion for fetal anemia due to red blood cell alloimmunization: 14 years experience in Leuven. Facts Views Vis Obgyn. 2015;7(2):129-136.
203. Mari G, Norton ME, Stone J, et al. Society for Maternal-Fetal Medicine (SMFM) Clinical Guideline #8: the fetus at risk for anemia—diagnosis and management. Am J Obstet Gynecol. 2015;212(6):697-710.
204. Daffos F, Forestier F, Mac Aleese J, et al. Fetal curarization for prenatal magnetic resonance imaging. Prenat Diagn. 1988;8(4):312-314.
205. Bernstein HH, Chitkara U, Plosker H, et al. Use of atracurium besylate to arrest fetal activity during intrauterine intravascular transfusions. Obstet Gynecol. 1988;72(5):813-816.
206. Yinon Y, Visser J, Kelly EN, et al. Early intrauterine transfusion in severe red blood cell alloimmunization. Ultrasound Obstet Gynecol. 2010;36(5):601-606.
207. Mandelbrot L, Daffos F, Forestier F, et al. Assessment of fetal blood volume for computer-assisted management of in utero transfusion. Fetal Ther. 1988; 3(1-2):60-66.
208. el-Azeem SA, Samuels P, Rose RL, et al. The effect of the source of transfused blood on the rate of consumption of transfused red blood cells in pregnancies affected by red blood cell alloimmunization. Am J Obstet Gynecol. 1997;177(4):753-757.
209. Mari G, Zimmermann R, Moise Jr KJ, Deter RL. Correlation between middle cerebral artery peak systolic velocity and fetal hemoglobin after 2 previous intrauterine transfusions. Am J Obstet Gynecol. 2005;193(3 Pt 2): 1117-1120.
210. Ruiz Villaespesa A, Suarez Mier MP, Lopez Ferrer P, et al. Nonimmunologic hydrops fetalis: an etiopathogenetic approach through the postmortem study of 59 patients. Am J Med Genet. 1990;35(2):274-279.
211. Knisely AS. The pathologist and the hydropic placenta, fetus, or infant. Semin Perinatol. 1995;19(6):525-531.
212. Steiner RD. Hydrops fetalis: role of the geneticist. Semin Perinatol. 1995;19(6):516-524.
213. Santolaya J, Alley D, Jaffe R, Warsof SL. Antenatal classification of hydrops fetalis. Obstet Gynecol. 1992;79(2):256-259.
214. Gudmundsson S, Huhta JC, Wood DC, et al. Venous Doppler ultrasonography in the fetus with nonimmune hydrops. Am J Obstet Gynecol. 1991; 164(1 Pt 1):33-37.
215. Kaiser IH. Ballantyne and triple edema. Am J Obstet Gynecol. 1971;110(1):115-120.
216. Kumar B, Nazaretian SP, Ryan AJ, Simpson I. Mirror syndrome: a rare entity. Pathology. 2007;39(3):373-375.
217. Vidaeff AC, Pschirrer ER, Mastrobattista JM, et al. Mirror syndrome. A case report. J Reprod Med. 2002;47(9):770-774.
218. Ordorica SA, Marks F, Frieden FJ, et al. Aneurysm of the vein of Galen: a new cause for Ballantyne syndrome. Am J Obstet Gynecol. 1990; 162(5):1166-1167.
219. Dorman SL, Cardwell MS. Ballantyne syndrome caused by a large placental chorioangioma. Am J Obstet Gynecol. 1995;173(5):1632-1633.
220. Livingston JC, Malik KM, Crombleholme TM, et al. Mirror syndrome: a novel approach to therapy with fetal peritoneal-amniotic shunt. Obstet Gynecol. 2007;110(2 Pt 2):540-543.

221. Duthie SJ, Walkinshaw SA. Parvovirus associated fetal hydrops: reversal of pregnancy induced proteinuric hypertension by in utero fetal transfusion. Br J Obstet Gynaecol. 1995;102(12):1011-1013.
222. Heyborne KD, Chism DM. Reversal of Ballantyne syndrome by selective second-trimester fetal termination. A case report. J Reprod Med. 2000; 45(4):360-362.
223. Espinoza J, Romero R, Nien JK, et al. A role of the anti-angiogenic factor sVEGFR-1 in the 'mirror syndrome' (Ballantyne's syndrome). J Matern Fetal Neonatal Med. 2006;19(10):607-613.
224. McCurdy Jr CM, Seeds JW. Route of delivery of infants with congenital anomalies. Clin Perinatol. 1993;20(1):81-106.
225. Kirshon B, Mari G, Moise Jr KJ. Indomethacin therapy in the treatment of symptomatic polyhydramnios. Obstet Gynecol. 1990;75(2):202-205.
226. Abrams ME, Meredith KS, Kinnard P, Clark RH. Hydrops fetalis: a retrospective review of cases reported to a large national database and identification of risk factors associated with death. Pediatrics. 2007;120(1):84-89.
227. Nakayama H, Kukita J, Hikino S, et al. Long-term outcome of 51 liveborn neonates with non-immune hydrops fetalis. Acta Paediatr. 1999; 88(1):24-28.
228. Haverkamp F, Noeker M, Gerresheim G, Fahnenstich H. Good prognosis for psychomotor development in survivors with nonimmune hydrops fetalis. BJOG. 2000;107(2):282-284.
229. Mari G, Abuhamad AZ, Cosmi E, et al. Middle cerebral artery peak systolic velocity: technique and variability. J Ultrasound Med. 2005;24(4): 425-430.
230. Machin GA. Hydrops revisited: literature review of 1,414 cases published in the 1980s. Am J Med Genet. 1989;34(3):366-390.
231. Santo S, Mansour S, Thilaganathan B, et al. Prenatal diagnosis of non-immune hydrops fetalis: what do we tell the parents? Prenat Diagn. 2011;31(2): 186-195.
232. Center for Disease Control (CDC). Risks associated with human parvovirum B19 infection. MMWR Morb Mortal Wkly Rep. 1989;38(6):81-88, 93-97.
233. Dijkmans AC, de Jong EP, Dijkmans BA, et al. Parvovirus B19 in pregnancy: prenatal diagnosis and management of fetal complications. Curr Opin Obstet Gynecol. 2012;24(2):95-101.
234. Cavoretto P, Molina F, Poggi S, et al. Prenatal diagnosis and outcome of echogenic fetal lung lesions. Ultrasound Obstet Gynecol. 2008;32(6): 769-783.
235. Wilson RD, Baxter JK, Johnson MP, et al. Thoracoamniotic shunts: fetal treatment of pleural effusions and congenital cystic adenomatoid malformations. Fetal Diagn Ther. 2004;19(5):413-420.
236. Loh KC, Jelin E, Hirose S, et al. Microcystic congenital pulmonary airway malformation with hydrops fetalis: steroids vs open fetal resection. J Pediatr Surg. 2012;47(1):36-39.
237. Society for Maternal-Fetal Medicine, Simpson LL. Twin-twin transfusion syndrome. Am J Obstet Gynecol. 2013;208(1):3-18.

CHAPTER 42

Fetal Measurements: Normal and Abnormal Fetal Growth and Assessment of Fetal Well-Being

Carol B. Benson and Peter M. Doubilet

SUMMARY OF KEY POINTS

- Accurate assignment of gestational age to a pregnancy is important for several reasons, including timing of screening tests for aneuploidy, monitoring fetal growth and diagnosing growth disturbances, and scheduling of delivery by elective induction or cesarean.
- If a woman has more than one sonogram during her pregnancy, the pregnancy should not be redated after the first scan; instead, the gestational age at the time of subsequent scans is the age at initial scan plus the time elapsed since that scan.
- In the first trimester, dating by sonographic findings or mean sac diameter prior to 6.0 weeks' gestation has an accuracy of ±0.5 weeks, while dating by crown-rump length at 6.0 weeks or later has an accuracy of ±0.7 weeks.
- Sonographic dating in the second and third trimesters has an accuracy of ±1.2 weeks at 14 to 20 weeks, ±1.9 weeks at 20 to 26 weeks, ±3.1 to 3.4 weeks at 26 to 32 weeks, and ±3.5 to 3.8 after 32 weeks.
- Fetal weight is estimated using a formula that incorporates measurements of the fetal head, abdomen, and femur and has an accuracy (95% confidence range) of ±15% to 18%.
- Estimated fetal weight should be assessed in relation to gestational age to determine whether the fetus is appropriate in size for gestational age.
- If a fetus is diagnosed as small-for-gestational-age, with an estimated fetal weight less than 10th percentile for gestational age, an attempt should be made to determine the cause through evaluation of both mother and fetus.
- When a fetus is suspected of being growth restricted, antenatal surveillance with biophysical profiles and fetal Doppler can guide management and improve outcome.

CHAPTER OUTLINE

GESTATIONAL AGE DETERMINATION
First Trimester
Second and Third Trimesters
Fetal Head Measurements
Femur Length
Abdominal Circumference
Composite Formulas
Gestational Age Estimation by Ultrasound: Most Accurate Approach at Each Stage of Pregnancy

WEIGHT ESTIMATION AND ASSESSMENT
Estimation of Fetal Weight
Recommended Approach
Weight Assessment in Relation to Gestational Age

FETAL GROWTH ABNORMALITIES
The Large Fetus
General Population
Diabetic Mothers
The Small-for-Gestational-Age Fetus and Fetal Growth Restriction

ASSESSMENT OF FETAL WELL-BEING
Biophysical Profile
Fetal Doppler
Umbilical Artery Doppler
Ductus Venosus Doppler
Middle Cerebral Artery Doppler
Summary of Fetal Doppler

Sonographic measurements of the fetus provide information about fetal age and growth. These data are used to assign gestational age, estimate fetal weight, and diagnose growth disturbances. As discussed in other chapters, fetal measurements are also used in the diagnosis of a number of fetal anomalies, such as skeletal dysplasias[1] and microcephaly.[2] Each of these abnormalities can be diagnosed or suspected on the basis of measurements that deviate from the "normal for dates."

It is important to begin by defining the various terms used in the evaluation of the age of a pregnancy. The true measure of a pregnancy's age is the number of days since conception, termed **conceptual age.** Historically, however, pregnancies were dated by the number of days since the first day of the last menstrual period (LMP), termed **menstrual age,** because for most of human history it was unknown when conception occurred. In women with regular 28-day cycles, menstrual age

is 2 weeks more than conceptual age, because conception occurs approximately 2 weeks after the LMP in such women. Currently, the term most often used to date pregnancies is **gestational age,** which is similar to menstrual age and is defined as follows:

$$\text{Gestational age} = \text{Conceptual age} + 2 \text{ weeks}$$

In women with 28-day cycles, gestational age and menstrual age are equal. In women with longer cycles, gestational age is less than menstrual age; the opposite holds in women with shorter cycles.

Accurate knowledge of gestational age is important for a number of reasons. The timing of screening tests in the first trimester, such as nuchal translucency measurement and maternal cell free fetal DNA analysis,[3,4] genetic amniocentesis in the second trimester, and elective induction or cesarean delivery in the third trimester are all based on the gestational age. The differentiation between term and preterm labor and the characterization of a fetus as "postdates" depend on gestational age. Knowledge of the gestational age can be critical in distinguishing normal from pathologic fetal development. Midgut herniation, for example, is normal up to 11 to 12 weeks of gestation[5] but signifies omphalocele thereafter. The normal size of a variety of fetal body parts depends on gestational age, as do levels of maternal serum alpha-fetoprotein,[6] human chorionic gonadotropin,[7] and estriol.[8] When a fetal anomaly is detected prenatally, the maternal choices and obstetric management are significantly influenced by gestational age.

Estimation of the fetal weight, on its own and in relation to the gestational age, can influence obstetric management decisions concerning the timing and route of delivery. A fetus growing poorly may benefit from close monitoring of fetal well-being to determine if early delivery is indicated. Such a fetus may be inadequately supplied by its placenta with oxygen and nutrients and, therefore, may do better in the care of a neonatologist than in utero. When a fetus is large, cesarean may be the preferred route of delivery, particularly in pregnancies complicated by maternal diabetes. In view of these considerations, fetal measurements should be a component of every complete obstetric sonogram.[9]

The well-being of the fetus at risk for perinatal morbidity and mortality, such as a growth-restricted fetus, can be monitored by ultrasound using the biophysical profile and Doppler. Abnormalities and changes in any of these surveillance tests may guide decisions about timing of delivery.[10,11]

GESTATIONAL AGE DETERMINATION

Clinical dating of a pregnancy is usually based on the patient's recollection of the first day of her LMP and on physical examination of uterine size. Unfortunately, both of these methods are imprecise, leading to inaccuracies in gestational age assignment. Dating by LMP (menstrual age) may be inaccurate because of variability in length of menstrual cycles, faulty memory,[12,13] recent exposure to oral contraceptives, or bleeding during early pregnancy.[14] Determining gestational age from the palpated dimension of the uterus may be affected by uterine fibroids, multiple pregnancy, and maternal body habitus.

Clinical dating is accurate only if either of the following two conditions apply: (1) the patient is a good historian with regular menstrual cycles, and the uterine size correlates closely with LMP; or (2) information is available specifying the time of conception, such as a basal body temperature chart or pregnancy achieved via assisted reproductive technologies in women treated for infertility.

Ultrasound provides an alternative and, in many cases, superior approach to gestational age estimation. Sonographic age estimation is based on sonographic findings or measurements taken during the ultrasound examination. Because biologic variability in the size of fetuses increases as pregnancy progresses, the accuracy of sonographic age estimates declines as pregnancy proceeds.[15-28] Thus, if a woman has more than one sonogram during a pregnancy, the pregnancy should never be redated after the first scan.

The decision as to whether to use clinical dating or sonographic dating at the time of the first scan is not well established for all pregnancies. In some cases, though, the decision is clear-cut: pregnancies achieved via *in vitro* fertilization should be dated based on the embryo transfer dates, and naturally conceived pregnancies in women with irregular menstrual cycles or with poor recollection of their LMP should be dated based on sonographic criteria. In other situations, however, particularly for pregnancies conceived naturally in women with regular cycles and good recollection of LMP, there are two reasonable alternatives. The first approach is to date the pregnancy based on LMP whenever the ages based on LMP and sonography are close to one another: within 5 days up to 8.9 weeks; within 7 days from 9.0 weeks to 15.9 weeks; within 10 days from 16.0 weeks to 21.9 weeks; within 14 days from 22.0 weeks to 27.9 weeks; and within 21 days from 28.0 weeks onward.[16] An alternative approach is to use sonographic dating routinely up to 24 weeks and the LMP thereafter, if the LMP is clearly recalled and within 21 days of sonographic dating.[15]

Whichever approach is used, it is important to know what sonographic criteria are available for gestational age estimation and which are the most accurate at each stage of pregnancy.

First Trimester

Sonographic findings and measurements allow highly accurate dating from 5 weeks' gestation until the end of the first trimester. The earliest sign of an intrauterine pregnancy is identification of a **gestational sac** in the uterine cavity. This appears as a round or oval fluid collection within the uterine cavity first seen on transvaginal sonography at approximately 5 weeks' gestation.[29] In some cases, the early gestational sac is surrounded by one or two echogenic rings, formed by the proliferating chorionic villi and the deeper layer of the decidua vera.[30,31] These rings are not consistently present, however, and any round or oval fluid collection in the mid uterus of a woman with a positive pregnancy test is highly likely to be a gestational sac[32] (Fig. 42.1).

From 5 to 6 weeks' gestation, two methods can be used to assign gestational age by ultrasound: (1) measurement of **mean sac diameter** (MSD) or (2) sonographic identification of gestational sac contents. The MSD is calculated as the average of the anteroposterior diameter, the transverse diameter, and the longitudinal diameter. It increases from 2 mm at 5 weeks to

FIG. 42.1 Gestational Sac. At 5.0 weeks' gestation, gestational sac *(arrow)* appears as a small, intrauterine fluid collection.

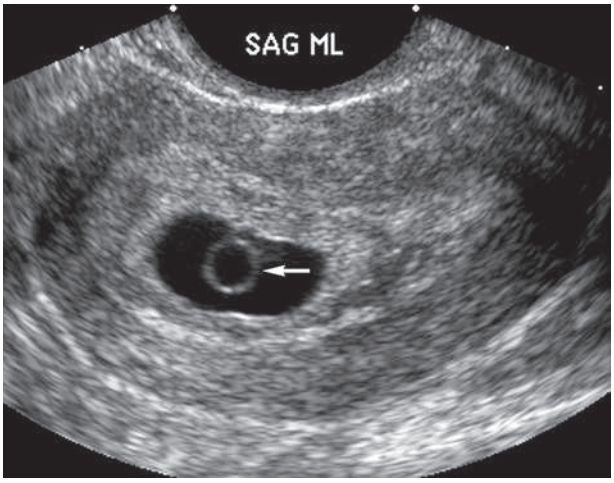

FIG. 42.2 Yolk Sac. Gestational sac contains yolk sac *(arrow)* on transvaginal sonogram at 5.5 weeks' gestation. No embryo is seen. *SAG ML,* Sagittal midline.

TABLE 42.1 Gestational Dating by Mean Sac Diameter (MSD) in the Early First Trimester

MSD (mm)	Gestational Age (Weeks)
2	5.0
3	5.1
4	5.2
5	5.4
6	5.5
7	5.6
8	5.7
9	5.9
10	6.0

95% Confidence interval = ±0.5 week.
Values from Daya S, Wood S, Ward S, et al. Early pregnancy assessment with transvaginal ultrasound scanning. CMAJ. 1991; 144(4):441-446.[33]

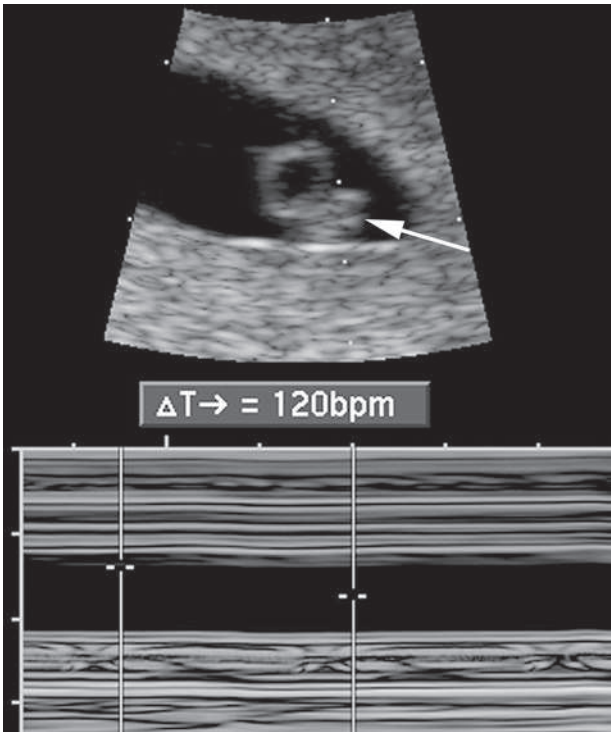

FIG. 42.3 Embryonic Heartbeat. Transvaginal sonogram and M-mode at 6 weeks demonstrate cardiac activity originating from tiny embryo *(arrow)* adjacent to the yolk sac. See also Video 42.1.

10 mm at 6 weeks,[33] a growth pattern that can be used to assign gestational age during this period (Table 42.1).

The second method, based on the sonographic findings within the gestational sac, is best done by transvaginal sonography and relies on the observation that, on average, the gestational sac is first identifiable at 5.0 weeks, the **yolk sac** at 5.5 weeks (Fig. 42.2), and the embryo and **embryonic heartbeat** at 6.0 weeks[34] (Fig. 42.3, Video 42.1). The timing of these milestones is subject to minimal variability, with a 95% confidence range of approximately 0.5 weeks.[31] Gestational age can be assigned based on these milestones (Table 42.2).

From 6 weeks until the end of the first trimester, gestational age correlates closely with the **crown-rump length** (CRL) of the embryo or fetus.[35,36] The term **embryo** is commonly used up to 10 weeks' gestation, and the term **fetus** applies thereafter.[37] The CRL is the length of the embryo or fetus from the top of its head to the bottom of its torso. It is measured as the longest dimension of the embryo, excluding the yolk sac and extremities. From 9 or 10 weeks onward, the CRL measurements are most accurate if taken with the fetus in neutral position[38] (Fig. 42.4). The CRL can be used to assign gestational age accurately up to 14 weeks because there is little biologic variability in fetal length up until that age[39] (Table 42.3). After that point, the CRL of the longer, more developed fetus becomes less reliable. At this later stage, the CRL is affected by the fetal position, measuring shorter in a fetus whose spine is flexed and longer in a fetus whose spine is extended.

TABLE 42.2 Gestational Dating by Ultrasound in the First Trimester

Sonographic Finding	Gestational Age (Weeks)
Gestational sac, no yolk sac, embryo, or heartbeat	5
Gestational sac with yolk sac, no embryo or heartbeat	5.5
Gestational sac with heartbeat and embryo <5 mm in length	6
Embryo/fetus ≥5 mm in length	Age based on crown-rump length (see Table 42.3)

FIG. 42.4 Crown-Rump Length Measurement. Cursors delineate the length of the fetus from the top of its head to the bottom of its torso.

Second and Third Trimesters

Many sonographic parameters have been proposed for estimating gestational age in the second and third trimesters. These include several fetal measurements: **biparietal diameter** (BPD),[40,41] **head circumference** (HC),[42] **abdominal circumference** (AC),[43] **femur length** (FL),[25,44-46] as well as combinations of two or more fetal measurements: the **corrected-BPD**[41] and **composite age formulas.**[43,47] Measurements of structurally abnormal fetal body parts should not be used in the assignment of gestational age.

Fetal Head Measurements

Three measurements or parameters involve the fetal head: BPD, **occipitofrontal diameter** (OFD), and HC. All three measurements are taken from transaxial sonograms of the fetal head at the level of the paired thalami and cavum septi pellucidi[48] (Fig. 42.5). These head measurements are most accurate if the image is a true axial plane demonstrating the head as oval with symmetry of the thalami and cerebral hemispheres and without visualization of the posterior fossa.[49] The BPD is measured from the outer edge of the cranium nearest the transducer to the inner edge of the cranium farthest from the transducer ("leading edge to leading edge") (Fig. 42.5). The OFD is obtained from the same transaxial image as the BPD and is measured from mid-skull to mid-skull along the long axis of the fetal head (Fig. 42.5). This latter measurement is used in conjunction with the BPD to calculate the corrected-BPD using the following formula[41]:

$$\text{Corrected-BPD} = \sqrt{(\text{BPD} \times \text{OFD})/1.265}$$

TABLE 42.3 Gestational Age Estimation by Crown-Rump Length (CRL)

CRL (mm)	Gestational Age (Weeks)	CRL (mm)	Gestational Age (Weeks)
5	6.0	45	11.1
6	6.2	46	11.2
7	6.4	47	11.3
8	6.6	48	11.4
9	6.8	49	11.4
10	7.0	50	11.5
11	7.2	51	11.6
12	7.4	52	11.7
13	7.5	53	11.8
14	7.7	54	11.8
15	7.8	55	11.9
16	8.0	56	12.0
17	8.1	57	12.1
18	8.3	58	12.2
19	8.4	59	12.2
20	8.5	60	12.3
21	8.7	61	12.4
22	8.8	62	12.4
23	8.9	63	12.5
24	9.0	64	12.6
25	9.1	65	12.7
26	9.3	66	12.7
27	9.4	67	12.8
28	9.5	68	12.9
29	9.6	69	12.9
30	9.7	70	13.0
31	9.8	71	13.1
32	9.9	72	13.2
33	10.0	73	13.2
34	10.1	74	13.3
35	10.2	75	13.4
36	10.3	76	13.4
37	10.4	77	13.5
38	10.5	78	13.5
39	10.6	79	13.6
40	10.7	80	13.7
41	10.8		
42	10.8		
43	10.9		
44	11.0		

Values derived from formula in Robinson HP, Fleming JE. A critical evaluation of sonar "crown-rump length" measurements. Br J Obstet Gynaecol. 1975;82(9):702-710.[35]

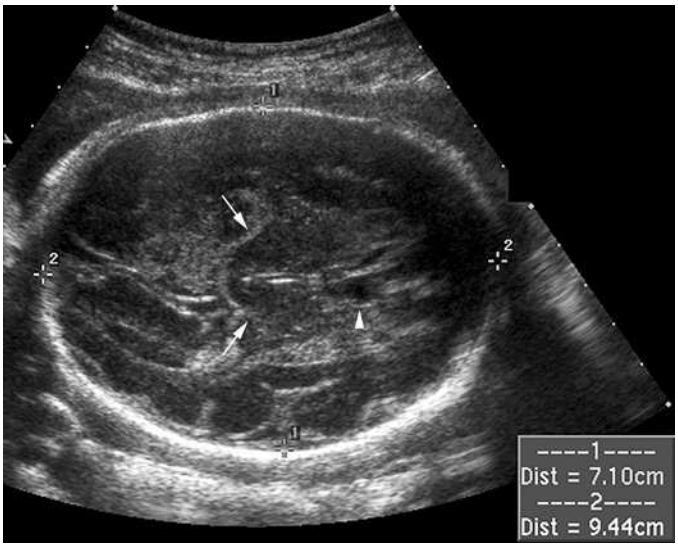

FIG. 42.5 Biparietal Diameter (BPD) and Occipitofrontal Diameter (OFD) Measurements. Transaxial sonogram of the fetal head at the level of the paired thalami *(arrows)* and cavum septi pellucidi *(arrowhead),* with BPD *(calipers 1)* and OFD *(calipers 2)*. Note how the calipers for the BPD are placed from the outer aspect of the skull to the inner aspect of the skull, "leading edge to leading edge."

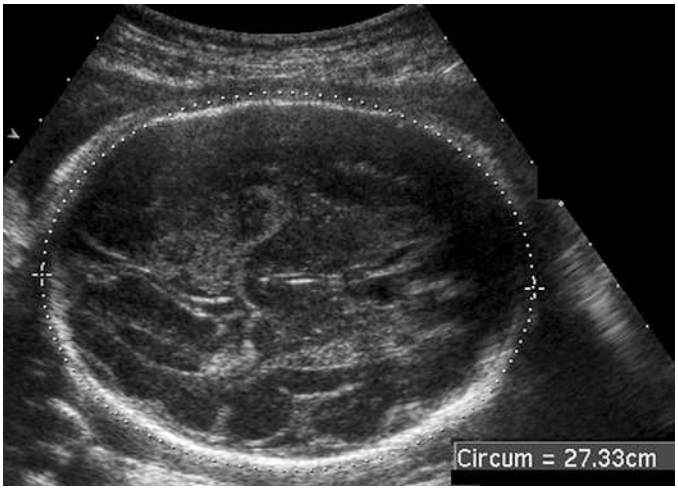

FIG. 42.6 Head Circumference (HC) Measurement. HC measurement (*calipers* and *tracing dots*) on transaxial sonogram of the fetal head at the same level as for the biparietal diameter measurement. Note how the HC measurement is obtained by tracing around the bone.

The rationale for the corrected-BPD is that it represents the BPD of the standard-shaped head (one with an OFD/BPD ratio of 1.265) of the same cross-sectional area.[41] The same tables or formulas used to determine gestational age from the BPD are used to determine gestational age from the corrected-BPD (Table 42.4).

The HC is the length of the outer perimeter of the cranium, made on the same transaxial image of the fetal head. It can be measured by using an electronic ellipse[50] (Fig. 42.6, Table 42.5) or calculated from the outer-edge-to-outer-edge analogs of the BPD and OFD:

$$HC = 1.57 \times [(\text{Outer-to-outer BPD}) + (\text{Outer-to-outer OFD})]$$

TABLE 42.4 Gestational Age Estimation by Biparietal Diameter (BPD)

BPD OR BPDc (mm)	Gestational Age (Weeks)	BPD OR BPDc (mm)	Gestational Age (Weeks)
20	13.2	60	24.2
21	13.4	61	24.5
22	13.6	62	24.9
23	13.8	63	25.3
24	14.0	64	25.7
25	14.3	65	26.1
26	14.5	66	26.5
27	14.7	67	26.9
28	14.9	68	27.3
29	15.1	69	27.7
30	15.4	70	28.1
31	15.6	71	28.5
32	15.8	72	29.0
33	16.1	73	29.4
34	16.3	74	29.9
35	16.6	75	30.3
36	16.8	76	30.8
37	17.1	77	31.2
38	17.3	78	31.7
39	17.6	79	32.2
40	17.9	80	32.7
41	18.1	81	33.2
42	18.4	82	33.7
43	18.7	83	34.2
44	19.0	84	34.7
45	19.3	85	35.2
46	19.6	86	35.8
47	19.9	87	36.3
48	20.2	88	36.9
49	20.5	89	37.4
50	20.8	90	38.0
51	21.1	91	38.6
52	21.4	92	39.2
53	21.7	93	39.8
54	22.1	94	40.4
55	22.4	95	41.0
56	22.8	96	41.6
57	23.1	≥97	42.0
58	23.5		
59	23.8		

BPDc, Corrected-BPD.
Values from Doubilet PM, Benson CB. Improved prediction of gestational age in the late third trimester. J Ultrasound Med. 1993;12(11):647-653.[44]

Although the BPD is simpler to measure than the corrected-BPD or HC, it has the disadvantage of being the only one of the three measurements that disregards head shape. This means that two heads of equal widths but different lengths will have the same BPD, but the longer head will have a greater corrected-BPD and HC than the shorter head (Fig. 42.7). The fetus with the longer head will therefore be assigned a greater gestational age based on the corrected-BPD or HC; however, both fetuses will

TABLE 42.5 Gestational Age Estimation by Head Circumference (HC)

HC (mm)	Gestational Age (Weeks)	HC (mm)	Gestational Age (Weeks)
80	13.4	225	24.5
85	13.7	230	25.0
90	14.0	235	25.5
95	14.3	240	26.1
100	14.7	245	26.6
105	15.0	250	27.1
110	15.3	255	27.7
115	15.6	260	28.3
120	16.0	265	28.9
125	16.3	270	29.4
130	16.6	275	30.0
135	17.0	280	30.7
140	17.3	285	31.3
145	17.7	290	31.9
150	18.1	295	32.6
155	18.4	300	33.3
160	18.8	305	33.9
165	19.2	310	34.6
170	19.6	315	35.3
175	20.0	320	36.1
180	20.4	325	36.8
185	20.8	330	37.6
190	21.3	335	38.3
195	21.7	340	39.1
200	22.2	345	39.9
205	22.6	350	40.7
210	23.1	355	41.6
215	23.6	360	42.4
220	24.0		

Values derived from formula in Law RG, MacRae KD. Head circumference as an index of fetal age. J Ultrasound Med. 1982;1(7):281-288.[42]

be assigned the same gestational age if the BPD is used as the basis for age assignment.

Femur Length

The length of the ossified diaphysis of the fetal femur is often used for gestational age estimation.[25,41,45] Careful measurement technique is necessary to obtain an accurate estimate of gestational age by FL (Fig. 42.8, Table 42.6). The transducer must be aligned to the long axis of the diaphysis, perpendicular to the beam, with both ends of the ossified diaphysis appearing squared off. The cursors should be positioned at the junction of the echogenic bone with the hypoechoic cartilage, and the thin, bright reflection of the cartilaginous epiphysis should not be included in the measurement.[49,51]

Abdominal Circumference

The fetal AC is the length of the outer perimeter of the fetal abdomen, measured on transverse view at the level of the intrahepatic portion of the umbilical vein. Ideally the stomach will also be visible (Fig. 42.9). Ideally, the abdomen should appear round. The level chosen should demonstrate only a short segment of the umbilical vein in the anterior third of the liver. Measurement of the AC involves placing the ellipse along the outer skin surface[49] (Fig. 42.9A). Alternatively, the AC may be calculated from two orthogonal **abdominal diameters** (AD_1, AD_2), one anteroposterior and the other transverse (Fig. 42.9B), measured on the same image, as follows[50,52]:

$$AC = 1.57 \times (AD_1 + AD_2)$$

Composite Formulas

Gestational age can be estimated from measurements of the head, abdomen, or femur by means of tables or formulas that present the mean value of each measurement for a given gestational age (Tables 42.4 to 42.6). Composite age formulas that combine several fetal measurements can also be used to estimate gestational age.[25,47]

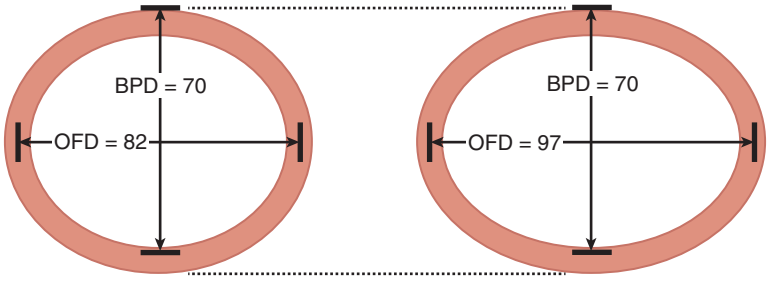

A Corrected BPD = 67 HC = 250

B Corrected BPD = 73 HC = 274

FIG. 42.7 Effect of Head Shape on Corrected-BPD and HC. Heads **A** and **B** have equal biparietal diameters *(BPD),* but **A** has a smaller occipitofrontal diameter *(OFD)* than **B.** Therefore the corrected-BPD and head circumference *(HC)* are smaller for **A** than **B.** Based on BPD, fetuses **A** and **B** would be assigned the same gestational age. Based on corrected-BPD or HC, however, fetus **A** would be assigned a lower gestational age than fetus **B.**

FIG. 42.8 Femur Length Measurement. Electronic calipers measure the ossified diaphysis of the femur. Note how the bone is imaged parallel to the transducer.

Because composite age formulas use a combination of two or more measurements in conjunction to estimate gestational age, a potential disadvantage of using such formulas is that an abnormal measurement or anomaly might be obscured. For example, in a fetus with a skeletal dysplasia manifested by shortened long bones and a normal head size, the gestational age based on the composite formula will be an underestimation, falling between that predicted by the HC and that predicted by the short FL. As a result, the FL might not appear to be abnormally small when compared to this improperly calculated gestational age.

Gestational Age Estimation by Ultrasound: Most Accurate Approach at Each Stage of Pregnancy

When sonographic, as opposed to clinical, dating is used to assign gestational age, it is important to use the most accurate method or measurement available (Table 42.7). This is most relevant at the time of the initial scan in a woman's pregnancy, since, as noted previously, it is inappropriate to reassign gestational age at the time of the second or subsequent scan during the pregnancy.

If the initial scan is performed in the early first trimester, when ultrasound demonstrates no embryo or an embryo less than 5 mm in length, two approaches to gestational age assignment are equal in accuracy, both with 95% confidence ranges of ±0.5 weeks: date the pregnancy based on MSD (see Table 42.1) or on sac contents (see Table 42.2). For the rest of the first trimester, when the CRL measures 5 to 80 mm, dating based on CRL (see Table 42.3) is very accurate, with a 95% confidence range of ±0.7 weeks.[53]

In the second and third trimesters, there are several options for sonographic dating, including measurements of the head, femur, or abdomen, as well as composite formulas based on measurements of two or more of these. When both the width and length of the head (BPD and OFD) are visible, the optimal approach to sonographic age assignment in the second trimester is to use either the corrected-BPD or the HC, and, in the third trimester, use the corrected-BPD, the HC, or the FL. When either the anterior or posterior aspects of the cranium are not well seen on ultrasound, so that the OFD and HC cannot be measured accurately, it is best to date based on the BPD or FL in the second trimester and on the FL in the third trimester.[44,54,55] These approaches are the most accurate single-body-part sonographic dating methods and are preferable to composite age formulas for reasons presented earlier.

TABLE 42.6 Gestational Age Estimation by Femur Length (FL)

FL (mm)	Gestational Age (Weeks)	FL (mm)	Gestational Age (Weeks)
10	13.7	45	24.5
11	13.9	46	24.9
12	14.2	47	25.3
13	14.4	48	25.7
14	14.6	49	26.2
15	14.9	50	26.6
16	15.1	51	27.0
17	15.4	52	27.5
18	15.6	53	28.0
19	15.9	54	28.4
20	16.2	55	28.9
21	16.4	56	29.4
22	16.7	57	29.9
23	17.0	58	30.4
24	17.3	59	30.9
25	17.6	60	31.4
26	17.9	61	31.9
27	18.2	62	32.5
28	18.5	63	33.0
29	18.8	64	33.6
30	19.1	65	34.1
31	19.4	66	34.7
32	19.7	67	35.3
33	20.1	68	35.9
34	20.4	69	36.5
35	20.7	70	37.1
36	21.1	71	37.7
37	21.4	72	38.3
38	21.8	73	39.0
39	22.2	74	39.6
40	22.5	75	40.3
41	22.9	76	40.9
42	23.3	77	41.6
43	23.7	≥78	42.0
44	24.1		

Values from Doubilet PM, Benson CB. Improved prediction of gestational age in the late third trimester. J Ultrasound Med. 1993;12(11):647-653.[44]

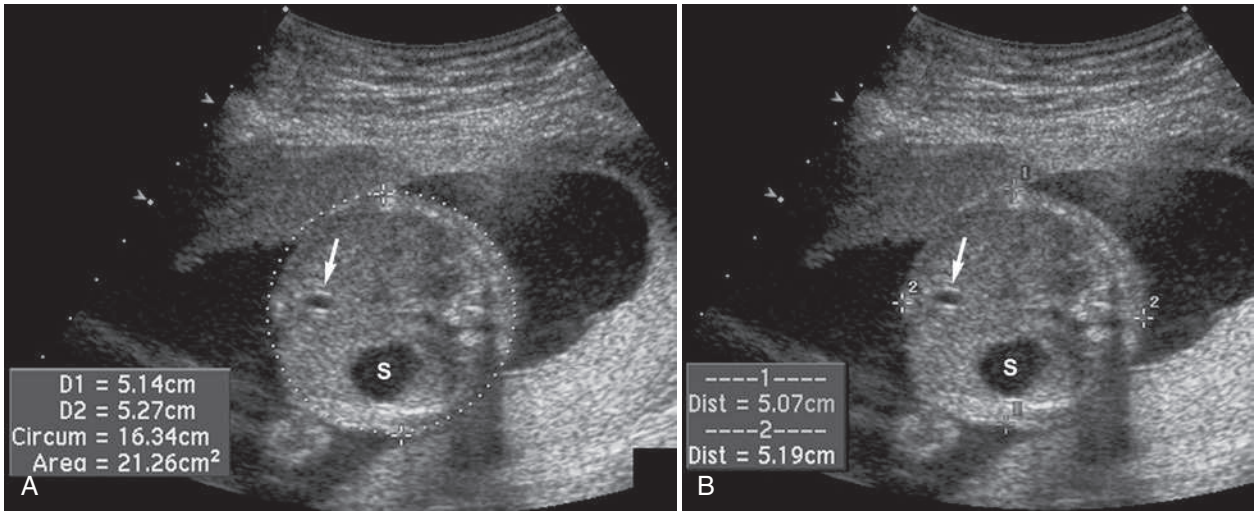

FIG. 42.9 Abdominal Circumference and Diameter Measurements. (A) and **(B)** Axial views of the fetal abdomen at the level of the stomach *(S)* and intrahepatic portion of the umbilical vein *(arrow)*. On **A** the circumference of the abdomen has been traced electronically (*calipers* and *tracing dots*). On **B** the transverse *(calipers 1)* and anteroposterior *(calipers 2)* diameters have been measured with electronic calipers.

TABLE 42.7 Gestational Age (GA) Assignment by Ultrasound: Most Accurate Approach at Each Stage of Pregnancy

Stage of Pregnancy	Basis for GA	Tables	Accuracy (Weeks)[a]
FIRST TRIMESTER			
Early (5-6 weeks)	Mean sac diameter or sonographic findings	42.1, 42.2	±0.5
Mid to late (6-13 weeks)	CRL	42.3	±0.7
SECOND TRIMESTER			
If OFD measurable	BPDc or HC	42.4, 42.5	±1.2 (14-20 weeks) ±1.9 (20-26 weeks)
If OFD not measurable	BPD or FL	42.4, 42.6	±1.4 (14-20 weeks) ±2.1-2.5 (20-26 weeks)
THIRD TRIMESTER			
If OFD measurable	BPDc, HC, or FL	42.4, 42.5, 42.6	±±3.1-3.4 (26-32 weeks) ±±3.5-3.8 (32-42 weeks)
If OFD not measurable	FL	42.6	±±3.1 (26-32 weeks) ±±3.5 (36-42 weeks)

[a]Two standard deviations (2 SD) or 95% confidence interval (CI).

BPD, Biparietal diameter; *BPDc,* corrected-BPD; *CRL,* crown-rump length; *FL,* femur length; *HC,* head circumference; *OFD,* occipitofrontal diameter.

With permission from Doubilet PM. Should a first trimester dating scan be routine for all pregnancies? Semin Perinatol. 2013;37(5):307-309[53]; Benson CB, Doubilet PM. Sonographic prediction of gestational age: accuracy of second- and third-trimester fetal measurements. AJR Am J Roentgenol. 1991;157(6):1275-1277.[54]

WEIGHT ESTIMATION AND ASSESSMENT

Before the availability of ultrasound, manual examination of the maternal abdomen was the approach used to estimate fetal size. The physical examination, however, provides only a general approximation of fetal weight because the palpated dimensions of the uterus are affected by several factors other than fetal size, including amniotic fluid volume, presence of fibroids, and maternal obesity.

Sonographic measurements of fetal body parts provide a direct way of assessing fetal weight and are used mainly in the third trimester. The approach to fetal weight estimation and assessment involves a number of steps: (1) estimate the fetal weight based on fetal measurements; (2) estimate the gestational age using the approach described earlier; (3) determine the weight percentile for gestational age using a formula or chart of weight norms as a function of gestational age; (4) if the fetus is above the 90th percentile or above 4000 g estimated weight, consider options for route of delivery; (5) if the weight is at or below the 10th

percentile, attempt to determine whether the fetus is constitutionally small or small because of a pathologic etiology, then manage the pregnancy accordingly.

Estimation of Fetal Weight

Numerous formulas have been published for estimating fetal weight based on sonographic measurements, most of which use one or more of these fetal body parts: head (BPD or HC), abdomen (AD or AC), and femur (FL).[19-24,26-28,56] Other measurements, such as thigh circumference, have been used as well.[28] Formulas that estimate fetal weight using three-dimensional (3D) sonography[57-59] and 3D magnetic resonance imaging (MRI) have also been published.[60,61]

The accuracy of a weight prediction formula is determined by assessing how well the formula works in a group of fetuses scanned close to delivery. An important measure of a formula's performance is its 95% confidence range. If the 95% confidence range is ±18%, for example, the estimated weight will fall within 18% of the actual weight in 95% of cases, and the error will be greater than 18% in only 5% of cases. The narrower the confidence range is, the more reliable is the formula.

Many published studies provide information on this measure of a formula's accuracy[62-65] (Table 42.8). The following points are noteworthy:

TABLE 42.8 Accuracy of Fetal Weight Prediction Formulas

Body Part(s) Included in Formula	Formula	95% Confidence Range (%)[a]
Abdomen	Campbell and Wilkin[19]	±17.1-23.8[56,62]
	Higginbottom et al.[20]	±23.8[56]
	Hadlock et al.[56]	±22.2[56]
	Vintzileos et al.[28]	±22.8[28]
Head and abdomen	Warsof et al.[21]	±17.4-21.2[21,56,69]
	Shepard et al.[22]	±18.2-18.3[22,62]
	Thurnau et al.[23]	±19.8[56]
	Jordaan[24]	±25.8[56]
	Hadlock et al.[56]	±18.2[56]
	Hadlock et al.[26]	±18.2[26]
	Birnholz[27]	±17.7[63,b]
	Vintzileos et al.[28]	±21.2[28]
Abdomen and femur	Hadlock et al.[56]	±16.4[56]
	Hadlock et al.[26]	±16.0[26]
Head, abdomen, and femur	Hadlock et al.[56]	±15.0-15.4[56]
	Hadlock et al.[26]	±14.8-15.0[26]
	Vintzileos et al.[28]	±17.6[28]
Head, abdomen, femur, and thigh	Vintzileos et al.[28]	±15.6-17.8[28]

[a]Computed as two standard deviations (2 SD) of the relative error, as reported in the study(ies) referenced, unless otherwise indicated.
[b]Based on the fraction of cases in which the estimated weight falls within 10% of the actual weight.

- The accuracy of weight prediction formulas improves as the number of measured body parts increases up to three, achieving greatest accuracy when measurements of the head, abdomen, and femur are used. There is no apparent improvement by adding the thigh circumference as a fourth measurement[66] and no proven benefit from using 3D sonography or MRI.
- Even when based on measurements of the head, abdomen, and femur, sonographic weight prediction has a rather wide 95% confidence range of at least ±15%. Based on the abdomen and either the head or femur, the range is at least ±16% to 18%. Precision is considerably worse when only the abdomen is used.
- A number of factors have been studied to determine their effect on accuracy of weight prediction. Accuracy appears to be worse in fetuses that weigh less than 1000 g than in larger fetuses.[63] Over the rest of the birth weight range, however, accuracy is fairly constant.[26,56,62,67] Weight prediction is less accurate in diabetic than in nondiabetic mothers: in diabetic mothers, formulas that use measurements of the head, abdomen, and femur have a 95% confidence range of ±24%,[68] wider than the range of ±15% in the general population.[26,56] The presence of oligohydramnios or polyhydramnios has no impact on accuracy.[23,63,69] Scan quality may have an effect on accuracy. Studies have shown a trend toward greater accuracy in scans that were rated "good" compared with those rated "poor" based on ability to visualize anatomic landmarks.[63,70]

Recommended Approach

An attempt should be made to image all three key fetal anatomic regions—head, abdomen, and femur—at the appropriate anatomic levels (Table 42.9). If measurements of all three structures can be obtained, Formula 1 in Table 42.9 should be used to estimate fetal weight. This formula should be used with the corrected-BPD when the OFD is available, and with the BPD itself if not. An alternative approach, equally accurate but more cumbersome, would be to use Formula 1 when the OFD is unavailable, and a formula based on HC, AC, and FL when the OFD is available. If the abdomen and only one of the head or the femur can be appropriately imaged, Formula 2 or 3 should be used. If the abdomen cannot be measured, or both the head and femur cannot be measured, then a weight estimate should not be calculated. Using the approach outlined in Table 42.9, an accuracy of ±15% to 18% can be achieved for weight estimation.

Weight Assessment in Relation to Gestational Age

When an ultrasound is performed in the third trimester, best estimates of gestational age and fetal weight should be established. The gestational age may be based on a prior ultrasound, clinical dating criteria, or current measurements; fetal weight is always calculated from current measurements. The two values should be assessed in relation to one another to determine whether the fetus is appropriate in size for dates. This can be accomplished by using a table that provides norms for fetal weight as a function

TABLE 42.9 Approach to Fetal Weight Estimation

Body Parts Imaged	Formula Used for Weight Estimate
HEAD, ABDOMEN, AND FEMUR	
OFD measurable	Formula 1, using corrected-BPD in place of BPD
OFD not measurable	Formula 1
HEAD AND ABDOMEN	
OFD measurable	Formula 2, using corrected-BPD in place of BPD
OFD not measurable	Formula 2
ABDOMEN AND FEMUR	
—	Formula 3

FORMULA 1[a]

$$\text{Log}_{10}(\text{EFW}>) = 1.4787 - 0.003343\ \text{AC} \times \text{FL} + \text{BPD}_2 + 0.0458\ \text{AC} + 0.158\ \text{FL}$$

FORMULA 2[a]

$$\text{Log}_{10}(\text{EFW}>) = 1.1134 + 0.05845\ \text{AC} - 0.000604\ \text{AC}^2 - 0.007365\ \text{BPD}^2 + \text{BPD}_2 + 0.00595\ \text{BPD} \times \text{AC} + 0.1694\ \text{BPD}$$

FORMULA 3[a]

$$\text{Log}_{10}(\text{EFW}) = 1.3598 + 0.051\ \text{AC} + 0.01844\ \text{FL} - 0.0037\ \text{AC} \times \text{FL}$$

[a]Formulas from Hadlock FP, Harrist RB, Sharman RS, et al. Estimation of fetal weight with the use of head, body, and femur measurements—a prospective study. Am J Obstet Gynecol. 1985;151(3):333-337.[26]

AC, Abdominal circumference (cm); *BPD,* biparietal diameter (cm); *EFW,* estimated fetal weight, in grams (g); *FL,* femur length (cm); *OFD,* occipitofrontal diameter (cm).

TABLE 42.10 Fetal Weight Percentiles in the Third Trimester

	WEIGHT PERCENTILES (GRAMS)		
Gestational Age (Weeks)	**10th**	**50th**	**90th**
25	490	660	889
26	568	760	1016
27	660	875	1160
28	765	1005	1322
29	884	1153	1504
30	1020	1319	1706
31	1171	1502	1928
32	1338	1702	2167
33	1519	1918	2421
34	1714	2146	2687
35	1919	2383	2959
36	2129	2622	3230
37	2340	2859	3493
38	2544	3083	3736
39	2735	3288	3952
40	2904	3462	4127
41	3042	3597	4254
42	3142	3685	4322
43	3195	3717	4324

With permission from Doubilet PM, Benson CB, Nadel AS, Ringer SA. Improved birth weight table for neonates developed from gestations dated by early ultrasonography. J Ultrasound Med. 1997;16(4):241-249.[71]

of gestational age (Table 42.10), several of which appear in the literature.[71-76]

There is some debate about a number of aspects of fetal weight assessment in relation to gestational age. Should a weight table or chart based on neonatal weights or on estimated fetal weights be used? Should the table or chart be derived solely from pregnancies of low-risk mothers? Should "population norms" or "customized norms" be used?

Most weight norms (tables or charts) are derived from large data sets of neonatal birth weights from babies born at a known gestational age.[71-76] At least one chart, on the other hand, was produced using estimated fetal weights instead of neonatal birth weights.[77,78] A rationale for the latter is that several studies have shown that fetuses that deliver preterm are smaller, on average, than those of the same gestational age that remain in utero.[79-83] Babies born preterm thus represent an abnormal group with a negatively skewed weight distribution. This supports the argument that fetuses should be compared to fetuses, not to babies.[84]

A large international study, INTERGROWTH-21st, used another approach to produce weight norms derived from a healthy population.[85,86] Although it is based on birth weights rather than fetal weights, the study population used to generate these norms consists of babies born at or beyond 33 weeks to mothers with no known pregnancy-related risk factors. The INTERGROWTH-21st norms, however, are of limited use for assessing fetal weight in relation to gestational age, because they do not cover the period prior to 33 weeks' gestation.

Perhaps the biggest controversy in weight assessment is whether the estimated weight of a fetus should be compared to norms from the overall population or to customized norms[87-91] derived from a subgroup of fetuses similar to that fetus. For example, if an African-American fetus has an estimated weight of 1200 g at 30 weeks' gestation, should the weight percentile be determined from overall population norms or from African-American norms? In that example, the population-based percentile would be lower than the customized percentile, because African-American fetuses and neonates are smaller, on average, than those in the general population.[92] Although there are proponents of customized norms,[93-95] a major concern with this approach is that it can do harm by inadvertently normalizing the weight of a fetus who is small on a pathologic basis.[96,97] This viewpoint is supported by the fact that at least some population groups with small babies have elevated rates of postnatal complications[98] and by the INTERGROWTH-21st finding that neonates of healthy mothers do not differ in size based on ethnic background.[99]

Overall, our recommended approach is to use population norms. Although it would theoretically be preferable to use norms

derived from estimated fetal weights,[77,78] norms derived from birth weights are better established and are based on larger study populations.[71-76]

The weight gain between two ultrasound examinations can be estimated as the difference between the two estimated weights. Adequacy of weight gain can be assessed by comparing this difference to established normal fetal growth rate as a function of gestational age. INTERGROWTH-21st data indicate that median fetal weight gain per week decreases progressively from 33 weeks of gestation onward, with a maximum rate of 270 g per week at 33 weeks, down to 100 g per week at 41 weeks.[86] Other older growth tables suggest that weight gain may increase until 36 weeks, then decline steadily thereafter.[71,72] The longer the time is between scans, the more accurate the sonographic estimate of interval weight gain will be. When two scans are performed within 1 week of each other, weight gain cannot be determined reliably, because weight prediction is too imprecise to detect small changes in growth. Furthermore, estimating weight too close to the time of the prior scan could raise unnecessary concern by a spurious finding that the fetus has grown subnormally or even lost weight. Thus there is little or no value in computing an estimated weight at the time of the second scan 1 week after the first. Instead, it is recommended that fetal weight gain only be assessed after an interval of at least 2 weeks' duration.[10,11]

When several examinations have been performed, fetal growth can be depicted graphically by means of a trend plot or growth curve. One form of growth curve plots the **estimated fetal weight versus gestational age,** with the curve for the fetus being examined superimposed on lines depicting the 1st, 10th, 50th, 90th, and 99th percentiles (Fig. 42.10A). An alternative mode of display plots the **estimated fetal weight percentile versus gestational age** (Fig. 42.10B). In this latter format, the graph for a normally growing fetus will be a horizontal line, indicating maintenance of a particular weight percentile throughout gestation. A down sloping line suggests subnormal growth rate.

Calculation of weight percentiles and plotting of growth curves are most easily accomplished by computer, using an obstetric ultrasound software package that performs these tasks.[100-102] Alternatively, similar results can be achieved by means of a calculator and manual plotting of data.

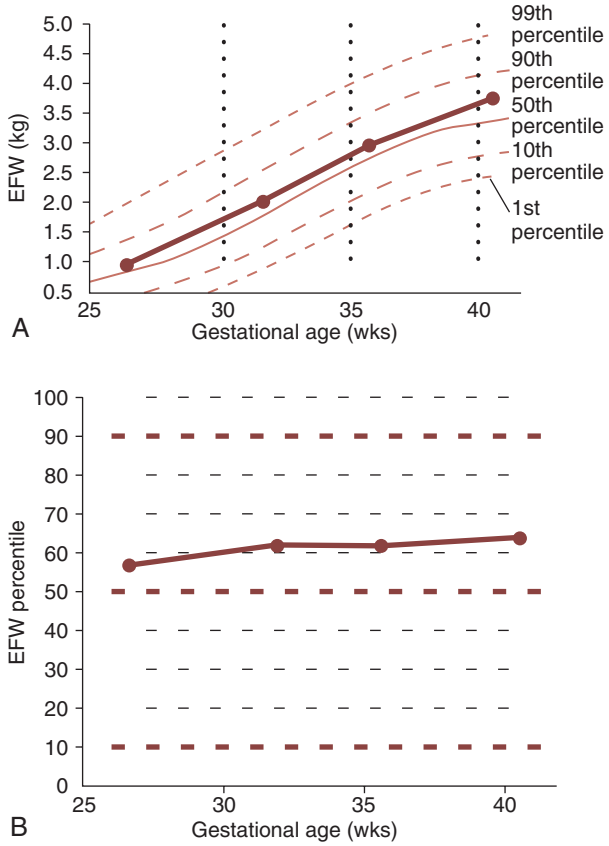

FIG. 42.10 Fetal Growth Curves. (A) Estimated fetal weight plotted against gestational age, superimposed on 1st, 10th, 50th, 90th, and 99th percentile curves. The fetus depicted here has a normal growth pattern, with estimated fetal weights between the 50th and 90th percentile over four sonograms. **(B)** Estimated fetal weight *(EFW)* percentile against gestational age.

FETAL GROWTH ABNORMALITIES

The Large Fetus

The **large-for-gestational-age** (LGA) neonate (or fetus) is defined as one whose weight is above the 90th percentile for gestational age.[71,103-105] **Macrosomia,** a related entity, is most often defined on the basis of a weight above 4000 g; other weight cutoffs (4100 g, 4500 g) are sometimes used.[74,76-80,106] These growth disturbances occur with different frequencies and are associated with different morbidities and mortalities in diabetic mothers as compared to the general population. Therefore these two patient populations are considered separately.

General Population

About 10% of all infants have birth weights above the 90th percentile for gestational age and are considered LGA infants. Of all newborns, 8% to 10% have birth weights over 4000 g and thus are classified as "macrosomic," and 2% weigh over 4500 g.[104,106-109] These rates, however, vary considerably among different patient subgroups, depending on presence or absence of risk factors. Risk factors for LGA and macrosomia include maternal obesity, history of a previous LGA infant, prolonged pregnancy (>40 weeks), excess pregnancy weight gain, multiparity, and advanced maternal age.[103,104,107,110-112]

Large fetuses have an increased incidence of perinatal morbidity and mortality, in large part because of obstetric complications. Shoulder dystocia, fractures, and facial and brachial plexus palsies occur more frequently as a result of traumatic delivery.[106,110,113,114] The incidence of perinatal asphyxia, meconium aspiration, neonatal hypoglycemia, and other metabolic complications is significantly increased in these pregnancies.[103,106,107,110]

The most straightforward approach to diagnosing fetal LGA and macrosomia is to use the estimated fetal weight computed from sonographic measurements. An estimated weight above the 90th percentile for gestational age suggests LGA, and a weight estimate above 4000 g suggests macrosomia. Although weight estimation is somewhat less accurate in large than in average-sized fetuses,[62,115] this approach has been demonstrated to be moderately good for diagnosing LGA and macrosomia. It has a **positive**

predictive value (PPV) of up to 51% for LGA and 67% for macrosomia. Other proposed sonographic parameters have lower sensitivity or lower PPV than the estimated fetal weight[62,103,106,116-124] (Table 42.11).

Diabetic Mothers

Fetuses of insulin-dependent and gestational diabetic mothers are exposed to high levels of glucose throughout pregnancy and, as a result, produce excess insulin. This leads to overgrowth of the fetal trunk and abdominal organs, while the head and brain grow at a normal rate.[104,105] Therefore these fetuses tend to have different body proportions than fetuses of nondiabetic mothers. Sonographic measurements of fetuses of diabetic mothers demonstrate accelerated growth of the fetal thorax and abdomen beginning between 28 and 32 weeks' gestation.[104,105,125]

An LGA weight occurs in 25% to 42% and macrosomia in 10% to 50% of infants of diabetic mothers.[104,105,126] As many as 12% of infants of mothers with diabetes weigh more than 4500 g at birth. Perinatal complications are more frequent in macrosomic fetuses of diabetic mothers than in those of nondiabetic mothers.[109,113,114,127,128] Shoulder dystocia, for example, occurs in 31% of macrosomic fetuses of diabetic mothers and only 3% to 10% of macrosomic fetuses of nondiabetic mothers.[110,113]

Many sonographic parameters, involving a variety of measurements, formulas, and ratios, have been proposed for diagnosing LGA and macrosomia in the fetus of the diabetic mother[117,129-131] (Table 42.12). As a group, these have higher sensitivities and PPVs than sonographic criteria in the general population, in part because of the higher prevalence of large fetuses in diabetic mothers.

As in the general population, the most straightforward approach to diagnosing LGA and macrosomia in the fetuses of diabetic mothers is by means of the sonographically estimated fetal weight.[68,117,129,132,133] A fetus whose estimated weight falls above the 90th percentile for gestational age has a 74% likelihood of being LGA, versus 19% if the estimated weight lies below the 90th percentile.[129] A weight estimate above 4000 g is associated with a 77% chance of macrosomia, and one above 4500 g with an 86% chance. The chance of macrosomia is only 16% when the weight estimate is less than 4000 g.[68] Thus, if vaginal delivery is believed to be contraindicated for the macrosomic fetuses of diabetic mothers, the estimated fetal weight should be considered when selecting the route of delivery.

The Small-for-Gestational-Age Fetus and Fetal Growth Restriction

Fetuses are termed *small for gestational age* (SGA) if their estimated weights are below the 10th percentile for gestational age. SGA fetuses are a heterogeneous group and can be subdivided into constitutionally small fetuses (e.g., those with small parents) and fetuses whose small size is due to a pathologic process.

Small-for-Gestational-Age Fetuses: Causes

CONSTITUTIONALLY SMALL
PATHOLOGICALLY SMALL
Placenta Mediated
Primary placental
Maternal

Fetal
Aneuploidy
Malformations
Infections

TABLE 42.11 Sonographic Criteria for Large-for-Gestational Age (LGA) and Macrosomia in the General Population: Performance Characteristics

	(%)		PREDICTIVE VALUES (%)[a]	
	Sensitivity	Specificity	Positive	Negative
CRITERIA TO PREDICT LGA[a]				
Elevated AD-BPD[115]	46	79	19	93
Low FL/AC[103,115]	24-75	44-93	13-26	92-94
Elevated AFV[119,123]	12-17	92-98	19-35	91
Elevated ponderal index[103,115]	13-15	85-98	13-36	91-94
High EFW[103,123]	20-74	93-96	6-51	88-94
Elevated growth score[103]	14	91	10	90
Elevated AFV, high EFW[123]	11	99	54	99
CRITERIA TO PREDICT MACROSOMIA				
Elevated FL[121]	24	96	52	88
Elevated AC[121]	53	94	63	89
High EFW[63,124,121]	11-65	89-96	38-67	83-91
Elevated BPD[121]	29	98	71	92

[a]Predictive values for criteria for LGA computed using Bayes' theorem,112 assuming an LGA prevalence rate of 10%.
AC, Abdominal circumference; *AD,* abdominal diameter; *AFV,* amniotic fluid volume; *BPD,* biparietal diameter; *EFW,* estimated fetal weight; *FL,* femur length; *FL/AC,* femur length to abdominal circumference ratio.
With permission from Doubilet PM, Benson CB. Fetal growth disturbances. Semin Roentgenol. 1990;25(4):309-316.[117]

As a group, SGA fetuses have a poor prognosis, with increased perinatal morbidity and mortality rates. Their mortality rate is four to eight times that of non-SGA fetuses.[134-136] Half of surviving SGA fetuses have serious short- or long-term morbidity, including meconium aspiration, pneumonia, and metabolic disorders.[134,137-139] The risk, however, is dependent on the cause of the small size. Constitutionally small fetuses carry no elevated risk, unlike those who are small because of a pathologic condition. Furthermore, the potential to improve outcome by appropriate management of pathologically small fetuses varies depending on causation. For example, when the small size is caused by placental insufficiency, early delivery may improve outcome, but this intervention is unlikely to affect outcome in chromosomally abnormal fetuses.

The term *fetal growth restriction* (FGR), also called *intrauterine growth restriction,* is used differently by different authors. Some use FGR and SGA synonymously, considering all fetuses below the 10th percentile for gestational age to be growth restricted. Others use FGR to refer to pathologically small fetuses.

Terminology aside, determination of the cause(s) of small fetal size is often difficult, so that all SGA fetuses should be classified as suspected FGR.[140] The approach to SGA or FGR involves three steps: (1) diagnosis: identify small fetuses; (2) classification: attempt to determine the cause of the small size; (3) management: institute monitoring and decide on timing of delivery.

The most direct approach to identifying SGA fetuses is to diagnose SGA if the estimated fetal weight falls below the 10th percentile for the best estimate of gestational age. Several other criteria for diagnosing SGA or FGR have been proposed, including sonographic measurements and ratios,[141] as well as a multiparameter scoring system.[142,143] None of the individual parameters has a high PPV,[141] and the performance characteristics of the scoring system[143] are not good enough to make up for its complexity and cumbersome nature. Thus the straightforward approach of using the estimated fetal weight percentile is the preferred method for diagnosing SGA fetuses.

Once SGA has been diagnosed, an attempt should be made to determine its cause through evaluation of both the mother and the fetus. Maternal assessment should include physical examination and blood tests, directed toward diagnosis of **hypertension, renal disease,** and other maternal conditions that can cause FGR. Fetal assessment begins with a careful sonographic examination, looking especially for findings suggestive of a **chromosomal** or **viral** cause (e.g., holoprosencephaly, clenched hands, rocker-bottom feet, intracranial calcifications). If such a finding is present, amniocentesis or umbilical blood sampling can confirm the diagnosis of a chromosomal abnormality. A viral cause of FGR may also be diagnosed by these procedures, in some cases.[144]

Growth-restricted fetuses, other than those with a lethal condition, such as **trisomy 13 or 18,** should be carefully monitored for the remainder of the pregnancy. The monitoring is typically performed at weekly or semiweekly intervals. Sonographic features to be followed include **amniotic fluid volume, biophysical profile score, estimated fetal weight percentile,** and **fetal Doppler.** A worsening trend in one or more of these features should prompt consideration of early delivery.

ASSESSMENT OF FETAL WELL-BEING

It has been shown that when a fetus is suspected of being growth restricted or having another condition that could affect the

TABLE 42.12 Sonographic Criteria for Large-for-Gestational Age (LGA) and Macrosomia in Diabetic Mothers: Performance Characteristics

	(%)		PREDICTIVE VALUES (%)	
	Sensitivity	**Specificity**	**Positive**	**Negative**
CRITERIA TO PREDICT LGA[a]				
Elevated HC[129]	50	80	64	70
Elevated AC/BPD[130]	83	60	71	75
High EFW[129]	78	78	74	81
Elevated BPD[129]	13	86	75	57
Elevated AC[105,127,129]	71-88	81-85	56-78	81-96
Elevated AC growth[105]	84	85	79	89
Low FL/AC[105,130]	58-79	75-80	68-83	75-76
Elevated AC, high EFW[129]	72	71	89	89
CRITERIA TO PREDICT MACROSOMIA				
Elevated AC[127]	84	78	41	96
Low FL/AC[131]	48-64	60-74	36-42	80-83
Elevated TD-BPD[126]	87	72	61	92
High EFW[68]	48	95	77	84

[a]Predicted values for criteria for LGA computed using Bayes theorem,[112] assuming an LGA prevalence rate of 10%.
AC, Abdominal circumference; *AC/BPD,* abdominal circumference to biparietal diameter ratio; *BPD,* biparietal diameter; *EFW,* estimated fetal weight; *FL,* femur length; *FL/AC,* femur length to abdominal circumference ratio; *HC,* head circumference; *TD,* thoracic diameter.
With permission from Doubilet PM, Benson CB. Fetal growth disturbances. Semin Roentgenol. 1990;25(4):309-316.[117]

Fetal and Placental Risk Factors Associated With Fetal Growth Restriction

FETAL FACTORS
Chromosomal Abnormalities
Trisomy 13, 18, 21
Monosomy (45,XO)
Deletions
Uniparental disomy
Confined placental mosaicism

Congenital Malformations
Absence of fetal pancreas
Anencephaly
Diaphragmatic hernia
Omphalocele
Gastroschisis
Renal agenesis/dysplasia
Multiple malformations

Multiple Gestations
Monochorionic twins
One fetus with malformations
Twin-to-twin transfusion
Discordant twins
Triplets

PLACENTAL FACTORS
Abnormal trophoblastic invasion
Multiple placental infarctions (chronic abruption)
Umbilical-placental vascular anomalies
Abnormal cord insertion (velamentous cord insertion)
Placenta previa
Circumvallate placenta
Chorioangiomata

With permission from Lin C. Current concepts of fetal growth restriction: part I. Causes, classification, and pathophysiology. Obstet Gynecol. 1998;92(6):1044-1055.[135]

Maternal Risk Factors Associated With Fetal Growth Restriction

GENETIC/CONSTITUTIONAL
NUTRITION/STARVATION
Inflammatory bowel disease
Ileojejunal bypass
Chronic pancreatitis
Low prepregnancy weight
Poor pregnancy weight gain, second and third trimesters

HYPOXIC
Severe lung disease
Cyanotic heart disease
Sickle cell anemia

VASCULAR
Chronic hypertension
Preeclampsia
Collagen vascular disease
Type 1 diabetes mellitus

RENAL
Glomerulonephritis
Lipoid nephritis
Arteriolar nephrosclerosis
Renal transplantation

ANTIPHOSPHOLIPID ANTIBODIES
ENVIRONMENT AND DRUGS
High altitude
Emotional stress
Physical stress
Cigarette smoking
Alcohol abuse
Substance abuse (heroin, cocaine)
Therapeutic drugs
Antimetabolites
Anticonvulsants
Anticoagulants

POOR OBSTETRIC HISTORY
Previous stillbirths
Recurrent aborters
Previous birth of growth-restricted fetus
Previous preterm births

With permission from Lin C. Current concepts of fetal growth restriction: part I. Causes, classification, and pathophysiology. Obstet Gynecol. 1998;92(6):1044-1055.[135]

oxygenation or nutrition to the fetus, antenatal surveillance can improve the outcome for these fetuses. Surveillance of such a fetus includes serial ultrasounds to monitor fetal growth, perform biophysical profiles (BPPs), and measure Doppler parameters. Nonstress tests (NSTs) are also used to monitor fetal well-being. The nature and frequency of monitoring tests depends on the apparent severity of fetal compromise.[10,11]

Biophysical Profile

The BPP, introduced in the 1980s, is a noninvasive test of fetal well-being based on four ultrasound parameters and the NST. The four ultrasound parameters are (1) fetal movement, (2) fetal tone, (3) fetal breathing movements, and (4) amniotic fluid volume (Table 42.13, Fig. 42.11, Videos 42.2 and 42.3). Each parameter receives 2 points if the fetus meets criteria and 0 points if it does not. Thus a perfect score for the ultrasound portion of the BPP is 8 out of 8, with 2 points given for each of the four parameters.[145,146] The parameters were chosen to assess both the acute and the chronic state of the fetus, with acute parameters being fetal tone, movement, and breathing movements, and amniotic fluid volume being a chronic marker of fetal well-being.[145] Studies have shown that the BPP is reliable and reproducible, and that scores of 8 out of 8 are associated with a low rate of stillbirths and low rate of fetal asphyxia within 1 week of testing.[11,145,147-150] Lower scores, those below 6 out of 8, are associated with increased risk for fetal asphyxia, low cord pH, cerebral palsy, and stillbirth. The lower the score is, the higher the risk of perinatal compromise will be.[11,145,148]

The BPP exam is performed within 30 minutes. If a fetus does not meet criteria for a parameter within the 30-minute time period, that parameter is given a score of 0. The BPP score

TABLE 42.13 Biophysical Profile Parameters for 30-Minute Ultrasound Examination

Parameter	2 Points Given	0 Points Given
Fetal movement	At least 3 discrete body or limb movements	Less than 3 discrete body or limb movements
Fetal tone	At least 1 episode of extension and flexion of extremity or spine	No episode of extension and flexion of extremity or spine
Fetal breathing movement	At least 30 seconds of continuous, rhythmic breathing movements	No episode of continuous breathing movement for 30 seconds
Amniotic fluid volume	Single pocket at least 1 cm across and 2 cm in vertical	No pocket 1 cm across and 2 cm in vertical

With permission from Manning FA, Platt LD, Sipos L. Antepartum fetal evaluation: development of a fetal biophysical profile. Am J Obstet Gynecol. 1980;136(6):787-795.[146]

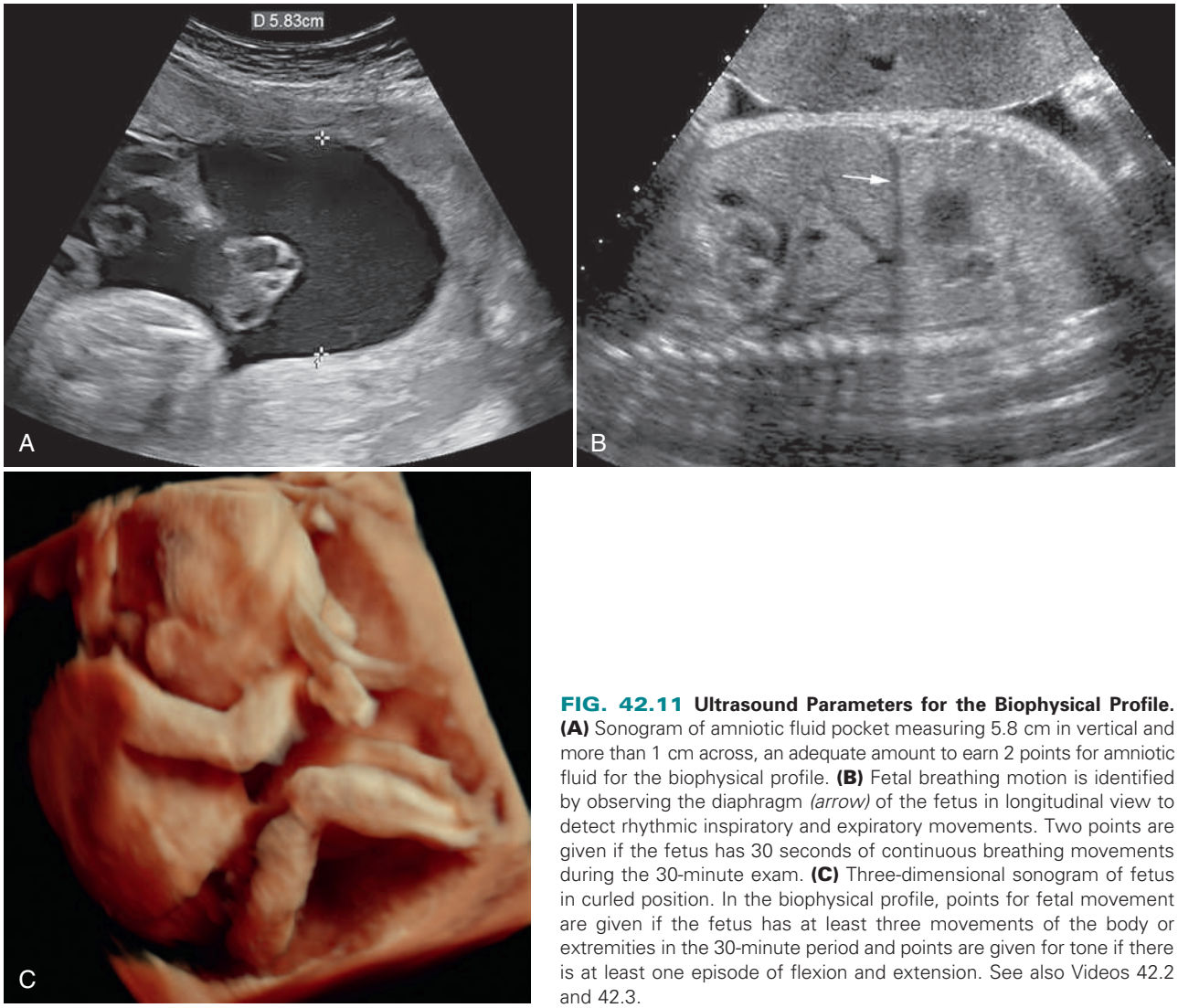

FIG. 42.11 Ultrasound Parameters for the Biophysical Profile. **(A)** Sonogram of amniotic fluid pocket measuring 5.8 cm in vertical and more than 1 cm across, an adequate amount to earn 2 points for amniotic fluid for the biophysical profile. **(B)** Fetal breathing motion is identified by observing the diaphragm *(arrow)* of the fetus in longitudinal view to detect rhythmic inspiratory and expiratory movements. Two points are given if the fetus has 30 seconds of continuous breathing movements during the 30-minute exam. **(C)** Three-dimensional sonogram of fetus in curled position. In the biophysical profile, points for fetal movement are given if the fetus has at least three movements of the body or extremities in the 30-minute period and points are given for tone if there is at least one episode of flexion and extension. See also Videos 42.2 and 42.3.

is reported as the number of points earned over the total for the study, which is 8 for an ultrasound BPP without NST. When a score of less than 8 out of 8 is given, the parameter or parameters for which no points were given should also be reported. For example, if a fetus has normal amniotic fluid volume with a pocket of fluid more than 2 cm vertical and 1 cm wide, demonstrates adequate fetal movement and tone to obtain 2 points for each, but does not demonstrate fetal breathing movement during the 30-minute exam, that BPP would be reported as 6 out of 8 with 2 points deducted for lack of fetal breathing movement. In

most cases, the BPP does not require a full 30 minutes of sonographic evaluation, because, given the short sleep cycles of the fetus, it typically meets criteria in less than that time, sometimes as short as 5 minutes.[145]

The BPP as a test of fetal well-being has several limitations. First, the test is less reliable in the severely premature fetus because of lack of brain maturity and should not be administered before 24 weeks' gestation.[145] Second, the biophysical state of the fetus is affected by administration of corticosteroids, which may cause depression of fetal breathing and movement for a few days after treatment.[151-155] This latter limitation must be kept in mind when using the BPP to guide management decisions shortly after steroid treatment.[145]

Fetal Doppler

Doppler parameters of a number of vessels, including the umbilical artery, umbilical vein, ductus venosus, middle cerebral artery, aortic isthmus, and uterine artery in the mother, have been studied to determine if Doppler parameters can be used to predict outcome and direct management.[140,156-160] Among vessels studied, umbilical artery Doppler has been shown to be the most useful for monitoring fetuses at risk for compromise, particularly those with suspected FGR.[11,140,148,156,160,161] When umbilical artery Doppler is incorporated into surveillance of fetuses with suspected growth restriction, overall outcome is improved, with fewer unnecessary interventions, inductions of labor, cesarean deliveries, and perinatal deaths.[10,148,160-162] Although umbilical artery Doppler has been shown to improve outcome in fetuses with suspected growth restriction and in mothers with preeclampsia or hypertension, routine screening with umbilical artery Doppler in low-risk pregnancies is not recommended, because it has not resulted in improved outcome in this patient population.[140,161]

Although some advocate adding middle cerebral artery and/or ductus venosus Doppler to the evaluation of fetuses with suspected growth restriction and abnormal umbilical artery Doppler,[161,163-165] studies have not yet shown improved outcomes when these additional Doppler studies are performed.[10,11,140,148,160]

Umbilical Artery Doppler

Umbilical artery Doppler is used to assess fetal well-being after 24 weeks' gestation for those fetuses with suspected growth restriction or in mothers with preeclampsia or hypertension.[140,148,156,160,161] To obtain a waveform, the Doppler gate is placed on a free loop of umbilical cord, away from the placental and fetal cord insertions and in the absence of fetal breathing movements. The ratio of peak systolic to end-diastolic velocity is calculated (S/D ratio). Flow in the umbilical artery is normally low resistance, with an S/D ratio of less than 3.5 up to 28 weeks' gestation and less than 3.0 thereafter[166] (Fig. 42.12A). With significant placental dysfunction, resistance in the placenta increases and flow in the umbilical artery demonstrates diminished diastolic flow, with an S/D ratio above the normal range (Fig. 42.12B). In such cases, the risk of fetal compromise and perinatal mortality is increased. The risk of fetal compromise is increased further when end-diastolic flow in the umbilical artery is absent (Fig. 42.12C), and is highest when end-diastolic flow is reversed (Fig. 42.12D). In particular, the risk of perinatal mortality within 1 week of diagnosing reversed end-diastolic flow in the umbilical artery of a growth-restricted fetus is so high, close to 50%, that delivery is generally recommended, regardless of the gestational age.[10,11,140,156,167-170]

Ductus Venosus Doppler

The ductus venosus is the short vessel connecting the umbilical vein near its junction with the left portal vein directly to the inferior vena cava. This allows shunting of umbilical venous blood directly to the heart, bypassing the liver. Normal flow in the ductus venosus is antegrade, toward the heart, throughout the cardiac cycle (Fig. 42.13A). Studies have shown that absent or reversed flow (Fig. 42.13B) in the ductus venosus at any time during the cardiac cycle is a sign of cardiovascular instability and is associated with increased morbidity and mortality rates in growth-restricted fetuses.[10,11,140,148,150,160] However, these same studies demonstrate poor sensitivities and specificities, and, therefore, the value of ductus venosus Doppler for directing the management of growth-restricted fetuses has not been established.[11,140,148,160]

Middle Cerebral Artery Doppler

Doppler of the middle cerebral artery (MCA) provides information about flow resistance in the fetal brain. For optimal interrogation of the MCA, the Doppler gate should be placed on the middle cerebral artery in the proximal third of the vessel, close to its origin from the circle of Willis. If peak systolic velocity is being measured, the Doppler angle must be zero or angle correction must be used. Normally, flow in the MCA is high resistance, with low diastolic flow (Fig. 42.14A). In the compromised fetus, vessels in the brain vasodilate, a response called "brain sparing," leading to decreased resistance to blood flow and increased diastolic flow in the MCA. This "brain-sparing" effect can be measured by calculating the resistive index (RI) of the MCA waveform. The RI is considered abnormal when it is less than the fifth percentile for gestational age[148,159,160] (Fig. 42.14B). An abnormal RI in the MCA is associated with perinatal mortality and morbidity, including acidosis at birth, low 5-minute Apgars, and neonatal intracranial hemorrhage.[148,159] However, the published studies are inconsistent, and an abnormal MCA Doppler is a poor predictor of adverse outcome in preterm infants. There is no convincing evidence that the use of MCA Doppler for guiding management of growth-restricted fetuses improves outcome.[10,148,160,171]

Some have advocated using the MCA Doppler in conjunction with umbilical artery Doppler to improve the identification of fetuses at risk for poor outcome. In particular, some have recommended comparing the RI or pulsatility index (PI) in the MCA to the corresponding RI or PI in the umbilical artery in a ratio called the "cerebroplacental ratio" (Fig. 42.15):

$$\text{Cerebroplacental ratio} = \frac{\text{Middle cerebral artery pulsatility index}}{\text{Umbilical artery pulsatility index}}$$

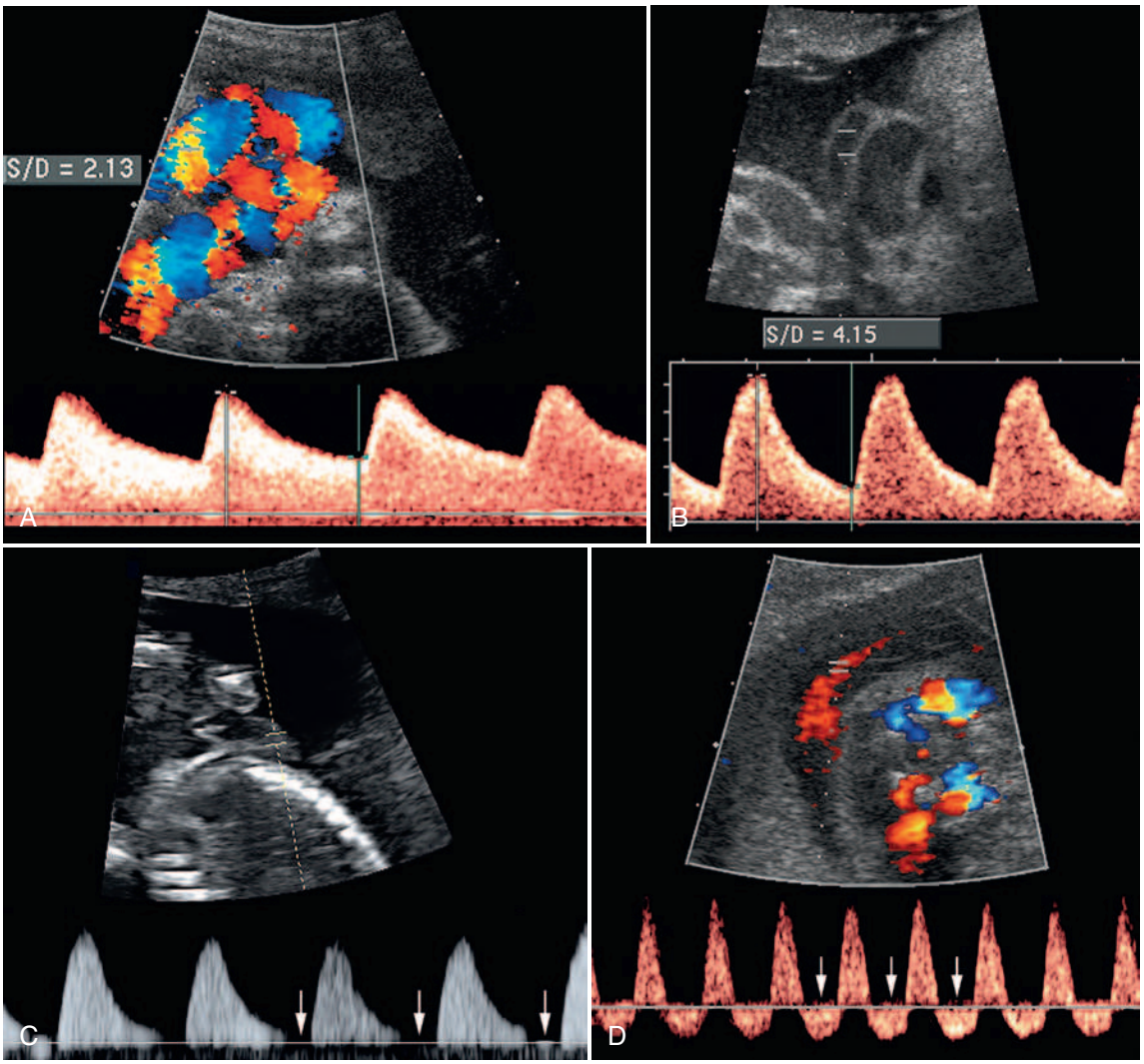

FIG. 42.12 Umbilical Artery Doppler. (A) Color and spectral Doppler of umbilical artery demonstrating normal flow with systolic to diastolic ratio *(S/D)* normal at 2.13. **(B)** Sonogram of term fetus showing Doppler gate on umbilical artery and spectral waveform with elevated S/D of 4.15 due to diminished diastolic flow. **(C)** Sonogram showing Doppler gate on umbilical artery and spectral waveform below demonstrating absent end-diastolic flow *(arrows)*. **(D)** Color and spectral Doppler demonstrating reversed end-diastolic flow *(arrows)*.

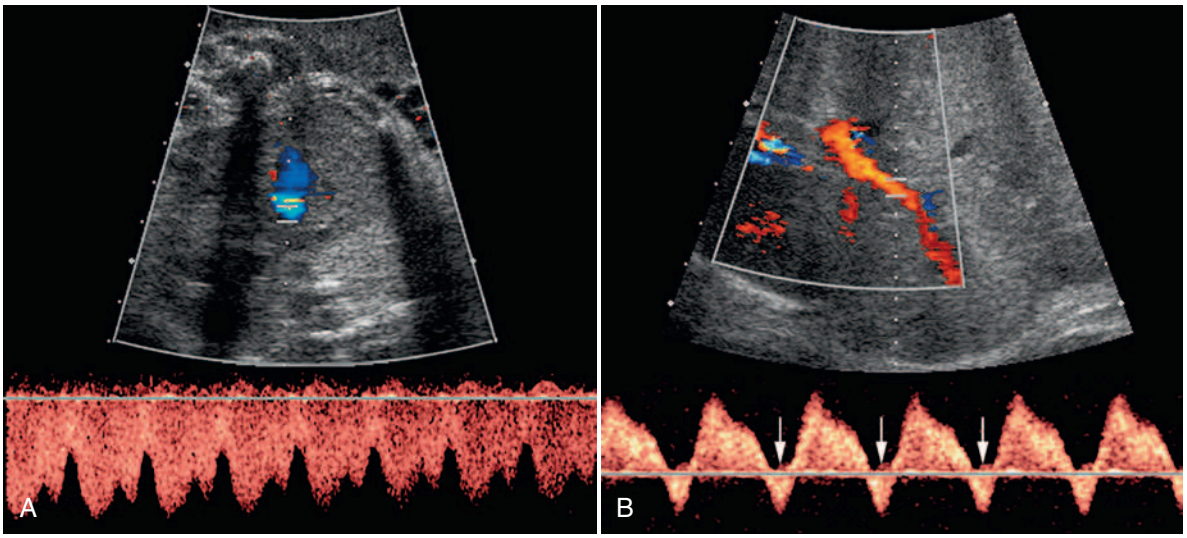

FIG. 42.13 Ductus Venosus Doppler. (A) Color and spectral Doppler of the ductus venosus demonstrating normal flow, toward the heart throughout the cardiac cycle. **(B)** Color and spectral Doppler of the ductus venosus demonstrating reversed flow *(arrows)* during part of the cardiac cycle, an abnormal finding.

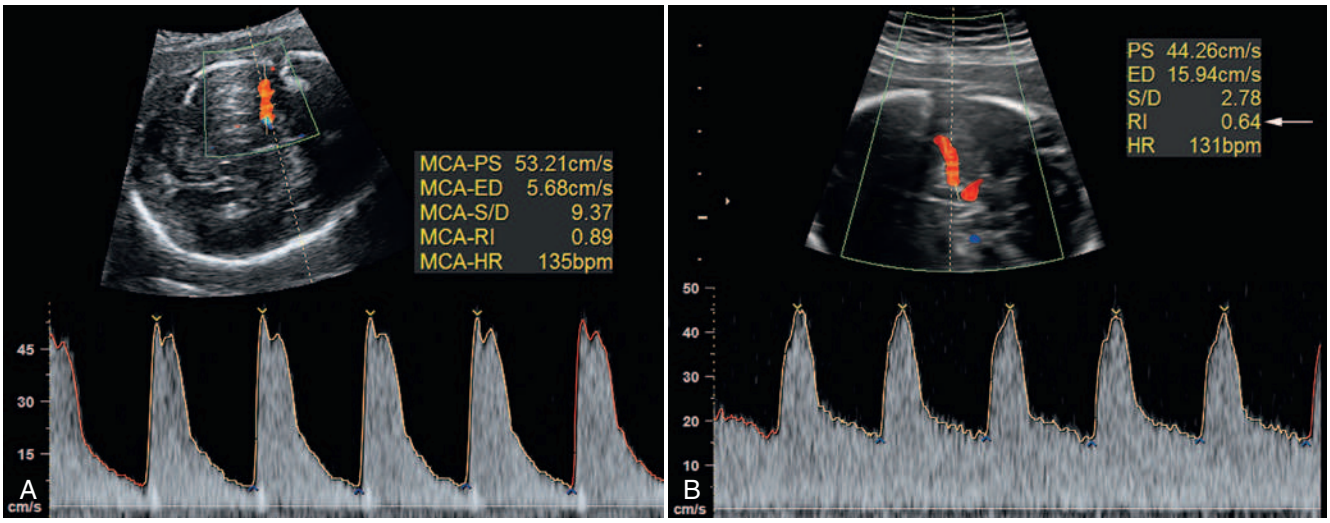

FIG. 42.14 Middle Cerebral Artery Doppler. (A) Color and spectral Doppler of normal fetal middle cerebral artery with normal resistive index *(RI)* of 0.89. **(B)** Color and spectral Doppler of abnormal fetal middle cerebral artery demonstrating abnormally low resistive index *(RI)* of 0.64 *(arrow)* as a result of elevated diastolic flow.

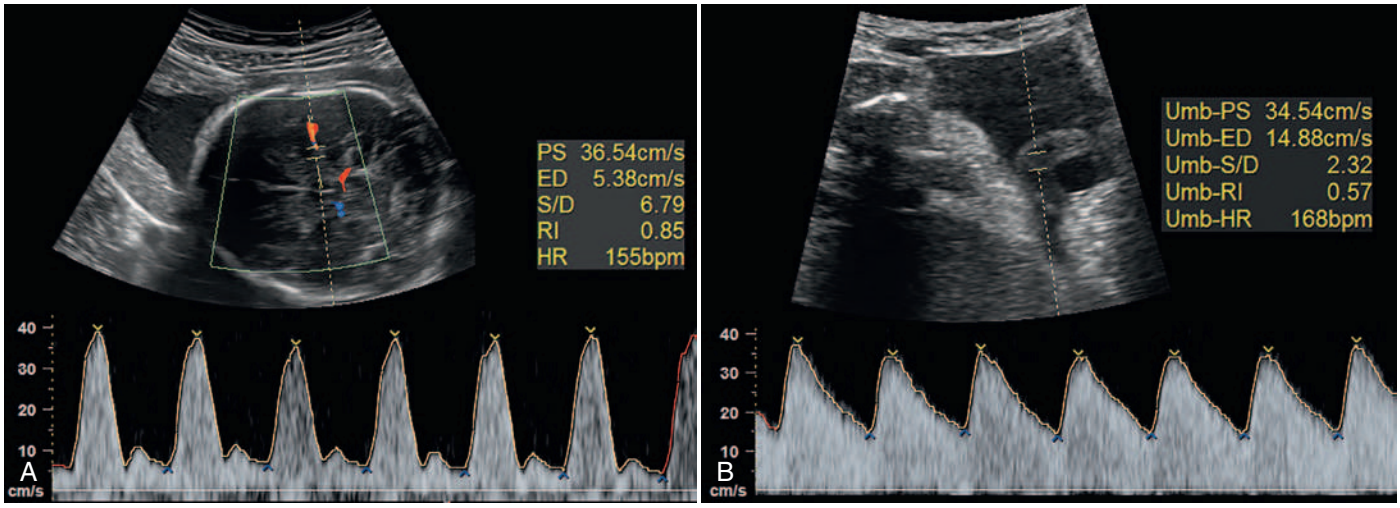

FIG. 42.15 Cerebroplacental Ratio. Normal cerebroplacental ratio of 1.49, calculated by taking the ratio of **A,** the resistive index in the middle cerebral artery (0.85) to **B,** the resistive index in the umbilical artery (0.57).

The cerebroplacental ratio is abnormal if it is less than 1.0.[161,163] This ratio takes into account the decreased MCA resistance with "brain sparing" and vasodilation and increased umbilical artery resistance from increased placental resistance associated with placental dysfunction. An abnormal cerebroplacental ratio is associated with increased fetal distress in labor, low cord pH, and high neonatal intensive care admissions.[10,140,159,160,163,172] However, the utility of this ratio in the surveillance of the growth-restricted fetus has not been well established.

Summary of Fetal Doppler

To date, the only Doppler surveillance study that has been shown to improve outcome in growth-restricted fetuses is umbilical artery Doppler. Although ductus venosus and MCA Doppler have been shown to demonstrate changes with fetal compromise, their use in guiding management of high-risk pregnancies with FGR has not been proven.

REFERENCES

1. Filly RA, Golbus MS, Carey JC, Hall JG. Short-limbed dwarfism: ultrasonographic diagnosis by mensuration of fetal femoral length. Radiology. 1981;138(3):653-656.
2. Chervenak FA, Rosenberg J, Brightman RC, et al. A prospective study of the accuracy of ultrasound in predicting fetal microcephaly. Obstet Gynecol. 1987;69(6):908-910.
3. ACOG Committee on Practice Bulletins. ACOG Practice Bulletin No. 77: screening for fetal chromosomal abnormalities. Obstet Gynecol. 2007;109(1):217-227.
4. Bianchi DW, Platt LD, Goldberg JD, et al. Genome-wide fetal aneuploidy detection by maternal plasma DNA sequencing. Obstet Gynecol. 2012;119(5):890-901.
5. Bowerman RA. Sonography of fetal midgut herniation: normal size criteria and correlation with crown-rump length. J Ultrasound Med. 1993;12(5):251-254.
6. Wald NJ, Cuckle HS, Densem JW, et al. Maternal serum screening for Down's syndrome in early pregnancy. BMJ. 1988;297(6653):883-887.
7. Osathanondh R, Canick JA, Abell KB, et al. Second trimester screening for trisomy 21. Lancet. 1989;2(8653):52.

8. Canick JA, Knight GJ, Palomak GE, et al. Low second trimester maternal serum unconjugated oestriol in pregnancies with Down's syndrome. Br J Obstet Gynaecol. 1988;95(4):330-333.
9. American Institute of Ultrasound in Medicine. AIUM practice guideline for the performance of obstetric ultrasound examinations. J Ultrasound Med. 2013;32(6):1083-1101.
10. Resnik R. Fetal growth restriction: evaluation and management. UpToDate. 2015.
11. Thompson JL, Kuller JA, Rhee EH. Antenatal surveillance of fetal growth restriction. Obstet Gynecol Surv. 2012;67(9):554-565.
12. Wegienka G, Baird DD. A comparison of recalled date of last menstrual period with prospectively recorded dates. J Womens Health (Larchmt). 2005;14(3):248-252.
13. Savitz D, Terry Jr J, Dole N, et al. Comparison of pregnancy dating by last menstrual period, ultrasound, or their combination. Am J Obstet Gynecol. 2002;187(6):1660-1666.
14. Campbell S, Warsof SL, Little D, Cooper DJ. Routine ultrasound screening for the prediction of gestational age. Obstet Gynecol. 1985;65(5): 613-620.
15. Verburg BO, Steegers EAP, De Ridder M, et al. New charts for ultrasound dating of pregnancy and assessment of fetal growth: longitudinal data from a population-based cohort study. Ultrasound Obstet Gynecol. 2008;31(4): 388-396.
16. American College of Obstetrics and Gynecologists (ACOG). Committee opinion no 611: method for estimating due date. Obstet Gynecol. 2014;124(4):863-866.
17. Caughey AB, Nicholson JM, Washington AE. First- vs second-trimester ultrasound: the effect on pregnancy dating and perinatal outcomes. Am J Obstet Gynecol. 2008;198(6):703.e1-703.e6.
18. Kalish RB, Thaler HT, Chasen ST, et al. First- and second-trimester ultrasound assessment of gestational age. Am J Obstet Gynecol. 2004;191(3): 975-978.
19. Campbell S, Wilkin D. Ultrasonic measurement of fetal abdomen circumference in the estimation of fetal weight. Br J Obstet Gynaecol. 1975;82(9):689-697.
20. Higginbottom J, Slater J, Porter G, Whitfield CR. Estimation of fetal weight from ultrasonic measurement of trunk circumference. Br J Obstet Gynaecol. 1975;82(9):698-701.
21. Warsof SL, Gohari P, Berkowitz RL, Hobbins JC. The estimation of fetal weight by computer-assisted analysis. Am J Obstet Gynecol. 1977;128(8): 881-892.
22. Shepard MJ, Richards VA, Berkowitz RL, et al. An evaluation of two equations for predicting fetal weight by ultrasound. Am J Obstet Gynecol. 1982;142(1):47-54.
23. Thurnau GR, Tamura RK, Sabbagha R, et al. A simple estimated fetal weight equation based on real-time ultrasound measurements of fetuses less than thirty-four weeks' gestation. Am J Obstet Gynecol. 1983;145(5):557-561.
24. Jordaan HV. Estimation of fetal weight by ultrasound. J Clin Ultrasound. 1983;11(2):59-66.
25. Hadlock FP, Deter RL, Harrist RB, Park SK. Estimating fetal age: computer-assisted analysis of multiple fetal growth parameters. Radiology. 1984;152(2): 497-501.
26. Hadlock FP, Harrist RB, Sharman RS, et al. Estimation of fetal weight with the use of head, body, and femur measurements—a prospective study. Am J Obstet Gynecol. 1985;151(3):333-337.
27. Birnholz JC. An algorithmic approach to accurate ultrasonic fetal weight estimation. Invest Radiol. 1986;21(7):571-576.
28. Vintzileos AM, Campbell WA, Rodis JF, et al. Fetal weight estimation formulas with head, abdominal, femur, and thigh circumference measurements. Am J Obstet Gynecol. 1987;157(2):410-414.
29. Doubilet PM, Benson CB. First, do no harm… To early pregnancies. J Ultrasound Med. 2010;29(5):685-689.
30. Bradley WG, Fiske CE, Filly RA. The double sac sign of early intrauterine pregnancy: use in exclusion of ectopic pregnancy. Radiology. 1982;143(1): 223-226.
31. Bree RL, Edwards M, Bohm-Velez M, et al. Transvaginal sonography in the evaluation of normal early pregnancy: correlation with HCG level. AJR Am J Roentgenol. 1989;153(1):75-79.
32. Doubilet PM, Benson CB. Double sac sign and intradecidual sign in early pregnancy: interobserver reliability and frequency of occurrence. J Ultrasound Med. 2013;32(7):1207-1214.
33. Daya S, Woods S, Ward S, et al. Early pregnancy assessment with transvaginal ultrasound scanning. CMAJ. 1991;144(4):441-446.
34. Jain KA, Hamper UM, Sanders RC. Comparison of transvaginal and transabdominal sonography in the detection of early pregnancy and its complications. AJR Am J Roentgenol. 1988;151(6):1139-1143.
35. Robinson HP, Fleming JE. A critical evaluation of sonar "crown-rump length" measurements. Br J Obstet Gynaecol. 1975;82(9):702-710.
36. MacGregor SN, Tamura RK, Sabbagha RE, et al. Underestimation of gestational age by conventional crown-rump length dating curves. Obstet Gynecol. 1987;70(3 Pt 1):344-348.
37. Moore KL, Persaud TVN, Torchia MG. The developing human: clinically oriented embryology. 9th ed. Philadelphia: Saunders; 2013.
38. Ioannou C, Sarris I, Hoch L, et al. Standardisation of crown-rump length measurement. Br J Obstet Gynaecol. 2013;120:38-41.
39. Doubilet PM. Should a first trimester dating scan be routine for all pregnancies? Semin Perinatol. 2013;37(5):307-309.
40. Kurtz AB, Wapner RJ, Kurtz RJ, et al. Analysis of biparietal diameter as an accurate indicator of gestational age. J Clin Ultrasound. 1980;8(4): 319-326.
41. Doubilet PM, Greenes RA. Improved prediction of gestational age from fetal head measurements. AJR Am J Roentgenol. 1984;142(4):797-800.
42. Law RG, MacRae KD. Head circumference as an index of fetal age. J Ultrasound Med. 1982;1(7):281-288.
43. Hadlock FP, Deter RL, Harrist RB, Park SK. Fetal abdominal circumference as a predictor of menstrual age. AJR Am J Roentgenol. 1982;139(2): 367-370.
44. Doubilet PM, Benson CB. Improved prediction of gestational age in the late third trimester. J Ultrasound Med. 1993;12(11):647-653.
45. Jeanty P, Rodesch F, Delbeke D, Dumont JE. Estimation of gestational age from measurements of fetal long bones. J Ultrasound Med. 1984; 3(2):75-79.
46. Honarvar M, Allahyari M, Dehbashi S. Assessment of gestational age based on ultrasonic femur length after the first trimester: a simple mathematical correlation between gestational age (GA) and femur length (FL). Int J Gynaecol Obstet. 2000;70(3):335-340.
47. Hadlock FP, Deter RL, Harrist RB, Park SK. Computer assisted analysis of fetal age in the third trimester using multiple fetal growth parameters. J Clin Ultrasound. 1983;11(6):313-316.
48. Hadlock FP, Deter RL, Harrist RB, Park SK. Fetal biparietal diameter: rational choice of plane of section for sonographic measurement. AJR Am J Roentgenol. 1982;138(5):871-874.
49. Papageorghiou AT, Sarris I, Ioannou C, et al. Ultrasound methodology used to construct the fetal growth standards in the INTERGROWTH-21st Project. Br J Obstet Gynaecol. 2013;120:27-32.
50. Hadlock FP, Kent WR, Loyd JL, et al. An evaluation of two methods for measuring fetal head and body circumferences. J Ultrasound Med. 1982;1(9):359-360.
51. Goldstein RB, Filly RA, Simpson G. Pitfalls in femur length measurements. J Ultrasound Med. 1987;6(4):203-207.
52. Smulian JC, Ranzini AC, Ananth CV, et al. Comparison of three sonographic circumference measurement techniques to predict birth weight. Obstet Gynecol. 1999;93(5 Pt 1):692-696.
53. Doubilet PM. Should a first trimester dating scan be routine for all pregnancies? Semin Perinatol. 2013;37(5):307-309.
54. Benson CB, Doubilet PM. Sonographic prediction of gestational age: accuracy of second- and third-trimester fetal measurements. AJR Am J Roentgenol. 1991;157(6):1275-1277.
55. Johnsen SL, Rasmussen S, Sollien R, Kiserud T. Fetal age assessment based on femur length at 10-25 weeks of gestation, and reference ranges for femur length to head circumference ratios. Acta Obstet Gynecol Scand. 2005;84(8):725-733.
56. Hadlock FP, Harrist RB, Carpenter RJ, et al. Sonographic estimation of fetal weight. The value of femur length in addition to head and abdomen measurements. Radiology. 1984;150(2):535-540.

57. Lee W, Deter RL, Ebersole JD, et al. Birth weight prediction by three-dimensional ultrasonography: fractional limb volume. J Ultrasound Med. 2001;20(12):1283-1292.
58. Song T. Fetal weight prediction by thigh volume measurement with three-dimensional ultrasonography. Obstet Gynecol. 2000;96(2): 157-161.
59. Schild RL, Fimmers R, Hansmann M. Fetal weight estimation by three-dimensional ultrasound. Ultrasound Obstet Gynecol. 2000;16(5): 445-452.
60. Uotila J, Dastidar P, Heinonen T, et al. Magnetic resonance imaging compared to ultrasonography in fetal weight and volume estimation in diabetic and normal pregnancy. Acta Obstet Gynecol Scand. 2000;79(4):255-259.
61. Hatab MR, Zaretsky MV, Alexander JM, Twickler DM. Comparison of fetal biometric values with sonographic and 3D reconstruction MRI in term gestations. AJR Am J Roentgenol. 2008;191(2):340-345.
62. Benacerraf BR, Gelman R, Frigoletto FD. Sonographically estimated fetal weights: accuracy and limitation. Am J Obstet Gynecol. 1988;159(5): 1118-1121.
63. Townsend RR, Filly RA, Callen PW, Laros RK. Factors affecting prenatal sonographic estimation of weight in extremely low birthweight infants. J Ultrasound Med. 1988;7(4):183-187.
64. Barel O, Vaknin Z, Tovbin J, et al. Assessment of the accuracy of multiple sonographic fetal weight estimation formulas: a 10-year experience from a single center. J Ultrasound Med. 2013;32(5):815-823.
65. Kehl S, Schmidt U, Spaich S, et al. What are the limits of accuracy in fetal weight estimation with conventional biometry in two-dimensional ultrasound? A novel postpartum study. Ultrasound Obstet Gynecol. 2012; 39(5):543-548.
66. Scioscia M, Scioscia F, Vimercati A, et al. Estimation of fetal weight by measurement of fetal thigh soft-tissue thickness in the late third trimester. Ultrasound Obstet Gynecol. 2008;31(3):314-320.
67. Hill LM, Breckle R, Wolfgram KR, O'Brien PC. Evaluation of three methods for estimating fetal weight. J Clin Ultrasound. 1986;14(3):171-178.
68. Benson CB, Doubilet PM, Saltzman DH. Sonographic determination of fetal weights in diabetic pregnancies. Am J Obstet Gynecol. 1987;156(2): 441-444.
69. Chauhan SP, Scardo JA, Hendrix NW, et al. Accuracy of sonographically estimated fetal weight with and without oligohydramnios. A case-control study. J Reprod Med. 1999;44(11):969-973.
70. Pineau JC, Grange G, Kapitaniak B, et al. Estimation of fetal weight: accuracy of regression models versus accuracy of ultrasound data. Fetal Diagn Ther. 2008;24(2):140-145.
71. Doubilet PM, Benson CB, Nadel AS, Ringer SA. Improved birth weight table for neonates developed from gestations dated by early ultrasonography. J Ultrasound Med. 1997;16(4):241-249.
72. Brenner WE, Edelman DA, Hendricks CH. A standard of fetal growth for the United States of America. Am J Obstet Gynecol. 1976;126(5): 555-564.
73. Lubchenco LO, Hansman C, Dressler M, Boyd E. Intrauterine growth as estimated from liveborn birth-weight data at 24 to 42 weeks of gestation. Pediatrics. 1963;32:793-800.
74. Gruenwald P. Growth of the human fetus. I. Normal growth and its variation. Am J Obstet Gynecol. 1966;94(8):1112-1119.
75. Thomson AM, Billewicz WZ, Hytten FE. The assessment of fetal growth. Br J Obstet Gynaecol. 1968;75(9):903-916.
76. Hutchins CJ. Delivery of the growth-retarded infant. Obstet Gynecol. 1980;56(6):683-686.
77. Deter RL, Harrist RB, Hadlock FP, Poindexter AN. Longitudinal studies of fetal growth with the use of dynamic image ultrasonography. Am J Obstet Gynecol. 1982;143(5):545-554.
78. Hadlock FP, Harrist RB, Martinez-Poyer J. In utero analysis of fetal growth: a sonographic weight standard. Radiology. 1991;181(1):129-133.
79. Doubilet PM, Benson CB, Wilkins-Haug L, Ringer S. Fetuses subsequently born premature are smaller than gestational age-matched fetuses not born premature. J Ultrasound Med. 2003;22(4):359-363.
80. Lysikiewicz A, Bracero LA, Tejani N. Sonographically estimated fetal weight percentile as a predictor of preterm delivery. J Matern Fetal Med. 2001;10(1):44-47.
81. Mercer BM, Merlino AA, Milluzzi CJ, Moore JJ. Small fetal size before 20 weeks' gestation: associations with maternal tobacco use, early preterm birth, and low birthweight. Am J Obstet Gynecol. 2008;198(6):673.e1-673.e8.
82. Bukowski R, Gahn D, Denning J, Saade G. Impairment of growth in fetuses destined to deliver preterm. Am J Obstet Gynecol. 2001;185(2):463-467.
83. Secher NJ, Hansen PK, Thomsen BL, Keiding N. Growth retardation in preterm infants. Br J Obstet Gynaecol. 1987;94(2):115-120.
84. Burkhardt T, Schaffer L, Zimmermann R, Kurmanavicius J. Newborn weight charts underestimate the incidence of low birthweight in preterm infants. Am J Obstet Gynecol. 2008;199(2):139.e1-139.e6.
85. Villar J, Altman DG, Purwar M, et al. The objectives, design and implementation of the INTERGROWTH-21st Project. Br J Obstet Gynaecol. 2013;120(Suppl. 2):9-26.
86. Villar J, Ismail LC, Victora CG, et al. International standards for newborn weight, length, and head circumference by gestational age and sex: the Newborn Cross-Sectional Study of the INTERGROWTH-21st Project. Lancet. 2014;384(9946):857-868.
87. Gardosi J, Chang A, Kalyan B, et al. Customised antenatal growth charts. Lancet. 1992;339(8788):283-287.
88. Gardosi J, Mongelli M, Wilcox M, Chang A. An adjustable fetal weight standard. Ultrasound Obstet Gynecol. 1995;6(3):168-174.
89. de Jong CL, Gardosi J, Dekker GA, et al. Application of a customised birthweight standard in the assessment of perinatal outcome in a high risk population. Br J Obstet Gynaecol. 1998;105(5):531-535.
90. Clausson B, Gardosi J, Francis A, Cnattingius S. Perinatal outcome in SGA births defined by customised versus population-based birthweight standards. Br J Obstet Gynaecol. 2001;108(8):830-834.
91. Figueras F, Figueras J, Meler E, et al. Customised birthweight standards accurately predict perinatal morbidity. Arch Dis Child Fetal Neonatal Ed. 2007;92(4):F277-F280.
92. Alexander GR, Wingate MS, Mor J, Boulet S. Birth outcomes of Asian-Indian-Americans. Int J Gynaecol Obstet. 2007;97(3):215-220.
93. Resnik R. One size does not fit all. Am J Obstet Gynecol. 2007;197(3):221-222.
94. Melamed N, Ray JG, Shah PS, et al. Should we use customized fetal growth percentiles in urban Canada? J Obstet Gynaecol Can. 2014;36(2): 164-170.
95. Steer PJ. Possible differences in fetal size by racial origin. Lancet Diabetes Endocrinol. 2014;2(10):766-767.
96. Hutcheon JA, Zhang X, Platt RW, et al. The case against customised birthweight standards. Paediatr Perinat Epidemiol. 2010;25(1):11-16.
97. McCarthy EA, Walker SP. International fetal growth standards: one size fits all. Lancet. 2014;384(9946):835-836.
98. Wong LF, Caughey AB, Nakagawa S, et al. Perinatal outcomes among different Asian-American subgroups. Am J Obstet Gynecol. 2008;199(4):382.e1-382.e6.
99. Villar J, Papageorghiou AT, Pang R, et al. The likeness of fetal growth and newborn size across non-isolated populations in the INTERGROWTH-21st Project: the Fetal Growth Longitudinal Study and Newborn Cross-Sectional Study. Lancet Diabetes Endocrinol. 2014;2(10):781-792.
100. Greenes RA. OBUS: a microcomputer system for measurement, calculation, reporting, and retrieval of obstetric ultrasound examinations. Radiology. 1982;144(4):879-883.
101. Jeanty P. A simple reporting system for obstetrical ultrasonography. J Ultrasound Med. 1985;4(11):591-593.
102. Ott WJ. The design and implementation of a computer-based ultrasound data system. J Ultrasound Med. 1986;5(1):25-32.
103. Ott WJ. The diagnosis of altered fetal growth. Obstet Gynecol Clin North Am. 1988;15(2):237-263.
104. Mintz MC, Landon MB. Sonographic diagnosis of fetal growth disorders. Clin Obstet Gynecol. 1988;31(1):44-52.
105. Landon MB, Mintz MC, Gabbe SG. Sonographic evaluation of fetal abdominal growth: predictor of the large-for-gestational-age infant in pregnancies complicated by diabetes mellitus. Int J Gynaecol Obstet. 1989;30(1):83.
106. Abramowicz JS. Fetal macrosomia. UpToDate. 2015.
107. Boyd ME, Usher RH, McLean FH. Fetal macrosomia: prediction, risks, proposed management. Obstet Gynecol. 1983;61(6):715-722.

108. Modanlou HD, Dorchester WL, Thorosian A, Freeman RK. Macrosomia—maternal, fetal, and neonatal implications. Obstet Gynecol. 1980;55(4):420-424.
109. Deter RL, Hadlock FP. Use of ultrasound in the detection of macrosomia: a review. J Clin Ultrasound. 1985;13(8):519-524.
110. Golditch IM, Kirkman K. The large fetus. Management and outcome. Obstet Gynecol Surv. 1979;34(2):137-139.
111. Rodriguez MH. Ultrasound evaluation of the postdate pregnancy. Clin Obstet Gynecol. 1989;32(2):257-261.
112. Arias F. Predictability of complications associated with prolongation of pregnancy. Obstet Gynecol. 1987;70(1):101-106.
113. Acker DB, Sachs BP, Friedman EA. Risk factors for shoulder dystocia in the average-weight infant. Obstet Gynecol. 1986;67(5):614-618.
114. Gross SJ, Shime J, Farine D. Shoulder dystocia: predictors and outcome. Am J Obstet Gynecol. 1987;156(2):334-336.
115. Miller JM Jr, Korndorffer Jr FA, Kissling GE, et al. Recognition of the overgrown fetus: in utero ponderal indices. Am J Perinatol. 1987;4(2):86-89.
116. Miller JM, Korndorffer FA, Gabert HA. Fetal weight estimates in late pregnancy with emphasis on macrosomia. J Clin Ultrasound. 1986;14(6):437-442.
117. Doubilet PM, Benson CB. Fetal growth disturbances. Semin Roentgenol. 1990;25(4):309-316.
118. Miller J, Korndorffer F, Kissling G, et al. Recognition of the overgrown fetus: in utero ponderal indices. Am J Perinatol. 1987;4(2):86-89.
119. Chamberlain PF, Manning FA, Morrison I, et al. Ultrasound evaluation of amniotic fluid volume. II. The relationship of increased amniotic fluid volume to perinatal outcome. Am J Obstet Gynecol. 1984;150(3):250-254.
120. Benson CB, Coughlin BF, Doubilet PM. Amniotic fluid volume in large-for-gestational-age fetuses of nondiabetic mothers. J Ultrasound Med. 1991;10(3):149-151.
121. Miller Jr JM, Brown HL, Khawli OF, et al. Ultrasonographic identification of the macrosomic fetus. Am J Obstet Gynecol. 1988;159(5):1110-1114.
122. Chauhan SP, West DJ, Scardo JA, et al. Antepartum detection of macrosomic fetus: clinical versus sonographic, including soft-tissue measurements. Obstet Gynecol. 2000;95(5):639-642.
123. Benson CB, Coughlin BF, Doubilet PM. Amniotic fluid volume in large-for-gestational-age fetuses of nondiabetic mothers. J Ultrasound Med. 1991;10(3):149-151.
124. Miller Jr JM, Kissling GA, Brown HL, Gabert HA. Estimated fetal weight: applicability to small- and large-for-gestational-age fetus. J Clin Ultrasound. 1988;16(2):95-97.
125. Basel D, Lederer R, Diamant YZ. Longitudinal ultrasonic biometry of various parameters in fetuses with abnormal growth rate. Acta Obstet Gynecol Scand. 1987;66(2):143-149.
126. Elliott JP, Garite TJ, Freeman RK, et al. Ultrasonic prediction of fetal macrosomia in diabetic patients. Obstet Gynecol. 1982;60(2):159-162.
127. Bochner CJ, Medearis AL, Williams J, et al. Early third-trimester ultrasound screening in gestational diabetes to determine the risk of macrosomia and labor dystocia at term. Am J Obstet Gynecol. 1987;157(3):703-708.
128. Sandmire HF, O'Halloin TJ. Shoulder dystocia: its incidence and associated risk factors. Int J Gynaecol Obstet. 1988;26(1):65-73.
129. Tamura RK, Sabbagha RE, Depp R, et al. Diabetic macrosomia: accuracy of third trimester ultrasound. Obstet Gynecol. 1986;67(6):828-832.
130. Bracero LA, Baxi LV, Rey HR, Yeh MN. Use of ultrasound in antenatal diagnosis of large-for-gestational age infants in diabetic gravid patients. Am J Obstet Gynecol. 1985;152(1):43-47.
131. Benson CB, Doubilet PM, Saltzman DH, et al. Femur length/abdominal circumference ratio. Poor predictor of macrosomic fetuses in diabetic mothers. J Ultrasound Med. 1986;5(3):141-144.
132. Combs CA, Rosenn B, Miodovnik M, Siddiqi TA. Sonographic EFW and macrosomia: is there an optimum formula to predict diabetic fetal macrosomia? J Matern Fetal Med. 2000;9(1):55-61.
133. Colman A, Maharaj D, Hutton J, Tuohy J. Reliability of ultrasound estimation of fetal weight in term singleton pregnancies. N Z Med J. 2006;119(1241):U2146.
134. Lockwood CJ, Weiner S. Assessment of fetal growth. Clin Perinatol. 1986;13(1):3-35.
135. Lin C. Current concepts of fetal growth restriction: part I. Causes, classification, and pathophysiology. Obstet Gynecol. 1998;92(6):1044-1055.
136. Pilliod RA, Cheng YW, Snowden JM, et al. The risk of intrauterine fetal death in the small-for-gestational-age fetus. Am J Obstet Gynecol. 2012;207(4):318.e1-318.e6.
137. Reed K, Droegmueller W. Intrauterine growth retardation. In: Centrullo CL, Sbarra AJ, editors. The problem-oriented medical record. New York: Plenum; 1984. p. 175-194.
138. Seeds JW. Impaired fetal growth: definition and clinical diagnosis. Obstet Gynecol. 1984;64(3):303-310.
139. Dobson PC, Abell DA, Beischer NA. Mortality and morbidity of fetal growth retardation. Austr N Z J Obstet Gynaecol. 1981;21(2):69-72.
140. Berkley E, Chauhan SP, Abuhamad A. Doppler assessment of the fetus with intrauterine growth restriction. Am J Obstet Gynecol. 2012;206(4):300-308.
141. Benson CB, Doubilet PM, Saltzman DH. Intrauterine growth retardation: predictive value of US criteria for antenatal diagnosis. Radiology. 1986;160(2):415-417.
142. Benson CB, Boswell SB, Brown DL, et al. Improved prediction of intrauterine growth retardation with use of multiple parameters. Radiology. 1988;168(1):7-12.
143. Benson CB, Belville JS, Lentini JF, et al. Intrauterine growth retardation: diagnosis based on multiple parameters—a prospective study. Radiology. 1990;177(2):499-502.
144. Doubilet PM, Benson CB. Sonographic evaluation of intrauterine growth retardation. AJR Am J Roentgenol. 1995;164(3):709-717.
145. Manning FA. The fetal biophysical profile. UpToDate. 2015.
146. Manning FA, Platt LD, Sipos L. Antepartum fetal evaluation: development of a fetal biophysical profile. Am J Obstet Gynecol. 1980;136(6):787-795.
147. Manning FA, Baskett TF, Morrison I, Lange I. Fetal biophysical profile scoring: a prospective study in 1,184 high-risk patients. Am J Obstet Gynecol. 1981;140(3):289-294.
148. Everett TR, Peebles DM. Antenatal tests of fetal wellbeing. Semin Fetal Neonatal Med. 2015;20(3):138-143.
149. Manning FA, Morrison I, Harman CR, et al. Fetal assessment based on fetal biophysical profile scoring: experience in 19,221 referred high-risk pregnancies. II. An analysis of false-negative fetal deaths. Am J Obstet Gynecol. 1987;157(4):880-884.
150. Seravalli V, Baschat AA. A uniform management approach to optimize outcome in fetal growth restriction. Obstet Gynecol Clin North Am. 2015;42(2):275-288.
151. Subtil D, Tiberghien P, Devos P, et al. Immediate and delayed effects of antenatal corticosteroids on fetal heart rate: a randomized trial that compares betamethasone acetate and phosphate, betamethasone phosphate, and dexamethasone. Am J Obstet Gynecol. 2003;188(2):524-531.
152. Mulder EJH, Derks JB, Visser GHA. Antenatal corticosteroid therapy and fetal behaviour: a randomised study of the effects of betamethasone and dexamethasone. Br J Obstet Gynaecol. 1997;104(11):1239-1247.
153. Senat MV, Minoui S, Multon O, et al. Effect of dexamethasone and betamethasone on fetal heart rate variability in preterm labour: a randomised study. Br J Obstet Gynaecol. 1998;105(7):749-755.
154. Rotmensch S, Liberati M, Vishne TH, et al. The effect of betamethasone and dexamethasone on fetal heart rate patterns and biophysical activities: a prospective randomized trial. Acta Obstet Gynecol Scand. 1999;78(6):493-500.
155. Rotmensch S, Lev S, Kovo M, et al. Effect of betamethasone administration on fetal heart rate tracing: a blinded longitudinal study. Fetal Diagn Ther. 2005;20(5):371-376.
156. Maulik D. Doppler ultrasound of the umbilical artery for fetal surveillance. UpToDate. 2015.
157. Maulik DEV, Mundy D, Heitmann E, Maulik D. Evidence-based approach to umbilical artery Doppler fetal surveillance in high-risk pregnancies: an update. Clin Obstet Gynecol. 2010;53(4):869-878.
158. Dahlbäck C, Pihlsgård M, Gudmundsson S. Abnormal ductus venosus pulsatility index in the absence of concurrent umbilical vein pulsations does not indicate worsening fetal condition. Ultrasound Obstet Gynecol. 2013;42(3):322-328.

159. Cruz-Martinez R, Figueras F, Hernandez-Andrade E, et al. Changes in myocardial performance index and aortic isthmus and ductus venosus Doppler in term, small-for-gestational age fetuses with normal umbilical artery pulsatility index. Ultrasound Obstet Gynecol. 2011;38(4):400-405.
160. Mone F, McAuliffe FM, Ong S. The clinical application of Doppler ultrasound in obstetrics. Obstet Gynaecol. 2014;17(1):13-19.
161. Copel JA, Bahtiyar MO. A practical approach to fetal growth restriction. Obstet Gynecol. 2014;123(5):1057-1069.
162. Alfirevic Z, Stampalija T, Gyte GML. Fetal and umbilical Doppler ultrasound in high-risk pregnancies. Cochrane Database Syst Rev. 2013;(11):CD007529.
163. DeVore GR. The importance of the cerebroplacental ratio in the evaluation of fetal well-being in SGA and AGA fetuses. Am J Obstet Gynecol. 2015;213(1):5-15.
164. Baschat AA. Venous Doppler for fetal assessment. UpToDate. 2015.
165. Cruz-Martinez R, Tenorio V, Padilla N, et al. Risk of ultrasound-detected neonatal brain abnormalities in intrauterine growth-restricted fetuses born between 28 and 34 weeks' gestation: relationship with gestational age at birth and fetal Doppler parameters. Ultrasound Obstet Gynecol. 2015;46(4):452-459.
166. Acharya G, Wilsgaard T, Berntsen GKR, et al. Reference ranges for serial measurements of umbilical artery Doppler indices in the second half of pregnancy. Am J Obstet Gynecol. 2005;192(3):937-944.
167. Karsdorp VHM, van Vugt JMG, van Geijn HP, et al. Clinical significance of absent or reversed end diastolic velocity waveforms in umbilical artery. Lancet. 1994;344(8938):1664-1668.
168. Valcamonico A, Danti L, Frusca T, et al. Absent end-diastolic velocity in umbilical artery: risk of neonatal morbidity and brain damage. Am J Obstet Gynecol. 1994;170(3):796-801.
169. Ertan AK, He JP, Tanriverdi HA, et al. Comparison of perinatal outcome in fetuses with reverse or absent enddiastolic flow in the umbilical artery and/or fetal descending aorta. J Perinat Med. 2003;31(4):307-312.
170. Gerber S, Hohlfeld P, Viquerat F, et al. Intrauterine growth restriction and absent or reverse end-diastolic blood flow in umbilical artery (Doppler class II or III): a retrospective study of short- and long-term fetal morbidity and mortality. Eur J Obstet Gynecol Reprod Biol. 2006;126(1):20-26.
171. Fieni S, Gramellini D, Piantelli G. Lack of normalization of middle cerebral artery flow velocity prior to fetal death before the 30th week of gestation: a report of three cases. Ultrasound Obstet Gynecol. 2004;24(4):474-476.
172. Figueras F, Savchev S, Triunfo S, et al. An integrated model with classification criteria to predict small-for-gestational-age fetuses at risk of adverse perinatal outcome. Ultrasound Obstet Gynecol. 2015;45(3):279-285.

CHAPTER 43

Sonographic Evaluation of the Placenta

Thomas D. Shipp

SUMMARY OF KEY POINTS

- The placenta undergoes tremendous development within the first half of pregnancy yet continues to mature and develop during the gestation.
- A placenta that lies near or over the internal cervical os is common early in gestation, yet most of these will resolve by the end of pregnancy. Ultrasound, especially transvaginal sonography, is instrumental to determine placental position.
- Placenta accreta is increasingly common and ultrasound is vital for its identification, especially in patients at high risk for its development. Sonographic findings most important for identifying placenta accreta are placental lacunae, loss of the placental-myometrial hypoechoic space, abnormalities of the uterine-bladder interface, and color Doppler abnormalities.
- Placental infarctions are commonly identified within the placenta, especially in patients at high risk for their development (e.g., those who have preeclampsia, maternal vascular disease, or thrombophilia).
- Abnormalities of placental shape are common, as are differences in location of the placental umbilical cord insertion.
- The presence of a vasa previa is associated with increased perinatal morbidity and mortality rates. Vasa previa should be evaluated for all gravidas, especially for those with an increased risk of its development.
- Those parturients with abnormal postpartum bleeding should be evaluated for the presence of retained products of conception. Echogenic endometrial masses in these patients strongly suggest the presence of retained products of conception.

CHAPTER OUTLINE

PLACENTAL DEVELOPMENT
Placental Appearance
Placental Size
Placental Vascularity and Doppler Ultrasound
Amnion-Chorion Separation
Elastography
PLACENTA PREVIA
PLACENTA ACCRETA
PLACENTAL ABRUPTION
PLACENTAL INFARCTION
PLACENTAL MASSES
MESENCHYMAL DYSPLASIA OF THE PLACENTA
MOLAR GESTATIONS
MORPHOLOGIC PLACENTAL ABNORMALITIES
Circumvallate Placenta
Succenturiate Lobe
Bilobed Placenta
UMBILICAL CORD
Size and Appearance
Insertion Into the Placenta
Velamentous and Marginal Cord Insertions
Vasa Previa
PLACENTA DURING LABOR AND POSTPARTUM
Third Stage of Labor
Retained Products of Conception
CONCLUSION

The use of ultrasound to evaluate the placenta is routine among the majority of pregnant American women because they have at least one ultrasound examination during pregnancy. A wide range of pregnancy complications result from abnormal placental development, including preeclampsia, intrauterine growth restriction (IUGR), and abruption. Other placental and umbilical cord abnormalities, such as placenta previa, placenta accreta/increta/percreta, or vasa previa, may cause major maternal and fetal complications, especially if not recognized antenatally. Timely recognition of these abnormalities can lead to improved management of pregnancy and delivery. Thus careful examination of the placenta by ultrasound can contribute directly to enhanced patient care and improved outcomes.

PLACENTAL DEVELOPMENT

The early developing embryo is surrounded by amnion and chorion. Villi cover the entire surface of the chorion up to about 8 weeks of gestation (Fig. 43.1). The villi, which are the basic structures of the placenta, initially form by 4 or 5 weeks' gestation. The villi next to the **decidua capsularis** degenerate, forming the **chorion laeve.** The villi contiguous with the **decidua basalis**

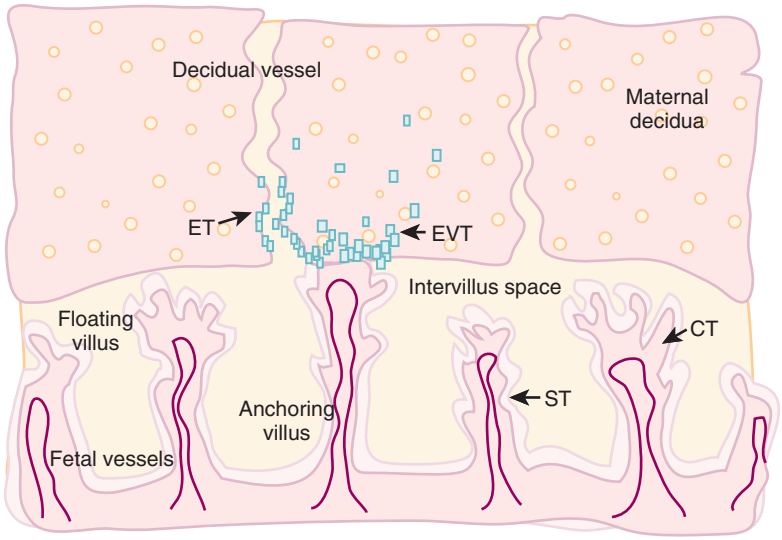

FIG. 43.1 Human Placenta Microarchitecture. Fetal derivatives in the placenta consist of fetal vessels and placental cotyledons (villi). Villi consist of fetal vessels surrounded by **cytotrophoblast** cells *(CT).* Covering the cytotrophoblast cells is a multinucleated cellular layer called the **syncytiotrophoblast** *(ST).* Anchoring villi are in direct contact with the maternal uterine lining, called the **decidua.** The decidua is traversed by maternal vasculature. Blood from these vessels empties into the intervillous space and bathes the placental villi. Note that maternal and fetal blood vessels are separated by trophoblast, villous stroma, and fetal vascular endothelium. Cytotrophoblast cells from anchoring villi can change into an invasive phenotype called extravillous cytotrophoblast cells *(EVT).* EVT invade deeply into the maternal decidua. Some EVT, called endovascular trophoblast cells *(ET),* embed within the walls of the maternal vasculature. (With permission from Comiskey M, Warner CM, Schust DJ. MHC molecules of the preimplantation embryo and trophoblast. In: Mor G, editor. Immunology of pregnancy. Austin/New York: Landes Bioscience, 2006.)

become the **chorion frondosum** and later the placenta. The fetal side of the placenta consists of the **chorionic plate** and **chorionic villi.** The maternal side consists of the decidua basalis, which opens up into large cisterns, the **intervillous spaces.** The fetal villi are immersed in maternal blood located in the intervillous spaces. Anchoring villi develop from the chorionic plate.[1] These attach to the decidua basalis, holding the placenta in place.[2,3] By the end of pregnancy, the villi have a surface area of 12 to 14 square meters.[4] This type of placentation, seen in humans and some rodents, is termed *hemochorial placentation.*

Placental Appearance

Sonographically, the placenta in the first and second trimesters is slightly more echogenic than the surrounding myometrium (Fig. 43.2A). The attachment site, or base of the placenta, should be clearly delineated from the underlying myometrium. The edges of the placenta usually have a small sinus, the **marginal sinus of the placenta** (Fig. 43.2B), where intervillous blood drains into the maternal venous circulation. This area should not be confused with a placental separation.

Placental lakes (venous lakes, at least 2 × 2 cm) occur in up to 5% of pregnancies[5-10] (Fig. 43.2C, Video 43.1). They represent areas of intervillous spaces devoid of placental villous trees and are seen as hypoechoic structures within the placenta. Moving blood flow can be seen in these areas. They may have irregular shapes or a narrow, cleftlike appearance and may change in appearance over the gestation. Large placental lakes (>5 cm in largest dimension) have been associated with IUGR.[10]

As the placenta matures, areas of echogenicity within the placenta are visualized (Fig. 43.2D and E). In cases of **placental infarction,** there may be hypoechoic lesions with echogenic borders.

Placental Size

The placenta typically has a round shape with a central umbilical cord insertion, but variability in the shape of the placenta is quite common.[11] Placental length is approximately six times its maximal width at 18 to 20 weeks' gestation. The mean thickness of the placenta in millimeters in the first half of pregnancy closely approximates the gestational age in weeks.[12] If the placenta thickness is greater than 4 cm (40 mm) before 24 weeks, an abnormality should be suspected. These abnormalities include **ischemic-thrombotic damage, intraplacental hemorrhage, chorioangioma,** and **fetal hydrops**[13] (Fig. 43.3, Video 43.2).

Given the variable shape of the placenta, calculating a placental volume from two-dimensional (2D) imaging can be complicated. Multiplanar volume calculation involves sequential sections of the placenta at intervals such as 1.0 mm. The margins are manually traced, and a volume is calculated.[14] Most current studies appraising the use of three-dimensional (3D) sonography have used the VOCAL (Virtual Organ Computer-aided AnaLysis) method,[14] in which the 3D volume in question is rotated and the area of interest traced at its margin, after which a volume is calculated (Fig. 43.4).

Placental volume approximation in the first trimester holds promise as an important part of early pregnancy evaluation. Uterine artery Doppler analysis provides limited information regarding IUGR and the effects of maternal hypertension, but it is insufficient as a sole indicator of trophoblast invasion, in part because it is typically performed late in the second trimester. Small placental volumes in the first trimester presage abnormal uterine artery perfusion.[15] Uterine artery Doppler ultrasound combined with assessment of placental volume may identify pregnant women at risk for hypertension, abruption, or IUGR.[16,17] First-trimester placental volumes correlate with both placental

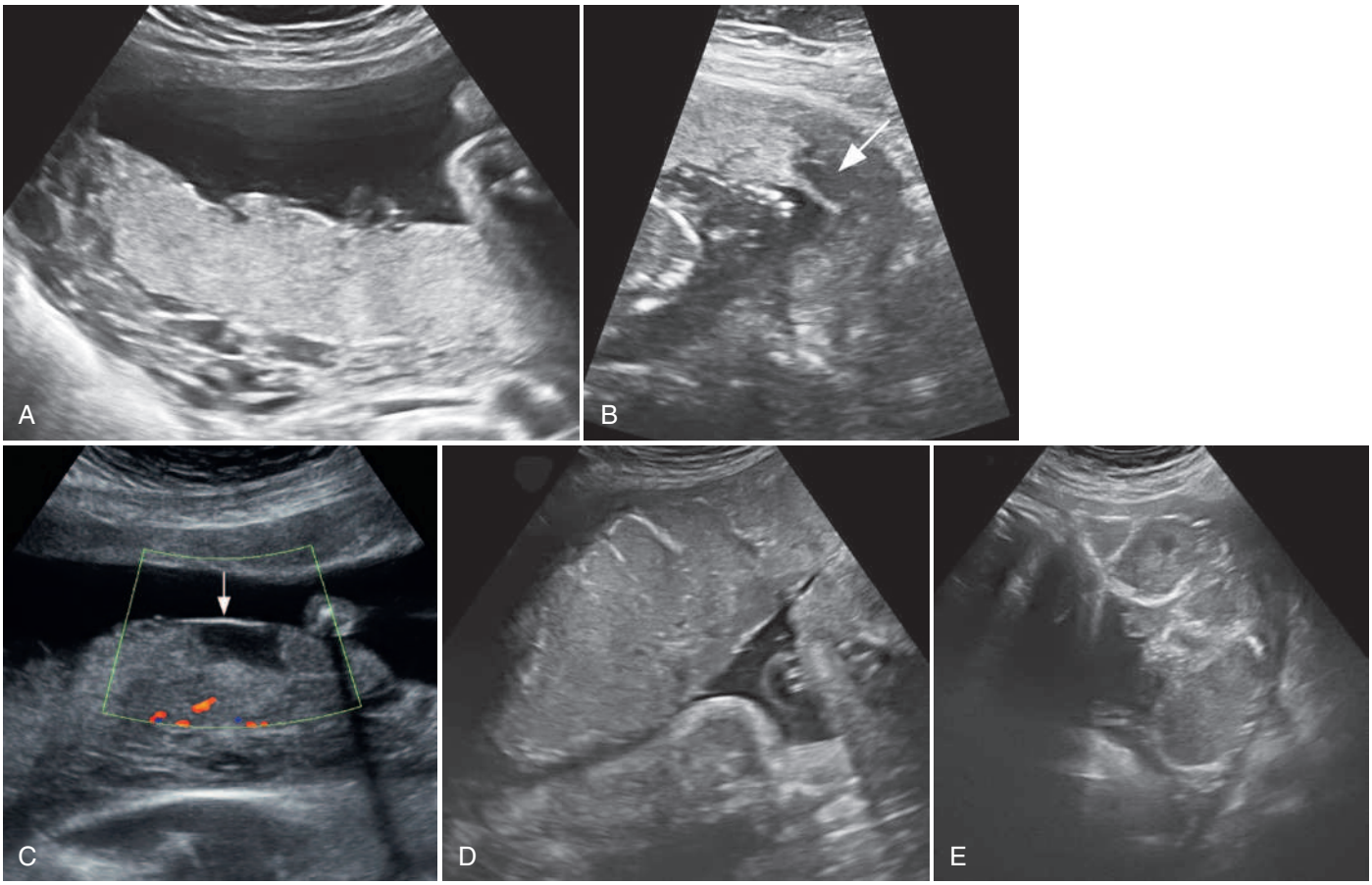

FIG. 43.2 Normal Appearance of Placenta. (A) At 18 weeks, note the uniformly echogenic appearance of the placenta. **(B)** Note **marginal sinus of placenta** *(arrow),* a circumferential venous drainage point into the maternal uterine veins that should not be mistaken for placental separation. **(C) Placental lake** *(arrow)* at 20 weeks. See also Video 43.1. **(D)** Placenta at 32 weeks' gestation. Note the diffuse placental calcifications. **(E)** Placenta at 39 weeks' gestation with defined linear calcifications outlining the placental cotyledons. Note the increasing echogenicity in the placenta as it matures.

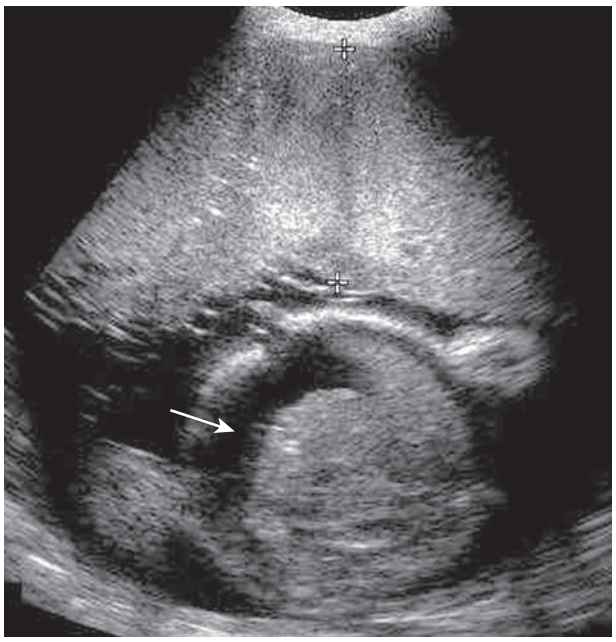

FIG. 43.3 Thick Placenta in Fetal Hydrops. The calipers indicate how one would measure the thickness of the placenta. Note the ascites *(arrow).* See also Video 43.2 for thick placenta in fetus with **villitis.**

weight and birth weight, but they have not been shown to predict the development of preeclampsia.[18,19] The first-trimester **placental volume quotient** (placental volume/crown-rump length) is low for aneuploid fetuses, with 53% having a quotient less than 10th percentile.[20] For twins, the placental volume is 83%, and for triplets 76%, that of singletons, for a given gestational age.[21]

The placenta dramatically increases in size until approximately 15 to 17 weeks' gestation. From this point, there is a fourfold increase in placental size until delivery, whereas over this same time period the fetus has a 50-fold increase in size.[22] Midtrimester placental volume is associated with maternal nutritional status, birth weight, and pregnancy outcome.[23-27]

Placental Vascularity and Doppler Ultrasound

The human placenta is a discoidal, villous, hemochorial structure. Nutrients are exchanged over many villi. Surrounding the villi are the **intervillous spaces,** which are bathed in maternal blood. The villi are sproutlike projections from the chorionic plate into the intervillous space. The villi are directly connected to the fetal vascular system, whereas the maternal blood emanates from the developing spiral arteries to the intervillous spaces to contact

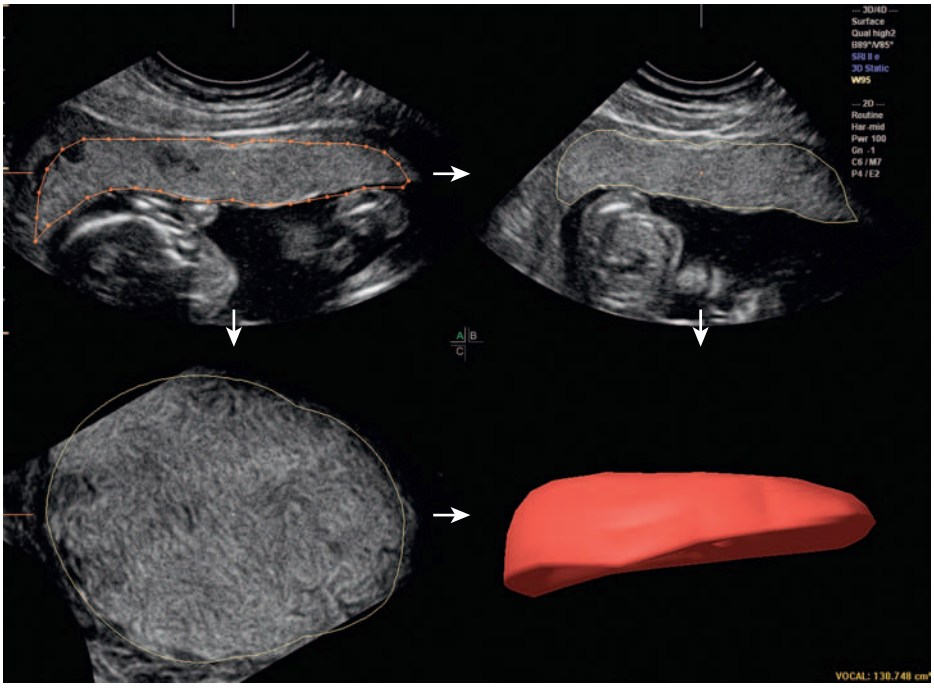

FIG. 43.4 **Three-Dimensional Assessment of Placental Volume in Second Trimester.**

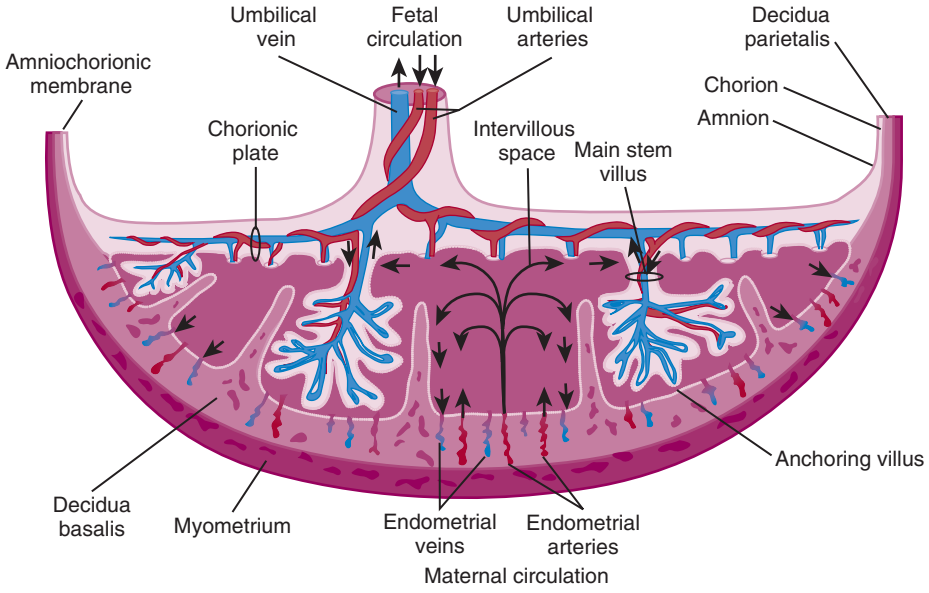

FIG. 43.5 **Schematic Drawing of Placental Vasculature.**

directly the trophoblasts of the villi[28] (Fig. 43.5). Maternal blood flow of the intervillous space depends on flow from the spiral arteries. Maternal vascular disease (e.g., hypertension) can directly affect the pregnancy by limiting this blood flow.[29]

Intervillous blood flow begins early in the first trimester.[30-32] Color Doppler ultrasound has been used to detect this intervillous and spiral artery flow by 12 weeks' gestation, but the flow, if any, that occurs before this time is not well understood.[33] Before 12 weeks, the presence of intervillous blood flow by gray-scale imaging may indicate failed pregnancy.[34]

Color and power Doppler sonography have been used to identify blood flow in intraplacental villous arteries.[35] A decrease in the number of detectable intraplacental villous arteries is associated with IUGR.[36] Three-dimensional power Doppler ultrasound provides a better appreciation of placental vascularity and pathophysiology by assessing placental flow and documenting the amount of flow in a given area. Because of its low variability between sampling sites in varied parts of the placenta, 3D imaging may have a future role in assessing flow in high-risk pregnancies (e.g., hypertension, IUGR).[37] Recent work by multiple researchers has shown that 3D placental vascularization indices are lower for those with preeclampsia,[19] are not aided by the inclusion of pregnancy-associated plasma protein A (PAPP-A) and uterine artery Doppler indices,[38] and may be improved with the addition

of 3D placental volume and computer analysis of placental calcification.[39] How well these indices can be used for the prediction of preeclampsia requires further investigation. First-trimester 3D power Doppler placental indices are unable to differentiate between those destined to have growth restriction as compared to normally grown fetuses.[40] Recent work in an animal model, however, demonstrating discrimination of maternal and fetal blood flow in the microvasculature of the placenta may allow further insights into placental blood flow and its effects on placental function.[41]

Amnion-Chorion Separation

The amnion normally "fuses" with the chorion early in the second trimester. Failure of the amnion and chorion to fuse after 17 weeks is a rare complication of pregnancy, associated with multiple abnormalities. Previous amniocentesis is a risk factor for amnion-chorion separation.[42] Associated factors may include IUGR, preterm delivery, oligohydramnios, placental abruption, and Down syndrome[43] (Fig. 43.6).

Elastography

A preliminary report has attempted to differentiate subchorionic hematoma from placenta previa using elastography.[44] More rigorous evaluations have shown that the use of both shear wave and strain elastography of the placenta was different between normal pregnancies and those that developed preeclampsia.[45,46] This exciting novel area of placental research offers much promise for the future.

PLACENTA PREVIA

The term *placenta previa* refers to a placenta that is "previous" to the fetus in the birth canal. The incidence at delivery is approximately 0.5% of all pregnancies.[47] **Bleeding** in the second and third trimesters is the hallmark of placenta previa. This bleeding can be life threatening to the mother and fetus. With antenatal detection, expectant management and cesarean delivery, both maternal and perinatal mortality rates have decreased over the past 40 years.[48,49] Accurate diagnosis of placenta previa is vital to improve the outcome for mother and neonate.

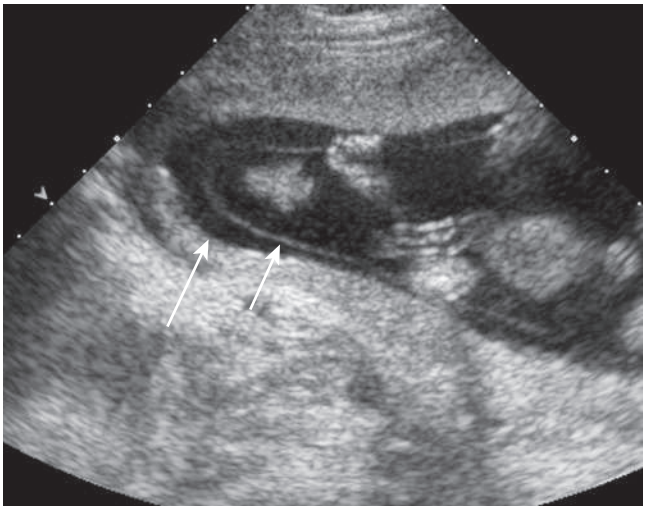

FIG. 43.6 Chorioamniotic Separation in Second Trimester. Amnion *(short arrow)* is separated from the chorion *(long arrow)*.

The differentiation of placental position has historically been performed by digital assessment of the lower uterine segment and placenta through the cervix. Using this potentially hazardous method of evaluation, placental position was classified as complete placenta previa, partial placenta previa, incomplete placenta previa, marginal placenta previa, low-lying placenta, and placenta distant from the internal cervical os. These classifications do not directly apply to the ultrasound examination of placental position relative to the cervix. The use of ultrasound to evaluate the position of the placenta in the uterus has both improved knowledge of the placenta within the uterus and simplified terminology with respect to placental position (Fig. 43.7). **Complete placenta previa** describes the situation in which the internal cervical os is totally covered by the placenta. Some differentiate those placentas that have a portion of placental substance that extends over the internal cervical os from those that are centrally placed over the cervix, a so-called central placenta previa. **Marginal placenta previa** denotes placental tissue at the edge of, or encroaching on, the internal cervical os. A **low placenta** is one in which the placental edge is within 2 cm, but not covering any portion, of the internal cervical os. The terms *incomplete placenta previa* and *partial placenta previa* have no place in the current sonographic assessment of placental position and should be used only by a clinician performing a digital examination when a "double setup" is necessary to determine where the leading edge of the placenta lies.

Transabdominal scanning can be used to visualize the internal cervical os and to determine the relation of the placenta to the cervix in most cases. Factors that can adversely affect the visualization of the cervix include prior abdominal surgery, obesity, deep or low position of the fetal head or presenting part, overfilled or underfilled maternal bladder, or uterine contractions. Transvaginal sonography (TVS) is safe[50] and accurate in depicting the internal cervical os. The proximity of the cervix to the vaginal probe allows higher-frequency probes to be used, with better resolution and thus better visualization of the internal cervical os. With improved resolution, clinicians can accurately determine the position of the leading placental edge to the internal cervical os. The use of TVS has been shown to change the assessment of the placental location in 25% of cases when the placenta is within 2 cm of the internal cervical os, as identified with transabdominal sonography.[51] A leading placental edge greater than 2 cm from the internal cervical os is associated with vaginal delivery, and distances less than 2 cm are associated with bleeding, potentially leading to cesarean delivery.[52,53]

Although placenta previa can occur in nulliparas, risk factors include number of prior cesarean deliveries (odds ratio: 4.5 for one; 44.9 for four[54]), increasing parity independent of number of prior cesarean deliveries,[55] and increasing maternal age.[56]

Early in the second trimester, the placenta occupies a relatively large portion of the uterine cavity and often is positioned near the cervix. As the uterus grows, a lesser proportion of placentas are located near the internal cervical os. This relative change in placental position is best understood by the placental migration

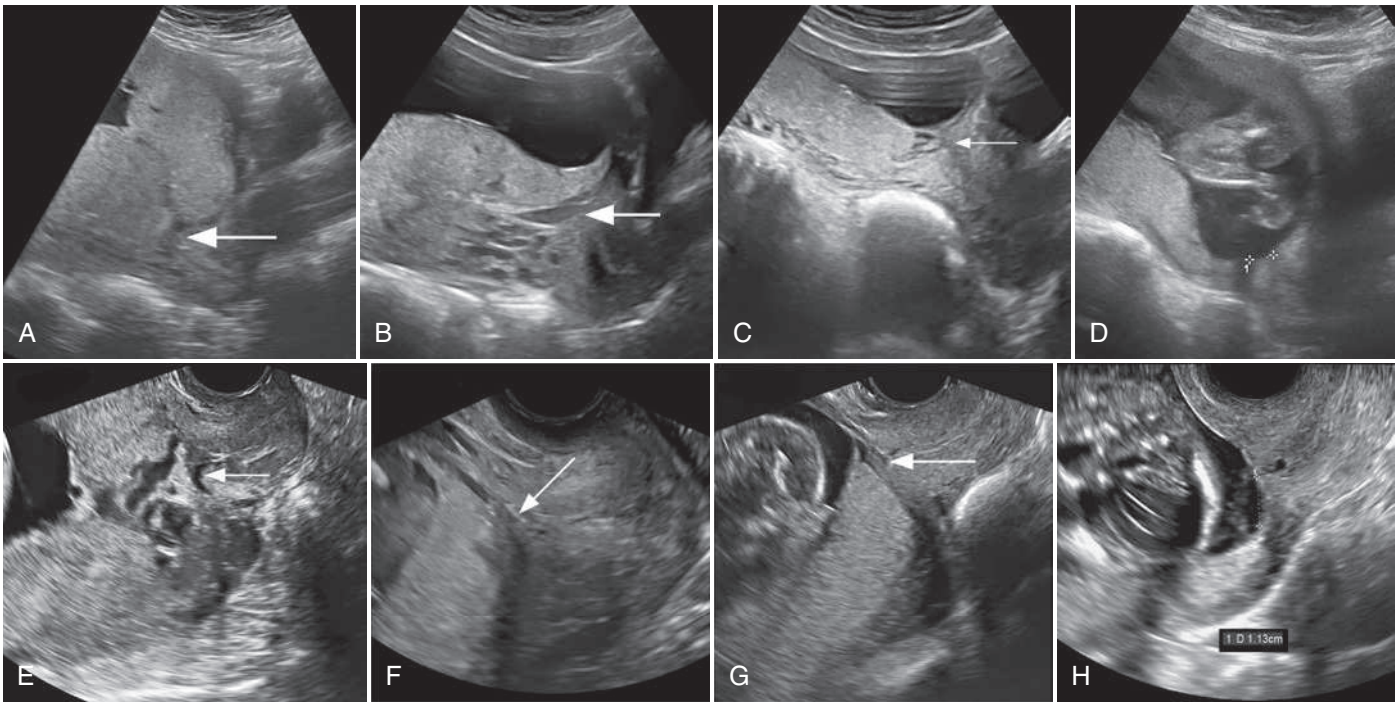

FIG. 43.7 Placental Position. (A)-(D) Transabdominal sonography (TAS) and **(E)-(H)** transvaginal sonography (TVS) can be used to determine placental position with respect to the internal os *(arrows)*. If the position is unclear with TAS, TVS should be used. **(A)** and **(E)** Complete central placenta previa. **(B)** and **(F)** Complete posterior placenta previa. **(C)** and **(G)** Marginal placenta previa. **(D)** and **(H)** Low placenta. The calipers show the distance from the internal cervical os to the leading placental edge.

theory.[57] This theory of "dynamic placentation" suggests that as the uterus develops, the placenta is "drawn away" from the internal cervical os. It is unclear whether the primary mechanism is disproportionate development of the lower uterine segment so that the placenta, although it does not detach from the uterine wall, comes to lie more distant from the internal cervical os. This theory would also be consistent with complete central placenta previas that do not resolve at a rate approaching that of other low-lying placentas, because the expansion of the lower uterine segment would not lead to the resolution of this type of placenta previa.

If the placenta overlaps the cervix by less than 2 cm at the end of the second trimester, more than 88% of patients deliver vaginally.[58] A rate of migration (in the second and third trimesters) away from the internal os of 3.0 to 5.4 mm per week is also associated with vaginal delivery, whereas a placental-internal os distance of less than 2 cm or a pattern of migration of 0.3 to 0.6 mm weekly are associated with interventional cesarean delivery and a higher rate of peripartum complications.[58,59]

The prediction of a placenta previa at delivery is best when the placenta overlaps the internal cervical os by 1.4 cm at 10 to 16 weeks' gestation,[60] or 2 cm at 20 to 23 weeks' gestation.[61] Mustafa et al.[62] demonstrated that if the placenta overlaps by 2.3 cm at 11 to 14 weeks, the probability of a placenta previa at term is 8%, with a sensitivity of 83% and a specificity of 86%.[62] Aside from a complete central placenta previa, given the current data, it is still difficult to predict precisely which patients will have resolution of their low placenta; therefore further ultrasound examinations are required to assess placental position if a low placenta is identified early in gestation. In a large retrospective study, if the placenta was low (<2 cm from the internal cervical os) at 16 to 24 weeks' gestation, 1.6% had a persistent low placenta or placenta previa at or near term.[63]

For women with a low placenta, the description of the leading edge of the placenta in the early third trimester as "thin" (≤1 cm in thickness and/or angle of placental edge <45 degrees) or "thick" (any other type of placenta) is predictive of delivery complications. Antepartum hemorrhage is more common with thick-edged placentas, as is the rate of cesarean delivery, placenta accreta, low birth weight, and earlier gestational age at delivery.[64] Interestingly, a more recent study performed in the first and second trimesters suggested that a thin-edged placenta with a smaller angle was more predictive of placenta previa.[65] Although not ready for clinical implementation, this parameter may help identify patients who can be reassured early in pregnancy that they will not have a placenta previa at delivery.

PLACENTA ACCRETA

The normal placenta attaches to but does not invade the myometrium. At delivery, the placenta separates at the decidual plane, with an abrupt cessation of intraplacental flow as the myometrium contracts.[66] A placenta that is abnormally adherent to the uterine wall after delivery is termed **placenta accreta. Placenta increta** occurs if the placenta invades the myometrium more deeply, and **placenta percreta** refers to a placenta that at least in part protrudes through the uterine serosa. Placenta accreta, increta, and percreta (hereafter referred to as "placenta accreta" unless

otherwise indicated) are serious complications of pregnancy associated with maternal blood loss, need for hysterectomy, and retained products of conception. With ultrasound, placenta accreta can be identified antenatally so that delivery plans can be made prospectively, improving the outcome for mother and child.

Although placenta accreta (or increta or percreta) can occur in any pregnancy, important risk factors include prior uterine surgery (with risk increasing with increasing number of prior cesarean deliveries), placenta previa, unexplained elevated maternal serum alpha-fetoprotein (MS-AFP), increased maternal cell-free placental lactogen, and advancing maternal age.[67-70] A woman with no placenta previa and no prior history of cesarean section has a baseline risk of 0.26% for placenta accreta. This increases almost linearly with number of prior cesarean sections, to 10% in patients with four or more.[71] Women with a placenta previa and an unscarred uterus have a 5% risk of clinical placenta accreta. With a placenta previa and one previous cesarean section, the risk of placenta accreta is 24%; this risk increases to 67% with a placenta previa and four or more cesarean deliveries.[71]

Several sonographic signs are associated with placenta accreta. The presence of a coexisting **placenta previa** in the majority of cases makes it particularly likely that the adherent portion of the placenta will be low in the uterus, in the region of a prior cesarean scar. This simple fact makes the evaluation of these placentas much more straightforward with TVS. Sonographic findings of placenta accreta include loss of the normal hypoechoic retroplacental-myometrial interface, thinning or disruption of the hyperechoic subvesicular uterine myometrium/serosa, presence of focal exophytic masses, and numerous placental lakes[72-75] (Fig. 43.8, Video 43.3).

The color Doppler ultrasound findings suggestive of placenta previa accreta include diffuse lacunar blood flow throughout the placenta, dilated vascular channels between the placenta and bladder or cervix, absence of the normal subplacental venous flow, and the demonstration of vessels crossing the placental-myometrial disruption site.[76,77] Three-dimensional sonography may also be helpful for evaluation of vascular anatomy in the setting of a placenta accreta.[78,79] The gray-scale and color Doppler sonographic findings described for placenta accreta are also present, but more exaggerated, in placenta increta and placenta percreta (Figs. 43.8 and 43.9; Videos 43.4 and 43.5). Three-dimensional color and power Doppler ultrasound are helpful to demonstrate the extensive torturous vascularity seen with such placentas. Greatly increased vascular lacunae with turbulent or "tornado" blood flow increases the likelihood of placenta increta or placenta percreta.[80]

Many recent studies have documented the use of ultrasound findings to identify women with placenta accreta. A recent meta-analysis documented that incorporation of sonographic abnormalities (placental lacunae, loss of the placental-myometrial hypoechoic space, abnormalities of the uterine-bladder interface, and color Doppler) led to a sensitivity of 91% and specificity of 97% for the detection of placenta accreta.[81] A "Placenta Accreta Index" was reported that included number of prior cesarean deliveries, placental location, presence and grade of lacunae, smallest myometrial thickness, and presence of bridging vessels, and constructed a receiver operating characteristic curve whereby the area under the curve was 0.87 (95% confidence interval [CI], 0.8, 0.95). A score of 0 to 9 had a range of probability of placenta accreta from 2% to 96%, respectively.[82] Further work is necessary to determine the historical and sonographic parameters needed to optimize prenatal diagnosis.

As in many aspects of obstetric sonography, early diagnosis is preferable. In women with a history of cesarean delivery, a gestational sac in the lower half of the uterus, at or before 10 weeks' gestation, is associated with placenta accreta,[83] as are first-trimester placental lacunae, an irregular placental-myometrial interface and placenta previa[84-86] (Fig. 43.10). Cesarean scar ectopic pregnancies appear to be precursors of placenta accreta.[87] When the diagnosis is unclear or nonspecific findings are present, magnetic resonance imaging (MRI) may be helpful,[88-93] particularly when the placenta is posterior over an area of prior uterine scar, such as from myomectomy (Fig. 43.11).

Information about placenta accreta and its variants is indispensable for delivery management. Accurate prenatal diagnosis allows uterine conservation and avoidance of massive blood loss at delivery. Strategies include preoperative placement of internal iliac artery balloon catheters and ultrasound-guided fundal classical cesarean incisions to deliver the fetus above the upper margin of the placenta.

PLACENTAL ABRUPTION

Placental abruption is one of the worrisome causes of vaginal bleeding in the latter part of pregnancy because it contributes to perinatal mortality. Patients typically present with third-trimester vaginal bleeding associated with abdominal or uterine pain and labor. The incidence is approximately 0.5% of pregnancies. History of prior abruption, hypertension, prolonged rupture of membranes, IUGR, chorioamnionitis, polyhydramnios, maternal thrombophilias, maternal substance use (tobacco, alcohol, cocaine), maternal trauma, and advanced maternal age are all risk factors for placental abruption.[94-96] The diagnosis of placental abruption is typically made based on clinical findings; the retroplacental clot is frequently isoechoic to the placenta or myometrium and cannot always be identified sonographically.

A **subplacental hematoma** between the placenta and uterine wall is a placental abruption (Fig. 43.12, Videos 43.6 and 43.7). This should be differentiated from a **subchorionic hematoma,** in which the hematoma is located beneath the chorion, not the placenta. Although a subchorionic hematoma can occur anytime during pregnancy, it is more common in the first half of pregnancy, and its appearance will change as the hematoma organizes (Fig. 43.13A). A **preplacental hematoma** is a rare condition likely caused by bleeding from fetal vessels and located on the fetal surface of the placenta under the chorion (Fig. 43.14, Videos 43.8 and 43.9). Because preplacental hematomas likely result from the accumulation of fetal blood, prognosis may be poorer.[97] When massive, these hematomas are sometimes termed **Breus mole.** Preplacental hematomas are associated with maternal hypertension.[98]

An acute hematoma has an echogenicity similar to that of the placenta, making sonographic visualization difficult. As the hematoma organizes, it becomes more hypoechoic (Fig. 43.13B)

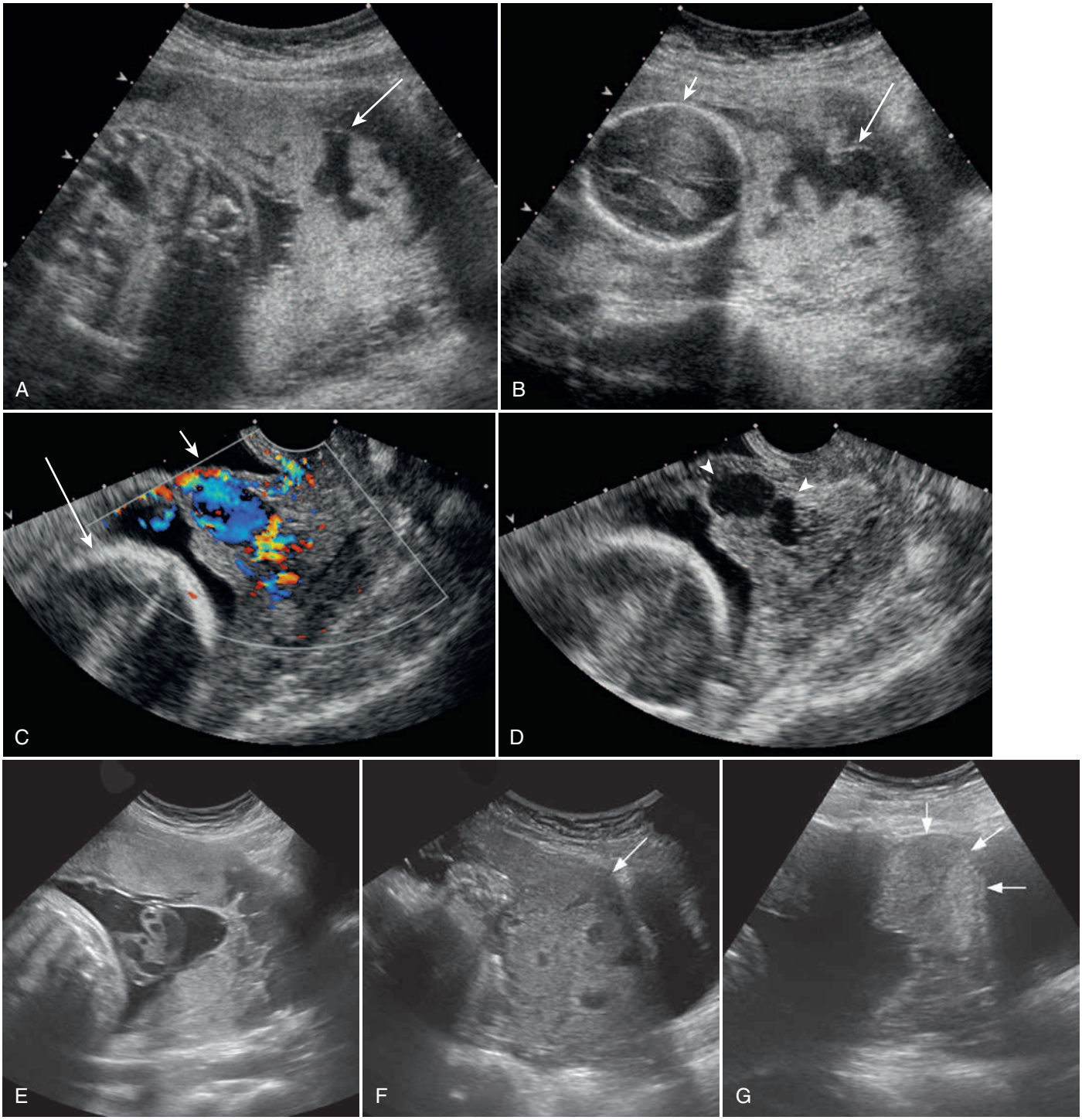

FIG. 43.8 Placenta Accreta With Placental Lakes. **(A)** Transabdominal sonogram of a third-trimester placenta shows a placental (venous) lake *(arrow).* **(B)** In a different patient, transabdominal sonogram of second-trimester placenta shows multiple placental lakes *(long arrow); short arrow,* fetal head. **(C)** In another patient, transvaginal sonogram of second-trimester placenta shows intense color flow within and below the placenta; *long arrow,* fetal head; *short arrow,* maternal bladder. **(D)** In the same patient as **C,** multiple placental lakes are visualized *(arrowheads).* **(E)** Placenta accreta. Note the multiple placental lakes in the lower uterine segment in the area of scar from a prior cesarean. **(F)** Placenta increta. Note the placental lakes and the loss of the hypoechoic zone between the placenta and myometrium *(arrow).* **(G)** Placenta percreta. Note the bulging of the placenta in the lower uterine segment including into the posterior wall of the bladder *(arrows).* See also Video 43.3 (accreta), Video 43.4 (increta), and Video 43.5 (percreta).

and can approach the echogenicity of the myometrium. An indirect sign of the presence of an acute hematoma is apparent thickening of the placenta, which is associated with worse outcome.[99,100]

Even though placental abruption remains a clinical diagnosis, ultrasound can play an important role. Larger hematomas are expected to be seen (Fig. 43.15), and these are more likely to be clinically important. Glantz and Purnell[101] reported that the identification of placental abruption by ultrasound had a sensitivity, specificity, positive predictive value, and negative predictive value of 24%, 96%, 88%, and 53%, respectively. They determined that if a hematoma was identified by sonography, there was an increased risk of preterm delivery, low birth weight, and neonatal intensive care unit admission. Increased size of the hematoma and percentage of placental involvement are associated with increased fetal mortality.[102]

PLACENTAL INFARCTION

Placental infarctions can occur focally or throughout the placenta and are thought to have a vascular etiology. **Maternal floor infarction** is a diffuse entity overtaking the villi with a fibrinoid deposition at the maternal surface and basal plate, reaching into the placental substance. The presence of this fibrin surrounding the villi obstructs nutrient exchange from mother to fetus. Both

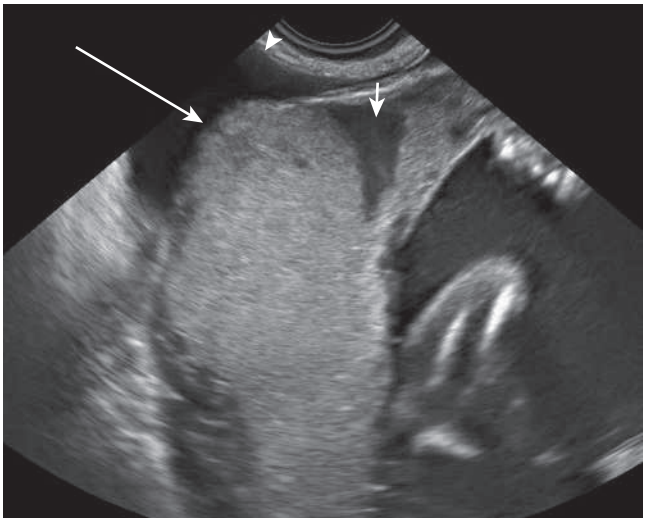

FIG. 43.9 Placenta Percreta. Transvaginal sonogram of a third-trimester placenta shows loss of the hypoechoic border between the placenta and the myometrium, with protrusion of the placenta *(long arrow)* into the maternal bladder *(arrowhead); short arrow,* placental lake.

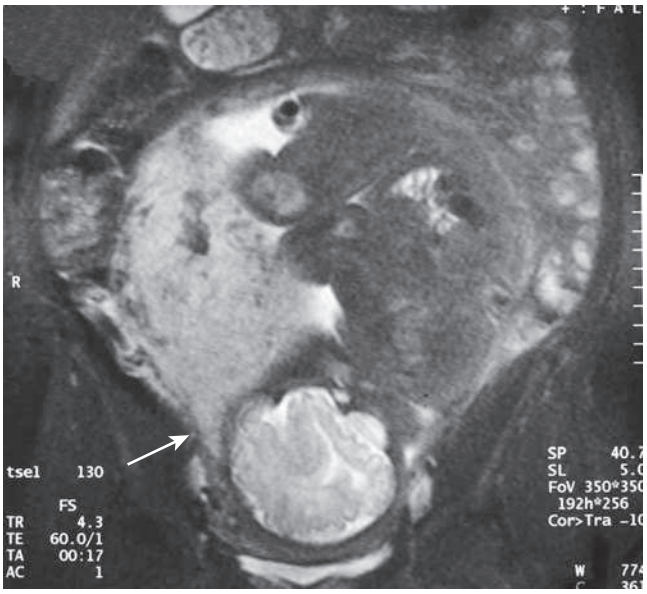

FIG. 43.11 Placenta Accreta. Coronal T2-weighted MR image shows an absent myometrial-placental interface in a posterolateral location *(arrow)* surrounded by normal myometrial-placental interface in a patient with previous posterior myomectomy. This region was not well evaluated with ultrasound. (With permission from Levine D. Placenta accreta: evaluation with color Doppler, power Doppler and fast MRI. Radiology. 1997;205:773-776.[89])

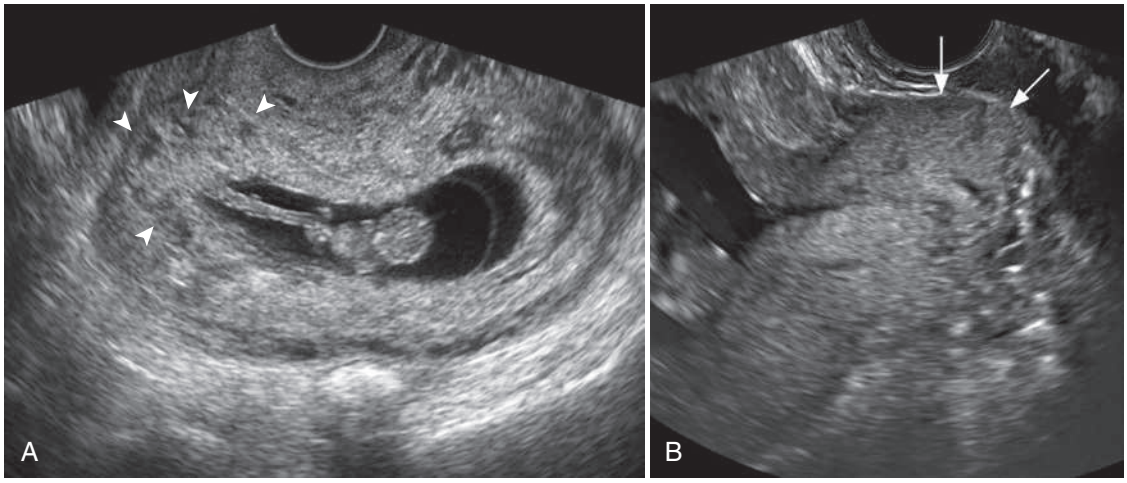

FIG. 43.10 First-Trimester Placenta Accreta. (A) The umbilical cord insertion is low in the uterus; arrowheads indicate multiple small placental lakes. This patient had a prior cesarean delivery and subsequently was shown to have a placental previa accreta. **(B)** A different patient with two prior cesarean deliveries. Note bulging of the placental tissue in the scar from a prior cesarean into the posterior wall of the bladder *(arrows).*

abnormalities are associated with oligohydramnios, umbilical artery Doppler abnormalities, IUGR, central nervous system injury, and fetal demise. Maternal floor infarction tends to recur in subsequent pregnancies.[28,103-105] Although peripheral infarctions are common at term, infarctions larger than 3 cm or involving more than 5% of the placenta are associated with increased perinatal morbidity. Both maternal and fetal thrombophilias can lead to placental infarctions.[106]

The sonographic findings of maternal floor infarction include a hyperechoic placental mass (Fig. 43.16A) or placental thickening. Hyperechoic areas of the placenta are especially prominent along the maternal surface of the placenta and can stretch into the placental substance itself. These can be a normal finding, especially with mature placentas. Hyperechoic placental masses may be associated with central hypoechoic spaces as they organize. **Subchorionic cysts** are also commonly present with maternal floor infarction (Fig. 43.16B). On this continuum are placental basal plate calcifications, which at times, can be quite prominent (Fig. 43.16C). The hyperechoic mass seen with maternal floor infarction resembles that seen with placental chorioangiomas.[107]

Placental infarctions caused by maternal vascular disease often result in uteroplacental ischemia and infarction of the villi. These appear as echogenic, rimmed cystic lesions within the placenta, not necessarily at the maternal side of the placenta or basal plate (Fig. 43.17, Videos 43.10 and 43.11). When identified early in gestation, anticoagulation with heparin may improve outcome; however, further investigation is necessary before establishing treatment guidelines.[108,109]

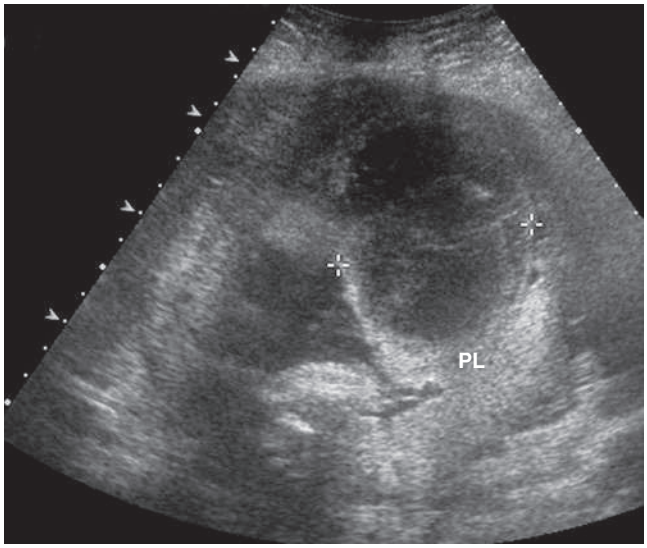

FIG. 43.12 Placental Abruption. Transabdominal sonogram of the placenta *(PL)* with a hematoma *(calipers)* lifting the placenta away from the uterine wall. See also Videos 43.6 and 43.7.

PLACENTAL MASSES

Solid-appearing placental masses include **chorioangioma, subamniotic hematoma, subchorionic hematoma,** and **placental hemorrhage.** These masses should be differentiated from fluid-filled placental regions of placental cysts and venous lakes. As previously discussed, placental infarctions may also have a masslike appearance.

Subchorionic placental cysts on the fetal surface of the placenta are predominantly innocuous findings on prenatal sonography, similar to cysts in the substance of the placenta (Fig. 43.18). Most fetuses whose placentas contain these cysts have normal outcomes. Larger cysts (>4.5 cm) are associated with IUGR. Maternal floor infarction may also be associated with placental cysts.[110,111]

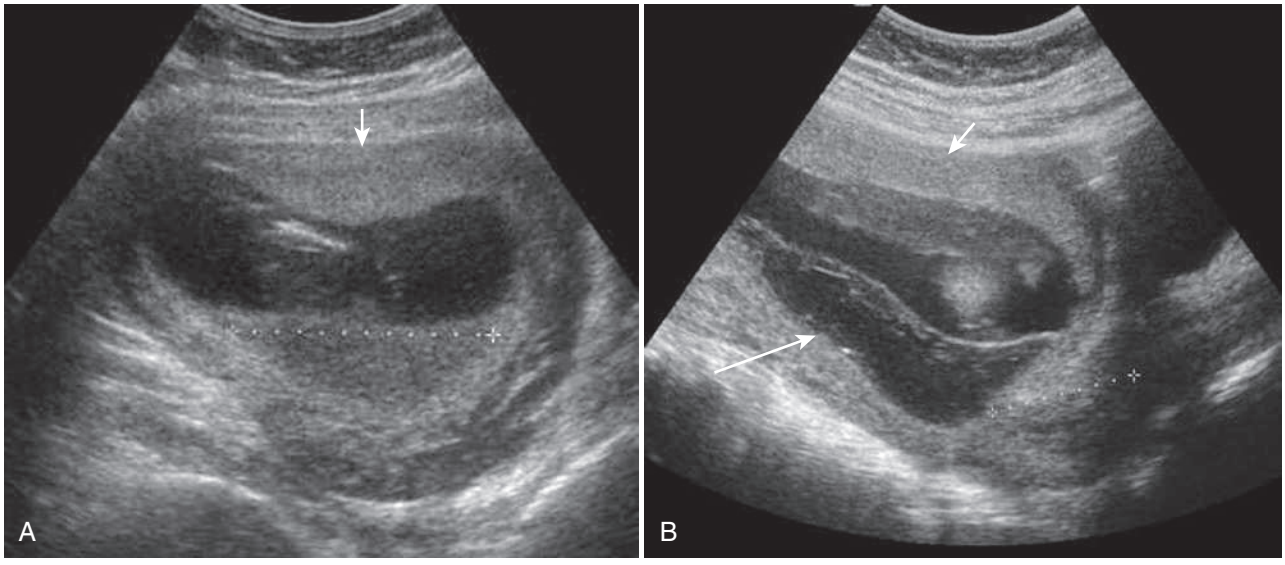

FIG. 43.13 Subchorionic Hematoma. (A) Transabdominal transverse view of the uterus in the second trimester shows acute subchorionic hematoma *(calipers).* The anterior placenta is shown by the short arrow. **(B)** Transabdominal midsagittal view of the same patient later in pregnancy demonstrates the subchorionic hematoma *(long arrow)* more hypoechoic and located overlying the cervix *(calipers); short arrow,* placenta.

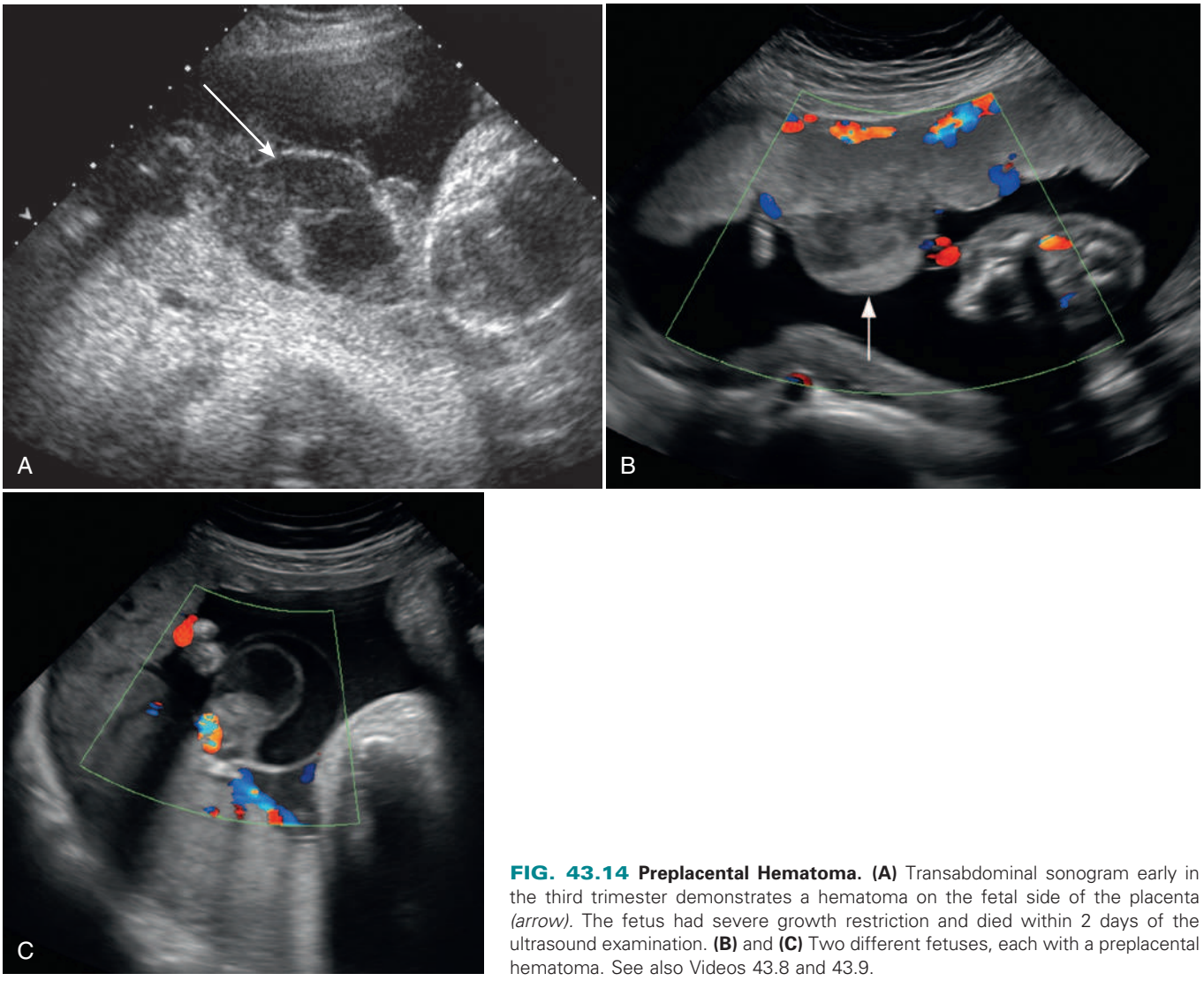

FIG. 43.14 Preplacental Hematoma. (A) Transabdominal sonogram early in the third trimester demonstrates a hematoma on the fetal side of the placenta *(arrow).* The fetus had severe growth restriction and died within 2 days of the ultrasound examination. **(B)** and **(C)** Two different fetuses, each with a preplacental hematoma. See also Videos 43.8 and 43.9.

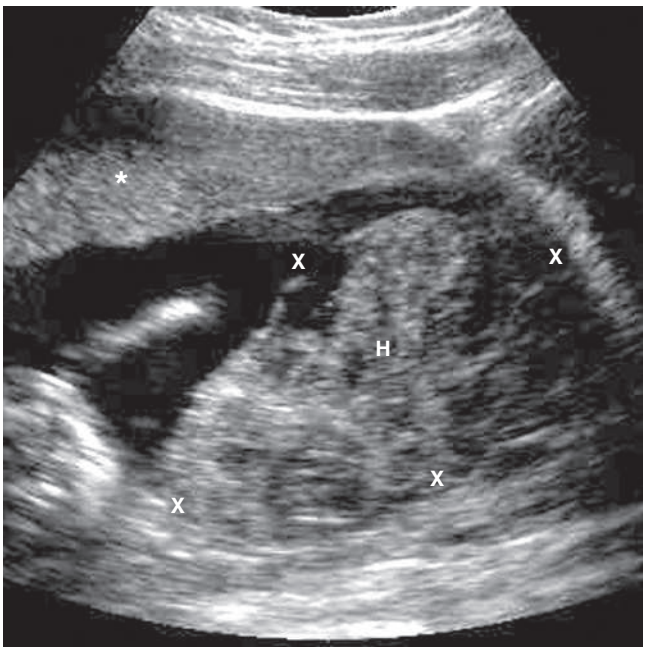

FIG. 43.15 Large Hematoma. Transabdominal sonogram shows large hematoma *(H, calipers).* The placenta (*) is anterior.

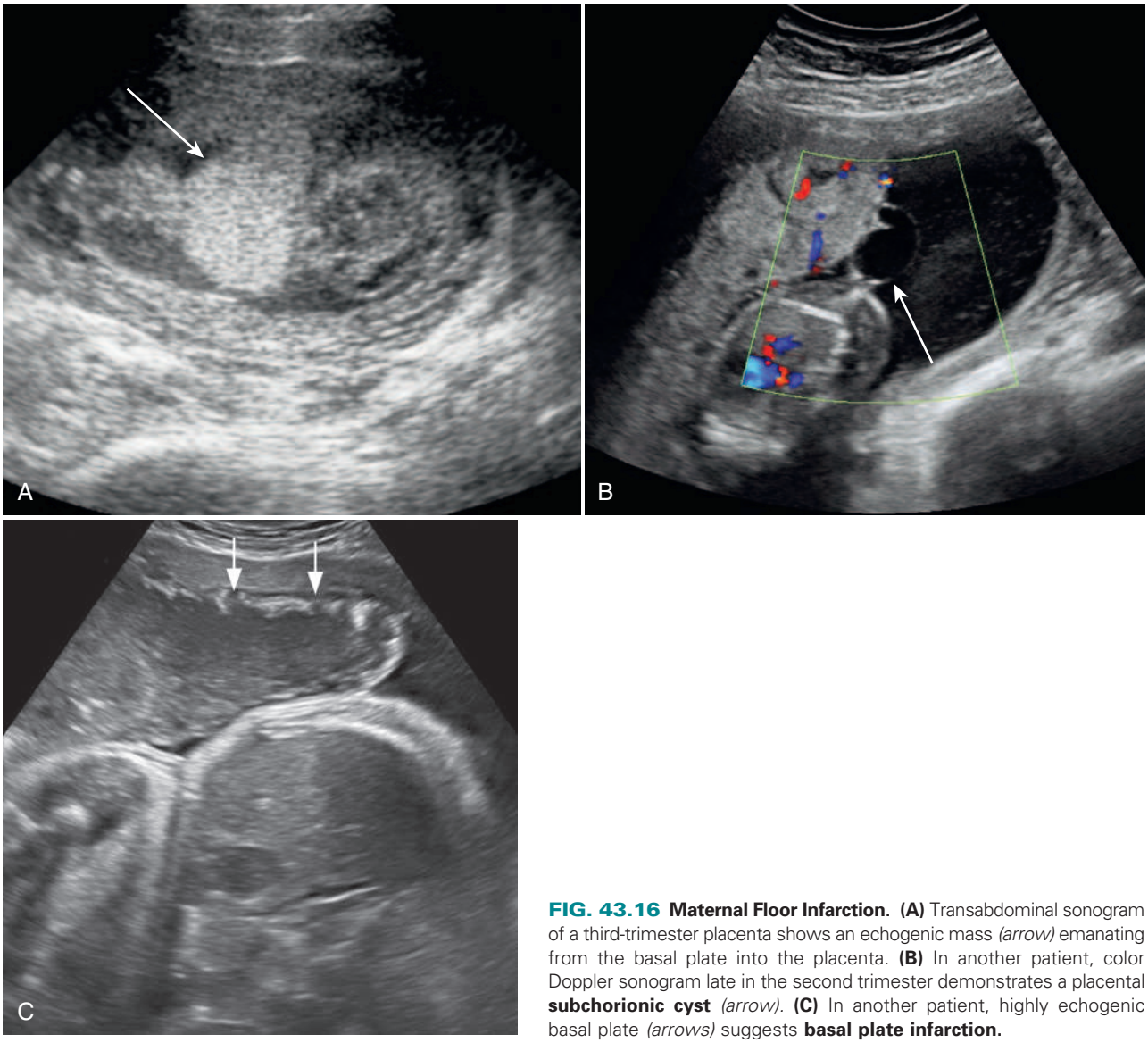

FIG. 43.16 Maternal Floor Infarction. (A) Transabdominal sonogram of a third-trimester placenta shows an echogenic mass *(arrow)* emanating from the basal plate into the placenta. **(B)** In another patient, color Doppler sonogram late in the second trimester demonstrates a placental **subchorionic cyst** *(arrow)*. **(C)** In another patient, highly echogenic basal plate *(arrows)* suggests **basal plate infarction.**

The most common benign tumor of the placenta is the **chorioangioma,** occurring in approximately 1% of pregnancies (Fig. 43.19). Although most are asymptomatic, large chorioangiomas can lead to high-output fetal cardiac failure, anemia, hydrops, and death.[112] Chorioangiomas appear as well-circumscribed solid tumors in the placenta. They can range from hypoechoic to hyperechoic compared to the echogenicity of the placenta. A threshold of 5 cm in diameter typically portends a high risk for adverse outcome.[113,114] Use of color or power Doppler ultrasound is helpful to identify increased blood flow within the solid mass, thereby distinguishing the mass as a chorioangioma.[115,116] Blood flow is not consistently demonstrable, especially with smaller chorioangiomas; those with low flow tend to have a better outcome, whereas chorioangiomas with extremely elevated flow usually are associated with adverse perinatal outcome, commonly through high-output heart failure. These pregnancies require close follow-up and surveillance for polyhydramnios and other signs of fetal hydrops.[117,118] Decreasing blood flow, as documented by color or power Doppler ultrasound, signals an improved prognosis.[118] Three-dimensional power Doppler can assist with the diagnosis of chorioangioma and can be used to quantitate blood flow to the tumor.[113]

In cases where the fetus is at risk for **hydrops,** in utero intervention improves perinatal outcomes. Interventions have included injection of thrombogenic material,[119] microcoil embolization,[120] and endoscopic laser devascularization,[121] in utero transfusion, amnioreduction (for those with polyhydramnios), and alcohol injection.[122]

Maternal **malignancies** rarely metastasize to the placenta. Malignant melanoma and adenocarcinoma of the breast, pancreas, and colon are most common.[123,124] These deposits are typically microscopic and do not interfere with placental function.

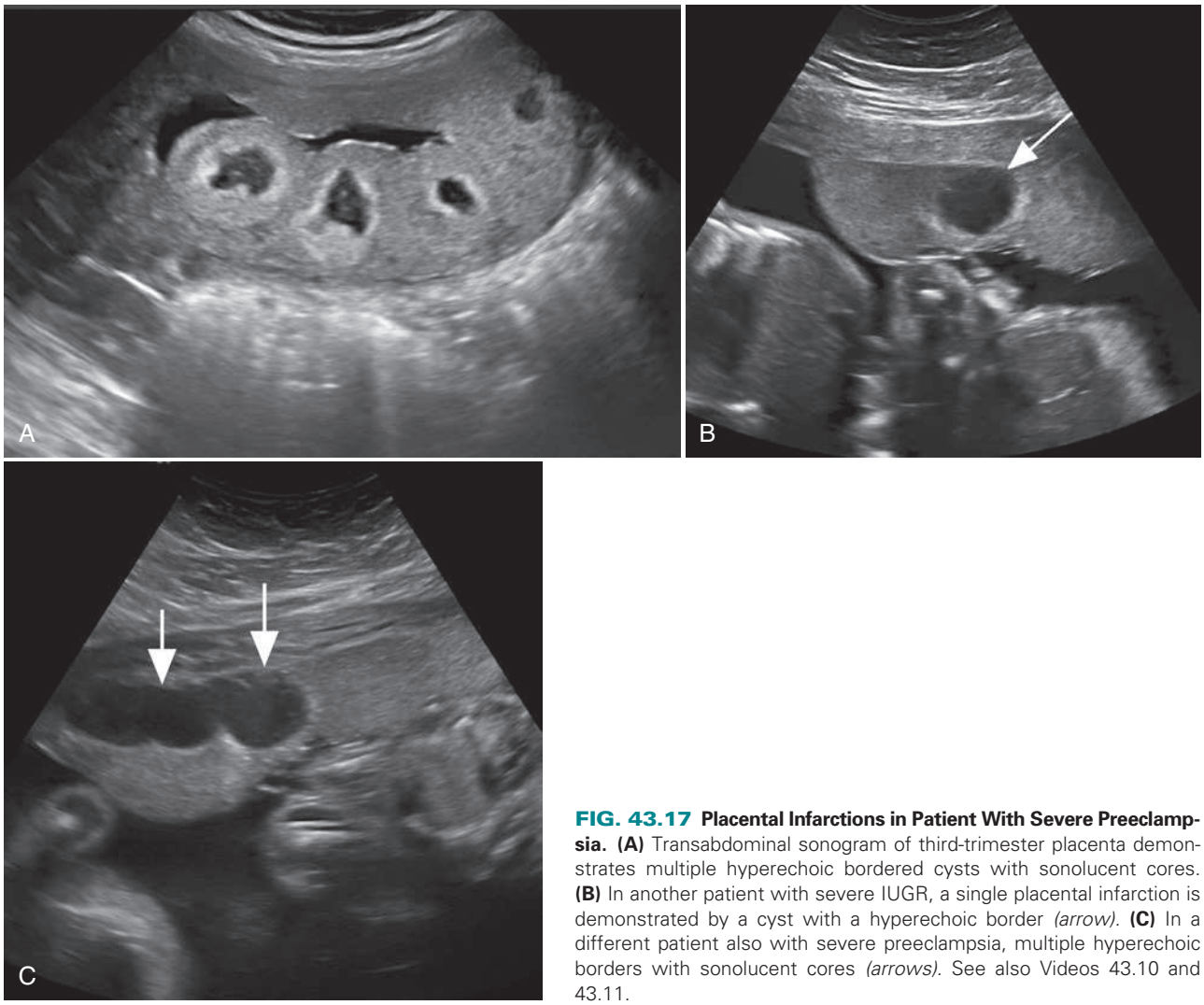

FIG. 43.17 Placental Infarctions in Patient With Severe Preeclampsia. (A) Transabdominal sonogram of third-trimester placenta demonstrates multiple hyperechoic bordered cysts with sonolucent cores. **(B)** In another patient with severe IUGR, a single placental infarction is demonstrated by a cyst with a hyperechoic border *(arrow)*. **(C)** In a different patient also with severe preeclampsia, multiple hyperechoic borders with sonolucent cores *(arrows)*. See also Videos 43.10 and 43.11.

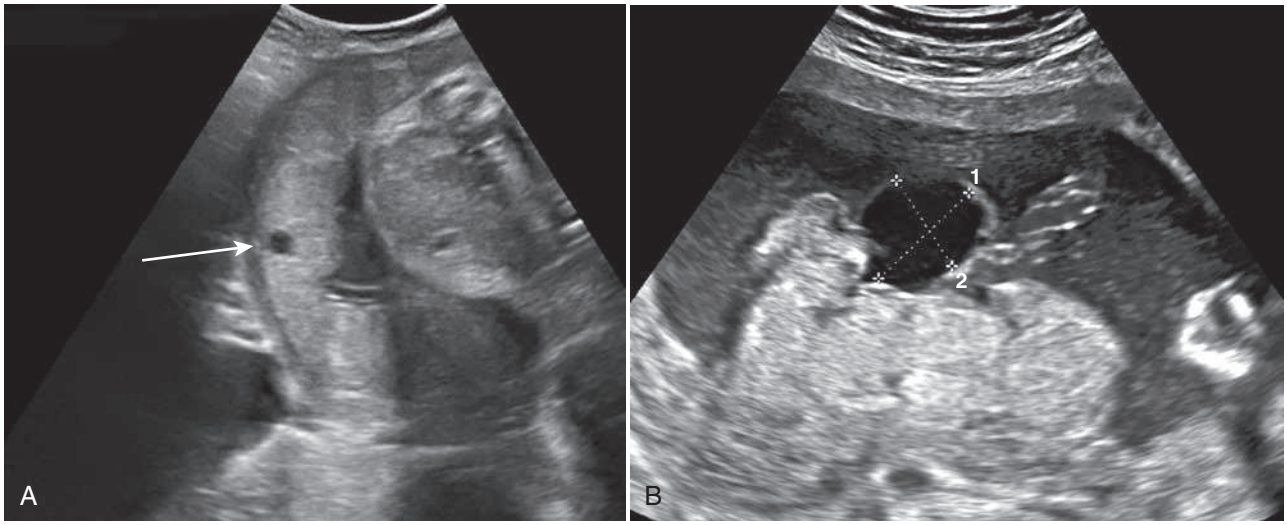

FIG. 43.18 Placental Cysts. (A) Transabdominal sonogram of a third-trimester placenta demonstrates a small placental cyst *(arrow)*. **(B)** Transabdominal sonogram of a second-trimester placenta with a surface cyst *(calipers)* located near the umbilical cord insertion.

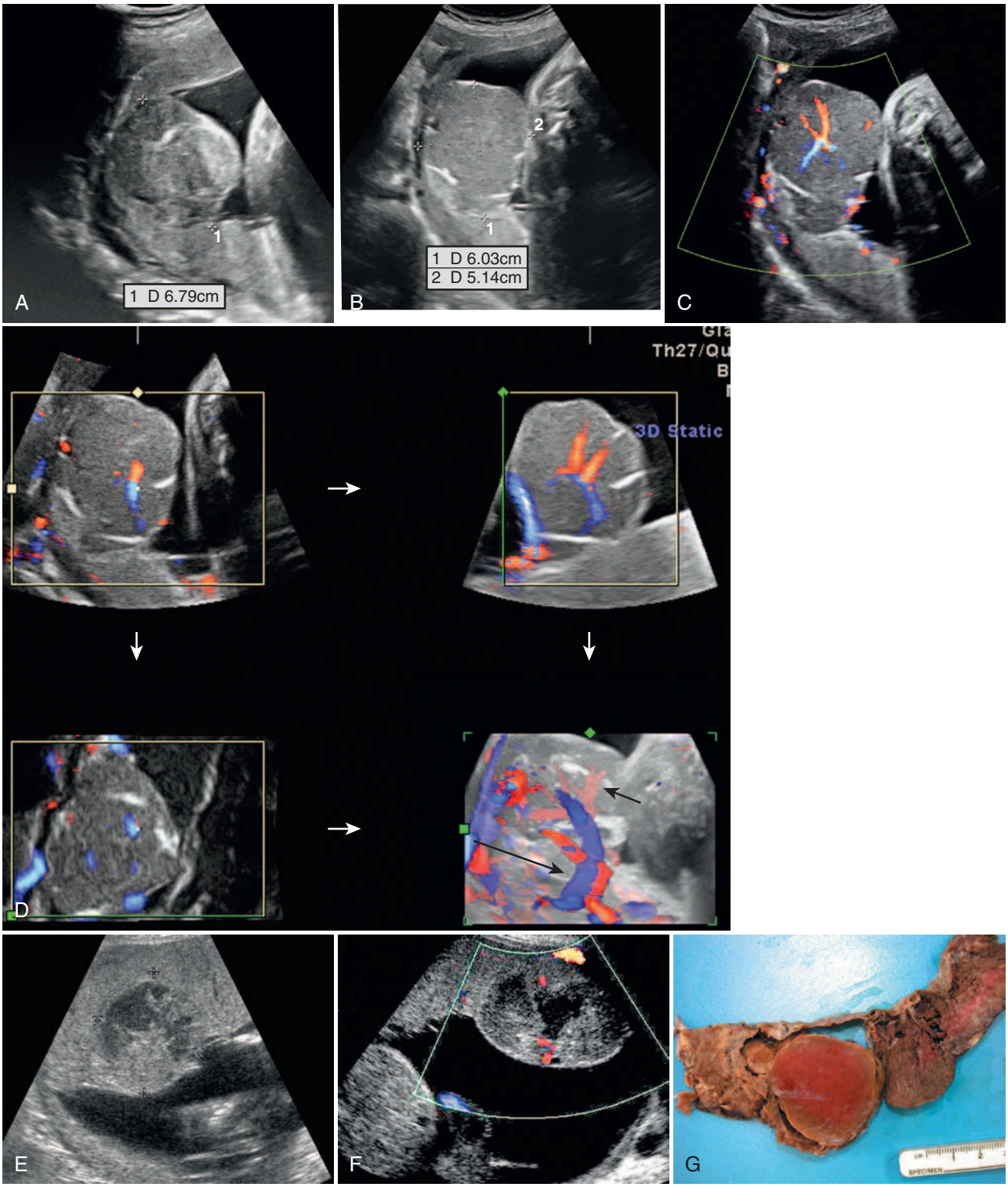

FIG. 43.19 Chorioangioma. **(A)** Transabdominal sonogram shows a heterogeneous placental mass *(calipers).* **(B)** In another patient, transabdominal sonogram of a more homogeneous and isoechoic placental mass *(calipers).* **(C)** In a different patient, transabdominal color Doppler sonogram shows blood flow within the tumor. **(D)** Same patient as **C;** 3D color Doppler sonography demonstrates feeding vessel *(long black arrow)* and vasculature *(short black arrow)* in the placental tumor. **(E)** and **(F)** Gray-scale and color Doppler sonograms show another patient with a small, hypovascular chorioangioma. **(G)** Specimen.

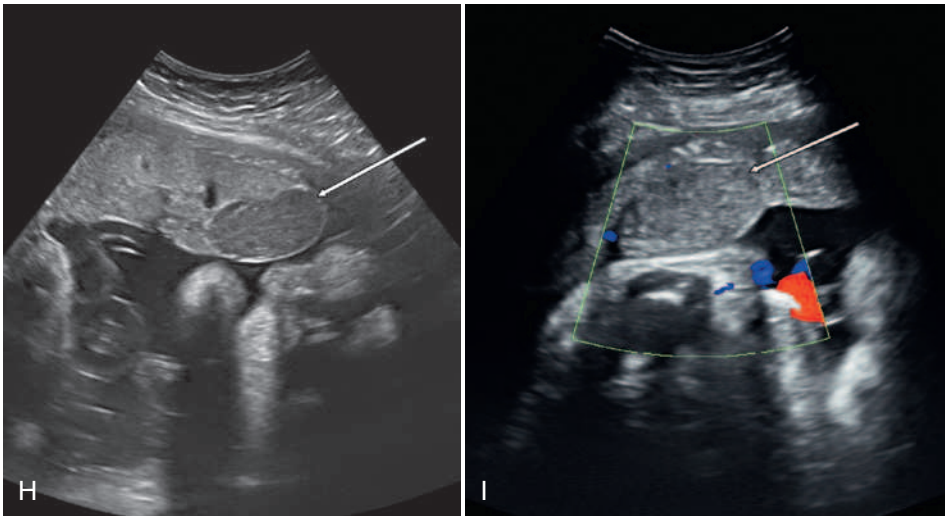

FIG. 43.19, cont'd **(H)** and **(I)** Placental chorioangioma *(arrow)* in another patient (**I** taken 4 weeks after **H**). The chorioangioma is relatively homogeneous and similar in echogenicity to the placenta.

MESENCHYMAL DYSPLASIA OF THE PLACENTA

Mesenchymal dysplasia of the placenta resembles a partial hydatidiform mole both grossly and microscopically, with a thickened placenta and small cystic lesions. The appearance of the placenta has been described as having a "stained-glass" appearance when color Doppler sonography is used, due to the flow noted in the multiple placental cysts.[125] In contrast to partial moles, mesenchymal dysplasia of the placenta may be associated with a normal fetus, although IUGR is common. There is also an association with **Beckwith-Wiedemann syndrome**[126] (Fig. 43.20). The villi in these cases are cystic with dilated vasculature. The karyotype is usually normal.[127]

FIG. 43.20 Mesenchymal Dysplasia of Placenta. Associated with Beckwith-Weidemann syndrome at 20 weeks' gestation. Note the enlarged placenta (8 cm, *calipers*) with multiple cystic spaces.

MOLAR GESTATIONS

Gestational trophoblastic disease consists of **complete mole** (Fig. 43.21) and **partial mole** and **choriocarcinoma.** These placental abnormalities are discussed in detail in Chapter 30.

MORPHOLOGIC PLACENTAL ABNORMALITIES

There are a number of placental shape abnormalities, some quite common, and some quite rare. New evidence suggests that the development of placental shape abnormalities originates from placental vascular abnormalities in the first trimester, also leading to umbilical cord insertion abnormalities.[11]

Circumvallate Placenta

In circumvallate placenta the membranes of the chorion laeve, instead of inserting at the margin of the placental disc, insert more toward the center of the disc. The pathologist can identify fibrin at the margin along with evidence of bleeding. With a complete circumvallate placenta, a ring may constrict the chorion frondosum.[28] Because of this placement, there is disproportionate folding of the placenta and fetal membranes. This results in the chorionic plate being smaller than the basal plate. Within the membrane fold, hyalinized villi may be seen after being incorporated into the fold.

Circumvallate placenta has the sonographic appearance of a rolled edge of membranes at the placental edge inserting toward the center of the placental chorionic disc (Fig. 43.22, Videos 43.12 and 43.13). Termed a **placental shelf,** this rolled edge of membranes can be thick and most often occupies only a small

portion of the placenta. Circumvallate placentas can also be confused with **uterine synechiae** (Fig. 43.23A), **uterine septum** (Fig. 43.23B), and **amniotic bands.** Carefully identifying the insertion of the membranes and determination of the echogenicity of the rolled edge of placenta, which should be similar to that of the placenta, should provide the correct diagnosis.

If a circumvallate placenta is identified, even if it seems to occupy only a small portion of the placenta, the rest of the placenta must be evaluated to determine whether the rolled edge of membranes involves the entire placenta. Three-dimensional sonography has been suggested as helpful for diagnosing a complete circumvallate placenta with the appearance of a "tire mounted on a wheel" or the "tire sign."[128] Complete circumvallate placentae are associated with adverse neonatal outcomes, including placental abruption, preterm delivery, oligohydramnios, IUGR, emergency cesarean delivery, Apgar scores less than 7, and perinatal death.[129,130] Fortunately, complete circumvallate placenta is rare, whereas partial circumvallate placentas are quite common and should be regarded as normal variants.

Evaluating second-trimester placental shelves to determine whether the sonographic finding persisted into the third trimester, Shen et al.[129] found an incidence of 11% for the identification of these shelves at the 13- to 16-week scan. Of note, none of the placental shelves occupied more than 25% of the placenta. Also, none of the partial circumvallate placentas could be sonographically appreciated in the third trimester. All neonates had a normal outcome. A recent large study of postdelivery placenta inspection yielded a complete circumvallate placenta incidence of 1.8%, none of which was detected antenatally.

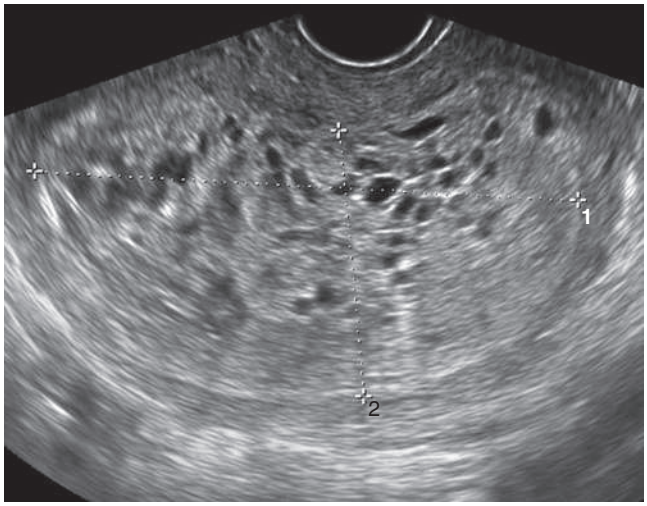

FIG. 43.21 Molar Pregnancy. Transvaginal sonogram in the late first trimester demonstrates a moderate amount of gestational tissue with multiple cystic spaces.

Succenturiate Lobe

Succenturiate lobes, or **accessory lobes,** of the placenta can be a single lobe or multiple lobes in addition to the main placental lobe (Fig. 43.24). Their incidence is as high as 6%.[28] Given that placental tissue is present in the accessory lobe, there must be arterial and venous connections to the main portion of the placenta. One concern involves a retained placental accessory lobe after delivery, if not expected from the antenatal sonogram. Succenturiate lobes can also lie over the cervix as a variant of **placenta previa.**[126] Even more important is the concern over the location of the vascular connection between the main placenta and the succenturiate lobe. If the vessels lie in proximity to the cervix, a **vasa previa** may be present.

When a succenturiate lobe of the placenta is identified, it is imperative that the vascular connection between the succenturiate lobe and placenta be identified. This can be difficult at times because of poor visualization, especially later in pregnancy, and because the closest distance between succenturiate lobe and placenta is not always the route taken by the vessels. At a

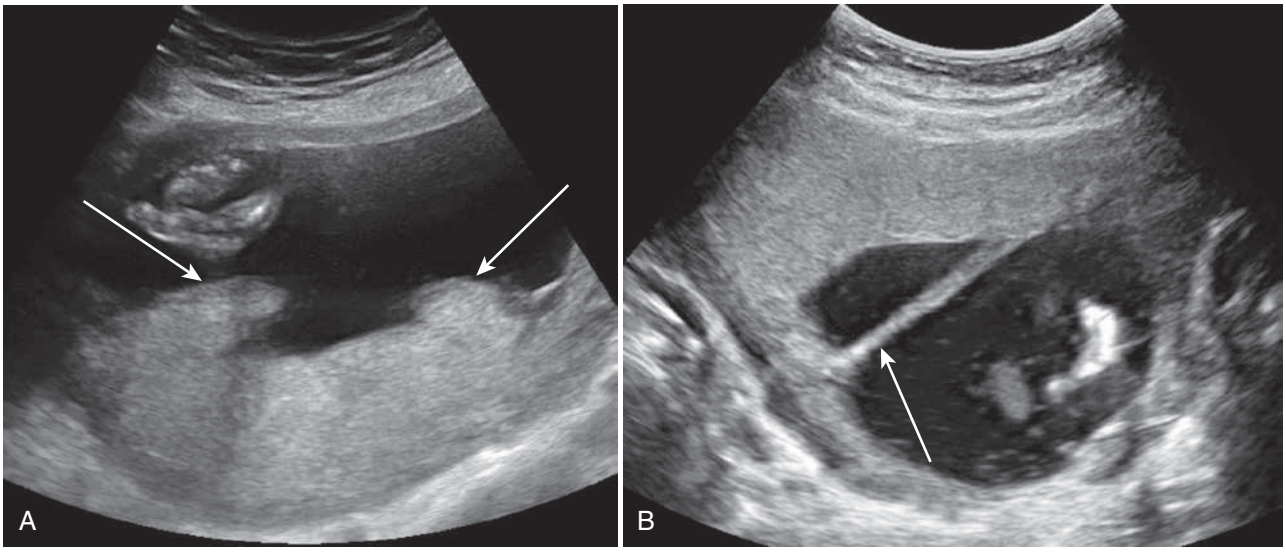

FIG. 43.22 Circumvallate Placenta. (A) Transabdominal sonogram in the early third trimester shows rolled edges of the placenta *(arrows).* **(B)** Transabdominal sonogram in the second trimester shows a placental shelf *(arrow),* which has echogenicity similar to the remainder of the placenta. See also Videos 43.12 and 43.13.

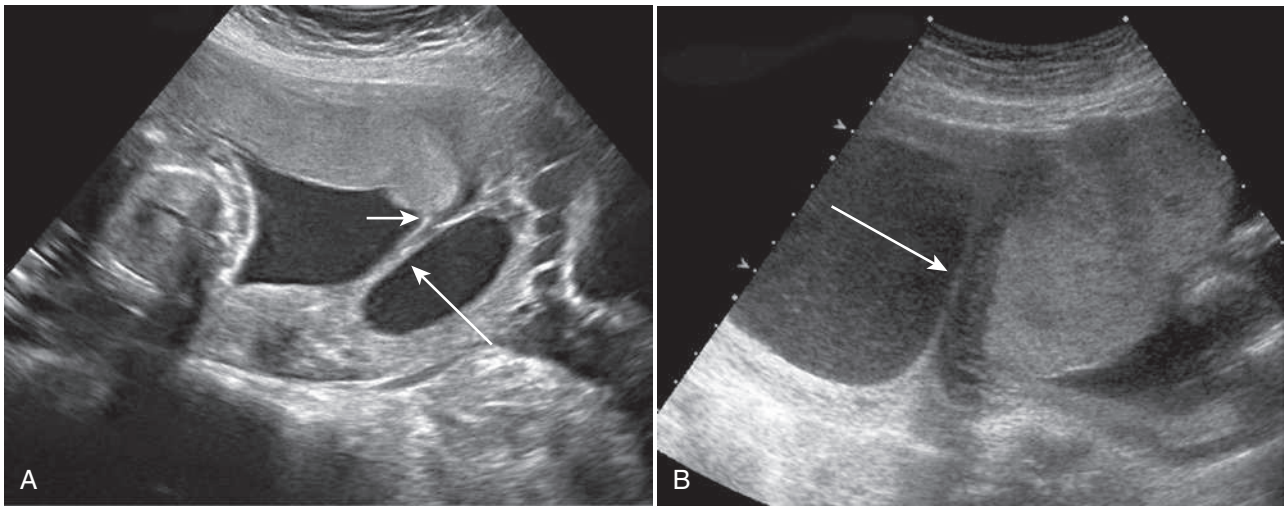

FIG. 43.23 Mimics of Circumvallate Placenta. (A) Placenta abutting a **uterine synechia** *(long arrow)* of myometrial tissue; *short arrow,* placental edge. **(B)** Transabdominal sonogram of a second-trimester pregnancy with a **uterine septum** *(arrow)*. The placenta partially inserts on the uterine septum.

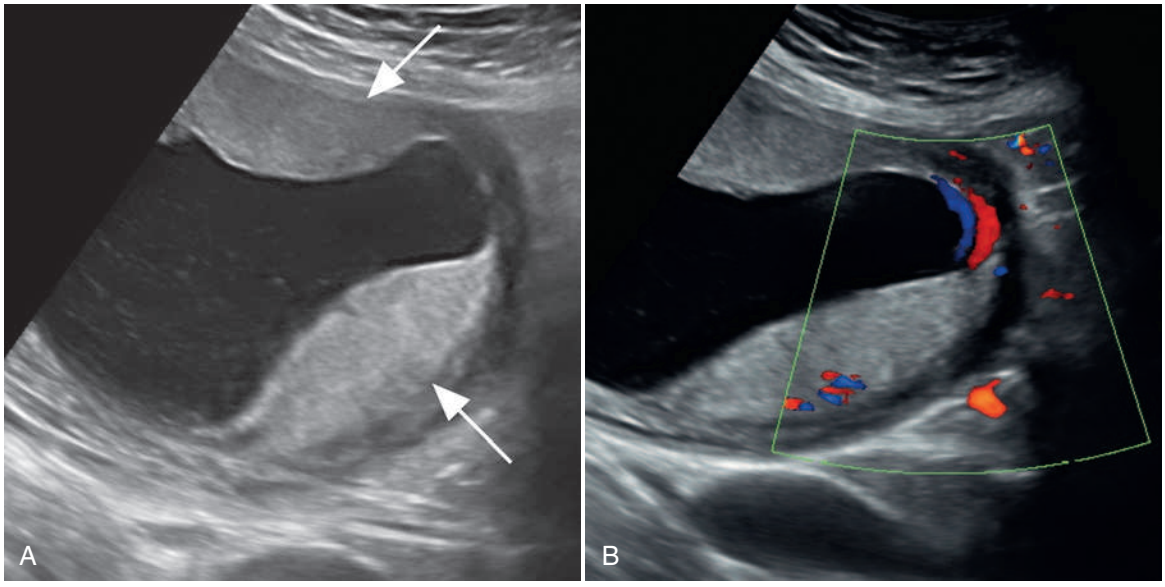

FIG. 43.24 Succenturiate Lobe. (A) Transabdominal sonogram shows two placental components *(arrows)*. **(B)** Color Doppler demonstrates the vascular connection between the succenturiate lobe and the main placental disc.

minimum, the internal cervical os should be evaluated to assess for the presence of fetal vessels.

Bilobed Placenta

Bilobed placentas consist of two similarly sized placental lobes separated by intervening membranes (Fig. 43.25, Video 43.14). There must be some vascular connection between the lobes, and the umbilical cord may insert in the membranes between the lobes. Although rare, a bilobed placenta can be regarded similar to succenturiate lobes, with similar risks. Bilobed placentas may have more unprotected vessels, however, reinforcing the need for careful evaluation of the placental vasculature in such cases.

UMBILICAL CORD

Size and Appearance

Umbilical cord length varies, and a normal length has not been established. However, extremes of cord length are associated with abnormal outcome. **Short umbilical cords** are associated with conditions that impair fetal movement early in gestation, such as akinesia syndromes, aneuploidy, and extreme IUGR. **Excessive cord length** is associated with asphyxia or death resulting from a variety of situations that compromise cord flow, including excessive coiling, true knots, multiple loops of nuchal cord, and cord prolapse.

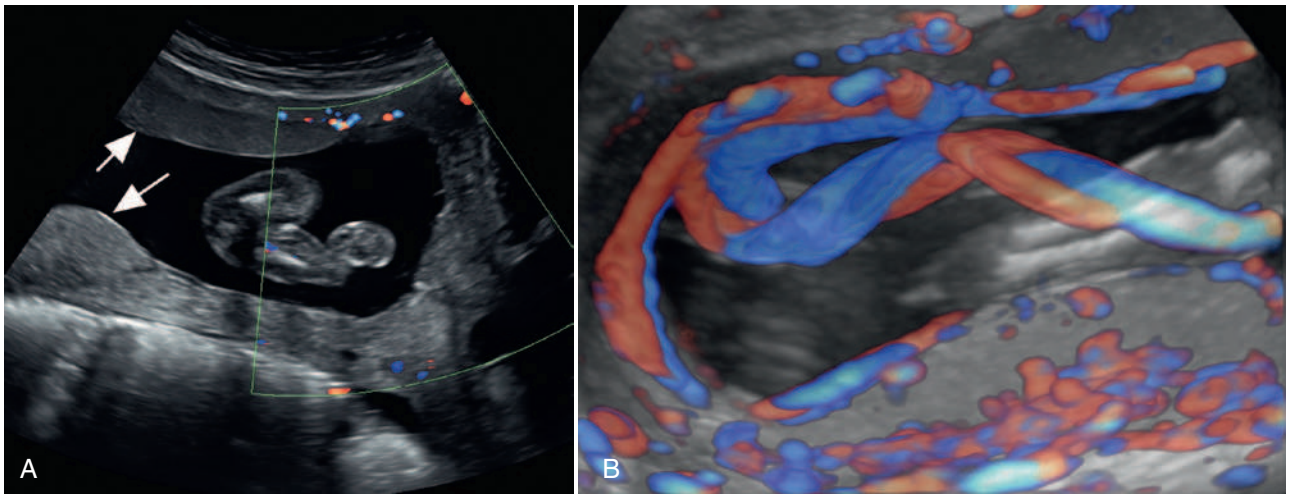

FIG. 43.25 Bilobed Placenta. (A) Transabdominal sonogram of a third-trimester bilobed placenta. Both placental discs are of comparable size *(arrows)*. **(B)** Three-dimensional color Doppler ultrasound demonstrates the umbilical cord inserting into the upper lobe and the fetal vascular connection between the lobes. See also Video 43.14.

The potential importance of the **diameter** of the umbilical cord is unclear. In the first trimester, fetal size correlates with cord diameter, and small diameter may be a marker for pregnancy loss.[131] Also, data from multiple centers suggest that cord diameter may be a marker for chromosomal abnormalities when larger[132] or smaller than expected.[133] In the second and third trimesters, the largest contributor to the size of the umbilical cord is **Wharton jelly,** the supportive substance surrounding the umbilical vessels. A nomogram has been developed for the area of Wharton jelly that correlates with fetal biometry up to 32 weeks' gestation.[134,135] In the second trimester, a larger-than-expected umbilical cord is associated with aneuploidy.[136] IUGR has been associated with thin cords; diabetes, fetal macrosomia, placental abruption, and rhesus isoimmunization have been associated with thicker cords.[137] The associations between fetal umbilical cord size and fetal growth overlap too greatly to be useful screening tools for these entities.[138]

Information on the umbilical cord and its manner of **twisting** comes from the pathology literature. Left twists occur in 83%, right twists in 12%, and absent twists in 5% of umbilical cords in live-born singletons. For the umbilical cords that have a twist, ascertainment of the degree of twist has been reported antenatally. The **umbilical coiling index** is calculated by dividing the number of helices by the cord length in centimeters (Fig. 43.26). The mean umbilical coiling index is 0.44 ± 0.11 antenatally and 0.28 ± 0.08 after delivery.[139] Umbilical coiling does not vary with respect to the amount of Wharton jelly present.[140] Assessment of the degree of coiling in the second trimester does not correlate well with the umbilical coiling index at term.[141]

Absent umbilical cord twists are associated with single umbilical arteries, multiple gestations, fetal demise, preterm delivery, aneuploidy, and both marginal and velamentous umbilical cord insertions[142-144] (Fig. 43.27). Lower degrees of coiling are associated with lesser degrees of fetal growth.[145]

True knots of the umbilical cord occur in 1% to 2% of pregnancies. Although some are normal variants,[146] these knots may also be associated with increased fetal mortality. Sonographic

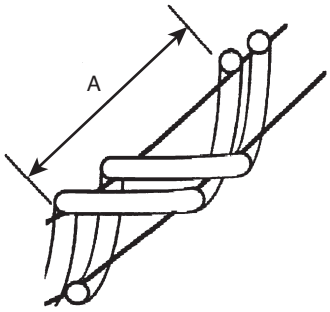

FIG. 43.26 Umbilical Coiling Index. Defined as the distance *(A)* between the same umbilical artery making one turn around the umbilical vein. (With permission from Otsubo Y, Yoneyama Y, Suzuki S, et al. Sonographic evaluation of umbilical cord insertion with umbilical coiling index. J Clin Ultrasound. 1999;27[6]:341-344.[143])

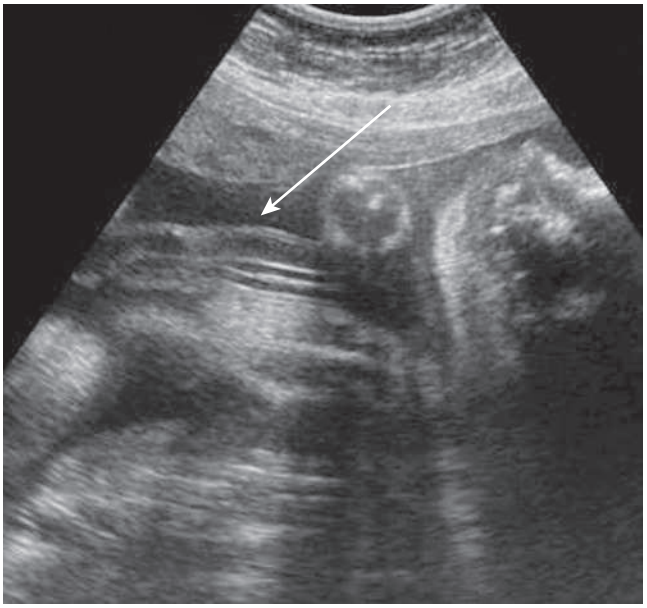

FIG. 43.27 Uncoiled Cord in Second Trimester.

features such as the "hanging noose sign" have been proposed to make this diagnosis antenatally, with 2D imaging as well as 3D and 4D sonography.[147,148] Although 3D sonography may be helpful for suggesting the presence of a true knot of the umbilical cord, multiple loops of cord lying next to each other can mimic the presence of a knot.[149,150]

Cysts of the umbilical cord can be seen throughout pregnancy, occurring most frequently on the portion closest to the fetus (Fig. 43.28). Many cysts develop from the allantois and omphalomesenteric duct, or **pseudocysts** may develop through liquefaction of Wharton jelly, giving the umbilical cord a hydropic appearance[151,152] (Fig. 43.29). All cord cysts are associated with both structural and chromosomal defects, so a detailed structural survey is required whenever a cyst is encountered.[153] However, cord cysts seen in the first trimester often resolve, without sequelae.[154] **Trisomies 13 and 18** are the most common chromosomal abnormalities associated with umbilical cord cysts,[152,155] and genitourinary and gastrointestinal anomalies are the most common structural defects.[156-159]

Vascular anomalies of the umbilical cord are associated with adverse fetal outcomes. **Umbilical artery aneurysms** are associated with vascular abnormalities, trisomy 18, and fetal demise.[152,160-162] **Spontaneous rupture** of the umbilical artery with a resultant umbilical cord hematoma has also been reported.[162]

Umbilical cord tumors are exceedingly rare. The most common is the umbilical cord **hemangioma,** which appears as a heterogeneous mass surrounded by multiple peripheral cystic areas. Cord hematomas are associated with an increased risk of fetal demise.[163,164]

Nuchal cord (cord around neck of the fetus) is often seen in the second and third trimesters and is a common finding at delivery. Multiple tight loops of nuchal cord indenting the skin late in the third trimester may prompt further evaluation

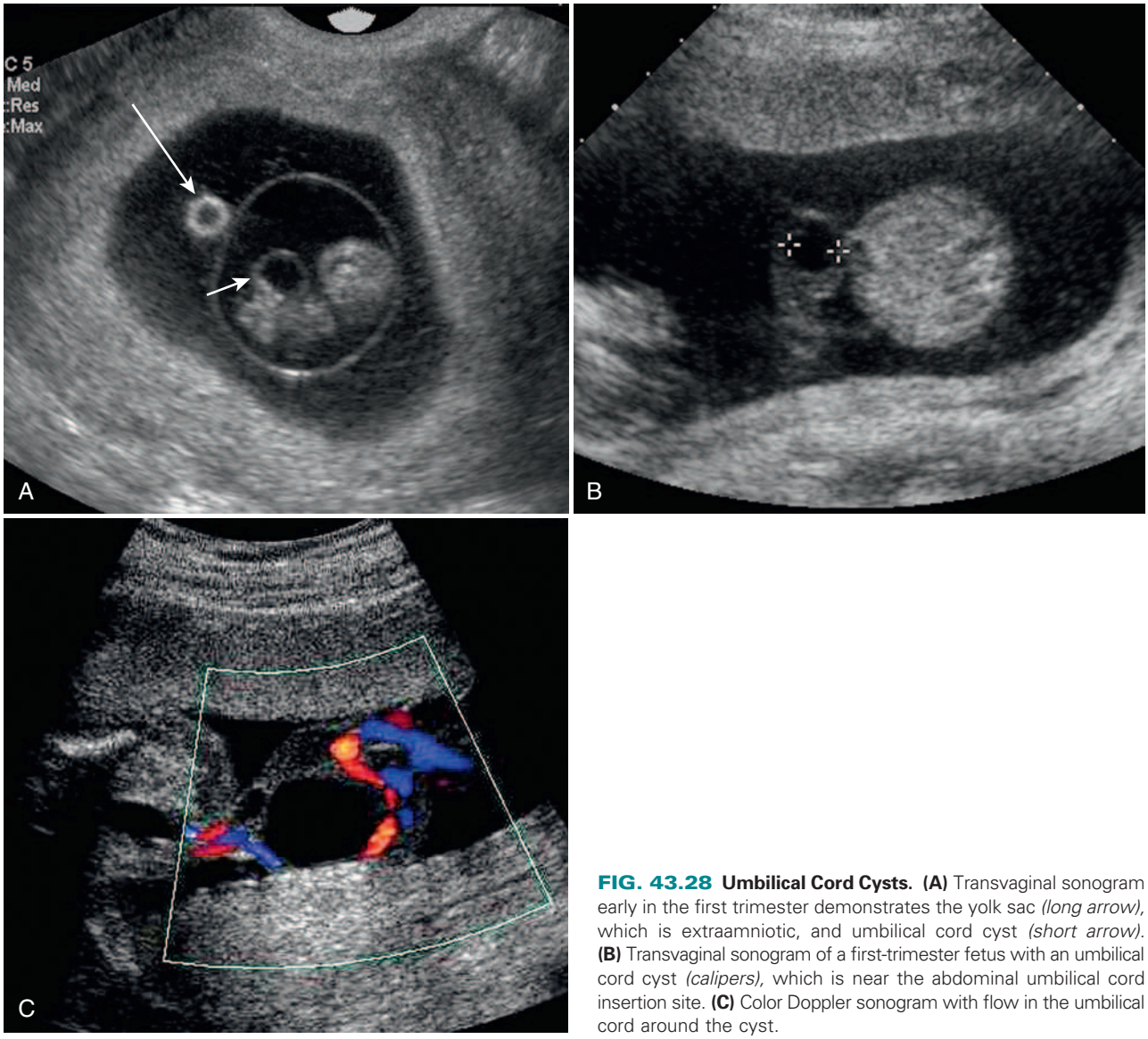

FIG. 43.28 Umbilical Cord Cysts. (A) Transvaginal sonogram early in the first trimester demonstrates the yolk sac *(long arrow),* which is extraamniotic, and umbilical cord cyst *(short arrow).* **(B)** Transvaginal sonogram of a first-trimester fetus with an umbilical cord cyst *(calipers),* which is near the abdominal umbilical cord insertion site. **(C)** Color Doppler sonogram with flow in the umbilical cord around the cyst.

but management is unclear, especially because documenting circumferential looping of the umbilical cord around the fetal neck is difficult because of the shadowing present late in gestation.

The normal umbilical cord has three vessels; one vein carries oxygenated blood to the fetus, and two arteries carry deoxygenated blood from the fetus. In 1% to 2% of pregnancies, however, there is only a **single umbilical artery** (Fig. 43.30, Video 43.15). The diagnosis is made either by examining a free loop of cord in the amniotic fluid or by assessing the umbilical arteries around the fetal bladder. Although associated with aneuploidy as well as many anomalies, especially renal and cardiac abnormalities, in isolation a single umbilical artery has no functional importance.

FIG. 43.29 Edematous Cord. Transabdominal sonogram of a third-trimester fetus shows an edematous area *(arrow)* of cord near the abdominal umbilical cord insertion.

Insertion Into the Placenta

The normal umbilical cord normally inserts into the central portion of the placenta. Identifying the placental umbilical cord insertion is important to recognize abnormalities of the umbilical cord vessels, as with gray-scale imaging and color or power Doppler sonography[165] (Fig. 43.31, Video 43.16).

Velamentous and Marginal Cord Insertions

A **velamentous umbilical cord insertion** refers to the situation where the umbilical cord inserts into the membranes and not the placental disc (Fig. 43.32, Video 43.15). A **marginal cord insertion** (Fig. 43.33), also known as a **battledore placenta,** occurs when the umbilical cord inserts into the very margin of the placenta. Velamentous umbilical cord insertions occur in approximately 1% of singleton pregnancies; marginal cord insertions occur in approximately 7% of singletons. Both of these cord insertions are more common in multiple gestations and are also associated with single umbilical arteries[28] and are associated with the smaller twins in monochorionic twin pregnancies with discordant growth.[166]

Velamentous umbilical cord insertions are sonographically identified throughout the second and third trimesters of pregnancy with great reliability. Sepulveda et al.[167] identified the placental cord insertion in more than 99% of pregnancies, correctly identifying all velamentous cord insertions using both gray-scale and color Doppler sonography.[167] A velamentous cord insertion has been identified as early as 10 weeks' gestation[168] and can be routinely identified on the 11- to 14-week first-trimester scan.[169] Velamentous cord insertions are associated with IUGR, preterm delivery, congenital anomalies, low Apgar scores, fetal and

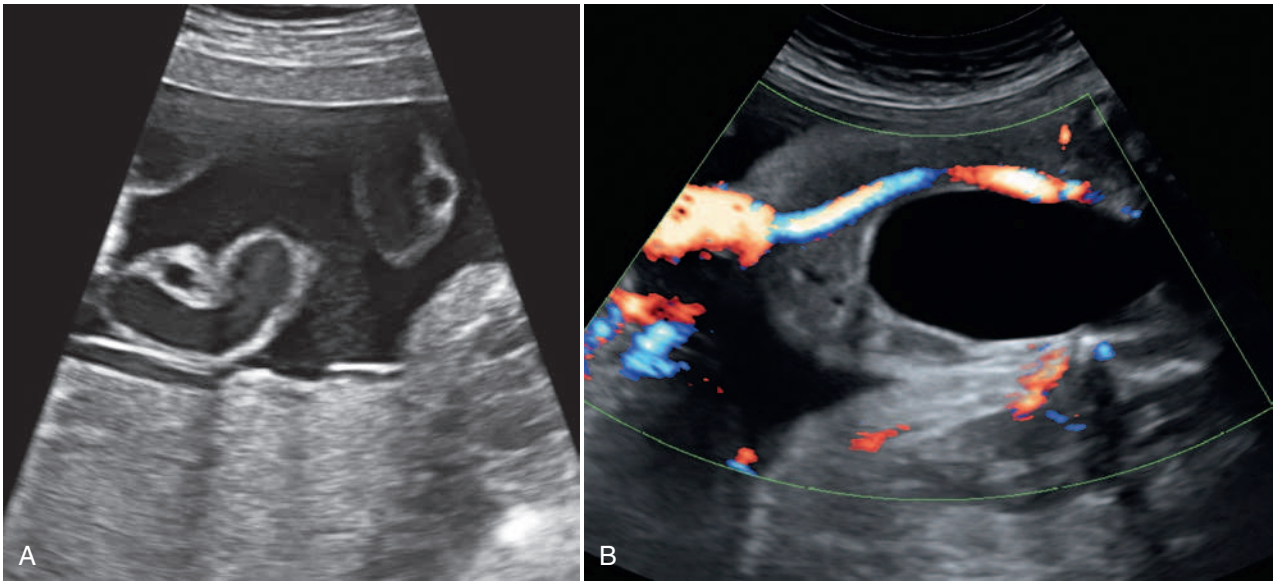

FIG. 43.30 Single Umbilical Artery. (A) Gray-scale sonogram shows a single artery and a single vein. **(B)** Color Doppler ultrasound adjacent to the fetal bladder shows a single umbilical artery. See also Video 43.15.

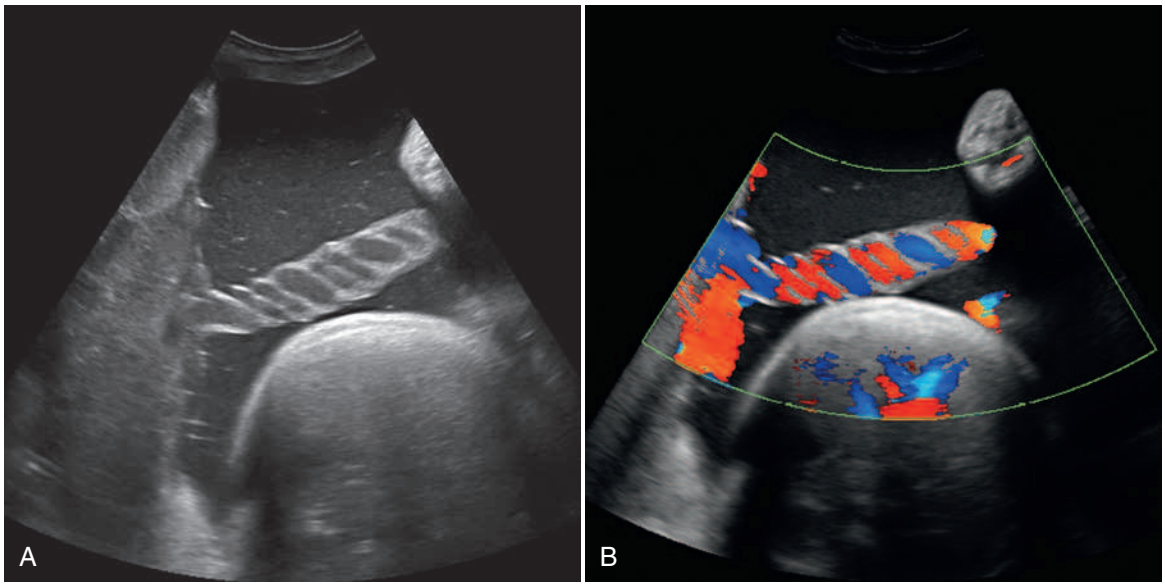

FIG. 43.31 Normal Cord Insertion Into Placenta. (A) Gray-scale sonogram demonstrates a normal umbilical cord insertion into the placenta. **(B)** Color Doppler sonogram shows the umbilical cord insertion into the placenta. See also Video 43.16.

neonatal death, retained placenta after delivery, and postpartum hemorrhage.[167,170,171] Marginal umbilical cord insertions are not associated with IUGR or preterm delivery[172] but are associated with vasa previa.

The insertion of the umbilical cord into the membranes leads to the unsupported coursing of the umbilical vessels to the placental disc and many complications. Wharton jelly supports and protects the umbilical vessels in the umbilical cord. With the vessels in the membranes, no Wharton jelly is present, leading to increased risk of compression or even rupture of these vessels. Intrapartum fetal heart rate patterns show more variable decelerations and no accelerations with velamentous cord insertions during the first and second stages of labor compared to controls.[170] Increasing length of the unsupported membrane vessels is associated with increasing rates of abnormal heart rate patterns, as is the umbilical cord insertion being in the lower portion rather than the middle or upper portion of the uterus.[170] Nonreassuring fetal heart rate patterns and emergency cesarean deliveries are more frequent with velamentous cord insertions in the lower third than in the middle or upper third of the uterus.[170] Because velamentous cord insertions are typically located low in the uterus, TVS can be critical to making this diagnosis.

A rare abnormality of umbilical cord insertion that overlaps with velamentous umbilical cord insertions is furcate umbilical cord insertion. This occurs when the umbilical cord vessels prematurely divide and insert into the membranes with vessels coursing to the placental substance (Fig. 43.34). The mangrove sign, so called because of the roots of a mangrove tree having a similar appearance, has been coined to denote furcate umbilical cord insertions.[173] A recent case report documents the association of a furcate umbilical cord insertion with retained placenta and a fetal syndrome.[174] Further research is necessary to better understand this rare entity.

Vasa Previa

Vasa previa is the situation where the umbilical cord vessels overlie the internal cervical os (Fig. 43.35, Video 43.17). The incidence is approximately 0.6 in 1000 pregnancies,[175] but approximately 25% that are diagnosed in the second trimester resolve.[176] Because these are fetal vessels, even a small amount of blood loss from rupture of these vessels can lead to fetal death. High-risk situations that require specific exclusion of vasa previa include velamentous umbilical cord insertions in which the membranous fetal umbilical vessels can traverse the internal cervical os somewhere along their length. Marginal umbilical cord insertions, especially those with aberrant vessels within the membranes, also are associated with vasa previa.[177] Presence of bilobed placentas[178] or the more common succenturiate lobes[179] requires that a vasa previa be excluded, given the potential for a poor neonatal outcome. Prior low placenta, placenta previa, multiple gestations, pregnancies resulting from *in vitro* fertilization, and pregnancies with umbilical cord insertions occurring in the lower third of the uterus in the first trimester are all associated with vasa previa.[175,177,179,180]

Once a vasa previa is diagnosed, obstetric management is critical to optimize outcome. Current recommendations are for antenatal corticosteroids between 28 and 32 weeks' gestation, consideration of hospitalization between 30 and 34 weeks' gestation, and delivery at 34 to 37 weeks' gestation, which is recommended to obviate the risks of vessel rupture that can occur with labor or rupture of the membranes.[181] If the patient has preterm labor, ruptured membranes, or bleeding before 35 weeks, delivery at the earlier gestational age should be considered.[180,182]

Vasa previa is diagnosed when a fetal vessel is identified overlying the internal cervical os. Although gray-scale ultrasound

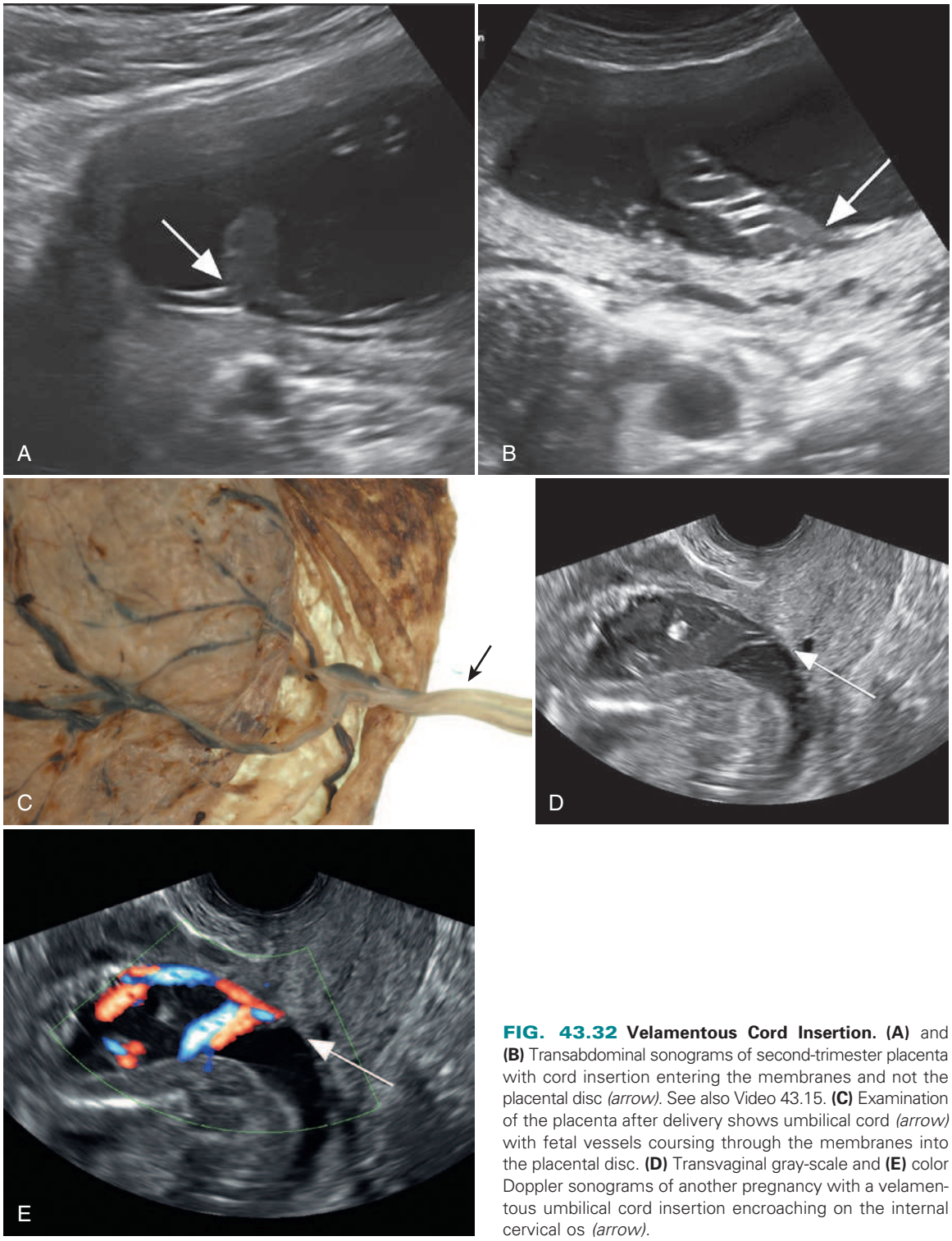

FIG. 43.32 Velamentous Cord Insertion. (A) and **(B)** Transabdominal sonograms of second-trimester placenta with cord insertion entering the membranes and not the placental disc *(arrow)*. See also Video 43.15. **(C)** Examination of the placenta after delivery shows umbilical cord *(arrow)* with fetal vessels coursing through the membranes into the placental disc. **(D)** Transvaginal gray-scale and **(E)** color Doppler sonograms of another pregnancy with a velamentous umbilical cord insertion encroaching on the internal cervical os *(arrow)*.

can identify the vessel, color or power Doppler sonography can assist with visualizing the vessel. Pulsed wave Doppler ultrasound should confirm a fetal artery, by demonstrating the heart rate of the fetus rather than that of the pregnant woman. Three-dimensional sonography may assist with making the diagnosis of a vasa previa,[177,183] especially using 3D power Doppler sonography to map out the aberrant vessels.[184] The clinician must be careful, however, especially when using color or power Doppler ultrasound, not to equate identification of the umbilical cord in the lower uterine segment or overlying the cervix with a vasa previa (Fig. 43.36). The cord could be free floating in this area, termed a **funic presentation,** and not a vasa previa (Fig. 43.37). Careful attention to detail, using movement of the probe or follow-up sonography, may be necessary to reach the correct diagnosis.[185]

FIG. 43.33 Marginal Cord Insertion. Gray-scale sonogram shows the umbilical cord inserting into the edge of the placenta *(arrows).*

PLACENTA DURING LABOR AND POSTPARTUM

Third Stage of Labor

Ultrasound may have some role during the third stage of labor, the time from delivery of the neonate to delivery of the placenta. A prolonged third stage, with the placenta retained, has various causes. If the placenta does not separate, a placenta accreta could be present.[66] A prolonged third stage may also be caused by retention of a detached placenta from poor contractility or atony of the uterus, sometimes from infection. These abnormalities are treated differently, and ultrasound may help differentiate the various causes of a prolonged third stage of labor and lead to improved patient care.[186]

The mechanism of placental separation has been reported using gray-scale sonography.[187] Color Doppler ultrasound provides information on the phases of placental separation during the third stage of labor by specifically assessing blood flow between the myometrium and the placenta.[188] The manner in which the placenta separates varies, based on prior cesarean delivery and a prolonged second stage of labor.[189]

Retained Products of Conception

Women with suspected retained products of conception (RPOC) typically present with abnormal bleeding. RPOC are most common after second-trimester spontaneous abortion, extreme preterm birth, medical termination of pregnancy, and unsuspected placenta accreta. RPOC are suggested when an echogenic endometrial mass is visualized within the uterine cavity (Fig. 43.38). This mass may extend into the myometrium[190] and can be differentiated from blood clot when blood flow is

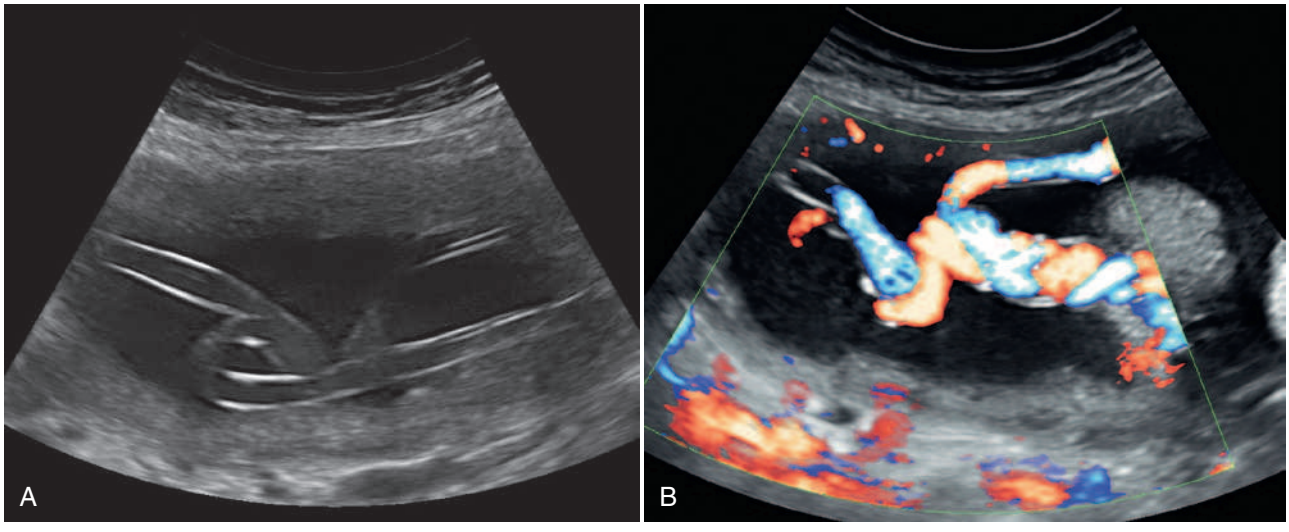

FIG. 43.34 Furcate Cord Insertion. (A) Gray-scale and **(B)** color Doppler sonograms of a patient with a furcate insertion of the umbilical cord. Note the separation of the vessels within the membranes.

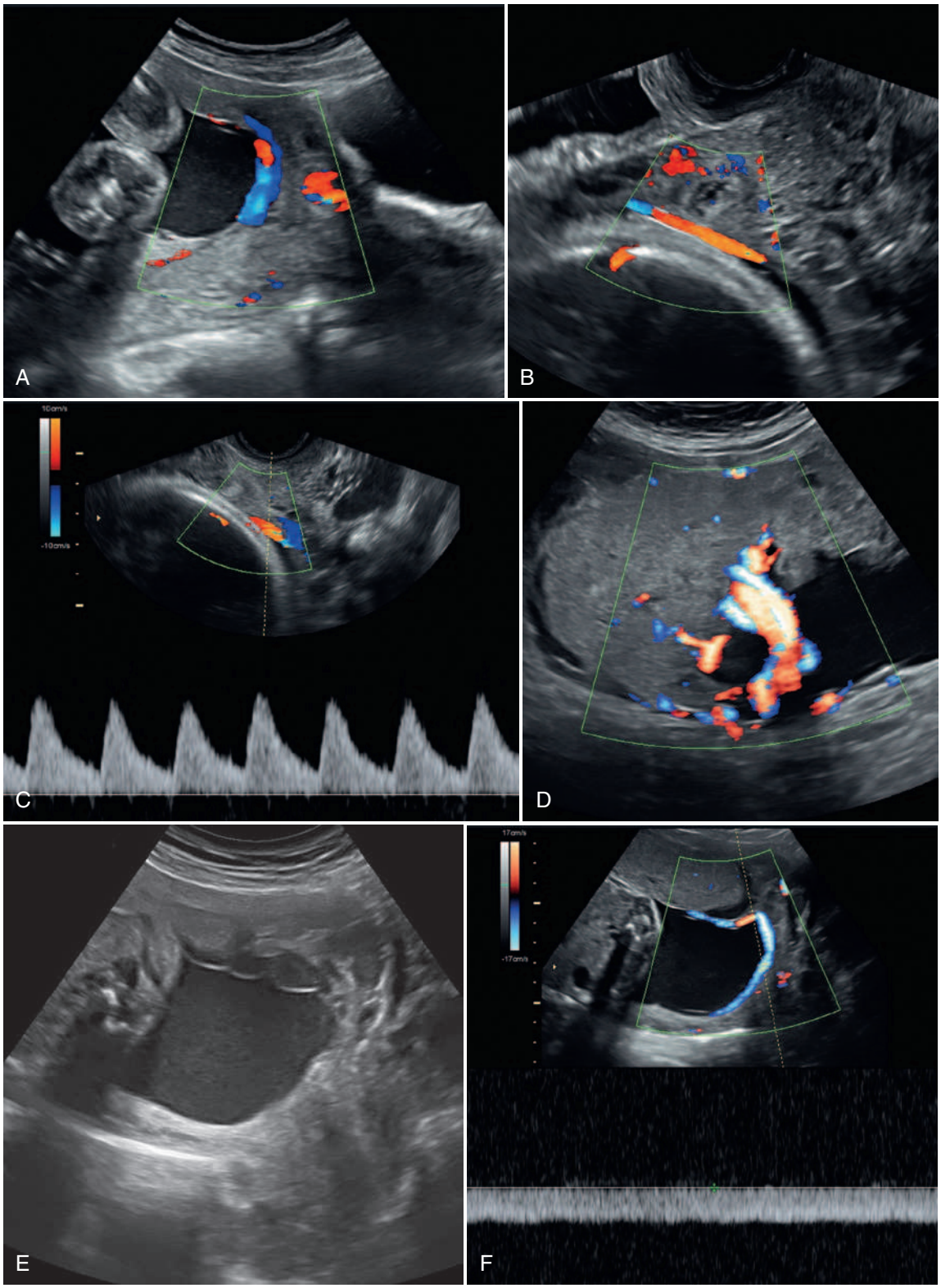

FIG. 43.35 Vasa Previa. (A) Transabdominal color Doppler demonstrating vessels overlying the internal cervical os. **(B)** Transvaginal color Doppler demonstrating a vessel overlying the internal cervical os. The fetal cranium is shown in the lower portion of the image. **(C)** Color and pulsed Doppler demonstrating a fetal artery overlying the internal cervical os consistent with a vasa previa. **(D)** Color Doppler sonogram demonstrating a normal placental umbilical cord insertion. **(E)** Gray-scale sonogram of the same patient in **D** demonstrating an apparently normal image of the internal cervical os. **(F)** Color and pulsed Doppler demonstrating a placental vessel overlying the internal cervical os consistent with a vasa previa. Placental vessels can emanate from the placental disc even in those with normal umbilical cord insertions. See also Video 43.17.

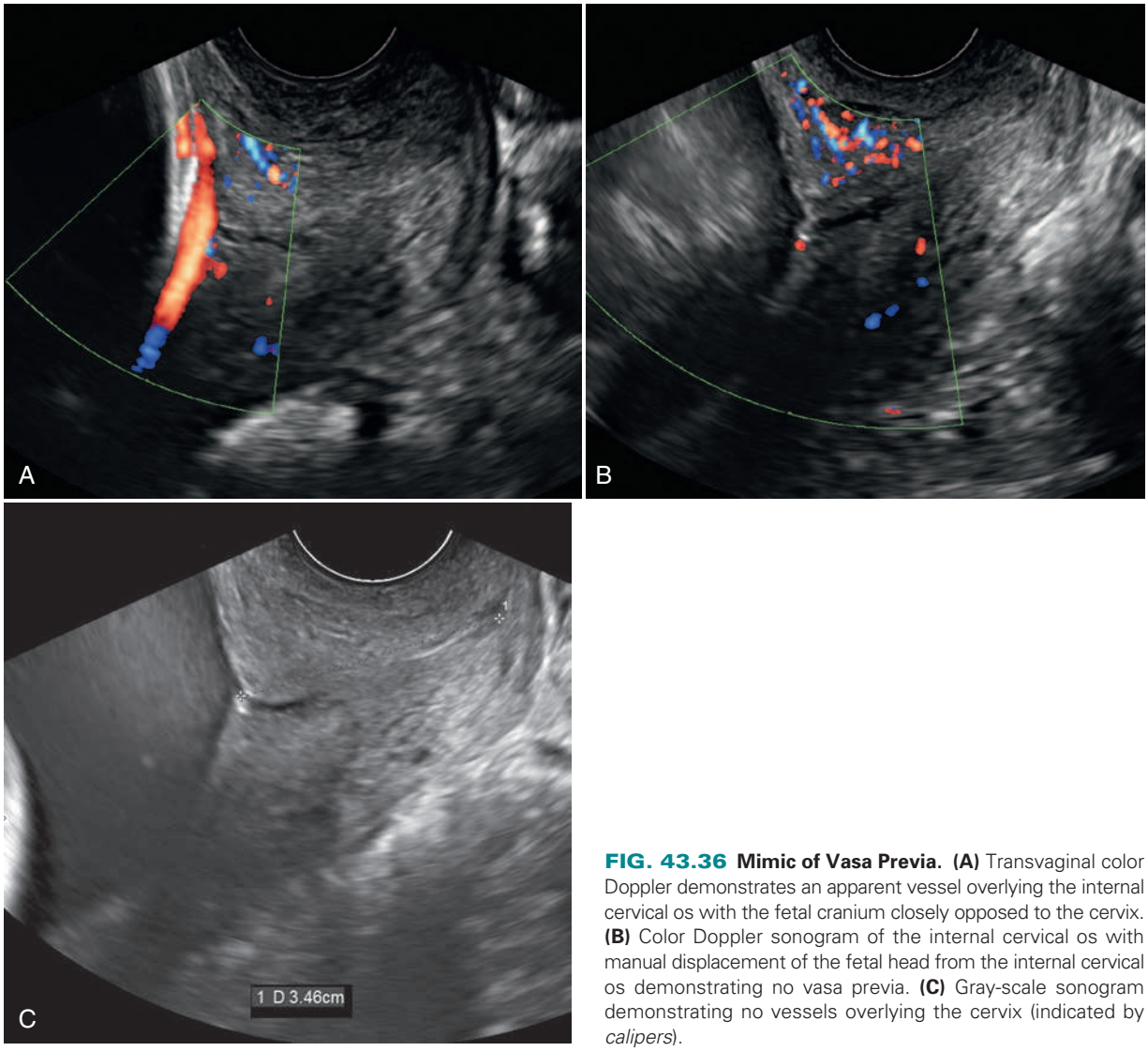

FIG. 43.36 Mimic of Vasa Previa. (A) Transvaginal color Doppler demonstrates an apparent vessel overlying the internal cervical os with the fetal cranium closely opposed to the cervix. **(B)** Color Doppler sonogram of the internal cervical os with manual displacement of the fetal head from the internal cervical os demonstrating no vasa previa. **(C)** Gray-scale sonogram demonstrating no vessels overlying the cervix (indicated by *calipers*).

FIG. 43.37 Funic Presentation. Transvaginal ultrasound of a single loop of normal umbilical cord, free floating and overlying the internal cervical os. The cervix is indicated by the calipers. The three vessels of the umbilical cord are seen in cross section.

demonstrated. However, lack of flow does not exclude RPOC. Care should be taken not to mistake vascularized RPOC for a uterine arteriovenous malformation, because prominent flow can be seen in RPOC.[190] In fact, the association of an endometrial mass with prominent blood flow strongly suggests RPOC.[191,192] Endometrial measurements less than 10 mm suggest the absence of RPOC, especially in the absence of blood flow, with high negative predictive values.[193] Calcifications in the endometrial mass are highly suggestive of RPOC. These calcifications represent normal placental maturation that occurred during pregnancy.

CONCLUSION

Multiple abnormalities associated with placental development and function can be identified by prenatal sonography. Sonographers and sonologists need to understand the basic anatomy and physiology of the placenta so that abnormal findings on prenatal sonography can be acknowledged, to achieve the best possible outcome for mother and neonate.

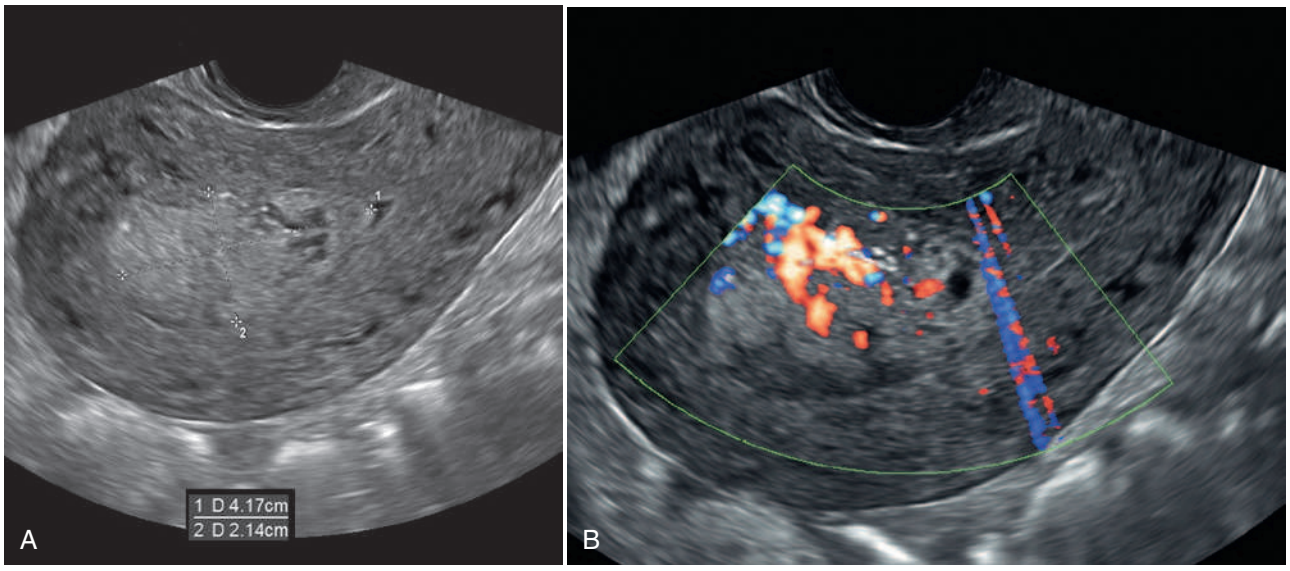

FIG. 43.38 Retained Products of Conception. (A) Transvaginal gray-scale sonogram shows a heterogeneous area of echogenic tissue in the endometrial cavity. **(B)** Transvaginal color Doppler sonogram in the same patient shows vascularization of an endometrial mass, consistent with retained products of conception.

REFERENCES

1. Pijnenborg R, Vercruysse L. Shifting concepts of the fetal-maternal interface: a historical perspective. Placenta. 2008;29(Suppl.A):S20-S25.
2. Moore KL. The developing human. 3rd ed. Philadelphia: Saunders; 1982.
3. Kanne JP, Lalani TA, Fligner CL. The placenta revisited: radiologic-pathologic correlation. Curr Probl Diagn Radiol. 2005;34(6):238-255.
4. Jauniaux E, Poston L, Burton GJ. Placental-related diseases of pregnancy: involvement of oxidative stress and implications in human evolution. Hum Reprod Update. 2006;12(6):747-755.
5. Fujikura T, Sho S. Placental cavities. Obstet Gynecol. 1997;90(1):112-116.
6. Reis NS, Brizot ML, Schultz R, et al. Placental lakes on sonographic examination: correlation with obstetric outcome and pathologic findings. J Clin Ultrasound. 2005;33(2):67-71.
7. Morikawa M, Cho K, Kataoka S, et al. Magnetic resonance image findings of placental lake: report of two cases. Prenat Diagn. 2005;25(3):250-252.
8. Has R, Yuksel A, Gunay S, et al. Antenatal sonographic detection of an unusual placental lake under the cord insertion. Arch Gynecol Obstet. 2005;271(1):59-61.
9. Thompson MO, Vines SK, Aquilina J, et al. Are placental lakes of any clinical significance? Placenta. 2002;23(8-9):685-690.
10. Hwang HS, Sohn IS, Kwon HS. The clinical significance of large placental lakes. Eur J Obstet Gynecol Reprod Biol. 2012;162(2):139-143.
11. Salafia CM, Yampolsky M, Shlakhter A, et al. Variety in placental shape: when does it originate? Placenta. 2012;33(3):164-170.
12. Tongsong T, Boonyanurak P. Placental thickness in the first half of pregnancy. J Clin Ultrasound. 2004;32(5):231-234.
13. Lee AJ, Bethune M, Hiscock RJ. Placental thickness in the second trimester: a pilot study to determine the normal range. J Ultrasound Med. 2012;31(2):213-218.
14. Nowak PM, Nardozza LM, Araujo Junior E, et al. Comparison of placental volume in early pregnancy using multiplanar and vocal methods. Placenta. 2008;29(3):241-245.
15. Hafner E, Metzenbauer M, Dillinger-Paller B, et al. Correlation of first trimester placental volume and second trimester uterine artery Doppler flow. Placenta. 2001;22(8-9):729-734.
16. Schuchter K, Metzenbauer M, Hafner E, Philipp K. Uterine artery Doppler and placental volume in the first trimester in the prediction of pregnancy complications. Ultrasound Obstet Gynecol. 2001;18(6):590-592.
17. Rizzo G, Capponi A, Cavicchioni O, et al. First trimester uterine Doppler and three-dimensional ultrasound placental volume calculation in predicting pre-eclampsia. Eur J Obstet Gynecol Reprod Biol. 2008;138(2):147-151.
18. Effendi M, Demers S, Giguere Y, et al. Association between first-trimester placental volume and birth weight. Placenta. 2014;35(2):99-102.
19. de Almeida Pimenta EJ, Silva de Paula CF, Duarte Bonini Campos JA, et al. Three-dimensional sonographic assessment of placental volume and vascularization in pregnancies complicated by hypertensive disorders. J Ultrasound Med. 2014;33(3):483-491.
20. Metzenbauer M, Hafner E, Schuchter K, Philipp K. First-trimester placental volume as a marker for chromosomal anomalies: preliminary results from an unselected population. Ultrasound Obstet Gynecol. 2002;19(3):240-242.
21. Wegrzyn P, Fabio C, Peralta A, et al. Placental volume in twin and triplet pregnancies measured by three-dimensional ultrasound at 11 + 0 to 13 + 6 weeks of gestation. Ultrasound Obstet Gynecol. 2006;27(6):647-651.
22. Hafner E, Schuchter K, van Leeuwen M, et al. Three-dimensional sonographic volumetry of the placenta and the fetus between weeks 15 and 17 of gestation. Ultrasound Obstet Gynecol. 2001;18(2):116-120.
23. Thame M, Osmond C, Wilks RJ, et al. Blood pressure is related to placental volume and birth weight. Hypertension. 2000;35(2):662-667.
24. Michailidis GD, Morris RW, Mamopoulos A, et al. The influence of maternal hematocrit on placental development from the first to the second trimesters of pregnancy. Ultrasound Obstet Gynecol. 2002;20(4):351-355.
25. Thame M, Osmond C, Bennett F, et al. Fetal growth is directly related to maternal anthropometry and placental volume. Eur J Clin Nutr. 2004;58(6):894-900.
26. Hafner E, Metzenbauer M, Hofinger D, et al. Comparison between three-dimensional placental volume at 12 weeks and uterine artery impedance/notching at 22 weeks in screening for pregnancy-induced hypertension, pre-eclampsia and fetal growth restriction in a low-risk population. Ultrasound Obstet Gynecol. 2006;27(6):652-657.
27. Wolf H, Oosting H, Treffers PE. Second-trimester placental volume measurement by ultrasound: prediction of fetal outcome. Am J Obstet Gynecol. 1989;160(1):121-126.
28. Benirschke K, Kaufmann P, Baergen RN. Pathology of the human placenta. New York: Springer; 2006. Available from: http://catalog.hathitrust.org/api/volumes/oclc/60776850.html.
29. Matijevic R, Kurjak A, Hafner T. Terminal parts of uteroplacental circulation in pregnancy: assessment by color/pulsed Doppler ultrasound. Ultrasound Rev Obstet Gynecol. 2001;1:262-274.
30. Valentin L, Sladkevicius P, Laurini R, et al. Uteroplacental and luteal circulation in normal first-trimester pregnancies: Doppler ultrasonographic and morphologic study. Am J Obstet Gynecol. 1996;174(2):768-775.

31. Craven CM, Ward K. Syncytiotrophoblastic fragments in first-trimester decidual veins: evidence of placental perfusion by the maternal circulation early in pregnancy. Am J Obstet Gynecol. 1999;181(2):455-459.
32. Guimaraes Filho HA, da Costa LL, Araujo Junior E, et al. Placenta: angiogenesis and vascular assessment through three-dimensional power Doppler ultrasonography. Arch Gynecol Obstet. 2008;277(3):195-200.
33. Carbillon L, Challier JC, Alouini S, et al. Uteroplacental circulation development: Doppler assessment and clinical importance. Placenta. 2001;22(10):795-799.
34. Jauniaux E, Greenwold N, Hempstock J, Burton GJ. Comparison of ultrasonographic and Doppler mapping of the intervillous circulation in normal and abnormal early pregnancies. Fertil Steril. 2003;79(1):100-106.
35. Campbell S. Placental vasculature as visualized by 3D power Doppler angiography and 3D color Doppler imaging. Ultrasound Obstet Gynecol. 2007;30(6):917-920.
36. Mu J, Kanzaki T, Tomimatsu T, et al. Investigation of intraplacental villous arteries by Doppler flow imaging in growth-restricted fetuses. Am J Obstet Gynecol. 2002;186(2):297-302.
37. Guiot C, Gaglioti P, Oberto M, et al. Is three-dimensional power Doppler ultrasound useful in the assessment of placental perfusion in normal and growth-restricted pregnancies? Ultrasound Obstet Gynecol. 2008;31(2):171-176.
38. Hannaford KE, Tuuli M, Goetzinger KR, et al. First-trimester 3-dimensional power Doppler placental vascularization indices from the whole placenta versus the placental bed to predict preeclampsia: does pregnancy-associated plasma protein a or uterine artery Doppler sonography help? J Ultrasound Med. 2015;34(6):965-970.
39. Moran MC, Mulcahy C, Zombori G, et al. Placental volume, vasculature and calcification in pregnancies complicated by pre-eclampsia and intrauterine growth restriction. Eur J Obstet Gynecol Reprod Biol. 2015;195:12-17.
40. Rosner M, Dar P, Reimers LL, et al. First-trimester 3D power Doppler of the uteroplacental circulation space and fetal growth restriction. Am J Obstet Gynecol. 2014;211(5):521.e1-521.e8.
41. Osmanski BF, Lecarpentier E, Montaldo G, et al. Discriminative imaging of maternal and fetal blood flow within the placenta using ultrafast ultrasound. Sci Rep. 2015;5:13394.
42. Levine D, Callen PW, Pender SG, et al. Chorioamniotic separation after second-trimester genetic amniocentesis: importance and frequency. Radiology. 1998;209(1):175-181.
43. Bromley B, Shipp TD, Benacerraf BR. Amnion-chorion separation after 17 weeks' gestation. Obstet Gynecol. 1999;94(6):1024-1026.
44. Ogawa M, Nagao D, Mori K, et al. Elastography for differentiation of subchorionic hematoma and placenta previa. Ultrasound Obstet Gynecol. 2012;39(1):112-114.
45. Cimsit C, Yoldemir T, Akpinar IN. Strain elastography in placental dysfunction: placental elasticity differences in normal and preeclamptic pregnancies in the second trimester. Arch Gynecol Obstet. 2015;291(4):811-817.
46. Cimsit C, Yoldemir T, Akpinar IN. Shear wave elastography in placental dysfunction: comparison of elasticity values in normal and preeclamptic pregnancies in the second trimester. J Ultrasound Med. 2015;34(1):151-159.
47. Mabie WC. Placenta previa. Clin Perinatol. 1992;19(2):425-435.
48. Silver R, Depp R, Sabbagha RE, et al. Placenta previa: aggressive expectant management. Am J Obstet Gynecol. 1984;150(1):15-22.
49. McShane PM, Heyl PS, Epstein MF. Maternal and perinatal morbidity resulting from placenta previa. Obstet Gynecol. 1985;65(2):176-182.
50. Timor-Tritsch IE, Yunis RA. Confirming the safety of transvaginal sonography in patients suspected of placenta previa. Obstet Gynecol. 1993;81(5 Pt 1):742-744.
51. Smith RS, Lauria MR, Comstock CH, et al. Transvaginal ultrasonography for all placentas that appear to be low-lying or over the internal cervical os. Ultrasound Obstet Gynecol. 1997;9(1):22-24.
52. Oppenheimer LW, Farine D, Ritchie JW, et al. What is a low-lying placenta? Am J Obstet Gynecol. 1991;165(4 Pt 1):1036-1038.
53. Bhide A, Prefumo F, Moore J, et al. Placental edge to internal os distance in the late third trimester and mode of delivery in placenta praevia. BJOG. 2003;110(9):860-864.
54. Ananth CV, Smulian JC, Vintzileos AM. The association of placenta previa with history of cesarean delivery and abortion: a metaanalysis. Am J Obstet Gynecol. 1997;177(5):1071-1078.
55. Gilliam M, Rosenberg D, Davis F. The likelihood of placenta previa with greater number of cesarean deliveries and higher parity. Obstet Gynecol. 2002;99(6):976-980.
56. Faiz AS, Ananth CV. Etiology and risk factors for placenta previa: an overview and meta-analysis of observational studies. J Matern Fetal Neonatal Med. 2003;13(3):175-190.
57. King DL. Placental migration demonstrated by ultrasonography. A hypothesis of dynamic placentation. Radiology. 1973;109(1):167-170.
58. Oppenheimer L, Holmes P, Simpson N, Dabrowski A. Diagnosis of low-lying placenta: can migration in the third trimester predict outcome? Ultrasound Obstet Gynecol. 2001;18(2):100-102.
59. Predanic M, Perni SC, Baergen RN, et al. A sonographic assessment of different patterns of placenta previa "migration" in the third trimester of pregnancy. J Ultrasound Med. 2005;24(6):773-780.
60. Rosati P, Guariglia L. Clinical significance of placenta previa detected at early routine transvaginal scan. J Ultrasound Med. 2000;19(8):581-585.
61. Becker RH, Vonk R, Mende BC, et al. The relevance of placental location at 20-23 gestational weeks for prediction of placenta previa at delivery: evaluation of 8650 cases. Ultrasound Obstet Gynecol. 2001;17(6):496-501.
62. Mustafa SA, Brizot ML, Carvalho MH, et al. Transvaginal ultrasonography in predicting placenta previa at delivery: a longitudinal study. Ultrasound Obstet Gynecol. 2002;20(4):356-359.
63. Heller HT, Mullen KM, Gordon RW, et al. Outcomes of pregnancies with a low-lying placenta diagnosed on second-trimester sonography. J Ultrasound Med. 2014;33(4):691-696.
64. Ghourab S. Third-trimester transvaginal ultrasonography in placenta previa: does the shape of the lower placental edge predict clinical outcome? Ultrasound Obstet Gynecol. 2001;18(2):103-108.
65. Shukunami K, Nishijima K, Kurokawa T, et al. A small-angled thin edge of the placenta predicts abnormal placentation at delivery. J Ultrasound Med. 2005;24(3):331-335.
66. Krapp M, Baschat AA, Hankeln M, Gembruch U. Gray scale and color Doppler sonography in the third stage of labor for early detection of failed placental separation. Ultrasound Obstet Gynecol. 2000;15(2):138-142.
67. Zelop C, Nadel A, Frigoletto Jr FD, et al. Placenta accreta/percreta/increta: a cause of elevated maternal serum alpha-fetoprotein. Obstet Gynecol. 1992;80(4):693-694.
68. Miura K, Miura S, Yamasaki K, et al. Increased level of cell-free placental mRNA in a subgroup of placenta previa that needs hysterectomy. Prenat Diagn. 2008;28(9):805-809.
69. Wu S, Kocherginsky M, Hibbard JU. Abnormal placentation: twenty-year analysis. Am J Obstet Gynecol. 2005;192(5):1458-1461.
70. Armstrong CA, Harding S, Matthews T, Dickinson JE. Is placenta accreta catching up with us? Aust N Z J Obstet Gynaecol. 2004;44(3):210-213.
71. Clark SL, Koonings PP, Phelan JP. Placenta previa/accreta and prior cesarean section. Obstet Gynecol. 1985;66(1):89-92.
72. Finberg HJ, Williams JW. Placenta accreta: prospective sonographic diagnosis in patients with placenta previa and prior cesarean section. J Ultrasound Med. 1992;11(7):333-343.
73. Comstock CH, Love Jr JJ, Bronsteen RA, et al. Sonographic detection of placenta accreta in the second and third trimesters of pregnancy. Am J Obstet Gynecol. 2004;190(4):1135-1140.
74. Yang JI, Lim YK, Kim HS, et al. Sonographic findings of placental lacunae and the prediction of adherent placenta in women with placenta previa totalis and prior cesarean section. Ultrasound Obstet Gynecol. 2006;28(2):178-182.
75. Kerr de Mendonca L. Sonographic diagnosis of placenta accreta. Presentation of six cases. J Ultrasound Med. 1988;7(4):211-215.
76. Chou MM, Ho ES, Lee YH. Prenatal diagnosis of placenta previa accreta by transabdominal color Doppler ultrasound. Ultrasound Obstet Gynecol. 2000;15(1):28-35.
77. Wong HS, Cheung YK, Strand L, et al. Specific sonographic features of placenta accreta: tissue interface disruption on gray-scale imaging and

evidence of vessels crossing interface- disruption sites on Doppler imaging. Ultrasound Obstet Gynecol. 2007;29(2):239-240.
78. Comstock CH. Antenatal diagnosis of placenta accreta: a review. Ultrasound Obstet Gynecol. 2005;26(1):89-96.
79. Mazouni C, Gorincour G, Juhan V, Bretelle F. Placenta accreta: a review of current advances in prenatal diagnosis. Placenta. 2007;28(7):599-603.
80. Chou MM, Tseng JJ, Hwang JI, et al. Sonographic appearance of tornado blood flow in placenta previa accreta/increta. Ultrasound Obstet Gynecol. 2001;17(4):362-363.
81. D'Antonio F, Iacovella C, Bhide A. Prenatal identification of invasive placentation using ultrasound: systematic review and meta-analysis. Ultrasound Obstet Gynecol. 2013;42(5):509-517.
82. Rac MW, Dashe JS, Wells CE, et al. Ultrasound predictors of placental invasion: the Placenta Accreta Index. Am J Obstet Gynecol. 2015;212(3):343.e1-343.e7.
83. Comstock CH, Lee W, Vettraino IM, Bronsteen RA. The early sonographic appearance of placenta accreta. J Ultrasound Med. 2003;22(1):19-23.
84. Shih JC, Cheng WF, Shyu MK, et al. Power Doppler evidence of placenta accreta appearing in the first trimester. Ultrasound Obstet Gynecol. 2002;19(6):623-625.
85. Chen YJ, Wang PH, Liu WM, et al. Placenta accreta diagnosed at 9 weeks' gestation. Ultrasound Obstet Gynecol. 2002;19(6):620-622.
86. Ballas J, Pretorius D, Hull AD, et al. Identifying sonographic markers for placenta accreta in the first trimester. J Ultrasound Med. 2012;31(11):1835-1841.
87. Timor-Tritsch IE, Monteagudo A, Cali G, et al. Cesarean scar pregnancy is a precursor of morbidly adherent placenta. Ultrasound Obstet Gynecol. 2014;44(3):346-353.
88. Taipale P, Orden MR, Berg M, et al. Prenatal diagnosis of placenta accreta and percreta with ultrasonography, color Doppler, and magnetic resonance imaging. Obstet Gynecol. 2004;104(3):537-540.
89. Levine D, Hulka CA, Ludmir J, et al. Placenta accreta: evaluation with color Doppler US, power Doppler US, and MR imaging. Radiology. 1997;205(3):773-776.
90. Warshak CR, Eskander R, Hull AD, et al. Accuracy of ultrasonography and magnetic resonance imaging in the diagnosis of placenta accreta. Obstet Gynecol. 2006;108(3 Pt 1):573-581.
91. Masselli G, Brunelli R, Casciani E, et al. Magnetic resonance imaging in the evaluation of placental adhesive disorders: correlation with color Doppler ultrasound. Eur Radiol. 2008;18(6):1292-1299.
92. Dwyer BK, Belogolovkin V, Tran L, et al. Prenatal diagnosis of placenta accreta: sonography or magnetic resonance imaging? J Ultrasound Med. 2008;27(9):1275-1281.
93. Riteau AS, Tassin M, Chambon G, et al. Accuracy of ultrasonography and magnetic resonance imaging in the diagnosis of placenta accreta. PLoS ONE. 2014;9(4):e94866.
94. Kramer MS, Usher RH, Pollack R, et al. Etiologic determinants of abruptio placentae. Obstet Gynecol. 1997;89(2):221-226.
95. Tikkanen M, Nuutila M, Hiilesmaa V, et al. Clinical presentation and risk factors of placental abruption. Acta Obstet Gynecol Scand. 2006;85(6):700-705.
96. Oyelese Y, Ananth CV. Placental abruption. Obstet Gynecol. 2006;108(4):1005-1016.
97. Loi K, Tan KT. Massive pre-placental and subchorionic haematoma. Singapore Med J. 2006;47(12):1084-1086.
98. Fisteag-Kiprono L, Foster K, McKenna D, Baptista M. Antenatal sonographic diagnosis of massive subchorionic hematoma: a case report. J Reprod Med. 2005;50(3):219-221.
99. Kikutani M, Ishihara K, Araki T. Value of ultrasonography in the diagnosis of placental abruption. J Nippon Med Sch. 2003;70(3):227-233.
100. Raio L, Ghezzi F, Cromi A, et al. The thick heterogeneous (jellylike) placenta: a strong predictor of adverse pregnancy outcome. Prenat Diagn. 2004;24(3):182-188.
101. Glantz C, Purnell L. Clinical utility of sonography in the diagnosis and treatment of placental abruption. J Ultrasound Med. 2002;21(8):837-840.
102. Nyberg DA, Mack LA, Benedetti TJ, et al. Placental abruption and placental hemorrhage: correlation of sonographic findings with fetal outcome. Radiology. 1987;164(2):357-361.
103. Vernof KK, Benirschke K, Kephart GM, et al. Maternal floor infarction: relationship to X cells, major basic protein, and adverse perinatal outcome. Am J Obstet Gynecol. 1992;167(5):1355-1363.
104. Adams-Chapman I, Vaucher YE, Bejar RF, et al. Maternal floor infarction of the placenta: association with central nervous system injury and adverse neurodevelopmental outcome. J Perinatol. 2002;22(3):236-241.
105. Kumazaki K, Nakayama M, Sumida Y, et al. Placental features in preterm infants with periventricular leukomalacia. Pediatrics. 2002;109(4):650-655.
106. Roberts D, Schwartz RS. Clotting and hemorrhage in the placenta—a delicate balance. N Engl J Med. 2002;347(1):57-59.
107. Mandsager NT, Bendon R, Mostello D, et al. Maternal floor infarction of the placenta: prenatal diagnosis and clinical significance. Obstet Gynecol. 1994;83(5 Pt 1):750-754.
108. Alkazaleh F, Viero S, Simchen M, et al. Ultrasound diagnosis of severe thrombotic placental damage in the second trimester: an observational study. Ultrasound Obstet Gynecol. 2004;23(5):472-476.
109. Aurioles-Garibay A, Hernandez-Andrade E, Romero R, et al. Prenatal diagnosis of a placental infarction hematoma associated with fetal growth restriction, preeclampsia and fetal death: clinicopathological correlation. Fetal Diagn Ther. 2014;36(2):154-161.
110. Raga F, Ballester MJ, Osborne NG, Bonilla-Musoles F. Subchorionic placental cyst: a cause of fetal growth retardation—ultrasound and color-flow Doppler diagnosis and follow-up. J Natl Med Assoc. 1996;88(5):285-288.
111. Brown DL, DiSalvo DN, Frates MC, et al. Placental surface cysts detected on sonography: histologic and clinical correlation. J Ultrasound Med. 2002;21(6):641-646.
112. Haak MC, Oosterhof H, Mouw RJ, et al. Pathophysiology and treatment of fetal anemia due to placental chorioangioma. Ultrasound Obstet Gynecol. 1999;14(1):68-70.
113. Shih JC, Ko TL, Lin MC, et al. Quantitative three-dimensional power Doppler ultrasound predicts the outcome of placental chorioangioma. Ultrasound Obstet Gynecol. 2004;24(2):202-206.
114. Taori K, Patil P, Attarde V, et al. Chorioangioma of placenta: sonographic features. J Clin Ultrasound. 2008;36(2):113-115.
115. Prapas N, Liang RI, Hunter D, et al. Color Doppler imaging of placental masses: differential diagnosis and fetal outcome. Ultrasound Obstet Gynecol. 2000;16(6):559-563.
116. Sepulveda W, Aviles G, Carstens E, et al. Prenatal diagnosis of solid placental masses: the value of color flow imaging. Ultrasound Obstet Gynecol. 2000;16(6):554-558.
117. Jauniaux E, Ogle R. Color Doppler imaging in the diagnosis and management of chorioangiomas. Ultrasound Obstet Gynecol. 2000;15(6):463-467.
118. Zalel Y, Gamzu R, Weiss Y, et al. Role of color Doppler imaging in diagnosing and managing pregnancies complicated by placental chorioangioma. J Clin Ultrasound. 2002;30(5):264-269.
119. Nicolini U, Zuliani G, Caravelli E, et al. Alcohol injection: a new method of treating placental chorioangiomas. Lancet. 1999;353(9165):1674-1675.
120. Lau TK, Leung TY, Yu SC, et al. Prenatal treatment of chorioangioma by microcoil embolisation. BJOG. 2003;110(1):70-73.
121. Quintero RA, Reich H, Romero R, et al. In utero endoscopic devascularization of a large chorioangioma. Ultrasound Obstet Gynecol. 1996;8(1):48-52.
122. Fan M, Skupski DW. Placental chorioangioma: literature review. J Perinat Med. 2014;42(3):273-279.
123. Eltorky M, Khare VK, Osborne P, Shanklin DR. Placental metastasis from maternal carcinoma. A report of three cases. J Reprod Med. 1995;40(5):399-403.
124. Ferreira CM, Maceira JM, Coelho JM. Melanoma and pregnancy with placental metastases. Report of a case. Am J Dermatopathol. 1998;20(4):403-407.
125. Kuwata T, Takahashi H, Matsubara S. Stained-glass' sign for placental mesenchymal dysplasia. Ultrasound Obstet Gynecol. 2014;43(3):355.
126. Gibson BR, Muir-Padilla J, Champeaux A, Suarez ES. Mesenchymal dysplasia of the placenta. Placenta. 2004;25(7):671-672.
127. Robertson M, Geerts LT, de Jong G, Wainwright H. Mesenchymal dysplasia in a monochorionic diamniotic twin pregnancy with review of the differential diagnosis of cystic changes in the placenta. J Ultrasound Med. 2007;26(5):689-693.

128. Arlicot C, Herve P, Simon E, Perrotin F. Three-dimensional surface rendering of the chorionic placental plate: the "tire" sign for the diagnosis of a circumvallate placenta. J Ultrasound Med. 2012;31(2):340-341.
129. Shen O, Golomb E, Lavie O, et al. Placental shelf—a common, typically transient and benign finding on early second-trimester sonography. Ultrasound Obstet Gynecol. 2007;29(2):192-194.
130. Suzuki S. Clinical significance of pregnancies with circumvallate placenta. J Obstet Gynaecol Res. 2008;34(1):51-54.
131. Ghezzi F, Raio L, Di Naro E, et al. First-trimester sonographic umbilical cord diameter and the growth of the human embryo. Ultrasound Obstet Gynecol. 2001;18(4):348-351.
132. Ghezzi F, Raio L, Di Naro E, et al. First-trimester umbilical cord diameter: a novel marker of fetal aneuploidy. Ultrasound Obstet Gynecol. 2002;19(3):235-239.
133. Rembouskos G, Cicero S, Papadopoulos V, et al. Umbilical cord diameter at 11-14 weeks of gestation: relation to chromosomal defects. Ultrasound Obstet Gynecol. 2004;23(3):237-239.
134. Ghezzi F, Raio L, Di Naro E, et al. Nomogram of Wharton's jelly as depicted in the sonographic cross section of the umbilical cord. Ultrasound Obstet Gynecol. 2001;18(2):121-125.
135. Togni FA, Araujo Junior E, Vasques FA, et al. The cross-sectional area of umbilical cord components in normal pregnancy. Int J Gynaecol Obstet. 2007;96(3):156-161.
136. Predanic M, Perni SC, Chasen S, Chervenak FA. Fetal aneuploidy and umbilical cord thickness measured between 14 and 23 weeks' gestational age. J Ultrasound Med. 2004;23(9):1177-1183.
137. Cromi A, Ghezzi F, Di Naro E, et al. Large cross-sectional area of the umbilical cord as a predictor of fetal macrosomia. Ultrasound Obstet Gynecol. 2007;30(6):861-866.
138. Barbieri C, Cecatti JG, Krupa F, et al. Validation study of the capacity of the reference curves of ultrasonographic measurements of the umbilical cord to identify deviations in estimated fetal weight. Acta Obstet Gynecol Scand. 2008;87(3):286-291.
139. Degani S, Lewinsky RM, Berger H, Spiegel D. Sonographic estimation of umbilical coiling index and correlation with Doppler flow characteristics. Obstet Gynecol. 1995;86(6):990-993.
140. Predanic M, Perni SC. Absence of a relationship between umbilical cord thickness and coiling patterns. J Ultrasound Med. 2005;24(11):1491-1496.
141. Qin Y, Lau TK, Rogers MS. Second-trimester ultrasonographic assessment of the umbilical coiling index. Ultrasound Obstet Gynecol. 2002;20(5):458-463.
142. Lacro RV, Jones KL, Benirschke K. The umbilical cord twist: origin, direction, and relevance. Am J Obstet Gynecol. 1987;157(4 Pt 1):833-838.
143. Otsubo Y, Yoneyama Y, Suzuki S, et al. Sonographic evaluation of umbilical cord insertion with umbilical coiling index. J Clin Ultrasound. 1999;27(6):341-344.
144. Strong Jr TH, Elliott JP, Radin TG. Non-coiled umbilical blood vessels: a new marker for the fetus at risk. Obstet Gynecol. 1993;81(3):409-411.
145. de Laat MW, van Alderen ED, Franx A, et al. The umbilical coiling index in complicated pregnancy. Eur J Obstet Gynecol Reprod Biol. 2007;130(1):66-72.
146. Maher JT, Conti JA. A comparison of umbilical cord blood gas values between newborns with and without true knots. Obstet Gynecol. 1996;88(5):863-866.
147. Ramon YCCL, Martinez RO. Prenatal diagnosis of true knot of the umbilical cord. Ultrasound Obstet Gynecol. 2004;23(1):99-100.
148. Ramon y Cajal CL, Martinez RO. Four-dimensional ultrasonography of a true knot of the umbilical cord. Am J Obstet Gynecol. 2006;195(4):896-898.
149. Hasbun J, Alcalde JL, Sepulveda W. Three-dimensional power Doppler sonography in the prenatal diagnosis of a true knot of the umbilical cord: value and limitations. J Ultrasound Med. 2007;26(9):1215-1220.
150. Stempel LE. Beyond the pretty pictures: giving obstetricians just enough (umbilical) cord to hang themselves. Am J Obstet Gynecol. 2006;195(4):888-890.
151. Kiran H, Kiran G, Kanber Y. Pseudocyst of the umbilical cord with mucoid degeneration of Wharton's jelly. Eur J Obstet Gynecol Reprod Biol. 2003;111(1):91-93.
152. Shipp TD, Bromley B, Benacerraf BR. Sonographically detected abnormalities of the umbilical cord. Int J Gynaecol Obstet. 1995;48(2):179-185.
153. Weissman A, Drugan A. Sonographic findings of the umbilical cord: implications for the risk of fetal chromosomal anomalies. Ultrasound Obstet Gynecol. 2001;17(6):536-541.
154. Skibo LK, Lyons EA, Levi CS. First-trimester umbilical cord cysts. Radiology. 1992;182(3):719-722.
155. Ghezzi F, Raio L, Di Naro E, et al. Single and multiple umbilical cord cysts in early gestation: two different entities. Ultrasound Obstet Gynecol. 2003;21(3):215-219.
156. Tong SY, Lee JE, Kim SR, Lee SK. Umbilical cord cyst: a prenatal clue to bladder exstrophy. Prenat Diagn. 2007;27(12):1177-1179.
157. Schiesser M, Lapaire O, Holzgreve W, Tercanli S. Umbilical cord edema associated with patent urachus. Ultrasound Obstet Gynecol. 2003;22(6):646-647.
158. Emura T, Kanamori Y, Ito M, et al. Omphalocele associated with a large multilobular umbilical cord pseudocyst. Pediatr Surg Int. 2004;20(8):636-639.
159. Sepulveda W. Beware of the umbilical cord 'cyst. Ultrasound Obstet Gynecol. 2003;21(3):213-214.
160. Berg C, Geipel A, Germer U, et al. Prenatal diagnosis of umbilical cord aneurysm in a fetus with trisomy 18. Ultrasound Obstet Gynecol. 2001;17(1):79-81.
161. Sepulveda W, Corral E, Kottmann C, et al. Umbilical artery aneurysm: prenatal identification in three fetuses with trisomy 18. Ultrasound Obstet Gynecol. 2003;21(3):292-296.
162. Shen O, Reinus C, Baranov A, Rabinowitz RR. Prenatal diagnosis of umbilical artery aneurysm: a potentially lethal anomaly. J Ultrasound Med. 2007;26(2):251-253.
163. Daniel-Spiegel E, Weiner E, Gimburg G, Shalev E. The association of umbilical cord hemangioma with fetal vascular birthmarks. Prenat Diagn. 2005;25(4):300-303.
164. Iyoob SD, Tsai A, Ruchelli ED, et al. Large umbilical cord hemangioma: sonographic features with surgical pathologic correlation. J Ultrasound Med. 2006;25(11):1495-1498.
165. Moshiri M, Zaidi SF, Robinson TJ, et al. Comprehensive imaging review of abnormalities of the umbilical cord. Radiographics. 2014;34(1):179-196.
166. Kent EM, Breathnach FM, Gillan JE, et al. Placental cord insertion and birthweight discordance in twin pregnancies: results of the national prospective esprit study. Am J Obstet Gynecol. 2011;205(4):376.e1-376.e7.
167. Sepulveda W, Rojas I, Robert JA, et al. Prenatal detection of velamentous insertion of the umbilical cord: a prospective color Doppler ultrasound study. Ultrasound Obstet Gynecol. 2003;21(6):564-569.
168. Monteagudo A, Sfakianaki AK, Timor-Tritsch IE. Velamentous insertion of the cord in the first trimester. Ultrasound Obstet Gynecol. 2000;16(5):498-499.
169. Sepulveda W. Velamentous insertion of the umbilical cord: a first-trimester sonographic screening study. J Ultrasound Med. 2006;25(8):963-968.
170. Hasegawa J, Matsuoka R, Ichizuka K, et al. Velamentous cord insertion and atypical variable decelerations with no accelerations. Int J Gynaecol Obstet. 2005;90(1):26-30.
171. Esakoff TF, Cheng YW, Snowden JM, et al. Velamentous cord insertion: is it associated with adverse perinatal outcomes? J Matern Fetal Neonatal Med. 2015;28(4):409-412.
172. Liu CC, Pretorius DH, Scioscia AL, Hull AD. Sonographic prenatal diagnosis of marginal placental cord insertion: clinical importance. J Ultrasound Med. 2002;21(6):627-632.
173. Kuwata T, Suzuki H, Matsubara S. The 'mangrove sign' for velamentous umbilical cord insertion. Ultrasound Obstet Gynecol. 2012;40(2):241-242.
174. Lamale-Smith LM, Snuttjer MJ, Harper TC. Furcate umbilical cord insertion: disparate outcomes of a rare obstetrical finding. A case report. J Reprod Med. 2015;60(7-8):365-368.
175. Ruiter L, Kok N, Limpens J, et al. Incidence of and risk indicators for vasa praevia: a systematic review. BJOG. 2016;123(8):1278-1287.
176. Rebarber A, Dolin C, Fox NS, et al. Natural history of vasa previa across gestation using a screening protocol. J Ultrasound Med. 2014;33(1):141-147.

177. Lee W, Lee VL, Kirk JS, et al. Vasa previa: prenatal diagnosis, natural evolution, and clinical outcome. Obstet Gynecol. 2000;95(4):572-576.
178. Stafford IP, Neumann DE, Jarrell H. Abnormal placental structure and vasa previa: confirmation of the relationship. J Ultrasound Med. 2004;23(11): 1521-1522.
179. Baulies S, Maiz N, Munoz A, et al. Prenatal ultrasound diagnosis of vasa praevia and analysis of risk factors. Prenat Diagn. 2007;27(7):595-599.
180. Oyelese Y, Spong C, Fernandez MA, McLaren RA. Second trimester low-lying placenta and in-vitro fertilization? Exclude vasa previa. J Matern Fetal Med. 2000;9(6):370-372.
181. Society of Maternal-Fetal Medicine Publications Committee, Sinkey RG, Odibo AO, Dashe JS. #37: Diagnosis and management of vasa previa. Am J Obstet Gynecol. 2015;213(5):615-619.
182. Catanzarite V, Maida C, Thomas W, et al. Prenatal sonographic diagnosis of vasa previa: ultrasound findings and obstetric outcome in ten cases. Ultrasound Obstet Gynecol. 2001;18(2):109-115.
183. Oyelese Y, Chavez MR, Yeo L, et al. Three-dimensional sonographic diagnosis of vasa previa. Ultrasound Obstet Gynecol. 2004;24(2):211-215.
184. Canterino JC, Mondestin-Sorrentino M, Muench MV, et al. Vasa previa: prenatal diagnosis and evaluation with 3-dimensional sonography and power angiography. J Ultrasound Med. 2005;24(5):721-724.
185. Seince N, Carbillon L, Perrot N, Uzan M. Various Doppler sonographic appearances and challenges in prenatal diagnosis of vasa praevia. J Clin Ultrasound. 2002;30(7):450-454.
186. Herman A. Complicated third stage of labor: time to switch on the scanner. Ultrasound Obstet Gynecol. 2000;15(2):89-95.
187. Herman A, Zimerman A, Arieli S, et al. Down-up sequential separation of the placenta. Ultrasound Obstet Gynecol. 2002;19(3):278-281.
188. Krapp M, Katalinic A, Smrcek J, et al. Study of the third stage of labor by color Doppler sonography. Arch Gynecol Obstet. 2003;267(4):202-204.
189. Mo A, Rogers MS. Sonographic examination of uteroplacental separation during the third stage of labor. Ultrasound Obstet Gynecol. 2008;31(4): 427-431.
190. Rufener SL, Adusumilli S, Weadock WJ, Caoili E. Sonography of uterine abnormalities in postpartum and postabortion patients: a potential pitfall of interpretation. J Ultrasound Med. 2008;27(3):343-348.
191. Atri M, Rao A, Boylan C, et al. Best predictors of grayscale ultrasound combined with color Doppler in the diagnosis of retained products of conception. J Clin Ultrasound. 2011;39(3):122-127.
192. Kamaya A, Krishnarao PM, Folkins AK, et al. Variable color Doppler sonographic appearances of retained products of conception: radiologic-pathologic correlation. Abdom Imaging. 2015;40(7):2683-2689.
193. Sellmyer MA, Desser TS, Maturen KE, et al. Physiologic, histologic, and imaging features of retained products of conception. Radiographics. 2013;33(3):781-796.

CHAPTER

44 Cervical Ultrasound and Preterm Birth

Hournaz Ghandehari and Phyllis Glanc

SUMMARY OF KEY POINTS

- There is a significant association between cervix length and the risk of preterm birth.
- A cervical length of more than 3 cm has a high negative predictive value for delivery at less than 34 weeks' gestation.
- The most reliable method of documenting cervical length is transvaginal ultrasound.
- The single most reliable parameter for cervical assessment is a short cervical length.
- The earlier in gestation, the shorter the cervix, the greater is the risk of spontaneous preterm birth before 34 weeks, with the best predictive value when cervical length measures less than 25 mm.
- Rate of cervical change may be a better predictor than cervical length.

CHAPTER OUTLINE

PRETERM BIRTH
SONOGRAPHY OF THE UTERINE CERVIX
Transabdominal Approach
Transperineal/Translabial Approach
Transvaginal Sonography
Technical Limitations and Pitfalls
Normal Cervix
"Short" Cervix
PREDICTION OF SPONTANEOUS PRETERM BIRTH
Obstetric Factors
Cervical Funneling
Rate of Cervical Change
Dynamic Cervical Change
Other Sonographic Features
CERVICAL ASSESSMENT IN SPECIFIC CLINICAL SCENARIOS
Asymptomatic Patients
General Obstetric Population Screening
High-Risk Obstetric Population Screening
Symptomatic Patients
Cervical Incompetence and Cervical Cerclage
Cervical Incompetence and Vaginal Pessary
Vaginal Progesterone and 17-Alpha Hydroxyprogesterone Caproate
MANAGEMENT PROTOCOLS FOR THE ABNORMAL CERVIX
CONCLUSION
Acknowledgment

PRETERM BIRTH

Preterm birth (PTB), defined as delivery before 37 weeks of gestation, occurs in 5% to 11% of all pregnancies, ranging from as low as 5% in some European countries to 15% in the United States and to as high as 18% in some African countries, attributable to geographic, socioeconomic, and racial disparities.[1-3] PTB is the leading cause of neonatal morbidity and mortality not attributable to congenital anomalies or aneuploidy. If an infant is born preterm, the risk of death in the first year of life is 40-fold greater compared with an infant born at term.[2]

Immediate consequences of PTB include respiratory distress, intraventricular hemorrhage, sepsis, and retinopathy of prematurity.[2] In the long term, infants born preterm represent one-half the children with cerebral palsy, one-third of those with abnormal vision, one-quarter of those with chronic lung disease, and one-fifth of children with mental retardation.[2,4,5] The morbidity of prematurity persists to adulthood, with an increased incidence of behavioral problems, lower levels of educational achievement, reduced rates of reproductive success (with incidence of both conception and live birth adversely affected), and an increased incidence of second-generation PTB.[6-8]

The risk of prematurity persists in subsequent pregnancies, with a twofold increased risk in the next pregnancy and up to 50% risk of PTB if the woman has experienced two or more prior PTBs.[2] Given the substantial and far-reaching impact of PTB, it is important to recognize patients at increased risk of **spontaneous preterm birth** (SPTB), such that therapeutic interventions can be implemented to improve neonatal outcome.

About 85% of preterm deliveries occur spontaneously and are traditionally classified as one of three discrete events: **preterm labor** (uterine activity with coordinated cervical effacement and dilation), **preterm premature ruptured membranes** (ruptured

fetal membranes in the absence of uterine activity and cervical change), or **cervical incompetence** (cervical dilation in the absence of uterine activity).[2,9,10] Cervical incompetence can be further defined as either a **mechanical failure** of the cervix to remain closed against the increasing intrauterine expansion or as a **functional failure,** with premature activation of the events of cervical ripening (dilation and effacement) that normally occur at term.[9] Although categorized in this manner, spontaneous premature delivery is best described along a continuum of biologic events leading to early delivery, given that the biochemical mediators that effect uterine contractions, fetal membrane disruption, and cervical ripening are similar: prostaglandins, the metallomatrix proteases and their inhibitors, and the families of proinflammatory and antiinflammatory cytokines.[2,10] As such, the events of prematurity often overlap; in particular, cervical change can precede fetal membrane rupture and uterine contractions, although the cervix may not be functionally or mechanically incompetent.

Evaluation of the cervix has been used as a tool to predict SPTB based on the concept that the cervix acts as an anatomic marker of the underlying pathologic processes leading to a premature delivery. Digital examination of the cervix measures only the length from the external cervical os to the cervical-vaginal junction, not the intrapelvic cervical-isthmus portion of the cervix. Therefore digital examination underestimates cervical length by a mean difference of 12 mm in more than 80% of women in the second and third trimesters compared with sonography.[11] Moreover, dilation of the cervix starts proximally so the distal portion may still appear normal on digital exam, even when the cervix has started to shorten and/or dilate. The current approach to evaluation of the cervix is by ultrasound, preferably via the transvaginal route. This chapter reviews the techniques of uterine cervix sonography and its relationship with PTB prediction.

SONOGRAPHY OF THE UTERINE CERVIX

There are three approaches to scanning the cervix: transabdominal sonography (TAS), transvaginal sonography (TVS) and transperineal (translabial) sonography. Each approach has advantages and limitations for different clinical scenarios. The closed length of the cervix is the single most important parameter to report, as it is most closely linked to the risk of PTB. Additional comments include any evidence of funneling.

Transabdominal Approach

TAS of the cervix is typically performed during the standard second- and third-trimester obstetric ultrasound examinations and is used as a routine screening tool for measurement of closed cervical length.

Longitudinal scanning is initiated in the midline of the lower abdomen, just above the symphysis pubis, using a transducer with a frequency of 3 MHz or higher.[12,13] Landmarks include the internal cervical os, the external cervical os, the outline of the cervical canal, and the outline of the cervical corpus[14] (Fig. 44.1).

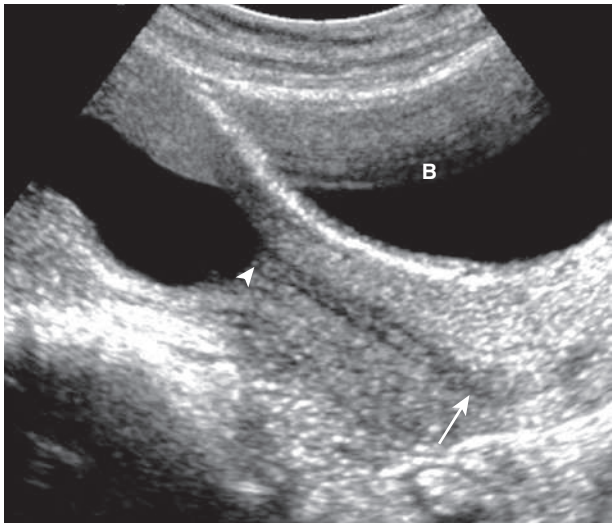

FIG. 44.1 Normal Cervix. TAS full-bladder technique. Longitudinal midline image of the cervix. The cervical canal is seen from the internal os *(arrowhead)* to the external os *(arrow). B,* Bladder.

FIG. 44.2 Normal Cervix. TAS empty-bladder technique. Longitudinal midline image of the cervix obtained by scanning through the amniotic fluid. The cervical canal is indicated by calipers.

Measurement of cervical length is affected by overdistention of the urinary bladder. Increased bladder pressure can compress the lower uterine segment and falsely elongate the cervix or mask cervical dilation.[12] Cervices less than 2 cm in length cannot be easily visualized against the vaginal and bladder tissue.[12]

In the second trimester, if the urinary bladder is empty, amniotic fluid can be used as an acoustic window to scan the cervix. Longitudinal scans are obtained with the transducer angled downward from just below the umbilicus. The cervix may assume a more vertical orientation and appear bulkier (Fig. 44.2) when the bladder is empty. Difficulty in identifying the external os can contribute to error in cervical length measurement.

Visualization of the cervix can be difficult because of large maternal habitus or an engaged position of the fetal head.[12,13,15] Regardless of the gestational age, there is relatively poor

reproducibility of TAS measurement of the cervix. Research has demonstrated conflicting results regarding the usefulness of TAS screens in that the cutoff in TAS to identify a cervix length of 25 mm or less is variable. This suggests that higher TAS cutoffs are required to achieve high sensitivity.[14,16] The challenge is that in a low-risk group, the prevalence of short cervix due to cervical incompetence is low and a large sample size is required to achieve meaningful statistics.

Transperineal/Translabial Approach

Transperineal sonography is reserved for patients for whom the cervix cannot be adequately visualized by TAS, and in whom TVS is unacceptable for personal or discomfort-related concerns. Scanning is performed with an empty urinary bladder. An abdominal transducer with a frequency of 3 MHz or higher can be used.[17-19] To minimize the risk of transmission of infection, the transducer is covered with plastic wrap. With the patient supine and hips abducted, the transducer is placed between the labia minora at the vaginal introitus. The ultrasound beam is oriented in a sagittal plane along the direction of the vagina. The vagina is seen in a vertical plane between the bladder and the rectum (Fig. 44.3).[15,20,21] The cervix is oriented horizontally, at a right angle with the vagina. The full length of the cervical canal can be visualized in 86% to 96% of patients with this technique[17,18]; however, in some cases the region of the external os can be obscured by rectal gas or the symphysis pubis. Although some reports have suggested that the reproducibility of the measurements is poor,[21-24] others have demonstrated improved reproducibility and accuracy in the hands of an experienced examiner.[15,22,25] This enhanced requirement for experience limits the utility of this study. This examination has a greater learning curve in order to perform reliably and reproducibly than TVS studies. Cicero et al.[25] showed that 50% of transperineal studies were inadequate because of shadowing in the learning phase of the first 200 patients. Subsequently in the second phase reliable images were obtained in 78% of cases. Because transperineal scanning of the cervix is more dependent on gestational age and the experience of the investigator, it should be reserved as an alternative study in patients for whom a TVS is deemed unacceptable for psychological, cultural, or medical reasons.

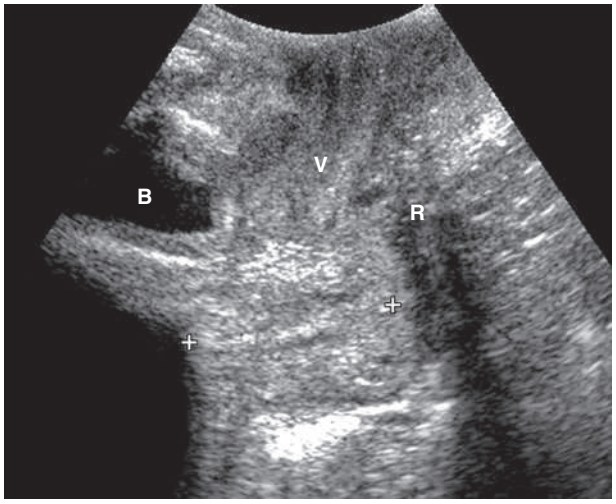

FIG. 44.3 Transperineal Scan of Normal Cervix. The cervix *(calipers)* is oriented horizontally, approximately perpendicular to the ultrasound beam. The vagina *(V)* is oriented in a nearly vertical plane. *B,* Bladder; *R,* rectum.

Transvaginal Sonography

TVS is the reference-standard technique for accurate determination of the dimensions and characteristics of the cervix.[26] The examination is performed with an empty urinary bladder. A gynecologic table fitted with stirrups is preferred, although the examination can be carried out with the patient's hips elevated on a thick cushion or wedge. With the patient in a dorsal lithotomy position, supine and hips abducted, an endovaginal transducer (5-MHz or higher frequency) covered with plastic wrap is placed in the vagina and oriented in a longitudinal plane. The probe is inserted under real-time visualization until the cervix comes into view. Usually, the transducer is inserted only 3 to 4 cm into the vagina so that the images of the cervix are within the effective focal range of the transducer (Fig. 44.4). Depending on the position of the cervix in the vagina, the probe may need to be moved anteriorly, posteriorly, and/or laterally.[27] There is a standardized method for obtaining reproducible cervical measurements (see box).

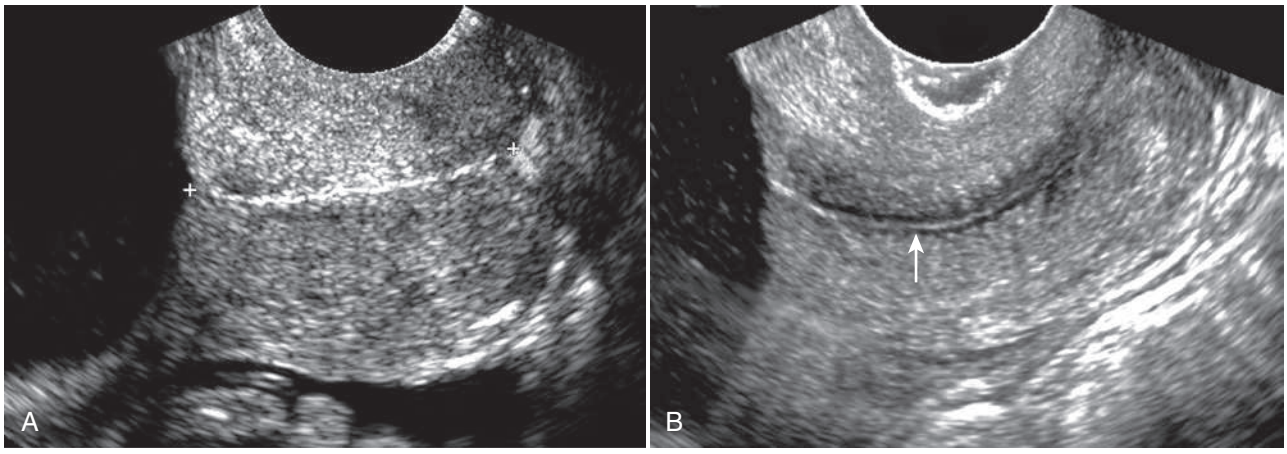

FIG. 44.4 TVS of Normal Cervix. (A) Suggested placement of cursors for measuring cervical length. **(B)** Normal cervical glandular area. The cervical canal is seen as an echogenic line *(arrow)* surrounded by a hypoechoic zone resulting from endocervical glands.

Standard Technique for Cervical Measurement

1. Place the probe in the anterior fornix of the vagina.
2. Obtain a sagittal view of the cervix, with the long-axis view of echogenic endocervical mucosa along the length of the canal.
3. Withdraw the probe until the image is blurred, and reapply just enough pressure to restore the image (to avoid excessive pressure on the cervix, which can elongate it).
4. Enlarge the image so that the cervix occupies at least two-thirds of the image and external and internal os are well seen.
5. Measure the cervical length from the internal to the external os along the endocervical canal.
6. Obtain at least three measurements, and record the shortest best measurement in millimeters.

With permission from Berghella V, Bega G, Tolosa JE, Berghella M. Ultrasound assessment of the cervix. Clin Obstet Gynecol. 2003; 46(4):947-962.[21]

A symmetrical image of the external os should be obtained, and the distance from the surface of the anterior lip to the cervical canal should be equal to the distance from the surface of the posterior lip to the cervical canal. If the anterior lip appears thinner than the posterior lip, there may be undue pressure placed on the cervix by the transvaginal probe. An additional sign of excessive pressure is increased echogenicity of the cervix[21] (Fig. 44.5).

When the cervix appears curved (deviation of the central canal of >5 mm from a straight line connecting the external and internal os), the cervical length can be either traced or the sum of two straight lines that follow the curve can be used.[21,28] Using these standard criteria, the interobserver coefficient of variation can be improved to 3.3%.[27]

TVS is superior to the TAS technique. Higher-frequency transducers and closer proximity to the structures studied allow for better resolution. Potential complications of TVS include an increased risk of bleeding in the presence of placenta previa, induction of uterine activity in women with cervical shortening caused by cervical stimulation, and chorioamnionitis in the presence of ruptured membranes. However, increased risk of chorioamnionitis or neonatal sepsis with TVS after preterm premature rupture of membranes (PPROM) has not been demonstrated.[29,30] TVS has also been deemed safe to use in patients with placenta previa with no increased risk for bleeding; however, caution is advised to ensure that the probe is always carefully inserted under real-time visualization.[31]

To date, TVS assessment of cervical length by three-dimensional sonography has been limited to the development of a normal distribution curve of cervical length through gestation. Overall, mean cervical length appears to be longer than the measurement by traditional two-dimensional scanning. However, there is to be high intra/interobserver variability.[32] Currently, there are no reported studies of the relationship between three-dimensional TVS and SPTB prediction.

Technical Limitations and Pitfalls

As mentioned previously, one limitation of TAS, especially in advanced gestation, is that the cervix may be obscured by the presenting part, in particular with a cephalic presentation. In addition, a short cervix or empty bladder may reduce the quality of the measurement obtained, whereas a full bladder may artificially elongate the cervix.

There are a number of technical limitations and pitfalls associated with TVS of the cervix. Large maternal body habitus can limit visualization. Bowel gas can obscure visualization.

A lower uterine segment myometrial contraction, immediately superior to the cervix, may result in a pseudoelongation of the cervix (Fig. 44.6). The classic tips to recognize this appearance is the artificially elongated length of the cervix (>5 cm), the thicker diameter of the "cervix" at the proximal extent, which actually incorporates the lower uterine muscle so that it appears thicker than at the external os. The thickness of the internal and external cervical os should be similar. Lower uterine segment contractions are transient and rarely persist beyond 15 minutes.

A second pitfall associated with the lower uterine segment contraction has been termed "pseudodilation" of the cervix. It

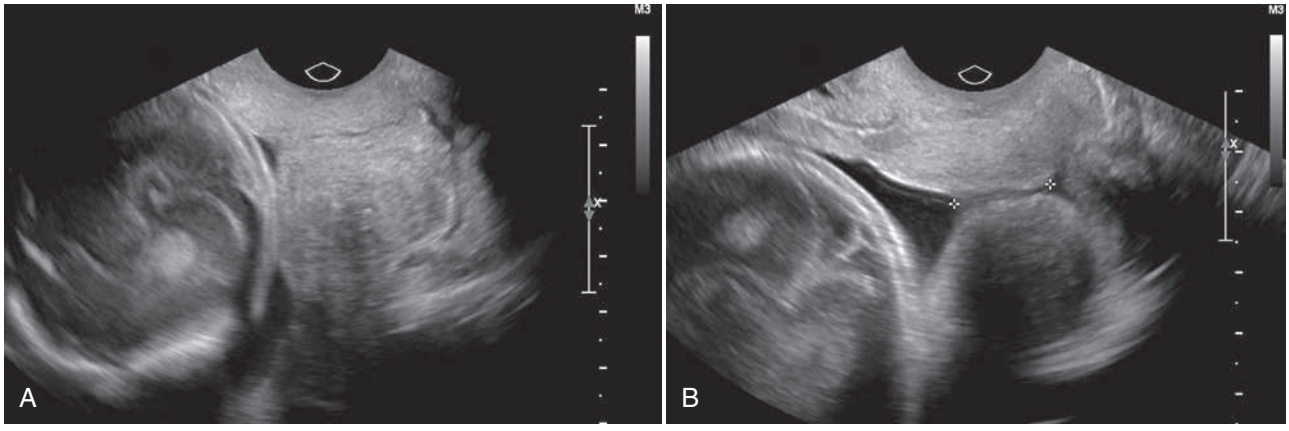

FIG. 44.5 Example of Poor Technique During TVS of Cervix. (A) Excessive pressure on the cervix with anterior lip appearing thinner than the posterior lip causing false elongation and increased echogenicity of the cervix. **(B)** Removal of pressure with equal anterior and posterior lips. Calipers measure appropriate cervical length.

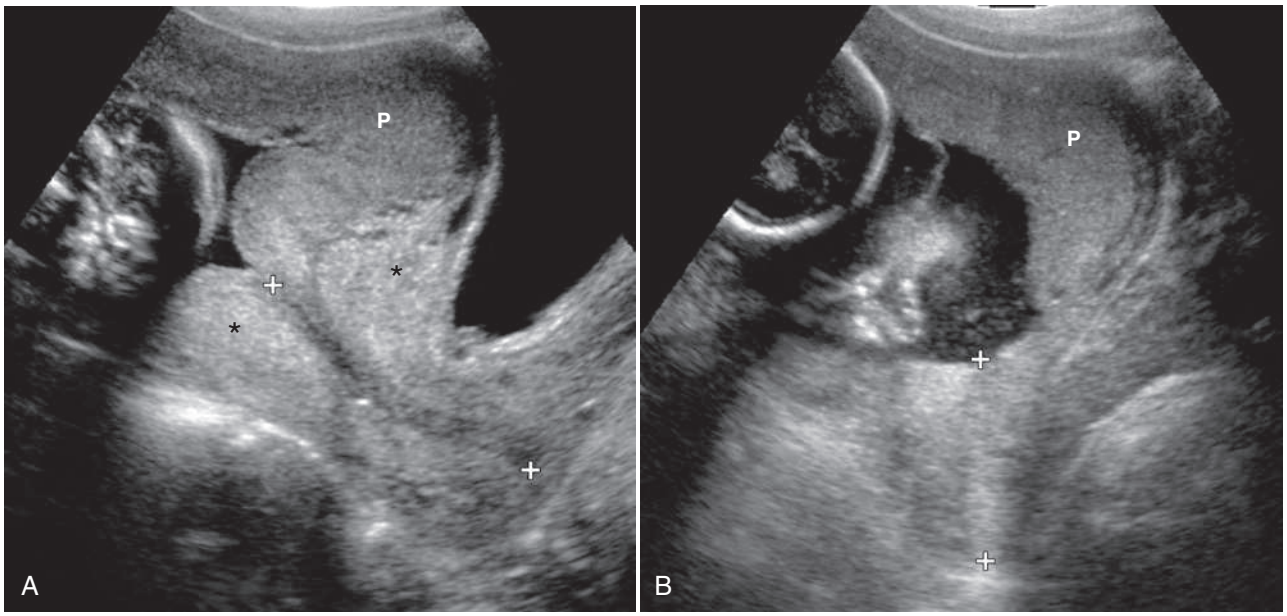

FIG. 44.6 Uterine Contractions. (A) TAS longitudinal image shows contraction (*) leading to a falsely elongated cervical canal *(calipers),* which measures 7.4 cm. **(B)** After relaxation of the contraction, the cervix *(calipers)* measures 4.2 cm. *P,* Placenta.

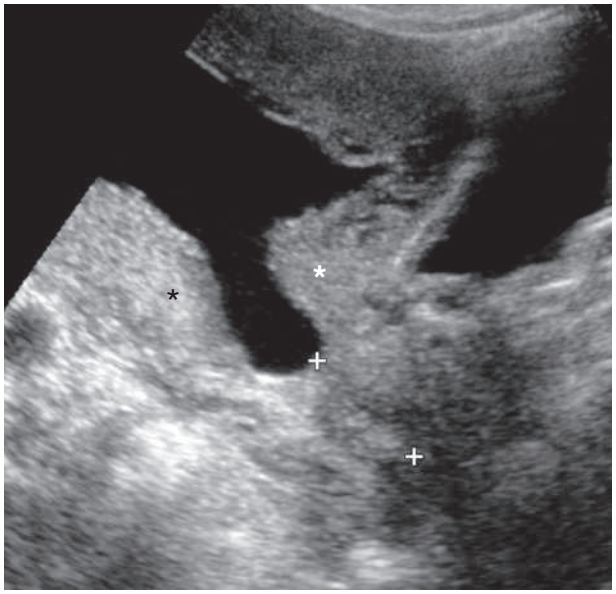

FIG. 44.7 Pseudodilation Caused by Uterine Contractions. Transabdominal longitudinal scan shows a lower uterine segment contraction (*) leading to a false appearance of dilated cervical canal. The closed cervix *(calipers)* measures 3.5 cm.

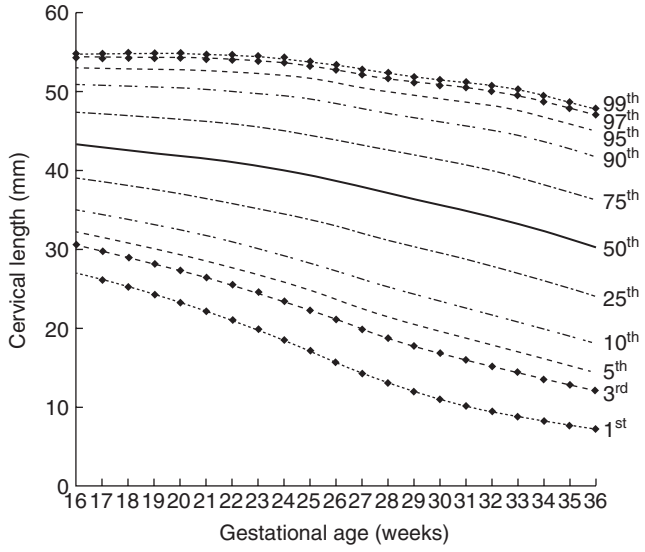

FIG. 44.8 Reference Ranges for Cervical Length Across Gestation. First to 99th percentiles are indicated. (With permission from Salomon LJ, Diaz-Garcia C, Bernard JP, Ville Y. Reference range for cervical length throughout pregnancy: non-parametric LMS-based model applied to a large sample. Ultrasound Obstet Gynecol. 2009;33[4]: 459-464.[33])

is caused by a lower uterine segment contraction with partial (Fig. 44.7) or complete approximation of the anterior and posterior myometrium with the resultant false appearance of a "funnel" above the closed cervix. The classic tips to recognize this appearance is the artificially elongated length of the cervix (>5 cm), the normal cervix lying caudal with respect to the pseudodilation, and the transient nature of this appearance.

Normal Cervix

Sonographically, the cervix appears as a distinct, soft tissue structure containing midrange echoes. The **endocervical canal** often appears as an echogenic line surrounded by a hypoechoic zone attributed to the endocervical glands (see Fig. 44.4B). Occasionally, the endocervical canal may appear hypoechoic and minimally dilated along its entire length. Benign **nabothian cysts** can be seen within the cervical soft tissues.

Numerous studies have evaluated **cervical length** in normal pregnancy. The typical cervix increases its length in the first trimester because of elaboration of the glandular content of the cervix.[27] Salomon et al.[33] published a reference curve of cervical length through gestation using TVS based on a large sample (Fig. 44.8). Based on this study, at about 20 weeks' gestation,

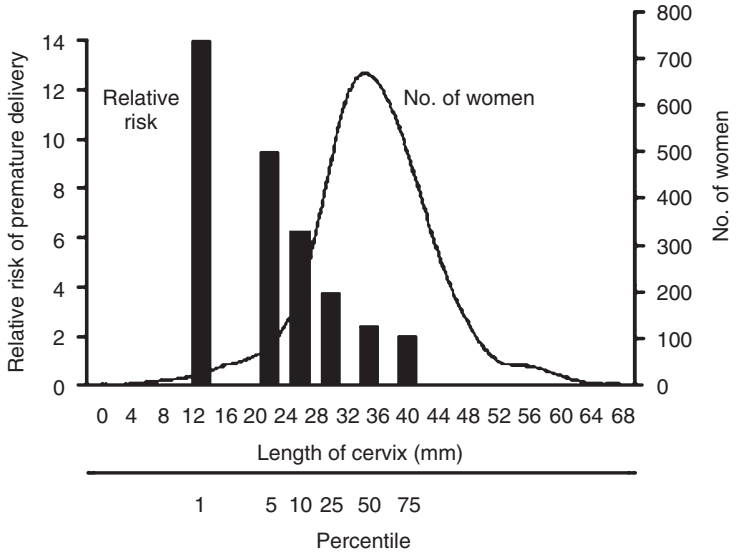

FIG. 44.9 Cervical Length and Risk of Preterm Delivery Percentile Ranking. Transvaginal ultrasound cervical length percentile rank, at 24 weeks' gestation, and relative risk of preterm delivery before 35 weeks. (With permission from Iams JD, Goldenberg RL, Meis PJ, et al. The length of the cervix and the risk of spontaneous premature delivery. National Institute of Child Health and Human Development Maternal Fetal Medicine Unit Network. N Engl J Med. 1996;334[9]:567-572.[34])

the 10th, 50th, and 90th percentiles of cervical length are 32.3, 41.9, and 50.5 mm, respectively.[33] A progressive linear reduction in cervical length occurs over the 10th to 40th week of gestation.

"Short" Cervix

With the goal of understanding the relationship between cervical length and SPTB (delivery before 35 weeks' gestation), in 1996, Iams et al.[34] published a prospective, multicenter study in which an unselected general population of women with singleton pregnancies underwent TVS at 24 and 28 weeks' gestation. Cervical length at both examinations was comparable and normally distributed, with a mean ±SD of 35.2 ± 8.3 mm at 24 weeks and 33.7 ± 8.5 mm at 28 weeks. A correlation between cervical length and the rate of SPTB was determined (Fig. 44.9); if the cervix was less than 26 mm (10th percentile) or less than 13 mm (1st percentile), risk of SPTB was increased by 6.49-fold and 13.99-fold, respectively, compared with the rate of SPTB if the cervix was at the 75th percentile length (40 mm) or greater.[34] Based on this landmark study, the definition of a **"short cervix" as less than 25 mm** (or <10th percentile length at 24-28 weeks) was accepted (Fig. 44.10).

Since then, more than 50 studies of TVS evaluation of the cervix and the risk of SPTB have been published. In 2003, Honest et al.[35] conducted a meta-analysis of 46 studies (including more than 31,000 asymptomatic singleton patients) and concluded that the utility of TVS assessment of cervical length for the prediction of SPTB varies with the gestational age at assessment and the definition of SPTB (birth before gestational age <32 weeks, <34 weeks, or <37 weeks). To summarize, the earlier in gestation, the shorter the cervix, the greater is the risk of SPTB, with the best predictive value when cervical length measures less than 25 mm and SPTB is defined as delivery earlier than 34 weeks' gestation (Table 44.1).

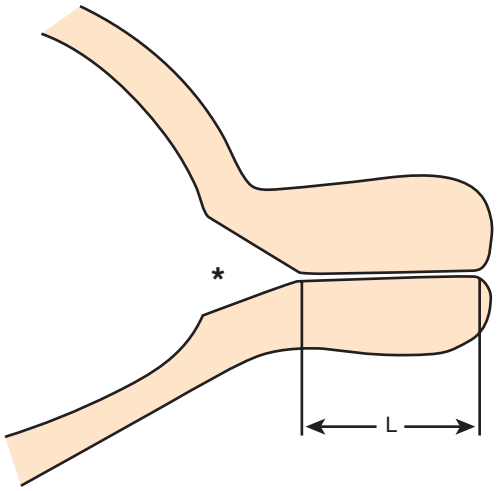

FIG. 44.10 Schematic of Abnormal Cervix. Length of the closed cervical canal *(L)* and the presence or absence of funneling (*) should be reported.

However, it should be recognized that the previous studies assessed cervical length at or before 28 weeks' gestation. Several reports have demonstrated no predictive value of TVS measurement of the cervix beyond 30 weeks of gestation for any definition of SPTB, likely because the cervix undergoes a gradual shortening process beyond this gestational age regardless of the timing of delivery.

The controversial aspect of TVS assessment of cervical length and the prediction of SPTB is that not all patients with a defined "short" cervix at any gestational age will deliver preterm. TVS is a reasonable tool for identifying patients who will deliver at or close to term with good negative predictive value. However, more than 50% of patients with a cervical length less than 25 mm measured at 20 weeks will deliver beyond 34 weeks' gestation.[34,35]

TABLE 44.1 Prediction of Spontaneous Preterm Birth Based on Gestational Age (GA) at Cervical Length Measurement (<25 mm)[a]

GA at Delivery	<20 Weeks	20-24 Weeks	24-28 Weeks
<32 weeks	4.1 (1.6-10.1)	4.19 (2.6-6.7)	No data
<34 weeks	6.2 (3.2-12.0)	4.40 (3.5-5.4)	4.0 (3.1-5.2)
<37 weeks	8.7 (3.8-19.9)	25.6 (8.5-76.7)	3.1 (1.1-8.9)

[a]Data presented as odds ratio ±95th percentile confidence intervals. Modified from Honest H, Bachmann LM, Coomarasamy A, et al. Accuracy of cervical transvaginal sonography in predicting preterm birth: a systematic review. Ultrasound Obstet Gynecol. 2003;22(3):305-322.[35]

Several studies have attempted to improve the predictive value of TVS by combining with other factors, including obstetric history and the concentration of fetal fibronectin in cervicovaginal secretions, to create a risk assessment formula.

PREDICTION OF SPONTANEOUS PRETERM BIRTH

Obstetric Factors

Celik et al.[36] presented a model to evaluate the ability of combinations of maternal demographics (age, race, weight, height, smoking status, history of cervical surgery, obstetric history) and cervical length between 20 and 24 weeks' gestation for prediction of SPTB in about 59,000 women with singleton pregnancies. The best prediction for SPTB was provided by cervical length alone, which was improved by adding obstetric history but not maternal characteristics. The estimated detection rates for extreme (<28 weeks), early (28-30 weeks), moderate (31-33 weeks), and mild (34-36 weeks) PTB by combining obstetric history and cervical length were 80.6%, 58.5%, 53.0%, and 28.6%, respectively, with a 10% false-positive rate. These data suggest that the combined screening model has better predictive value than either factor alone; similar findings in smaller-scale studies have been reported.[37]

Fetal fibronectin (FFN) is a glycoprotein that binds the amniochorion to the decidua and is released into cervicovaginal fluid in response to inflammation or separation of amniochorion from the decidua. Recent studies suggest that the combined use of cervical length and FFN improves the diagnostic performance of each test.[38,39] However, it has been shown that positive or negative FFN is relevant only when the sonographic cervical length is less than 30 mm.[40] Risk of SPTB remains low in women with cervical length of 30 mm or more and in those with cervical length of between 15 and 30 mm and negative FFN.[38,39,41]

Cervical Funneling

Much controversy surrounds the utility of measuring the **cervical "funnel,"** which is defined as the dilation of the internal os and the herniation of the fetal membranes into the cervical canal by more than 5 mm[42] (Figs. 44.11 and 44.12, Video 44.1). To et al.[43] reported that **funneling** of the internal os was present in 4% of all pregnancies; the shorter the cervix was, the greater was the likelihood of funneling, with 98% prevalence if the length was less than 15 mm and only 1% if greater than 30 mm. The rate of SPTB was increased in pregnancies demonstrating cervical funneling. However, funneling did not provide any significant contribution to the prediction of SPTB when combined with cervical length.[44,45] As an isolated finding compared with cervical length, the residual closed length measurements have a better predictive value than funneling. In addition, the shape or size of the funnel was not correlated to SPTB. As such, funneling is best reported as a categorical variable (present or absent) and best interpreted in the context of overall cervical length and obstetrical history.

Rate of Cervical Change

In their meta-analysis, Honest et al.[35] correlated a single measurement of cervical length at a single time point in gestation with the risk of SPTB. However, the events of prematurity occur along a continuum and likely develop over an as-yet undefined and variable period. Therefore **progressive shortening of the cervix** may be more important than a single abnormal cervical length measurement. A "short and shortening" cervical length may be a more effective tool for SPTB prediction than a "short but stable" cervical length. In a cohort of unselected patients, Naim et al.[46] demonstrated that if cervical length decreased on serial scans, the odds ratio for SPTB increased 6.8-fold per unit of change (one unit = decline of 10 mm per month). In women at increased risk of PTB, Owen at el.[28] reported that serial measurements up to 24 weeks' gestation significantly improved the prediction of SPTB compared with a single cervical measurement at 16 to 18 weeks. Similarly, in women at increased risk of SPTB (based on obstetric history), if cervical length remained stable from 12 to 20 weeks and greater than 25 mm, all patients delivered at term.[47] Patients in whom cervical length became serially shorter (ultimately <15 mm) and the decrease in length occurred before 20 weeks were offered and accepted a cervical cerclage, and all delivered after 30 weeks' gestation. Groom et al.[48] and Szychowski et al[49] reported similar results. These studies suggest three important points:

1. Serial cervical assessment is important to predict SPTB.
2. Progressive cervical shortening in patients at increased risk may begin before the typical timing of routine cervical assessment at the second-trimester fetal anatomic scan, advocating for initiation of serial cervical assessment early in the second trimester.
3. Serial cervical shortening in the second trimester may identify patients with true mechanical failure of the cervix, who may benefit from the placement of a cerclage to prevent SPTB.

Dynamic Cervical Change

A **dynamic cervix** is defined as having spontaneous shortening, lengthening, or funneling observed during real-time TVS[50] (Fig. 44.13). However, the value of a dynamic cervix for the prediction of SPTB is less clearly defined than that of a short cervix. Owen et al.[28] demonstrated that dynamic cervical length shortening in

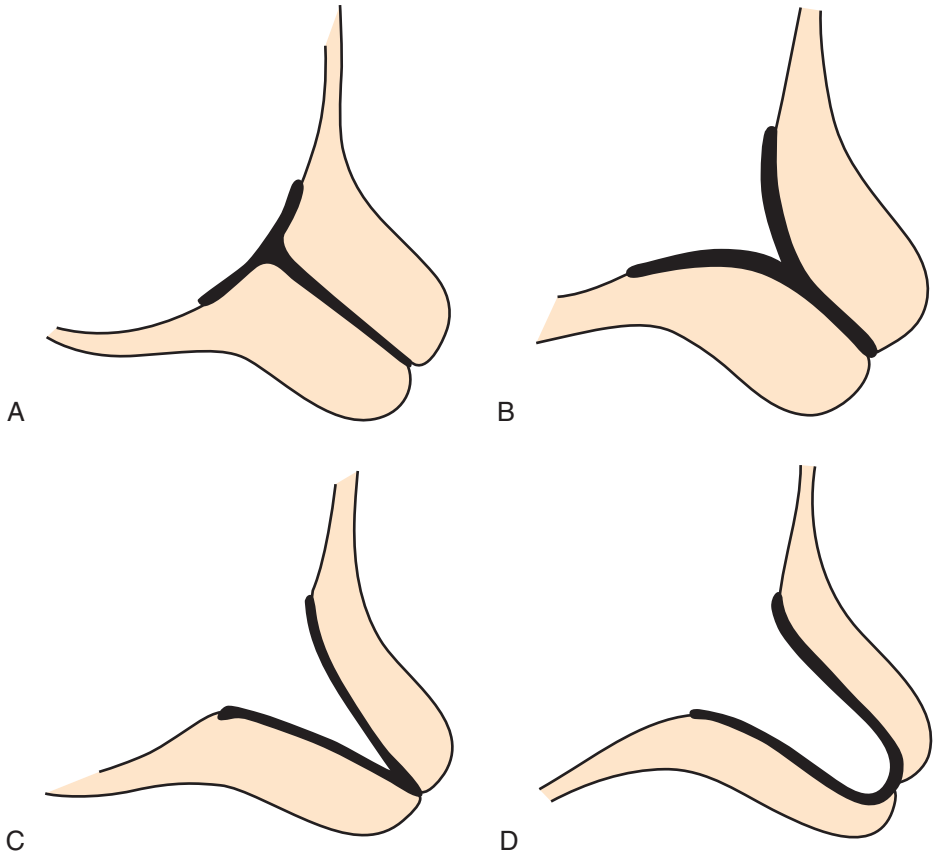

FIG. 44.11 Schematic of Normal Cervix and Cervical Funnel Shapes. (A) The normal closed internal os and the cervical canal appear T shaped. **(B)-(D)** Different stages of funneling resemble the letters Y, V, and U.

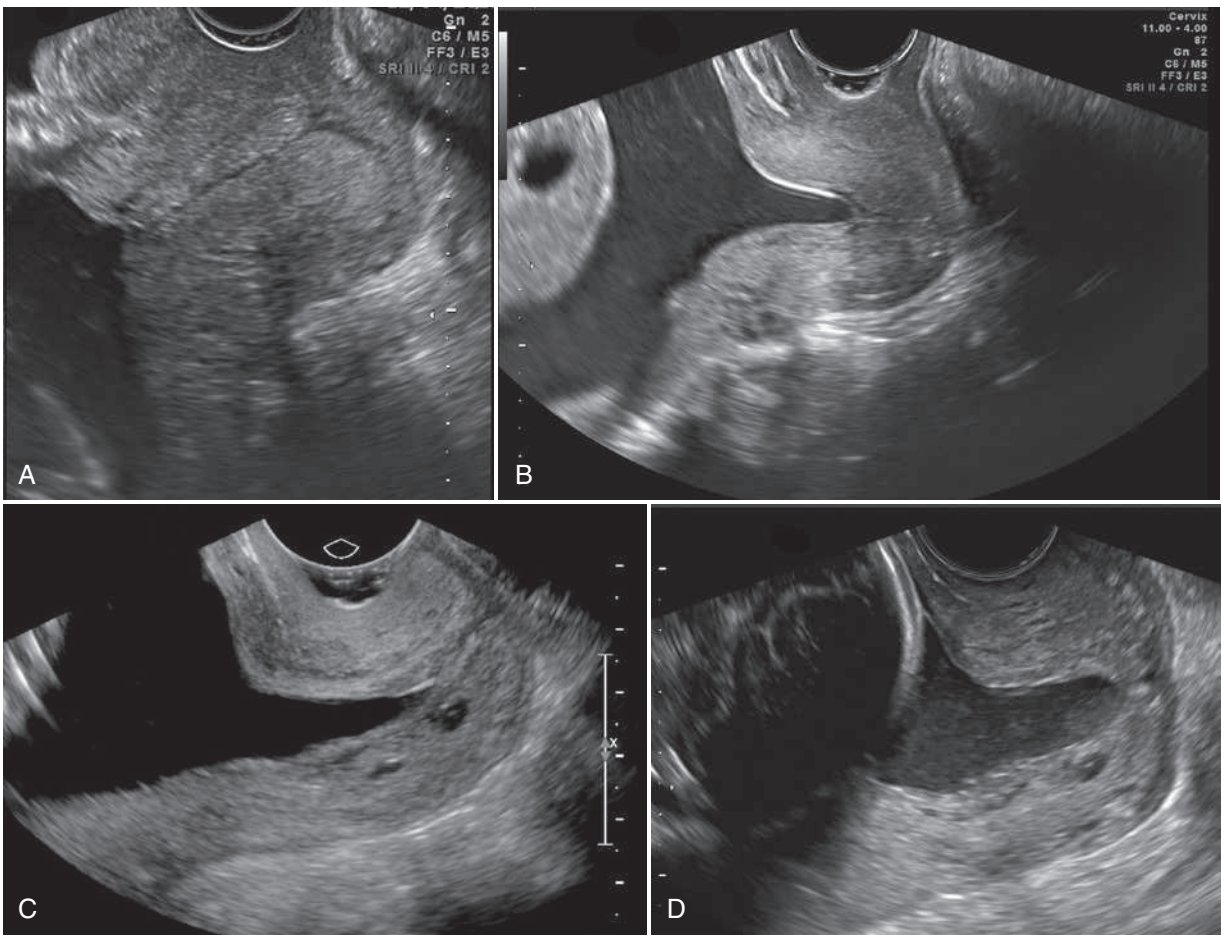

FIG. 44.12 Normal Cervix and Cervical Funneling. (A) Transvaginal scan of normal cervix, showing a T-shaped closed internal os. **(B)-(D)** Transvaginal scan shows different types of herniation of membranes, which respectively resemble the letters Y, V, and U. In **D,** with the U configuration, in this case the "U" is so deep there is no residual measurable closed cervical length.

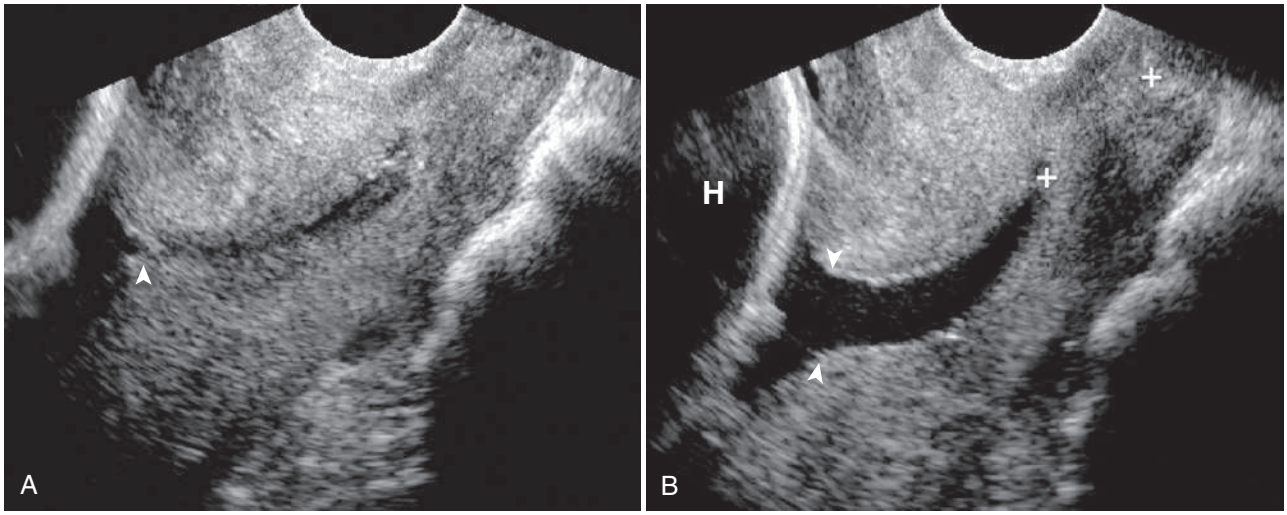

FIG. 44.13 Dynamic Dilation of the Cervix, Transvaginal Ultrasound. (A) Initially, the internal os appears closed *(arrowhead).* **(B)** Image obtained 30 seconds later shows funneling of the internal os *(arrowheads).* The residual closed cervix *(calipers)* measures 12 mm. *H,* Fetal head.

asymptomatic high-risk women during serial evaluations significantly improved the prediction of PTB. Patients with uterine contractions also had a greater incidence of dynamic cervical change than asymptomatic patients.[51] In both clinical scenarios, the minimal closed cervical length, not the "dynamic change," was the better predictor of SPTB. Several noninvasive stress techniques have been suggested to elicit cervical change and improve the ability of TVS to predict cervical incompetence. These stressors include **transfundal pressure** (pressure applied at the fundus for 15 seconds that elicits >5 mm in cervical length shortening), standing, and coughing. Several small studies found that transfundal pressure was the most effective tool in cervical assessment and the most sensitive tool to predict progressive cervical shortening.[52,53]

Other Sonographic Features

Several sonographic features other than cervical length have been studied to predict SPTB, including canal dilation, absence of the glandular area along the length of the canal, and amniotic fluid debris. Each feature is associated with an increased risk of PTB independent of cervical length. **Cervical canal dilation** of 2 to 4 mm was associated with a 5.5-fold increased risk of SPTB.[54] The **cervical glandular area** is a hypoechoic zone that runs along the length of the cervical canal (see Fig. 44.4B). In 388 unselected women, an absent cervical glandular area at 21 to 24 weeks' gestation predicted SPTB before 35 weeks (odds ratio of 129), suggesting a strong association.[55]

Cervix: Abnormal Findings on TVS[a]

Shortest closed cervical length <25 mm
Presence of funneling
Presence of positive response to fundal pressure
Presence of amniotic fluid debris ("sludge")
Shortening of 8-10 mm since previous TVS

[a]Gestational age less than 30 weeks.

"Sludge" or **debris** can be observed at ultrasound examination as free-floating echogenic material in close proximity to the cervix (Fig. 44.14, Videos 44.2 and 44.3). Samples of the sludge in patients with impending preterm delivery have been aspirated under ultrasound guidance, and the microbiologic examination reveals clusters of inflammatory cells and bacteria. Presence of sludge is an independent risk factor for **SPTB,**[56] PPROM, increased concentration of microbes within the amniotic fluid, and histologic chorioamnionitis in asymptomatic patients at high risk for spontaneous preterm delivery. Furthermore, the combination of "sludge" and a short cervix conferred a greater risk for SPTB than a short cervix alone.[57]

CERVICAL ASSESSMENT IN SPECIFIC CLINICAL SCENARIOS

Asymptomatic Patients

General Obstetric Population Screening

The prevention of PTB is a major health care priority. Only about 10% of spontaneous early PTBs occur in women with a prior history.[58] This leaves approximately 90% of PTBs occurring in women with no prior history of PTB, that is, the "low-risk" population.

It has been shown that over 95% of women without a prior PTB and with a singleton gestation have additional risk factors that would place them at increased risk for PTB, regardless of cervical length.[59] Therefore perhaps the term "low risk" needs to be redefined. Two large randomized clinical trials have demonstrated that in women with no prior history of PTB, a combined approach in which mid-trimester TVS screening for cervical length is used to identify patients at risk for preterm delivery (cervical length of <20 mm), followed by the administration of vaginal progesterone gel from the mid-trimester pregnancy until term reduces the rate of PTB before 33 weeks of gestation up to 45%.[60,61]

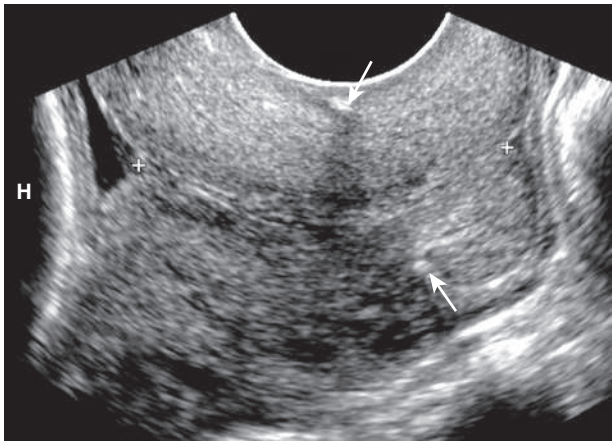

FIG. 44.14 Cervical Cerclage. Transvaginal scan demonstrates a closed cervix that measures 28 mm *(calipers)*. The cerclage sutures *(arrows)* appear hyperechoic. *H,* Fetal head.

Moreover, this protocol resulted in decreased rates of respiratory distress syndrome (the most common complication of preterm neonates), significant reduction in proportion of infants with any mortality or morbidity event, decreased rates of low birth weight (<1500 g), and improved neonatal outcomes.[60] An individual patient data meta-analysis of five large randomized controlled trial studies, including the two studies mentioned earlier, indicates that vaginal progesterone is effective in women with or without a history of PTB and a short cervix and therefore recommends that universal transvaginal sonographic measurement of cervical length be performed at 19 to 24 weeks of gestation.[62] Cost-effectiveness of this approach has been demonstrated in two separate studies, one of which demonstrated that 19 million dollars can be saved for every 100,000 women screened.[63,64]

Thus there is level I evidence for prevention of PTB and neonatal benefits based on treating with vaginal progesterone of low-risk singleton gestations identified with TVS screening to have a short cervical length. Cervical length TVS of singleton gestations fulfills many criteria for an effective screening test. However, the issue of universal screening of singleton gestations without prior PTB for the prevention of PTB remains a topic of debate because of insufficient data.[65]

During TAS for fetal anatomy or other indications, if the closed cervical length is less than 25 mm any time before 28 weeks of gestation, or suspicion of findings such as a dilated cervical canal, a ballooned fluid-filled lower segment with no visible cervix, or a cord or fetal part in the canal are noted, then further evaluation of the cervix by TVS is indicated.

As will be further discussed in subsequent sections, randomized controlled studies of cerclage placement in low-risk women identified with a "short cervix" have not demonstrated benefit of the cerclage for the prolongation of pregnancy.[66] Antibiotic therapy and bed rest have not been demonstrated to be effective at reducing the rate of SPTB in women with a "short cervix."[2]

High-Risk Obstetric Population Screening

Prior Preterm Birth. Once a patient has experienced an SPTB, the risk of recurrence is increased twofold based on history alone. TVS assessment of cervical length has been suggested as a tool of surveillance to evaluate the risk of SPTB specific to the individual patient and to identify those at greatest risk. Iams et al.[34] reported that cervical length was more predictive of PTB when other risk factors were also present. For a cervical length less than 25 mm at 22 to 24 weeks of gestation in a woman with a previous PTB, the relative risk was approximately 10-fold greater than that of women in the unselected population. Berghella et al.[45] demonstrated that the risk of recurrent SPTB varies with the gestational age at the time of measurement and the total length of cervix, but is not affected by the number of previous PTBs or the gestational age at delivery of the previous PTB. The risk of SPTB was decreased by 5.5% per week of gestation gained and by 6.0% per mm increase in cervical length. Crane and Hutchens[67] performed a systematic review of 14 studies involving 2258 asymptomatic high-risk women. In women with previous SPTB, for cervical length less than 25 mm, the likelihood ratios for SPTB were 4.3 and 2.8 when gestational age at assessment was less than 20 weeks and 20 to 24 weeks, respectively. Following that review, Seaward et al.[68] found limited utility of cervical length after 24 weeks' gestation in 75 high-risk patients; cervical length less than 25 mm or less than 15 mm measured at 24 to 30 weeks did not predict SPTB (defined as either <32 or <35 weeks' gestation) or adverse perinatal outcome. As discussed previously, the rate of cervical change may be a better predictive tool to identify those at greatest (and conversely lower) risk.

Multiple Gestations. Twin and higher-order multiple gestations are at increased risk of SPTB; 50% of twin gestations deliver before 35 weeks of gestation, and the mean gestational age for a triplet gestation is 32 weeks. Several studies have attempted to define individual patient risk by using TVS assessment of the cervix. For the twin gestation, when measured at 20 to 22 weeks, both length less than 25 mm and presence of funneling were predictive of SPTB, but at 27 weeks, only length less than 25 mm predicted SPTB.[69-72] The likelihood ratio of SPTB for cervical length less than 25 mm was 5.4-fold, but if the cervix

TAS Findings That Indicate TVS Follow-Up

- Closed cervical length less than 25 mm (any time <28 weeks)
- Dilated cervical canal
- Ballooned, fluid-filled lower segment with no visible cervix
- Suspicion of cord or fetal parts prolapse into the cervical canal

Risk Factors for Preterm Birth

- Short cervical length
- Prior preterm birth
- Uterocervical anomalies (such as müllerian duct abnormalities)
- Prior cervical surgery such as LEEP
- Multiple gestations
- Polyhydramnios

LEEP, Loop electrosurgical excision procedure.

measured greater than 30 mm, rate of SPTB was as low as 4%. For the triplet gestation, using the same cutoff length of less than 25 mm, a positive predictive value of 83% for SPTB was reported when the cervix was measured at 14 to 20 weeks' gestation.[69-72]

Uterocervical Anomalies and Cervical Surgery. Previous cervical surgery (cone biopsy or laser excisional therapy) and a known uterine or cervical congenital anomaly (uterine didelphys, bicornuate uterus, or diethylstilbestrol [DES] exposure in utero) are factors that significantly increase the risk of SPTB. Several researchers have sought to determine if the cutoff cervical length value of less than 25 mm provides the best predictive for SPTB for women with known congenital uterine anomalies. As expected, women with a unicornuate uterus had the shortest mean cervical length and the highest rate of SPTB, compared with women with a bicornuate or septate uterus. However, the mean gestational age at delivery was typically longer than 30 weeks' gestation. Using a cervical length cutoff of 30 mm when measured after 20 weeks, rate of SPTB was increased by 13-fold; at 14 to 23 weeks, if the cervix was less than 25 mm, rate of SPTB was as high as 50%.[73] After cervical amputation by cone biopsy or laser excisional surgery (loop electrosurgical excision procedure [LEEP]), the mean cervical length is shorter.[74] LEEP and cone biopsy therapy are associated with increased risk of SPTB by 3.45-fold, presumably from effects on cervical length and function. Again, a longer cervical cutoff of greater than 30 mm gave the best predictive value for identifying patients not at risk of SPTB, with a negative predictive value of 97%.

Preterm Premature Rupture of Membranes. Although the odds ratio for prediction of PPROM by TVS cervical assessment increases in relation to serial decreases in cervical length less than 20 mm, the positive and negative predictive values are low compared with the prediction of SPTB in general. TVS after PPROM can be performed without increased risk of chorioamnionitis or neonatal sepsis.[29] A cervical length less than 20 mm was associated with a latency period of less than 48 hours following PPROM.[29]

Polyhydramnios. Given that polyhydramnios is a risk factor for SPTB, presumably related to uterine distention triggering of uterine activity or mechanical cervical incompetence, one small study examined the relationship among the severity of polyhydramnios, cervical length, and SPTB.[75] A gradual shortening of cervical length was associated with advancing gestational age but not the severity of the polyhydramnios. Cervical length less than 15 mm was associated with an earlier gestational age at delivery.

Fetal Therapy. Based on the assumption that cervical length is an anatomic marker of underlying pathologic processes that lead to SPTB, clinicians have sought to use the cervical length measurement to quantify risk in patients undergoing a fetal therapeutic intervention that in itself increases the risk of SPTB. A cervical length less than 30 mm at multipregnancy reduction from triplet to twin gestation (at <14 weeks) has a positive predictive value of 67% for delivery less than 33 weeks after the procedure.[76-78] Similarly, a cervical length less than 30 mm before laser treatment of twin-twin transfusion syndrome was associated with SPTB, independent of parity, intrauterine death of one fetus, disease severity, or volume of the amniotic fluid reduction as part of the procedure.[76-78]

Symptomatic Patients

A patient presenting with symptoms consistent with preterm labor (uterine contractility, vaginal discharge or bleeding) is considered at increased risk of SPTB, although two-thirds of women admitted with the diagnosis of threatened PTB deliver at term.[2] Honest et al.[35] summarized the risk of SPTB before 34 weeks' gestation as follows: if the cervix measured less than 30 mm, risk increased by 2.0-fold if measured before 20 weeks and increased by 2.3-fold after 20 weeks. The presence of funneling, regardless of gestational age, increased the likelihood ratio to 4.7-fold. Alternatively, a TVS cervical length of longer than 30 mm makes the diagnosis of preterm labor extremely unlikely, with a negative predictive value of 98% to 99%. Multiple studies have shown the importance of sonographic assessment of cervical length in distinguishing between true and false labor in patients presenting with symptoms of preterm labor.[79]

As previously stated, assessment of FFN in the cervical-vaginal secretions improves the prediction of delivery provided by cervical length evaluation in patients with a cervical length of less than 30 mm.[38,40,41]

Cervical Incompetence and Cervical Cerclage

Cervical incompetence is defined as the inability to support a full-term pregnancy because of a functional or mechanical defect of the cervix.[80] It is characterized clinically by acute painless dilation of the cervix usually in the mid-trimester, culminating in prolapse and/or PPROM with resultant preterm delivery. This occurs in 0.5% to 1.0% of all pregnancies, with a recurrence risk of 30%.[2,9] **Functional failure** of the cervix is premature cervical ripening (shortening and dilation normally occurring at the end of gestation) and most often is related to urogenital or intrauterine infection or inflammation and thus has a low risk of recurrence. **Mechanical failure** of the cervix, defined as a defect in the structural integrity of the cervix, may result from traumatic injury to the cervix, including cervical laceration, amputation, conization, excessive cervical dilation before diagnostic curettage, or therapeutic abortion.[2] It may also be associated with DES in utero or uterine malformations. Serial cervical shortening in the second trimester and a positive response to fundal pressure may be used to unmask specific cervical mechanical incompetence during pregnancy.[48,49,53]

Certain nonsurgical approaches, including activity restriction, bed rest, and pelvic rest have not been proved to be effective for the treatment of cervical insufficiency.[81,82] These patients may benefit from the placement of a **cervical cerclage,** a suture used to reinforce the structural integrity of the cervical canal.

Indications for cerclage include[83]:

- History indicated (prophylactic) cerclage: in patients with unexplained second-trimester delivery in the absence of labor or abruptio placentae. Three randomized controlled trials have reported on the efficacy of this approach; two found no significant improvement in outcomes[84,85] and one found fewer preterm deliveries before 33 weeks in the cerclage group.[86]

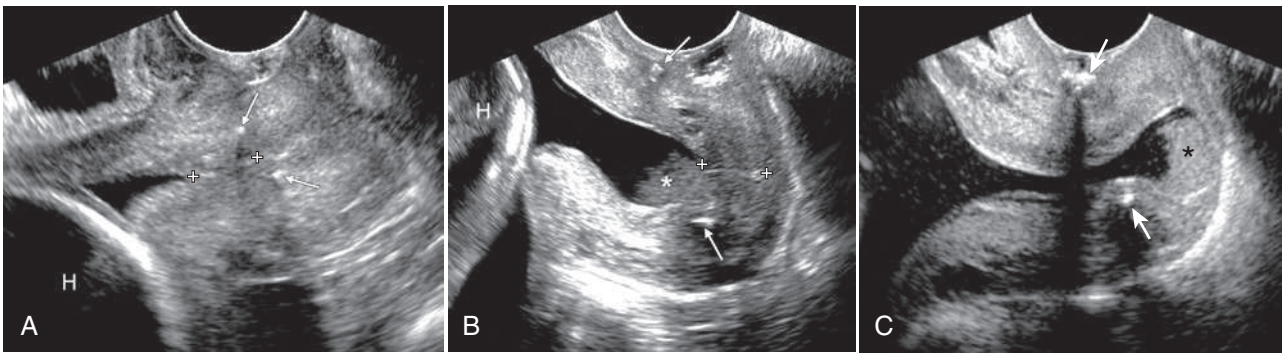

FIG. 44.15 Funneling After Cervical Cerclage. (A) Transvaginal scan demonstrates mild protrusion of the membranes. There remains 10-mm closed cervix length *(calipers)* above the sutures *(arrows)*. **(B)** Transvaginal scan demonstrates protrusion of the membranes to the level of the sutures *(arrows)*. The residual closed cervix length below the cerclage sutures measures 10 mm *(calipers)*. **(C)** Transvaginal scan demonstrates protrusion of the membranes beyond the sutures *(arrows)*. *H,* Fetal head; * indicates amniotic fluid sludge.

- Physical examination indicated ("rescue") cerclage: in patients presenting with advanced cervical dilation in the absence of labor or abruptio placentae. Limited data from one small randomized trial and retrospective studies have suggested the possibility of benefit from cerclage placement in these women.[83]
- Sonographic finding of a short cervix (<25 mm) before 24 weeks of gestation in patient with singleton pregnancy and prior history of PTB less than 34 weeks of gestation.

Numerous studies have compared perinatal outcome in cerclage patients treated with history-indicated cerclage versus those monitored with serial TVS examinations that have been treated with an ultrasound-indicated cerclage as needed. Two recent summaries of the results of these multiple studies have drawn the following conclusions, which are limited to singleton pregnancies:

1. Most patients at risk of cervical insufficiency can be safely monitored with serial TVS examinations in the second trimester.[87,88]
2. History-indicated cerclage procedures can be avoided in more than one-half of the patients who undergo serial TVS cervical length monitoring.[87,89]
3. Duration of surveillance should begin at 16 weeks and end at 24 weeks of gestation.[87]
4. Although women with a current singleton pregnancy, prior SPTB at less than 34 weeks of gestation, and short cervical length (<25 mm) before 24 weeks of gestation do not meet the diagnostic criteria for cervical insufficiency, available evidence suggests that cerclage placement may be effective in this setting[90,91] Cerclage is associated with significant decreases in PTB outcomes, as well as improvements in composite neonatal morbidity and mortality.

Sonography has been used in the operating room to guide the placement of cervical cerclage, especially when the cervix is short, to ensure that the suture material is placed within the cervical tissue and does not encroach on bladder mucosa or rectum. Once in place, the cervical cerclage will appear as one or more echodense "dots" along the length of the cervical canal

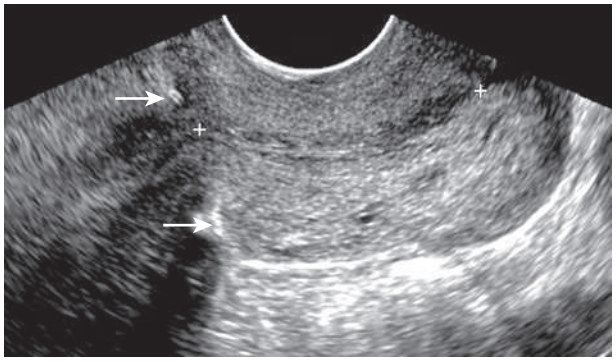

FIG. 44.16 Abdominal Cervical Cerclage. Transvaginal longitudinal scan demonstrates hyperechoic sutures *(arrows)* at the internal os in this woman with a history of incompetent cervix. The cervix is closed and long, measuring 4.5 cm *(calipers)*.

(Fig. 44.14). Postcerclage evaluation includes location of the sutures in relation to both the internal and the external cervical os and measurement of the length of the closed cervical canal both above and below the level of the suture line. Once the cerclage has been placed, cervical length assessment continues to have value in the prediction of SPTB. Several studies reported that if the residual total closed cervical length after cerclage placement was less than 15 mm, or if "funneling to stitch" (open canal to level of suture line) was present (Fig. 44.15), the patient was at significantly increased risk of delivery before 32 weeks' gestation, regardless of the indication for stitch placement.[68,92,93] Beyond 30 weeks, there was no predictive value of cervical assessment in women with a cerclage.

When the vaginal portion of the cervical tissue is absent or damaged (trachelectomy, cone biopsy, birth trauma), the placement of a cerclage in the vaginal component of the cervix is not possible. Alternatively, a cerclage can be placed at the level of the cervicouterine isthmus either by laparoscopy or laparotomy. On TVS assessment, the echodense dots of this "abdominal" cerclage will be visualized close to the bladder and adjacent to the lower uterine segment (Fig. 44.16).

Who Should Not Get a Cerclage? Incidentally detected short cervical length in the second trimester in the absence of a prior singleton PTB is not diagnostic of cervical insufficiency,

and cerclage is not clearly indicated in this setting.[94] Cerclage may increase the risk of PTB in women with a twin pregnancy and an ultrasonographically detected cervical length less than 25 mm and thus is not recommended.[88,95] In addition, evidence is lacking for the benefit of cerclage solely for the following indications: prior LEEP, cone biopsy, or müllerian anomaly.

Cervical Incompetence and Vaginal Pessary

Cervical pessary is a silicone device that has been used in the past 50 years to prevent PTB. Two randomized controlled studies have assessed the effectiveness of this treatment option in women with singleton gestations and a mid-trimester short cervical length detected by TVS and with no prior history of PTB, one of which is in favor (PECEP trial)[62] and the other one from China, which did not show significant benefit to using this device.[96]

A Cochrane review in 2010 (before these two trials were published)[97] did not identify any well-designed randomized clinical trial in order to confirm or refute the benefit of cervical pessary in singleton gestations. However, it was noted that there is evidence from nonrandomized trials that showed some benefit of cervical pessary in preventing PTB. At this time, evidence remains controversial.

Vaginal Progesterone and 17-Alpha Hydroxyprogesterone Caproate

It is important to note that progesterone and 17-alpha hydroxyprogesterone caproate (17α-OHPC) have different chemical structures, pharmacologic effects, clinical indications, and safety profiles.[98] Progesterone is a natural progestogen, whereas 17α-OHPC is a synthetic progestogen. Vaginal progesterone is recommended for the prevention of PTB in women with a short cervix (with or without a history of PTB). 17α-OHPC is currently recommended for the prevention of PTB in women with a singleton gestation and a history of PTB. Currently, there is a safety warning for 17α-OHPC based on a nonsignificant increased rate of stillbirth and miscarriages in women who received 17α-OHPC,[99] whereas no such issues have been reported with vaginal progesterone.

MANAGEMENT PROTOCOLS FOR THE ABNORMAL CERVIX

Because of improved test characteristics in women at increased risk of SPTB, and because interventions such as cerclage and progesterone therapy may have a potential benefit in the high-risk patient, cervical length measurement is currently used as a screening test in high-risk pregnancies and perhaps in the future, universally for all pregnancies. What remains to be determined is the frequency of evaluation, the gestational age of first evaluation, and the utility of the measurements after 30 weeks of gestation. Based on the previous discussions, specific management protocols are suggested (Figs. 44.17 and 44.18).

CONCLUSION

TVS is the reference-standard approach for cervical assessment in pregnancy. Cervical length is used most often to predict SPTB. Cervical length should be taken in the context of maternal risk factors for SPTB (obstetric history, uterine contractions), gestational age, funneling, response to fundal pressure, previous measurement, presence of cervical glandular area, and amniotic fluid debris. The cervical length cutoff of 25 mm at mid-trimester provides the best predictive values for SPTB before 34 weeks. A "short" (<25 mm) cervical length is not a diagnosis of impending SPTB, but rather a tool to quantify the increased risk of such an event.

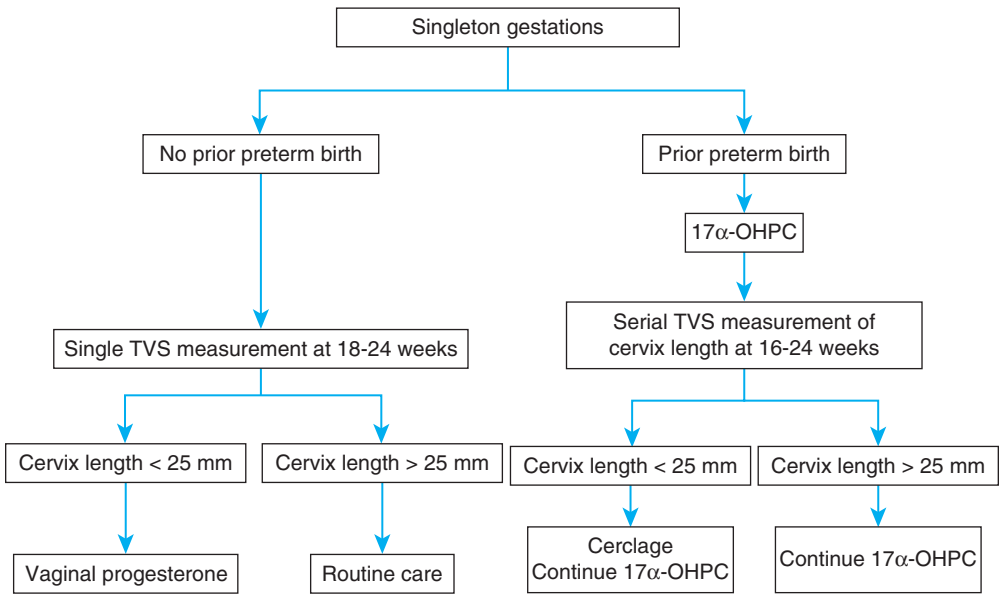

FIG. 44.17 Management Protocol: General Obstetric Population. Proposed algorithm to guide response to cervical length measurements at transvaginal sonography (at 18-24 weeks' gestation). *17α-OHPC,* 17-alpha Hydroxyprogesterone caproate. *TVS,* transvaginal sonography.

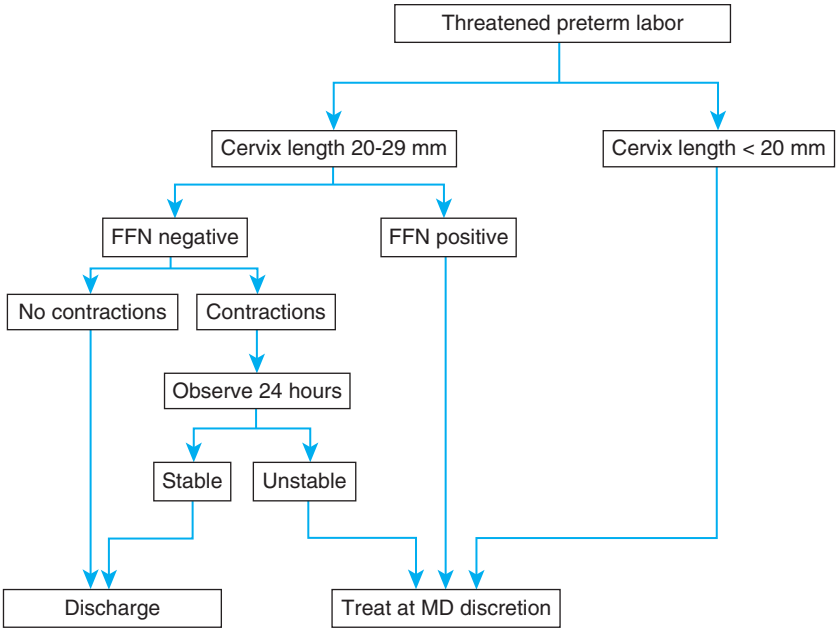

FIG. 44.18 Management Protocol: High-Risk Obstetric Population. Algorithm to guide management in threatened preterm labor. *FFN,* Fetal fibronectin.

Acknowledgment

The authors would like to thank Drs. Whittle, Fong, and Windrim, whose chapter in the previous edition of this book formed the backbone of the current chapter.

REFERENCES

1. Blencowe H, Cousens S, Oestergaard MZ, et al. National, regional, and worldwide estimates of preterm birth rates in the year 2010 with time trends since 1990 for selected countries: a systematic analysis and implications. Lancet. 2012;379(9832):2162-2172.
2. Spong CY. Prediction and prevention of recurrent spontaneous preterm birth. Obstet Gynecol. 2007;110(2 Pt 1):405-415.
3. Blondel B, Macfarlane A, Gissler M, et al. Preterm birth and multiple pregnancy in European countries participating in the PERISTAT project. BJOG. 2006;113(5):528-535.
4. Kramer MS, Demissie K, Yang H, et al. The contribution of mild and moderate preterm birth to infant mortality. Fetal and Infant Health Study Group of the Canadian Perinatal Surveillance System. JAMA. 2000;284(7):843-849.
5. O'Shea TM, Klinepeter KL, Goldstein DJ, et al. Survival and developmental disability in infants with birth weights of 501 to 800 grams, born between 1979 and 1994. Pediatrics. 1997;100(6):982-986.
6. Saigal S, Hoult LA, Streiner DL, et al. School difficulties at adolescence in a regional cohort of children who were extremely low birth weight. Pediatrics. 2000;105(2):325-331.
7. Buck GM, Msall ME, Schisterman EF, et al. Extreme prematurity and school outcomes. Paediatr Perinat Epidemiol. 2000;14(4):324-331.
8. Botting N, Powls A, Cooke RW, Marlow N. Attention deficit hyperactivity disorders and other psychiatric outcomes in very low birthweight children at 12 years. J Child Psychol Psychiatry. 1997;38(8):931-941.
9. Golan A, Barnan R, Wexler S, et al. Incompetence of the uterine cervix. Obstet Gynecol Surv. 1989;44(2):96-107.
10. Romero R, Espinoza J, Goncalves LF, et al. The role of inflammation and infection in preterm birth. Semin Reprod Med. 2007;25(1):21-39.
11. Sonek JD, Iams JD, Blumenfeld M, et al. Measurement of cervical length in pregnancy: comparison between vaginal ultrasonography and digital examination. Obstet Gynecol. 1990;76(2):172-175.
12. Mason GC, Maresh MJ. Alterations in bladder volume and the ultrasound appearance of the cervix. Br J Obstet Gynaecol. 1990;97(5):457-458.
13. Andersen HF. Transvaginal and transabdominal ultrasonography of the uterine cervix during pregnancy. J Clin Ultrasound. 1991;19(2):77-83.
14. Friedman AM, Schwartz N, Ludmir J, et al. Can transabdominal ultrasound identify women at high risk for short cervical length? Acta Obstet Gynecol Scand. 2013;92(6):637-641.
15. Meijer-Hoogeveen M, Stoutenbeek P, Visser GH. Transperineal versus transvaginal sonographic cervical length measurement in second- and third-trimester pregnancies. Ultrasound Obstet Gynecol. 2008;32(5):657-662.
16. Hernandez-Andrade E, Romero R, Ahn H, et al. Transabdominal evaluation of uterine cervical length during pregnancy fails to identify a substantial number of women with a short cervix. J Matern Fetal Neonatal Med. 2012;25(9):1682-1689.
17. Mahony BS, Nyberg DA, Luthy DA, et al. Translabial ultrasound of the third-trimester uterine cervix. Correlation with digital examination. J Ultrasound Med. 1990;9(12):717-723.
18. Hertzberg BS, Bowie JD, Weber TM, et al. Sonography of the cervix during the third trimester of pregnancy: value of the transperineal approach. AJR Am J Roentgenol. 1991;157(1):73-76.
19. Hertzberg BS, Kliewer MA, Baumeister LA, et al. Optimizing transperineal sonographic imaging of the cervix: the hip elevation technique. J Ultrasound Med. 1994;13(12):933-936.
20. Gauthier T, Marin B, Garuchet-Bigot A, et al. Transperineal versus transvaginal ultrasound cervical length measurement and preterm labor. Arch Gynecol Obstet. 2014;290(3):465-469.
21. Berghella V, Bega G, Tolosa JE, Berghella M. Ultrasound assessment of the cervix. Clin Obstet Gynecol. 2003;46(4):947-962.
22. Kurtzman JT, Goldsmith LJ, Gall SA, Spinnato JA. Transvaginal versus transperineal ultrasonography: a blinded comparison in the assessment of cervical length at midgestation. Am J Obstet Gynecol. 1998;179(4):852-857.
23. Owen J, Neely C, Northen A. Transperineal versus endovaginal ultrasonographic examination of the cervix in the midtrimester: a blinded comparison. Am J Obstet Gynecol. 1999;181(4):780-783.
24. Okun N. Is transperineal ultrasonography of cervical length in pregnant women as accurate as endovaginal ultrasonography? A prospective, blinded comparison of level of agreement of two techniques. J Obstet Gynaecol Can. 2001;23:592-596.
25. Cicero S, Skentou C, Souka A, et al. Cervical length at 22-24 weeks of gestation: comparison of transvaginal and transperineal-translabial ultrasonography. Ultrasound Obstet Gynecol. 2001;17(4):335-340.

26. Kushnir O, Vigil DA, Izquierdo L, et al. Vaginal ultrasonographic assessment of cervical length changes during normal pregnancy. Am J Obstet Gynecol. 1990;162(4):991-993.
27. Gramellini D, Fieni S, Molina E, et al. Transvaginal sonographic cervical length changes during normal pregnancy. J Ultrasound Med. 2002;21(3): 227-232.
28. Owen J, Yost N, Berghella V, et al. Mid-trimester endovaginal sonography in women at high risk for spontaneous preterm birth. JAMA. 2001; 286(11):1340-1348.
29. Odibo AO, Berghella V, Reddy U, et al. Does transvaginal ultrasound of the cervix predict preterm premature rupture of membranes in a high-risk population? Ultrasound Obstet Gynecol. 2001;18(3):223-227.
30. Carlan SJ, Richmond LB, O'Brien WF. Randomized trial of endovaginal ultrasound in preterm premature rupture of membranes. Obstet Gynecol. 1997;89(3):458-461.
31. Timor-Tritsch IE, Yunis RA. Confirming the safety of transvaginal sonography in patients suspected of placenta previa. Obstet Gynecol. 1993;81(5 Pt 1):742-744.
32. Rovas L, Sladkevicius P, Strobel E, Valentin L. Reference data representative of normal findings at three-dimensional power Doppler ultrasound examination of the cervix from 17 to 41 gestational weeks. Ultrasound Obstet Gynecol. 2006;28(6):761-767.
33. Salomon LJ, Diaz-Garcia C, Bernard JP, Ville Y. Reference range for cervical length throughout pregnancy: non-parametric LMS-based model applied to a large sample. Ultrasound Obstet Gynecol. 2009;33(4):459-464.
34. Iams JD, Goldenberg RL, Meis PJ, et al. The length of the cervix and the risk of spontaneous premature delivery. National Institute of Child Health and Human Development Maternal Fetal Medicine Unit Network. N Engl J Med. 1996;334(9):567-572.
35. Honest H, Bachmann LM, Coomarasamy A, et al. Accuracy of cervical transvaginal sonography in predicting preterm birth: a systematic review. Ultrasound Obstet Gynecol. 2003;22(3):305-322.
36. Celik E, To M, Gajewska K, et al. Cervical length and obstetric history predict spontaneous preterm birth: development and validation of a model to provide individualized risk assessment. Ultrasound Obstet Gynecol. 2008;31(5): 549-554.
37. To MS, Skentou CA, Royston P, et al. Prediction of patient-specific risk of early preterm delivery using maternal history and sonographic measurement of cervical length: a population-based prospective study. Ultrasound Obstet Gynecol. 2006;27(4):362-367.
38. Gomez R, Romero R, Medina L, et al. Cervicovaginal fibronectin improves the prediction of preterm delivery based on sonographic cervical length in patients with preterm uterine contractions and intact membranes. Am J Obstet Gynecol. 2005;192(2):350-359.
39. Hermans FJ, Bruijn MM, Vis JY, et al. Risk stratification with cervical length and fetal fibronectin in women with threatened preterm labor before 34 weeks and not delivering within 7 days. Acta Obstet Gynecol Scand. 2015;94(7):715-721.
40. van Baaren GJ, Vis JY, Wilms FF, et al. Predictive value of cervical length measurement and fibronectin testing in threatened preterm labor. Obstet Gynecol. 2014;123(6):1185-1192.
41. Audibert F, Fortin S, Delvin E, et al. Contingent use of fetal fibronectin testing and cervical length measurement in women with preterm labour. J Obstet Gynaecol Can. 2010;32(4):307-312.
42. Mancuso MS, Szychowski JM, Owen J, et al. Cervical funneling: effect on gestational length and ultrasound-indicated cerclage in high-risk women. Am J Obstet Gynecol. 2010;203(3):259.e1-259.e5.
43. To MS, Skentou C, Liao AW, et al. Cervical length and funneling at 23 weeks of gestation in the prediction of spontaneous early preterm delivery. Ultrasound Obstet Gynecol. 2001;18(3):200-203.
44. Meijer-Hoogeveen M, Stoutenbeek P, Visser GH. Methods of sonographic cervical length measurement in pregnancy: a review of the literature. J Matern Fetal Neonatal Med. 2006;19(12):755-762.
45. Berghella V, Roman A, Daskalakis C, et al. Gestational age at cervical length measurement and incidence of preterm birth. Obstet Gynecol. 2007;110(2 Pt 1):311-317.
46. Naim A, Haberman S, Burgess T, et al. Changes in cervical length and the risk of preterm labor. Am J Obstet Gynecol. 2002;186(5):887-889.
47. Iqbal S, Kfouri J, Whittle WL, Windrim R. Early serial cervical length measurement as a toll to select candidates for cervical cerclage in a population of patients at increased risk for spontaneous preterm birth. Presented at Society for Obstetricians and Gynecologists of Canada Annual Meeting, Ottawa 2007.
48. Groom KM, Shennan AH, Bennett PR. Ultrasound-indicated cervical cerclage: outcome depends on preoperative cervical length and presence of visible membranes at time of cerclage. Am J Obstet Gynecol. 2002;187(2): 445-449.
49. Szychowski JM, Owen J, Hankins G, et al. Timing of mid-trimester cervical length shortening in high-risk women. Ultrasound Obstet Gynecol. 2009; 33(1):70-75.
50. Wong G, Levine D, Ludmir J. Maternal postural challenge as a functional test for cervical incompetence. J Ultrasound Med. 1997;16(3):169-175.
51. Pugatsch R, Elad D, Jaffa AJ, Eytan O. Analysis of cervical dynamics by ultrasound imaging. Ann N Y Acad Sci. 2007;1101:203-214.
52. Guzman ER, Rosenberg JC, Houlihan C, et al. A new method using vaginal ultrasound and transfundal pressure to evaluate the asymptomatic incompetent cervix. Obstet Gynecol. 1994;83(2):248-252.
53. Guzman ER, Pisatowski DM, Vintzileos AM, et al. A comparison of ultrasonographically detected cervical changes in response to transfundal pressure, coughing, and standing in predicting cervical incompetence. Am J Obstet Gynecol. 1997;177(3):660-665.
54. Hartmann K, Thorp Jr JM, McDonald TL, et al. Cervical dimensions and risk of preterm birth: a prospective cohort study. Obstet Gynecol. 1999;93(4):504-509.
55. Pires CR, Moron AF, Mattar R, et al. Cervical gland area as an ultrasonographic marker for preterm delivery. Int J Gynaecol Obstet. 2006;93(3): 214-219.
56. Hatanaka AR, Mattar R, Kawanami TE, et al. Amniotic fluid "sludge" is an independent risk factor for preterm delivery. J Matern Fetal Neonatal Med. 2016;29(1):120-125.
57. Kusanovic JP, Espinoza J, Romero R, et al. Clinical significance of the presence of amniotic fluid 'sludge' in asymptomatic patients at high risk for spontaneous preterm delivery. Ultrasound Obstet Gynecol. 2007;30(5):706-714.
58. Mercer BM, Goldenberg RL, Moawad AH, et al. The preterm prediction study: effect of gestational age and cause of preterm birth on subsequent obstetric outcome. National Institute of Child Health and Human Development Maternal-Fetal Medicine Units Network. Am J Obstet Gynecol. 1999;181(5 Pt 1):1216-1221.
59. Mella MT, Mackeen AD, Gache D, et al. The utility of screening for historical risk factors for preterm birth in women with known second trimester cervical length. J Matern Fetal Neonatal Med. 2013;26(7):710-715.
60. Hassan SS, Romero R, Vidyadhari D, et al. Vaginal progesterone reduces the rate of preterm birth in women with a sonographic short cervix: a multicenter, randomized, double-blind, placebo-controlled trial. Ultrasound Obstet Gynecol. 2011;38(1):18-31.
61. Fonseca EB, Celik E, Parra M, et al. Progesterone and the risk of preterm birth among women with a short cervix. N Engl J Med. 2007;357(5): 462-469.
62. Goya M, Pratcorona L, Merced C, et al. Cervical pessary in pregnant women with a short cervix (PECEP): an open-label randomised controlled trial. Lancet. 2012;379(9828):1800-1806.
63. Werner EF, Han CS, Pettker CM, et al. Universal cervical-length screening to prevent preterm birth: a cost-effectiveness analysis. Ultrasound Obstet Gynecol. 2011;38(1):32-37.
64. Cahill AG, Odibo AO, Caughey AB, et al. Universal cervical length screening and treatment with vaginal progesterone to prevent preterm birth: a decision and economic analysis. Am J Obstet Gynecol. 2010;202(6):548.e1-548.e8.
65. Society for Maternal-Fetal Medicine. Publications Committee. Progesterone and preterm birth prevention: translating clinical trials data into clinical practice. Am J Obstet Gynecol. 2012;206(5):376-386.
66. Pramod R, Okun N, McKay D, et al. Cerclage for the short cervix demonstrated by transvaginal ultrasound: current practice and opinion. J Obstet Gynaecol Can. 2004;26(6):564-570.
67. Crane JM, Hutchens D. Use of transvaginal ultrasonography to predict preterm birth in women with a history of preterm birth. Ultrasound Obstet Gynecol. 2008;32(5):640-645.

68. Seaward A, Kfouri J, Dodd J, et al. Does transvaginal ultrasound assessment of the total cervical length and/or "funnelling to the stitch" predict preterm birth in women with a cervical cerclage in situ? Presented at Society for Maternal-Fetal Medicine Annual Meeting, 2008.
69. Maslovitz S, Hartoov J, Wolman I, et al. Cervical length in the early second trimester for detection of triplet pregnancies at risk for preterm birth. J Ultrasound Med. 2004;23(9):1187-1191.
70. Vayssiere C, Favre R, Audibert F, et al. Cervical assessment at 22 and 27 weeks for the prediction of spontaneous birth before 34 weeks in twin pregnancies: is transvaginal sonography more accurate than digital examination? Ultrasound Obstet Gynecol. 2005;26(7):707-712.
71. Vayssiere C, Favre R, Audibert F, et al. Cervical length and funneling at 22 and 27 weeks to predict spontaneous birth before 32 weeks in twin pregnancies: a French prospective multicenter study. Am J Obstet Gynecol. 2002;187(6):1596-1604.
72. Guzman ER, Walters C, O'Reilly-Green C, et al. Use of cervical ultrasonography in prediction of spontaneous preterm birth in triplet gestations. Am J Obstet Gynecol. 2000;183(5):1108-1113.
73. Airoldi J, Berghella V, Sehdev H, Ludmir J. Transvaginal ultrasonography of the cervix to predict preterm birth in women with uterine anomalies. Obstet Gynecol. 2005;106(3):553-556.
74. Crane JM, Delaney T, Hutchens D. Transvaginal ultrasonography in the prediction of preterm birth after treatment for cervical intraepithelial neoplasia. Obstet Gynecol. 2006;107(1):37-44.
75. Hershkovitz R, Sheiner E, Maymon E, et al. Cervical length assessment in women with idiopathic polyhydramnios. Ultrasound Obstet Gynecol. 2006;28(6):775-778.
76. Fait G, Har-Toov J, Gull I, et al. Cervical length, multifetal pregnancy reduction, and prediction of preterm birth. J Clin Ultrasound. 2005; 33(7):329-332.
77. Robyr R, Boulvain M, Lewi L, et al. Cervical length as a prognostic factor for preterm delivery in twin-to-twin transfusion syndrome treated by fetoscopic laser coagulation of chorionic plate anastomoses. Ultrasound Obstet Gynecol. 2005;25(1):37-41.
78. Rebarber A, Carreno CA, Lipkind H, et al. Cervical length after multifetal pregnancy reduction in remaining twin gestations. Am J Obstet Gynecol. 2001;185(5):1113-1117.
79. Tsoi E, Akmal S, Rane S, et al. Ultrasound assessment of cervical length in threatened preterm labor. Ultrasound Obstet Gynecol. 2003;21(6): 552-555.
80. Rand L, Norwitz ER. Current controversies in cervical cerclage. Semin Perinatol. 2003;27(1):73-85.
81. Grobman WA, Gilbert SA, Iams JD, et al. Activity restriction among women with a short cervix. Obstet Gynecol. 2013;121(6):1181-1186.
82. Sciscione AC. Maternal activity restriction and the prevention of preterm birth. Am J Obstet Gynecol. 2010;202(3):232.e1-232.e5.
83. American College of Obstetricians and Gynecologists. ACOG. Practice Bulletin No.142: Cerclage for the management of cervical insufficiency. Obstet Gynecol. 2014;123(2 Pt 1):372-379.
84. Lazar P, Gueguen S, Dreyfus J, et al. Multicentred controlled trial of cervical cerclage in women at moderate risk of preterm delivery. Br J Obstet Gynaecol. 1984;91(8):731-735.
85. Rush RW, Isaacs S, McPherson K, et al. A randomized controlled trial of cervical cerclage in women at high risk of spontaneous preterm delivery. Br J Obstet Gynaecol. 1984;91(8):724-730.
86. Anonymous. Final report of the Medical Research Council/Royal College of Obstetricians and Gynaecologists multicentre randomised trial of cervical cerclage. MRC/RCOG Working Party on Cervical Cerclage. Br J Obstet Gynaecol. 1993;100(6):516-523.
87. Brown JA, Pearson AW, Veillon EW, et al. History- or ultrasound-based cerclage placement and adverse perinatal outcomes. J Reprod Med. 2011;56(9-10):385-392.
88. Berghella V, Odibo AO, To MS, et al. Cerclage for short cervix on ultrasonography: meta-analysis of trials using individual patient-level data. Obstet Gynecol. 2005;106(1):181-189.
89. Berghella V, Mackeen AD. Cervical length screening with ultrasound-indicated cerclage compared with history-indicated cerclage for prevention of preterm birth: a meta-analysis. Obstet Gynecol. 2011;118(1):148-155.
90. Berghella V, Rafael TJ, Szychowski JM, et al. Cerclage for short cervix on ultrasonography in women with singleton gestations and previous preterm birth: a meta-analysis. Obstet Gynecol. 2011;117(3):663-671.
91. Owen J, Hankins G, Iams JD, et al. Multicenter randomized trial of cerclage for preterm birth prevention in high-risk women with shortened midtrimester cervical length. Am J Obstet Gynecol. 2009;201(4):375.e1-375.e8.
92. Scheib S, Visintine JF, Miroshnichenko G, et al. Is cerclage height associated with the incidence of preterm birth in women with an ultrasound-indicated cerclage? Am J Obstet Gynecol. 2009;200(5):e12-e15.
93. O'Brien JM, Hill AL, Barton JR. Funneling to the stitch: an informative ultrasonographic finding after cervical cerclage. Ultrasound Obstet Gynecol. 2002;20(3):252-255.
94. To MS, Alfirevic Z, Heath VC, et al. Cervical cerclage for prevention of preterm delivery in women with short cervix: randomised controlled trial. Lancet. 2004;363(9424):1849-1853.
95. Roman AS, Rebarber A, Pereira L, et al. The efficacy of sonographically indicated cerclage in multiple gestations. J Ultrasound Med. 2005;24(6): 763-768.
96. Hui SY, Chor CM, Lau TK, et al. Cerclage pessary for preventing preterm birth in women with a singleton pregnancy and a short cervix at 20 to 24 weeks: a randomized controlled trial. Am J Perinatol. 2013;30(4): 283-288.
97. Abdel-Aleem H, Shaaban OM, Abdel-Aleem MA. Cervical pessary for preventing preterm birth. Cochrane Database Syst Rev. 2010;(9):CD007873.
98. Romero R, Stanczyk FZ. Progesterone is not the same as 17alpha-hydroxyprogesterone caproate: implications for obstetrical practice. Am J Obstet Gynecol. 2013;208(6):421-426.
99. Meis PJ, Klebanoff M, Thom E, et al. Prevention of recurrent preterm delivery by 17 alpha-hydroxyprogesterone caproate. N Engl J Med. 2003;348(24): 2379-2385.

CHAPTER 45

Neonatal and Infant Brain Imaging

Carol M. Rumack and Amanda K. Auckland

SUMMARY OF KEY POINTS

- Brain ultrasound of premature infants is best performed for germinal matrix hemorrhage and hydrocephalus at 10 to 14 days of life and for cystic periventricular leukomalacia at 30 days of life.
- The best time to assess for white matter injury of prematurity is at term-equivalent age.
- Cerebellar hemorrhage is missed if mastoid views of the posterior fossa are not obtained.
- High-resolution images are needed to fully study the brain parenchyma for white matter injury.
- Multiple acoustic windows are essential for accurate detailed ultrasound imaging of the brain.
- Doppler evaluation is key for any cystic lesion to exclude vascular malformations.
- Computed tomography of the newborn brain is not indicated except in the case of a traumatic birth.
- Congenital anomalies are well evaluated with ultrasound and, if further information is needed, are an indication for magnetic resonance imaging.

CHAPTER OUTLINE

EQUIPMENT
SONOGRAPHIC TECHNIQUE
Coronal Imaging
Sagittal Imaging
Posterior Fontanelle Imaging
Mastoid Fontanelle Imaging
Three-Dimensional Ultrasound
STANDARDIZED REPORTS
Standardized Views for Display
DEVELOPMENTAL ANATOMY
Brain Sulcal Development and Subarachnoid Spaces
Cavum Septi Pellucidi and Cavum Vergae
Cavum Veli Interpositi
Frontal Horn Variants
Choroid Plexus and Variants
Germinal Matrix
Calcar Avis
Cerebellar Vermis
Cisterna Magna
CONGENITAL BRAIN MALFORMATIONS
DISORDERS OF NEURAL TUBE CLOSURE
Chiari Malformations
Agenesis of Corpus Callosum
Corpus Callosum Lipoma
Dandy-Walker Spectrum
DISORDERS OF DIVERTICULATION AND CLEAVAGE: HOLOPROSENCEPHALY
Septo-Optic Dysplasia
Alobar Holoprosencephaly
Semilobar Holoprosencephaly
Lobar Holoprosencephaly
Middle Interhemispheric Form of Holoprosencephaly
DISORDERS OF SULCATION AND CELLULAR MIGRATION
Schizencephaly
Lissencephaly
DESTRUCTIVE LESIONS
Porencephalic Cyst
Hydranencephaly
Cystic Encephalomalacia
Metabolic Disorders
HYDROCEPHALUS
Cerebrospinal Fluid Production and Circulation
Level of Obstruction
HYPOXIC-ISCHEMIC EVENTS
Arterial Watershed Determines Regional Pattern of Brain Damage
Germinal Matrix Hemorrhage
Subependymal Hemorrhage (Grade I Hemorrhage)
Intraventricular Hemorrhage (Grade II Hemorrhage)
Intraventricular Hemorrhage With Hydrocephalus (Grade III Hemorrhage)
Intraparenchymal Hemorrhage (Grade IV Hemorrhage)
Cerebellar Hemorrhage
Subarachnoid Hemorrhage
Cerebral Edema and Infarction
White Matter Injury of Prematurity or Periventricular Leukomalacia
Term Infants With Hypoxic Ischemic Injury
Focal Infarction
Lenticulostriate Vasculopathy
Hyperechoic Caudate Nuclei
POSTTRAUMATIC INJURY
Subdural and Epidural Hematomas
INFECTION
Congenital Infections
Neonatal Acquired Infections
Meningitis and Ventriculitis
INTRACRANIAL MASSES
Brain Tumors
Cystic Intracranial Lesions
Arachnoid Cysts
Porencephalic Cysts
Choroid Plexus Cysts
Supratentorial Periventricular Cystic Lesions
Frontal Horn Cysts
Subependymal Cysts
Periventricular Leukomalacia
Galenic Venous Malformations

Neonatal sonography of the brain is an essential part of newborn care, particularly in high-risk and unstable premature infants.[1,2] Current ultrasound technology allows for rapid evaluation of infants in the intensive care nursery with virtually no risk. The advantages of sonography over computed tomography (CT) or magnetic resonance imaging (MRI) include portability, lower cost, speed, no ionizing radiation, no sedation, and real-time visualization with video clips saved for later review. Screening of premature infants for intracranial hemorrhage has proven highly sensitive and specific. Daneman and colleagues have reported that optimal imaging of the neonatal brain requires delineation of structures in both the near and far fields. Thus magnification of selected areas with focal zone and higher resolution megahertz adjustments are essential for these detailed regional assessments.[3,4] Real-time assessment is essential to detect subtle changes in echogenicity of the brain parenchyma, especially common in white matter injury of prematurity (WMIP). MRI is very sensitive and specific with regard to identification of brain injuries but, because of the cost and need for transfer of very unstable premature infants, is typically performed at term-equivalent age if concerns regarding neurodevelopmental outcomes are present.

Ultrasound is essential to the neonatal evaluation and follow-up of hydrocephalus and periventricular leukomalacia (PVL). Prenatal ultrasound and MRI diagnosis[5] of central nervous system (CNS) malformations, infection, or masses is now followed up by ultrasound in the neonatal period. When major anomalies are present, associated anomalies may need evaluation by neonatal MRI. CT is not indicated in premature infants because of the lack of good gray versus white matter differentiation from the high water content in the newborn brain.[6] For the same reason, CT is rarely used for term infants unless there is a history of birth trauma.

Ultrasound can be useful for the follow-up of ventricular shunt therapy or possible complications. Color and spectral Doppler ultrasound of cranial blood flow may prove valuable, particularly for cystic lesions when the differential diagnosis includes a vascular lesion, or for possible subdural hematomas, and to separate normal vascular structures from clot. Doppler ultrasound is also useful in infants receiving extracorporeal membrane oxygenation (ECMO) or when decreased blood flow is a risk for infarction (see Chapter 46).

EQUIPMENT

In the premature infant, a 7.5-MHz or higher transducer is recommended to obtain the highest resolution possible. A 5-MHz transducer may be necessary to allow for adequate sound penetration of a larger infant head.[7] Electronic phased array transducers with a 120-degree sector angle and multifocal zone capabilities are generally used for imaging through the anterior fontanelle. **Small-footprint, linear array, high-frequency transducers** (up to 12 MHz) can provide high-quality images for scanning of near-field pathology through the anterior fontanelle. These transducers are best for subdural hematomas, meningitis, superior sagittal sinus thrombosis, and cerebral edema, and in some cases, migrational abnormalities,[8] or for scanning over the mastoid fontanelle, posterior fontanelle, and foramen magnum. The squamosal portion of the temporal bone is thin but may require a 5-MHz transducer if not imaged through the mastoid fontanelle. The multifocal zone capability provides excellent resolution throughout the field of view, but requires a cooperative patient because the frame rate is slowed significantly. **Compound imaging,** allowing for multiple angles of insonation, is also useful when imaging through small spaces such as the fontanelles. Video clip capabilities are invaluable in an uncooperative infant or when documenting motion, such as blood flow.

It has become routine to save video clips for later review, to prevent repeating an examination if there is a questionable finding and to be certain that each view has been completely evaluated. Clips can greatly improve the understanding of the pathology. Areas of increased or decreased echogenicity may be extremely subtle on single images, but they become much more apparent when integrated with cine or video that captures real-time ultrasound findings and the relationship to normal structures.

SONOGRAPHIC TECHNIQUE

Currently, most brain sonographic examinations are performed through the **anterior fontanelle** in both the coronal and the sagittal planes. It has become clear that the neonatal brain is not fully examined unless the posterior fossa is evaluated through the **posterior and mastoid fontanelles.** In fact, cerebellar hemorrhage has been proven by MRI correlation to be missed without the mastoid views of the posterior fossa.[9] Posterior fossa malformations may not be well understood without these highly detailed views of the cerebellum, fourth ventricle, and cisterna magna.[10-12] Thus the posterior fossa views from the mastoid fontanelle are extremely important in the evaluation of cerebellar hemorrhage or posterior fossa anomalies, which are quite common. Good skin-to-transducer coupling can be achieved by an acoustic coupling gel. Occasionally, a standoff pad can be useful to evaluate superficial abnormalities such as subdural hemorrhage, but a higher resolution transducer is a better option to evaluate the near field in detail.

It is very important to use color Doppler ultrasound imaging to evaluate **fluid collections** because some cystic areas are actually vessels. If extracerebral fluid collections are expected, they are better evaluated with CT or MRI. Axial ultrasound scanning has been used extensively in utero, particularly for accurate measurements of fetal ventricular dimensions. In the newborn, axial scanning is used in evaluation of the posterior fossa through the mastoid fontanelle and to evaluate the circle of Willis with color Doppler ultrasound.[7,13-15] Doppler evaluation of the major cerebral arteries may be indicated with particular attention to the resistive index changes that can indicate cerebral blood flow abnormalities. Color and spectral Doppler may show hyperemia, and they can be used to depict patency and flow in the major dural sinuses (see Chapter 46). The posterior scanning techniques are the best approach to evaluate the occipital horns for ventricular clot. The foramen magnum approach may be useful when evaluating the upper spinal canal, as in patients with a Chiari malformation.

The anterior fontanelle remains open until approximately 2 years of age but is suitable for scanning only until about 12 to 14 months. The smaller the fontanelle, the smaller is the acoustic window and the more difficult the examination will be.[7,13]

Every effort should be made to maintain normal body temperature in premature infants when performing ultrasound. Their small size results in a high surface-to-volume ratio and rapid heat loss when they are exposed. Overhead warming lamps, blankets, and warmed coupling gel should be routinely used. If the infant is in an Isolette, heat loss may be minimized by using access side holes as an entry site for the transducer.

Handwashing and cleansing of the transducer between patients are of paramount importance to avoid the spread of infection in the intensive care nursery. Simple cleansing of the transducer head with a manufacturer-approved disinfectant should be adequate. When absolute sterility is required, such as during operative sonography, the transducer can be placed inside a sterile surgical glove or sterile transducer cover with coupling gel. Sterile aqueous gel or saline solution can be used as a coupler outside the sterile cover.

Standard brain scanning includes sagittal and coronal planes through the anterior fontanelle and should also routinely include at least two axial views: through the posterior fontanelle and the mastoid fontanelle. Coronal images acquired through the posterior fontanelle may be useful as well, to compare ventricular size. Magnified views with high-frequency transducers are essential to study near-field pathology such as extraaxial fluid for hemorrhage or infection and dural venous sinuses. Whenever possible, the transducer should be held firmly between the thumb and index finger, and the lateral aspect of the hand should rest on the infant's head for stability. Video clips should be obtained routinely for any abnormality to improve ultrasound diagnosis, avoid repeating a scan on an unstable newborn, and allow review of complex images and prompt diagnosis without delaying the patient workflow. Real-time imaging enables the appreciation of subtle changes in echogenicity more easily than static images. Lesions that affect gray-white matter differentiation as well as focal nonhemorrhagic infarcts may cause mild changes in echogenicity.[3]

Coronal Imaging

Coronal images are obtained by placing the scan head of the transducer transversely across the anterior fontanelle (Fig. 45.1, Video 45.1). The plane of the ultrasound beam should then sweep in an anterior-to-posterior direction, completely through the brain. Care must be taken to maintain symmetrical imaging of the brain and skull. An initial sweep of the brain to obtain parallel alignment of the thick glomus of the choroid plexus in each trigone is a good method to obtain symmetry. At least six standard coronal images should be obtained during this anterior-to-posterior sweep.[13]

Coronal Brain Scans: Normal Structures

MIDLINE STRUCTURES
Interhemispheric fissure
Cingulate sulcus
Corpus callosum
Cavum septi pellucidi
Cavum vergae (when present)
Third ventricle
Fourth ventricle
Brainstem
Vermis of cerebellum

PARAMEDIAN STRUCTURES
Frontal lobe
Parietal lobe
Occipital lobe
Frontal horn of lateral ventricle
Body of lateral ventricle
Temporal horn of lateral ventricle
Trigone of lateral ventricle
Choroid plexus
Glomus of choroid plexus
Caudate nucleus
Internal capsule
Thalamus
Lentiform nucleus
Tentorium cerebelli
Cerebellar hemisphere
Sylvian fissure
Cisterna magna

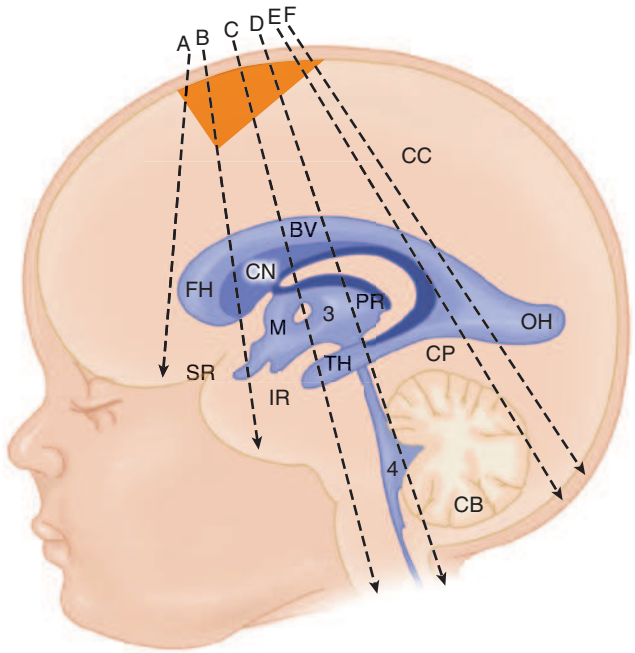

FIG. 45.1 Coronal Brain Ultrasound Planes Through Anterior Fontanelle. *A* to *F* correspond to front to back. *3,* Third ventricle; *4,* fourth ventricle; *BV,* body of lateral ventricle; *CB,* cerebellum; *CC,* cerebral cortex; *CN,* caudate nucleus; *CP,* choroid plexus; *FH,* frontal horn; *IR,* infundibular recess; *M,* massa intermedia; *OH,* occipital horn; *PR,* pineal recess; *SR,* supraoptic recess; *TH,* temporal horn. See also Video 45.1. (With permission from Rumack CM, Manco-Johnson ML. Perinatal and infant brain imaging: role of ultrasound and computed tomography. St Louis: Mosby; 1984.[7])

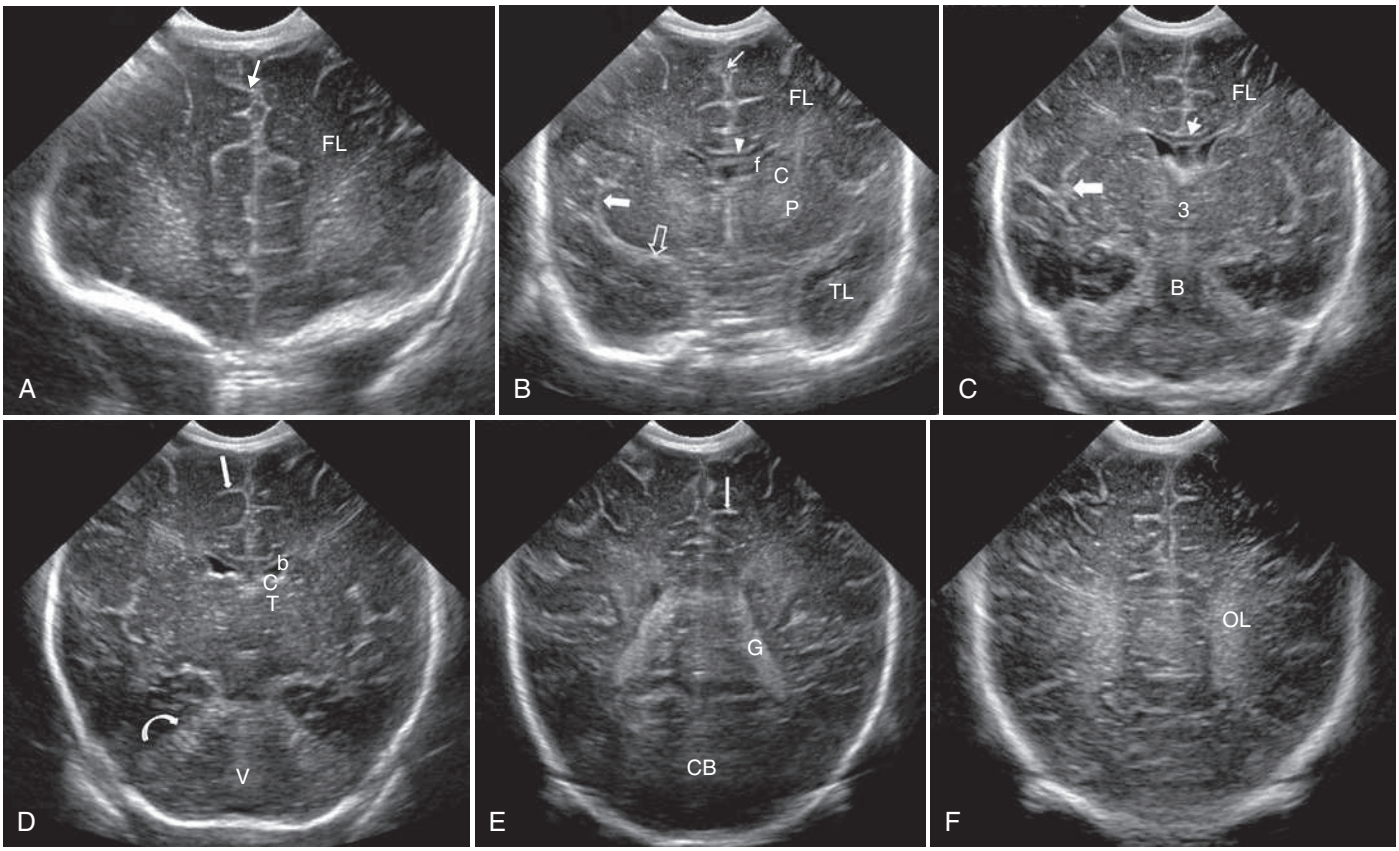

FIG. 45.2 Normal Coronal Brain Images: Full-Term Infant. Anterior to posterior corresponds to sections *A* to *F* in Fig. 45.1. **(A)** *FL,* Frontal lobes; *small white arrow* in **B,** interhemispheric fissure. **(B)** *C,* Caudate nucleus; *f,* frontal horn of lateral ventricle *(thin arrow)*; *P,* putamen; *TL,* temporal lobe; *arrowhead,* corpus callosum; *closed arrow,* sylvian fissure; *open arrow,* bifurcation of internal carotid artery. **(C)** *3,* Location of third ventricle; *B,* brainstem; *FL,* frontal lobe; *arrowhead,* corpus callosum. **(D)** *b,* Body of lateral ventricle; *c,* choroid plexus; *T,* thalamus; *V,* vermis of cerebellum; *curved arrow,* tentorium cerebelli; *straight arrow,* cingulate sulcus. **(E)** *CB,* Cerebellum; *G,* glomus of choroid plexus; *arrow,* cingulate sulcus. **(F)** *OL,* Occipital lobe.

The most anterior image is acquired just **anterior to the frontal horns** of the lateral ventricles[16] (Fig. 45.2A). Visualization of the anterior cranial fossa is obtained, including the frontal lobes of the cerebral cortex with the orbits deep to the floor of the skull base.

Moving posteriorly, the **frontal horns of the lateral ventricles** appear as symmetrical, anechoic, comma-shaped structures with the hypoechoic caudate heads within the concave lateral border (see Fig. 45.2B). Structures visualized from superior to inferior in the midline include the interhemispheric fissure, cingulate sulcus, genu and anterior body of the corpus callosum, and septum pellucidum between the ventricles. Moving laterally from the midline, the caudate nucleus is separated from the putamen by the internal capsule. Lateral to the putamen, the sylvian fissure is echogenic because it contains the **middle cerebral artery** (MCA). The sylvian fissure separates the frontal from the temporal lobe. Inferiorly, the internal carotid arteries bifurcate to form the echogenic anterior cerebral artery and MCA.

Progressing farther posteriorly to the level above the midbrain, the **body of the lateral ventricles** is visible on either side of the cavum septi pellucidi (see Fig. 45.2C). Below this, the thalami lie on either side of the third ventricle, which is usually too thin to visualize in normal infants. Deep to the thalami, the brainstem begins to be visualized. Lateral to the midline, the **thalami** are separated from the lentiform nuclei **(caudate and putamen)** by the **internal capsule.** Lateral to the lentiform nuclei is the deep white matter region of brain called the **centrum semiovale.** Again, the sylvian fissures are visible.

A slightly more posterior transducer angulation results in a plane that includes the **cerebellum.** The body of the lateral ventricles becomes somewhat more rounded as the size of the caudate nucleus decreases once posterior to the foramen of Monro (see Fig. 45.2D). At this level in the midline, the body of the corpus callosum is deep to the cingulate sulcus, and the third ventricle is located between the anterior portions of the thalami. Echogenic material visualized in the floor of the lateral ventricles is the **choroid plexus.** Echogenic choroid plexus is also seen in the roof of the third ventricle, resulting in three echogenic foci of choroid. The thalami are now more prominent on either side of the third ventricle. Midline structures are unchanged, except that deep to the thalami, the tentorium covering the cerebellum can be visualized. Below this, in the posterior fossa, the **vermis** is the echogenic structure in the midline surrounded by the more hypoechoic cerebellar hemispheres. When the septum pellucidum is cystic posteriorly, it is called the **cavum vergae.** Because the cystic center of the septum pellucidum closes from posterior to anterior as the brain matures, late-gestation neonates often have only the more anterior cavum septi pellucidi. The

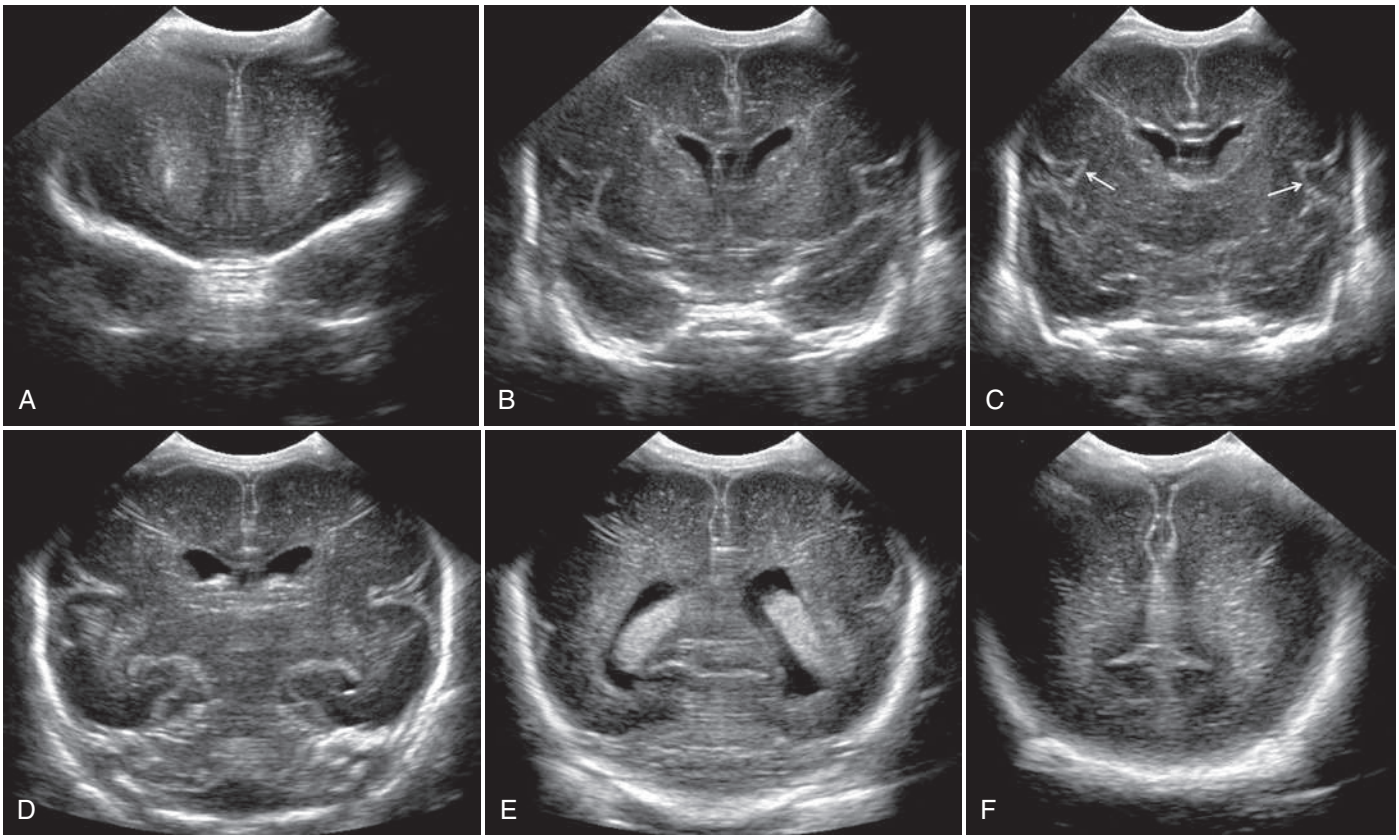

FIG. 45.3 Normal Coronal Brain Images: Premature Newborn Infant. (A)-(F) Coronal images in very premature infant; ventricles can be larger with extreme prematurity. **(C)** Sylvian fissures *(arrows)* appear boxlike.

lentiform nuclei may no longer be seen at this level. The **temporal horns** of the lateral ventricles may be seen lateral and inferior to the thalami, but are usually not seen unless there is hydrocephalus.

Further posteriorly, the **trigone** or **atrium of the lateral ventricles** and **occipital horns** are visualized (see Fig. 45.2E). The extensive echogenic glomus of the choroid plexus nearly obscures the lumen of the cerebrospinal fluid (CSF)–filled ventricle at the trigone. In the midline—the visualized portion of the corpus callosum deep to the cingulate sulcus—is the splenium. Inferiorly, the cerebellum is separated from the occipital cortex by the tentorium cerebelli.

The most posterior section visualizes predominantly **occipital lobe cortex** and the most posterior aspect of the occipital horns of the lateral ventricles that do not contain choroid plexus (see Fig. 45.2F). This section is angled posterior to the cerebellum.

Normal premature brain ultrasound images in the same planes are shown in Fig. 45.3. The lateral ventricles are slightly larger; the cavum septi pellucidi extends back to become the cavum vergae between the lateral ventricle bodies and occipital horns. There are only a few sulci, and the sylvian fissures are wider and typically appear boxlike rather than as thin fissures. The basal ganglia in premature infants are normally diffusely homogeneously echogenic, an appearance that is more prominent than in the thalami and typically more echogenic than the cerebral cortex. Basal ganglia and thalami do not show increased echogenicity at term-equivalent age.[17]

Sagittal Imaging

The sagittal images are obtained by placing the transducer longitudinally across the anterior fontanelle and angling it to each side (Fig. 45.4, Video 45.2). The **midline** is first identified through the interhemispheric fissure by recognition of the curving line of the corpus callosum above the cystic cavum septi pellucidi and cavum vergae. Below the cavum lies the choroid plexus in the roof of the third ventricle. If there is third ventricular enlargement, the massa intermedia will be outlined by CSF and the **aqueduct of Sylvius** may be visualized. The **fourth ventricle** is identified as a notch in the anterior surface of the highly echogenic **cerebellar vermis**[18] (Fig. 45.5).

The **cingulate sulcus** lies parallel to and above the corpus callosum. The highly echogenic falx can be difficult to scan directly through and obtain a clear midline sagittal image; therefore a very slight movement to either side of the falx may be necessary to adequately visualize midline brain structures. In this view, the size of the cerebellar vermis has been used to assess gestational age.[19] However, the degree of sulcal development is the most reliable method for gestational age based on established pathologic standards.[20] Shallow angulation to each side of about 10 degrees will show the normally small **lateral ventricles** (Fig. 45.6A-B). The ventricles are not located in a perfectly straight plane anterior to posterior. The transducer must be angled so that the anterior portion of the sector is directed more medially and the posterior portion more laterally, to include the entire lateral ventricle in a single image.[13]

Above the lateral ventricle is the cerebral cortex, and below it is the cerebellar hemisphere. The **caudate nucleus** and the **thalamus** surround the third ventricle and are within the arms of the ventricle (see Fig. 45.6B). The **caudothalamic groove** at the junction of these two structures is an important area to

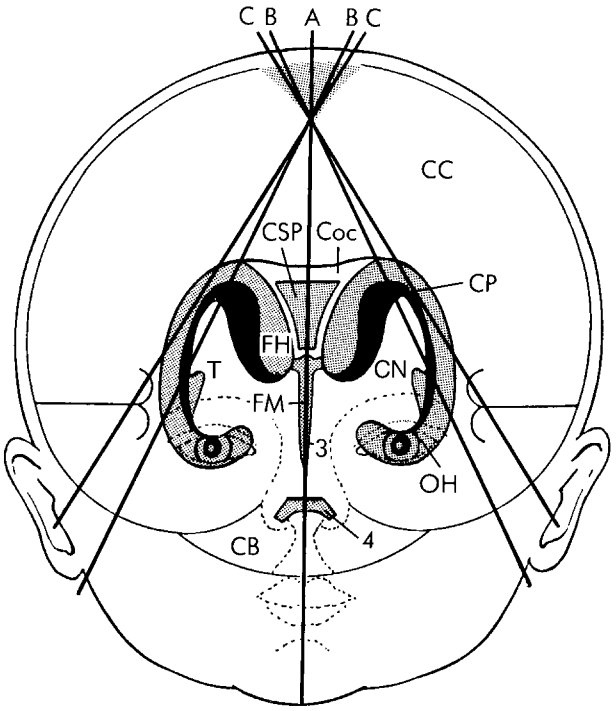

FIG. 45.4 Sagittal Planes Used in Brain Scanning Through Anterior Fontanelle. *A* to *C* correspond to midline to lateral. *3,* Third ventricle; *4,* fourth ventricle; *CB,* cerebellum; *CC,* cerebral cortex; *CN,* caudate nucleus; *Coc,* corpus callosum; *CP,* choroid plexus; *CSP,* cavum septi pellucidi; *FH,* frontal horn; *FM,* foramen of Monro; *OH,* occipital horn; *T,* temporal horn. See also Video 45.2. (Modified from Rumack CM, Manco-Johnson ML. Perinatal and infant brain imaging: role of ultrasound and computed tomography. St Louis: Mosby; 1984.[7])

Sagittal Brain Scans: Normal Structures

MIDLINE STRUCTURES
Frontal lobe
Parietal lobe
Occipital lobe
Cingulate sulcus
Pericallosal artery
Corpus callosum
Cavum septi pellucidi
Cavum vergae[a]
Cavum velum interpositum[a]
Third ventricle
Fourth ventricle
Tentorium
Choroid plexus, third ventricle
Aqueduct
Occipitoparietal fissure
Brainstem
Vermis of cerebellum

PARAMEDIAN STRUCTURES
Frontal lobe
Parietal lobe
Occipital lobe
Frontal horn of lateral ventricle
Body of lateral ventricle
Atrium of lateral ventricle (trigone)
Temporal horn of lateral ventricle
Occipital horn of lateral ventricle
Choroid plexus
Caudate nucleus
Thalamus
Caudothalamic groove
Cerebellum

[a]Not always visible.

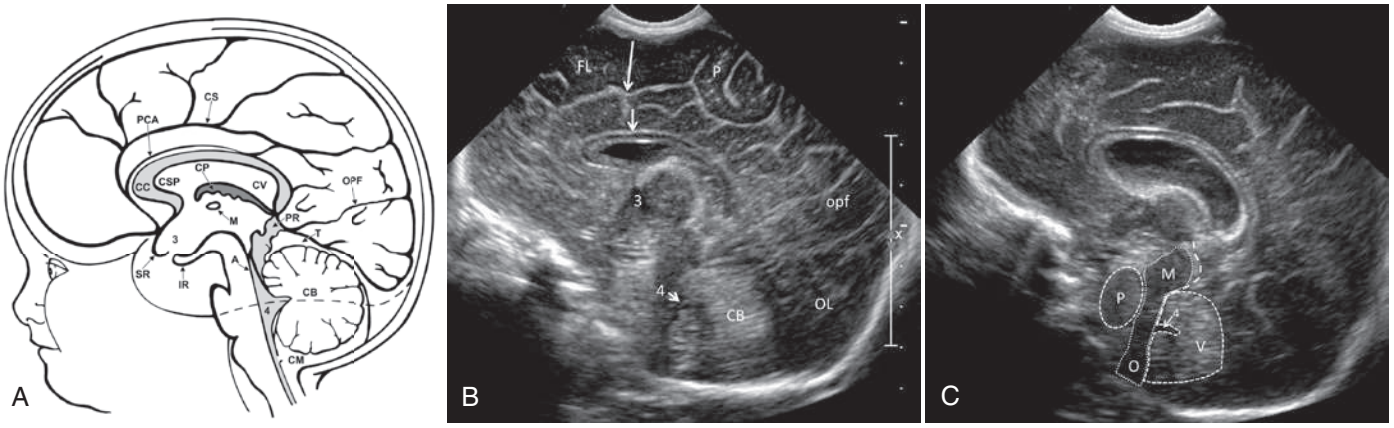

FIG. 45.5 Normal Midline Sagittal Anatomy. (A) Schematic drawing. *3,* Third ventricle; *4,* fourth ventricle; *A,* aqueduct; *CB,* cerebellum (vermis); *CC,* corpus callosum; *CM,* cisterna magna; *CP,* choroid plexus; *CS,* cingulate sulcus; *CSP,* cavum septi pellucidi; *CV,* cavum vergae; *IR,* infundibular recess; *M,* massa intermedia; *OPF,* occipitoparietal fissure; *PCA,* pericallosal artery; *PR,* pineal recess; *SR,* supraoptic recess; *T,* tentorium. **(B)** Normal midline sagittal ultrasound brain scan. *3,* Third ventricle; *4,* fourth ventricle; *CB,* cerebellar vermis; *FL,* frontal lobe; *OL,* occipital lobe; *opf,* occipitoparietal fissure; *P,* parietal lobe; *long arrow,* cingulate sulcus; *short arrow,* corpus callosum. **(C)** Sagittal midline sonogram. *4,* Fourth ventricle; *M,* midbrain; *O,* medulla oblongata; *P,* pons; *V,* cerebellar vermis; *dotted line,* aqueduct of Sylvius.

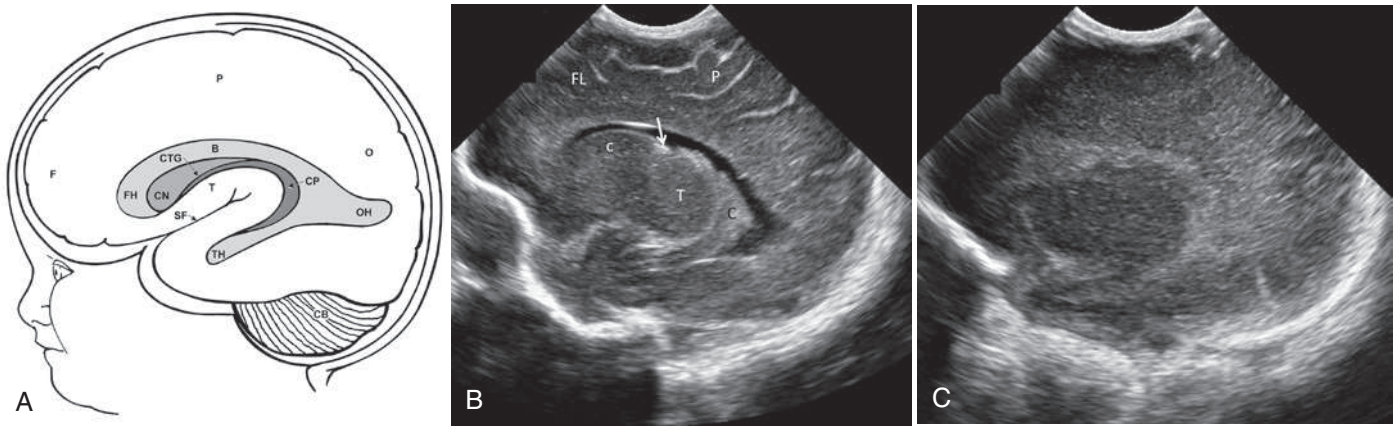

FIG. 45.6 Normal Paramedian Sagittal Anatomy. (A) Schematic drawing. *B,* Body of lateral ventricle; *CB,* cerebellum; *CN,* caudate nucleus; *CP,* choroid plexus; *CTG,* caudothalamic groove; *F,* frontal lobe; *FH,* frontal horn; *O,* occipital lobe; *OH,* occipital horn; *P,* parietal lobe; *SF,* sylvian fissure; *T,* thalamus; *TH,* temporal horn. **(B)** Sagittal sonogram, paramedian view. *Black C,* Choroid plexus; *FL,* frontal lobe; *P,* parietal lobe; *T,* thalamus; *white c,* caudate nucleus; *arrow,* caudothalamic groove. **(C)** Parasagittal sonogram of cerebral cortex.

recognize, because this is the most common site of germinal matrix hemorrhage (GMH) in the subependymal region of the ventricle.

More pronounced lateral angulation will demonstrate the peripheral aspect of the ventricles and the more lateral **cerebral hemisphere,** including the temporal lobes (see Fig. 45.6C) where the MCA branches extend toward the ventricle.

Sagittal sonography almost always reveals a normal hyperechoic **peritrigonal blush**[21] in the parietal lobe just posterior and superior to the ventricular trigones on parasagittal views (see Fig. 45.6B). It is caused by the interface of numerous parallel fibers that are perpendicular to the longitudinal angle of the ultrasound beam passing through the anterior fontanelle. This is an **anisotropic effect** artifact that occurs when the beam is perpendicular to the fibers through the anterior fontanelle. A similar area of increased echogenicity is not seen on sonograms obtained through the posterior fontanelle, because with that angulation, the long axis of the ultrasound beam and the fiber tracts are almost parallel.

Posterior Fontanelle Imaging

Posterior fontanelle imaging is very useful to evaluate the occipital horns for the diagnosis of intraventricular hemorrhage (IVH). The posterior fontanelle lies in the midline at the junction of the lambdoid and sagittal sutures; it is open only until about 3 months of age[22] (Fig. 45.7). The transducer should be angled slightly off midline with the anterior portion of the probe directed slightly medially, to demonstrate the lateral ventricular trigone with its occipital horn in the near field (Fig. 45.8). The choroid glomus will be seen with extensions into the ventricular body and temporal horn. The **occipital horn** does not contain choroid plexus and should be completely anechoic. Angling the transducer into the left and right parasagittal planes will display each occipital horn. These planes are extremely useful for detecting dependently layering clot and clot attached to the choroid plexus.

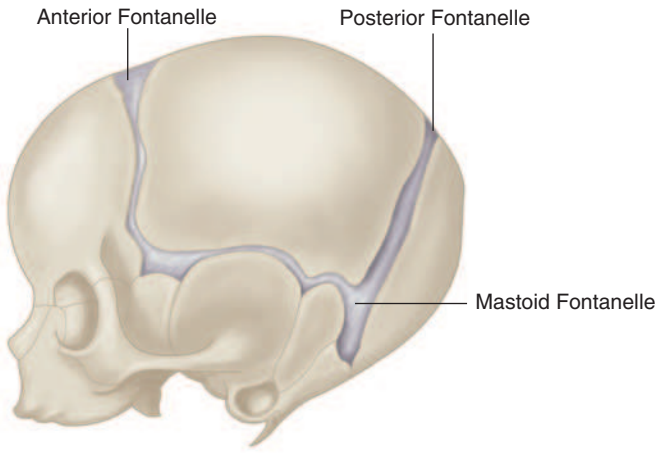

FIG. 45.7 Acoustic Windows: Anterior, Posterior, and Mastoid Fontanelles.

Mastoid Fontanelle Imaging

The mastoid fontanelle allows assessment of the brainstem and posterior fossa, which are not well demonstrated in the standard planes through the anterior fontanelle. The ultrasound transducer is placed about 1 cm behind the helix of the ear and 1 cm above the tragus. The mastoid fontanelle is located at the junction of the squamosal, lambdoidal, and occipital sutures (see Fig. 45.7, Video 45.3). Posterior fossa axial images, with the anterior portion of the transducer angled slightly cephalad, will demonstrate the **fourth ventricle, posterior cerebellar vermis, cerebellar hemispheres,** and the **cisterna magna.** These axial images should be displayed with the top of the head to the left (Fig. 45.9). The radiating folia of the cerebellar hemispheres contain relatively hypoechoic neural tissue and are surrounded by echogenic leptomeninges in the multiple cerebellar fissures.[23] In the roof of the fourth ventricle lies the normal echogenic **fourth ventricular choroid plexus.**[24] Behind the fourth ventricle is the

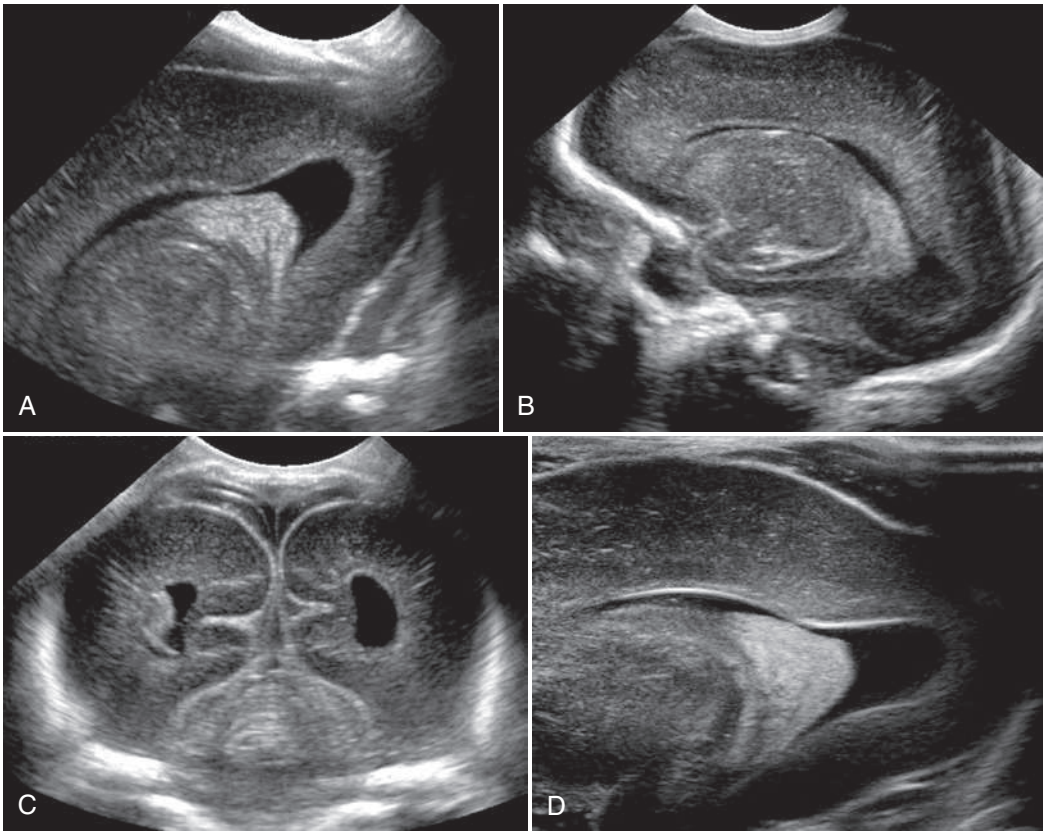

FIG. 45.8 Occipital Horn. (A) Sagittal occipital horn from the posterior fontanelle. **(B)** Same sagittal occipital horn from the anterior fontanelle. **(C)** Coronal occipital horns from the posterior fontanelle; echogenic clot visible in right occipital horn. **(D)** Same occipital horn; linear transducer shows increased resolution.

echogenic midline vermis, which appears less echogenic in the axial view compared with midline sagittal scans. When angled axial images are obtained through the lower parts of the cerebellum below the fourth ventricle, the (normally thin) **vallecula** may be seen in the midline as a space between the cerebellar hemispheres (see Fig. 45.9C), particularly in the presence of hydrocephalus. In steeply angled axial scans, the **foramen of Magendie** can be seen in the midline as a thin sonolucent line between the cerebellar hemispheres extending from the fourth ventricle to the cisterna magna. It should not be mistaken for a Dandy-Walker variant.[25] The presence of an intact vermis on higher images and the marked caudal angulation required to see the vallecula allow differentiation of this normal variant.[11,12,14] Color Doppler ultrasound in this view allows evaluation of flow in the transverse and straight sinuses to exclude venous thrombosis.

A slightly higher axial scan should include the thalami, midbrain, third ventricle, aqueduct of Sylvius, and quadrigeminal plate cistern, with the transducer angled from the standard axial plane and placed cephalad to the external auricle (Fig. 45.10). At this level, the **thalami** are hypoechoic, inverted, heart-shaped structures. The midbrain, including the **cerebral peduncles** and **corpora quadrigemina,** consists of paired hypoechoic lenticular structures just caudal to the thalami. The third ventricle is usually a thin cleft, barely visible between the thalami. The aqueduct is usually a thin echogenic line but may occasionally be a thin slit in the midbrain. The **quadrigeminal cistern** is echogenic and surrounds the midbrain.

Three-Dimensional Ultrasound

Three-dimensional (3-D) ultrasound may be a useful adjunct to standard two-dimensional (2-D) imaging of the neonatal brain.[26] A volume of brain can be acquired in a few seconds, and then reconstructed displays of three octagonal slices at any angle can be viewed, in addition to coronal, sagittal, and axial planes. Brain lesions can be tracked in three views at once, which can better identify the position in the brain and the most likely diagnosis. Some authors recommend 3-D volume measurement of the ventricles[27,28]; the standard method is still a qualitative assessment based on typical normal ventricles of different age groups.

STANDARDIZED REPORTS

Standardized Views for Display

Brain anatomy images should be displayed in a consistent manner so that comparisons can be easily made. At our institution, routine sagittal images are always shown with the infant's face to the left. Labels on sagittal scans should be "left" or "right." Video clips are more difficult to label and might be best done separately on the left and right, in addition to a full sweep through the entire brain from side to side.

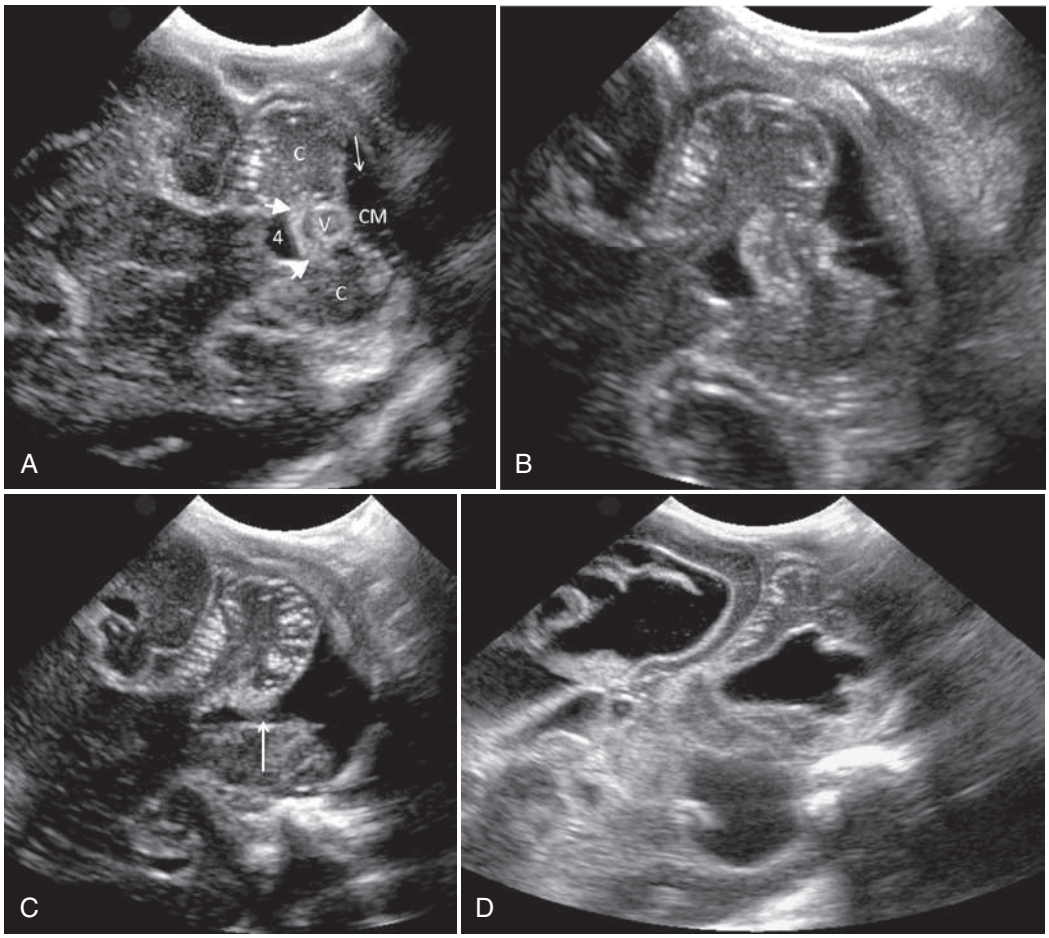

FIG. 45.9 Mastoid Fontanelle Images at Fourth Ventricle Level in Posterior Fossa. (A) Normal cerebellar hemispheres *(C),* cerebellar vermis *(V),* fourth ventricle *(4),* cisterna magna *(CM),* cisterna magna septa *(arrow),* choroid plexus in roof of fourth ventricle *(arrowheads).* **(B)** Normal axial cisterna magna. Note the radiating folia of the cerebellar hemispheres that contain relatively hypoechoic neural tissue and are surrounded by echogenic leptomeninges in the multiple cerebellar fissures. **(C)** Low posterior fossa view through the vallecula *(arrow).* **(D)** Severe enlargement of the fourth ventricle in an infant with **posthemorrhagic hydrocephalus.**

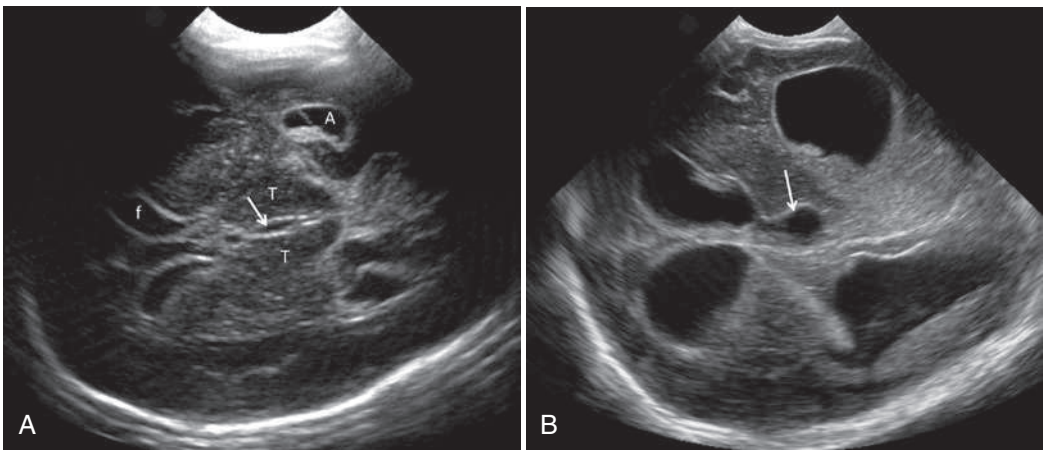

FIG. 45.10 Mastoid Fontanelle Images of the Midbrain Level Above Fourth Ventricle in Neonates With Posthemorrhagic Hydrocephalus. (A) Mild posthemorrhagic hydrocephalus, axial plane at the level of the atria of the lateral ventricle *(A),* frontal horns *(f),* thalami *(T),* and third ventricle *(arrow).* **(B)** Axial plane in an infant with moderate posthemorrhagic hydrocephalus, third ventricle *(arrow).*

With use of the American College of Radiology (ACR) and American Institute of Ultrasound Medicine (AIUM) practice parameters for the performance of neurosonography in neonates and infants,[29] there are specific questions to answer. Developing a template for reports is a useful task to ensure complete reporting.

DEVELOPMENTAL ANATOMY

Brain Sulcal Development and Subarachnoid Spaces

In the very premature infant, the brain sulci are not fully developed and the brain appears quite smooth[20,30] (Figs. 45.11 and 45.12).

Ultrasound of the Brain: Standard Report Template

The ventricular size and configuration are <normal>.
The corpus callosum is <present> <above the cavum septum pellucidi and/or cavum vergae>.
There is <no hemorrhage in the caudothalamic groove or in the ventricular system>.
The cerebellar vermis, fourth ventricle, and cerebellar hemispheres <appear normal>.
Sulcal development is <normal> for gestational age.

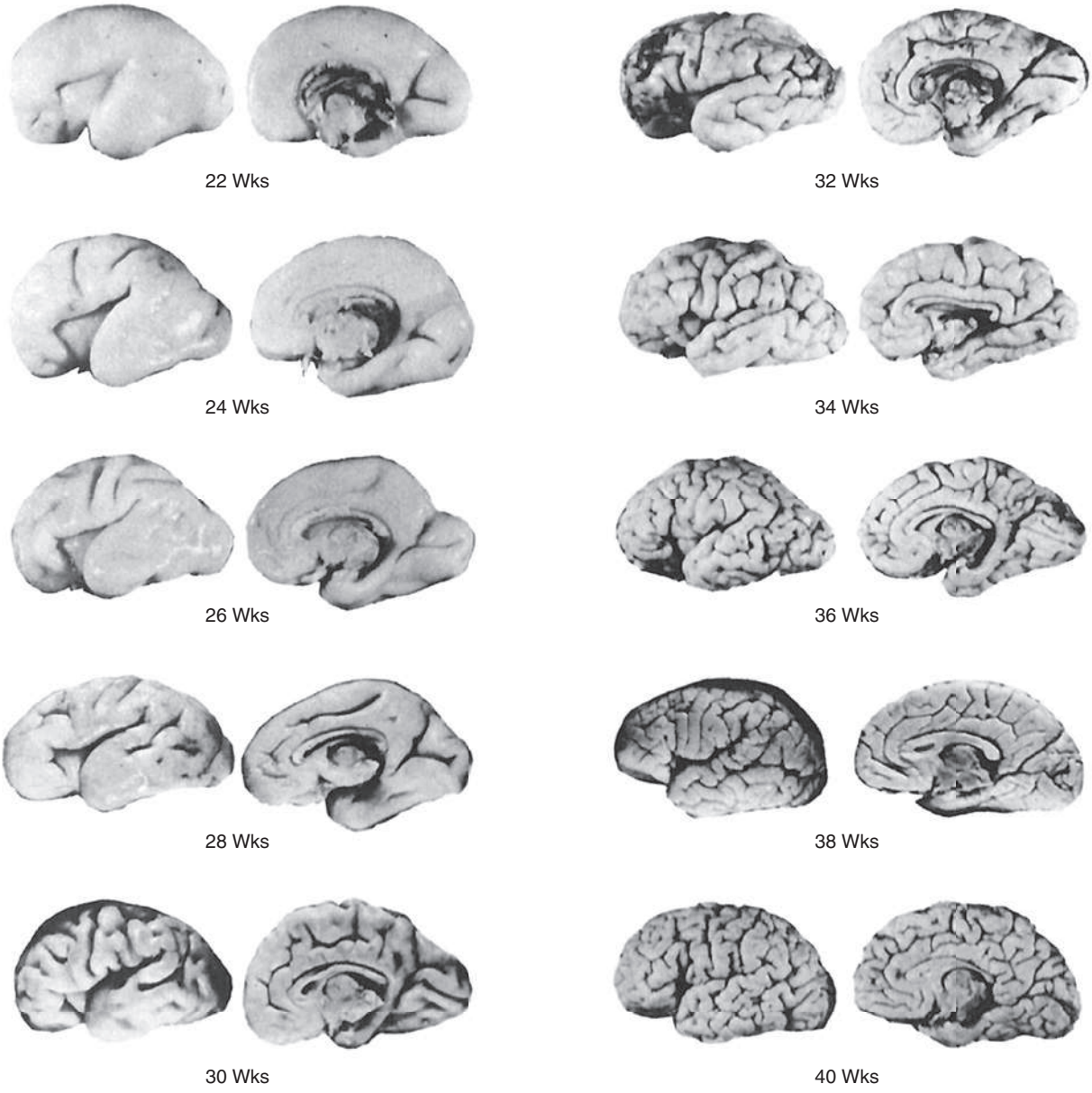

FIG. 45.11 Normal Sulcal Pattern Development. At 22 to 40 weeks' gestation. (With permission from Dorovini-Zis K, Dolman CL. Gestational development of brain. Arch Pathol Lab Med. 1977;101[4]:192-195.[20])

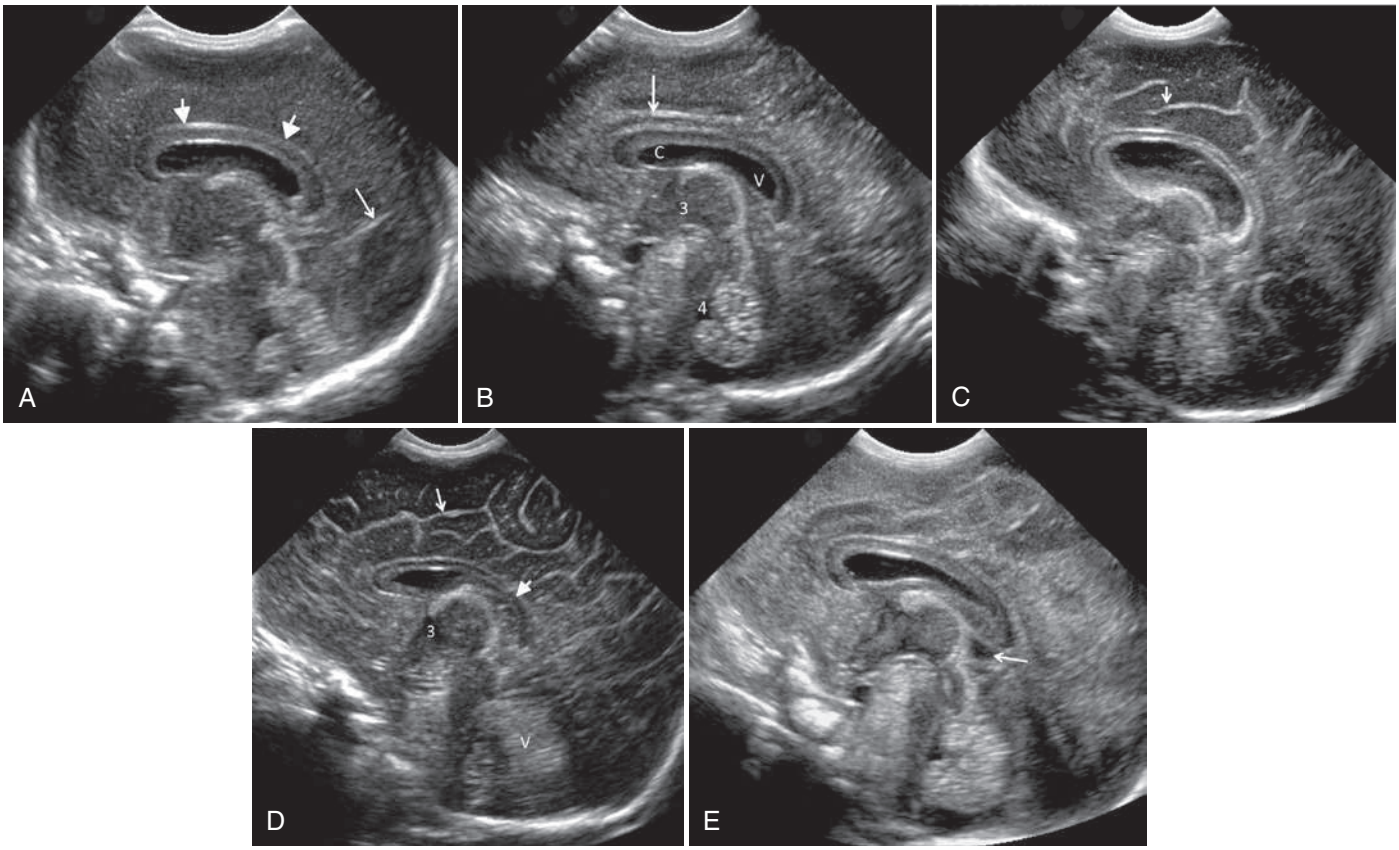

FIG. 45.12 Development of Sulci in a Premature Infant Brain. (A) At 24 weeks. No sulci; occipitoparietal fissure *(arrow)* can be seen; corpus callosum *(short arrows)* lies above the cavum septi pellucidi and cavum vergae. **(B)** At 27 weeks. Cingulate sulcus *(arrow)* is visible. Cavum septi pellucidi *(C),* cavum vergae *(V),* third ventricle *(3),* and fourth ventricle *(4)* are shown in this midline sagittal image. **(C)** At 33 weeks. Cingulate sulcus *(arrow)* now has a few branches. **(D)** At 39 weeks. Cingulate sulcus *(medium arrow)* has many branches. Cavum vergae *(short arrow)* is closed; third ventricle *(3)* and cerebellar vermis *(V)* are shown. **(E)** Cavum veli interpositum *(arrow).*

The first sulcus to form is the primitive, almost square, **sylvian fissure,** best seen on coronal images[31] (see Fig. 45.3C). Later, after infolding of the insula (opercularization), the sylvian fissure becomes a narrow, echogenic fissure filled with MCA branches.[30,32] Sulcal development, best evaluated on midline sagittal images, then extends to the **calcarine fissure** as a simple straight line in the fifth gestational month (20 weeks).[33] By 24 to 25 weeks' gestation, the **occipitoparietal fissure** is present, but no actual sulci. By 28 weeks, the **callosomarginal sulcus** over the corpus callosum and a simple linear **cingulate sulcus** superior and parallel to the corpus callosum are seen (see Fig. 45.12B). By 30 weeks, the cingulate sulcus is branched. Between 33 and 40 weeks' gestation, sulci bend, branch, and anastomose so that a full-term infant has many peripheral branches over the brain surface (see Fig. 45.12D).

Although not used routinely, measurement of the subarachnoid space on a magnified view of the brain can be done from the triangular sagittal sinus to the surface of the cortex. Armstrong and colleagues[34] have reported that the subarachnoid space is normally less than 3.5 mm in 95% of preterm infants before 36 weeks' gestation. Closer to term, the values tended to be at the higher end of the range, increasing slightly on a weekly basis, which suggests that premature infants have reduced brain growth during extrauterine life.

Cavum Septi Pellucidi and Cavum Vergae

There is one continuous cystic midline structure in the septum pellucidum during fetal life. The septum contains the cavum septi pellucidi anterior to the foramen of Monro (see Fig. 45.12) and the cavum vergae posteriorly. Both parts are normally present early in gestation, but they close from back to front, starting at approximately 6 months' gestation (Fig. 45.13). By full term, closure has occurred posteriorly in 97% of infants so that there is only a cavum septi pellucidi at birth. By 3 to 6 months after birth, this septum is completely closed in 85% of infants, although in some the septum remains open into adulthood.[35] In fetal brain imaging, Callen and colleagues[36] reported that the columns of the **fornix** can be mistaken for the cavum septi pellucidi. On axial views below the frontal horns, the fornix appears as a cystic structure with a central linear echo. Absence of the corpus callosum may not be identified because the fornices are present and simulate the cavum between the two frontal horns. Careful evaluation of the inferior position of the fornices below the frontal horns will avoid this error.

Cavum Veli Interpositi

The cavum of the velum interpositum represents a potential space above the choroid in the roof of the third ventricle and

below the columns of the fornices.[2,37] It may appear as an anechoic, inverted, helmetlike space just inferior and posterior to the splenium in the pineal region (see Fig. 45.12E). Blasi and colleagues[38] have described the prenatal diagnosis of the cavum veli interpositi on 2-D and 3-D ultrasound with color flow Doppler. Careful study of the anatomic location of the cystic structure, its size, and changes over time is required to be certain this is a normal variant, not an arachnoid cyst with mass effect or associated anomaly of the corpus callosum. Chen and colleagues[37] reported that 21% of neonates have a cavum veli interpositi on sonography. By 2 years of age, this cystic area is an uncommon finding and thus is thought to be a normal stage of brain development. Rarely, a cyst is found in this area that causes compression of other structures.

Frontal Horn Variants

A few newborns have cysts exactly parallel (not above or below) and adjacent to the frontal horns (Fig. 45.14). These cysts are typically bilateral and have septations between the cyst and the frontal horns. **Frontal horn cysts,** also called **coarctation of the frontal horn**[39] and **connatal cysts,**[40] are caused by folding of the frontal horn on itself, resulting in kinking (seen as a septation). Typical normal frontal horns are directly lateral to the cavum septi pellucidi on coronal images, below the corpus callosum. The frontal horns are relatively thin compared with the occipital horns.

Choroid Plexus and Variants

The choroid plexus is the site of CSF production in the ventricles (Fig. 45.15). The largest portion of the choroid plexus is the **glomus,** a highly echogenic structure attached to the trigone of each lateral ventricle. The choroid tapers as it extends anteriorly to the foramen of Monro and continues from each lateral ventricle into and along the roof of the third ventricle. The choroid plexus tapers laterally as it extends into the temporal horn of the lateral ventricle. The choroid plexus does not extend into the frontal

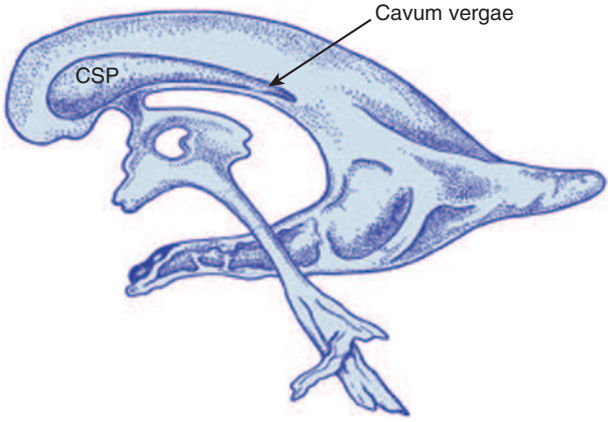

FIG. 45.13 Cavum Septi Pellucidi *(CSP).* Arrow indicates **cavum vergae** projecting on the medial surface of the lateral ventricles. (With permission from Rumack CM, Manco-Johnson ML. Perinatal and infant brain imaging: role of ultrasound and computed tomography. St Louis: Mosby; 1984.[7])

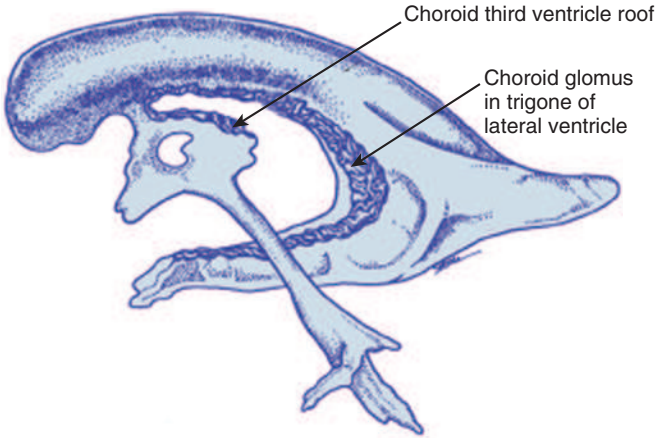

FIG. 45.15 Choroid Plexus. Drawing shows choroid plexus as it courses through the third and lateral ventricles *(arrows).* (With permission from Rumack CM, Manco-Johnson ML. Perinatal and infant brain imaging: role of ultrasound and computed tomography. St Louis: Mosby; 1984.[7])

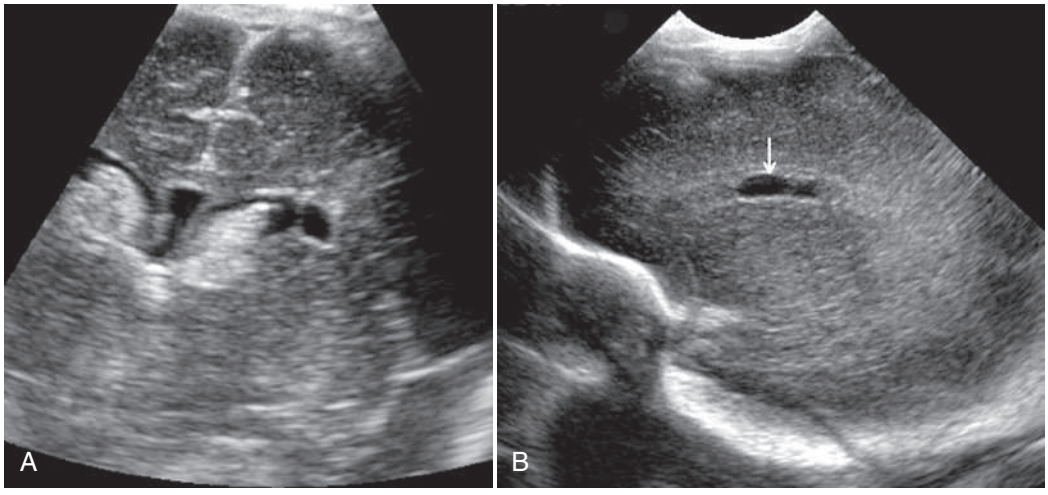

FIG. 45.14 Frontal Horn Cysts. (A) and **(B)** Coronal and sagittal sonograms show the uncommon normal variant, also called "coarctation of the frontal horn" or "connatal cysts," which are immediately lateral *(arrow)* to the ventricle. They are thought to be caused by folding of the frontal horn on itself. (There is also bilateral **subependymal and intraventricular hemorrhage** in both frontal horns.)

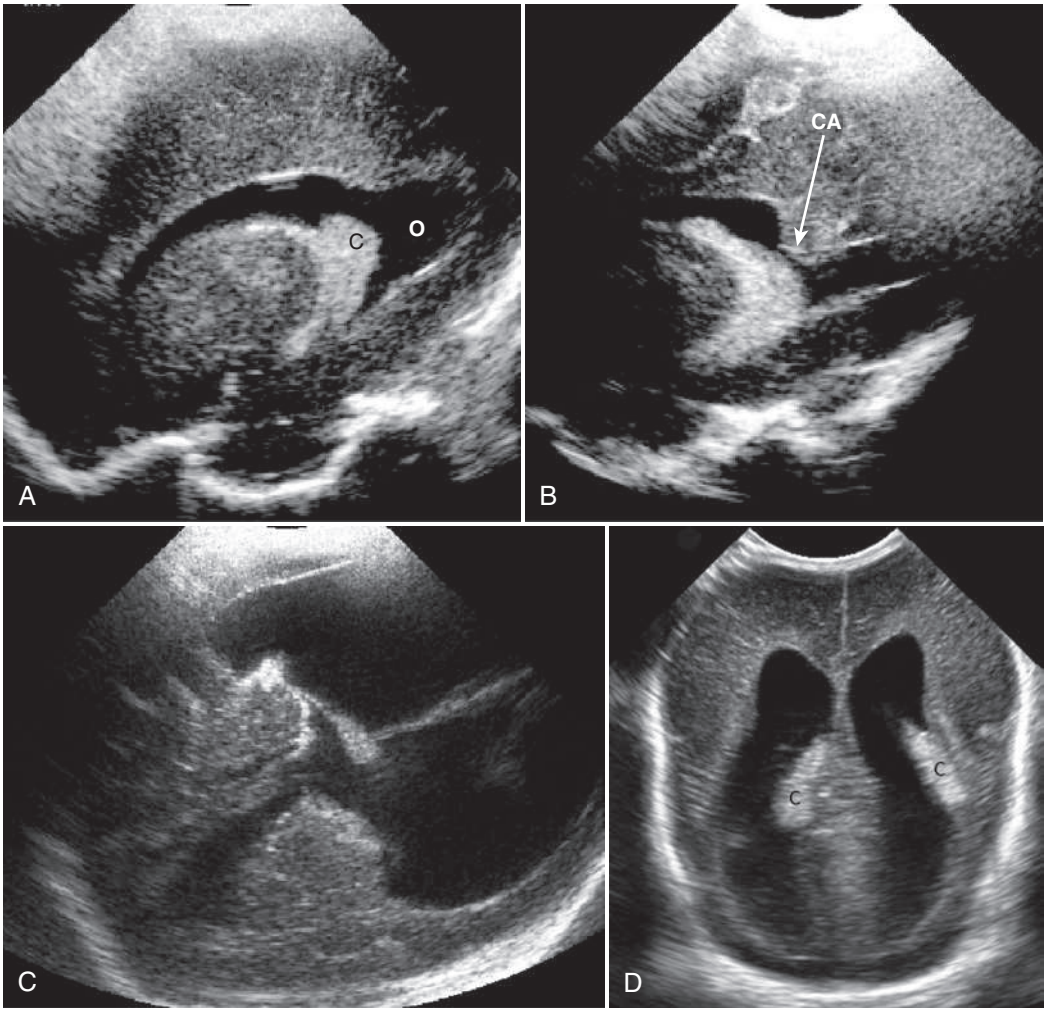

FIG. 45.16 Choroid Plexus and Calcar Avis. (A) and **(B)** Posterior fontanelle views of lateral ventricle. **(A)** Normal choroid plexus glomus *(c)* does not extend into the occipital horn *(O)*. **(B)** Calcar avis *(CA)* can be seen projecting into the occipital horn and imitates hemorrhage. Continuity with the adjacent brain identifies this structure. **(C)** Axial view of the lateral ventricles shows "dangling" choroid plexus in a newborn with hydrocephalus from **aqueductal stenosis. (D)** Coronal view of the lateral ventricles shows dependent choroid plexus.

or occipital horn. The choroid plexus is also present in the roof of the fourth ventricle.[24] (see 45.9A) Small cysts in the choroid plexus are common, but at times areas that appear to be cysts are in fact small vessels.

The glomus of the choroid plexus is often doubled and thus appears **lobulated** (Fig. 45.16). Some authors have termed this appearance a **"split" choroid plexus.**[41] It may be mistaken for clot adhering to the choroid plexus. Color Doppler ultrasound will differentiate the normal highly vascular choroid from similarly echogenic, but avascular, clot (see Fig. 45.8C). Coronal views may also show a flattened or truncated choroid plexus at the level of the thickest portion at the trigone, probably related to the angle of the transducer to the choroid.[41] If there is a large ventricle, the choroid will normally "dangle," or hang down toward the dependent ventricle, when the infants are lying on their side (see Fig. 45.16D).

Pitfalls in Neurosonography

Peritrigonal blush on sagittal view (anisotrophic effect)
Choroid plexus shapes affected by position
- Normal choroid plexus: split, lobulated, or truncated
- Dangling choroid (in hydrocephalus)
- Normal choroidal vessels vs. choroid plexus cyst
- Normal choroid plexus vs. hemorrhage around the choroid

Asymmetrical normal-sized ventricles
Dandy-Walker malformation false-positive diagnosis due to angled view through the lower cerebellum

Germinal Matrix

The germinal matrix develops deep to the ependyma and consists of loosely organized, proliferating cells that give rise to the neurons and glia of the cerebral cortex and basal ganglia (Fig. 45.17). Its vascular bed is the most richly perfused region of the developing brain. Vessels in this region form an immature vascular rete of fine capillaries, extremely thin-walled veins, and larger irregular vessels.[42] The capillary network is best developed on the periphery of the germinal matrix and becomes less well developed toward the central glioblastic mass. Although the germinal matrix is not visualized on sonography, it is important as the typical anatomic site over the caudate nucleus where GMH occurs in premature infants.

Early in gestation, the germinal matrix forms the entire wall of the ventricular system. After the third month of gestation, the germinal matrix regresses, first around the third ventricle, then around the temporal and occipital horns and trigone. By 24 weeks' gestation, the germinal matrix persists only over the head of the caudate nucleus and to a lesser extent over the body of the caudate. By 32 weeks' gestation, it is unusual to see GMH because these cells migrate out to the cerebral cortex. This regression continues until 40 weeks' gestation, when the germinal matrix ceases to exist as a discrete structure, and the immature vascular rete has been remodeled to form adult vascular patterns.

Calcar Avis

On posterior fontanelle views, a normal gyrus, the calcar avis, frequently protrudes into the medial aspect of the lateral ventricle at the junction of the trigone and occipital horn (see Fig. 45.16B). Although this normal brain gyrus may mimic intraventricular clot, slightly turning the transducer will show its continuity with the brain. It can be recognized because of a central echogenic sulcus **(calcarine fissure),** its continuity with the adjacent brain, and normal vascularity on color Doppler ultrasound.[41]

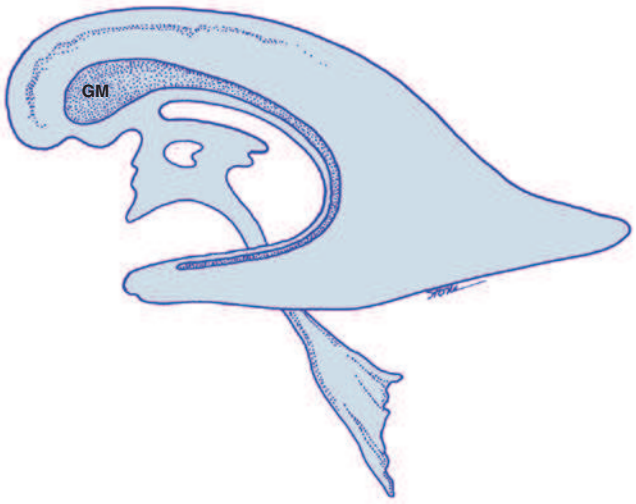

FIG. 45.17 Germinal Matrix. Drawing shows germinal matrix *(GM)* at 30 to 32 weeks' gestation, with largest amount near the caudate nucleus. (With permission from Rumack CM, Manco-Johnson ML. Perinatal and infant brain imaging: role of ultrasound and computed tomography. St Louis: Mosby; 1984.[7])

Cerebellar Vermis

Because the cerebellum develops late in gestation, a mistaken fetal diagnosis of cerebellar vermian hypoplasia is occasionally made. If axial scans are done below the normal level of the fourth ventricle, the vallecula between the cerebellar hemispheres may be mistaken for a Dandy-Walker variant. Pseudoabsence of the inferior vermis[41] or pseudo–vermian hypoplasia can be appreciated on axial views through the posterior fossa. There may appear to be a small or absent cerebellar vermis and a wide communication between the fourth ventricle and cisterna magna. Slightly more superior axial views will show the normal cerebellar vermis. The appearance of a missing or hypoplastic vermis can be evaluated carefully by moving the transducer superiorly to depict the normal vermis, and by obtaining sagittal midline views. The cerebellar vallecula is a variably sized subarachnoid space below and not continuous with the fourth ventricle. The foramen of Magendie is thinner than the vermian cleft in a Dandy-Walker variant[14] (see Fig. 45.9C).

Cisterna Magna

Cisterna magna septa are typically seen inferior and posterior to the cerebellar vermis, usually straight and parallel (see Fig. 45.9). These septa arise at the cerebellovermian angle and continue to the occipital bone. Robinson and Goldstein[43] proposed that these septa are a remnant of Blake pouch cysts and thus a marker of normal cerebellar development.[44,45]

CONGENITAL BRAIN MALFORMATIONS

Congenital brain malformations are the most common anomalies in humans.[42,46,47] Malformations can be classified based on brain development and the types of anomalies that result when development is altered. Brain development can be divided into three stages.[46] **Cytogenesis** involves the formation of cells from molecules. **Histogenesis** is the formation of cells into tissues and involves neuronal proliferation and differentiation. **Organogenesis** is the formation of tissues into organs.

Organogenesis can be subdivided into further stages[48] (Fig. 45.18). The first stage, **neural tube formation and closure,** occurs at 3 to 4 weeks' gestation. The neural plate folds in on itself, fusing dorsally and giving rise to the earliest recognizable brain and spinal cord. In the next stage, **segmentation and diverticulation** of the forebrain occur at 5 to 6 weeks. The single central fetal ventricle separates into two lateral ventricles, and the brain divides into two cerebral hemispheres. Anterior diverticulation results in the formation of the olfactory bulbs and optic vesicles and the induction of facial development. The pituitary and pineal gland also develop by diverticulation from the ventricle at this stage.

Neuronal proliferation and migration occur at 8 to 24 weeks' gestation. Tremendous cellular proliferation is necessary to provide

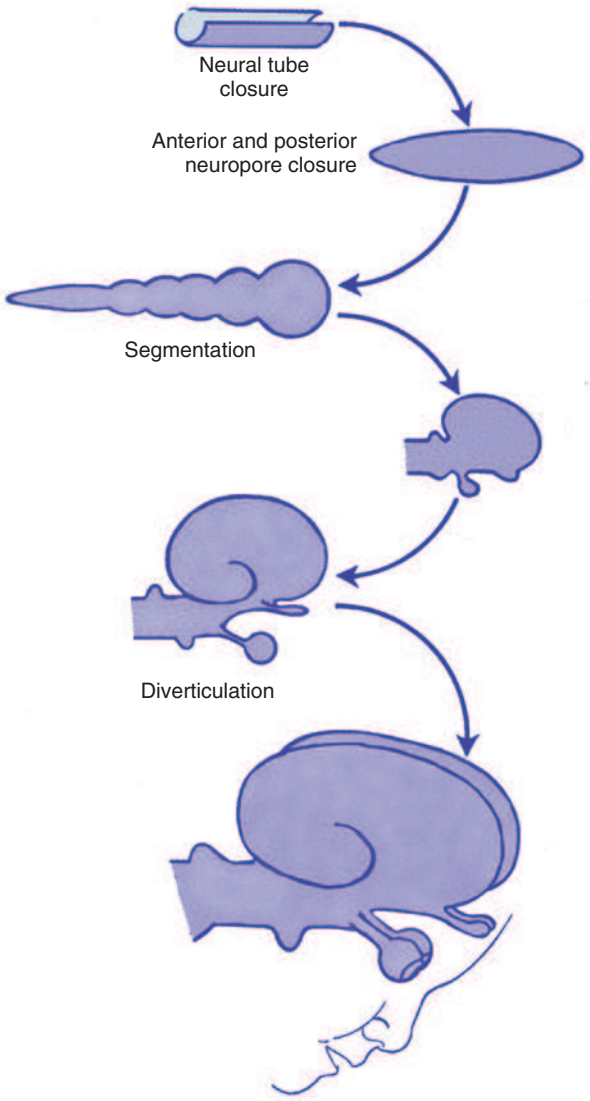

FIG. 45.18 Stages of Organogenesis. The neural tube closure at 3 to 4 weeks' gestation, including closure of the anterior and posterior neuropores. At 5 to 6 weeks, the brain segments and five types of diverticula form. First, the paired olfactory tracts, optic tracts, and cerebral ventricles develop, then the unpaired pineal and pituitary. Neural proliferation, migration, organization, and myelination occur after these stages. (With permission from DeMyer W. Classification of cerebral malformations. Birth Defects Orig Artic Ser. 1971;7[1]:78-93.[48])

Congenital Brain Malformations

DISORDERS OF ORGANOGENESIS
Disorders of Neural Tube Closure
Chiari malformation
Agenesis of the corpus callosum
Lipoma of the corpus callosum
Dandy-Walker malformation or variant
Posterior fossa arachnoid cyst
Teratoma

Disorders of Diverticulation and Cleavage
Septo-optic dysplasia
Holoprosencephaly (alobar, semilobar, lobar)

Disorders of Sulcation/Cellular Migration
Lissencephaly
Schizencephaly
Heterotopias
Pachymicrogyria or polymicrogyria

DISORDERS OF SIZE
DISORDERS OF MYELINATION
DESTRUCTIVE LESIONS
DISORDERS OF HISTOGENESIS

Neurocutaneous Syndromes (Phakomatoses)
Tuberous sclerosis
Neurofibromatosis
Congenital Vascular Malformations

DISORDERS OF CYTOGENESIS
Congenital neoplasms

Modified from DeMeyer classification of anomalies.[21,22,48]

Stages of Brain Development

Cytogenesis: development of molecules into cells
Histogenesis: development of cells into tissues
Organogenesis: development of tissues into organs
- Neural tube closure (dorsal induction: 3-4 weeks' gestation)
- Diverticulation (ventral induction: 5-6 weeks' gestation)
- Neuronal proliferation (8-16 weeks' gestation)
- Neuronal migration (24 weeks' gestation to years)
- Organization (6 months' gestation to years after birth)
- Myelination (birth to years after birth)

[a]Stages overlap in time but may be individually abnormal.
Modified from Volpe JJ. Brain injury in premature infants: a complex amalgam of destructive and developmental disturbances. Lancet Neurol. 2009;8(1):110-124.[46]

a growing brain with the necessary building blocks to form properly. Finally, millions of cells must migrate into the organized functional structure that is recognized as a normal brain. The germinal matrix is a source of many of the migrating cells and eventually disappears as they migrate out. **Myelination** occurs from the second trimester to adulthood but is most active from directly after birth until 2 years of age.[46,47] Migration and myelination defects are best evaluated with MRI and have been well described by Barkovich.[31] MRI has greatly increased our understanding of brain development, and many genetic and environmental factors may interfere with normal development.

Destructive lesions can occur at any point in brain development. Congenital malformations of the brain are often diagnosed in utero, and neonatal sonographic imaging may be needed to confirm or further evaluate the prenatal diagnosis. In most cases, MRI may be required to clarify the ultrasound findings. In general, MRI is preferred over CT because it best demonstrates sulcal patterns, migrational anomalies, and abnormal myelination. Disorders of cerebellar growth and development are now better

understood with major advances in fetal magnetic resonance neuroimaging and with major advances in genetics. Examples of reviews of cerebellar development and malformations are those by Limperopoulos and du Plessis[49] and Patel and Barkovich.[50]

DISORDERS OF NEURAL TUBE CLOSURE

Chiari Malformations

There are three classic Chiari malformations. **Chiari I** malformation is simply the downward displacement of the cerebellar tonsils, without displacement of the fourth ventricle or medulla. **Chiari II** malformation is the most common and of greatest clinical importance because of its almost universal association with myelomeningocele. **Chiari III** malformation is a high cervical encephalomeningocele in which the medulla, fourth ventricle, and virtually the entire cerebellum reside.

Classic sonographic findings of the Chiari II malformation involve the entire brain. Present theories propose that a failure in neural tube closure results in a small posterior fossa.[31,50] In early brain development, abnormal neural tube closure may result in a spinal defect such as a myelomeningocele. This decompresses the ventricles and leads to underdevelopment of the posterior fossa bony structures. The intracranial findings are the result of the small posterior fossa. The tentorial attachment is low, and the combined effect causes compression of the upper cerebellum by the tentorium. The inferior cerebellum is compressed and displaced into the foramen magnum. The cerebellar tonsils and vermis herniate into the spinal canal through an enlarged foramen magnum. The pons and medulla are inferiorly displaced, as is the elongated fourth ventricle (Figs. 45.19 and 45.20; Video 45.4 and Video 45.5).

Chiari II Malformation: Sonographic Findings

- Anterior and inferior pointed frontal horns
  - Batwing configuration
- Enlarged lateral ventricles
  - (colpocephaly if associated corpus callosum agenesis or dysgenesis)
- Enlarged massa intermedia fills third ventricle
- Elongation and caudal displacement of fourth ventricle, pons, medulla, and vermis
- Nonvisualization of fourth ventricle due to compression

There is usually marked **enlargement of the massa intermedia** on the coronal and midline sagittal ultrasound images. Although the third ventricle is often enlarged and the aqueduct is kinked, the enlarged massa intermedia often fills the third ventricle, causing it to appear only slightly larger than normal. The fourth ventricle is often not visualized because it is thin, elongated, compressed, and displaced into the upper spinal canal. The frontal horns are typically small and pointed. The corpus callosum is frequently either dysgenetic or absent. When callosal abnormalities are present, the posterior horns of the lateral ventricles often are disproportionately large, called "colpocephaly." The **anterior and inferior pointing of the frontal horns** has often been referred to as a **"bat wing" configuration** see (Figs. 45.19 and 45.20, Video 45.6). The septum pellucidum may be completely or partially absent. The interhemispheric fissure usually appears to be widened on coronal images, particularly after shunting. There may also be **gyral interdigitation** when the corpus callosum is absent (see Fig. 45.20). The posterior fossa is usually small, and the tentorium appears relatively low and hypoplastic. Hydrocephalus resulting from the Chiari II malformation is frequently mild in utero but may be progressive over time and associated with a tethered spinal cord (Video 45.7). When CSF circulation can no longer decompress into the myelomeningocele after the repair, hydrocephalus typically worsens. Neonatal screening for hydrocephalus will be best done routinely about 2 days after the myelomeningocele repair, as the ventricles may appear undilated before this. Ultrasound diagnosis of **craniolacunia** (lacuna skull, lückenschädel) is possible. Lacunar skull is a dysplasia that is often present at birth in the Chiari II malformation. The lacunar skull has a wavy, irregular appearance of the inner calvaria.[51] Craniolacunia will disappear over the first year of life even without shunting.

Routine prenatal screening for maternal serum alpha-fetoprotein (MS-AFP), which is elevated with neural tube defects, and the widespread use of sonography in pregnancy allow for the prenatal diagnosis of most Chiari malformations.[52] Because of its classic appearance, the Chiari II brain malformation is often recognized in utero and alerts the sonographer to look closely for a myelomeningocele. In less than 2% of myelomeningoceles, the neural tube defect is covered by skin, so there is no elevation of MS-AFP and there may be no Chiari II malformation (Fig. 45.21). Sonography or CT is reliable for follow-up of shunting procedures. MRI may be necessary to evaluate infants with symptoms suggesting brainstem compression because this may require decompression of the foramen magnum. Fetal myelomeningocele repair in selected patients may decrease the severity of the Chiari II malformation after birth.[53]

Agenesis of Corpus Callosum

The corpus callosum forms broad bands of connecting fibers between the cerebral hemispheres. Development of the corpus callosum occurs between 8 and 20 weeks of gestation. Magnetic resonance images from early fetuses show that the genu and anterior body develop first, and development proceeds both anteriorly to the rostrum and posteriorly to develop the splenium.[31,54] Therefore, depending on the timing of the intrauterine insult, development may be partially arrested, or complete agenesis may occur. If development is partial, the genu is usually present and the dorsal splenium or the anterior rostrum is absent. Because insults causing anomalies of the corpus callosum occur early (8-20 weeks) in development, other CNS anomalies occur in up to 80% of cases.[28,54] These associated anomalies include **Chiari II** and **Dandy-Walker** malformation, **holoprosencephaly, encephalocele, lipoma, arachnoid cyst, migrational abnormalities,** and **Aicardi syndrome** (female infants with agenesis of the corpus callosum, ocular abnormalities, and infantile spasms). If the corpus callosum is absent, MRI will be valuable either in

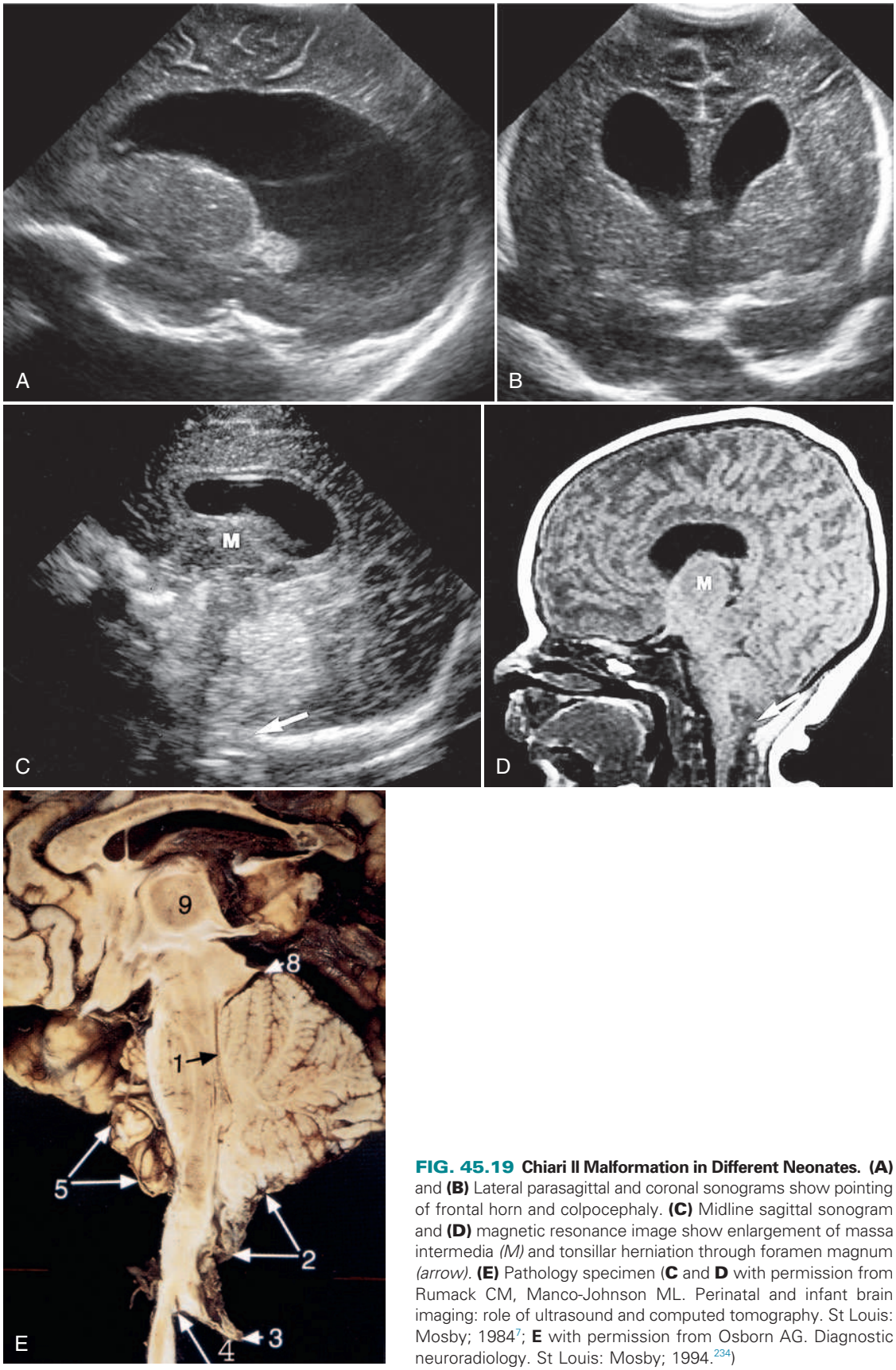

FIG. 45.19 Chiari II Malformation in Different Neonates. (A) and **(B)** Lateral parasagittal and coronal sonograms show pointing of frontal horn and colpocephaly. **(C)** Midline sagittal sonogram and **(D)** magnetic resonance image show enlargement of massa intermedia *(M)* and tonsillar herniation through foramen magnum *(arrow)*. **(E)** Pathology specimen (**C** and **D** with permission from Rumack CM, Manco-Johnson ML. Perinatal and infant brain imaging: role of ultrasound and computed tomography. St Louis: Mosby; 1984[7]; **E** with permission from Osborn AG. Diagnostic neuroradiology. St Louis: Mosby; 1994.[234])

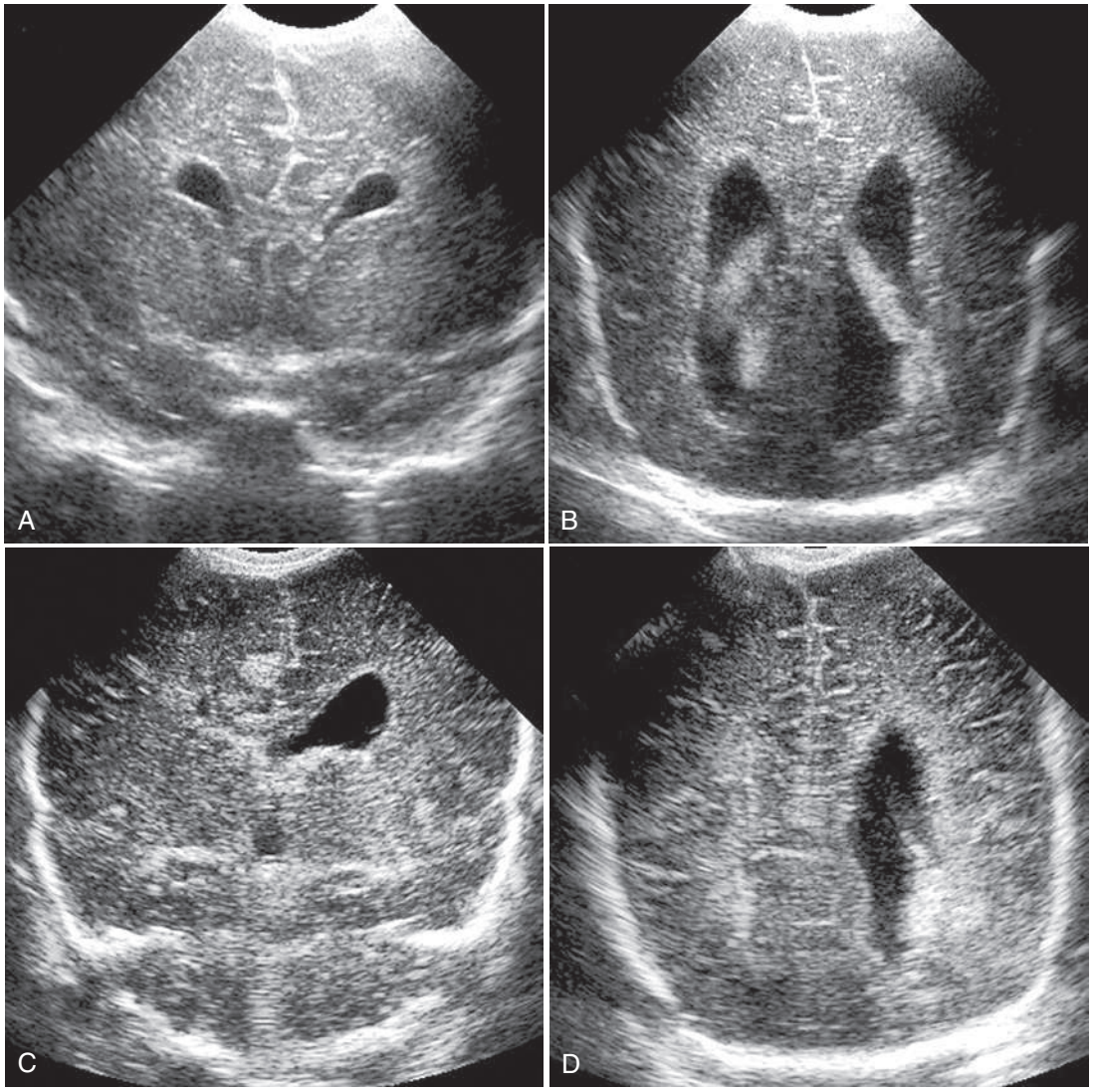

FIG. 45.20 Chiari II and Absent Corpus Callosum. (A) Anterior coronal image shows widely separated frontal horns. **(B)** Posterior coronal view shows the parallel orientation of the ventricles. Gyral interdigitation is best seen before shunting in this patient. **(C)** and **(D)** Anterior and posterior coronal ultrasound scans show Chiari II malformation after ventriculoperitoneal shunting for hydrocephalus. The right lateral ventricle is much smaller, typical of the side with the shunt. See also Video 45.4, Video 45.5, and Video 45.6.

utero or at birth to delineate associated findings that may cause a poor prognosis and change patient management.[31,55] Isolated agenesis of the corpus callosum may have a normal prognosis. However, Barkovich[31] has reported that symptomatic patients with absence of the corpus callosum typically have seizures, microcephaly, delayed development, mental retardation, or hypothalamic dysfunction.

The key diagnostic clues to agenesis of the corpus callosum on sonography are the widely spaced, parallel-oriented lateral ventricles that have extremely narrow, often slitlike frontal horns[56] (Fig. 45.22). Coronally, the frontal horns and ventricular bodies have sharply angled, lateral peaks. There may be relative enlargement of the occipital horns (colpocephaly) and often, enlarged temporal horns. **Probst bundles,** longitudinal callosal fibers that failed to decussate or cross to the other cerebral hemisphere, bulge into the ventricles along the superomedial aspect of the lateral ventricles. These are best seen on coronal images as the concave medial border to the lateral ventricles. There is no septum pellucidum. The third ventricle is often dilated and elevated; its roof extends superiorly between the lateral ventricles and into the interhemispheric fissure and may be associated with a dorsal midline cyst (Fig. 45.23). The medial cerebral sulci are typically radially arranged, perpendicular to the expected course of the corpus callosum, causing a **"sunburst" sign** on sagittal midline images (Fig. 45.24). The pericallosal sulcus is missing, and the cingulate sulcus is absent or present only as unconnected segments. Because agenesis of the corpus callosum has additional brain anomalies in more than 75% of patients, further evaluation with postnatal MRI is indicated. **Cerebellar hypoplasia, gyral anomalies,** and **heterotopia** are seen most often on MRI.[28]

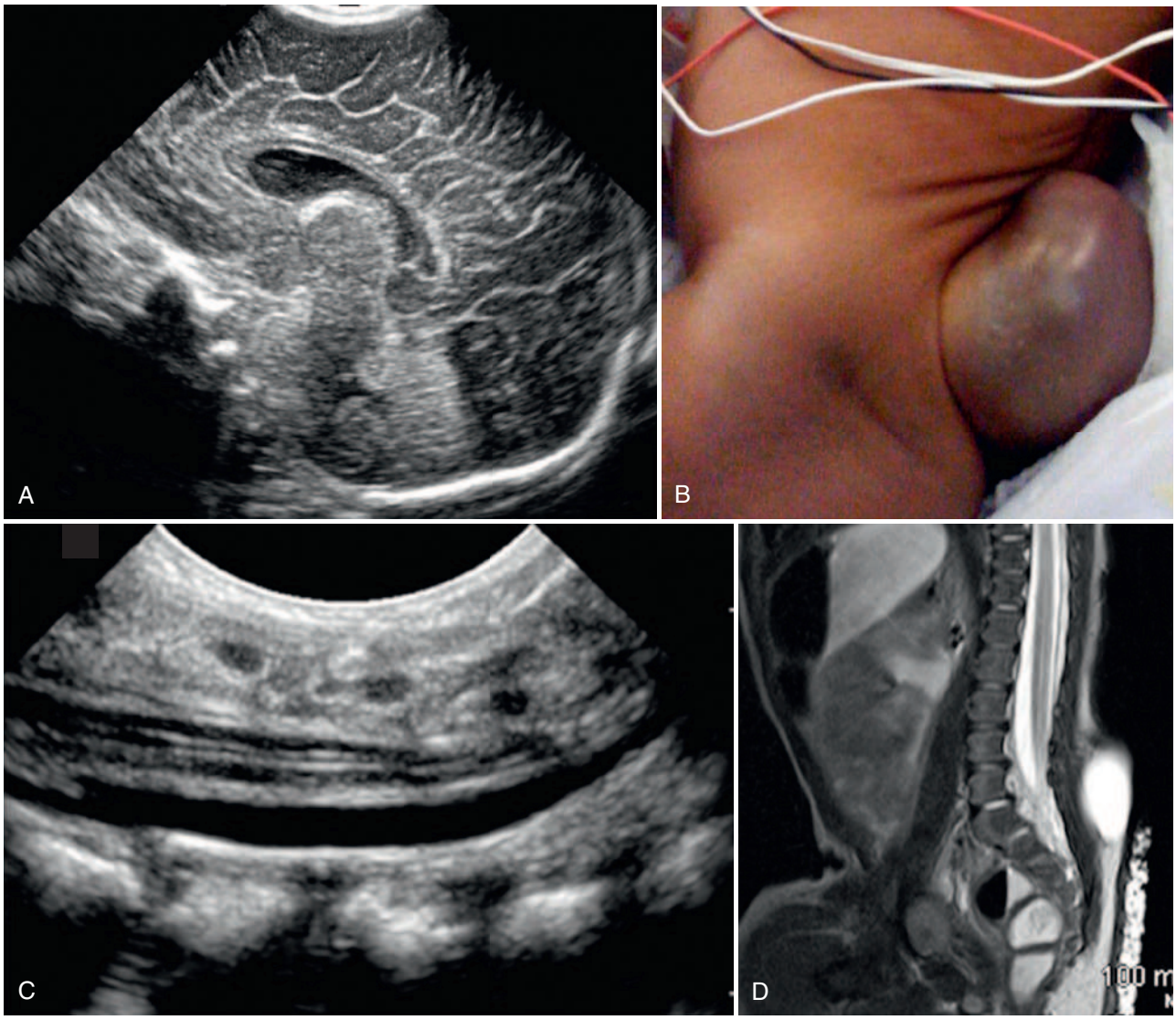

FIG. 45.21 Myelomeningocele, Skin Covered, With No Chiari II Malformation. (A) Midline sagittal brain ultrasound and **(B)** photograph of myelomeningocele. **(C)** Sagittal spine ultrasound and **(D)** T2-weighted magnetic resonance imaging show tethered cord extending almost to the sacrum. See also Video 45.7.

Agenesis of Corpus Callosum: Sonographic Findings

Absent corpus callosum
Absent cingulate gyrus and sulcus
Radial arrangement of medial sulci above third ventricle ("sunburst" sign)
Widely spaced, parallel lateral ventricles
Extremely narrow frontal horns (slitlike)
Concave or straight medial borders secondary to Probst bundles
Colpocephaly (dilated atria and occipital horns)
Elevated third ventricle extending between lateral ventricles, continuous with interhemispheric fissure, with or without dorsal cyst
Absent septum pellucidum

Corpus Callosum Lipoma

Maldevelopment of embryonic neural crest tissues may result in lipomas of the interhemispheric fissure. These lipomas have no mass effect and thus do not require surgery. Corpus callosum lipomas account for 30% to 50% of intracranial lipomas and are associated with dysgenesis of the corpus callosum[31] (Fig. 45.25).

Dandy-Walker Spectrum

Dandy-Walker malformation appears as a dilated fourth ventricle in direct communication with the cisterna magna (Fig. 45.26). The posterior fossa is enlarged, with elevation of the tentorium cerebelli, straight sinus, and torcular Herophili at the venous sinus confluence. The vermis of the cerebellum is hypoplastic to absent, and the cerebellar hemispheres are variably hypoplastic and displaced laterally by the enlarged fourth ventricle. The brainstem may be compressed anteriorly or hypoplastic.

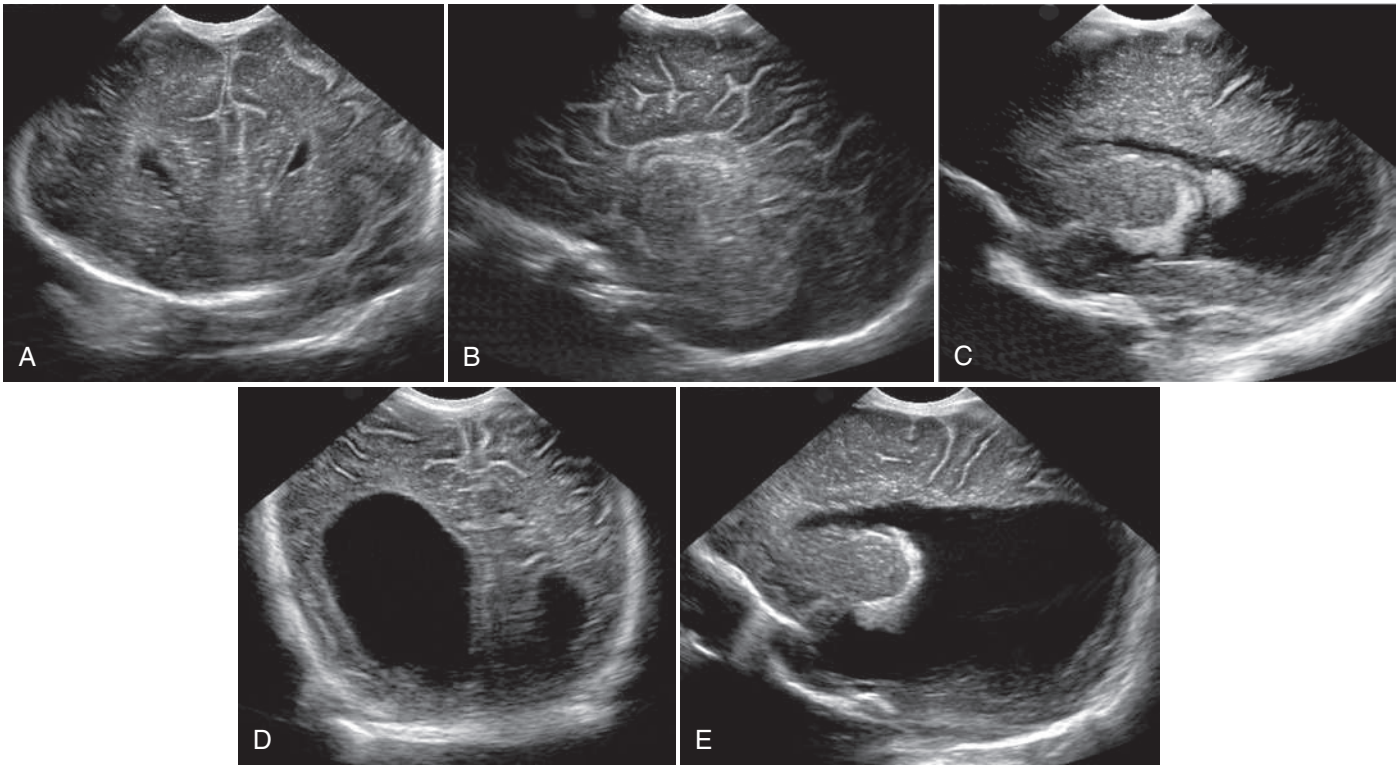

FIG. 45.22 Agenesis of the Corpus Callosum, Isolated Anomaly in Two Neonates. *Neonate 1:* **(A)** Small frontal horns are widely separated. **(B)** Sulci radiate in sunburst pattern in parasagittal just off midline view. **(C)** Colpocephaly seen in parasagittal view of lateral ventricle. *Neonate 2:* **(D)** Coronal view of the occipital horns shows enlarged right occipital horn. **(E) Colpocephaly** seen in parasagittal view of right lateral ventricle.

Generalized obstructive hydrocephalus occurs in up to 80% of cases. If there is also agenesis of the corpus callosum, colpocephaly is typically present.[7,57]

Dandy-Walker Malformation: Sonographic Findings

- Enlarged fourth ventricle connects to Dandy-Walker cyst posteriorly
- Large posterior fossa
- Hypoplastic cerebellar vermis
- Hypoplastic cerebellar hemispheres displaced laterally by fourth ventricle
- Small brainstem
- Hydrocephalus (80%)
- Obstruction above and below fourth ventricle
- Absent or dysgenetic corpus callosum (up to 70%)

The etiology of Dandy-Walker malformation is not definitively known. Theories include agenesis of the foramina of Luschka and Magendie in the first trimester, malformation of the roof of the fourth ventricle, and delayed opening of the foramen of Magendie.[31] The prenatal diagnosis of Dandy-Walker malformation, with differentiation from Dandy-Walker variant, a posterior fossa arachnoid cyst, and mega–cisterna magna, is usually possible. Some severe cases may be diagnosed early, but typically Dandy-Walker malformation is diagnosed after 17 weeks' gestation, when the inferior vermis has normally completely formed.[40,58]

The Dandy-Walker malformation is associated with other CNS anomalies in up to 70% of cases. These include partial or complete agenesis of the corpus callosum, encephalocele, holoprosencephaly, microcephaly, gray matter heterotopia, and gyral malformations. Chromosomal abnormalities are described in up to 20% to 50% of cases and include trisomy 13, 18, and 21. Other associated anomalies include gastrointestinal, genitourinary, cardiac, musculoskeletal, and pulmonary malformations, including congenital diaphragmatic hernia and cystic hygroma.[57,59,60]

Therapy for the Dandy-Walker malformation includes ventriculoperitoneal shunting, which will decompress the lateral ventricles but may not decompress the posterior fossa cyst. The cyst may require a separate shunt for decompression. Sonography can be used to follow these procedures until the infant is approximately 18 months of age, but this method is rarely used after the first few months of life.

In the **Dandy-Walker Spectrum,** there is variable hypoplasia of the posterior inferior vermis and communication between the fourth ventricle and cisterna magna. The fourth ventricle may be slightly to moderately enlarged. In the mildest form, the posterior fossa is normal in size, and although the vermis is small, the cerebellar hemispheres are normal. There is no associated hydrocephalus. Mastoid fontanelle views should be taken in this setting through the fourth ventricle so that the normal

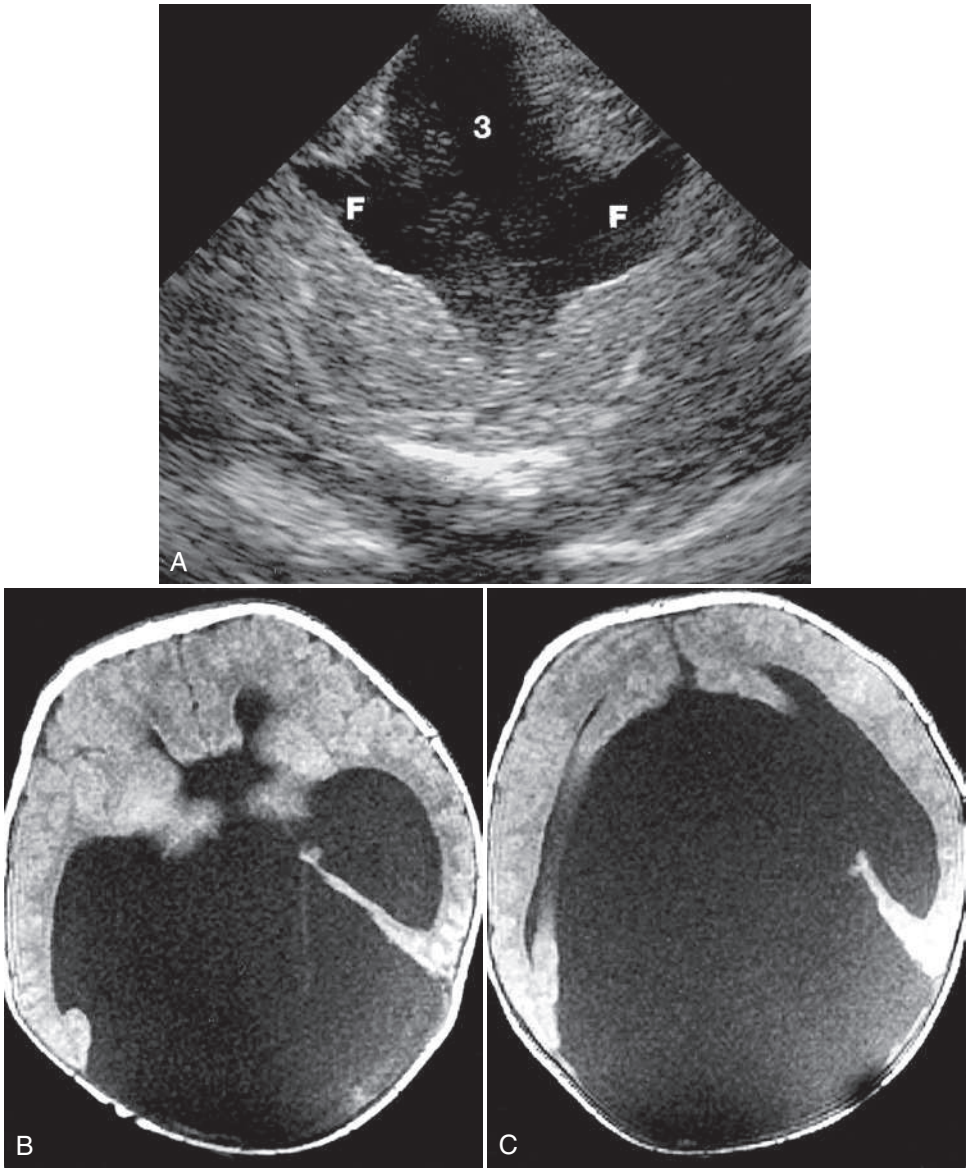

FIG. 45.23 Agenesis of Corpus Callosum (ACC) With Elevation of Third Ventricle and Continuation Into a Large Dorsal Cyst. (A) Coronal sonogram and **(B)** and **(C)** computed tomography scans show widely separated frontal horns *(F)*, a large third ventricle that extends superiorly as a dorsal cyst *(3)* between the lateral ventricles in a newborn who also had Dandy-Walker malformation.

foramen of Magendie and vallecula, which may be enlarged with hydrocephalus, are not mistaken for a Dandy-Walker anomaly[25] (see Fig. 45.9C). The Dandy-Walker spectrum varies greatly with vermian hypoplasia, an enlarged fourth ventricle, a large aqueduct, and a large third ventricle.[14] Chromosomal abnormalities occur in up to 30% of these infants. Associated CNS or extra-CNS anomalies may affect the outcome of the infant more than the Dandy-Walker spectrum.[31,57]

Two differential diagnoses of posterior fossa cystic lesions mimic Dandy-Walker syndrome. A **mega–cisterna magna** is described as the mildest form of this spectrum and includes no mass effect, no hydrocephalus, and a normal cerebellar vermis, fourth ventricle, and cerebellar hemisphere (Fig. 45.27). A **posterior fossa subarachnoid cyst** can be differentiated from Dandy-Walker malformation or spectrum by the lack of communication of the cyst with the fourth ventricle. The normal fourth ventricle, vermis, and cerebellum are displaced by the arachnoid cyst.[58,59]

Posterior Fossa Cystic Lesions

Dandy-Walker Malformation
Hypoplastic vermis with rotation
Blake pouch cyst
Mega–cisterna magna
Posterior fossa subarachnoid cyst

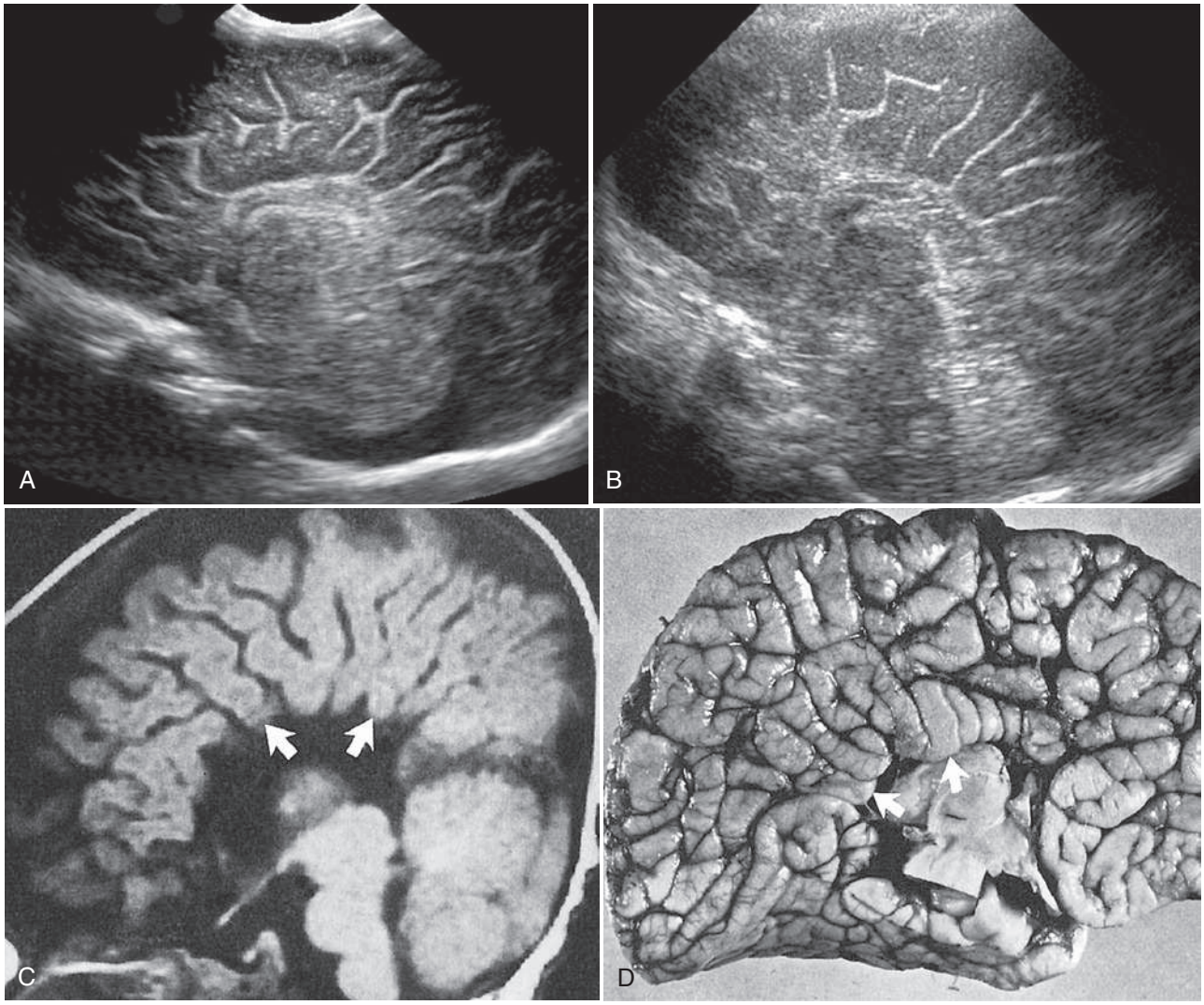

FIG. 45.24 "Sunburst" or Radial Arrangement of Sulci in Agenesis of the Corpus Callosum. (A) and **(B)** Midsagittal sonograms. **(C)** Midsagittal magnetic resonance image. **(D)** Sagittal pathologic specimen. Arrows indicate radial array of sulci. (**C** with permission from Osborn AG. Diagnostic neuroradiology. St Louis: Mosby; 1994[234]; **D** with permission from Friede R. Developmental neuropathology. 2nd ed. New York: Springer-Verlag; 1975.[42])

Complete agenesis of the cerebellar vermis without hydrocephalus occurs in **Joubert syndrome,** with associated symptoms including episodic hyperpnea, ataxia, abnormal eye movements, and mental retardation.[31] This anomaly is thought to be caused by the inability of the posterior fossa axons to cross the midline. There is a Meckel-like syndrome with Dandy-Walker malformation, polycystic kidneys, hepatic fibrosis, and hand and genital anomalies. True **Meckel-Gruber syndrome** includes an encephalocele, renal cystic dysplasia, short limbs, and polydactyly.[60]

DISORDERS OF DIVERTICULATION AND CLEAVAGE: HOLOPROSENCEPHALY

Holoprosencephaly results from a failure of diverticulation when the primitive prosencephalon does not divide into the telencephalon and the diencephalon between the fourth and eighth weeks of gestation. The telencephalon normally develops into the cerebral hemispheres, ventricles, putamen, and caudate nuclei. The diencephalon becomes the third ventricle, thalami, hypothalamus, and lateral globus pallidus. Holoprosencephaly represents a spectrum of malformations that form a continuum from most severe, with no separation of the telencephalon into hemispheres (**alobar** holoprosencephaly), to least severe, with partial separation of the dorsal aspects of the brain (**lobar** holoprosencephaly). The septum pellucidum is absent in all forms of holoprosencephaly (Fig. 45.28).

Septo-Optic Dysplasia

Some consider the mildest form of lobar holoprosencephaly to be **septo-optic dysplasia,** with absence of the septum pellucidum and optic nerve hypoplasia (Fig. 45.29, Video 45.8). About two-thirds of these infants have hypothalamic-pituitary dysfunction. They may have visual symptoms and growth restriction. In

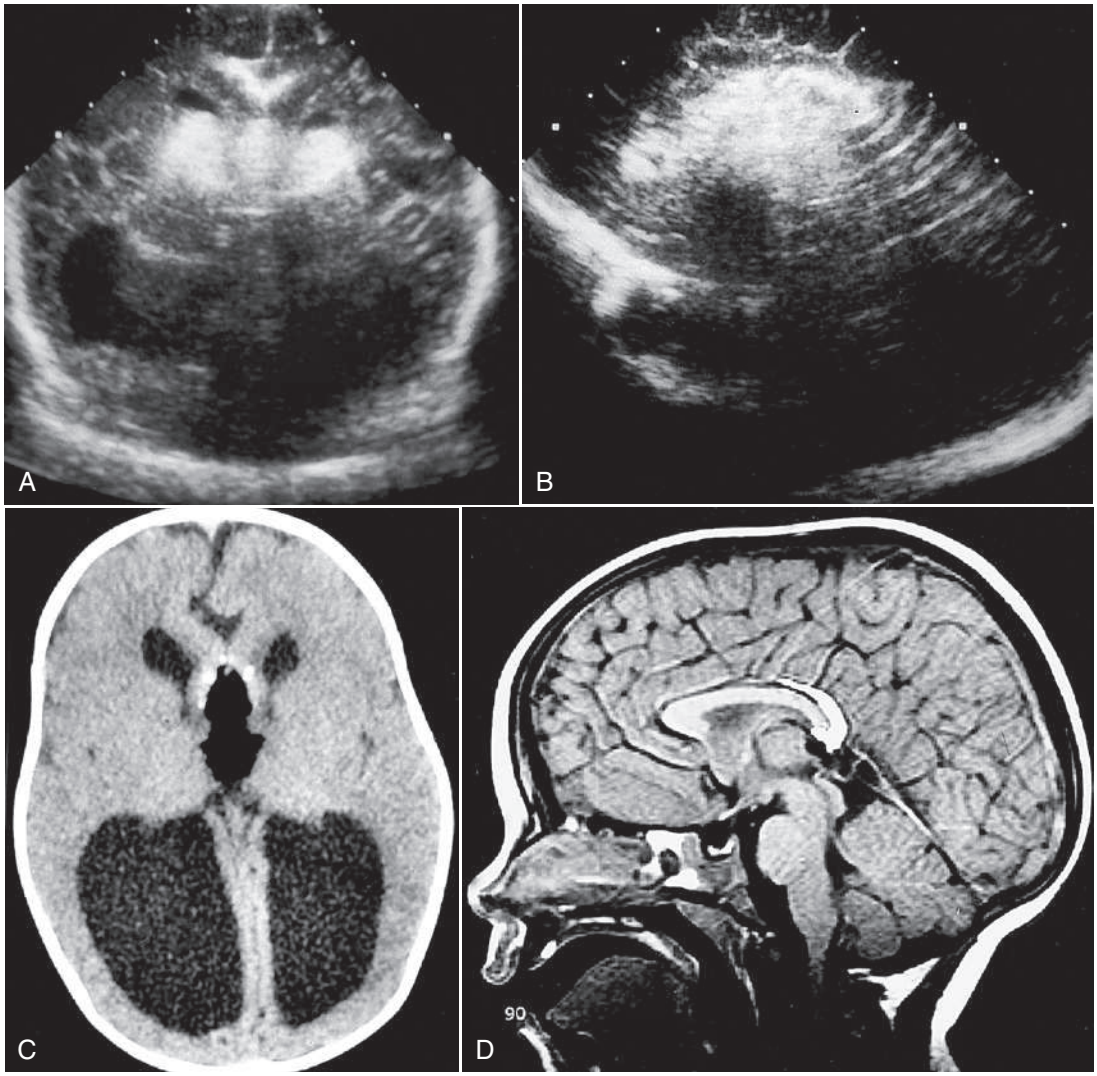

FIG. 45.25 Lipoma of Corpus Callosum. (A) and **(B)** Coronal and sagittal sonograms show highly echogenic fat surrounded by calcification; both are causing major acoustic shadowing. **(C)** Computed tomography scan shows black central fat surrounded by white flecks of calcium. **(D)** Sagittal magnetic resonance scan shows fat (bright white on T1-weighted image) extending over the corpus callosum.

FIG. 45.26 Dandy-Walker Complex Compared With Normal Posterior Fossa. (A) and **(B)** Axial posterior fossa sonograms in two infants with Dandy-Walker complex show a wide continuity between the fourth ventricle and the cisterna magna. **(C)** Normal axial sonogram of the fourth ventricle and slightly echogenic cerebellar vermis.

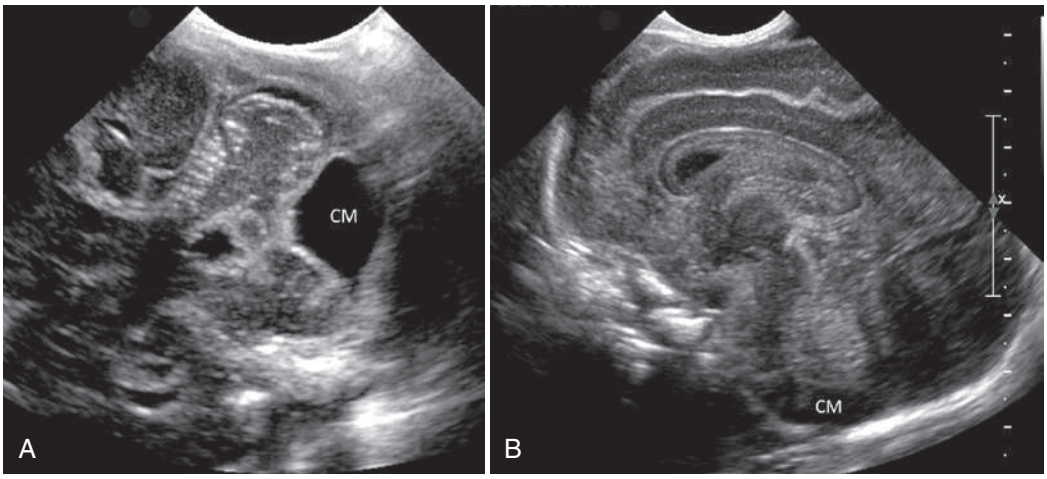

FIG. 45.27 Mega–Cisterna Magna. (A) and **(B)** Axial and sagittal sonograms show an enlarged cisterna magna *(CM)* with no connection to the fourth ventricle and no ventriculomegaly.

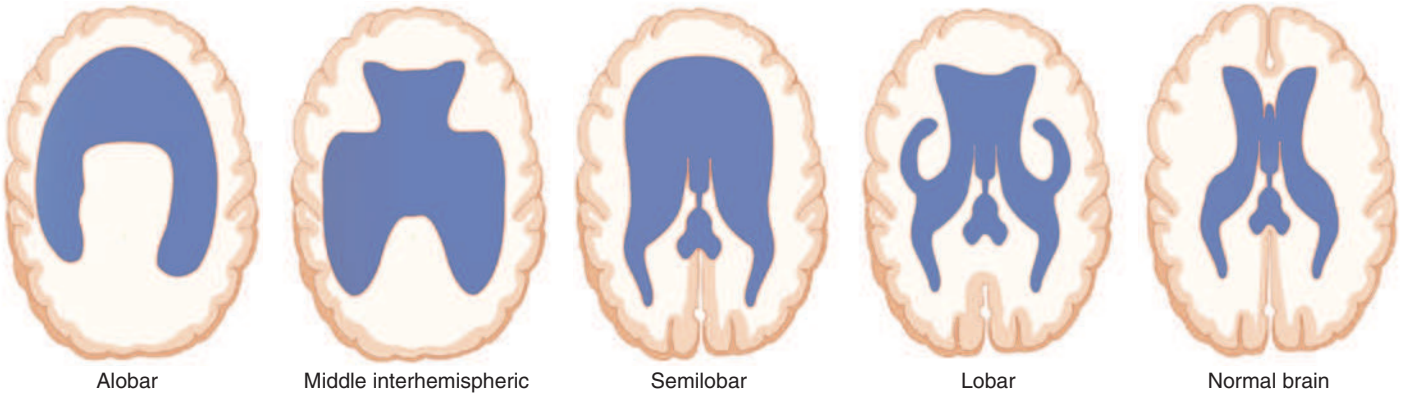

FIG. 45.28 Holoprosencephaly Classification. Holoprosencephaly classification. Normal versus four types—alobar (most severe), middle interhemispheric, semilobar, and lobar.

addition to occurrence with holoprosencephaly, callosal agenesis, and Chiari II malformations, other associations suggest that septo-optic dysplasia may occur from destructive processes that cause schizencephaly and chronic severe hydrocephalus.[31] Intermediate in severity between alobar and lobar is **semilobar** holoprosencephaly, with fusion of the cortex and ventricle anteriorly but variable separation posteriorly; facial anomalies are mild or absent. Anomalies of the face and calvaria accompany and help predict the severity of the brain malformation, because the face develops at the same time as the brain during diverticulation. Cases of holoprosencephaly are usually suspected as a result of the accompanying facial anomalies, with more severe facial anomalies predicting more severe intracranial anomalies. Holoprosencephaly is most frequently seen in **trisomy 13 and 18 syndromes** and can also be caused by **teratogens,** the most common mechanism in **infants of diabetic mothers.**[31,60-62]

Alobar Holoprosencephaly

Alobar holoprosencephaly is the most severe form of this disorder. Infants with this defect usually die within the first months of life or are stillborn. Facial features may include **cebocephaly** (hypotelorism and malformed nose; Fig. 45.30D), **cyclopia,** and **ethmocephaly** (cyclopia or hypotelorism with a midline proboscis above the eyes). The brain surrounds a single midline horseshoe- or crescent-shaped ventricle with a surrounding thin, primitive cerebral cortex[59] (Fig. 45.30). The hemispheres are fused as a pancakelike mass of tissue in the most anterior portion of the calvaria. Only in holoprosencephaly will the splenium of the corpus callosum be the only segment present.[31] The thalami are fused, and there is no falx, corpus callosum, or interhemispheric

Alobar Holoprosencephaly: Sonographic Findings

Single midline crescent-shaped ventricle
Thin layer of cerebral cortex
No falx
No interhemispheric fissure
No corpus callosum
Fused thalami and basal ganglia
Fused echogenic choroid plexus
Absent third ventricle
Large dorsal cyst

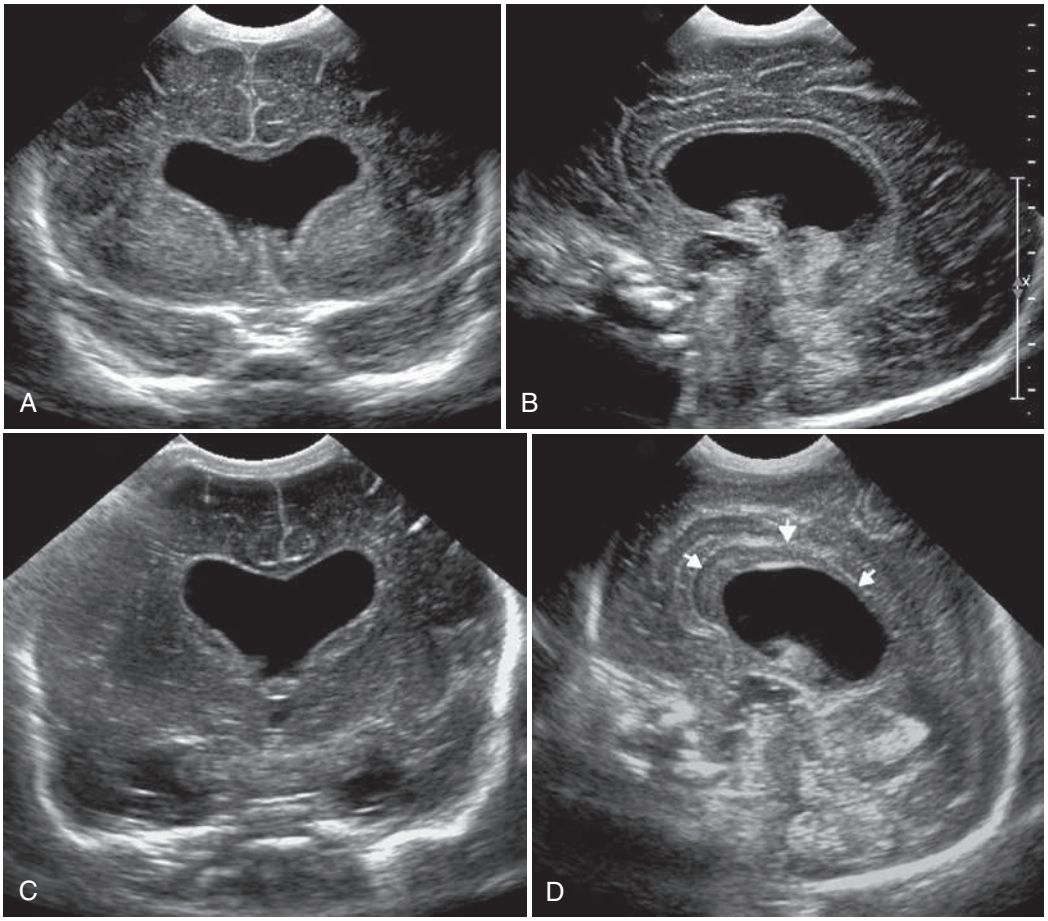

FIG. 45.29 Septo-Optic Dysplasia in Two Infants. (A) and **(B)** Coronal and sagittal sonograms. Although the cavum septum pellucidum is absent, the corpus callosum is present and complete. **(C)** Coronal sonogram shows continuity between frontal horns resulting from absence of the septum pellucidum. **(D)** Sagittal midline sonogram shows the corpus callosum *(arrows),* which is thinned posteriorly. See also Video 45.8.

fissure. Midline, moderately echogenic, fused thalami are seen anterior to the fused, hyperechogenic choroid plexus. The third ventricle is usually absent, so the large, single, central holoventricle communicates inferiorly with the aqueduct and may also connect posteriorly with a dorsal cyst. Pachygyria may be seen. Posterior fossa structures may be normal.

Semilobar Holoprosencephaly

In semilobar holoprosencephaly, more brain parenchyma is present, but the single ventricle persists. There may be separate occipital and temporal horns. A small portion of the falx and interhemispheric fissure develops in the occipital cortex posteriorly. The splenium and genu of the corpus callosum are often formed and may be seen on midline sagittal sections. The thalami are partially separated, and the third ventricle is rudimentary. Facial anomalies are less severe than in alobar holoprosencephaly, usually with only mild hypotelorism and median or lateral cleft lip.

Lobar Holoprosencephaly

Lobar holoprosencephaly is the least severe form of this disorder. There is almost complete separation of hemispheres, with development of a falx and interhemispheric fissure, but these may be shallow anteriorly, and the frontal lobes are fused. The septum pellucidum is absent. The anterior horns of the lateral ventricles are fused and square, but the occipital horns are separated. Temporal horns may be present. The third ventricle is usually present, separating the thalami. The splenium and body of the corpus callosum are often present, with absence of the genu and rostrum. Facial anomalies are mild and similar to the semilobar form or absent.

Middle Interhemispheric Form of Holoprosencephaly

A fourth variant of holoprosencephaly, the **middle interhemispheric form** of holoprosencephaly, also called **syntelencephaly,** occurs in less than 5% of cases. This has a separation of the anterior and posterior parts of the hemispheres, but fusion is present in the central region of the brain between parietal hemispheres, and the face is generally normal. Cases typically show mild ventriculomegaly, absence of parts of the septi pellucidi, abnormality of the midpart of the corpus callosum, and dorsal cysts. The middle interhemispheric form can resemble mild ventriculomegaly with septal fenestration. Coronal scanning may show fusion of the central parts of the hemisphere. MRI helps

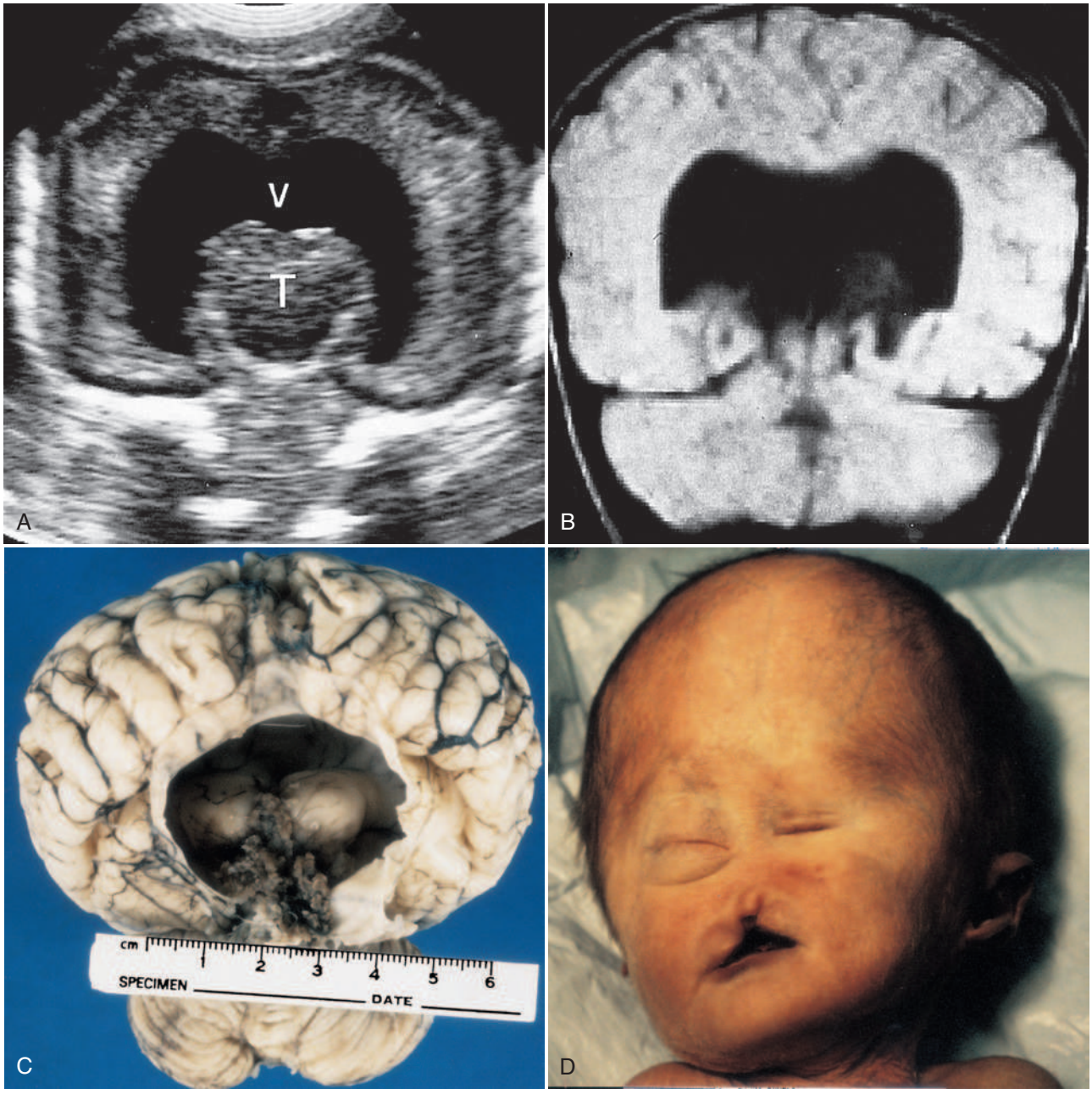

FIG. 45.30 Alobar Holoprosencephaly. (A) Coronal sonogram shows single central ventricle *(V)* and fused thalami *(T)*. No falx or interhemispheric fissure is present. **(B)** Magnetic resonance image and **(C)** pathology specimen show single central ventricle and fused thalami. **(D)** Autopsy specimen shows **cebocephaly** (severe hypotelorism and malformed nose).

confirm this appearance and typically shows sylvian fissures connecting abnormally across the midline.[63-66]

DISORDERS OF SULCATION AND CELLULAR MIGRATION

Schizencephaly

Believed to be caused by a primary neuronal migration malformation in utero, schizencephaly has been reported in familial cases and in early prenatal injury from drug abuse and abdominal trauma, vascular insult, or toxin.[67] It causes gray matter–lined clefts that extend through the entire hemisphere, from the ependymal lining of the lateral ventricles to the pial covering of the cortex. The clefts may be bilateral or unilateral (Fig. 45.31). There may be wide openings of the clefts **(open-lip schizencephaly).** In some cases the cleft is closed **(closed-lip schizencephaly)** and may require MRI for diagnosis, because gray matter–white matter differentiation is not well demonstrated on sonography. Most of these patients develop seizures, hemiparesis, and variable developmental delay. The severity is related to the amount of brain involved. Some patients with schizencephaly

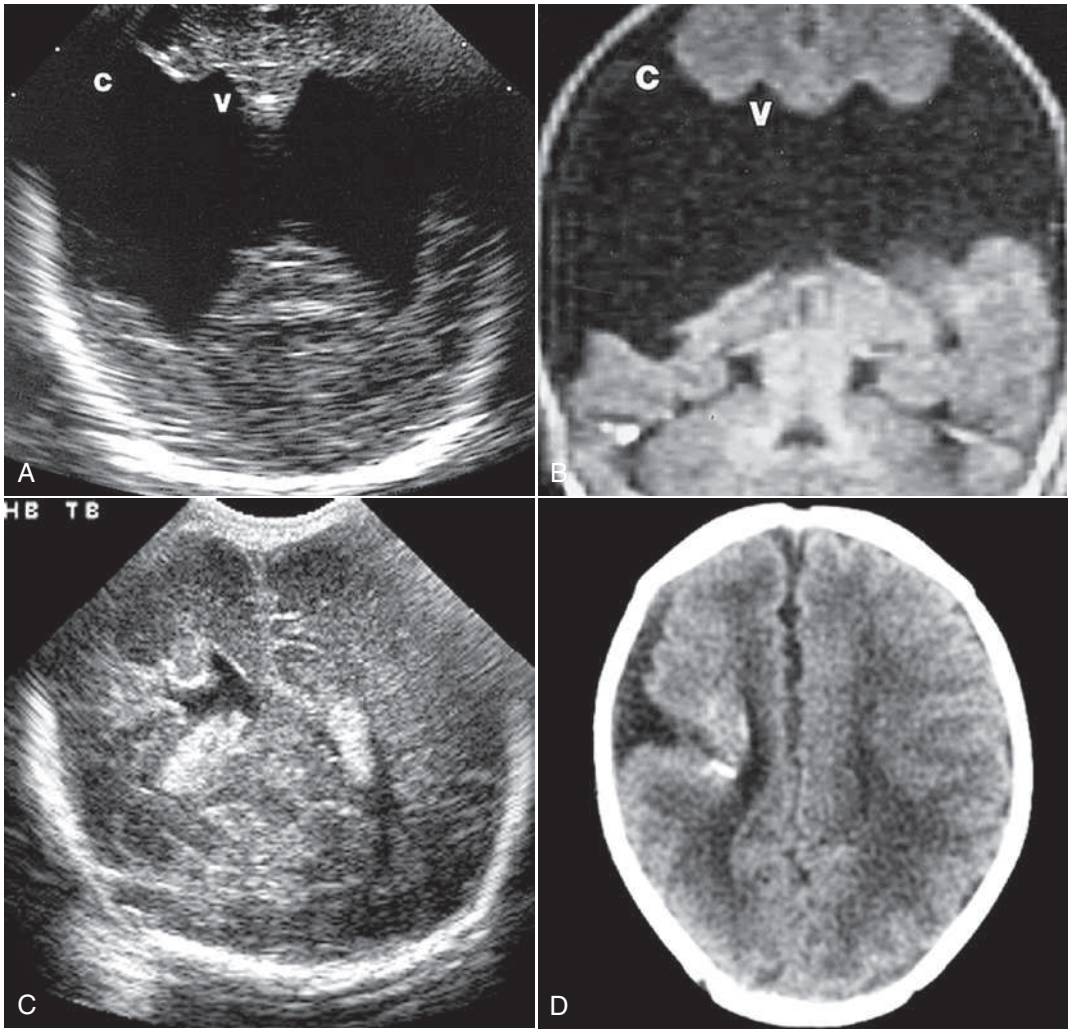

FIG. 45.31 Schizencephaly. (A) Coronal sonogram and **(B)** coronal magnetic resonance image of open-lip schizencephaly show bilateral clefts *(c)* with wide openings to the ventricular *(v)* system. **(C)** Sonogram and **(D)** computed tomography image show closed-lip schizencephaly with calcification from in utero infection.

have blindness, thought to be related to absence of the septum pellucidum and associated optic nerve hypoplasia. This is thought to be an acquired septo-optic dysplasia. There are genetic cases from the *EMX2* homeobox gene[31] and other patients with possible in utero injury during the second trimester. **Cytomegalovirus** (CMV) has been reported to cause schizencephaly as would be expected for those maternal infections that occur in the first trimester at the time of initial brain development.[68,69] In patients with unilateral involvement, recent reports show reorganization of the motor area so that the unaffected hemisphere takes over function.[70]

Lissencephaly

Complete lack of sulcal formation caused by lissencephaly can be recognized on ultrasound when the sulcal pattern does not match that expected for gestational age. Hourglass or "figure 8" has been described as typical of the cortical surface. The sylvian fissures are often open owing to failure of the opercularization process.[30-33] The arrested myelination results in only four layers of cortex and a smooth brain. Because these patients typically have microcephaly, it is important to study these patients very carefully. Although lissencephaly is associated with many genetic syndromes, CMV and other infections have also been reported to cause lissencephaly.

DESTRUCTIVE LESIONS

Porencephalic Cyst

Before 26 weeks' gestation, focal brain destruction will typically heal with dysplastic gray matter and result in schizencephaly, usually associated with migrational defects.[42] After 26 weeks' gestation, a porencephalic cyst will develop in an area of normally developed brain that has been damaged and heals with scarring because of a lining of gliotic white matter. By definition, porencephalic cysts always connect with the ventricular system but do not extend to the surface cortex. They usually occur after birth, secondary to intraparenchymal hemorrhage (IPH), infection (focal vasculitis, abscess), or trauma.

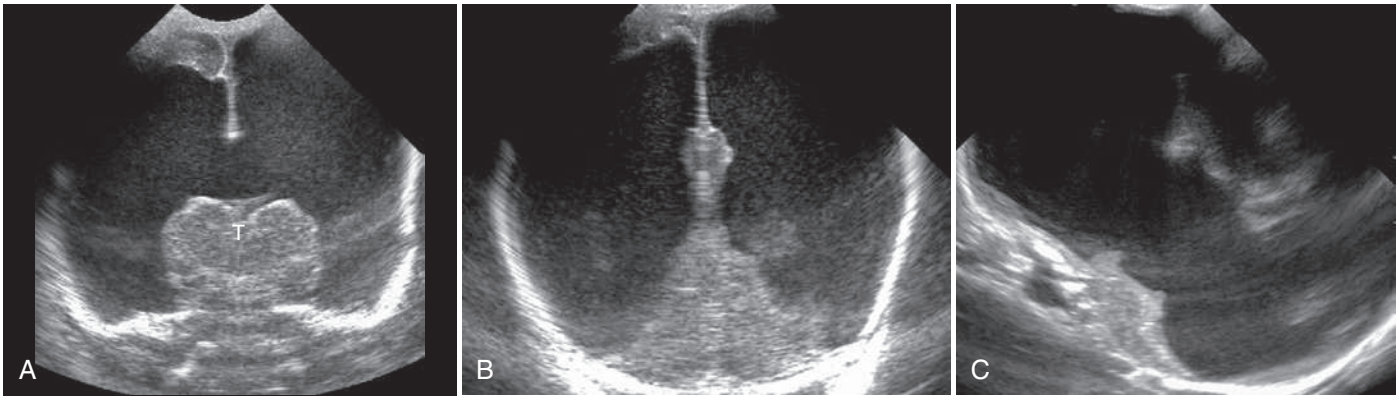

FIG. 45.32 Hydranencephaly Versus Severe Ventriculomegaly. (A) and **(B)** Coronal anterior. **(C)** Midline sagittal. Note that only cerebrospinal fluid is seen above thalamus *(T),* except for a small amount of tissue in the right high parietal region. This at first looks like holoprosencephaly, but an echogenic falx is seen in the midline.

Hydranencephaly

Classically, hydranencephaly is believed to be caused by bilateral occlusion of the internal carotid arteries during fetal development, but it may result from any of several intracranial destructive processes[71] (Fig. 45.32). Hydranencephaly is the severest form of porencephaly in that there is almost total destruction of the cerebral cortex.[72] These infants may appear surprisingly normal at birth but are developmentally delayed from an early age and frequently die within the first year of life.

The sonographic findings include a calvaria filled with CSF, but little else. Structures that receive their blood supply from the posterior cerebral artery and vertebral artery, such as the thalamus, cerebellum, brainstem, and posterior choroid plexus, are spared and are usually identifiable. Blood flow will not be appreciated by color or spectral Doppler in the carotid arteries. An incomplete or complete falx may be identifiable. The presence of the falx helps differentiate this lesion from alobar holoprosencephaly, in which the falx does not form. It can be difficult to differentiate hydranencephaly from severe hydrocephalus, but a thin rim of cortex should be visualized by sonography in hydrocephalus.[72] If there is an enlarging head circumference, ventriculoperitoneal shunting may be indicated, regardless of the actual diagnosis, to control CSF accumulation and severe skull enlargement.

Cystic Encephalomalacia

Encephalomalacia is an area of focal brain damage that pathologically has astrocytic proliferation and glial septations. In diffuse brain damage, there may be large areas of cystic encephalomalacia (Fig. 45.33). The location of the damage depends on the type of insult. Typically, there is no connection to the ventricular system. In neonates, infection or anoxia can cause widespread damage, whereas a thrombus may cause focal damage.

Metabolic Disorders

A wide range of abnormalities are seen on neonatal brain ultrasound in metabolic disorders,[73] including cysts, calcifications, structural brain abnormalities, and white matter echogenicity. Significant hypoglycemia can manifest in the first 3 days of life with seizures. Hyperechoic areas of the brain are seen in the posterior parietal regions bilaterally—not in the typical watershed areas.[53]

HYDROCEPHALUS

Hydrocephalus results from an imbalance between CSF production and its drainage by the arachnoid villi. Hydrocephalus can result from **intraventricular obstruction,** when CSF flow is obstructed within the ventricular system, or from **extraventricular obstruction** to CSF circulation, which occurs within the subarachnoid spaces and cisterns or is secondary to decreased CSF absorption at the arachnoid villi in the sagittal sinus. **Overproduction** of CSF from a choroid plexus papilloma is an unusual cause. Other causes include venous obstruction or vascular malformations; vein of Galen malformation often obstructs. The most common causes of **intraventricular obstructive hydrocephalus** (IVOH) include infection or hemorrhage (causing obstruction to the exiting foramina of the third or fourth ventricle), congenital anomalies (e.g., aqueductal stenosis [Fig. 45.34], Dandy-Walker malformation), and tumors. Aqueductal stenosis occurs in males from an X-linked gene *(L1-CAM)* and may be diagnosed by about 18 weeks of gestation with hydrocephalus and adducted thumbs.[74] The most common causes of **extraventricular obstructive hydrocephalus** (EVOH) are hemorrhage and infection with fibrosis at the basal cisterns, incisura, convexity cisterns, or parasagittal region.

Cerebrospinal Fluid Production and Circulation

CSF provides a chemically controlled protective environment that continually bathes and circulates around the CNS. Although mainly produced by the choroid plexus, CSF is also produced by the ventricular ependyma, the intracranial subarachnoid lining, and the spinal subarachnoid lining. CSF normally flows from the lateral ventricles, through the foramina of Monro, third ventricle, aqueduct of Sylvius, fourth ventricle, lateral foramina of Luschka or medial foramen of Magendie, and into the basal cisterns. From there, a small quantity circulates down into the

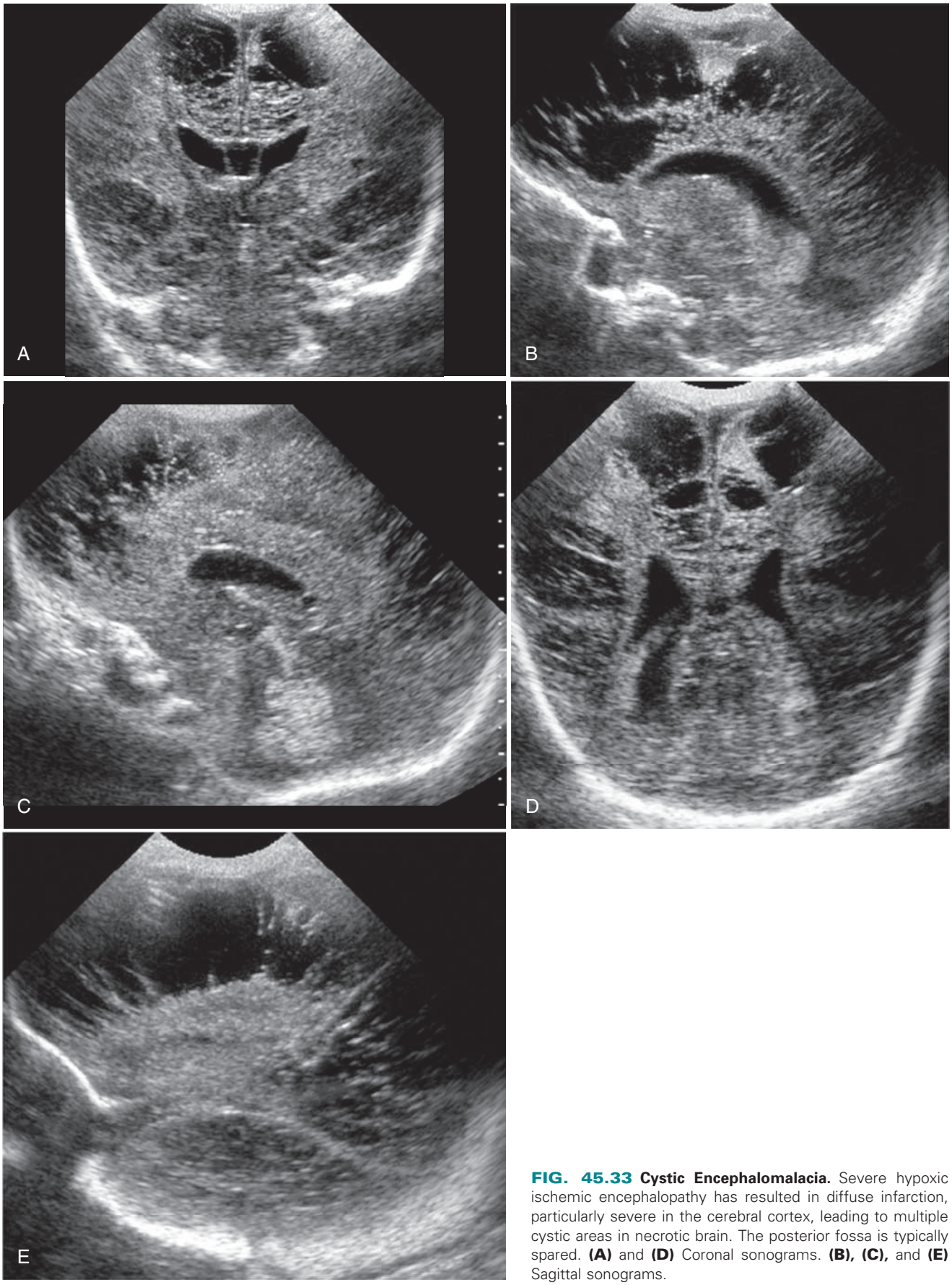

FIG. 45.33 Cystic Encephalomalacia. Severe hypoxic ischemic encephalopathy has resulted in diffuse infarction, particularly severe in the cerebral cortex, leading to multiple cystic areas in necrotic brain. The posterior fossa is typically spared. **(A)** and **(D)** Coronal sonograms. **(B), (C),** and **(E)** Sagittal sonograms.

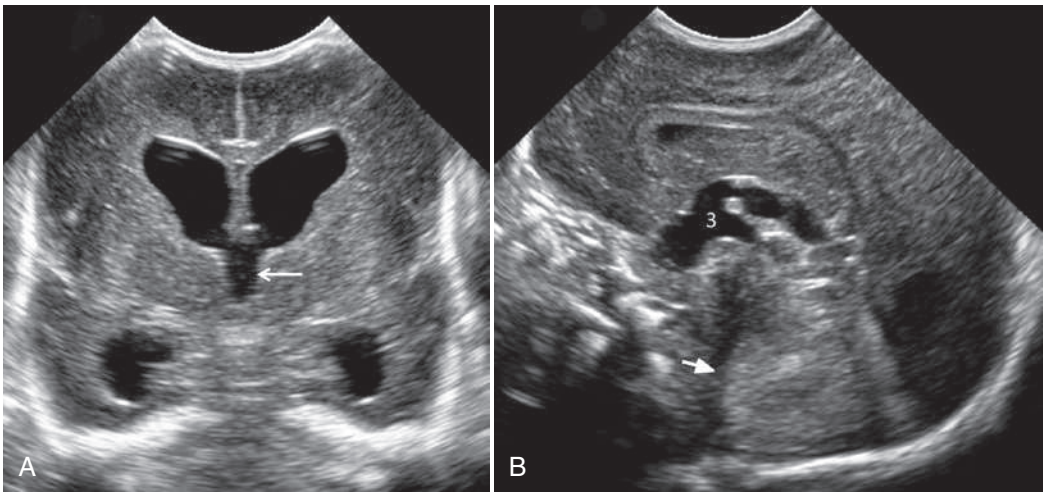

FIG. 45.34 Aqueductal Stenosis. (A) Coronal sonogram shows dilation of lateral ventricles and third ventricle *(arrow).* **(B)** Sagittal midline sonogram shows marked third ventricle *(3)* dilation and normal fourth ventricle *(short arrow).*

spinal subarachnoid space. CSF flows upward around the brain anteriorly and posteriorly to reach the vertex, where it is resorbed by the arachnoid granulations into the superior sagittal sinus.

Hydrocephalus often can be diagnosed in utero by 15 weeks' gestation.[75-77] The size of the atrium of the ventricle and the glomus of the choroid plexus remains constant in the second and third trimesters in the transaxial plane. In utero an upper limit of 10 mm for the ventricular atrium has been established and well reviewed.[78,79] However, ventricles can be enlarged (ventriculomegaly) owing to a dysgenetic process involving the white and/or gray matter rather than a fluid imbalance. Once hydrocephalus is recognized, close inspection for spinal dysraphism and other CNS or extra-CNS anomalies is warranted. Chromosome evaluation is often recommended if other anomalies are recognized. Signs of the Chiari II malformation should be especially sought because this is associated with a myelomeningocele in almost 100% of cases.

Neonatal hydrocephalus is easily recognized by routine coronal and sagittal imaging.[78,79] Ventricular size is slightly larger in premature newborns than in term infants. Progression of hydrocephalus can best be estimated by comparison with previous studies. Sonography is also helpful in following ventricular decompression in patients shunted for hydrocephalus. In following ventricular size in cases of hydrocephalus, care must be taken so that changes in ultrasound sector depth do not result in apparent enlargement or decompression of the ventricles related to magnification differences when different depth scales are used.

Level of Obstruction

Asymmetry of the lateral ventricles can cause a ventricle to be slightly larger as a normal variant. The entire ventricular system should be evaluated to identify the level at which a transition occurs from a large to a small ventricle.[80] Dilation of the lateral and third ventricles indicates an aqueduct of Sylvius obstruction, often an X-linked recessive trait, and at times caused by IVH. The rare case of isolated dilation of the fourth ventricle also requires ventricular system evaluation. Dilation of all ventricles suggests an extraventricular source.

Causes of Hydrocephalus

INTRAVENTRICULAR OBSTRUCTION
Posthemorrhagic
Aqueductal obstruction
Fourth ventricle obstruction
Posterior fossa subdural hematoma
Chiari II malformation
Dandy-Walker malformation
Aqueductal stenosis
Postinfectious scarring
Vein of Galen malformation
Tumor or cyst

EXTRAVENTRICULAR OBSTRUCTION
Posthemorrhagic scarring
Postinfectious scarring
Achondroplasia
Absence or hypoplasia of arachnoid granulations
Venous obstruction

OVERPRODUCTION OF CEREBROSPINAL FLUID
Choroid plexus papilloma

Ventricular enlargement does not always mean obstruction. Severe cases of **hypoxic-ischemic injury** result in large ventricles due to brain atrophy 2 to 4 weeks after the insult rather than obstructive hydrocephalus. One rare cause of ventricular enlargement is **glutaric aciduria type 1.**[81] These patients actually have macrocephaly at birth or within the first few weeks of life. Cystlike bilateral widening of the sylvian fissures may be the first sign, followed by progressive frontotemporal subarachnoid and ventricular enlargement, thought to be caused by atrophy. If glutaric aciduria is diagnosed in early infancy, rigorous dietary control may allow normal neurologic development. Some believe that the cystic changes represent focal areas of edema causing the macrocephaly and later atrophy as the head size becomes

smaller, apparently from brain destruction. It is essential to recognize this pattern and test for glutaric aciduria.

HYPOXIC-ISCHEMIC EVENTS

Hypoxic-ischemic events in the neonate can be divided into maternal causes and causes attributable to the neonate. **Maternal causes** include chronic cardiac or pulmonary lung disease, placental insufficiency, shock, placental abruption, and cardiorespiratory arrest, all of which can cause severe birth asphyxia. An uncommon cause is maternal cocaine use.[82] Some **therapeutic maneuvers** in these extremely sick, hypoxic neonates have also been associated with an increased risk for GMH secondary to increased venous obstruction.[83] Increased venous pressure has been demonstrated in infants breathing out of sequence with a mechanical ventilator, during endotracheal tube suctioning, and with high peak inspiratory pressure.[84] Tension pneumothorax, exchange transfusions, rapid infusions of colloid, and myocardial injury caused by asphyxia are other factors that may greatly affect hemodynamics and venous pressure.[84-86]

Arterial Watershed Determines Regional Pattern of Brain Damage

The sonographic findings are varied depending on the cause and the age of the neonate when the hypoxic-ischemic event occurs, because the watershed areas of the brain change in location during the last trimester[46,87] (Table 45.1). In premature infants the watershed is in the immediate periventricular region, and thus **GMH** and **PVL** are common pathologic findings. With the advantage of MRI examinations, noncystic forms of white matter injury have been increasingly diagnosed in premature infants that extend beyond the periventricular space to affect the diffuse cerebral white matter, thalamus, basal ganglia, brainstem, and cerebellum.[46] In full-term infants, damage tends to occur more in the cortical or subcortical regions, because the watershed moves to these areas more toward the brain surface, resulting in **parasagittal infarction** regions in term infants.[88] How to study hypoxic-ischemic encephalopathy (HIE) depends on the brain maturity and stability of the newborn infant. Findings at MRI complement ultrasound and may more often predict noncystic white matter lesions.[89-93]

Lack of autoregulation of cerebral blood pressure, which typically occurs in premature infants and less often in asphyxiated full-term infants, will cause cerebral perfusion to be directly affected by hypertensive or hypotensive episodes. This pressure-passive system can result in sudden focal hemorrhage or, with hypotension, diffuse or focal infarction.

The neurologic manifestations of brain injury in the premature infant range from the less severe motility and cognitive deficits to major spastic motor deficits, including spastic diplegia and spastic quadriplegia with more profound intellectual deficits. In the full-term infant the hypoxic-ischemic events may manifest as seizures, movement disorders including arching and fisting, altered tone, absent suck, and, depending on the severity, intellectual deficits.

TABLE 45.1 Patterns of Hypoxic-Ischemic Injury in Newborns

Hypotension	Premature Infant	Term Infant
Mild to moderate	GMH or periventricular hemorrhagic infarction White matter injury of prematurity (WMIP a.k.a. PVL)	Parasagittal cortical or subcortical injury
Severe	Deep gray matter Brainstem and cerebellar infarct	Lateral thalamus Posterior putamen hippocampus Corticospinal and sensorimotor tracts

WMIP formerly periventricular leukomalacia (PVL) has more extensive injury into cerebral white matter and cortex, thalamus, basal ganglia, brainstem, and cerebellum.
GMH, Germinal matrix hemorrhage.
Modified from Volpe JJ. Brain injury in premature infants: a complex amalgam of destructive and developmental disturbances. Lancet Neurol. 2009;8(1):110-124.[46]

Germinal Matrix Hemorrhage

GMH may lead to **IVH, hydrocephalus,** and **porencephaly.** GMH is a common event that occurs primarily in premature infants less than 32 weeks' gestational age. Although the incidence once was as high as 55%, most nurseries have experienced a significant drop in GMH, such that the range is now 10% to 25% in very-low-birth-weight infants (<1000 g) in most neonatal intensive care units.[94,95] Infants at greatest risk are those at gestational ages of less than 30 weeks, with birth weight less than 1500 g, or both.[96] Severe grades of hemorrhage with hydrocephalus (grade III) and IPH (grade IV) have stabilized at about 11%, according to a large outcome study of very-low-birth-weight infants (<1500 g) by the National Institute of Child Health and Human Development (NICHD).[97]

Multiple factors are associated with GMH, including prematurity with complications caused by altered cerebral blood flow such as hypoxia, hypertension, hypercarbia, hypernatremia, rapid volume increase, and pneumothorax.[84-86] Other causes include increases in cerebral venous pressure at delivery, congestive heart failure, increased ventilator pressures, and coagulopathies.[53] Factors associated with decreased incidence of GMH include increased use of antenatal steroids[98,99] and improved neonatal respiratory care, such as the effective use of high-frequency ventilators, oscillators, and surfactant, which decrease pressure to the lung.

GMH originates below the subependymal layer and may be contained by the ependyma or may rupture into the ventricular system or less often into the adjacent parenchyma and thus can

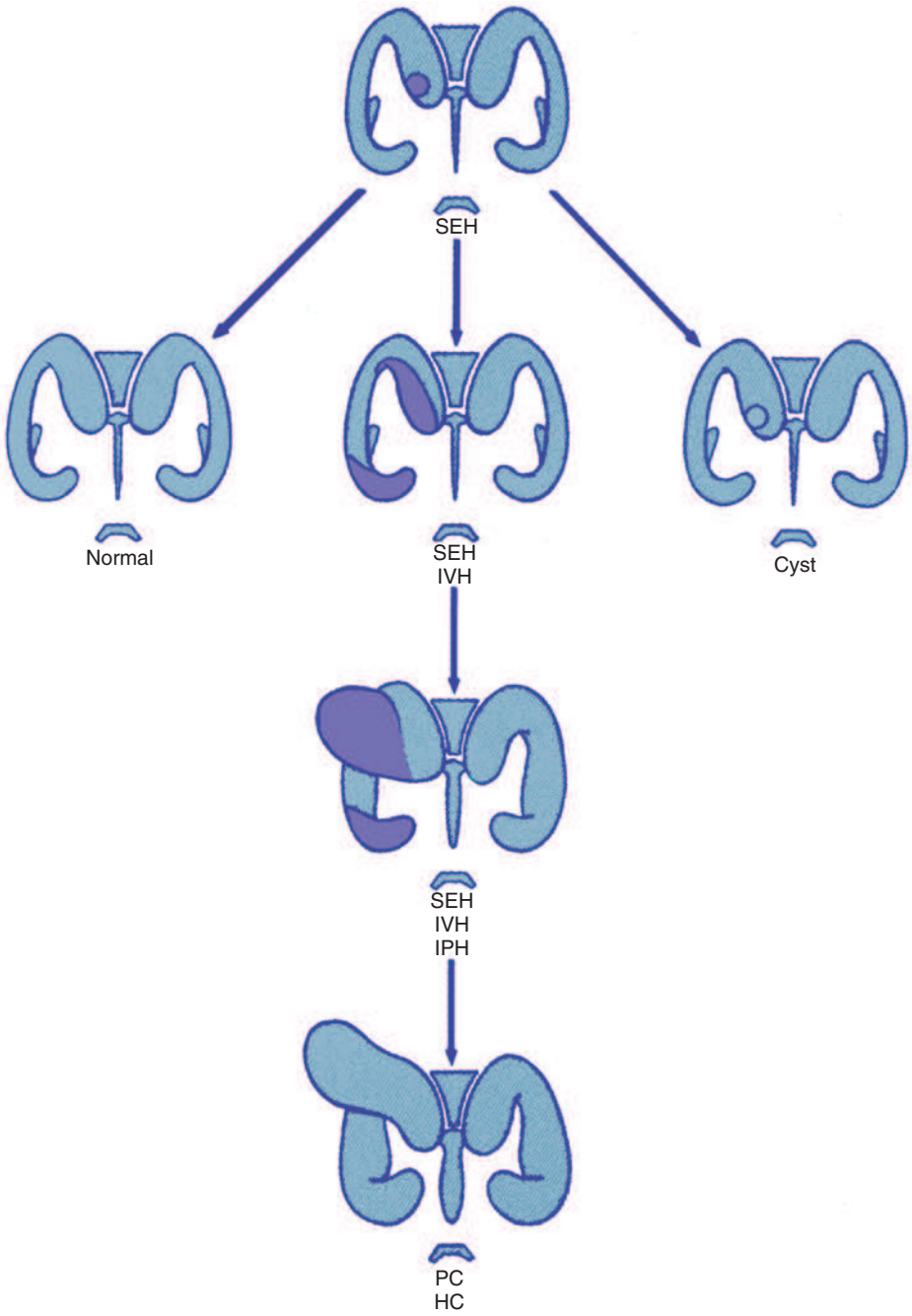

FIG. 45.35 Sequelae of Subependymal Hemorrhage *(SEH).* SEH may resolve, leaving a normal scan; may resolve, leaving a small subependymal cyst; or may progress, rupturing into the ventricle, causing intraventricular hemorrhage *(IVH),* or extending into the parenchyma, causing intraparenchymal hemorrhage *(IPH).* Hydrocephalus *(HC)* and porencephaly *(PC)* are common sequelae of SEH. (With permission from Rumack CM, Manco-Johnson ML. Perinatal and infant brain imaging: role of ultrasound and computed tomography. St Louis: Mosby; 1984.[7])

manifest as subependymal hemorrhage (SEH), IVH, or IPH[100] (Fig. 45.35). The **germinal matrix** is a fine network of blood vessels and primitive neural tissue that lines the ventricular system in the subependymal layer during fetal life. As the fetus matures, the germinal matrix regresses toward the foramen of Monro so that, by full term, only a small amount of germinal matrix is present in the caudothalamic groove between the thalamus and the caudate nucleus. This fine network of blood vessels is highly susceptible to pressure and metabolic changes, which can lead to rupture of the vessels. The germinal matrix is rarely a site of hemorrhage after 32 weeks' gestation because it has almost disappeared. Thus full-term infants rarely experience this type of hemorrhage.

The classification of GMH most widely used was proposed by Burstein and colleagues.[100] Other systems are used as well, but the **anatomic description** of exactly where the brain damage

occurs is more important than the classification. The key causes of poor neurologic outcome relate to hydrocephalus and parenchymal extension into the descending white matter tracts (Table 45.2).

Sonography is the most effective method for detecting this hemorrhage in the newborn period and for follow-up in the subsequent weeks. Most hemorrhage (90%) occurs in the first 7 days of life, but only one-third of these occur in the first 24 hours.[101] The optimal cost-effective timing to screen premature infants is at 10-14 days of life, to identify patients with significant hemorrhage as well as those developing hydrocephalus.[102] Small SEHs (grade I) might be missed when screening late if they resolve quickly, but these have not proven clinically important. A late screen for PVL should performed at 1 month to search for the cystic changes of PVL,[103,104] because the clinical course or first brain ultrasound will not predict the later development of hydrocephalus or PVL. An examination should be performed earlier if required by the patient's condition. Term-equivalent age studies with MRI are now frequently done to determine the extent of damage. Careful recent studies with ultrasound done at term-equivalent age by Daneman and colleagues[3] have demonstrated that many of the noncystic findings can be identified with high-resolution transducers focused on the brain parenchyma in areas that are not periventricular where the noncystic WMIP occurs.

TABLE 45.2 Grades of Germinal Matrix Hemorrhage

Grade	Type and Description
I	Subependymal hemorrhage
II	Intraventricular extension without hydrocephalus
III	Intraventricular hemorrhage with hydrocephalus
IV	Intraparenchymal hemorrhage with or without hydrocephalus

Optimal Brain Ultrasound Screening in Premature Infants (Less Than 30 Weeks' Gestation or Less Than 1500 g)

FIRST SCAN: 10 TO 14 DAYS
Germinal matrix hemorrhage
Posthemorrhagic hydrocephalus

SECOND SCAN: 4 WEEKS OF AGE
Cystic PVL
Cystic PVL lesions coalesce, leaving only thin white matter after 4 weeks
Ventricular enlargement

THIRD SCAN: TERM-EQUIVALENT AGE
White matter injury of prematurity (beyond only PVL)
Best seen by ultrasound or magnetic resonance imaging

PVL, Periventricular leukomalacia.

Complications of SHE and IVH are IVOH, usually at the foramina of Monro or the sylvian aqueduct, and EVOH, at the arachnoid granulations. Complications of IPH are permanent areas of damaged brain that can become necrotic, leading to porencephalic cysts.

Subependymal Hemorrhage (Grade I Hemorrhage)

On sonographic examination, acute SEH appears as a homogeneous, moderately to highly echogenic mass (Fig. 45.36). The echogenic clot often causes focal hemorrhage in the caudothalamic groove. The choroid plexus is normally quite thick at the trigone of the lateral ventricle and tapers progressively anteriorly, descending between the head of the caudate and the thalamus just above the foramen of Monro. SEH may appear as a bulge in the choroid plexus (Fig. 45.37, Video 45.9 and Video 45.10). As the hematoma ages, the clot becomes less echogenic, with its center becoming sonolucent. Over time the clot retracts, and necrosis

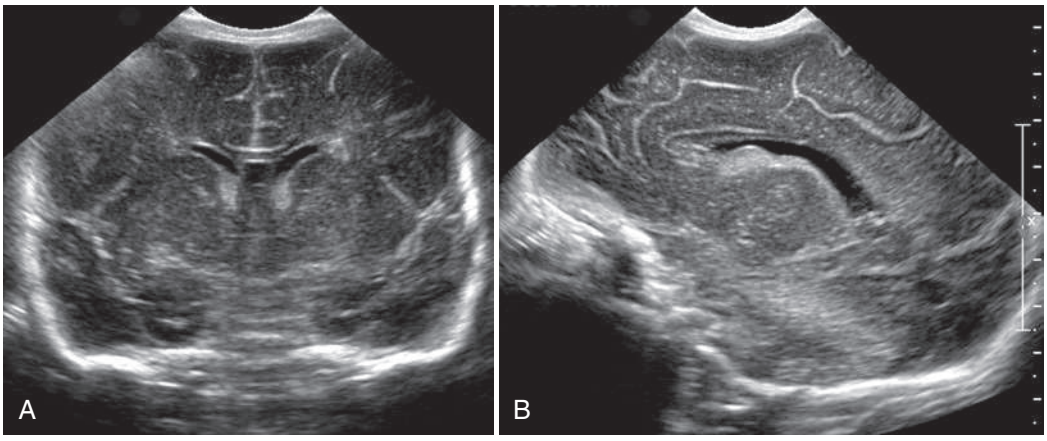

FIG. 45.36 Subependymal Hemorrhage (SEH), Bilateral. (A) Coronal sonogram shows echogenic SEH bilaterally. **(B)** Parasagittal sonogram shows the hemorrhage located in the caudothalamic notch. See also Video 45.9 and Video 45.10.

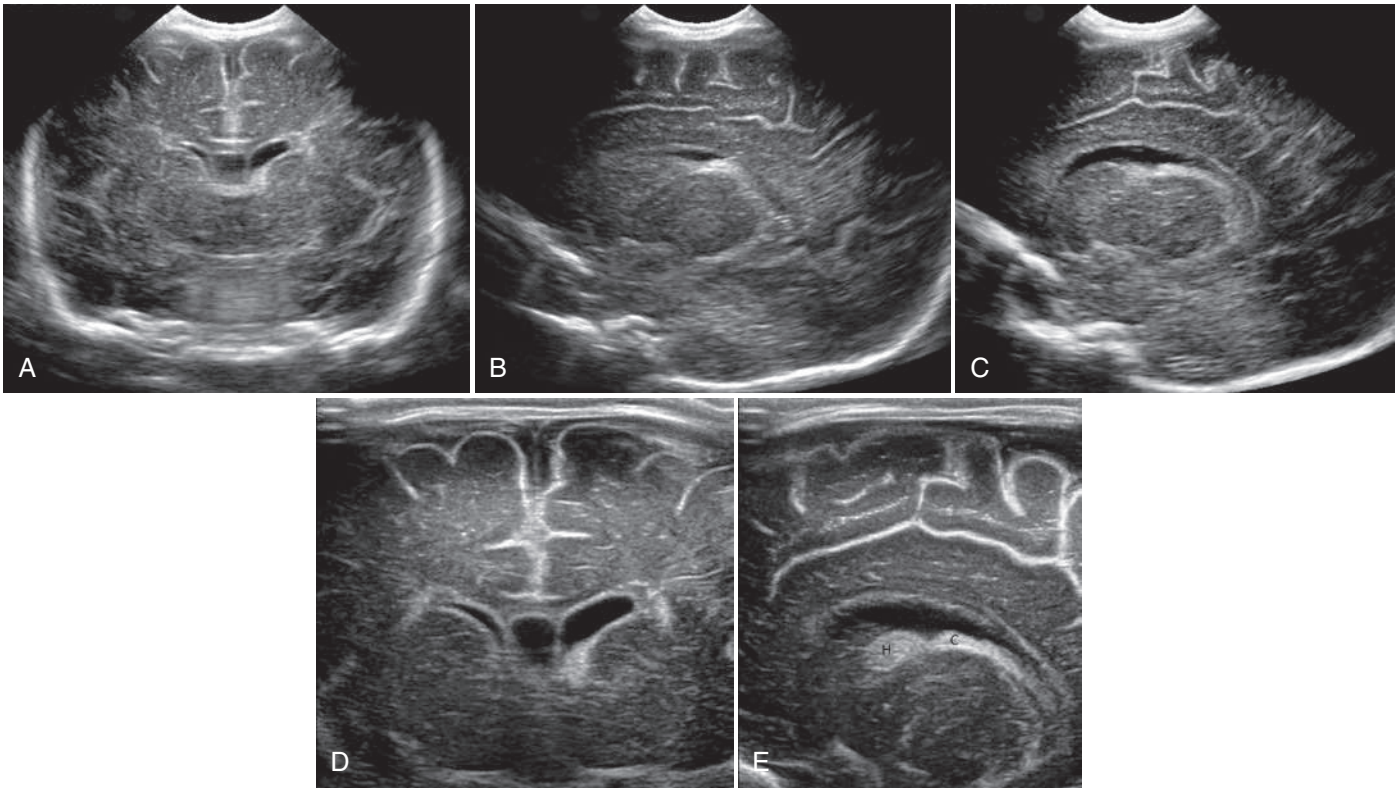

FIG. 45.37 Subependymal Hemorrhage (SEH), Unilateral. (A) Coronal sonogram showing a subtle unilateral SEH. **(B)** Parasagittal sonogram of normal caudothalamic notch. **(C)** Parasagittal sonogram of SEH. **(D)** Coronal sonogram obtained with a higher frequency linear transducer clarifies the SEH. **(E)** Parasagittal sonogram obtained with linear transducer shows the SEH *(H)* clearly separate from the choroid plexus *(C)*.

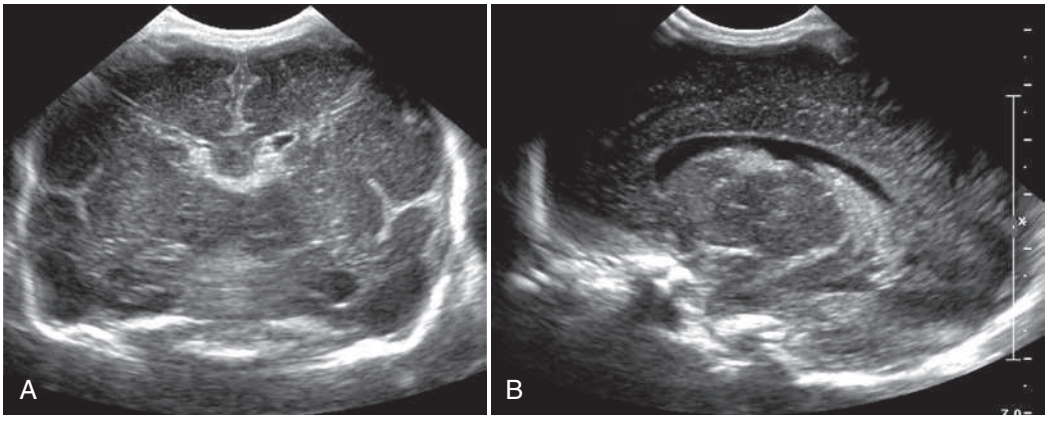

FIG. 45.38 Intraventricular Hemorrhage. (A) and **(B)** Coronal and sagittal sonograms show intraventricular hemorrhage from bilateral SEH breaking into the lateral ventricles.

occurs with complete resolution of hemorrhage or occasionally development of a **subependymal cyst.** SEH may persist as a linear echo adjacent to the ependyma. Hemorrhage is still evident for months on MRI but becomes isodense on CT at about 10 days so that these comparison studies may suggest different findings.

Intraventricular Hemorrhage (Grade II Hemorrhage)

When SEH bursts into the lateral ventricle, IVH appears as hyperechoic clot that fills a portion of the ventricular system or all of a ventricle when the clot forms a cast of the ventricle (Fig. 45.38). The clot itself may obscure the ventricle owing to complete filling of the lumen. The normally thick, echogenic choroid plexus may appear asymmetrically thick and may be difficult to define within the ventricle separate from the densely echogenic hemorrhage (Fig. 45.39). As the clot matures, it becomes echolucent centrally and more well defined and separable from the more echogenic choroid plexus. Low-level echoes from debris floating in a ventricle may occur as the clot breaks apart. Use of the posterior fontanelle or mastoid fontanelle axial views will increase the detection of IVH in normal-sized ventricles, because at times there are only small clots or **CSF-blood fluid levels** in the occipital horn (Fig. 45.39D-E).

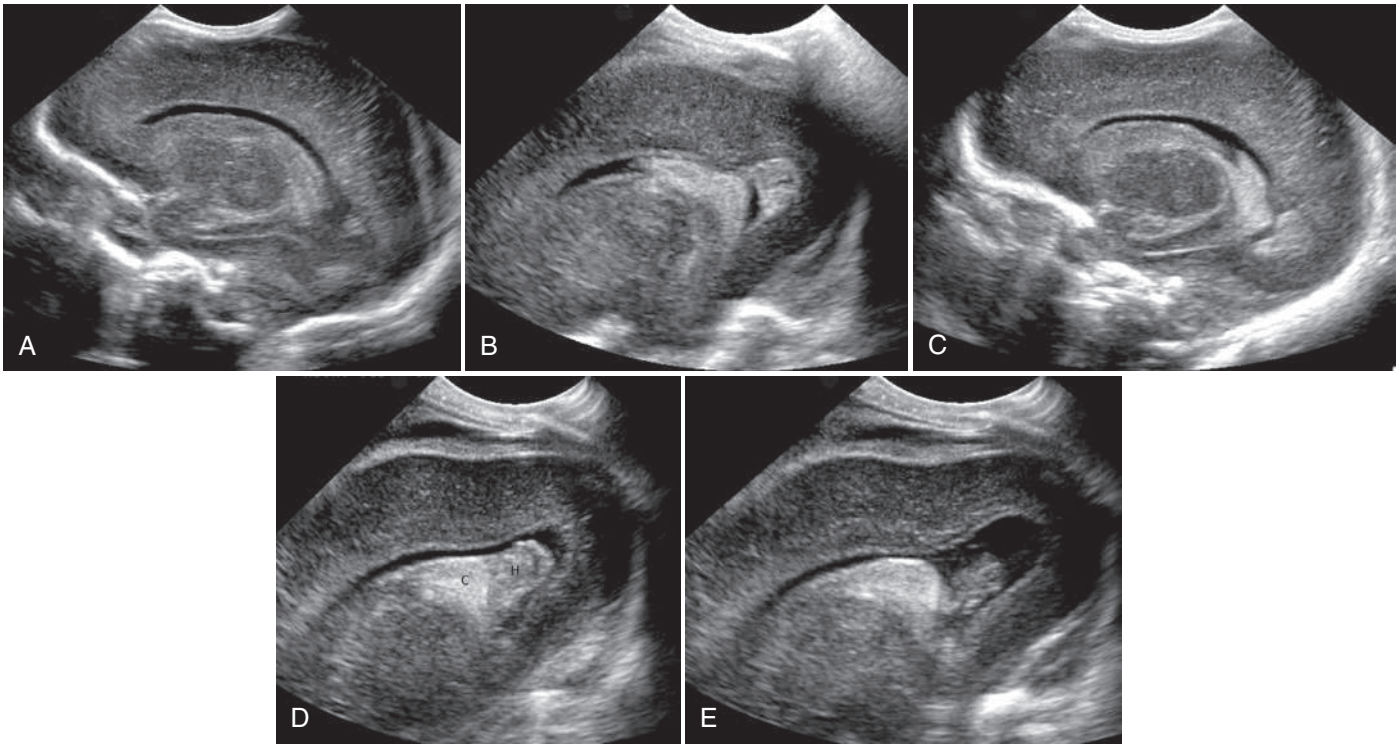

FIG. 45.39 Intraventricular Hemorrhage: Anterior and Posterior Fontanelle in Two Neonates. *Neonate 1:* **(A)** Sagittal sonogram through the anterior fontanelle shows intraventricular hemorrhage within the occipital horn. **(B)** Occipital horn hemorrhage better visualized through the posterior fontanelle. *Neonate 2:* **(C)** Sagittal sonogram through the anterior fontanelle vaguely shows clot in occipital horn. **(D)** Sagittal sonogram through the posterior fontanelle clearly shows hemorrhage *(H)* and choroid plexus *(C)* better than the previous image. **(E)** Hemorrhage seen separate from the choroid plexus. Note how the echogenicity of the clot is lower than that of the choroid plexus in neonate 2, suggesting older hemorrhage than that seen in neonate 1.

Signs of Intraventricular Hemorrhage

Hyperechoic material fills portion of ventricular system
Clot forms a cast of the ventricle
  May obscure ventricle because lumen completely filled
Thick, echogenic choroid plexus
Echolucent centrally later, as clot matures
Low-level echoes floating in a ventricle
Cerebrospinal fluid–blood fluid levels

Blood in the third or fourth ventricle may be missed and is much more clearly identified on posterior fossa ultrasound with mastoid views. If the blood extends into the subarachnoid space and cisterna magna, there is an increased risk for posthemorrhagic hydrocephalus[105,106] (Fig. 45.40, Video 45.11 and Video 45.12). **Cisterna magna clot** is a better predictor of posthemorrhagic hydrocephalus than initial hydrocephalus. Early-onset IVH, in the first 6 hours of life, is uncommon and is associated with a higher risk for both cognitive and motor impairment, including cerebral palsy.[107] Neurodevelopmental outcomes in extremely premature infants have shown increased rates of neurosensory impairment, developmental delay, cerebral palsy, blindness, and deafness at 2 to 3 years corrected age in an Australian cohort study,[108] even when the original injury was grade 1 or II IVH.

Intraventricular Hemorrhage With Hydrocephalus (Grade III Hemorrhage)

The ventricular enlargement that occurs after IVH allows for clear visualization of clot, which often assumes a dependent location but may be adherent to ventricular walls and/or choroid plexus (Figs. 45.41 and 45.42, Video 45.13, Video 45.14, Video 45.15). Change in position may lead to change in location of mobile clot. Posterior fontanel le images may show IVH in the occipital horn in subtler cases. As with SEH, in time the echogenic clot will become more echolucent centrally and may eventually resolve. A **chemical ventriculitis** as a response to blood in the CSF typically causes thickening and increased echogenicity of the subependymal lining of the ventricle. Posthemorrhagic hydrocephalus may require shunting if it is progressive. Follow-up scans should be obtained weekly unless the head grows rapidly or another crisis intervenes. Typically, the most severe degree of hydrocephalus occurs after several weeks. As the blood clears from the ventricles, particularly with a block at the aqueduct, the ventricular size may return to normal. In one series, posthemorrhagic ventricular dilation required surgical treatment with a ventriculoperitoneal reservoir or shunt in only 34% of very-low-birth-weight infants with hydrocephalus.[109] Another series reported a marked decrease in both temporary and permanent shunts in extremely low-gestational-age newborns, such that only 16% of these infants required a permanent shunt after

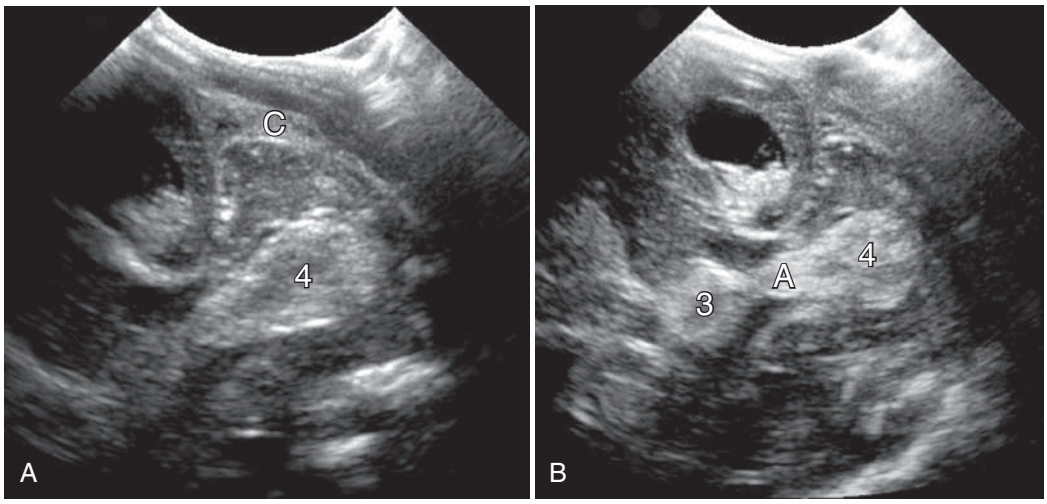

FIG. 45.40 Cisterna Magna and Fourth Ventricle Clot. (A) Axial sonogram shows echogenic clot within the cisterna magna *(C)* and fourth ventricle *(4)*. **(B)** Expansive clot within the aqueduct of Sylvius *(A)* between the third *(3)* and fourth *(4)* ventricles.

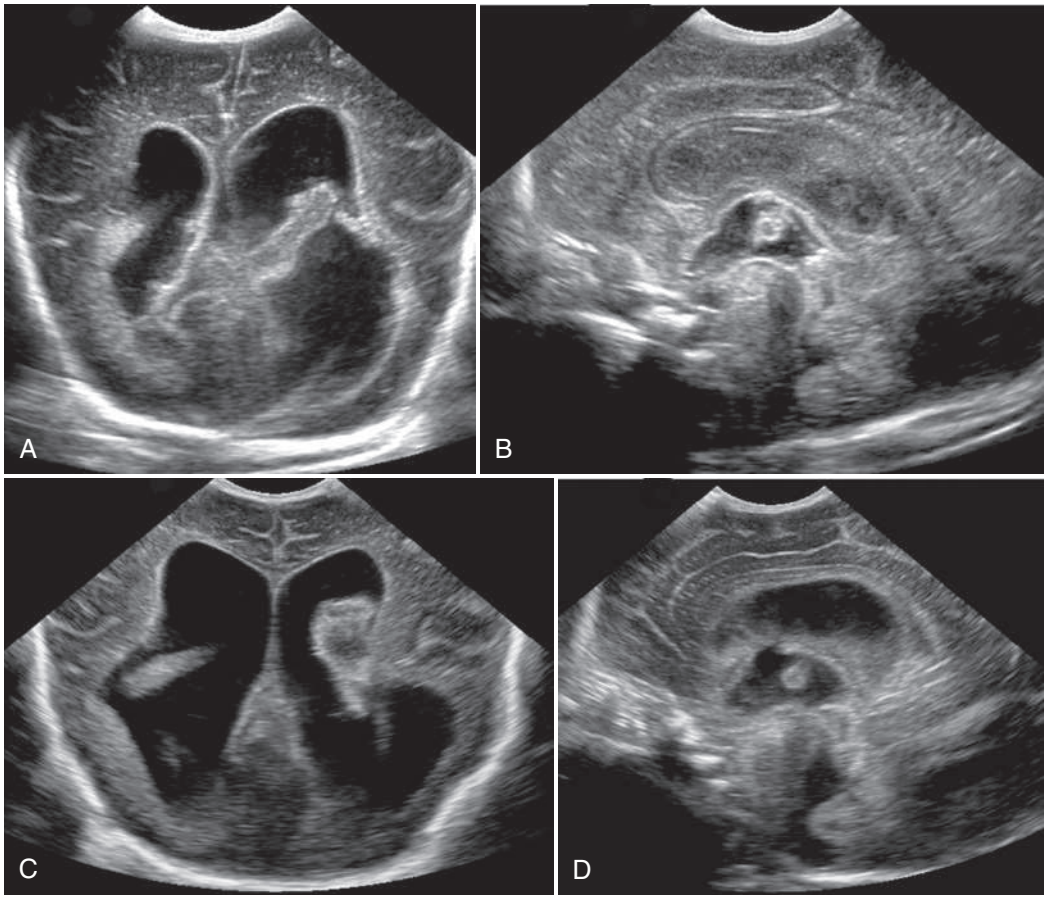

FIG. 45.41 Intraventricular Hemorrhage and Hydrocephalus. (A) and **(B)** Coronal and sagittal sonograms show enlarged lateral ventricles and third ventricle; clot is causing intraventricular obstructive hydrocephalus. Note the echogenic lining of the lateral ventricles due to ventriculitis associated with the hemorrhage. **(C)** and **(D)** Coronal and sagittal sonograms shows extraventricular obstructive hydrocephalus; the lateral ventricles, third ventricle, and fourth ventricle are all enlarged.

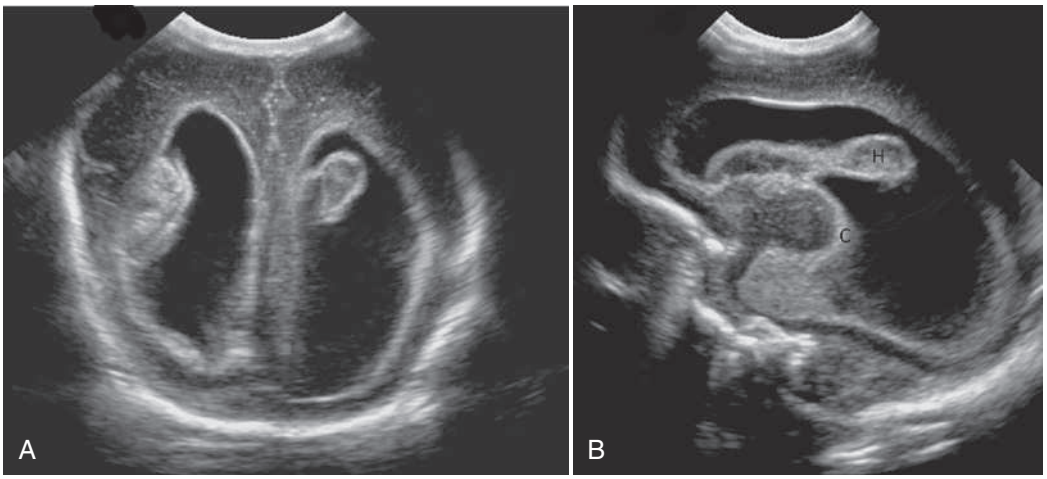

FIG. 45.42 Intraventricular Hemorrhage: Dependent Clot. (A) Coronal sonogram shows dependent clot in an infant with the right side of the head down. **(B)** Sagittal sonogram of the left lateral ventricle shows dependent clot *(H)* separate from the choroid plexus *(C)*. Note also the extensive echogenicity lining the ventricles, likely due to ventriculitis and blood clot.

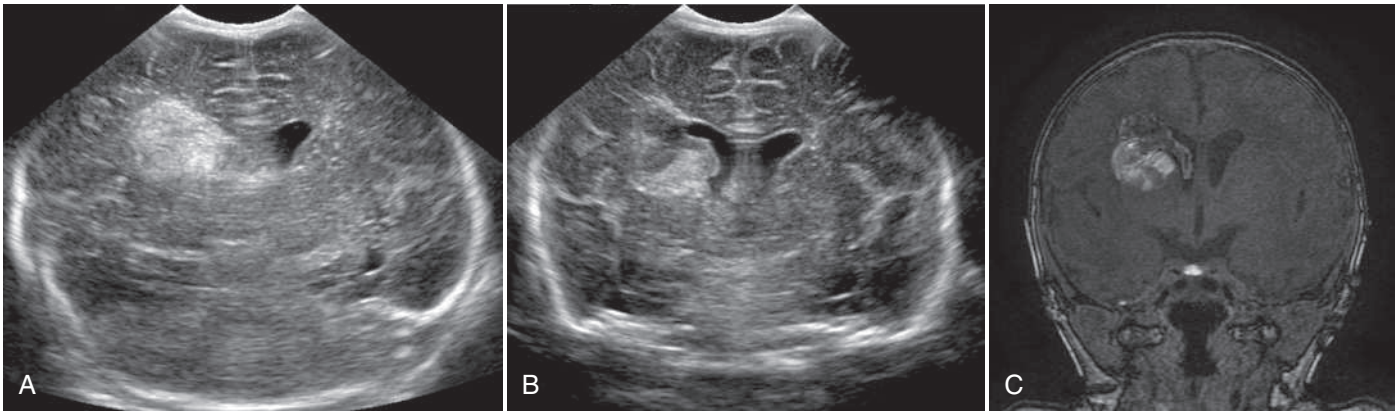

FIG. 45.43 Intraparenchymal Hemorrhage. (A) and **(B)** Coronal sonograms show acute intraparenchymal hemorrhage in the right parietal lobe and follow-up 8 days later. Note the change in echogenicity of the clot over time, with some areas that are still echogenic but other areas that are now more isoechoic to brain parenchyma. **(C)** Coronal magnetic resonance image shows the clot. See also Video 45.11 and Video 45.12.

severe posthemorrhagic hydrocephalus.[110] Occasionally, a **trapped fourth ventricle** may be caused by obstruction of both the aqueduct and the outlets of the fourth ventricle. In these cases a ventriculoperitoneal shunt will decompress only the lateral and third ventricles. Shunting can have long-term side effects, especially if there is a multiloculated hydrocephalus after shunt infection.[111]

Intraparenchymal Hemorrhage (Grade IV Hemorrhage)

IPH is usually in the cerebral cortex and located in the frontal or parietal lobes, because it often extends from the subependymal layer over the **caudothalamic groove** (Fig. 45.43). Studies suggest that IPH is caused by hemorrhagic venous infarction.[84,85] **Periventricular hemorrhagic infarction** (PVI) is believed to be venous infarction secondary to a large SEH compressing subependymal veins. These focal periventricular white matter infarcts are typically frontal to parieto-occipital and are asymmetrical, usually unilateral, and if bilateral, asymmetrical in size. PVI in the temporal lobe is associated with a greater risk of cognitive, behavioral, and visual problems.[112] Infants with IPH associated with GMH typically develop hemiparesis, and if there is periventricular hyperintensity, they may develop cerebral palsy.[113-118] It is thought that this hyperintensity may relate to pressure from hydrocephalus. This is in contrast to infants with periventricular echogenicity and minimal or no IVH, who are at much higher risk for PVL. These infarcts typically cause spastic hemiparesis.[31,113]

Acutely, IPH appears as an echogenic homogeneous mass extending into the brain parenchyma. As the clot retracts, the edges form an echogenic rim around the center, which becomes sonolucent. The clot may move to a dependent position, and by 2 to 3 months after the injury, an area of **porencephaly** (if there is communication with the ventricle) or encephalomalacia develops (Figs. 45.44 and 45.45).

Unusual types and sites of IPH, acute cystic changes, midline shift, and downward extension of hemorrhage into the thalamus may result from hemorrhage into PVL, secondary to infarction or thromboembolism, from a bleeding diathesis (e.g., vitamin

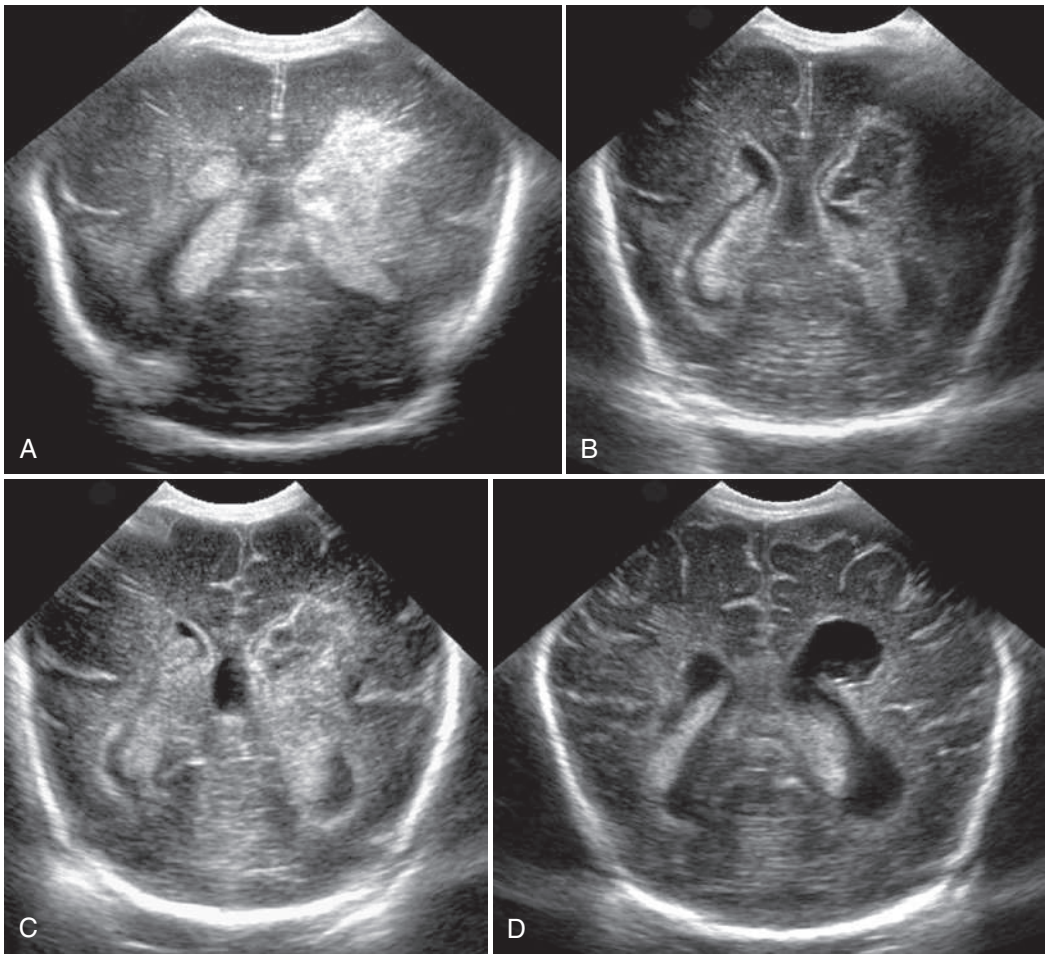

FIG. 45.44 Intraparenchymal Hemorrhage: Development of Porencephaly. (A) Coronal sonogram of 2-day-old infant shows intraparenchymal hemorrhage in the left parietal lobe. **(B)** At 17 days old. **(C)** At 29 days old. **(D)** At 2 months old.

K deficiency), hemophilia, alloimmune thrombocytopenia or Rh immune incompatibility, and hypernatremia.[119,120] Hemophilia has been associated with intracranial hemorrhage. A review of 102 newborns with hemorrhage in 33 publications found 65% intracranial and 35% extracranial.[121] Spontaneous IPH has been reported in term infants but was associated with signs of trauma or venous compression. If a unilateral thalamic hemorrhage appears in a newborn, **cerebral sinovenous thrombosis** should be strongly considered.[122,123]

Extracorporeal membrane oxygenation (ECMO) complications include IPH secondary to infarction, ischemia, and thromboembolism. GMH or IVH is less common after ECMO because premature infants are at high risk for these types of hemorrhage and thus this procedure is typically not done in premature infants.[124] These complications may be from the hypoxic brain damage secondary to the underlying lung disease, even before initiation of ECMO therapy. The complications from ECMO are also caused by heparinization and transient hypertension.[125]

Ultrasound is used for daily evaluation of the newborn receiving ECMO. The portability and ease of use in the critically ill infant without the need for transport are the main advantages. A 20-year study in Netherlands demonstrated 17% brain abnormalities with 8% hemorrhage and 5% stroke, particularly on the left. Sonography can alert the clinician to intracranial hemorrhage and the option to stop ECMO therapy.

Cerebellar Hemorrhage

Cerebellar hemorrhage has been diagnosed more frequently with special sonographic views through the mastoid fontanelle and from MRI evaluation of disrupted cerebellar development.[126-131] **Posterior fossa hemorrhage** is a reported complication of a traumatic delivery in full-term infants, in ECMO therapy, or with a coagulopathy. However, cerebellar hemorrhage can occur in premature infants because there is germinal matrix in the fourth ventricle (Fig. 45.46). The periphery of the cerebellar hemisphere is also a typical site of cerebellar hemorrhage. Mastoid fontanelle imaging is now routinely used to visualize the cerebellum in the optimum focal zone to allow cerebellar hemorrhage to be seen and the posterior fossa fully evaluated. Resolution of cerebellar hemorrhage into a cyst in the posterior fossa may allow easier diagnosis; the normal echogenic cerebellum may obscure hemorrhage when acute but is more clearly visualized with an "optimized examination" to look for subtle

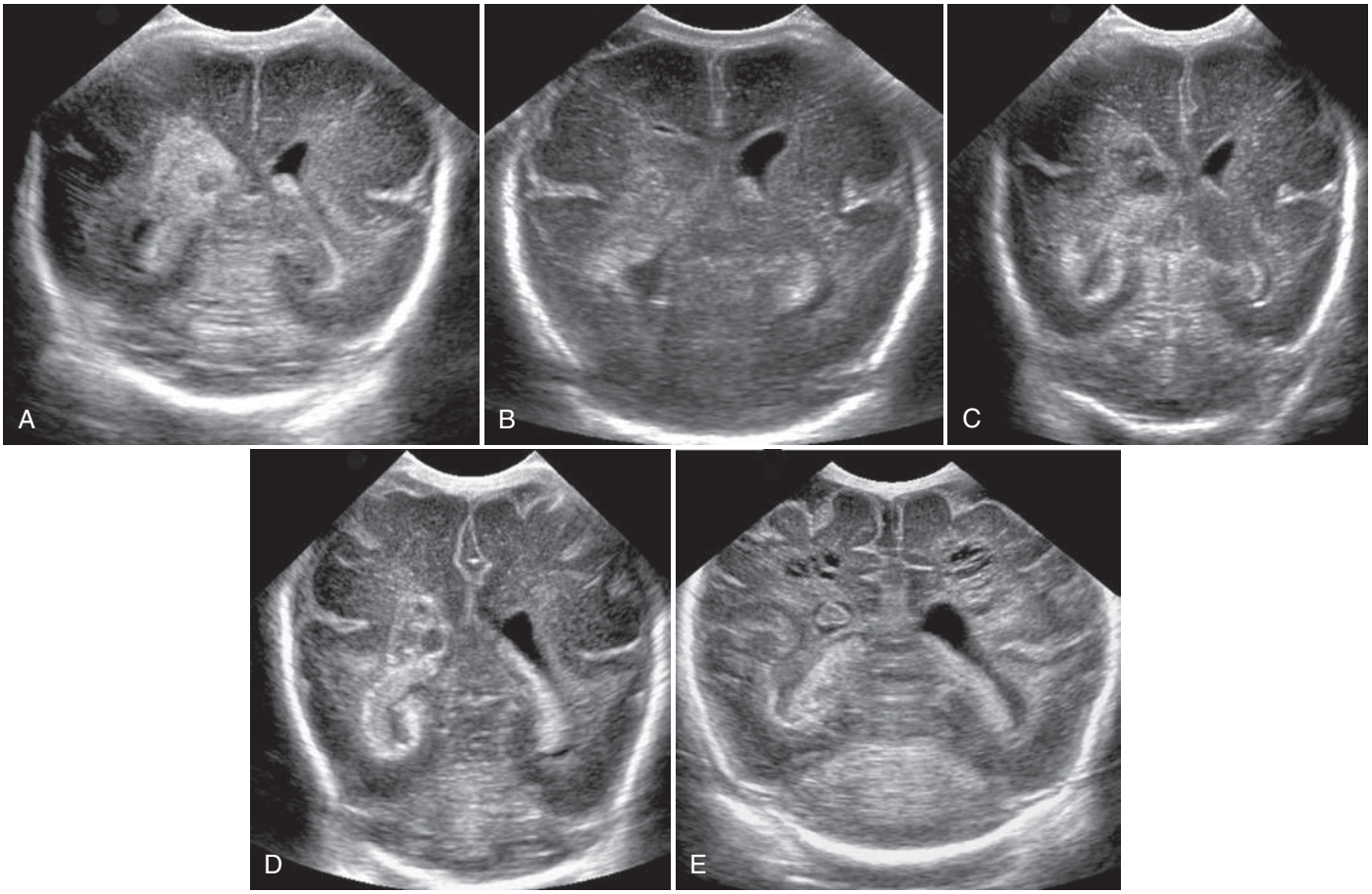

FIG. 45.45 Intraparenchymal Hemorrhage (IPH): Periventricular Hemorrhagic Infarction (PVI) and Later Periventricular Leukomalacia (PVL). (A) Coronal sonogram of 3-day-old infant shows IPH in the right parietal lobe. **(B)** At 12 days old. IPH is becoming sonolucent centrally. **(C)** At 19 days old. IPH has echogenic rind around lucent center. **(D)** At 1 month old. **(E)** At 2 months old, extensive PVL white matter damage is visible bilaterally.

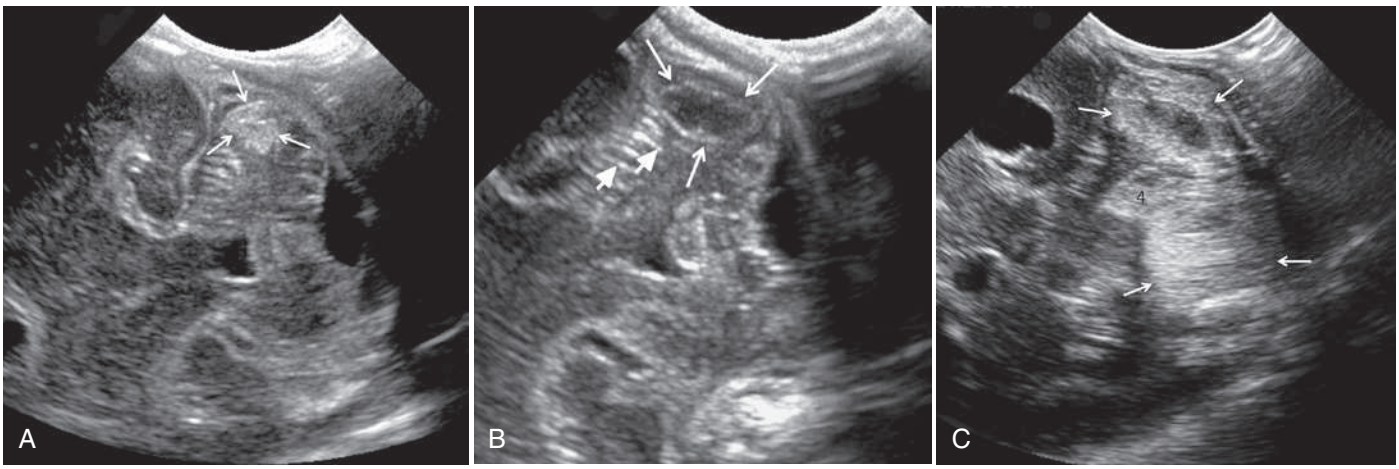

FIG. 45.46 Cerebellar Hemorrhage. (A) Axial sonogram of the cerebellum shows small acute echogenic cerebellar hemispheric hemorrhage on the periphery *(arrows)*. **(B)** Same patient. Chronic sonolucent cerebellar hemorrhage *(arrows)*. Normal pattern of alternating hypoechoic and hyperechoic linear cerebellar folia and fissures *(arrowheads)* seen through the mastoid fontanelle. **(C)** Bilateral severe cerebellar hemorrhage *(arrows),* and IVH in fourth ventricle *(4)*.

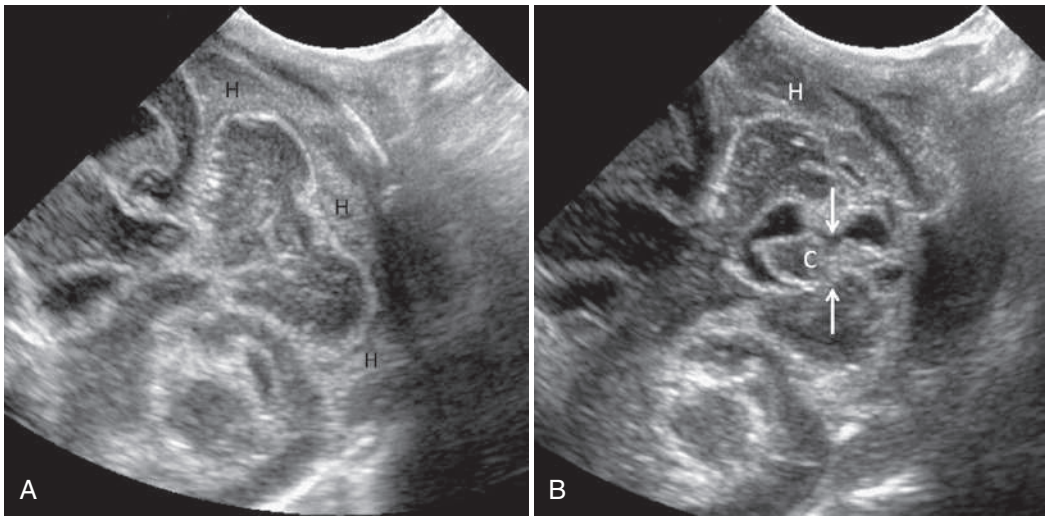

FIG. 45.47 Subarachnoid Hemorrhage Is a Secondary Process Following IVH When Blood Flows From the Fourth Ventricle Into the Cisterna Magna. (A) Axial sonogram of the posterior fossa shows hemorrhage in the subarachnoid space *(H)* and cisterna magna. **(B)** Axial sonogram shows blood in the subarachnoid space and clot *(C)* within the fourth ventricle and dilated foramen of Magendie *(arrows)*.

parenchymal hemorrhage or injury as described by Daneman[3] and others.[132]

Merrill and colleagues[133] reported 13 cerebellar hemorrhages in 525 infants under 1500 g. Each of these occurred in the first week of life in unstable neonates with acidosis or hypotension requiring intensive resuscitation, but not always associated with supratentorial hemorrhage. On follow-up to 2 years, four infants had cognitive deficits and developmental delay without signs of motor abnormalities. Cerebellar hemorrhage has been followed to term with MRI in some studies, and cerebellar volume loss has been reported that has been more extensive than the initial hemorrhage. The exact mechanism is not known, but Volpe has postulated that it may be due to selective neuronal necrosis.[134] Three cases of prenatally diagnosed posterior fossa cysts were found to result from hemorrhage. These were initially thought to be congenital posterior fossa arachnoid cysts but were recognized because of debris in the cysts and hemosiderin on MRI.[135] In neonates, cerebellar hemorrhage has rarely required surgical intervention, although older children may require emergency drainage.

Subarachnoid Hemorrhage

The presence of enlarged interhemispheric and sylvian fissures with thickened sulci and increased echogenicity can suggest the diagnosis of subarachnoid hemorrhage (SAH). SAH may occur in neonates who have experienced asphyxia, trauma, or disseminated intravascular coagulation and may be the only hemorrhage in full-term infants who are not at risk for GMH. Cisternal SAH has been found after IVH but can be a difficult diagnosis on ultrasound. Posterior fossa views can aid in making the diagnosis (Fig. 45.47). Spread of blood from the ventricular system into the spinal subarachnoid space after GMH is common and can be seen within 24 hours of the initial, severe IVH in premature infants.[107]

Cerebral Edema and Infarction

White Matter Injury of Prematurity or Periventricular Leukomalacia

WMIP, previously known as "periventricular leukomalacia," the principal ischemic lesion of the premature infant, is infarction and necrosis of the periventricular white matter. In MRI studies[136] the use of diffusion-weighted imaging (which shows hyperintense areas of restricted diffusion) have demonstrated that white matter damage to premature infants often extends beyond the periventricular areas into the cerebral white matter and cortex, the thalamus, basal ganglia, brainstem, and cerebellum. This premature pattern has been termed "white matter injury of prematurity."[31,46,54] In some cases, there is a history of cardiorespiratory compromise, resulting in hypotension and severe hypoxia and ischemia. The pathogenesis of PVL has been found to relate to three major factors: (1) the immature vasculature in the periventricular watershed; (2) the absence of vascular autoregulation in premature infants, particularly in the cerebral white matter; and (3) the maturation-dependent vulnerability of the oligodendroglial precursor cell. These cells are extremely vulnerable to attack by free radicals generated in the ischemia-reperfusion sequence.[46,97]

The prevalence of PVL in the very-low-birth-weight infant (<1000 g) was previously reported as 25% to 40%.[87] Later, Ment and colleagues[94] reported that PVL incidence decreased to 7%. However, with both ultrasound and MRI comparison, cystic and noncystic white matter damage has been shown in 50% of preterm infants.[31] Because more infants are surviving with WMIP/PVL (and thus are at risk for cerebral palsy) than in the past, it becomes even more important to diagnose these lesion. WMIP consists of cystic changes of PVL, which are more often visualized on ultrasound, and noncystic white matter damage, which is better seen on MRI[137] (Fig. 45.48).

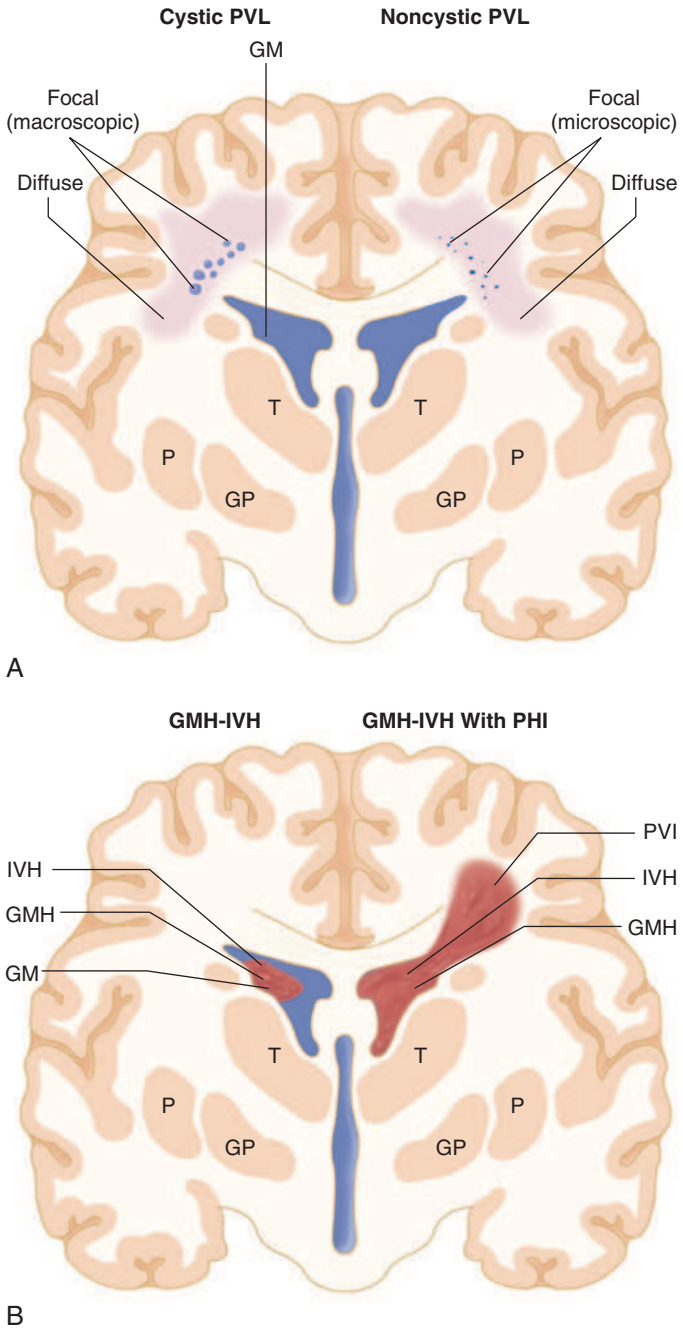

FIG. 45.48 Cystic and Noncystic Periventricular Leukomalacia *(PVL)* and Germinal Matrix Hemorrhage–Intraventricular Hemorrhage *(GMH-IVH)* and Periventricular Hemorrhagic Infarction *(PVI).* Diagram illustrates coronal sections from the brain of a 28-week-old premature infant. The dorsal cerebral subventricular zone, the ventral germinative epithelium of the germinal matrix *(GM),* thalamus *(T),* and putamen *(P)* and globus pallidus *(GP)* are shown. **(A)** The focal necrotic lesions in cystic PVL are macroscopic in size and evolve to cysts. The focal necrotic lesions in noncystic PVL are microscopic in size and evolve to glial scars. The diffuse component of both cystic and noncystic PVL *(pink)* is characterized by the cellular changes. **(B)** Hemorrhage *(red)* into the GM results in GMH, which could burst through the ependyma to cause an IVH *(left).* When the GHM-IVH is large, PHI might result *(right).* (Adapted from Volpe JJ. Brain injury in premature infants: a complex amalgam of destructive and developmental disturbances. Lancet Neurol. 2009;8[1]:110-124.[46])

In the cystic pattern of PVL, the white matter most affected is in the arterial border zones at the level of the optic radiations adjacent to the trigones of the lateral ventricles and the frontal cerebral white matter near the foramina of Monro. This cystic pattern can involve the white matter diffusely as well. The prevalence of PVL has been noted to increase with the duration of survival in premature infants, raising the possibility of cumulative postnatal insults, including circulatory compromise, patent ductus arteriosus, apneic spells, and sepsis.[101,138,139]

In the noncystic pattern of WMIP/PVL, there may be diffuse cerebral cortex white matter damage, microscopic focal white matter damage, and basal ganglia, thalamic,[140] and cerebellar damage that evolves to glial scars. Typically, the white matter is thinned with irregular ventricular walls. There may also be corpus callosum injury. Epelman and colleagues[141] have shown that careful ultrasound evaluation may show increased callosal echogenicity, which reflects corpus callosum damage and can be used as a specific marker for this injury early when MRI is less often used. Near-term ultrasound and MRI at term-equivalent age have been shown to predict neurodevelopmental outcomes in extremely premature infants.[142]

Maternal chorioamnionitis has been associated with WMIP/PVL, possibly the result of vasoactive proteins being released into the fetal circulation, causing fluctuations in cerebral blood flow. Inflammatory responses to infection in the fetus or the neonate that activate astrocytes and microglia may cause PVL,[143,144] or these may represent a pathologic response to repair the tissue injury in PVL.[145] Proinflammatory cytokines found after chorioamnionitis correlate with PVL development.[146] Prevention of PVL may depend on treatment with maternal antibiotics (in the case of chorioamnionitis before delivery) or anticytokine agents and therapy with free-radical scavengers.

Cystic PVL can been anticipated to follow a severe hemodynamic event in 56% of premature infants with PVL. Unexpected PVL (without a specific clinical neonatal event) has been reported in as many as 44% of cases.[147] This series of PVL patients had been treated for preterm delivery and often had maternal chorioamnionitis. It is proposed that the maternal infection predisposes to preterm delivery and PVL. Antenatal steroids have been shown to decrease the incidence of PVL and the incidence of IPH from GMH.[148-151]

Later neurologic problems from cystic PVL/WMIP include developmental delay and spastic diplegia involving both legs, often noticeable by 6 months of age. Spastic diplegia occurs because the pyramidal tracts from the motor cortex that innervate the legs pass through the internal capsule and travel close to the lateral ventricular wall. Severe cases of PVL will also affect the arms, resulting in spastic quadriplegia, and also cause vision and intellectual deficits.[152-155] The prevalence of cerebral palsy was evaluated in the French EPIPAGE cohort study of 2364 children born at 22 to 32 weeks' gestation; 1954 (83%) were studied at 2 years of age. Twenty percent had cerebral palsy if born at 24 to 26 weeks' gestation, whereas only 4% had cerebral palsy if born at 32 weeks. For those with neonatal head ultrasound and follow-up, 17% of children with neonatal IVH (grade III) and 25% with neonatal white matter damage had cerebral palsy, compared with 4% with normal ultrasound scans.[156]

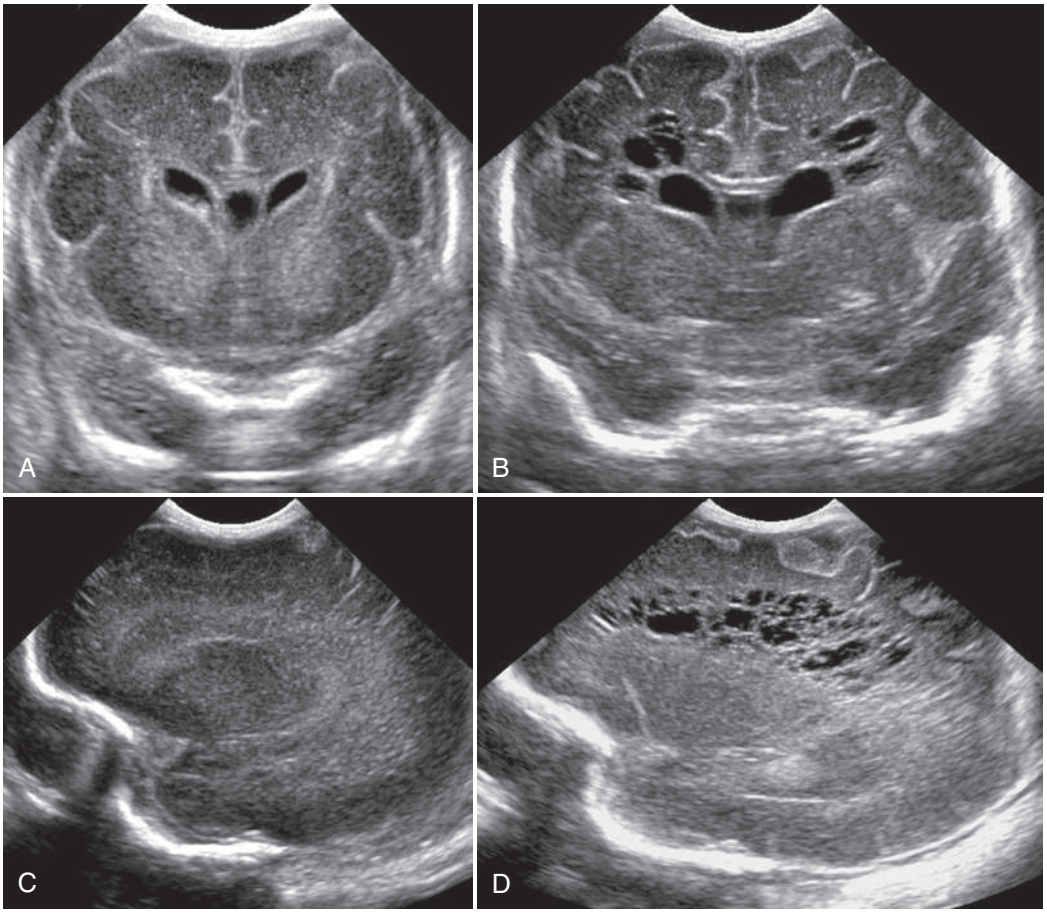

FIG. 45.49 Periventricular Leukomalacia (PVL): Echogenic to Cystic. (A) Coronal sonogram shows acute increased areas of echogenicity. **(B)** Development of cystic PVL 1 month later. **(C)** and **(D)** Sagittal sonograms. See also Video 45.16.

Pathologically, the periventricular white matter undergoes coagulation necrosis, followed by phagocytosis of the necrotic tissue. This necrosis usually occurs in the white matter adjacent to the external angles of the lateral ventricles. This results in decreased myelination in these areas and focal dilated lateral ventricles. In more severe cases of PVL, cystic cavities develop.[40,152,154] Petechial hemorrhages can complicate PVL. In fact, hemorrhagic PVL has been shown to be much more common (64%) than thought when there is MRI-ultrasound correlation.[157]

The initial sonographic examination findings in infants who ultimately develop cystic PVL may be normal. Within 2 weeks of the initial insult, however, the periventricular white matter increases in echogenicity until it is greater than the adjacent choroid plexus. This increased echogenicity is usually caused by edema from infarction and may also result from hemorrhage[158] (Fig. 45.49A). Two to 4 weeks after the insult, cystic changes may develop in the area of abnormal echogenic parenchyma (Fig. 45.49B-D; Video 45.16). The cysts can be single or multiple and are parallel to the ventricular border in the deep white matter and often lateral and/or superior to the top of the ventricles. These cysts measure from millimeters to 2 cm in diameter. The cystic changes are usually bilateral and often symmetrical. Cystic changes in the corpus callosum can progress to later thinning.[139,159]

Pathologic studies suggest that sonography actually underestimates the incidence of PVL.[158,160] In 51 cases of postmortem-proven PVL, Adcock and colleagues[160] found that in 44% the neurosonogram failed to make the diagnosis for two main reasons: (1) most often the ultrasound examinations were performed before 1 month of age and missed the cystic stage of PVL, and (2) the lesions were microcystic and not large enough to find on ultrasound.

On subsequent sonograms, the cystic lesions may enlarge or resolve.[154] Therefore normal-appearing white matter on sonograms obtained several weeks to months after the insult does not exclude the occurrence of PVL. MRI becomes more sensitive than either CT or ultrasound for long-term follow-up of parenchymal injury, because when myelination progresses, **glial scarring** from damaged white matter can be diagnosed (Fig. 45.50), typically with thinning of the white matter adjacent to an enlarged ventricle where the cysts have coalesced and are no longer visible. Because the initial ultrasound examination findings are often normal in infants who have sustained a significant hypoxic-ischemic event, late sonograms should be obtained at about 4 weeks after birth to exclude evolving PVL. The characteristic distribution of cystic lesions that are clearly separate from the ventricle in PVL should distinguish them from the parenchymal hemorrhage that occurs in grade IV GMH. However, PVL and GMH can occur

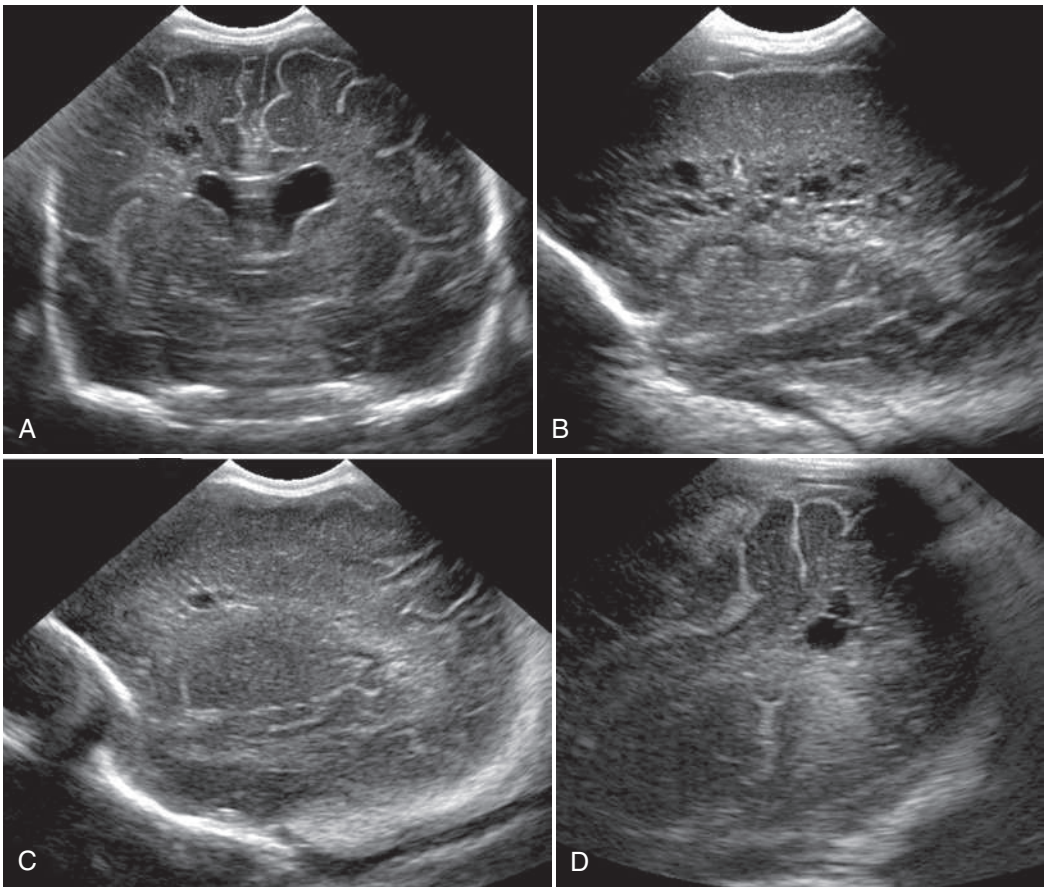

FIG. 45.50 Periventricular Leukomalacia (PVL). (A) Coronal sonogram of cystic PVL. **(B)** and **(C)** Sagittal sonograms show large and small affected areas of PVL. **(D)** Sagittal sonogram shows cystic PVL in the occipital lobe.

simultaneously.[161] Periventricular white matter damage can be studied with cranial ultrasound if technical factors include careful attention to focal areas of hyperechogenicity. Leijser and colleagues[162] divided white matter into **grade 0,** less echogenicity than choroid plexus; **grade 1,** same echogenicity as choroid plexus; and **grade 2,** brighter than choroid plexus. Only severe grade (grade 2) predicted a poor neurologic outcome.

MRI has proven to be the best method for WMIP/PVL diagnosis when done at term-equivalent age in the very-low-birth-weight infants most at risk for PVL.[163,164] The increasing use of MRI has been controversial as a standard of care but clearly adds to the prognostic value in predicting neurodevelopmental outcomes of very premature infants.[165,166] The addition of diffusion-weighted imaging[167] and diffusion tensor imaging[168] have also been shown to add value in predicting more extensive white matter injury. Delayed myelination, ventricular enlargement, and width of extracerebral spaces were not found to be good predictors of cerebral palsy.

Term Infants With Hypoxic Ischemic Injury

Diffuse cerebral edema with or without SAH is a common result of hypoxic-ischemic events in full-term infants. In some cases, acute very focal areas of edema may cause increased gray matter–white matter differentiation. However, it is common that when brain edema can be diagnosed on ultrasound, there are typically slitlike ventricles in a diffusely echogenic brain with poorly defined sulci. This echogenicity may cause **effacement of the sulci** so that the sulci seem to disappear (Fig. 45.51).[4] The brain parenchyma appears echogenic in the distribution of the injury, and the sulci are difficult to appreciate because of surrounding echogenic edematous brain. The mechanism of the increased echogenicity of the brain parenchyma from cerebral edema is not understood completely. One possibility is that the increased intracellular fluid causes more interfaces.

Color Doppler ultrasound evaluation of severely asphyxiated infants has demonstrated earlier and at times more focal abnormalities than gray-scale evaluation alone (see Chapter 46). Investigators have used Doppler sonography to classify brain edema and to predict outcome. Outcome of children with significantly abnormal cerebral blood flow was noted in 47 patients, from newborns to 4 years of age. However, loss or reversal of diastolic flow did not necessarily imply a lethal outcome. Survival was associated with prompt and effective treatment.[169] A few studies have shown MRI changes early in neonatal life from asphyxia, but most neonatologists resist moving a very unstable newborn for magnetic resonance scanning. If the ischemic event was severe enough to lead to infarction, diffuse brain volume loss occurs within 2 weeks, with ventricular enlargement

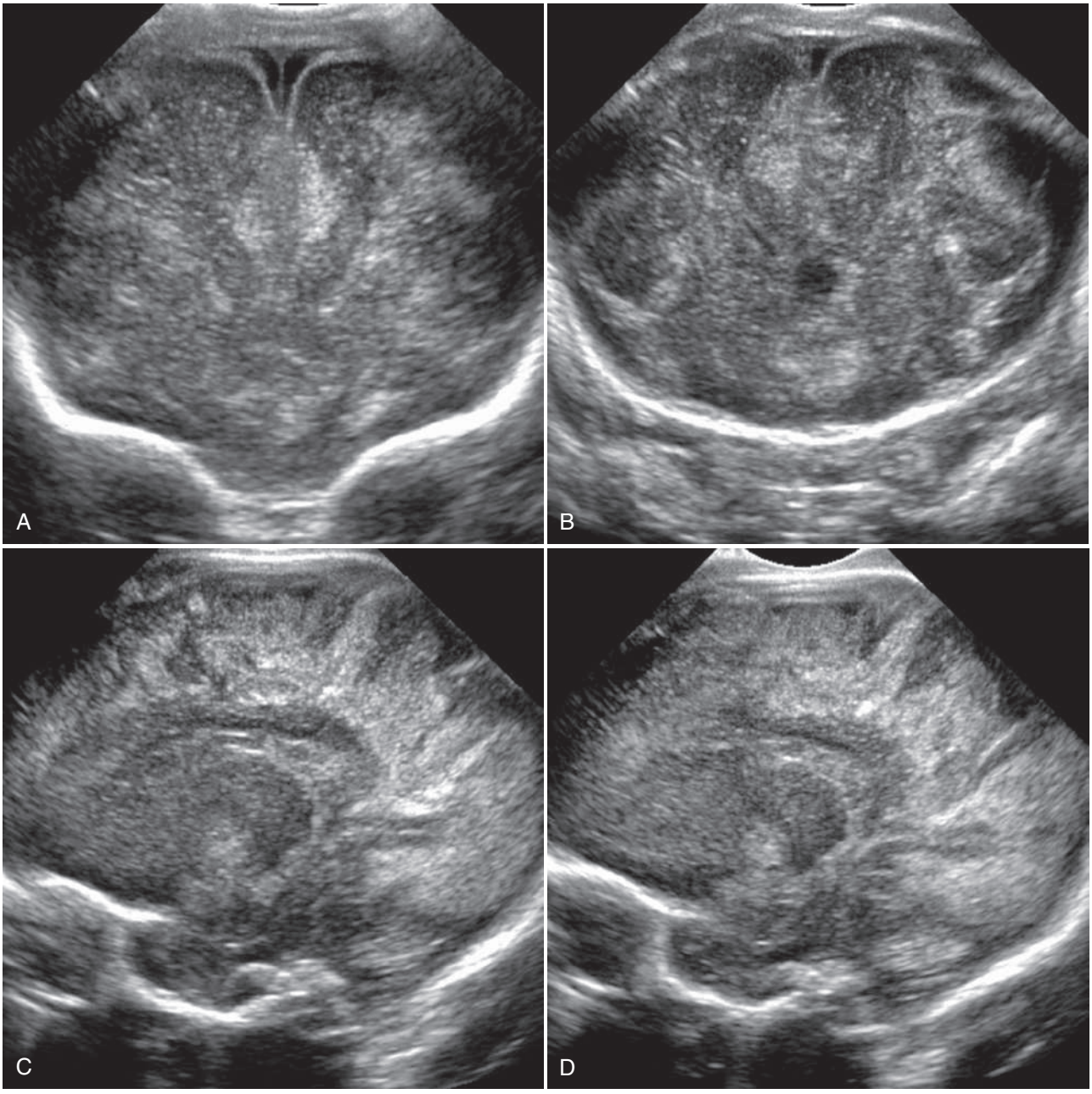

FIG. 45.51 Cerebral Edema. (A) and **(B)** Coronal sonograms; **(C)** and **(D)** sagittal sonograms. Severe cerebral edema has caused effacement and silhouetting of the sulci from acute, near-total intrauterine asphyxia after placental abruption. Diffuse increased echogenicity from edema obscures sulci. Ventricles are slitlike because of the severe edema.

secondary to atrophy.[31] Enlarged extraaxial fluid spaces also develop as a consequence of the atrophic changes. The head circumference is very helpful to distinguish diffuse atrophy from hydrocephalus, because the head circumference is normal to small in patients who have undergone diffuse brain atrophy. Depending on the type of insult, generalized brain atrophy or focal areas of porencephaly or encephalomalacia may occur. With **acute near-total intrauterine asphyxia** in the newborn, an unusual pattern of basal ganglia damage with sparing of the cerebral cortex and white matter has been reported. This may be difficult to diagnose with ultrasound if it is not hemorrhagic until late changes of atrophy develop[31] (Fig. 45.52).

Sonography can detect these complications of hypoxic-ischemic events, but MRI is more sensitive to the full extent of the insult near the cortical surface.[31,170] To optimize ultrasound imaging of the term neonatal brain, Daneman and colleagues[171] used higher frequencies (8-17 MHz) with multiple focal planes in near-field, midfield, and far-field magnified views with spectral and color Doppler ultrasound, searching for abnormal resistive indices on spectral Doppler ultrasound. They also emphasized the need to perform the ultrasound examination within 2 hours of MRI for an accurate comparison. Special features to be evaluated on every ultrasound study in neonates with hypoxic-ischemic insult should include gray matter–white matter differentiation

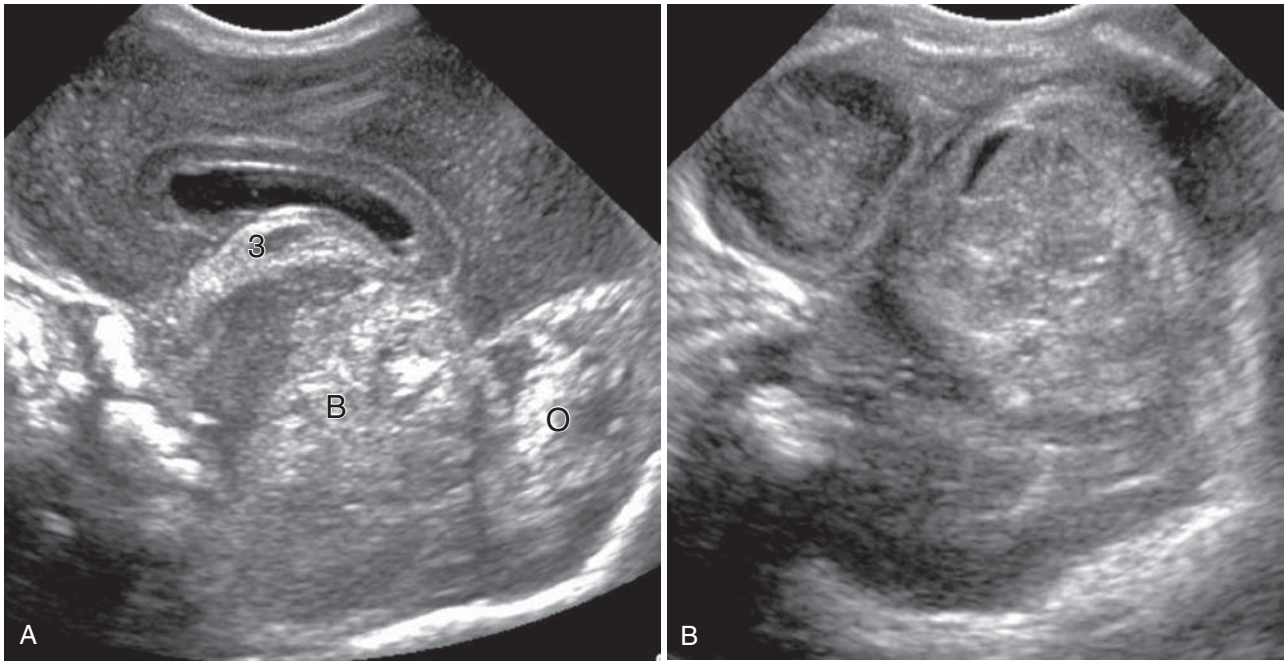

FIG. 45.52 Brainstem and Cerebellar Hemorrhage. (A) and **(B)** Sagittal and axial sonograms show highly echogenic hemorrhage in the brainstem *(B),* cerebellar vermis, and hemispheres, and posteriorly in the occipital cortex *(O),* after acute, near-total intrauterine asphyxia. Clot is also seen in the third ventricle *(3)* just below the cavum septi pellucidi.

and focal abnormal echogenicity in cerebral cortex and deeper structures. Doppler ultrasound to look for flow fluctuations in resistive indices and flow in the dural sinuses is valuable.

In term infants treated with **hypothermia for hypoxic ischemic encephalopathy,** there have been rare reports of IVH.[166,172,173] However, outcomes after hypothermia for HIE from the NICHD Neonatal Research Network studies show that there is a decrease in deaths and that hypothermia does not increase rates of severe disability among survivors.

Neonatal HIE is best evaluated with ultrasound in the first few days of life. MRI is the most sensitive and specific imaging technique, and is useful in stable term infants. Some authors suggest that MRI late in the first week of life may be useful but term-equivalent age is best for prognosis. However, the brain may appear normal or near normal at 5 to 7 days after the event. For severe hypotensive episodes, thalami, brainstem, and cerebellum are most sensitive owing to their high metabolic activity. In premature infants, HIE injury appears as increased echogenicity on ultrasound, hypoattenuation on CT (may be missed because of high neonatal brain water content), and hyperintensity from restricted diffusion on diffusion-weighted imaging. In term infants, the lateral thalami, posterior putamen, hippocampus, brainstem, corticospinal tracts, and sensorimotor cortex are most affected.[88,89,174]

Focal Infarction

Cerebral infarction in the neonate, aside from PVL or periventricular hemorrhagic venous infarction, is uncommon. Risk factors are prematurity, severe birth asphyxia, congenital heart disease (resulting in a left-to-right shunt), meningitis, emboli (from the placenta or systemic circulation), polycythemia, hypernatremia, and trauma.[120,175,176] Symptoms vary, ranging from asymptomatic to seizures with lethargy and coma. The MCA distribution is the most frequent site, although the anterior and posterior circulations have also been affected.[46] Single areas of infarction are more frequently seen in full-term infants, whereas premature infants often demonstrate multiple sites of injury. Cerebral blood flow evaluation with color and or power Doppler sonography are used in unstable neonates, and diffusion-weighted MRI is used in stable infants to identify the earliest signs of stroke.[177-182]

Cerebellar infarction is much less common than cerebral infarction. However, six cases were reported in 3 years at Hammersmith Hospital in London, diagnosed by MRI in patients at several years of age who were born prematurely.[183] All these patients also had IVH, and thus cerebellar damage was likely a result of diffuse ischemic injury. Only one of the six patients was diagnosed on sonography as having cerebellar damage. Because the vermis is so echogenic, edema or hemorrhage can be a difficult diagnosis in this region. Cerebellar infarction was also diagnosed with MRI in 13 patients with severe cerebral palsy who had cerebellar hemispheric and vermian damage.[184] Now that we are routinely evaluating the posterior fossa in detail, we are more aware of cerebellar infarction at the time of the injury in premature infants.[185]

On sonography, the infarcted brain parenchyma demonstrates specific findings within the first 2 weeks (see Fig. 45.52; Fig. 45.53). These include echogenic parenchyma, lack of arterial pulsation, lack of blood flow appreciated by pulsed or color Doppler sonography, mass effect from edema, arterial territorial distribution of injury, and decreased sulcal definition. After 2 weeks, the echogenic lesions begin to show cystic changes, and

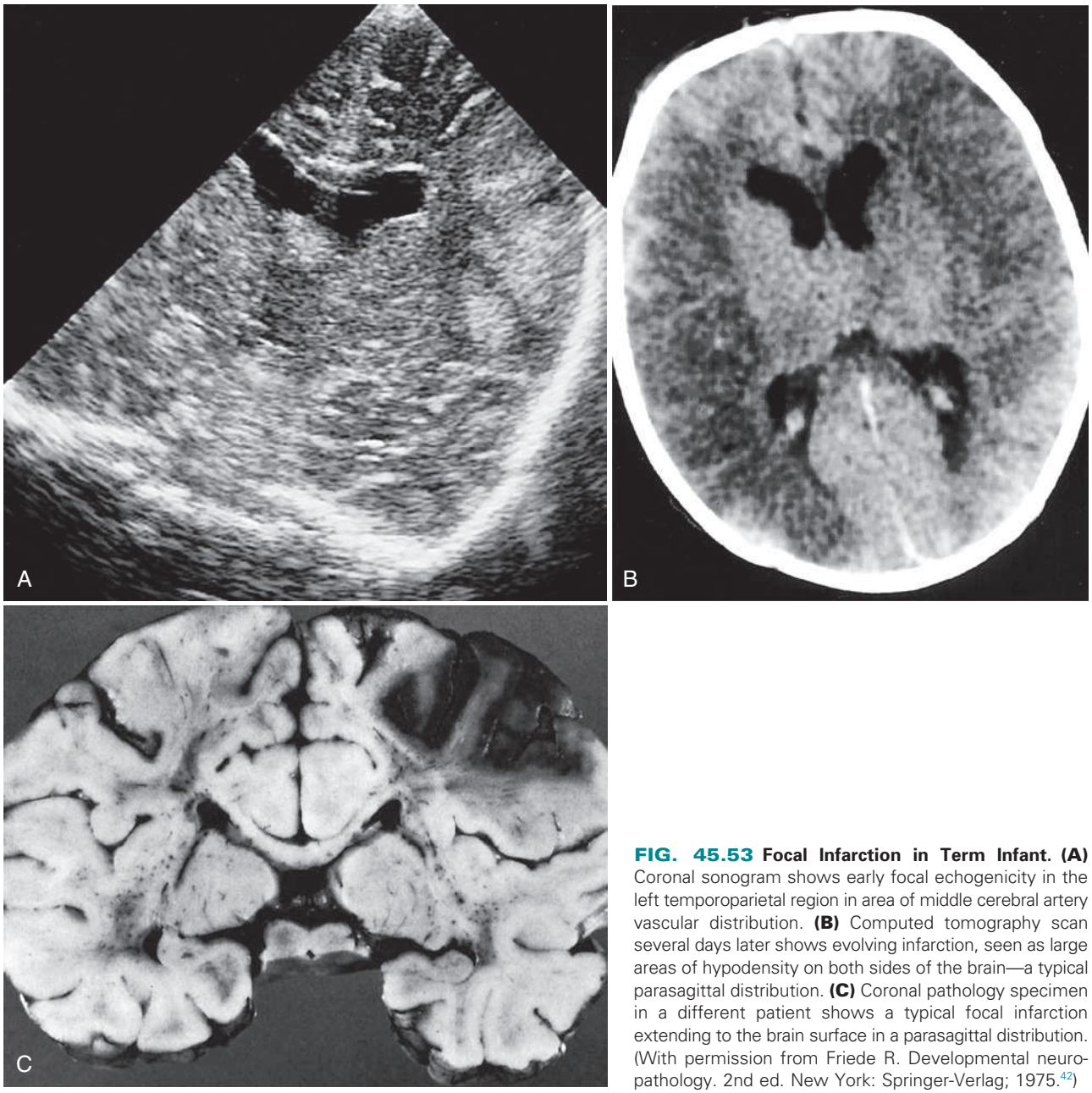

FIG. 45.53 Focal Infarction in Term Infant. (A) Coronal sonogram shows early focal echogenicity in the left temporoparietal region in area of middle cerebral artery vascular distribution. **(B)** Computed tomography scan several days later shows evolving infarction, seen as large areas of hypodensity on both sides of the brain—a typical parasagittal distribution. **(C)** Coronal pathology specimen in a different patient shows a typical focal infarction extending to the brain surface in a parasagittal distribution. (With permission from Friede R. Developmental neuropathology. 2nd ed. New York: Springer-Verlag; 1975.[42])

Cerebral Infarction: Sonographic Signs

Echogenic parenchyma
Lack of flow on color Doppler and pulsed Doppler
Mass effect from edema
Arterial territorial distribution of injury
Decreased sulcal definition
Increased pulsation in periphery of infarcted section
Early collateral arterial vessels within hours of insult

ipsilateral ventricular enlargement from evolving atrophy (hydrocephalus ex vacuo), as well as a gradual return of arterial pulsations in the major branches from proximal to peripheral distribution. Cerebellar lesions are typically peripheral and thus do not lead to local ventricular enlargement. Using color Doppler imaging, **luxury perfusion** has been identified within hours of a focal vascular insult, both experimentally and in newborn infants. Power Doppler may be more sensitive than color Doppler in detecting the increase in the size and number of vessels seen with luxury perfusion.

Lenticulostriate Vasculopathy

Linear branching echogenicity in the lenticulostriate arteries of the thalamus and basal ganglia is uncommon but has been described in intrauterine viral infections (CMV, rubella, syphilis) (Video 45.17 and Video 45.18), neonatal asphyxia, nonimmune hydrops, fetal alcohol syndrome, and trisomies 13 and 21. Coley and colleagues[186] reported that hypoxic-ischemic conditions accounted for 30 of 63 cases. In a study by Amir, of 92 infants

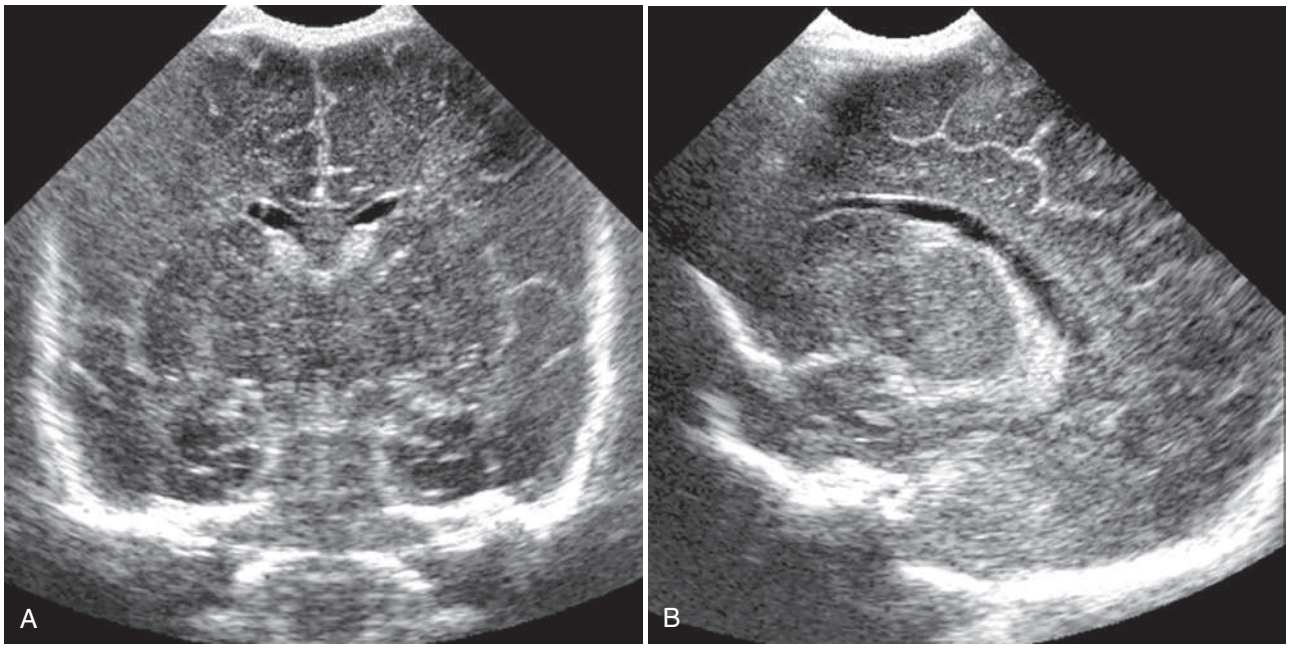

FIG. 45.54 Hyperechoic Caudate Nucleus (Bilateral). (A) and **(B)** Coronal and sagittal sonograms show echogenic caudate nuclei that did not appear abnormal until the premature infant was about 1 month of age (postulated to be remote ischemic damage).

with congenital CMV, half had lenticulostriate vasculopathy on an initial head ultrasound, and this was a marker for sensorineural hearing loss.[187] In a study by Chamnanvanakij and colleagues, of 10 preterm infants who ultimately developed linear hyperechogenicity in the basal ganglia and thalamus, the mean age of diagnosis was 1 month and it was a marker for more diffuse brain injury and for poor neurologic outcome.[188]

Hyperechoic Caudate Nuclei

Bilateral hyperechoic foci in the caudate nuclei develop in the characteristic location of GMH but are atypical in that they are sharply marginated, teardrop shaped, bilateral, and symmetrical (Fig. 45.54). Schlesinger and colleagues[189] reported that five of nine infants had ischemia and two were normal in this area, based on MRI and histopathologic review. Hyperechoic caudate nuclei seem to occur late, usually after the first week of life, when most GMH occurs.

POSTTRAUMATIC INJURY

Subdural and Epidural Hematomas

Subdural and epidural hemorrhage can be a difficult diagnosis on sonography compared with CT or MRI.[7] On sonographic examination, these hematomas appear as unilateral or bilateral hypoechoic fluid collections surrounding the brain parenchyma (Fig. 45.55). Subdural hematomas are uncommon in newborns and not necessarily indicative of birth trauma—13 of 26 affected infants diagnosed on CT had a history of trauma.[190] Fortunately, surgery is rarely required. Small amounts of fluid may be difficult to detect secondary to the near-field artifact inherent in every transducer. However, this is less of a problem if a high-frequency transducer (10-12 MHz) is used. With a lower-frequency transducer, interposing an acoustic gel pad between the transducer and the fontanelle can assist in eliminating the near-field artifact. Magnified coronal sections with high-frequency linear transducers (at least 10-12 MHz) are best for appreciating the epidural and subdural collections in the supratentorial space. Imaging through the foramen magnum or posterior fontanelle can assist in diagnosing infratentorial extraaxial fluid collections.

Color Doppler sonography has been shown to distinguish subarachnoid and subdural fluid and hemorrhage based on displacement of vessels on the brain surface (see Fig. 45.55; see Chapter 46). Doppler ultrasound may be useful in determining which patients may be simply observed and which require MRI for a more specific diagnosis of hemorrhage.

After the neonatal period, when birth trauma may cause hemorrhage, the presence of new subdural fluid collections should suggest preexisting meningitis (most often from *Haemophilus influenzae*) or nonaccidental trauma. If an infant's head circumference increases abnormally quickly after the first 2 weeks of life, a CT examination is usually performed to search for extraaxial fluid, because the most common cause is subdural hemorrhage, not hydrocephalus. If a sonographic examination is performed, the clinician should carefully search the near field with magnified views for extracerebral fluid and cerebral tears, as well as membranes seen in chronic subdural fluid collections.

INFECTION

Congenital Infections

Congenital infections can have serious consequences for the developing fetus. Death of the fetus, congenital malformations,

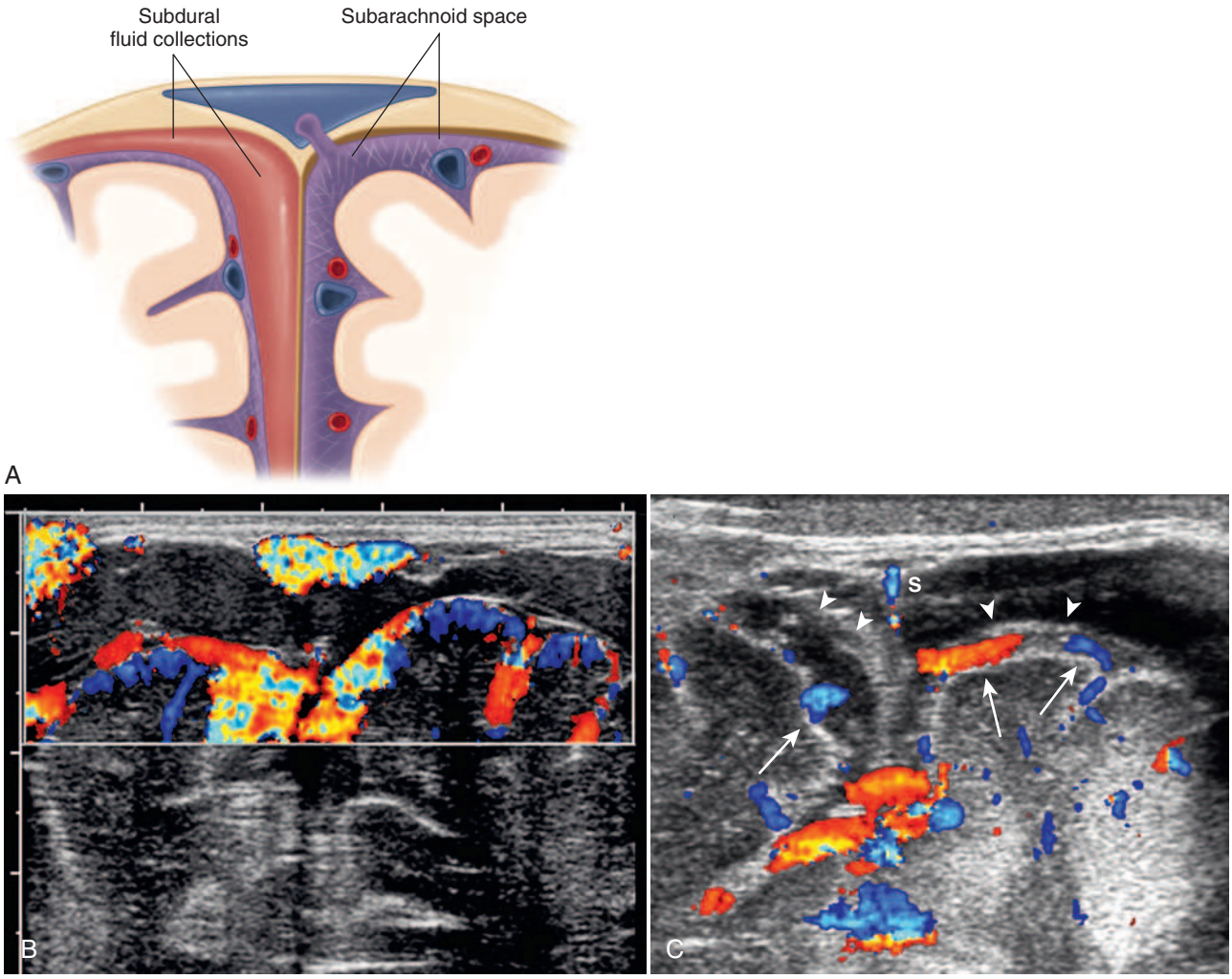

FIG. 45.55 Subdural and Subarachnoid Fluid Collections. (A) Drawing shows vessels are compressed onto the surface of the brain in subdural fluid collections and vessels cross the fluid in subarachnoid space. **(B)** Magnified coronal color Doppler image of interhemispheric fissure in a 2-week-old infant. Large bilateral echogenic subdural effusions from **meningitis** compress the superficial cortical vessels onto the cortical surface. **(C)** Coronal color Doppler image of interhemispheric fissure in a 1-month-old infant. Large left and small right hypoechoic chronic subdural hematomas *(S)* from **nonaccidental trauma** lie above the echogenic subarachnoid fluid. The cortical surface is compressed by the echogenic subarachnoid fluid, which surrounds superficial cortical vessels *(arrows)* separated from the relatively lucent subdural fluid by echogenic and thickened pia-arachnoid *(arrowheads).* Note the echogenic subcortical white matter and superior sagittal sinus.

mental retardation or developmental delay, and spasticity or seizures may result from infection at critical times during gestation. Ultrasound plays an important role in identifying and following both antenatal and neonatal complications from congenital infections, with MRI showing additional findings in many cases.[191,192]

The most frequent congenital infections are commonly referred to by the acronym TORCH. This refers to the infections *Toxoplasma gondii,* rubella, CMV, and herpes simplex virus type 2 (HSV-2). The O stands for "other," such as syphilis. Syphilis causes acute meningitis, infrequently resulting in parenchymal lesions in the newborn.[193]

Of the TORCH group, congenital infection by CMV is the most common, occurring in approximately 1% of all births.[194] CMV may be acquired at or after birth with little or no consequence, but prenatal infections may result in serious damage to the developing brain.[195,196] Maternal infection is usually subclinical. Maternal immunity to CMV reduces the risk of CMV in utero, and vaccines are being considered.[197] Toxoplasmosis is the second common congenital infection and is caused by the unicellular parasite *T. gondii.*[198,199]

The severity of the infection with either CMV or toxoplasmosis depends on the timing of the infection during gestation. Earlier infection, before 20 to 24 weeks, results in more devastating outcomes: microcephaly, lissencephaly with abnormal myelination, a hypoplastic cerebellum, polymicrogyria and cortical dysplasias, porencephaly, and multicystic encephalomalacia.[200] CMV has been reported to cause schizencephaly in some patients[69,70] (Fig. 45.56). Ventriculomegaly may result from brain volume loss. Later infection, after 24 weeks, will result in less severe neurologic damage.

To differentiate CMV from toxoplasmosis, serum titers for antibodies against these organisms are useful. Other differentiating criteria include the petechial skin lesions and hepatomegaly

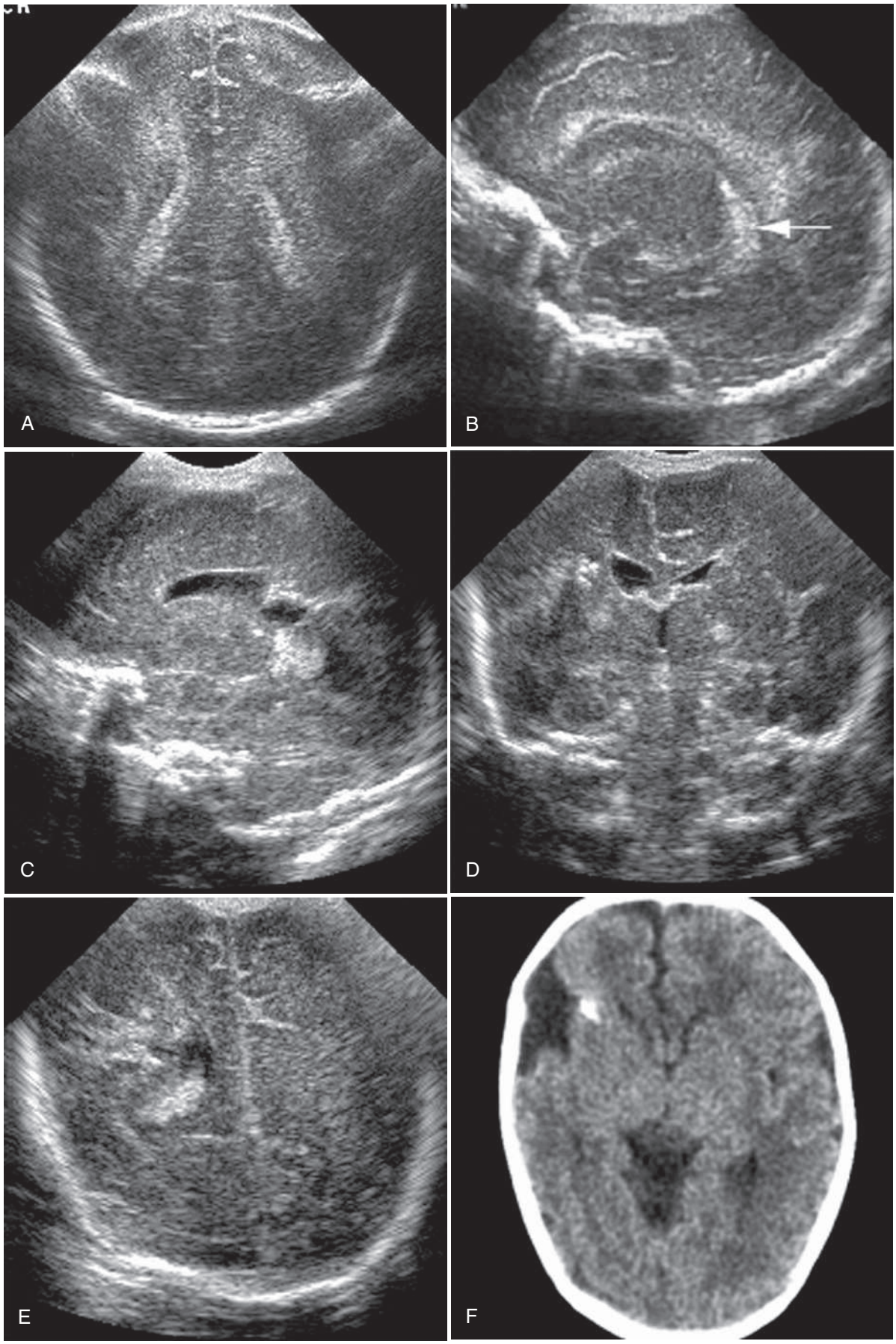

FIG. 45.56 Cytomegalovirus Encephalitis. (A) and **(B)** Periventricular echogenicity and focal calcification *(arrow)* with little acoustic shadowing. **(C)-(E)** In another patient, focal calcifications on ultrasound. **(F)** Computed tomography scan. See also Video 45.17, Video 45.18, and Video 45.19.

associated with CMV and chorioretinitis associated with toxoplasmosis. Intracranial calcifications have been described in both infections. CMV classically causes periventricular calcifications (see Fig. 45.56, Videos 45.17 and 45.18). Ventricular septations have also been described (Video 45.19). Toxoplasmosis causes more scattered calcifications with a predilection for the basal ganglia. However, both patterns have been seen in both infections.[201] Resolution of intracranial calcification has been reported after treatment of congenital toxoplasmosis, consistent with improved neurologic outcome.[202]

Sonography can demonstrate the periventricular or scattered cerebral calcifications as echogenic foci with or without acoustic shadowing. In eight proven cases of CMV, Malinger and colleagues[200] reported periventricular hyperintensity in all cases, as well as calcification, ventriculomegaly, hypoplastic vermis, periventricular cysts, intraventricular adhesions, and echogenic vasculature in the basal ganglia. Cerebellar calcification was seen in one patient.[200] The brain parenchyma may appear disorganized, with poorly defined sulci and corpus callosum. CT demonstrates the calcifications to a better extent, but MRI shows abnormal myelination or cortical dysplasias most reliably.

Recently, maternal **Zika virus infection** has been described in Brazil and many other countries and is associated with fetal microcephaly and severe cerebral damage.[203] Sonographic findings are similar to severe forms of CMV with microcephaly, ventriculomegaly, corpus callosum abnormalities, gray and white matter loss, and cerebral calcifications.[204-213]

HSV-1 or HSV-2 may cause disease of the CNS, although HSV-2 is more common in the neonate, and HSV-1 occurs primarily in older children and adults. HSV-2 may be acquired transplacentally or by vaginal exposure to herpetic genital lesions during birth. The resulting encephalitis is typically diffuse, resulting in loss of gray matter–white matter differentiation. (This differs from the temporal lobe disease seen in older children and adults with HSV-1.) Cystic encephalomalacia of periventricular white matter and hemorrhagic infarction with scattered parenchymal calcifications frequently result.[214] Relative sparing of the lower neural axis, including the basal ganglia, thalamus, cerebellum, and brainstem, is typical. Infections acquired in utero may lead to microcephaly, intracranial calcifications, and retinal dysplasias.[215]

Since the widespread availability of rubella vaccine after 1967, congenital rubella has fortunately become extremely uncommon in the Western world. Unfortunately, it remains a significant problem in many other parts of the world. Subependymal cysts, microcephaly, and vasculopathy have been described.[216]

Neonatal Acquired Infections

Meningitis and Ventriculitis

Despite the development of antibiotics to treat bacterial infections, there are now cases of methicillin-resistant infections,[217] and bacterial meningitis remains a serious concern for infants and children. Neonatal sepsis has a major impact on neurodevelopmental outcome of extremely premature infants independent of other risk factors.[218] Schlapbach and colleagues[218] found three times the risk for cerebral palsy after sepsis; proposed mechanisms included direct brain damage from infection and secondary arterial hypotension from septic shock.

During the first month of an infant's life, the two most common infections result from *Escherichia coli* and group B streptococci. Between 4 and 12 weeks, *E. coli* and *Streptococcus pneumoniae* are the most common, and from 3 months to 3 years, *H. influenzae* is most frequent. Enteroviruses have been reported to cause encephalitis as well.[219] Meningitis is usually a clinical diagnosis; imaging is needed only to evaluate for complications or when the patient's clinical situation deteriorates.[31,216]

Complications of meningitis include subdural empyemas or fluid collections (Figs. 45.57 and 45.58), cerebritis, abscess formation, and venous sinus thrombosis. Infarctions can occur from either arterial vasculitis or venous obstruction, as a result of venous sinus thrombosis. Sonography can identify these complications but is not specific. Areas of increased or decreased echogenicity of brain parenchyma or sulci may represent edema, cerebritis, or evolving infarction (Fig. 45.59).

Ventriculitis, another complication of meningitis seen in 60% to 95% of cases, is suggested by the sonographic findings of hydrocephalus, echogenic debris within the ventricles, increased echogenicity, or a shaggy ependymal lining or fibrous septa within the ventricles (Fig. 45.60). Ultrasound is best for identifying intraventricular septa formation compared with CT or MRI. These septations can result in shunt failure or allow bacteria to escape antibiotic exposure. MRI and CT with enhancement are more sensitive for localizing the complications of infection, such as infarcts, venous sinus thrombosis, and extraaxial fluid collections.

INTRACRANIAL MASSES

Brain Tumors

In only 11% of children are brain neoplasms seen before 2 years of age. Tumors that do occur before the age of 2 years are usually congenital and may appear on prenatal ultrasound as polyhydramnios.[220] Tumors can be difficult to diagnosis in the neonate. If the neoplasm causes hydrocephalus, signs and symptoms of increased intracranial pressure, such as enlarging head size, vomiting, or behavioral alteration, it may be recognized. More specific signs and symptoms depend on the location of the tumor, such as cranial nerve findings or pituitary gland and hypothalamic dysfunctions. In general, MRI is the imaging modality of choice in these infants. However, with nonspecific signs and symptoms, including an enlarging head from hydrocephalus, ultrasound may be the first imaging procedure performed. Sonography can delineate the tumor site and size and evaluate cystic and solid components.

Tumors may manifest initially because of hemorrhage into the tumor. In fact, because hemorrhage is so much more common than tumor in newborns, it may be extremely difficult to differentiate a simple hematoma from a tumor; both can be quite echogenic. Any hemorrhage present in unusual circumstances or in an unusual location should be investigated by contrast-enhanced CT or MRI, searching for an occult tumor.[7] For unusual hemorrhage, follow-up scans are also helpful because clotting

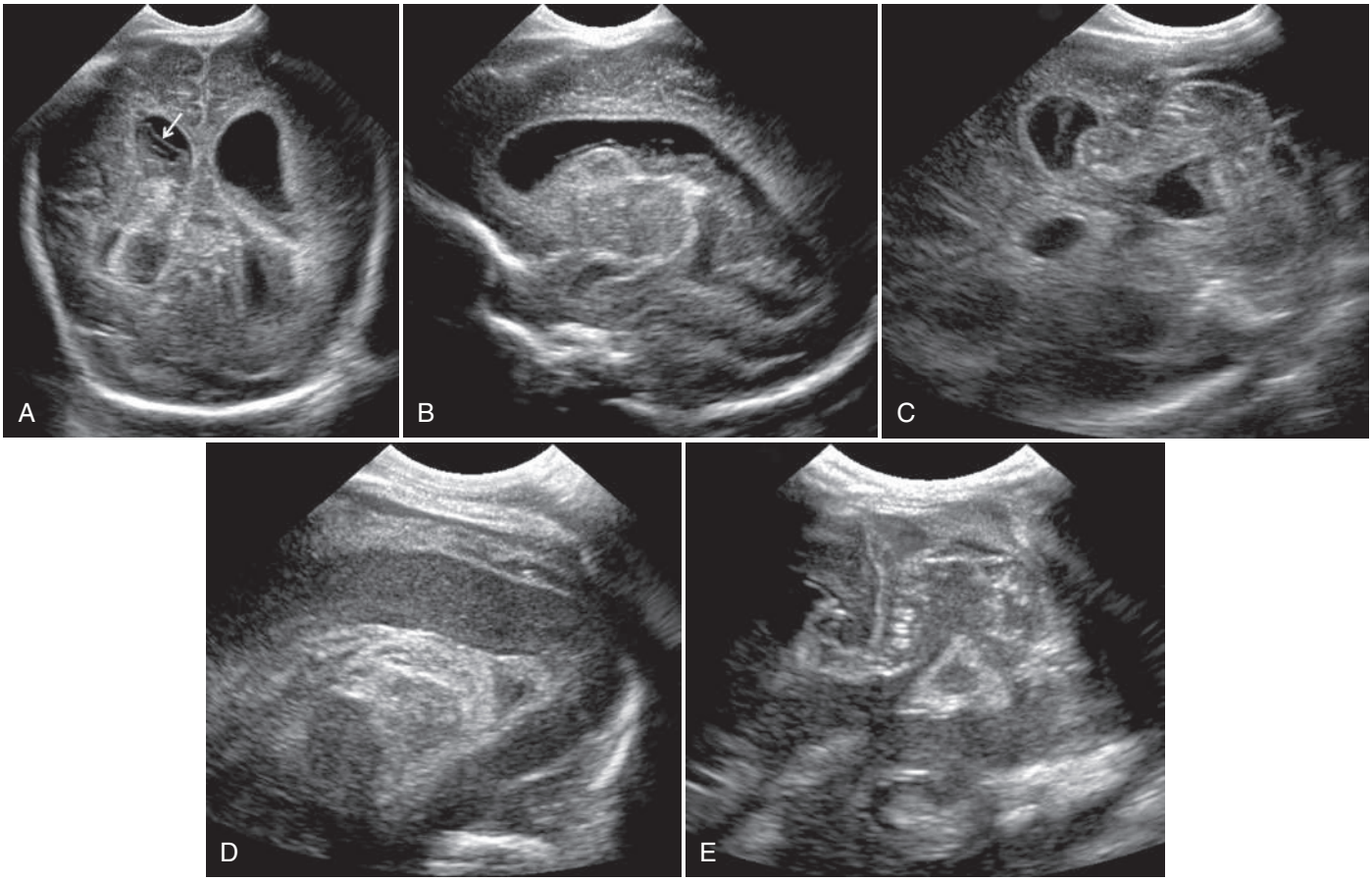

FIG. 45.57 Ventriculitis: *Escherichia Coli* Meningitis and *Chlamydia* Chorioamnionitis. (A)-(C) *E. coli* meningitis–affected infant with echogenic ventricular walls and intraventricular septations *(arrow).* **(D)** and **(E)** Thick, echogenic walls of the lateral ventricle and fourth ventricle in an infant of a mother with chlamydia, causing severe chorioamnionitis; at the time of cesarean section the uterus contained copious amounts of purulent fluid. Note echogenic material in the extraaxial space as well.

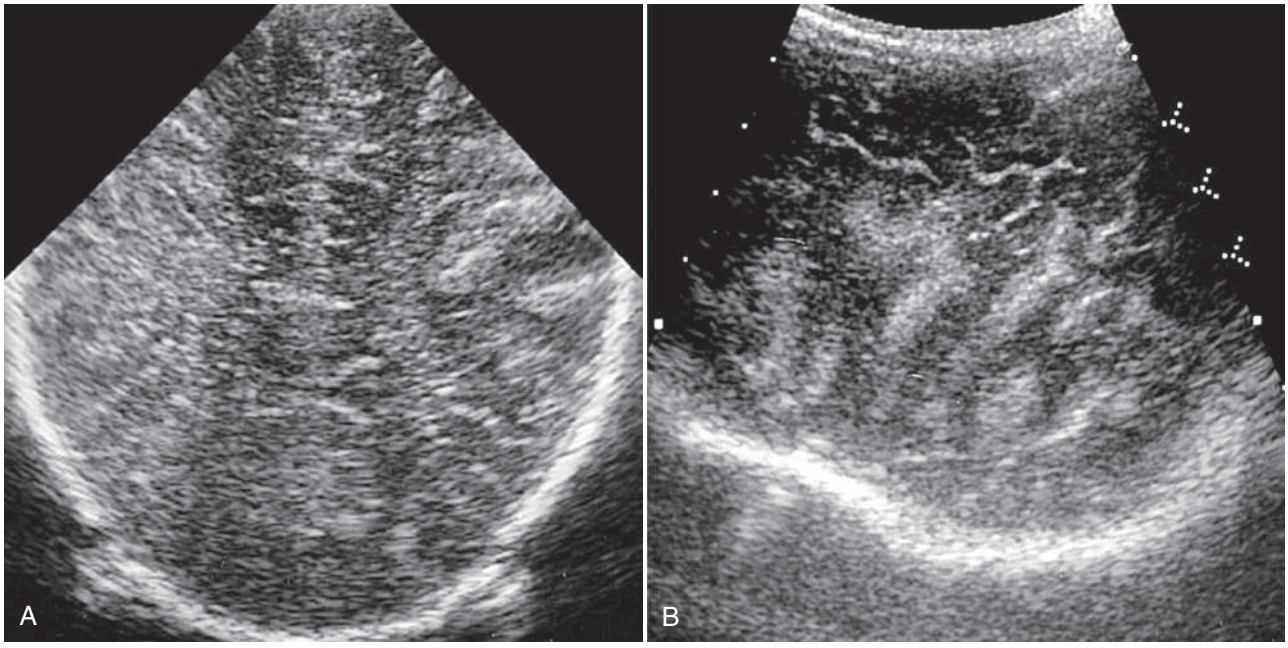

FIG. 45.58 Group B Streptococcal Meningitis. (A) and **(B)** Coronal and sagittal sonograms show diffusely echogenic sulci that appear thicker than normal.

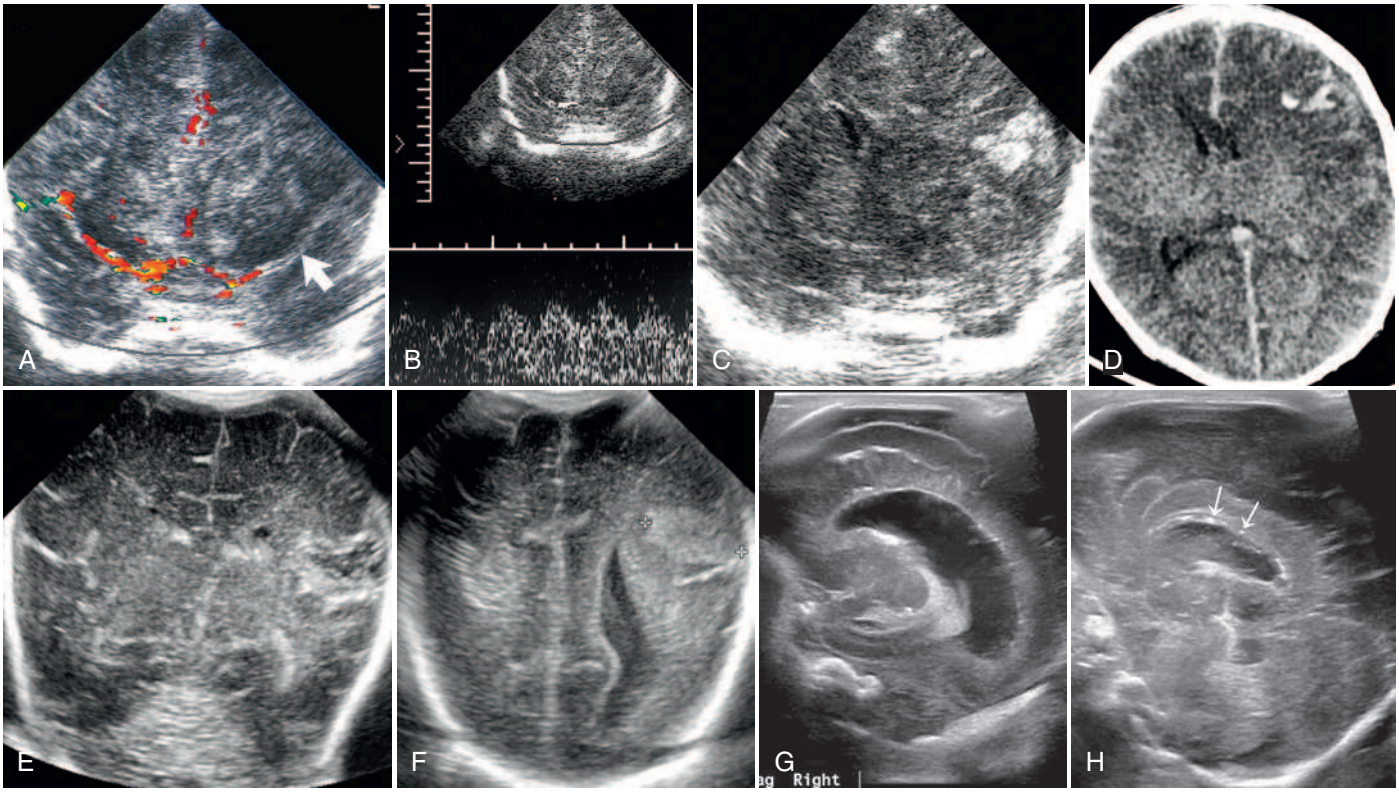

FIG. 45.59 Infections. (A)-(D) Group B streptococcal meningitis with focal infarction. (A) Coronal sonogram with color Doppler shows lack of flow in the left middle cerebral artery (MCA; *arrow*); gray-scale imaging alone showed symmetrical, increased echogenicity. **(B)** Pulsed Doppler image in the right MCA (opposite side) shows greatly increased diastolic flow. **(C)** Coronal sonogram and **(D)** computed tomography scan later show hemorrhage into an infarction with midline shift from left to right. **(E)** and **(F)** Coronal anterior and posterior sonograms show left MCA focal echogenic infarct *(calipers)*, cause unknown, in another premature infant at 2 weeks after birth. **(G)** and **(H)** Sagittal sonogram in fetus with unknown infection, but the pattern of calcification at gray-white junction suggests Zika. Note also the calcifications in the corpus callosum *(arrows)*. (**G** and **H** courtesy of I. Castro-Aragon, MD, Boston.)

from the hemorrhage will resolve over time, allowing the tumor to be visualized.

Spectral and color Doppler imaging can identify vascular components of the tumor. Follow-up with MRI is then performed to evaluate the full extent of the neoplasm, assist with differential diagnosis, and evaluate for therapeutic approaches. Differentiating the histologic type of the neoplasm is not possible, but localizing the tumor usually allows a differential diagnosis.

Tumor location in infants younger than 1 year differs from that in older children and differs by series.[31,221-223] **Supratentorial neoplasms** are more common than infratentorial tumors by approximately 2.5:1. **Teratomas** are the most frequent neoplasms reported in the first year of life. **Astrocytomas** (astrocytic gliomas) are second in most series, usually arising from the optic chiasm and nerves or the hypothalamus (Figs. 45.61 and 45.62). Other neoplasms include **atypical teratomas or rhabdoid tumors** (rather than medulloblastomas), **primitive neuroectodermal tumors** (PNETs), **ependymomas,**[224] and **choroid plexus papillomas** (Fig. 45.63). Sporadic cases of oligodendroglioma, hemangioblastoma, hemangioma, dermoid cyst, lipoma, primary neuroblastoma, teratoma, and meningioma have been reported.[224] A few cases of diffuse neonatal hemangiomatosis have been reported, with numerous hemangiomas of the brain, skin, spinal cord, liver, and heart. Although these may cause congestive heart failure, the greatest risk is bleeding into the lesions and possible disseminated intravascular coagulopathy. These infants do not usually live long enough for steroid therapy to cause involution of the lesions, which typically helps in neonatal hemangiomas.[225]

Common Brain Tumors in First Year of Life

Teratoma
Suprasellar astrocytoma (hypothalamic)
Teratoma or rhabdoid tumor
Ependymoma
Choroid plexus tumor

Cystic Intracranial Lesions

Cystic intracranial lesions are quite common, and ultrasound is the best method for evaluating such lesions (short of surgical proof). Fortunately, most cystic masses of the brain are

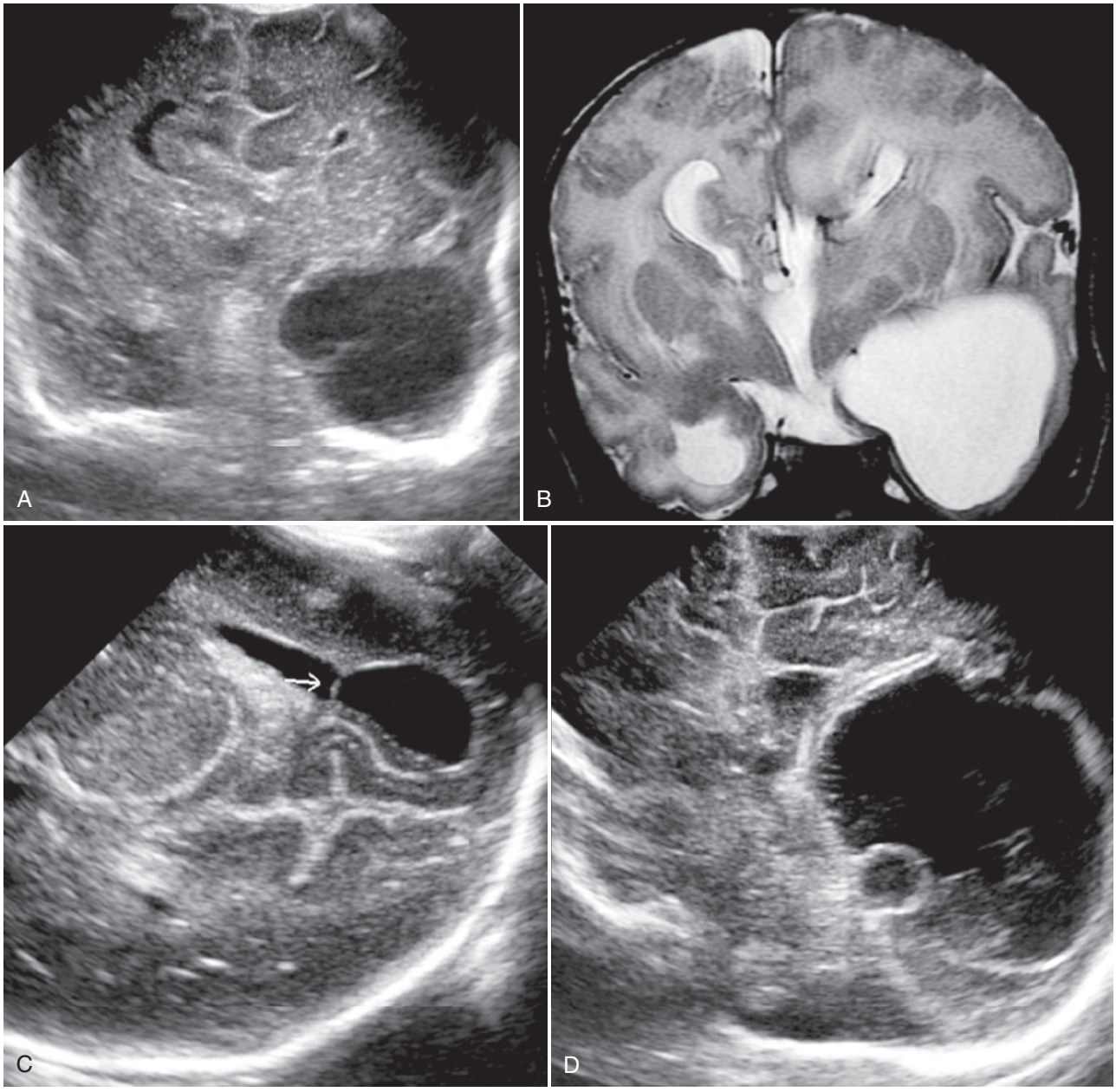

FIG. 45.60 Antenatal Infection: Ventriculitis. (A-D) Term infant with diffusely echogenic cerebral cortex and hydrocephalus. **(C)** Septations *(arrow)* have isolated the left temporal horn into a cystic mass, in addition to absence of the corpus callosum and vermian hypoplasia.

benign.[31,39,40,226,227] First, it is important to recognize the **normal cystic structures** and the variants discussed earlier under Developmental Anatomy, including the cavum septi pellucidi and vergae, cavum veli interpositi, frontal horn cysts, and cisterna magna (Table 45.3). Second, a normal variant, a large cisterna magna or **mega–cisterna magna,** is not a true cyst (see Fig. 45.27).

Arachnoid Cysts

Arachnoid cysts are the most common true cysts of the brain but make up only 1% of all space-occupying lesions in children.[31] Arachnoid cysts are CSF-containing spaces between two layers of arachnoid membrane. Primary and secondary cysts are believed to develop by different mechanisms. Primary cysts are believed to result from abnormal splitting of the arachnoid and from CSF collecting between the two layers. Secondary arachnoid cysts may develop when CSF is trapped between arachnoid adhesions. Arachnoid cysts, particularly those in the midline, may grow and cause obstruction of the ventricular system.[31] These midline arachnoid cysts most often manifest with hydrocephalus in infancy. The ultrasound appearance of an arachnoid cyst is an anechoic area with discrete walls. Midline arachnoid cysts are

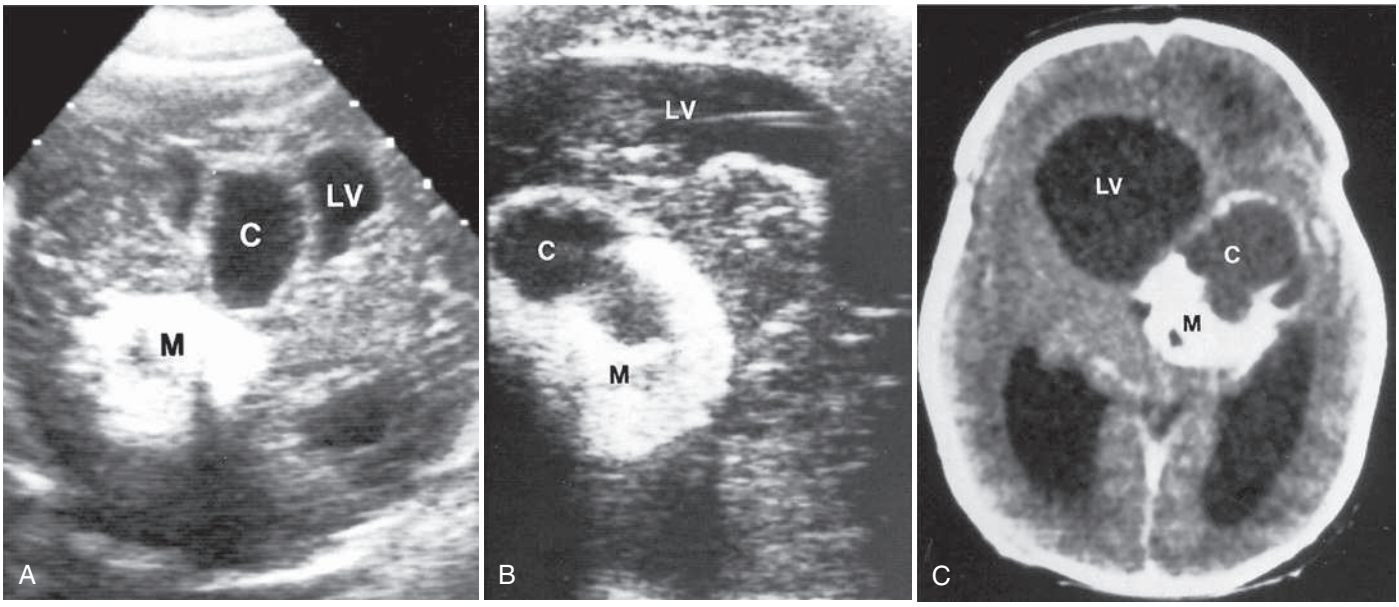

FIG. 45.61 Astrocytic Glioma (Astrocytoma). (A) and **(B)** Coronal and sagittal scans show echogenic mass *(M)* with cystic component *(C)* extending superiorly between lateral ventricles *(LV)*. **(C)** Axial enhanced computed tomography scan. (Courtesy of T. Stoeker, MD, Roanoke, VA.)

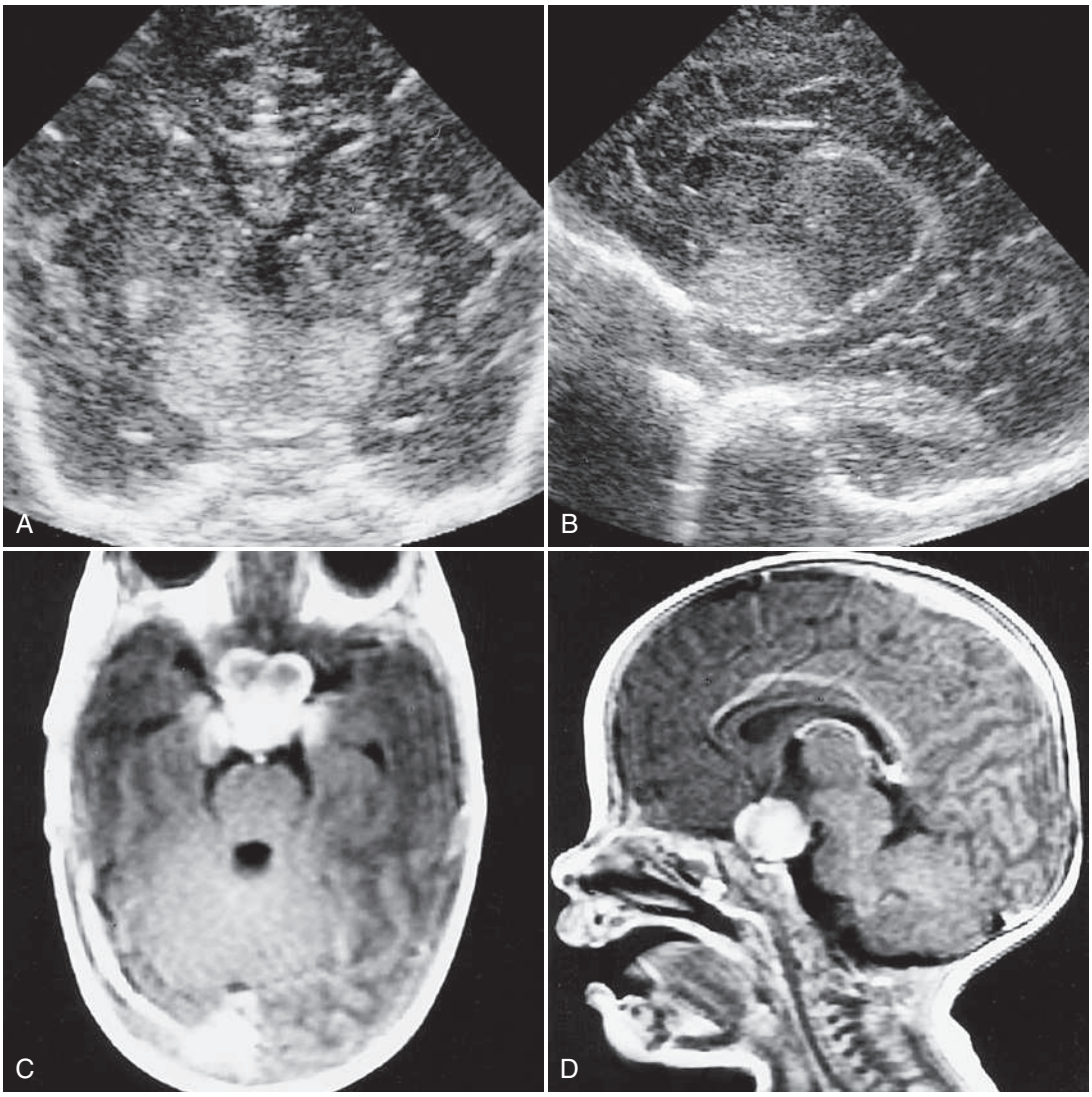

FIG. 45.62 Optic Glioma. (A) and **(B)** Coronal and sagittal sonograms show midline echogenic mass. **(C)** Computed tomography scan and **(D)** sagittal T1-weighted magnetic resonance image, with contrast, show enhancement of midline optic glioma.

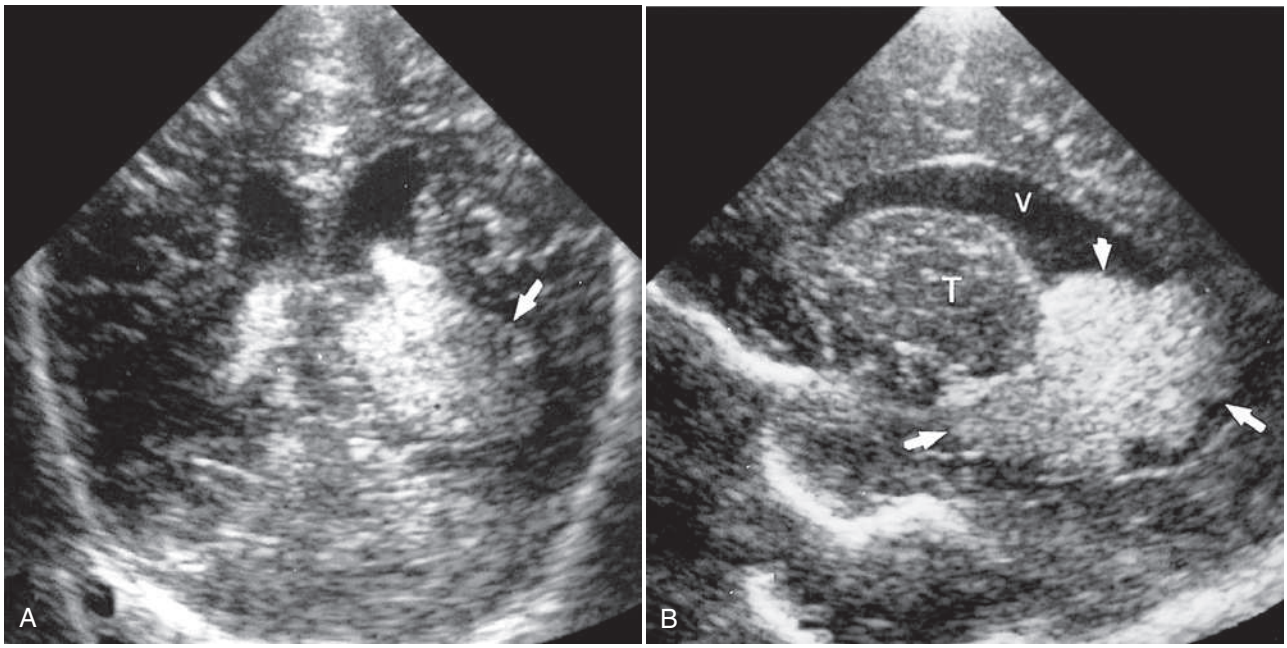

FIG. 45.63 Choroid Plexus Papilloma *(Arrows)* in Left Lateral Ventricle. (A) and **(B)** Coronal and sagittal sonograms. *T,* Thalamus; *V,* lateral ventricle. (Courtesy of D. Pretorius, MD, University of California at San Diego.)

TABLE 45.3 Cystic Brain Lesions

Category	Specific Lesions
Normal variants	Frontal horn cysts (connatal cysts, coarctation of the lateral ventricle)
	Choroid plexus cysts
Congenital	Primary arachnoid cyst
	Dandy-Walker malformation
	Hydranencephaly
	Holoprosencephaly
Periventricular	Periventricular leukomalacia
	Subependymal cyst
	Porencephalic cyst
Neoplastic	Cerebellar astrocytoma (cystic type)
	Craniopharyngioma
	Teratoma
Inflammatory	Abscess
	Subdural empyema
Other	Secondary arachnoid cysts
	Vein of Galen malformation

Sites of Arachnoid Cysts

Anterior portions of middle cranial fossa
Suprasellar region
Posterior fossa
Quadrigeminal region
Cerebral convexities
Interhemispheric fissure

[a]In decreasing order of frequency.

frequently associated with other brain anomalies. With agenesis of the corpus callosum, midline cysts are frequently continuous with an elevated third ventricle. In alobar holoprosencephaly, a dorsal cyst may be continuous with the single central ventricle.

Porencephalic Cysts

Porencephalic cysts are a result of brain necrosis and cavitation, which is continuous with the ventricular system (see Fig. 45.44). These lesions are usually caused by brain parenchymal hemorrhage, infection, or surgery.[7]

Choroid Plexus Cysts

Choroid plexus cysts are common and usually asymptomatic. Choroid cysts occur in all age groups and are found in 34% of fetuses and infants at autopsy. However, prenatal and neonatal ultrasound reports have identified choroid cysts in only approximately 1% of the populations studied. Choroid plexus cysts tend to be single and occur as an isolated finding. However, large (>10 mm) and multiple choroid cysts are occasionally associated with chromosomal anomalies, particularly trisomy 18,[2] trisomy 21, and Aicardi syndrome.[228] Many other anomalies are typically present in these newborns.

A choroid plexus cyst appears as a cyst with well-defined walls within the choroid plexus (Fig. 45.64). Choroid cysts vary in size from less than 4 mm to over 1 cm and are usually unilateral, left greater than right, and situated in the dorsal aspect of the choroid plexus. Rare cases of symptomatic choroid cysts causing obstructive hydrocephalus have been reported but are probably related to some specific cause rather than a normal variant.[228] Occasional choroid cysts develop after choroid plexus hemorrhage into the ventricle. Color Doppler is helpful to distinguish vessels in the choroid from cysts.

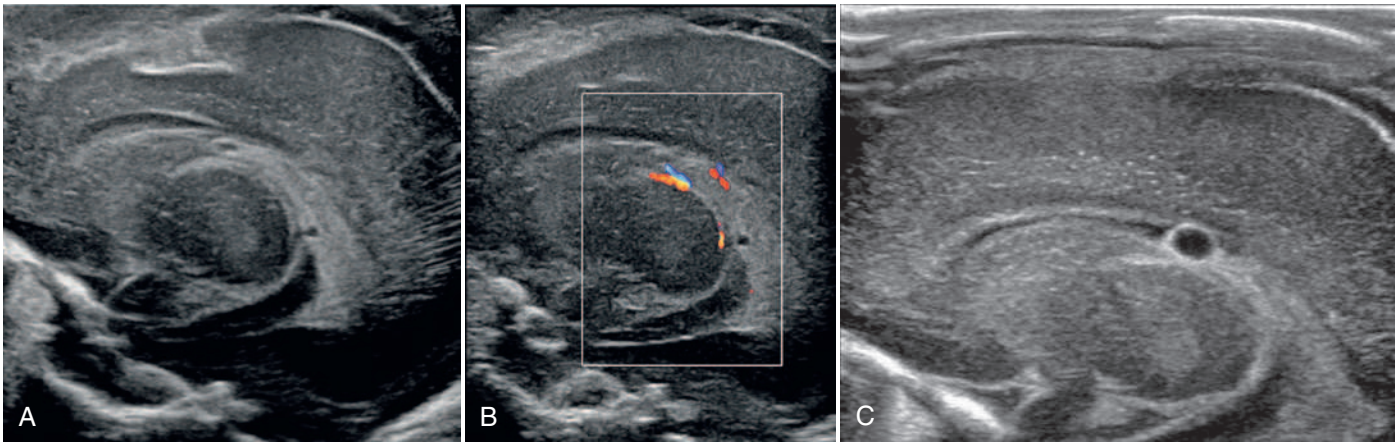

FIG. 45.64 Choroid Plexus Cysts. (A)-(C) Sagittal sonograms show varying sizes of cysts. Normal vascularity of the choroid plexus and avascularity of the cyst are demonstrated.

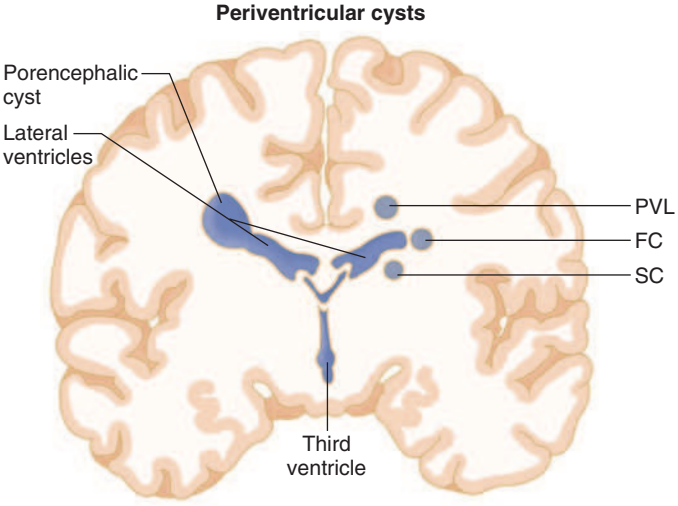

FIG. 45.65 Periventricular Cysts. These cysts include the normal-variant frontal horn cyst *(FC),* the subependymal cyst *(SC),* cystic periventricular leukomalacia *(PVL),* and porencephalic cysts that communicate directly with the ventricle, caused by intraparenchymal hemorrhage or infection (cerebritis).

Supratentorial Periventricular Cystic Lesions

Many periventricular cysts are found in and around the normal ventricles (Fig. 45.65).

Frontal Horn Cysts

The frontal horn cysts that are attached directly lateral to the frontal horn have also been called **coarctation of the lateral ventricles** and **connatal cysts**[40] (see Fig. 45.14A). Although these frontal horn cysts were previously thought to be postischemic, it is now believed that they form as a normal variant anterior to the foramen of Monro. The ventricle seems to have folded on itself, causing the wall to lie against the frontal horn.

Subependymal Cysts

Subependymal cysts are discrete cysts in the lining of the ventricles (Fig. 45.66). These cysts most often result from the sequelae of GMH in premature infants.[229] Other causes include infection, including CMV and rubella, and the rare **cerebrohepatorenal (Zellweger) syndrome.**[61,84] Subependymal cysts can also be an isolated finding with no apparent predisposing event. Cocaine exposure has been reported to increase the incidence of subependymal cysts in premature infants.[230]

Periventricular Leukomalacia

Periventricular cysts also result from PVL (see Fig. 45.50). These cysts develop lateral to and above the entire lateral ventricle, typically above the frontal horn and body of the ventricle.

Galenic Venous Malformations

Galenic venous malformations are frequently referred to as "vein of Galen aneurysms," but this is a misnomer because these are not true aneurysms. These abnormalities actually represent dilation of the vein of Galen caused by a vascular malformation that is fed by large arteries off the anterior or posterior cerebral artery circulation.[231] Infants with large shunts usually are presented in the first month of life with **congestive heart failure.** In later childhood, smaller shunts manifest with seizure, cranial bruit, hydrocephalus, and cardiomegaly.

Sonographically, a galenic venous malformation appears as an anechoic cystic mass between the lateral ventricles (Fig. 45.67). It lies posterior to the foramen of Monro, superior to the third ventricle, and primarily in the midline. These malformations are differentiated from other cystic masses by identification of a large feeding vessel. Spectral or color Doppler sonography can be used to identify blood flow filling the mass, thus confirming the diagnosis. Hydrocephalus may or may not be present. Calcification may occur, especially if there is thrombosis in the malformation.[232] MRI and magnetic resonance angiography may be valuable in planning treatment.[233,234]

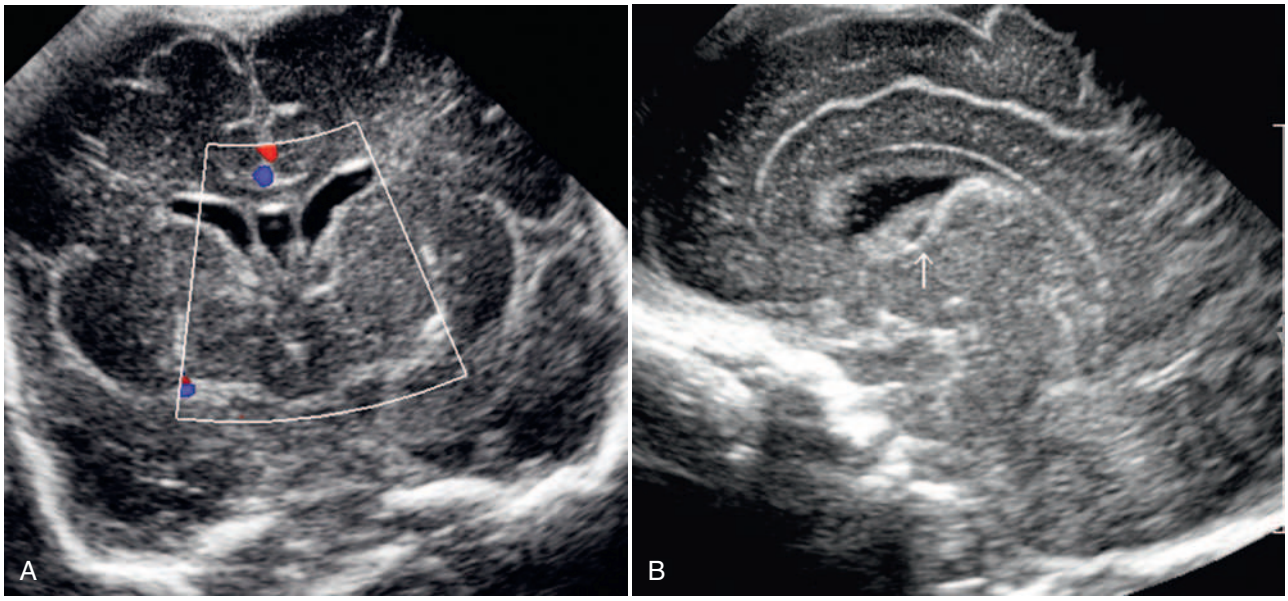

FIG. 45.66 Subependymal Cyst. (A) and **(B)** Coronal and midline sagittal sonograms show cyst *(arrow),* which formed after cytomegalovirus antenatal infection in the region of the caudothalamic notch, where we typically expect to see germinal matrix hemorrhage. The cyst was present at birth.

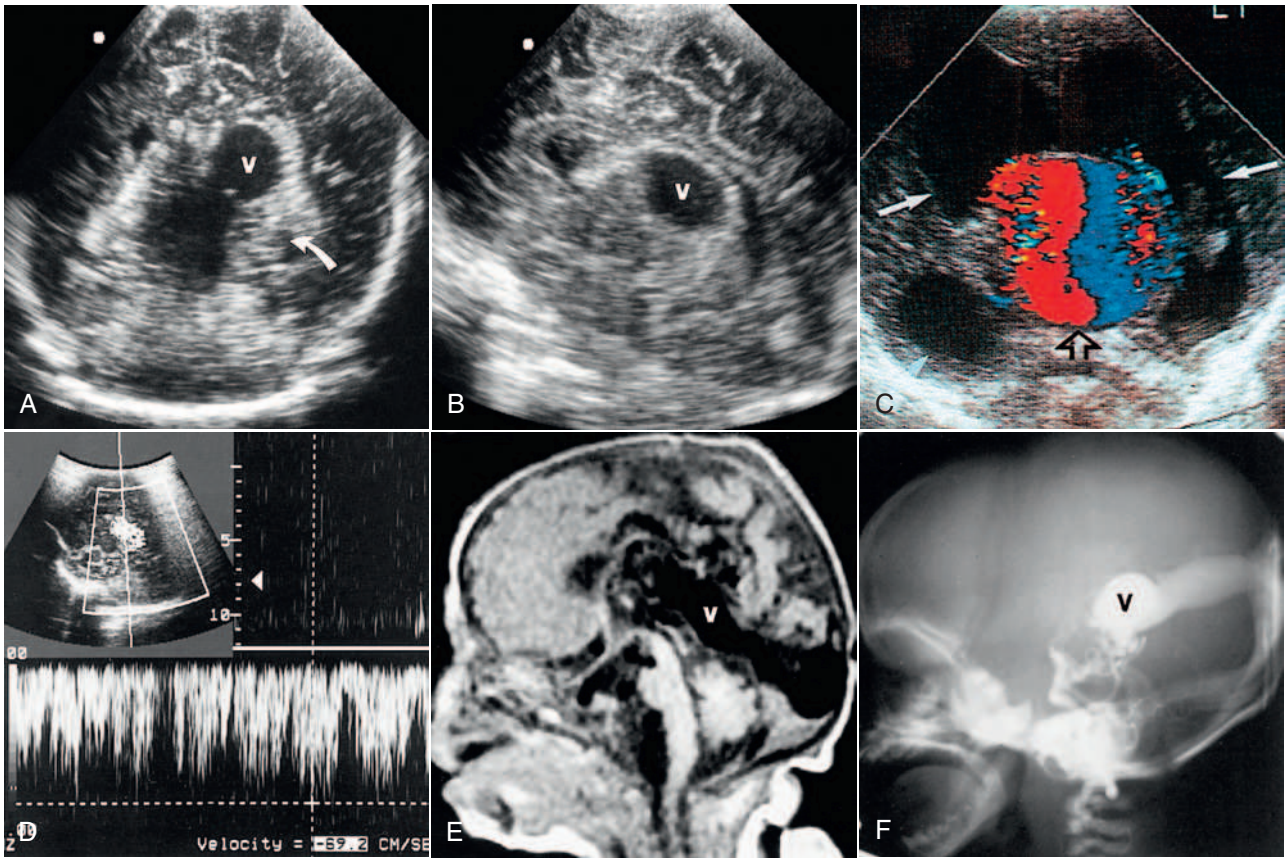

FIG. 45.67 Vein of Galen Malformation. (A) and **(B)** Coronal and sagittal sonograms show enlarged vein of Galen *(V)* and straight sinus. Echogenic arterial feeding vessels below and anterior to dilated vein of Galen *(curved arrow).* **(C)** and **(D)** Color Doppler and duplex Doppler ultrasound scans show turbulent flow, which clearly defines this cystic-appearing mass as vascular. **(E)** Sagittal magnetic resonance scan and **(F)** angiogram, in a different patient, show that the echogenic region is a tortuous tangle of abnormal feeding vessels; cystic mass is dilated vein of Galen *(V).*

REFERENCES

1. Barr LL. Neonatal cranial ultrasound. Radiol Clin North Am. 1999;37(6):1127-1146, vi.
2. Benson JE, Bishop MR, Cohen HL. Intracranial neonatal neurosonography: an update. Ultrasound Q. 2002;18(2):89-114.
3. Daneman A, Epelman M. Neurosonography: in pursuit of an optimized examination. Pediatr Radiol. 2015;45(Suppl. 3):S406-S412.
4. Epelman M, Daneman A, Kellenberger CJ, et al. Neonatal encephalopathy: a prospective comparison of head US and MRI. Pediatr Radiol. 2010; 40(10):1640-1650.
5. Bulas D. Fetal magnetic resonance imaging as a complement to fetal ultrasonography. Ultrasound Q. 2007;23(1):3-22.
6. Barnette AR, Horbar JD, Soll RF, et al. Neuroimaging in the evaluation of neonatal encephalopathy. Pediatrics. 2014;133(6):e1508-e1517.
7. Rumack CM, Manco-Johnson ML. Perinatal and infant brain imaging: role of ultrasound and computed tomography. St Louis: Mosby; 1984.
8. Thomson GD, Teele RL. High-frequency linear array transducers for neonatal cerebral sonography. AJR Am J Roentgenol. 2001;176(4):995-1001.
9. de Vries LS, Benders MJ, Groenendaal F. Imaging the premature brain: ultrasound or MRI? Neuroradiology. 2013;55(Suppl. 2):13-22.
10. Angtuaco TL. Navigating the neonatal brain through the base of the skull: an effective sonographic teaching tool. Ultrasound Q. 2004;20(2): 38-44.
11. Enriquez G, Correa F, Aso C, et al. Mastoid fontanelle approach for sonographic imaging of the neonatal brain. Pediatr Radiol. 2006;36(6): 532-540.
12. Correa F, Enriquez G, Rossello J, et al. Posterior fontanelle sonography: an acoustic window into the neonatal brain. AJNR Am J Neuroradiol. 2004;25(7):1274-1282.
13. Pigadas A, Thompson JR, Grube GL. Normal infant brain anatomy: correlated real-time sonograms and brain specimens. AJR Am J Roentgenol. 1981;137(4):815-820.
14. Di Salvo DN. A new view of the neonatal brain: clinical utility of supplemental neurologic US imaging windows. Radiographics. 2001;21(4):9439-9455.
15. Luna JA, Goldstein RB. Sonographic visualization of neonatal posterior fossa abnormalities through the posterolateral fontanelle. AJR Am J Roentgenol. 2000;174(2):561-567.
16. Rumack CR, Horgan JG, Hay TC, et al. Pocket atlas of pediatric ultrasound. Philadelphia: Lippincott-Raven; 1990.
17. van Wezel-Meijler G, Leijser LM, Wiggers-de Bruine FT, et al. Diffuse hyperechogenicity of basal ganglia and thalami in preterm neonates: a physiologic finding? Radiology. 2011;258(3):944-950.
18. Ginath S, Lerman-Sagie T, Haratz Krajden K, et al. The fetal vermis, pons and brainstem: normal longitudinal development as shown by dedicated neurosonography. J Matern Fetal Neonatal Med. 2013;26(8):757-762.
19. Cuddihy SL, Anderson NG, Wells JE, Darlow BA. Cerebellar vermis diameter at cranial sonography for assessing gestational age in low-birth-weight infants. Pediatr Radiol. 1999;29(8):589-594.
20. Dorovini-Zis K, Dolman CL. Gestational development of brain. Arch Pathol Lab Med. 1977;101(4):192-195.
21. DiPietro MA, Brody BA, Teele RL. Peritrigonal echogenic "blush" on cranial sonography: pathologic correlates. AJR Am J Roentgenol. 1986;146(5): 1067-1072.
22. Buckley KM, Taylor GA, Estroff JA, et al. Use of the mastoid fontanelle for improved sonographic visualization of the neonatal midbrain and posterior fossa. AJR Am J Roentgenol. 1997;168(4):1021-1025.
23. Burger IM, Filly RA, Bowie J, Barkovich AJ. The grand unifying theory of bright echoes in the fetal and neonatal brain. J Ultrasound Med. 2012; 31(10):1665-1673.
24. Teele RL, Taylor GA. Demonstration of fourth ventricular choroid plexus on neonatal cranial ultrasonography. Pediatr Radiol. 2012;42(5):620-623.
25. Steggerda SJ, de Bruine FT, Smits-Wintjens VE, et al. Ultrasound detection of posterior fossa abnormalities in full-term neonates. Early Hum Dev. 2012;88(4):233-239.
26. Romero JM, Madan N, Betancur I, et al. Time efficiency and diagnostic agreement of 2-D versus 3-D ultrasound acquisition of the neonatal brain. Ultrasound Med Biol. 2014;40(8):1804-1809.
27. Csutak R, Unterassinger L, Rohrmeister C, et al. Three-dimensional volume measurement of the lateral ventricles in preterm and term infants: evaluation of a standardised computer-assisted method in vivo. Pediatr Radiol. 2003;33(2):104-109.
28. Glenn OA, Goldstein RB, Li KC, et al. Fetal magnetic resonance imaging in the evaluation of fetuses referred for sonographically suspected abnormalities of the corpus callosum. J Ultrasound Med. 2005;24(6):791-804.
29. American Institute of Ultrasound in Medicine, American College of Radiology, Society of Radiologists in Ultrasound. AIUM practice guideline for the performance of neurosonography in neonates and infants. J Ultrasound Med. 2014;33(6):1103-1110.
30. Ghai S, Fong KW, Toi A, et al. Prenatal US and MR imaging findings of lissencephaly: review of fetal cerebral sulcal development. Radiographics. 2006;26(2):389-405.
31. Barkovich AJ. Pediatric neuroimaging. 4th ed. Philadelphia: Lippincott-Williams & Wilkins; 2012.
32. Govaert P, Swarte R, De Vos A, Lequin M. Sonographic appearance of the normal and abnormal insula of Reil. Dev Med Child Neurol. 2004;46(9): 610-616.
33. Worthen NJ, Gilbertson V, Lau C. Cortical sulcal development seen on sonography: relationship to gestational parameters. J Ultrasound Med. 1986;5(3):153-156.
34. Armstrong DL, Bagnall C, Harding JE, Teele RL. Measurement of the subarachnoid space by ultrasound in preterm infants. Arch Dis Child Fetal Neonatal Ed. 2002;86(2):F124-F126.
35. Shaw CM, Alvord Jr EC. Cava septi pellucidi et vergae: their normal and pathological states. Brain. 1969;92(1):213-223.
36. Callen PW, Callen AL, Glenn OA, Toi A. Columns of the fornix, not to be mistaken for the cavum septi pellucidi on prenatal sonography. J Ultrasound Med. 2008;27(1):25-31.
37. Chen CY, Chen FH, Lee CC, et al. Sonographic characteristics of the cavum velum interpositum. AJNR Am J Neuroradiol. 1998;19(9):1631-1635.
38. Blasi I, Henrich W, Argento C, Chaoui R. Prenatal diagnosis of a cavum veli interpositi. J Ultrasound Med. 2009;28(5):683-687.
39. Rosenfeld DL, Schonfeld SM, Underberg-Davis S. Coarctation of the lateral ventricles: an alternative explanation for subependymal pseudocysts. Pediatr Radiol. 1997;27(12):895-897.
40. Epelman M, Daneman A, Blaser SI, et al. Differential diagnosis of intracranial cystic lesions at head US: correlation with CT and MR imaging. Radiographics. 2006;26(1):173-196.
41. Enriquez G, Correa F, Lucaya J, et al. Potential pitfalls in cranial sonography. Pediatr Radiol. 2003;33(2):110-117.
42. Friede R. Developmental neuropathology. 2nd ed. New York: Springer-Verlag; 1975.
43. Robinson AJ, Goldstein R. The cisterna magna septa: vestigial remnants of Blake's pouch and a potential new marker for normal development of the rhombencephalon. J Ultrasound Med. 2007;26(1):83-95.
44. Oh KY, Rassner UA, Frias Jr AE, Kennedy AM. The fetal posterior fossa: clinical correlation of findings on prenatal ultrasound and fetal magnetic resonance imaging. Ultrasound Q. 2007;23(3):203-210.
45. Robinson AJ, Blaser S, Toi A, et al. The fetal cerebellar vermis: assessment for abnormal development by ultrasonography and magnetic resonance imaging. Ultrasound Q. 2007;23(3):211-223.
46. Volpe JJ. Brain injury in premature infants: a complex amalgam of destructive and developmental disturbances. Lancet Neurol. 2009;8(1):110-124.
47. Gilles FH, Leviton A, Dooling EC. The developing human brain. Boston: John Wright–PSG; 1983.
48. DeMyer W. Classification of cerebral malformations. Birth Defects Orig Artic Ser. 1971;7(1):78-93.
49. Limperopoulos C, du Plessis AJ. Disorders of cerebellar growth and development. Curr Opin Pediatr. 2006;18(6):621-627.
50. Patel S, Barkovich AJ. Analysis and classification of cerebellar malformations. AJNR Am J Neuroradiol. 2002;23(7):1074-1087.
51. Coley BD. Ultrasound diagnosis of lückenschädel (lacunar skull). Pediatr Radiol. 2000;30(2):82-84.
52. Babcook CJ, Goldstein RB, Barth RA, et al. Prevalence of ventriculomegaly in association with myelomeningocele: correlation with gestational age and severity of posterior fossa deformity. Radiology. 1994;190(3):703-707.

53. Barkovich AJ. Diagnostic imaging: pediatric neuroradiology. 2nd ed. Philadelphia: Elsevier; 2015.
54. Kier EL, Truwit CL. The normal and abnormal genu of the corpus callosum: an evolutionary, embryologic, anatomic, and MR analysis. AJNR Am J Neuroradiol. 1996;17(9):1631-1641.
55. Goodyear PW, Bannister CM, Russell S, Rimmer S. Outcome in prenatally diagnosed fetal agenesis of the corpus callosum. Fetal Diagn Ther. 2001; 16(3):139-145.
56. Babcock DS. The normal, absent, and abnormal corpus callosum: sonographic findings. Radiology. 1984;151(2):449-453.
57. Aletebi FA, Fung KF. Neurodevelopmental outcome after antenatal diagnosis of posterior fossa abnormalities. J Ultrasound Med. 1999;18(10):683-689.
58. Estroff JA, Parad RB, Barnes PD, et al. Posterior fossa arachnoid cyst: an in utero mimicker of Dandy-Walker malformation. J Ultrasound Med. 1995;14(10):787-790.
59. Hart MN, Malamud N, Ellis WG. The Dandy-Walker syndrome. A clinicopathological study based on 28 cases. Neurology. 1972; 22(8):771-780.
60. Lachman RS, Taybi H. Taybi and Lachman's radiology of syndromes, metabolic disorders, and skeletal dysplasias. 5th ed. St Louis: Mosby-Elsevier; 2007.
61. DeMyer W, Zeman W, Palmer CG. The face predicts the brain: diagnostic significance of median facial anomalies for holoprosencephaly (arhinencephaly). Pediatrics. 1964;34:256-263.
62. Stashinko EE, Clegg NJ, Kammann HA, et al. A retrospective survey of perinatal risk factors of 104 living children with holoprosencephaly. Am J Med Genet A. 2004;128a(2):114-119.
63. Volpe P, Campobasso G, De Robertis V, Rembouskos G. Disorders of prosencephalic development. Prenat Diagn. 2009;29(4):340-354.
64. Lewis AJ, Simon EM, Barkovich AJ, et al. Middle interhemispheric variant of holoprosencephaly: a distinct cliniconeuroradiologic subtype. Neurology. 2002;59(12):1860-1865.
65. Hahn JS, Barnes PD. Neuroimaging advances in holoprosencephaly: refining the spectrum of the midline malformation. Am J Med Genet C Semin Med Genet. 2010;154C(1):120-132.
66. Malinger G, Lev D, Kidron D, et al. Differential diagnosis in fetuses with absent septum pellucidum. Ultrasound Obstet Gynecol. 2005; 25(1):42-49.
67. Oh KY, Kennedy AM, Frias Jr AE, Byrne JL. Fetal schizencephaly: pre- and postnatal imaging with a review of the clinical manifestations. Radiographics. 2005;25(3):647-657.
68. Sener RN. Schizencephaly and congenital cytomegalovirus infection. J Neuroradiol. 1998;25(2):151-152.
69. Iannetti P, Nigro G, Spalice A, et al. Cytomegalovirus infection and schizencephaly: case reports. Ann Neurol. 1998;43(1):123-127.
70. Lee HK, Kim JS, Hwang YM, et al. Location of the primary motor cortex in schizencephaly. AJNR Am J Neuroradiol. 1999;20(1):163-166.
71. Cecchetto G, Milanese L, Giordano R, et al. Looking at the missing brain: hydranencephaly case series and literature review. Pediatr Neurol. 2013;48(2):152-158.
72. Pretorius DH, Russ PD, Rumack CM, et al., editors. Diagnosis of brain neuropathology in utero. Berlin: Springer-Verlag; 1987.
73. Leijser LM, de Vries LS, Rutherford MA, et al. Cranial ultrasound in metabolic disorders presenting in the neonatal period: characteristic features and comparison with MR imaging. AJNR Am J Neuroradiol. 2007;28(7): 1223-1231.
74. Senat MV, Bernard JP, Delezoide A, et al. Prenatal diagnosis of hydrocephalus-stenosis of the aqueduct of Sylvius by ultrasound in the first trimester of pregnancy. Report of two cases. Prenat Diagn. 2001;21(13):1129-1132.
75. Benacerraf BR, Shipp TD, Bromley B, Levine D. What does magnetic resonance imaging add to the prenatal sonographic diagnosis of ventriculomegaly? J Ultrasound Med. 2007;26(11):1513-1522.
76. Lee CS, Hong SH, Wang KC, et al. Fetal ventriculomegaly: prognosis in cases in which prenatal neurosurgical consultation was sought. J Neurosurg. 2006;105(4 Suppl.):265-270.
77. Levine D, Feldman HA, Tannus JF, et al. Frequency and cause of disagreements in diagnoses for fetuses referred for ventriculomegaly. Radiology. 2008;247(2):516-527.
78. Filly RA, Goldstein RB. The fetal ventricular atrium: fourth down and 10 mm to go. Radiology. 1994;193(2):315-317.
79. Alagappan R, Browning PD, Laorr A, McGahan JP. Distal lateral ventricular atrium: reevaluation of normal range. Radiology. 1994;193(2):405-408.
80. Rosenfeld DL, Lis E, DeMarco K. Transtentorial herniation of the fourth ventricle. Pediatr Radiol. 1995;25(6):436-439.
81. Forstner R, Hoffmann GF, Gassner I, et al. Glutaric aciduria type I: ultrasonographic demonstration of early signs. Pediatr Radiol. 1999;29(2): 138-143.
82. Dogra VS, Shyken JM, Menon PA, et al. Neurosonographic abnormalities associated with maternal history of cocaine use in neonates of appropriate size for their gestational age. AJNR Am J Neuroradiol. 1994;15(4): 697-702.
83. Dean LM, Taylor GA. The intracranial venous system in infants: normal and abnormal findings on duplex and color Doppler sonography. AJR Am J Roentgenol. 1995;164(1):151-156.
84. Taylor GA. New concepts in the pathogenesis of germinal matrix intraparenchymal hemorrhage in premature infants. AJNR Am J Neuroradiol. 1997;18(2):231-232.
85. Ghazi-Birry HS, Brown WR, Moody DM, et al. Human germinal matrix: venous origin of hemorrhage and vascular characteristics. AJNR Am J Neuroradiol. 1997;18(2):219-229.
86. Taylor GA. Effect of germinal matrix hemorrhage on terminal vein position and patency. Pediatr Radiol. 1995;25(Suppl. 1):S37-S40.
87. Chao CP, Zaleski CG, Patton AC. Neonatal hypoxic-ischemic encephalopathy: multimodality imaging findings. Radiographics. 2006;26(Suppl. 1): S159-S172.
88. Huang BY, Castillo M. Hypoxic-ischemic brain injury: imaging findings from birth to adulthood. Radiographics. 2008;28(2):417-439.
89. Hintz SR, O'Shea M. Neuroimaging and neurodevelopmental outcomes in preterm infants. Semin Perinatol. 2008;32(1):11-19.
90. Leijser LM, de Bruine FT, Steggerda SJ, et al. Brain imaging findings in very preterm infants throughout the neonatal period: part I. Incidences and evolution of lesions, comparison between ultrasound and MRI. Early Hum Dev. 2009;85(2):101-119.
91. Rutherford M, Srinivasan L, Dyet L, et al. Magnetic resonance imaging in perinatal brain injury: clinical presentation, lesions and outcome. Pediatr Radiol. 2006;36(7):582-592.
92. Liauw L, van der Grond J, van den Berg-Huysmans AA, et al. Hypoxic-ischemic encephalopathy: diagnostic value of conventional MR imaging pulse sequences in term-born neonates. Radiology. 2008;247(1):204-212.
93. Inder TE, Anderson NJ, Spencer C, et al. White matter injury in the premature infant: a comparison between serial cranial sonographic and MR findings at term. AJNR Am J Neuroradiol. 2003;24(5):805-809.
94. Ment LR, Schneider KC, Ainley MA, Allan WC. Adaptive mechanisms of developing brain. The neuroradiologic assessment of the preterm infant. Clin Perinatol. 2000;27(2):303-323.
95. Paul DA, Pearlman SA, Finkelstein MS, Stefano JL. Cranial sonography in very-low-birth-weight infants: do all infants need to be screened? Clin Pediatr (Phila). 1999;38(9):503-509.
96. Khwaja O, Volpe JJ. Pathogenesis of cerebral white matter injury of prematurity. Arch Dis Child Fetal Neonatal Ed. 2008;93(2):F153-F161.
97. Lemons JA, Bauer CR, Oh W, et al. Very low birth weight outcomes of the National Institute of Child Health and Human Development Neonatal Research Network, January 1995 through December 1996. NICHD Neonatal Research Network. Pediatrics. 2001;107(1):E1.
98. Shankaran S, Bauer C, Bain R, et al. Relationship between antenatal steroid administration and grades III and IV intracranial hemorrhage in low birth weight infants. Am J Obstet Gynecol. 1995;173:305-312.
99. Maher JE, Cliver SP, Goldenberg RL, et al. The effect of corticosteroid therapy in the very premature infant. March of Dimes multicenter study. Am J Obstet Gynecol. 1994;170:869-873.
100. Burstein J, Papile LA, Burstein R. Intraventricular hemorrhage and hydrocephalus in premature newborns: a prospective study with CT. AJR Am J Roentgenol. 1979;132(4):631-635.

101. Rumack CM, Manco-Johnson ML, Manco-Johnson MJ, et al. Timing and course of neonatal intracranial hemorrhage using real-time ultrasound. Radiology. 1985;154(1):101-105.
102. Boal DK, Watterberg KL, Miles S, Gifford KL. Optimal cost-effective timing of cranial ultrasound screening in low-birth-weight infants. Pediatr Radiol. 1995;25(6):425-428.
103. Townsend SF, Rumack CM, Thilo EH, et al. Late neurosonographic screening is important to the diagnosis of periventricular leukomalacia and ventricular enlargement in preterm infants. Pediatr Radiol. 1999;29(5):347-352.
104. Perlman JM, Rollins N. Surveillance protocol for the detection of intracranial abnormalities in premature neonates. Arch Pediatr Adolesc Med. 2000; 154(8):822-826.
105. Cramer BC, Walsh EA. Cisterna magna clot and subsequent post-hemorrhagic hydrocephalus. Pediatr Radiol. 2001;31(3):153-159.
106. Rudas G, Varga E, Meder U, et al. Changes in echogenicity of spinal subarachnoid space associated with intracranial hemorrhage: new observations. Pediatr Radiol. 2000;30(11):739-742.
107. Vohr B, Allan WC, Scott DT, et al. Early-onset intraventricular hemorrhage in preterm neonates: incidence of neurodevelopmental handicap. Semin Perinatol. 1999;23(3):212-217.
108. Bolisetty S, Dhawan A, Abdel-Latif M, et al. Intraventricular hemorrhage and neurodevelopmental outcomes in extreme preterm infants. Pediatrics. 2014;133(1):55-62.
109. Murphy BP, Inder TE, Rooks V, et al. Posthaemorrhagic ventricular dilatation in the premature infant: natural history and predictors of outcome. Arch Dis Child Fetal Neonatal Ed. 2002;87(1):F37-F41.
110. Alan N, Manjila S, Minich N, et al. Reduced ventricular shunt rate in very preterm infants with severe intraventricular hemorrhage: an institutional experience. J Neurosurg Pediatr. 2012;10(5):357-364.
111. Tsitouras V, Sgouros S. Infantile posthemorrhagic hydrocephalus. Childs Nerv Syst. 2011;27(10):1595-1608.
112. Salamon N. Neuroimaging of cerebral small vessel disease. Brain Pathol. 2014;24(5):519-524.
113. Bass WT, Jones MA, White LE, et al. Ultrasonographic differential diagnosis and neurodevelopmental outcome of cerebral white matter lesions in premature infants. J Perinatol. 1999;19(5):330-336.
114. Bassan H, Limperopoulos C, Visconti K, et al. Neurodevelopmental outcome in survivors of periventricular hemorrhagic infarction. Pediatrics. 2007; 120(4):785-792.
115. O'Shea TM, Kuban KC, Allred EN, et al. Neonatal cranial ultrasound lesions and developmental delays at 2 years of age among extremely low gestational age children. Pediatrics. 2008;122(3):e662-e669.
116. Bassan H, Benson CB, Limperopoulos C, et al. Ultrasonographic features and severity scoring of periventricular hemorrhagic infarction in relation to risk factors and outcome. Pediatrics. 2006;117(6):2111-2118.
117. Wood NS, Costeloe K, Gibson AT, et al. The EPICure study: associations and antecedents of neurological and developmental disability at 30 months of age following extremely preterm birth. Arch Dis Child Fetal Neonatal Ed. 2005;90(2):F134-F140.
118. Kobayashi S, Fujimoto S, Fukuda S, et al. Periventricular leukomalacia with late-onset circulatory dysfunction of premature infants: correlation with severity of magnetic resonance imaging findings and neurological outcomes. Tohoku J Exp Med. 2006;210(4):333-339.
119. Korkmaz A, Yigit S, Firat M, Oran O. Cranial MRI in neonatal hypernatraemic dehydration. Pediatr Radiol. 2000;30(5):323-325.
120. Dean LM, McLeary M, Taylor GA. Cerebral hemorrhage in alloimmune thrombocytopenia. Pediatr Radiol. 1995;25(6):444-445.
121. Kulkarni R, Lusher JM. Intracranial and extracranial hemorrhages in newborns with hemophilia: a review of the literature. J Pediatr Hematol Oncol. 1999;21(4):289-295.
122. Huang AH, Robertson RL. Spontaneous superficial parenchymal and leptomeningeal hemorrhage in term neonates. AJNR Am J Neuroradiol. 2004;25(3):469-475.
123. Kersbergen KJ, Groenendaal F, Benders MJ, de Vries LS. Neonatal cerebral sinovenous thrombosis: neuroimaging and long-term follow-up. J Child Neurol. 2011;26(9):1111-1120.
124. Raets MM, Dudink J, Ijsselstijn H, et al. Brain injury associated with neonatal extracorporeal membrane oxygenation in the Netherlands: a nationwide evaluation spanning two decades. Pediatr Crit Care Med. 2013; 14(9):884-892.
125. Rollins MD, Yoder BA, Moore KR, et al. Utility of neuroradiographic imaging in predicting outcomes after neonatal extracorporeal membrane oxygenation. J Pediatr Surg. 2012;47(1):76-80.
126. Messerschmidt A, Brugger PC, Boltshauser E, et al. Disruption of cerebellar development: potential complication of extreme prematurity. AJNR Am J Neuroradiol. 2005;26(7):1659-1667.
127. Steggerda SJ, Leijser LM, Wiggers-de Bruine FT, et al. Cerebellar injury in preterm infants: incidence and findings on US and MR images. Radiology. 2009;252(1):190-199.
128. Messerschmidt A, Fuiko R, Prayer D, et al. Disrupted cerebellar development in preterm infants is associated with impaired neurodevelopmental outcome. Eur J Pediatr. 2008;167(10):1141-1147.
129. Muller H, Beedgen B, Schenk JP, et al. Intracerebellar hemorrhage in premature infants: sonographic detection and outcome. J Perinat Med. 2007;35(1):67-70.
130. Limperopoulos C, Bassan H, Gauvreau K, et al. Does cerebellar injury in premature infants contribute to the high prevalence of long-term cognitive, learning, and behavioral disability in survivors? Pediatrics. 2007;120(3): 584-593.
131. Limperopoulos C, Benson CB, Bassan H, et al. Cerebellar hemorrhage in the preterm infant: ultrasonographic findings and risk factors. Pediatrics. 2005;116(3):717-724.
132. Pekcevik Y, Ozer EA, Guleryuz H. Cranial sonography in extremely preterm infants. J Clin Ultrasound. 2014;42(5):283-290.
133. Merrill JD, Piecuch RE, Fell SC, et al. A new pattern of cerebellar hemorrhages in preterm infants. Pediatrics. 1998;102(6):E62.
134. Volpe JJ. Neurology of the newborn. 5th ed. Philadelphia: Saunders-Elsevier; 2008.
135. Folkerth RD, McLaughlin ME, Levine D. Organizing posterior fossa hematomas simulating developmental cysts on prenatal imaging: report of 3 cases. J Ultrasound Med. 2001;20(11):1233-1240.
136. Kidokoro H, Kubota T, Ohe H, et al. Diffusion-weighted magnetic resonance imaging in infants with periventricular leukomalacia. Neuropediatrics. 2008;39(4):233-238.
137. Mirmiran M, Barnes PD, Keller K, et al. Neonatal brain magnetic resonance imaging before discharge is better than serial cranial ultrasound in predicting cerebral palsy in very low birth weight preterm infants. Pediatrics. 2004;114(4):992-998.
138. Silveira RC, Procianoy RS, Dill JC, da Costa CS. Periventricular leukomalacia in very low birth weight preterm neonates with high risk for neonatal sepsis. J Pediatr (Rio J). 2008;84(3):211-216.
139. Veyrac C, Couture A, Saguintaah M, Baud C. Brain ultrasonography in the premature infant. Pediatr Radiol. 2006;36(7):626-635.
140. Ligam P, Haynes RL, Folkerth RD, et al. Thalamic damage in periventricular leukomalacia: novel pathologic observations relevant to cognitive deficits in survivors of prematurity. Pediatr Res. 2009;65(5):524-529.
141. Epelman M, Daneman A, Halliday W, et al. Abnormal corpus callosum in neonates after hypoxic-ischemic injury. Pediatr Radiol. 2012;42(3): 321-330.
142. Hintz SR, Barnes PD, Bulas D, et al. Neuroimaging and neurodevelopmental outcome in extremely preterm infants. Pediatrics. 2015;135(1):e32-e42.
143. Gibbs RS. The relationship between infections and adverse pregnancy outcomes: an overview. Ann Periodontol. 2001;6(1):153-163.
144. Bracci R, Buonocore G. Chorioamnionitis: a risk factor for fetal and neonatal morbidity. Biol Neonate. 2003;83(2):85-96.
145. Rezaie P, Dean A. Periventricular leukomalacia, inflammation and white matter lesions within the developing nervous system. Neuropathology. 2002;22(3):106-132.
146. Vigneswaran R. Infection and preterm birth: evidence of a common causal relationship with bronchopulmonary dysplasia and cerebral palsy. J Paediatr Child Health. 2000;36(4):293-296.
147. Batton DG, Kirtley X, Swails T. Unexpected versus anticipated cystic periventricular leukomalacia. Am J Perinatol. 2003;20(1):33-40.
148. Leviton A, Dammann O, Allred EN, et al. Antenatal corticosteroids and cranial ultrasonographic abnormalities. Am J Obstet Gynecol. 1999;181(4): 1007-1017.

149. Verma U, Tejani N, Klein S, et al. Obstetric antecedents of intraventricular hemorrhage and periventricular leukomalacia in the low-birth-weight neonate. Am J Obstet Gynecol. 1997;176(2):275-281.
150. Perlman JM. White matter injury in the preterm infant: an important determination of abnormal neurodevelopment outcome. Early Hum Dev. 1998;53(2):99-120.
151. Cooke RW. Trends in incidence of cranial ultrasound lesions and cerebral palsy in very low birthweight infants 1982-93. Arch Dis Child Fetal Neonatal Ed. 1999;80(2):F115-F117.
152. Stannard MW, Jimenez JF. Sonographic recognition of multiple cystic encephalomalacia. AJR Am J Roentgenol. 1983;141(6):1321-1324.
153. Schellinger D, Grant EG, Richardson JD. Cystic periventricular leukomalacia: sonographic and CT findings. AJNR Am J Neuroradiol. 1984;5(4):439-445.
154. Dubowitz LM, Bydder GM, Mushin J. Developmental sequence of periventricular leukomalacia. Correlation of ultrasound, clinical, and nuclear magnetic resonance functions. Arch Dis Child. 1985;60(4):349-355.
155. Melhem ER, Hoon Jr AH, Ferrucci Jr JT, et al. Periventricular leukomalacia: relationship between lateral ventricular volume on brain MR images and severity of cognitive and motor impairment. Radiology. 2000;214(1):199-204.
156. Ancel PY, Livinec F, Larroque B, et al. Cerebral palsy among very preterm children in relation to gestational age and neonatal ultrasound abnormalities: the EPIPAGE cohort study. Pediatrics. 2006;117(3):828-835.
157. Sie LT, van der Knaap MS, van Wezel-Meijler G, et al. Early MR features of hypoxic-ischemic brain injury in neonates with periventricular densities on sonograms. AJNR Am J Neuroradiol. 2000;21(5):852-861.
158. Carson SC, Hertzberg BS, Bowie JD, Burger PC. Value of sonography in the diagnosis of intracranial hemorrhage and periventricular leukomalacia: a postmortem study of 35 cases. AJR Am J Roentgenol. 1990;155(3):595-601.
159. Coley BD, Hogan MJ. Cystic periventricular leukomalacia of the corpus callosum. Pediatr Radiol. 1997;27(7):583-585.
160. Adcock LM, Moore PJ, Schlesinger AE, Armstrong DL. Correlation of ultrasound with postmortem neuropathologic studies in neonates. Pediatr Neurol. 1998;19(4):263-271.
161. de Vries LS, Dubowitz LM, Pennock JM, Bydder GM. Extensive cystic leucomalacia: correlation of cranial ultrasound, magnetic resonance imaging and clinical findings in sequential studies. Clin Radiol. 1989;40(2):158-166.
162. Leijser LM, Liauw L, Veen S, et al. Comparing brain white matter on sequential cranial ultrasound and MRI in very preterm infants. Neuroradiology. 2008;50(9):799-811.
163. Valkama AM, Paakko EL, Vainionpaa LK, et al. Magnetic resonance imaging at term and neuromotor outcome in preterm infants. Acta Paediatr. 2000;89(3):348-355.
164. Aida N, Nishimura G, Hachiya Y, et al. MR imaging of perinatal brain damage: comparison of clinical outcome with initial and follow-up MR findings. AJNR Am J Neuroradiol. 1998;19(10):1909-1921.
165. El-Dib M, Massaro AN, Bulas D, Aly H. Neuroimaging and neurodevelopmental outcome of premature infants. Am J Perinatol. 2010;27(10):803-818.
166. Whyte HE, Blaser S. Limitations of routine neuroimaging in predicting outcomes of preterm infants. Neuroradiology. 2013;55(Suppl. 2):3-11.
167. de Vries LS, van Haastert IC, Benders MJ, Groenendaal F. Myth: cerebral palsy cannot be predicted by neonatal brain imaging. Semin Fetal Neonatal Med. 2011;16(5):279-287.
168. Ferriero DM. Neonatal brain injury. N Engl J Med. 2004;351(19):1985-1995.
169. Chiu NC, Shen EY, Ho CS. Outcome in children with significantly abnormal cerebral blood flow detected by Doppler ultrasonography: focus on the survivors. J Neuroimaging. 2003;13(1):53-56.
170. Barkovich AJ, Sargent SK. Profound asphyxia in the premature infant: imaging findings. AJNR Am J Neuroradiol. 1995;16(9):1837-1846.
171. Daneman A, Epelman M, Blaser S, Jarrin JR. Imaging of the brain in full-term neonates: does sonography still play a role? Pediatr Radiol. 2006;36(7):636-646.
172. Shankaran S, Pappas A, McDonald SA, et al. Childhood outcomes after hypothermia for neonatal encephalopathy. N Engl J Med. 2012;366(22):2085-2092.
173. Al Yazidi G, Srour M, Wintermark P. Risk factors for intraventricular hemorrhage in term asphyxiated newborns treated with hypothermia. Pediatr Neurol. 2014;50(6):630-635.
174. Shroff MM, Soares-Fernandes JP, Whyte H, Raybaud C. MR imaging for diagnostic evaluation of encephalopathy in the newborn. Radiographics. 2010;30(3):763-780.
175. Han BK, Lee M, Yoon HK. Cranial ultrasound and CT findings in infants with hypernatremic dehydration. Pediatr Radiol. 1997;27(9):739-742.
176. Triulzi F, Parazzini C, Righini A. Patterns of damage in the mature neonatal brain. Pediatr Radiol. 2006;36(7):608-620.
177. Mader I, Schoning M, Klose U, Kuker W. Neonatal cerebral infarction diagnosed by diffusion-weighted MRI: pseudonormalization occurs early. Stroke. 2002;33(4):1142-1145.
178. Huppi PS, Murphy B, Maier SE, et al. Microstructural brain development after perinatal cerebral white matter injury assessed by diffusion tensor magnetic resonance imaging. Pediatrics. 2001;107(3):455-460.
179. Seibert JJ, Avva R, Hronas TN, et al. Use of power Doppler in pediatric neurosonography: a pictorial essay. Radiographics. 1998;18(4):879-890.
180. Blankenberg FG, Loh NN, Norbash AM, et al. Impaired cerebrovascular autoregulation after hypoxic-ischemic injury in extremely low-birth-weight neonates: detection with power and pulsed wave Doppler US. Radiology. 1997;205(2):563-568.
181. Allison JW, Faddis LA, Kinder DL, et al. Intracranial resistive index (RI) values in normal term infants during the first day of life. Pediatr Radiol. 2000;30(9):618-620.
182. Nishimaki S, Iwasaki S, Minamisawa S, et al. Blood flow velocities in the anterior cerebral artery and basilar artery in asphyxiated infants. J Ultrasound Med. 2008;27(6):955-960.
183. Mercuri E, He J, Curati WL, et al. Cerebellar infarction and atrophy in infants and children with a history of premature birth. Pediatr Radiol. 1997;27(2):139-143.
184. Johnsen SD, Tarby TJ, Lewis KS, et al. Cerebellar infarction: an unrecognized complication of very low birthweight. J Child Neurol. 2002;17(5):320-324.
185. Bulas DI, Vezina GL. Preterm anoxic injury. Radiologic evaluation. Radiol Clin North Am. 1999;37(6):1147-1161.
186. Coley BD, Rusin JA, Boue DR. Importance of hypoxic/ischemic conditions in the development of cerebral lenticulostriate vasculopathy. Pediatr Radiol. 2000;30(12):846-855.
187. Amir J, Schwarz M, Levy I, et al. Is lenticulostriated vasculopathy a sign of central nervous system insult in infants with congenital CMV infection? Arch Dis Child. 2011;96(9):846-850.
188. Chamnanvanakij S, Rogers CG, Luppino C, et al. Linear hyperechogenicity within the basal ganglia and thalamus of preterm infants. Pediatr Neurol. 2000;23(2):129-133.
189. Schlesinger AE, Shackelford GD, Adcock LM. Hyperechoic caudate nuclei: a potential mimic of germinal matrix hemorrhage. Pediatr Radiol. 1998;28(5):297-302.
190. Chamnanvanakij S, Rollins N, Perlman JM. Subdural hematoma in term infants. Pediatr Neurol. 2002;26(4):301-304.
191. Lequin MH, Vermeulen JR, van Elburg RM, et al. *Bacillus cereus* meningoencephalitis in preterm infants: neuroimaging characteristics. AJNR Am J Neuroradiol. 2005;26(8):2137-2143.
192. Capretti MG, Lanari M, Tani G, et al. Role of cerebral ultrasound and magnetic resonance imaging in newborns with congenital cytomegalovirus infection. Brain Dev. 2014;36(3):203-211.
193. Filippi L, Serafini L, Dani C, et al. Congenital syphilis: unique clinical presentation in three preterm newborns. J Perinat Med. 2004;32(1):90-94.
194. Benoist G, Salomon LJ, Mohlo M, et al. Cytomegalovirus-related fetal brain lesions: comparison between targeted ultrasound examination and magnetic resonance imaging. Ultrasound Obstet Gynecol. 2008;32(7):900-905.
195. Ancora G, Lanari M, Lazzarotto T, et al. Cranial ultrasound scanning and prediction of outcome in newborns with congenital cytomegalovirus infection. J Pediatr. 2007;150(2):157-161.

196. de Vries LS, Gunardi H, Barth PG, et al. The spectrum of cranial ultrasound and magnetic resonance imaging abnormalities in congenital cytomegalovirus infection. Neuropediatrics. 2004;35(2):113-119.
197. Fowler KB, Stagno S, Pass RF. Maternal immunity and prevention of congenital cytomegalovirus infection. JAMA. 2003;289(8):1008-1011.
198. Nowakowska D, Respondek-Liberska M, Golab E, et al. Too late prenatal diagnosis of fetal toxoplasmosis: a case report. Fetal Diagn Ther. 2005;20(3):190-193.
199. Moinuddin A, McKinstry RC, Martin KA, Neil JJ. Intracranial hemorrhage progressing to porencephaly as a result of congenitally acquired cytomegalovirus infection—an illustrative report. Prenat Diagn. 2003;23(10):797-800.
200. Malinger G, Lev D, Zahalka N, et al. Fetal cytomegalovirus infection of the brain: the spectrum of sonographic findings. AJNR Am J Neuroradiol. 2003;24(1):28-32.
201. Shaw CM, Alvord Jr EC. Subependymal germinolysis. Arch Neurol. 1974;31(6):374-381.
202. Patel DV, Holfels EM, Vogel NP, et al. Resolution of intracranial calcifications in infants with treated congenital toxoplasmosis. Radiology. 1996;199(2):433-440.
203. Campos GS, Bandeira AC, Sardi SI. Zika virus outbreak, Bahia, Brazil. Emerg Infect Dis. 2015;21(10):1885-1886.
204. Mlakar J, Korva M, Tul N, et al. Zika virus associated with microcephaly. N Engl J Med. 2016;374(10):951-958.
205. Brasil P, Pereira Jr JP, Raja Gabaglia C, et al. Zika virus infection in pregnant women in Rio de Janeiro—preliminary report. N Engl J Med. 2016.
206. Sarno M, Sacramento GA, Khouri R, et al. Zika virus infection and stillbirths: a case of hydrops fetalis, hydranencephaly and fetal demise. PLoS Negl Trop Dis. 2016;10(2):e0004517.
207. Driggers RW, Ho CY, Korhonen EM, et al. Zika virus infection with prolonged maternal viremia and fetal brain abnormalities. N Engl J Med. 2016;374(22):2142-2151.
208. Calvet G, Aguiar RS, Melo AS, et al. Detection and sequencing of Zika virus from amniotic fluid of fetuses with microcephaly in Brazil: a case study. Lancet Infect Dis. 2016;16(6):653-660.
209. Schuler-Faccini L, Ribeiro EM, Feitosa IM, et al. Possible association between Zika virus infection and microcephaly—Brazil, 2015. MMWR Morb Mortal Wkly Rep. 2016;65(3):59-62.
210. Hazin AN, Poretti A, Turchi Martelli CM, et al. Computed tomographic findings in microcephaly associated with Zika virus. N Engl J Med. 2016;374(22):2193-2195.
211. de Fatima Vasco Aragao M, van der Linden V, Brainer-Lima AM, et al. Clinical features and neuroimaging (CT and MRI) findings in presumed Zika virus related congenital infection and microcephaly: retrospective case series study. BMJ. 2016;353:i1901.
212. Melo A, Aguiar R, Amorim M, et al. Congenital Zika virus infection: beyond neonatal microcephaly. JAMA Neurol. 2016;73(12):1407-1416.
213. Oliveira Melo AS, Malinger G, Ximenes R, et al. Zika virus intrauterine infection causes fetal brain abnormality and microcephaly: tip of the iceberg? Ultrasound Obstet Gynecol. 2016;47(1):6-7.
214. Gray PH, Tudehope DI, Masel J. Cystic encephalomalacia and intrauterine herpes simplex virus infection. Pediatr Radiol. 1992;22(7):529-532.
215. George R, Andronikou S, du Plessis J, et al. Central nervous system manifestations of HIV infection in children. Pediatr Radiol. 2009;39(6):575-585.
216. Ben-Ami T, Yousefzadeh D, Backus M, et al. Lenticulostriate vasculopathy in infants with infections of the central nervous system sonographic and Doppler findings. Pediatr Radiol. 1990;20(8):575-579.
217. Woodlief RS, Markowitz JE. Unrecognized invasive infection in a neonate colonized with methicillin-resistant staphylococcus aureus. J Pediatr. 2009;155(6):943-e1.
218. Schlapbach LJ, Aebischer M, Adams M, et al. Impact of sepsis on neurodevelopmental outcome in a Swiss National Cohort of extremely premature infants. Pediatrics. 2011;128(2):e348-e357.
219. Wu T, Fan XP, Wang WY, Yuan TM. Enterovirus infections are associated with white matter damage in neonates. J Paediatr Child Health. 2014;50(10):817-822.
220. Hwang SW, Su JM, Jea A. Diagnosis and management of brain and spinal cord tumors in the neonate. Semin Fetal Neonatal Med. 2012;17(4):202-206.
221. Jooma R, Kendall BE. Intracranial tumours in the first year of life. Neuroradiology. 1982;23(5):267-274.
222. Ambrosino MM, Hernanz-Schulman M, Genieser NB, et al. Brain tumors in infants less than a year of age. Pediatr Radiol. 1988;19(1):6-8.
223. Jooma R, Hayward RD, Grant DN. Intracranial neoplasms during the first year of life: analysis of one hundred consecutive cases. Neurosurgery. 1984;14(1):31-41.
224. Mazewski CM, Hudgins RJ, Reisner A, Geyer JR. Neonatal brain tumors: a review. Semin Perinatol. 1999;23(4):286-298.
225. Dotan M, Lorber A. Congestive heart failure with diffuse neonatal hemangiomatosis—case report and literature review. Acta Paediatr. 2013;102(5):e232-e238.
226. Pal BR, Preston PR, Morgan ME, et al. Frontal horn thin walled cysts in preterm neonates are benign. Arch Dis Child Fetal Neonatal Ed. 2001;85(3):F187-F193.
227. Malinger G, Lev D, Ben Sira L, et al. Congenital periventricular pseudocysts: prenatal sonographic appearance and clinical implications. Ultrasound Obstet Gynecol. 2002;20(5):447-451.
228. Naeini RM, Yoo JH, Hunter JV. Spectrum of choroid plexus lesions in children. AJR Am J Roentgenol. 2009;192(1):32-40.
229. Shackelford GD, Fulling KH, Glasier CM. Cysts of the subependymal germinal matrix: sonographic demonstration with pathologic correlation. Radiology. 1983;149(1):117-121.
230. Smith LM, Qureshi N, Renslo R, Sinow RM. Prenatal cocaine exposure and cranial sonographic findings in preterm infants. J Clin Ultrasound. 2001;29(2):72-77.
231. Litvak J, Yahr MD, Ransohoff J. Aneurysms of the great vein of Galen and midline cerebral arteriovenous anomalies. J Neurosurg. 1960;17:945-954.
232. Chapman S, Hockley AD. Calcification of an aneurysm of the vein of Galen. Pediatr Radiol. 1989;19(8):541-542.
233. Jones BV, Ball WS, Tomsick TA, et al. Vein of Galen aneurysmal malformation: diagnosis and treatment of 13 children with extended clinical follow-up. AJNR Am J Neuroradiol. 2002;23(10):1717-1724.
234. Osborn AG. Diagnostic neuroradiology. St Louis: Mosby; 1994.

CHAPTER

46 Duplex Sonography of the Neonatal and Infant Brain

Thierry A.G.M. Huisman and Andrea Poretti

SUMMARY OF KEY POINTS

- Duplex sonography is a valuable, functional addition to anatomic sonography of the pediatric brain.
- Various quantitative metrics can be extracted from the flow curves, including peak systolic, end-diastolic flow velocity, time average maximum mean blood flow velocity, and resistive index.
- The quantitative markers may be influenced or altered by mechanical ventilation, patent ductus arteriosus, extracorporeal membrane oxygenation (ECMO), arteriovenous shunting, and pathologies that are affected by cerebral hemodynamic autoregulation.
- In hypoxic ischemic injury and general brain edema, the resistive index values typically drop to low values.
- Duplex sonography may help to identify and explore arterial and venous malformations such as the vein of Galen aneurysmal malformation.

CHAPTER OUTLINE

SONOGRAPHIC TECHNIQUE
Approaches
Doppler Optimization
Safety Considerations
Doppler Measurements and Factors That Change Resistive Index
NORMAL HEMODYNAMICS
Normal Arterial Blood Flow Patterns
Normal Venous Blood Flow Patterns
INTENSIVE CARE THERAPIES AND CEREBRAL HEMODYNAMICS
Mechanical Ventilation
Extracorporeal Membrane Oxygenation
Therapeutic Hypothermia and Brain Cooling
DIFFUSE NEURONAL INJURY
Hypoxic Ischemic Injury and Asphyxia
Cerebral Edema
Brain Death
INTRACRANIAL HEMORRHAGE AND STROKE
Focal Arterial Ischemic Stroke
HYDROCEPHALUS
VASCULAR MALFORMATIONS
INTRACRANIAL TUMORS
NEAR-FIELD STRUCTURES
Differentiation of Subarachnoid From Subdural Fluid Collections
Dural Venous Sinus Thrombosis
UNCOMMON VASCULAR APPLICATIONS
PITFALLS OF DUPLEX SONOGRAPHY

Continuous and pulsed echo technique, or **duplex sonography** in which gray-scale tissue imaging is combined with blood flow sampling, has been in use for the past decades in the evaluation of normal and abnormal neonatal intracranial hemodynamics.[1-3] In addition, **color Doppler sonography** renders valuable information about the direction of the blood flow in relation to the transducer. This technique allows better understanding of altered intracranial flow or exploring the complex angioarchitecture of vascular malformations. Continuing improvements in transducer design and sensitivity allow routine imaging of the intracranial vasculature in newborns and young infants, including the identification of flow in submillimeter arteries (e.g., lenticulostriate arteries) and patency of dural venous sinuses (e.g., superior and inferior sagittal sinus) of the brain.[4] The wide dynamic range and high sensitivity of **power Doppler sonography,** in which blood flow is represented as various shades of a single color (amplitude-coded color or color flow Doppler energy), is especially helpful to depict low-velocity and low-amplitude blood flow. Power Doppler sonography, however, lacks information about flow direction. Furthermore, analysis of the sampled **flow spectra/curves** and postprocessing software programs offer extraction of objective semiquantitative data (e.g., **peak systolic velocity** [PSV], **end-diastolic flow velocity** [EDV], **resistive index** [RI], and **time-averaged mean blood flow velocity** [TAV]). These semiquantitative data can be collected serially, giving valuable real-time information about progression of disease or recovery. Analysis of the shape of the spectral pattern with delayed systolic flow acceleration, flattened systolic upstroke, slow diastolic deceleration, or reversal of flow during diastole may provide important information about the cerebral hemodynamics. This chapter describes how brain ultrasonography combining multiplanar, multiapproach anatomic and functional/hemodynamic

data has become an invaluable noninvasive bedside imaging modality supporting diagnosis, monitoring, guidance of treatment options, and estimation of prognosis for neonates with a wide variety of neurologic diseases.

SONOGRAPHIC TECHNIQUE

Approaches

Three different scanning approaches to the neonatal brain have worked well, each with its own advantages and limitations.[5-9] The **anterior fontanelle approach** is the most common and easiest to use. The basilar, internal carotid, and anterior cerebral arteries, as well as the internal cerebral veins, vein of Galen, and superior sagittal, inferior, and straight sinus, can be routinely sampled on **midsagittal scans** (Fig. 46.1A-B). The smaller thalamostriate arteries and opercular branches of the middle cerebral artery (MCA) may be seen on angled parasagittal images.

On **coronal scans** through the anterior fontanelle, the supraclinoid internal carotid arteries, M1 segments of the MCAs, thalamostriate arteries, A1 segments of the anterior cerebral arteries, and the cavernous sinus can almost always be visualized on anteriorly angled scans (see Fig. 46.1C). Paired terminal, caudothalamic/thalamostriate, and internal cerebral veins, the basilar artery, straight sinus, and transverse sinuses can be seen on more posteriorly angled scans. A major drawback of the coronal plane is the near perpendicular angle between the MCA and the ultrasound beam, such that measured frequency shifts from flowing red blood cells approach zero, making the MCA appear to have no flow.

The **temporal bone approach** is best for the MCA. The transducer is placed in axial orientation approximately 1 cm anterior and superior to the helix of the ear. Using the thin temporal bone as an acoustic window, adequate penetration for imaging and Doppler studies can be achieved in most full-term neonates. This approach allows visualization of the major branches of the circle of Willis (see Fig. 46.1D). In most premature infants, both MCAs can be easily insonated from one side of the head.

The **mastoid fontanelle approach** is an angled axial scan. This acoustic window is located approximately 1 cm behind and superior to the helix of the ear at the junction of the posterior parietal, temporal, and occipital bones. It is the preferred approach for imaging flow in the transverse dural sinuses, and the torcular Herophili in selected patients (see Fig. 46.1E).

Dedicated images of the posterior fossa circulation may be obtained using the **foramen magnum approach or suboccipital approach** (see Fig. 46.1F). The neonate is placed in lateral recumbent position with the head gently flexed. The transducer is placed in the midline, just inferior to the occipital protuberance, and angled cephalad in either sagittal or axial orientation. Alternatively, the **posterior fontanelle** (see Fig. 46.1G) at the junction between the lambdoid and sagittal suture can be used as an acoustic window. The posterior fossa arterial and venous vasculature can be depicted in most children.

Finally, a **transorbital approach** (see Fig. 46.1H) may be selected to evaluate the ophthalmic artery and the internal carotid siphon. Typically, the transducer is positioned over the closed eyelid and angled slightly medially and upward toward the region of the orbital apex/optic nerve canal.

Doppler Optimization

- Acoustic window should match sampled vessel.
- Electronically magnify image.
- Restrict color region of interest to enhance color sensitivity and frame rate.
- Adjust color gain to maximize vascular signal and minimize aliasing and tissue artifact.
- Use lowest bandpass filter to maximize low-flow sensitivity and evaluate venous structures.
- Use 7- to 15-MHz linear transducer for superior sagittal sinus.
- Use power-mode Doppler for smallest vessels when flow direction is not needed.
- Insonication angle for spectral data collection should be less than 60 degrees.
- Sample volume box should be centered to vessel lumen, avoiding sharp curves of vessel.

Doppler Optimization

For the best visualization of the intracranial vascular system, the image should be electronically magnified and the color region of interest restricted to enhance color sensitivity and frame rate. Color gain should be carefully adjusted and balanced to maximize vascular signal, limit flow aliasing, and minimize tissue motion artifacts, and the lowest bandpass filter should be used to maximize low-flow sensitivity necessary for evaluating venous structures. A 7- to 15-MHz linear transducer is recommended for examining the superficially located superior sagittal sinus. Visualization of the smaller arterial branches of the middle and anterior cerebral arteries can also be accomplished in the majority of normal premature and full-term infants but often requires a higher frequency (7 or 10 MHz) vector or sector transducers capable of detecting lower velocity and amplitude signal. The use of power Doppler sonography is recommended when directional information is of secondary importance and detection of flow is primary.

For specific vessel evaluation, spectral Doppler imaging can be performed using 3.5- to 15-MHz probes, depending on the depth and location of the target vessel. To ensure reliable and reproducible quantitative hemodynamic metrics, care should be given to maintain an angle of insonication of less than 60 degrees while sampling the intravascular flow. Furthermore, comparison of serial data requires a standardized, uniform angle of insonication of the same vessel during subsequent studies. In addition, factors that may alter the diameter of the sampled vessels should be taken into account, such as acute changes in systemic blood pressure, $Paco_2$, Pao_2, and hematocrit.

Safety Considerations

During pulsed wave and color flow Doppler examinations, signal is obtained by imparting energy into tissues. Although intracranial Doppler ultrasound is safe, biologic effects may be identified in

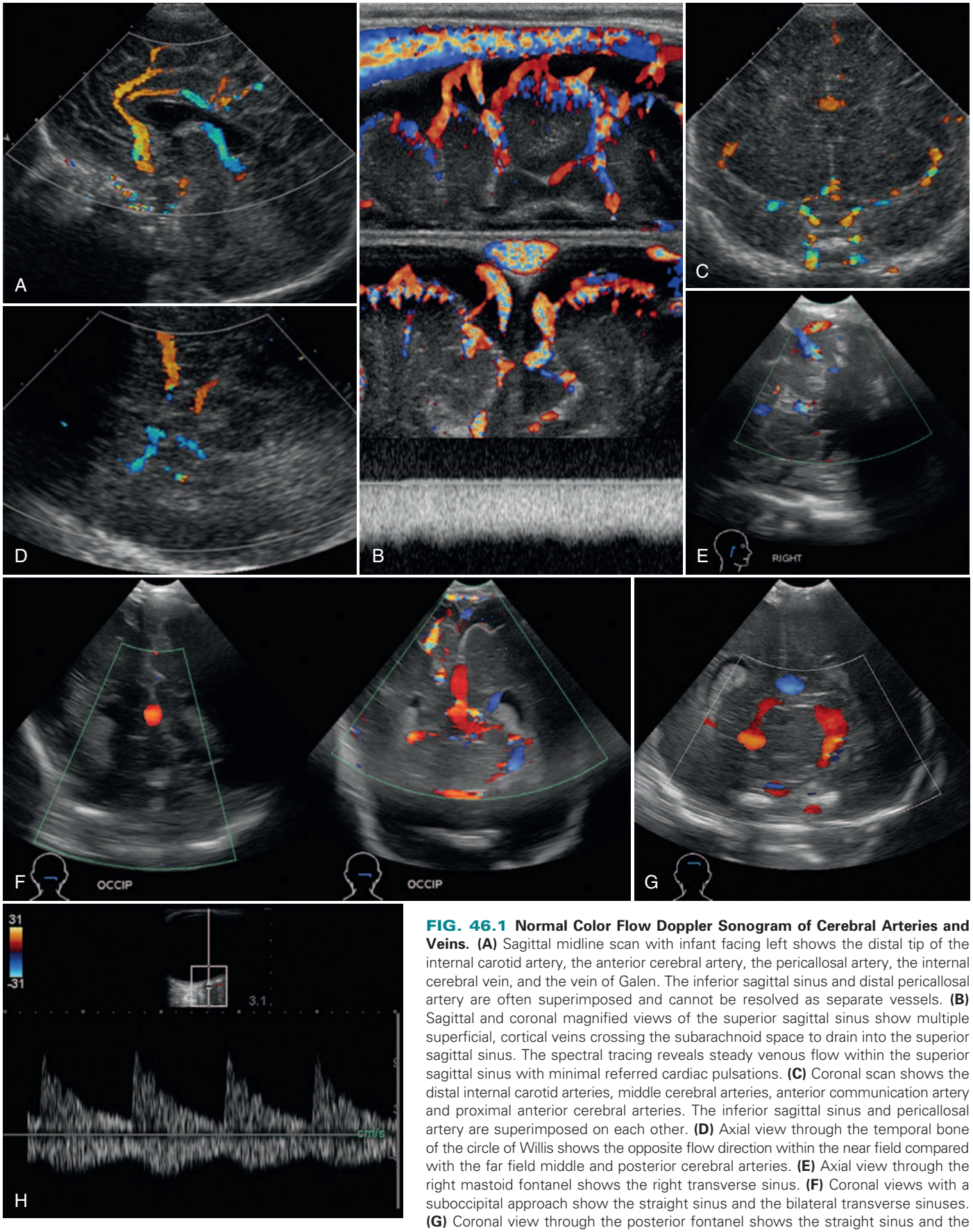

FIG. 46.1 Normal Color Flow Doppler Sonogram of Cerebral Arteries and Veins. **(A)** Sagittal midline scan with infant facing left shows the distal tip of the internal carotid artery, the anterior cerebral artery, the pericallosal artery, the internal cerebral vein, and the vein of Galen. The inferior sagittal sinus and distal pericallosal artery are often superimposed and cannot be resolved as separate vessels. **(B)** Sagittal and coronal magnified views of the superior sagittal sinus show multiple superficial, cortical veins crossing the subarachnoid space to drain into the superior sagittal sinus. The spectral tracing reveals steady venous flow within the superior sagittal sinus with minimal referred cardiac pulsations. **(C)** Coronal scan shows the distal internal carotid arteries, middle cerebral arteries, anterior communication artery and proximal anterior cerebral arteries. The inferior sagittal sinus and pericallosal artery are superimposed on each other. **(D)** Axial view through the temporal bone of the circle of Willis shows the opposite flow direction within the near field compared with the far field middle and posterior cerebral arteries. **(E)** Axial view through the right mastoid fontanel shows the right transverse sinus. **(F)** Coronal views with a suboccipital approach show the straight sinus and the bilateral transverse sinuses. **(G)** Coronal view through the posterior fontanel shows the straight sinus and the bilateral transverse sinuses. **(H)** Normal Doppler waveform produced by the central retinal artery and the central retinal vein (**H** courtesy of Dr. Rebecca Riggs, The Johns Hopkins Hospital, Baltimore, MD).

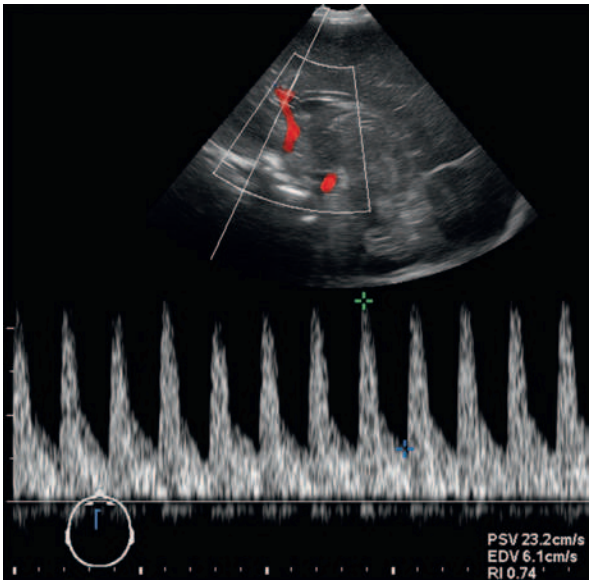

FIG. 46.2 Determination of Peak Systolic Flow Velocity (PSV), End-Diastolic Flow Velocity (EDV) and Resistive Index (RI) Within an Arterial Branch of the Anterior Arterial Circulation. The RI can be derived by placing the Doppler cursor at PSV *(green cross),* and at EDV, or minimum velocity *(blue cross).* The RI is calculated as (PSV – EDV)/PSV.

the future. Thus Doppler exposure should be time limited, and the signal intensity should be maximized by increasing gain and not transducer power output settings. The ALARA principle (as low as reasonably achievable) should be followed to limit energy exposure to tissues.

Doppler Measurements and Factors That Change Resistive Index

The **peak systolic velocity, end-diastolic flow velocity, resistive index,** and **time-averaged mean flow velocity** (TAV) are the most commonly used semiquantitative spectral Doppler measures for monitoring intracranial hemodynamics (Fig. 46.2).

One should, however, be aware of the various factors that may modify the measured or calculated RI values, which include both technical causes and patient comorbidities outside of the brain[10-12] (Fig. 46.3, Table 46.1).

With **increasing filter settings,** lower velocities are not depicted, resulting in a falsely elevated RI. **Transducer pressure** on the anterior fontanelle may transiently increase intracranial pressure (ICP), which in turn preferentially reduces flow during diastole and increases RI, especially in neonates with impaired cerebral autoregulation (e.g., secondary to hypoxic ischemic injury [HII]). In infants with symptomatic **patent ductus arteriosus,** resistance to flow in the cerebrovascular bed is higher than pulmonary vascular resistance. This results in shunting of blood away from the brain during diastole and an elevated intracranial RI. During **tachycardia,** the arterial pressure wave has less time to dissipate before another systolic ejection occurs. Intracranial RI is artificially lower because diastolic velocities are measured at middiastole, when velocities are higher, rather than during end diastole. **Left ventricular dysfunction** (decreased cardiac output) results in a decreased systolic pressure wave, lowered systolic velocities, and a reduced RI.

TABLE 46.1 Factors That Change Resistive Index (RI)

Factor	Effect on RI
High-pass filter settings	Increased
Transducer scanning pressure	Increased
Patent ductus arteriosus	Increased
Elevated heart rate	Decreased
Decreased cardiac output	Decreased

The RI is only a weak predictor of cerebrovascular resistance under most physiologic conditions. Mean blood flow velocity measures are the most informative indices of **cerebral blood flow** (CBF). Although accurate placement of the sample volume and angle of insonation are required, a strong correlation has been demonstrated between mean blood flow velocity and changes in global CBF under a variety of clinical and experimental conditions.[13-16]

NORMAL HEMODYNAMICS

Normal Arterial Blood Flow Patterns

Arterial hemodynamics in the cerebral circulation are affected by normal maturational events in the healthy newborn. The RI in the **anterior cerebral artery** decreases from a mean of 0.78 (range, 0.5-1.0) in **preterm infants** to a mean of 0.71 (range, 0.6-0.8) in full-term newborns.[2,3,17-19] This trend is associated with increasing diastolic flow velocities and may be related to peripheral changes in cerebrovascular resistance or to changes proximal to the site of recording, such as a closing ductus arteriosus and a diminishing left-to-right shunt. In **full-term infants,** RI may also change over the first few days of life.[2] In a study of 476 normal newborns weighing over 2500 g at birth, anterior cerebral artery RI decreased from a mean of 70.6 ± 7 (range, 51-87) to 68.3 ± 6 (range, 51-83) within the first 24 hours.[20]

Table 46.2 provides the range of published peak systolic and end diastolic velocities and RI values in several intracranial arteries. Although the range of normal values is broad, no great variability should be seen in the individual patient. Changes of more than 50% from baseline values should be considered abnormal. There are no consistent differences in instantaneous blood flow velocity among the major branches of the circle of Willis or between right-sided and left-sided structures. The measured blood flow velocities may, however, vary with pressure applied to the anterior fontanel. In healthy preterm and term neonates a tendency toward higher RI values can be observed with anterior fontanel compression, and a statistically significant increase in RI values may be observed in children with presumed impaired autoregulation of brain perfusion caused by hydrocephalus or brain edema related to HII.[11,21]

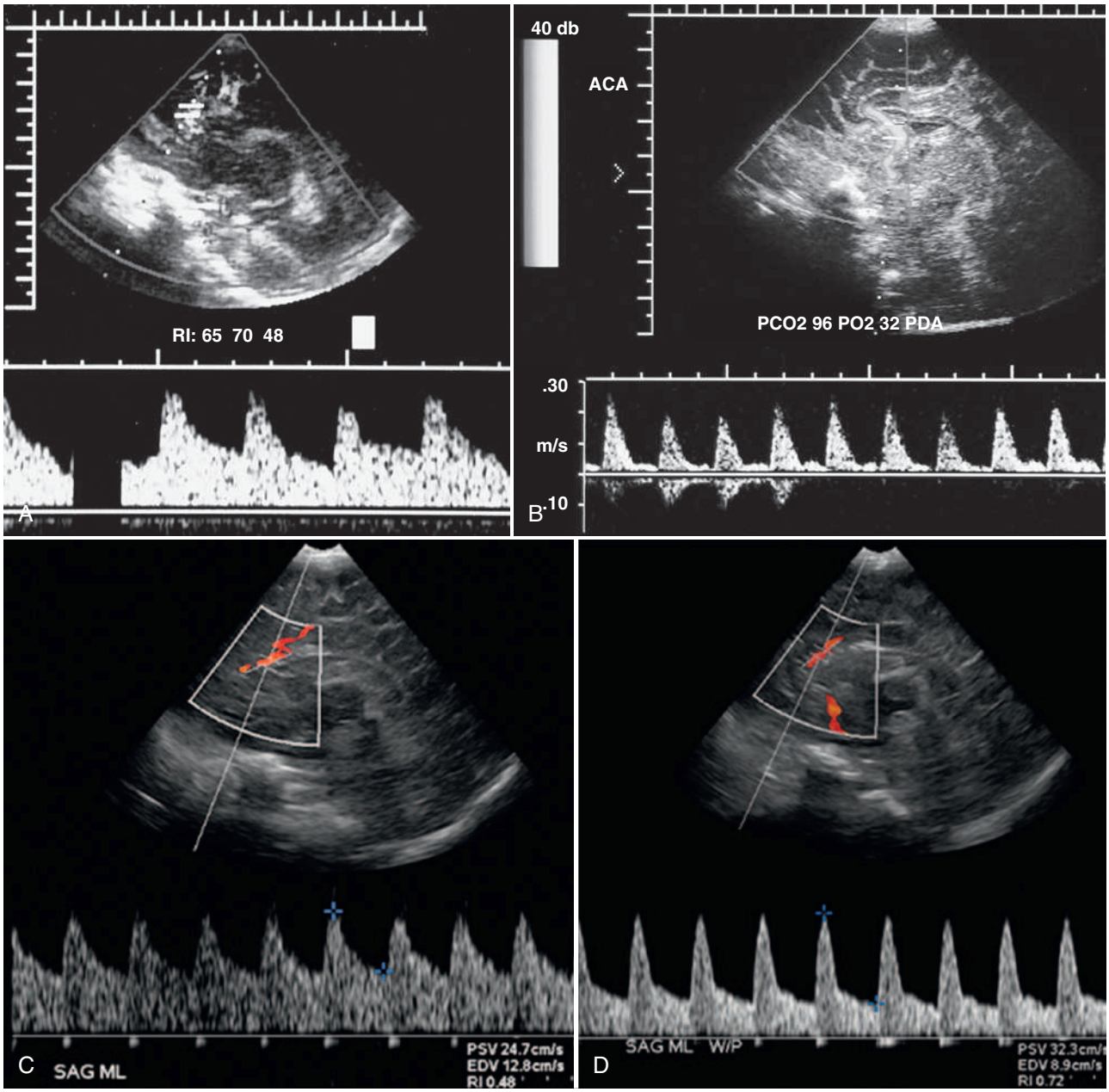

FIG. 46.3 Factors Affecting Intracranial Resistive Index (RI). (A) High variability in pulsatility of flow related to left ventricular dysfunction in an infant with congenital heart disease. **(B)** Absent diastolic flow in an infant with symptomatic patent ductus arteriosus. **(C)** and **(D)** High variability in spectral Doppler flow measurements and RI values occur in neonatal hypoxic ischemic injury as a result of impaired hemodynamic autoregulation; RI values increase significantly when sampled without (**[C]** RI = 0.48) and with (**[D]** RI = 0.72) gentle pressure to the anterior fontanelle.

TABLE 46.2 Range of Arterial Blood Flow Velocities in Full-Term Infants[a]

Artery	Peak Systolic Velocity (cm/sec)	End-Diastolic Velocity (cm/sec)	Resistive Index
Internal carotid	12-80	3-20	0.5-0.8
Basilar	30-80	5-20	0.6-0.8
Middle cerebral	20-70	8-20	0.6-0.8
Anterior cerebral	12-35	6-20	0.6-0.8
Posterior cerebral	20-60	8-25	0.6-0.8

[a]Values modified from Archer LN, Evans DH, Levene MI. Doppler ultrasound examination of the anterior cerebral arteries of normal newborn infants: the effect of postnatal age. Early Hum Dev. 1985;10(3-4):255-260[2]; Horgan JG, Rumack CM, Hay T, et al. Absolute intracranial blood-flow velocities evaluated by duplex Doppler sonography in asymptomatic preterm and term neonates. Am J Roentgenol. 1989;152(5):1059-1064[17]; Allison JW, Faddis LA, Kinder DL, et al. Intracranial resistive index (RI) values in normal term infants during the first day of life. Pediatr Radiol. 2000;30(9):618-620[18]; and Raju TN, Zikos E. Regional cerebral blood velocity in infants. A real-time transcranial and fontanellar pulsed Doppler study. J Ultrasound Med. 1987;6(9):497-507.[19]

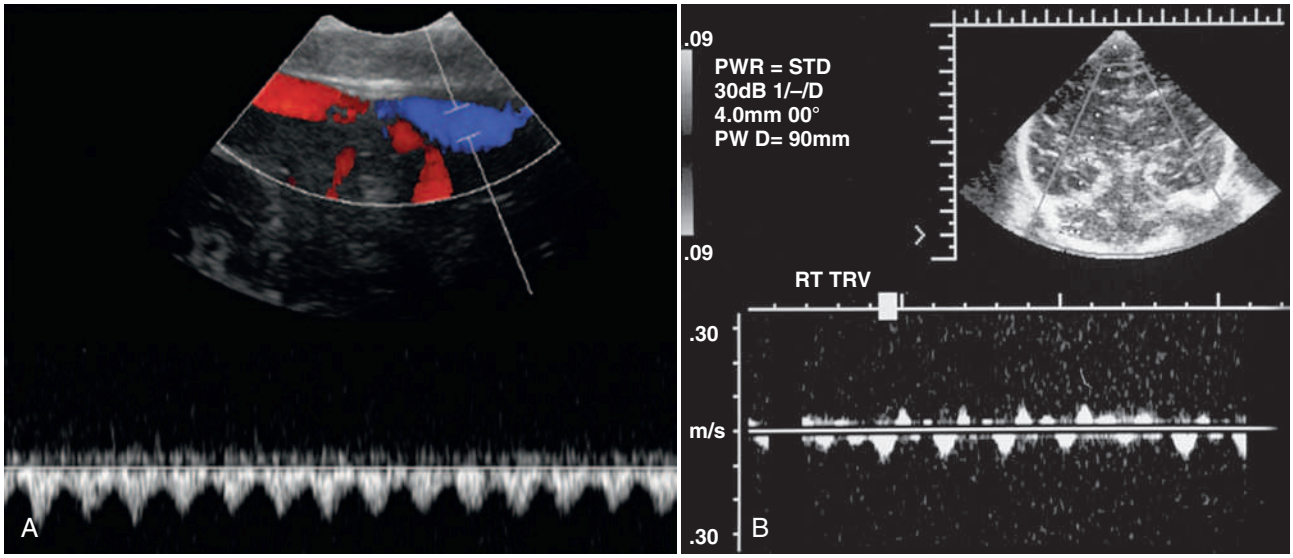

FIG. 46.4 Referred Cardiac Pulsations in Veins. **(A)** Doppler tracing from the superior sagittal sinus in a full-term newborn shows low-amplitude pulsatility. **(B)** Exaggerated venous pulsations from tricuspid regurgitation.

Normal Venous Blood Flow Patterns

Venous blood flow is continuous in the intracerebral veins and dural sinuses.[22] Cardiac pulsations of variable amplitude may occasionally be propagated into the larger venous structures, such as the vein of Galen and the sagittal and transverse sinuses (Fig. 46.4). High-amplitude or sawtooth patterns of pulsatility are not normal and may be seen in infants with **elevated right-sided heart pressures** or **tricuspid regurgitation.** Although respiratory changes are not usually observed during normal quiet respiration, marked changes in velocity can occur during **forceful crying** or are seen secondary to high-frequency ventilation settings.[8,22,23] Table 46.3 provides ranges for mean blood flow velocities in several intracranial veins and sinuses.

TABLE 46.3 Mean Venous Blood Flow Velocities in Full-Term Newborns

Vessel	Mean TAV[a] (cm/sec)
Terminal veins	3.0 ± 0.3
Internal cerebral veins	3.3 ± 0.3
Vein of Galen	4.3 ± 0.7
Straight sinus	5.9 ± 1.0
Superior sagittal sinus	9.2 ± 1.1
Inferior sagittal sinus	3.5 ± 0.3

[a]Time-averaged mean blood flow velocity (± standard error of the mean). Values modified from Taylor GA. Intracranial venous system in the newborn: evaluation of normal anatomy and flow characteristics with color Doppler US. Radiology. 1992;183(2):449-452.[8]

INTENSIVE CARE THERAPIES AND CEREBRAL HEMODYNAMICS

Mechanical Ventilation

Cerebral hemodynamics can be greatly affected by mechanical ventilation. Changes in venous return to the heart caused by **breathing out of synchrony** with the ventilator may result in significant beat-to-beat variability in arterial waveforms.[24]

Similarly, **high peak inspiratory pressures** can impede venous return to the heart and result in reversal of flow in the intracranial veins. Treatment with **high-frequency ventilation** exerts its effects on both arterial and venous hemodynamics in the form of short-amplitude oscillations (Fig. 46.5).[9,25] **Endotracheal suctioning** has been associated with marked increases in mean arterial blood pressure and arterial blood flow velocities in premature infants and has been attributed to the relative pressure-passive cerebral circulation (lack of autoregulation) in these patients.[26] Treatment with **inhaled nitric oxide** has also been reported to decrease CBF velocities in newborns with pulmonary hypertension. These infants experience an acute improvement in pulmonary hemodynamics and gas exchange at the onset of nitric oxide therapy.[27]

Extracorporeal Membrane Oxygenation

Extracorporeal membrane oxygenation (ECMO) may be used for the treatment of infants with severe, refractory respiratory and/or cardiac failure who have not responded to maximal conventional treatment. ECMO is also used for postoperative support in children with cardiopulmonary failure after surgical repair of congenital heart disease or congenital diaphragmatic hernia. During venoarterial ECMO **(VA-ECMO),** infants typically undergo cannulation and ligation of the right common carotid artery and jugular vein for vascular access and are placed on **nonpulsatile partial cardiopulmonary bypass.** This results in significant alterations in intracranial hemodynamics[28,29] (Fig. 46.6A). As the amount of flow through the ECMO bypass circuit increases, arterial pulsatility decreases proportionately and may

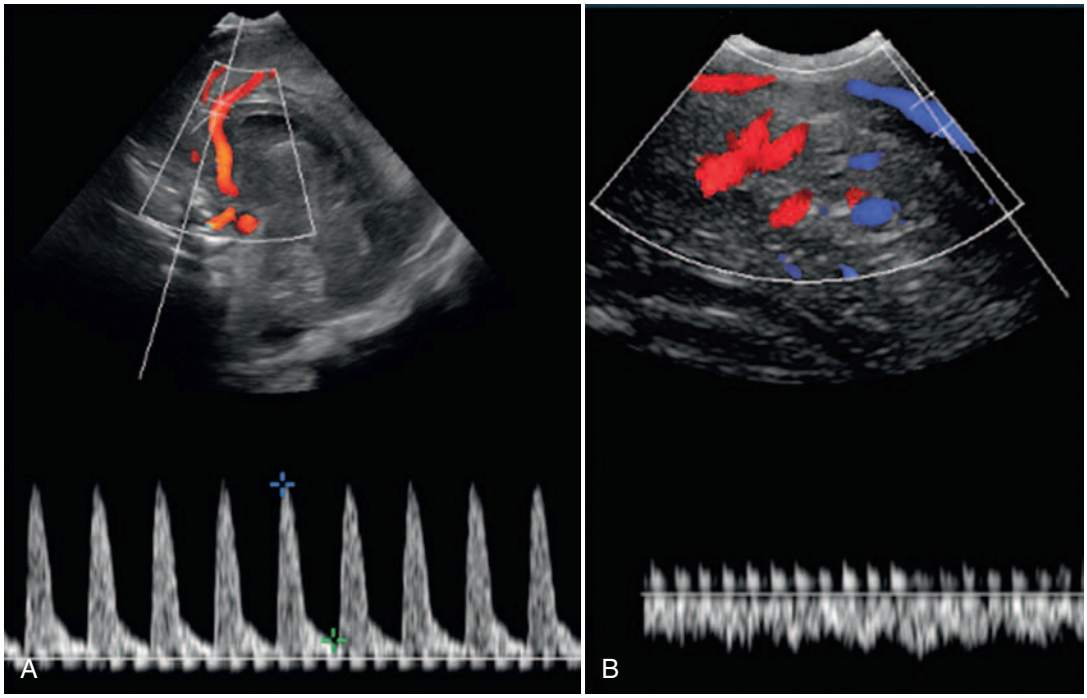

FIG. 46.5 High-Frequency Ventilation of Premature Infants. Pulsed wave Doppler tracing shows ventilation-related oscillations next to the arterial flow **(A)** and venous flow **(B).**

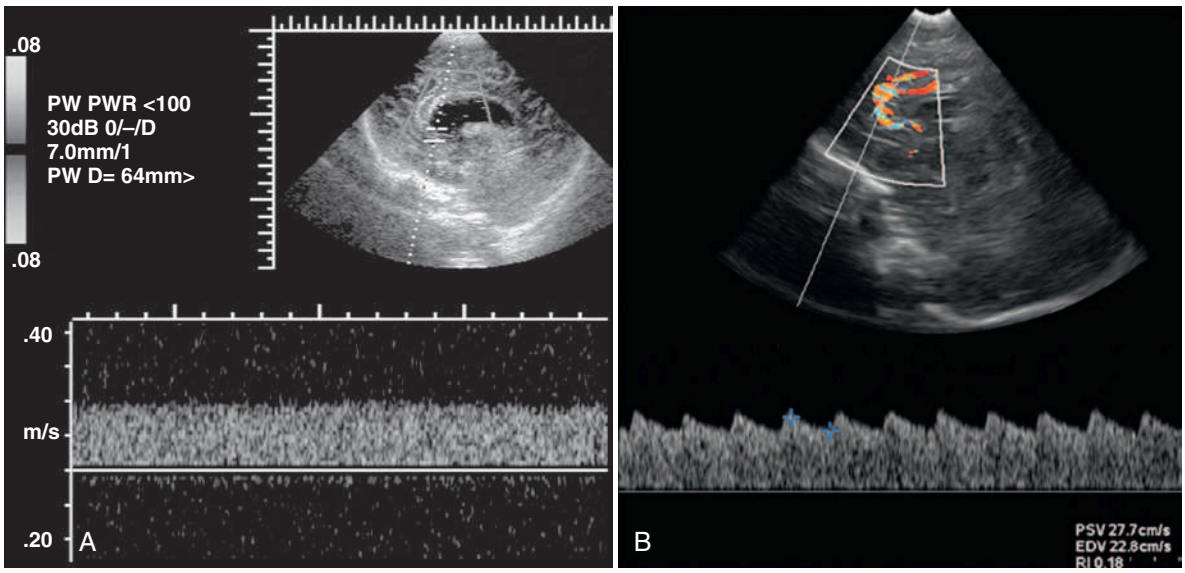

FIG. 46.6 Doppler Changes During Extracorporeal Membrane Oxygenation (ECMO). (A) Continuous nonpulsatile flow on pulsed wave Doppler tracing from the anterior cerebral artery in an infant with congenital heart disease and severe cardiac dysfunction during venoatrial ECMO shows absent arterial pulsatility. **(B)** In a different infant, residual pulsatile flow on pulsed wave Doppler tracing from the anterior cerebral artery in an infant with congenital heart disease and moderate cardiac dysfunction during venovenous ECMO shows minimal arterial pulsatility.

disappear altogether, especially in association with severe cardiac dysfunction.[30] Venous drainage and flow are typically also affected, partially as a result of the jugular vein ligation.[27,31]

More recently, double-lumen venous cannulas have allowed the use of venovenous circuits (venovenous extracorporeal membrane oxygenation [**VV-ECMO**]) in which the functionally intact left side of the heart pumps the oxygenated blood (delivered to the right side of the heart by the VV-ECMO circuit) into the systemic circulation. Major differences between the VV-ECMO circuit and the VA-ECMO circuit are the maintenance of pulsatile blood flow (see Fig. 46.6B), avoidance of ligation of the carotid artery, and perfusion of the pulmonary and coronary circulation by well-oxygenated blood.[32] VV-ECMO is used when there is only pulmonary dysfunction.

Duplex sonography may serve as a bedside monitoring modality for brain injury in a patient on ECMO. Studies have shown that in neonates without apparent neurologic injury, cerebral blood flow velocity (CBFV) was significantly lower than normal while on ECMO support and that CBFV increased after decannulation. Children who developed cerebral hemorrhage had higher CBFV for days before clinical recognition of a cerebral hemorrhage.[33]

Therapeutic Hypothermia and Brain Cooling

Brain temperature has been shown to be tightly linked to brain perfusion. Few data are available on the impact of brain cooling on the neonatal cerebral hemodynamics. Previous studies have primarily focused on patients who received cooling for cardiac surgery or treatment of traumatic brain injury. Hypothermia was noted to decrease CBFV, whereas increased temperatures increased CBFV.[34]

DIFFUSE NEURONAL INJURY

Hypoxic Ischemic Injury and Asphyxia

The cerebral hemodynamic changes associated with HII or asphyxia depend on many complex interacting factors including the severity, time, and duration of the insult; ongoing hypercapnia and hypoxemia; and maturity of the brain. In the setting of severe or prolonged asphyxia, brain tissue HII results in the excessive release of excitatory amino acids, such as glutamate and aspartate. The subsequent complex cascade of neurometabolic events results in cerebral vasodilation with subsequent cerebral edema.[35] In addition to the conventional gray-scale imaging findings of increased echogenicity of the hemispheric white matter, increased corticomedullary differentiation, slitlike ventricles, and effaced subarachnoid spaces, significant changes in hemodynamic metrics may be observed on duplex sonography. **Increased mean CBFV** and **decreased RI values** (<0.55-0.60) may be seen on spectral Doppler imaging within 12 hours of injury, lasting up to several days after the initial insult (Fig. 46.7).[36,37] Furthermore, RI measurements, in conjunction with clinical markers, may serve as a safe and cost-efficient method for prognostication of outcome and success of hypothermic treatment after HII (Fig. 46.8). RI values below 0.60 **before cooling** may broadly differentiate neonates who are more likely to have outcomes of severe neurodevelopmental disability or death by age 20 to 32 months.[38] Persistent hypoxia or hypercapnia will also contribute to generalized vasodilation and abnormal Doppler spectra. Fluctuation of systolic velocities may be caused by hypoxia-related cardiac ischemia.[39,40]

Cerebral Edema

Cerebral edema may be seen in HII, congestive heart failure, and many infectious processes. In the early phases of brain edema the RI values typically decrease owing to related vascular vasodilation.[41] As cerebral edema worsens, cerebrovascular resistance increases, with resultant dampening of the diastolic blood flow velocities. Pulsed wave Doppler imaging typically shows subsequent progressive elevation of the RI values and may eventually be accompanied by a reversal of the diastolic flow in the intracranial arteries.[40,42]

Brain Death

Depending on local legislation, several strict criteria have to be fulfilled for clinical determination of brain death. Typically, absent pupillary responses, no cranial nerve reflexes, no spontaneous respiration, and a "flat" electroencephalogram are combined with neuroimaging techniques confirming absent brain perfusion on a radionuclide CBF study. Several studies have focused on the value of duplex sonography for determination of brain death.

Duplex sonography typically shows markedly elevated RI values (>1.0) with reversal of diastolic flow in brain death, likely secondary to increased ICP. However, it should be recognized that reversal of the diastolic blood flow may also be seen in children with significant hydrocephalus and patent ductus arteriosus.[43] In brain death, in addition, the pulsations of the middle and anterior cerebral arteries appear diminished. Eventually, flow during systole becomes diminished and present only during a brief portion of the cardiac cycle. This represents **nonviable brain blood flow**[42] (Fig. 46.9).

Although absence of intracranial flow demonstrated by Doppler techniques is a reliable sign of absent cortical function, the presence of flow does not guarantee functional integrity, and brain death may be present despite preserved intracranial blood flow.[43,44]

INTRACRANIAL HEMORRHAGE AND STROKE

Color flow Doppler imaging may be used to show initial displacement, gradual encasement, and **obstruction of the subependymal and terminal veins** by germinal matrix hemorrhage (GMH; Fig. 46.10). In one study, displacement or occlusion of the terminal vein could be demonstrated in 50% of GMHs and in 92% of periventricular white matter hemorrhages.[45] This finding may be useful in the early prediction of infants at risk for worsening intracranial hemorrhage.

Focal Arterial Ischemic Stroke

Focal disruption of CBF causes **arterial ischemic stroke** in the neonatal period. Perinatal complications are the most common cause of stroke in newborns. Other factors are meningitis, trauma, polycythemia, dehydration, hypercoagulability, and cerebral vasculitis.[46,47] These lesions typically occur in full-term infants, mostly affect the vascular territory of the MCAs (>50%), and are usually unilateral.

Not all cerebral infarcts show alterations in regional blood flow. Although magnetic resonance imaging (MRI) and catheter angiography are the imaging reference standards, during the subacute phase cranial Doppler sonography can show hypervascularity characterized by an increased size and number of visible vessels, and increased mean CBFV in the peripheral, penumbral region of the ischemic area[47-49] (Fig. 46.11). This

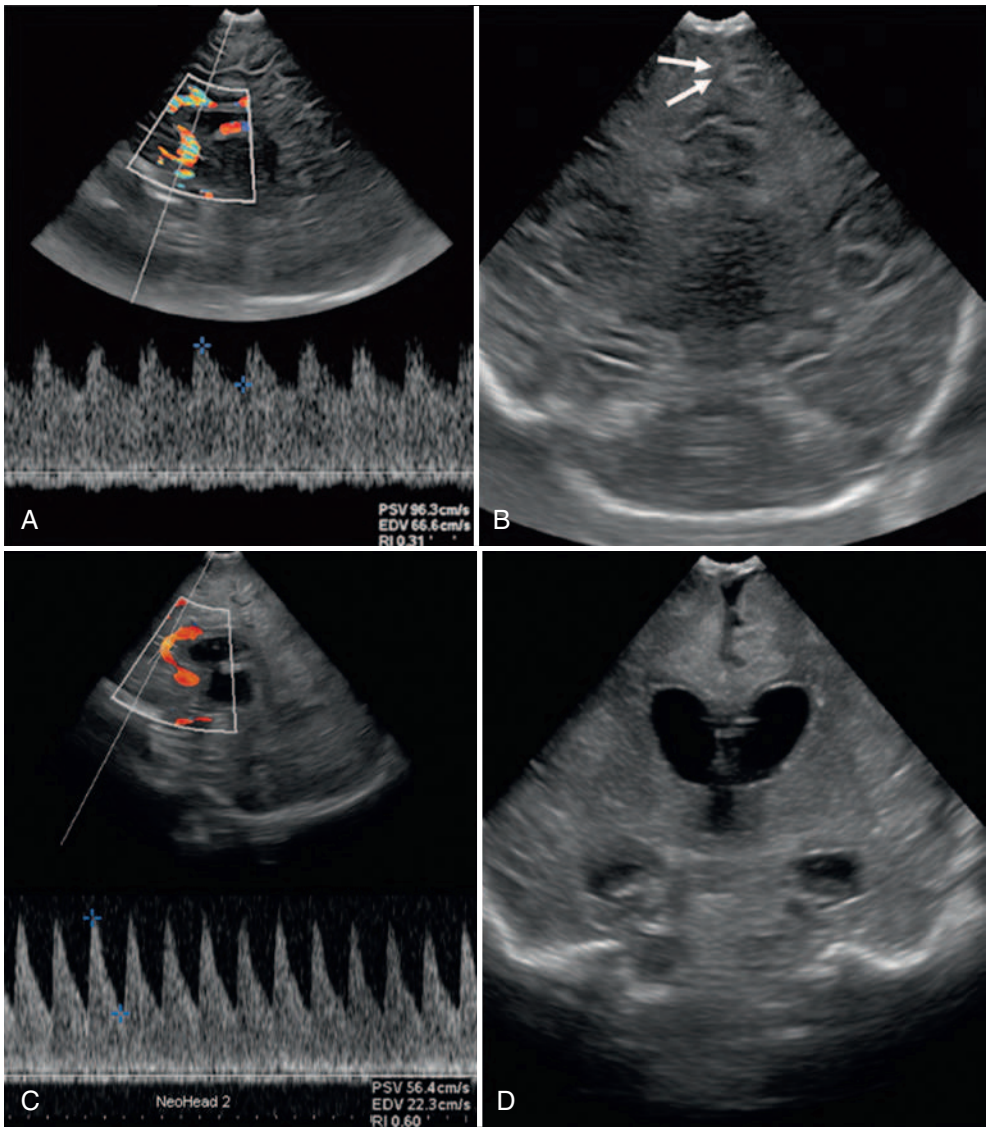

FIG. 46.7 Severe Perinatal Hypoxic Ischemic Injury in a Full-Term Infant With Additional Respiratory Distress Due to Meconium Aspiration. (A) and **(B)** Initial ultrasound study shows diffuse brain edema with increased echogenicity of the cerebral white matter, accentuated corticomedullary differentiation, partially interrupted cortex along the midline *(arrows),* and slitlike ventricles. Anterior cerebral artery Doppler shows elevated flow during diastole and a reduced resistive index (RI) value (0.31). **(C)** and **(D)** Follow-up imaging shows a progressive severe tissue injury with global gray and white matter echogenicity (loss of corticomedullary differentiation) and ventriculomegaly with pseudonormalization of the RI value (0.60).

pattern of vasodilation is thought to be caused by the uncoupling of CBF from local metabolic demands and is known as **luxury perfusion.**[50,51]

HYDROCEPHALUS

As ICP rises, arterial flow tends to be more affected during diastole than during systole, resulting in an elevated pulsatility of flow and increased RI. Seibert and colleagues showed that **increasing RI** correlates well with ICP elevation in an experimental canine model of hydrocephalus.[52] Also, significant decreases in pulsatility and RI values have been shown to occur after ventricular tapping and shunting in infants with hydrocephalus.[53,54] However, elevated ICP may not always be present in infants with ventricular dilation, and the RI values may be well within the normal range. Furthermore, the RI values vary with gestational and postnatal age, cardiac function, heart rate, patency of the ductus arteriosus, and executed treatment. Consequently, care should be taken to not use the RI value as a sole indicator of raised ICP.[54]

Several additional variations of the duplex Doppler technique can be applied to enhance the diagnostic sensitivity and specificity of the imaging. Doppler sonography of the anterior cerebral artery or MCA during fontanelle compression may be useful in the early identification of infants with abnormal intracranial compliance before development of increased ICP, as shown by elevated baseline RI.[21] Taylor and Madsen directly measured changes in ICP and intracranial RI before and after ventricular drainage procedures.[55,56] These studies showed that the change

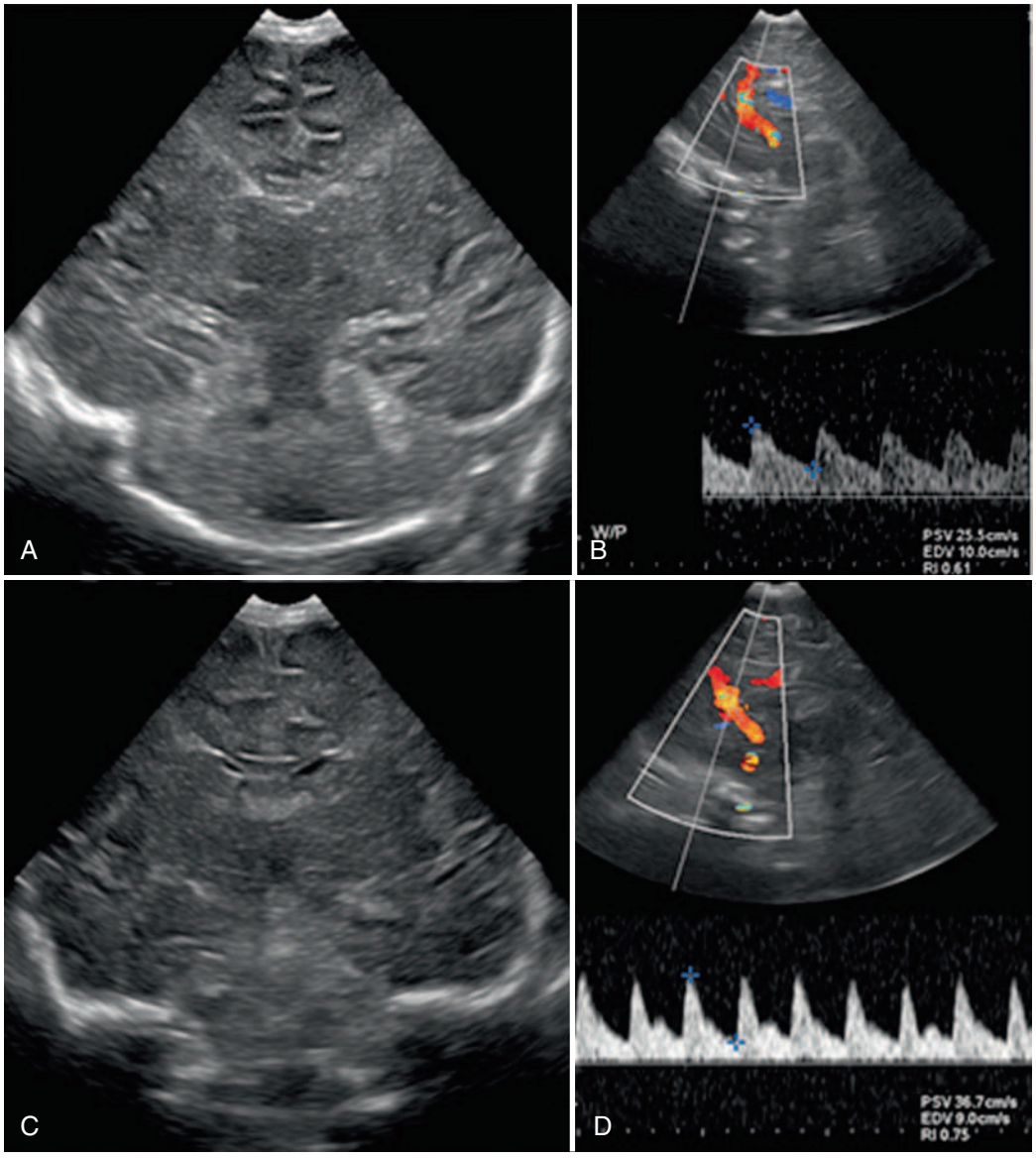

FIG. 46.8 Serial Imaging in a Neonate With Perinatal Hypoxic Ischemic Injury Treated With Therapeutic Hypothermia. (A) and **(B)** Initial ultrasound study shows diffuse brain edema with increased echogenicity of the cerebral white matter, accentuated corticomedullary differentiation, and slitlike ventricles. Anterior cerebral artery Doppler shows a resistive index (RI) value of 0.61. **(C)** and **(D)** Follow-up imaging shows normalization of the B-mode imaging findings after completion of hypothermic therapy and a normal RI value of 0.75. These findings matched the normal neurologic examination findings.

in RI during graded anterior fontanelle compression is a strong predictor of ICP and can help predict the need for shunt placement. This technique has also been used successfully to evaluate intracranial compliance in young children with **craniosynostosis** before surgical repair.[57]

According to the Monro-Kellie hypothesis, the volume of brain, cerebrospinal fluid (CSF), blood, and other intracranial components is constant.[58] During graded fontanelle compression in normal infants, CSF or blood can be readily displaced to compensate for the small increase in volume delivered by compression of the anterior fontanelle, causing no increase in ICP. In infants with hydrocephalus, however, the increase in intracranial volume with fontanelle compression is translated into a transient increase in ICP and an **acute increase in arterial pulsatility resulting in an increased RI** (Fig. 46.12). Serial examinations using this technique can follow an individual infant's ability to compensate for minor changes in intracranial volume, providing a noninvasive, indirect measure of intracranial compliance[59] (Fig. 46.13).

Karl-Heinz Deeg and his group showed that calculating the ratios of the peak systolic flow velocity, EDV, and time average flow velocity measured in the intracranial and extracranial carotid arteries (I/E ratio) can serve as an additional helpful method for semiquantitative estimation of ICP. Slightly increased ICPs below 20 cm H_2O were linked to an increase of the I/E ratio above 1, while the RI values remained unchanged. ICP increases above 20 cm H_2O lowered the I/E ratio significantly below normal values of 0.8, while the RI values increased. The

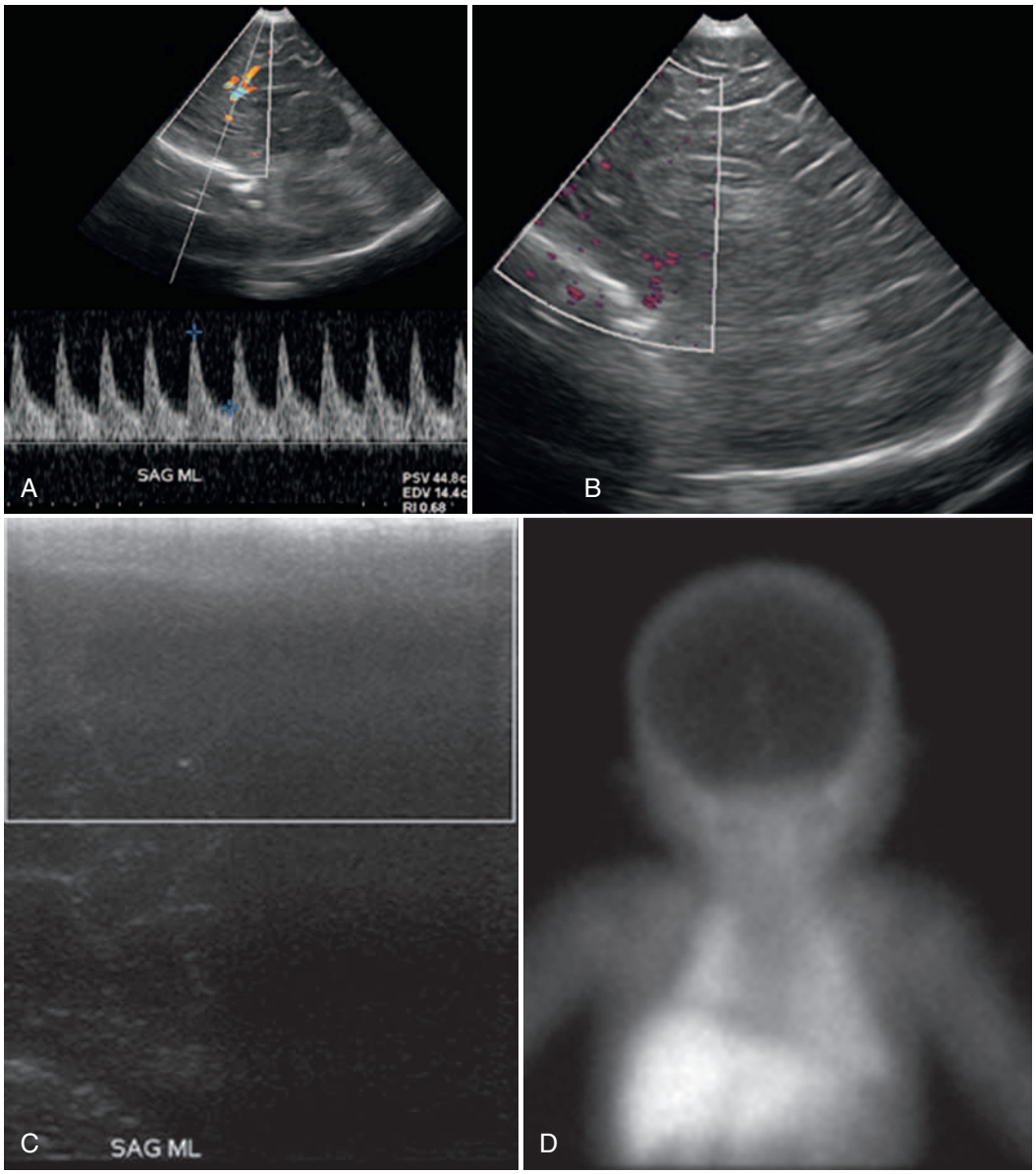

FIG. 46.9 Seven-Week-Old Infant With Progressive Liver Failure, Severe Neurologic Deterioration, and Brain Death. **(A)** Initial ultrasound study and pulsed wave Doppler tracing from anterior cerebral artery appear unremarkable. **(B)** Follow-up imaging during devastating neurologic deterioration shows no relevant brain perfusion on power Doppler imaging. **(C)** Sagittal midline power Doppler imaging also fails to show venous flow within the superior sagittal sinus, confirming lack of brain perfusion. **(D)** Complete lack of brain perfusion was also confirmed by nuclear medicine perfusion study.

decrease in the I/E ratio was more prominent for the EDV compared with the peak systolic flow velocity and time average flow velocity.[60]

VASCULAR MALFORMATIONS

Pediatric cerebral **arteriovenous malformations** (AVMs) differ substantially from adult forms in their angioarchitecture, clinical presentation, systemic hemodynamic impact, and overall functional outcome.[61] Pediatric AVMs are frequently fistulous or multifocal, often exert a hemodynamic effect on the entire venous system, and rarely manifest with high flow–related vasculopathy or flow-related aneurysms. Systemic manifestations with cardiac overload are a key clinical feature increasing morbidity and mortality. Chronic venous stasis and/or ischemia in combination with a vascular steal may cause chronic cardiac insufficiency and result in irreversible brain damage. The so-called **"melting brain"** is a well-known devastating complication of the **vein of Galen aneurysmal malformation** (VGAM), which is the most common neonatal intracranial vascular malformation. Differentiation between "true" and "false" VGAM is essential.[62] In the true VGAM, arteries drain directly into a dilated, persisting interhemispheric prosencephalic vein (Markowski vein) without connection to the deep venous system. In "false" VGAM, subpial AVMs adjacent to the cerebellum, brainstem, or deep supratentorial territories drain into a normally developed vein of Galen,

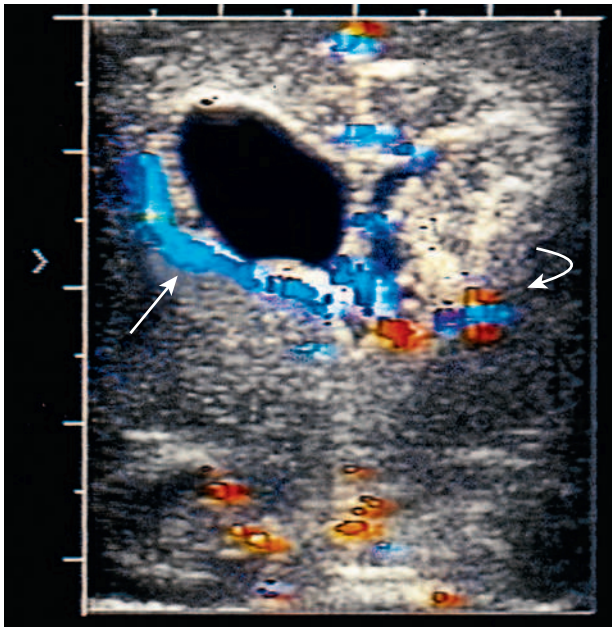

FIG. 46.10 Left-Sided Germinal Matrix Hemorrhage (GMH) With Obstruction of Terminal Vein Resulting in Periventricular Venous Stasis and Hemorrhagic Infarction. Flow in left subependymal vein *(curved arrow)* is obliterated by the hematoma. Flow in normal right subependymal vein *(straight arrow)* is shown.

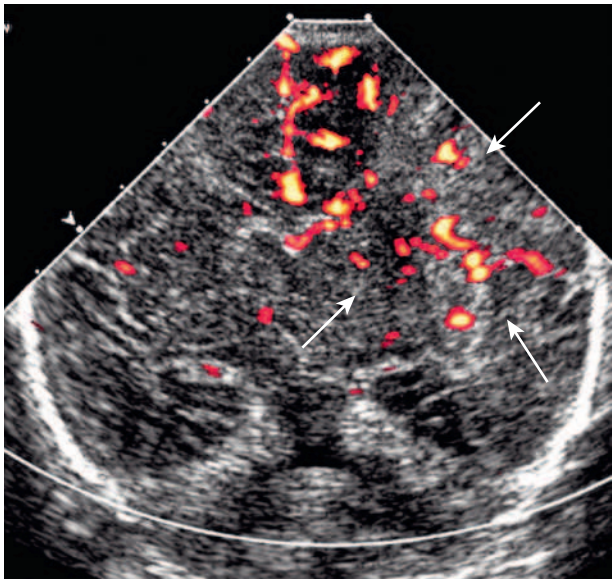

FIG. 46.11 Luxury Perfusion Secondary to Left Middle Cerebral Artery Ischemic Stroke in Full-Term Neonate. Coronal amplitude-mode Doppler image shows greatly increased blood flow to the ischemic mildly hyperechogenic area *(arrows),* consistent with luxury perfusion.

which may dilate owing to the venous overload. Consequently, the correct terminology would be **"vein of Galen aneurysmal dilation"** (VGAD). Ultrasound is an important imaging tool that allows the direct visualization of the dilated vessels of vein of Galen aneurysms as well as possible complications such as brain edema and hydrocephalus. VGAM and VGAD are typically diagnosed prenatally by ultrasound screening.[63] Prenatal and postnatal color flow sonography and spectral analysis of the blood flow curves within the supplying and draining vessels give

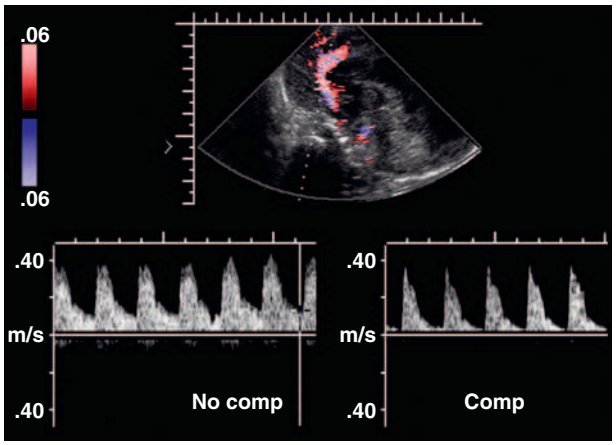

FIG. 46.12 Hydrocephalus Causes Increased Resistive Index (RI) When Gentle Anterior Fontanelle Pressure Is Added. Pulsed wave Doppler tracing of the anterior cerebral artery with transducer held lightly over anterior fontanelle *(No comp)* shows an RI of 0.69. Repeat tracing obtained a few seconds later with transducer firmly held over fontanelle *(Comp).* RI has increased to 0.99, indicating abnormal intracranial compliance. *Comp,* Compression.

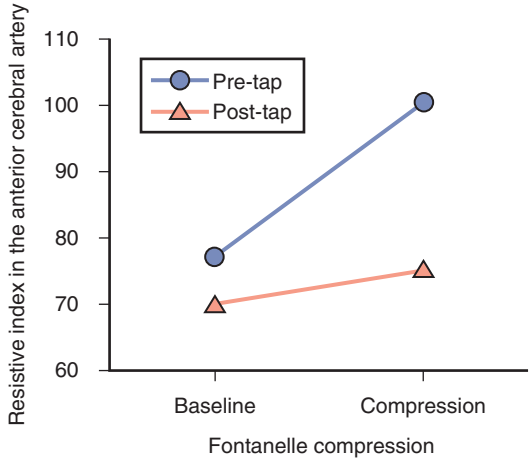

FIG. 46.13 Shunted Hydrocephalus Is Less Sensitive to Pressure Effects on Fontanelle. Graph of serial resistive index (RI) determinations in an infant with hydrocephalus before *(Pre-tap)* and after *(Post-tap)* shunt shows greatly diminished hemodynamic response to fontanelle compression after ventricular drainage. Note that RI is quite similar at baseline and increases with fontanelle compression.

important hemodynamic data both before and after treatment (Figs. 46.14 and 46.15). Spectral Doppler imaging typically shows arterialization of venous flow and increased flow velocities, with reduced pulsatility of the arterial feeders. Blood flow in the more peripheral portions of brain may show diminished or absent flow as a result of a "vascular steal" away from the normal cerebral circulation through the low-resistance malformation.[64,65]

Sinus pericranii is a congenital venous vascular malformation characterized by a fluctuating, compressible subcutaneous venous mass lesion in which the intracranial and extracranial veins are connected through a calvarial defect (Fig. 46.16). The lesion typically increases in size during crying. Duplex Doppler sonography easily differentiates the lesion from various differential diagnoses including meningoencephaloceles, dermoids (Fig.

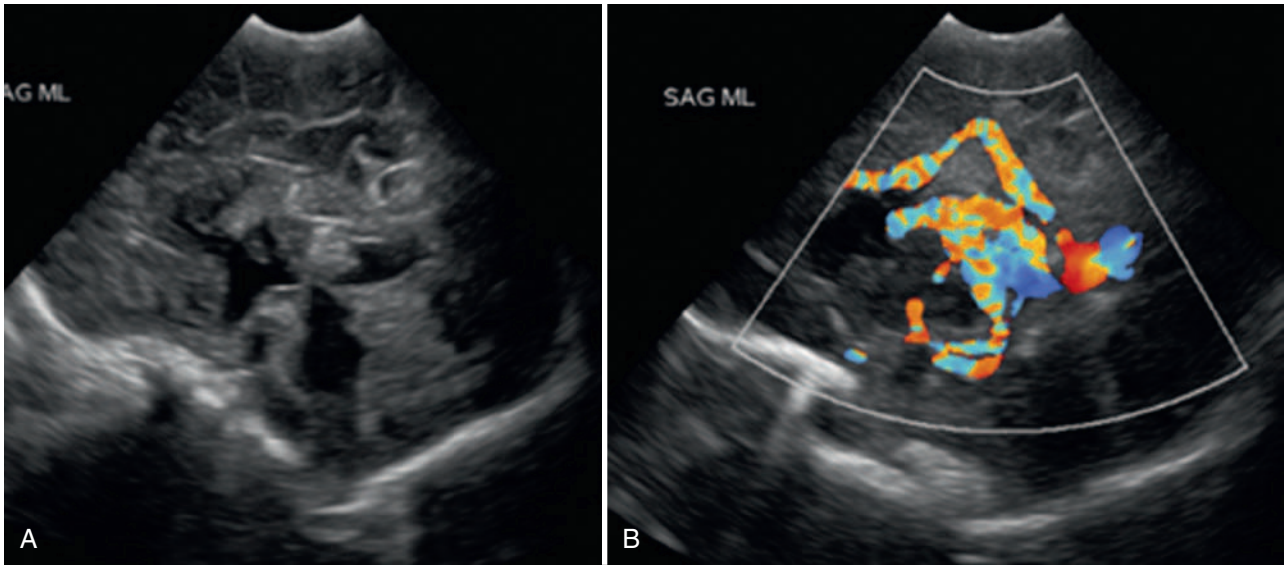

FIG. 46.14 Vein of Galen Aneurysmal Malformation. (A) Gray-scale and **(B)** color Doppler sagittal images show a vascular mass that on color flow Doppler is a dilated vein of Galen supplied by a dilated pericallosal artery and posterior choroidal artery. The vascular malformation appears hypoechoic on B-mode imaging and could be overlooked.

46.17), lipomas, AVMs, hemangiomas, cephalohematomas, or subgaleal effusions. On conventional gray-scale sonography the sinus pericranii is typically anechoic, whereas duplex Doppler sonography shows the venous nature of the lesion. A bidirectional, turbulent venous flow may be seen across the connecting, dilated transcalvarial veins.[66]

INTRACRANIAL TUMORS

Neonatal intracranial tumors are uncommon, and experience with Doppler characterization of these lesions is limited.[67] Doppler sonography may be helpful in characterizing the degree of intratumoral vascularity and in identifying its vascular supply[68] (Fig. 46.18).

NEAR-FIELD STRUCTURES

Differentiation of Subarachnoid From Subdural Fluid Collections

Color flow Doppler ultrasound with high-frequency linear transducers can be used to characterize extracerebral fluid collections as **subarachnoid, subdural,** or **combined.** Because superficial cortical blood vessels lie within the pia-arachnoid, fluid in the subarachnoid space surrounds and lifts the cortical vessels up and away from the brain surface (Fig. 46.19). Fluid in the subdural space pushes cortical vessels down toward the brain surface and is separated from these vessels by a thin membrane. Correlation with MRI and computed tomography (CT) suggests that color flow Doppler imaging is reliable in making this differentiation.[69] However, cortical veins drain into the superior sagittal sinus through emissary veins that course through the extra-axial spaces and can be mistaken for vessels in the subarachnoid space.[70]

Dural Venous Sinus Thrombosis

Dural venous sinus thrombosis may occur in the neonate as the result of systemic or localized infection, congenital heart disease, coagulation disorders, vascular malformations, trauma, and dehydration. Color flow Doppler ultrasound can be used as a noninvasive tool for initial identification and monitoring of dural sinus thrombosis.[46,52,71]

UNCOMMON VASCULAR APPLICATIONS

Duplex Doppler sonography may be helpful for the exploration and confirmation of the vascular nature of the linear hyperechogenic lesions that may be seen in the central gray matter of neonates, also known as **lenticulostriate "vasculopathy"**[72] (Fig. 46.20). Doppler may be used for various rare anatomic vascular anomalies such as hypoplasia of the internal carotid artery. Duplex sonography may also prove to be helpful in diagnosing and monitoring vasomotor reactivity and vasospasm after subarachnoid hemorrhage or traumatic brain injury.

PITFALLS OF DUPLEX SONOGRAPHY

As with any advanced imaging tool, the sonographer and radiologist should be aware of the potential pitfalls and limitations of duplex sonography. The insonication angle should be adapted to the course of the sampled vessel, the sample volume box should be centered within the vessel, and sharp curves should be avoided (turbulent flow with aliasing). Furthermore, the close proximity of the arterial circle of Willis and venous circle of Trolard may result in a simultaneous sampling of both the arterial and venous waveforms, affecting correct calculation of various hemodynamic markers such as the RI values (Fig. 46.21).[73,74] In addition,

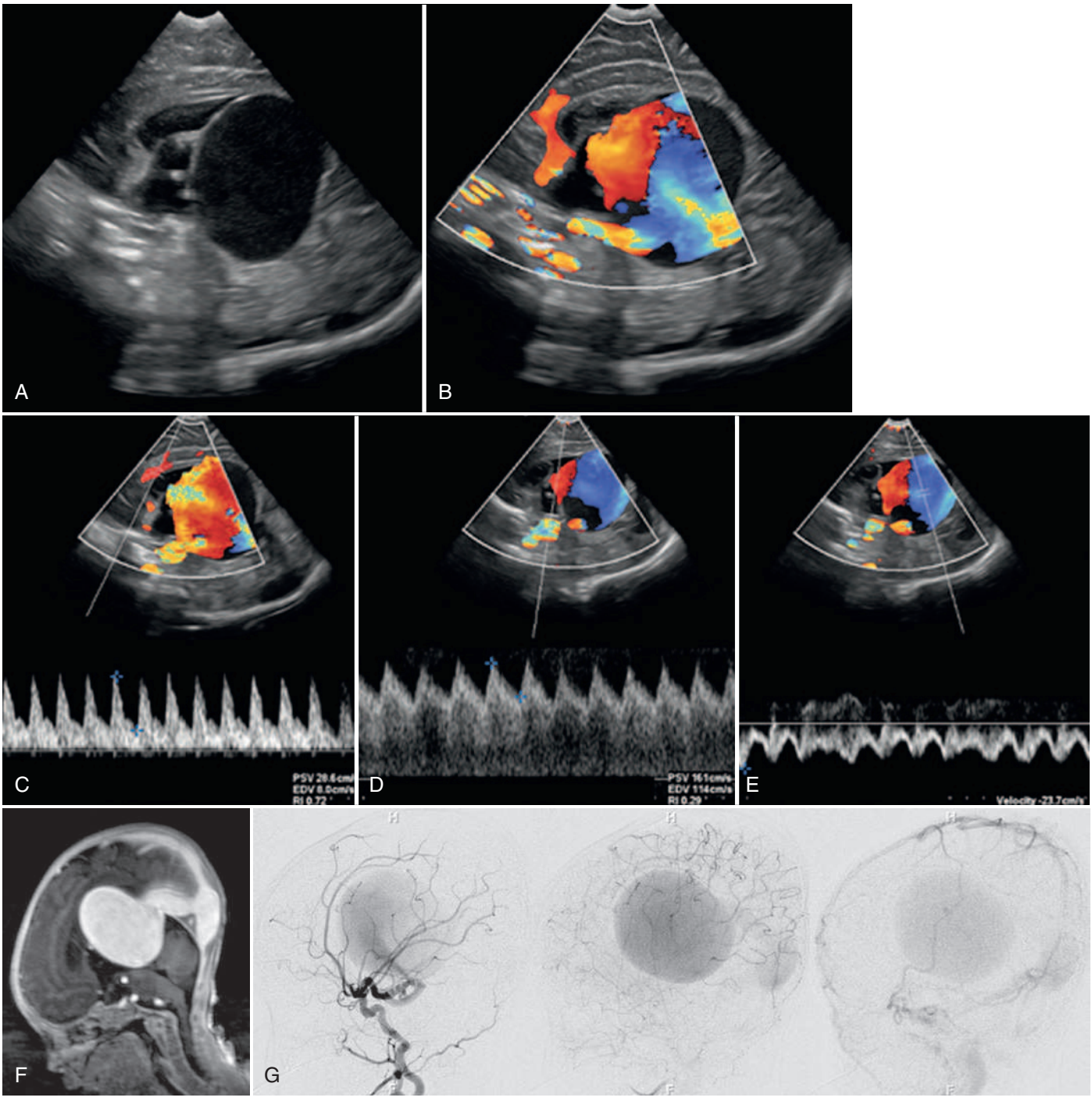

FIG. 46.15 Vein of Galen Aneurysmal Malformation. (A) Sagittal gray-scale and **(B)** color Doppler images show a vascular mass due to aneurysmal enlargement of the vein of Galen with prominent turbulent flow. The tectal plate is compressed downward and the supratentorial ventricles are dilated because of aqueductal obstruction and venous hypertension. **(C)-(E)** Color Doppler sonography with spectral analysis of the malformation allows study of the hemodynamic angioarchitecture of the malformation. Normal flow is noted within the pericallosal artery **(C),** whereas a high flow is noted within the feeding posterior choroidal artery **(D)** with matching low resistive index (RI) value (RI = 0.29) as a result of the arteriovenous shunting. Within the dilated vein of Galen **(E),** extensive referred cardiac pulsations are noted. **(F)** Contrast-enhanced magnetic resonance venography confirms the malformation. **(G)** Digital subtraction angiography shows that the vein of Galen aneurysmal malformation is supplied by dilated bilateral posterior choroidal arteries.

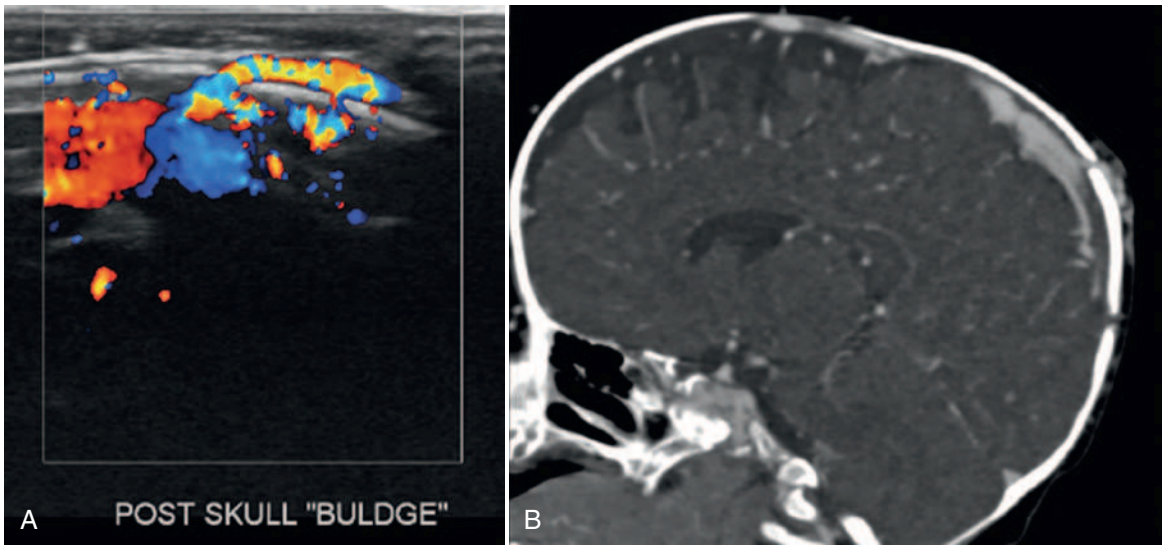

FIG. 46.16 Sinus Pericranii. (A) Midsagittal color flow Doppler sonography shows a prominent vein connecting the intracranial superior sagittal sinus with the subcutaneous venous network. **(B)** Correlative contrast-enhanced computed tomography scan with vessels crossing the calvarium through a small posterior bony defect.

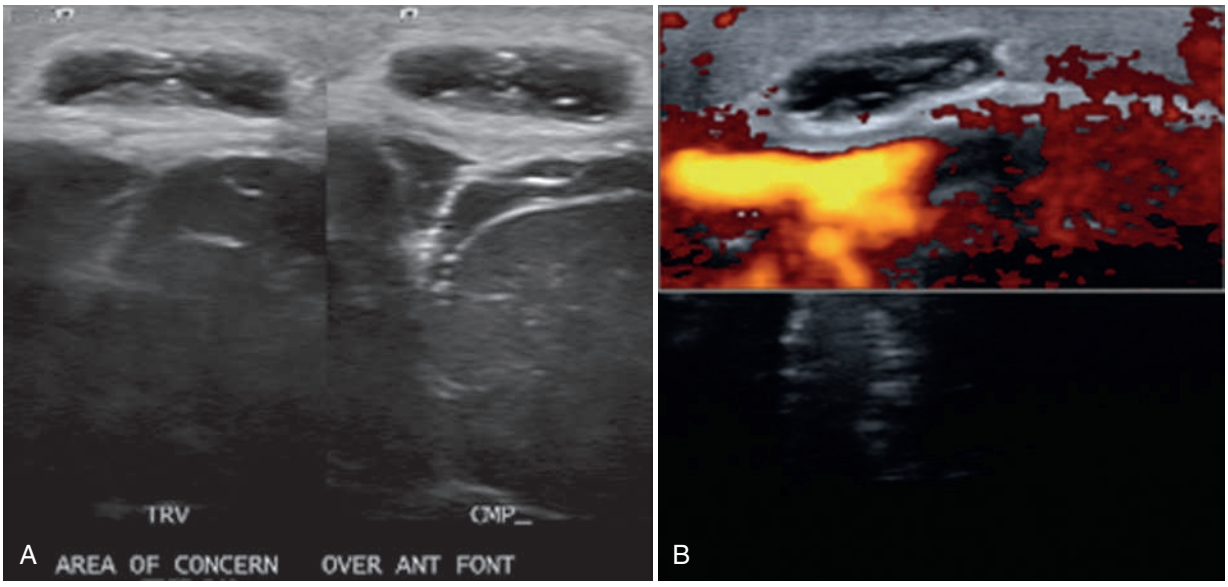

FIG. 46.17 Dermoid in the Sagittal Suture. (A) Gray-scale sonography shows a focal hypoechogenic lesion overlying the sagittal suture. **(B)** Power Doppler sonography shows the nonvascular nature of the focal "bump," excluding a sinus pericranii.

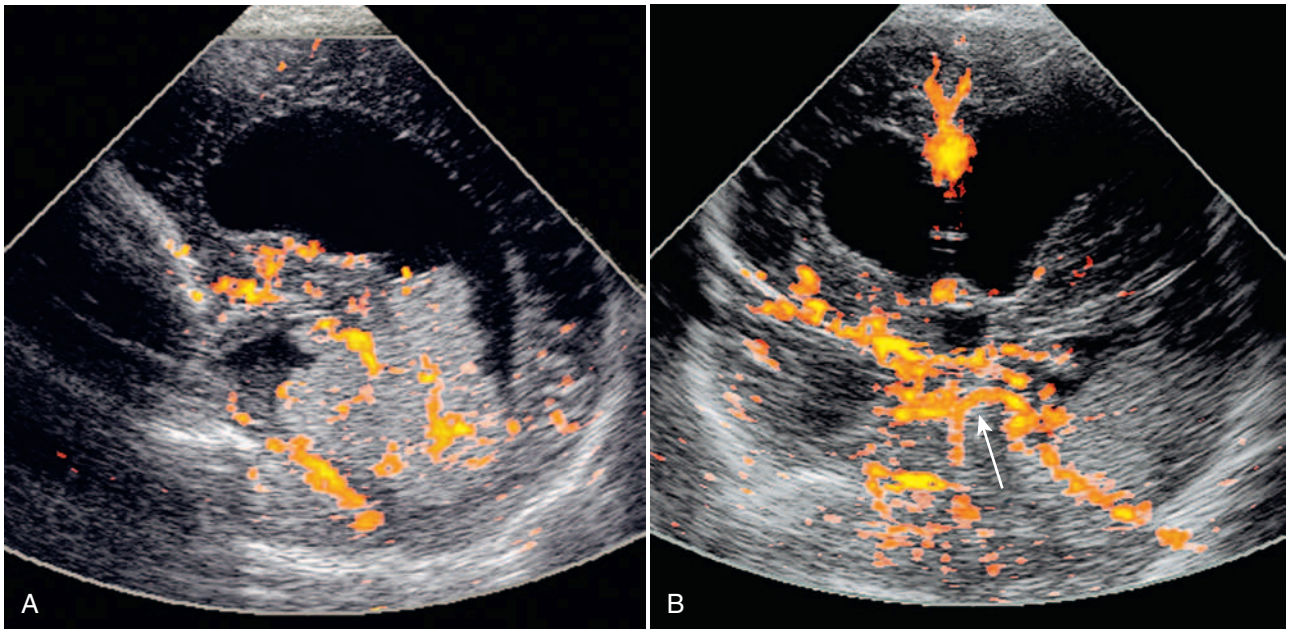

FIG. 46.18 Choroid Plexus Papilloma in 6-Week-Old Infant. (A) Angled sagittal and **(B)** coronal color amplitude (power) Doppler images show increased tumor vascularity within the echogenic mass, with arterial supply arising from a branch of the basilar artery *(arrow)*.

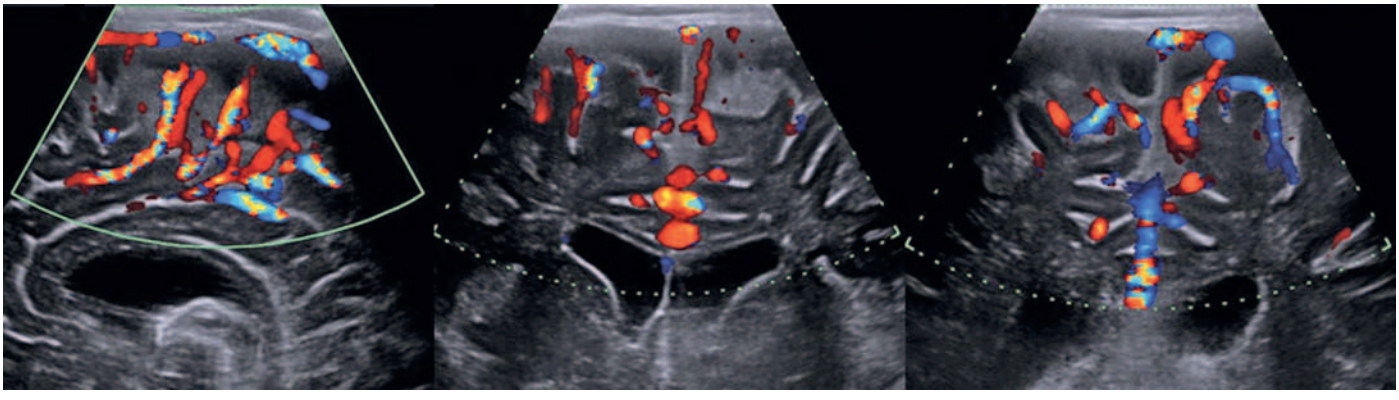

FIG. 46.19 Subdural and Subarachnoid Effusions From Meningitis. Magnified sagittal and coronal color Doppler images of interhemispheric fissure. Large bilateral partially hypoechogenic, partially hyperechogenic subdural and subarachnoid effusions. Superficial cortical vessels cross the subarachnoid and subdural space to drain into the superior sagittal sinus. The ventricles are mildly dilated; the leptomeninges are thickened and hyperechogenic.

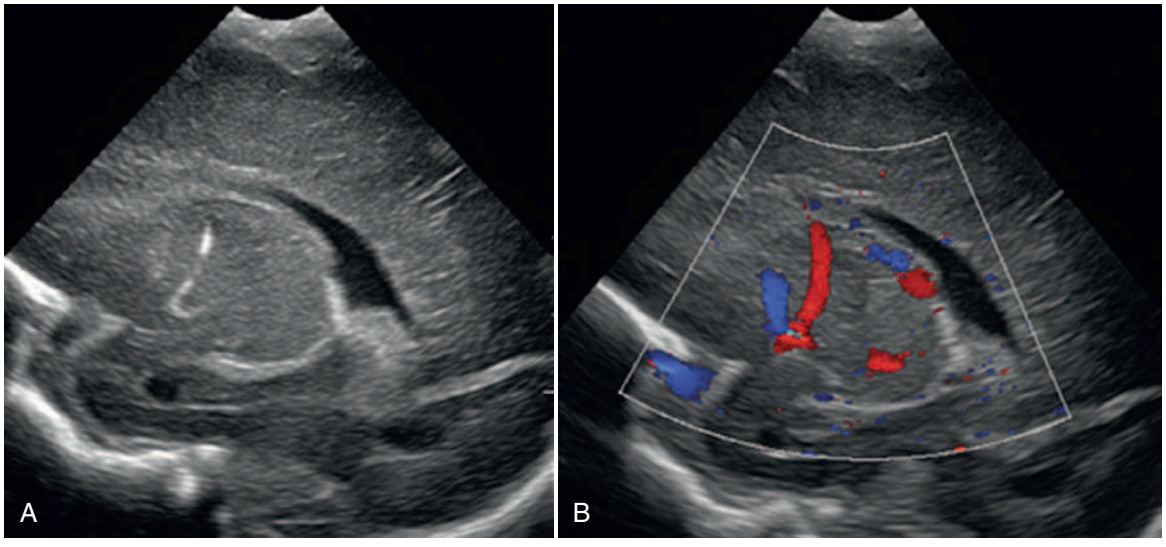

FIG. 46.20 Lenticulostriate Vasculopathy. (A) Gray-scale sagittal sonography shows moderately hyperechogenic linear lesions within the basal ganglia that prove to be prominent lenticulostriate vessels on color flow Doppler sonography **(B).**

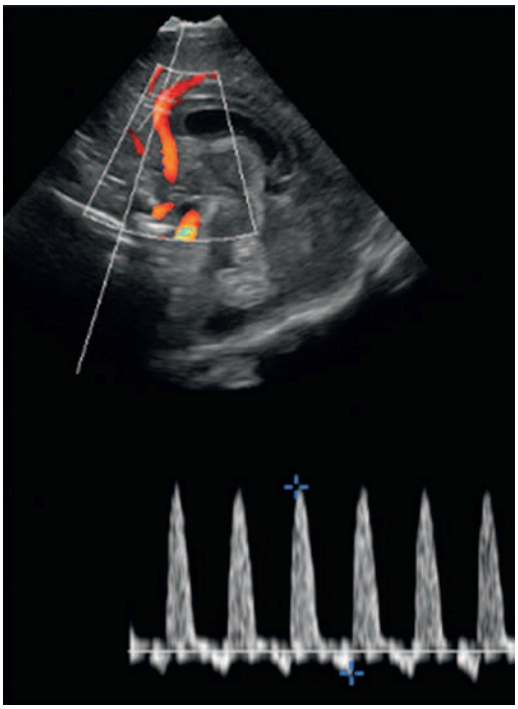

FIG. 46.21 Pitfall: Arterial and Venous Overlay on Spectral Flow Curve. Simultaneous sampling of the arterial flow within the pericallosal artery and adjacent inferior sagittal sinus may mimic a reversal of the diastolic flow with incorrect calculation of the resistive index values.

slow-flow vessels, deep-seated vessels, and superficial vessels obscured by the calvarial bone or outside the acoustic window may be overlooked. A dedicated familiarity with the studied pathologies is a sine qua non for sensitive and specific duplex sonography.

REFERENCES

1. Bada HS, Hajjar W, Chua C, Sumner DS. Noninvasive diagnosis of neonatal asphyxia and intraventricular hemorrhage by Doppler ultrasound. J Pediatr. 1979;95(5 Pt 1):775-779.
2. Archer LN, Evans DH, Levene MI. Doppler ultrasound examination of the anterior cerebral arteries of normal newborn infants: the effect of postnatal age. Early Hum Dev. 1985;10(3-4):255-260.
3. Grant EG, White EM, Schellinger D, et al. Cranial duplex sonography of the infant. Radiology. 1987;163(1):177-185.
4. Taylor G. Current concepts in neonatal cranial Doppler sonography. Ultrasound Q. 1992;223-244.
5. Wong WS, Tsuruda JS, Liberman RL, et al. Color Doppler imaging of intracranial vessels in the neonate. Am J Roentgenol. 1989;152(5):1065-1070.
6. Mitchell DG, Merton D, Needleman L, et al. Neonatal brain: color Doppler imaging. Part I. Technique and vascular anatomy. Radiology. 1988;167(2):303-306.
7. Mitchell DG, Merton DA, Mirsky PJ, Needleman L. Circle of Willis in newborns: color Doppler imaging of 53 healthy full-term infants. Radiology. 1989;172(1):201-205.
8. Taylor GA. Intracranial venous system in the newborn: evaluation of normal anatomy and flow characteristics with color Doppler US. Radiology. 1992;183(2):449-452.
9. Dean LM, Taylor GA. The intracranial venous system in infants: normal and abnormal findings on duplex and color Doppler sonography. Am J Roentgenol. 1995;164(1):151-156.
10. Perlman JM, Hill A, Volpe JJ. The effect of patent ductus arteriosus on flow velocity in the anterior cerebral arteries: ductal steal in the premature newborn infant. J Pediatr. 1981;99(5):767-771.
11. Taylor GA. Effect of scanning pressure on intracranial hemodynamics during transfontanellar duplex US. Radiology. 1992;185(3):763-766.
12. Taylor GA, Martin GR, Short BL. Cardiac determinants of cerebral blood flow during extracorporeal membrane oxygenation. Invest Radiol. 1989;24(7):511-516.
13. Taylor GA, Short BL, Walker LK, Traystman RJ. Intracranial blood flow: quantification with duplex Doppler and color Doppler flow US. Radiology. 1990;176(1):231-236.
14. Greisen G, Johansen K, Ellison PH, et al. Cerebral blood flow in the newborn infant: comparison of Doppler ultrasound and 133xenon clearance. J Pediatr. 1984;104(3):411-418.
15. Hansen NB, Stonestreet BS, Rosenkrantz TS, Oh W. Validity of Doppler measurements of anterior cerebral artery blood flow velocity: correlation with brain blood flow in piglets. Pediatrics. 1983;72(4):526-531.
16. Lundell BP, Lindstrom DP, Arnold TG. Neonatal cerebral blood flow velocity I. An in vitro validation of the pulsed Doppler technique. Acta Paediatr Scand. 1984;73(6):810-815.
17. Horgan JG, Rumack CM, Hay T, et al. Absolute intracranial blood-flow velocities evaluated by duplex Doppler sonography in asymptomatic preterm and term neonates. Am J Roentgenol. 1989;152(5):1059-1064.
18. Allison JW, Faddis LA, Kinder DL, et al. Intracranial resistive index (RI) values in normal term infants during the first day of life. Pediatr Radiol. 2000;30(9):618-620.
19. Raju TN, Zikos E. Regional cerebral blood velocity in infants. A real-time transcranial and fontanellar pulsed Doppler study. J Ultrasound Med. 1987;6(9):497-507.
20. Agoestina T, Humphrey JH, Taylor GA, et al. Safety of one 52-mumol (50,000 IU) oral dose of vitamin A administered to neonates. Bull World Health Organ. 1994;72(6):859-868.
21. Taylor GA, Phillips MD, Ichord RN, et al. Intracranial compliance in infants: evaluation with Doppler US. Radiology. 1994;191(3):787-791.
22. Winkler P, Helmke K. Duplex-scanning of the deep venous drainage in the evaluation of blood flow velocity of the cerebral vascular system in infants. Pediatr Radiol. 1989;19(2):79-90.
23. Cowan F, Thoresen M. Changes in superior sagittal sinus blood velocities due to postural alterations and pressure on the head of the newborn infant. Pediatrics. 1985;75(6):1038-1047.
24. Rennie JM, South M, Morley CJ. Cerebral blood flow velocity variability in infants receiving assisted ventilation. Arch Dis Child. 1987;62(12):1247-1251.
25. Laubscher B, van Melle G, Fawer CL, et al. Haemodynamic changes during high frequency oscillation for respiratory distress syndrome. Arch Dis Child Fetal Neonatal Ed. 1996;74(3):F172-F176.
26. Perlman JM, Volpe JJ. Suctioning in the preterm infant: effects on cerebral blood flow velocity, intracranial pressure, and arterial blood pressure. Pediatrics. 1983;72(3):329-334.
27. Day RW. Cerebral blood flow velocity acutely decreases in newborns who respond to inhaled nitric oxide. Am J Perinatol. 2001;18(4):185-194.
28. Taylor GA, Short BL, Glass P, Ichord R. Cerebral hemodynamics in infants undergoing extracorporeal membrane oxygenation: further observations. Radiology. 1988;168(1):163-167.
29. Mitchell DG, Merton D, Desai H, et al. Neonatal brain: color Doppler imaging. Part II. Altered flow patterns from extracorporeal membrane oxygenation. Radiology. 1988;167(2):307-310.
30. Taylor GA, Walker LK. Intracranial venous system in newborns treated with extracorporeal membrane oxygenation: Doppler US evaluation after ligation of the right jugular vein. Radiology. 1992;183(2):453-456.
31. Weber TR, Kountzman B. The effects of venous occlusion on cerebral blood flow characteristics during ECMO. J Pediatr Surg. 1996;31(8):1124-1127.
32. Barnacle AM, Smith LC, Hiorns MP. The role of imaging during extracorporeal membrane oxygenation in pediatric respiratory failure. Am J Roentgenol. 2006;186(1):58-66.
33. O'Brien NF, Hall MW. Extracorporeal membrane oxygenation and cerebral blood flow velocity in children. Pediatr Crit Care Med. 2013;14(3):e126-e134.

34. Stretti F, Gotti M, Pifferi S, et al. Body temperature affects cerebral hemodynamics in acutely brain injured patients: an observational transcranial color-coded duplex sonography study. Crit Care. 2014;18(5):552.
35. Taylor GA, Trescher WH, Johnston MV, Traystman RJ. Experimental neuronal injury in the newborn lamb: a comparison of *N*-methyl-D-aspartic acid receptor blockade and nitric oxide synthesis inhibition on lesion size and cerebral hyperemia. Pediatr Res. 1995;38(5):644-651.
36. van Bel F, van de Bor M, Stijnen T, et al. Cerebral blood flow velocity pattern in healthy and asphyxiated newborns: a controlled study. Eur J Pediatr. 1987;146(5):461-467.
37. Ilves P, Lintrop M, Metsvaht T, et al. Cerebral blood-flow velocities in predicting outcome of asphyxiated newborn infants. Acta Paediatr. 2004;93(4):523-528.
38. Gerner GJ, Burton VJ, Poretti A, et al. Transfontanellar duplex brain ultrasonography resistive indices as a prognostic tool in neonatal hypoxic-ischemic encephalopathy before and after treatment with therapeutic hypothermia. J Perinatol. 2016;36(3):202-206.
39. van Bel F, van de Bor M, Baan J, Ruys JH. The influence of abnormal blood gases on cerebral blood flow velocity in the preterm newborn. Neuropediatrics. 1988;19(1):27-32.
40. Deeg KH, Rupprecht T, Zeilinger G. Doppler sonographic classification of brain edema in infants. Pediatr Radiol. 1990;20(7):509-514.
41. Vannucci RC. Mechanisms of perinatal hypoxic-ischemic brain damage. Semin Perinatol. 1993;17(5):330-337.
42. McMenamin JB, Volpe JJ. Doppler ultrasonography in the determination of neonatal brain death. Ann Neurol. 1983;14(3):302-307.
43. Glasier CM, Seibert JJ, Chadduck WM, et al. Brain death in infants: evaluation with Doppler US. Radiology. 1989;172(2):377-380.
44. Taekuchi K, Iinuma K, Satoh H, et al. Report on the criteria for the determination of brain death in children. Part II. Determination of brain death in children in Japan. Japan Med Assoc J. 2002;336-357.
45. Taylor GA. Effect of germinal matrix hemorrhage on terminal vein position and patency. Pediatr Radiol. 1995;25(Suppl. 1):S37-S40.
46. Yikilmaz A, Taylor GA. Sonographic findings in bacterial meningitis in neonates and young infants. Pediatr Radiol. 2008;38(2):129-137.
47. Soetaert AM, Lowe LH, Formen C. Pediatric cranial Doppler sonography in children: non–sickle cell applications. Curr Probl Diagn Radiol. 2009;38(5):218-227.
48. Hernanz-Schulman M, Cohen W, Genieser NB. Sonography of cerebral infarction in infancy. Am J Roentgenol. 1988;150(4):897-902.
49. Taylor GA. Alterations in regional cerebral blood flow in neonatal stroke: preliminary findings with color Doppler sonography. Pediatr Radiol. 1994;24(2):111-115.
50. Savoiardo M. CT scanning. In: Barnett H, Stein B, Mohr J, et al., editors. Stroke: pathophysiology, diagnosis and management. New York: Churchill Livingstone; 1986. p. 189-219.
51. Taylor GA, Trescher WA, Traystman RJ, Johnston MV. Acute experimental neuronal injury in the newborn lamb: US characterization and demonstration of hemodynamic effects. Pediatr Radiol. 1993;23(4):268-275.
52. Seibert JJ, McCowan TC, Chadduck WM, et al. Duplex pulsed Doppler US versus intracranial pressure in the neonate: clinical and experimental studies. Radiology. 1989;171(1):155-159.
53. Bada HS, Miller JE, Menke JA, et al. Intracranial pressure and cerebral arterial pulsatile flow measurement in neonatal intraventricular hemorrhage. J Pediatr. 1982;100(2):291-296.
54. Hanlo PW, Gooskens RH, Nijhuis IJ, et al. Value of transcranial Doppler indices in predicting raised ICP in infantile hydrocephalus. A study with review of the literature. Childs Nerv Syst. 1995;11(10):595-603.
55. Taylor GA, Madsen JR. Neonatal hydrocephalus: hemodynamic response to fontanelle compression—correlation with intracranial pressure and need for shunt placement. Radiology. 1996;201(3):685-689.
56. Westra SJ, Lazareff J, Curran JG, et al. Transcranial Doppler ultrasonography to evaluate need for cerebrospinal fluid drainage in hydrocephalic children. J Ultrasound Med. 1998;17(9):561-569.
57. Westra S, Stotland M, Lazareff J, et al. Perioperative transcranial Doppler US to evaluate intracranial compliance in young children undergoing craniosynostosis repair surgery. Radiology. 2001;218(3):816-823.
58. Bruce DA, Berman WA, Schut L. Cerebrospinal fluid pressure monitoring in children: physiology, pathology and clinical usefulness. Adv Pediatr. 1977;24:233-290.
59. de Oliveira R, Machado H. Transcranial color-coded Doppler ultrasonography for evaluation of children with hydrocephalus. Neurosurg Focus. 2003;15(4):1-7.
60. Deeg KH, Wolf A. Doppler ultrasound diagnosis of increased intracranial pressure by comparison of 2 blood flow velocities in the extra- and intracranial segment of the internal carotid artery. 2: Findings in children with increased intracranial pressure. Ultraschall Med. 2001;22(2):66-74.
61. Batista L, Ozanne A, Barbosa M, et al. Arteriovenous malformations: diagnosis and endovascular treatment. In: Tortori-Donati P, Rossi A, Biancheri R, editors. Pediatric Neuroradiology: Brain. Berlin: Springer; 2005. 287-317.
62. Alvarez H, Garcia Monaco R, Rodesch G, et al. Vein of Galen aneurysmal malformations. Neuroimaging Clin N Am. 2007;17(2):189-206.
63. Ruano R, Benachi A, Aubry MC, et al. Perinatal three-dimensional color power Doppler ultrasonography of vein of Galen aneurysms. J Ultrasound Med. 2003;22(12):1357-1362.
64. Soto G, Daneman A, Hellman J. Doppler evaluation of cerebral arteries in a galenic vein malformation. J Ultrasound Med. 1985;4(12):673-675.
65. Westra SJ, Curran JG, Duckwiler GR, et al. Pediatric intracranial vascular malformations: evaluation of treatment results with color Doppler US. Work in progress. Radiology. 1993;186(3):775-783.
66. Kim YJ, Kim IO, Cheon JE, et al. Sonographic features of sinus pericranii in 4 pediatric patients. J Ultrasound Med. 2011;30(3):411-417.
67. Chow PP, Horgan JG, Burns PN, et al. Choroid plexus papilloma: detection by real-time and Doppler sonography. AJNR Am J Neuroradiol. 1986;7(1):168-170.
68. Simanovsky N, Taylor G. Sonography of brain tumors in infants and young children. Pediatr Radiol. 2001;31(6):392-398.
69. Chen CY, Chou TY, Zimmerman RA, et al. Pericerebral fluid collection: differentiation of enlarged subarachnoid spaces from subdural collections with color Doppler US. Radiology. 1996;201(2):389-392.
70. Amodio J, Spektor V, Pramanik B, et al. Spontaneous development of bilateral subdural hematomas in an infant with benign infantile hydrocephalus: color Doppler assessment of vessels traversing extra-axial spaces. Pediatr Radiol. 2005;35(11):1113-1117.
71. Bezinque SL, Slovis TL, Touchette AS, et al. Characterization of superior sagittal sinus blood flow velocity using color flow Doppler in neonates and infants. Pediatr Radiol. 1995;25(3):175-179.
72. Makhoul IR, Eisenstein I, Sujov P, et al. Neonatal lenticulostriate vasculopathy: further characterisation. Arch Dis Child Fetal Neonatal Ed. 2003;88(5):F410-F414.
73. Cullen S, Demengie F, Ozanne A, et al. The anastomotic venous circle of the base of the brain. Interv Neuroradiol. 2005;11(4):325-332.
74. Tubbs RS, Loukas M, Shoja MM, et al. The venous circle of Trolard. Bratisl Lek Listy. 2008;109(4):180-181.

CHAPTER 47

Doppler Sonography of the Brain in Children

Dorothy Bulas and Alexia Egloff

SUMMARY OF KEY POINTS

- Transcranial Doppler (TCD) can be performed, with or without imaging. Four windows are available after closure of the anterior fontanelle—temporal, orbital, transforaminal, and submandibular.
- Physiologic variables including age, gender, hematocrit, viscosity, carbon dioxide, temperature, blood pressure, and mental or motor activity can impact flow velocity.
- There are several established clinical applications for TCD and many potential applications for the assessment of cerebral blood flow in the pediatric and adult age groups.
- TCD can be used as a screening test to assess for stroke risk in children with sickle cell disease. Those children with time-averaged maximum mean velocities higher than 200 cm/sec or peak systolic velocities greater than 250 cm/sec in the middle cerebral artery (MCA) or distal internal carotid artery are at highest risk for stroke.
- TCD can be used to assess for vasospasm and help guide therapy. A peak systolic velocity greater than 200 cm/sec is considered abnormal in the appropriate setting. The accuracy of TCD in the diagnosis of vasospasm can be increased by using the Lindegaard ratio (MCA/cervical internal carotid artery ratio). A ratio of higher than 6 suggests severe vasospasm; a ratio between 3 and 6 is associated with mild to moderate vasospasm, and less than 3 in patients with elevated flow velocities is likely secondary generalized hyperemia.

CHAPTER OUTLINE

SONOGRAPHIC TECHNIQUE
ULTRASOUND POWER SETTINGS
LIMITATIONS AND PITFALLS IN TRANSCRANIAL DOPPLER
CONTRAST ENHANCEMENT
INDICATIONS FOR TRANSCRANIAL DOPPLER IMAGING
Sickle Cell Disease
Vasospasm
Evaluation of Collateral Flow
Headaches
Sleep Apnea
Hydrocephalus
Vascular Malformations
Asphyxia
Cerebral Edema and Hyperventilation Therapy
Evaluation of Right-to-Left Shunt
Brain Death
Neuromonitoring and Intraoperative Neuroradiologic Procedures
Transcranial Doppler and Tissue Plasminogen Activator
Functional Transcranial Doppler
Other Potential Uses

Duplex Doppler sonography with color flow imaging through the anterior fontanelle is simple and has proved useful in evaluating abnormalities of cerebral blood flow in the neonate and young child.[1-4] Once the fontanelle closes, transcranial Doppler (TCD) sonography can still be performed noninvasively using a low MHz (2- to 2.5-MHz) pulsed wave Doppler transducer through the thin temporal bone, the orbits, and the foramen magnum. This technique can be used to measure the velocity and pulsatility of blood flow within the intracranial arteries of the circle of Willis and the vertebrobasilar system.[5] TCD sonography has become a key tool in the management of children with sickle cell disease (SCD) and has proved to be a valuable adjunct in the evaluation of various intracranial pathologies in children, including vasospasm, vascular malformations, and brain death, as well as the assessment of cerebral hemodynamics after trauma, asphyxia, migraine, and stroke.

Two types of TCD sonographic equipment are available: **nonimaging** (TCD) and **imaging** (TCDI). The nonimaging technique uses continuous wave and pulsed wave Doppler to insonate specific vessels using strict criteria for vessel identification based on the depth and direction of flow for intracranial vessels through the temporal bone.[6,7] This blinded technique requires meticulous skill in obtaining the highest achievable audible Doppler frequency and the ability to maintain the mental image of the circle of Willis. Advantages of nonimaging TCD include the fact that the units designed for this exam are small, portable, and inexpensive; have good Doppler sensitivity; and have superior window maneuverability due to small transducer size. Limitations

include the need for intensive training, difficulty in finding specific vessels by sound, and lack of unit availability in radiology departments. Duplex Doppler sonography with color imaging using low MHz transducers via the temporal bone has increased the utility of TCD sonography. Advantages of TCDI include rapid vessel identification, a shorter learning curve, and availability of units in radiology departments. This imaging technique allows more confident vessel identification, resulting in easier, more reliable, and reproducible information.[8-11] However, with training and experience, both techniques have been shown to be reliable and reproducible.[12,13]

SONOGRAPHIC TECHNIQUE

The **anterior fontanelle** typically remains open through the first year of life. Once closed, three cranial windows (in addition to burr holes and surgical defects) can be used routinely to insonate the intracranial circulation: the **transtemporal window, orbital window,** and the **suboccipital window.** The **submandibular window** can also be used to complete the examination of the cervical segment of the internal carotid artery (ICA).[14]

The transtemporal approach is through the thin suprazygomatic portion of the temporal bone using a low MHz (2- to 2.5-MHz) transducer. The transtemporal acoustic window is usually found on the temporal bone just cephalad to the zygomatic arch and anterior to the ear. The intracranial anatomic landmark in this plane by gray-scale imaging is the heart-shaped **cerebral peduncles** (Fig. 47.1A). Just anterior to the peduncles is the star-shaped, echogenic interpeduncular or suprasellar **cistern.** Anteriorly and laterally from this basilar cistern lies the echogenic fissure for the **middle cerebral artery** (MCA). Color Doppler sonographic imaging (Fig. 47.1B, Video 47.1) and spectral analysis (Figs. 47.1C and 47.2A, Video 47.2) of this vessel show flow toward the transducer. Insonating the vessel deeper toward the midline directs the operator into the bifurcation of the A1 segment of the **anterior cerebral artery** (ACA) and the MCA (Video 47.3). Spectral analysis at this bifurcation landmark will show bidirectional flow, that is, flow toward the transducer in the MCA and flow in the ACA away from the transducer (Fig. 47.2B). As the Doppler gate is moved more medial anteriorly, flow is seen entirely in the ACA away from the transducer (Fig. 47.2C). The MCA should be studied from its most peripheral location to the point of bifurcation, and the ACA studied as medially as possible. The **distal internal carotid artery** (DICA) is just inferior to the bifurcation. The flow of the DICA may be dampened with a harsher sound from the increased angle of insonation, with flow typically directed toward the transducer (Fig. 47.2D). The **posterior cerebral artery** (PCA) can be visualized as it circles around the cerebral peduncles. Flow in this vessel may be away or toward the transducer depending on curser placement (Fig. 47.2E). At times, the MCA, the ACA, and the PCA on the opposite side may also be visualized. Ideally, each side should be studied through the ipsilateral window whenever possible.

The vertebral and basilar arteries can be studied through the suboccipital window via the **foramen magnum** with a low MHz transducer. The patient lies on one side or prone, and the head is bowed slightly so the chin touches the chest, causing a gap between the cranium and the atlas to enlarge. The transducer is placed midline in the nape of the neck and angled through the foramen magnum toward the orbits. The normal landmark is the rounded hypoechoic **medulla** just anterior to the echogenic **clivus** (Fig. 47.3A). The vertebral arteries appear in a V-shaped manner as they rise to the medullopontine junction to form the basilar artery between the hypoechoic medulla-pons junction and the echogenic clivus (Fig. 47.3B). From this posterior view, flow in the vertebral and basilar arteries should be directed away from the transducer (Fig. 47.3C).

The **transorbital window** allows for evaluation of the **ophthalmic artery** (OA), the retinal artery, and the **carotid siphon.** This evaluation is performed with the eyes closed using a higher MHz (5- to 7.5-MHz) transducer on its lowest power setting (Fig. 47.4). Unlike the temporal approach in which the bone attenuates a majority of sound thus requiring a low MHz transducer, the fluid-filled globe only minimally attenuates the sound waves. Although no bioeffects from the ultrasound evaluation of the eye are known, ocular damage can potentially occur as ultrasound energy can create cavitation and heat. The U.S. Food and Drug Administration (FDA) guidelines suggest limiting spatial peak temporal average to 17 mW/cm^2 for orbital imaging and limit the mechanical index to 0.28.[15,16] The time of insonation must also be as minimal as possible to decrease risk of damage to soft tissues.[17] The FDA has approved certain imaging transducers on various manufacturer equipment for the evaluation of the orbit. It is important for operators to determine which transducer is approved for orbital imaging for their system.

A liberal amount of gel is needed on the eyelid with only light pressure utilized on the globe. The orientation marker should be pointed medially toward the nose. Flow in the OA should be toward the transducer. The OA enters the optic foramen and lies lateral and slightly inferior to the optic nerve. It then usually crosses superior to the optic nerve and proceeds anteriorly on the medial side of the orbit. The color pulse repetition frequency should be decreased to visualize the OA. The mean velocity of the OA is 21 + 5 cm/sec with high pulsatility.[18] The central retinal artery branch of the OA is the easiest branch to interrogate with color flow Doppler imaging, just posterior to the retina. Because visualization of this central retinal artery entails directing sound waves through the lens, the lowest power setting must be used to minimize the risk of lens injury and subluxation. However, a large OA branch proceeds along the nasal or medial wall of the orbit. Because interrogating this vessel does not involve directing the sound beam through the lens, a higher power setting may be used for this branch. In the carotid siphon, flow direction varies depending on the segment: toward the probe in the infraclinoid segment, bidirectional in the genu, and away from the probe in the supraclinoid segment. The mean velocity of the carotid siphon is 47 + 14 cm/sec with a low resistance signal.[18]

The **submandibular window,** located at the angle of the jaw, allows for examination of the extracranial ICA, including morphology, flow direction, and velocities. Once the vessels have been identified, different information can be obtained through evaluation of the spectral waveform. Flow direction is one of the first parameters obtained with evaluations (by convention,

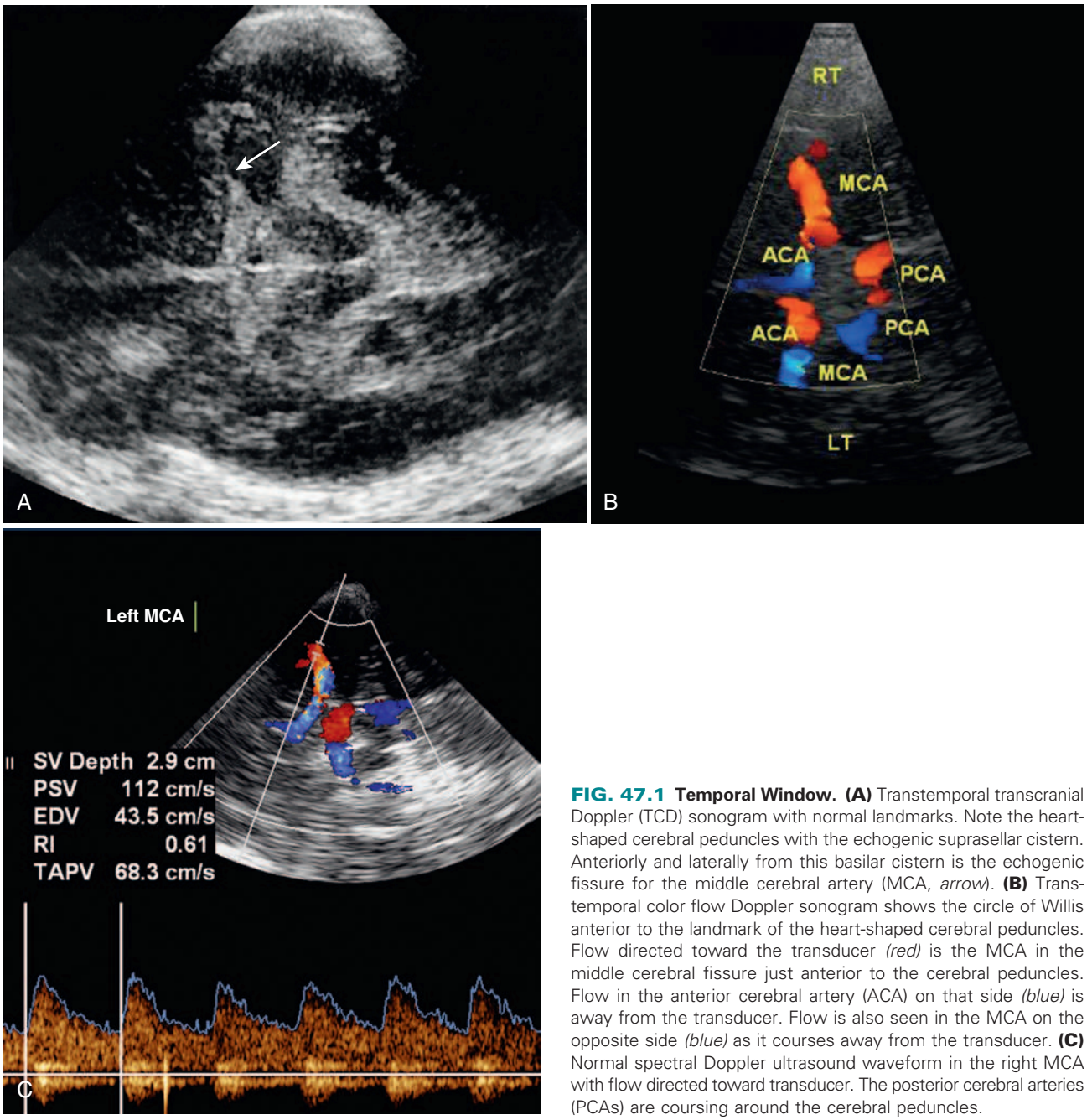

FIG. 47.1 Temporal Window. (A) Transtemporal transcranial Doppler (TCD) sonogram with normal landmarks. Note the heart-shaped cerebral peduncles with the echogenic suprasellar cistern. Anteriorly and laterally from this basilar cistern is the echogenic fissure for the middle cerebral artery (MCA, *arrow*). **(B)** Transtemporal color flow Doppler sonogram shows the circle of Willis anterior to the landmark of the heart-shaped cerebral peduncles. Flow directed toward the transducer *(red)* is the MCA in the middle cerebral fissure just anterior to the cerebral peduncles. Flow in the anterior cerebral artery (ACA) on that side *(blue)* is away from the transducer. Flow is also seen in the MCA on the opposite side *(blue)* as it courses away from the transducer. **(C)** Normal spectral Doppler ultrasound waveform in the right MCA with flow directed toward transducer. The posterior cerebral arteries (PCAs) are coursing around the cerebral peduncles.

flow toward the transducer is coded red and above the baseline, whereas flow away from the transducer is coded blue and below the baseline). A large sample volume (4-6 mm) allows for good signal to noise ratio. Velocities, such as peak systolic velocity (PSV), end diastolic velocity (EDV), and mean flow velocity, and indices reflecting vascular resistance including pulsatility index and resistive index are evaluated.

On spectral analysis of the waveform, the maximum, minimum, and mean velocities can be measured in centimeters per second. It is important to remember which velocity measures are used for various applications. For the STOP study assessing stroke risk in the sickle cell population, the **time-averaged mean of the maximum** (TAMM) **velocity** is followed, and is sometimes called the **time-averaged peak velocity.** This is not the same value as the mean velocity. PSV is the value followed for vasospasm. Terminology of the various mean and TAMM velocities can be vendor specific and need to be clarified dependent on the application TCD is being used for. At least two tracings should be made for each vessel. The highest velocity obtained is likely the most accurate, because it is believed to be the velocity obtained at the best insonating angle to the vessel.[19]

Angle correction cannot be performed with the nonimaging technique, and a 0-degree angle is assumed. Although angle correction is possible with the imaging technique because of visualization of the vessel course, published velocities typically have not been angle-corrected. In clinical applications such as

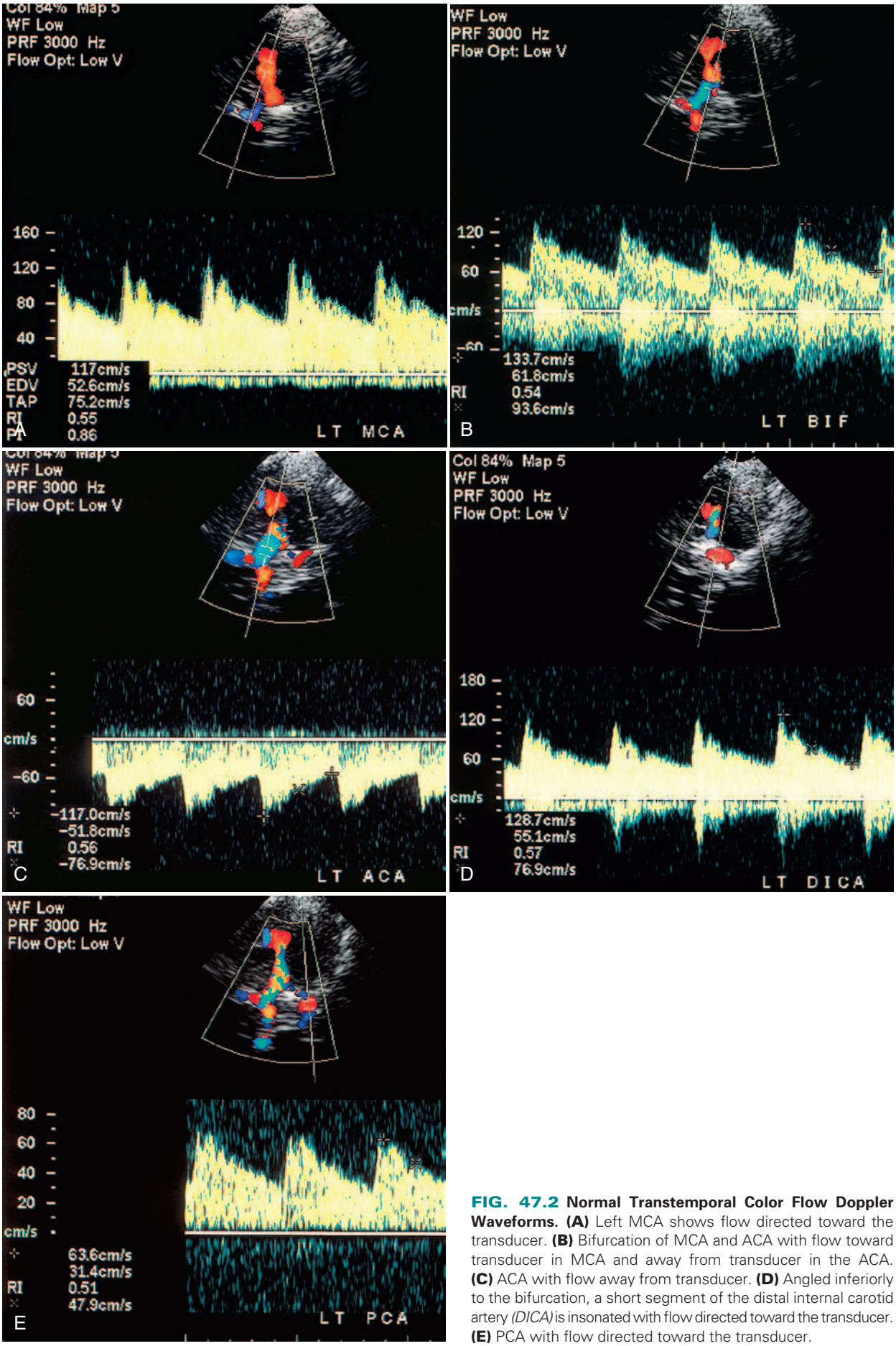

FIG. 47.2 Normal Transtemporal Color Flow Doppler Waveforms. (A) Left MCA shows flow directed toward the transducer. **(B)** Bifurcation of MCA and ACA with flow toward transducer in MCA and away from transducer in the ACA. **(C)** ACA with flow away from transducer. **(D)** Angled inferiorly to the bifurcation, a short segment of the distal internal carotid artery *(DICA)* is insonated with flow directed toward the transducer. **(E)** PCA with flow directed toward the transducer.

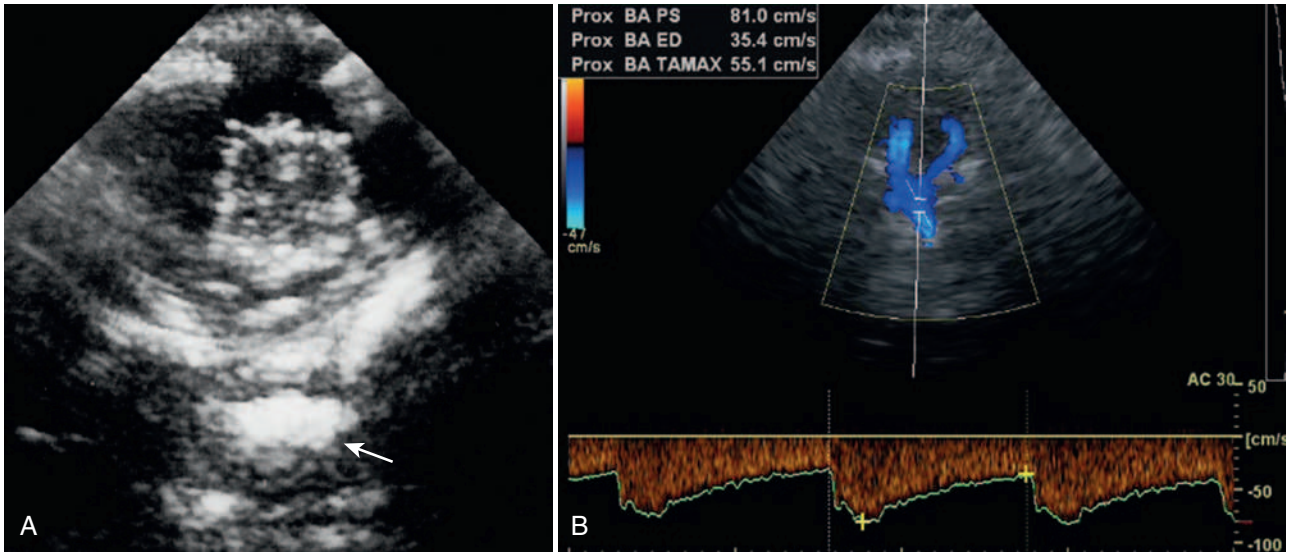

FIG. 47.3 Occipital View Through Foramen Magnum. (A) Normal landmark in the foramen magnum view shows rounded medulla just anterior to the very echogenic clivus *(arrow).* **(B)** With color flow Doppler imaging, the V-shaped vertebral arteries *(blue)* join to form the basilar artery at the medulla-pons junction. Cursor is on the left vertebral artery. Spectral Doppler ultrasound waveforms in the basilar artery show flow away from the transducer.

assessing stroke risk in children with sickle cell anemia, guidelines regarding normal versus abnormal/conditional velocities were validated in large clinical trials using nonduplex equipment that was not angle-corrected.[20-23] Angle correction can significantly increase velocities in vessels that are not coursing directly toward the transducer.[24] Although angle correction has been suggested as a way to correct for variations between the imaging and nonimaging examinations, the lack of published data for angle-corrected velocities currently limits this approach.[12,13,25] Audible optimization for curser placement is key in obtaining similar values with TCD and TCDI without angle correcting. Placing a cursor on a two-dimensional color image may not result in the most optimized tracing because the third dimension of the vessel may be out of the image plane. For this reason, curser placement based solely on a color image may result in a lower velocity than curser placement utilizing the highest achievable audible Doppler frequency. Because the MCA and OA usually course almost directly toward or away from the transducer using the technique described here, angle correction is less of an issue in these vessels. ACA and PCA velocities are more variable because of their tortuous course.

An index of pulsatility, either the **pulsatility index** (PI) (PSV – DV [diastolic velocity]/mean velocity) or **resistive index** (RI) (PSV – DV/PSV), can also be evaluated. Both of these indices are ratios and therefore minimize the effect of vessel angulation.

Physiologic variables including age, gender, hematocrit, viscosity, carbon dioxide, temperature, blood pressure, and mental or motor activity can impact flow velocity.[17] Age-dependent reference values are available for velocities of the various intracranial vessels.[26,27] Early in life, velocities increase with age, demonstrating a rapid increase after birth and a slower increase until 6 to 8 years of age. Afterward and through adolescence, a slow decrease is seen until 70% of the maximal velocity is reached around 18 years of age. Regarding gender, slightly higher velocities are observed in pubertal girls when compared to boys.[28] An inverse relationship is present between hematocrit and viscosity and flow velocity; a decrease in 30% to 40% of the hematocrit will result in an increase in velocities around 20%.[17] If anemia is the cause of elevated velocities, the changes should be detected in all of the intracranial arteries. A focal velocity increase suggests a focal cause.

Changes in arterial carbon dioxide (CO_2) affect cerebral blood flow and arterial velocities. **Hyperventilation** causes a decrease in the MCA mean velocity and an increase in the PI. **Hypoventilation** causes an increase in MCA mean velocity and decrease in PI. If a child is sleeping or in pain and is hyperventilating, TCD results may be affected.

Heart rate also influences intracranial arterial velocities. The sonographer may need to adjust Doppler display sweep time in extreme cases of bradycardia or tachycardia. If autoregulation is intact, cardiac output should not have an affect on TCD velocities.

Velocities can demonstrate daily and interobserver variability. Studies evaluating these variations suggest that normal daily changes should be less than 10 cm/sec and interobserver variability can be 7.5% (measured at the same time) to 13% (daily variation). They suggest that a variation of more than 14% be considered abnormal.[29]

Normal mean velocity in the MCA in adults range from 50 to 80 cm/sec; in the ACA, 35 to 60 cm/sec; in the PCA, 30 to 50 cm/sec; and in the basilar artery, 25 to 50 cm/sec. PSVs up to 150 cm/sec have been described in patients with SCD secondary to anemia.[30,31] The velocity in the OA is normally about one-fourth

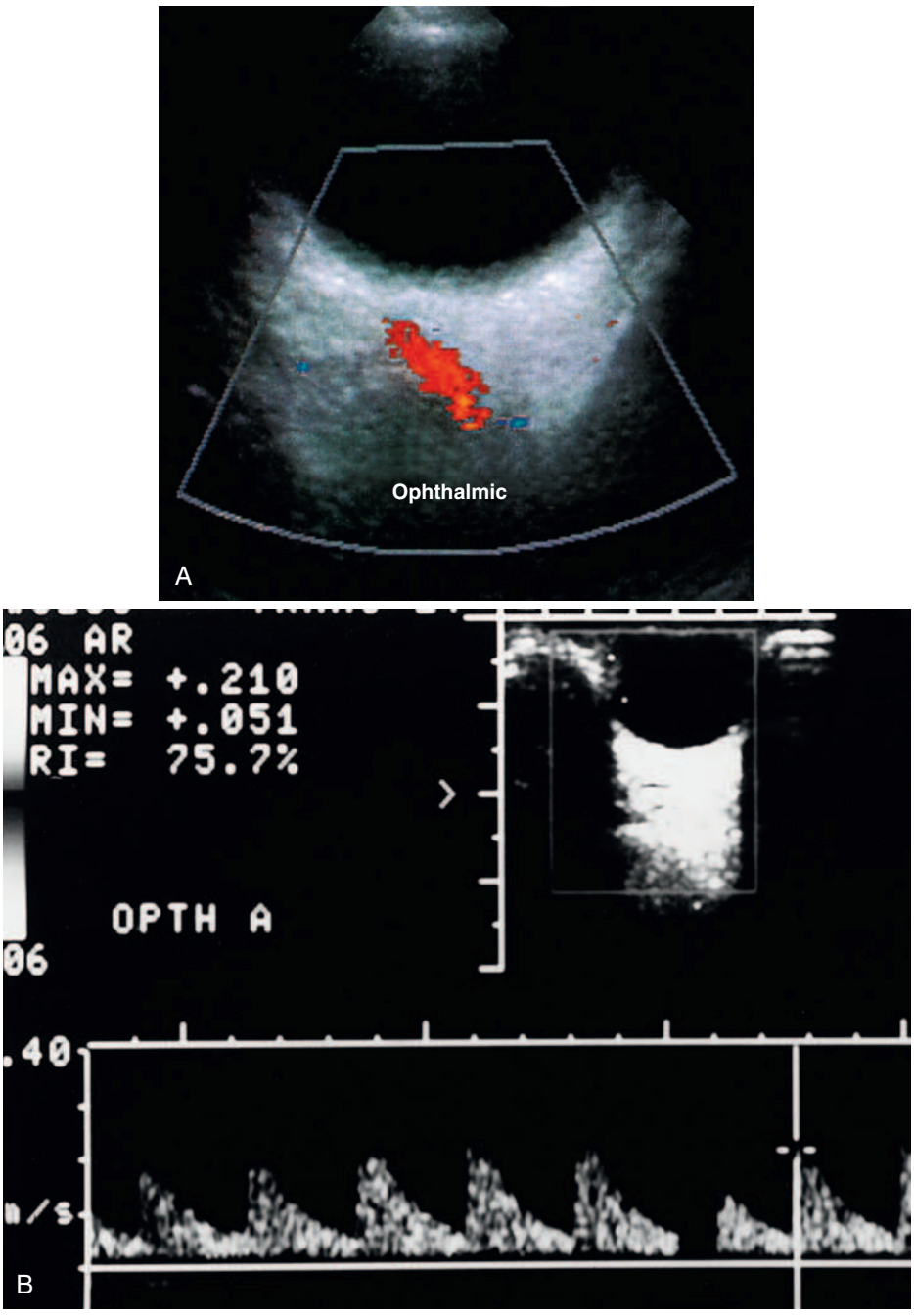

FIG. 47.4 Normal Transcranial Doppler Sonography Through Eye. (A) Color flow Doppler sonogram visualizing the ophthalmic artery (OA) posterior to the globe with flow directed toward the transducer *(red)*. **(B)** Normal waveform of OA with RI of 0.76.

the velocity in the MCA. The velocity in the PCA and vertebral and basilar arteries should be about one-half the velocity in the MCA.

The normal PI ranges from 0.7 to 1.1 and the normal RI ranges from 0.43 to 0.58 after fontanelle closure.[27] The OA has a higher RI, usually between 0.70 and 0.79, and less diastolic flow because it supplies a muscular bed[14] (see Fig. 47.4B). An increase in diastolic flow will result in a decrease in the RI, whereas a decrease in diastolic flow will result in an increase in the RI. As intracranial pressure increases above mean arterial pressure, diastolic flow may become reversed, demonstrating an RI of greater than 1.[32]

The **Lindegaard ratio** is a ratio between the velocity of the MCA or ACA and the ipsilateral extracranial ICA and can help differentiate changes caused by generalized hyperemia from vasospasm. A similar ratio can also be obtained between the basilar artery and the extracranial vertebral artery.[33]

ULTRASOUND POWER SETTINGS

The American Institute of Ultrasound and Medicine and the U.S. federal guidelines of the spatial peak temporal average intensity (I_{SPTA}) for the pediatric head recommend not to exceed 94 mW/cm^2. The limit decreases to 17mW/cm^2 when evaluating vessels in the eye.[34] A maximum mechanical index of 0.28 is also recommended with a limit in the time OA of insonation. The power settings of transducers of various manufacturers are different for each piece of equipment and each probe.[35] Depending on the manufacturer and transducer, energy levels may be within the guidelines only on the low power setting.

When the transtemporal approach is used, at least 65% (and likely more) of the energy is attenuated by the skull. Lower MHz transducers are thus needed for adequate penetration of the skull, and higher settings may therefore be used. It is important when moving to OA insonation that a different transducer with lower setting be used.[36] At any time, the "as low as reasonably achievable" (ALARA) principle should be followed by limiting the exposure time and increasing gain to improve signal and avoiding an increase in power output.

LIMITATIONS AND PITFALLS IN TRANSCRANIAL DOPPLER

TCD and TCDI are inexpensive, noninvasive, and widely available, but they are highly operator dependent. Thorough training and knowledge are required to adequately perform this type of examination.[37,38] Finding the best transtemporal window can be difficult. The transtemporal window varies in size and location. Anywhere from 10% to 37% of patients do not have a good acoustic window.[39] The inability to penetrate the temporal bone is influenced by age, sex, and race. Hyperostosis of the skull is most common in African Americans, Asians, and older females.[38] Contrast agents have been used in an attempt to improve vessel visualization.[40]

There are numerous pitfalls to performing a TCD sonographic examination in children (Table 47.1).[13,41,42] Low wall filter adjustments, high Doppler ultrasound frequency, and critical assessment of velocity spectral analysis are crucial for accurate interpretation of the data.[10] If the examiner becomes lost, it is best to start over, using a systematic search for a better window. First, with TCDI, identify the cerebral peduncles on gray scale. Then add color, optimizing color control settings, angling the transducer, and locating the MCA-ACA bifurcation. Then follow the exam protocol. Remember that although the clinician can assume a patent circle of Willis in children, one artery should not be used to represent the entire cerebral circulation.

TABLE 47.1 Tips for Performing Transcranial Doppler Sonography in Children

Issue	Suggested Tips
Child too active	Put the child at ease and answer all questions before starting the exam. Use distractors such as TV. Let younger children sit on the mother's lap.
Doppler signal is weak	Search for a better window. Change the angle of the transducer. Change the sample volume depth. Use maximum power if needed and adjust color gain/PRF setting. Use headphones to hear subtle Doppler signals.
Multiple Doppler signals are noted	Decrease sample volume size. Search for a better window.
Background noise is high	Adjust gain.
Motion artifact	Check for patient motion or transducer motion. Adjust sample volume.
Doppler signal aliasing	Increase PRF setting. Lower baseline.

PRF, Pulse repetition frequency.

CONTRAST ENHANCEMENT

Insufficient temporal bone windows, unfavorable insonation angles, and low flow velocities can result in nonvisualization of normal or pathologic flow with TCD sonography. In adult studies, echocontrast agents such as galactose microbubble suspensions and sulfur hexafluoride microbubbles have been used in an attempt to increase the applications of transcranial studies.[43-46] These contrast agents have been shown to facilitate visualization of vessel patency, stenosis, occlusion, and collateral flow.[47-49] Small-caliber arteries and vessels that run at unfavorable angles may be identified.[50] Velocities obtained using this method provide reliable data regarding stenosis and occlusion and comparisons with digital subtraction angiography have been favorable.[43,50,51]

Indications for echo-enhancing agents include depiction of vessel anatomy of tumors, vascular malformations, and stenosis. In the evaluation of brain death, use of contrast may improve the level of confidence of documenting low flow. Limitations of this technique include short duration of some of the contrast agents, blooming artifact, and limited availability for pediatric studies in the United States.

Contrast-enhanced three-dimensional power Doppler sonography has also been shown to improve identification of vessels. Using this technique in adults with inadequate windows, Postert et al.[50] noted clear three-dimensional visualization of most major intracranial vascular segments. The addition of contrast resulted in more sensitive sonographic imaging than unenhanced three-dimensional reconstructions. These studies were found to be easy to perform and interpret, increasing the level of operator diagnostic confidence.[52]

INDICATIONS FOR TRANSCRANIAL DOPPLER IMAGING

Indications for Transcranial Doppler in Adults

Detection and follow-up of stenosis or occlusion in major intracranial arteries
Monitoring of thrombolytic therapy
Detection of cerebral vasculopathy and evaluation of collateral intracranial flow
Detection and monitoring vasospasm
Detection right-to-left shunts and/or circulating cerebral microemboli
Assessment of cerebral vasomotor reactivity
Adjunct in evaluation of cerebral death
Intraoperative evaluation of embolization, thrombosis, and hyper/hypoperfusion
Assessment of arteriovenous malformations and intracranial aneurysms
Evaluation of positional vertigo or syncope

Additional Indications for Transcranial Doppler in Children

Evaluation of stroke risk in sickle cell disease
Detection and monitoring vasospasm
Assessment of intracranial pressure and hydrocephalus
Assessment of hypoxic ischemic encephalopathy
Assessment of cerebral vasomotor reactivity
Adjunct in evaluation of cerebral death
Assessment of dural venous patency and arteriovenous fistula
Intraoperative monitoring

Sickle Cell Disease

Neurologic manifestations are common in SCD and include overt infarction or stroke, **silent cerebral infarcts,** and hemorrhage (rare in children, more often seen secondary to aneurysm rupture in adults).[53] Stroke results in neurologic deficits, and silent cerebral infarcts can result in academic and behavioral difficulties and increase the risk of having a future stroke.[54] Patients present with vasculopathy involving the large intracranial arteries, most frequently the distal internal carotid artery and proximal middle and anterior cerebral arteries. The vasculopathy can progress for months to years before symptoms develop and can result in formation of numerous small collateral vessels, consistent with **moyamoya syndrome.** This occlusive vasculopathy is characterized by endothelial damage with intimal thickening, muscular proliferation, and inflammatory changes with or without in situ thrombosis.[53,55,56] Hemodynamic abnormalities in sickle cell anemia (including hyperemia, hypervolemia, and cerebral vascular dilation) play a role in the development of neurologic injuries, especially in the pathogenesis of silent cerebral infarcts.[54]

The incidence of stroke varies depending on the origin of the patient and haplotype of SCD; for example, the incidence is 4.1% in Mediterranean patients, 6.7% in first-generation African patients living in France, and 10% in African Americans younger than 20 years of age.[57] Silent cerebral infarcts are the more common type of cerebral injury in patients with SCD. They are described as a 3 mm or larger lesion seen on at least two T2-weighted magnetic resonance imaging (MRI) sequences with no history or clinical evidence of focal neurologic deficit.[56] Silent cerebral infarcts can be seen in patients younger than 1 year of age with reported incidences of 13% by 13.7 months, 27% in patients younger than 6 years and 37% in 14-year-olds.[54] First and recurrent strokes can be prevented, but not completely suppressed, by transfusion therapy in patients at risk.[19,58] With transfusion treatment the anemia is partially corrected and cerebrovascular reserve is improved,[59] resulting in a decrease in TCD velocities[60] and a reduction in the risk of stroke to less than 1%,[61] although patients may still develop new silent cerebral infarcts (18% at 1-year follow-up and 28% at 2-year follow-up).[54] **Bone marrow transplantation** has proved curative in young patients with symptomatic SCD and has led to stabilization of nervous system vasculopathy.[62]

TCD sonography has proved to be a safe, reliable, and cost-effective screening method for children at risk of stroke. A sensitivity of 90% and specificity of 100% detecting arteriopathy after stroke when compared to angiography has been described.[63] No significant association has been identified between silent infarcts and TCD velocities[54,64] or magnetic resonance angiography (MRA).[54]

Adams et al. first showed the effectiveness of nonimaging Doppler sonographic studies in screening for cerebrovascular disease in patients with SCD.[19,30,31,65] Using the transtemporal and suboccipital approach, Adams et al. screened 190 asymptomatic SCD patients and found in clinical follow-up that a TAMM velocity in the MCA of 170 cm/sec or greater indicated a patient at risk for development of cerebrovascular accident (CVA, stroke).[65]

Using duplex Doppler imaging, MRA, and MRI, Seibert et al.[66] described five indicators of cerebrovascular disease in patients with SCD: (1) maximum velocity in the OA of more than 35 cm/sec (Fig. 47.5), (2) mean velocity in the MCA of more than 170 cm/sec (Fig. 47.6), (3) RI in the OA less than 0.6 (Fig. 47.7), (4) velocity in the OA greater than that of the ipsilateral MCA, and (5) maximum velocity in the PCA or the vertebral or basilar arteries greater than maximum velocity in the MCA. An 8-year follow-up of 27 neurologically symptomatic and 90 asymptomatic sickle cell patients showed all five original TCD indicators of disease were still significant.[67] Four additional factors were also significant: (1) turbulence, (2) PCA or ACA visualized without seeing the MCA (Figs. 47.8, 47.9, 47.10), (3) any RI less than 0.3, and (4) maximum MCA velocity greater than 200 cm/sec (Fig. 47.11). The sensitivity of Doppler ultrasound as a predictor of stroke was 94% with a specificity of 51%.

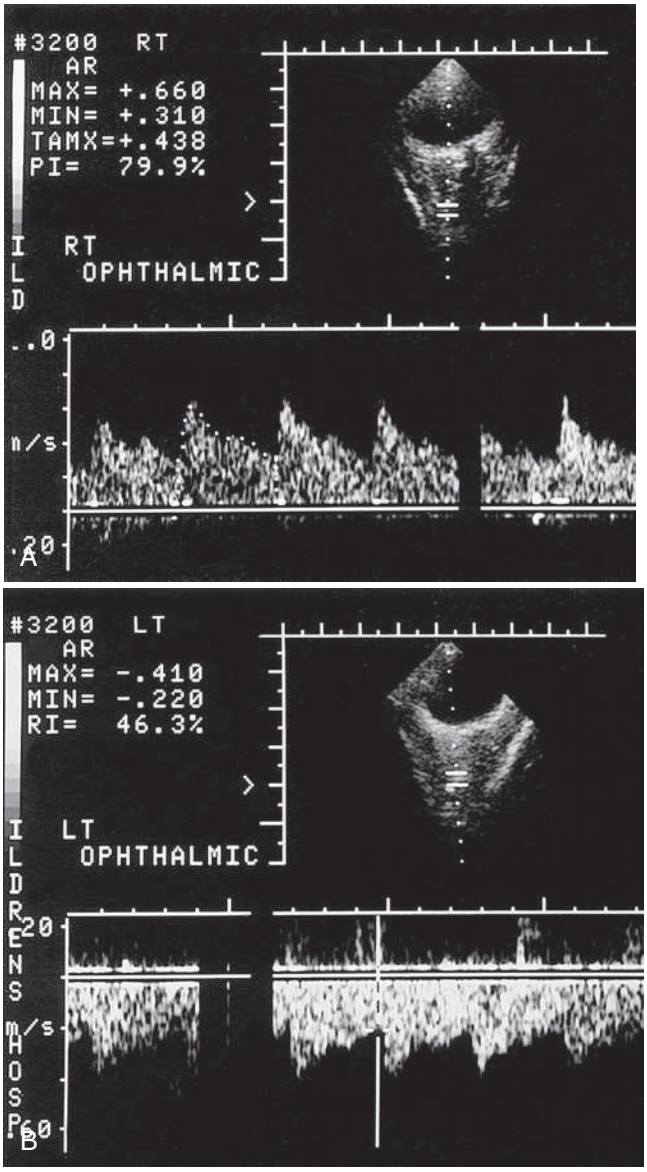

FIG. 47.5 Abnormal Ophthalmic Artery (OA) Flow in 16-Year-Old Boy With Sickle Cell Disease. Patient had his first left cerebrovascular accident (CVA, stroke) at age 7 years. Spectral Doppler ultrasound waveforms through the eye show increased diastolic flow in both OAs. **(A)** Increased velocity in the right OA with maximum velocity of 66 cm/sec; **(B)** reversed flow in the left OA.

Cerebrovascular Disease: Indicators in Children With Sickle Cell Disease

Maximum velocity, OA ≥ 35 cm/sec
TAMM velocity, MCA ≥ 170 cm/sec
RI in OA ≤ 0.6
Velocity in OA greater than velocity in ipsilateral MCA
Maximum velocity in PCA, vertebral, or basilar arteries greater than or equal to MCA velocity
Turbulence
Visualization of PCA or ACA without visualization of MCA
Any RI < 0.3
Maximum MCA PSV ≥ 200 cm/sec

ACA, Anterior cerebral artery; *MCA,* middle cerebral artery; *OA,* ophthalmic artery; *PCA,* posterior cerebral artery; *PSV,* peak systolic velocity; *RI,* resistive index, *TAMM,* time-averaged mean of the maximum.

Data from Seibert JJ, Miller SF, Kirby RS, et al. Cerebrovascular disease in symptomatic and asymptomatic patients with sickle cell anemia: screening with duplex transcranial Doppler US—correlation with MR imaging and MR angiography. Radiology. 1993;189(2):457-466[66]; Seibert JJ, Glasier CM, Kirby RS, et al. Transcranial Doppler, MRA, and MRI as a screening examination for cerebrovascular disease in patients with sickle cell anemia: an 8-year study. Pediatr Radiol. 1998;28(3):138-142.[67]

Siegel et al.[68] compared transtemporal TCD to neurologic examination and also found a maximum flow in the MCA of more than 200 cm/sec or less than 100 cm/sec (including no flow) as significant for disease. Verlhac et al.[63] studied SCD with duplex Doppler imaging with a 3-MHz transducer transtemporally and suboccipitally, as well as with MRA and MRI. Arteriography was performed in patients with suspected stenosis on TCD sonography. They found that patients with a mean velocity greater than 190 cm/sec had stenosis on arteriography. Kogutt et al.[69] evaluated symptomatic SCD patients and found 91% sensitivity and 22% specificity of TCD using MRA as the reference standard. Abnormal TCD values were (1) maximum and mean velocity (V_{max} and V_{mean}) greater than 2 standard deviations (SD) from normal values reported by Adams et al.[65,70] in SCD: V_{max} MCA > 168 ± −38 cm/sec and V_{mean} MCA 115 ± −31 cm/sec, and V_{max} ACA 138 ± 34 cm/sec and V_{mean} ACA 94 ± 28 cm/sec; (2) RI < 0.40; and (3) V_{max} MCA < V_{max} ACA (Fig. 47.12).

Screening sickle cell patients with the nonimaging pulsed Doppler ultrasound technique involves scanning the patient transtemporally to evaluate the MCA, bifurcation, DICA, ACA, and PCA. The OA can be evaluated through the orbit. The basilar and vertebral arteries can be evaluated from the occipital approach. The PSV, EDV, TAMM velocity, and RI of each of these vessels should be measured at least twice to obtain the most accurate measurement.[71] The MCA should be tracked from the peripheral branch to the bifurcation with velocities obtained every 2 mm. Optimizing the tracing is crucial in identifying regions of stenosis.[72] Color Doppler flow imaging (TCDI) can also be used to screen SCD patients. This technique is faster to learn, allows for quicker vessel identification, and improves gate placement. Because image-based probes tend to be larger than nonimaging probes, however, optimizing the tracing may be more difficult and can result in slightly lower velocities than those obtained by nonimaging methods.[20,21]

The Stroke Prevention Trial in Sickle Cell Anemia (STOP) study led by Robert Adams showed that regular transfusion of children at risk for stroke (based on Doppler sonography) could prevent CVA.[19,72-75] Adams studied children age 2 to 16 years, from 14 medical centers, who had MCA mean velocities higher than 200 cm/sec and were at risk of developing stroke. Half received blood transfusions every 3 to 4 weeks, enough to lower sickle cell hemoglobin to below 30%. After 1 year, the transfusions

Text continued on p. 1604.

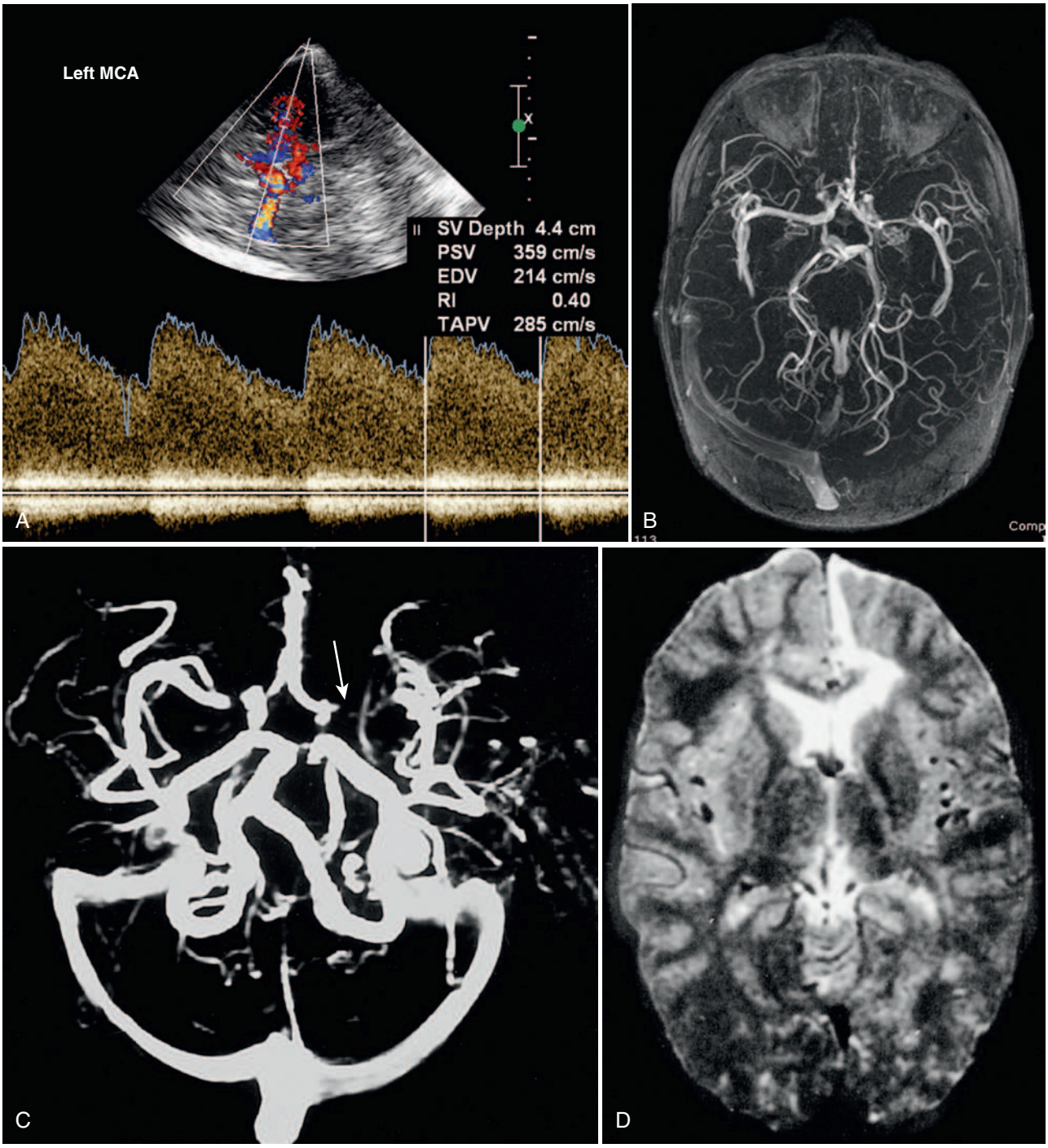

FIG. 47.6 Middle Cerebral Artery (MCA) Stenosis in 9-Year-Old With Sickle Cell Disease. (A) TCD sonogram demonstrates extremely elevated velocities in the left MCA, including a PSV of 359 cm/sec and time-averaged peak velocity of 285 cm/sec. **(B)** MRA 3D time-of-flight image of the circle of Willis demonstrates diffuse narrowing of the left MCA, with multiple small vessels suggestive of **moyamoya angiopathy. (C)** Reformatted maximum-intensity projection image of the same patient confirms narrowing of the left MCA *(arrow)*. **(D)** Axial fast spin-echo T2-weighted MR image demonstrates volume loss of the left basal ganglia and left hemispheric white matter, with signal voids secondary to multiple collaterals.

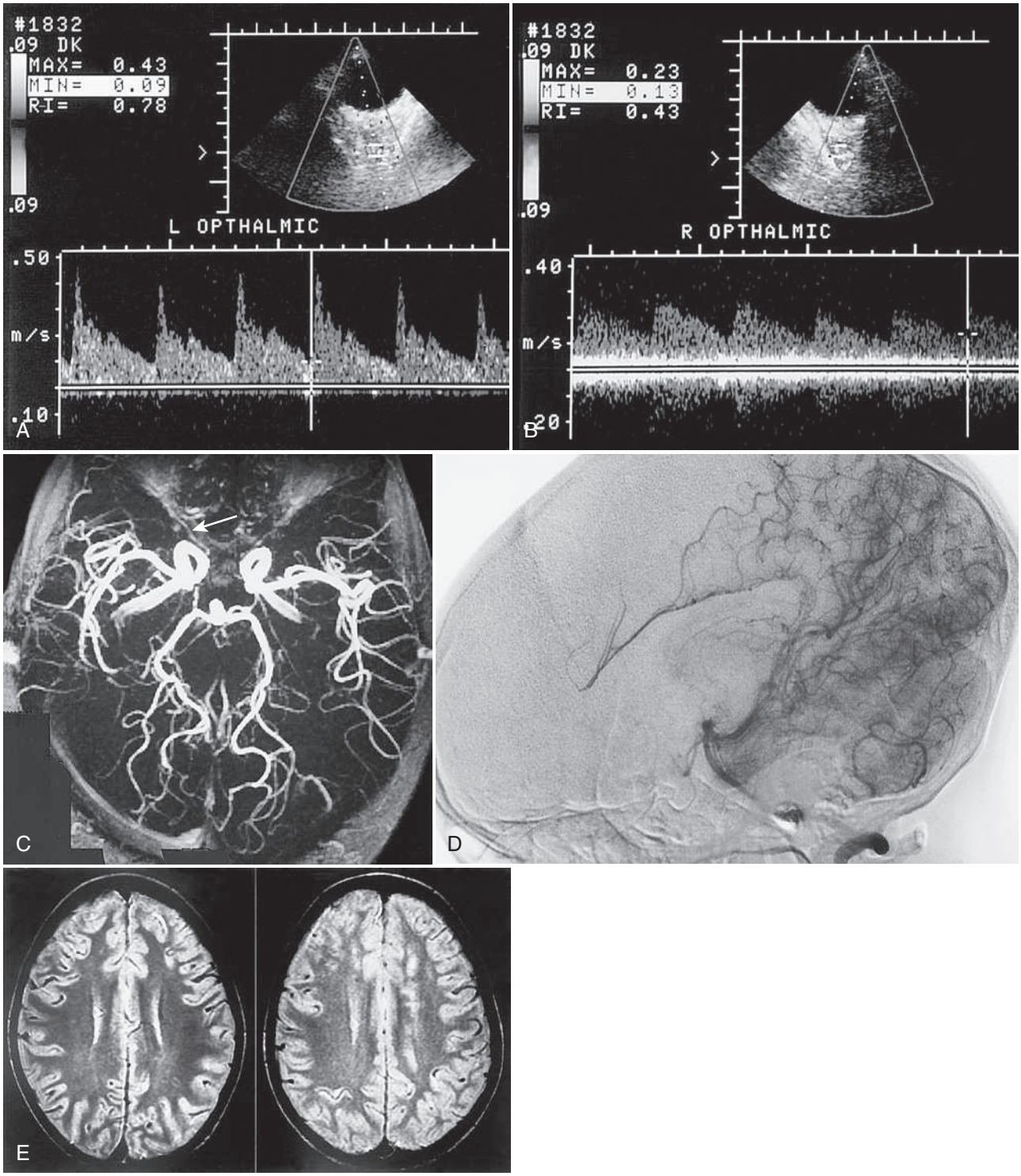

FIG. 47.7 Developing Stroke in Asymptomatic 13-Year-Old Boy With Sickle Cell Anemia. (A) TCD sonogram through the left eye shows relatively normal ophthalmic waveform with normal RI of 0.78 but increased flow with a maximum velocity of 43 cm/sec. **(B)** TCD sonogram through the right eye shows more abnormal waveform with increased diastolic flow in the right ophthalmic artery (OA) with a low RI of 0.43. **(C)** Axial 3D time-of-flight MR angiogram shows absent ACAs bilaterally with prominent right OA *(arrow).* **(D)** Vertebral arteriogram demonstrates retrograde filling of the ACA. **(E)** Initial image (on *left*) obtained at time of MRA is normal. Six months later, patient had acute stroke, and second MR angiogram now shows bilateral, spotty, hyperintense areas in the ACA distribution. Both images are axial proton density weighted.

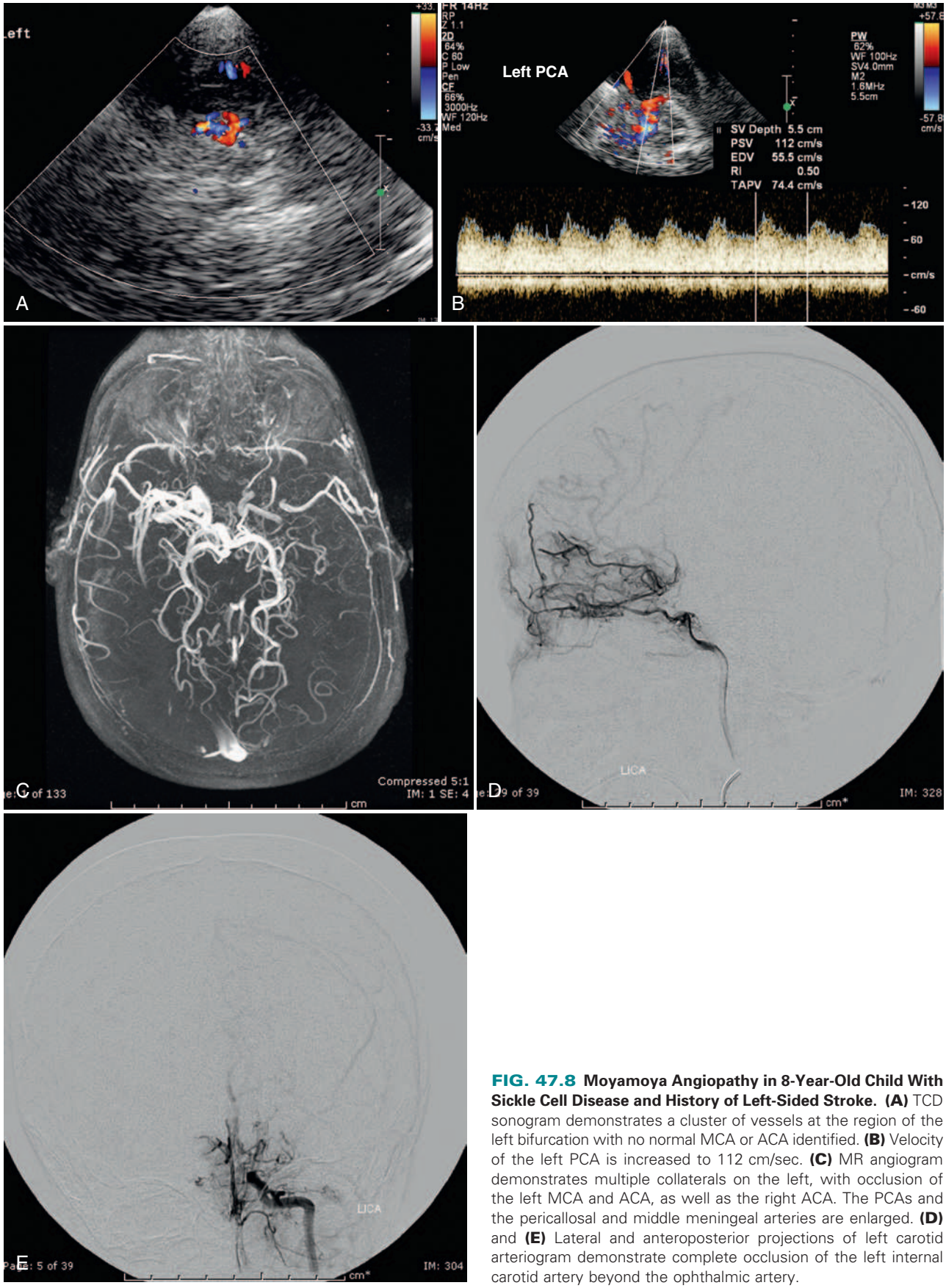

FIG. 47.8 Moyamoya Angiopathy in 8-Year-Old Child With Sickle Cell Disease and History of Left-Sided Stroke. (A) TCD sonogram demonstrates a cluster of vessels at the region of the left bifurcation with no normal MCA or ACA identified. **(B)** Velocity of the left PCA is increased to 112 cm/sec. **(C)** MR angiogram demonstrates multiple collaterals on the left, with occlusion of the left MCA and ACA, as well as the right ACA. The PCAs and the pericallosal and middle meningeal arteries are enlarged. **(D)** and **(E)** Lateral and anteroposterior projections of left carotid arteriogram demonstrate complete occlusion of the left internal carotid artery beyond the ophthalmic artery.

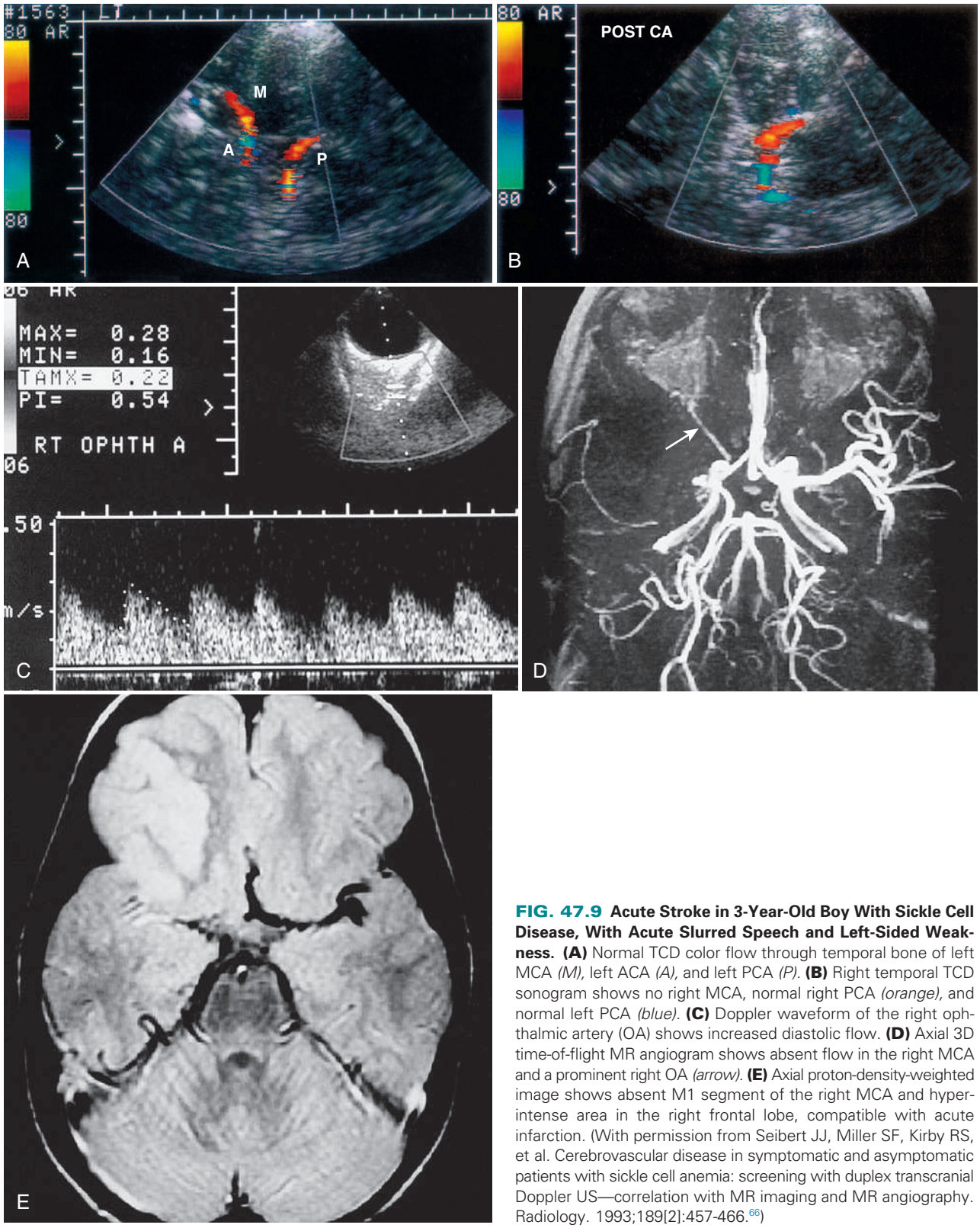

FIG. 47.9 Acute Stroke in 3-Year-Old Boy With Sickle Cell Disease, With Acute Slurred Speech and Left-Sided Weakness. (A) Normal TCD color flow through temporal bone of left MCA *(M),* left ACA *(A),* and left PCA *(P).* **(B)** Right temporal TCD sonogram shows no right MCA, normal right PCA *(orange),* and normal left PCA *(blue).* **(C)** Doppler waveform of the right ophthalmic artery (OA) shows increased diastolic flow. **(D)** Axial 3D time-of-flight MR angiogram shows absent flow in the right MCA and a prominent right OA *(arrow).* **(E)** Axial proton-density-weighted image shows absent M1 segment of the right MCA and hyperintense area in the right frontal lobe, compatible with acute infarction. (With permission from Seibert JJ, Miller SF, Kirby RS, et al. Cerebrovascular disease in symptomatic and asymptomatic patients with sickle cell anemia: screening with duplex transcranial Doppler US—correlation with MR imaging and MR angiography. Radiology. 1993;189[2]:457-466.[66])

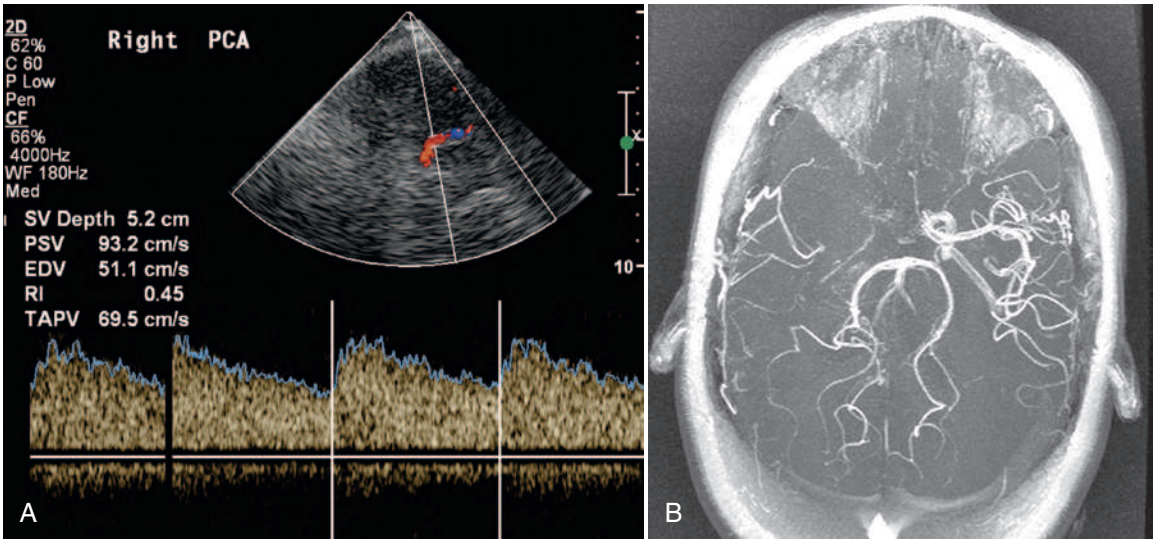

FIG. 47.10 Chronic Right ICA and MCA Stenosis in a 16-Year-Old Child Status Post Bilateral Encephaloduroarteriosynangiosis. (A) Color Doppler imaging demonstrates nonvisualization of the right ACA and MCA with flow documented in the right PCA suggesting an adequate window and appropriate optimization of settings. **(B)** Axial three-dimensional time-of-flight MR angiogram demonstrates absent flow in the right ICA, MCA, and ACA with peripheral collaterals.

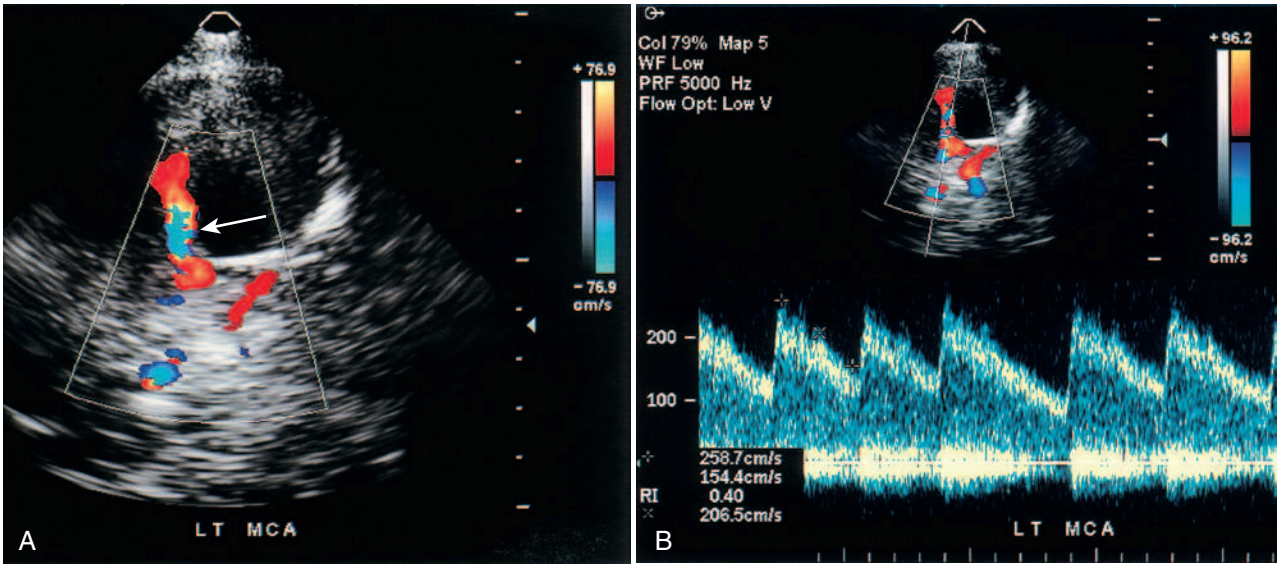

FIG. 47.11 Maximum MCA Velocity Greater Than 200 cm/sec Indicates Cerebrovascular Disease in 4-Year-Old Girl With Sickle Cell Disease. (A) Color Doppler imaging demonstrates a region of aliasing *(arrow)* at the proximal left MCA. **(B)** Doppler waveform confirms the presence of abnormally high mean and peak velocities (TAMM velocity, 206 cm/sec; PSV, 259 cm/sec), which stratify into the "high" stroke risk category. The child started receiving transfusion therapy.

lowered the stroke risk by 90%. Although only one transfusion patient had a stroke (1.6%), 11 (16%) nontransfusion children sustained a CVA (Table 47.2).

After early termination of the study, patients were offered to start or continue transfusion treatment, and an extended evaluation was performed confirming the efficacy of TCD in prediction of stroke risk (even during transfusion treatment) and the benefit of transfusion treatment reducing this risk.[76] This observation period also suggested that the risk of stroke decreases with age progression, even in the absence of transfusion treatment.[76] Reviewing the STOP data, Jones et al.[77] reported that a PSV greater than 250 cm/sec may be useful for assessing stroke risk in SCD patients.

The SIT trial, a multicenter clinical study aimed at evaluating the usefulness of transfusion therapy in the prevention of recurrence of silent clinical infarcts demonstrated that children with silent clinical infarcts and normal TCD who undergo transfusion therapy have a 58% relative risk reduction of infarct recurrence.[59] The results were positive although not as significant as those seen with STOP (92% relative risk reduction).[73]

Verlhac et al.[78] describe the use of evaluation of the extracranial ICA in patients with SCD and suggest that tortuosities of the

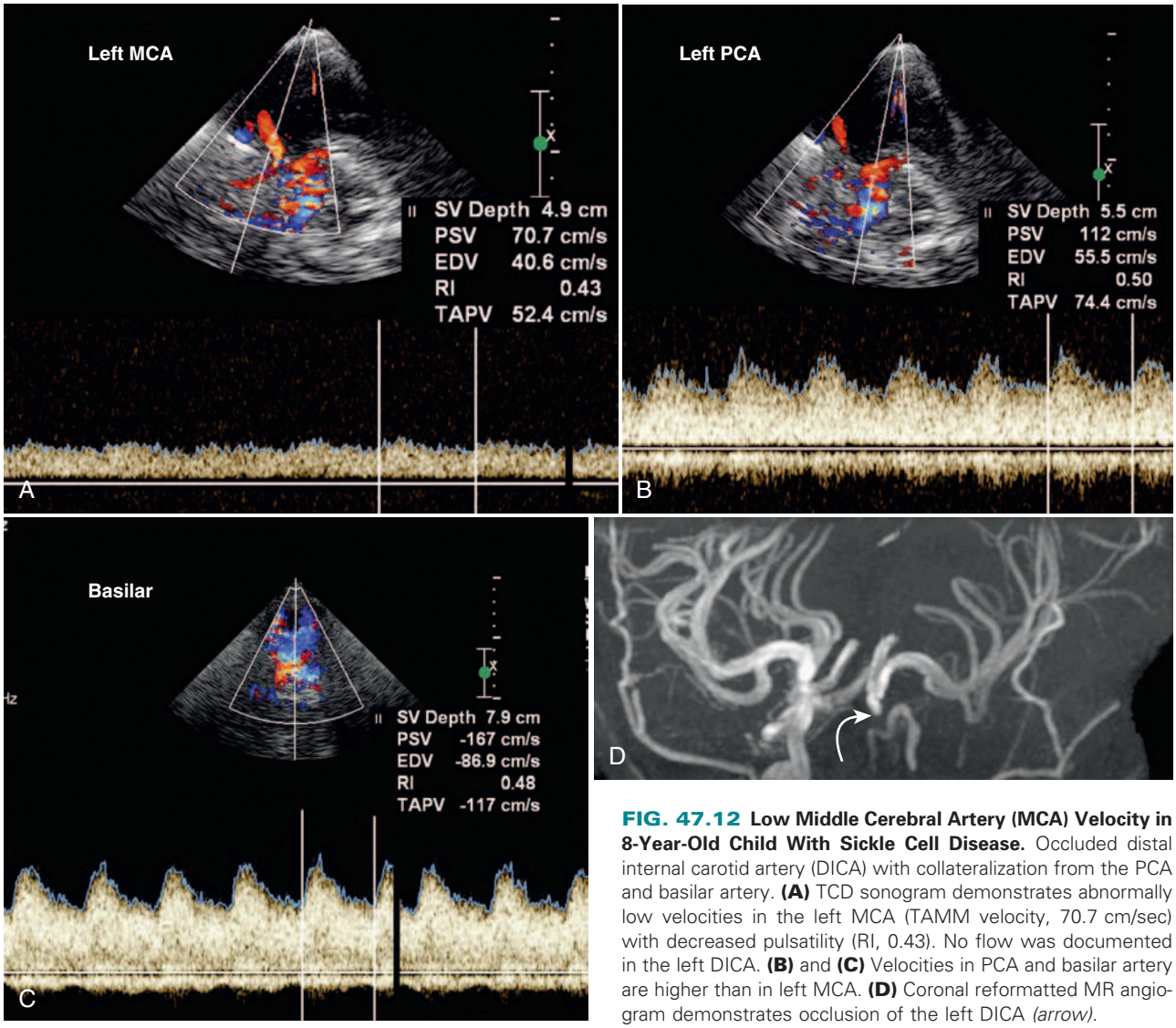

FIG. 47.12 Low Middle Cerebral Artery (MCA) Velocity in 8-Year-Old Child With Sickle Cell Disease. Occluded distal internal carotid artery (DICA) with collateralization from the PCA and basilar artery. **(A)** TCD sonogram demonstrates abnormally low velocities in the left MCA (TAMM velocity, 70.7 cm/sec) with decreased pulsatility (RI, 0.43). No flow was documented in the left DICA. **(B)** and **(C)** Velocities in PCA and basilar artery are higher than in left MCA. **(D)** Coronal reformatted MR angiogram demonstrates occlusion of the left DICA *(arrow)*.

TABLE 47.2 STOP Stroke Risk Categories

Category	Definition
Low	<170 cm/sec TAMM velocity
Conditional	170-199 cm/sec TAMM velocity
Abnormal	≥200 cm/sec TAMM velocity *or* >250 cm/sec PSV

PSV, Peak systolic velocity; *STOP,* Stroke Prevention Trial in Sickle Cell Anemia; *TAMM,* time-averaged maximum mean.
With permission from Adams RJ, McKie VC, Hsu L, et al. Prevention of a first stroke by transfusions in children with sickle cell anemia and abnormal results on transcranial Doppler ultrasonography. N Engl J Med. 1998;339(1):5-11.[73]

ICA increase the risk of developing stenosis. They also report that increased extracranial ICA velocities (>160 cm/sec), even in the absence of abnormal intracranial velocities, should be a considered risk factor for cerebrovascular complications.

TCD is recommended as a screening test for all 2- through 16-year-old children with SCD.[79,80] Optimal timing and frequency vary depending on the presence of velocities used as thresholds (TAMM velocity range cutoff of 155-170 cm/sec) and age.[56,81] It has been suggested that SCD patients with a normal TCD can be followed every 12 months, but closer follow-up should be performed in patients with results at or near the threshold ("conditional" velocities, at 3-6 months).[56] Patients with a TAMM velocity of greater than 200 cm/sec or a PSV greater than 250 cm/sec in the MCA on two examinations are at high risk of stroke and are recommended for transfusion therapy.[77]

All patients with abnormal TCD have vasculopathy, but some patients with vasculopathy and silent stroke can have normal TCD examinations. These patients have more than two times the risk of developing a stroke compared to the unscreened population.[61] In a study comparing the use of PSV versus TAMM velocity in predicting MRI/MRA abnormalities performed by Naffaa et al.,[61] PSV had a higher sensitivity (73% vs. 41%) and TAMM velocity had a higher specificity (100% vs. 81%). They suggest using the PSV as the measurement of choice for TCD screening and lowering the TAMM velocity threshold to 165 cm/sec to obtain a higher sensitivity in the prediction of vasculopathy apparent on MRI (92%). Correlation with MRI and MRA findings are useful because an association of abnormal TCD and MRI findings increases the risk for developing a new silent infarct or stroke when compared to those whose initial MRI is normal.[82] In the STOP trial, the rate of stroke was higher for patients with presence of silent cerebral ischemia and abnormal TCD (52%) compared to patients with abnormal TCD but no evidence of silent ischemia on MRI (21%).[54]

Low mean velocities may also be a marker for a high risk of stroke in the SCD population if the stenosis is so tight that minimal flow courses through the vessel (Fig. 47.13). Buchanan et al.[83] described cerebral insults in five patients with low TCD velocities (<70 cm/sec) and suggest these abnormal results also require further evaluation with MRI/MRA and closer follow-up examinations.

Elevated ACA velocity, although not part of the STOP criteria, also suggests an increased stroke risk (Fig. 47.14). Kwiatkowski et al.[84] found that an elevated ACA TAMM velocity higher than 170 cm/sec was associated with an increased risk of stroke. In subjects with normal ICA-MCA velocities and an elevated ACA velocity, the risk of stroke was greater than 10-fold, whereas the risk more than doubled with those who had both elevated ACA and elevated ICA-MCA velocities.

Although the STOP recommendations are for yearly exams from age 2 to 16, patients younger than 2 years of age can also benefit from TCD evaluation. The BABY HUG study[85] demonstrated that infants with lower hemoglobin levels at baseline have higher TCD velocities and a higher incidence of clinical events. Hydroxyurea treatment has been shown to reduce both the rise in TCD velocities and the presence of clinical events.[85] Further evaluation of the BABY HUG trial data may help determine whether early TCD evaluation can identify infants at risk of having a stroke during childhood.[86]

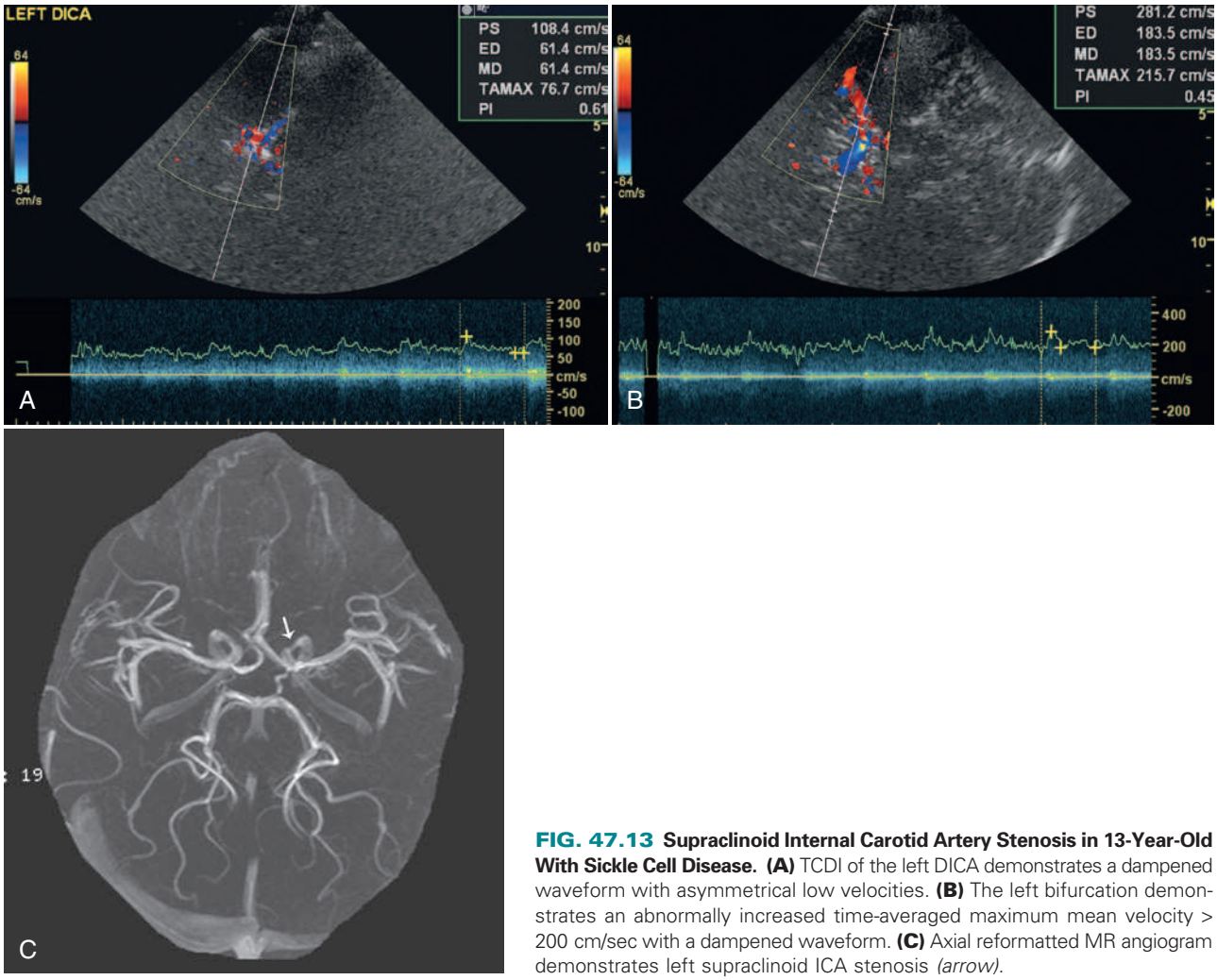

FIG. 47.13 Supraclinoid Internal Carotid Artery Stenosis in 13-Year-Old With Sickle Cell Disease. (A) TCDI of the left DICA demonstrates a dampened waveform with asymmetrical low velocities. **(B)** The left bifurcation demonstrates an abnormally increased time-averaged maximum mean velocity > 200 cm/sec with a dampened waveform. **(C)** Axial reformatted MR angiogram demonstrates left supraclinoid ICA stenosis *(arrow)*.

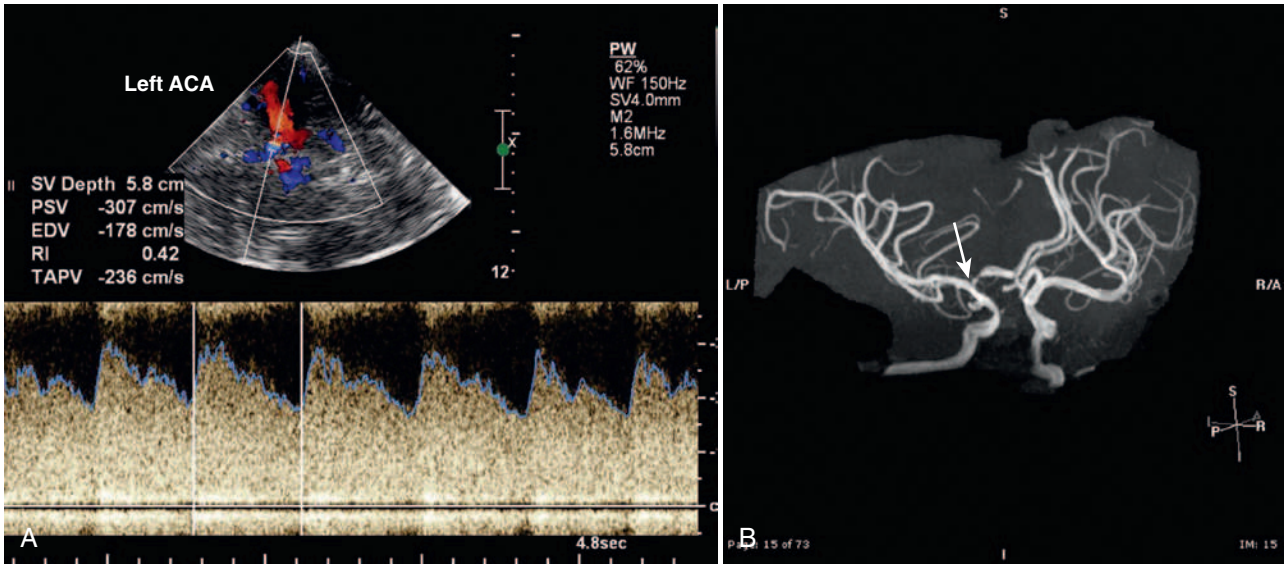

FIG. 47.14 Anterior Cerebral Artery (ACA) Stenosis in 11-Year-Old Child With Sickle Cell Disease. (A) TCD sonogram demonstrates abnormally elevated left ACA velocities. **(B)** Three-dimensional time-of-flight MR angiogram demonstrates stenosis at the origin of the A1 segment of the left ACA *(arrow)*.

When assigning the risk of stroke based on TCD velocities, it is important to consider how velocities may differ with the overall health of the patient, patient ethnicity, and the specific equipment used compared to those obtained with nonduplex equipment in the initial STOP studies. When ill, comorbidities including hypoxia, fever, hypoglycemia, and worsening anemia can increase the cerebral blood flow velocities, making the results invalid if conditional or abnormal.[56] In these cases, repeating the study when the patient is no longer ill will help verify the results. Because different ethnicities and haplotypes of the disease have different average velocities, risk of stroke, and prognosis, it is possible that different criteria have to be determined to assess risk for a specific ethnicity.[87]

Regarding the equipment used, studies have evaluated the differences in nonimaging TCD versus imaging TCD techniques. In studies performed in the early 2000s, nonangle-corrected velocities obtained with Acuson and ATL TCDI equipment were approximately 10% lower in the MCA than those obtained with Nicolet (Vascular, Madison, WI) nonimaging equipment.[20,21] Later studies showed no significant difference in TAMM velocity measurements obtained with General Electric TCDI equipment compared with Nicolet nonimaging equipment.[22,23] The reasons for these differing results are likely multifactorial. Early imaging probes were bulkier, making it more difficult to optimize Doppler tracings. Padayachee et al.[88] discussed how the TAMM velocity is quantified using the Doppler equation. Optimizing the waveform without angle correction can result in similar results compared to the nonimaging TCD technique negating the need for decreasing the threshold for TCDI cutoffs.[88] A 10% lower cutoff point for TAMM velocities has been suggested depending on the protocol and machine used.[13] Besides appropriate curser placement, instrument settings (volume size, gain, waveform display) should be optimized. Close attention to technique can reduce the differences between velocity data acquired with different ultrasound machines. Centers should be aware of these potential differences and perform their own comparison studies when using various imaging equipment before changing velocity thresholds for TCDI.[88]

Although **angle correction** with TCDI may be a way to correct for lower velocities obtained by TCDI compared with nonimaging TCD, this technique has not yet been validated and may overestimate stroke risk in children with SCD.[25] Therefore angle correction currently is not recommended when performing and interpreting TCDI for stroke risk assessment in pediatric SCD.[12,13]

The natural history of TCD velocities in sickle cell patients continues to be studied.[89-91] The STOP 2 trail was performed to assess when discontinuation of transfusion therapy was appropriate. After 30 months of transfusion treatment and normalization of TCD velocities, patients were randomized to continue or suspend transfusion therapy. STOP 2 demonstrated that patients in whom transfusion therapy was suspended after normalization of TCD have a return to abnormal TCD velocities with a higher occurrence of stroke, and are more likely to develop silent clinical infarcts, indicating the need to continue transfusion treatment.[92,93]

Optimal management for children with abnormal velocities remains problematic, with no consensus regarding long-term therapy in children with persistently abnormal velocities. The side effects of prolonged transfusion therapy have clinicians searching for other methods of improving stroke risk, including the use of hydroxycarbamide (hydroxyurea) therapy and bone marrow transplant.[62,94-96] Hydroxyurea with phlebotomy proved to be useful in the prevention of stroke recurrence during the SWiTCH protocol, but not as good as transfusion therapy with chelation.[97,98] Other studies (TWiTCH trial) are evaluating the use of hydroxyurea in the prevention of primary stroke in patients with abnormal TCD velocities.

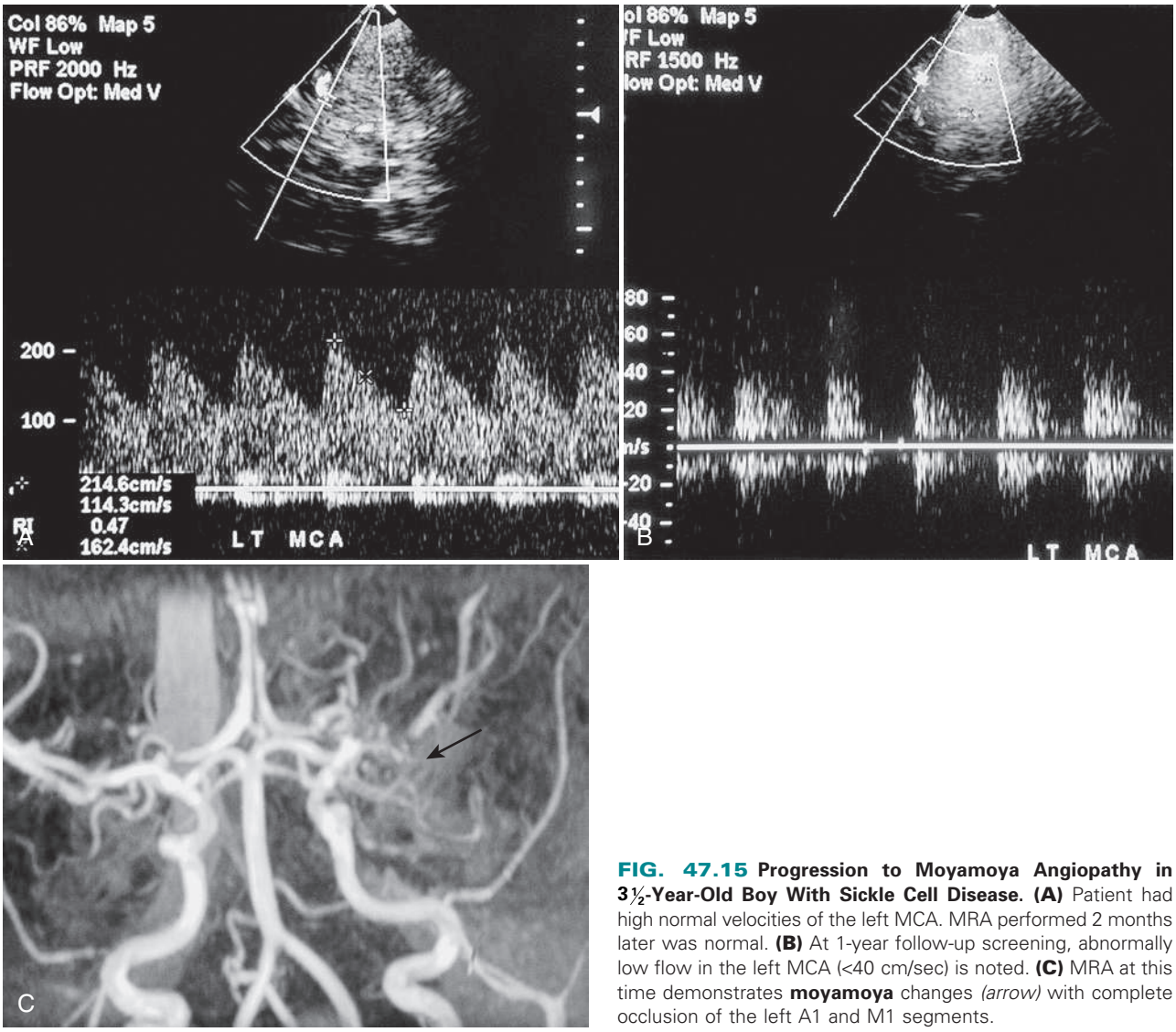

FIG. 47.15 Progression to Moyamoya Angiopathy in 3½-Year-Old Boy With Sickle Cell Disease. (A) Patient had high normal velocities of the left MCA. MRA performed 2 months later was normal. **(B)** At 1-year follow-up screening, abnormally low flow in the left MCA (<40 cm/sec) is noted. **(C)** MRA at this time demonstrates **moyamoya** changes *(arrow)* with complete occlusion of the left A1 and M1 segments.

The management of children with conditional velocities is also being studied. Many remain in the conditional range for years or eventually normalize, but up to 23% of this cohort convert over time to abnormal velocities[89,90] (Fig. 47.15). Protocols using less invasive therapies such as hydroxycarbamide (e.g., hydroxyurea therapy) in children with conditional velocities show promise and suggest that following these patients with TCD may be useful to assess treatment response.[94-96]

Vasospasm

Cerebral vasospasm can present as a complication of subarachnoid hemorrhage secondary to rupture of an intracranial aneurysm,[99] secondary to trauma with or without hemorrhage or secondary to other pathology.[33,100,101] TCD sonography has become an important tool in detecting vasospasm before the patient develops ischemic neurologic deficits or infarct.[37,102] High specificity has been described (100%) for vertebral/basilar vasospasm with PSV greater than 80 and 95 cm/sec, respectively,[102] and with high specificity in the diagnosis of MCA vasospasm (98%-100%) when PSV is greater than 200 cm/sec[103,104] but a sensitivity of only 59%.[105] Digital subtraction angiography continues to be the reference standard, but because of the cost, high radiation, and risk of the procedure, it is not as widely used.[37]

In adults with aneurysm rupture causing subarachnoid hemorrhage, vasospasm typically develops 4 to 14 days after the rupture,[33] gradually increasing and peaking between days 5 and 14.[99] Following traumatic brain injury, vasospasm can occur (19%-68% incidence) but usually without clinical deficits (4%-17%). Cerebral vasospasm in adults with traumatic brain injury presents in the first 2 days after the injury,[99] peaks around day 5 to 7 and has a shorter overall duration. Posttraumatic vasospasm can also occur in the absence of subarachnoid hemorrhage and has an even shorter duration (1.25 days).[99,106] Vasospasm has been seen in 17% of patients with ruptured brain arteriovenous malformation and presents in 4 to 11 days following rupture.[107] Patients with persistent severe vasospasm may develop permanent deficits from cerebral infarction with morbidity and mortality rates of 10% to 30%.[33] In a 2010 study of pediatric patients with moderate

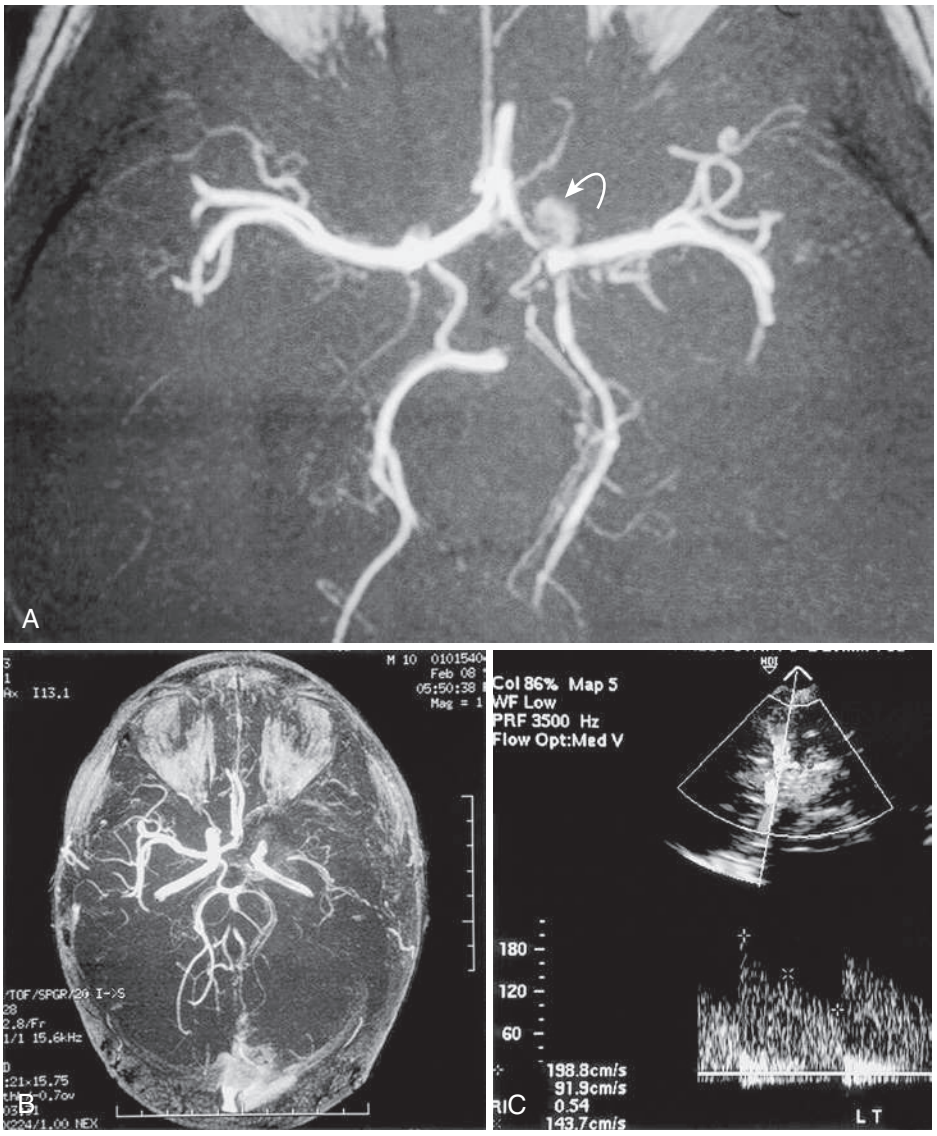

FIG. 47.16 Vasospasm With Aneurysm. Ten-year-old boy with acute headache. **(A)** MR angiogram demonstrates narrow supraclinoid carotid, narrow A1 segment, and small left bifurcation aneurysm *(arrow)*. **(B)** After clipping of aneurysm, susceptibility metal artifact limits MRA evaluation of the left proximal M1 segment. **(C)** On day 15, TCD sonogram demonstrates high PSV of 199 cm/sec, consistent with moderate vasospasm. Patient did well after medical management.

to severe head trauma, vasospasm peaked at day 2 or 3 and lasted for 2 to 4 days.[108]

In the presence of vasospasm, blood flow velocity increases because of a decrease in the luminal cross-sectional area of the affected vessel. Thus TCD can be used to optimize timing of therapy and is useful in following the effects of therapy (Fig. 47.16). When a hemodynamically significant vasospasm is suggested, emergency cerebral angiography with balloon dilation angioplasty or intraarterial infusion of vasodilating agents may be helpful.[109] Serial TCD studies showing reduction in velocities indicate the appropriate time to withdraw therapy, minimizing complications and shortening intensive care unit stays. TCD is most accurate in detecting vasospasm of the MCA. TCD cannot be used to assess the ACA beyond its A1 segment and is limited in the evaluation of the peripheral branches of the MCA.

It is important to remember that studies evaluating vasospasm assess the PSV. Depending on the mean velocities measured, vasospasm can be considered mild, moderate, or severe as demonstrated by angiography (Table 47.3).[29] Philip et al.[110] described increased arterial flow velocities as those elevated by more than 2 SD above normal for age and sex. TCD values should always be combined with clinical and laboratory data.[111,112]

A steep increase (>25 cm/sec/day) in velocity in the first few days after subarachnoid hemorrhage is associated with a worse prognosis. Sources of error in the detection of vasospasm by TCD sonography (vs. arteriography) include missing peripheral vasospasm, copresence of increased **intracranial pressure** (ICP), and low volume flow.[7] The **Lindegaard ratio** (ratio of velocities of the MCA/ipsilateral ICA) can be used to differentiate increased velocities due to vasospasm versus other causes. A Lindegaard ratio of 3 to 6 is suggestive of mild to moderate cerebral vasospasm

TABLE 47.3 Severity of Vasospasm With Typical Velocities[29]

	Mild (cm/sec)	Moderate (cm/sec)	Severe (cm/sec)
Terminal ICA	120-130	>130	
MCA	120-130	130-200	>200
Basilar	60-80	80-115	>115
Vertebral	60-80	>80	>80
ACA		>50% increase in 24 h	>50% increase in 24 h
PCA		>110	>110

ACA, Anterior cerebral artery; *ICA,* internal carotid artery; *MCA,* middle cerebral artery; *PCA,* posterior cerebral artery.
With permission from Kalanuria A, Nyquist P, Armonda R, Razumovsky A. Use of transcranial Doppler (TCD) ultrasound in the neurocritical care unit. Neurosurg Clin N Am. 2013;24:441-456.[29]

and a ratio greater than 6 is suggestive of severe vasospasm. A ratio less than 3 in patients with elevated flow velocities is seen as a result of physiologic processes such as hyperemia or autoregulation.[29,113] In a similar way, a ratio between the basilar artery and the extracranial vertebral artery can also be obtained.[33] A basilar artery to vertebral artery ratio of 2.0 to 3.0 is associated with mild to moderate vasospasm and a ratio greater than 3 is suggestive of severe vasospasm.[113]

Evaluation of Collateral Flow

When stenosis or occlusive disease is present, collateral flow via the circle of Willis can be identified with TCD evaluation. Angiographic examinations provide a better evaluation and diagnosis, but TCD can help with screening and reduce the number of negative invasive procedures.[38]

Collateral flow can be seen in the anterior communicating artery with a high sensitivity (95%) and specificity (100%) (Fig. 47.17). It is difficult to distinguish from adjacent ACA flow but indirect signs can be identified.[38] It is slightly more difficult to evaluate the posterior communicating artery for collateral flow, with a sensitivity of 87% and specificity of 95%. Reversed OA flow with low pulsatility with or without delayed systolic flow acceleration helps in the diagnosis of occlusion or critical stenosis with high specificity (100%) and good sensitivity (75%); normal flow direction does not exclude proximal occlusion/stenosis of ICA or a stenosis of less than 80%.[38]

Leptomeningeal collaterals more commonly originate from the ACA and can be seen in patients with proximal MCA occlusion. **Leptomeningeal collateral** presence has a sensitivity of 81% and specificity of 77% for MCA occlusion. In the presence of leptomeningeal collaterals secondary to MCA occlusion, high velocity and low resistance flow in the ipsilateral ACA or PCA can be seen; a 30% velocity difference can be noted between the right and left ACA or PCA.[38] In the setting of basilar artery occlusion, reversal of basilar artery flow can be seen characterized by low resistance flow toward the probe via suboccipital window and decreased velocity and high resistance flow in vertebral arteries. Reversal of vertebral artery flow can also be seen as a collateral pathway.

Moyamoya angiopathy is a progressive stenosis of the terminal ICA and proximal MCA and ACA with development of a network of abnormal collateral vessels. It can be idiopathic (moyamoya disease) or associated with another disease (moyamoya syndrome) such as SCD, neurofibromatosis I, Down syndrome, or Turner syndrome (see Fig. 47.15). In patients with moyamoya angiopathy, TCD might be useful in monitoring, but more studies are needed to validate its use.[114]

Headaches

Prevalence of headache in children varies depending on the population studied and has been reported to range between 8% and 60%. Prevalence increases with age and the most common causes are tension and migraine. No statistical difference has been identified in the overall prevalence in SCD when compared to control population.

TCD has been used in the evaluation of adults with vascular headaches.[7] Thie et al.[115] found a significant increase in mean velocity in migraine patients compared to controls during headache-free periods. They then continued to evaluate the patients during headache episodes and demonstrated that those with common migraines had decreased intracranial velocities and increased pulsatility, whereas symptomatic patients with classic migraines demonstrated opposite findings with an increase in velocities and a decrease in pulsatility[116] (Fig. 47.18). Different studies have shown migraine headaches to be associated with mild to moderate vascular narrowing and/or decreased blood flow[117] as well as a decrease in RI and PI.[118]

In pediatric patients, Wang et al.[119] evaluated the utility of TCD sonography in the assessment of isolated headaches and demonstrated a sensitivity and specificity in detecting intracranial lesions of 75% and 99.7%, respectively. Another study evaluated children between 5 and 17 years of age and suggested the possibility of cerebral vasospasm in the headache-free periods.[120]

In a study of 1176 pediatric patients with SCD, 36% had recurrent headaches, with migraine in 15%. In this study, no association was seen between headaches and silent stroke. On the other hand, recurrent headaches and migraines were associated with lower hemoglobin concentration and higher pain event rates.[121] Lower hemoglobin levels are associated with increased cerebral blood flow velocities in children with SCD with normal neurologic examinations and vascular headaches when compared to those without headaches. Similar findings have been described in adults with SCD and severe/frequent headaches versus mild or absent headaches.[121] TCD sonography may assist in the

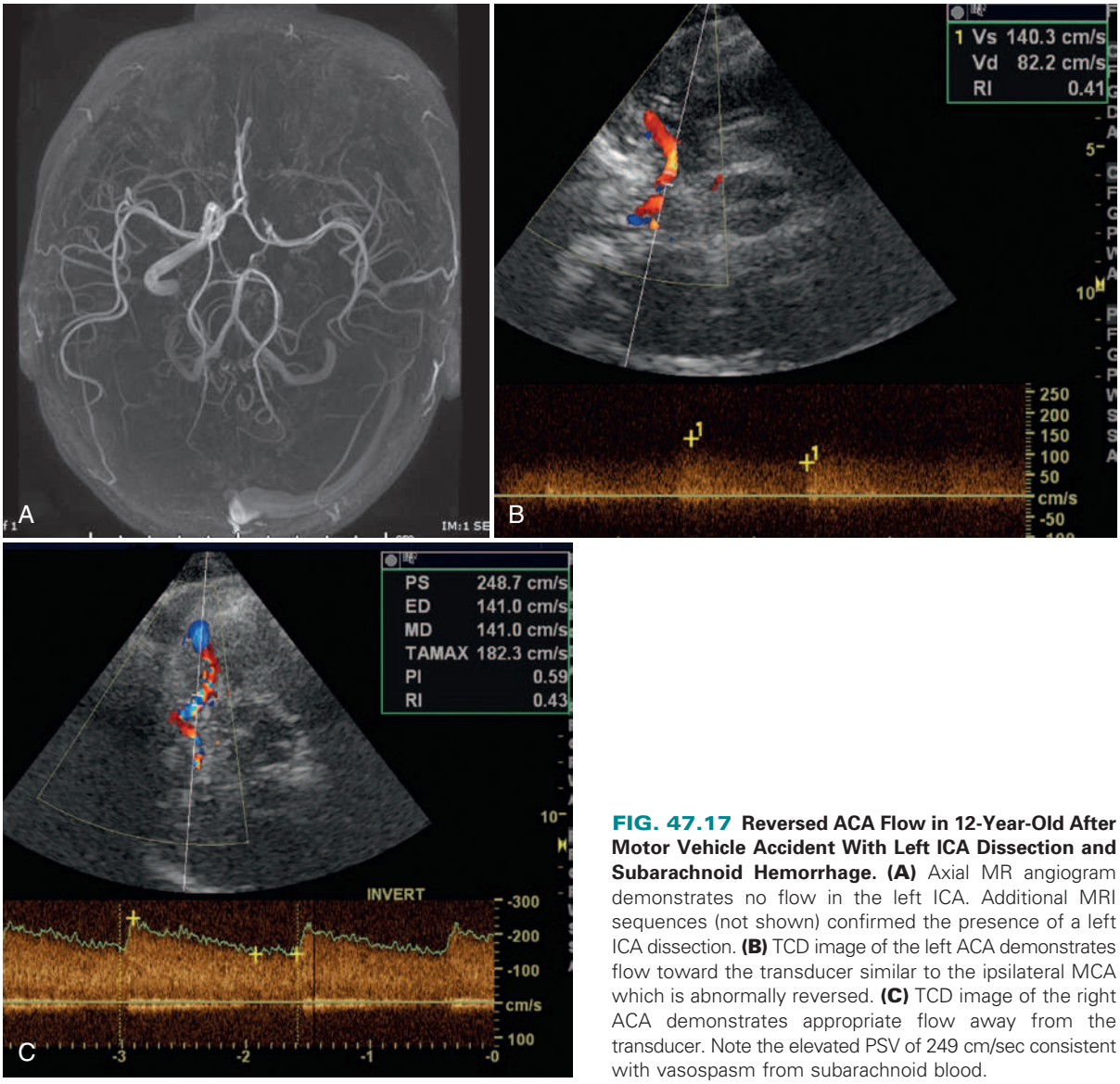

FIG. 47.17 Reversed ACA Flow in 12-Year-Old After Motor Vehicle Accident With Left ICA Dissection and Subarachnoid Hemorrhage. (A) Axial MR angiogram demonstrates no flow in the left ICA. Additional MRI sequences (not shown) confirmed the presence of a left ICA dissection. **(B)** TCD image of the left ACA demonstrates flow toward the transducer similar to the ipsilateral MCA which is abnormally reversed. **(C)** TCD image of the right ACA demonstrates appropriate flow away from the transducer. Note the elevated PSV of 249 cm/sec consistent with vasospasm from subarachnoid blood.

differential diagnosis of headaches of unknown causes and could prove useful in therapeutic interventions.

Sleep Apnea

Several studies have demonstrated changes in MCA velocities in children with **sleep-disordered breathing,** a spectrum of upper airway obstruction ranging from primary snoring to obstructive sleep apnea. Increases in MCA flow velocity have been documented in children with mild sleep-disordered breathing.[122] In a group of children with sleep-disordered breathing followed after adenotonsillectomy, MCA velocities decreased (suggesting a normalization of MCA velocities) with a resultant increase in mean overnight oxyhemoglobin saturation postoperatively. These children demonstrated an improvement in processing speed and visual attention postoperatively as well.[123]

In patients with SCD, sleep-disordered breathing and snoring have a high prevalence, with 37% snoring and 24% positive polysomnography findings.[124] In a study evaluating overnight pulse oximetry, TCD, and central nervous system events in patients with SCD, an association between nocturnal oxyhemoglobin desaturation and central nervous system event risk was seen. Evidence of obstructive sleep apnea, seen as dips in overnight pulse oximetry, was not useful to predict central nervous system events.[125] Another study evaluating the prevalence of sleep-disordered breathing and the association with high-risk TCD velocities in patients with SCD showed no significant difference in the TCD velocities and percentage of patients with high-risk velocities when comparing the snorers with the nonsnorers. Overall, there was no association between sleep-disordered breathing or snoring and cerebrovascular risk.[124]

Hydrocephalus

The ability to differentiate between **ventriculomegaly** and **hydrocephalus** (increasing ventriculomegaly and increasing ICP) can be difficult. When hydrocephalus develops, ICP increases, resulting in a decrease in diastolic flow. Stable ventriculomegaly

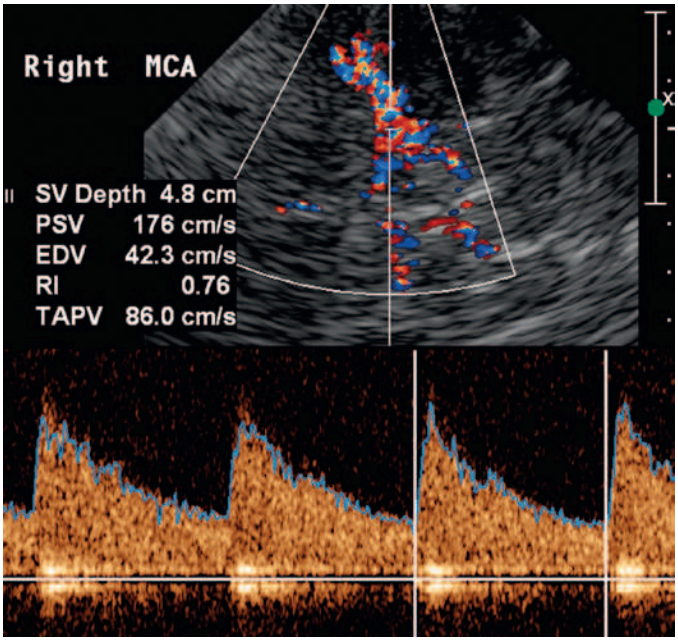

FIG. 47.18 Elevated Pulsatility of the MCA in 12-Year-Old With Headaches. TCD image of the right MCA demonstrates an elevated RI of 0.76. Normal RI values should range from 0.43 to 0.58 after fontanelle closure.

should have normal pulsatility; thus an elevated RI in cases where ventricular size is increased may imply the need for a shunt. Hill and Volpe[126] first described a decrease in diastolic/systolic flow in 11 hydrocephalic infants. Because it is noninvasive and repeatable, Doppler sonography has been increasingly used to assess changes in cerebral hemodynamics in hydrocephalus through the anterior fontanelle in infants. It can be used through the temporal bone in older children as well.[4,127,128] There is a direct correlation between the ICP (from experimental fontanometric and direct measurement evidence) and the RI. The increasing RI is predominantly caused by a reduction in the EDV.[128,129] The vascular indices most often applied in hydrocephalic patients are RI and PI. Both ratios minimize the error in estimating true velocity caused by a varying angle of insonation. This is particularly important in hydrocephalus because vascular anatomy can be distorted by ventricular enlargement, and a small angle of insonation cannot be assumed.[130] Difficulties with using the RI to determine hydrocephalus have occurred because (1) there is a wide range of normal RI values (0.65-0.85 in the neonate, 0.60-0.70 in the child before fontanelle closure, and 0.50-0.60 in older children and adults through temporal window after fontanelle closure),[14] and (2) many other intracranial and extracranial factors can change the RI other than increased ICP[131] (Table 47.4). Therefore the RI must be correlated closely with the clinical condition of the patient.

TABLE 47.4 Factors That Change Cerebral Doppler Indices

	Resistive Index	Systolic Velocity
INTRACRANIAL ABNORMALITIES		
Intracranial bleed	Increased	Beat-to-beat variation, risk factor for IVH
Periventricular leukomalacia	Increased	
Asphyxia	Decreased initially	
Brain edema	Increased	
Hydrocephalus	Increased, reverses after drainage	
Subdural	Increased	
Brain death	Increased	Decreased, reversed diastolic flow
ECMO	Decreased	
Vascular malformations	Decreased	Increased, turbulence
EXTRACRANIAL ABNORMALITIES		
P_{CO_2}	Inverse relationship	
Heart rate	Inverse relationship	
Shock		Decreased systolic/diastolic
Patent ductus arteriosus	Increased	
Pneumothorax	Increased	
Cardiac ischemia	Increased	
Gastrointestinal bleed	Increased	
Polycythemia, hyperviscosity	Increased	Decreased
Anemia	Increased	
DRUGS		
Indomethacin	Increased	Decreased
Maternal cocaine	Increased	
Exogenous surfactant	Increased	

ECMO, Extracorporeal membrane oxygenation; *IVH,* intraventricular hemorrhage; *P_{CO_2},* carbon dioxide partial pressure (tension).

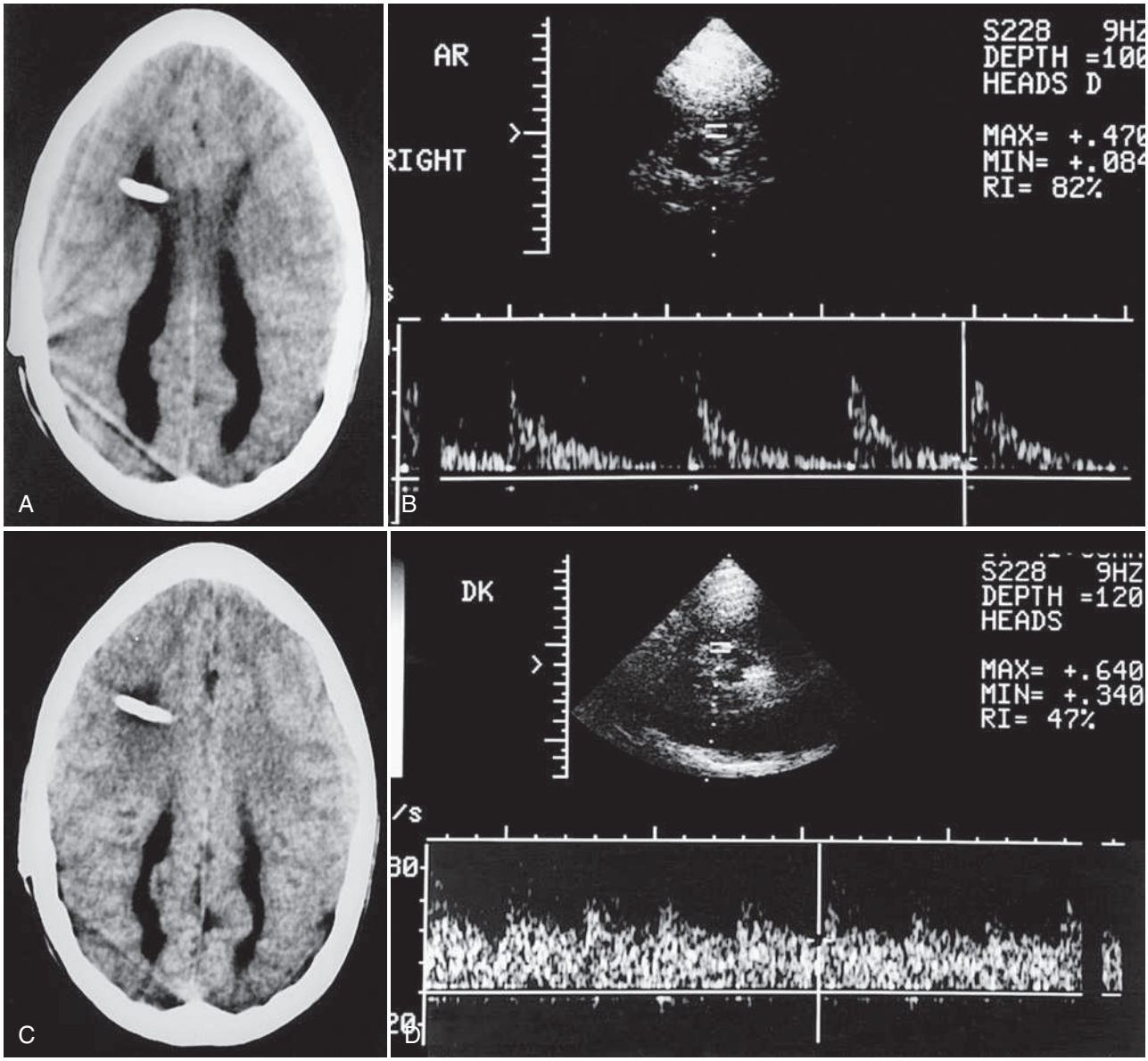

FIG. 47.19 Shunt Dysfunction in 8-Year-Old. (A) CT scan shows mildly dilated ventricles. **(B)** TCD image through the temporal window shows an increased RI of 0.82 in the MCA. **(C)** CT scan after shunt revision shows decrease in ventricular size. **(D)** TCD image of the MCA demonstrates a decrease in RI to 0.47, now in the normal range (after age 2 years with fontanelle closure, normal RI is 0.5). (With permission from Seibert JJ, Glasier CM, Leithiser JRE, et al. Transcranial Doppler using standard duplex equipment in children. Ultrasound Q. 1990;8:167-176.[14])

Goh et al.[128] used an RI of greater than 0.8 as a sign of increased ICP in the neonate and an RI of greater than 0.65 in children. Because of varying normal values and overlapping normal and abnormal values, RI is most useful on an individual basis following a patient's course to determine whether clinical changes and ventricular dilation are secondary to increased pressure (such as with shunt malfunction) or atrophy (Fig. 47.19). Any increase in RI should be considered as potentially important in terms of shunt malfunction. False-normal values may be the result of cerebral spinal fluid tracking along the shunt. Excessive thickness of the skull may prevent TCD ultrasound from being obtained successfully in some of these patients.[132,133]

Pediatric patients with tuberculous meningitis often have raised ICP and cerebral vasculopathies, and attempts to obtain a noninvasive technique to replace invasive ICP monitoring have been studied.[134] Some researchers have suggested that TCDI can help monitor pressure changes over time in these patients.[135] However, a study performed in children with tuberculous meningitis with communicating hydrocephalus demonstrated that PI obtained by TCD was not accurate in the assessment of ICP and might not change even in cases in which a change in ICP has been documented.[134]

The use of TCD has been studied in adult patients with idiopathic normal pressure hydrocephalus as a way of evaluating positive results of the cerebrospinal fluid tap and predict usefulness of a shunt. In a small study performed by Sedighi et al.,[136] patients with idiopathic normal pressure hydrocephalus underwent TCD evaluation before and after a cerebrospinal fluid tap test. In patients

with idiopathic normal pressure hydrocephalus, baseline TCD velocities were higher than in controls and demonstrated a significant decrease in those who reported clinical improvement after the tap.

Vascular Malformations

Intracranial Doppler imaging is useful for detecting vascular malformations in the unstable neonate.[3,137] The vascular malformation may be imaged with color or power Doppler ultrasound. Spectral analysis of the involved vessels will show high velocity, with low pressure and low pulsatility caused by increased diastolic flow. These hemodynamic qualities result in higher-than-normal mean and PSV, in conjunction with turbulence and lower-than-normal RIs (Fig. 47.20). TCD sonography can assess **arteriovenous malformation** (AVM) with a sensitivity of 87% to 95%,[126-133,137-140] particularly when contrast enhancement is used.[46] A study performed in adults comparing intraoperative contrast-enhanced TCD with angiography demonstrated that TCD is less sensitive (detected only 91.3% of AVMs diagnosed by angiography), underestimates the size of the AVM, and provides limited information regarding blood supply and venous drainage.[141] Because MRI affords an even higher sensitivity than TCD in screening, Doppler imaging is used more often to quantitate the hemodynamics of AVMs and to monitor the effects of surgical or endoluminal interventions.[142] After surgical or embolization treatment, the decrease in systolic velocity and increase in RI in the feeding arteries can be followed. In a study performed by Kaspera et al.[143] in patients after surgical resection or embolization of the AVM, an increase and normalization of PI was noted before a decrease in velocity. No correlation was seen between the degree of normalization of the parameters and the extent of the embolization of the AVM.

TCD ultrasound has also been used to assess other vascular anomalies, such as **Sturge-Weber syndrome, dural arteriovenous fistulas,** and **carotid-cavernous fistulas.**[144-146] In a series of patients with Sturge-Weber syndrome, decreased arterial flow velocity and increased PI was noted in the affected MCA, suggesting chronic hypoperfusion of the tissue secondary to venous stasis or cortical vessel hypoplasia due to cortical atrophy.[145] The fact that these findings were present even before the onset of symptoms suggests that venous stasis results in cortical injury.[147] A different study demonstrated increased velocities on the affected side during seizures and a fourfold to sixfold increase in flow in the contralateral side.[147] In cases of arteriovenous fistulas, an increase in flow velocity is present in at least one cerebral vein or venous sinus, which decreases after embolization. A venous flow velocity of more than 50 cm/sec is considered abnormal and should be further evaluated.[40] In patients with carotid cavernous fistulas, Doppler can be used for detection and to follow treatment.

Asphyxia

TCD sonography has been used in the evaluation of hypoxic-ischemic brain injury. Mild asphyxia typically does not alter cerebral hemodynamics.[148] Severe or prolonged asphyxia may result in impairment of cerebral autoregulation, producing an increase in diastolic blood flow and a decrease in cerebrovascular resistance.[2] Intracranial Doppler imaging in the neonate has been particularly helpful in predicting significant hypoxic-ischemic brain injury.[1,149-152] Archer et al.[151] found 100% sensitivity of a low RI caused by increased diastolic flow in the ACA and MCA and an adverse neurologic outcome when performed within the first 48 hours of the insult in the neonate. Stark and Seibert[149] reported 10 in 13 neonates with an initially low RI who later developed severe neurodevelopmental handicaps. The finding of increased diastolic flow can also be useful in evaluating the older child after head injury or cardiac arrest to predict significant cerebral injury before computed tomography (CT) findings become evident (Fig. 47.21).

Cerebral Edema and Hyperventilation Therapy

Head trauma initiates several pathologic processes that may result in significant changes in cerebral hemodynamics. Diagnosis of these abnormalities can be crucial for the appropriate management of such cases. After a significant cerebral hypoxic insult, vasodilation may initially occur with a resultant increase in diastolic flow velocity and a reduced RI during this early hyperemic phase. As ICP increases, however, the diastolic flow velocity begins to decrease, and the systolic peak velocity has a "spiky" appearance.[2] As cerebral edema develops, there is further loss of forward diastolic flow, and RI increases.[129] Sequential TCD readings after a cerebral insult have been helpful in evaluating the presence of edema and the course of treatment[153] (Fig. 47.22).

Treatment for cerebral edema includes hyperventilation. An inverse relationship exists between carbon dioxide partial pressure (P_{CO_2}) and the RI. The higher the P_{CO_2}, the greater the vasodilation, the greater the diastolic flow, and the lower the RI. When the P_{CO_2} is reduced, vasoconstriction results, with decreased diastolic flow and increased RI. Thus CO_2 reactivity can be measured assessing the RI. The cerebral blood flow increases 4% per mm Hg rise in P_{CO_2}.[1,26,129,152] The absence of change in the RI as the patient's ventilation is increased is described as an absent "CO_2 reactivity test" and is a sign of severe brain injury.[154] Because of this, RI can be used to monitor hyperventilation therapy in cerebral edema associated with head trauma.[2,155] As hyperventilation decreases the P_{CO_2}, the RI should increase with the concomitant vasoconstriction of cerebral vessels. The clinician must take into account, however, that increasing cerebral edema will also increase the RI. Therefore this measurement should be closely correlated with other clinical and laboratory findings. For example, hyperventilation treatment in a patient who has an increasing RI in the face of no change in ICP suggests that the treatment is causing too much cerebral vasoconstriction. In this scenario the patient may benefit from a decrease in the hyperventilation.

Evaluation of Right-to-Left Shunt

Although transesophageal echocardiogram provides a direct evaluation of the cardiac structures, TCD can also be used in the evaluation of right-to-left shunts.[156-158] TCD provides visualization of emboli through the cerebral circulation. Valsalva maneuver can be performed noninvasively at the bedside without requiring sedation.[29] The observation of 10 microbubbles of agitated saline

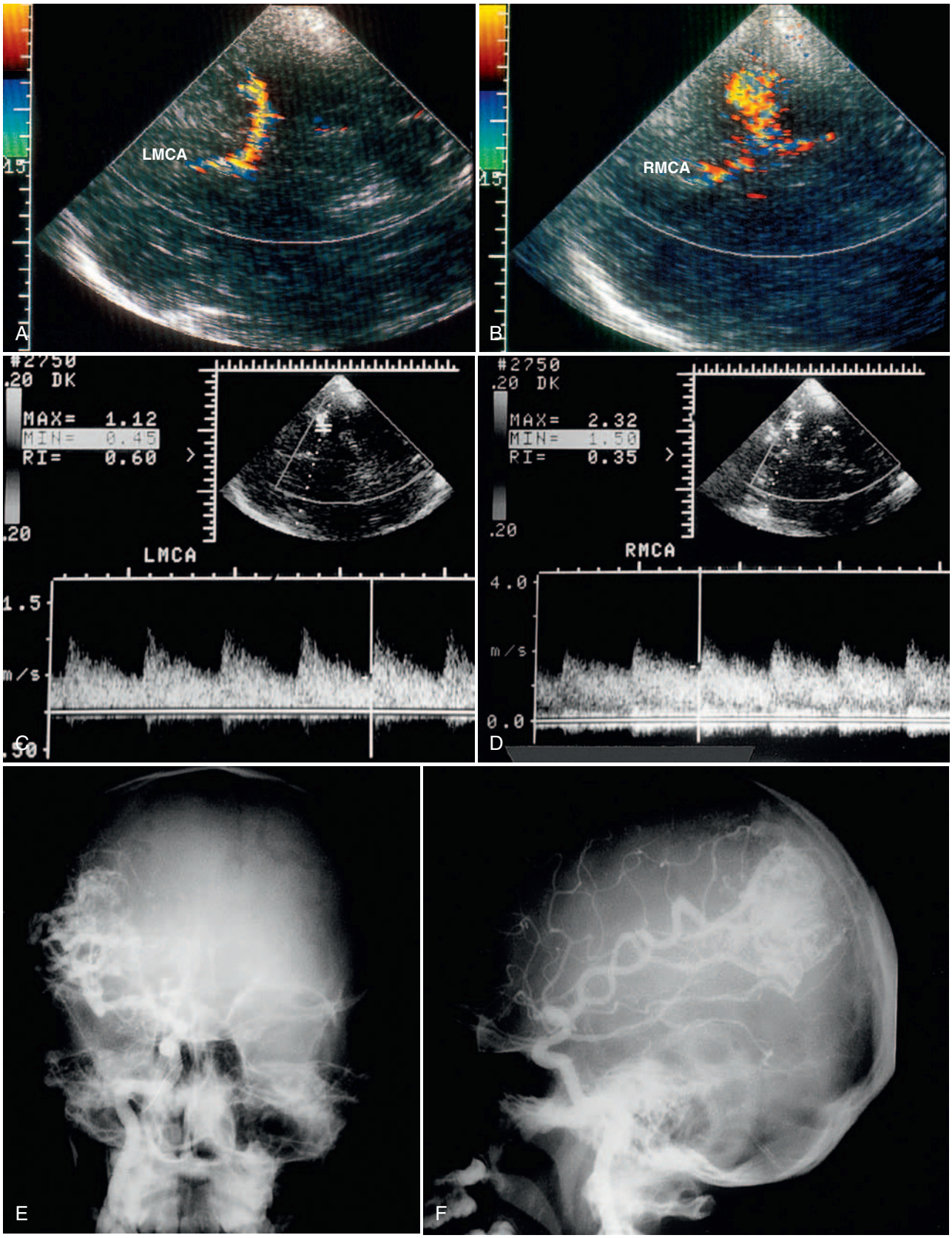

FIG. 47.20 Arteriovenous Malformation (AVM). (A) Normal color flow Doppler image of the left MCA. **(B)** Increased number of vessels in the region of AVM at the right MCA. **(C)** TCD spectral Doppler sonogram of left MCA shows normal maximum velocity of 112 cm/sec. **(D)** Velocity on the right is increased, with a maximum velocity of 232 cm/sec. **(E)** and **(F)** Anteroposterior and lateral views of an arteriogram demonstrates the large AVM.

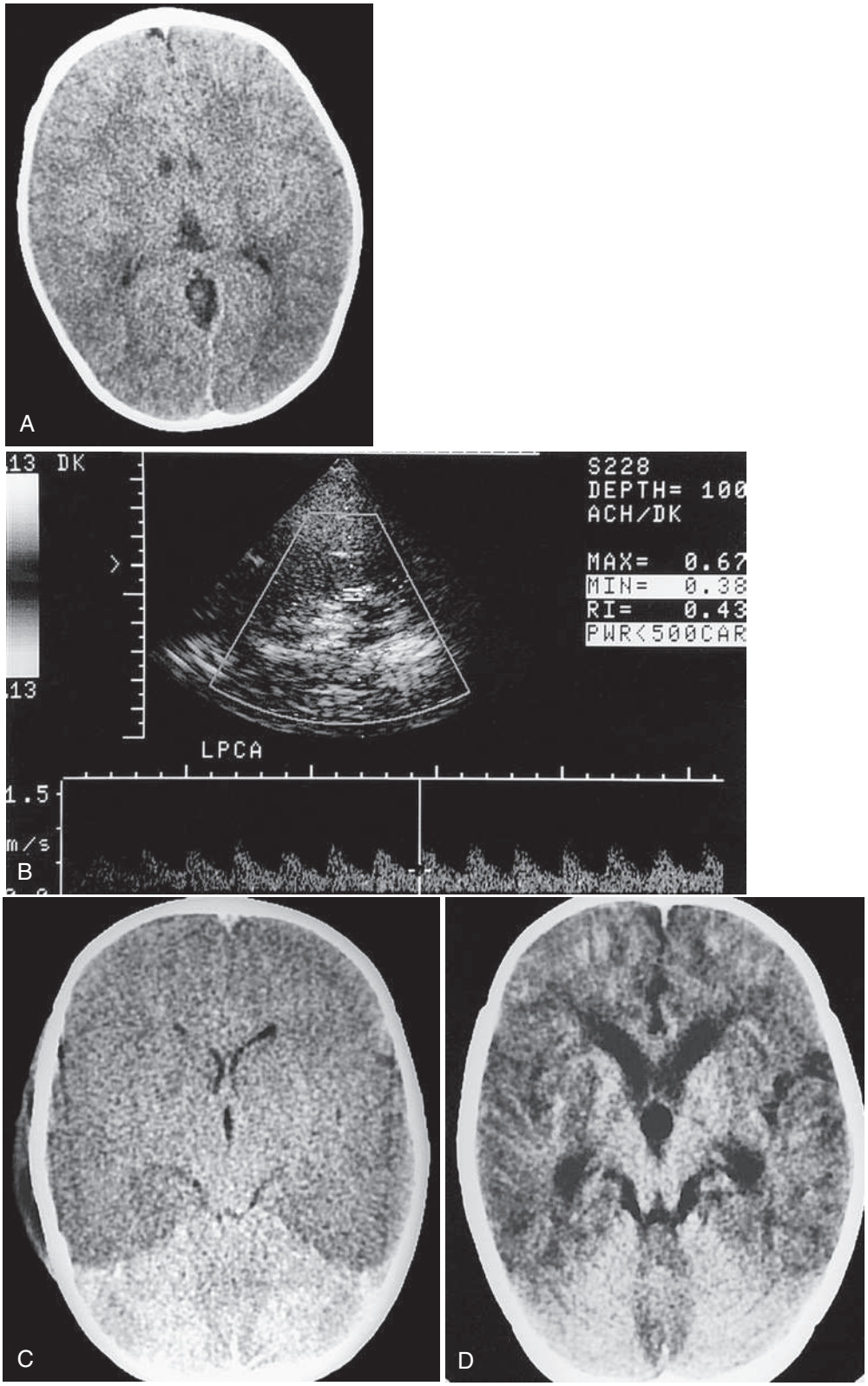

FIG. 47.21 Asphyxia. (A) One-year-old child after a respiratory arrest demonstrates mild cerebral edema on CT scan. **(B)** However, the RI in the left PCA is abnormally low, measuring 0.43, consistent with loss of autoregulation (normal range is 0.5-0.6). **(C)** CT scan 2 days later shows severe cerebral edema. **(D)** CT scan 1 month later shows marked atrophy.

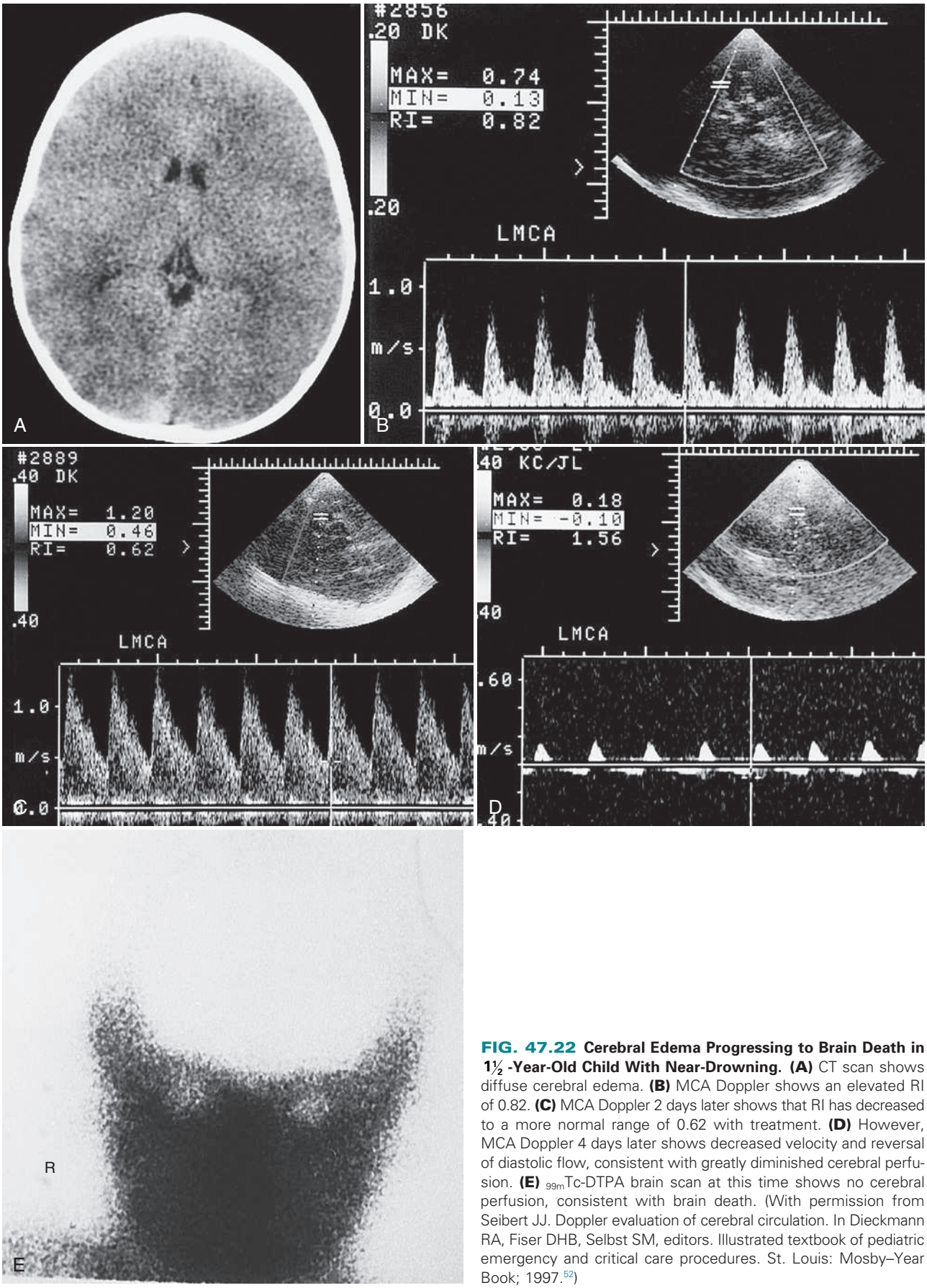

FIG. 47.22 Cerebral Edema Progressing to Brain Death in 1½ -Year-Old Child With Near-Drowning. (A) CT scan shows diffuse cerebral edema. **(B)** MCA Doppler shows an elevated RI of 0.82. **(C)** MCA Doppler 2 days later shows that RI has decreased to a more normal range of 0.62 with treatment. **(D)** However, MCA Doppler 4 days later shows decreased velocity and reversal of diastolic flow, consistent with greatly diminished cerebral perfusion. **(E)** $_{99m}$Tc-DTPA brain scan at this time shows no cerebral perfusion, consistent with brain death. (With permission from Seibert JJ. Doppler evaluation of cerebral circulation. In Dieckmann RA, Fiser DHB, Selbst SM, editors. Illustrated textbook of pediatric emergency and critical care procedures. St. Louis: Mosby–Year Book; 1997.[52])

at less than 10 seconds following contrast injection on TCD examination with Valsalva maneuver is diagnostic of right-to-left shunt with high sensitivity and specificity.[29] In pediatric patients, TCD can detect shunt resolution in patients with a moderate to large patent ductus arteriosus by a decrease in RI as the duct closes.[159]

Brain Death

Establishing brain death can be problematic, with rapid identification useful when considering organ transplant donation. Neurologic examination, electroencephalography, brainstem-evoked potentials, and nuclear blood flow studies can be used at times to establish brain death. TCD is another noninvasive tool, which can be repeated as often as required, is portable, inexpensive, and easy to perform. For patients in phenobarbital coma in which electroencephalography is not diagnostic, TCD is particularly helpful in demonstrating the severity of cerebrovascular compromise.[160-162]

After a severe asphyxiating event, an initial drop in RI may be caused by vasodilation from loss of autoregulation. As cerebral edema develops, there is loss of forward diastolic flow, followed by reversal of diastolic flow. Cessation of cerebral blood flow then occurs at the microcirculation level. The larger vessels will distend, then constrict, and eventually thrombose or collapse. As ICP increases above mean arterial pressure, arrest of cerebral circulation results in a decrease in antegrade systolic velocity. Small, early systolic spikes and complete cessation of antegrade flow then develops. Eventually, no systolic or diastolic flow can be detected[142,161] (Fig. 47.23, Videos 47.4 and 47.5).

Sonographic Criteria for Brain Death After Fontanelle Closure

Sustained reversal of diastolic flow
Small, early systolic spikes
No flow in middle cerebral artery (MCA), with reversal of diastolic flow in extracranial internal carotid artery (in patient with previously documented flow)
Mean velocity in MCA < 10 cm/sec for more than 30 minutes

There is some concern as to the reliability of TCD sonography in assessing infant brain death. Many factors are associated with reversal of diastolic flow (thus RI > 1.0) in the neonate, most often increased ICP with or without hydrocephalus and a patent ductus arteriosus[4,163] (see Table 47.4). In neonates, low RI has been described in patients clinically dead, whereas infants with high RIs have survived.[163,164] A greatly elevated RI (1-2) in a term infant with no evidence of hydrocephalus or a patent ductus arteriosus strongly suggests brain death.[165]

Sustained reversal of diastolic flow is characteristic of essentially absent effective cerebral blood flow in the adult and older child[164,166] (Fig. 47.24). In two independent studies of a total of 91 comatose patients, Petty et al.[167] and Feri et al.[168] found a TCD waveform of absent or complete reversed diastolic flow or small, early systolic spikes in at least two intracranial arteries in all 43 brain-dead patients, but in none of other patients with coma (age range, 2-88 years). Bulas et al.[169] reported a study in 19 children (aged 4-14 years) who sustained severe closed-head injury. All seven children with complete retrograde diastolic flow on the initial examination met brain death criteria within 24 hours of that study. Feri et al.[168] and Shiogai et al.[166] described three unstable patients who briefly showed diastolic reversal flow followed by a forward diastolic flow in the same waveform who improved, but of the patients Feri et al. observed, none with complete reversal of diastolic flow survived.

There have been a few reported pediatric cases of mild diastolic reversed flow who later demonstrate recovery of forward diastolic flow and brainstem function. Kirkham et al.[160] therefore suggested using a **direction of flow index** (DFI = 1 − maximum diastolic velocity area/maximum systolic velocity area). All children with substantial diastolic reversed flow and a time-averaged velocity of less than 10 cm/sec over a 30-minute period died. Some investigators have advocated continuous TCD monitoring. Powers et al.[161] showed that a mean velocity in the MCA of less than 10 cm/sec for longer than 30 minutes was not compatible with survival. Qian et al.[170] found that in children, reversed diastolic flow, small systolic forward flow, or a direction of flow index less than 0.8 in the MCA for more than 2 hours was a reliable indicator of brain death. Undetectable flow in the brain has also been described in brain death.[166,168-171] The occurrence of undetectable MCA flow, however, could sometimes be caused by technical factors, including absence of an appropriate acoustic window. The use of contrast agents may improve the level of confidence when no flow is encountered.

Some investigators have studied both the extracranial and the intracranial carotid circulation simultaneously in their evaluation of brain death. Feri et al.[168] described three waveform patterns in the MCA as well as in the extracranial internal carotid and vertebral arteries as **specific for brain death:** (1) diastolic reversed flow without systolic forward flow, (2) brief systolic forward flow, and (3) undetectable flow. Absence of MCA flow on TCD sonography, with a simultaneous recording of complete reversal of diastolic flow in the extracranial ICA, was a reliable sign of cerebral circulatory arrest. Some investigators have studied only the extracranial carotid circulation in the neck. Jalili et al.[172] reported 100% specificity for brain death with bilateral reversal of diastolic flow in the ICA of children with brain death.

The ease of performing TCD sonography and the ability to repeat the study as often as necessary also assist in proving the **absence of brain death,** particularly when a patient has taken sedative drugs (Fig. 47.25). It is important to remember that TCD examination is a proven useful confirmatory examination and is not used in isolation[173]; when used in combination with electroencephalography, specificity is up to 100%.[174] A recent study by Sharma et al.[175] evaluated the utility of TCD as a diagnostic test when clinical diagnosis was not possible due to confounding factors. They demonstrated that TCD can help make an early diagnosis of brain death and can also be used to assess prognosis. Thus, in patients where brain dead criteria are not met, the presence of a waveform consistent with cerebral circulatory arrest in at least one major cerebral artery is associated with

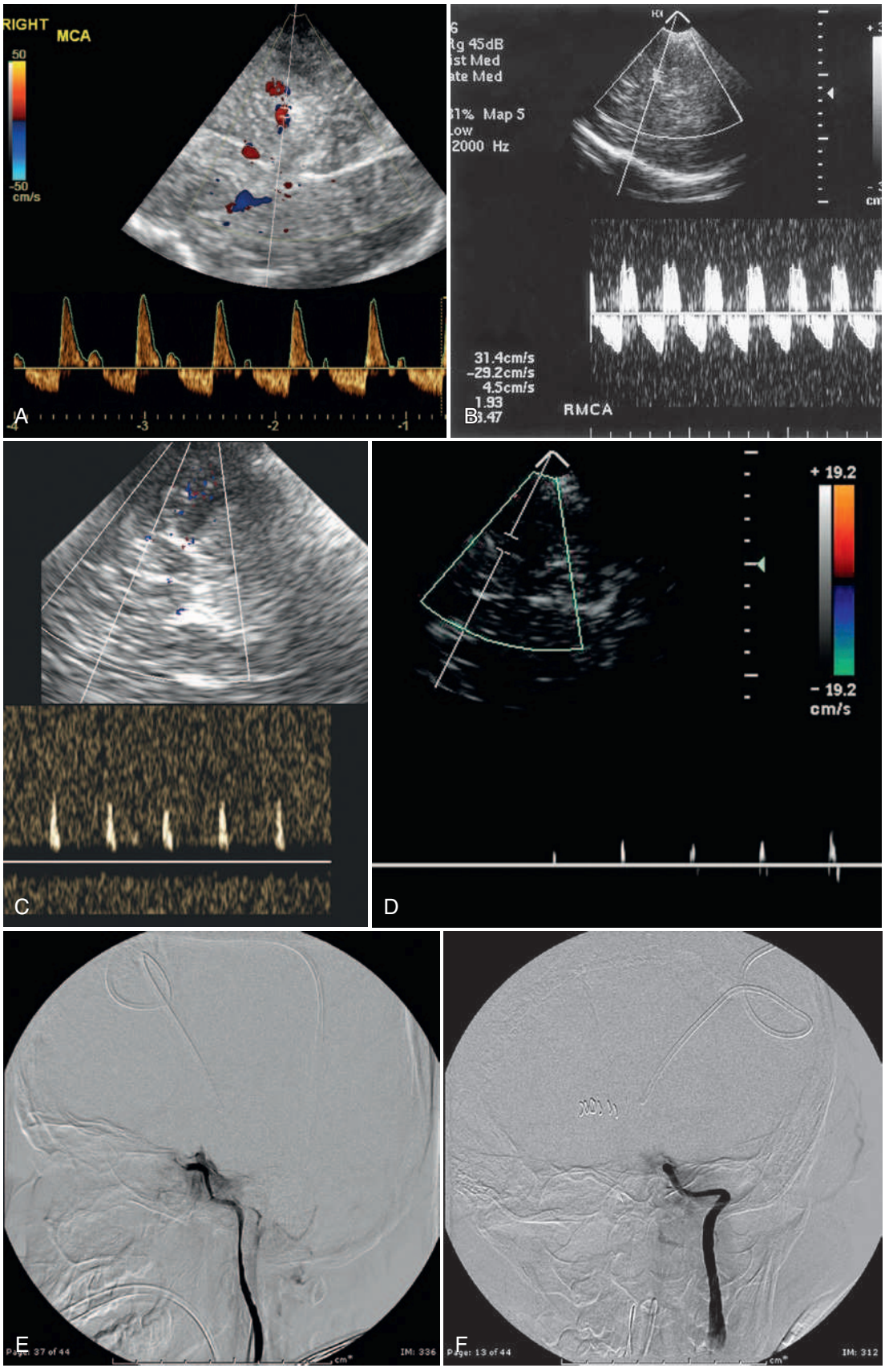

FIG. 47.23 Patterns of Pediatric TCD Spectral Doppler Waveforms in Impending Brain Death. (A) and **(B)** Reversal of diastolic flow. See also Videos 47.4 and 47.5. **(C)** Brief systolic forward flow with diminished peak velocity and no diastolic flow. **(D)** No discernible systolic or diastolic flow. **(E)** and **(F)** Lateral and anteroposterior projections of a carotid arteriogram in a 13-year-old status post motor vehicle accident demonstrate lack of intracranial circulation confirming brain death.

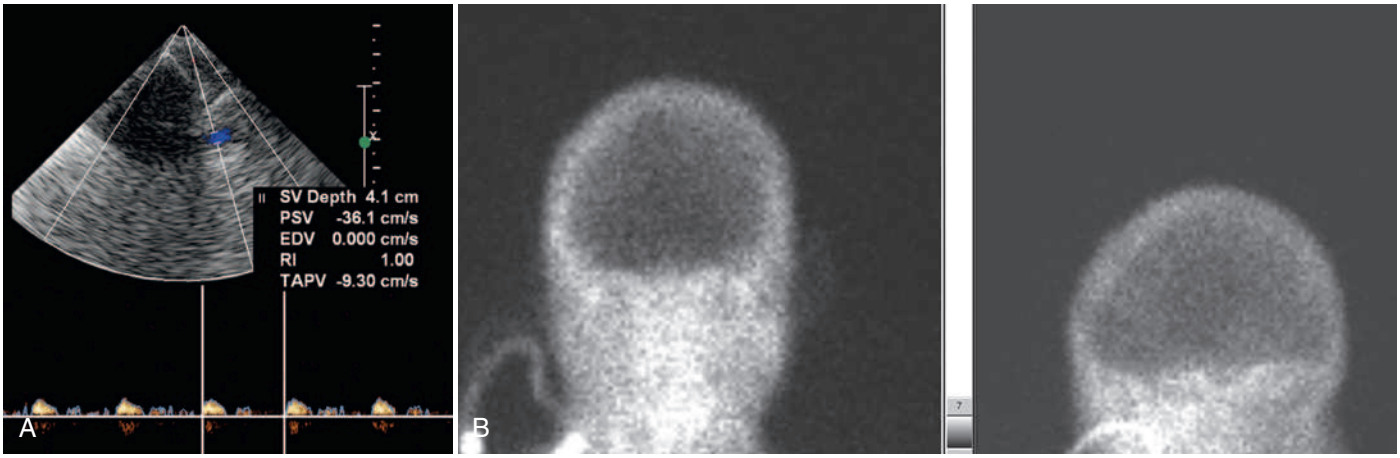

FIG. 47.24 Brain Death Following Hypoxic Insult in a 17-Year-Old Child. (A) TCD spectral waveform of the right MCA demonstrates no significant antegrade flow. **(B)** $_{99m}$Tc-HMPAO brain scan the same day demonstrates no intracranial update. Tracer in the convexity of the head is from the external carotid circulation.

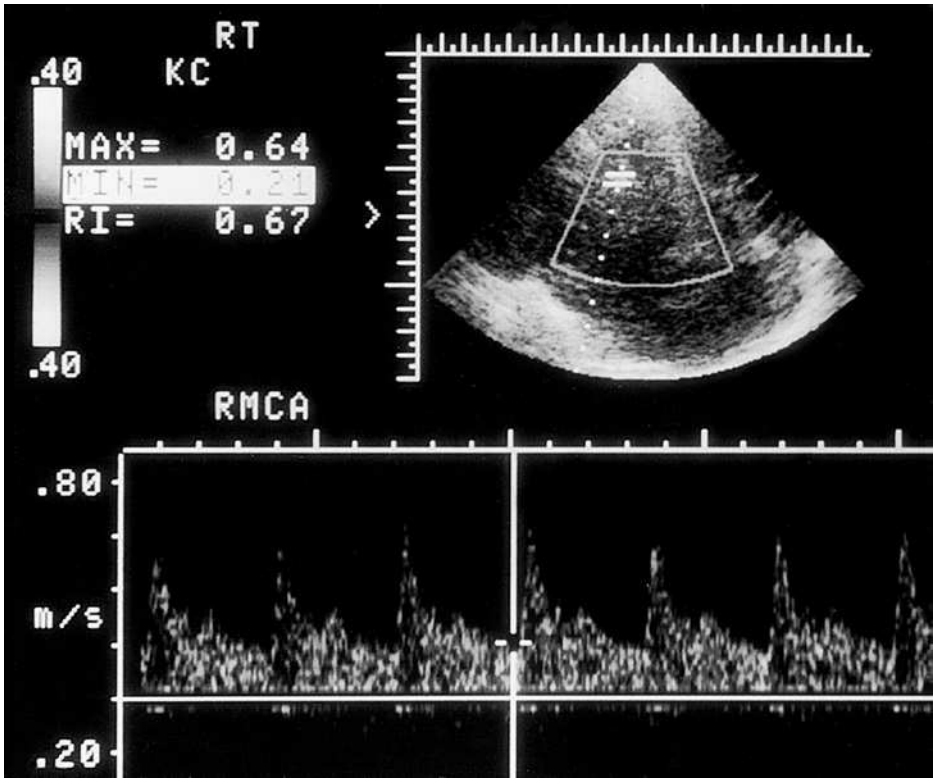

FIG. 47.25 Coma, Not Brain Death. Teenager in status epilepticus with flat electroencephalogram in phenobarbital coma with carbon dioxide tension (P_{CO_2}) of 27 mm Hg. TCD spectral waveform shows antegrade diastolic flow in the right MCA with slightly elevated RI of 0.67 but no evidence of brain death. Patient recovered without sequelae.

a poor prognosis and can help family and clinicians make decisions regarding care.

Neuromonitoring and Intraoperative Neuroradiologic Procedures

Neuromonitoring includes identifying loss of neurologic functions or appearance of secondary cerebral insults that could benefit from early intervention. Neuromonitoring provides physiologic information that can help clinicians better understand the affect of the illness on the brain, assess prognosis, and allow guidance of individualized therapy.[176]

TCD monitoring has been used in the evaluation of cerebral autoregulation in pediatric patients undergoing anesthesia. Blood pressure limits of autoregulation are poorly defined in pediatrics and multiple factors may have substantial impact on the capability of appropriate cerebral autoregulation, including age, gender, temperature, anesthesia, vasopressors, carbon dioxide, inflammation, and brain injury. By identifying the mean arterial pressure

range that has the most robust autoregulation, better neuroprotection can be provided during a procedure.[177]

Intraoperative TCD monitoring of the velocity in the MCA during **carotid endarterectomy** is an accepted clinical application in adults.[6] Intraoperative complications of carotid endarterectomy relate mainly to ischemia during cross-clamping, hyperemic phenomena, or embolization of atheromatous or gaseous materials. After ischemia, hyperemia can occur and is characterized by a sudden increase in flow velocity. High-amplitude spikes seen on TCD spectral waveform and associated with an audible chirping sound are caused by solid or gaseous microemboli as small as 30 to 50 µm.[178] Ischemia during cross-clamping is a classic complication occurring in up to 10% of patients; it is caused by incompetent intracranial collateral circulation, mainly the anterior and posterior communicating arteries and the leptomeningeal vessels. TCD ultrasound can be used to assess the effect of carotid cross-clamping on the MCA in both children and adults (Fig. 47.26).

TCD monitoring during **cardiopulmonary bypass** for cardiac surgery has also been studied. TCD sonography can demonstrate **emboli showers** that occur during aortic cannulation, cardiac manipulation, or other surgical maneuvers.[179-181] Doppler ultrasound has been used to monitor flow patterns during cardiopulmonary bypass with a decrease in mean velocity with increasing hypothermia noted.[182] Profound hypothermic circulatory arrest and profound hypothermia with continuous low-flow cardiopulmonary bypass are used to facilitate repair of complex congenital heart lesions. Extended periods of profound hypothermic arrest may impair cerebral function and metabolism and produce ischemic brain injury. TCD has enabled the noninvasive intraoperative monitoring of cerebral perfusion when using either circulatory arrest or low-flow bypass.

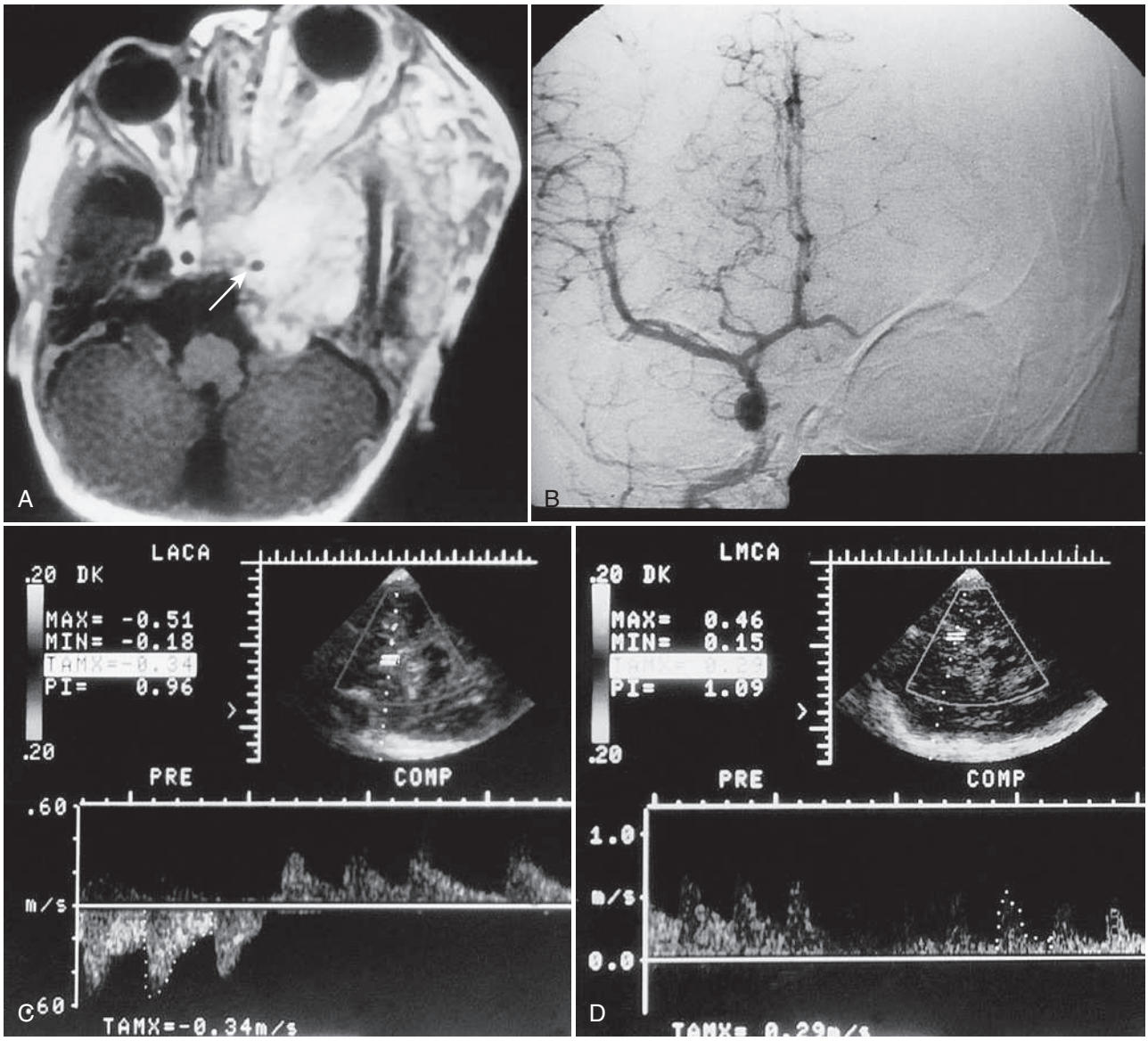

FIG. 47.26 Plexiform Neurofibroma. (A) Left internal carotid artery *(arrow)* is patent but surrounded by the plexiform neurofibroma on MRI. **(B)** Compression of left carotid artery at arteriography shows cross-filling from right side into left ACA. **(C)** TCD spectral waveform at time of compression also shows good filling of left ACA from right side (reverse flow in the left ACA). **(D)** Good filling of left MCA.

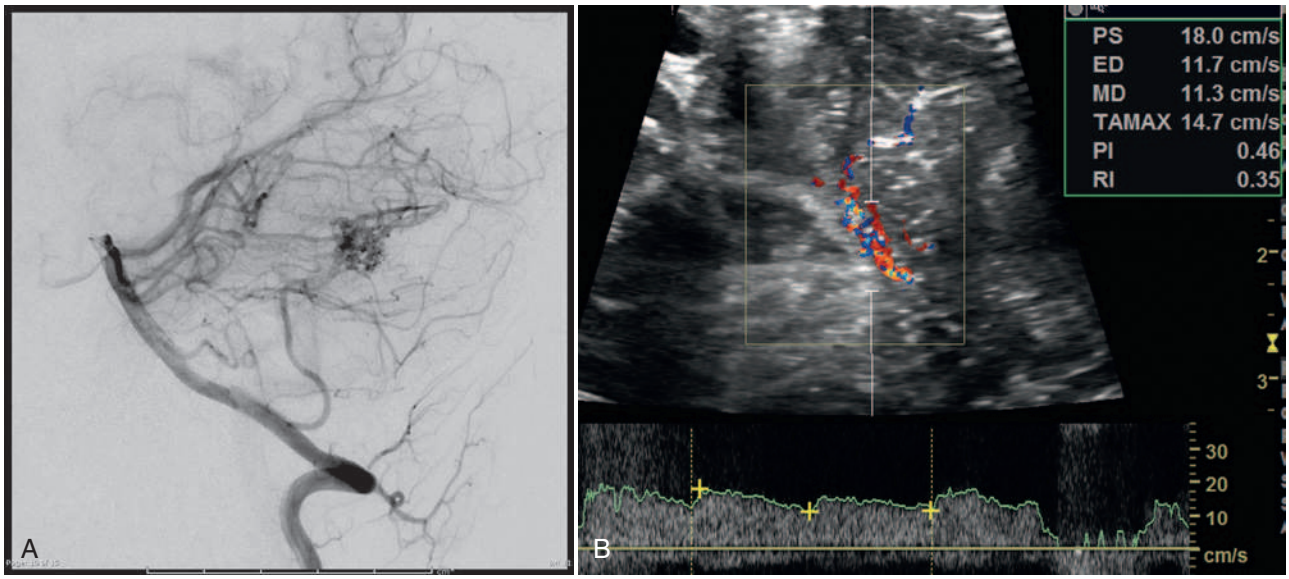

FIG. 47.27 Intraoperative Guidance for Resection of a Supracerebellar Arteriovenous Malformation With Residual Feeders Status After Glue Embolization. (A) Angiogram demonstrates a residual supracerebellar vascular malformation. **(B)** Intraoperative TCD via craniotomy helped identify the vascular nidus *(cursor)*.

A study evaluating the neurodevelopmental outcome in infants undergoing surgery for congenital heart defects indicates that low cerebral blood flow velocities on TCD obtained in the postoperative period is a marker of suboptimal cerebral perfusion.[183] Future TCD studies may help to develop improved methods of cerebral protection during repair of complex congenital heart lesions.[182,184,185]

TCD has also been used during diagnostic and therapeutic neuroangiographic and surgical procedures.[185] Asymptomatic **microemboli** have been shown to enter the cerebral circulation in large numbers during "routine" carotid angiography as well as pediatric scoliosis surgery. High rates of microemboli may be related to the presence of right-to-left cardiac shunts.[186] Intraoperative guidance using contrast agents and three-dimensional TCD is being investigated to improve the demonstration of vascular anatomy (Fig. 47.27).

Outside of surgery, neuromonitoring by TCD has also been done in patients with traumatic brain injury, intracranial hemorrhage, diabetic ketoacidosis,[187] and sepsis in the intensive care unit.[188] By evaluating flow velocity responses to spontaneous or induced changes in cerebral perfusion pressure, TCD can help modify treatment.[176]

A study evaluating the cerebral blood flow velocity in children on **extracorporeal membrane oxygenation** (ECMO) demonstrated that higher velocities suggested to be secondary to hyperemia were identified 2 to 6 days prior to recognizing cerebral hemorrhage. Further studies might demonstrate usefulness of TCD in the monitoring and management of patients on ECMO.[189]

Transcranial Doppler and Tissue Plasminogen Activator

Ultrasound enhances the activity of **tissue plasminogen activator** (TPA). TCD sonography can identify residual blood flow signals around thrombi and, by delivering mechanical pressure waves, expose more thrombus surface to circulating TPA. The CLOT-BUST international multicenter trial[190] showed that ultrasound can enhance the thrombolytic activity of a drug with clinical recovery from stroke with recanalization 2 hours after TPA bolus. This was seen in 25% of patients treated with TPA and TCD compared with 8% who received TPA alone ($p = .02$). The use of contrast-enhanced ultrasound and TPA was recently evaluated in animals and proved to be more effective than TPA with nonenhanced ultrasound, contrast-enhanced ultrasound without TPA, or ultrasound alone.[190] Current ongoing clinical trials include phase II studies of 2-MHz TCD ultrasound with contrast agents or microbubbles.[191,192] Future applications using contrast agents may include evaluating perfusion of brain tumors after chemotherapy and radiation.

Functional Transcranial Doppler

The use of TCD in functional evaluation of the brain is a complementary tool. It is useful in the measurement of the lateralization during cognitive tasks. It is noninvasive, has excellent temporal resolution, and is not affected by motion artifact.[193] Perfusion can also be evaluated and has a significant correlation with findings on functional MRI and positron emission tomography studies. Functional TCD is considered a useful examination in the elucidation of the hemispheric organization of cognitive, motor, and sensory functions in adults and children.[102]

Other Potential Uses

Patients with beta-thalassemia (minor) have an increased risk of stroke and may benefit from transfusion and splenectomy as treatment. Studies demonstrate an increase in mean arterial velocities in patients compared to controls.[194]

Using TCD alone thus far has not predicted stroke risk in patients with thalassemia major.[195] More studies are needed

in this area to better understand the potential benefits of TCD in the management of these patients.[194,195]

Another area of research is the use of TCD in the evaluation of the cognitive function of children. Various studies have associated cerebrovascular function using TCD measurements with cognitive performance. In neonates, a decrease in blood flow velocities is associated with poor cognitive performance and in patients with SCD, an increase in flow velocities is associated with poor outcomes.[102,196]

REFERENCES

1. Raju TN. Cranial Doppler applications in neonatal critical care. Crit Care Clin. 1992;8(1):93-111.
2. Saliba EM, Laugier J. Doppler assessment of the cerebral circulation in pediatric intensive care. Crit Care Clin. 1992;8(1):79-92.
3. Taylor GA. Current concepts in neonatal cranial Doppler sonography. Ultrasound Q. 1992;4:223-244.
4. Seibert JJ, McCowan TC, Chadduck WM, et al. Duplex pulsed Doppler US versus intracranial pressure in the neonate: clinical and experimental studies. Radiology. 1989;171(1):155-159.
5. Aaslid R, Markwalder TM, Nornes H. Noninvasive transcranial Doppler ultrasound recording of flow velocity in basal cerebral arteries. J Neurosurg. 1982;57(6):769-774.
6. Lupetin AR, Davis DA, Beckman I, Dash N. Transcranial Doppler sonography. Part 1. Principles, technique, and normal appearances. Radiographics. 1995;15(1):179-191.
7. Katz ML, Comerota AJ. Transcranial Doppler: a review of technique, interpretation and clinical applications. Ultrasound Q. 1991;8:241-265.
8. Byrd SM. An overview of transcranial Doppler color flow imaging: a technique comparison. Ultrasound Q. 1996;13:197-210.
9. Rosendahl T, Muller C, Wagner W, et al. Transcranial imaging: a new angle on transcranial Doppler video. J Color Flow Imaging. 1995;5:58.
10. Fujioka KA, Douville CM. Transcranial Doppler: anatomy and free hand examination techniques. New York: Raven Press; 1992.
11. Neulen A, Greke C, Prokesch E, et al. Image guidance to improve reliability and data integrity of transcranial Doppler sonography. Clin Neurol Neurosurg. 2013;115(8):1382-1388.
12. McCarville MB. Comparison of duplex and nonduplex transcranial Doppler ultrasonography. Ultrasound Q. 2008;24(3):167-171.
13. Bulas D. Screening children for sickle cell vasculopathy: guidelines for transcranial Doppler evaluation. Pediatr Radiol. 2005;35(3):235-241.
14. Seibert JJ, Glasier CM, Leithiser JRE, et al. Transcranial Doppler using standard duplex equipment in children. Ultrasound Q. 1990;8:167-176.
15. Erickson SJ, Hendrix LE, Massaro BM, et al. Color Doppler flow imaging of the normal and abnormal orbit. Radiology. 1989;173(2):511-516.
16. Baxter GM, Williamson TH. Color Doppler imaging of the eye: normal ranges, reproducibility, and observer variation. J Ultrasound Med. 1995;14(2):91-96.
17. Purkayastha S, Sorond F. Transcranial Doppler ultrasound: technique and application. Semin Neurol. 2012;32(4):411-420.
18. Otis S, Ringelstein EB. Principles and applications of TCD. In: Tegeler C, Babikian V, Gomez C, editors. Neurosonology. St. Louis: Mosby–Year Book; 1996. p. 117.
19. Adams R, McKie V, Nichols F, et al. The use of transcranial ultrasonography to predict stroke in sickle cell disease. N Engl J Med. 1992;326(9):605-610.
20. Bulas DI, Jones A, Seibert JJ, et al. Transcranial Doppler (TCD) screening for stroke prevention in sickle cell anemia: pitfalls in technique variation. Pediatr Radiol. 2000;30(11):733-738.
21. McCarville MB, Li C, Xiong X, Wang W. Comparison of transcranial Doppler sonography with and without imaging in the evaluation of children with sickle cell anemia. AJR Am J Roentgenol. 2004;183(4):1117-1122.
22. Neish AS, Blews DE, Simms CA, et al. Screening for stroke in sickle cell anemia: comparison of transcranial Doppler imaging and nonimaging US techniques. Radiology. 2002;222(3):709-714.
23. Malouf Jr AJ, Hamrick-Turner JE, Doherty MC, et al. Implementation of the STOP protocol for stroke prevention in sickle cell anemia by using duplex power Doppler imaging. Radiology. 2001;219(2):359-365.
24. Fujioka KA, Gates DT, Spencer MP. A comparison of transcranial color Doppler imaging and standard static pulsed wave Doppler in the assessment of intracranial hemodynamics. J Vasc Tech. 1994;18:29.
25. Krejza J, Rudzinski W, Pawlak MA, et al. Angle-corrected imaging transcranial Doppler sonography versus imaging and nonimaging transcranial Doppler sonography in children with sickle cell disease. AJNR Am J Neuroradiol. 2007;28(8):1613-1618.
26. Bode H. Pediatric applications of transcranial Doppler sonography. New York: Springer-Verlag; 1988.
27. Verlhac S. Transcranial Doppler in children. Pediatr Radiol. 2011;41(Suppl. 1):S153-S165.
28. Vavilala M, Kincaid M, Muangman S, et al. Gender differences in cerebral bloodflow velocity and autoregulation between the anterior and posterior circulations in healthy children. Pediatr Res. 2005;58(3):574-578.
29. Kalanuria A, Nyquist P, Armonda R, Razumovsky A. Use of transcranial Doppler (TCD) ultrasound in the neurocritical care unit. Neurosurg Clin N Am. 2013;24:441-456.
30. Adams RJ, Nichols FT, McKie VC, et al. Transcranial Doppler: influence of hematocrit in children with sickle cell anemia without stroke. J Cardiovasc Tech. 1989;8:97-101.
31. Adams RJ, Nichols 3rd FT, Aaslid R, et al. Cerebral vessel stenosis in sickle cell disease: criteria for detection by transcranial Doppler. Am J Pediatr Hematol Oncol. 1990;12(3):277-282.
32. Chadduck WM, Seibert JJ. Intracranial duplex Doppler: practical uses in pediatric neurology and neurosurgery. J Child Neurol. 1989;4(Suppl.):S77-S86.
33. Mills J, Mehta V, Russin J, et al. Advanced imaging modalities in the detection of cerebral vasospasm. Neurol Res Int. 2013;2013:415960.
34. Lizzi R, Mortimer A, Carstensen E, et al. Bioeffects considerations for the safety of diagnostic ultrasound. American Institute of Ultrasound in Medicine. Bioeffects Committee. J Ultrasound Med. 1988;7(9 Suppl.):S1-S38.
35. Rabe H, Grohs B, Schmidt RM, et al. Acoustic power measurements of Doppler ultrasound devices used for perinatal and infant examinations. Pediatr Radiol. 1990;20(4):277-281.
36. Aaslid R. Transcranial Doppler sonography. New York: Springer-Verlag; 1986.
37. Lee Y, Zuckerman S, Mocco J. Current controversies in prediction, diagnosis and management of cerebral vasospasm: Where do we stand? Neurol Res Int. 2013;2013:373458.
38. Guan J, Zhang S, Zhou Q, et al. Usefulness of transcranial Doppler ultrasound in evaluating cervical-cranial collateral circulations. Interv Neurol. 2013;2(1):8-18.
39. Brunser A, Silva C, Cárcamo D, et al. Transcranial Doppler in a Hispanic-Mestizo population with neurological diseases: a study of sonographic window and its determinants. Brain Behav. 2012;2(3):231-236.
40. Harrer J, Popescu O, Henkes H, et al. Assessment of dural arteriovenous fistulae by transcranial color-coded duplex sonography. Stroke. 2005;36:976-979.
41. Winkler P, Helmke K. Major pitfalls in Doppler investigations with particular reference to the cerebral vascular system. Part I. Sources of error, resulting pitfalls and measures to prevent errors. Pediatr Radiol. 1990;20(4):219-228.
42. Winkler P, Helmke K, Mahl M. Major pitfalls in Doppler investigations. Part II. Low flow velocities and colour Doppler applications. Pediatr Radiol. 1990;20(5):304-310.
43. Bazzocchi M, Quaia E, Zuiani C, Moroldo M. Transcranial Doppler: state of the art. Eur J Radiol. 1998;27(Suppl. 2):S141-S148.
44. Totaro R, Marini C, Sacco S, et al. Contrast-enhanced transcranial Doppler sonography in patients with acute cerebrovascular diseases. Funct Neurol. 2001;16(1):11-16.
45. Postert T, Federlein J, Przuntek H, Buttner T. Insufficient and absent acoustic temporal bone window: potential and limitations of transcranial contrast-enhanced color-coded sonography and contrast-enhanced power-based sonography. Ultrasound Med Biol. 1997;23(6):857-862.

46. Wang L, He W, Wang HS, et al. Comparison of transcranial color-coded real-time sonography and contrast enhanced color-coded sonography for detection and characterization of intracranial arteriovenous malformations. J Ultrasound Med. 2014;33:273-280.
47. Griewing B, Schminke U, Motsch L, et al. Transcranial duplex sonography of middle cerebral artery stenosis: a comparison of colour-coding techniques—frequency- or power-based Doppler and contrast enhancement. Neuroradiology. 1998;40(8):490-495.
48. Droste DW, Llull JB, Pezzoli C, et al. SonoVue (BR1), a new long-acting echocontrast agent, improves transcranial colour-coded duplex ultrasonic imaging. Cerebrovasc Dis. 2002;14(1):27-32.
49. Droste DW, Jurgens R, Weber S, et al. Benefit of echocontrast-enhanced transcranial color-coded duplex ultrasound in the assessment of intracranial collateral pathways. Stroke. 2000;31(4):920-923.
50. Postert T, Braun B, Pfundtner N, et al. Echo contrast-enhanced three-dimensional power Doppler of intracranial arteries. Ultrasound Med Biol. 1998;24(7):953-962.
51. Gerriets T, Seidel G, Fiss I, et al. Contrast-enhanced transcranial color-coded duplex sonography: efficiency and validity. Neurology. 1999;52(6): 1133-1137.
52. Seibert JJ. Doppler evaluation of cerebral circulation. In: Dieckmann RA, Fiser DHB, Selbst SM, editors. Illustrated textbook of pediatric emergency and critical care procedures. St. Louis: Mosby–Year Book; 1997.
53. Thust S, Burke C, Siddiqui A. Neuroimaging findings in sickle cell disease. Br J Radiol. 2014;87(1040):20130699.
54. DeBaun M, Armstrong D, McKinstry R, et al. Silent cerebral infarcts: a review on a prevalent and progressive cause of neurologic injury in sickle cell anemia. Blood. 2012;119(20):4587-4596.
55. Kato G, Hebbel R, Steinberg M, et al. Vasculopathy in sickle cell disease. Am J Hematol. 2009;84(9):618-625.
56. Jordan L, Casella J, DeBaun M. Prospects for primary stroke prevention in children with sickle cell anemia. Br J Haematol. 2012;157(1):14-25.
57. Colombatti R, Meneghetti G, Ermani M, et al. Primary stroke prevention for sickle cell disease in north-east Italy: the role of ethnic issues in establishing a transcranial Doppler screening program. Ital J Pediatr. 2009;35:15.
58. Bader-Meunier B, Verlhac S, Elmaleh-Berges M, et al. Effect of transfusion therapy on cerebral vasculopathy in children with sickle-cell anemia. Hematologica. 2009;94(1):123-126.
59. DeBaun M, Armstrong D, McKinstry R, et al. Controlled trial of transfusions for silent cerebral infarcts in sickle cell anemia. N Engl J Med. 2014;371(8): 699-710.
60. Kwiatkowski J, Ym E, Miller S, et al. Effect of transfusion therapy on transcranial Doppler ultrasonography velocities in children with sickle cell disease. Pediatr Blood Cancer. 2011;56(5):777-782.
61. Naffaa L, Tandon Y, Irani N. Transcranial Doppler screening in sickle cell disease: the implications of using peak systolic criteria. World J Radiol. 2015;7(2):52-56.
62. Walters MC, Patience M, Leisenring W, et al. Bone marrow transplantation for sickle cell disease. N Engl J Med. 1996;335(6):369-376.
63. Verlhac S, Bernaudin F, Tortrat D, et al. Detection of cerebrovascular disease in patients with sickle cell disease using transcranial Doppler sonography: correlation with MRI, MRA and conventional angiography. Pediatr Radiol. 1995;25(Suppl. 1):S14-S19.
64. Kwiatkowski J, Zimmerman R, Pollock A, et al. Silent infarcts in young children with sickle cell disease. Br J Haematol. 2009;146(3):300-305.
65. Adams RJ, Aaslid R, el Gammal T, et al. Detection of cerebral vasculopathy in sickle cell disease using transcranial Doppler ultrasonography and magnetic resonance imaging. Case report. Stroke. 1988;19(4):518-520.
66. Seibert JJ, Miller SF, Kirby RS, et al. Cerebrovascular disease in symptomatic and asymptomatic patients with sickle cell anemia: screening with duplex transcranial Doppler US—correlation with MR imaging and MR angiography. Radiology. 1993;189(2):457-466.
67. Seibert JJ, Glasier CM, Kirby RS, et al. Transcranial Doppler, MRA, and MRI as a screening examination for cerebrovascular disease in patients with sickle cell anemia: an 8-year study. Pediatr Radiol. 1998;28(3): 138-142.
68. Siegel MJ, Luker GD, Glauser TA, DeBaun MR. Cerebral infarction in sickle cell disease: transcranial Doppler US versus neurologic examination. Radiology. 1995;197(1):191-194.
69. Kogutt MS, Goldwag SS, Gupta KL, et al. Correlation of transcranial Doppler ultrasonography with MRI and MRA in the evaluation of sickle cell disease patients with prior stroke. Pediatr Radiol. 1994;24(3):204-206.
70. Adams RJ, Nichols FT, Figueroa R, et al. Transcranial Doppler correlation with cerebral angiography in sickle cell disease. Stroke. 1992;23(8): 1073-1077.
71. Brambilla D, Miller S, Adams R. Intra-individual variation in blood flow velocities in cerebral arteries of children with sickle cell disease. Pediatr Blood Cancer. 2007;49(3):318-322.
72. Nichols FT, Jones AM, Adams RJ. Stroke prevention in sickle cell disease (STOP) study guidelines for transcranial Doppler testing. J Neuroimaging. 2001;11(4):354-362.
73. Adams RJ, McKie VC, Hsu L, et al. Prevention of a first stroke by transfusions in children with sickle cell anemia and abnormal results on transcranial Doppler ultrasonography. N Engl J Med. 1998;339(1):5-11.
74. Adams RJ, McKie VC, Brambilla D, et al. Stroke prevention trial in sickle cell anemia. Control Clin Trials. 1998;19(1):110-129.
75. Pegelow CH, Wang W, Granger S, et al. Silent infarcts in children with sickle cell anemia and abnormal cerebral artery velocity. Arch Neurol. 2001;58:2017-2021.
76. Lee M, Piomelli S, Granger S, et al. Stroke Prevention Trial in Sickle Cell Anemia (STOP): extended follow-up and final results. Blood. 2006;108(3): 847-852.
77. Jones A, Granger S, Brambilla D, et al. Can peak systolic velocities be used for prediction of stroke in sickle cell anemia? Pediatr Radiol. 2005;35(1): 66-72.
78. Verlhac S, Balandra S, Cussenot I, et al. Extracranial carotid arteriopathy in strokefree children with sickle cell anemia: detection by submandibular Doppler sonography. Pediatr Radiol. 2014;44(5):587-596.
79. Leite A, de Oliveira R, de Moura P, et al. Abnormal transcranial Doppler ultrasonography in children with sickle cell disease. Rev Bras Hematol Hemoter. 2012;34(4):307-310.
80. McGann P, Nero A, Ware R. Current management of sickle cell anemia. Cold Spring Harb Perspect Med. 2013;3(8):a011817.
81. Enningful-Eghan H, Moore R, Ichord R, et al. Transcranial Doppler screening and prophylactic transfusion program is effective in preventing overt stroke in children with sickle cell disease. J Padiatr. 2010;157(3):479-484.
82. Wang WC, Gallagher DM, Pegelow CH, et al. Multicenter comparison of magnetic resonance imaging and transcranial Doppler ultrasonography in the evaluation of the central nervous system in children with sickle cell disease. J Pediatr Hematol Oncol. 2000;22(4):335-339.
83. Buchanan I, James-Herry A, Osunkwo I. The other side of abnormal: a case series of low transcranial Doppler velocities associated with stroke in children with sickle cell disease. J Pediatr Hematol Oncol. 2013;35(7):543-546.
84. Kwiatkowski JL, Granger S, Brambilla DJ, et al. Elevated blood flow velocity in the anterior cerebral artery and stroke risk in sickle cell disease: extended analysis from the STOP trial. Br J Haematol. 2006;134(3): 333-339.
85. Lebensburger J, Miller S, Howard T, et al. Influence of severity of anemia on clinical findings in infants with sickle cell anemia: analyses from the BABY HUG study. Pediatr Blood Cancer. 2012;59(4):675-678.
86. Pavlakis S, Rees R, Huang X, et al. Transcranial Doppler ultrasonography (TCD) in infants with sickle cell anemia: baseline data from the BABY HUG trial. Pediatr Blood Cancer. 2010;54(2):256-259.
87. Shahripour R, Mortazavi M, Barlinn K, et al. Can STOP trial velocity criteria be applied to Iranian children with sickle cell disease? J Stroke. 2014; 16(2):97-101.
88. Padayachee ST, Thomas N, Arnold AJ, Inusa B. Problems with implementing a standardised transcranial Doppler screening programme: impact of instrumentation variation on STOP classification. Pediatr Radiol. 2012;42(4):470-474.
89. Hankins JS, Fortner GL, McCarville MB, et al. The natural history of conditional transcranial Doppler flow velocities in children with sickle cell anaemia. Br J Haematol. 2008;142(1):94-99.

90. Adams RJ, Brambilla DJ, Granger S, et al. Stroke and conversion to high risk in children screened with transcranial Doppler ultrasound during the STOP study. Blood. 2004;103(10):3689-3694.
91. McCarville MB, Goodin GS, Fortner G, et al. Evaluation of a comprehensive transcranial Doppler screening program for children with sickle cell anemia. Pediatr Blood Cancer. 2008;50(4):818-821.
92. Adams R, Brambilla D, Optimizing Primary Stroke Prevention in Sickle Cell Anemia (STOP 2) Trial Investigators. Discontinuing prophylactic transfusions used to prevent stroke in sickle cell disease. N Engl J Med. 2005;353(26):2769-2778.
93. Abboud M, Yim E, Musallam K, et al. Discontinuing prophylactic transfusions increases the risk of silent brain infarction in children with sickle cell disease: data from STOP II. Blood. 2011;118(4):894-898.
94. Bernaudin F, Verlhac S, Coïc L, et al. Long-term follow-up of pediatric sickle cell disease patients with abnormal high velocities on transcranial Doppler. Pediatr Radiol. 2005;35(3):242-248.
95. Zimmerman SA, Schultz WH, Burgett S, et al. Hydroxyurea therapy lowers transcranial Doppler flow velocities in children with sickle cell anemia. Blood. 2007;110(3):1043-1047.
96. Kratovil T, Bulas D, Driscoll MC, et al. Hydroxyurea therapy lowers TCD velocities in children with sickle cell disease. Pediatr Blood Cancer. 2006;47(7):894-900.
97. Ware R, Zimmerman S, Sylvestre P, et al. Prevention of secondary stroke and resolution of transfusional iron overload in children with sickle cell anemia using hydroxyurea and phlebotomy. J Pediatr. 2014;145: 346-352.
98. Ware RE, Helms RW, SWiTCH Investigators. Stroke With Transfusions Changing to Hydroxyurea (SWiTCH). Blood. 2012;119(17):3925-3932.
99. Kramer D, Winer J, Pease B, et al. Cerebral vasospasm in traumatic brain injury. Neurol Res Int. 2013;2013:415813.
100. Kincaid MS. Transcranial Doppler ultrasonography: a diagnostic tool of increasing utility. Curr Opin Anaesthesiol. 2008;21(5):552-559.
101. Rigamonti A, Ackery A, Baker AJ. Transcranial Doppler monitoring in subarachnoid hemorrhage: a critical tool in critical care. Can J Anaesth. 2008;55(2):112-123.
102. Alexandrov AV, Sloan MA, Tegeler CH, et al. Practice standards for transcranial Doppler (TCD) ultrasound. Part II. Clinical indications and expected outcomes. J Neuroimaging. 2012;22(3):215-224.
103. Lennihan L, Petty GW, Mohr JP, et al. Transcranial Doppler detection of anterior cerebral artery vasospasm (abstract). Stroke. 1989;20:151.
104. Sloan MA, Haley Jr EC, Kassell NF, et al. Sensitivity and specificity of transcranial Doppler ultrasonography in the diagnosis of vasospasm following subarachnoid hemorrhage. Neurology. 1989;39(11):1514-1518.
105. Kassab M, Majid A, Farooq M, et al. Transcranial Doppler: an introduction for primary care physicians. J Am Board Fam Med. 2007;20:65-71.
106. Martin N, Doberstein C, Zane C, et al. Posttraumatic cerebral arterial spasm: transcranial Doppler ultrasound, cerebral blood flow and angiographic findings. J Neurosurg. 1992;77(4):575-583.
107. Chhor V, Le Manach Y, Clarençon F, et al. Admission risk factors for cerebral vasospasm in ruptured brain arteriovenous malformations: an observational study. Crit Care. 2011;15(4):R190.
108. O'Brien N, Reuter-Rice K, Khanna S, et al. Vasospasm in children with traumatic brain injury. Intensive Care Med. 2010;36(4):680-687.
109. Topcuoglu MA, Pryor JC, Ogilvy CS, Kistler JP. Cerebral vasospasm following subarachnoid hemorrhage. Curr Treat Options Cardiovasc Med. 2002;4(5):373-384.
110. Philip S, Chaiwat O, Udomphorn Y, et al. Variation in cerebral blood flow velocity with cerebral perfusion pressure >40 mm Hg in 42 children with severe traumatic brain injury. Crit Care Med. 2009;37(11):2973-2978.
111. Lysakowski C, Walder B, Costanza MC, Tramer MR. Transcranial Doppler versus angiography in patients with vasospasm due to a ruptured cerebral aneurysm: a systematic review. Stroke. 2001;32(10):2292-2298.
112. Kincaid MS, Souter MJ, Treggiari MM, et al. Accuracy of transcranial Doppler ultrasonography and single-photon emission computed tomography in the diagnosis of angiographically demonstrated cerebral vasospasm. J Neurosurg. 2009;110(1):67-72.
113. Kirsch J, Mathur M, Johnson M, et al. Advances in transcranial Doppler US: imaging ahead. Radiographics. 2013;33:E1-E14.
114. Guey S, Tournier-Lasserve E, Herve D, et al. Moyamoya disease and syndrome: from genetics to clinical management. Appl Clin Genet. 2015;8:49-68.
115. Thie A, Fuhlendorf A, Spitzer K, Kunze K. Transcranial Doppler evaluation of common and classic migraine. Part I. Ultrasonic features during the headache-free period. Headache. 1990;30(4):201-208.
116. Thie A, Fuhlendorf A, Spitzer K, Kunze K. Transcranial Doppler evaluation of common and classic migraine. Part II. Ultrasonic features during attacks. Headache. 1990;30(4):209-215.
117. Min Y, Lee J, Mon B, et al. Clinical predictors for migraine in patients presenting with nausea and/or vomiting. J Neurogastroenterol Motil. 2013;19(4):516-520.
118. Askhonov UG, Askhonov GH. EEG and transcranial dopplerography of middle cerebral artery in patients with primary headaches. J Headache Pain. 2013;14(Suppl. 1):134.
119. Wang HS, Kuo MF, Huang SC, et al. Transcranial ultrasound diagnosis of intracranial lesions in children with headaches. Pediatr Neurol. 2002;26(1):43-46.
120. Boasso L, Aq F. Cerebral vasospasm in childhood migraine during the intermigrainous period. J Neuroimaging. 2004;14(2):158-161.
121. Dowling M, Noetzel M, Rodeghier M. Headache and migraine in children with sickle cell disease are associated with lower hemoglobin and higher pain events rates but not silent cerebral infarction. J Pediatr. 2014;164(5): 1175-1180.
122. Hill CM, Hogan AM, Onugha N, et al. Increased cerebral blood flow velocity in children with mild sleep-disordered breathing: a possible association with abnormal neuropsychological function. Pediatrics. 2006;118(4): e1100-e1108.
123. Hogan AM, Hill CM, Harrison D, Kirkham FJ. Cerebral blood flow velocity and cognition in children before and after adenotonsillectomy. Pediatrics. 2008;122(1):75-82.
124. Goldstein NA, Keller R, Rey K, et al. Sleep-disordered breathing and transcranial Dopplers in sickle cell disease. Arch Otolaryngol Head Neck Surg. 2011;137(12):1263-1268.
125. Kirkham FJ, Hewes DK, Prengler M, et al. Nocturnal hypoxaemia and central-nervous-system events in sickle-cell disease. Lancet. 2001;357(9269): 1656-1659.
126. Hill A, Volpe JJ. Decrease in pulsatile flow in the anterior cerebral arteries in infantile hydrocephalus. Pediatrics. 1982;69(1):4-7.
127. Goh D, Minns RA. Intracranial pressure and cerebral arterial flow velocity indices in childhood hydrocephalus: current review. Childs Nerv Syst. 1995;11(7):392-396.
128. Goh D, Minns RA, Hendry GM, et al. Cerebrovascular resistive index assessed by duplex Doppler sonography and its relationship to intracranial pressure in infantile hydrocephalus. Pediatr Radiol. 1992;22(4):246-250.
129. Klingelhofer J, Conrad B, Benecke R, et al. Evaluation of intracranial pressure from transcranial Doppler studies in cerebral disease. J Neurol. 1988;235(3): 159-162.
130. Finn JP, Quinn MW, Hall-Craggs MA, Kendall BE. Impact of vessel distortion on transcranial Doppler velocity measurements: correlation with magnetic resonance imaging. J Neurosurg. 1990;73(4):572-575.
131. Hanlo PW, Gooskens RH, Nijhuis IJ, et al. Value of transcranial Doppler indices in predicting raised ICP in infantile hydrocephalus. A study with review of the literature. Childs Nerv Syst. 1995;11(10):595-603.
132. Rodríguez-Nuñez A, Somoza-Martín M, Gómez-Lado C, et al. Therapeutic criteria in communicating childhood hydrocephalus. J Neurosurg Sci. 2008;52(1):17-21.
133. Pople IK. Doppler flow velocities in children with controlled hydrocephalus: reference values for the diagnosis of blocked cerebrospinal fluid shunts. Childs Nerv Syst. 1992;8(3):124-125.
134. Van Toorn R, Schaaf H, Solomons R, et al. The value of transcranial Doppler imaging in children with tuberculous meningitis. Child Nerv Syst. 2014;30(10):1711-1716.
135. Wakerley B, Sharma V. Transcranial Doppler derived pulsatility index in the assessment of intracranial pressure: the trend is your friend. Neurosurgery. 2013;72(2):E319-E320.
136. Sedighi B, Shafiee K, Seifaldini R, Abdi A. Changing cerebral blood flow in normal pressure hydrocephalus after the tap test can predict clinical improvement. Iran J Neurol. 2014;13(4):245-249.

137. Westra SJ, Curran JG, Duckwiler GR, et al. Pediatric intracranial vascular malformations: evaluation of treatment results with color Doppler US. Work in progress. Radiology. 1993;186(3):775-783.
138. Grolimund P, Seiler RW, Aaslid R, et al. Evaluation of cerebrovascular disease by combined extracranial and transcranial Doppler sonography. Experience in 1,039 patients. Stroke. 1987;18(6):1018-1024.
139. Lindegaard KF, Aaslid R, Nornes H, editors. Cerebral arteriovenous malformations. New York: Springer-Verlag; 1986.
140. Lindegaard KF, Grolimund P, Aaslid R, Nornes H. Evaluation of cerebral AVM's using transcranial Doppler ultrasound. J Neurosurg. 1986;65(3):335-344.
141. Hong-zhi X, Zhi-yong Q, Yu-xiang G, et al. Diagnostic value of contrast enhanced intraoperative Doppler sonography for cerebral arteriovenous malformations compared with angiography. Chinese Med J. 2010;123(20): 2812-2815.
142. Petty GW, Massaro AR, Tatemichi TK, et al. Transcranial Doppler ultrasonographic changes after treatment for arteriovenous malformations. Stroke. 1990;21(2):260-266.
143. Kaspera W, Ladzinski P, Larysz P, et al. Transcranial color coded Doppler assessment of cerebral arteriovenous malformation hemodynamics in patients treated surgically or with staged embolization. Clin Neurol Neurosurg. 2014;116:46-53.
144. Jordan LC, Wityk RJ, Dowling MM, et al. Transcranial Doppler ultrasound in children with Sturge-Weber syndrome. J Child Neurol. 2008;23(2): 137-143.
145. Duan YY, Zhou XY, Liu X, et al. Carotid and transcranial color-coded duplex ultrasonography for the diagnosis of dural arteriovenous fistulas. Cerebrovasc Dis. 2008;25(4):304-310.
146. Kilic T, Elmaci I, Bayri Y, et al. Value of transcranial Doppler ultrasonography in the diagnosis and follow-up of carotid-cavernous fistulae. Acta Neurochir. 2001;143(12):1257-1264.
147. Lo W, Marchuk D, Ball K, et al. Updates and future horizons on the understanding, diagnosis and treatment of Sturge Weber syndrome brain involvement. Dev Med Child Neurol. 2012;54(3):214-223.
148. Bulas DI. Transcranial Doppler: applications in neonates and children. Ultrasound Clin. 2009;4(4):533-551.
149. Stark JE, Seibert JJ. Cerebral artery Doppler ultrasonography for prediction of outcome after perinatal asphyxia. J Ultrasound Med. 1994;13(8): 595-600.
150. Gray PH, Tudehope DI, Masel JP, et al. Perinatal hypoxic-ischaemic brain injury: prediction of outcome. Dev Med Child Neurol. 1993;35(11): 965-973.
151. Archer LN, Levene MI, Evans DH. Cerebral artery Doppler ultrasonography for prediction of outcome after perinatal asphyxia. Lancet. 1986;2(8516): 1116-1118.
152. Raju TN. Cerebral Doppler studies in the fetus and newborn infant. J Pediatr. 1991;119(2):165-174.
153. Bellner J, Romner B, Reinstrup P, et al. Transcranial Doppler sonography pulsatility index (PI) reflects intracranial pressure (ICP). Surg Neurol. 2004;62(1):45-51.
154. Bode H, Wais U. Age dependence of flow velocities in basal cerebral arteries. Arch Dis Child. 1988;63(6):606-611.
155. Newell DW, Seiler RW, Aaslid R, editors. Head injury and cerebral circulatory arrest. New York: Raven Press; 1992.
156. Komar M, Olszowska M, Przewlocki T, et al. Transcranial Doppler ultrasonography should it be the first choice for persistent foramen ovale screening? Cardiovasc Ultrasound. 2014;12:16.
157. Van H, Poommipanit P, Shalaby M, et al. Sensitivity of transcranial Doppler versus intracardiac echocardiography in the detection of right-to-left shunt. JACC Cardiovasc Imaging. 2010;3(4):343-348.
158. Naqvi J, Yap K, Ahmad G, et al. Transcranial Doppler ultrasound: a review of the physical principles and major applications in critical care. Int J Vasc Med. 2013;2013:629378.
159. Rodriguez R, Cornel G, Hosking M, et al. Cerebral blood flow velocity during occlusive manipulation of patent ductus arteriosus in children. J Neuroimaging. 1999;9(1):23-29.
160. Kirkham FJ, Neville BG, Gosling RG. Diagnosis of brain death by transcranial Doppler sonography. Arch Dis Child. 1989;64(6):889-890.
161. Powers AD, Graeber MC, Smith RR. Transcranial Doppler ultrasonography in the determination of brain death. Neurosurgery. 1989;24(6):884-889.
162. Valentin A, Karnik R, Winkler WB, et al. Transcranial Doppler for early identification of potential organ transplant donors. Wien Klin Wochenschr. 1997;109(21):836-839.
163. Chiu NC, Shen EY, Lee BS. Reversal of diastolic cerebral blood flow in infants without brain death. Pediatr Neurol. 1994;11(4):337-340.
164. Ducrocq X, Hassler W, Moritake K, et al. Consensus opinion on diagnosis of cerebral circulatory arrest using Doppler-sonography: Task Force Group on cerebral death of the Neurosonology Research Group of the World Federation of Neurology. J Neurol Sci. 1998;159(2):145-150.
165. Glasier CM, Seibert JJ, Chadduck WM, et al. Brain death in infants: evaluation with Doppler US. Radiology. 1989;172(2):377-380.
166. Shiogai T, Sato E, Tokitsu M, et al. Transcranial Doppler monitoring in severe brain damage: relationships between intracranial haemodynamics, brain dysfunction and outcome. Neurol Res. 1990;12(4):205-213.
167. Petty GW, Wiebers DO, Meissner I. Transcranial Doppler ultrasonography: clinical applications in cerebrovascular disease. Mayo Clin Proc. 1990;65(10): 1350-1364.
168. Feri M, Ralli L, Felici M, et al. Transcranial Doppler and brain death diagnosis. Crit Care Med. 1994;22(7):1120-1126.
169. Bulas D, Chadduck WM, Vezina GL. Pediatric closed head injury: evaluation with transcranial Doppler ultrasound. Eighty-First Scientific Assembly and Annual Meeting. Chicago: Radiological Society of North America; 1995.
170. Qian SY, Fan XM, Yin HH. Transcranial Doppler assessment of brain death in children. Singapore Med J. 1998;39(6):247-250.
171. Hassler W, Steinmetz H, Gawlowski J. Transcranial Doppler ultrasonography in raised intracranial pressure and in intracranial circulatory arrest. J Neurosurg. 1988;68(5):745-751.
172. Jalili M, Crade M, Davis AL. Carotid blood-flow velocity changes detected by Doppler ultrasound in determination of brain death in children. A preliminary report. Clin Pediatr (Phila). 1994;33(11):669-674.
173. Wang K, Yuan Y, Xu ZQ, et al. Benefits of combination of electroencephalography, short latency somatosensory evoked potentials, and transcranial Doppler techniques for confirming brain death. J Zhejiang Univ Sci B. 2008;9(11):916-920.
174. Dhanwate A. Brainstem death: a comprehensive review in Indian perspective. Indian J Crit Care Med. 2014;18(9):596-605.
175. Sharma D, Souter MJ, Moore AE, Lam AM. Clinical experience with transcranial Doppler ultrasonography as a confirmatory test for brain death: a retrospective analysis. Neurocrit Care. 2011;14(3):370-376.
176. Stocchetti N, Le Roux P, Vespa P, et al. Clinical review: neuromonitoring—an update. Crit Care. 2013;17(1):201.
177. Williams M, Lee J. Intraoperative blood pressure and cerebral perfusion: strategies to clarify hemodynamic goals. Paediatr Anaesth. 2014;24(7): 657-667.
178. Albin MS, Bunegin L, Garcia C, McKay W. The transcranial Doppler can image microaggregates of intracranial air and particulate matter. J Neurosurg Anesthesiol. 1989;1(2):134-135.
179. Pugsley W. The use of Doppler ultrasound in the assessment of microemboli during cardiac surgery. Perfusion. 1986;4:115.
180. Jordan Jr WD, Voellinger DC, Doblar DD, et al. Microemboli detected by transcranial Doppler monitoring in patients during carotid angioplasty versus carotid endarterectomy. Cardiovasc Surg. 1999;7(1):33-38.
181. Dagirmanjian A, Davis DA, Rothfus WE, et al. Silent cerebral microemboli occurring during carotid angiography: frequency as determined with Doppler sonography. AJR Am J Roentgenol. 1993;161(5):1037-1040.
182. Burrows FA. Transcranial Doppler monitoring of cerebral perfusion during cardiopulmonary bypass. Ann Thorac Surg. 1993;56(6):1482-1484.
183. Cheng H, Wypij D, Laussen P, et al. Cerebral blood flow velocity and neurodevelopmental outcome in infants undergoing surgery for congenital heart disease. Ann Thorac Surg. 2014;98(1):125-132.
184. Williams GD, Ramamoorthy C. Brain monitoring and protection during pediatric cardiac surgery. Semin Cardiothorac Vasc Anesth. 2007;11(1): 23-33.
185. Abdul-Khaliq H, Uhlig R, Bottcher W, et al. Factors influencing the change in cerebral hemodynamics in pediatric patients during and after corrective

cardiac surgery of congenital heart diseases by means of full-flow cardiopulmonary bypass. Perfusion. 2002;17(3):179-185.
186. Rodriguez RA, Letts M, Jarvis J, et al. Cerebral microembolization during pediatric scoliosis surgery: a transcranial Doppler study. J Pediatr Orthop. 2001;21(4):532-536.
187. Ma L, Roberts J, Pihoker T, et al. Transcranial Doppler-based assessment of cerebral autoregulation in critically ill children during diabetic ketoacidosis treatment. Pediatr Crit Care Med. 2014;15(8):742-749.
188. Oddo M, Taccone FS. How to monitor the brain in septic patients? Minerva Anestesiol. 2015;81:776-788.
189. O'Brien N, Hall M. Extracorporeal membrane oxygenation and cerebral blood flow velocity in children. Pediatr Crit Care Med. 2013;14(3):e126-e134.
190. Nedelman M, Ritschel N, Doenges S, et al. Combined contrast-enhanced ultrasound and rt-PA treatment is safe and improves impaired microcirculation after reperfusion of middle cerebral artery occlusion. J Cereb Blood Flow Metab. 2010;30(10):1712-1720.
191. Tsivgoulis G, Alexandrov AV. Ultrasound-enhanced thrombolysis in acute ischemic stroke: potential, failures, and safety. Neurother. 2007;4(3):420-427.
192. Alexandrov AV. Ultrasound enhanced thrombolysis for stroke. Int J Stroke. 2006;1(1):26-29.
193. Meyer G, Spray A, Fairlie JE, Uomini NT. Inferring common cognitive mechanisms from brain blood-flow lateralization data: a new methodology for fTCD analysis. Front Psychol. 2014;5:552.
194. Ashjazadeh N, Emami S, Petramfar P, et al. Intracranial blood flow velocity in patients with β-thalassemia intermedia using transcranial Doppler sonography: a case-control study. Anemia. 2012;2012:798296.
195. Shariat A, Nazeri M, Abolhasani Foroughi A, Karimi M. Transcranial Doppler ultrasonography in beta-thalassemia major patients without and with thrombocytosis. Iran Red Crescent Med J. 2013;15(3):234-238.
196. Bakker M, Hofman J, Churches O, et al. Cerebrovascular function and cognition in childhood: a systematic review of transcranial Doppler studies. BMC Neurol. 2014;14:43.

CHAPTER 48

The Pediatric Head and Neck

Rupa Radhakrishnan and Beth M. Kline-Fath

SUMMARY OF KEY POINTS

- Ultrasound is an excellent modality to evaluate head and neck masses in children because of its accessibility and lack of ionizing radiation.
- Lesion location is an important factor to consider in evaluation of head and neck masses in children.
- Common head and neck masses in children are related to lymph nodes, thyroglossal duct anomalies, branchial anomalies, inclusion cysts, and vascular anomalies.
- Use of spectral Doppler waveforms can aid in identification of arterial components in vascular anomalies to narrow the differential diagnoses.

CHAPTER OUTLINE

NORMAL CERVICAL ANATOMY
SUPRAHYOID SPACE
Salivary Glands
Normal Anatomy
Inflammatory Lesions
Masses
Suprahyoid Cystic Lesions
Masticator Space
INFRAHYOID SPACE
Thyroid Gland
Normal Anatomy
Congenital Thyroid Lesions
Inflammatory Thyroid Disease
Thyroid Masses
Parathyroid Glands
Other Cystic Lesions
LACKING DEFINITION BY THE HYOID
Congenital Lesions
Branchial Anomalies
Ectopic Thymus
Dermoid and Epidermoid Lesions
Teratomas
Vascular Lesions
Vascular Anomalies
Vascular Tumors
Vascular Malformations
Other Congenital Lesions
Iatrogenic Lesions
Inflammatory Lesions
Lymph Nodes
Fibromatosis Colli
Masses
Pilomatricoma
Congenital Infantile Myofibromatosis
Malignant Neoplasms

NORMAL CERVICAL ANATOMY

The goal in pediatric imaging is to perform a study with the lowest possible radiation exposure and least sedation to adequately answer the clinical question.[1-4] Sonography, given a lack of ionizing radiation and its noninvasive approach, is almost invariably the initial imaging modality in a child with a neck lesion. Sonography is cost-effective, widely available, and portable. Ultrasound can illustrate normal cervical anatomy, evaluate vascular structures and lesions with spectral Doppler imaging, and delineate pathology with regard to location, size, and presence of calcification. Cystic masses are common pediatric neck lesions, and sonography is also exceptional at distinguishing solid from cystic lesions and assessing compressibility of lesions. Transducers with frequencies of 7.5 to 10 MHz are excellent for examination of the neck.

Limitations of ultrasound technique include the inability to evaluate bone, small field of view, and degree of soft tissue contrast. Because of these limitations, magnetic resonance imaging (MRI) and computed tomography (CT) are excellent adjunct modalities that can provide additional soft tissue and bone detail and further delineate extent of disease.[5]

An understanding of normal cervical anatomy is essential to appropriately evaluate head and neck pathology. The soft tissues of the neck can be separated into boundaries of the superficial and deep spaces.[6-8] The **superficial fascia** is primarily composed of subcutaneous fat. The platysma muscle, subcutaneous lymph nodes, and nerves lie within the superficial space. The **deep cervical fascia,** encircled by the superficial tissues, contains the major structures of the neck (Fig. 48.1). The deep cervical fascia includes superficial, middle, and deep layers (Fig. 48.2).

Simplifying the deep cervical fascial anatomy is best achieved by dividing the neck into suprahyoid and infrahyoid locations.[6,7] The **suprahyoid space** includes the areas of the neck between the skull base and hyoid bone.[6] The **infrahyoid space** is the area of the neck between the hyoid bone and clavicles.[7] Some deep

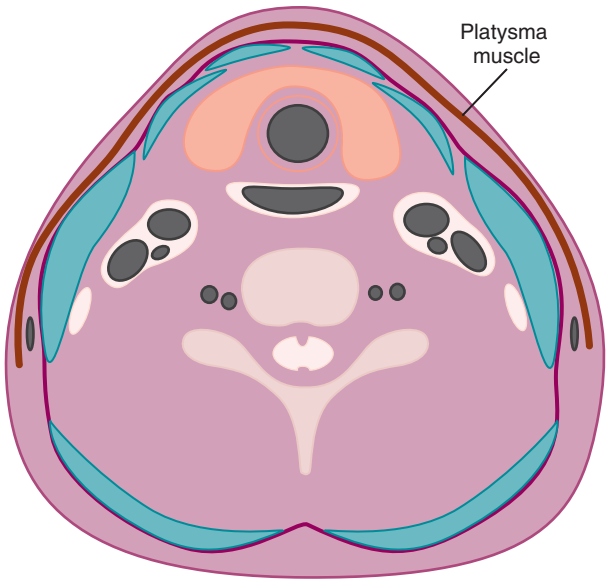

FIG. 48.1 Superficial and Deep Cervical Boundaries. Axial image of the neck at the level of the thyroid demonstrates the platysma muscle, which separates the peripheral superficial from central deep cervical fascial layers.

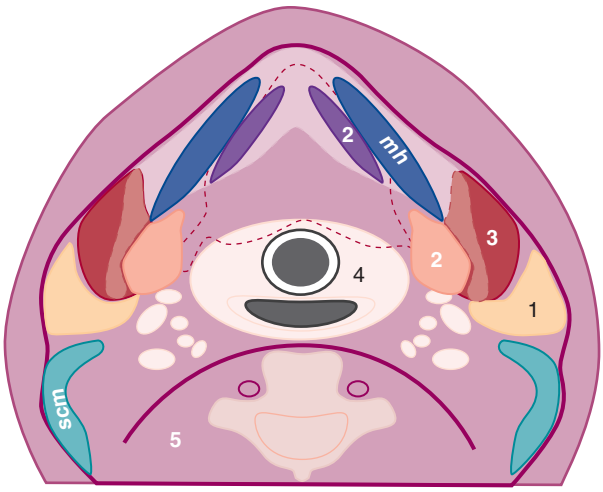

FIG. 48.3 Deep Cervical Fascial Layers of Suprahyoid Neck, Axial Image. The parotid, masticator, and submandibular spaces represent the superficial layer. *1,* Parotid gland. *2,* Submandibular space contains the sublingual *(brown)* and submandibular *(orange)* glands. *3,* Masticator space contains the masseter muscle. *4,* Middle layer; *5,* Deep fascial layer; *mh,* Mylohyoid muscle; *scm,* sternocleidomastoid muscle.

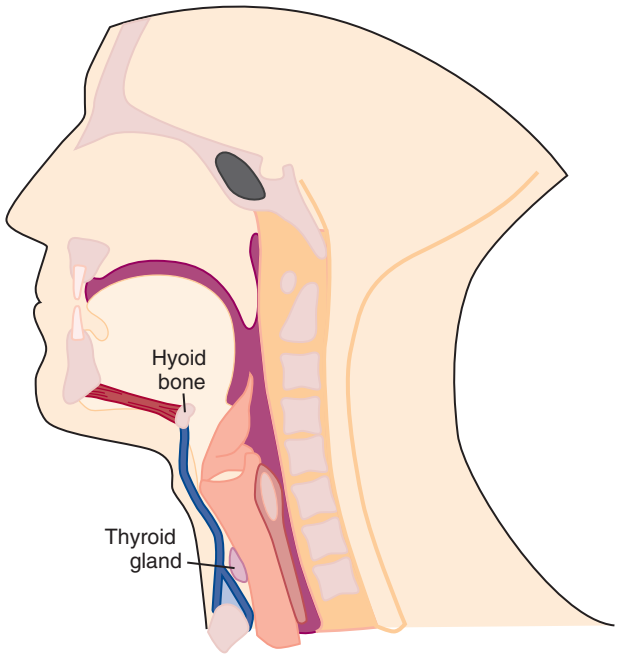

FIG. 48.2 Deep Cervical Fascial Layers. Sagittal image of the neck separates the deep cervical fascia into three boundaries: superficial *(blue),* middle *(orange),* and deep *(yellow).*

fascial planes and lesions extend within both the infrahyoid and the suprahyoid space. These spaces and lesions are described as "lacking definition by the hyoid." Using this organization, with the knowledge of the normal anatomic elements in each space, the appropriate differential diagnosis for a mass can be proposed.

SUPRAHYOID SPACE

The suprahyoid space includes the superficial, middle, and deep layers of the deep cervical fascia[9] (Fig. 48.3). The superficial layer envelops three spaces. The **parotid space** includes the parotid gland, intraparotid facial nerve, retromandibular vein, lymph nodes, and external carotid artery. The **masticator space** includes muscles of mastication and the posterior body of the mandible. The **submandibular space** includes the sublingual and submandibular glands, as well as the adjacent lymph nodes, muscles of the tongue, and hypoglossal nerve. Ultrasound is most useful in evaluation of the spaces in the superficial fascial layer.

The middle territory of the suprahyoid space lies between fascial layers and includes the **parapharyngeal** and **pharyngeal** spaces. This middle layer, which includes lymphoid tissue, minor salivary glands, and fat encircling the pharynx, is difficult to visualize with ultrasound and is not discussed separately. The **carotid space** is formed from fibers of the middle and deep layers of cervical fascia. The **retropharyngeal space** is contained by layers of the middle cervical space anteriorly and deep cervical layers posteriorly. However, because the retropharyngeal space and **prevertebral** layer, a deep cervical space, cannot be separated, it is easiest to consider these layers together in the deep cervical facial layer as the retropharyngeal space. The carotid space and retropharyngeal space extend above and below the hyoid and are discussed later.

Salivary Glands

Because the parotid and submandibular areas primarily contain salivary tissue and thus have similar pathology, these two spaces are considered together. The major salivary glands that occupy these spaces include the parotid glands, the submandibular glands, and the sublingual glands.

Normal Anatomy

The **parotid gland** is the largest salivary gland. This encapsulated gland, containing lymphoid tissue, vessels, and nerves, wraps around the angle of the mandible anterior to the mastoid tip (Fig. 48.4). Most parotid tissue lies superficial to the masseter muscle. In 20% of patients, an **accessory** parotid gland, which is a nodule of salivary tissue separate from the main parotid, can be identified on the masseter muscle.[10] The parotid gland contains acini that drain through the **Stensen duct,** a structure that extends anteriorly to exit above the upper second molar.[11] The duct lies approximately 1 cm below the inferior margin of the zygomatic arch.[12] The **facial nerve** travels within the parotid gland, lying lateral to the retromandibular vein and posterior belly of the digastric muscle, which is the muscle deep to the mastoid tip. The facial nerve acts a boundary to divide the parotid gland into superficial and deep components. The **deep lobe** of the parotid, which accounts for 20% of the gland, lies adjacent to the parapharyngeal space and beneath the angle of the mandible.

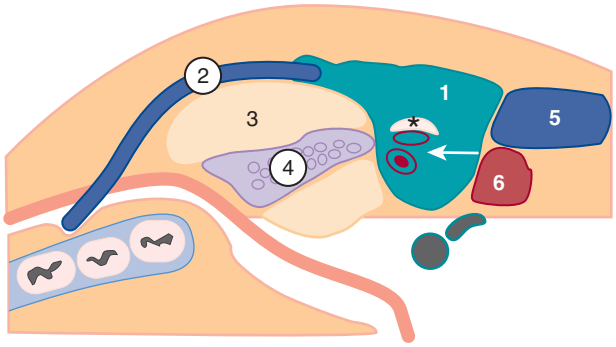

FIG. 48.4 Diagram of Parotid Space. *1,* Parotid gland; *2,* Stensen duct; *3,* masseter muscle; *4,* angle of mandible; *5,* mastoid; *6,* posterior belly of digastric muscle. Arrow points between the retromandibular vein *(open circle)* and external carotid artery *(partly solid circle),* demarcating superficial and deep lobes. Lenticular tan structure with * is the facial nerve.

Imaging of the parotid should be performed with a high-frequency transducer. Usually, linear transducers of 5 to 12 MHz are used. The entire gland should be evaluated in two perpendicular planes. Because the facial nerve is poorly delineated on ultrasound, the **retromandibular vein,** which lies directly deep to the nerve and lateral to the external carotid artery, is an excellent landmark to separate the superficial and deep lobes.[12,13] Typically, the deep lobe can only be partially visualized, concealed by acoustic shadowing of the mandibular ramus. On sonography, the parotid gland is generally homogeneous and hyperechoic with regard to the adjacent muscle (Fig. 48.5). The degree of echogenicity of the gland depends on the amount of intraglandular fatty tissue; the greater the fat content, the higher the echogenicity.

Normal intraparotid ducts may be visualized as linear reflective structures. The Stensen duct is usually not visible in the absence of dilation. In the parotid parenchyma, normal lymph nodes may be observed. Most nodes are identified at the upper or lower pole, are oval in shape, measure 5 to 6 mm in the short axis, and appear hypoechoic with a hyperechoic central hilum.[12] Ultrasound is especially useful in differentiating intraparotid lesions from extraparotid masses and separating solid and cystic lesions in this location.

The submandibular space contains both the submandibular glands and the sublingual glands in addition to submandibular lymph nodes. The submandibular glands lie within the posterior submandibular space, whereas the sublingual glands are anterior (Fig. 48.6). The **submandibular glands** are bordered by the mandible laterally and the mylohyoid muscle superiorly and medially. A small portion of the gland may pass posterior to the mylohyoid muscle to lie within the sublingual area. The space anterior to the submandibular gland contains lymph nodes. The torturous facial artery typically crosses the parenchyma laterally. The anterior facial vein can often be identified along the anterosuperior aspect of the gland.[14] Medially, the lingual artery and vein may be evident. The **Wharton duct,** the excretory duct for the gland, extends along the mylohyoid and medial part of the sublingual gland to its orifice at the floor of the mouth. On sonography, the submandibular glands should be examined in

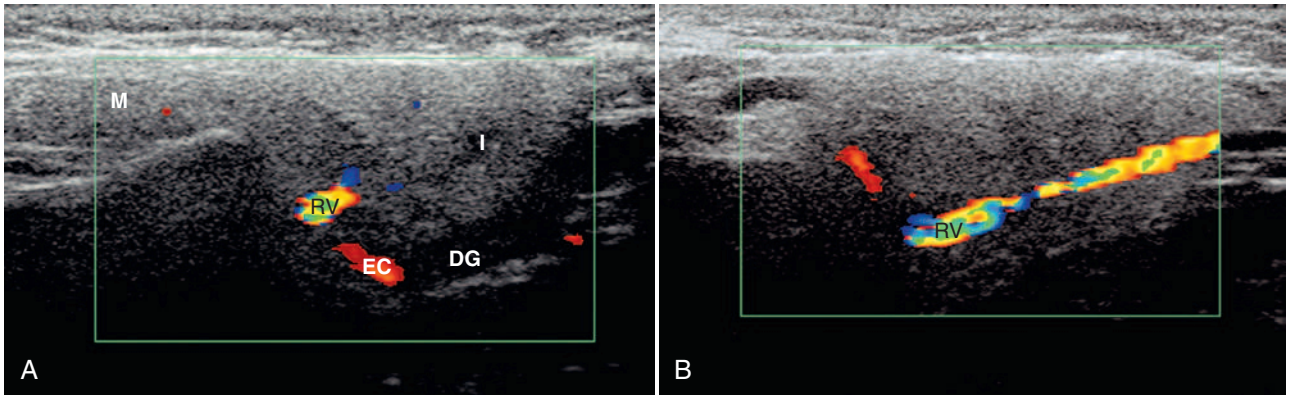

FIG. 48.5 Normal Parotid Gland. (A) Transverse color Doppler ultrasound shows mildly increased echogenicity compared with adjacent masseter muscle *(M).* Deep and superficial portions of the gland are separated by the retromandibular vein *(RV)* found lateral to the external carotid artery *(EC)* and posterior belly of the digastric muscle *(DG).* Small, hypoechoic intraparotid lesion is consistent with normal lymph node *(I).* **(B)** Longitudinal color Doppler sonogram shows normal parotid displaying homogeneous hyperechoic texture and retromandibular vein *(RV).*

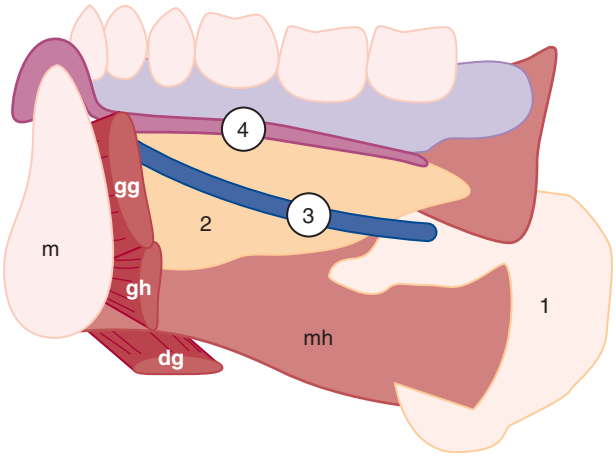

FIG. 48.6 Normal Submandibular Space. Sagittal diagram shows submandibular gland *(1)*, sublingual gland *(2)*, submandibular (Wharton) duct *(3)*, sublingual duct *(4)*, mylohyoid muscle *(mh)*, genioglossus muscle *(gg)*, geniohyoid muscle *(gh)*, anterior belly of digastric muscle *(dg)*, and mandible *(m)*.

two perpendicular planes, usually long and transverse, with a high-frequency linear transducer. The glands are triangular, homogeneous, and more echogenic than muscle but less echogenic than the parotids[15] (Fig. 48.7). On high-resolution sonography, **fine linear streaks** can be observed, representing intraglandular ductules. The Wharton duct may be visualized as a thin echogenic wall medial to the sublingual gland. Movement of the patient's tongue may aid in visualization of the duct.[16]

The **sublingual gland** lies on the mylohyoid muscle between the mandible and genioglossus muscle. In addition to the gland, the sublingual area includes the submandibular duct and sublingual vessels, which lie medial to the gland. Scanning of the gland should be performed with a high-frequency linear transducer submental in two perpendicular planes with the patient supine and the head retroflexed.[17] A standoff pad can be helpful in accessing the anatomy. On transverse imaging the gland is oval, whereas on long sections the gland has a lentiform shape (Fig. 48.8). The echogenicity of the sublingual gland is similar to the parotid and submandibular glands.[17]

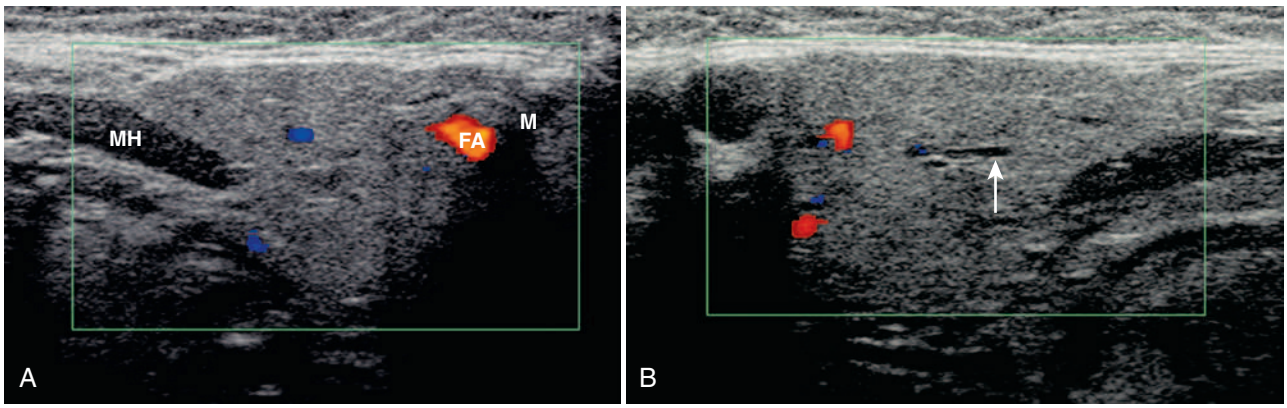

FIG. 48.7 Normal Submandibular Gland. (A) Transverse color Doppler scan shows homogeneous triangular gland with mandible *(M)* laterally and mylohyoid muscle *(MH)* medially. Facial artery *(FA)* is also present laterally along the gland. **(B)** Longitudinal color Doppler imaging shows central linear structure without color *(arrow)*, representing nondilated Wharton duct.

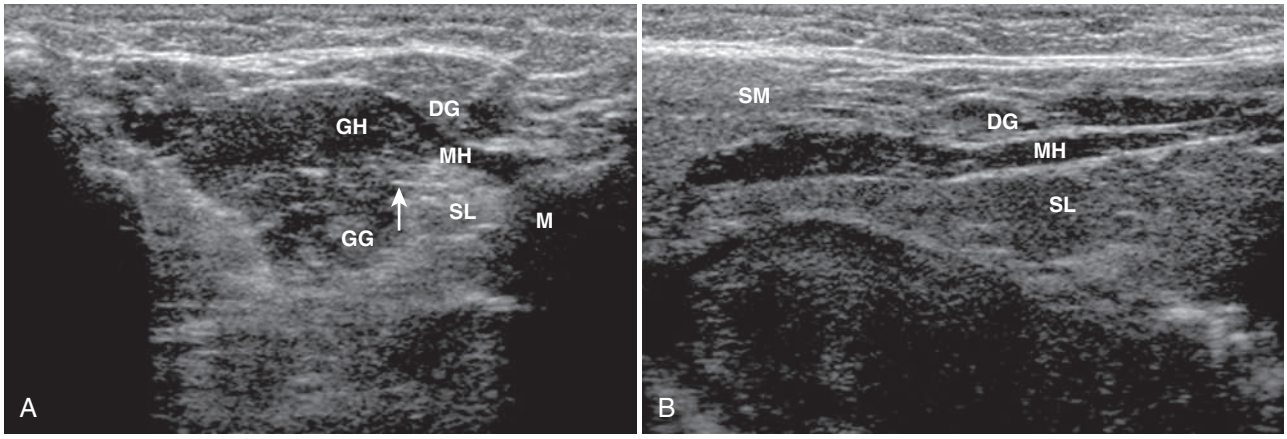

FIG. 48.8 Normal Sublingual Gland. (A) Transverse image shows triangular homogeneous sublingual glands laterally adjacent to mandible. *Arrow*, Wharton duct; *DG*, anterior belly of digastric muscle; *GG*, genioglossus; *M*, mandible; *MH*, mylohyoid; *GH*, geniohyoid; *SL*, sublingual gland. **(B)** Longitudinal ultrasound shows the submandibular gland *(SM)* posteriorly and the lenticular homogeneous sublingual gland *(SL)*.

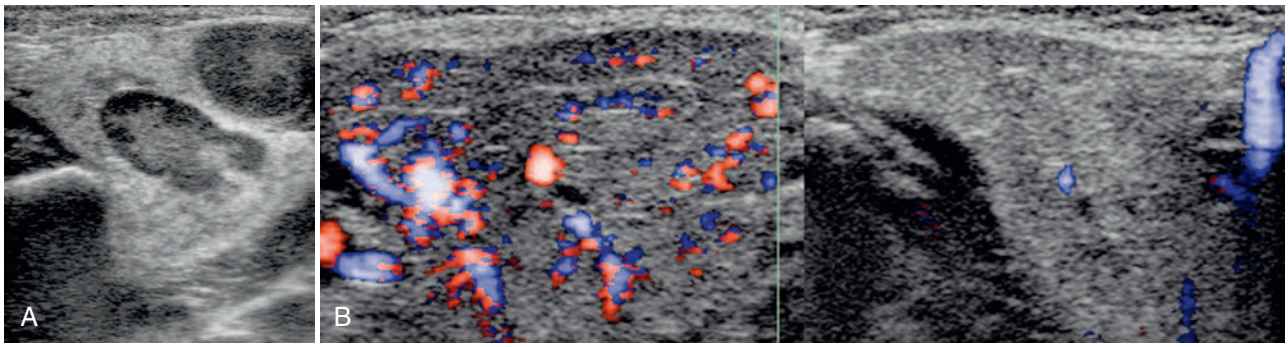

FIG. 48.9 Viral Salivary Gland Infection. (A) Mononucleosis of parotid gland in 10-year-old child. Transverse scan shows a swollen, mildly inhomogeneous parotid with enlarged intraparotid lymph nodes. **(B)** Color Doppler comparison sonograms of the submandibular glands shows decreased echogenicity and increased vascularity in the left and normal appearance of the right.

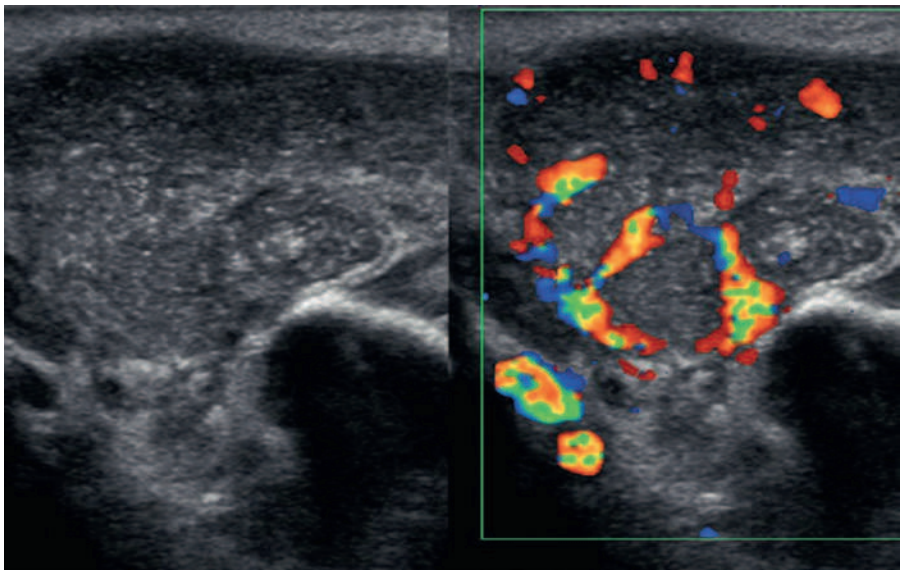

FIG. 48.10 Bacterial Parotid Infection. Split screen gray-scale and color Doppler images show a swollen, heterogeneous hypervascular parotid gland in a 17-day-old neonate infected with *Staphylococcus.*

Inflammatory Lesions

Most salivary gland pathology in children is caused by inflammatory lesions, which can be acute or chronic. The acute form may be secondary to viral or bacterial etiologies. The chronic form includes a long differential diagnosis (e.g., **human immunodeficiency virus [HIV], Sjögren syndrome, sialoadenitis, sarcoidosis,** other **granulomatous processes**).

Acute Salivary Gland Inflammation. In children, **viral salivary gland infections** are the most common cause of acute inflammation.[18] Endemic viruses, including mumps, mononucleosis, and cytomegalovirus (CMV), are the most common viral causes, causing painful unilateral or bilateral swelling of the salivary tissue. In 85% of cases, the parotid gland is involved. Although less prevalent with the advent of immunization, **mumps** is still the most common cause of **parotitis.**[11] Mumps, a highly contagious worldwide infection spread by airborne droplets, is typically encountered in the winter and spring and primarily affects children younger than 15 years.[18] The incubation period for this virus is 14 to 21 days, but the infection is contagious 3 days before the onset of swelling until the resolution of the swelling.[19] With ultrasound, viral salivary infections show a diffusely enlarged gland that may have a normal, heterogeneous and/or hypoechoic echotexture with increased vascularity[20,21] (Fig. 48.9). Frequently there is bilateral involvement, although unilateral involvement may be seen in up to one-third of patients.[21]

Bacterial infection is rare in children, primarily affecting the parotid gland. *Staphylococcus aureus* is the most common cause.[11,15,18,22] Children younger than age 1 year, especially premature infants (35%-40% cases), immunosuppressed patients, and children with severe dental and gingival disease are particularly vulnerable. Infection is typically unilateral and associated with fever, dehydration, and gland pain and edema. Proposed etiologies include infection in the mouth or stasis of salivary flow through the ducts.[18] Using ultrasound, the parotid gland appears enlarged and heterogeneous in echotexture with discrete, hypoechoic nodules representing enlarged intraparotid lymph nodes[11-13] (Fig. 48.10). There may be dilation of the central parotid ducts.[21] Adjacent cervical lymphadenopathy is common. In patients with uncomplicated parotitis, treatment is primarily

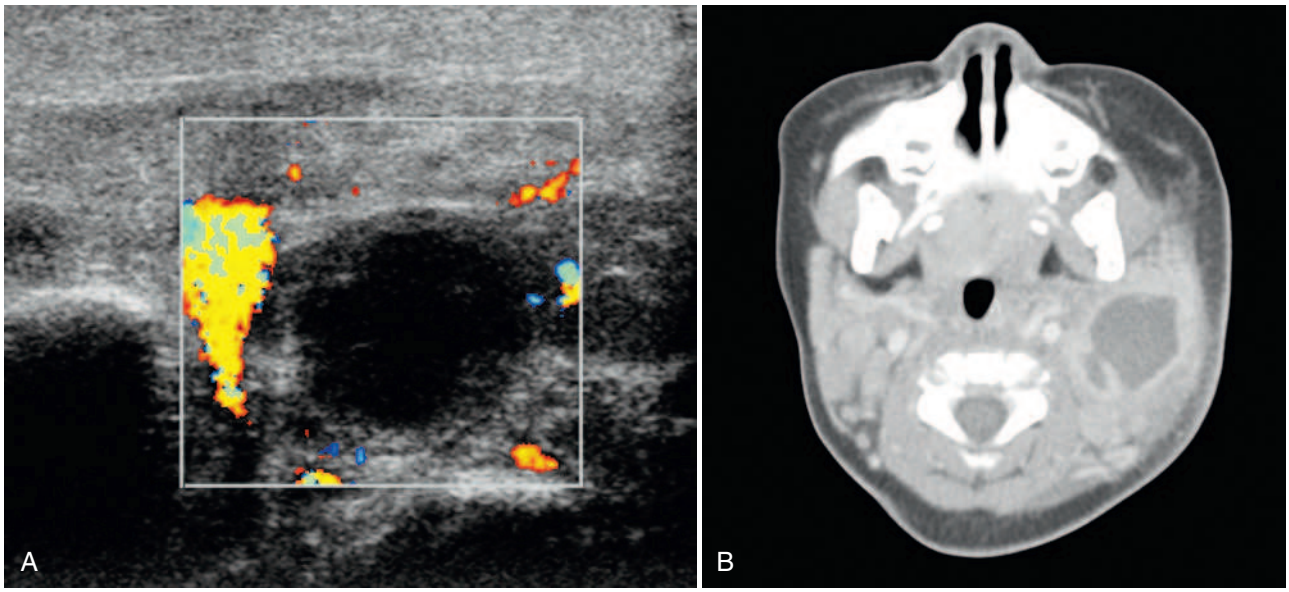

FIG. 48.11 Parotid Abscess. (A) Two-month-old infant developed swelling along the left ear. Sonogram of the parotid area demonstrates a round, well-defined, hypoechoic mass without internal blood flow within the deep parotid. **(B)** Contrast computed tomography scan performed 2 days later because of lack of response to intravenous antibiotics demonstrates a large, round, hypoattenuated lesion with partial enhancing peripheral wall within inflamed left parotid.

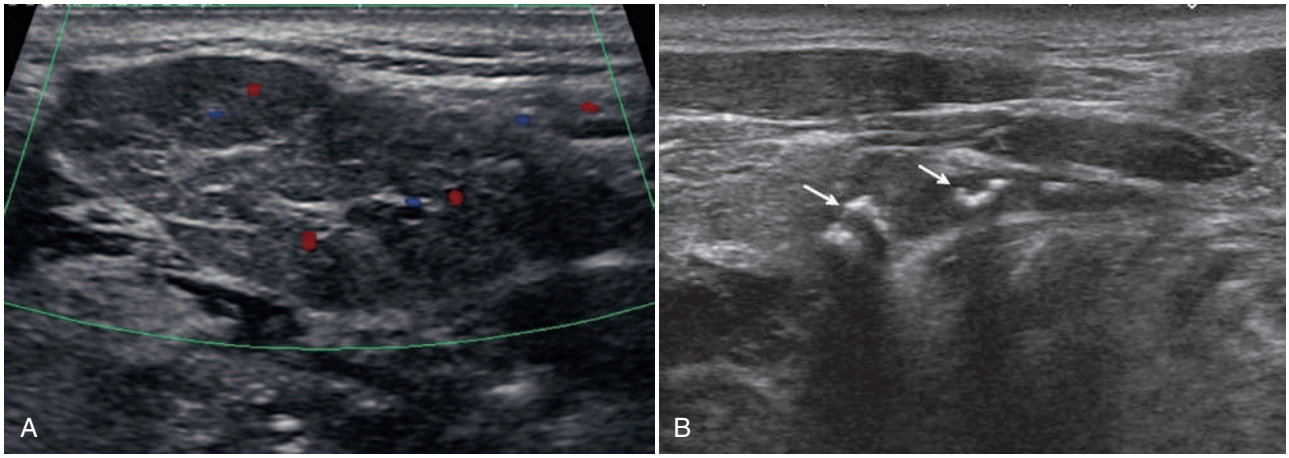

FIG. 48.12 Submandibular Gland Sialolithiasis. (A) Color Doppler of enlarged hypoechoic submandibular gland containing echogenic foci. **(B)** Dilated submandibular (Wharton) duct due to multiple obstructing echogenic shadowing foci, consistent with stones *(arrows)*. See also Video 48.1.

supportive with administration of intravenous (IV) antibiotics.[20] In the presence of severe dehydration and especially in neonates 7 to 14 days old with bacterial infection, an intraparotid abscess may develop. These collections typically appear hypoechoic or anechoic with posterior acoustic enhancement and occasionally a hyperechoic halo[12] (Fig. 48.11). Internal debris may be noted, and in some patients, hyperechoic foci consistent with gas bubbles. Ultrasound-guided drainage is useful when abscess is present. Recurrence is uncommon.

Sialolithiasis is uncommon in children, with 90% in the submandibular gland and 10% in the parotid.[12,18,20] In 25% of patients, stones are often multiple and intraglandular or intraductal in location. Submandibular glands are prone to calculi because of the alkaline nature and high viscosity of their secretions. The Wharton duct is long with an upward course and thus also has a higher propensity for stone formation. Clinically, recurrent swelling during eating and superimposed infection may result from partial or complete obstruction of the duct by a stone. Sonography is as sensitive as 94% in the detection of salivary calculi. Features include hyperechoic foci with acoustic shadowing representing stones (Fig. 48.12, Video 48.1). With duct occlusion, hypoechoic tubular areas are typically consistent with dilated ducts.[12,23] About 50% of patients have inflammation of the gland in conjunction with the calculus,[12] and the gland will demonstrate a heterogeneous architecture. Although 80% of submandibular and 60% of parotid stones are radiopaque on x-ray examination, when more information is needed beyond ultrasound, a CT scan provides the best detail.[24]

Nodal enlargement in the parotid is often present in association with cervical adenopathy caused by infection or neoplasm.

Parinaud oculoglandular syndrome presents with conjunctivitis and ipsilateral intraparotid or periauricular adenopathy and can result from ***Chlamydia*** **infection** or **cat-scratch disease.** In the submandibular space, sonography is useful to differentiate nodal from glandular disease.

Chronic Inflammatory Disease. Juvenile (recurrent) parotitis is the most common cause of childhood parotid swelling in developed countries.[22] This disorder manifests with intermittent pain, fever, and unilateral or bilateral parotid swelling. The submandibular and sublingual glands are not affected, and there is no known cause for the recurrent parotitis. Differential diagnosis includes mumps or suppurative parotitis, which is excluded by lack of pus from the parotid duct.[25] Age at presentation is typically 3 to 6 years, and the episodes tend to cease near puberty or in late adolescence.[26] Boys are more often affected than girls.[26,27] Some patients acquire superimposed acute infection, typically with *Streptococcus viridans.*[25,26]

Ultrasound is the favored imaging approach, demonstrating enlarged parotid glands containing multiple round, hypoechoic areas measuring 2 to 4 mm in diameter, likely representing peripheral sialectasis and lymphocytic infiltration[28] (Fig. 48.13). Some glands may be hypervascular, secondary to acute inflammation.[27] Treatment is generally supportive with analgesics and antibiotic administration.

Chronic sialadenitis is caused by an inflammatory process that damages the acini, altering the drainage system of the gland. The etiology may be infectious or noninfectious. Clinically, patients have gland swelling and pain, particularly postprandial. Patients with **chronic sialadenitis** on sonography often demonstrate a heterogeneous gland with small, punctate, echogenic areas or with multiple hypoechoic areas[15] (Fig. 48.14). Punctate areas are believed to represent mucus in the dilated ducts or walls of the dilated ducts. The hypoechoic areas likely represent edema and sialectasis. Increased vascularity can be demonstrated in areas of abnormal echotecture.[29] Findings may be bilateral and associated with intraglandular or adjacent lymph node involvement.

Infectious etiologies include granulomatous diseases such as **mycobacterial, actinomycosis,** and **histoplasmosis.** Primary tuberculosis of the salivary gland is rare; however, nontuberculous salivary gland infection, typically secondary to *Mycobacterium avium-intracellulare,* is more common, usually manifesting at age 16 to 36 months. It is important to remember that tuberculosis and actinomycosis can mimic neoplasm because as the disease progresses, the lesions may appear as hypoechoic masses with poorly defined margins. On color Doppler sonography, these infectious lesions, unlike neoplasms, show no color flow. Complications with actinomycosis and mycobacteria include draining sinuses and fistulas. Treatment is typically with antimicrobial therapy, although surgery may be necessary.

The most common **noninfectious** salivary gland inflammatory processes include autoimmune disease, sarcoid, and recurrent sialolithiasis (see Fig. 48.14). **Sjögren syndrome** is an autoimmune disorder that results in inflammation and destruction of the exocrine glands, primarily lacrimal and salivary tissue.[30] These patients are usually monitored with ultrasound because of increased risk for lymphoma. **Sarcoid** is an idiopathic granulomatous disease that is uncommon in children. Parotid involvement, noted in 30% of patients, may be the only initial finding. **Heerfordt disease** is the combination of parotid involvement,

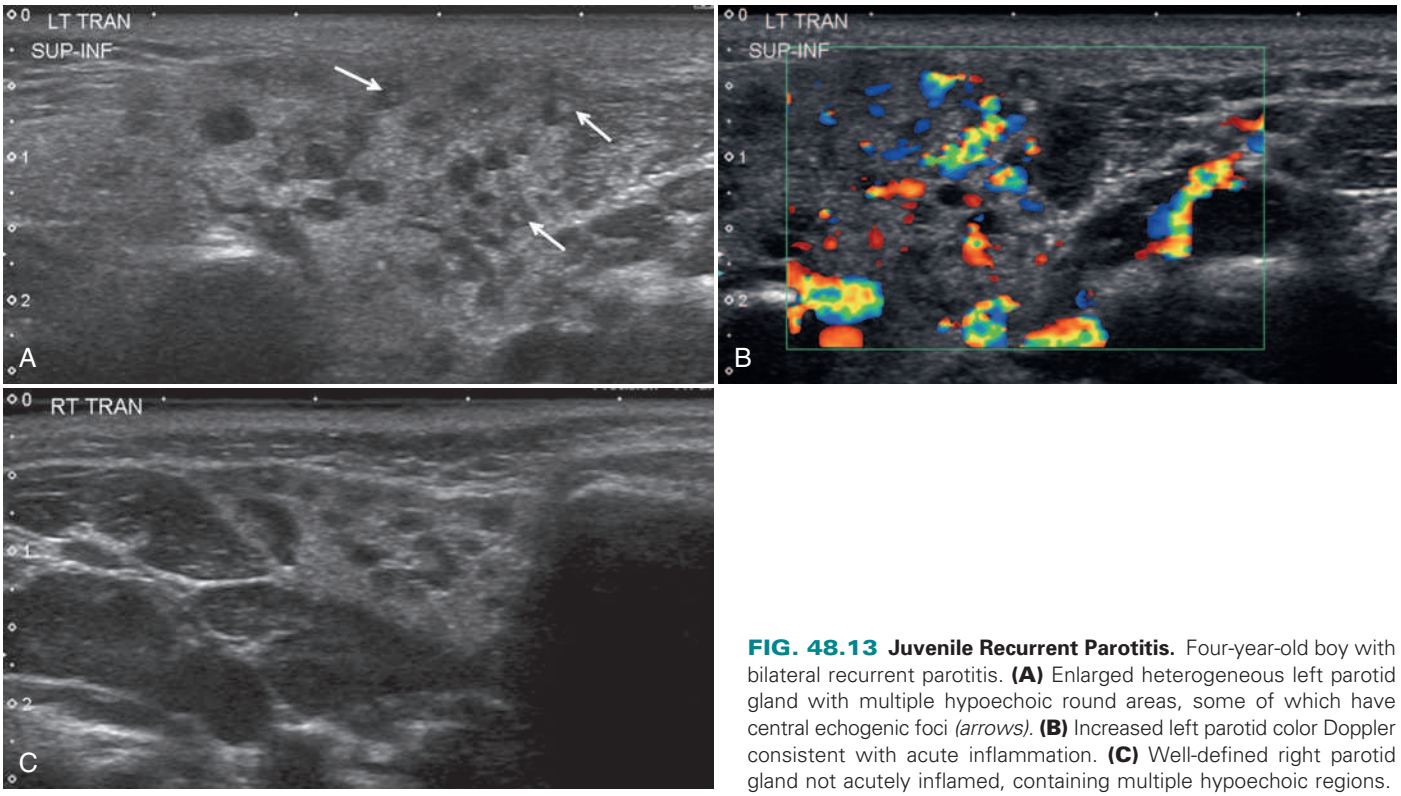

FIG. 48.13 Juvenile Recurrent Parotitis. Four-year-old boy with bilateral recurrent parotitis. **(A)** Enlarged heterogeneous left parotid gland with multiple hypoechoic round areas, some of which have central echogenic foci *(arrows).* **(B)** Increased left parotid color Doppler consistent with acute inflammation. **(C)** Well-defined right parotid gland not acutely inflamed, containing multiple hypoechoic regions.

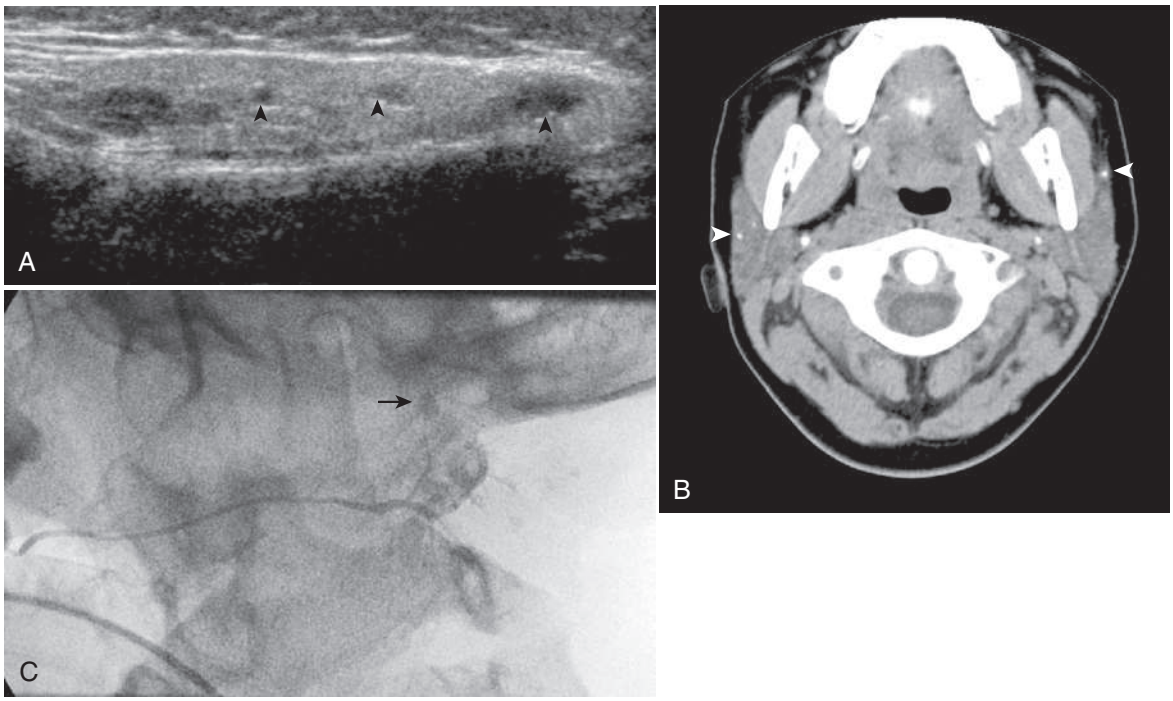

FIG. 48.14 Chronic Parotid Sialadenitis Secondary to Sialolithiasis. (A) Parotid contains round areas of decreased echogenicity typical of dilated ducts and small areas of increased echogenicity consistent with mucus and small calculi *(arrowheads).* **(B)** Computed tomography scan shows multiple calculi in the right and left parotid *(arrowheads)* and inhomogeneous density of the right parotid. **(C)** Sialogram excludes stone obstructing Stensen duct but shows pooling in peripheral dilated ducts, sialectasis *(arrow).*

uveitis, and facial paralysis.[20] Calcified hypoechoic lesions may be present. Treatment is primarily with steroids.

Salivary glands can also be involved in the spectrum of immunoglobulin G4 (IgG4)–associated disease **(IgG4-associated disease),** a systemic disease characterized by abundant infiltration of IgG4-positive plasma cells and lymphocytes with associated fibrosis resulting in multiorgan dysfunction.[31] There can be multiple sites of involvement in the head and neck. **Mikulicz disease** and chronic sclerosing sialadenitis **(Küttner tumor)** are the two manifestations of IgG4-associated disease in the salivary glands.[31] Both these conditions are more common in elderly men, but pediatric cases of Küttner tumor have been reported.[32-34] Mikulicz disease is characterized by painless swelling of the parotid, submandibular, and sublingual salivary glands, as well as the lacrimal glands. Küttner tumor is a hard masslike enlargement frequently involving the submandibular glands, either unilateral or bilateral.[31] In Mikulicz disease, sonography reveals multiple hypoechoic areas in enlarged salivary glands.[35] On sonography **Küttner tumor** often shows diffuse involvement of the salivary gland with heterogeneous echogenicity, dilated ducts, calculi, and prominent intraglandular vessels. Focal salivary gland lesions show hypoechoic heterogeneous regions with a radial branching vascular pattern demonstrated by Doppler.[36]

Kimura disease is a rare, possibly autoimmune inflammatory disorder with slow-growing painless soft tissue masses frequently in the subcutaneous tissues over the parotid, periauricular, and submandibular regions.[37,38] There can be contiguous extension of the lesions into the parotid gland.[39] These lesions are frequently described in adolescent and young adult Asian males.[37] There may be associated intraparotid, submental, and submandibular lymphadenopathy, with normal node morphology. On sonography the soft tissue masses are found to be heterogeneous hypoechoic centrally with echogenic hypervascular rim. Lymph nodes show exaggerated hilar and capsular vascularity.[37,38]

Human immunodeficiency virus (HIV) infection can affect all salivary glands, but primarily the parotid. The patient may demonstrate bilateral parotid swelling and lung disease from lymphocytic interstitial pneumonitis.[15] Infection is characterized by benign lymphoepithelial lesions, consisting of lymphoid hyperplasia accompanied by an intranodal cyst lined by epithelial cells.[40,41] Prevalence of salivary gland abnormalities in pediatric HIV can be as high as 58%, and they can be present even in the absence of a history of parotid enlargement.[42] Bilateral cystic enlargement of the parotid glands is a widely recognized cause of parotid gland swelling in patients with HIV infection but can be difficult to differentiate from recurrent parotitis, Sjögren syndrome, lymphoma, and Warthin tumor.[24,40] In 70% of patients, on sonography an enlarged gland is noted containing small, hypoechoic areas without acoustic enhancement and with thick septations consistent with lymphoid infiltration[15,43,44] (Fig. 48.15). In 30% there are large, anechoic areas consistent with lymphoepithelial cysts replacing the gland. From 40% to 70% of HIV patients have associated symmetrical cervical adenopathy and enlarged adenoids.[45]

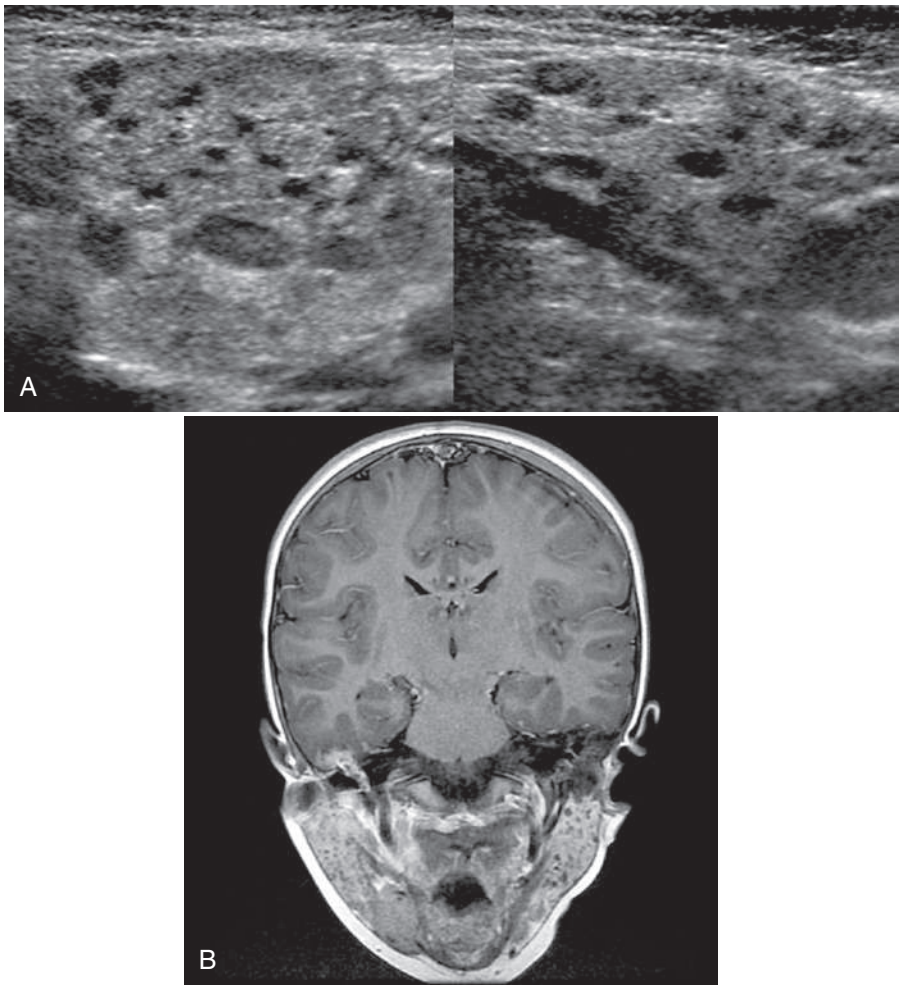

FIG. 48.15 Human Immunodeficiency Virus (HIV) Parotitis. (A) Transverse images of mildly enlarged right and left parotid glands containing small, hypoechoic areas. **(B)** Coronal postgadolinium T1-weighted magnetic resonance image demonstrates multiple lymphoepithelial cysts within enhancing parotid tissue bilaterally.

Masses

Vascular Masses. The common childhood salivary gland vascular masses include vascular neoplasms such as hemangiomas, and vascular malformations such as venous or lymphatic malformations. **Hemangiomas** represent 60% of all salivary gland neoplasms.[46,47] About 80% arise in the parotid, and 18% are present in submandibular tissue.[20] On ultrasound, the lesions are infiltrative or well circumscribed, usually hypoechoic relative to the glandular tissue, and may involve all or part of the gland (Fig. 48.16). In the proliferative phase, on color Doppler sonography there is a high vessel density, with both increased arteries and increased veins. Arterial spectral Doppler demonstrates high flow velocity and low resistive index (RI) with spectral broadening.[43,47] Because most infantile hemangiomas spontaneously regress, medical management with propranolol, laser therapy, or surgical excision is used only when symptoms warrant.[48,49] **Lymphatic malformations** may involve the parotid gland or may infiltrate the submandibular space. On ultrasound, a lymphatic malformation within the parotid gland shows cystic spaces of varying sizes, with or without solid elements, septations, and internal layering debris[11] (Fig. 48.17). **Venous malformations** can be small, involving only a portion of the salivary gland, or may be diffuse, involving multiple spaces of the neck. These lesions contain multiple cystic areas, ectatic venous channels, and often phleboliths, which aid in sonographic diagnosis.

Neoplasms. Tumors of the salivary glands account for only 1% of all pediatric tumors.[50] About 8% of primary tumors of the head and neck in children originate within the salivary glands[15]; 90% to 95% occur in the parotid and the rest in the submandibular and sublingual glands.[11] Most masses of the salivary gland are benign and have a vascular etiology, with only 13% reported to be solid salivary gland tumors.[20,50,51] Pediatric epithelial salivary masses tend to occur in children older than 10 years, with 23% to 50% of them reported to be malignant.[18,20,50] Most malignant tumors in children are of lower grade compared with adults, although children younger than 10 years tend to have higher grade tumors.[20]

In children, sonography is the first step, especially for palpable lesions because the majority of space-occupying lesions in the salivary glands are well delineated.[23] There are no specific sonographic findings differentiating malignant from benign salivary

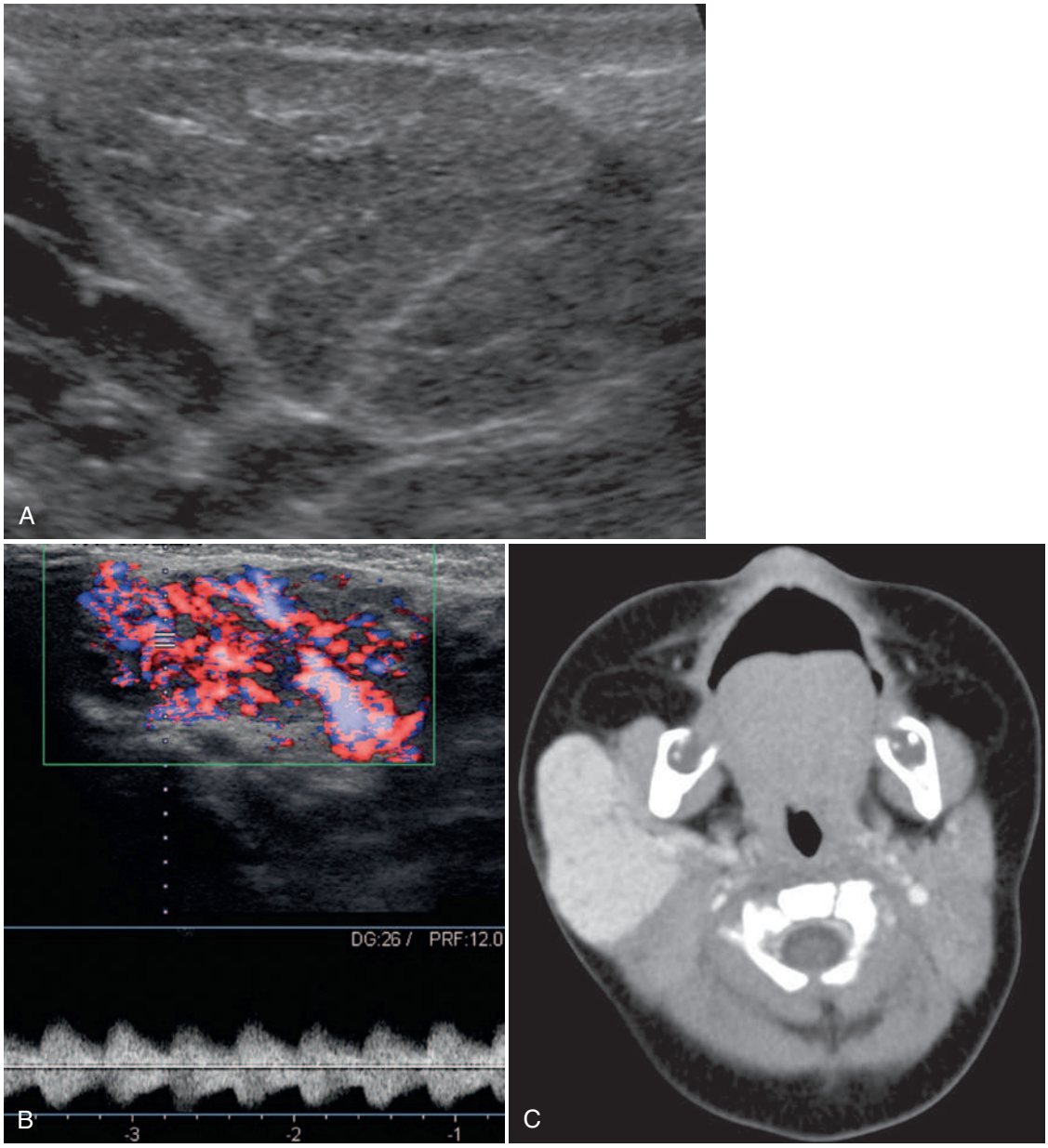

FIG. 48.16 Parotid Hemangioma. (A) Enlarged hypoechoic parotid gland with a few internal linear striations. **(B)** Color Doppler sonogram shows high vessel density with low–arterial resistance spectral waveform. **(C)** Computed tomography scan demonstrates intense enhancement of the right parotid mass.

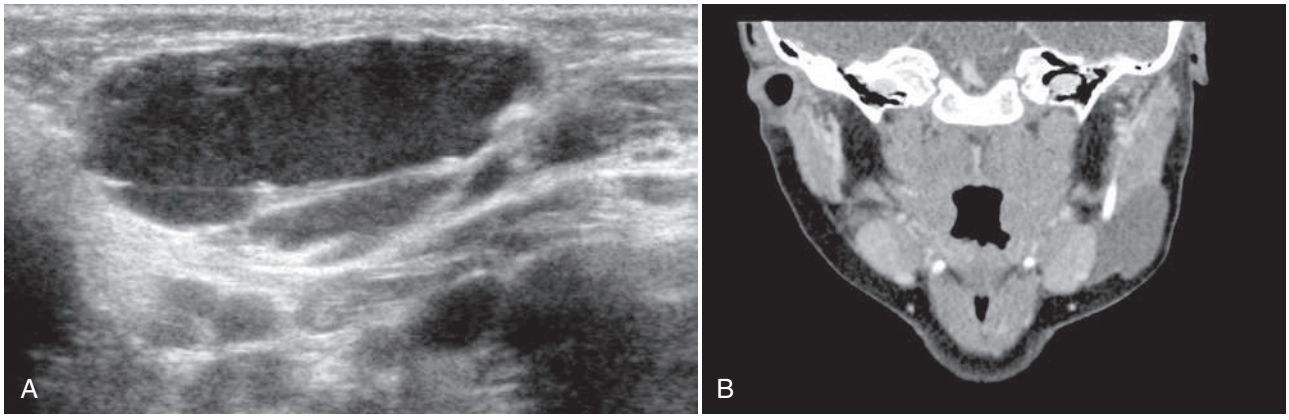

FIG. 48.17 Parotid Lymphatic Malformation. (A) Cystic septated mass within the superficial parotid. **(B)** Coronal computed tomography scan shows the cystic lesion lateral to and inseparable from the normally enhancing left parotid.

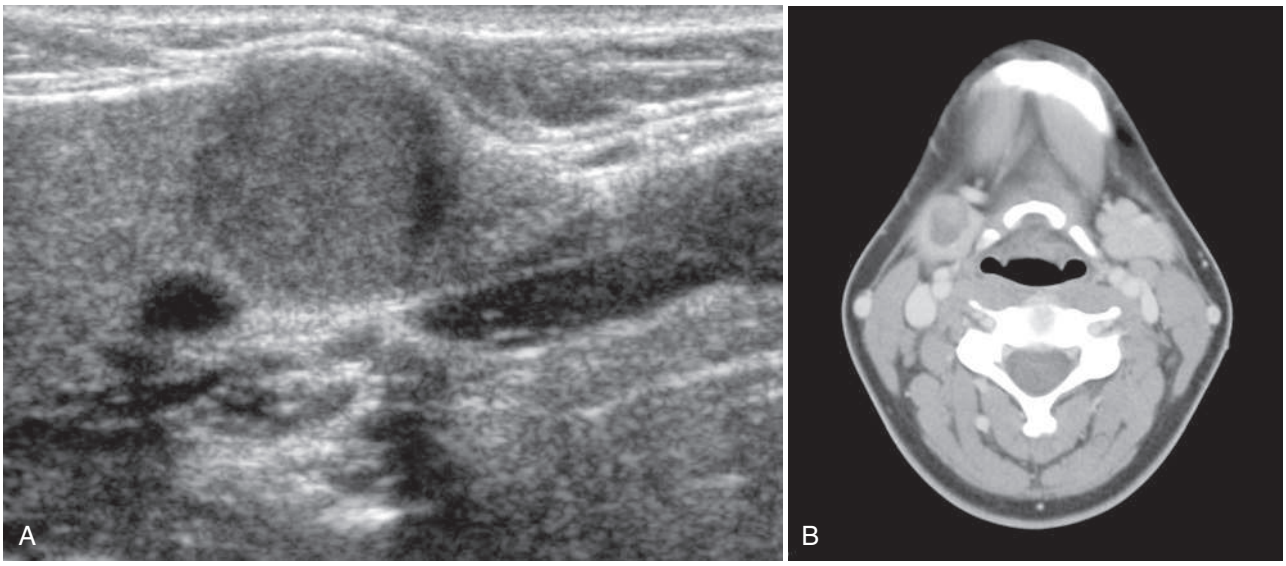

FIG. 48.18 Submandibular Pleomorphic Adenoma. (A) Submandibular gland containing a well-defined hypoechoic mass. **(B)** Computed tomography scan shows a well-defined low-density lesion centered within the right submandibular gland.

gland neoplasms, although ill-defined tumor margins and adjacent lymphadenopathy are suspicious features.[52,53] For further definition of a lesion, MRI is the method of choice because it provides precise information with regard to the nature of the mass as well as its extent, especially the presence of perineural invasion.[15,24]

Pleomorphic adenomas, also referred to as **benign mixed-cell tumors,** contain both mesenchymal and epithelial cell lines. These neoplasms are the most common benign salivary gland tumor in childhood and occur in all pediatric age groups (median, 15 years).[18,23] Most occur as a solitary, hard, painless, slow-growing mass.[54] Approximately 60% to 90% of these lesions originate in the parotid gland and 10% to 30% in the submandibular gland.[12,15] These lesions can recur (1%-50%) as multiple masses or rarely can develop late metastatic deposits.[54] On sonography, the lesion appears lobulated, well defined, and hypoechoic or isoechoic (with respect to normal salivary tissue) (Fig. 48.18). Cystic areas and hyperechoic shadowing foci representing small calcifications may be noted.[11] Typically, pleomorphic adenomas demonstrate peripheral vascularity with a hypovascular center.[13,24,29] Treatment includes surgical resection with facial nerve sparing procedures if in the parotid gland.

Warthin tumor, also referred to as papillary cystadenoma lymphomatosum or **adenolymphoma,** is a rare benign salivary gland neoplasm of children and solely identified in the parotid gland.[55,56] The lesion contains a double layer of epithelial cells resting on a dense lymphoid stroma and is believed to result from incorporation of lymphatic elements and heterotopic ductal epithelium within the parotid lymph nodes. Ultrasound findings include an oval, hypoechoic, well-defined mass containing multiple microcystic or anechoic areas, given the high propensity for cystic change.[12,13,55] With color and Doppler sonography, the tumor typically is hypervascular. Technetium 99m scintigraphy shows intense uptake in the tumor but is almost never performed in children.[11,12] Treatment is surgical resection; however, recurrence is possible from multifocality.

Mucoepidermoid carcinoma, the most common malignant salivary gland neoplasm in children, consists of cords, sheets, or cystic spaces lined by squamous and mucous cells.[11,15] Of the malignant salivary gland lesions, 60% are diagnosed as mucoepidermoid carcinomas, and about 50% arise from the parotid.[15] Clinically, these lesions may be tender, may grow rapidly, and may cause facial nerve paralysis.[12] Most (76%) mucoepidermoid carcinomas in children are of low grade.[57] Ultrasound characteristics depend on histologic grade. However, increased intratumoral RI and high peak systolic flow velocity (>60 cm/sec) should increase suspicion for malignancy.[29] Sonography should also be performed in the area of the lesion to assess for metastatic-appearing lymph nodes.[58]

Acinic cell carcinoma accounts for approximately 10% of malignant salivary gland tumors, most commonly arising from the parotid gland and less frequently from the submandibular or minor salivary glands.[57] On ultrasound, these lesions are usually irregular in shape with discrete margins, heterogeneous, hypoechoic, and poorly vascularized[59] (Fig. 48.19). Lesions may also demonstrate a mixed cystic and solid appearance and have posterior acoustic enhancement. Importantly, these lesions may be difficult to differentiate from other benign masses.[59] Treatment is usually wide surgical resection with radiotherapy reserved for extraglandular extension, lymph node metastases, or local recurrences.[57] This tumor has the best prognosis of all malignant salivary gland neoplasms.[60]

Adenoid cystic carcinoma accounts for approximately 9% of malignant salivary gland tumors in children, almost always in the parotid gland.[57] These are slow-growing tumors but have increased association with perineural invasion. No specific sonographic characteristics are described. Pain and numbness are present in 40% of children with adenoid cystic carcinoma and strongly correlate with perineural invasion.

Sialoblastoma is a rare neonatal neoplasm of the salivary gland, with less than 50 cases described in the literature.[61,62] This

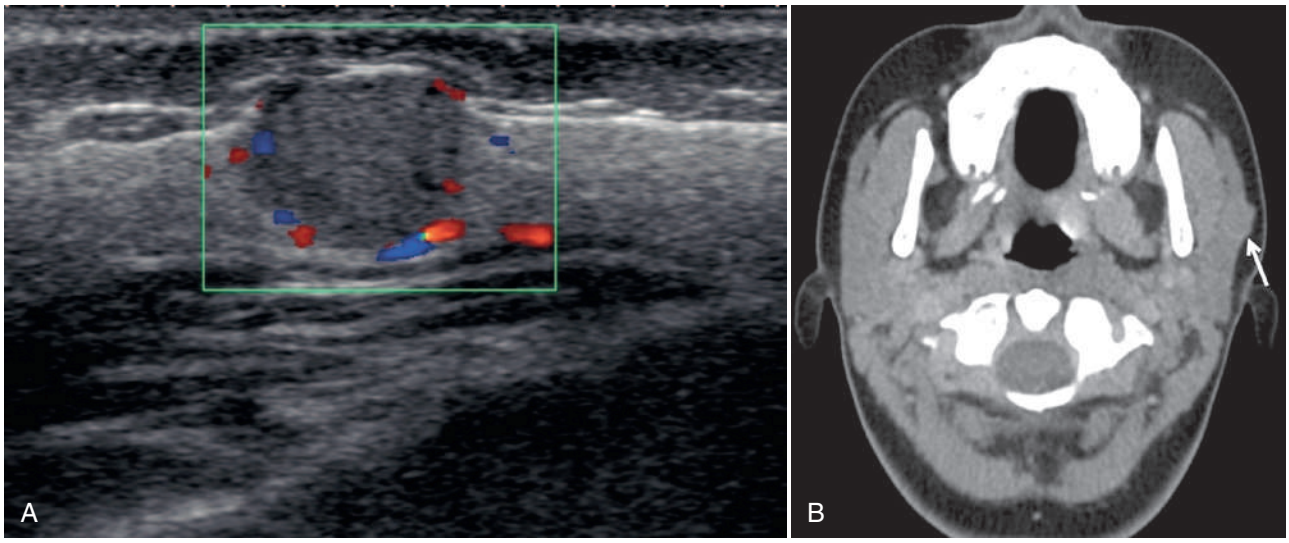

FIG. 48.19 Parotid Acinic Cell Carcinoma. (A) Color Doppler shows a round hypoechoic mass arising from the left parotid gland. The mass is hypovascular, but there is peripheral increased vascularity on color Doppler. **(B)** The mass in the left parotid gland is moderately enhancing and difficult to separate from the parotid gland *(arrow)*.

lesion consists of basaloid and myoepithelial cells that are reminiscent of the developing salivary anlage.[61] The lesion is most frequent in the parotid gland and less common in the submandibular gland. This lesion often manifests as a large parotid mass identified in early infancy or childhood, although prenatal and some adult cases have also been described. Sialoblastoma is a focally aggressive tumor, with local recurrences and infrequent distant metastases.[62] Sonographic characteristics are not well described. However, descriptions include that of a multinodular well-defined predominantly hypoechoic salivary gland mass with multiple septations and without increased vascularity.[63,64] On MRI, heterogeneous appearance is often described, with areas of hemorrhage or necrosis.[61,65,66] There are few case reports of combined sialoblastoma and hepatoblastoma.[63,67,68]

Other Salivary Gland Lesions. Lingual thyroid may appear as a homogeneous solid mass in the midline dorsum of the tongue. In 70% of patients, this ectopic tissue is the only functioning thyroid tissue.

Rhabdomyosarcoma occurs 40% of the time in the head and neck and can arise from any muscle. This is the second most common malignancy in the parotid and submandibular spaces in the pediatric population.[50] Salivary gland involvement is frequently by direct extension.[69]

Primary lymphoma of the salivary glands is termed MALToma, denoting origin from mucosa-associated lymphoid tissue. Patients with Sjögren syndrome and other autoimmune disease, including HIV, are at risk for primary lymphoma. Secondary involvement of lymphoma is rare, but more common in the parotid.[70] Ultrasound demonstrates a focal mass or diffuse infiltration with an enlarged gland. Lesions may consist of multiple small, hypoechoic nodules or an irregularly shaped, heterogeneous mass without calcification or cystic degeneration.[70] A reported case of submandibular gland involvement by MALToma showed hypoechoic compartments surrounded by hyperechoic lines, creating a tortoiseshell appearance.[71] Increased color Doppler flow is typical.

Lipomas represent 1% of parotid tumors; 57% of lipomas in the parotid area arise within the gland. These lesions are compressible, oval, and well defined. On ultrasound, lipomas contain striped or feathered internal echoes devoid of color and Doppler flow.[23] In younger children, lipoblastomas are more common.[72]

Leukemic infiltration is rare, with a presentation similar to lymphoma on ultrasound.[73]

Metastatic disease is rare in children but would include neuroblastoma and thyroid cancer.[43,74]

Peripheral nerve sheath tumors including neurofibroma and schwannoma can occur in the parotid gland, often in relation to the facial nerve.[75,76] Multiple or plexiform neurofibromas are typical in patients with neurofibromatosis type 1.[69] Sonography demonstrates multiple hypoechoic areas within the gland.[77]

Suprahyoid Cystic Lesions

In the parotid space, **type I branchial cysts** are most common. Simple cysts of the salivary glands are rare and likely caused by **mucous retention.** On ultrasound, the lesions are well defined and anechoic, with posterior acoustic enhancement and no internal blood flow.[12,74] In the preauricular region, superficial to the parotid gland, dermoid and epidermoid cysts may also occur.

In the submandibular space laterally, **type II branchial cysts** can be identified posterior to the submandibular gland. **Lymphatic malformations** may also extend into the space. **Ranulae** (sublingual cysts) are mucous retention cysts resulting from obstruction of the sublingual gland or duct. They present paramidline, in the area of the sublingual gland, as a painless swelling along the floor of the mouth. When large, sublingual cysts can extend

Differential Diagnosis of Suprahyoid Cystic Lesions

PAROTID SPACE
Branchial apparatus cyst type I
Parotid mucus retention cyst
Tumors with cystic components
Parotid abscess
Lymph node necrosis
Lymphatic malformation

SUBMANDIBULAR SPACE
Branchial apparatus cyst type II
Ranulae
Dermoid or epidermoid
Thyroglossal duct cyst
Vallecular cyst
Lymph node necrosis
Lymphatic malformation

below the level of the mylohyoid muscle, termed "plunging ranulae."[20] Rarely, the lesions are bilateral, and some large lesions extend into the parapharyngeal space. Imaging of a simple ranula on ultrasound demonstrates a unilocular cyst. If infected, the lesion may show internal debris, poorly defined borders, and adjacent inflammation (Fig. 48.20). These lesions are managed with intraoral marsupialization or surgical resection.

Midline lesions in the suprahyoid area include **dermoid** or **epidermoid** tumors and **thyroglossal duct cysts.** A **cyst of the vallecula** results from retained secretions in the mucous glands of the pharyngeal wall.[78] These cysts can be congenital or acquired and can cause upper airway obstruction resulting in death.[79,80] The lesions are midline and on sonography appear as a hypoechoic or an anechoic cystic mass, behind and below the tongue[81] (Fig. 48.21).

Masticator Space

Ultrasound is helpful in evaluating pathology in the masticator space as well as excluding parotid gland involvement. The two most common soft tissue masses to consider in the masticator space are **sarcomas** and **vascular malformations.** It is important to remember that the masseter and pterygoid muscles are often involved in venous malformations.[82] An uncommon homogeneous mass to consider is benign hypertrophy of the masseter muscle.[74] However, tumor infiltration of the muscle from leukemia or lymphoma can mimic hypertrophy; thus, clinical correlation is essential (Fig. 48.22). In the presence of trauma, a hematoma appearing as a hypoechoic area may be demonstrated. Inflammatory lesions also may develop, including secondary or primary myositis or osteomyelitis of the mandible, often in the presence of an infected tooth. Cellulitis and soft tissue abscesses may accompany these infections.[15]

INFRAHYOID SPACE

The infrahyoid deep cervical fascia is split into superficial, middle, and deep compartments[7] (Fig. 48.23). The superficial layer at this level is the **suprasternal space,** lying above the sternum and anterior to the sternothyroid and sternohyoid muscles. The **visceral space** is delineated by the middle layer of deep cervical fascia. The visceral space contains the thyroid, parathyroid, trachea, esophagus, paraesophageal lymph nodes, and recurrent laryngeal nerve.

Thyroid Gland

Normal Anatomy

The thyroid gland originates as an outpouching in the foramen cecum at the base of the tongue. The tissue descends by the seventh week of gestation to lie anterior to the larynx and upper

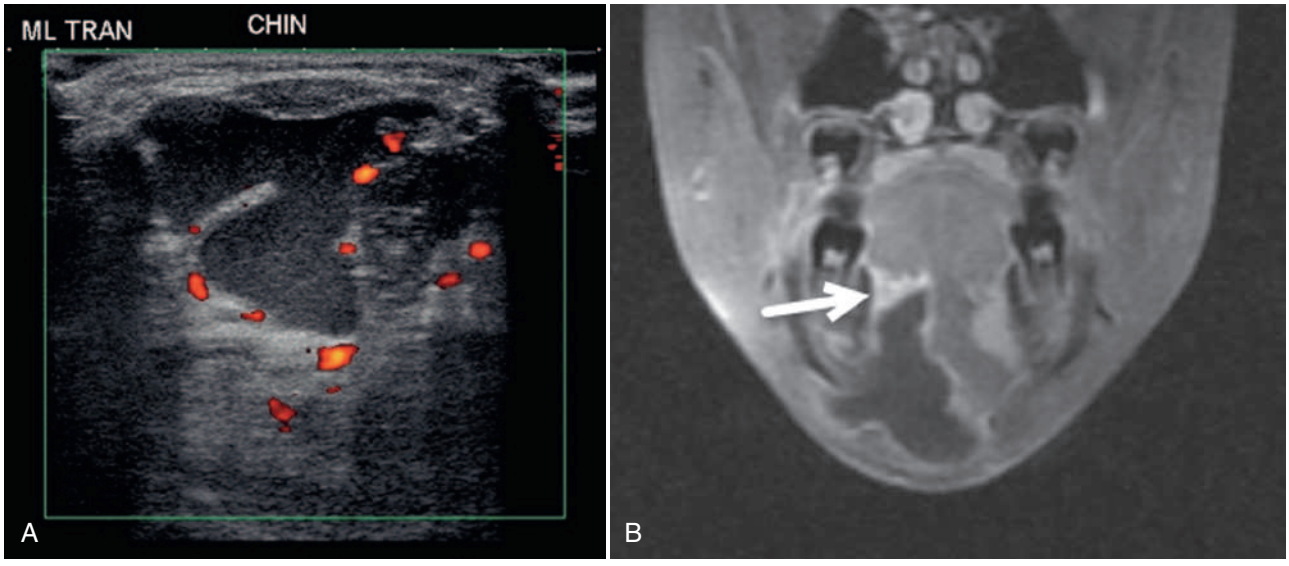

FIG. 48.20 Ranula. Ten-year-old child with neck pain. **(A)** Well-defined lobular hypoechoic lesion containing debris but with acoustic enhancement and lack of internal flow centered between the right sublingual gland and floor of the mouth. **(B)** Coronal fat-saturated T1-weighted magnetic resonance image after contrast showing the wall-enhancing cyst in continuity with the sublingual gland *(arrow),* plunging below the tongue.

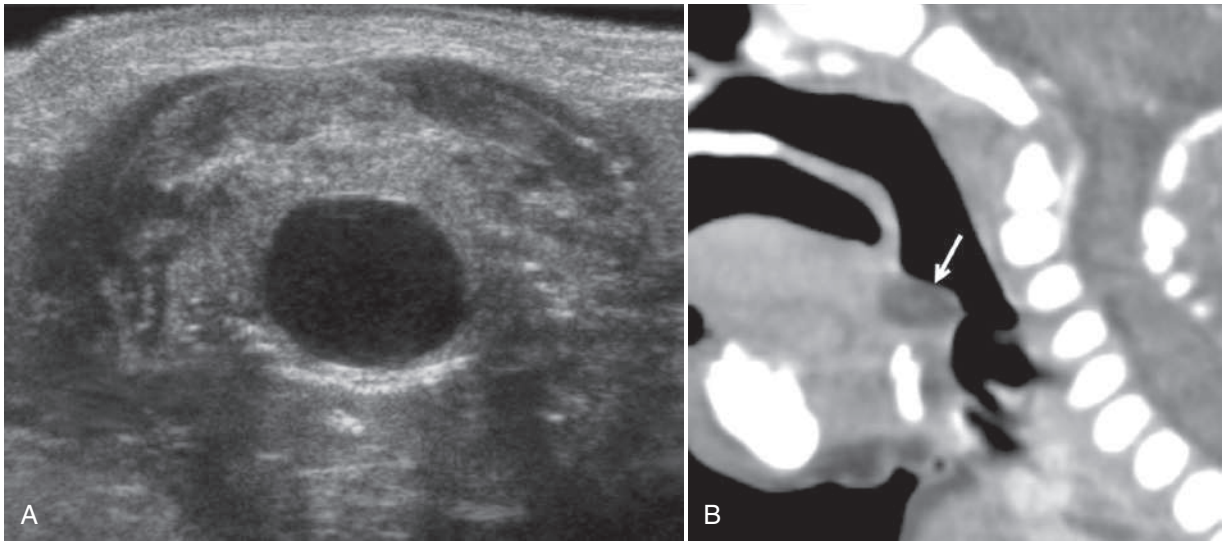

FIG. 48.21 Cyst of Vallecula. (A) Gray-scale ultrasound through the base of the tongue demonstrates a unilocular cyst with good through transmission. **(B)** Sagittal computed tomography image shows a simple cyst *(arrow)* along the base of the tongue at the level of the vallecula.

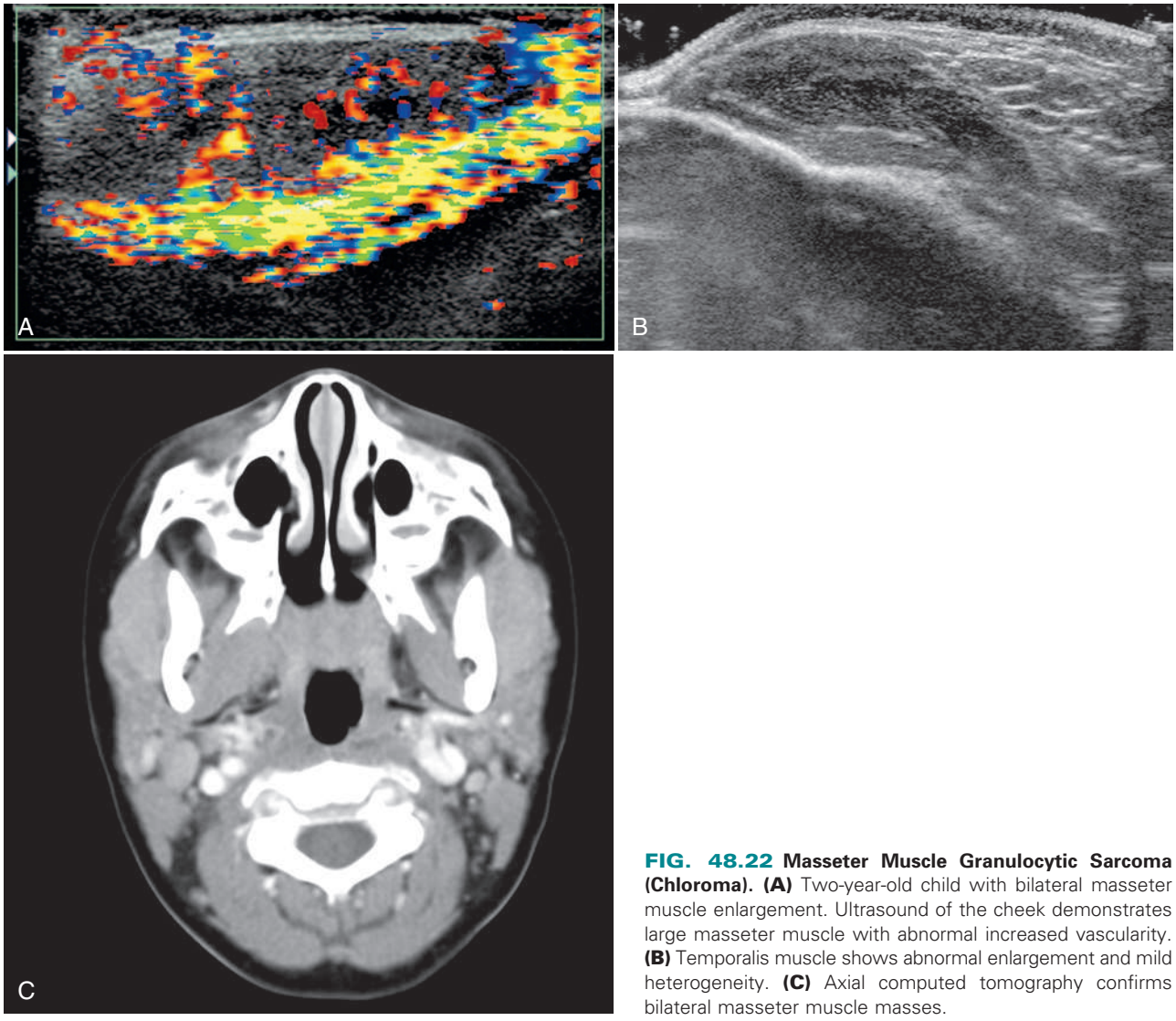

FIG. 48.22 Masseter Muscle Granulocytic Sarcoma (Chloroma). (A) Two-year-old child with bilateral masseter muscle enlargement. Ultrasound of the cheek demonstrates large masseter muscle with abnormal increased vascularity. **(B)** Temporalis muscle shows abnormal enlargement and mild heterogeneity. **(C)** Axial computed tomography confirms bilateral masseter muscle masses.

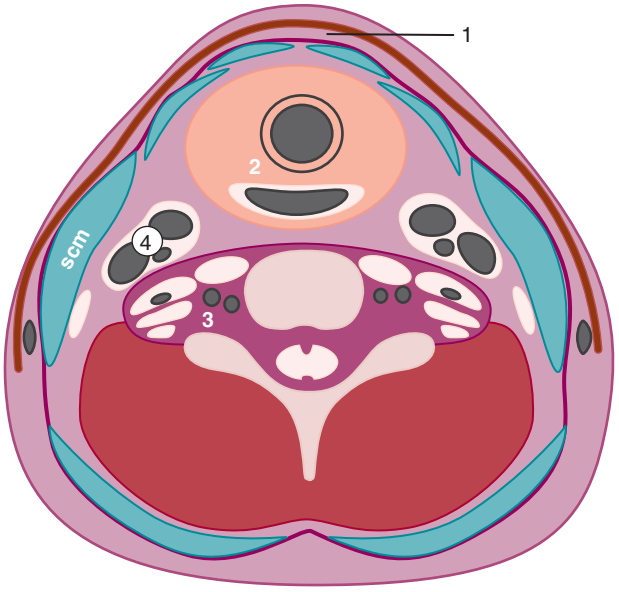

FIG. 48.23 Deep Cervical Fascial Layers of Infrahyoid Space. Axial diagram: *1,* superficial; *2,* middle (visceral); *3,* deep; *4,* carotid; *scm,* sternocleidomastoid muscle.

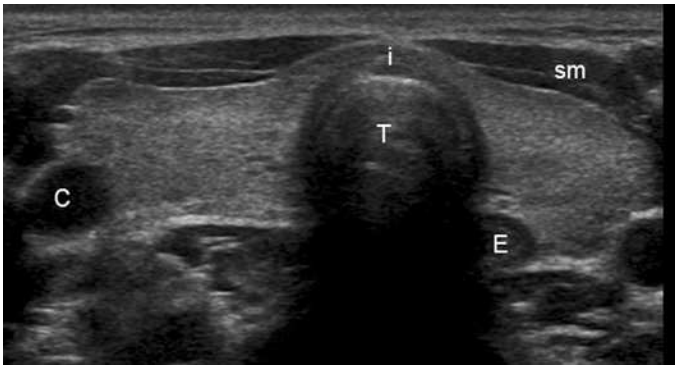

FIG. 48.24 Normal Thyroid. Transverse sonogram of the thyroid gland demonstrates homogeneous, increased echotexture compared with the sternohyoid and sternothyroid *(sm)* muscles. Normal right lobe, left lobe, and isthmus *(i).* Trachea *(T)* is midline and esophagus *(E)* is posterior to left lobe. Common carotid artery *(C)* is present along the peripheral margin.

trachea.[83] The common carotid arteries and internal jugular veins are present on the lateral edges, and the cervical esophagus is midline or to the left of the trachea. The thyroid gland contains two lobes and is connected by an **isthmus.** In 50% of patients, a **pyramidal lobe** extends superiorly from the isthmus. Four parathyroid glands lie along the posterior surface of the thyroid lobes.

Ultrasound is performed with the patient supine and the neck slightly hyperextended. A high-frequency linear array transducer (10-15 MHz) is necessary.[84] A standoff pad may be helpful. Longitudinal and transverse imaging of the entire thyroid tissue should be performed. Doppler imaging may be considered in the examination of masses or nodules. Adjacent neck structures, especially the jugular chain and supraclavicular nodes, should be imaged.

On ultrasound, the normal thyroid gland is homogeneous and hyperechoic compared with adjacent muscle (Fig. 48.24). The lobes of tissue are triangular on transverse and elliptical on sagittal images. The size of the thyroid gland changes with age; Tables 48.1 and 48.2 list normal values.[85,86]

Congenital Thyroid Lesions

Although some congenital thyroid lesions extend into both the suprahyoid and the infrahyoid space, the pathology is described here as it is inherent to the thyroid.

Because untreated hypothyroidism can result in severe mental retardation and delayed bone development, there is a nationwide program in the United States for neonatal screening. **Congenital hypothyroidism** is present in 1 per 4000 infants and is twice as common in girls as in boys.[87,88] Causes include agenesis, dysgenesis, and goiter from inborn error of metabolism, maternal thyrotoxicosis, or maternal ingestion of iodine, antithyroid medication, or lithium.[29,87] About 85% of cases are caused by **dysgenesis** (structural defects of the thyroid gland), either hypoplasia or ectopia.[88] Sonography is the best imaging modality in congenital hypothyroidism because it correctly defines presence of the thyroid gland, which may be classified as large, normal, small, or absent.[89] Large glands are typically goitrous. Normal-sized glands in children with congenital hypothyroidism have been observed in patients with pseudohypoparathyroidism, trisomy 21, hypopituitarism, maternal antibody–induced

TABLE 48.1 Normal Dimensions of the Thyroid Gland[a]

	No. of Subjects (Male-to-Female Ratio)	Thickness (cm)[b]	Width (cm)[b]
CORRECTED GESTATIONAL WEEKS			
30-33	5 (4:1)	0.8 ± 0.1	1.1 ± 0.3
33-37	19 (13:6)	1.1 ± 0.3[c]	1.4 ± 0.3[d]
HEIGHT (cm)			
45-50	42 (20:22)	1.4 ± 0.2[c]	1.7 ± 0.2[c]
50-70	42 (27:15)	1.4 ± 0.1	1.8 ± 0.2
70-90	8 (6:2)	1.4 ± 0.1	1.9 ± 0.1
90-100	8 (3:5)	1.4 ± 0.1	1.8 ± 0.2
100-110	34 (12:22)	1.5 ± 0.3	2.1 ± 0.3
110-120	35 (20:15)	1.7 ± 0.3	2.3 ± 0.3
120-130	45 (23:22)	1.8 ± 0.4	2.4 ± 0.3
130-140	36 (21:15)	1.9 ± 0.5	2.7 ± 0.2
140-150	42 (20:22)	2.1 ± 0.4	2.8 ± 0.3
150-160	59 (25:34)	2.2 ± 0.4	2.8 ± 0.4
160-170	16 (14:2)	2.4 ± 0.4	3.0 ± 0.4

[a]As a function of corrected gestational weeks in premature neonates and as a function of height from neonates to adolescence.
[b]Mean ±1 standard deviation.
[c]Compared with 30-33 weeks: $p < .01$.
[d]Compared with 30-33 weeks: $p < .05$.
With permission from Ueda D, Mitamura R, Suzuki N, Yano K, Okuno A. Sonographic imaging of the thyroid gland in congenital hypothyroidism. Pediatr Radiol. 1992;22(2):102-105.[86]

TABLE 48.2 Volume of Thyroid Gland and Thickness of Each Lobe[a]

Height (cm)	No. of Subjects	Volume (cm)	RLT (cm)[b]	LLT (cm)[b]
≤99	16	2.3 ± 0.7	0.8 ± 0.17	0.8 ± 0.18
100-109	34	3.3 ± 1.0	0.8 ± 0.19	0.8 ± 0.21
110-119	35	4.1 ± 1.1	0.9 ± 0.17	0.9 ± 0.19
120-129	45	4.9 ± 1.1	0.9 ± 0.18	0.9 ± 0.20
130-139	36	6.3 ± 2.0	0.9 ± 0.25	1.0 ± 0.25
140-149	42	7.4 ± 2.2	1.0 ± 0.23	1.0 ± 0.23
150-159	59	8.5 ± 2.3	1.1 ± 0.23	1.0 ± 0.24
≥160	20	10.9 ± 2.5	1.2 ± 0.24	1.2 ± 0.25

[a]As a function of body height.
[b]Mean ±1 standard deviation.
LLT, Left lobe thickness; *RLT,* right lobe thickness.
With permission from Ueda D. Normal volume of the thyroid gland in children. J Clin Ultrasound. 1990;18(6):455-462.[85]

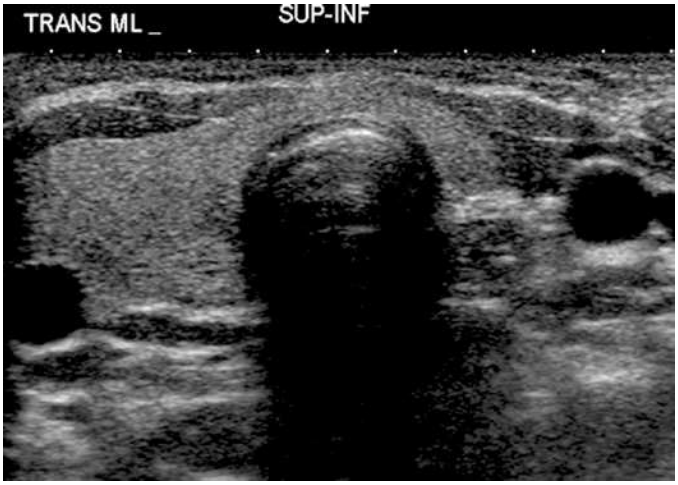

FIG. 48.25 Thyroid Hemiagenesis. Normal right lobe and isthmus of the thyroid are identified, but the left lobe is absent. Note that the left carotid vessel lies in the anatomic area of the left lobe.

hypothyroidism, and transient elevated thyrotropin.[88,89] Rarely (0.2% of cases), **thyroid hemiagenesis** can occur, with failure of development in either lobe, the left being absent in 60% of cases[88,90] (Fig. 48.25). On ultrasound, if no thyroid gland can be identified in the expected location, imaging should be performed superiorly in the midline to the base of the tongue because ectopic thyroid tissue may be present anywhere along the embryologic descent. **Ectopic thyroid tissue** is lingual and thus suprahyoid in 90% of cases, lying close to the hyoid bone and deep to the muscles of the tongue.[90] Ultrasound imaging in the neonate with ectopic thyroid typically shows a well-defined ovoid structure equal in echotexture to normal thyroid tissue and hyperemic on color Doppler (Fig. 48.26). In older children treated for hypothyroidism in the presence of ectopic tissue, the gland may appear hypoechoic with no vascularity.[91] Some children with ectopic tissue are euthyroid and have a mass at the base of the tongue. It is important to identify this tissue as thyroid because removal in the absence of other thyroid tissue will result in a hypothyroid individual. When ultrasound is unable to identify ectopic thyroid tissue, a nuclear medicine scan, given the high sensitivity, may be employed.[91,92] Scintigraphic studies are also useful in assessing thyroid function when apparently normal thyroid tissue is identified on ultrasound.[89]

Thyroglossal duct cyst, representing 70% of all congenital neck masses, is the most common midline cyst and developmental anomaly identified on ultrasound.[43,90,93] The anatomy of the thyroglossal duct follows the pathway of embryology from the foramen cecum of the tongue, along the inferior and posterior surface of the midline hyoid, to the pyramidal lobe of the thyroid. Persistence of the duct, which is lined by secretory epithelium, results in cyst or sinus formation. The classic presentation of a thyroglossal duct cyst is that of an asymptomatic mass adjacent to the hyoid bone, although the cyst can be located at any point of descent.[49,94] Anatomically, most are located in a midline or parasagittal position, particularly to the left of midline. The thyroglossal duct cyst may move with swallowing, and if suprahyoid, the lesion will classically elevate with tongue movement.[43] Congenital fistulas in association with these cysts are infrequent but can occur after inflammation.[95]

The classic sonographic appearance of a thyroglossal duct cyst is noted in less than half of cases and includes a thin-walled, anechoic unilocular cyst (Fig. 48.27). Typically, however, these cysts are caused by high protein content rather than inflammation so they are hypoechoic or heterogeneous, some appearing pseudosolid and mimicking ectopic tissue[95-97] (Fig. 48.28). Posterior acoustic enhancement is present in most cysts, and absence of color Doppler flow can be helpful in the diagnosis. However, demonstration of a normal thyroid gland while imaging a thyroglossal duct cyst is recommended to exclude the diagnosis of ectopic tissue. Up to one-third of patients with these cysts will develop superimposed infection and demonstrate imaging findings of thick walls, internal septation, and heterogeneous echotexture from debris.[95,98] There is a slightly increased risk of cancer, primarily papillary, and calcification or a soft tissue mass in the presence of a cyst should raise suspicion of malignancy.[82,93,99] Therapy is surgical resection with the Sistrunk procedure, which involves excision of the cyst, the remnant tract, and part of the hyoid bone. Recurrent thyroglossal duct cysts occur after a Sistrunk procedure in approximately 11% of patients.[100]

Differential diagnosis for cystic lesions in the infrahyoid space includes thyroglossal duct cyst, dermoid, epidermoid, branchial cyst, lymphatic malformation, laryngocele, necrotic adenopathy, teratoma, and thymic cyst.

Inflammatory Thyroid Disease

Acute bacterial infection of the thyroid is rare because the gland is highly resistant to infection by virtue of its high iodine content.[101,102] If present, infection is usually caused by staphylococci, streptococci, or anaerobic bacteria. On sonography, the gland demonstrates heterogeneous, poorly defined echotexture. If the left lobe of the thyroid is abnormal, a congenital piriform sinus, type III or IV branchial apparatus remnant, should be

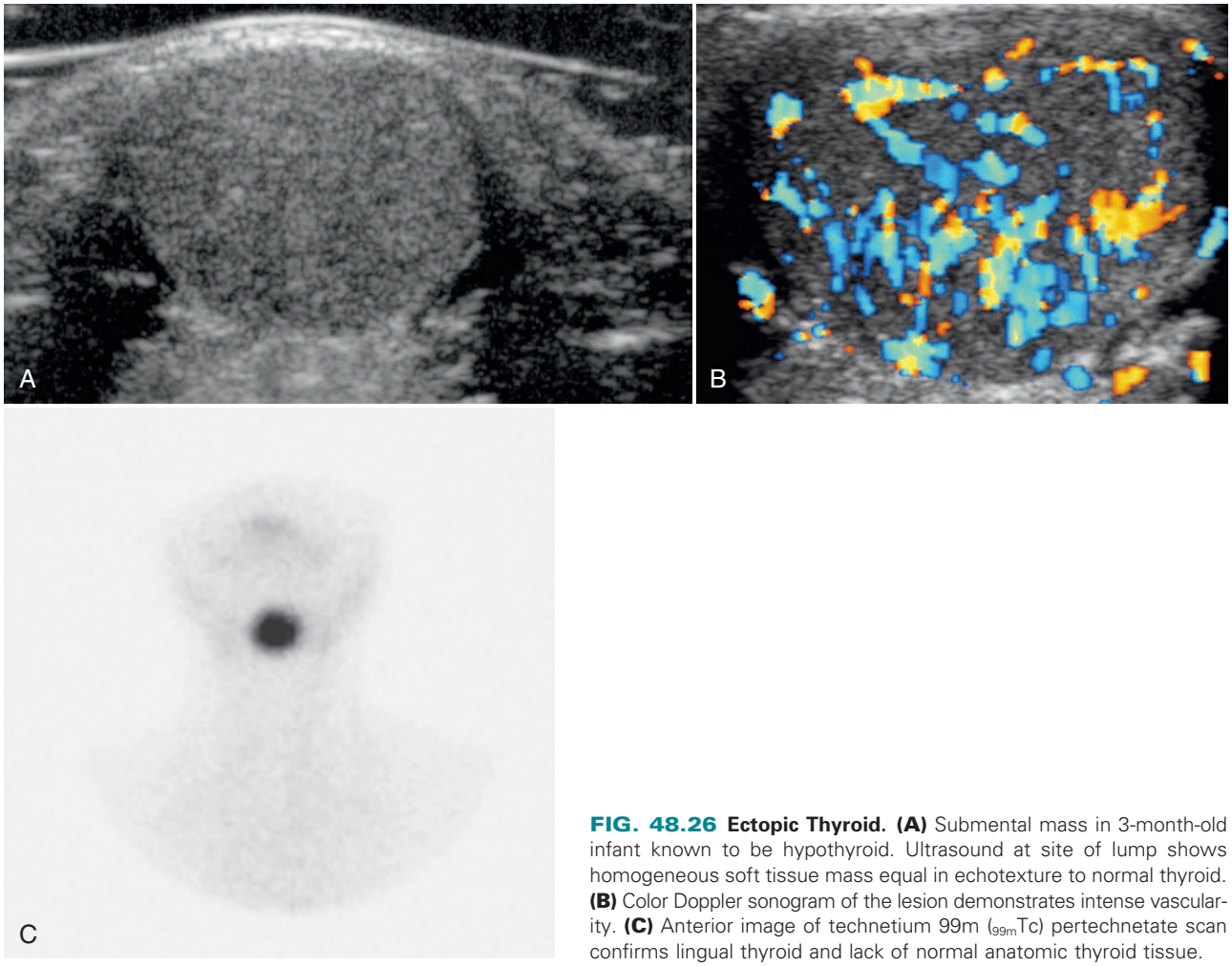

FIG. 48.26 Ectopic Thyroid. (A) Submental mass in 3-month-old infant known to be hypothyroid. Ultrasound at site of lump shows homogeneous soft tissue mass equal in echotexture to normal thyroid. **(B)** Color Doppler sonogram of the lesion demonstrates intense vascularity. **(C)** Anterior image of technetium 99m ($_{99m}$Tc) pertechnetate scan confirms lingual thyroid and lack of normal anatomic thyroid tissue.

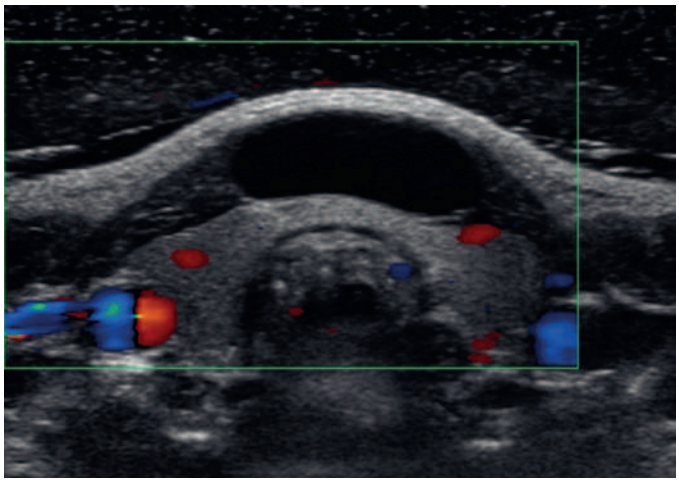

FIG. 48.27 Thyroglossal Duct Cyst. Color Doppler shows a large anechoic midline cyst immediately anterior to the thyroid gland and partly encased by the strap muscles.

Differential Diagnosis for Infrahyoid Cystic Lesions

MIDLINE
Thyroglossal duct cyst
Dermoid or epidermoid

LATERAL
Branchial cyst
Lymphatic malformation (may be midline)
Laryngocele
Thyroglossal duct cyst
Necrotic lymphadenopathy
Teratoma
Thymic cyst

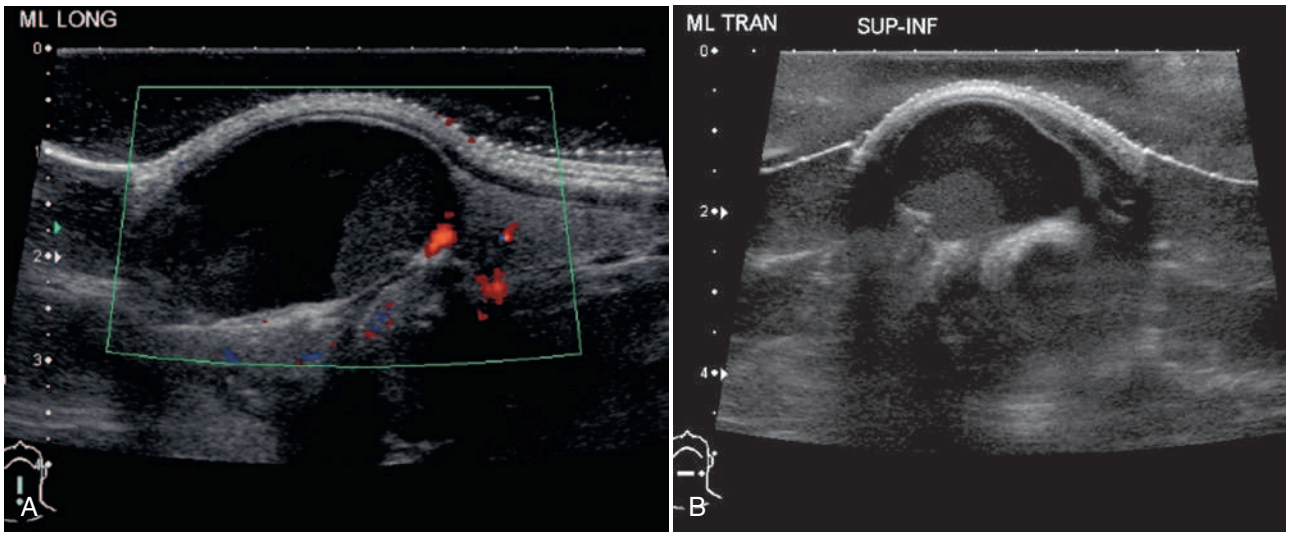

FIG. 48.28 Complex Thyroglossal Duct Cyst. (A) Sagittal color Doppler image of a complex cystic avascular lesion anterior to the trachea and superior to the isthmus of the thyroid. The lesion is hypoechoic with debris inferiorly. **(B)** Gray-scale axial ultrasound demonstrates heterogeneous mass with both hypoechoic and isoechoic components.

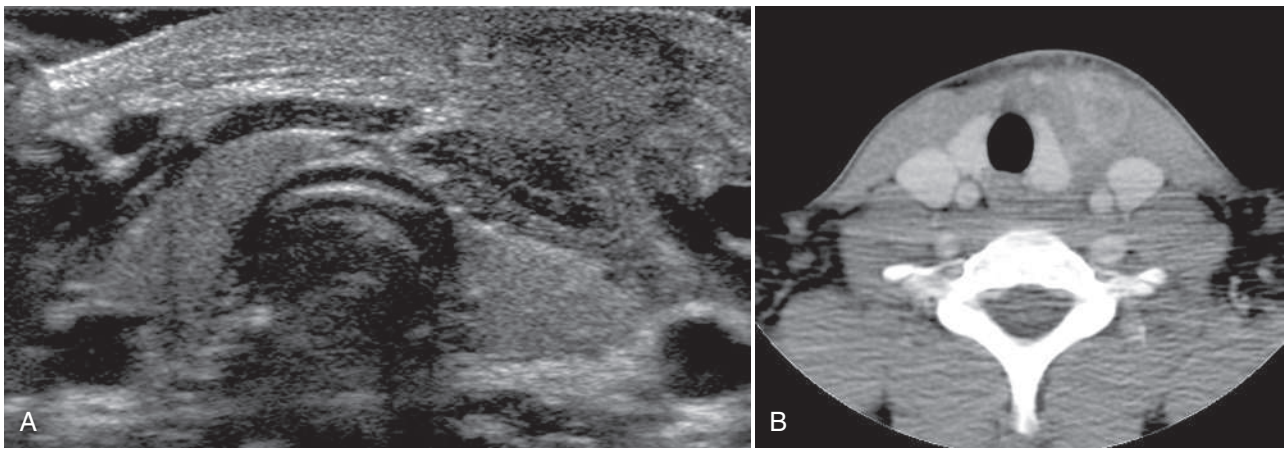

FIG. 48.29 Type IV Branchial Sinus Abscess. (A) Hypoechoic, poorly defined collection in left anterior neck distorting muscle and soft tissue planes, compressing the left thyroid gland. **(B)** Axial computed tomography scan at same level demonstrates inhomogeneously enhancing phlegmon adjacent to left lobe of the thyroid.

considered[101,102] (Fig. 48.29). These patients usually are presented at age 2 to 12 years with fever, sore throat, and swelling in the lower neck. On ultrasound, the left lobe of the thyroid gland may be heterogeneous. If an abscess has developed, typically a focal hypoechoic lesion is surrounded by hyperemia in the left perithyroid area.[87,90,101,102]

de Quervain thyroiditis, also known as **focal thyroiditis,** is an uncommon form of subacute thyroiditis likely caused by a viral infection.[83] Granulomatous inflammation of the gland can result in thyromegaly and heterogeneous echogenicity.

Hashimoto thyroiditis is the most common cause of thyroid disease in children and adolescents.[74] It is an autoimmune disorder caused by circulating antibodies. Injury to the gland results in a diffuse lymphocytic and plasma cell infiltration. The process is more common in girls than in boys, with a family history of thyroid disease in one-fourth of cases.[88,103] Clinically, the patient has painless enlargement of the thyroid. Although in the acute phase the patient may be hyperthyroid, most patients are hypothyroid at presentation. Hashimoto thyroiditis may be associated with several syndromes (e.g., Turner, Noonan, Down) and has been described in patients with juvenile diabetes, those receiving phenytoin therapy, and those with Hodgkin disease.[87] On ultrasound, the gland is enlarged with lobular margins and contains coarse septations and multiple hypoechoic micronodules measuring 1 to 6 mm in diameter[90] (Fig. 48.30). Normal, increased, or deceased color Doppler waveforms may be present. Adjacent cervical adenopathy is often noted. The majority of these patients have spontaneous resolution of symptoms. Suspicious nodules identified on thyroid ultrasound in the setting of Hashimoto thyroiditis are generally followed owing to increased risk of malignancy.[104,105]

Graves disease is the most common cause of hyperthyroidism in children. It is an autoimmune disease caused by thyroid-stimulated immunoglobulin binding to the thyroid-stimulating hormone (TSH) receptor, increasing the production of thyroid hormone. There is frequently a family history. It is more common in girls (5:1 female-to-male ratio) and has a peak incidence in adolescence, ages 11 to 15 years.[87,88] Diagnosis is usually clinical; children have an enlarged thyroid gland, exophthalmos, and hyperthyroidism. Fetuses and neonates born to mothers with Graves disease are also at risk for transient thyroid dysfunction and goiter because of transfer of thyroid-stimulating immunoglobulins.[88,103] During ultrasound examination, patients with Graves disease demonstrate diffuse enlargement of the thyroid gland, which appears heterogeneous and diffusely hypoechoic. Doppler imaging demonstrates intense hypervascularity, also known as "thyroid inferno"[90] (Fig. 48.31). Doppler waveform shows increased peak systolic velocity and decreased RI.[106]

Thyroid Masses

Thyroid nodules in pediatrics are uncommon, with an incidence of 1.5%.[107] Children with an asymptomatic palpable nodule typically have normal thyroid function.[108] In a child or adolescent, a solitary nodule should be approached with suspicion because there is a 33% risk of malignancy.[103] Ultrasound and radionuclide scintigraphy are the primary methods of imaging thyroid nodules. Fine-needle aspiration (FNA), especially with ultrasound guidance, may be helpful and has 80% to 95% accuracy for defining pathology in pediatric patients.[107-109] If FNA is not diagnostic, surgical excision may be required.[83] On sagittal imaging, the cricoid can appear as a round or oval mass, similar in echotexture to the normal thyroid and posteromedial to the gland.[110] A **pseudonodule** of the thyroid can be produced by uncalcified cricoid cartilage.

During ultrasound inspection, color Doppler flow imaging may be helpful to evaluate for injury to adjacent vessels.[111]

Thyroid cysts are the most common incidentally detected thyroid lesions in children.[112] These cysts are rarely true epithelial-lined cysts, usually degenerative because of necrosis within benign thyroid nodules. Most of these lesions are complex with mixed echotexture, thick irregular walls, septations, and in some cases, fluid-fluid levels from previous hemorrhage. Bright, echogenic internal areas result from **colloid** material, sometimes creating **comet-tail artifacts**[84,87] (Fig. 48.32). Calcifications in degenerative lesions may create echogenic foci of acoustic shadowing or peripheral eggshell calcifications. Doppler sonography typically shows peripheral vascularity, and nuclear medicine studies demonstrate variable uptake.

Although uncommon, **hemorrhage** within the thyroid, related to direct or indirect trauma, can mimic a nodule. The hematoma on sonography typically appears heterogeneous and hypoechoic (Fig. 48.33). Many of these masses contain cystic areas resulting from hemorrhage or necrosis. Nuclear medicine studies show variable uptake, with some follicular adenomas demonstrating intense activity. Because malignancy may appear as a cystic mass, close follow-up imaging and surgical diagnosis are typically indicated.[103,113]

Follicular adenomas, the most common benign lesions of the thyroid, arise from an overproliferation of follicular cells (hyperplasia).[90,107] Lesions may be solitary or multinodular, are round and well defined, and have decreased, increased, or honeycomb echotexture. About 60% of adenomas demonstrate a peripheral, 1- to 2-mm hypoechoic halo caused by a fibrous capsule and peripheral blood vessels best delineated with color Doppler sonography[90] (Fig. 48.34). Despite benign imaging

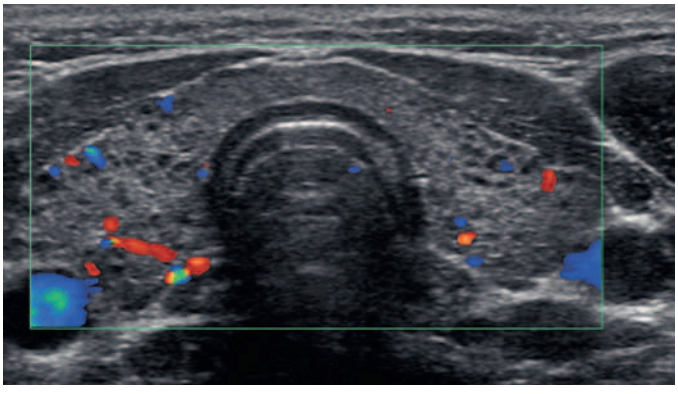

FIG. 48.30 Hashimoto Thyroiditis. Thyroid imaging with color Doppler shows coarse heterogeneous pattern with multiple hypoechoic micronodular areas, and mildly increased vascularity.

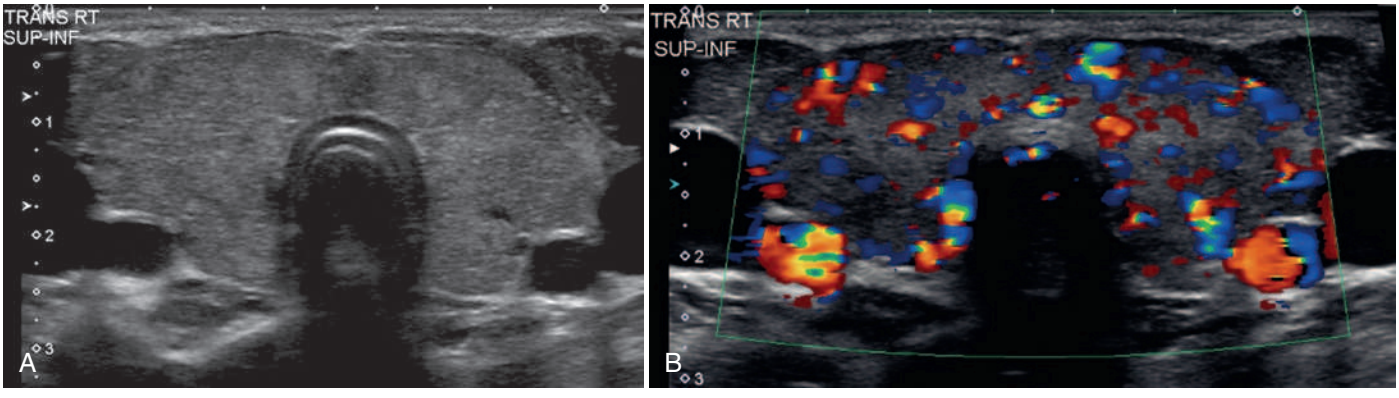

FIG. 48.31 Graves Disease. (A) Thyroid is diffusely enlarged and heterogeneously hypoechoic. **(B)** Color Doppler ultrasound demonstrates "thyroid inferno."

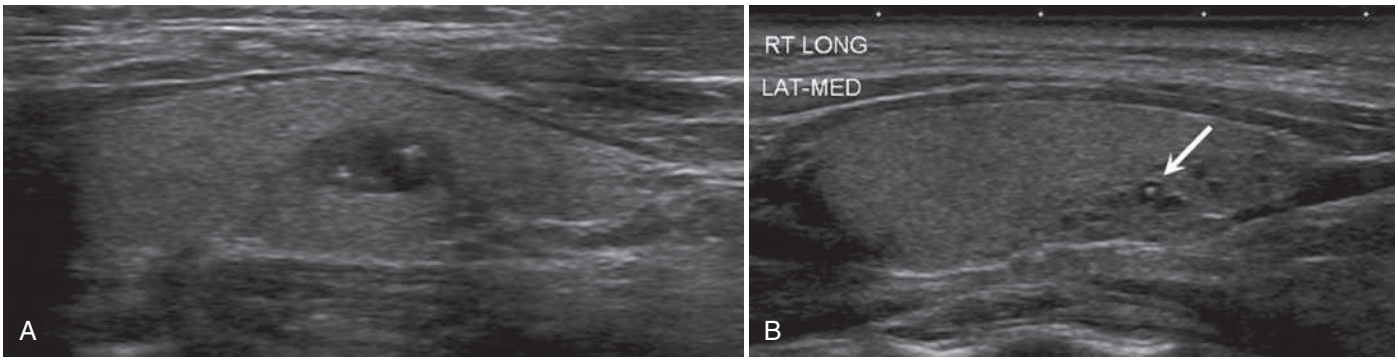

FIG. 48.32 Thyroid Degenerative (Colloid) Cyst. (A) Five-year-old with palpable mass demonstrates complex elliptical hypoechoic lesion with internal echogenic foci in the left lobe of the thyroid proven to represent colloid cyst. On color Doppler *(not shown),* no internal flow was present. **(B)** Smaller hypoechoic lesions were noted in right lobe of thyroid, one demonstrating comet-tail artifact *(arrow).*

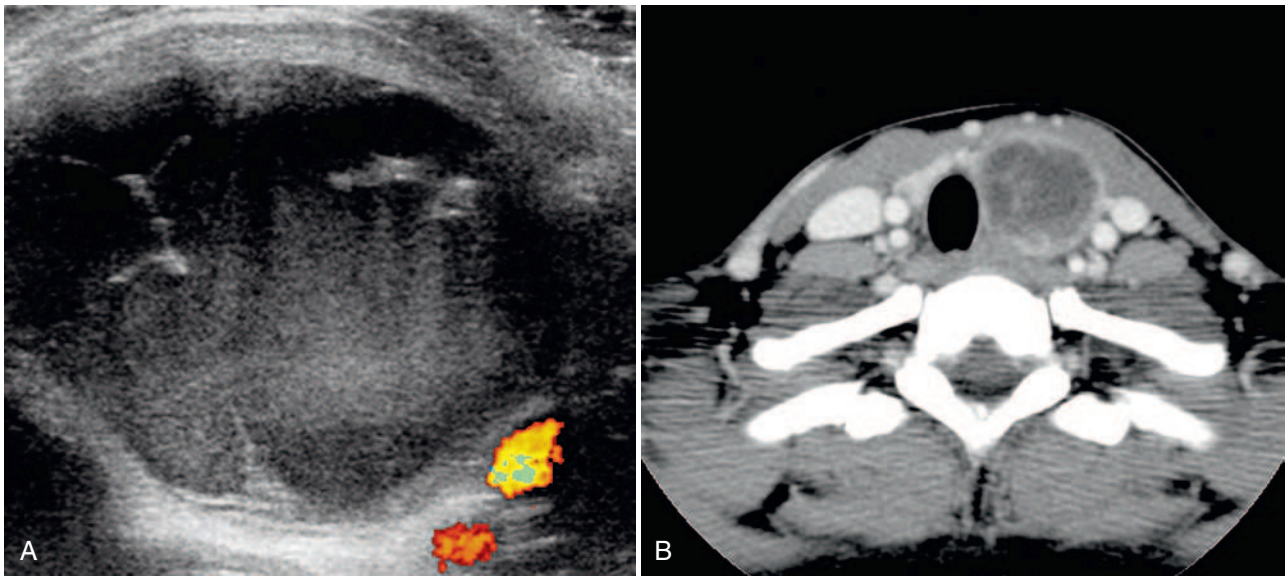

FIG. 48.33 Thyroid Hematoma. (A) Teenage girl was elbowed in the left side of the neck and developed a lump. Imaging of left lobe of thyroid demonstrates heterogeneous, well-defined, round avascular lesion. **(B)** Axial computed tomography scan shows hematoma replacing most of the left lobe.

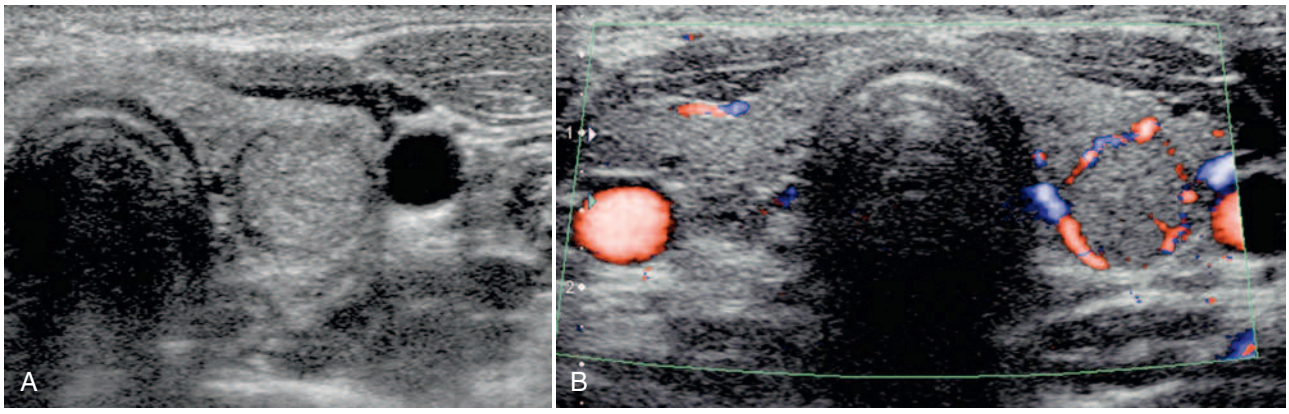

FIG. 48.34 Thyroid Follicular Adenoma. (A) Round, well-defined, almost-isoechoic lesion in the left lobe of the thyroid demonstrates a peripheral halo of decreased echogenicity. **(B)** Color Doppler sonogram demonstrates peripheral vascularity.

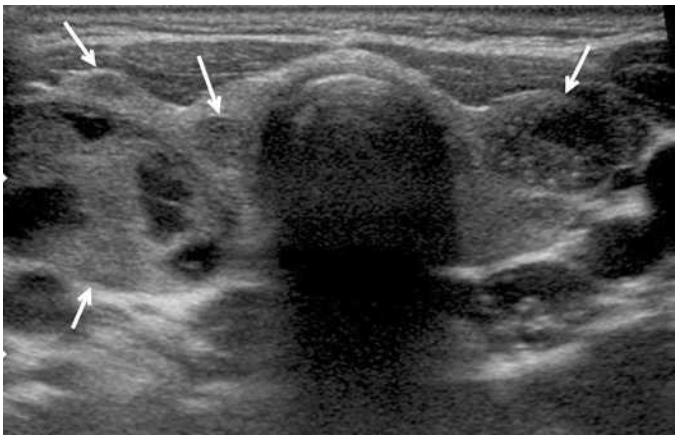

FIG. 48.35 Multinodular Goiter. Seventeen-year-old with thyroid enlargement. Thyroid ultrasound image shows multiple nodules within both lobes of the thyroid, some of which are small and hypoechoic and others large and complex. See also Video 48.2.

characteristics, these lesions can be difficult to differentiate from malignancy.[87,112]

Multinodular (adenomatous) goiter in children is uncommon but typically is diagnosed in adolescent girls near puberty.[114] In adults the etiology has been linked to iodine deficiency. In children, genetic susceptibility is more common, although autoimmune factors are also implicated.[115] Multinodular goiter has been described in patients with renal cystic disease, polydactyly, Hashimoto thyroiditis, McCune-Albright syndrome, and previous radiation therapy.[114] At presentation, children are typically euthyroid and clinically are diagnosed with a palpable nodule or nodules. On ultrasound, the nodules show variable heterogeneity with macronodular or micronodular formation (Fig. 48.35, Video 48.2). Some may become cystic because of necrosis or hemorrhage.[114] Continued ultrasound monitoring of these patients is warranted given the increased risk for nonmedullary cancer.[115]

Thyroid cancer is rare in children and represents only 1.5% of all malignancies in patients younger than 15 years.[90,106] However, there is a 1.5- to 5-fold greater chance of a thyroid nodule being malignant in children when compared with adults.[116,117] Among girls 15 to 19 years of age, thyroid cancer is the second most common malignancy.[118] Factors that are associated with increased risk of thyroid cancer include a positive family history of thyroid cancer, genetic predisposition, and radiation exposure, especially in patients with history of bone marrow transplant.[87,119] Multiple syndromes such as the PTEN hamartoma tumor syndromes (which are caused by germline mutations of the *PTEN* tumor suppressor gene), Cowden and Bannayan-Riley-Ruvalcaba syndromes, familial adenomatous polyposis, Gardner syndrome, Peutz-Jeghers syndrome, and Carney complex are associated with thyroid nodules and cancers.[120] Autoimmune thyroiditis has also been shown to be associated with a greater incidence of thyroid cancers.[120,121] The irradiated thyroid can show a spectrum of abnormalities, from cysts to benign or malignant nodules. Incidence of thyroid cancer after irradiation may increase more than 20-fold, with a mean latency period of about 15 years.[109] Risk factors in the presence of radiation include female gender, younger age at irradiation, and longer time since irradiation.[122]

Patients with thyroid cancer usually have a palpable nodule or cervical adenopathy and, rarely, hoarseness or pain. **Papillary cancer,** the most common pediatric thyroid neoplasm, represents 80% of all cases and is multicentric in 20% of cases[121] (Fig. 48.36). Metastatic disease with papillary tumor is through the lymphatics. **Follicular cancer** represents 17% of thyroid cancers and metastasizes through the bloodstream. **Medullary cancers** comprise 2% to 3% of thyroid cancers, secrete calcitonin, and are typically diagnosed in patients with a strong family history or features of multiple endocrine neoplasia type II (MEN IIa and IIb). At presentation, children with medullary cancer are usually at an advanced tumor stage, with lymph node involvement in 50% to 80% and metastasis to the lung in 6% to 18%.[90,109,123]

Children with thyroid cancer have cervical and pulmonary metastasis more frequently than adults. They also have more advanced disease and higher rate of recurrence.[116] Bone metastases are, however, rare in children. With sonography, it can be difficult to differentiate benign from malignant thyroid masses. Helpful differentiating ultrasound criteria for malignancy include a predominantly solid lesion, the presence of calcification (especially microcalcifications), hypoechogenicity, irregular margins, large height-to-width ratio, absence of peripheral halo, intranodular vascularity, and associated abnormal lymph nodes.[124-128] Unfortunately, no size criteria are provided to distinguish benign from malignant thyroid nodules. Needle biopsy or surgical resection should be considered in children with suspicious sonographic or clinical features, owing to the high increased risk (25%-50%) of thyroid malignancy.[129] Follicular cancers often mimic adenomas. Adjacent lymph nodes should always be inspected, as the presence of lymphadenopathy or calcification is concerning for metastatic disease.

Malignant Thyroid Nodule: Sonographic Characteristics

Predominantly solid lesion
Presence of calcification, especially microcalcifications
Hypoechogenicity
Irregular margins
Large height-to-width ratio
Absence of peripheral halo
Intranodular vascularity
Associated abnormal lymph nodes

Nuclear medicine (frequently iodine-123 and iodine-131 scintigraphy) has been used to guide therapy because "cold" nodules on scintigraphy are suspicious for malignancy. Although "hot" nodules on nuclear medicine scintigraphy are usually not malignant, exceptions can occur[103] (Fig. 48.37). In general, thyroid neoplasms (excluding the medullary type) have a good prognosis, with 10-year survival greater than 95% when treated with total thyroidectomy, lymph node dissection, and postoperative iodine-131 radioiodine therapy.[109]

Other pediatric thyroid neoplasms include **lymphoma** and **teratoma.** In pediatric patients with Hashimoto thyroiditis and a solitary or multiple hypoechoic lesions, lymphoma should considered.[90]

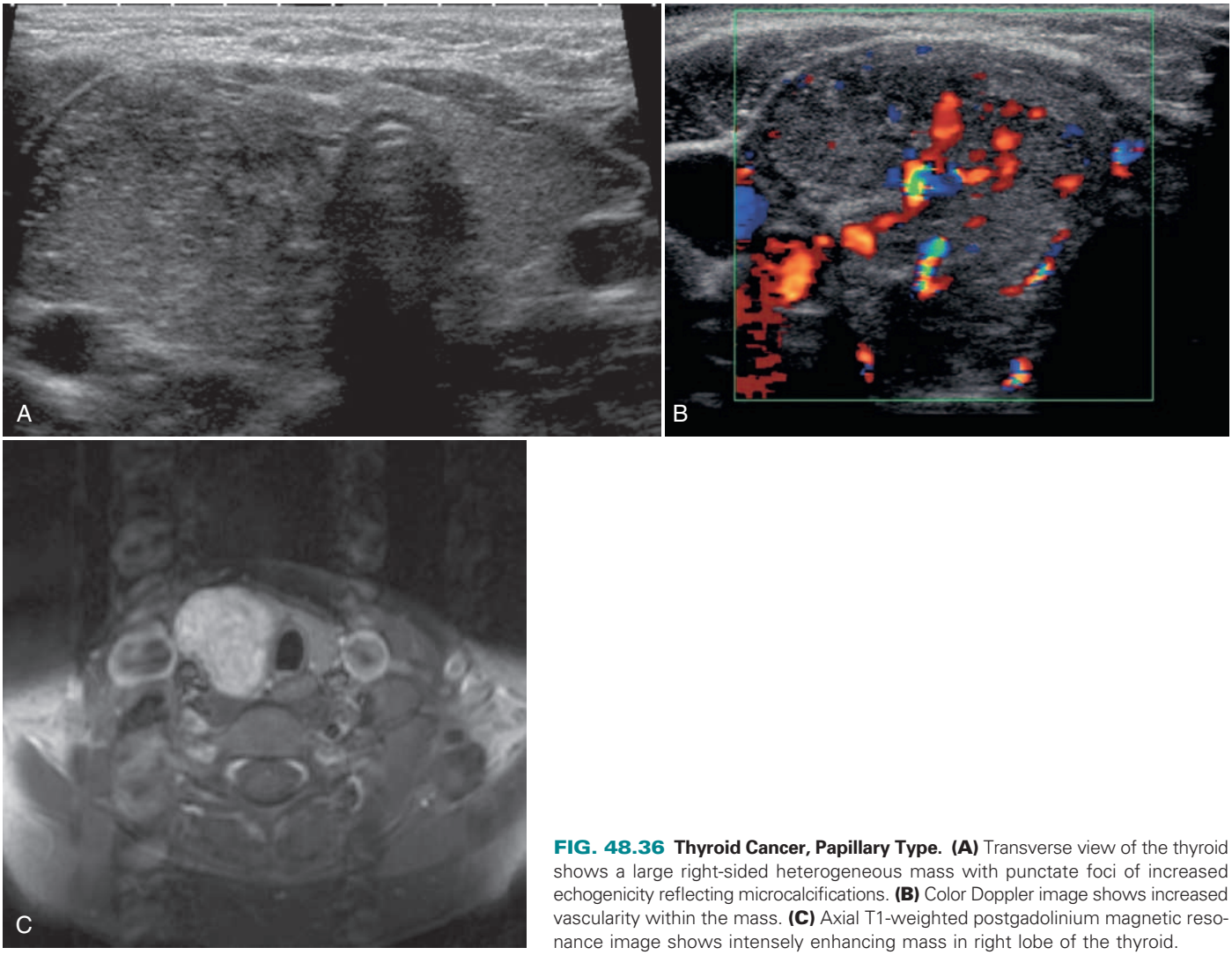

FIG. 48.36 Thyroid Cancer, Papillary Type. (A) Transverse view of the thyroid shows a large right-sided heterogeneous mass with punctate foci of increased echogenicity reflecting microcalcifications. **(B)** Color Doppler image shows increased vascularity within the mass. **(C)** Axial T1-weighted postgadolinium magnetic resonance image shows intensely enhancing mass in right lobe of the thyroid.

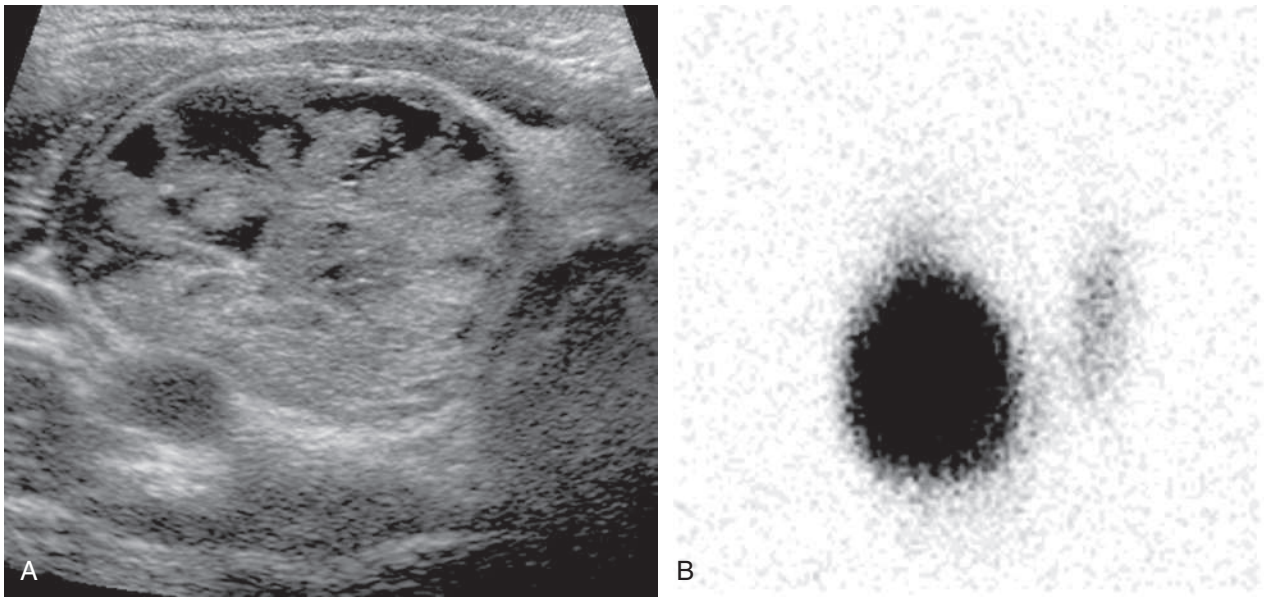

FIG. 48.37 Thyroid Cancer, Papillary Type. (A) Heterogeneous, well-defined right thyroid lobe nodule with peripheral halo, favored to represent follicular adenoma. **(B)** Technetium 99m ($_{99m}$Tc) pertechnetate scan demonstrates increased uptake suggesting hyperfunctioning adenoma, but pathology diagnosis was cancer.

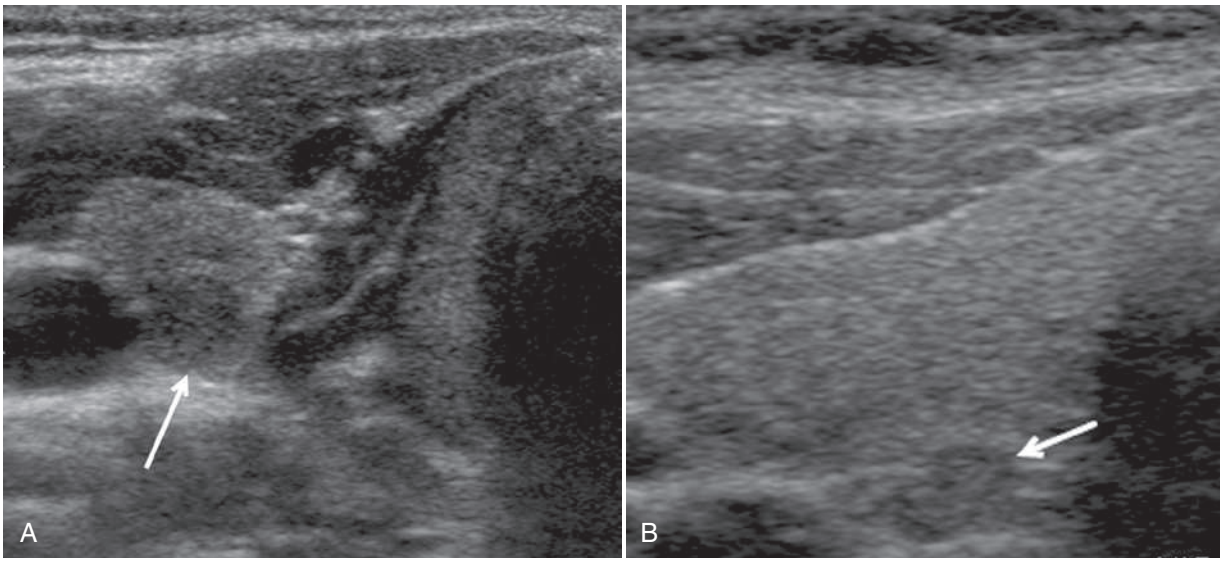

FIG. 48.38 Parathyroid Adenoma and Hyperplasia. (A) Patient with hyperparathyroidism demonstrates a hypoechoic nodule *(arrow)* posterior to the thyroid gland. **(B)** Patient with renal failure shows hypoechoic lenticular lesion *(arrow)* posterior to thyroid, consistent with parathyroid gland hyperplasia.

Parathyroid Glands

The parathyroid glands are two paired endocrine glands arising from the third and fourth branchial pouches.[130] **Normal parathyroid tissue** is infrequently identified separate from the thyroid because their echotexture is similar. Sonographic imaging of the parathyroid may be helpful in the presence of primary or secondary **hyperparathyroidism.** Parathyroid **adenomas** are rare in children but are the most common cause of primary hyperparathyroidism.[131,132] Children with chronic renal failure may develop parathyroid gland hyperplasia caused by secondary hyperparathyroidism.[133] Four-gland parathyroid hyperplasia is more common in patients with MEN I.[134] Ultrasound is 80% to 90% sensitive in detecting parathyroid tumors and gland enlargement.[131] Typical sonographic imaging findings of an adenoma and hyperplasia are similar, appearing as an oblong, sharply demarcated, hypoechoic solid mass aligned craniocaudal and posterior to the thyroid (Fig. 48.38). Less frequently, the mass may be cystic, calcified, multilobular, and giant.[43] Enlargement of the adjacent inferior thyroid artery may be identified as an **arc of vascularity,** providing clues to diagnosis of an adenoma.[135] Because 20% of the parathyroid tissue can be ectopic, MRI may be considered if ultrasound is unsuccessful in identifying the lesion.[136]

Other Cystic Lesions

Foregut cysts represent defective budding of the respiratory or intestinal tract. **Bronchogenic cysts** are usually mediastinal and rarely may occur as a mass in the lower neck.[94,137] **Esophageal cysts** are typically centered close to the esophageal wall. Foregut lesions usually occur as a palpable lump but can enlarge rapidly, causing airway obstruction and dysphagia. With sonography, the lesions are typically unilocular but may be complicated by hemorrhage and infection, especially in the presence of persistent communication with the airway or esophagus.

Laryngoceles are air- or fluid-filled dilations of the laryngeal saccule, a small pouch arising from the roof of the laryngeal ventricle.[93] Internal laryngoceles remain within the larynx, whereas external masses project through the thyrohyoid membrane.[138] When the laryngeal saccule is totally obstructed, the outpouching will appear as a smooth-walled anechoic mass projecting into the endolaryngeal or preepiglottic space.[138] In 8% to 10% of cases, laryngoceles develop superimposed infection, and there is a 15% association with neoplasm.[93] Children typically have airway obstruction or feeding difficulties.

LACKING DEFINITION BY THE HYOID

The carotid space and deep cervical fascial layers extend above and below the hyoid bone.[6,7] The **carotid space,** enveloped by all three layers, extends from the skull base to the aortic arch. Its contents include the internal carotid artery, jugular vein, cranial nerves IX to XII (vagus nerve, X), and deep cervical lymph node chain. The **retropharyngeal and prevertebral spaces** extend from the skull base to the level of the third thoracic vertebral body. The **danger space** is within the retropharyngeal space where a pathway exists for infection to spread inferiorly into the posterior mediastinum. The retropharyngeal space contains primarily lymph nodes, whereas the prevertebral space contains vertebral bodies, spinal cord, paraspinal and scalene muscles, and vertebral artery and vein. These spaces are not discussed separately because many diseases, especially nodal, involve multiple spaces simultaneously. It should be noted that ultrasound is especially useful in assessment of superficial lesions. Ultrasound is of limited value in deep space lesions involving the retropharyngeal space and prevertebral space, which typically require CT or MRI for better evaluation.[139]

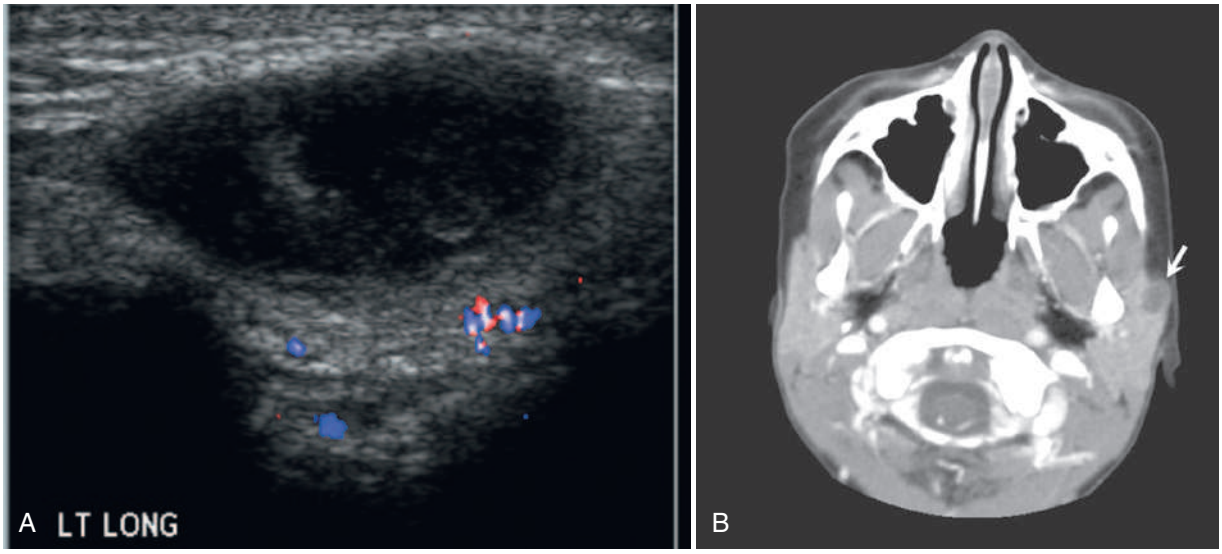

FIG. 48.39 Type I Branchial Cyst. (A) Four-year-old child with swelling and pain inferior to the left ear. Longitudinal sonogram demonstrates an elliptical heterogeneous hypoechoic lesion lacking color flow, superficial and inseparable from the parotid gland. **(B)** Axial computed tomography scan obtained 2 months later after treatment with antibiotics confirms well-defined cystic lesion *(arrow)* embedded in the superficial lobe of the left parotid.

Congenital Lesions

Branchial Anomalies

The **branchial (pharyngeal) apparatus** develops between the fourth and sixth week of gestation. The structure consists of six pairs of mesodermal **branchial arches** separated by five paired internal endodermal **pharyngeal pouches** and five paired external ectodermal **branchial clefts,** or grooves. Abnormalities in development of this apparatus may result in the formation of a cyst, sinus tract, or fistula, although most branchial lesions present as cysts.[140,141] Sinus tracts communicate with either skin or mucosa of the upper airway when a pouch or groove fails to obliterate; if both pouch and groove fail, then a fistula between skin and mucosa develops. A cyst occurs when a groove remnant forms an epithelial line space without communication.[142] Branchial anomalies, after thyroglossal duct cysts, are the second most common congenital head and neck lesions in children, with the majority arising from the type II apparatus.[141,142] Branchial anomalies, particularly when bilateral, may be part of branchio-oto-renal syndrome, a disorder that also manifests with bilateral preauricular pits and renal abnormalities.[143] On sonography, branchial malformations typically appear as a simple or complex cyst with through transmission. These lesions are susceptible to hemorrhage or superimposed infection, but predisposition to cancer remains controversial.[93] Treatment of choice is surgical resection or fistulectomy, with a 4% rate of recurrence.[143,144]

First branchial anomalies represent 8% to 10% of all anomalies and appear as a cyst or sinus adjacent to the external auditory canal, the pinnae, or the parotid gland, extending to the level of the mandible angle[143] (Fig. 48.39). These lesions can be superficial or deep, even embedded into the parotid gland with variable relationship to the facial nerve.[144,145] Some demonstrate a tract to the external auditory canal.

Second branchial anomalies represent 90% of all branchial apparatus malformations.[143] Cysts of the type II branchial anomaly result from persistence of the cervical sinus.[144-146] During development of the branchial apparatus, the second arch expands downward to meet and merge with the fifth arch, thus covering the second, third, and fourth arches and forming a cervical sinus of His.[130,146] Because of this embryology, many anatomic type II cysts are possible. These cysts are differentiated (Bailey) into four types.[144] Type I is deep to the platysma muscle. Type II, the most common, is anterior to the sternocleidomastoid, posterior to the submandibular gland, and lateral to the carotid sheath. Type III cysts are anatomically between the internal and external carotid arteries, posteromedial to the sternocleidomastoid and lateral to the pharynx (Fig. 48.40). Type IV cysts are adjacent to the pharyngeal wall.

Third and fourth branchial anomalies are rare, with incidence of type III 2% to 8% and type IV 1% to 2%.[143] Third branchial apparatus anomalies originate at the base of the pyriform sinus and pass above the superior laryngeal nerve (Fig. 48.41), whereas fourth branchial anomalies originate at the apex of the pyriform sinus and extend through the cricothyroid membrane and beneath the superior laryngeal nerve.[143,147] Third and fourth anomalies may manifest as a cyst in the lower anterior neck but more commonly appear as a pyriform sinus or fistula (Fig. 48.42). The anatomy of the lesion is typically a left-sided tract (89%) extending from the pyriform sinus to the anterior lower neck adjacent to the thyroid.[148] Patients may have recurrent neck infection, abscess (39%), or suppurative thyroiditis (33%).[101,148] On sonography, the thyroid often appears heterogeneous because of adjacent inflammation. In some cases, an air-containing intrathyroid or perithyroid cystic mass may be present, representing a complicating abscess.[49] A barium swallow study or CT with oral barium may be beneficial to define the tract, usually inconspicuous on sonography.[149]

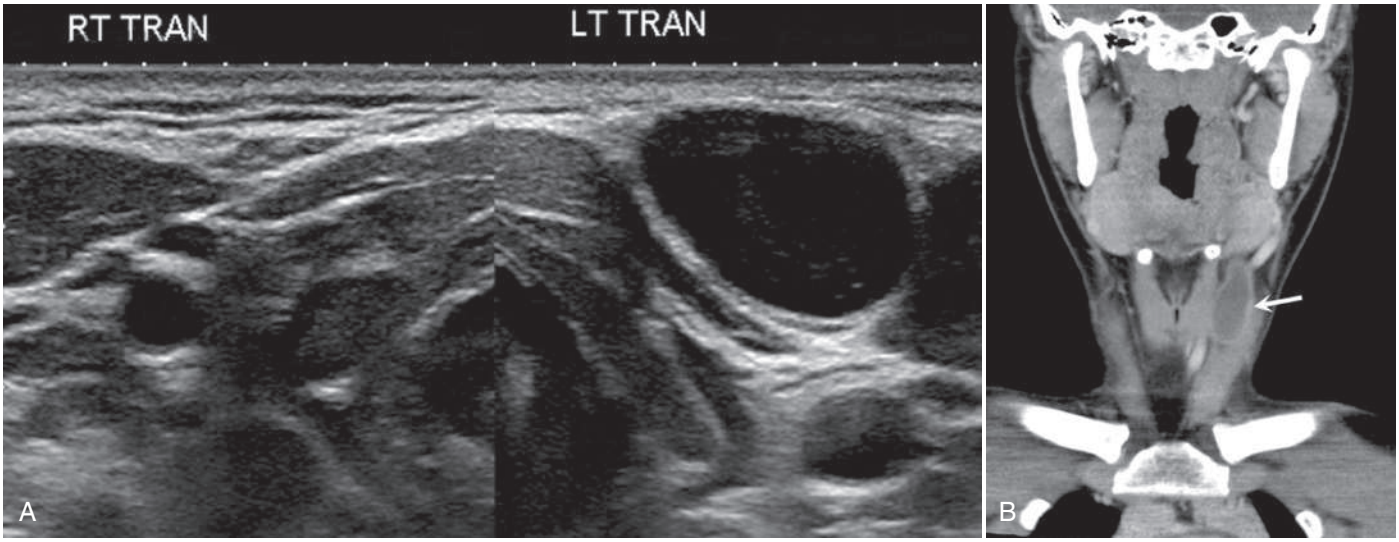

FIG. 48.40 Type II Branchial Cyst. (A) Transverse side-by-side image of the right and left sides of the neck. There is a unilocular, anechoic, encapsulated cystic lesion with through transmission in the left neck medial to the left sternocleidomastoid muscle. **(B)** Coronal computed tomography scan demonstrates the elliptical cyst *(arrow)* medial to the sternocleidomastoid muscle and lateral to the pharynx, type III of the second branchial apparatus anomalies.

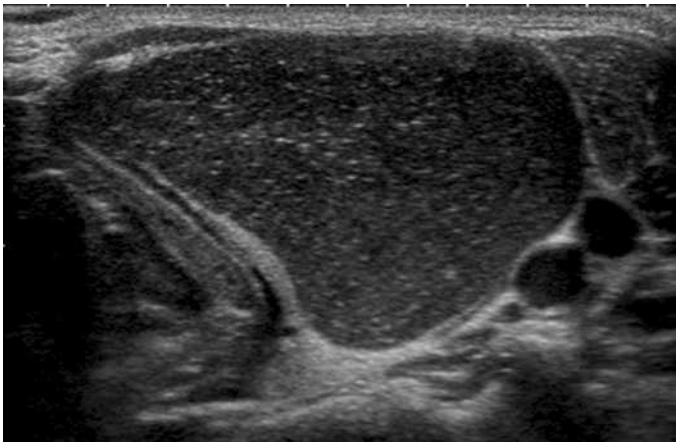

FIG. 48.41 Type III Branchial Apparatus Cyst. There is a unilocular complex hypoechoic cyst in the lower neck adjacent to the thyroid cartilage, suggesting hemorrhage or infection. No flow was present on color Doppler.

Ectopic Thymus

The thymus gland arises in the sixth week of gestation as outpouchings of primarily the third and a small portion of the fourth pharyngeal pouches.[93] Caudal elongation leads to the formation of tubular structures known as the **thymopharyngeal ducts.** By the ninth week, migration due to attachment to the pericardium is followed by obliteration of the duct from the angle of the mandible, along the carotid sheath, to the level of the superior mediastinum. The resulting migrating solid masses fuse to form thymus tissue anatomically located below the thyroid gland.[150] Superior cervical extension of the thymus is normal in children and young adults, seen in nearly 66% of these patients anywhere along the course of descent.[146,150,151] The ectopic thymus can be differentiated from other masses via sonography because of isoechogenicity and sometimes continuity with normal thymus, sharp angulated margins, parallel septa, pliability, lack of mass effect, and absence of central hilum with color Doppler imaging[43,150] (Fig. 48.43).

With persistence of the thymopharyngeal duct or progressive cystic degeneration of the thymic tissue, a **thymic cyst** may occur.[99,130] Most thymic cysts occur in the first decade of life, with a male and left-sided predominance.[152] Approximately 50% of cervical cysts are in continuity with a mediastinal mass.[43,153] On ultrasound, the lesions are typically large, unilocular or multilocular cysts intimately associated with the carotid space, often splaying the carotid artery and jugular vein[144,153] (Fig. 48.44). Intralesional debris can occur in the presence of hemorrhage or infection.[101] There are no reports of associated neoplasm, but surgical resection is the treatment of choice.[93,152]

Dermoid and Epidermoid Lesions

Dermoid and epidermoid lesions represent 7% of head and neck lesions and 25% of midline cervical anomalies.[93,98] These lesions develop when there is inclusion of ectodermal tissue during the fusion of the branchial arches.[146,154] **Dermoid cysts** contain two germ layers, both ectoderm and mesoderm, whereas **epidermoid cysts** consist of only one germ layer, ectoderm.[99,140] Although the majority of these masses are found around the orbit or adjacent to the nose, approximately 11% of these cysts occur in the floor of the mouth in the submandibular space.[93] With regard to imaging of the neck, most occur as a painless, slow-growing midline neck mass in the floor of the mouth, or less often in the thyroidal or suprasternal area.[43] Ultrasound of these lesions mimics a "pseudosolid" appearance, demonstrating a well-circumscribed, thin-walled unilocular mass with internal echoes and minimal posterior echo enhancement[152] (Fig. 48.45). Sometimes, there may be mixed echoes owing to internal fat or posterior shadowing in the presence of calcification.[152] Surgical resection is

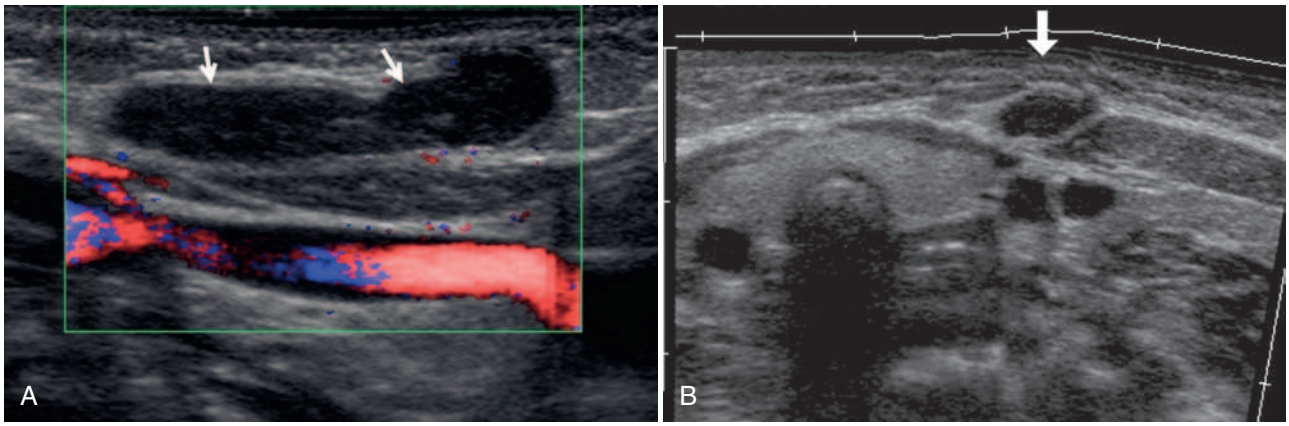

FIG. 48.42 Branchial Sinus. One-month-old child with draining sinus in the left neck. **(A)** Longitudinal ultrasound image shows a hypovascular tubular structure in the superficial soft tissues of the left side of the neck *(arrows)*. **(B)** Panoramic ultrasound of the neck shows the relationship of the branchial sinus *(arrow)* to the left lobe of the thyroid gland.

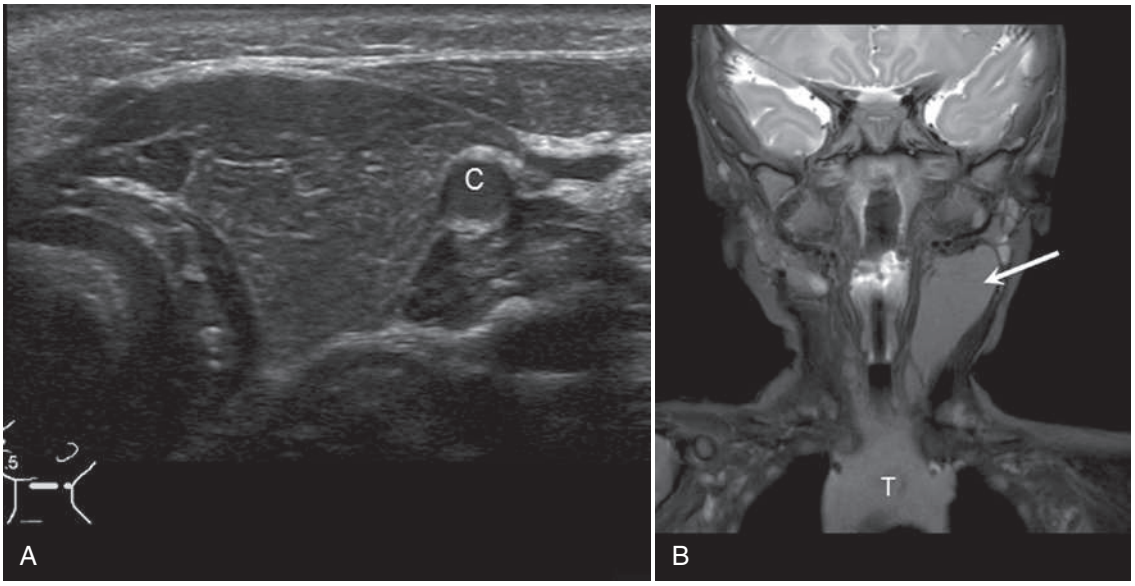

FIG. 48.43 Ectopic Thymus Tissue. Five-month-old child with fullness in the left side of the neck. **(A)** Ultrasound demonstrates an angular soft tissue mass with thin parallel septae medial to the carotid *(C)*. **(B)** Coronal short-tau inversion recovery (STIR) magnetic resonance image shows soft tissue in the left side of the neck *(arrow),* which is equal in signal to thymus *(T)* in the superior mediastinum.

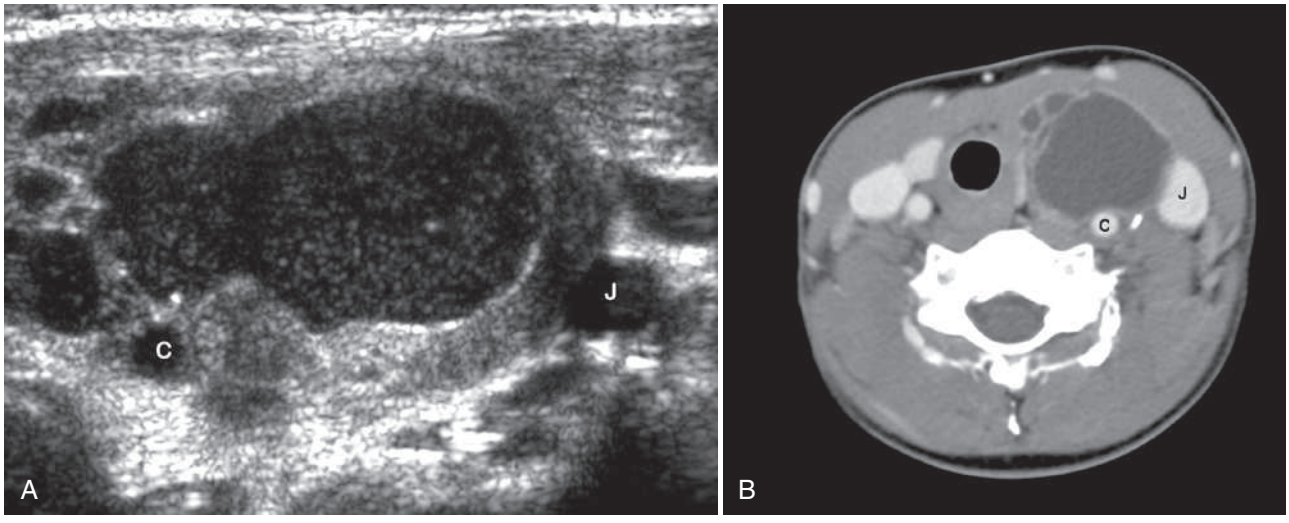

FIG. 48.44 Complicated Thymic Cyst. (A) Complex cystic mass with septation and thick peripheral wall splaying carotid artery *(C)* and jugular vein *(J)*. **(B)** Axial computed tomography scan shows complex mass at thoracic inlet displacing thyroid and airway.

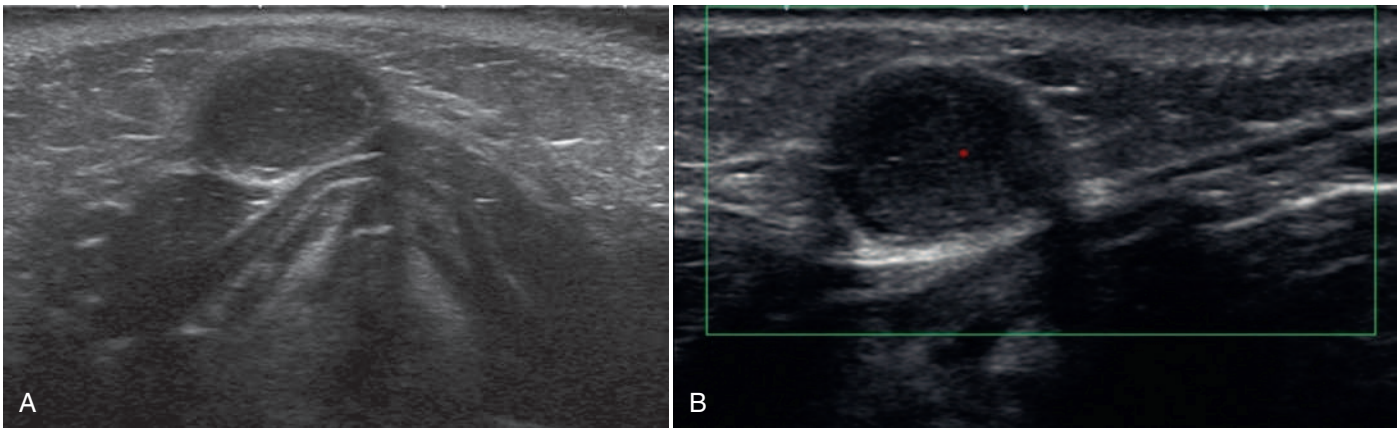

FIG. 48.45 Dermoid Cyst. Gray-scale **(A)** and color Doppler **(B)** transverse images show a well-defined, right paramidline, avascular infrahyoid lesion containing internal echoes and posterior through transmission. The lesion is in the deep subcutaneous layer, immediately superficial to the strap muscles.

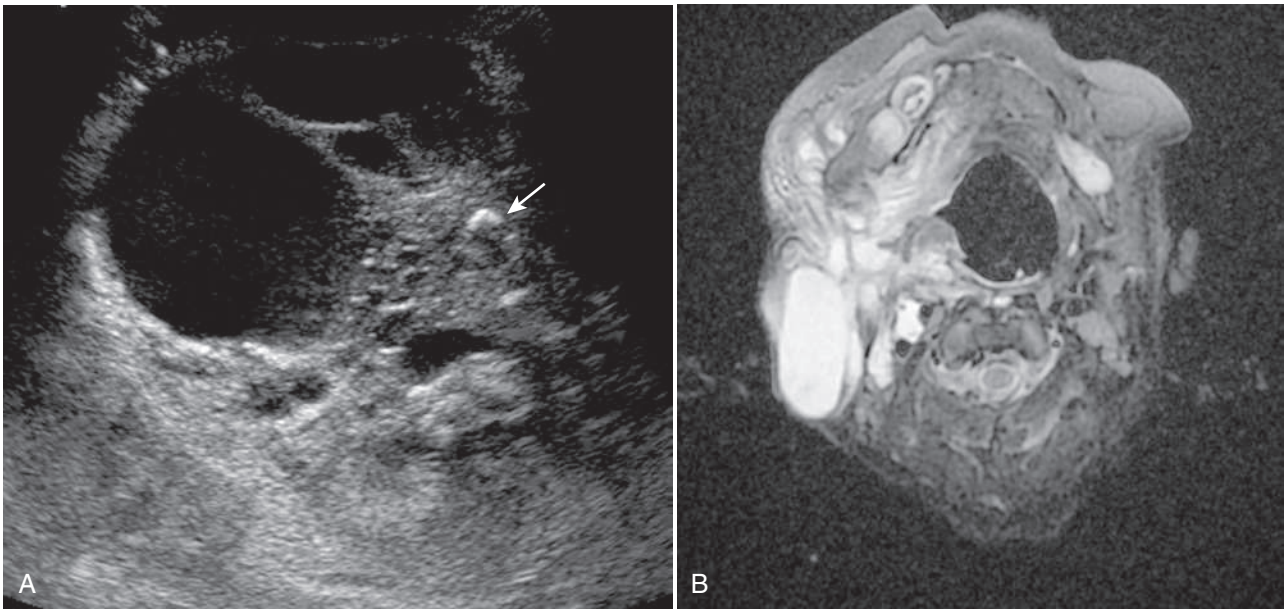

FIG. 48.46 Cervical Teratoma. (A) Poor definition of soft tissue planes caused by a complex infiltrative mass containing cystic, solid, and calcified areas *(arrow)*. **(B)** Axial T2-weighted magnetic resonance image shows complex cystic and solid mass infiltrating the parotid, masseter, submandibular, parapharyngeal, and carotid space soft tissues.

recommended because these anomalies are at risk for rupture or infection, and 5% will undergo malignant degeneration to squamous cell neoplasms.[93,98]

Teratomas

Cervical teratomas are rare, occurring in 1 per 40,000 live births but representing 5% to 14% of all neonatal teratomas.[154-156] These lesions are believed to arise from pluripotential cells of two or three germ layers isolated at sites distant to the anatomic site of origin.[154,157] About 90% of childhood teratomas consist of all three germ layers with variable differentiation, and 75% to 85% of head and neck tumors contain neuroectodermal tissue.[154] Most cervical teratomas are benign, with rare malignant diagnosis.[156,157] These lesions typically occur as a large, infiltrative cystic and solid mass in the anterior and lateral neck.[5,156] Airway impingement is the most common cause of morbidity; therefore, prenatal identification of the lesion may help define management at delivery.[156,158] Sonography demonstrates a multilocular heterogeneous mass containing solid and cystic components, with calcifications in 50% of cases[156,158,159] (Fig. 48.46). Mortality approaches 100% if the lesions are not immediately managed and resected.[158,160]

Vascular Lesions

Vascular Anomalies

In 1982, Mulliken and Glowacki[161] proposed a classification separating vascular anomalies into two groups, tumors versus

malformations, based on lesion growth patterns. Vascular masses that proliferate rapidly and can involute are regarded as **tumors.**[48] Vascular lesions that grow in proportion to the child and do not involute are considered **malformations.** With emerging knowledge about these vascular lesions, the International Society for the Study of Vascular Anomalies (ISSVA) provided a classification on vascular anomalies in 1996, and updated it in 2014. They acknowledge the fact that this classification scheme would be modified as new scientific information became available.[162]

Vascular Anomalies[ISSVA]

VASCULAR TUMORS
Benign
Locally aggressive or borderline
Malignant

VASCULAR MALFORMATIONS
Simple
Combined
Of major named vessels
Associated with other anomalies

Gray-scale and color and duplex Doppler ultrasound can help determine whether the anomaly is cystic or solid, evaluate for intralesional calcifications or phleboliths, and identify the presence of high-flow vessels.[163] CT scans may be helpful when a patient cannot be sedated, to confirm intralesional calcification and evaluate associated bone changes. Because of soft tissue definition, multiplanar capabilities, and ability to define high-flow vessels, MRI is the preferred imaging modality for vascular malformations.[161,163]

Vascular Tumors

Benign vascular tumors include infantile and congenital hemangiomas, pyogenic granuloma (lobular capillary hemangioma), tufted angioma, and a few other rare lesions. Kaposiform hemangioendothelioma is a locally aggressive vascular tumor seen in infants. Angiosarcoma and epithelioid hemangioendothelioma are malignant vascular tumors that may be seen in childhood.[162] The locally aggressive or malignant vascular lesions are extremely rare and frequently characterized by rapid growth. These lesions are best evaluated with MRI.

Infantile hemangiomas are the most common vascular lesions in infancy and childhood. These high-flow masses are benign neoplasms composed of proliferating endothelial cells.[161] Infantile hemangiomas represent 60% of head and neck hemangiomas.[47] Hemangiomas occur three times more often in girls than boys.[48] Most occur as a painless, compressible, growing mass, and half have a bluish or red stain in the skin superficial to the lesion.[157] These lesions typically become apparent within the first few weeks of life, undergo a phase of proliferation and peak in size at 1 year of age, then undergo spontaneous, slow involution over the first decade.[161] On ultrasound, these lesions are lobulated, well marginated, heterogeneously echogenic and compressible when superficial. On color Doppler imaging during the proliferative phase, there is exuberant vascularity within the lesion, with high vessel density of greater than five vessels per square centimeter[164] (Fig. 48.47, Video 48.3). These lesions are supplied by high-flow vessels with low-resistance arterial waveforms. Prominent draining veins are present, but there is no arterialization of venous waveforms.[164] Clinical and sonographic evaluation is generally sufficient for diagnosis, and biopsy is rarely indicated. During the involutional phase, there is a decrease in size of the lesion as well as a decrease in the vascularity and the high systolic flow.[164]

Hemangiomas are common in premature infants, usually evident shortly after birth, but 95% of these lesions manifest during the first 6 months.[157,163] Endothelial glucose transporter 1 (GLUT 1) is a diagnostic marker for infantile hemangioma. If one or multiple hemangiomas are present in a trigeminal dermatome distribution (frequently V1), the clinician should consider **PHACES syndrome** (*p*osterior fossa malformations, *h*emangiomas, *a*rterial anomalies, *c*oarctation of aorta and cardiac defects, *e*ye abnormalities, *s*ternal notching).[165] Infantile hemangiomas are treated only if symptomatic or if they endanger vital structures. Treatment options include propranolol, laser therapy, and surgery.

Congenital hemangiomas, less common than infantile hemangiomas, will be present at full size at birth. They are GLUT 1 negative, lack a gender predisposition, and commonly occur in the head or extremity joints.[166] They may subsequently involute before 1 year of age (rapidly involuting congenital hemangioma [RICH]), may be static (noninvoluting congenital hemangioma [NICH]), or may partially involute (partially involuting congenital hemangioma [PICH]). On Doppler sonography, congenital hemangiomas are heterogeneous and highly vascular with fast-flow low-resistance arterial vessels as well as channels with venous flow[166,167] (Fig. 48.48). Calcifications may occasionally be seen in RICH and NICH, differentiating these lesions from infantile hemangiomas.[166]

Vascular Malformations

Simple vascular malformations may be composed of only one type of vessel such as capillaries, lymphatics, or veins or, as in the case of arteriovenous malformations (AVMs) or arteriovenous fistulas (AVFs), may involve more than one type of vessel.[162] Simple capillary malformations frequently appear as cutaneous lesions, are diagnosed clinically, and are rarely imaged. Capillary malformations can occur combined with other anomalies, such as the Sturge-Weber syndrome with facial cutaneous capillary malformation (port-wine stain) frequently in the distribution of the ophthalmic segment of the trigeminal nerve.[162]

Lymphatic malformations, originating from a sequestered embryonic lymph sac, are composed of primitive lymphatic spaces of varying sizes separated by connective tissue stroma.[140] Lymphatic malformations may be macrocystic with large cysts (previously called **cystic hygromas**), microcystic (previously called **lymphangiomas**), or mixed cystic. There is no specific size criterion separating microcystic from macrocystic lymphatic malformations, but in general, if the size of the cyst is large enough for sclerotherapy, it is considered macrocystic. Lesion cyst size is likely caused by the stromal environment rather than lesion behavior.[99] Some lymphatic malformations are diagnosed

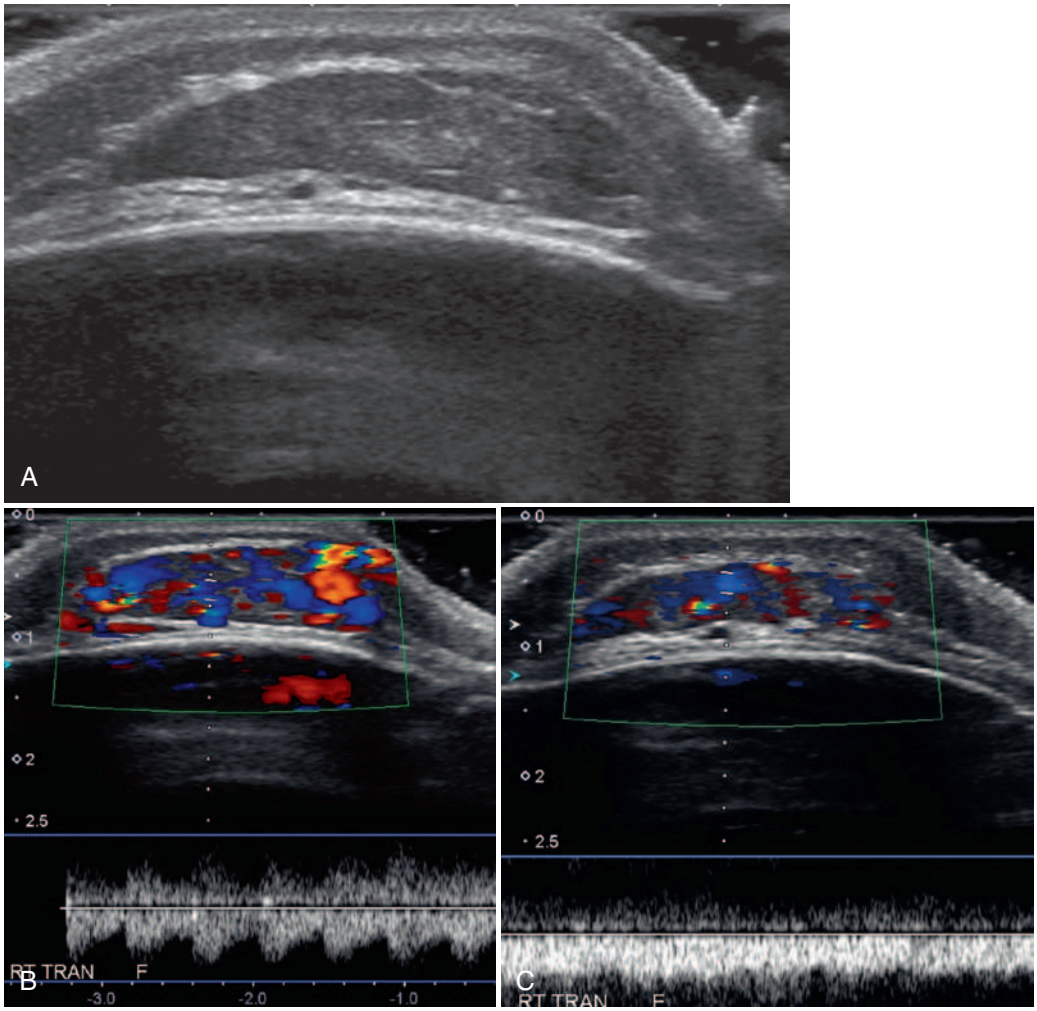

FIG. 48.47 Infantile Hemangioma. (A) Oblong heterogeneous echogenic right scalp mass in a 5-month-old infant. **(B)** The lesion is intensely vascular with low-resistance arterial waveforms. **(C)** Prominent veins are present without arterialization of flow. See also Video 48.3.

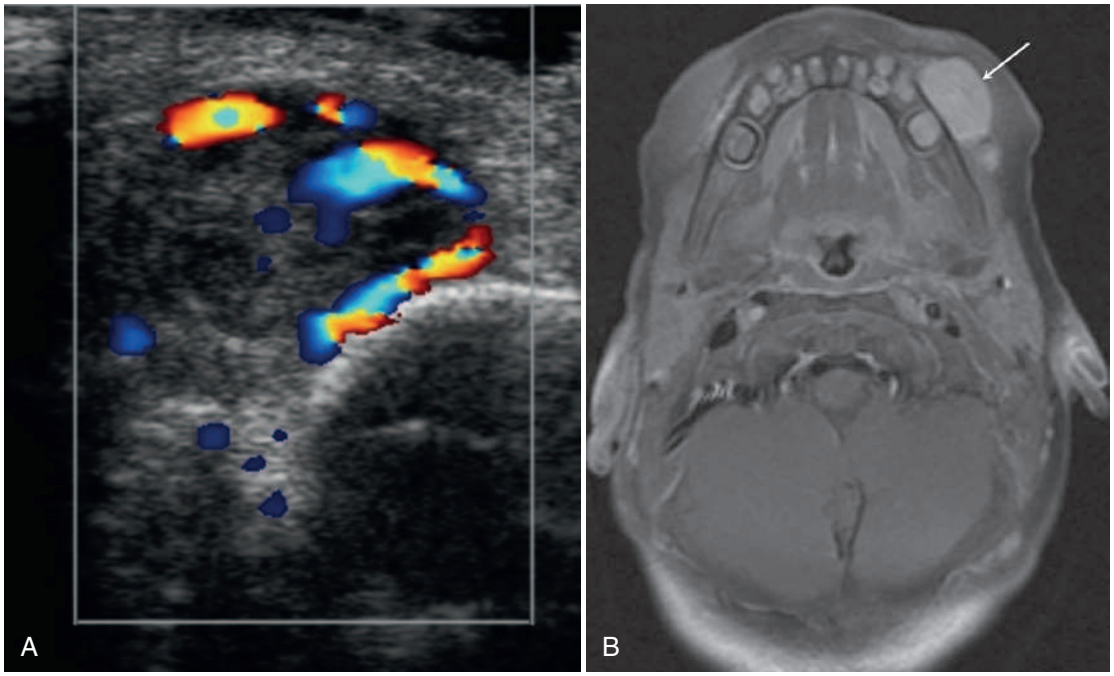

FIG. 48.48 Noninvoluting Congenital Hemangioma (NICH). (A) Heterogeneous hypoechoic mass with increased vascularity in an 8-month-old infant. The lesion was present since birth, and there was superficial cutaneous discoloration. **(B)** Postcontrast T1-weighted magnetic resonance image shows uniform enhancement of the left cheek mass. *(arrow).*

prenatally, with 90% presenting by age 2 years. Clinically, the skin is usually normal but may have a bluish hue, puckering, or tiny vesicles.[163] These lesions can be diffuse or focal, tend to invade multiple anatomic facial planes, and will rapidly enlarge if complicated by hemorrhage or infection. Hypertrophy and intraosseous invasion of adjacent bone, usually the mandible, can occur.

About 75% of lymphatic lesions occur in the neck, and most originate within the posterior triangle or oral cavity, with lesions occurring on the left side twice as often as on the right side.[43,48,82] Of infants with lymphatic malformations, 3% to 10% have airway compromise from respiratory obstruction or mediastinal extension.[47,157] Although most children with lymphatic malformation have a normal karyotype, several syndromes are associated, such as Turner, Down, Noonan, Roberts, and trisomy 13 and 18.[144] On ultrasound, most lymphatic malformations are multiloculated cystic masses with septa of variable thickness and solid components[47] (Fig. 48.49, Video 48.4). Fluid-fluid levels or echogenic debris can result from superimposed hemorrhage or infection. MRI provides optimum tissue characterization and lesion delineation before surgical intervention.[168] Surgical resection is the treatment of choice but can be difficult if the lesion invades neural, vascular, and muscular structures; therefore sclerotherapy, radiofrequency ablation, and laser therapy are other options.[48,168] Other malformations involving the lymphatic system include generalized lymphatic anomaly, Gorham-Stout disease, channel-type lymphatic malformation, primary lymphedema, and others.[162]

Venous malformations are soft, compressible lesions that may distend with increased venous pressure (Valsalva maneuver). About 40% of these lesions occur in the head and neck, and many invade multiple fascial planes and involve osseous structures.[163] These lesions, appearing clinically as soft, bluish, compressible masses, consist of thin-walled, dilated, dysplastic, small and large venous channels deficient in smooth muscle.[43] Rapid enlargement may occur secondary to phlebothrombosis. Multiple venous malformations are seen in **Maffucci syndrome** and **blue rubber bleb nevus syndrome, cerebral cavernous malformation,** and **glomuvenous malformation.**[162,169] **Phleboliths** are present in 16% of cases and can help confirm the diagnosis. Ultrasound demonstrates hypoechoic lesions with heterogeneous architecture. Acoustic shadowing secondary to phleboliths and fluid-fluid levels may be identified[48] (Fig. 48.50). On Doppler sonography, venous low-velocity flow is identified. Treatment includes elastic compression, sclerotherapy, and surgical excision.

Arteriovenous malformations (AVMs) represent collections of a nidus of tortuous abnormal, thin-walled vessels connecting dilated feeding arteries to draining veins. These lesions may be centered in cutaneous, muscular, or intraosseous structures.

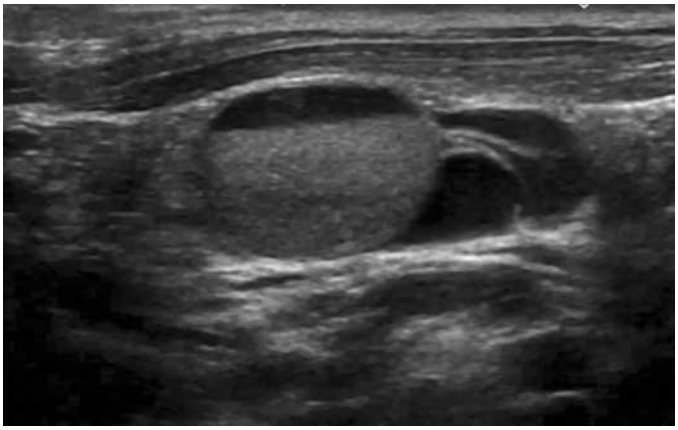

FIG. 48.49 Lymphatic Malformation. Lymphatic malformation in a 5-year-old child with long-standing left neck mass. Ultrasound shows a multilocular cystic lesion with a fluid-fluid level in one of the locules, indicating internal hemorrhage. See also Video 48.4.

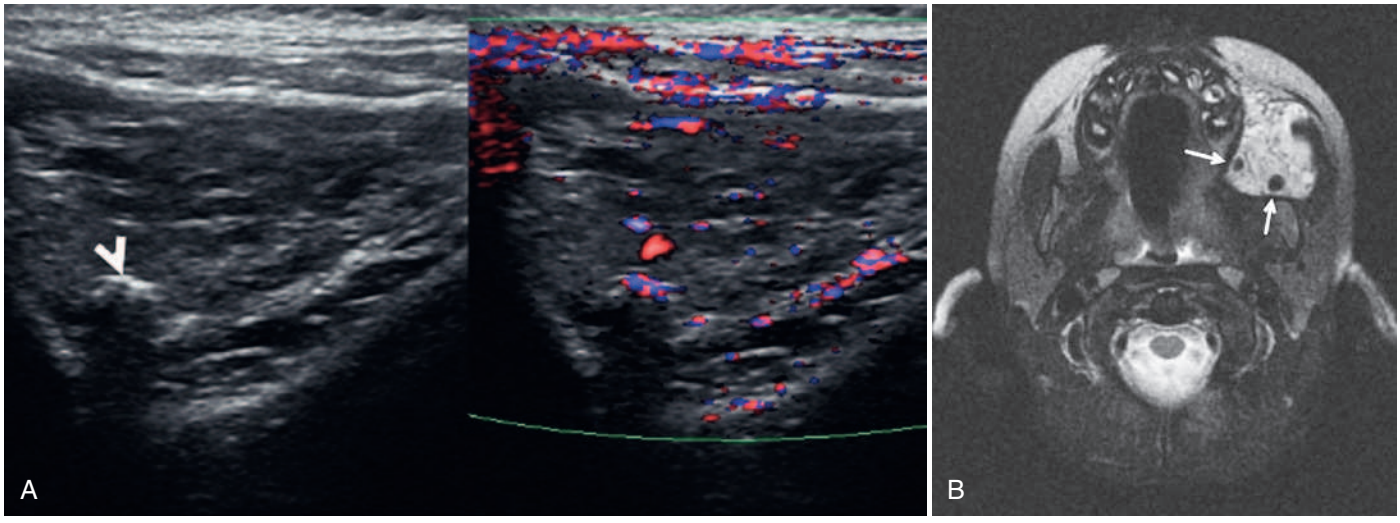

FIG. 48.50 Venous Malformation. (A) Side-by-side gray-scale and color Doppler. Masseter muscle is enlarged and heterogeneous with hypoechoic areas and a hyperechoic focus that shadows *(arrowhead),* consistent with phlebolith. Color Doppler demonstrates mild increase in vascularity. **(B)** Axial T2-weighted fat-saturated magnetic resonance image demonstrates high-signal lesion infiltrating the masseter muscle and parapharyngeal space. Dark foci are consistent with phleboliths *(arrows).*

Clinically, a blush hyperemia and thrill or bruit may be present. AVMs can enlarge acutely from increased blood flow, obstruction, or infection. An extensive lesion may cause congestive heart failure. AVMs also are affected by hormones, often increasing in size at puberty and during pregnancy.[48] The most common sites of AVMs in the head and neck include the cheek, followed by the ear, nose, and forehead.[43] On gray-scale ultrasound, AVMs demonstrate heterogeneity, with multiple hypoechoic channels and absence of soft tissue mass. Doppler sonograms show a high-flow lesion with low-resistance arteries and arterialized venous waveforms[47] (Fig. 48.51). Transcatheter embolization, sclerotherapy, and surgical excision are the mainstays of management.[48]

In **arteriovenous fistulas** (AVFs), there is direct communication between the arteries and veins without an intervening tangle of vessels; AVFs are frequently acquired during trauma. However, both AVMs and AVFs can occur sporadically, in the setting of hereditary hemorrhagic telangiectasia or capillary malformation–arteriovenous malformation (CM-AVM) syndrome.[162]

A combination of two or more simple vascular malformations is classified as a combined vascular malformation. Vascular malformations are also categorized based on involvement of major named vessels. It is important to recognize that both vascular tumors and vascular malformations can be associated with other anomalies and syndromes.[162]

Other Congenital Lesions

Cervical aortic arch is a rare congenital anomaly in which the arch is positioned high, above the clavicle, usually in the right side of the neck. This developmental variant occurs because of persistence of the embryonic third arch with regression of the fourth.[170] These patients are often asymptomatic but can have a pulsatile anechoic mass, dysphasia, and respiratory symptoms.[43]

Internal jugular phlebectasia is a rare congenital saccular or fusiform dilation of the internal jugular vein.[43,171] The lesion typically occurs on the right side with a history of asymptomatic neck swelling, although uncommon complications such as thrombosis and Horner syndrome have been reported.[172,173] Ultrasound demonstrates an echo-free, slow-flow vessel on color Doppler sonography that measures greater than 15 mm in anterior-to-posterior dimension and increases in size with Valsalva maneuver[171,172] (Fig. 48.52). Treatment is typically conservative.[173]

Iatrogenic Lesions

Color and duplex Doppler ultrasound are noninvasive techniques that provide information about blood vessel patency, size, and direction of blood flow.[174-176] Vascular lines are typically placed through the subclavian or jugular vein into the superior vena cava. Gray-scale and color Doppler sonograms can demonstrate **arterial** and **venous stenosis, thrombosis,** or **pseudoaneurysms,** which can result from central line placement or prior extracorporeal membrane oxygenation (ECMO) therapy[177] (Fig. 48.53). Ultrasound guidance has also proved useful for insertion of central venous and ECMO catheters to prevent morbidity related to malposition.[178-180]

Inflammatory Lesions

Lemierre syndrome is rare and typically occurs in young adults, more commonly male, after a primary oropharyngeal infection.[181] It is hypothesized that **thrombophlebitis** of tonsillar veins propagates into the internal jugular vein, resulting in *Fusobacterium necrophorum or streptococcal* **septicemia** and **septic emboli,** primarily to the lungs.[182,183] Ultrasound demonstrates an engorged, noncompressible vein that may contain echogenic thrombus. Color Doppler ultrasound can document absent flow and may show a lack of pulsation with Valsalva maneuver (Fig. 48.54). Blood cultures and chest radiography or CT scan secure the diagnosis so that appropriate antibiotic therapy can be instituted.[184]

Lymph Nodes

Lymph nodes consist of an outer cortex of lymphoid follicles and hilum containing lymphatic sinus, connective tissue, and blood vessels. Cervical lymph nodes, which number about 300, are located along the lymphatic vessels in the neck.[185] A normal infant lymph node measures less than 3 mm in diameter.[43] In children, lymph nodes larger than 1 cm in maximum dimension are considered enlarged. On ultrasound, a normal node is ovoid and hypoechoic, with an echogenic hilum containing central vascularity (Fig. 48.55). The normal length exceeds its width by 2 : 1.[74]

Lymph nodes can enlarge as a result of reactive hyperplasia, infection, inflammation, or malignancy.[186] Cervical lymphadenopathy is common and frequently a normal finding in children. From 47% to 55% of children of all ages and 80% to 90% of children aged 4 to 8 years have palpable reactive hyperplastic lymph nodes not originating from infection or systemic illness. Palpable lymph nodes in infants, however, are not normal and should be evaluated further. **Supraclavicular lymphadenopathy and large nodes** are concerning, associated with high risk of malignancy and requiring FNA and/or biopsy.[186-188]

The diagnosis of lymphadenitis is often clinical, and most cases are uncomplicated; therefore most patients are treated medically and require no additional imaging. If imaging is performed, key features include location, extent of cellulitis, myositis, presence of abscess, and vascular compromise.[144] With ultrasound imaging, **lymphadenitis** demonstrates multiple enlarged lymph nodes, normal in shape but with reduced echogenicity and increased central and peripheral vascularity[74,144,189] (Fig. 48.56). With progressive enlargement of the nodes and **cellulitis,** there is blurring of soft tissue planes, some septa may stand out, and color Doppler imaging shows increased blood flow[45] (Fig. 48.57). When an **abscess** forms, the nodes coalesce, central vascularity disappears, and a hypoechoic center, sometimes with posterior enhancement, is present and surrounded by a thick, hyperechoic, hypervascular irregular capsule (Fig. 48.58). Pus-fluid levels, fluid movement on Doppler ultrasound, and hyperechoic foci with comet-tail artifacts, signifying air, help confirm the diagnosis.[74] In severe cases, adenitis may spread to the deep cervical spaces such as retropharyngeal, parapharyngeal, or submandibular space.[190] In rare instances, sinus tracts and

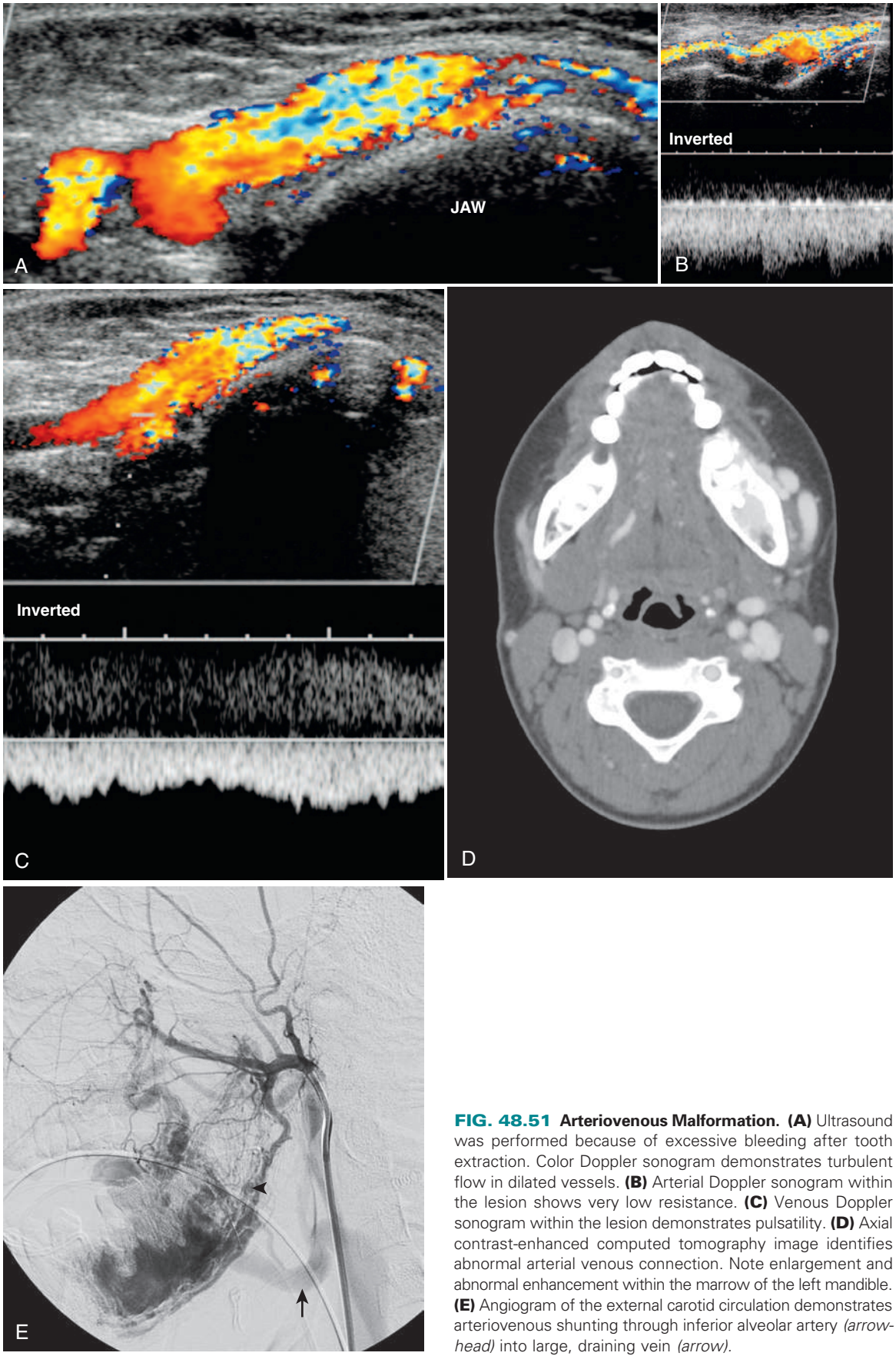

FIG. 48.51 Arteriovenous Malformation. (A) Ultrasound was performed because of excessive bleeding after tooth extraction. Color Doppler sonogram demonstrates turbulent flow in dilated vessels. **(B)** Arterial Doppler sonogram within the lesion shows very low resistance. **(C)** Venous Doppler sonogram within the lesion demonstrates pulsatility. **(D)** Axial contrast-enhanced computed tomography image identifies abnormal arterial venous connection. Note enlargement and abnormal enhancement within the marrow of the left mandible. **(E)** Angiogram of the external carotid circulation demonstrates arteriovenous shunting through inferior alveolar artery *(arrowhead)* into large, draining vein *(arrow)*.

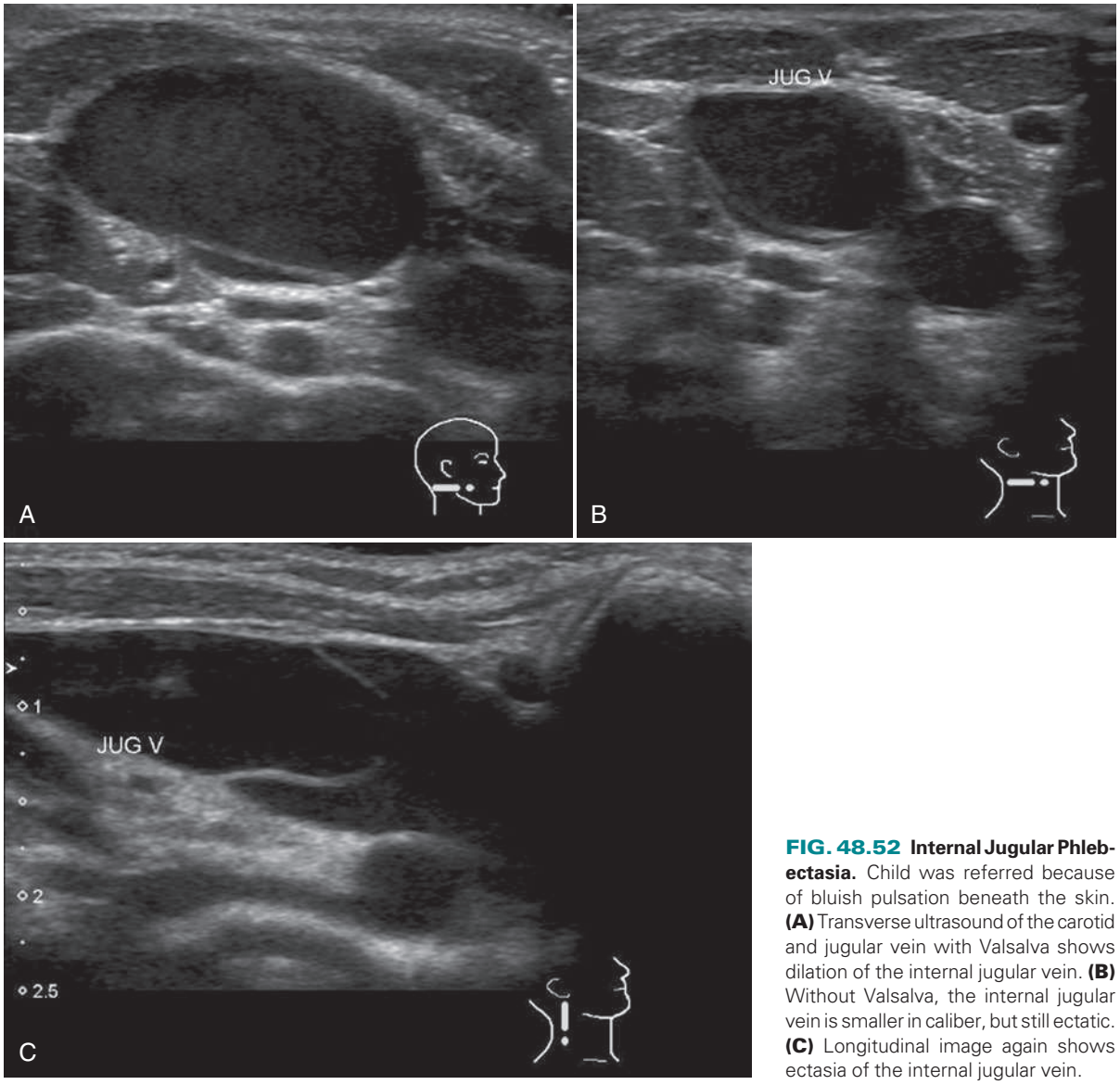

FIG. 48.52 Internal Jugular Phlebectasia. Child was referred because of bluish pulsation beneath the skin. **(A)** Transverse ultrasound of the carotid and jugular vein with Valsalva shows dilation of the internal jugular vein. **(B)** Without Valsalva, the internal jugular vein is smaller in caliber, but still ectatic. **(C)** Longitudinal image again shows ectasia of the internal jugular vein.

fistulas may develop.[45] FNA and surgical incision may be necessary to resolve the infection.[187]

Acute lymph node enlargement in children can be unilateral or bilateral. The anterior cervical nodes, which drain the mouth and pharynx, are most often affected.[187] In 80% of cases, acute **unilateral pyogenic lymphadenitis** is secondary to *S. aureus* or group A beta-hemolytic streptococci.[74,187,191] Many patients have respiratory tract infection, pharyngitis, tonsillitis, or otitis media in conjunction with tender, warm, and erythematous lymph nodes. A less common cause of acute bacterial lymphadenitis includes actinomycosis in a patient with poor dental hygiene.

The etiology of **bilateral cervical lymphadenopathy** tends to be viral, including rhinovirus, parainfluenza virus, and influenza.[191] **Epstein-Barr virus** can be difficult to differentiate from bacterial infections because the infection may be associated with exudative tonsillitis. In a patient with Epstein-Barr virus, the presence of diffuse lymphadenopathy and hepatosplenomegaly may help confirm the diagnosis.[5] Noting the age of the child and the sites involved may provide other clues[192] (Tables 48.3 and 48.4).

Subacute or chronic infection occurs when cervical lymph nodes enlarge slowly and are only minimally tender without substantial cellulitis. Differential diagnosis includes bacterial causes such as atypical mycobacteria, *Mycobacterium tuberculosis, Nocardia,* or cat-scratch disease; viral pathogens; or fungal infection such as histoplasmosis.[187,190] Most **mycobacterial infections** are caused by variant strains of *Mycobacterium avium-intracellulare-scrofulaceum* complex.[187] Infection typically is unilateral and occurs in children aged 1 to 5 years. *M. tuberculosis,* when it involves the cervical nodes, is thought to represent an extension of the primary pulmonary lesion or to be associated with acquired immunodeficiency syndrome (AIDS).[45] Nodes on sonography with low attenuation centers and small calcifications suggest mycobacterial infection.[77,144] *Nocardia* typically is seen

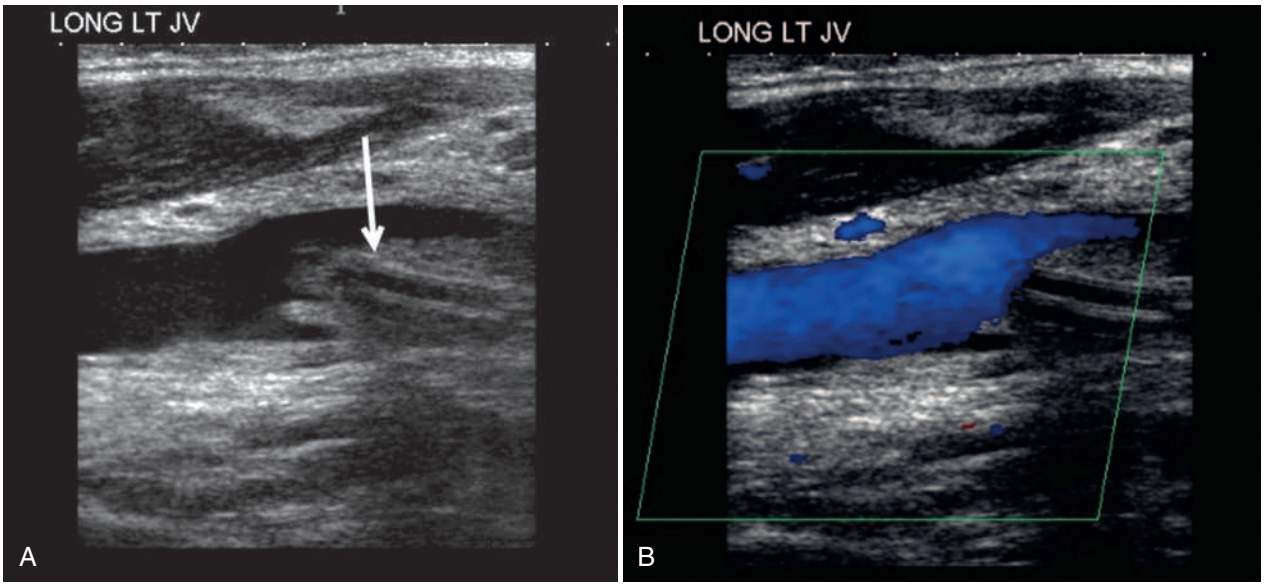

FIG. 48.53 Jugular Vein Thrombosis Caused by Central Line. (A) Longitudinal image of internal jugular vein with thrombus surrounding a vascular catheter *(arrow)*. **(B)** Color Doppler image shows partial occlusion at site of thrombus.

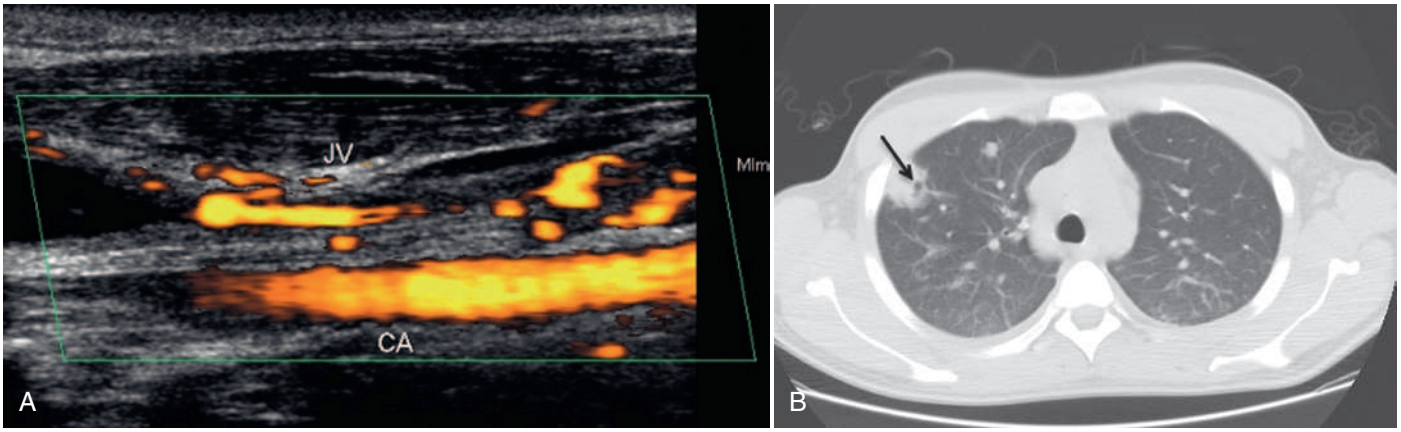

FIG. 48.54 Lemierre Syndrome. (A) Color Doppler sonogram of the internal jugular vein demonstrates near-occlusive clot within the lumen. **(B)** Axial chest computed tomography image shows two parenchymal nodules in the right upper lung with an area of central cavitation *(arrow)* caused by septic emboli.

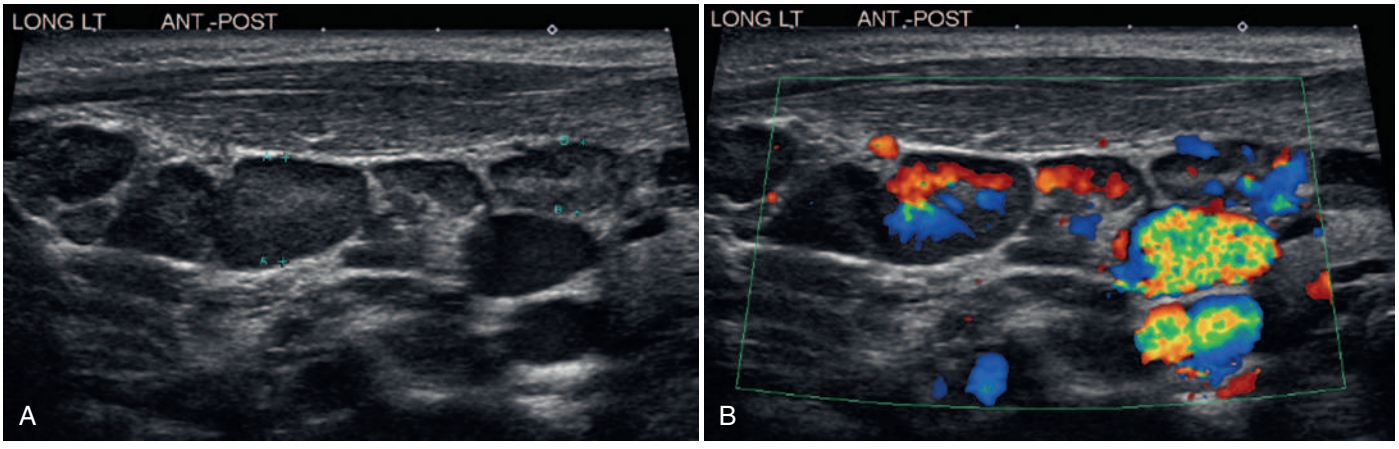

FIG. 48.55 Lymph Node Morphology. (A) Longitudinal scan of multiple normal sized (<1 cm) lymph nodes, ovoid and hypoechoic, with an echogenic hilum. **(B)** Color Doppler sonogram demonstrates central hilar vessels.

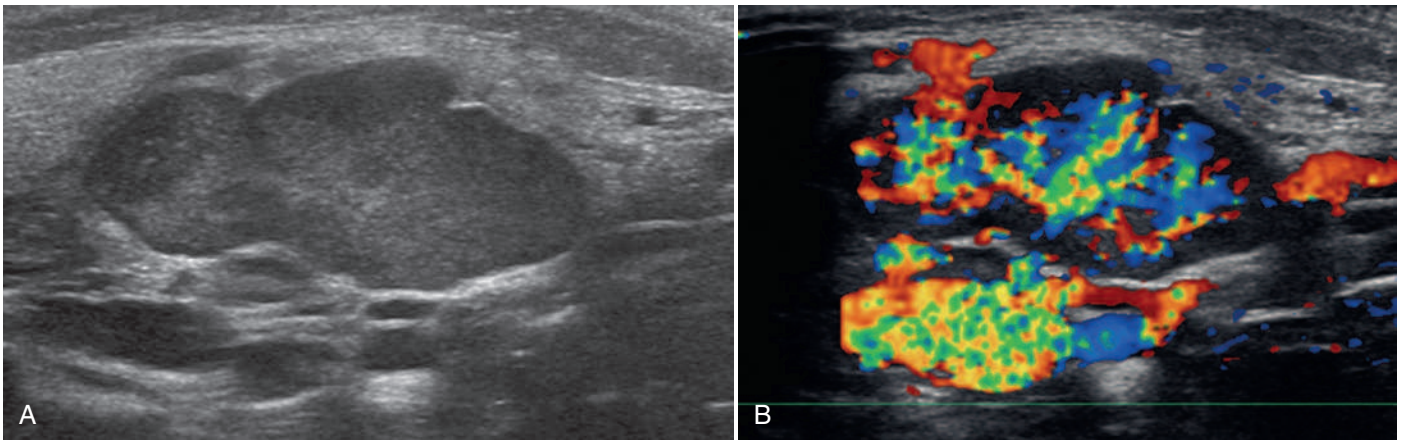

FIG. 48.56 Lymphadenopathy Related to Epstein-Barr Virus. (A) Left anterior cervical chain demonstrates enlarged hypoechoic nodal mass. **(B)** Color Doppler demonstrates increased central vascularity.

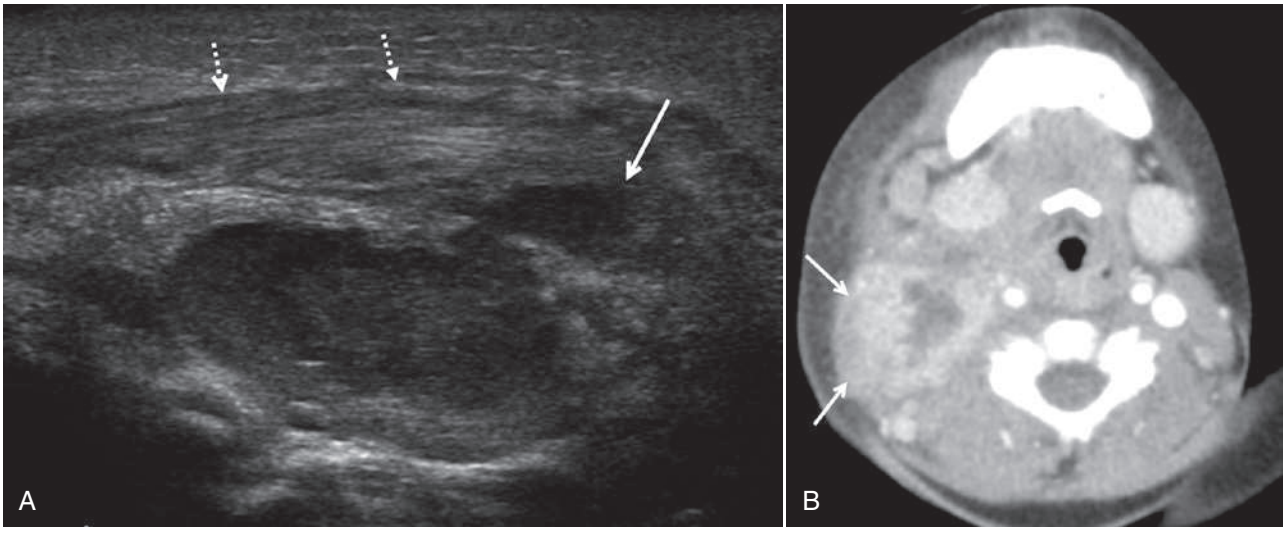

FIG. 48.57 Complicated Lymphadenitis With Myositis. (A) Ultrasound image shows a hypoechoic collection deep to the sternocleidomastoid muscle with extension of inflammatory material into muscle *(arrow).* The sternocleidomastoid *(dotted arrows)* is heterogeneous and swollen, consistent with myositis. **(B)** Axial contrast-enhanced computed tomography confirms presence of an abscess in the right upper neck and associated adjacent cellulitis and right sternocleidomastoid myositis *(arrows).*

TABLE 48.3 Age and Causes of Lymphadenopathy

Pediatric Category	Common Infectious Causes
Newborn	*Staphylococcus aureus* most common Occasionally, late-onset group B streptococci
Infant and child younger than 5 years	Group A streptococci and *S. aureus* Nontuberculous *Mycobacterium*
School-age child and adolescent	Epstein-Barr virus, cytomegalovirus, toxoplasmosis Tuberculosis or infectious mononucleosis

TABLE 48.4 Site of Node and Causes of Lymphadenopathy

Node Site	Common Causes
Occipital	Roseola, rubella, scalp infections
Periauricular	Eye infections, cat-scratch disease
Cervical	Streptococcal or staphylococcal adenitis or tonsillitis Mononucleosis, toxoplasmosis, malignancies, Kawasaki disease
Submandibular	Hodgkin or non-Hodgkin lymphoma, tuberculosis, histoplasmosis

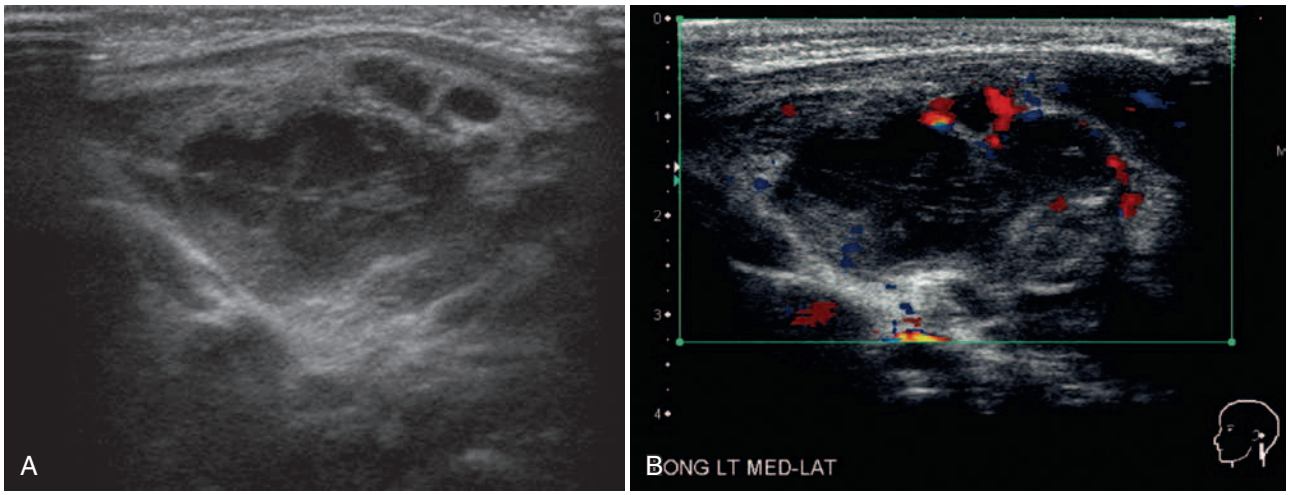

FIG. 48.58 Complicated Lymphadenitis With Abscess. (A) Gray-scale ultrasound image shows multilobulated, hypoechoic area with thick wall in the left upper cervical region. **(B)** Color Doppler image shows lack of vessels in the center of the collection but with peripheral vascularity.

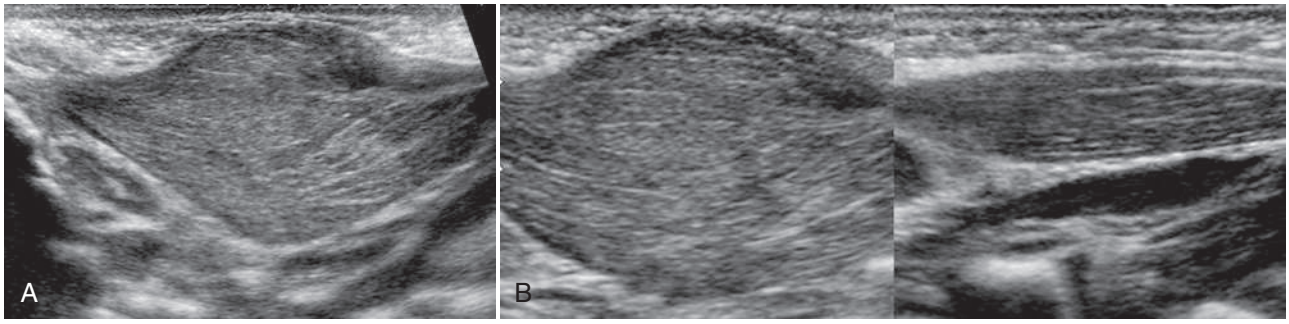

FIG. 48.59 Fibromatosis Coli. (A) Longitudinal ultrasound shows sternocleidomastoid muscle with enlargement, attenuation of striations, and mild increase in echotexture. **(B)** Longitudinal view shows comparison of abnormal left and normal right sternocleidomastoid muscle.

in immunocompromised children.[190] **Cat-scratch disease,** caused by the organism *Bartonella henselae,* manifests typically with a dominant unilateral node 2 to 4 weeks after a minor cat scratch, usually from a kitten.[187] **Histoplasmosis,** an infection prevalent in the Mississippi Valley and northeastern United States, manifests with cervical adenitis and a mediastinal mass and is typically asymptomatic but may be fatal if acutely disseminated.[190] FNA for cytopathology and culture may help confirm the diagnosis; these nodes often can persist for months, making distinction from neoplasm difficult.[45,190] Other inflammatory causes of lymphadenopathy in children include collagen vascular disease, sarcoid, immunologic deficiencies (HIV and chronic granulomatous disease), and postvaccination syndrome.[192] **Kawasaki disease,** a multisystem vasculitis of unknown origin, causes cervical adenopathy in 50% to 70% of patients with the disease.[193] Children with Kawasaki disease typically are presented before 5 years of age with enlarged unilateral lymph nodes greater than 1.5 cm in diameter.[193]

Fibromatosis Colli

Fibromatosis colli occurs in 0.3% to 1.9% of children. The etiology is still unclear but may involve intramuscular hemorrhage, venous occlusion, birth trauma, or in utero torticollis.[82,144,187,194] Pathologically, fibromatosis colli results from fibrosis and shortening of the sternocleidomastoid muscle, producing a soft tissue mass.[195] Peak incidence of presentation is 2 to 8 weeks after birth. Fibromatosis colli typically affects the firstborn boy with breech presentation or difficult delivery. Most infants have ipsilateral head tilt, contralateral chin deviation, and a palpable soft tissue mass.[196,197] From 6% to 20% of patients have associated musculoskeletal anomalies, including hip dysplasia and facial asymmetry.[49]

Sonography is the best technique to image the fibromatosis colli lesion. A normal sternocleidomastoid muscle demonstrates decreased echogenicity and long, thin, echogenic lines denoting the muscle fascicles along the length of the muscle. In the presence of fibromatosis colli, there is a focal or diffuse enlargement of the sternocleidomastoid, which typically shows homogeneous or heterogeneous increased echogenicity; however, mixed and hypoechoic lesions have been described[194,195] (Fig. 48.59). Focal lesions tend to involve the inferior third of the muscle.[194] In larger masses, there is distorted architecture with disruption of the normal muscle bundles.[195] Some cases may resolve spontaneously; however, physical therapy is the first line of therapy and

effective in 95% of children.[49] If head tilt persists, muscle release or tenotomy is performed to prevent development of significant craniofacial asymmetry and scoliosis.[5]

Masses

Pilomatricoma

Pilomatricomas (previously called "pilomatrixomas") are benign neoplasms arising from the hair follicles.[198] They are the second most frequently resected mass in the head and neck in children, after lymph nodes.[198] However, pilomatricomas are infrequently imaged because diagnosis is often made clinically. Imaging is often requested when the clinician is unfamiliar with the diagnosis or the lesion is in the preauricular region and needs to be excluded from an intraparotid mass or branchial apparatus remnant.[198,199] These lesions typically occur in the head and neck in children younger than 10 years, with a smaller peak occurring in the sixth and seventh decades.[199] Multiple pilomatricomas can be seen in the setting of Gardner syndrome, myotonic dystrophy, Steinert disease, Turner syndrome, and sarcoidosis.[199] Clinically, the lesions are firm nodules attached to the skin and are freely mobile over the subcutaneous tissues. On ultrasound, these lesions are frequently well-defined, hypoechoic lesions with mild internal heterogeneous echogenicity, speckled or chunky internal calcifications, and hypoechoic rim. The lesions may have internal vascularity demonstrated by spectral Doppler (Fig. 48.60). Rarely, when the lesion has ruptured, the mass has an irregular heterogeneous sonographic appearance, indistinguishable from other subcutaneous lesions.[200,201] There may be some perilesional hypoechogenicity, which is found to correlate with perilesional inflammation.[202] Complete surgical resection is curative.

Congenital Infantile Myofibromatosis

Congenital infantile myofibromatosis, although rare, is the most common fibrous tumor in the neonate and infant. The cause is unknown, although some familial cases have been reported.[203,204] Histologically, these lesions are composed of well-circumscribed nodules of plump spindle-shaped cells with staining characteristics intermediate between smooth muscle cells and fibroblasts. Often, there is central necrosis with focal calcifications.[203] These masses can occur in the skin, muscle, bone, or viscera or intracranially.[203,205,206] Infantile myofibromatosis lesions almost exclusively affect infants and young children, with 88% occurring before 2 years of age.[203] Over half of the lesions are identified in the neonatal period, and some cases are diagnosed prenatally.[203,207] The World Health Organization (WHO) classifies congenital infantile myofibromatosis into three types: the solitary type, also called "infantile myofibroma"; the multicentric form without visceral involvement; and the multicentric form with visceral involvement.[203,206] The solitary infantile myofibroma is more common in males (69%) and frequently occurs in the head, neck, and trunk. The multicentric form is more common in females (63%). The solitary form of infantile myofibromatosis and the multicentric form without visceral involvement generally have a good prognosis, and recurrence is rare. Surgical excision is the treatment of choice when feasible; chemotherapy is used in inoperable cases. Some cases may show spontaneous regression.[203]

On ultrasound, the lesions often show a lobulated heterogeneous appearance with central anechoic and hyperechoic structures (Fig. 48.61). Thick septations may separate the anechoic regions. The lesions are typically hypovascular.[205] CT and MRI are useful in assessment of disease extent and bone and soft tissue involvement and to screen for additional lesions.

Other, less common fibrous lesions that can occur in the head and neck include nodular fasciitis and inflammatory myofibroblastic tumor. These lesions have a nonspecific soft tissue mass imaging appearance and require additional imaging and biopsy for definitive diagnosis.

Malignant Neoplasms

Malignant neoplasms of the head and neck represent 12% of all childhood cancers. Lymphomas and sarcomas encompass 50%

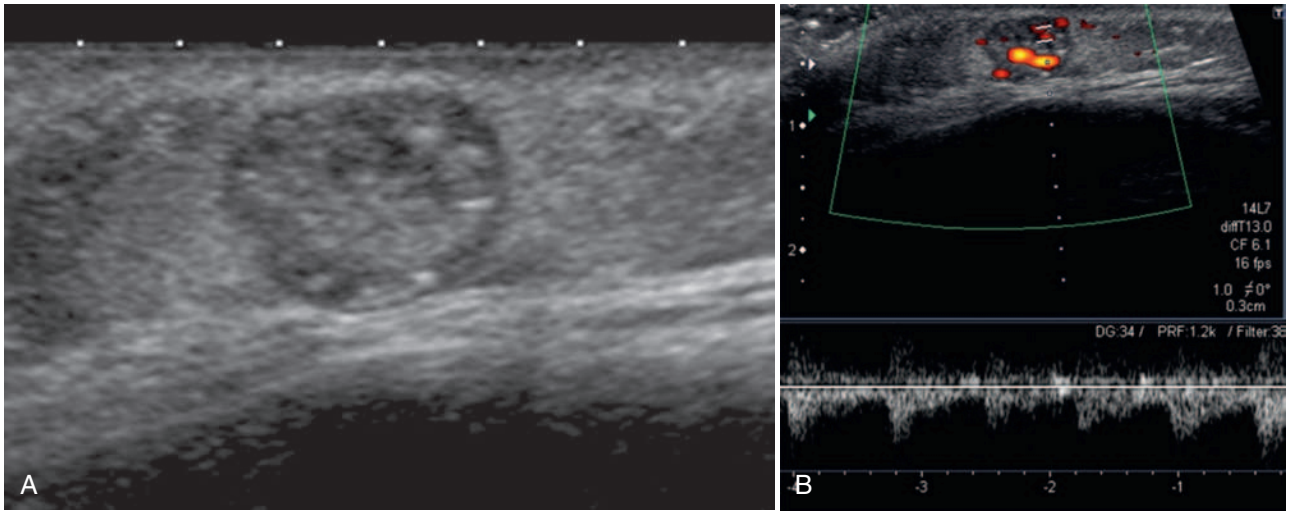

FIG. 48.60 Pilomatricoma. Seven-year-old girl with right scalp bump for 4 months. **(A)** Gray-scale ultrasound image shows a well demarcated heterogeneous hypoechoic lesion with internal echogenic foci. **(B)** Color Doppler image shows presence of internal vascularity within the lesion.

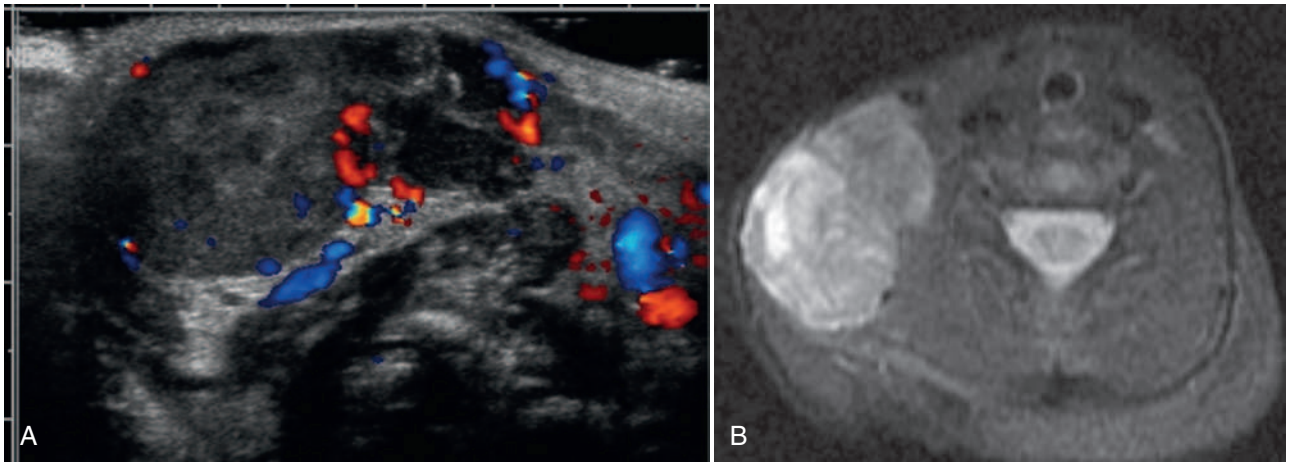

FIG. 48.61 Infantile Myofibroma. One-month-old with right neck mass since birth. **(A)** Ultrasound shows lobulated heterogeneous mass with solid and cystic components and predominantly peripheral vascularity. **(B)** On fat-suppressed T2-weighted magnetic resonance imaging, there is a heterogeneous lobulated hyperintense mass, with suggestion of cystic component superficially.

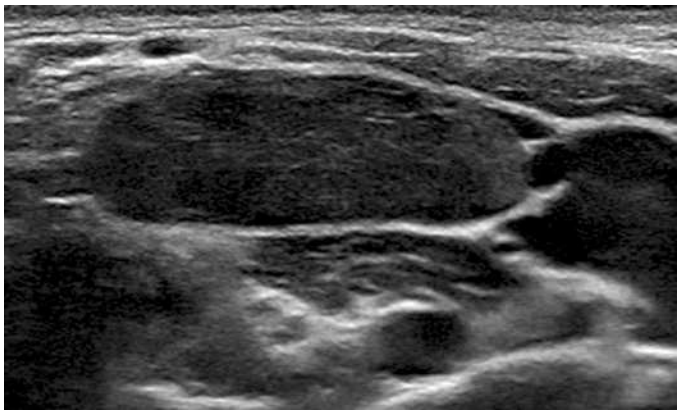

FIG. 48.62 Hodgkin Lymphoma. Sixteen-year-old with fullness in the right supraclavicular area. Ultrasound demonstrates large hypoechoic "pseudocystic" lymph node with loss of normal architecture, concerning for malignancy.

of these neoplasms. After puberty, lymphoma is the most common neoplasm.[187]

Lymphoma. **Lymphoma** is the most common head and neck malignancy, accounting for 27% of head and neck malignancies in children.[116] There is an equal 50% distribution of Hodgkin lymphoma and non-Hodgkin lymphoma.[144] Pediatric lymphoma has a greater association with Epstein-Barr virus and has a 2:1 male preponderance.[116] **Hodgkin lymphoma** typically manifests in adolescence as upper cervical and less frequently supraclavicular masses.[208,209] **Non-Hodgkin lymphoma** usually manifests at age 2 to 12 years with extranodal masses, diffuse nodal involvement, and rapid growth.[208,209] On gray-scale ultrasound, lymphoma often demonstrates a hypoechoic, pseudocystic appearance with sharp borders caused by reduced fat in lymph nodes, and lack of calcifications[210] (Fig. 48.62). Lymphomas do not necessarily follow malignant color vascular distribution, often with exaggerated hilar flow containing large, central branching vessels.[210] Extensive axillary and mediastinal adenopathy may be noted at presentation.[144] Imaging of these patients should include CT scans of the neck, chest, abdomen, and pelvis. Gallium-67 citrate scintigraphy and fluorodeoxyglucose–positron emission tomography (FDG-PET) are also helpful in further depiction of disease extent.[209]

Rhabdomyosarcoma. Rhabdomyosarcoma is a malignant tumor that arises from skeletal muscle cells. It is the third most common soft tissue tumor of childhood, after Wilms tumor and neuroblastoma, with 40% of cases originating in the head and neck.[116,144,211] About 85% of patients with rhabdomyosarcoma are younger than age 15 years.[212] A bimodal peak incidence occurs at age 1 to 3 years and in early adolescence.[74] The two main histologic types are embryonal and alveolar.[211] Embryonal rhabdomyosarcoma represents 60% of cases, is most common in the young child, and frequently arises in the head and neck.[212,213] Alveolar rhabdomyosarcoma, 20% of tumors, is more common in the older child and has a poorer prognosis. The most common sites of origin include the orbit, nasopharynx, middle ear or mastoid, and sinonasal cavity. These tumors tend to be aggressive, metastasize to lymph nodes, and rapidly invade bone, often with intracranial extension. Because of this aggressive course, MRI and CT scans are typically the first line of imaging to define the full extent of the lesion and exclude intracranial extension.[82] If a lesion is detected with ultrasound, however, the tumors typically are poorly vascularized and heterogeneous, with ill-defined hypoechoic areas caused by necrosis[74] (Fig. 48.63).

Neuroblastoma. **Neuroblastoma** is a neoplasm derived from the sympathetic neural crest cells, with the most common site of origin being the adrenal gland.[82] Primary cervical neuroblastoma can arise in the retropharyngeal area and is seen in only 5% of cases but usually has a favorable prognosis. Metastatic disease from a primary mass outside of the neck is more common and can occur in the cervical lymph nodes, calvaria, and facial bones.[74,214] Head and neck manifestations of neuroblastoma include Horner syndrome, proptosis, opsoclonus, and periorbital soft tissue masses.[215,216] Soft tissue or lymph node metastasis on ultrasound typically appears as an echogenic mass with or without calcification that displaces the great vessels of the neck and may extend into the mediastinum, spine, or skull base.[215] Expansile

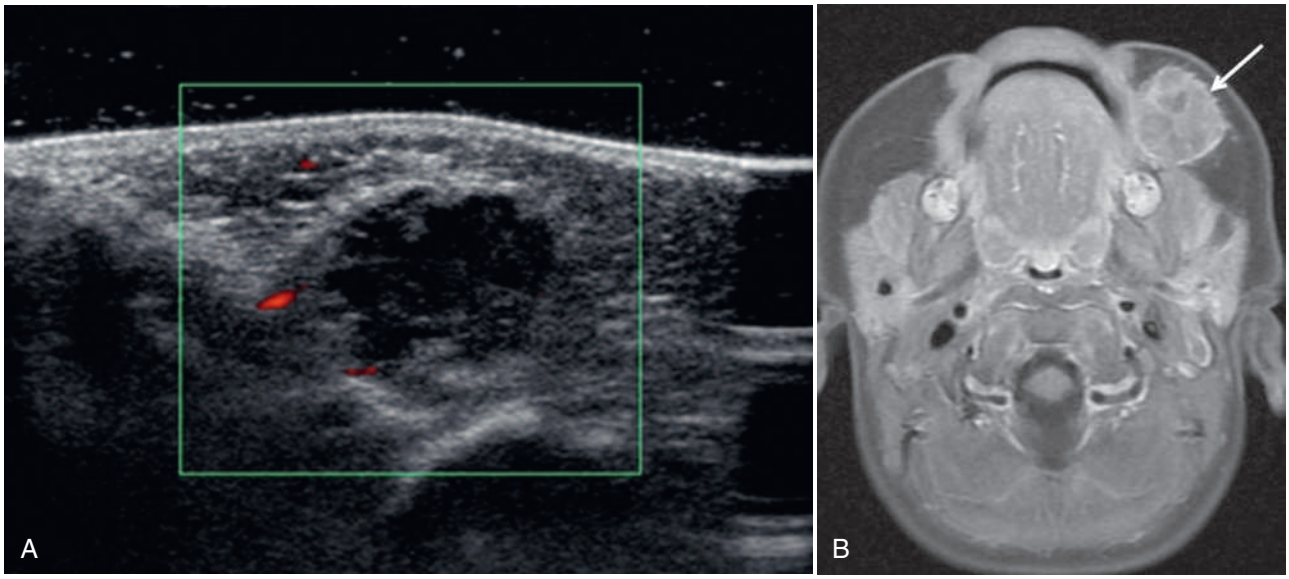

FIG. 48.63 Rhabdomyosarcoma. Five-month-old with hard mass in the left cheek. **(A)** Color Doppler ultrasound image shows a hypoechoic, hypovascular, irregular, poorly marginated mass in the left cheek. **(B)** T1-weighted postcontrast magnetic resonance image shows a heterogeneously enhancing mass in the left cheek *(arrow).* The mass had increased in size compared with the ultrasound performed 3 weeks beforehand.

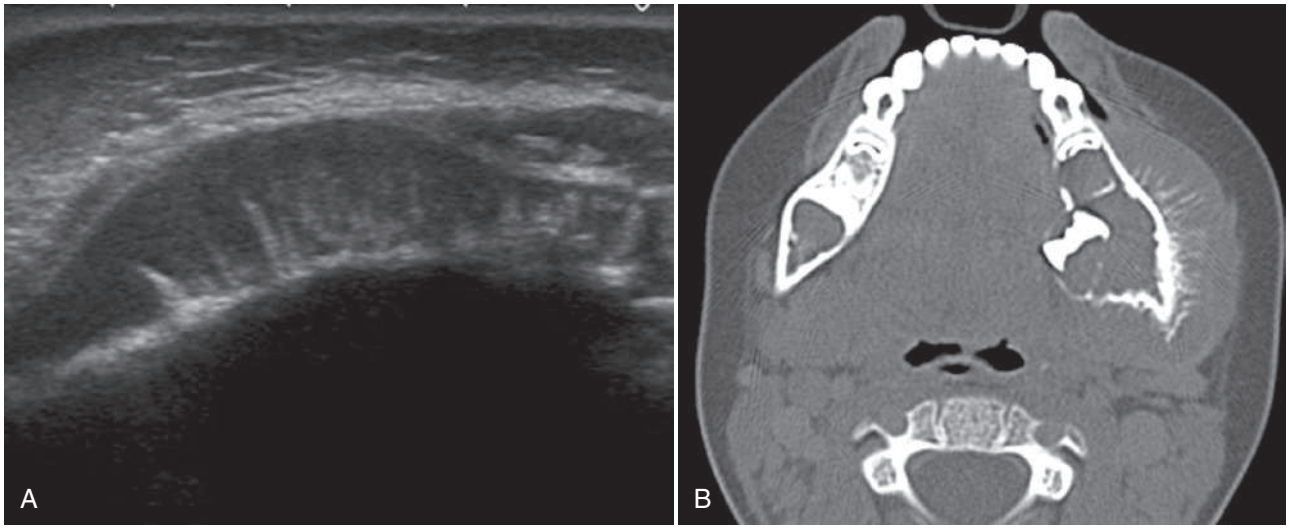

FIG. 48.64 Neuroblastoma. Three-year-old with left cheek swelling. **(A)** Ultrasound image shows a hypoechoic mass in the deep soft tissues of the left cheek inseparable from the left mandibular ramus, which is poorly defined and contains radiating echogenic bands consistent with aggressive periostitis. **(B)** Computed tomography image through the mandible shows expansion of the left hemimandible with aggressive periosteal reaction and soft tissue mass.

bony lesions may also manifest as facial or calvarial bumps referred for sonographic evaluation. Orbital metastasis of neuroblastoma is most frequent, but other facial bones such as the maxilla and mandible can be involved as well.[214] It is important to recognize underlying osseous involvement, which can be seen as radiating echogenic bands reflecting the aggressive periosteal reaction[214] (Fig. 48.64).

Other Neoplasms. An unusual soft tissue mass in the head and neck should raise concern for malignancy in children. Leukemic soft tissue deposits or granulocytic sarcomas (previously called "chloromas") should be considered (Fig. 48.65) in children with leukemia. Less common malignancies include other rare soft tissue sarcomas such as infantile fibrosarcoma, osteosarcoma, or Ewing sarcoma. The presentation and sonographic appearances may be nonspecific, and additional imaging with biopsy is frequently needed for diagnosis.

Metastatic Disease. Metastatic nodal disease is uncommon in pediatrics.[144] Neuroblastoma, rhabdomyosarcoma, and thyroid cancer are the most likely causes. Imaging usually cannot differentiate reactive, inflammatory, or neoplastic disease.[144,208] Clinical concerns for neoplasm include onset in neonatal period, rapid growth, skin ulceration, fixation to skin, and large, hard masses.[191] With ultrasound, suspicious findings have been defined. Tumor invasion typically starts in the cortex, so changes in the

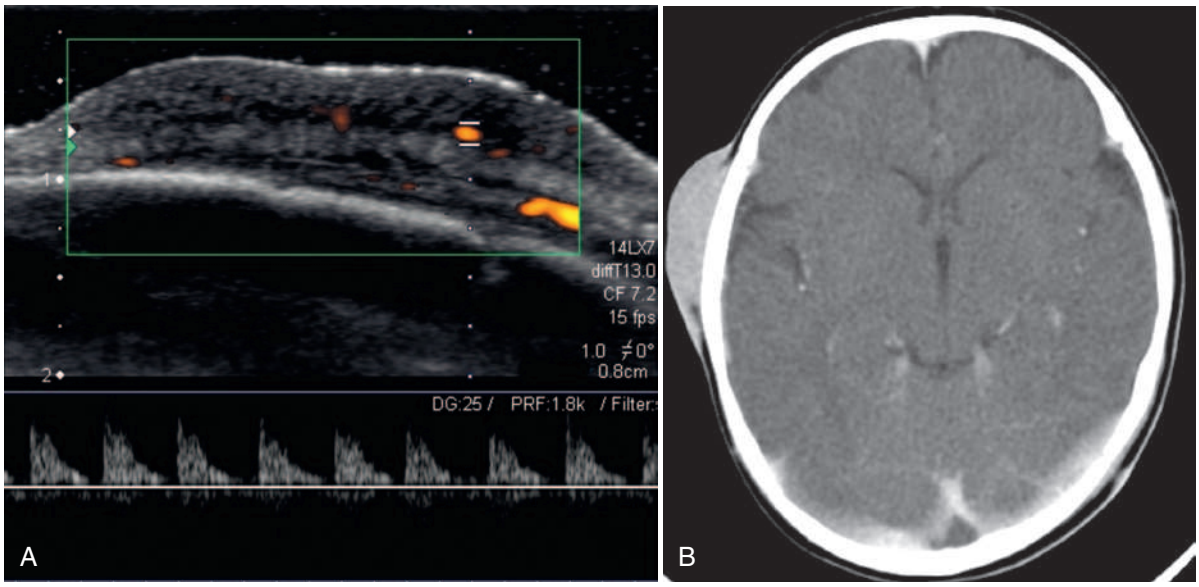

FIG. 48.65 Granulocytic Sarcoma (Chloroma). Three-month-old with right scalp bump for 2 weeks. **(A)** Ultrasound demonstrates an ill-defined mass that was not hypervascular, but had arterial waveforms. **(B)** Head computed tomography image shows avidly enhancing mass involving skin and soft tissues of the right scalp. Peripheral blood smear in this infant showed blast cells, and diagnosis was granulocytic sarcoma in the setting of acute myelogenous leukemia.

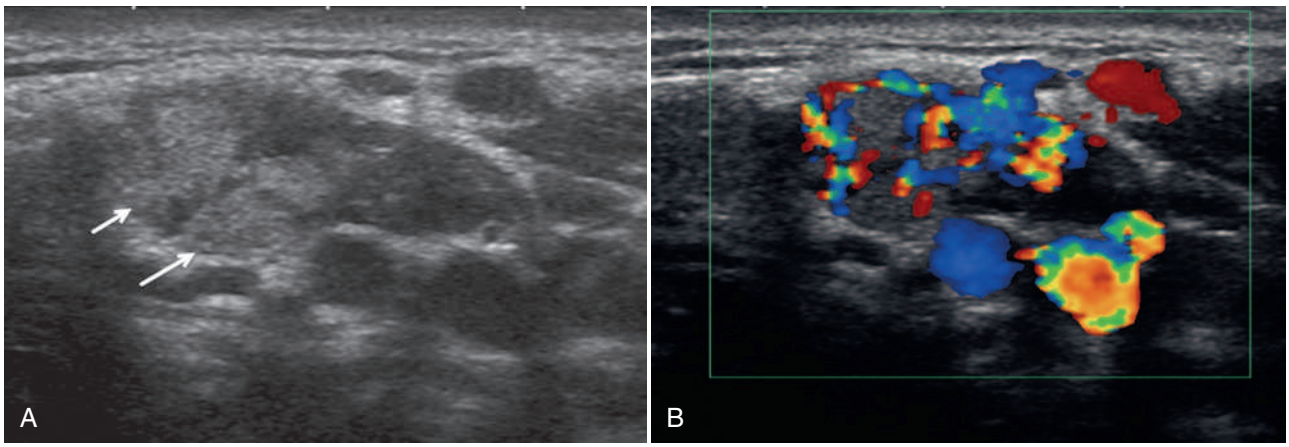

FIG. 48.66 Lymph Node Metastasis From Thyroid Cancer. (A) Enlarged node demonstrates lobular areas of increase echogenicity *(arrows),* poor definition of borders, and asymmetrical shape. **(B)** Color Doppler of the node shows increased asymmetrical vascularity in the area of abnormal echogenicity.

normal nodal shape from ovoid to round or asymmetrical are a concern.[43] Other imaging clues to malignant diagnosis include large size (>3 cm), heterogeneous echotexture, lack of echogenic hilum, and perinodal invasion.[156,158] Matted nodes and soft tissue edema are common findings in infectious or inflammatory disorders. Necrosis and calcification can be a sign of malignancy, but similar findings are noted in granulomatous lesions.[156] Thyroid nodal metastases are typically identified in the low neck and supraclavicular area.[217] On sonography, thyroid nodal disease demonstrates the same neoplastic findings, as well as increased echogenicity and cystic degeneration, with greater than 50% containing internal calcifications[185,217] (Fig. 48.66).

Color Doppler sonography of lymph nodes can be helpful when classified into four categories: hilar, peripheral, mixed, and avascular.[146,155] Color Doppler sonograms of benign lesions are typically avascular or hilar, whereas malignant nodes demonstrate peripheral or mixed vascular flow.[106,155,156] High Doppler RIs and pulsatility index have been noted in neoplastic adenopathy; however, other studies have not supported this finding. Therefore the accuracy of this technique is controversial.[146] Ultrasound is useful in guiding FNA biopsy.[156,160]

REFERENCES

1. Koch BL. Avoiding sedation in pediatric radiology. Pediatr Radiol. 2008;38(Suppl. 2):S225-S226.
2. Pappas JN, Donnelly LF, Frush DP. Reduced frequency of sedation of young children with multisection helical CT. Radiology. 2000;215(3):897-899.
3. Reed MH. Imaging utilization commentary: a radiology perspective. Pediatr Radiol. 2008;38(Suppl. 4):S660-S663.
4. Strauss KJ, Kaste SC. The ALARA (as low as reasonably achievable) concept in pediatric interventional and fluoroscopic imaging: striving to keep radiation

doses as low as possible during fluoroscopy of pediatric patients—a white paper executive summary. Radiology. 2006;240(3):621-622.
5. Malik A, Odita J, Rodriguez J, Hardjasudarma M. Pediatric neck masses: a pictorial review for practicing radiologists. Curr Probl Diagn Radiol. 2002;31(4):146-157.
6. Harnsberger HR, Osborn AG. Differential diagnosis of head and neck lesions based on their space of origin. 1. The suprahyoid part of the neck. AJR Am J Roentgenol. 1991;157(1):147-154.
7. Smoker WR, Harnsberger HR. Differential diagnosis of head and neck lesions based on their space of origin. 2. The infrahyoid portion of the neck. AJR Am J Roentgenol. 1991;157(1):155-159.
8. Bergeron RT. In re: Harnsberger HR, Osborn AG. Differential diagnosis of head and neck lesions based on their space of origin. 1. The suprahyoid part of the neck. AJR Am J Roentgenol 1991;157:147-154 and Smoker WRK, Harnsberger HR. Differential diagnosis of head and neck lesions based on their space of origin. 2. the infrahyoid portion of the neck. AJR Am J Roentgenol 1991;157:155-159. AJNR Am J Neuroradiol. 2001;22(8):1628-1629.
9. Gamss C, Gupta A, Chazen JL, Phillips CD. Imaging evaluation of the suprahyoid neck. Radiol Clin North Am. 2015;53(1):133-144.
10. Currarino G, Votteler TP. Lesions of the accessory parotid gland in children. Pediatr Radiol. 2006;36(1):1-7.
11. Lowe LH, Stokes LS, Johnson JE, et al. Swelling at the angle of the mandible: imaging of the pediatric parotid gland and periparotid region. Radiographics. 2001;21(5):1211-1227.
12. Bialek EJ, Jakubowski W, Karpinska G. Role of ultrasonography in diagnosis and differentiation of pleomorphic adenomas: work in progress. Arch Otolaryngol Head Neck Surg. 2003;129(9):929-933.
13. Howlett DC. High resolution ultrasound assessment of the parotid gland. Br J Radiol. 2003;76(904):271-277.
14. Weissman JL, Carrau RL. Anterior facial vein and submandibular gland together: predicting the histology of submandibular masses with CT or MR imaging. Radiology. 1998;208:441-446.
15. Garcia CJ, Flores PA, Arce JD, et al. Ultrasonography in the study of salivary gland lesions in children. Pediatr Radiol. 1998;28(6):418-425.
16. Ching AS, Ahuja AT. High-resolution sonography of the submandibular space: anatomy and abnormalities. AJR Am J Roentgenol. 2002;179(3):703-708.
17. Yasumoto M, Inoue H, Ohashi I, et al. Simple new technique for sonographic measurement of the thyroid in neonates and small children. J Clin Ultrasound. 2004;32(2):82-85.
18. McQuone SJ. Acute viral and bacterial infections of the salivary glands. Otolaryngol Clin North Am. 1999;32(5):793-811.
19. Thoeny HC. Imaging of salivary gland tumours. Cancer Imaging. 2007;7:52-62.
20. Mehta D, Willging JP. Pediatric salivary gland lesions. Semin Pediatr Surg. 2006;15(2):76-84.
21. Kanekar SG, Mannion K, Zacharia T, Showalter M. Parotid space: anatomic imaging. Otolaryngol Clin North Am. 2012;45(6):1253-1272.
22. Saarinen RT, Kolho KL, Pitkaranta A. Cases presenting as parotid abscesses in children. Int J Pediatr Otorhinolaryngol. 2007;71(6):897-901.
23. Gritzmann N. Sonography of the salivary glands. AJR Am J Roentgenol. 1989;153(1):161-166.
24. Yousem DM, Kraut MA, Chalian AA. Major salivary gland imaging. Radiology. 2000;216(1):19-29.
25. Leerdam CM, Martin HC, Isaacs D. Recurrent parotitis of childhood. J Paediatr Child Health. 2005;41(12):631-634.
26. Chitre VV, Premchandra DJ. Recurrent parotitis. Arch Dis Child. 1997;77(4):359-363.
27. Sitheeque M, Sivachandran Y, Varathan V, et al. Juvenile recurrent parotitis: clinical, sialographic and ultrasonographic features. Int J Paediatr Dent. 2007;17(2):98-104.
28. Nozaki H, Harasawa A, Hara H, et al. Ultrasonographic features of recurrent parotitis in childhood. Pediatr Radiol. 1994;24(2):98-100.
29. Martinoli C, Derchi LE, Solbiati L, et al. Color Doppler sonography of salivary glands. AJR Am J Roentgenol. 1994;163(4):933-941.
30. Kawamura H, Taniguchi N, Itoh K, Kano S. Salivary gland echography in patients with Sjogren's syndrome. Arthritis Rheum. 1990;33(4):505-510.
31. Fujita A, Sakai O, Chapman MN, Sugimoto H. IgG4-related disease of the head and neck: CT and MR imaging manifestations. Radiographics. 2012;32(7):1945-1958.
32. Hamano H, Kawa S, Horiuchi A, et al. High serum IgG4 concentrations in patients with sclerosing pancreatitis. N Engl J Med. 2001;344(10):732-738.
33. Tabata T, Kamisawa T, Takuma K, et al. Serum IgG4 concentrations and IgG4-related sclerosing disease. Clin Chim Acta. 2009;408(1-2):25-28.
34. Melo JC, Kitsko D, Reyes-Mugica M. Pediatric chronic sclerosing sialadenitis: Kuttner tumor. Pediatr Dev Pathol. 2012;15(2):165-169.
35. Takagi Y, Nakamura H, Origuchi T, et al. IgG4-related Mikulicz's disease: ultrasonography of the salivary and lacrimal glands for monitoring the efficacy of corticosteroid therapy. Clin Exp Rheumatol. 2013;31(5):773-775.
36. Ahuja AT, Richards PS, Wong KT, et al. Kuttner tumour (chronic sclerosing sialadenitis) of the submandibular gland: sonographic appearances. Ultrasound Med Biol. 2003;29(7):913-919.
37. Ahuja A, Ying M, Mok JS, Anil CM. Gray scale and power Doppler sonography in cases of Kimura disease. AJNR Am J Neuroradiol. 2001;22(3):513-517.
38. Takeishi M, Makino Y, Nishioka H, et al. Kimura disease: diagnostic imaging findings and surgical treatment. J Craniofac Surg. 2007;18(5):1062-1067.
39. Horikoshi T, Motoori K, Ueda T, et al. Head and neck MRI of Kimura disease. Br J Radiol. 2011;84(1005):800-804.
40. Rosso R, Pretolesi F, del Bono V, et al. Benign lymphoepithelial parotid lesions in vertically HIV-infected patients. AIDS Patient Care STDS. 2006;20(8):536-541.
41. Mandel L, Bijoor R. Imaging (computed tomography, magnetic resonance imaging, ultrasound, sialography) in a case of recurrent parotitis in children. J Oral Maxillofac Surg. 2006;64(6):984-988.
42. da Silva Rath IB, Beltrame AP, Carvalho AP, et al. HIV-associated salivary gland disease—clinical or imaging diagnosis? Int J Paediatr Dent. 2015;25(4):233-238.
43. Toma PL, Rossi UG. Paediatric ultrasound. II. Other applications. Eur Radiol. 2001;11(12):2369-2398.
44. Goddart D, Francois A, Ninane J, et al. Parotid gland abnormality found in children seropositive for the human immunodeficiency virus (HIV). Pediatr Radiol. 1990;20(5):355-357.
45. Hudgins PA. Nodal and nonnodal inflammatory processes of the pediatric neck. Neuroimaging Clin N Am. 2000;10(1):181-192, ix.
46. Seibert RW, Seibert JJ. High resolution ultrasonography of the parotid gland in children. Pediatr Radiol. 1986;16(5):374-379.
47. Petrovic S, Petrovic D, Pesic Z, Kovacevic P. Sonography of congenital neck masses in children. Med Biol. 2005;12:164-169.
48. Fordham LA, Chung CJ, Donnelly LF. Imaging of congenital vascular and lymphatic anomalies of the head and neck. Neuroimaging Clin N Am. 2000;10(1):117-136, viii.
49. Turkyilmaz Z, Karabulut R, Bayazit YA, et al. Congenital neck masses in children and their embryologic and clinical features. B-ENT. 2008;4(1):7-18.
50. Bentz BG, Hughes CA, Ludemann JP, Maddalozzo J. Masses of the salivary gland region in children. Arch Otolaryngol Head Neck Surg. 2000;126(12):1435-1439.
51. Hockstein NG, Samadi DS, Gendron K, et al. Pediatric submandibular triangle masses: a fifteen-year experience. Head Neck. 2004;26(8):675-680.
52. Gerwel A, Kosik K, Jurkiewicz D. US in preoperative evaluation of parotid gland neoplasms. Otolaryngol Pol. 2015;69(2):27-33.
53. de Ru JA, van Leeuwen MS, van Benthem PP, et al. Do magnetic resonance imaging and ultrasound add anything to the preoperative workup of parotid gland tumors? J Oral Maxillofac Surg. 2007;65(5):945-952.
54. Koral K, Sayre J, Bhuta S, et al. Recurrent pleomorphic adenoma of the parotid gland in pediatric and adult patients: value of multiple lesions as a diagnostic indicator. AJR Am J Roentgenol. 2003;180(4):1171-1174.
55. Kim J, Kim EK, Park CS, et al. Characteristic sonographic findings of Warthin's tumor in the parotid gland. J Clin Ultrasound. 2004;32(2):78-81.

56. Fang QG, Shi S, Li ZN, et al. Epithelial salivary gland tumors in children: a twenty-five-year experience of 122 patients. Int J Pediatr Otorhinolaryngol. 2013;77(8):1252-1254.
57. Lennon P, Silvera VM, Perez-Atayde A, et al. Disorders and tumors of the salivary glands in children. Otolaryngol Clin North Am. 2015;48(1): 153-173.
58. Aro K, Leivo I, Makitie AA. Management and outcome of patients with mucoepidermoid carcinoma of major salivary gland origin: a single institution's 30-year experience. Laryngoscope. 2008;118(2):258-262.
59. Li J, Gong X, Xiong P, et al. Ultrasound and computed tomography features of primary acinic cell carcinoma in the parotid gland: a retrospective study. Eur J Radiol. 2014;83(7):1152-1156.
60. Wahlberg P, Anderson H, Biorklund A, et al. Carcinoma of the parotid and submandibular glands—a study of survival in 2465 patients. Oral Oncol. 2002;38(7):706-713.
61. Choudhary K, Panda S, Beena VT, et al. Sialoblastoma: a literature review from 1966-2011. Natl J Maxillofac Surg. 2013;4(1):13-18.
62. Saravakos P, Hartwein J, Fayyazi A. Sialoblastoma of the parotid gland in a 13-year-old girl with multiple recurrences and long-term follow-up. Head Neck. 2016;38(1):E13-E15.
63. Stones DK, Jansen JC, Griessel D. Sialoblastoma and hepatoblastoma in a newborn infant. Pediatr Blood Cancer. 2009;52(7):883-885.
64. Cristofaro M, Giudice A, Amentea M, Giudice M. Diagnostic and therapeutic approach to sialoblastoma of submandibular gland: a case report. J Oral Maxillofac Surg. 2008;66(1):123-126.
65. Som PM, Brandwein M, Silvers AR, Rothschild MA. Sialoblastoma (embryoma): MR findings of a rare pediatric salivary gland tumor. AJNR Am J Neuroradiol. 1997;18(5):847-850.
66. Yekeler E, Dursun M, Gun F, et al. Sialoblastoma: MRI findings. Pediatr Radiol. 2004;34(12):1005-1007.
67. Cheng YK, Chu WC, Law LW, et al. A fetus with a huge neck mass and a large abdominal circumference—a rare case of sialoblastoma and hepatoblastoma. Prenat Diagn. 2012;32(9):915-917.
68. Siddiqi SH, Solomon MP, Haller JO. Sialoblastoma and hepatoblastoma in a neonate. Pediatr Radiol. 2000;30(5):349-351.
69. Koch BL, Myer 3rd CM. Presentation and diagnosis of unilateral maxillary swelling in children. Am J Otolaryngol. 1999;20(2):106-129.
70. Yasumoto M, Yoshimura R, Sunaba K, Shibuya H. Sonographic appearances of malignant lymphoma of the salivary glands. J Clin Ultrasound. 2001;29(9): 491-498.
71. Asai S, Okami K, Nakamura N, et al. Tortoiseshell appearance of bilateral submandibular glands by infiltration of mucosa-associated lymphoid tissue lymphoma. J Ultrasound Med. 2008;27(6):969-973.
72. Xie CM, Kubba H. Parotidectomy in children: indications and complications. J Laryngol Otol. 2010;124(12):1289-1293.
73. Saha A, Dandekar S, Milla S, et al. Bilateral parotid gland enlargement and palpable nephromegaly in infant acute lymphoblastic leukemia: case report and review of the literature. J Pediatr Hematol Oncol. 2014;36(3): 246-248.
74. Dubois J, Patriquin H. Doppler sonography of head and neck masses in children. Neuroimaging Clin N Am. 2000;10(1):215-252, ix.
75. Khilnani AK, Thaddanee R, Parmar B, Majmundar P. Intraparotid schwannoma: a rare case report. Int J Appl Basic Med Res. 2015;5(2): 154-156.
76. McGuirt Sr WF, Johnson PE, McGuirt WT. Intraparotid facial nerve neurofibromas. Laryngoscope. 2003;113(1):82-84.
77. Vazquez E, Enriquez G, Castellote A, et al. US, CT, and MR imaging of neck lesions in children. Radiographics. 1995;15(1):105-122.
78. Woodfield CA, Levine MS, Rubesin SE, et al. Pharyngeal retention cysts: radiographic findings in seven patients. AJR Am J Roentgenol. 2005;184(3): 793-796.
79. Gutierrez JP, Berkowitz RG, Robertson CF. Vallecular cysts in newborns and young infants. Pediatr Pulmonol. 1999;27(4):282-285.
80. Leonardo GD, Federico M, Stefania N, et al. Endoscopic treatment of vallecular cyst in a newborn. Int J Pediatr Otorhinolaryngol. 2009;4: 10-13.
81. Cuillier F, Bidault J. Vallecular cyst. Reunion Island, France: Hospital Felix Guyon; 2001.
82. Meuwly JY, Lepori D, Theumann N, et al. Multimodality imaging evaluation of the pediatric neck: techniques and spectrum of findings. Radiographics. 2005;25(4):931-948.
83. Schneider K. Sonographic imaging of the thyroid in children. Prog Pediatr Surg. 1991;26:1-14.
84. Tessler FN, Tublin ME. Thyroid sonography: current applications and future directions. AJR Am J Roentgenol. 1999;173(2):437-443.
85. Ueda D. Normal volume of the thyroid gland in children. J Clin Ultrasound. 1990;18(6):455-462.
86. Ueda D, Mitamura R, Suzuki N, et al. Sonographic imaging of the thyroid gland in congenital hypothyroidism. Pediatr Radiol. 1992;22(2):102-105.
87. Babcock DS. Thyroid disease in the pediatric patient: emphasizing imaging with sonography. Pediatr Radiol. 2006;36(4):299-308.
88. Garel C, Leger J, editors. Thyroid imaging in children. Paris: S Karger, AG Basel; 2007.
89. Chang YW, Lee DH, Hong YH, et al. Congenital hypothyroidism: analysis of discordant US and scintigraphic findings. Radiology. 2011;258(3): 872-879.
90. Toma P, Rossi UG, Magnaguagno F, Granata C. Imaging of the normal and affected thyroid in children with emphasis on sonography. Pediatr Endocrinol Rev. 2003;1(Suppl. 2):237-243.
91. Marinovic D, Garel C, Czernichow P, Leger J. Ultrasonographic assessment of the ectopic thyroid tissue in children with congenital hypothyroidism. Pediatr Radiol. 2004;34(2):109-113.
92. De Bruyn R, Ng WK, Taylor J, et al. Neonatal hypothyroidism: comparison of radioisotope and ultrasound imaging in 54 cases. Acta Paediatr Scand. 1990;79(12):1194-1198.
93. Masters F, Given CA. Cystic neck masses: a pictorial review of unusual presentations and complicating features. Appl Radiol. 2008;37:26-32.
94. Hsieh YY, Hsueh S, Hsueh C, et al. Pathological analysis of congenital cervical cysts in children: 20 years of experience at Chang Gung Memorial Hospital. Chang Gung Med J. 2003;26(2):107-113.
95. Kutuya N, Kurosaki Y. Sonographic assessment of thyroglossal duct cysts in children. J Ultrasound Med. 2008;27(8):1211-1219.
96. Wadsworth DT, Siegel MJ. Thyroglossal duct cysts: variability of sonographic findings. AJR Am J Roentgenol. 1994;163(6):1475-1477.
97. Ahuja AT, King AD, Metreweli C. Sonographic evaluation of thyroglossal duct cysts in children. Clin Radiol. 2000;55(10):770-774.
98. Foley DS, Fallat ME. Thyroglossal duct and other congenital midline cervical anomalies. Semin Pediatr Surg. 2006;15(2):70-75.
99. Lev S, Lev MH. Imaging of cystic lesions. Radiol Clin North Am. 2000;38(5):1013-1027.
100. Ducic Y, Chou S, Drkulec J, et al. Recurrent thyroglossal duct cysts: a clinical and pathologic analysis. Int J Pediatr Otorhinolaryngol. 1998;44(1): 47-50.
101. Wang HK, Tiu CM, Chou YH, Chang CY. Imaging studies of pyriform sinus fistula. Pediatr Radiol. 2003;33(5):328-333.
102. Bar-Ziv J, Slasky BS, Sichel JY, et al. Branchial pouch sinus tract from the piriform fossa causing acute suppurative thyroiditis, neck abscess, or both: CT appearance and the use of air as a contrast agent. AJR Am J Roentgenol. 1996;167(6):1569-1572.
103. Rogers DG. Thyroid disease in children. Am Fam Physician. 1994;50(2): 344-350.
104. Bas VN, Aycan Z, Cetinkaya S, et al. Thyroid nodules in children and adolescents: a single institution's experience. J Pediatr Endocrinol Metab. 2012;25(7-8):633-638.
105. Koibuchi H, Omoto K, Fukushima N, et al. Coexistence of papillary thyroid cancer and Hashimoto thyroiditis in children: report of 3 cases. J Ultrasound Med. 2014;33(7):1299-1303.
106. Mahmutyazicioglu K, Turgut M. Doppler evaluation of the thyroid in pediatric goiter. J Clin Ultrasound. 2004;32(1):24-28.
107. Niedziela M. Pathogenesis, diagnosis and management of thyroid nodules in children. Endocr Relat Cancer. 2006;13(2):427-453.
108. Ardito G, Pintus C, Revelli L, et al. Thyroid tumors in children and adolescents: preoperative study. Eur J Pediatr Surg. 2001;11(3):154-157.
109. Reiners C, Demidchik YE. Differentiated thyroid cancer in childhood: pathology, diagnosis, therapy. Pediatr Endocrinol Rev. 2003;1(Suppl. 2): 230-235.

110. Donohoo JH, Wallach MT. Cricoid cartilage on sonography in pediatric patients mimics a thyroid mass. J Ultrasound Med. 2006;25(7):907-911.
111. Park CH, Oh KK, Kim EK, et al. Thyroid gland rupture after blunt cervical trauma. J Ultrasound Med. 2006;25(7):943-946.
112. Avula S, Daneman A, Navarro OM, et al. Incidental thyroid abnormalities identified on neck US for non-thyroid disorders. Pediatr Radiol. 2010;40(11): 1774-1780.
113. Bachrach LK, Daneman D, Daneman A, Martin DJ. Use of ultrasound in childhood thyroid disorders. J Pediatr. 1983;103(4):547-552.
114. Garcia CJ, Daneman A, Thorner P, Daneman D. Sonography of multinodular thyroid gland in children and adolescents. Am J Dis Child. 1992; 146(7):811-816.
115. Al-Fifi S, Rodd C. Multinodular goiter in children. J Pediatr Endocrinol Metab. 2001;14(6):749-756.
116. Qaisi M, Eid I. Pediatric head and neck malignancies. Oral Maxillofac Surg Clin North Am. 2016;28(1):11-19.
117. Gupta A, Ly S, Castroneves LA, et al. A standardized assessment of thyroid nodules in children confirms higher cancer prevalence than in adults. J Clin Endocrinol Metab. 2013;98(8):3238-3245.
118. Lyshchik A, Drozd V, Demidchik Y, Reiners C. Diagnosis of thyroid cancer in children: value of gray-scale and power Doppler US. Radiology. 2005;235(2):604-613.
119. Roy R, Kouniavsky G, Schneider E, et al. Predictive factors of malignancy in pediatric thyroid nodules. Surgery. 2011;150(6):1228-1233.
120. Corrias A, Mussa A. Thyroid nodules in pediatrics: which ones can be left alone, which ones must be investigated, when and how. J Clin Res Pediatr Endocrinol. 2013;5(Suppl. 1):57-69.
121. Hogan AR, Zhuge Y, Perez EA, et al. Pediatric thyroid carcinoma: incidence and outcomes in 1753 patients. J Surg Res. 2009;156(1):167-172.
122. Crom DB, Kaste SC, Tubergen DG, et al. Ultrasonography for thyroid screening after head and neck irradiation in childhood cancer survivors. Med Pediatr Oncol. 1997;28(1):15-21.
123. Segal K, Arad-Cohen A, Mechlis S, et al. Cancer of the thyroid in children and adolescents. Clin Otolaryngol Allied Sci. 1997;22(6):525-528.
124. Brkljacic B, Cuk V, Tomic-Brzac H, et al. Ultrasonic evaluation of benign and malignant nodules in echographically multinodular thyroids. J Clin Ultrasound. 1994;22(2):71-76.
125. Shin JH, Han BK, Ko EY, Kang SS. Sonographic findings in the surgical bed after thyroidectomy: comparison of recurrent tumors and nonrecurrent lesions. J Ultrasound Med. 2007;26(10):1359-1366.
126. Jun P, Chow LC, Jeffrey RB. The sonographic features of papillary thyroid carcinomas: pictorial essay. Ultrasound Q. 2005;21(1):39-45.
127. Chammas MC, Gerhard R, de Oliveira IR, et al. Thyroid nodules: evaluation with power Doppler and duplex Doppler ultrasound. Otolaryngol Head Neck Surg. 2005;132(6):874-882.
128. Frates MC, Benson CB, Charboneau JW, et al. Management of thyroid nodules detected at US: Society of Radiologists in Ultrasound consensus conference statement. Radiology. 2005;237(3):794-800.
129. Goldfarb M, Gondek SS, Sanchez Y, Lew JI. Clinic-based ultrasound can predict malignancy in pediatric thyroid nodules. Thyroid. 2012;22(8): 827-831.
130. Benson MT, Dalen K, Mancuso AA, et al. Congenital anomalies of the branchial apparatus: embryology and pathologic anatomy. Radiographics. 1992;12(5):943-960.
131. Winzelberg GG, Hydovitz JD, O'Hara KR, et al. Parathyroid adenomas evaluated by Tl-201/Tc-99m pertechnetate subtraction scintigraphy and high-resolution ultrasonography. Radiology. 1985;155(1):231-235.
132. Prasad TR, Bhatnagar V. Giant solitary parathyroid adenoma presenting with bone disease. Indian Pediatr. 2002;39(11):1044-1107.
133. Scheible W. Recent advances in ultrasound: high-resolution imaging of superficial structures. Head Neck Surg. 1981;4(1):58-63.
134. Roizen J, Levine MA. Primary hyperparathyroidism in children and adolescents. J Chin Med Assoc. 2012;75(9):425-434.
135. Wolf RJ, Cronan JJ, Monchik JM. Color Doppler sonography: an adjunctive technique in assessment of parathyroid adenomas. J Ultrasound Med. 1994;13(4):303-308.
136. Lee VS, Spritzer CE. MR imaging of abnormal parathyroid glands. AJR Am J Roentgenol. 1998;170(4):1097-1103.
137. Sarin YK, Thambudorai R. Ectopic bronchogenic cyst. Indian Pediatr. 1997;34(11):1035-1036.
138. Da Cunha Pinho M, Viana PC, Omokawa M, et al. External laryngocele: sonographic appearance—a case report. Radiol Bras. 2007;40:279-282.
139. Maroldi R, Farina D, Ravanelli M, et al. Emergency imaging assessment of deep neck space infections. Semin Ultrasound CT MR. 2012;33(5): 432-442.
140. Koch BL. The child with a neck mass. Appl Radiol. 2005;34:8-22.
141. Waldhausen JH. Branchial cleft and arch anomalies in children. Semin Pediatr Surg. 2006;15(2):64-69.
142. Goff CJ, Allred C, Glade RS. Current management of congenital branchial cleft cysts, sinuses, and fistulae. Curr Opin Otolaryngol Head Neck Surg. 2012;20(6):533-539.
143. Spinelli C, Rossi L, Strambi S, et al. Branchial cleft and pouch anomalies in childhood: a report of 50 surgical cases. J Endocrinol Invest. 2015.
144. Koch BL. Cystic malformations of the neck in children. Pediatr Radiol. 2005;35(5):463-477.
145. Miller MB, Rao VM, Tom BM. Cystic masses of the head and neck: pitfalls in CT and MR interpretation. AJR Am J Roentgenol. 1992;159(3): 601-607.
146. Nicollas R, Guelfucci B, Roman S, Triglia JM. Congenital cysts and fistulas of the neck. Int J Pediatr Otorhinolaryngol. 2000;55(2):117-124.
147. Mukherji SK, Fatterpekar G, Castillo M, et al. Imaging of congenital anomalies of the branchial apparatus. Neuroimaging Clin N Am. 2000;10(1):75-93, viii.
148. Nicoucar K, Giger R, Jaecklin T, et al. Management of congenital third branchial arch anomalies: a systematic review. Otolaryngol Head Neck Surg. 2010;142(1):21-28, e2.
149. Mou JW, Chan KW, Wong YS, et al. Recurrent deep neck abscess and piriform sinus tract: a 15-year review on the diagnosis and management. J Pediatr Surg. 2014;49(8):1264-1267.
150. Fitoz S, Atasoy C, Turkoz E, et al. Sonographic findings in ectopic cervical thymus in an infant. J Clin Ultrasound. 2001;29(9):523-526.
151. Costa NS, Laor T, Donnelly LF. Superior cervical extension of the thymus: a normal finding that should not be mistaken for a mass. Radiology. 2010;256(1):238-242.
152. Gaddikeri S, Vattoth S, Gaddikeri RS, et al. Congenital cystic neck masses: embryology and imaging appearances, with clinicopathological correlation. Curr Probl Diagn Radiol. 2014;43(2):55-67.
153. Ballal HS, Mahale A, Hegde V, et al. Case report: cervical thymic cyst. Indian J Radiol Imaging. 1999;9:187-189.
154. Smirniotopoulos JG, Chiechi MV. Teratomas, dermoids, and epidermoids of the head and neck. Radiographics. 1995;15(6):1437-1455.
155. Al-Khateeb TH, Al Zoubi F. Congenital neck masses: a descriptive retrospective study of 252 cases. J Oral Maxillofac Surg. 2007;65(11):2242-2247.
156. Kerner B, Flaum E, Mathews H, et al. Cervical teratoma: prenatal diagnosis and long-term follow-up. Prenat Diagn. 1998;18(1):51-59.
157. Guarisco JL. Congenital head and neck masses in infants and children. Part II. Ear Nose Throat J. 1991;70(2):75-82.
158. Hasiotou M, Vakaki M, Pitsoulakis G, et al. Congenital cervical teratomas. Int J Pediatr Otorhinolaryngol. 2004;68(9):1133-1139.
159. Kogutt MS, Cohen S. Cervical teratoma in infants and children. South Med J. 1977;70(1):122-123.
160. Herman TE, Siegel MJ. Cervical teratoma. J Perinatol. 2008;28(9): 649-651.
161. Mulliken JB, Glowacki J. Hemangiomas and vascular malformations in infants and children: a classification based on endothelial characteristics. Plast Reconstr Surg. 1982;69(3):412-422.
162. Wassef M, Blei F, Adams D, et al. Vascular anomalies classification: recommendations from the International Society for the Study of Vascular Anomalies. Pediatrics. 2015;136(1):e203-e214.
163. Robertson RL, Robson CD, Barnes PD, Burrows PE. Head and neck vascular anomalies of childhood. Neuroimaging Clin N Am. 1999;9(1):115-132.
164. Restrepo R, Palani R, Cervantes LF, et al. Hemangiomas revisited: the useful, the unusual and the new. Part 1: overview and clinical and imaging characteristics. Pediatr Radiol. 2011;41(7):895-904.
165. Metry DW, Dowd CF, Barkovich AJ, Frieden IJ. The many faces of PHACE syndrome. J Pediatr. 2001;139(1):117-123.

166. Gorincour G, Kokta V, Rypens F, et al. Imaging characteristics of two subtypes of congenital hemangiomas: rapidly involuting congenital hemangiomas and non-involuting congenital hemangiomas. Pediatr Radiol. 2005;35(12): 1178-1185.
167. Rogers M, Lam A, Fischer G. Sonographic findings in a series of rapidly involuting congenital hemangiomas (RICH). Pediatr Dermatol. 2002; 19(1):5-11.
168. Edwards PD, Rahbar R, Ferraro NF, et al. Lymphatic malformation of the lingual base and oral floor. Plast Reconstr Surg. 2005;115(7):1906-1915.
169. Boukobza M, Enjolras O, Guichard JP, et al. Cerebral developmental venous anomalies associated with head and neck venous malformations. AJNR Am J Neuroradiol. 1996;17(5):987-994.
170. Jacob JL. Left cervical aortic arch associated with multiple vascular anomalies. Cardiol Young. 2011;21(6):700-702.
171. Hu X, Li J, Hu T, Jiang X. Congenital jugular vein phlebectasia. Am J Otolaryngol. 2005;26(3):172-174.
172. Eksioglu AS, Senel S, Cinar G, Karacan CD. Sonographic measurement criteria for the diagnosis of internal jugular phlebectasia in children. J Clin Ultrasound. 2013;41(8):486-492.
173. Bora MK. Internal jugular phlebectasia: diagnosis by ultrasonography, Doppler and contrast CT. J Clin Diagn Res. 2013;7(6):1194-1196.
174. Babcock DS. Sonographic evaluation of suspected pediatric vascular diseases. Pediatr Radiol. 1991;21(7):486-489.
175. Taylor BJ, Seibert JJ, Glasier CM, et al. Evaluation of the reconstructed carotid artery following extracorporeal membrane oxygenation. Pediatrics. 1992;90(4):568-572.
176. Simonetti G, Bozzao A, Floris R, Silvestrini M. Non-invasive assessment of neck-vessel pathology. Eur Radiol. 1998;8(5):691-697.
177. Jacobs JP, Goldman AP, Cullen S, et al. Carotid artery pseudoaneurysm as a complication of ECMO. Ann Vasc Surg. 1997;11(6):630-633.
178. Kuenzler KA, Arthur LG, Burchard AE, et al. Intraoperative ultrasound reduces ECMO catheter malposition requiring surgical correction. J Pediatr Surg. 2002;37(5):691-694.
179. Liberman L, Hordof AJ, Hsu DT, Pass RH. Ultrasound-assisted cannulation of the right internal jugular vein during electrophysiologic studies in children. J Interv Card Electrophysiol. 2001;5(2):177-179.
180. Lamperti M, Caldiroli D, Cortellazzi P, et al. Safety and efficacy of ultrasound assistance during internal jugular vein cannulation in neurosurgical infants. Intensive Care Med. 2008;34(11):2100-2105.
181. Righini CA, Karkas A, Tourniaire R, et al. Lemierre syndrome: study of 11 cases and literature review. Head Neck. 2014;36(7):1044-1051.
182. De Sena S, Rosenfeld DL, Santos S, Keller I. Jugular thrombophlebitis complicating bacterial pharyngitis (Lemierre's syndrome). Pediatr Radiol. 1996;26(2):141-144.
183. Schubert AD, Hotz MA, Caversaccio MD, Arnold A. Septic thrombosis of the internal jugular vein: Lemierre's syndrome revisited. Laryngoscope. 2015;125(4):863-868.
184. Castro-Marin F, Kendall JL. Diagnosis of Lemierre syndrome by bedside emergency department ultrasound. J Emerg Med. 2007;10:44.
185. Ahuja AT, Ying M. Sonographic evaluation of cervical lymph nodes. AJR Am J Roentgenol. 2005;184(5):1691-1699.
186. Jordan N, Tyrrell J. Management of enlarged cervical lymph nodes. Curr Paediatr. 2004;14:154-159.
187. Brown RL, Azizkhan RG. Pediatric head and neck lesions. Pediatr Clin North Am. 1998;45(4):889-905.
188. Locke R, Comfort R, Kubba H. When does an enlarged cervical lymph node in a child need excision? A systematic review. Int J Pediatr Otorhinolaryngol. 2014;78(3):393-401.
189. Turkington JR, Paterson A, Sweeney LE, Thornbury GD. Neck masses in children. Br J Radiol. 2005;78(925):75-85.
190. Penn Jr EB, Goudy SL. Pediatric inflammatory adenopathy. Otolaryngol Clin North Am. 2015;48(1):137-151.
191. Moore SW, Schneider JW, Schaaf HS. Diagnostic aspects of cervical lymphadenopathy in children in the developing world: a study of 1,877 surgical specimens. Pediatr Surg Int. 2003;19(4):240-244.
192. Peters TR, Edwards KM. Cervical lymphadenopathy and adenitis. Pediatr Rev. 2000;21(12):399-405.
193. Kao HT, Huang YC, Lin TY. Kawasaki disease presenting as cervical lymphadenitis or deep neck infection. Otolaryngol Head Neck Surg. 2001;124(4):468-470.
194. Bedi DG, John SD, Swischuk LE. Fibromatosis colli of infancy: variability of sonographic appearance. J Clin Ultrasound. 1998;26(7):345-348.
195. Cheng JC, Metreweli C, Chen TM, Tang S. Correlation of ultrasonographic imaging of congenital muscular torticollis with clinical assessment in infants. Ultrasound Med Biol. 2000;26(8):1237-1241.
196. Hsu TC, Wang CL, Wong MK, et al. Correlation of clinical and ultrasonographic features in congenital muscular torticollis. Arch Phys Med Rehabil. 1999;80(6):637-641.
197. Lin JN, Chou ML. Ultrasonographic study of the sternocleidomastoid muscle in the management of congenital muscular torticollis. J Pediatr Surg. 1997;32(11):1648-1651.
198. Knight PJ, Reiner CB. Superficial lumps in children: what, when, and why? Pediatrics. 1983;72(2):147-153.
199. Lan MY, Lan MC, Ho CY, et al. Pilomatricoma of the head and neck: a retrospective review of 179 cases. Arch Otolaryngol Head Neck Surg. 2003;129(12):1327-1330.
200. Choo HJ, Lee SJ, Lee YH, et al. Pilomatricomas: the diagnostic value of ultrasound. Skeletal Radiol. 2010;39(3):243-250.
201. Hwang JY, Lee SW, Lee SM. The common ultrasonographic features of pilomatricoma. J Ultrasound Med. 2005;24(10):1397-1402.
202. Lim HW, Im SA, Lim GY, et al. Pilomatricomas in children: imaging characteristics with pathologic correlation. Pediatr Radiol. 2007;37(6): 549-555.
203. Chung EB, Enzinger FM. Infantile myofibromatosis. Cancer. 1981;48(8): 1807-1818.
204. Cheung YH, Gayden T, Campeau PM, et al. A recurrent *PDGFRB* mutation causes familial infantile myofibromatosis. Am J Hum Genet. 2013;92(6): 996-1000.
205. Koujok K, Ruiz RE, Hernandez RJ. Myofibromatosis: imaging characteristics. Pediatr Radiol. 2005;35(4):374-380.
206. Holzer-Fruehwald L, Blaser S, Rossi A, et al. Imaging findings in seven cases of congenital infantile myofibromatosis with cerebral, spinal, or head and neck involvement. Neuroradiology. 2012;54(12):1389-1398.
207. Coleman AM, Calvo-Garcia MA, Zbojniewicz AM, et al. Prenatal diagnosis of infantile myofibroma with postnatal imaging correlation. Fetal Diagn Ther. 2014.
208. Imhof H, Czerny C, Hormann M, Krestan C. Tumors and tumor-like lesions of the neck: from childhood to adult. Eur Radiol. 2004;14(Suppl. 4):L155-L165.
209. Toma P, Granata C, Rossi A, Garaventa A. Multimodality imaging of Hodgkin disease and non-Hodgkin lymphomas in children. Radiographics. 2007;27(5):1335-1354.
210. Evans RM. Ultrasound of cervical lymph nodes. Imaging. 2003;15:101-108.
211. McCarville MB, Spunt SL, Pappo AS. Rhabdomyosarcoma in pediatric patients: the good, the bad, and the unusual. AJR Am J Roentgenol. 2001;176(6):1563-1569.
212. Ng WK. Embryonal rhabdomyosarcoma in a young boy. Mcgill J Med. 2007;10(1):16-19.
213. Bellah R. Ultrasound in pediatric musculoskeletal disease: techniques and applications. Radiol Clin North Am. 2001;39(4):597-618, ix.
214. D'Ambrosio N, Lyo J, Young R, et al. Common and unusual craniofacial manifestations of metastatic neuroblastoma. Neuroradiology. 2010;52(6):549-553.
215. Cardesa-Salzmann TM, Mora-Graupera J, Claret G, Agut T. Congenital cervical neuroblastoma. Pediatr Blood Cancer. 2004;43(7):785-787.
216. Gallet BL, Egelhoff JC. Unusual CNS and orbital metastases of neuroblastoma. Pediatr Radiol. 1989;19(5):287-289.
217. Kuna SK, Bracic I, Tesic V, et al. Ultrasonographic differentiation of benign from malignant neck lymphadenopathy in thyroid cancer. J Ultrasound Med. 2006;25(12):1531-1537.

CHAPTER 49

The Pediatric Spinal Canal

Ilse Castro-Aragon, Deborah Levine, and Carol M. Rumack

SUMMARY OF KEY POINTS

- Spine ultrasound is used in the evaluation of neonates and infants (up to 3-4 months) with high- or moderate-risk cutaneous manifestations of closed spinal dysraphism, clinical signs of a tethered cord, or congenital anomalies that are frequently associated with spinal dysraphism.
- Additional indications for spine ultrasound include evaluation after failed lumbar puncture, guidance for lumbar puncture, and intraoperative guidance.
- The conus medullaris is usually at L1-2 and can extend to the superior endplate of L3.
- Neural tube defects can be open (nonskin-covered) or closed (skin-covered) spinal lesions, with or without a subcutaneous mass or other cutaneous stigmata.
- Understanding anatomy, embryology, normal variants, and scanning technique is important for accurate diagnosis.

CHAPTER OUTLINE

EMBRYOLOGY
SONOGRAPHIC TECHNIQUE AND NORMAL ANATOMY
SPINAL ANOMALIES
Tethered Spinal Cord
SPINAL DYSRAPHISM
Open Spinal Dysraphism
Closed Spinal Dysraphism With a Subcutaneous Mass
Closed Spinal Defects Without a Subcutaneous Mass
Simple Dysraphic States
Complex Dysraphic States (Disorders of Gastrulation)
TUMORS
HEMORRHAGE AND INFECTION
ARACHNOID CYSTS
INTRAOPERATIVE AND OTHER USES OF SPINAL SONOGRAPHY

In normal infants, the spinal canal and contents can be visualized because the nonossified state of the posteromedian intraneural synchondrosis provides an ample acoustic window (Fig. 49.1). The abnormal configuration of vertebral bodies in infants with certain dysraphic abnormalities opens the window even further. Although magnetic resonance imaging (MRI) is considered the examination of choice when evaluating the spine in children and adults, sonography of the spine in the newborn period can reveal details that are difficult to define with MRI. Several authors have recommended ultrasound as the initial imaging modality in patients younger than 6 months suspected of having a spinal disorder.[1] Others have recommended ultrasound in asymptomatic infants with cutaneous stigmata and MRI in the presence of deficits and cutaneous stigmata.[2] Fatty masses, cord position, and relationship of the cord to any mass, as well as presence or absence of nerve root pulsations, can be seen clearly.

EMBRYOLOGY

For a better understanding of spinal pathology, a general knowledge of the process of spinal cord and vertebral column formation is helpful. The trilaminar disc is formed by **gastrulation.** This is followed by **primary neurulation,** which forms the spinal cord from cervical through S5 sacral segments.[3] Distal to this level, the conus and the filum terminale are formed by a process termed **canalization and retrogressive differentiation** of the caudal cell mass, also referred to as **secondary neurulation.**

During weeks 2 and 3, the bilaminar embryonic disc (formed by layers of endoderm and ectoderm) is converted into a trilaminar disc through the process of **gastrulation.** The process starts with the appearance of the primitive streak, which forms caudally, adjacent to the area that eventually becomes the cloaca. The primitive streak actively forms mesenchymal cells that give rise to the mesoderm. Some mesenchymal cells migrate laterally, and the paired anlagen eventually fuse in the midline to form the notochord process, which contains a central lumen (notochordal canal).[4,5] The neuroenteric canal, which is the proximal part of the notochordal canal, normally obliterates when development of the notochord is complete.

The nervous system develops from the neural plate, which differentiates from the ectoderm overlying the notochord and paraxial mesoderm.[6] The neural plate is composed of neural ectoderm and is contiguous with the cutaneous ectoderm on both sides. The cells at the junction of the neural and cutaneous

ectoderm differentiate into neural crest cells. Primary neurulation (closure of the neural tube) begins during days 22 and 23. The lateral margins of the neural plate thicken to form the neural folds, and the thinner midline of the neural plate forms the neural groove. The neural folds bend dorsally, converge, and fuse in the midline to form the neural tube. The process of tube closure begins in the region of the craniocervical junction and extends cephalad and caudad with several fusion sites, and the posterior neuropore closes last by day 27. After closure of the neural tube, the overlying ectoderm separates from the neural tissue and fuses in the midline, forming a continuous ectodermal covering of the neural structures; this process is known as **disjunction.** After the neural tube has closed and separates from the superficial ectoderm, mesenchyme also migrates dorsal to the neural tube and forms precursors of the neural arches, in addition to meninges and paraspinous muscles. At the time of closure, the lateral edges of the neural plate, which form the neural crest cells, are extruded from the neural tube, move to the dorsum of the neural tube, and eventually migrate laterally and give rise to the sensory dorsal root ganglia, the autonomic nervous system, and other structures[7,8] (Fig. 49.2).

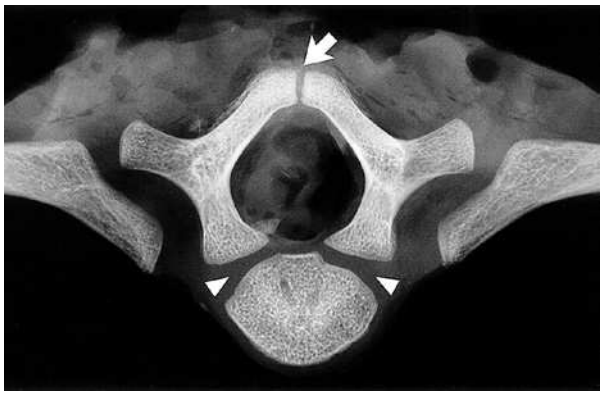

FIG. 49.1 Cartilaginous Gaps in Vertebral Ring Allow Penetration by Scanning Beam. Transverse radiograph through a thoracic vertebral body specimen from an infant demonstrates the cartilaginous posterior median intraneural synchondrosis *(arrow)* and the paired neurocentral synchondroses *(arrowheads).* (Courtesy of Dr. Paul Kleinman, Children's Hospital, Boston.)

The distal neural tube is formed by secondary neurulation. Distal to the posterior neuropore, undifferentiated cells from the primitive streak form the caudal cell mass (day 30). Microcysts develop and coalesce to form a tubular structure that unites with the more distal neural tube that was formed by primary neurulation. At 38 days the process of retrogressive differentiation occurs, with decrease in size of the cell mass and central lumen of the caudal neural tube. The segment formed by this process eventually forms the **filum terminale** and **cauda equina** and ascends to form the **conus medullaris** and **ventriculus terminalis.** The regression process continues into the postnatal period with minimal migration, and the conus reaches the adult level of L1-2 by approximately 3 months of age.[9]

The spinal column develops in parallel with the spinal cord beginning at the future occipital region and sweeps caudally.

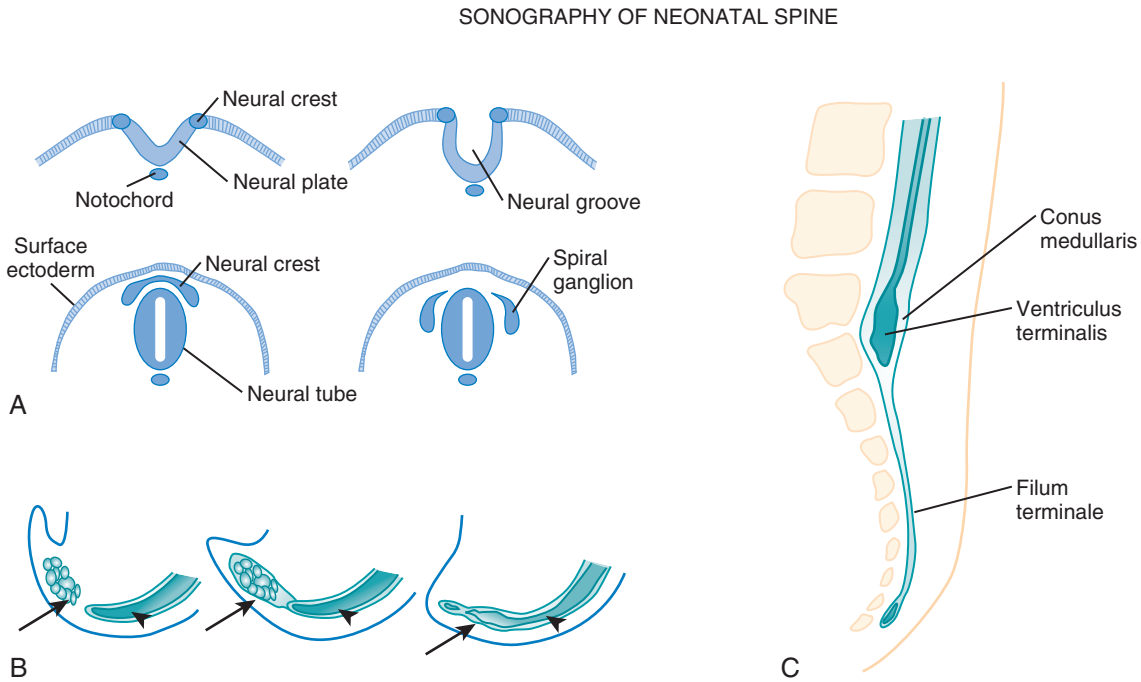

FIG. 49.2 Three Stages of Spinal Cord Development. (A) Neurulation (closure of neural tube) is the process of progression from neural plate to neural groove to neural tube. **(B) Canalization** occurs when multiple microcysts form and coalesce in caudal cell mass *(arrows),* which fuses to distal neural tube *(arrowheads),* forming the primitive spinal cord. **(C) Retrogressive differentiation** (programmed cell death) is the process by which the caudal cell mass and neural tube regress in size to form the **fetal conus medullaris, ventriculus terminalis,** and **filum terminale.** (**A** with permission from Sadler T. Langman's medical embryology. 5th ed. Baltimore: Lippincott; 1985; **B** and **C** with permission from Barkovich AJ. The nervous system. Pediatric neuroimaging. 3rd ed. Philadelphia: Lippincott Williams & Wilkins; 2000.[8])

The mesenchyme lateral to the closing neural tube organizes into somites. The dorsolateral portion of each somite will become skeletal muscle and dermis, whereas the ventromedial portion will become the cartilage, bone, and ligaments of the vertebral column. The formation of the vertebrae at the caudal end of the embryo proceeds by a different process with a mass of cells of notochord, mesenchyme, and neural tissue that divides into somites.

One can readily see how failure of completion or error in organization at any of these levels might lead to anomalies in spinal formation. Complete nondisjunction of the cutaneous ectoderm and the neuroectoderm prevents mesenchymal migration and results in a nonskin-covered posterior dysraphism such as **myelomeningocele.** A focal nondisjunction results in a focal **ectodermal-neuroectodermal tract** or **dermal sinus tract.** In focal unilateral premature disjunction, the neural tube separates from cutaneous ectoderm before complete neural tube closure, and this allows access of mesenchymal cells to the neural groove and ependymal lining. The mesenchyme differentiates into fat and develops skin-covered abnormalities such as **lipomyelomeningoceles. Filum terminale lipomas** likely occur from abnormal development of the caudal cell mass. The caudal cell mass forms in close proximity to the **cloaca** (origin of the lower genitourinary and anorectal structures), which explains the high incidence of **lumbosacral hypogenesis** and **tethered spinal cords** in patients with anorectal and urogenital anomalies. Aberrations in gastrulation, which can interfere with primary and/or secondary neurulation, explain **diastematomyelia, neurenteric fistula, caudal agenesis,** and **segmental spinal dysgenesis.**[10]

SONOGRAPHIC TECHNIQUE AND NORMAL ANATOMY

In general, infants are scanned in the prone position, although it is possible to scan in a decubitus position while the infant is fed with a bottle or even breast-fed. A much better scan will be obtained if the caregiver is allowed to feed a struggling infant and return to the prone position in the postprandial state. A pacifier dipped in glucose can also be used to calm the patient during imaging. If possible, the lumbar lordosis is accentuated by elevating the shoulders, to aid determination of vertebral body level by defining the lumbosacral junction.[11] For an accurate definition of the level of the cord termination, an anteroposterior (AP) and lateral spine radiograph using a metal marker at the level of the end of the spinal cord by ultrasound can aid in documentation of the level, because the estimated level on ultrasound may be in error in the presence of spinal anomalies such as six lumbar vertebrae. In addition, elevation of the upper trunk and head can further distend the dependent caudal portion of the thecal sac. An excellent alternative approach is to place a rolled blanket under the lower abdomen in a prone position, to widen the acoustic window by separating the spinous processes.[12] The posterior elements of the spine ossify after birth (from caudally to cranially). There is reduced penetration of sound in the lumbar spine at 3 to 4 months, and in most patients the quality significantly decreases after 6 months. In the older infant and child, parasagittal scanning can better visualize the canal contents relative to midline sagittal scanning.[13]

High-frequency linear transducers allow visualization of fine details of anatomy, with the additional aid of saved clips and extended–field-of-view images, which are useful for counting vertebral segments (Fig. 49.3). A split screen can document the landmarks used for counting vertebral bodies and determining the level of the conus medullaris. Movement of the spinal cord and cauda equina with crying, respiration, and the cardiac cycle is seen in real time and documented with saved clips (Video 49.1). The normal movement can be seen in newborns but might not be noticeably brisk until approximately 2 postnatal months.[12] Although different indications for imaging may require varying views, it is best to scan the entire back in both the longitudinal and the transverse planes, with right and left labels on transverse images (which can be confusing when scanning in the prone position). This allows a thorough search for contiguity of vertebral body rings, an assessment of contour and position of the spinal cord, and a survey of the paraspinous musculature and overlying skin. A standoff pad or a good amount of gel can be used to evaluate a subcutaneous mass or other structures in the near field.

If the acoustic window is small, as occurs during the evaluation of the craniocervical junction, a smaller-footprint curvilinear, sector, or small linear transducer allows scanning at the base of the skull and through the foramen magnum. This view allows visualization of the cisterna magna, brainstem, inferior cerebellum, and proximal cervical cord[14-16] (Fig. 49.4).

The fine anatomic display possible with sonography has been shown in correlative studies between ultrasound and specimen anatomy.[17] Fig. 49.5 demonstrates the basic landmarks that should be visible. The cartilaginous spinous processes are hypoechoic (Fig. 49.6), and the epidural space, which contains a variable amount of fat, is visible anterior to the posterior dura mater. The dura is seen on longitudinal images as an echogenic line parallel to the posterior anechoic subarachnoid space that is anterior to the spinal cord. The cord is surrounded anteriorly by anterior subarachnoid space and echogenic vertebral bodies. The cord is hypoechoic, whereas the interfaces created by the fanning nerve rootlets are echogenic.

The central echo complex in the otherwise hypoechoic cord has been shown with ultrasound and histoanatomic correlation to be produced by the interface between the myelinated ventral white commissure and central end of the anterior median fissure.[18,19] Images obtained with high-frequency transducers sometimes reveal a column of fluid within the center of the central echo complex within the conus medullaris. The **ventriculus terminalis** is a persistent fetal terminal ventricle and appears as smooth dilation of the central echo complex within the conus medullaris. This normal finding is seen often in the neonate and regresses or disappears soon after birth (Fig. 49.7).[12,20]

The normal **filum terminale** is visible and mobile with cerebrospinal fluid (CSF) pulsations. The center of the filum tends to be relatively hypoechoic compared with its bright outer margins. The filum terminale extends from the tip of the conus medullaris, crosses the subarachnoid space, and inserts on the first coccygeal vertebral body. The filum is surrounded by the

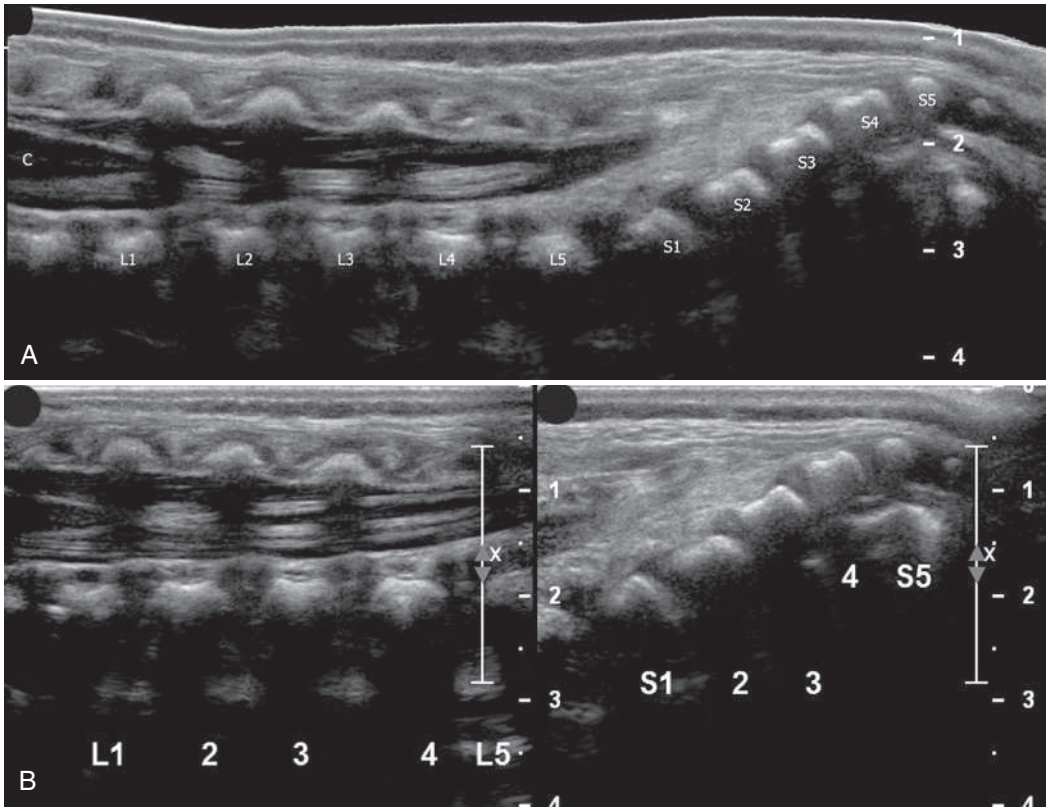

FIG. 49.3 Lumbosacral Spine in a 2-Week-Old Infant. (A) Extended–field-of-view image reveals detailed anatomy of the course and contour of the lumbosacral spine. The hypoechoic cord is visible *(C),* sacral and lumbar vertebral bodies are labeled, and the lumbosacral junction can be determined where S1 tilts posteriorly. **(B)** Split image in the same patient. The same landmarks can be documented with a dual image. Often this is technically easier than the panoramic view. See also Video 49.1.

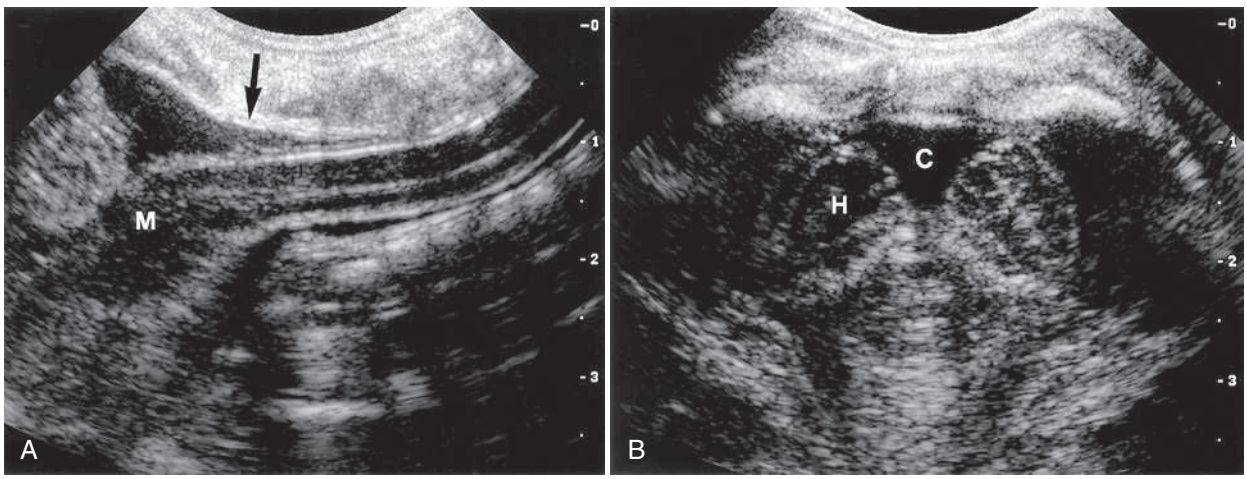

FIG. 49.4 Brainstem, Cisterna Magna, and Cerebellar Hemispheres. (A) Sagittal view of the craniocervical junction using the foramen magnum as a window. The arrow indicates the posterior margin of the foramen magnum. Visualization of the cerebellum and medulla *(M)* is also possible on this view. **(B)** On transverse view, the cisterna magna *(C)* and cerebellar hemispheres *(H)* are well shown.

cauda equina, and the normal thickness is 1 to 2 mm[21] (Fig. 49.8, Video 49.2). Sometimes it can be difficult to separate the filum terminale from the nerve roots in the cauda equina to obtain a good measurement. **Filar cysts** (Fig. 49.9) can be seen within or on the filum terminale and caudal to the conus medullaris and should be considered a variant of normal development when there is no other suggestion of pathology.[7,22] The incidence of filar cyst is up to 11.8% in the newborn period.[20] Detection is inversely related to age up to 6 months. These cysts are not seen on most neonatal or adult MRI studies. There is no proven explanation for their origin; possibilities include a true cyst, a pseudocyst, an embryonic remnant, or a developmental phenomenon that regresses with age. They do not require further imaging or follow-up.[20]

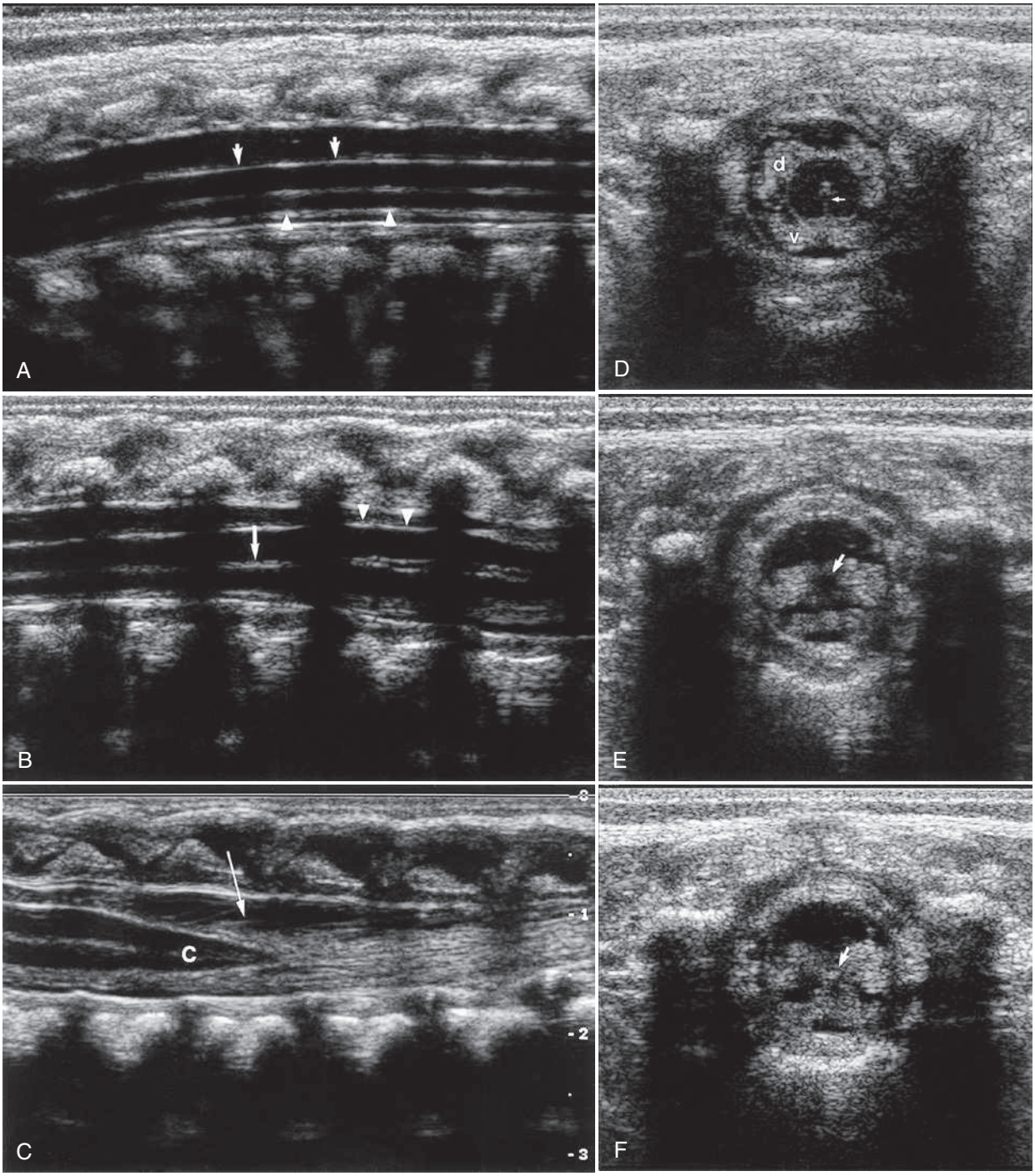

FIG. 49.5 Normal Spinal Cord. (A) Sagittal view shows posterior aspect *(arrows)* and anterior aspect of the thoracic spinal cord *(arrowheads).* Normal thoracic spinal cord is more anteriorly positioned within the vertebral canal than the more distal spinal cord. **(B)** Normal widening of the lumbar spinal cord *(arrowheads).* The central echo complex is visible as an echogenic line *(arrow).* **(C)** Tip of the conus medullaris *(C)* should taper gradually. Individual nerve rootlets are visible *(arrow).* **(D)** On transverse view of the lumbar spinal cord, dorsal *(d)* and ventral *(v)* nerve rootlets, as well as the anterior median fissure, are visible *(arrow).* **(E)** Transverse view near the tip of the conus medullaris demonstrates the hypoechoic substance of the cord *(arrow)* in the center of the more echogenic nerve rootlets. **(F)** The beginning of the filum terminale is seen as a central, slightly echogenic focus *(arrow)* in the transverse plane.

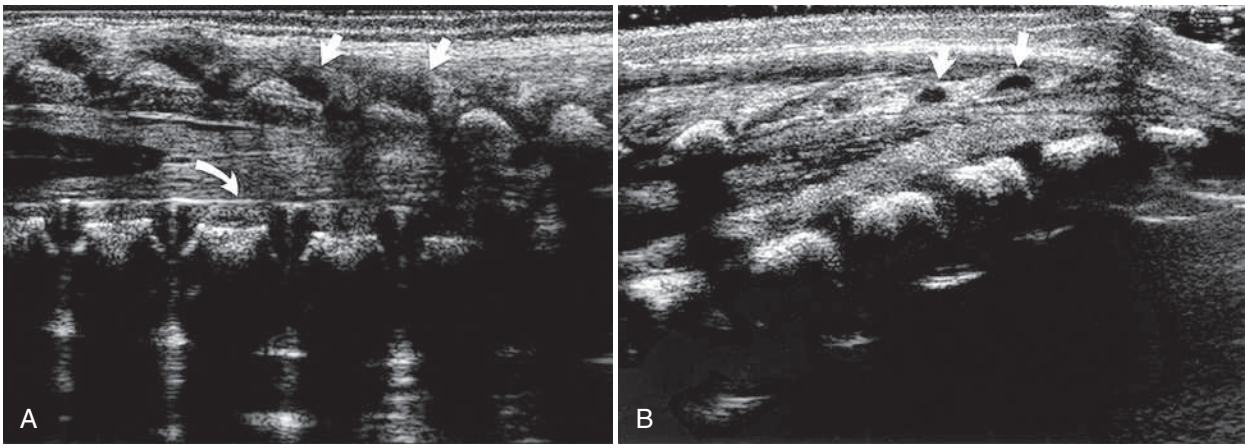

FIG. 49.6 Normal Vertebral Sonographic Anatomy. (A) Sagittal view of the distal lumbar spine shows fine definition of vertebral body anatomy. The cartilaginous tips of the posterior spinous processes are visible *(arrows),* as well as the posterior margin of the cartilaginous portion of the L3 vertebral body *(curved arrow).* **(B)** More distal sagittal view shows the cartilaginous posterior elements of the midsacral spine *(arrows).*

FIG. 49.7 Fluid Within Central Canal (Ventriculus Terminalis). Sagittal view of the lumbar spine. This is a common, normal variant *(arrow)* observed in many infants.

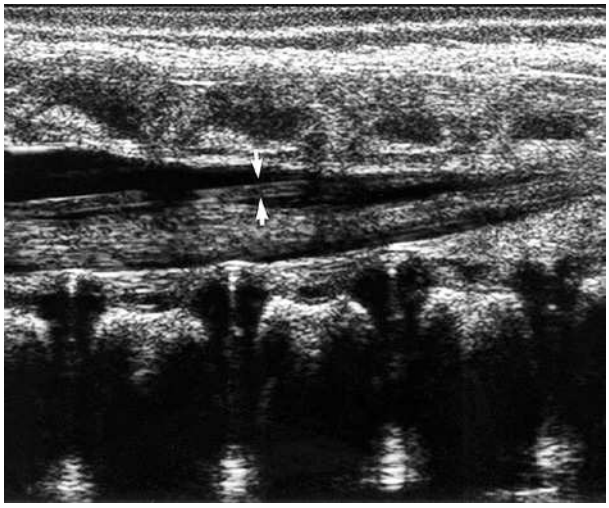

FIG. 49.8 Normal Filum Terminale. This can be clearly distinguished from the nerve roots and should be less than 2 mm in diameter *(arrows).* The external edges of the filum are relatively bright compared with the central portion of the filum. See also Video 49.2.

Some infants have more prominent epidural fat, which also should be considered a normal variant unless other signs suggest an abnormal fatty mass (Fig. 49.10). Color Doppler ultrasound can help localize the epidural venous plexus, anterior spinal arteries, and paired posterior spinal arteries. Malposition, compression, or distention of these vessels may help to distinguish an abnormal mass within the vertebral canal from normal nerve rootlets or epidural fat.

Determination of the **position of the tip of the conus medullaris** is the most common indication for spinal ultrasound and should always be included in a neonatal spine sonographic examination. Approaches, all of which presume normal anatomy, include (1) finding the lowest rib (presumably the 12th rib) on lateral parasagittal scanning, following medially to the vertebral body and counting down from this level; (2) defining the longitudinal lumbosacral junction where S1 is the first vertebral body that tilts posteriorly (similar to a lateral spine radiograph) and using that as a reference[12]; (3) defining the distal end of the thecal sac which is usually at S2[12]; and (4) counting upward from the last ossified "sacral" vertebral body. The fourth approach can be inaccurate because of the great variability in the ossification of the coccygeal vertebral bodies.[23] In general, ossified coccygeal vertebral bodies have a rounded central nucleus, whereas sacral ossification centers take on a more squared contour. If at least two methods are applied and the vertebral assignment is the same, it is likely correct. If these methods prove problematic owing to variants of ossification or segmentation anomalies, the ultrasound transducer can be used to locate the tip of the conus, mark the skin at that level with a **radiopaque BB marker,** and obtain AP and lateral radiographs of the entire spine to determine the corresponding vertebral level (Fig. 49.11). If this is done, a lateral film is helpful because distortion from beam angulation is less problematic. The AP spine view allows counting of ribs and vertebral bodies with accuracy. The degree of ossification of the coccyx can also be assessed with this film. As the sonographer gains experience in scanning the neonatal spine, the variability in the shape of the cartilaginous coccyx becomes evident (Fig. 49.12 and Video 49.3).

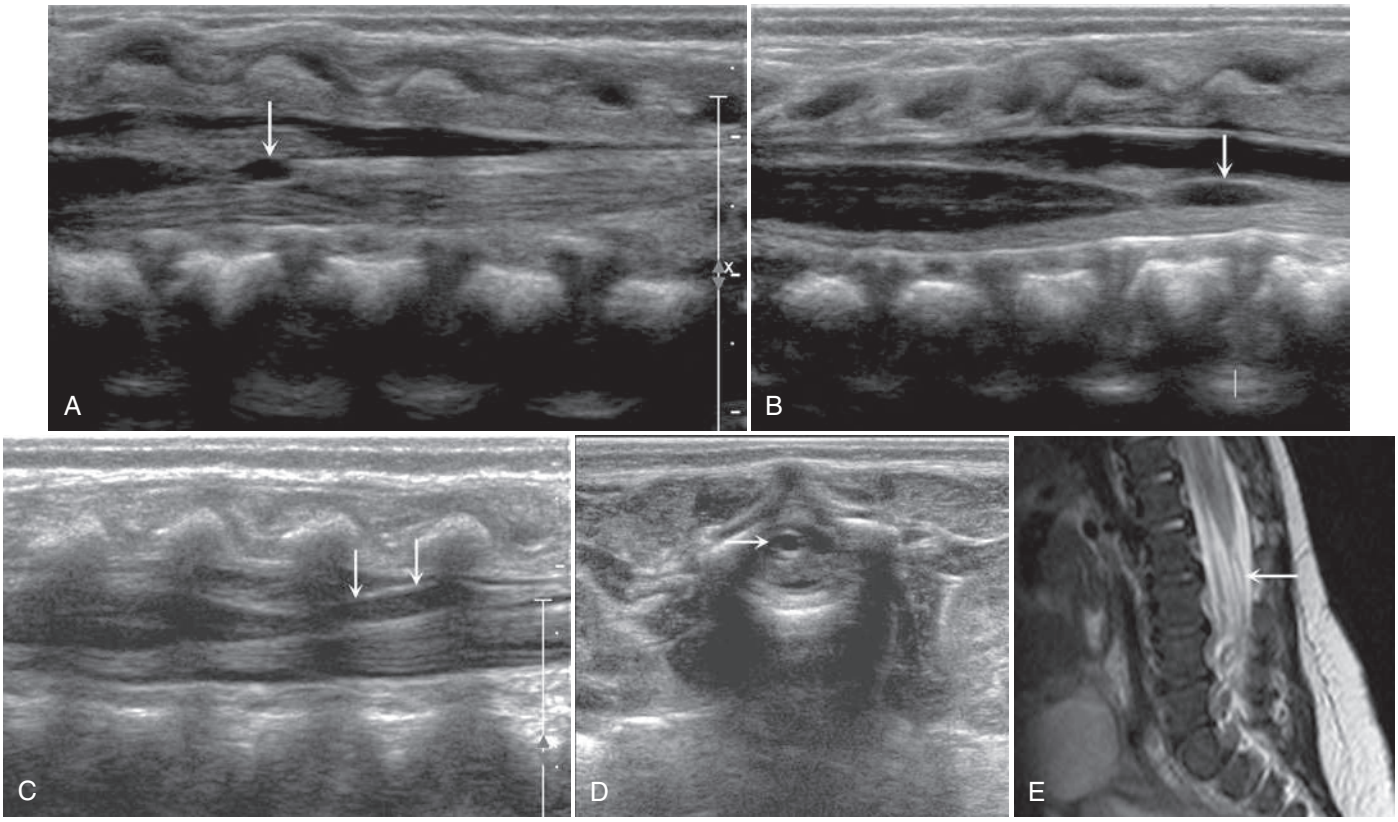

FIG. 49.9 Filar Cysts. (A) Small round cyst *(arrow)* distal to the conus medullaris is a normal variant. The rest of the filum terminale is seen distal to the cyst, has slightly echogenic borders and central hypoechogenicity, and can be distinguished from the nerve roots of the cauda equina. **(B)** Another patient with an oval filar cyst *(arrow);* in another patient, **(C)** and **(D)** sagittal and axial views of the spine and **(E)** T2-weighted sagittal magnetic resonance image show a large filar cyst *(arrow)*.

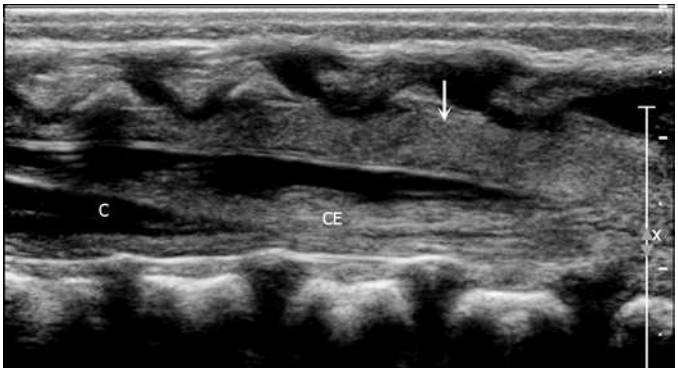

FIG. 49.10 Normal Epidural Fat. Epidural fatty layer can sometimes be prominent *(arrow)*. Note the distal cord *(C)* and the cauda equina *(CE)*.

The normal conus is typically located in the ventral thecal sac on prone position, between L1 and L2 and occasionally extending to the superior endplate of L3. However, the range of normal varies in children from T10-T11 to the superior end plate of L3.[24] On MRI, the position of the conus ascends from 20 to 38 weeks. The mean conus position is L4 from 21 to 25 weeks, L3-4 from 26 to 30 weeks, L2-3 from 31 to 35 weeks, and L2 after 36 weeks.[25] A conus position at the third lumbar vertebra (L3) or above by the beginning of the third trimester should be considered normal.[26-28] A conus tip at the L3-L4 disc space level is too low.[24,29-35] Therefore a conus position of L3 proper in the late preterm infant is equivocal, requiring follow-up.[8,32] Factors other than conus position alone need to be considered when determining the need, if any, for further evaluation with MRI. When an experienced spine sonographer finds that the tip of the conus medullaris is positioned over the upper third of the L3 vertebral body with normal nerve root pulsation, and if no other abnormalities are noted and the physical examination findings are not suspicious, we do not generally recommend further imaging.

If subsequent MRI is deemed prudent after an equivocal ultrasound examination, many pediatric neuroradiologists support waiting until the infant is at least 3 months old because there is poor tissue contrast (low signal to noise) in the newborn spine.[36] Greater anatomic detail can be displayed with MRI in the larger infant using standard techniques.

As vertebral ossification progresses and the infant becomes more active, fewer details are visible with ultrasound.

SPINAL ANOMALIES

Tethered Spinal Cord

Tethered cord syndrome is a clinical condition that can be seen with a spectrum of pathologic causes that tether the spinal cord in a lower-than-normal position and may lead to neurologic,

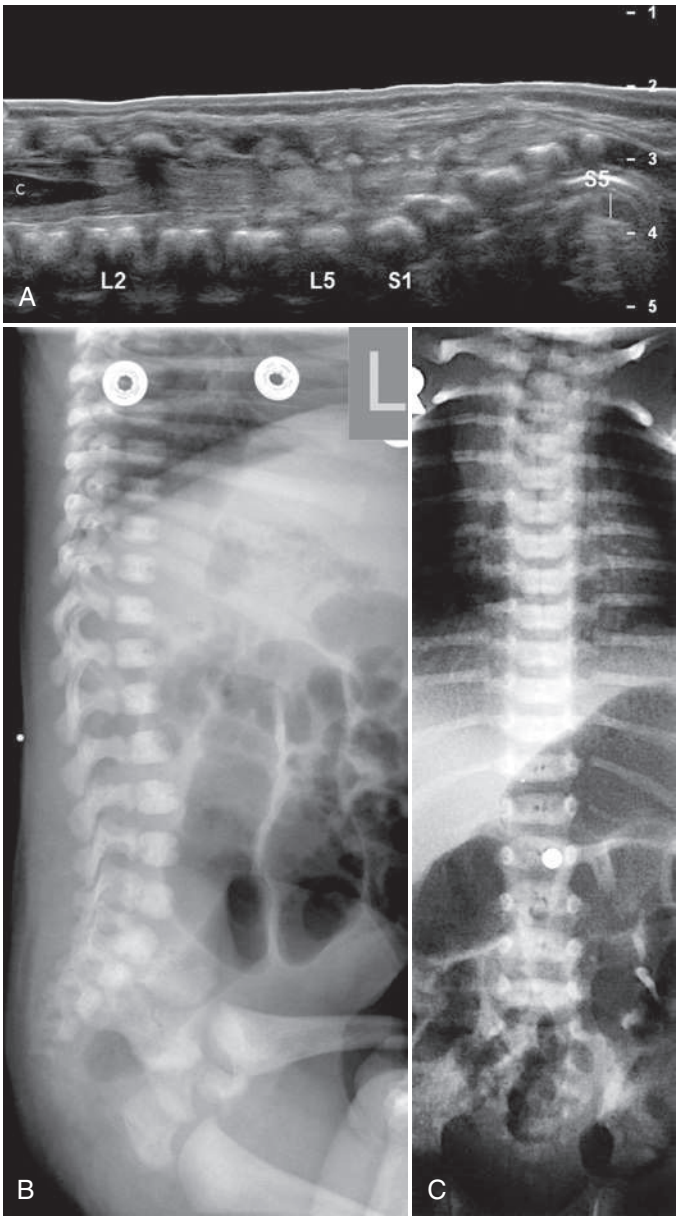

FIG. 49.11 Determining Level of Conus Medullaris. When it is difficult to determine the level of the conus medullaris by ultrasound alone, plain radiographs are often helpful. **(A)** Panoramic view shows round ossification center at S5; margins of other sacral vertebral bodies are square. BB is placed on the skin of the infant at L2, at the position of the tip of conus medullaris during sonography. **(B)** Lateral radiograph of the lower thoracic, lumbar, and sacral spine shows the marker at L2, confirming the counting done by ultrasound. Notice the inferior ribs at T12, the normal lumbosacral junction, and the round ossification at S5. **(C)** Frontal radiography in another patient. A BB was placed on the skin of an infant corresponding to the position of the tip of the conus medullaris during sonography, to help determine the associated vertebral body level.

musculoskeletal, urologic, or gastrointestinal abnormalities (Fig. 49.13). The clinical signs and symptoms are age dependent and develop as a complication of open neural tube repair or as the presentation of a closed spinal dysraphism. Spinal cord injury is theorized to result from cord ischemia caused by excessive tension or stretching of nerve fibers. The signs and symptoms have also been described in patients that have a conus medullaris in a normal position, although they usually have cutaneous stigmata, vertebral anomalies, or intradural lipomas.[9]

The treatment of a tethered cord in symptomatic patients is surgical release with total or near-total resection of the tethering mass and depending on the lesion repair of the dura. In asymptomatic patients with imaging abnormalities or in symptomatic patients with normal imaging, there is controversy with regard to treatment.[37-41]

Because newborns may have no neurologic deficits on presentation, the role of ultrasound is to identify the tethering lesion or condition and evaluate the position of the conus medullaris in patients with high- or intermediate-risk cutaneous markers. High-risk cutaneous markers include **focal hypertrichosis, infantile hemangioma, atretic meningocele, dermal sinus tract, subcutaneous lipoma, caudal appendage,** and **segmental hemangiomas** in association with **LUMBAR syndrome** (lower body hemangiomas, urogenital abnormalities, ulcerations, myelopathy, bony defects, anorectal malformations, arterial anomalies, and renal anomalies). Intermediate-risk cutaneous markers include **capillary malformations** (**salmon patches** or **port-wine stains**). Low-risk cutaneous markers do not require routine neuroimaging or follow-up and include coccygeal dimples, light hair, isolated café au lait spots, mongolian spots, hypomelanotic and hypermelanotic macules or papules, and deviated or forked gluteal clefts.[42]

Coccygeal dimples are present in 2% to 4% of newborns and are defined as a soft tissue depression located up to 2.5 cm above the anus, in proximity with the coccyx. They can be classified as shallow if the bottom is visible or deep if the bottom is not visible. A study of 84 infants with deep and shallow coccygeal dimples who underwent MRI at a mean age of 1 year identified **fibrolipomas** of the terminal filum in 16.7% of patients. The fibrolipomas were more common in patients with deep dimples. In addition, these researchers found a 7% incidence of a low conus, defined as conus below the L3 vertebral body.[43] A study of 50 neonates who underwent ultrasound examination and MRI showed no pathologic findings in infants with simple coccygeal dimples and deviated gluteal folds. In a group of 109 infants with simple dimples, ultrasound revealed no pathologic findings that needed surgery, but did show 20 cases of low dermal tracts, which had no continuity with intraspinal structures and no cord tethering.[44] These likely fibrous tracts track anteriorly and inferiorly from the dimple to the coccyx tip (see Fig. 49.12A).[12] In the group of 42 infants with deviated or split gluteal folds that were not caused by an underlying soft or bony mass, ultrasound revealed no pathologic findings.[44] Therefore in low-risk patients, if the need for imaging is questionable but imaging is desired, ultrasound provides a reliable screening tool.[44,45]

SPINAL DYSRAPHISM

The term "spinal dysraphism" stems from the Greek roots meaning bad ("dys") seam or suture ("raphe") and was first used in the literature by Tulpuis in 1641.[46] Currently, the **dysraphic lesions** describe a broad group of abnormalities that might be explained by an error in the embryologic processes of gastrulation, primary

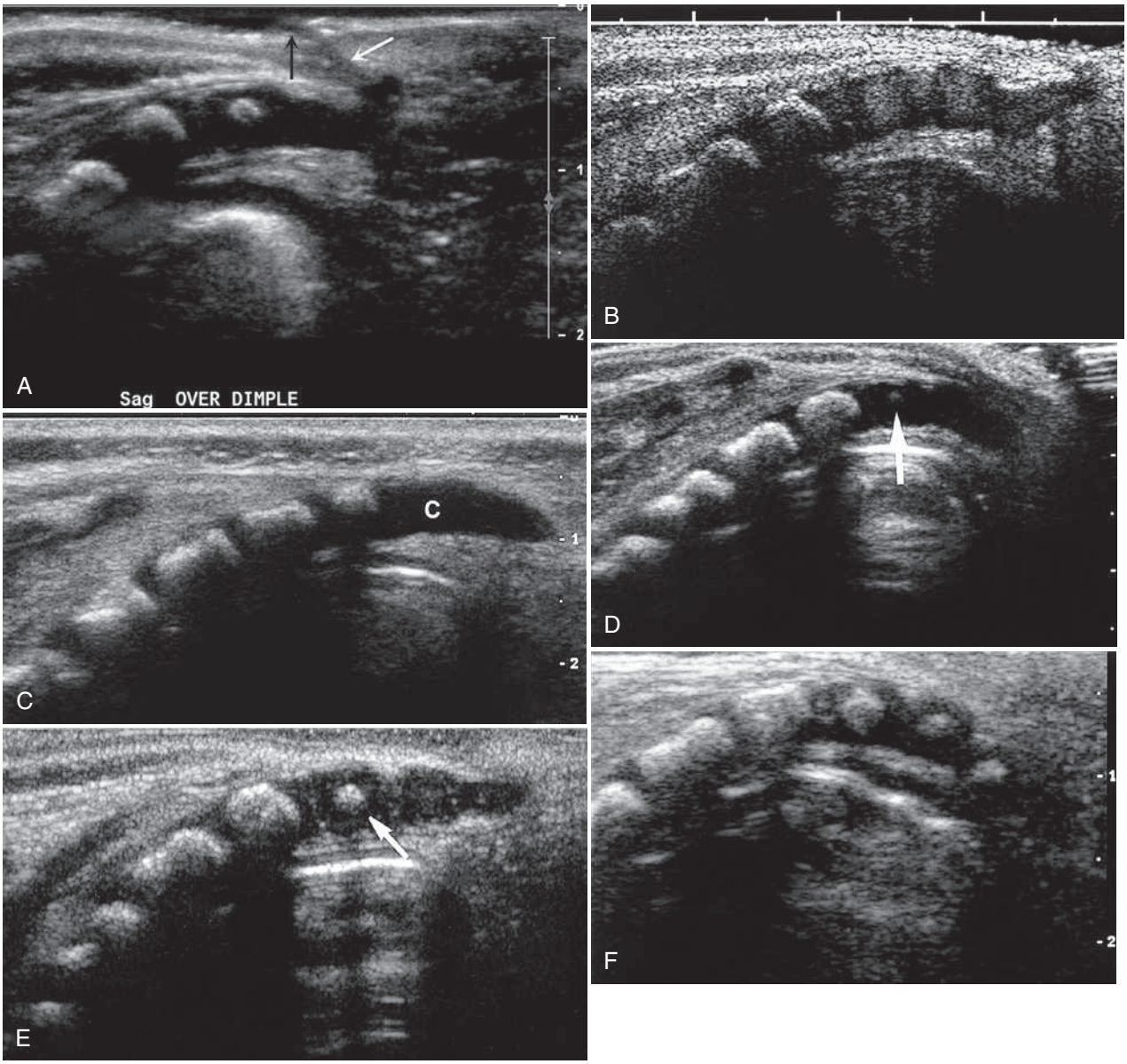

FIG. 49.12 Variation in Normal Development of Coccyx in Six Infants. (A) Dorsal curve of the distal coccyx. Notice coccygeal skin dimple *(black arrow)* and hypoechoic tract in the subcutaneous tissue *(white arrow)* that extends to the tip of the coccyx. See also Video 49.3. **(B)** The coccygeal curve is less severe. **(C)** Smooth, classic curve of the cartilaginous coccyx *(C)*. **(D)** A tiny ossification nucleus is seen in the C1 segment *(arrow)*. **(E)** Larger focus of ossification *(arrow)* and **(F)** ossification nuclei are visible within all coccygeal segments.

neurulation, disjunction, canalization, and/or retrogressive differentiation of the caudal cell mass. They can be grouped based on clinical characteristics: nonskin-covered open neural tube defects or skin-covered closed spinal lesions with or without a subcutaneous mass or other cutaneous stigmata.

The terminology used to describe this spectrum of anomalies can be confusing because there is a tendency to use the terms imprecisely and there are several proposed classifications. This can lead to confusion in interpreting the literature, inaccurate assumptions about prognosis, inappropriate management, and confusion in analyzing results of treatment.[39,47] Posterior **spina bifida** refers to incomplete closure of the posterior neural arch of a vertebra. It may be isolated, incidental, and of no clinical significance. The normal laminae at L5 remain unfused until 5 to 6 years. In the past, "spina bifida aperta" was used to refer to open spinal dysraphism and "spina bifida occulta" to refer to closed spinal dysraphism, but these terms are no longer favored.

A **placode** is a segment of flattened embryonic neural tissue that did not undergo normal neurulation. A placode can be terminal, if it is at the caudal end of the spinal cord, or segmental, lying at any level of the spinal cord. A terminal placode can be apical, involving the apex of the cord, or parietal if it involves a longer segment.

The first step of a clinical-neuroradiologic classification of spinal dysraphisms proposed by Tortori-Donati and Rossi,[5,10] is to determine whether the malformation is exposed to air (open

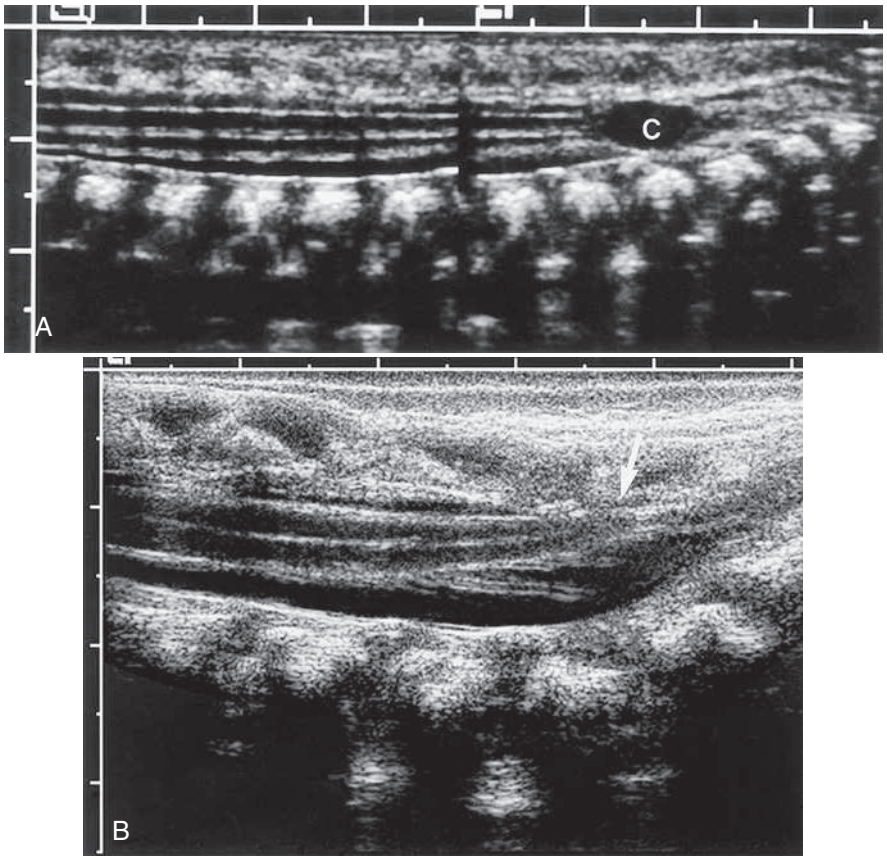

FIG. 49.13 Tethered Cord in Two Infants. (A) Newborn with tethered cord ending at S2 and an interposed filar cyst *(C).* **(B)** Newborn with a tethered cord in the setting of the VATER association (*v*ertebral defects, imperforate *a*nus, *t*racheo*e*sophageal fistula, and *r*adial and *r*enal anomalies). *Arrow* indicates the point of tethering.

spinal dysraphism) or covered by intact skin (closed spinal dysraphism) (Table 49.1). The abnormalities can be further characterized by the presence of a subcutaneous mass, which can be formed by neural elements, subarachnoid fluid, or fat.

Open Spinal Dysraphism

Open defects can occur at any level but are most common in the lumbosacral region. The diagnosis is often first suspected on maternal screening tests for elevated levels of alpha-fetoprotein (AFP) during pregnancy in maternal blood or amniotic fluid. Sonography of the fetus being screened for this condition is well established.[48-50] Open defects are generally repaired on the first or second day of life without preoperative imaging because the defect is readily apparent. Preoperative MRI can be performed to detect other abnormalities such as **syrinx, diastematomyelia,** and hydrocephalus and to understand the relationship between the placode and nerve roots.[10] Postoperative MRI can be also done to document associated anomalies. Ultrasound examination of the newborn spine with unrepaired defects is infrequently performed, in order to avoid the risk of ulceration or infection. In transverse prone views one would see the dorsal roots lateral and the ventral roots medial and posterior to the placode.[12] Ultrasound can be performed to detect other abnormalities of the spine above the open defect such as syrinx, atrophy of the thoracic and lumbar cord, arachnoid cyst, diastematomyelia, and intradural lipoma. Ultrasound and MRI of the brain are usually obtained to follow up hydrocephalus and Chiari II malformations before and after repair.

The most common open spine defect is **myelomeningocele** (98% of cases). The true incidence of neural tube defects is difficult to estimate and is approximately 2 per 1000 live births, with significant geographic and ethnic variations and increased incidence in certain high-risk groups.[51] The incidence has decreased over time, possibly the result of periconceptual folic acid, other environmental factors, and/or termination of affected pregnancies.[52] A myelomeningocele occurs when a placode is displaced dorsally by expanded subarachnoid space and is exposed to the environment by a bony defect in the midline (Fig. 49.14). Infants with **myelocele** have a flat neural placode (at the level of the skin of the back) that is exposed to the environment. The lack of expansion of the subarachnoid space distinguishes this lesion from the myelomeningocele (Fig. 49.15).

Hemimyelomeningoceles or hemimyeloceles are very rare causes of open neural tube defects that can be present if one side of a split cord malformation fails to neurulate. They are likely related to embryologic failures in gastrulation with superimposed neurulation.[5]

Open spinal defects are always associated with the **Chiari II malformation.** The proposed mechanism of this association is that leakage of CSF by the open spinal defect collapses the

TABLE 49.1 Clinical-Radiologic Classification System for Spinal Dysraphism

OPEN SPINAL DYSRAPHISM
Myelomeningocele (or hemimyelomeningocele)
Myelocele (myeloschisis)

CLOSED SPINAL DYSRAPHISM
With a Subcutaneous Mass
Lipomyelomeningocele
Lipomyelocele
Myelocystocele (terminal or cervical)
Meningocele
Cervical myelomeningocele

Without a Subcutaneous Mass
Simple dysraphic states
- Spina bifida
- Persistence of terminal ventricle
- Intraspinal lipoma
- Tight filum terminale

Complex dysraphic states
- Dorsal dermal sinus
- Caudal regression syndrome
- Split notochord syndrome (dorsal enteric fistula and neurenteric cyst)
- Split cord malformation (diastematomyelia)
- Segmental spinal dysgenesis

Modified from Barkovich AJ. Pediatric neuroimaging. 4th ed. Philadelphia: Lippincott Williams & Wilkins; 2012.[36]

embryonic ventricular system and the lack of distention disrupts normal brain development.[53] The findings of hindbrain herniation can be mild early in pregnancy,[54] and although findings may progress, the severity of the hindbrain malformation varies and can lead to delay in diagnosis if the spinal abnormality is not recognized. The Chiari II malformation is absent in all types of closed spinal defects with the possible exception of large myelocystoceles.[5] The Chiari II malformation consists of a small posterior fossa with upward transincisural herniation of the superior cerebellum, as well as downward herniation through the foramen magnum with associated compression and distortion of the brainstem. This posterior fossa distortion can be seen by sonography of the brain through the anterior fontanelle and of the craniocervical junction through the foramen magnum.[55] Hydrocephalus may develop early in the second trimester but usually develops postnatally, typically after closure of the skin opening because this closes the CSF leak.[56] Sonography also has a potential role in the evaluation of the spinal cord in patients with repaired myelomeningocele. Specifically, real-time imaging, cine clips, or M-mode ultrasound, in conjunction with MRI, has the potential to suggest the redevelopment of the tethered cord syndrome, based on dampened nerve root pulsation in this high-risk group. The scarring that adheres the caudal cord to the dura rarely occurs in neonates. The cord should be central in the dependent portion of the canal, and cord and roots should move normally in both the anterior-posterior direction with normal respiration and craniocaudally with neck flexion.[12,57-60]

Closed Spinal Dysraphism With a Subcutaneous Mass

Closed spinal dysraphisms are defined as the group of spinal dysraphisms that exist beneath an intact covering of dermis and epidermis and that are therefore not discovered with AFP screening. Many patients are clearly identified by abnormal physical examination findings, but some defects are not clinically evident at birth and may manifest later in infancy (around 6 months of age) with tethered cord syndrome. Common closed spinal defects that manifest with a lumbar **subcutaneous mass** include lipomas with a dural defect (**lipomyelocele** and **lipomyelomeningocele**) and rare entities including **meningocele** and terminal **myelocystocele.** The main differential diagnosis for lumbar masses is sacrococcygeal teratoma and overgrowing fatty tissue in caudal regression. Cervical masses that occur as a closed dysraphism with a subcutaneous mass are very rare and include cervical myelomeningocele, myelocystocele, and meningocele. The differential diagnosis includes occipitocervical cephalocele and subcutaneous lymphatic malformations.

In **lipomyelocele** (lipomyeloschisis; Fig. 49.16, Video 49.4, Video 49.5, and Video 49.6), the neural placode-lipoma interface is within or at the edge of the spinal canal and the associated lipoma is continuous with the subcutaneous fat through a posterior bony defect; the overlying skin is frequently abnormal. The subcutaneous fatty mass is located above the intergluteal crease and usually extends asymmetrically into one buttock. The placode is terminal (apical or parietal) and may be asymmetrical, involving one edge of the neural plate. The placode-lipoma interface may extend over several vertebral levels. The size of the spinal canal may be increased depending on the size of the lipoma, but the size of the subarachnoid space ventral to the cord is normal.[10]

In **lipomyelomeningocele,** the ventral subarachnoid space is enlarged, the interface of the placode-lipoma is outside the spinal canal, and the lipoma is continuous with the subcutaneous fat through a posterior bony defect (Fig. 49.17, Video 49.7, Video 49.8). The placode is frequently segmental and may be deformed, stretched and rotated asymmetrically toward the lipoma on one side, with meninges herniating on the opposite side; therefore the lengths of the spinal roots can be asymmetrical. The spinal cord below the placode is normal and lies within the canal.

In both entities of lipomyelocele and lipomyelomeningocele, the mass is more commonly formed by mature adipocytes separated by collagen bands. Other tissues such as aberrant neuroglial tissue, cartilage, bone, or fibrous, muscular, or vascular structures can be present and form **"dysraphic hamartomas."** The lipoma can invade the extradural space **(lipomatous dura mater)** and hydromyelia can be present. The subcutaneous and intraspinal components of the lipomas can grow as part of normal increase in adipose tissue in childhood, with obesity or pregnancy.

A **posterior meningocele** is less common than lipomyeloceles and lipomyelomeningoceles and forms from extension of a CSF-filled sac lined by dura and arachnoid through a dorsal bony defect. Nerve roots or part of the filum terminale may course in the sac, but no part of the spinal cord is in the sac. The spinal cord itself is normal but can be tethered to the neck

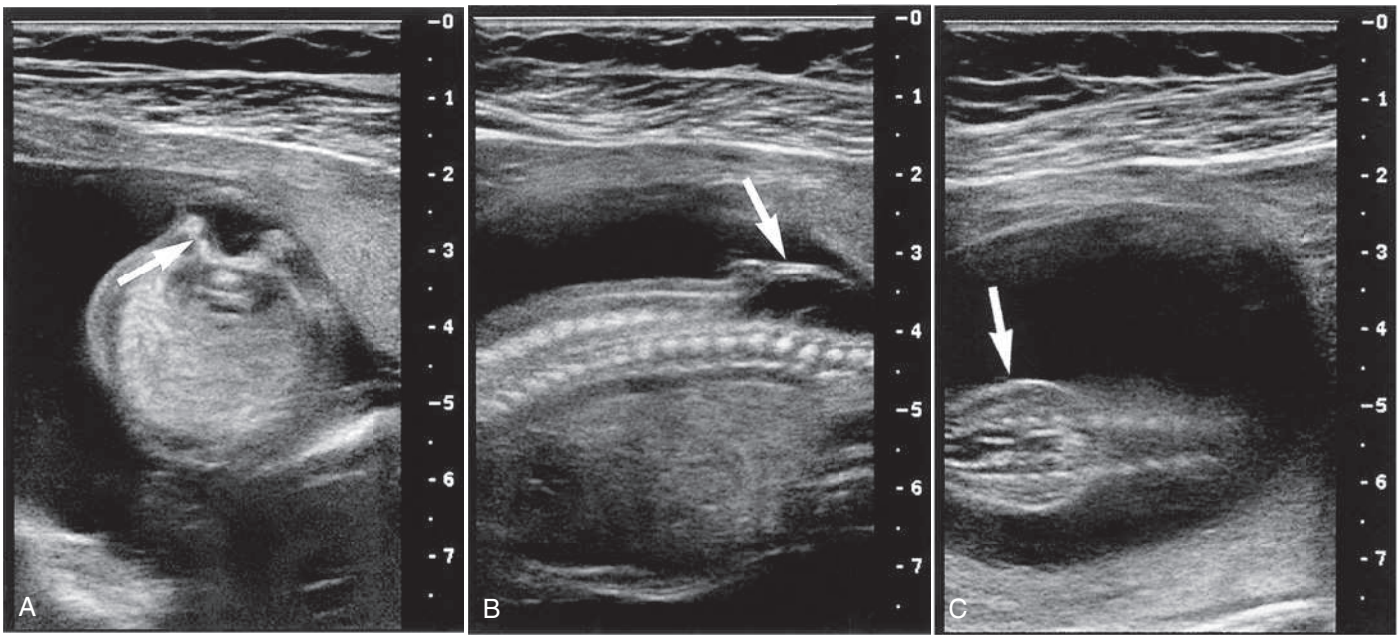

FIG. 49.14 Lumbosacral Myelomeningocele in 18-Week Fetus. (A) Transverse view shows the open nature of the posterior elements of the affected vertebral ring *(arrow)*. **(B)** Sagittal view shows the protuberance of the covering membrane and neural placode *(arrow)*. **(C)** Coronal view shows the thin nature of the covering membrane *(arrow)*.

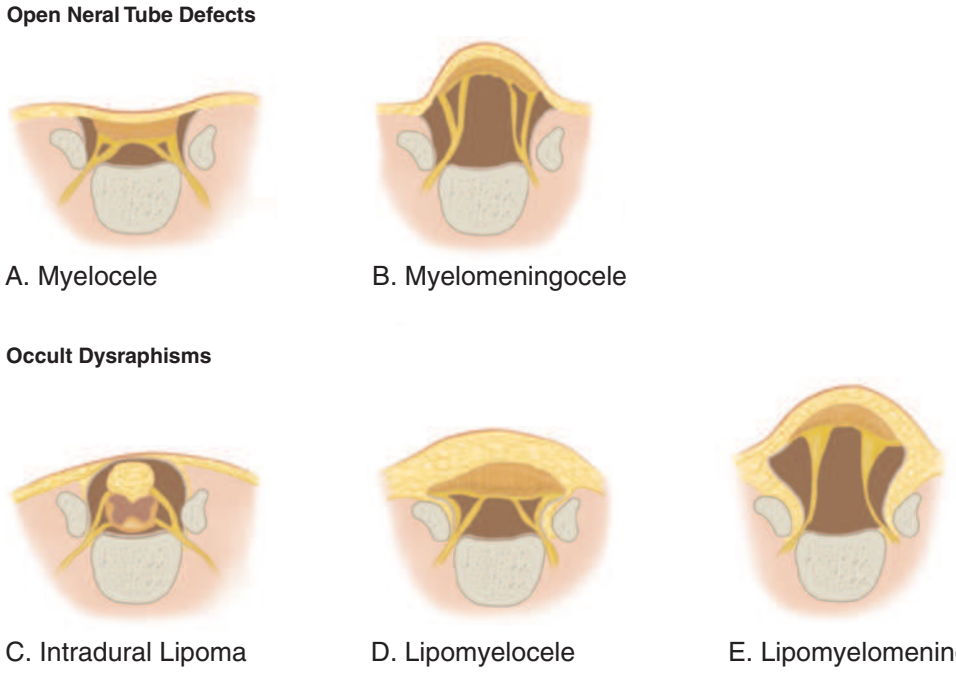

FIG. 49.15 Examples of Open Neural Tube Defects (A and B) and Examples of Closed Spinal Defects Without a Subcutaneous Mass (C) or With Subcutaneous Mass (D and E). Each diagram is positioned with the dorsal side up as one would scan the spine of an infant.

of a sacral meningocele. Their most common location is in the lumbar or sacral spine, but they can be seen in the thoracic or cervical spine. On ultrasound, the CSF-filled sac has a small neck and is continuous with the thecal sac. Small bands of pia, arachnoid, or dura can be seen, not nerves. An atretic meningocele is the condition in which an aberrant nerve adheres to the neck of the meningocele and is a cause of low conus with no apparent cause of tethering. Atretic meningoceles are associated with a midline scar that resembles a cigarette burn.[12]

Myelocystocele is a rare malformation in which the dilated central canal of the spinal cord protrudes dorsally through a dorsal bony defect. Myelocystoceles can occur at the cervical, thoracic, or lumbosacral levels. They are distinct from myelomeningoceles and are skin covered.[61,62] When occurring at the

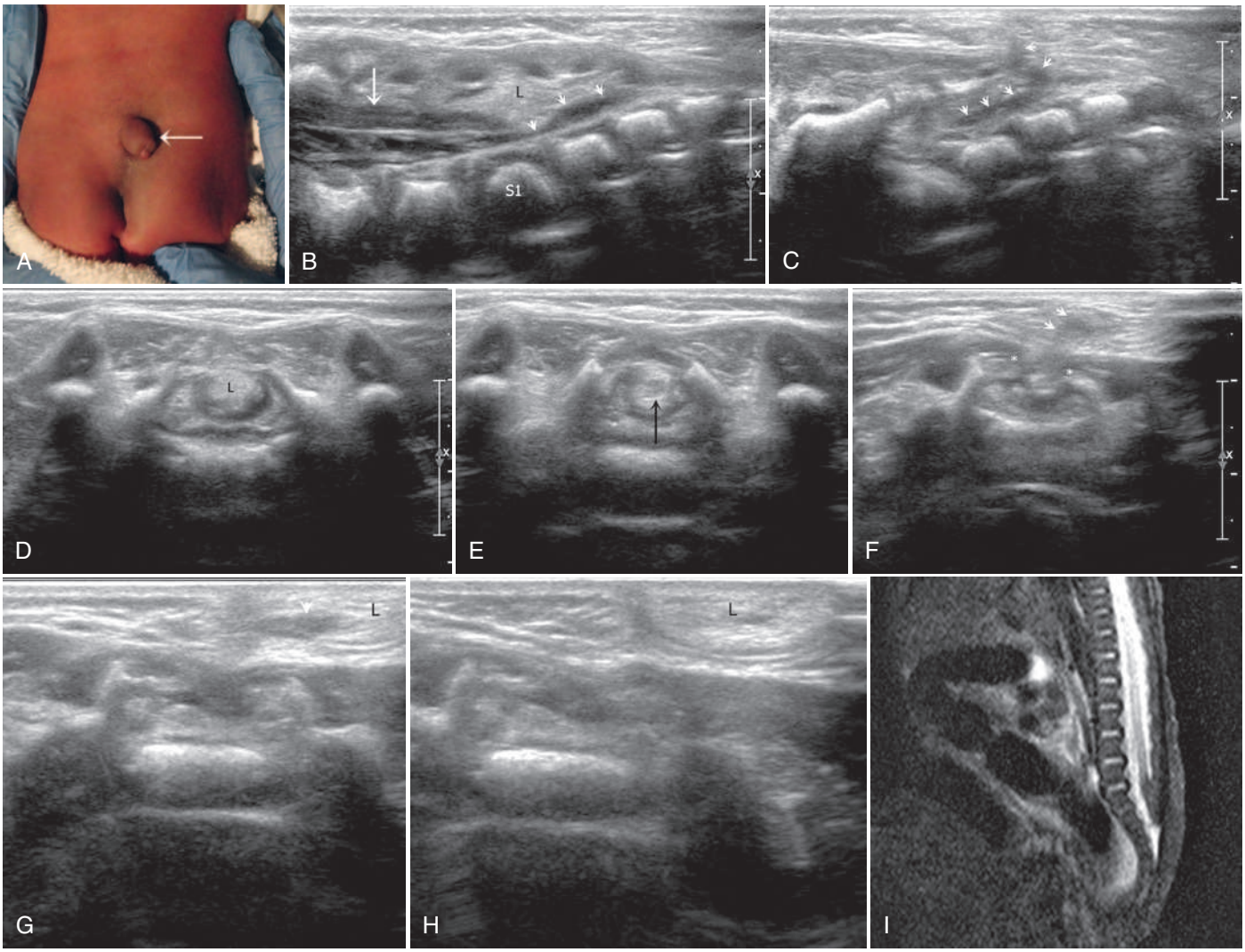

FIG. 49.16 Lipomyelocele. (A) Newborn with subcutaneous mass *(white arrow)* over the right sacrum and deviated gluteal cleft. **(B)** Sagittal view demonstrates a low-lying tethered cord that ends at S1 *(arrow points to the cord).* There is a terminal placode, and the placode-lipoma *(L)* interface lies within the canal. The lipoma and the fibrofatty filum terminale cannot be separated on this view. There is a small amount of fluid ventral to the lipoma *(small white arrows).* **(C)** Sagittal view shows fluid *(small white arrows)* extending through a defect in the right posterior elements of S2 and into the subcutaneous lipoma. **(D)** Transverse view showing intradural lipoma *(L)* extending dorsal and inferior to the conus medullaris. **(E)** Transverse view of the lipoma shows a central, tubular hypoechoic structure with more echogenic margins *(black arrow),* which corresponds to the fibrofatty filum. Note the intact cartilaginous posterior elements. **(F)** Transverse view at the level of the small right S2 posterior element defect *(outlined by *).* Note small amount of fluid extending in the central aspect of the subcutaneous mass *(small white arrows).* Transverse images are oriented with the right side of the patient to the left of the screen to maintain consistency with the position of the subcutaneous mass on the initial photograph. **(G)** Transverse view at the level of the subcutaneous mass shows central hypoechoic fluid *(white arrowhead)* and subcutaneous lipoma *(L).* **(H)** Transverse view at the level of the subcutaneous lipoma *(L).* **(I)** Sagittal T2 weighted image with fat saturation demonstrates the tip of the conus at the lumbosacral junction, and a hypointense terminal lipoma adjacent to the filum terminale. The subcutaneous mass is not seen at this level because it was to the right of midline. See also Video 49.4, Video 49.5, and Video 49.6.

lumbosacral level, they are designated **terminal myelocystoceles** (Fig. 49.18); these are quite rare.[63] The diagnosis can be established with ultrasound or MRI when the low-lying cord terminus ends in a cyst that is in communication with the central canal of the spinal cord **(syringocele).** Expanded subarachnoid space (meningocele) surrounds the distal cord and terminal cyst. Fluid within the terminal cyst does not communicate with the expanded subarachnoid space. They have a high association with cloacal exstrophy.[64-66]

Closed Spinal Defects Without a Subcutaneous Mass

Simple Dysraphic States

Filum terminale lipomas are characterized by fibrolipomatous thickening of the filum terminale. Both the intradural and extradural portions of the filum terminale can be involved, and the amount of fatty infiltration varies. Frequently the filum is slightly off midline as seen on transverse images. In this entity,

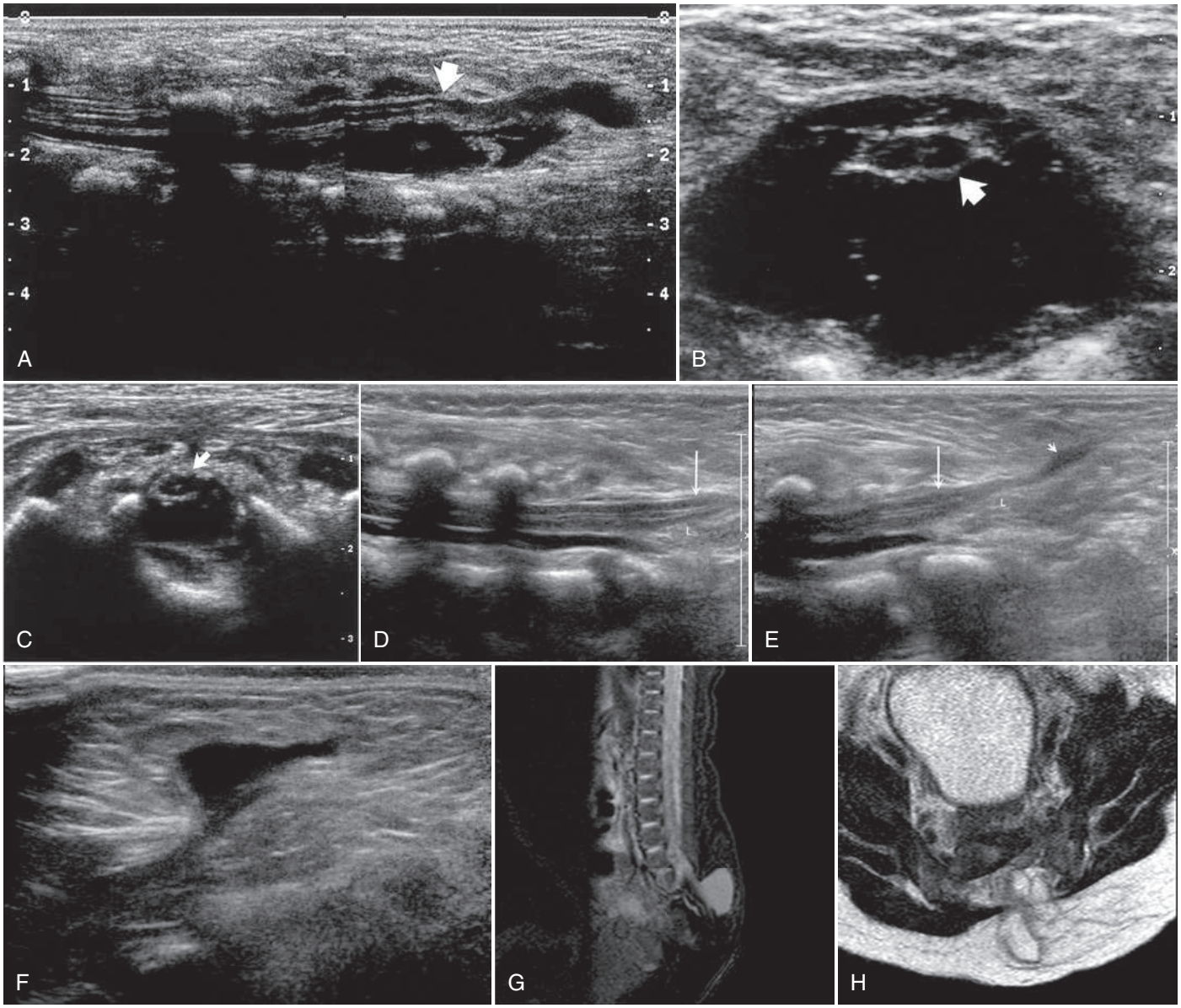

FIG. 49.17 Lipomyelomeningocele. (A) Sagittal split-screen collage of the low spinal cord *(arrow).* **(B)** Transverse view shows the neural placode posteriorly displaced *(arrow)* and the cerebrospinal fluid (CSF)–filled meningocele surrounding the placode. **(C)** Distal end of the tethered cord is incorporated into the lipoma *(arrow).* In another patient, **(D)** sagittal view shows a tethered cord *(arrow)* and a lipoma *(L)* that extends ventral to the terminal placode. Note the small ventriculus terminalis. **(E)** Sagittal view of the spine demonstrates a low-lying cord *(arrow)* with a placode that extends outside of the canal, fluid that extends to the subcutaneous mass *(small white arrow),* and a large lipoma *(L)* that extends ventral to the placode. **(F)** Sagittal view of the subcutaneous mass shows large amount of central fluid and subcutaneous fat. **(G)** Sagittal T2-weighted, fat-saturated image shows fluid in the subcutaneous fat, the placode, and hypointense ventral lipoma extending outside the spinal canal. **(H)** Axial T2 view of the pelvis shows the subcutaneous fatty and fluid mass extending beyond the spinal canal through a defect in the posterior elements of the sacrum. See also Video 49.7 and Video 49.8.

fatty tissue expands the filum terminale beyond 2 mm.[21,67] On ultrasound, this is seen as a thickened, echogenic filum terminale, sometimes with an undulating contour[68] (Fig. 49.19). In adults, "incidental" fatty infiltration of the filum has been found in 0.2% to 4% of asymptomatic patients who had no evidence of cord tethering and is considered a normal variant.[69,70]

The **abnormally long spinal cord** is a variant in which the conus medullaris does not taper and at the sacrum it connects with the lower end of the thecal sac. It may occur with intradural lipomas or lipomyelomeningoceles.

A **persistent terminal ventricle** (fifth ventricle) is a small ependyma-lined cavity in the conus medullaris. It is commonly considered a normal variant. If large, it may cause symptoms such as low back pain, sciatica, or bladder disturbance and it should be distinguished from an intramedullary tumor by its lack of enhancement and stable size.

Intradural lipomas (Fig. 49.20) can be found anywhere in the spinal canal but are more frequently lumbosacral. Their embryology and pathology is similar to lipomas with dural defects, but they are contained within an intact dural sac. They are located in the midline along the dorsal surface of the placode. They are generally subpial and may bulge posteriorly in the subarachnoid space. If large they can displace the cord laterally.[10] Their size can vary and they can be multifocal. **Intramedullary** lipoma refers to fatty infiltration within the cord; the lipoma does not extend beyond the pia.

Dorsal dermal sinuses (Fig. 49.21) are epithelium-lined fistulas that connect the skin to the central nervous system and meninges and are thought to result from focal incomplete disjunction of cutaneous ectoderm from neuroectoderm. They should be suspected on physical examination if there is a midline dimple or ostium above the gluteal cleft and more than 2.5 cm above the anus, which can be associated with a hairy nevus, capillary hemangioma, or hyperpigmented patch. The sinus is seen as a hypoechoic band that extends across the subcutaneous tissues, through an osseous defect, and into the spinal canal to the dural sac and may end in the subarachnoid space, the conus medullaris, the filum terminale, a nerve root, a dermoid, or an epidermoid cyst. The cord is usually low and tethered.[12] Sinuses can cause leakage of CSF if they are open to the subarachnoid space. In this situation, sterile gel and a probe cover should be used. The dermal sinus can originate from the skin overlying a lipomyelocele. Dermoids are common (11%).[5,10] They can be infected and are usually in the cauda equina or conus medullaris. The lumbosacral region is the most common site of such sinuses, and if present, the skin opening tends to be positioned cephalad to the point of contact with the dura. The sinus is easier to recognize in the midline sagittal plane than on transverse images. On sagittal views, the sinus is seen as a hypoechoic stipe in the subcutaneous fat. Occipital, cervical, and thoracic sinuses can all occur but are less common. The chief risks of undiagnosed dorsal dermal sinuses are infection, chemical meningitis from rupture into the subarachnoid space, and compression injury from any associated intradural mass.[71-76]

FIG. 49.18 Terminal Myelocystocele in a Fetus at 31 Weeks' Gestation. Oblique coronal view shows the well-defined, echogenic skin covering characteristic of these lesions *(arrows).*

Complex Dysraphic States (Disorders of Gastrulation)

Disorders of Midline Notochordal Integration. Abnormal development of the notochord results in complex malformations that involve the spinal cord and other organs. These disorders are present without a subcutaneous mass, except for the rare hemimyelocele and hemimyelomeningocele. The disorders of midline notochordal integration cause failure of fusion in the midline to form a single notochordal process and result in longitudinal notochordal splitting.[77]

The rarest and most severe entity is **dorsal enteric fistula,** in which an abnormal neurenteric canal connects the skin with the bowel and crosses a space between a duplicated spine and cord.[4] **Neurenteric cysts** are in the spinal canal, can remain trapped between a split notochord, and are lined by alimentary tract epithelium; their internal contents, although variable, are usually similar to CSF. They are typically intradural, in the

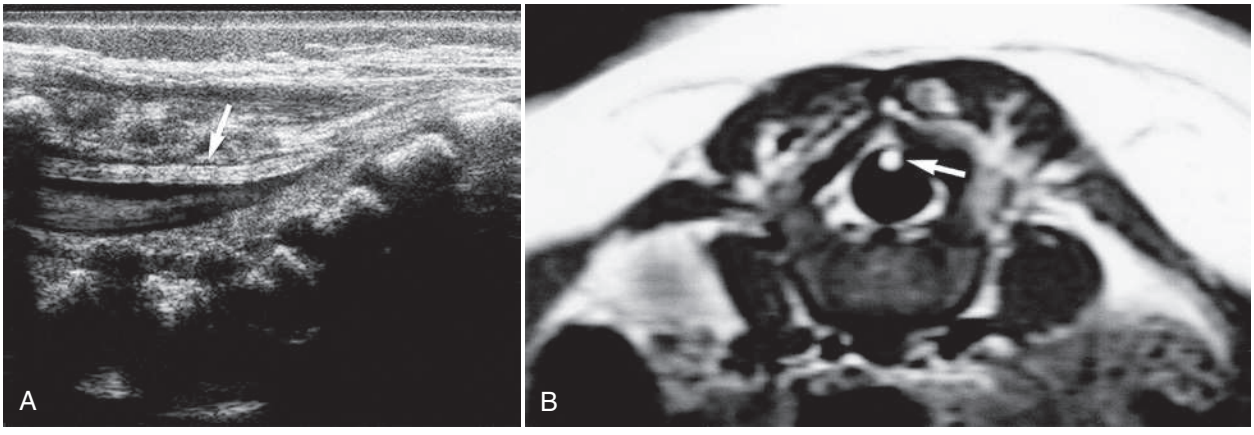

FIG. 49.19 Fibrolipoma of Filum Terminale. (A) Sagittal ultrasound and **(B)** transverse T1-weighted magnetic resonance image show that the filum terminale is abnormally thickened and echogenic *(arrow),* with high T1 signal in the filum *(arrow)* on magnetic resonance imaging.

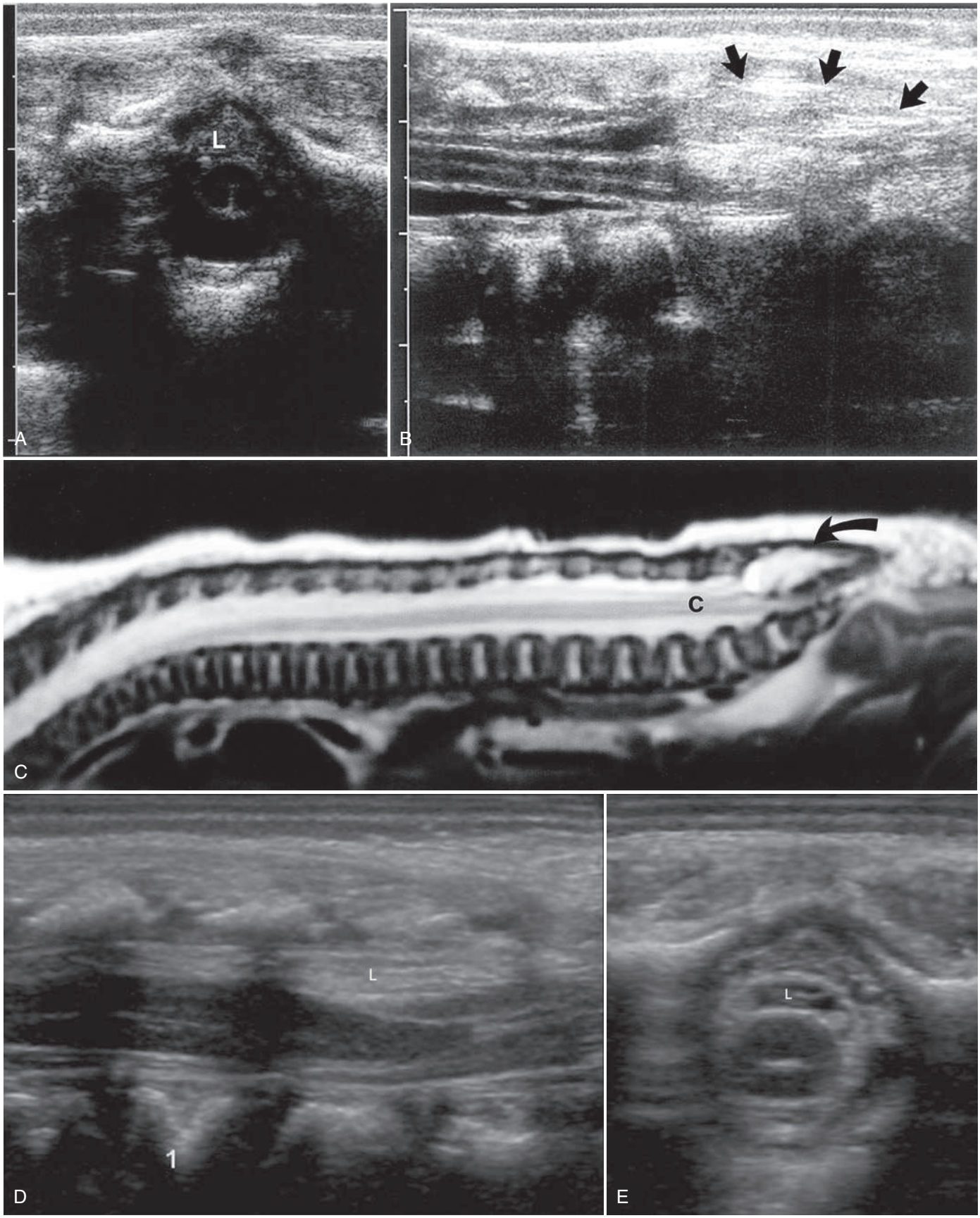

FIG. 49.20 Intradural Lipomas. (A) Transverse views in a 2-week-old girl demonstrate mild rightward deviation of the low spinal cord, which is also pulled into an abnormally dorsal position by the lipoma *(L).* **(B)** Sagittal views of the low cord with the clearly visible tethering lipoma *(black arrows).* **(C)** The correlative sagittal T2-weighted magnetic resonance image, oriented to match the ultrasound, reveals the abnormally low cord *(C)* and the lipoma *(curved black arrow).* In another newborn, **(D)** sagittal and **(E)** transverse views of the spine demonstrate a dorsal intradural lipoma tethering the spinal cord; the tip ends at mid L3. *1* indicates the 1st lumbar vertebral body. *L,* Lipoma. (**D** and **E** courtesy of Dr. Kathy McCarten.)

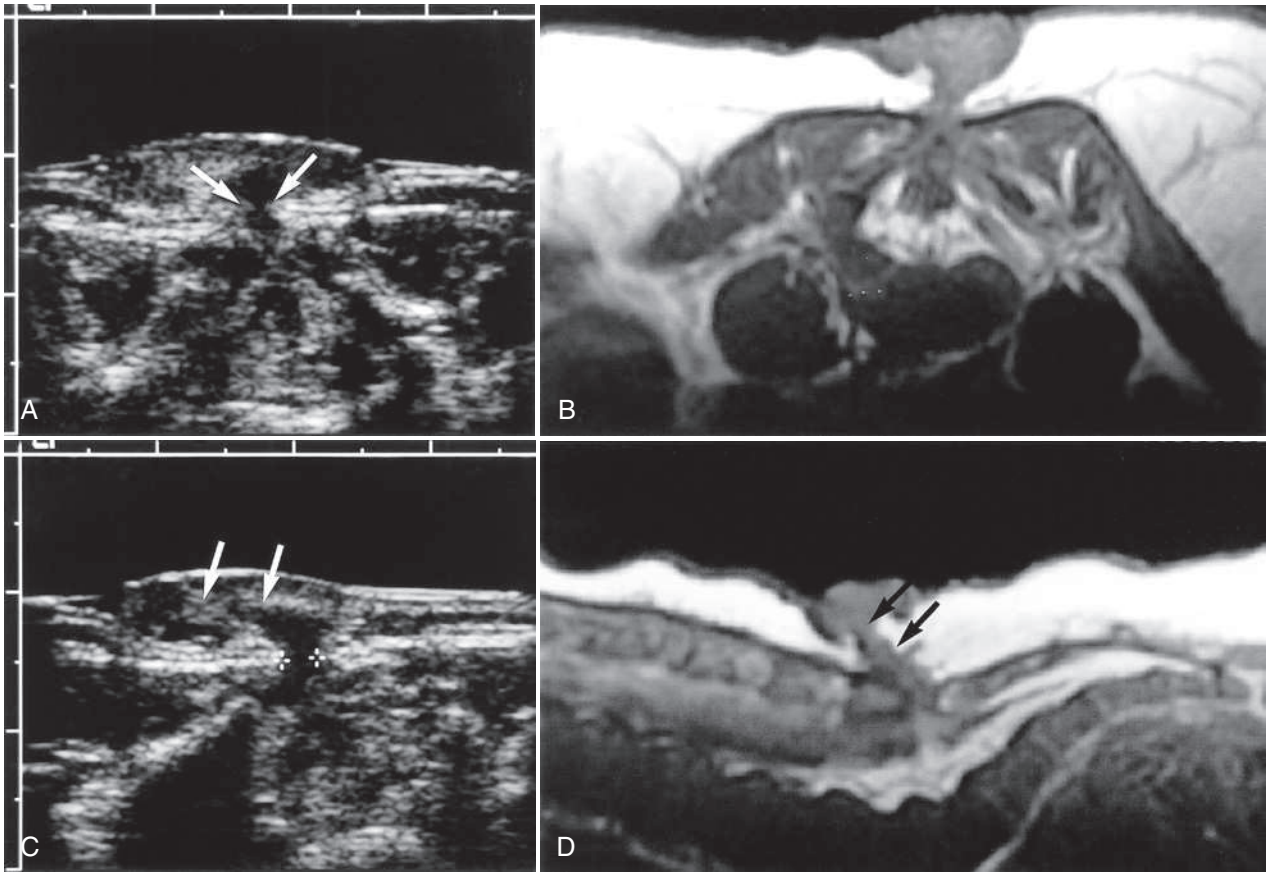

FIG. 49.21 Dorsal Dermal Sinus. Transverse and sagittal views, pairing ultrasound and T1-weighted magnetic resonance imaging. **(A)** and **(B)** Transverse views reveal the open connection among the subcutaneous fatty layer, overlying muscles, and vertebral canal *(arrows).* **(C)** and **(D)** Sagittal views show the obliquity of the connecting sinus *(arrows).* The skin-side opening is superior to the level of dural connection. This is a typical configuration.

cervicothoracic spine (less common in the lumbar spine or posterior fossa), and tend to be seen anterior to the vertebral column at a level well inferior to the associated vertebral anomaly.[5,78]

Diastematomyelia or split cord malformations are a spectrum of abnormalities in which there is sagittal division of the cord (Fig. 49.22). In **diastematomyelia type 1,** the two hemicords are contained in individual dural tubes. There is an extradural intervening bony or osteocartilaginous spur that extends from the vertebral body to the neural arches. Spurs can be complete or incomplete and are usually seen in the caudal end of the cord splitting. The hemicords can reunite caudal to the cleft or extend to the conus. **Hydromyelia** occurs in 50% of cases. Vertebral anomalies include **bifid lamina, widened interpediculate distance, hemivertebrae, fused vertebrae, intersegmental laminar fusion** (which limits acoustic window), and **scoliosis.**

In **diastematomyelia type II,** there are two hemicords and a single dural tube. Three variants consist of absent septum, fibrous septum, and partial cord splitting. The most common variant is absent septum, and the least common is when the cleft is partial and the splitting incomplete, which is best seen on

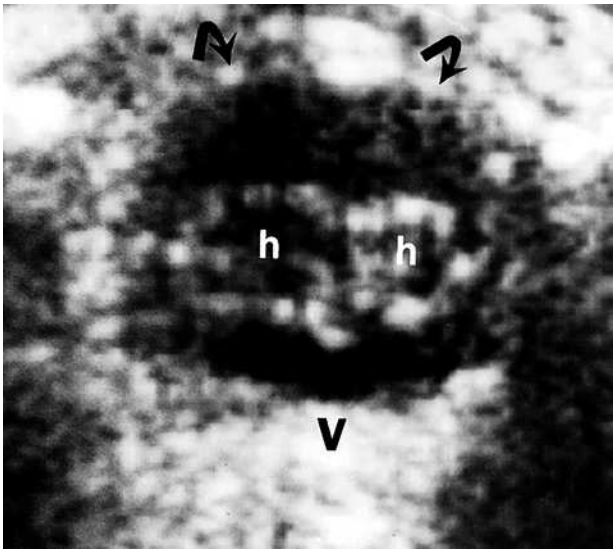

FIG. 49.22 Diastematomyelia in 3-Year-Old Girl. Transverse scan of lumbar canal shows two hemicords *(h),* confirmed on magnetic resonance imaging and at surgery. *V,* Vertebral body; *curved arrows,* dorsal dura.

transverse views. A fibrous septum can be seen on axial high-resolution magnetic resonance images. Hydromyelia may be present and the conus is typically low, strongly associated with filar lipomas and tight filum terminale. Vertebral anomalies are usually milder than in type I.[10,79,80]

The diagnosis of diastematomyelia can be made with ultrasound in the newborn period.[62,64,81,82] About one-half of patients with diastematomyelia have some surface stigmata of an underlying malformation, such as a **cranial hairy tuft, nevi, lipomas, dimples, or vascular lesions.**[61,79,80] Despite this, it is not unusual for the diagnosis to be delayed until older childhood because scoliosis or other characteristic neurologic or orthopedic symptoms develop. MRI is necessary beyond the neonatal period to establish the diagnosis. Definition of any dividing cartilaginous or bony septum is an important part of surgical planning and can be difficult to visualize with ultrasound,[45] sometimes necessitating the additional step of spinal computed tomography (CT).

Diastematomyelia may occur in isolation or in conjunction with other anomalies, such as myelomeningocele, lipoma, dermal sinus, and dermoid or teratoma.[61,83]

Disorders of Midline Notochordal Formation. The notochord induces the development of the spinal cord, spinal vertebrae, and other organs. If there are abnormal notochordal segments, vertebral malformations and segmental abnormalities of neurulation can exist. Most commonly the caudal segment is involved and caudal agenesis develops. If an intermediate segment is involved, this results in segmental spinal dysgenesis.

Caudal agenesis refers to a heterogeneous group of caudal anomalies that include **total or partial agenesis of the spinal column** (the majority involve the sacrum and coccyx), **imperforate anus, genital anomalies, renal dysplasia, pulmonary hypoplasia, and lower limb anomalies.**[84] Agenesis of the sacrum and coccyx may be part of syndromic associations including **Currarino triad**[85-88] (partial sacral agenesis, anorectal malformation, presacral teratoma or anterior meningocele), **OEIS**[89] (omphalocele, exstrophy of the cloaca, imperforate anus, spinal defects) and **VACTERL** (vertebral anomalies, imperforate anus, cardiac malformations, tracheoesophageal fistula, renal and limb abnormalities). Lipomyelomeningocele and terminal myelocystocele can be seen in up to 20%. Caudal agenesis is associated with maternal diabetes. It is seen in about 1% of babies born to mothers with uncontrolled type I diabetes mellitus; 16% of cases are associated with maternal diabetes.

Depending on the location and shape of the conus medullaris, caudal agenesis has been classified into two types.[3,90,91-95] **Type 1 or high-position caudal agenesis** (T12 or L1) involves a wedge-shaped or blunted contour of the conus owing to loss of anterior horn cells and small sacral nerve roots.[45,96] The degree of vertebral aplasia varies from absence of the coccyx to the lower thoracic vertebra, but most commonly the last vertebra is from L5 to S2. The dural sac ends at a high level. Clinically, neurologic deficits are stable. If the sacral vertebrae are absent, the iliac wings become closely opposed. There is often associated **dislocation of the hips** (Fig. 49.23).

Type II is **caudal agenesis** with **low and tethered conus medullaris** with mild vertebral dysgenesis (last vertebra up to S4). The partial agenesis of the conus may not be recognized owing to stretched conus and tethering to a tight filum, lipoma, or anterior meningocele. These patients clinically have tethered cord syndrome.[97]

Segmental spinal dysgenesis refers to a clinical and radiologic syndrome that includes segmental agenesis or dysgenesis of the lumbar or thoracolumbar spine, segmental abnormality of the underlying spinal cord and nerve roots, congenital paraplegia or paraparesis, and congenital lower limb deformities. The spine and cord can form an acute-angle kyphosis and the canal can be narrow or interrupted. The lower spinal cord is low lying and bulky and can be hypoplastic or interrupted (Fig. 49.24, Video 49.8, Video 49.9). Typically a horseshoe kidney and equinovarus feet are present.[10,98]

Several anomalies are associated with high incidence of dysraphism.[99] About one-third of infants with **high imperforate anus,** one-half with the **cloacal malformation,** and essentially all with **cloacal exstrophy** have associated spinal cord anomalies. One could argue that the cloacal exstrophy group should forgo the ultrasound step and go straight to MRI. A large percentage of the other groups can avoid sedated MRI if they are shown on ultrasound to have a normal-appearing spine in the newborn period. Because patients with spinal dysraphism often have associated renal anomalies, the kidneys should be examined as well as the spine.

Anomalies at Risk for Spinal Dysraphism

Cloacal exstrophy (100%)
Cloacal malformation (50%)
High imperforate anus (30%)
Ectopic or low imperforate anus

Hemivertebrae result from a disruption of the primary ossification center and pairing defects of the involved sclerotomes. Disorders of vertebral segmentation include **block vertebrae** and **unilateral unsegmented bars** (Figs. 49.25 and 49.26). Fusion can occur at myriad sites, including the anterior and posterior spinal column, or at facet joints.[100] Ultrasound can characterize many of the formational vertebral anomalies and is probably an underused tool.[101-104] The suspicion of a subtle vertebral anomaly seen on radiographs in the newborn period when ossification is incomplete can often be proved or refuted with spine sonography.

TUMORS

Tumors positioned in and around the vertebral canal are rare. In the neonatal period, **intraspinal neuroblastoma** is the most likely diagnosis when such a mass is discovered.[105] These lesions tend to calcify and extend into the vertebral canal from the retroperitoneum. Both the calcium and the course of extension can be observed with sonography (Fig. 49.27). These infants may have a palpable abdominal mass or signs of spinal cord compression. Other differential possibilities in the situation of intraspinal tumor extension include **hemangioma** and **rhabdoid tumor.**[106]

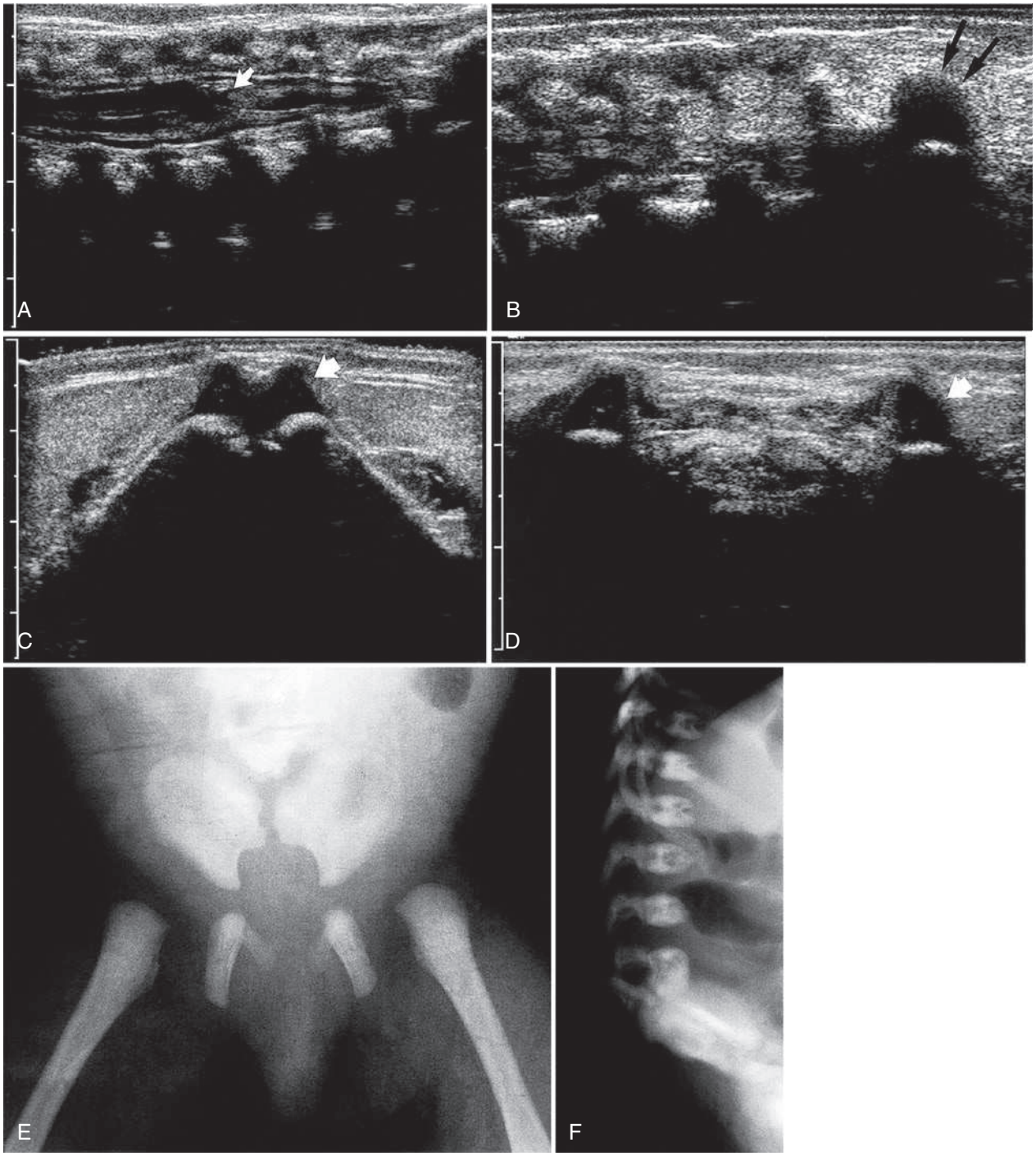

FIG. 49.23 Caudal Regression Syndrome in 4-Week-Old Girl. (A) Sagittal view of the conus medullaris reveals its tip is abnormally blunted *(arrow)*. **(B)** Sagittal view of the truncated, distal end of the vertebral column reveals an abnormally upturned and truncated cartilaginous tip *(black arrows)*. **(C)** Transverse view of absent sacrum at the expected position of the sacral spine shows the cartilaginous posterior margin of the iliac wings to be directly apposed *(arrow)* with no separating sacrum. **(D)** Normal comparison of the relationship of the posterior, cartilaginous iliac wings *(arrow)* in most infants. **(E)** Frontal radiograph of the pelvis demonstrates the directly apposed medial aspects of the iliac wings, absent distal lumbar and sacral spine, and dislocated hips. **(F)** Lateral radiograph demonstrates the truncated vertebral column.

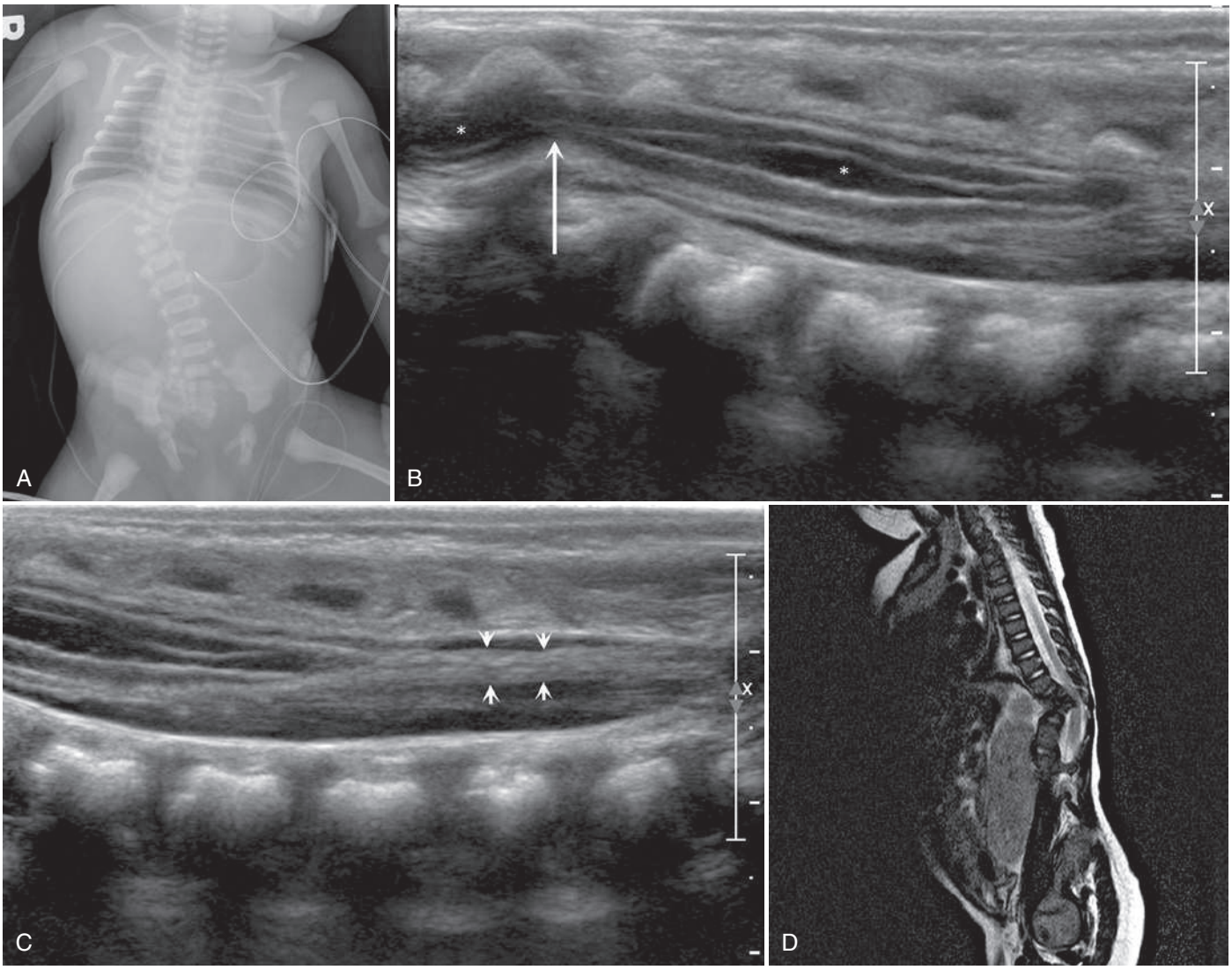

FIG. 49.24 Segmental Spinal Dysgenesis in a Newborn With Imperforate Anus, Clubfeet, and Gibbus Deformity. (A) Frontal radiograph demonstrates a kyphoscoliosis at the thoracolumbar junction with multiple hemivertebrae. There are fused sacral segments. **(B)** Sagittal view of the spine at the level of the thoracolumbar vertebral anomalies demonstrates thinning of the spinal cord, **syringomyelia** (*) above and below the area of narrowing *(white arrow)*, and a low conus medullaris. **(C)** Sagittal view of the spine shows a low lying conus medullaris that ends at L4. Note the dilation of the central canal. The filum terminale is thickened and echogenic *(arrowheads)* and showed little movement with respiration. **(D)** Sagittal T1-weighted image of the thoracolumbar spine demonstrates vertebral anomalies and marked kyphosis. There is significant segmental thinning of the spinal cord and segmental obliteration of the spinal canal. See also Video 49.8 and Video 49.9.

There are a few reports of primary intramedullary neoplasms, such as gliofibroma.[107]

Sacrococcygeal teratomas (Figs. 49.28, 49.29, and 49.30) most often are discovered in the fetal or newborn period and are the most common presacral tumors in that age group. These heterogeneous teratomas tend to recur and are generally described as **mature** or **immature.**[108-111] Altman's classification of sacrococcygeal teratomas is helpful for presurgical planning and describes the extent of the mass, which can be large and external or small and internal (Table 49.2)[112] These masses tend to have a very heterogeneous appearance on ultrasound, including solid, cystic components, fat, or foci of calcification.[113] Sacrococcygeal teratomas do not generally enter the vertebral canal, but there have been rare reports of such extension.[114]

TABLE 49.2 Altman's Classification of Sacrococcygeal Teratomas

Type	Description
I	The bulk of the mass is external, with only a minimal presacral component.
II	Both large external and large internal components are present.
III	A relatively small amount of tumor is external, but the bulk of the mass is internal.
IV	There is no external mass because the tumor is exclusively presacral.

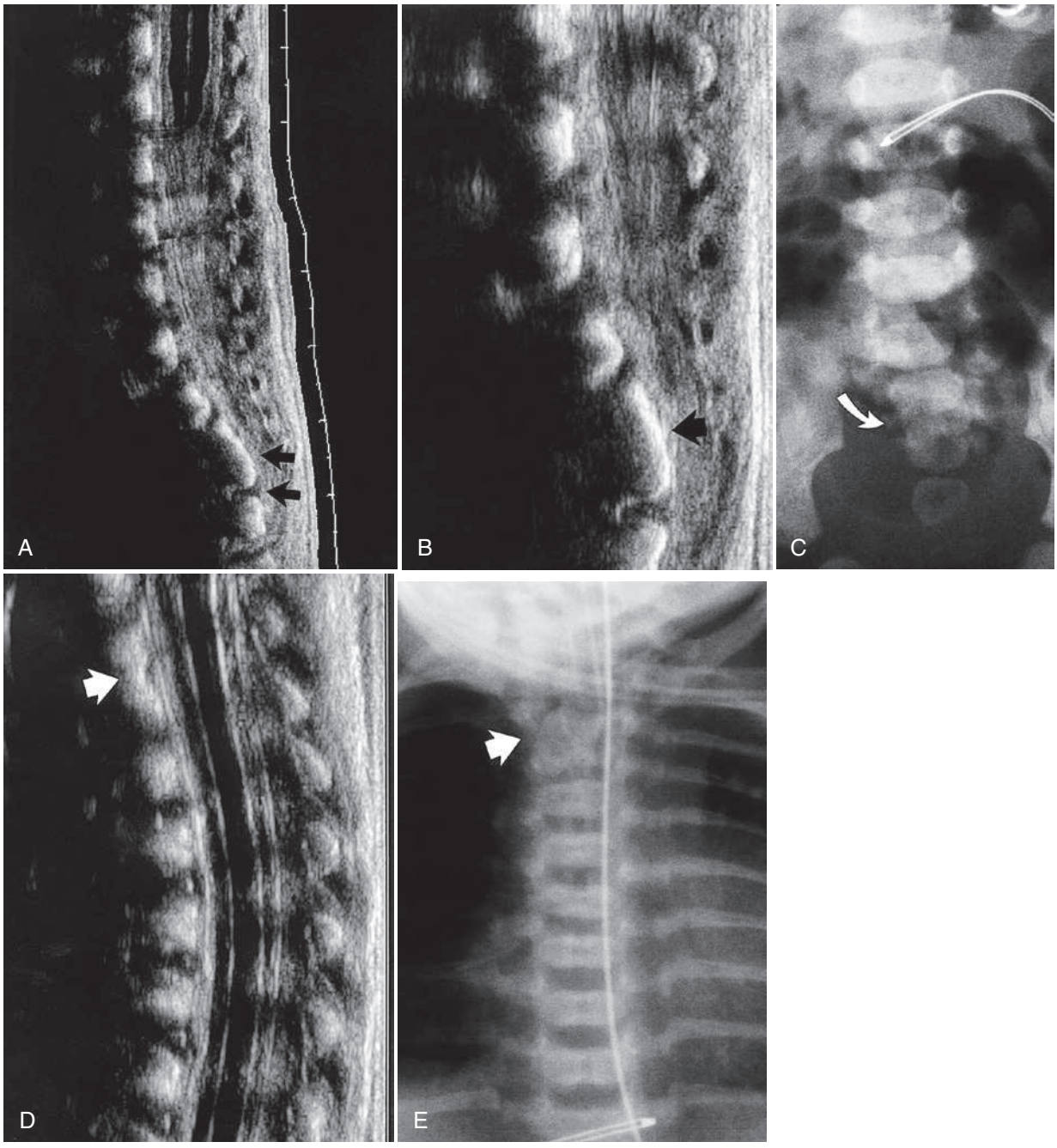

FIG. 49.25 Imperforate Anus With Block Vertebrae. (A) Extended–field-of-view image reveals the abnormal sacral truncation and block vertebrae *(arrows).* **(B)** Enlarged view of the same region. **(C)** Radiograph shows the area of vertebral fusion *(curved arrow).* **(D)** Sagittal view of the thoracic spine and **(E)** frontal radiograph reveal an additional block vertebrae *(arrows).*

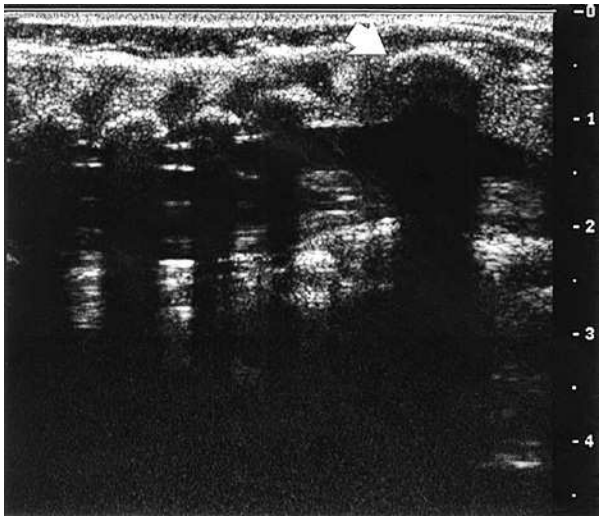

FIG. 49.26 Abnormal Fusion in 9-Week-Old Boy. Abnormal fusion of the posterior elements *(arrow)* created a firm mass to palpation.

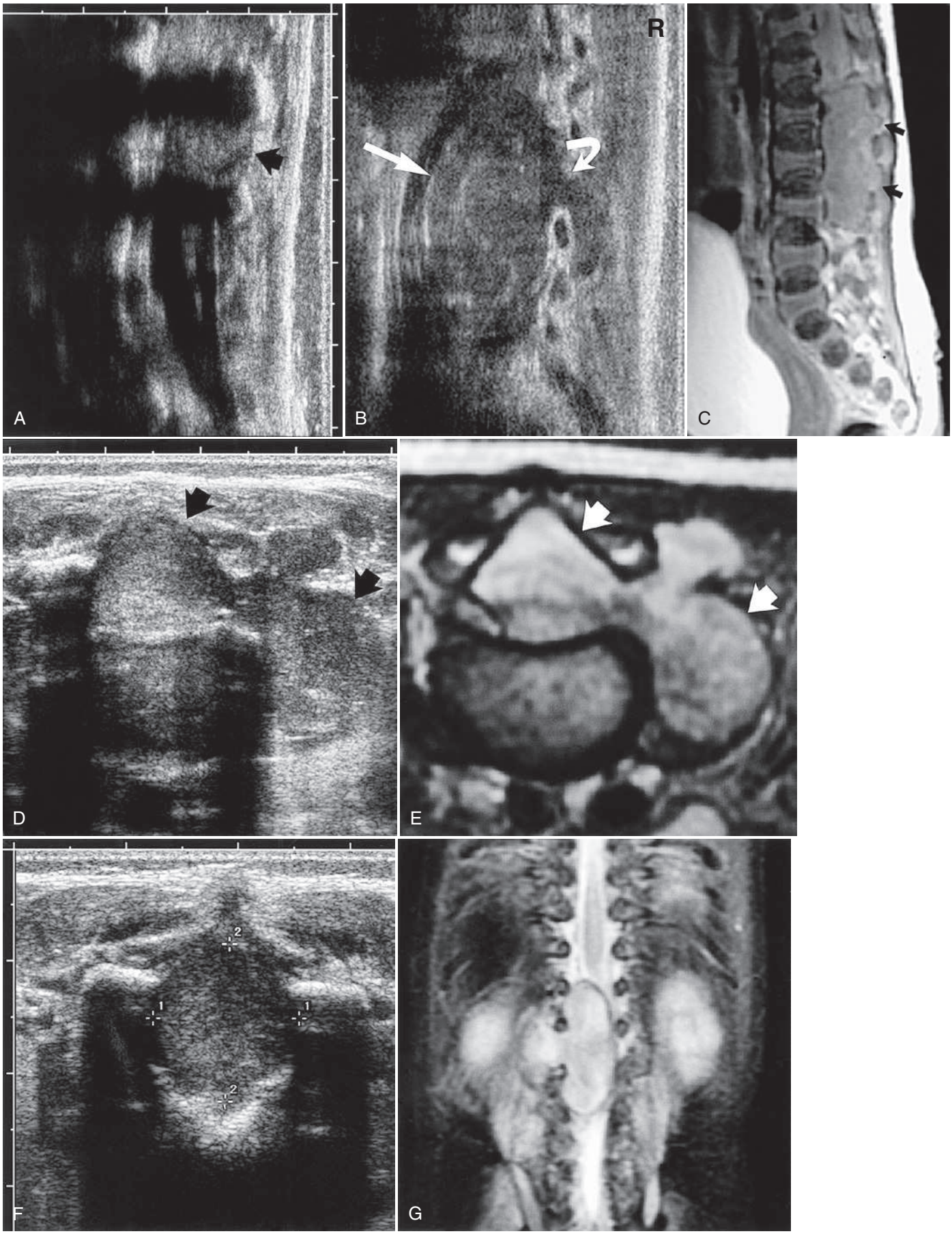

FIG. 49.27 Neuroblastoma With Intraspinal Extension. This 4-week-old girl had rectal prolapse. Initial imaging included spinal sonography. **(A)** and **(B)** On sagittal views (oriented to match magnetic resonance image), a homogeneously echogenic mass was discovered within the lumbar vertebral canal *(straight arrows)* and protrudes through the neural foramen *(curved arrow)*. **(C)** Corresponding T2-weighted magnetic resonance image shows hypointense intraspinal lumbar mass *(black arrows)*. Corresponding transverse sonogram **(D)** and magnetic resonance image **(E)** show the dumbbell-shaped mass with an intraspinal component and paraspinal/retroperitoneal extension *(arrows)*. **(F)** Axial ultrasound shows intraspinal component *(calipers)*. **(G)** Coronal T2-weighted magnetic resonance image reveals the intraspinal mass compressing the conus medullaris and extension into retroperitoneum.

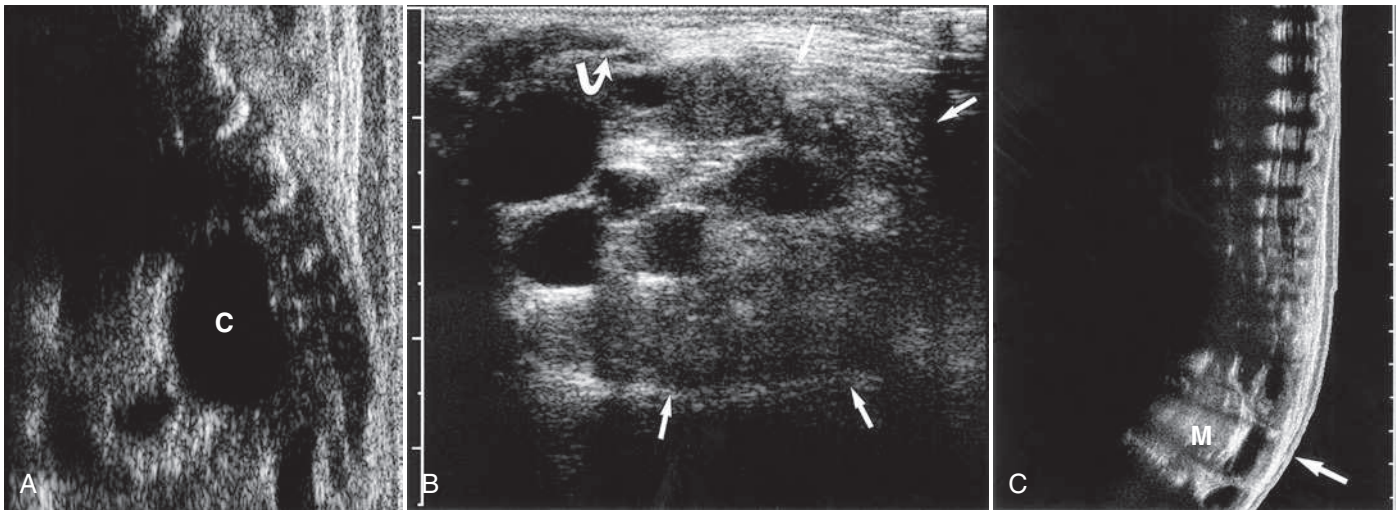

FIG. 49.28 Sacrococcygeal Teratoma. A 3-day-old infant girl with "fullness" in the buttocks. **(A)** Sagittal view shows a complex mass immediately anterior to the cartilaginous coccyx. Portions of the mass are cystic *(C).* **(B)** More distal view reveals the tip of the coccyx *(curved arrow).* The large mass extended even below the end of the coccyx *(straight arrows).* **(C)** Extended–field-of-view image gives another sense of the relative size of the mass *(M)* compared with the rest of the spine (*arrow,* end of coccyx), but the contour of the skin of the buttocks was not distorted.

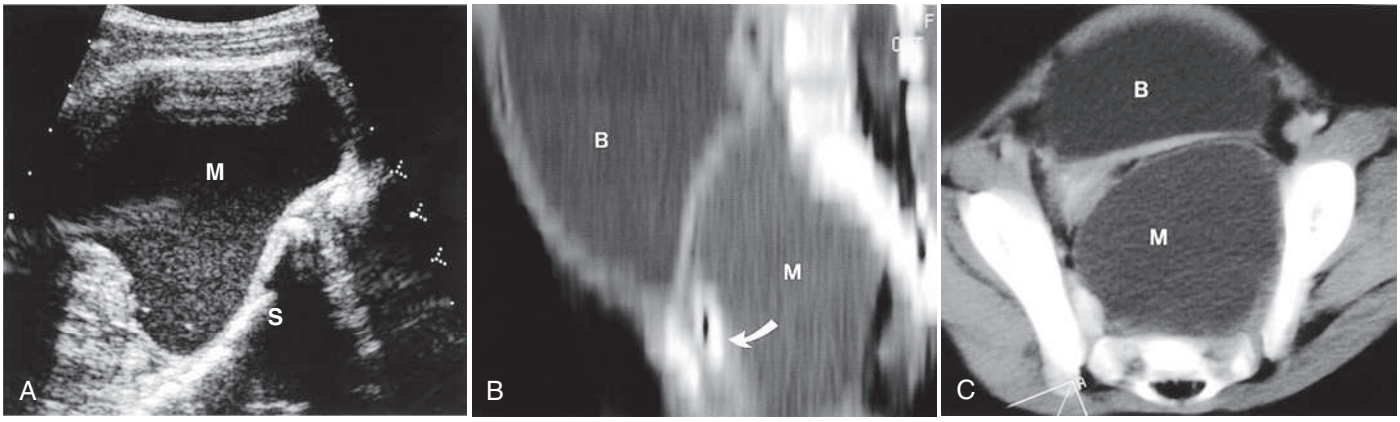

FIG. 49.29 Intrapelvic Sacrococcygeal Teratoma. A 3-year-old girl with bladder outlet obstruction. **(A)** Sagittal ultrasound view of the pelvis shows a complex cystic mass *(M)* that might have been mistaken for the urinary bladder. The mass was compressed immediately against the anterior wall of the sacrum *(S).* **(B)** Reconstructed sagittal and **(C)** direct axial computed tomography views reveal the mass *(M)* and the distended urinary bladder *(B).* High-intensity material is barium within the anteriorly displaced rectum *(curved arrow).*

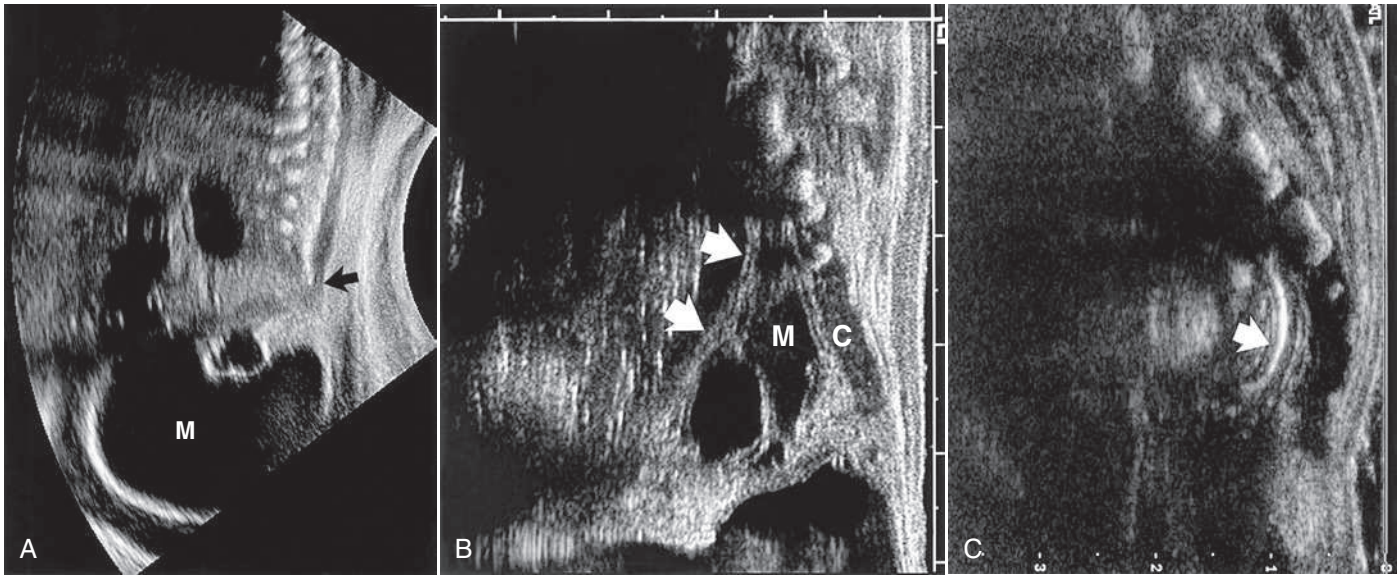

FIG. 49.30 Cystic Sacrococcygeal Teratoma. (A) Fetus at 25 weeks' gestation. The distal end of the calcified spine *(black arrow)* and the cystic portion of the mass *(M)* are demonstrated. **(B)** Postnatal ultrasound. The mass *(M)* is positioned immediately anterior to the coccyx *(C)* and immediately posterior to the posterior wall of the rectum *(arrows).* A large portion of the mass was external, and a small tongue of the tumor extended into a presacral, retrorectal position. **(C) Normal infant,** sagittal view, shows air within the rectum *(arrow),* which hugs the anterior aspect of the coccyx.

HEMORRHAGE AND INFECTION

Hemorrhage within the vertebral canal can occur in newborns in association with trauma, such as a birth injury, or with an invasive procedure such as failed lumbar puncture ("bloody taps"). Hemorrhage from birth trauma can be centered at any vertebral level. Hemorrhage related to lumbar puncture is originally centered at the point of needle placement but can extend superiorly and inferiorly for some distance. These primarily epidural collections can be visualized acutely as echogenic fluid that becomes heterogeneous and then anechoic in appearance, resolving in 2 to 4 days.[45,115] (Fig. 49.31). Injury to the spinal cord itself is also visible with ultrasound as a hyperechoic focus in the acute phase.[116] Echogenic debris within the subarachnoid space is sometimes visible with ultrasound after lumbar puncture (Fig. 49.32). This may represent hemorrhage from the trauma of the procedure or may be caused by redistribution of hemorrhage originally found in the cerebral ventricles of infants with known intraventricular hemorrhage.[117]

Ultrasound is useful for guiding percutaneous lumbar puncture[118] and for guiding anesthesiologists for caudal anesthesia in infants and neonates.[119] With a high-resolution transducer, the spinal needle can be followed from the skin to the thecal sac using midline sagittal scanning in the neonate and young infant and parasagittal scanning in the older infant and child.[45,120]

The importance of prompt recognition and treatment of epidural abscesses is well documented in the literature.[121] In the newborn and infant period, ultrasound is useful in detecting such collections.[122,123] This is particularly true if the infant is medically unstable and transfer to the MRI suite is deemed too risky. It is important to scan the entire length of the vertebral column and to pay special attention to the integrity of the vertebral bodies in these patients.

ARACHNOID CYSTS

Arachnoid cysts are infrequently found in infants, children and young adults. They can be incidental findings or they can cause

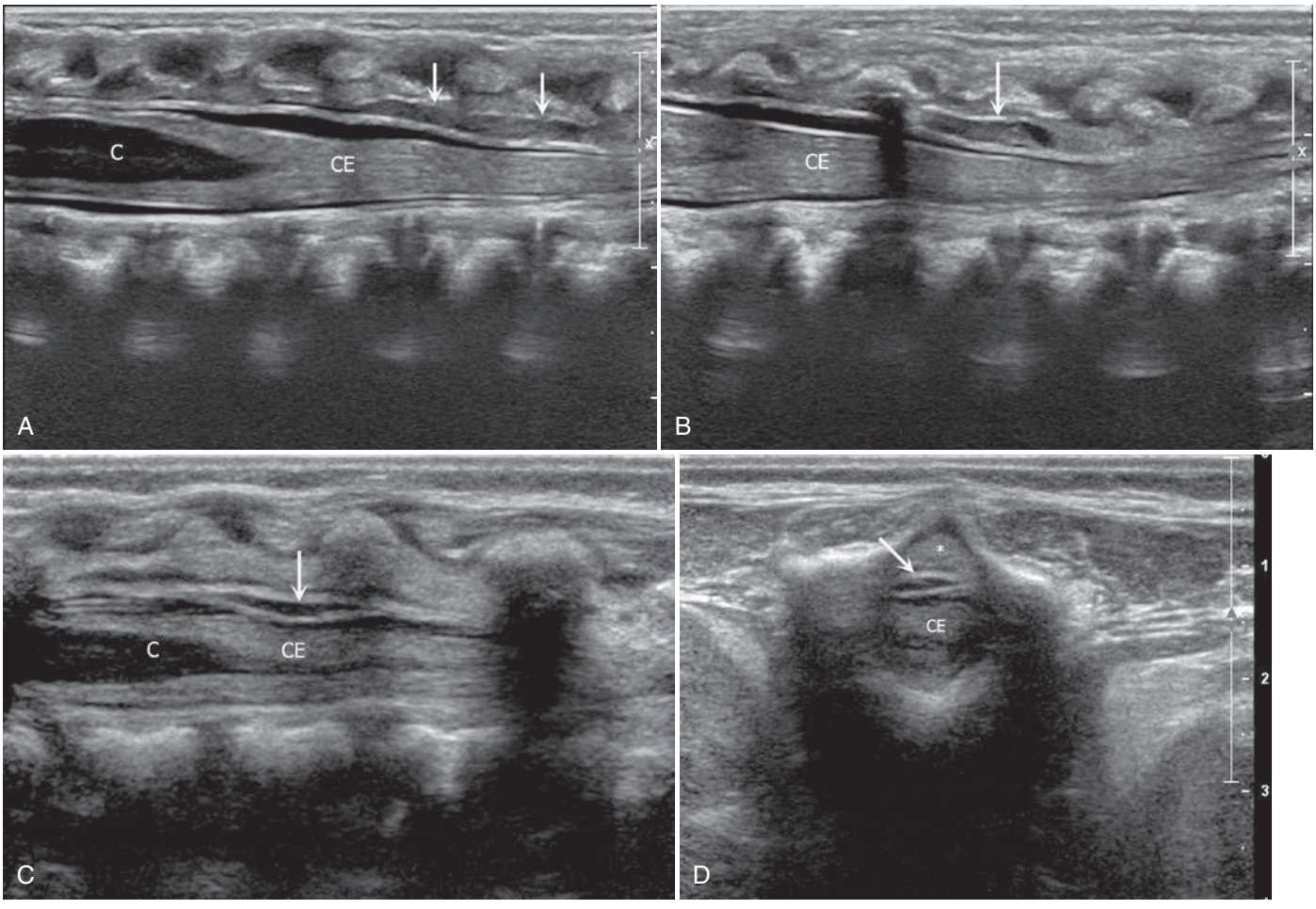

FIG. 49.31 Collections After Failed Lumbar Puncture. Epidural collection. (A) and **(B)** Sagittal views of the lumbar spine show the distal cord *(C)*. There is a large hypoechoic epidural collection *(arrows)*. The dura is the echogenic horizontal line deep to the collection. There is a small amount of subarachnoid fluid surrounding the nerve roots in the cauda equina *(CE)*. **Subdural collection. (C)** Sagittal view of the lumbar spine shows the distal cord *(C)* and cauda equina *(CE)*. There is a small subdural fluid collection seen between the dura and the arachnoid *(arrow)*. **(D)** Transverse view of the subdural collection confirms location of the fluid *(arrow)* below the dura. Note the fat (*) in the epidural space and the nerve roots in the cauda equina *(CE)*.

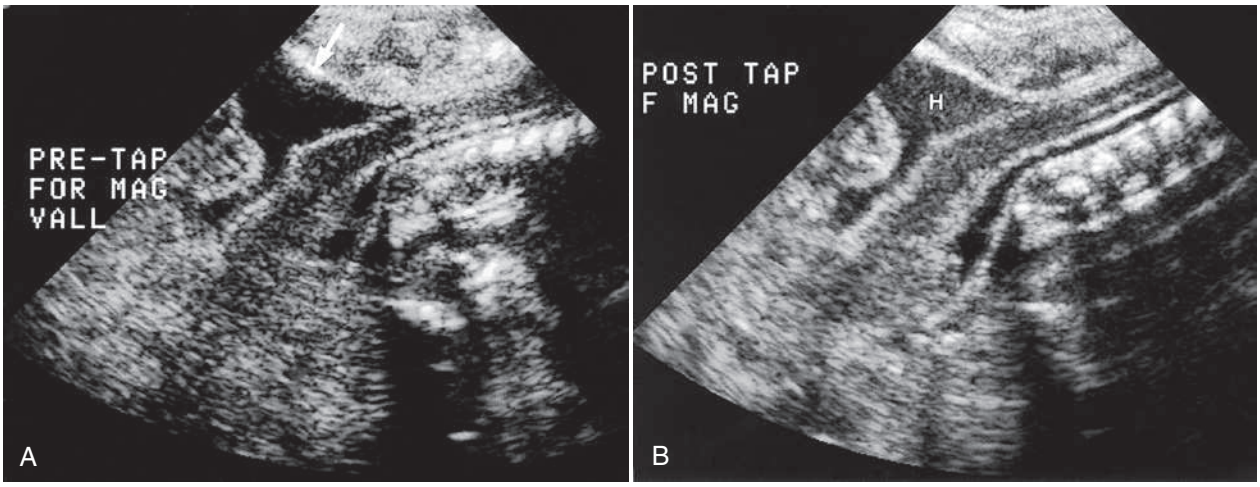

FIG. 49.32 Hemorrhage in Cisterna Magna After Lumbar Tap. (A) Sagittal view of the craniocervical junction before a lumbar tap using the foramen magnum as a window reveals anechoic fluid in the cisterna magna *(arrow)*. **(B)** The same region contains internal echoes, indicating the presence of hemorrhage *(H)*, after lumbar tap.

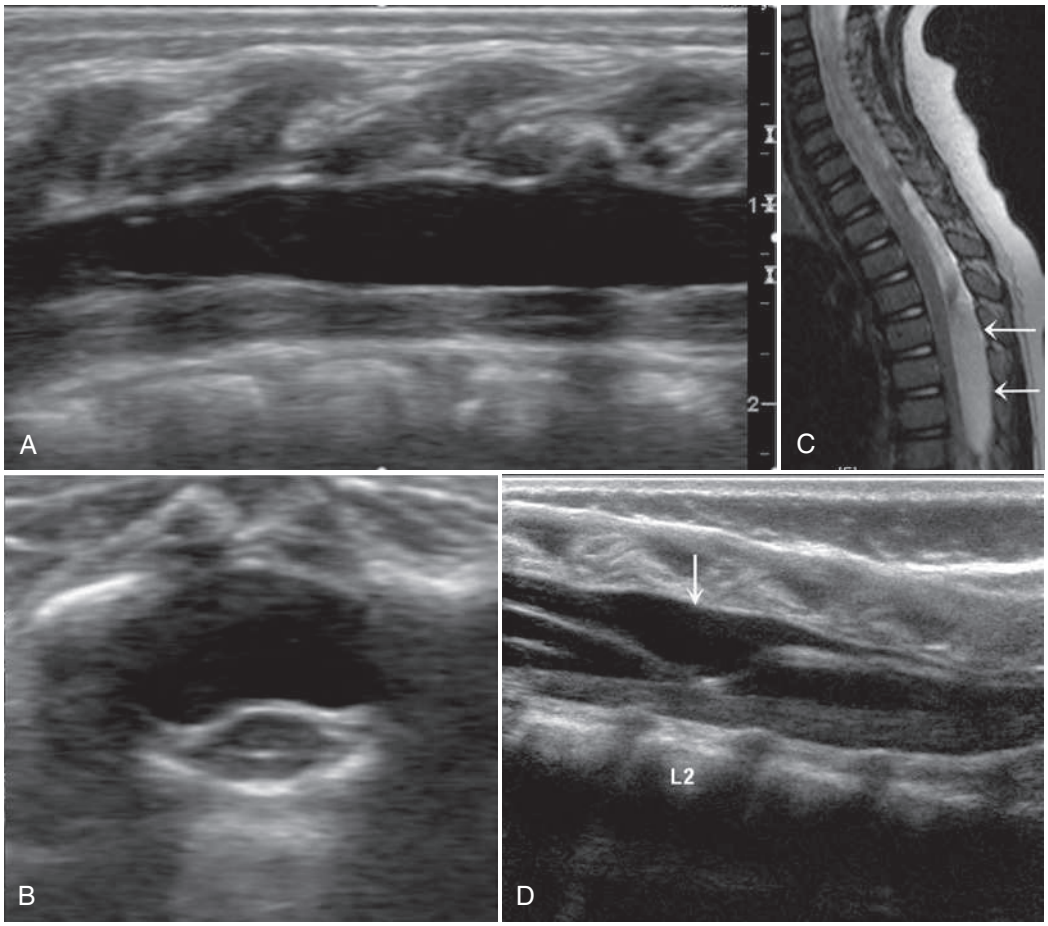

FIG. 49.33 Arachnoid Cysts. (A) and **(B)** Sagittal and transverse views of the thoracic spine in a 1-month-old demonstrate a large dorsal arachnoid cyst causing ventral displacement and compression of the spinal cord. **(C)** Sagittal T2-weighted image of the thoracic spine confirms a large arachnoid cyst *(arrows)* ventrally displacing the cord and causing thinning and compression of the cord. **(D)** Sagittal view in another newborn patient shows a small intradural arachnoid cyst *(arrow)* dorsal to the conus medullaris and proximal filum terminale. (**C** and **D** courtesy of Dr. Kathy McCarten.)

myelopathy and radiculopathy. They can be congenital or associated with trauma, surgery, arachnoiditis, neural tube defects, or neurocutaneous melanosis.

Arachnoid cysts can be intradural or less commonly extradural. Intradural cysts result from alterations of the arachnoid trabeculae, and extradural cysts from a defect in the dura that allows the subarachnoid space to herniate. They can occur in areas of prior surgery from arachnoid adhesions or abnormal CSF flow. They are most common in the thoracic spine (Fig. 49.33). When there are symptoms of cord compression, they should be treated with excision of the cyst wall. Widening of the spinal canal, bone erosion, displacement of the epidural fat, displacement of the thecal sac, and anterior compression of the cord can occur. The cysts are posterolateral to the spinal cord, and the walls can be difficult to differentiate from the fluid.[124-126]

INTRAOPERATIVE AND OTHER USES OF SPINAL SONOGRAPHY

Real-time ultrasound guidance is a valuable resource used by neurosurgeons during spine surgery to guide procedures and assess results in the setting of confined surgical fields. Many authors have described the use of intraoperative spinal sonography in minimizing surgical invasion of the vulnerable spinal cord and in analyzing normal and abnormal cord motion.[127-130] Once a **laminectomy** has been performed, the extended window into the vertebral canal makes highly detailed imaging possible, even in older patients.[131] Posterior fossa decompression for Chiari 1 malformation can be assessed intraoperatively with ultrasound if a water bath is created in the surgical bed after suboccipital craniectomy. Adequate cerebellar tonsillar motion and CSF pulsation is valuable information that can determine the need for dural incision without compromising the outcome of the decompression.[132] Masses can be precisely localized, and optimal position of the cervical cord can be determined before cervical vertebral fusion. Ultrasound has successfully guided fine-needle aspiration biopsy of lytic vertebral body and paraspinal mass lesions.[133] Definition of postoperative collections is also possible (Fig. 49.34). In general, the superficial soft tissues of the back are well defined by ultrasound. Superficial **hemangiomas** of the back, frequently the impetus to perform spine sonography, are well delineated on ultrasound (Fig. 49.35).

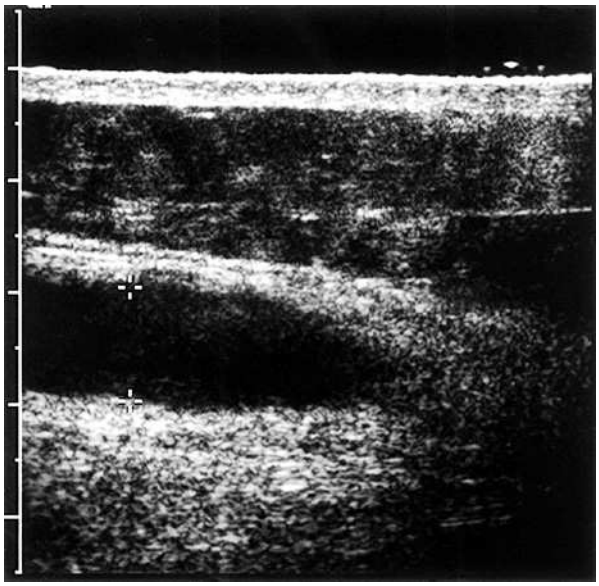

FIG. 49.34 Seroma. Transverse view of the back in a 6-year-old child after posterior spinal fusion for scoliosis. Cursors indicate the presence of a seroma.

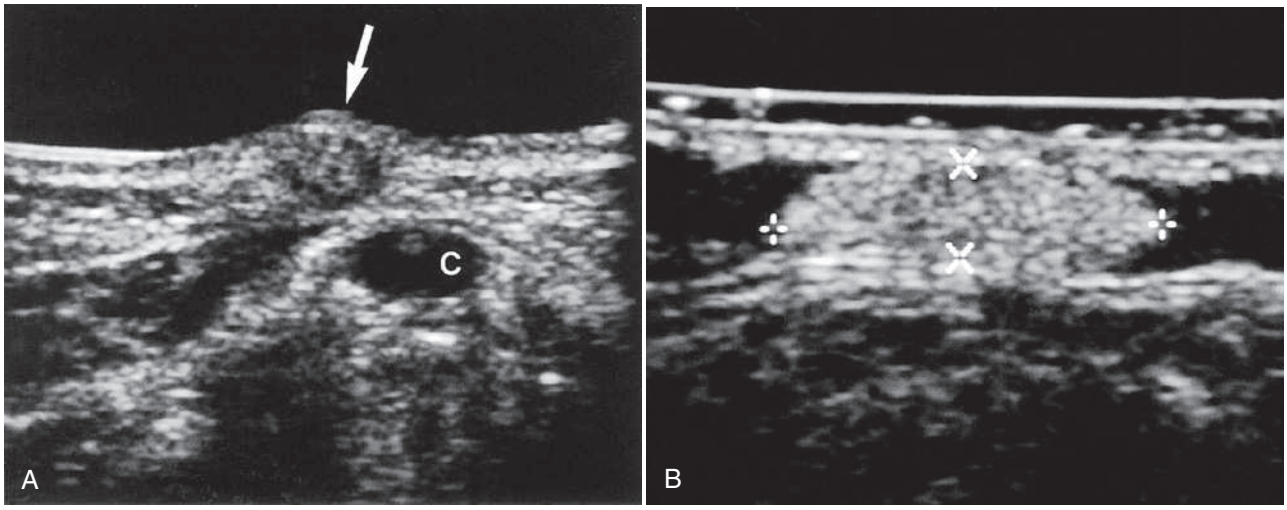

FIG. 49.35 Subcutaneous Hemangiomas. (A) Transverse ultrasound of a palpable, red mass adjacent to the coccyx *(C)* in a newborn. There is no extension into the vertebral canal, and the underlying spinal cord *(arrow)* is normal. **(B)** Sagittal ultrasound view of another infant shows an echogenic lesion *(calipers)* that does not distort the skin surface. The standoff pad is helpful to demonstrate or exclude changes in skin contour.

REFERENCES

1. Rohrschneider WK, Forsting M, Darge K, Troger J. Diagnostic value of spinal US: comparative study with MR imaging in pediatric patients. Radiology. 1996;200(2):383-388.
2. Pierre-Kahn A, Zerah M, Renier D, et al. Congenital lumbosacral lipomas. Childs Nerv Syst. 1997;13(6):298-334.
3. Nievelstein RA, Hartwig NG, Vermeij-Keers C, Valk J. Embryonic development of the mammalian caudal neural tube. Teratology. 1994;49(6):445.
4. Hoffman CH, Dietrich RB, Pais MJ, et al. The split notochord syndrome with dorsal enteric fistula. AJNR Am J Neuroradiol. 1993;14(3):622-627.
5. Tortori-Donati P, Rossi A, Cama A. Spinal dysraphism: a review of neuroradiological features with embryological correlations and proposal for a new classification. Neuroradiology. 2000;42(7):471-491.
6. Moore KL, Persaud TV. The nervous system. The developing human: clinically oriented embryology. Philadelphia: Saunders; 2003. p. 427-463.
7. Lowe LH, Johanek AJ, Moore CW. Sonography of the neonatal spine: part 1, Normal anatomy, imaging pitfalls, and variations that may simulate disorders. AJR Am J Roentgenol. 2007;188(3):733-738.
8. Barkovich AJ. The nervous system. Pediatric neuroimaging. Philadelphia: Lippincott Williams & Wilkins; 2000. p. 13-69.
9. Hertzler DA 2nd, DePowell JJ, Stevenson CB, Mangano FT. Tethered cord syndrome: a review of the literature from embryology to adult presentation. Neurosurg Focus. 2010;29(1):E1.
10. Rossi A, Biancheri R, Cama A, et al. Imaging in spine and spinal cord malformations. Eur J Radiol. 2004;50(2):177-200.
11. Beek FJ, van Leeuwen MS, Bax NM, et al. A method for sonographic counting of the lower vertebral bodies in newborns and infants. AJNR Am J Neuroradiol. 1994;15(3):445-449.
12. Ladino Torres MF, DiPietro MA. Spine ultrasound imaging in the newborn. Semin Ultrasound CT MR. 2014;35(6):652-661.
13. Alvarado E, Leach J, Care M, et al. Pediatric spinal ultrasound: neonatal and intraoperative applications. Semin Ultrasound CT MR. 2017;38(2):126-142.
14. Goodwin L, Quisling RG. The neonatal cisterna magna: ultrasonic evaluation. Radiology. 1983;149(3):691-695.
15. Cramer BC, Jequier S, O'Gorman AM. Sonography of the neonatal craniocervical junction. AJR Am J Roentgenol. 1986;147(1):133-139.
16. Harlow CL, Drose JA. A special technique for cervical spine sonography. Illustrated by a patient with meningoencephalocele, Dandy-Walker variant, and syringomyelia. J Ultrasound Med. 1992;11(9):502-506.
17. Gusnard DA, Naidich TP, Yousefzadeh DK, Haughton VM. Ultrasonic anatomy of the normal neonatal and infant spine: correlation with cryomicrotome sections and CT. Neuroradiology. 1986;28(5-6):493-511.
18. St Amour TE, Rubin JM, Dohrmann GJ. The central canal of the spinal cord: ultrasonic identification. Radiology. 1984;152(3):767-769.
19. Nelson Jr MD, Sedler JA, Gilles FH. Spinal cord central echo complex: histoanatomic correlation. Radiology. 1989;170(2):479-481.
20. Irani N, Goud AR, Lowe LH. Isolated filar cyst on lumbar spine sonography in infants: a case-control study. Pediatr Radiol. 2006;36(12):1283-1288.
21. Yundt KD, Park TS, Kaufman BA. Normal diameter of filum terminale in children: in vivo measurement. Pediatr Neurosurg. 1997;27(5):257-259.
22. Lowe LH, Johanek AJ, Moore CW. Sonography of the neonatal spine: part 2, Spinal disorders. AJR Am J Roentgenol. 2007;188(3):739-744.
23. Beek FJ, Bax KM, Mali WP. Sonography of the coccyx in newborns and infants. J Ultrasound Med. 1994;13(8):629-634.
24. DiPietro MA. The conus medullaris: normal US findings throughout childhood. Radiology. 1993;188(1):149-153.
25. Huang YL, Wong AM, Liu HL, et al. Fetal magnetic resonance imaging of normal spinal cord: evaluating cord visualization and conus medullaris position by T2-weighted sequences. Biomed J. 2014;37(4):232-236.
26. Ballantyne JW. The spinal column of the infant. Edinburgh Med J. 1892;37:913-922.
27. Miller MM. Prenatal growth of the human spinal cord. J Comp Neurol. 1913;23:39-70.
28. Streeter GL. Factors involved in the formation of the filum terminale. Am J Anat. 1919;25:1-11.
29. Barson AJ. The vertebral level of termination of the spinal cord during normal and abnormal development. J Anat. 1970;106(Pt 3):489-497.
30. Wilson DA, Prince JR. John Caffey award. MR imaging determination of the location of the normal conus medullaris throughout childhood. AJR Am J Roentgenol. 1989;152(5):1029-1032.
31. Hawass ND, el-Badawi MG, Fatani JA, et al. Myelographic study of the spinal cord ascent during fetal development. AJNR Am J Neuroradiol. 1987;8(4):691-695.
32. Robbin ML, Filly RA, Goldstein RB. The normal location of the fetal conus medullaris. J Ultrasound Med. 1994;13(7):541-546.
33. Hill CA, Gibson PJ. Ultrasound determination of the normal location of the conus medullaris in neonates. AJNR Am J Neuroradiol. 1995;16(3):469-472.
34. Sahin F, Selcuki M, Ecin N, et al. Level of conus medullaris in term and preterm neonates. Arch Dis Child Fetal Neonatal Ed. 1997;77(1):F67-F69.
35. Kesler H, Dias MS, Kalapos P. Termination of the normal conus medullaris in children: a whole-spine magnetic resonance imaging study. Neurosurg Focus. 2007;23(2):E7.
36. Barkovich AJ. Pediatric neuroimaging. 4th ed. Philadelphia: Lippincott Williams & Wilkins; 2012.
37. Chapman PH, Davis KR. Surgical treatment of spinal lipomas in childhood. Pediatr Neurosurg. 1993;19(5):267-275.
38. Drake JM. Surgical management of the tethered spinal cord—walking the fine line. Neurosurg Focus. 2007;23(2):E4.
39. Muthukumar N. Congenital spinal lipomatous malformations: part I—classification. Acta Neurochir (Wien). 2009;151(3):179-188.
40. Pang D, Zovickian J, Oviedo A. Long-term outcome of total and near-total resection of spinal cord lipomas and radical reconstruction of the neural placode, part II: outcome analysis and preoperative profiling. Neurosurgery. 2010;66(2):253-272.
41. Harrison MJ, Mitnick RJ, Rosenblum BR, Rothman AS. Leptomyelolipoma: analysis of 20 cases. J Neurosurg. 1990;73(3):360-367.
42. Dias M, Partington M; Section on Neurologic Surgery. Congenital brain and spinal cord malformations and their associated cutaneous markers. Pediatrics. 2015;136(4):e1105-e1119.
43. Harada A, Nishiyama K, Yoshimura J, et al. Intraspinal lesions associated with sacrococcygeal dimples. J Neurosurg Pediatr. 2014;14(1):81-86.
44. Ben-Sira L, Ponger P, Miller E, et al. Low-risk lumbar skin stigmata in infants: the role of ultrasound screening. J Pediatr. 2009;155(6):864-869.
45. Coley BD, Shiels WE 2nd, Hogan MJ. Diagnostic and interventional ultrasonography in neonatal and infant lumbar puncture. Pediatr Radiol. 2001;31(6):399-402.
46. Leveuf J. Etudes sur le spina bifida. Paris: Masson & Cie; 1937.
47. Muthukumar N. Congenital spinal lipomatous malformations: part II—clinical presentation, operative findings, and outcome. Acta Neurochir (Wien). 2009;151(3):189-197.
48. Fiske CE, Filly RA. Ultrasound evaluation of the normal and abnormal fetal neural axis. Radiol Clin North Am. 1982;20(2):285-296.
49. Russ PD, Pretorius DH, Manco-Johnson ML, Rumack CM. The fetal spine. Neuroradiology. 1986;28(5-6):398-407.
50. Dennis MA, Drose JA, Pretorius DH, Manco-Johnson ML. Normal fetal sacrum simulating spina bifida: "pseudodysraphism". Radiology. 1985;155(3):751-754.
51. Frey L, Hauser WA. Epidemiology of neural tube defects. Epilepsia. 2003;44(Suppl. 3):4-13.
52. Smithells RW, Sheppard S, Schorah CJ, et al. Possible prevention of neural-tube defects by periconceptional vitamin supplementation. Lancet. 1980;1(8164):339-340.
53. McLone DG, Knepper PA. The cause of Chiari II malformation: a unified theory. Pediatr Neurosci. 1989;15(1):1-12.
54. Husler MR, Danzer E, Johnson MP, et al. Prenatal diagnosis and postnatal outcome of fetal spinal defects without Arnold-Chiari II malformation. Prenat Diagn. 2009;29(11):1050-1057.
55. de la Cruz R, Millan JM, Miralles M, Munoz MJ. Cranial sonographic evaluation in children with meningomyelocele. Childs Nerv Syst. 1989;5(2):94-98.

56. Bulas D. Fetal evaluation of spine dysraphism. Pediatr Radiol. 2010;40(6): 1029-1037.
57. Levy LM, Di Chiro G, McCullough DC, et al. Fixed spinal cord: diagnosis with MR imaging. Radiology. 1988;169(3):773-778.
58. Schumacher R, Kroll B, Schwarz M, Ermert JA. M-mode sonography of the caudal spinal cord in patients with meningomyelocele. Work in progress. Radiology. 1992;184(1):263-265.
59. Brunelle F, Sebag G, Baraton J, et al. Lumbar spinal cord motion measurement with phase-contrast MR imaging in normal children and in children with spinal lipomas. Pediatr Radiol. 1996;26(4):265-270.
60. Gerscovich EO, Maslen L, Cronan MS, et al. Spinal sonography and magnetic resonance imaging in patients with repaired myelomeningocele: comparison of modalities. J Ultrasound Med. 1999;18(9):655-664.
61. Barkovich AJ. Congenital anomalies of the spine. Pediatric neuroimaging. Philadelphia: Lippincott Williams & Wilkins; 2000. p. 621-683.
62. Korsvik HE, Keller MS. Sonography of occult dysraphism in neonates and infants with MR imaging correlation. Radiographics. 1992;12(2): 297-306.
63. McLone DG, Naidich TP. Terminal myelocystocele. Neurosurgery. 1985; 16(1):36-43.
64. Unsinn KM, Geley T, Freund MC, Gassner I. US of the spinal cord in newborns: spectrum of normal findings, variants, congenital anomalies, and acquired diseases. Radiographics. 2000;20(4):923-938.
65. Peacock WJ, Murovic JA. Magnetic resonance imaging in myelocystoceles. Report of two cases. J Neurosurg. 1989;70(5):804-807.
66. Nishino A, Shirane R, So K, et al. Cervical myelocystocele with Chiari II malformation: magnetic resonance imaging and surgical treatment. Surg Neurol. 1998;49(3):269-273.
67. Raghavan N, Barkovich AJ, Edwards M, Norman D. MR imaging in the tethered spinal cord syndrome. AJR Am J Roentgenol. 1989;152(4): 843-852.
68. Rypens F, Avni EF, Matos C, et al. Atypical and equivocal sonographic features of the spinal cord in neonates. Pediatr Radiol. 1995;25(6): 429-432.
69. Brown E, Matthes JC, Bazan 3rd C, Jinkins JR. Prevalence of incidental intraspinal lipoma of the lumbosacral spine as determined by MRI. Spine. 1994;19(7):833-836.
70. Uchino A, Mori T, Ohno M. Thickened fatty filum terminale: MR imaging. Neuroradiology. 1991;33(4):331-333.
71. Martinez-Lage JF, Esteban JA, Poza M, Casas C. Congenital dermal sinus associated with an abscessed intramedullary epidermoid cyst in a child: case report and review of the literature. Childs Nerv Syst. 1995;11(5): 301-305.
72. Walker AE, Bucy PC. Congenital dermal sinuses: a source of spinal meningeal infection and subdural abscesses. Brain. 1934;57:401-421.
73. Mount LA. Congenital dermal sinuses as a cause of meningitis, intraspinal abscess and intracranial abscess. J Am Med Assoc. 1949;139(18): 1263-1268.
74. Haworth JC, Zachary RB. Congenital dermal sinuses in children; their relation to pilonidal sinuses. Lancet. 1955;269(6879):10-14.
75. Wright RL. Congenital dermal sinuses. Prog Neurol Surg. 1971;4: 175-191.
76. Barkovich AJ, Edwards M, Cogen PH. MR evaluation of spinal dermal sinus tracts in children. AJNR Am J Neuroradiol. 1991;12(1):123-129.
77. Schijman E. Split spinal cord malformations: report of 22 cases and review of the literature. Childs Nerv Syst. 2003;19(2):96-103.
78. Fernandes ET, Custer MD, Burton EM, et al. Neurenteric cyst: surgery and diagnostic imaging. J Pediatr Surg. 1991;26(1):108-110.
79. Pang D. Split cord malformation: Part II: Clinical syndrome. Neurosurgery. 1992;31(3):481-500.
80. Pang D, Dias MS, Ahab-Barmada M. Split cord malformation: Part I: A unified theory of embryogenesis for double spinal cord malformations. Neurosurgery. 1992;31(3):451-480.
81. Glasier CM, Chadduck WM, Burrows PE. Diagnosis of diastematomyelia with high-resolution spinal ultrasound. Childs Nerv Syst. 1986;2(5): 255-257.
82. Raghavendra BN, Epstein FJ, Pinto RS, et al. Sonographic diagnosis of diastematomyelia. J Ultrasound Med. 1988;7(2):111-113.
83. Ugarte N, Gonzalez-Crussi F, Sotelo-Avila C. Diastematomyelia associated with teratomas. Report of two cases. J Neurosurg. 1980;53(5):720-725.
84. Duhamel B. From the mermaid to anal imperforation: the syndrome of caudal regression. Arch Dis Child. 1961;36(186):152-155.
85. Currarino G, Coln D, Votteler T. Triad of anorectal, sacral, and presacral anomalies. AJR Am J Roentgenol. 1981;137(2):395-398.
86. Deprest JA, Lerut TE, Vandenberghe K. Operative fetoscopy: new perspective in fetal therapy? Prenat Diagn. 1997;17(13):1247-1260.
87. O'Riordain DS, O'Connell PR, Kirwan WO. Hereditary sacral agenesis with presacral mass and anorectal stenosis: the Currarino triad. Br J Surg. 1991; 78(5):536-558.
88. Gaskill SJ, Marlin AE. The Currarino triad: its importance in pediatric neurosurgery. Pediatr Neurosurg. 1996;25(3):143-146.
89. Smith NM, Chambers HM, Furness ME, Haan EA. The OEIS complex (omphalocele-exstrophy-imperforate anus-spinal defects): recurrence in sibs. J Med Genet. 1992;29(10):730-732.
90. Long FR, Hunter JV, Mahboubi S, et al. Tethered cord and associated vertebral anomalies in children and infants with imperforate anus: evaluation with MR imaging and plain radiography. Radiology. 1996;200(2):377-382.
91. Carson JA, Barnes PD, Tunell WP, et al. Imperforate anus: the neurologic implication of sacral abnormalities. J Pediatr Surg. 1984;19(6):838-842.
92. Warf BC, Scott RM, Barnes PD, Hendren 3rd WH. Tethered spinal cord in patients with anorectal and urogenital malformations. Pediatr Neurosurg. 1993;19(1):25-30.
93. Chestnut R, James HE, Jones KL. The VATER association and spinal dysraphia. Pediatr Neurosurg. 1992;18(3):144-148.
94. Karrer FM, Flannery AM, Nelson Jr MD, et al. Anorectal malformations: evaluation of associated spinal dysraphic syndromes. J Pediatr Surg. 1988;23 (1 Pt 2):45-48.
95. Beek FJ, Boemers TM, Beek FJ, et al. Spine evaluation in children with anorectal malformations. Pediatr Radiol. 1995;25(Suppl. 1):S28-S32.
96. Barkovich AJ, Raghavan N, Chuang S, Peck WW. The wedge-shaped cord terminus: a radiographic sign of caudal regression. AJNR Am J Neuroradiol. 1989;10(6):1223-1231.
97. Muthukumar N. Surgical treatment of nonprogressive neurological deficits in children with sacral agenesis. Neurosurgery. 1996;38(6):1133-1137.
98. Tortori-Donati P, Fondelli MP, Rossi A, et al. Segmental spinal dysgenesis: neuroradiologic findings with clinical and embryologic correlation. AJNR Am J Neuroradiol. 1999;20(3):445-456.
99. Appignani BA, Jaramillo D, Barnes PD, Poussaint TY. Dysraphic myelodysplasias associated with urogenital and anorectal anomalies: prevalence and types seen with MR imaging. AJR Am J Roentgenol. 1994;163(5): 1199-1203.
100. Brockmeyer DL, Smith JT. Congenital vertebral anomalies. In: McLone DG, editor. Pediatric neurosurgery: surgery of the developing nervous system. Philadelphia: Saunders; 2001. p. 428-441.
101. Abrams SL, Filly RA. Congenital vertebral malformations: prenatal diagnosis using ultrasonography. Radiology. 1985;155(3):762.
102. Benacerraf BR, Greene MF, Barss VA. Prenatal sonographic diagnosis of congenital hemivertebra. J Ultrasound Med. 1986;5(5):257-259.
103. Rouse GA, Filly RA, Toomey F, Grube GL. Short-limb skeletal dysplasias: evaluation of the fetal spine with sonography and radiography. Radiology. 1990;174(1):177-180.
104. Zelop CM, Pretorius DH, Benacerraf BR. Fetal hemivertebrae: associated anomalies, significance, and outcome. Obstet Gynecol. 1993;81(3): 412-416.
105. Patel RB. Sonographic diagnosis of intraspinal neuroblastoma. J Clin Ultrasound. 1985;13(8):565-569.
106. Garcia CJ, Keller MS. Intraspinal extension of paraspinal masses in infants: detection by sonography. Pediatr Radiol. 1990;20(6):437-439.
107. Windisch TR, Naul LG, Bauserman SC. Intramedullary gliofibroma: MR, ultrasound, and pathologic correlation. J Comput Assist Tomogr. 1995;19(4): 646-648.
108. Gonzalez-Crussi F, Winkler RF, Mirkin DL. Sacrococcygeal teratomas in infants and children: relationship of histology and prognosis in 40 cases. Arch Pathol Lab Med. 1978;102(8):420-425.
109. Ein SH, Adeyemi SD, Mancer K. Benign sacrococcygeal teratomas in infants and children: a 25 year review. Ann Surg. 1980;191(3):382-384.

110. Lahdenne P, Heikinheimo M, Nikkanen V, et al. Neonatal benign sacrococcygeal teratoma may recur in adulthood and give rise to malignancy. Cancer. 1993;72(12):3727-3731.
111. Altman RP, Randolph JG, Lilly JR. Sacrococcygeal teratoma: American Academy of Pediatrics Surgical Section Survey—1973. J Pediatr Surg. 1974;9(3):389-398.
112. Noseworthy J, Lack EE, Kozakewich HP, et al. Sacrococcygeal germ cell tumors in childhood: an updated experience with 118 patients. J Pediatr Surg. 1981;16(3):358-364.
113. Kocaoglu M, Frush DP. Pediatric presacral masses. Radiographics. 2006;26(3):833-857.
114. Ribeiro PR, Guys JM, Lena G. Sacrococcygeal teratoma with an intradural and extramedullary extension in a neonate: case report. Neurosurgery. 1999;44(2):398-400.
115. Leadman M, Seigel S, Hollenberg R, Caco C. Ultrasound diagnosis of neonatal spinal epidural hemorrhage. J Clin Ultrasound. 1988;16(6):440-442.
116. Filippigh P, Clapuyt P, Debauche C, Claus D. Sonographic evaluation of traumatic spinal cord lesions in the newborn infant. Pediatr Radiol. 1994;24(4):245-247.
117. Rudas G, Almassy Z, Papp B, et al. Echodense spinal subarachnoid space in neonates with progressive ventricular dilatation: a marker of noncommunicating hydrocephalus. AJR Am J Roentgenol. 1998;171(4):1119-1121.
118. Oulego-Erroz I, Mora-Matilla M, Alonso-Quintela P, et al. Ultrasound evaluation of lumbar spine anatomy in newborn infants: implications for optimal performance of lumbar puncture. J Pediatr. 2014;165(4):862-865.e1.
119. Mirjalili SA, Taghavi K, Frawley G, Craw S. Should we abandon landmark-based technique for caudal anesthesia in neonates and infants? Paediatr Anaesth. 2015;25(5):511-516.
120. Wang PI, Wang AC, Naidu JO, et al. Sonographically guided lumbar puncture in pediatric patients. J Ultrasound Med. 2013;32(12):2191-2197.
121. Stammers FA. Spinal epidural suppuration, with special reference to osteomyelitis of the vertebrae. Br J Surg. 1938;26:366-374.
122. Gudinchet F, Chapuis L, Berger D. Diagnosis of anterior cervical spinal epidural abscess by US and MRI in a newborn. Pediatr Radiol. 1991;21(7):515-517.
123. Rubaltelli L, De Gerone E, Caterino G. Echographic evaluation of tubercular abscesses in lumbar spondylitis. J Ultrasound Med. 1990;9(2):67-70.
124. Rabb CH, McComb JG, Raffel C, Kennedy JG. Spinal arachnoid cysts in the pediatric age group: an association with neural tube defects. J Neurosurg. 1992;77(3):369-372.
125. Myles LM, Gupta N, Armstrong D, Rutka JT. Multiple extradural arachnoid cysts as a cause of spinal cord compression in a child. Case report. J Neurosurg. 1999;91(1 Suppl.):116-120.
126. Rimmelin A, Clouet PL, Salatino S, et al. Imaging of thoracic and lumbar spinal extradural arachnoid cysts: report of two cases. Neuroradiology. 1997;39(3):203-206.
127. Rubin JM, DiPietro MA, Chandler WF, Venes JL. Spinal ultrasonography. Intraoperative and pediatric applications. Radiol Clin North Am. 1988;26(1):1-27.
128. Jokich PM, Rubin JM, Dohrmann GJ. Intraoperative ultrasonic evaluation of spinal cord motion. J Neurosurg. 1984;60(4):707-711.
129. Maiuri F, Iaconetta G, de Divitiis O. The role of intraoperative sonography in reducing invasiveness during surgery for spinal tumors. Minim Invasive Neurosurg. 1997;40(1):8-12.
130. Theodotou BC, Powers SK. Use of intraoperative ultrasound in decision making during spinal operations. Neurosurgery. 1986;19(2):205-211.
131. Braun IF, Raghavendra BN, Kricheff II. Spinal cord imaging using real-time high-resolution ultrasound. Radiology. 1983;147(2):459-465.
132. Narenthiran G, Parks C, Pettorini B. Management of Chiari I malformation in children: effectiveness of intra-operative ultrasound for tailoring foramen magnum decompression. Childs Nerv Syst. 2015;31(8):1371-1376.
133. Gupta S, Takhtani D, Gulati M, et al. Sonographically guided fine-needle aspiration biopsy of lytic lesions of the spine: technique and indications. J Clin Ultrasound. 1999;27(3):123-129.

CHAPTER 50

The Pediatric Chest

Chetan Chandulal Shah and S. Bruce Greenberg

SUMMARY OF KEY POINTS

- Ultrasound of the chest plays an important role in diagnosis and treatment of pleural effusion and empyema.
- Real-time ultrasound is very useful in evaluation of diaphragmatic motion disorders.
- Ultrasound can determine if a neoplastic lesion is solid or cystic.
- Doppler and color ultrasound can evaluate vascularity of a lesion and vascular thrombosis.
- Ultrasound of the chest is very useful in differentiating among (1) solid mass and large or persistent pleural effusion when there is a totally or partially opaque hemithorax on chest radiographs; (2) round pneumonia and mediastinal mass; and (3) normal thymus and mediastinal mass.
- Ultrasound guidance is helpful for interventional chest procedures.

CHAPTER OUTLINE

ULTRASOUND TECHNIQUE
PLEURAL EFFUSION AND EMPYEMA
Sonographic Signs of Pleural Fluid
Free Fluid Movement With Respiration
Fluid Color Flow Doppler Signal
Diaphragm Sign
Displaced-Crus Sign
Bare-Area Sign
Sonography Versus Computed Tomography Scan
Mass Versus Fluid
Parapneumonic Collections and Empyema
Lung Abscess Versus Empyema
LUNG PARENCHYMAL DISORDERS
Pneumonia
Round Pneumonia
Chest Radiograph or Ultrasound?
Atelectasis
Congenital Pulmonary Airway Malformation
Bronchopulmonary Foregut Malformation
DIAPHRAGM DISORDERS
VASCULAR DISORDERS
Vascular Thrombosis
Lymphovascular Malformation
MEDIASTINAL MASSES
Thymic Index
Abnormal Location of Thymus Mimicking Mass Lesion
Anterior Mediastinal Masses
Lymphadenopathy
Posterior Mediastinal Masses
ULTRASOUND-GUIDED INTERVENTIONAL PROCEDURES
OTHER LESS ESTABLISHED INDICATIONS

Extracardiac chest sonography is limited by air in the lungs and bone in the thoracic cage. However, ultrasound is valuable for evaluating the abnormal chest in which fluid and solid structures interpose between the chest wall and lung. Sonography is particularly well suited for the evaluation of **pleural effusion and empyema.** The thymus, liver, and spleen provide windows for chest sonography. Any radiographically opaque chest can be further evaluated by sonography to determine whether there is pleural fluid, a chest mass, atelectasis, consolidation, or lung hypoplasia. Ultrasound may show the pulmonary mass reaching the periphery but may not be able to provide a specific diagnosis. Computed tomography (CT) is required for evaluation of the extent of the mass. Biopsy might be required to arrive at a specific diagnosis.

Ultrasound can be used to guide thoracentesis, chest tube placement, or biopsy of the pleura, the lung, or a mediastinal mass. The indications for extracardiac chest sonography are listed in the accompanying box. Breast, cardiac, and pericardial lesions are beyond the scope of this chapter.

ULTRASOUND TECHNIQUE

Linear transducers with frequencies ranging from 5 to 15 MHz are used for chest ultrasound.[1] Diaphragmatic motion can best be assessed using real-time ultrasound comparison of the diaphragmatic motion on the right and the left sides. Color flow Doppler sonographic imaging is useful to demonstrate vascular supply, which is important in the diagnosis of sequestration. The selection of the frequency of the transducer is inversely dependent on patient size. Higher frequencies are used for infants, and lower frequencies for adolescents.[2]

Indications for Extracardiac Chest Sonography

FLUID ACCUMULATION IN THE PLEURA
Pleural effusion
Empyema

LUNG DISORDERS
Pneumonia
Atelectasis
Sequestration
Congenital pulmonary airway malformation
Bronchopulmonary foregut malformation

DIAPHRAGM DISORDERS
Diaphragmatic paralysis
Diaphragmatic hernia or defect
Diaphragmatic rupture

VASCULAR DISORDERS
Vascular thrombosis
Vascular malformation

MASSES
Mediastinal, chest wall, and at times pulmonary masses

INTERVENTIONAL INDICATIONS
Thoracentesis
Biopsy of chest mass
Sclerotherapy of lymphatic malformation
Vascular access

OTHER INDICATIONS
Catheter position in vessels
Pneumothorax
Rib fracture
Rib osteomyelitis
Bronchiolitis

Sector or vector transducers are used for intercostal and suprasternal approaches. Linear transducers with the long axis of the transducer aligned with the intercostal space can also be used. We have found that the smaller footprint of newer linear transducers provides improved resolution compared with vector transducers using the intercostal window (Fig. 50.1). Newer technology has allowed for increased portability of ultrasound equipment such that some ultrasound probes can connect directly to a tablet or smart phone device. The resolution of these newer devices is currently a limiting factor.

In children younger than 1 year, sternal ossification centers are unfused, the mineral content of the bones and cartilage is lower than in older children, and the thymus is much larger relative to other structures. Acoustic windows through the sternum, costal cartilages, and thymus allow ultrasound evaluation of mediastinal structures. In older children transabdominal ultrasound of the lower chest, including the diaphragm, can be performed using the liver, spleen, or fluid-filled stomach as an acoustic window. Sector, vector, or linear array transducers can be used for this purpose.

Free pleural fluid is dependent in position and will shift with patient positioning. Ultrasound of the dependent areas will identify free pleural fluid. Loculated fluid will necessarily be in a dependent position but may move with positioning.

Three longitudinal planes are used for assessment of the mediastinum (Fig. 50.2): right parasagittal plane through the superior vena cava (SVC), sagittal plane through the aortic root, and left parasagittal plane through the pulmonary outflow tract. **Two distinct transverse planes** through the mediastinum are also routinely used (Fig. 50.3): the superior plane at the confluence of the brachiocephalic veins and SVC and a lower transverse plane where the SVC, aorta, and pulmonary outflow tract are visualized.

PLEURAL EFFUSION AND EMPYEMA

The most frequent use of chest sonography is for the evaluation of a completely radiopaque hemithorax (Fig. 50.4) or a partially radiopaque hemithorax (Fig. 50.5). Ultrasound distinguishes pleural from pulmonary causes of opacification. Chest ultrasound is more sensitive than decubitus radiographs for detecting small amounts of pleural fluid (Fig. 50.6). Pleural fluid collections less than 4 mm in thickness can be physiologic and detected in normal children placed on their elbow after lying for 5 minutes in a left lateral decubitus position.[3] Because pleural effusions transmit sound waves, they allow for visualization of structures deep to the pleura that are not normally identifiable.

Intercostal and subdiaphragmatic windows are used to access the pleural space. The **spleen** and **liver** are good windows to the pleural space because they are relatively homogeneous solid organs that provide good through transmission (Figs. 50.7 and 50.8). The classic appearance of transudative pleural effusion is an echo-free or hypoechoic collection without septations immediately deep to the chest wall. However, it should be recognized that exudates can also be anechoic and that transudative pleural effusions are anechoic and nonseptated in only 45% of patients.[4] Therefore echogenicity in pleural collections does not exclude the diagnosis of a transudate.

Exudates are usually complex collections with internal echoes and associated fibrin septations. The collections may be multiloculated with a honeycomb appearance.[5] Exudates are associated with pleural thickening and underlying parenchymal abnormality.[6] Complex collections such as a **hemothorax** (Fig. 50.9) or **empyema** (Fig. 50.10) have thicker fluid with **septations** (Fig. 50.11). Underlying consolidated or atelectatic lung is more echogenic than an effusion. Complicated effusions are characterized by an irregular or indistinct interface between pleura and the adjacent lung. A **fibrothorax** has a thick pleural rind that is echogenic. Multiple hyperechoic foci in the lung are caused by residual air within bronchi and alveoli and are called **sonographic air bronchograms** (Fig. 50.12).

Text continued on p. 1709.

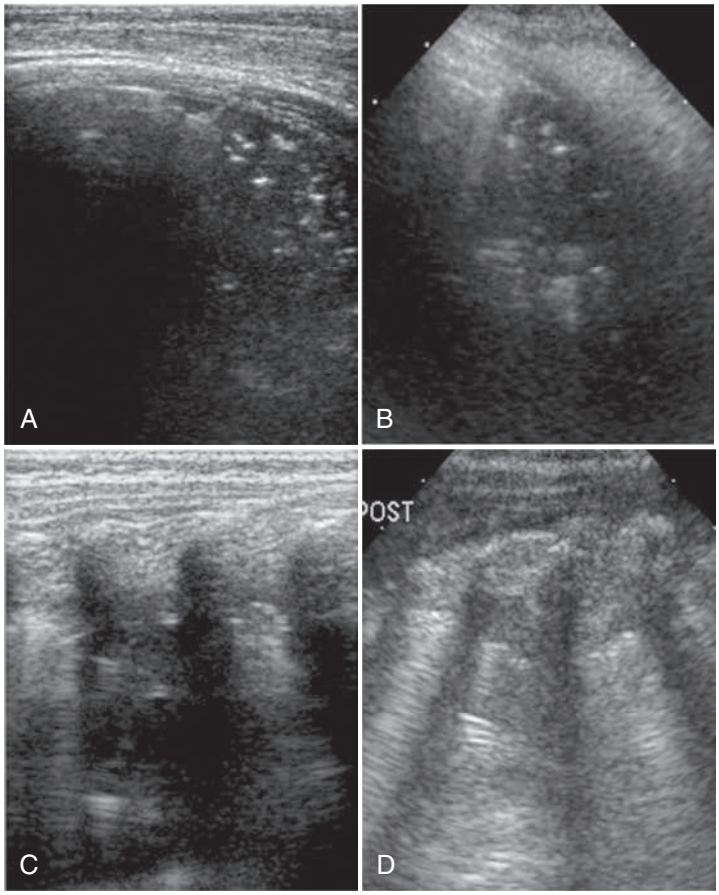

FIG. 50.1 Pneumonia on Chest Ultrasound. (A) Linear transducer. **(B)** Vector transducer. **Air bronchograms** from pneumonia are seen better with linear transducers than vector transducers, especially when the **air bronchograms** are closer to the chest wall and there is no intervening pleural fluid. **(C)** and **(D)** Air bronchograms within a **round pneumonia** in another child are better visualized with a linear transducer **(C)** than with a vector transducer **(D),** despite the intervening rib shadows.

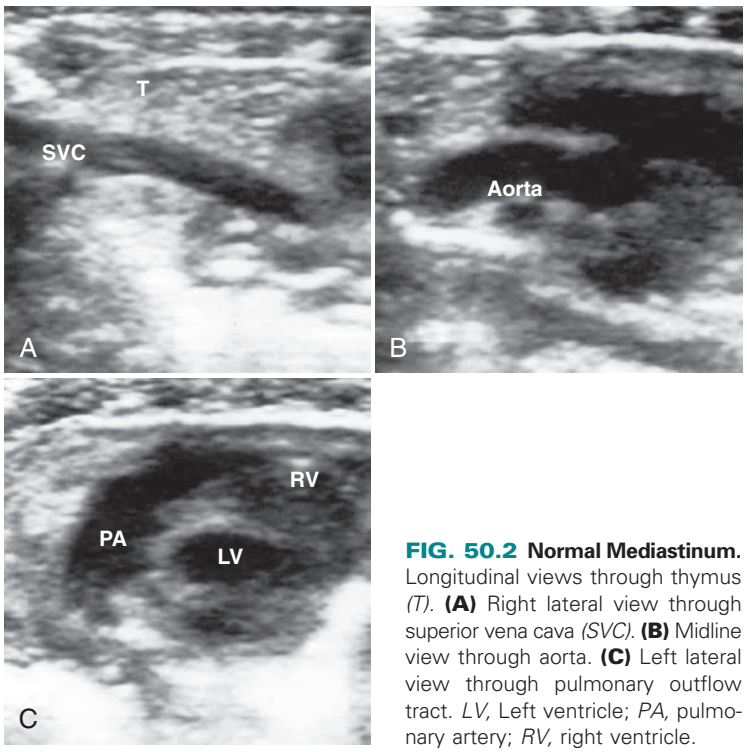

FIG. 50.2 Normal Mediastinum. Longitudinal views through thymus *(T).* **(A)** Right lateral view through superior vena cava *(SVC).* **(B)** Midline view through aorta. **(C)** Left lateral view through pulmonary outflow tract. *LV,* Left ventricle; *PA,* pulmonary artery; *RV,* right ventricle.

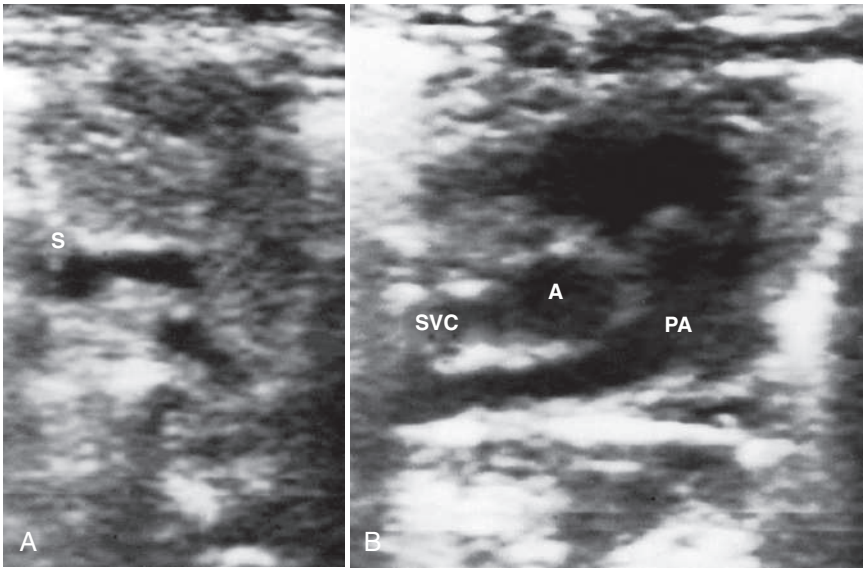

FIG. 50.3 Normal Mediastinum, Transverse View. (A) Superior plane with innominate vein catheter running through thymus to superior vena cava *(S).* **(B)** Inferior plane through superior vena cava *(SVC),* aorta *(A),* and pulmonary artery *(PA).*

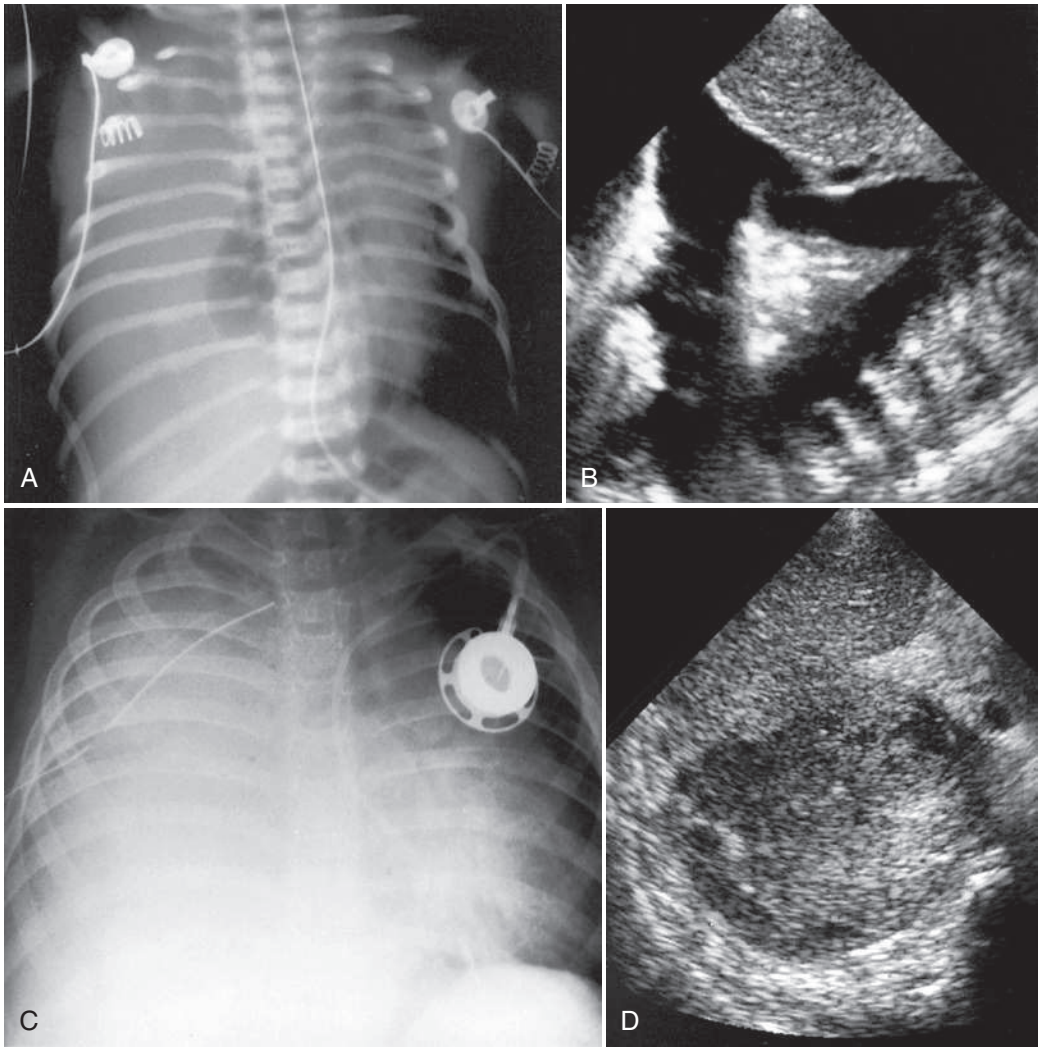

FIG. 50.4 Radiopaque Hemithorax: Neonatal Chylothorax. (A) Anteroposterior chest radiograph in 2-week-old infant shows opacified right chest and shift of heart and mediastinum to left. **(B)** Sonogram through liver shows that the opacity is a large accumulation of fluid around a collapsed lung. **(C)** Right chest opacification with shift of the heart to the left side, suggesting fluid in the right pleural space. No drainage was obtained from a chest tube. **(D)** Sonogram through liver shows that the right chest is filled with solid tissue, which at surgery was infected with **aspergillosis** extending from the liver. (With permission from Seibert RW, Seibert JJ, Williamson SL. The opaque chest: when to suspect a bronchial foreign body. Pediatr Radiol. 1986;16[3]:193-196.[76])

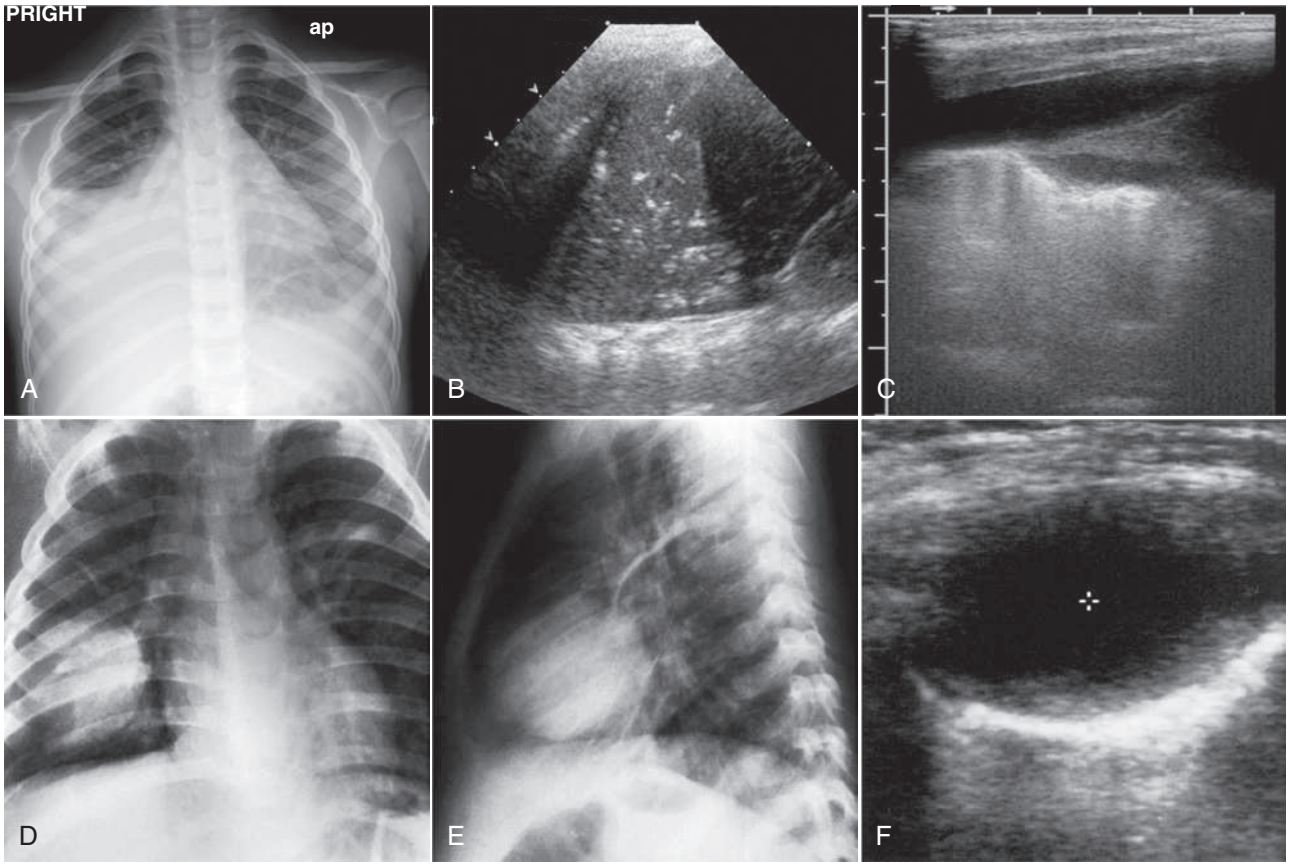

FIG. 50.5 Partially Radiopaque Hemithorax. (A) Radiograph. **(B)** and **(C)** Sonograms show left upper lobe pneumonia with left pleural fluid. **(D)-(F)** Another patient with partially opaque right hemithorax. **(D)** and **(E)** Posteroanterior and lateral chest radiographs. **(F)** Sonogram shows that the radiopacity is a hypoechoic, loculated fluid collection (+) in the minor fissure.

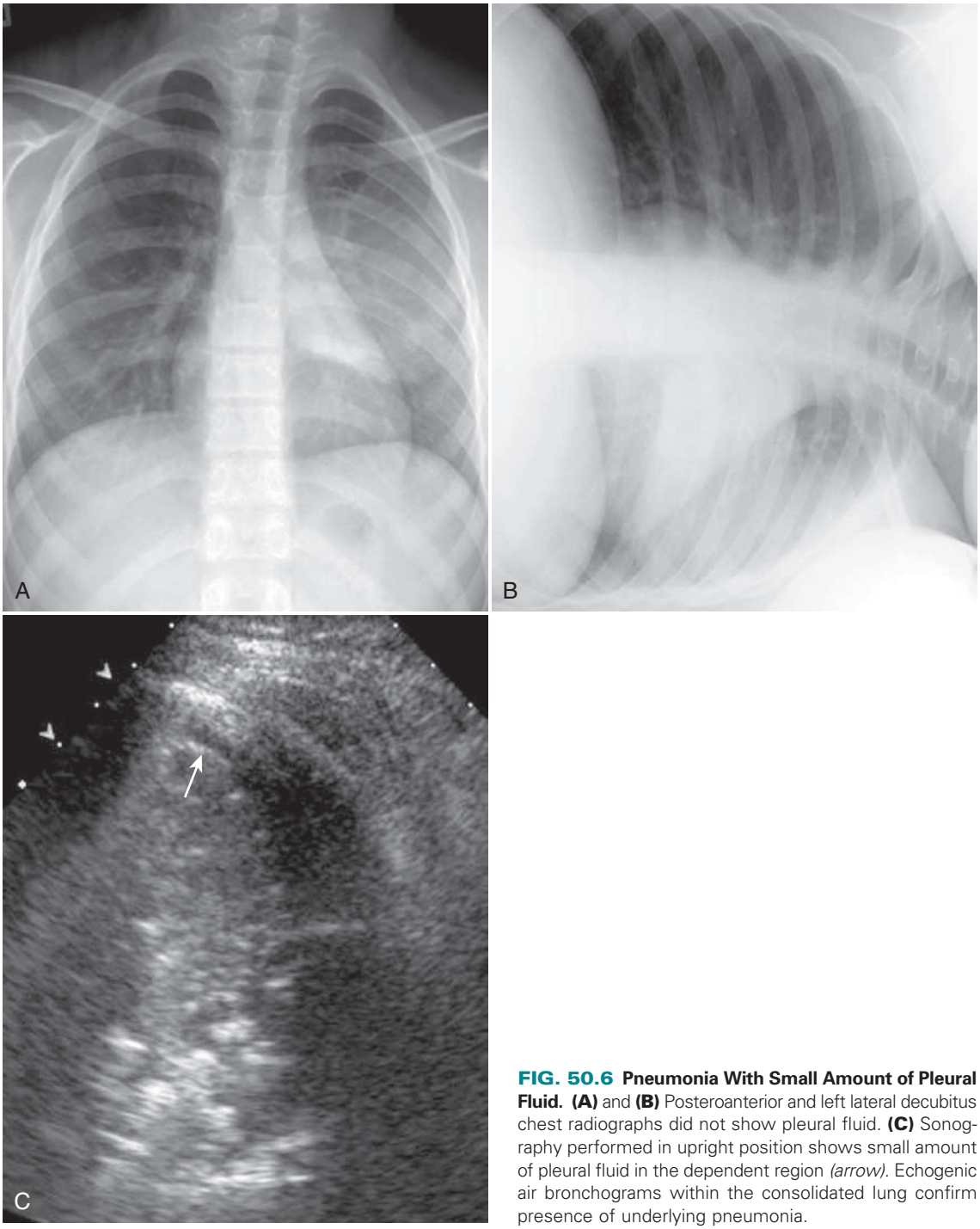

FIG. 50.6 Pneumonia With Small Amount of Pleural Fluid. (A) and **(B)** Posteroanterior and left lateral decubitus chest radiographs did not show pleural fluid. **(C)** Sonography performed in upright position shows small amount of pleural fluid in the dependent region *(arrow)*. Echogenic air bronchograms within the consolidated lung confirm presence of underlying pneumonia.

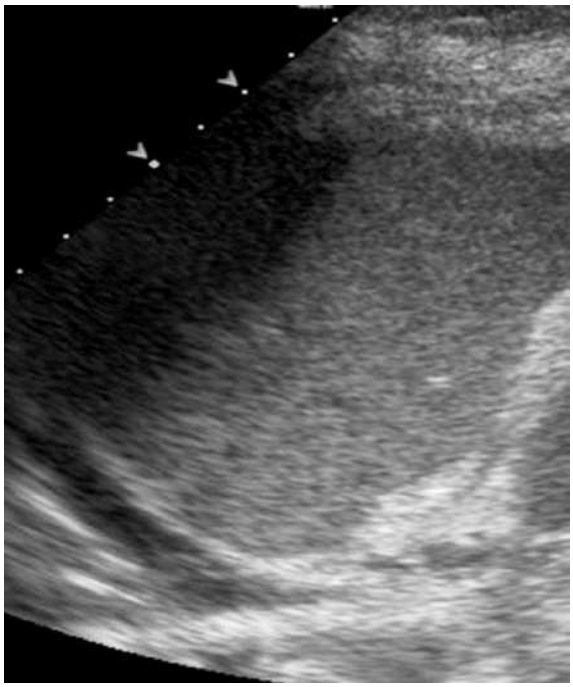

FIG. 50.7 Pleural Fluid Seen Through Splenic Window. Longitudinal sonogram shows a small amount of fluid in the left pleural space.

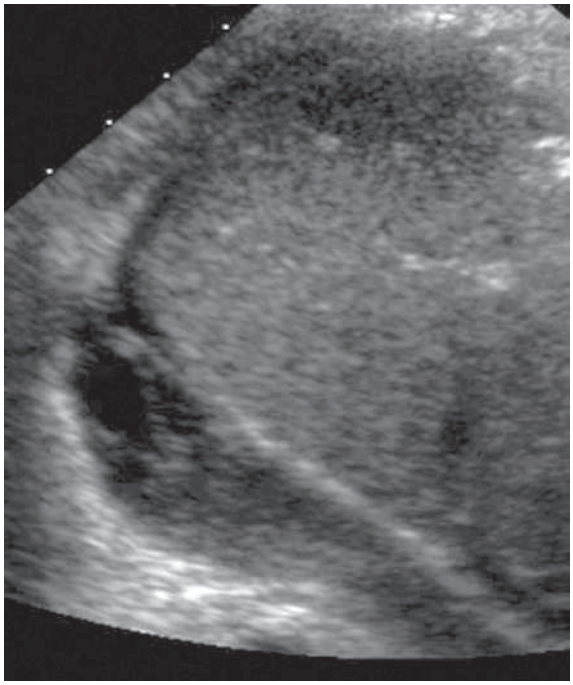

FIG. 50.8 Empyema Seen Through Hepatic Window. Sonography of pleural space through the hepatic window shows presence of echogenic fluid in the right pleural space.

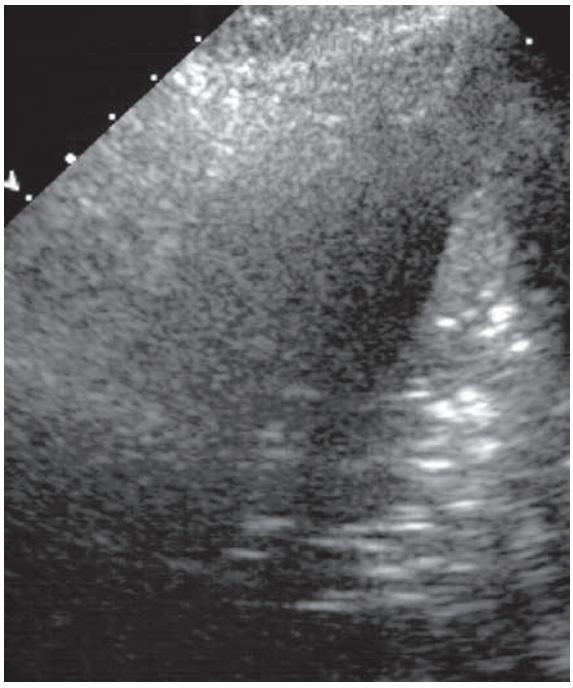

FIG. 50.9 Hemothorax. Moderately echogenic right effusion is present after trauma from four-wheeler crash. Atelectasis of the right lower lung is present, with some hyperechoic air bronchograms visible.

FIG. 50.10 Empyema Caused by Pneumonia. Longitudinal sonogram shows echogenic fluid in the right pleural space above the diaphragm. Purulent drainage contained gram-positive and gram-negative rods and gram-positive cocci.

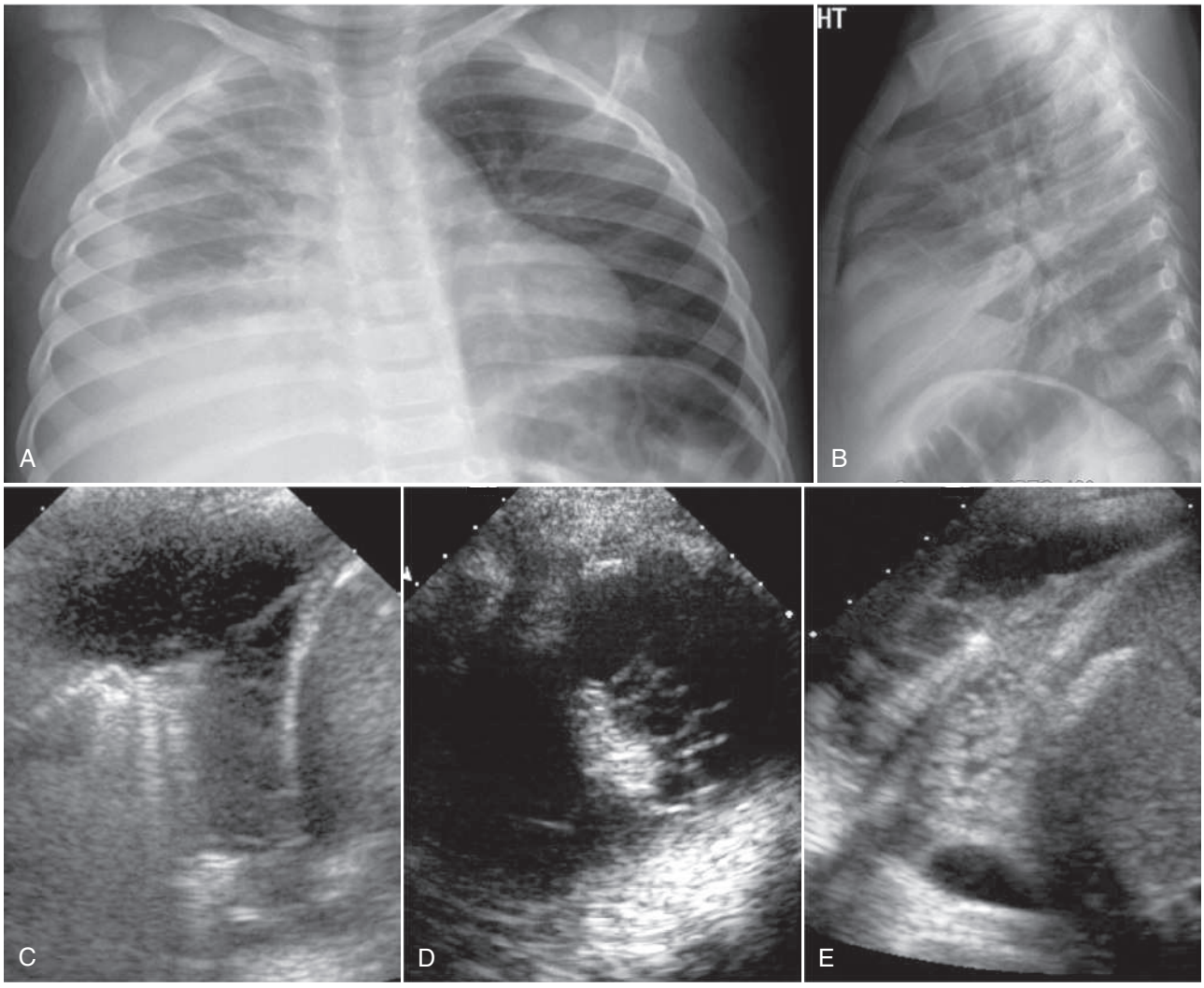

FIG. 50.11 Septated Pleural Fluid. (A) and **(B)** Posteroanterior and lateral radiographs show right pleural fluid with obliterated right hemidiaphragm. **(C)** Longitudinal sonogram shows septated pleural fluid. **(D)** and **(E)** Transverse and longitudinal sonograms of two other patients with septated pleural fluid.

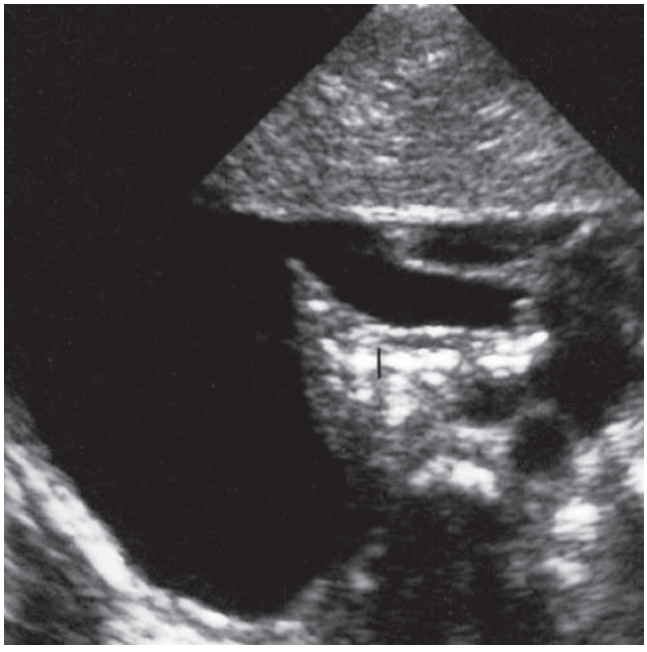

FIG. 50.12 Sonographic Air Bronchograms Within Pneumonia. Multiple echogenic linear air shadows called "sonographic air bronchograms" are seen within the consolidated lung *(l)* in this child with pneumonia.

Sonographic Signs of Pleural Fluid

Sonographic Signs of Pleural Fluid

- Fluid collection deep to the chest wall and/or above the diaphragm
- Posterior chest wall visualized behind the fluid
- Free fluid moves with respiration
- Septations move if fluid is loculated
- Color Doppler signal between visceral and parietal pleura and/or at costophrenic angle
- Diaphragm sign (fluid outside or peripheral to diaphragm)
- Displaced-crus sign
- Bare-area sign

Free Fluid Movement With Respiration

Free fluid changes position with changes in the patient's position. Fluid will move posterior to the liver and lungs when the patient is in a supine position (Fig. 50.13). When the patient is upright, the fluid will move between the lung and the diaphragm. Free fluid is indicated by change in the shape of pleural fluid with inspiration and expiration and the presence of **moving septations** within the pleural fluid[7] (Video 50.1). These septations are fibrin strands.

Fluid Color Flow Doppler Signal

Color flow Doppler ultrasound aids in distinguishing pleural effusion from pleural thickening.[7] Color Doppler signal is identified during respiratory motion between the visceral and parietal pleura in the presence of pleural effusion. Cell movement, debris, and fibrin scatter sound waves, producing the color flow Doppler signal in the pleural fluid collection (Fig. 50.14). Organized pleural thickening will appear as a colorless pleural lesion with no Doppler signal. The color flow Doppler signal has high sensitivity and specificity in determining if a fluid collection can be aspirated.[8] The fluid color flow Doppler signal is particularly useful in distinguishing if small, loculated collections can be aspirated.

Diaphragm Sign

When the liver or spleen is used as an acoustic window and fluid is seen adjacent to these organs, the location of the fluid is determined in reference to the diaphragmatic position. If the fluid is below the diaphragm and more centrally located, it is **ascites.** If the fluid is above the diaphragm and more peripherally located, it is in the pleural space (see Fig. 50.7).

Displaced-Crus Sign

There is fluid in the pleural space if the fluid is interposed between the crus and the vertebral column, displacing the crus away from the spine.

Bare-Area Sign

The posterior aspect of the right lobe of the liver is directly attached to the posterior diaphragm without peritoneum. Thus ascitic fluid in the subhepatic or subphrenic space cannot extend behind the liver at the level of the bare area. Pleural fluid will extend behind the liver at the level of the bare area (see Fig. 50.13).

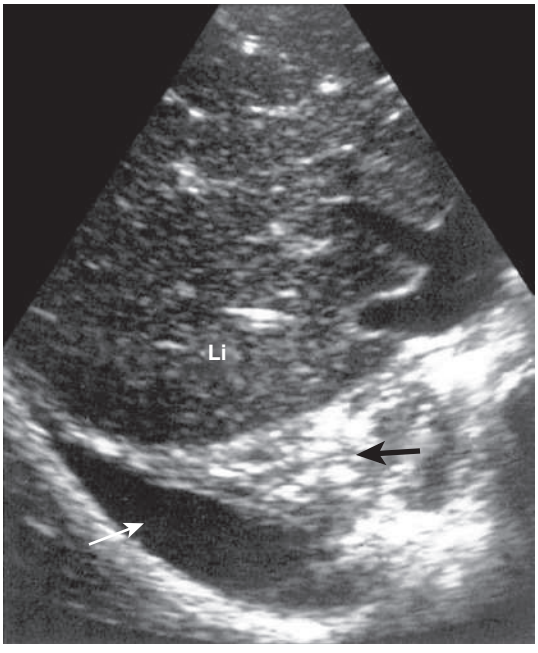

FIG. 50.13 Posterior Pleural Fluid Over Bare Area of Liver. Transverse scan through liver with patient in supine position shows triangular consolidated lung with air bronchograms *(black arrow)* behind the liver *(Li).* Fluid *(white arrow)* is posterior to lung and is behind the bare area of the liver, and therefore is in the pleural space.

Sonography Versus Computed Tomography Scan

Ultrasound, unlike CT, is a portable, bedside technique, making it ideal for evaluating chest opacification detected by conventional radiographs in the critically ill infant or child, to distinguish pulmonary from pleural disease (Fig. 50.15). Septations are better visualized by ultrasound than CT (Fig. 50.16). CT is better at identifying pulmonary parenchymal abnormalities, but this does not improve the outcome in managing empyema.[9]

Mass Versus Fluid

A limitation of chest sonography is that very homogeneous, solid, hypoechoic lesions may appear fluid filled. The criteria for fluid-filled structures are (1) lack of internal echoes; (2) a sharp posterior wall; and (3) increased through transmission of sound deep to the collection of fluid. The lack of echogenicity is a relative phenomenon that is judged by the echogenicity of the surrounding structures. The air-filled lung deep to a pleural collection will have a strong echogenic interface regardless of the nature of the pleural collection. Fluid in the pleural space produces **acoustic enhancement.** The lack of referenced solid or cystic structures in the chest makes detection of increased through transmission difficult to judge within the chest. Observing a change in shape of the pleural fluid during respiration, the movement of echogenic particles, and the fluid color flow Doppler signal is helpful in

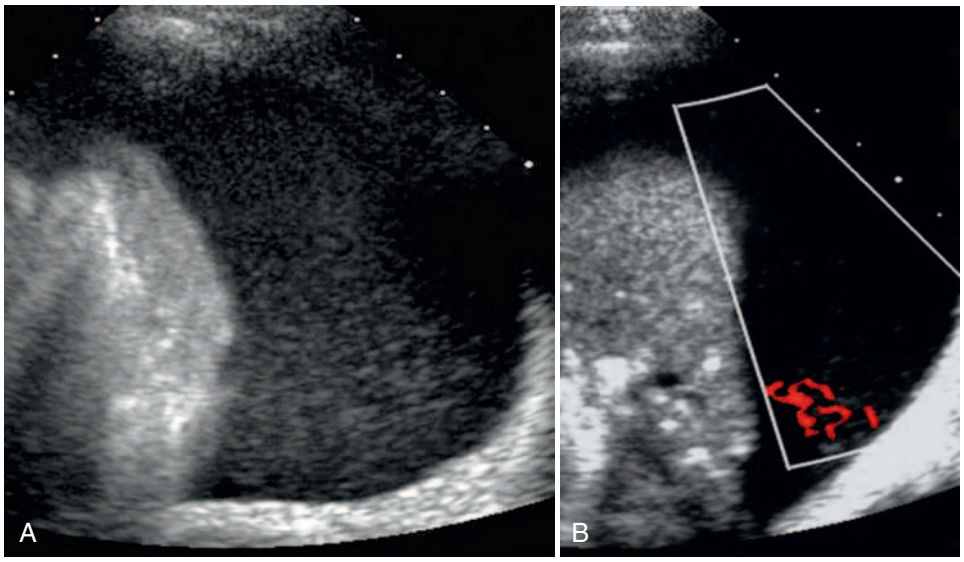

FIG. 50.14 Color Flow Doppler Signal in Pleural Fluid With Debris. (A) Gray-scale sonogram shows left pleural fluid with much debris. **(B)** Color flow Doppler signal.

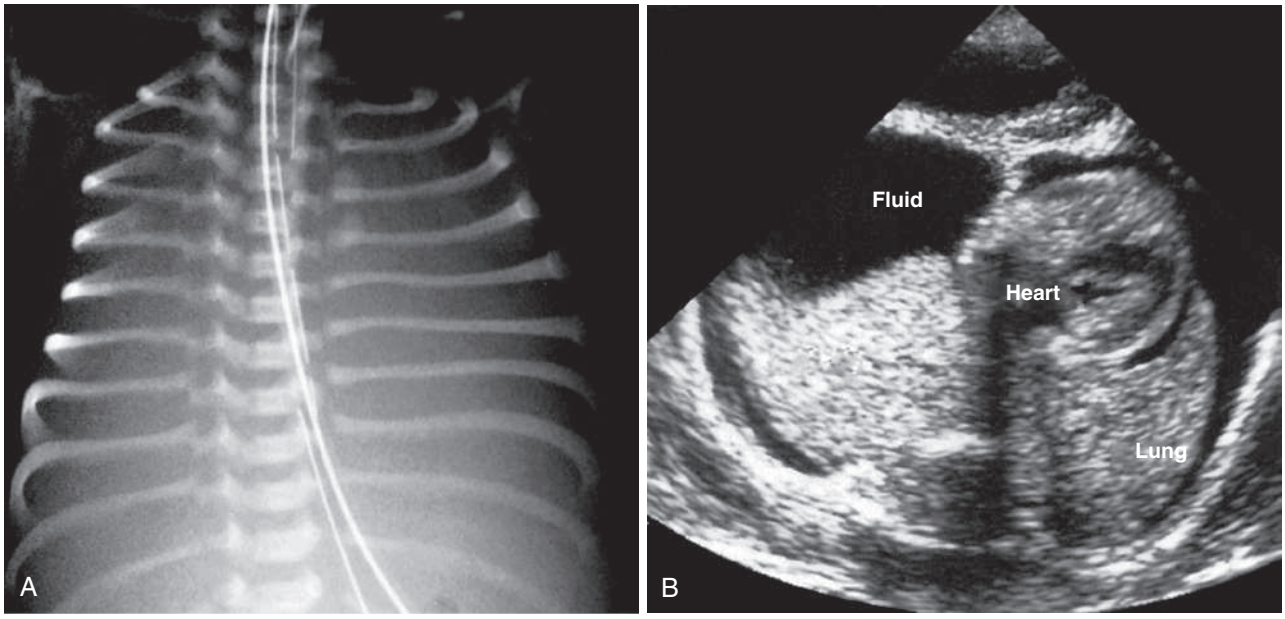

FIG. 50.15 Bilateral Pleural Fluid and Pericardial Fluid in Critically Ill Patient. (A) Chest radiograph of infant receiving extracorporeal membrane oxygenation (ECMO) shows complete lung opacification. **(B)** Transverse sonogram shows pleural fluid around both collapsed lungs and a small amount of pericardial fluid.

distinguishing thick pleural fluid from solid masses. Consolidated lung superficial to aerated lung will have increased through transmission compared with the aerated lung and can be identified as lung parenchyma by the presence of **air or fluid bronchograms.** Collapsed or consolidated lung tissue often has the appearance of the liver or spleen. A patient with persistent pleural fluid not responding to drainage can be evaluated by ultrasound for a possible underlying tumor (Fig. 50.17).

Another pitfall in the sonographic evaluation of the chest is the acoustic shadow cast by a rib **(rib shadowing),** which may confuse the inexperienced sonographer into misinterpreting that a mass is anechoic. The transducer should be placed between the ribs to avoid this pitfall. The echogenicity of the mass or pleural lesion can be compared with that of the liver.

Parapneumonic Collections and Empyema

Parapneumonic collections occur in up to 40% of children with bacterial pneumonia and are especially common in those younger than 4 years.[10] Most collections are not infected, but many evolve into **empyemas** with frank pus. Parapneumonic effusions detected by ultrasound can be prognostic in children with pneumonia. Children with complicated collections characterized by septations

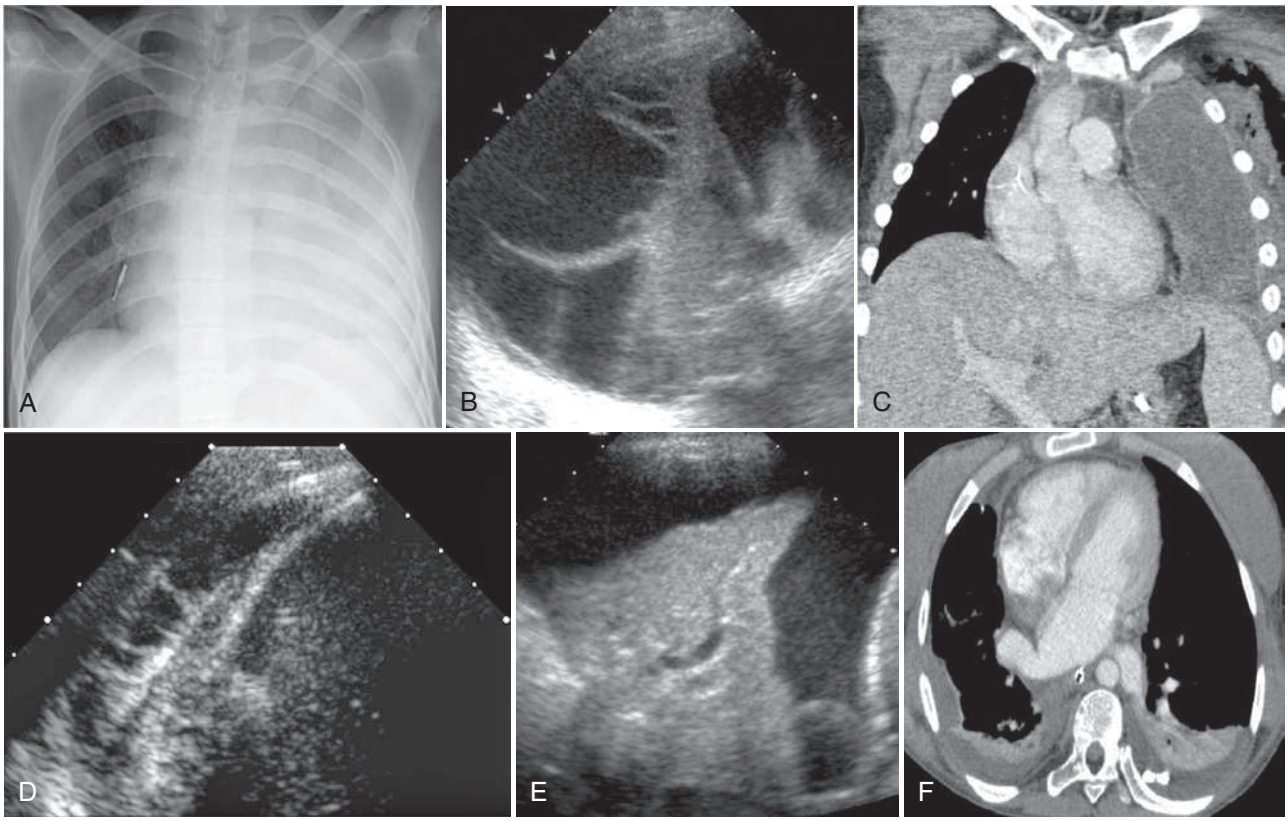

FIG. 50.16 Septations in Pleural Space Are Seen Better on Sonograms Than Computed Tomography (CT) Scans. (A) Chest radiograph shows opacified left hemithorax. **(B)** Sonogram shows a septated fluid collection. **(C)** CT scan shows pleural fluid, but the septa are not well visualized. **(D)** In another child with cystic fibrosis and lung transplant, sonogram shows septated pleural fluid on the right side, in addition to **(E)** echogenic pleural fluid with few septations on the left side. **(F)** CT scan shows bilateral pleural fluid, but septations at the right base are not well visualized.

have longer hospital stays and benefit from intrapleural fibrinolytic therapy or surgical procedures.[11]

Lung Abscess Versus Empyema

Lung abscess adjacent to the chest wall or to an acoustic window such as the liver or spleen usually appears as a complex collection with fluid-debris levels and septations just like an empyema. Abscesses and empyemas usually exhibit different types of motion when visualized by ultrasound. An abscess demonstrates expansion of the entire circumference with inspiration, whereas with an empyema, only the internal wall adjacent to the lung shows slight motion. Lung abscesses may be difficult to differentiate from empyema when the empyema contains multiple, loculated air collections caused by thoracentesis. Air-fluid collections move with patient repositioning, which can aid in distinguishing empyema from abscess (Figs. 50.18 and 50.19).

LUNG PARENCHYMAL DISORDERS

Pneumonia

Consolidated lung is hypoechoic relative to the highly reflective, air-filled, normal surrounding lung. Consolidated lung echogenicity is similar to that of liver (Fig. 50.20), but sonographic air bronchograms differentiate it from liver. Strong, nonpulsatile, branching, linear echoes produced by air-filled bronchi converge toward the root of the lung. The linear pattern of bright echoes is observed when scanning parallel to the long axis of the bronchi (Fig. 50.21). When the scanning is done at more acute angles, scattered echoes of variable lengths produced by the sonographic air bronchograms are observed (Fig. 50.22). If there is adjacent pleural fluid, the hypoechoic consolidated lung can be differentiated from the hypoechoic-to-anechoic pleural effusion by identification of these sonographic air bronchograms.

Round Pneumonia

Round pneumonia is more common in children younger than 8 years, but 15% occur between 8 and 12 years.[12] Young children do not have well-formed pores of Kohn and channels of Lambert for collateral air circulation. The inflammation spreads centrifugally as the strands of fibrin usually spread during the red hepatization phase of pneumonia through the pores of Kohn and channels of Lambert.[13] Owing to underdevelopment of these collateral circulations, the advancing front is sharply demarcated from the unaffected lung parenchyma and causes a focal round mass like pneumonia that mimics a posterior mediastinal mass on the radiograph of the chest. Most round pneumonias are posteriorly located and in lower lobes.

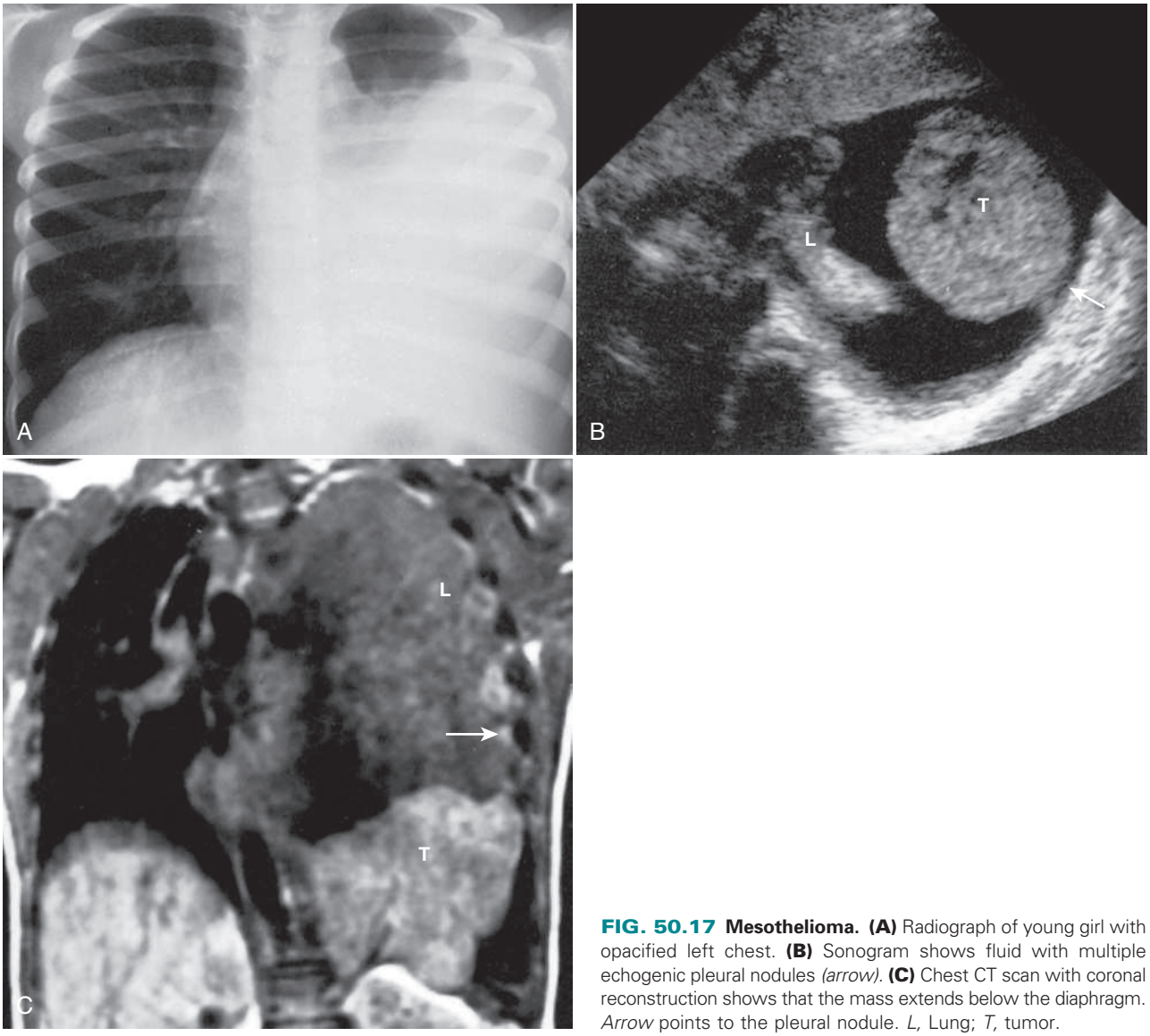

FIG. 50.17 Mesothelioma. (A) Radiograph of young girl with opacified left chest. **(B)** Sonogram shows fluid with multiple echogenic pleural nodules *(arrow)*. **(C)** Chest CT scan with coronal reconstruction shows that the mass extends below the diaphragm. *Arrow* points to the pleural nodule. *L,* Lung; *T,* tumor.

Unlike adults, children may not have typical signs and symptoms of pneumonia. A common etiological agent for round pneumonia is pneumococcus (streptococcus pneumonia). The diagnosis becomes clearer if the radiograph is repeated after a few days. On the follow-up radiograph after antibiotic therapy, most round pneumonias resolve without progression to lobar pneumonia.

Ultrasound can show the air bronchograms and confirm that it is a round pneumonia on the day of the presentation (Fig. 50.23), and one can avoid CT scan of the chest. However, a follow-up chest radiograph may still be indicated to exclude the remote possibility of mass or congenital anomaly.

Chest Radiograph or Ultrasound?

Many recent studies have reported that pneumonia can be diagnosed with ultrasound.[14-25] Ultrasound may supplement chest radiographs in certain circumstances, such as differentiation of round pneumonia from a mediastinal mass (see Fig. 50.23). However, replacing chest radiographs with ultrasound in suspected cases of pneumonia is not practical at many institutions. Meta-analysis[14] of eight studies performed from 2008 to 2014 shows that for most of these studies[15-21] the ultrasound examination was performed by a skilled physician or skilled sonographer. These studies did not specify the time required to perform the ultrasound examinations and interpret the findings. It is obvious that the time required to perform an ultrasound study is substantially longer than to obtain a radiograph. Professional time involvement of the physician in interpreting ultrasound findings is typically greater than for interpreting radiographs. Ultrasound is operator dependent, and interobserver variability has not been studied. A recent study[22] showed that pneumonia was missed by ultrasound in 5 of 76 children with pneumonia seen on radiographs. Missing these 6.6% of pneumonia cases to avoid minimal ionizing radiation from a chest radiograph probably

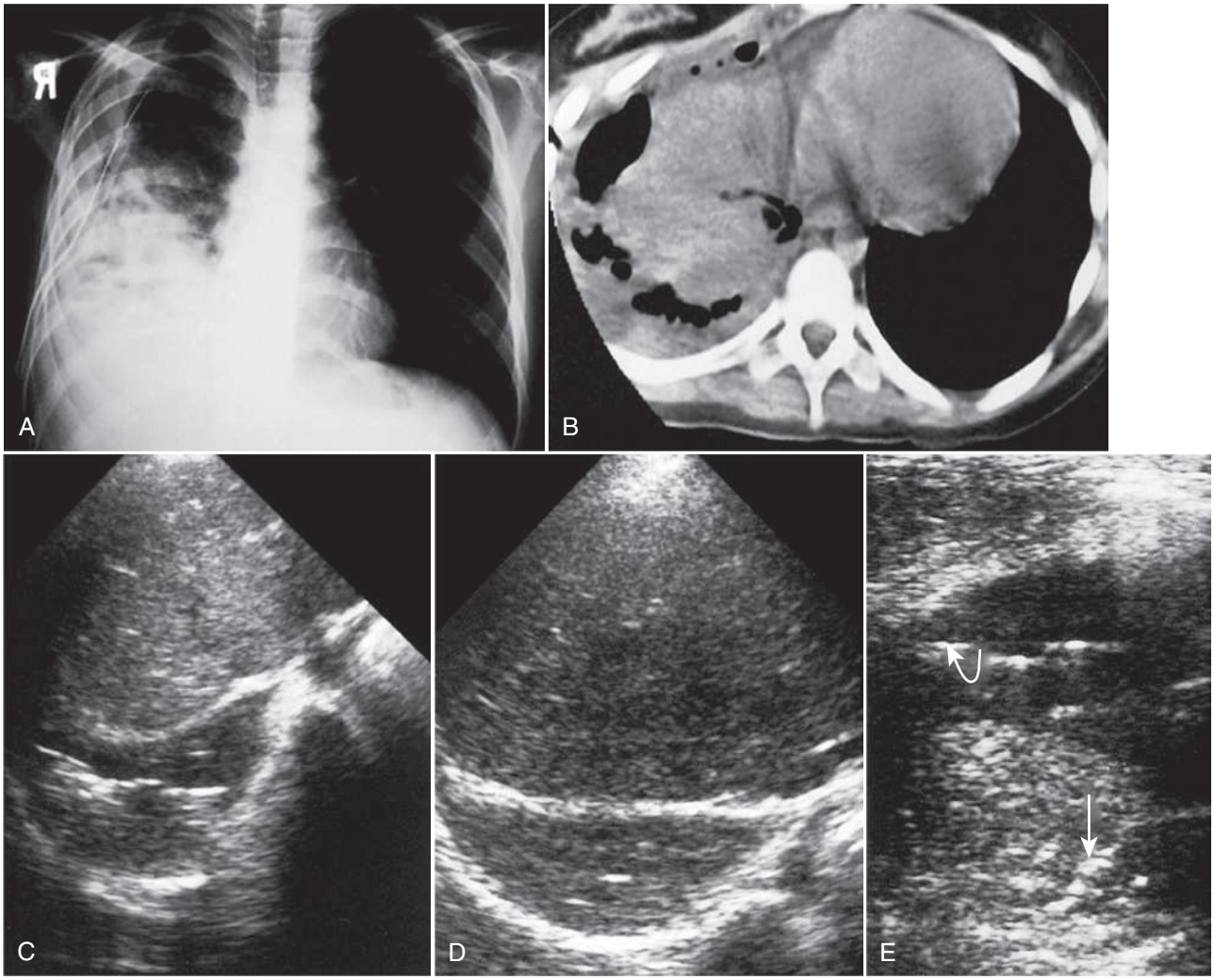

FIG. 50.18 Air-Fluid Levels in Complex Empyema. (A) Chest radiograph. **(B)** Computed tomography (CT) scan and **(C)** sonogram with patient supine and. **(D)** Upright. Air-fluid levels are seen on the supine view, but are out of the plane of the lower fluid in the upright view. **(E)** Transverse intercostal supine scan through anterior chest wall shows both the linear lines of bronchi *(arrow)* at random pattern and the linear lines of air *(curved arrow)* in the pleural fluid.

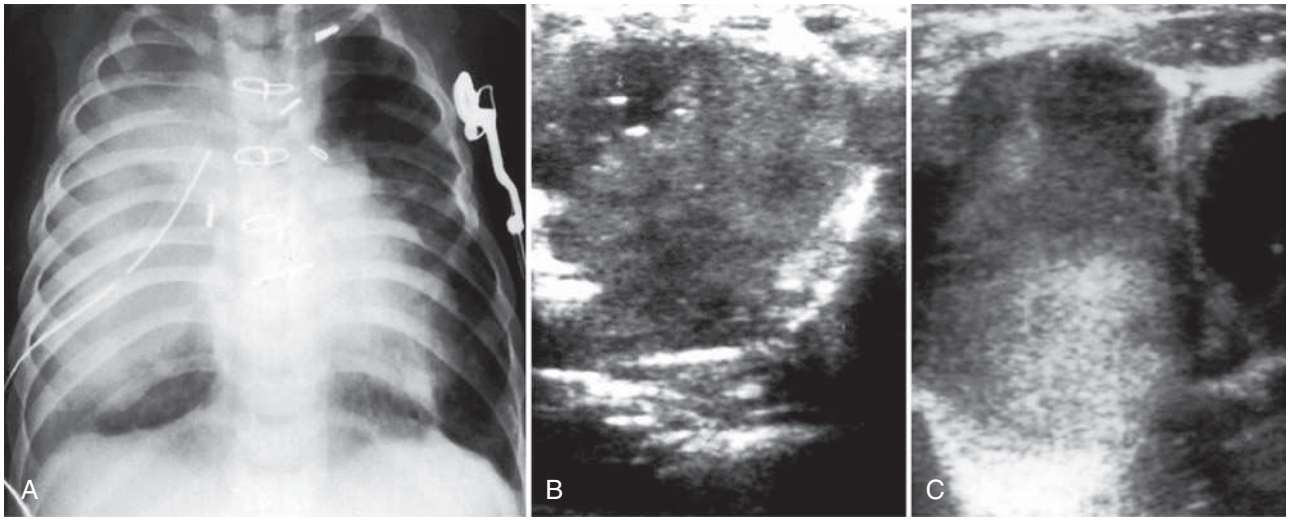

FIG. 50.19 Thick Pleural Fluid With Changing Appearance in Empyema. (A) Chest radiograph shows pleural fluid that is not draining by chest tube. **(B)** Transverse sonogram shows very thick fluid with no air bronchograms. **(C)** Differential thick fluid-fluid level caused by change in position.

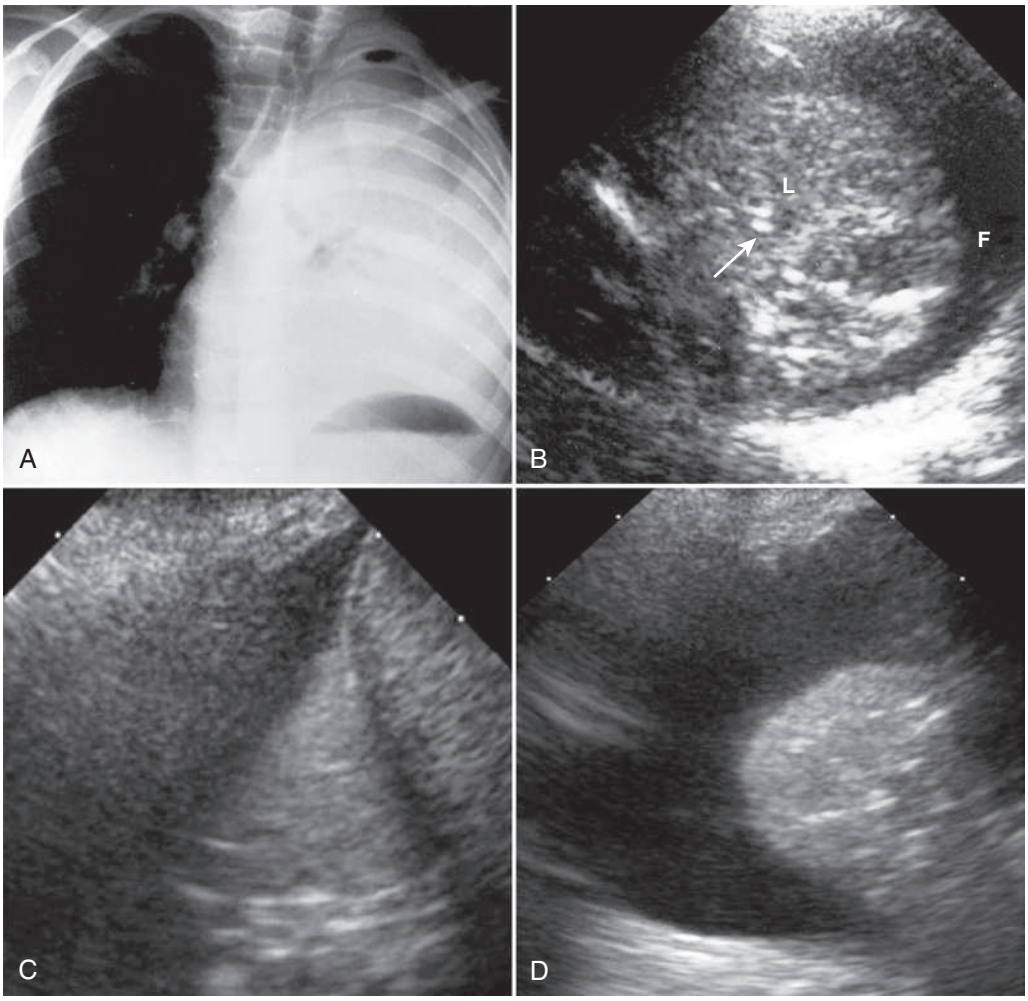

FIG. 50.20 Echogenicity of Air Bronchograms in Consolidated Lung. (A) Chest radiograph shows an opacified left chest with some air bronchograms. **(B)** Transverse scan shows fluid *(F)* around consolidated lung *(L),* which has echogenicity similar to the liver. Air bronchograms within the consolidated lung *(arrow).* **(C)** and **(D)** Sonograms of another patient show consolidated lung with air bronchograms and surrounded by fluid.

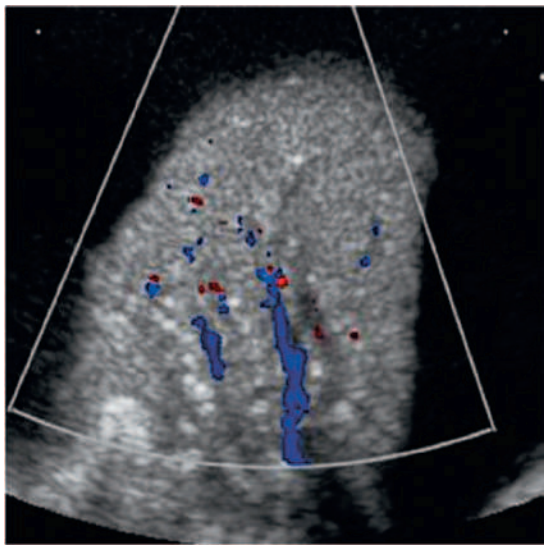

FIG. 50.21 Pneumonia Showing Tubular Air Bronchograms. Color flow Doppler sonogram shows echogenic branching air bronchograms with intervening branching vessels in consolidated lung surrounded by fluid.

defies the "reasonably achievable" part of the ALARA (as low as reasonably achievable) principle.[26] Typical radiation dose with a pediatric exposure setting for a frontal view chest radiograph is less than 0.1 mSv, which corresponds to natural background radiation for less than 10 days and is considered minimal risk.[26-28]

Atelectasis

Atelectatic lung is similar in echogenicity to liver (Fig. 50.24). Sonographic air bronchograms may be present in atelectatic lung, but the air bronchograms are more crowded than in pneumonia because the lung volume is decreased. Bronchi can be filled with fluid rather than air, creating fluid bronchograms. The echogenic, parallel, branching walls are filled with hypoechoic fluid, without the acoustic shadowing and reverberation artifacts normally seen with air. Color flow Doppler sonography differentiates fluid-filled bronchi from vessels because there will be no flow in the bronchi.

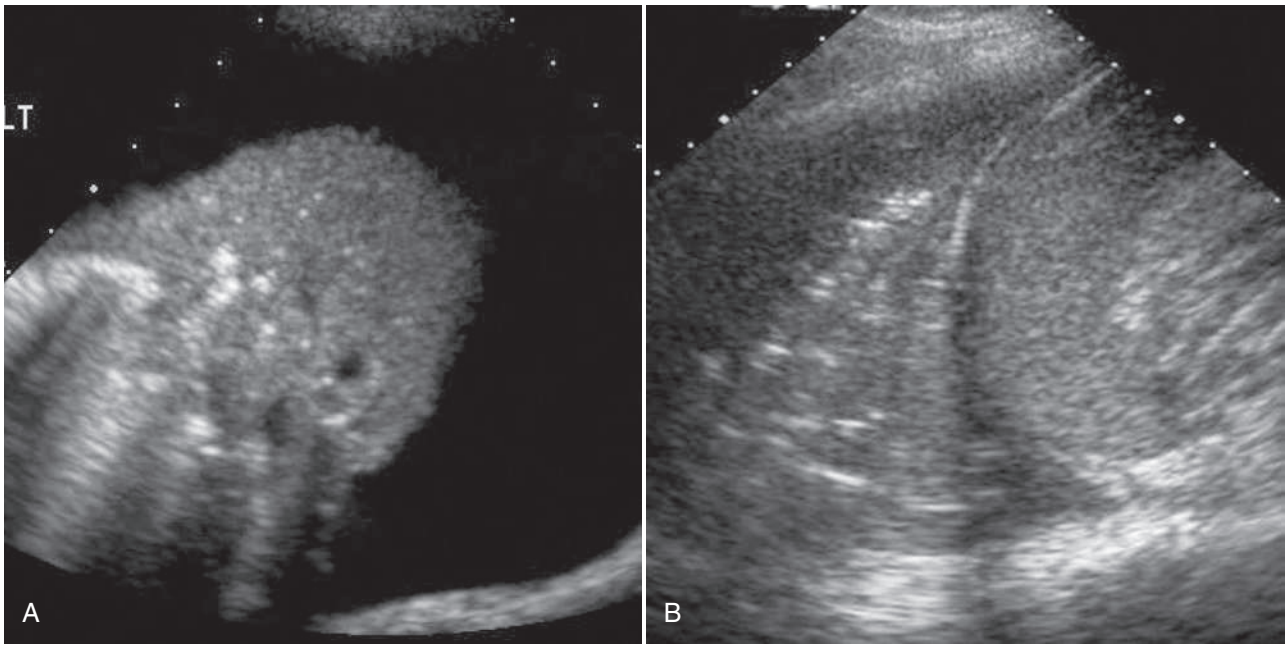

FIG. 50.22 Pneumonia Showing Scattered Air Bronchograms. (A) and **(B)** Transverse and longitudinal sonograms of two patients in a plane that is not parallel to the long axis of the bronchi show scattered echoes of variable lengths from scattered air bronchograms. Fluid surrounds the consolidated lung.

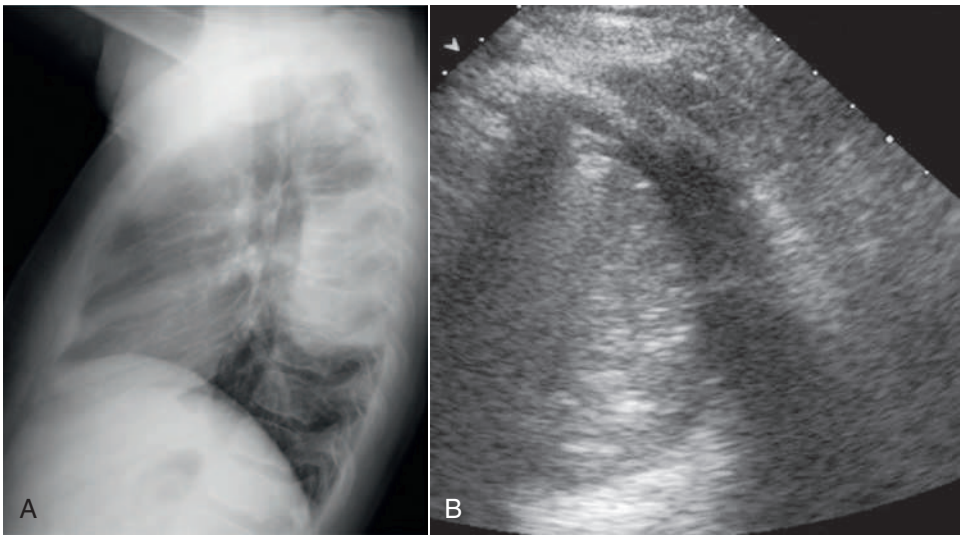

FIG. 50.23 Round Pneumonia. (A) Lateral chest radiograph shows a rounded opacity posteriorly in this 12-year-old child. **(B)** Transverse sonogram shows air bronchograms within the lesion, confirming it as round pneumonia, with a small amount of pleural fluid surrounding the consolidated lung. Ultrasound diagnosis helped avoid ionizing radiation from a computed tomography scan.

Congenital Pulmonary Airway Malformation

Congenital pulmonary airway malformation (CPAM) comprises a spectrum of disorders that include bronchopulmonary malformation, hybrid lesions (CPAM and sequestration), and congenital lobar overinflation.

Bronchopulmonary malformations may contain systemic and/or pulmonary vascularity and cysts. When only cysts are present with no systemic vascularity, these were previously called congenital **cystic adenomatoid malformation** (CCAM). Type I has one or more large cysts measuring more than 2 cm in size. Type II has multiple small cysts, less than 2 cm. Type III has microcysts but appears solid on ultrasound and on gross examination.[1]

Pulmonary sequestrations may be extralobar or intralobar, and have systemic vascular supply.[29,30] Extralobar sequestration[31] is congenital and has pulmonary tissue with a separate pleura. Extralobar sequestration typically manifests in infancy. Intralobar sequestration is acquired after recurrent infections causing

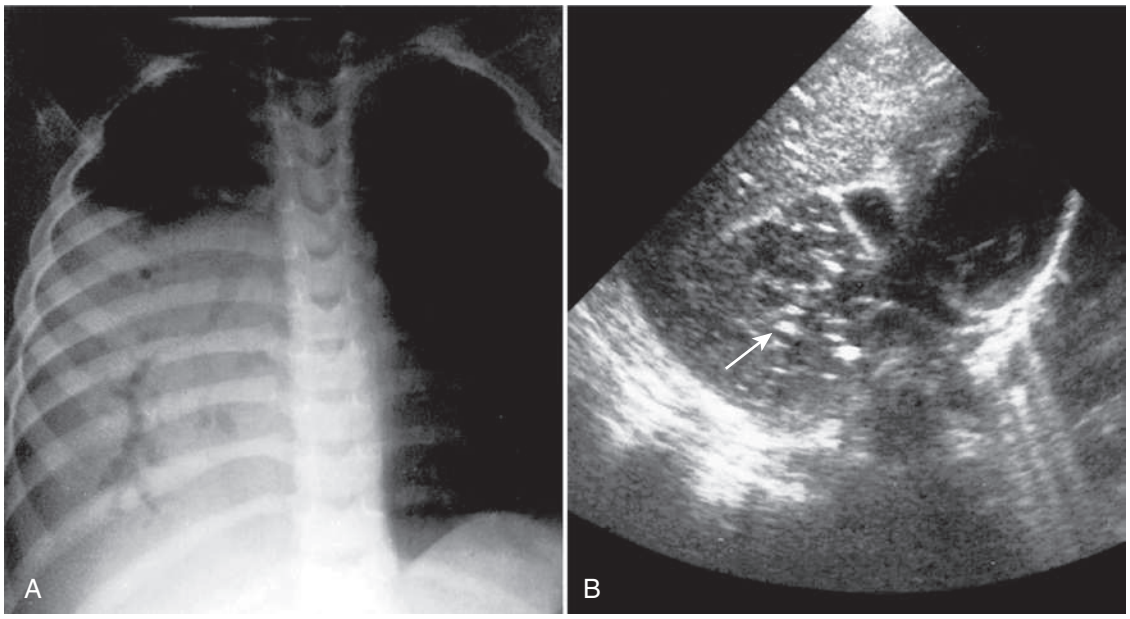

FIG. 50.24 Atelectasis From Foreign Body. (A) Chest radiograph shows air bronchograms in opacified right side of chest with shift of the heart to the right, indicating volume loss. **(B)** Transverse sonogram through liver shows no fluid in chest. Multiple air bronchograms *(arrow)* are visible within collapsed lung. At endoscopy, foreign body was found in right main stem bronchus. (With permission from Seibert RW, Seibert JJ, Williamson SL. The opaque chest: when to suspect a bronchial foreign body. Pediatr Radiol. 1986;16[3]:193-196.[76])

bronchial obstruction and compromised pulmonary artery supply as a result of inflammation. Inferior pulmonary ligament artery and phrenic artery normally supply inferomedial and diaphragmatic visceral pleura, respectively. These normal arteries may become parasitized to supply the infected portion of a lower lobe if the normal pulmonary arterial supply is compromised. The intralobar sequestered lung is typically present in the lower lobes and is enclosed by the visceral pleura of the parent lung. Ultrasound may show a hypoechoic mass in the lower lobe (Fig. 50.25). Color Doppler can demonstrate a systemic vessel supplying the hypoechoic mass in both extralobar and intralobar sequestration.

Bronchopulmonary Foregut Malformation

Bronchogenic cysts or **bronchopulmonary foregut malformations**[32] may be identified by chest ultrasound if they are adjacent to the chest wall (Fig. 50.26).

DIAPHRAGM DISORDERS

Sonography is particularly valuable in evaluating a paradiaphragmatic lesion, which may be a **diaphragm eventration,**[33] a **diaphragmatic hernia** (Fig. 50.27), a **subphrenic abscess,**[34,35] or an **intrathoracic kidney.**[36] These abnormalities frequently are associated with respiratory compromise, making bedside, portable sonography the study of choice. Less common diaphragmatic masses detected by sonography include hemangioma,[37] primitive neuroectodermal tumor, and primary embryonal rhabdomyosarcoma.[38-40]

Ultrasound is the bedside examination of choice for evaluation of suspected diaphragmatic motion abnormalities. Comparison of hemidiaphragm motion can be observed by placing the transducer in the subxiphoid position in a transverse orientation, angled upward toward the posterior leaflets of the hemidiaphragms. Such comparison can be done with transverse sonographic scanning in infants (Video 50.2), but in older children (Video 50.3), unilateral sagittal scanning of each diaphragm is necessary. A comparison of the maximal excursion of the diaphragm for each side using real-time ultrasound is more accurate than fluoroscopy in demonstrating diaphragmatic movement abnormality.[41] In the artificially ventilated patient, the respirator must be disconnected for 5 to 10 seconds to observe unassisted respiration. With paralysis, there is absent or **paradoxical motion** on one side and exaggerated excursions on the opposite side. **Diaphragm paralysis** is a frequent concern after cardiac surgery[42] (Video 50.4). Severe eventration and a diaphragmatic hernia may also show paradoxical motion. During real-time evaluation of diaphragm motion,[43] M-mode sonography can also be used in assessment of diaphragm function[44] (Figs. 50.28 and 50.29). Sonography can demonstrate **rupture of the diaphragm**[45] (Fig. 50.30).

VASCULAR DISORDERS

Vascular Thrombosis

The normal thymus is an excellent acoustic window to view normal mediastinal structures and mediastinal masses. The thymus is anterior to the great vessels and extends inferiorly to the upper portion of the heart. The great vessels, including the SVC, aorta, and pulmonary artery, are well imaged through the thymus. These vessels are more conspicuous with color Doppler ultrasound (Fig. 50.31). The left brachiocephalic vein courses

Text continued on p. 1721.

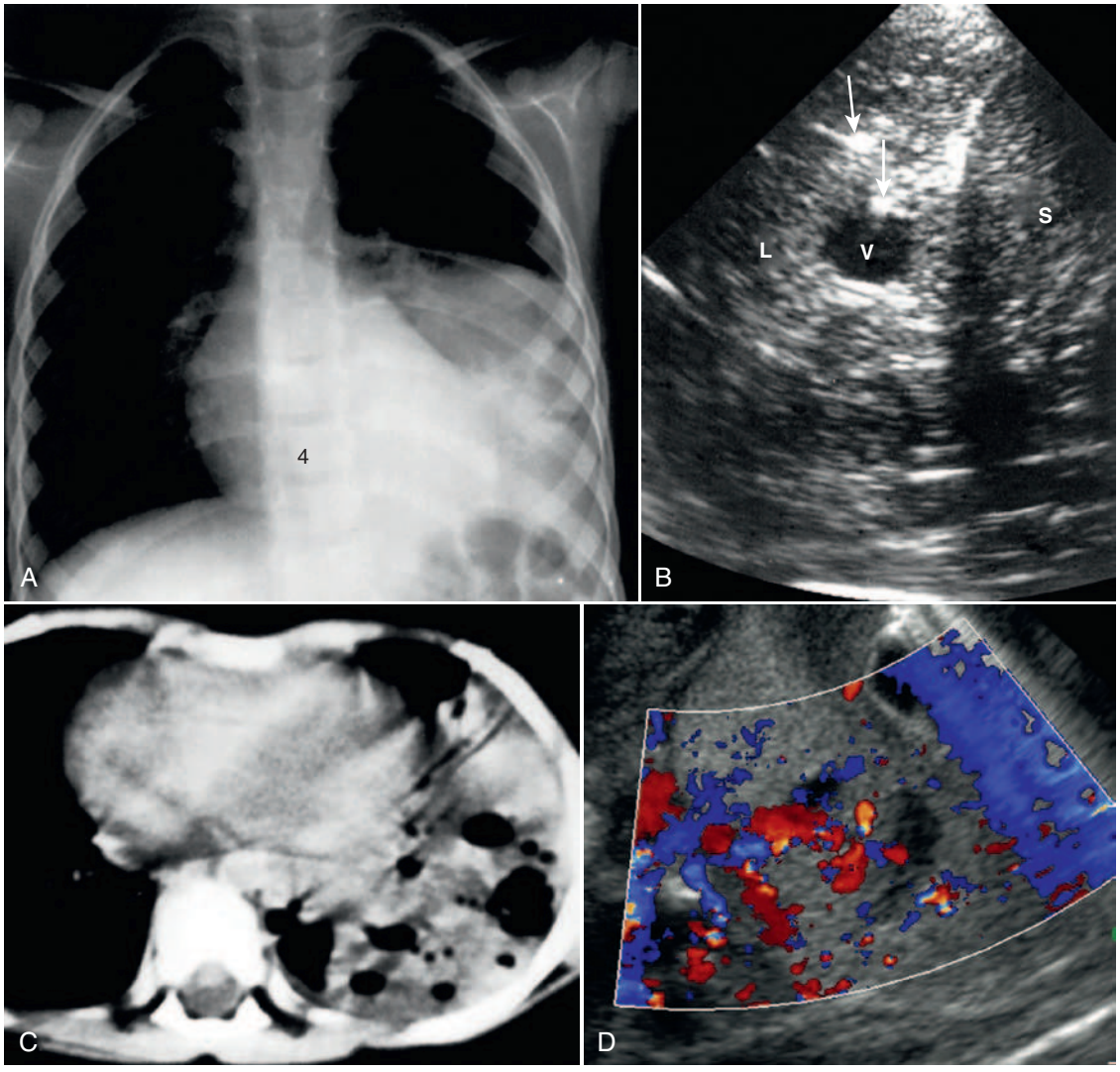

FIG. 50.25 Sequestration. (A) Chest radiograph of 4-year-old child shows large mass in left lower chest. **(B)** Left longitudinal sonogram shows solid mass with air bronchograms *(arrows)* and appearance of lung *(L)* above spleen *(S). V,* Blood vessel in mass. **(C)** Computed tomography (CT) scan shows diffuse areas of bronchiectasis throughout mass. **(D)** Color Doppler ultrasound shows arterial feeding vessel from aorta to sequestration in another patient. (Courtesy of Carol M. Rumack, MD.)

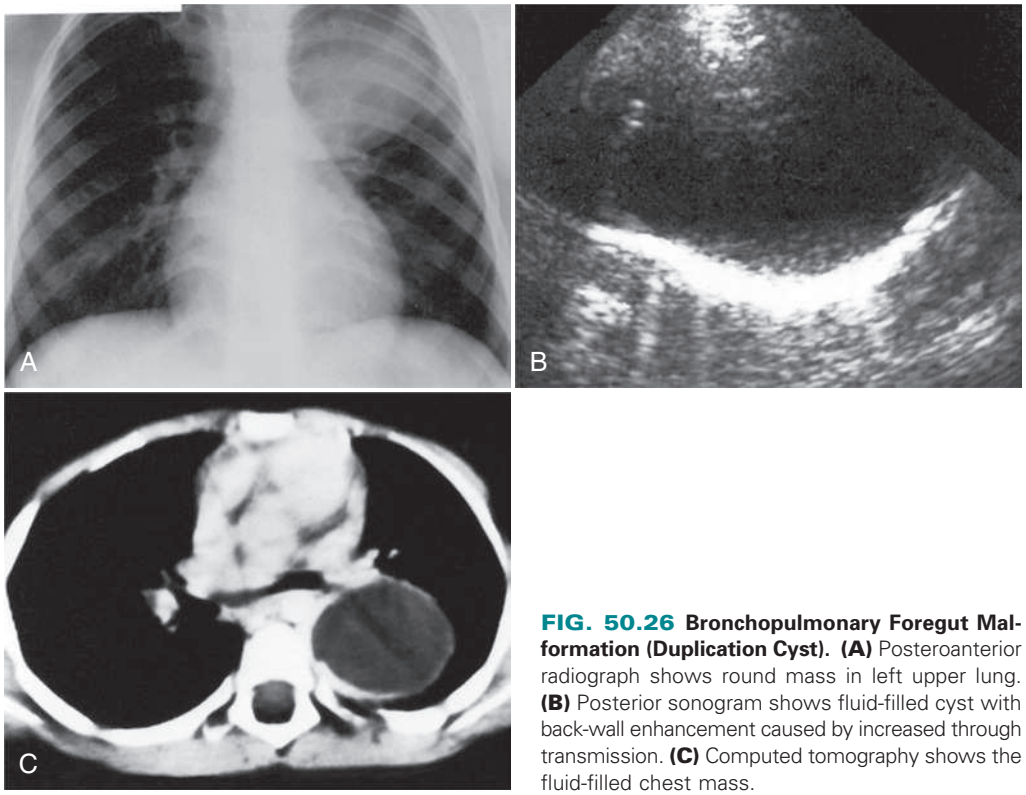

FIG. 50.26 Bronchopulmonary Foregut Malformation (Duplication Cyst). (A) Posteroanterior radiograph shows round mass in left upper lung. **(B)** Posterior sonogram shows fluid-filled cyst with back-wall enhancement caused by increased through transmission. **(C)** Computed tomography shows the fluid-filled chest mass.

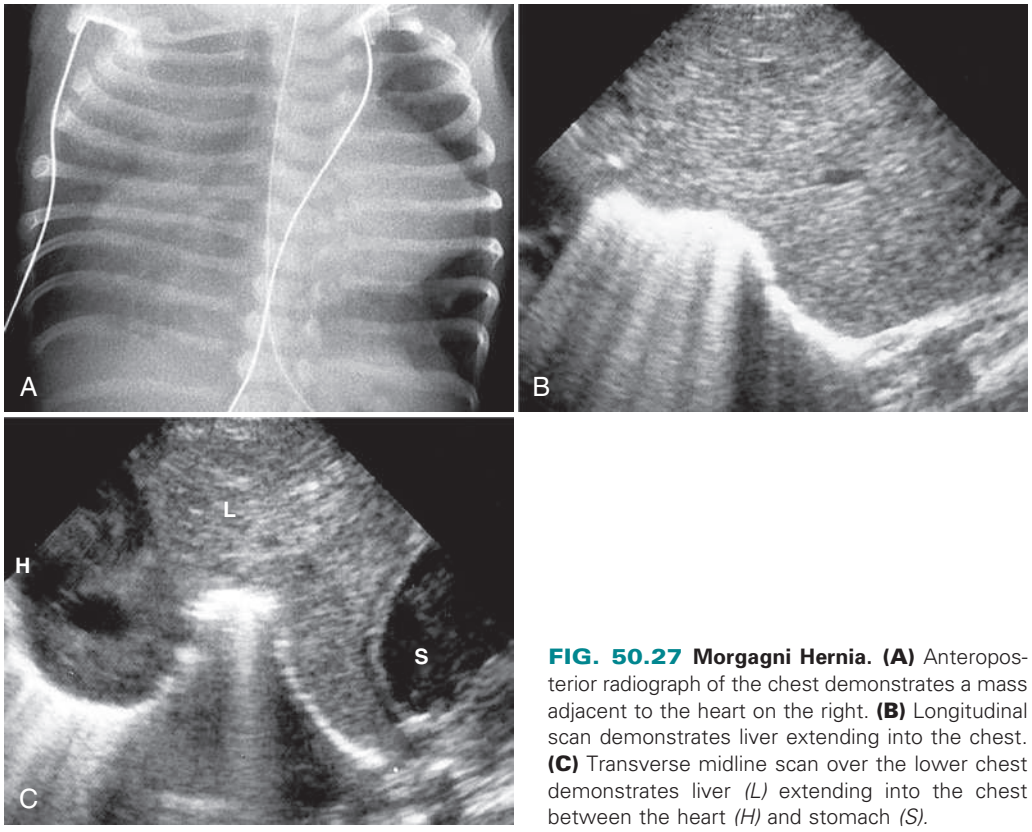

FIG. 50.27 Morgagni Hernia. (A) Anteroposterior radiograph of the chest demonstrates a mass adjacent to the heart on the right. **(B)** Longitudinal scan demonstrates liver extending into the chest. **(C)** Transverse midline scan over the lower chest demonstrates liver *(L)* extending into the chest between the heart *(H)* and stomach *(S)*.

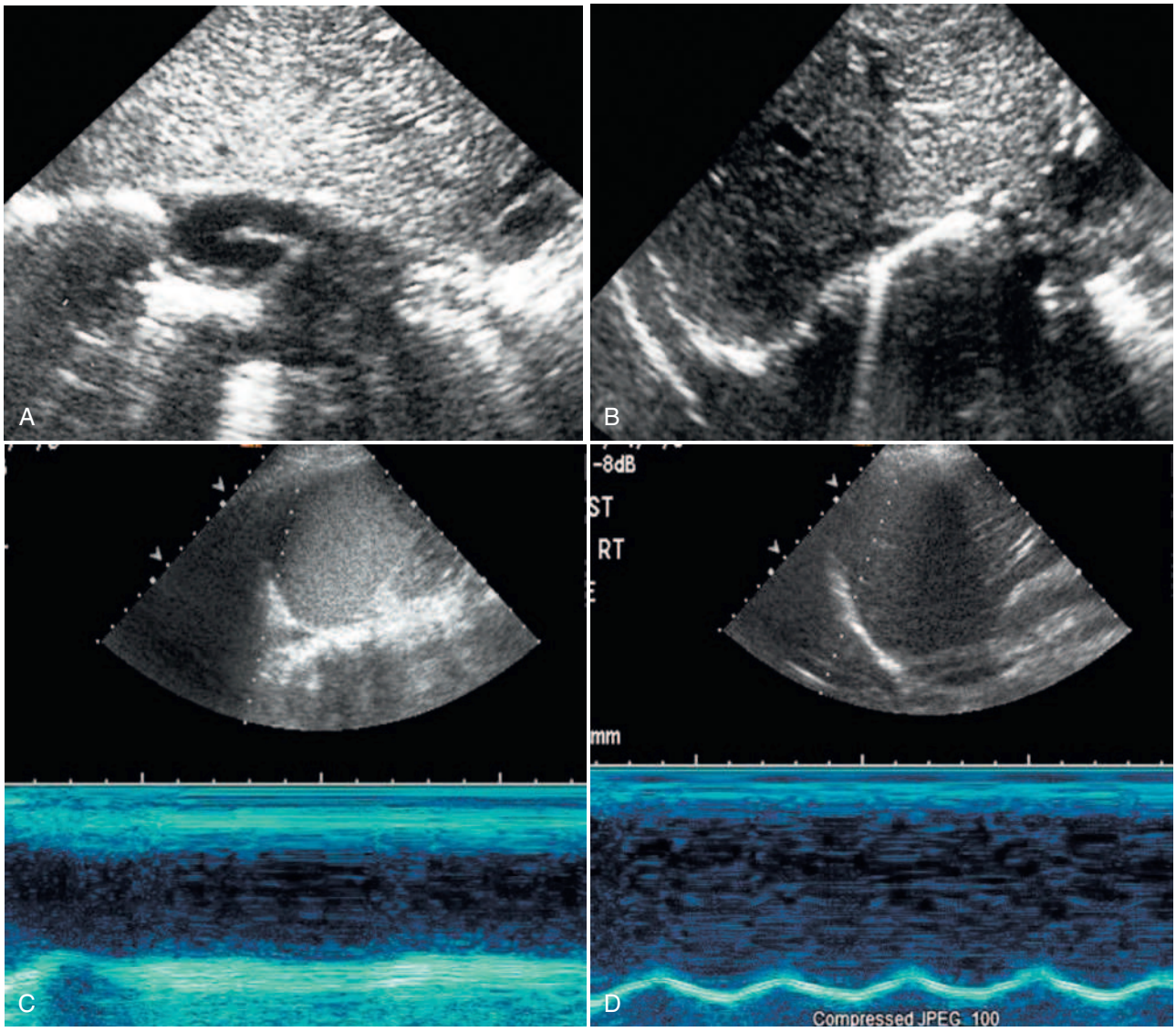

FIG. 50.28 Paralyzed Left Hemidiaphragm Compared With Normal Right Hemidiaphragm. B-mode sonogram of **(A)** left and **(B)** right hemidiaphragm. M-mode sonogram shows **(C)** left hemidiaphragmatic paralysis and **(D)** normal excursion of right hemidiaphragm.

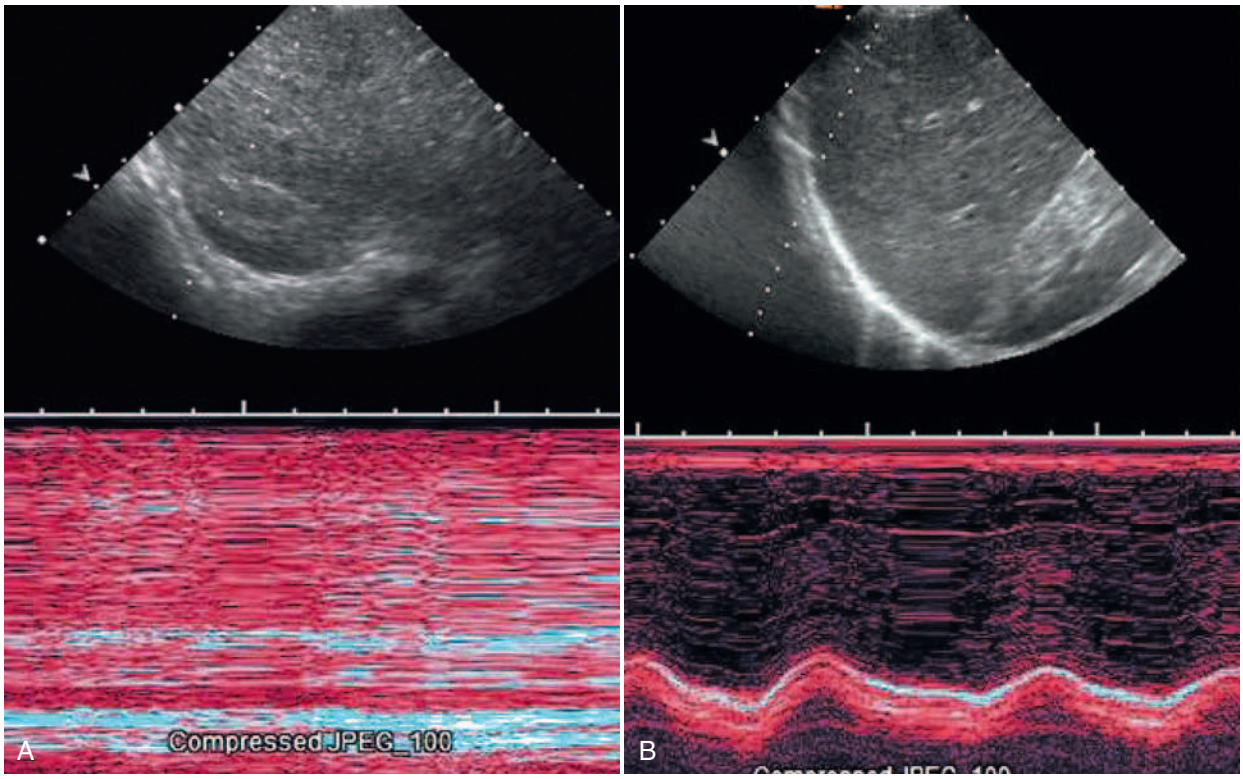

FIG. 50.29 Follow-Up of Diaphragmatic Paralysis. Gray-scale real-time and M-mode ultrasound. **(A)** Child with complex congenital heart disease shows left hemidiaphragmatic paralysis. **(B)** Spontaneous recovery of left hemidiaphragmatic motion was observed on follow-up sonogram.

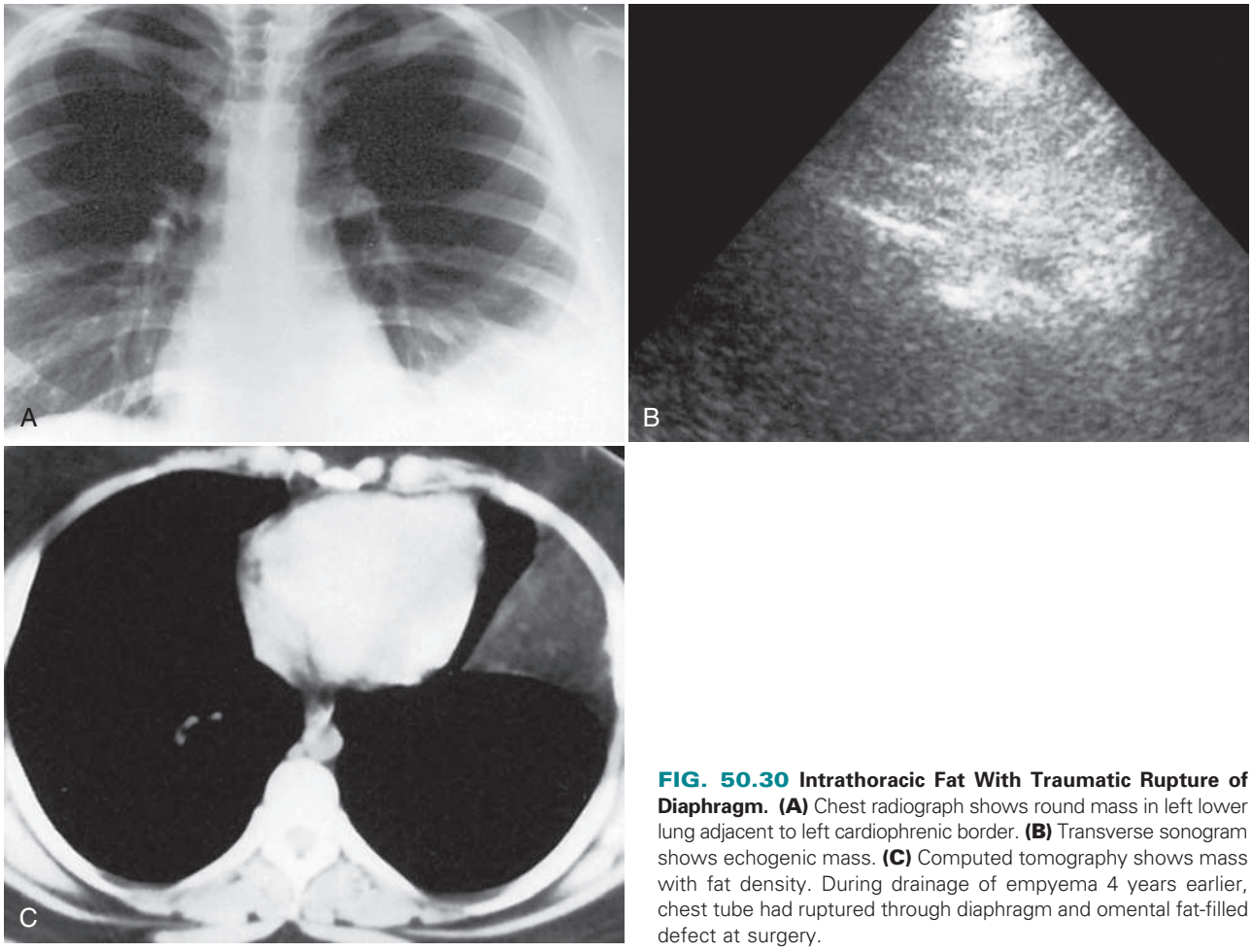

FIG. 50.30 Intrathoracic Fat With Traumatic Rupture of Diaphragm. (A) Chest radiograph shows round mass in left lower lung adjacent to left cardiophrenic border. **(B)** Transverse sonogram shows echogenic mass. **(C)** Computed tomography shows mass with fat density. During drainage of empyema 4 years earlier, chest tube had ruptured through diaphragm and omental fat-filled defect at surgery.

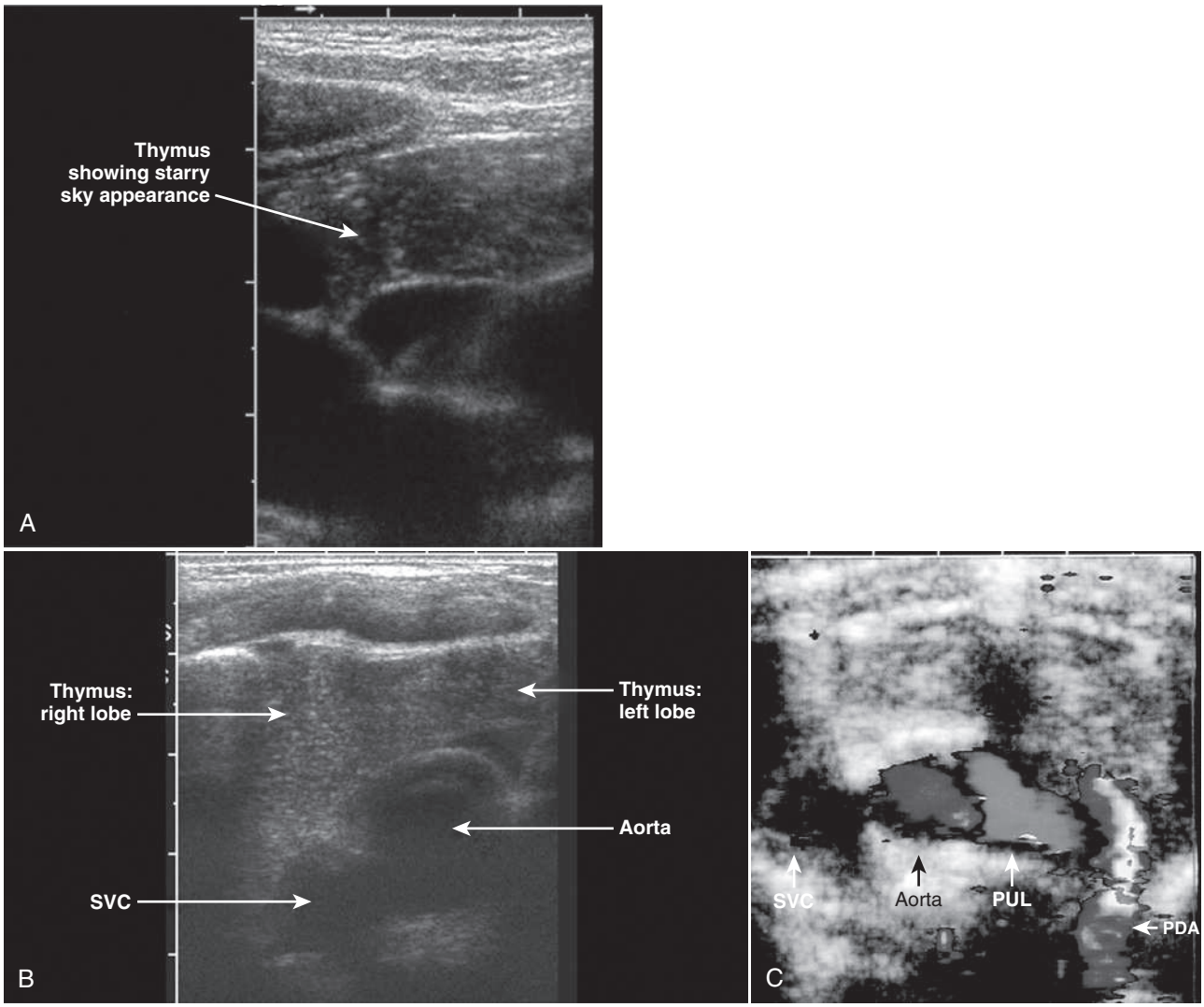

FIG. 50.31 Normal Thymus and Great Vessels of Chest. (A) and **(B)** Longitudinal and transverse sonograms show normal thymus echotexture in a 31-month-old boy. Superior vena cava *(SVC)* and aorta are visible through the thymic window. **(C)** Gray-scale rendering of a color Doppler image shows normal great vessels in the chest in transverse scan through the thymus in another child. *PDA,* Posterior descending artery; *PUL,* pulmonary artery.

transversely from left to right, posterior to the thymus, to enter the SVC. This is useful to determine catheter position (Fig. 50.32) and the presence of a thrombus in children with central venous catheters.

Doppler examination is useful in identifying **thrombus** within the subclavian vein, SVC, and pulmonary artery (Fig. 50.33). Thrombosis of the axillary or subclavian vein secondary to thoracic outlet syndrome[46] is seen on ultrasound Doppler study in **Paget-Schroetter syndrome**[47] (Fig. 50.34). It results from an abnormal insertion of the costoclavicular ligament laterally on the first rib, along with hypertrophy of the scalenus anticus muscle.

The Doppler waveform is abnormal when **thrombosis** or **obstruction** of the SVC is present. Doppler ultrasound findings include (1) loss of biphasic SVC waveform, (2) continuous forward flow rather than distinct systolic and diastolic peaks, (3) a turbulent flow profile, (4) increased velocity downstream, and (5) decreased velocity upstream.[48] Venous thrombosis is reported in 20% of children receiving extracorporeal membrane oxygenation (ECMO).[49] Doppler waveforms may be different in patients receiving ECMO because their resistive indices are low. Recurrent SVC thrombosis has been reported in a child with activated protein C resistance.[50]

Superior Vena Cava Thrombosis: Doppler Sonographic Findings

Loss of biphasic waveform
Continuous forward flow (no systolic or diastolic peaks)
Turbulent flow
Increased downstream velocity
Decreased upstream velocity

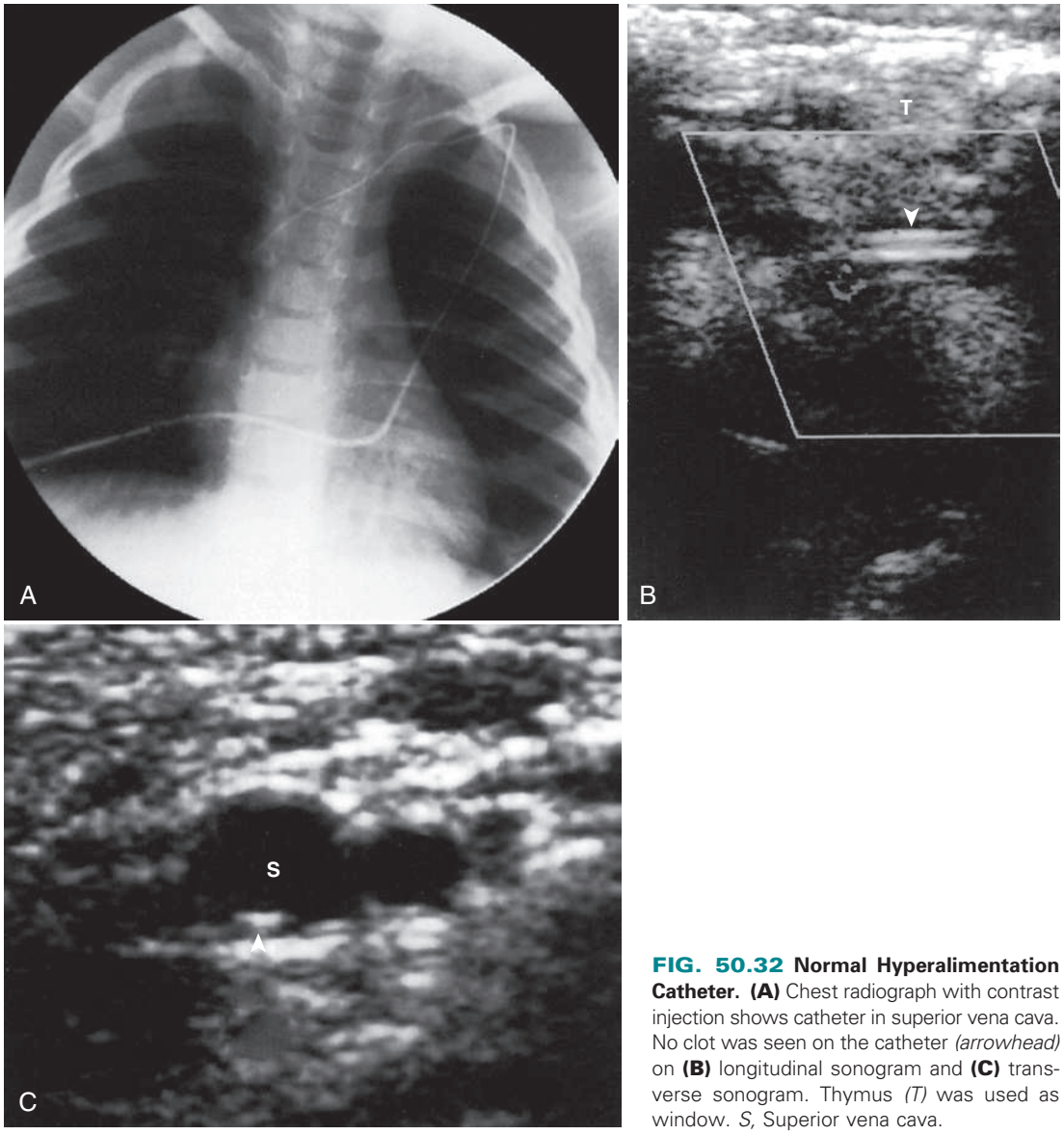

FIG. 50.32 Normal Hyperalimentation Catheter. (A) Chest radiograph with contrast injection shows catheter in superior vena cava. No clot was seen on the catheter *(arrowhead)* on **(B)** longitudinal sonogram and **(C)** transverse sonogram. Thymus *(T)* was used as window. *S,* Superior vena cava.

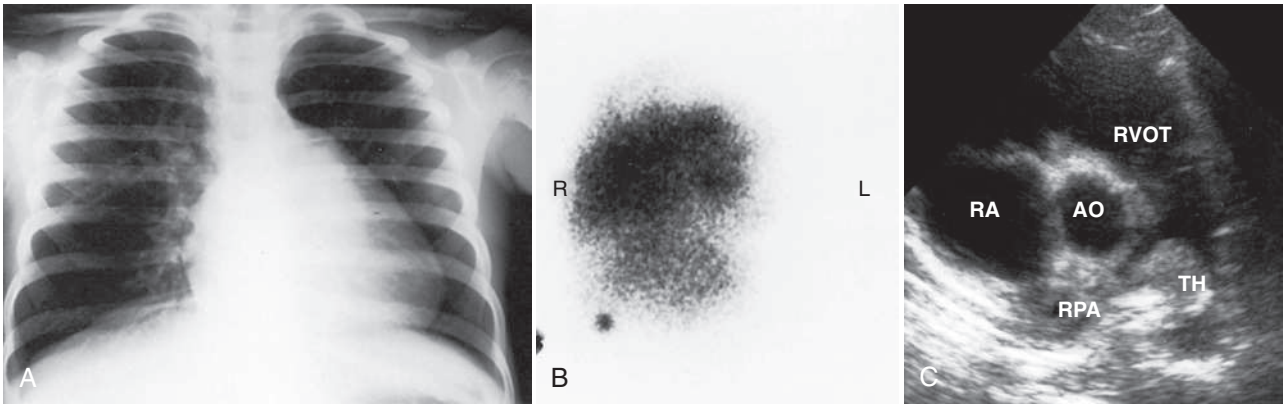

FIG. 50.33 Pulmonary Embolus. (A) Chest radiograph shows hyperlucent left lung in 4-year-old child. **(B)** Pulmonary perfusion scan shows no perfusion to left lung. **(C)** Transverse sonogram through heart shows saddle embolus in main pulmonary artery. *AO,* Aorta; *RA,* right atrium; *RPA,* right pulmonary artery; *RVOT,* right ventricular outflow tract; *TH,* thrombus.

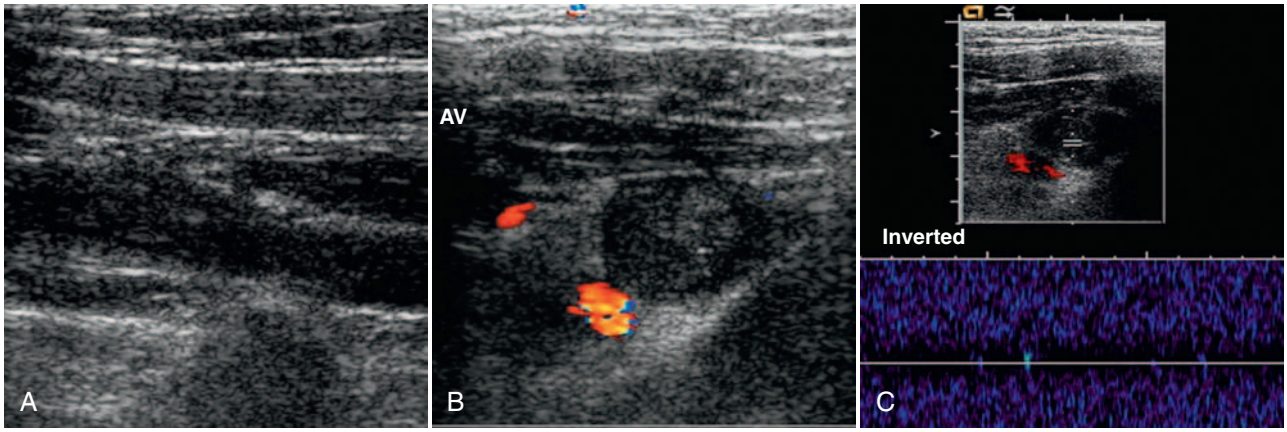

FIG. 50.34 Paget-Schroetter Syndrome. (A) Gray-scale, **(B)** color flow, and **(C)** spectral Doppler waveform images show subclavian vein thrombosis with absence of color flow and absence of Doppler signal secondary to a thoracic outlet syndrome in a 17-year-old female equestrian. (Courtesy of Dr. Charles A. James, Arkansas Children's Hospital, Little Rock, AK.)

Lymphovascular Malformation

Lymphatic malformations[51] (Fig. 50.35) are composed of dilated lymphatic sacs of variable size, which may appear unilocular or multilocular. Lymphatic malformations may undergo hemorrhage, in which case the lesion appears as a uniformly echogenic mass or multiple cysts containing echogenic debris. Septations in cystic lesions are better identified by ultrasound than by CT or magnetic resonance imaging (MRI).

MEDIASTINAL MASSES

CT and MRI are the primary modalities for evaluation of mediastinal masses detected by chest radiography. Suprasternal sonography[52] can be useful for detecting small and large mediastinal masses, particularly lymphoma. Mediastinal sonography for masses should include major vessels or cardiac chambers in the field of view so that mass and vessel echogenicity can be compared directly. This prevents the pitfall created by reducing the gain setting in response to the hyperechoic appearance of adjacent lung. The reduced gain setting gives a falsely anechoic appearance to a solid mass. **Juxtaphrenic paravertebral masses** may be detected with a subxiphoid or transdiaphragmatic approach.

Mediastinal ultrasound can also determine whether chest masses extend into the neck. **Retrosternal thyroid** mass extension detection by ultrasound is helpful for surgical planning. Ultrasound allows characterization of masses as solid or cystic. Doppler imaging may be helpful in evaluating whether a chest mass is vascular in origin. Malignant chest masses demonstrate a low-impedance, high–diastolic-flow Doppler signal.[53] Color Doppler ultrasound before percutaneous biopsy can rule out vascular lesions that would preclude biopsy.

A widened superior mediastinum detected on chest radiography can be evaluated initially by sonography. Detection of a normal but prominent thymus rather than a mediastinal mass precludes the need for CT. The thymus is normally located in the superior mediastinum anterior to the great vessels in the superior mediastinum, from the superior edge of the manubrium to the fourth costal cartilage. The thymus is mildly hypoechoic relative to liver, spleen, and thyroid. It shows some echogenic strands. A fine granular echotexture gives the thymus a "starry sky" appearance (see Fig. 50.31). A fibrous capsule gives the thymus a smooth, well-defined margin.

Thymic Index

Thymic index is the product of thymic width measured on transverse images and the area of the largest lobe measured on a longitudinal image[54-56] (Table 50.1). The thymic index has acceptable correlation with actual thymus weight and volume. The measurement is performed during expiration to obtain a standardized size. Thymic index is greater in children with active atopic dermatitis than in healthy controls[57] (Fig. 50.36). Larger thymic index at birth is associated with lower infant mortality rate.[58] Thymic size varies with age, and normal thymic index values have been established[54-56] (Table 50.2).

Abnormal Location of Thymus Mimicking Mass Lesion

Superior herniation of thymus into the neck is a rare entity in which there is intermittent migration of the broadest part of the normal thymus out of the thorax into the suprasternal region. Real-time ultrasound shows that the mass moves into the neck during Valsalva maneuver, with an increase in the intrathoracic pressure, and has typical echotexture of thymus, thereby avoiding unnecessary biopsy and surgery.[59] **Cervical ectopic thymus** is an uncommon variant. A hypoechoic mass with characteristic thymic ultrasound echotexture is identified along the track of the thymopharyngeal duct.[60,61] The thymus can **protrude into the chest wall** as a bulging mass because of a congenital sternal defect. Real-time ultrasound can demonstrate movement of herniated thymus during respiratory cycles.

Anterior Mediastinal Masses

Benign abnormalities of the thymus in children include thymic cyst, intrathymic hemorrhage, thymolipoma, and thymoma. The thymus may also be involved by a hemangioma, lymphatic

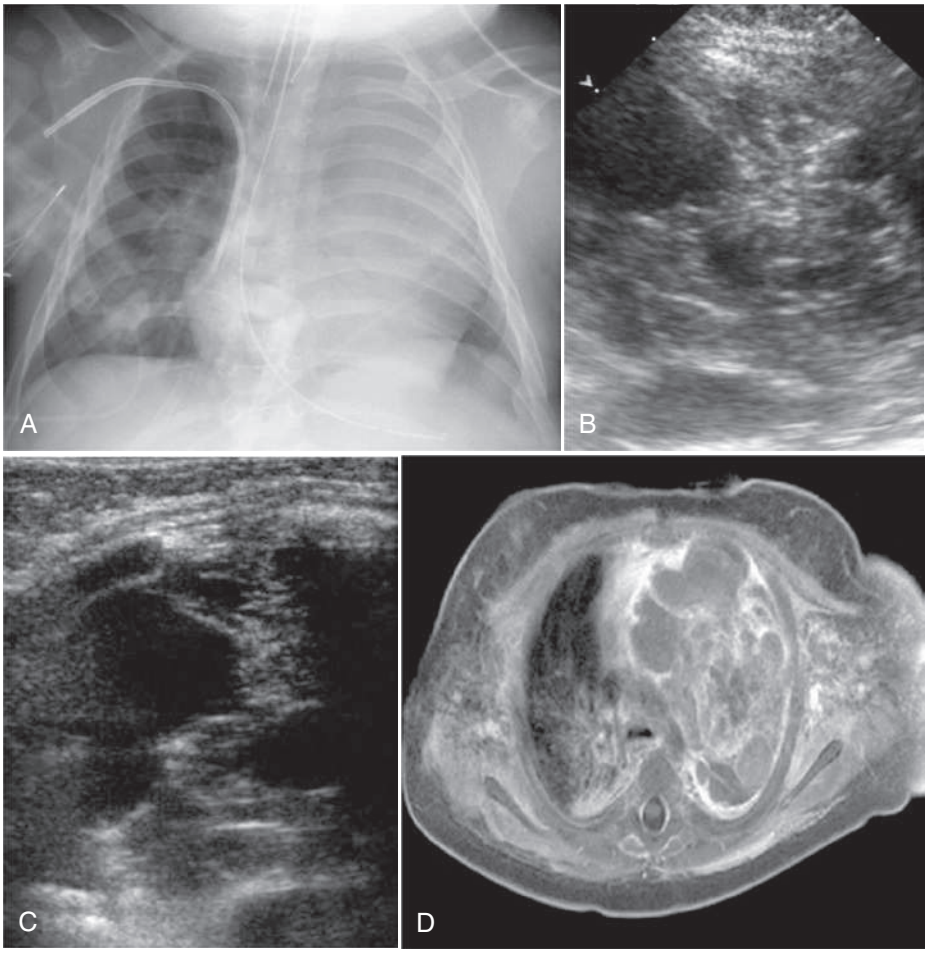

FIG. 50.35 Macrocystic Lymphatic Malformation in 7-Month-Old Girl. (A) Chest radiograph shows opacity in left upper chest and neck. **(B)** and **(C)** Sonograms show multiple cystic spaces. **(D)** T1-weighted postcontrast, axial magnetic resonance image defines the extent of the lesion.

TABLE 50.1 Formula for Calculation of Thymic Index

Thymic index (cm^3)	=	Area of the largest lobe (cm^2)	×	Transverse dimension of thymus from right lateral edge to left lateral edge (cm)
Area of the lobe of thymus (cm^2)	=	Craniocaudad dimension (cm)	×	Anteroposterior dimension (cm)

malformation, or Langerhans cell histiocytosis. Malignant infiltration of the thymus is also seen in lymphoma and leukemia. **Thymic cysts** are anechoic. Other abnormalities of the thymus may show irregular or lobular margin, heterogeneous echogenicity, and coarse echotexture. **Germ cell tumors** can have variable appearance. **Teratomas** are heterogeneous masses that contain fat, bone, calcification, and cystic elements.

Lymphadenopathy

The most common mediastinal mass in older children is lymphadenopathy resulting from **leukemia** or **lymphoma. Lymphadenopathy** appears as hypoechoic nodules. Lymph nodes in lymphoma are more hypoechoic and more hypovascular than inflammatory lymph nodes.[62]

Posterior Mediastinal Masses

Posterior mediastinal masses, including neurogenic tumors, make up the majority of mediastinal masses in young infants. **Neurogenic tumors** appear as a lobulated or well-defined hypoechoic mass with granular or flecklike calcifications. Neurenteric cysts are well-defined, anechoic lesions with thin walls. When inflammation and hemorrhage occur, the cyst may contain echogenic debris from proteinaceous fluid, mucus, or blood.

ULTRASOUND-GUIDED INTERVENTIONAL PROCEDURES

Sonography is an excellent method for guiding postoperative fluid collections[63] (Fig. 50.37), **pleural fluid aspiration,**[64]

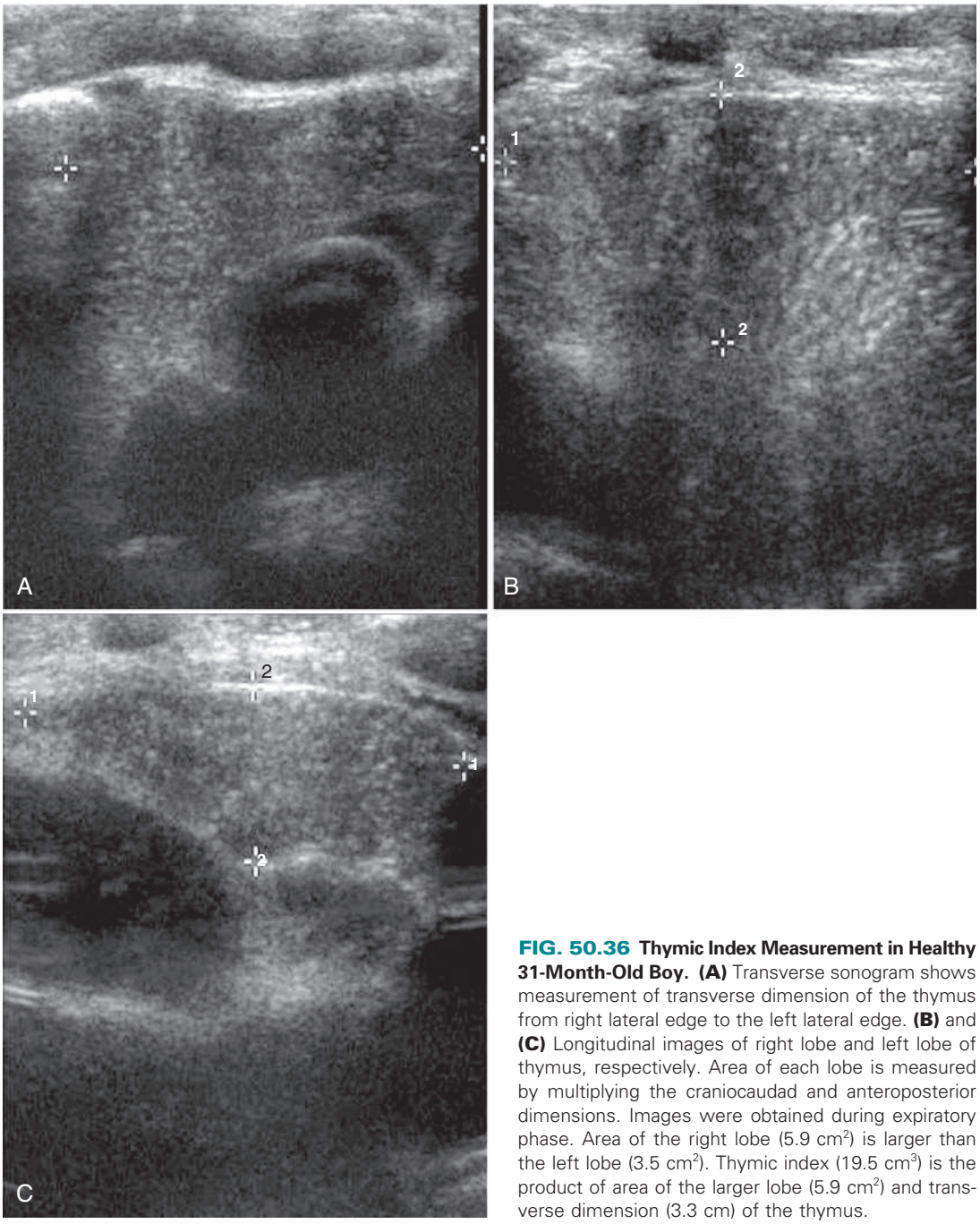

FIG. 50.36 Thymic Index Measurement in Healthy 31-Month-Old Boy. (A) Transverse sonogram shows measurement of transverse dimension of the thymus from right lateral edge to the left lateral edge. **(B)** and **(C)** Longitudinal images of right lobe and left lobe of thymus, respectively. Area of each lobe is measured by multiplying the craniocaudad and anteroposterior dimensions. Images were obtained during expiratory phase. Area of the right lobe (5.9 cm^2) is larger than the left lobe (3.5 cm^2). Thymic index (19.5 cm^3) is the product of area of the larger lobe (5.9 cm^2) and transverse dimension (3.3 cm) of the thymus.

mediastinal mass biopsy, and chest wall **lesion biopsy.** Ultrasound can be used either for marking the skin overlying a fluid collection or for directly visualizing a needle during insertion into a collection (Fig. 50.37). Ultrasound is particularly helpful in determining whether the pleural effusion will respond to **simple drainage** or will require **surgical decortication.**[65] If the fluid is relatively anechoic or clear, simple drainage with thoracentesis or chest tube drainage is an adequate treatment. If the fluid is thick with multiple septations, and if the patient does not respond promptly to antibiotic therapy, decortication or video-assisted thoracic surgery may be required.[11,66] Complicated parapneumonic effusions and empyemas have been successfully treated in up to 93% of children, using tissue plasminogen activator administered through a small-bore chest tube.[67]

Empyema surrounded by lung may appear to be a pulmonary abscess on sonography. Changing the patient position and the viewing planes can help distinguish an empyema from a lung abscess (Fig. 50.38). Ultrasound can be used to guide needle aspiration for etiologic diagnosis in patients with complicated pneumonia, as well as aspiration of microabscesses in necrotizing pneumonia.

Sonography can detect **pneumothoraces**[68] after thoracentesis.[69] Before and after thoracentesis, the ipsilateral pulmonary apex and adjacent lung should be examined in the upright position

for normal pleural respiratory movement. If the pleural respiratory motion is absent, a pneumothorax should be suspected.

Central venous catheters can be placed under ultrasound guidance, and the catheter tip position can be determined using ultrasound.[70] **Sclerotherapy** for macrocystic lymphatic malformation under ultrasound guidance has the advantage of dynamically visualizing the procedure reaction that causes obliteration of the macrocysts[71] (Fig. 50.39). Unlike fluoroscopy guidance, the residual cysts are easily seen under ultrasound guidance and can be targeted for further sclerotherapy.

TABLE 50.2 Normal Thymic Index Values for Children Younger Than 2 Years

Age in Months	THYMIC INDEX (cm^3)	
	Average	Standard Deviation (SD)
Premature	11.9	3.9
0-1	18.1	6.7
1-2	25.4	9.4
2-3	22.3	6.9
3-4	26.8	10.3
4-5	29.7	17.6
5-6	24.2	9.3
6-8	22.2	8.9
8-10	21.5	6.8
10-12	23.2	7.2
12-18	17.2	6.4
18-24	15.4	5.6

Modified from Yekeler E, Tambag A, Tunaci A, et al. Analysis of the thymus in 151 healthy infants from 0 to 2 years of age. J Ultrasound Med. 2004;23(10):1321-1326.[56]

Acute rib pain from cystic fibrosis exacerbation has been managed with ultrasound-guided placement of a continuous thoracic paravertebral catheter.[23,28]

OTHER LESS ESTABLISHED INDICATIONS

Pneumothorax,[2,24,25,72,73] rib fracture,[74] and bronchiolitis[75] can be detected sonographically. However, use of ultrasound may not

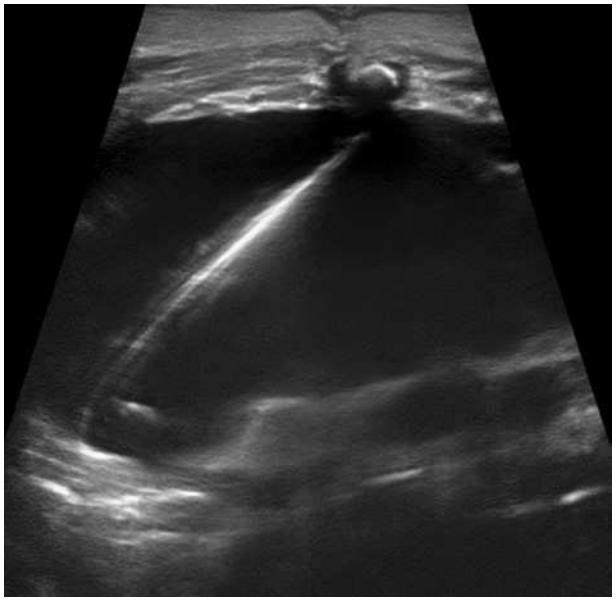

FIG. 50.37 Retrosternal Seroma. Sonogram shows anechoic fluid collection in retrosternal space in 7-week-old girl with history of surgery for ventricular septal defect and hypoplastic aortic arch performed 5 weeks before the ultrasound. Needle is visible within the fluid collection during ultrasound-guided aspiration of the fluid.

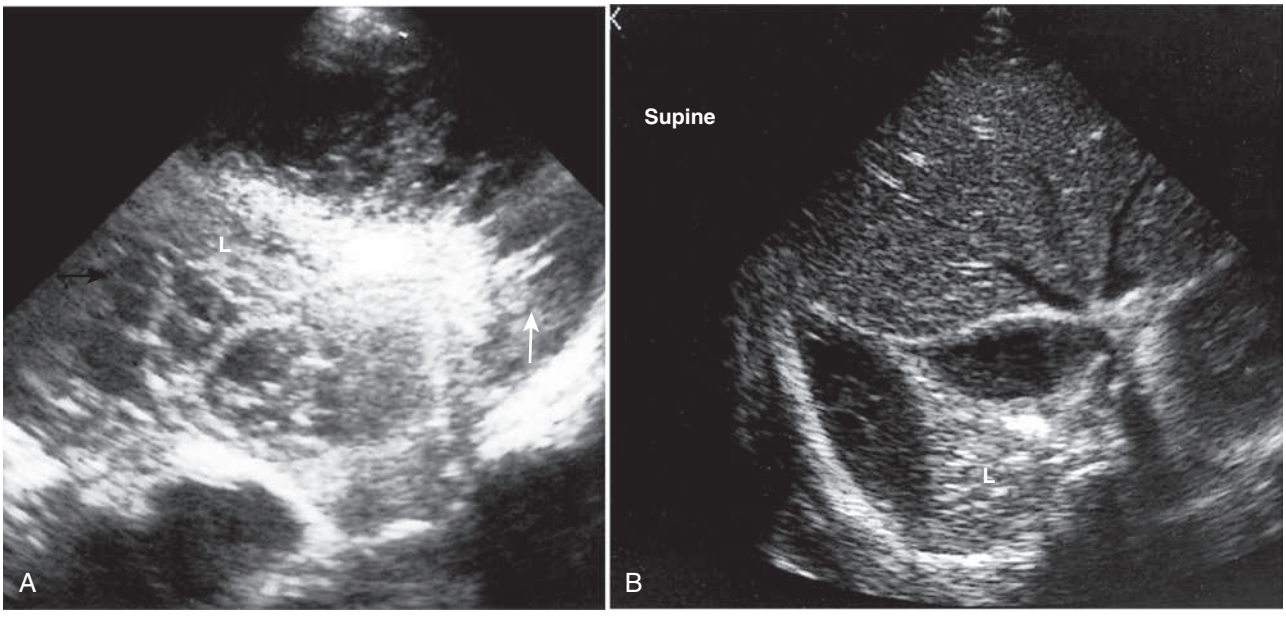

FIG. 50.38 Empyema Requiring Surgical Decortications in Patient With Sickle Cell Anemia. (A) Thick fluid *(black arrow)* around lung *(L)* with multiple loculations. Thick putty rind was found at surgery. Possible intraparenchymal abscesses *(white arrow)* on upright transverse scan. **(B)** On supine scan through the liver, only empyema surrounds the lung *(L);* no abscess is present.

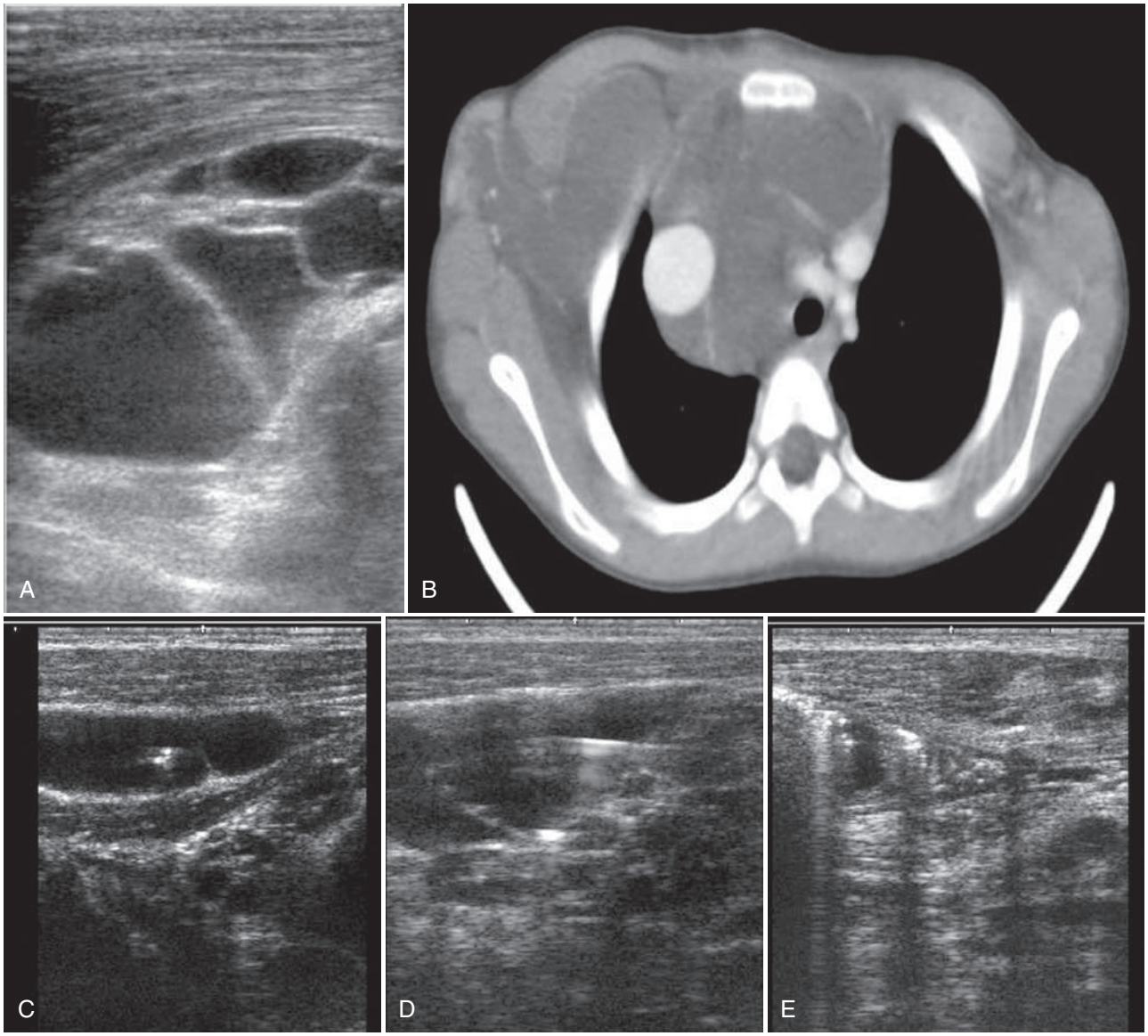

FIG. 50.39 Ultrasound-Guided Sclerotherapy of Macrocystic Lymphatic Malformation. (A) Sonogram shows multiple cysts within the right chest wall and axilla extending into the mediastinum. **(B)** Computed tomography scan shows extent of the lesion. **(C)** and **(D)** Sonograms show needle and dilator, respectively, within the lesion. **(E)** Sonogram immediately after sclerotherapy injection shows excellent response.

be practical compared with the current usual diagnostic methods because chest radiographs are quickly and cheaply performed compared with ultrasound, with a very low radiation dose. Ultrasound requires more time to perform, is operator dependent, and may not be practical in critically ill children or in very young children.

Pneumomediastinum may be misinterpreted on ultrasound as pneumothorax.[72] In a patient with suspected rib fractures, radiographs may still be required to look for other fractures. Severity of bronchiolitis can be determined by ultrasound.[75] However, it can easily be determined by clinical scoring by evaluating respiratory rate, dyspnea, use of accessory respiratory muscles, and auscultation. Moderate and severe cases are given supplementary oxygen. Why would we want to replace a stethoscope with ultrasound at unnecessary additional cost without any incremental additional benefit?

REFERENCES

1. Coley BD. Pediatric chest ultrasound. Radiol Clin North Am. 2005;43(2):405-418.
2. Trinavarat P, Riccabona M. Potential of ultrasound in the pediatric chest. Eur J Radiol. 2014;83(9):1507-1518.
3. Kocijancic K. Ultrasonographic forms of pleural space in healthy children. Coll Antropol. 2007;31(4):999-1002.
4. Chen HJ, Tu CY, Ling SJ, et al. Sonographic appearances in transudative pleural effusions: not always an anechoic pattern. Ultrasound Med Biol. 2008;34(3):362-369.
5. Kim OH, Kim WS, Kim MJ, et al. US in the diagnosis of pediatric chest diseases. Radiographics. 2000;20(3):653-671.
6. Feller-Kopman D. Ultrasound-guided thoracentesis. Chest. 2006;129(6):1709-1714.
7. Wu RG, Yang PC, Kuo SH, Luh KT. "Fluid color" sign: a useful indicator for discrimination between pleural thickening and pleural effusion. J Ultrasound Med. 1995;14(10):767-769.
8. Riccabona M. Ultrasound of the chest in children (mediastinum excluded). Eur Radiol. 2008;18(2):390-399.

9. Jaffe A, Calder AD, Owens CM, et al. Role of routine computed tomography in paediatric pleural empyema. Thorax. 2008;63(10):897-902.
10. Pinotti KF, Ribeiro SM, Cataneo AJ. Thorax ultrasound in the management of pediatric pneumonias complicated with empyema. Pediatr Surg Int. 2006;22(10):775-778.
11. Chen KY, Liaw YS, Wang HC, et al. Sonographic septation: a useful prognostic indicator of acute thoracic empyema. J Ultrasound Med. 2000;19(12):837-843.
12. Kim YW, Donnelly LF. Round pneumonia: imaging findings in a large series of children. Pediatr Radiol. 2007;37(12):1235-1240.
13. Gaston B. Pneumonia. Pediatr Rev. 2002;23(4):132-140.
14. Pereda MA, Chavez MA, Hooper-Miele CC, et al. Lung ultrasound for the diagnosis of pneumonia in children: a meta-analysis. Pediatrics. 2015;135(4):714-722.
15. Copetti R, Cattarossi L. Ultrasound diagnosis of pneumonia in children. Radiol Med. 2008;113(2):190-198.
16. Esposito S, Papa SS, Borzani I, et al. Performance of lung ultrasonography in children with community-acquired pneumonia. Ital J Pediatr. 2014;40:37.
17. Shah VP, Tunik MG, Tsung JW. Prospective evaluation of point-of-care ultrasonography for the diagnosis of pneumonia in children and young adults. JAMA Pediatr. 2013;167(2):119-125.
18. Iuri D, De Candia A, Bazzocchi M. Evaluation of the lung in children with suspected pneumonia: usefulness of ultrasonography. Radiol Med. 2009;114(2):321-330.
19. Reali F, Sferrazza Papa GF, et al. Can lung ultrasound replace chest radiography for the diagnosis of pneumonia in hospitalized children? Respiration. 2014;88(2):112-115.
20. Liu J, Liu F, Liu Y, et al. Lung ultrasonography for the diagnosis of severe neonatal pneumonia. Chest. 2014;146(2):383-388.
21. Caiulo VA, Gargani L, Caiulo S, et al. Lung ultrasound characteristics of community-acquired pneumonia in hospitalized children. Pediatr Pulmonol. 2013;48(3):280-287.
22. Urbankowska E, Krenke K, Drobczynski L, et al. Lung ultrasound in the diagnosis and monitoring of community acquired pneumonia in children. Respir Med. 2015;109(9):1207-1212.
23. Cutshall C, Hutchins J. Ultrasound-guided continuous thoracic paravertebral catheter management of acute rib pain secondary to cystic fibrosis exacerbation in a pediatric patient. A A Case Rep. 2015;4(3):29-30.
24. Sawires HK, Abdel Ghany EA, Hussein NF, Seif HM. Use of lung ultrasound in detection of complications of respiratory distress syndrome. Ultrasound Med Biol. 2015;41(9):2319-2325.
25. Balesa J, Rathi V, Kumar S, Tandon A. Chest sonography in the diagnosis of pneumothorax. Indian J Chest Dis Allied Sci. 2015;57(1):7-11.
26. Cohen MD. CT radiation dose reduction: can we do harm by doing good? Pediatr Radiol. 2012;42(4):397-398.
27. Amis Jr ES. CT radiation dose: trending in the right direction. Radiology. 2011;261(1):5-8.
28. Krane EJ. Editorial comment: Thoracic paravertebral blockade for the management of pain associated with cystic fibrosis. A A Case Rep. 2015;4(3):33.
29. Frazier AA, Rosado de Christenson ML, Stocker JT, Templeton PA. Intralobar sequestration: radiologic-pathologic correlation. Radiographics. 1997;17(3):725-745.
30. Gosselin MV. Intralobar sequestration. In: Gurney JW, Winer-Muram HT, editors. Diagnostic imaging: chest. Salt Lake City: Amirsys; 2006. p. II-2-14-7.
31. Choe J, Goo HW. Extralobar pulmonary sequestration with hemorrhagic infarction in a child: preoperative imaging diagnosis and pathological correlation. Korean J Radiol. 2015;16(3):662-667.
32. Liu R, Adler DG. Duplication cysts: diagnosis, management, and the role of endoscopic ultrasound. Endosc Ultrasound. 2014;3(3):152-160.
33. Ghribi A, Bouden A, Braiki M, et al. Diaphragmatic eventration in children. Tunis Med. 2015;93(2):76-78.
34. Boultbee JE, Lloyd DA. The ultrasound appearance of subdiaphragmatic rupture of a right lobe liver abscess in a two-year-old child. Br J Radiol. 1979;52(623):899-901.
35. Kapoor R, Saha MM, Talwar S. Ultrasonic evaluation of intra-abdominal abscesses. Indian Pediatr. 1991;28(7):757-760.
36. Szmigielska A, Ksiezopolska A, Roszkowska-Blaim M, et al. Rare renal ectopia in children—intrathoracic ectopic kidney. Dev Period Med. 2015;19(2):186-188.
37. Yao Q, Hu X, Huang G, Pa M. A case of diaphragmatic infantile hemangioma. J Perinatol. 2013;33(7):576-577.
38. Chavhan GB, Babyn PS, Cohen RA, Langer JC. Multimodality imaging of the pediatric diaphragm: anatomy and pathologic conditions. Radiographics. 2010;30(7):1797-1817.
39. Gupta AK, Mitra DK, Berry M. Primary embryonal rhabdomyosarcoma of the diaphragm in a child: case report. Pediatr Radiol. 1999;29(11):823-825.
40. Kim MP, Hofstetter WL. Tumors of the diaphragm. Thorac Surg Clin. 2009;19(4):521-529.
41. Houston JG, Fleet M, Cowan MD, McMillan NC. Comparison of ultrasound with fluoroscopy in the assessment of suspected hemidiaphragmatic movement abnormality. Clin Radiol. 1995;50(2):95-98.
42. Lerolle N, Guerot E, Dimassi S, et al. Ultrasonographic diagnostic criterion for severe diaphragmatic dysfunction after cardiac surgery. Chest. 2009;135(2):401-407.
43. Epelman M, Navarro OM, Daneman A, Miller SF. M-mode sonography of diaphragmatic motion: description of technique and experience in 278 pediatric patients. Pediatr Radiol. 2005;35(7):661-667.
44. Gerscovich EO, Cronan M, McGahan JP, et al. Ultrasonographic evaluation of diaphragmatic motion. J Ultrasound Med. 2001;20(6):597-604.
45. Eren S, Kantarci M, Okur A. Imaging of diaphragmatic rupture after trauma. Clin Radiol. 2006;61(6):467-477.
46. Arthur LG, Teich S, Hogan M, et al. Pediatric thoracic outlet syndrome: a disorder with serious vascular complications. J Pediatr Surg. 2008;43(6):1089-1094.
47. Trenor 3rd CC, Fisher JG, Khan FA, et al. Paget-Schroetter syndrome in 21 children: outcomes after multidisciplinary care. J Pediatr. 2015;166(6):1493-1497 e1.
48. Lv FQ, Duan YY, Yuan LJ, et al. Doppler superior vena cava flow evolution and respiratory variation in superior vena cava syndrome. Echocardiography. 2008;25(4):360-365.
49. Riccabona M, Kuttnig-Haim M, Dacar D, et al. Venous thrombosis in and after extracorporeal membrane oxygenation: detection and follow-up by color Doppler sonography. Eur Radiol. 1997;7(9):1383-1386.
50. Provenzale JM, Frush DP, Ortel TL. Recurrent thrombosis of the superior vena cava associated with activated protein C resistance: imaging findings. Pediatr Radiol. 1998;28(8):597-598.
51. Odibo IN, Linam LE, Richter GE, et al. Extensive fetal congenital subcutaneous mixed venous lymphatic lesion: prenatal diagnosis and postnatal management. AJP Rep. 2015;5(1):e37-e42.
52. Moseme T, Andronikou S. Through the eye of the suprasternal notch: point-of-care sonography for tuberculous mediastinal lymphadenopathy in children. Pediatr Radiol. 2014;44(6):681-684.
53. Hsu WH, Yu YH, Tu CY, et al. Color Doppler US pulmonary artery vessel signal: a sign for predicting the benign lesions. Ultrasound Med Biol. 2007;33(3):379-388.
54. Hasselbalch H, Ersboll AK, Jeppesen DL, Nielsen MB. Thymus size in infants from birth until 24 months of age evaluated by ultrasound. A longitudinal prediction model for the thymic index. Acta Radiol. 1999;40(1):41-44.
55. Jeppesen DL, Hasselbalch H, Nielsen SD, et al. Thymic size in preterm neonates: a sonographic study. Acta Paediatr. 2003;92(7):817-822.
56. Yekeler E, Tambag A, Tunaci A, et al. Analysis of the thymus in 151 healthy infants from 0 to 2 years of age. J Ultrasound Med. 2004;23(10):1321-1326.
57. Olesen AB, Andersen G, Jeppesen DL, et al. Thymus is enlarged in children with current atopic dermatitis. A cross-sectional study. Acta Derm Venereol. 2005;85(3):240-243.
58. Aaby P, Marx C, Trautner S, et al. Thymus size at birth is associated with infant mortality: a community study from Guinea-Bissau. Acta Paediatr. 2002;91(6):698-703.
59. Senel S, Erkek N, Otgun I, et al. Superior herniation of the thymus into the neck—a familial pattern. J Thorac Imaging. 2008;23(2):131-134.
60. De Foer B, Vercruysse JP, Marien P, et al. Cervical ectopic thymus presenting as a painless neck mass in a child. JBR-BTR. 2007;90(4):281-283.

61. Chu WC, Metreweli C. Ectopic thymic tissue in the paediatric age group. Acta Radiol. 2002;43(2):144-146.
62. Na DG, Lim HK, Byun HS, et al. Differential diagnosis of cervical lymphadenopathy: usefulness of color Doppler sonography. Am J Roentgenol. 1997;168(5):1311-1316.
63. Cantinotti M, Giordano R, Assanta N, et al. Chest ultrasound: a new, easy, and radiation-free tool to detect retrosternal clot after pediatric cardiac surgery. J Cardiothorac Vasc Anesth. 2015;29(5):e59-e60.
64. Miraglia R, Maruzzelli L, Piazza M, et al. Real-time ultrasound-guided placement of a pigtail catheter in supine position for draining pleural effusion in pediatric patients who have undergone liver transplantation. J Clin Ultrasound. 2016;44(5):284-289.
65. McBride SC. Management of parapneumonic effusions in pediatrics: current practice. J Hosp Med. 2008;3(3):263-270.
66. Chiu CY, Wong KS, Huang YC, et al. Echo-guided management of complicated parapneumonic effusion in children. Pediatr Pulmonol. 2006;41(12):1226-1232.
67. Feola GP, Shaw LC, Coburn L. Management of complicated parapneumonic effusions in children. Tech Vasc Interv Radiol. 2003;6(4):197-204.
68. Migliaro F, Sodano A, Capasso L, Raimondi F. Lung ultrasound-guided emergency pneumothorax needle aspiration in a very preterm infant. BMJ Case Rep. 2014;2014.
69. Pihlajamaa K, Bode MK, Puumalainen T, et al. Pneumothorax and the value of chest radiography after ultrasound-guided thoracocentesis. Acta Radiol. 2004;45(8):828-832.
70. Alonso-Quintela P, Oulego-Erroz I, Rodriguez-Blanco S, et al. Location of the central venous catheter tip with bedside ultrasound in young children: can we eliminate the need for chest radiography? Pediatr Crit Care Med. 2015;16(9):e340-e345.
71. Duman L, Karnak I, Akinci D, Tanyel FC. Extensive cervical-mediastinal cystic lymphatic malformation treated with sclerotherapy in a child with Klippel-Trenaunay syndrome. J Pediatr Surg. 2006;41(1):e21-e24.
72. Saracino C, Tessaro M. Pneumomediastinum as a sonographic mimic of pneumothorax. J Ultrasound Med. 2015;34(8):1521-1522.
73. Jalli R, Sefidbakht S, Jafari SH. Value of ultrasound in diagnosis of pneumothorax: a prospective study. Emerg Radiol. 2013;20(2):131-134.
74. Kelloff J, Hulett R, Spivey M. Acute rib fracture diagnosis in an infant by US: a matter of child protection. Pediatr Radiol. 2009;39(1):70-72.
75. Basile V, Di Mauro A, Scalini E, et al. Lung ultrasound: a useful tool in diagnosis and management of bronchiolitis. BMC Pediatr. 2015;15:63.
76. Seibert RW, Seibert JJ, Williamson SL. The opaque chest: when to suspect a bronchial foreign body. Pediatr Radiol. 1986;16(3):193-196.

CHAPTER 51

The Pediatric Liver and Spleen

Sara M. O'Hara

SUMMARY OF KEY POINTS

- Infants with neonatal jaundice should be imaged before 2 months of age to optimize surgical treatment of biliary atresia, if present.
- Steatosis and cirrhosis both attenuate the ultrasound beam, making imaging challenging, but it is important for determining the underlying cause of disease.
- Approximately 40% of liver tumors in children are benign, and hemangiomas are the most common of these.
- Among malignant liver tumors in children, hepatoblastoma is most common.
- Doppler assessment of the liver provides critical information used to differentiate among numerous causes of hepatic disease.
- Knowledge of common spontaneous portosystemic collateral pathways facilitates the sonographic examination and a search for root causes of cirrhosis.
- Effective examination of pediatric segmental liver transplants requires familiarity with their substantially altered anatomy.

CHAPTER OUTLINE

ANATOMY
Portal Vein Anatomy
Left Lobe of Liver
Right Lobe of Liver
Hepatic Vein Anatomy
NEONATAL JAUNDICE
Choledochal Cyst
Spontaneous Rupture of Bile Duct
Paucity of Interlobular Bile Ducts and Alagille Syndrome
Biliary Atresia
Neonatal Hepatitis
Neonatal Jaundice and Urinary Tract Infection or Sepsis
Inborn Errors of Metabolism
STEATOSIS
CIRRHOSIS
CHOLELITHIASIS
LIVER TUMORS
Identification
Benign Liver Tumors
Hemangiomas
Infantile Hemangioendotheliomas
Mesenchymal Hamartomas
Adenomas
Focal Nodular Hyperplasia
Malignant Liver Tumors
Hepatoblastoma
Hepatocellular Carcinoma
Undifferentiated Embryonal Sarcoma
Biliary Rhabdomyosarcoma
Metastases
Detection of Tumor Angiogenesis
LIVER ABSCESS AND GRANULOMAS
Pyogenic Abscess
Parasitic Abscesses
Amebiasis
Echinococcosis
Schistosomiasis
Granulomas of the Liver
DOPPLER ASSESSMENT OF LIVER DISEASE AND PORTAL HYPERTENSION IN CHILDREN
Basic Principles
Normal Flow Patterns in Splanchnic Vessels
Possibilities and Pitfalls
Sonographic Technique
Child With Liver Disease: Doppler Examination for Portal Hypertension
Abnormal Flow Patterns Within the Portal System
Absent Doppler Signal
Arterialized Portal Venous Flow
Reversed or To-and-Fro Flow
Abnormal Hepatic Arterial Doppler Patterns
Portal Venous Hypertension
Prehepatic Portal Hypertension
Intrahepatic Portal Hypertension
Suprahepatic (Posthepatic) Portal Hypertension
Surgical Portosystemic Shunts
Hepatic Shear Wave Elastography
DOPPLER SONOGRAPHY IN CHILDREN RECEIVING LIVER TRANSPLANT
Pretransplantation Evaluation
Posttransplantation Evaluation
Multiorgan Transplants
THE SPLEEN
Acknowledgment

ANATOMY

The anatomy of the liver can be explored in many planes with sonography. The usual course of intrahepatic vessels and their normal variants can be traced.[1] There is a simple sonographic approach to the segmental anatomy of the liver based on the nomenclature of the French surgeon Couinaud,[2] who described the segments according to the distribution of the portal and hepatic veins. Each segment has a branch (or a group of branches) of the **portal vein** at its center and a **hepatic vein** at its periphery.

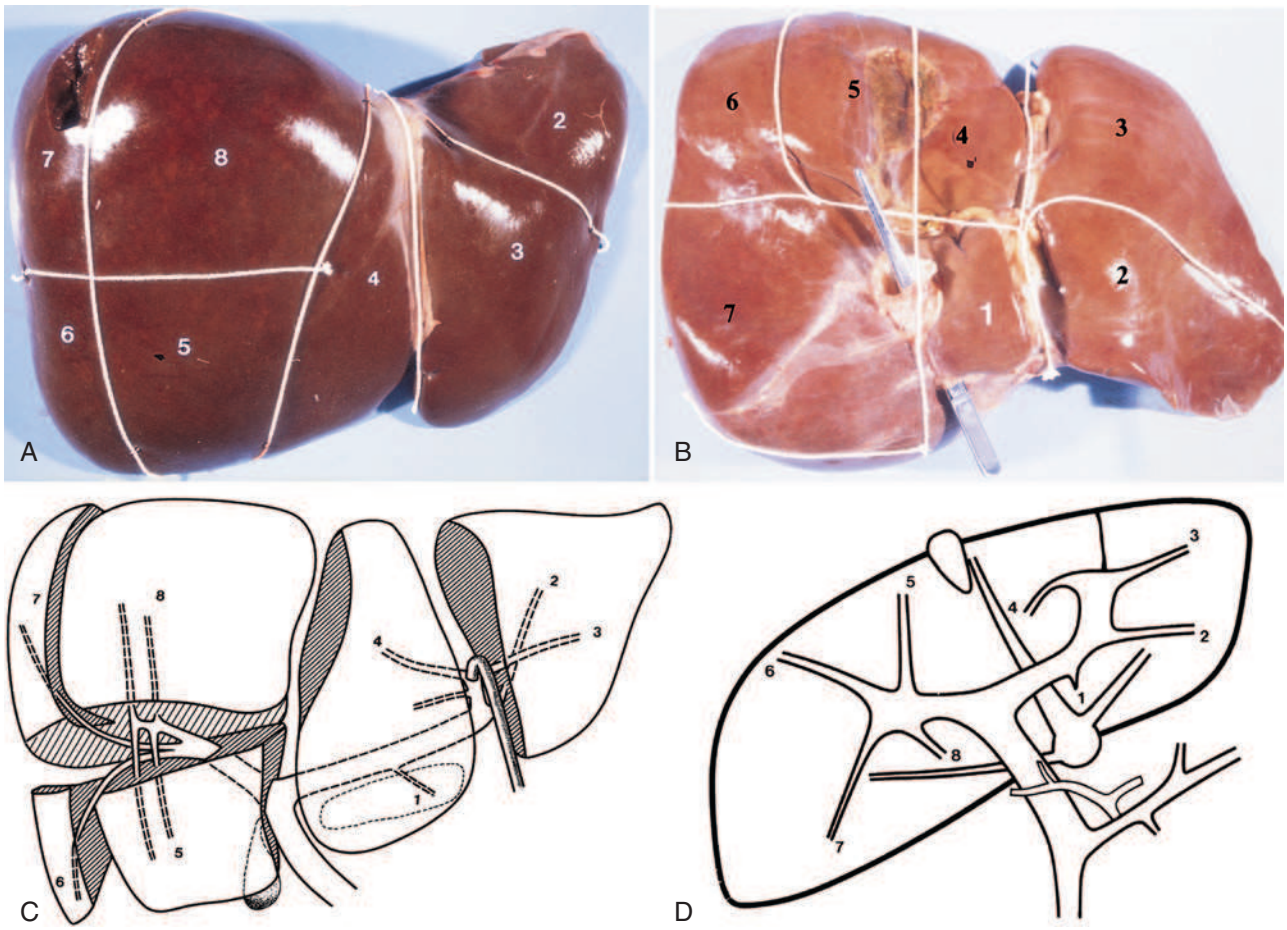

FIG. 51.1 External Segmental Anatomy of the Liver. Segments are numbered in a counterclockwise direction. Their borders are marked with string. **(A)** Upper and anterior surface. Note the whitish falciform ligament that separates segments 3 and 4. **(B)** Lower surface: the forceps are in the main portal vein. The gallbladder has been removed from its bed, which separates segments 4 and 5. The vertical string between segments 4 and 5 and between 1 and 7 follows the gallbladder/middle hepatic vein axis and marks the main hepatic fissure, the division between right and left lobes. Segment 1, the caudate lobe, is to the right of the forceps. Segments 3 and 4 are separated by the falciform ligament; 1 and 2 by the ligamentum venosum. **(C)** Schema of the hepatic segments with their portal venous branches (upper anterior, viewed as in **[A]**). **(D)** Diagram of the portal and hepatic veins and their relationship to the segments (lower liver surface, viewed as in **[B]**). (With permission from Ikeda S, Sera Y, Yamamoto H, Ogawa M. Effect of phenobarbital on serial ultrasonic examination in the evaluation of neonatal jaundice. Clin Imaging. 1994;18[2]:146-148.[4])

Each lobe of the liver contains **four segments.** The segments are numbered counterclockwise: 1 through 4 make up the **left lobe,** and 5 through 8, the **right lobe.** Segment 1 is the **caudate lobe** or Spiegel lobe. The right and left lobes are separated by the **main hepatic fissure,** a line connecting the neck of the gallbladder and the left side of the inferior vena cava (IVC) (Fig. 51.1).

The segmental branches of the portal vein (each one of which leads into a segment) can be outlined in the form of two Hs turned sideways, one for the left lobe (segments 1-4) and one for the right lobe (segments 5-8) (Fig. 51.2).

Portal Vein Anatomy

Left Lobe of Liver

The H of the left lobe is visualized with an oblique, upwardly tilted subxiphoid view. The H is formed by the left portal vein, the branch entering segment 2, the umbilical portion of the left portal vein, and the branches to segments 3 and 4. To this recumbent H are attached two ligaments, the **ligamentum venosum,** also called the "lesser omentum" or the "hepatogastric ligament," and the **falciform ligament.** The ligamentum venosum separates segment 1 from segment 2. The falciform ligament is visible between the umbilical portion of the left portal vein[2] and the outer surface of the liver. It separates segment 3 from segment 4.

Segment 1, the caudate lobe, is bordered posteriorly by the IVC, laterally by the ligamentum venosum, and anteriorly by the left portal vein. Unlike the other segments of the liver, segment 1 may receive branches of the left and right portal veins. The portal veins to segment 1 are usually small and are rarely seen sonographically. The caudate lobe has one or more hepatic veins that drain directly into the IVC, separately from the three main hepatic veins.[3] This special vascularization is a distinctive characteristic of segment 1.

The portal vein leading to **segment 2** is a linear continuation of the left portal vein, completing the lower horizontal limb of the H. Segmental branches to segments 3 and 4 form the other horizontal limb. **Segments 2 and 3** are thus located to the left

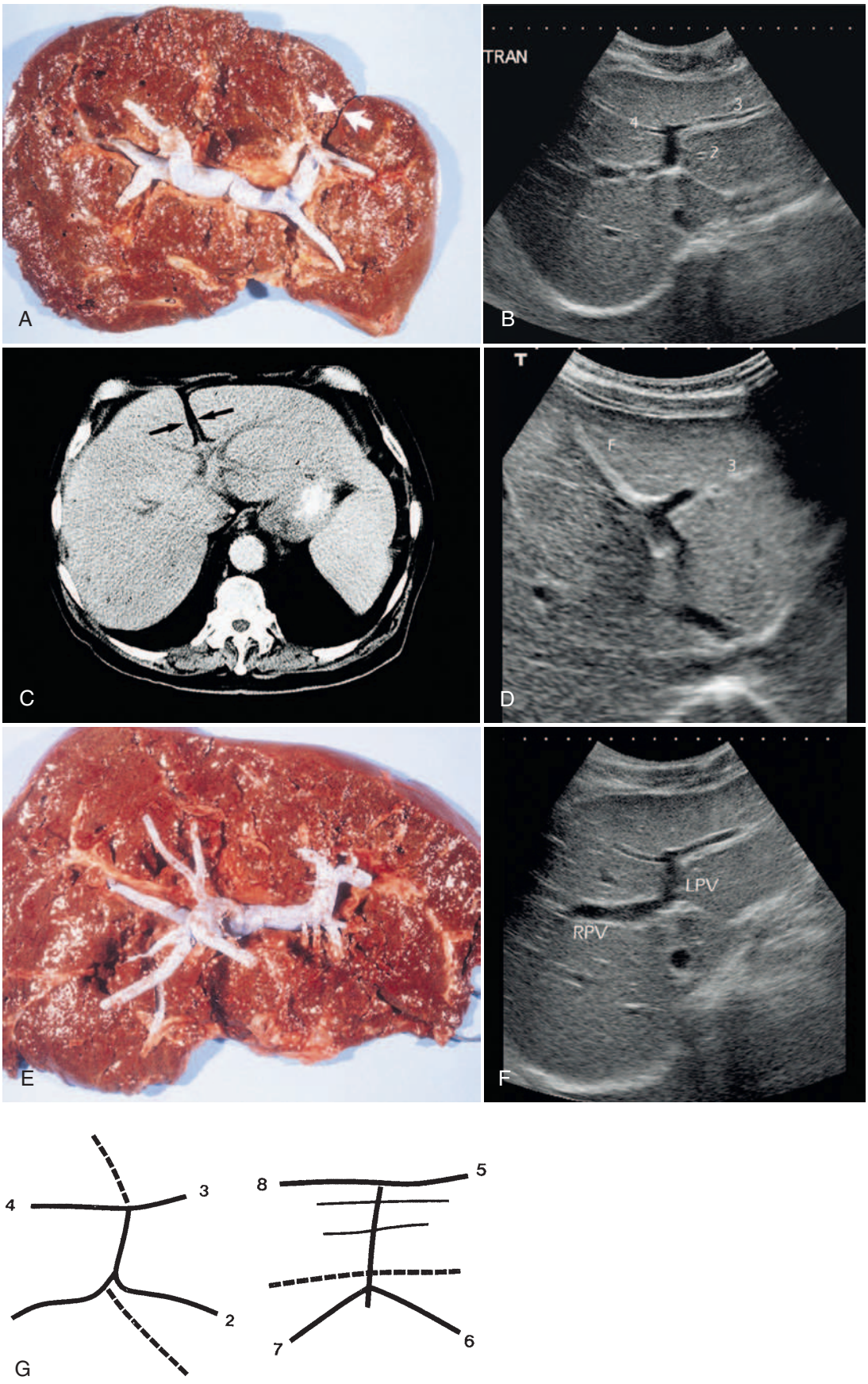

FIG. 51.2 Anatomy of Segmental Portal Veins. (A) Left hepatic lobe, shown on a dissected specimen (with pale-blue dye in portal vein); **(B)** on a subxiphoid transverse sonogram; **(C)** on computed tomography (CT) scan; and **(D)** on more cephalad transverse sonogram. The left portal vein, with branches to segments 2, 3, and 4, forms a horizontally placed H. The umbilical portion of the left portal vein forms the crossbar of the H. Falciform ligament (*arrows* in **[A]** and **[C]** and *F* in **[D]**) is an extension of the umbilical part of the left portal vein. **(E)** Right hepatic lobe of a dissected specimen, and **(F)** on a transverse sonogram obtained at the branch point of the main portal vein into right and left branches. **(G)** *Left* and *right,* Diagrams of the portal vein branches to the left and right lobes. Portal vein branches to segments 5 through 8 and 6 and 7 form the main limbs of the H, and the right portal vein forms its crossbar. Once again, the H is turned horizontally. (With permission from Bismuth H. Surgical anatomy and anatomical surgery of the liver. World J Surg. 1982;6[1]:3-9.[1])

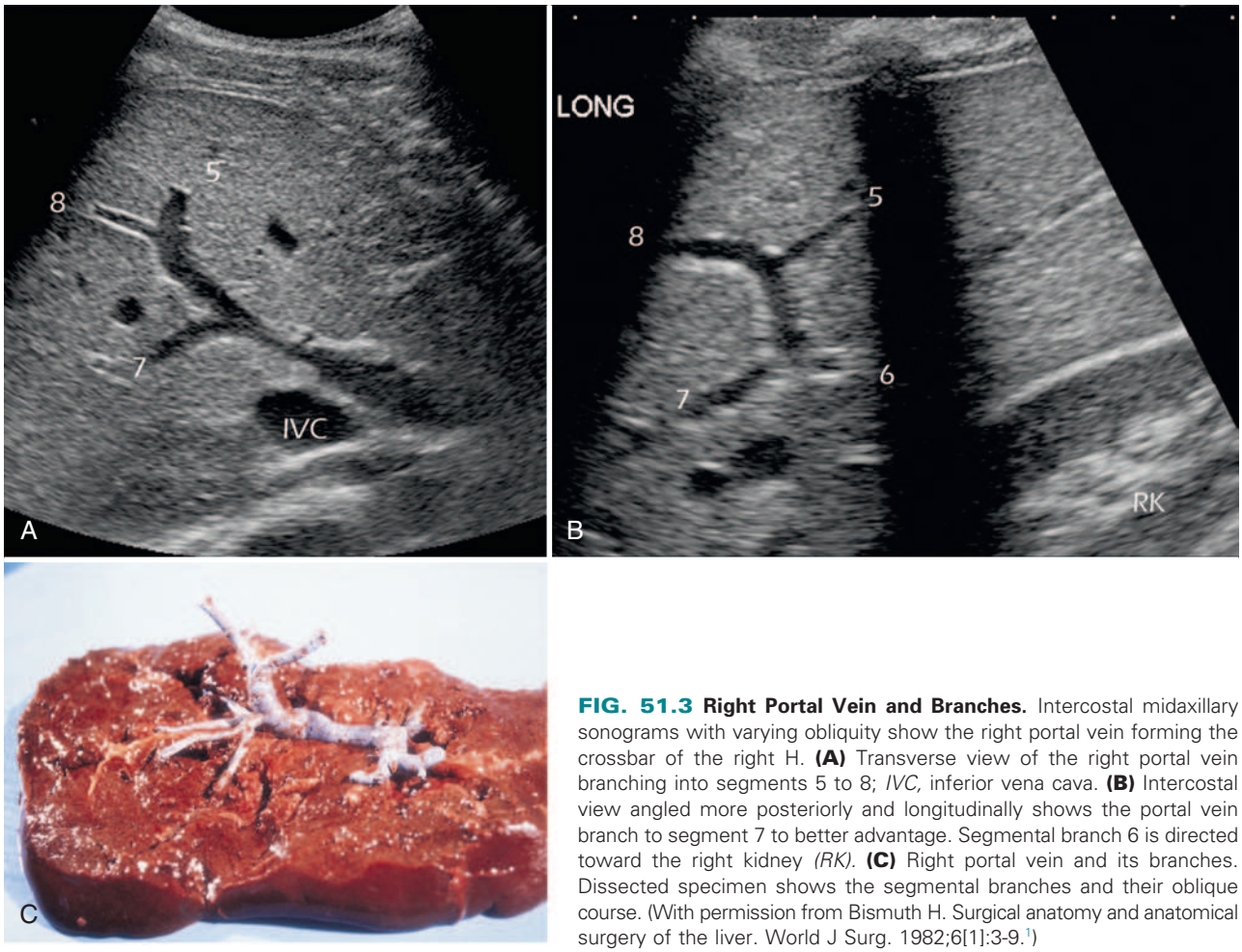

FIG. 51.3 Right Portal Vein and Branches. Intercostal midaxillary sonograms with varying obliquity show the right portal vein forming the crossbar of the right H. **(A)** Transverse view of the right portal vein branching into segments 5 to 8; *IVC,* inferior vena cava. **(B)** Intercostal view angled more posteriorly and longitudinally shows the portal vein branch to segment 7 to better advantage. Segmental branch 6 is directed toward the right kidney *(RK).* **(C)** Right portal vein and its branches. Dissected specimen shows the segmental branches and their oblique course. (With permission from Bismuth H. Surgical anatomy and anatomical surgery of the liver. World J Surg. 1982;6[1]:3-9.[1])

of the umbilical portion of the left portal vein, the ligamentum venosum, and the falciform ligament. **Segment 4,** the **quadrate lobe,** is situated around the right anterior limb of the portal venous H, to the right of the umbilical portion of the left portal vein and the falciform ligament. Segment 4 is separated from segment 5 by the main hepatic fissure and from segments 5 and 8 by the middle hepatic vein. The quadrate lobe is separated from segment 1 by the left portal vein.

Right Lobe of Liver

The right portal vein and its branches are best seen with a sagittal or oblique midaxillary intercostal approach. In some patients a subcostal approach is also useful. The right portal vein follows an oblique or vertical course, directed anteriorly.

The branches leading to the segments of the right lobe of the liver are also distributed in the shape of a sideways H. The right portal vein forms the crossbar of the H. The branches to segments 5 and 8 form the upper limb of the H, and the branches to segments 6 and 7 form its lower portion. The branches of segments 6 and 7 are more obliquely oriented, and the transducer should be rotated slightly upward for segment 7 and downward in the direction of the right kidney for segment 6.

The middle hepatic vein separates segments 5 and 8 from segment 4. The right hepatic vein separates segments 5 and 8 from segments 6 and 7 (Fig. 51.3). **Segment 5** is bordered medially by the gallbladder and the middle hepatic vein and laterally by the right hepatic vein. The right portal vein serves as a landmark for the separation of segment 5 from segment 8. Segment 8 is separated from segment 7 by the right hepatic vein and from segment 4 by the middle hepatic vein.

Segments 6 and 7 are separated from segments 5 and 8 by the right hepatic vein. **Segment 6** is the part of the liver closest to the kidney; its lateral border is the rib cage. **Segment 7** is separated from segment 8 by the right hepatic vein and is bordered laterally by the rib cage and cephalically by the dome of the diaphragm.

Hepatic Vein Anatomy

When seen with an oblique coronal subxiphoid view, the three hepatic veins form a W, with its base on the IVC. The left and middle hepatic veins join the left anterior part of the IVC (Fig. 51.4). The hepatic veins separate the following segments: the **left hepatic vein** separates segment 2 from segment 3; the **middle hepatic vein** separates segment 4 from segments 5 and

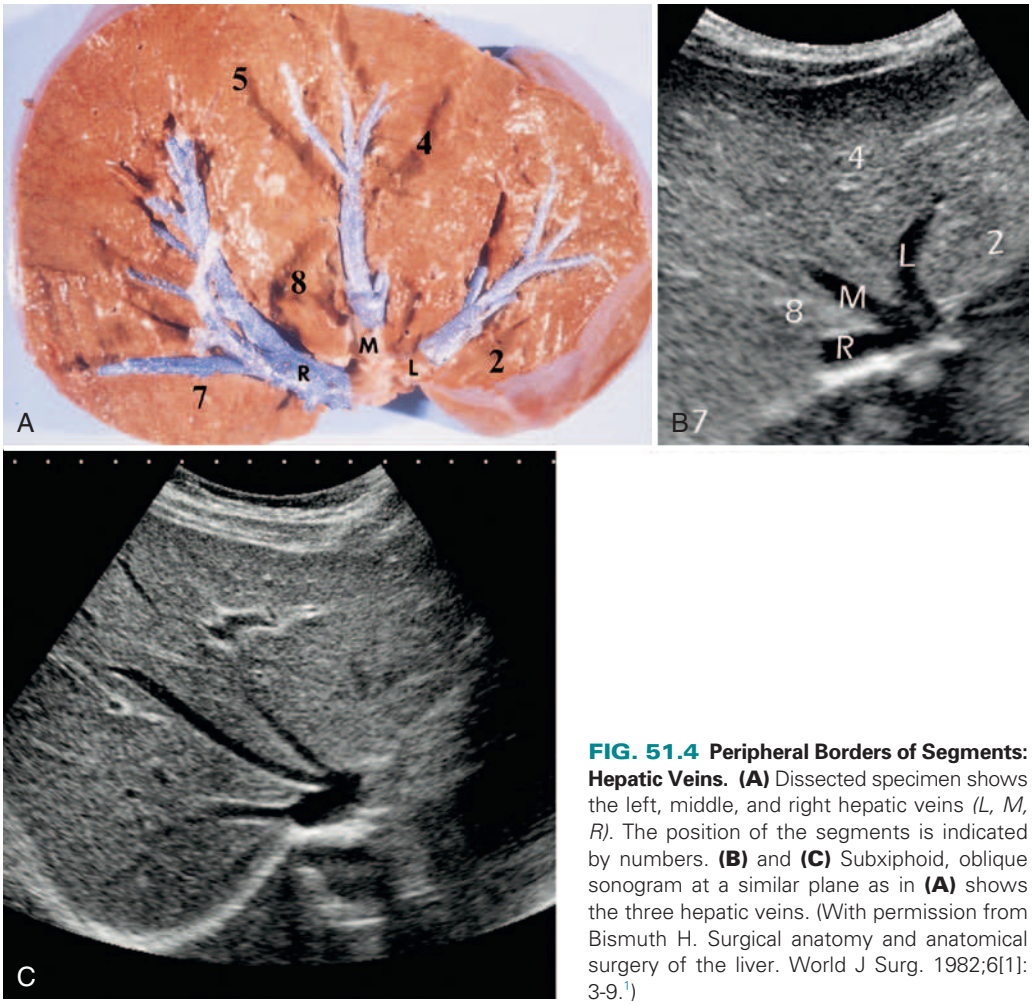

FIG. 51.4 Peripheral Borders of Segments: Hepatic Veins. (A) Dissected specimen shows the left, middle, and right hepatic veins *(L, M, R)*. The position of the segments is indicated by numbers. **(B)** and **(C)** Subxiphoid, oblique sonogram at a similar plane as in **(A)** shows the three hepatic veins. (With permission from Bismuth H. Surgical anatomy and anatomical surgery of the liver. World J Surg. 1982;6[1]: 3-9.[1])

8; and the **right hepatic vein** separates segments 5 and 8 from segments 6 and 7. With the oblique subxiphoid view, the right portal vein is seen en face, which helps separate the superficial segment 5 from the more deeply situated segment 8.

The sonographic examination of the child's liver should include visualization of the **right and left portal veins** and their segmental branches, as well as the hepatic veins. Not only can focal lesions be identified and accurately localized, but thrombosis, compression, or tumor invasion of vessels can be outlined. Doppler sonography is added when the presence and direction of blood flow within these veins need to be assessed. Exploring the liver through its vessels is an excellent way to ensure that the sonographic examination is complete and not just an arbitrary glance at this otherwise homogeneous organ with variable contours and few landmarks except for its veins. Because the branches of the hepatic artery and the bile ducts are neighbors of the portal veins, the examination of the lobar and segmental portal veins ensures a complete assessment of these structures as well.

NEONATAL JAUNDICE

The cause of persistent jaundice in the newborn is often difficult to define because clinical and laboratory features may be similar in hepatocellular and obstructive jaundice. If bile obstruction, biliary atresia, or metabolic diseases such as galactosemia and tyrosinemia are to be treated effectively with surgery or specific diet and medication, the diagnosis must be made early, in the first 2 to 3 months, before irreversible cirrhosis has occurred.

Sonography plays an important role in defining causes of **extrahepatic obstruction to bile flow** that may be effectively treated with early surgery, including **choledochal cyst, biliary atresia,** and **spontaneous perforation of the bile ducts.** (Other causes of bile duct obstruction, such as cholelithiasis, tumors of the bile ducts or pancreas, and congenital stenosis of the common bile duct (CBD), usually appear later in childhood.) Intrahepatic causes of neonatal jaundice include **hepatitis** (bacterial, viral, or parasitic) and **metabolic diseases** (e.g., galactosemia, tyrosinemia, fructose intolerance, α_1-antitrypsin deficiency, cystic fibrosis, paucity of interlobular bile ducts, North American Indian cirrhosis). **Systemic diseases** that cause cholestasis include heart failure, shock, sepsis, neonatal lupus, histiocytosis, and severe hemolytic disease.

The infant with jaundice is usually screened with sonography. When dilation of the bile ducts is found, percutaneous cholangiography or cholecystography may be performed if the cause

Causes of Neonatal Jaundice

OBSTRUCTION OF BILE DUCTS
Choledochal cyst
Biliary atresia
Spontaneous perforation of the bile ducts
Paucity of interlobular bile ducts (Alagille syndrome)

HEPATOCELLULAR DAMAGE (CHOLESTASIS)
Hepatitis
Bacterial
Syphilis
Listeria
Staphylococcus

Viral
Hepatitis B
Hepatitis C
Cytomegalovirus
Human immunodeficiency virus
Rubella
Herpesvirus
Epstein-Barr virus

Parasitic
Toxoplasma

Systemic Diseases
Shock
Sepsis
Heart failure
Neonatal lupus
Histiocytosis
Hemolytic diseases

METABOLIC LIVER DISEASES
Galactosemia
Tyrosinemia
Fructose intolerance
α_1-Antitrypsin deficiency
Cystic fibrosis

and anatomy of the obstruction are unclear. If sonography fails to outline an anatomic abnormality, hepatobiliary scintigraphy may define patency of the CBD, unless hepatocyte damage is extensive. If no radionuclide reaches the gut, liver biopsy is typically performed. Both scintigraphy and the sonographic search for the gallbladder are enhanced by the bile-stimulating effect of phenobarbital administered for 3 to 5 days before the test.[4] The **triangular cord sign,** an echogenic cone-shaped density just cranial to the portal vein bifurcation on longitudinal or transverse scans, is highly predictive of biliary atresia. An **absent or small gallbladder** (<1.5 cm in length) coupled with the triangular cord sign is even more specific for the diagnosis.[5]

Choledochal Cyst

Dilation of varying lengths and severity of the CBD, termed "choledochal cyst," usually manifests as jaundice in infancy,

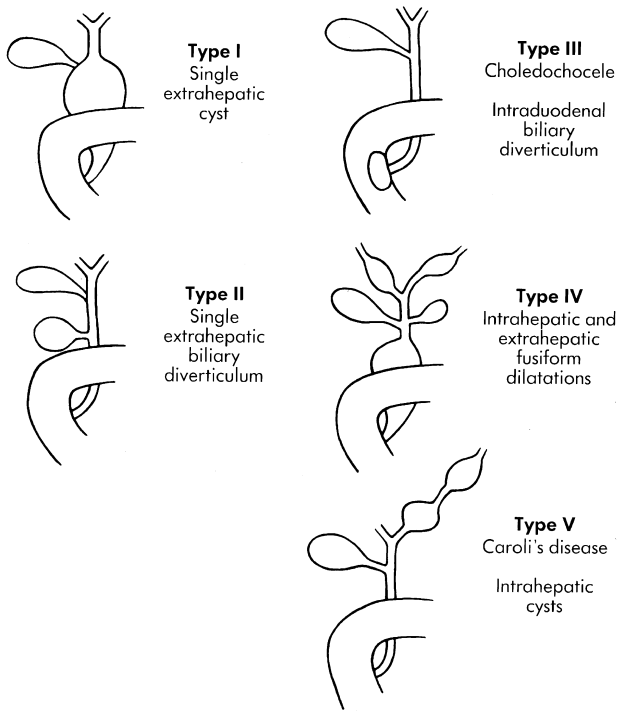

FIG. 51.5 Choledochal Cyst Classification.

clinically mimicking neonatal hepatitis and biliary atresia (Fig. 51.5). Todani's classification describes five types.[6] Type I, **cylindrical or saccular dilation of the common bile duct,** is most common (80%-90%) and is thought to be caused by an abnormal insertion of the CBD into the pancreatic duct, forming a common channel and facilitating reflux of enzymes into the CBD, with consequent inflammation. Because choledochal cysts have been detected in 15-week gestational age fetuses, when amylase is not yet present, and because surgically treated cysts in the newborn period show minimal inflammation, there must be causative factors (as yet unknown) other than the common-channel theory. Two rare but well-documented causes of bile duct dilation (choledochal cyst) in the newborn are localized atresia of the CBD and multiple intestinal atresias in which the CBD empties into a blind pouch of bowel.[7] A choledochal cyst manifesting later in childhood may have a different pathogenesis. It is usually complicated by cholangitis and classically causes abdominal pain, obstructive jaundice, and fever. In some cases the cyst is palpable as a mass.

Choledochal cyst type II consists of one or more **diverticula** of the CBD (2% of cysts). **Choledochocele** (type III) is a dilation of the intraduodenal part of the CBD (1%-5%). **Multiple intrahepatic and extrahepatic cysts** make up type IV (10%), sometimes subcategorized into types IVa and IVb, which has only extrahepatic cysts. **Caroli disease** (type V) affects intrahepatic bile ducts.

Sonographic screening of the jaundiced infant shows one or several thin-walled cysts at the liver hilum or within the liver (choledochal cyst type I; Fig. 51.6). The gallbladder is identified separately. Dilation of intrahepatic ducts, as well as stones, may occur later as a result of bile stasis and cholangitis. Scintigraphy

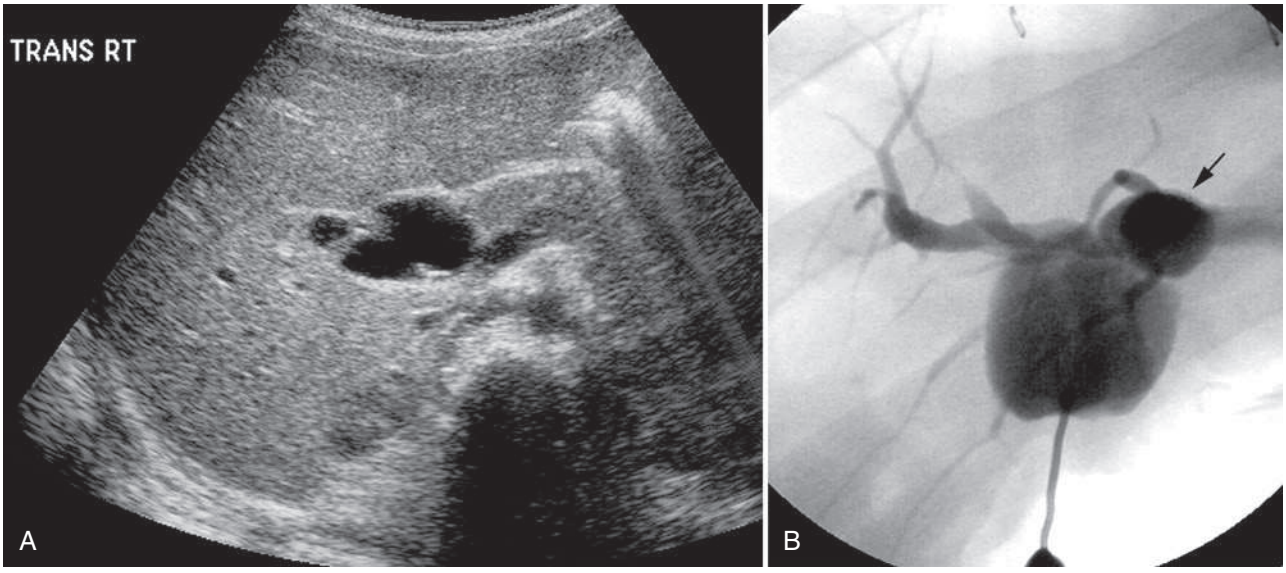

FIG. 51.6 Choledochal Cyst Type I in Infant With Jaundice. (A) Transverse sonogram. A large cyst that is the greatly dilated common bile duct is visible entering the pancreatic head. **(B)** Intraoperative cholangiogram shows injection of the gallbladder and filling of the choledochal cyst *(arrow).*

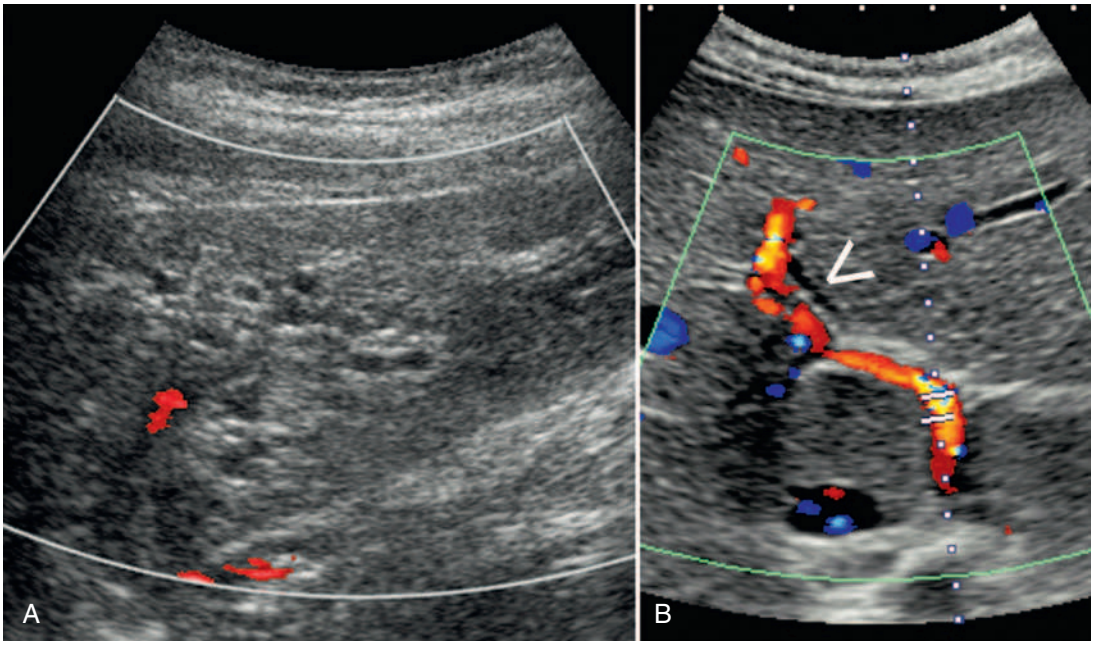

FIG. 51.7 Biliary Ductal Dilation. (A) Caroli disease, type V choledochal cyst. Longitudinal color Doppler image of the left lobe of the liver shows saccular dilation of bile ducts with thickened echogenic walls and few vessels in the deeper aspect of the liver. Cholangitis, caused by obstruction of the bile ducts or by ascending infection, leads to dilation of the intrahepatic and common bile ducts. **(B)** Central bile duct dilation on transverse sonogram in a different patient, with concentric smooth dilation of main intrahepatic duct *(arrowhead)* caused by distal common bile obstruction.

is used to document bile flow into the cyst, and percutaneous cholecystography/cholangiography or endoscopic retrograde cholangiopancreatography is performed if detailed mapping of the bile system is deemed necessary before surgery.

Caroli disease (type V choledochal cyst) consists of nonobstructive dilation of intrahepatic bile ducts[8,9] and is often associated with congenital hepatic fibrosis and autosomal recessive polycystic kidney disease.[10] The disease is caused by the arrest of or derangement in embryologic remodeling of ducts, resulting in segmental dilation. Patients tend to seek medical attention later than with other types of choledochal cysts, usually after cholangitis and stones have formed in childhood (Fig. 51.7). At sonography, Caroli disease has dilated ducts surrounding branches of the portal vein.[9] Sludge and stones are often visible within

the dilated ducts. Abscesses complicating cholangitis are seen as cavities with walls thicker than those of the ducts and filled with heterogeneous material. Polycystic kidneys, when present, are another clue to the diagnosis of Caroli disease; Caroli disease and autosomal recessive polycystic kidney disease may occur together because both are associated with mutation in the *PKHD1* gene.[11]

Spontaneous Rupture of Bile Duct

Rupture of the bile duct is rare. Rupture in newborns leads to jaundice, abdominal distention, and substantial morbidity. Because the site of rupture is usually the junction of the cystic duct and CBD, it is believed that a developmental weakness at this site leads to the rupture. The biliary system is undilated, but there are ascites and loculated fluid collections around the gallbladder. Although the condition was previously treated surgically, the recent trend is toward percutaneous drainage and conservative management.[12]

Paucity of Interlobular Bile Ducts and Alagille Syndrome

Manifesting with chronic cholestasis, usually within the first 3 months of life, ductal paucity and **arteriohepatic dysplasia** (Alagille syndrome [ALGS]) are diagnosed histologically by noting a reduced number of interlobular bile ducts compared with the total number of portal areas. Because of cholestasis, the gallbladder may be very small (disuse). The CBD is normal (Video 51.1). The liver is usually enlarged, especially the left lobe. Portal hypertension ensues, with splenomegaly and esophageal varices. In children with ALGS, paucity of bile ducts is associated with a characteristic facies, pulmonary artery stenosis, butterfly vertebrae, segmentation anomalies, and, infrequently, renal abnormalities (renal tubular acidosis).[13] ALGS is inherited as an autosomal dominant disease with variable penetrance, most commonly due to mutation in *JAG1* (ALGS type 1), but in a small proportion of cases mutation in *NOTCH2* (ALGS type 2).[14]

Biliary Atresia

The incidence of biliary atresia varies from 1 in 8000 to 1 in 10,000 births. Boys and girls are equally affected. Biliary cirrhosis occurs early, often in the first weeks after birth. Biliary atresia is characterized by absence or obliteration of the lumen of the extrahepatic and intrahepatic bile ducts (Fig. 51.8). It is associated with the **polysplenia syndrome** (biliary atresia, situs inversus, polysplenia, symmetrical liver, interrupted IVC, preduodenal portal vein) in about 20% of patients,[15] as well as with **trisomy 17 or 18.** Because the disease is extremely rare, and because the pancreatic duct, which develops with the bile ducts, is normal in affected children, biliary atresia likely develops after the bile ducts have formed. The etiology of biliary atresia is still unclear, although there is evidence pointing to viral, toxic, and multiple genetic factors. An in utero insult to the hepatobiliary system may result in a progressive sclerosis of the extrahepatic and intrahepatic bile ducts. In addition, certain drugs (e.g., carbamazepine) have been associated with biliary atresia.[16]

Jaundice classically develops gradually, 2 to 3 weeks after birth. The diagnosis is readily made if there are radiologic or sonographic signs of the polysplenia syndrome (see Fig. 51.8C-G). Because the flow of bile is interrupted, the gallbladder is typically very small (20%) or absent (80%).[15] After having the infant fast for 4 to 6 hours, a specific search with a high-frequency transducer will demonstrate a very small gallbladder **(microgallbladder)** in about 20% of patients. When the gallbladder is visible, the "ghost triad" appearance has been reported to help in making the correct diagnosis of biliary atresia.[17] The **ghost triad** consists of gallbladder length less than 1.9 cm, irregular or incomplete mucosal lining, and irregular or lobular contour. The echogenic fibrotic remnant of the CBD seen adjacent to the portal vein has been called the **triangular cord sign.** The combination of a small gallbladder, less than 1.5 cm in length, and the triangular cord sign are very specific for the diagnosis of biliary atresia.[5] Any intrahepatic bile duct remnants may dilate and be visible at sonography as bile duct dilation or small cysts. In addition, the cholangitis that complicates biliary atresia may result in cystic areas within the liver.[18]

Surgical treatment creates communication between a loop of jejunum (transposed to the liver after a Roux-en-Y anastomosis) and any patent bile "ductules" at the liver hilum. This is the classic hepatoportoenterostomy described by Kasai in 1959.[19] Even if there is no mucosal contact between intestine and the bile ducts, the procedure permits bile drainage, with complete clinical remission in 30% and partial drainage in 30% of affected children. The prognosis becomes much more guarded when the Kasai procedure is delayed to more than 60 days after birth.[20] Despite successful Kasai procedures, 75% of patients require liver transplantation before age 20 years.[21] Biliary atresia remains the most common reason for liver transplant in pediatric patients.

Neonatal Hepatitis

Defined as an infection of the liver occurring before the age of 3 months, neonatal hepatitis is now considered an entity distinct from toxic or metabolic diseases affecting the neonate. The causative agent (bacterium, virus, or parasite) reaches the liver through the placenta, via the vagina from infected maternal secretions, or through catheters or blood transfusions. Transplacental infection occurs most readily during the third trimester, and syphilis, *Toxoplasma,* rubella, and cytomegalovirus (CMV) are the most common agents[16] (Fig. 51.9, Video 51.2).

Neonatal bacterial hepatitis is usually secondary to upward spread of organisms from the vagina, infecting endometrium, placenta, and amniotic fluid. In twin pregnancies, the fetus nearest the cervix is more frequently affected. *Listeria* and *Escherichia coli* are the usual organisms. During vaginal delivery, direct contact with herpesvirus, CMV, human immunodeficiency virus (HIV), and *Listeria* organisms may lead to hepatitis. Blood transfusions may contain hepatitis virus B or C, CMV, Epstein-Barr virus, and HIV. Infected umbilical vein catheterization usually results in bacterial hepatitis or abscesses.[16]

With the exception of diffuse hepatomegaly, there are no specific sonographic signs of hepatitis, unless abscesses (usually

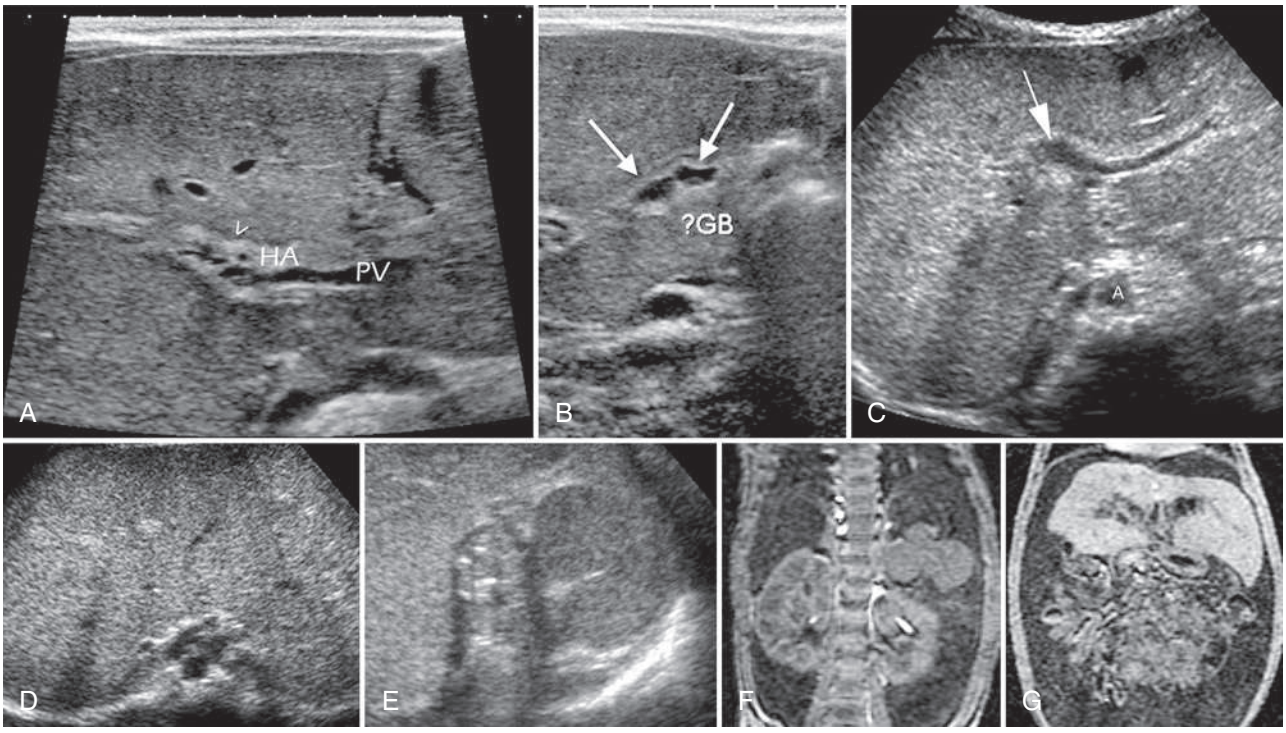

FIG. 51.8 Biliary Atresia Spectrum. (A) Transverse sonogram near the porta hepatis. **Triangular cord sign** is linear, echogenic fibrous tissue *(arrowhead)* anterior to a normal portal vein *(PV)* and hepatic artery *(HA)*. Failure to visualize the common bile duct in a newborn with jaundice is strongly suggestive of biliary atresia. **(B) Gallbladder ghost triad:** small gallbladder *(arrows),* irregular and incomplete echogenic lining, and indistinct lobular wall. Highly specific finding for biliary atresia. **(C)** to **(G) Polysplenia syndrome** in a different patient, with preduodenal portal vein and interruption of inferior vena cava (IVC). **(C)** Transverse liver sonogram shows aorta *(A)* anterior and left of the spine in newborn girl. The bifurcation of the portal vein *(arrow)* is more anterior than usual. **(D)** Right transverse sonogram shows liver extending across the entire upper abdomen. IVC is missing on both views. **(E)** In left upper quadrant, several small spleens are present. No gallbladder was found in this patient with biliary atresia. **(F)** Coronal magnetic resonance spoiled gradient echo (SPGR) images performed for ascites and elevated liver enzymes shows polysplenia. **(G)** Transverse liver with anteriorly positioned portal vein several months after Kasai procedure.

bacterial in origin) occur.[22,23] The gallbladder wall may be thickened, probably from hypoalbuminemia. Dystrophic calcifications in the hepatic parenchyma may be seen.

Neonatal Jaundice and Urinary Tract Infection or Sepsis

The association of jaundice with urinary tract infection or sepsis occurs more often in male than female newborns. Jaundice, hepatomegaly, and vomiting are common clinical signs. Urinary tract symptoms are uncommon, as are shock and fever. A thorough examination of the kidneys, ureters, and bladder should therefore accompany sonography of the liver in the infant with jaundice. Similarly, the diaphragm and lung bases should be examined to look for pleural effusions and pneumonia, which may be accompanied by sepsis and jaundice in the newborn.

Inborn Errors of Metabolism

Because these disorders cause liver damage in the newborn, some rapidly destroying the liver if untreated, and because several can be treated effectively with diet or drugs once diagnosed, pediatricians and radiologists should be well acquainted with inborn errors of metabolism. Liver damage is caused by storage of a hepatotoxic metabolite or by absence of an essential enzyme that impairs the detoxification process of the liver.

Steatosis is especially prominent in the **glycogen storage diseases, galactosemia, tyrosinemia,** and **cystic fibrosis. Cirrhosis** eventually develops in all the diseases that cause liver damage, and portal hypertension then follows. The risk of **hepatocellular carcinoma** is significantly increased in **α_1-antitrypsin deficiency,** in **tyrosinemia,** and in **glycogen storage disease type I. Liver adenomas** also develop in the last two entities, as does **renal tubular disease,** which is usually characterized by acidosis and nephrocalcinosis.[16]

Tyrosinemia is best treated by transplantation. Until drug therapy became available for the treatment of the acute neurologic crises in infants with acute tyrosinemia, transplantation was performed as a lifesaving procedure as soon as surgically feasible. Currently, transplantation is done once liver nodules appear because hepatocellular carcinoma develops in about 30% of children with tyrosinemia who survive the neonatal period. A review of livers dissected at liver transplantation found that preoperative sonograms and computed tomography (CT) scans were not accurate in distinguishing regeneration nodules, adenomas, and carcinomas, nor was alpha-fetoprotein (AFP) analysis[24] (Fig. 51.10).

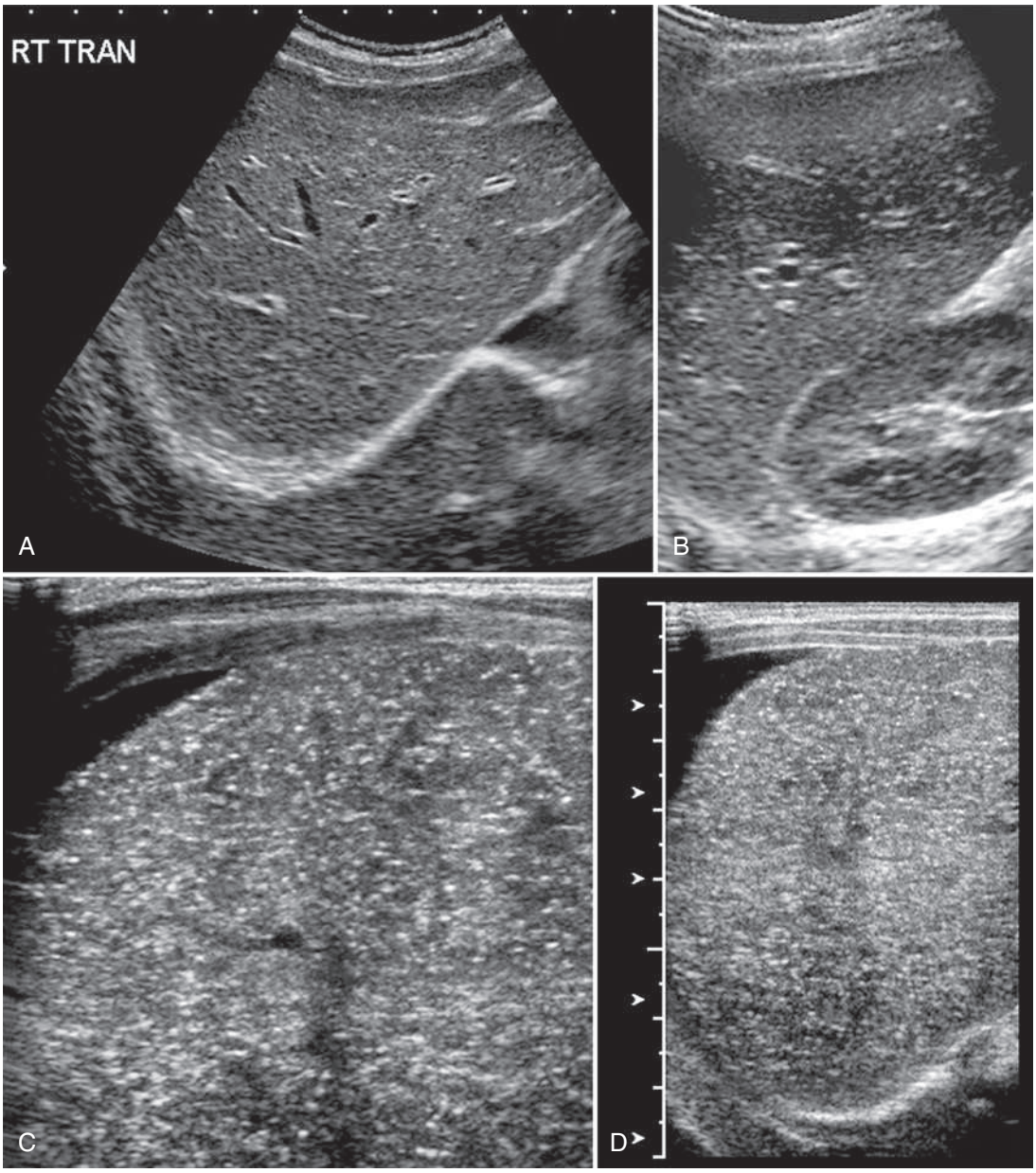

FIG. 51.9 Hepatitis. (A) Transverse sonogram in a teenage boy with acute hepatitis shows echogenic portal triads and hypoechoic parenchyma. **(B)** Longitudinal image in same patient showing hepatic hypoechoic echotexture similar to adjacent right kidney. **(C)** Transverse magnified sonogram and **(D)** conventional linear array image show **congenital herpes infection** in an infant with dystrophic calcification throughout the liver. See also Video 51.2.

Inborn Errors of Metabolism

HEPATOCYTE INJURY CONSISTENTLY
Glycogen storage disease type IV
Galactosemia
Fructose intolerance
Tyrosinemia
Wolman disease
Zellweger syndrome
Neonatal iron storage disease
Wilson disease

HEPATOCYTE INJURY SOMETIMES
α_1-Antitrypsin deficiency
Cystic fibrosis
Glycogen storage disease (I and III)

NO HEPATOCYTE DAMAGE (STORE METABOLITES)
Mucopolysaccharidoses
Gaucher disease

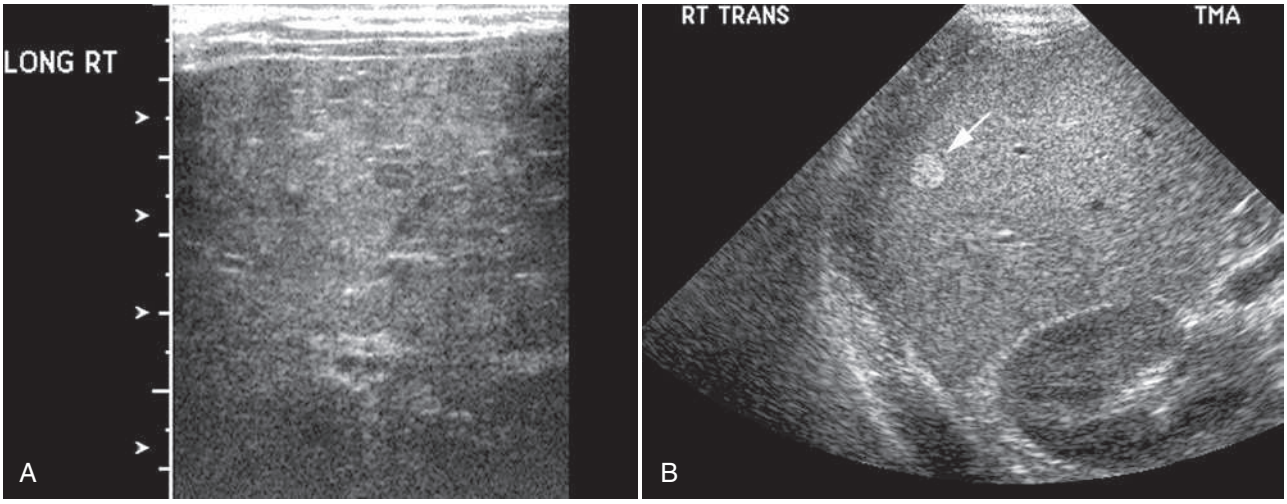

FIG. 51.10 Tyrosinemia and Glycogen Storage Disease (Type I, von Gierke Disease). (A) Longitudinal sonogram shows heterogeneous echotexture, likely a combination of regenerating nodules and adenomas of the liver, in a patient with tyrosinemia awaiting liver transplant. **(B) Echogenic adenoma** *(arrow)* in the liver of another child with glycogen storage disease type I. Follow-up was done because of this patient's increased risk of hepatocellular carcinoma.

The sonographic examination of children with possible metabolic disease includes a careful analysis of liver size and architecture, searching for steatosis, cirrhosis, and nodules; an analysis of renal architecture, searching for increased size and nephrocalcinosis; and a Doppler examination of the abdomen searching for signs of portal hypertension.

STEATOSIS

Fat accumulates in hepatocytes after cellular damage **(fatty degeneration),** through the overloading of previously healthy cells with excess fat **(fatty infiltration),** or in certain enzyme deficiency syndromes, through the inability of fat to be mobilized out of the liver. Drugs (acetylsalicylic acid, tetracycline, valproate, warfarin [Coumadin]) and toxins (aflatoxin, hypoglycine) as well as alcohol abuse lead to fatty degeneration of liver cells. Steatosis is also seen in metabolic liver disorders such as galactosemia, fructose intolerance, and Reye syndrome. Obesity (Video 51.3), corticosteroid therapy, hyperlipidemia, and diabetes are examples of increased fat mobilization and its entry into the liver. In malnutrition, nephrotic syndrome, and cystic fibrosis, not only does excess fat enter the liver, but mobilization of fat out of the hepatocyte is deficient as well. When parenteral nutrition does not include lipids, steatosis results from a deficiency of essential fatty acids. Most inherited disorders of the liver mentioned previously involve an enzyme deficiency and result in steatosis.

Fatty changes are reversible, may be diffuse or focal, and are often detected on ultrasonography before clinically suspected.[25] On sonography, areas of steatosis are highly echogenic, blurring vessel walls. The nearby kidney cortex appears much less echogenic. When focal, steatosis usually has smooth, geometric, or fingerlike borders[26] (Fig. 51.11). Intervening normal liver may appear hypoechogenic and masquerade as mass lesions (metastases or abscesses), especially if the ultrasound gain is adjusted by using the fatty areas as a normal reference. Segments 4 and 5 are often spared in steatosis, perhaps because of favorable blood supply by the gallbladder and its vessels.[27] Nodules of steatosis may mimic metastases on CT. Areas of abnormal echotexture on sonographic studies can be further evaluated with CT; the two modalities are complementary in this situation. Ultrasound grading of steatosis is subjective; magnetic resonance spectroscopy can reliably quantify fat content. Magnetic resonance imaging (MRI) sequences and various MRI contrast agents can characterize focal lesions in the liver. Despite sophisticated imaging, occasionally biopsy may be necessary.

FIG. 51.11 Fatty Infiltration of Liver (Steatosis) in Patient With Cystic Fibrosis. Sagittal view shows increased hepatic echotexture, with some sparing posteriorly. The cortex of the right kidney is much less echogenic than the fatty liver.

Causes of Steatosis

Drugs
- Acetylsalicylic acid
- Tetracycline
- Valproate (and other antiepileptic medications)
- Warfarin (Coumadin)
- Toxins
- Aflatoxin
- Hypoglycine

Alcohol abuse
Metabolic liver disease
- Galactosemia
- Fructose intolerance
- Reye syndrome

Obesity
Corticosteroid therapy
Hyperlipidemia
Diabetes
Malnutrition
Nephrotic syndrome
Cystic fibrosis

CIRRHOSIS

The usual forms of cirrhosis in childhood are **biliary** and **post necrotic.** Morphologically, the cirrhotic liver consists of regenerating nodules devoid of central veins and surrounded by variable amounts of connective tissue. Hepatic architecture is sufficiently distorted to disturb hepatic circulation and hepatocellular function. Increased resistance to blood flow through the liver leads to portal hypertension.

The sonographic appearance of the liver depends on the severity of the cirrhosis. With progressive replacement of hepatocytes by fibrous tissue, the liver attenuates sound increasingly, and sound penetration of the liver, even with low-frequency (2 or 3 MHz) transducers, becomes difficult. The macronodules of advanced cirrhosis become visible sonographically at the surface of the liver (contrasted to the neighboring lesser omentum, peritoneum, or ascites, if present) or within its substance (nodular architecture, increased hyperechogenic fibrous tissue around portal vein branches and the ligamentum teres).[26] The caudate lobe is often prominent[28] (Fig. 51.12). Parts of segment 4 of the right lobe of the liver may atrophy in advanced disease.

CHOLELITHIASIS

Gallstones are less common in children than in adults and are usually related to an associated disease. Their composition can be mixed or of calcium bilirubinate. The "adult" cholesterol stone is rare except in children with cystic fibrosis.[29] Gallstones are mobile and hyperechogenic, and they cast acoustic shadows only if they are of appropriate size and composition.

In some children, especially those receiving total parenteral nutrition, thick bile can be observed to form **sludge,** loosely formed "sludge balls" or **"tumefactive sludge,"** and finally **stones,** when serial sonograms are performed over several weeks (Fig. 51.13). **Stasis of bile flow** is the probable cause of sludge and stone formation, also seen in utero and in premature infants and usually regressing spontaneously.[30]

Gallbladder wall thickening occurs in children with acute hepatitis, hypoalbuminemia, obstructed hepatic venous return, and ascites.[22,23] The classic signs of impacted gallstone, thick gallbladder wall, and fluid around the gallbladder seen in adults with **acute cholecystitis** are rare in children. The gallbladder becomes dilated and rounded (rather than the normal oval shape) in fasting children (especially infants receiving total parenteral nutrition), children with sepsis (especially streptococcal), and those in the acute phase of **Kawasaki disease.** When distended, the gallbladder may become tender and painful. It heals with the underlying disease. **Acalculous cholecystitis** in children is rare and should be diagnosed only if no disease causing gallbladder distention or wall edema is found.[31]

Diseases Associated With Gallstones in Children

HEMATOPOIETIC
Hemolytic anemias or hemolysis (artificial heart valve)
Rh incompatibility
Blood transfusions
Sickle cell anemia

GASTROINTESTINAL
Cystic fibrosis
Bile duct anomalies
Ileal dysfunction (Crohn disease, short bowel)
Total parenteral nutrition
Metabolic liver diseases

OTHER
Immobilization (scoliosis surgery)
Dehydration
Obesity
Sepsis
Oral contraceptives

LIVER TUMORS

Identification

It is sometimes difficult to define the origin of an abdominal mass, especially when it is large. The following questions are helpful in tracing a mass to hepatic origin:

- **Vascular anatomy:** Can a feeding hepatic vessel be identified by means of Doppler sonography? Are segmental portal veins displaced or invaded by the tumor[32]? What liver segments are involved? Is the main hepatic artery enlarged? (This usually signals the presence of a highly vascular hemangioendothelioma.)
- **Biliary anatomy:** Are the bile ducts normal? Has the gallbladder been identified?
- **Anatomy of the abdomen:** Does the mass move with the liver during respiration? Is the liver parenchyma normal or

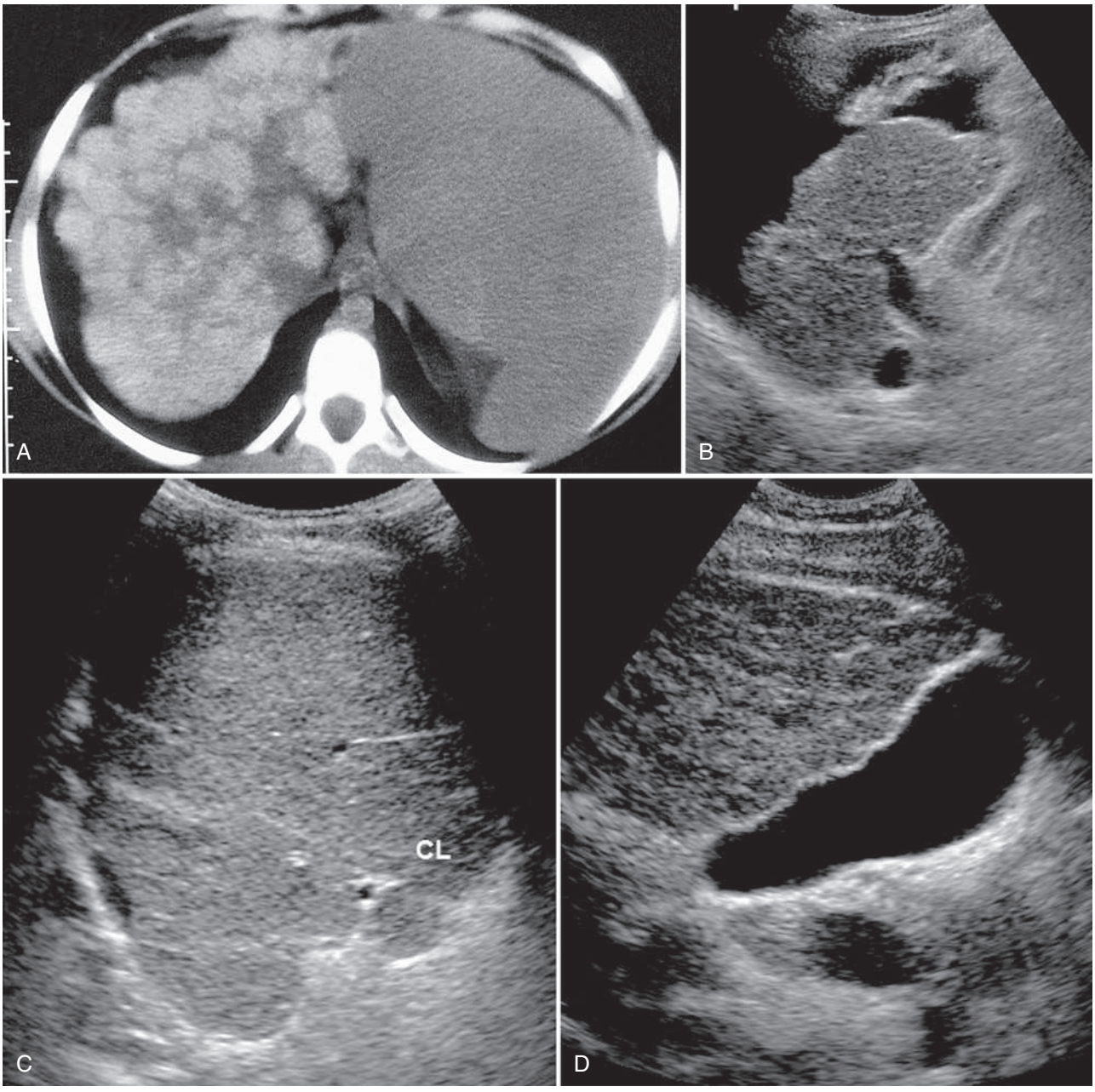

FIG. 51.12 Cirrhosis. (A) Computed tomography (CT) scan of the upper abdomen in a 6-year-old child shows a small liver with multiple nodules visible both along the cortex and within the liver. Microscopy of the native liver after transplantation showed regenerating nodules and severe cirrhosis (portal hypertension). **(B)** Sonogram of another child shows macronodules of cirrhosis at the surface of the liver outlined by ascitic fluid. **(C)** Sonogram in a teenager with cystic fibrosis and cirrhosis shows diffusely increased echotexture of the liver. Note the nodular lateral surface of the liver and the larger caudate lobe *(CL)*. **(D)** Nodular contour may also be appreciated against a fluid-filled gallbladder margin in patients without ascites. This 17-year-old patient had autoimmune hepatitis and developing cirrhosis.

cirrhotic? Is there ascitic fluid available for cytology? Is there another abdominal, retroperitoneal, para-aortic, or pelvic mass that could be a primary tumor?

Benign Liver Tumors

About 40% of primary liver tumors in children are benign. Hemangiomas are by far the most common. Mesenchymal hamartomas, adenomas, and focal nodular hyperplasia together constitute about one-half of benign liver tumors in the child.[33]

Hemangiomas

Hemangiomas are vascular, mesenchymal masses that may be focal (solitary), multifocal, or diffuse. All are characterized initially by active endothelial growth (angiogenesis). During this stage, the tumor is highly vascular and may cause sufficient arteriovenous (AV) shunting to result in high-output heart failure. When associated with hydrops or congestive heart failure and thrombocytopenia, this lesion may be called **neonatal hemangiomatosis.** Hemangiomas in the liver are often associated with cutaneous

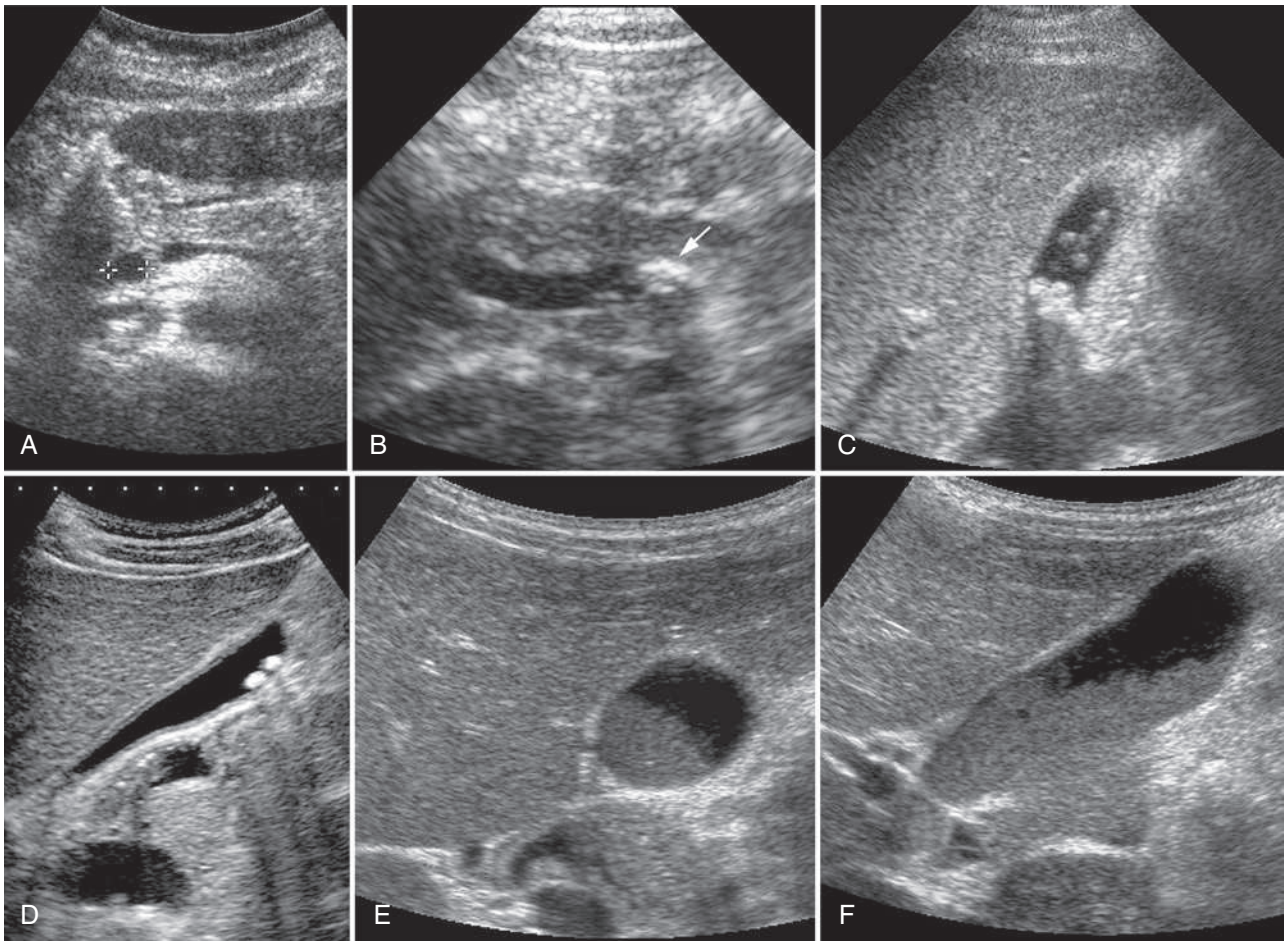

FIG. 51.13 Cholelithiasis. (A) Transverse and **(B)** longitudinal views of a dilated common bile duct (between cursors in **[A]**) containing an echogenic shadowing stone (stone seen only on **[B]** *[arrow]*) in a teenager with acute right upper quadrant pain. **(C)** and **(D)** Multiple echogenic, shadowing gallstones in two other patients, with hemolytic anemia. Note that the stones show variable degrees of shadowing, likely related to their mineral composition. **(E)** and **(F)** Gallbladder sludge without stones or gallbladder wall thickening in a patient receiving total parenteral nutrition.

Liver Masses in Children

SOLID
Hemangioendothelioma (single or multiple)
Adenoma, hamartoma
Focal nodular hyperplasia
Regeneration nodules in cirrhosis
Hepatoblastoma
Hepatocellular carcinoma
Biliary rhabdomyosarcoma (can be cystic)
Lymphoma
Metastasis

CYSTS IN OR NEAR THE LIVER
Congenital cysts
Congenital hepatic fibrosis
Choledochal cysts
Duodenal duplication cyst
Hydatid cyst ("sand," daughter cysts)
Caroli disease
Hamartoma

hemangiomas as well (Fig. 51.14, Video 51.4, Video 51.5). Solitary hemangiomas are now recognized to be the hepatic form of **cutaneous rapidly involuting congenital hemangiomas** (RICH), which are fully developed at birth and demonstrate an accelerated involution over the first year of life. Multifocal and diffuse hemangiomas are still actively proliferating lesions, also known as **infantile hemangiomas.** Diffuse hemangiomas are more likely to have complications of hemorrhage, cardiac compromise, hepatic failure, hypothyroidism, or coagulopathy, and may be treated with propranolol, embolization, resection, or transplant. Steroids and chemotherapy are less frequently used.[34,35] As a typical solitary hemangioma matures, vessel growth slows. Existing vessels may enlarge and form "lakes" with minimal blood flow. This is the cavernous hemangioma typically seen in adults and rarely in children.[36]

Infantile Hemangioendotheliomas

Infantile hemangioendotheliomas are single or multiple solid masses of varying echogenicity, often containing fine, linear foci of calcium.[37] Doppler sonography shows blood flow in multiple tortuous vessels both within and at the periphery

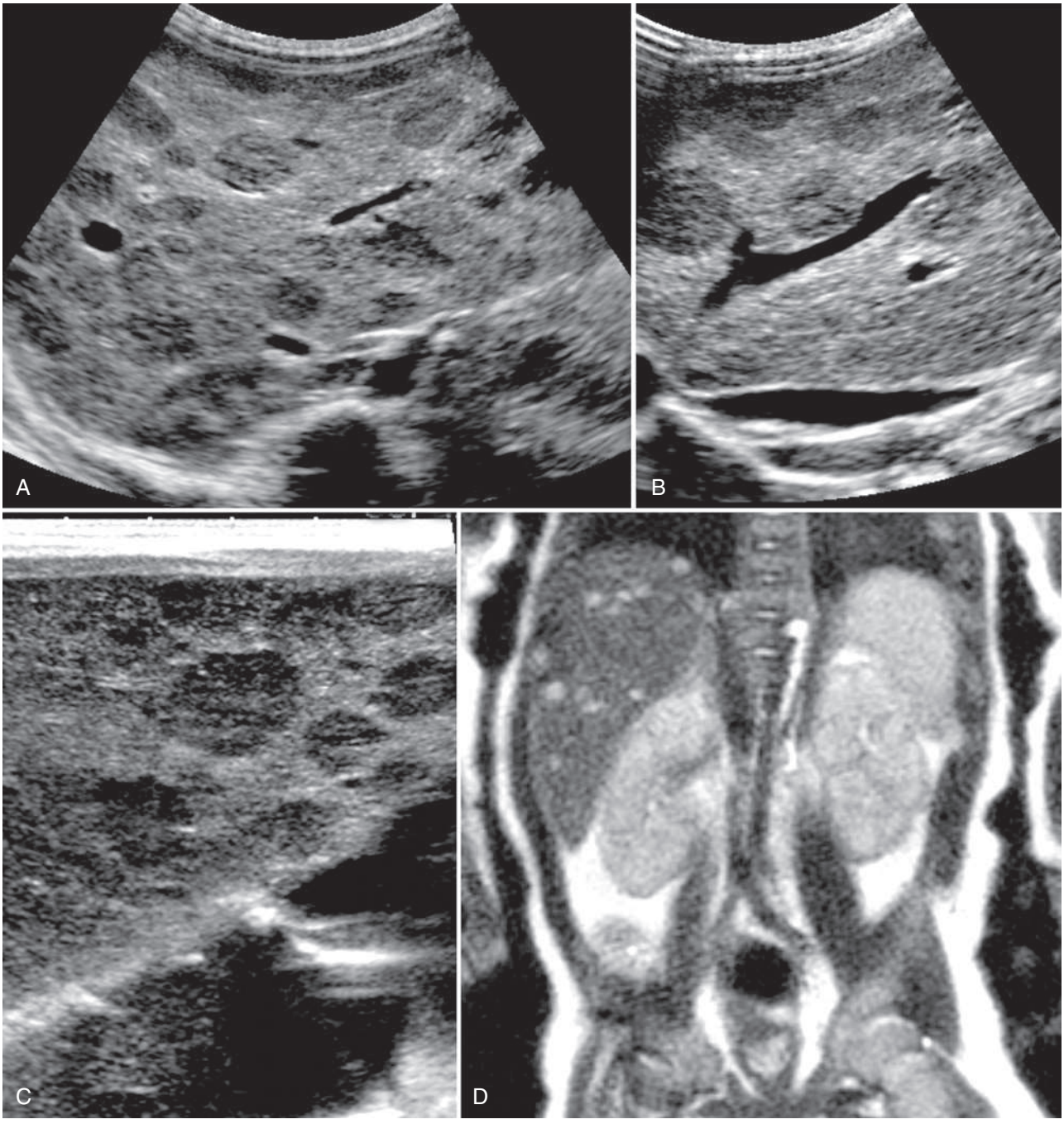

FIG. 51.14 Hemangiomas. Multiple visceral and cutaneous hemangiomas were found in this newborn with enlarged liver at birth. **(A)** Transverse sonogram showing innumerable hypoechoic lesions enlarging the liver. **(B)** Longitudinal sonogram of the liver showing one hemangioma deforming the adjacent hepatic vein. **(C)** Transverse linear array image showing the lesions in greater detail. **(D)** Coronal magnetic resonance single shot fast spin echo (SSFSE) image shows only a few remaining liver lesions several months after treatment. See also Video 51.4 and Video 51.5.

of the mass (Fig. 51.15). Doppler shifts exceed those seen in normal intrahepatic arteries. When AV shunting is severe, the celiac axis, hepatic artery, and veins are dilated, and the infraceliac aorta is small. Doppler shifts (low-resistance high-diastolic flow) from hemangioendothelioma vessels may resemble those from malignant tumors.[38] The vascular nature of these lesions is confirmed by bolus injection CT and the search for rapid filling and rapid washout in these masses. Angiography is usually reserved for patients considered for embolization.

Mesenchymal Hamartomas

Mesenchymal hamartomas are rare, usually multiseptate, cystic masses derived from periportal mesenchyma. Calcifications occur rarely. Hamartoma typically manifests as an asymptomatic mass in the right lobe of the liver in children younger than 2 years.[39]

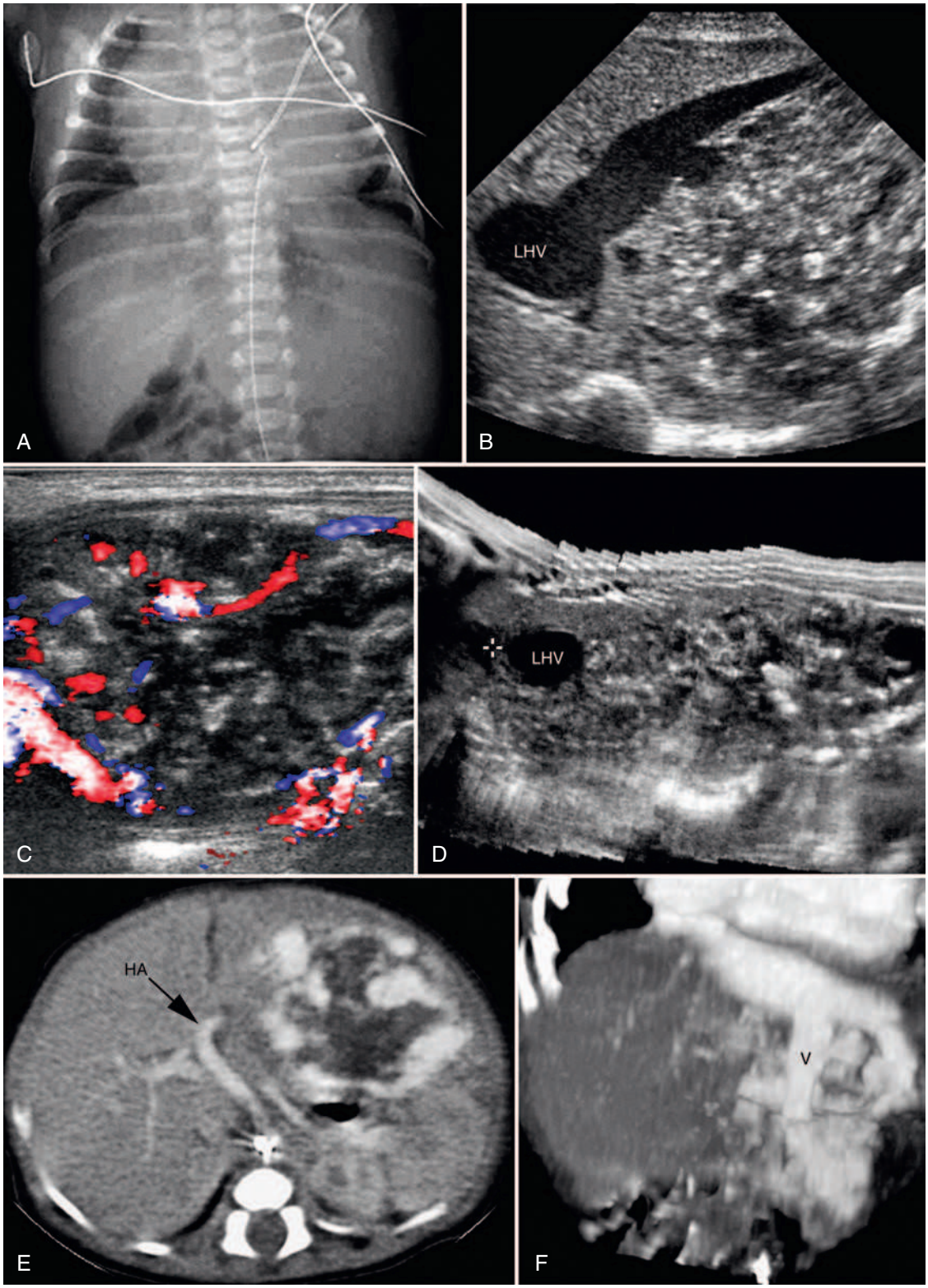

FIG. 51.15 Infantile Hemangioendothelioma. (A) Chest and abdominal radiograph of newborn shows left upper quadrant soft tissue mass and congestive heart failure. **(B)** Longitudinal gray-scale ultrasound; *LHV,* left hepatic vein. **(C)** Color Doppler ultrasound. **(D)** Extended-view longitudinal ultrasound. **(E)** Contrast medium–enhanced axial computed tomography (CT) scan. **(F)** Images of the mass show an enlarged hepatic artery (*HA* in **[E]**) feeding the lesion and large veins (*V* in **[F]**) draining into the right atrium and creating a left-to-right shunt and heart failure.

Adenomas

Adenomas are rare except in association with metabolic liver disease, especially **glycogen storage disease type I**[40]; **oral contraceptive therapy;** and **anabolic steroid therapy** for **Fanconi anemia,** which may result in development of hepatocellular carcinoma. Serum AFP levels are normal. Sonographic appearance varies from hyperechoic to hypoechoic. Malignant degeneration is rare. The distinction between adenoma and a malignant mass is difficult with sonography, CT, and MRI because imaging findings vary and are nonspecific. In patients with Fanconi anemia after bone marrow transplant, adenomas may mimic abscess during sepsis evaluation.

Focal Nodular Hyperplasia

Focal nodular hyperplasia is a benign tumor caused by a hyperplastic response to a vascular abnormality, most often following chemotherapy. It typically shows a central scar, which may be visible sonographically or at CT or MRI. The pattern of contrast uptake and washout on CT and MRI is very characteristic.[41]

Malignant Liver Tumors

Most solid liver tumors in children are malignant and are derived from epithelium. When tumor involvement is locally extensive, liver transplant is a consideration.

Hepatoblastoma

Hepatoblastoma, the most common primary liver tumor in childhood, occurs in children younger than 3 years and may be considered the infantile form of hepatocellular carcinoma. There is an association with **Beckwith-Wiedemann syndrome, hemihypertrophy,** and the **11p13 chromosome.**[42] Serum AFP levels are almost always elevated. Some tumors secrete gonadotropins and lead to **precocious puberty.**

The tumor is usually single, solid, large, of mixed echogenicity, and poorly marginated, with small cysts and rounded or irregularly shaped deposits of calcium (Fig. 51.16). These calcifications are quite different from the fine, linear calcifications seen in hemangioendotheliomas.[43] The remaining liver is usually normal, although metastases are found in 20% at diagnosis. Intrahepatic vessels are displaced and amputated by the mass. Tumor thrombi are less common than in hepatocellular carcinoma. Doppler sonography is helpful in diagnosing vessel invasion and detecting flow in malignant neovasculature.[44,45] Complete resection of the tumors results in a cure rate of 83% to 95%. Resectability depends on the number of segments and vessels involved and is best determined with MRI.[46]

Hepatocellular Carcinoma

The incidence of hepatocellular carcinoma, the second most common primary malignant liver tumor in children, has two peaks, at 4 to 5 years and at 12 to 14 years. About one-half of affected children have preexisting liver disease, especially tyrosinemia, glycogen storage disease type I, α_1-antitrypsin deficiency, Byler disease, and ALGS. Approximately one-third have hepatitis B or C cirrhosis or biliary cirrhosis related to biliary atresia. Serum AFP levels are usually elevated. The tumor is often multicentric; masses are solid, rarely calcify, and have variable echogenicity. Portal venous invasion is common and easily detected with Doppler sonography, as is the high-velocity flow in peripheral neovasculature.[44,45,47,48]

Undifferentiated Embryonal Sarcoma

Undifferentiated embryonal sarcoma (malignant mesenchymoma) is considered the malignant counterpart of the hamartoma. It is rare; occurs in children 6 to 10 years of age, which is older than those with hamartomas; grows rapidly; and develops central necrosis and cysts. Serum AFP levels are normal. Masses are typically large and appear heterogeneous (Fig. 51.17).

Biliary Rhabdomyosarcoma

An unusual site for primary rhabdomyosarcoma, tumors of the biliary tree tend to occur in young children, with a mean age of 3½ years. Rhabdomyosarcoma may originate in the intrahepatic and extrahepatic ducts, gallbladder, cystic duct, or ampulla of Vater. Children typically have intermittent obstructive jaundice, hepatomegaly, abdominal distention and pain, weight loss, dark urine, and acholic stools. Intraductal location is the best imaging clue to the diagnosis of this otherwise heterogeneous, occasionally cystic mass (Fig. 51.18). Tumors spread locally and metastasize to lung and bone.

Metastases

Metastases to the liver usually arise from **neuroblastoma** (Fig. 51.19), **Wilms tumor, leukemia,** or **lymphoma.** Diffuse infiltration of the liver (or multiple nodules) in stage 4S neonatal neuroblastoma is remarkable for its good prognosis.

Detection of Tumor Angiogenesis

Hepatoblastoma and hepatocellular carcinoma frequently produce a network of microscopic, parasitic tumor vessels at their periphery. Flow in these vessels, which lack a normal muscularis, produces Doppler shifts (low-resistance, high-velocity flow) greater than those seen in the aorta.[45,47] New Doppler techniques that are more sensitive, **superb microvascular imaging** (SMI) and **intravenous ultrasound contrast agents,** have potential to improve visibility of primary liver tumors and metastases.

LIVER ABSCESS AND GRANULOMAS

Pyogenic Abscess

Pyogenic liver abscesses are rare in the typical child. Abscesses generally occur in association with sepsis, in children with depressed immunity (leukemia, drugs), in those with primary immune defects (chronic granulomatous disease, dysgammaglobulinemia), and with contiguous infection (appendicitis, cholangitis). At sonography, abscesses are generally well-defined masses, with or without heterogeneous fluid content and small air bubbles producing ring-down artifacts (Fig. 51.20, Video 51.6). Abscesses displace but do not invade neighboring vessels. A Doppler examination may be used to confirm the patency of nearby portal venous branches. Fluid in the pleural space or Morison pouch should be sought in the supine position.

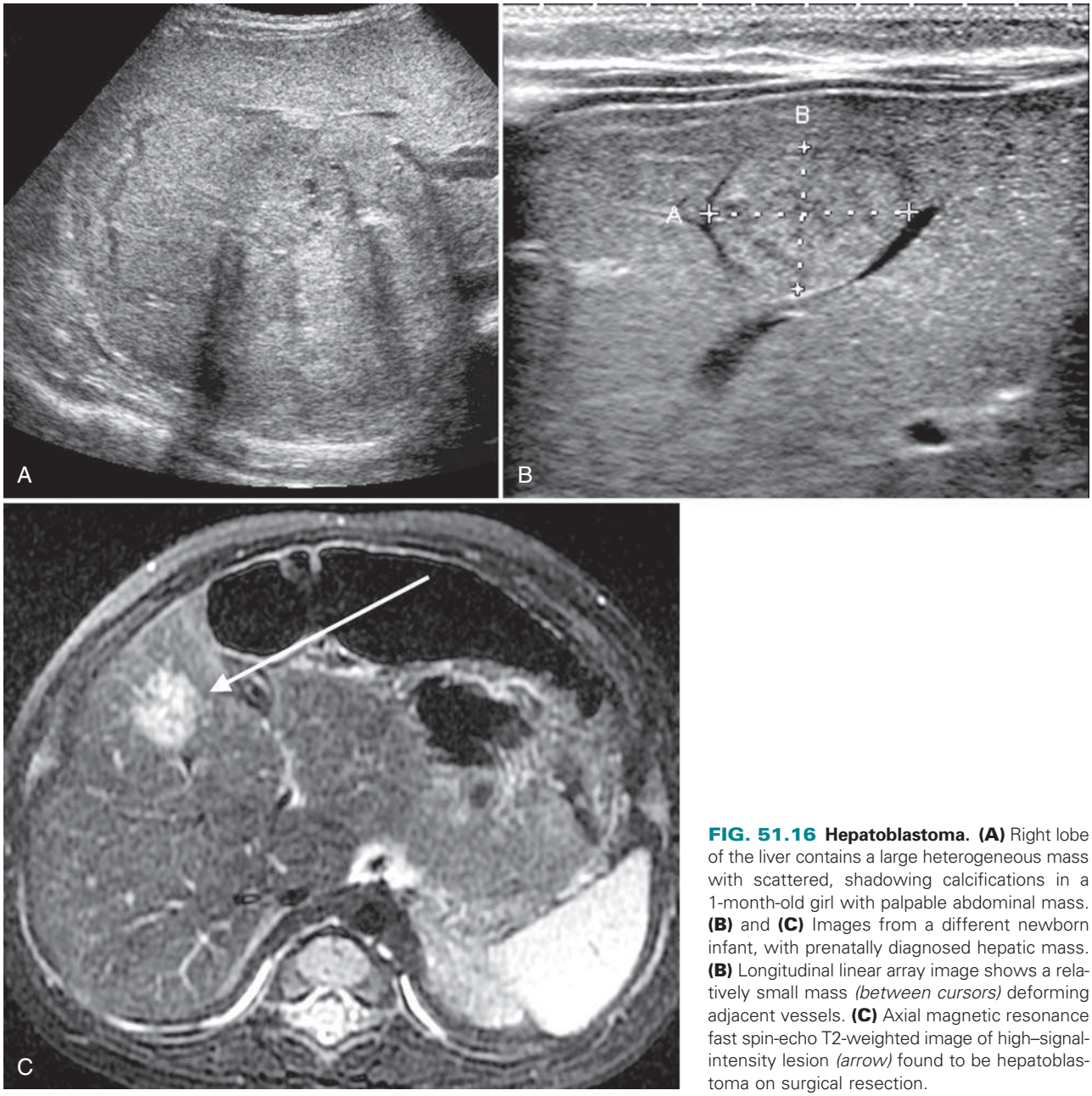

FIG. 51.16 Hepatoblastoma. (A) Right lobe of the liver contains a large heterogeneous mass with scattered, shadowing calcifications in a 1-month-old girl with palpable abdominal mass. **(B)** and **(C)** Images from a different newborn infant, with prenatally diagnosed hepatic mass. **(B)** Longitudinal linear array image shows a relatively small mass *(between cursors)* deforming adjacent vessels. **(C)** Axial magnetic resonance fast spin-echo T2-weighted image of high–signal-intensity lesion *(arrow)* found to be hepatoblastoma on surgical resection.

Aspiration, with or without drainage of abscesses, under sonographic or CT guidance is the preferred treatment in many centers. Some abscesses, especially those accompanying chronic granulomatous disease, gradually calcify during medical treatment.[49] Multiple small abscesses, usually seen in the immunosuppressed child, may result in an enlarged, painful liver. Distinguishing these tiny hypoechogenic lesions from normal liver parenchyma is a challenge to the resolution of the equipment and the skill of the examiner. Scanning the anterior surface of the liver with a high-frequency linear transducer often outlines some of the multiple lesions that are otherwise missed. I routinely complement the ultrasound examination with high-resolution CT in these children because small abscesses are often better seen with CT. Use of sensitive Doppler techniques and intravenous microbubbles may decrease the need for CT.

Parasitic Abscesses

Amebiasis

The incidence of parasitic abscesses in children, although low, is increasing because of expanding travel and immigration. Amebiasis is endemic in the tropics and spreads through person-to-person contact. The protozoan *Entamoeba histolytica* is ingested, invades the colonic mucosa, enters intestinal veins, and spreads into portal venous branches. The organism secretes proteolytic enzymes, and hepatic abscess formation occurs rapidly.

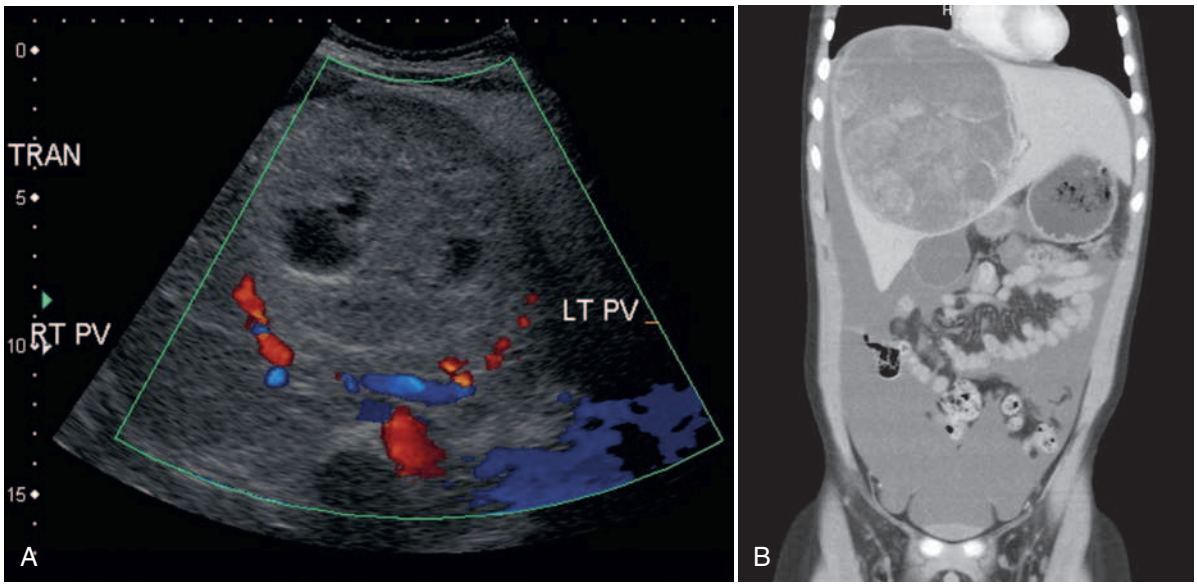

FIG. 51.17 Undifferentiated Embryonal Sarcoma. (A) Transverse color Doppler ultrasound shows a large heterogeneous echotexture mass, splaying the right and left portal veins in the liver of a 10-year-old child. **(B)** Coronal reformatted computed tomography scan shows variable contrast enhancement in the large mass, which replaces most of the right lobe. A large amount of ascites may be related to biopsy or spontaneous hemorrhage.

It is the most frequent extraintestinal complication of **amebic infection.** In children, abscesses are usually multiple and occur most often in infants younger than 1 year and are life-threatening. Fever spikes and hepatomegaly without jaundice are the usual forms of presentation. Diagnosis is made by serologic testing, although the result is not always positive in infants.

Both sonographic and CT imaging modalities are highly sensitive but fail to differentiate amebic from pyogenic abscesses. The sonographic pattern of hypoechoic, homogeneous, or heterogeneous target masses may mimic that of hematoma or neoplasm. Abscess rupture into the thorax, although rare in childhood, is pathognomonic for amebic abscess. Extension into subphrenic or perihepatic spaces, peritoneum, and nearby abdominal organs is more frequent. Diagnostic puncture is disappointing because of the low yield of organisms. Because pyogenic abscesses usually occur in the immunodeficient child, an abscess occurring in an otherwise healthy infant should be considered amebic until proven otherwise. In the past, high mortality rates (60% in infants) have been caused by late diagnosis. They have been reduced to near zero with early detection through the use of cross-sectional imaging (sonography, CT, and MRI).[50]

Echinococcosis

The adult tapeworm, *Echinococcus,* lives in the jejunum of the dog, where it lays its eggs, which are spread through feces and then swallowed by the intermediate host (usually sheep but sometimes humans). Endemic areas include the Middle East, the southern United States, and northern Canada. Embryos, freed in the duodenum, invade the mucosa to enter a mesenteric vein, which flows to the liver, where a slowly growing cyst composed of an acellular outer layer and an endothelialized inner layer may develop. Compressed surrounding liver tissue forms a third layer. The inner layer forms freely floating embryos (scolices), "snowflakes" or "hydatid sand," which are visible with sonography. **Daughter cysts** form within the main cyst under certain circumstances and, when seen sonographically, suggest the diagnosis of **hydatid cyst.** Ruptured daughter cysts form floating membranes. A dead cyst decreases in size and gradually calcifies.[51-53]

Schistosomiasis

Invasion of the portal vein by the ova of *Schistosoma* leads to portal hypertension without cirrhosis. Liver disease progresses so slowly that portal hypertension is rarely seen in a child.

Granulomas of the Liver

Granulomas are circumscribed, focal, inflammatory lesions that may be of bacterial (*Mycobacterium tuberculosis,* other mycobacteria, *Listeria,* spirochetes), fungal *(Candida, Histoplasma, Aspergillus),* parasitic *(Toxocara, Ascaris),* or malignant (lymphoma) origin. Clinical features are those of the underlying disease, and the liver is usually enlarged. Confluent granulomas or abscesses may be recognized as distinct masses at sonography.

DOPPLER ASSESSMENT OF LIVER DISEASE AND PORTAL HYPERTENSION IN CHILDREN

Basic Principles

The physics of Doppler ultrasound and the details of instrumentation have been well described.[54,55] The principles essential to the performance of a successful clinical examination with real-time

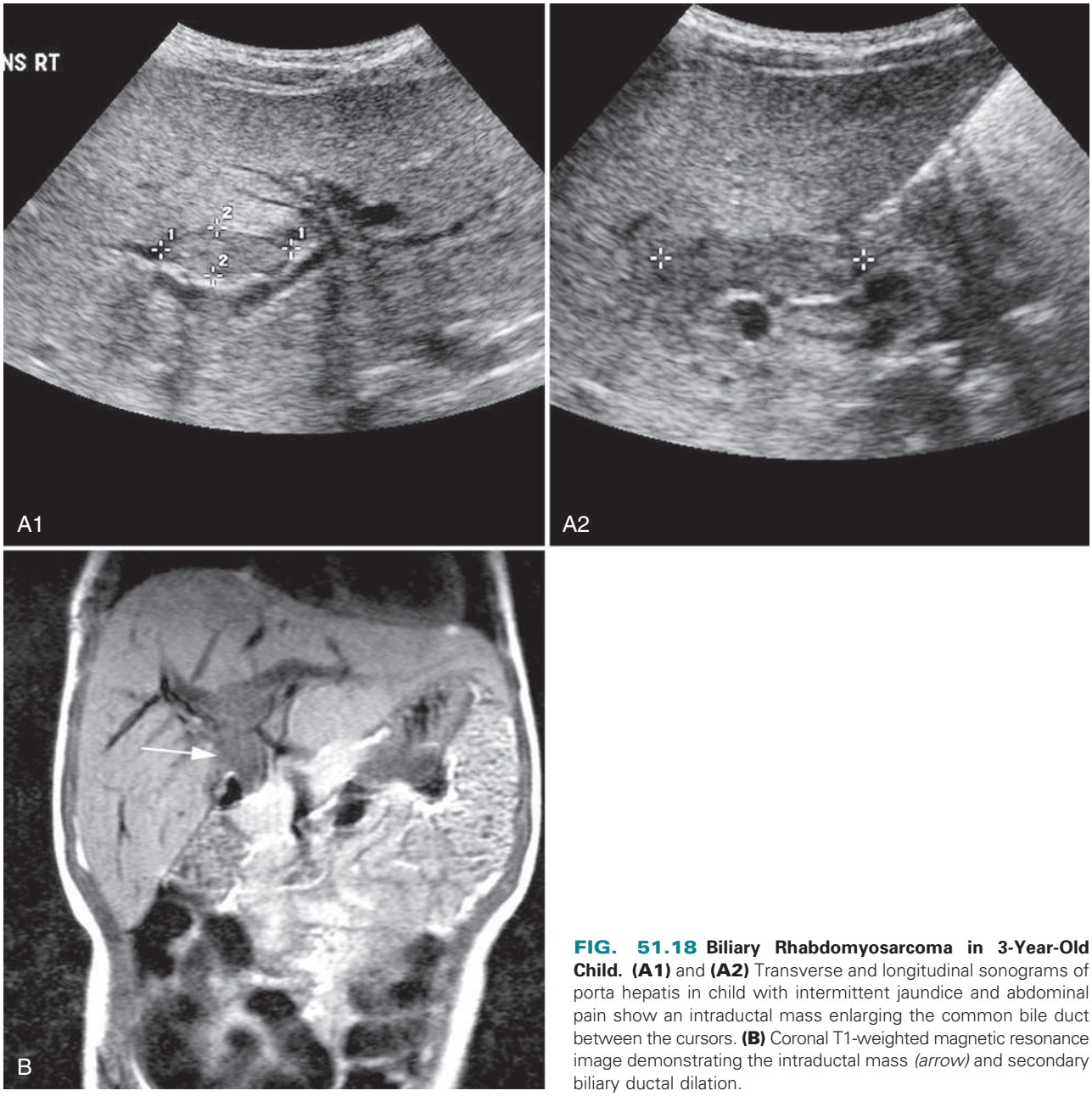

FIG. 51.18 Biliary Rhabdomyosarcoma in 3-Year-Old Child. (A1) and **(A2)** Transverse and longitudinal sonograms of porta hepatis in child with intermittent jaundice and abdominal pain show an intraductal mass enlarging the common bile duct between the cursors. **(B)** Coronal T1-weighted magnetic resonance image demonstrating the intraductal mass *(arrow)* and secondary biliary ductal dilation.

ultrasound coupled to a spectral or color Doppler display are discussed in Chapter 1.

Most of the abdominal vessels studied in children have a low flow velocity. Therefore the wall filter should be as low as possible, preferably at 50 Hz or less. The pulse repetition frequency should be as low as possible for the same reason, unless there is **aliasing.**

There are great advantages to color mapping (Video 51.7) because entire segments of vessels are seen at a glance (e.g., portosystemic collateral veins in portal hypertension or stenoses of vessels). When examining small vessels in children, motion may produce flashes or dots of color artifact. Pulsed Doppler sampling of such doubtful signals distinguishes these artifacts from flow signals. Because of their small body size and ready access to the Doppler beam, children are particularly suited to color, power, and pulsed Doppler abdominal examinations.

New Doppler techniques that are more sensitive to low-velocity flow, which was previously obscured by noise or "signal clutter," have the potential to reveal isoechoic lesions in the liver, including metastases. **Superb microvascular imaging** shows third- and fourth-order branches of the portal veins[56] (Fig. 51.21, Video 51.8, Video 51.9). SMI takes the same returning ultrasound signal and declutters the information to depict very-low-velocity flow. **Intravenous Doppler contrast agents,** various formulations of microbubbles, are now approved by the U.S. Food and Drug Administration (FDA) for cardiac and liver use in the United

FIG. 51.19 Metastatic Liver Disease in 4-Year-Old Child. Transverse sonogram in right upper quadrant shows well-defined right adrenal neuroblastoma *(cursors)* and multiple echogenic hepatic metastases.

States and have been shown to be efficacious. Guidelines for Doppler contrast agent use have been published by the European Federation of Societies for Ultrasound in Medicine and Biology (EFSUMB) at www.efsumb.org. Contrast-enhanced ultrasound requires intravenous access, and the cost of the microbubble agent is added to the cost of the examination.[57]

Normal Flow Patterns in Splanchnic Vessels

Arteries to the liver and spleen supply a low-resistance vascular bed and normally show forward flow throughout the cardiac cycle. Blood flow in the mesenteric arteries shows few or no diastolic Doppler shifts. The superior mesenteric artery in the fasting person has very little forward flow during diastole. Shortly after a meal, its diastolic flow increases considerably.[58] The Doppler profile of the abdominal aorta changes throughout its course. Continuous forward diastolic flow in the upper abdominal aorta is no longer seen beyond the origins of the low-resistance branches to the liver, spleen, intestine, and kidneys. In the distal abdominal aorta, flow reverses during diastole. Fig. 51.22 shows Doppler spectral waveforms of some arteries and veins pertinent to this discussion.[59]

The **systemic veins of the abdomen** (IVC and hepatic and renal veins) show a pulsatile flow pattern that reflects cardiac contractions; two flow peaks toward the heart occur during atrial and ventricular diastole (filling). A short spurt of reversed flow occurs in the hepatic veins and proximal IVC with atrial systole. In addition, the phase of respiration will influence the flow pattern of the systemic intraabdominal veins (with increasing velocity in expiration). Consequently, the Doppler sonographic characteristics of these veins are variable in the breathing child.

Flow in splanchnic veins is steadier, with only gentle undulations that mirror cardiac motion.[59] Blood is constantly directed toward the portal vein and into the liver. Flow velocity in the portal vein increases greatly after a meal and decreases with exercise.[60,61] **Hepatofugal** portal venous flow (away from liver) can be reversed to **hepatopetal** (into liver) flow after a meal.[61]

Possibilities and Pitfalls

The hepatic veins, difficult to outline with angiography, are easily identified with sonography and their flow pattern outlined. The major splanchnic vessels, such as the splenic, mesenteric, and portal veins, are readily opacified with arterioportography, but small vessels are difficult to explore. This is particularly true of the branches of the **left portal vein,** which often are not opacified. The intrahepatic portal circulation can be readily studied with Doppler sonography, both in health and in disease. Each segmental branch of the portal vein is usually accessible to the Doppler beam. Regional flow patterns and the result of compression, obstruction of flow, reversal of flow, or AV fistulas can be assessed. With angiography and MRI, to-and-fro flow in a splanchnic vein is difficult to perceive. The Doppler examination yields clear signals of to-and-fro flow motions both on spectral display and with color. If questions remain about examination details or changes in the patient's condition, the Doppler examination can be repeated without risk.

These advantages are counterbalanced by certain limitations, most of which are identical to those of real-time sonography. The examination is operator dependent and requires training not only in sonography but also in the physics of Doppler and in the normal anatomy and physiology of the liver and splanchnic circulation. Doppler sonography is subject to the same physical laws as is real-time ultrasound. One cannot expect a good Doppler examination in a patient who just had a poor real-time sonogram. The child's cirrhotic liver may be enlarged with increased sound attenuation. Penetrating all this tissue with a real-time or Doppler beam can be a challenge.

Quantitative analysis of splanchnic blood flow with Doppler instrumentation could allow more intensive study of physiologic flow as well as portal hypertension and response to various drugs. However, because the technique depends on exact vessel beam angle and vessel diameter measurements, it is currently fraught with inaccuracies.[54,62]

In the present state of the art, despite the limitations just cited, the Doppler examination of the splanchnic circulation is valuable. If a noninvasive test can determine whether the patient has portal hypertension, the location of the level of obstruction to blood flow, and whether esophageal varices exist, it is indeed a useful clinical tool. For this reason, the Doppler examination has become the screening method of choice for children with liver disease and potential portal hypertension.

Sonographic Technique

Children older than 5 years are usually examined after a 4- to 6-hour fast. Normally, their cooperation can be obtained if the procedure is explained to them and distractions are provided. Sedation is seldom necessary. Whenever possible, respiration is stopped during the Doppler examination of a vessel so as to

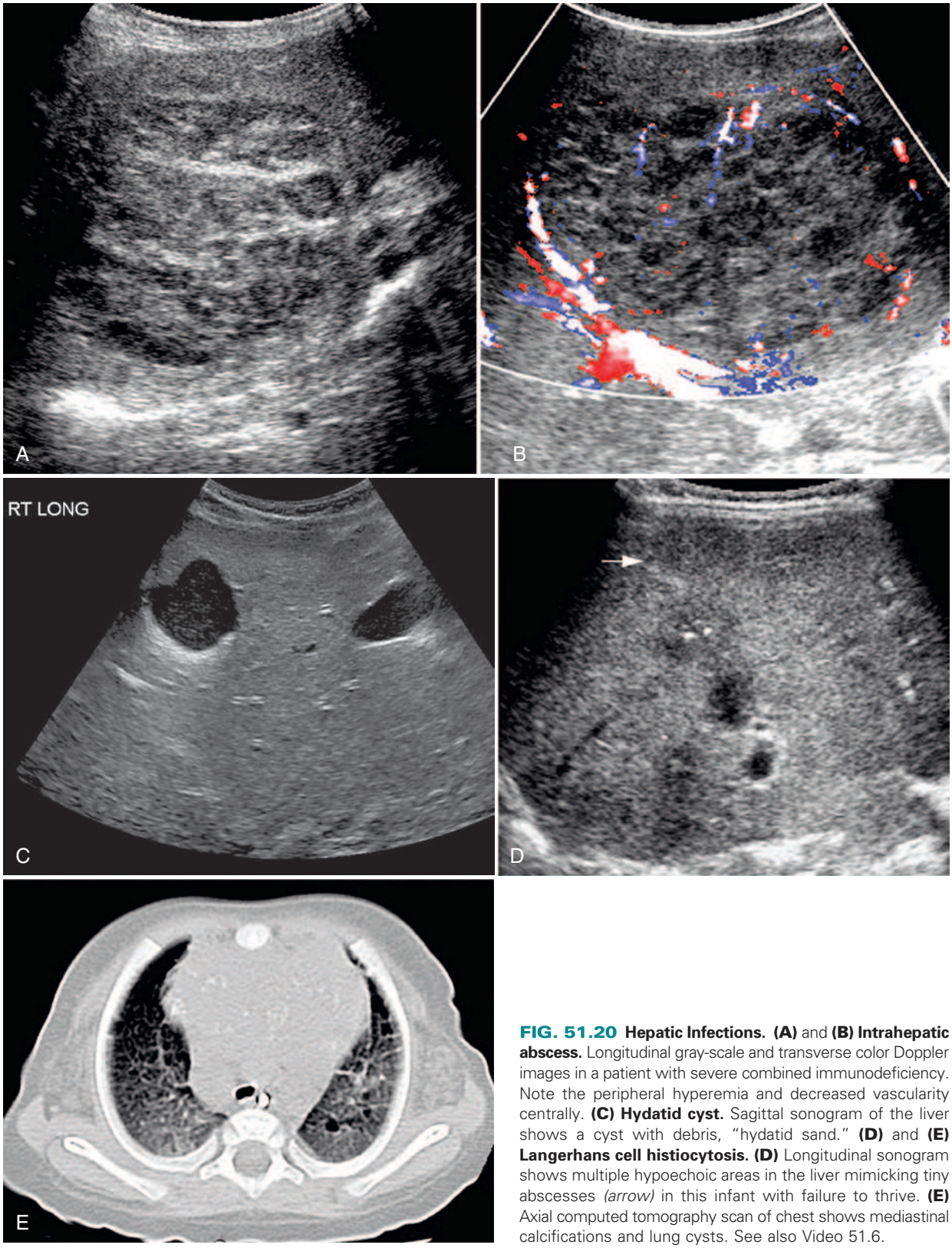

FIG. 51.20 Hepatic Infections. (A) and **(B) Intrahepatic abscess.** Longitudinal gray-scale and transverse color Doppler images in a patient with severe combined immunodeficiency. Note the peripheral hyperemia and decreased vascularity centrally. **(C) Hydatid cyst.** Sagittal sonogram of the liver shows a cyst with debris, "hydatid sand." **(D)** and **(E) Langerhans cell histiocytosis. (D)** Longitudinal sonogram shows multiple hypoechoic areas in the liver mimicking tiny abscesses *(arrow)* in this infant with failure to thrive. **(E)** Axial computed tomography scan of chest shows mediastinal calcifications and lung cysts. See also Video 51.6.

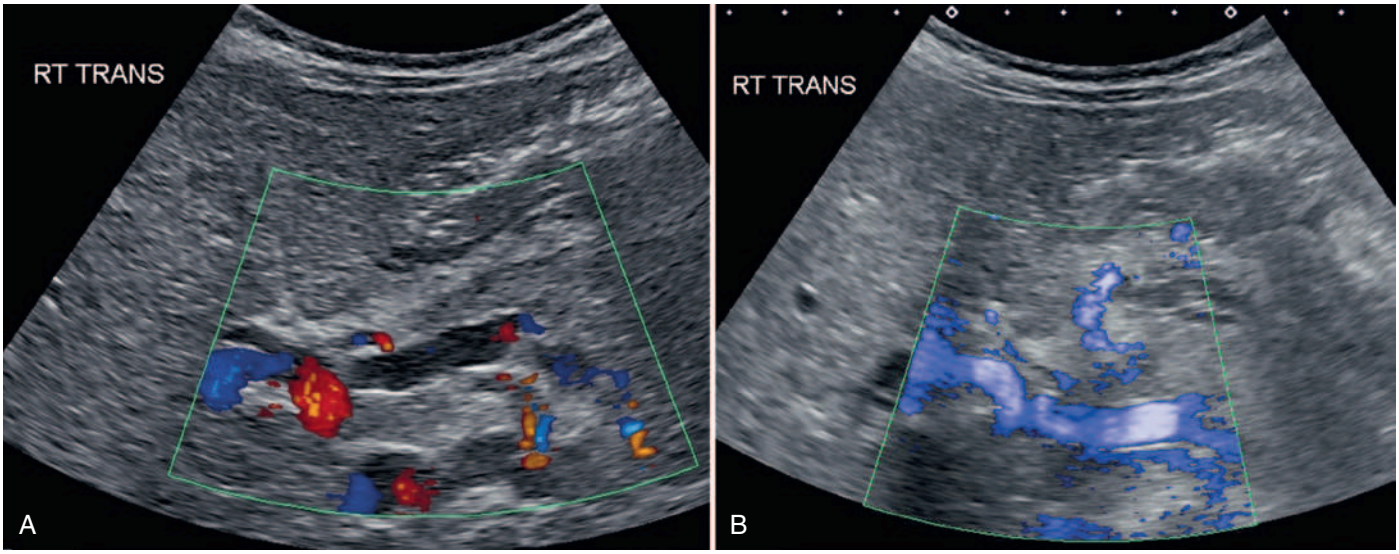

FIG. 51.21 Superb Microvascular Imaging (SMI). (A) Color Doppler images show lack of color flow in the main extrahepatic portal vein in a patient with chronic liver disease **(B)** SMI images show filling of the portal vein with blue color, reflecting the very-low-velocity flow in this still-patent portal vein. See also Video 51.8 and Video 51.9.

minimize its movement. The frequency for the examination may vary from 3.0 to 7.5 MHz, depending on the child's size and transducer availability. Because a small or upset child tends to breathe rapidly, the examiner must be familiar with the Doppler equipment to manipulate it quickly. All technical settings should be preadjusted or preprogrammed to minimize examination time. The vessel to be examined is identified with real-time sonography. Color Doppler ultrasound can be used to guide the placement of the sample volume. A spectral display of the Doppler shift is then usually readily obtained, even though it may disappear during part of the respiratory cycle.

Child With Liver Disease: Doppler Examination for Portal Hypertension

The aim of the Doppler examination is to assess the presence and direction of flow in splanchnic veins, the main portal vein and its segmental intrahepatic branches, the hepatic veins, and the IVC[63-66] (Fig. 51.23). In addition, the presence of flow in the main hepatic artery and its intrahepatic branches should be determined. When the clinical or basic Doppler examination raises suspicion for **portal hypertension,** a systematic search for portosystemic collateral veins follows. Fig. 51.24 outlines the usual sites for spontaneous portosystemic shunts.[65,67] The lesser omentum[68] (from splenomesenteric junction to esophagus) and the renal, splenic, and hepatic hila as well as the pelvis are screened for the presence of dilated, tortuous veins. If hepatofugal (reversed) flow is found in a splanchnic vein, this vein is traced to the recipient systemic vessel. In cases of portal hypertension, the **left gastric vein** drains blood into the inferior esophageal vein; the **splenic vein** drains into the renal (or pararenal) veins; the **superior and inferior mesenteric veins** drain into gonadal, retroperitoneal, or hemorrhoidal veins; and the **paraumbilical veins** follow the round and falciform ligaments to drain into the anterior abdominal and iliac veins to form the classic **caput medusae** or into veins of the anterior chest wall and the internal mammary vein.

Direction of flow in one or several veins of the portal venous system may change in portal hypertension, and it is essential to record the flow direction accurately. The Doppler sample volume should be placed in the center of the vessel lumen. If the direction of flow within a vessel is difficult to ascertain, a nearby vessel with known flow direction can be used as a reference (e.g., splenic or hepatic artery or adjacent vein).

The **main portal vein** and its right hepatic branches are best studied through a right intercostal approach. Sometimes the superior mesenteric vein is also clearly seen from this position. The **left portal vein** and three of its four branches (portal branch to caudate lobe is rarely seen) and the **hepatic veins** are best seen through an oblique subcostal approach. The **splenic vein** is explored through a transverse approach over the spleen. The **superior mesenteric vein** and **main portal vein** are best visualized through a sagittal right paramedian approach. The **left gastric vein** usually ends near the splenoportal junction and, when enlarged, is easily observed through a sagittal left paramedian view. The **inferior mesenteric vein,** when normal, can rarely be visualized sonographically. When enlarged, it may be traced through a left lateral approach to its junction with the splenic or superior mesenteric vein.

The various possible origins of the **hepatic artery** may be difficult to recognize. We first look for the artery at its usual origin from the celiac axis and also as it passes between the portal vein and the CBD. When the left hepatic artery arises from the superior mesenteric artery, it passes through the ligamentum venosum. The intrahepatic arterial branches accompany branches of the portal vein and can be detected with a slightly enlarged Doppler sample volume placed over a portal venous branch, even when the arterial branch cannot be seen with

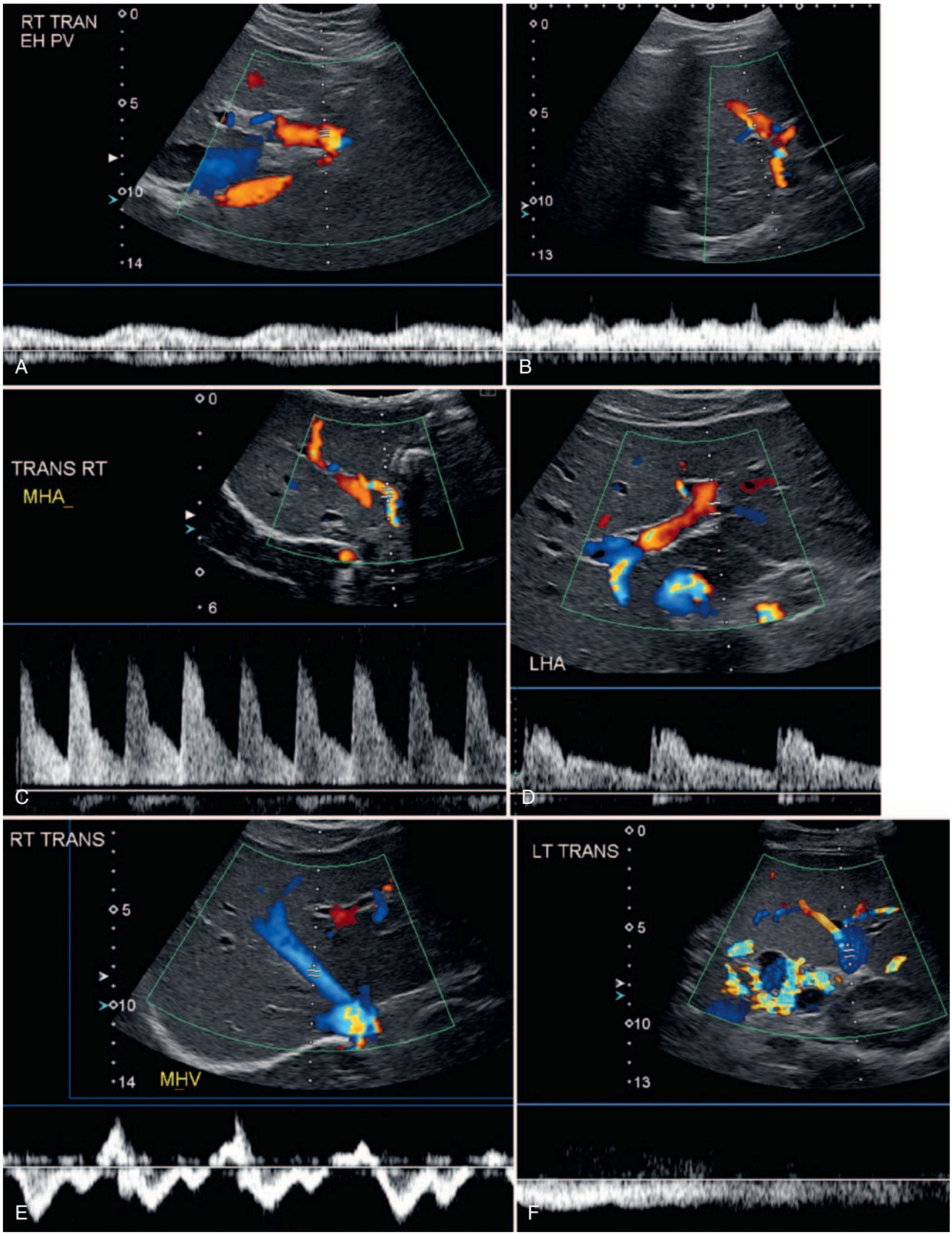

FIG. 51.22 Typical Duplex Doppler Images of Splanchnic Vessels. (A) Normal portal vein examined through a transverse, paramedian, subcostal approach. Flow fluctuates slightly with cardiac systole. Note aliasing artifact from low pulse repetition frequency. **(B)** Normal right branch of portal vein seen from an oblique right subcostal approach. Note that a few arterial pulsations are seen as a result of respiratory motion. **(C)** Normal main hepatic artery at the porta hepatis, with typical forward flow throughout systole and diastole. **(D)** Normal left hepatic artery branch with preservation of the dicrotic notch during systole. **(E)** Normal hepatic vein, transverse subcostal view, with triphasic flow, away from transducer except during right atrial systole when flow is toward the transducer. **(F)** Enlarged splenic vein at hilum with monophasic flow away from the spleen and numerous adjacent varices medially.

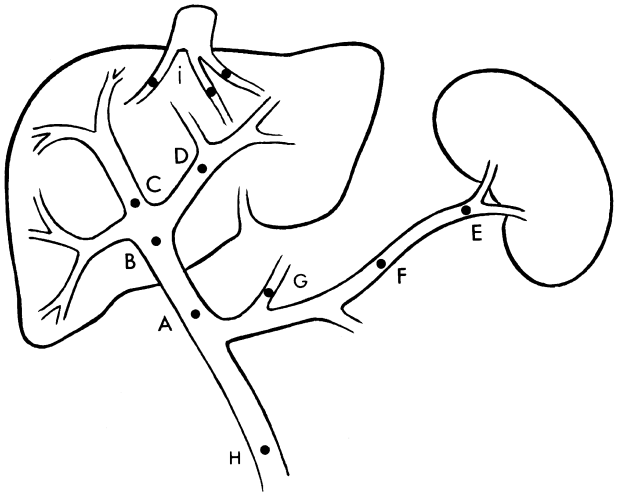

FIG. 51.23 Essential Splanchnic Vein Reference Points in Doppler Sampling for Possible Portal Hypertension in Children With Liver Disease. *A,* Main portal vein; *B,* intrahepatic portal vein; *C,* right portal vein; *D,* left portal vein; *E,* splenic vein at hilum; *F,* splenic vein; *G,* left coronary vein; *H,* superior mesenteric vein; *I,* hepatic veins. Evaluation of the hepatic artery and inferior vena cava should be done as well. (With permission from Patriquin H, Lafortune M, Burns PN, Dauzat M. Duplex Doppler examination in portal hypertension: technique and anatomy. Am J Roentgenol. 1987;149[1]:71-76.[64])

real-time ultrasound. The arteries to the right lobe of the liver (especially segments 5, 7, and 8) are usually easy to identify in this manner. The hepatic arterial branch accompanying the umbilical portion of the left portal vein (to segment 4) is especially easy to examine with Doppler imaging because of the almost ideal vessel beam angle, which can be obtained through an anterior abdominal approach (Fig. 51.25). For this reason, I routinely look for arterial Doppler signals at this site in children who have undergone liver transplantation.

Abnormal Flow Patterns Within the Portal System

Absent Doppler Signal

Proof of absence of a Doppler signal is much more difficult to establish than is its presence. The examiner who fails to obtain a Doppler signal from a given vessel usually questions the sensitivity of the machine and tests other nearby vessels. Failure to obtain a pulsed, color, or power Doppler signal from a splanchnic vein examined at an angle of less than 60 degrees, full Doppler gain, and low pulse repetition frequency, with 50-Hz wall filter and restricted Doppler window, means that blood is flowing at a velocity of less than 4 cm/sec (extremely slow). Thus absence of a Doppler signal in this situation generally means absence of flow or a prethrombotic state.

Arterialized Portal Venous Flow

When the normal, gently undulating flow within a portal vein is replaced by systolic peaks and high diastolic Doppler shifts, this is termed an "arterialized flow pattern" and may signal the presence of an arterioportal fistula.[69]

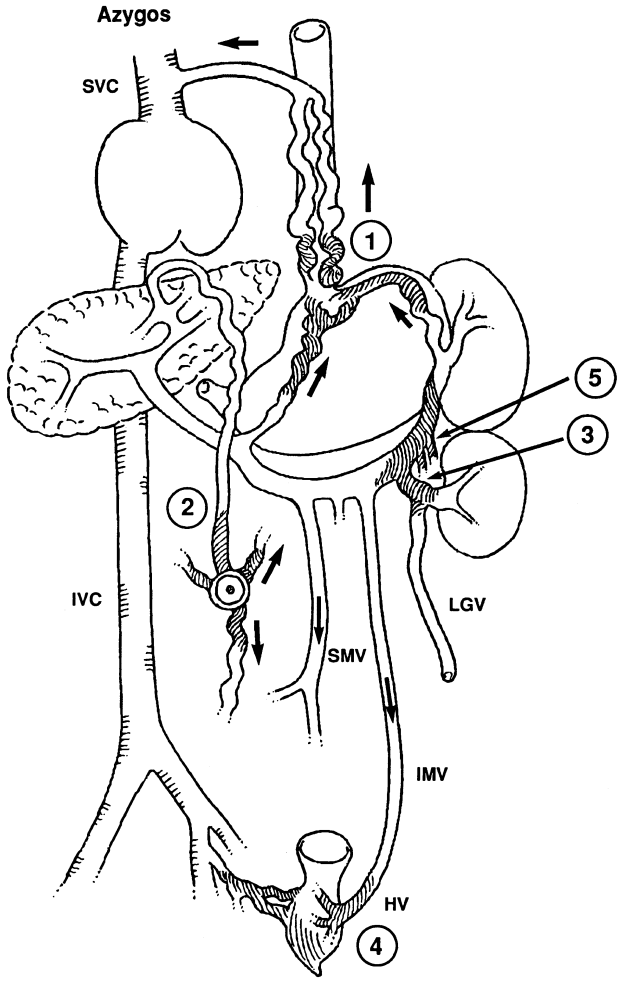

FIG. 51.24 Diagram of Common Spontaneous Portosystemic Collateral Routes. *HV,* Hemorrhoidal vein; *IMV,* inferior mesenteric vein; *IVC,* inferior vena cava; *LGV,* left gonadal vein; *SMV,* superior mesenteric vein; *SVC,* superior vena cava; *1,* left gastric-azygos route (esophageal varices); *2,* paraumbilical-hypogastric/internal mammary route (caput medusa); *3,* splenorenal route; *4,* IMV-hemorrhoidal route; *5,* spleno-retroperitoneal-gonadal route. (With permission from Patriquin HB, LaFortune M. SPR Annual Meeting Syllabus. Pediatr Radiol. 1994.[67])

Causes of Absent Doppler Signal

Doppler angle greater than 60 degrees
Low Doppler gain
Low pulse repetition frequency
High filter (best is 50 Hz)
Small sample volume
Portal vein flow decreases when fasting
Hepatic artery flow decreases after a meal

Reversed or To-and-Fro Flow

Reversed flow in a splanchnic or intrahepatic portal vein is the most reliable Doppler sign of portal hypertension. However, hepatofugal flow in the portal vein occurs late and relatively rarely in patients with liver disease. To-and-fro flow in the portal vein also suggests the presence of portal hypertension. Highly

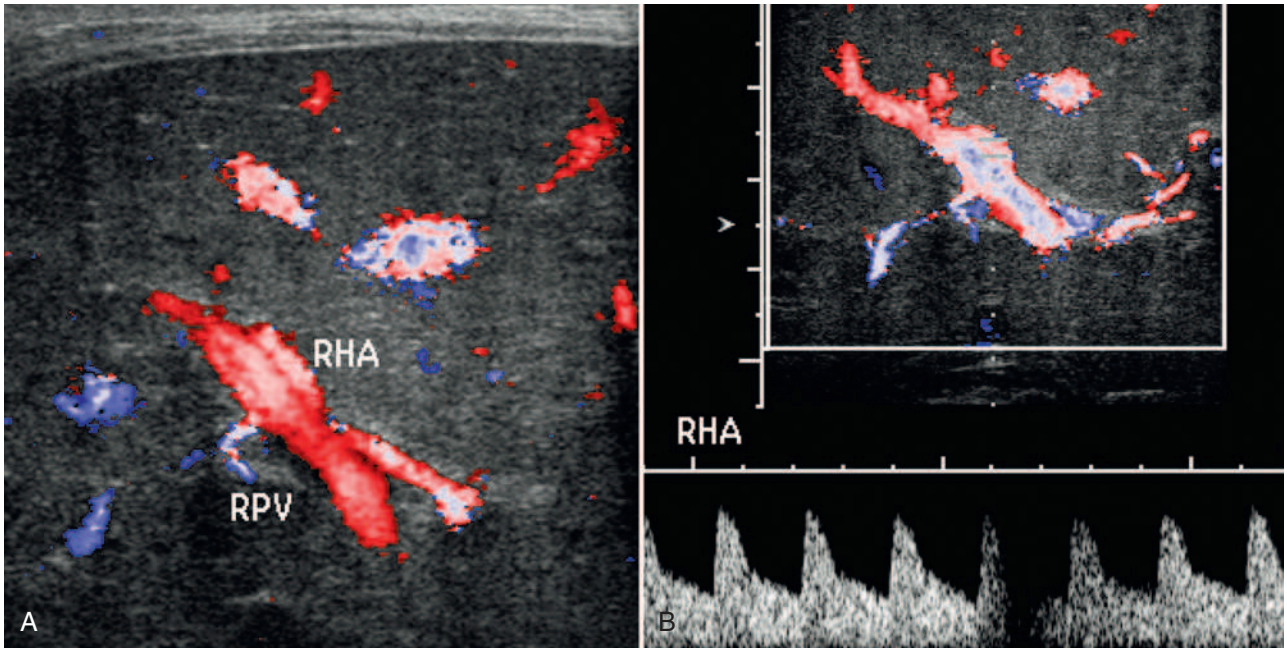

FIG. 51.25 Normal Liver and Right Hepatic Artery *(RHA)* in an Infant. Oblique subcostal color Doppler sonograms. **(A)** Right portal vein *(RPV)*. **(B)** Cursor in RHA shows normal arterial flow waveform. Doppler shifts from normal hepatic artery and portal vein have identical directions of flow.

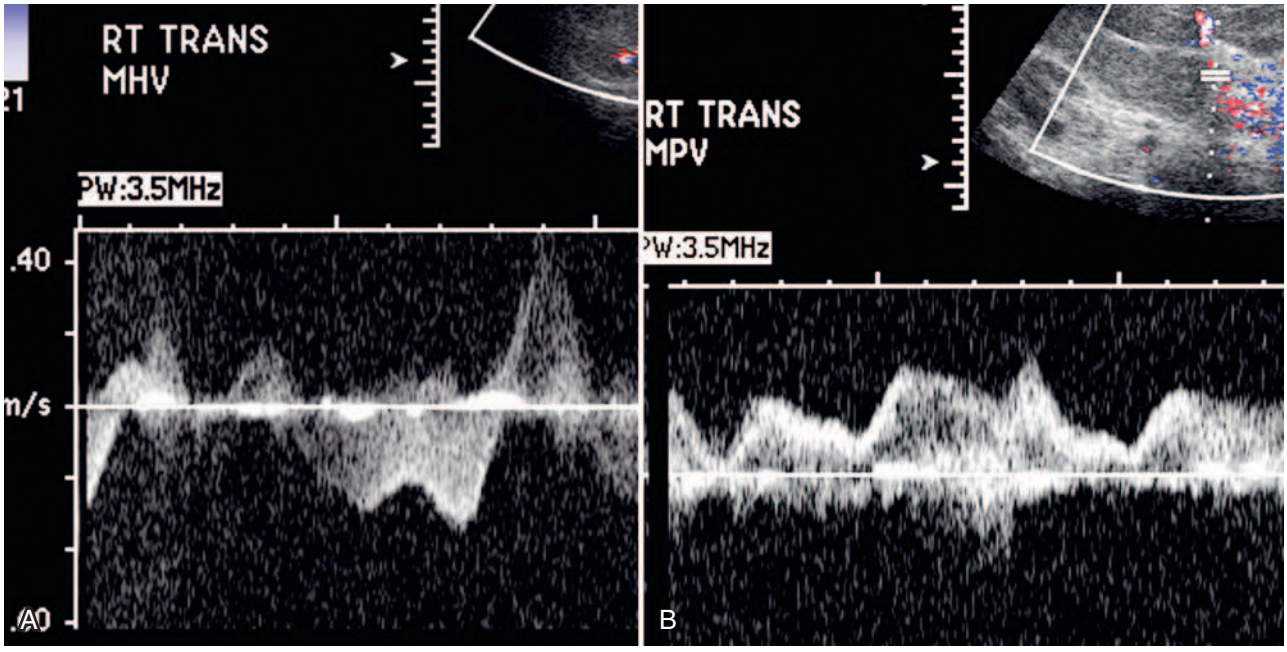

FIG. 51.26 Postfontan Procedure Hepatic and Portal Venous Flow Increase in a Child With Congenital Heart Disease. (A) Highly pulsatile hepatic venous flow and **(B)** portal venous flow. Right atrial pressure is transmitted through the hepatic veins, across the hepatic sinusoids to the portal vein.

pulsatile or to-and-fro flow in the portal vein may also be seen in right-sided heart failure (Fig. 51.26) or tricuspid insufficiency, resulting from transmitted pressure across the hepatic sinusoids.

Abnormal Hepatic Arterial Doppler Patterns

Absence of a hepatic artery Doppler signal suggests arterial thrombosis, spasm, or reduced flow in prethrombotic states.[69] Locally increased systolic Doppler shifts or peripheral tardus-parvus curves may be the result of stenosis or spasm of the hepatic artery, as at any other arterial site.

The portal vein and hepatic artery act in concert to nourish the liver. Changes in flow volumes in one affect the other. After a meal, portal venous flow increases and hepatic arterial flow diminishes, probably by vasoconstriction. Postprandially, hepatic arterial diastolic flow is decreased and systolic peaks are lower

when measured at the same sites in the same person.[70] Arterial signals within the liver may be difficult to find after a meal. This is particularly disturbing in the patient who has received a liver transplant, in whom a false diagnosis of thrombosis may be considered.

Portal Venous Hypertension

Portal venous hypertension is a pathologic condition characterized by increased pressure in the portal vein or one of its tributaries. The normal pressure in the portal vein is between 5 and 10 mm Hg. When the pressure in the portal vein is more than 5 mm Hg above IVC pressure, portal hypertension is present.

The many sequelae of portal hypertension include splenomegaly, collateral vein formation, and a thickened lesser omentum. In children the lesser omentum is observed between the left lobe of the liver and the aorta on sagittal images. Lesser omentum thickness should not exceed the diameter of the aorta[70,71] (Fig. 51.27). In portal hypertension it is thickened by lymphatic stasis and an engorged left gastric vein. Morphologic changes of the liver architecture are usually present as well.

An increased caliber of the portal vein and a lack of variation in the caliber of the splenic and mesenteric veins have been described in portal hypertension in adults. The accuracy of these findings in the assessment of portal hypertension in children

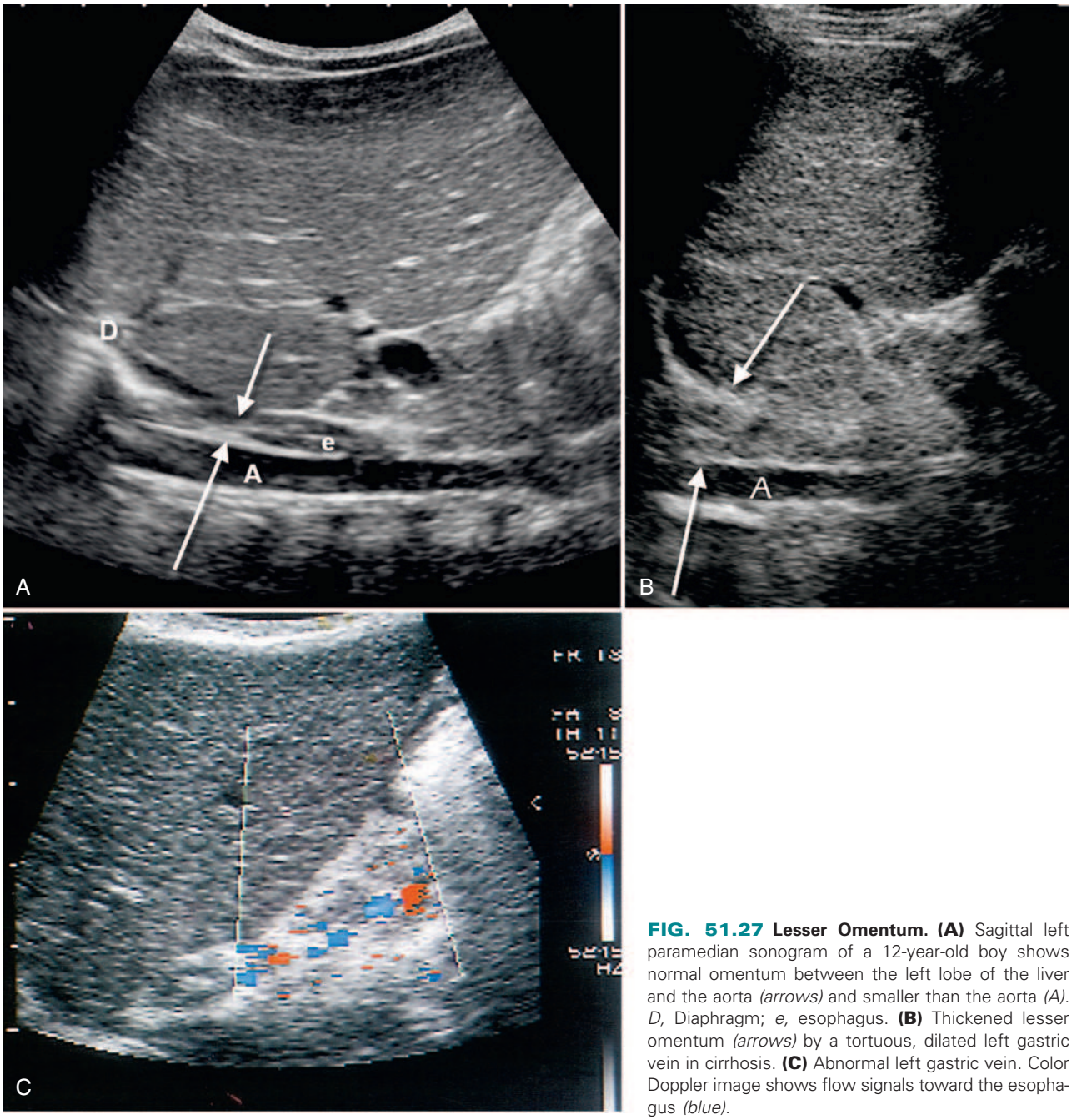

FIG. 51.27 Lesser Omentum. (A) Sagittal left paramedian sonogram of a 12-year-old boy shows normal omentum between the left lobe of the liver and the aorta *(arrows)* and smaller than the aorta *(A). D,* Diaphragm; *e,* esophagus. **(B)** Thickened lesser omentum *(arrows)* by a tortuous, dilated left gastric vein in cirrhosis. **(C)** Abnormal left gastric vein. Color Doppler image shows flow signals toward the esophagus *(blue).*

has not been established. Anecdotally, in children with biliary cirrhosis, portal venous caliber has decreased as cirrhosis progressed.

The hemodynamic information gleaned from the Doppler examination usually answers the following questions: Is portal hypertension present? What is the level of obstruction? What is the direction of flow within the system? Are there portosystemic collaterals?

Hepatofugal flow away from the liver in a portosystemic collateral vein establishes the diagnosis of portal hypertension. Clinically, the most important route is through the left gastric vein, which supplies esophageal varices. The **left gastric vein** is rarely visible sonographically in the normal child. When it dilates to a diameter of greater than 2 to 3 mm, it can be traced from the splenic vein near the splenomesenteric junction through the lesser omentum (behind left lobe of liver and anterior to aorta) to the esophagus. A venous Doppler flow pattern makes it possible to distinguish the vein from the nearby left gastric or hepatic arteries. Flow direction is determined at the same time. The caliber of the left gastric vein is usually related to the size of esophageal varices, and increased diameter is associated with increased risk of bleeding.[72]

The **paraumbilical vein** classically shunts blood from the left portal vein to the periumbilical venous network. It follows a vertical, right paramedian course to enter the falciform ligament through the left lobe of the liver[73,74] (Fig. 51.28). With a high-frequency transducer (7.5-10 MHz), its subcutaneous course is easily seen on sonography from the lower tip of the left lobe of the liver to the umbilicus. Other spontaneous portosystemic collateral veins should be sought near the spleen, left kidney, and flanks, where splenorenal shunts (Fig. 51.29) or dilated perirenal, retroperitoneal, or gonadal veins receive blood from the splenic or mesenteric veins; in the pelvis (Fig. 51.30), around the right kidney; and near the porta hepatis and gallbladder (Fig. 51.31, Video 51.10), where portocaval, paraduodenorenal, or veins of Sappey may shunt the blood between portal and hepatic veins. The variety of spontaneous portosystemic collaterals is almost limitless.

All portosystemic collaterals should be traced to their recipient systemic vein, which is usually dilated where the shunt enters. The "donor" splanchnic vein is also dilated. When portal hypertension decreases after shunt surgery or transplantation, portosystemic collaterals decrease in size (as do the enlarged spleen and lesser omentum).

If a spontaneous or surgical portosystemic shunt is large, **hepatic encephalopathy** may ensue. The Doppler examination, being "physiologic," may reveal unusual portosystemic collateral routes difficult to demonstrate with arterioportographic studies (locally inverted flow in intrahepatic portal venous branches, "neo" veins leading from portal veins to abdominal wall, or hepatofugal flow in splenic vein).

Prehepatic Portal Hypertension

Prehepatic portal hypertension results from obstruction of the splenic, mesenteric, or portal vein. As with other venous thromboses, predisposing factors involve the vessel wall (trauma, catheters), stagnant blood flow, and abnormal clotting factors. Principal causes of **thrombosis of the portal vein** include (1) trauma such as umbilical venous catheterization; (2) dehydration or shock; (3) pyophlebitis following appendicitis or abdominal sepsis; (4) coagulopathy, with protein C deficiency increasingly recognized; (5) portal vein invasion by adjacent tumors; (6) compression of the vein by pancreatitis, lymph nodes, or tumor; and (7) increased resistance to portal venous flow into the liver in cirrhosis or the Budd-Chiari syndrome.

Recanalization of portal venous thrombi usually occurs rapidly in children. In addition, paraportal venous channels and the cystic veins draining the gallbladder dilate and channel blood into the liver if there is no obstruction at this site (in cirrhosis or hepatic vein thrombosis). The resultant collection of tortuous veins is called **cavernous transformation** of the portal vein or a **cavernoma** (see Fig. 51.31). Hepatopetal flow toward the liver in these vessels is easily detected with Doppler sonography. Despite these collateral channels, portal hypertension follows, often with esophageal varices.[75]

Causes of Portal Vein Thrombosis

Trauma
Catheters
Dehydration
Shock
Pyelophlebitis
Coagulopathy, especially protein C deficiency
Portal vein invasion
Portal vein compression
Cirrhosis
Budd-Chiari syndrome

After thrombosis of the portal vein, the peripheral intrahepatic portal veins become small and threadlike. The lumen of portal branches may not be visible. Careful examination of these vessels with Doppler sonography usually shows hepatopetal venous flow, likely the result of shunting through the vessels at the porta hepatis, which constitute the "cavernoma." Because the obstruction to venous flow occurs at the porta hepatis, it is not surprising that children with portal venous thrombosis do not have enlarged paraumbilical veins and a caput medusa; this portosystemic route relies on abundant flow in the left portal vein.[75]

Another cause of prehepatic (or intrahepatic "presinusoidal") portal hypertension in children is **congenital hepatic fibrosis** (Fig. 51.32). This autosomal recessive disease is characterized by fibrosis at the portal triad, where terminal branches of the portal vein and small bile ducts are compressed. Hepatocytes and liver function are normal.[10] Liver architecture is disturbed by linear or cystlike structures representing variable bile duct ectasia, as well as paraportal collaterals (cavernoma).[76,77] These children usually have bleeding esophageal varices. Sonography shows hallmarks of portal hypertension: splenomegaly and a thick lesser omentum in which a dilated tortuous left gastric vein may be visible, with hepatofugal flow detected with Doppler sonography. Congenital hepatic fibrosis is usually associated with

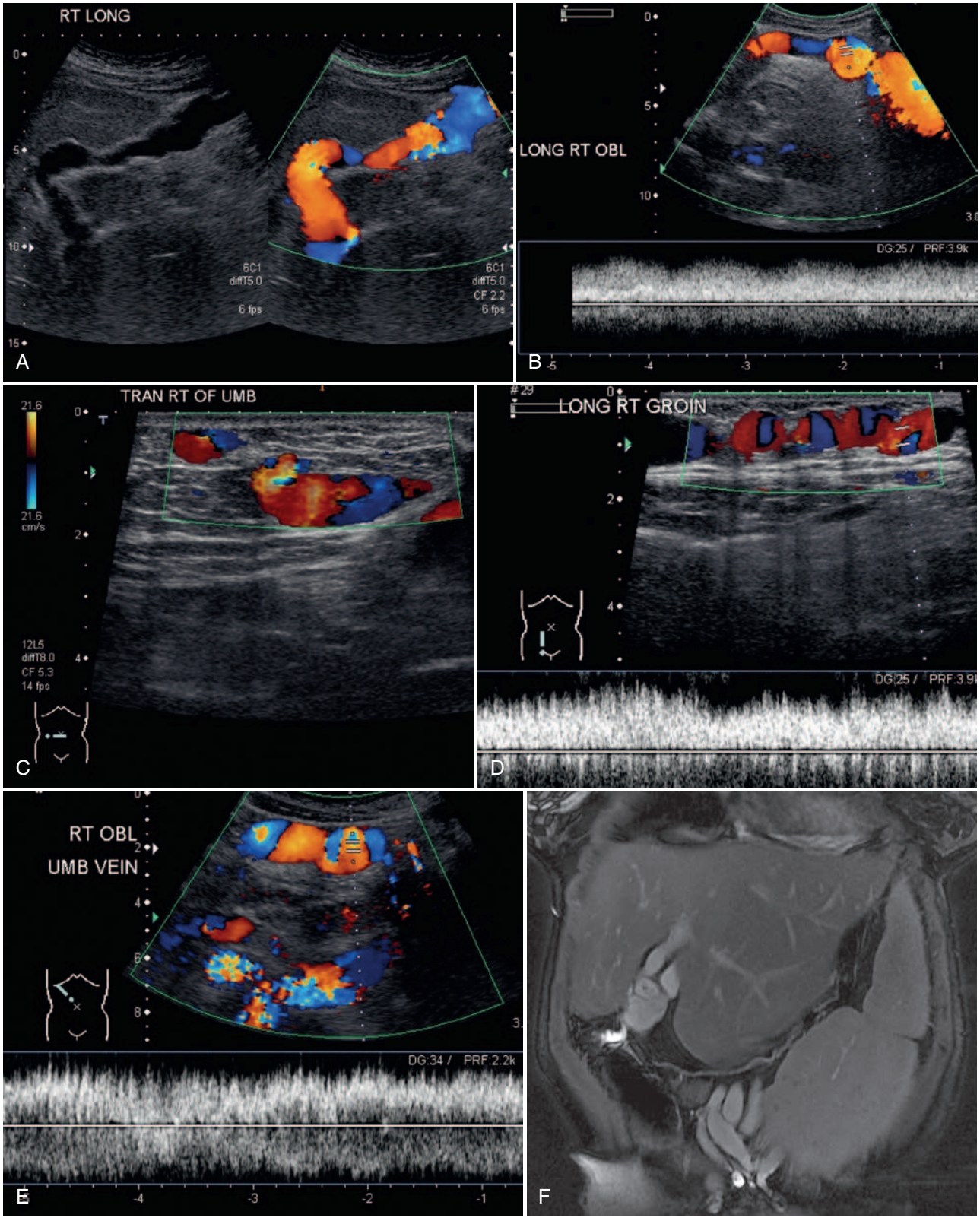

FIG. 51.28 Paraumbilical Collateral Route. (A) and **(B)** Transverse paramedian gray-scale and color Doppler sonograms show left lobe of liver in a child with cirrhosis and portal hypertension. **Recanalized umbilical vein,** with venous flow signals directed toward the transducer, anteriorly out of the liver. **(C)-(E)** Sagittal and oblique color Doppler images showing flow leaving the liver through a patent paraumbilical vein that courses to the periumbilical area and right groin area. Pulsed Doppler waveforms show low velocity venous flow "hum" in these vessels. **(F)** Coronal Fiesta magnetic resonance image shows pericholecystic tortuous varices and infraumbilical vessels in the same patient.

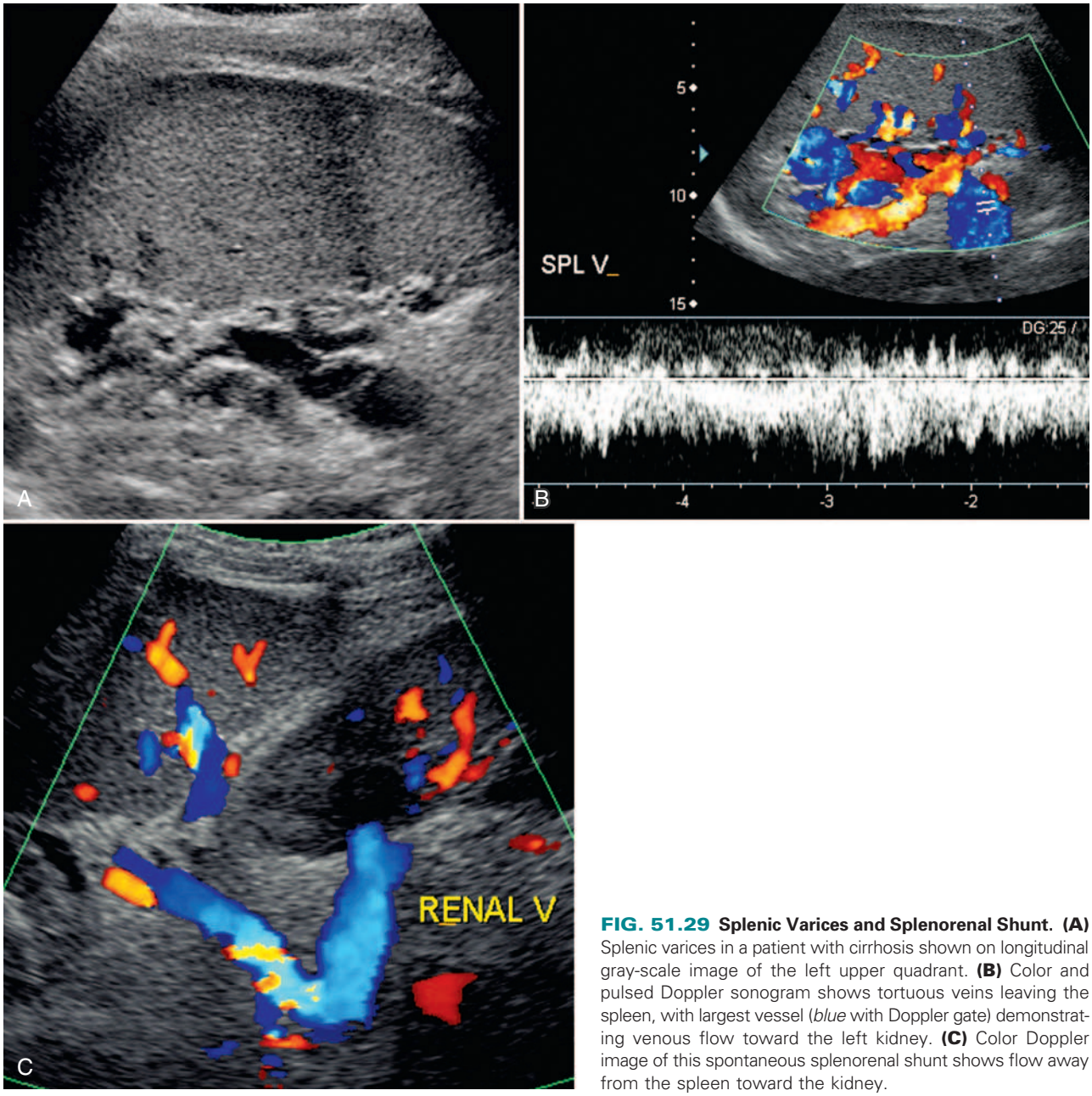

FIG. 51.29 Splenic Varices and Splenorenal Shunt. (A) Splenic varices in a patient with cirrhosis shown on longitudinal gray-scale image of the left upper quadrant. **(B)** Color and pulsed Doppler sonogram shows tortuous veins leaving the spleen, with largest vessel (*blue* with Doppler gate) demonstrating venous flow toward the left kidney. **(C)** Color Doppler image of this spontaneous splenorenal shunt shows flow away from the spleen toward the kidney.

autosomal recessive polycystic kidney disease.[78] The dilation of renal collecting ducts in these children is variable and less severe than in the neonatal form, and renal impairment is less marked. However, renal architecture is greatly disturbed. The pyramids are hyperechoic and may contain calcium; small cysts may be seen; and the kidneys are usually enlarged. These features enable informed sonographers to find the cause of upper intestinal bleeding in these children during their first abdominal sonogram.

Intrahepatic Portal Hypertension

Serious insult to the hepatocyte results in **necrosis.** Unless necrosis is overwhelming, scarring and the formation of multiple regenerating nodules follow. The process of **cirrhosis** results in scarred and obstructed sinusoids and abnormal portal venous blood flow through the regenerated nodules. In children, cirrhosis may result from the following:

- Hepatitis
- Destruction of the hepatocyte by toxins accumulated in inherited metabolic diseases, such as tyrosinemia, some forms of glycogen storage disease, and Wilson disease
- Bile stasis, as in biliary atresia and cystic fibrosis

Although different types of cirrhosis cause initial obstruction at presinusoidal (schistosomiasis, biliary cirrhosis), sinusoidal (Laennec cirrhosis), and postsinusoidal levels, progressive scarring usually spreads to the entire sinusoid. As intrahepatic portal venous flow stagnates, portosystemic collaterals open. Portal blood flow decreases. Total hepatic blood supply is usually maintained by an increase of blood flow in the hepatic artery.

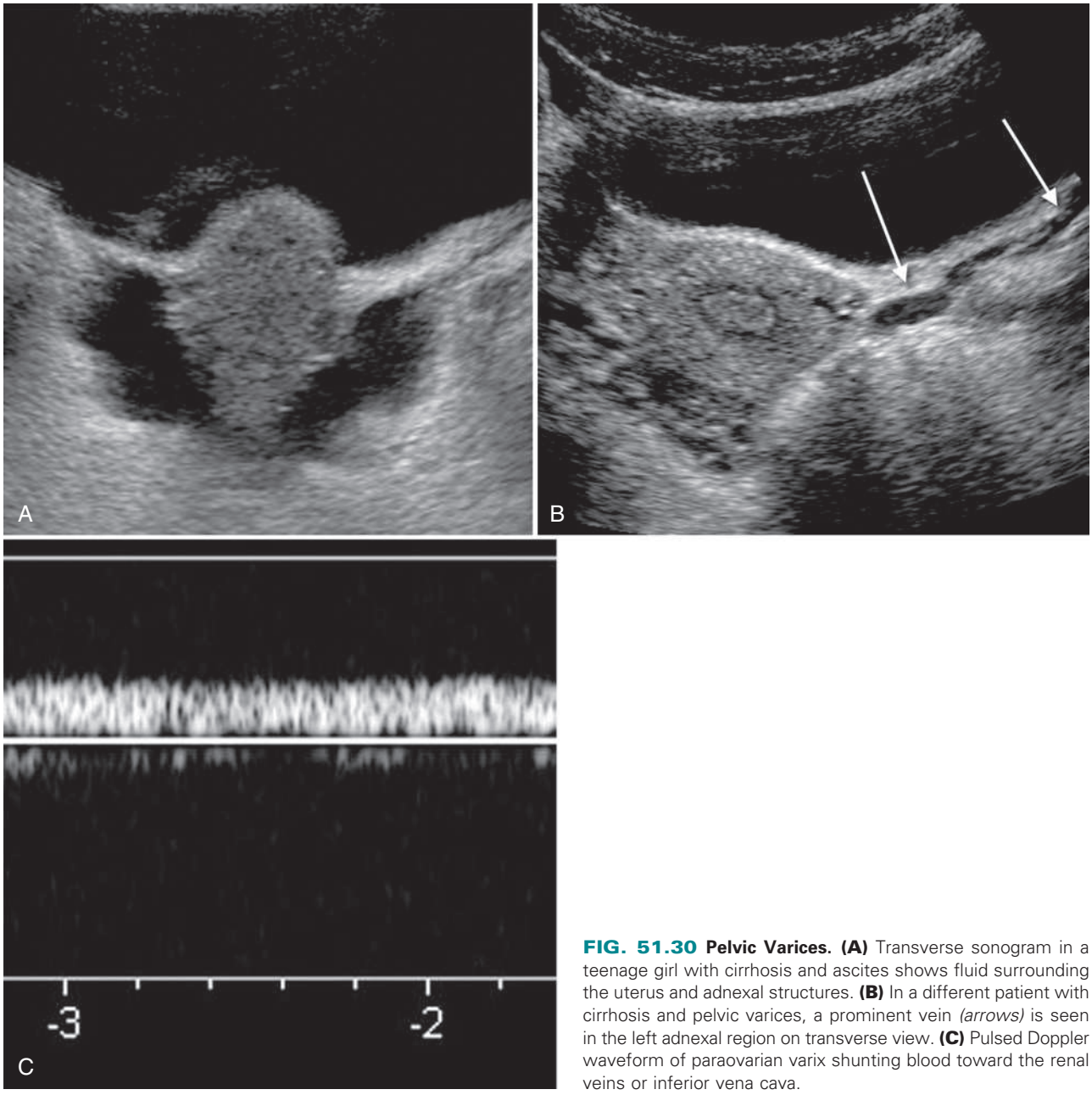

FIG. 51.30 Pelvic Varices. (A) Transverse sonogram in a teenage girl with cirrhosis and ascites shows fluid surrounding the uterus and adnexal structures. **(B)** In a different patient with cirrhosis and pelvic varices, a prominent vein *(arrows)* is seen in the left adnexal region on transverse view. **(C)** Pulsed Doppler waveform of paraovarian varix shunting blood toward the renal veins or inferior vena cava.

Causes of Cirrhosis in Children

Hepatitis
Toxins accumulated in inherited metabolic diseases
Biliary atresia
Cystic fibrosis

Sonographically, these changes in hemodynamics are signaled by decreasing diameter of the portal vein and its segmental branches, to the point at which they are reduced to threadlike structures. Flow velocity, when measurable, is reduced. Conversely, branches of the hepatic artery (normally difficult to see in children) may become visible with gray-scale sonography. Doppler sonography mirrors the increased hepatic arterial caliber and flow seen angiographically. Doppler shifts from segmental arteries are increased compared with their portal venous neighbors.

Two hemodynamic mechanisms appear to operate in patients with portal hypertension, especially in those with cirrhosis. The **backward-flow theory** explains portal hypertension by the increased resistance to portal venous flow caused by the intrahepatic block described earlier. In response to stagnating intrahepatic flow, portosystemic collaterals form and drain blood away from the liver, finally resulting in hepatofugal flow in some or all segmental branches and in the main portal vein, which is easily demonstrated with Doppler sonography. Why does the portal pressure remain elevated despite the presence of such a

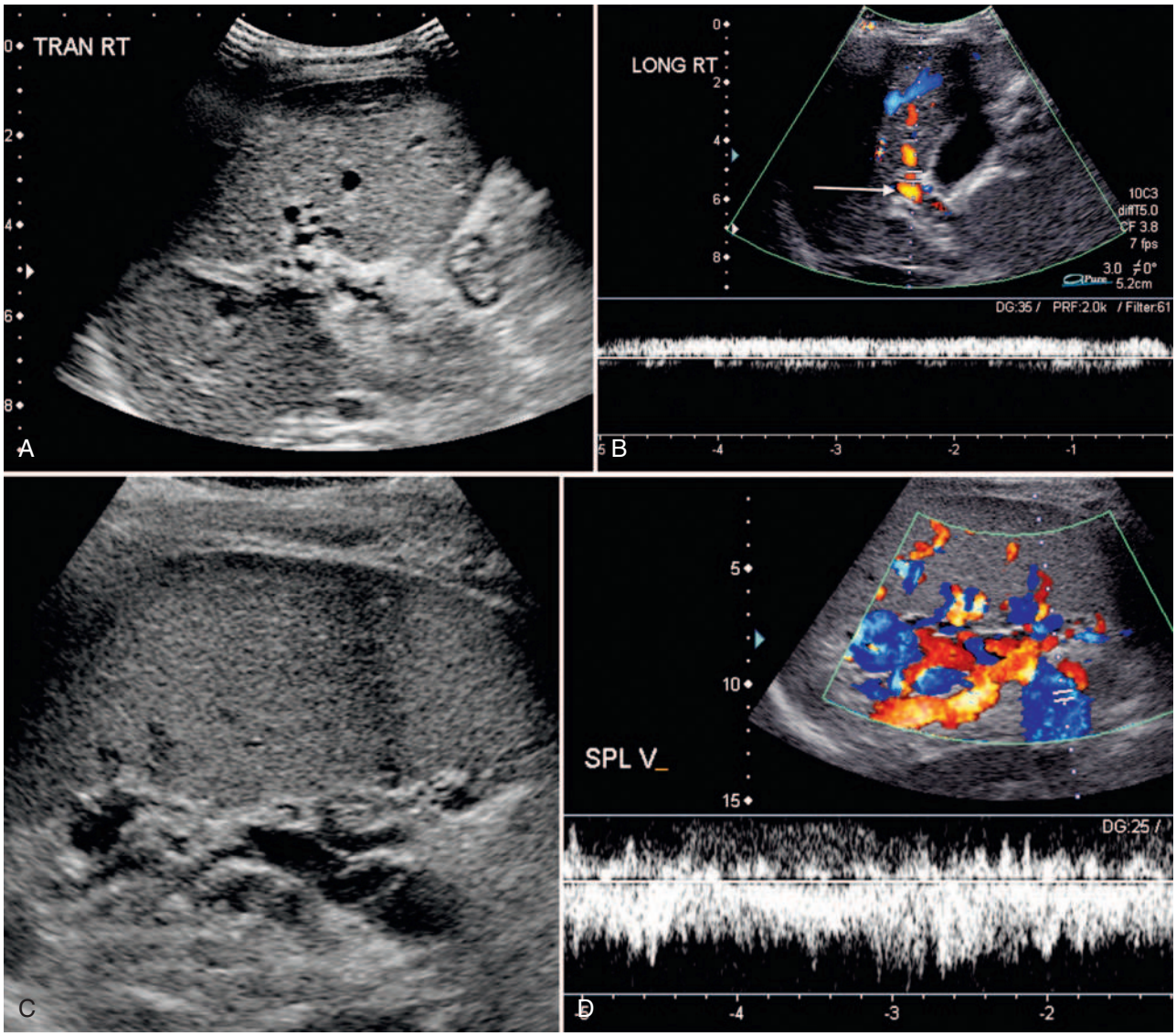

FIG. 51.31 Cavernous Transformation of Portal Vein in Child After Umbilical Vein Catheterization in Infancy. (A) Transverse sonogram of the liver shows several tortuous tubular veins, but no large main portal vein at the porta hepatis. **(B)** Color and pulsed Doppler waveform within one of these veins shows slow hepatopetal flow. The **main hepatic artery** is large *(arrow)* just deep to the vein being interrogated, a typical finding in cavernous transformation of the portal vein. **(C)** Despite the venous collaterals transporting blood into the liver around the thrombosed main portal vein, the child had **splenic varices** seen on longitudinal sonogram. **(D)** Color and pulsed Doppler waveform of the splenic varices shows brisker venous flow than that seen in the porta. See also Video 51.10.

decompression mechanism? This question may be answered by the **forward-flow theory.** In the backward-flow theory, portal blood flow is unchanged or even diminished. The forward-flow theory proposes that splanchnic arterioles dilate in patients with cirrhosis. The resultant decreased splanchnic resistance leads to increased flow in the intestinal arteries and veins, with subsequently increased portal venous blood flow. This would explain why portal hypertension is maintained despite extensive portosystemic shunting.

Because the obstruction to portal blood flow in cirrhosis is within the liver, periportal and pericholecystic venous collaterals rarely develop. However, blood is often shunted from the left portal vein through one or several tortuous **paraumbilical veins** to veins of the anterior wall of the abdomen and thorax. Documenting hepatofugal flow in such a vein situated within the falciform ligament is an easy way to establish the diagnosis of portal hypertension in children. The superficial abdominal (thoracic) wall collaterals are readily traced with color Doppler sonography if a high-frequency transducer is used.

The **left gastric vein,** shunting blood from the liver to esophageal varices, although dilated, becomes increasingly difficult to detect sonographically in children with advanced cirrhosis. Atrophy of the left lobe of the liver abolishes the acoustic window through which the lesser omentum is normally explored.

All the other portosystemic shunts described in Fig. 51.24 are possible in children with cirrhosis; thus the entire abdomen

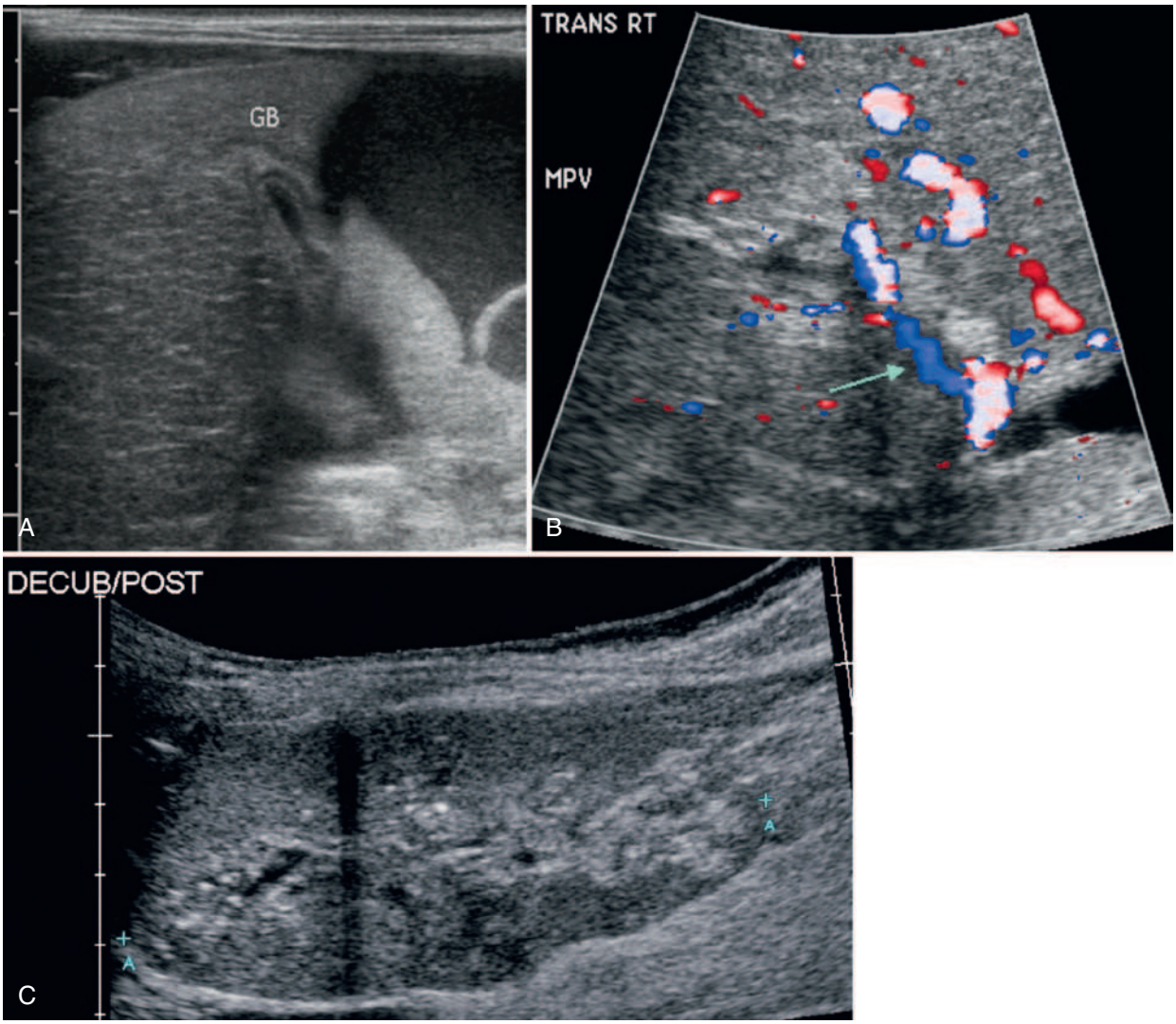

FIG. 51.32 Congenital Hepatic Fibrosis Causes Portal Vein and Biliary Obstruction. (A) Transverse grey-scale ultrasound shows ascites, gallbladder wall thickening, and coarse hepatic echotexture reflecting biliary ductal ectasia. **(B)** Color Doppler image in the same infant shows flow away from the liver in tortuous vessels *(arrow)* in the porta hepatis due to cavernous transformation of the portal vein. **(C)** Longitudinal prone image of the kidney in this infant shows abnormal renal echotexture with echogenic foci related to dilated collecting ducts, microscopic cysts, and dystrophic calcification.

and pelvis should be explored with sonography. The principle of **shunting** is constant in all portosystemic collaterals; a dilated, often tortuous splanchnic vein with reversed (hepatofugal) flow shunts blood into a systemic vein that is equally dilated at the site of the shunt. Rapid venous blood flow produces high, steady Doppler shifts. Turbulence and bidirectional flow often occur at the shunt site. A diagram that summarizes the Doppler findings is extremely helpful in visualizing the entire shunt route as well as the intrahepatic circulation. A few patients with severe portal hypertension develop reversal of flow in the main portal vein, sometimes because of the proximity of a large shunt near the porta hepatis. However, it must be recognized that if one were to depend on reversed portal venous flow to make the diagnosis of portal hypertension, one would miss the diagnosis in the majority of such patients.[79]

Suprahepatic (Posthepatic) Portal Hypertension

The clinical quartet of ascites, abdominal pain, jaundice, and hepatomegaly that follows obstruction of the hepatic veins is called the **Budd-Chiari syndrome** (Fig. 51.33). It is rare in children. Doppler sonography is particularly useful in excluding the diagnosis, because the four clinical signs that make up the syndrome are quite common in children with other forms of portal hypertension. The first patients with thrombosis of the hepatic veins described by Budd (1846), Fredrichs, Lange, and Chiari (1899) were thought to have hepatic phlebitis secondary to sepsis or syphilis, with primary involvement of small branches of the hepatic veins. Since then, other causes have been recognized, now classified as obstruction of the central and sublobular veins,

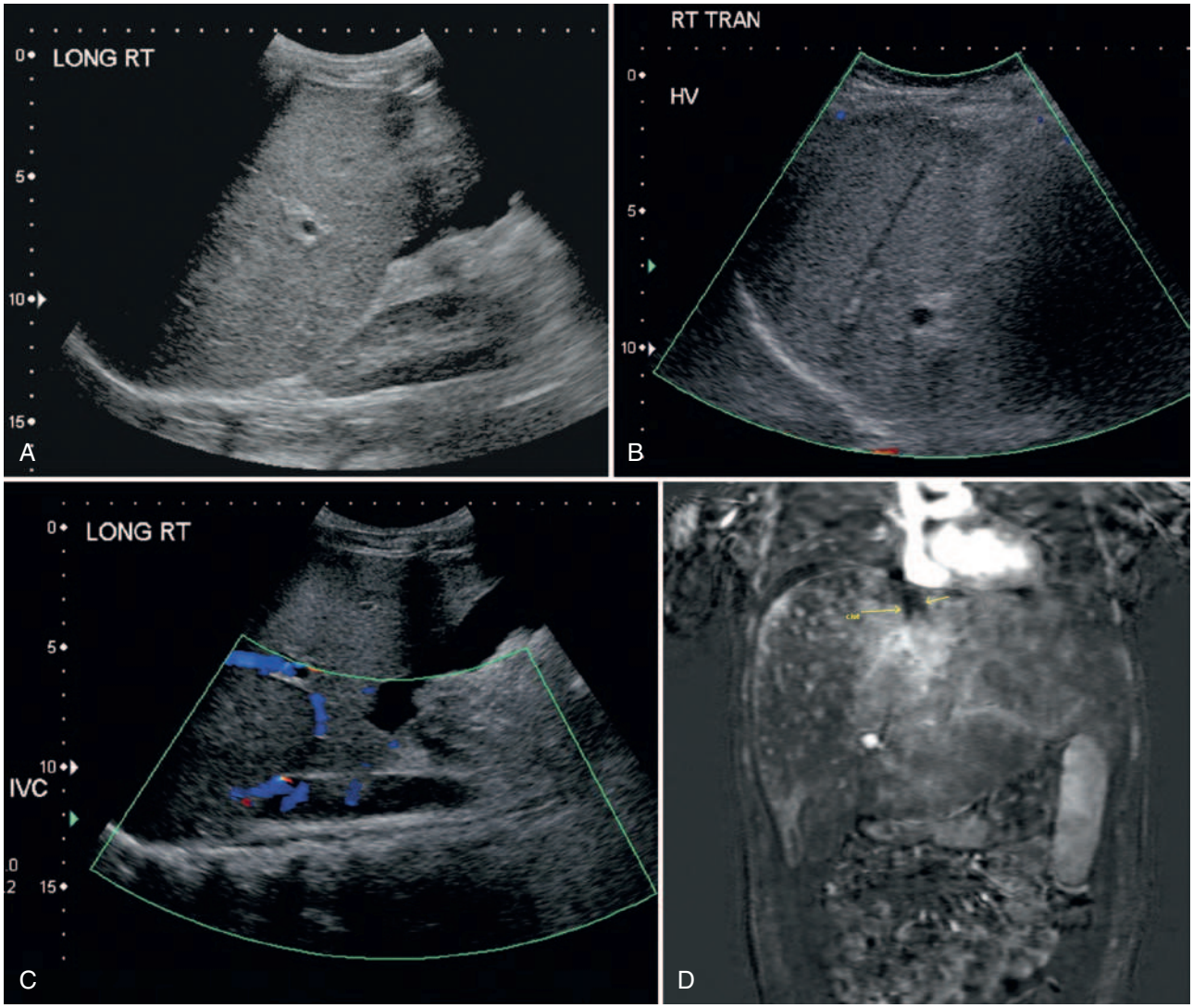

FIG. 51.33 Budd-Chiari Syndrome. (A) Acute appearance: the liver is enlarged, surrounded by ascitic fluid. **(B)** The diagonal course of a hepatic vein is filled with echogenic clot. **(C)** Longitudinal image of the inferior vena cava shows abrupt truncation and lack of intrahepatic flow. **(D)** Thrombus at the hepatic venous confluence *(arrows)* was confirmed with magnetic resonance flow-sensitive imaging.

the major hepatic veins, or the IVC near the hepatic vein ostia.[80] **Small-vessel hepatic venous occlusive disease** (VOD), also known as **sinusoidal obstruction syndrome** (SOS), is caused by toxins (pyrrolizidine alkaloids contained in ragwort or Jamaican bush tea); chemotherapy; bone marrow and stem cell transplantation; lupus erythematosus; hepatic irradiation; and oral contraceptives. This VOD involves primarily small hepatic venous radicles, although the major branches may be secondarily involved.

Sonographic findings of VOD include splenomegaly, ascites, small-caliber hepatic veins, and flow in paraumbilical veins. The sonographic diagnosis of VOD remains difficult; clinical and laboratory criteria are better indicators of the severity of VOD and its response to medical therapy.[81] **Thrombosis of the main hepatic veins** is usually caused by coagulation abnormalities or congenital malformations of the hepatic vein ostia. Obstruction of the hepatic portion of the IVC may result in thrombosis of the hepatic veins. Congenital membranes of the IVC resulting from faulty embryologic fenestration of its lumen can also lead to obstruction of hepatic veins.[82,83] The most common position for such a membrane is below an obstructed left hepatic vein and above a patent right hepatic vein, probably a result of an obstructing fibrous remnant of the left umbilical vein and ductus venosus.

Causes of Hepatic Venous Occlusive Disease

- Toxins
  - Pyrrolizidine alkaloid
  - Ragwort or Jamaican bush tea
- Chemotherapy
- Bone marrow transplantation
- Lupus erythematosus
- Hepatic irradiation
- Oral contraceptives
- Coagulation abnormalities
- Congenital malformations of hepatic vein ostia
- Obstruction of hepatic portion of inferior vena cava
- Congenital membranes of inferior vena cava

After any obstruction of the hepatic veins, the liver becomes enlarged and congested. Because the caudate lobe has its own hepatic vein that drains into the IVC below the others, it is often spared and serves as the only initial venous drainage route for the entire liver. The caudate lobe enlarges quickly and often compresses the IVC. This is followed by ascites, often pleural effusions, splenomegaly, and the formation of portosystemic collaterals. Doppler sonography shows absence or reversal of flow in the hepatic veins. Areas of high-velocity flow near stenoses of hepatic veins are easily detected with color-guided, pulsed Doppler sonography. In the absence of hepatic venous drainage, arterial blood may be shunted into the portal vein through microscopic shunts at the portal triad or through larger intrahepatic shunts. Portal venous flow may reverse. Alternately, the portal vein may thrombose when liver congestion is severe. **Wedge hepatic venography,** which shows a spider web network of intrahepatic veins instead of the usual hepatic venous lumens, is now rarely performed, because the hepatic vasculature is well assessed with Doppler sonography.

The patient with acute Budd-Chiari syndrome rarely has time to form portosystemic collateral routes. If present, shunt routes are similar to those seen in cirrhosis. Periportal and pericholecystic veins do not usually serve as shunt routes because they drain into the segmental branches of the right portal vein, which are highly congested in response to hepatic vein obstruction. Extensive intrahepatic shunts may form.

The treatment of hepatic vein occlusion is anticoagulant therapy, defibrotide, ablation of obstructive webs, or emergency portocaval shunting. The recanalization of hepatic veins, the regression of portal hypertension (decreased caliber and flow velocity in portosystemic shunts, smaller spleen, absorption of ascites), and the patency of therapeutic shunts can be assessed with Doppler sonography.

Surgical Portosystemic Shunts

Previously, definitive treatment of children with bleeding esophageal varices was surgical portosystemic shunts. These shunts are now created only when sclerotherapy of varices has failed or liver transplantation is not feasible. Children with healthy livers and prehepatic portal hypertension are still candidates for shunt procedures. **Transjugular intrahepatic portosystemic shunt** (TIPS) procedures are being performed as an alternate to classic surgical shunts in adults, with increasing use in children. The patency of transjugular shunts is monitored with Doppler sonography, which shows blood flowing from the "donor" right portal vein through the intrahepatic stent and into the right (or another) hepatic vein. Shunt stenoses, thrombosis, and flow around the stent are readily visible with Doppler sonography.

Surgical portosystemic shunts can be total or partial. **Total shunts** direct the entire venous blood flow from the congested splanchnic system into a systemic vein, as in the end-to-side portocaval shunt, in which the main portal vein is redirected. The hepatic end is ligated and the splanchnic end is connected to the IVC. In this situation, portal venous perfusion of the liver is minimal. **Partial shunts** divert only some of the splanchnic blood into a systemic vein, thereby yielding better liver perfusion and reducing the incidence of hepatic encephalopathy. The distal splenorenal (Warren) shunt connects the splenic vein to the left renal vein. The side-to-side, H-type, portocaval shunt connects the portal vein to the IVC at the porta hepatis. The REX shunt connects the left portal vein to the IVC using a donor vein. Many variants of these surgical procedures exist.

Doppler study of the intrahepatic portal veins is invaluable in the assessment of **portocaval shunt patency.** In the majority of patent shunts, flow in the intrahepatic portal veins is hepatofugal.[84] It is easy to understand why this should be so in side-to-side portocaval shunts, in which high-pressure intrahepatic venous blood flows through the shunt into the low-pressure vena cava. It is more difficult to explain hepatofugal flow in the intrahepatic portal veins in patients with an end-to-side portocaval shunt, in which the hepatic end of the portal vein has been ligated and cut. Blood may leave the liver through a system of collateral veins between intrahepatic branches of the portal vein and low-pressure systemic veins. This phenomenon has been demonstrated on angiography.[85]

Signs of shunt obstruction include the following:

- The shunt site is difficult or impossible to detect, and no Doppler signals can be obtained.
- Blood in the splanchnic vein feeding the shunt no longer flows toward the shunt.
- The direction of intrahepatic portal venous flow returns to normal.
- Spontaneous portosystemic shunts and other signs of portal hypertension reappear.

Hepatic Shear Wave Elastography

Real-time shear wave elastography (SWE) is a rapidly expanding method to assess liver stiffness or fibrosis in cirrhosis, inflammatory conditions, and tumors. An earlier technique for **mechanical compression without imaging** (Fibroscan), **transient elastography** (TE), was rapidly adopted by gastroenterologists and hepatologists but has been shown to be less reliable and reproducible than **shear wave elastography** (SWE) (Fig. 51.34). A third type of elastography, **acoustic radiation force imaging** (ARFI) (Fig. 51.35), uses a B-mode ultrasound image to position a fixed region of interest (ROI) box, which is measured in real time during a button push (which sends the shear wave pulse). ARFI is similar to TE with the added benefit of seeing the segment of liver being interrogated. Ultrasound elastography is readily performed in children without sedation, and measurements can be timed during respiratory pauses. Ultrasound elastography has shown good correlation with magnetic resonance elastography (MRE) and liver biopsy. Both techniques have potential to decrease the need for liver biopsy in children.[86-89]

DOPPLER SONOGRAPHY IN CHILDREN RECEIVING LIVER TRANSPLANT

Pretransplantation Evaluation

Before liver transplantation can be considered, the caliber and patency of the main portal vein and IVC must be assessed. This is usually done with Doppler sonography and supplemented with MRI.[90-92] If the portal vein diameter is less than 4 mm (as

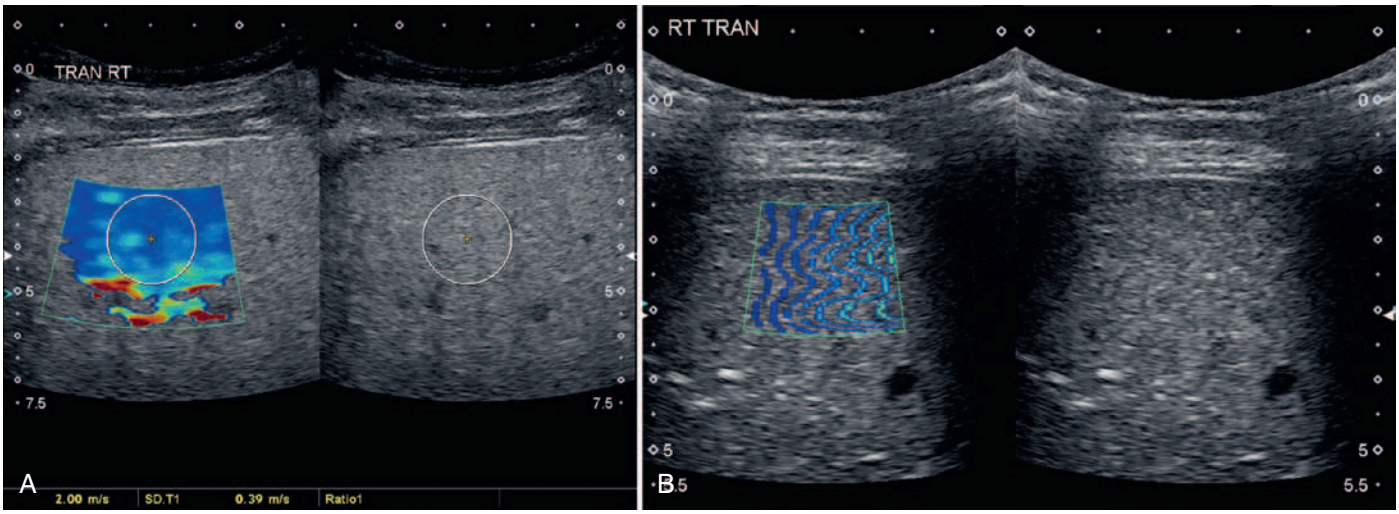

FIG. 51.34 Chronic Liver Disease Due to Hepatitis B. (A) Shear wave elastography color map and circular region of interest placed over a relatively homogenous area of liver, yielding a shear wave velocity of 2 m/sec. **(B) Propagation wave display** shows vertical blue bands of the shear wave front passing through the liver. Regular wave contours and intervals favor a homogenous site for measurements.

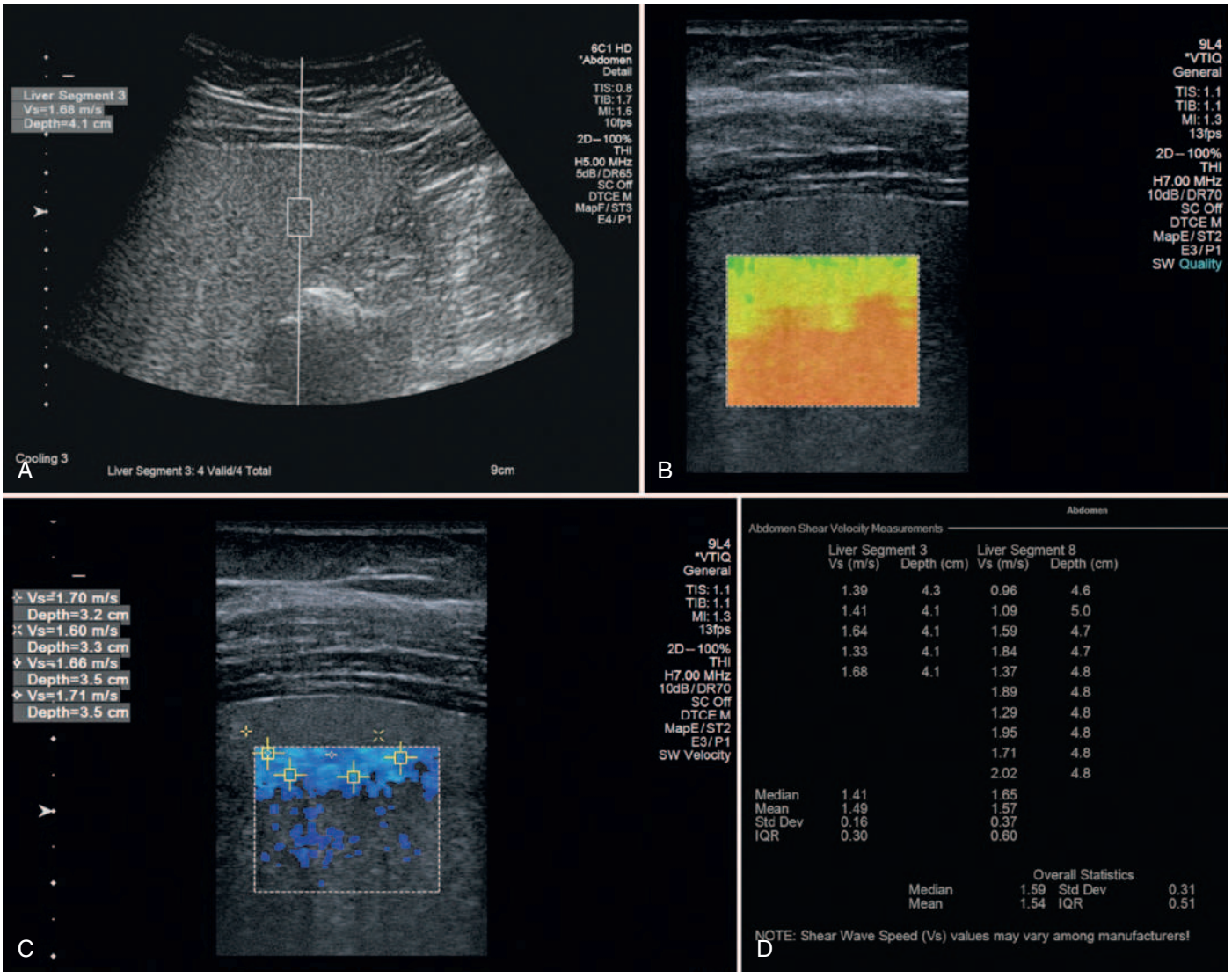

FIG. 51.35 Acoustic Radiation Force Imaging (ARFI). (A) Shear wave region of interest is selected perpendicular to the liver capsule and more than 1 cm deep to the liver margin. **(B)** Color display of elastography to aid in selecting an appropriate site. **(C)** Larger box in which multiple shear wave measurements have been made. **(D)** Table of results to look for erroneous data and spurious results, average values, standard deviation, and interquartile range (IQR).

in advanced cirrhosis) or if Doppler flow studies are equivocal, MRI or angiography may be performed. Children with biliary atresia may have an associated **polysplenia syndrome** (see Fig. 51.8C-G), which includes intestinal malrotation, bilaterally symmetrical patterns of the major bronchi, abnormal location of the portal vein anterior to the duodenum, and interruption of the IVC.[15,90] Liver transplantation may be more difficult in these children. It is essential that the surgeon be aware of this anatomic abnormality before transplantation.

In addition, portocaval or mesenteric-caval shunts, whether created surgically or occurring naturally, change both the flow pattern and the caliber of the main portal vein and may alter the surgical approach to transplantation. The anatomic variants of the hepatic artery are not always demonstrated on sonography, but angiography is rarely performed for the purpose of outlining the anatomy of the hepatic artery. The examination of the child before transplantation should also include several organs: the kidneys, lungs, heart, and intestinal tract.[90,92] During liver transplantation in the child, the donor hepatic artery is sometimes removed with a cuff of aorta and anastomosed to the recipient's abdominal aorta or iliac artery. An adult liver is usually divided before being transplanted into a small child. Although the left lobe (segments 2 and 3) is preferred, an adult liver may be divided and used for two recipients. A **transient fluid collection** often forms around the cut surface of the transplanted lobe or segments, even though the cut is packed with hemostatic material such as Gelfoam or fibrin glue. Because the anatomy involved in segmental or lobar liver transplantation differs considerably from the normal anatomy and from the anatomy involved in whole-organ transplantation, a diagram of the procedure is a useful guide for the sonographer assessing patency of anastomosed vessels.

Posttransplantation Evaluation

The most common complications in the immediate postoperative period are **hepatic artery stenosis, spasm,** and **thrombosis.** Although collateral vessels may form in the child and shunt arterial blood into the liver, bile duct injury frequently occurs, followed by the formation of bile lakes and recurrent infection. Retransplantation is almost invariably necessary.

Immediate Doppler examination either in the surgical suite or at the child's bedside soon after surgery and then daily for 5 to 7 days is typically performed to confirm patency of the anastomosed vessels, before clinical or biochemical liver examination findings become abnormal.[93] The hepatic arterial anastomosis can be difficult to see adjacent to the Roux loop, so it is important to examine the intrahepatic arterial branches adjacent to intrahepatic portal veins, with both gray-scale and Doppler techniques. Optimal sites for the detection of hepatic arterial Doppler signals in whole-liver transplants are adjacent to the umbilical branch of the left portal vein and adjacent to the branch to segments 3 and 4, and alongside the right portal vein and the branches to segments 6 and 7. The presence of arterial signals at these sites usually establishes patency of the hepatic artery. In segmental liver transplants, the "porta hepatis" is located eccentrically along the right lateral costal margin.[94-96] Given the variability of graft size and orientation in the right upper quadrant, the sonographer must find optimal imaging windows by trial and error. In the immediate postoperative period, hepatic arterial flow (both systolic and diastolic) is generally brisk. However, in the next 2 to 3 days, graft edema may result in transiently decreased diastolic flow. As long as systolic upstroke remains sharp and there are other signs of graft swelling (i.e., periportal edema), patients are watched expectantly. If the patient's liver enzyme levels rise, further Doppler evaluation or surgical reexploration is generally performed. Tardus-parvus waveforms in the hepatic artery in the immediate perioperative period are most likely related to arterial spasm and are treated pharmacologically.

Children with clinically undetected, chronic obstruction of the main hepatic artery have been reported in whom dampened intrahepatic arterial flow was detected with Doppler sonography. Angiography in these patients shows obstruction of the hepatic artery and liver perfusion through extensive arterial collaterals around the site of a portoenterostomy at the porta hepatis.

In patients well enough to eat or receive gastric tube feedings, remember that hepatic arterial Doppler shifts are difficult to detect after a meal.[70] A repeat examination after a fast may show much stronger signals. Failure to detect intrahepatic arterial Doppler shifts indicates thrombosis or a prethrombotic state. Given the risk of graft injury, arteriography is generally performed in this situation, with the intent to treat with thrombolytics or angioplasty.

Although hepatic artery interrogation is the most important part of the posttransplant examination, the Doppler study is also helpful in assessing the patency of the venous anastomoses—the portal and hepatic veins and the IVC. The sites of venous anastomosis are clearly visible with gray-scale sonography and should be demonstrated (Fig. 51.36). **Portal venous thrombosis** at the anastomosis may occur but is less frequent than arterial occlusion. Turbulence may be expected at the anastomotic site of the portal vein, especially when there is discrepancy in the size of anastomosed vessels. **Stenosis** or compression of the portal vein is accompanied by locally increased Doppler shifts (Fig. 51.37). Portal hypertension may follow. Poststenotic dilation of the portal vein may occur without serious sequelae. In some patients with a small portal vein from a segmental transplant, prolonged fasting may increase hepatic arterial flow and make visualization of the portal vein difficult. A limited follow-up scan, after feeding the patient, can vastly improve visualization of portal venous flow.

Inferior vena cava thrombosis is usually asymptomatic in the child because collateral flow through the paravertebral venous system is quickly established. The sonographic diagnosis of an IVC thrombus in a child with liver transplantation can be difficult. The IVC lumen is obliterated by thrombus, and the vessel becomes very difficult to visualize (Fig. 51.38). However, even a patent IVC can be difficult to find because anatomic relationships are greatly altered in these children. At Doppler sonography, flow in a hemiazygos vein is easily mistaken for flow in the IVC. The IVC is frequently compressed by a large donor graft, so careful examination of the draining hepatic veins is important.

During segmental transplantation, the recipient's IVC is left intact and the hepatic vein(s) directly anastomosed to the

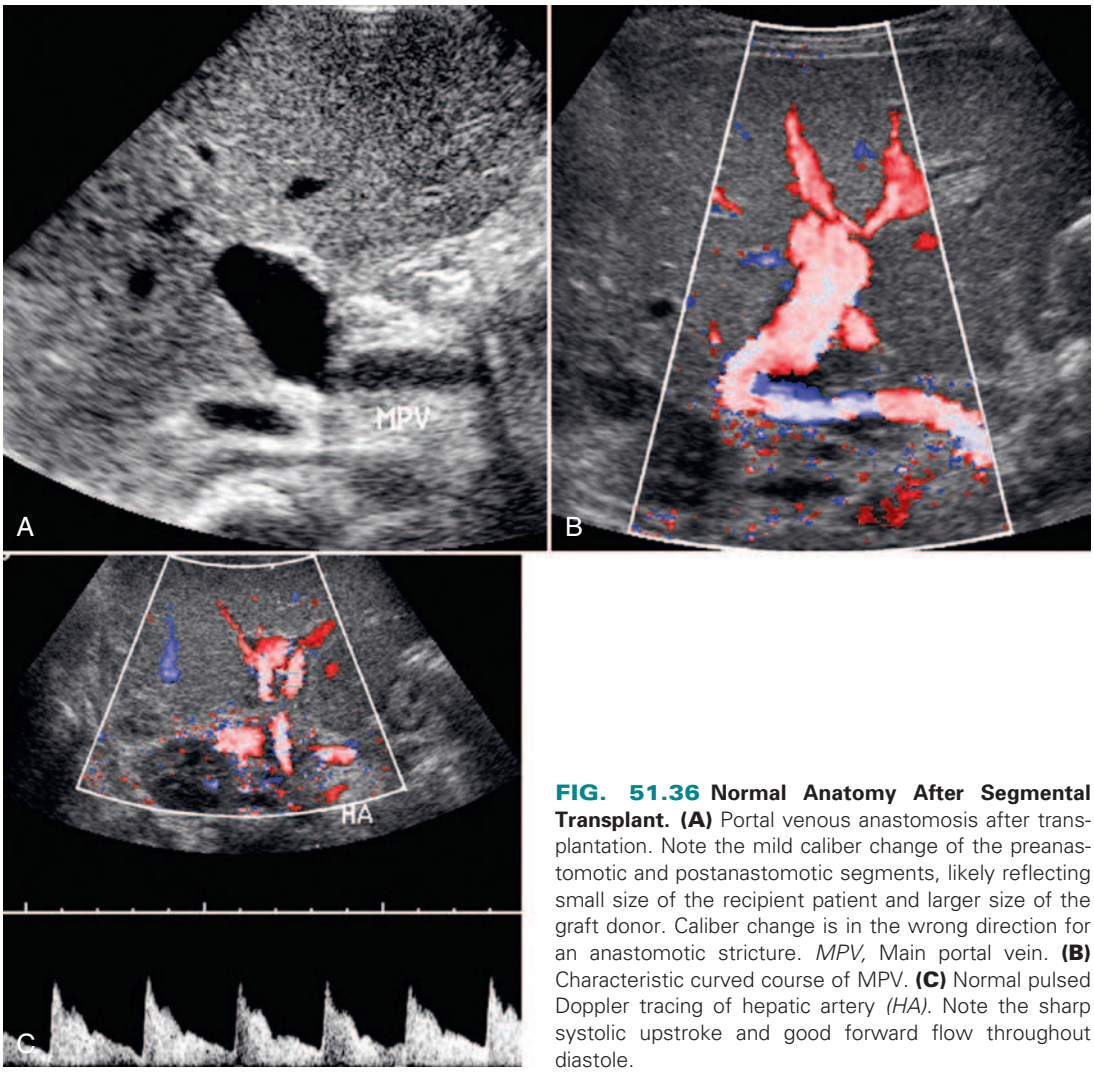

FIG. 51.36 Normal Anatomy After Segmental Transplant. (A) Portal venous anastomosis after transplantation. Note the mild caliber change of the preanastomotic and postanastomotic segments, likely reflecting small size of the recipient patient and larger size of the graft donor. Caliber change is in the wrong direction for an anastomotic stricture. *MPV,* Main portal vein. **(B)** Characteristic curved course of MPV. **(C)** Normal pulsed Doppler tracing of hepatic artery *(HA).* Note the sharp systolic upstroke and good forward flow throughout diastole.

IVC or right atrium. Both the hepatic veins and the IVC may thrombose, starting at the anastomosis. The immediate postoperative examination outlines the surgical anatomy in these children and serves as a useful standard for comparison in assessing the continued patency of the anastomosed vessels. Stumps of oversewn graft IVC are also frequently encountered, lying between the liver parenchyma and native IVC. Thrombus in the remnant of donor IVC seldom propagates but can be seen as intraluminal echoes perioperatively. With time, these donor IVC remnants become less visible, collapsing and blending into the medium-level echoes of the retroperitoneum.

Graft rejection does not result in predictable flow alterations of the hepatic artery, unlike the increased intrarenal resistance to flow noted in acute renal allograft rejection. However, changes in the normal phasicity of hepatic venous blood flow have been linked to graft rejection. Specifically, when normal triphasic hepatic venous blood flow becomes monophasic, biopsy specimens show evidence of acute rejection (sensitivity 92%, specificity 48%) or other hepatic disease (cholangitis, fibrosis, centrilobular congestion and necrosis, lymphoproliferative disease, cholestasis, hepatitis).[95,97] Some liver transplant recipients never demonstrate triphasic flow, presumably because of poor elasticity in the donor graft, and thus these criteria are not useful in this subgroup.

Biliary air or **pneumobilia** is another common finding in patients after liver transplant (see Fig. 51.38H, Video 51.11). Anecdotally, it is less frequent in the immediate postoperative period (despite routine stenting of the duct) and is more likely to be noted on routine follow-up scans several months later. The source of air is retrograde passage from the gastrointestinal tract, through the Roux loop and choledochoenterostomy and into the bile ducts. Careful examination of the liver parenchyma on routine follow-up sonography is important to exclude biliary tree abnormalities, abscess, focal areas of ischemia, and complications of percutaneous biopsy (e.g., bile lake, AV shunts, hemorrhage). Biliary ductal dilation may be caused by stenosis of the choledochoenterostomy, bile duct ischemia with secondary stricture, stone disease, and compression of ducts by external

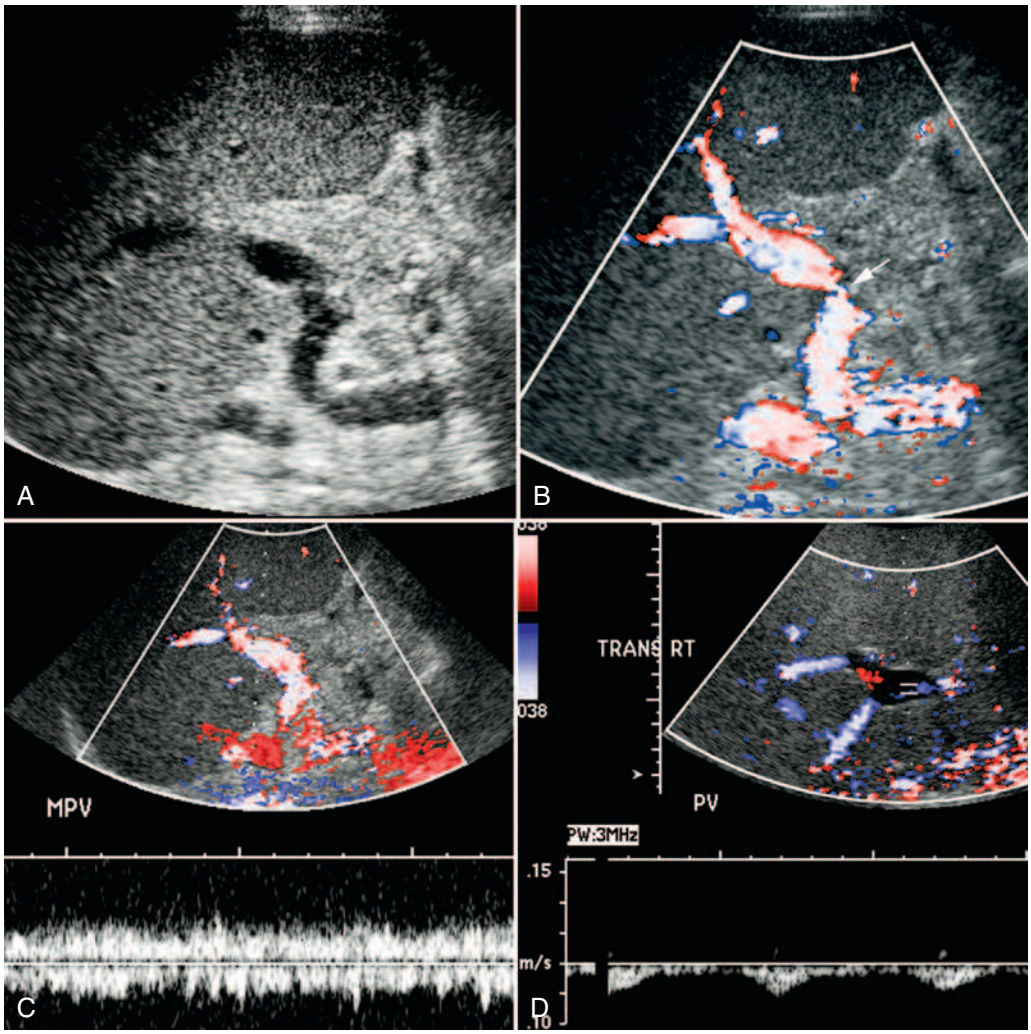

FIG. 51.37 Portal Vein Stenosis After Transplantation. (A) Subcostal oblique sonogram and **(B)** color Doppler image show a narrowed segment of the portal vein at the anastomotic site *(arrow).* **(C)** Pulsed Doppler tracing just beyond the site of stenosis shows turbulent, high-velocity, bidirectional flow. *MPV,* Main portal vein. **(D)** Color and pulsed Doppler images in a different transplant patient show impending thrombosis of the portal vein *(PV),* with absent color signal and minimal flow on low scale settings.

masses, fluid collections, or adenopathy. Perioperative **fluid collections** are common and typically resolve in weeks to months. Persistent collections may represent lymphocele or persistent bile leak. New collections are most often related to infection, iatrogenic injury, trauma, or graft failure.

Long-term survival of pediatric liver transplant patients continues to improve, bringing a new set of long-term complications to search out during imaging examinations. **Aneurysms** may develop in the portal vein or hepatic arteries (see Fig. 51.38E-G), particularly at anastomoses or where segments of donor vessel were used. A careful search of the entire length of donor portal vein and hepatic artery to the point of connection to native vasculature is recommended. In the case of infrarenal aortic anastomoses, the entire length of the hepatic artery conduit may be difficult to identify. Intervening bowel gas may be compressed out of the way, or a far lateral, midaxillary line of scanning through the flank may show the graft site along the anterior surface of the aorta just below the renal arteries. Cross-sectional imaging with CT angiography, MRI, and occasionally angiography are sometimes needed. Hepatic vein stenosis can also be a cause of cryptic graft failure. Careful examination of the hepatic venous outflow may still show only indirect evidence of stenosis: loss of phasicity in the hepatic veins, with change in phasicity in only one of the three hepatic veins. Given the location of the upper hepatic venous or caval anastomosis, sonographic evaluation is challenging. Occasionally, venography will clearly show a tight stenosis where one was only suspected sonographically. Fortunately, venous access in these cases can also be used to treat the lesion with angioplasty.

Additional complications in long-term liver transplant survivors include renal cystic disease,[96] chronic renal failure, graft-versus-host disease, lymphoproliferative disorders, and other complications of immune suppression.

Multiorgan Transplants

A growing new subset of liver transplant recipients involves those receiving combined liver–small intestine transplants. Sonographic evaluation of the whole-liver transplant is unchanged, although the addition of a second donor pancreas and donor aorta with

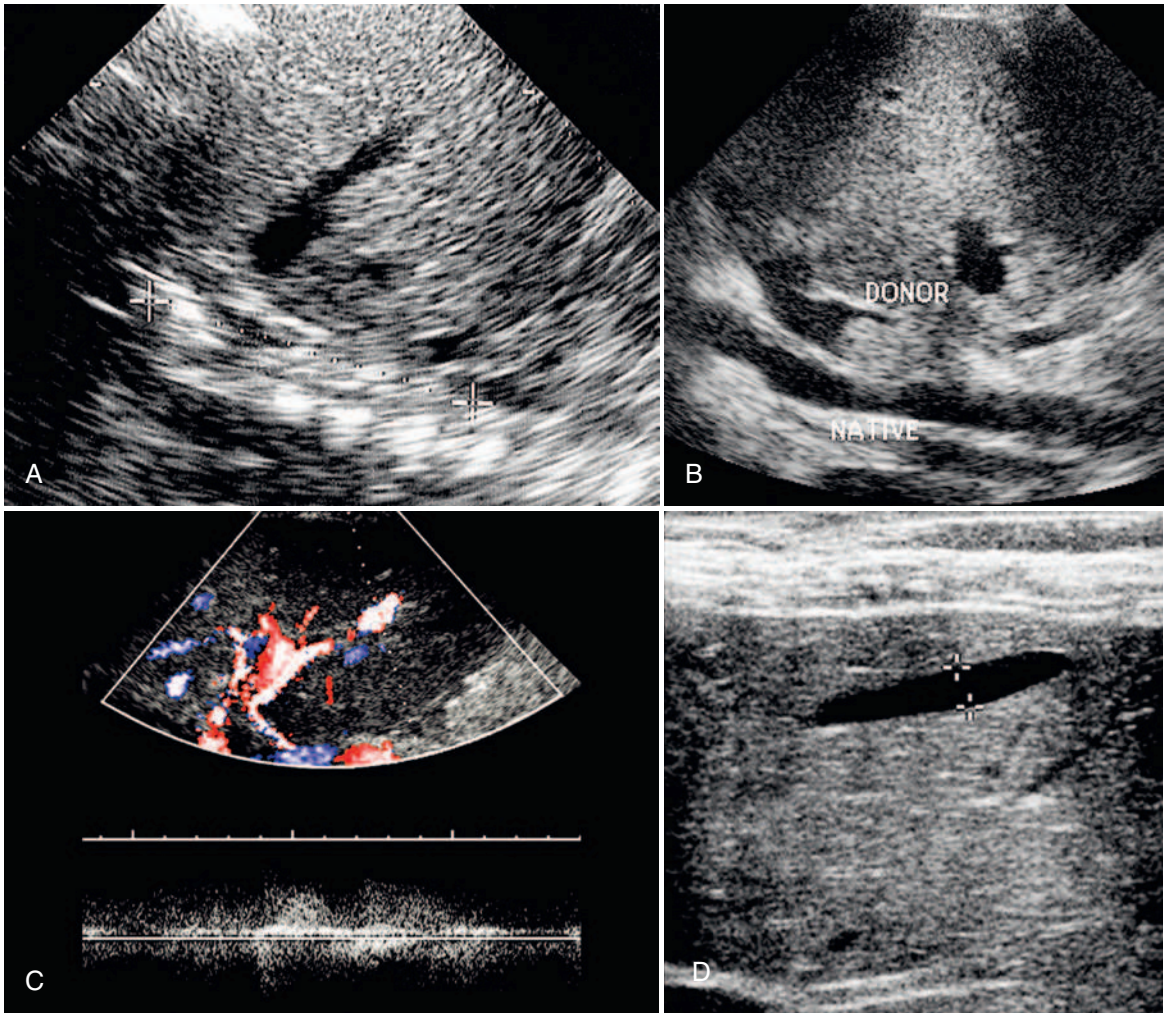

FIG. 51.38 Transplant Complications. (A) Thrombosis *(cursors)* of inferior vena cava (IVC) after bisegmental liver transplantation in a 2-year-old child contrasts with the hypoechoic lumen of a nearby patent hepatic vein. **(B) Partial thrombosis** of oversewn donor IVC interposed between native IVC and hepatic parenchyma. This is not usually problematic unless the clot propagates. **(C)** Color and pulsed Doppler image shows **arteriovenous fistula** with turbulent flow in a transplant liver after biopsy. **(D)** Focal dilation *(cursors)* of a bile duct in the left lobe of the transplant liver. This may be caused by hepatic arterial compromise and duct stenosis or ductal injury from previous percutaneous biopsy.

Continued

celiac and superior mesenteric arteries can create Doppler imaging challenges.[97] Evaluation of the small bowel is limited when there is postoperative ileus. Color Doppler evaluation of donor small bowel wall perfusion is useful in the immediate perioperative period. As bowel function returns, other clinical parameters replace Doppler evaluation of bowel viability. When complications arise, sonographic evaluation of the small bowel is similar to the approach used for necrotizing enterocolitis, looking for pneumatosis, poor perfusion, complicated ascites, and signs suggesting perforation. Sonographic imaging experience with these patients continues to expand.

THE SPLEEN

Examination of the spleen is an integral part of the sonographic assessment of the child with liver or pancreatic disease or with infection or trauma.

Cysts of the spleen are congenital (epithelial lined),[98] posttraumatic (pseudocyst without lining),[99] or hydatid (unilocular and later daughter cysts).[51] Splenic cysts associated with polycystic kidney disease are rare in childhood. Splenic **abscesses** are found most frequently in immunosuppressed or leukemic children with candidiasis. The abscesses within the enlarged spleen usually become visible long after the diagnosis of *Candida* sepsis has been made. Cat-scratch disease is another cause of multiple splenic abscesses. Splenic **calcifications** may be the result of granulomatous infections (histoplasmosis, tuberculosis) or chronic granulomatous disease of childhood.

Splenic enlargement accompanies many systemic infections, including infectious **mononucleosis** and other viral infections, typhoid fever, malaria, and fungal infections. Both the length and the width of the spleen increase (Fig. 51.39). The lower tip of the spleen becomes rounded. Other causes of enlargement include congestion in portal hypertension and infiltration with leukemic or lymphomatous tissue, which is usually impossible to distinguish from normal splenic parenchyma sonographically. These conditions underline the importance of examining the spleen in the context of the entire abdomen (e.g., for liver disease and portosystemic collaterals or for lymphadenopathy).[31]

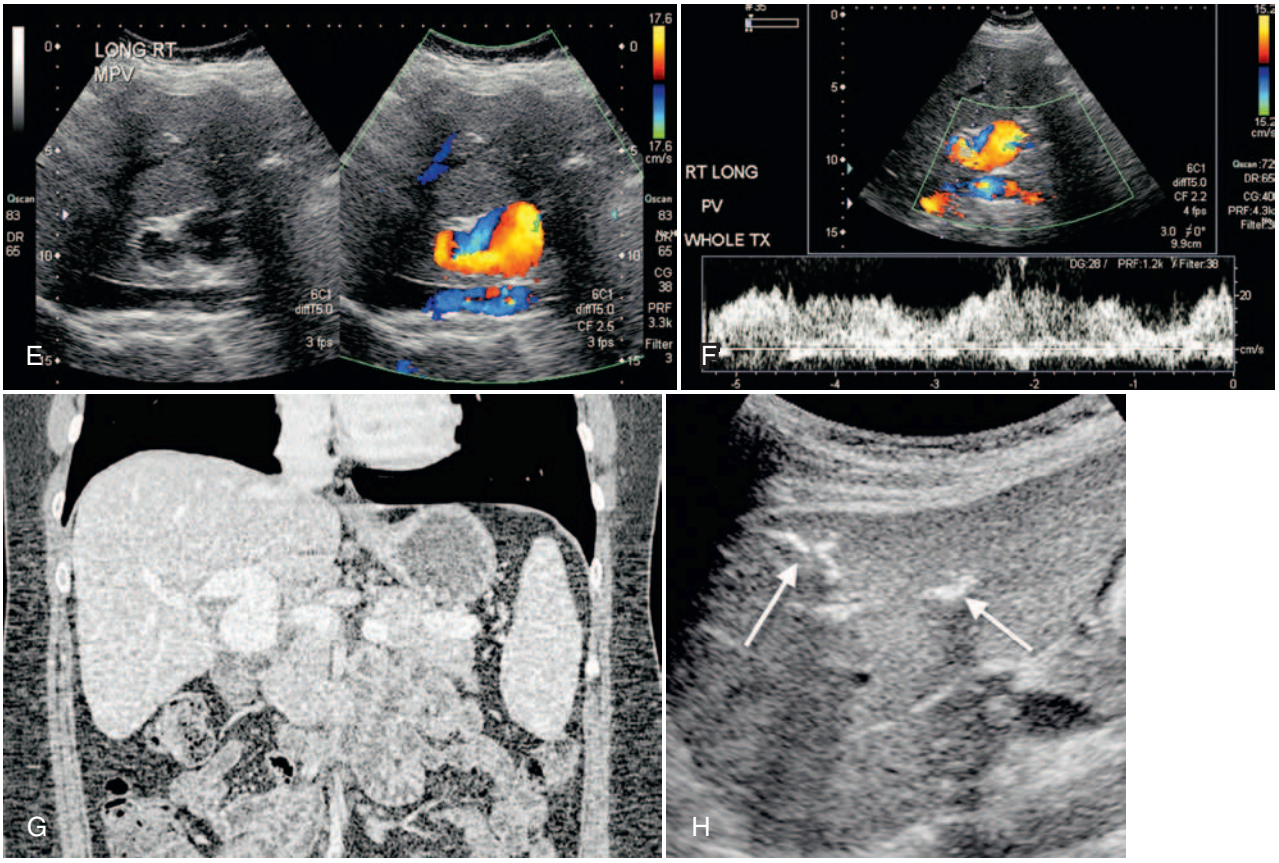

FIG. 51.38, cont'd **(E)-(H)** Portal vein **aneurysm** several years after whole-liver transplant. **(E)** Twin screen (gray-scale and color Doppler) display of swirling blood flow in the main portal vein. **(F)** Color and pulsed Doppler waveform shows turbulent flow within the aneurysm. **(G)** Coronal computed tomography (CT) image of same patient shows the portal vein aneurysm displacing the hepatic artery. Note the perisplenic and perigastric varices, best seen on the coronal reformatted CT image. **(H) Pneumobilia.** Transverse sonogram shows branching echogenic lines of air with "dirty" shadowing *(arrows)*. Air within the biliary tree is common after choledochoenterostomy and is not itself a complication, although it can impair sonographic evaluation of the transplant liver. See also Video 51.11.

Causes of Splenic Enlargement

Infection (bacterial, viral, protozoal, fungal)
Lymphoma, leukemia
Lymphoproliferative disorders
  Chronic granulomatous disease
Cirrhosis, portal hypertension
Sequestration
  Sickle cell disease
Hemolytic anemia, extramedullary hematopoiesis
Langerhans cell histiocytosis
Storage diseases
  Gaucher disease
  Niemann-Pick disease
  Mucopolysaccharidoses
Collagen vascular disease
Congestive heart failure
Sarcoidosis

The spleen is one of the most frequently injured organs when abdominal trauma has occurred. **Splenic hematomas** are usually hypoechoic lesions, often located under the capsule (Fig. 51.40C). Fresh hematomas may be isoechoic or hyperechoic, and some linear lacerations are difficult to see on sonography. Hemoperitoneum is almost always present. Sonography is being used as the initial screening examination in children with abdominal trauma with variable results.[100,101] CT may be used only in doubtful cases or when there is concomitant spinal or head trauma. Proponents of sonography state that despite underdiagnosis of some pancreatic and exceptional splenic hematomas as well as some mesenteric tears, the surgical management of the children was not affected, and no child died because lesions were missed at the initial examination.[101] In these cases, CT was performed if sonography was difficult because of rib fractures, or if there was doubt or increasing unexplained hemoperitoneum. CT remains the standard of care for pediatric abdominal trauma in the United States, whereas ultrasound is favored in Canada and some European countries.

Spontaneous rupture of the spleen occurs in the enlarged fragile organ in infectious mononucleosis and is heralded by hemoperitoneum.[102]

Splenic infarcts occur frequently in children with sickle cell anemia and also in children with various forms of vasculitis (see Fig. 51.40D). Lesions are usually triangular and hypoechoic. If the ligamentous attachments of the spleen are lax or absent, the spleen may move about in the abdomen **(wandering spleen)** and occasionally may undergo torsion on its pedicle. Torsion

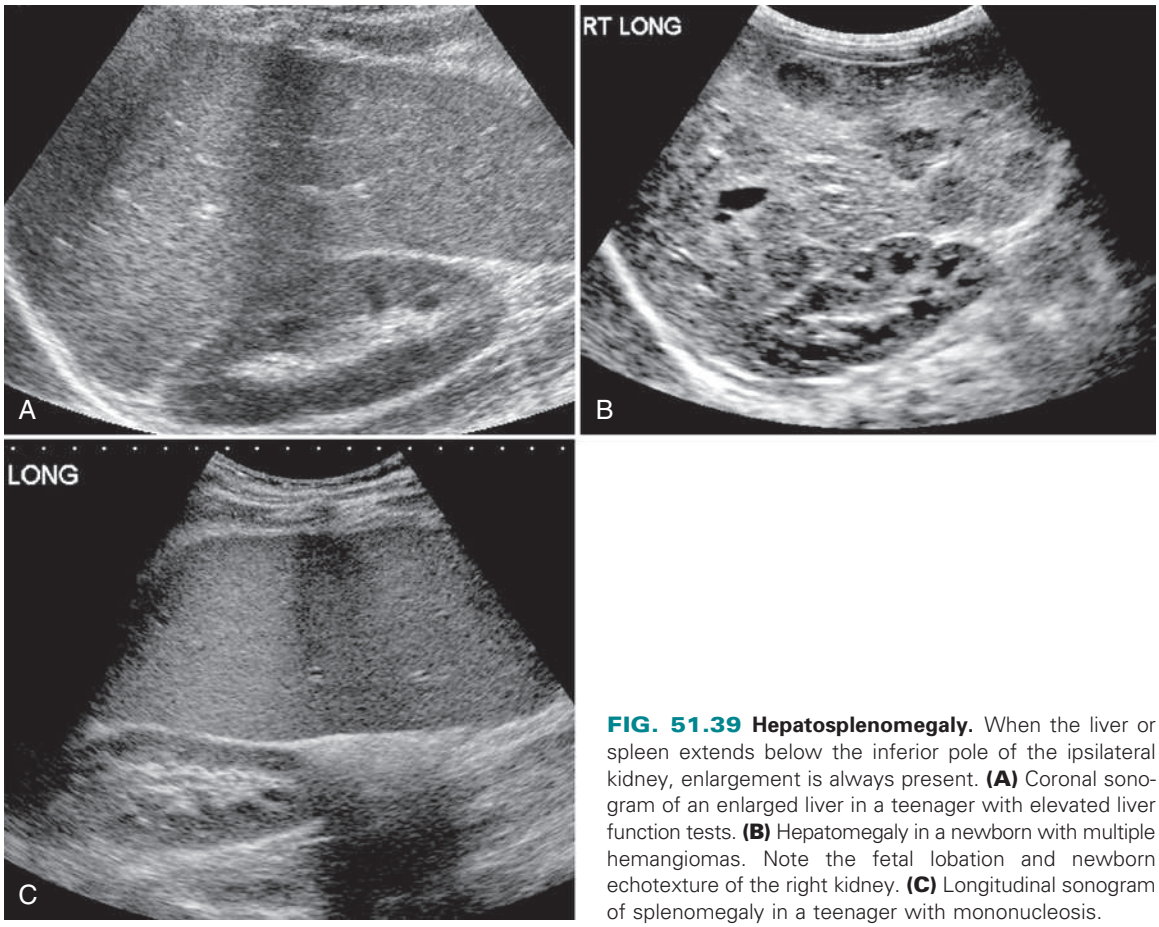

FIG. 51.39 Hepatosplenomegaly. When the liver or spleen extends below the inferior pole of the ipsilateral kidney, enlargement is always present. **(A)** Coronal sonogram of an enlarged liver in a teenager with elevated liver function tests. **(B)** Hepatomegaly in a newborn with multiple hemangiomas. Note the fetal lobation and newborn echotexture of the right kidney. **(C)** Longitudinal sonogram of splenomegaly in a teenager with mononucleosis.

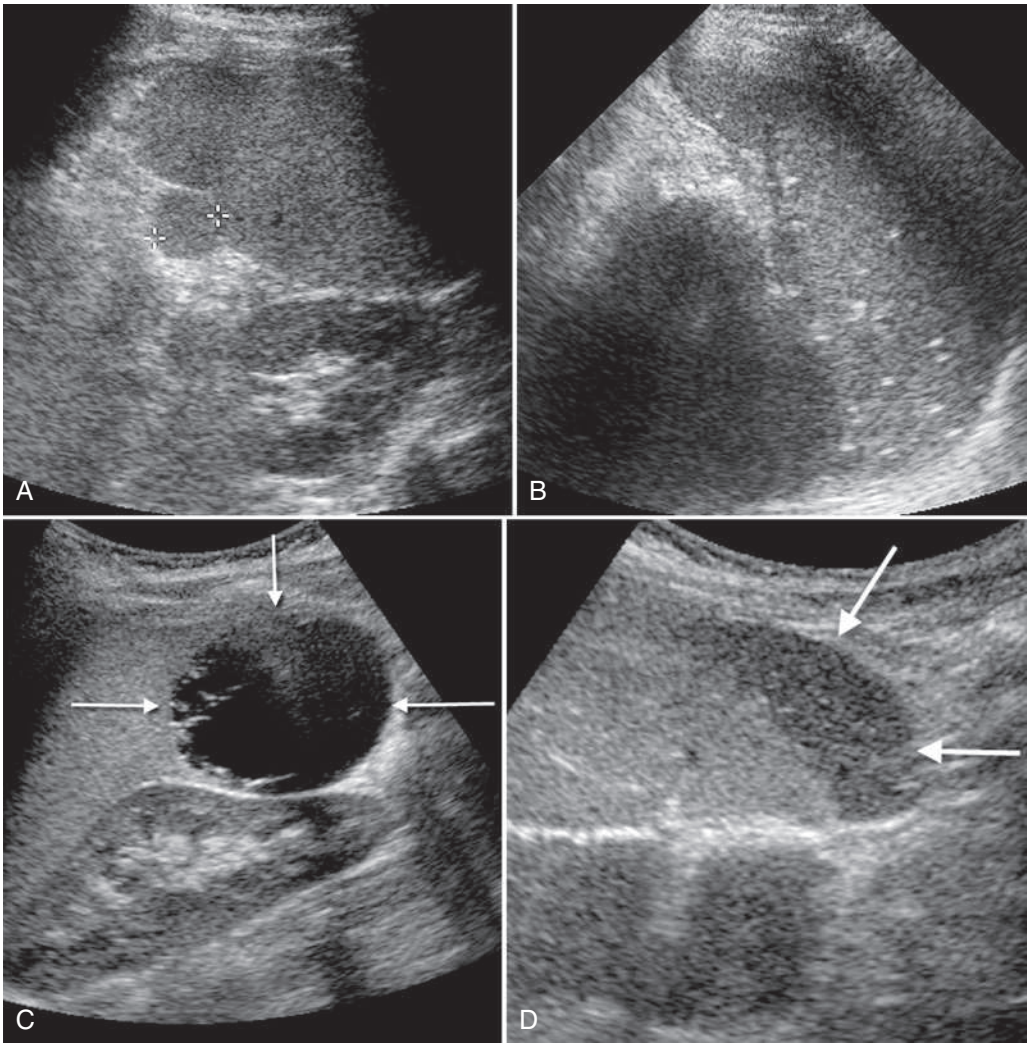

FIG. 51.40 Splenic Abnormalities. (A) Transverse sonogram shows small **accessory spleen** near the splenic hilum *(cursors).* **(B) Granulomas.** Multiple echogenic, faintly shadowing foci. **(C)** Subacute **hematoma/contusion,** which is evolving into a posttraumatic cyst *(arrows).* A well-defined hypoechoic area in the splenic tip after sports trauma in a teenager. **(D) Splenic infarct** *(arrows)* in a patient after bone marrow transplant with sepsis.

and splenic infarction can manifest as acute abdominal pain or a palpable mass.

Acknowledgment

This chapter is an update and revision of the previous excellent work by Heidi Patriquin, MD, who died in November 2000. Dr. Patriquin was a pioneer in pediatric ultrasound and particularly in abdominal visceral Doppler. She developed novel techniques for evaluating blood flow, and described important differences in pediatric and adult sonography. I had the pleasure of knowing her briefly and found her enthusiasm for pediatric ultrasound contagious. I think she would enjoy the advances described and new images included in the chapter.

REFERENCES

1. Bismuth H. Surgical anatomy and anatomical surgery of the liver. World J Surg. 1982;6(1):3-9.
2. Couinaud CLF. Etudes anatomiques et chirurgicales. Paris: Masson; 1957.
3. Dodds WJ, Erickson SJ, Taylor AJ, et al. Caudate lobe of the liver: anatomy, embryology, and pathology. AJR Am J Roentgenol. 1990;154(1):87-93.
4. Ikeda S, Sera Y, Yamamoto H, Ogawa M. Effect of phenobarbital on serial ultrasonic examination in the evaluation of neonatal jaundice. Clin Imaging. 1994;18(2):146-148.
5. Tan Kendrick AP, Phua KB, Ooi BC, et al. Making the diagnosis of biliary atresia using the triangular cord sign and gallbladder length. Pediatr Radiol. 2000;30(2):69-73.
6. Todani T, Watanabe Y, Narusue M, et al. Congenital bile duct cysts: classification, operative procedures, and review of thirty-seven cases including cancer arising from choledochal cyst. Am J Surg. 1977;134(2):263-269.
7. McHugh K, Daneman A. Multiple gastrointestinal atresias: sonography of associated biliary abnormalities. Pediatr Radiol. 1991;21(5):355-357.
8. Caroli J, Soupault R, Kossakowski J, et al. Congenital polycystic dilation of the intrahepatic bile ducts; attempt at classification. Sem Hop. 1958;34(8/2):488-495.
9. Levy AD, Rohrmann Jr CA, Murakata LA, Lonergan GJ. Caroli's disease: radiologic spectrum with pathologic correlation. AJR Am J Roentgenol. 2002;179(4):1053-1057.
10. Davies CH, Stringer DA, Whyte H, et al. Congenital hepatic fibrosis with saccular dilatation of intrahepatic bile ducts and infantile polycystic kidneys. Pediatr Radiol. 1986;16(4):302-305.
11. Adeva M, El-Youssef M, Rossetti S, et al. Clinical and molecular characterization defines a broadened spectrum of autosomal recessive polycystic kidney disease (ARPKD). Medicine (Baltimore). 2006;85(1):1-21.
12. Pereira EC, Yan J, Asaid M, et al. Conservative management of spontaneous bile duct perforation in infancy: case report and literature review. J Pediatr Surg. 2012;47(9):1757-1759.
13. Alagille D, Estrada A, Hadchouel M, et al. Syndromic paucity of interlobular bile ducts (Alagille syndrome or arteriohepatic dysplasia): review of 80 cases. J Pediatr. 1987;110(2):195-200.
14. Turnpenny PD, Ellard S. Alagille syndrome: pathogenesis, diagnosis and management. Eur J Hum Genet. 2012;20(3):251-257.
15. Abramson SJ, Berdon WE, Altman RP, et al. Biliary atresia and noncardiac polysplenic syndrome: US and surgical considerations. Radiology. 1987;163(2):377-379.
16. Roy CC, Silverman A, Alagille D. Pediatric clinical gastroenterology. 4th ed. St Louis: Mosby; 1994.
17. Mittal V, Saxena AK, Sodhi KS, et al. Role of abdominal sonography in the preoperative diagnosis of extrahepatic biliary atresia in infants younger than 90 days. AJR Am J Roentgenol. 2011;196(4):W438-W445.
18. Betz BW, Bisset 3rd GS, Johnson ND, et al. MR imaging of biliary cysts in children with biliary atresia: clinical associations and pathologic correlation. AJR Am J Roentgenol. 1994;162(1):167-171.
19. Kasai M, Suzuki S. A new operation for 'non-correctable' biliary atresia: hepatic porto-enterostomy. Shuiyutsu. 1959;(13):733-739.
20. Kasai M, Suzuki H, Ohashi E, et al. Technique and results of operative management of biliary atresia. World J Surg. 1978;2(5):571-579.
21. Bezerra JA, Balistreri WF. Cholestatic syndromes of infancy and childhood. Semin Gastrointest Dis. 2001;12(2):54-65.
22. Maresca G, De Gaetano AM, Mirk P, et al. Sonographic patterns of the gallbladder in acute viral hepatitis. J Clin Ultrasound. 1984;12(3):141-146.
23. Patriquin HB, DiPietro M, Barber FE, Teele RL. Sonography of thickened gallbladder wall: causes in children. AJR Am J Roentgenol. 1983;141(1):57-60.
24. Dubois J, Garel L, Patriquin H, et al. Imaging features of type 1 hereditary tyrosinemia: a review of 30 patients. Pediatr Radiol. 1996;26(12):845-851.
25. Henschke CI, Goldman H, Teele RL. The hyperechogenic liver in children: cause and sonographic appearance. AJR Am J Roentgenol. 1982;138(5):841-846.
26. Tchelepi H, Ralls PW, Radin R, Grant E. Sonography of diffuse liver disease. J Ultrasound Med. 2002;21(9):1023-1032.
27. Aubin B, Denys A, Lafortune M, et al. Focal sparing of liver parenchyma in steatosis: role of the gallbladder and its vessels. J Ultrasound Med. 1995;14(2):77-80.
28. Patriquin HB, Roy CC, Weber AM, Filiatrault D. Liver diseases and portal hypertension. Clin Diagn Ultrasound. 1989;24:103-127.
29. Lobe TE. Cholelithiasis and cholecystitis in children. Semin Pediatr Surg. 2000;9(4):170-176.
30. Keller MS, Markle BM, Laffey PA, et al. Spontaneous resolution of cholelithiasis in infants. Radiology. 1985;157(2):345-348.
31. Littlewood TR, Chrestman SJ. Ultrasonography of infants and children. Philadelphia: Saunders; 1991.
32. Brunelle F, Chaumont P. Hepatic tumors in children: ultrasonic differentiation of malignant from benign lesions. Radiology. 1984;150(3):695-699.
33. Isaacs Jr H. Fetal and neonatal hepatic tumors. J Pediatr Surg. 2007;42(11):1797-1803.
34. Gottschling S, Schneider G, Meyer S, et al. Two infants with life-threatening diffuse neonatal hemangiomatosis treated with cyclophosphamide. Pediatr Blood Cancer. 2006;46(2):239-242.
35. Hsi Dickie B, Fishman SJ, Azizkhan RG. Hepatic vascular tumors. Semin Pediatr Surg. 2014;23(4):168-172.
36. Mulliken JB, Glowacki J. Hemangiomas and vascular malformations in infants and children: a classification based on endothelial characteristics. Plast Reconstr Surg. 1982;69(3):412-422.
37. Dachman AH, Lichtenstein JE, Friedman AC, Hartman DS. Infantile hemangioendothelioma of the liver: a radiologic-pathologic-clinical correlation. AJR Am J Roentgenol. 1983;140(6):1091-1096.
38. Paltiel HJ, Patriquin HB, Keller MS, et al. Infantile hepatic hemangioma: Doppler US. Radiology. 1992;182(3):735-742.
39. Ros PR, Goodman ZD, Ishak KG, et al. Mesenchymal hamartoma of the liver: radiologic-pathologic correlation. Radiology. 1986;158(3):619-624.
40. Brunelle F, Tammam S, Odievre M, Chaumont P. Liver adenomas in glycogen storage disease in children. Ultrasound and angiographic study. Pediatr Radiol. 1984;14(2):94-101.
41. Cha DI, Lee MW, Kim YK, et al. Assessing patients with hepatocellular carcinoma meeting the Milan criteria: is liver 3 tesla MR with gadoxetic acid necessary in addition to liver CT? J Magn Reson Imaging. 2014;39(4):842-852.
42. Koufos A, Hansen MF, Copeland NG, et al. Loss of heterozygosity in three embryonal tumours suggests a common pathogenetic mechanism. Nature. 1985;316(6026):330-334.
43. Dachman AH, Pakter RL, Ros PR, et al. Hepatoblastoma: radiologic-pathologic correlation in 50 cases. Radiology. 1987;164(1):15-19.
44. Bates SM, Keller MS, Ramos IM, et al. Hepatoblastoma: detection of tumor vascularity with duplex Doppler US. Radiology. 1990;176(2):505-507.
45. Van Campenhout I, Patriquin H. Malignant microvasculature in abdominal tumors in children: detection with Doppler US. Radiology. 1992;183(2):445-448.
46. Boechat MI, Kangarloo H, Ortega J, et al. Primary liver tumors in children: comparison of CT and MR imaging. Radiology. 1988;169(3):727-732.

47. Taylor KJ, Ramos I, Morse SS, et al. Focal liver masses: differential diagnosis with pulsed Doppler US. Radiology. 1987;164(3):643-647.
48. Chung EM, Lattin Jr GE, Cube R, et al. From the archives of the AFIP: Pediatric liver masses: radiologic-pathologic correlation. Part 2. Malignant tumors. Radiographics. 2011;31(2):483-507.
49. Garel LA, Pariente DM, Nezelof C, et al. Liver involvement in chronic granulomatous disease: the role of ultrasound in diagnosis and treatment. Radiology. 1984;153(1):117-121.
50. Lee SH, Tomlinson C, Temple M, et al. Imaging-guided percutaneous needle aspiration or catheter drainage of neonatal liver abscesses: 14-year experience. AJR Am J Roentgenol. 2008;190(3):616-622.
51. Andronikou S, Welman CJ, Kader E. Classic and unusual appearances of hydatid disease in children. Pediatr Radiol. 2002;32(11):817-828.
52. Czermak BV, Akhan O, Hiemetzberger R, et al. Echinococcosis of the liver. Abdom Imaging. 2008;33(2):133-143.
53. Lewall DB, McCorkell SJ. Hepatic echinococcal cysts: sonographic appearance and classification. Radiology. 1985;155(3):773-775.
54. Burns PN, Jaffe CC. Quantitative flow measurements with Doppler ultrasound: techniques, accuracy, and limitations. Radiol Clin North Am. 1985;23(4): 641-657.
55. Nelson TR, Pretorius DH. The Doppler signal: where does it come from and what does it mean? AJR Am J Roentgenol. 1988;151(3):439-447.
56. Machado P, Segal S, Lyshchik A, Forsberg F. A novel microvascular flow technique: initial results in thyroids. Ultrasound Q. 2016;32(1):67-74.
57. Claudon M, Dietrich CF, Choi BI, et al. Guidelines and good clinical practice recommendations for contrast enhanced ultrasound (CEUS) in the liver—update 2012: a WFUMB-EFSUMB initiative in cooperation with representatives of AFSUMB, AIUM, ASUM, FLAUS and ICUS. Ultrasound Med Biol. 2013;39(2):187-210.
58. Sato S, Ohnishi K, Sugita S, Okuda K. Splenic artery and superior mesenteric artery blood flow: nonsurgical Doppler US measurement in healthy subjects and patients with chronic liver disease. Radiology. 1987;164(2):347-352.
59. Patriquin HB, Paltiel H. Abdominal Doppler ultrasound in children: clinical applications. Pediatric radiology categorical course syllabus. Chicago: Radiological Society of North America; 1989. p. 185-196.
60. Ohnishi K, Saito M, Nakayama T, et al. Portal venous hemodynamics in chronic liver disease: effects of posture change and exercise. Radiology. 1985;155(3):757-761.
61. Tochio H, Kudo M, Nishiuma S, Okabe Y. Intrahepatic spontaneous retrograde portal flow in patients with cirrhosis of the liver: reversal by food intake. AJR Am J Roentgenol. 2001;177(5):1109-1112.
62. Burns P, Taylor K, Blei AT. Doppler flowmetry and portal hypertension. Gastroenterology. 1987;92(3):824-826.
63. Lafortune M, Madore F, Patriquin H, Breton G. Segmental anatomy of the liver: a sonographic approach to the Couinaud nomenclature. Radiology. 1991;181(2):443-448.
64. Patriquin H, Lafortune M, Burns PN, Dauzat M. Duplex Doppler examination in portal hypertension: technique and anatomy. AJR Am J Roentgenol. 1987;149(1):71-76.
65. Subramanyam BR, Balthazar EJ, Madamba MR, et al. Sonography of portosystemic venous collaterals in portal hypertension. Radiology. 1983;146(1):161-166.
66. van Leeuwen MS. Doppler ultrasound in the evaluation of portal hypertension. Clin Diagn Ultrasound. 1990;26:53-76.
67. Patriquin HB, LaFortune M. SPR Annual Meeting Syllabus. Pediatr Radiol. 1994.
68. Patriquin H, Tessier G, Grignon A, Boisvert J. Lesser omental thickness in normal children: baseline for detection of portal hypertension. AJR Am J Roentgenol. 1985;145(4):693-696.
69. Segel MC, Zajko AB, Bowen A, et al. Hepatic artery thrombosis after liver transplantation: radiologic evaluation. AJR Am J Roentgenol. 1986;146(1): 137-141.
70. Lafortune M, Dauzat M, Pomier-Layrargues G, et al. Hepatic artery: effect of a meal in healthy persons and transplant recipients. Radiology. 1993;187(2):391-394.
71. Brunelle F, Alagille D, Pariente D, Chaumont P. An ultrasound study of portal hypertension in children. Ann Radiol (Paris). 1981;24(2):121-130.
72. Lebrec D, De Fleury P, Rueff B, et al. Portal hypertension, size of esophageal varices, and risk of gastrointestinal bleeding in alcoholic cirrhosis. Gastroenterology. 1980;79(6):1139-1144.
73. Patriquin H. Current concepts in pediatric radiology. Chicago: Radiological Society of North America; 1994.
74. Taylor KJW, Burns PN, Wells PNT, editors. Clinical applications of Doppler ultrasound. Philadelphia: Lippincott-Raven; 1996.
75. De Gaetano AM, Lafortune M, Patriquin H, et al. Cavernous transformation of the portal vein: patterns of intrahepatic and splanchnic collateral circulation detected with Doppler sonography. AJR Am J Roentgenol. 1995;165(5): 1151-1155.
76. Besnard M, Pariente D, Hadchouel M, et al. Portal cavernoma in congenital hepatic fibrosis. Angiographic reports of 10 pediatric cases. Pediatr Radiol. 1994;24(1):61-65.
77. Odievre M, Chaumont P, Montagne JP, Alagille D. Anomalies of the intrahepatic portal venous system in congenital hepatic fibrosis. Radiology. 1977;122(2):427-430.
78. Patriquin HB. Pediatric diseases test and syllabus. Reston, VA: American College of Radiology; 1993.
79. Bolondi L, Gandolfi L, Arienti V, et al. Ultrasonography in the diagnosis of portal hypertension: diminished response of portal vessels to respiration. Radiology. 1982;142(1):167-172.
80. Stanley P. Budd-Chiari syndrome. Radiology. 1989;170(3 Pt 1):625-627.
81. Lassau N, Auperin A, Leclere J, et al. Prognostic value of Doppler-ultrasonography in hepatic veno-occlusive disease. Transplantation. 2002;74(1):60-66.
82. Kotecha RS, Buckland A, Phillips MB, et al. Hepatic sinusoidal obstruction syndrome during chemotherapy for childhood medulloblastoma: report of a case and review of the literature. J Pediatr Hematol Oncol. 2014;36(1): 76-80.
83. Hosoki T, Kuroda C, Tokunaga K, et al. Hepatic venous outflow obstruction: evaluation with pulsed duplex sonography. Radiology. 1989;170(3 Pt 1):733-737.
84. Novak D, Butzow GH, Becker K. Hepatic occlusion venography with a balloon catheter in patients with end-to-side portacaval shunts. AJR Am J Roentgenol. 1976;127(6):949-953.
85. Ledesma-Medina J, Dominguez R, Bowen A, et al. Pediatric liver transplantation. Part I. Standardization of preoperative diagnostic imaging. Radiology. 1985;157(2):335-338.
86. Dillman JR, Heider A, Bilhartz JL, et al. Ultrasound shear wave speed measurements correlate with liver fibrosis in children. Pediatr Radiol. 2015;45(10):1480-1488.
87. Barr RG, Ferraioli G, Palmeri ML, et al. Elastography assessment of liver fibrosis: Society of Radiologists in Ultrasound Consensus Conference statement. Radiology. 2015;276(3):845-861.
88. Xanthakos SA, Podberesky DJ, Serai SD, et al. Use of magnetic resonance elastography to assess hepatic fibrosis in children with chronic liver disease. J Pediatr. 2014;164(1):186-188.
89. Leschied JR, Dillman JR, Bilhartz J, et al. Shear wave elastography helps differentiate biliary atresia from other neonatal/infantile liver diseases. Pediatr Radiol. 2015;45(3):366-375.
90. Hernanz-Schulman M, Ambrosino MM, Genieser NB, et al. Pictorial essay. Current evaluation of the patient with abnormal visceroatrial situs. AJR Am J Roentgenol. 1990;154(4):797-802.
91. Longley DG, Skolnick ML, Zajko AB, Bron KM. Duplex Doppler sonography in the evaluation of adult patients before and after liver transplantation. AJR Am J Roentgenol. 1988;151(4):687-696.
92. Squires RH, Ng V, Romero R, et al. Evaluation of the pediatric patient for liver transplantation: 2014 practice guideline by the American Association for the Study of Liver Diseases, American Society of Transplantation and the North American Society for Pediatric Gastroenterology, Hepatology, and Nutrition. J Pediatr Gastroenterol Nutr. 2014;59(1): 112-131.
93. American College of Radiology (ACR), Society for Pediatric Radiology (SPR), Society of Radiologists in Ultrasound (SRU), American Institute of Ultrasound in Medicine (AIUM). AIUM practice guideline for the performance of an ultrasound examination of solid-organ transplants. J Ultrasound Med. 2014;33(7):1309-1320.

94. Caron KH, Strife JL, Babcock DS, Ryckman FC. Left-lobe hepatic transplants: spectrum of normal imaging findings. AJR Am J Roentgenol. 1992;159(3):497-501.
95. Jequier S, Jequier JC, Hanquinet S, et al. Orthotopic liver transplants in children: change in hepatic venous Doppler wave pattern as an indicator of acute rejection. Radiology. 2003;226(1):105-112.
96. Calvo-Garcia MA, Campbell KM, O'Hara SM, et al. Acquired renal cysts after pediatric liver transplantation: association with cyclosporine and renal dysfunction. Pediatr Transplant. 2008;12(6):666-671.
97. Sudan DL, Iyer KR, Deroover A, et al. A new technique for combined liver/small intestinal transplantation. Transplantation. 2001;72(11):1846-1848.
98. Daneman A, Martin DJ. Congenital epithelial splenic cysts in children. Emphasis on sonographic appearances and some unusual features. Pediatr Radiol. 1982;12(3):119-125.
99. Paterson A, Frush DP, Donnelly LF, et al. A pattern-oriented approach to splenic imaging in infants and children. Radiographics. 1999;19(6):1465-1485.
100. Emery KH, McAneney CM, Racadio JM, et al. Absent peritoneal fluid on screening trauma ultrasonography in children: a prospective comparison with computed tomography. J Pediatr Surg. 2001;36(4):565-569.
101. Filiatrault D, Longpre D, Patriquin H, et al. Investigation of childhood blunt abdominal trauma: a practical approach using ultrasound as the initial diagnostic modality. Pediatr Radiol. 1987;17(5):373-379.
102. Johnson MA, Cooperberg PL, Boisvert J, et al. Spontaneous splenic rupture in infectious mononucleosis: sonographic diagnosis and follow-up. AJR Am J Roentgenol. 1981;136(1):111-114.

CHAPTER 52

The Pediatric Urinary Tract and Adrenal Glands

Harriet J. Paltiel and Diane S. Babcock

SUMMARY OF KEY POINTS

- Ultrasound can reliably characterize renal duplication, fusion, and rotational anomalies.
- Ultrasound is useful in evaluating renal, ureteral, and bladder anatomy in patients with suspected hydronephrosis.
- Contrast-enhanced voiding urosonography (CEVUS) is a promising technique that may eventually replace conventional voiding cystourethrography (VCUG) in selected cases.
- Ultrasound is used to assess renal size and to exclude anatomic abnormalities as the cause of acute kidney injury (AKI).
- Ultrasound is the initial imaging study of choice in patients with suspected urolithiasis, with noncontrast computed tomography reserved for cases in which ultrasound is nondiagnostic.
- Intravenous contrast-enhanced ultrasound may provide valuable information regarding renal injury in patients with blunt abdominal trauma.
- Ultrasound plays a key role in the evaluation of patients with renal transplants, in both early and later postoperative periods.
- Renal ultrasound is often helpful in distinguishing among different types of renal cystic disease.
- Ultrasound is employed to distinguish cystic (usually benign) from solid (often malignant) renal masses.
- Ultrasound is used to differentiate between neonatal adrenal hemorrhage and neuroblastoma.

CHAPTER OUTLINE

PEDIATRIC URINARY TRACT SONOGRAPHY
Technique
Normal Renal Anatomy
Normal Bladder Anatomy
CONGENITAL ANOMALIES OF THE URINARY TRACT
Renal Duplication
Other Renal Anomalies
CAUSES OF HYDRONEPHROSIS
Ureteropelvic Junction Obstruction
Ureteral Obstruction
Bladder Outlet Obstruction
Vesicoureteral Reflux
Prune-Belly Syndrome
Megacystis-Microcolon-Malrotation–Intestinal Hypoperistalsis Syndrome
Bladder Exstrophy
Urachal Anomalies
URINARY TRACT INFECTION
Acute Pyelonephritis
Chronic Pyelonephritis
Neonatal Candidiasis
Cystitis
MEDICAL RENAL DISEASE
Acute Kidney Injury
Chronic Kidney Disease
URINARY TRACT CALCIFICATION
Renal Cortical Calcification
Medullary Nephrocalcinosis
Urinary Stasis
Renal Vein Thrombosis Calcifications
Dystrophic Calcification
Urolithiasis
RENAL TRAUMA
RENAL VASCULAR DISEASE
Doppler Sonographic Examination Technique
Normal Vascular Anatomy and Flow Patterns
Causes of Increased Resistance to Intrarenal Arterial Flow
Clinical Applications
Vessel Patency
Acute Renal Vein Thrombosis
Renal Artery Stenosis
Intrarenal Arterial Disease
RENAL TRANSPLANTATION
Vascular Complications
Perinephric Fluid Collections
Parenchymal Abnormalities
Urologic Complications
Tumors
RENAL CYSTIC DISEASE
Autosomal Recessive Polycystic Kidney Disease
Autosomal Dominant Polycystic Kidney Disease
Multicystic Renal Dysplasia
Nephronophthisis and Medullary Cystic Disease
Congenital Renal Cysts
Tuberous Sclerosis and Von Hippel–Lindau Disease
Acquired Cysts
RENAL TUMORS
Wilms Tumor
Mesoblastic Nephroma
Renal Cell Carcinoma
Angiomyolipoma
Multilocular Cystic Nephroma
Renal Lymphoma
Bladder Tumors
PEDIATRIC ADRENAL SONOGRAPHY
Normal Anatomy
Congenital Adrenal Hyperplasia
Neonatal Adrenal Hemorrhage
Neuroblastoma
Pheochromocytoma
Adrenocortical Neoplasm

PEDIATRIC URINARY TRACT SONOGRAPHY

Technique

Sonography plays a major role in the evaluation of the pediatric urinary tract and adrenal glands. Ultrasound examination of the pediatric urinary tract should include imaging of the kidneys, ureters (if visualized), and urinary bladder. For most patients, no special preparation is required. The child's parents are asked to bring the patient for the study with a full urinary bladder when a study is performed for evaluation of hematuria or urinary tract stones (Table 52.1). These children are requested to drink fluids during the hour before the examination. Patients scheduled for renal Doppler examination should have nothing to eat or drink (NPO) before the study for a time period determined according to patient age. For a young child who is not yet toilet-trained, the bladder should be checked first and frequently because it may fill and empty suddenly.

Although children vary in their ability to hold still, sedation is rarely needed. Infants younger than 1 year can be fed or given a pacifier during the examination. The patient older than 1 year can be distracted or entertained by watching movies, playing with toys, or reading a book. The addition of cine clips often compensates for movement of the child.

A variety of ultrasound equipment can be used. The highest frequency transducer that will penetrate the area being examined is optimal. Harmonic imaging may aid in visualization of the difficult-to-scan patient. Different types of transducers are used for different parts of the body. Scans of the kidneys from the back are best performed with a linear or curved linear transducer, whereas frontal scans of the kidney are best performed with a curved linear or sector transducer that penetrates between the ribs. Views of the bladder are obtained with a curved linear transducer. The ureters are evaluated as they leave the renal pelvis and enter the bladder. Images are recorded and stored on digital media.

Routine examination includes longitudinal and transverse views of both kidneys (Fig. 52.1). In the pediatric patient, the kidneys are imaged in the supine and prone positions. The supine sagittal or coronal image allows optimal visualization of the upper pole, which may be obscured by ribs in the prone position. The echogenicity of the kidney should always be compared with the adjacent liver and spleen. Decubitus positioning is helpful to visualize the upper pole for measurement when the upper kidney is obscured by the ribs. The prone image allows optimal visualization of the lower pole of the kidney, but the upper pole may be obscured by overlying ribs or aerated lung in the costophrenic angle. **Kidney volumes** can be determined by obtaining a transverse image through the midkidney and measuring its anteroposterior (AP) and transverse dimensions (see Fig. 52.1C). The formula for determining the volume of a prolate ellipsoid is used:

$$\text{Kidney volume} = \text{Length} \times \text{Width} \times \text{Height} \times 0.523$$

Normal sonographic measurements of **renal length** and volume in comparison to patient age, height, weight, and/or body surface area have been determined and are useful in evaluation of the abnormal kidney[1-6] (Fig. 52.2, Tables 52.2, 52.3, 52.4, and 52.5). Length and volume data for single functioning kidneys in children have also been reported.[7,8] Compensatory renal growth of a single functional kidney occurs in utero, and its relative size difference

TABLE 52.1 Patient Preparation for Urinary Tract Ultrasound

Indication	Preparation
Hematuria	Full bladder
Urinary tract stones	Full bladder
Renal Doppler examination	NPO for time period determined according to age <1 year of age: NPO for 2 hours >1 year and <5 years of age: NPO for 4 hours ≥5 years of age: NPO for 6 hours
All other indications	None

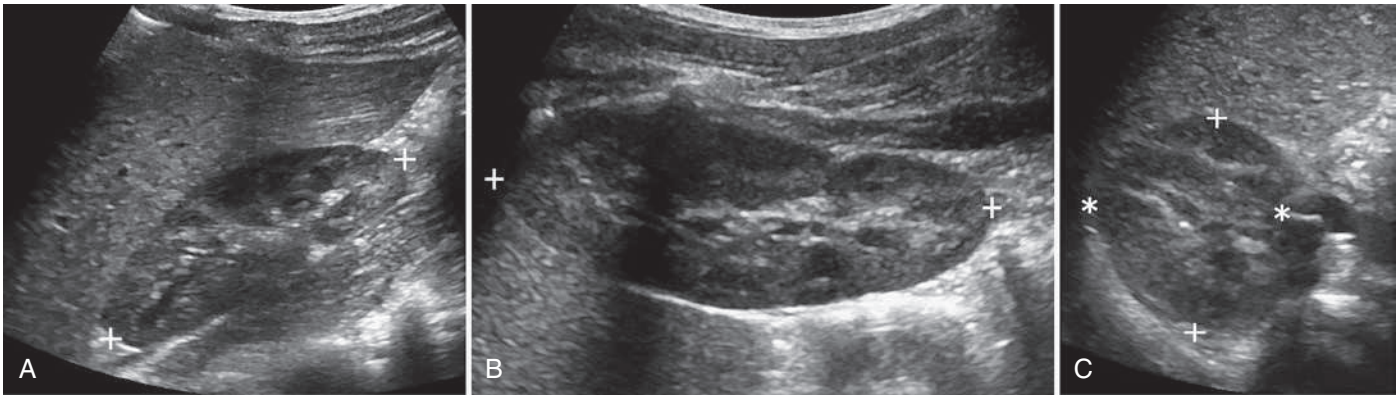

FIG. 52.1 Renal Length and Volume. (A) Longitudinal supine image. **(B)** Longitudinal prone image. Length measurements are obtained from either the supine or prone view (+). **(C)** Transverse image through the midkidney with anteroposterior height (+) and width (*) measurements (volume = length × width × height × 0.52).

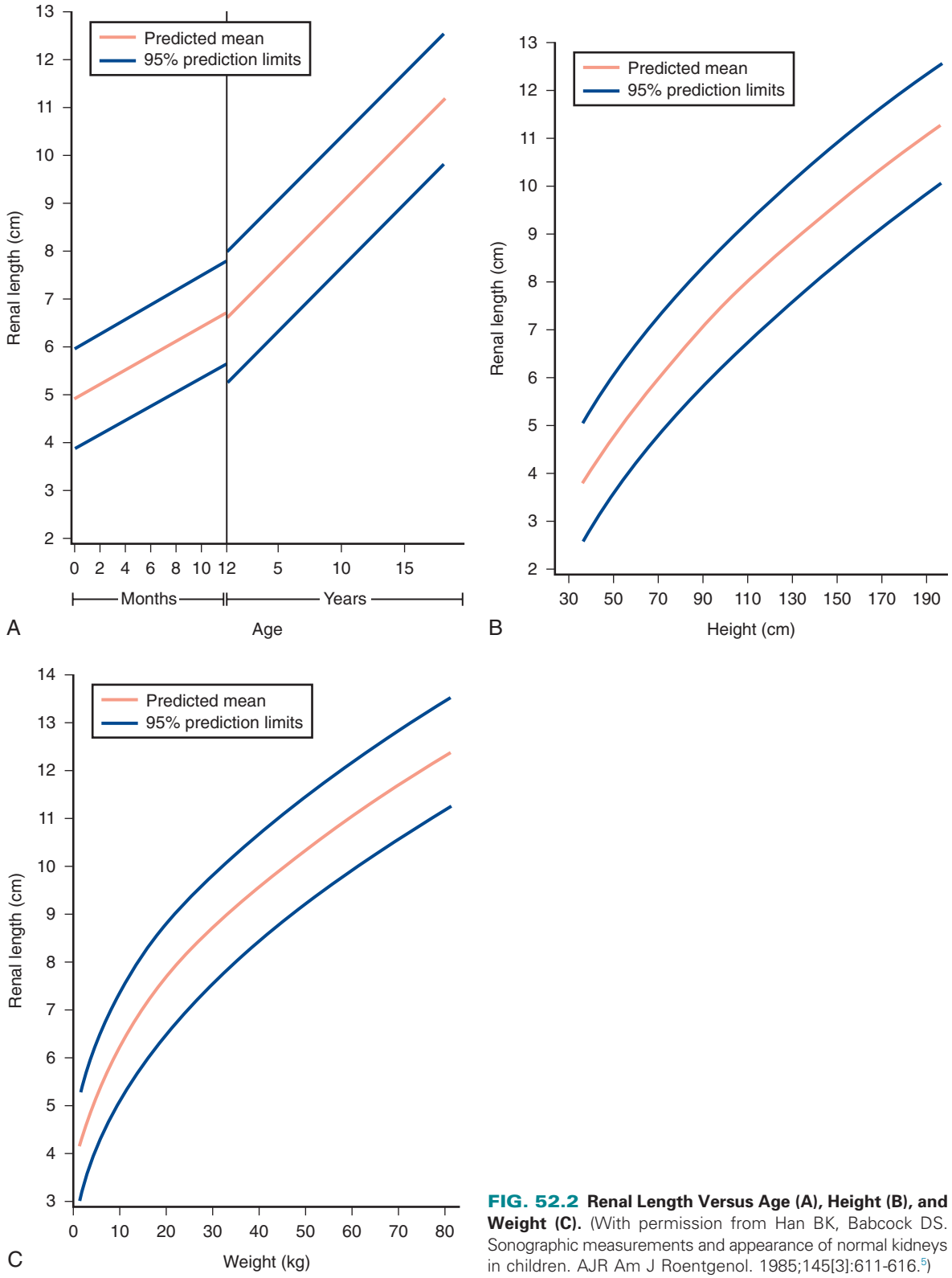

FIG. 52.2 Renal Length Versus Age (A), Height (B), and Weight (C). (With permission from Han BK, Babcock DS. Sonographic measurements and appearance of normal kidneys in children. AJR Am J Roentgenol. 1985;145[3]:611-616.[5])

TABLE 52.2 Reference Values for Infant Kidney Length (in Centimeters) According to Age (in Months) and Gender

				95% CI FOR MEAN		PERCENTILE	
Gender	Age (Months)	Number	Mean ± SD	Lower Limit	Upper Limit	3rd	97th
Male	0-3	336	4.88 ± 0.56	4.82	4.94	3.9	6.0
	3-6	238	5.69 ± 0.40	5.64	5.74	5.0	6.5
	6-9	246	5.90 ± 0.41	5.85	5.96	5.1	6.8
	9-12	220	5.93 ± 0.50	5.86	6.00	5.0	6.9
Female	0-3	246	4.75 ± 0.62	4.67	4.83	3.6	6.1
	3-6	210	5.70 ± 0.39	5.64	5.75	5.0	6.5
	6-9	250	5.73 ± 0.40	5.68	5.78	5.1	6.6
	9-12	238	6.17 ± 0.50	6.10	6.23	5.1	7.0

CI, Confidence interval; *SD,* standard deviation.
With permission from Vujic A, Kosutic J, Bogdanovic R, et al. Sonographic assessment of normal kidney dimensions in the first year of life—a study of 992 healthy infants. Pediatr Nephrol 2007;22(8):1143-1150.[3]

TABLE 52.3 Reference Values for Infant Kidney Volume (in Milliliters) According to Age (in Months) and Gender

				95% CI FOR MEAN		PERCENTILE	
Gender	Age (Months)	Number	Mean ± SD	Lower Limit	Upper Limit	3rd	97th
Male	0-3	336	14.32 ± 4.52	13.84	14.81	7.48	24.14
	3-6	238	19.30 ± 4.40	18.74	19.86	12.18	30.04
	6-9	246	21.50 ± 3.98	21.01	22.00	15.08	30.60
	9-12	220	24.59 ± 7.17	23.64	25.54	14.68	42.49
Female	0-3	246	13.22 ± 4.31	12.68	13.77	6.20	21.88
	3-6	210	18.58 ± 3.85	18.06	19.09	12.43	26.74
	6-9	250	20.20 ± 3.82	19.73	20.68	13.88	28.19
	9-12	238	26.48 ± 7.60	25.51	27.45	15.45	46.77

CI, Confidence interval; *SD,* standard deviation.
With permission from Vujic A, Kosutic J, Bogdanovic R, et al. Sonographic assessment of normal kidney dimensions in the first year of life—a study of 992 healthy infants. Pediatr Nephrol 2007;22(8):1143-1150.[3]

continues throughout infancy and childhood (Table 52.6). Renal size in premature infants has also been compared with gestational age or birth weight[9-12] (Fig. 52.3). In patients with chronic problems, such as recurrent urinary tract infection (UTI), reflux, or neurogenic bladder, renal growth can be monitored on follow-up examinations.

Doppler ultrasound of the kidneys is performed in select patients when renal arterial or venous disease is suspected, using techniques similar to those employed in adults (see **Renal Vascular Disease** below).

Longitudinal and transverse views of the urinary bladder are obtained in both distended and postvoid states. Images are obtained with a convex linear transducer using the highest frequency that will penetrate the patient. Harmonic imaging may be useful to minimize artifacts. Bladder volume may be determined on longitudinal and transverse views of the urinary bladder when maximally but comfortably distended (Fig. 52.4). Because the bladder varies in shape, various formulas have been suggested to calculate its volume.[13,14] The most commonly used method calculates bladder volume using the formula for determining the volume of a prolate ellipsoid, noted earlier.

Bladder wall thickness in children has been evaluated in only a few studies using different techniques and leading to somewhat different results and conclusions.[15,16] A retrospective study by Jequier and Rousseau[16] measured the wall posterolateral to the trigone on transverse or sagittal images in 410 children and 10 adults whose bladders were filled to a variable degree. They determined that the normal mean wall thickness is 2.8 mm when the bladder is almost empty, and 1.5 mm when it is distended. There was a linear relationship between bladder fullness and wall thickness, with upper limits of 3 mm and 5 mm for a full or empty bladder, respectively. In a more recent prospective study of children with full bladders by Uluocak and colleagues,[15] thickness measurements were obtained from the anterior, posterior, and lateral walls. Mean anterior, posterior, and lateral wall thicknesses were 1.4 mm (range 0.8-2.8), 1.6 mm (range 0.7-3.1),

TABLE 52.4 Mean Total Renal Volumes (Values Are Mean ± Standard Deviation)

Age (Years)	Mean Age (Years)	No. of Subjects	Total Renal Volume (cm^3)
0.00-0.249	0.0	99	30.83 ± 7.98
0.25-0.49	0.25	81	44.76 ± 11.03
0.50-0.99	0.5	121	55.44 ± 6.82
1.00-1.49	1.0	111	62.80 ± 9.23
1.50-1.99	1.5	56	68.35 ± 10.64
2.00-2.49	2.0	87	74.49 ± 10.04
2.50-2.99	2.5	98	82.47 ± 9.22
3.00-3.49	3.0	135	89.60 ± 11.89
3.50-3.99	3.5	77	94.89 ± 9.50
4.00-4.49	4.0	115	102.01 ± 10.41
4.50-4.99	4.5	79	106.81 ± 10.90
5.00-5.49	5.0	109	112.62 ± 13.47
5.50-5.99	5.5	129	118.44 ± 13.18
6.00-6.49	6.0	173	123.79 ± 12.04
6.50-6.99	6.5	130	132.18 ± 12.01
7.00-7.49	7.0	142	137.00 ± 12.11
7.50-7.99	7.5	137	144.05 ± 13.26
8.00-8.49	8.0	127	151.08 ± 14.40
8.50-8.99	8.5	79	156.15 ± 11.37
9.00-9.49	9.0	147	163.69 ± 11.93
9.50-9.99	9.5	79	168.57 ± 11.28
10.00-10.49	10.0	125	174.16 ± 10.39
10.50-10.99	10.5	79	183.18 ± 12.69
11.00-11.49	11.0	104	188.03 ± 12.13
11.50-11.99	11.5	50	195.24 ± 11.12
12.00-12.49	12.0	90	201.82 ± 11.65
12.50-12.99	12.5	50	208.46 ± 12.56
13.00-13.49	13.0	87	215.00 ± 16.63
13.50-13.99	13.5	42	218.30 ± 14.83
14.00-14.49	14.0	90	225.39 ± 16.98
14.50-14.99	14.5	45	230.14 ± 14.43
15.00-15.49	15.0	85	236.43 ± 14.58
15.50-15.99	15.5	44	244.36 ± 14.37
16.00-16.49	16.0	50	251.99 ± 16.42
16.50-16.99	16.5	24	257.75 ± 17.54
17.00-17.49	17.0	41	262.69 ± 12.67
17.50-17.99	17.5	59	271.26 ± 11.10

Adapted from Leung VY, Chu WC, Yeung CK, et al. Nomograms of total renal volume, urinary bladder volume and bladder wall thickness index in 3,376 children with a normal urinary tract. Pediatr Radiol. 2007;37(2):181-188.[2]

TABLE 52.5 New Centiles for Renal Growth of the Solitary or Single Functioning Kidney: Renal Length and Renal Volume

	RENAL LENGTH, LEFT KIDNEY (mm)		RENAL LENGTH, RIGHT KIDNEY (mm)			RENAL VOLUME, LEFT KIDNEY (mL)		RENAL VOLUME, RIGHT KIDNEY (mL)	
Body Height (cm)	5th Centile	95th Centile	5th Centile	95th Centile	Body Surface Area (m^2)	5th Centile	95th Centile	5th Centile	95th Centile
55 (<60)	36.6	67.6	39.9	69.5	<0.4	10.0	37.1	11.8	41.0
70 (60-79.9)	51.9	82.2	51.5	74.0	0.4-<0.7	29.5	85.0	28.7	77.0
90 (80-99.9)	67.0	96.7	65.7	87.3	0.7-<1	49.5	161.0	54.0	129.6
110 (100-119.9)	70.1	104.4	73.0	100.0	1-<1.3	81.8	259.2	81.4	173.6
130 (120-139.9)	85.0	120.0	81.0	107.2	1.3-<1.6	102.3	273.1	99.0	174.0
150 (140-159.9)	90.3	135.8	93.8	124.4	>1.6	115.4	315.5	130.0	274.7
170 (≥160)	96.8	145.8	104.0	140.0					

With permission from Spira EM, Jacobi C, Frankenschmidt A, et al. Sonographic long-term study: paediatric growth charts for single kidneys. Arch Dis Child. 2009;94(9):693-698.[8]

TABLE 52.6 Shape and Correction Coefficient *(k)* for Bladder Volume

Bladder Shape	*k* (SE)	Pearson *r*	*P* Value	Mean Percentage Error ± SD
Whole sample[a]	0.66 (0.011)	0.927	<.01	19.19 ± 9.59
Round	0.561 (0.013)	0.940	<.01	5.10 ± 8.30
Cuboid	0.923 (0.012)	0.982	<.01	5.53 ± 6.86
Ellipsoid	0.802 (0.006)	0.992	<.01	3.09 ± 3.52
Triangular	0.623 (0.007)	0.988	<.01	7.71 ± 8.66
Undefined	0.749 (0.048)	0.976	<.01	15.18 ± 17.21

[a]Regardless of shape.
SD, Standard deviation; *SE,* standard error.
With permission from Kuzmic AC, Brkljacic B, Ivankovic D. The impact of bladder shape on the ultrasonographic measurement of bladder volume in children. Pediatr Radiol 2003;33:530-534.[13]

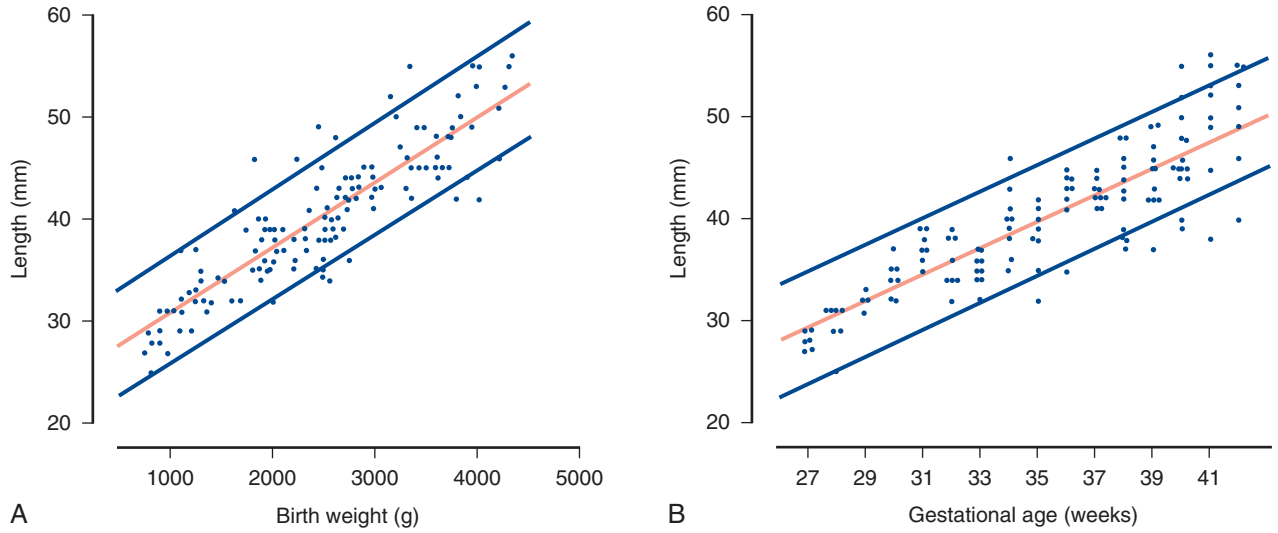

FIG. 52.3 Kidney Length Versus Birth Weight (A) and Gestational Age (B). (With permission from Chiara A, Chirico G, Barbarini M, et al. Ultrasonic evaluation of kidney length in term and preterm infants. Eur J Pediatr. 1989;149[2]:94-95.[11])

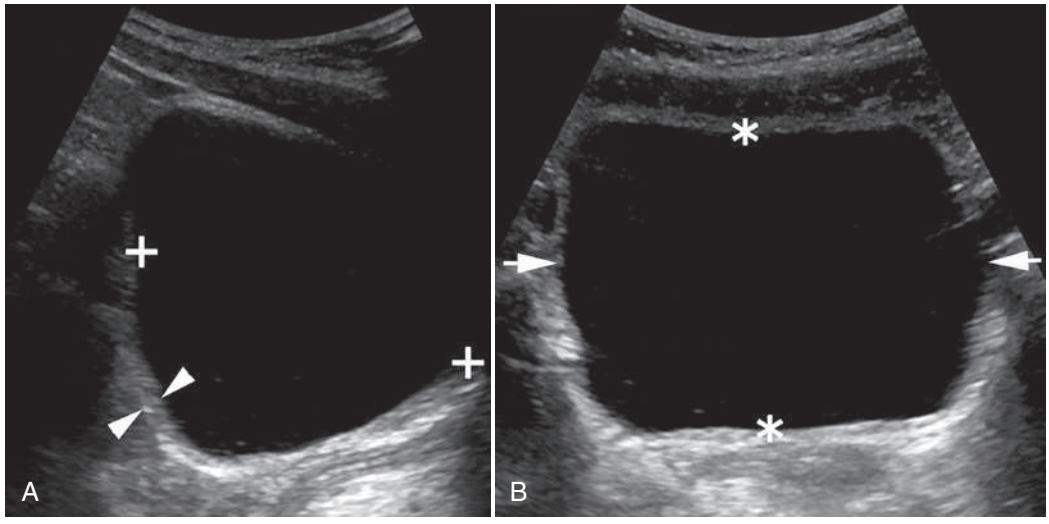

FIG. 52.4 Bladder Volume. (A) Longitudinal midline image. **(B)** Transverse image. Length (+), width *(arrows),* and anteroposterior dimension (*) measured along the inner wall. Bladder wall thickness *(arrowheads)* measured along posterior wall.

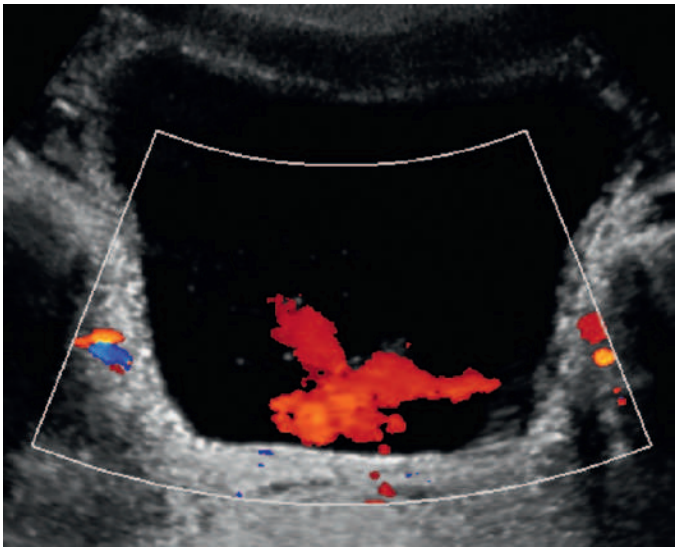

FIG. 52.5 Ureteral Jets. Transverse bladder image shows bilateral ureteral jets crossing each other.

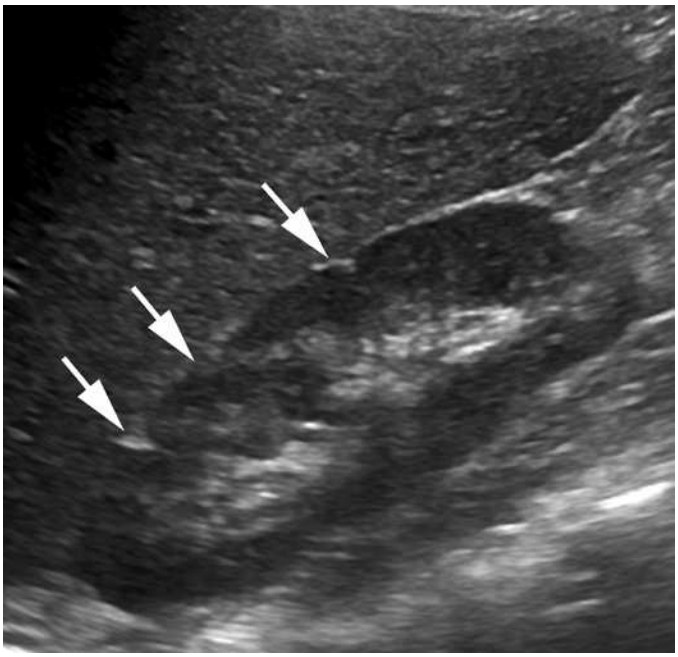

FIG. 52.6 Fetal Lobulation. Longitudinal image of the right kidney depicts a mildly undulating contour due to parenchymal indentations that spare the pyramids *(arrows)*.

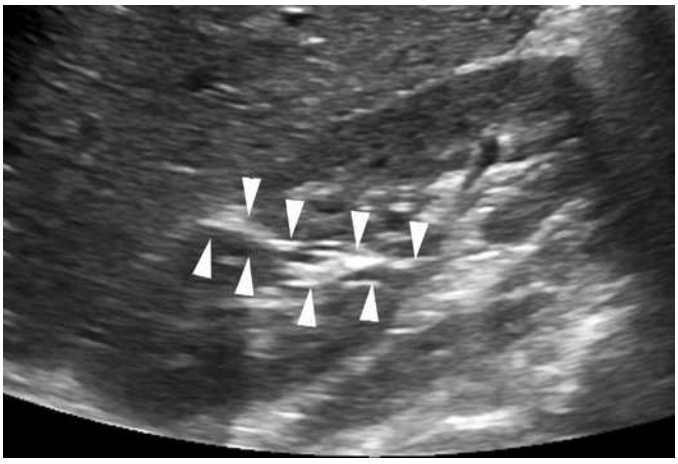

FIG. 52.7 Renal Junctional Parenchymal Defect. Longitudinal image of the right kidney reveals an echogenic groove extending obliquely through the parenchyma *(arrowheads)*.

and 1.5 mm (range 0.6-2.6), respectively. Strong positive correlations were found between anterior and posterior wall thickness and increased age and body mass index (BMI). However, in contrast to the study of Jequier and Rousseau, there was no correlation between bladder volume and anterior or posterior wall thickness. Further studies are required in order to better delineate the effects of measurement technique as well as patient age, height, and BMI on bladder wall thickness.

Scans of the bladder are best performed with the bladder comfortably full so that abnormalities, including wall thickening and trabeculation, can be seen. Dilation of the distal **ureters** and **ureteroceles** is also sought. The thickness of the bladder wall may be increased with inflammation or muscular hypertrophy. Postvoid views of the bladder and kidneys may be helpful in patients with a **neurogenic bladder** or **dilated upper collecting system,** because a distended bladder may cause increased dilation but improve after voiding.

Color Doppler sonography is used in selected clinical situations to evaluate the ureteral jets[17,18] (Fig. 52.5).

Normal Renal Anatomy

Throughout the second trimester, the fetal kidney consists of a collection of renunculi (small kidneys), each composed of a central large pyramid with a thin peripheral rim of cortex. As the renunculi progressively fuse, their adjoining cortices form a **column of Bertin.** The former renunculi are then called "lobes." Remnants of these lobes with incomplete fusion are recognized by a lobulated surface of the kidney. This **"persistent fetal lobulation"** (Fig. 52.6) should not be confused with renal scarring[19] and may persist into adulthood.[20] Fetal lobulation is distinguished from scarring by the presence of a smooth renal contour, regular spacing, and absence of calyceal blunting. The indentations spare the renal pyramids, unlike scarring, in which the renal parenchyma overlying the pyramids appears thinned.

The **renal junctional parenchymal defect** (interrenicular septum or fissure) is the most prominent of these grooves, extending from the hilum to the cortex, and is caused by perirenal fat adherent to the renal capsule along a cleft on the renal surface. It is frequently seen in the anterosuperior aspect of the kidney[20] (Fig. 52.7). At birth, the pyramids are still large and hypoechoic compared with the thin rim of echogenic cortex that surrounds them. Glomerular filtration rate shortly after birth is low and increases rapidly after the first week postpartum. Throughout childhood, there is significant growth of the cortex, and the pyramids gradually become proportionately smaller.

The anatomy and sonographic appearance of the pediatric kidney depend on age.[5,21,22] The **normal infant kidney** has several features that differ from the normal adult kidney (Fig. 52.8). The

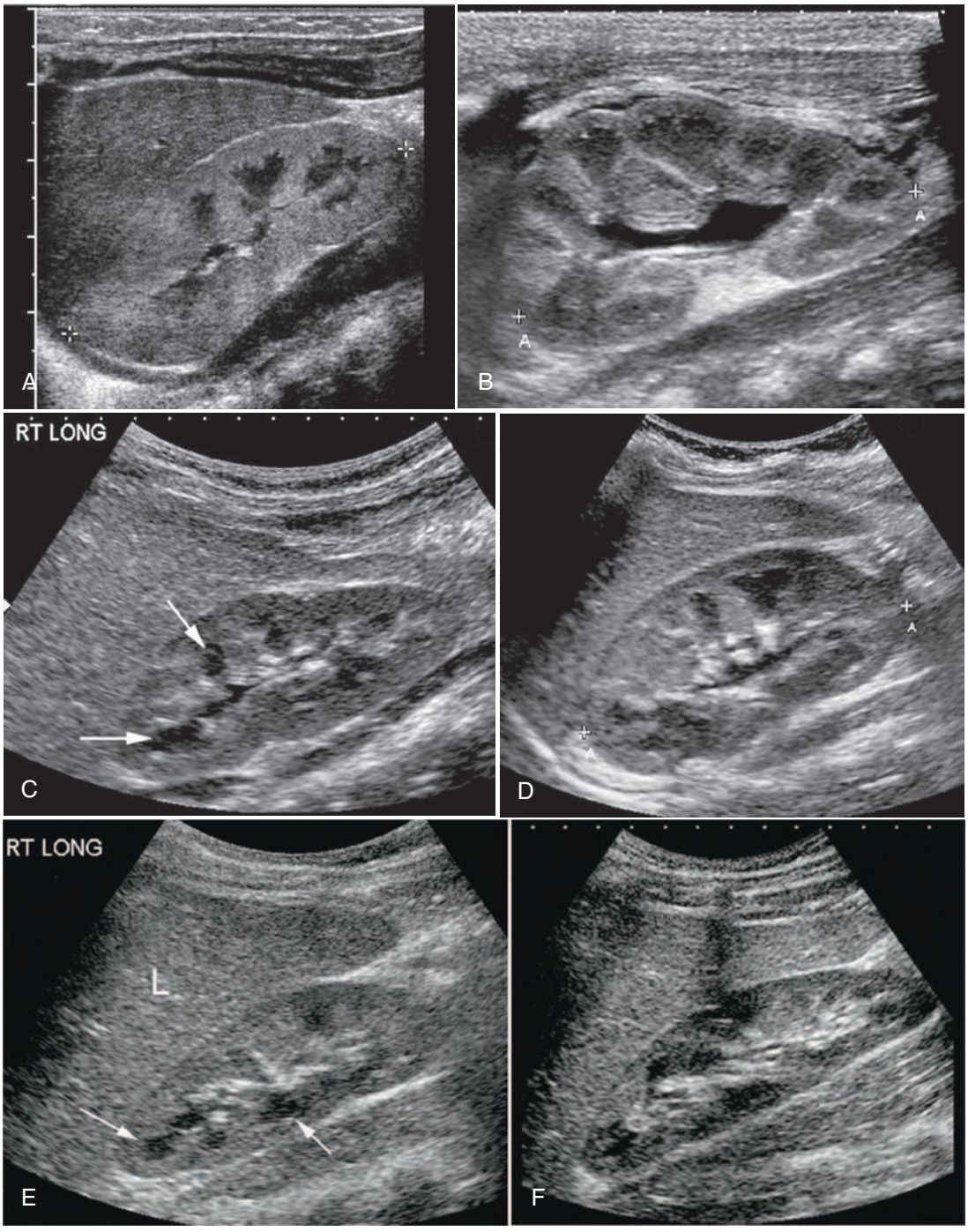

FIG. 52.8 Normal Renal Appearances at Different Ages. (A) Premature infant. Cortex is prominent and more echogenic than the liver. Prominent hypoechoic renal pyramids. **(B) Term infant.** Normal fetal lobulations of renal cortex are isoechoic or slightly hyperechoic to liver and spleen. Prominent renal pyramids are hypoechoic. **(C) Term infant.** Central echo complex is not prominent because of less peripelvic fat. Renal cortex equals the liver in echogenicity. Medullary pyramids *(arrows)* are relatively larger and appear more prominent. **(D) Two-year-old child.** Renal cortex is slightly less echogenic than liver. Renal sinus fat begins to develop central echogenicity around vessels. **(E) Ten-year-old child.** Normal cortex is less echogenic than liver *(L)* or spleen. Medullary pyramids *(arrows)* are relatively hypoechoic around the central echo complex of strong specular echoes. **(F) Fourteen-year-old child.** Renal cortex is less echogenic than liver or spleen. Pyramids are much less prominent. Renal sinus fat is increased.

central echo complex is much less prominent compared with the renal parenchyma because there is less peripelvic fat in the infant than in the adult. Renal cortical echogenicity is typically increased in the **normal premature infant kidney** compared with the liver and spleen. The echogenicity of the renal cortex in the **normal term infant kidney** is often the same as the echogenicity of the adjacent normal liver, whereas in the **older child and adult kidney,** the renal cortex is less echogenic than the liver. The medullary pyramids in the infant are relatively larger and tend to appear more prominent (more hypoechoic). The corticomedullary differentiation is greater in the infant and child's kidney than in the adult, possibly because of increased resolution from higher frequency transducers and less overlying body fat tissue. It may also result from differences in the cellular composition of the renal parenchyma in the infant. These prominent pyramids in the pediatric kidney can easily be mistaken for multiple cysts or dilated calyces by those not familiar with the differences. Normal pyramids line up around the central echo complex in a characteristic pattern and can therefore be differentiated from cysts. The position of the arcuate artery at the corticomedullary junction can also help to identify a structure as a pyramid.

Renal anatomy in the teenager and older child is similar to that in the adult[5,21,22] (see Fig. 52.8). The renal parenchyma consists of the cortex, which is peripheral, contains the glomeruli, and has several extensions to the edge of the renal sinus (the septa or column of Bertin); and the medulla (containing the renal pyramids), which is more central and adjacent to the calyces. The normal cortex produces low-level, backscattered echoes. The medullary pyramids are relatively hypoechoic and arranged around the central, echo-producing renal sinus. The arcuate vessels can be demonstrated as intense specular echoes at the corticomedullary junction. This corticomedullary differentiation can be identified in most children but occasionally cannot be visualized in those with increased overlying soft tissues. The central echo complex consists of strong specular echoes from the renal sinus, including the renal collecting system, calyces and infundibula, arteries, veins, lymphatics, peripelvic fat, and part of the renal pelvis. With distention of the renal collecting system, these echoes become separated and small degrees of hydronephrosis can be demonstrated. Mild degrees of distention can be seen in normal children, particularly after recent high intake of fluids or diuretics. A normally distended urinary bladder can also cause functional ureteral obstruction and mild distention of the renal collecting systems. Rescanning when the bladder is empty will usually result in resolution of both collecting system and ureteral distention in an otherwise normal urinary tract.

Normal Bladder Anatomy

The normal urinary bladder is thin walled. Bladder volume and wall thickness are influenced by the degree of bladder distention.[15,16] The distal ureters may be visible at the bladder base, especially if the child is well hydrated, likely related to the normal transient passage of urine associated with peristalsis (Fig. 52.9). Bladder wall thickness may increase with inflammation or muscular hypertrophy.

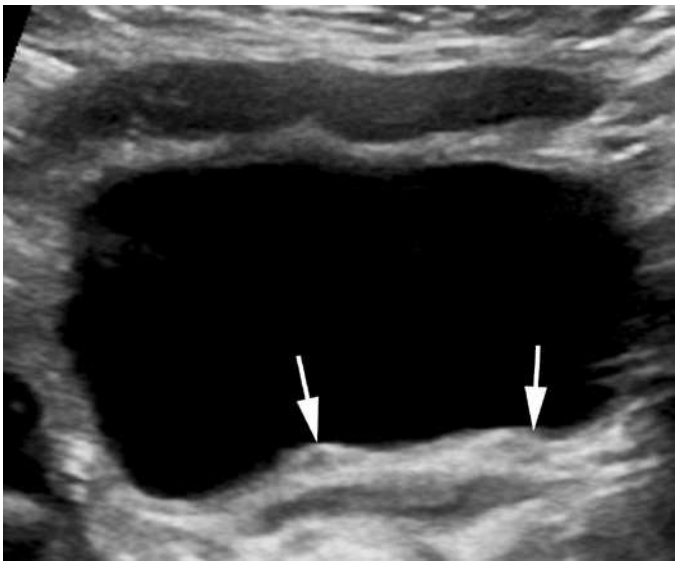

FIG. 52.9 Normal Distal Ureters. Transverse bladder image depicts distal ureteral insertions at the level of the trigone *(arrows)*.

CONGENITAL ANOMALIES OF THE URINARY TRACT

Renal Duplication

A common congenital anomaly of the urinary tract is duplication of the collecting system, which may be partial or complete. In complete duplication, two pelves and two separate ureters drain the kidney. The lower-pole ureter usually inserts into the bladder at the normal site. However, the intramural portion of the ureter may be shorter than usual, and vesicoureteral reflux (VUR) frequently results.[23] The upper-pole ureter often inserts ectopically, inferior and medial to the site of the normal ureteral insertion **(Weigert-Meyer rule).** Its orifice may be stenotic and obstructed. Ballooning of the submucosal portion of this upper-pole ureter causes a **ureterocele.** In some patients, the upper-pole ureter may have an insertion entirely outside the bladder including the urethra (above, at, or below the external urinary sphincter), in the uterus or vagina, or in the ejaculatory duct, seminal vesicle, or vas deferens.[24]

Patients with unobstructed duplications have no more clinical problems than their normal counterparts. Patients with complicated renal duplications may have UTI, failure to thrive, abdominal mass, hematuria, or symptoms of bladder outlet obstruction from a ureterocele. Female patients with urethral insertion of the upper-pole ureter below the external urinary sphincter or with vaginal or uterine insertion may have chronic, constant urinary incontinence or frequent dribbling.

Duplication of the renal collecting system is diagnosed on sonography when the central echo complex separates into two parts with an interposed column of normal renal parenchyma **(column of Bertin)** (Fig. 52.10). Unless collecting system dilation and/or ureteral dilation are present, it is usually impossible to distinguish a partial, uncomplicated duplication from a complete duplication because a normal ureter is difficult to visualize sonographically.[25]

With obstruction of an upper-pole moiety, dilation of the upper-pole collecting system and its entire ureter is seen. The renal parenchyma may be thinned over the upper-pole collecting system. If the obstruction is associated with a ureterocele, views of the bladder may demonstrate the ureterocele as a rounded, anechoic structure within the bladder in addition to the dilated distal ureter adjacent to the bladder (Fig. 52.11). A large ureterocele may cross the midline and obstruct the contralateral ureter or bladder outlet and cause bilateral hydronephrosis. Ureteroceles can be difficult to diagnose if they are large enough to mimic the bladder. If this is a concern, a postvoid scan will be diagnostic. With reflux into the lower-pole moiety, the lower-pole collecting system and its ureter will be dilated to a varying degree. If reflux is mild, there may be no lower-pole dilation.

Other Renal Anomalies

Other renal anomalies include congenital absence of the kidney, abnormal position of the kidney (e.g., pelvic kidney, crossed ectopia), and horseshoe kidney with fusion of the lower poles in the midline.[26] **Congenital absence of the kidney** or ectopia of the kidney is suspected when no renal tissue can be identified in the renal fossa on sonography. At birth, the adrenal gland will not present as the usual inverted V above the kidney but assumes a flat shape often called a **"lying-down adrenal"** (Fig. 52.12). Care must be taken to search for the kidney not only in its usual location in the renal fossa, but also in the lower abdomen or pelvis. The contralateral kidney, when healthy, shows compensatory hypertrophy when one kidney is absent or severely damaged. Nuclear scintigraphy may be helpful in identifying a small, functioning kidney not visualized by ultrasound.

With a **horseshoe kidney** the longitudinal axis of the kidneys is abnormal. The lower poles are rotated medially and will be fused in the midline anterior to the spine by a fibrous band or renal parenchyma (Fig. 52.13). The kidney is also positioned somewhat lower than usual. A horseshoe kidney can be overlooked if the abnormal renal axes are not recognized. The central fused renal tissue may also be thin and easily missed, particularly if it solely fibrous in nature.

Crossed renal ectopia is a rare congenital anomaly wherein both kidneys are located on the same side of the abdomen. There is at least some degree of fusion in approximately 90% of cases, with the usual pattern consisting of fusion of the orthotopic

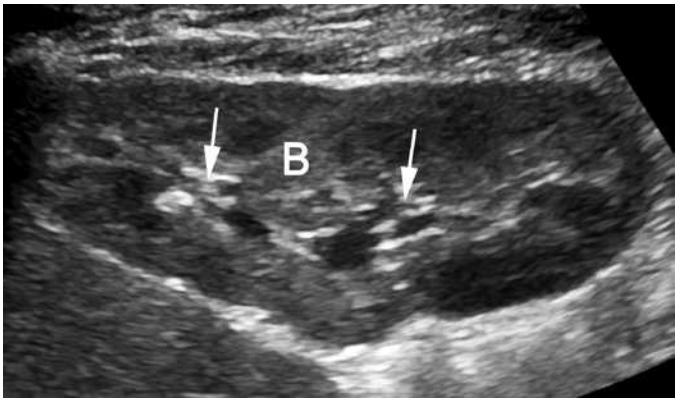

FIG. 52.10 Renal Duplication. Longitudinal prone image of the right kidney demonstrates normal renal parenchyma, a column of Bertin *(B)* dividing the central echo complex into two parts *(arrows)*.

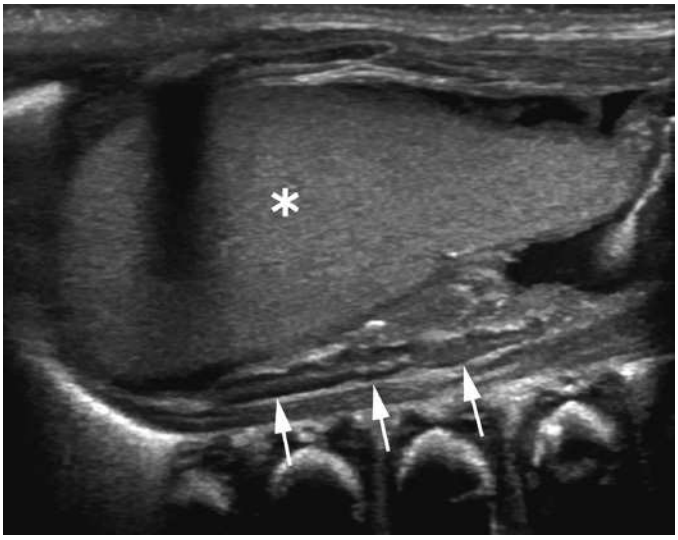

FIG. 52.12 "Lying Down" Adrenal Sign in a Neonate With Absence of the Left Kidney. Longitudinal image depicts an elongated and flattened adrenal gland *(arrows)* along the spine. *, Spleen.

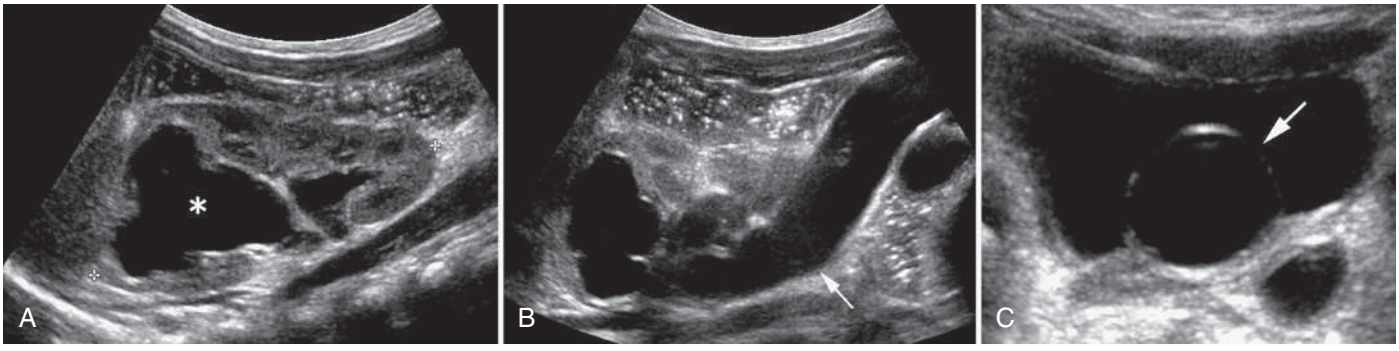

FIG. 52.11 Renal Duplication With Ectopic Ureterocele of Upper-Pole Moiety. (A) Longitudinal image of left kidney reveals dilation of the upper-pole collecting system (*) and less dilated lower-pole renal pelvis. **(B)** Longitudinal image of left flank depicts dilated upper-pole ureter *(arrow)* extending from renal pelvis. **(C)** Transverse bladder image shows **ureterocele** within the bladder *(arrow)*.

lower renal pole to the ectopic upper renal pole (Fig. 52.14, Video 52.1). The ureter of the ectopic kidney crosses the midline to insert normally within the bladder. Crossed renal ectopia is more frequent in boys than girls (male-to-female ratio is 1.4:1), and is two to three times more common on the right side than on the left.[27] As with other renal anomalies, crossed ectopia can be an incidental finding but is also associated with other congenital anomalies.[28]

Rarer patterns include crossed unfused ectopia and solitary or unfused bilateral crossed ectopy. Another pattern of combined ectopy and fusion of two pelvic kidneys is variably referred to as a **"pancake"** or **"cake"** kidney, depending on the extent of fusion and the resultant appearance. These more complex abnormalities can be isolated or associated with other congenital conditions.

CAUSES OF HYDRONEPHROSIS

Dilation of the renal collecting system—hydronephrosis—is a fairly common problem in the pediatric patient. It is frequently, but not always, associated with obstruction, and ultrasound is particularly sensitive for its detection. Investigation of a child with suspected hydronephrosis usually begins with sonography to evaluate the anatomy of the kidneys, ureters, and bladder.[29] The degree of functional obstruction is evaluated by diuretic renography.[30] If the obstruction is mild, the patient is followed because the obstruction and dilation often resolve as the patient grows older.[31,32]

Congenital hydronephrosis is almost always initially detected on fetal sonography and the infant referred for evaluation after birth. Fetal hydronephrosis may be due to obstruction, VUR, or a physiologic variant without obstruction.[33] Small amounts of fluid may be detected in the normal renal pelvis. However, dilation of the renal calyces is abnormal and suggests significant pathology. To make a more precise diagnosis and to estimate severity, information regarding renal length, parenchymal thickness and echogenicity, degree of pelvicalyceal and ureteral dilation, bladder wall thickness, and volume should be obtained with sonography.[31] Voiding cystourethrography (VCUG) and nuclear scintigraphy using technetium 99m (^{99m}Tc) mercaptoacetyltriglycine (MAG3) with furosemide (diuretic renography) are often performed for complete evaluation.[30,34]

Significant variation currently exists in the clinical management of infants and children with prenatally diagnosed urinary tract dilation (UTD) that is related to a lack of evidence-based information correlating the severity of prenatal dilation to postnatal urologic abnormalities. To address the perceived need for a unified classification system with a widely accepted terminology for the diagnosis and management of prenatal and postnatal UTD, a UTD classification system was devised in 2014 during a consensus meeting of eight medical societies concerned with the prenatal and postnatal diagnosis and management of UTD.[35,36] This grading system is correlated with the risk of postnatal uropathies and is based on six sonographic features: (1) anterior-posterior renal pelvic diameter (APRPD), (2) calyceal dilation with distinction between central and peripheral calyceal dilation postnatally, (3) renal parenchymal thickness, (4) renal parenchymal appearance, (5) bladder abnormalities, and (6) ureteral abnormalities. For prenatal studies, the seventh

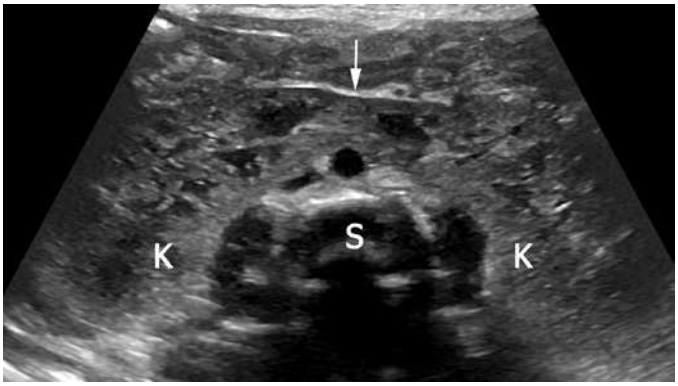

FIG. 52.13 Horseshoe Kidney. Transverse supine image depicts fusion of the medially rotated lower poles of the right and left kidneys *(K)* by a parenchymal band *(arrow)* extending anterior to the spine *(S)*.

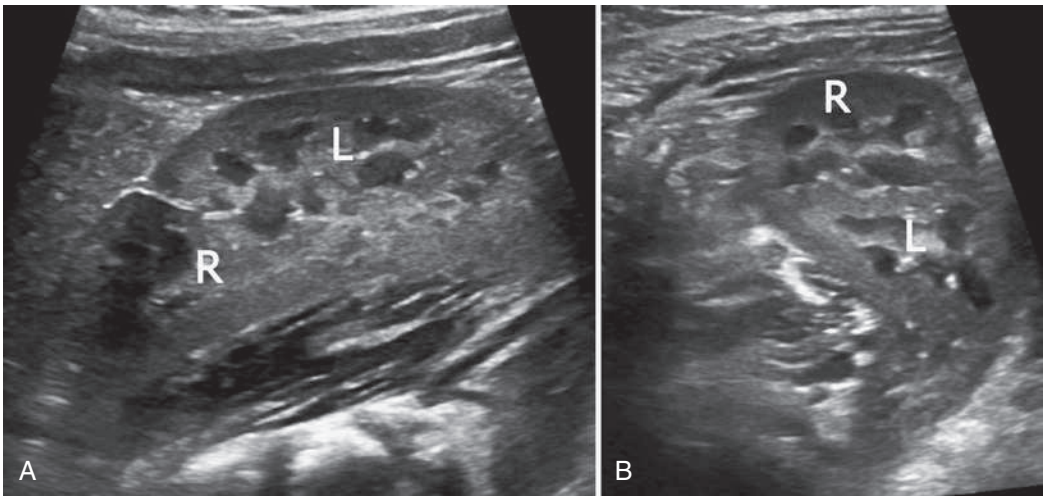

FIG. 52.14 Crossed Renal Ectopia. (A) Longitudinal and **(B)** transverse images of the right flank reveal fusion of the lower pole of the orthotopic right kidney *(R)* to the upper pole of the ectopic left kidney *(L)*. The left kidney is medially rotated. See also Video 52.1.

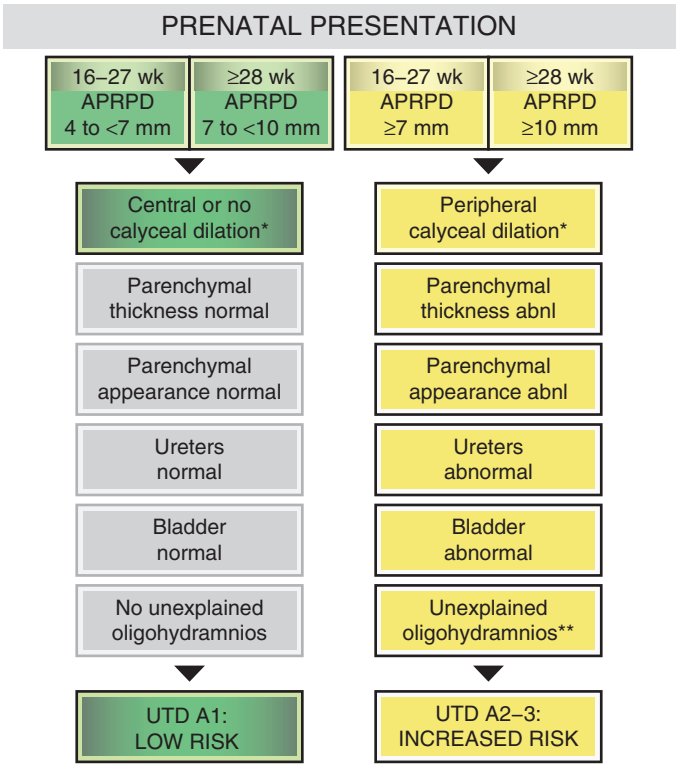

FIG. 52.15 Urinary Tract Dilation *(UTD)* Risk Stratification—Prenatal Presentation for UTD A1 (Low Risk) and UTD A2-3 (Increased Risk). Classification is based on the presence of the most concerning feature. *abnl,* Abnormal; *APRPD,* anterior-posterior renal pelvic diameter; *GU,* genitourinary. (With permission from Nguyen HT, Benson CB, Bromley B, et al. Multidisciplinary consensus on the classification of prenatal and postnatal urinary tract dilation [UTD classification system]. J Pediatr Urol. 2014;10[6]:982-998.[36])

sonographic finding to report is the quantity of amniotic fluid. Normal imaging parameters are also defined (Figs. 52.15 and 52.16). It is anticipated that future research will result in a refinement of this classification system that can be correlated with other clinical outcomes such as renal function and the need for surgical intervention.

Ureteropelvic Junction Obstruction

Ureteropelvic junction obstruction (UPJO) is the most common cause of significant prenatal hydronephrosis. It is usually results from a functional stricture at the ureteropelvic junction (UPJ) or a crossing lower-pole renal vessel. UPJO results in a functional disturbance in either the initiation or the propagation of normal peristaltic activity within the ureter. The obstruction produces proximal dilation of the renal collecting system. There is also an associated increased incidence of congenital anomalies of the contralateral kidney.

Ultrasound diagnosis of hydronephrosis is based on the presence of a dilated renal pelvis and caliectasis. A variable amount of renal parenchymal tissue can be visualized. The ureter is normal in size and is not usually visualized by ultrasound (Fig. 52.17).

Ureteral Obstruction

Congenital ureterovesical junction obstruction (UVJO) is a result of narrowing and aperistalsis of the distal ureter, or an ectopic insertion. With so-called **"primary megaureter"** the juxtavesicular ureter may be devoid of ganglion cells or may demonstrate muscular hypoplasia and/or mural fibrosis.[37-39] The submucosal tunnel and ureteral orifice are normal. There is a variable degree of dilation of the intrarenal collecting system and of the ureter proximal to the narrowing. Ultrasound typically shows hydronephrosis and hydroureter with a narrow segment of the distal ureter behind the bladder (Fig. 52.18). MAG3 diuretic renography

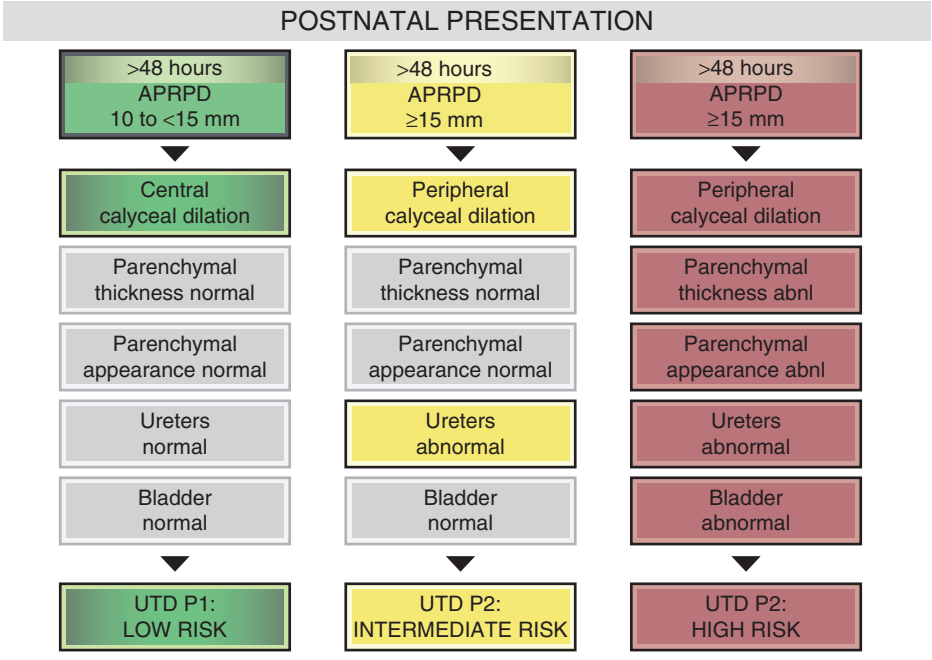

FIG. 52.16 Urinary Tract Dilation *(UTD)* Risk Stratification—Postnatal Presentation for UTD P1 (Low Risk), UTD P2 (Intermediate Risk), and UTD P3 (High Risk). Stratification is based on the most concerning ultrasound finding. *abnl,* Abnormal; *APRPD,* anterior-posterior renal pelvic diameter. (With permission from Nguyen HT, Benson CB, Bromley B, et al. Multidisciplinary consensus on the classification of prenatal and postnatal urinary tract dilation [UTD classification system]. J Pediatr Urol. 2014;10[6]:982-998.[36])

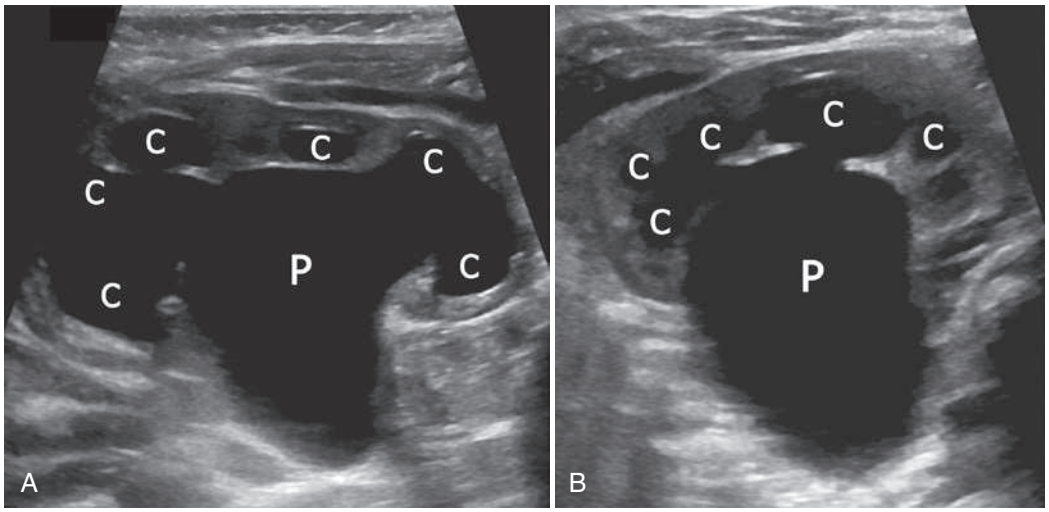

FIG. 52.17 Ureteropelvic Junction Obstruction. (A) and **(B)** Longitudinal and transverse images show marked renal collecting system dilation with the medially dilated pelvis *(P)* communicating with dilated calyces *(C)*.

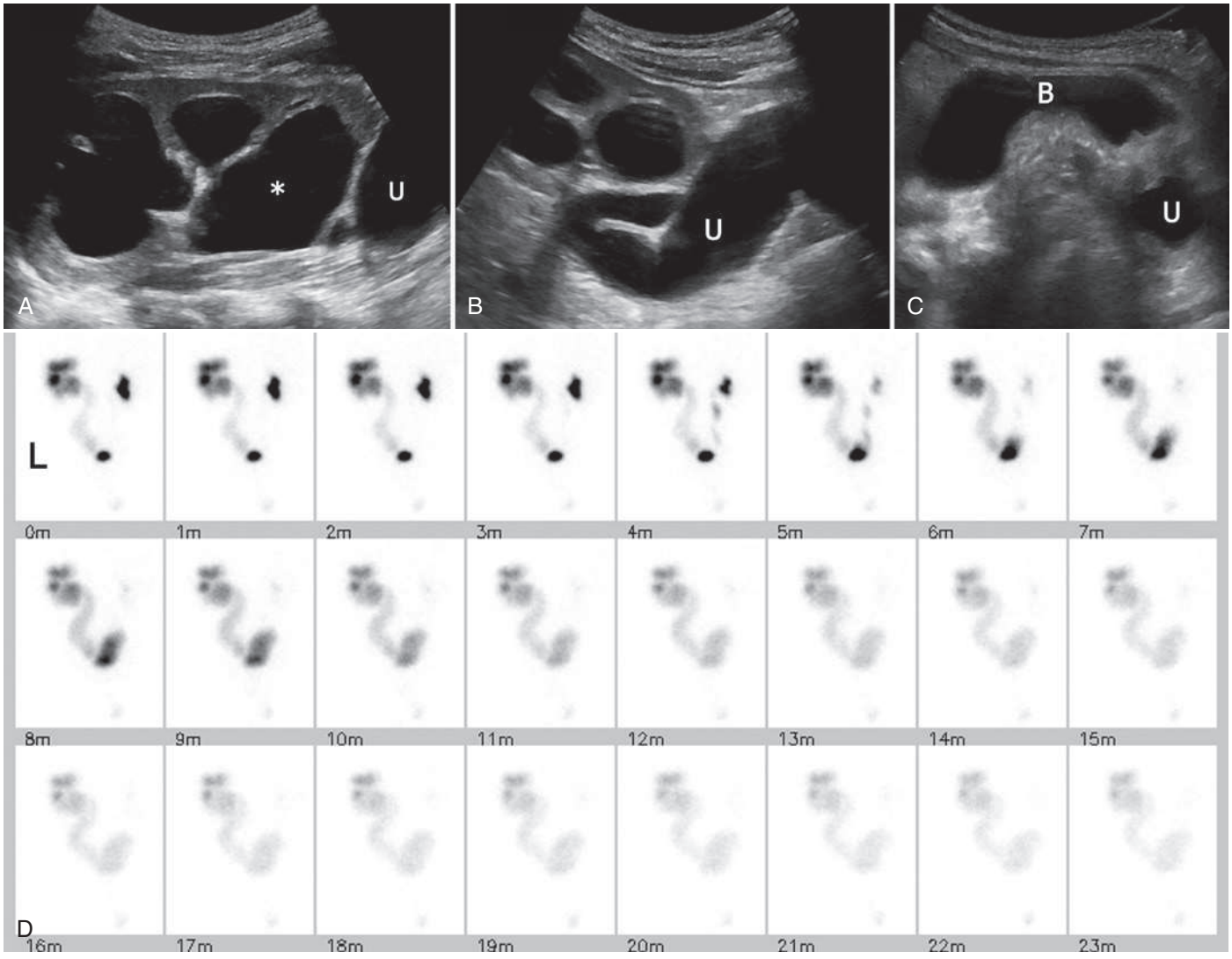

FIG. 52.18 Ureterovesical Junction Obstruction. (A) Longitudinal image of the left kidney reveals severe hydronephrosis and proximal hydroureter *(U)*. *, Renal pelvis. **(B)** Longitudinal image shows the dilated, tortuous ureter *(U)* in the left flank. **(C)** Transverse image depicts the dilated left ureter *(U)* near its insertion into the bladder *(B)*. **(D) MAG3 diuretic renography** images demonstrate left-sided pelvocaliectasis and ureteral tortuosity with delayed washout of activity compared with the right. *L*, Left side.

is typically used to clarify whether the dilation is caused by obstruction.

An obstructed ureter can result from many causes. **Ectopic insertion of a ureter** can cause obstruction either with or without a ureterocele and may result in dilation of the more proximal collecting system and ureter, typically manifesting with ureteral duplication. The ureter can also be obstructed by an intraluminal abnormality, such as a stone, blood clot, or fungus ball. Increased peristalsis in the ureter proximal to the obstruction may be detected with real-time sonography. Doppler sonography may show a diminished or abnormal ureteral jet on the side of obstruction.[18,40,41] The ureter can also be obstructed anywhere along its course by extrinsic compression from a mass, such as a lymphoma or abscess. The exact site of obstruction may be difficult to visualize by ultrasound because of overlying bowel gas.

Bladder Outlet Obstruction

Bilateral hydronephrosis is frequently caused by obstruction at the level of the bladder or bladder outlet. Congenital obstruction due to **posterior urethral valves** (PUVs) results in an irregular, thick-walled bladder. PUV can occasionally be diagnosed by ultrasound, with demonstration of a dilated posterior urethra. Transperineal contrast-enhanced ultrasound (CEUS) diagnosis of PUV has also been described[42,43] (Fig. 52.19). However, VCUG should be performed for optimal visualization of the valves.

Patients with spinal dysraphism and hyperreflexive detrusor muscle activity will have a functional obstruction due to a neurogenic bladder that produces high bladder pressure during voiding. These patients may develop a thick-walled, trabeculated bladder[44] (Fig. 52.20, Video 52.2, Video 52.3, Video 52.4). Congenital anomalies of the spine should be sought with radiographs and spinal ultrasound in neonates, if not obvious clinically.

A pelvic mass that obstructs the bladder outlet, such as **rhabdomyosarcoma,** or less commonly, a **fibroepithelial polyp,** can also be associated with bilateral hydronephrosis and hydroureter.[45]

Vesicoureteral Reflux

Dilation of the renal collecting system is not always caused by obstruction, and other abnormalities, such as VUR, should be considered. In a child with hydronephrosis detected by ultrasound, the bladder size and contractility and the urethra should be further evaluated with VCUG. In addition, VUR can be diagnosed and may be the cause of the UTD.

Contrast-enhanced voiding urosonography is a safe, nonionizing, radiation-free alternative to the fluoroscopic VCUG that is used by experienced investigators in some centers throughout the world for the management of VUR. Its sensitivity is comparable to or greater than that of VCUG or radionuclide cystography in the diagnosis of VUR.[46] Published studies reporting use of this technique in the United States to date have been limited.[47,48] Contrast-enhanced voiding urosonography is performed after bladder catheterization and intravesical infusion of normal saline containing the ultrasound contrast agent. Sequential imaging of the bladder, kidneys, and urethra is performed during bladder filling and voiding. Ultrasound contrast-specific settings are used to image the microbubbles. Digital ultrasound still images as well as image clips are used for documentation purposes (see Fig. 52.20). The severity of VUR can be graded using a scale similar to the International Grading System used for conventional VCUG.[49] Patients with reflux are often treated endoscopically with a submucosal, subureteric injection of a bulking agent. Follow-up sonography of the bladder will depict the implants, which over time may undergo changes in size and shape as well as calcification[50,51] (Fig. 52.21). Paltiel and colleagues[52] showed that nonvisualization of the implant or a multilobed contour is associated with persistent reflux.

Prune-Belly Syndrome

Prune-belly syndrome, also known as **Eagle-Barrett syndrome,** is a rare congenital disorder that occurs almost exclusively in males and is thought to result from urethral obstruction early in development. Abnormalities include absence or deficiency of the abdominal musculature; large, hypotonic, dilated and tortuous ureters; a large bladder; a patent urachus bilateral cryptorchidism; and a dilated prostatic urethra. There are decreased muscular fibers throughout the urinary tract and prostate, resulting in dilation and hypoperistalsis. Renal dysplasia and hydronephrosis can occur to varying degrees. Associated malformations of the cardiopulmonary, gastrointestinal, and skeletal systems are common.[53]

Megacystis-Microcolon-Malrotation–Intestinal Hypoperistalsis Syndrome

Megacystis-microcolon-malrotation–intestinal hypoperistalsis syndrome (MMIHS), a rare syndrome, is an inherited, autosomal recessive disorder that falls on the spectrum of chronic intestinal pseudo-obstructive disorders, which includes **chronic adynamic ileus, hypoganglionosis, Hirschsprung disease, intestinal neuronal dysplasia, and total colonic aganglionosis.** It is more common in girls than boys. Presentation is usually in the neonatal period, although the diagnosis can also be suspected on prenatal sonography.[54] Typical clinical features include abdominal distention, hypoactive or absent bowel sounds, and an inability to void spontaneously. A markedly dilated, nonobstructed bladder, a microcolon, and decreased or absent intestinal peristalsis are characteristic findings. Other frequent abnormalities include hydroureteronephrosis, VUR, intestinal malrotation, and a shortened bowel. Although the exact etiology has not yet been elucidated, smooth muscle myopathic changes have been demonstrated at pathology. Marked abnormality of the detrusor muscle of the bladder results in voiding dysfunction.[55] Most patients with MMIHS eventually succumb to sepsis, malnutrition, or multiorgan failure. Recurrent UTIs result from the need for chronic bladder catheterization. Intestinal function is resistant to surgical intervention. Children who survive beyond the neonatal period require long-term total parenteral nutrition (TPN), which eventually results in TPN-associated chronic liver disease. Transplantation is currently the only successful management option for those patients who cannot tolerate TPN. The

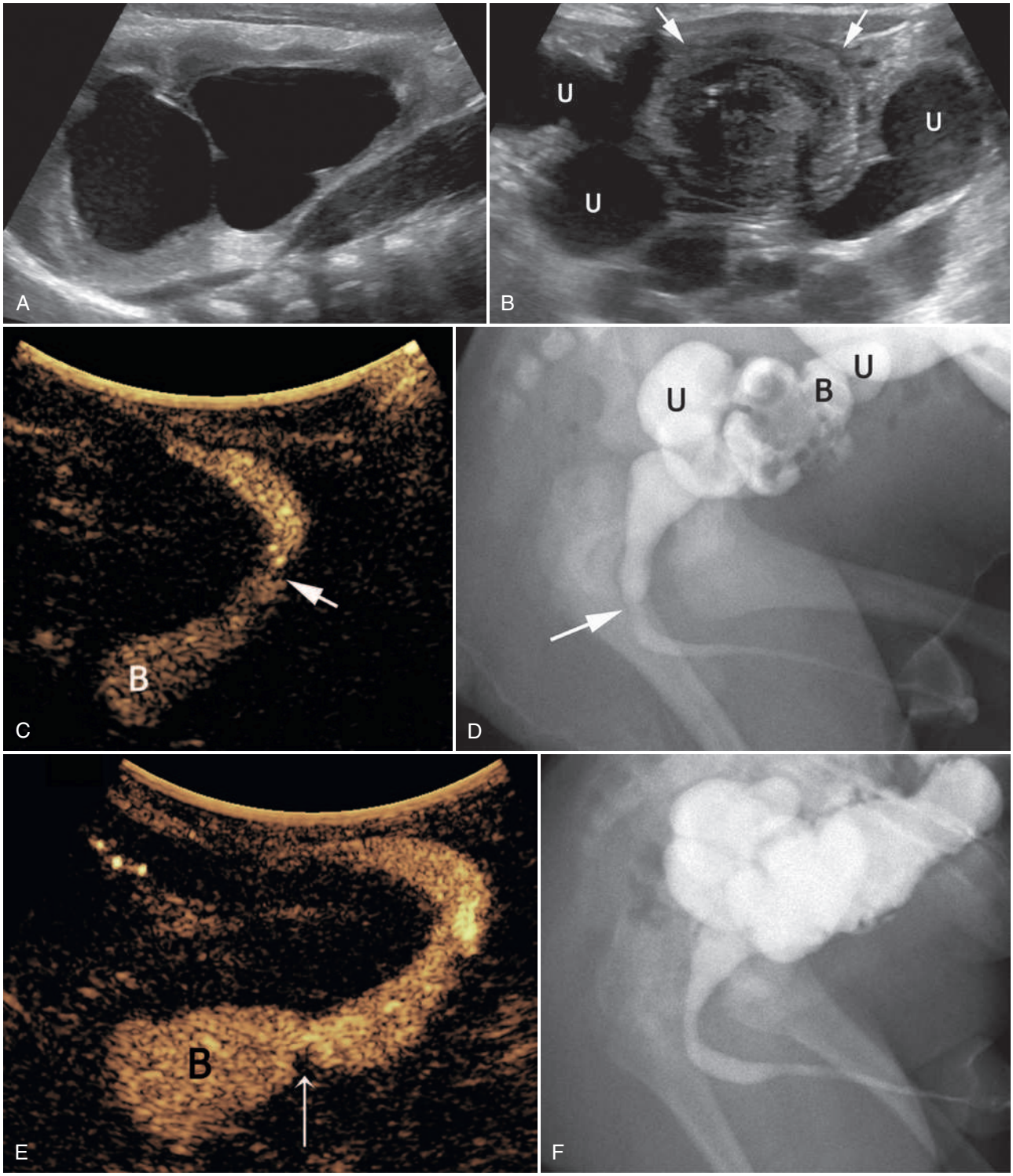

FIG. 52.19 Bilateral Hydronephrosis Secondary to Posterior Urethral Valves. (A) Longitudinal image of kidney shows hydronephrosis, which was present bilaterally. **(B)** Transverse image of the pelvis reveals thick-walled bladder *(arrows)* and tortuous, dilated ureters *(U)*. **(C)** Transperineal contrast-enhanced ultrasound image and **(D)** voiding cystourethrogram demonstrate dilated posterior urethra with indentation at the site of the obstructing valves *(arrows)*. *B,* Bladder; *U,* ureter. **(E)** Postoperative transperineal contrast-enhanced ultrasound image and **(F)** Postoperative voiding cystourethrogram reveal improvement in urethral contour.

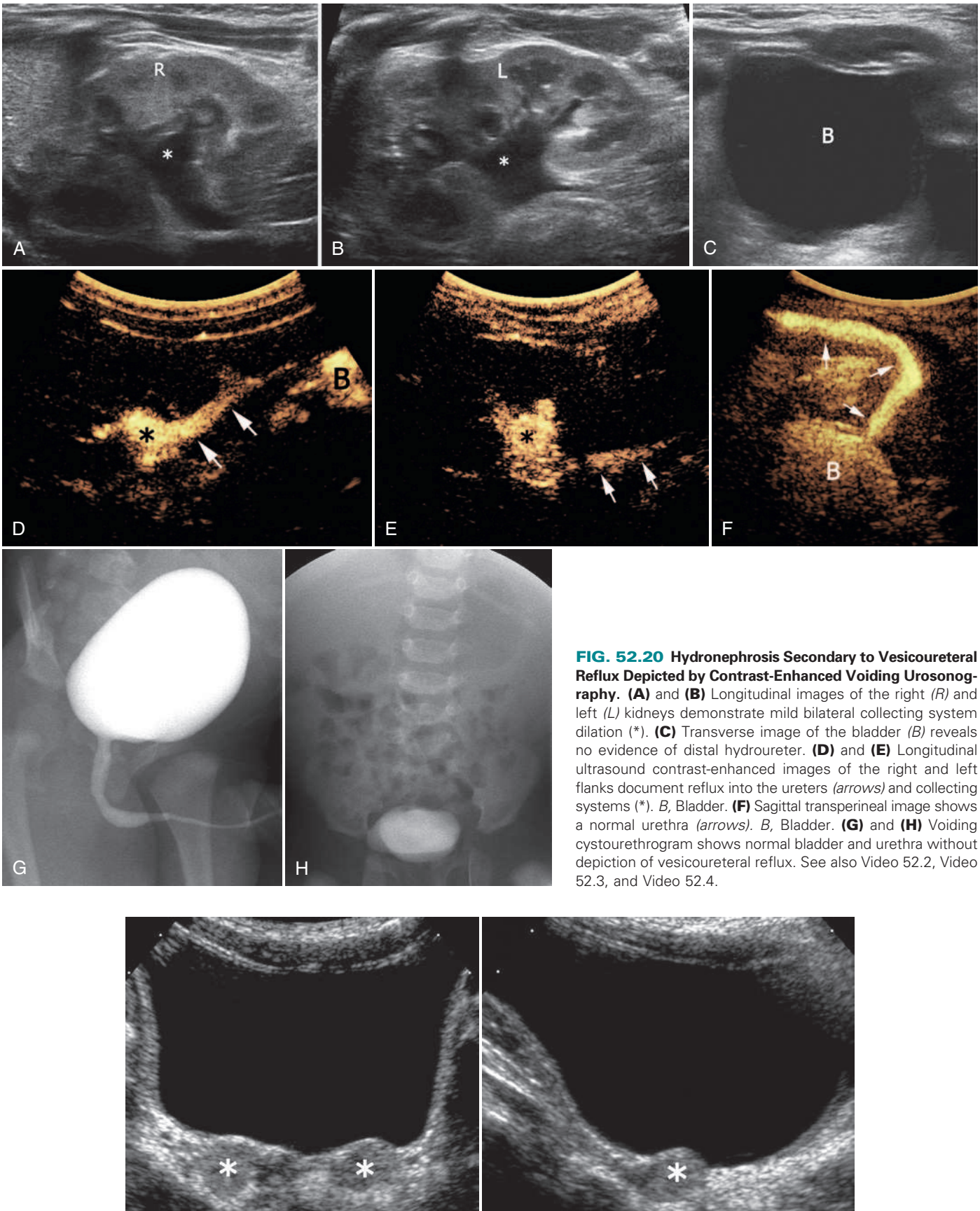

FIG. 52.20 Hydronephrosis Secondary to Vesicoureteral Reflux Depicted by Contrast-Enhanced Voiding Urosonography. (A) and **(B)** Longitudinal images of the right *(R)* and left *(L)* kidneys demonstrate mild bilateral collecting system dilation (*). **(C)** Transverse image of the bladder *(B)* reveals no evidence of distal hydroureter. **(D)** and **(E)** Longitudinal ultrasound contrast-enhanced images of the right and left flanks document reflux into the ureters *(arrows)* and collecting systems (*). *B,* Bladder. **(F)** Sagittal transperineal image shows a normal urethra *(arrows)*. *B,* Bladder. **(G)** and **(H)** Voiding cystourethrogram shows normal bladder and urethra without depiction of vesicoureteral reflux. See also Video 52.2, Video 52.3, and Video 52.4.

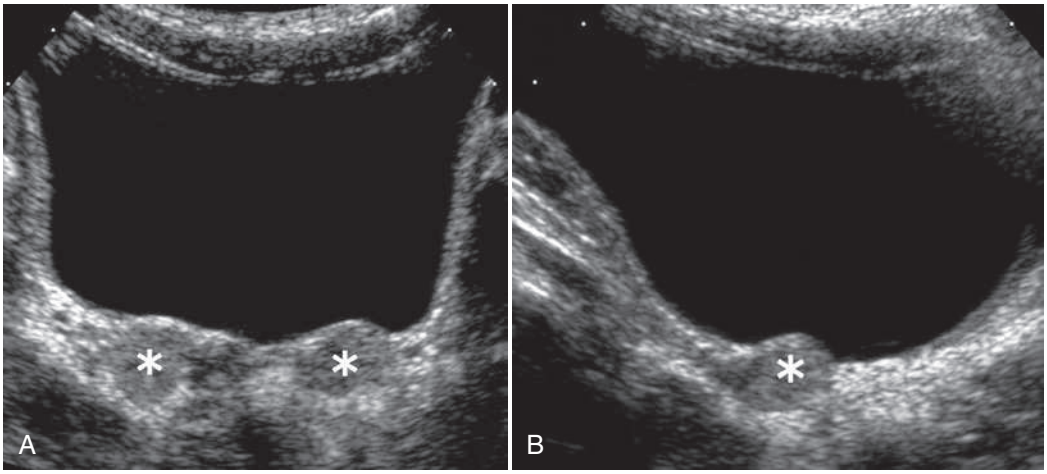

FIG. 52.21 Subureteric Implants Used to Treat Vesicoureteral Reflux. (A) and **(B)** Transverse and longitudinal bladder images reveal bilateral subureteric mounds (*) associated with the bulking agent.

appropriate choice of transplant is dictated by the presence or absence of coexistent TPN-related chronic liver disease or chronic kidney failure resulting from urologic disease.[56] These options include isolated intestinal transplantation, combined liver-intestinal transplantation, and multivisceral transplantation.

Bladder Exstrophy

Bladder exstrophy is a rare congenital malformation characterized by an infraumbilical abdominal wall defect, incomplete bladder closure with mucosal continuity with the anterior abdominal wall, epispadias, and associated abnormalities of the pelvic bones and musculature. This disorder is a component of the **exstrophy-epispadias complex,** with epispadias at the mild end of the spectrum and cloacal exstrophy at the severe end. Bladder exstrophy is the most common of these abnormalities and occurs most often in boys.[57] Clinical features include bladder eversion, epispadias, wide diastasis of the pubic bones, and anterior displacement of the anus as a result of muscular deficiency. In boys, the penis will be shortened with wide separation of the corporal attachments and dorsal curvature. In girls, there is a bifid clitoris. The ureters have a low bladder insertion with a characteristic J-shaped course due to an enlarged pouch of Douglas that displaces the ureters inferolaterally. Unless ureteral reimplantations are performed, these patients will all develop VUR after exstrophy closure.[57]

Modern staged repair of bladder exstrophy is a two-step process in girls and a three-step process in boys. In stage I, the bladder and abdominal wall defects are closed in both sexes 48 to 72 hours after birth, with epispadias repair only in girls. If the pubic diastasis is greater than 4 cm or the malleability of the pelvis is poor, iliac osteotomies may be performed at this time. In stage II, the male urethra is closed, usually between 6 and 12 months of age. In stage III, bladder neck reconstruction and bilateral ureteral reimplantation are performed, generally at 4 to 5 years of age, when the child can take part in a voiding program.[58]

After repair, the bladder will appear small on ultrasound imaging with irregular contours and a thickened wall. The kidneys generally have a normal appearance, although hydronephrosis may occur as a result of VUR, bladder outlet obstruction, or urethral stricture. Renal scarring can develop from recurrent pyelonephritis or obstructive uropathy after bladder neck reconstruction.

Bladder augmentation using a segment of bowel is an option for children who cannot undergo bladder neck reconstruction because of a low bladder capacity, abnormal bladder compliance, or incontinence.[59] Ileocystoplasty is the most popular choice, although other bowel segments can be used. By ultrasound, the augmented bladder segment will be identified superior to the native bladder, and will demonstrate an undulating contour. The characteristic "gut signature" of the augmented segment is readily identified[59] (Fig. 52.22). Echogenic intraluminal mucus or debris is often noted.

Urachal Anomalies

The fetal urachus is a tubular structure extending from the umbilicus to the bladder. It normally closes by birth, and a urachal remnant may be visible as a hypoechoic, elliptical mass on the anterosuperior aspect of the bladder (Fig. 52.23). A **patent urachus** is present if there is a complete tubular connection from the bladder to the skin surface at the umbilicus (about 50%), or only a portion may be open as a blind-ending **urachal sinus** arising either from the bladder dome (**vesicourachal diverticulum,** about 3%-5%, Fig. 52.24) or from the umbilicus (umbilicourachal sinus, about 15%). When only the midportion of the urachus remains patient, a **urachal cyst** is the result (about 30%)[60] (Fig. 52.25).

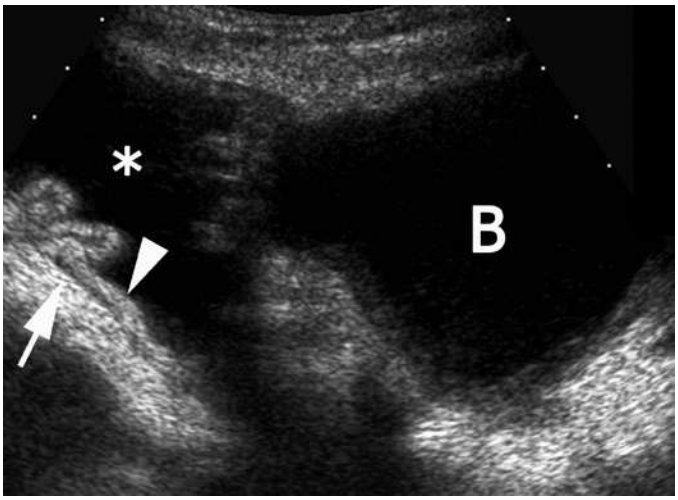

FIG. 52.22 Sigmoid Cystoplasty in Patient With History of Bladder Exstrophy. Longitudinal image demonstrates bladder *(B)* with augmented segment located superiorly (*). Note the undulating contour of the augmented segment with the outer hypoechoic muscular layer *(arrow)* and the inner hyperechoic layer of bowel mucosa *(arrowhead)*.

The literature is inconclusive on how to manage pediatric urachal lesions, especially those discovered incidentally. Both the therapeutic and the prophylactic value of surgical resection are ill defined. A recent retrospective review of 721 patients by Gleason and colleagues concluded that urachal anomalies are more common than previously reported, and that children with asymptomatic lesions do not appear to benefit from prophylactic excision, as the risk of malignancy later in life is remote.[61]

URINARY TRACT INFECTION

UTI is a common clinical problem in children and a frequent indication for renal sonography. The imaging workup of the child with a UTI is usually performed after the first culture has documented infection in an infant or child. The purpose of the workup is to identify congenital anomalies, obstruction, and other abnormalities that may predispose the patient to infection. Sonography of the urinary tract, including the kidneys and bladder, is used for initial screening. VCUG is indicated after a first UTI only if ultrasound reveals hydronephrosis, scarring, or other abnormalities suggestive of high-grade VUR or obstructive uropathy or in patients with complex clinical conditions. VCUG is also recommended if there is a recurrence of a febrile UTI.[62]

In most centers in the United States, conventional fluoroscopic VCUG is performed for evaluation of the bladder and urethra

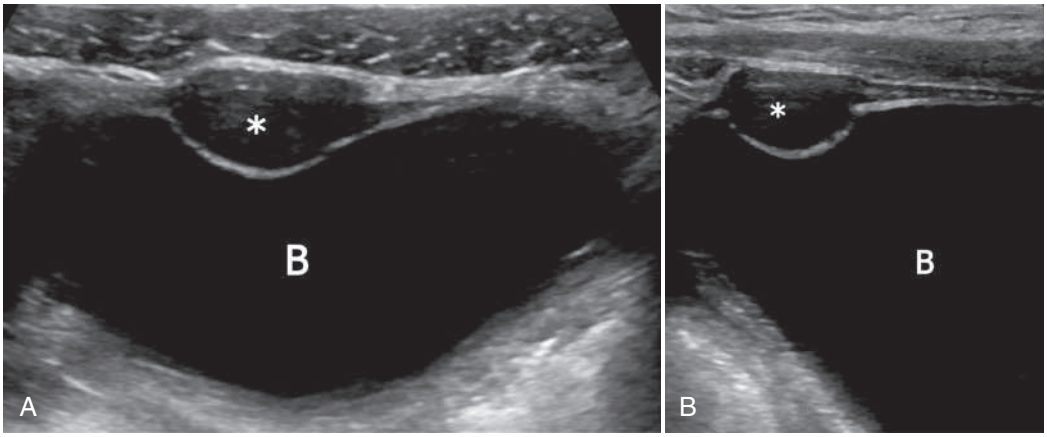

FIG. 52.23 Urachal Remnant. (A) and **(B)** Transverse and longitudinal images depict the hypoechoic, elliptical urachal remnant (*) in the anterosuperior bladder wall. *B,* Bladder.

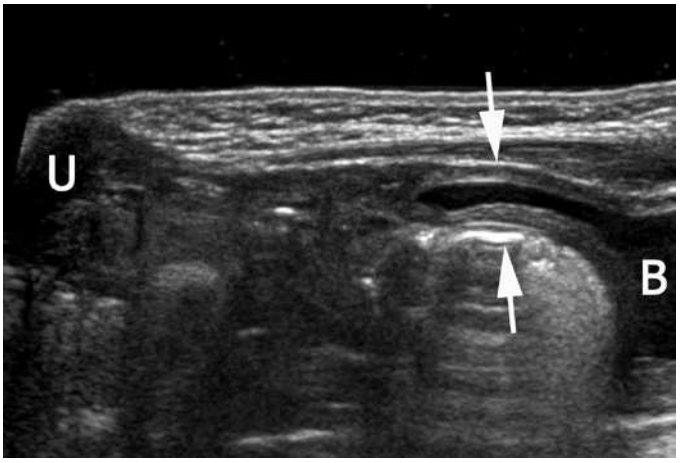

FIG. 52.24 Vesicourachal Diverticulum. Longitudinal image reveals a diverticulum *(arrows)* arising from the bladder dome and extending superiorly. *B,* Bladder; *U,* umbilicus.

and to detect the presence of VUR. Nuclear cystography can also be used for diagnosis of VUR and is associated with a lower radiation dose to the gonads in boys. In some centers nuclear cystography is used as the initial study for girls with normal renal and bladder sonograms, because girls rarely have urethral abnormalities. Some centers also use it to follow reflux in all children. At Boston Children's Hospital, we recently introduced contrast-enhanced VCUG and plan to eventually pilot its use in the follow-up of patients with prior VCUG documentation of VUR, as an initial imaging study in selected patients with normal ultrasound imaging of the kidneys and bladder, and in patients whose parents have serious concerns about radiation exposure (see Fig. 52.20, Video 52.2, Video 52.3, Video 52.4).

Diuretic renography with MAG3 can be performed to differentiate between obstructive and nonobstructive causes of renal or ureteral dilation, and to assess renal function.[30,63] Renal nuclear scintigraphy with ^{99m}Tc dimercaptosuccinic acid (DMSA) is extremely sensitive for demonstrating focal areas of inflammation and parenchymal scarring. Although mild scarring may be missed with sonography, power Doppler sonography increases the sensitivity of scar detection.[64,65] Because mild scars do not alter the course of therapy, the radiation dose of a renal cortical scan is not required[66-69] and the increased time and expense of Doppler sonography may also be avoided.

Acute Pyelonephritis

Acute pyelonephritis is one of the most serious bacterial illnesses of childhood. It may be diagnosed clinically in patients with a sudden onset of fever, flank pain, costovertebral angle tenderness, and microscopic evidence of urinary infection. VUR is clearly a risk factor for the development of acute pyelonephritis, which often starts as an ascending infection from the bladder. It can also occur by hematogenous spread. In infants, symptoms are often ambiguous, and fever is not always helpful in identifying patients at risk for complications of acute pyelonephritis such as sepsis and meningitis.[70,71]

In general, there are few findings of acute pyelonephritis on conventional gray-scale sonography. There may be swelling of the infected kidney and altered renal parenchymal echogenicity from edema causing triangular areas of increased echogenicity or rounded hypoechoic zones. **Focal pyelonephritis** can appear sonographically as a localized mass with abnormal echogenicity compared with the remainder of the kidney and loss of corticomedullary differentiation (Fig. 52.26). There may be thickening of the wall of the renal pelvis and ureter, also caused by edema and inflammation[72] (Fig. 52.27). Sequential examinations of these focal infected areas will typically demonstrate a rapid change, with resolution of the mass in response to antibiotic therapy.

Power Doppler sonography, DMSA scintigraphy, computed tomography (CT), and magnetic resonance imaging (MRI) may all show absent or decreased perfusion in a diffuse or lobar distribution, especially in the upper or lower poles.[73] CEUS has also been used to identify adults with acute pyelonephritis,[74] but there have been no reports yet regarding its use in children. When patients with UTIs do not respond rapidly to antibiotic therapy, repeat sonographic and/or CT examinations are indicated to search for complications that require drainage.

Acute lobar nephronia is a localized, nonliquefactive, severe interstitial bacterial infection of the renal parenchyma. Sonography

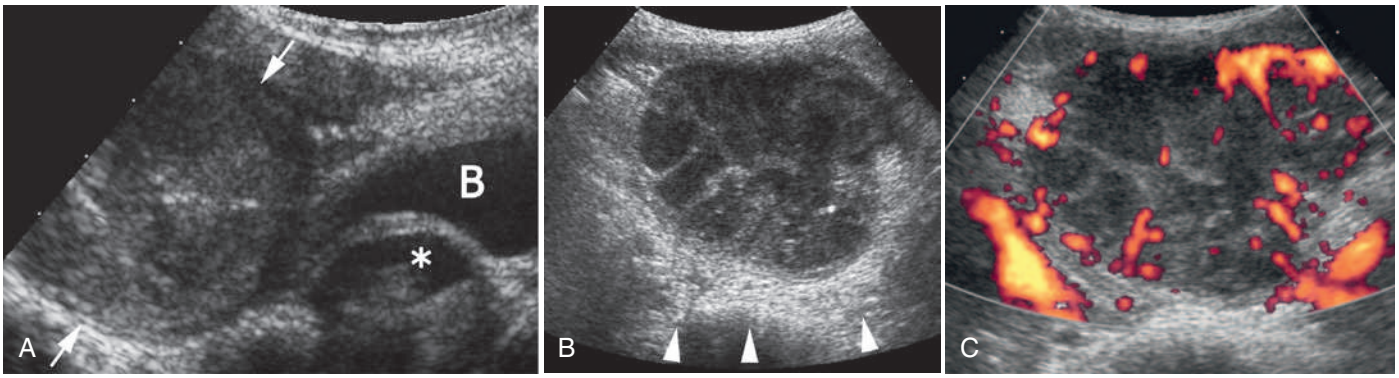

FIG. 52.25 Infected Urachal Cyst. (A) Longitudinal image shows a complex, lobulated mass *(arrows)* adjacent to the superior aspect of the bladder *(B)*. *, Free pelvic fluid. **(B)** Transverse image of the mass depicts increased through transmission of sound *(arrowheads)* in keeping with the fluid nature of the lesion. **(C)** Color Doppler image depicts hyperemia at the periphery of the lesion indicative of its inflammatory nature.

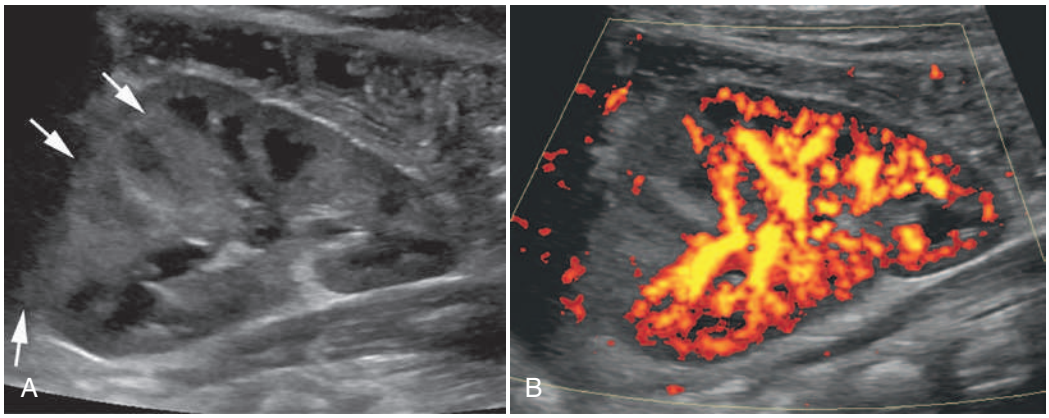

FIG. 52.26 Acute Pyelonephritis in 2-Month-Old Girl. (A) Longitudinal image demonstrates a swollen, echogenic upper pole with loss of normal corticomedullary differentiation *(arrows)*. **(B)** Power Doppler sonography reveals markedly diminished blood flow in this region.

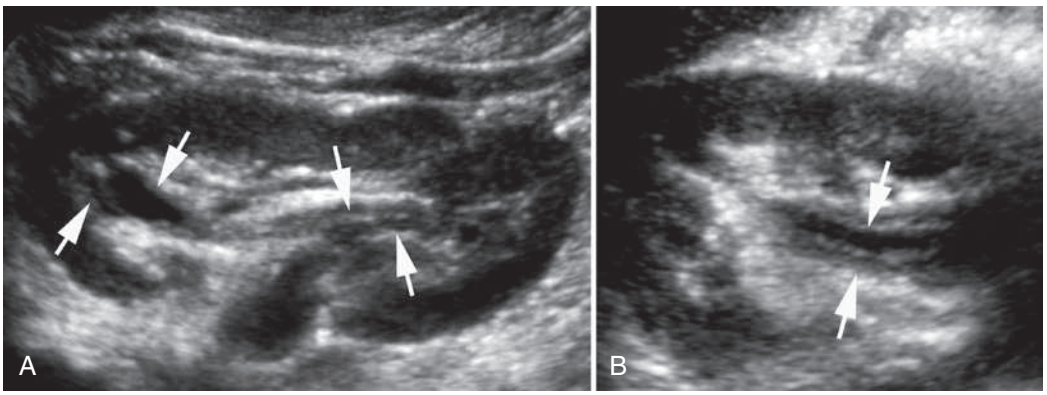

FIG. 52.27 Thickening of the Renal Pelvic Wall. (A) and **(B)** Longitudinal and transverse images demonstrate thickening of the renal pelvic wall *(arrows)*, which can occur as a result of inflammation or reflux, as well as after relief of obstruction.

may demonstrate a focal mass of variable echogenicity with ill-defined borders. CT is considered a more sensitive and accurate imaging modality for the diagnosis of acute lobar nephronia. Affected patients have a more protracted clinical course than those with acute pyelonephritis, and there is a higher incidence of renal scarring.[75] If response to antibiotic therapy is inadequate, the mass may liquefy centrally and become a renal abscess that requires drainage. Sonography of an abscess shows a focal mass with a hypoechoic central area representing liquefied pus (Fig. 52.28).

Another potential complication of acute pyelonephritis that requires drainage is pyonephrosis, which appears on sonography as echogenic material filling a dilated collecting system (Fig. 52.29).

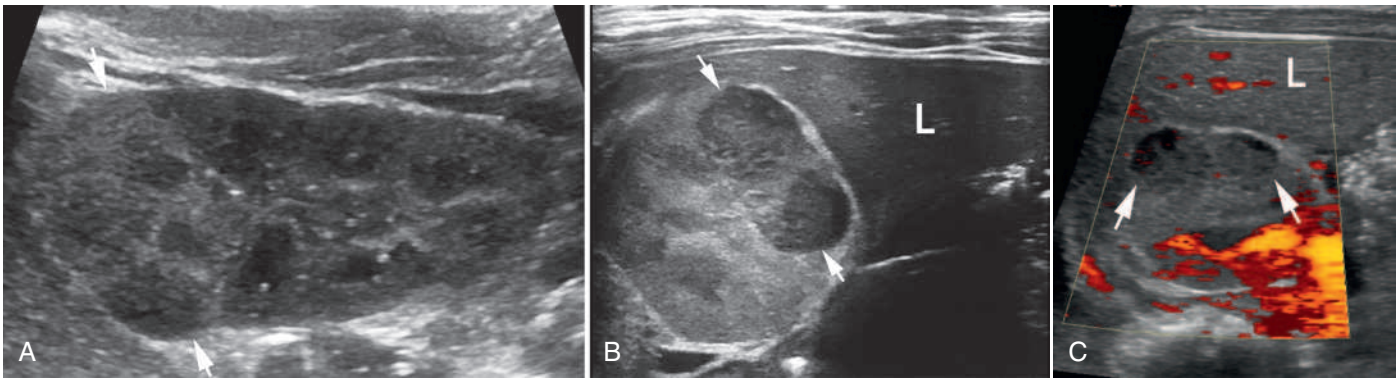

FIG. 52.28 Renal Abscess. (A) Longitudinal image of the right kidney reveals upper-pole swelling with loss of normal corticomedullary differentiation *(arrows).* **(B)** Transverse image of the right upper renal pole depicts an irregular intraparenchymal fluid collection *(arrows).* **(C)** Power Doppler image of the right upper pole shows diminished blood flow as well as the intraparenchymal fluid collection *(arrows). L,* Liver.

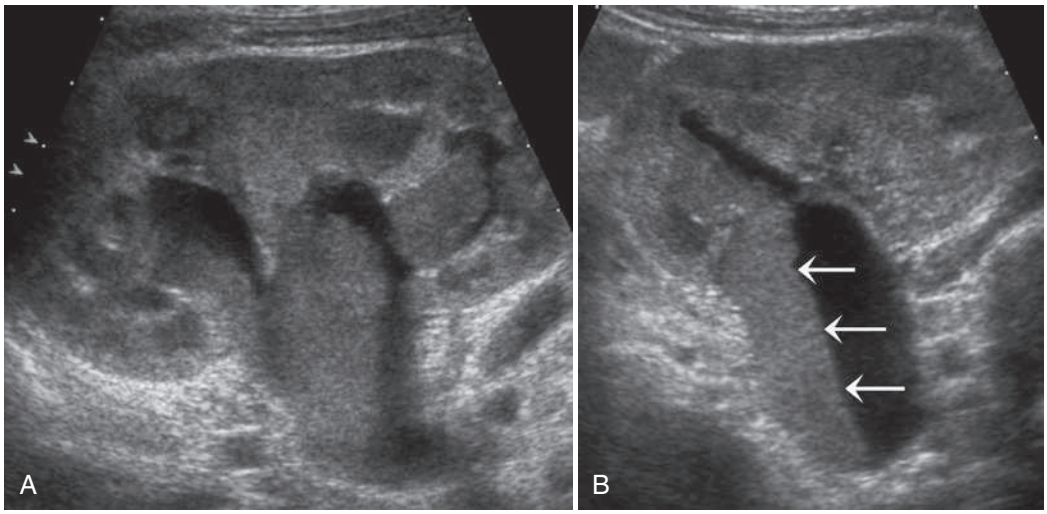

FIG. 52.29 Pyonephrosis in a 4-Month-Old Infant With Underlying Ureteropelvic Junction Obstruction. (A) and **(B)** Sagittal and transverse images of the left kidney depict moderate hydronephrosis with echogenic material in the collecting system and a prominent fluid-fluid level in the renal pelvis *(arrows).*

Chronic Pyelonephritis

Chronic pyelonephritis is caused by repeated episodes of acute pyelonephritis and results in a small, scarred kidney, indicative of end-stage renal disease. The kidney is usually irregular in outline because of focal parenchymal loss. The renal cortex is typically more echogenic than the adjacent hepatic or splenic parenchyma, and there may be decreased corticomedullary differentiation (Fig. 52.30). These findings are not specific and can also be seen in children with **chronic glomerulonephritis, renal dysplasia, hypertension, or renal ischemia.**

Neonatal Candidiasis

Candida albicans is a saprophytic fungus that usually infects immunocompromised patients, particularly neonates with indwelling catheters receiving broad-spectrum antibiotics. Systemic candidiasis leads to infection of multiple organs, including the kidneys, and neonates may have anuria, oliguria, a flank mass, or hypertension. Sonography may show diffuse enlargement of the kidney, with loss of normal architecture and increased parenchymal echogenicity. Fungus ball formation due to mycelial clumping may occur in the collecting system, resulting in echogenic masses and hydronephrosis secondary to obstruction[76] (Fig. 52.31).

Cystitis

Inflammation of the urinary bladder may occur in children as a result of infection or drug therapy, as with the antineoplastic agent cyclophosphamide. The bladder wall becomes thickened and irregular, with hypervascularity identified with color and power Doppler imaging. Echogenic debris or blood clot may be seen in the bladder lumen[77] (Fig. 52.32). Rarely, an **inflammatory pseudotumor** may result, with visualization of a bladder mass[78] (Fig. 52.33, Video 52.5).

MEDICAL RENAL DISEASE

The term "medical renal disease" refers to disorders that primarily affect the renal parenchyma and may be acute or chronic. Ultrasound is usually the initial imaging study performed in the

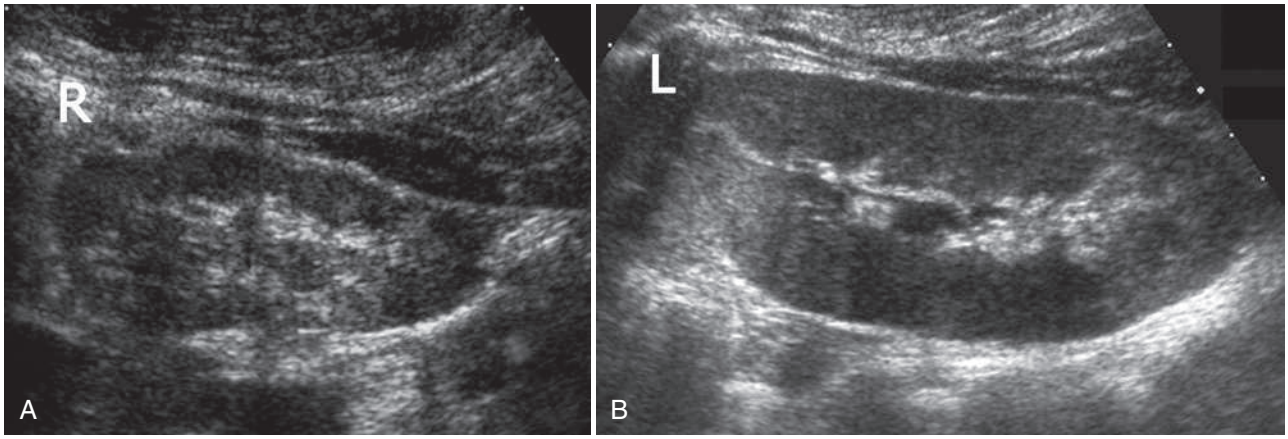

FIG. 52.30 Chronic Pyelonephritis in 12-Year-Old Boy With a History of Urinary Tract Infection. (A) and **(B)** The right kidney *(R)* is small (7.6 cm) compared with the left kidney (*L;* 11.5 cm), and demonstrates thin, echogenic parenchyma. The left kidney is hypertrophied but otherwise appears normal.

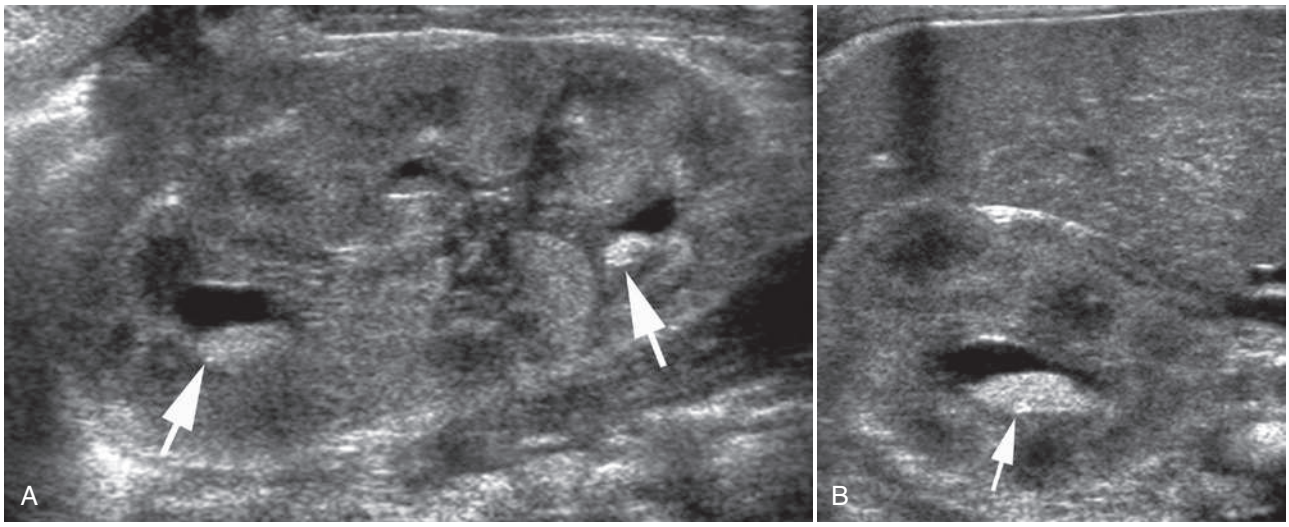

FIG. 52.31 Renal Candidiasis in a Premature Neonate. (A) and **(B)** Longitudinal and transverse images show echogenic material within the calyces **(A)** and pelvis **(B)** of the right kidney *(arrows)* representing **fungus balls.**

evaluation of patients who typically have hematuria, proteinuria, or renal failure.[79]

Acute Kidney Injury

Acute kidney injury (AKI), defined as a sudden loss of renal function, may be caused by inadequate renal perfusion, renal cell injury, or urinary tract obstruction. AKI usually develops in hospitalized children as a consequence of systemic illness or its treatment, and not from primary renal disease. The most common causes of AKI in children are renal ischemia, nephrotoxic drugs, and sepsis. Other important causes are listed in the accompanying box. All forms of AKI can lead to chronic kidney disease (CKD). Recovery of renal function depends on the underlying events leading to injury.[80]

Ultrasound is usually the initial diagnostic imaging study performed in the workup of children with AKI, and is often the only imaging required. The role of ultrasound is to assess renal size and to exclude anatomic abnormalities as the cause of AKI. Pathologic changes of the renal cortex, medulla, and collecting system are readily detected and correlate well with histologic findings. Doppler ultrasound yields information about renal perfusion and vascular abnormalities. Ultrasound is also used to localize the kidneys for percutaneous biopsy. Functional information may be obtained with nuclear medicine studies that can aid in more precisely differentiating among prerenal, renal, and postrenal causes of AKI.[80]

In the setting of prerenal injury, the kidney is intrinsically normal, and renal function is diminished as a result of decreased renal perfusion. The kidneys are sonographically normal, and restoration of renal perfusion results in a prompt return of renal function.

Renal ischemia caused by prolonged prerenal injury or by a severe hypoxic or ischemic insult can result in **acute tubular necrosis** (ATN). Imaging findings depend on the severity of parenchymal injury. A generalized increase in renal cortical echogenicity indicates intrinsic renal disease (Fig. 52.34). In mild

Common Causes of Acute Kidney Injury

PRERENAL FAILURE
Decreased true intravascular volume
Decreased effective intravascular volume

INTRINSIC RENAL DISEASE
Acute tubular necrosis (vasomotor neuropathy)
- Hypoxic or ischemic insults
- Drug induced
- Toxin mediated
  - Endogenous toxins—hemoglobin, myoglobin
  - Exogenous toxins—ethylene glycol, methanol

URIC ACID NEPHROPATHY AND TUMOR LYSIS SYNDROME
INTERSTITIAL NEPHRITIS
Drug induced
Idiopathic

GLOMERULONEPHRITIS
VASCULAR LESIONS
Renal artery thrombosis
Renal vein thrombosis
Cortical necrosis
Hemolytic uremic syndrome

HYPOPLASIA OR DYSPLASIA WITH OR WITHOUT OBSTRUCTIVE UROPATHY
Idiopathic
Exposure to nephrotoxic drugs in utero

HEREDITARY RENAL DISEASE
Autosomal dominant polycystic kidney disease
Autosomal recessive polycystic kidney disease
Alport syndrome
Sickle cell nephropathy
Juvenile nephronophthisis

OBSTRUCTIVE UROPATHY AND LOWER TRACT LESIONS
Obstruction in a solitary kidney
Bilateral ureteral obstruction
Urethral obstruction
Bladder rupture

With permission from Andreoli S. Clinical evaluation of acute kidney injury in children. In: Avner ED, editor. Pediatric nephrology. 6th ed. Berlin: Springer-Verlag; 2009.[81]

FIG. 52.32 Hemorrhagic Cystitis Caused by the Polyomavirus BK Virus in Patient With Leukemia. Transverse bladder image shows thick-walled bladder containing echogenic debris and blood clot (*).

cases, the kidneys may appear normal or may demonstrate slightly increased renal cortical echogenicity. Loss of corticomedullary differentiation can occur. Doppler flow may be normal in mild disease, whereas poor peripheral perfusion and diminished arterial diastolic flow due to increased peripheral vascular resistance occur in more severe cases.[80] Decreased renal cortical echogenicity is typical of **acute cortical necrosis.**

Nephrotoxic drugs commonly associated with AKI include antibiotics, chemotherapeutic agents, and nonsteroidal antiinflammatory medications. Some medications such as aminoglycoside antibiotics cause tubular injury. Methicillin and other penicillin analogues, cimetidine, sulfonamides, rifampin, and nonsteroidal antiinflammatory drugs may cause acute interstitial nephritis, which in some cases leads to a hypersensitivity reaction with development of antitubular basement membrane antibodies.

Children with **B-cell lymphoma** and **acute lymphocytic leukemia** are at risk for the development of uric acid nephropathy and tumor lysis syndrome. In patients with **septic shock,** AKI can develop from hypotension, leading to renal ischemia and ATN.[80]

Chronic Kidney Disease

The classification of CKD published by the National Kidney Foundation Kidney Disease Outcomes Quality Initiative is based on estimated glomerular filtration rate and is applicable to children older than 2 years and to adults[82] (Table 52.7). The most common causes of pediatric CKD in North America are congenital disorders such as **obstructive uropathy, renal dysplasia,** and **reflux nephropathy.** In contrast, in Japan, 34% of pediatric CKD is due to **glomerulonephritis, primary focal segmental glomerulosclerosis,** and **immunoglobulin A nephropathy.** In Jordan and Iran, where consanguinity is more common, heritable disorders such as **cystic kidney disease, primary hyperoxaluria, cystinosis, Alport syndrome,** and **congenital nephrotic syndrome** represent a greater proportion of cases of CKD. In the

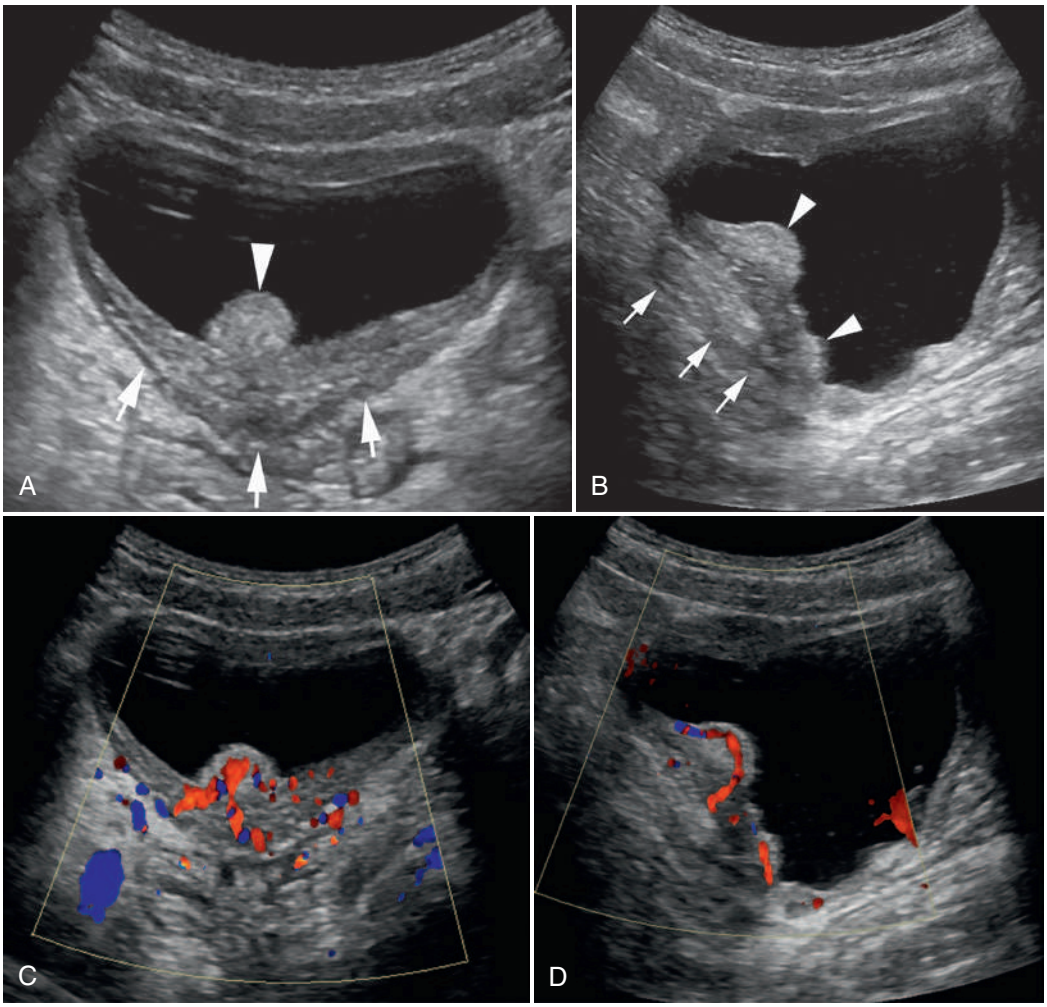

FIG. 52.33 Inflammatory Pseudotumor in Patient With Hemorrhagic Cystitis Secondary to Cyclophosphamide Treatment. (A) and **(B)** Transverse and longitudinal images demonstrate diffuse thickening and irregularity of the bladder wall *(arrows)* as well as multiple nonmobile, echogenic lesions *(arrowheads)*. **(C)** and **(D)** Transverse and longitudinal color Doppler images reveal hyperemia of both bladder wall and lesions. Complete resolution of mural abnormalities documented on follow-up study performed 6 months later. See also Video 52.5.

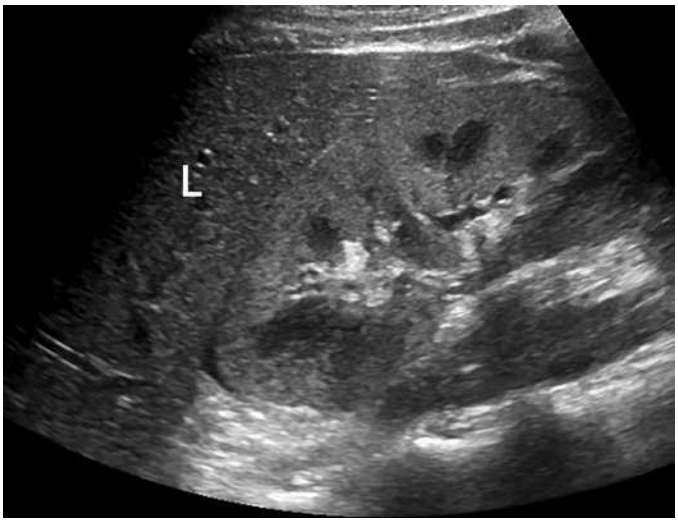

FIG. 52.34 Acute Kidney Injury in a 17-Year-Old Male Athlete Who Became Severely Dehydrated After Intense Competition. Longitudinal image of right kidney depicts increased cortical echogenicity, greater than that of the adjacent liver *(L)*.

TABLE 52.7 Kidney Disease Outcomes Quality Initiative—Stages of Chronic Kidney Disease

Stage	Description	GFR (mL/min/1.73 m^2)
1	Kidney damage with normal or increased GFR	≥90
2	Kidney damage with mild decrease in GFR	60-89
3	Moderate decrease in GFR	30-59
4	Severe decrease in GFR	15-29
5	Kidney failure	<15 (or dialysis)

GFR, Glomerular filtration rate.

With permission from VanDeVoorde RG, Warady BA. Management of chronic kidney disease. In: Avner ED, editor. Pediatric nephrology. 6th ed. Berlin: Springer-Verlag; 2009.[242]

developing world, acquired causes of CKD predominate, particularly infection-related glomerulopathies. The worldwide incidence and prevalence of CKD are greater for boys than for girls because of the higher incidence of congenital causes of CKD in boys.[80]

As with AKI, ultrasound is the primary imaging modality used to investigate CKD. Congenital anomalies such as UPJO, PUV, duplex collecting systems and ureters, and ectopic ureteral insertion are well depicted by sonography. Determination of kidney size is critical for long-term follow-up. Enlarged kidneys can occur in the setting of obstruction, cystic disease, and glomerulonephritis. Hypoplastic and scarred kidneys usually are small. A gradual reduction in kidney size usually occurs in patients with CKD. With progressive CKD, a concomitant loss of corticomedullary differentiation usually occurs, and most kidneys will have echogenic parenchyma. However, increased renal parenchymal echogenicity is a nonspecific finding and is not correlated with the severity of disease. **Dysplastic kidneys** have disordered development that usually results in a combination of echogenic parenchyma and cysts (Fig. 52.35). Dysplasia may be focal or diffuse and is usually depicted sonographically as echogenic tissue without identifiable corticomedullary differentiation.[80] Renal vascularity reflects functional status and will decrease in persons with CKD. The renal arterial resistive index (RI) correlates with creatinine levels and appears to be an independent risk factor for the progression of CKD.[83]

URINARY TRACT CALCIFICATION

Renal Cortical Calcification

Renal cortical calcification most commonly occurs as a result of acute cortical necrosis or chronic glomerulonephritis.[84] Additional causes are listed in the accompanying box. In the setting of acute cortical necrosis, the renal cortex will appear echogenic by ultrasound within a few weeks of injury, with calcification increasing over time (Fig. 52.36). Progressive renal atrophy also occurs.[85]

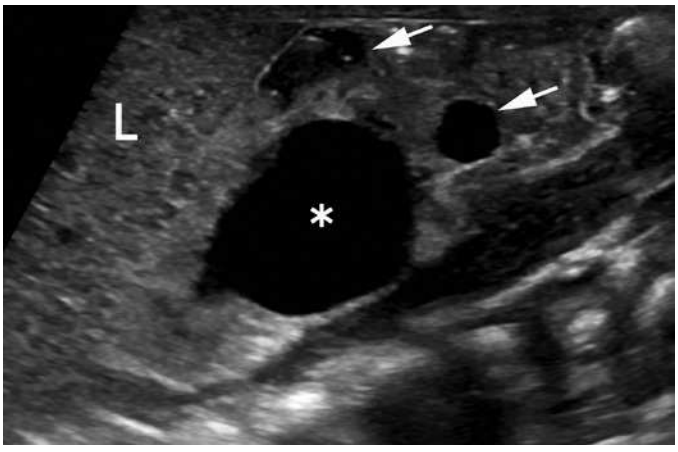

FIG. 52.35 Renal Dysplasia. Longitudinal image of right kidney demonstrates echogenic parenchyma with absent corticomedullary differentiation and peripheral cysts *(arrows)*. *, Dilated renal pelvis; *L*, liver.

Causes of Cortical Nephrocalcinosis

Renal cortical necrosis
Chronic glomerulonephritis
Renal transplant rejection
Alport syndrome
Ethylene glycol poisoning
Hyperoxaluria
Acquired immunodeficiency syndrome–associated infections

With permission from Bedard M, Wildman S, Dillman J. Embryology, anatomy, and variants of the genitourinary tract. In: Coley BD, editor. Caffey's pediatric diagnostic imaging. 12th ed. Philadelphia: Elsevier Saunders; 2013.[86]

Medullary Nephrocalcinosis

In more than 90% of children with nephrocalcinosis, calcification is mainly located in the medullary pyramids. The most common causes in children are metabolic disorders resulting in **hypercalcemia** and **hypercalciuria, renal tubular acidosis,** and **diuretic therapy.** Additional causes are listed in Table 52.8.

Prolonged administration of diuretics such as furosemide is a significant cause of medullary nephrocalcinosis in neonates. In these conditions an increased calcium load is presented to the kidney. The mineral content within the kidney increases progressively from the glomerulus to the collecting ducts, and thus the greatest concentration of calcium is found in the pyramids, especially at their tips. The **"Anderson-Carr-Randall progression"** of calculus formation postulates that microscopic calcifications within a renal pyramid may fuse to form a plaque that migrates toward the calyceal epithelium, eventually

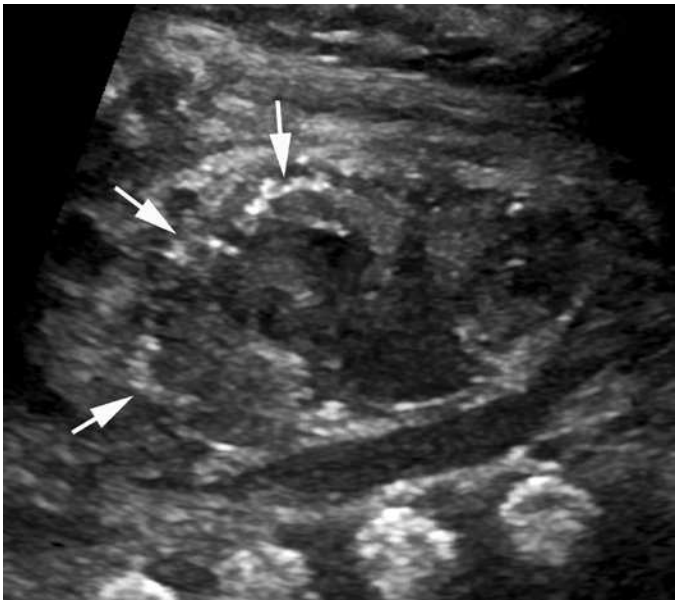

FIG. 52.36 Acute Cortical Necrosis in Infant With History of Aortic and Vena Caval Thromboses and Severe Renal Functional Impairment. Longitudinal image reveals thin, echogenic parenchyma with loss of corticomedullary differentiation and cortical calcifications *(arrows)*.

TABLE 52.8 Causes of Medullary Nephrocalcinosis[86]

Category	Examples
Hypercalciuria	
Endocrine	Hyperparathyroidism
	Cushing syndrome
	Diabetes insipidus
	Hyperthyroidism
Renal	Renal tubular acidosis
Alimentary	Milk alkali syndrome
	Hypervitaminosis D
Skeletal	Immobilization
	Metastatic disease
Drugs	Furosemide
	Steroids
Miscellaneous	Idiopathic hypercalciuria
	Idiopathic hypercalcemia
	Nephropathic cystinosis
Urinary Stasis	Obstructive uropathy
	Medullary sponge kidney
Hyperoxaluria	Primary
Hyperuricosuria	Secondary

perforating it and thereby providing a nidus for urinary stone formation.[87] Sonography readily demonstrates calcium deposits within the renal medullae (Fig. 52.37).

Urinary Stasis

Any form of urinary stasis predisposes not only to infection, but to calcium deposition as well. Thus the tubular ectasia encountered in **medullary sponge kidney** and in **autosomal recessive polycystic kidney disease** (ARPKD) often shows deposits of calcium in the pyramids, at the site of the dilated tubules. Similarly, milk of calcium, a viscous colloidal suspension of various calcium salts, may deposit in calyceal diverticula or in the renal pelvis in the setting of UPJO[88] (Fig. 52.38). **Staghorn calculi** occasionally occur in children with renal obstruction and infection (Fig. 52.39).

Renal Vein Thrombosis Calcifications

The finely branching calcifications within the cortex and medulla of the kidney that develop after renal vein thrombosis represent microthrombi in the intrarenal veins[89] (Fig. 52.40).

Dystrophic Calcification

Dystrophic calcification of abnormal tissue can occur anywhere in the urinary tract, including sites of inflammation resulting from chronic infection or within a tumor or the wall of a cyst.

Urolithiasis

"Urolithiasis" refers to the presence of stones at any site within the renal collecting system, ureter, bladder, or urethra. The prevalence of urolithiasis varies according to age, sex, race, and geographic region.[90] In the United States, urolithiasis occurs in about 50 per 100,000 adolescents.[91] It is more common in Caucasians than in African Americans. In adults, the highest

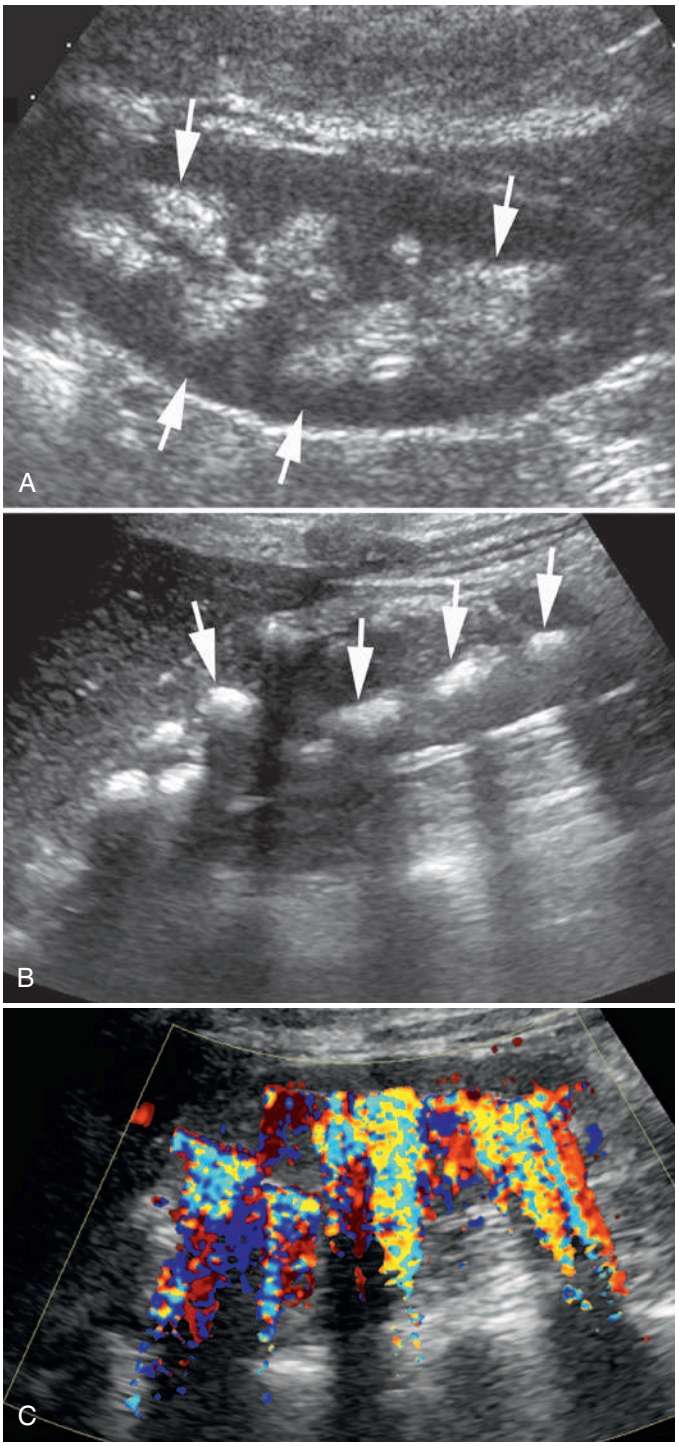

FIG. 52.37 (A) Renal medullary nephrocalcinosis in 13-year-old boy with **hypervitaminosis D.** Longitudinal image of the left kidney demonstrates echogenic calcium deposits completely filling the renal pyramids *(arrows).* **(B) Nephrocalcinosis in 18-year-old girl with Bartter syndrome.** Longitudinal image of the right kidney shows multiple shadowing stones at the tips of the renal pyramids *(arrows).* **(C)** Longitudinal color Doppler image of the right kidney reveals the **twinkling artifact** associated with the stones.

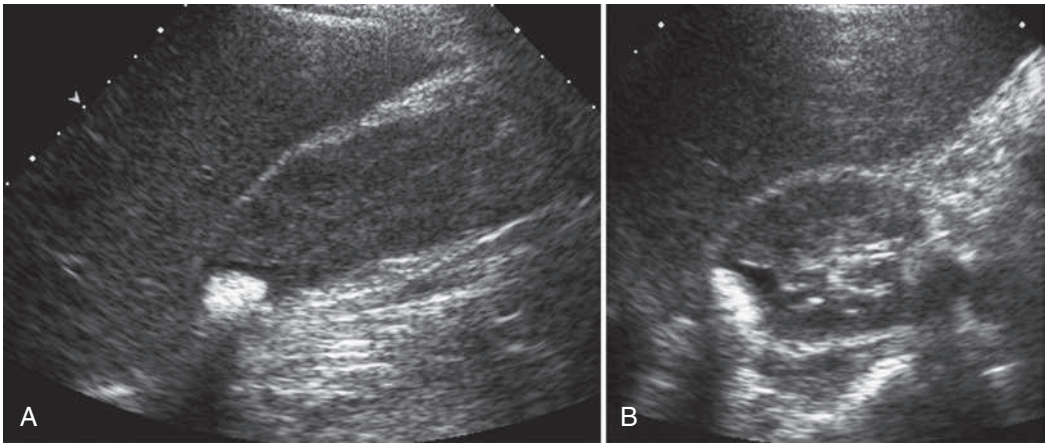

FIG. 52.38 Renal Milk of Calcium. (A) and **(B)** Longitudinal and transverse decubitus images of the right kidney demonstrate echogenic, dependently layering material within an upper-pole **calyceal diverticulum.**

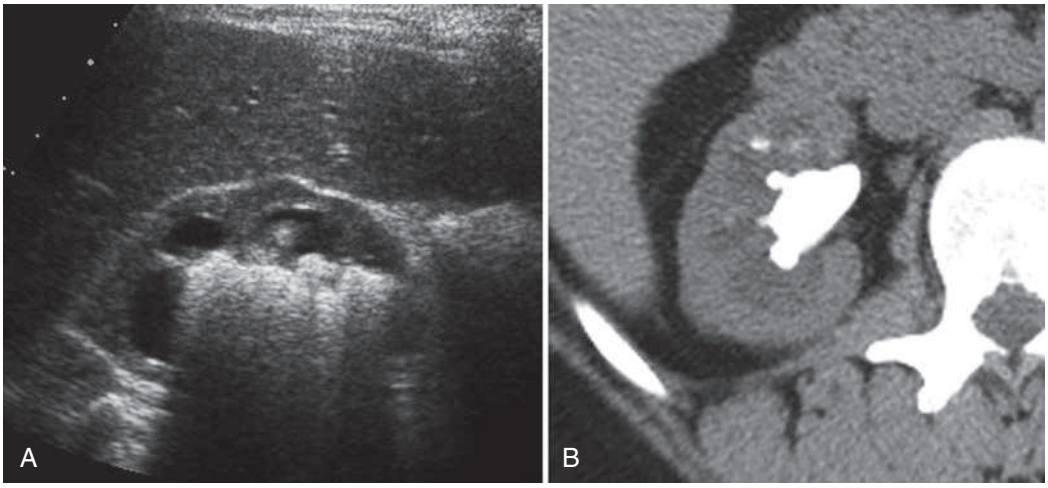

FIG. 52.39 Staghorn Calculus in 18-Year-Old Female Patient With Tyrosinemia. (A) Longitudinal image of the right kidney shows extensive echogenic foci filling the collecting system with prominent distal shadowing. **(B)** Axial computed tomography image confirms the presence of a large branching stone within the right renal calyces and pelvis.

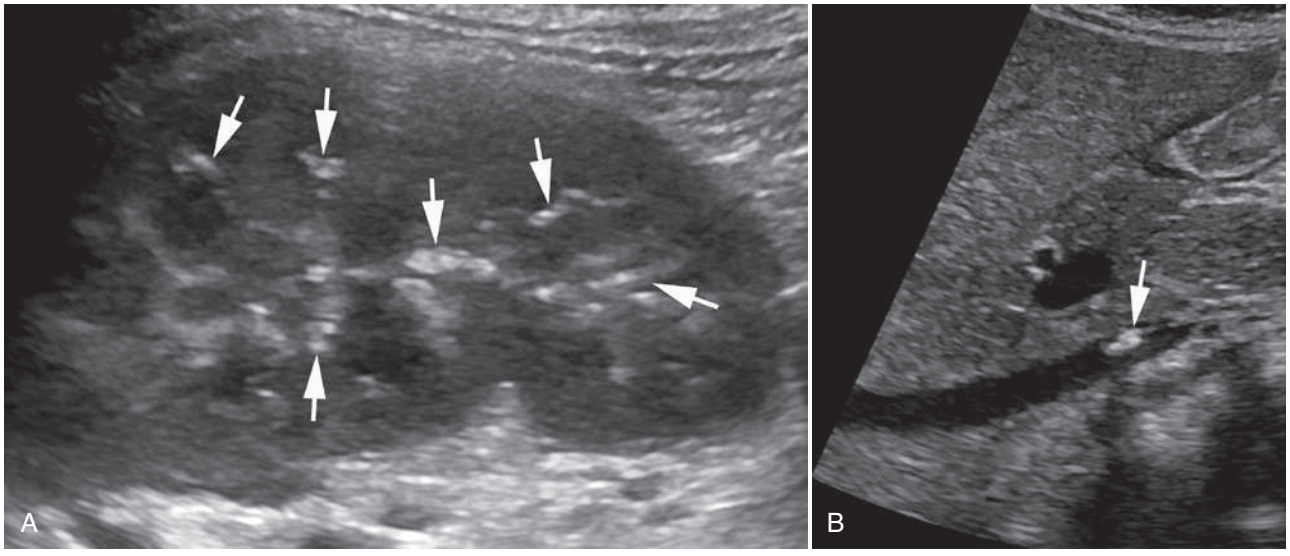

FIG. 52.40 Three-Year-Old Girl With a History of Congenital Vena Caval and Bilateral Renal Vein Thrombosis. (A) Longitudinal image of left kidney depicts multiple linear, branching, echogenic foci representing small, calcified veins *(arrows)*. **(B)** Longitudinal image of the inferior vena cava shows a residual calcified mural thrombus *(arrow)*.

prevalence of stones occurs in the southeastern United States; the geographic distribution of stone disease in children has not been reported.[92] Approximately 70% of children with urolithiasis have an underlying predisposing condition such as **urinary stasis, hypercalciuria, or chronic infection.** Approximately 40% to 60% of stones are predominantly composed of calcium oxalate, 10% to 20% are mainly calcium phosphate, 10% to 25% are mixed stones containing both calcium oxalate and calcium phosphate, 17% to 30% are magnesium ammonium phosphate (struvite or infection related), 6% to 10% are cystine, and 2% to 10% are uric acid.[93] Ultrasound is the initial imaging study of choice, with noncontrast CT reserved for cases in which ultrasound is nondiagnostic.[94] Urinary tract stones appear as foci of increased echogenicity with or without associated acoustic shadowing. In general, acoustic shadowing is present when the stone is 5 mm or more in diameter.[95] The color comet tail artifact **"twinkle sign"** is a rapidly alternating color Doppler signal that occurs immediately deep to the object that causes it, and appears as a linear aliased band of color[96] (see Fig. 52.37C). This artifact can be useful in the diagnosis of small stones in the absence of hydronephrosis or hydroureter. Color Doppler evaluation of the ureteral jet may be helpful in diagnosing obstruction because it is absent or of diminished velocity in the setting of high-grade obstruction.[17]

RENAL TRAUMA

After blunt abdominal trauma, the kidney is the most commonly injured organ in children. The pediatric kidney is believed to be at increased risk of injury compared with the adult kidney because of its larger size relative to the abdomen, and less protection from unossified ribs, weaker abdominal muscles, and minimal perinephric fat.[97] Renal trauma in children is often associated with other organ injury, particularly of the liver and spleen.

Most children with clinically significant kidney trauma have hematuria. Asymptomatic, microscopic hematuria is a low-yield sign for the presence of renal injury, whereas patients with gross hematuria have a much higher incidence of renal injury (22%) than those who do not (8%).[98] Preexisting and often clinically silent renal abnormalities such as hydronephrosis or ectopic kidney may make the kidney more susceptible to injury by minor trauma.

CT is the primary imaging modality for suspected blunt abdominal trauma in the pediatric patient.[99,100] Ultrasound is used primarily in the follow-up of injuries found on CT.[101] Parenchymal contusion is the most common kidney injury. It is characterized by microscopic hemorrhage and edema and is best depicted by CT, although ultrasound may show distortion of the normal renal architecture. Perirenal hematoma may occur as a complication of renal injury, and is subcapsular or perinephric in location. Renal hematoma can vary in appearance, but is usually echogenic at first and becomes hypoechoic as it liquefies. Injury to the renal collecting system leads to extravasation of urine. A urinoma results when the extravasated urine is limited to the perirenal space, which can be difficult to distinguish from hypoechoic blood by ultrasound. When the hematoma results from injury to the vascular pedicle, there will also be absent flow in the renal vessels and/or within the renal parenchyma.

The introduction of ultrasound contrast agents into clinical practice has permitted their use in the assessment of patients with mild to moderate blunt abdominal trauma, particularly when there is clinical concern but conventional ultrasound reveals no solid organ injury (Fig. 52.41, Video 52.6). Menichini and colleagues[102] and Valentino and colleagues[103] have shown that CEUS is nearly as accurate as contrast-enhanced CT in depicting solid organ injuries in children. One important limitation of the technique, however, is that the ultrasound contrast agent is not filtered by the kidney, so a urinoma cannot be readily distinguished from a hematoma.

RENAL VASCULAR DISEASE

Doppler Sonographic Examination Technique

Infants and small children are examined without special preparation, but they may be given clear liquids to drink during the examination to calm them, to increase hydration, and to provide an acoustic window through the fluid-filled stomach. Sedation is rarely necessary. The older child is best examined after a 4- to 6-hour fast (to reduce intestinal gas) only if a detailed examination of the main renal artery is planned. Color and spectral Doppler examinations are performed. Power Doppler may also be useful to evaluate the presence of vascular flow. Doppler settings should be adjusted for maximal detection of slow flow using the highest possible transducer frequency, relatively small color area of interest, low pulse repetition frequency, and low wall filter. Pulse repetition frequency is augmented if aliasing occurs. A small sample volume and an insonating angle of 60 degrees or less are needed.[104]

The aorta is examined by means of an anterior left paramedian as well as a left axillary approach, with longitudinal and transverse views. The main renal arteries are often best imaged through the flanks, although an anterior midline approach can also be used. Color Doppler is used to trace the renal arteries, which are then examined with serial pulsed Doppler samples, especially in areas of high-velocity flow. Even if the entire renal artery cannot be outlined because of overlying intestinal gas, the retrocaval portion of the right renal artery and the hilar arteries can usually be analyzed. A segmental or interlobar artery in each third of the kidney (upper, middle, and lower) is then studied with spectral Doppler, and the RI or pulsatility index is calculated.

Normal Vascular Anatomy and Flow Patterns

The intrarenal arteries and veins and their relationship to the renal cortex, pyramids, and calyces are exceptionally well outlined with color Doppler ultrasound.[105] The main renal artery or arteries divide in the renal hilum to form several pairs (anterior and posterior) of segmental arteries. These course toward the pyramids and divide into the interlobar branches, which follow the periphery

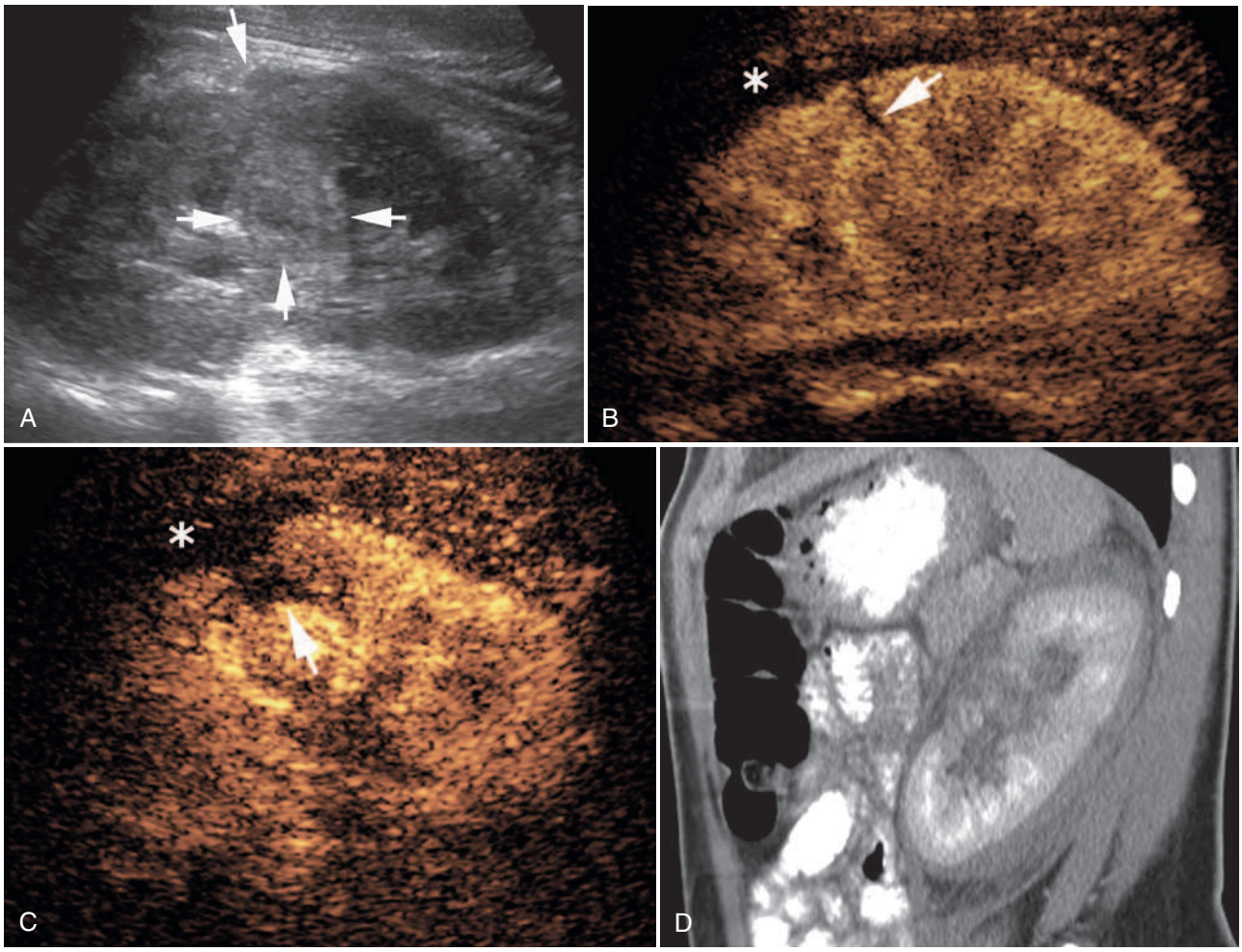

FIG. 52.41 Renal Laceration and Perirenal Hematoma. (A) Longitudinal gray-scale image shows swelling, contour irregularity, and loss of corticomedullary differentiation in the midportion of the left kidney *(arrows)*. **(B)** and **(C)** Longitudinal intravenous (IV) contrast-enhanced ultrasound images readily depict the parenchymal defect *(arrow)* and adjacent hematoma (*). **(D)** Longitudinal reformatted IV contrast-enhanced computed tomography image demonstrates the midrenal laceration and surrounding hematoma. See also Video 52.6.

of the pyramids. At the outer edge of the pyramids, the interlobar arteries give rise to the arcuate arteries, which follow the outer contour of the pyramids. Cortical arteries arise from the arcuate arteries and radiate into the cortex, following a direction similar to that of the interlobar vessels. The venous circulation follows that of the arteries, and simultaneous adjacent signals are often depicted with both color Doppler sonography and on spectral analysis (Fig. 52.42).

The renal arterial bed normally has low resistance, and there is a constant flow of blood into the kidney throughout the cardiac cycle. The normal adult renal arterial RI is estimated at 0.58 ± 0.05. Renal RI is age dependent, with children having higher RI values and a trend toward decreasing values with increasing age. This age dependency of the renal RI and, therefore of renal vascular resistance, has been postulated to be dependent on serum levels of active renin, because the maturational profile of the renal RI more closely parallels that of active renin than of other renal functional parameters.[106] Because there is a range of normal RI values in children, and the renal RI is highest in the first 3 months of life,[106] the diagnosis of abnormal intrarenal resistance is much more reliably made in children by comparing waveforms from the pathologic kidney with those of the normal kidney, or tracings of the pathologic kidney obtained from one day to the next.

Pulsed Doppler ultrasound tracings from the normal intrarenal and main renal veins are somewhat variable: in some children the pulsations from right atrial systole and diastole are clearly visible, whereas in others the flow is steadier. To-and-fro venous flow throughout the cardiac cycle may be seen in right-sided heart failure or in the absence of arterial perfusion, as in the setting of end-stage renal disease.

Causes of Increased Resistance to Intrarenal Arterial Flow

Any increase in intrarenal arterial pressure results in decreased flow. Diastolic flow occurs at the lowest pressure during the cardiac cycle, so it will decrease or disappear before systolic Doppler flow curves are appreciably affected. The causes of increased intrarenal resistance to flow can be classified as

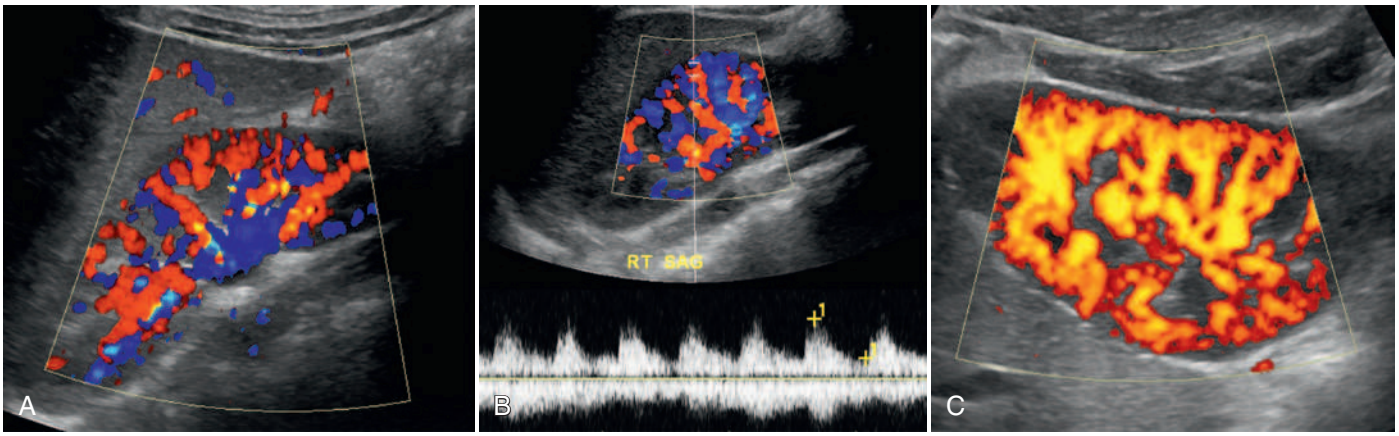

FIG. 52.42 Normal Intrarenal Circulation in a 3-Year-Old Boy. (A) Longitudinal color Doppler sonogram shows the segmental vessels at the hilum, the interlobar vessels alongside the pyramids, and the arcuate vessels at the inner edge of the cortex. **(B)** Spectral display from a normal interlobar artery (low resistance, high diastolic flow) and vein (pulsatile, reflecting right atrial pulsations). **(C)** Power Doppler sonogram displays blood flow extending to the periphery of the renal cortex.

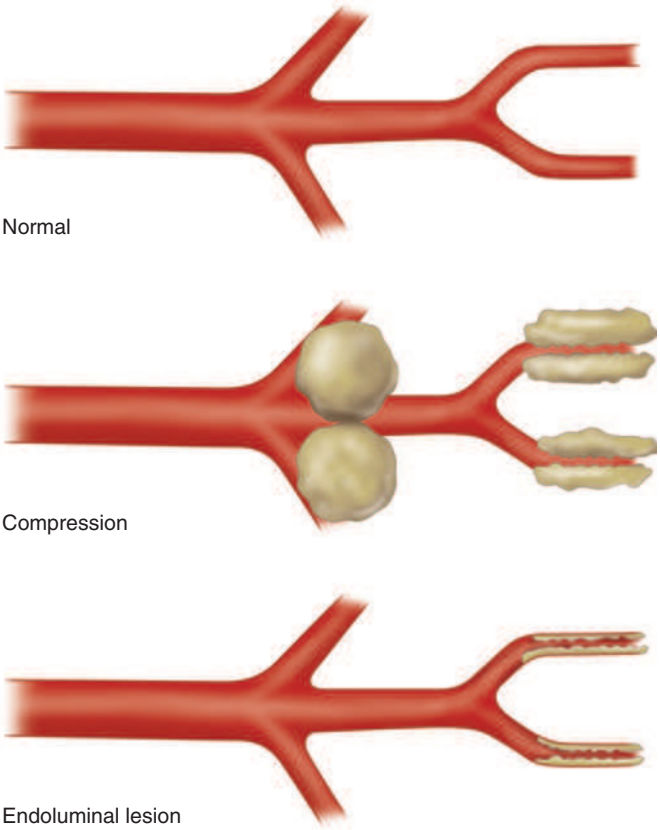

FIG. 52.43 Causes of Increased Resistance to Intrarenal Arterial Flow.

intravascular, perivascular, and perirenal (Fig. 52.43). Any decrease in the size of the lumen of small intrarenal arteries or arterioles (spasm, as in shock; endothelial inflammation, as in hemolytic-uremic syndrome [HUS]) leads to increased resistance to arterial inflow. Compression of small vessels by intrarenal edema (e.g., secondary to renal vein thrombosis) may result in identical arterial Doppler tracings. Back pressure from an acutely obstructed ureter has the same result. Finally, significant compression from a hematoma, lymphocele, or the tight abdominal wall around an adult kidney transplanted into a small child can also cause compression of vessels and decrease intrarenal arterial flow.

The successful Doppler examination of intrarenal arteries therefore includes the following two steps:

1. Comparing the RI with either the RI on the other side or the RI from a previous examination
2. Reviewing the pertinent pathophysiologic factors involved in a patient with high RI

Causes of Increased Resistive Index in Renal Arteries

INTRAVASCULAR
Vascular spasm in shock
Endothelial inflammation in hemolytic-uremic syndrome

PERIVASCULAR
Intrarenal edema
Renal vein thrombosis
Acutely obstructed ureter

PERIRENAL COMPRESSION
Hematoma
Lymphocele
Tight abdominal wall

Clinical Applications

Vessel Patency

The Doppler examination is a reliable indicator of the patency of the renal arteries, of the veins, and of the presence of intrarenal perfusion. Therefore the examination is particularly useful in the evaluation of renal allograft perfusion immediately after surgery. It is also useful in the exclusion of arterial injury after trauma, especially when the renal architecture is sonographically normal and other, more invasive examinations are not indicated.

Color Doppler sonography is especially valuable in the search for postbiopsy arteriovenous fistulas (AVFs) and aneurysms.[107]

Acute Renal Vein Thrombosis

Acute renal vein thrombosis may follow shock or occur as a complication of the nephrotic syndrome, secondary to abnormal coagulation, or in the presence of a nearby malignant mass, such as **Wilms tumor.** In the neonate, thrombosis is usually associated with dehydration, decreased renal perfusion and oxygenation, and polycythemia. It is more prevalent in infants of diabetic mothers. The clinical presentation includes hematuria, palpable flank mass, proteinuria, and decreased renal function. Sonography typically shows an enlarged kidney with altered parenchymal echogenicity (Fig. 52.44). The normal corticomedullary differentiation is obliterated. Patchy areas of decreased and increased echogenicity are secondary to edema and parenchymal hemorrhage. Sonography may demonstrate echogenic thrombus within the renal vein and inferior vena cava. Thrombi are initiated in small venules and propagate toward the hilum, so that renal parenchymal abnormalities are often present without clear visualization of a thrombus.[89,108] In contrast, in the renal allograft, thrombosis usually starts at the venous anastomosis.

Causes of Acute Renal Vein Thrombosis

Shock
Nephrotic syndrome
Coagulopathy
Adjacent tumors (e.g., Wilms tumor)
Neonatal dehydration, especially infants of diabetic mothers

Doppler sonography may show decreased or absent flow in the renal veins, as well as a significantly increased RI in the involved renal arteries. This decreased renal arterial diastolic

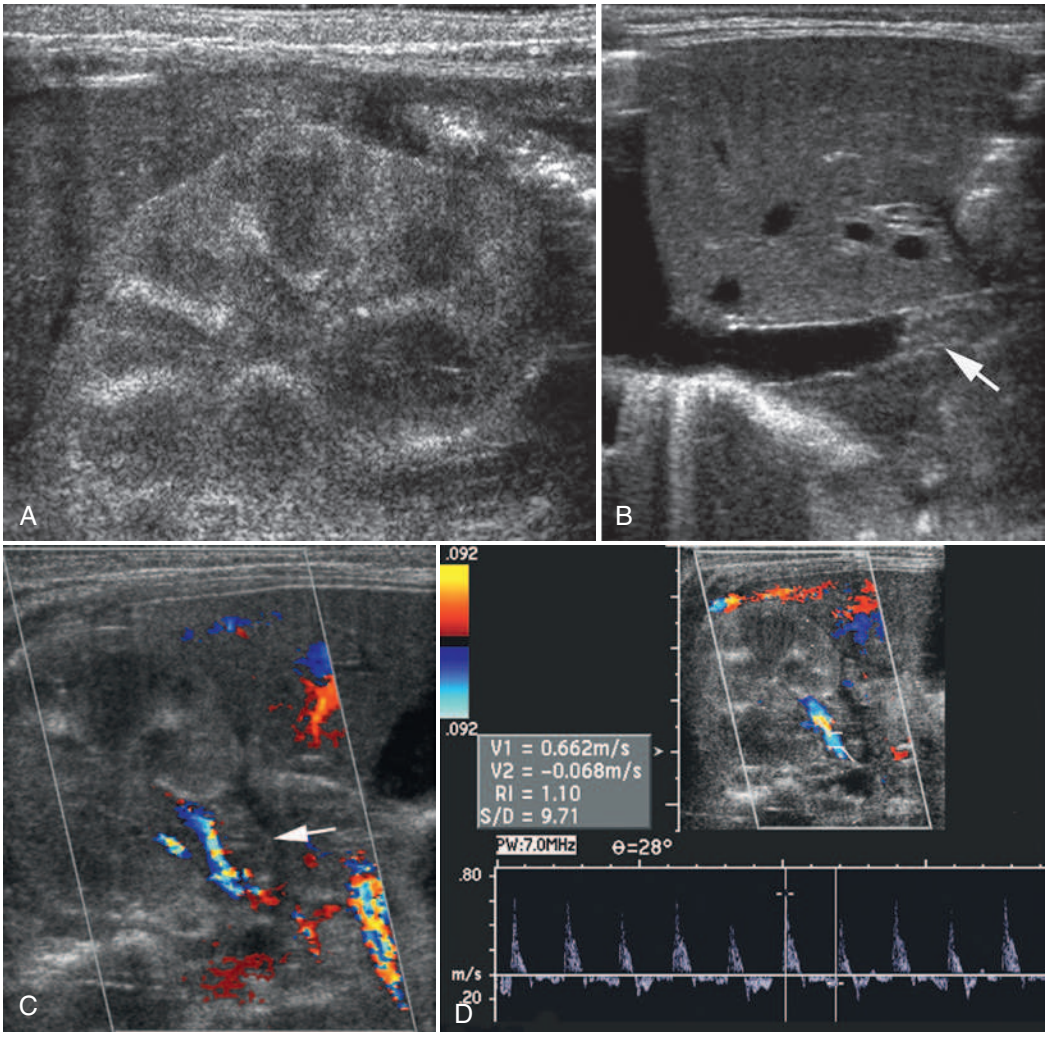

FIG. 52.44 Acute Renal Vein Thrombosis in Premature Infant. (A) Longitudinal image of the right flank demonstrates an edematous kidney with echogenic parenchyma and decreased corticomedullary differentiation. **(B)** Longitudinal image of the inferior vena cava reveals a large intraluminal clot *(arrow).* **(C)** and **(D)** Color and spectral Doppler images of the right renal artery reveal high-velocity arterial blood flow with diastolic reversal due to increased perivascular resistance secondary to intrarenal edema. No flow is documented within the thrombosed main renal vein *(arrow).*

flow is caused by edema and obstruction to outflow of arterial blood entering the kidney. In babies, these signs are much less reliable because flow is rapidly reestablished in the main renal vein, as well as within intrarenal veins. The pathophysiologic response of the kidney to renal vein thrombosis depends on the acuity of the occlusion, extent of thrombosis, and the development of venous collateral circulation. This reestablishment of venous flow occurs not only in native kidneys but also in renal transplants, although the process takes much longer, up to 3 weeks in the transplanted kidney. The degree of recovery of the affected kidney after acute renal vein thrombosis ranges over a wide spectrum, from full recovery to a variety of abnormalities, including complete absence of function, to tubular disorders and renovascular hypertension.[89]

Renal Artery Stenosis

Approximately 1% to 3% of children have hypertension, with an increasing prevalence caused by the childhood obesity epidemic. Most hypertensive children are at low risk for renovascular hypertension, which accounts for approximately 5% to 10% of all childhood hypertension.[109] The most common underlying cause of renovascular hypertension in infants is thromboembolism related to umbilical artery catheterization,[110] whereas renal arterial fibromuscular dysplasia and Takayasu arteritis are the most common causes in older children.[111] There are many other developmental and acquired causes of renovascular hypertension in the pediatric population (Table 52.9).

The precise role of noninvasive imaging in children with suspected renovascular hypertension is unclear. There is no imaging technique currently available that can reliably exclude every potentially treatable cause of renovascular hypertension.[113] Ultrasound of the abdominal aorta and depiction of renal size and architecture are useful to exclude global nephropathy, focal scarring, or tumor. Doppler ultrasound can be used to demonstrate an increase in blood velocity as it passes through a stenotic arterial lumen. The presence of a proximal stenosis can also be inferred from the depiction of a *tardus* (late) and/or *parvus* (flat) arterial waveform in vessels distal to a stenosis.[114,115] However, even in experienced hands, localization of an accessory renal artery stenosis or branch vessel stenosis can be time-consuming and challenging.

The classic signs of stenosis described in adults and also applied to children include increased resistance to flow proximally (decreased or absent diastolic or even systolic flow), high velocity at the site of narrowing (>180 cm/sec), turbulence immediately distally, and flow possibly returning to normal at some distance from the stenosis (Fig. 52.45). The following renal arterial Doppler criteria have been found to suggest significant stenosis[114]:

1. Flow velocity measurements exceeding 180 cm/sec
2. Velocity ratio between renal artery and abdominal aorta greater than 3.5:1

Doppler ultrasound waveforms return to normal immediately after repair of stenosis. It must be remembered that the parvus-tardus waveforms identified in the downstream circulation will reflect any stenosis occurring upstream, including Takayasu aortitis and aortic coarctation.

TABLE 52.9 Causes of Renovascular Hypertension[112]

Category	Examples
Fibromuscular dysplasia	
Inflammatory disease	Takayasu arteritis
	Kawasaki disease
	Moyamoya disease
	Irradiation
Genetic disorders	Williams syndrome
	Neurofibromatosis
	Klippel-Trénaunay-Weber syndrome
	Feuerstein-Mims syndrome
	Rett syndrome
	Degos-Kohlmeier disease
	Marfan syndrome
Atherosclerosis	Hyperlipidemias
Vascular anomaly	Renal arteriovenous malformation
	Renal artery aneurysm
	Renal artery hypoplasia
	Renal arteriovenous malformation
Thromboembolism	Umbilical artery catheterization
	Neonate of diabetic mother
	Sepsis, dehydration
Renal transplantation	Rejection
	Arterial narrowing
Other	Congenital rubella
	Compression by mass
	Congenital fibrous band
	Posttraumatic cause
	Retroperitoneal fibrosis

Intrarenal Arterial Disease

Hemolytic-uremic syndrome is one of the most common causes of AKI in nonhospitalized infants and children. It is characterized by endothelial cell injury, intravascular platelet-fibrin thrombi, and vascular damage. It may occur sporadically, in epidemic outbreaks, or as a genetic or familial disorder. Patients with typical HUS will experience bloody diarrhea associated with Shiga toxin–producing bacteria, predominately *Escherichia coli* O157:H7.[116] Atypical HUS occurs without bloody diarrhea and is due to defective complement system activation and regulation.[117]

The lesions of HUS cause increased resistance to renal arterial inflow. At sonography, the renal cortex is uniformly hyperechoic, and the pyramids are sharply demarcated (Fig. 52.46). The kidneys may greatly enlarge. A study of 20 children with HUS found that during the phase of anuria there was no diastolic flow.[118] As the acute vascular lesions healed, diastolic flow returned, followed by diuresis within 24 to 48 hours. Because the Doppler examinations predicted the onset of diuresis, the duration of peritoneal dialysis was kept to a minimum, thereby reducing the risk of complications.

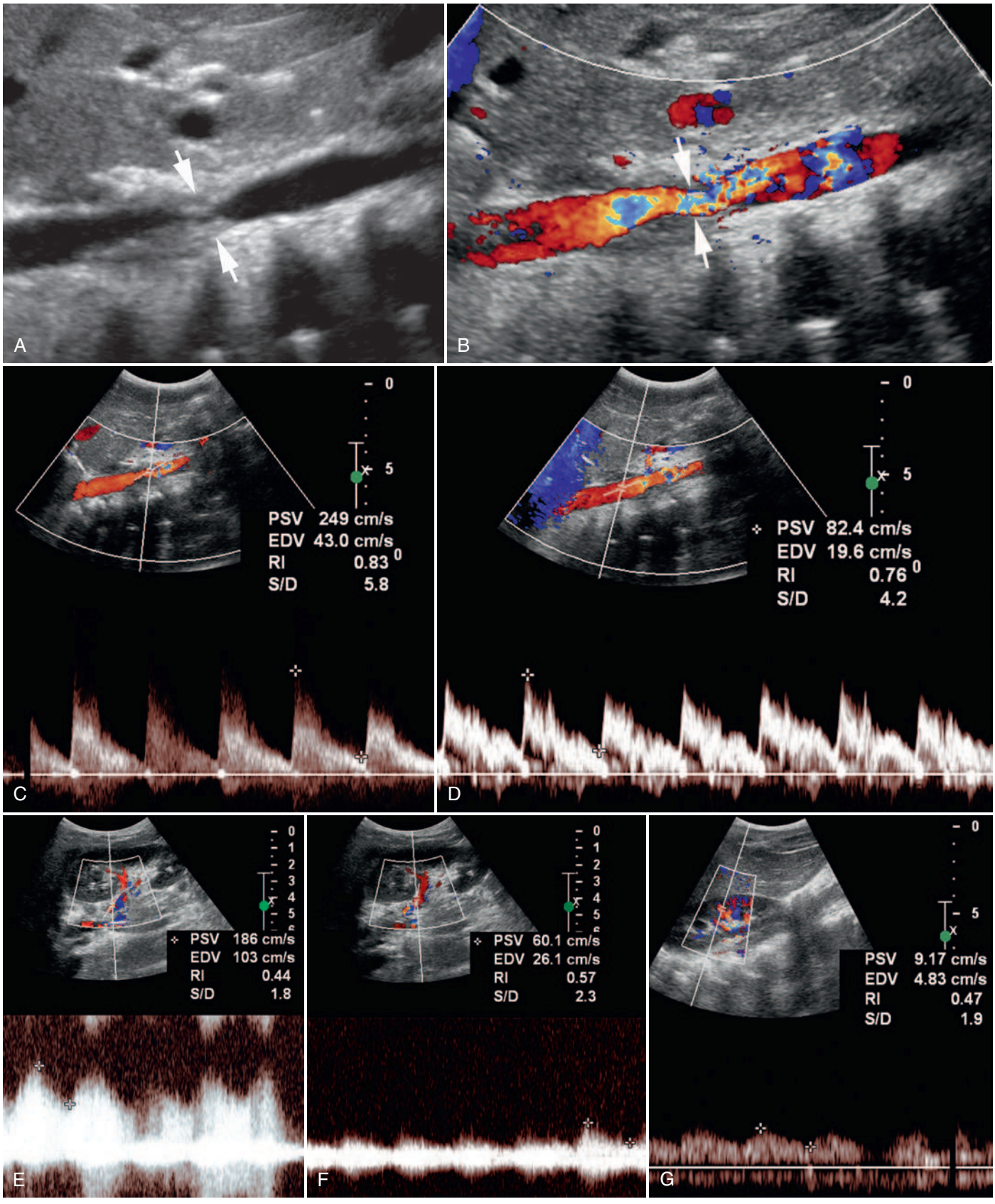

FIG. 52.45 Renal Artery Stenosis in a 4-Year-Old Boy With Midaortic Syndrome and Hypertension. (A) and **(B)** Longitudinal gray-scale and color Doppler images of the abdominal aorta show focal marked mural thickening and significant luminal narrowing as well as color aliasing at the site of stenosis *(arrows).* **(C)** and **(D)** Spectral Doppler display reveals an elevated peak systolic velocity within the aorta at the site of narrowing **(C)** compared with the peak systolic velocity within a more proximal portion of the aorta **(D).** Peak systolic velocity within the proximal right main renal artery is elevated **(E)** compared with the velocity obtained from a more distal portion of the artery **(F).** The distal artery also demonstrates a delayed systolic upstroke with diminished amplitude and rounding of the systolic peak (tardus-parvus waveform). **(G)** A similar tardus-parvus spectral Doppler waveform is obtained from the interlobar vessels of the right kidney.

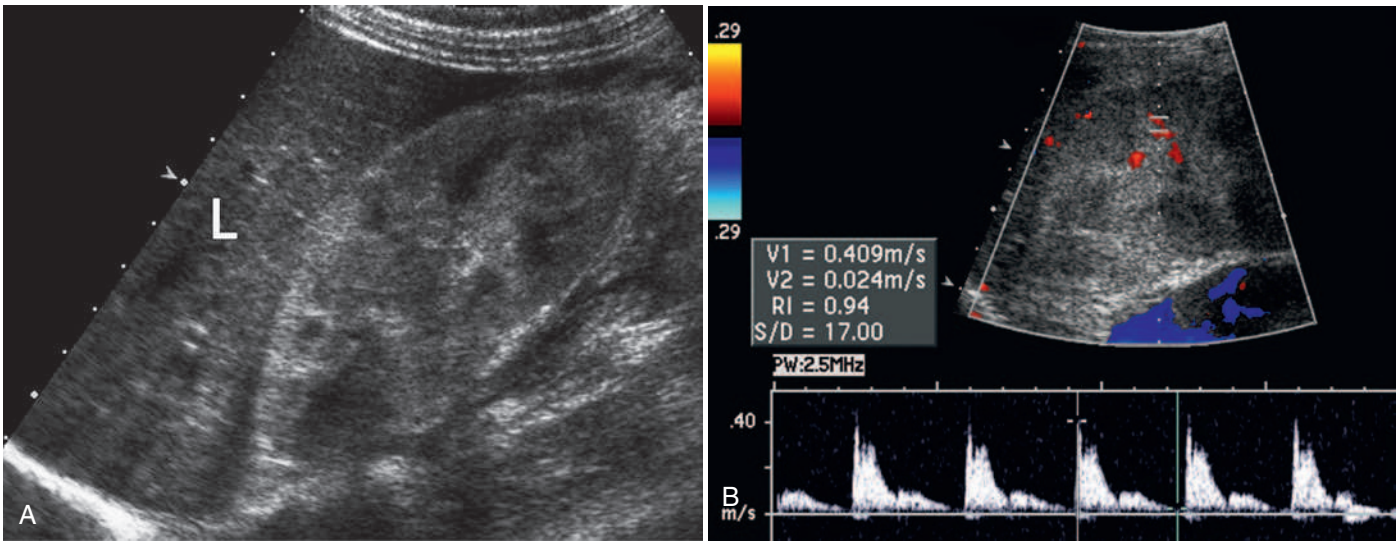

FIG. 52.46 Hemolytic-Uremic Syndrome in a 6-Year-Old Girl. (A) Longitudinal image reveals increased right renal cortical echogenicity, greater than that of the adjacent liver *(L)*. **(B)** Spectral Doppler display reveals diminished diastolic blood flow with an elevated resistive index in a right renal interlobar artery.

RENAL TRANSPLANTATION

Renal transplantation is the treatment of choice for end-stage kidney disease in children. Gray-scale and color Doppler ultrasound imaging provide a comprehensive assessment of transplant morphology, depiction of perirenal and pelvic fluid collections, and evaluation of graft vascularity. At our hospital, an initial postoperative ultrasound examination is performed with short-term follow-up studies performed as clinically indicated. Long-term follow-up consists of yearly ultrasound studies. Ultrasound is also used to guide allograft biopsy.

Approximately half of all renal transplants in children are obtained from living donors, usually a parent.[119,120] In older children, surgical technique is identical to that used in adults, with the allograft placed in an extraperitoneal location in the right or left iliac fossa, and end-to-side vascular anastomoses to the ipsilateral external iliac artery and vein. If there is a significant size discrepancy between the donor and an infant or small child recipient, the allograft may be placed intraperitoneally, with an end-to-side anastomosis of the transplant renal artery to the aorta and of the transplant renal vein to the inferior vena cava, in order to optimize graft perfusion.

Ultrasound evaluation of a normal renal allograft demonstrates an intraabdominal or intrapelvic kidney with gray-scale and Doppler imaging features identical to those of a native kidney. Immediately postoperatively, moderately elevated peak systolic velocity and turbulent flow in the main renal artery are common and probably related to edema at the arterial anastomosis with functional narrowing. Associated diminished downstream peak systolic velocities can result in diminished arterial RIs at the level of the interlobar arteries. Conversely, elevated arterial RIs can occur as a result of diffuse graft edema and diminished diastolic flow. These abnormalities often improve or normalize within in the first 24 hours after transplantation.[121] Recently, CEUS has been used to provide both qualitative and quantitative assessment of renal allograft blood flow and perfusion. CEUS has been shown to be superior to conventional ultrasound in combination with Doppler imaging in detecting even subtle microvascular disturbances in allograft perfusion. In addition, quantitative perfusion parameters derived from CEUS show predictive capability regarding long-term kidney function.[122,123] To date, there is limited experience in the use of CEUS for evaluation of renal allografts in the United States.

Vascular Complications

Vascular complications occur in 0.8% to 13.9% of pediatric renal transplants,[124,125] and include renal artery thrombosis, renal vein thrombosis, renal artery stenosis, AVF, and arterial pseudoaneurysm. Children are at increased risk of early vascular thrombosis compared with adults because of their small size and frequent discrepancies between the size of the donor and recipient vessels.[126] According to data from the North American Pediatric Renal Transplant Cooperative Study, graft thrombosis is the most common cause of first-year allograft loss in children, accounting for as many as 35% of cases.[127] Sonographic assessment of the transplanted pediatric kidney is an important and useful tool in the detection of early vascular complications.[121]

Renal artery thrombosis with associated graft infarction is an unusual complication of renal transplantation, occurring in only 3% to 4% of all pediatric renal transplants.[128,129] It usually develops within the first 48 hours after transplantation and is associated with en bloc transplants from young cadaveric donors that contain paired renal allografts as well as the ureters, main renal arteries and veins, and segments of the juxtarenal aorta and inferior vena cava. Most cases are related to arterial kinking or intimal dissection (Fig. 52.47). Segmental infarctions sometimes occur in the early postoperative period in allografts with multiple renal arteries, but these lesions more commonly develop as a late complication in association with acute or chronic rejection[130] (Fig. 52.48). Clinical symptoms of infarction include tenderness

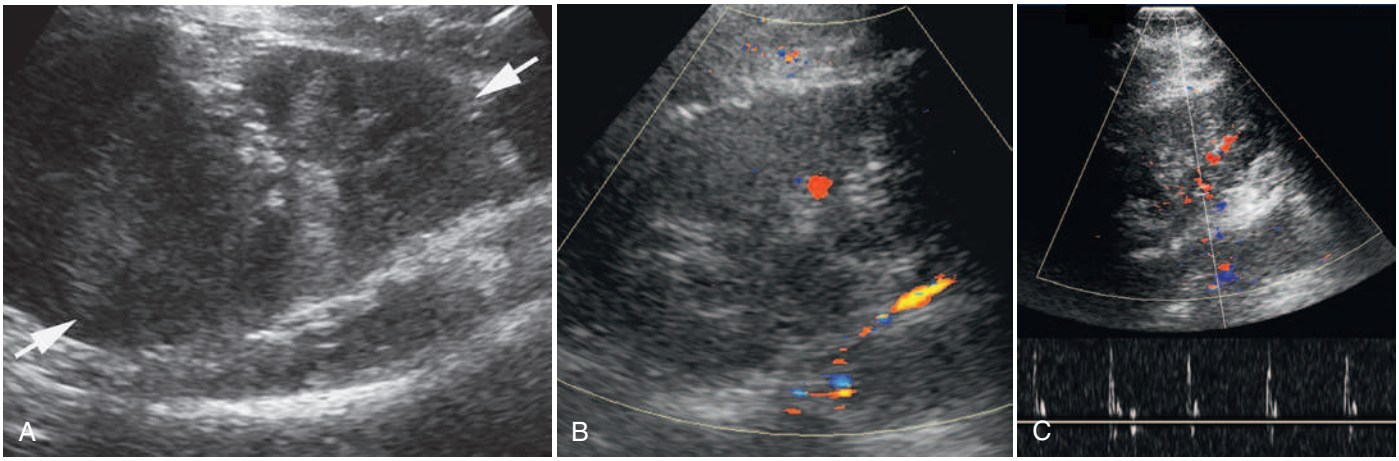

FIG. 52.47 Arterial Thrombosis in a 15-Year-Old Boy 1 Day After Kidney Transplantation. (A) Longitudinal sonogram of renal allograft shows a swollen kidney with poor corticomedullary differentiation *(arrows)*. **(B)** Color Doppler imaging reveals minimal intrarenal flow. **(C)** Spectral Doppler analysis of the main renal artery in the hilum of the kidney depicts systolic spikes with no appreciable diastolic flow.

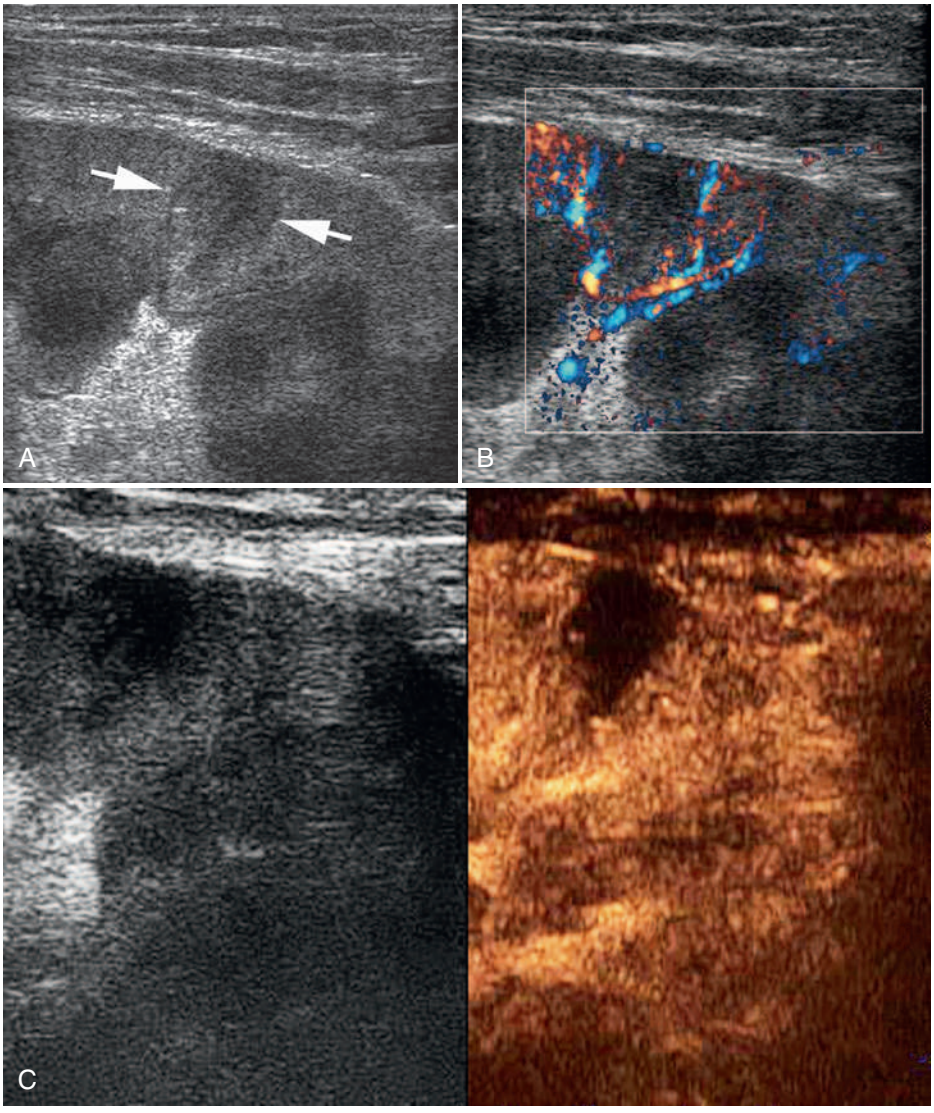

FIG. 52.48 Segmental Infarction of Renal Allograft 5 Years After Transplantation. (A) Longitudinal gray-scale image demonstrates a hypoechoic, triangular zone in the renal cortex *(arrows)*. **(B)** Color Doppler image shows displacement of vessels around this zone. **(C)** Contrast-enhanced ultrasound reveals focal absence of perfusion in keeping with infarction (reference gray-scale image in left panel). (Courtesy of Dr. Ákos Járay, University of Pécs, Hungary.)

and swelling over the graft and anuria. However, severe rejection has been reported to cause markedly diminished blood flow that mimics arterial thrombosis. Thus optimization of Doppler imaging parameters for the detection of slow flow is mandatory to prevent misdiagnosis of arterial thrombosis when acute rejection is present.[131] Unfortunately, graft failure is the usual outcome of arterial thrombosis, although urgent thrombolytic therapy or thrombectomy can be attempted.

Renal vein thrombosis is also uncommon in pediatric renal transplants, occurring in approximately 2% of allografts.[129] Virtually all cases occur within the first postoperative month.[127] The clinical symptoms are similar to those associated with renal artery thrombosis. Sonography often shows edema and abnormally increased echogenicity of the renal parenchyma. Venous flow is absent within the main renal vein, and there is associated reverse diastolic flow within the main renal artery. Early recognition of renal vein thrombosis is critical because graft salvage is potentially possible with either thrombolytic therapy or thrombectomy.[132]

Renal artery stenosis is a late complication, with a reported incidence of 4% to 18%.[124,133] Clinical presentations include new or progressive hypertension, marked hypertension refractory to medical therapy, hypertension associated with graft dysfunction in the absence of rejection, and hypertension associated with a systolic bruit audible over the graft.[134] The incidence of renal artery stenosis in children is difficult to determine because there is no consensus as to what degree of arterial narrowing is clinically significant. The most widely accepted criterion is elevation of peak systolic velocity at the site of narrowing, although there is conflicting literature regarding optimal cutoff values.[135-137] In adults, peak systolic values greater than 250 or 300 cm/sec have been shown to be highly sensitive and specific for the diagnosis of renal artery stenosis.[138,139] However, there are minimal data regarding the usefulness of these criteria in children.[140]

Sonographic evaluation with color and spectral Doppler reveals elevated velocities in the narrowed segment with spectral broadening of the arterial waveform. There is sometimes an associated downstream tardus-parvus waveform in the intrarenal arteries with associated low RIs. There may be color aliasing within the stenotic portion of the artery and perivascular soft tissue vibration artifacts caused by turbulent flow in the stenotic segment.[141] For this reason, the velocity measurements in the main renal artery, the iliac artery, and the segmental renal arteries should be interpreted together.[142] Magnetic resonance angiography (MRA) or CT angiography can be performed before conventional angiography, the current reference standard imaging test. These investigations may detect a significant stenosis of the transplant main renal artery. However, even in these patients there can be stable graft function with conservative treatment.[124,138]

Renal biopsies are routinely performed for graft surveillance and for assessment of graft dysfunction. An **arteriovenous fistula** (AVF) is the most common complication of graft biopsy, reported in 8% of cases by Schwarz and colleagues,[143] and is almost always inconsequential. Most AVFs are asymptomatic, and more than three-quarters will resolve spontaneously. Symptomatic fistulas resulting in ischemia because of a vascular steal phenomenon are treated with embolization. Sonographically, an AVF may be missed on gray-scale imaging but obvious with color and spectral Doppler evaluation (Fig. 52.49). Pseudoaneurysm is another complication of renal biopsy, and also tends to be asymptomatic and usually resolves spontaneously. With gray-scale sonography, pseudoaneurysms appear as simple or complex cystic structures. Color Doppler imaging reveals the classic **"yin-yang" pattern** of to-and-fro flow (Fig. 52.50). Spectral Doppler analysis at the neck of the pseudoaneurysm demonstrates disordered bidirectional blood flow. Progressive enlargement of the pseudoaneurysm or a diameter greater than 2 cm is an indication for embolic therapy.[130,144]

Perinephric Fluid Collections

Perinephric fluid collections are the most common nonrenovascular complications of kidney transplantation in children and occur with a frequency similar to that observed in adults.[129] ultrasound cannot definitively differentiate among hematoma, seroma, lymphocele, and abscess.

Lymphocele is the most common perinephric collection, and is usually an incidentally noted, well-defined, anechoic fluid collection adjacent to the graft (Fig. 52.51). A urine leak, or **urinoma,** can appear as an amorphous, anechoic fluid collection surrounding the graft or can have a more complex appearance **Hematomas** and **abscesses** usually appear as complex perinephric collections. Follow-up studies are useful in documenting changes in collection size. Progressive decrease in size can obviate the need for further workup, and ultrasound-guided percutaneous aspiration can be performed when further characterization of the fluid is necessary.[142]

Parenchymal Abnormalities

In the immediate postoperative period, diffuse parenchymal abnormality of the renal graft is caused by **acute tubular necrosis** (ATN), **rejection,** and **drug toxicity.** ATN occurs to some degree in most renal grafts immediately after surgery, wherein it is also referred to as "preservation injury." It is characterized clinically by oliguria and poor renal function and is more pronounced in kidneys obtained from cadaveric donors and from donors with prolonged ischemic times.[144]

Acute rejection, humoral or cellular, is the most common type of rejection. Symptoms commonly include poor renal function, tenderness over the graft, oliguria, and edema. Improvements in immunosuppressive therapy have resulted in a substantial decrease in the incidence of acute rejection over the last 10 to 15 years.[145] The cornerstone of immunosuppressive therapy in pediatric renal transplantation is the calcineurin inhibitors cyclosporine and tacrolimus, but their nephrotoxic potential can lead to graft injury. Clinical findings are similar to those associated with ATN and rejection—commonly, decreasing urine output, rising serum creatinine, abdominal pain, and fever. The imaging features of these disorders also overlap with one another, including graft enlargement, loss of corticomedullary differentiation, and decreased diastolic arterial blood flow with increased RIs. Sonography is most helpful in ruling out other causes of graft dysfunction such as compression from a perinephric fluid collection, urinary collecting system obstruction, or large vessel abnormality.[130] When there is significant graft dysfunction and

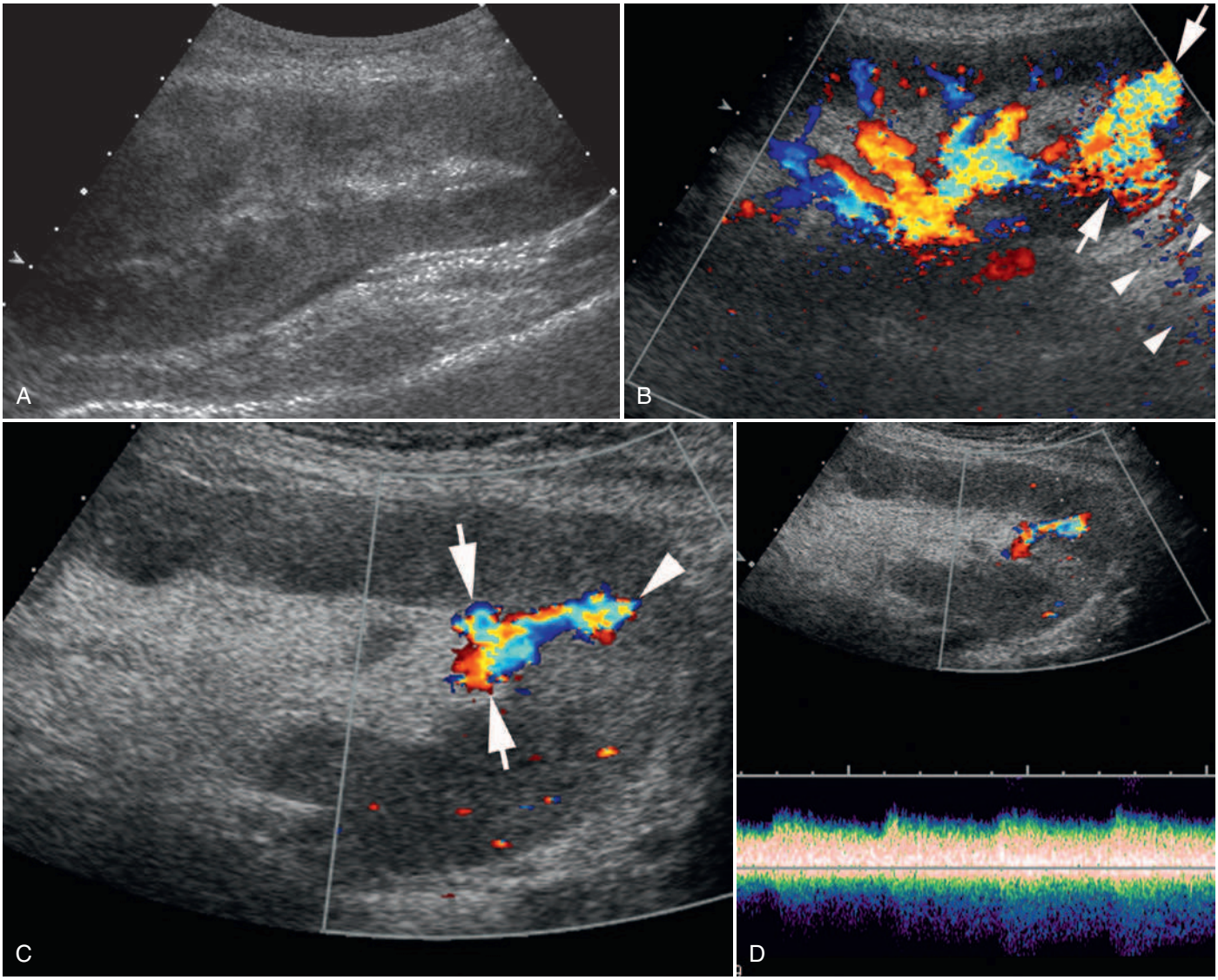

FIG. 52.49 Postbiopsy Arteriovenous Fistula (AVF). (A) Longitudinal gray-scale image of a renal allograft reveals no abnormality. **(B)** Color Doppler image shows markedly increased lower-pole blood flow *(arrows)* with adjacent soft tissue color artifact related to tissue vibration *(arrowheads).* **(C)** Color Doppler image with significantly increased velocity setting shows a focal, rounded AVF in the lower pole *(arrowhead)* with associated feeding and draining vessels *(arrows).* **(D)** Spectral Doppler waveform analysis depicts AVF high-amplitude, low-resistance arterial blood flow above the baseline, and arterialized venous flow below the baseline.

nonspecific sonographic findings, renal biopsy is usually indicated for a definitive diagnosis.

With improving early graft survival in children, **chronic rejection** currently represents the most common cause of overall pediatric graft failure, accounting for one-third of all graft loss.[146] This fact is particularly important in the pediatric population because of high rates of medication noncompliance during adolescence. Noncompliant periods are believed to increase the risk for chronic rejection by permitting subclinical chronic immune injury.[147]

Chronic allograft injury demonstrates similar imaging findings regardless of cause. Sonography demonstrates progressive volume loss with diffuse cortical atrophy, often with superimposed focal cortical scarring. Mild to moderate collecting system dilation can be seen in the absence of obstruction (Fig. 52.52).

Urologic Complications

Urologic complications are the most frequent cause of surgical morbidity in the pediatric transplant population, occurring in up to 23% of transplant recipients. There is a higher incidence in children with underlying malformations of the urinary tract, such as obstructive lesions, lower urinary tract dysfunction, and/or previous urologic reconstruction.[148-152] Common complications include urine leak, ureteral obstruction, VUR, and pyelonephritis.

A **urine leak** usually develops as a complication of ischemic necrosis or increased urinary pressure due to obstruction, and can occur anywhere in the urinary tract, from the renal calyces to the site of the ureterocystostomy.[153] It typically manifests within the first 2 weeks after transplantation with oliguria and azotemia, frequently associated with severe pain in the region of the graft.

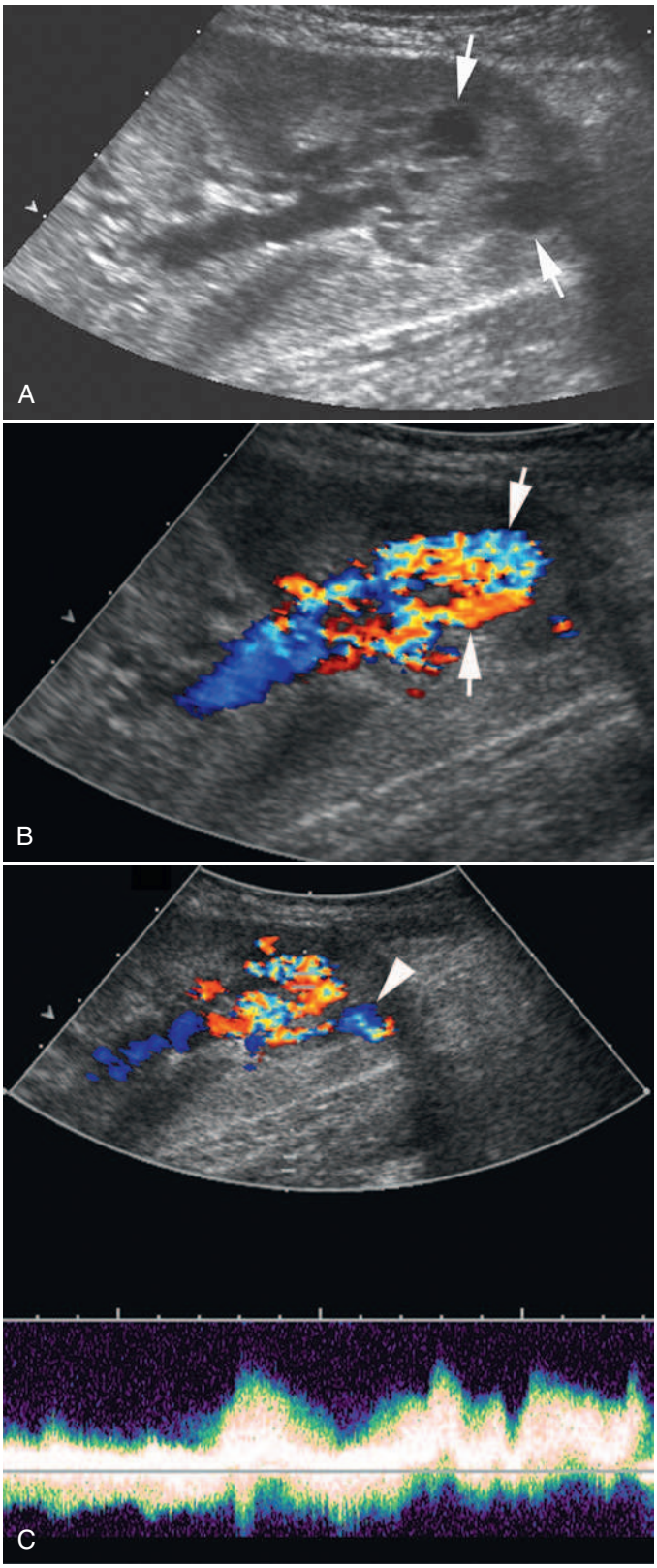

FIG. 52.50 Postbiopsy Pseudoaneurysms. (A) Longitudinal gray-scale image of a renal allograft shows two rounded lower-pole anechoic cystic structures *(arrows).* **(B)** Color Doppler imaging reveals a "yin-yang" sign caused by swirling blood flow within the upper pseudoaneurysm *(arrows).* **(C)** Spectral Doppler analysis depicts disordered blood flow above and below the baseline. Arrowhead indicates lower pseudoaneurysm.

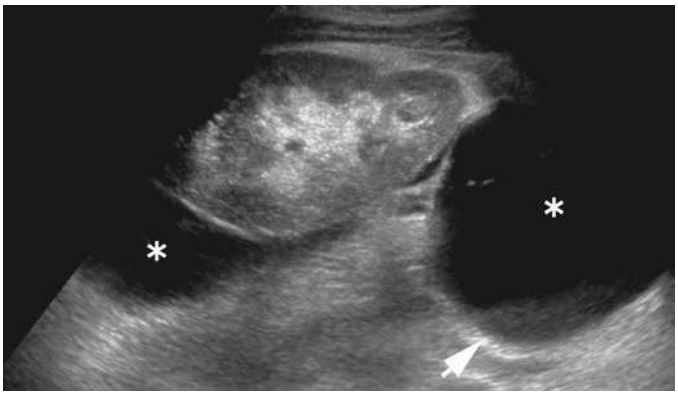

FIG. 52.51 Lymphocele. Longitudinal gray-scale image demonstrates two anechoic fluid collections adjacent to the upper and lower poles of a renal allograft (*). The lower collection is separate from the bladder *(not shown)* and contains a small amount of echogenic, dependent debris *(arrow).*

Depending on whether the allograft is located intraperitoneally or extraperitoneally, the leak can result in a localized perinephric urinoma or urine ascites.[130] A urinoma will usually appear as an anechoic, well-circumscribed, perinephric fluid collection. If clinically indicated, ^{99m}Tc-mertiatide renal scintigraphy, contrast-enhanced CT, or magnetic resonance urography can be performed to differentiate urinoma from seroma or lymphocele.

Urinary tract obstruction usually becomes apparent in the first few months after transplantation, and in general manifests clinically with nonspecific graft dysfunction. About 50% of the time, obstruction is related to an **ischemic stricture** at the ureteroneocystostomy. Other causes include midureteral stenosis, stone, blood clot, fungus ball, and extrinsic compression. Midureteral stenosis usually occurs in the setting of chronic rejection. Some degree of hydronephrosis is commonly identified after renal transplantation in both children and adults as a result of denervation with loss of muscle tone of the donor collecting system. The presence or absence of mild to moderate collecting system dilation has been shown to correlate poorly with the presence or absence of urinary tract obstruction in the post-transplant patient.[154] However, sonographic depiction of moderate to severe hydronephrosis and hydroureter that increase progressively over time warrants further evaluation for posttransplant urinary tract obstruction. MAG3 renal scintigraphy or magnetic resonance urography can be performed, with the more invasive method of percutaneous antegrade urography used to localize the site of obstruction. A nephrostomy tube can be placed for purposes of urinary tract decompression and to permit stent placement or balloon ureteroplasty.[130]

Vesicoureteral reflux (VUR) has been documented in approximately one-third to one-half of children after renal transplantation.[155,156] However, the presence of VUR does not appear to be associated with either an increased frequency of posttransplant urinary tract infection or decreased long-term graft function.[149,156] Patients with VUR into the transplant kidney usually have an underlying urologic abnormality, most commonly PUVs.[157,158]

Allograft infection may manifest as pyelonephritis, perinephric or parenchymal abscess, pyonephrosis, or fungus ball. Although

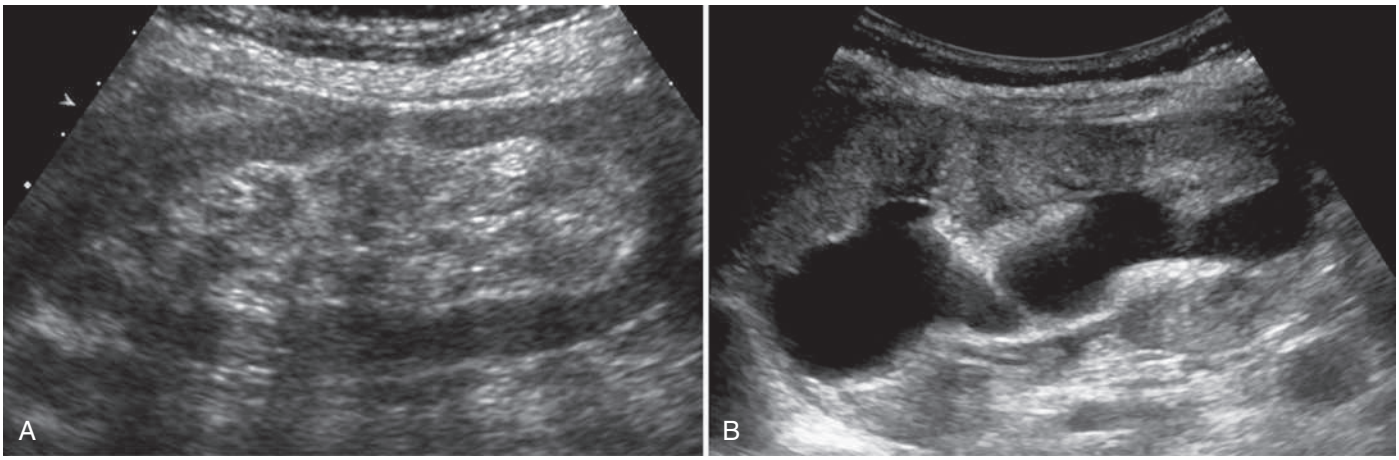

FIG. 52.52 Chronic Allograft Nephropathy. (A) Longitudinal gray-scale image of a renal allograft reveals diffuse cortical atrophy. **(B)** Longitudinal gray-scale image of a different patient demonstrates echogenic cortex and decreased corticomedullary differentiation. There is also moderate collecting system dilation.

pyelonephritis after renal transplantation in children is relatively common in comparison to adult transplant recipients, if treated promptly it does not appear to adversely affect graft function.[159,160] Pyelonephritis is associated with VUR in pediatric renal transplant recipients.[160] As with the native kidney, the sonographic appearance of pyelonephritis is variable, ranging from normal to swelling and altered parenchymal echogenicity related to edema.

A **perinephric** or **parenchymal abscess** is an uncommon complication of graft pyelonephritis. Other causes include infection of the surgical site or spontaneous or iatrogenic infection of a previously sterile fluid collection. They commonly appear within the first postoperative month. Although the sonographic appearance of an abscess is relatively nonspecific, a complex appearance with prominent septations, internal debris, and mural hyperemia documented with color and spectral Doppler is suggestive of an infectious etiology. In the setting of pyelonephritis, the presence of mobile, hyperechoic foci within a dilated collecting system should raise concern for pyonephrosis.[161] Fungus balls manifest as discrete intraluminal masses.[153]

Urinary tract stones occur with the same frequency in renal transplant recipients as in the general population.[162] Sonography is helpful in identifying stones within the renal parenchyma, collecting system, ureter, and bladder, as well as documenting any associated hydronephrosis or hydroureter.

Tumors

Long-term immunosuppression predisposes renal transplant recipients to the development of neoplasia, both within the transplant kidney and in other organs.[80] **Posttransplant lymphoproliferative disorder (PTLD)** and **inflammatory myofibroblastic tumor** have been reported.

The imaging appearance of PTLD depends on the site of involvement (Fig. 52.53). When the allograft is affected, it typically appears as multiple ill-defined, hypoechoic parenchymal masses.[130] Inflammatory myofibroblastic tumor is a rare and usually benign neoplasm that can develop after bone marrow solid organ and bone marrow transplantation.[163] It may occur anywhere in the body, although it favors certain locations, including the lung, liver, gastrointestinal tract, and bladder.

RENAL CYSTIC DISEASE

The category of renal cystic diseases includes a large group of disorders with variable phenotypic expression. Cystic diseases may be diagnosed in utero or may be seen in infancy, childhood or adulthood. They can usually be differentiated on the basis of clinical findings, including age at presentation, renal imaging features (including cyst distribution), and the presence and nature of extrarenal manifestations. Ultrasound evaluation plays a central role in the diagnostic evaluation of patients with renal cysts. In individuals with an atypical presentation, additional imaging studies and/or genetic testing may be necessary to establish a diagnosis.[164]

Autosomal Recessive Polycystic Kidney Disease

ARPKD is a severe hepatorenal fibrocystic disorder characterized by nonobstructive renal collecting duct dilation and malformation of the portobiliary system.[164] It is caused by mutations in the polycystic and hepatic disease gene 1 *(PKHD1),* which encodes fibrocystin-polyductin complex, a protein expressed in primary cilia of kidney and bile duct epithelial cells.[165] ARPKD occurs in approximately 1 : 20,000 live births.[166] In general, it is diagnosed prenatally in association with oligohydramnios or at birth when it is characterized by progressive renal insufficiency and portal hypertension. Oligohydramnios results in the so-called "Potter sequence" consisting of pulmonary hypoplasia, limb defects, and characteristic dysmorphic facies. There is an estimated perinatal mortality rate of 30% as a result of respiratory insufficiency.[167,168] However, in infants who survive the first month of life, 1-year survival rates of 92% to 95% have been reported.[166] The kidneys are enlarged and echogenic, with loss of normal parenchymal corticomedullary differentiation. Medullary echogenicity is increased as a result of the multiple interfaces associated with the

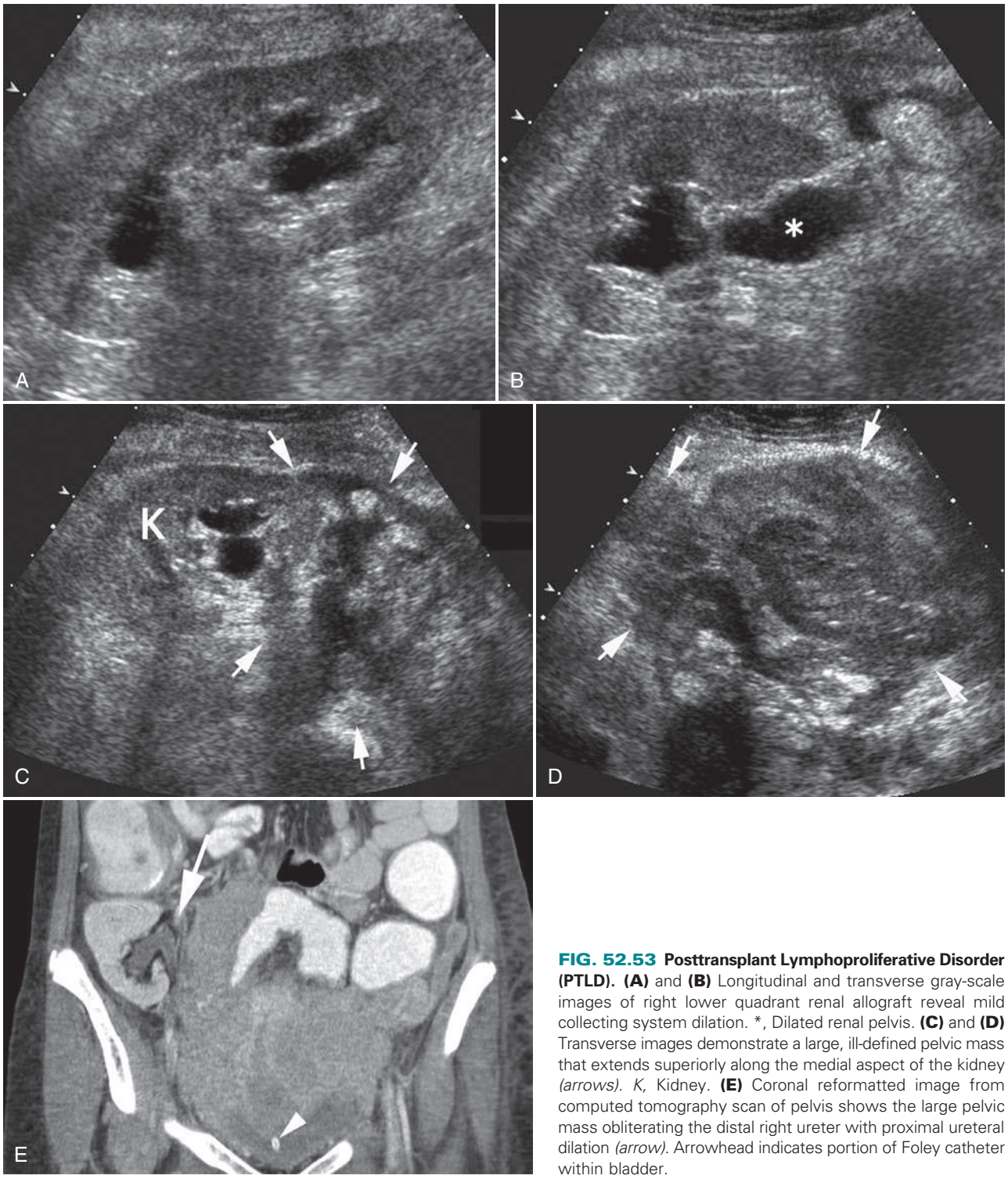

FIG. 52.53 Posttransplant Lymphoproliferative Disorder (PTLD). (A) and **(B)** Longitudinal and transverse gray-scale images of right lower quadrant renal allograft reveal mild collecting system dilation. *, Dilated renal pelvis. **(C)** and **(D)** Transverse images demonstrate a large, ill-defined pelvic mass that extends superiorly along the medial aspect of the kidney *(arrows). K,* Kidney. **(E)** Coronal reformatted image from computed tomography scan of pelvis shows the large pelvic mass obliterating the distal right ureter with proximal ureteral dilation *(arrow).* Arrowhead indicates portion of Foley catheter within bladder.

dilated collecting ducts that reflect sound. The cortex is frequently compressed by the dilated medullary collecting ducts, leading to a hypoechoic halo. Dilated cortical collecting ducts located immediately beneath the renal capsule may be seen with high-resolution ultrasound (Fig. 52.54). They tend to lie in parallel columns with a distribution that is radial to the kidney as a whole.[169] Renal size stabilizes or decreases over time. Macrocysts are not usually noted at birth but may develop later in childhood.

Histologic hepatic involvement is present in all patients with ARPKD. In embryonic life, biliary precursor cells form a periportal sheet known as the "ductal plate" that is progressively remodeled to generate intrahepatic bile ducts. A remodeling defect in patients with ARPKD leads to intrahepatic ductal dilation and progressive portal tract fibrosis. Patients who survive the neonatal period may develop portal hypertension as a result of the periportal fibrosis.

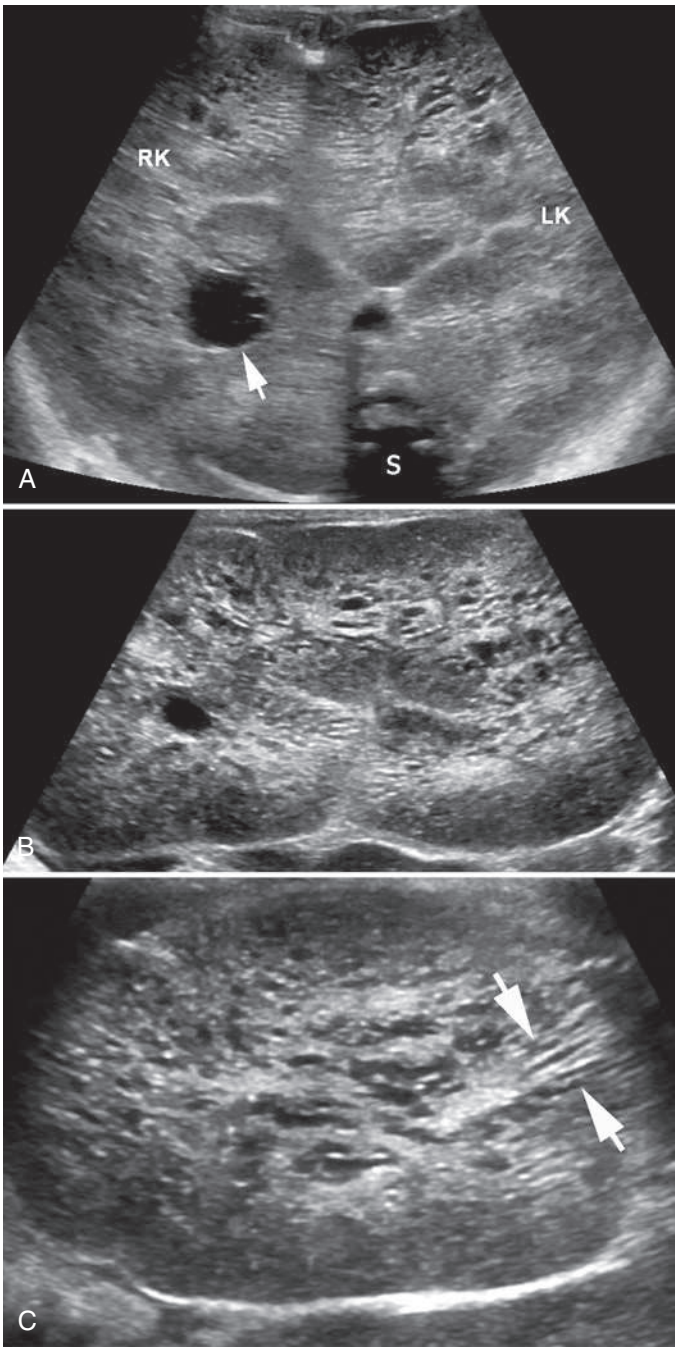

FIG. 52.54 Autosomal Recessive Polycystic Kidney Disease (ARPKD). (A) Transverse image of neonate shows symmetrically enlarged kidneys filling the abdomen. *LK,* Left kidney; *RK,* right kidney; *S,* spine. A macrocyst is present in the right kidney *(arrow).* **(B)** Longitudinal image of right kidney demonstrates loss of normal corticomedullary differentiation, hypoechoic subcapsular cortex, and multiple cysts of varying size within the medullary region. **(C)** High-resolution transverse image of left kidney reveals multiple dilated subcapsular cortical collecting ducts *(between arrows).*

Autosomal Dominant Polycystic Kidney Disease

Autosomal dominant polycystic kidney disease (ADPKD) is the most common inherited form of kidney failure that eventually results in end-stage renal disease. It is characterized by bilateral, progressive enlargement of focal cysts that occur in all portions of the nephron, and variable extrarenal manifestations also occur. Approximately 600,000 individuals in the United States are affected, and 13 million people worldwide.[170]

ADPKD is usually asymptomatic until middle age. However, in about 2% to 5% of patients, ADPKD is seen in the neonatal period, with substantial morbidity and mortality. These early manifestations of ADPKD may be indistinguishable from ARPKD and can be differentiated only on the basis of histologic or genetic analysis. There is a familial incidence of childhood presentation, with siblings of affected children demonstrating a greater risk of early disease.[171]

ADPKD is caused by dominant transmission of one of two defective genes, *PKD1* (mapped to chromosome 16p13.3 in 85% of patients) or *PKD2* (mapped to chromosome 4q13–23 in 15% of patients). *PKD1* encodes the protein polycystin-1 and *PKD2* encodes polycystin-2. These two proteins are localized to the primary cilia in the epithelial cells that line the renal tubules and interact to form a calcium channel receptor. Both are important in the differentiation, maintenance, and repair of renal tubular cells and in determining the morphology of the renal tubules. *PKD1*-associated disease is generally more severe than *PKD2*-associated disease. However, there is significant phenotypic heterogeneity. Unusually mild cases are believed to be due to the transmission of so-called "hypomorphic" alleles (i.e., those that have retained partial activity).[170,172]

Most children with ADPKD are born with normal kidneys. Normal ultrasound examination findings cannot exclude ADPKD until after the age of 35 years, particularly for *PKD2* mutations.[173] The presence of at least two renal cysts (unilateral or bilateral) in an individual younger than 30 years of age with a 1 in 2 risk of *PKD1* is sufficient to establish the diagnosis.[174] Even a single cyst in a genetically predisposed child is highly suspicious for ADPKD because the prevalence of renal cysts in the general pediatric population is low[175,176] (Fig. 52.55). The concomitant presence of an extrarenal cyst in the liver or pancreas indicates the diagnosis of ADPKD, although these are rare at initial presentation in children.[176,177] Older children have larger and more numerous renal cysts and develop progressive renal enlargement (Fig. 52.56). Results from the Consortium of Renal Imaging Studies in Polycystic Kidney Disease have shown that the larger the cyst mass or renal volume, the worse the prognosis, regardless of whether the cysts derive from an *ADPKD1* or *ADPKD2* gene defect.[178]

In third-trimester fetuses and infants with ADPKD in the neonatal period, the kidneys are normal in size to mildly enlarged. The cortex is hyperechoic compared with the liver or spleen with hypoechoic medulla resulting in increased corticomedullary differentiation[179] (see Fig. 52.55). This appearance differs from the usual appearance of ARPKD, in which the kidneys are markedly rather than mildly enlarged and the medullae are hyperechoic. A few small cysts may be seen in the cortex, medulla, or both in ADPKD. Unlike the tubular cysts of ARPKD, the cysts in the dominant form appear round.[167,180]

Extrarenal manifestations include cysts of the liver, spleen, pancreas, seminal vesicles, and arachnoid membrane. The liver is the most common extrarenal site of involvement. Aneurysms

of the intracranial vessels and aorta and aortic dissection are additional associations.[181]

Multicystic Renal Dysplasia

Multicystic dysplastic kidney (MCDK) is a congenital malformation, with an incidence of about 1 per 4000 live births.[182] Histologically, multiple noncommunicating cysts are separated by dysplastic parenchyma. The etiology of MCDK is uncertain, although various theories have been proposed. The "ureteric bud theory" of Mackie and Stephens hypothesizes that MCDK may result from a ureteric bud that is atretic or connects abnormally with the metanephric mesenchyme and the developing bladder, resulting in obstruction.[183] Work by Batourina and colleagues[184] and Viana and colleagues[185] suggests that an abnormal interaction between the developing bladder trigone and the distal ureter may result in dysfunction at the ureterovesical junction and subsequent obstruction. Bilateral MCDK disease is usually lethal shortly after birth, owing to associated pulmonary hypoplasia secondary to prolonged oligohydramnios in utero. With unilateral MCDK, renal function is usually maintained by the contralateral kidney.[186] Although MCDK can be an isolated finding, it frequently occurs in association with other anomalies of the urinary tract, most commonly VUR, UPJO, and UVJO.[186] It is also a common or characteristic finding in multisystemic genetic disorders such as **branchio-oto-renal syndrome** and **renal-coloboma syndrome.**[183]

MCDK is usually diagnosed by prenatal sonography (Fig. 52.57, Video 52.7), or if unilateral may be found as an abdominal mass at birth. The common pelvoinfundibular form of MCDK manifests as numerous, randomly distributed noncommunicating cysts of varying size. There is no renal pelvis or renal sinus, and renal parenchyma is absent or dysplastic. The less common hydronephrotic form of MCDK consists of multiple small, peripheral cysts and a larger central cyst, with some connections between the peripheral cysts and the central cyst. The entire kidney is usually involved and may be small, normal in size, or enlarged. There is no or minimal functional renal tissue.[187] The contralateral kidney usually demonstrates compensatory hypertrophy. Segmental involvement may occur, most often in the upper-pole moiety of a duplex kidney.[188] In patients with no other urologic abnormalities, MCDK is managed nonoperatively, as the risk of associated malignancy is low. Most affected kidneys will undergo partial or complete involution.[189]

FIG. 52.55 Autosomal Dominant Polycystic Kidney Disease (ADPKD). Longitudinal gray-scale image of 33-week gestational age fetus of a mother with ADPKD reveals a small, round cyst in the upper pole of the right kidney consistent with ADPKD *(arrow)*. Renal parenchymal echogenicity is slightly increased and the medullary pyramids are hypoechoic. Both right and left kidneys were mildly enlarged for gestational age.

Nephronophthisis and Medullary Cystic Disease

Nephronophthisis (NPHP) is an autosomal recessive tubulointerstitial disorder, and one of the most common causes of inherited end-stage kidney disease in children and young adults.[190] To date, 19 causative genes have been identified, although the causative genes are still unknown in approximately 70% of affected patients.[164] At presentation children usually are 4 to 6 years of

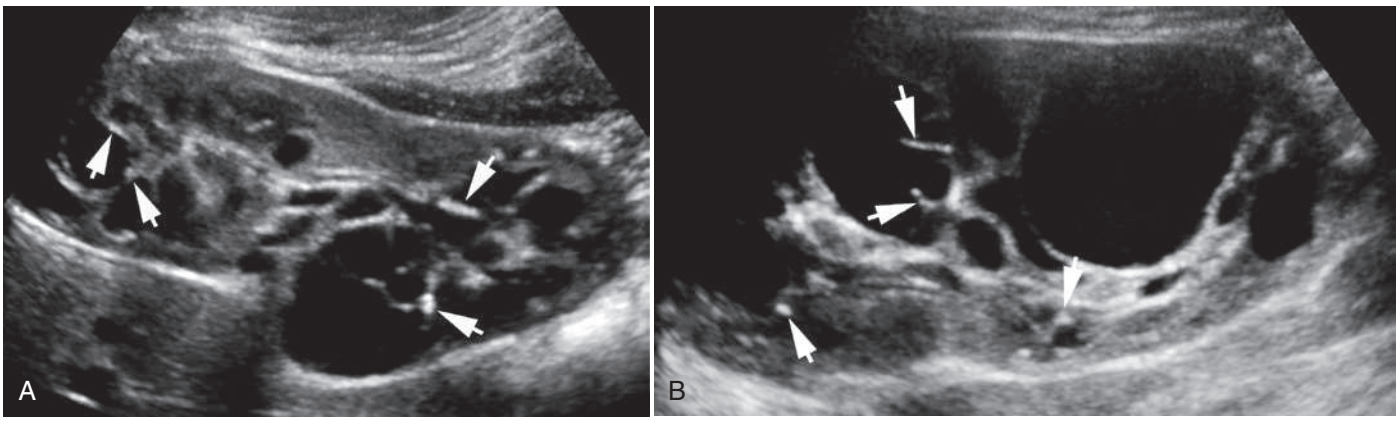

FIG. 52.56 Autosomal Dominant Polycystic Kidney Disease (ADPKD). (A) and **(B)** Longitudinal prone gray-scale images in a 17-year-old girl demonstrate enlarged right and left kidneys, respectively, containing multiple cysts of varying size. Scattered linear and punctate echogenic foci may represent mural calcifications and/or stones *(arrows)*.

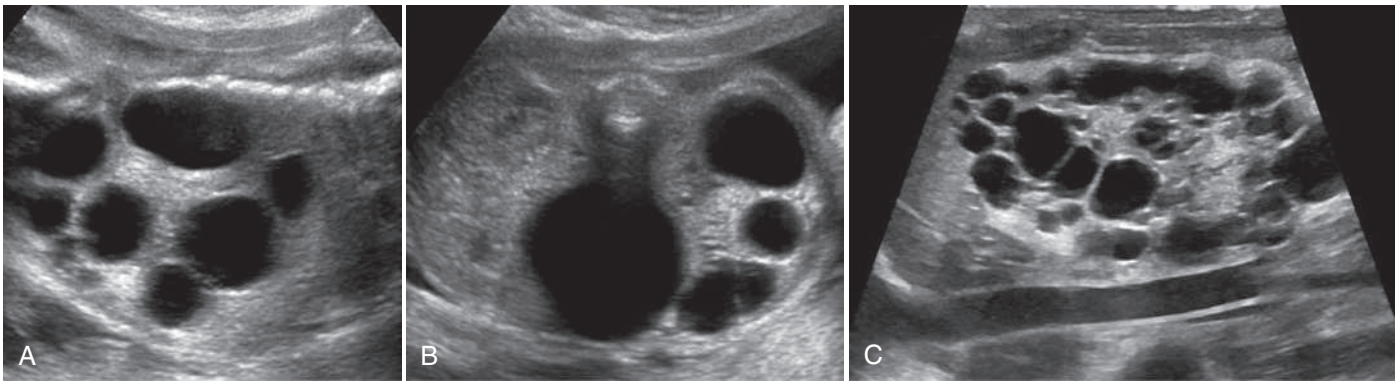

FIG. 52.57 Multicystic Dysplastic Kidney (MCDK). (A) and **(B)** Longitudinal and transverse gray-scale images of a 27-week gestational age fetus depict the presence of multiple cysts of varying size surrounded by echogenic cortex. **(C)** Longitudinal gray-scale image of a different patient at birth shows near-complete replacement of the left kidney by numerous cysts. See also Video 52.7.

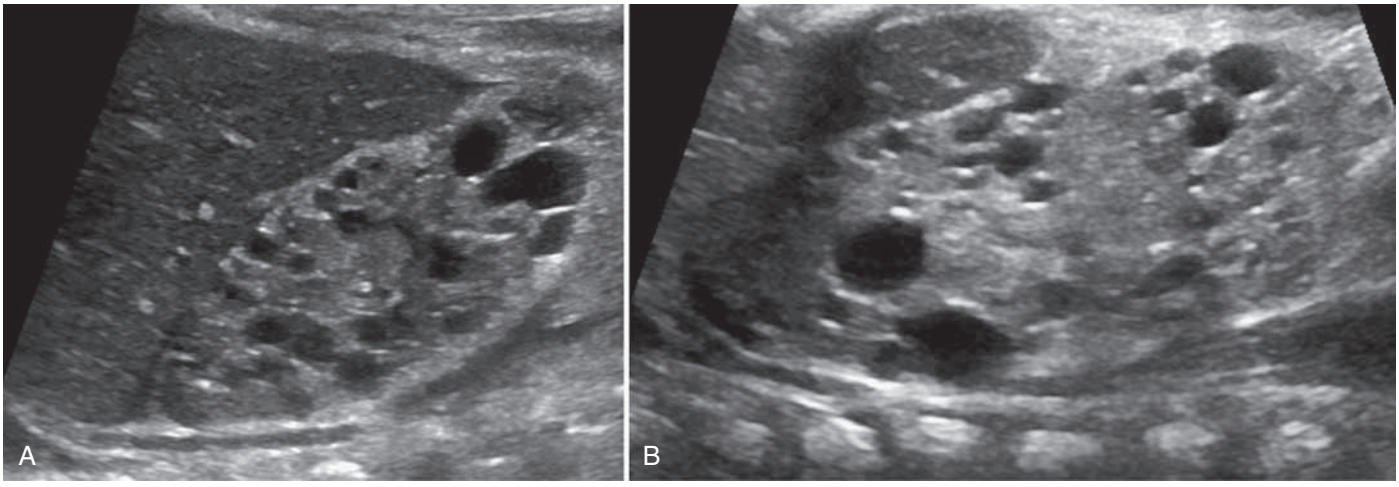

FIG. 52.58 Nephronophthisis. Neonate With Homozygous NPH3 Mutations Associated With Anuria and Pulmonary Hypoplasia. (A) and **(B)** Longitudinal gray-scale images of the right and left flanks, respectively, reveal echogenic parenchyma with loss of corticomedullary differentiation and multiple cysts located throughout both kidneys.

age and have polydipsia and polyuria and decreased urinary concentration. A slowly progressive decline in renal function typically occurs. An exception to this clinical presentation is the infantile variant, usually a result of mutation in the *NPHP2* or *NPHP3* gene, which is seen in patients in the first few months of life with renal insufficiency and hypertension, and rapid progression to end-stage renal disease.[191] The kidneys are normal in size or small, except in the infantile form, in which they are enlarged.[192] On ultrasound, the kidneys are echogenic with decreased corticomedullary differentiation (Fig. 52.58). Cysts may be observed at the corticomedullary junction.

Medullary cystic kidney disease is an autosomal dominant tubulointerstitial disorder that usually manifests in the third to sixth decades of life. As with NPHP, there may be a history of polydipsia and polyuria, and urinary concentrating ability is decreased. Type 1 disease is caused by heterozygous mutations in the *MUC1* gene. Type 2 disease is caused by heterozygous mutations in the uromodulin gene.[164] On ultrasound, the kidneys are normal to small in size, and often echogenic. Similar to NPHP, cysts can occur at the corticomedullary junction (Fig. 52.59).

Congenital Renal Cysts

Tuberous Sclerosis and Von Hippel–Lindau Disease

Although renal cysts occur in many syndromes, two of the most common are tuberous sclerosis and Von Hippel–Lindau Disease. **Tuberous sclerosis** is an autosomal dominant disease consisting of mental retardation, epilepsy, adenoma sebaceum, multiple ectodermal lesions, and mesodermal hamartomas. Renal lesions are present in more than 40% of patients and include cysts, which can be multiple and resemble ADPKD with renal enlargement (Fig. 52.60).

Von Hippel–Lindau disease is an autosomal dominant disorder characterized by the formation of tumors and cysts in many different organs throughout the body. Renal cysts and renal cell carcinoma are common visceral manifestations of this disorder, with the latter a significant cause of mortality.[193]

Acquired Cysts

Patients with **chronic renal failure,** especially those receiving long-term dialysis, often develop renal cysts (Fig. 52.61).

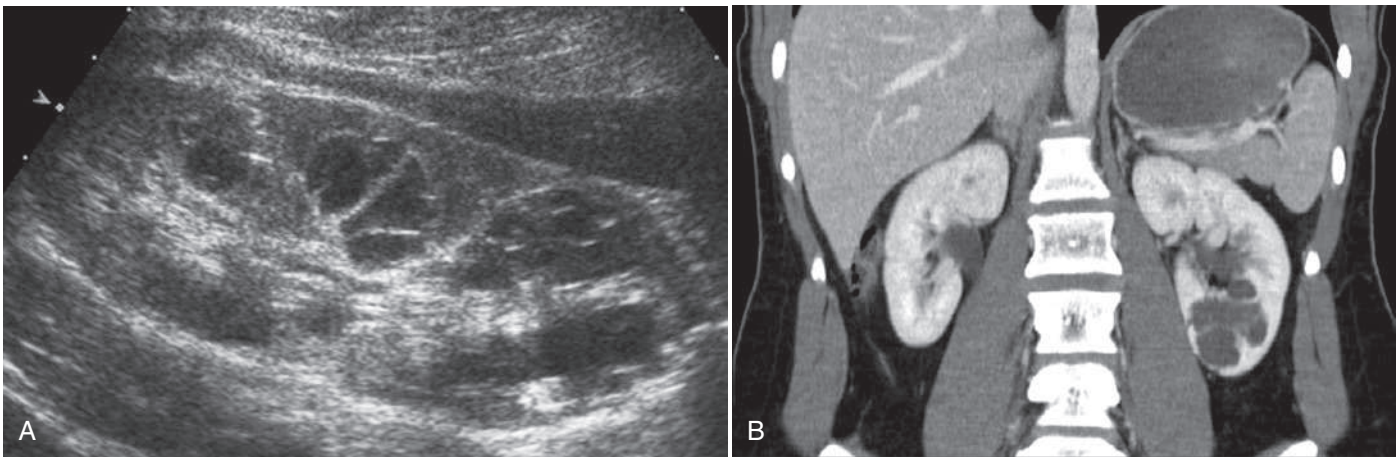

FIG. 52.59 Medullary Cystic Disease. Asymptomatic 17-year-old girl who underwent renal imaging after trauma. **(A)** Longitudinal gray-scale image of left kidney demonstrates multiple anechoic cysts within the medullary pyramids. **(B)** Coronal reformatted intravenous contrast-enhanced computed tomography image depicts the medullary cysts in the lower left renal pole.

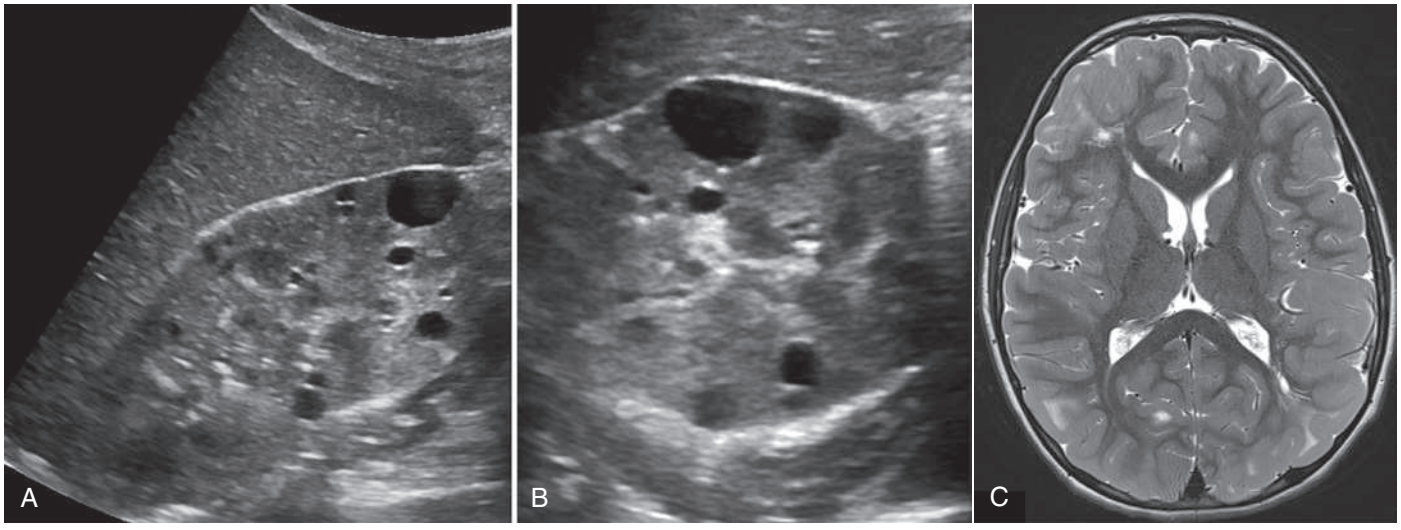

FIG. 52.60 Tuberous Sclerosis. **(A)** and **(B)** Longitudinal and transverse gray-scale images of the right kidney in a 6-year-old boy show multiple anechoic parenchymal cysts. **(C)** Axial T2 fluid-attenuated inversion recovery (FLAIR) magnetic resonance image of the brain demonstrates multiple foci of abnormally high signal in the subependymal and subcortical regions typical of tubers.

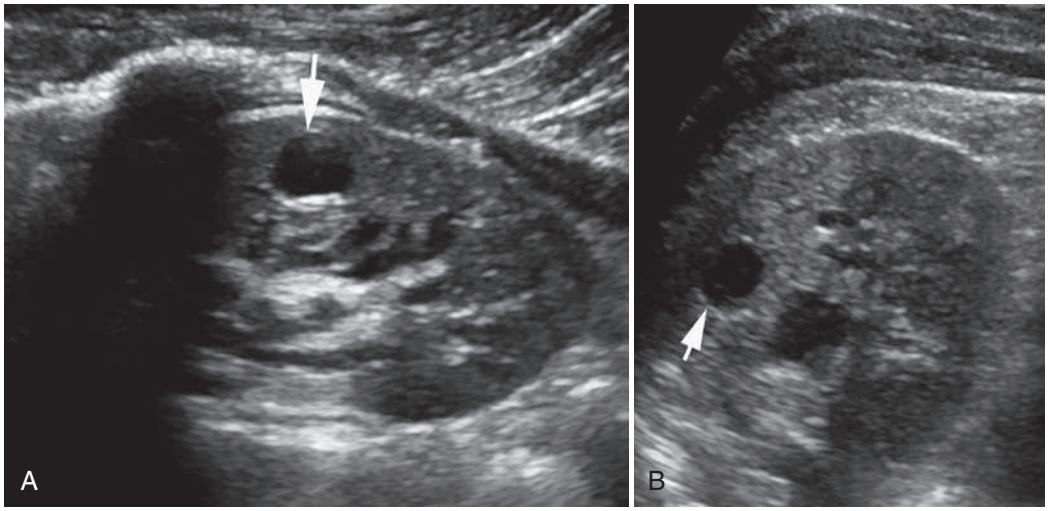

FIG. 52.61 Dialysis-Associated Renal Cyst. A 17-year-old boy on chronic hemodialysis for end-stage renal disease (ESRD). **(A)** and **(B)** Longitudinal and transverse images reveal a single anechoic cyst in the upper pole of the right kidney *(arrows).* There is loss of normal renal corticomedullary differentiation in keeping with ESRD.

Spontaneous hemorrhage within the cysts may also occur.[194,195] Renal cysts have also been reported to develop after **liver transplantation.** Patients at risk are at least 10 years posttransplant, have been treated with cyclosporine, and have impaired renal function.[196,197]

Simple cysts are generally asymptomatic and are much less common in children than in adults. They typically appear as a single mass arising from the renal parenchyma.[198] They may occasionally be complicated by infection, hemorrhage, or calcification.[199]

RENAL TUMORS

The most common abdominal masses in the child are of renal origin: hydronephrosis and MCDK. Solid tumors are less common. Initial imaging includes sonography and often a plain film of the abdomen. The site of origin of the mass, its architecture (cystic or solid), and vascularization can usually be determined with sonography.

If the mass is cystic and arises from the kidney, the usual differential diagnosis is between a hydronephrotic kidney and MCDK. The configuration of the cysts on sonography and, if needed, presence of function on nuclear renography help distinguish these two entities. If the mass is solid and related to the kidney, Wilms tumor is the most likely diagnosis. Metastases and tumoral invasion of the renal vein or inferior vena cava are sought during the sonographic survey of the abdomen. Staging of the tumor is usually done with CT or MRI.[200,201] If the kidney is normal and the mass is related to another organ, the workup continues with imaging that is optimal for that organ.

Wilms Tumor

Wilms tumor, or **nephroblastoma,** is the most common intra-abdominal malignant tumor of childhood. Approximately 80% of patients are aged 1 to 5 years at presentation, with a peak incidence at 3 to 4 years of age.[202] When the tumor is large, it may be difficult to differentiate from **neuroblastoma,** which frequently arises from the adrenal gland and occurs in a similar age group. Wilms tumor is usually bulky and expands within the renal parenchyma, resulting in distortion and displacement of the collecting system and capsule. It is usually sharply marginated. Five percent to 10% of patients have bilateral tumors, and **nephroblastomatosis** may be present in both kidneys in children with unilateral Wilms tumor. Screening is recommended for children at high risk for the development of Wilms tumor, including those with **hemihypertrophy, sporadic aniridia, Beckwith-Wiedemann syndrome, WAGR syndrome** (Wilms tumor, aniridia, genitourinary anomalies, and intellectual disability [mental retardation]), and nephroblastomatosis.[202]

Typically, Wilms tumor is a large solid mass distorting the renal sinus, pyramids, cortex, and contour of the kidney as depicted with sonography. Although usually quite hyperechoic and homogeneous, there may be hypoechoic areas that represent hemorrhage and necrosis. Decreased blood flow compared with the adjacent renal parenchyma is usually seen with color and power Doppler ultrasound (Fig. 52.62).

Wilms tumor spreads via direct extension into the renal sinus and peripelvic soft tissues, the lymph nodes in the renal hilum, and the paraaortic regions. Because extension is possible into the renal vein, inferior vena cava, right atrium, and liver, these areas should also be examined for the presence of tumor (Fig. 52.63). Color and spectral Doppler sonography are useful in detecting residual flow around a tumor clot, as well as tumor arterial signals both from the periphery of the tumor and from within the tumor thrombus. The opposite kidney should be carefully examined for the presence of tumor. Although to date there have been few reports on the use of CEUS in the diagnosis of pediatric renal masses, this modality is potentially of great usefulness (Fig. 52.64). CT and MRI are usually performed for further workup and staging.[202]

Mesoblastic Nephroma

Mesoblastic nephroma or **fetal renal hamartoma** is the most common neonatal renal neoplasm, and is sometimes detected in the fetus. It is a benign tumor but can spread through local

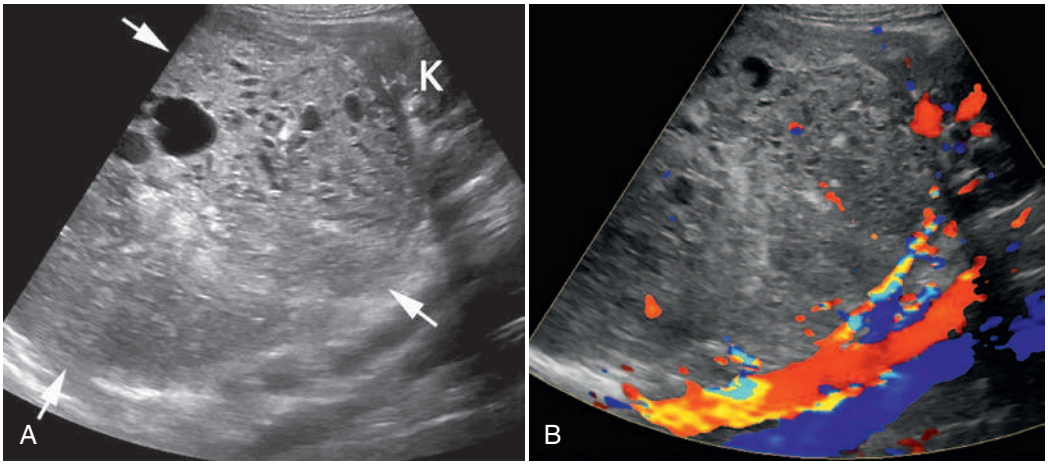

FIG. 52.62 Wilms Tumor. (A) Longitudinal gray-scale image depicts a large, hyperechoic mass *(arrows)* arising from the upper and middle portions of the left kidney *(K).* Multiple anechoic zones within the tumor are the sequelae of hemorrhage and/or necrosis. **(B)** Longitudinal color Doppler image depicts less blood flow within the tumor than in the adjacent renal parenchyma.

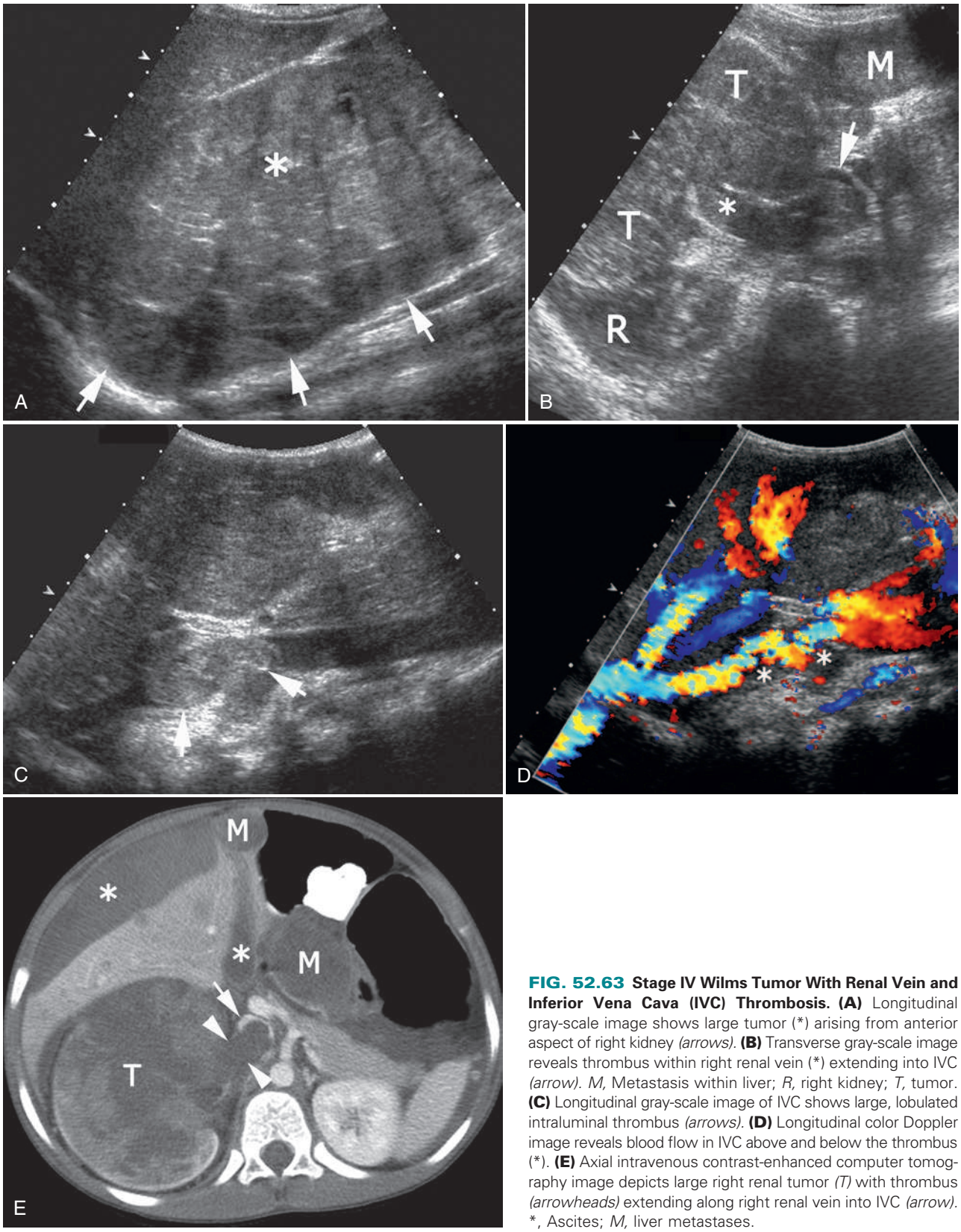

FIG. 52.63 Stage IV Wilms Tumor With Renal Vein and Inferior Vena Cava (IVC) Thrombosis. (A) Longitudinal gray-scale image shows large tumor (*) arising from anterior aspect of right kidney *(arrows)*. **(B)** Transverse gray-scale image reveals thrombus within right renal vein (*) extending into IVC *(arrow)*. *M,* Metastasis within liver; *R,* right kidney; *T,* tumor. **(C)** Longitudinal gray-scale image of IVC shows large, lobulated intraluminal thrombus *(arrows)*. **(D)** Longitudinal color Doppler image reveals blood flow in IVC above and below the thrombus (*). **(E)** Axial intravenous contrast-enhanced computer tomography image depicts large right renal tumor *(T)* with thrombus *(arrowheads)* extending along right renal vein into IVC *(arrow)*. *, Ascites; *M,* liver metastases.

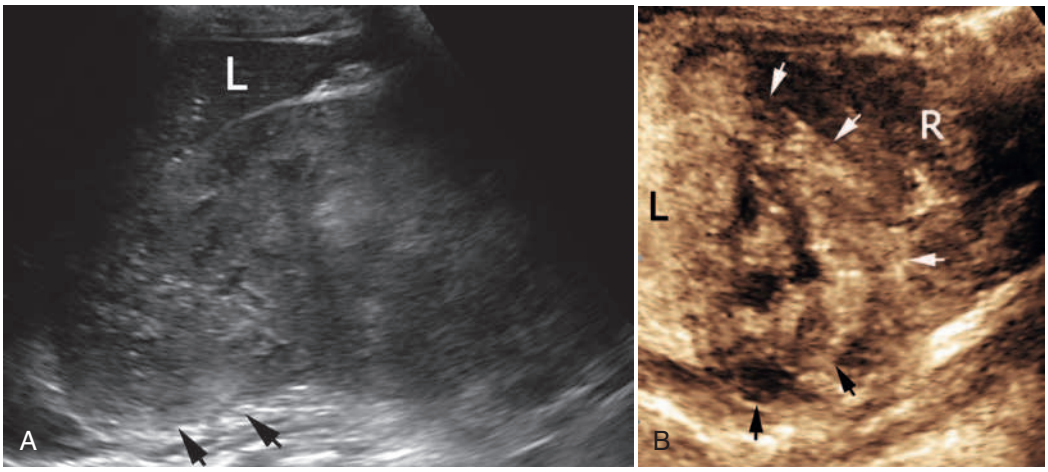

FIG. 52.64 Contrast-Enhanced Ultrasound (CEUS) of Wilms Tumor. (A) Longitudinal gray-scale image of right kidney reveals a bulbous appearance of the upper pole *(arrows)* without a clearly-defined mass. *L,* Liver. **(B)** Longitudinal CEUS image better defines the upper-pole mass *(arrows). L,* Liver; *R,* right kidney. (Courtesy of Dr. Erika Rubesova, Stanford University.)

invasion and is usually treated by simple nephrectomy. Sonography demonstrates a mass arising within the kidney, similar in appearance to a Wilms tumor. It is solid but may have cystic-appearing areas of hemorrhage and necrosis (Fig. 52.65). There are two main pathological types: the classic variant, and the more aggressive cellular variant. The cellular variant is characterized by hemorrhage and necrosis, with invasion of perirenal fat and adjacent organs, and local recurrence. Cystic components are readily identified by ultrasound, whereas central hemorrhage is better depicted by CT. MRI shows high sensitivity for both.[203]

Renal Cell Carcinoma

Renal cell carcinoma is rare in childhood. It occurs later than Wilms tumor, with a median age at diagnosis ranging between 8 and 17 years. Unlike adults, in whom up to 67% of renal cell carcinomas are found incidentally, most children are symptomatic, and approximately 30% have metastatic disease on presentation. There is also no gender predominance in children. Children and adolescents with renal cell carcinoma have much higher rates of translocation tumors than adults. Children with translocation tumors tend to have indolent disease with good outcomes compared with adults, even those with advanced disease.[204] Renal cell carcinoma cannot be distinguished from Wilms tumor by imaging, but calcification is more common (25%-53%) in renal cell carcinoma (Fig. 52.66) than in Wilms tumor (9%).[205]

Angiomyolipoma

Angiomyolipoma is a form of hamartoma that can be complicated by hemorrhage and/or rupture. In children, these tumors are usually multiple and are associated with tuberous sclerosis. Sonography typically shows multiple masses of varying echogenicity depending on their fat content. Masses containing a large amount of fat are very echogenic[206,207] (Fig. 52.67).

Multilocular Cystic Nephroma

Multilocular cystic nephroma is a rare lesion that is generally considered benign. It can occur at any age but is uncommon in children younger than 2 years. The mass is composed of multiple cysts of varying size joined by connective tissue septa. It may be difficult to distinguish from a cystic, well-differentiated Wilms tumor containing nephroblastoma components in the walls of the cysts. Sonography demonstrates a well-circumscribed, multiloculated cystic mass with septations (Fig. 52.68). Some suggest a malignant potential for these lesions and recommend nephrectomy.[208-210]

Renal Lymphoma

Lymphomatous involvement of the kidney is usually a secondary process and can be seen on sonography as single or multiple, relatively hypoechoic or slightly echogenic masses within the kidney. The kidney may be enlarged and lobulated in outline. Diffuse infiltration of the kidney can also occur[211,212] (Fig. 52.69, Video 52.8).

Bladder Tumors

Primary tumors of the lower urinary tract are uncommon in children. **Sarcoma botryoides** is a **rhabdomyosarcoma** arising in the bladder base in males, manifesting with bladder outlet obstruction (Fig. 52.70). In girls, this rare tumor typically occurs in the uterus or vagina.[78,213,214]

PEDIATRIC ADRENAL SONOGRAPHY

Normal Anatomy

The adrenal gland is relatively prominent in the neonate and is easily visualized with ultrasound above the kidneys. At birth, the adrenal gland is relatively large, representing 0.2% to 0.3% of total body weight, compared with 0.001% in adults. There is a linear relationship between body weight and gland length in healthy neonates. However, in premature neonates, gestational age and gland length have a linear relationship. In the neonate, there is a thick fetal zone that occupies about 80% of the adrenal cortex. After birth, the fetal zone of the adrenal cortex undergoes involution. The linear dimensions of the adrenal continually decrease during the first 6 months of life (Table 52.10). In addition, the appearance of the adrenal gland changes as the cortex involutes, the overall echogenicity of the gland increases, and

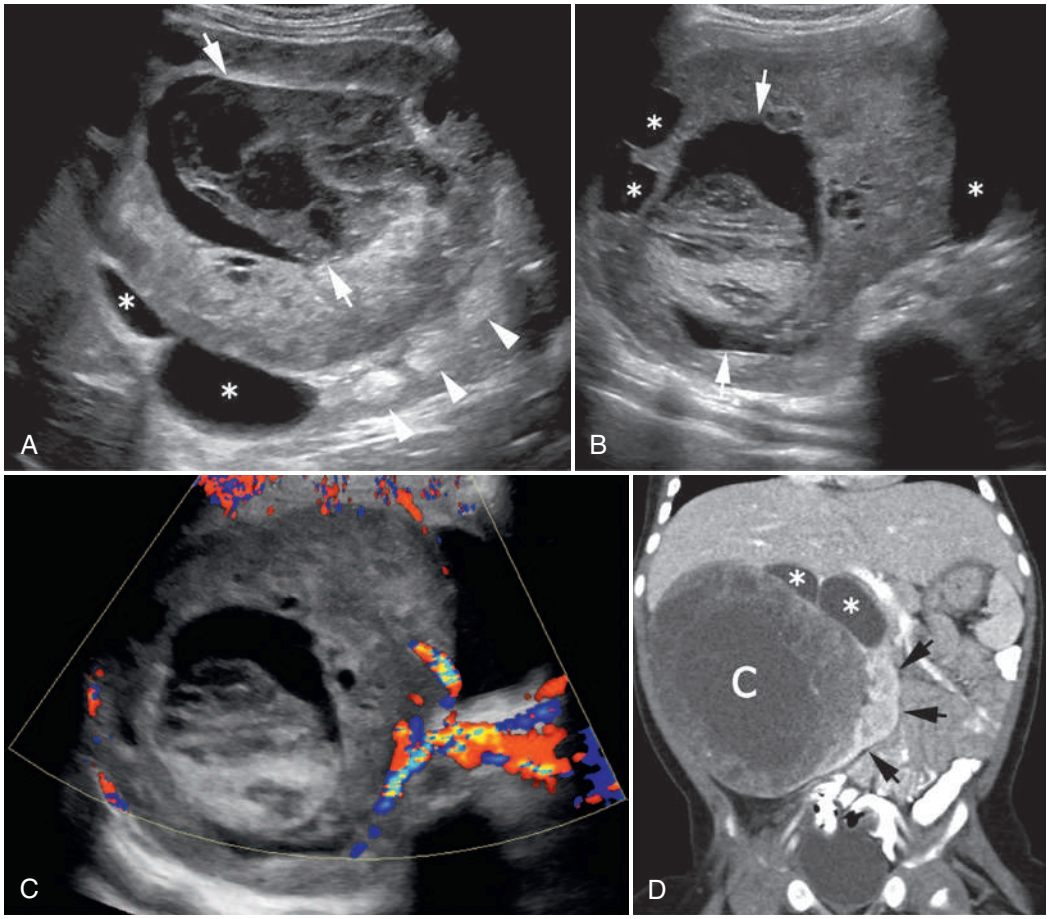

FIG. 52.65 Mesoblastic Nephroma. (A) and **(B)** Longitudinal and transverse gray-scale images of the right kidney depict a mass with peripheral cysts (*) and a centrally located, heterogeneous zone surrounded by fluid *(arrows)*. Incidental echogenic renal pyramids due to medullary nephrocalcinosis *(arrowheads)*. **(C)** Transverse color Doppler image shows no flow within the heterogeneous central portion of the tumor typical of cystic necrosis or resolving hemorrhage. **(D)** Coronal intravenous contrast-enhanced computed tomography image demonstrates a large right renal mass with little contrast enhancement compared with the adjacent compressed renal parenchyma *(arrows)*, a relatively low-attenuating central zone *(C)*, and peripheral cysts (*).

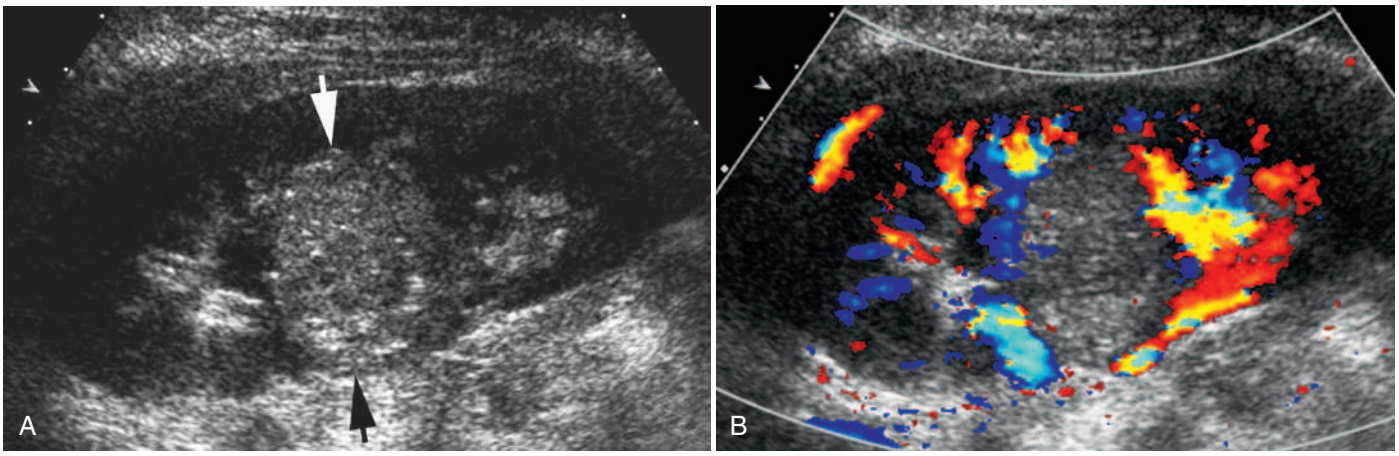

FIG. 52.66 Renal Cell Carcinoma. Eleven-year-old girl with prior history of medulloblastoma. Renal tumor detected incidentally during surveillance imaging. **(A)** Longitudinal gray-scale image reveals a round mass in the renal sinus *(arrows)* that contains multiple tiny calcifications. **(B)** Longitudinal color Doppler image shows peripheral displacement of the renal hilar vessels around the mass.

there is decreased sonographic differentiation between the cortex and medulla.[215,216]

Longitudinal and transverse images of the adrenal gland are best obtained with a high-frequency convex or sector transducer. From the transverse images of the gland, AP and transverse dimensions are measured. From the longitudinal images, the cephalocaudal length is measured from the apex to the midpoint of the base of the gland (Fig. 52.71).

If there is renal agenesis or ectopia, the neonatal gland will appear flattened and "lying down" along the psoas muscle on

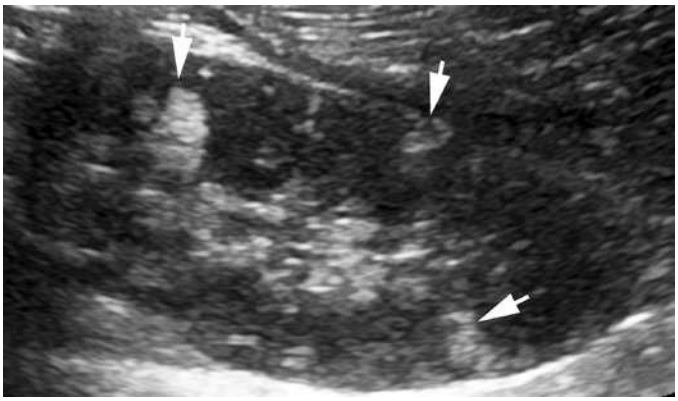

FIG. 52.67 Angiomyolipomas. Twelve-year-old boy with **tuberous sclerosis.** Longitudinal gray-scale image demonstrates multiple hyperechoic masses in keeping with angiomyolipoma *(arrows).*

longitudinal sonograms, the so-called "lying down" adrenal sign[217] (see Fig. 52.12).

In the older child and teenager, the adrenal gland is not easily depicted by ultrasound, and other imaging modalities are preferable for evaluation.

Congenital Adrenal Hyperplasia

Congenital adrenal hyperplasia (CAH) is an inherited form of adrenal insufficiency caused by autosomal recessive mutation of genes that encode the production of enzymes involved in the corticosteroid synthetic pathway. There is impaired synthesis of cortisol by the adrenal cortex that results in an excessive accumulation of androgenic precursors and adrenal gland enlargement. The majority of cases are caused by a mutation of the *CYP21A2* gene that leads to a deficiency of the 21-hydroxylase enzyme. Infants may have salt-wasting, virilization of the external genitalia in girls, and precocious puberty in boys.[218]

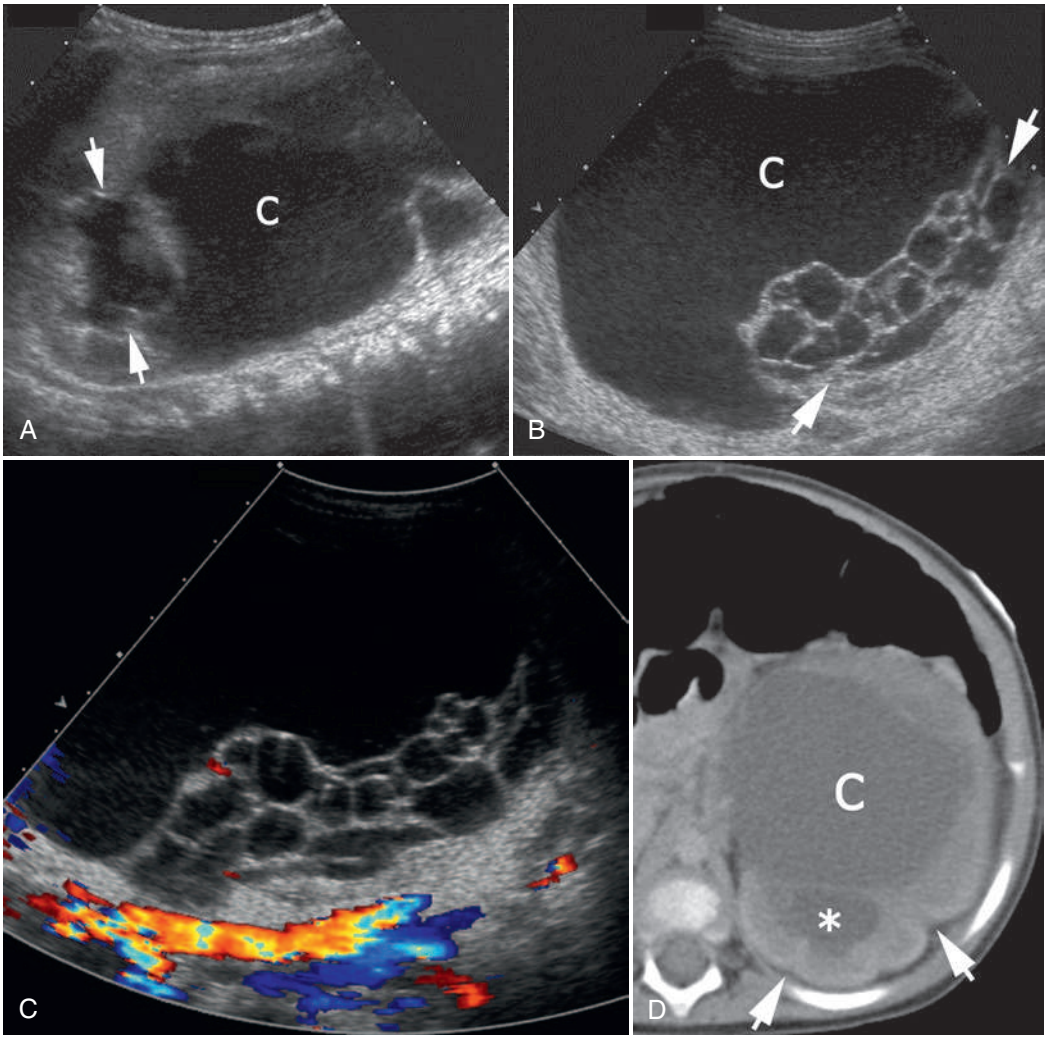

FIG. 52.68 Multilocular Cystic Nephroma. A 10-month-old boy with large abdominal mass. **(A)** Longitudinal gray-scale image depicts a large cyst *(C)* arising from the left kidney. The upper-pole calyces are dilated *(arrows)* secondary to obstruction by the cyst. **(B)** Longitudinal gray-scale image reveals complex nature of the lesion with the large central cyst *(C)* and multiple smaller mural cysts *(arrows).* **(C)** Longitudinal color Doppler image confirms the cystic, avascular nature of the lesion. **(D)** Axial intravenous contrast-enhanced computed tomography image reveals cyst (C) surrounded by compressed renal parenchyma *(arrows)* and dilated posterior calyces (*).

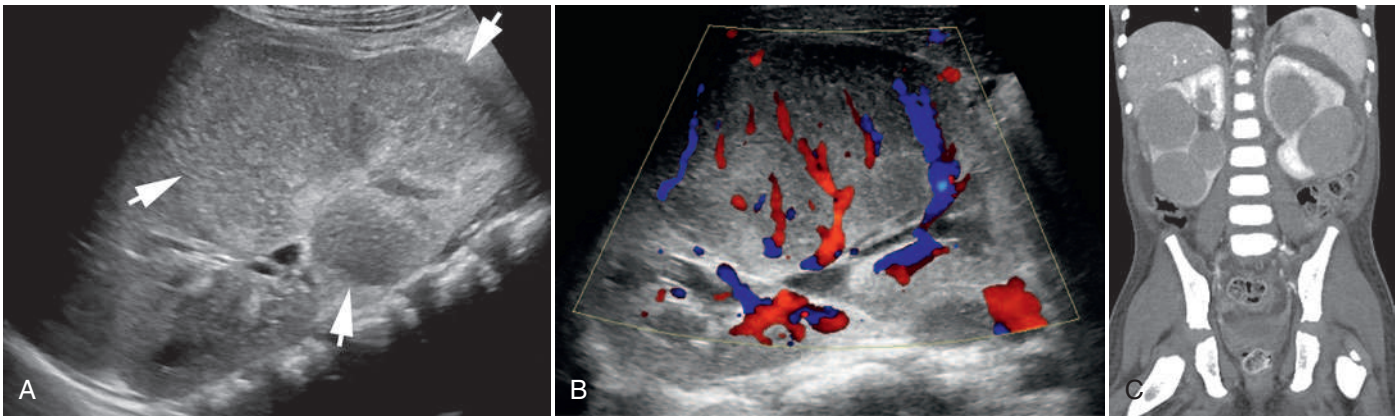

FIG. 52.69 Renal Lymphoma. A 4-year-old boy with **Burkitt lymphoma and secondary involvement of the kidneys. (A)** Longitudinal gray-scale image demonstrates several rounded, echogenic masses in the middle and lower portions of the right kidney *(arrows)*. **(B)** Longitudinal color Doppler image of the right kidney depicts prominent blood flow within one of the masses. **(C)** Coronal intravenous contrast-enhanced image shows multiple hypoenhancing masses of both kidneys. See also Video 52.8.

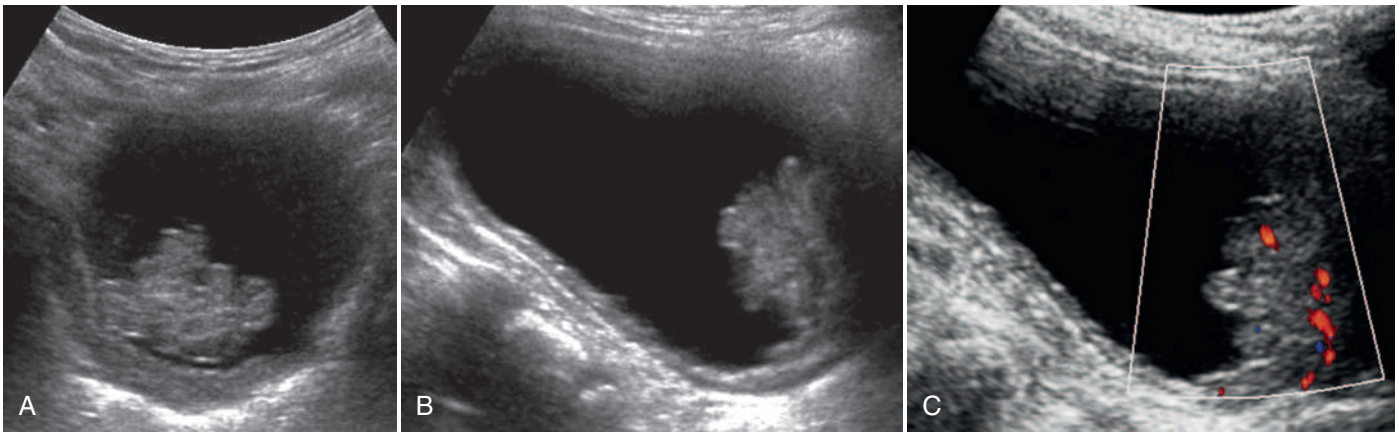

FIG. 52.70 Bladder Rhabdomyosarcoma. An 18-month-old boy with urinary tract infection (UTI). **(A)** and **(B)** Transverse and longitudinal gray-scale images reveal a lobulated, soft tissue mass containing small calcifications arising from the trigone of the bladder. **(C)** Longitudinal color Doppler image depicts blood vessels within the tumor.

TABLE 52.10 Adrenal Measurements in Neonates: Mean ± SD (Mean Percentage Change ± SD)

Day	Transverse	Anteroposterior	Circumference	Area (cm^2)	Length
1	17.0 ± 2.7	9.6 ± 2.1	44.5 ± 5.3	1.3 ± 0.3	17.3 ± 1.8
3	14.8 ± 3.3	7.5 ± 2.2	36.7 ± 8.4	0.95 ± 0.5	12.8 ± 3.2
	(84.0 ± 19.9)	(78.6 ± 16.9)	(82.4 ± 16.3)	(68.3 ± 24.5)	(73.9 ± 18.7)
5	13.7 ± 2.1	6.9 ± 1.6	33.4 ± 5.1	0.75 ± 0.2	11.4 ± 2.7
	(77.5 ± 11.3)	(62.0 ± 20.6)	(65.2 ± 19.4)	(44.5 ± 29.2)	(51.9 ± 12.6)
11	11.8 ± 2.5	5.9 ± 1.4	28.6 ± 6.1	0.57 ± 0.3	8.9 ± 2.0
	(67.4 ± 17.2)	(62.0 ± 20.6)	(65.2 ± 19.4)	(44.5 ± 19.4)	(51.9 ± 12.6)
21	10.8 ± 1.9	5.6 ± 0.5	25.3 ± 3.9	0.45 ± 0.1	8.2 ± 1.2
	(61.5 ± 13.4)	(61.1 ± 16.3)	(57.8 ± 11.3)	(35.7 ± 13.7)	(47.9 ± 8.0)
42	9.5 ± 1.5	5.7 ± 1.0	23.8 ± 2.8	0.4 ± 0.1	7.7 ± 0.9
	(53.9 ± 11.6)	(61.3 ± 14.8)	(54.4 ± 10.4)	(32.5 ± 11.5)	(45.0 ± 6.4)

SD, Standard deviation.

With permission from Scott EM, Thomas A, McGarrigle HH, Lachelin GC. Serial adrenal ultrasonongraphy in normal neonates. J Ultrasound Med 1990; 9:279-283.[215]

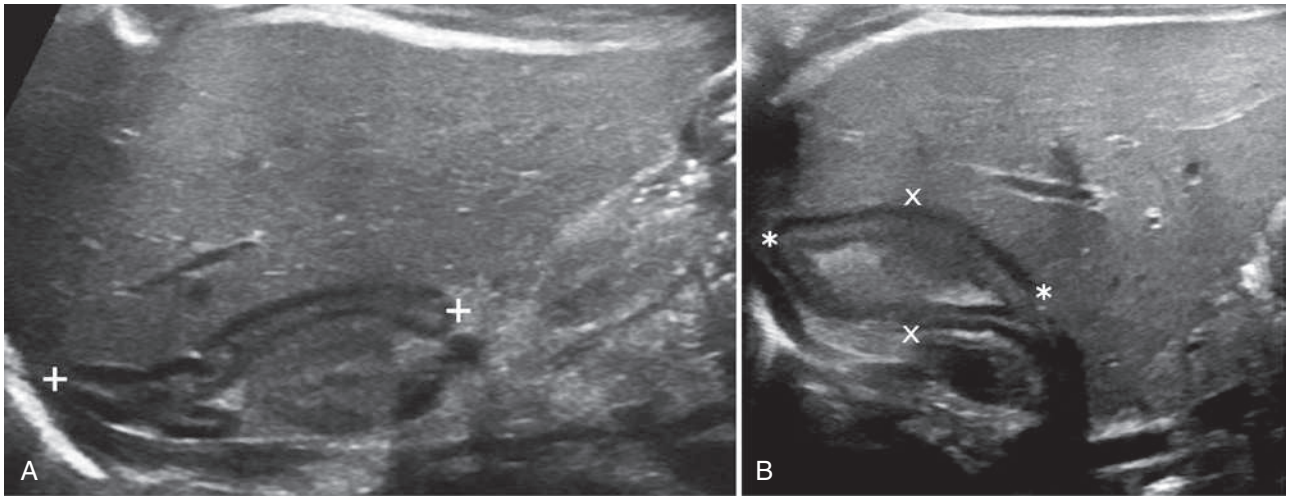

FIG. 52.71 Normal Neonatal Adrenal Gland. (A) and **(B)** Longitudinal and transverse gray-scale images of the right adrenal gland show a Y-shaped configuration with a hypoechoic rim representing the fetal adrenal cortex and a central echogenic adrenal medulla. +, Length; *, width; x, thickness.

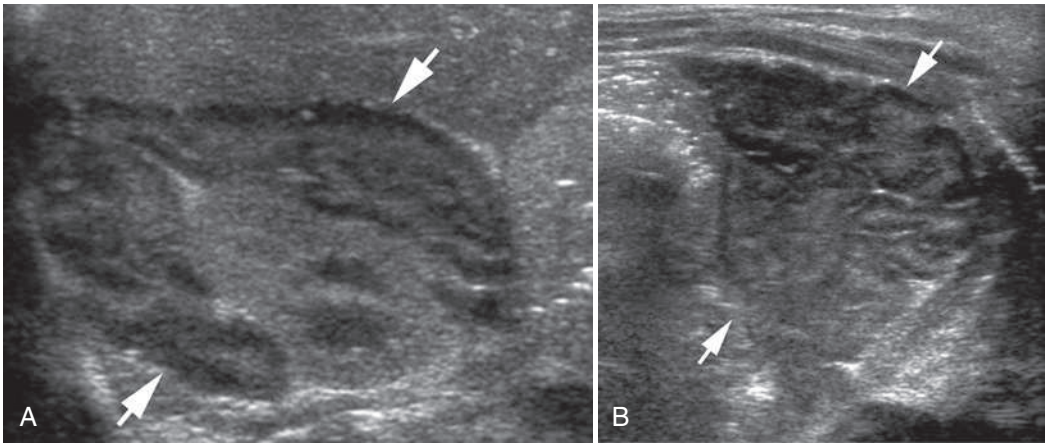

FIG. 52.72 Congenital Adrenal Hyperplasia. Neonate With Ambiguous Genitalia. (A) and **(B)** Transverse images of the right and left adrenals, respectively, reveal enlarged glands with a cerebriform appearance *(arrows)*.

CAH causes bilateral adrenal gland enlargement, which may be asymmetrical. An adrenal gland limb thicker than 4 mm is considered enlarged, even in the neonatal period.[219] However, adrenal gland enlargement alone is not sensitive or specific for the diagnosis of CAH. A normal-sized adrenal gland does not exclude the diagnosis of CAH, and some healthy babies have adrenal glands in the size range typical of CAH.[219] Specific features in the evaluation of the adrenal glands can make ultrasound a sensitive and specific presumptive test for CAH pending the results of laboratory studies. These include a cerebriform appearance of the gland[220] (Fig. 52.72) and stippled echoes, or diffusely increased central glandular echogenicity[221] rather than the normal central echogenic stripe. Pelvic sonography is extremely valuable in the evaluation of female infants with suspected CAH and if there are ambiguous genitalia. Although the external genitalia are masculinized, the internal female genitalia are present. In neonates, the presence of the uterus is exceptionally well demonstrated because of the normal maternal hormones that stimulate development of a prominent echogenic endometrial stripe in the uterine cavity.

Testicular adrenal rest tumors are very common, particularly in postpubertal boys with poorly controlled **congenital adrenal hyperplasia.** These tumors are small, generally multiple, and often bilateral. The involved testis may be enlarged, but its contour is not distorted. The masses are eccentric and commonly surround the mediastinum testis.[222,223]

Neonatal Adrenal Hemorrhage

Hemorrhage into the adrenal gland occurs in the neonate and may even start in utero. It is associated with fetal macrosomia, fetal acidemia, stress, birth trauma, asphyxia, sepsis, bleeding disorders, and maternal diabetes.[224] It occurs most frequently between the second and seventh day of life, with an abdominal mass, hyperbilirubinemia, and occasionally, hypovolemic shock. In some cases, the hemorrhage is asymptomatic and may be discovered incidentally or appear as a palpable mass. About 70% of adrenal hemorrhages are right-sided.[225] Sonography demonstrates a suprarenal mass of variable echogenicity, depending on the age of the bleed. Acute hemorrhage usually appears echogenic or isoechoic to the normal gland, without internal vascularity

on color Doppler imaging. Over several weeks, the hemorrhage becomes anechoic, reflecting blood clot lysis and liquefaction (Fig. 52.73). The hemorrhage gradually decreases in size and may result in adrenal calcification. Differentiation from a neonatal neuroblastoma is important.[226] Follow-up demonstrating a progressive decrease in size and eventual resolution confirms the diagnosis of an adrenal hemorrhage.

Neuroblastoma

Neuroblastoma is the most common extracranial solid tumor of childhood. It arises from neural crest tissue and represents the malignant end of a spectrum of related tumors that includes the **benign ganglioneuroma** and **ganglioneuroblastoma,** an intermediate-grade neoplasm with mixed histology. Neuroblastoma may demonstrate spontaneous regression from an undifferentiated state to a totally benign appearance. It is classified into three risk categories: low, intermediate, and high risk. Low-risk disease is common in infants and good outcomes frequently occur with observation or surgery. High-risk disease is very difficult to treat successfully, even with intensive, multimodal therapy.[227] Neuroblastoma is associated with the **Beckwith-Wiedemann syndrome, Hirschsprung disease, neurofibromatosis type 1, DiGeorge syndrome,** and **central hypoventilation syndrome.**[228]

Two-thirds of the time, neuroblastoma develops in the abdomen, with approximately two-thirds of the tumors arising from the adrenal gland. The remainder may develop anywhere along the sympathetic nerve chain.[229] In the majority of children with neuroblastoma the disease is found between 1 and 5 years of age, with the most common age at presentation being 18 months. Boys and girls are equally affected.[230]

At sonography, adrenal neuroblastoma is heterogeneous in echotexture, with irregular, hyperechoic areas caused by calcification. Its margins tend to be poorly defined. Extension of tumor around the aorta and celiac and superior mesenteric arteries helps to distinguish neuroblastoma from Wilms tumor, which is usually well defined and relatively homogeneous in echotexture (Fig. 52.74, Video 52.9). Sonography needs to be followed by CT or MRI for disease staging. MRI is particularly useful because the tumor can extend into the spinal canal and cause neurologic symptoms. It is critical to know if this extension has occurred before the tumor is surgically removed because the child may

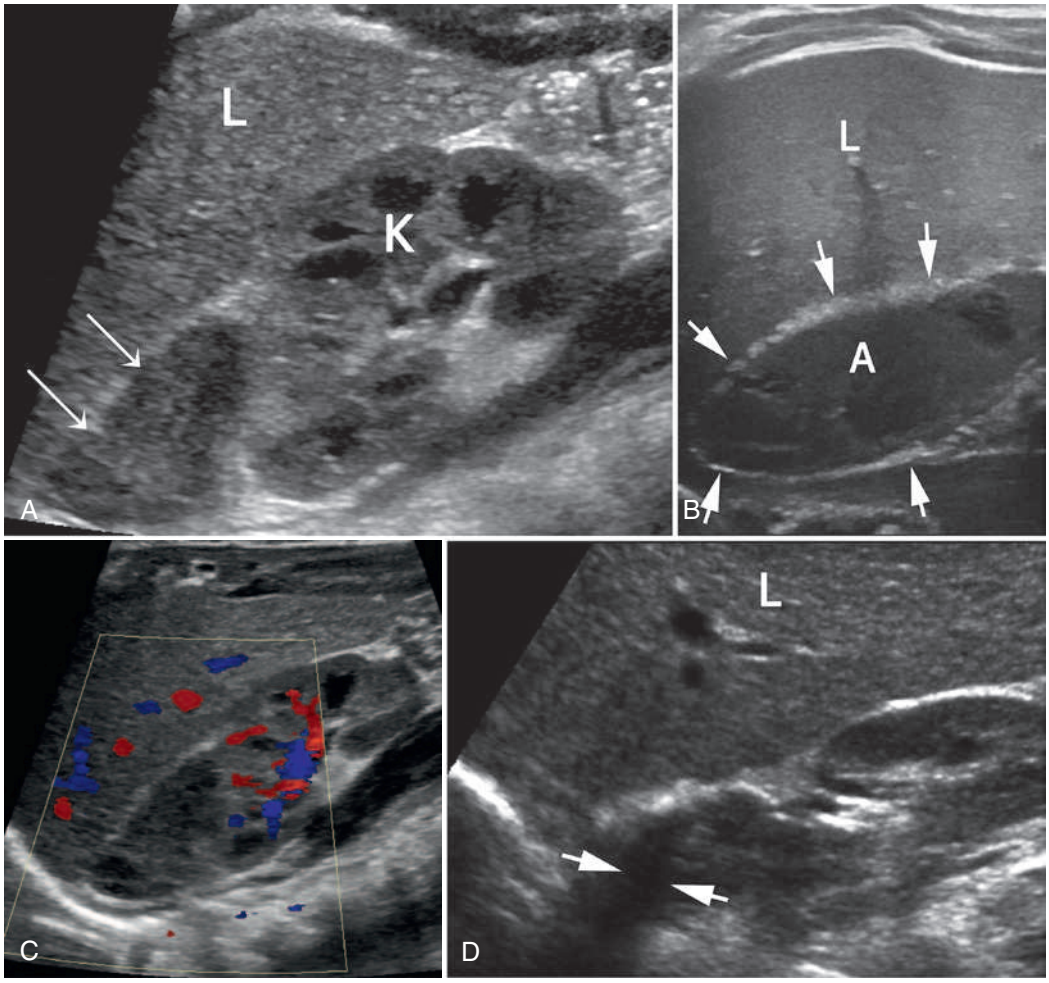

FIG. 52.73 Neonatal Adrenal Hemorrhage. (A) and **(B)** Longitudinal gray-scale images of the right flank demonstrate a suprarenal hypoechoic "mass." The overall shape of the adrenal gland is preserved and there is peripheral calcification *(arrows). A,* Adrenal; *K,* kidney; *L,* liver. **(C)** Longitudinal color Doppler image demonstrates the avascular nature of the adrenal lesion. **(D)** Longitudinal gray-scale image 18 months later reveals complete involution of the "mass" and replacement by dense calcification with distal shadowing *(arrows),* typical of a resolved hemorrhage.

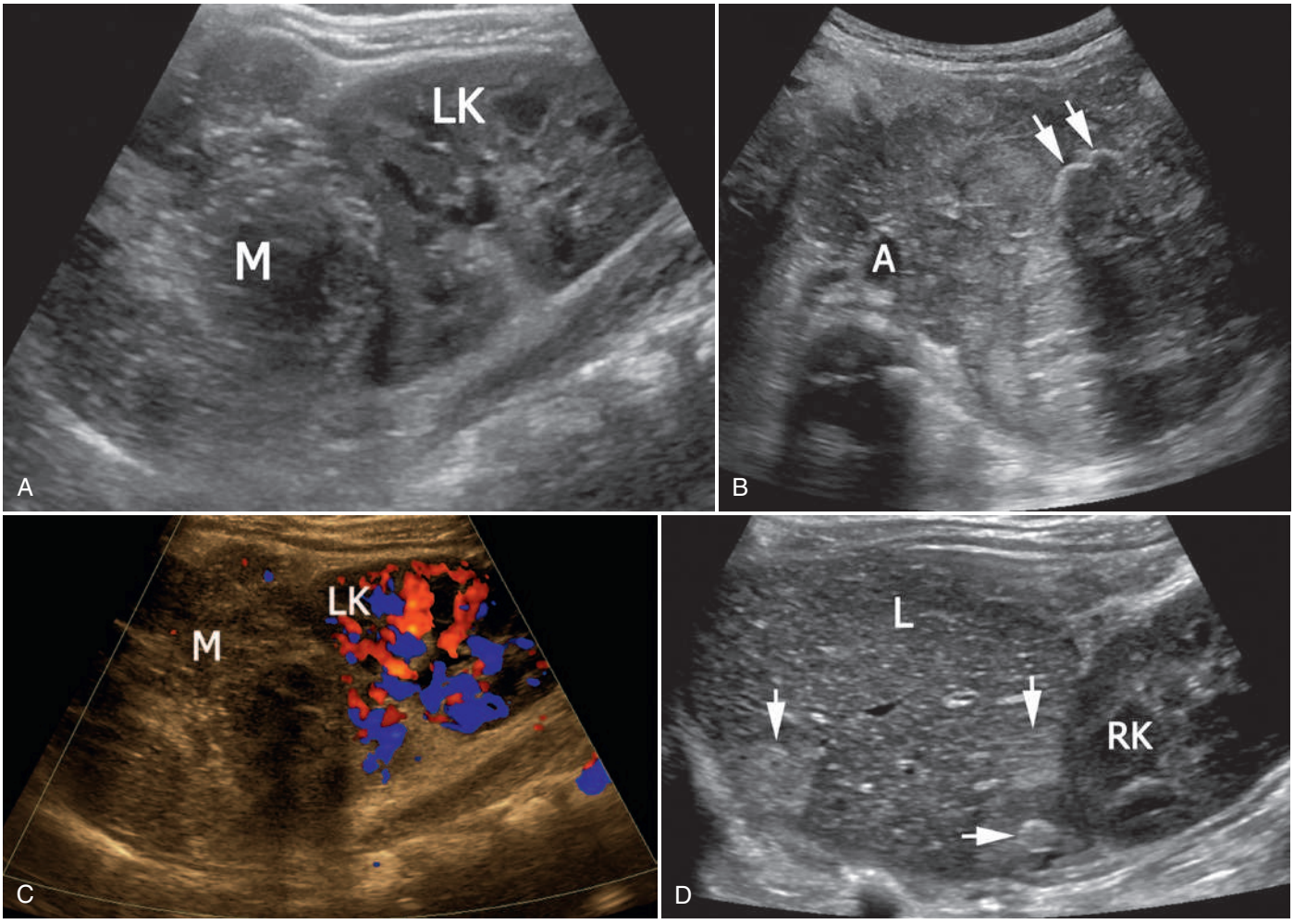

FIG. 52.74 Neuroblastoma in 4-Month-Old Boy With Stage IV Disease. (A) Longitudinal gray-scale image demonstrates a heterogeneous, lobulated mass arising from the left adrenal gland *(M)* and compressing the upper pole of the left kidney *(LK)*. **(B)** Transverse gray-scale image depicts the mass crossing the midline and encasing the aorta *(A)*. The mass contains calcifications with associated distal shadowing *(arrows)*. **(C)** Longitudinal color Doppler image shows hypovascularity of the mass *(M)* compared with the underlying left kidney *(LK)*. **(D)** Longitudinal gray-scale image of the liver *(L)* depicts three hyperechoic metastatic deposits *(arrows)*. *RK,* Right kidney. See also Video 52.9.

develop neurologic symptoms postoperatively, including paralysis, if the tumor is not carefully resected.

Pheochromocytoma

According to the World Health Organization classification of endocrine tumors, a pheochromocytoma is an intraadrenal paraganglioma arising from catecholamine-producing chromaffin cells in the adrenal medulla.[231,232] These tumors may occur sporadically, or as a component of a hereditary tumor syndrome, including **von Hippel–Lindau disease, multiple endocrine neoplasia** (MEN) types IIA and IIB, and the **familial paraganglioma syndromes.** Rarer associations include **neurofibromatosis type 1, MEN type I, tuberous sclerosis complex,** and **Carney triad.**[231,233]

About 56% of apparently sporadic pheochromocytomas in children 18 years of age or younger are caused by a mutation in the germline DNA, and the percentage of children younger than 10 years of age with hereditary disease is as high as 70%.[234] Hereditary pheochromocytoma is often bilateral and is more common in children than adults.[235,236]

Pheochromocytoma in children usually is discovered as a result of catecholamine hypersecretion, because of tumor mass effect, as an incidental finding at imaging, or after family screening for one of the hereditary syndromes. Signs and symptoms suggestive of pheochromocytoma include sustained hypertension, paroxysmal episodes of headache, palpitations and diaphoresis, pallor, orthostatic hypotension and syncope, tremor, and anxiety.[231] Quantification of plasma free metanephrine and normetanephrine, or measurement of 24-hour urinary fractionated metanephrines are the most accurate biochemical tests used for diagnosis of pheochromocytoma in adults. Although fewer studies have been performed in children, metanephrine quantification is thought to be a superior method in this population as well.[237]

At sonography, a pheochromocytoma will appear as a solid, highly vascular, round or oval mass of variable echogenicity.[225]

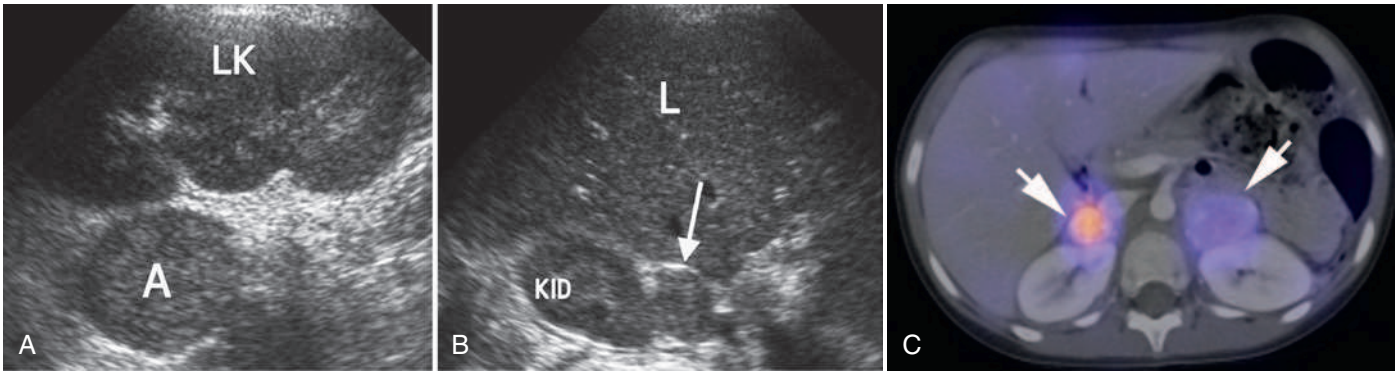

FIG. 52.75 Pheochromocytoma in 6-Year-Old Boy With von Hippel-Lindau Syndrome and Bilateral Adrenal Pheochromocytoma. (A) Longitudinal gray-scale image of the left flank reveals the presence of a solid, round adrenal mass *(A)* medial to the left kidney *(LK)*. **(B)** Transverse gray-scale image demonstrates a solid, rounded mass *(arrow)* medial to the right kidney *(KID)*. *L,* Liver. **(C)** Iodine-123 metaiodobenzylguanidine (MIBG) image fused to an intravenous axial contrast-enhanced computed tomography image depicts the bilateral adrenal tumors *(arrows)*. The right-sided mass shows greater radiopharmaceutical uptake than the left-sided mass.

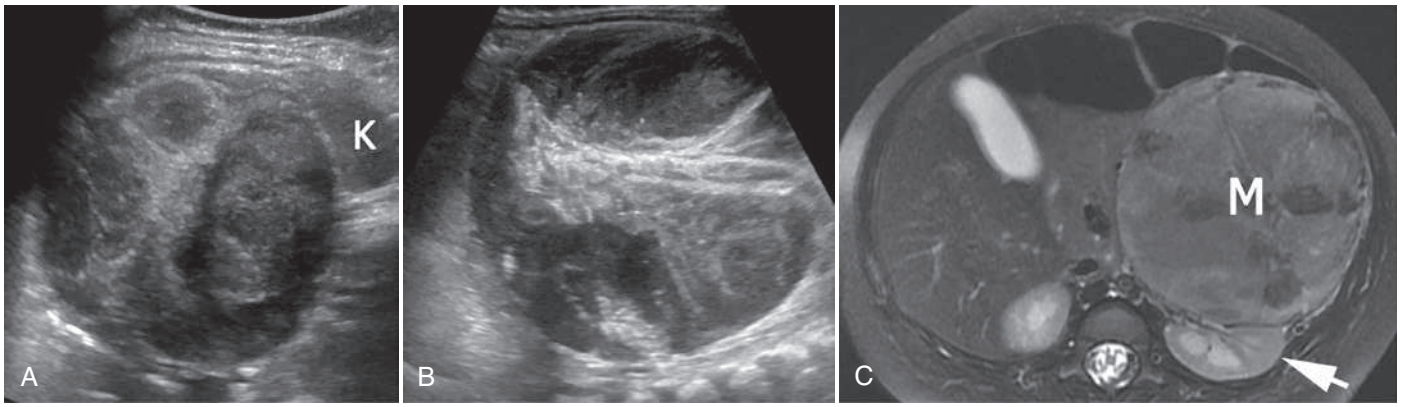

FIG. 52.76 Adrenal Carcinoma in 8-Month-Old Girl With Virilization and Precocious Puberty. (A) and **(B)** Transverse and longitudinal gray-scale images of the left flank demonstrate a large, round, heterogeneous mass replacing the adrenal gland. *K,* Left kidney. **(C)** Intravenous contrast-enhanced axial computed tomography image shows the left adrenal mass *(M)* displacing and rotating the left kidney *(arrow)*.

Masses generally range from 2 to 5 cm in diameter at presentation, although they may exceed 10 cm. Larger lesions tend to be heterogeneous as a result of hemorrhage, necrosis, and/or calcification (Fig. 52.75). Cross-sectional imaging of the abdomen and pelvis with CT or MRI is performed for surgical planning. Functional imaging with ^{123}I-labeled metaiodobenzylguanidine (MIBG) is a highly specific test that can confirm the catecholamine-secreting nature of a tumor, localize tumors not seen with cross-sectional imaging, and identify other sites of disease. Because MIBG testing is not 100% sensitive, additional nuclear medicine imaging tests may need to be performed. Chest CT is performed in patients with suspected lung metastases.[238]

Adrenocortical Neoplasm

Primary tumors of the adrenal cortex are rare in children, with an incidence of 0.3 to 0.4 cases per million per year before the age of 15 years.[239] Because reliable histologic differentiation between cortical adenomas and carcinomas in children may be difficult, the inclusive term "adrenocortical neoplasm" is often used.[240] Most tumors develop before 5 years of age, with a female predominance, although the sex ratio is equal in adolescence. In contrast to adults, most pediatric adrenocortical neoplasms are hormonally active. The presence of increased hormone levels is useful both for initial diagnosis and in the detection of tumor recurrence. Androgen overproduction leads to virilization in girls and precocious puberty in boys; most tumors also cause an overproduction of mineralocorticoids.[238] Although the majority of affected children will not have an underlying disorder, there is a known association with **Beckwith-Wiedemann syndrome** and **Li-Fraumeni syndrome.**[238]

Tumors larger than 5 to 10 cm in diameter; a tumor weight greater than 200 g; and aggressive growth features such as invasion into the periadrenal soft tissues, kidneys, and/or inferior vena cava (IVC) suggest malignancy. Small lesions tend to be homogeneous, whereas larger lesions often contain foci of hemorrhage, necrosis, or calcification.[241] **Adrenal carcinoma** in an 8-month-old girl with virilization and precocious puberty is typical of these rare lesions (Fig. 52.76). Metastases occur most often to the liver, lung, and bone.[238] Sonography is particularly helpful in the detection of tumor invasion into the IVC. Cross-sectional imaging with CT and MRI is used for more precise delineation.

REFERENCES

1. Kadioglu A. Renal measurements, including length, parenchymal thickness, and medullary pyramid thickness, in healthy children: what are the normative ultrasound values? AJR Am J Roentgenol. 2010;194(2):509-515.
2. Leung VY, Chu WC, Yeung CK, et al. Nomograms of total renal volume, urinary bladder volume and bladder wall thickness index in 3,376 children with a normal urinary tract. Pediatr Radiol. 2007;37(2):181-188.
3. Vujic A, Kosutic J, Bogdanovic R, et al. Sonographic assessment of normal kidney dimensions in the first year of life—a study of 992 healthy infants. Pediatr Nephrol. 2007;22(8):1143-1150.
4. Schmidt IM, Main KM, Damgaard IN, et al. Kidney growth in 717 healthy children aged 0-18 months: a longitudinal cohort study. Pediatr Nephrol. 2004;19(9):992-1003.
5. Han BK, Babcock DS. Sonographic measurements and appearance of normal kidneys in children. AJR Am J Roentgenol. 1985;145(3):611-616.
6. Rosenbaum DM, Korngold E, Teele RL. Sonographic assessment of renal length in normal children. AJR Am J Roentgenol. 1984;142(3):467-469.
7. Krill A, Salami S, Rosen L, et al. Evaluating compensatory hypertrophy: a growth curve specific for solitary functioning kidneys. J Urol. 2012;188 (4 Suppl.):1613-1617.
8. Spira EM, Jacobi C, Frankenschmidt A, et al. Sonographic long-term study: paediatric growth charts for single kidneys. Arch Dis Child. 2009;94(9): 693-698.
9. Schmidt IM, Chellakooty M, Boisen KA, et al. Impaired kidney growth in low-birth-weight children: distinct effects of maturity and weight for gestational age. Kidney Int. 2005;68(2):731-740.
10. Chiara A, Chirico G, Barbarini M, et al. Ultrasonic evaluation of kidney volume in term and preterm infants. Am J Perinatol. 1993;10(2):109-111.
11. Chiara A, Chirico G, Barbarini M, et al. Ultrasonic evaluation of kidney length in term and preterm infants. Eur J Pediatr. 1989;149(2):94-95.
12. Schlesinger AE, Hedlund GL, Pierson WP, Null DM. Normal standards for kidney length in premature infants: determination with US. Work in progress. Radiology. 1987;164(1):127-129.
13. Kuzmic AC, Brkljacic B, Ivankovic D. The impact of bladder shape on the ultrasonographic measurement of bladder volume in children. Pediatr Radiol. 2003;33(8):530-534.
14. Hvarness H, Skjoldbye B, Jakobsen H. Urinary bladder volume measurements: comparison of three ultrasound calculation methods. Scand J Urol Nephrol. 2002;36(3):177-181.
15. Uluocak N, Erdemir F, Parlaktas BS, et al. Bladder wall thickness in healthy school-aged children. Urology. 2007;69(4):763-766.
16. Jequier S, Rousseau O. Sonographic measurements of the normal bladder wall in children. AJR Am J Roentgenol. 1987;149(3):563-566.
17. Burge HJ, Middleton WD, McClennan BL, Hildebolt CF. Ureteral jets in healthy subjects and in patients with unilateral ureteral calculi: comparison with color Doppler US. Radiology. 1991;180(2):437-442.
18. Jequier S, Paltiel H, Lafortune M. Ureterovesical jets in infants and children: duplex and color Doppler US studies. Radiology. 1990;175(2):349-353.
19. Patriquin H, Lefaivre JF, Lafortune M, et al. Fetal lobation. An anatomo-ultrasonographic correlation. J Ultrasound Med. 1990;9(4):191-197.
20. Currarino G. Lowichik A. The Oddono's sulcus and its relation to the renal "junctional parenchymal defect" and the "interrenicular septum." Pediatr Radiol. 1997;27(1):6-10.
21. Vade A, Lau P, Smick J, et al. Sonographic renal parameters as related to age. Pediatr Radiol. 1987;17(3):212-215.
22. Hricak H, Slovis TL, Callen CW, et al. Neonatal kidneys: sonographic anatomic correlation. Radiology. 1983;147(3):699-702.
23. Bisset 3rd GS, Strife JL. The duplex collecting system in girls with urinary tract infection: prevalence and significance. AJR Am J Roentgenol. 1987;148(3):497-500.
24. Mackie GG, Awang H, Stephens FD. The ureteric orifice: the embryologic key to radiologic status of duplex kidneys. J Pediatr Surg. 1975;10(4): 473-481.
25. Schaffer RM, Shih YH, Becker JA. Sonographic identification of collecting system duplications. J Clin Ultrasound. 1983;11(6):309-312.
26. Decter RM. Renal duplication and fusion anomalies. Pediatr Clin North Am. 1997;44(5):1323-1341.
27. McDonald JH, McClellan DS. Crossed renal ectopia. Am J Surg. 1957;93(6):995-1002.
28. Glodny B, Petersen J, Hofmann KJ, et al. Kidney fusion anomalies revisited: clinical and radiological analysis of 209 cases of crossed fused ectopia and horseshoe kidney. BJU Int. 2009;103(2):224-235.
29. Riccabona M. Potential of modern sonographic techniques in paediatric uroradiology. Eur J Radiol. 2002;43(2):110-121.
30. Rossleigh MA. Renal cortical scintigraphy and diuresis renography in infants and children. J Nucl Med. 2001;42(1):91-95.
31. Barbosa JA, Chow JS, Benson CB, et al. Postnatal longitudinal evaluation of children diagnosed with prenatal hydronephrosis: insights in natural history and referral pattern. Prenat Diagn. 2012;32(13):1242-1249.
32. Vandervoort K, Lasky S, Sethna C, et al. Hydronephrosis in infants and children: natural history and risk factors for persistence in children followed by a medical service. Clin Med Pediatr. 2009;3:63-70.
33. Pohl HG, Belman AB. Congenital anomalies of the urinary tract. Curr Pediatr Rev. 2014;10(2):123-132.
34. Abdulnour HA, Williams JL, Kairalla JA, Garin EH. Does hydronephrosis predict the presence of severe vesicoureteral reflux? Eur J Pediatr. 2012;171(11):1605-1610.
35. Chow JS, Darge K. Multidisciplinary consensus on the classification of antenatal and postnatal urinary tract dilation (UTD classification system). Pediatr Radiol. 2015;45(6):787-789.
36. Nguyen HT, Benson CB, Bromley B, et al. Multidisciplinary consensus on the classification of prenatal and postnatal urinary tract dilation (UTD classification system). J Pediatr Urol. 2014;10(6):982-998.
37. Arena E, Nicotina PA, Arena S, et al. Interstitial cells of Cajal network in primary obstructive megaureter. Pediatr Med Chir. 2007;29(1):28-31.
38. Payabvash S, Kajbafzadeh AM, Tavangar SM, et al. Myocyte apoptosis in primary obstructive megaureters: the role of decreased vascular and neural supply. J Urol. 2007;178(1):259-264.
39. Berrocal T, Lopez-Pereira P, Arjonilla A, Gutierrez J. Anomalies of the distal ureter, bladder, and urethra in children: embryologic, radiologic, and pathologic features. Radiographics. 2002;22(5):1139-1164.
40. Jandaghi AB, Falahatkar S, Alizadeh A, et al. Assessment of ureterovesical jet dynamics in obstructed ureter by urinary stone with color Doppler and duplex Doppler examinations. Urolithiasis. 2013;41(2):159-163.
41. Summers RM, Adler RS, Fowlkes JB, Rubin JM. Laminar submerged jets by color Doppler ultrasound. A model of the ureteral jet phenomenon. Invest Radiol. 1992;27(12):1044-1051.
42. Duran C, Valera A, Alguersuari A, et al. Voiding urosonography: the study of the urethra is no longer a limitation of the technique. Pediatr Radiol. 2009;39(2):124-131.
43. Mate A, Bargiela A, Mosteiro S, et al. Contrast ultrasound of the urethra in children. Eur Radiol. 2003;13(7):1534-1537.
44. Fotter R. Neurogenic bladder in infants and children—a new challenge for the radiologist. Abdom Imaging. 1996;21(6):534-540.
45. Huppmann AR, Pawel BR. Polyps and masses of the pediatric urinary bladder: a 21-year pathology review. Pediatr Dev Pathol. 2011;14(6): 438-444.
46. Darge K. Voiding urosonography with US contrast agent for the diagnosis of vesicoureteric reflux in children: an update. Pediatr Radiol. 2010;40(6): 956-962.
47. Colleran GC, Barnewolt CE, Chow JS, Paltiel HJ. Intrarenal reflux: diagnosis at contrast-enhanced voiding urosonography. J Ultrasound Med. 2016;35(8):1811-1819.
48. Atala A, Ellsworth P, Share J, et al. Comparison of sonicated albumin enhanced sonography to fluoroscopic and radionuclide voiding cystography for detecting vesicoureteral reflux. J Urol. 1998;160(5):1820-1822.
49. Lebowitz RL, Olbing H, Parkkulainen KV, et al. International system of radiographic grading of vesicoureteric reflux. International Reflux Study in Children. Pediatr Radiol. 1985;15(2):105-109.
50. Cerwinka WH, Kaye JD, Scherz HC, et al. Radiologic features of implants after endoscopic treatment of vesicoureteral reflux in children. AJR Am J Roentgenol. 2010;195(1):234-240.
51. Gargollo PC, Paltiel HJ, Rosoklija I, Diamond DA. Mound calcification after endoscopic treatment of vesicoureteral reflux with autologous

chondrocytes—a normal variant of mound appearance? J Urol. 2009;181(6):2702-2707.
52. Paltiel HJ, Diamond DA, Zurakowski D, et al. Endoscopic treatment of vesicoureteral reflux with autologous chondrocytes: postoperative sonographic features. Radiology. 2004;232(2):390-397.
53. Jennings RW. Prune belly syndrome. Semin Pediatr Surg. 2000;9(3):115-120.
54. Osborne NG, Bonilla-Musoles F, Machado LE, et al. Fetal megacystis: differential diagnosis. J Ultrasound Med. 2011;30(6):833-841.
55. Ballisty MM, Braithwaite KA, Shehata BM, Dickson PN. Imaging findings in megacystis-microcolon–intestinal hypoperistalsis syndrome. Pediatr Radiol. 2013;43(4):454-459.
56. Loinaz C, Rodriguez MM, Kato T, et al. Intestinal and multivisceral transplantation in children with severe gastrointestinal dysmotility. J Pediatr Surg. 2005;40(10):1598-1604.
57. Pierre K, Borer J, Phelps A, Chow JS. Bladder exstrophy: current management and postoperative imaging. Pediatr Radiol. 2014;44(7):768-786.
58. Gearhart J, Mathews R. Exstrophy-epispadias complex. In: Wein AJ, Kavoussi LR, Partin AW, Peters CA, editors. Campbell-Walsh urology. 11th ed. Philadelphia: Elsevier; 2016. p. 3182-3233.
59. Breen M, Phelps A, Estrada C, Chow JS. The role of imaging in pediatric bladder augmentation. Pediatr Radiol. 2015;45(10):1440-1447.
60. Yu JS, Kim KW, Lee HJ, et al. Urachal remnant diseases: spectrum of CT and US findings. Radiographics. 2001;21(2):451-461.
61. Gleason JM, Bowlin PR, Bagli DJ, et al. A comprehensive review of pediatric urachal anomalies and predictive analysis for adult urachal adenocarcinoma. J Urol. 2015;193(2):632-636.
62. Subcommittee on Urinary Tract Infection, Steering Committee on Quality Improvement and Management, Roberts KB. Urinary tract infection: clinical practice guideline for the diagnosis and management of the initial UTI in febrile infants and children 2 to 24 months. Pediatrics. 2011;128(3):595-610.
63. Shulkin BL, Mandell GA, Cooper JA, et al. Procedure guideline for diuretic renography in children 3.0. J Nucl Med Technol. 2008;36(3):162-168.
64. Brader P, Riccabona M, Schwarz T, et al. Value of comprehensive renal ultrasound in children with acute urinary tract infection for assessment of renal involvement: comparison with DMSA scintigraphy and final diagnosis. Eur Radiol. 2008;18(12):2981-2989.
65. Stogianni A, Nikolopoulos P, Oikonomou I, et al. Childhood acute pyelonephritis: comparison of power Doppler sonography and Tc-DMSA scintigraphy. Pediatr Radiol. 2007;37(7):685-690.
66. Karmazyn B, Coley B, Binkovitz L, et al. ACR Appropriateness Criteria: urinary tract infection—child. [online publication]. Reston, VA: American College of Radiology (ACR); 2016. Available from: https://acsearch.acr.org/docs/69444/Narrative. Accessed February 26, 2017.
67. Lebowitz RL, Mandell J. Urinary tract infection in children: putting radiology in its place. Radiology. 1987;165(1):1-9.
68. Jequier S, Forbes PA, Nogrady MB. The value of ultrasonography as a screening procedure in a first-documented urinary tract infection in children. J Ultrasound Med. 1985;4(8):393-400.
69. Mason Jr WG. Urinary tract infections in children: renal ultrasound evaluation. Radiology. 1984;153(1):109-111.
70. Morello W, La Scola C, Alberici I, Montini G. Acute pyelonephritis in children. Pediatr Nephrol. 2016;31(8):1253-1265.
71. Montini G, Tullus K, Hewitt I. Febrile urinary tract infections in children. N Engl J Med. 2011;365(3):239-250.
72. Dacher JN, Hitzel A, Avni FE, Vera P. Imaging strategies in pediatric urinary tract infection. Eur Radiol. 2005;15(7):1283-1288.
73. Paterson A. Urinary tract infection: an update on imaging strategies. Eur Radiol. 2004;14(Suppl. 4):L89-L100.
74. Mitterberger M, Pinggera GM, Colleselli D, et al. Acute pyelonephritis: comparison of diagnosis with computed tomography and contrast-enhanced ultrasonography. BJU Int. 2008;101(3):341-344.
75. Sheu JN. Acute lobar nephronia in children. Pediatr Neonatol. 2015;56(3):141-142.
76. Bisht V, Voort JV. Clinical practice: obstructive renal candidiasis in infancy. Eur J Pediatr. 2011;170(10):1227-1235.
77. McCarville MB, Hoffer FA, Gingrich JR, Jenkins 3rd JJ. Imaging findings of hemorrhagic cystitis in pediatric oncology patients. Pediatr Radiol. 2000;30(3):131-138.
78. Snow A, Estrada C, Chow J. Ultrasonography of the pediatric bladder. Ultrasound Clin. 2013;8(3):423-439.
79. Quaia E, Bertolotto M. Renal parenchymal diseases: is characterization feasible with ultrasound? Eur Radiol. 2002;12(8):2006-2020.
80. Paltiel H. Renal failure and transplantation. In: Coley BD, editor. Caffey's pediatric diagnostic imaging. 12th ed. Philadelphia.: Elsevier; 2013. p. 1236-1241.
81. Andreoli S. Clinical evaluation of acute kidney injury in children. In: Avner ED, editor. Pediatric nephrology. 6th ed. Berlin: Springer-Verlag; 2009.
82. National Kidney Foundation. Definition and classification of stages of chronic kidney disease. Am J Kidney Dis. 2002;39(2 Suppl. 1):S46-S74.
83. Sugiura T, Wada A. Resistive index predicts renal prognosis in chronic kidney disease: results of a 4-year follow-up. Clin Exp Nephrol. 2011;15(1):114-120.
84. Dyer RB, Chen MY, Zagoria RJ. Abnormal calcifications in the urinary tract. Radiographics. 1998;18(6):1405-1424.
85. Wells R. Acquired abnormalities (stone disease and infection). In: Coley BD, editor. Caffey's pediatric diagnostic imaging. 12th ed. Philadelphia.: Elsevier; 2013. p. 1209-1217.
86. Bedard M, Wildman S, Dillman J. Embryology, anatomy, and variants of the genitourinary tract. In: Coley BD, editor. Caffey's pediatric diagnostic imaging. 12th ed. Philadelphia: Elsevier Saunders; 2013.
87. Patriquin H, Robitaille P. Renal calcium deposition in children: sonographic demonstration of the Anderson-Carr progression. AJR Am J Roentgenol. 1986;146(6):1253-1256.
88. Patriquin H, Lafortune M, Filiatrault D. Urinary milk of calcium in children and adults: use of gravity-dependent sonography. AJR Am J Roentgenol. 1985;144(2):407-413.
89. Elsaify WM. Neonatal renal vein thrombosis: grey-scale and Doppler ultrasonic features. Abdom Imaging. 2009;34(3):413-418.
90. Routh JC, Graham DA, Nelson CP. Trends in imaging and surgical management of pediatric urolithiasis at American pediatric hospitals. J Urol. 2010;184(4 Suppl.):1816-1822.
91. Tasian GE, Copelovitch L. Evaluation and medical management of kidney stones in children. J Urol. 2014;192(5):1329-1336.
92. Sas DJ. An update on the changing epidemiology and metabolic risk factors in pediatric kidney stone disease. Clin J Am Soc Nephrol. 2011;6(8):2062-2068.
93. Hernandez JD, Ellison JS, Lendvay TS. Current trends, evaluation, and management of pediatric nephrolithiasis. JAMA Pediatr. 2015;169(10):964-970.
94. Smith-Bindman R, Aubin C, Bailitz J, et al. Ultrasonography versus computed tomography for suspected nephrolithiasis. N Engl J Med. 2014;371(12):1100-1110.
95. Kraus SJ, Lebowitz RL, Royal SA. Renal calculi in children: imaging features that lead to diagnoses: a pictorial essay. Pediatr Radiol. 1999;29(8):624-630.
96. Tchelepi H, Ralls PW. Color comet-tail artifact: clinical applications. AJR Am J Roentgenol. 2009;192(1):11-18.
97. Brown SL, Elder JS, Spirnak JP. Are pediatric patients more susceptible to major renal injury from blunt trauma? A comparative study. J Urol. 1998;160(1):138-140.
98. Taylor GA, Eichelberger MR, Potter BM. Hematuria. A marker of abdominal injury in children after blunt trauma. Ann Surg. 1988;208(6):688-693.
99. Gaines BA. Intra-abdominal solid organ injury in children: diagnosis and treatment. J Trauma. 2009;67(2 Suppl.):S135-S139.
100. American College of Radiology. ACR–ASER–SCBT-MR–SPR practice parameter for the performance of pediatric computed tomography (CT). 2014. Available from: https://www.acr.org/~/media/ACR/Documents/PGTS/guidelines/CT_Pediatric.pdf. Accessed March 1, 2017.
101. Bennett MK, Jehle D. Ultrasonography in blunt abdominal trauma. Emerg Med Clin North Am. 1997;15(4):763-787.
102. Menichini G, Sessa B, Trinci M, et al. Accuracy of contrast-enhanced ultrasound (CEUS) in the identification and characterization of traumatic

solid organ lesions in children: a retrospective comparison with baseline US and CE-MDCT. Radiol Med. 2015;120(11):989-1001.
103. Valentino M, Serra C, Pavlica P, et al. Blunt abdominal trauma: diagnostic performance of contrast-enhanced US in children—initial experience. Radiology. 2008;246(3):903-909.
104. Burns P. Interpreting and analyzing the Doppler examination. In: Taylor K, Burns P, Wells P, editors. Clinical applications of Doppler ultrasound. New York: Raven; 1995. p. 55-98.
105. Chavhan GB, Parra DA, Mann A, Navarro OM. Normal Doppler spectral waveforms of major pediatric vessels: specific patterns. Radiographics. 2008;28(3):691-706.
106. Bude RO, DiPietro MA, Platt JF, et al. Age dependency of the renal resistive index in healthy children. Radiology. 1992;184(2):469-473.
107. Brandenburg VM, Frank RD, Riehl J. Color-coded duplex sonography study of arteriovenous fistulae and pseudoaneurysms complicating percutaneous renal allograft biopsy. Clin Nephrol. 2002;58(6):398-404.
108. Kraft JK, Brandao LR, Navarro OM. Sonography of renal venous thrombosis in neonates and infants: can we predict outcome? Pediatr Radiol. 2011; 41(3):299-307.
109. Tullus K, Brennan E, Hamilton G, et al. Renovascular hypertension in children. Lancet. 2008;371(9622):1453-1463.
110. Batisky DL. Neonatal hypertension. Clin Perinatol. 2014;41(3):529-542.
111. Tullus K. Renovascular hypertension—is it fibromuscular dysplasia or Takayasu arteritis? Pediatr Nephrol. 2013;28(2):191-196.
112. Wells R. Vascular conditions. In: Coley BD, editor. Caffey's pediatric diagnostic imaging. 2nd ed. Philadelphia: Elsevier Saunders; 2013.
113. Vo NJ, Hammelman BD, Racadio JM, et al. Anatomic distribution of renal artery stenosis in children: implications for imaging. Pediatr Radiol. 2006;36(10):1032-1036.
114. Stavros AT, Parker SH, Yakes WF, et al. Segmental stenosis of the renal artery: pattern recognition of tardus and parvus abnormalities with duplex sonography. Radiology. 1992;184(2):487-492.
115. Patriquin HB, Lafortune M, Jequier JC, et al. Stenosis of the renal artery: assessment of slowed systole in the downstream circulation with Doppler sonography. Radiology. 1992;184(2):479-485.
116. Tarr PI, Gordon CA, Chandler WL. Shiga-toxin–producing *Escherichia coli* and haemolytic uraemic syndrome. Lancet. 2005;365(9464):1073-1086.
117. Tsai HM. Untying the knot of thrombotic thrombocytopenic purpura and atypical hemolytic uremic syndrome. Am J Med. 2013;126(3):200-209.
118. Patriquin HB, O'Regan S, Robitaille P, Paltiel H. Hemolytic-uremic syndrome: intrarenal arterial Doppler patterns as a useful guide to therapy. Radiology. 1989;172(3):625-628.
119. Gulati A, Sarwal MM. Pediatric renal transplantation: an overview and update. Curr Opin Pediatr. 2010;22(2):189-196.
120. Shapiro R, Sarwal MM. Pediatric kidney transplantation. Pediatr Clin North Am. 2010;57(2):393-400. table of contents.
121. Herz DB, McLorie GA, Hafez AT, et al. High resolution ultrasound characterization of early allograft hemodynamics in pediatric living related renal transplantation. J Urol. 2001;166(5):1853-1858.
122. Zeisbrich M, Kihm LP, Druschler F, et al. When is contrast-enhanced sonography preferable over conventional ultrasound combined with Doppler imaging in renal transplantation? Clin Kidney J. 2015;8(5):606-614.
123. Harvey CJ, Alsafi A, Kuzmich S, et al. Role of US contrast agents in the assessment of indeterminate solid and cystic lesions in native and transplant kidneys. Radiographics. 2015;35(5):1419-1430.
124. Irtan S, Maisin A, Baudouin V, et al. Renal transplantation in children: critical analysis of age related surgical complications. Pediatr Transplant. 2010;14(4):512-519.
125. Shokeir AA, Osman Y, Ali-El-Dein B, et al. Surgical complications in live-donor pediatric and adolescent renal transplantation: study of risk factors. Pediatr Transplant. 2005;9(1):33-38.
126. Singh A, Stablein D, Tejani A. Risk factors for vascular thrombosis in pediatric renal transplantation: a special report of the North American Pediatric Renal Transplant Cooperative Study. Transplantation. 1997;63(9): 1263-1267.
127. Smith JM, Stablein D, Singh A, et al. Decreased risk of renal allograft thrombosis associated with interleukin-2 receptor antagonists: a report of the NAPRTCS. Am J Transplant. 2006;6(3):585-588.
128. van Lieburg AF, de Jong MC, Hoitsma AJ, et al. Renal transplant thrombosis in children. J Pediatr Surg. 1995;30(4):615-619.
129. Sheldon CA, Churchill BM, Khoury AE, McLorie GA. Complications of surgical significance in pediatric renal transplantation. J Pediatr Surg. 1992;27(4):485-490.
130. Nixon JN, Biyyam DR, Stanescu L, et al. Imaging of pediatric renal transplants and their complications: a pictorial review. Radiographics. 2013;33(5): 1227-1251.
131. Irshad A, Ackerman SJ, Campbell AS, Anis M. An overview of renal transplantation: current practice and use of ultrasound. Semin Ultrasound CT MR. 2009;30(4):298-314.
132. Ponticelli C, Moia M, Montagnino G. Renal allograft thrombosis. Nephrol Dial Transplant. 2009;24(5):1388-1393.
133. Stringer DA, O'Halpin D, Daneman A, et al. Duplex Doppler sonography for renal artery stenosis in the post-transplant pediatric patient. Pediatr Radiol. 1989;19(3):187-192.
134. Dodd 3rd GD, Tublin ME, Shah A, Zajko AB. Imaging of vascular complications associated with renal transplants. AJR Am J Roentgenol. 1991;157(3):449-459.
135. de Morais RH, Muglia VF, Mamere AE, et al. Duplex Doppler sonography of transplant renal artery stenosis. J Clin Ultrasound. 2003;31(3): 135-141.
136. Loubeyre P, Abidi H, Cahen R, Tran Minh VA. Transplanted renal artery: detection of stenosis with color Doppler US. Radiology. 1997;203(3): 661-665.
137. Merkus JW, Hoitsma AJ, van Asten WN, et al. Echo-Doppler diagnosis of renal allograft artery stenosis. Clin Transplant. 1995;9(5):383-389.
138. Baxter G. Renal transplantation. In: Clinical ultrasound. 3rd ed. Edinburgh (United Kingdom): Churchill Livingstone; 2011. p. 528-549.
139. Patel U, Khaw KK, Hughes NC. Doppler ultrasound for detection of renal transplant artery stenosis-threshold peak systolic velocity needs to be higher in a low-risk or surveillance population. Clin Radiol. 2003;58(10): 772-777.
140. Cook A, Khoury A, Kader K, et al. Does peak systolic velocity correlate with renal artery stenosis in a pediatric renal transplant population? Pediatr Transplant. 2006;10(5):608-612.
141. Surratt JT, Siegel MJ, Middleton WD. Sonography of complications in pediatric renal allografts. Radiographics. 1990;10(4):687-699.
142. McGuire M, Phelps A, Paltiel H. Pediatric visceral transplantation. Ultrasound Clin. 2008;8(3):375-401.
143. Schwarz A, Hiss M, Gwinner W, et al. Course and relevance of arteriovenous fistulas after renal transplant biopsies. Am J Transplant. 2008;8(4): 826-831.
144. Stanescu AL, Hryhorczuk AL, Chang PT, et al. Pediatric abdominal organ transplantation: current indications, techniques, and imaging findings. Radiol Clin North Am. 2016;54(2):281-302.
145. Horslen S, Barr ML, Christensen LL, et al. Pediatric transplantation in the United States, 1996–2005. Am J Transplant. 2007;7(5 Pt 2):1339-1358.
146. North American Pediatric Renal Trials and Collaborative Studies. NAPRTCS 2010 annual transplant report. Rockville, Md: North American Pediatric Renal Trials and Collaborative Studies; 2010.
147. Smith JM, Ho PL, McDonald RA. North American Pediatric Renal Transplant Cooperative Study. Renal transplant outcomes in adolescents: a report of the North American Pediatric Renal Transplant Cooperative Study. Pediatr Transplant. 2002;6(6):493-499.
148. Rossi V, Torino G, Gerocarni Nappo S, et al. Urological complications following kidney transplantation in pediatric age: a single-center experience. Pediatr Transplant. 2016;20(4):485-491.
149. Sierralta MC, Gonzalez G, Nome C, et al. Kidney transplant in pediatric patients with severe bladder pathology. Pediatr Transplant. 2015;19(7): 675-683.
150. Aki FT, Aydin AM, Dogan HS, et al. Does lower urinary tract status affect renal transplantation outcomes in children? Transplant Proc. 2015;47(4):1114-1116.
151. Englesbe MJ, Lynch RJ, Heidt DG, et al. Early urologic complications after pediatric renal transplant: a single-center experience. Transplantation. 2008;86(11):1560-1564.

152. Torricelli FC, Watanabe A, Piovesan AC, et al. Urological complications, vesicoureteral reflux, and long-term graft survival rate after pediatric kidney transplantation. Pediatr Transplant. 2015;19(8):844-848.
153. Akbar SA, Jafri SZ, Amendola MA, et al. Complications of renal transplantation. Radiographics. 2005;25(5):1335-1356.
154. Chu L, Jacobs BL, Schwen Z, Schneck FX. Hydronephrosis in pediatric kidney transplant: clinical relevance to graft outcome. J Pediatr Urol. 2013;9(2):217-222.
155. Ranchin B, Chapuis F, Dawhara M, et al. Vesicoureteral reflux after kidney transplantation in children. Nephrol Dial Transplant. 2000;15(11): 1852-1858.
156. Fontana I, Ginevri F, Arcuri V, et al. Vesico-ureteral reflux in pediatric kidney transplants: clinical relevance to graft and patient outcome. Pediatr Transplant. 1999;3(3):206-209.
157. Routh JC, Yu RN, Kozinn SI, et al. Urological complications and vesicoureteral reflux following pediatric kidney transplantation. J Urol. 2013;189(3): 1071-1076.
158. Barrero R, Fijo J, Fernandez-Hurtado M, et al. Vesicoureteral reflux after kidney transplantation in children. Pediatr Transplant. 2007;11(5): 498-503.
159. Esezobor CI, Nourse P, Gajjar P. Urinary tract infection following kidney transplantation: frequency, risk factors and graft function. Pediatr Nephrol. 2012;27(4):651-657.
160. Neuhaus TJ, Schwobel M, Schlumpf R, et al. Pyelonephritis and vesicoureteral reflux after renal transplantation in young children. J Urol. 1997;157(4): 1400-1403.
161. Stuck KJ, Jafri SZ, Adler DD, et al. Ultrasound evaluation of uncommon renal transplant complications. Urol Radiol. 1986;8(1):6-12.
162. Sutherland T, Temple F, Chang S, et al. Sonographic evaluation of renal transplant complications. J Med Imaging Radiat Oncol. 2010;54(3): 211-218.
163. Harel Z, Perl J, Herzenberg AM, Bargman JM. Inflammatory pseudotumor of the kidney allograft. Am J Kidney Dis. 2009;54(3):533-537.
164. Cramer MT, Guay-Woodford LM. Cystic kidney disease: a primer. Adv Chronic Kidney Dis. 2015;22(4):297-305.
165. Onuchic LF, Furu L, Nagasawa Y, et al. *PKHD1,* the polycystic kidney and hepatic disease 1 gene, encodes a novel large protein containing multiple immunoglobulin-like plexin-transcription-factor domains and parallel beta-helix 1 repeats. Am J Hum Genet. 2002;70(5):1305-1317.
166. Hartung EA, Guay-Woodford LM. Autosomal recessive polycystic kidney disease: a hepatorenal fibrocystic disorder with pleiotropic effects. Pediatrics. 2014;134(3):e833-e845.
167. Bergmann C, Senderek J, Windelen E, et al. Clinical consequences of PKHD1 mutations in 164 patients with autosomal-recessive polycystic kidney disease (ARPKD). Kidney Int. 2005;67(3):829-848.
168. Guay-Woodford LM, Desmond RA. Autosomal recessive polycystic kidney disease: the clinical experience in North America. Pediatrics. 2003;111(5 Pt 1):1072-1080.
169. Traubici J, Daneman A. High-resolution renal sonography in children with autosomal recessive polycystic kidney disease. AJR Am J Roentgenol. 2005;184(5):1630-1633.
170. Sweeney Jr WE, Avner ED. Diagnosis and management of childhood polycystic kidney disease. Pediatr Nephrol. 2011;26(5):675-692.
171. Sedman A, Bell P, Manco-Johnson M, et al. Autosomal dominant polycystic kidney disease in childhood: a longitudinal study. Kidney Int. 1987;31(4):1000-1005.
172. Yee J. Autosomal dominant polycystic disease: more than just empty space. Adv Chronic Kidney Dis. 2010;17(2):113-114.
173. Gunay-Aygun M. Liver and kidney disease in ciliopathies. Am J Med Genet C Semin Med Genet. 2009;151C(4):296-306.
174. Ravine D, Gibson RN, Walker RG, et al. Evaluation of ultrasonographic diagnostic criteria for autosomal dominant polycystic kidney disease 1. Lancet. 1994;343(8901):824-827.
175. Bergmann C. Educational paper: ciliopathies. Eur J Pediatr. 2012;171(9): 1285-1300.
176. Gabow PA, Kimberling WJ, Strain JD, et al. Utility of ultrasonography in the diagnosis of autosomal dominant polycystic kidney disease in children. J Am Soc Nephrol. 1997;8(1):105-110.
177. Tee JB, Acott PD, McLellan DH, Crocker JF. Phenotypic heterogeneity in pediatric autosomal dominant polycystic kidney disease at first presentation: a single-center, 20-year review. Am J Kidney Dis. 2004;43(2):296-303.
178. O'Neill WC, Robbin ML, Bae KT, et al. Sonographic assessment of the severity and progression of autosomal dominant polycystic kidney disease: the Consortium of Renal Imaging Studies in Polycystic Kidney Disease (CRISP). Am J Kidney Dis. 2005;46(6):1058-1064.
179. Brun M, Maugey-Laulom B, Eurin D, et al. Prenatal sonographic patterns in autosomal dominant polycystic kidney disease: a multicenter study. Ultrasound Obstet Gynecol. 2004;24(1):55-61.
180. Avni FE, Guissard G, Hall M, et al. Hereditary polycystic kidney diseases in children: changing sonographic patterns through childhood. Pediatr Radiol. 2002;32(3):169-174.
181. Loftus H, Ong AC. Cystic kidney diseases: many ways to form a cyst. Pediatr Nephrol. 2013;28(1):33-49.
182. Hains DS, Bates CM, Ingraham S, Schwaderer AL. Management and etiology of the unilateral multicystic dysplastic kidney: a review. Pediatr Nephrol. 2009;24(2):233-241.
183. Mackie GG, Stephens FD. Duplex kidneys: a correlation of renal dysplasia with position of the ureteral orifice. J Urol. 1975;114(2):274-280.
184. Batourina E, Tsai S, Lambert S, et al. Apoptosis induced by vitamin A signaling is crucial for connecting the ureters to the bladder. Nat Genet. 2005;37(10):1082-1089.
185. Viana R, Batourina E, Huang H, et al. The development of the bladder trigone, the center of the anti-reflux mechanism. Development. 2007;134(20): 3763-3769.
186. Rudnik-Schoneborn S, John U, Deget F, et al. Clinical features of unilateral multicystic renal dysplasia in children. Eur J Pediatr. 1998;157(8): 666-672.
187. Roach PJ, Paltiel HJ, Perez-Atayde A, et al. Renal dysplasia in infants: appearance on 99mTc DMSA scintigraphy. Pediatr Radiol. 1995;25(6): 472-475.
188. Han JH, Lee YS, Kim MJ, et al. Conservative management of segmental multicystic dysplastic kidney in children. Urology. 2015;86(5):1013-1018.
189. Eickmeyer AB, Casanova NF, He C, et al. The natural history of the multicystic dysplastic kidney—is limited follow-up warranted? J Pediatr Urol. 2014;10(4):655-661.
190. Hildebrandt F, Otto E. Cilia and centrosomes: a unifying pathogenic concept for cystic kidney disease? Nat Rev Genet. 2005;6(12):928-940.
191. Tory K, Rousset-Rouviere C, Gubler MC, et al. Mutations of NPHP2 and NPHP3 in infantile nephronophthisis. Kidney Int. 2009;75(8):839-847.
192. Wolf MT, Hildebrandt F. Nephronophthisis. Pediatr Nephrol. 2011; 26(2):181-194.
193. Wood 3rd CG, Stromberg 3rd LJ, Harmath CB, et al. CT and MR imaging for evaluation of cystic renal lesions and diseases. Radiographics. 2015;35(1):125-141.
194. Choyke PL. Acquired cystic kidney disease. Eur Radiol. 2000;10(11): 1716-1721.
195. Querfeld U, Schneble F, Wradzidlo W, et al. Acquired cystic kidney disease before and after renal transplantation. J Pediatr. 1992;121(1):61-64.
196. Calvo-Garcia MA, Campbell KM, O'Hara SM, et al. Acquired renal cysts after pediatric liver transplantation: association with cyclosporine and renal dysfunction. Pediatr Transplant. 2008;12(6):666-671.
197. Franchi-Abella S, Mourier O, Pariente D, et al. Acquired renal cystic disease after liver transplantation in children. Transplant Proc. 2007;39(8): 2601-2602.
198. Bayram MT, Alaygut D, Soylu A, et al. Clinical and radiological course of simple renal cysts in children. Urology. 2014;83(2):433-437.
199. Siegel M. Urinary tract. In: Siegel MJ, editor. Pediatric sonography. 4th ed. Lippincott Williams & Wilkins; 2011. p. 384-460.
200. Malkan AD, Loh A, Bahrami A, et al. An approach to renal masses in pediatrics. Pediatrics. 2015;135(1):142-158.
201. Gee MS, Bittman M, Epelman M, et al. Magnetic resonance imaging of the pediatric kidney: benign and malignant masses. Magn Reson Imaging Clin N Am. 2013;21(4):697-715.
202. Geller E, Kochan PS. Renal neoplasms of childhood. Radiol Clin North Am. 2011;49(4):689-709, vi.

203. Chaudry G, Perez-Atayde AR, Ngan BY, et al. Imaging of congenital mesoblastic nephroma with pathological correlation. Pediatr Radiol. 2009;39(10):1080-1086.
204. Young EE, Brown CT, Merguerian PA, Akhavan A. Pediatric and adolescent renal cell carcinoma. Urol Oncol. 2016;34(1):42-49.
205. Renshaw AA, Granter SR, Fletcher JA, et al. Renal cell carcinomas in children and young adults: increased incidence of papillary architecture and unique subtypes. Am J Surg Pathol. 1999;23(7):795-802.
206. O'Callaghan FJ, Noakes MJ, Martyn CN, Osborne JP. An epidemiological study of renal pathology in tuberous sclerosis complex. BJU Int. 2004;94(6):853-857.
207. Casper KA, Donnelly LF, Chen B, Bissler JJ. Tuberous sclerosis complex: renal imaging findings. Radiology. 2002;225(2):451-456.
208. Granja MF, O'Brien AT, Trujillo S, et al. Multilocular Cystic nephroma: a systematic literature review of the radiologic and clinical findings. AJR Am J Roentgenol. 2015;205(6):1188-1193.
209. Karmazyn B, Tawadros A, Delaney LR, et al. Ultrasound classification of solitary renal cysts in children. J Pediatr Urol. 2015;11(3):149 e1-149 e6.
210. Boybeyi O, Karnak I, Orhan D, et al. Cystic nephroma and localized renal cystic disease in children: diagnostic clues and management. J Pediatr Surg. 2008;43(11):1985-1989.
211. Ganeshan D, Iyer R, Devine C, et al. Imaging of primary and secondary renal lymphoma. AJR Am J Roentgenol. 2013;201(5):W712-W719.
212. Sheth S, Ali S, Fishman E. Imaging of renal lymphoma: patterns of disease with pathologic correlation. Radiographics. 2006;26(4):1151-1168.
213. Shah RU, Lawrence C, Fickenscher KA, et al. Imaging of pediatric pelvic neoplasms. Radiol Clin North Am. 2011;49(4):729-748.
214. Defoor W, Minevich E, Sheldon C. Unusual bladder masses in children. Urology. 2002;60(5):911.
215. Scott EM, Thomas A, McGarrigle HH, Lachelin GC. Serial adrenal ultrasonography in normal neonates. J Ultrasound Med. 1990;9(5):279-283.
216. Oppenheimer DA, Carroll BA, Yousem S. Sonography of the normal neonatal adrenal gland. Radiology. 1983;146(1):157-160.
217. Hoffman CK, Filly RA, Callen PW. The "lying down" adrenal sign: a sonographic indicator of renal agenesis or ectopia in fetuses and neonates. J Ultrasound Med. 1992;11(10):533-536.
218. Chung EM, Biko DM, Schroeder JW, et al. From the radiologic pathology archives: precocious puberty: radiologic-pathologic correlation. Radiographics. 2012;32(7):2071-2099.
219. Al-Alwan I, Navarro O, Daneman D, Daneman A. Clinical utility of adrenal ultrasonography in the diagnosis of congenital adrenal hyperplasia. J Pediatr. 1999;135(1):71-75.
220. Avni EF, Rypens F, Smet MH, Galetty E. Sonographic demonstration of congenital adrenal hyperplasia in the neonate: the cerebriform pattern. Pediatr Radiol. 1993;23(2):88-90.
221. Daneman D, Daneman A. Diagnostic imaging of the thyroid and adrenal glands in childhood. Endocrinol Metab Clin North Am. 2005;34(3):745-768, xi.
222. Claahsen-van der Grinten HL, Dehzad F, Kamphuis-van Ulzen K, de Korte CL. Increased prevalence of testicular adrenal rest tumours during adolescence in congenital adrenal hyperplasia. Horm Res Paediatr. 2014;82(4):238-244.
223. Delfino M, Elia J, Imbrogno N, et al. Testicular adrenal rest tumors in patients with congenital adrenal hyperplasia: prevalence and sonographic, hormonal, and seminal characteristics. J Ultrasound Med. 2012;31(3):383-388.
224. Gyurkovits Z, Maroti A, Renes L, et al. Adrenal haemorrhage in term neonates: a retrospective study from the period 2001–2013. J Matern Fetal Neonatal Med. 2015;28(17):2062-2065.
225. Bittman ME, Lee EY, Restrepo R, Eisenberg RL. Focal adrenal lesions in pediatric patients. AJR Am J Roentgenol. 2013;200(6):W542-W556.
226. Deeg KH, Bettendorf U, Hofmann V. Differential diagnosis of neonatal adrenal haemorrhage and congenital neuroblastoma by colour coded Doppler sonography and power Doppler sonography. Eur J Pediatr. 1998;157(4):294-297.
227. Maris JM, Hogarty MD, Bagatell R, Cohn SL. Neuroblastoma. Lancet. 2007;369(9579):2106-2120.
228. Lonergan GJ, Schwab CM, Suarez ES, Carlson CL. Neuroblastoma, ganglioneuroblastoma, and ganglioneuroma: radiologic-pathologic correlation. Radiographics. 2002;22(4):911-934.
229. Paterson A. Adrenal pathology in childhood: a spectrum of disease. Eur Radiol. 2002;12(10):2491-2508.
230. Davenport KP, Blanco FC, Sandler AD. Pediatric malignancies: neuroblastoma, Wilm's tumor, hepatoblastoma, rhabdomyosarcoma, and sacroccygeal teratoma. Surg Clin North Am. 2012;92(3):745-767.
231. Waguespack SG, Rich T, Grubbs E, et al. A current review of the etiology, diagnosis, and treatment of pediatric pheochromocytoma and paraganglioma. J Clin Endocrinol Metab. 2010;95(5):2023-2037.
232. Pacak K, Eisenhofer G, Ahlman H, et al. Pheochromocytoma: recommendations for clinical practice from the First International Symposium. October 2005. Nat Clin Pract Endocrinol Metab. 2007;3(2):92-102.
233. Carney JA. Carney triad: a syndrome featuring paraganglionic, adrenocortical, and possibly other endocrine tumors. J Clin Endocrinol Metab. 2009;94(10):3656-3662.
234. Neumann HP, Bausch B, McWhinney SR, et al. Germ-line mutations in nonsyndromic pheochromocytoma. N Engl J Med. 2002;346(19):1459-1466.
235. Barontini M, Levin G, Sanso G. Characteristics of pheochromocytoma in a 4- to 20-year-old population. Ann N Y Acad Sci. 2006;1073:30-37.
236. Beltsevich DG, Kuznetsov NS, Kazaryan AM, Lysenko MA. Pheochromocytoma surgery: epidemiologic peculiarities in children. World J Surg. 2004;28(6):592-596.
237. Havekes B, Romijn JA, Eisenhofer G, et al. Update on pediatric pheochromocytoma. Pediatr Nephrol. 2009;24(5):943-950.
238. Balassy C, Navarro OM, Daneman A. Adrenal masses in children. Radiol Clin North Am. 2011;49(4):711-727, vi.
239. Bonfig W, Bittmann I, Bechtold S, et al. Virilising adrenocortical tumours in children. Eur J Pediatr. 2003;162(9):623-628.
240. Agrons GA, Lonergan GJ, Dickey GE, Perez-Monte JE. Adrenocortical neoplasms in children: radiologic-pathologic correlation. Radiographics. 1999;19(4):989-1008.
241. Flynt KA, Dillman JR, Davenport MS, et al. Pediatric adrenocortical neoplasms: can imaging reliably discriminate adenomas from carcinomas? Pediatr Radiol. 2015;45(8):1160-1168.
242. VanDeVoorde R, Warady B. Management of chronic kidney disease. In: Avner ED, editor. Pediatric Nephrology. 6th ed. Berlin: Springer-Verlag; 2009.

CHAPTER 53

The Pediatric Gastrointestinal Tract

Susan D. John and Martha Mappus Munden

SUMMARY OF KEY POINTS

- Successful bowel ultrasound is facilitated by use of high-frequency transducers and real-time viewing of the bowel activity. Oral fluid administration and graded compression techniques help displace interfering bowel gas.
- Accurate measurement of the pyloric muscle thickness with adequate distention of the stomach with fluid is the key to correct diagnosis of hypertrophic pyloric stenosis. When the pylorus is normal, the duodenum should be examined, as well as the mesenteric vessels.
- The diagnosis of ileocolic intussusception can be made with ultrasound with a high degree of accuracy, precluding the need for a diagnostic enema when normal. Transient small bowel intussusceptions are common, have a different appearance on ultrasonography, and do not require treatment or follow-up unless very long or persistent.
- Inflammatory conditions of the small and large intestine can be easily evaluated with ultrasound. Specific features such as mucosal or transmural edema, echogenicity, and blood flow assessment with Doppler imaging can help to narrow the range of differential diagnoses and can be used to monitor therapy.
- Ultrasound findings of bowel wall thickening and pneumatosis intestinalis can help make the diagnosis of necrotizing enterocolitis when not evident on radiographs. Complex fluid in the abdomen helps to diagnose perforation in infants with a gasless abdomen.
- Ultrasound is the procedure of choice for the initial evaluation of the child with acute abdominal pain. Appendicitis can be detected in the majority of children with experience and proper technique. Secondary findings such as absent bowel peristalsis, mesenteric edema, and free or loculated fluid collections can help make the diagnosis of appendicitis, even when the appendix itself is not visible.
- Cystic abdominal masses are well seen with ultrasound and may be associated with the gastrointestinal tract. Wall characteristics and presence of internal septations, debris, calcifications, or fat can help to determine the etiology of the mass.
- Ultrasound of the pancreas in children is most helpful for identifying peripancreatic fluid collections or pseudocysts resulting from pancreatitis and detecting cystic pancreatic masses.

CHAPTER OUTLINE

ESOPHAGUS AND STOMACH
Normal Anatomy and Technique
Esophagus
Stomach
Hypertrophic Pyloric Stenosis
Pylorospasm and Minimal Muscular Hypertrophy
Pitfalls in Sonographic Diagnosis
Gastric Diaphragm
Gastritis and Ulcer Disease
Bezoar
DUODENUM AND SMALL BOWEL
Normal Anatomy and Technique
Congenital Duodenal Obstruction
Duodenal Hematoma
Small Bowel Obstruction
Intussusception
COLON
Normal Anatomy and Technique
Ectopic or Imperforate Anus
INTESTINAL INFLAMMATORY DISEASE
Appendicitis
Gastrointestinal Neoplasms and Cysts
PANCREAS
Normal Anatomy and Technique
Pancreatitis
Pancreatic Masses

ESOPHAGUS AND STOMACH

Normal Anatomy and Technique

Sonography has become an important diagnostic imaging modality in the evaluation of the gastrointestinal (GI) tract of children. Ultrasound permits direct visualization of the various mural layers of the GI tract. The ability to observe GI dynamics without exposure to ionizing radiation is an added asset of sonography. Video clips made during scanning can be a valuable resource to view peristalsis and to capture subtle abnormalities in mobile children. Ultrasound is most suitable for portions of the GI tract that are not surrounded by or filled with large amounts of gas. The stomach is best evaluated after allowing the patient to ingest clear fluids. Sugar water works well for infants.

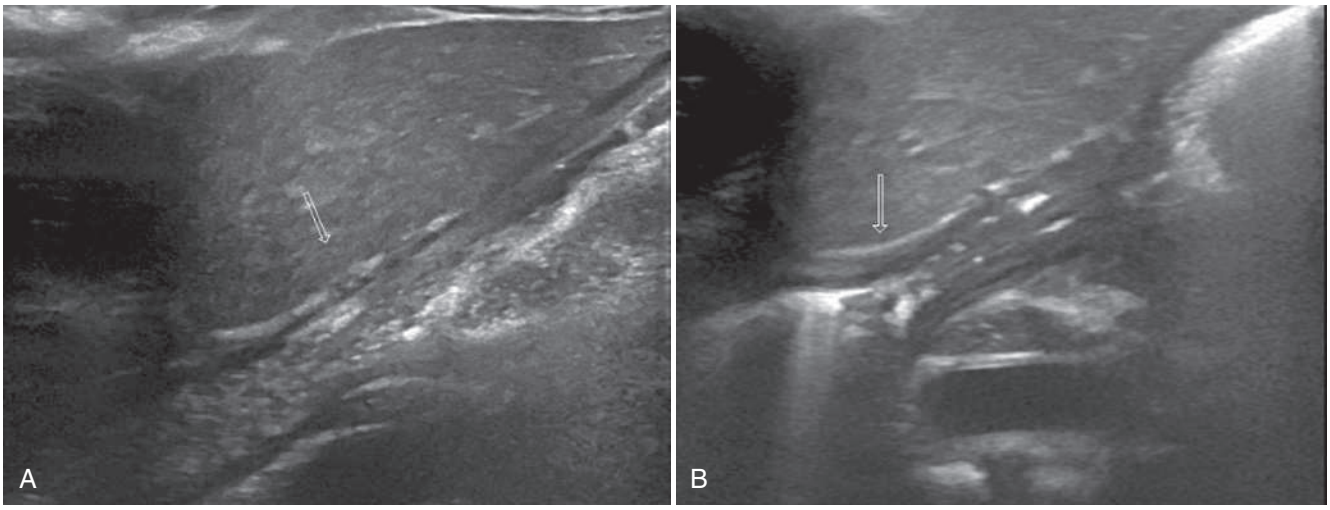

FIG. 53.1 Gastroesophageal Reflux. (A) Normal contracted gastroesophageal junction *(arrow)*. **(B)** Later, the lower esophageal sphincter opens, and reflux of fluid and formula into the esophagus is visible *(arrow)*.

Stomach: Optimal Measurements

Normal pyloric muscle thickness ≤2 mm
Normal gastric mucosa thickness ≤2-3 mm
Peristalsis through pylorus

Esophagus

Most of the esophagus is inaccessible by sonography because of surrounding aerated lung. Only the subdiaphragmatic portion of the esophagus is usually visible (Fig. 53.1A). The gastroesophageal junction can be seen by examining the patient with sagittal images in the supine or right-side-down decubitus position.[1-3] This technique permits observation of the function of the gastroesophageal junction and can be used to detect gastroesophageal reflux. Reflux is noted when fluid is regurgitated into the retrocardiac portion of the esophagus (Fig. 53.1B). Color Doppler sonography may facilitate the detection of gastroesophageal reflux.[4] **Hiatal hernias** can also be detected with sonography, which may be more sensitive than barium studies for detecting small degrees of herniation[5,6] (Fig. 53.2). However, the sonographic techniques required are operator dependent and have not gained much popularity. Therefore esophageal abnormalities are usually assessed with other imaging modalities, such as fluoroscopy or endoscopy.

Stomach

Most abnormalities of the stomach in infants and children involve the gastric antrum and distal third of the stomach. This portion of the stomach is easily evaluated using the liver as an acoustic window. Distending the stomach with clear fluid facilitates evaluation of the mucosal, submucosal, and muscular layers of the stomach (Fig. 53.3). Furthermore, gastric peristalsis and emptying can be evaluated.

FIG. 53.2 Hiatal Hernia. The fluid-distended stomach extends through the esophageal hiatus *(arrow)*.

Normal gastric mucosa, including the muscularis mucosae and submucosal layers, measures 2 to 3 mm, whereas the outer circular muscle layer measures between 1 to 2 mm in thickness.[7,8] These measurements should be obtained with the stomach fully distended with fluid, and the scan should be performed in the midlongitudinal plane of the stomach or, on cross section, proximal to the pyloric canal, measuring the single muscle wall thickness, excluding the mucosa. On cross-sectional imaging, if the image obtained is too close to the contracted pyloric canal,

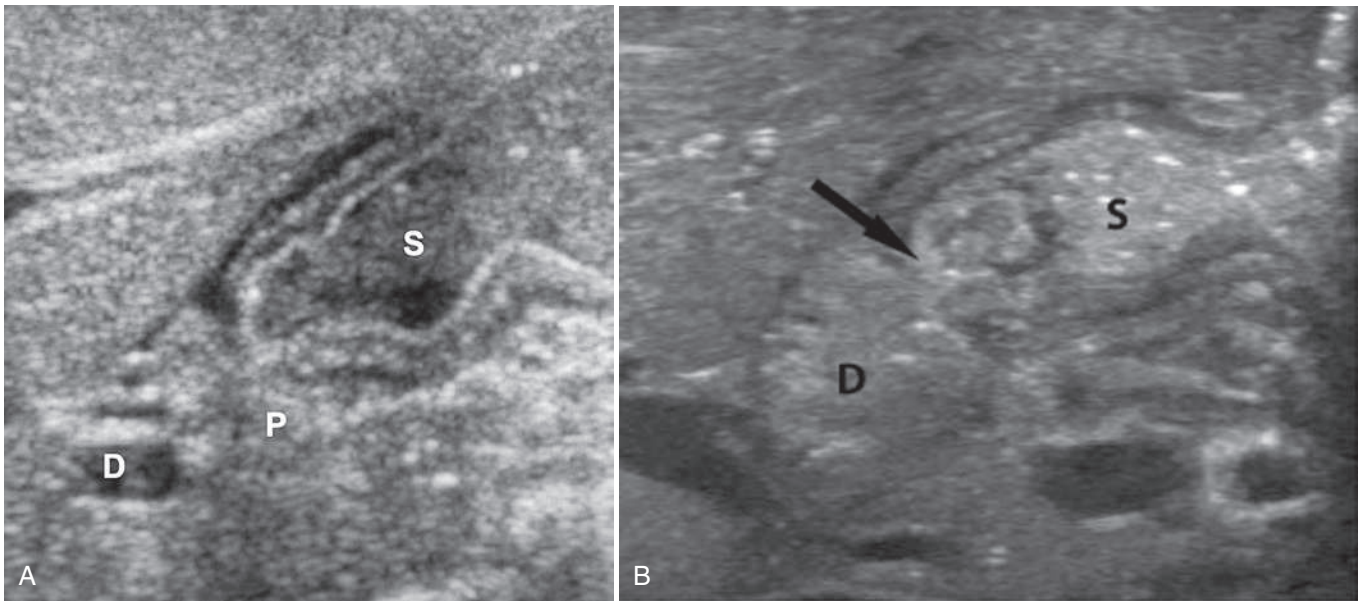

FIG. 53.3 Normal Stomach. (A) Normal antrum of stomach *(S),* pyloric canal *(P),* and proximal duodenum *(D).* Four gastric wall layers are visible (from inside out): echogenic mucosa, hypoechoic muscularis mucosae, echogenic submucosa, and hypoechoic outer circular muscle. **(B)** Fluid passes freely through the normal pylorus *(arrow). D,* Duodenum; *S,* stomach.

thickening of the pyloric muscle can be suggested erroneously. Similarly, if tangential images are obtained on the longitudinal plane, the muscle may erroneously appear thickened (Fig. 53.4). This same phenomenon is also seen with the echogenic mucosal layer.

Hypertrophic Pyloric Stenosis

Muscle width ≥3 mm
Pyloric canal length ≥1.5 cm
No peristalsis through pylorus

Hypertrophic Pyloric Stenosis

During the past decade, sonography has replaced the radiographic upper GI series for the diagnosis of infantile hypertrophic pyloric stenosis (HPS). Unlike the upper GI series, which demonstrates only the indirect effects of pyloric muscle hypertrophy on the gastric lumen, ultrasound allows direct visualization of the gastric muscle thickening that is the hallmark of the disease. Although a few pitfalls in the sonographic diagnosis of HPS exist, the technique is relatively easily mastered and results in greatly improved accuracy of diagnosis and patient outcome. Indeed, the accuracy approaches 100%, and ultrasound is now the procedure of choice for the detection of pyloric stenosis.[9-12]

After the initial documentation of the sonographic detection of the hypertrophied pyloric muscle in pyloric stenosis by Teele and Smith,[13] many studies described the characteristic findings of HPS.[14-18] Increased pyloric muscle thickness and canal length; increased transverse diameter of the pylorus; thickened, redundant mucosa; estimation of the degree of gastric outlet obstruction; and calculation of pyloric muscle volume have all been used to diagnose pyloric stenosis. However, of all the criteria, thickening of the pyloric muscle and elongation of the pyloric canal have emerged as the most consistently useful. The thickness at which the muscle is considered **hypertrophied is 3 mm or greater when measuring the hypoechoic single muscle layer transversely.**[7] Pyloric canal length of 1.5 cm is considered diagnostic of pyloric stenosis when seen in conjunction with thickened pyloric muscle.

In the classic case of HPS, the thickened muscle mass is seen as a hypoechoic layer just superficial to the more echogenic mucosal layer of the pyloric canal (Fig. 53.5). In cross section, this **"olive,"** on clinical palpation, resembles a sonolucent **"doughnut"** medial to the gallbladder and anterior to the right kidney. Often, small amounts of fluid are visible trapped between the thickened echogenic mucosal folds, corresponding to the **"string"** (elongated canal) and **"double tract"** (folded mucosa) signs previously described on radiographic upper GI series.[19] In longitudinal section, sonography also permits evaluation of functional alterations at the pylorus. Active gastric peristalsis that ends abruptly at the margin of the hypertrophied muscle, absence of a normal opening of the pylorus, and diminished passage of fluid from the stomach into the duodenum are useful adjunctive findings in pyloric stenosis. Thickened mucosa within the pylorus often accompanies the muscle hypertrophy.[20] Although most often an isolated abnormality, HPS occasionally accompanies other obstructive antropyloric lesions, such as duodenal feeding tubes (Fig. 53.6), eosinophilic gastroenteritis, antral polyps,[21] and idiopathic or prostaglandin-induced foveolar hyperplasia.[22]

The length of the pyloric channel is typically shorter in premature infants with pyloric stenosis, but normal pyloric measurements for premature infants are not well established. At surgery of premature infants with HPS, the mass is reportedly

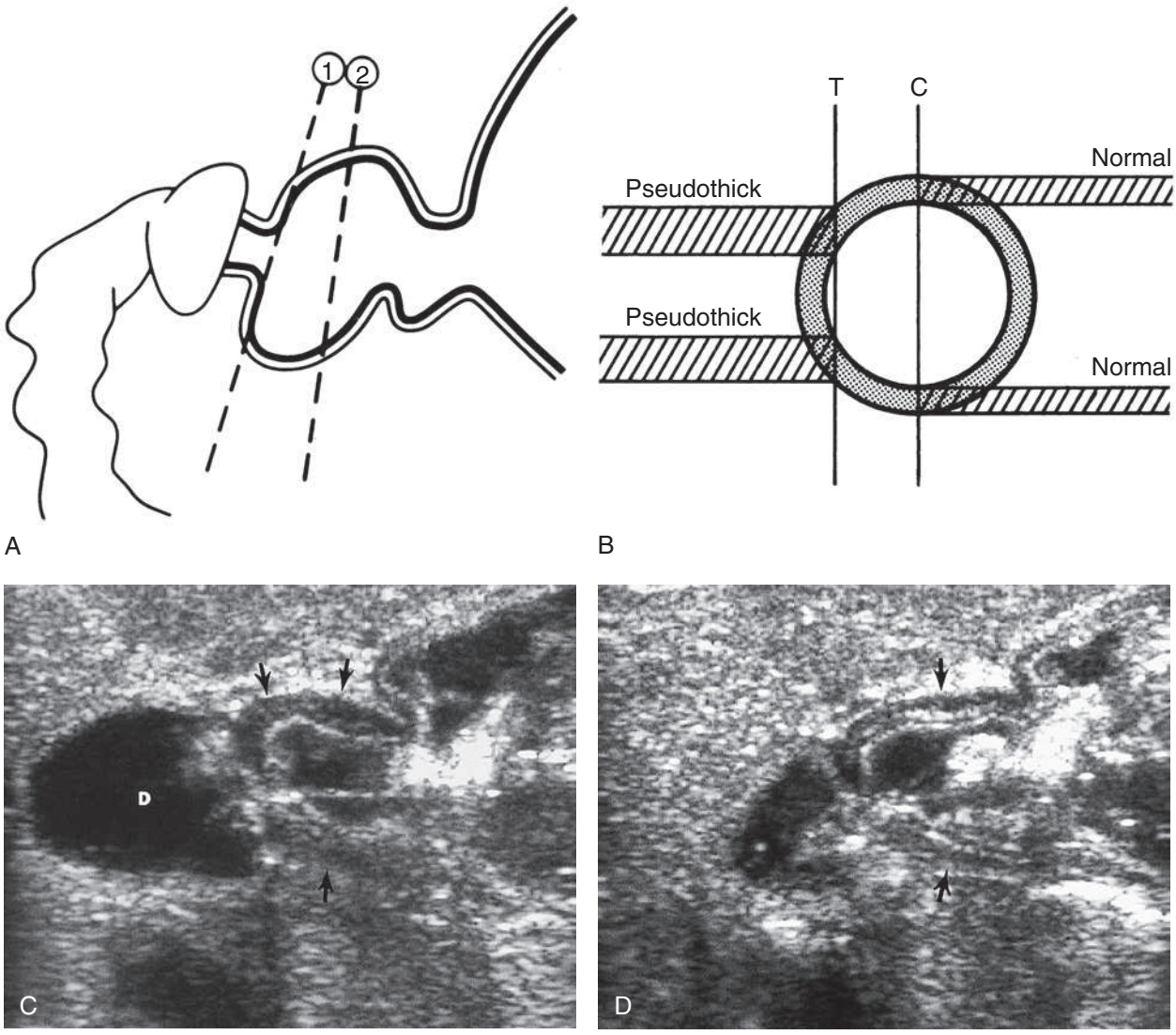

FIG. 53.4 Pyloric Muscle Tangential Imaging Artifacts. (A) When imaging the antrum in cross section, the muscle will appear thickened if obtained through plane 1, but will show normal thickness if obtained through plane 2. **(B)** Longitudinal scan, tangential plane *(T),* shows pseudothickening. Imaging in center *(C)* shows true normal muscle thickness. **(C)** Tangential scan shows muscle pseudothickening *(arrows). D,* Duodenum. **(D)** Antrum distended with fluid shows normal muscle *(arrows).*

softer, more pliable, and thinner. Rarely, HPS manifests during the first 14 days of life and can be challenging to diagnose because most consider HPS to occur after 2 weeks of age. These infants are often thought to have severe reflux, and ultrasound criteria for these younger infants are also not established. Those with presentation before the expected age range are more likely to have a positive family history than those with presentation after 2 weeks of age, and more of these infants have been breast fed. The muscle thickness is also decreased relative to the older HPS patient, with some advocating a muscle thickness of greater than or equal to 2.5 mm and channel length of greater than or equal to 14 mm for criteria in these younger patients.[23-25]

Ultrasound also is very useful for the evaluation of persistent vomiting in the postpyloromyotomy patient. The fluoroscopic upper GI series is of limited value in such cases because it tends to show persistent deformity and narrowing of the canal even in asymptomatic patients. However, sonography can definitively identify persistently thickened muscle, although cautious interpretation in postpyloromyotomy patients is recommended because the pyloric muscle may not reach its normal thickness until 8 months after surgery[26] (Fig. 53.7).

Pylorospasm and Minimal Muscular Hypertrophy

In some vomiting infants, sonography shows a persistently contracted and elongated canal, but the degree of muscular thickening is less than the criterion of 3 mm for surgically correctible HPS. With extended observation, eventually the canal opens and fluid is seen to pass into the duodenum,[27] but the periods of spasm predominate (Fig. 53.8). In the vast majority of cases, there is no thickening of the pyloric muscle or mucosa, and the problem is primarily nonspecific **pylorospasm (antral**

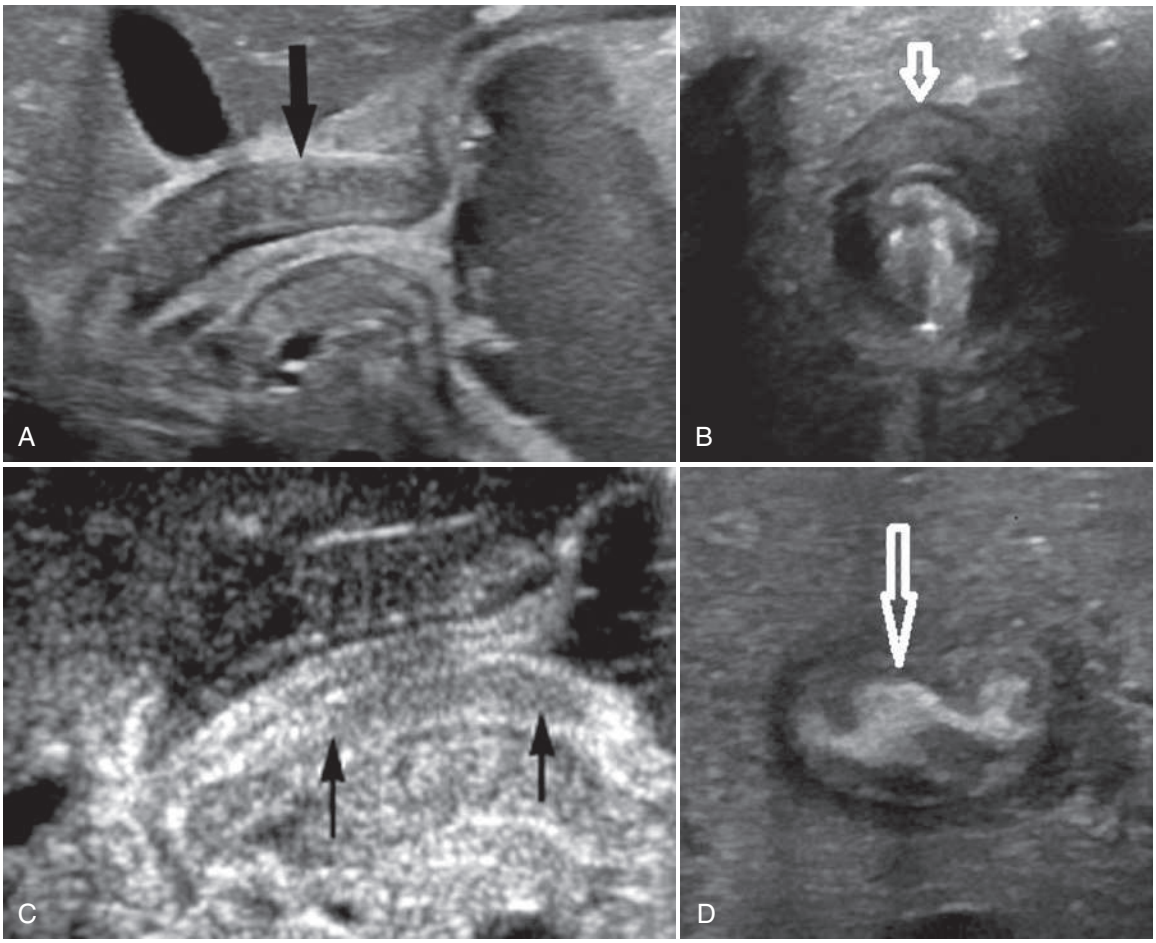

FIG. 53.5 Hypertrophic Pyloric Stenosis. (A) Longitudinal scan shows markedly thickened, hypoechoic gastric antral muscle *(arrow)*. Elongated canal is nearly 2 cm in length. **(B)** Transverse scan shows typical, hypoechoic "doughnut" *(arrow)*. Central echogenic mucosa with anechoic fluid-filled crevices. **(C)** In another patient, longitudinal image of the pylorus shows the thick echogenic mucosa *(arrows)* within the thickened muscle mass. **(D)** Transverse image shows similar echogenic mucosal thickening *(arrow)*.

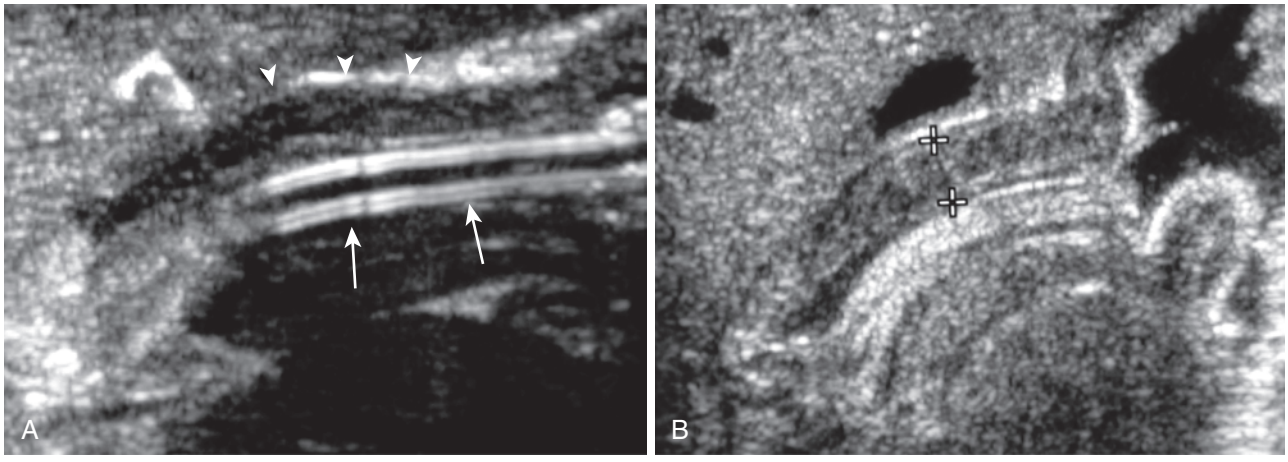

FIG. 53.6 Minimal Pyloric Muscle Thickening Progresses to Hypertrophic Pyloric Stenosis. (A) Longitudinal scan in infant with a duodenal feeding tube *(arrows)* shows contracted pyloric canal and 2.3-mm-thick pyloric muscle *(arrowheads)*. **(B)** Two weeks later the muscle was hypertrophied (4 mm).

dyskinesia). This condition can accompany milk allergy or other forms of gastritis.

In some cases the pyloric muscle is mildly thickened, measuring 2 to 3 mm.[7] Such patients should be distinguished from those with normal muscle thickness (<2 mm) because in some patients minimal muscle hypertrophy can eventually progress to classic pyloric stenosis. In other infants, minimal muscle thickening will resolve spontaneously, but such patients should be followed closely with ultrasound until the muscle regresses to a normal thickness.

Pitfalls in Sonographic Diagnosis

The echogenicity of the pyloric muscle varies according to the angle at which the ultrasound beam crosses the muscle fibers. During sonography of HPS, the hypertrophied muscle appears echogenic rather than hypoechoic when imaged in the midlongitudinal plane. This alteration of echogenicity is caused by an artifact called the **anisotropic effect,** which occurs at about the 6 and 12 o'clock positions of the muscle, where the ultrasound beam is perpendicular to the muscle fibers.[28] With current high-resolution linear array transducers, the echogenic appearance of the muscle does not substantially decrease its visibility (Fig. 53.9A). The position of the antropyloric canal can change during the examination, especially if the stomach becomes overly distended with fluid. The distended antrum causes the pylorus to become more posteriorly directed, making it more difficult to follow with ultrasound. In such cases the gastric antrum may have a squared-off configuration (Fig. 53.9B). When this occurs, the pylorus may be located by cephalad angulation of the transducer or by imaging from a more lateral position on the abdomen.

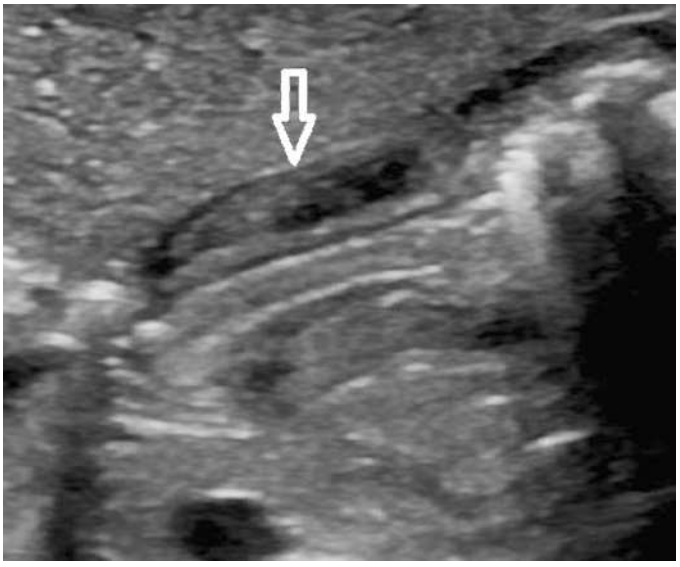

FIG. 53.7 Muscle Thickening After Pyloromyotomy. Note the persistent muscle thickening *(arrow)* in this infant 21 days after surgery.

Pitfalls in Diagnosis of Hypertrophic Pyloric Stenosis (HPS)

- Echogenic muscle at 90 degrees to beam (anisotropic effect)
- Posteriorly oriented antropyloric canal (overdistended stomach)
- Prostaglandin-induced HPS (mucosal, not muscular thickening)
- Minimal pyloric muscle thickening; may progress to HPS

Perhaps the most common pitfall in the sonographic diagnosis of pyloric muscle hypertrophy is inadequate distention of the gastric antrum with fluid. When the antrum is relatively empty, it remains contracted, and the muscle layer can appear falsely thickened (Fig. 53.10). When administering oral fluids for this study, keeping the infant in a right posterior oblique position helps to ensure that the fluid will fully distend the antrum. Despite these occasional pitfalls, the sonographic diagnosis of pyloric stenosis is generally straightforward.

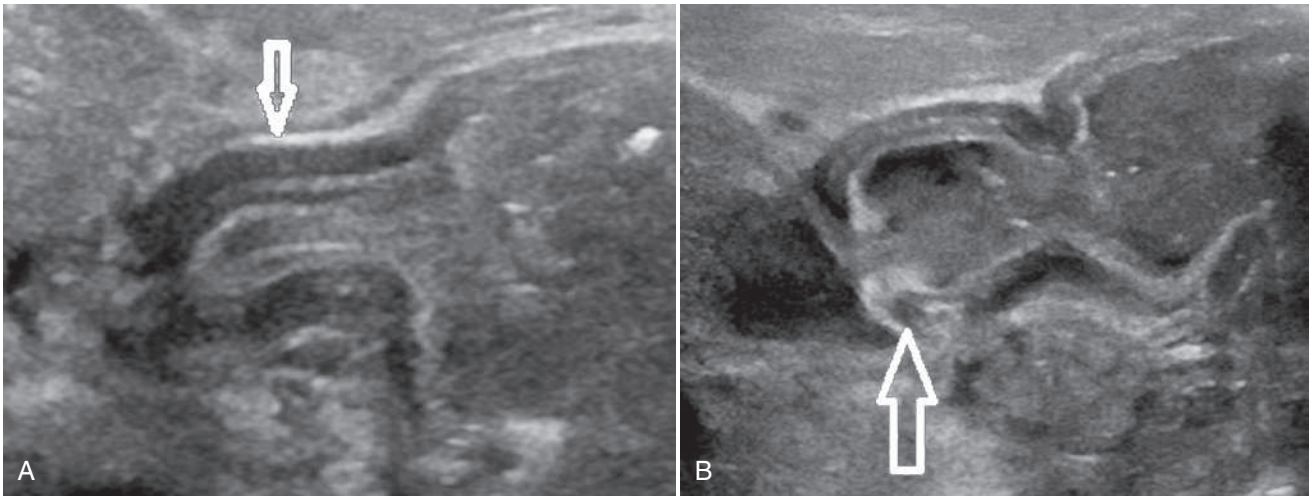

FIG. 53.8 Pylorospasm. (A) The pylorus remained contracted early in the examination of this infant, causing the muscle to appear slightly thickened *(arrow).* **(B)** After giving more oral water and a slightly extended period of viewing, the pylorus relaxed and appeared normal *(arrow).*

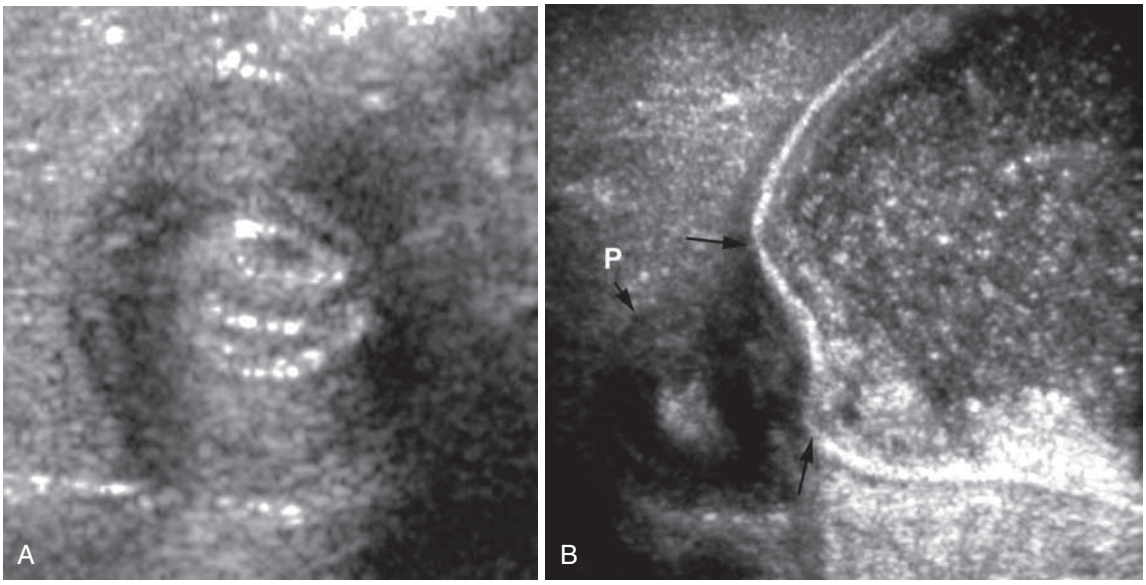

FIG. 53.9 Hypertrophic Pyloric Stenosis. (A) Echogenicity artifact at 6 and 12 o'clock positions (anisotropic effect). Cross-sectional image through the pylorus shows the thickened muscle with increased echogenicity at 6 and 12 o'clock positions. **(B)** Posteriorly directed canal artifact. Note the squared-off appearance of the gastric antrum *(arrows)*. The thickened pylorus *(P)* is only partially visible in this imaging plane.

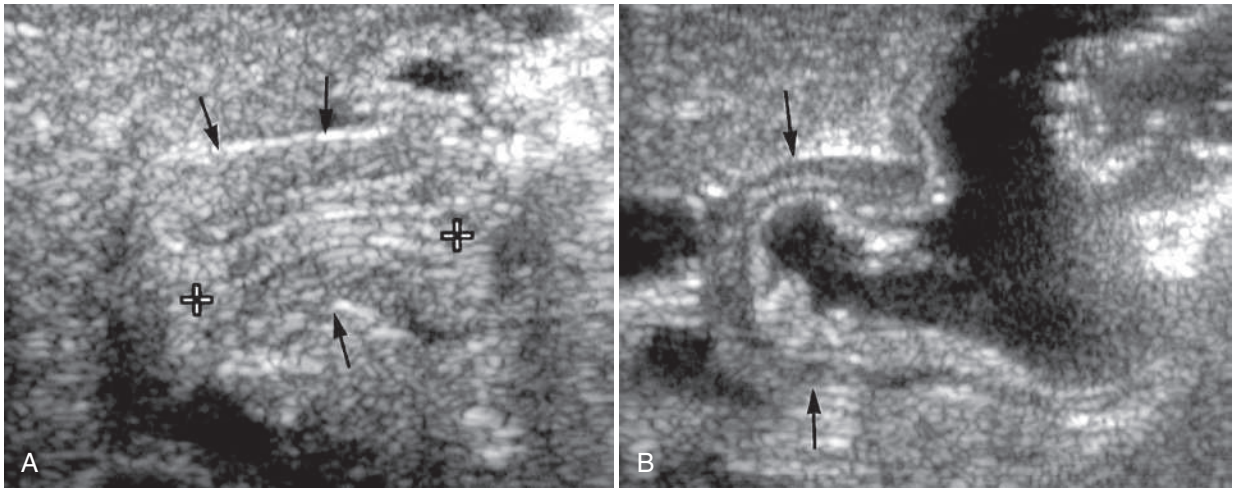

FIG. 53.10 Empty Stomach Artifact. (A) Before fluid is administered, the antrum is contracted and the pyloric muscle appears thickened *(arrows)*. **(B)** When fluid distends the antrum, the true normal thickness of the muscle is seen *(arrows)*.

Gastric Diaphragm

The gastric diaphragm, or antral web, consists of a congenital membrane that extends across the gastric antrum. These diaphragms most often lie less than 2 cm from the pylorus and are therefore usually visible on ultrasound examination. Complete diaphragms are considered one form of gastric atresia, but many diaphragms are incomplete and cause variable degrees of obstruction. On sonography, the web appears as an echogenic band across the distal gastric antrum (Fig. 53.11). Care must be taken to image such webs in the true midlongitudinal plane because if an incomplete diaphragm is imaged at its periphery, a complete diaphragm may be erroneously suggested.

Gastritis and Ulcer Disease

Peptic ulcer disease in pediatric patients is probably more common than generally is appreciated.[29] **Gastric ulcers** are more common than duodenal ulcers in younger children (median age of 6.5 years) and ***Helicobacter pylori*** infection is less prevalent with gastric ulcers than with duodenal ulcers.[29] Sonography is not particularly helpful with duodenal ulcers, but gastric inflammatory disease may be visible sonographically. Barium radiographic studies often reveal nothing more than persistent deformity or spasm of the antropyloric region. Ultrasound of the fluid-filled stomach permits direct visualization of the thickened gastric mucosa and submucosa,[30] which often is accompanied by loss

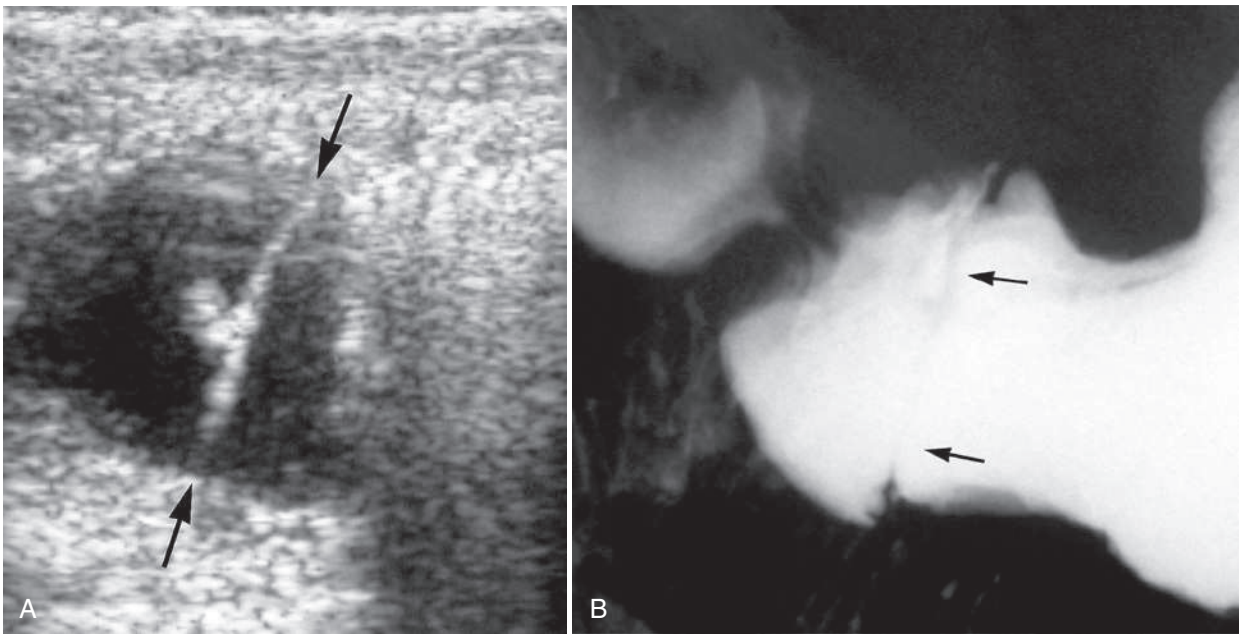

FIG. 53.11 Gastric Diaphragm. (A) Note the thin membrane *(arrows)* crossing the fluid-filled gastric antrum. **(B)** The same diaphragm seen during a contrast upper gastrointestinal series *(arrows)*.

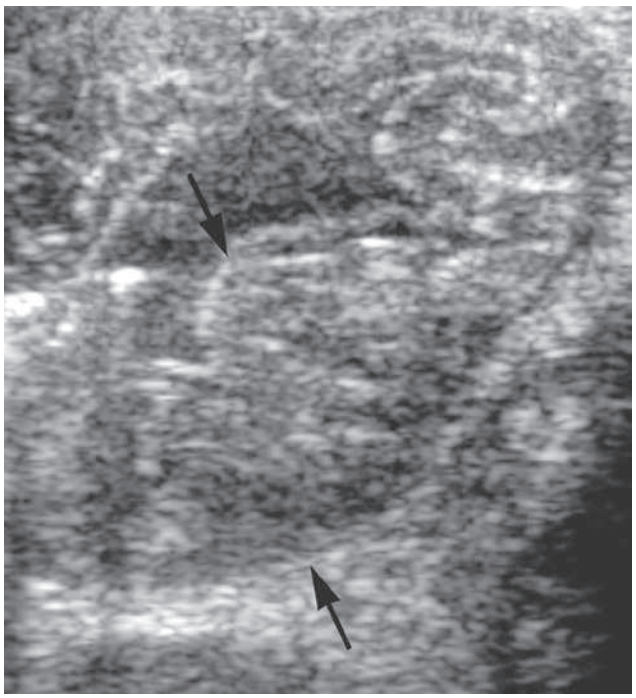

FIG. 53.12 Gastritis. Marked thickening of the gastric mucosa *(arrows)* is visible in this immunosuppressed transplant patient.

of definition of the individual layers of the gastric wall (Fig. 53.12). The ulcer crater itself usually is not visualized sonographically. Ultrasound can also be used to follow therapy, showing a return of the normal gastric wall layers as the ulcer heals. Thickening of the gastric mucosa is not a specific finding and can be seen with other conditions, such as **eosinophilic gastritis, inflammatory pseudotumor,**[31] **chronic granulomatous disease, Ménétrier disease,**[32] **milk allergy,** and **prostaglandin-induced antral foveolar hyperplasia.**[33,34] The last condition is self-limiting and can be seen in asymptomatic infants.[35]

Bezoar

Lactobezoars are the most common form of bezoar in children, occurring predominantly in infants who are fed improperly reconstituted powdered formula. In older children, **trichobezoars,** caused by the ingestion of hair, are more common. Both types of bezoar can be easily identified with ultrasound, especially if the patient is given clear fluid to help outline the mass. Lactobezoars appear as a solid, heterogeneous, echogenic intraluminal mass[36] (Fig. 53.13). With trichobezoars, air tends to be trapped in and around the hair fibers, which causes a characteristic arc of echogenicity that obscures the mass but conforms to the shape of the distended stomach. Distending the stomach with water and scanning in decubitus and upright positions allows the bezoar to be separated from the gastric wall, clinching the diagnosis[37] (Fig. 53.14). Trichobezoars can rarely lead to small bowel obstruction in cases where the bezoar extends beyond the stomach, called **Rapunzel syndrome** when extending through a large portion of the small intestine.[38]

In the case of small bowel obstruction, a bezoar proximal to the obstruction has a **twinkling artifact,** a characteristic arclike shadow with strong posterior acoustic shadowing, whereas fecal material has neither the posterior shadowing nor the twinkling artifact. Bezoars can be difficult to differentiate from fecal material proximal to a small bowel obstruction by computed tomography (CT).[39]

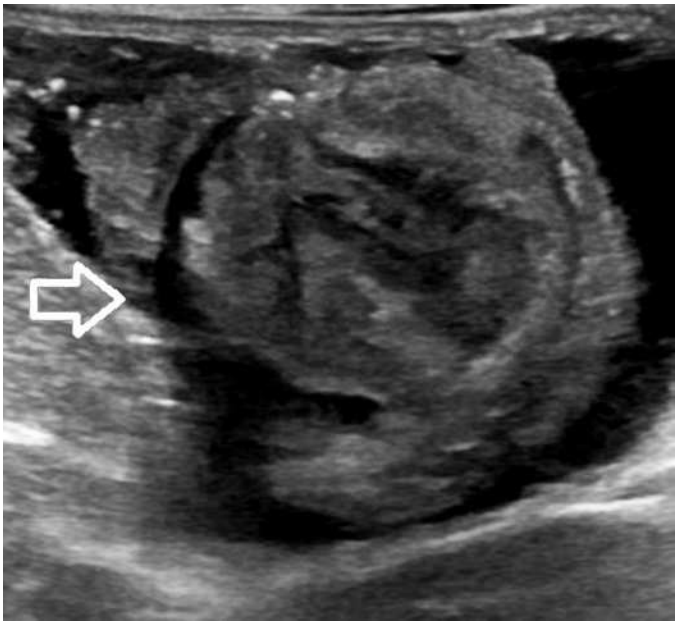

FIG. 53.13 Lactobezoar. Longitudinal ultrasound of the stomach. Note large filling defect caused by the lactobezoar in an otherwise fluid-filled stomach *(arrow).* The child had had nothing by mouth for 6 hours.

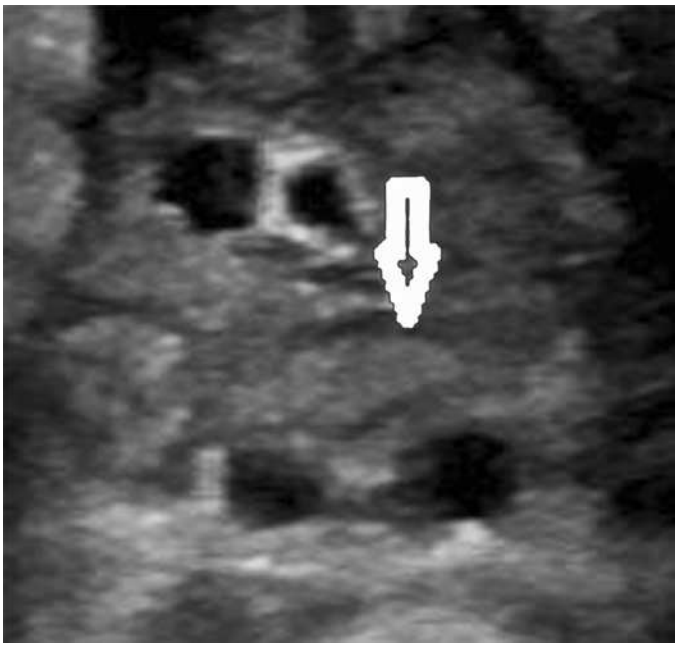

FIG. 53.15 Normal Duodenum. The third portion of the duodenum *(arrow)* is visible between the aorta and superior mesenteric vessels.

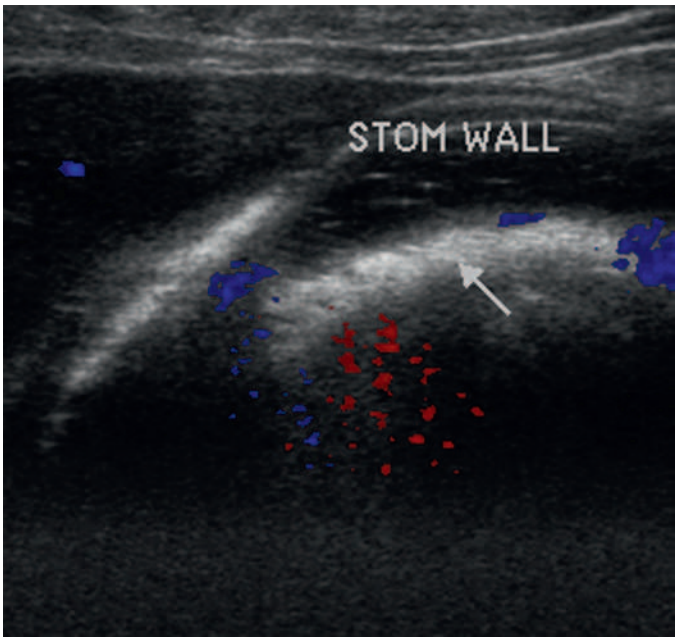

FIG. 53.14 Trichobezar. Echogenic arc is caused by air trapped within the mass of hair fibers *(arrow).*

DUODENUM AND SMALL BOWEL

Normal Anatomy and Technique

Normally, intestinal gas prevents complete visualization of the duodenum and small bowel with ultrasound. However, if the stomach is filled with fluid, it is often possible to identify the duodenal bulb, descending duodenum, and third portion of duodenum located between the aorta and the superior mesenteric vessels (Fig. 53.15). In addition, gradual compression of the abdomen with the transducer during scanning often encourages the gas to move to other areas, allowing previously obscured small bowel loops to be examined. The mucosa, submucosa, and muscular layers can be delineated,[28] especially in those loops that contain fluid (Fig. 53.16).

Congenital Duodenal Obstruction

Sonography can readily identify an obstructed, fluid-filled, distended duodenum, and frequently the level of obstruction can be determined. Complete duodenal obstruction in the newborn is often readily apparent on radiographs, and ultrasound generally provides little additional useful information. However, in patients in whom the stomach and duodenum are filled with fluid rather than air, ultrasound can be quite useful.

Proximal duodenal obstruction resulting in the classic double-bubble sign occurs with **duodenal atresia,** with or without associated annular pancreas (Fig. 53.17). Plain radiograph findings usually are diagnostic, showing two air-filled bubbles representing the dilated stomach and proximal duodenum. Similar findings can be seen with **severe duodenal stenosis** and **duodenal diaphragms or webs.** Usually, sonography is not needed to identify obstructions in this portion of the duodenum. However, when duodenal atresia is associated with esophageal atresia, air cannot reach the stomach and duodenum, making radiographic diagnosis more difficult. Sonography is diagnostic in such infants by demonstrating the grossly distended, fluid-filled duodenal bulb, stomach, and distal esophagus.[40,41]

Sonography has been used for diagnosis of **intestinal malrotation with midgut volvulus** in an infant with bilious vomiting, although the fluoroscopic upper GI series remains the reference standard. If an ultrasound is performed in a patient with volvulus,

FIG. 53.16 Normal Small Bowel. High-frequency ultrasound images show the thin, distinct layers of normal bowel loops.

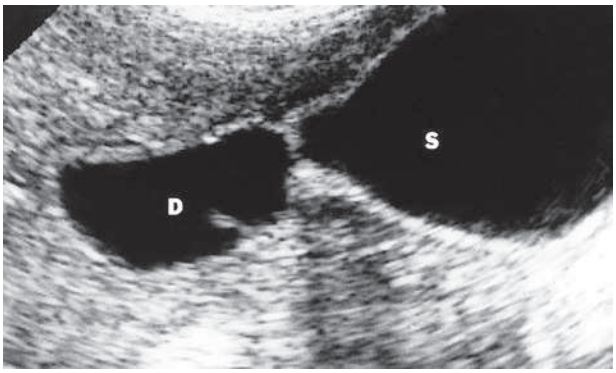

FIG. 53.17 Duodenal Atresia. The presence of grossly distended duodenal bulb *(D)* and stomach *(S)* constitutes the sonographic "double bubble" sign.

vigorous peristalsis of the dilated, obstructed duodenal C-loop is seen (Fig. 53.18) and characteristic tapering of the distal, twisted end can be visualized.[42] Color Doppler will show the **"whirlpool" sign** of twisted mesenteric veins around the superior mesenteric artery (SMA) (Fig. 53.19). Obstruction from **peritoneal (Ladd) bands,** which also accompanies rotational anomalies of the intestine, can have a similar appearance. In addition to these findings, an abnormal position of the superior mesenteric vein (SMV) and artery can be seen in patients with intestinal malrotation, with or without volvulus (Fig. 53.20). Failure of normal embryologic bowel rotation leaves the SMV anterior to or to the left of the SMA[43,44] as opposed to its normal position to the right of the artery. Although this finding is not always present in volvulus,[45] it is probably worthwhile to observe the relationship of these vessels in any child who is undergoing sonography for the evaluation of vomiting. In addition, documentation of the normal position of the third portion of the duodenum posterior to the SMA and anterior to the aorta can be used to exclude malrotated bowel. With practice, this becomes easier.[46,47] Although these findings are valuable for suggesting the diagnosis, absence of these findings does not exclude malrotation or volvulus.[48]

A final cause of distal duodenal obstruction is a **duodenal diaphragm** that has stretched into a **windsock configuration** (Fig. 53.21). The distal end of the obstructed duodenum will have a rounded shape in this condition,[49] as opposed to the tapered end, which is seen more often with midgut volvulus.

Duodenal Hematoma

Duodenal hematoma is a common complication of blunt abdominal trauma in children, including those with battered child syndrome. Sonography can demonstrate the dilated, obstructed duodenum and more specifically can show evidence of an intramural hematoma[50-52] (Fig. 53.22). The intramural hemorrhage initially causes echogenic thickening of the wall of the duodenum, but as time passes, the hematoma undergoes liquefaction and the thickened wall becomes hypoechoic. Similar hematomas can occur with **Henoch-Schönlein purpura.**[53]

Small Bowel Obstruction

The diagnosis of small bowel obstruction is usually accomplished with plain radiographs. At times, however, ultrasound can be used to help determine the site or cause of the obstruction. In cases of mechanical small bowel obstruction, the fluid-filled, dilated, hyperperistaltic loops of small bowel proximal to the obstruction are usually clearly visible with ultrasound (Fig. 53.23). One can also assess small bowel in both lower quadrants in an attempt to ascertain the level of obstruction and also try to determine the cause of obstruction if lesions such as duplication cysts, small bowel intussusception, or even interloop collections from a perforated appendix are present.

In neonates with congenital causes of small bowel obstruction (e.g., ileal atresia, meconium ileus), prenatal intestinal perforation can occur, releasing variable amounts of meconium into the peritoneal cavity. In some of these fetuses, the perforation heals in utero, and the only clues that remain after birth are scattered

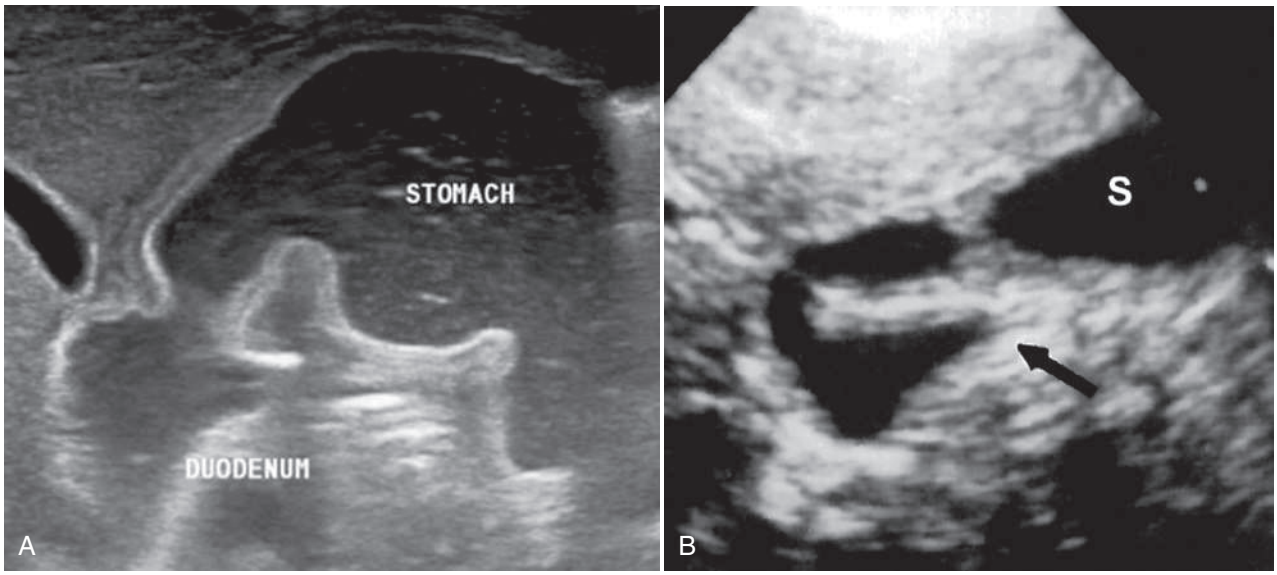

FIG. 53.18 Midgut Volvulus. (A) The pylorus is widely patent and the proximal duodenum is dilated and shows vigorous peristalsis. The point of obstruction is not clearly visible in this patient. **(B)** In a different child, vigorous peristaltic activity fails to empty the duodenum, and the third portion of the duodenum has **beak deformity** *(arrow). S,* Stomach.

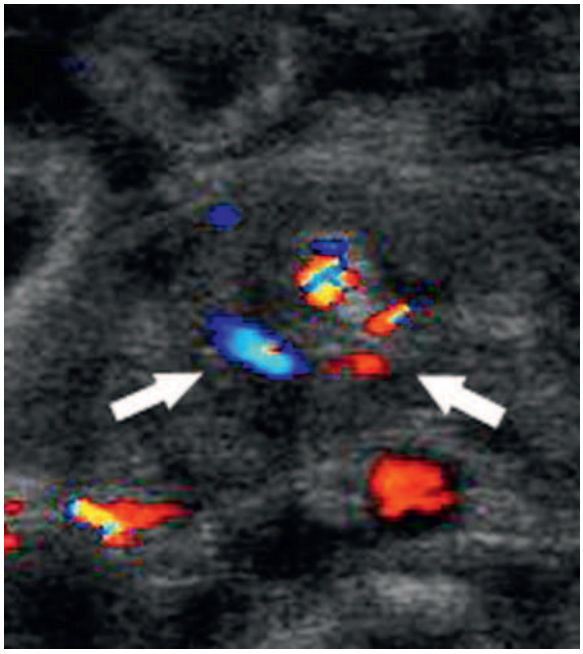

FIG. 53.19 Midgut Volvulus "Whirlpool" Sign. Color Doppler shows a clockwise **whirlpool** of vessels *(arrows)* around a volvulus.

calcifications in the peritoneal cavity. In patients in whom larger amounts of meconium have leaked, or in whom an active leak remains after birth, cystic masses can be found in the peritoneal cavity, giving rise to the term **cystic meconium peritonitis.** Sonographically, these cysts are of variable size and are fairly well defined, often with very heterogeneous cystic fluid.[54,55] The highly echogenic calcifications can also be found with ultrasound (Fig. 53.24). Echogenic ascitic fluid may also be present after perforation, whether in utero or neonatal.

Small bowel obstruction from **intestinal hematomas** usually occurs as a result of **Henoch-Schönlein purpura, blunt abdominal trauma, or coagulopathies.** In any of these conditions, the mural hemorrhage can be detected sonographically as asymmetric or circumferential areas of intestinal wall thickening that can vary from echogenic to hypoechoic.[53]

Intussusception

Intussusception is the most common cause of small bowel obstruction in children between the ages of 6 months and 4 years. Clinical findings of crampy, intermittent abdominal pain, vomiting, palpable abdominal mass, and "currant jelly" stools are classic. Patients with these characteristic symptoms probably do not require ultrasound diagnosis before attempted enema reduction. Many of these clinical features are present in young children with abdominal pain for other reasons, and some children with intussusception do not exhibit all the classic features. In such children, sonography can help confirm or exclude intussusception. Sensitivity and specificity for the diagnosis of intussusception with ultrasound are very high, approaching 100%.[56-60] If an intussusception is not demonstrated sonographically, an enema need not be performed unless clinical suspicion is high. False positives can occur occasionally in other conditions causing thickened bowel wall[61] (Fig. 53.25).

Sonographic Signs of Intussusception

Oval hypoechoic mass
  Pseudokidney or doughnut sign
Hypoechoic rim with central echogenicity
Multiple layers and concentric rings
Small amount of peritoneal fluid
Large amount of peritoneal fluid suggests perforation, especially echogenic ascites

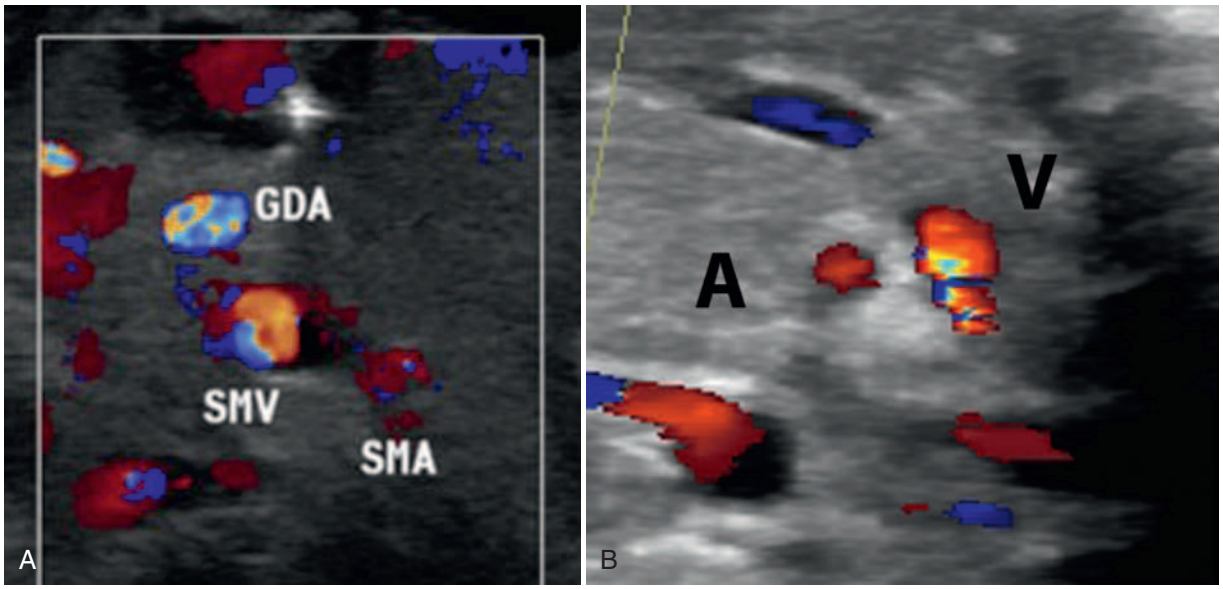

FIG. 53.20 Midgut Volvulus: Altered Relationship of Mesenteric Vessels. (A) Normal relationship of superior mesenteric artery *(SMA)* and the superior mesenteric vein *(SMV). GDA,* Gastroduodenal artery. **(B)** Intestinal malrotation and midgut volvulus; the vein *(V)* lies to the left of the artery *(A).*

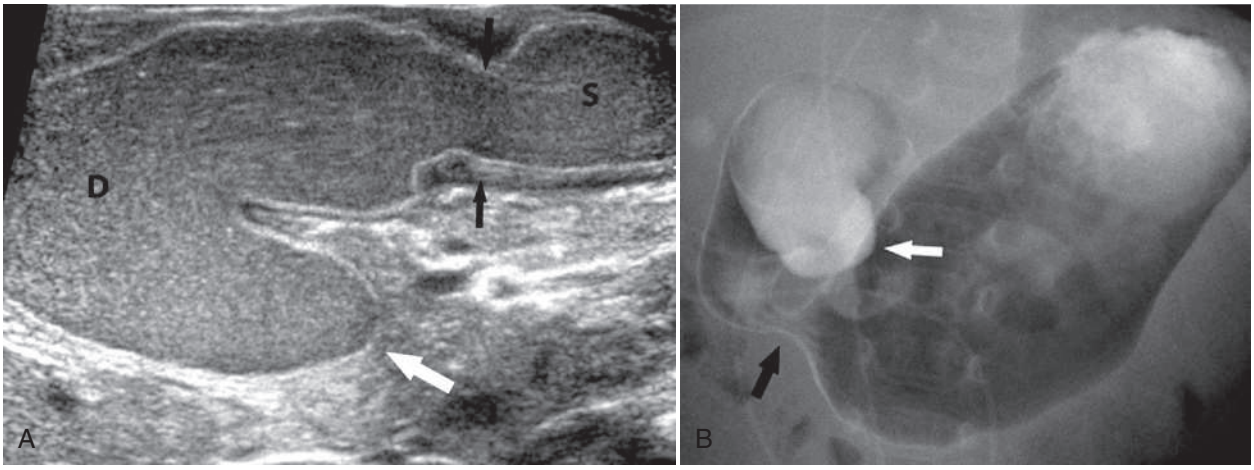

FIG. 53.21 Duodenal Web. (A) Ultrasound shows a markedly dilated duodenum *(D)* filled with fluid. Note the rounded configuration at the point of obstruction in the duodenum *(white arrow)* and the widely patent pylorus *(black arrows). S,* Stomach. **(B)** Contrast upper gastrointestinal image shows similar findings, with the rounded end of the duodenum *(white arrow). Black arrow,* Pylorus.

Ultrasound for suspected intussusception is best performed with a 5- to 10-MHz curved array or linear transducer. The intussusception appears as an oval, hypoechoic mass with bright, central echoes on longitudinal imaging (i.e., **pseudokidney**) and a **hypoechoic doughnut,** or **target configuration with echogenic central echoes.**[62-64] The hypoechoic rim represents the edematous walls of the loops of bowel comprising the intussusceptum, and the central echogenicity represents compressed mesentery, mucosa, and intestinal contents. Linear array transducers display the intussusceptum with greater clarity, showing multiple layers and concentric rings representing the bowel wall, mesentery, and even lymph nodes that have been drawn into the intussusception[65,66] (Fig. 53.26D). In some cases, anechoic fluid is also seen trapped within the incompletely compressed head of the intussusception. Rarely, the lead point of an intussusception can be identified within the intussusceptum (Fig. 53.27).

Once an intussusception has been documented by sonography, the patient usually proceeds to nonsurgical reduction, unless clinical or radiographic evidence of perforation is found. Currently, air reduction is the most popular method of treatment, although hydrostatic reduction using water-soluble contrast remains a viable alternative. **Ultrasound-guided hydrostatic reduction** is an alternative method that avoids the ionizing radiation of standard fluoroscopic examinations.[67-70] Sonography can also be used to identify the ileo-ileal intussusception that sometimes remains after the successful hydrostatic reduction of

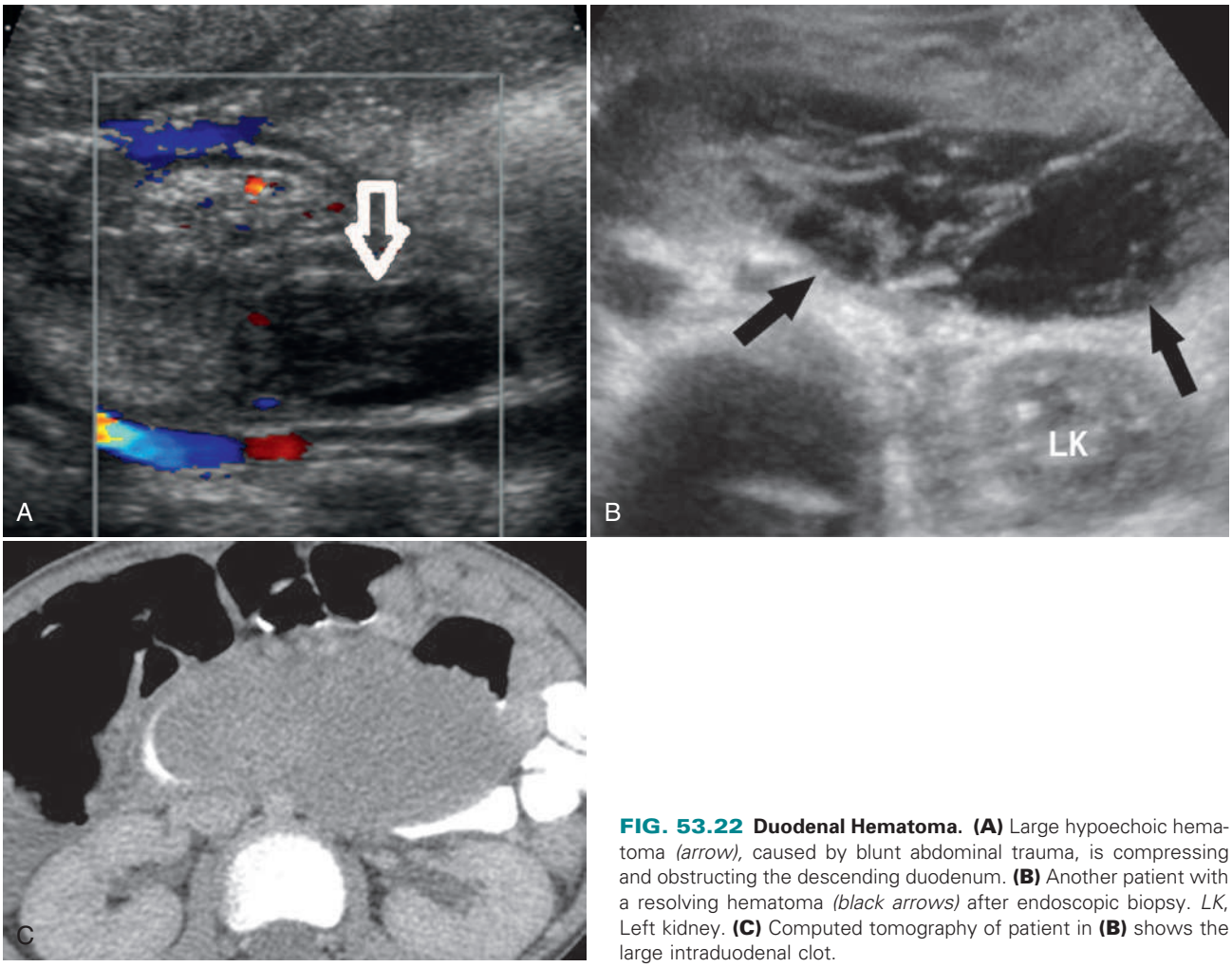

FIG. 53.22 Duodenal Hematoma. (A) Large hypoechoic hematoma *(arrow),* caused by blunt abdominal trauma, is compressing and obstructing the descending duodenum. **(B)** Another patient with a resolving hematoma *(black arrows)* after endoscopic biopsy. *LK,* Left kidney. **(C)** Computed tomography of patient in **(B)** shows the large intraduodenal clot.

the ileocolic portion of an intussusception. **Recurrent intussusception** occurs in 4% to 10% of cases, and thus ultrasound is worthwhile in children with recurrent symptoms after successful enema reduction. Fixed small bowel intussusception is less common in children but can occur when lead points such as **polyps** or **Meckel diverticulum** are present or may occur as a postoperative complication of major abdominal surgeries[71] (Fig. 53.28). Enema examinations are not helpful for diagnosis or treatment of intussusceptions restricted to small bowel, but ultrasound can provide prompt identification of the abnormality in most cases.[64]

Spontaneous reduction of intussusception is a well-known phenomenon that has been documented sonographically. In such patients, when symptoms subside between the time the diagnosis is made and the time a reduction procedure is begun, ultrasound can verify resolution of the intussusception and spare the patient an unnecessary enema procedure.[72] **Transient small bowel intussusception** is a common occurrence, especially in patients with hyperperistalsis. These intussusceptions are not associated with substantial edema in the intussuscepted loops, and therefore the peripheral rim of the intussusception appears thinner and more echogenic than firmly impacted intussusceptions.[73,74] The patient is usually asymptomatic, and spontaneous resolution of the intussusception usually can be observed at ultrasound with a little patience. Intussusception of the small bowel associated with gastrojejunal feeding tubes can also be identified sonographically.[75]

The only absolute contraindication to nonsurgical reduction of an intussusception is radiographic evidence of rupture (free intraperitoneal air or a large amount of complex ascites) or clinical signs of peritonitis. A small amount of free peritoneal fluid is typically seen during ultrasound in patients with intussusception, even in the absence of perforation.[76,77] Therefore a small amount of ascites is not a contraindication to nonsurgical reduction. However, if a large amount of ascites is found or the fluid appears complex, perforation should be considered.

Investigators have attempted to correlate certain ultrasound features of intussusception with the subsequent ability to reduce them nonsurgically. Findings such as peripheral rim thickness of greater than 1 cm, large amounts of internal trapped fluid, and lymph nodes larger than 1 cm within the intussusception have shown some correlation with decreased success of enema reduction.[66,78] Color Doppler assessment of blood flow to the intussusceptum has been used to identify patients who have

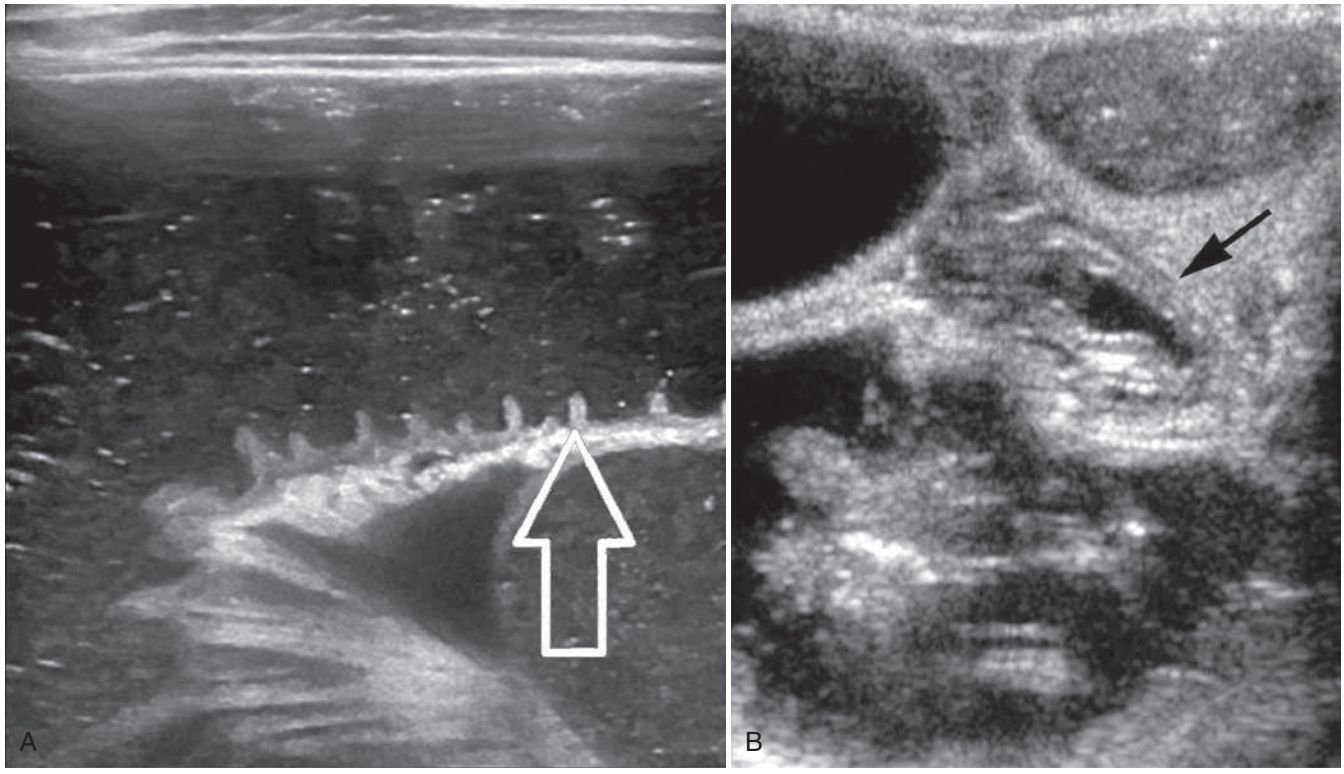

FIG. 53.23 Small Bowel Obstruction. (A) The dilated, obstructed small bowel is clearly seen with ultrasound. Note the closely spaced mucosal folds typical of small bowel *(arrow).* **(B)** Another child with dilated, fluid-filled, obstructed small bowel loops surrounding the small tubular diverticulum *(arrow).*

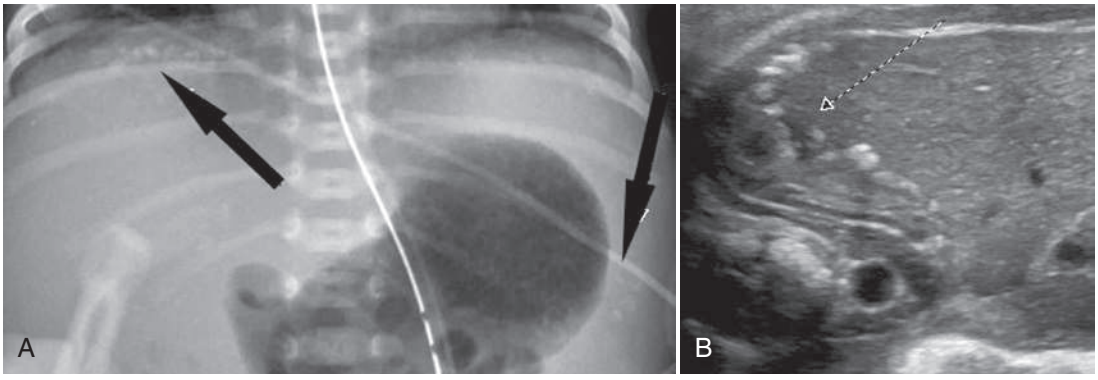

FIG. 53.24 Meconium Peritonitis With Calcification. (A) Stippled calcifications in the right upper quadrant *(arrows)* of the distended abdomen in a newborn. **(B)** Sonography revealed echogenic calcifications lining the peritoneal surface around the liver *(arrow).*

FIG. 53.25 False-Positive Intussusception. Thickened loops of small bowel secondary to an adjacent perforated appendicitis resembles an intussusception.

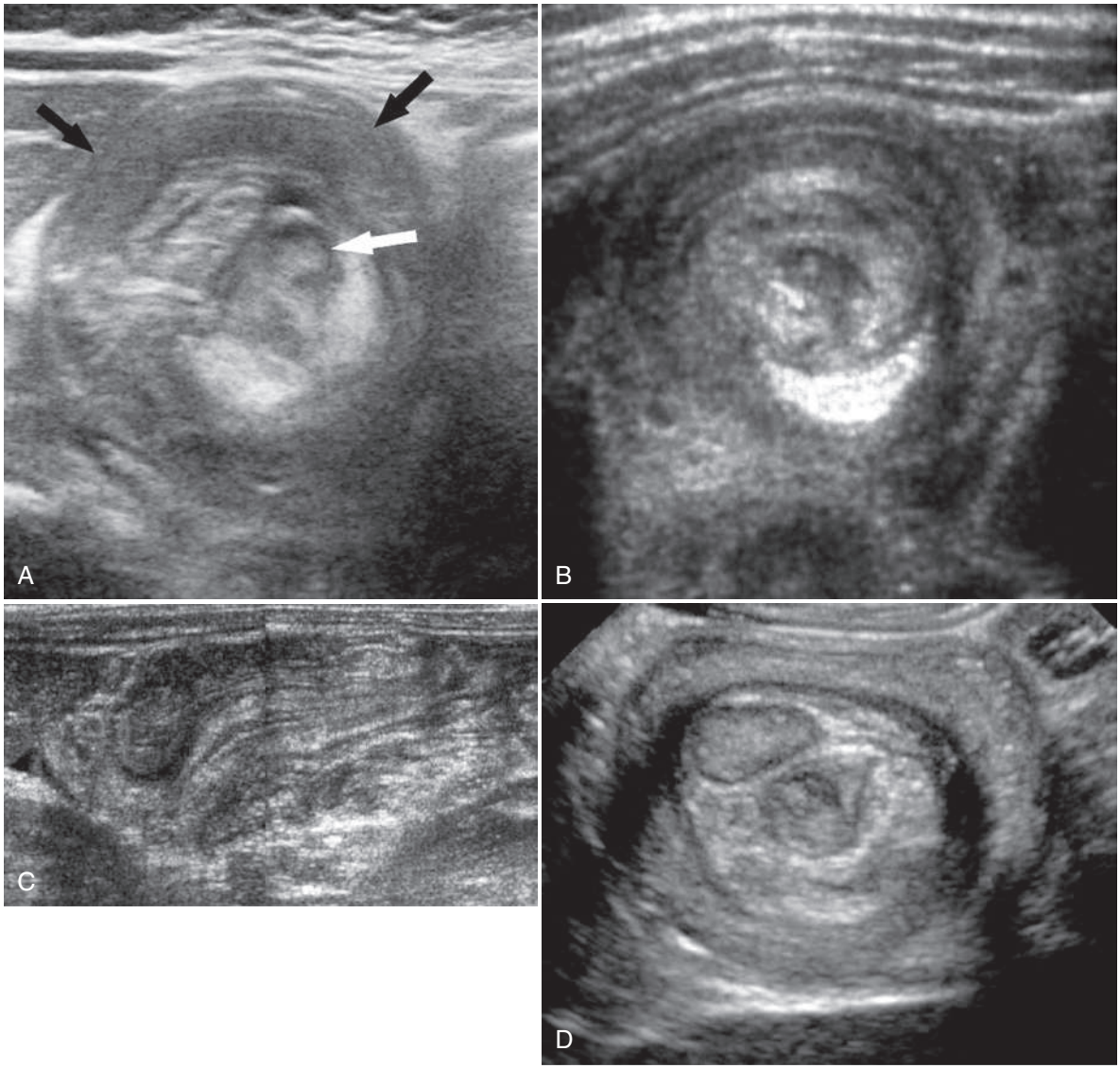

FIG. 53.26 Ileocolic Intussusception. (A) Linear transducers clearly show the concentric rings of the edematous intussusceptum *(black arrows)* with echogenic fat, mesenteric lymph nodes *(white arrow),* and a small amount of fluid trapped in the center. **(B)** Intussusception, showing concentric rings of bowel within bowel. **(C)** Longitudinal image of intussusception. **(D)** In another patient, transverse ultrasound shows ileocolic intussusception with multiple lymph nodes that have been drawn into the intussusception.

substantial bowel ischemia and who may be at greater risk of perforation during attempted nonsurgical reduction[79,80] (Fig. 53.29). Although such findings may portend more difficult enema reduction or increased risk of perforation, none are considered contraindications to nonsurgical reduction procedures.

COLON

Normal Anatomy and Technique

Sonographic evaluation of the colon can be compromised by the gas and excessive fecal material. However, in most patients the characteristic haustral markings in the multilayered wall of the ascending colon can easily be identified (Fig. 53.30). When pathologic wall thickening occurs, ultrasound can be used to assess degree and distribution of wall thickening of the ascending and descending colon and rectum, whereas the transverse colon can be more difficult to assess because of bowel gas. Patterns of inflammation and mural stratification have been described to assist in the diagnosis of colitis, with **pseudomembranous colitis** easy to diagnose based on its typical pancolonic distribution[81] (Fig. 53.30B). Some authors advocate graded compression for sonographic evaluation of colonic polyps, although this can be challenging.[82]

Ectopic or Imperforate Anus

Sonography in the neonate can also be used to study imperforate or ectopic anus.[83-85] In patients with ectopic or imperforate anus, it is important to determine where the distal end of the hindgut terminates. Well-known pitfalls in attempting this with plain

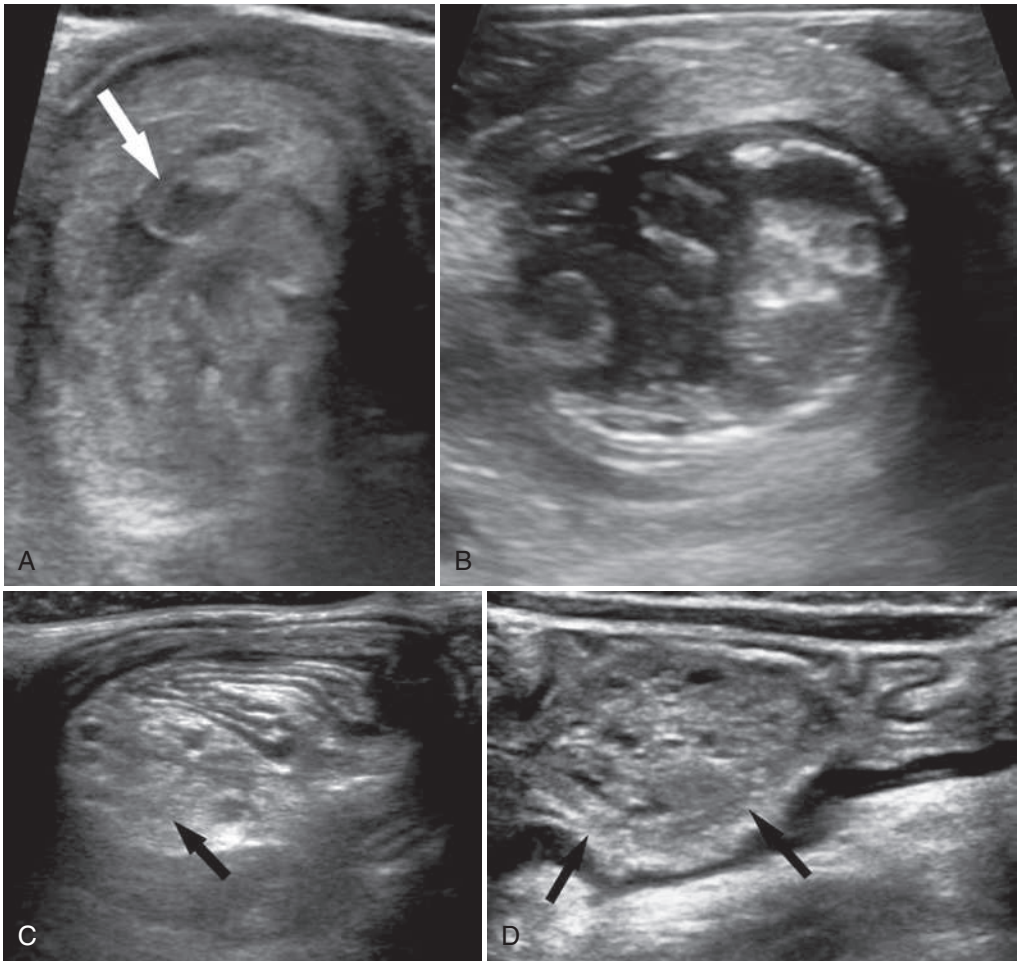

FIG. 53.27 Ileocolic Intussusception With Lead Point. (A) A small fluid-filled structure within this intussusception *(arrow)* represents the Meckel diverticulum found at surgery. **(B)** Intussusception with internal mass representing Burkitt lymphoma. **(C)** Another patient with intussusception caused by a juvenile polyp. The mass is difficult to see within the intussusception *(arrow)*. **(D)** Same patient as in **(C).** The polyp is easily visible after the intussusception is reduced *(arrows)*. (**C** and **D** courtesy of Clara Neira, MD.)

radiographs include those taken in the cross-table prone position. Radiographically, the colon can erroneously appear to end in a high position if the air column fails to progress to the end of the colon because of impacted meconium. Imperforate anus in the newborn can be assessed sonographically via a perineal approach. The low type of imperforate anus passes through the levator ani muscle complex and is managed with transperineal anoplasty. Intermediate and high imperforate anus are supralevator and are managed by initial diverting colostomy. Scanning with a high-resolution transducer via a midsagittal transperineal approach gives excellent detail of the wall of the distal rectal pouch. Fistula location can also be detected in some sonographically (Fig. 53.31). The study should not be performed in a crying infant because the increased abdominal pressure moves the rectal pouch closer to the perineal surface. Haber and colleagues used a pouch-to-perineum distance of 15 mm with a sensitivity and specificity of 100% and 86% in separation of low from high and intermediate imperforate anus and found that with lack of an anocutaneous fistula and rectal pouch–to–perineal distance of greater than 15 mm, the diagnoses of intermediate or high imperforate anus can be made.[83]

INTESTINAL INFLAMMATORY DISEASE

Ultrasound and magnetic resonance imaging (MRI) are being used more often to evaluate GI disorders in the pediatric patient, with decreasing emphasis on CT because of associated exposure to ionizing radiation. High-resolution linear array transducers allow direct and detailed evaluation of the intestinal wall, showing up to five distinct layers in the wall of normal intestine. Lower-frequency transducers can be used to evaluate for mesenteric edema or abscess collections. Intravenous microbubble ultrasound contrast has added to the capability of ultrasound in assessment of inflammatory conditions, especially in the assessment and follow-up of therapy in Crohn disease. Wall thickening is nonspecific[86] and can be seen in a variety of inflammatory

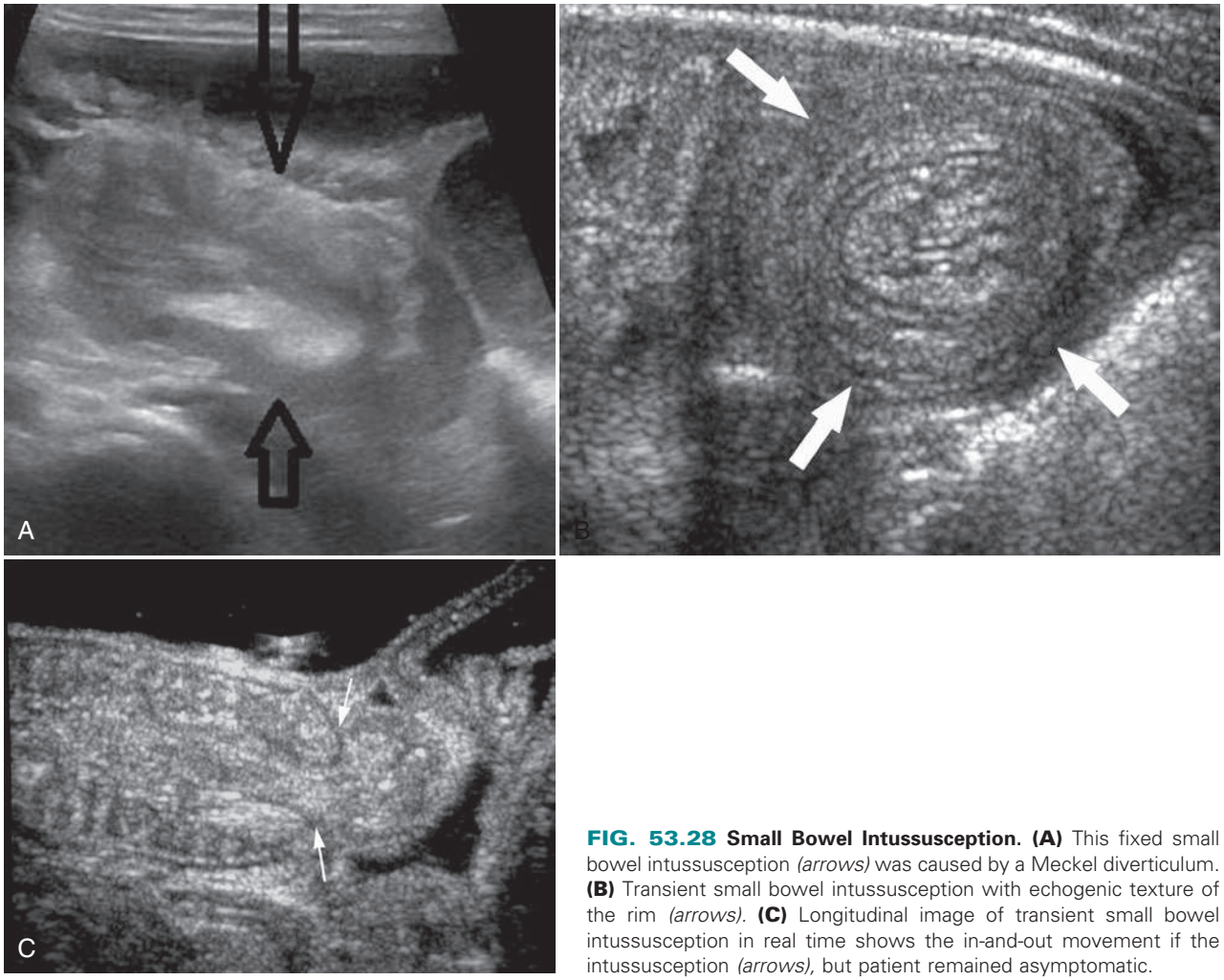

FIG. 53.28 Small Bowel Intussusception. (A) This fixed small bowel intussusception *(arrows)* was caused by a Meckel diverticulum. **(B)** Transient small bowel intussusception with echogenic texture of the rim *(arrows).* **(C)** Longitudinal image of transient small bowel intussusception in real time shows the in-and-out movement if the intussusception *(arrows),* but patient remained asymptomatic.

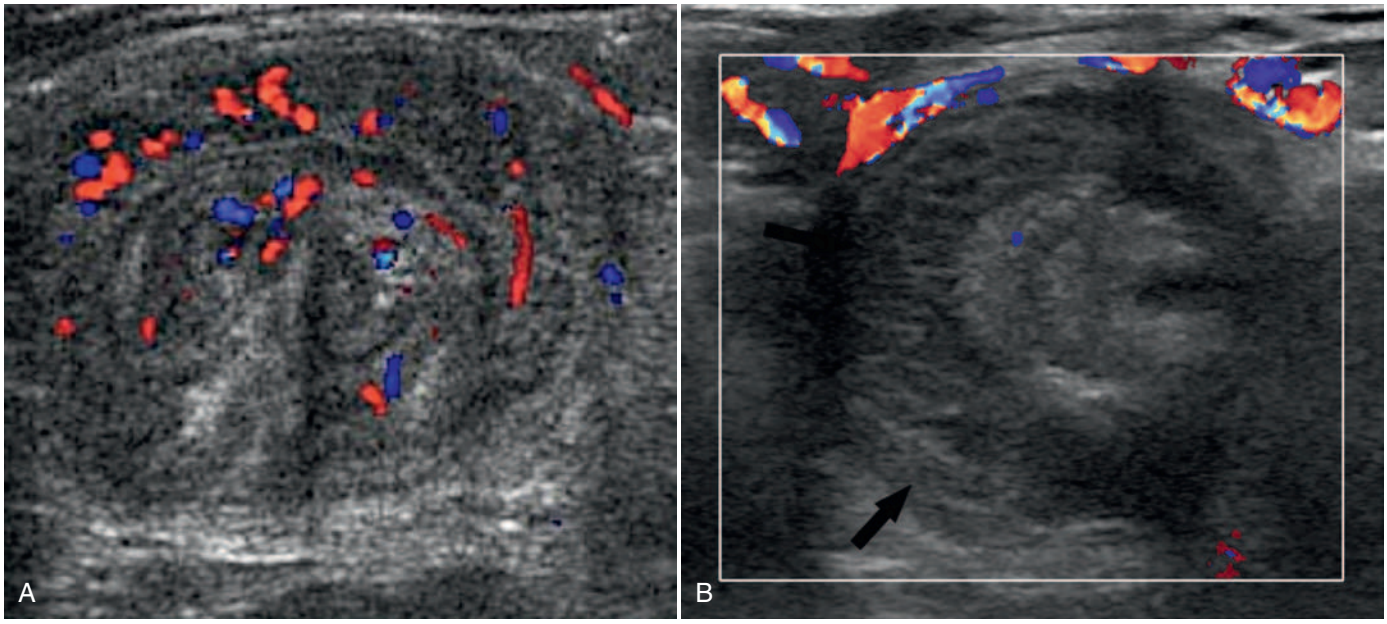

FIG. 53.29 Intussusception: Doppler Imaging. (A) Color Doppler ultrasound demonstrates substantial blood flow within the wall of the intussusceptum. Hydrostatic reduction was successful in this patient without complication. **(B)** Color Doppler ultrasound in another patient shows no flow within the wall of the intussusceptum *(arrows).* At surgery, the bowel was necrotic.

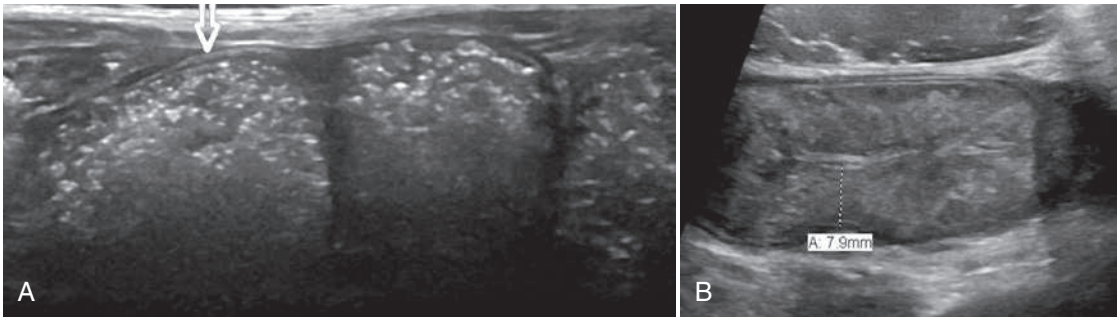

FIG. 53.30 Normal Colonic Wall Ultrasound. (A) Note the thin, multilayered wall of this normal colon *(arrow),* which is filled with fecal material. **(B)** Marked colonic wall thickening and loss of haustral marking in a child with pseudomembranous colitis.

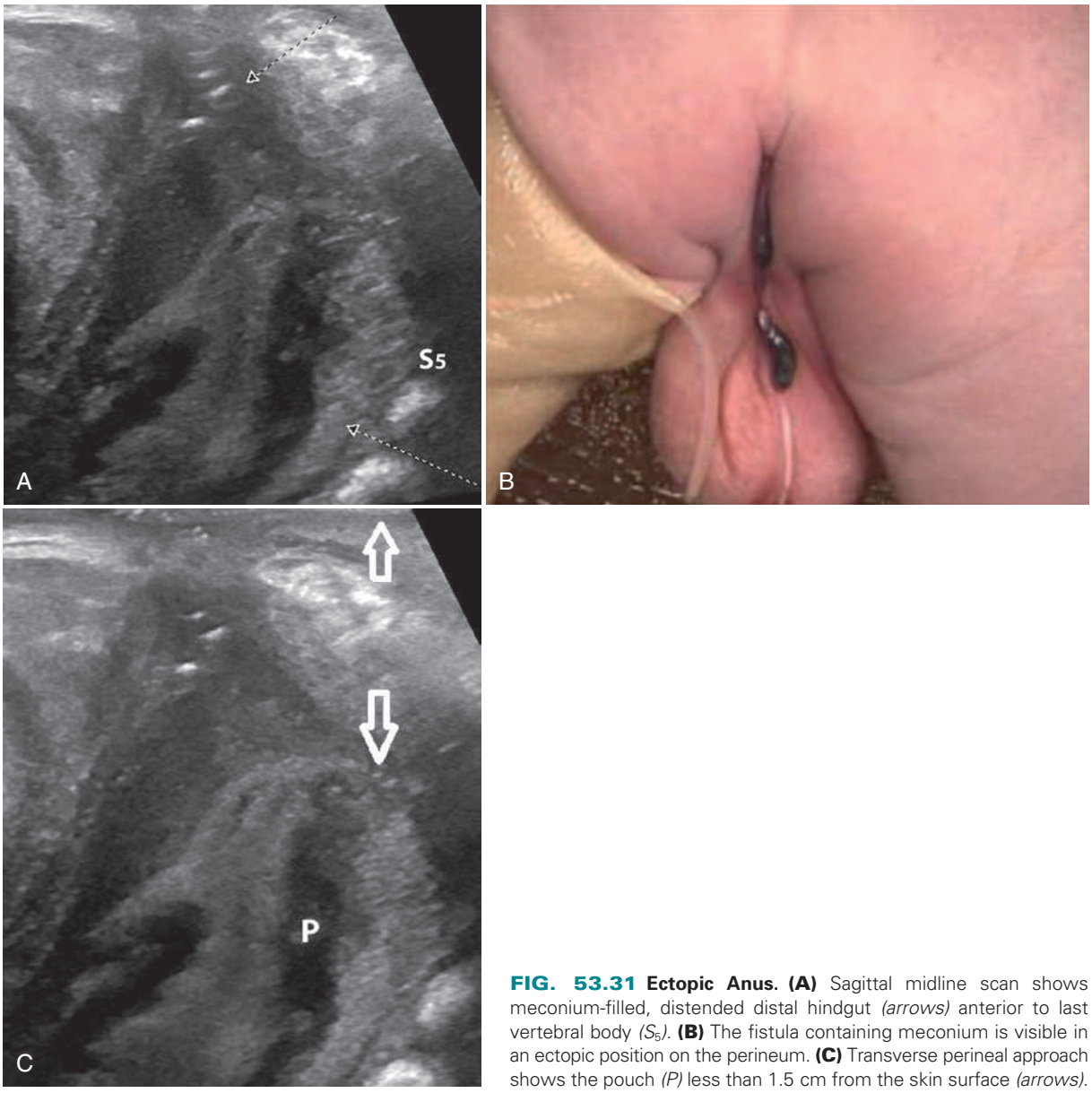

FIG. 53.31 Ectopic Anus. (A) Sagittal midline scan shows meconium-filled, distended distal hindgut *(arrows)* anterior to last vertebral body *(S_5).* **(B)** The fistula containing meconium is visible in an ectopic position on the perineum. **(C)** Transverse perineal approach shows the pouch *(P)* less than 1.5 cm from the skin surface *(arrows).*

conditions, including Crohn disease,[87,88] ulcerative colitis,[88] pseudomembranous colitis,[89,90] neutropenic colitis (typhlitis),[91] infectious colitis,[92-94] allergic colitis,[95] Kawasaki disease,[96] necrotizing enterocolitis (NEC),[97] hemolytic uremic syndrome,[98] graft-versus-host disease,[99,100] glycogen storage disease type 1B,[101] and chronic granulomatous disease of childhood.

Causes of Intestinal Wall Thickening

Inflammatory bowel disease (Crohn disease or regional enteritis, ulcerative colitis)
Yersinia, Campylobacter ileocolitis
Colitis
Perforated appendicitis
Rotavirus
Cytomegalovirus (CMV) infection
Typhlitis
Chronic granulomatous disease
Eosinophilic enteritis
Hematoma (Henoch-Schönlein purpura, trauma)
Hemolytic uremic syndrome
Graft-versus-host disease
Intussusception
Lymphoma
Benign tumor
Tuberculosis (rare)
Celiac disease

Sonography can sometimes differentiate **mucosal** from **transmural** inflammation. If the inflammatory process involves primarily the mucosa (e.g., **ulcerative colitis, pseudomembranous colitis, typhlitis**), the inner echogenic mucosal layer becomes thickened and sometimes nodular or irregular, but the outer muscular layer of the wall remains thin (Fig. 53.32). When the inflammation involves the entire intestinal wall (e.g., **regional enteritis**), thickening of the entire wall is seen (Fig. 53.33). Color Doppler sonography demonstrates increased blood flow to the thickened intestinal loops with most inflammatory bowel conditions, with the submucosa containing the main vascular channels[102] (Fig. 53.34). Hypovascularity is more typical in hemolytic uremic syndrome.[98] Normal bowel wall also shows little signal with color or power Doppler imaging.

For elective procedures, patients should avoid eating solid foods for 4 hours before the examination, but noncarbonated liquids are encouraged to help displace bowel gas and partially fill the urinary bladder to displace small bowel from the pelvis. Compression techniques to displace bowel gas are well established for the evaluation of the cecum and appendix, ascending colon, descending colon, rectosigmoid colon, and small bowel loops in the left upper quadrant and right lower and left lower quadrants. Normal small bowel wall thickness is less than 2.5 mm and less than 2 mm for large bowel.[103] Wall thickness of greater than 3 mm is considered abnormal for the colon.[104] Stratification of wall layers is well depicted in normal small and large bowel. Loss of stratification

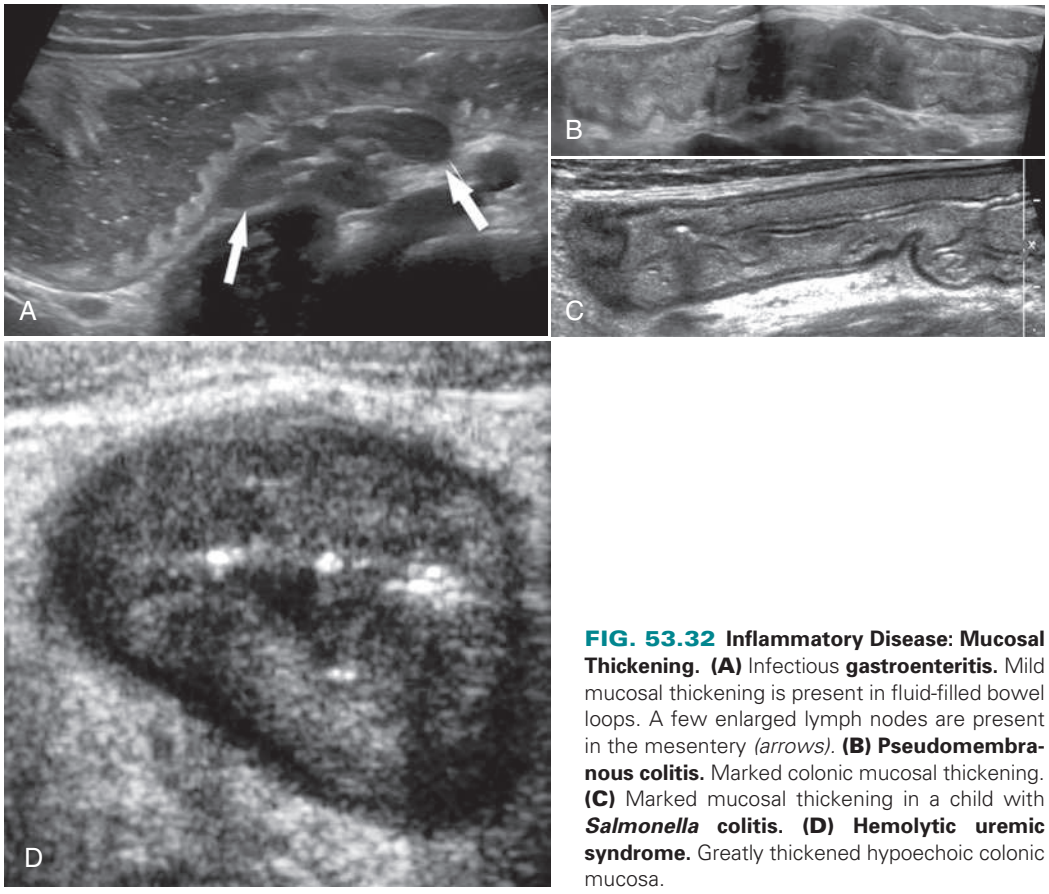

FIG. 53.32 Inflammatory Disease: Mucosal Thickening. (A) Infectious **gastroenteritis.** Mild mucosal thickening is present in fluid-filled bowel loops. A few enlarged lymph nodes are present in the mesentery *(arrows).* **(B) Pseudomembranous colitis.** Marked colonic mucosal thickening. **(C)** Marked mucosal thickening in a child with ***Salmonella* colitis. (D) Hemolytic uremic syndrome.** Greatly thickened hypoechoic colonic mucosa.

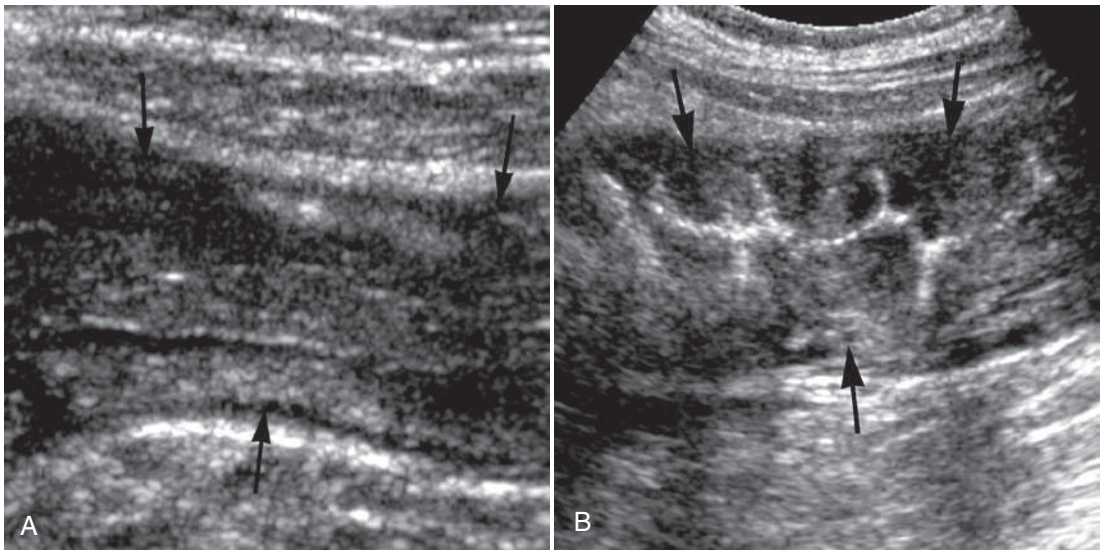

FIG. 53.33 Inflammatory Disease: Transmural Thickening. (A) Hypoechoic thickening of the wall of the ileum *(arrows)* in a 13-year-old child with regional enteritis. **(B)** Colitis. Note greatly thickened colonic wall *(arrows)*.

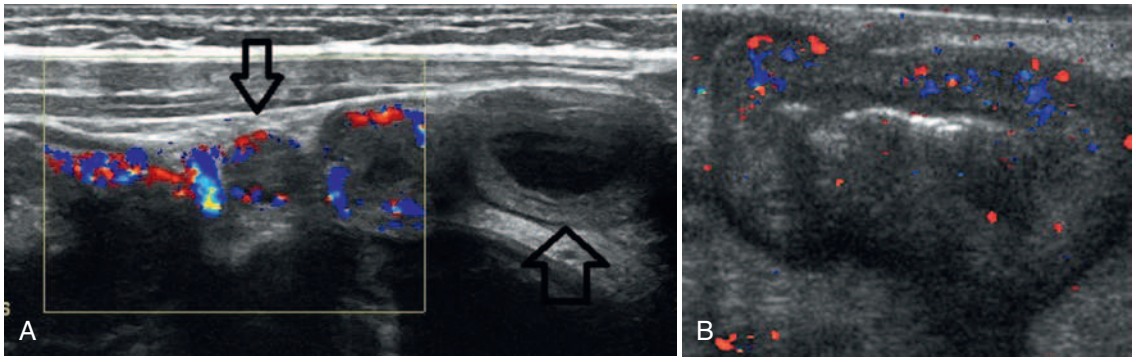

FIG. 53.34 Hyperemia With Bowel Inflammation. (A) Note the increased blood flow in the intestinal wall *(arrows)* in a child with nonspecific enteritis, demonstrated with color Doppler imaging. **(B)** Colonic wall thickening and hyperemia caused by **Shiga toxin–positive colitis.**

and loss of haustration are important indicators of wall inflammation.

Infectious colitis is a common cause of acute abdominal pain in children, primarily diagnosed by stool culture. However, ultrasound is helpful in distinguishing infectious bowel pathology from other causes such as intussusception and appendicitis in the young child and appendicitis or Crohn disease in the older child. Viral infections and gram-negative bacterial infections such as ***Shigella, Salmonella, Campylobacter, Escherichia coli,*** and ***Yersinia*** are common causes of enteritis.[105] Enterohemorrhagic ***E. coli*** can cause hemorrhagic colitis after ingestion of contaminated foods.

Lymphoid hyperplasia can be detected within the small bowel, and mesenteric lymph node enlargement may also be seen, especially with *Yersinia* and *Salmonella* (Fig. 53.35). History and immune status are important in creating a differential diagnosis, with ultrasound primarily used to exclude appendicitis, intussusception, and Crohn disease while confirming that there is an underlying enteritis present. Pneumatosis intestinalis can

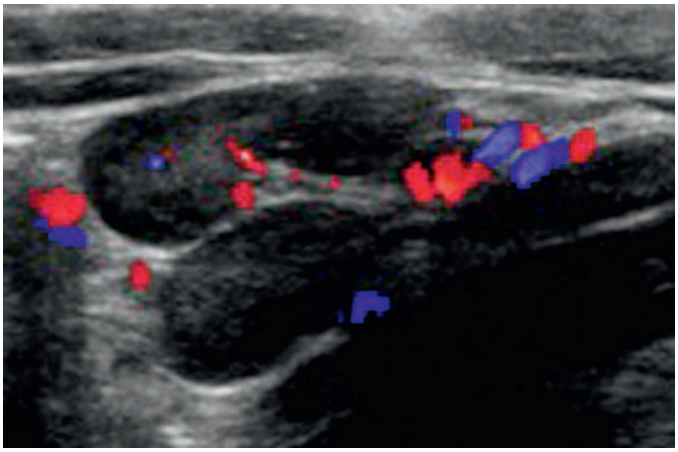

FIG. 53.35 Hypertrophied Lymphoid Tissue. A cluster of enlarged mesenteric lymph nodes in a child with ***Yersinia*** **colitis.**

FIG. 53.36 Ascariasis. The long slender parasite is clearly visible within the bowel on ultrasound *(arrows)*.

sometimes occur in infants and children with inflammatory conditions such as rotavirus infection or milk allergy.[106] *Mycobacterium tuberculosis,* a rare entity in developed countries, can be transmitted to bowel, with 90% of GI tuberculosis involving the distal ileum or cecum owing to the abundant lymphoid tissue. However, GI tuberculosis is an increasingly common disease in developing countries.[107]

On occasion, parasites may be found unexpectedly on ultrasound. **Ascariasis** is one of the most common intestinal infestations, prevalent in areas with poor sanitation. Eggs are passed with the feces of an infected person and can be transmitted by the fecal-oral route. Eggs hatch in the small intestine and can penetrate the intestinal mucosa and travel to the lung. On occasion, the worms can be identified in the bowel by their characteristic slender appearance and thin echogenic line within the body, representing the alimentary tract[108] (Fig. 53.36).

Enterobius vermicularis organisms, or **pinworms,** are the most common helminthic infection in the United States and Western Europe. Mobile pinworms have been seen within the appendix during sonographic studies as well as in the surgical setting.[109]

Crohn disease is the most common form of chronic inflammatory bowel disease in children. Ultrasound can be used as a screening tool for inflammatory bowel disease and also has value for assessing success of treatment and potential complications. Ultrasound sensitivity for the diagnosis of Crohn disease is comparable to that of other imaging modalities such as magnetic resonance enterography or CT,[110,111] and ultrasound is probably more suitable for use in young children. Bowel wall inflammation in Crohn disease is segmental and transmural and tends to be asymmetrical, with greater involvement of the mesenteric border of bowel (Fig. 53.37). A wall thickness of greater than 3 mm is a sign of active disease on follow-up ultrasound examinations.[112] In early Crohn disease, wall stratification may be preserved with thickening of the submucosal layer.[113] With more advanced disease, actively inflamed bowel wall shows loss of normal stratification and is hyperemic with decreased peristalsis. Skip areas and mesenteric inflammatory changes are characteristic of the disease. Lymph node hypertrophy and mesenteric fibrofatty proliferation also favor Crohn disease (Fig. 53.37B). Mesenteric inflammation that accompanies Crohn disease can be profound and can mimic other diagnoses in children on initial presentation with the disease.

Contrast-enhanced ultrasound (CEUS) has been shown to improve identification of the affected bowel loops in children with Crohn disease and can also depict the microvasculature of the bowel wall and surrounding mesentery.[114,115] Some studies have suggested that CEUS may help to distinguish inflammatory strictures from fibrotic strictures, which can help solve a common therapeutic dilemma in resolving Crohn disease.[116] Doppler measurement of the resistive index in the SMA has been used to assess progression of disease in patients with active Crohn disease with only partial correlation.[117] Investigations into use of ultrasound elastography to detect diminished tissue elasticity in the affected bowel are in the early stages. Sonography is indicated in children with suspected complications of regional enteritis. Ultrasound may identify distal right ureteral involvement by the inflammatory mass that can result in hydronephrosis. Although the fistulas and sinus tracts that develop in regional enteritis are usually not discernible sonographically, ultrasound can be used to identify associated intraabdominal abscesses (see Fig. 53.37C).

Henoch-Schönlein purpura, a condition caused by an **autoimmune vasculitis** involving small vessels in a variety of body systems, frequently involves the GI tract. Of these patients, 50% to 60% develop abdominal pain from intramural hemorrhage in the intestines, and this symptom may precede the development of the more characteristic purpuric skin rash. In such patients, sonography may detect the involved intestinal loops, which usually show circumferential, echogenic wall thickening, sometimes associated with small amounts of free abdominal fluid[53] (Fig. 53.38). Sonography also can be used to follow the resolution of the intestinal hemorrhage. **Intussusception** is a major complication of Henoch-Schönlein purpura, and sonography is highly useful to identify such an intussusception,[118] which usually involves only the small bowel and does not extend into the colon. Intestinal hemorrhage may also complicate bleeding diatheses or blunt abdominal trauma.

A variety of other conditions can result in thickening of the wall of the small bowel or colon, but few show distinguishing characteristics at imaging. **Hemolytic uremic syndrome** is associated with *E. coli* 0157:H7 infection, characterized by hemolytic anemia, thrombocytopenia, and renal failure. Hemolytic uremic syndrome is usually preceded by a severe hemorrhagic colitis. Color Doppler imaging reveals that the thickened bowel segments are hypovascular,[98] probably secondary to fibrin microthrombi that develop from factors released by the damaged endothelium (see Fig. 53.32D). **Graft-versus-host disease** in bone marrow transplant patients occurs when the transplanted tissue mounts an attack on host tissues. Skin, liver, and GI involvement is common. Acute graft-versus-host disease occurs within 100 days and involves the small intestine in 75% to 100% of cases.[119] Circumferential bowel wall thickening and mucosal hyperemia, representing the neovascularization driven by

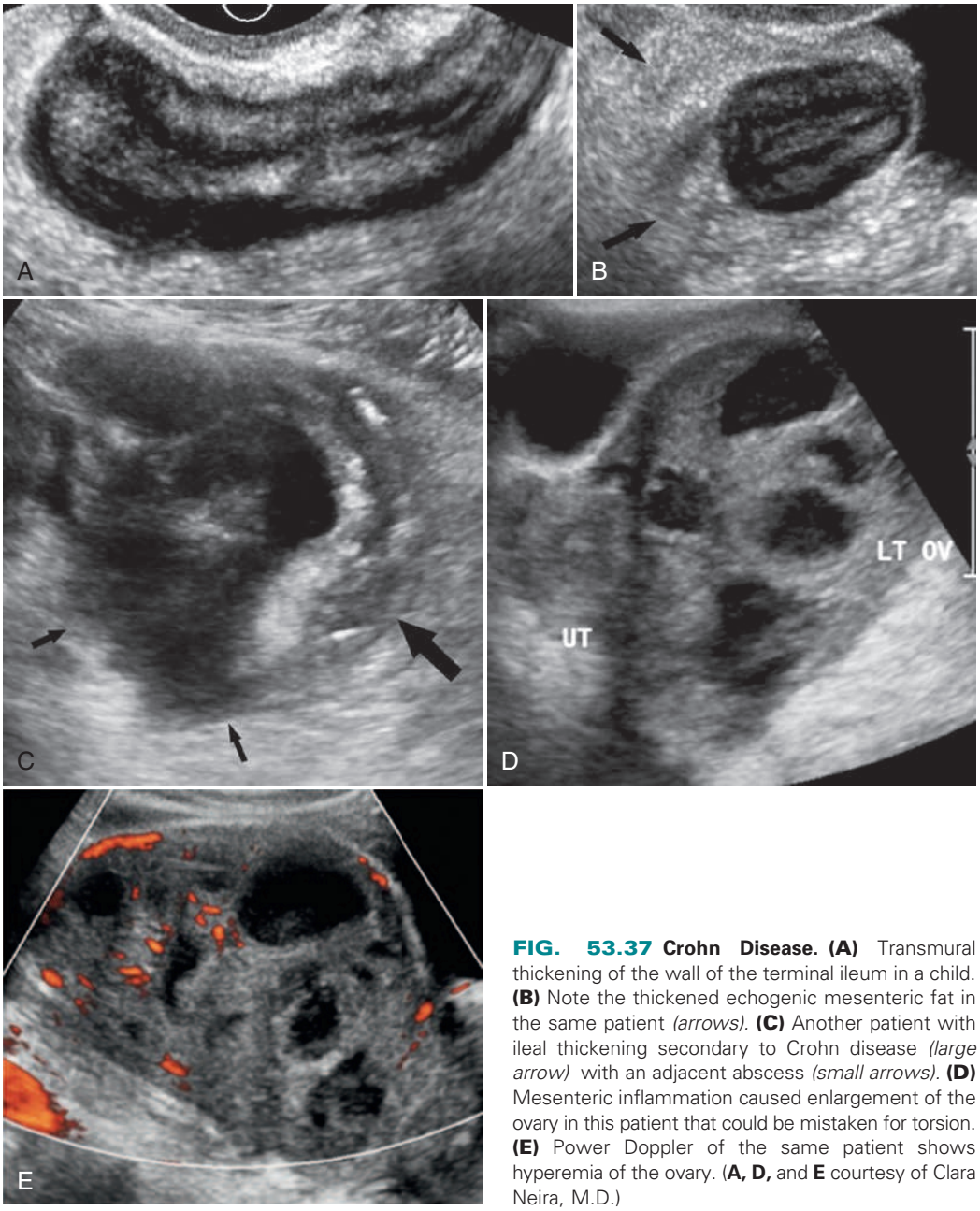

FIG. 53.37 Crohn Disease. (A) Transmural thickening of the wall of the terminal ileum in a child. **(B)** Note the thickened echogenic mesenteric fat in the same patient *(arrows)*. **(C)** Another patient with ileal thickening secondary to Crohn disease *(large arrow)* with an adjacent abscess *(small arrows)*. **(D)** Mesenteric inflammation caused enlargement of the ovary in this patient that could be mistaken for torsion. **(E)** Power Doppler of the same patient shows hyperemia of the ovary. (**A, D,** and **E** courtesy of Clara Neira, M.D.)

vasculogenesis in the early stages, are the predominant findings on ultrasound with mild bowel dilation. Graft-versus-host disease involves diffuse long segments of bowel and may extend from duodenum to rectum. Intestinal injury results in abdominal pain, vomiting, and diarrhea. The thickened, featureless intestinal loops are visible with ultrasound. A thin rim of echogenic material lining the mucosal surface of the affected loops has been described[99] (Fig. 53.39). This membrane is thought to represent the fibrinous exudate often seen covering the ulcerated mucosa at endoscopy in this condition.

Necrotizing enterocolitis (NEC) is an important problem in premature newborns, affecting close to 10% of infants weighing less than 1500 g. NEC can also affect term and near-term infants. The etiology is believed to be multifactorial involving altered bacterial flora, ischemia, and activated proinflammatory intracellular cascades. NEC is usually detected radiographically, but early in the disease, the classic findings of bowel dilation and pneumatosis intestinalis may not be apparent. In such cases, high-resolution sonography can assess the thickness of the intestinal loops, pattern of bowel wall perfusion, pneumatosis, peristalsis, free air, and subsequent fluid collections with perforation (Fig. 53.40). Early in NEC, there is bowel thickening, but wall thinning of less than 1 mm was seen by Faingold and colleagues as highly suggestive of severe ischemia.[120,121] **Pneumatosis intestinalis** may be visible on sonography before it is seen on radiographs, appearing as small, punctate, echogenic foci in the nondependent wall

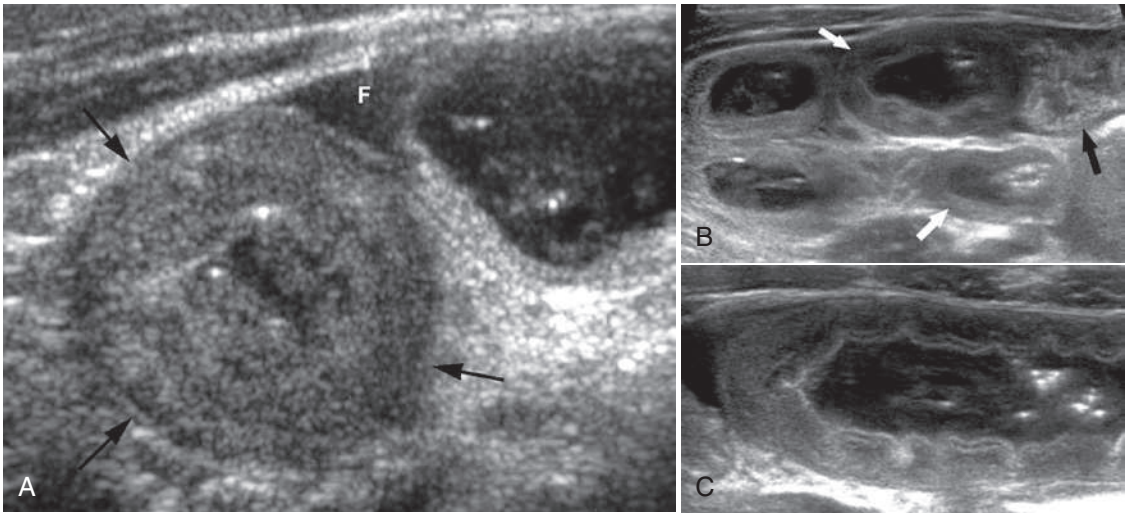

FIG. 53.38 Henoch-Schönlein Purpura. (A) Slightly hypoechoic, circumferential wall thickening of a single intestinal loop *(arrows),* with a small amount of adjacent anechoic free fluid *(F)* in a child with Henoch-Schönlein purpura. Note the normal thin wall of the adjacent bowel loop. **(B)** Another child with echogenic, small bowel thickening caused by Henoch-Schönlein purpura *(white arrows).* Note the normal wall on an adjacent loop of small bowel *(black arrow).* **(C)** Hypoechoic wall thickening in a different child with Henoch-Schönlein purpura.

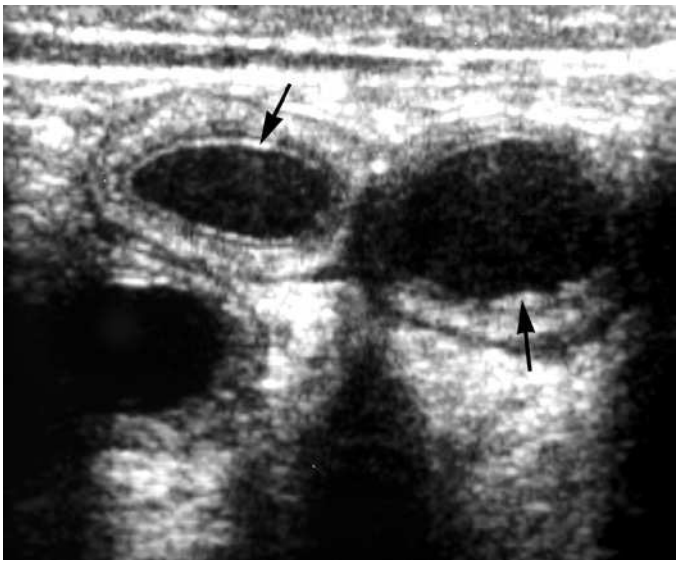

FIG. 53.39 Graft-Versus-Host Disease. Multiple thick-walled small bowel loops. A thin echogenic layer on the superficial surface of the mucosa *(arrows)* represents characteristic fibrinous deposit.

or as a granular echogenic ring within the bowel wall with posterior reverberation when more diffuse.[99,100] Intramural gas will not change with peristalsis or shift with change in positioning of the patient, which helps distinguish intramural from intraluminal gas. In addition, sonography can detect small amounts of gas within the portal venous system, which appear as small echogenic mobile foci within the liver, well before the gas is evident on plain films.[120-122] The patchy pattern with large amounts of mobile gas within the liver can be quite striking. **Pericholecystic hyperechogenicity** has also been described in infants with NEC.[123] The most serious complication is **bowel necrosis with perforation.** Increased flow velocity in the splanchnic arteries, most likely caused by vasoconstriction, has been suggested as a reliable early finding on Doppler sonography in NEC infants.[124] Free intra-abdominal air is detectable in infants who have minimal intestinal gas that has escaped through the perforation. Early free intraperitoneal gas can be detected most easily along the surface of the liver or within free intraperitoneal fluid.[100] The sonographic demonstration of **complex fluid collections with debris** can suggest perforation in such patients[125] (see Fig. 53.40E).

Sonographic Signs of Necrotizing Enterocolitis

- Thickened bowel loops with thinning of loops a late finding
- Echogenic foci caused by portal venous air
- Echogenic ring of intramural pneumatosis
- Pericholecystic hyperechogenicity
- Increased flow in superior mesenteric artery and celiac artery
- Complex fluid collections with perforation of bowel

Appendicitis

Ultrasound is now the recommended initial examination for those suspected of having appendicitis.[126] MRI is being used more often for those with large body habitus when ultrasound is unsuccessful.[127] Although CT is effective in diagnosing appendicitis, the growing trend to avoid unnecessary ionizing radiation is causing a shift away from the frequent use of CT.[128,129]

When appendicitis is not found, ultrasound often can help to suggest or confirm an alternative diagnosis.[130] In the end, the diagnostic approach to the acute abdomen remains a surgical management decision, but sonography is increasingly used to help diagnose appendicitis and to help manage postoperative complications.

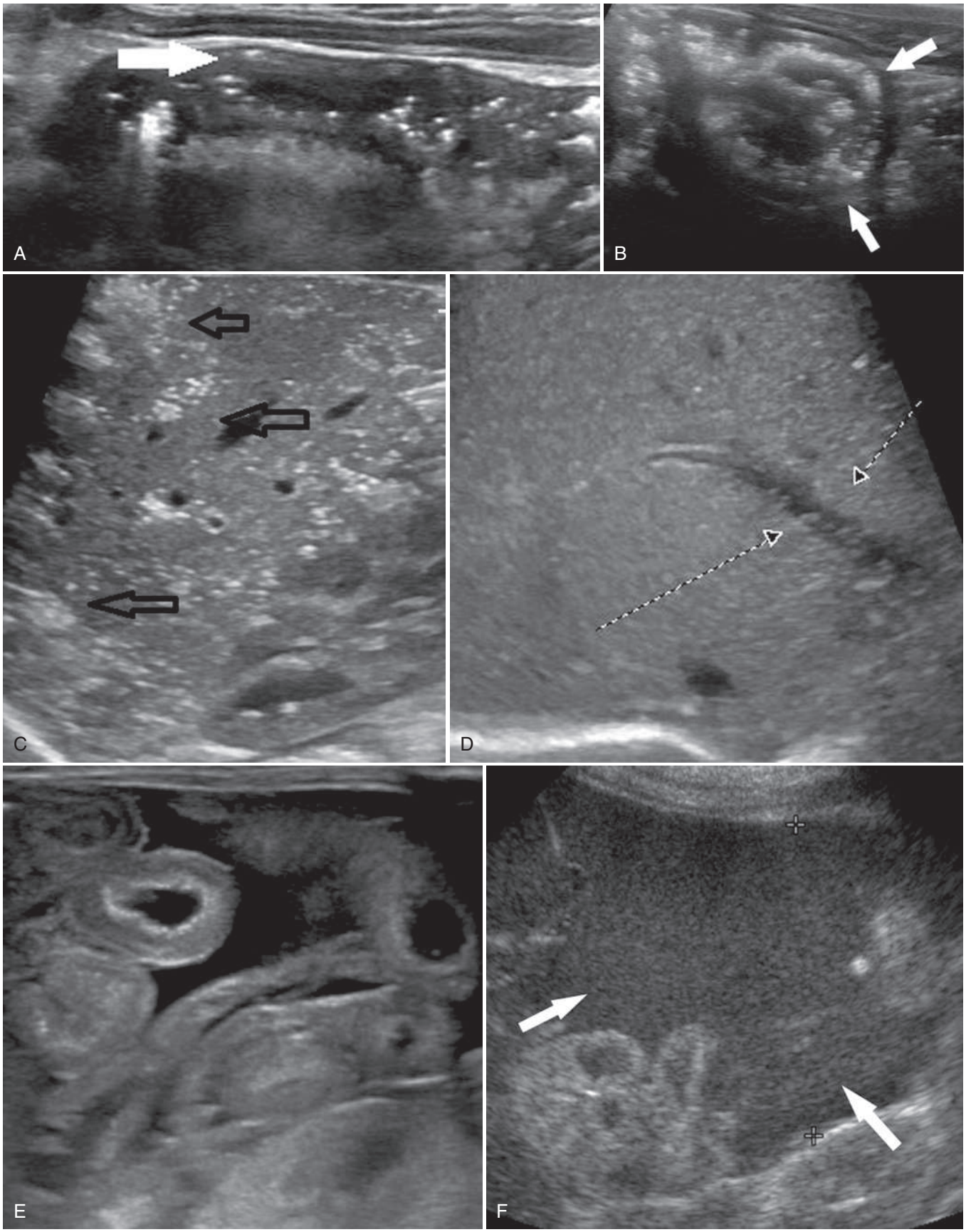

FIG. 53.40 Necrotizing Enterocolitis. (A) Mucosal and submucosal wall thickening with echogenic gas bubbles *(arrow)*. **(B)** Intramural gas (pneumatosis intestinalis) creates an echogenic ring *(arrows)*. **(C)** Widespread echogenic bubbles of gas in the portal venous system within the liver *(arrows)*. **(D)** Gas bubbles in the portal vein *(arrows)*. **(E)** Another infant shows thickened bowel loops with no pneumatosis and anechoic free fluid. **(F)** Fluid with echogenic debris *(arrows)* was caused by perforation in this infant.

Sonographic Signs of Appendicitis

Noncompressible, blind-ended, tubular structure
Diameter of tube ≥6 mm
Fluid trapped within nonperforated appendix
Target appearance of echogenic mucosa around fluid center surrounded by hypoechoic muscle
Fecalith: echogenic focus with pronounced posterior acoustic shadowing
Hypervascular appendix on color Doppler ultrasound
Gangrenous appendix: lack of flow on color Doppler ultrasound

Sonography of a child with acute abdominal pain is a procedure that requires patience and experience. The examination is facilitated by clinically localizing the pain, and even young children can help to guide the examination if asked to point with one finger to the site of maximal tenderness. Posterior manual compression and left lateral decubitus positioning may help to identify the appendix in patients whose appendix is not initially seen with graded-compression technique.[131] The ascending colon can be used as a helpful landmark, following the lateral border identified by haustrations to identify the cecum, then localizing the terminal ileum as the appendix, which arises 1 to 2 cm below the origin of the terminal ileum. The appendix is retrocecal in position in up to 68% of cases and within the pelvis in up to 53%.[132,133] Thus the examination should include the paracolic gutter, and a larger curvilinear probe may be needed to assess a low-positioned pelvic appendix. The normal appendix is easily compressible and smaller than the inflamed appendix, usually measuring less than 6 mm in diameter (Fig. 53.41). When the appendix cannot be found sonographically, the study findings are generally considered indeterminate. Standardized interpretive schemes that evaluate integrity of the appendix and assess inflammatory changes of the right lower quadrant have been shown to improve diagnostic accuracy.[134,135]

Sonographically, the acute, inflamed appendix appears as a blind-ending tubular structure that is noncompressible and measures 6 mm or greater in diameter[136] (Fig. 53.42). Size of the appendix can vary significantly in patients with both normal and abnormal appendices, and the 6-mm criterion is more useful for excluding appendicitis than for confirming it.[137] Viral-associated lymphoid hyperplasia thickens the hypoechoic appendiceal wall and can increase the maximum outer diameter of the appendix but should have no intraluminal fluid and no periappendiceal fat because the serosa is not involved (Fig. 53.43). However, there can be mural hyperemia and recurrent pain, sometimes leading to surgical intervention, although typically the lymphoid hyperplasia spontaneously resolves.[105] It is interesting to note that this was described by Symmers in *JAMA* in 1919.[138] Careful examination of the appendiceal tip should be performed in the presence of lymphoid hyperplasia, because the lymphoid tissue can predispose to appendicitis of the tip in some cases.[139] Fecal material impacted within the appendix, a nonsurgical condition treated with a bowel cleansing regimen, also increases the outer diameter, but the wall stratification of the appendix should be preserved and there should be no inflammatory change or hyperemia.[140]

Demonstration of other, associated sonographic abnormalities improves confidence in the diagnosis of appendicitis. **Fluid** is often seen trapped within a nonperforated appendix, and the surrounding echogenic mucosal layer and hypoechoic muscular layer of the appendiceal wall, combined with the central anechoic fluid, give the appendix a target appearance in cross section. **Fecaliths,** even those not calcified, can often be identified, appearing as echogenic foci with pronounced posterior acoustic shadowing (see Fig. 53.42D). A small amount of fluid may be seen adjacent to the appendix, even in the absence of perforation. Mesenteric lymphadenopathy frequently accompanies appendicitis, but alone is a nonspecific finding seen with other types of abdominal inflammation.[141] Thickening and increased echogenicity of the periappendiceal mesenteric fat is a valuable secondary finding, and the presence of more than one ultrasound sign of inflammation should be considered strong evidence of appendicitis, even if other definitive signs are absent.[142-144]

An advantage of sonography over other imaging modalities is the ability to correlate the pain of appendicitis with the imaging findings. Pinpoint tenderness with compression over the appendix is diagnostic in many children.[136] In cases of **perforated** appendicitis, the appendix itself is often more difficult to identify than in acute nonperforated appendicitis.[145] With perforation, the appendix becomes decompressed, and increasing intestinal gas from adynamic ileus and functional obstruction can interfere with the ultrasound examination Nevertheless, a careful, graded-compression technique may allow detection of focal aperistaltic bowel in the right lower quadrant, or a complex fluid collection representing an **abscess**[146] (Fig. 53.44A). Loss of the normal echogenic mucosal integrity suggests a **gangrenous appendix** (Fig. 53.44B-C), often associated with signs of perforation including echogenic periappendiceal fluid, abscess, interloop fluid collections, marked periappendiceal fat thickening, and aperistaltic bowel loops (Fig. 53.44D-E).

The risk of appendiceal perforation is greater in children younger than 4 years, because of many factors including limited verbal skills and lower incidence and thus less suspicion at younger ages.[147] The omentum is also poorly developed and almost devoid of fat in young children and thus is unable to contain a perforation. Diarrhea is a common presenting sign in young children and often confused with gastroenteritis, leading to a delay in diagnosis and the greater incidence of perforation.[148,149] After perforation, increasing flow may be seen in the soft tissues surrounding the appendix, and widespread abdominal fluid collections may be present at time of diagnosis owing to the lack of omental containment.[150,151]

Sonographic Signs of Appendiceal Perforation

Abscess formation
Loss of integrity of mucosal layer of the appendix
Presence of a fecalith in children younger than 8 years
Large amount of periappendiceal echogenic fat

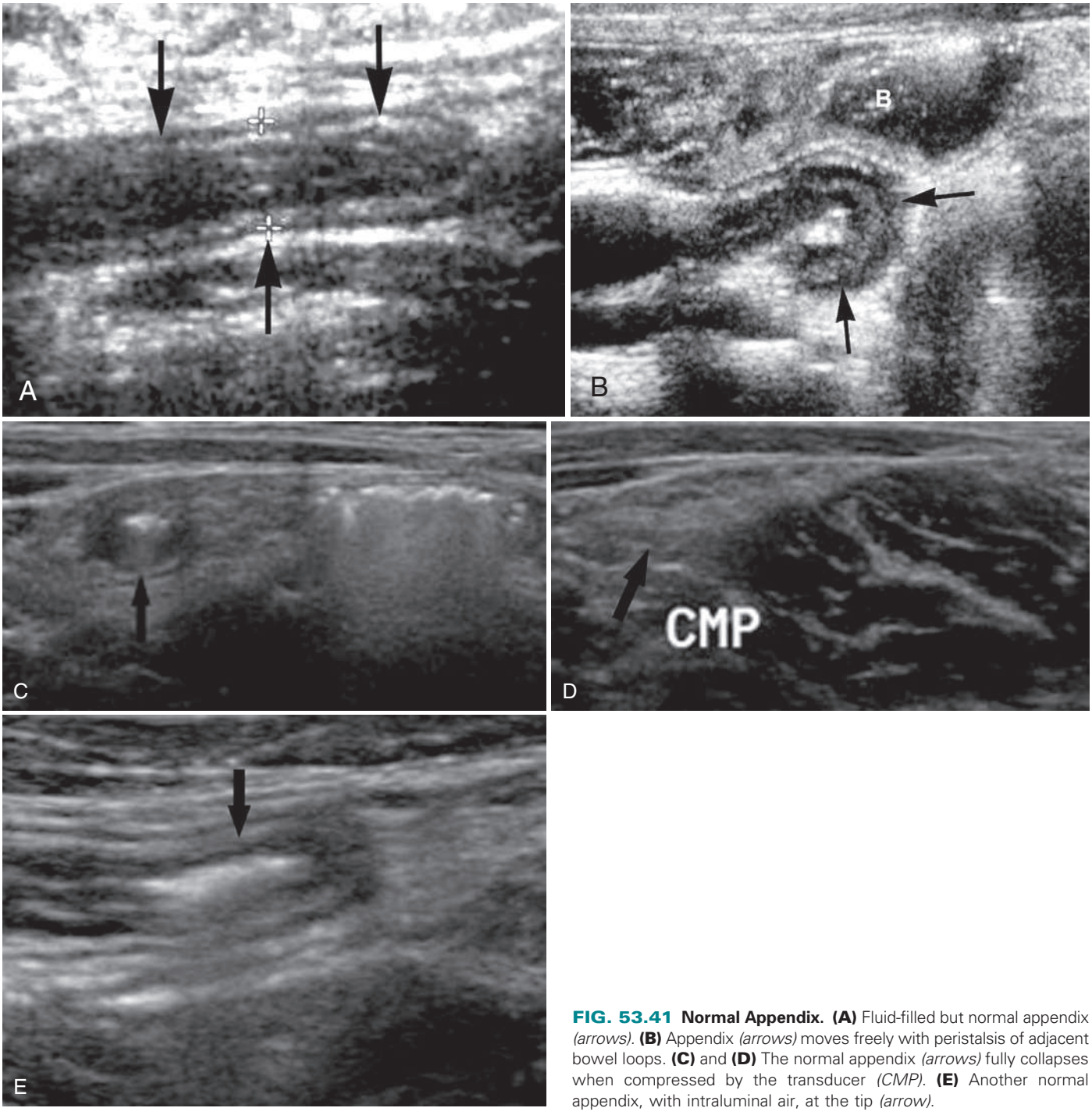

FIG. 53.41 Normal Appendix. (A) Fluid-filled but normal appendix *(arrows)*. **(B)** Appendix *(arrows)* moves freely with peristalsis of adjacent bowel loops. **(C)** and **(D)** The normal appendix *(arrows)* fully collapses when compressed by the transducer *(CMP)*. **(E)** Another normal appendix, with intraluminal air, at the tip *(arrow)*.

It is important to remember that many inflammatory conditions of the intestine other than appendicitis may be associated with small amounts of **free fluid surrounding the bowel loops.** Therefore small collections of simply echolucent fluid without other definitive evidence of appendicitis should not necessarily suggest an appendiceal abscess.

Other inflammatory conditions in the right lower quadrant may resemble appendicitis clinically but may be identified sonographically. **Mesenteric adenitis** refers to inflammation confined to the mesenteric lymph nodes in patients with a normal appendix. The condition is often associated with viral infection and usually is self-limited. Clusters of enlarged mesenteric lymph nodes that number more than five and are tender with compression suggest the diagnosis,[102] especially when a normal appendix is also seen. Mild mucosal thickening in the distal ileum is a common associated finding (Fig. 53.45). Isolated mesenteric lymph nodes are common and should not be considered abnormal. **Omental infarction** is a less common cause of acute abdominal

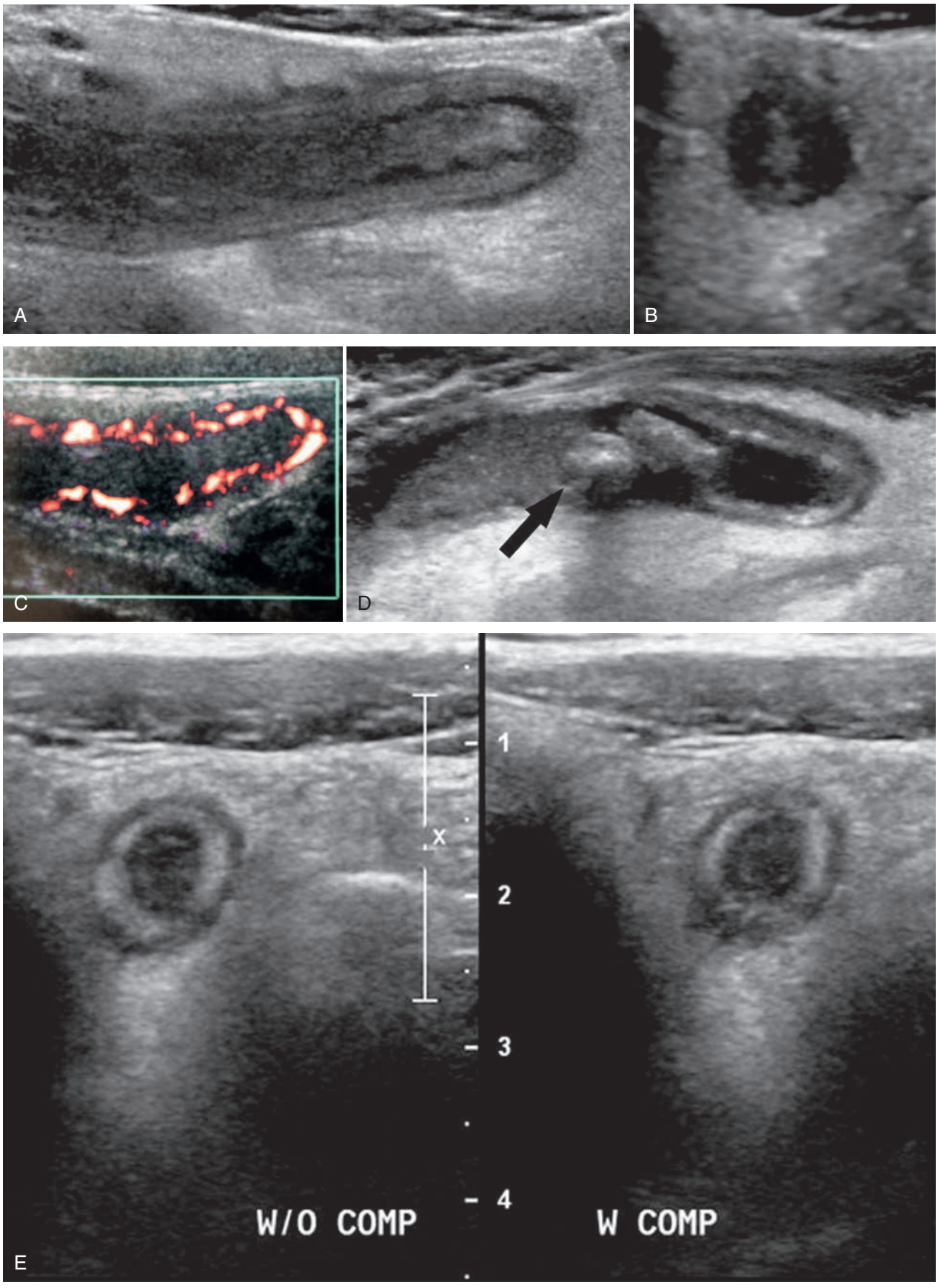

FIG. 53.42 Acute Appendicitis. (A) and **(B)** Longitudinal and transverse scans show a distended, fluid-filled appendix that measures 7 mm in diameter. **(C)** Power Doppler imaging reveals hyperemia of the appendiceal wall. **(D)** Echogenic fecalith with posterior shadowing *(arrow)* within a fluid-filled dilated appendix. Note the surrounding echogenic fat, indicating edema. **(E)** The inflamed appendix does not collapse with compression.

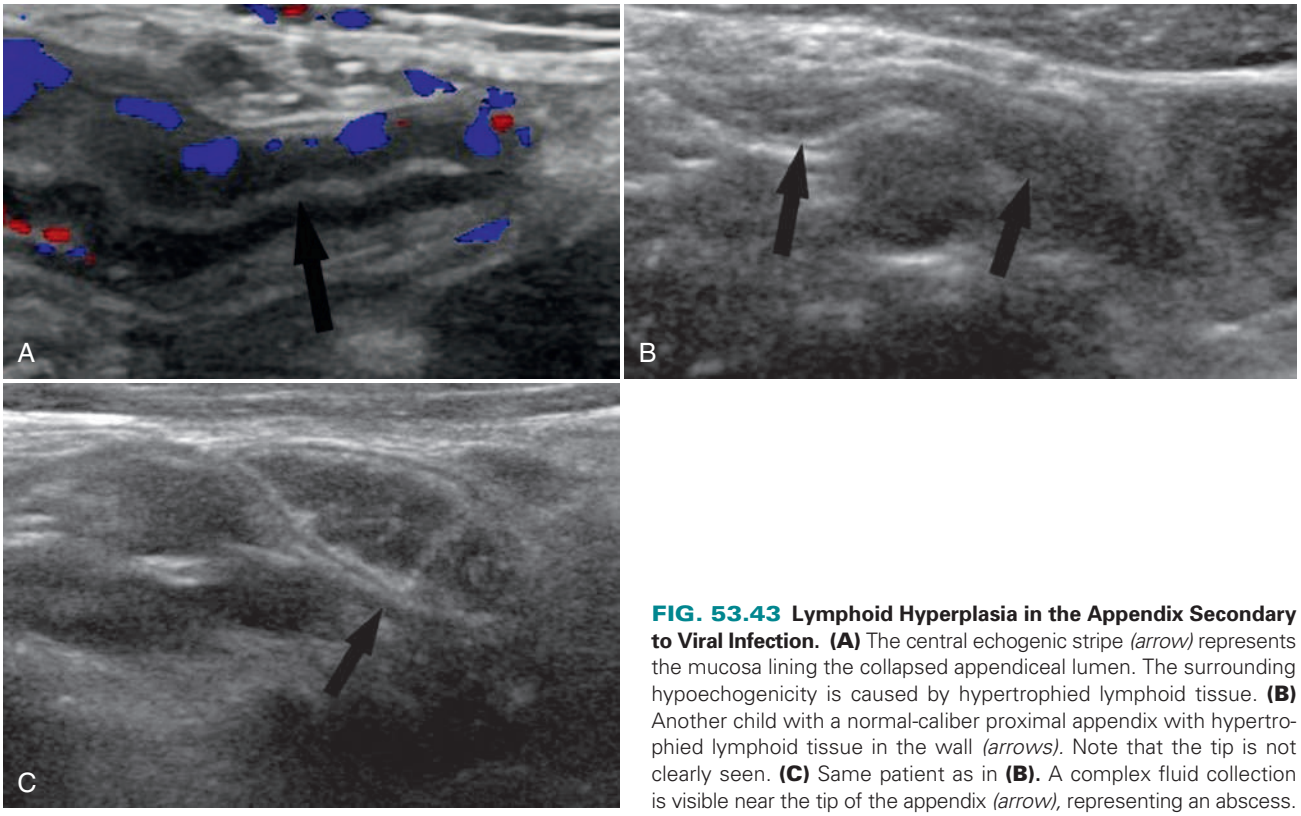

FIG. 53.43 Lymphoid Hyperplasia in the Appendix Secondary to Viral Infection. (A) The central echogenic stripe *(arrow)* represents the mucosa lining the collapsed appendiceal lumen. The surrounding hypoechogenicity is caused by hypertrophied lymphoid tissue. **(B)** Another child with a normal-caliber proximal appendix with hypertrophied lymphoid tissue in the wall *(arrows).* Note that the tip is not clearly seen. **(C)** Same patient as in **(B).** A complex fluid collection is visible near the tip of the appendix *(arrow),* representing an abscess.

pain in children. Ultrasound may reveal a heterogeneous mass or a localized focus of increased echogenicity in the omentum, characteristically located between the anterior abdominal wall and the colon.[151,152] **Meckel diverticulum** may become torsed or inflamed and may resemble an inflamed appendix or a complex pelvic mass sonographically[153,154] (Fig. 53.46A). The initial presentation of Crohn disease can be mistaken for appendicitis (Fig. 53.46B).

Gastrointestinal Neoplasms and Cysts

The superior ability of sonography to distinguish solid from cystic masses makes this examination an excellent choice for the diagnosis of the various types of cysts that can occur in the abdomen. The most common cysts associated with the GI tract are mesenteric cysts and GI duplication cysts. Characteristically, GI **duplication cysts** are filled with anechoic fluid and have a well-defined, double-layered wall that consists of an inner echogenic mucosal layer and a thin, outer hypoechoic muscular layer (Fig. 53.47A-C). These two layers are usually continuous throughout the cyst wall,[155,156] helping to distinguish GI duplication cysts from other simple-walled cysts, such as **mesenteric cysts** or **pseudocysts** (Fig. 53.47D-E). Occasionally, single-walled cysts appear to have a double-layered wall because of a fibrinous layer that can be deposited along the inner cyst wall after intracystic bleeding, but this is a relatively uncommon occurrence. Duplication cysts frequently contain foci of ectopic gastric mucosa, which can become inflamed and ulcerated. In such cases, intracystic hemorrhage may occur, and the resulting debris within the cystic fluid can cause the cyst to appear solid.[157] Some GI duplication cysts are pedunculated and therefore may be located at a site remote from the actual point of origin. Occasionally, active peristalsis of the cyst wall can be seen at real-time ultrasound.

Burkitt lymphoma is the most rapidly growing tumor in childhood, with a doubling time of about 24 hours.[158] The GI tract is involved in 22.5% of patients, with abdominal or pelvic masses in 45%. Burkitt lymphoma primarily affects the ileocecal region, unlike desmoplastic small round cell tumors, and can lead to secondary intussusception. Diffuse bowel wall thickening with adjacent nodal mass lesions in the mesentery and retroperitoneum are often seen at presentation. Ascites and rare peritoneal involvement can be seen. A solid mesenteric mass could be confused with a desmoplastic small round cell tumor. The appendix is infrequently involved, but appendiceal intussusception of the appendix secondary to Burkitt lymphoma has been observed (see Fig. 53.27B). Burkitt lymphoma does not commonly have calcifications at presentation.

Desmoplastic small round cell tumors represent a rare but highly malignant neoplasm, most commonly found in the peritoneal cavity with a male preponderance.[159] Disseminated tumor is often present at time of diagnosis, and distinguishing this from Burkitt lymphoma is difficult, although desmoplastic small round cell tumors have frequent calcification and extensive peritoneal involvement at presentation with a tendency to involve the retrovesical region.[159]

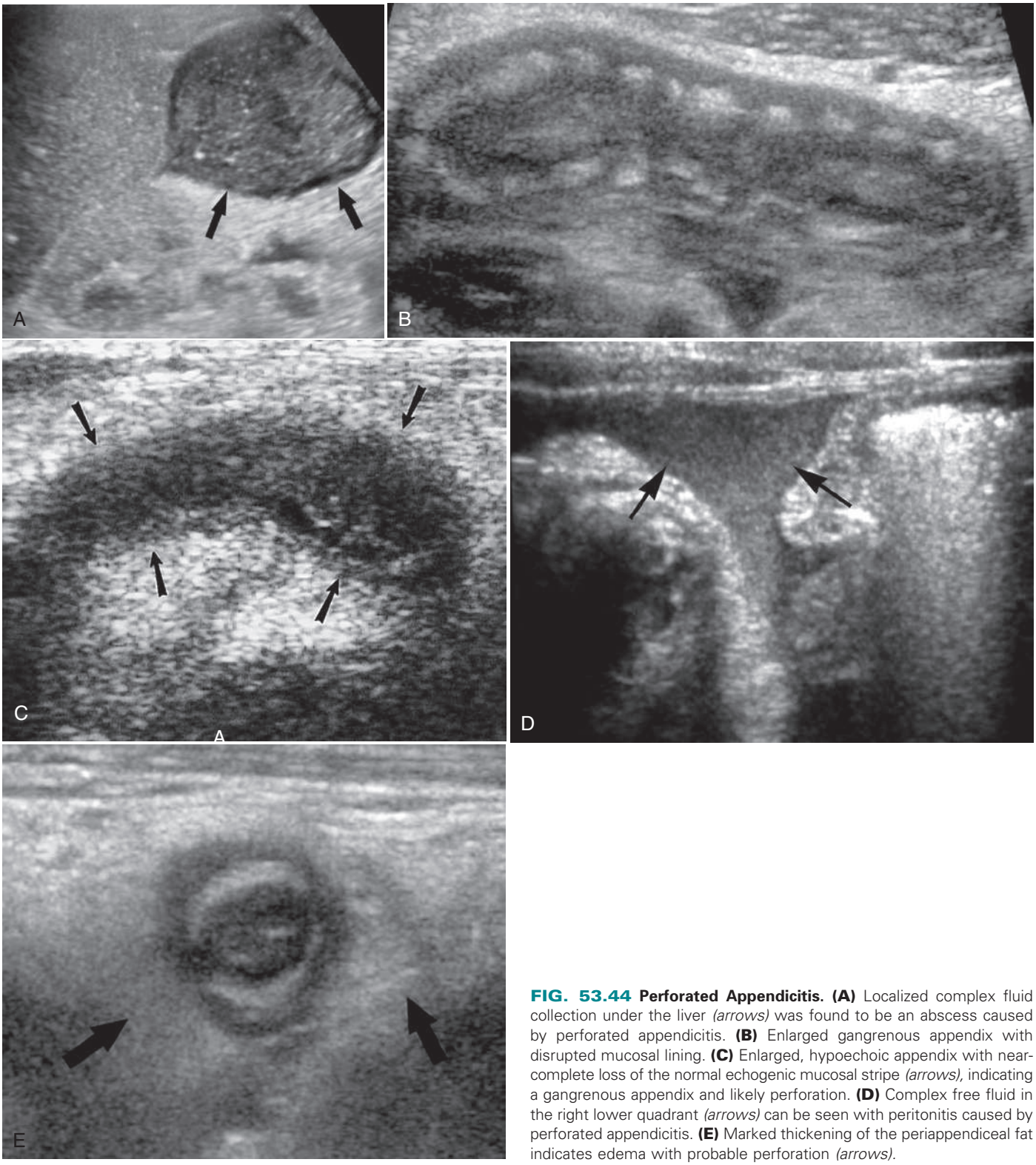

FIG. 53.44 Perforated Appendicitis. (A) Localized complex fluid collection under the liver *(arrows)* was found to be an abscess caused by perforated appendicitis. **(B)** Enlarged gangrenous appendix with disrupted mucosal lining. **(C)** Enlarged, hypoechoic appendix with near-complete loss of the normal echogenic mucosal stripe *(arrows),* indicating a gangrenous appendix and likely perforation. **(D)** Complex free fluid in the right lower quadrant *(arrows)* can be seen with peritonitis caused by perforated appendicitis. **(E)** Marked thickening of the periappendiceal fat indicates edema with probable perforation *(arrows).*

Abdominal desmoid tumors are a rare, benign type of tumor that can occur as a mass or masses in the mesentery, abdominal wall, retroperitoneum, and pelvis. There is an association with Gardner syndrome, and these will not have metastatic lesions.

Gastrointestinal stromal tumors rarely occur in the pediatric population and have a propensity to occur in females with a mean age of 12.6 years.[160] They arise in the muscularis propria, most commonly in the antrum and body of the stomach. Internal cystic areas are common and can represent hemorrhage or necrosis.

Sonography does not play a major role in the evaluation of GI neoplasms, but masses or polyps may be identified in some patients when the bowel is filled with fluid.[82,161] More often, intraluminal GI masses in children manifest with obstruction caused by intussusception. The mass that acts as a lead point for the intussusception may not always be sonographically discernible. Most solid tumors appear with a variably echogenic pattern and cannot be reliably distinguished by their sonographic characteristics.[45,162-164] **Lymphoma** tends to be hypoechoic and may be associated with ulceration. The tumors most likely to appear predominantly cystic are teratomas and lymphangiomas.[165-169] **Abdominal lymphangiomas** most frequently occur in the mesentery and can appear as solitary cysts or as multiloculated cystic masses[168] (Fig. 53.48A-B). **Gastrointestinal teratomas** usually have large cystic components, but echogenic fat and calcifications are also often visible[165,167,168] (Fig. 53.48C). **Hemangiomas** may involve the mesentery and are usually associated with hypervascularity and large feeding vessels.

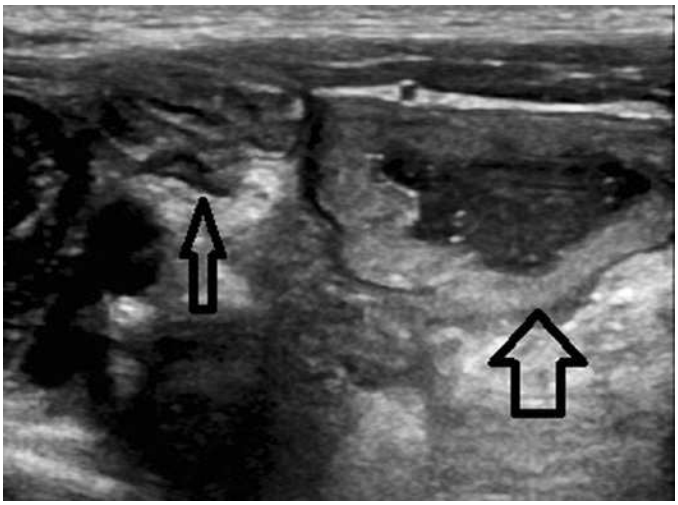

FIG. 53.45 Mesenteric Adenitis/Ileitis. Thickened mucosa in a small bowel loop *(large arrow)* with a normal appendix nearby *(small arrow)*.

PANCREAS

Normal Anatomy and Technique

The pancreas is easily imaged in children and normally appears relatively generous in size compared with the pancreas of an adult. The normal echotexture of the pancreas in childhood is homogeneous and most often isoechoic or hyperechoic compared with the liver. The normal pancreatic duct is usually not visible sonographically, unless a high-resolution linear transducer is used.

Pancreatitis

Pancreatitis is less common in children than in adults and is more likely to be acute rather than chronic. The most common causes of acute pancreatitis in children include blunt abdominal trauma (including abusive abdominal trauma), viral infection, and drug toxicity. Regardless of the cause, sonographic findings are usually sparse unless a complicating pseudocyst arises. The most common abnormal sonographic finding is pancreatic enlargement (Fig. 53.49A), but a normal-sized pancreas does not exclude the diagnosis. Decreased echogenicity of the pancreas can occur with pancreatitis,[170,171] but this is a difficult finding to substantiate because of the variable echogenicity of the normal pancreas in children.[171] Occasionally, increased echogenicity of the pararenal space may be encountered, the result of lipolysis of normal fat by pancreatic enzymes that have leaked into the hepatorenal space.[172]

Chronic or recurrent pancreatitis in children is most likely caused by congenital abnormalities affecting the biliary tract (e.g., **choledochal cysts, pancreas divisum, cystic**

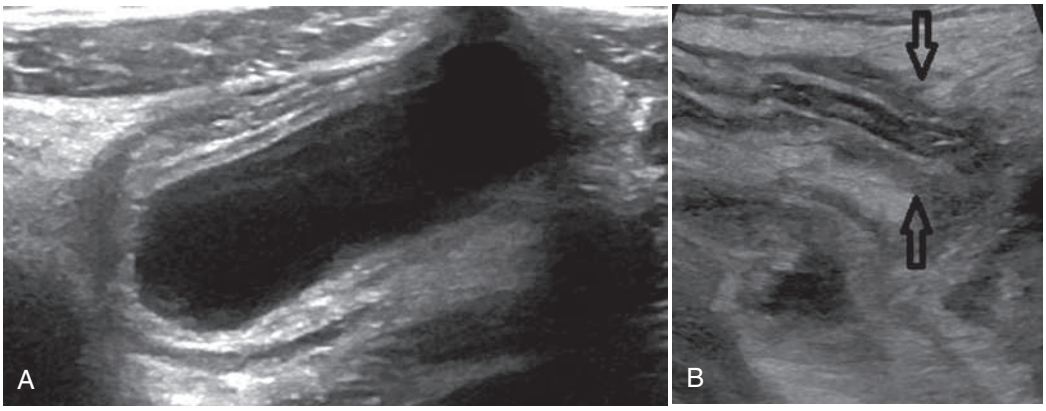

FIG. 53.46 Other Conditions Resembling Appendicitis. (A) Inflamed Meckel diverticulum. Transverse ultrasound of the right lower quadrant in a child with clinically suspected acute appendicitis. **(B)** Profound mesenteric inflammation in the region of the appendix was actually caused by **Crohn disease** *(arrows)*. The appendix was normal.

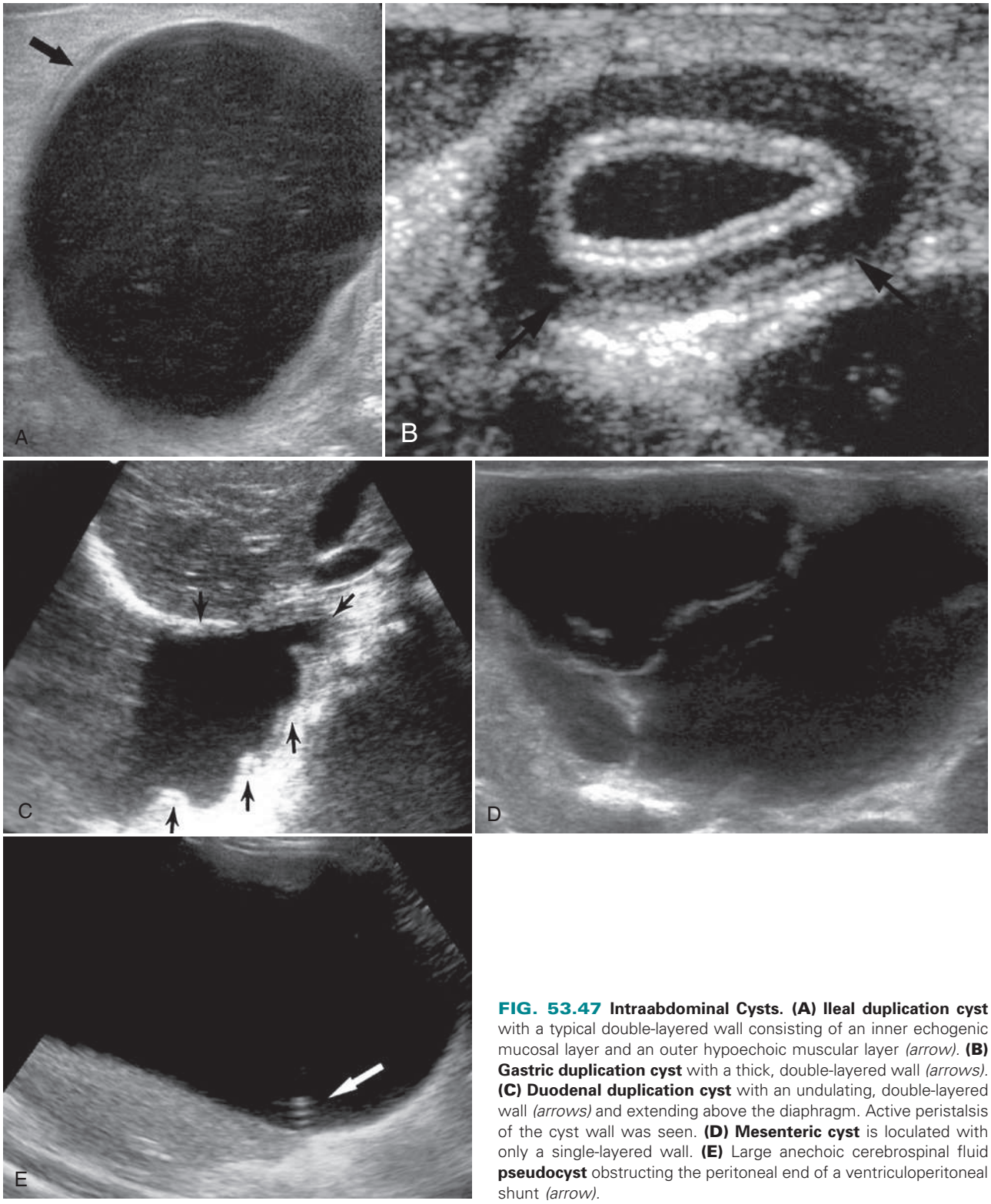

FIG. 53.47 Intraabdominal Cysts. (A) Ileal duplication cyst with a typical double-layered wall consisting of an inner echogenic mucosal layer and an outer hypoechoic muscular layer *(arrow).* **(B) Gastric duplication cyst** with a thick, double-layered wall *(arrows).* **(C) Duodenal duplication cyst** with an undulating, double-layered wall *(arrows)* and extending above the diaphragm. Active peristalsis of the cyst wall was seen. **(D) Mesenteric cyst** is loculated with only a single-layered wall. **(E)** Large anechoic cerebrospinal fluid **pseudocyst** obstructing the peritoneal end of a ventriculoperitoneal shunt *(arrow).*

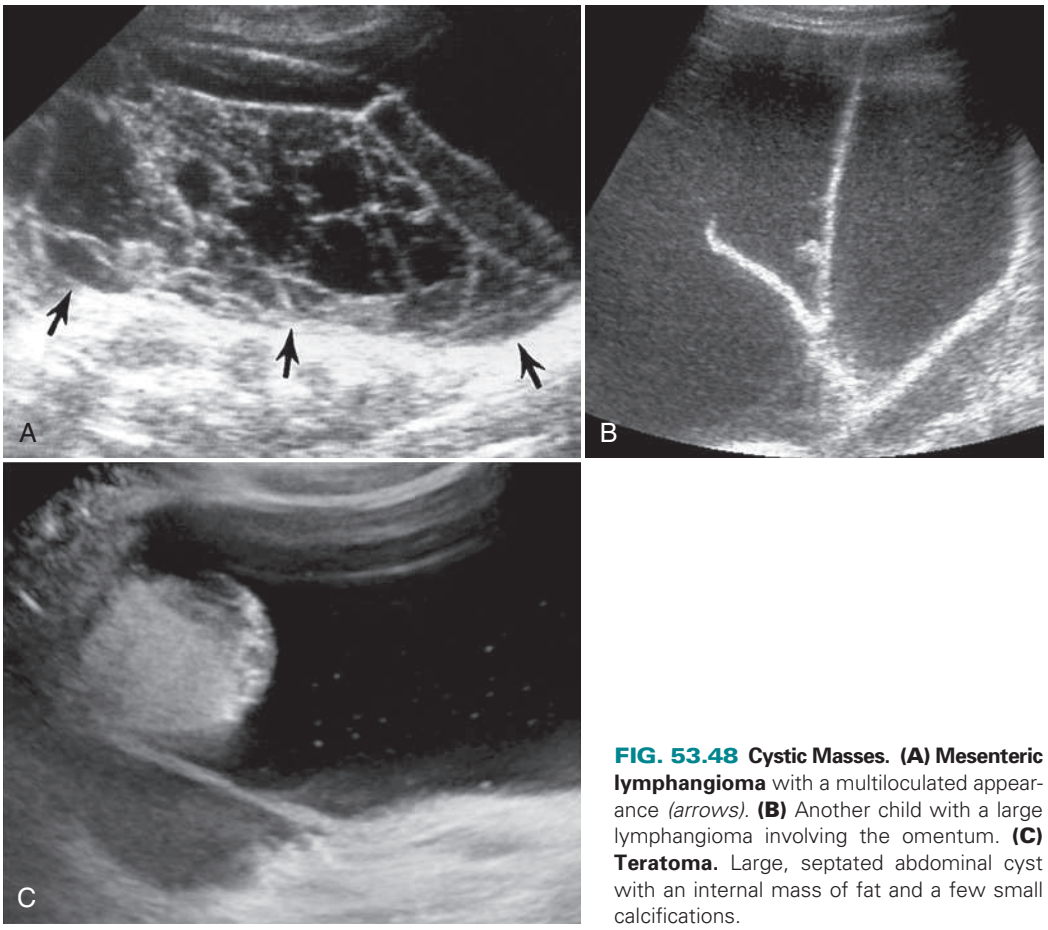

FIG. 53.48 Cystic Masses. (A) Mesenteric lymphangioma with a multiloculated appearance *(arrows)*. **(B)** Another child with a large lymphangioma involving the omentum. **(C) Teratoma.** Large, septated abdominal cyst with an internal mass of fat and a few small calcifications.

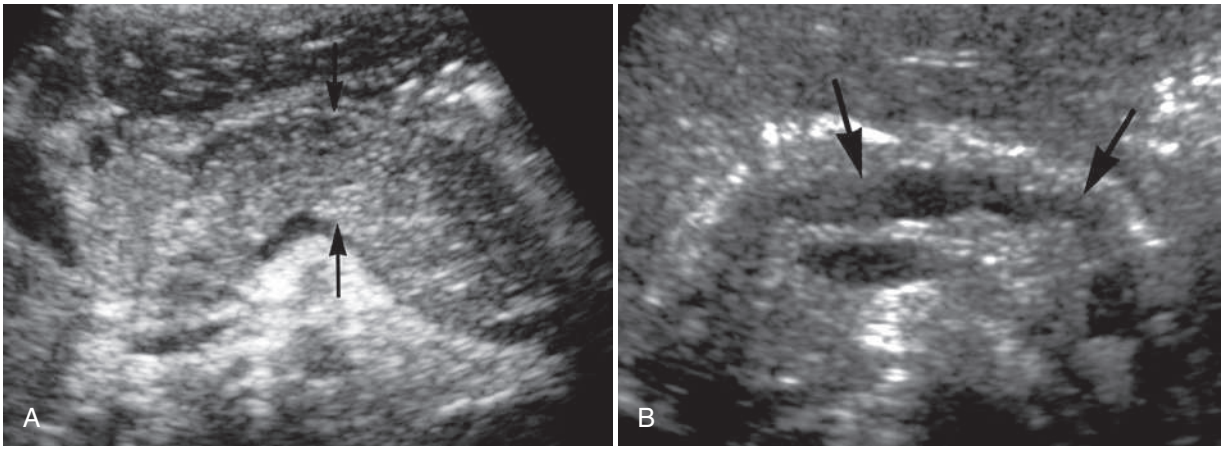

FIG. 53.49 Pancreatitis. (A) Child with pancreatic enlargement secondary to viral pancreatitis *(arrows)*. **(B)** Chronic pancreatitis in a 7-year-old child with **pancreas divisum** shows atrophic pancreas and a dilated pancreatic duct *(arrows)*.

fibrosis). With **cystic fibrosis,** precipitation or coagulation of secretions in the small pancreatic ducts leads to ductal concretions and obstruction. Distention of the ducts and acini leads to degeneration and replacement by small cysts. This ductal obstruction, along with atrophy of glandular elements and ensuing fibrosis, creates increased echogenicity of the pancreas[173-175] (see Fig. 53.49B). The gland is often small, and calcifications may be seen as punctate, echogenic foci within the hyperechoic pancreas. A similar appearance may be found in patients with hereditary autosomal dominant pancreatitis.[176]

Peripancreatic fluid collections often accompany acute pancreatitis, but such collections are not considered **pseudocysts** until they become persistent and are surrounded by a well-defined echogenic wall (Fig. 53.50). Many pancreatic pseudocysts are now treated conservatively, and sonography is useful for following

such patients to verify the spontaneous resolution of the fluid collection.[177] When the pseudocysts do not adequately resolve, sonography can be used to suggest suitability for percutaneous or endoscopic drainage.[178,179]

Pancreatic Masses

Tumors of the pancreas are extremely uncommon in children. The most common primary neoplasms are the benign insulinoma and adenocarcinoma.[180] **Insulinomas** are often difficult to detect sonographically, but intraoperative sonography has been used with success. Carcinoma of the pancreas usually appears as an echogenic or complex pancreatic mass. **Pancreatoblastoma** is a rare invasive tumor that is heterogeneous in texture, can encase vessels, and may metastasize widely.[181-183] Cystic masses of the pancreas include **lymphangioma, solid pseudopapillary tumor of the pancreas** (Fig. 53.51), and the rare **congenital pancreatic cyst.**[184,185] **Autoimmune pancreatitis** can cause focal enlargement of the pancreas that resembles a mass.[186]

Diffuse echogenic enlargement of the pancreas can be seen with **nesidioblastosis.** This is a tumorlike condition of the pancreas characterized by diffuse proliferation and persistence of primitive ductal epithelial cells. Nesidioblastosis is often associated with hypoglycemia and the **Beckwith-Wiedemann syndrome.** Diffusely increased echogenicity of the pancreas can also occur with fatty infiltration in the **Shwachman-Diamond syndrome** (Fig. 53.52), but in this condition the pancreas usually remains normal in size. Fatty replacement of the pancreas also can occur in children with cystic fibrosis or nonalcoholic fatty liver disease. Rarely, other types of tumors, such as in **leukemia,**[187] can infiltrate and enlarge the pancreas.

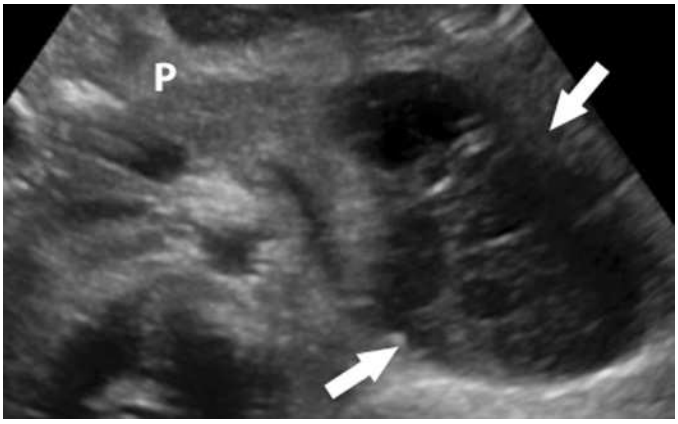

FIG. 53.50 Pancreatic Pseudocyst in Battered Child. Loculated fluid collection *(arrows)* in the region of the tail of the pancreas *(P).*

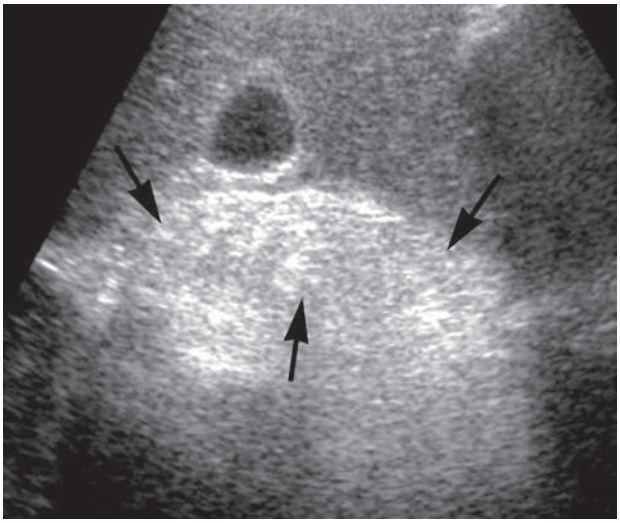

FIG. 53.52 Pancreatic Enlargement. Lipomatosis associated with Shwachman-Diamond syndrome. Echogenic enlargement of the pancreas *(arrows).*

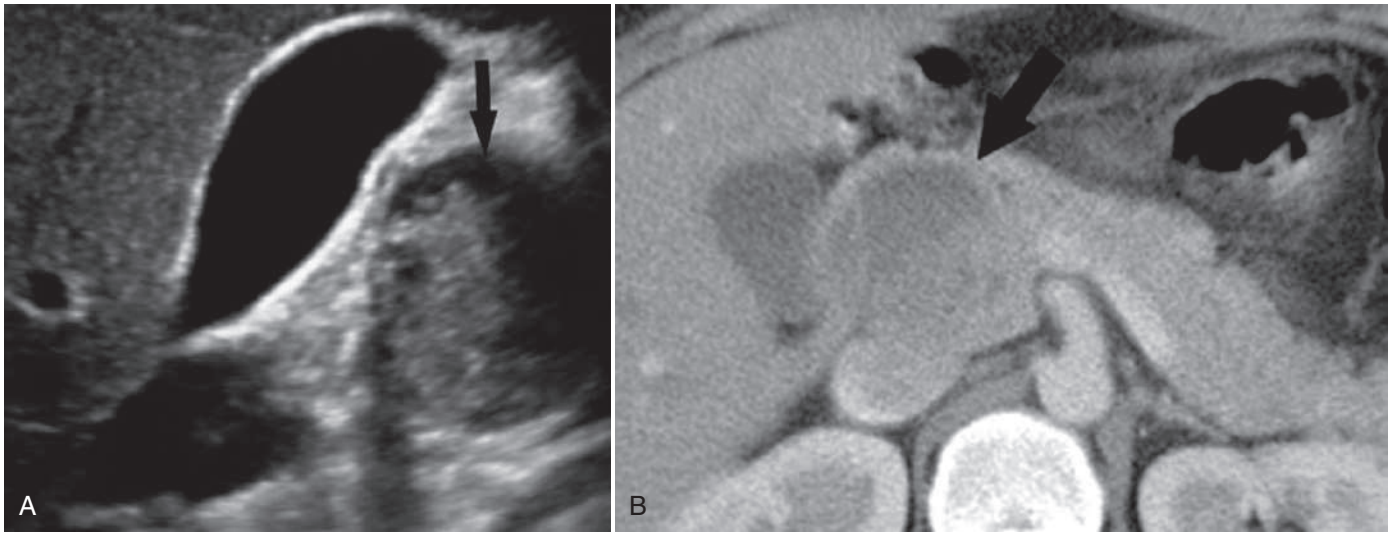

FIG. 53.51 Solid Pseudopapillary Tumor of the Pancreas. (A) Ultrasound shows a heterogeneous but predominantly cystic mass in the head of the pancreas that is only partially visible because of intestinal gas *(arrows).* **(B)** Computed tomography shows the partially cystic mass in the same child *(arrow).*

REFERENCES

1. Wright LL, Baker KR, Meny RG. Ultrasound demonstration of gastroesophageal reflux. J Ultrasound Med. 1988;7(8):471-475.
2. Gomes H, Lallemand A, Lallemand P. Ultrasound of the gastroesophageal junction. Pediatr Radiol. 1993;23(2):94-99.
3. Esposito F, Lombardi R, Grasso AC, et al. Transabdominal sonography of the normal gastroesophageal junction in children. J Clin Ultrasound. 2001; 29(6):326-331.
4. Farina R, Pennisi F, La Rosa M, et al. Contrast-enhanced colour-Doppler sonography versus pH-metry in the diagnosis of gastro-oesophageal reflux in children. Radiol Med. 2008;113(4):591-598.
5. Hirsch W, Kedar R, Preiss U. Color Doppler in the diagnosis of the gastroesophageal reflux in children: comparison with pH measurements and B-mode ultrasound. Pediatr Radiol. 1996;26(3):232-235.
6. Jang HS, Lee JS, Lim GY, et al. Correlation of color Doppler sonographic findings with pH measurements in gastroesophageal reflux in children. J Clin Ultrasound. 2001;29(4):212-217.
7. O'Keeffe FN, Stansberry SD, Swischuk LE, Hayden Jr CK. Antropyloric muscle thickness at US in infants: what is normal? Radiology. 1991;178(3): 827-830.
8. Hulka F, Campbell JR, Harrison MW, Campbell TJ. Cost-effectiveness in diagnosing infantile hypertrophic pyloric stenosis. J Pediatr Surg. 1997;32(11): 1604-1608.
9. Swischuk LE, Hayden Jr CK, Stansberry SD. Sonographic pitfalls in imaging of the antropyloric region in infants. Radiographics. 1989;9(3):437-447.
10. Hernanz-Schulman M, Sells LL, Ambrosino MM, et al. Hypertrophic pyloric stenosis in the infant without a palpable olive: accuracy of sonographic diagnosis. Radiology. 1994;193(3):771-776.
11. Hernanz-Schulman M, Zhu Y, Stein SM, et al. Hypertrophic pyloric stenosis in infants: US evaluation of vascularity of the pyloric canal. Radiology. 2003;229(2):389-393.
12. Rohrschneider WK, Mittnacht H, Darge K, Troger J. Pyloric muscle in asymptomatic infants: sonographic evaluation and discrimination from idiopathic hypertrophic pyloric stenosis. Pediatr Radiol. 1998;28(6): 429-434.
13. Teele RL, Smith EH. Ultrasound in the diagnosis of idiopathic hypertrophic pyloric stenosis. N Engl J Med. 1977;296(20):1149-1150.
14. Blumhagen JD, Maclin L, Krauter D, et al. Sonographic diagnosis of hypertrophic pyloric stenosis. AJR Am J Roentgenol. 1988;150(6): 1367-1370.
15. Cohen HL, Blumer SL, Zucconi WB. The sonographic double-track sign: not pathognomonic for hypertrophic pyloric stenosis; can be seen in pylorospasm. J Ultrasound Med. 2004;23(5):641-646.
16. Haller JO, Cohen HL. Hypertrophic pyloric stenosis: diagnosis using US. Radiology. 1986;161(2):335-339.
17. Lund Kofoed PE, Host A, Elle B, Larsen C. Hypertrophic pyloric stenosis: determination of muscle dimensions by ultrasound. Br J Radiol. 1988;61(721): 19-20.
18. Stunden RJ, LeQuesne GW, Little KE. The improved ultrasound diagnosis of hypertrophic pyloric stenosis. Pediatr Radiol. 1986;16(3):200-205.
19. Cohen HL, Schechter S, Mestel AL, et al. Ultrasonic "double track" sign in hypertrophic pyloric stenosis. J Ultrasound Med. 1987;6(3):139-143.
20. Hernanz-Schulman M, Neblett 3rd WW, Polk DB, Johnson JE. Hypertrophied pyloric mucosa in patients with hypertrophic pyloric stenosis. Pediatr Radiol. 1998;28(11):901.
21. Kim S, Chung CJ, Fordham LA, Specter BB. Coexisting hyperplastic antral polyp and hypertrophic pyloric stenosis. Pediatr Radiol. 1997;27(12): 912-914.
22. Callahan MJ, McCauley RG, Patel H, Hijazi ZM. The development of hypertrophic pyloric stenosis in a patient with prostaglandin-induced foveolar hyperplasia. Pediatr Radiol. 1999;29(10):748-751.
23. Janik JS, Wayne ER, Janik JP. Pyloric stenosis in premature infants. Arch Pediatr Adolesc Med. 1996;150(2):223-224.
24. Stark C, Rogers P, Eberly M, Nylund C. Association of prematurity with the development of infantile hypertrophic pyloric stenosis. Pediatr Res. 2015;78(2):218-222.
25. Demian M, Nguyen S, Emil S. Early pyloric stenosis: a case control study. Pediatr Surg Int. 2009;25(12):1053-1057.
26. Muramori K, Nagasaki A, Kawanami T. Ultrasonographic serial measurements of the morphologic resolution of the pylorus after Ramstedt pyloromyotomy for infantile hypertrophic pyloric stenosis. J Ultrasound Med. 2007;26(12): 1681-1687.
27. Yoshizawa J, Eto T, Higashimoto Y, et al. Ultrasonographic features of normalization of the pylorus after pyloromyotomy for hypertrophic pyloric stenosis. J Pediatr Surg. 2001;36(4):582-586.
28. Cohen HL, Zinn HL, Haller JO, et al. Ultrasonography of pylorospasm: findings may simulate hypertrophic pyloric stenosis. J Ultrasound Med. 1998;17(11):705-711.
29. Roma E, Kafritsa Y, Panayiotou J, et al. Is peptic ulcer a common cause of upper gastrointestinal symptoms? Eur J Pediatr. 2001;160(8):497-500.
30. Hayden CK, Swischuk LE, Rytting JE. Gastric ulcer disease in infants: US findings. Radiology. 1987;164(1):131-134.
31. Maves CK, Johnson JF, Bove K, Malott RL. Gastric inflammatory pseudotumor in children. Radiology. 1989;173(2):381-383.
32. Goldwag S, Bellah R, Ward K. Kogutt M. Sonographic detection of Ménétrier's disease in children. J Clin Ultrasound. 1994;22(9):567-570.
33. Mercado-Deane MG, Burton EM, Brawley AV, Hatley R. Prostaglandin-induced foveolar hyperplasia simulating pyloric stenosis in an infant with cyanotic heart disease. Pediatr Radiol. 1994;24(1):45-46.
34. McAlister WH, Katz ME, Perlman JM, Tack ED. Sonography of focal foveolar hyperplasia causing gastric obstruction in an infant. Pediatr Radiol. 1988;18(1):79-81.
35. Joshi A, Berdon W, Brudnicki A, et al. Gastric thumbprinting: diffuse gastric wall mucosal and submucosal thickening in infants with ductal-dependent cyanotic congenital heart disease maintained on long-term prostaglandin therapy. Ped Radiol. 2002;32(6):405-408.
36. Naik DR, Bolia A, Boon AW. Demonstration of a lactobezoar by ultrasound. Br J Radiol. 1987;60(713):506-508.
37. Ripolles T, Garcia-Aguayo J, Martinez MJ, Gil P. Gastrointestinal bezoars: sonographic and CT characteristics. AJR Am J Roentgenol. 2001; 177(1):65-69.
38. Naik S, Gupta V, Naik S, et al. Rapunzel syndrome reviewed and redefined. Dig Surg. 2007;24(3):157-161.
39. Lee KH, Han HY, Kim HJ, et al. Ultrasonographic differentiation of bezoar from feces in small bowel obstruction. Ultrasonography. 2015;34(3): 211-216.
40. Crowe JE, Sumner TE. Combined esophageal and duodenal atresia without tracheoesophageal fistula: characteristic radiographic changes. AJR Am J Roentgenol. 1978;130(1):167-168.
41. Hayden CK, Schwartz MZ, Davis M, Swischuk LE. Combined esophageal and duodenal atresia: sonographic findings. AJR Am J Roentgenol. 1983;140(2):225-226.
42. Hayden CK, Boulden TF, Swischuk LE, Lobe TE. Sonographic demonstration of duodenal obstruction with midgut volvulus. AJR Am J Roentgenol. 1984;143(1):9-10.
43. Loyer E, Dunne Eggli K. Sonographic evaluation of superior mesenteric vascular relationship in malrotation. Pediatr Radiol. 1989;19(3):173-175.
44. Zerin JM, DiPietro MA. Superior mesenteric vascular anatomy at US in patients with surgically proved malrotation of the midgut. Radiology. 1992;183(3):693-694.
45. Weinberger E, Winters WD, Liddell RM, et al. Sonographic diagnosis of intestinal malrotation in infants: importance of the relative positions of the superior mesenteric vein and artery. AJR Am J Roentgenol. 1992;159(4): 825-828.
46. Yousefzadeh D. The position of the duodenojejunal junction: the wrong horse to bet on in diagnosing or excluding malrotation. Pediatr Radiol. 2009;39(S2):172-177.
47. Menten R, Reding R, Godding V, et al. Sonographic assessment of the retroperitoneal position of the third portion of the duodenum: an indicator of normal intestinal rotation. Pediatr Radiol. 2012;42(8):941-945.
48. Ashley LM, Allen S, Teele R. A normal sonogram does not exclude malrotation. Pediatr Radiol. 2001;31(5):354-356.
49. Cremin BJ, Solomon DJ. Ultrasonic diagnosis of duodenal diaphragm. Pediatr Radiol. 1987;17(6):489-490.

50. Hayashi K, Futagawa S, Kozaki S, et al. Ultrasound and CT diagnosis of intramural duodenal hematoma. Pediatr Radiol. 1988;18(2):167-168.
51. Hernanz-Schulman M, Genieser NB, Ambrosino M. Sonographic diagnosis of intramural duodenal hematoma. J Ultrasound Med. 1989;8(5):273-276.
52. Orel SG, Nussbaum AR, Sheth S, et al. Duodenal hematoma in child abuse: sonographic detection. AJR Am J Roentgenol. 1988;151(1):147-149.
53. Couture A, Veyrac C, Baud C, et al. Evaluation of abdominal pain in Henoch-Schönlein syndrome by high frequency ultrasound. Pediatr Radiol. 1992;22(1):12-17.
54. Carroll BA, Moskowitz PS. Sonographic diagnosis of neonatal meconium cyst. AJR Am J Roentgenol. 1981;137(6):1262-1264.
55. Bowen A, Mazer J, Zarabi M, Fujioka M. Cystic meconium peritonitis: ultrasonographic features. Pediatr Radiol. 1984;14(1):18-22.
56. Applegate KE. Clinically suspected intussusception in children: evidence-based review and self-assessment module. AJR Am J Roentgenol. 2005;185(3 Suppl.):S175-S183.
57. Bhisitkul DM, Listernick R, Shkolnik A, et al. Clinical application of ultrasonography in the diagnosis of intussusception. J Pediatr. 1992;121(2):182-186.
58. Verschelden P, Filiatrault D, Garel L, et al. Intussusception in children: reliability of US in diagnosis—a prospective study. Radiology. 1992;184(3):741-744.
59. Shanbhogue R, Hussain S, Meradji M, et al. Ultrasonography is accurate enough for the diagnosis of intussusception. J Pediatr Surg. 1994;29(2):324-328.
60. Pracros JP, Tran-Minh VA, Morin de Finfe CH, et al. Acute intestinal intussusception in children. Contribution of ultrasonography (145 cases). Ann Radiol (Paris). 1987;30(7):525-530.
61. Newman B, Schmitz M, Gawande R, et al. Perforated appendicitis: an underappreciated mimic of intussusception on ultrasound. Pediatr Radiol. 2014;44(5):535-541.
62. Parienty RA, Lepreux JF, Gruson B. Sonographic and CT features of ileocolic intussusception. AJR Am J Roentgenol. 1981;136(3):608-610.
63. Morin M, Blumenthal D, Tan A, Li Y. The ultrasonic appearance of ileocolic intussusception. J Clin Ultrasound. 1981;9(9):516-518.
64. Swischuk LE, Hayden CK, Boulden T. Intussusception: indications for ultrasonography and an explanation of the doughnut and pseudokidney signs. Pediatr Radiol. 1985;15(6):388-391.
65. del Pozo G, Albillos JC, Tejedor D. Intussusception: US findings with pathologic correlation—the crescent-in-doughnut sign. Radiology. 1996;199(3):688-692.
66. del Pozo G, González-Spinola J, Gómez-Ansón B, et al. Intussusception: trapped peritoneal fluid detected with US—relationship to reducibility and ischemia. Radiology. 1996;201(2):379-383.
67. Riebel TW, Nasir R, Weber K. US-guided hydrostatic reduction of intussusception in children. Radiology. 1993;188(2):513-516.
68. Rohrschneider WK, Tröger J. Hydrostatic reduction of intussusception under US guidance. Pediatr Radiol. 1995;25(7):530-534.
69. Wood SK, Kim JS, Suh SJ, et al. Childhood intussusception: US-guided hydrostatic reduction. Radiology. 1992;182(1):77-80.
70. Flaum V, Schneider A, Gomes Ferreira C, et al. Twenty years' experience for reduction of ileocolic intussusceptions by saline enema under sonography control. J Pediatr Surg. 2016;51(1):179-182.
71. Carnevale E, Graziani M, Fasanelli S. Post-operative ileo-ileal intussusception: sonographic approach. Pediatr Radiol. 1994;24(3):161-163.
72. Swischuk LE, John SD, Swischuk PN. Spontaneous reduction of intussusception: verification with US. Radiology. 1994;192(1):269-271.
73. Munden MM, Bruzzi JF, Coley BD, Munden RF. Sonography of pediatric small-bowel intussusception: differentiating surgical from nonsurgical cases. AJR Am J Roentgenol. 2007;188(1):275-279.
74. Park NH, Park SI, Park CS, et al. Ultrasonographic findings of small bowel intussusception, focusing on differentiation from ileocolic intussusception. Br J Radiol. 2007;80(958):798-802.
75. Hughes UM, Connolly BL, Chait PG, Muraca S. Further report of small-bowel intussusceptions related to gastrojejunostomy tubes. Pediatr Radiol. 2000;30(9):614-617.
76. Feinstein KA, Myers M, Fernbach SK, Bhisitkul DM. Peritoneal fluid in children with intussusception: its sonographic detection and relationship to successful reduction. Abdom Imaging. 1993;18(3):277-279.
77. Swischuk LE, Stansberry SD. Ultrasonographic detection of free peritoneal fluid in uncomplicated intussusception. Pediatr Radiol. 1991;21(5):350-351.
78. Koumanidou C, Vakaki M, Pitsoulakis G, et al. Sonographic detection of lymph nodes in the intussusception of infants and young children: clinical evaluation and hydrostatic reduction. AJR Am J Roentgenol. 2002;178(2):445-450.
79. Lam AH, Firman K. Value of sonography including color Doppler in the diagnosis and management of long standing intussusception. Pediatr Radiol. 1992;22(2):112-114.
80. Lim HK, Bae SH, Lee KH, et al. Assessment of reducibility of ileocolic intussusception in children: usefulness of color Doppler sonography. Radiology. 1994;191(3):781-785.
81. Ledermann HP, Borner N, Strunk H, et al. Bowel wall thickening on transabdominal sonography. AJR Am J Roentgenol. 2000;174(1):107-117.
82. Baldisserotto M, Spolidoro JV, Bahu Mda G. Graded compression sonography of the colon in the diagnosis of polyps in pediatric patients. AJR Am J Roentgenol. 2002;179(1):201-205.
83. Haber HP, Seitz G, Warmann SW, Fuchs J. Transperineal sonography for determination of the type of imperforate anus. AJR Am J Roentgenol. 2007;189(6):1525-1529.
84. Donaldson JS, Black CT, Reynolds M, et al. Ultrasound of the distal pouch in infants with imperforate anus. J Pediatr Surg. 1989;24(5):465-468.
85. Oppenheimer DA, Carroll BA, Shochat SJ. Sonography of imperforate anus. Radiology. 1983;148(1):127-128.
86. Lim JH, Ko YT, Lee DH, et al. Sonography of inflammatory bowel disease: findings and value in differential diagnosis. AJR Am J Roentgenol. 1994;163(2):343-347.
87. Dinkel E, Dittrich M, Peters H, Baumann W. Real-time ultrasound in Crohn's disease: characteristic features and clinical implications. Pediatr Radiol. 1986;16(1):8-12.
88. Worlicek H, Lutz H, Heyder N, Matek W. Ultrasound findings in Crohn's disease and ulcerative colitis: a prospective study. J Clin Ultrasound. 1987;15(3):153-163.
89. Ros PR, Buetow PC, Pantograg-Brown L, et al. Pseudomembranous colitis. Radiology. 1996;198(1):1-9.
90. Downey DB, Wilson SR. Pseudomembranous colitis: sonographic features. Radiology. 1991;180(1):61-64.
91. Alexander JE, Williamson SL, Seibert JJ, et al. The ultrasonographic diagnosis of typhlitis (neutropenic colitis). Pediatr Radiol. 1988;18(3):200-204.
92. Puylaert JB, Lalisang RI, van der Werf SD, Doornbos L. Campylobacter ileocolitis mimicking acute appendicitis: differentiation with graded-compression US. Radiology. 1988;166(3):737-740.
93. Ueda D, Sato T, Yoshida M. Ultrasonographic assessment of *Salmonella* enterocolitis in children. Pediatr Radiol. 1999;29(6):469-471.
94. Matsumoto T, Iida M, Sakai T, et al. Yersinia terminal ileitis: sonographic findings in eight patients. AJR Am J Roentgenol. 1991;156(5):965-967.
95. Patenaude Y, Bernard C, Schreiber R, Sinsky AB. Cow's-milk-induced allergic colitis in an exclusively breast-fed infant: diagnosed with ultrasound. Pediatr Radiol. 2000;30(6):379-382.
96. Chung CJ, Rayder S, Meyers W, Long J. Kawasaki disease presenting as focal colitis. Pediatr Radiol. 1996;26(7):455-457.
97. Kodroff MB, Hartenberg MA, Goldschmidt RA. Ultrasonographic diagnosis of gangrenous bowel in neonatal necrotizing enterocolitis. Pediatr Radiol. 1984;14(3):168-170.
98. Friedland JA, Herman TE, Siegel MJ. *Escherichia coli* O157:H7–associated hemolytic-uremic syndrome: value of colonic color Doppler sonography. Pediatr Radiol. 1995;25(Suppl. 1):S65-S67.
99. Haber HP, Schlegel PG, Dette S, et al. Intestinal acute graft-versus-host disease. AJR Am J Roentgenol. 2000;174(1):118-120.
100. Klein SA, Martin H, Schreiber-Dietrich D, et al. A new approach to evaluating intestinal acute graft-versus-host disease by transabdominal sonography and colour Doppler imaging. Br J Haematol. 2001;115(4):929-934.

101. Schulman H, Weizman Z, Barki Y, et al. Inflammatory bowel disease in glycogen storage disease type 1 B. Pediatr Radiol. 1995;25(Suppl. 1): S160-S162.
102. Quillin SP, Siegel MJ. Gastrointestinal inflammation in children: color Doppler ultrasonography. J Ultrasound Med. 1994;13(10):751-756.
103. Anupindi SA, Halverson M, Khwaja A, et al. Common and uncommon applications of bowel ultrasound with pathologic correlation in children. AJR Am J Roentgenol. 2014;202(5):946-959.
104. Hata J, Haruma K, Yamanaka H, et al. Ultrasonographic evaluation of the bowel wall in inflammatory bowel disease: comparison of in vivo and in vitro studies. Abdom Imaging. 1994;19(5):395-399.
105. Couture A, Larroque A, Faure J, et al. Gastrointestinal tract sonography in fetuses and children. Berlin Heidelberg: Springer Science and Business Media. p. 577-604.
106. Esposito F, Senese R, Salvatore P, Vallone G. Intrahepatic portal-vein gas associated with rotavirus infection. J Ultrasound. 2011;14(1):10-13.
107. Debi U, Ravisankar V, Prasad KK, et al. Abdominal tuberculosis of the gastrointestinal tract: revisited. World J Gastroenterol. 2014;20(40): 14831-14840.
108. Ghonge NP. Gastric migration of intestinal ascariasis: B-mode sonographic depiction. J Ultrasound Med. 2008;27(12):1799-1801.
109. Arkoulis N, Zerbinis H, Simatos G, Nisiotis A. *Enterobius vermicularis* (pinworm) infection of the liver mimicking malignancy: Presentation of a new case and review of current literature. Int J Surg Case Rep. 2012; 3(1):6-9.
110. Horsthuis K, Bipat S, Bennink RJ, Stoker J. Inflammatory bowel disease diagnosed with US, MR, scintigraphy, and CT: meta-analysis of prospective studies. Radiology. 2008;247(1):64-79.
111. Anupindi SA, Podberesky DJ, Towbin AJ, et al. Pediatric inflammatory bowel disease: imaging issues with targeted solutions. Abdom Imaging. 2015;40(5):975-992.
112. Fraquelli M, Colli A, Casazza G, et al. Role of ultrasound in detection of Crohn's disease: meta-analysis. Radiology. 2005;236(1):95-101.
113. Chiorean L, Schreiber-Dietrich D, Braden B, et al. Ultrasonographic imaging of inflammatory bowel disease in pediatric patients. World J Gastroenterol. 2015;21(17):5231-5241.
114. Allison M, Kheniche A, Azoulay R, et al. Ultrasonography of Crohn disease in children. Pediatr Radiol. 2007;37(11):1071-1082.
115. Pallotta N, Civitelli F, Di Nardo G, et al. Small intestine contrast ultrasonography in pediatric Crohn's disease. J Pediatr. 2013;163(3): 778-784.
116. Yekeler E, Danalioglu A, Movasseghi B, et al. Crohn disease activity evaluated by Doppler ultrasonography of the superior mesenteric artery and the affected small-bowel segments. J Ultrasound Med. 2005;24(1):59-65.
117. Giovagnorio F, Diacinti D, Vernia P. Doppler sonography of the superior mesenteric artery in Crohn's disease. AJR Am J Roentgenol. 1998; 170(1):123-126.
118. Hu SC, Feeney MS, McNicholas M, et al. Ultrasonography to diagnose and exclude intussusception in Henoch-Schönlein purpura. Arch Dis Child. 1991;66(9):1065-1067.
119. McLaughlin PD, Maher MM. Nonneoplastic diseases of the small intestine: clinical, pathophysiologic, and imaging characteristics. AJR Am J Roentgenol. 2013;201(3):W382-W390.
120. Goske MJ, Goldblum JR, Applegate KE, et al. The "circle sign": a new sonographic sign of pneumatosis intestinalis—clinical, pathologic and experimental findings. Pediatr Radiol. 1999;29(7):530-535.
121. Epelman M, Daneman A, Navarro OM, et al. Necrotizing enterocolitis: review of state-of-the-art imaging findings with pathologic correlation. Radiographics. 2007;27(2):285-305.
122. Faingold R, Daneman A, Tomlinson G, et al. Necrotizing enterocolitis: assessment of bowel viability with color Doppler US. Radiology. 2005;235(2): 587-594.
123. Avni EF, Rypens F, Cohen E, Pardou A. Pericholecystic hyperechogenicities in necrotizing enterocolitis: a specific sonographic sign. Pediatr Radiol. 1991;21(3):179-181.
124. Deeg KH, Rupprecht T, Schmid E. Doppler sonographic detection of increased flow velocities in the celiac trunk and superior mesenteric artery in infants with necrotizing enterocolitis. Pediatr Radiol. 1993;23(8):578-582.
125. Miller SF, Seibert JJ, Kinder DL, Wilson AR. Use of ultrasound in the detection of occult bowel perforation in neonates. J Ultrasound Med. 1993;12(9):531-535.
126. Rosen MP, Ding A, Blake MA, et al. ACR Appropriateness Criteria right lower quadrant pain—suspected appendicitis. J Am Coll Radiol. 2011; 8(11):749-755.
127. Herliczek TW, Swenson DW, Mayo-Smith WW. Utility of MRI after inconclusive ultrasound in pediatric patients with suspected appendicitis: retrospective review of 60 consecutive patients. AJR Am J Roentgenol. 2013;200(5):969-973.
128. Pearce MS, Salotti JA, Little MP, et al. Radiation exposure from CT scans in childhood and subsequent risk of leukaemia and brain tumours: a retrospective cohort study. Lancet. 2012;380(9840):499-505.
129. Blitman NM, Anwar M, Brady KB, et al. Value of focused appendicitis ultrasound and Alvarado score in predicting appendicitis in children: can we reduce the use of CT? Am J Roentgenol. 2015;204(6):W707-W712.
130. Siegel MJ, Carel C, Surratt S. Ultrasonography of acute abdominal pain in children. JAMA. 1991;266(14):1987-1989.
131. Lee JH, Jeong YK, Hwang JC, et al. Graded compression sonography with adjuvant use of a posterior manual compression technique in the sonographic diagnosis of acute appendicitis. AJR Am J Roentgenol. 2002;178(4): 863-868.
132. Rothrock S, Pagane J. Acute appendicitis in children: emergency department diagnosis and management. Ann Emerg Med. 2000;36(1):39-51.
133. Baldisserotto M, Marchiori E. Accuracy of noncompressive sonography of children with appendicitis according to the potential positions of the appendix. AJR Am J Roentgenol. 2000;175(5):1387-1392.
134. Larson DB, Trout AT, Fierke SR, Towbin AJ. Improvement in diagnostic accuracy of ultrasound of the pediatric appendix through the use of equivocal interpretive categories. AJR Am J Roentgenol. 2015;204(4):849-856.
135. Fallon SC, Orth RC, Guillerman RP, et al. Development and validation of an ultrasound scoring system for children with suspected acute appendicitis. Pediatr Radiol. 2015;45(13):1945-1952.
136. Kao SC, Smith WL, Abu-Yousef MM, et al. Acute appendicitis in children: sonographic findings. AJR Am J Roentgenol. 1989;153(2):375-379.
137. Trout A, Towbin A, Zhang B. Journal Club: The pediatric appendix: defining normal. AJR Am J Roentgenol. 2014;202(5):936-945.
138. Symmers D. The clinical significance of lymphoid hyperplasia of the appendix. JAMA. 1919;72(7):468.
139. Swischuk L, Chung D, Hawkins H, et al. Non-fecalith-induced appendicitis: etiology, imaging, and pathology. Emerg Radiol. 2015;22(6):643-649.
140. Park NH, Park CS, Lee EJ, et al. Ultrasonographic findings identifying the faecal-impacted appendix: differential findings with acute appendicitis. Br J Radiol. 2007;80(959):872-877.
141. Puylaert JB. Mesenteric adenitis and acute terminal ileitis: US evaluation using graded compression. Radiology. 1986;161(3):691-695.
142. Trout A, Sanchez R, Ladino-Torres M. Reevaluating the sonographic criteria for acute appendicitis in children. Acad Radiol. 2012;19(11):1382-1394.
143. Wiersma F, Toorenvliet B, Bloem J, et al. US examination of the appendix in children with suspected appendicitis: the additional value of secondary signs. Eur Radiol. 2008;19(2):455-461.
144. Estey A, Poonai N, Lim R. Appendix not seen: the predictive value of secondary inflammatory sonographic signs. Pediatr Emerg Care. 2013;29(4): 435-439.
145. Hayden Jr CK, Kuchelmeister J, Lipscomb TS. Sonography of acute appendicitis in childhood: perforation versus nonperforation. J Ultrasound Med. 1992;11(5):209-216.
146. Quillin SP, Siegel MJ, Coffin CM. Acute appendicitis in children: value of sonography in detecting perforation. AJR Am J Roentgenol. 1992;159(6): 1265-1288.
147. Lee S, Stark R, Yaghoubian A, et al. Does age affect the outcomes and management of pediatric appendicitis? J Pediatr Surg. 2011;46(12): 2342-2345.
148. Lin YL, Lee CH. Appendicitis in infancy. Pediatr Surg Int. 2003; 19(1-2):1-3.
149. Blumfield E, Nayak G, Srinivasan R, et al. Journal Club: Ultrasound for differentiation between perforated and nonperforated appendicitis in pediatric patients. AJR Am J Roentgenol. 2013;200(5):957-962.

150. Patriquin HB, Garcier JM, Lafortune M, et al. Appendicitis in children and young adults: Doppler sonographic-pathologic correlation. AJR Am J Roentgenol. 1996;166(3):629-633.
151. Quillin SP, Siegel MJ. Diagnosis of appendiceal abscess in children with acute appendicitis: value of color Doppler sonography. AJR Am J Roentgenol. 1995;164(5):1251-1254.
152. Schlesinger A, Dorfman S, Braverman R. Sonographic appearance of omental infarction in children. Pediatr Radiol. 1999;29(8):598-601.
153. Daneman A, Lobo E, Alton DJ, Shuckett B. The value of sonography, CT and air enema for detection of complicated Meckel diverticulum in children with nonspecific clinical presentation. Pediatr Radiol. 1998;28(12): 928-932.
154. Farris SL, Fernbach SK. Axial torsion of Meckel's diverticulum presenting as a pelvic mass. Pediatr Radiol. 2001;31(12):886-888.
155. Barr LL, Hayden CK, Stansberry SD, Swischuk LE. Enteric duplication cysts in children: are their ultrasonographic wall characteristics diagnostic? Pediatr Radiol. 1990;20(5):326-328.
156. Hur J, Yoon C, Kim M, Kim O. Imaging features of gastrointestinal tract duplications in infants and children: from oesophagus to rectum. Pediatr Radiol. 2007;37(7):691-699.
157. Segal SR, Sherman NH, Rosenberg HK, et al. Ultrasonographic features of gastrointestinal duplications. J Ultrasound Med. 1994;13(11):863-870.
158. Hamrick-Turner JE, Saif MF, Powers CI, et al. Imaging of childhood non-Hodgkin lymphoma: assessment by histologic subtype. Radiographics. 1994;14(1):11-28.
159. Bellah R, Suzuki-Bordalo L, Brecher E, et al. Desmoplastic small round cell tumor in the abdomen and pelvis: report of CT findings in 11 affected children and young adults. AJR Am J Roentgenol. 2005;184(6): 1910-1914.
160. Siegel M. Pediatric Sonography. Philadelphia, PA: Lippincott Williams & Wilkins.; 2009.
161. Walter DF, Govil S, Korula A, et al. Pedunculated colonic polyp diagnosed by colonic sonography. Pediatr Radiol. 1992;22(2):148-149.
162. Park JM, Yeon KM, Han MC, et al. Diffuse intestinal arteriovenous malformation in a child. Pediatr Radiol. 1991;21(4):314-315.
163. Schneider K, Dickerhoff R, Bertele R. Malignant gastric sarcoma—diagnosis by ultrasound and endoscopy. Pediatr Radiol. 1986;16(1):69-70.
164. Cremin BJ, Brown RA. Carcinoma of the colon: diagnosis by ultrasound and enema. Pediatr Radiol. 1987;17(4):319-320.
165. Bowen B, Ros PR, McCarthy MJ, et al. Gastrointestinal teratomas: CT and US appearance with pathologic correlation. Radiology. 1987;162(2): 431-433.
166. McCullagh M, Keen C, Dykes E. Cystic mesothelioma of the peritoneum: a rare cause of 'ascites' in children. J Pediatr Surg. 1994;29(9):1205-1207.
167. Prieto ML, Casanova A, Delgado J, Zabalza R. Cystic teratoma of the mesentery. Pediatr Radiol. 1989;19(6-7):439.
168. Shah RS, Kaddu SJ, Kirtane JM. Benign mature teratoma of the large bowel: a case report. J Pediatr Surg. 1996;31(5):701-702.
169. Steyaert H, Guitard J, Moscovici J, et al. Abdominal cystic lymphangioma in children: benign lesions that can have a proliferative course. J Pediatr Surg. 1996;31(5):677-680.
170. Restrepo R, Hagerott HE, Kulkarni S, et al. Acute pancreatitis in pediatric patients: demographics, etiology, and diagnostic imaging. AJR Am J Roentgenol. 2016;206(3):632-644.
171. Nijs E, Callahan M, Taylor G. Disorders of the pediatric pancreas: imaging features. Pediatr Radiol. 2004;35(4):358-373.
172. Siegel MJ, Martin KW, Worthington JL. Normal and abnormal pancreas in children: US studies. Radiology. 1987;165(1):15-18.
173. Swischuk LE, Hayden CK. Pararenal space hyperechogenicity in childhood pancreatitis. AJR Am J Roentgenol. 1985;145(5):1085-1086.
174. Shilyansky J, Sena L, Kreller M, et al. Nonoperative management of pancreatic injuries in children. J Pediatr Surg. 1998;33(2):343-349.
175. Slovis TL, VonBerg VJ, Mikelic V. Sonography in the diagnosis and management of pancreatic pseudocysts and effusions in childhood. Radiology. 1980;135(1):153-155.
176. Daneman A, Gaskin K, Martin DJ, Cutz E. Pancreatic changes in cystic fibrosis: CT and sonographic appearances. AJR Am J Roentgenol. 1983;141(4):653-655.
177. Patty I, Kalaoui M, Al-Shamali M, et al. Endoscopic drainage for pancreatic pseudocyst in children. J Pediatr Surg. 2001;36(3):503-505.
178. Phillips HE, Cox KL, Reid MH, McGahan JP. Pancreatic sonography in cystic fibrosis. AJR Am J Roentgenol. 1981;137(1):69-72.
179. Willi UV, Reddish JM, Teele RL. Cystic fibrosis: its characteristic appearance on abdominal sonography. AJR Am J Roentgenol. 1980;134(5): 1005-1010.
180. Chung E, Travis M, Conran R. Pancreatic tumors in children: radiologic-pathologic correlation. Radiographics. 2006;26(4):1211-1238.
181. Berrocal T, Prieto C, Pastor I, et al. Sonography of pancreatic disease in infants and children. Radiographics. 1995;15(2):301-313.
182. Gupta A, Mitra D, Berry M, et al. Sonography and CT of pancreatoblastoma in children. AJR Am J Roentgenol. 2000;174(6):1639-1641.
183. Montemarano H, Lonergan G, Bulas D, Selby D. Pancreatoblastoma: imaging findings in 10 patients and review of the literature. Radiology. 2000;214(2): 476-482.
184. Auringer S, Ulmer J, Sumner T, Turner C. Congenital cyst of the pancreas. J Pediatr Surg. 1993;28(12):1570-1571.
185. Crowley JJ, McAlister WH. Congenital pancreatic pseudocyst: a rare cause of abdominal mass in a neonate. Pediatr Radiol. 1996;26(3):210-211.
186. Long J, Birken G, Migicovsky B. Autoimmune pancreatitis in a child presenting as a pancreatic mass. J Pediatr Surg Case Rep. 2015;3(3):111-113.
187. Rausch D, Norton K, Glass R, Kogan D. Infantile leukemia presenting with cholestasis secondary to massive pancreatic infiltration. Ped Radiol. 2002; 32(5):360-361.

CHAPTER 54

Pediatric Pelvic Sonography

William L. Simpson, Jr., Humaira Chaudhry, and Henrietta Kotlus Rosenberg

SUMMARY OF KEY POINTS

- Ultrasound is well suited for evaluation of the pediatric pelvis by providing excellent image quality without the use of radiation or the routine use of contrast material and without the need for sedation or anesthesia.
- Sonography of the pelvis is an excellent modality for serial assessment of pediatric pelvic abnormalities.
- Ultrasound can be used to evaluate congenital, infectious, inflammatory, endocrine, and neoplastic abnormalities of the pediatric pelvis.
- The appearance of the gonads of both sexes undergoes changes throughout the pediatric age range as they grow and develop adult characteristics.
- Water can be used as a contrast agent to distend structures that are normally collapsed (e.g., bladder, ureter, vagina, rectum) to facilitate evaluation and diagnosis.
- Although transvaginal ultrasound (TVS) provides high-resolution imaging of the female pelvis, its use in most pediatric female patients is precluded because they are not sexually active.

CHAPTER OUTLINE

SONOGRAPHIC TECHNIQUE
NORMAL FEMALE ANATOMY
The Uterus
The Vagina
The Ovary
OVARIAN ABNORMALITIES
Ovarian Cysts
Complications: Torsion, Hemorrhage, Rupture
Polycystic Ovarian Disease (Stein-Leventhal)
Massive Ovarian Edema
Ovarian Neoplasms
UTERINE AND VAGINAL ABNORMALITIES
Congenital Anomalies
Neoplasm
Pregnancy
Infection
Pelvic Inflammatory Disease
Foreign Bodies
ENDOCRINE ABNORMALITIES
Causes of Primary Amenorrhea
Precocious Puberty
NORMAL MALE ANATOMY
The Prostate
The Scrotum
The Testes
CONGENITAL MALE ABNORMALITIES
ACUTE SCROTAL PAIN OR SWELLING
Color Doppler Sonography in Testicular Torsion
SCROTAL MASSES
Intratesticular Causes
Extratesticular Causes
Paratesticular Tumors
LOWER URINARY TRACT
Congenital Anomalies
The Ureter
Neurogenic or Dysfunctional Bladder
Infection
Neoplasm
Trauma
Postoperative Bladder
PRESACRAL MASSES

SONOGRAPHIC TECHNIQUE

High-resolution, real-time, gray-scale and color Doppler sonography has emerged as the modality of choice for the evaluation of the pelvis in infants, children, and adolescents. Using the distended bladder as an acoustic window, the lower urinary tract, uterus, adnexa, prostate gland, seminal vesicles, and pelvic musculature and vessels can be easily evaluated.[1-6]

Depending on the size of the child, a 5-2, 9-4, or 8-5 MHz real-time curvilinear broad-bandwidth or sector transducer is used to obtain scans, usually in the transverse and sagittal planes. Linear probe technology is useful for evaluation of the bowel, peritoneum, perineum, and superficial lesions using a 12-5 MHz, 17-5 MHz, or other high-frequency linear broad-bandwidth probes.

Patients should be well hydrated before pelvic sonography so that the bladder will be optimally filled. In infants and young children who are unable to maintain a full bladder despite drinking clear liquids, it may be necessary to catheterize and fill the bladder with sterile water through a 5- or 8-French feeding tube, although this is rarely necessary. The use of sterile water as a contrast agent to outline the vagina **(hydrosonovaginography)** (Fig. 54.1, Video 54.1), rectum (water enema)[7,8] (Fig. 54.2), or urogenital sinus may be very helpful in the evaluation of the pediatric patient with a pelvic mass or complex congenital anomalies of the genitourinary tract. Meticulous real-time scanning is essential

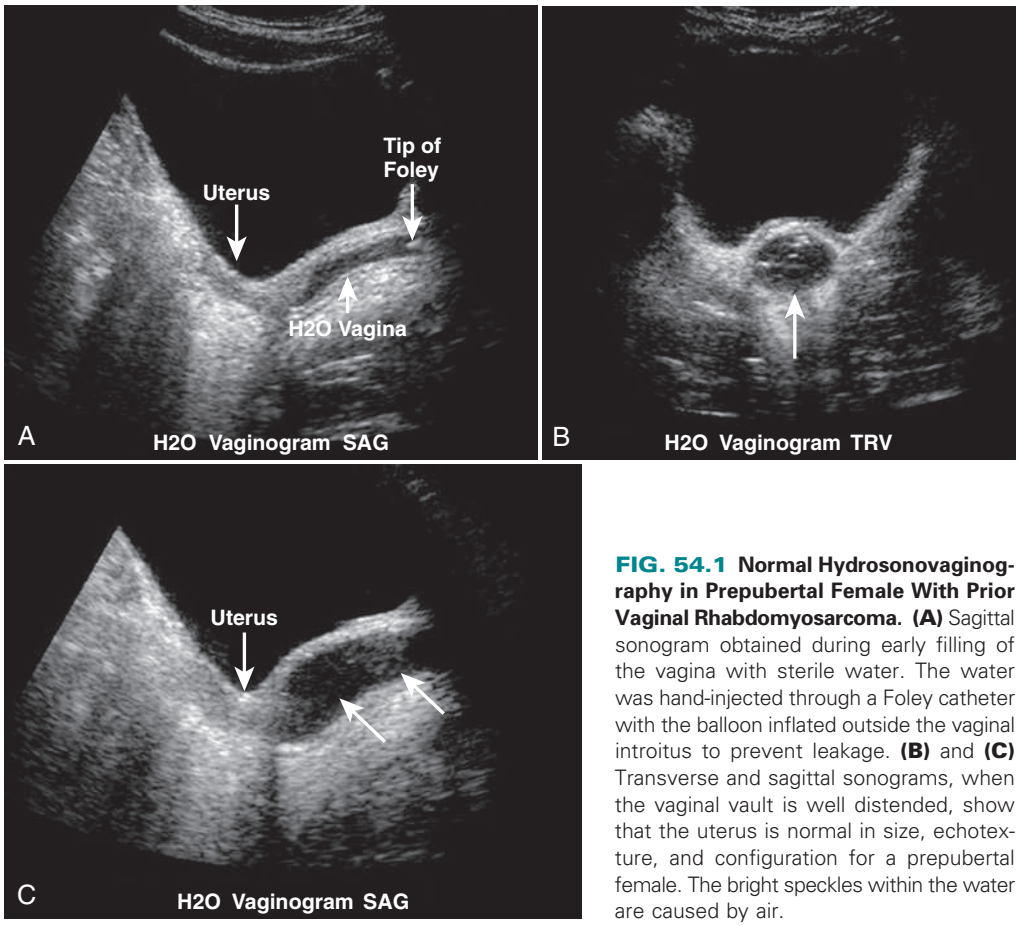

FIG. 54.1 Normal Hydrosonovaginography in Prepubertal Female With Prior Vaginal Rhabdomyosarcoma. (A) Sagittal sonogram obtained during early filling of the vagina with sterile water. The water was hand-injected through a Foley catheter with the balloon inflated outside the vaginal introitus to prevent leakage. **(B)** and **(C)** Transverse and sagittal sonograms, when the vaginal vault is well distended, show that the uterus is normal in size, echotexture, and configuration for a prepubertal female. The bright speckles within the water are caused by air.

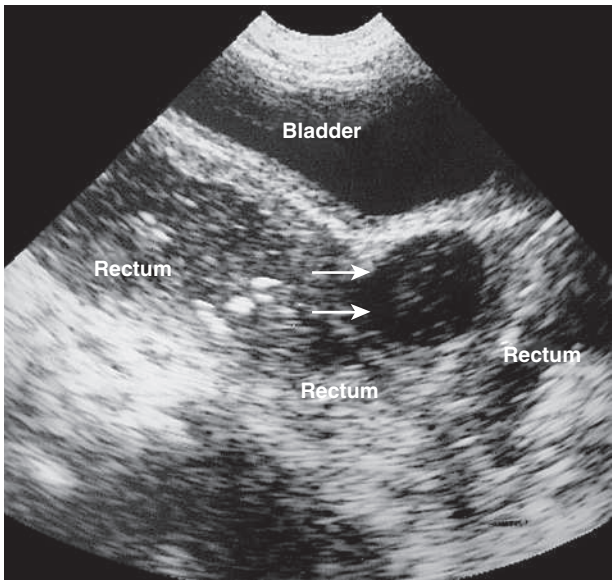

FIG. 54.2 Water Enema Technique in 5-Year-Old Boy With Appendiceal Abscess. Sagittal sonogram shows a small, hypoechoic fluid collection *(arrows)* located posterior to the bladder and anterior to the water-filled rectum.

because these structures are filled in a retrograde manner. When transabdominal sonography (TAS) provides suboptimal images in mature, sexually active teenage girls, **transvaginal ultrasound** (TVS) can provide higher resolution with more detailed images, thus aiding in the elucidation of the origin and characteristics of pelvic masses and complex adnexal lesions.[6,9]

The wall of the urinary bladder should be smooth in a distended state, with the wall thickness not greater than 3 mm during bladder distention, with a mean of 1.5 mm.[10] The wall should not be greater than 5 mm thick with the bladder empty or partially distended. In the nondistended state the internal aspect of the bladder wall generally appears slightly irregular sonographically. A **urachal remnant** may be visualized on sonography, as a structure of variable form and size, lying ventral to the peritoneum and situated between the umbilicus and the apex of the urinary bladder.[11] The distal ureters, with the exception of the submucosal intravesical portion, are not usually visualized unless abnormally dilated.[12] The **trigone,** however, is easily demonstrated (Fig. 54.3). The bladder neck and urethra can be demonstrated in both males and females by angling the transducer inferiorly[13] (Fig. 54.4). If a urethral abnormality is noted on suprapubic imaging, scans through the perineum or transrectally can confirm these findings using a different imaging plane.[14]

Hydrosonourethrography may be used to detect anterior urethral abnormalities (strictures, calculi, anterior or posterior urethral valves, foreign bodies, bladder neck dyssynergia, diverticula, trauma) by scanning the penis with a linear array transducer during real-time observation during voiding or during a retrograde hand-injection of saline into the urethra.[15] **Postvoid scanning** of the bladder can provide information about bladder function, differentiate the bladder from cystic masses or fluid collections in the pelvis, and evaluate the degree of drainage from dilated upper urinary tracts. When children cannot void, films taken after a Credé maneuver or catheterization indicate the effectiveness of these bladder-emptying procedures. We measure the postvoid residual of the bladder using the following formula:

$$\text{Length} \times \text{Width} \times \text{Depth (in cm)} \div 2 = \text{Volume (in mL)}$$

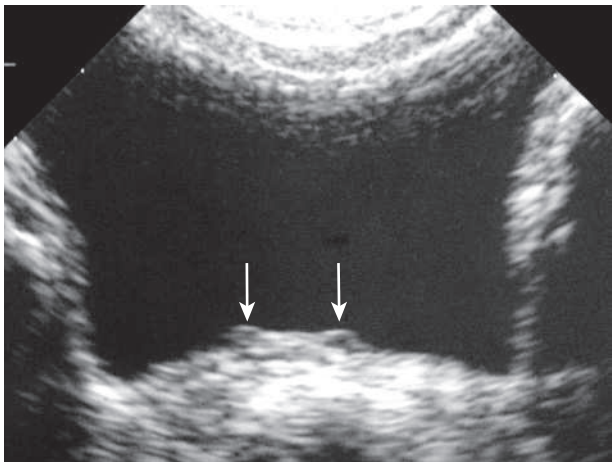

FIG. 54.3 Normal Trigone. With meticulous scanning, it is possible to identify the trigone *(arrows)* in pediatric patients.

NORMAL FEMALE ANATOMY

The Uterus

The uterus and ovaries undergo a series of changes in size and configuration during normal growth and development.[5,13] The **newborn female uterus** is prominent and thickened with a brightly echogenic endometrial lining caused by in utero hormonal stimulation[16] (Fig. 54.5). In the first 3 days of life, mean length and mean volume of the uterus are 4.2 cm and 10.0 cm^3.[17] The uterine configuration is spade shaped with a fundus-to-cervix ratio of 1:2. At 2 to 3 months of age the prepubertal uterus regresses to a smaller size and flat configuration (Fig. 54.6), with a length of 2.5 to 3 cm and a fundus-to-cervix ratio of 1:1, and with the endometrial stripe (when seen) appearing as thin as a pencil line. This tubular uterine configuration is maintained until puberty. The **postpubertal uterine length** gradually increases

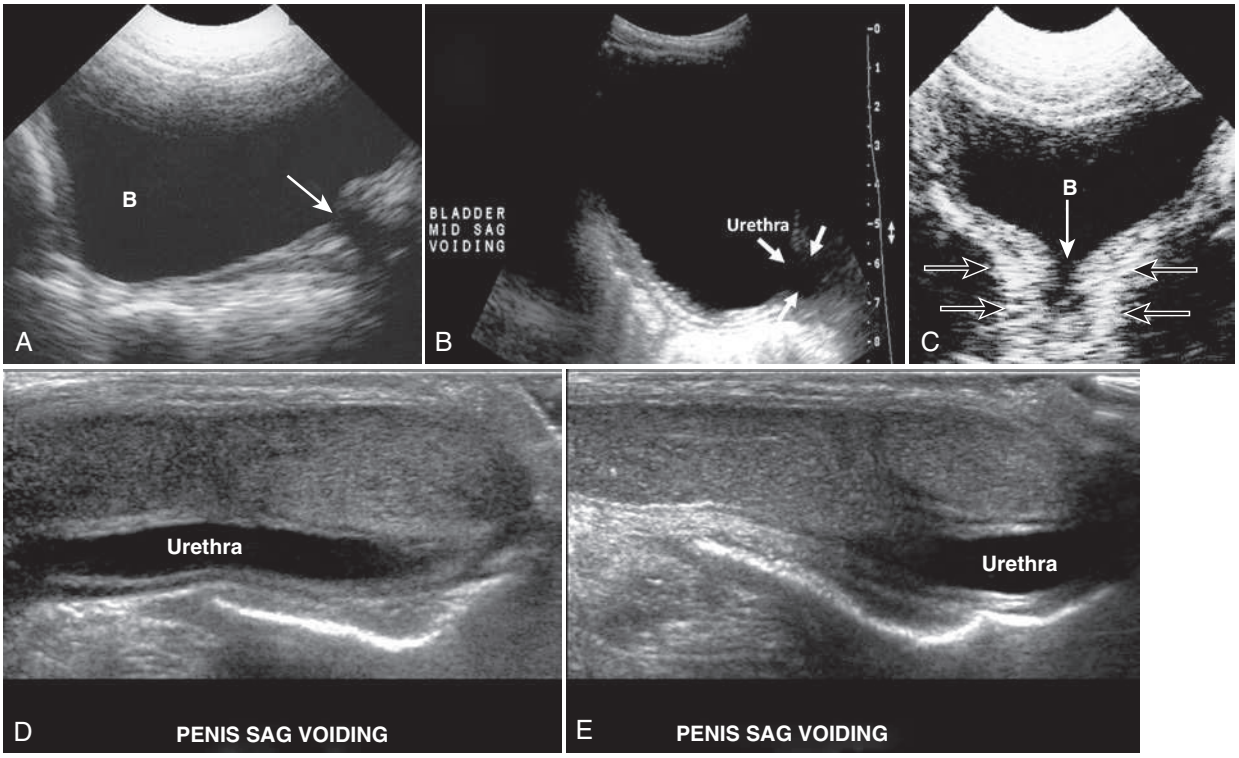

FIG. 54.4 Normal Urethras. (A) Normal female urethra. Using bladder *(B)* as an acoustic window, urethra *(arrow)* may be seen. **(B)** Voiding sonourethrography findings in a female. With use of a sagittal suprapubic approach during voiding, the female urethra can be seen as a fluid-distended structure. **(C)** Normal posterior urethra in young boy. Transverse scan through moderately distended bladder *(B)* shows posterior urethra *(white arrow)* and prostate gland *(black arrowheads)* surrounding the urethra. **(D)** and **(E)** Voiding sonourethrography findings in a male. Sagittal scan demonstrating normal-appearing penile urethra in **(D)**, and the normal-appearing, most distal urethra at the fossa navicularis in the glans of the penis. (**C** with permission from Rosenberg H. Sonography of the pediatric urinary tract. In: Bush WH, editor. Urologic imaging and interventional techniques. Baltimore: Urban & Schwarzenberg; 1989. p 164-179.[16])

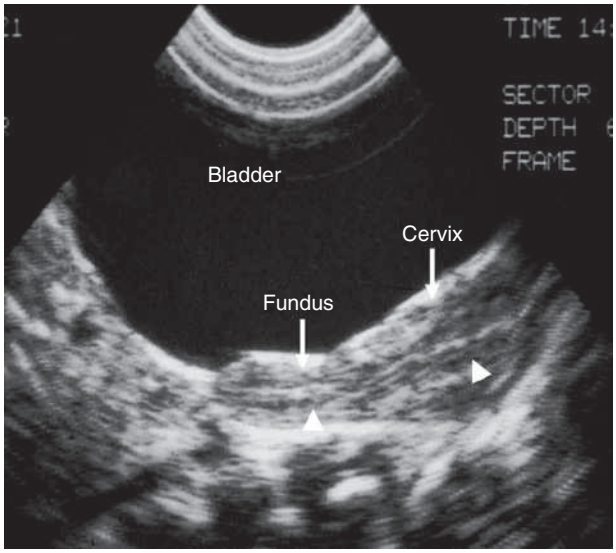

FIG. 54.5 Normal Newborn Uterus. Sagittal view shows that ratio of fundus to cervix is 1:2 for length, and the somewhat thick endometrial lining is prominently echogenic as a result of in utero hormonal stimulation *(arrowheads)*.

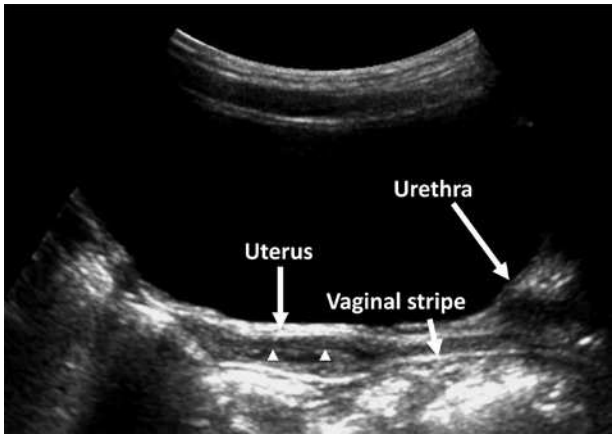

FIG. 54.6 Normal Prepubertal Uterus in 2-Year-Old Girl. Sagittal sonogram through the bladder demonstrates a fundus-to-cervix ratio of 1:1 and shows a pencil-line thin, unstimulated endometrial stripe *(arrowheads)*.

to 5 to 7 cm, and the fundus-to-cervix ratio becomes 3:1[13,16] (Table 54.1). The echogenicity and thickness of the endometrial lining then vary according to the phase of the menstrual cycle, as in adult women. The uterus is supplied by bilateral uterine arteries, which are branches of the internal iliac arteries. Color Doppler imaging generally demonstrates flow in the myometrium, with little or no flow in the endometrium.[15]

The Vagina

In children, digital and visual examination of the vagina is difficult. Often, physical examination of the vagina is performed with the patient under general anesthesia. High-resolution, real-time sonography can now obviate this need in many cases. In the infant or young girl with an interlabial mass, sonography in conjunction with other imaging modalities can usually determine the cause. The vagina is best visualized on midline longitudinal scans through the distended bladder. It appears as a long, tubular structure in continuity with the uterine cervix. The apposed mucosal surfaces cause a long, bright, slender, central linear echo. Hydrosonovaginography (see Fig. 54.1) under real-time sonography guidance can provide additional information about vaginal patency or confirm the presence or absence of a vaginal mass.

TABLE 54.1 Pediatric Uterine Measurements

Age	Uterine Length	Fundus-to-Cervix Ratio
Newborn	3.5 cm	1:2
Prepubertal[a]	2.5-3 cm	1:1
Postpubertal	5-8 cm	3:1

[a]Beginning at age 2-3 months.
Data from Comstock CH, Boal DK. Pelvic sonography of the pediatric patient. Semin Ultrasound. 1984;5:54-67[13]; and Rosenberg HK. Sonography of the pediatric urinary tract. In: Bush WH, editor. Urologic imaging and interventional techniques. Baltimore: Urban & Schwarzenberg; 1989. p. 164-179.[16]

The Ovary

Sonographic visualization of the ovaries in children can vary, depending on their location, size, and the age of the patient (Fig. 54.7, Video 54.2). Because of a typically long pedicle and a small pelvis, the neonatal ovaries may be found anywhere between the lower pole of the kidneys and the true pelvis (Fig. 54.8). Ovarian size is most reproducible and best described by measurement of the ovarian volume, which is calculated by a prolate ellipse formula (Length × Depth × Width [in cm] × 0.523 = Volume [in mL]).

The **mean ovarian volume** in neonates and girls younger than 6 years is usually 1 mL or less.[18] Ovarian volume gradually begins to increase at about age 6 years. The mean ovarian volume measurement in **premenarchal girls** aged 6 to 11 years ranges from 1.2 to 2.5 mL (Table 54.2). There is marked enlargement in ovarian size after puberty; thus ovarian sizes in **menstruating females** in late childhood will be larger than their premenarchal counterparts. Cohen and colleagues[19] reported a mean ovarian volume of 9.8 mL, with a 95% confidence interval between 2.5 and 21.9 mL, in menstruating females.

Beginning in the neonatal period, the appearance of the typical ovary is heterogeneous secondary to small cysts. Cohen and colleagues[17] reported observing **ovarian cysts** in 84% of children 1 day to 2 years of age and 68% of children 2 to 12 years of age. **Macrocysts** (>9 mm) were more frequently seen in the ovaries of girls in their first year of life compared with those in their second year. This probably accounts for the larger mean and top-normal ovarian volume measurements obtained in girls up to 3 months of age (mean ovarian volume, 1.06 mL; range, 0.7-3.6 mL) versus those 13 to 24 months of age (mean ovarian volume, 0.67 mL; range, 0.1-1.7 mL). These findings probably result from the higher residual maternal hormone level in younger infants. Orbak and colleagues[20] concluded that ovarian volume

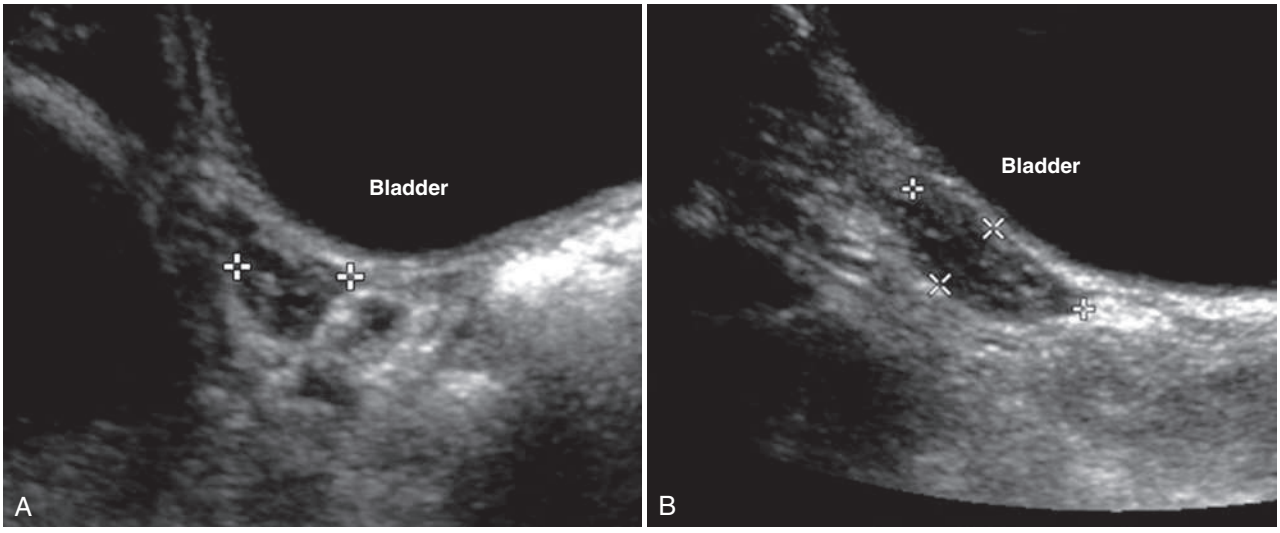

FIG. 54.7 Normal Ovary in 2-Year-Old Child. (A) and **(B)** Transverse and sagittal views of the ovary *(calipers)*. Note that small follicles are normal in the prepubertal ovary and can be easily visualized with high-resolution technology.

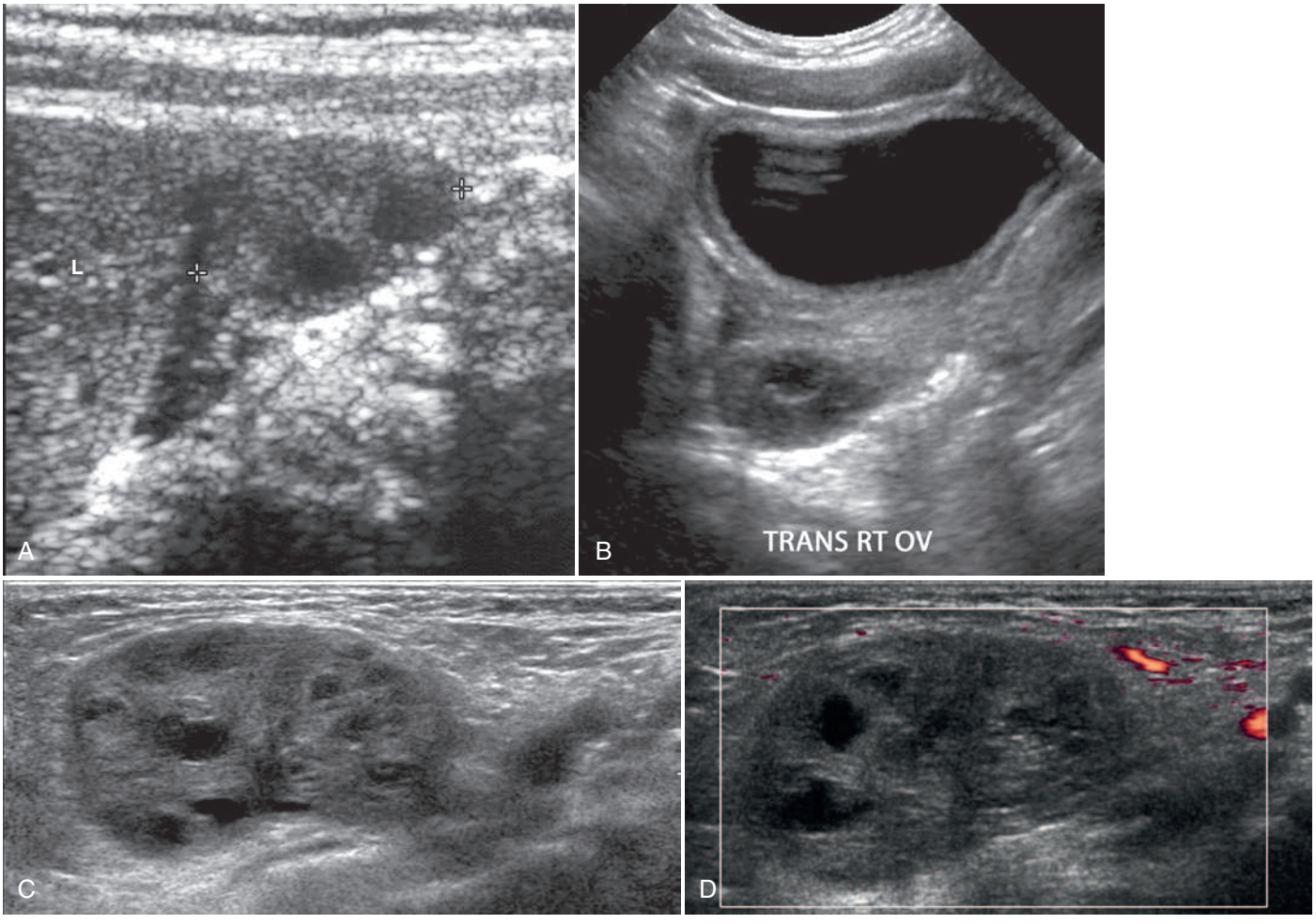

FIG. 54.8 Ectopic Ovary. (A) Ectopic ovary in 18-year-old female with cyclic right upper quadrant pain thought to be caused by recurrent "gallbladder attacks." The liver and gallbladder were normal *(not shown)*. The ectopic right ovary *(cursors)* is just below the inferior edge of the right lobe of the liver *(L)*. **(B)-(D)** Ectopic ovary in the left inguinal canal in a 4-month-old girl with groin mass and vomiting. Transabdominal sonography **(B)** revealed a normal right ovary in the right adnexa, but the left ovary was not seen. An oval structure with no internal vascularity was identified within the left groin (**[C]** and **[D]**); it contains multiple follicles and was enlarged compared with the normally positioned right ovary, consistent with a **torsed herniated left ovary.**

TABLE 54.2 Pediatric Ovarian Volume Measurements

Age	Mean Ovarian Volume, mL (±SD)
PREMENARCHAL	
0-5 yr	**≤1 mL**
1 day to 3 mo	1.06 (±0.96)
4-12 mo	1.05 (±0.67)
13-24 mo	0.67 (±0.35)
3 yr	0.7 (±0.4)
4 yr	0.8 (±0.4)
5 yr	0.9 (±0.02)
6-8 yr	**1.2 mL**
6 yr	1.2 (±0.4)
7 yr	1.3 (±0.6)
8 yr	1.1 (±0.5)
9-10 yr[a]	**2.1 mL**
9 yr	2.0 (±0.8)
10 yr	2.2 (±0.7)
11 yr[a]	**2.5 mL (±1.3)**
12 yr[a]	3.8 mL (±1.4)
13 yr[a]	4.2 mL (±2.3)
MENSTRUAL	
	9.8 mL (±5.8)

[a]Note that these measurements may differ, depending on degree of maturation and presence of menarche.
SD, Standard deviation.
Data from Cohen HL, Shapiro MA, Mandel FS, Shapiro ML. Normal ovaries in neonates and infants: a sonographic study of 77 patients 1 day to 24 months old. AJR Am J Roentgenol. 1993;160(3):583-586[17]; and Rosenberg H. Sonography of the pediatric urinary tract. In: Bush WH, editor. Urologic imaging and interventional techniques. Baltimore: Urban & Schwarzenberg; 1989. p. 164-179.[16]

was reduced in newborns with relatively low birth weight and intrauterine growth restriction, and that functional cysts were more prevalent among low-birth-weight girls.

The blood supply of the ovary is dual, arising from the **ovarian artery,** which originates directly from the aorta, and from the **uterine artery,** which supplies an adnexal branch to each ovary. Blood flow can be seen in 90% of the adolescent ovary, but Doppler imaging cannot distinguish between the two blood supplies. Typically, on color Doppler imaging the intraovarian arteries appear as short, straight branches located centrally within the normal ovary.[21]

OVARIAN ABNORMALITIES

Ovarian Cysts

Simple ovarian cysts in children are relatively common.[22] Small cysts (1-7 mm) have been detected on sonograms in the third-trimester fetus and the neonate and are secondary to maternal and placental chorionic gonadotropin. There is a higher incidence of larger ovarian cysts in infants of mothers with toxemia, diabetes, and Rh isoimmunization, all of which are associated with a greater-than-normal release of placental chorionic gonadotropin.[23] Large ovarian cysts in the fetus can cause mechanical complications during vaginal delivery. As a result of the small size of the true pelvis in infants and young children, ovarian cysts are often intraabdominal in location and must be differentiated from **mesenteric** or **omental cysts, gastrointestinal duplication cysts,**[24] and **urachal cysts.** Ovarian cysts are associated with **cystic fibrosis, congenital juvenile hypothyroidism,**[25] **McCune-Albright syndrome** (fibrous dysplasia and patchy cutaneous pigmentation), and **peripheral sexual precocity.** Autonomously functioning ovarian cysts can cause **precocious pseudopuberty.**

Although neonatal ovarian cysts were surgically removed in the past, spontaneous resolution of some cysts has been demonstrated on sonography[23] (Fig. 54.9). When a follicle continues to grow after failed ovulation or when it does not collapse after ovulation, follicular and corpus luteal cysts may result. Most **follicular cysts** are unilocular, contain clear serous fluid, and range in size from 3 to 20 cm. **Corpus luteal cysts** can contain serous or hemorrhagic fluid and generally range in size from 5 to 11 cm. **Theca lutein cysts** are thought to represent hyperstimulated follicles caused by gestational trophoblastic disease or a complication of drug therapy to stimulate ovulation. Rarely, **parovarian cysts** are diagnosed in childhood (Fig. 54.10). They are of mesothelial or paramesonephric origin and arise in the broad ligament or fallopian tubes.

Complications: Torsion, Hemorrhage, Rupture

Most ovarian cysts are asymptomatic. Symptoms of pain, tenderness, nausea, vomiting, and low-grade fever usually indicate complications of torsion, hemorrhage, or rupture. **Torsion** can occur in normal ovaries but is more often caused by an ovarian cyst or tumor. In children, torsion of the normal ovary can occur because the fallopian tube is relatively long and the ovary is more mobile. The typical presentation is sudden onset of acute lower abdominal pain, often associated with nausea, vomiting, and leukocytosis. Torsion of **normal adnexa** usually occurs in prepubertal girls and is thought to be related to excessive mobility of the adnexa, allowing torsion at the mesosalpinx with changes in intraabdominal pressure or body position. Torsion of the **ovary and fallopian tube** results from partial or complete rotation of the ovary on its vascular pedicle. This results in compromise of arterial and venous flow, congestion of the ovarian parenchyma, and, ultimately, hemorrhagic infarction.[26] The sonographic findings in **acute ovarian torsion** are often nonspecific and include ovarian enlargement, fluid in the cul-de-sac, and other adnexal pathologic findings, such as cyst or tumor (Fig. 54.11 and see Fig. 54.8C-D). A predominantly cystic or complex adnexal mass with a fluid-debris level or septa correlates with pathologic evidence of ovarian hemorrhage or infarction. In 28 of 32 patients, Lee and colleagues[27] showed that ultrasound could demonstrate preoperatively the twisted vascular pedicle in surgically proven torsion, giving a diagnostic accuracy of 87%. This appeared as a round, hyperechoic structure with multiple concentric hypoechoic stripes (target appearance), as a beaked structure with concentric hypoechoic stripes, or as an ellipsoid or tubular structure with internal heterogeneous echoes. Concentric hypoechoic intrapedicular structures could be identified as

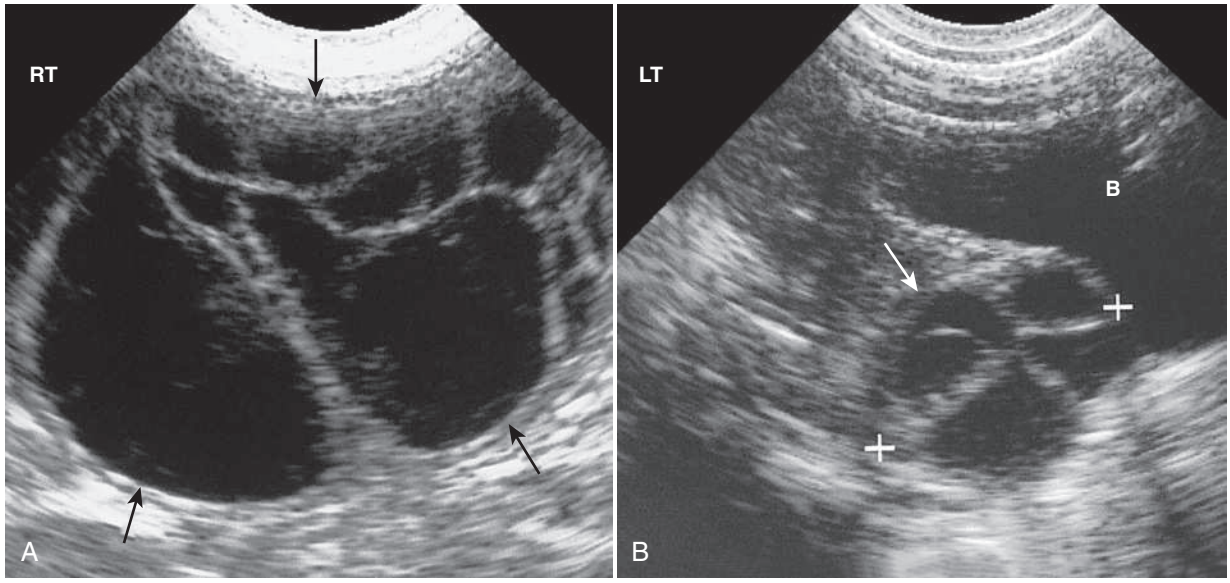

FIG. 54.9 Ovarian Cysts in Newborn Girl. (A) Right ovary. **(B)** Left ovary. Cysts manifested as a lower abdominopelvic mass. Multiple anechoic cystic areas with septations are noted in ovaries bilaterally *(arrows)*. Ovarian cysts were believed to be secondary to in utero hormonal stimulation. Follow-up studies *(not shown)* showed complete regression. *B,* Bladder.

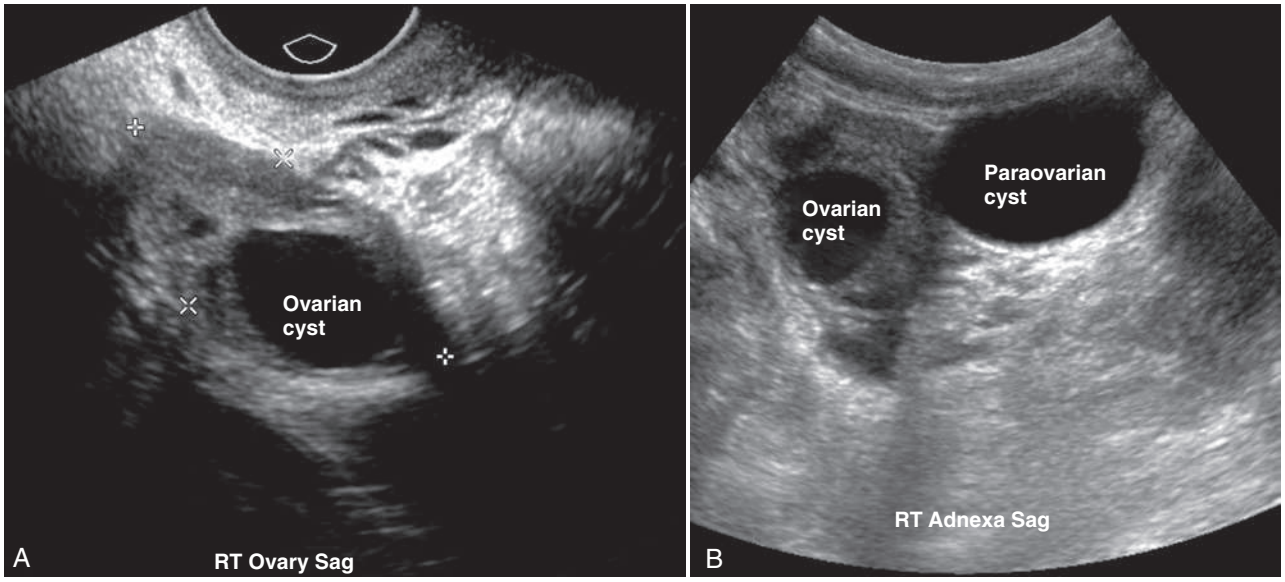

FIG. 54.10 Adnexal Cysts in Teenager. (A) and **(B)** Sonograms demonstrate a simple cyst within the right ovary. In addition, a simple parovarian cyst is demonstrated in **(B)**.

vascular structures on color Doppler sonography ("whirlpool sign"). The absence of flow on color Doppler ultrasound is not a reliable diagnostic criterion because peripheral (or even central) arterial flow can be seen in surgically proven twisted ovaries. This may be explained by the duality of the ovarian arterial perfusion.[28] The demonstration of **multiple follicles** (8-12 mm in size) **in the cortical or peripheral portion of a unilaterally enlarged ovary** has been reported as a specific sonographic sign of torsion.[29-31] These cystic changes occur in up to 74% of twisted ovaries and are attributed to transudation of fluid into follicles secondary to vascular congestion. At times, isolated fallopian tube torsion occurs in perimenarcheal girls with acute pelvic pain and in whom a cystic mass in a midline position is demonstrated (either in the cul-de-sac or superior to the uterus) in association with a normal ipsilateral ovary.[32]

Acute Ovarian Torsion: Sonographic Findings

Ovarian enlargement
Fluid in cul-de-sac
Adnexal mass (ovarian hemorrhage or infarction)
Cystic or complex
Fluid-debris level
Multiple peripheral follicles
"Whirlpool sign" on color Doppler

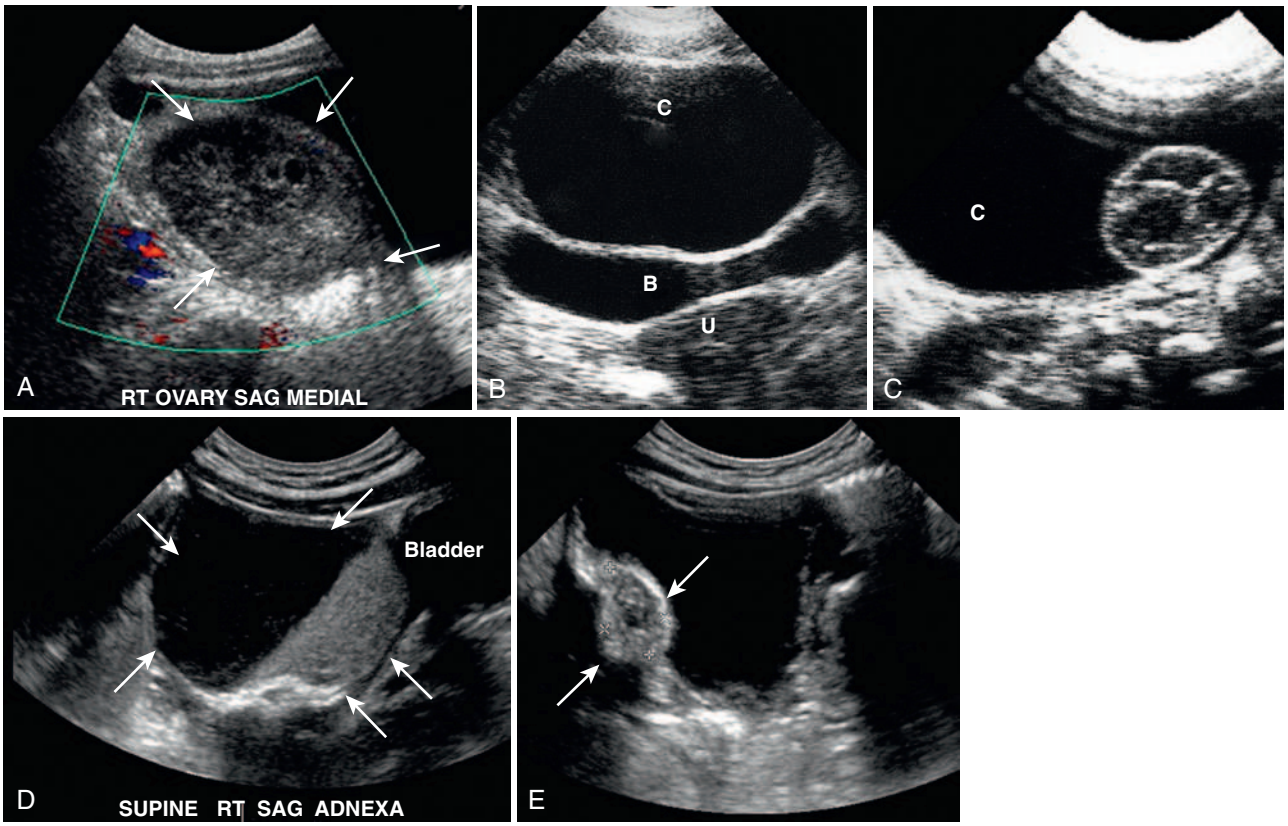

FIG. 54.11 Ovarian Torsion. (A) Sagittal sonogram in 9-year-old girl with right lower quadrant pain demonstrates a greatly enlarged avascular right ovary that contains multiple, variably sized cysts. The ovary was easily untwisted at surgery and immediately regained normal color. **(B)** Ovarian torsion complicating an ovarian cyst in a 16-year-old girl with pelvic pain. Transverse view of the pelvis shows the large anterior ovarian cyst *(C)* compressing the bladder *(B)* (surgical proof of torsion). No ovarian parenchymal tissue was seen sonographically. *U,* Uterus. **(C)** Infarcted, encysted, ovarian torsion in a 6-day-old girl with an abdominal mass. Sonogram of the right lower abdomen and pelvis demonstrates an oval, complex structure within a larger cystic mass *(C).* **(D)** Sagittal view shows infarcted, encysted, torsed right ovary in newborn with cystic mass noted on prenatal sonogram. A fluid-debris level is noted within the cyst *(arrows).* **(E)** Transverse left decubitus scan shows encysted right ovary *(arrows)* embedded in the wall of the cyst.

Hemorrhagic ovarian cysts occur in adolescents and have a variety of sonographic patterns caused by internal blood clot formation and lysis (Fig. 54.12). The most common appearance is a heterogeneous mass that is predominantly anechoic and contains hypoechoic material. Less often, hemorrhagic ovarian cysts are homogeneous, either hypoechoic or hyperechoic. Almost all hemorrhagic cysts (92%) have increased sound through transmission, indicating the cystic nature of the lesion. Additional sonographic features include a thick wall (e.g., 4 mm), septations, and fluid in the cul-de-sac. Although the sonographic findings are nonspecific, the changing appearance of hemorrhagic ovarian cysts over time, as a result of clot lysis, can help establish the diagnosis.[33] In some cases the diagnosis can be confused with **appendiceal abscess, dermoid cyst,** or **teratoma.** Rarely, **pelvic varices** can masquerade as a multiseptated cystic mass (Fig. 54.13).

Polycystic Ovarian Disease (Stein-Leventhal)

The primary clinical manifestations of polycystic ovarian disease (polycystic ovary syndrome [PCOS], Stein-Leventhal syndrome) are hirsutism and irregular menstrual bleeding caused by excess ovarian androgens and chronic anovulation.[34] These features emerge late in puberty or shortly thereafter. In patients with obesity or insulin resistance, the severity of the presentation is amplified. The evolution of this condition during early adolescence is not well understood, but it appears that abnormal activation of the hypothalamic-pituitary-ovarian-adrenal axis occurs, accompanied by specific morphologic changes in the ovaries.[34] The changes in the ovaries have been termed "polycystic ovarian morphology." It was defined in adults by the Rotterdam criteria as (a) one or both ovaries demonstrate 12 or more follicles measuring 2 to 9 mm in diameter, or (b) the ovarian volume exceeds 10 cm[35] (Fig. 54.14, Video 54.3). However, there is controversy as to whether the same criteria can be applied to adolescents.[36-39] These criteria are based on TVS in adults. In the adolescents, sonography is predominately performed transabdominally. The transabdominal approach has decreased resolution compared with TVS, which can limit evaluation of follicle number, especially in obese patients.[36,39] However, sonography is still valuable and frequently is used in the evaluation of an adolescent girl suspected of having PCOS.[39,40] Long-term follow-up is important in these patients because of the increased incidence

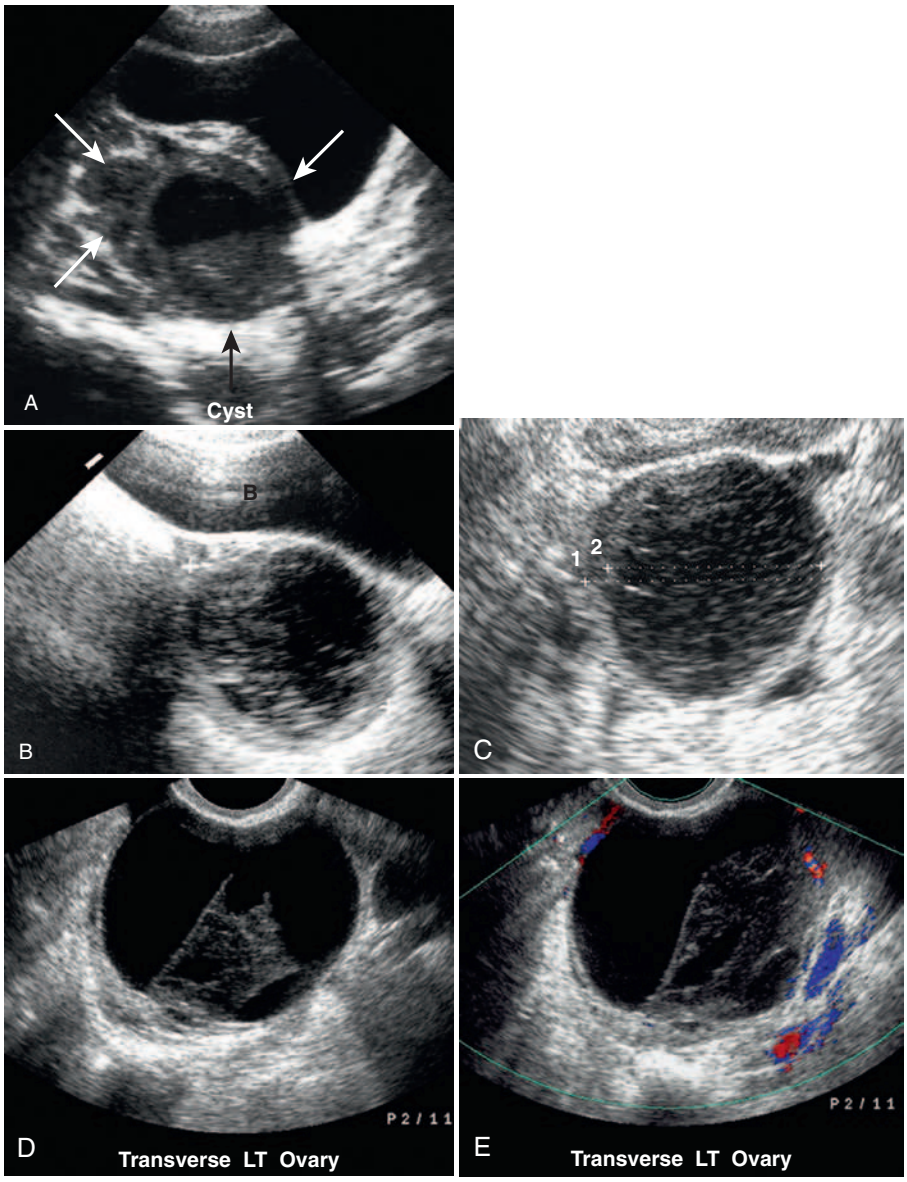

FIG. 54.12 Hemorrhagic Ovarian Cysts in Four Teenagers With Left Pelvic Pain: Spectrum of Appearances. (A) Transverse view of the pelvis reveals a large, round cyst within the ovary (*arrows,* ovary) that contains a fluid-debris level representing a hemorrhagic cyst. **(B)** Sagittal transabdominal sonography (TAS) shows enlargement of the left ovary with a rim of ovary surrounding a cyst that contains multiple, echogenic, streaky densities. *B,* Bladder. **(C)** Transvaginal ultrasound (TVS) confirms the presence of surrounding ovarian tissue and the heterogeneous appearance of the contained fluid. **(D)** and **(E)** TVS images of left ovary demonstrate jagged material within the clearly defined cyst.

of **endometrial carcinoma** from long-term unopposed estrogen.[37,41]

Massive Ovarian Edema

Massive edema of the ovary manifests with marked enlargement of the affected ovary caused by accumulation of edema fluid in the stroma, separating normal follicular structures (Fig. 54.15). It is thought to result from partial or intermittent torsion that interferes with venous and lymphatic drainage. It affects patients during their second to third decades of life and causes acute abdominal pain, palpable adnexal mass, menstrual disturbances at times, masculinization, and Meigs syndrome. Two-thirds of patients have right-sided ovarian edema, thought to be related to high pressure in the right ovarian vein caused by direct drainage into the inferior vena cava (IVC) or increased pressure secondary to uterine dextroposition. The ovaries may be massively enlarged, with diameter up to 35 cm. Grossly, the external surface is soft and pearly white and appears similar to **fibromatosis,** a condition likely to occur in young women (up to 25 years of age) in which primary proliferation of the ovarian stroma may result in torsion and ultimately edema. The sonographic features of ovarian edema include a solid, hypoechoic mass, enhanced through transmission, and cystic follicles within the lesion.[42,43] The masculinization is thought to be caused by stromal luteinization that results from mechanical stretching of the stromal cells by the edema fluid. In addition, human chorionic gonadotropin–like substance may

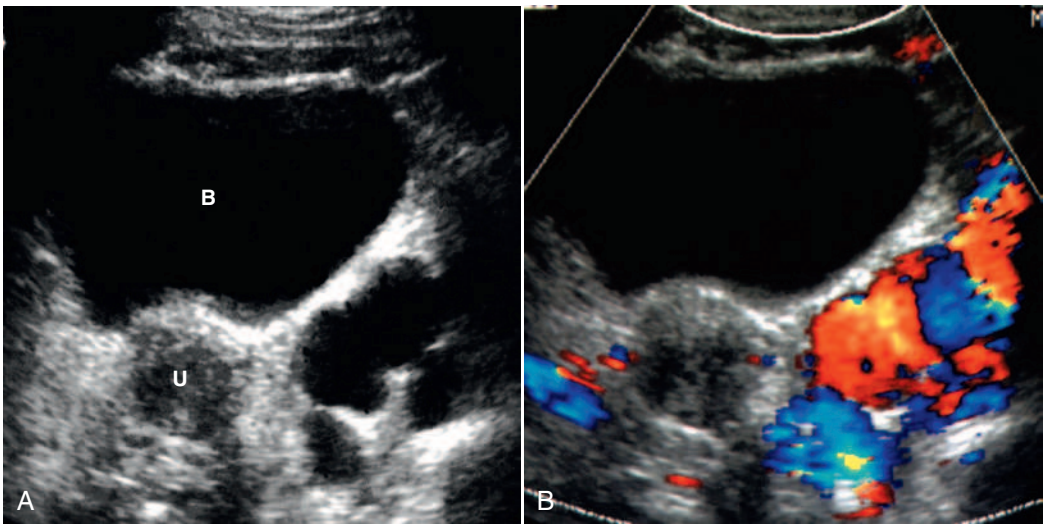

FIG. 54.13 Pelvic Varices Mimicking a Multiseptated Ovarian Cyst. Young woman with chronic liver disease and portal hypertension. **(A)** Transverse sonogram of pelvis shows a multiseptated left adnexal mass. *B,* Bladder; *U,* uterus. **(B)** Transverse color Doppler sonography of pelvis clearly demonstrates the vascular nature of the lesion. Pulsed Doppler showed venous waveforms *(not shown).*

FIG. 54.14 Polycystic Ovarian Disease: Stein-Leventhal Syndrome. Sagittal sonogram of the left ovary in 21-year-old woman with secondary amenorrhea, obesity, and hirsutism. The ovary is round and contains multiple peripheral follicles ("string of pearls"), each of which measures greater than 5 mm (and less than 9 mm).

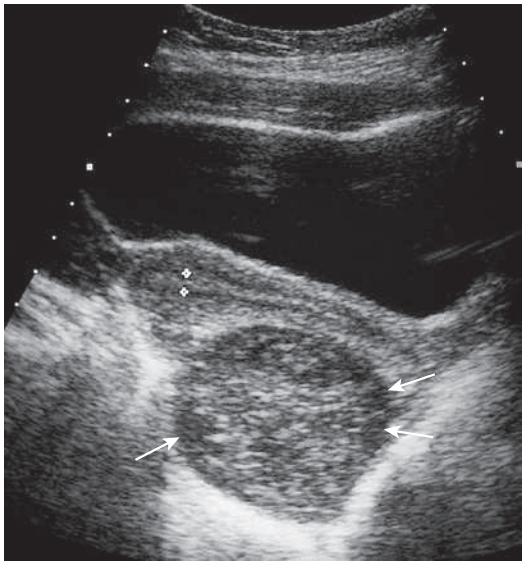

FIG. 54.15 Ovarian Edema. Massive ovarian edema in a 13-year-old girl with masculinization and intermittent pelvic and abdominal pain. Sagittal sonographic image demonstrates a large, heterogeneous, primarily hypoechoic mass posterior and separate from the uterus. This mass contains marked sound through transmission and multiple tiny follicles *(arrows). Calipers,* Endometrial stripe. (Courtesy of Marilyn Goske, MD.)

accumulate in edema fluid and promote luteinization, and level of 17-ketosteroids may be increased.

Ovarian Neoplasms

Ovarian neoplasms account for 1% of all childhood tumors, and 10% to 30% of these are malignant. These neoplasms may develop at any age but most frequently occur at puberty. Abdominal pain or a palpable abdominal or pelvic mass is the usual presenting symptom. Symptoms may develop as a result of torsion or hemorrhage into the tumor. Ovarian torsion is more common in adolescents than in adults; however, ascites is less common in girls.[44,45]

Primary ovarian tumors can be classified into three types of cell origins: **germ cells, epithelial cells,** and **stromal cells.** In children, 60% of primary ovarian tumors are of germ cell origin, in contrast to adults, in whom 90% are epithelial in origin. About 75% to 95% of germ cell tumors in childhood are benign teratomas. However, there is a higher incidence of malignancy in younger patients. In girls younger than 10 years, 84% of ovarian germ cell tumors are malignant. The presence of ascites suggests malignancy.

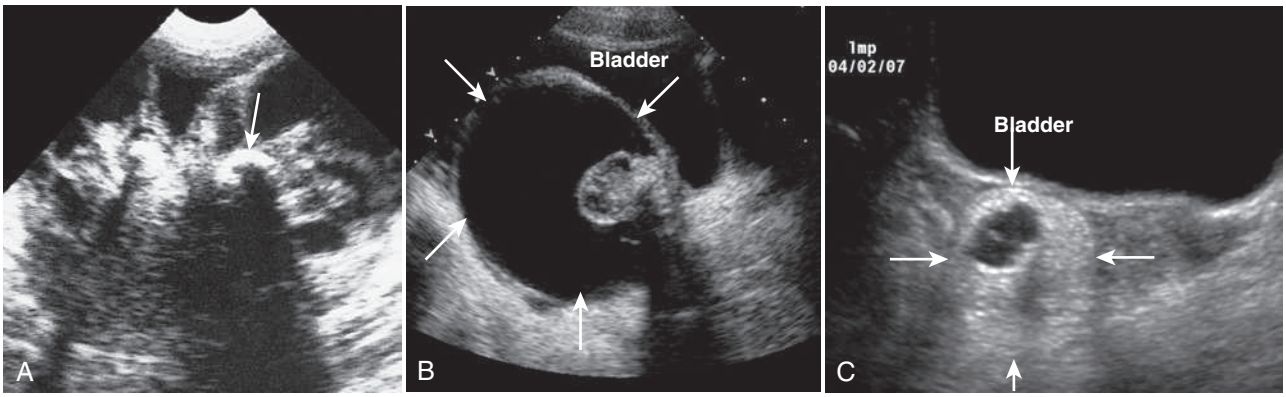

FIG. 54.16 Benign Ovarian Teratomas. (A) Transverse sonogram of pelvis in 6-year-old girl with constipation and large abdominal mass revealed very large, complex mass filling pelvis and lower two-thirds of abdomen, containing multiple shadowing, echogenic foci *(arrow)* consistent with calcifications. **(B)** Midline sonogram in a 12-year-old girl with right lower quadrant pelvic pain demonstrates a complex, primarily cystic mass *(arrows)* that contains a small area of shadowing calcification in the dermal plug. **(C)** Young girl with a history of urinary tract infection. Sonography demonstrates a complex, round, primarily brightly echoic mass *(arrows)* with smaller, hypoechoic cystic areas.

Ovarian Masses in Children

Benign ovarian teratomas (almost 60%)
Dysgerminoma
Embryonal carcinoma
Endodermal sinus tumor
Epithelial tumors of ovary (postpuberty)
Granulosa theca cell tumor (precocious puberty)
Arrhenoblastoma (rare, virilizing)
Gonadoblastoma (in dysplastic gonads—e.g., Turner syndrome)
Acute leukemia

Benign teratomas have a wide spectrum of sonographic characteristics (Fig. 54.16). Teratomas may be predominantly cystic. The most common sonographic appearance is a cystic mass with an echogenic mural nodule, the so-called "Rokitansky nodule" or "dermoid plug."[46-49] Cystic teratomas are usually freely mobile on a pedicle; 10% are bilateral, and 90% are less than 15 cm in diameter.[50]

Dysgerminoma is the most common malignant germ cell tumor of the ovary in childhood. This tumor frequently occurs before puberty, and 10% are bilateral. The tumor is usually a large, solid, encapsulated, rapidly growing mass containing hypoechoic areas as a result of hemorrhage, necrosis, and cystic degeneration. Retroperitoneal lymph node metastases may occur. Dysgerminoma is more radiosensitive than the other malignant ovarian tumors.[47,48]

Embryonal carcinoma and **endodermal sinus tumors** are less common malignant germ cell tumors. **Choriocarcinoma** is rare in children. All these are rapidly growing, highly malignant, solid neoplasms. Embryonal carcinoma is often associated with abnormal hormonal stimulation. These tumors tend to spread by direct extension to the opposite adnexa and retroperitoneal lymph nodes. Peritoneal seeding and hematogenous metastases to liver, lung, bone, and mediastinum are common.

Epithelial tumors of the ovary, which include serous and mucinous **cystadenoma** or **cystadenocarcinoma,** represent 20% of ovarian tumors in children.[51] Epithelial lesions are rare before puberty. On sonography, they are predominantly cystic masses with septa of variable thickness. It is often difficult to differentiate benign from malignant and serous from mucinous cystadenomas or cystadenocarcinomas based only on sonographic criteria.

Granulosa theca cell tumor is the most common stromal tumor in children. It is often associated with feminizing effects and precocious puberty as a result of estrogen production. Of these tumors, 10% are bilateral; only 3% are malignant. Sonographic appearance is nonspecific, and they may be solid, cystic, or mixed.[47-49] **Arrhenoblastoma** (Sertoli-Leydig cell tumor) is rare but may result in virilization. **Gonadoblastoma** is composed of germ cells admixed with sex cell and stromal elements and usually arises in dysplastic gonads. Bilateral involvement occurs in one-third of cases, and 50% contain dysgerminoma elements.

In **leukemic infiltration,** the ovaries, as well as the testes and central nervous system, are sanctuary sites for acute leukemia. Ovarian involvement in autopsy series ranges from 11% to 50%. In leukemia with ovarian relapse, most patients have large, hypoechoic, pelvic masses with smooth, lobulated margins. The tumor can infiltrate the pelvic organs and bowel loops to such a degree that the uterus and ovaries cannot be separately identified. Secondary hydronephrosis may develop. Bickers and colleagues[52] suggested that pelvic sonography should be used to monitor and detect early leukemic relapse in the ovaries of children in clinical remission. The ovaries may also be a site for metastatic spread from **neuroblastoma, lymphoma,** and **colon carcinoma.** The tumors rarely grow large enough to produce a mass and are usually asymptomatic. Typically, the secondary neoplasms appear on sonography as enlargement of one or both ovaries, which are hypoechoic or hyperechoic to the uterus. Less often, a discrete solid or complex mass is seen.

It was originally thought that Doppler sonography would serve to differentiate between benign and malignant ovarian masses. In adolescents and adult women, malignant ovarian

tumors generally have central, low-resistance arterial Doppler waveforms (resistive index [RI] < 0.4, or pulsatility index [PI] < 1.0), thought to be caused by a relative paucity of a muscular layer in the neoplastic vessels,[53] thereby limiting the specificity of Doppler imaging.[54] Benign ovarian masses tend to have peripheral, high-resistance flow (RI > .7 or PI > 1.0). However, nonneoplastic lesions (e.g., tubo-ovarian abscess, ectopic pregnancy, functioning corpus luteum) also have low-resistance flow, and some malignant tumors show high-resistance flow.

UTERINE AND VAGINAL ABNORMALITIES

Congenital Anomalies

Congenital anomalies of the uterus and vagina in children are uncommon and usually manifest as an abdominal or pelvic mass secondary to obstruction. There is a high incidence of associated renal anomalies (50%) and an increased incidence of skeletal anomalies (12%).[55] The uterus, cervix, and upper two-thirds of the vagina are formed by the fused caudal ends of the müllerian (paramesonephric) duct. The paired fallopian tubes are formed by the unfused upper ends. The lower third of the vagina is derived from the urogenital sinus. Müllerian duct development into the uterus is dependent on the formation of the wolffian (mesonephric) duct. Therefore abnormal development of the müllerian duct, resulting in uterine and vaginal anomalies, is often associated with renal anomalies.[56,57]

The **bicornuate uterus** is the most common congenital uterine anomaly. It results when the two müllerian ducts fuse only inferiorly[58] (Fig. 54.17). The two separate uterine horns, which are joined at a variable level above the cervix, are best demonstrated on transverse sonograms through the superior portion of the uterus. Most often only one cervix is visualized (when there are two, this is a bicornis bicollis) and one vagina is identified. With **complete duplication of the müllerian ducts (didelphys),** there is a septated vagina and duplicated cervix and uterus. In either anomaly, obstruction of one uterine horn can result in a pelvic mass from unilateral hydrometra or hematometra. Other septation anomalies of the uterus can result from incomplete involution of the midline septum between the paired müllerian ducts. A **unicornuate uterus** is formed from the agenesis of one müllerian duct.[59] In utero exposure to **diethylstilbestrol** (DES) has been associated with development of a **T-shaped uterus.** Sonography shows a narrow uterus caused by absence of the normal, superior, bulbous expansion of the uterine fundus. Three-dimensional sonography is an excellent modality for obtaining planar reformatted sections through the uterus, which allows for precise evaluation of the anatomy.[57]

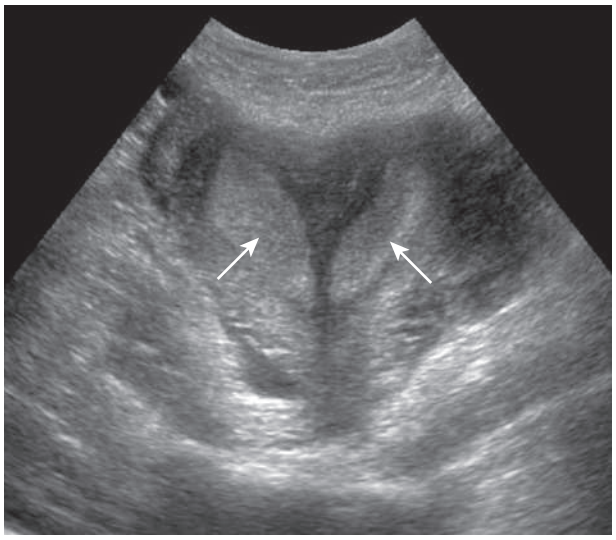

FIG. 54.17 Bicornuate Uterus. Transverse image of the uterus in a 20-year-old woman with acute lower abdominal and pelvic pain reveals two separate endometrial cavities *(arrows)* in the middle to fundal region of the uterus.

Hydrocolpos or **hydrometrocolpos,** caused by obstruction of the vagina, accounts for 15% of abdominal masses in newborn girls (Fig. 54.18). The obstruction is secondary to an **imperforate hymen,** a **transverse vaginal septum,** or a **stenotic or atretic vagina.** There is an accumulation of mucous secretions proximal to the obstruction. The secretions are secondary to intrauterine and postnatal stimulation of uterine and cervical glands by maternal estrogens. A simple imperforate hymen is not usually associated with other congenital anomalies. However, there is a high incidence of genitourinary, gastrointestinal, and skeletal anomalies associated with **vaginal atresia** or a **midtransverse or high-transverse vaginal septum.** Combined perineal-abdominal sonography is an excellent method for accurate assessment of these anomalies.[60] Although TAS is useful to determine if hydrocolpos or hydrometrocolpos is present, this method does not allow measurement of the thickness of a caudally placed obstructive septum. On sonographic examination, hydrocolpos appears as a large, tubular, cystic mass posterior to the bladder and extending inferior to the symphysis pubis.[61] Low-level echoes within the fluid represent mucous secretions in neonates and blood in postpubertal girls[62] (Fig. 54.19). There may be secondary urinary retention and hydronephrosis. Imperforate anus, cloacal exstrophy, and persistent urogenital sinus often have associated hydrometrocolpos.[63-65] Rarely, one may see peritoneal calcifications complicating hydrometrocolpos because of a sterile inflammatory reaction to spillage into the peritoneal cavity of accumulated secretions.[66]

The **Mayer-Rokitansky-Küster-Hauser syndrome,** the second most common cause of primary amenorrhea, comprises vaginal atresia, rudimentary uterus, normal fallopian tubes and ovaries, and broad and round ligaments.[55] The spectrum of uterine anomalies (hypoplasia or duplication) ranges from a partial lumen to a septate or bicornuate uterus with unilateral or bilateral obstruction. These girls have a normal female karyotype, secondary sexual development, and external genitalia. There are high incidences of unilateral renal (50%) and skeletal (12%) anomalies. Unilateral renal agenesis and ectopia are the most common renal anomalies. The most common sonographic findings are uterine didelphys with unilateral hydrometrocolpos and ipsilateral renal agenesis. Water vaginography can help identify the septated vagina with unilateral vaginal obstruction[55] (Fig. 54.20). The analogous genitourinary defects in the male result in duplicated müllerian

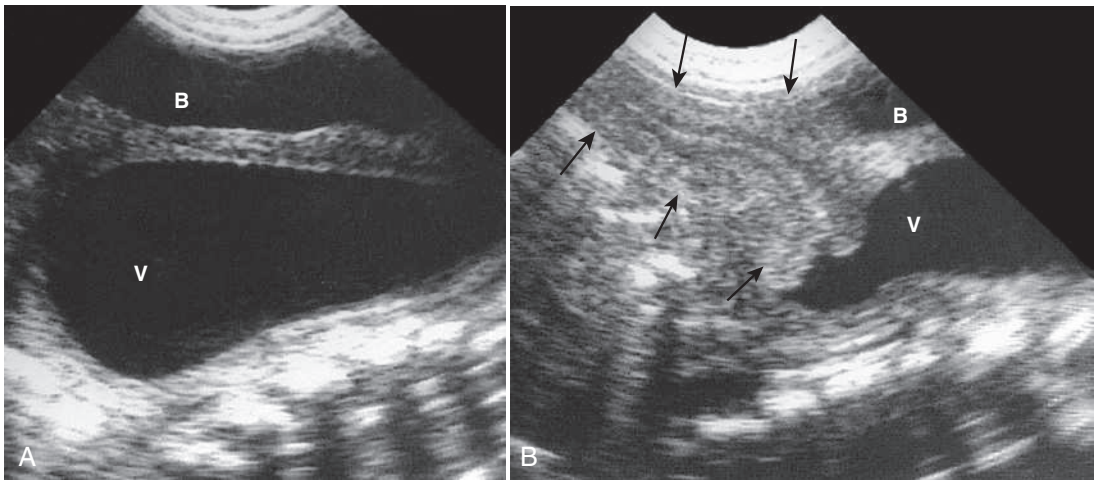

FIG. 54.18 Hydrocolpos. (A) Sagittal scan of pelvis in newborn showing large, conical, fluid-filled mass representing obstructed vagina *(V)* behind bladder *(B).* **(B)** Sagittal scan, angled higher than in **(A)**, shows uterus *(arrows)* with cervix projecting into dilated vagina *(V). B,* Bladder. (With permission from Rosenberg H. Sonography of pediatric urinary tract abnormalities. Part I. Am Urol Assoc Weekly Update Series. 1986;35:1-8.[231])

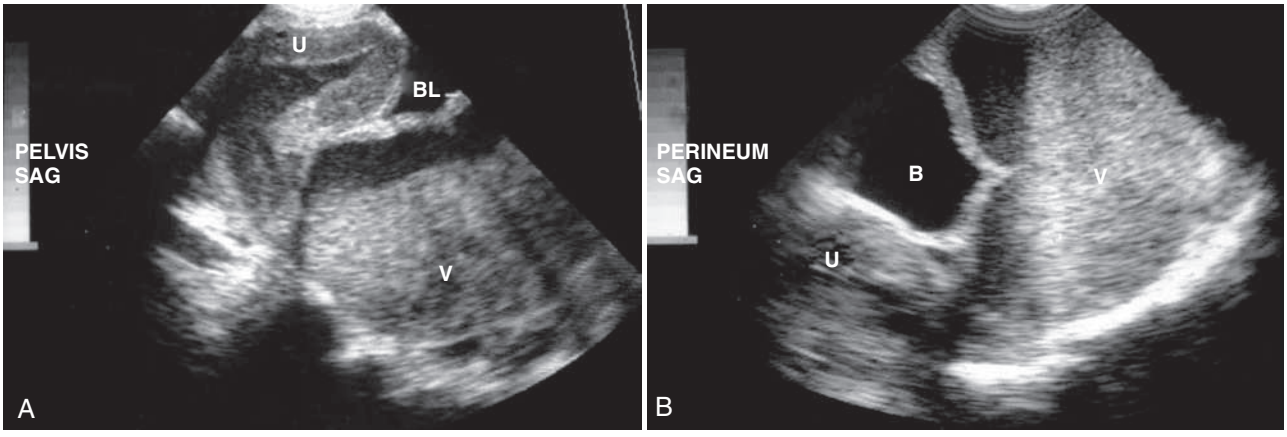

FIG. 54.19 Hematometrocolpos. (A) Sagittal scan of pelvis shows dilated uterine cavity *(U)* filled with echogenic debris (blood). Fluid-debris level is seen in dilated, obstructed vagina *(V). BL,* Bladder. **(B)** Perineal scan confirming the massively dilated vagina with the distal end immediately below the skin surface. *B,* Bladder; *U,* uterus, *V,* vagina. (With permission from Fisher MR, Kricun ME, editors. Imaging of the pelvis. Gaithersburg, Md: Aspen; 1989.[62])

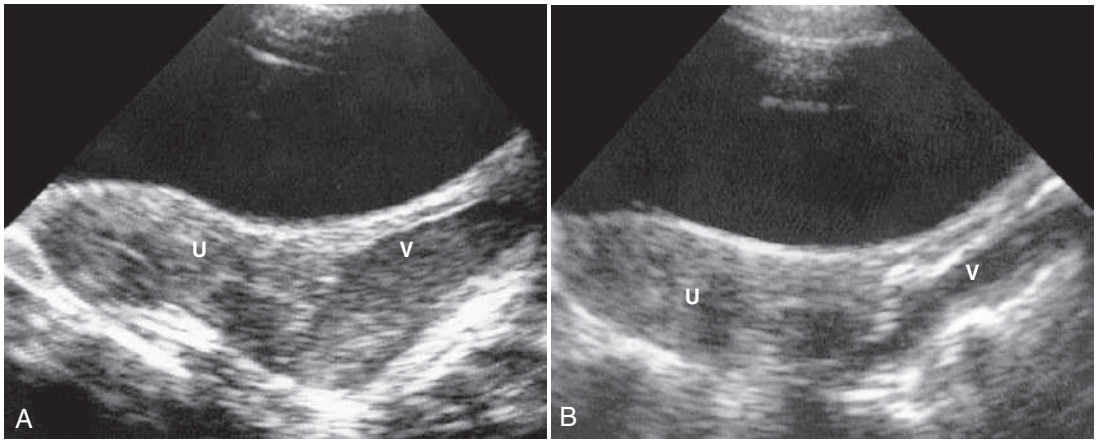

FIG. 54.20 Mayer-Rokitansky-Kuster-Hauser Syndrome. This 13-year-old girl had duplication of uterus and vagina, obstructed right-sided vagina, and fenestrated vaginal septum with cyclic pelvic pain and normal menstrual periods. **(A)** Sagittal scan of pelvis demonstrates a normal right uterus *(U)* and a distended vagina *(V)* filled with echogenic material that moved at real time. **(B)** Left-sided uterus *(U)* is clearly seen in the sagittal plane, and following hand-injection of sterile water into the single introitus, the left-sided vagina *(V)* was demonstrated. During real-time observation, tiny amounts of water could be seen intermittently in the right-sided vagina, suggesting the presence of a fenestrated vaginal septum.

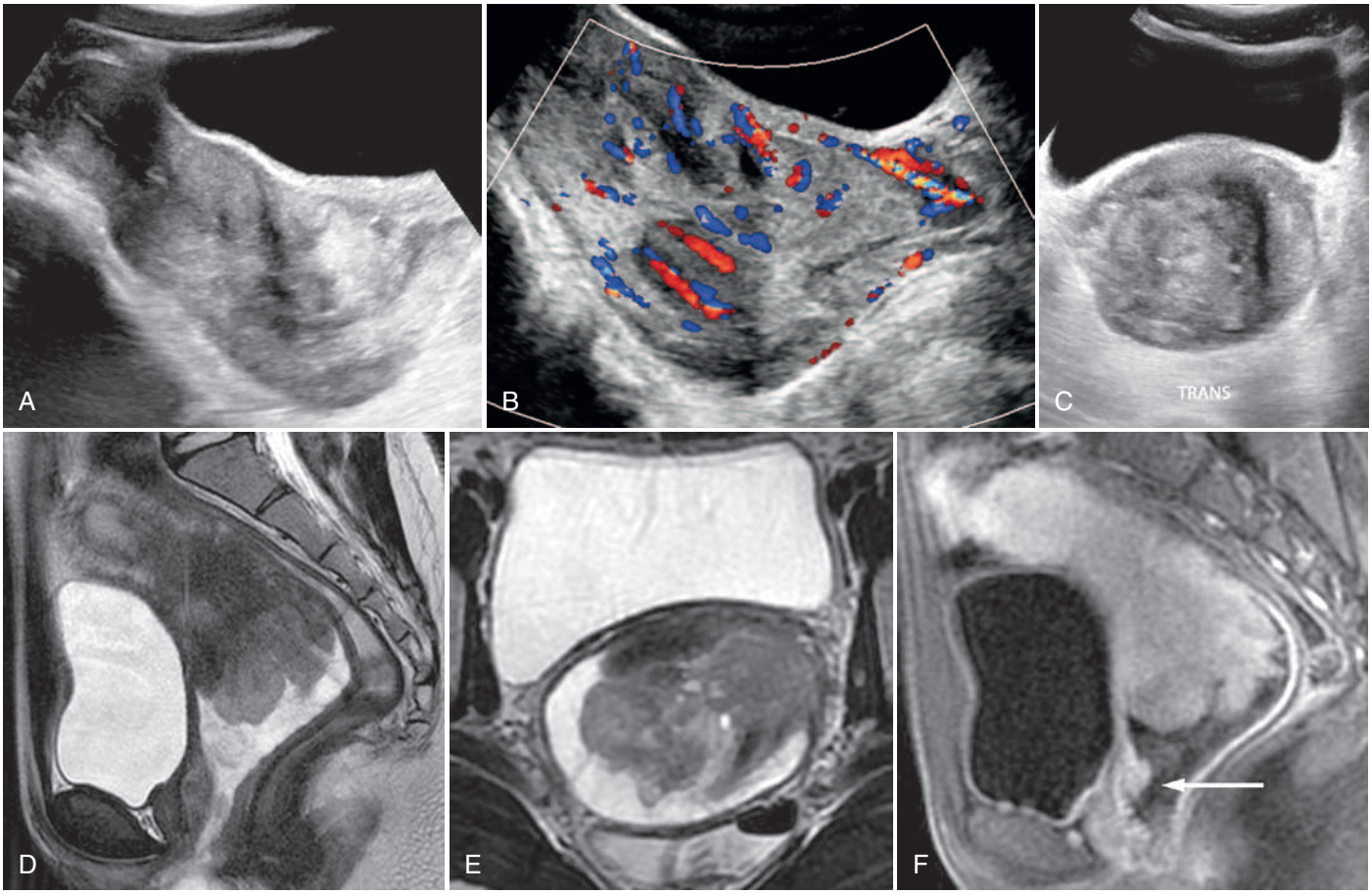

FIG. 54.21 Rhabdomyosarcoma of Vagina. Sagittal **(A)** scan through the uterus shows a heterogeneous solid mass in the upper vagina inseparable from the cervix. Normal fundus and endometrial echo are visible superior to the mass, with significant vascularity on color Doppler imaging **(B)**. Transverse scan **(C)** shows a heterogeneous mass that expands the upper vagina and cervix. Magnetic resonance image shows intermediate signal mass with a frondlike configuration on sagittal **(D)** and transverse **(E)** T2-weighted imaging with high signal in the surrounding vagina as a result of fluid and blood. The mass avidly enhances after gadolinium administration **(F)** with extension along the anterior vaginal wall *(arrow)*.

duct remnants (müllerian cyst and dilated prostatic utricle) with unilateral renal agenesis.

Neoplasm

Tumors of the uterus and vagina are uncommon in the pediatric patient. Malignant tumors are more common than are benign tumors, and the vagina is a more common site than is the uterus. **Rhabdomyosarcoma** is the most common primary malignant neoplasm (Fig. 54.21).[67] It can arise from the uterus or vagina, although uterine involvement is more frequent by direct extension from a vaginal tumor. Presentation is usually at 6 to 18 months of age with vaginal bleeding or protrusion of a polypoid cluster of masses **(sarcoma botryoides)** through the introitus. Rhabdomyosarcoma most often arises from the anterior wall of the vagina near the cervix. It may also arise in the distal vagina or labia. Direct extension of the tumor into the bladder neck is common, but posterior invasion of the rectum is infrequent. Lymphadenopathy and distant metastases are uncommon at presentation. On sonographic examination, these tumors are solid, homogeneous masses that fill the vaginal cavity or cause enlargement of the uterus with an irregular contour.

Endodermal sinus tumor, a less common genital neoplasm, is a highly malignant germ cell tumor that can arise in the vagina. It has clinical and sonographic presentations similar to those of rhabdomyosarcoma Other malignant tumors of the uterus and vagina are rare. Adenocarcinoma of the cervix in adults arises from the endocervix, whereas in children it is a polypoid lesion that originates from the ectocervix and upper vagina. **Carcinoma of the vagina** (usually clear cell adenocarcinoma) usually occurs in teenagers with a history of in utero DES exposure. Leukemic infiltration of the uterus can occur secondary to contiguous extension from an ovarian relapse. Sonography shows a large, homogeneous, hypoechoic, pelvic mass incorporating the uterus and ovaries, which cannot be separately identified. There may be associated hydronephrosis caused by distal ureteral obstruction.

Benign, solid neoplasms of the uterus and vagina are rare in children. However, benign cystic vaginal masses can occur. The most common cystic lesion of the vagina is **Gartner cyst.** A remnant of the distal wolffian (mesonephric) duct, Gartner cysts may be single or multiple and typically arise from the anterolateral vaginal wall. They appear as fluid-filled cysts within the vagina

on ultrasound. Other cystic vaginal masses include **paraurethral cysts, inclusion cysts,** and **paramesonephric** (müllerian) **duct cysts.**

Pregnancy

Intrauterine pregnancy must always be considered in the differential diagnosis of a pelvic mass in girls 9 years of age or older. There is an increased incidence of complications in pediatric pregnancy. These include **toxemia, preeclampsia, placental abruption, lacerations,** and **cesarean section.** Prematurity and perinatal mortality are also increased in infants of teenage mothers.

When the sonographic findings show a distended endometrial cavity in a sexually active girl, molar pregnancy should be considered (Fig. 54.22). In girls postpartum, a well-defined, heterogeneous endometrial mass raises the possibility of **retained products of conception** (Fig. 54.23).

Although **ectopic pregnancy** accounts for approximately 2% of all pregnancies and is less common in young adolescents, the diagnosis should be considered in the presence of pelvic pain, an abnormal **beta human chorionic gonadotropin** (β-hCG) level, irregular vaginal bleeding, and missed menstrual period. An ectopic pregnancy is most likely located in a fallopian tube (ampulla 70%, isthmus 12%, fimbria 11.1%). The two most common sonographic signs of ectopic pregnancy include an **adnexal mass** that is separate from the ovary and the **tubal ring sign** (Fig. 54.24). The diagnosis is more certain when a yolk sac or a living embryo is demonstrated within the adnexal mass.[68] The tubal ring sign consists of a hyperechoic ring surrounding an extrauterine gestational sac. The additional demonstration

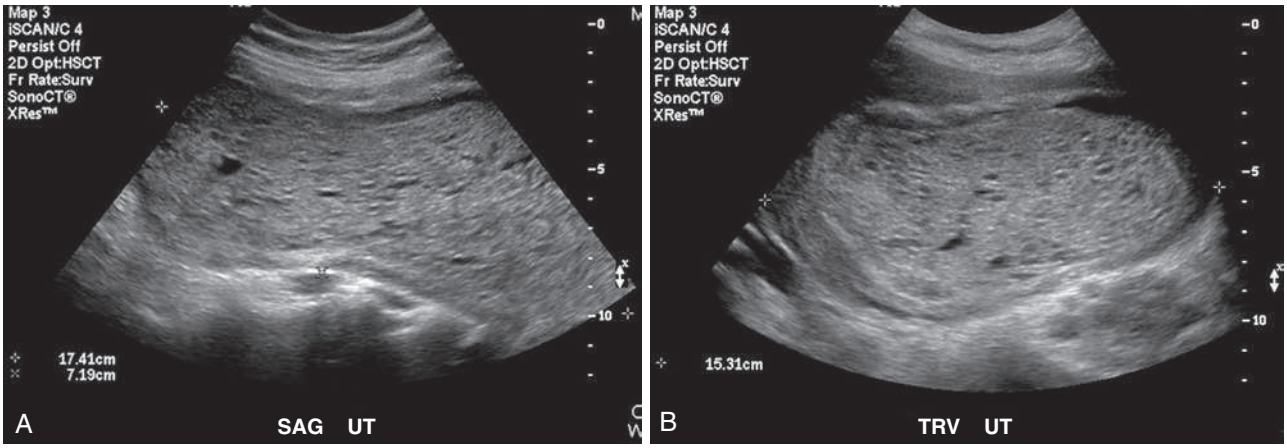

FIG. 54.22 Molar Pregnancy in 20-Year-Old Patient With Vaginal Bleeding and Abdominal Pain. (A) and **(B)** Sagittal and transverse sonograms of the uterus demonstrate a 17.4 × 15.3 × 7.2–cm complex, mainly solid mass, throughout the uterus with the exception of the distal end of the cervix, which is characterized by diffuse heterogeneity from myriad tiny cystic spaces. The mass is hypovascular and does not contain calcifications.

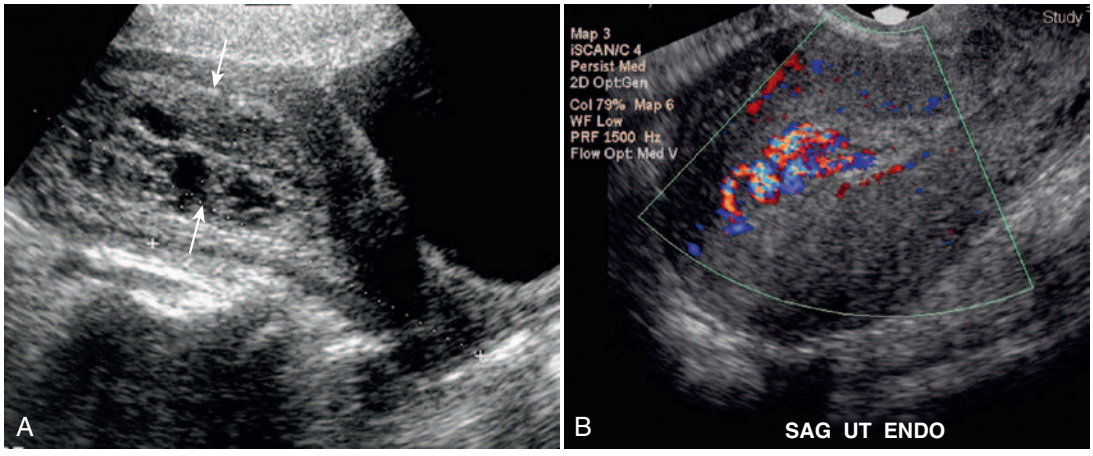

FIG. 54.23 Retained Products of Conception. (A) This 15-year-old girl had ongoing cramps and vaginal bleeding after a spontaneous abortion. Sagittal sonography shows elongation of the uterus (13 cm) with a heterogeneous, fairly well-defined, oval masslike area *(arrows)* occupying the fundus. **(B)** Another teenager with vaginal bleeding a few days after a therapeutic abortion. Sagittal color Doppler sonogram of the uterus demonstrates endometrial hypervascularity, consistent with retained products of conception.

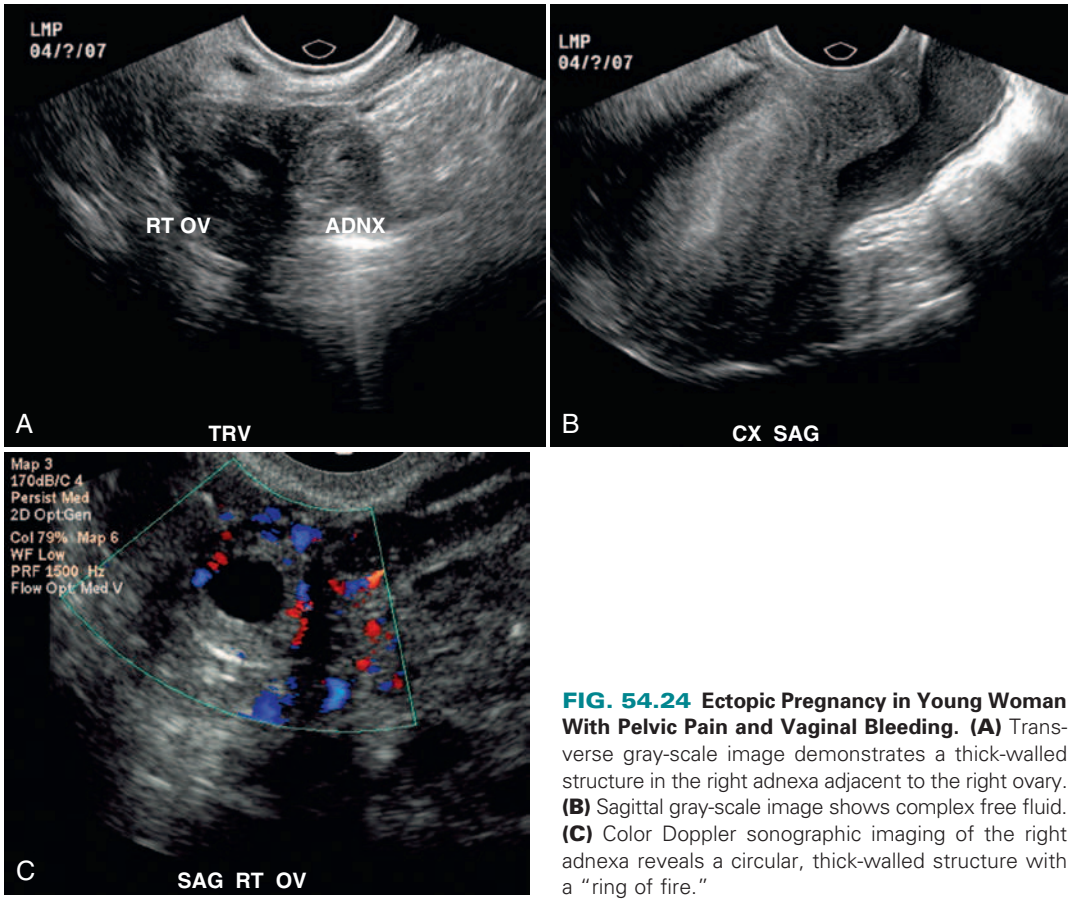

FIG. 54.24 Ectopic Pregnancy in Young Woman With Pelvic Pain and Vaginal Bleeding. (A) Transverse gray-scale image demonstrates a thick-walled structure in the right adnexa adjacent to the right ovary. **(B)** Sagittal gray-scale image shows complex free fluid. **(C)** Color Doppler sonographic imaging of the right adnexa reveals a circular, thick-walled structure with a "ring of fire."

of the **"ring of fire" sign,** which consists of high-velocity, low-impedance flow within the hyperechoic ring, may be another useful finding.[69] However, this sign is nonspecific and may be seen surrounding a normal corpus luteal cyst. Hypotension or overt shock suggests ruptured ectopic pregnancy. Although TVS has greatly improved the diagnostic evaluation of suspected ectopic pregnancy, TAS plays a complementary role by providing a global view of the pelvis and abdominal contents.[70] β-hCG measurements are essential for establishing the diagnosis. This glycoprotein hormone begins to increase in a curvilinear fashion early in pregnancy and continues to increase until approximately 9 to 11 weeks, when it normally reaches a plateau. The plateau lasts for a few days and declines at 20 weeks. β-hCG level doubles on an average of approximately 48 hours when the pregnancy is normal. In the presence of an ectopic pregnancy, however, serum β-hCG levels often rise much more slowly, and a plateau is reached early in the pregnancy. A less than 50% increase in β-hCG level in a 48-hour period is almost always associated with a nonviable pregnancy, whether intrauterine or extrauterine.[71]

Infection

Pelvic Inflammatory Disease

Pelvic inflammatory disease (PID) is an infection of the upper genital tract, usually related to *Neisseria gonorrhoeae* or *Chlamydia trachomatis* infection. The serious sequelae of this disease include ectopic pregnancy, infertility, and chronic pelvic pain. Adolescent females are in a higher-risk group, and thus PID should be considered in sexually active females with pelvic pain. The ascending infection may affect uterus, fallopian tubes, and ovaries, causing endometritis, salpingitis, oophoritis, pelvic peritonitis, and tubo-ovarian abscess.

In a study by Bulas of PID in adolescents,[72] anatomic detail was improved with TVS compared with TAS. Transvaginal scans showed new abnormalities in 71% of patients, and the level of disease severity was changed in 33% of patients, which affected treatment decisions in many of these patients.

Acutely, the pelvic sonogram may be normal.[70,73] In the **endometritis** stage of PID, the uterus may be enlarged and more hyperechoic, may contain a small amount of fluid in the endometrial canal, and may have indistinct margins. The normal fallopian tube is usually not visualized on sonography. As the infection ascends, however, the fallopian tubes become thick walled and fill with purulent material[72] (Fig. 54.25). A **pyosalpinx** is a dilated, occluded fallopian tube that contains echogenic purulent fluid. A residual **hydrosalpinx** is a tubular or round structure with anechoic fluid. Ovarian changes from PID may include enlargement secondary to the production of inflammatory exudate and edema and development of many tiny cysts, which may represent small follicles or abscesses (Fig. 54.26).

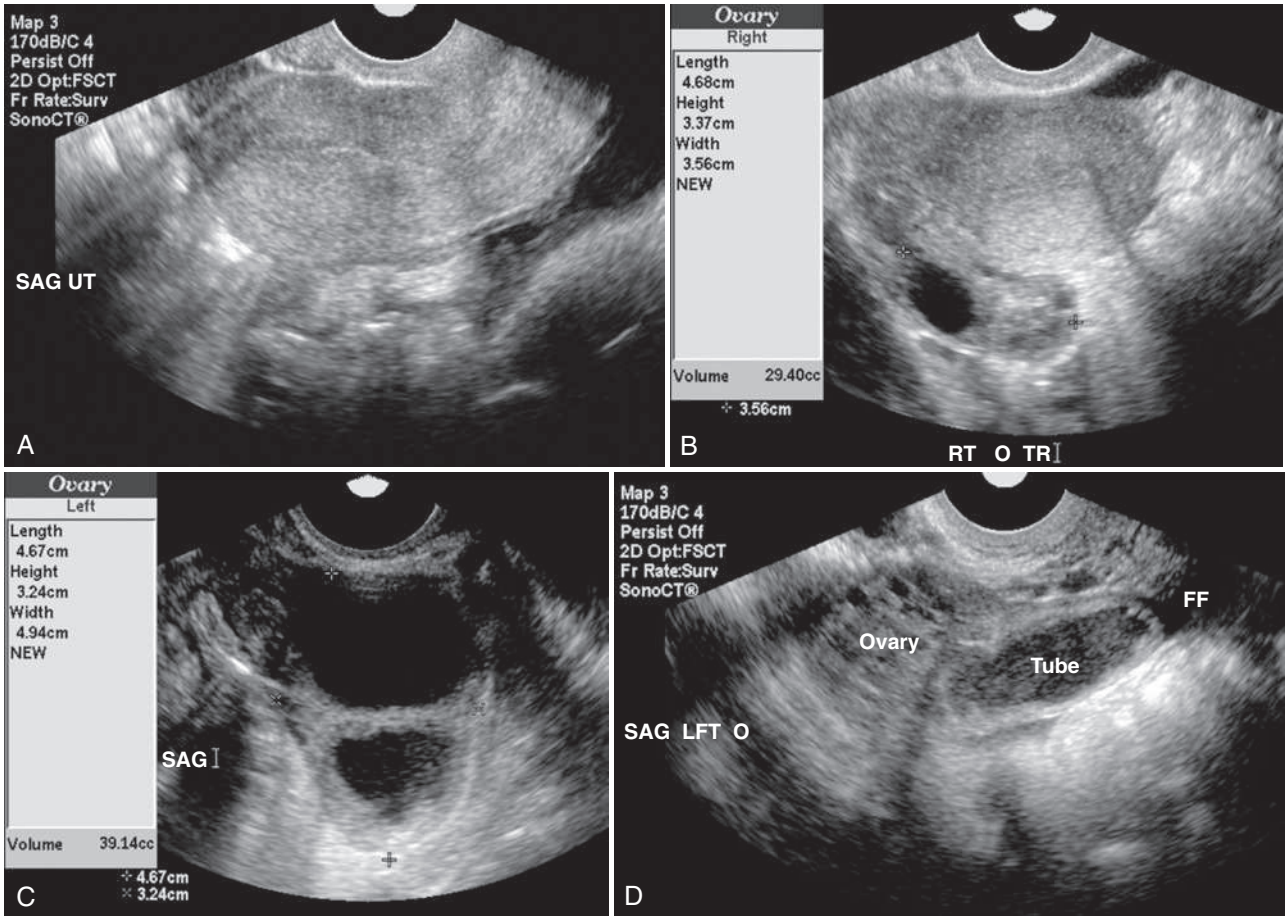

FIG. 54.25 Pelvic Inflammatory Disease With Tubo-Ovarian Complex. Transvaginal ultrasound in 16-year-old girl with pelvic pain. **(A)** Sagittal image of the uterus shows free fluid in the cul-de-sac. **(B)** The right ovary is normal sized *(calipers)*, although there is an anechoic dominant cyst. **(C)** Sagittal image of greatly enlarged left adnexa demonstrates a tubo-ovarian complex (one cyst within ovary and one anterior to ovarian border). **(D)** Fluid-distended fallopian tube is noted with surrounding free fluid *(FF)*. The fluid within the tube is complex with heterogeneous internal echoes, implying purulent material.

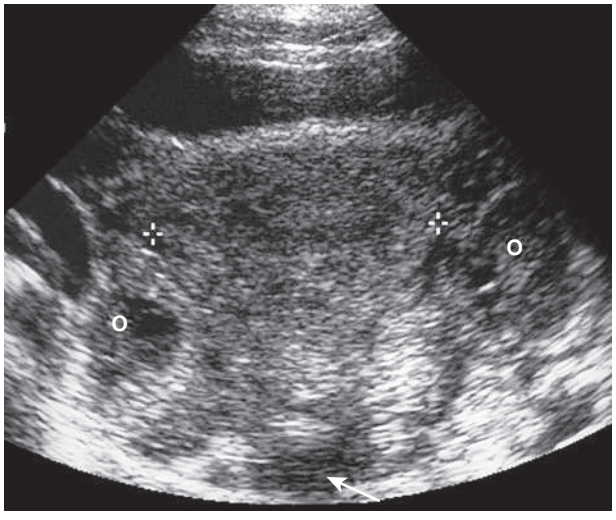

FIG. 54.26 Pelvic Inflammatory Disease. Transverse transabdominal sonography reveals increased, poorly defined, soft tissue echogenicity representing inflammatory material causing indistinct uterine and ovarian margins and haziness in the parametrial area. A small amount of echogenic fluid is seen posteriorly *(arrow)*. *Calipers,* Uterus; *O,* ovary.

Pelvic Inflammatory Disease: Sonographic Findings

Enlarged, hyperechoic uterus
Indistinct uterine margins
Fluid in endometrial cavity
Pyosalpinx (dilated tube with thick walls with echogenic fluid)
Ovarian enlargement with tiny cysts
Tubo-ovarian abscess (heterogeneous adnexal mass)

Periovarian adhesions may form, resulting in fusion of the ovary and thickened tube, forming a tubo-ovarian complex. Further progression leads to tissue breakdown and formation of a **tubo-ovarian abscess,** which usually appears as a heterogeneous, adnexal mass with enhanced through transmission, internal debris, and septations. Color Doppler evaluation of pelvic masses in patients with PID is not specific and overlaps with other entities. Flow in an abscess may be seen along its periphery;

however, this pattern may also be seen in other cystic lesions.[21,72] In **extensive cases of PID** the pelvis is diffusely filled with a heterogeneous echo pattern containing cystic and solid components that obscure tissue planes and uterine margins.

A complication of PID is **gonococcal or chlamydial perihepatitis (Fitz-Hugh–Curtis syndrome).** The patient has right upper quadrant pain caused by localized peritonitis of the anterior liver surface and parietal peritoneum of the anterior abdominal wall. Sonographic findings include the presence of ascitic fluid and thickening of the right anterior extrarenal tissue between the liver and right kidney.[74,75]

Foreign Bodies

A vaginal discharge may be a sign of vaginal infection or trauma. Foreign bodies in the vagina are a cause of 4% of cases of **vaginitis.** A wad of toilet paper is the most common foreign body in the vagina in the pediatric population. Vaginal foreign bodies are seen in 18% of children with vaginal bleeding and discharge and in 50% of children with vaginal bleeding and no discharge. Sonography, either transabdominal or transperineal, with or without water vaginography, can identify both radiopaque and nonradiopaque foreign bodies within the vagina as echogenic material with distal acoustic shadowing. A retained vaginal foreign body can be demonstrated on sonography as a slight indentation on the posterior bladder wall. Acoustic shadowing is characteristic but may not be present.[76,77]

ENDOCRINE ABNORMALITIES

Ultrasound is integral to the evaluation of children with endocrine abnormalities. In the newborn with ambiguous genitalia, pelvic sonography can quickly determine the presence or absence of the uterus and vagina. Identification of the ovaries or testes is more difficult because normal neonatal ovaries are difficult to visualize with ultrasound. Using a high-resolution (12-17 MHz) linear transducer, the gonads may be found in the inguinal canal or in the ambiguous labioscrotal folds. **Differentiation of the gonads** between ovaries and testes may be possible because ovaries often have small, hypoechoic follicles and testes have a solid, homogeneous echotexture.[78]

Causes of Primary Amenorrhea

Sonographic assessment of the uterine size, shape, and maturity and ovarian development can provide a clue to the many causes of primary amenorrhea. A small or absent uterus may be an indication of gonadal dysgenesis, **chromosomal abnormalities, decreased hormonal states, testicular feminization,** or **isolated uterine hypoplasia or agenesis.** In **Turner syndrome** (45,XO karyotype), the most common form of **gonadal dysgenesis,** there is delayed or absent puberty associated with short stature, webbed neck, renal anomalies, and coarctation of the aorta. Turner syndrome is almost always mosaic (45,XO/46,XX). The ovaries vary from nonvisualized streak ovaries to normal-appearing ovaries. The uterine configuration also varies from prepubertal to an intermediate length that is less than that of the normal adult female. Cleeman and colleagues[79] demonstrated in a group of 41 patients with Turner syndrome that one or both ovaries were detected in 37% by ultrasound. The mean ovarian volume was lower in those with Turner syndrome than in the controls ($p = .001$) (1.1 mL vs. 11.52 mL). The mean uterine volume was not significantly different from that in the normal controls.

Other forms of gonadal dysgenesis are also associated with nonvisualization of the ovaries as a result of absent or streak gonads. In **pure gonadal dysgenesis (Swyer syndrome),** the patients have 46,XX or 46,XY karyotypes and normal height. **Mixed gonadal dysgenesis** is a genetic mosaic of karyotypes 45,XO/46,XY with a streak ovary and a contralateral intra-abdominal testicle. Both these forms of gonadal dysgenesis have an increased risk of gonadal tumors as a result of the presence of the Y chromosome. **Noonan syndrome (pseudo–Turner syndrome)** is characterized by phenotypic changes of Turner syndrome, normal ovarian function, and normal ovaries on ultrasound.

Testicular feminization is another cause of primary amenorrhea. It is a sex-linked recessive abnormality, resulting in end-organ insensitivity to androgens. These patients are phenotypic females with a 46,XY karyotype. The uterus and ovaries are absent, the vagina ends blindly, and the testes are ectopic (usually pelvic or within inguinal canals or in labia majora).

Precocious Puberty

Precocious puberty is the development of secondary sexual characteristics, gonadal enlargement, and ovulation before age 8 years. In true precocious puberty, the endocrine profile is similar to that of normal puberty, with elevated levels of estrogen and gonadotropins. The uterus has an enlarged, postpubertal configuration (fundus-to-cervix ratio of 2:1 to 3:1) with a more prominent echogenic endometrial canal than seen in prepubertal females. The ovarian volume is greater than 1 mL, and functional cysts are often present. Precocious puberty is classified into two types: central and peripheral. **Central precocious puberty** (true precocious puberty) is gonadotropin dependent.[80,81] More than 80% of these cases are idiopathic. Intracranial tumors, usually a **hypothalamic glioma or hamartoma,** account for 5% to 10% of cases. There are occasional cases that follow development of increased intracranial pressure, such as **postmeningitis hydrocephalus.** The augmented uterine and ovarian volumes shown on ultrasound occur before the typical changes in secretion patterns of luteinizing hormone (LH) and follicle-stimulating hormone (FSH) revealed with the luteinizing hormone–releasing hormone (LHRH) test. Pelvic sonography during treatment with long-acting gonadotropin-releasing hormone analogues will show decreased uterine and ovarian volume compared with pretreatment values, and the hormonal status will become appropriate for age.[82,83]

In **pseudoprecocious puberty,** the peripheral type, the endocrine profile is variable because this type is gonadotropin independent. Usually, the estrogen levels are elevated and the gonadotropin levels are low. The cause is outside the hypothalamic-pituitary axis—usually an **ovarian tumor. Granulosa tumor** is the most common lesion. Other, less frequent causes are functioning ovarian cysts, **dysgerminoma, teratoma,** and **choriocarcinoma.** Ultrasound will identify the ovarian mass and a mature uterus.

Although **feminizing adrenal tumors** are a rare cause of pseudoprecocious puberty, sonographic examination of the adrenal areas should be performed in all patients with precocious puberty who are referred for pelvic ultrasound. The liver should be examined as well because precocious puberty has been associated with **hepatoblastoma.** In isolated premature **thelarche** (breast development) or premature **adrenarche** (pubic or axillary hair development), sonography shows normal prepubertal uterus and ovaries.

NORMAL MALE ANATOMY

The Prostate

The configuration of the prostate is ellipsoid in boys compared with the more conical shape seen in men. The prostatic echogenicity is hypoechoic and more homogeneous than in the adult prostate, which is frequently heterogeneous secondary to central gland nodules, calcifications, and corpora amylacea.[84,85] Prostate volume may be calculated by using the formula for a prolate ellipsoid (mentioned earlier for ovarian volume).

Ingram and colleagues[86] showed that in a group of 36 boys, ages 7 months to 13.5 years (mean 7.7 years), the prostatic volume ranged from 0.4 to 5.2 mL (mean 1.2 mL). The seminal vesicles may be identified in young boys and adolescents and are best seen in the transverse plane as small, hypoechoic structures giving an appearance similar to a bow tie or the wings of a seagull (Fig. 54.27).

The Scrotum

Before sonographic examination of the scrotum, the clinician should carefully palpate the entire scrotum. The pediatric scrotum is examined with a high-frequency linear array broadband transducer, generally a 12-5 MHz for children and teenagers and a 17-5 MHz, small-footprint, "hockey stick" probe for very small testes in infants and young children and for atrophic testes. It is helpful to elevate and immobilize the testes by gently placing a rolled-up towel posterior to the scrotum between the legs. For accurate measurements of larger adolescent testes, a curvilinear, broad-bandwidth probe, either a 9-4 or 5-2 MHz, and a stepoff pad may be necessary. In infants or any patient with a painful scrotum, a stepoff pad is essential to perform this valuable study. Both hemiscrota should be routinely examined so that differences in size and echogenicity of the intrascrotal contents can be recognized. Color Doppler imaging parameters should be optimized for the best detection of low-velocity and low-volume blood flow typically seen in the scrotum (color gain settings are maximized until background noise becomes visible, and wall filter and pulse repetition frequencies are adjusted to the lowest settings). Power Doppler imaging, with its increased sensitivity for the detection of blood flow, is useful for examination of slow flow states in the cooperative patient and particularly in very young children who normally have low testicular flow. In very small testes, power output may need to be increased to detect flow. Color flow in the two hemiscrota should be compared for symmetry. The addition of pulsed Doppler imaging allows for quantitative evaluation of arterial waveforms and measurements of velocity.

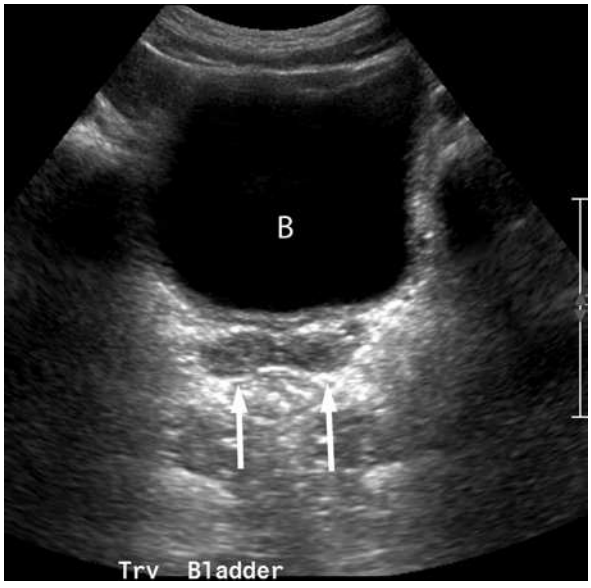

FIG. 54.27 Seminal Vesicles. Through a well-distended bladder *(B)*, the seminal vesicles *(arrows)* are seen as hypoechoic, bilaterally symmetrical structures with a "bow tie" appearance.

The Testes

The normal **newborn testes** have a homogeneous low- to medium-level echogenicity and are spherical or oval in shape with a length of 7 to 10 mm (Fig. 54.28). The epididymis and **mediastinum testis** are usually not seen in the neonate. By puberty, the testis contains homogeneous medium-level echoes and an echogenic linear structure along its superoinferior axis, which represents the mediastinum testis (Fig. 54.29, Video 54.4). The testis measures 3 to 5 cm in length and 2 to 3 cm in depth and width after puberty. Studies of testicular sizes during infancy and adolescence performed using orchidometers report the range of mean testicular volumes as 1.10 mL (standard deviation [SD] ± 0.14) and 30.25 mL (SD ± 9.64).[87] Normal testes smaller than 1 mL can be present in young infants and children.[88,89] The **tunica albuginea** may be seen as a thin echogenic line around the testis. Occasionally, a hypoechoic linear band is noted in the normal testis, usually in the middle third, corresponding to sites of **intratesticular vessels.**[90]

The normal color Doppler appearance of the testes changes with age. Despite optimized slow-flow settings, it may not be possible to detect color flow in normal, small, prepubertal testes.[88,89,91] Atkinson and colleagues[88] reported that centripetal arterial flow could be identified with color Doppler imaging in only 6 (46%) of 13 testes measuring less than 1 mL and in all testes measuring greater than 1 mL. When color flow is seen in prepubertal testes, it generally appears as pulsatile foci of color without the linear or branching pattern seen in adolescents or adults[88] (see Fig. 54.29). The recurrent rami arteries are usually too small to be identified in children, although they may be seen in adolescents. Color Doppler can demonstrate flow in 60% to 83% of prepubertal testes, and power Doppler imaging can demonstrate flow in 73% to 92% of prepubertal testes. Luker and Siegel[91] showed that power mode Doppler ultrasound

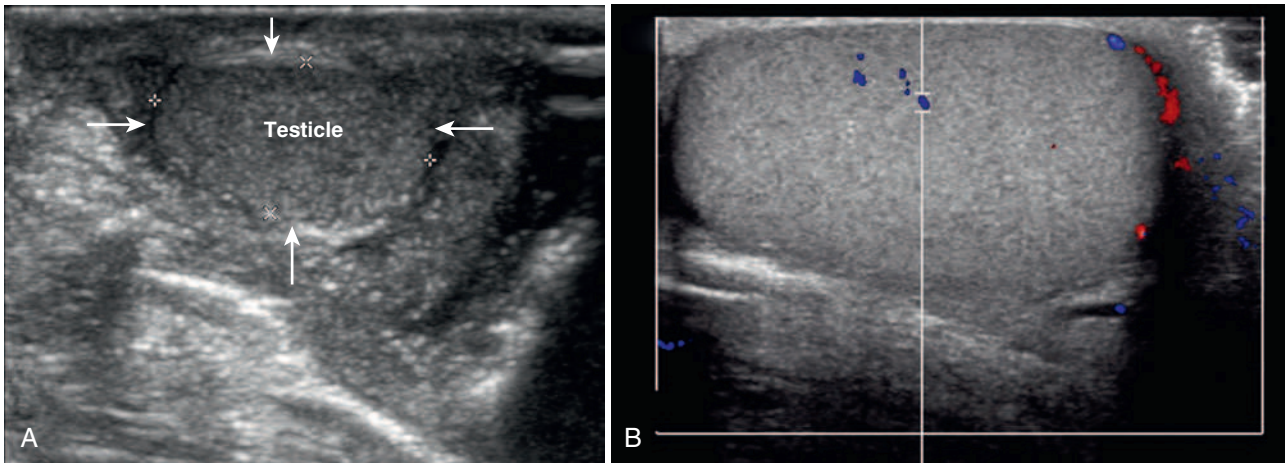

FIG. 54.28 Normal Infant Testis. (A) Gray-scale sagittal image shows the normal, homogeneous, relatively low-level echogenicity of this normal infant testis. **(B)** Some color Doppler flow is demonstrated within the testis.

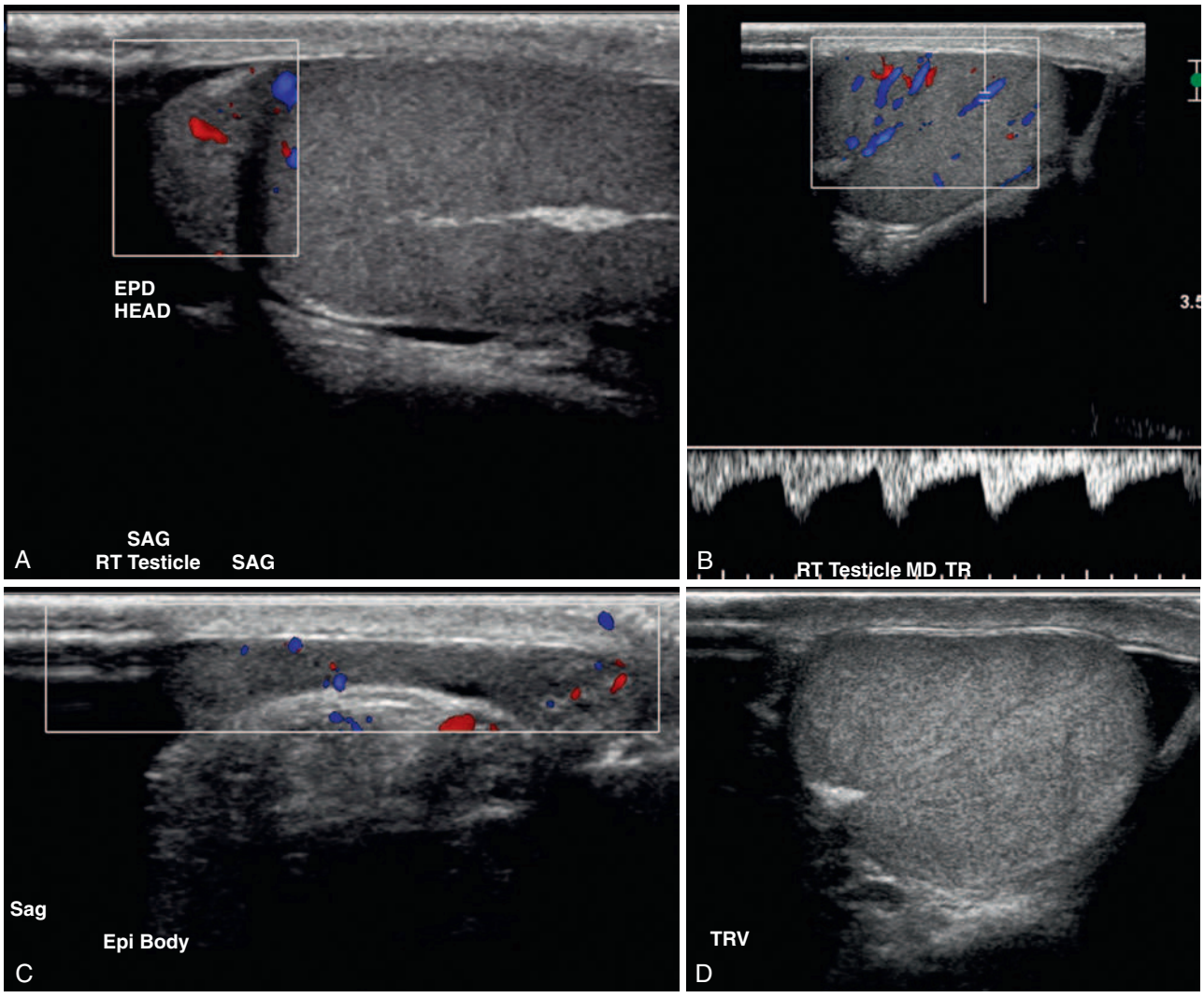

FIG. 54.29 Normal Postpubertal Testis. (A) Color Doppler image demonstrates flow within the head of the epididymis. The testis demonstrates normal homogenous echogenicity, with the mediastinal testis appearing as a white stripe. *EPD*, Epididymal; *Sag*, sagittal. **(B)** Normal duplex color Doppler flow in the centripetal arteries of this normal-appearing testis. *MD*, Mid; *TR*, transverse. **(C)** There is also normal flow in the body and tail of the epididymis. **(D)** Transverse image of testis. A small hydrocele is present. See also Video 54.4.

improved depiction of intratesticular vessels in normal prepubertal and postpubertal testes, but that there was still a lack of visualized flow in several normal prepubertal testes.

Normal pulsed wave Doppler testicular flow reflects its supply from the testicular artery, which has a low-resistance pattern (low peak systolic velocities and relatively high diastolic velocities). Flow in extratesticular vessels reflects supply from the cremaster and deferential arteries and has a higher resistance pattern (low diastolic flow). Because the periphery of the testis contains capsular branches of the testicular artery and branches of the cremasteric and deferential arteries, the patency of the testicular artery can be established reliably only by placing the Doppler sample volume in the center of the testis. The RI of the testicular artery in young men ranges from 0.48 to 0.75 (mean 0.62), and the RI of the capsular arteries ranges from 0.46 to 0.78 (mean 0.66). The RI of the supratesticular arteries varies from 0.63 to 1.00 (mean 0.84). The RI in intratesticular arteries is lower in postpubertal than in prepubertal boys.[92]

The examiner must compare the symmetry of color Doppler flow in both testes to detect disease more accurately and to ensure the system is optimally set to detect flow in the clinically normal testis. Absent flow may not be valid if the ultrasound equipment being used is insufficiently sensitive to detect low flow or if faulty technical settings are used (e.g., high wall filter, low gain, high pulse repetition frequency, low transducer frequency). Power Doppler is often better than color Doppler sonography in assessing symmetry of blood flow.[93]

The **epididymis** lies along the posterolateral aspect of the testis. The triangular epididymal head is isoechoic with the testis or slightly hyperechoic, whereas the echogenicity of the epididymal body is isoechoic or slightly hypoechoic in relationship to the testis. Flow may not be detected in the normal prepubertal epididymis but is generally seen on both color flow and power mode Doppler imaging in postpubertal epididymides.[91]

CONGENITAL MALE ABNORMALITIES

In **cryptorchidism** the testis does not descend through the inguinal canal into the scrotum as expected between the 25th and 32nd week of gestation. In most cases the testes are located within the scrotum at birth or within 4 to 6 weeks after birth. Undescended testes are seen in 4% of full-term newborns and in approximately 33% of premature male infants weighing less than 2500 grams. Testicular descent continues during the first year of life, so that by the end of the first year, only 0.7% to 0.8% of these infants have true cryptorchidism, and in 10% to 25%, it is bilateral cryptorchidism.[94] Although the malpositioned testis may lie anywhere along its course from the retroperitoneum to the scrotum, most undescended testes (80%-90%) are located at or below the inguinal canal and thus are amenable to sonographic localization[95] (Fig. 54.30). Magnetic resonance imaging (MRI) may be employed for localizing intraabdominal cryptorchid testes.[96] Localization of the undescended testis is important in disease prevention because cryptorchidism is associated with increased risks of malignancy, infertility, and torsion.[95] Rarely, the testis is found in the perineum or at the base of the penis.

Aberrations in testicular descent may result in **transverse testicular ectopia,** an anomaly in which both testes are located in the same hemiscrotum. Clinical presentation includes a nonpalpable testis on one side and a scrotal "mass" on the other.[97] About 20% of patients have associated anomalies, such as seminal vesicle cysts, renal dysplasia, hypospadias, ureteropelvic junction obstruction, and ipsilateral inguinal hernia.

Anorchidism, bilateral testicular absence, occurs in 1 per 20,000 newborn males. **Monorchidism,** unilateral testicular absence, occurs in 1 per 5000 boys and is usually left sided. This is thought to result from an in utero torsion or vascular accident because of the associated blind-ending spermatic vessels and spermatic cords.[98]

FIG. 54.30 Undescended Right Testis. The right testis *(between calipers)* is located in the right hemipelvis inside the inguinal ring between a bowel loop and the bladder. A normal left testis was seen in the left hemiscrotum; the right testis was not seen in the right hemiscrotum *(not shown)*.

The number of testes may vary. **Polyorchidism (testicular duplication)** typically manifests in the older child as an asymptomatic scrotal mass, but occasionally it will manifest with pain due to torsion. The testes share a common epididymis, vas deferens, and tunica albuginea. Usually, a single, small, **accessory testis** is demonstrated within the scrotum in addition to two normal testes **(triorchidism).**[99] A **bilobed testis** may mimic a duplicated testis. Polyorchid and bilobed testes have medium-level homogeneous echogenicity and are smaller than the contralateral testis.

Testes smaller than normal may result from cryptorchidism, torsion, inflammation, varicocele, prior inguinal hernia repair, radiation treatment, and trauma. Congenital causes include **Klinefelter syndrome** and **primary hypopituitarism.** These small gonads may have normal, increased, or decreased echogenicity.[97]

True hermaphroditism is an intersex condition in which the patient has both ovarian and testicular tissue, in the form of either separate structures or an **ovotestis.** Ultrasound can demonstrate the textural difference within an ovotestis in that the testicular portion is more homogeneous with medium-level echoes, whereas the ovarian tissue is more heterogeneous with small, anechoic, cystic follicles interspersed with the low- to medium-level parenchymal echogenicity[100] (Fig. 54.31). These patients are seen either prepubertally with ambiguous genitalia or postpubertally with the development of gynecomastia, cyclic hematuria, or cryptorchidism in a patient reared as a boy, or amenorrhea in a patient reared as a girl (Fig. 54.32).

Cystic dysplasia of the testis is a rare congenital condition consisting of dilated rete testis and efferent ducts, as well as adjacent parenchymal atrophy. Patients typically have painless scrotal enlargement at a mean age of 5.8 years.[101] The ultrasound appearance consists of multiple, small, anechoic, cysts predominantly in the region of the mediastinum testis (Fig. 54.33). The

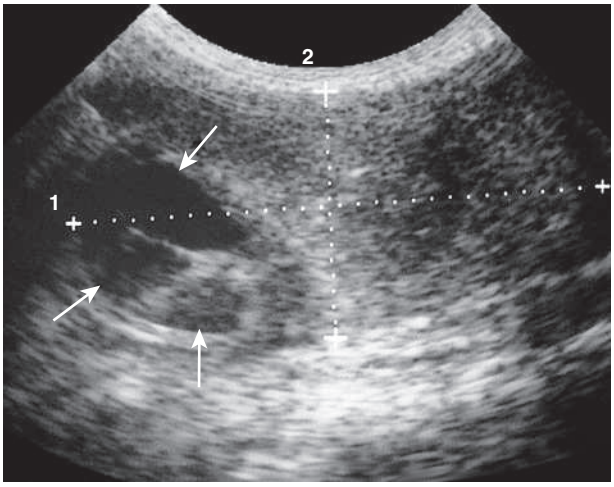

FIG. 54.31 Ovotestis. Ovotestis in a 15-year-old phenotypic boy with gynecomastia, intermittent scrotal pain and swelling, and recent scrotal trauma. Sagittal sonography of the right hemiscrotum revealed a heterogeneous right gonad *(calipers)* with focal cystic areas representing follicles in the upper pole *(arrows).* This gonad contained ovarian and testicular tissue.

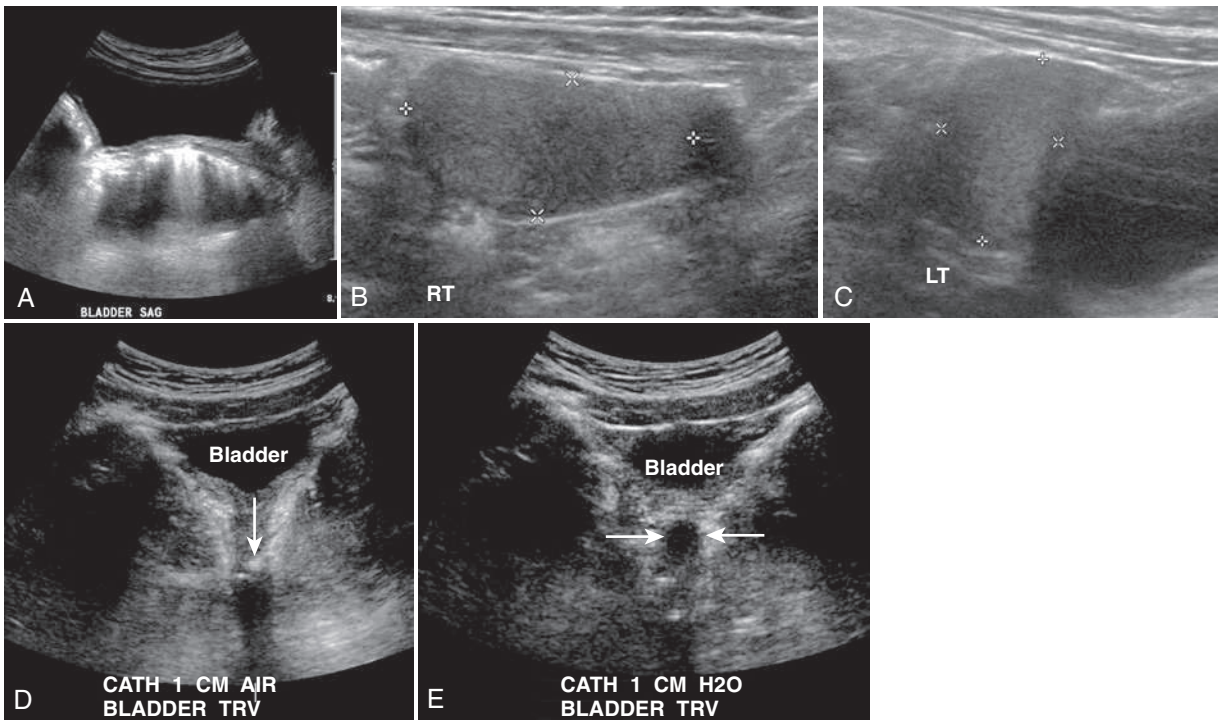

FIG. 54.32 Testicular Feminization Syndrome. This 5-year-old girl underwent bilateral inguinal herniorrhaphies. At surgery, the tissue within each of the inguinal canals felt firmer than expected in the presence of normal herniated ovaries, and thus both were biopsied. **(A)** Sagittal scan of the normal-appearing urinary bladder reveals no evidence of a uterus or ovaries. **(B)** and **(C)** Male-type gonads are seen bilaterally, as evidenced by the homogeneity and lack of follicles in either gonad. Biopsy of both gonads revealed normal, male-type gonads. **(D)** and **(E)** Using the bladder as a sonic window, the length of the vaginal canal was assessed by injecting air and then sterile water into the vaginal opening during sonographic observation. The vaginal canal was extremely short, approximately 1 cm in length.

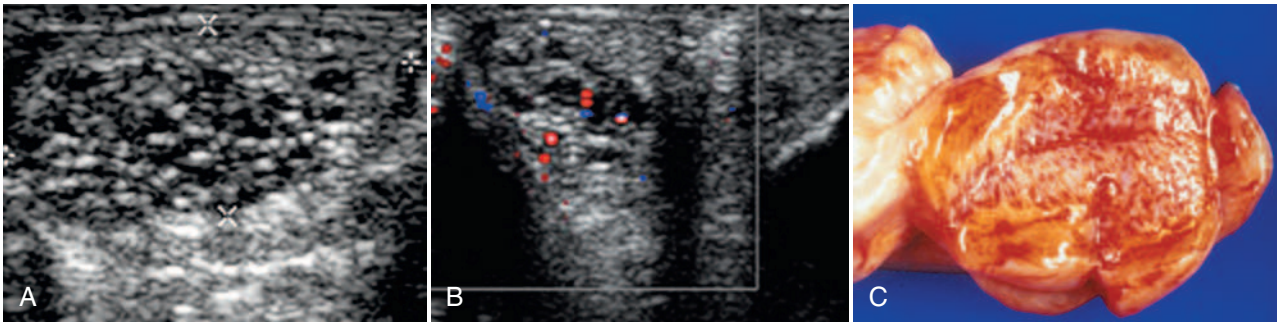

FIG. 54.33 Cystic Dysplasia of Testis. (A) Sagittal sonogram and **(B)** color Doppler sonography show multiple tiny cysts in the testicle. **(C)** Pathologic specimen shows tiny cysts. (Courtesy of Janet Strife, MD, Cincinnati Children's Hospital.)

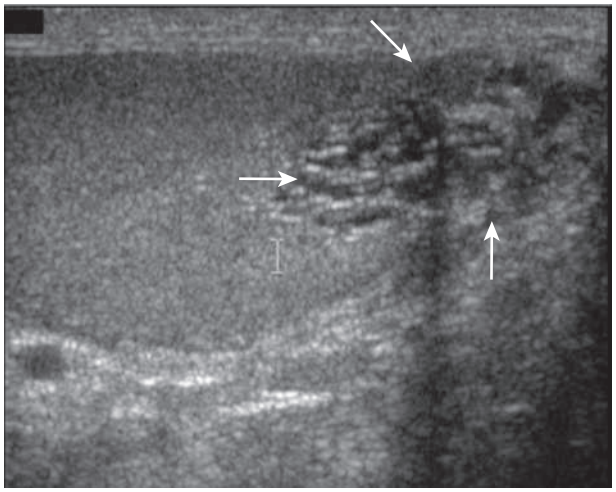

FIG. 54.34 Tubular Ectasia of the Rete Testis. This 9-year-old boy had left scrotal pain. Sagittal sonogram demonstrates a focal cluster of tiny, oval cysts *(arrows)* in the symptomatic area.

defect may result from an embryologic defect preventing fusion between the rete testis tubule (arising from the gonadal blastema) and efferent ductules (arising from the mesonephros). Several reported cases in children were associated with ipsilateral renal agenesis, multicystic dysplastic kidney, or renal dysplasia.[101,102] The appearance in the scrotum is similar to the incidentally noted condition of tubular ectasia of the rete testis described in adults, which probably represents an acquired condition secondary to prior inflammation or trauma[102,103] (Fig. 54.34). The lack of color flow within these cystic structures distinguishes tubular ectasia from **intratesticular varicocele,** which can have a similar gray-scale appearance but demonstrates venous flow on color Doppler imaging.[104] This condition may mimic a cystic neoplasm such as teratoma. If filled with mucoid material or debris instead of anechoic fluid, the cysts may mimic a solid mass.

ACUTE SCROTAL PAIN OR SWELLING

The most common causes of acute pain and swelling in the pediatric scrotum include **testicular torsion, epididymitis** with or without **orchitis, torsion of the testicular appendages, testicular trauma, acute hydrocele, and incarcerated hernia.** Less common causes are idiopathic scrotal edema, **Henoch-Schönlein purpura, scrotal fat necrosis, familial Mediterranean fever,** and secondary scrotal involvement from abdominal pathology.[102-106] It is often impossible clinically to differentiate between the conditions that require conservative medical treatment and those that demand immediate surgery.[107] However, the combination of gray-scale and color Doppler sonography provides information about morphology and testicular perfusion.[108-111]

Acute Scrotal Pain or Swelling

COMMON
Testicular torsion
Epididymitis with and without orchitis
Torsion of testicular appendages
Testicular trauma
Acute hydrocele
Incarcerated hernia

UNCOMMON
Idiopathic scrotal edema
Henoch-Schönlein purpura
Scrotal fat necrosis
Familial Mediterranean fever
Abdominal pathology

Testicular torsion and **epididymitis** (with or without orchitis) are the two most frequently encountered causes of the acute scrotum in the pediatric population. High-resolution ultrasound with color Doppler imaging is the method preferred for distinguishing between these two entities.[108-117] This is crucial because testicular torsion is treated surgically and epididymitis with or without orchitis is treated medically. To confirm the diagnosis of testicular torsion unequivocally, the clinician must demonstrate absence of flow in the painful testis and normal flow in the asymptomatic normal testis,[89] keeping in mind that the presence of flow in the painful testis does not exclude torsion. In the patient with incomplete or partial spermatic cord torsion (twist of ≤360 degrees), normal arterial flow may be demonstrated, although it is usually quantitatively diminished compared with the asymptomatic contralateral testis.[115,117]

Torsion of the spermatic cord is found in 14% to 31% of children and adolescents with an acute scrotum. Testicular torsion results when the testis and spermatic cord twist one or more

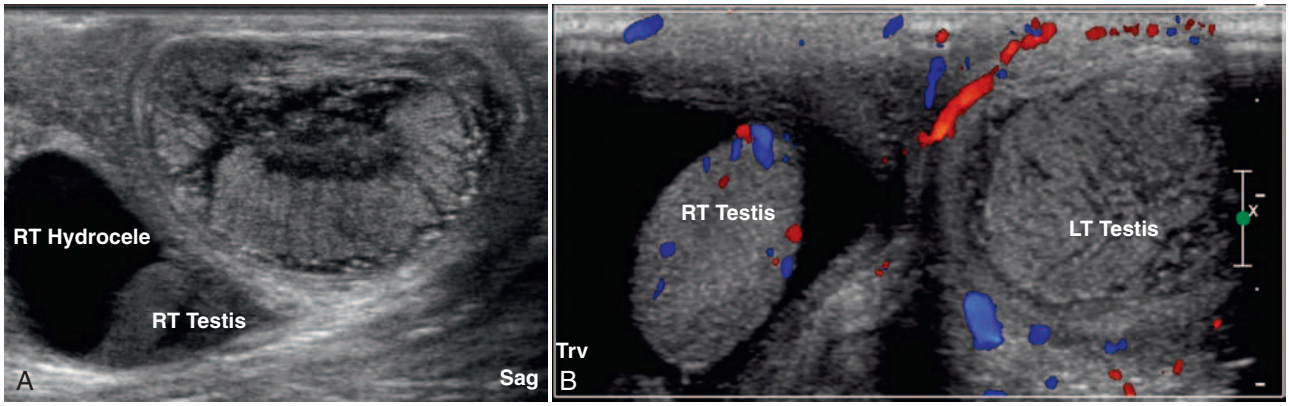

FIG. 54.35 Extravaginal Testicular Torsion. Newborn with hard, nontender, left testicular mass. **(A)** Sagittal sonogram of the scrotum reveals an enlarged, heterogeneous left testis with dilated rete testes. There are multiple foci of bright echogenicity surrounding the left testis, suggesting an intrauterine torsion—"missed" torsion. Note the normal right testis with surrounding hydrocele. **(B)** Normal flow is shown in the normal-appearing right testis. However, a surrounding rim of color Doppler flow can be seen around the avascular, swollen left testis.

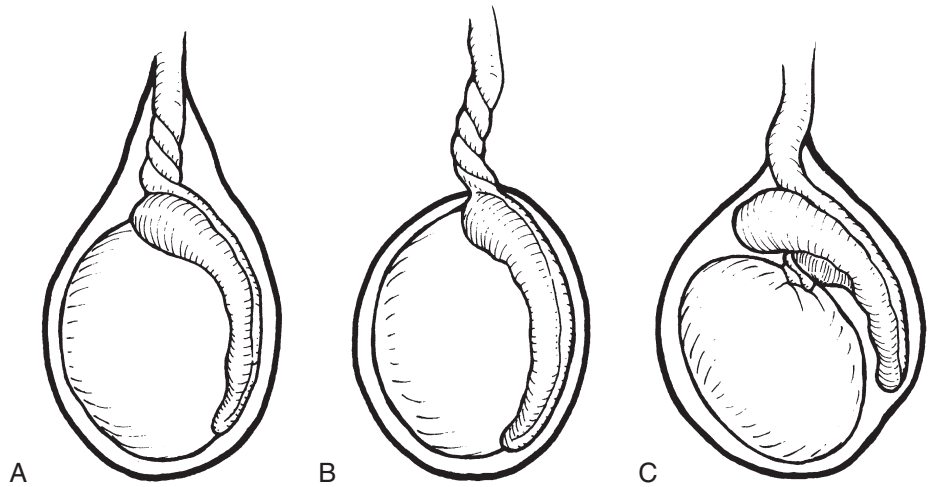

FIG. 54.36 Types of Testicular Torsion. (A) Intravaginal torsion above the epididymis. **(B)** Extravaginal torsion. **(C)** Torsion of the testis below the epididymis. (With permission from Leape LL. Torsion of the testis. In: Welch KJ, Randolph JG, Ravitch MM, editors. Pediatric surgery. St. Louis, 1986, Mosby.[123])

times, obstructing blood flow. Torsion of the testis has the highest prevalence during two age peaks—infancy and adolescence.[89] Two types of torsion have been described—extravaginal and intravaginal, with the latter being more common. **Extravaginal torsion** is generally found in neonates at the level of the spermatic cord, which is poorly fixed in the inguinal canal. All the scrotal contents are strangulated in this type of torsion.[89,100,118] Extravaginal torsion is thought to occur in utero.[119] The loose attachment of the spermatic cord and testes to surrounding structures may account for increased mobility and may predispose to the extravaginal type of torsion seen in neonates (Fig. 54.35). The scrotum is swollen and red with a firm, painless enlarged testicle, which is generally unilateral. Surgical salvage at birth is unlikely because the testis is already necrotic, but occurrence of extravaginal torsion after birth demands emergency surgery.[120] The ultrasound findings vary according to the duration of the torsion. In more recent torsion, the testis is heterogeneously enlarged with hypoechoic and hyperechoic areas. When the torsion is less acute, the testis may be normal or slightly enlarged, with peripheral echogenicity corresponding to calcifications in the tunica albuginea. Often, associated scrotal skin thickening and hydroceles are present.[118,119] There is no Doppler signal in the spermatic cord or the testis. Chronic torsion ultimately leads to small testicular size. Contralateral compensatory hypertrophy may be seen.[121] Other conditions that mimic extravaginal torsion in patients with a swollen scrotum in the neonatal period include **meconium peritonitis,** intraperitoneal bleeding tracking through the patent processus vaginalis, and tumor.

With **intravaginal torsion** the tunica vaginalis completely surrounds the testis and inserts high on the spermatic cord, preventing fixation of the testis to the scrotum and allowing the testis to rotate freely on its vascular pedicle, known as the **bell-and-clapper deformity.**[122] Another, less frequently encountered type of intravaginal torsion is **torsion of the mesorchium,** the tissue attachment between the testis and epididymis[89,97,123] (Fig. 54.36). In this situation, the testis twists within the tunica vaginalis without torsion of the epididymis. **Torsion within the scrotal sac,** or intravaginal torsion, may occur in any age group but is seen more often in adolescents and young adults.[89] The boys develop sudden onset of scrotal or lower abdominal pain. There

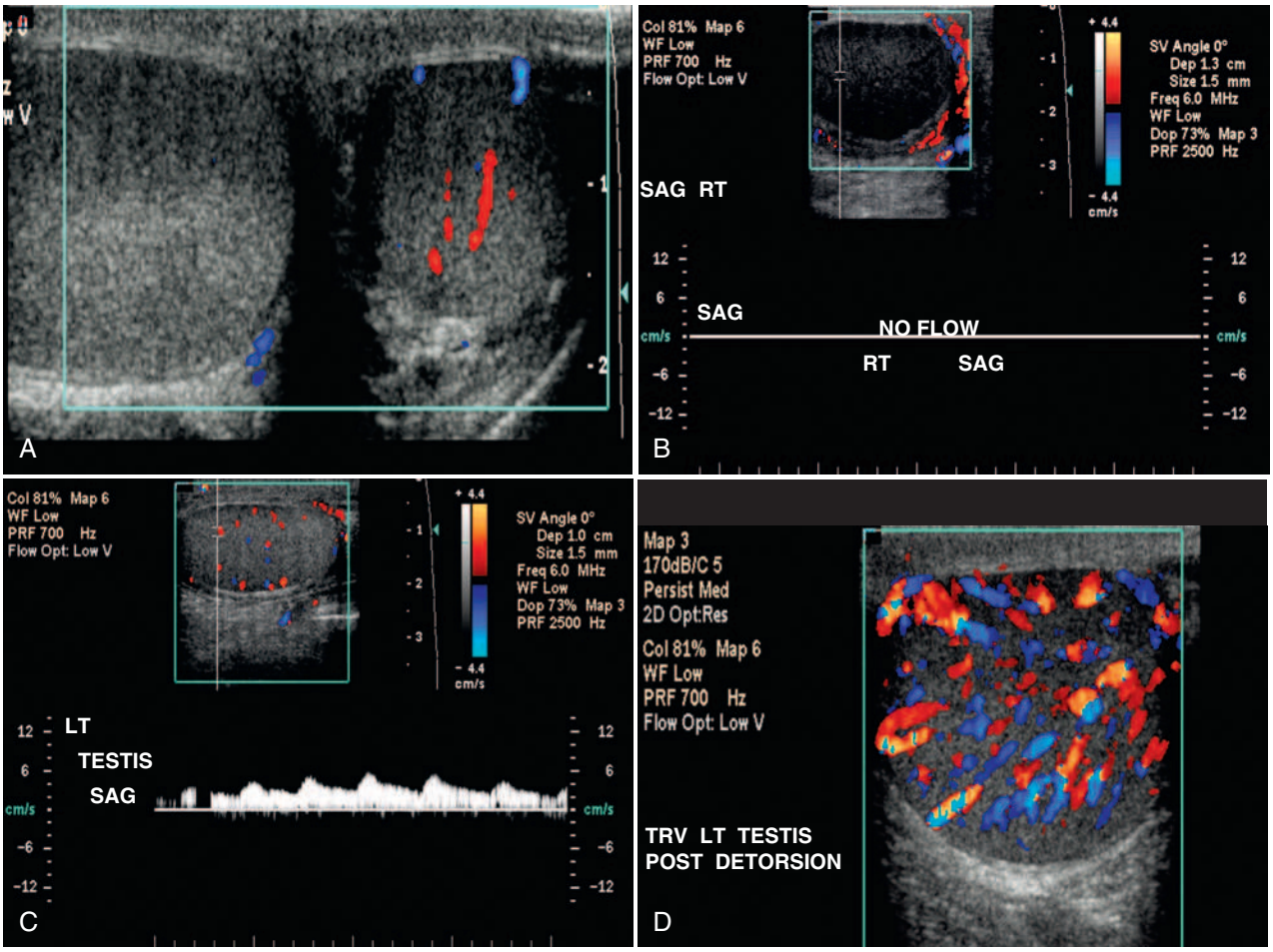

FIG. 54.37 Acute Testicular Torsion. This 13-year-old boy had acute, excruciating right-sided scrotal pain. **(A)** Transverse gray-scale image of both testes demonstrates enlargement of the avascular right testis. **(B)** Absence of both color and pulsed Doppler flow is noted on this sagittal image of the right testis. **(C)** Normal pulsed and color Doppler flow confirmed in asymptomatic, normal-appearing left testis. **(D)** Teenage boy with acute left-sided testicular torsion. Closed manual detorsion of the left testis was done at diagnosis in the ultrasound suite. Color Doppler sonogram of the left testis obtained immediately after detorsion shows dramatic hyperemia throughout the left testis.

is often a history of similar previous self-limited episodes, suggesting prior torsion and detorsion. Nausea and vomiting are more frequently seen in testicular torsion than in other causes of acute scrotum, with a positive predictive value of more than 96%. The boys may also have anorexia and low-grade fever. Physical examination is difficult because of severe tenderness. The affected hemiscrotum is swollen and erythematous with the affected testis often oriented transversely. The cremasteric reflex may be absent.[114] Most important, patients with suspected intravaginal torsion require emergency surgery to optimize testicular salvage. If it is clinically obvious that a patient has an acute torsion, emergency surgery should be done, even without imaging, because any delay in surgical treatment reduces the likelihood of testicular salvage. Some believe that closed manual detorsion may improve salvage rates and convert an emergent situation to an elective surgical procedure for future orchiopexy (Fig. 54.37); however, this is controversial.[124,125] The best results are obtained in those who have immediate detorsion and fixation to the scrotal wall and orchiopexy of the contralateral testis.[97] The salvage rate is greater than 80% when surgery is performed within 6 hours of the onset of symptoms; approximately 70% when performed within 6 to 12 hours of symptoms; and less than 20% if surgery is delayed for 12 to 24 hours after the onset of pain.[89,115,126] After 24 hours, the testis is virtually never salvageable. The sonographic features in testicular torsion depend on the duration and severity of the vascular compromise.

Sonographic Signs of Testicular Torsion

TESTES
Normal early
Hypoechoic after 4-6 hours from edema
Heterogeneous after 24 hours from hemorrhage and infarction ("missed" torsion)

PERITESTICULAR
Hypoechoic epididymis
Reactive hydrocele
Skin thickening
Enlarged, twisted spermatic cord

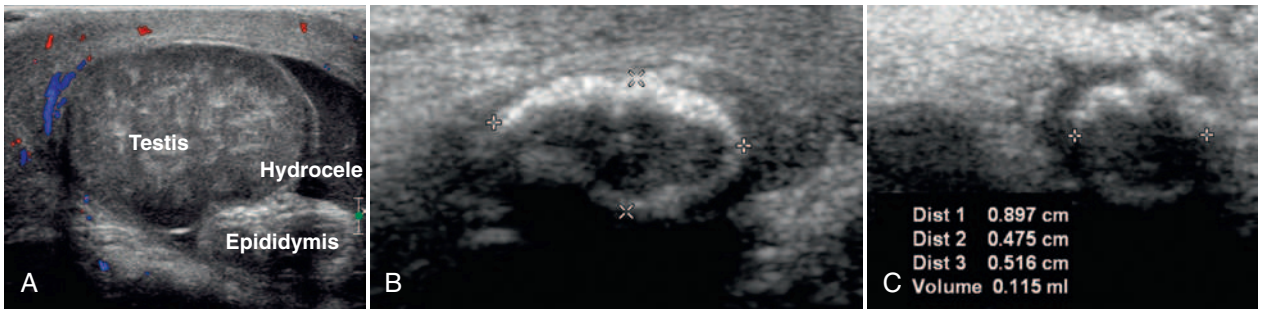

FIG. 54.38 "Missed" Testicular Torsion. (A) This 18-year-old male patient had a 2-day history of left scrotal pain and swelling. Sagittal sonogram demonstrates an enlarged (volume, 22.6 mL), hypoechoic, heterogeneous left testis and epididymis with increased echogenicity and thickening of the tunica albuginea. There is no arterial or venous flow within the left testis or epididymis, although there is hyperemia around the testis. This constellation of findings is consistent with a missed testicular torsion of a subacute nature. A reactive hydrocele is seen around the left testis, which contains complicated fluid. **(B)** and **(C)** Sagittal and transverse sonograms in 5-month-old male infant with missed torsion of the left testis, with history since birth of a normal size right testis *(not shown)* and a small hard left testis. The tiny left testis (volume, 0.1 mL) is shown in the left hemiscrotum, with the tunica albuginea appearing brightly echoic and demonstrating partial shadowing of the ultrasound beam, consistent with delayed (missed) torsion, the insult presumably having occurred in utero.

The gray-scale appearance of the torsed testis ranges from normal (early) to enlarged and hypoechoic secondary to edema (usually after 4-6 hours) and then to a heterogeneous appearance with areas of increased echogenicity secondary to vascular congestion, hemorrhage, and ischemia (usually after 24 hours)[89,115] (Fig. 54.38). The last appearance is also known as **"missed" torsion.** Surgical removal is recommended if the testis is clearly necrotic because if left in situ, the contralateral testis may be adversely affected because of a presumed antibody-induced immunologic process.[97] Other gray-scale findings in the presence of torsion include abnormal orientation of the testis within the scrotum (e.g., transverse lie) as well as abnormally thickened paratesticular structures. The epididymis is usually enlarged because of vascular congestion and may be isoechoic, hypoechoic, or hyperechoic to the testis. There may be scrotal wall thickening and reactive hydrocele formation. Another associated finding includes an enlarged, twisted spermatic cord.[116]

Color Doppler Sonography in Testicular Torsion

To make the diagnosis of acute testicular torsion, the clinician must unequivocally demonstrate absent blood flow in the painful testis and normal blood flow in the contralateral asymptomatic testis. The color flow examination includes careful comparison of the symmetry of flow in both testes. The sensitivity of color Doppler for detecting acute testicular torsion in pediatric patients is 90% to 100%, whereas the sensitivity of scintigraphy approaches 100%.[124,125,127] In technically adequate studies performed on state-of-the-art equipment, the specificity of color flow imaging is almost 100%.[115] Important to note, presence of flow in the painful testis does not exclude the diagnosis of torsion.[126,128,129] In patients with incomplete or partial spermatic cord torsion (≤360 degrees), arterial flow may be demonstrated, although diminished in quantity compared with the asymptomatic testis.[126] Power Doppler, with its greater sensitivity to minimal flow, may be helpful.[120]

In cases of **detorsion,** color Doppler may demonstrate increased flow within the painful testis and paratesticular soft tissues caused by **reactive hyperemia.** This phenomenon may mimic the reactive hyperemia that occurs in inflammatory conditions such as epididymo-orchitis.[126] The clinical findings should help to differentiate between torsion and inflammation. In the patient with acute scrotal pain that spontaneously resolves and in whom color Doppler imaging shows hyperemia, detorsion is likely. Spontaneously or manually reduced torsion does not require emergency surgery, but these patients are at risk for subsequent torsion and can benefit from orchiopexy.[126,130] In cases of **late torsion** (>24 hours), color Doppler typically shows marked hyperemia of the scrotal wall and paratesticular soft tissues with absent testicular flow, analogous to the scintigraphic doughnut sign. Pulsed Doppler waveform analysis is unnecessary for the diagnosis of torsion. The sensitivity of pulsed Doppler for detecting torsion ranges from 67% to 100%. In small children, identification of flow can be difficult in normal testes because of the small size of the testicular arteries. In addition, it may be difficult to distinguish between paratesticular and intratesticular arterial pulsations, and thus scrotal wall hyperemia associated with torsion may be mistaken for normal flow.

With **chronic torsion** the testis will begin to atrophy after 14 days. During this phase, the testis may remain hypoechoic, or it may become hyperechoic if fibrosis or calcification develops.[126] The ipsilateral epididymis is often enlarged and echogenic, often with an accompanying hydrocele. Other causes of **testicular infarction** include trauma, polyarteritis nodosa, and subacute bacterial endocarditis. Extrinsic compression of the cord or testis leading to testicular infarction can occur with hernias,[115] hydroceles,[131,132] and epididymitis.

Acute epididymitis accounts for 28% to 47% of cases of acute scrotal pain in children and is more common in pubertal than prepubertal boys. It is thought that many cases of prepubertal epididymitis are actually cases of **appendiceal torsion,** especially in patients with a negative urine culture.[114] Patients with epididymitis typically have a more gradual onset of pain with fewer

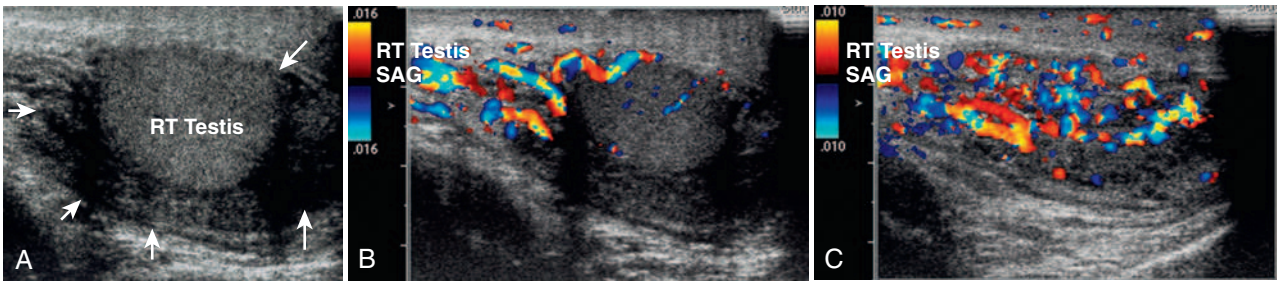

FIG. 54.39 Acute Epididymitis in 8-Year-Old Boy With Right Scrotal Pain. (A) Sagittal sonogram of the right testis shows a normal-appearing testis surrounded posterolaterally by a prominent, hypoechoic heterogeneous epididymis *(arrows)*. **(B)** Longitudinal color Doppler image of the scrotum reveals increased flow in the head of the epididymis with normal flow in the testis. **(C)** Marked hypervascularity is noted throughout the body and tail of the epididymis. Skin thickening is also present.

constitutional symptoms compared with patients with testicular or appendiceal torsion.[115,133]

On sonography, the inflamed epididymis may be focally or diffusely enlarged with coarse echoes. The overall echo pattern is usually decreased, but normal or increased echogenicity may be observed.[134] Associated orchitis is more often diffuse; when focal, however, it is usually close to the inflamed epididymis. The involved portion of the testis is usually hypoechoic and enlarged. On color Doppler imaging, the inflamed epididymis and testis are typically hyperemic (Fig. 54.39), although occasionally, normal flow may be seen in the involved organs.[14,133,134] Pulsed Doppler evaluation is not necessary to establish the diagnosis of acute epididymitis, but when performed, there is elevated diastolic flow in the epididymal arteries, a low-resistance waveform (RI < 0.7 for epididymal arteries), and detectable venous flow.[134,135]

With **orchitis** there may also be abnormally decreased vascular resistance (RI < 0.5) for testicular arteries. In testicular tumors, there may be hyperemia, but the RI is usually greater than 0.5. Therefore **pulsed Doppler** may be useful to differentiate hyperemic tumor from testicular hyperemia.[133,135] Associated sonographic findings include reactive simple or complex hydrocele and skin thickening. Complications of severe epididymo-orchitis include abscess formation and ischemia leading to infarction. Testicular infarction secondary to severe epididymo-orchitis is indistinguishable from infarction secondary to torsion.

Torsion on Color Doppler Ultrasound

Decreased or absent flow
Spontaneous detorsion—normal or increased flow
Incomplete torsion—normal or decreased flow

Because there is overlap in the gray-scale appearance of both testicular torsion and epididymo-orchitis, their differentiation depends on color Doppler imaging.[127,136] **Torsion** typically is characterized on Doppler imaging by decreased or absent flow within the involved testis. The classic appearance of **epididymitis and orchitis** is increased flow within the epididymis and the involved testis if orchitis is present.

Epididymitis on Color Doppler Ultrasound

Increased flow in epididymis
Increased flow in testes if also infected
Ischemia may cause decreased flow

However, the overlap between the two may lead to false-positive or false-negative diagnoses. The hyperemia or normal color flow seen in testes with **spontaneous detorsion** may be confused for epididymitis.[133] **Incomplete torsion** of the testis may reveal normal or decreased color flow.[116] **Ischemia** and **infarction** may also be seen with severe epididymitis, although this is usually less of a diagnostic dilemma because these patients also require surgery. Because Doppler imaging is limited in young patients with testes less than 1 mL, power and contrast agents may be helpful in distinguishing between torsed and normal testes.[124,127]

With **chronic epididymitis** the epididymis becomes enlarged and heterogeneous, and the testicular tunica becomes thickened, appearing as an echogenic hyperemic rim around the testis. Small calcifications may develop in the epididymis and the tunica albuginea. Ultimately, the testis may atrophy and become diffusely or focally hypoechoic.[97] **Isolated orchitis** is unusual and in general has a viral etiology. **Mumps orchitis** is seen in about 30% of prepubertal boys infected with mumps. The testes are usually enlarged and hyperechoic bilaterally during the initial phase, resulting in testicular atrophy and reduced fertility.

Clinical findings should aid in the differentiation of detorsion and scrotal inflammation. Detorsion is more likely in the presence of spontaneously resolved acute scrotal pain and hyperemia on color Doppler imaging. Pulsed Doppler waveform analysis is not necessary to establish the diagnosis of epididymitis, but if used, it shows elevated diastolic flow in the epididymal arteries, a low-resistance waveform (RI < 0.7 for epididymal arteries), and detectable venous flow. Abnormally decreased vascular resistance (RI < 0.5 for testicular arteries) is also seen in orchitis.[135] When surgery is not done to remove an infarcted testis, the infarcted testis will begin to atrophy after 14 days. During this chronic phase, the testis may be hypoechoic, but when fibrosis and calcification develop, the gonad may become hyperechoic.

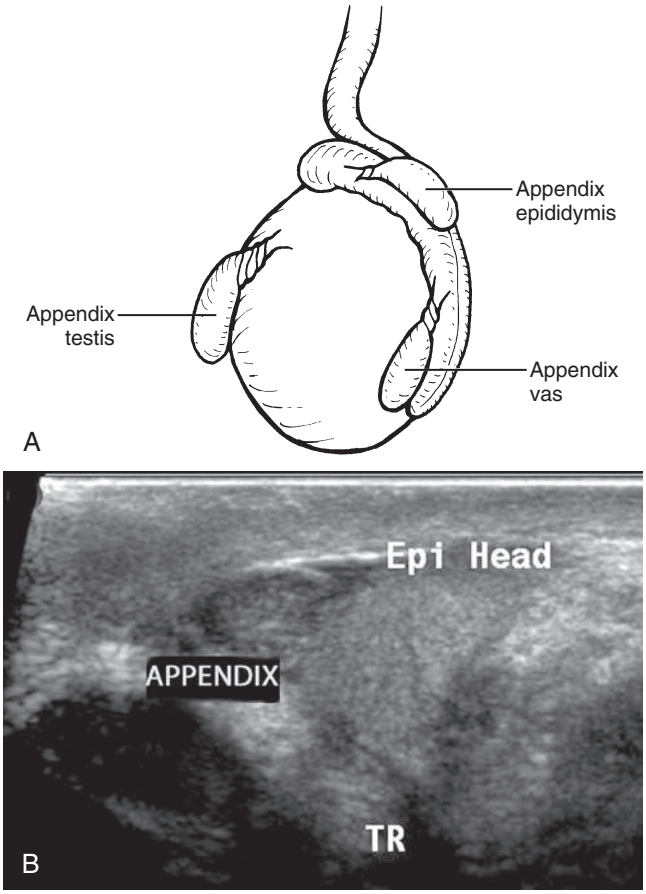

FIG. 54.40 Testicular Appendages. (A) Appendix testis, appendix epididymis, and appendix vas **(vas aberrans of Haller). (B)** Transverse image in a normal male through the epididymal head shows the epididymal appendage to be an isoechoic nodule adjacent to but separate from the head. (**A** with permission from Leape LL. Torsion of the testis. In: Welch KJ, Randolph JG, Ravitch MM, editors. Pediatric surgery. St. Louis, 1986, Mosby.[123])

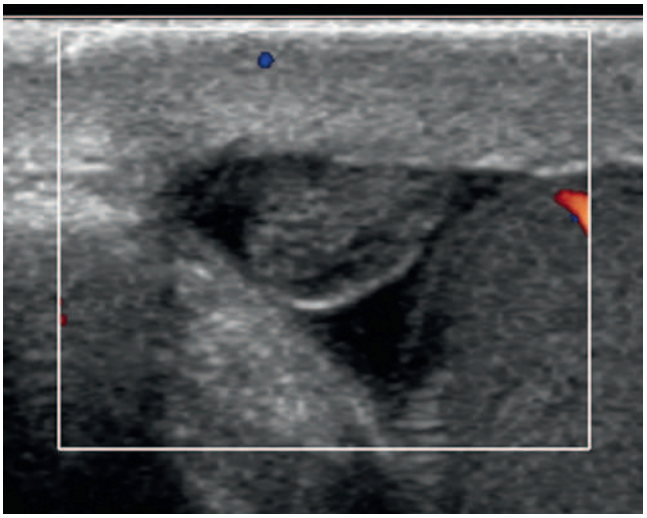

FIG. 54.41 Torsion of Appendix Epididymis in 12-Year-Old Boy With 10 Hours of Scrotal Pain. Transverse power Doppler image through the superior scrotum reveals an enlarged paratesticular mass with no vascularity consistent with a torsed epididymal appendix. Flow is detected in the adjacent testicle, excluding testicular torsion.

In younger boys, epididymitis is more often secondary to genitourinary abnormalities, such as ectopic ureter draining into the vas deferens or seminal vesicles.[137] **Bladder outlet obstruction** (e.g., posterior urethral valve and dysfunctional voiding) can cause reflux of urine into the ejaculatory ducts and lead to epididymitis even if the urine is sterile.[128,138] Epididymitis may also follow **trauma.** With epididymitis, patients typically have a more gradual onset of symptoms and fewer constitutional symptoms than with torsion. There may be mild scrotal tenderness to severe scrotal pain and tenderness with fever and pyuria. In adolescent boys, most cases are secondary to **sexually transmitted organisms** (e.g., *C. trachomatis, N. gonorrhoeae*). In young boys, *Escherichia coli* is found in 10% to 25% of patients.[114,136]

Torsion of a testicular appendage, or appendix epididymis, is the most common cause of acute scrotal pain in prepubertal boys, with an incidence of 26% to 67% peaking between 6 and 12 years of age[88,138,139] (Fig. 54.40). Torsion of a testicular appendage may produce the same clinical signs and symptoms of testicular torsion or epididymitis, but there is generally no nausea and vomiting. If the classic clinical finding of a small, firm, round, mobile, tender paratesticular mass, which often exhibits bluish discoloration visible through the skin **(blue-dot sign),** in the superior aspect of the scrotum is not found, then ultrasound is recommended to avoid unnecessary surgery.[97,140,141] The diagnostic sonographic appearance of a **torsed appendage** is that of a solid, ovoid mass with a variably sized hypoechoic center and hyperechoic rim adjacent to the superior aspects of a testis or epididymis that is avascular[138,142] (Fig. 54.41). Reactive hydroceles, scrotal skin thickening, testicular and epididymal enlargement, and hypoechogenicity may be seen, as well.[142,143] In acute torsion of an appendix, the torsed appendix appears avascular and the epididymis hyperemic. In late torsion (>1 day), a zone of reactive hyperemia may surround the torsed appendage.[140,141] Depending on the extent of the associated inflammatory process, the testis may have normal or increased vascularity.[90,142-145] The testicular appendages are embryologic remnants of blind-ending mesonephric tubules.[138] The **appendix testis** is attached to the tunica albuginea on the superior pole of the testis, and the **appendix epididymis** is located on the epididymal head. Both appendages are pedunculated and thus predisposed to torsion; 92% of males have an appendix testis, and 25% have an appendix epididymis.[97] Most torsed appendices atrophy, with resolution of symptoms with supportive care. Surgery is reserved for persistently symptomatic appendages. Eventually, infarcted appendages shrink in size, may calcify, and may break free to become **scrotoliths.**[90,139]

Trauma to the scrotum most often results from sporting injuries but may be seen in straddle or handlebar injuries, motor vehicle crashes, child abuse, or birth trauma. Trauma can cause a testicular hematoma, fracture, or rupture.[146,147] Testicular rupture is a surgical emergency. Improved salvage rates have been shown if surgery to repair a ruptured testis is performed within 72 hours of the traumatic event.[138] Sonographic findings of rupture (Fig. 54.42) include diffuse parenchymal heterogeneity with loss of a normal, smooth contour and disruption of the tunica

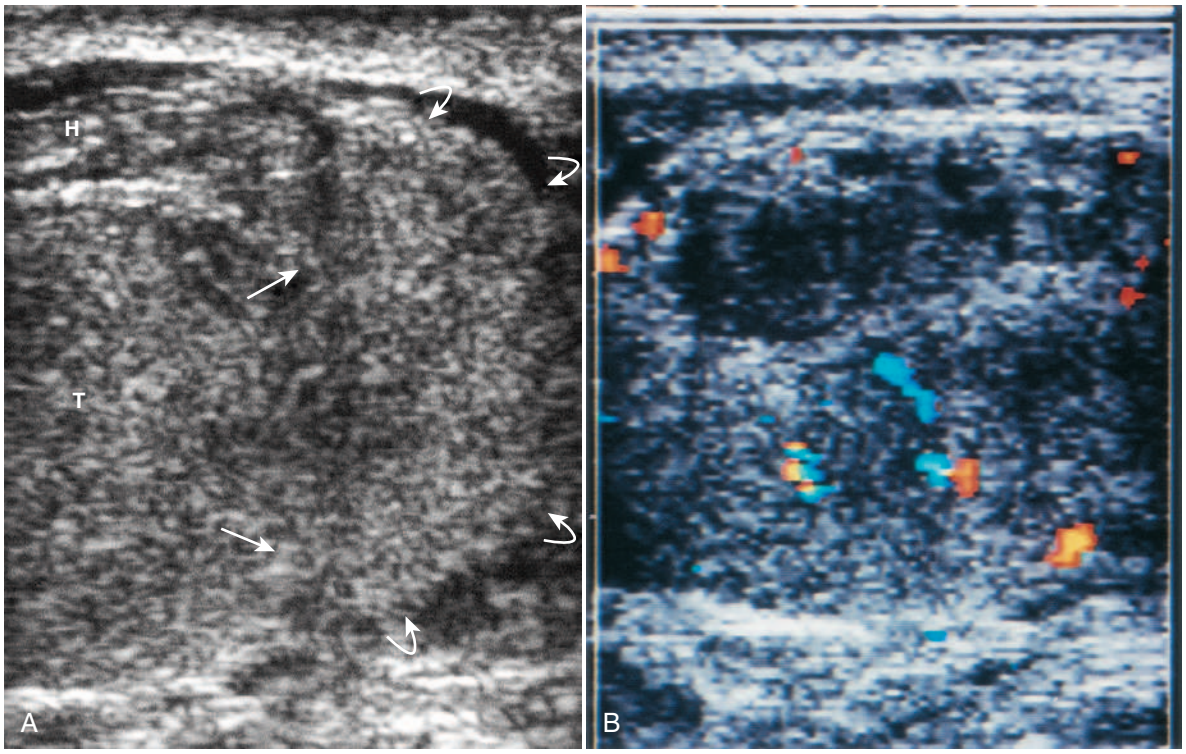

FIG. 54.42 Testicular Rupture in Patient With Scrotal Pain After Groin Kick. (A) Longitudinal view of the inferior aspect of the left testis shows disruption of the tunica albuginea *(straight arrows)* with extrusion of seminiferous tubules *(curved arrows)*. Associated hematocele *(H)* is present. *T,* Testis. **(B)** Color Doppler image of the left testis reveals heterogeneity, representing contusion and hemorrhage within the testicular parenchyma. Intratesticular flow excludes infarction.

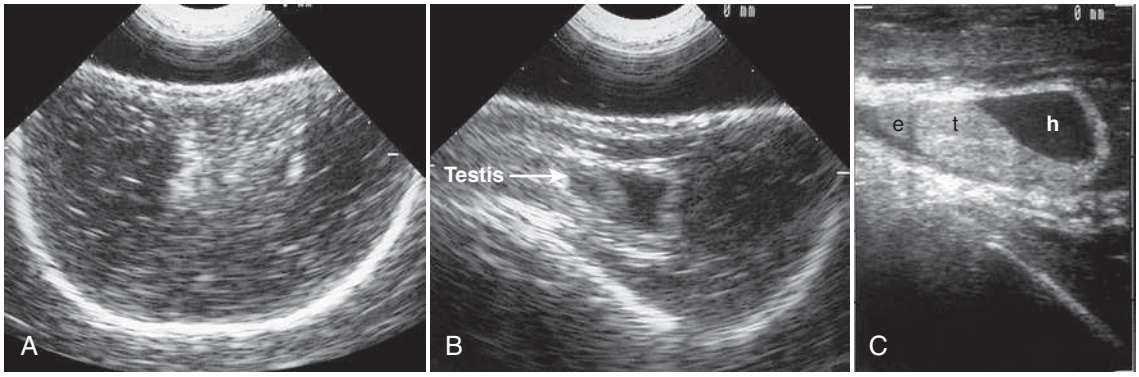

FIG. 54.43 Acute Idiopathic Scrotal Edema With Normal Testes in 4-Year-Old Boy With Sudden, Painless, Scrotal Swelling. Transverse **(A)** sonogram of the scrotum and sagittal (**[B]** and **[C]**) images of the left hemiscrotum using a stepoff pad reveal marked scrotal swelling, normal right testis *(t),* and epididymis *(e)* with an adjacent hydrocele *(h)*. The left testis and epididymis *(not shown)* were also normal.

albuginea, extrusion of seminiferous tubules, and nonvisualization of the testis. The presence of flow on color Doppler imaging in the traumatized testis is helpful in excluding testicular ischemia. Conversely, with testicular fracture, there is discontinuity of the normal testicular parenchyma, but the tunica albuginea remains intact. On ultrasound, a fracture is seen as a hypoechoic line within a normally shaped testicle.[117,129] **Testicular hematomas** appear as avascular masses, the echogenicity of which varies depending on the age of the hematoma.[90] Associated findings include scrotal hematomas, hematoceles, and wall thickening. Complications of testicular rupture include infarction, chronic pain, abscess, and infertility. Although ultrasound may aid in evaluating the traumatized scrotum, controversy surrounds its usefulness because some clinicians question its accuracy and recommend early surgical exploration even in the absence of testicular rupture.[146]

Acute **idiopathic scrotal edema** is a rare cause of scrotal edema that may involve one or both testes. It typically affects boys 5 to 11 years of age, and presenting signs and symptoms include scrotal swelling, erythema, and typically no pain[148] (Fig. 54.43). Swelling may extend to the anterior abdominal wall and perineum. Sonographic findings include marked thickening of the scrotal wall, with normal testes and epididymides.[91,97,148,149] Color Doppler imaging may show normal or slightly increased

flow to the scrotal wall with normal flow to the testes and epididymides.[122,148-151] Acute scrotal edema resolves spontaneously within several days without sequelae.

Scrotal or testicular involvement is estimated in 15% of patients with **Henoch-Schönlein purpura,** a vasculitis involving small vessels and affecting the skin, gastrointestinal tract, joints, and kidneys. Sonographic findings include diffuse swelling of the scrotum and contents with intact testicular flow, obviating the need for surgery in this entity, which usually resolves spontaneously and completely.[152] The echotexture of the testes is normal, but there is generally bilateral epididymal enlargement with a heterogeneous echo pattern, reactive hydrocele, and scrotal wall thickening.[150,151] Color Doppler imaging reveals hypervascularity, especially in the thickened scrotal wall and epididymis with normal intratesticular flow.[153] Careful examination for the classic purpuric rash over the buttocks, lower extremities, and perineum aids in diagnosis.[92]

Scrotal swelling and pain may also be secondary to an intraabdominal process, especially in neonates with a patent processus vaginalis. Various fluids, such as blood, chyle, pus, dialysis fluid, cerebrospinal fluid from ventriculoperitoneal shunt, or other intraperitoneal fluids can drain into the scrotum. Blood from the abdomen can enter the scrotum through extravasation into the tissue planes or through a patent processus vaginalis and can be the presenting sign in patients with adrenal hemorrhage,[109] hepatic laceration, or delayed splenic rupture in a battered child. Scrotal swelling has been reported in association with inflammatory or infectious conditions, such as acute appendicitis, perforated appendicitis,[108] or Crohn disease.[111] Another unusual cause for scrotal swelling is testicular vein thrombosis from a femoral venous line during cardiac catheterization. In the neonate with scrotal swelling and in older children with scrotal swelling of uncertain cause, abdominal sonography may help diagnose a primary abdominal event as the cause for secondary scrotal pathology.[109]

SCROTAL MASSES

Intratesticular Causes

Sonography plays an important role in the evaluation of scrotal masses by confirming the presence of a lesion, determining its site of origin, and characterizing its contents. Ultrasound has almost 100% sensitivity in detecting testicular tumors.[154,155] Ultrasound is able to distinguish intratesticular from extratesticular tumors in 90% to 100% of cases.[103] This distinction is important because most intratesticular masses are malignant and most extratesticular masses are benign. Benign and malignant testicular tumors are the seventh most common neoplasm in children. **About 80% of testicular tumors are malignant.** In the pediatric age group, there are two peak incidences of testicular neoplasms: in children younger than 2½ years (60%) and in late adolescence (40%). The incidence of malignancy in a cryptorchid (abdominal) testis is increased by a factor of 30 to 50. Both **seminomas** (malignant) and **gonadoblastomas** (the majority of which are benign) often develop in dysplastic gonads associated with **undescended testes, testicular feminization syndrome, male pseudohermaphroditism,** and **true hermaphroditism.**[151]

Testicular tumors account for about 1% of all childhood neoplasms and for 2% of solid malignant tumors in boys.[156,157] **Primary testicular neoplasms** are divided into those of germ cell and non–germ cell origin. In prepubertal children, 70% to 90% of primary testicular neoplasms are of germ cell origin, and most of these (66%-82%) are **endodermal sinus tumors** (yolk sac carcinomas). Yolk sac tumor is localized to the scrotum at presentation in most patients (≥80%).[156,157] The remaining 20% of patients have lymphatic spread to regional and retroperitoneal lymph nodes or hematogenous spread to distant sites. Survival is 70% or greater with disease restricted to the testis.[156] **Embryonal cell carcinomas, teratocarcinomas,** and **choriocarcinomas** are more aggressive tumors and metastasize early through lymphatic and hematogenous routes. **Endodermal sinus tumors** occur primarily as a painless scrotal mass in infants 12 to 24 months of age. There may be an associated ipsilateral **hydrocele** (25%) or **inguinal hernia** (21%). The tumor may metastasize to the lungs, especially in older children, but retroperitoneal lymph node metastasis is rare. **Embryonal carcinoma** usually occurs in adolescence or young adulthood. It is highly malignant and usually spreads to retroperitoneal and mediastinal lymph nodes, with hematogenous metastases to the lung, liver, and brain.[151] Elevated serum alpha-fetoprotein levels are common in yolk sac and embryonal cell tumors, whereas elevated serum levels of β-hCG are seen most often with embryonal cell tumors and teratocarcinomas.[156,157]

The remaining germ cell tumors seen in adolescents and adults are benign teratomas, teratocarcinomas, and choriocarcinomas.[156] **Testicular teratoma** is the most common benign germ cell tumor of the testis in infants and young children. Teratomas are most often seen in children younger than 4 years. Patients with testicular neoplasms usually have painless scrotal or testicular enlargement. Pain secondary to torsion or hemorrhage into the tumor is rare.[99] About 85% of benign teratomas contain well-differentiated elements from all three germ cell layers. There are poorly differentiated elements in approximately 15% of these tumors, but even so, the tumor usually has a benign course.[156] In pubertal patients, however, teratomas are often malignant and tend to behave more aggressively, necessitating orchiectomy.

Seminoma, the most common testicular tumor in adults, is rare in children, is most often associated with cryptorchidism, and when present, is usually in adolescents. In general, seminomas are uniformly hypoechoic masses, rarely containing areas of necrosis and hemorrhage[103,158] (Fig. 54.44). On the other hand, **teratomas** and **teratocarcinomas** are complex masses with hypoechoic areas from serous fluid and hyperechoic areas representing fat and calcifications.[103,157-159] The remaining germ cell tumors have nonspecific, variable appearances.[158] When the tunica is invaded by aggressive tumors, the testicular contour appears irregular. Testicular tumors are accompanied by reactive hydroceles in 20% to 25% of cases.[156,160] The scrotal skin is rarely thickened in the presence of tumors, and when observed in the presence of a mass, is usually indicative of an inflammatory process.

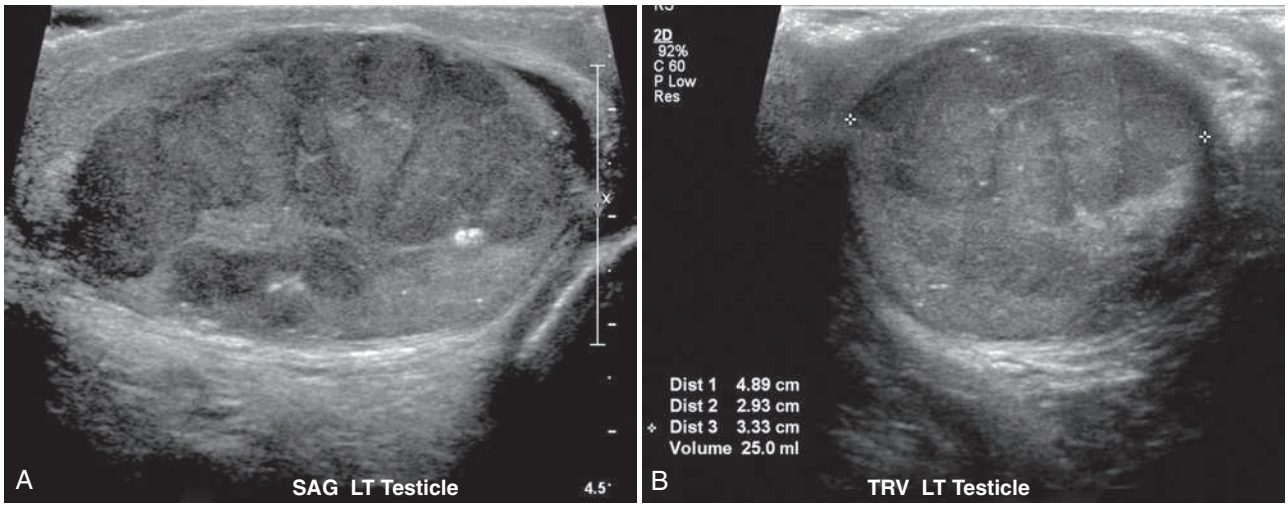

FIG. 54.44 Seminoma in 18-Year-Old Patient With Painless Left Scrotal Mass. (A) and **(B)** Sagittal and transverse sonograms of the left testis demonstrate a testicular volume of 25 mL, with a lobulated, heterogeneous, relatively hypoechoic mass occupying most of the testis with a thin rim of normal testis and a few tiny clusters of calcification, as well as multiple tiny echogenicities both inside and outside the mass **(microlithiasis).**

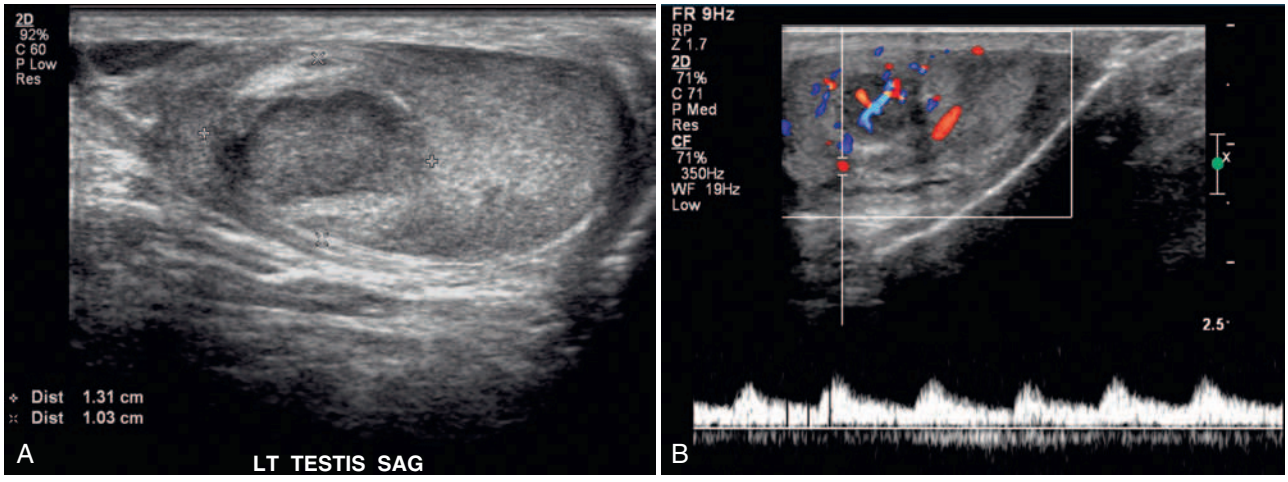

FIG. 54.45 Leydig Cell Tumor in 8-Year-Old Boy With 6-Month History of Precocious Puberty. (A) Sagittal sonogram of left testis demonstrates a 1.3 × 1.0 × 1.0–cm hypoechoic, well-defined mass with peripheral areas of brighter echogenicity. **(B)** Color and spectral Doppler demonstrate arterial flow within the mass.

Doppler is useful in the evaluation of testicular tumors, with degree of vascularity dependent on tumor size. Larger tumors are usually hypervascular, but tumors less than 1.5 cm in diameter tend to be avascular or hypovascular.[161] One may demonstrate tumor vascular displacement or compression or a normal vascular course. In some cases a tumor may not be obvious on gray-scale imaging but is obvious with color Doppler imaging. RI determinations do not aid in diagnosis.[162]

The most common primary non–germ cell tumors of the testes are **Leydig cell and Sertoli cell tumors.**[163] These stromal tumors account for about 10% of testicular neoplasms and are usually hormone secreting.[157] Leydig cell tumors account for about 60% of the non–germ cell tumors, and Sertoli cell tumors about 40%. Leydig cell tumors are typically seen in patients aged 3 to 6 years and produce testosterone, which results in precocious virilization. Patients with Sertoli cell tumors usually develop painless masses within the first year of life. Most are hormonally inactive, but some secrete estrogen, which results in gynecomastia. Both these non–germ cell tumors are slow growing and virtually always benign in prepubertal patients.[151] These tumors are usually small, well-circumscribed hypoechoic lesions[103,158] (Fig. 54.45). In larger lesions, cystic spaces may develop secondary to hemorrhage and necrosis. Orchiectomy is curative, although tissue-sparing surgery is possible for Leydig cell tumors.

Another rare tumor is the **gonadoblastoma,** which is found in phenotypic females with streak gonads or in patients with a male karyotype and testes.[97,156,157] These tumors are usually small, well circumscribed, and hypoechoic.[103,158] In larger lesions, cystic spaces may develop secondary to hemorrhage and necrosis. They are generally benign and are usually found at surgery to remove intraabdominal dysplastic gonads.[156,164] Other benign testicular masses include hemangiomas, neurofibromas, lipomas, fibromas,

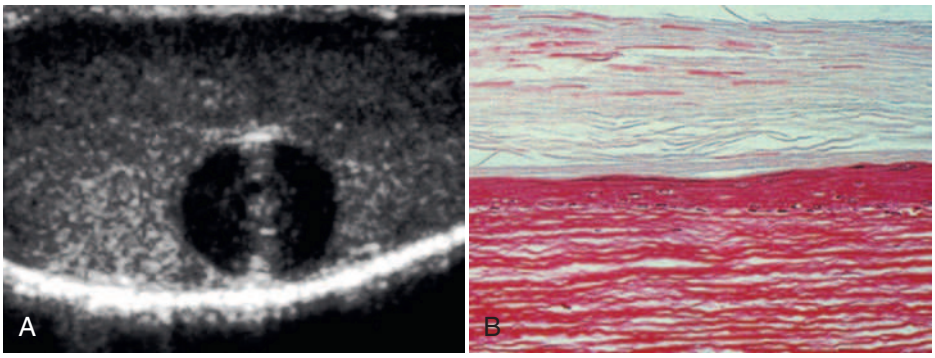

FIG. 54.46 Epidermoid Cyst. (A) Sagittal, magnified sonogram shows a sharply defined lesion composed of multiple circular layers caused by epidermal tissue. **(B)** Histologic specimen. (Courtesy of Janet Strife, MD, Cincinnati Children's Hospital.)

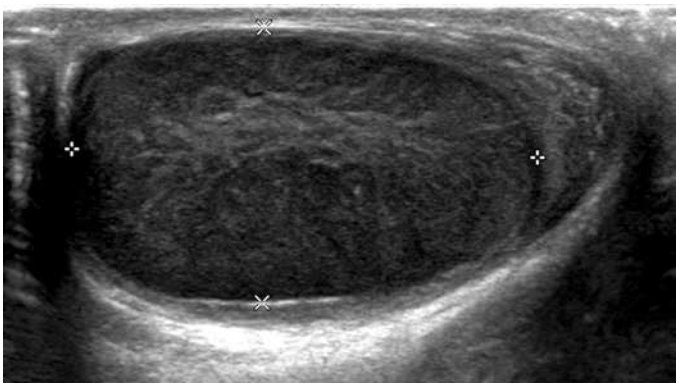

FIG. 54.47 Leukemic Infiltration of Testis in 13-Year-Old Male With B-Cell Leukemia Relapse and an Enlarged Right Testis. Sagittal image reveals a predominately hypoechoic and enlarged (6.7 mL) right testis representing diffuse leukemic infiltration. The normal left testis *(not shown)* was 1.1 mL in volume.

epidermoids, and cysts.[156,165] There are also nonneoplastic lesions that resemble benign solid neoplasms, including **cystic dysplasia, adrenal rests, hematomas,** and **Leydig cell hyperplasia.**[166] The sonographic appearance is quite variable, but characteristically the **epidermoid cyst** is hypoechoic, is well circumscribed, and contains internal echoes or an onion-skin lamellated appearance[167] (Fig. 54.46). **Adrenal rests** appear in the testes when fetal adrenal cortical cells migrate coincidentally with the gonadal tissue during embryologic development. Adrenal rests form tumorlike masses in response to increased levels of adrenocortical hormones, usually caused by **congenital adrenal hyperplasia** or **Cushing syndrome.** On sonography, adrenal rests appear as round, variably sized, hypoechoic, solid intratesticular nodules, usually located near the mediastinum testis.[166,168,169] They are usually bilateral intratesticular nodules that may enlarge or regress over time.[169] The rests resemble Leydig cell tumors histologically and sonographically, but the clinical setting of abnormal hormonal levels associated with hyperfunctioning adrenals usually clarifies the diagnosis.[170]

The testes are a well-known sanctuary site for **leukemia** and **lymphoma** (Fig. 54.47). Clinically silent testicular involvement may be seen in 25% of boys with newly diagnosed acute lymphoblastic leukemia. The testes may be enlarged and homogeneously hypoechoic or may contain focal hypoechoic masses.[171,172] Bilateral involvement is most common, and color Doppler flow is almost always increased, with a disorganized vascularity.[173] **Neuroblastoma, Wilms tumor, Langerhans cell histiocytosis, retinoblastoma, rhabdomyosarcoma,** and **sinus histiocytosis** may metastasize to the testes.[174] The spread may be lymphatic or hematogenous or by direct extension from contiguous tumor. The masses are painless and firm, or there may be diffuse testicular enlargement. The sonographic findings in these testicular tumors are not specific. The involved testicle is usually enlarged with a globular or lobulated contour. Both primary and metastatic tumors may result in focal masses or diffuse involvement. The echogenicity ranges from hypoechoic to hyperechoic, and the parenchyma may be homogeneous or heterogeneous with areas of decreased echogenicity, reflecting hemorrhage or necrosis or areas of increased echogenicity reflecting calcification.[162,171,173,175,176] At times, the echogenicity will be normal.[173] Gray-scale abnormalities may be seen more frequently in the testes of older postpubertal patients with testicular tumors. This may reflect the histologically different tumors affecting different age groups.

Color Doppler imaging is helpful in the evaluation of pediatric testicular tumors. Disorganized hypervascular blood flow was seen in six (86%) of seven patients in a study of pediatric patients with testicular tumors by Luker and Siegel.[173] Although all the patients had testicular enlargement, the testicular echotexture in four (57%) of seven patients was normal; thus color Doppler was helpful in depicting the tumor in these patients. Hypervascularity with normal echogenicity may be seen in orchitis; however, orchitis without epididymitis is uncommon, especially in prepubertal children, and history helps in distinguishing the two entities because tumor frequently manifests as an enlarged, nontender mass.[173] The management of testicular tumors in childhood has evolved during the last 20 years as a result of a multicenter retrospective survey that identified the preoperative and intraoperative criteria of nonmalignancy and analyzed the results of conservative management of a testicular mass. Valla[177] reported the findings of the Study Group in Pediatric Urology. A testicular tumor in children had a 50% chance of being benign, and ultrasound results were more conclusive than clinical criteria in limiting the preoperative diagnosis to teratoma, epidermoid cyst, and, particularly, simple cyst. The group concluded that treatment selection according to clinical, biologic, radiologic, and frozen-section findings should allow appropriate decision

FIG. 54.48 Bilateral Hydroceles in Newborn. Transverse view of the scrotum shows both testes outlined by large, anechoic fluid collections.

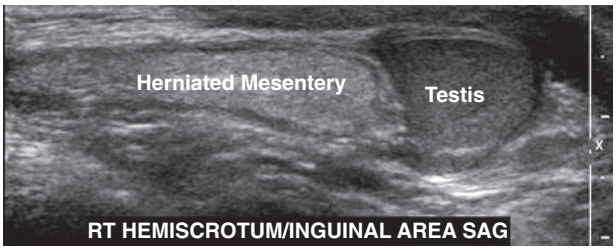

FIG. 54.49 Inguinal Hernia in Baby With Right Inguinal Mass. Sagittal sonogram of the right hemiscrotum and inguinal area demonstrates brightly echoic fatty mesentery extending from the peritoneal cavity into the right inguinal canal, abutting the right testis.

making regarding testis-sparing surgery without additional oncologic risk, and with an esthetic, psychological, and functional benefit.[177] Patients with **solitary simple cysts,** which are uncommon testicular masses, have painless scrotal enlargement.[178] The cysts are anechoic masses with smooth walls, no nodular or solid elements, and increased sound transmission. They differ from epidermoid cysts and other cystic neoplasms that contain internal echoes. These simple cysts are benign and thus may be followed with sonography. In infants, growth of the cyst may cause compression and replacement of testicular parenchyma. Thus early conservative surgery with removal of the cyst and preservation of the adjacent parenchyma may be performed.[179] Simple enucleation suffices when sonography demonstrates that the cyst is undoubtedly simple.

Extratesticular Causes

Hydroceles are an abnormal collection of serous fluid in the scrotal sac and represent the most common cause of painless scrotal enlargement in children. Hydroceles may be congenital or acquired. In neonates and infants, virtually all hydroceles are congenital. As the testis descends into the scrotum, it becomes invested with a portion of peritoneum, the **processus vaginalis.** At birth, the processus vaginalis normally closes off proximally and forms the **tunica vaginalis.** A variable amount of peritoneal fluid may be trapped within the tunica vaginalis, forming a stable hydrocele in the neonate. This fluid is resorbed slowly during the first 18 months of life. If the processus vaginalis fails to close, an open communication exists between the peritoneal cavity and the scrotum. This can result in a **scrotal hernia** or a **communicating hydrocele** with a varying amount of fluid. Extension of the hydrocele into the pelvis can be seen in a communicating hydrocele. Surgical ligation is required to close the **patent processus vaginalis.**[180]

The usual sonographic appearance of a hydrocele is anechoic fluid in the scrotum (Fig. 54.48). In older children, hydroceles are usually acquired. The presence of echoes or septations in the fluid suggests a **reactive hydrocele** caused by infection, torsion, trauma, or tumor. Other collections, such as chronic hemorrhage or lymphoceles (associated with ipsilateral renal transplantation), may be seen and mistaken for a reactive hydrocele. These result from lymphatic disruption with leakage of lymph fluid into the tunica vaginalis or from direct extension of a periallograft lymphocele through the inguinal canal.[181] They appear on ultrasound as septated fluid collections surrounding the testes.

Hematoceles are collections of blood in the tunica vaginalis. Most are the result of surgery or trauma,[180] but they may also be secondary to bleeding disorders or malignant tumors.[182,183] They appear on sonography as fluid collections with low-level internal debris, septations, or fluid-debris levels. Scrotal wall thickening may be present with chronic hematoceles.

Scrotal hernia is a common mass in boys that is usually evident clinically. **Inguinal hernias** are almost always the result of a patent processus vaginalis **(indirect hernia)** into the scrotal sac. Hernias are more frequently right-sided because the right processus vaginalis closes after the left. Sonography may demonstrate bowel loops in the scrotum, normal testis, and epididymis, and an echogenic area representing herniated omentum[184] (Fig. 54.49). Lack of peristalsis within herniated bowel loops suggests ischemia. Ischemia and incarceration (nonreducibility of bowel loops) convert an elective procedure to emergent surgery. Extratesticular pathology, such as **hematoceles, loculated hydroceles, scrotal abscesses,** and **urinomas,** can mimic fluid-filled bowel loops, and **herniated omentum** can be confused for a primary scrotal mass. Thus examination of the inguinal canal and the region of the Hesselbach triangle is recommended to evaluate for a hernia sac and exclude a primary scrotal pathology.

Other scrotal masses often identified in adolescent and postpubertal males are varicoceles, spermatoceles, and epididymal cysts.[184] **Varicoceles** represent dilated veins in the pampiniform plexus positioned posterior to the testis. The majority (85%-98%) are on the left side.[185] The presence of varicoceles in young boys is uncommon and may result from compression of the spermatic cord by tumor. Sonographic evaluation reveals small serpentine structures that display flow on color Doppler imaging and venous waveforms on spectral Doppler imaging. Augmentation of Doppler flow occurs with a Valsalva maneuver and upright positioning (Fig. 54.50). **Spermatoceles** occur in the epididymal head and consist of fluid, spermatozoa, and sediment. **Epididymal cysts** contain no spermatozoa and can occur in the epididymal head, body, or tail. Sonographic examination shows round structures with good through transmission and well-defined back

FIG. 54.50 Left Varicocele in Postpubertal Patient Complaining of Feeling "Wormlike" Structures in Left Side of Scrotum. (A) Transverse color Doppler sonogram of the left testis shows multiple areas filled with color in the paratesticular tissues lateral to the normal-appearing left testis. **(B)** Sagittal scan of the paratesticular tissues demonstrates prominent, anechoic, tortuous, tubular structures. **(C)** Exuberant color Doppler flow and enlargement of these paratesticular veins is seen after Valsalva maneuver.

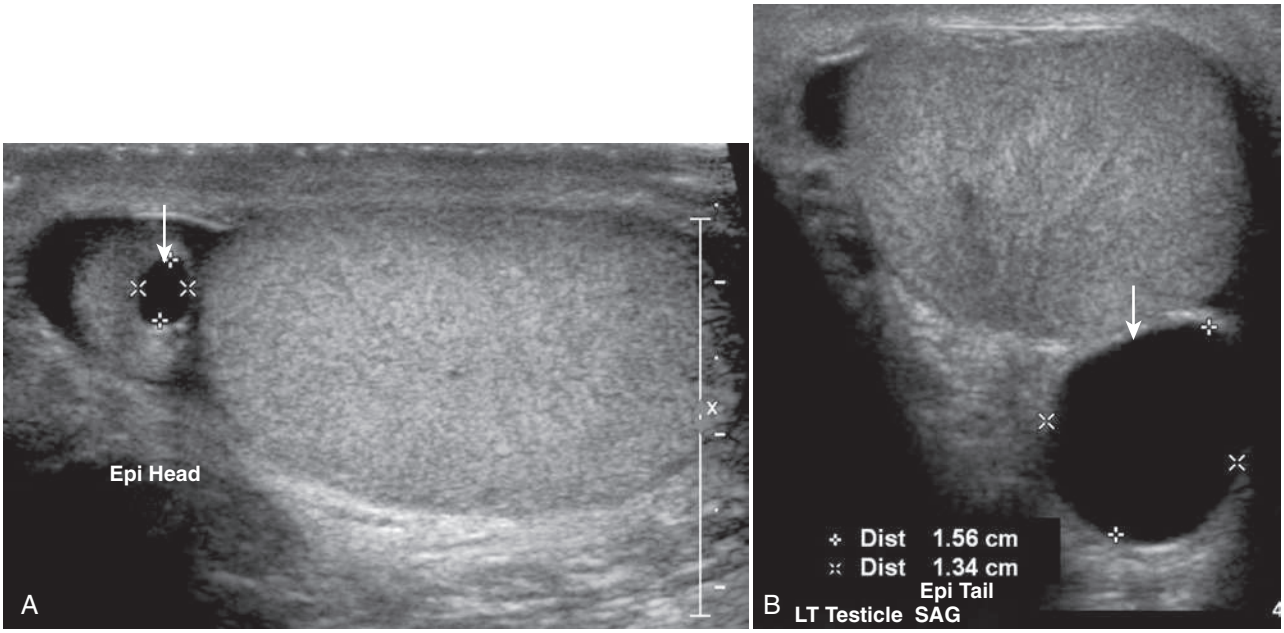

FIG. 54.51 Epididymal Cysts. Teenage boy with left-sided scrotal masses. **(A)** Sagittal scan demonstrates a small cyst *(arrow)* in the head of the epididymis and a normal left testis. **(B)** Transverse scan of the inferior aspect of the left testis demonstrates a larger cyst *(arrow)* in the adjacent tail of the epididymis. A small hydrocele is present.

walls, which may contain debris (Fig. 54.51). They range in size from a few millimeters to several centimeters.[182] Other cystic lesions include **spermatic cord cysts** and **cysts of the tunica vaginalis.**

Paratesticular Tumors

Both benign and malignant paratesticular tumors are rare and typically involve the epididymis or spermatic cord. They may also arise in the appendix testis or the tunica. About 30% of spermatic cord tumors are malignant and in general are caused by **embryonal rhabdomyosarcoma**[156,186] (Fig. 54.52). This tumor usually appears as a rapidly growing, painless, intrascrotal mass in boys younger than 5 years. Up to 40% have retroperitoneal lymph node involvement at diagnosis.[186] Other malignant lesions include **metastatic neuroblastoma, lymphoma, leiomyosarcoma,** and **fibrosarcoma.**[175,187,188] They are usually well-defined, homogeneous or heterogeneous, hypoechoic solid masses. Benign paratesticular tumors include **fibromas, hemangiomas, lipomas, leiomyomas, lymphangiomas,** and **neurofibromas.** Both benign and malignant paratesticular tumors may appear hypoechoic,

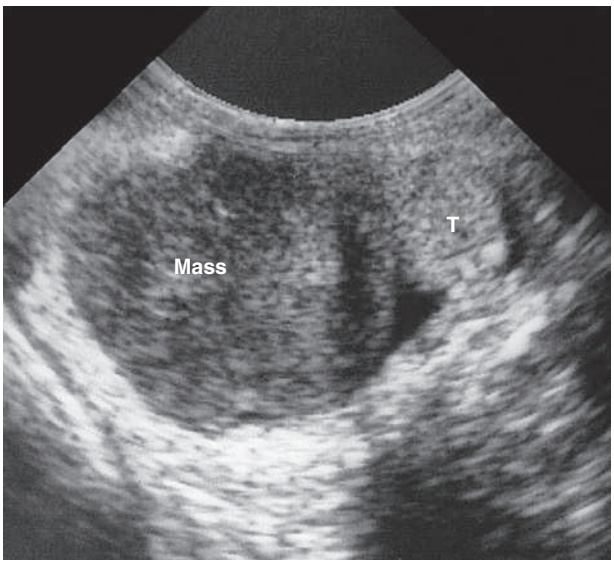

FIG. 54.52 Paratesticular Rhabdomyosarcoma. Large, solid mass was identified medial to left testis *(T)* with a small hydrocele in this 18-month-old boy.

hyperechoic, or heterogeneous. Ultrasound cannot clearly distinguish benign from malignant lesions.[189] Increased vascularity on Doppler imaging in a paratesticular rhabdomyosarcoma may mimic that seen with epididymitis.[186] Thus follow-up should be performed in cases of suspected epididymitis to ensure resolution of any mass because rhabdomyosarcoma can manifest this way.[189]

The most common benign paratesticular masses include adenomatoid tumors as well as fluid-filled masses, such as **spermatoceles** and cysts of the epididymis or tunica albuginea. **Adenomatoid tumors** are usually seen in the body of the epididymis and less often in the spermatic cord or testicular tunics. They are solid, well-circumscribed, with variable echogenicity. **Epididymal cystadenomas** (associated with **von Hippel–Lindau disease**)[190] and **lymphangiomas** are septated cystic masses.[182,191] With **splenogonadal fusion,** a rare congenital anomaly, a mass of ectopic splenic tissue may be noted adjacent to the left testis.[192]

Focal calcifications from meconium periorchitis may appear as palpable scrotal masses (Fig. 54.53). These dystrophic calcifications result from in utero bowel perforation during the second or third trimester of gestation. Sterile intestinal contents (meconium) leak into the peritoneal cavity and enter the scrotum through a patent processus vaginalis and elicit a foreign body inflammatory response that results in focal calcifications. As with calcification elsewhere, these areas are echogenic with strong posterior shadows and may mimic a solid neoplasm, particularly a teratoma. Differentiation is based on the finding of additional intraperitoneal calcifications on sonography or plain film radiography of the abdomen.[189] Eventually, spontaneous regression of these calcifications occurs, and thus conservative management is recommended.[193] Differential diagnosis of scrotal or testicular calcifications in the pediatric patient includes teratoma, gonadoblastoma, Leydig cell tumor, testicular microlithiasis, calcified loose bodies, phleboliths, meconium peritonitis, calcified hematomas, and postinflammatory or infectious scrotal calculi.

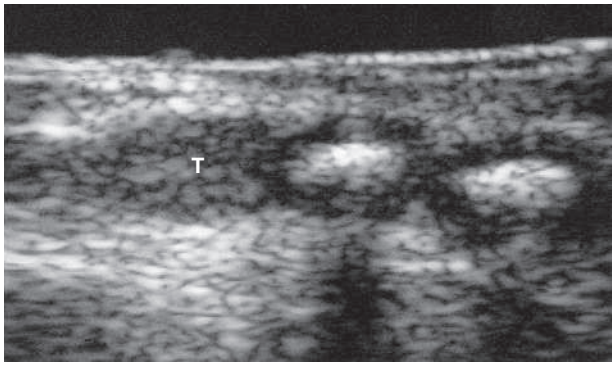

FIG. 54.53 Meconium Periorchitis in 5-Year-Old Boy With Painless Scrotal Masses. Sagittal view of the left hemiscrotum using a stepoff pad shows two well-defined, oval, brightly echogenic masses with hypoechoic halos and acoustic shadows, which lie inferior to the normal left testis *(T)*. (With permission from Mene M, Rosenberg HK, Ginsberg PC. Meconium periorchitis presenting as scrotal nodules in a five year old boy. J Ultrasound Med. 1994;13[6]:491-494.[193])

Testicular microlithiasis is an asymptomatic condition that has a characteristic sonographic appearance and usually is discovered incidentally. It has been reported in normal patients and those with **Down syndrome, cryptorchidism,** and **Klinefelter syndrome.** Testicular microlithiasis represents calcified debris within the seminiferous tubules. The cellular debris has a calcific core and surrounding lamellated collagen, resulting from a failure of Sertoli cell phagocytosis. On ultrasound there are tiny (1-3 mm), hyperechoic, most often nonshadowing foci[189] (Fig. 54.54, Video 54.5). The number of echogenic foci within the testis can range from a few to many, but at least five microliths on a single image should be visualized to meet ultrasonographic criteria.[194] The association between testicular microlithiasis and malignancy remains unclear. Ultrasound follow-up should be considered in symptomatic patients, in patients with a history of malignancy, or on patient request. Self-examinations can be used to follow asymptomatic patients.[195]

LOWER URINARY TRACT

Congenital Anomalies

Duplication anomalies of the collecting systems and ureters are the most common congenital anomalies of the urinary tract. In **complete ureteral duplication** the lower ureter inserts orthotopically into the trigone, often resulting in vesicoureteral reflux. The upper-pole ureter usually inserts ectopically in the bladder (at the bladder neck) or in the trigone (inferomedial to the normal location). It can also insert into the urethra, vagina, or uterus

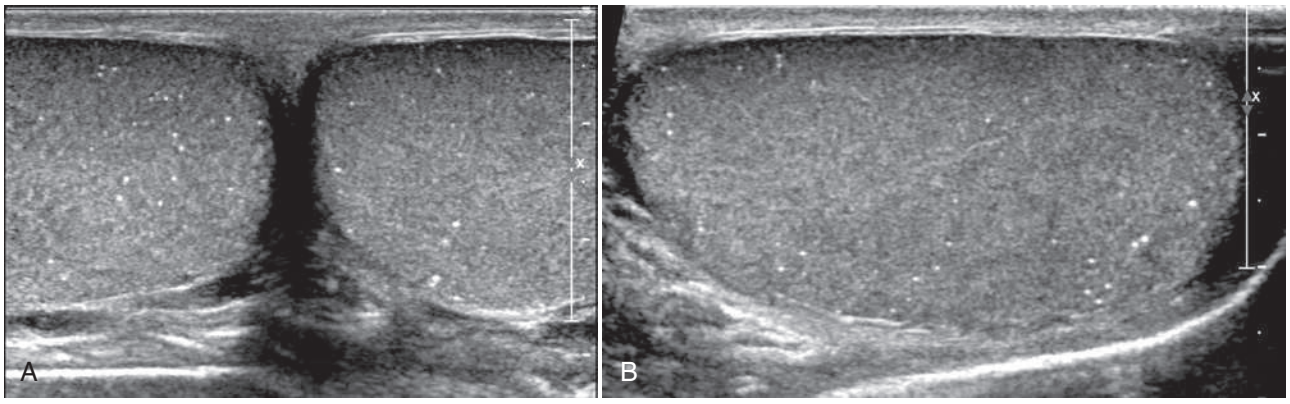

FIG. 54.54 Testicular Microlithiasis. Transverse image of both testicles **(A)** and sagittal image of the right testicle **(B)** in an 18-year-old male with testicular pain reveal multiple punctate echogenic foci without acoustic shadowing. See also Video 54.5.

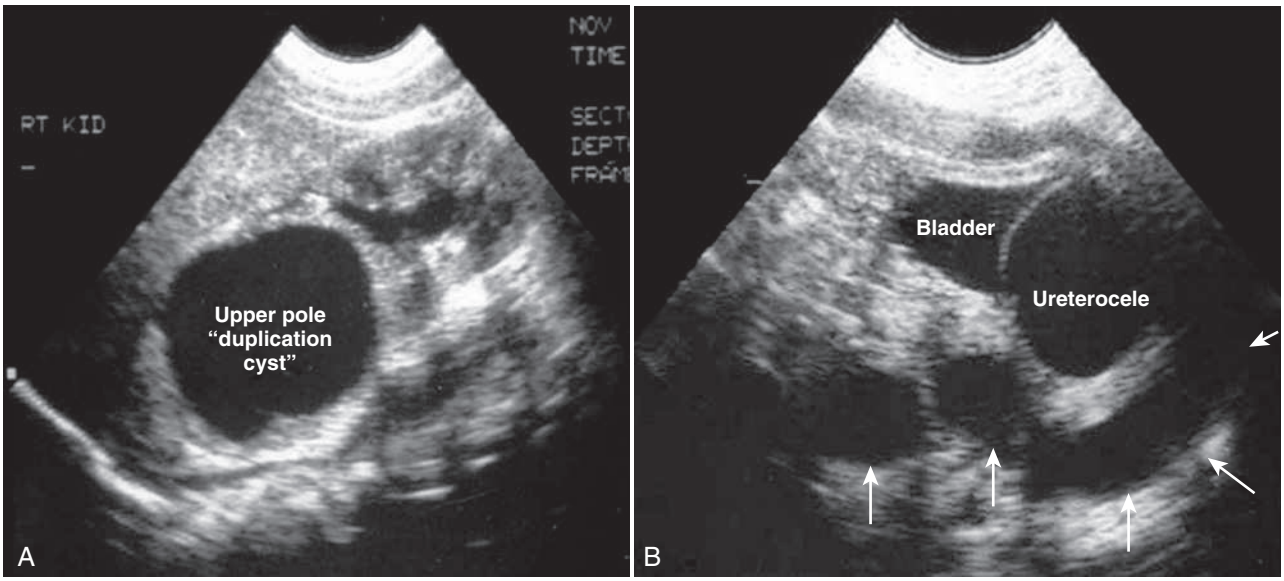

FIG. 54.55 Ectopic Ureterocele. Obstructed upper-pole moiety of a duplex kidney in a baby with urinary tract infection. **(A)** Sagittal sonogram of right kidney showing upper-pole "duplication cyst" and mild dilation of the intrarenal collecting system in the lower pole surrounded by normal parenchyma. **(B)** Sagittal view of the pelvis demonstrates a large, ectopic ureterocele within the urinary bladder, which is in continuity with the greatly dilated, tortuous, upper-pole ureter *(arrows).*

in girls, resulting in urinary dribbling. In boys the **ectopic ureter** can insert in the proximal urethra, seminal vesicle, vas deferens, or ejaculatory duct. Urinary incontinence is not a presenting symptom in boys because the ectopic insertion is always proximal to the external sphincter. Duplication anomalies are often asymptomatic; **urinary tract infection** (UTI) is the most common initial presentation. The upper-pole moiety often becomes obstructed as a result of an **ectopic ureterocele.** Sonography demonstrates a dilated upper-pole collecting system and ureter that ends distally as a well-defined, thin-walled cystic protuberance into the bladder base (Fig. 54.55). The lower-pole system is often dilated secondary to reflux.[196] Less frequently, the lower-pole moiety may be dilated from obstruction of the ureteral orifice by the adjacent ectopic ureterocele or because of vesicoureteral reflux. About 10% to 20% of ectopic ureters are associated with a single collecting system (Fig. 54.56). The renal parenchyma associated with an ectopic ureter may be dysplastic (containing echogenic parenchyma, loss of corticomedullary junction, and variably sized cysts).

Sonography is well suited for screening siblings of patients with **vesicoureteral reflux,** who are at greater risk of having reflux than the general population. Giel and colleagues[197] showed that given the seemingly innocuous nature of vesicoureteral reflux in older asymptomatic siblings of known patients with reflux, observation alone in this group is an acceptable form of management.

Posterior urethral valves are a common cause of urinary tract obstruction in boys. Signs and symptoms at presentation include palpable flank masses caused by hydronephrosis or urinoma, poor urine stream, UTI, and failure to thrive. On sonography, the bladder has a thick, trabeculated wall, and the posterior urethra is dilated (Fig. 54.57). There may be marked hydronephrosis with dilated, tortuous ureters secondary to vesicoureteral reflux. Occasionally, the reflux is unilateral, resulting

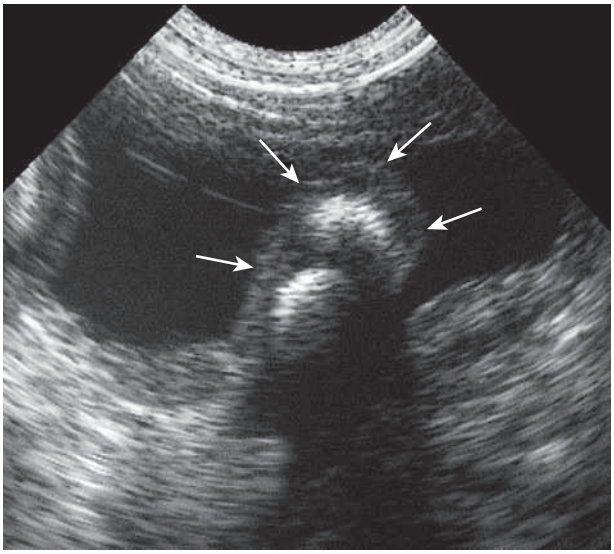

FIG. 54.56 Simple Ureterocele With Stones in 7-Year-Old Child With Recent Mild Trauma. Sagittal view of the left side of the bladder demonstrates a simple ureterocele *(arrows)* protruding into the bladder lumen, containing two brightly echogenic, shadowing calculi.

Causes of Bladder Outlet Obstruction

Posterior urethral valves
Prune-belly syndrome
Anterior urethral valves
Urethral duplication or ureterocele
Congenital urethral stricture
Anterior urethral diverticulum
Posterior urethral polyp

in ipsilateral hydroureteronephrosis. The renal parenchyma may be thin and the echogenicity may be abnormally increased as a result of long-standing reflux or obstructive nephropathy. Many infants with posterior urethral valves have secondary renal dysplasia, manifesting on sonography as brightly echogenic kidneys usually devoid of corticomedullary differentiation and often containing tiny cysts.[198] The appearance of the renal parenchyma has predictive value in infants with posterior urethral valves with regard to potential renal function.[199]

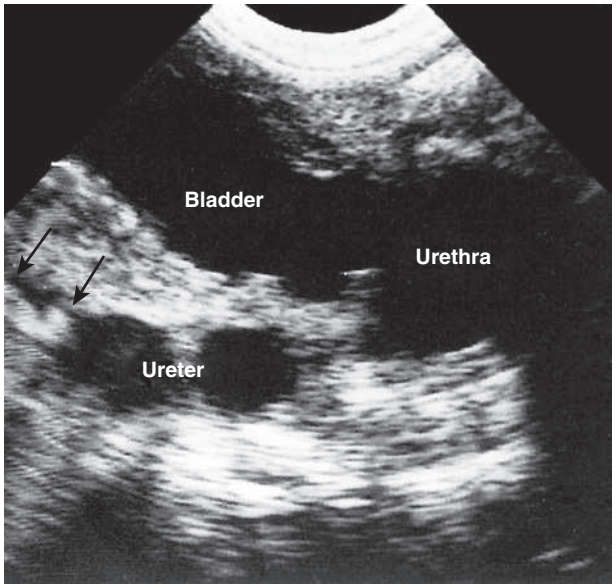

FIG. 54.57 Posterior Urethral Valves in Newborn Boy. Midline sagittal scan shows irregularly thickened bladder wall (caused by obstruction), massively dilated posterior urethra, and moderately dilated tortuous distal ureter. Arrows show the serosal surface of the bladder wall. (With permission from Rosenberg H. Sonography of pediatric urinary tract abnormalities. Part I. Am Urol Assoc Weekly Update Series. 1986;35: 1-8.[231])

The **prune-belly syndrome** (abdominal muscle deficiency or **Eagle-Barrett syndrome**) is another common cause of urinary tract obstruction in infant boys. The syndrome is composed of a triad of absent abdominal musculature, bilateral hydroureteronephrosis, and cryptorchidism. There are three forms of urinary tract abnormality. In the most severe form, urethral atresia and renal dysplasia are present; these children have a very poor prognosis and typically die in infancy. Associated congenital anomalies are frequent and include intestinal malrotation or atresia, imperforate anus, Hirschsprung disease, congenital heart defects, skeletal anomalies, and cystic adenomatoid malformation of the lung. In the less severe form of urinary tract abnormality, the bladder is large and atonic, and there is bilateral hydroureteronephrosis, impaired renal function, and no urethral obstruction. The changes are thought to be caused by a neurogenic dysfunction rather than a mechanical obstruction. There are usually no associated congenital anomalies, and these infants have a better prognosis.[200] In the mildest type of prune-belly syndrome, the urinary tract is only mildly affected.

Other uncommon forms of bladder outlet obstruction include anterior urethral valves, urethral duplication, congenital urethral stricture, anterior urethral diverticulum, posterior urethral polyp[201] (Fig. 54.58), and stones[202] (Fig. 54.59). Rarely, a giant bladder diverticulum many descend below the bladder neck and lead to bladder outlet obstruction.[203] Voiding cystourethrography (VCUG), in addition to sonography, is usually necessary to identify these urethral obstructions.

The Ureter

The ureters cannot be visualized on ultrasound unless they are dilated. Real-time sonography can sometimes differentiate between

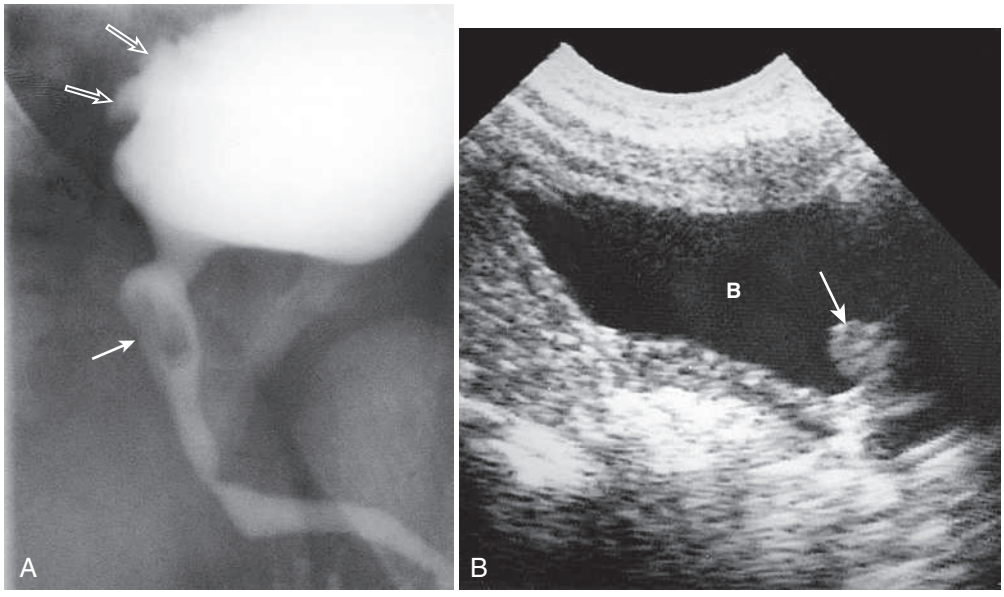

FIG. 54.58 Congenital Urethral Polyp That Caused Prenatal Hydroureteronephrosis in Newborn Boy. (A) Voiding cystourethrography demonstrates an oval, polypoid mass in the posterior urethra *(solid arrow)* and posterior bladder wall thickening *(open arrows)*. **(B)** Sagittal sonogram of the bladder *(B)* 4 months later shows a solid polypoid mass *(arrow)* protruding from the bladder neck into the bladder lumen. (With permission from Caro PA, Rosenberg HK, Snyder 3rd HM. Congenital urethral polyp. AJR Am J Roentgenol. 1986;147[5]:1041-1042.[201])

mechanical obstruction and vesicoureteral reflux. In **ureterovesical junction obstruction** the distal ureter is dilated but may taper, making it difficult to visualize at the level of the bladder trigone, and at times, ureteral peristalsis is absent (Fig. 54.60). Sonography is useful for identification of a stone as the cause of distal ureteral obstruction (Fig. 54.61). With **vesicoureteral reflux** the ureterovesical junction is often gaping or patulous, and active peristalsis is demonstrated.[94,204] In patients with a dilated tubular structure posterior to the bladder, Doppler ultrasound can be used to differentiate a ureter, artery, or vein. In addition, color Doppler sonography allows reliable visualization of the **ureteric jet phenomenon.**

Marshall and colleagues[205] found that the distance of the ureteric orifice from the midline of the bladder correlated with vesicoureteric reflux when the mean distance was 10.25 mm ± 2.40 SD. Jequier and colleagues[206] used color Doppler imaging to show that (1) the duration of the ureteric jet varied from 0.4 to 7.5 seconds and depended largely on fluid intake, (2) the direction of the normal jet was anteromedial and upward, (3) jets from refluxing ureters could appear normal, and (4) Doppler analyses of the ureteric jet do not allow either the diagnosis or the exclusion of vesicoureteral reflux.[206] Berrocal and colleagues[207] demonstrated that cystosonography with SHU 508A appears comparable to VCUG in the depiction of vesicoureteral reflux. Darge and colleagues[208] showed that the number of VCUG procedures was significantly reduced as a result of implementation of voiding urosonography using the intravesical application of the ultrasound contrast agent Levovist.

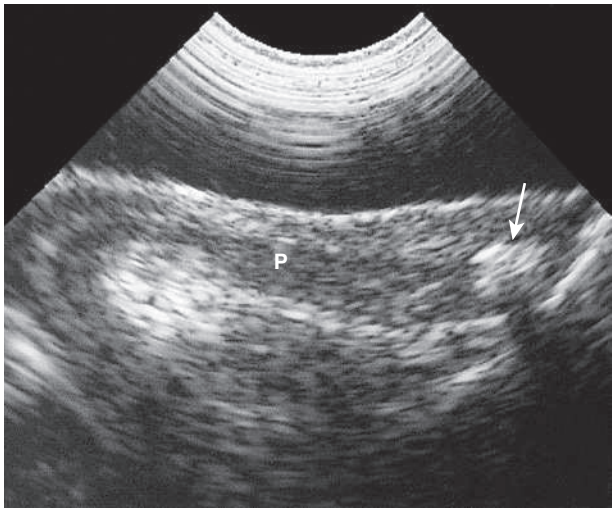

FIG. 54.59 Urethral Stone in Fossa Navicularis. Sagittal image of penis *(P)* using stepoff pad reveals a 7-mm calculus *(arrow)* in the distal urethra of this 6-year-old boy with gross hematuria, dysuria, and suprapubic pain.

Neurogenic or Dysfunctional Bladder

Urinary tract sonography has become a routine screening procedure in children with neurogenic or dysfunctional bladders. The most common cause of neurogenic bladder in children is **myelomeningocele.** Other acquired forms of dysfunctional bladder include **traumatic paraplegia, cerebral palsy, spinal cord tumor,** and **encephalitis** or **transverse myelitis.** These children have a higher incidence of UTI, bladder stones, and reflux. Sonography of a neurogenic bladder demonstrates an irregularly thickened, trabeculated bladder wall, often with multiple diverticula. Echogenic material within the bladder lumen may represent complications of infection, hemorrhage, stone formation, or foreign body insertion via the urethra.[209] Ultrasound can also be used to assess the patient's ability to empty the bladder spontaneously or after Credé maneuver or catheterization. Residual urine volumes can be measured.[210]

Urachal anomalies can be identified on ultrasound when there is persistence of the embryonic tract between the dome of the bladder and umbilicus. Cacciarelli and colleagues[211] identified a normal urachal remnant in 62% of bladder sonograms in children.[10,212] A normal urachal remnant appears as a small (6 mm depth × 13 mm length × 12 mm width), elliptical, hypoechoic structure located posterior to the rectus abdominis muscle and

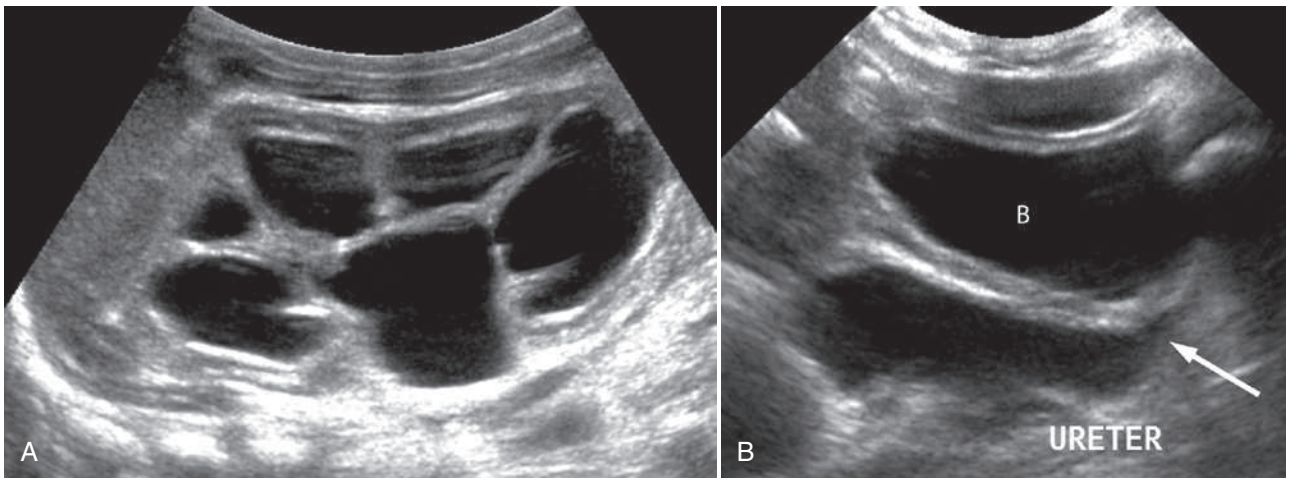

FIG. 54.60 Congenital Ureterovesical Junction (UVJ) Obstruction in Infant With Urinary Tract Infection. (A) Sagittal view of the left kidney reveals severe hydronephrosis with a markedly thin parenchyma with compression of the corticomedullary differentiation. **(B)** Sagittal sonogram of the bladder *(B)* shows the dilated ureter, which tapers inferiorly at the UVJ *(arrow).*

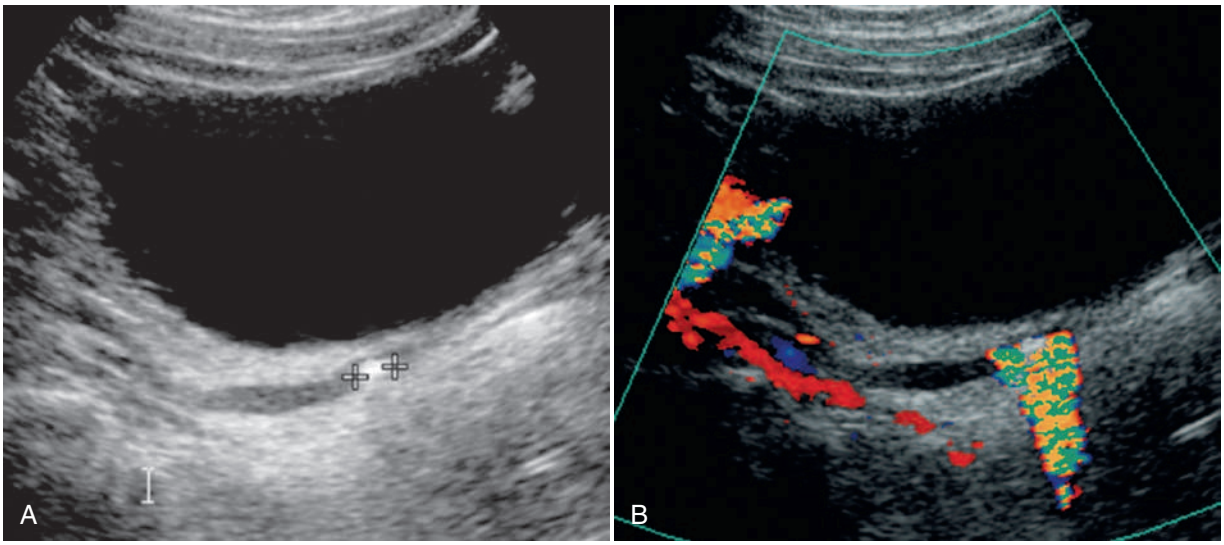

FIG. 54.61 Distal Ureter Stone. This 14-year-old patient had hematuria and right flank pain that radiated to the right groin. Mild right-sided hydronephrosis *(not shown)* was present. **(A)** Small stone *(arrow)* is lodged in the mildly dilated distal ureter, with distal acoustic shadowing. **(B)** Color Doppler shows "twinkle" artifact, confirming the presence of a stone.

on the midanterosuperior surface of the distended bladder. Involution of the urachus is not complete at birth and can be followed on sonography during the first months of life. Thus young infants with a discharging umbilicus or an infected urachus may benefit from a conservative approach using serial sonography as a guide because sonography can document spontaneous involution as well as abnormal development.[10] There are four types of urachal anomalies: **patent urachus** (completely open urachal lumen associated with urinary drainage from umbilicus), **urachal sinus** (opening to umbilicus), **urachal diverticulum** (opening to bladder), and **urachal cyst** (urachus obliterated at both ends with extraperitoneal position of isolated cyst)[213] (Fig. 54.62). Two sonographic patterns have been described in urachal anomalies: (1) a cystic mass, often with internal echoes or septations caused by infection, and (2) an echogenic, thickened, tubular sinus tract (8-15 mm in diameter).[213]

Other anomalies of the lower urinary tract that can be identified on ultrasound include **ectopic pelvic kidney, seminal vesicle cysts** (Fig. 54.63), **müllerian duct (prostatic utricle) cysts** (Fig. 54.64), and congenital or acquired **bladder diverticula.**[214]

Infection

UTIs are common in children, especially girls, and are usually the result of cystitis. Clinically, these children have urinary frequency, incontinence, dysuria, and/or hematuria.[215,216] The UTI is usually bacterial. **Hemorrhagic cystitis** can develop secondary to a viral infection (Fig. 54.65), chemotherapy with cyclophosphamide, or indwelling catheters. **Granulomatous cystitis** in a patient with chronic granulomatous disease of childhood can be detected on ultrasound. On sonography, the bladder may appear normal in mild cases of cystitis. More specific signs of cystitis are diffuse or focal bladder wall thickening and irregularity (Fig. 54.66). Echogenic material in the bladder lumen may represent purulent or hemorrhagic urine. **Bladder calculi** are more common with *Proteus* or *Pseudomonas* infections. With **cystitis cystica** or **cystitis glandularis,** rounded, isoechoic or hypoechoic, polypoid lesions may protrude into the lumen, mimicking a bladder tumor (Fig. 54.67). Rosenberg and colleagues[217] reported that in children with hematuria, dysuria, and frequency plus cystographic or sonographic demonstration of a bladder with reduced capacity and circumferential wall thickening, or sonographic findings of isoechoic bladder wall thickening (focal, multifocal, or circumferential distribution), intact mucosa, and bullous lesions, these findings should strongly suggest inflammation and not malignancy. In addition, changing mass contour and thickness with increasing bladder filling are particularly suggestive of inflammatory thickening. When an inflammatory lesion is suspected, follow-up imaging should be performed in 2 weeks, which will preclude biopsy if findings are normal.[217]

Neoplasm

Rhabdomyosarcoma is the most common tumor of the lower urinary tract in children, with 21% arising from the genitourinary tract. The most frequent primary sites are the bladder trigone or prostate. Less frequent sites of origin are the seminal vesicles, spermatic cord, vagina, uterus, vulva, pelvic musculature, urachus, and paratesticular area.[44,218] There is a male predominance of 1.6:1. The peak incidence occurs at 3 to 4 years of age; a second, smaller peak is seen in adolescence. The most common rhabdomyosarcoma cell type is the embryonal form, of which **sarcoma botryoides** is a subtype. The **alveolar** form is next in frequency; **undifferentiated** and **pleomorphic types** are uncommon. Tumors arising from the bladder, prostate, or both usually manifest early with symptoms from urinary tract obstruction and hematuria. Rhabdomyosarcoma has been reported to be associated with **neurofibromatosis, fetal alcohol syndrome,** and **basal cell nevus syndrome.**

On sonographic examination, rhabdomyosarcoma appears as a homogeneous, solid mass with an echotexture similar to

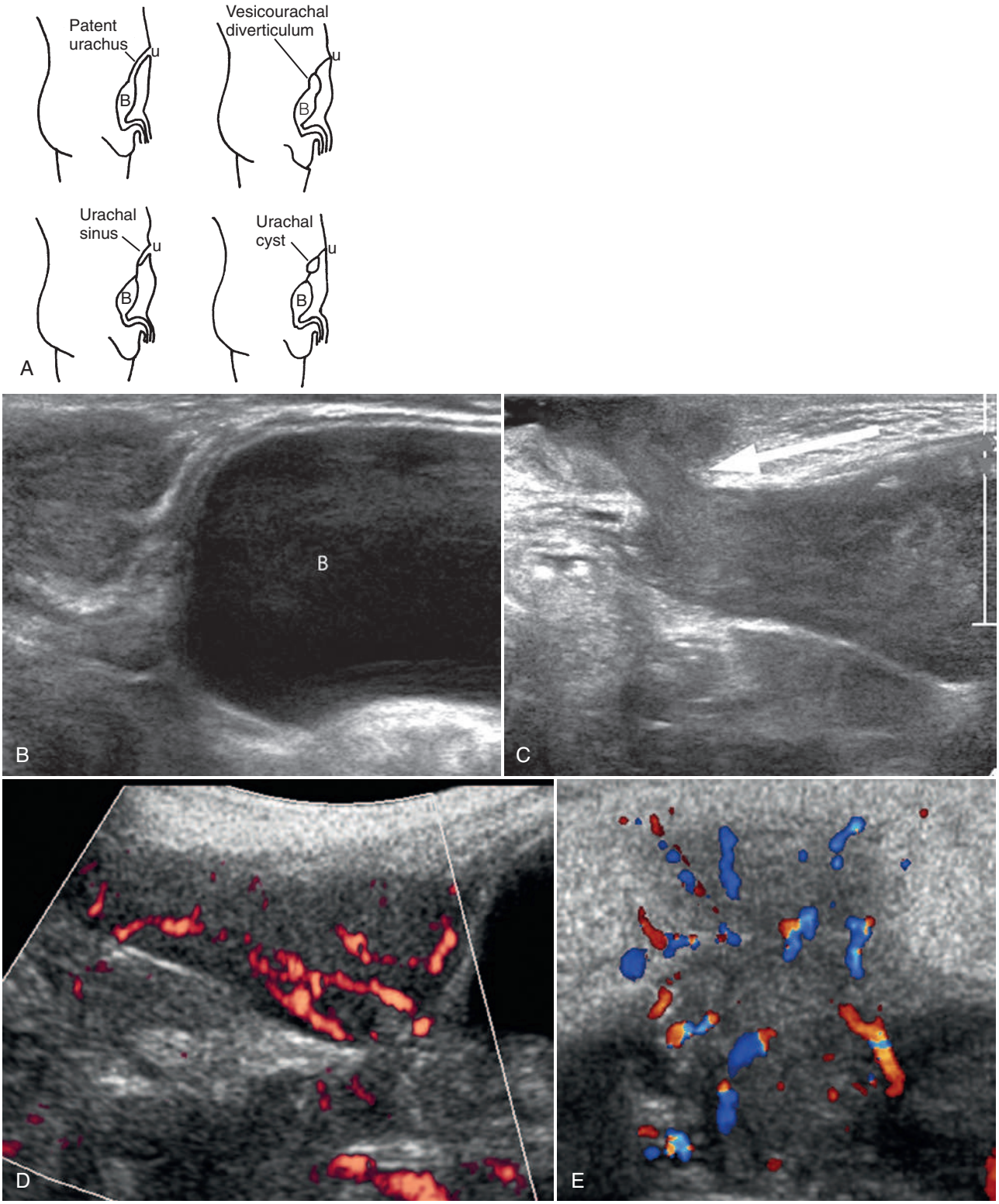

FIG. 54.62 Urachal Abnormalities. (A) Patent urachus (urachal lumen communicates with both umbilicus and bladder); **vesicourachal diverticulum** (urachal lumen communicates only with bladder); **urachal sinus** (urachal lumen communicates only with umbilicus); and **urachal cyst** (does not communicate with bladder or umbilicus). **(B)-(D) Infected urachal cyst.** Eight-year-old boy with lower abdominal pain, fever, and inflammation around the umbilicus with occasional drainage. **(B)** Sagittal image of the supravesicular region shows a tubular hypoechoic urachal cyst extending from the bladder *(B)* dome superiorly. **(C)** Just superior to image in **(B)**, the urachal cyst is seen extending to the umbilicus *(arrow).* **(D)** Power Doppler image shows hyperemia. **(E)** Transverse color Doppler shows hyperemia extends thru umbilicus into subcutaneous fat which is hyperechogenic. (**A** with permission from Boyle G, Rosenberg HK, O'Neill J. An unusual presentation of an infected urachal cyst. Review of urachal anomalies. Clin Pediatr [Phila]. 1988;27[3]:130-134.[213])

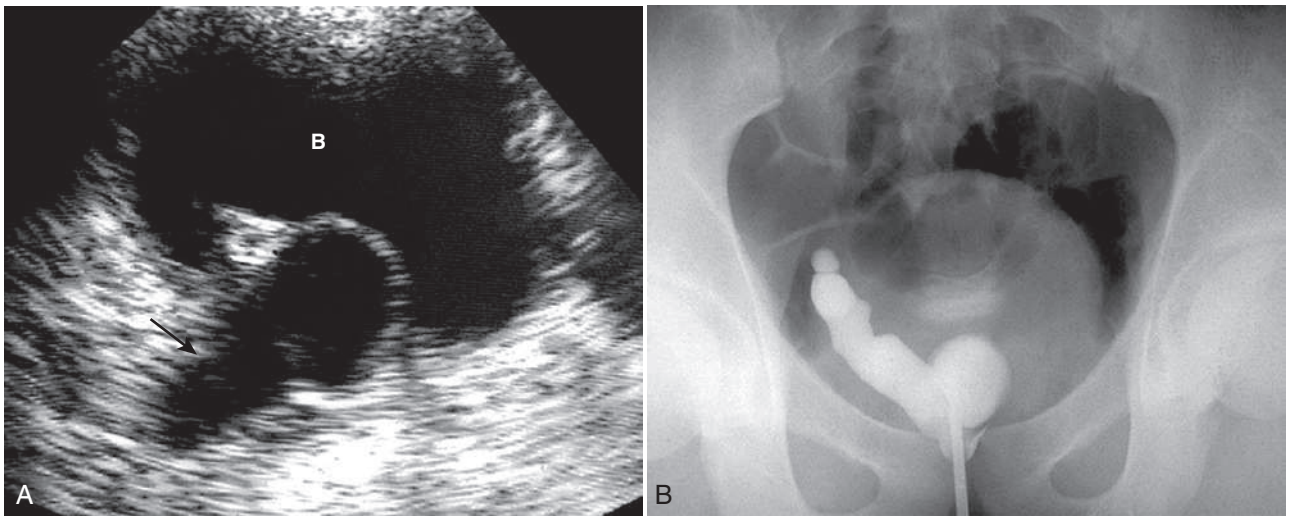

FIG. 54.63 Seminal Vesicle Cyst in 17-Year-Old Male With Right Renal Agenesis. (A) Transverse sonogram shows tubular structure *(arrow)* with a rounded portion projected over bladder *(B)*. **(B)** Intraoperative cystoscopic retrograde injection of contrast material confirms the presence of a seminal vesicle cyst.

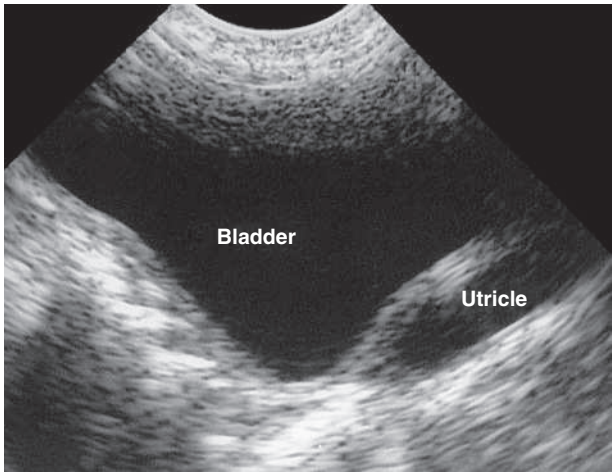

FIG. 54.64 Prostatic Utricle in 4-Year-Old True Hermaphrodite. This child was reared as a boy after external genitalia reconstruction. Sagittal view of the bladder reveals a fluid-filled, tubular utricle posterior to the bladder base.

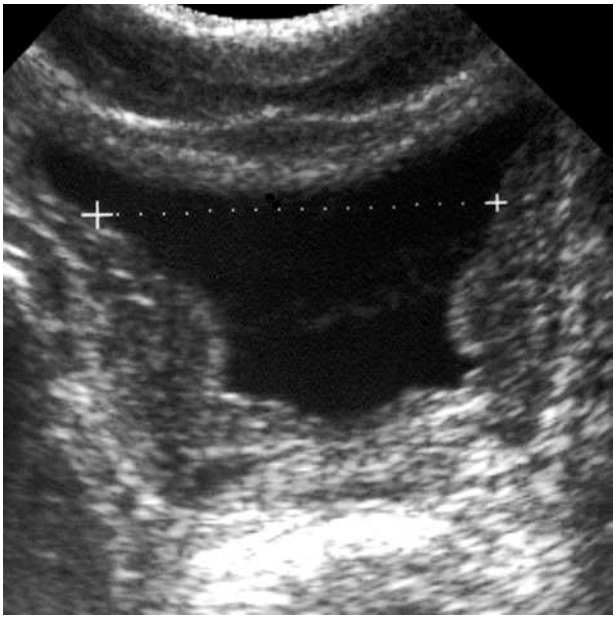

FIG. 54.65 Viral Cystitis in 11-Year-Old Boy With Frequency, Hematuria, and Dysuria. Transverse sonogram shows lobulated thickening *(cursors)* of the bladder wall.

muscle. Anechoic spaces caused by necrosis and hemorrhage are occasionally seen (Fig. 54.68). Calcification is uncommon. Bladder lesions originate in the submucosa, infiltrate the bladder wall, and produce polypoid projections into the lumen (sarcoma botryoides). Tumors arising in the prostate cause concentric or asymmetrical enlargement of the prostate and often infiltrate the bladder neck, posterior urethra, and perirectal tissues (Fig. 54.69). Regional and retroperitoneal lymph node metastases are common. Rarely, leiomyosarcoma may arise from the bladder wall and is more likely to have calcifications.

Benign tumors of the lower urinary tract are extremely rare and include **transitional cell papilloma** (**neurofibroma, fibroma, hemangioma,** and **leiomyoma**).[219,220] Neurofibromatosis can be invasive, with diffuse involvement of the pelvic organs.[221] **Pheochromocytoma** of the bladder is a rare tumor that probably arises in the paraganglia of the visceral (autonomic) nervous system and is located submucosally either in the dome or in the posterior wall close to the trigone. In children, 2% of bladder pheochromocytomas are malignant. Pheochromocytomas can be seen in the context of familial syndromes or diseases, which include neurofibromatosis, **von Hippel–Lindau disease, Sturge-Weber syndrome, tuberous sclerosis, multiple endocrine neoplasia type A** (medullary thyroid carcinoma and hyperparathyroidism), and **multiple endocrine neoplasia type IIB** (medullary thyroid carcinoma, mucosal neuromas, and pheochromocytoma). Pheochromocytomas of the bladder may cause headache, blurred vision, diaphoresis, palpitations, intermittent hypertension (70%), and hematuria (6%). Any of these symptoms

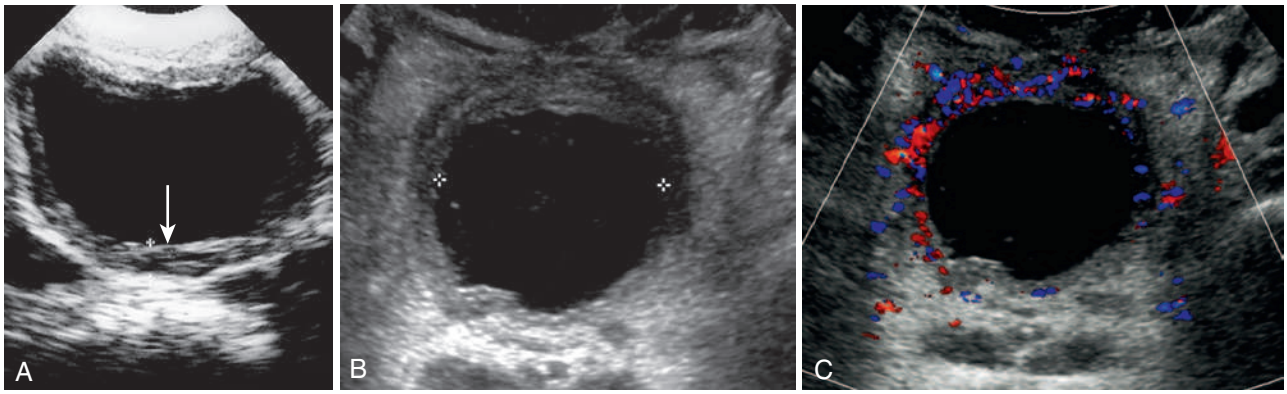

FIG. 54.66 Cystitis. (A) Chronic bacterial cystitis. Transverse sonogram demonstrates bladder wall thickening *(arrow)*. **(B)** and **(C)** Cyclophosphamide (Cytoxan) cystitis in child after bone marrow transplant. The bladder wall is thickened and hyperemic. Debris is noted within the bladder lumen.

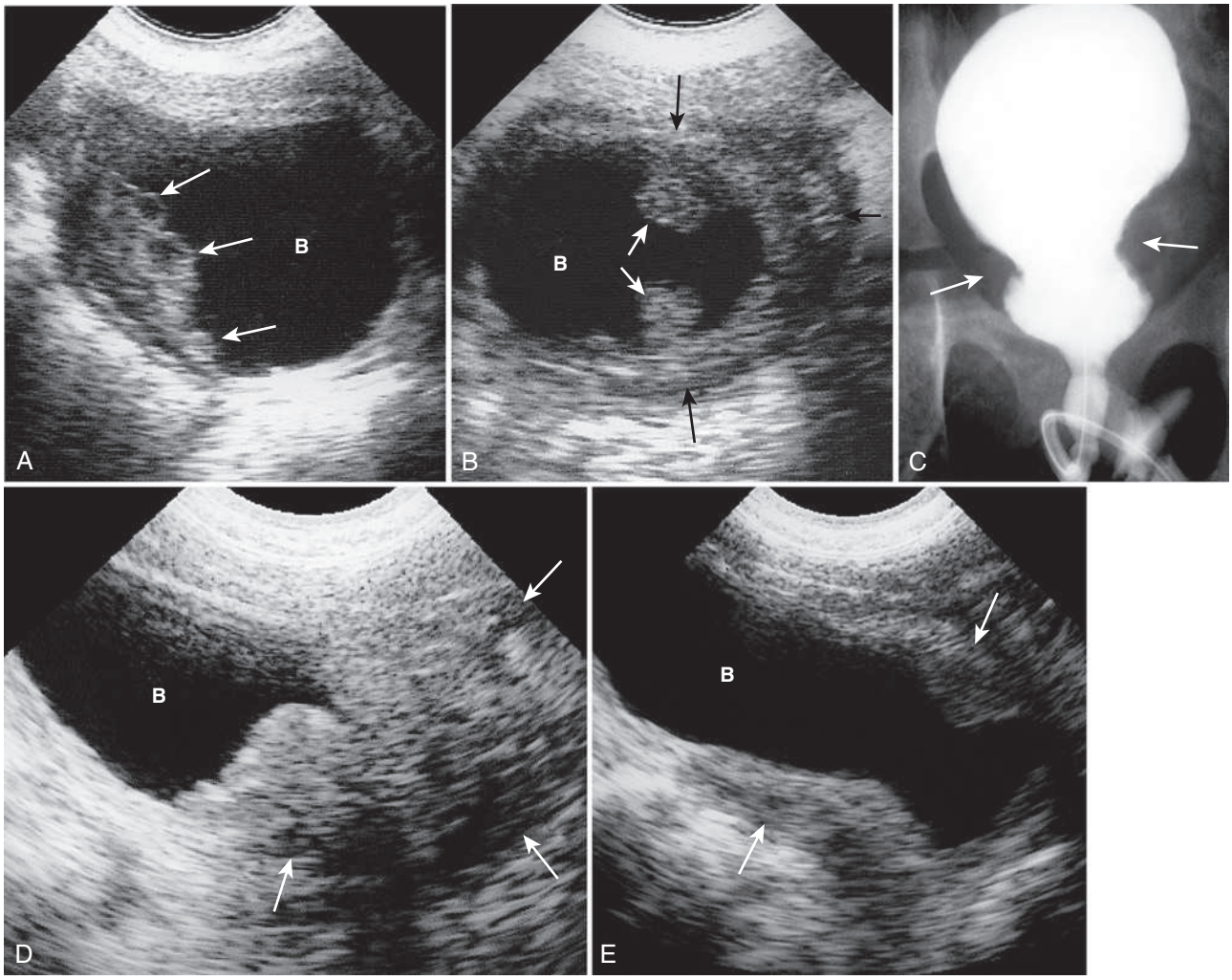

FIG. 54.67 Bullous, Benign Cystitis From Cytomegalovirus After 24 Hours of Dysuria and Hematuria. (A) Sagittal sonogram of the bladder *(B)*. Complex mass containing multiple, well-circumscribed, hypoechoic and anechoic, polypoid lesions *(arrows)* arising from the dome and projecting into the lumen. **(B)** Hemorrhagic cystitis. Transverse view of the bladder *(B)* shows asymmetrical bladder wall thickening involving the left half of the bladder *(black arrows)* with polypoidlike protrusions of thickened wall *(small white arrows)* into bladder lumen. **(C)** Frontal image from voiding cystourethrography shows concentric narrowing. **(D)** Sagittal sonogram with partial bladder *(B)* filling shows masslike thickening of the posteroinferior bladder walls *(arrows)*. **(E)** Sagittal sonogram obtained after further bladder *(B)* filling shows a decrease in the apparent size of the mass *(arrows)* with increased bladder distention. (**B** and **E** with permission from Rosenberg HK, Eggli KD, Zerin JM, et al. Benign cystitis in children mimicking rhabdomyosarcoma. J Ultrasound Med. 1994;13[12]:921-932.[217])

may be seen with micturition.[222] Benign polyps in the male urethra can arise from a stalk near the verumontanum and cause urinary tract obstruction.

Trauma

Trauma to the lower urinary tract in children is most often caused by blunt trauma. Foreign bodies and complications of surgery are less frequent causes. The bladder in children is in a more intraabdominal position than in adults, and therefore bladder rupture is usually intraperitoneal. **Spontaneous bladder rupture** is rare in children and is seen primarily in neonates with urinary ascites secondary to urethral obstruction or neurogenic bladder.

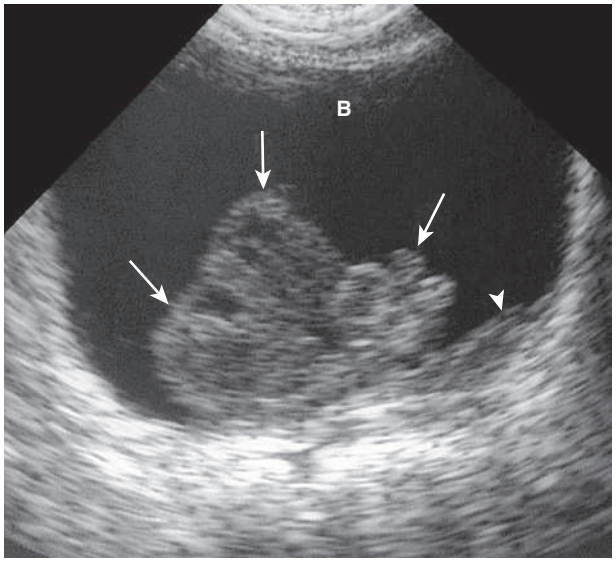

FIG. 54.68 Rhabdomyosarcoma of Bladder Wall. Large, complex, polypoidlike mass *(arrows)* arises from base of the bladder *(B)* in this 9-year-old boy with painless hematuria. Asymmetrical bladder wall thickening was noted posterolaterally on patient's left *(arrowhead)*.

Preexisting abnormalities of the vesical wall, such as tumors, stones, tuberculosis, diverticula, and surgical scars, can predispose a child to spontaneous rupture of the bladder.[223] Sonography can demonstrate urinary ascites in cases of intraperitoneal rupture or a loculated fluid collection **(urinoma)** in the retropubic or perivesical space in extraperitoneal rupture.

Postoperative Bladder

Sonography has assumed an important role in the evaluation of the postoperative bladder. **Ureteral reimplantation** is a common surgical procedure for the correction of persistent vesicoureteral reflux. The reimplanted ureteral segment is submucosal and contiguous to the bladder mucosa. Sonograms reveal an echogenic, fixed, tubular, submucosal structure without acoustic shadowing at or just above the trigone. Occasionally the reimplanted ureter appears only as an area of focal thickening of the posterior bladder wall.[224] Sonography is also useful for the demonstration of the echogenic mound present after treatment with Deflux (dextranomer–hyaluronic acid copolymer) as a first-line treatment for high-grade vesicoureteral reflux[225] (Fig. 54.70).

Bladder augmentation is now a widely accepted surgical procedure for the reconstruction of small-capacity bladders caused by exstrophy, neurogenic bladder, or tumor. Segments of bowel, usually the sigmoid, cecum, or ileum or the ileocecal segment, are anastomosed to the bladder to increase the size of the urinary reservoir. Sonography of the augmented bladder reveals a thick or irregularly shaped bladder wall (Fig. 54.71). Pseudomasses within the bladder lumen, representing bowel folds, mucous collections, or bowel that was surgically intussuscepted into the reconstructed bladder to prevent reflux, are a common finding. Fine debris and linear strands often float within the urine and probably represent mucus. Active peristalsis within the bowel segment can be identified on real-time imaging. Complications of bladder reconstructive surgery can be detected on ultrasound and include enterocystic **anastomotic strictures, ureteral reflux**

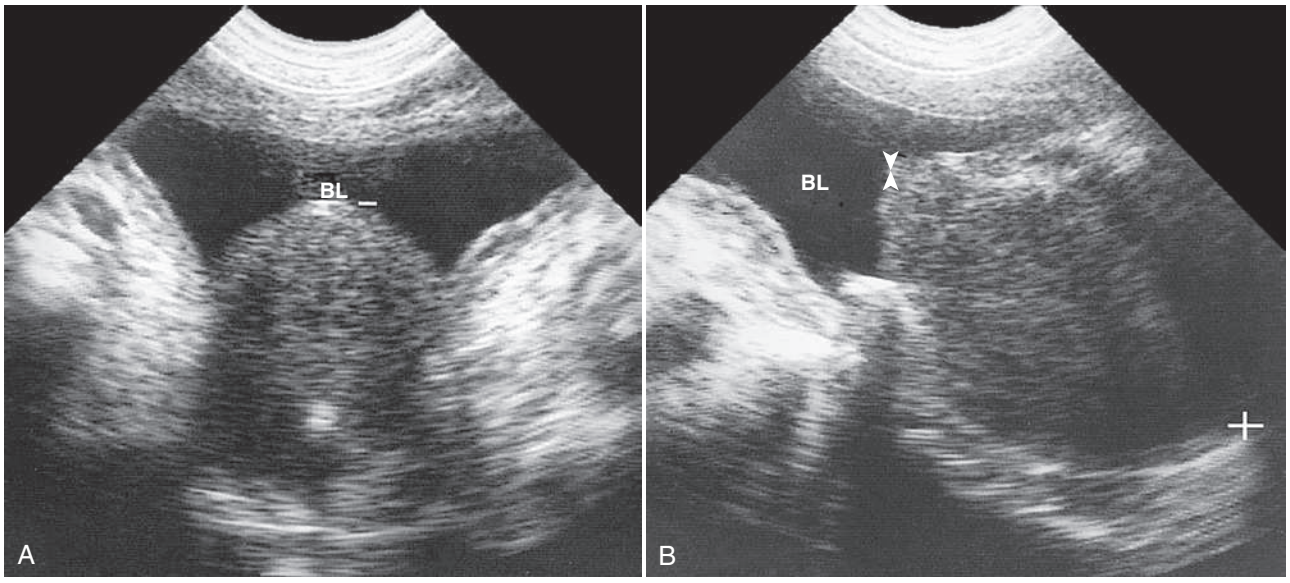

FIG. 54.69 Prostatic Rhabdomyosarcoma With Bladder Invasion in 11-Month-Old Boy With Pelvic Pain. (A) and **(B)** Transverse and sagittal sonograms of the pelvis demonstrate a large, solid mass arising inferior to the bladder neck *(BL)* invading the bladder base.

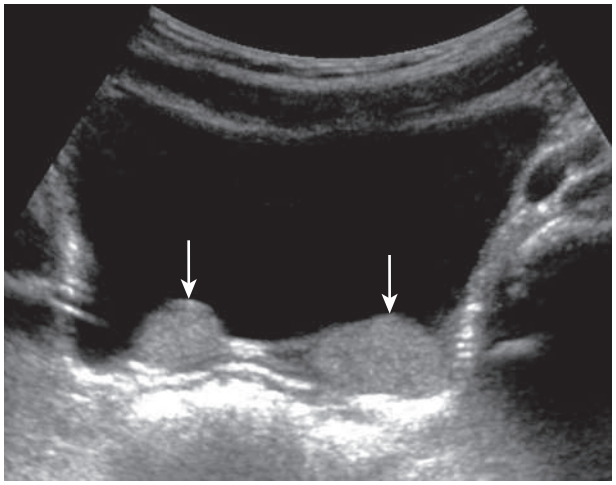

FIG. 54.70 Bilateral Injections of Deflux Into Ureterovesical Junctions. This 2-year-old girl had a history of recurrent urinary tract infection and bilateral vesicoureteral reflux. Note the round, brightly hyperechoic mounds of Deflux *(arrows)* at the trigones bilaterally.

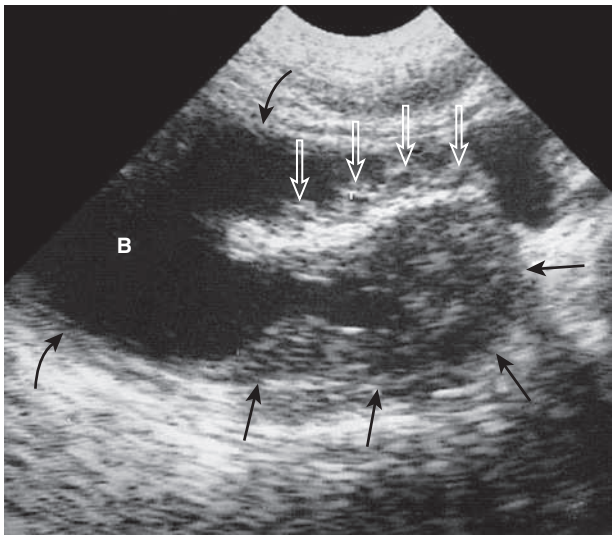

FIG. 54.71 Augmented Bladder. Transverse view of the bladder *(B)* shows the thick wall of the anatomic bladder *(straight black arrows)* and the large augmentation *(curved arrows); open arrows,* haustral markings.

or obstruction, calculi, extravasation, abscess, urinoma, hematoma, and large amounts of residual urine after voiding.[226,227]

PRESACRAL MASSES

The presacral space is a potential space between the perirectal fascia and the fibrous coverings of the anterior sacrum. A lesion in the presacral space can usually be identified on routine sonography through a distended bladder. To confirm the origin of the mass, a water enema can be performed to identify the rectosigmoid colon in relation to the lesion. Additional scans through the buttocks are often helpful to determine the true extent of the tumor.

Presacral Masses in Children

SOLID
Sacrococcygeal teratoma
Neuroblastoma
Rhabdomyosarcoma
Fibroma
Lipoma
Leiomyoma
Lymphoma
Hemangioendothelioma
Sacral bone tumors

CYSTIC
Abscess
Rectal duplication
Hematoma
Lymphocele
Neurenteric cyst
Sacral osteomyelitis
Ulcerative colitis
Anterior meningocele

Sacrococcygeal teratoma is the most common presacral neoplasm in the pediatric age group. About 50% are noted at birth, with a 4:1 female-to-male incidence. Sacrococcygeal teratoma arises from multipotential cells in Hensen nodes that migrate caudally and come to lie within the coccyx. Radiographic evidence of bony abnormalities of the sacrum or coccyx may be present (Fig. 54.72). There is a 75% incidence of associated congenital anomalies, most often involving the musculoskeletal system. Some sacrococcygeal teratomas are familial, with autosomal dominant inheritance. These teratomas have a high frequency of twins.[228]

Sacrococcygeal teratomas can be benign or malignant. Tumors detected before age 2 months are most likely benign. Those detected after 2 months have a 50% to 90% incidence of malignancy. Malignancy is more common in boys and in lesions that are predominantly solid. Cystic lesions are more likely benign. All teratomas have a malignant potential, regardless of their texture, location, or size. Recurrence of a benign teratoma after incomplete surgical removal leads to increased risk of malignant transformation; therefore the coccyx must be removed completely at surgery to prevent recurrence. Sacrococcygeal teratomas can be divided into the following four types, based on their location:

Type I: Predominantly external
Type II: External with a substantial intrapelvic component
Type III: Small external mass with predominant intrapelvic portion
Type IV: Entirely presacral with no external component

Type I lesions are usually benign and appear at birth. Types II, III, and IV have a higher incidence of malignancy, probably because the large intrapelvic component goes unrecognized and

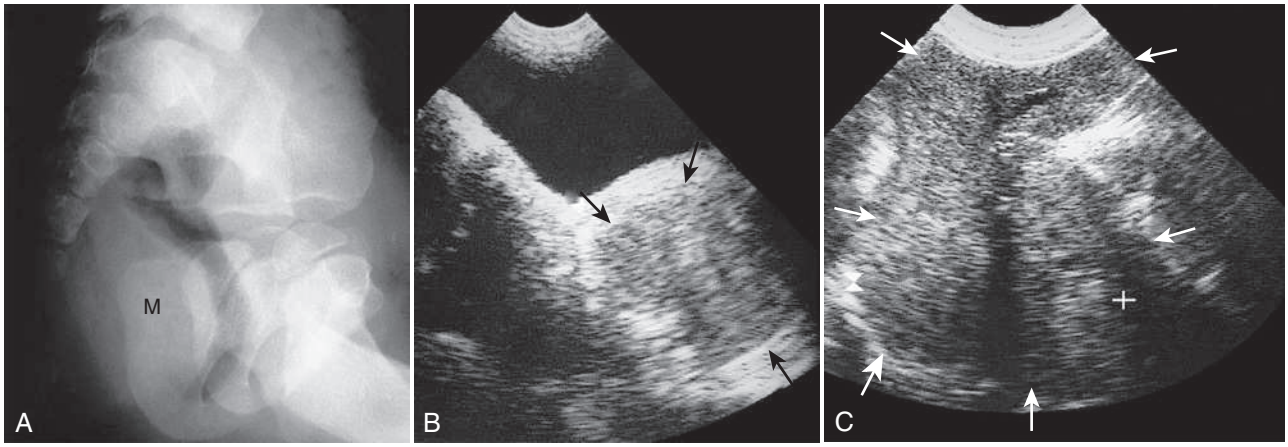

FIG. 54.72 Sacrococcygeal Teratoma in 2-Year-Old Boy With Palpable Mass at Base of Spine. (A) Lateral radiograph of the pelvis shows lack of coccygeal ossification and large, retrorectal, soft tissue mass *(M)* with anterior displacement of the rectum. **(B)** Sagittal ultrasound shows a solid mass *(arrows)* deep in the pelvis posteroinferior to the bladder. **(C)** Transverse ultrasound over the base of the spine posteriorly shows a primarily solid mass *(arrows)* with one small cystic area extending deep into the pelvis.

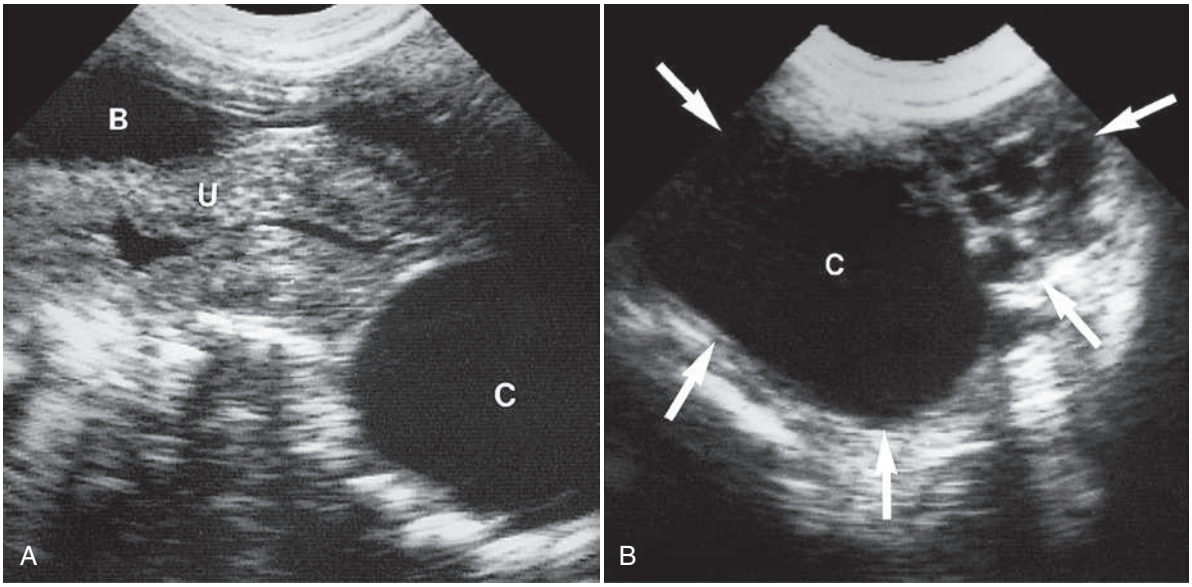

FIG. 54.73 Sacrococcygeal Teratoma in Newborn Girl With Buttock Mass. (A) Sagittal sonogram demonstrates a large, cystic mass *(C),* deep in the pelvis, posteroinferior to the uterus *(U).* The small amount of fluid noted in the endometrial canal is secondary to residual material hormonal stimulation. *B,* Bladder. **(B)** Transverse image over the base of the spine posteriorly demonstrates a complex mass *(arrows)* with a predominantly large cystic *(C)* component.

undetected for longer periods than the large, exophytic masses.[49,228] Malignant teratomas are usually **endodermal sinus tumors.**

There is a wide spectrum of ultrasound appearances of sacrococcygeal teratomas, ranging from purely cystic to mixed or purely solid (Figs. 54.73 and 54.74). Calcifications, seen in one-third of cases, can be amorphous, punctate, or spiculated and suggest the lesion is benign. Fat within the tumor appears as bright areas of heterogeneous echogenicity. Large tumors may displace and compress the bladder anteriorly and superiorly, causing urinary retention and hydronephrosis.

Neuroblastoma and other neurogenic tumors can arise in the presacral space in children. Five percent of neuroblastomas arise in the pelvis. Because of their midline location, they are considered stage III tumors. Pelvic neuroblastoma has a better prognosis than intraabdominal neuroblastoma. The pelvic lesions have a similar sonographic appearance to the adrenal lesions. They are solid, echogenic, heterogeneous masses with a 70% incidence of calcification. Areas of cystic necrosis and hemorrhage are uncommon[229,230] (see Fig. 54.74).

Rhabdomyosarcoma arising from the pelvic musculature can manifest as a solid presacral mass. It is usually an infiltrating tumor with poorly defined margins. Anechoic spaces within a predominantly solid mass suggest areas of necrosis and hemorrhage. Calcification is rare.[229] Ultrasound is an excellent method for identifying and staging rhabdomyosarcoma arising from the genitourinary tract. However, computed tomography (CT) and MRI provide more complete information for those tumors arising from the pelvic side walls. Other predominantly **solid presacral**

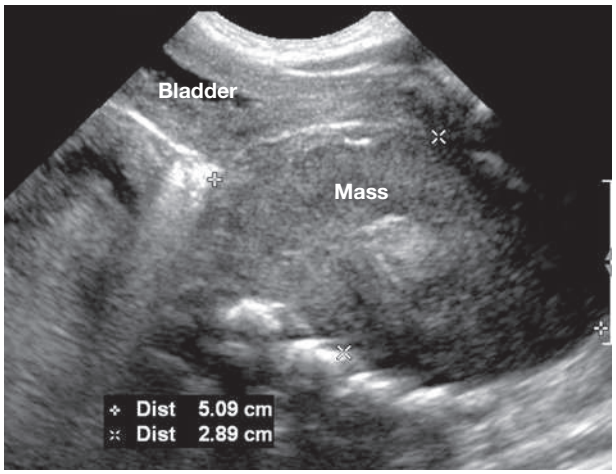

FIG. 54.74 Neuroblastoma. Full-term male baby with a prenatal diagnosis of a large (5 × 3 × 4 cm), solid, deep, pelvic mass that contains a central, nonshadowing calcification. The mass flattens the urinary bladder while displacing it anteriorly.

masses to be considered in the differential diagnosis include fibroma, lipoma, leiomyoma (and their malignant counterparts), lymphoma, hemangioendothelioma, and metastatic disease. **Sacral bone tumors,** such as Ewing sarcoma, osteosarcoma, chondrosarcoma, giant cell tumor, and aneurysmal bone cyst, may also appear as presacral masses. Chordomas of the sacrococcygeal region are rare in children.

Cystic presacral lesions, in addition to sacrococcygeal teratomas, can be detected on sonography. These include abscess, rectal duplication, hematoma, lymphocele, neurenteric cyst, sacral osteomyelitis, and ulcerative colitis. An anterior sacral meningocele also manifests as a cystic presacral mass. It represents herniation of the meninges through an anterior defect in the sacrum. The sacrum usually has a scimitar- or sickle-shaped configuration. A solid mural nodule within the cystic meningocele represents glial or lipomatous tissue.

REFERENCES

1. Stranzinger E, Strouse PJ. Ultrasound of the pediatric female pelvis. Semin Ultrasound CT MR. 2008;29(2):98-113.
2. Garel L, Dubois J, Grignon A, et al. US of the pediatric female pelvis: a clinical perspective. Radiographics. 2001;21(6):1393-1407.
3. Siegel MJ. Female pelvis. In: Siegel MJ, editor. Pediatric sonography. 3rd ed. Philadelphia: Lippincott Williams & Wilkins; 2002. p. 530-577.
4. Siegel MJ. Male genital tract. In: Siegel MJ, editor. Pediatric sonography. 3rd ed. Philadelphia: Lippincott Williams & Wilkins; 2002. p. 579-624.
5. Asavoaie C, Fufezan O, Cosarca M. Ovarian and uterine ultrasonography in pediatric patients. Pictorial essay. Med Ultrason. 2014;16(2):160-167.
6. Paltiel HJ, Phelps A. US of the pediatric female pelvis. Radiology. 2014;270(3):644-657.
7. Teele RL, Share JC. Ultrasonography of the female pelvis in childhood and adolescence. Radiol Clin North Am. 1992;30(4):743-758.
8. Rubin C, Kurtz AB, Goldberg BB. Water enema: a new ultrasound technique in defining pelvic anatomy. J Clin Ultrasound. 1978;6(1):28-33.
9. Bellah RD, Rosenberg HK. Transvaginal ultrasound in a children's hospital: is it worthwhile? Pediatr Radiol. 1991;21(8):570-574.
10. Jequier S, Rousseau O. Sonographic measurements of the normal bladder wall in children. AJR Am J Roentgenol. 1987;149(3):563-566.
11. Zieger B, Sokol B, Rohrschneider WK, et al. Sonomorphology and involution of the normal urachus in asymptomatic newborns. Pediatr Radiol. 1998;28(3):156-161.
12. Marchal GJ, Baert AL, Eeckels R, Proesmans W. Sonographic evaluation of the normal ureteral submucosal tunnel in infancy and childhood. Pediatr Radiol. 1983;13(3):125-129.
13. Comstock CH, Boal DK. Pelvic sonography of the pediatric patient. Semin Ultrasound. 1984;5:54-67.
14. Cohen HL, Susman M, Haller JO, et al. Posterior urethral valve: transperineal US for imaging and diagnosis in male infants. Radiology. 1994;192(1):261-264.
15. Schiller VL, Grant EG. Doppler ultrasonography of the pelvis. Radiol Clin North Am. 1992;30(4):735-742.
16. Rosenberg HK. Sonography of the pediatric urinary tract. In: Bush WH, editor. Urologic imaging and interventional techniques. Baltimore: Urban & Schwarzenberg; 1989. p. 164-179.
17. Kaplan SL, Edgar JC, Ford EG, et al. Size of testes, ovaries, uterus and breast buds by ultrasound in healthy full-term neonates ages 0–3 days. Pediatr Rad. 2016;46:1837-1847.
18. Cohen HL, Shapiro MA, Mandel FS, Shapiro ML. Normal ovaries in neonates and infants: a sonographic study of 77 patients 1 day to 24 months old. AJR Am J Roentgenol. 1993;160(3):583-586.
19. Cohen HL, Tice HM, Mandel FS. Ovarian volumes measured by US: bigger than we think. Radiology. 1990;177(1):189-192.
20. Orbak Z, Kantarci M, Yildirim ZK, et al. Ovarian volume and uterine length in neonatal girls. J Pediatr Endocrinol Metab. 2007;20(3):397-403.
21. Quillin SP, Siegel MJ. Transabdominal color Doppler ultrasonography of the painful adolescent ovary. J Ultrasound Med. 1994;13(7):549-555.
22. de Silva KS, Kanumakala S, Grover SR, et al. Ovarian lesions in children and adolescents—an 11-year review. J Pediatr Endocrinol Metab. 2004;17(7):951-957.
23. Nussbaum AR, Sanders RC, Benator RM, et al. Spontaneous resolution of neonatal ovarian cysts. AJR Am J Roentgenol. 1987;148(1):175-176.
24. Kuo HC, Lee HC, Shin CH, et al. Clinical spectrum of alimentary tract duplication in children. Acta Paediatr Taiwan. 2004;45(2):85-88.
25. Riddlesberger Jr MM, Kuhn JP, Munschauer RW. The association of juvenile hypothyroidism and cystic ovaries. Radiology. 1981;139(1):77-80.
26. Rosado Jr WM, Trambert MA, Gosink BB, Pretorius DH. Adnexal torsion: diagnosis by using Doppler sonography. AJR Am J Roentgenol. 1992;159(6):1251-1253.
27. Lee EJ, Kwon HC, Joo HJ, et al. Diagnosis of ovarian torsion with color Doppler sonography: depiction of twisted vascular pedicle. J Ultrasound Med. 1998;17(2):83-89.
28. Hurh PJ, Meyer JS, Shaaban A. Ultrasound of a torsed ovary: characteristic gray-scale appearance despite normal arterial and venous flow on Doppler. Pediatr Radiol. 2002;32(8):586-588.
29. Graif M, Itzchak Y. Sonographic evaluation of ovarian torsion in childhood and adolescence. AJR Am J Roentgenol. 1988;150(3):647-649.
30. Cass DL. Ovarian torsion. Semin Pediatr Surg. 2005;14(2):86-92.
31. Servaes S, Zurakowski D, Laufer MR, et al. Sonographic findings of ovarian torsion in children. Pediatr Radiol. 2007;37(5):446-451.
32. Harmon JC, Binkovitz LA, Binkovitz LE. Isolated fallopian tube torsion: sonographic and CT features. Pediatr Radiol. 2008;38(2):175-179.
33. Baltarowich OH, Kurtz AB, Pasto ME, et al. The spectrum of sonographic findings in hemorrhagic ovarian cysts. AJR Am J Roentgenol. 1987;148(5):901-905.
34. Hann LE, Hall DA, McArdle CR, Seibel M. Polycystic ovarian disease: sonographic spectrum. Radiology. 1984;150(2):531-534.
35. Rotterdam ESHRE/ASRM-Sponsored PCOS Consensus Workshop Group. Revised 2003 consensus on diagnostic criteria and long-term health risks related to polycystic ovary syndrome. Fertil Steril. 2004;81(1):19-25.
36. Agapova SE, Cameo T, Sopher AB, Oberfield SE. Diagnosis and challenges of polycystic ovary syndrome in adolescence. Semin Reprod Med. 2014;32(3):194-201.
37. Lee TT, Rausch ME. Polycystic ovarian syndrome: role of imaging in diagnosis. Radiographics. 2012;32(6):1643-1657.

38. Siklar Z, Berberoglu M, Camtosun E, Kocaay P. Diagnostic characteristics and metabolic risk factors of cases with polycystic ovary syndrome during adolescence. J Pediatr Adolesc Gynecol. 2015;28(2):78-83.
39. Youngster M, Ward VL, Blood EA, et al. Utility of ultrasound in the diagnosis of polycystic ovary syndrome in adolescents. Fertil Steril. 2014;102(5): 1432-1438.
40. Powers SE, Uliassi NW, Sullivan SD, et al. Trends in standard workup performed by pediatric subspecialists for the diagnosis of adolescent polycystic ovary syndrome. J Pediatr Adolesc Gynecol. 2015;28(1): 43-46.
41. Jeffrey Chang R, Coffler MS. Polycystic ovary syndrome: early detection in the adolescent. Clin Obstet Gynecol. 2007;50(1):178-187.
42. Lee AR, Kim KH, Lee BH, Chin SY. Massive edema of the ovary: imaging findings. AJR Am J Roentgenol. 1993;161(2):343-344.
43. Roth LM, Deaton RL, Sternberg WH. Massive ovarian edema. A clinicopathologic study of five cases including ultrastructural observations and review of the literature. Am J Surg Pathol. 1979;3(1):11-21.
44. Sty JR, Wells RG. Other abdominal and pelvic masses in children. Semin Roentgenol. 1988;23(3):216-231.
45. Guzel AB, Gulec UK, Gumurdulu D, et al. Unusual adnexal masses in adolescents and young women: massive ovarian oedema. J Obstet Gynaecol. 2013;33(6):635-636.
46. Sisler CL, Siegel MJ. Ovarian teratomas: a comparison of the sonographic appearance in prepubertal and postpubertal girls. AJR Am J Roentgenol. 1990;154(1):139-141.
47. Heo SH, Kim JW, Shin SS, et al. Review of ovarian tumors in children and adolescents: radiologic-pathologic correlation. Radiographics. 2014;34(7): 2039-2055.
48. Kelleher CM, Goldstein AM. Adnexal masses in children and adolescents. Clin Obstet Gynecol. 2015;58(1):76-92.
49. Shah RU, Lawrence C, Fickenscher KA, et al. Imaging of pediatric pelvic neoplasms. Radiol Clin North Am. 2011;49(4):729-748, vi.
50. Patel MD, Feldstein VA, Lipson SD, et al. Cystic teratomas of the ovary: diagnostic value of sonography. AJR Am J Roentgenol. 1998;171(4): 1061-1065.
51. Stankovic ZB, Djukic MK, Sedlecki K, et al. Rapidly growing bilateral ovarian cystadenoma in a 6-year-old girl: case report and literature review. J Pediatr Adolesc Gynecol. 2006;19(1):35-38.
52. Bickers GH, Siebert JJ, Anderson JC, et al. Sonography of ovarian involvement in childhood acute lymphocytic leukemia. AJR Am J Roentgenol. 1981;137(2): 399-401.
53. Fleischer AC, Rodgers WH, Kepple DM, et al. Color Doppler sonography of benign and malignant ovarian masses. Radiographics. 1992;12(5): 879-885.
54. Carter J, Saltzman A, Hartenbach E, et al. Flow characteristics in benign and malignant gynecologic tumors using transvaginal color flow Doppler. Obstet Gynecol. 1994;83(1):125-130.
55. Rosenberg HK, Sherman NH, Tarry WF, et al. Mayer-Rokitansky-Kuster-Hauser syndrome: US aid to diagnosis. Radiology. 1986;161(3):815-819.
56. Blask AR, Sanders RC, Gearhart JP. Obstructed uterovaginal anomalies: demonstration with sonography. Part I. Neonates and infants. Radiology. 1991;179(1):79-83.
57. Blask AR, Sanders RC, Rock JA. Obstructed uterovaginal anomalies: demonstration with sonography. Part II. Teenagers. Radiology. 1991;179(1): 84-88.
58. Wilson SR, Beecham CT, Carrington ER, editors. Obstetrics and gynecology. 8th ed. St Louis: Mosby; 1987.
59. Brody JM, Koelliker SL, Frishman GN. Unicornuate uterus: imaging appearance, associated anomalies, and clinical implications. AJR Am J Roentgenol. 1998;171(5):1341-1347.
60. Scanlan KA, Pozniak MA, Fagerholm M, Shapiro S. Value of transperineal sonography in the assessment of vaginal atresia. AJR Am J Roentgenol. 1990;154(3):545-548.
61. Messina M, Severi FM, Bocchi C, et al. Voluminous perinatal pelvic mass: a case of congenital hydrometrocolpos. J Matern Fetal Neonatal Med. 2004;15(2):135-137.
62. Fisher MR, Kricun ME, editors. Imaging of the pelvis. Gaithersburg, Md: Aspen; 1989.
63. Meglin AJ, Balotin RJ, Jelinek JS, et al. Cloacal exstrophy: radiologic findings in 13 patients. AJR Am J Roentgenol. 1990;155(6):1267-1272.
64. Capito C, Echaieb A, Lortat-Jacob S, et al. Pitfalls in the diagnosis and management of obstructive uterovaginal duplication: a series of 32 cases. Pediatrics. 2008;122(4):e891-e897.
65. Mirkovic L, Mirkovic D, Boskovic V, Markovic Z. Uterus didelphys with obstructed hemivagina and ipsilateral renal agenesis. Acta Chir Iugosl. 2007;54(3):137-139.
66. Hu MX, Methratta S. An unusual case of neonatal peritoneal calcifications associated with hydrometrocolpos. Pediatr Radiol. 2001;31(10):742-744.
67. Andrassy RJ, Wiener ES, Raney RB, et al. Progress in the surgical management of vaginal rhabdomyosarcoma: a 25-year review from the Intergroup Rhabdomyosarcoma Study Group. J Pediatr Surg. 1999;34(5):731-734.
68. Lin EP, Bhatt S, Dogra VS. Diagnostic clues to ectopic pregnancy. Radiographics. 2008;28(6):1661-1671.
69. Pellerito JS, Taylor KJ, Quedens-Case C, et al. Ectopic pregnancy: evaluation with endovaginal color flow imaging. Radiology. 1992;183(2):407-411.
70. Zinn HL, Cohen HL, Zinn DL. Ultrasonographic diagnosis of ectopic pregnancy: importance of transabdominal imaging. J Ultrasound Med. 1997;16(9):603-607.
71. Lipscomb GH, Stovall TG, Ling FW. Nonsurgical treatment of ectopic pregnancy. N Engl J Med. 2000;343(18):1325-1329.
72. Bulas DI, Ahlstrom PA, Sivit CJ, et al. Pelvic inflammatory disease in the adolescent: comparison of transabdominal and transvaginal sonographic evaluation. Radiology. 1992;183(2):435-439.
73. Wherry KL, Dubinsky TJ, Waitches GM, et al. Low-resistance endometrial arterial flow in the exclusion of ectopic pregnancy revisited. J Ultrasound Med. 2001;20(4):335-342.
74. Schoenfeld A, Fisch B, Cohen M, et al. Ultrasound findings in perihepatitis associated with pelvic inflammatory disease. J Clin Ultrasound. 1992;20(5): 339-342.
75. Dinerman LM, Elfenbein DS, Cumming WA. Clinical Fitz-Hugh-Curtis syndrome in an adolescent. Ultrasonographic findings. Clin Pediatr (Phila). 1990;29(9):532-535.
76. Caspi B, Zalel Y, Katz Z, et al. The role of sonography in the detection of vaginal foreign bodies in young girls: the bladder indentation sign. Pediatr Radiol. 1995;25(Suppl. 1):S60-S61.
77. Deligeoroglou E, Deliveliotou A, Laggari V, et al. Vaginal foreign body in childhood: a multidisciplinary approach. J Paediatr Child Health. 2006;42(10): 649-651.
78. Goske MJ, Emmens RW, Rabinowitz R. Inguinal ovaries in children demonstrated by high resolution real-time ultrasound. Radiology. 1984;151(3):635-636.
79. Cleemann L, Holm K, Fallentin E, et al. Uterus and ovaries in girls and young women with Turner syndrome evaluated by ultrasound and magnetic resonance imaging. Clin Endocrinol (Oxf). 2011;74(6):756-761.
80. Eksioglu AS, Yilmaz S, Cetinkaya S, et al. Value of pelvic sonography in the diagnosis of various forms of precocious puberty in girls. J Clin Ultrasound. 2013;41(2):84-93.
81. Yu J, Shin HY, Lee SH, et al. Usefulness of pelvic ultrasonography for the diagnosis of central precocious puberty in girls. Korean J Pediatr. 2015;58(8): 294-300.
82. Ambrosino MM, Hernanz-Schulman M, Genieser NB, et al. Monitoring of girls undergoing medical therapy for isosexual precocious puberty. J Ultrasound Med. 1994;13(7):501-508.
83. Jensen AM, Brocks V, Holm K, et al. Central precocious puberty in girls: internal genitalia before, during, and after treatment with long-acting gonadotropin-releasing hormone analogues. J Pediatr. 1998;132(1): 105-108.
84. Mong A, Bellah R. Imaging the pediatric prostate. Radiol Clin North Am. 2006;44(5):749-756, ix.
85. Shapiro E, Hartanto V, Perlman EJ, et al. Morphometric analysis of pediatric and nonhyperplastic prostate glands: evidence that BPH is not a unique stromal process. Prostate. 1997;33(3):177-182.
86. Ingram S, Hollman AS, Azmy AF. Ultrasound evaluation of the paediatric prostate. Br J Urol. 1994;74(5):601-603.
87. Daniel Jr WA, Feinstein RA, Howard-Peebles P, Baxley WD. Testicular volumes of adolescents. J Pediatr. 1982;101(6):1010-1012.

88. Atkinson Jr GO, Patrick LE, Ball Jr TI, et al. The normal and abnormal scrotum in children: evaluation with color Doppler sonography. AJR Am J Roentgenol. 1992;158(3):613-617.
89. Patriquin HB, Yazbeck S, Trinh B, et al. Testicular torsion in infants and children: diagnosis with Doppler sonography. Radiology. 1993;188(3): 781-785.
90. Fakhry J, Khoury A, Barakat K. The hypoechoic band: a normal finding on testicular sonography. AJR Am J Roentgenol. 1989;153(2):321-323.
91. Luker GD, Siegel MJ. Scrotal US in pediatric patients: comparison of power and standard color Doppler US. Radiology. 1996;198(2):381-385.
92. Paltiel HJ, Rupich RC, Babcock DS. Maturational changes in arterial impedance of the normal testis in boys: Doppler sonographic study. AJR Am J Roentgenol. 1994;163(5):1189-1193.
93. Barth RA, Shortliffe LD. Normal pediatric testis: comparison of power Doppler and color Doppler US in the detection of blood flow. Radiology. 1997;204(2):389-393.
94. Sherman NH, Boyle GK, Rosenberg HK. Sonography in the neonate. Ultrasound Q. 1988;6:91-150.
95. Christensen JD, Dogra VS. The undescended testis. Semin Ultrasound CT MR. 2007;28(4):307-316.
96. Maghnie M, Vanzulli A, Paesano P, et al. The accuracy of magnetic resonance imaging and ultrasonography compared with surgical findings in the localization of the undescended testis. Arch Pediatr Adolesc Med. 1994; 148(7):699-703.
97. Kogan S, Kadziselimovic F, Howards SS, et al. Pediatric andrology. In: Gillenwater JY, Grayback JT, Howards SS, et al., editors. Adult and pediatric urology. 3rd ed. St Louis: Mosby; 1996. p. 2623-2674.
98. Gong M, Geary ES, Shortliffe LM. Testicular torsion with contralateral vanishing testis. Urology. 1996;48(2):306307.
99. Finkelstein MS, Rosenberg HK, Snyder 3rd HM, Duckett JW. Ultrasound evaluation of scrotum in pediatrics. Urology. 1986;27(1):1-9.
100. Eberenz W, Rosenberg HK, Moshang T, et al. True hermaphroditism: sonographic demonstration of ovotestes. Radiology. 1991;179(2): 429-431.
101. Eberli D, Gretener H, Dommann-Scherrer C, et al. Cystic dysplasia of the testis: a very rare paediatric tumor of the testis. Urol Int. 2002;69(1):1-6.
102. Piotto L, LeQuesne GW, Gent R, et al. Congenital cystic dysplasia of the rete testis. Pediatr Radiol. 2001;31(10):724-726.
103. Hamm B, Fobbe F, Loy V. Testicular cysts: differentiation with US and clinical findings. Radiology. 1988;168(1):19-23.
104. Weiss AJ, Kellman GM, Middleton WD, Kirkemo A. Intratesticular varicocele: sonographic findings in two patients. AJR Am J Roentgenol. 1992;158(5): 1061-1063.
105. Pimpalwar A, Chowdhary S, Huskisson J, Corkery JJ. Cysts of the ejaculatory system—a treatable cause of recurrent epididymo-orchitis in children. Eur J Pediatr Surg. 2002;12(4):281-285.
106. Galejs LE, Kass EJ. Color Doppler ultrasound evaluation of the acute scrotum. Tech Urol. 1998;4(4):182-184.
107. Makela E, Lahdes-Vasama T, Rajakorpi H, Wikstrom S. A 19-year review of paediatric patients with acute scrotum. Scand J Surg. 2007;96(1): 62-66.
108. Friedman SC, Sheynkin YR. Acute scrotal symptoms due to perforated appendix in children: case report and review of literature. Pediatr Emerg Care. 1995;11(3):181-182.
109. Yang WT, Ku KW, Metreweli C. Case report: neonatal adrenal haemorrhage presenting as an acute right scrotal swelling (haematoma)—value of ultrasound. Clin Radiol. 1995;50(2):127-129.
110. Schroder CH, Rieu P, de Jong MC. Peritoneal laceration: a rare cause of scrotal edema in a 2-year-old boy. Adv Perit Dial. 1993;9:329-330.
111. Simoneaux SF, Ball TI, Atkinson Jr GO. Scrotal swelling: unusual first presentation of Crohn's disease. Pediatr Radiol. 1995;25(5):375-376.
112. Older RA, Watson LR. Ultrasound diagnosis of testicular torsion: beware the swollen epididymis. J Urol. 1997;157(4):1369-1370.
113. Kilkenny TE. Acute scrotum in an infant: post-herniorrhaphy complication. Sonographic evaluation. Pediatr Radiol. 1993;23(6):481-482.
114. Kadish HA, Bolte RG. A retrospective review of pediatric patients with epididymitis, testicular torsion, and torsion of testicular appendages. Pediatrics. 1998;102(1 Pt 1):73-76.
115. Gronski M, Hollman AS. The acute paediatric scrotum: the role of colour Doppler ultrasound. Eur J Radiol. 1998;26(2):183-193.
116. Hollman AS, Ingram S, Carachi R, Davis C. Colour Doppler imaging of the acute paediatric scrotum. Pediatr Radiol. 1993;23(2):83-87.
117. Bhatt S, Dogra VS. Role of US in testicular and scrotal trauma. Radiographics. 2008;28(6):1617-1629.
118. Brown SM, Casillas VJ, Montalvo BM, Albores-Saavedra J. Intrauterine spermatic cord torsion in the newborn: sonographic and pathologic correlation. Radiology. 1990;177(3):755-757.
119. Groisman GM, Nassrallah M, Bar-Maor JA. Bilateral intra-uterine testicular torsion in a newborn. Br J Urol. 1996;78(5):800-801.
120. Zinn HL, Cohen HL, Horowitz M. Testicular torsion in neonates: importance of power Doppler imaging. J Ultrasound Med. 1998;17(6):385-388.
121. Koff SA. Does compensatory testicular enlargement predict monorchism? J Urol. 1991;146(2 Pt 2):632-633.
122. Klin B, Lotan G, Efrati Y, et al. Acute idiopathic scrotal edema in children—revisited. J Pediatr Surg. 2002;37(8):1200-1202.
123. Leape LL. Torsion of the testis. In: Welch KJ, Randolph JG, Ravitch MM, editors. Pediatric surgery. St. Louis: Mosby; 1986.
124. Paltiel HJ, Connolly LP, Atala A, et al. Acute scrotal symptoms in boys with an indeterminate clinical presentation: comparison of color Doppler sonography and scintigraphy. Radiology. 1998;207(1):223-231.
125. Chen DC, Holder LE, Kaplan GN. Correlation of radionuclide imaging and diagnostic ultrasound in scrotal diseases. J Nucl Med. 1986;27(11): 1774-1781.
126. Prando D. Torsion of the spermatic cord: the main gray-scale and Doppler sonographic signs. Abdom Imaging. 2009;34(5):648-661.
127. Coley BD, Frush DP, Babcock DS, et al. Acute testicular torsion: comparison of unenhanced and contrast-enhanced power Doppler US, color Doppler US, and radionuclide imaging. Radiology. 1996;199(2):441-446.
128. Siegel MJ. The acute scrotum. Radiol Clin North Am. 1997;35(4): 959-976.
129. Deurdulian C, Mittelstaedt CA, Chong WK, Fielding JR. US of acute scrotal trauma: optimal technique, imaging findings, and management. Radiographics. 2007;27(2):357-369.
130. Haynes BE, Haynes VE. Manipulative detorsion: beware the twist that does not turn. J Urol. 1987;137(1):118-119.
131. Erbay N, Brown SL, Spencer RP. Hydrocele mimicking testicular torsion on radionuclide and ultrasound studies. Clin Nucl Med. 1997;22(8): 570-571.
132. Nye PJ, Prati Jr RC. Idiopathic hydrocele and absent testicular diastolic flow. J Clin Ultrasound. 1997;25(1):43-46.
133. Nussbaum Blask AR, Rushton HG. Sonographic appearance of the epididymis in pediatric testicular torsion. AJR Am J Roentgenol. 2006;187(6): 1627-1635.
134. Horstman WG, Middleton WD, Melson GL. Scrotal inflammatory disease: color Doppler US findings. Radiology. 1991;179(1):55-59.
135. Jee WH, Choe BY, Byun JY, et al. Resistive index of the intrascrotal artery in scrotal inflammatory disease. Acta Radiol. 1997;38(6):1026-1030.
136. Lee JC, Bhatt S, Dogra VS. Imaging of the epididymis. Ultrasound Q. 2008;24(1):3-16.
137. Karmazyn B, Kaefer M, Kauffman S, Jennings SG. Ultrasonography and clinical findings in children with epididymitis, with and without associated lower urinary tract abnormalities. Pediatr Radiol. 2009;39(10): 1054-1058.
138. Bukowski TP, Lewis AG, Reeves D, et al. Epididymitis in older boys: dysfunctional voiding as an etiology. J Urol. 1995;154(2 Pt 2):762-765.
139. Cohen HL, Shapiro MA, Haller JO, Glassberg K. Torsion of the testicular appendage. Sonographic diagnosis. J Ultrasound Med. 1992;11(3):81-83.
140. Baldisserotto M, de Souza JC, Pertence AP, Dora MD. Color Doppler sonography of normal and torsed testicular appendages in children. AJR Am J Roentgenol. 2005;184(4):1287-1292.
141. Singh AK, Kao SC. Torsion of testicular appendage. Pediatr Radiol. 2010;40(3):373.
142. Strauss S, Faingold R, Manor H. Torsion of the testicular appendages: sonographic appearance. J Ultrasound Med. 1997;16(3):189-192.
143. Hesser U, Rosenborg M, Gierup J, et al. Gray-scale sonography in torsion of the testicular appendages. Pediatr Radiol. 1993;23(7):529-532.

144. Monga M, Scarpero HM, Ortenberg J. Metachronous bilateral torsion of the testicular appendices. Int J Urol. 1999;6(11):589-591.
145. Black JA, Patel A. Sonography of the normal extratesticular space. AJR Am J Roentgenol. 1996;167(2):503-506.
146. Jeffrey RB, Laing FC, Hricak H, McAninch JW. Sonography of testicular trauma. AJR Am J Roentgenol. 1983;141(5):993-995.
147. Corrales JG, Corbel L, Cipolla B, et al. Accuracy of ultrasound diagnosis after blunt testicular trauma. J Urol. 1993;150(6):1834-1836.
148. Lee A, Park SJ, Lee HK, et al. Acute idiopathic scrotal edema: ultrasonographic findings at an emergency unit. Eur Radiol. 2009;19(8):2075-2080.
149. Herman TE, Shackelford GD, McAlister WH. Acute idiopathic scrotal edema: role of scrotal sonography. J Ultrasound Med. 1994;13(1):53-55.
150. Ben-Sira L, Laor T. Severe scrotal pain in boys with Henoch-Schönlein purpura: incidence and sonography. Pediatr Radiol. 2000;30(2):125-128.
151. Sudakoff GS, Burke M, Rifkin MD. Ultrasonographic and color Doppler imaging of hemorrhagic epididymitis in Henoch-Schönlein purpura. J Ultrasound Med. 1992;11(11):619-621.
152. Grainger AJ, Hide IG, Elliott ST. The ultrasound appearances of scrotal oedema. Eur J Ultrasound. 1998;8(1):33-37.
153. Munden MM, Trautwein LM. Scrotal pathology in pediatrics with sonographic imaging. Curr Probl Diagn Radiol. 2000;29(6):185-205.
154. Begley MG, Shawker TH, Robertson CN, et al. Fournier gangrene: diagnosis with scrotal US. Radiology. 1988;169(2):387-389.
155. Kocakoc E, Bhatt S, Dogra V. Ultrasound evaluation of testicular neoplasms. Ultrasound Clin. 2007;2:27-44.
156. Castleberry RP, Cushing B, Perlman E, et al., editors. Germ cell tumors. 3rd ed. Philadelphia: Lippincott-Raven; 1997.
157. Skoog SJ. Benign and malignant pediatric scrotal masses. Pediatr Clin North Am. 1997;44(5):1229-1250.
158. Geraghty MJ, Lee Jr FT, Bernsten SA, et al. Sonography of testicular tumors and tumor-like conditions: a radiologic-pathologic correlation. Crit Rev Diagn Imaging. 1998;39(1):1-63.
159. Liu P, Phillips MJ, Edwards VD, et al. Sonographic findings of testicular teratoma with pathologic correlation. Pediatr Radiol. 1992;22(2):99-101.
160. Worthy L, Miller EI, Chinn DH. Evaluation of extratesticular findings in scrotal neoplasms. J Ultrasound Med. 1986;5(5):261-263.
161. Horowitz MB, Abiri MM. US case of the day. Benign cystic teratoma and testicular microlithiasis. Radiographics. 1997;17(3):793-796.
162. Horstman WG, Melson GL, Middleton WD, Andriole GL. Testicular tumors: findings with color Doppler US. Radiology. 1992;185(3):733-737.
163. Castleberry RP, Kelly DR, Joseph DB, et al., editors. Gonadal and extragonadal germ cell tumors. 4th ed. Chicago: Mosby–Year Book; 1991.
164. Luisiri A, Vogler C, Steinhardt G, Silberstein M. Neonatal cystic testicular gonadoblastoma. Sonographic and pathologic findings. J Ultrasound Med. 1991;10(1):59-61.
165. Hertzberg BS, Mahony BS, Bowie JD, Anderson EE. Sonography of an intratesticular lipoma. J Ultrasound Med. 1985;4(11):619-621.
166. Seidenwurm D, Smathers RL, Kan P, Hoffman A. Intratesticular adrenal rests diagnosed by ultrasound. Radiology. 1985;155(2):479-481.
167. Moghe PK, Brady AP. Ultrasound of testicular epidermoid cysts. Br J Radiol. 1999;72(862):942-945.
168. Avila NA, Premkumar A, Merke DP. Testicular adrenal rest tissue in congenital adrenal hyperplasia: comparison of MR imaging and sonographic findings. AJR Am J Roentgenol. 1999;172(4):1003-1006.
169. Avila NA, Shawker TS, Jones JV, et al. Testicular adrenal rest tissue in congenital adrenal hyperplasia: serial sonographic and clinical findings. AJR Am J Roentgenol. 1999;172(5):1235-1238.
170. Walker BR, Skoog SJ, Winslow BH, et al. Testis sparing surgery for steroid unresponsive testicular tumors of the adrenogenital syndrome. J Urol. 1997;157(4):1460-1463.
171. Mazzu D, Jeffrey Jr RB, Ralls PW. Lymphoma and leukemia involving the testicles: findings on gray-scale and color Doppler sonography. AJR Am J Roentgenol. 1995;164(3):645-647.
172. Patriquin HB, editor. Leukemic infiltration of the testis. Reston, Va: American College of Radiology; 1993.
173. Luker GD, Siegel MJ. Pediatric testicular tumors: evaluation with gray-scale and color Doppler US. Radiology. 1994;191(2):561-564.
174. Casola G, Scheible W, Leopold GR. Neuroblastoma metastatic to the testis: ultrasonographic screening as an aid to clinical staging. Radiology. 1984;151(2):475-476.
175. Koseoglu V, Akata D, Kutluk T, et al. Neuroblastoma with spermatic cord metastasis in a child: sonographic findings. J Clin Ultrasound. 1999;27(5):287-289.
176. McEniff N, Doherty F, Katz J, et al. Yolk sac tumor of the testis discovered on a routine annual sonogram in a boy with testicular microlithiasis. AJR Am J Roentgenol. 1995;164(4):971-972.
177. Valla JS. Testis-sparing surgery for benign testicular tumors in children. J Urol. 2001;165(6 Pt 2):2280-2283.
178. Garcia CJ, Zuniga S, Rosenberg H, et al. Simple intratesticular cysts in children: preoperative sonographic diagnosis and histological correlation. Pediatr Radiol. 1999;29(11):851-855.
179. Altadonna V, Snyder 3rd HM, Rosenberg HK, Duckett JW. Simple cysts of the testis in children: preoperative diagnosis by ultrasound and excision with testicular preservation. J Urol. 1988;140(6):1505-1507.
180. Holloway BJ, Belcher HE, Letourneau JG, Kunberger LE. Scrotal sonography: a valuable tool in the evaluation of complications following inguinal hernia repair. J Clin Ultrasound. 1998;26(7):341-344.
181. Dierks PR, Moore PT. Scrotal lymphocele: a complication of renal transplant surgery. J Ultrasound Med. 1985;4(2):91-92.
182. Chung SE, Frush DP, Fordham LA. Sonographic appearances of extratesticular fluid and fluid-containing scrotal masses in infants and children: clues to diagnosis. AJR Am J Roentgenol. 1999;173(3):741-745.
183. Miele V, Galluzzo M, Patti G, et al. Scrotal hematoma due to neonatal adrenal hemorrhage: the value of ultrasonography in avoiding unnecessary surgery. Pediatr Radiol. 1997;27(8):672-674.
184. Aso C, Enriquez G, Fite M, et al. Gray-scale and color Doppler sonography of scrotal disorders in children: an update. Radiographics. 2005;25(5):1197-1214.
185. Niedzielski J, Paduch D, Raczynski P. Assessment of adolescent varicocele. Pediatr Surg Int. 1997;12(5-6):410-413.
186. Wood A, Dewbury KC. Case report: paratesticular rhabdomyosarcoma—colour Doppler appearances. Clin Radiol. 1995;50(2):130-131.
187. Frates MC, Benson CB, DiSalvo DN, et al. Solid extratesticular masses evaluated with sonography: pathologic correlation. Radiology. 1997;204(1):43-46.
188. Zwanger-Mendelsohn S, Shreck EH, Doshi V. Burkitt lymphoma involving the epididymis and spermatic cord: sonographic and CT findings. AJR Am J Roentgenol. 1989;153(1):85-86.
189. Akbar SA, Sayyed TA, Jafri SZ, et al. Multimodality imaging of paratesticular neoplasms and their rare mimics. Radiographics. 2003;23(6):1461-1476.
190. Choyke PL, Glenn GM, Wagner JP, et al. Epididymal cystadenomas in von Hippel–Lindau disease. Urology. 1997;49(6):926-931.
191. Alaminos-Mingorance M, Sanchez-Lopez-Tello C, Castejon-Casado J, et al. Scrotal lymphangioma in children. Urol Int. 1998;61(3):181-182.
192. Cirillo Jr RL, Coley BD, Binkovitz LA, Jayanthi RV. Sonographic findings in splenogonadal fusion. Pediatr Radiol. 1999;29(1):73-75.
193. Mene M, Rosenberg HK, Ginsberg PC. Meconium periorchitis presenting as scrotal nodules in a five year old boy. J Ultrasound Med. 1994;13(6):491-494.
194. Sung EK, Setty BN, Castro-Aragon I. Sonography of the pediatric scrotum: emphasis on the Ts—torsion, trauma, and tumors. AJR Am J Roentgenol. 2012;198(5):996-1003.
195. Chiang LW, Yap TL, Asiri MM, et al. Implications of incidental finding of testicular microlithiasis in paediatric patients. J Pediatr Urol. 2012;8(2):162-165.
196. Nussbaum AR, Dorst JP, Jeffs RD, et al. Ectopic ureter and ureterocele: their varied sonographic manifestations. Radiology. 1986;159(1):227-235.
197. Giel DW, Noe HN, Williams MA. Ultrasound screening of asymptomatic siblings of children with vesicoureteral reflux: a long-term followup study. J Urol. 2005;174(4 Pt 2):1602-1604.
198. Macpherson RI, Leithiser RE, Gordon L, Turner WR. Posterior urethral valves: an update and review. Radiographics. 1986;6(5):753-791.
199. Hulbert WC, Rosenberg HK, Cartwright PC, et al. The predictive value of ultrasonography in evaluation of infants with posterior urethral valves. J Urol. 1992;148(1):122-124.

200. Garris J, Kangarloo H, Sarti D, et al. The ultrasound spectrum of prune-belly syndrome. J Clin Ultrasound. 1980;8(2):117-120.
201. Caro PA, Rosenberg HK, Snyder 3rd HM. Congenital urethral polyp. AJR Am J Roentgenol. 1986;147(5):1041-1042.
202. Kessler A, Rosenberg HK, Smoyer WE, Blyth B. Urethral stones: US for identification in boys with hematuria and dysuria. Radiology. 1992;185(3): 767-768.
203. Shukla AR, Bellah RA, Canning DA, et al. Giant bladder diverticula causing bladder outlet obstruction in children. J Urol. 2004;172(5 Pt 1): 1977-1979.
204. Keller MS, Weiss RM, Rosenfield NS. Sonographic evaluation of ureterectasis in children: the significance of peristalsis. J Urol. 1993;149(3):553-555.
205. Marshall JL, Johnson ND, De Campo MP. Vesicoureteric reflux in children: prediction with color Doppler imaging. Work in progress. Radiology. 1990;175(2):355-358.
206. Jequier S, Paltiel H, Lafortune M. Ureterovesical jets in infants and children: duplex and color Doppler US studies. Radiology. 1990;175(2):349-353.
207. Berrocal T, Gaya F, Arjonilla A, Lonergan GJ. Vesicoureteral reflux: diagnosis and grading with echo-enhanced cystosonography versus voiding cystourethrography. Radiology. 2001;221(2):359-365.
208. Darge K, Ghods S, Zieger B, et al. Reduction in voiding cystourethrographies after the introduction of contrast enhanced sonographic reflux diagnosis. Pediatr Radiol. 2001;31(11):790-795.
209. Benz MR, Stehr M, Kammer B, et al. Foreign body in the bladder mimicking nephritis. Pediatr Nephrol. 2007;22(3):467-470.
210. Erasmie U, Lidefelt KJ. Accuracy of ultrasonic assessment of residual urine in children. Pediatr Radiol. 1989;19(6-7):388-390.
211. Cacciarelli AA, Kass EJ, Yang SS. Urachal remnants: sonographic demonstration in children. Radiology. 1990;174(2):473-475.
212. Choi YJ, Kim JM, Ahn SY, et al. Urachal anomalies in children: a single center experience. Yonsei Med J. 2006;47(6):782-786.
213. Boyle G, Rosenberg HK, O'Neill J. An unusual presentation of an infected urachal cyst. Review of urachal anomalies. Clin Pediatr (Phila). 1988;27(3): 130-134.
214. Heaney JA, Pfister RC, Meares Jr EM. Giant cyst of the seminal vesicle with renal agenesis. AJR Am J Roentgenol. 1987;149(1):139-140.
215. Hayden Jr CK, Swischuk LE, Fawcett HD, et al. Urinary tract infections in childhood: a current imaging approach. Radiographics. 1986;6(6): 1023-1038.
216. Rifkin MD, Kurtz AB, Pasto ME, Goldberg BB. Unusual presentations of cystitis. J Ultrasound Med. 1983;2:25-28.
217. Rosenberg HK, Eggli KD, Zerin JM, et al. Benign cystitis in children mimicking rhabdomyosarcoma. J Ultrasound Med. 1994;13(12):921-932.
218. Wexler LH, Helman LJ, editors. Rhabdomyosarcoma and the undifferentiated sarcomas. Philadelphia: Lippincott-Raven; 1997.
219. Williams JL, Cumming WA, Walker 3rd RD, Hackett RL. Transitional cell papilloma of the bladder. Pediatr Radiol. 1986;16(4):322-323.
220. Bornstein I, Charboneau JW, Hartman GW. Leiomyoma of the bladder: sonographic and urographic findings. J Ultrasound Med. 1986;5(7): 407-408.
221. Shapeero LG, Vordermark JS. Bladder neurofibromatosis in childhood. Noninvasive imaging. J Ultrasound Med. 1990;9(3):177-180.
222. Crecelius SA, Bellah R. Pheochromocytoma of the bladder in an adolescent: sonographic and MR imaging findings. AJR Am J Roentgenol. 1995;165(1): 101-103.
223. Zerin JM, Lebowitz RL. Spontaneous extraperitoneal rupture of the urinary bladder in children. Radiology. 1989;170(2):487-488.
224. Mezzacappa PM, Price AP, Kassner EG, et al. Cohen ureteral reimplantation: sonographic appearance. Radiology. 1987;165(3):851-852.
225. Puri P, Pirker M, Mohanan N, et al. Subureteral dextranomer/hyaluronic acid injection as first line treatment in the management of high grade vesicoureteral reflux. J Urol. 2006;176(4 Pt 2):1856-1859.
226. Hertzberg BS, Bowie JD, King LR, Webster GD. Augmentation and replacement cystoplasty: sonographic findings. Radiology. 1987;165(3):853-856.
227. Gundeti MS, Eng MK, Reynolds WS, Zagaja GP. Pediatric robotic-assisted laparoscopic augmentation ileocystoplasty and Mitrofanoff appendicovesicostomy: complete intracorporeal—initial case report. Urology. 2008;72(5): 1144-1147.
228. Rescorla FJ, Sawin RS, Coran AG, et al. Long-term outcome for infants and children with sacrococcygeal teratoma: a report from the Childrens Cancer Group. J Pediatr Surg. 1998;33(2):171-176.
229. Kocaoglu M, Frush DP. Pediatric presacral masses. Radiographics. 2006;26(3):833-857.
230. Watanabe M, Komuro H, Kaneko M, et al. A rare case of presacral cystic neuroblastoma in an infant. J Pediatr Surg. 2008;43(7):1376-1379.
231. Rosenberg H. Sonography of pediatric urinary tract abnormalities. Part I. Am Urol Assoc Weekly Update Series. 1986;35:1-8.

CHAPTER 55

The Pediatric Hip and Other Musculoskeletal Ultrasound Applications

Leslie E. Grissom and H. Theodore Harcke

SUMMARY OF KEY POINTS

- Ultrasound is the preferred technique in the diagnosis and management of development dysplasia of the hip (DDH).
- DDH is multifactorial: the highest risk factor is female breech delivery.
- The two basic methods, morphologic and dynamic, share the need for recognition of critical anatomic landmarks of the hip. The dynamic technique emphasizes stability.
- The American Institute of Ultrasound in Medicine Practice Parameter standard examination includes assessment of hip position, stability, and morphology.
- In the United States, general screening of infants for DDH is by physical examination. Ultrasound is recommended for infants with abnormal physical examination findings or risk factors.
- Radiographs may be used for assessment of bony acetabular development after 4 to 6 months of age.
- Congenital and other musculoskeletal abnormalities of the developing bones can be assessed with ultrasound because of the superior visualization of cartilage.
- Sonography can serve as a screening tool for diagnosis of musculoskeletal infection and trauma.

CHAPTER OUTLINE

DEVELOPMENT DYSPLASIA OF THE HIP
Clinical Overview
Dynamic Sonographic Technique: Normal and Pathologic Anatomy
History
Technical Factors
Coronal/Neutral View
Coronal/Flexion View
Transverse/Flexion View
Alternative Views
Evaluation of the Infant at Risk
Evaluation During Treatment

OTHER PEDIATRIC MUSCULOSKELETAL ULTRASOUND APPLICATIONS
Nondevelopmental Dysplasia Hip Abnormalities
Painful Hip and Hip Joint Effusion
Teratologic Hip Dislocation
Atypical Hips
Congenital Foot Deformities
Club Foot
Vertical Talus
Congenital Limb Deformities
Proximal Focal Femoral Deficiency
Tibial Hemimelia
Congenital Nonhip Dislocations
Elbow and Knee Dislocations
Patellar Dislocation
Brachial Plexus Injury
Inflammation
Infection
Noninfectious Inflammation
Trauma
Popliteal Cysts
SUMMARY

Ultrasound has been widely used in the diagnosis and management of **development dysplasia of the hip** (DDH), although many other applications for sonography of the pediatric musculoskeletal system have been developed. Ultrasound is ideally suited to the evaluation of the immature skeleton and associated soft tissues because of visualization of the cartilage found in large amounts in developing bones and because of the lack of ionizing radiation. Other advantages include the ability to perform dynamic evaluations and to examine children without sedation. With some applications, including DDH, sonography may replace other imaging studies; in other cases, sonography complements radiography to aid in the diagnosis. In this chapter, we review the use of ultrasound in DDH and also describe briefly its use in other musculoskeletal conditions. Ultrasound of the pediatric spine is discussed in Chapter 49; fetal spine sonography is discussed in Chapter 35; and musculoskeletal ultrasound in nonpediatric patients is reviewed in Chapters 23 and 24.

DEVELOPMENT DYSPLASIA OF THE HIP

Clinical Overview

Development dysplasia of the hip (DDH), formerly called "congenital dislocation of the hip," usually manifests in the first year of life. The **incidence of DDH** varies throughout the world.

In whites, overt dislocation is reported to be 1.5 to 1.7 per 1000 live births.[1,2] When lesser degrees of abnormality such as subluxation are included, as many as 10 infants per 1000 live births may show some features of the disorder.[3] Early detection of an abnormality in the infant hip is the key to successful management. If treatment is begun at a young age, most of the sequelae that occur when DDH goes unrecognized until walking age can be prevented. Clinical screening programs have been instituted, and primary care physicians are taught to evaluate the hips as part of the newborn physical examination. Historically, infants with abnormal clinical examination findings were referred for plain radiographic film examinations. Ultrasound has now become the preferred technique for diagnosis and management of DDH in the first 6 months of life.[4] Hip sonography offers clear advantages over other imaging techniques in DDH. At the early age of initial diagnosis in the first 6 months of life, the femoral head and acetabulum consist of cartilage components that are clearly identified by ultrasound. Real-time sonography allows assessment of the hip in multiple planes, both at rest and with movement. Ultrasound can replace radiographic studies and reduce radiation exposure to the young infant.

The **cause of DDH** is multifactorial, with both physiologic and mechanical factors playing a role. Maternal-fetal interaction influences the development of hip problems in both categories. Maternal estrogens and hormones that affect pelvic relaxation just before delivery are believed to lead to temporary laxity of the hip capsule in the perinatal period. Most fetuses are exposed to extrinsic forces in the later weeks of pregnancy because of their increasing size and the diminishing volume of amniotic fluid. It is theorized that these forces, although gentle, can lead to deformation if persistently applied.[5] An increased incidence of DDH is reported in infants born in the breech position, in infants with a positive family history of DDH, in firstborns, and in pregnancy with oligohydramnios. Infants with skull-molding deformities, congenital torticollis, and foot deformities are also at increased risk for DDH.[6] Current reviews of risk have focused on female breech delivery as the highest risk for DDH, and imaging is recommended for these infants in published guidelines from the major U.S. societies.[7-9] There is some evidence of familial acetabular dysplasia,[10] although this is not considered a cause in most cases.

Risk Factors for Development Dysplasia of the Hip (DDH)

Family history of DDH
Firstborn child
Oligohydramnios
Breech delivery (female breech is the highest DDH risk category)
Skull-molding deformities
Congenital torticollis
Foot deformities

The mechanism of a typical dislocation is thought to be a gradual migration of the femoral head from the acetabulum because of the loose, elastic joint capsule. In the newborn period, the femoral head usually dislocates in a lateral and posterosuperior position relative to the acetabulum. The displaced femoral head can usually be reduced, and the joint components typically do not have any major deformity. When dislocation is not recognized in early infancy, the muscles tighten and limit movement. The acetabulum becomes dysplastic because it lacks the stimulus of the femoral head. Ligamentous structures stretch, and fibrofatty tissue occupies the acetabulum. Thus it becomes impossible to return the femoral head to the acetabulum with simple manipulation; a pseudoacetabulum may form along the inferior ilium laterally where the dislocated femoral head rests.

Sonography is most often used for evaluation of an infant with an abnormal physical examination or a DDH risk factor, such as positive family history, breech delivery, foot deformity, or torticollis. Many reports attest to greater efficacy of sonography compared with the clinical and radiographic examination.[11-15]

The routine screening of all newborn infant hips with ultrasound has been a controversial issue. Based on a comparison between clinical and sonographic screening with sonography, Tonnis and colleagues[11] concluded that all newborns should be screened for DDH with ultrasound because it detects more pathologic joints than the clinical examination. In some European countries, routine screening has been tried on a regional basis. Critics of **newborn screening programs** note the high number of infants undergoing treatment or requiring follow-up studies (whether for minor instability or immaturity in acetabular development), but it is also recognized that studying only infants at risk will not eliminate late cases of DDH.[16,17]

The current consensus in the United States is that the net benefits of universal sonographic screening are not clearly established. This opinion is based on the fact that there is a high rate of spontaneous resolution of neonatal hip instability and dysplasia and lack of evidence that intervention affects outcomes for the population.[18] The American Academy of Pediatrics (AAP) has published guidelines for pediatric examinations for the diagnosis of DDH.[7] Screening by clinical examination is recommended, and ultrasound is reserved for infants having abnormal examination findings or risk factors.[19-22] If a frankly dislocated hip is present, referral to orthopedic specialists is appropriate. When the abnormal physical examination findings suggest less severe hip instability shortly after birth, sonography should not be done until at least 3 to 4 weeks of age because hip instability may resolve on its own. Experience has indicated that many infants younger than 30 days have hip laxity that becomes normal after a few weeks without treatment. This is not a new observation; the phenomenon was recognized clinically by Barlow.[1] It identifies, however, a group of infants who need follow-up. Not all infants' hips become normal, and these patients require continued observation.[11]

Newborns with a risk factor for DDH should be checked at 4 to 6 weeks. This avoids multiple examinations in cases of transient neonatal instability and immaturity related to maternal hormones.

Indications for Hip Ultrasound

- Abnormal findings on physical or imaging examination of the hip
- Monitoring of patients with development dysplasia of the hip (DDH) treated with a Pavlik harness or other splint device
- Any family history of DDH
- Breech presentation regardless of gender
- Oligohydramnios and other uterine causes of postural molding
- Neuromuscular conditions

Dynamic Sonographic Technique: Normal and Pathologic Anatomy

History

The first in-depth use of sonography was performed by Graf,[23] an Austrian orthopedic surgeon. Scanning was performed from the lateral approach with the femur in its anatomic position. Graf's method, which keyed on acetabular morphology, established ultrasound's ability to distinguish the cartilage, bone, and soft tissue structures that compose the immature hip joint. When real-time sonographic equipment became available, sonographers experimented with different approaches to the hip[24] and the use of dynamic assessment. Both approaches recognize the need for critical landmarks of the femur and acetabulum. The dynamic technique, as proposed by Harcke and colleagues, mirrored the physical examination.[25]

Although two basic assessment strategies evolved, morphologic and dynamic, the two methods have common features,[25,26] in addition to stressing positional relationships and stability and assessment of critical acetabular landmarks. This formed the basis for an examination drawing on elements from both techniques,[26,27] which has become part of the practice parameter recommended by the American College of Radiology (ACR), the American Institute of Ultrasound in Medicine (AIUM), Society of Pediatric Radiology (SPR), and Society of Radiologists in Ultrasound (SRU).[8]

Technical Factors

Hip sonography should be performed with real-time linear array transducers. One should use the highest frequency transducer that provides adequate penetration of the soft tissues to the depth required. For infants up to 6 months of age, the 15-8 MHz broadband digital transducer is successful. A lower-frequency transducer may be required for infants older than 6 months.

Standard scanning is performed from the lateral or posterolateral aspect of the hip, moving the hip from the neutral position at rest to a position in which the hip is flexed. With the hip flexed, the femur is moved through a range of abduction and adduction, with stress views performed in the flexed position. One aspect of hip sonography relevant to dynamic examinations is the shift of the transducer between the examiner's hands when examining the right and left hip. The infant is lying supine with the feet toward the sonographer. When examining the left hip, the sonographer grasps the infant's left leg with the left hand, and the transducer is held in the right hand. When the right hip is examined, we recommend that the sonographer hold the transducer in the left hand and use the right hand to manipulate the infant's right leg. Although some sonographers find this awkward at first, ambidexterity in this context is easily mastered. We found that this technique makes it possible to perform the stress maneuver more reliably and better maintain the planes of interest.

For a satisfactory examination, the infant should be relaxed. Infants can be fed before or during the examination. Toys and other devices to attract the infant's attention are helpful and can be used as sonography is being performed. A parent can hold the infant's arms or head and can talk to the infant. There is no need for sedation. The upper body may remain clothed. Our standard practice is to leave the infant diapered and expose only the side of the hip being examined (strongly recommended for boys).

The **anatomy** is considered in orthogonal views. It is our routine practice to record images in each of these views for permanent records. This standardizes the examination and, in our institution, provides a guideline for the technologist who performs the initial examination. In describing views, we use a

Minimum Standard Examination for Development Dysplasia of the Hip (DDH) According to Guidelines From the American College of Radiology (ACR), American Institute of Ultrasound in Medicine (AIUM), Society for Pediatric Radiology (SPR), and Society of Radiologists in Ultrasound (SRU)

- The minimum standard is two orthogonal planes: a coronal view in the standard plane at rest (in flexion or extension) and a transverse view of the flexed hip with and without stress. This enables an assessment of hip position, stability,[4] and morphology when the study is correctly performed and interpreted. It should be noted that additional views and maneuvers can be obtained and that these may enhance the confidence of the examiner.
- Morphology is assessed at rest. The stress maneuvers follow those prescribed in the clinical examination of the hip and assess femoral stability.
- The attempts to dislocate the femoral head or reduce a displaced head are analogous to the Barlow and Ortolani tests used in the clinical examination. It is acceptable to perform the standard examination with the infant in a supine or lateral position.[8]

[a]Modified from ACR-AIUM-SPR-SRU practice parameter for the performance of the ultrasound examination for detection and assessment of developmental dysplasia of the hip. American College of Radiology. 2013. Available from: https://www.acr.org/~/media/ACR/Documents/PGTS/guidelines/US_Hip_Dysplasia.pdf. Accessed 2/21/2017.[8]

two-word combination that indicates the plane of the transducer with respect to the body (coronal or transverse) and the position of the hips (neutral or flexed).

It is the objective of the dynamic hip assessment to determine the position and stability of the femoral head, as well as the development of the acetabulum. With a normally positioned hip, the femoral head is congruently positioned within the acetabulum. Mild displacement, such as when the head is in contact with part of the acetabulum or is displaced but partly covered, is referred to as **subluxation.** The **dislocated hip** has no contact with or coverage by the acetabulum. A change in position of the femur may change the relationship of the femoral head and acetabulum. A hip that is subluxated in the neutral or rest position may seat itself with flexion and abduction. A dislocated hip may improve its position and partially reduce to a subluxated position. This is, in fact, a principle of treatment.

The **stability of the hip** is determined through motion and the application of stress. The stress maneuvers are the imaging counterparts of the clinical Barlow and Ortolani maneuvers, which are the basis for the clinical detection of a hip abnormality. The **Barlow test** determines whether the hip can be dislocated. The hip is flexed and the thigh brought into the adducted position. The gentle push posteriorly can demonstrate instability by causing the femoral head to move out of the acetabulum.[1] The **Ortolani test** determines whether the dislocated hip can be reduced. As the flexed, dislocated hip is abducted into a frog-leg position, the examiner feels a vibration or "clunk" that results when the femoral head returns to the acetabulum.[28] The **normal hip** is always seated at rest, with motion, and during the application of stress. The lax hip is normally positioned at rest and shows mild subluxation with stress. It must, however, invariably remain within the confines of the acetabulum. The subluxated hip is displaced laterally at rest and is loose; it may be dislocatable with stress and reducible with flexion and abduction. The **dislocated hip** may be able to be returned to the acetabulum with traction and abduction. This hip is distinguished from the most severe form of DDH, in which the femoral head is dislocated and cannot be reduced.

At birth, the proximal femur and much of the acetabulum are composed of cartilage. On sonographic examination, cartilage is hypoechoic compared with soft tissue, so it is easy to distinguish. A few scattered specular echoes can be visualized within the cartilage when high-frequency transducers are used and technique adjustments are optimally set. The **acetabulum** is composed of both bone and cartilage. At birth, the bony ossification centers in the ilium, ischium, and pubis are separated by the **triradiate cartilage,** which has a Y configuration. A cartilaginous acetabular rim (the **labrum**) extends outward from the acetabulum to form the cup that normally contains the femoral head. Most of the acetabular cartilage has an echogenicity similar to the femoral head. It is still possible to determine the joint line, which distinguishes the cartilaginous acetabulum from the femoral head, by simply rotating the femur. More pronounced movement of the hip often creates echoes within the joint space, probably as a result of the formation of microbubbles. At the lateral margin of the **labrum,** the hyaline cartilage changes to fibrocartilage, and this shows increased echogenicity. The echogenic hip capsule, composed of fibrous tissue, borders the femoral head laterally. The bony components of the hip reflect all of the sound beam from their surface. This creates a bright linear or curvilinear appearance on the sonogram, indicating the contour of the osseous surfaces in that plane.

Radiographically, the ossification center of the femoral head is recognized between the second and eighth months of life. It is typically seen earlier in females than in males, and there is a wide normal variation for the time of appearance. Although some asymmetry between the left and right hips can be normal, both in time of appearance and in size, delayed appearance and development are associated with DDH. Hip sonograms reflect the development of the ossification center and can be used to document the development of the center.[29] The ossification center can be found with ultrasound several weeks before it is visible radiographically. Initially, a confluence of blood vessels produces increased echoes within the cartilage. This precedes actual ossification. As ossification begins, the calcium content is insufficient to produce a visible radiographic density; however, the sound waves are reflected. With maturation, the size of the ossification center increases. In early development, the echoes from the center have a punctate appearance, whereas later in the first year of life, the growth in size gives it a curvilinear margin. As the normal infant approaches 1 year of age, the size of the ossification center precludes accurate determination of medial acetabular landmarks.

Sonography of the hip is practical only up to 8 months of age, unless there is delayed ossification of the femoral head. Between 4 months and 6 months, radiography becomes more reliable. Usually by 1 year of age, the femoral ossification center is large enough to prevent good sonographic visualization of the acetabulum.[9] The presence and size of the ossific nucleus can be evaluated in all views.

Coronal/Neutral View

The **coronal/neutral view,** which forms the basis for the morphologic technique, is performed from the lateral aspect of the joint with the plane of the ultrasound beam oriented coronally with respect to the hip joint. The femur is maintained with a physiologic amount of flexion. The coronal/neutral view is performed with the patient supine. The transducer is placed on the lateral aspect of the hip, and the hip is scanned until a standard plane of section is obtained (Fig. 55.1). The plane must precisely demonstrate the midportion of the acetabulum, with the straight iliac line superiorly and the inferior tip of the os ilium seen medially within the acetabulum. The echogenic tip of the labrum should also be visualized. The alpha and beta angles, if measured, relate to fixed points on the bony and cartilaginous components of the acetabulum[30] (see Fig. 55.1), and the exact plane must be obtained for the measurements to be reliable. The similarity can be noted between the appearance of the acetabulum in this coronal/neutral view and in the coronal/flexion view (Fig. 55.2). The difference is that the bony shaft (metaphysis) of the femoral neck is visualized below the femoral head in the coronal/neutral projection. In the coronal/flexion view, the femoral shaft is not in the plane of examination because the femur is flexed. A stability test can be performed in the coronal/neutral view

by gently pushing and pulling the infant's leg. This helps to verify deformity of the acetabulum and to identify craniodorsal movement of the femoral head under pressure. Zieger and colleagues[31] proposed a further adaptation of this view, advocating flexion and adduction of the hip to identify lateral displacement when instability is present. This is similar to the coronal/flexion stress view.

In the normal coronal/neutral view, the femoral head is resting against the bony acetabulum. The acetabular roof should have a concave configuration and cover at least half the femoral head. The cartilage of the acetabular roof is hypoechoic and extends lateral to the acetabular lip, terminating in the labrum, which is composed of fibrocartilage and is echogenic (see Fig. 55.1C). When a hip becomes subluxated or dislocated, the femoral head gradually migrates laterally and superiorly, with progressively decreased coverage of the femoral head (see Fig. 55.1E). In hip dysplasia, the acetabular roof is irregular and angled, and the labrum is deflected superiorly and becomes echogenic and thickened. When the hip is frankly dislocated, the labrum may be deformed. Echogenic soft tissue is interposed between the femoral head and the bony acetabulum. A combination of deformed labrum, fibrofatty tissue (pulvinar), and thickened ligamentum teres prevents the hip from being reduced.

The acetabulum can be assessed visually or with measurements, noting the depth and angulation of the acetabular roof, as well as the appearance of the labrum (see Fig. 55.1F). This can be seen in both coronal/neutral and coronal/flexion views and should be described in the report. Morin and colleagues[32,33] correlated coverage of the femoral head by the bony acetabulum with measurements of the acetabular angle. This assessment relates acetabular depth (d) to the diameter of the femoral head (D) and is expressed as percent ($d/D \times 100$) coverage of the femoral head. These data showed that normal radiographic measurements always had a femoral head coverage that exceeded 56%, and that clearly abnormal radiographic measurements had coverage of less than 40%.[33] This information should be used with caution because there are intermediate values for which sonographic and radiographic measurements do not correlate. We have also noted cases in which sonography showed the acetabulum to be better developed than it appeared radiographically, and vice versa.[34] This discrepancy occurs because the radiograph is a two-dimensional projection of the three-dimensional pelvis, and selected sonographic images illustrate a single coronal slice that may not match the projection.

Classification of hip joints may also be based on the measurement of the alpha and beta angles (see Fig. 55.1D-F). The alpha angle measures the inclination of the osseous acetabular roof with respect to the lateral margin of the iliac bone (baseline). The beta angle is formed by the baseline iliac bone and the inclination of the anterior cartilaginous acetabular roof, for which the tip of the labrum is its key landmark. Ultrasound units may contain software that facilitates measurement of these angles. Four basic hip types have been proposed on the basis of alpha and beta measurements.[30] Most of these subtypes have been subdivided, and small changes in angular measurements can result in a change in category. The reproducibility of angular measurements and subtypes has been a point of considerable discussion. In Europe, classification by measurement has been based on large numbers of infants examined. Some examiners have experienced problems with the use of measurements,[31,32,34-36] but those who adhere strictly to the technique find acceptable reproducibility.[11,37,38]

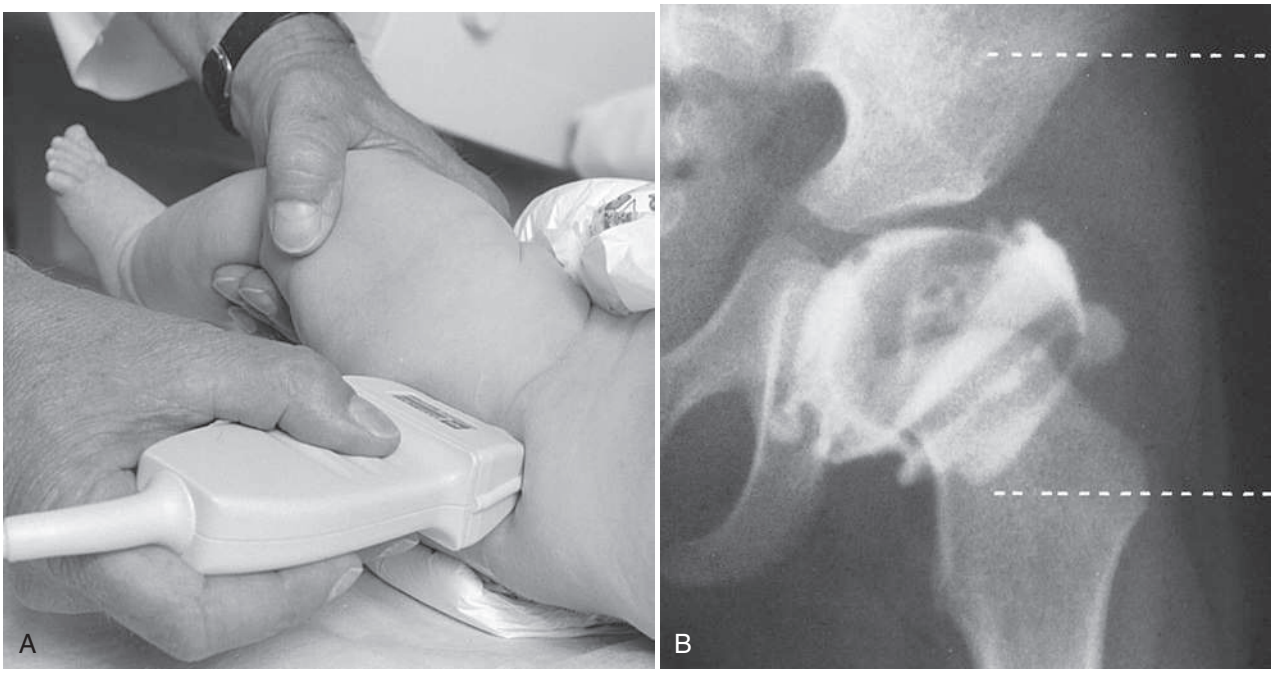

FIG. 55.1 Coronal/Neutral Hip View. (A) Linear array transducer is placed coronal and lateral with respect to the hip. The femur is in "physiologic neutral" for the infant (slight hip flexion). **(B)** Scan area *(dotted lines)* on arthrogram.

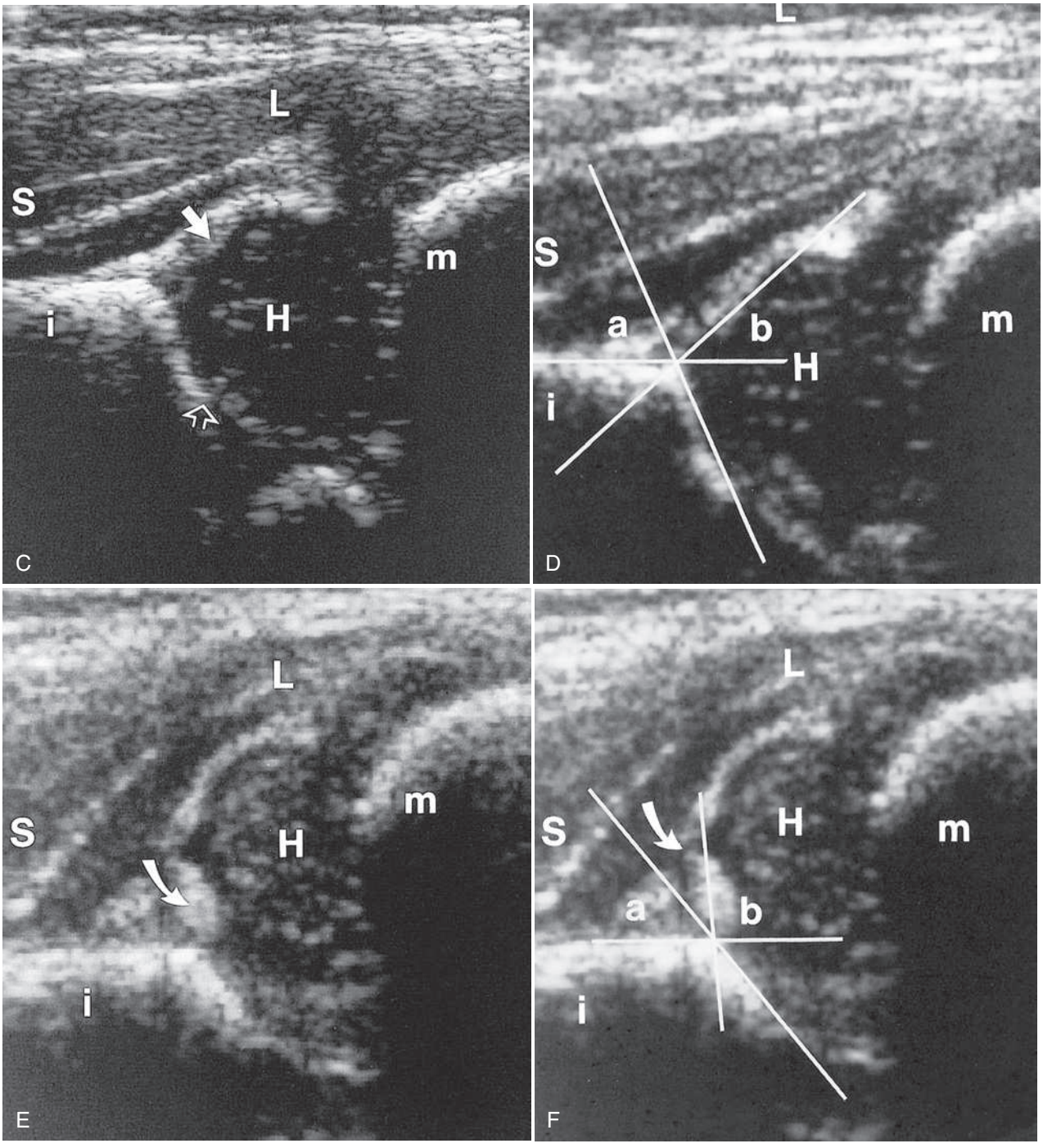

FIG. 55.1, cont'd **(C) Normal hip** sonogram shows sonolucent femoral head *(H)* resting against the bony acetabulum. Note fibrocartilaginous tip of labrum *(solid arrow)* and junction of bony ilium and triradiate cartilage *(open arrow)*. **(D) Normal hip** sonogram with alpha *(a)* and beta *(b)* angles used in measurement. **(E) Dislocated hip** sonogram shows displacement of femoral head *(H)* laterally with deformity of labrum *(curved arrow)*. **(F) Dislocated hip** sonogram with abnormal alpha and beta angles. *H,* Femoral head; *i,* iliac line; *L,* lateral; *m,* femoral metaphysis; *S,* superior.

Coronal/Flexion View

In the **coronal/flexion view** the transducer is maintained in a coronal plane with respect to the acetabulum (Fig. 55.2A) while the hip is moved to a 90-degree angle of flexion. During the assessment in this view, the transducer is moved in an anteroposterior direction with respect to the body to visualize the entire hip. Anterior to the femoral head, the curvilinear margin of the bony femoral shaft is identified. In the midportion of the acetabulum, the normally positioned femoral head is surrounded by echoes from the bony acetabular components (see Fig. 55.2B). Superiorly, the lateral margin of the iliac bone is seen, and the transducer position must be adjusted so the iliac bone becomes a straight horizontal line on the monitor. This landmark (**iliac**

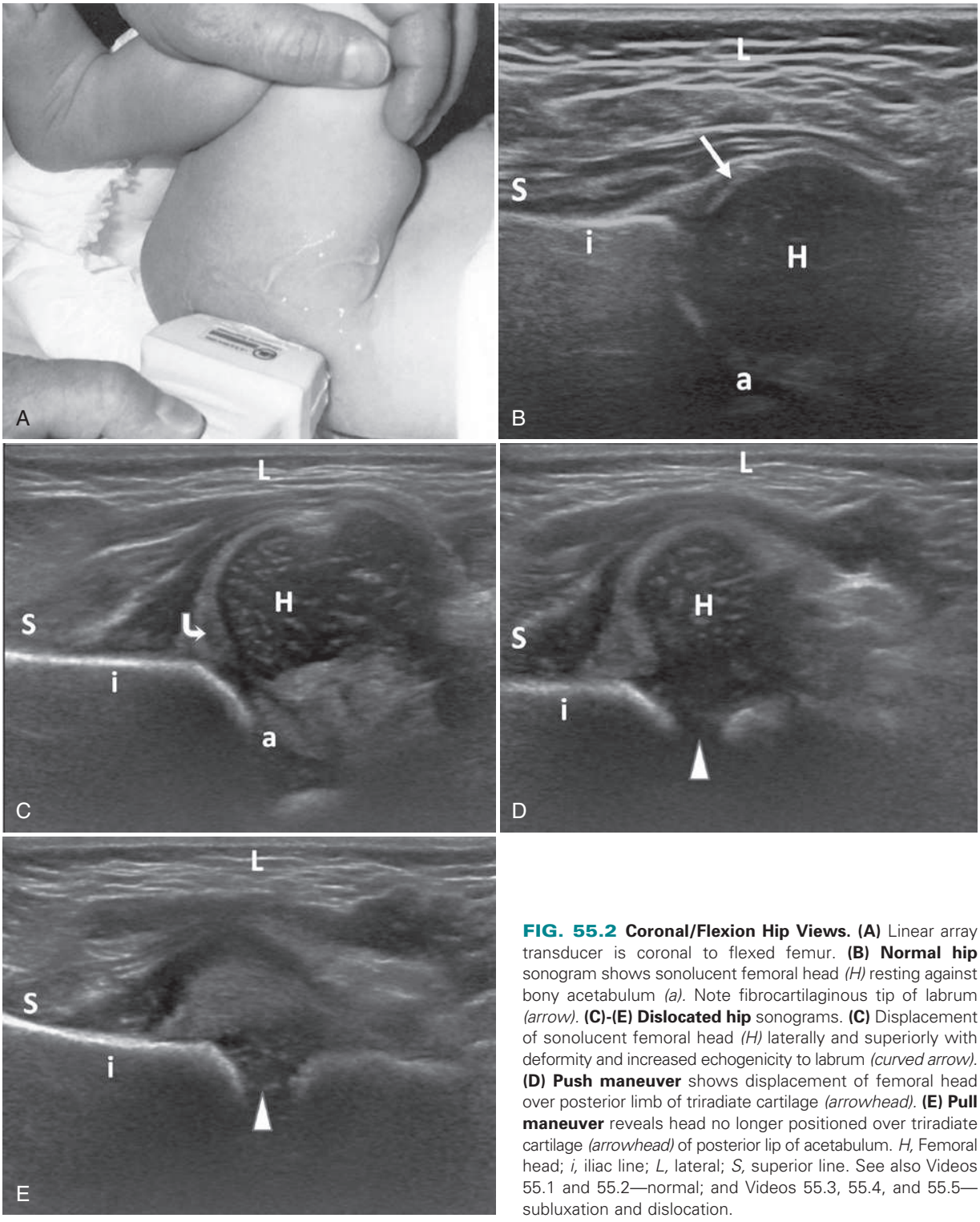

FIG. 55.2 Coronal/Flexion Hip Views. (A) Linear array transducer is coronal to flexed femur. **(B) Normal hip** sonogram shows sonolucent femoral head *(H)* resting against bony acetabulum *(a)*. Note fibrocartilaginous tip of labrum *(arrow)*. **(C)-(E) Dislocated hip** sonograms. **(C)** Displacement of sonolucent femoral head *(H)* laterally and superiorly with deformity and increased echogenicity to labrum *(curved arrow)*. **(D) Push maneuver** shows displacement of femoral head over posterior limb of triradiate cartilage *(arrowhead)*. **(E) Pull maneuver** reveals head no longer positioned over triradiate cartilage *(arrowhead)* of posterior lip of acetabulum. *H,* Femoral head; *i,* iliac line; *L,* lateral; *S,* superior line. See also Videos 55.1 and 55.2—normal; and Videos 55.3, 55.4, and 55.5—subluxation and dislocation.

bone line: flat and straight) is a key to accurately visualizing the midacetabulum and to obtaining the maximum depth of the acetabulum. When the transducer is positioned too anteriorly, the iliac line is inclined laterally; and if positioned too posteriorly, the iliac line exhibits concavity. When the plane is not correctly selected, it could be falsely concluded that the acetabulum is maldeveloped. A **normal hip** gives the appearance of a "ball on a spoon" in the midacetabulum. The femoral head represents the ball, the acetabulum forms the bowl of the spoon, and the iliac line is the handle. When the transducer is moved posteriorly and the scan plane is over the posterior margin of the acetabulum, the posterior limb of the triradiate cartilage, also known as the "posterior lip," becomes an easily recognized landmark. The bone above and below the cartilage notch is flat, and the normally

positioned femoral head is not visualized (Videos 55.1 and 55.2).

In **subluxation,** the femoral head is displaced laterally, posteriorly, or both, with respect to the acetabulum. Soft tissue echoes are seen between the femoral head and the bony reflections from the medial acetabulum. In **dislocation,** the femoral head is completely out of the acetabulum (see Fig. 55.2C). With superior dislocations, the femoral head may rest against the iliac bone. In posterior dislocations, the femoral head is seen lateral to the posterior lip. The acetabulum is usually not visualized in a dislocation because the bony shaft of the femur blocks the view.

Dynamic examination in the coronal/flexion view has two components. The first is performed over the posterior lip using a push-and-pull maneuver (see Fig. 55.2D-E). In the normal hip the femoral head is never seen over the posterior lip of the acetabulum. When there is instability, a portion of the femoral head appears over the posterior lip of the triradiate cartilage as the femur is pushed. With a pull, the head disappears from the plane. In a dislocated hip, the femoral head may be located over the posterior lip and may or may not move out of the plane with traction. The second component of the dynamic examination is performed over the midacetabulum. The Barlow-type maneuver is performed with **adduction** and gentle pushing against the knee. In the normal hip the femoral head will remain in place against the acetabulum. With subluxation or dislocation, the head will migrate laterally and posteriorly, and there will be echogenic soft tissue between the femoral head and the acetabulum (Videos 55.3, 55.4, and 55.5).

Transverse/Flexion View

Transition from the coronal/flexion view to the **transverse/flexion view** is accomplished by rotating the transducer 90 degrees and moving the transducer posteriorly so it is in a posterolateral position over the hip joint. The orientation of the scan plane is parallel to the flexed femoral shaft (Fig. 55.3A). The plane of the transducer and the landmarks are demonstrated on a computed tomography (CT) scan of a patient in a spica cast with a normal left and dislocated right hip (see Fig. 55.3B). Sonographically, the bony shaft and metaphysis of the femur give bright reflected echoes anteriorly, adjacent to the sonolucent femoral head. The echoes from the bony acetabulum appear posterior to the femoral head, and in the normal hip, a **U-shaped configuration** is produced by the metaphysis and the ischium (see Fig. 55.3C). The relationship of the femoral head and acetabulum is observed while the flexed hip is moved from maximum adduction to wide abduction. The sonogram changes its appearance in abduction and adduction. The deep, U-shaped configuration is produced with maximum abduction, whereas in adduction, a shallower, V-shaped appearance is observed. It is important to have the transducer positioned posterolaterally over the hip to see the medial acetabulum. When the transducer is not posterior enough, the view of the acetabulum is blocked by the femoral metaphysis, and the hip can appear falsely displaced. In adduction, the hip is stressed with a gentle posterior push (a **Barlow test**). In the normal hip, the femoral head will remain deeply in the acetabulum in contact with the ischium with stress. In **subluxation,** the hip will be normally positioned or mildly displaced at rest, and there will be increased lateral displacement from the medial acetabulum with stress, but the femoral head will remain in contact with a portion of the ischium. With **frank dislocation,** the hip will be laterally and posteriorly displaced to the extent that the femoral head has no contact with the acetabulum, and the normal U-shaped configuration cannot be obtained (see Fig. 55.3D). The process of dislocation and reduction is able to be visualized in unstable hips in the transverse/flexion view. With abduction, the dislocated hip may be reduced, representing the sonographic counterpart of the Ortolani maneuver. With adduction, the subluxated hip may be dislocatable, corresponding to the Barlow maneuver (Videos 55.6, 55.7, and 55.8).

Alternative Views

A **transverse/neutral view** is still used in our examination protocol, but this view has not been included in published guidelines. The transducer is directed horizontally into the acetabulum from the lateral aspect of the hip; the leg is in physiologic neutral position. The plane of interest is one that passes through the femoral head into the acetabulum at the center of the triradiate cartilage.[26] The position of the head with respect to the triradiate cartilage is evident and can confirm findings on the coronal/neutral view.

A number of **anterior views** have been described, and sonographers experienced in their use have indicated success with these views.[12,24] The anterior approach of Dahlstrom and colleagues[13] is performed with the patient supine and the hips flexed and abducted. The transducer is placed anterior to the hip joint and is centered over the femoral head with the plane of the sound beam parallel to the femoral neck (Fig. 55.4A-B). A Barlow or push maneuver can be performed to detect instability. **Complete dislocation** is considered to be present when femoral head displacement exceeds 50% of its diameter (see Fig. 55.4C). The image produced in a normal hip is an axial section through the acetabulum and a longitudinal section through the femoral head and neck.[11] The anterior view is particularly useful in rigid abduction splints and casts in which the posterior aspect of the hip is covered.

Evaluation of the Infant at Risk

We examine each hip in multiple views and report our findings with an emphasis on position and stability. Femoral head position is described as normal, subluxated, or dislocated. Dislocations are easy to determine, and we have had no difficulty with their identification. Sometimes it can be problematic to decide whether an abnormal hip that is widely displaced should be called "subluxated" or "dislocated." Stability testing is reported as normal, lax, subluxatable, dislocatable (for subluxated hips), and reducible or irreducible (for dislocated hips). When stress maneuvers are performed, it is important that the infant be relaxed; otherwise, inconsistency may be found between the sonographic and clinical examination findings and in serial ultrasound studies.

The acetabulum is assessed visually and is described as normal, immature, or dysplastic. More important are the development of the cartilaginous labrum and its coverage of the femoral head. Situations in which the bony component is steeply angled but the cartilage is well developed and covers the femoral head should

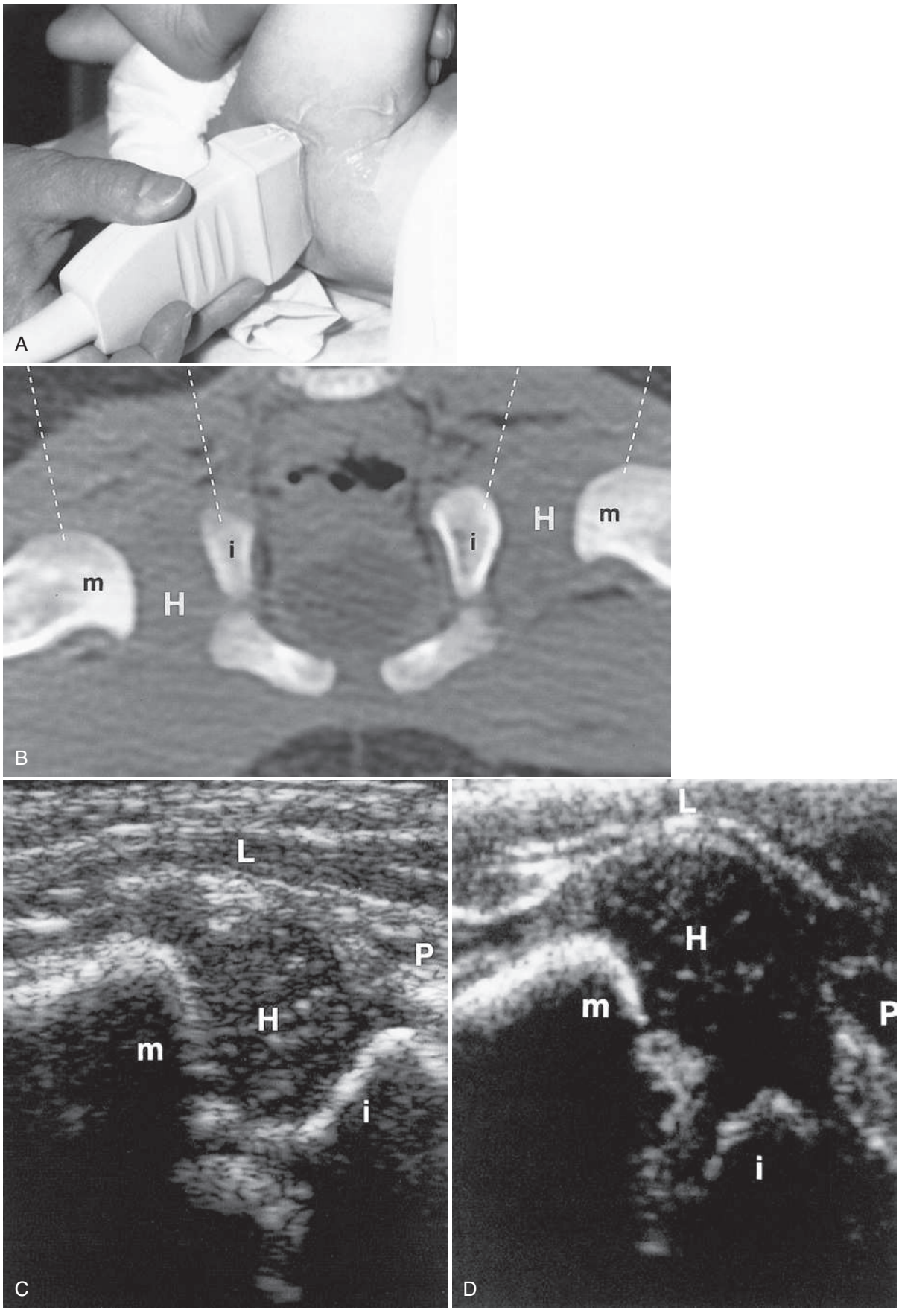

FIG. 55.3 Transverse/Flexion Hip View. (A) Linear array transducer is in the axial plane posterolaterally over the hip joint with the hip flexed. **(B)** Scan area *(dotted lines)* on a prone computed tomography (CT) scan. Scan demonstrates relationship of femoral head *(H),* metaphysis *(m),* and ischium *(i)* in the normal hip on the left and the dislocated hip on the right. **(C) Normal hip** sonogram shows echolucent femoral head *(H)* surrounded by metaphysis *(m)* (anterior) and ischium *(i)* (posterior), forming a U around the femoral head. *L,* Lateral; *P,* posterior. **(D) Dislocated hip** sonogram shows sonolucent femoral head *(H)* displaced posterolaterally. The U configuration of normal metaphysis *(m)* and ischium *(i)* is not seen. See also Video 55.6—normal; Video 55.7—subluxation; Video 55.8—dislocation.

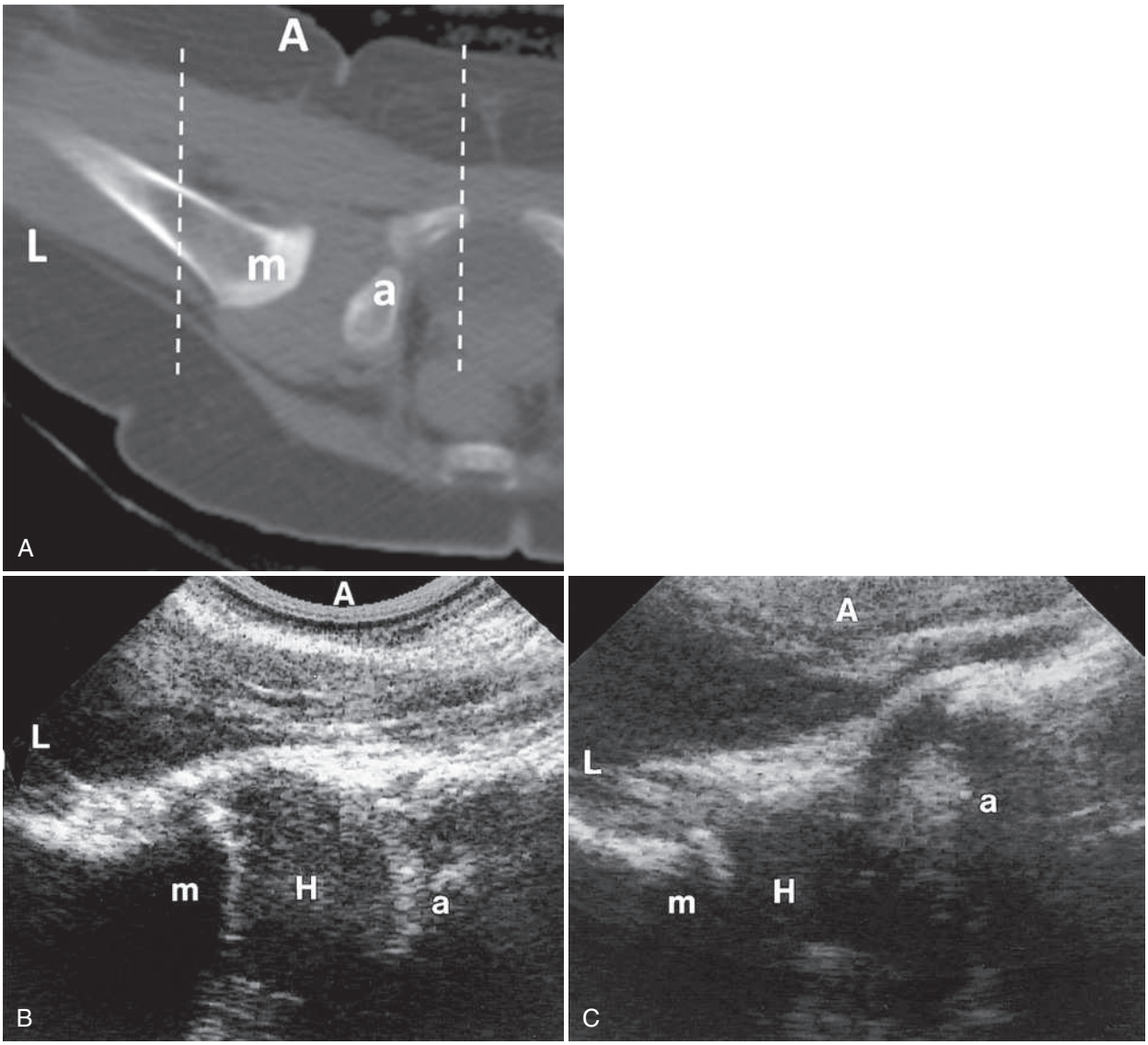

FIG. 55.4 Hip Anterior Views—Anterior Axial With Flexion and Abduction. (A) Scan area *(dotted lines)* on a computed tomography (CT) scan. *a,* Acetabulum; *A,* anterior; *L,* lateral; *m,* metaphysis. **(B) Normal hip** sonogram shows sonolucent femoral head *(H)* bordered by metaphysis *(m)* laterally and acetabulum *(a)* medially. **(C) Dislocated hip** sonogram shows posterior displacement of femoral head *(H)* and metaphysis *(m).*

be noted. Deformity and increased echogenicity of the cartilage are indications of more severe acetabular dysplasia.

Evaluation During Treatment

The usefulness of **sonography in the follow-up of infants with DDH,** whether for observation of resolving abnormality or in conjunction with a defined treatment regimen, is widely accepted. Currently, sonography is routinely used to follow borderline cases, particularly in very young infants, before a commitment is made to a treatment regimen. When treatment is indicated, ultrasound is typically used to monitor hip position during treatment. Dynamic splints, such as the Pavlik harness, hold the hip in a flexed abducted position. These restraints and similar devices are popular, and ultrasound has been tested as a way of monitoring hip position for infants in splint devices.[34,39,40] The sonographic examination in these patients is limited to the transverse/flexion and coronal/flexion views. The stress portion of the examination should not be performed unless requested. Typically, stress is not used until the conclusion of treatment, when weaning from the harness is instituted.

One of the problems with follow-up sonography has been its reliability in morphologic assessment of the bony acetabulum. Reports of discrepancies between the sonographic appearance of the bony acetabulum and the radiographic appearance indicate inexact correlation.[34] This may result from observer variation and the nature of the ultrasound measurements. The American Academy of Orthopaedic Surgeons (AAOS) guideline states that at 4 to 6 months of age it is appropriate to shift to the radiograph when following a patient.[41] We have chosen to include the pelvic radiograph as a baseline toward the end of the treatment protocol. The older the infant, the more we tend to consider radiography, particularly when the ossification centers are large. After successful treatment, continued monitoring of acetabular development by periodic radiographs is prudent. Residual acetabular dysplasia is reported in a small number of patients.[42]

At one time, we performed ultrasound in severe cases of DDH after casting through a window cut in the cast posteriorly. Now, cross-sectional imaging with CT or magnetic resonance imaging (MRI) is done after casting. The localizer CT film enables the technologist to select the appropriate level to assess hip position with attention to keeping the radiation dose low. MRI is increasingly used and gives no ionizing radiation, although its high cost and limited availability are disadvantages.[43] Our MRI protocols include T2-weighted images in axial and coronal planes.[44] Vascularity of the femoral head after reduction can be evaluated by adding contrast to the examination.[45]

Avascular necrosis of the femoral head is a recognized complication of DDH treatment devices. Both color and power Doppler ultrasound have been used to assess the vascularity of the femoral head during treatment. Because of the microvascular architecture in the cartilage canals, power Doppler sonography is thought to have the best potential. Normal hips show a radial pattern of flow from the center of the unossified head. The central collection of vessels is the precursor of the ossification center and is seen before the center is apparent on radiographs. Bearcroft and colleagues[46] reported that diminished flow can be demonstrated when the hip is placed in wide abduction, compressing the medial circumflex artery. This may correlate with development of avascular necrosis, and thus assessment of flow has been proposed as an aid in determining a safe abduction position for treatment. The examination is technically difficult and currently performed primarily in the research arena. Magnetic resonance imaging has become the preferred method for diagnosis of avascular necrosis.[45]

OTHER PEDIATRIC MUSCULOSKELETAL ULTRASOUND APPLICATIONS

In pediatric musculoskeletal sonography, knowledge of the normal appearance of cartilage, soft tissues, and developing osseous structures is essential. Use of a high-frequency linear transducer is advised, and comparison to the contralateral unaffected side is recommended. The focal zones should be over the area of interest with the appropriate depth, and gain should be optimized for the tissues scanned.[47] This section reviews ultrasound use in the diagnosis and management of congenital musculoskeletal abnormalities, including foot deformities, teratologic hip, congenital limb deformities, congenital nonhip dislocations, and brachial plexus injury. It also describes sonographic findings in other conditions such inflammation and trauma specific to children. Tumors and sports injuries are discussed in other musculoskeletal ultrasound chapters (see Chapters 23 and 24).

Nondevelopmental Dysplasia Hip Abnormalities

Painful Hip and Hip Joint Effusion

A variety of conditions cause hip pain in pediatric patients, including transient synovitis, osteomyelitis, Perthes disease, slipped capital femoral epiphysis, fracture, and arthritis. Although radiography is performed initially and is often diagnostic, the plain radiographic film often is normal in the presence of small joint effusions. Sonography can be used to determine if an effusion is present and to guide arthrocentesis. Several large studies of sonographic hip joint effusion detection have been reported. They show the technique to be easy to master and rapidly performed. The results have been highly sensitive in the detection of effusion, with as little as 1 mm of fluid recognized experimentally. False-negative results have been reported in infants younger than 1 year,[48] probably because the femoral neck has not developed and the capsule is small. Fluid tends to surround the femoral head instead.

Although hip sonography is sensitive in the detection of effusion, its place in the workup of the painful hip varies from center to center. In one large series, although ultrasound facilitated early diagnosis or prompted further investigation in some patients, it altered the therapy or outcomes in only 1% of the patients.[49] Clinicians use a number of physical signs (oral temperature, weight bearing) and laboratory findings (white blood cell count, C-reactive protein, erythrocyte sedimentation rate) to distinguish septic arthritis from transient synovitis in children.[47,50,51] They employ these parameters when making the decision to perform joint aspiration or seek additional imaging.

At our institution, the workup of the painful hip is individualized, and we find hip sonography to be helpful in certain circumstances. When the clinical picture is unclear, the presence or absence of an effusion can guide the clinician in the diagnosis and the need for further evaluation. For example, in the patient with clinical and laboratory signs of transient synovitis, hip sonography may be used to demonstrate an effusion; however, the patient does not usually undergo joint aspiration. In a patient with hip pain and signs of sepsis, MRI may be performed, regardless of the results of hip ultrasound, to exclude osteomyelitis and other soft tissue infection sites. MRI provides a more detailed evaluation of localized disease beyond the hip joint.

The patient is examined in the supine position with the hips in the neutral position with as little flexion as possible. A high-frequency linear transducer is recommended. The hip is scanned in a sagittal, oblique plane along the long axis of the femoral neck (Fig. 55.5). The brightly echogenic anterior cortex of the femoral head and neck with the intervening echolucent physis is seen; the anterior margin of the bony acetabulum is visualized superiorly. The anterior recess of the joint capsule parallels the femoral neck in this area, with the outer margin forming an echogenic line anterior to the cortex of the femoral neck and extending over the femoral head. The iliopsoas muscle is superficial to the capsule.

In the normal hip, the joint capsule has a concave contour and the thickness of the capsule from the outer margin to the cortex of the femoral neck measures 2 to 5 mm. When there is joint effusion, the anterior recess of the capsule becomes distended with a convex outer margin, and fluid is seen between the anterior and posterior layers of the capsule.[52] There is increased thickness of the abnormal joint capsule of at least 2 mm compared with the normal contralateral capsule.[53-55] The use of measurements alone is problematic when both hips are abnormal, although this occurs infrequently.

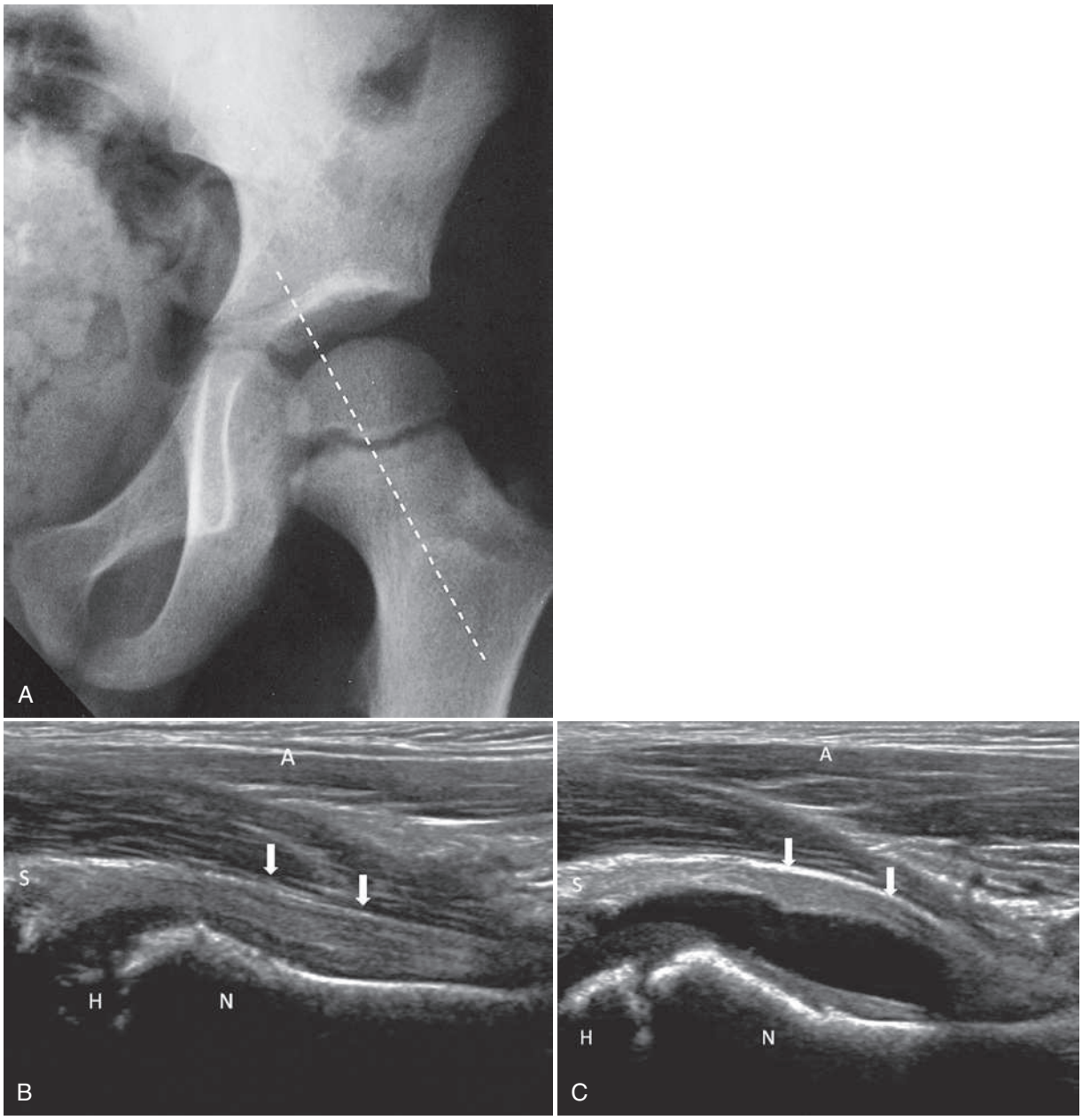

FIG. 55.5 Hip Joint Transient Synovitis. (A) Transducer position parallels femoral neck. Scan plane is shown by dashed line. **(B)** Normal hip sonogram shows joint capsule *(arrows)* following contours of femoral head *(H)* and neck *(N)*. **(C)** Hip effusion sonogram shows bulging joint capsule *(arrows)* with hypoechoic fluid in anterior recess extending along femoral neck *(N)* and cephalad over femoral head. *A,* Anterior; *S,* superior.

Fluid of varying echogenicity is visible within the capsule. The echoes are created by inflammatory debris or hemorrhage.[54] Zieger and colleagues[48] concluded that if the fluid is anechoic, the diagnosis of septic arthritis can be excluded. Other investigators have found the character of the fluid to be nonspecific,[49,53] describing echoes (probably representing hemorrhage) in the fluid in transient synovitis and anechoic fluid in cases of septic arthritis. Color Doppler sonography has also been used in an attempt to distinguish between infectious and noninfectious effusions, but the technique has proved to be unreliable.[56]

When fluid is detected, arthrocentesis can be performed using sonographic guidance; a saline lavage can be used if fluid cannot be withdrawn. Although the procedure requires patient cooperation, it is relatively easy to perform and avoids the ionizing radiation required in fluoroscopic arthrocentesis. Some clinicians use arthrocentesis therapeutically in Perthes disease, which can be recognized by fragmentation of the femoral head and thickened articular cartilage.[57] Sonograms to check for effusion may show other pathology, such as slippage of the head in **slipped capital femoral epiphysis** and cortical disruption in fracture or osteomyelitis, but these findings are better evaluated radiographically.

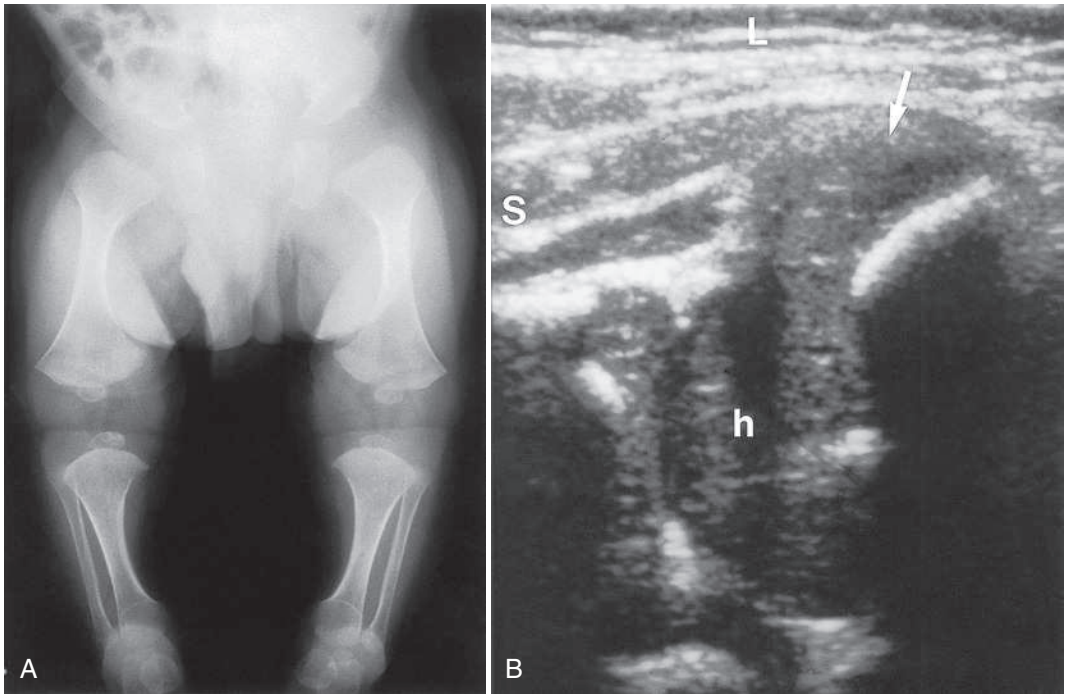

FIG. 55.6 Atypical Hip. (A) Radiograph of a 4-month-old infant with **Kniest dysplasia** shows shortening of the long bones and bulbous ends of the bones. **(B)** Coronal/neutral sonogram shows increased echogenicity of the cartilage and coxa vara with elevation of the greater trochanter *(arrow)* and narrowing of the acoustic window of the hip joint. *h,* Femoral head; *L,* lateral; *S,* superior.

Soft tissue swelling and other soft tissue abnormalities outside the joint capsule have also been diagnosed.

Teratologic Hip Dislocation

Teratologic hip dislocation is considered a different entity from DDH. Teratologic hips are dislocated earlier in utero than DDH and are seen in patients with various syndromes and neuromuscular diseases such as **arthrogryposis, Larsen syndrome,** and **chromosomal abnormalities.** Sonographic examination is the same as for DDH, but the planes of interrogation may require adjustment if there are contractures. Sonographic findings at rest resemble frank dislocation in DDH, but teratologic dislocation is more severe with contractures and limited movement. The acetabulum is small, typically obscured by the proximal femur, and the femoral head is distorted from chronic dislocation.[58,59]

Atypical Hips

Other patients with "atypical hips" include those with **skeletal dysplasias, congenital myopathy,** or **congenital coxa vara.** These patients have displacement of the hips, acetabular dysplasia, and coxa vara. There is delayed ossification of the bones, allowing examination at a later age, but the cartilage and soft tissues often show abnormal increased echogenicity, which obscures the osseous anatomy. With coxa vara, there is narrowing of the sonographic window, and the cartilage of the greater trochanter is elevated. The greater trochanter can be mistaken for a dislocated femoral head, so careful scanning is required. Adduction of the femur during scanning can widen the sonographic window and allow visualization of the normally located femoral head[60-63] (e.g., Kniest dysplasia) (Fig. 55.6).

Congenital Foot Deformities

Club Foot

The treatment of **equinovarus deformity** has dramatically improved with the development of the Ponseti technique of serial casting followed by limited surgery when necessary,[64] and similar changes have occurred with treatment of vertical talus. Imaging of foot anomalies has traditionally been radiographic, but ultrasound is now recognized as an accurate alternative for examination of both unossified and ossified tarsal bones at rest and with movement to assess alignment before and after treatment.

In clubfoot, there is medial displacement of the navicular and anterior displacement of the medial malleolus in relation to the talus with narrowing of the space between the bones.[65] The most commonly used sonographic measurement is the distance between the medial malleolus and the navicular (MMN), measured at rest and with abduction in the medial coronal plane. The measurement is lower than normal in clubfoot, and there is decreased movement with abduction. Other views and measurements include the calcaneocuboid (CC) joint, the length of the talus (TL), the talonavicular joint, the posterior sagittal view for measurement of the tibiocalcaneal distance, and the navicular morphology.[66-69] Normal measurements have been established for some of the views (MMN, CC, TL) for comparison.[70]

Vertical Talus

Congenital vertical talus is a less common anomaly of the foot, frequently occurring in patients with neuromuscular or genetic abnormalities in which there is dorsal dislocation of the navicular

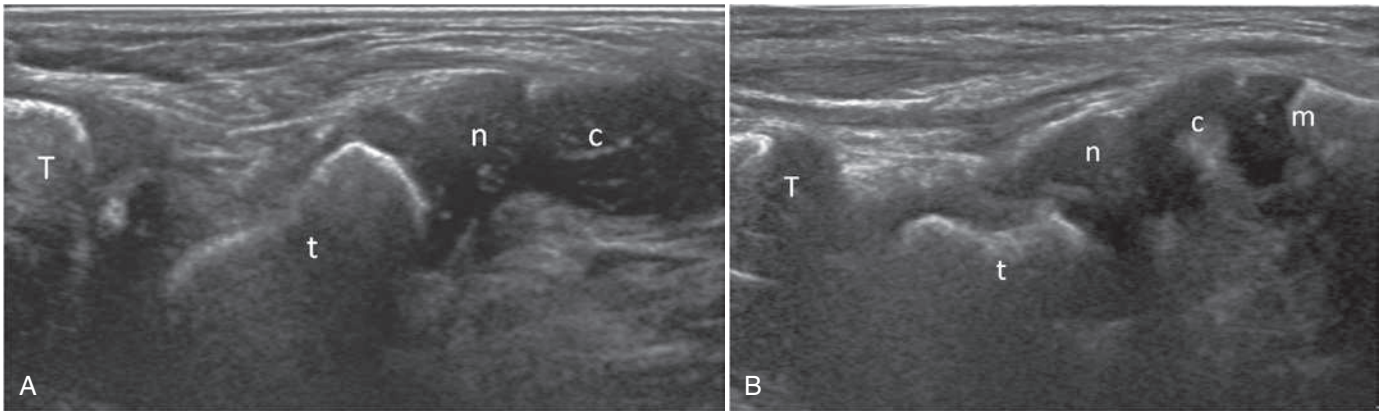

FIG. 55.7 Normal Foot Compared With Congenital Vertical Talus. (A) Sagittal view of the dorsum of the normal foot. The tibia *(T)* is visible proximally, and the talus *(t),* navicular *(n),* and cuneiform *(c)* in a line distally. **(B) Congenital vertical talus.** Sagittal view of the dorsum of the foot. The navicular *(n)* is displaced dorsally and superiorly overlying the head of the talus *(t).* The cuneiform *(c)* and metatarsal *(m)* distally are aligned with the navicular. The tibia *(T)* is visible superiorly.

bone with respect to the plantarflexed (vertical) talus, and it is not reducible. Oblique talus is similar in that the talus is more vertical than normal, and there is dorsal displacement of the navicular in dorsiflexion, reducible in plantarflexion. In the infant with unossified navicular and small talus, it can be difficult to determine the alignment of the joint radiographically, but with ultrasound the joint is easily seen when scanning in the sagittal plane dorsally. Normally, the navicular is located at the head of the talus in a straight line with the first metatarsal. In congenital vertical talus and oblique talus at rest, the navicular is dorsally displaced, projecting anterior to the head of the talus. With plantar flexion, the alignment will not change in vertical talus but corrects with oblique talus.[71] Some investigators use serial manipulation to correct vertical talus,[72] and ultrasound can be used to confirm improving alignment in these patients (Fig. 55.7). Other foot deformities that can be evaluated sonographically include skewfoot and metatarsus adductus.[66]

Congenital Limb Deformities

Proximal Focal Femoral Deficiency

Proximal focal femoral deficiency (PFFD) is a rare congenital anomaly with variable hypoplasia or absence of the proximal femur, usually unilateral and most often isolated. Prenatal diagnosis focuses on the diagnosis of a short femur based on routine femur measurements. If both femurs are short, it suggests skeletal dysplasia. After birth, ultrasound can be used to determine the subtype of PFFD, and thus the treatment, based on what cartilaginous components are present before they are ossified. Scanning includes the standard views of the hip with additional longitudinal and transverse views of the proximal femur. If there is a cartilaginous femoral head, it is essential to determine if it is connected to the proximal femur (Fig. 55.8). This is a difficult examination because of flexion contractures, the small size of the structures, and patient movement, but it can be helpful until the patient can undergo definitive MRI.[73-75]

Tibial Hemimelia

Tibial hemimelia is a rare defect in which there is hypoplasia or aplasia of the tibia, often associated with other congenital anomalies. As in PFFD, evaluation of cartilaginous and soft tissue components is important in the determination of surgical treatment and prognosis, and sonography can be used for this before ossification, scanning anteriorly in longitudinal and transverse planes with flexion and extension of the knee. The osseous defect in the tibia may be proximal or distal, and there may be a substantial cartilaginous component that can be seen sonographically.[76,77] The presence and function of the quadriceps tendon and the extensor mechanism are key; when the mechanism is intact, the cartilaginous patella will be visible overlying the intercondylar notch of the distal femur, and the patellar tendon will extend from the lower pole of the patella to the proximal tibia. The presence of an intact quadriceps mechanism allows reconstructive surgery and preservation of the knee joint, often with below-knee amputation and use of a prosthesis. The absence of the quadriceps mechanism may lead to disarticulation of the knee and use of a prosthesis without the benefit of knee extension.[76,78]

Congenital Nonhip Dislocations

Elbow and Knee Dislocations

Elbow and knee dislocations are rare, usually occurring secondary to malposition in utero and various syndromes, especially **arthrogryposis** and **Larsen syndrome.** Radial head dislocation can also be isolated. Diagnosis of **knee dislocation** can be problematic radiographically because of the large amount of cartilage making up the joints, and ultrasound is an easy way to diagnose displacement or dislocation, scanning anteriorly in longitudinal and transverse planes (Fig. 55.9). Circumferential scanning may be helpful when the orientation of the joint is uncertain. Comparison views of the contralateral side can be used for confirmation, but dislocation is often bilateral. Dynamic

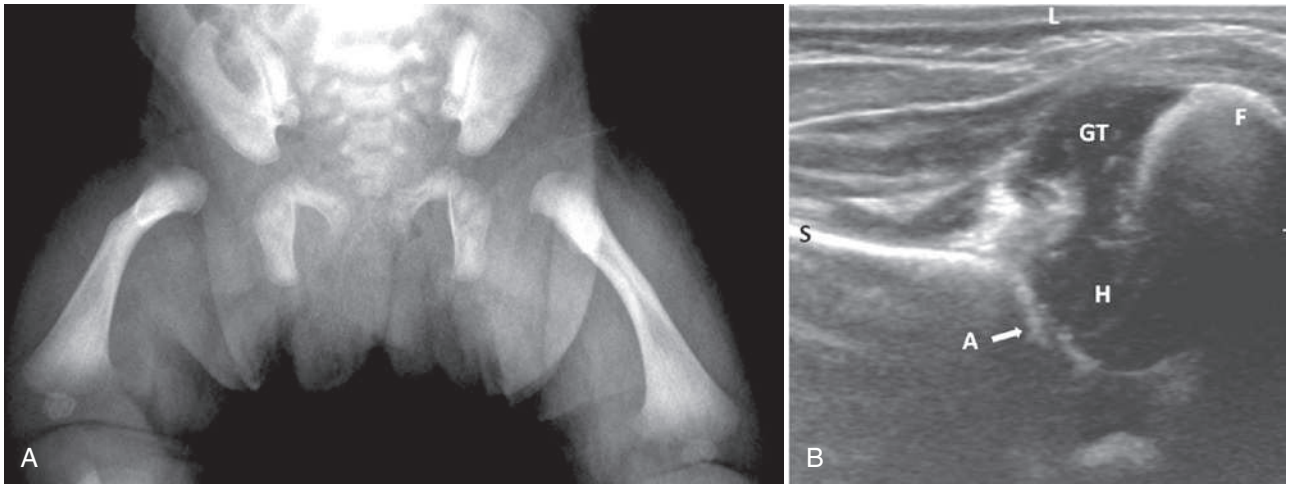

FIG. 55.8 Proximal Femoral Focal Deficiency (PFFD). (A) Pelvic radiograph shows PFFD on the right with a hypoplastic bowed right femur. Right hip appears laterally displaced. Left side normal. **(B)** Coronal/neutral sonogram of the right hip shows coxa vara with elevation of the greater trochanter. Femoral head seated. *A,* Acetabular roof; *F,* femur; *GT,* greater trochanter; *H,* femoral head; *L,* lateral; *S,* superior.

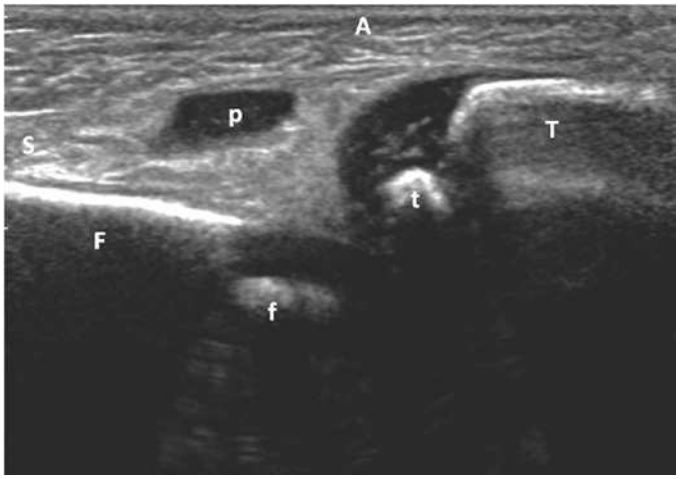

FIG. 55.9 Knee Dislocation With Anterior Displacement of the Tibia. Anterior longitudinal view in extension. *A,* Anterior; *f,* distal femoral epiphysis; *F,* femur; *p,* patella; *S,* superior; *t,* proximal tibial epiphysis; *T,* tibia.

sonography can be used to determine optimal position for reduction, splinting, and physical therapy.[79-81]

Patellar Dislocation

Congenital patellar dislocation is a rare anomaly of variable severity characterized by flexion contracture, genu valgum, and external rotation of the tibia. When suspected, diagnosis is easily made with ultrasound, scanning in sagittal and transverse planes anteriorly with the knee partially flexed. The patella normally lies in the intercondylar notch of the femur; the quadriceps muscle is visible superiorly and the patellar tendon inferiorly extending from the lower pole to the tibial tuberosity. In dislocation the patella may be elevated and/or laterally displaced, and it may be small, requiring more extensive search of the thigh. The patellar tendon may be thin and may appear "stretched," and the quadriceps muscle may be thin. Early diagnosis and treatment can lead to improved joint function[82] (Figs. 55.10 and 55.11).

Brachial Plexus Injury

Brachial plexus injury due to shoulder dystocia, also called **Erb palsy,** is the most common indication for shoulder ultrasound in the infant. Advanced imaging such as CT or MRI is reserved for older children in whom abnormalities persist. Brachial plexus birth injury manifests with weakness of the arm, limited external rotation, and in some cases progressive posterior displacement of the humeral head. It is relatively common, with an incidence of 3.8 per 1000 births. Although many cases resolve spontaneously, 7.3% of patients with birth injury progress to develop shoulder dislocation in the first year of life.[83] When symptoms persist, it is important to monitor the condition so that appropriate treatment can be initiated before there is substantial deformity of the osseous structures and soft tissues.[84]

We scan the shoulder in infants by using multiple views,[85] for conditions such as fracture, infection, or masses (Fig. 55.12). However, the most commonly used protocol for evaluation of brachial plexus injury is posterior scanning of the glenohumeral joint, first described by Hunter and colleagues[86] The technique was subsequently refined, adding dynamic scanning with internal and external rotation of the arm to elicit instability and reduction.[87] Martinoli and colleagues developed a technique for direct visualization of the brachial plexus in the neck.[88]

The patient is examined lying on the side or seated, supported by the parent, and the glenohumeral joint is scanned posteriorly in the transverse plane at rest and with maximum internal and external rotation. The humeral head rests on the cartilage of the glenoid with the triangular labrum extending posteriorly from the lip of the glenoid. The glenoid has a well-defined bony margin with approximately 90 degrees of angulation with respect to the posterior aspect of the scapula, similar in appearance to the coronal/flexion view of the infant hip. The humeral head normally protrudes beyond a line drawn parallel to the scapula; the degree

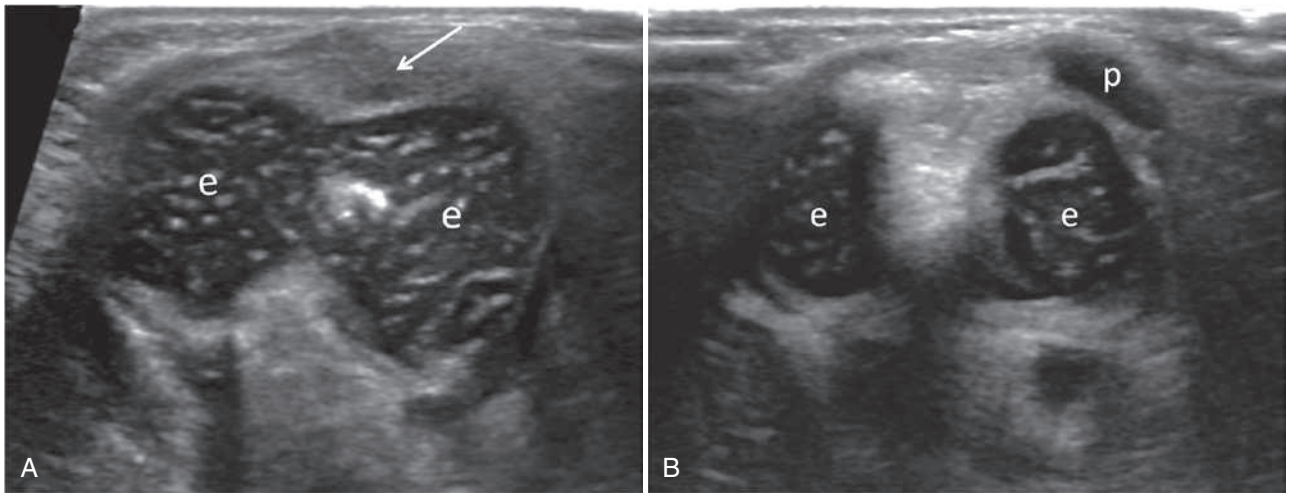

FIG. 55.10 Lateral Dislocation of the Patella. (A) Transverse ultrasound of the knee shows the cartilage of the femoral epiphysis *(e)* and empty intercondylar notch *(arrow).* **(B)** More inferior image shows cartilaginous femoral condyles *(e)* and laterally dislocated patellar cartilage *(p).*

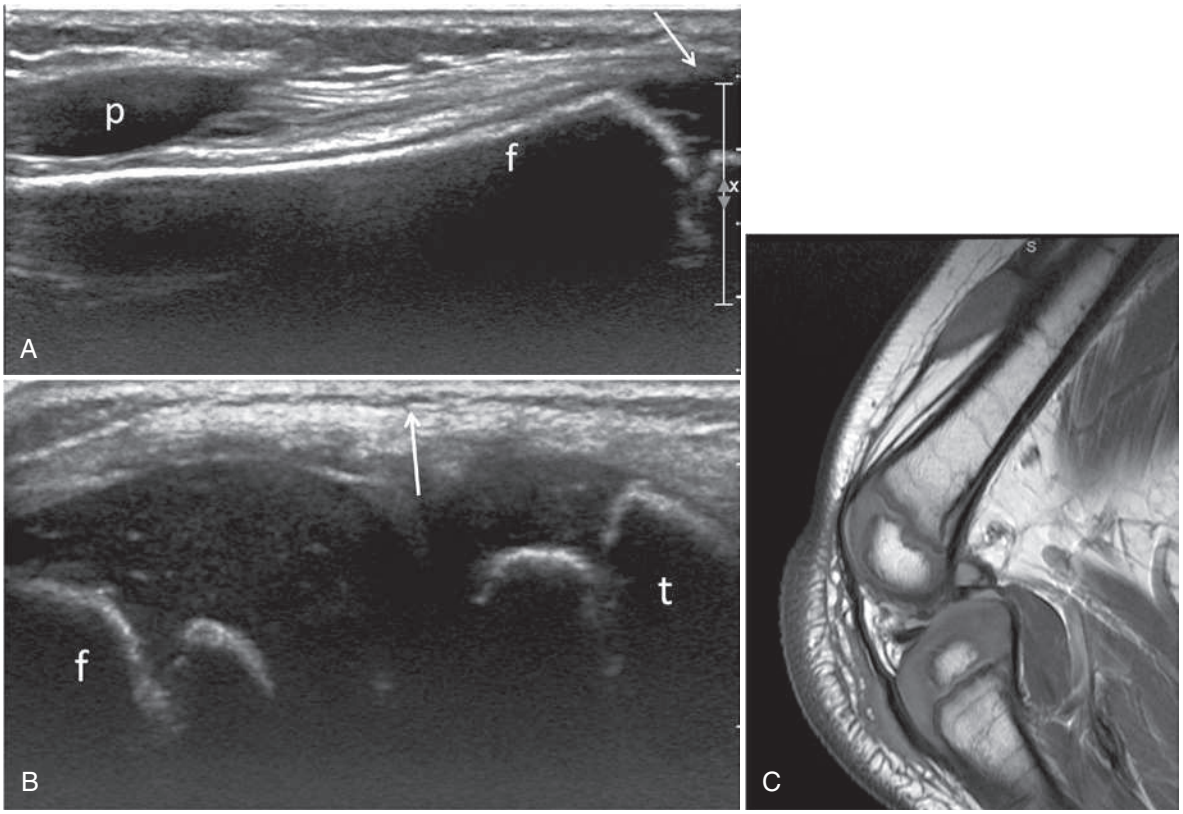

FIG. 55.11 Superior Dislocation of the Patella. (A) Anterior sagittal sonogram of the dislocated patella *(p). f,* Distal femur; *arrow,* knee joint. **(B)** Anterior sagittal view of the knee joint. The femur *(f)* and the tibia *(t)* are normally aligned with a very thin hypoechoic band anteriorly representing a dysplastic patellar tendon *(arrow).* The patella is not visible. **(C)** Sagittal magnetic resonance imaging demonstrates the superiorly dislocated patella and very thin patellar tendon.

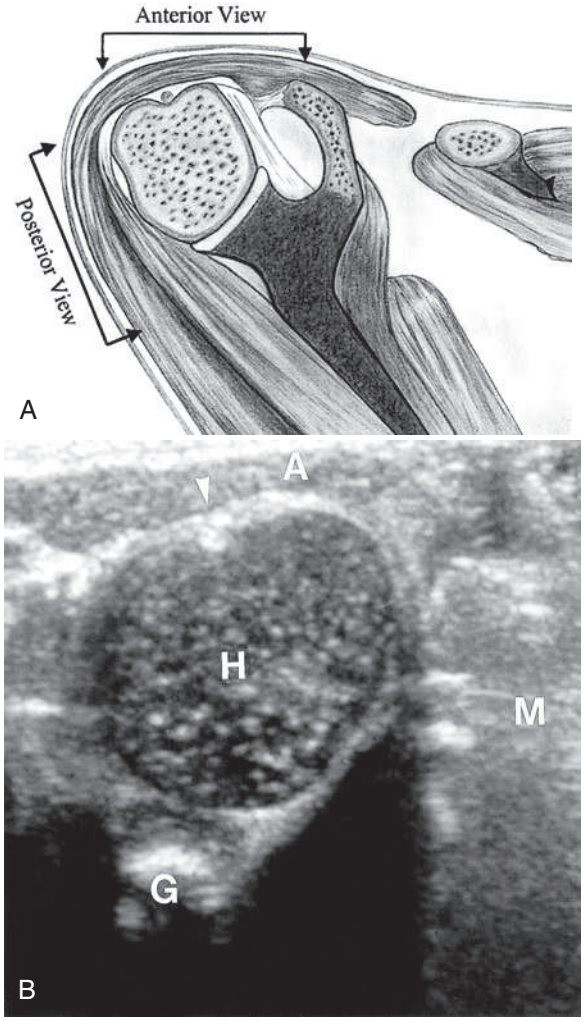

FIG. 55.12 Normal Neonatal Shoulder. (A) Illustration of anterior and posterior axial planes of interrogation of the shoulder. **(B)** Anterior axial image. Cartilaginous humeral head *(H)* anteriorly rests on glenoid *(G)* posteriorly. Biceps tendon *(arrowhead)* can be seen in the bicipital groove. *M,* Medial. (**A** reproduced with permission from Grissom LE, Harcke HT. Infant shoulder sonography: technique, anatomy, and pathology. Pediatr Radiol. 2001;31[12]:863-868.[85])

of protrusion is measured between the scapular line and a line connecting the osseous lip of the glenoid and the posterior margin of the humeral head cartilage as the alpha angle, normally less than 30 degrees.[89] The subluxated shoulder shows increased protrusion, deflection of the labrum, and deformity of the glenoid, which becomes irregular and angled, and the dislocated shoulder is not in contact with the glenoid surface. With internal rotation the position may worsen, and with external rotation the shoulder position may improve. This examination is technically challenging because of patient movement and agitation, but with experience it can be accomplished quickly and reproducibly.[87,90] One of the difficulties is determining the correct plane and angulation of interrogation. Repeat examination is recommended at 1, 3, 6, and 12 months of age, during which time there can be increasing displacement of the humeral head[90] (Fig. 55.13).

Inflammation

Infection

Ultrasound is increasingly used to evaluate pediatric patients for infection of the soft tissues,[91] often to supplement other modalities. Cellulitis (infection of subcutaneous soft tissues) and pyomyositis (infection of skeletal muscle) may be hematogenous or may originate from a puncture wound. Sonographically, there is heterogeneous soft tissue thickening and increased echogenicity in the affected area, and there may be regional adenopathy. If there is a puncture wound, foreign material or air may be present. Comparison with the contralateral unaffected side is helpful to make the diagnosis. The inflammatory process can progress to abscess formation or necrosis. Although inflammatory debris within the abscess may be hypoechoic, it can also be isoechoic or even hyperechoic and difficult to appreciate.[92] Color and power Doppler may also assist in the diagnosis in that the rim of the abscess will demonstrate increased flow, and the debris within the cavity should be avascular.[93] If the fluid is mobile, motion may cause color or power signal on Doppler sonography, but spectral analysis will not reveal any true vascularity. Sonographic guidance can be used to biopsy or drain an abscess.[94] A recent hematoma, early myositis ossificans, or a necrotic mass can have a similar appearance to an abscess, and the best way to distinguish infection from these entities is by clinical history and laboratory tests. In myositis ossificans and hematoma, after calcification has developed, the echo pattern changes, and being mistaken for abscesses becomes unlikely.

Septic arthritis can be an isolated abnormality or can be secondary to infection in the adjacent soft tissues or bone. Fluid is visible in the joint, and debris may or may not be seen within it. When joint fluid is anechoic or hypoechoic, it may be difficult to distinguish from the cartilage that caps the ends of the bones forming the joint. In addition, if there is debris in the fluid, it may be difficult to detect the septic effusion, similar to the soft tissue abscess (Fig. 55.14). Movement of the joint will show the cartilage-fluid interface clearly. Application of pressure to the tissue around a joint will cause joint fluid to shift, making the fluid easier to recognize. Pressure along the sides of the knee, for example, can force fluid into the suprapatellar bursa, thereby confirming an effusion. Color or power Doppler sonography may help because there is typically hyperemia in the capsule with infection.[95] The absence of hyperemia does not exclude septic arthritis.[56] As with hip effusions, sonography can be used to aspirate from the joints.[96]

Lyme disease, caused by the spirochete *Borrelia burgdorferi* and spread by deer ticks, can result in arthritis. This usually occurs in the subacute or chronic phase of the infection and is characterized by relapsing effusions, particularly in the knee joint. There may be synovial thickening, and cartilage loss is seen late in the course. This can be confused with juvenile rheumatoid arthritis, and the diagnosis should be considered in patients with oligoarticular joint effusions.[97]

Osteomyelitis typically occurs in the metaphyses of the long bones. The earliest sonographic sign is deep soft tissue swelling. Later signs are fluid along the cortex of the bone or, subperiosteally, fluid in the adjacent joint (either sterile or septic),

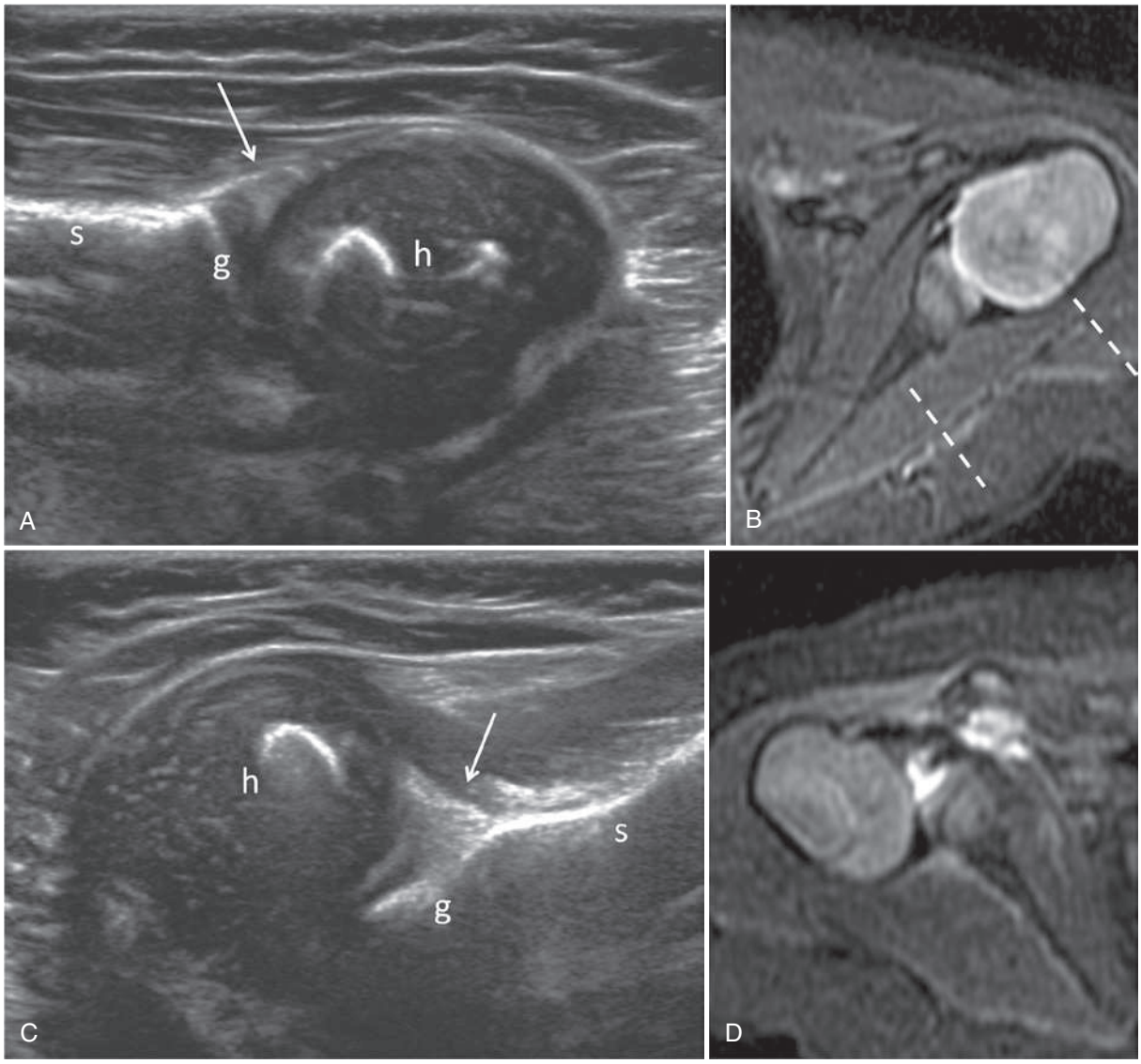

FIG. 55.13 Normal and Dislocated Shoulder. (A) Normal shoulder posterior axial sonogram. The humeral head *(h)* projects only minimally beyond the margin of the scapula. The glenoid *(g)* is well formed, and the labrum *(arrow)* is small. *s,* Scapula. **(B) Normal shoulder.** Axial T2-weighted magnetic resonance image shows the field of view in the plane of sonographic interrogation *(dashed lines).* **(C)** and **(D) Posterior dislocated shoulder. (C)** Posterior axial ultrasound. Note the posterior protrusion of the humeral head *(h),* the dysplastic glenoid *(g),* and the echogenic labrum *(arrow). s,* Scapula. **(D)** Dislocated humeral head with glenoid dysplasia. Axial T2-weighted magnetic resonance image.

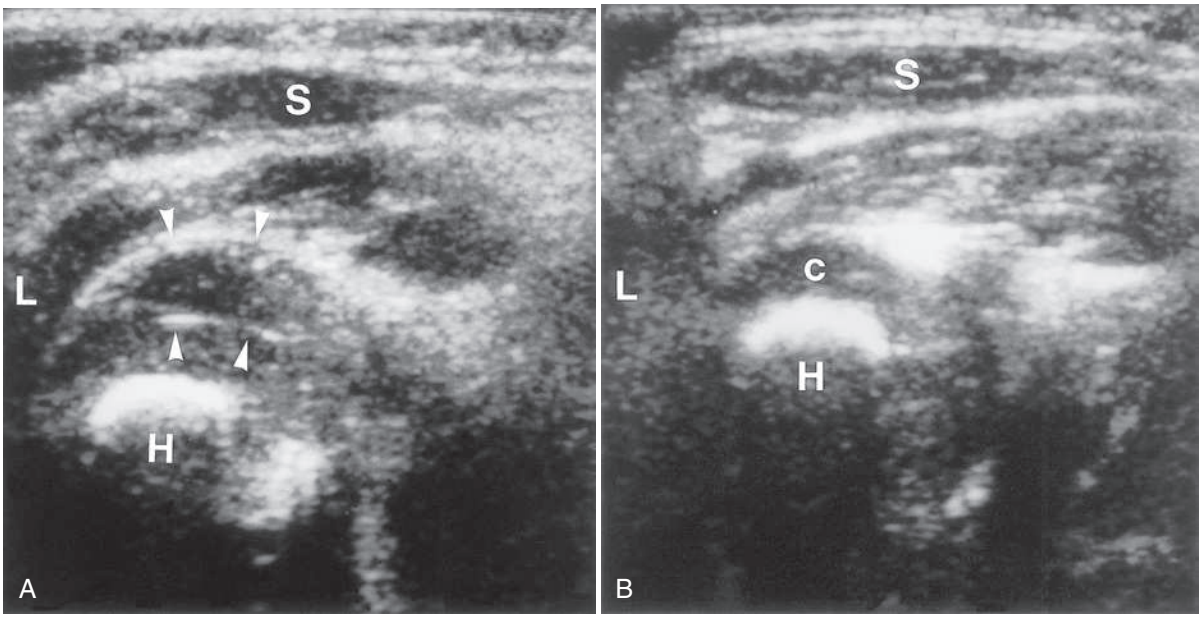

FIG. 55.14 Septic Arthritis. Coronal images of the shoulder. **(A)** Echogenic fluid within the shoulder joint *(arrowheads)* superior to the humeral head *(H). c,* Cartilage of humeral head; *L,* lateral; *S,* superior. **(B)** Normal side for comparison.

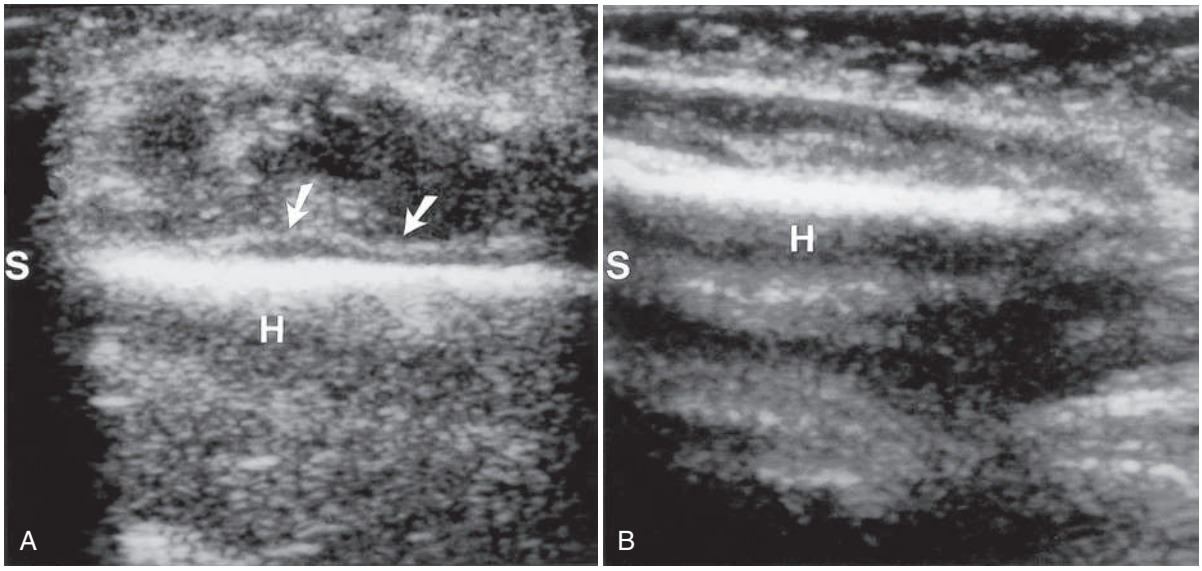

FIG. 55.15 Osteomyelitis. Longitudinal sonogram of the humerus *(H).* **(A)** Thickening and abnormal echogenicity of the soft tissues with fluid along the bone *(arrows).* **(B)** Normal side for comparison. *S,* Superior.

and cortical disruption (Fig. 55.15). Color and power Doppler sonography show increased flow at the margin of the elevated periosteum in advanced infection.[98-100] Osteomyelitis often spreads hematogenously in pediatric patients, so when it is detected in one location, examination of any other symptomatic areas is recommended. Some investigators examine all the extremities in this situation, particularly in infants who are difficult to assess clinically. Negative ultrasound findings do not exclude osteomyelitis.

Cat-scratch fever is caused by a gram-negative bacillus and is characterized by fever and regional, sometimes suppurative, adenopathy occurring proximal to the affected area—for example, in the groin related to scratches on the leg or in the epitrochlear area from scratches on the upper extremity. These infected nodes are highly vascular[101-103] (Fig. 55.16). Patients with cat-scratch disease may also develop hypoechoic hepatic and splenic lesions.[104]

Noninfectious Inflammation

Sonography has been used to evaluate and to monitor the effects of treatment in pediatric patients with arthritis. Synovitis and effusion are often seen, and there is increased Doppler signal in the inflamed, thickened synovium. The cartilage can also be examined for decreased thickness, increased echogenicity, and erosive changes.[105-107] Baker cysts occur in these patients, most often in the knee, and must be differentiated from a mass or deep venous thrombosis.

Trauma

Radiographs are the initial diagnostic modality used in evaluation of trauma, but sonography is a useful problem-solving tool when symptoms are present and radiographs are unrevealing. This applies to abnormalities such as growth plate fracture, soft tissue injury, and retained nonopaque foreign body.

Sonography is an excellent means to detect a fracture through the growth plate, particularly in the infant in whom the epiphyses

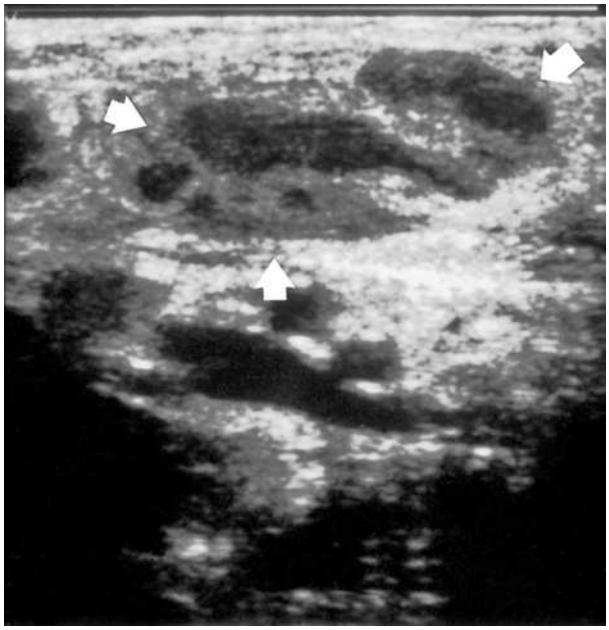

FIG. 55.16 Cat-Scratch Disease. Enlarged inguinal lymph nodes *(arrows)* with increased vascularity *(gray areas).*

are not ossified. When searching for a fracture, it is important to study the bone from all possible angles. In the extremities, this may mean 360-degree visualization. By careful examination of the affected area and comparison with the contralateral normal side, one can confirm fracture findings and assessment alignment. An avulsion or metaphyseal fracture may be detected that is not seen radiographically. This can be especially useful in **nonaccidental trauma** (Fig. 55.17). The joint can be examined to differentiate fracture from dislocation and to diagnose secondary effusion. Care must be taken to distinguish fluid from cartilage because both are hypoechoic. Passive motion and compression help to eliminate confusion. With fracture, there is virtually

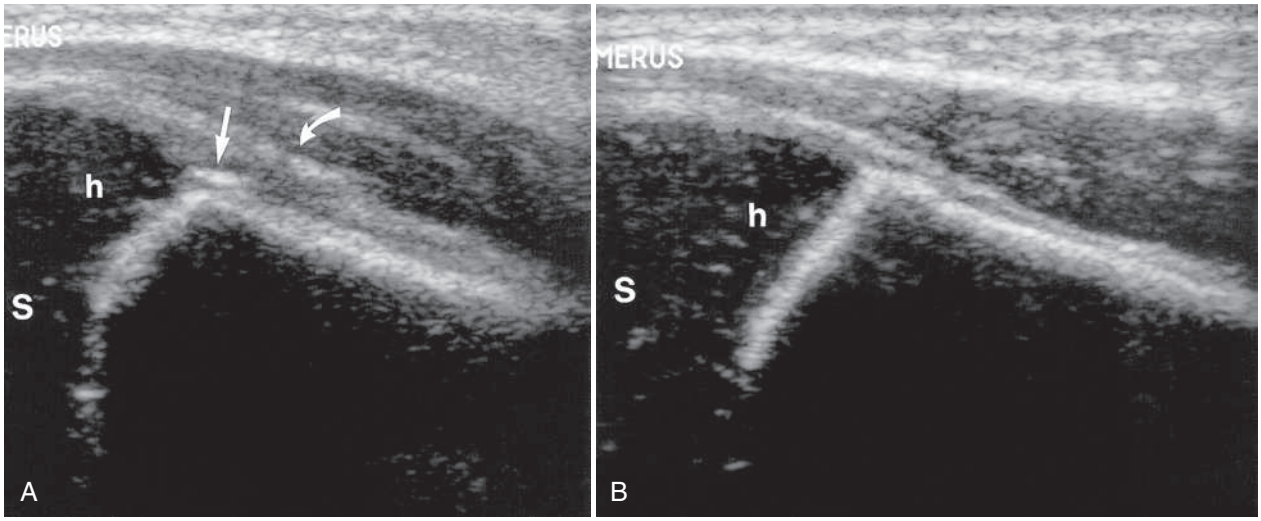

FIG. 55.17 Infant With Nonaccidental Trauma. Longitudinal sonogram of shoulder. **(A)** Metaphyseal fracture fragment *(straight arrow)* and soft tissue swelling *(curved arrow)* not detected on radiograph. **(B)** Normal side for comparison. *H,* Humeral head; *S,* superior.

always associated soft tissue abnormality, although this may be subtle and localized. The soft tissue planes become thickened by edema, and a small fluid collection may be present. Hematoma is initially hyperechoic with disruption of normal soft tissue planes, and later more complex as it organizes and resorbs. If myositis ossificans develops, it will gradually ossify, starting peripherally, but the early appearance will be identical.[108-110]

Ultrasound is also useful in evaluation of soft tissue structures such as tendons, ligaments, and muscles, and this is described in the other musculoskeletal chapters (see Chapters 23 and 24). In the pediatric population, sonography can be used to diagnose and grade Osgood-Schlatter disease.[111,112] Ultrasound can also be used for examination for foreign bodies.

Popliteal Cysts

Popliteal cysts often manifest in pediatric patients as a painless "swelling" or "soft tissue mass" behind the knee joint. Ultrasound is used to confirm the cystic nature of the mass. The cysts arise from the gastrocnemius-semimembranosus bursa lined with synovial fluid. They are deemed idiopathic, and although many practitioners think they are posttraumatic, a trauma history is rarely elicited, and associated intraarticular pathology is rare. Popliteal cysts are considered to be different from those found in childhood arthritis. These cysts are usually oval with a few septations but no solid tissue, located posteromedially in the popliteal fossa. Popliteal cysts can persist for years but do not rupture or become symptomatic. The natural history is spontaneous regression, so typically no treatment is recommended.[113-115] Whenever a cyst is seen in the area of a joint, ganglion cyst should also be considered.

SUMMARY

Although DDH was the first and continues to be the most common single indication for musculoskeletal ultrasound in pediatric patients, many other uses have been explored and developed. The ability to differentiate soft tissue structures from cartilage makes ultrasound especially helpful in infants. In this age of increasing concern regarding radiation, sonography has become an attractive alternative in the evaluation of the musculoskeletal system.

REFERENCES

1. Barlow TG. Early diagnosis and treatment of congenital dislocation of the hip. J Bone Joint Surg Br. 1962;44B:292-301.
2. VonRosen S. Prevention of congenital dislocation of the hip joint in Sweden. Acta Orthop Scand. 1970;130(Suppl.):1-64.
3. Tredwell SJ, Bell HM. Efficacy of neonatal hip examination. J Pediatr Orthop. 1981;1(1):61-65.
4. Harcke HT. Screening newborns for developmental dysplasia of the hip: the role of sonography. AJR Am J Roentgenol. 1994;162(2):395-397.
5. Dunn PM. Perinatal observations on the etiology of congenital dislocation of the hip. Clin Orthop Relat Res. 1976;119:11-22.
6. MacEwen GD, Bassett GS. Current trends in the management of congenital dislocation of the hip. Int Orthop. 1984;8(2):103-111.
7. Committee on Quality Improvement, Subcommittee on Developmental Dysplasia of the Hip, American Academy of Pediatrics. Clinical practice guideline: early detection of developmental dysplasia of the hip. Pediatrics. 2000;105(4):896-905.
8. ACR-AIUM-SPR-SRU practice parameter for the performance of the ultrasound examination for detection and assesssment of developmental dysplasia of the hip. American College of Radiology; 2013. Available from: https://www.acr.org/~/media/ACR/Documents/PGTS/guidelines/US_Hip_Dysplasia.pdf. Accessed 2/21/2017.
9. American Academy of Orthopaedic surgeons. Detection and nonoperative management of pediatric developmental dysplasia of the hip in infants up to six months of age. Evidence-based clinical practice guideline; September 5, 2014. Available from: http://www.aaos.org/research/guidelines/DDHGuidelineFINAL.pdf. Accessed 2/20/2017.
10. Wynne-Davies R. Acetabular dysplasia and familial joint laxity: two etiological factors in congenital dislocation of the hip. A review of 589 patients and their families. J Bone Joint Surg Br. 1970;52(4):704-716.
11. Tonnis D, Storch K, Ulbrich H. Results of newborn screening for CDH with and without sonography and correlation of risk factors. J Pediatr Orthop. 1990;10(2):145-152.
12. Gomes H, Menanteau B, Motte J, Robiliard P. Sonography of the neonatal hip: a dynamic approach. Ann Radiol (Paris). 1987;30(7):503-510.
13. Dahlstrom H, Oberg L, Friberg S. Sonography in congenital dislocation of the hip. Acta Orthop Scand. 1986;57(5):402-406.

14. Clarke NM, Harcke HT, McHugh P, et al. Real-time ultrasound in the diagnosis of congenital dislocation and dysplasia of the hip. J Bone Joint Surg Br. 1985;67(3):406-412.
15. Berman L, Klenerman L. Ultrasound screening for hip abnormalities: preliminary findings in 1001 neonates. Br Med J (Clin Res Ed). 1986;293(6549):719-722.
16. Clarke NM, Clegg J, Al-Chalabi AN. Ultrasound screening of hips at risk for CDH. Failure to reduce the incidence of late cases. J Bone Joint Surg Br. 1989;71(1):9-12.
17. Rosendahl K, Markestad T, Lie RT. Ultrasound screening for developmental dysplasia of the hip in the neonate: the effect on treatment rate and prevalence of late cases. Pediatrics. 1994;94(1):47-52.
18. Shipman SA, Helfand M, Moyer VA, Yawn BP. Screening for developmental dysplasia of the hip: a systematic literature review for the U.S. Preventive Services Task Force. Pediatrics. 2006;117(3):e557-e576.
19. Boeree NR, Clarke NM. Ultrasound imaging and secondary screening for congenital dislocation of the hip. J Bone Joint Surg Br. 1994;76(4):525-533.
20. Harcke HT. The role of ultrasound in diagnosis and management of developmental dysplasia of the hip. Pediatr Radiol. 1995;25(3):225-227.
21. Laborie L, Markestad T, Davidsen H, et al. Selective ultrasound screening for developmental hip dysplasia: effect on management and late detected cases. A prospective survey during 1991-2006. Pediatr Radiol. 2013;44(4):410-424.
22. Holen KJ, Tegnander A, Bredland T, et al. Universal or selective screening of the neonatal hip using ultrasound? A prospective, randomised trial of 15,529 newborn infants. J Bone Joint Surg Br. 2002;84(6):886-890.
23. Graf R. The diagnosis of congenital hip-joint dislocation by the ultrasonic compound treatment. Arch Orthop Trauma Surg. 1980;97(2):117-133.
24. Novick G, Ghelman B, Schneider M. Sonography of the neonatal and infant hip. AJR Am J Roentgenol. 1983;141(4):639-645.
25. Harcke HT, Clarke NM, Lee MS, et al. Examination of the infant hip with real-time ultrasonography. J Ultrasound Med. 1984;3(3):131-137.
26. Harcke HT, Grissom LE. Performing dynamic sonography of the infant hip. AJR Am J Roentgenol. 1990;155(4):837-844.
27. Graf R. Ultrasonography of the infantile hip. In: Sanders RC, Hill MC, editors. Ultrasound annual. New York: Raven Press; 1985. p. 177-186.
28. Hensinger RN. Congenital dislocation of the hip. Treatment in infancy to walking age. Orthop Clin North Am. 1987;18(4):597-616.
29. Harcke HT, Lee MS, Sinning L, et al. Ossification center of the infant hip: sonographic and radiographic correlation. AJR Am J Roentgenol. 1986;147(2):317-321.
30. Graf R. Classification of hip joint dysplasia by means of sonography. Arch Orthop Trauma Surg. 1984;102(4):248-255.
31. Zieger M, Hilpert S, Schulz RD. Ultrasound of the infant hip. Part 1. Basic principles. Pediatr Radiol. 1986;16(6):483-487.
32. Morin C, Harcke HT, MacEwen GD. The infant hip: real-time US assessment of acetabular development. Radiology. 1985;157(3):673-677.
33. Morin C, Zouaoui S, Delvalle-Fayada A, et al. Ultrasound assessment of the acetabulum in the infant hip. Acta Orthop Belg. 1999;65(3):261-265.
34. Polanuer PA, Harcke HT, Bowen JR. Effective use of ultrasound in the management of congenital dislocation and/or dysplasia of the hip. Clin Orthop Relat Res. 1990;252:176-181.
35. Bialik V, Pery M, Kaftori JK, Fishman J. The use of ultrasound scanning in the management of developmental disorders of the hip. Int Orthop. 1988;12(1):75-78.
36. Engesaeter LB, Wilson DJ, Nag D, Benson MK. Ultrasound and congenital dislocation of the hip. The importance of dynamic assessment. J Bone Joint Surg Br. 1990;72(2):197-201.
37. Langer R. Ultrasonic investigation of the hip in newborns in the diagnosis of congenital hip dislocation: classification and results of a screening program. Skeletal Radiol. 1987;16(4):275-279.
38. Szoke N, Kuhl L, Heinrichs J. Ultrasound examination in the diagnosis of congenital hip dysplasia of newborns. J Pediatr Orthop. 1988;8(1):12-16.
39. Grissom LE, Harcke HT, Kumar SJ, et al. Ultrasound evaluation of hip position in the Pavlik harness. J Diag Med Sonograph. 1988;7(1):1-6.
40. Dahlstrom H, Friberg S, Oberg L. Stabilisation and development of the hip after closed reduction of late CDH. J Bone Joint Surg Br. 1990;72(2):186-189.
41. Mulpuri K, Song KM, Gross RH, et al. The American Academy of Orthopaedic Surgeons evidence-based guideline on detection and nonoperative management of pediatric developmental dysplasia of the hip in infants up to six months of age. J Bone Joint Surg Am. 2015;97(20):1717-1718.
42. Alexiev VA, Harcke HT, Kumar SJ. Residual dysplasia after successful Pavlik harness treatment: early ultrasound predictors. J Pediatr Orthop. 2006;26(1):16-23.
43. McNally EG, Tasker A, Benson MK. MRI after operative reduction for developmental dysplasia of the hip. J Bone Joint Surg Br. 1997;79(5):724-726.
44. Gould SW, Grissom LE, Niedzielski A, et al. Protocol for MRI of the hips after spica cast placement. J Pediatr Orthop. 2012;32(5):504-509.
45. Tiderius C, Jaramillo D, Connolly S, et al. Post-closed reduction perfusion magnetic resonance imaging as a predictor of avascular necrosis in developmental hip dysplasia: a preliminary report. J Pediatr Orthop. 2009;29(1):14-20.
46. Bearcroft PW, Berman LH, Robinson AH, Butler GJ. Vascularity of the neonatal femoral head: in vivo demonstration with power Doppler US. Radiology. 1996;200(1):209-211.
47. Harcke H, Grissom L. Musculoskeletal ultrasound in pediatrics. Semin Musculoskelet Radiol. 1998;2(03):321-329.
48. Zieger M, Dorr U, Schulz R. Ultrasonography of hip joint effusions. Skeletal Radiol. 1987;16(8):607-611.
49. Miralles M, Gonzalez G, Pulpeiro JR, et al. Sonography of the painful hip in children: 500 consecutive cases. AJR Am J Roentgenol. 1989;152(3):579-582.
50. Kocher MS, Mandiga R, Zurakowski D, et al. Validation of a clinical prediction rule for the differentiation between septic arthritis and transient synovitis of the hip in children. J Bone Joint Surg Am. 2004;86-A(8):1629-1635.
51. Caird MS, Flynn JM, Leung YL, et al. Factors distinguishing septic arthritis from transient synovitis of the hip in children. A prospective study. J Bone Joint Surg Am. 2006;88(6):1251-1257.
52. Robben SF, Lequin M, Diepstraten AM, et al. Anterior joint capsule of the normal hip and in children with transient synovitis: US study with anatomic and histologic correlation. Radiology. 1999;210(2):499-507.
53. Marchal GJ, Van Holsbeeck MT, Raes M, et al. Transient synovitis of the hip in children: role of US. Radiology. 1987;162(3):825-828.
54. Alexander JE, Seibert JJ, Glasier CM, et al. High-resolution hip ultrasound in the limping child. J Clin Ultrasound. 1989;17(1):19-24.
55. Kallio P, Ryoppy S, Jappinen S, et al. Ultrasonography in hip disease in children. Acta Orthop Scand. 1985;56(5):367-371.
56. Strouse PJ, DiPietro MA, Adler RS. Pediatric hip effusions: evaluation with power Doppler sonography. Radiology. 1998;206(3):731-735.
57. Futami T, Kasahara Y, Suzuki S, et al. Ultrasonography in transient synovitis and early Perthes' disease. J Bone Joint Surg Br. 1991;73:635-639.
58. Gruel CR, Birch JG, Roach JW, Herring JA. Teratologic dislocation of the hip. J Pediatr Orthop. 1986;6(6):693-702.
59. Canavese F, Sussman MD. Strategies of hip management in neuromuscular disorders: Duchenne muscular dystrophy, spinal muscular atrophy, Charcot-Marie-Tooth disease and arthrogryposis multiplex congenita. Hip Int. 2009;19(Suppl. 6):S46-S52.
60. Grissom LE, Harcke HT. Ultrasonography of nondevelopmental dysplasia of the hips. Pediatr Radiol. 1997;27(1):70-74.
61. De Pellegrin MP, Mackenzie WG, Harcke HT. Ultrasonographic evaluation of hip morphology in osteochondrodysplasias. J Pediatr Orthop. 2000;20(5):588-593.
62. Lamminen A, Jaaskelainen J, Rapola J, Suramo I. High-frequency ultrasonography of skeletal muscle in children with neuromuscular disease. J Ultrasound Med. 1988;7(9):505-509.
63. Haake M, Wirth T, Griss P. False-positive sonographic hip examinations in newborns with congenital varus deformity of the proximal femur. Arch Orthop Trauma Surg. 1995;114(5):274-277.
64. Ponseti IV. Congenital clubfoot: fundamentals of treatment. London: Oxford University Press; 1996.

65. Ippolito E. Update on pathologic anatomy of clubfoot. J Pediatr Orthop B. 1995;4(1):17-24.
66. Miron M, Grimard G. Ultrasound evaluation of foot deformities in infants. Pediatr Radiol. 2015;46(2):193-209.
67. Shiels W, Coley B, Kean J, Adler B. Focused dynamic sonographic examination of the congenital clubfoot. Pediatr Radiol. 2007;37(11):1118-1124.
68. El-Adwar KL, Taha Kotb H. The role of ultrasound in clubfoot treatment: correlation with the Pirani score and assessment of the Ponseti method. Clin Orthop Relat Res. 2010;468(9):2495-2506.
69. Chami M, Daoud A, Maestro M, et al. Ultrasound contribution in the analysis of the newborn and infant normal and clubfoot: a preliminary study. Pediatr Radiol. 1996;26(4):298-302.
70. Aurell Y, Johansson A, Hansson G, et al. Ultrasound anatomy in the normal neonatal and infant foot: an anatomic introduction to ultrasound assessment of foot deformities. Eur Radiol. 2002;12(9):2306-2312.
71. Supakul N, Loder R, Karmazyn B. Dynamic US study in the evaluation of infants with vertical or oblique talus deformities. Pediatr Radiol. 2012;43(3): 376-380.
72. Dobbs MB, Purcell DB, Nunley R, Morcuende JA. Early results of a new method of treatment for idiopathic congenital vertical talus. J Bone Joint Surg Am. 2006;88(6):1192-1200.
73. Grissom LE, Harcke HT. Sonography in congenital deficiency of the femur. J Pediatr Orthop. 1994;14(1):29-33.
74. Filly AL, Robnett-Filly B, Filly RA. Syndromes with focal femoral deficiency: strengths and weaknesses of prenatal sonography. J Ultrasound Med. 2004;23(11):1511-1516.
75. Camera G, Dodero D, Parodi M, et al. Antenatal ultrasonographic diagnosis of a proximal femoral focal deficiency. J Clin Ultrasound. 1993;21(7): 475-479.
76. Weber M. New classification and score for tibial hemimelia. J Child Orthop. 2008;2(3):169-175.
77. Grissom LE, Harcke HT, Kumar SJ. Sonography in the management of tibial hemimelia. Clin Orthop Relat Res. 1990;251:266-270.
78. Kalamchi A, Dawe RV. Congenital deficiency of the tibia. J Bone Joint Surgery Br. 1985;76B:581-583.
79. Parsch K. Ultrasound diagnosis of congenital knee dislocation. Orthopade. 2002;31(3):306-307.
80. Abdelaziz TH, Samir S. Congenital dislocation of the knee: a protocol for management based on degree of knee flexion. J Child Orthop. 2011;5(2):143-149.
81. Kaas L, Struijs PA. Congenital radial head dislocation with a progressive cubitus valgus: a case report. Strategies Trauma Limb Reconstr. 2012; 7(1):39-44.
82. Koplewitz B, Babyn P, Cole W. Congenital dislocation of the patella. AJR Am J Roentgenol. 2005;184(5):1640-1646.
83. Dahlin L, Erichs K, Andersson C, et al. Incidence of early posterior shoulder dislocation in brachial plexus birth palsy. J Brachial Plex Peripher Nerve Inj. 2014;02(01):e38-e42.
84. Moukoko D, Ezaki M, Wilkes D, Carter P. Posterior shoulder dislocation in infants with neonatal brachial plexus palsy. J Bone Joint Surg Am. 2004;86-A(4):787-793.
85. Grissom LE, Harcke HT. Infant shoulder sonography: technique, anatomy, and pathology. Pediatr Radiol. 2001;31(12):863-868.
86. Hunter JD, Franklin K, Hughes PM. The ultrasound diagnosis of posterior shoulder dislocation associated with Erb's palsy. Pediatr Radiol. 1998; 28(7):510-511.
87. Zhang S, Ezaki M. Sonography as a preferred diagnostic tool to assess shoulder displacement in brachial plexus palsy. J Diagn Med Sonogr. 2008;24(6):339-343.
88. Martinoli C, Gandolfo N, Perez M, et al. Brachial plexus and nerves about the shoulder. Semin Musculoskelet Radiol. 2010;14(05):523-546.
89. Poyhia TH, Lamminen AE, Peltonen JI, et al. Brachial plexus birth injury: US screening for glenohumeral joint instability. Radiology. 2010; 254(1):253-260.
90. Vathana T, Rust S, Mills J, et al. Intraobserver and interobserver reliability of two ultrasound measures of humeral head position in infants with neonatal brachial plexus palsy. J Bone Joint Surg Am. 2007;89(8):1710-1715.
91. Adhikari S, Blaivas M. Sonography first for subcutaneous abscess and cellulitis evaluation. J Ultrasound Med. 2012;31(10):1509-1512.
92. Bureau N, Chhem R, Cardinal É. Musculoskeletal infections: US manifestations. Radiographics. 1999;19(6):1585-1592.
93. Gottlieb RH, Meyers SP, Hall C, et al. Pyomyositis: diagnostic value of color Doppler sonography. Pediatr Radiol. 1995;25(Suppl. 1):S109-S111.
94. Ramirez-Schrempp D, Dorfman DH, Baker WE, Liteplo AS. Ultrasound soft-tissue applications in the pediatric emergency department: to drain or not to drain? Pediatr Emerg Care. 2009;25:44-48.
95. Breidahl WH, Newman JS, Taljanovic MS, Adler RS. Power Doppler sonography in the assessment of musculoskeletal fluid collections. AJR Am J Roentgenol. 1996;166(6):1443-1446.
96. Fessell DP, Jacobson JA, Craig J, et al. Using sonography to reveal and aspirate joint effusions. AJR Am J Roentgenol. 2000;174(5):1353-1362.
97. Czupryna P, Moniuszko A, Czeczuga A, et al. Ultrasonographic evaluation of knee joints in patients with Lyme disease. Int J Infect Dis. 2012; 16(4):e252-e255.
98. Pineda C, Espinosa R, Pena A. Radiographic imaging in osteomyelitis: the role of plain radiography, computed tomography, ultrasonography, magnetic resonance imaging, and scintigraphy. Semin Plast Surg. 2009; 23(2):80-89.
99. Azam Q, Ahmad I, Abbas M, et al. Ultrasound and colour Doppler sonography in acute osteomyelitis in children. Acta Orthop Belg. 2005; 71(5):590-596.
100. Robben SG. Ultrasonography of musculoskeletal infections in children. Eur Radiol. 2004;14(Suppl. 4):L65-L77.
101. Garcia CJ, Varela C, Abarca K, et al. Regional lymphadenopathy in cat-scratch disease: ultrasonographic findings. Pediatr Radiol. 2000;30(9):640-643.
102. Melville DM, Jacobson JA, Downie B, et al. Sonography of cat scratch disease. J Ultrasound Med. 2015;34(3):387-394.
103. Ridder GJ, Richter B, Disko U, Sander A. Gray-scale sonographic evaluation of cervical lymphadenopathy in cat-scratch disease. J Clin Ultrasound. 2001;29(3):140-145.
104. Danon O, Duval-Arnould M, Osman Z, et al. Hepatic and splenic involvement in cat-scratch disease: imaging features. Abdom Imaging. 2000;25(2): 182-183.
105. Ramos PC, Ceccarelli F, Jousse-Joulin S. Role of ultrasound in the assessment of juvenile idiopathic arthritis. Rheumatology. 2012;51(Suppl. 7): vii10-vii12.
106. Sheybani E, Khanna G, White A, Demertzis J. Imaging of juvenile idiopathic arthritis: a multimodality approach. Radiographics. 2013;33(5): 1253-1273.
107. Szer IS, Klein-Gitelman M, DeNardo BA, McCauley RG. Ultrasonography in the study of prevalence and clinical evolution of popliteal cysts in children with knee effusions. J Rheumatol. 1992;19(3):458-462.
108. Tyler P, Saifuddin A. The imaging of myositis ossificans. Semin Musculoskelet Radiol. 2010;14(02):201-216.
109. Ryu JK, Jin W, Kim GY. Sonographic appearances of small organizing hematomas and thrombi mimicking superficial soft tissue tumors. J Ultrasound Med. 2011;30(10):1431-1436.
110. Fornage BD, Eftekhari F. Sonographic diagnosis of myositis ossificans. J Ultrasound Med. 1989;8(8):463-466.
111. Carr J, Hanly S, Griffin J, Gibney R. Sonography of the patellar tendon and adjacent structures in pediatric and adult patients. AJR Am J Roentgenol. 2001;176(6):1535-1539.
112. Lanning P, Heikkinen E. Ultrasonic features of the Osgood-Schlatter lesion. J Pediatr Orthop. 1991;11(4):538-540.
113. Dinham JM. Popliteal cysts in children. The case against surgery. J Bone Joint Surg Br. 1975;57(1):69-71.
114. Harcke HT, Niedzielski A, Thacker MM. Popliteal cysts in children: another look. J Pediatr Orthop B. 2016;25(6):539-542.
115. Akagi R, Saisu T, Segawa Y, et al. Natural history of popliteal cysts in the pediatric population. J Pediatr Orthop. 2013;33(3):262-268.

CHAPTER 56

Pediatric Interventional Sonography

Neil Johnson and Allison Aguado

SUMMARY OF KEY POINTS

- Understanding of the different needs of the parents and the child being treated is essential for pediatric interventions.
- Multimodality interventional suites allow for procedural guidance with varied modalities at different points during the procedure.
- Although needle guides may be used, they add to the expense of the procedure. Therefore we typically advocate for a single-operator freehand technique with needle entry point chosen after careful consideration of the anatomy and important structures such as ribs, large vessels, diaphragm, and bowel.
- Many needles and devices are available, and each practitioner should select and become very familiar with a limited selection of these devices.
- Few children younger than 12 years will cooperate during an invasive procedure, and a thorough familiarity with pediatric sedation is necessary, together with skilled personnel and adequate resuscitation facilities.
- In general, it is the external covering of an organ or muscle, the pleura, the peritoneum, the perimysium, or the deep fascia that registers pain sensation. Therefore local anesthesia is particularly important in these deep areas.
- Procedures such as abscess drainage, peripherally inserted central catheter (PICC) lines, pleural drainage, percutaneous cholangiography, targeted organ lesion biopsy, and musculoskeletal procedures can all benefit from ultrasound guidance.

CHAPTER OUTLINE

GENERAL PRINCIPLES
The Patient
Personnel and Equipment
GUIDANCE METHODS
Multimodality Interventional Suites
ULTRASOUND TECHNIQUES
Equipment and Transducers
One Operator Versus Two
Freehand Versus Mechanical Guides
Color Doppler Ultrasound
FREEHAND TECHNIQUE
Initial Needle Placement and Localization
Locating the Needle After Insertion
Correcting the Needle Angle
Correcting the Off-Target Needle
Training Aids for Freehand Sonographic Intervention
NEEDLES, WIRES, CATHETERS, AND BIOPSY DEVICES
Chiba Needles
Drainage Catheters
Initial Puncture Device
Biopsy Devices
ANATOMY
Diaphragm
Colon or Bowel
SEDATION
LOCAL ANESTHETIC TECHNIQUE
Ultrasound-Guided Deep Local Anesthetic Administration
ANTIBIOTICS
THE TYPICAL PROCEDURE
Prior Consultation and Prior Studies
Coagulation Studies
Aims and Expectations
Initial Ultrasound Scan Should Occur Before Sedation
Pus
Catheter Fixation May Be Difficult in Infants
Postprocedure Care and Follow-Up
SPECIFIC PROCEDURES
Abscess Drainage
Transrectal Drainage
Peripherally Inserted Central Catheter Lines
Central Venous Access
Pleural and Peritoneal Drainage
Percutaneous Cholangiography and Drainage
Mediastinal Mass Biopsy
Appendiceal Abscess Drainage
Targeted Organ Lesion Biopsy
Musculoskeletal Procedures
Head and Neck Lesions
NOTE FROM THE AUTHORS

GENERAL PRINCIPLES

The Patient

Unlike many adult patients, most pediatric patients are medically robust, without multiple comorbidities such as superimposed coronary, peripheral vascular, or cerebral disease. The smaller the patient, the more appropriate is the use of ultrasound for interventional procedure guidance of at least the initial access phase of an interventional procedure. Physicians whose practice includes mostly adults often regard a baby as a fragile, dangerous

patient. On the contrary, children tolerate levels of pH, creatinine, Po_2, and sedation that might cause major complications in adults. The pediatric patient is often quite unconcerned with the details of the disease and treatment, and all but the sickest patients simply want to leave the imaging department with the greatest amount of play and the least amount of anxiety and discomfort possible. Conversely, the parents are often more difficult to manage than the child. Understanding of the different needs of the parents and the child is essential from the beginning of the interaction.

Personnel and Equipment

Adequate equipment and experienced assistants are essential for successful and safe pediatric intervention. Although most interventional radiologists should be able to perform basic ultrasound-guided procedures on children, some cases are not appropriate for the inexperienced or occasional operator. A commitment to careful, graded learning, including the use of training phantoms, is needed, as is a good knowledge of regional anatomy or the willingness to learn and review the relevant anatomy before attempting challenging procedures.

By its nature, the timing of interventional practice is not always predictable or convenient, and it is common for the general ultrasound department to resent calls for borrowing ultrasound equipment on short notice. Despite the inconvenience, the interventionist should insist on the best technical ultrasound equipment available. The ideal situation is to have dedicated interventional ultrasound equipment housed in the interventional suite. Some major pediatric radiology departments have moved the interventional suite to the operating room environment. This integration of interventional radiology services within the operating room environment has generally resulted in increased cooperation between interventional radiologists and surgeons, especially involving intraoperative ultrasound assistance during traditional surgical procedures.

GUIDANCE METHODS

Computed tomography (CT) is necessary for some procedures, especially for procedures involving bone, but in most other cases, ultrasound-guided access with either ultrasound or fluoroscopic monitoring of wire and catheter placement is ideal (Table 56.1). Ultrasound can be used in the CT suite to complement a predominantly CT-guided procedure. Radiation dose to children undergoing CT procedures has recently aroused significant controversy, so ultrasound can be used to lower the need for CT.[1]

Multimodality Interventional Suites

The recent availability of cone-beam CT software installed on advanced angiography equipment with virtual three-dimensional (3-D) guidance enables combined complex interventional procedures involving ultrasound guided access, CT-like 3D imaging, live guidance graticules superimposed over 3-D images, and conventional fluoroscopy, all in the same interventional radiology suite.[2]

TABLE 56.1 Computed Tomography (CT) Versus Ultrasound for Interventional Procedures

	CT	Ultrasound
Ionizing radiation	Radiation dose to pediatric patients is an important current issue in pediatric imaging, particularly for interventional procedures, when more than one scan may be needed	None
Scan plane	Typically limited to initial axial images (especially difficult near the diaphragm)	Unlimited, except by bone or gas
Resolution	Excellent, although lack of fat in children can limit visualization	Excellent except for membranes in fluid collections
Convenience	More difficult to schedule	High
Cost	High	Intermediate
Monitoring	By repeat scan; no real-time ability; recovery from kinked wires difficult	Real time
Gas and bowel	Excellent, especially with contrast	Poor

Magnetic resonance imaging (MRI) guidance in pediatrics is uncommon. An example of multimodality guidance is shown in Fig. 56.1.

ULTRASOUND TECHNIQUES

Equipment and Transducers

A selection of transducers is essential. Small patient size and lack of subcutaneous fat in most children allow use of high-frequency transducers. Procedures performed around ribs, such as thoracentesis, are best done with small-footprint sector transducers. Vascular access procedures are best performed with a linear high-frequency transducer. Color Doppler is useful for localization of major blood vessels. Transducers with good near-field resolution are used for superficial lesions and for initial accurate placement of local anesthetic on the peritoneum, deep fascia, or organ capsule.

One Operator Versus Two

It is common for inexperienced operators to require a technologist or another radiologist to perform the ultrasound scanning. This should be vigorously discouraged. Although large, simple fluid

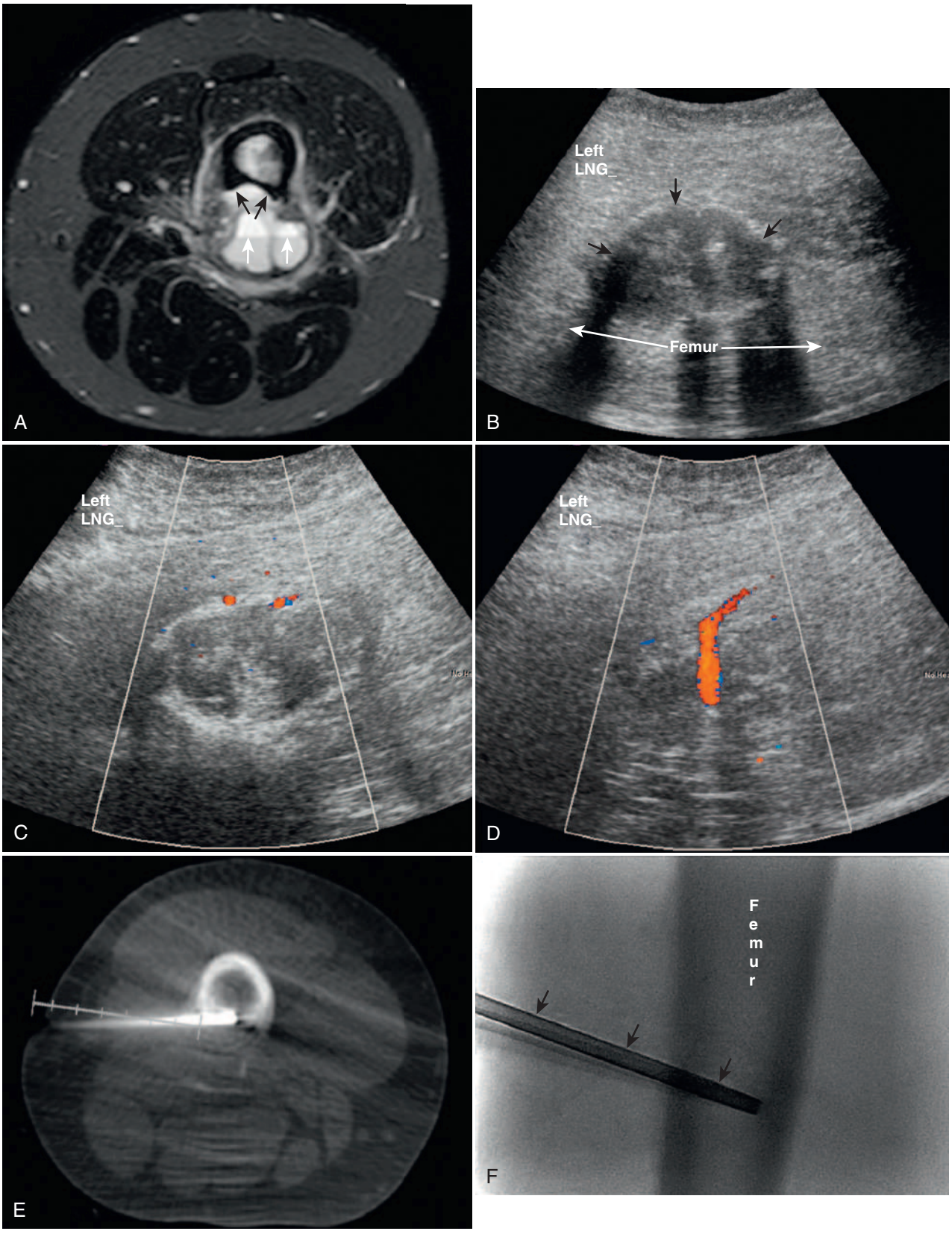

FIG. 56.1 Multimodality Interventional Procedure Guidance. Biopsy of posterior femur cortical aneurysmal bone cyst in a 15-year-old with 3 months of left thigh pain initially treated as a knee sports injury. **(A)** Transverse short-tau inversion recovery (STIR) magnetic resonance image mid left femur. Black arrows show eroded posterior bone cortex. White arrows show fluid-fluid levels. **(B)** Longitudinal ultrasound showing the soft tissue component of the lesion *(black arrows)*. **(C)** Color Doppler showed little internal blood flow, but **(D)** moderate-size peripheral arterial vessels were identified and avoided during the biopsy. **(E)** Axial cone-beam computed tomography scan showing initial guidance graticule and bone biopsy device entering the posterior bone cortex to obtain initial soft tissue samples for frozen section analysis to minimize the risk of more aggressive biopsy of a malignant lesion. Frozen section revealed a benign lesion. **(F)** Conventional fluoroscopy then allowed further sampling from all quadrants of the lesion.

collections can be drained this way, the necessary skills for accurate needle placement in small organs or near critical structures will never be learned. A single practitioner using an ultrasound transducer in one hand and the access needle or other device in the other hand is far superior to the "where's my needle now?"–type verbal communication required when there are two operators.

Freehand Versus Mechanical Guides

Most ultrasound equipment manufacturers supply well-designed mechanical guides that attach to a transducer and allow a predictable needle path to be visualized. These guides are useful for keeping the needle in the plane of the ultrasound beam and can be used for lesions with a simple approach path or a wide access window. Most devices require a disposable sterile kit when the device is used, adding to the cost of the procedure. Special needle guides are useful for the initial puncture for transrectal abscess drainage,[3] although many practitioners use simple freehand ultrasound guidance imaging of the rectal puncture needle using an anterior view through the filled bladder.

Freehand guidance is more difficult to learn but allows much more flexibility of approach. When the needle can be positioned 45 to 90 degrees to the beam, even fine, 30-gauge needles are easily visible. Freehand guidance allows the operator to choose the most advantageous transducer geometry and to steer the needle or biopsy device around other structures on the way to the lesion. Accurate placement of local anesthetic on the peritoneum, pleura, and other sensitive structures is made easier by freehand technique.

Color Doppler Ultrasound

Color Doppler has been advocated for visualization of the moving needle during interventional procedures, but our experience has been that the potential for better visualization of the needle tip is outweighed by the degradation of the gray-scale image and flash artifacts when color Doppler is active. Various needle tracking devices are available to enhance the visualization of the needle, but with the exception of the Yueh (Cook, Bloomington, IN) and Skater (InterV, Stenlose, Denmark) type sheathed access devices, which have very small holes in the catheter tip, these devices all add complexity and expense and are generally unnecessary if accurate ultrasound technique is learned.

FREEHAND TECHNIQUE

Freehand technique requires that the transducer be held in one hand and the needle or biopsy device in the other. The interventional physician needs to be able to use either hand as the needle or operating hand. For example, a biopsy specimen of the liver might be obtained by placing the transducer on the anterior abdominal wall using the right hand and making the needle approach from the patient's right lateral position, parallel to the table, using the left hand. A left-sided biopsy would best be performed by using the left hand for the transducer and the right hand for the needle approach from the left flank. With some practice and some simple rules, it is not difficult to use the nondominant hand as the needle hand.

Initial Needle Placement and Localization

The most important technique to learn in freehand sonography is needle localization. These rules work equally well for a needle entry site near the transducer or one at a distance (Fig. 56.2). The entry point is chosen after careful consideration of the anatomy and important structures such as ribs, large vessels, diaphragm, and bowel. Indentation of the entry site using a finger to compress the skin (Fig. 56.3) allows the exact entry site to be assessed. Once the entry site is chosen, a last check can be made by placing the transducer exactly over the marked entry point for a "needle's-eye view" to ensure that there will be no surprises such as the internal mammary artery during mediastinal biopsy or inferior epigastric artery during paracentesis or abdominal abscess drainage, which may be overlooked unless specifically localized. Once the entry path has been chosen and after proper application of local anesthetic, the needle or biopsy device is

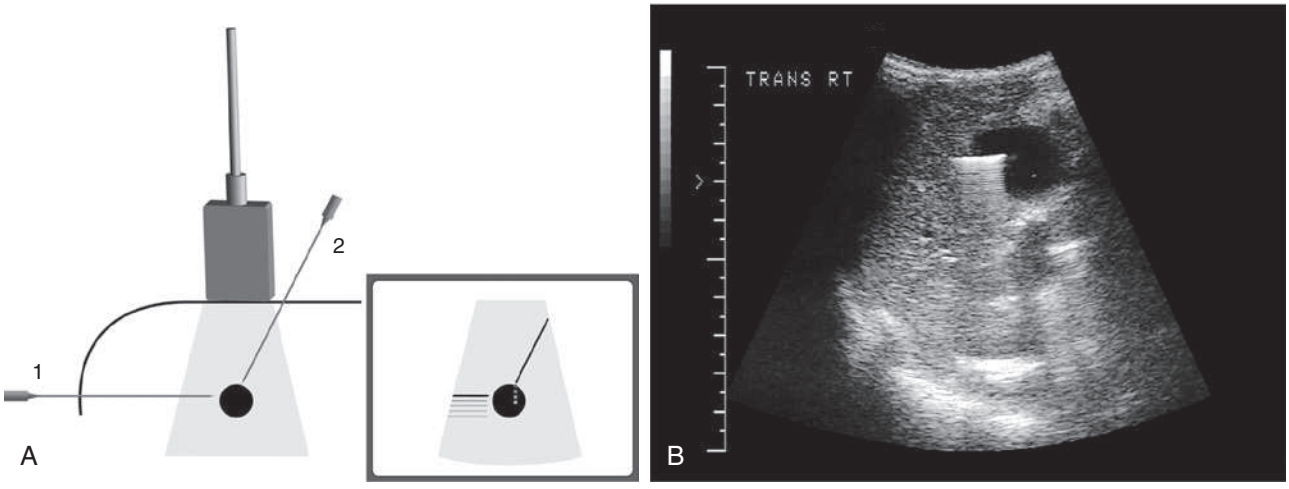

FIG. 56.2 Common Approaches. (A) The most common entry sites are either *(1)* lateral (parallel to the transducer face) or *(2)* adjacent to the transducer. **(B)** When the needle is parallel to the transducer face, a prominent reverberation artifact is seen, or a "comet-tail" artifact is seen when the needle is not parallel. The needle can be more difficult to locate in position 2.

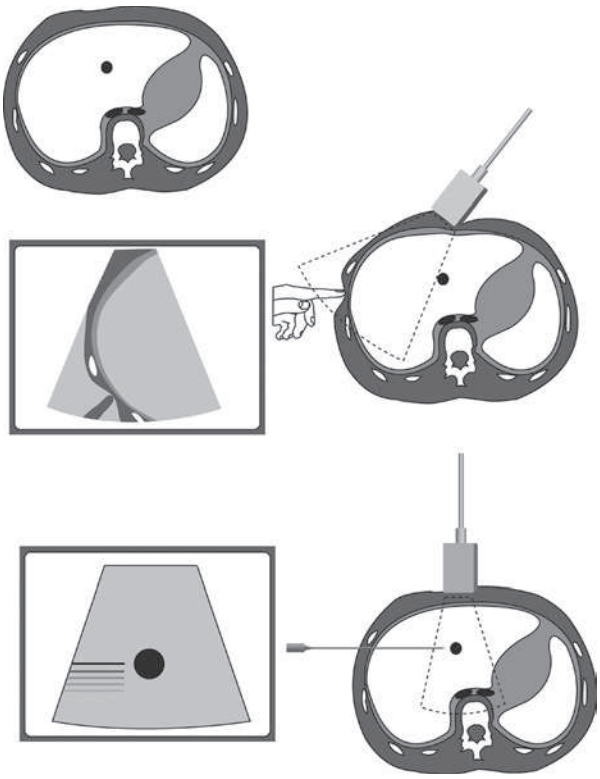

FIG. 56.3 Locating the Entry Site Laterally. The exact point of entry can be tested by rotating the transducer toward the body wall and palpating potential entry sites with a finger that is readily visible on the ultrasound real-time images.

placed through the skin toward the target. The needle and transducer need to be precisely in the same plane. This can be checked by looking directly down onto the top of the transducer and needle just before the initial placement is made (Fig. 56.4). The depth of the target should be measured and remembered before needle placement.

The needle should be initially advanced about one-half of the distance to the target under direct ultrasound monitoring. If necessary, the preplanned distance of insertion can be marked on the needle with a Steri-Strip. Inexperienced operators often have an uncontrollable urge to keep pushing the needle, hoping that it will magically make the needle visible. Radiologists who usually work with adults may not appreciate the short insertion distances required in small children and babies.

Locating the Needle After Insertion

With experience, it is possible to keep the needle visible starting from the moment of insertion, but if not, the needle must be localized before any further advancement is made. Check that the transducer and needle are parallel to each other by looking down the cable of the transducer with one eye closed. If the two are not parallel, adjust the position of the transducer, not the needle. Once the transducer and needle are parallel, keep the transducer in that plane and move the transducer a few millimeters back and forth strictly in the plane of the needle (Fig. 56.5). It is often useful to anchor the transducer hand on the patient by placing the fourth and fifth digits or the hypothenar border of

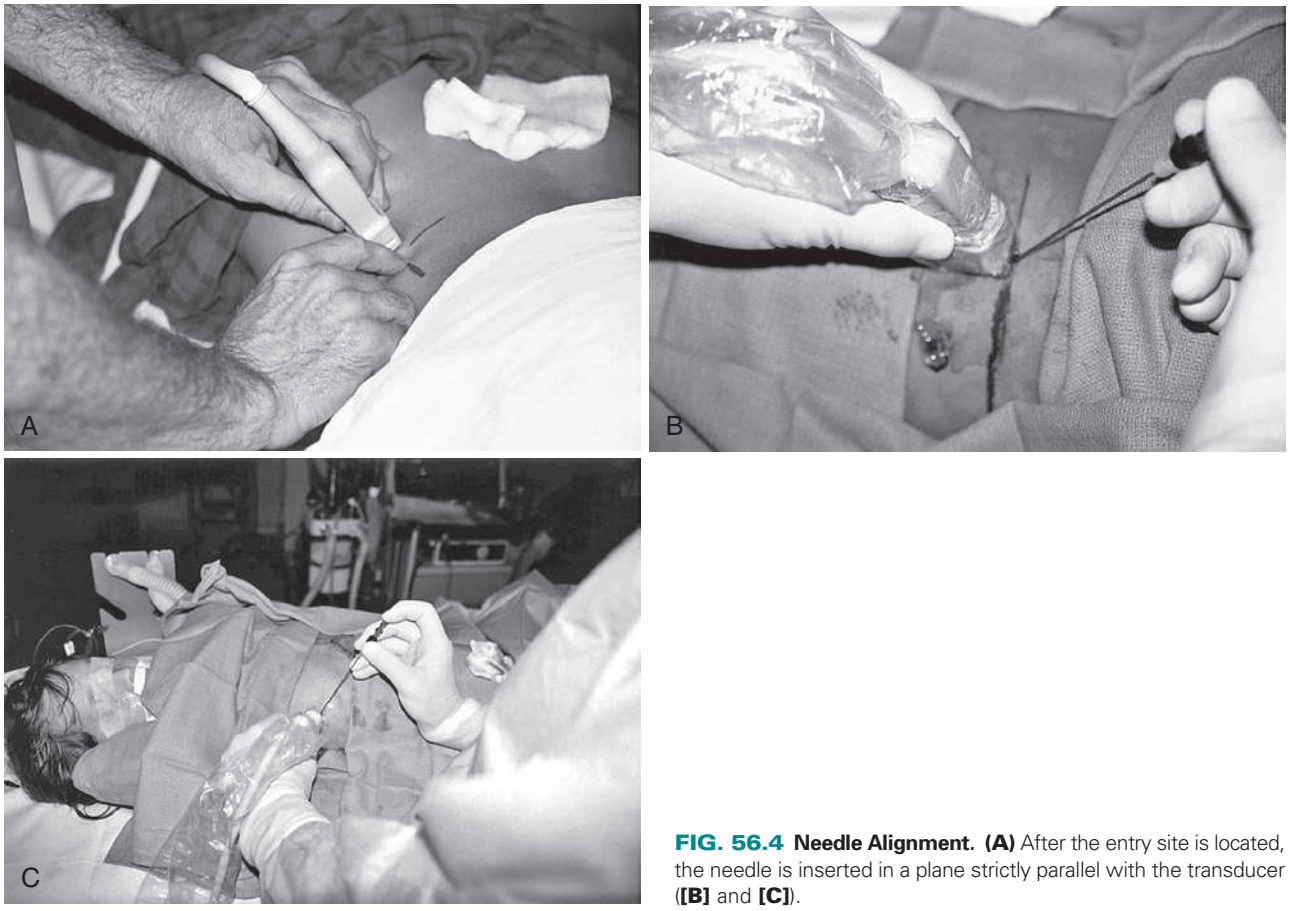

FIG. 56.4 Needle Alignment. (A) After the entry site is located, the needle is inserted in a plane strictly parallel with the transducer (**[B]** and **[C]**).

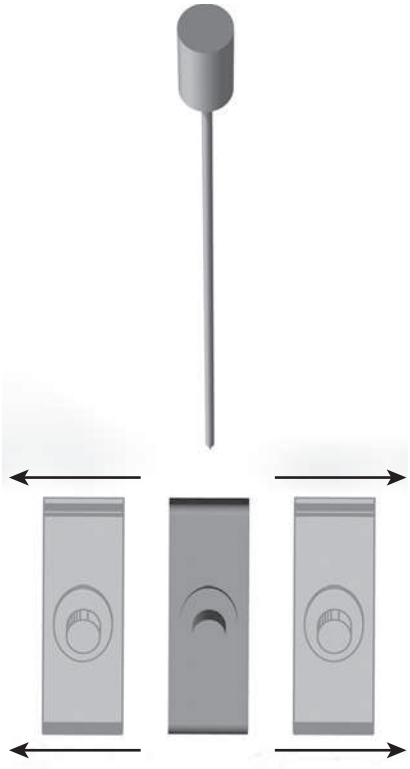

FIG. 56.5 Transducer Motion. After the needle is inserted, if the needle is no longer visible on the ultrasound image, the transducer is translated backward and forward in the plane of the needle, without rotating the transducer, until the needle is localized. The actual amount of movement required is much less than shown in this diagram; typically, it is only a few millimeters.

the transducer-holding hand firmly on the patient's skin, using the thumb and the second and third digits to hold and move the transducer. It is important not to jab the needle in and out aggressively or to try to move the needle and transducer in complex directions or angles all at once in a hopeful, and usually ineffective, attempt to localize the needle tip.

If the whole length of the needle is not visible, it may be at an angle oblique to the plane of the transducer, resulting in an erroneous impression of the position of the needle's tip (Fig. 56.6). Usually, only a few degrees of transducer rotation are required to obtain an image of the whole of the needle shaft.

The localization of the needle after initial placement must be a thoughtful and purposeful process that involves moving the transducer back and forth ("translation"), then adjusting and rotating its position in small increments until the whole length of the needle is visible.

If the needle is visible and the target is visible and the needle is pointing at the target, the needle is simply advanced toward the target. The needle may need a short sharp jab to enter the target, particularly if the target is a normal structure such as the gallbladder, a renal calyx, or a bile duct. The organs and tissue planes of children are soft and compliant (ballotable) and can sometimes "float" away from the needle tip as it is advanced, but the short jab required to puncture such organs or structures must always be made under control and with a purpose. Conditions such as some collagen disorders and prune belly syndrome cause even greater difficulties in initial organ or structure puncture.

The most common problem is that either the needle is not pointing at the target or the target is no longer visible in the scan plane.

Correcting the Needle Angle

If the needle and target are visible in the one image, but the needle angle is incorrect, do not attempt to radically change the angle of the needle while it is deep in an organ. Doing so, especially with a rigid biopsy needle, may result in significant bleeding and other complications. Instead, the needle is partly withdrawn until it is subcutaneous, the angle is adjusted, and the device is reinserted under direct ultrasound monitoring as before (Fig. 56.7).

If the transducer is not vertical, it is sometimes difficult to decide which way to adjust the needle's angle. The following simple rule will always work. Consider the position of the transducer cable and move the needle in relation to it (Fig. 56.7D-E). It is important, however, to know which side of the transducer belongs to which side of the ultrasound monitor screen. One should always test the orientation of the image before beginning a procedure by running a finger over the transducer face and noting where the finger appears on the screen. Otherwise the image of the needle is expected on one side of the screen but is actually on the other side of the screen where it is not noticed and is well on its way toward the aorta or some other significant structure.

Correcting the Off-Target Needle

If the needle is visible but the target is not, move the transducer parallel to the plane of the needle, first one way and then the other, until the target is reestablished. Remember which way the transducer needed to be moved to reimage the target, then withdraw the needle to the skin, move the skin entry site in the same direction by moving the needle tip in the subcutaneous tissues, and advance the needle once again into the patient.

Training Aids for Freehand Sonographic Intervention

These techniques can be practiced on various phantoms. The most readily available and practical practice phantom consists of a turkey breast and various materials, such as beef kidney, olives, cocktail onions, or artificial cysts made by tying off the finger of a surgical glove that has been filled with water. These materials are placed in the plane between the pectoralis major and minor muscles while the turkey breast is under water.[4-6]

NEEDLES, WIRES, CATHETERS, AND BIOPSY DEVICES

Many needles and devices are available, and each practitioner should select and become very familiar with a limited selection of these devices.

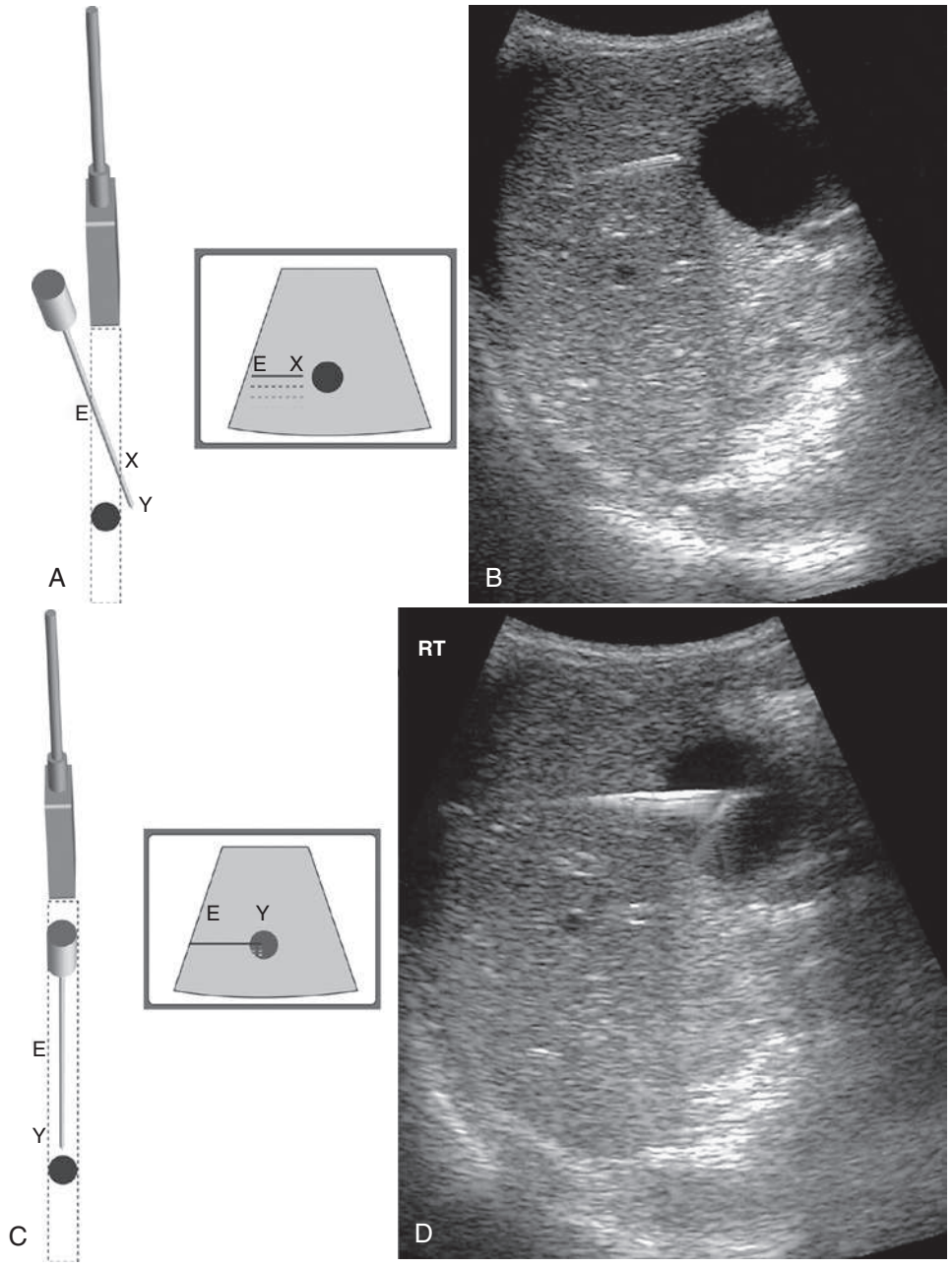

FIG. 56.6 Off-Plane Needle Position. (A) This off-plane position results in a shortened view *(E-X)* of the needle and a false sense of needle tip position at point *X,* whereas the real position of the tip is at point *Y.* **(B)** Off-plane view of part of the shaft of the needle during gallbladder puncture. **(C)** With needle in the exact plane of the transducer, the whole of the needle *(E-Y)* is visible. **(D)** It is now clear that the needle tip is actually in the gallbladder. Normally, the tip is accurately localized before puncture of the gallbladder. These images were obtained for illustration purposes, after successful gallbladder puncture.

Chiba Needles

Chiba needles are a class of relatively safe, very useful, flexible, small-diameter (usually 22-gauge) needles used for diagnostic contrast studies or for initial puncture of a target, especially if the target is near a vital structure. If the procedure involves subsequent placement of a guidewire or catheter, only a thin guide (typically 0.018 inch) can be placed through the needle. This is a relative disadvantage because a dilator will have to be placed over the 0.018-inch wire, and the thin wires are subject to kinking, especially when the dilator meets the deep fascia or capsule of an organ. We have found the Aprima Access set (Cook, Bloomington, IN) (formerly Neff set) to be especially useful and easy to use.

Drainage Catheters

Modern commercial catheters are of high quality, and usually a general purpose or locking loop catheter will suffice. For thick pus or old blood, a large-caliber catheter may need to be placed.

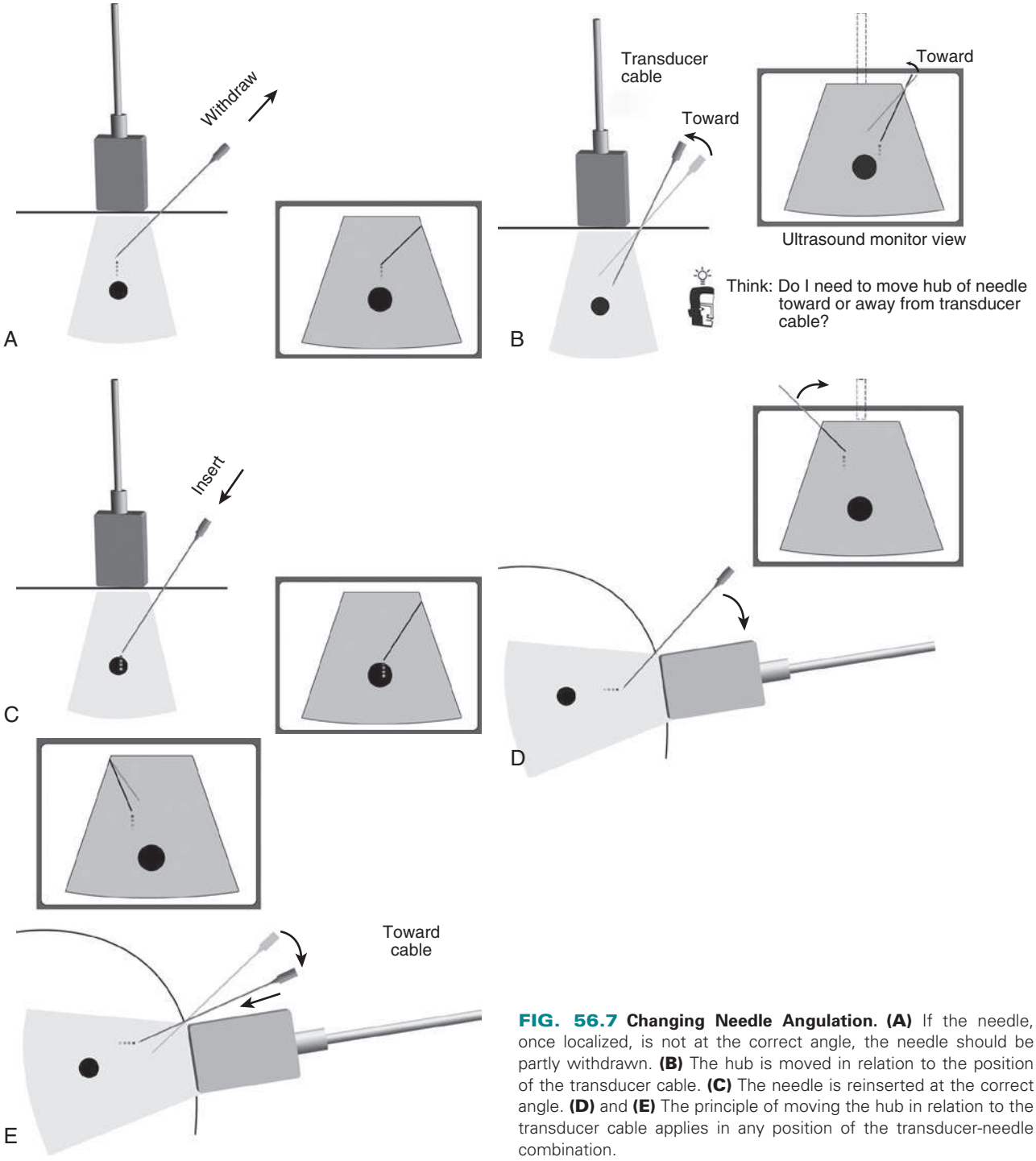

FIG. 56.7 Changing Needle Angulation. (A) If the needle, once localized, is not at the correct angle, the needle should be partly withdrawn. **(B)** The hub is moved in relation to the position of the transducer cable. **(C)** The needle is reinserted at the correct angle. **(D)** and **(E)** The principle of moving the hub in relation to the transducer cable applies in any position of the transducer-needle combination.

Initial Puncture Device

Most drainage catheters need to be placed over at least a 0.035-inch-diameter guidewire. An initial puncture with a small-caliber needle and placement of a 0.018-inch wire requires an exchange maneuver, and each passage of a wire or dilator adds to the time and complexity of the procedure, increasing the risk of losing position or kinking the wire, especially with most 0.018-inch wires, which are not robust.

Various prepackaged exchange sets are available commercially. Some sets (i.e., micropuncture, Aprima Access set) have a dilator/sheath that is placed over the 0.018-inch wire and then the dilator is removed, leaving the larger sheath in place, which allows placement of the 0.035-inch wire. These systems are used for some biliary procedures or where vital structures are very close to the target.

The Yueh needle (Cook, Bloomington, IN) is a needle/sheath device with small holes drilled in the end of the catheter, making

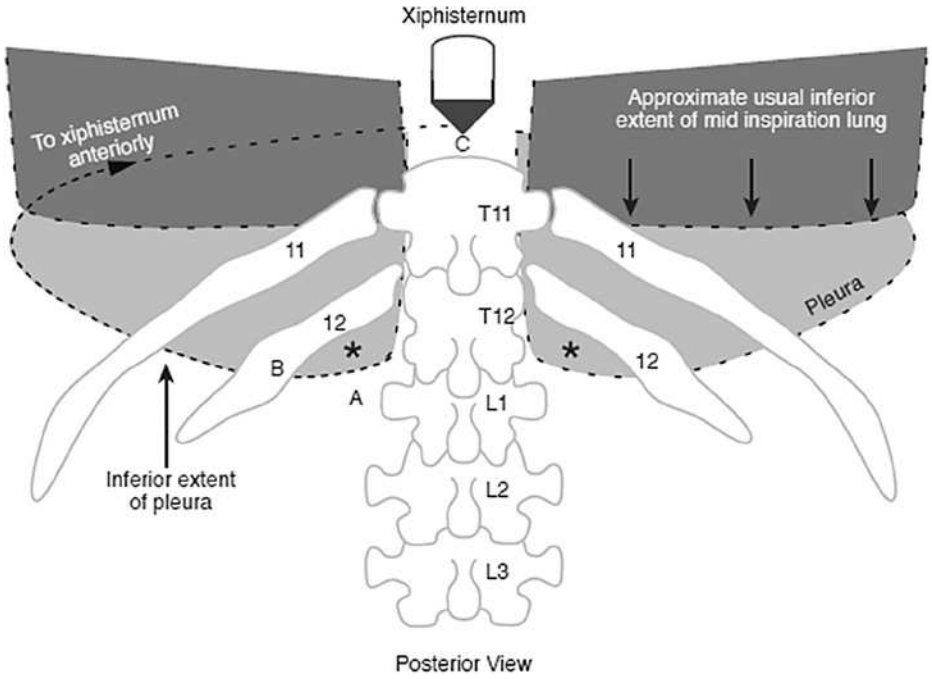

FIG. 56.8 The Surface Anatomy of the Diaphragm—Posterior View. The pleural space normally extends inferior to the 12th rib medially (position *A*), and superior to the lateral third of the 12th rib (position *B*). A line drawn from position *B* to the xiphoid process of the sternum (the xiphisternum) (position *C*) will map out the surface markings of the peripheral attachment of both the normal and the pathologically elevated diaphragm. Even if the dome of the diaphragm is grossly elevated by a pathologic process, the peripheral attachment remains unchanged.

it more conspicuous during ultrasound guidance. The holes also aid in aspiration of fluid.

Biopsy Devices

Aspiration cytology is not widely used in children because there is a much more diverse group of potential lesions in children than in adults. Many of the pediatric tumors depend partly on cellular arrangement for diagnosis, and pediatric pathologists are generally uncomfortable with making important diagnoses based on cytology specimens alone. Automated suction-core or slotted needle instruments are most often used.

Although it may seem logical that small-diameter devices should be used in children, in general, 16- to 18-gauge needles are most commonly used in order to obtain sufficient material for pathology examination. The larger needles may seem more dangerous, but if they are placed and monitored under ultrasound guidance, the risk is minimized.

ANATOMY

Diaphragm

A thorough knowledge of regional anatomy is essential. If a procedure is to take place in an unfamiliar area, there is always time to look up the anatomy in a text before proceeding. The surface anatomy of the diaphragm must be thoroughly understood (Fig. 56.8). It is important to remember that even if the apex of the diaphragm is grossly elevated by a mass or a subphrenic fluid collection, the diaphragm is still attached to the chest wall in the same relative position as it was at birth. If the pleural space is to be avoided, one must still enter a subphrenic collection below the peripheral attachment of the diaphragm. The diaphragm generally passes posteriorly across the junction of the middle and outer thirds of the 12th or last palpable rib posteriorly. From this point, a line drawn around the chest to the xiphoid process of the sternum (xiphisternum) will trace out the peripheral attachment of the diaphragm. It is important to be aware that the pleural space extends inferior to the medial third of the 12th rib (see Fig. 56.8).

Colon or Bowel

The colon lies just anterior to the kidneys and may be inadvertently punctured when entering from the posterior-lateral position during percutaneous nephrostomy. A nondistended colon may not be easily detectable by ultrasound, and one must be careful to avoid placing a nephrostomy too laterally or too anteriorly. If there is any doubt, a contrast enema can be performed and the position of the colon can be localized by fluoroscopy before or during the procedure. If available, cross-sectional imaging should be referenced before the procedure.

SEDATION

Few children younger than 12 years will cooperate during an invasive procedure, and a thorough familiarity with pediatric sedation is necessary, together with skilled personnel and adequate resuscitation facilities. It is better to perform a procedure using general anesthesia than to attempt the procedure without adequate sedation. If the child is uncomfortable or moving excessively,

the sedation should be increased, help should be obtained, or the procedure should be terminated.

Our previous sedation protocol has been published,[7] although we no longer manage our own sedation, preferring to use the anesthesia service that is readily available in our interventional suite. The anesthesiologists have been very flexible in accommodating our needs. Details of radiologist-supervised sedation are beyond the scope of this chapter. Specific publications should be consulted and adequate training acquired before performing deep sedation in children. A well-organized and experienced team that performs sedation regularly, with appropriate guidelines and limits, is more important than which particular drugs are used.

LOCAL ANESTHETIC TECHNIQUE

The most commonly used agent is lidocaine (Abbott Laboratories, Chicago, IL) 1% solution. The usual maximum adult dose for local anesthesia is 4.5 mg/kg (0.45 mL/kg of 1% solution). A maximum dose of 3 to 4 mg/kg (0.3-0.4 mL/kg of 1% solution) for children older than 3 years is noted in the product insert dosage recommendations, but there is no recommendation for younger children. We routinely use 3 to 4 mg/kg for all but extremely premature babies. Lidocaine is chemically stable only in a slightly acidic solution, so lidocaine is often combined with sodium bicarbonate 8.4% solution in a ratio of 10:1 immediately before injection. This effectively neutralizes the pH and reduces the sensation of stinging as the local anesthetic is injected. Liberal use of topical local anesthetic creams is also useful, but they must be applied 20 minutes before the procedure, and the entry site for a procedure is not always known in advance.

It is a common error to inject the local anesthetic and then immediately commence the procedure. All clinically useful local anesthetics work by diffusing across the lipid myelin and nerve cell membrane and block the sodium channel from the intracellular side of the sodium channel. It is therefore not surprising that lidocaine needs 5 to 8 minutes to achieve full effect. We usually place the local anesthetic, at least in the deep subcutaneous tissues, before gowning and gloving and preparing equipment. This allows time for the anesthetic to achieve maximal effect. Dentists are well aware of the time needed for maximal local anesthetic effect (they would lose their business if they did not practice good local anesthetic technique), but for obscure reasons, many physicians seem unaware of the need for waiting to achieve good local anesthetic effect.

The pain and stretch receptors are mostly in the epidermal layer. Discomfort associated with local anesthetic administration arises mostly from the rapid stretching of the epidermal sensors, before the local anesthetic agent has had time to block the axons. Thus the common practice of "raising a wheal" in the epidermis is contraindicated. Use of 30-gauge or smaller needles for initial slow deep subcutaneous injection minimizes the discomfort and often allows initial injection without the patient being aware of the skin puncture. Initial local anesthetic application to the deep subcutaneous layers allows the local anesthetic agent to first block the axons of the pain and other epidermal sensory nerve endings. Once this has been achieved, later local anesthetic application to the epidermis is usually painless. Care must be taken to exclude air from the syringe and needle before injecting the local anesthetic because even the amount of residual air in a 30-gauge needle, injected subcutaneously, may seriously degrade the ultrasound image.

Ultrasound-Guided Deep Local Anesthetic Administration

One of the keys to successful percutaneous procedures in children is adequate local anesthetic control of deep sensation. Many practitioners anesthetize only the skin and subcutaneous tissues and are then surprised when the patient moves or complains vigorously as a dilator is passing through the peritoneum, deep fascia, or the capsule of the organ. The solution is to place the majority of the local anesthetic on the peritoneum, fascia, or capsule. In general, it is the external covering of an organ or muscle, the pleura, the peritoneum, the perimysium, or the deep fascia that registers pain sensation. Subcutaneous fat, organs, and the muscle belly have very few nerve endings. Deep local anesthetic application is best achieved by using sonographic guidance. Surprisingly, even 30-gauge needles can be easily identified close to the skin with high-quality 7-or 10-MHz transducers. The focal zone must be adjusted appropriately, but with optimal conditions the local anesthetic can be deposited where it will have the most effect. This reduces the depth of sedation required and allows some procedures to be completed faster and without general anesthesia when it would otherwise have been required (Fig. 56.9).

ANTIBIOTICS

Antibiotics are routinely needed only when draining an infected collection or when the patient is immunosuppressed. We usually use periprocedural antibiotics for liver and renal transplant patients. The choice of antibiotics is individualized after consultation with the referring service, and they are usually given intravenously at the time of sedation or anesthesia induction. The basis for timing and duration of antibiotic prophylaxis of interventional radiology procedure is derived from the surgical literature. There is greatest suppression of infection when antibiotics are administered before inoculation. The likelihood of postprocedure infection increases with lengthening delay between the initiation of antibiotic prophylaxis and the procedure.[8] If a procedure is likely to be prolonged (i.e., >2 hours), a supplemental dose of antibiotics should be considered, depending on the half-life of the agent being administered.[9,10]

THE TYPICAL PROCEDURE

Prior Consultation and Prior Studies

It is important to review previous imaging or interventional radiology studies before the procedure. One should know what difficulties were encountered the previous time, or if there was a contrast reaction at a previous scan. Picture archiving and communications systems (PACSs) with integrated radiology

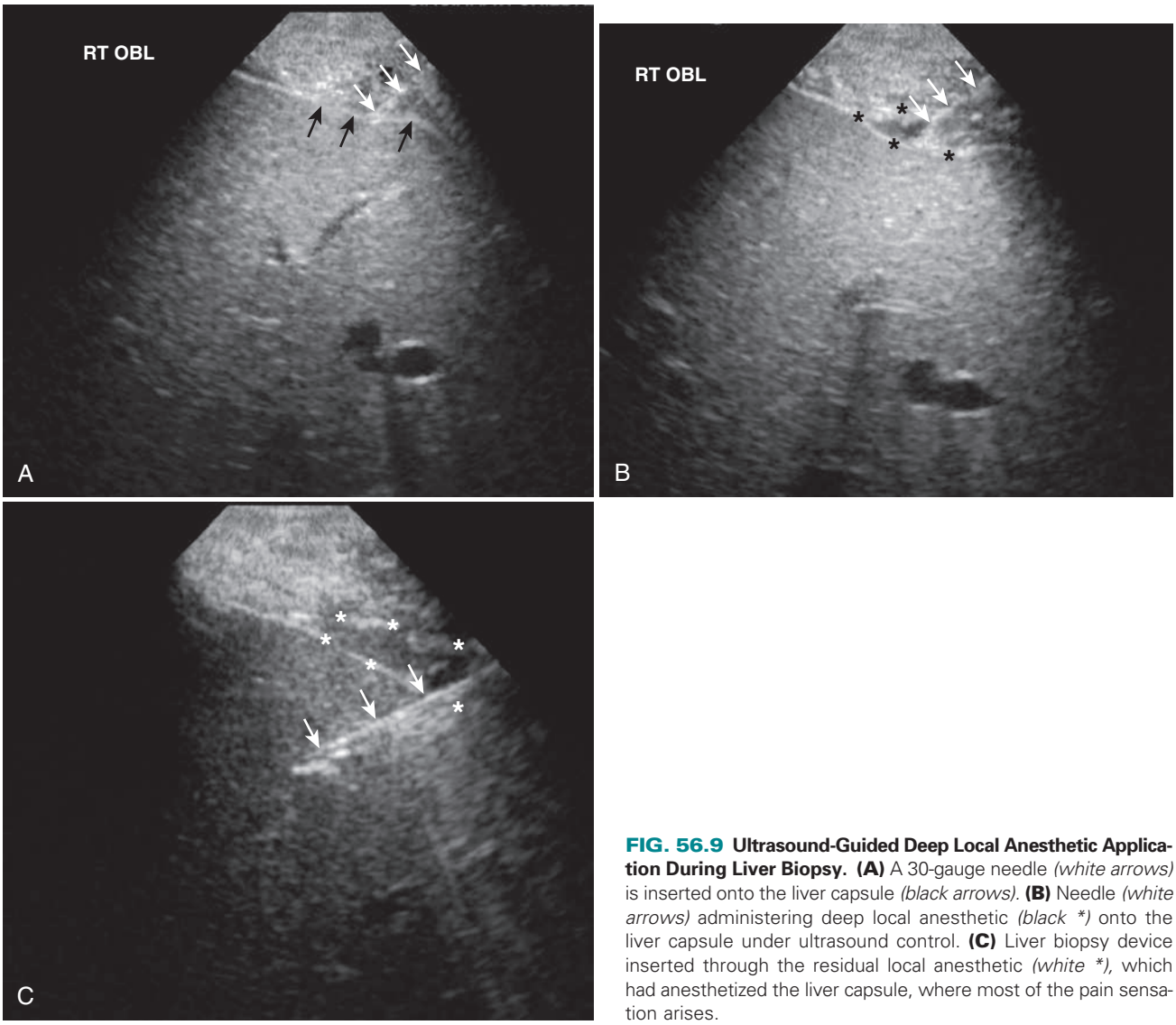

FIG. 56.9 Ultrasound-Guided Deep Local Anesthetic Application During Liver Biopsy. (A) A 30-gauge needle *(white arrows)* is inserted onto the liver capsule *(black arrows)*. **(B)** Needle *(white arrows)* administering deep local anesthetic *(black *)* onto the liver capsule under ultrasound control. **(C)** Liver biopsy device inserted through the residual local anesthetic *(white *)*, which had anesthetized the liver capsule, where most of the pain sensation arises.

reports and other clinical data make this easy. The interventional radiologist is responsible for having a clear understanding of the clinical reasons for the procedure and the expected benefits. At times, it is the duty of the interventional radiologist to insist on, or convene, a combined-care conference before undertaking a major procedure. This can be the greatest contribution a radiologist can make to the medical care of the child.

Coagulation Studies

Hematologic management in the patient undergoing percutaneous image-guided intervention is complex because of the wide range of procedures and equally wide range of patient demographics and comorbidities. Coagulation studies are indicated for most intraabdominal, chest wall, or retroperitoneal abscess drainage or biopsy procedures, which carry a moderate risk of bleeding; it should also be noted that renal biopsy carries a significant bleeding risk.[11] The management guidelines recommend correcting the international normalized ratio (INR) to below 1.5.[12] A platelet count is usually obtained in oncology patients; underlying malignancy appears to be an independent risk factor for bleeding after liver biopsy.[13] Caution should be exercised when the platelet count is below 50,000, and it is important to remember that platelet function may be affected by some chemotherapy, by nonsteroidal antiinflammatory agents, by uremia, and by other medical conditions. Patients with Wilms tumor may rarely have an undiagnosed transient acquired von Willebrand syndrome. Caution should be exercised if the skin incision continues to bleed vigorously for more than a minute or so. It is better to cancel a procedure and do a full coagulation workup than to continue and cause a major hemorrhage.

Aims and Expectations

Anticipation of problems is good practice, not a sign of weakness. No procedure should be undertaken without a clear understanding

of the aims, the expected benefit, and a reasonably detailed plan for completing the task. If an abscess is difficult to localize by ultrasound (e.g., in the psoas muscle in a large adolescent), then a transfer to the CT suite should be considered. Fluoroscopy after initial ultrasound-guided access allows a kinked wire to be withdrawn into the dilator and replaced or advanced into the abscess. CT is essential in some areas, notably pelvic abscesses requiring transgluteal drainage,[14] although transgluteal drainage of pelvic abscess has been almost exclusively replaced by ultrasound-guided transrectal catheter drainage at our institution.

A well-thought-out alternate plan is important, especially in complex procedures, such as renal stone removal or ureteric stent placement. What happens if the patient moves or the wire is dislodged? A second safety wire tucked up in an upper-pole calyx is always good insurance in complex renal procedures. Expect the unexpected, and the procedure will usually go as planned.

Initial Ultrasound Scan Should Occur Before Sedation

Understand the individual patient's anatomy before sedation or general anesthesia. Spending enough time to consider the most effective approach and the adjacent anatomy is as important as proper needle placement. It is less-than-perfect technique to pass a needle through the colon when a little time and care would have avoided the problem. The radiologist should have a good three-dimensional understanding of the patient's regional anatomy before commencing a procedure.

Pus

Pus is the liquefied products of inflammation. "Liquefied" is the most important word for the interventional radiologist. Unlike CT, which generates a static image, real-time ultrasound allows exploration of the liquidity and therefore of the drainability of a lesion. Urinomas are notoriously echogenic when first examined, but if the operator vigorously prods the collection with the ultrasound probe, the free-flowing nature of the collection becomes apparent and it can be drained by a simple 8-French catheter, rather than by the large-caliber sump catheter one may have thought would be needed.

Catheter Fixation May Be Difficult in Infants

Catheters are objects of wonder for small children and babies and are great chewing material if left in the grasp of tiny hands. Often, when a catheter "just falls out by itself," there has been some lapse in care on the part of professional staff. Either the catheter was not properly secured in the first place or a health care practitioner forgot to undo the safety pin when taking the child to the bathroom.

Some methods of fixation include standard sutures, sutures secured to the catheter by waterproof tape, or various commercial skin fixation devices. If the catheter is sutured in place, the suture must be placed deeply in the subcutaneous tissues. In babies and infants, the catheter is hidden out of reach, if possible, and secured with transparent plastic adhesive film. The joint between the catheter shaft and the hub of a drainage catheter is its weakest point, so we routinely affix the hub to the skin with adhesive tape or film, and train the patient's nurses to always retape this hub when performing routine catheter care.

Postprocedure Care and Follow-Up

Apart from bad communication skills, the quickest way to destroy an interventional referral pattern is to ignore the patient or the referring physician or surgeon once the patient has left the radiology department. The interventional radiologist is responsible for accepting the patient, for being satisfied that the procedure is justified and likely to be of significant benefit to the patient, and for follow-up, both in the immediate postprocedure period and for the long term. Leaving a pager number in the medical notes may result in a few trivial calls, but overall it will benefit the patient and increase referrals and satisfaction. If a complication occurs, either deal with it or consult another service, but do the consultation personally.

Be cautious of blood loss in children after liver or other biopsy. A hematocrit before and 2 hours after biopsy is a prudent precaution. Blood loss is typically slow and self-limiting, but if bleeding persists, often the only objective signs are pain and a rising pulse rate. Children who are experiencing blood loss notoriously maintain blood pressure and brain perfusion until very late and then suddenly deteriorate.

SPECIFIC PROCEDURES

Abscess Drainage

When entering an abscess cavity, a pus sample is usually obtained for culture, but the cavity should not be aspirated completely before placement of the catheter. Once the catheter is in position, simple aspiration with ultrasound monitoring for completeness is all that is required. Flushing with large volumes of saline or performing a contrast study could result in intravasation of infected material through the raw granulation tissue that always lines these abscesses. Contrast studies and flushing can be done later, once the cavity is healing, although we rarely do any postprocedure study for the majority of uncomplicated abscess drainages. During initial aspiration, it is not uncommon to get blood return near the end of aspiration. This is probably blood arising from the granulation tissue, and at times it can be alarming in amount. If active aspiration is ceased, the bleeding usually stops. The catheter should be left in place until the aspirate is straw colored and less than a few milliliters per day.

Transrectal Drainage

Deep pelvic abscesses can be drained by means of surgery or by a catheter inserted under ultrasound control.[15] The ultrasound-guided method is particularly appropriate for high collections that are beyond the reach of surgeons, but at our institution,

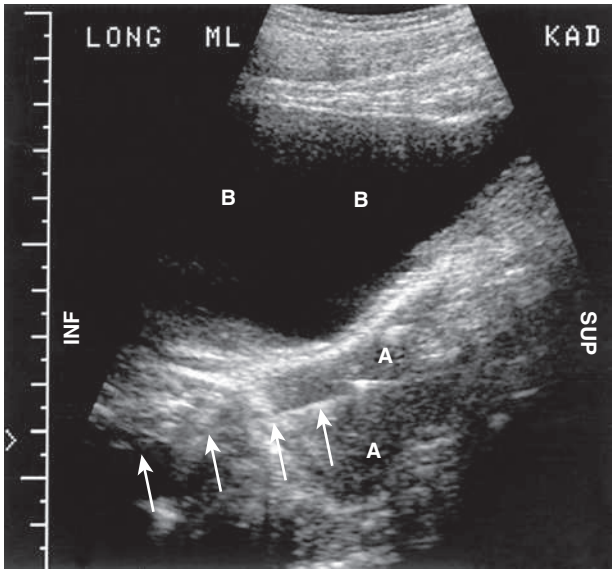

FIG. 56.10 Ultrasound-Guided Transrectal Abscess Drainage. The needle *(arrows)* has been inserted through the rectum and has punctured the high pelvic abscess *(A)* under ultrasound guidance. The bladder *(B)* is anterior to the abscess.

ultrasound-guided transrectal abscess drainage has substantially replaced the surgical procedure (Fig. 56.10). The catheter can either be withdrawn after complete aspiration of the cavity or left in place and secured to the leg with tape.[3]

Peripherally Inserted Central Catheter Lines

Peripherally inserted central catheters (PICCs) are a useful way of obtaining safe central access for short- to medium-term use.[16] The catheters range from 2 French to 5 French in size, and various commercial units are available, with insertion sets containing either a peel-away cannula similar to an intravenous catheter or a peel-away Seldinger-style sheath.

After insertion of the sheath into a peripheral vein (arm, leg, or scalp), the catheter is placed through the sheath and positioned in the central veins. Visual access to the arm veins is often easy in the older individual, but the veins of corpulent babies and infants can be notoriously difficult to identify and cannulate. Ultrasound guidance in these patients has become an essential skill for the PICC line service, and most PICC line nurses can successfully be taught the technique. In infants, the technique of ultrasound guidance for venous access is different from previously described parallel techniques. Because of beam-width issues, it is best to monitor the needle position by constantly adjusting the transverse or axial position of the transducer in a sweeping manner (Figs. 56.11 and 56.12, Video 56.1). The veins are usually so small that monitoring the needle position with the transducer in the plane of the needle and vein usually results in malpositioning of the needle because of the width of the ultrasound beam.

In older patients with larger veins, scanning in the plane of the vein can be useful, and safe passage of the guidewire can be observed (Fig. 56.13).

Central Venous Access

Placement of long-term central venous access devices is one of the most common vascular interventional procedures. Central venous access is used in infectious disease, dialysis, transplant, and oncology patients. The preferred vein is the right internal jugular vein (RIJV); it is large, is close to the skin, and provides a short, straight route to the superior vena cava. The RIJV should be used whenever possible for dialysis catheters or in renal failure patients to avoid compromise of the subclavian veins and the left brachiocephalic vein, which are important for the success of upper arm surgical dialysis access.[17] The RIJV also avoids the risk of pneumothorax and reduces the rate of symptomatic central venous stenoses when compared with the subclavian vein.[18,19] Use of the RIJV also avoids catheter pinch-off syndrome, seen exclusively in subclavian venous access, which is subject to repetitive trauma in the costoclavicular space and can result in catheter fracture.[20] When compared with the nonimage-guided surgical landmark technique (e.g., carotid artery, sternocleidomastoid muscle), the use of ultrasound has been reported to improve successful RIJV catheterization and achieves access with fewer attempts, a reduced incidence of carotid artery punctures, and increased success rate and a decreased duration of procedure.[21-25]

Ultrasound guidance allows accurate oblique access to the jugular vein, enabling a smoother curve to the tunneled part of the central catheter, which minimizes the risk of kinking or pinch-off obstruction of the catheter.

Pleural and Peritoneal Drainage

Ultrasound-guided diagnostic aspiration of pleural fluid is a common and useful procedure. Simple catheter drainage of parapneumonic complex fluid collection or empyema can result in complete cure if performed early enough, but the pleura has a remarkable ability to thicken and produce fibrin. These infected collections often loculate and become difficult to drain using a simple catheter technique. CT scanning does not usually show the loculations, and therefore referring clinicians often believe that the parapneumonic fluid should be easy to drain. The administration of thrombolytics, typically tissue plasminogen activator (tPA), through the pleural tube in order to change the physical characteristics of the thick fluid[26,27] is now a routine procedure. Any chest tube for empyema drainage must be monitored frequently by radiography, ultrasound, or occasionally postprocedure CT, to ensure that loculation has not recurred (Fig. 56.14).

Peritoneal fluid drainage for diagnostic and/or therapeutic reasons is usually not difficult and can often be achieved at the bedside with minimal or no sedation and good local anesthetic technique. When accessing the fluid via the lower quadrants, care must be taken to accurately localize and mark the position of the inferior epigastric vessels, which can cause substantial and difficult-to-control bleeding into the peritoneal fluid if injured during an otherwise "simple" aspiration procedure. Occasionally, debris obstructs the draining catheter and needs to be dislodged, either by vigorous movement of the needle and catheter or by

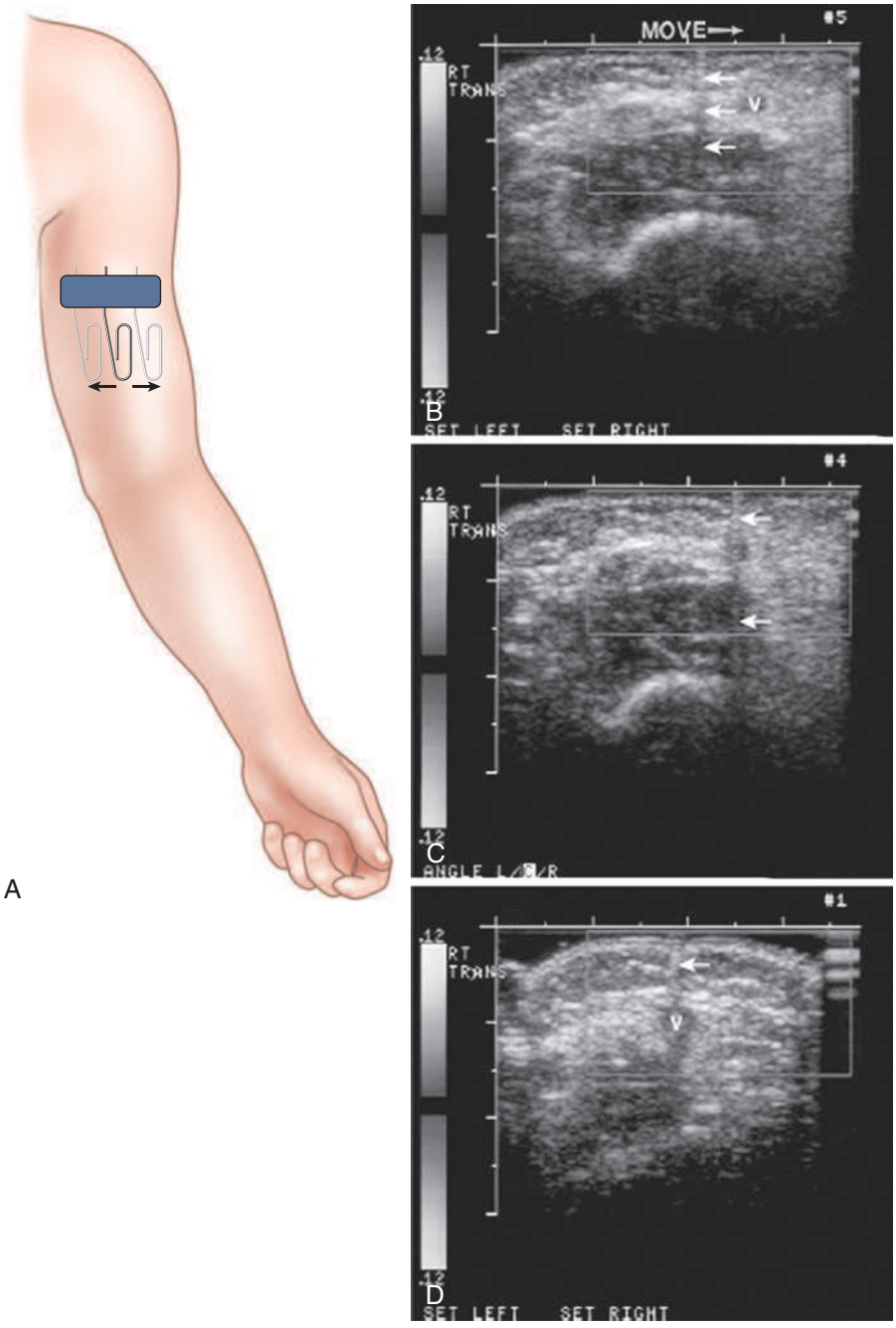

FIG. 56.11 Technique for Locating Exact Position of a Deep Vein Prior to Peripherally Inserted Central Catheter (PICC) Line Placement. **(A)** With the transducer held transverse to the direction of the target vein, a partly unfolded paper clip, placed between the skin and the transducer face, is moved backward and forward (**[B]** and **[C]**) to locate the vein for accurate application of subcutaneous local anesthetic. The transducer is held transverse to the needle path to avoid beam-width errors. The thin paperclip artifact *(arrows)* localizes the vein *(V)*. Note that with a tourniquet in place, especially in a small baby **([B]-[D]),** color Doppler sonography may show no flow. A tight tourniquet in a baby can obstruct even arterial flow, resulting in erroneous placement of an intraarterial PICC line, a very dangerous event, if unrecognized.

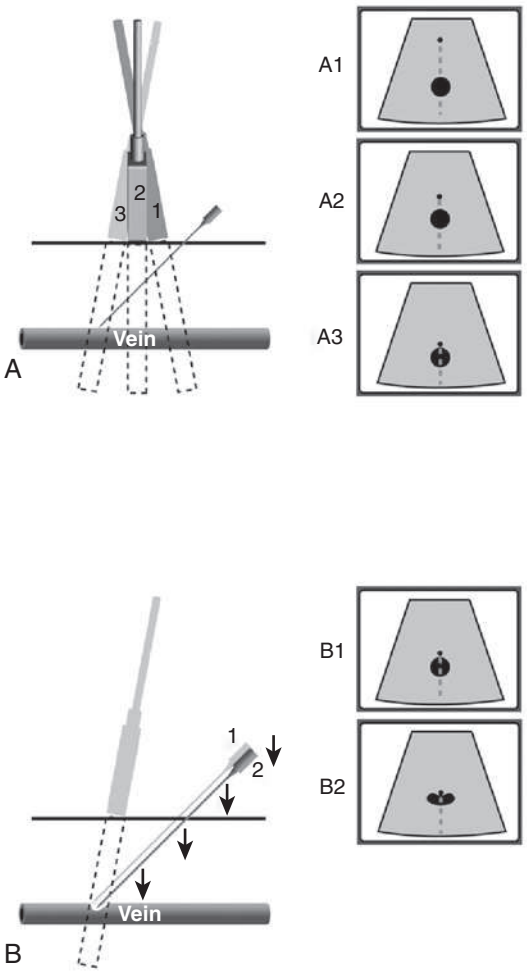

FIG. 56.12 Localizing the Needle Tip Near the Vein. (A) As the needle is advanced toward the vein, the transducer is used in transverse orientation and rocked back and forth *(A1-A3)* to sequentially track the tip of the needle as it is advanced toward the vein. In the illustration, the needle is depicted only as it is about to enter the vein (position *3*). **(B)** Trapping and puncturing the vein. The needle can easily slip to the side of the vein if it is simply advanced, especially when attempting to puncture a deep brachial vein. The loose soft tissue surrounding deep veins allows the vein to slide out of the way of the needle. When the tip of the needle is positioned correctly, adjacent to the anterior wall of the vein *(B1)*, gentle downward movement of the needle, without trying to puncture the vein, will "trap" the vein with the needle tip *(B2)*. Once the vein is trapped, a quick thrust will puncture both walls. Careful withdrawal usually results in venous blood return through the needle, allowing successful peripherally inserted central catheter (PICC) line placement.

passage of a guidewire to dislodge the obstructing debris (Video 56.2, Video 56.3).

Percutaneous Cholangiography and Drainage

Percutaneous transhepatic cholangiography can be successfully performed in children with or without duct dilation. Ultrasound is used to guide the Chiba needle toward the bile ducts, which lie in the portal tracts. The optimal diagnostic puncture site is at the junction of the middle and peripheral thirds of the duct, well away from the central portal veins and hepatic artery. If the ducts are dilated, the needle can be guided directly into the duct with the usual ultrasound techniques. Puncture should be made at a site and at an angle that will allow conversion of the track to a catheter drain should the diagnostic study reveal bile duct stenosis or complete obstruction, especially in liver transplant patients. Initial puncture of minimally dilated bile ducts in pediatric liver transplant patients is one of the most technically demanding ultrasound-guided procedures (Fig. 56.15).

Mediastinal Mass Biopsy

Lymphoma is a common childhood malignancy often manifesting with a mediastinal mass. In many cases, cervical, abdominal or axillary lymphadenopathy is seen at presentation enabling histologic diagnosis by surgical lymph node biopsy. In some cases, however, the patient has respiratory difficulty as a result of tracheal compression and there are no convenient enlarged lymph nodes available for biopsy. Many of these patients are unable to lie flat without respiratory distress. The mediastinal mass can enlarge very rapidly, such that a child who could lie flat for the initial CT scan cannot lie flat a few hours later. In these cases, ultrasound-guided mediastinal biopsy is often the safest option. Emergency radiotherapy and steroid administration can also be used to shrink the mass, but these maneuvers can result in inability to subtype the cells of the lymphoma, which is becoming more important for treatment decisions and prognosis.

These patients are managed in the operating room in a semi-erect position and need to be supervised and sedated by experienced anesthesia staff. We typically use copious local anesthesia and only minimal intravenous sedation, avoiding intubation if at all possible.

Doppler ultrasound is used to locate and avoid the internal mammary artery and vein. The mass is usually approached through a paramanubrial intercostal space under direct ultrasound guidance using a small-footprint sector probe. The great vessels and lung must be clearly visualized before biopsy. Multiple samples can be obtained with remarkably low risk of complication (Fig. 56.16).

Appendiceal Abscess Drainage

Initial ultrasound-guided drainage of an appendix-associated abscess is a well-documented procedure. Occasionally a secondary abscess occurs after interval endoscopic surgery for removal of the appendix, usually caused by a retained or unrecognized fecalith. Ultrasound guidance can also be used to drain these recurrent abscesses. In one case, we were able to precisely target the retained fecalith, drain the abscess, and then remove the fecalith by a second interventional procedure using an Amplatz biliary sheath (Cook, Bloomington, IN) and Fogarty balloon retrieval of the fecalith through the sheath (Fig. 56.17, Video 56.4).

Text continued on p. 1961.

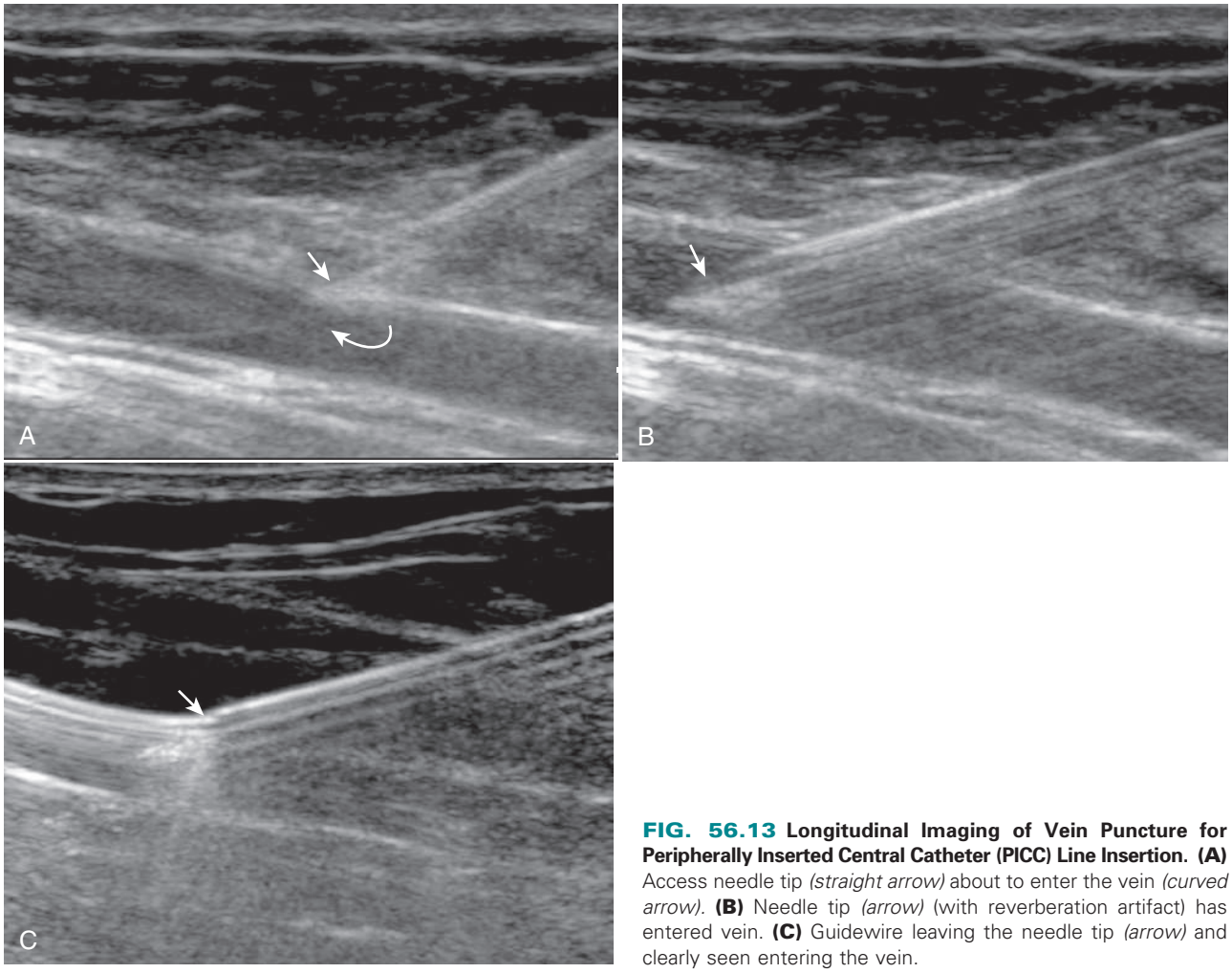

FIG. 56.13 Longitudinal Imaging of Vein Puncture for Peripherally Inserted Central Catheter (PICC) Line Insertion. (A) Access needle tip *(straight arrow)* about to enter the vein *(curved arrow)*. **(B)** Needle tip *(arrow)* (with reverberation artifact) has entered vein. **(C)** Guidewire leaving the needle tip *(arrow)* and clearly seen entering the vein.

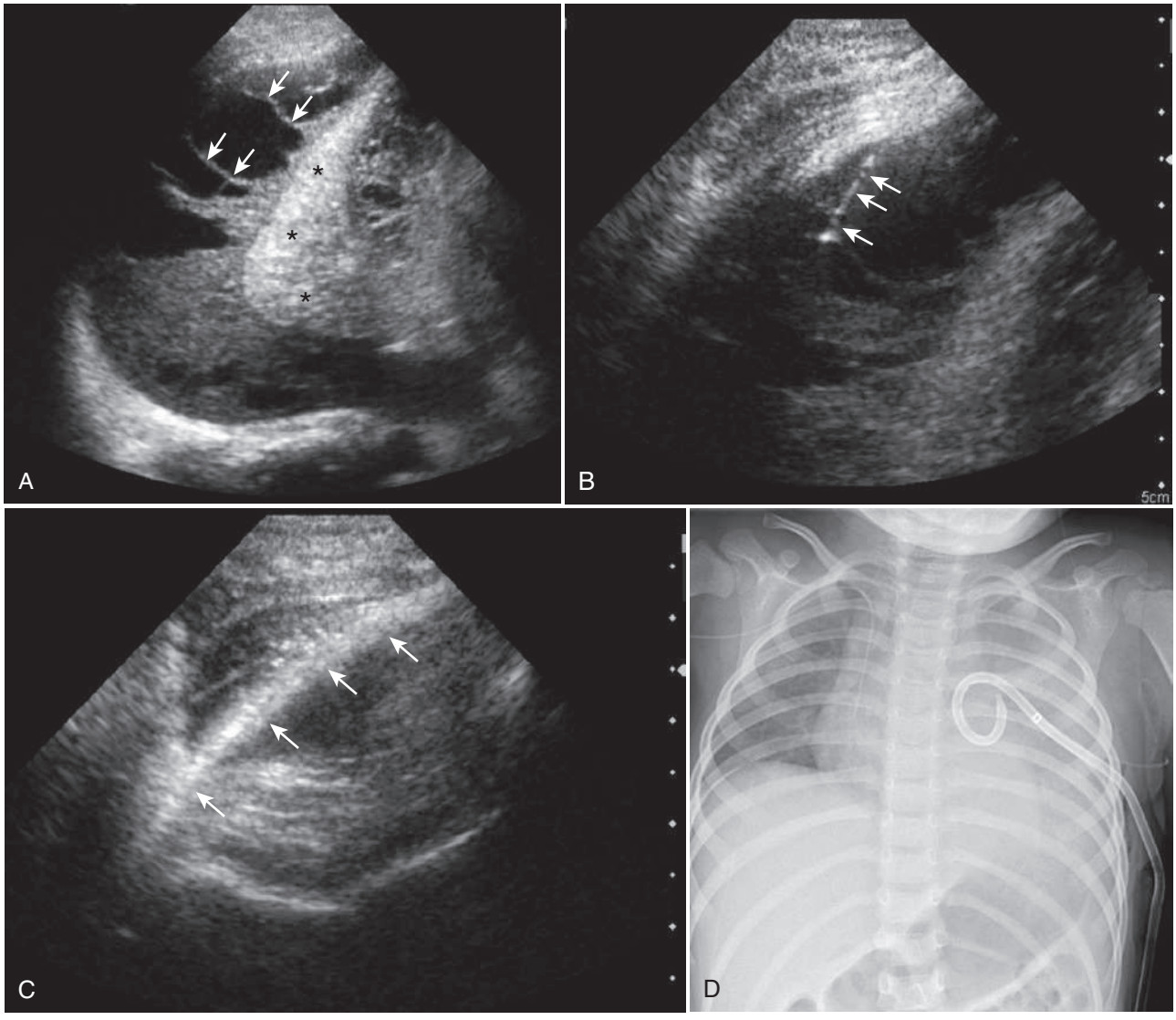

FIG. 56.14 Ultrasound Guidance for Treatment of Loculated Chest Empyema. (A) Semisolid extrapleural inflammatory material with septae *(arrows)* compressing the airless adjacent left lung *(black *).* **(B)** Access needle *(arrows)* entering the empyema. **(C)** Left chest tube *(arrows)* inserted for drainage and for installation of tissue plasminogen activator (tPA), a very successful combined treatment of this condition formerly treated by thoracotomy. **(D)** Radiograph showing left chest tube position.

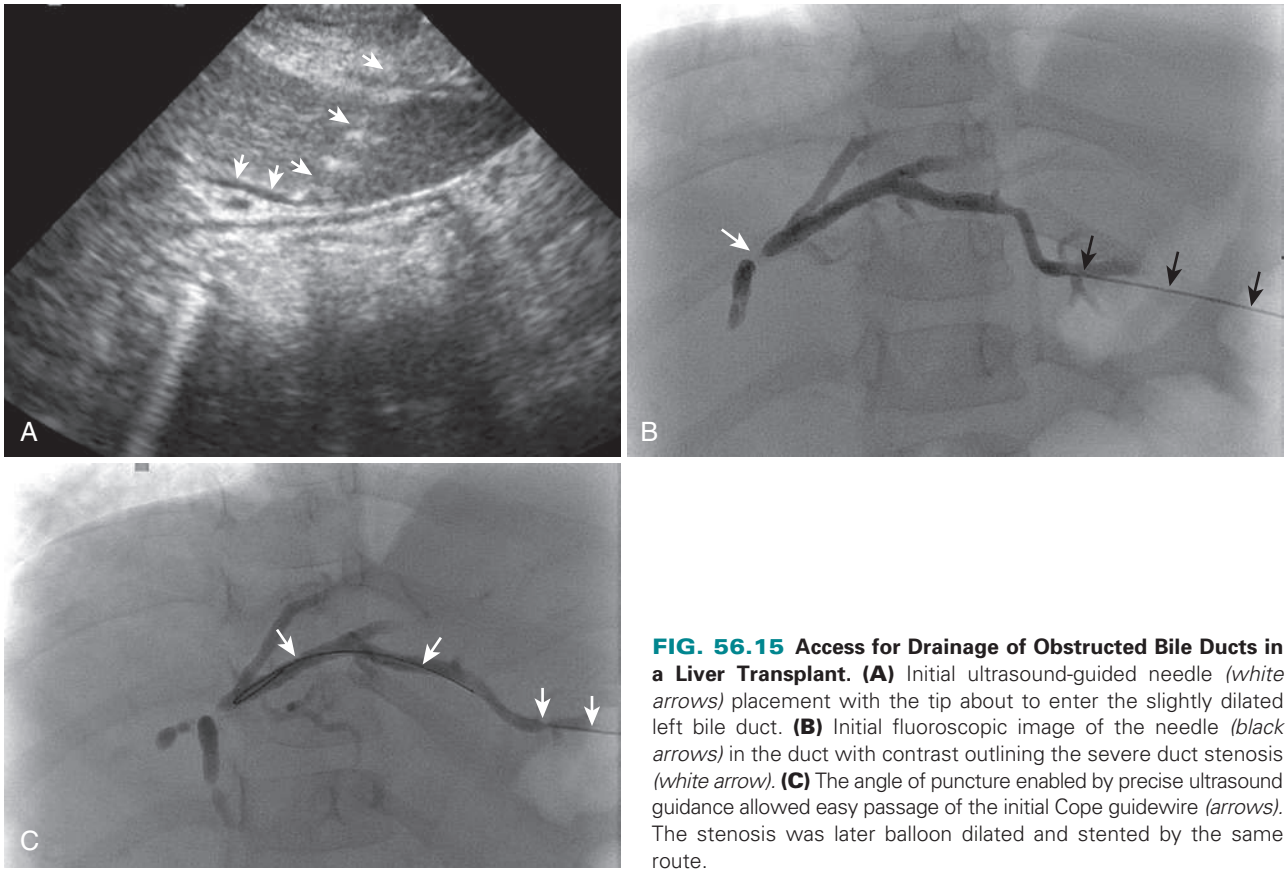

FIG. 56.15 Access for Drainage of Obstructed Bile Ducts in a Liver Transplant. (A) Initial ultrasound-guided needle *(white arrows)* placement with the tip about to enter the slightly dilated left bile duct. **(B)** Initial fluoroscopic image of the needle *(black arrows)* in the duct with contrast outlining the severe duct stenosis *(white arrow)*. **(C)** The angle of puncture enabled by precise ultrasound guidance allowed easy passage of the initial Cope guidewire *(arrows)*. The stenosis was later balloon dilated and stented by the same route.

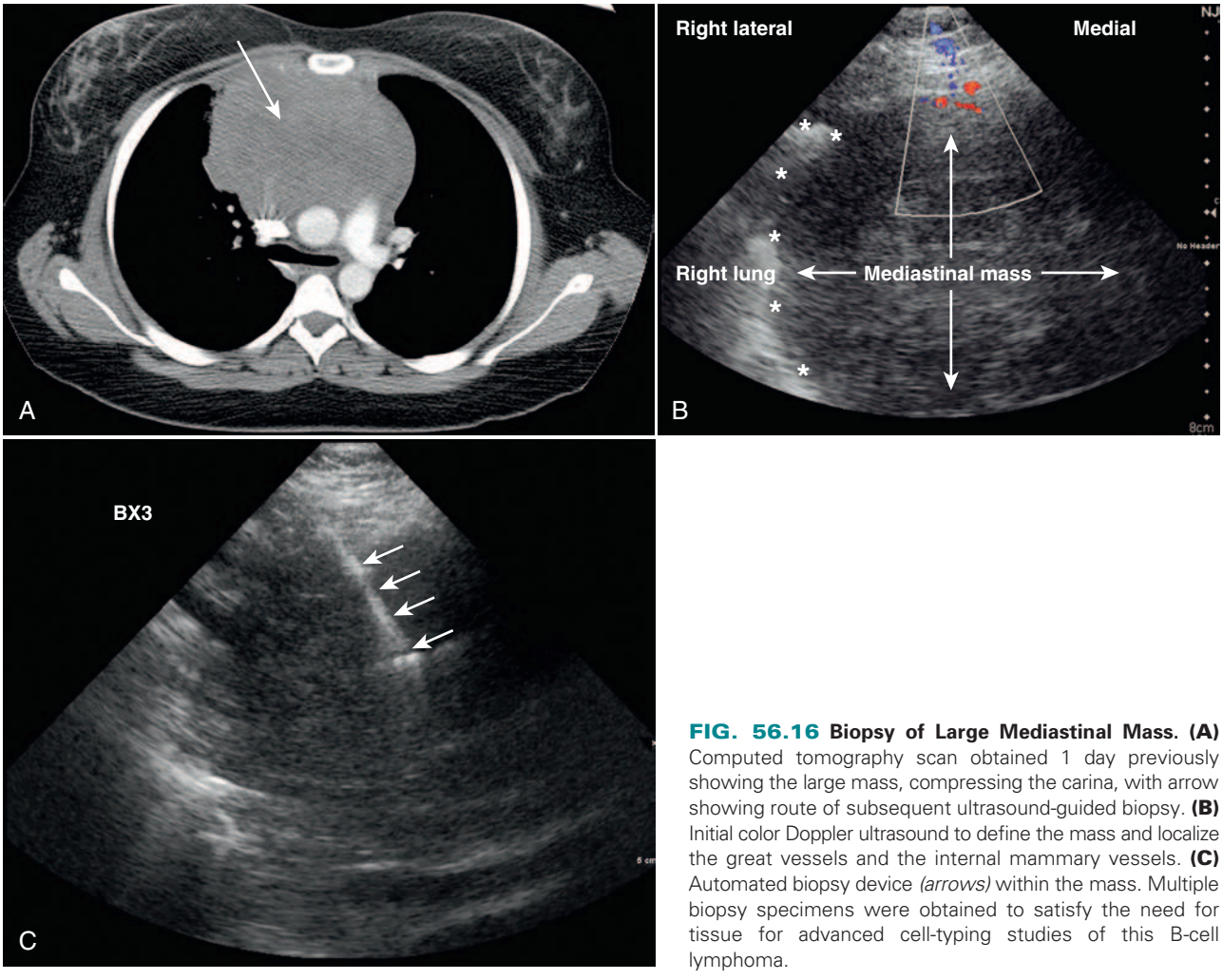

FIG. 56.16 Biopsy of Large Mediastinal Mass. (A) Computed tomography scan obtained 1 day previously showing the large mass, compressing the carina, with arrow showing route of subsequent ultrasound-guided biopsy. **(B)** Initial color Doppler ultrasound to define the mass and localize the great vessels and the internal mammary vessels. **(C)** Automated biopsy device *(arrows)* within the mass. Multiple biopsy specimens were obtained to satisfy the need for tissue for advanced cell-typing studies of this B-cell lymphoma.

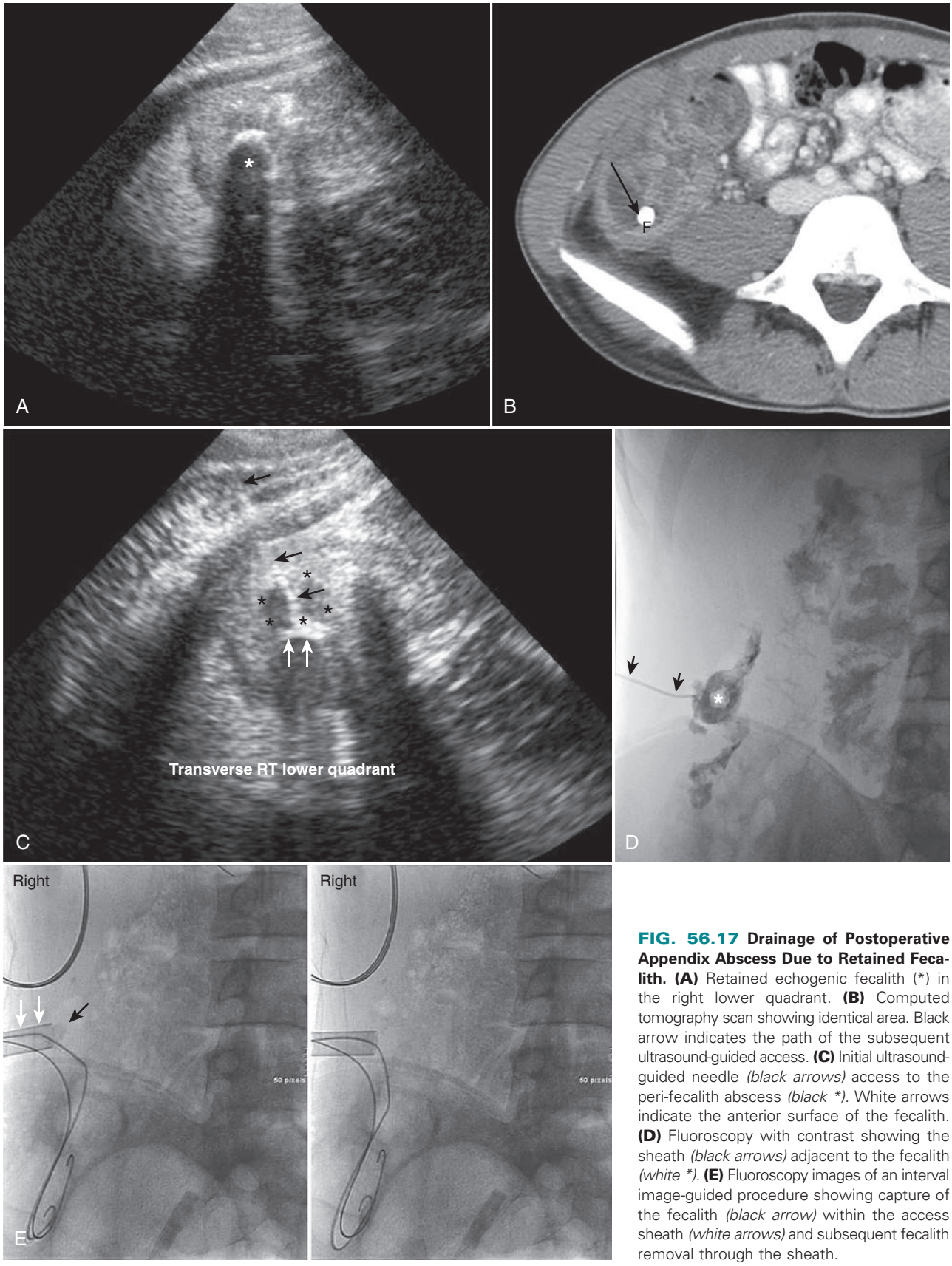

FIG. 56.17 Drainage of Postoperative Appendix Abscess Due to Retained Fecalith. (A) Retained echogenic fecalith (*) in the right lower quadrant. **(B)** Computed tomography scan showing identical area. Black arrow indicates the path of the subsequent ultrasound-guided access. **(C)** Initial ultrasound-guided needle *(black arrows)* access to the peri-fecalith abscess *(black *)*. White arrows indicate the anterior surface of the fecalith. **(D)** Fluoroscopy with contrast showing the sheath *(black arrows)* adjacent to the fecalith *(white *)*. **(E)** Fluoroscopy images of an interval image-guided procedure showing capture of the fecalith *(black arrow)* within the access sheath *(white arrows)* and subsequent fecalith removal through the sheath.

Targeted Organ Lesion Biopsy

Ultrasound-guided nontarget-organ biopsy such as for suspected liver or kidney abnormality is a well-established procedure. Targeted intraorgan lesion biopsy is more demanding. Each case must be assessed on its merits, but caution should be exercised for lesions close to the diaphragm or major intraorgan or extraorgan vasculature. Figs. 56.18 and 56.19 illustrate two such targeted lesion biopsies.

Musculoskeletal Procedures

Whereas CT or cone-beam CT is the usual guidance modality for deep bone procedures, ultrasound can be useful for certain periosteal or cartilage-related lesions (see Fig. 56.1; Fig. 56.20, Video 56.5, Video 56.6, and Video 56.7).

Steroid injection for local treatment of specific joints in diseases such as juvenile rheumatoid arthritis can be achieved by nonimage-guided access in large joints such as the knee, but increasingly, rheumatologists are referring patients for image-guided steroid injection for smaller or technically difficult joints such as the subtalar, temporomandibular, or interphalangeal joints. Ultrasound guidance can be used for accurate access to these small joints.[28,29] Ultrasound-guided steroid injection of tendon sheaths is a valuable procedure (Fig. 56.21, Video 56.8).

Some deep foreign bodies can be removed under ultrasound guidance (Fig. 56.22). It is important that the ultrasound-guided procedure be done before the wound is opened and probed in the emergency room or operating room. Otherwise, air degrades the ability of ultrasound to visualize the foreign body and the case must be cancelled and rescheduled.

Head and Neck Lesions

Certain vascular and lymphatic malformations are amenable to ultrasound-guided access and treatment, usually by sclerosing agents.[30] Orbital lymphatic malformations are difficult to treat surgically but respond well to percutaneous ultrasound-guided sclerosis (Fig. 56.23).

Ranulas are rare lesions consisting of saliva-containing cysts most commonly due to trauma or obstruction of the sublingual duct. The sublingual duct secretes saliva continuously, whereas the submandibular and parotid duct secrete only with oral stimuli such as eating, and therefore the sublingual gland is more prone to formation of ranula. Plunging ranula can be treated successfully by ultrasound and fluoroscopically guided sclerosis (Fig. 56.24).

NOTE FROM THE AUTHORS

The authors dedicate this chapter to the memory of Dr. William (Bill) Shiels. Dr. Shiels was an interventional ultrasound innovator, an extreme enthusiast, and co-author of this chapter in the fourth edition. He pioneered many new and innovative techniques in pediatric interventional radiology, often involving ultrasound guidance and monitoring. He established a popular system of training phantoms and established and maintained active leadership of the annual "hands-on" sessions at the RSNA for many years. He inspired many young pediatric interventionalists and taught us all. He will be remembered by all who came into contact with this unique and inspiring person. Thank you, Bill.

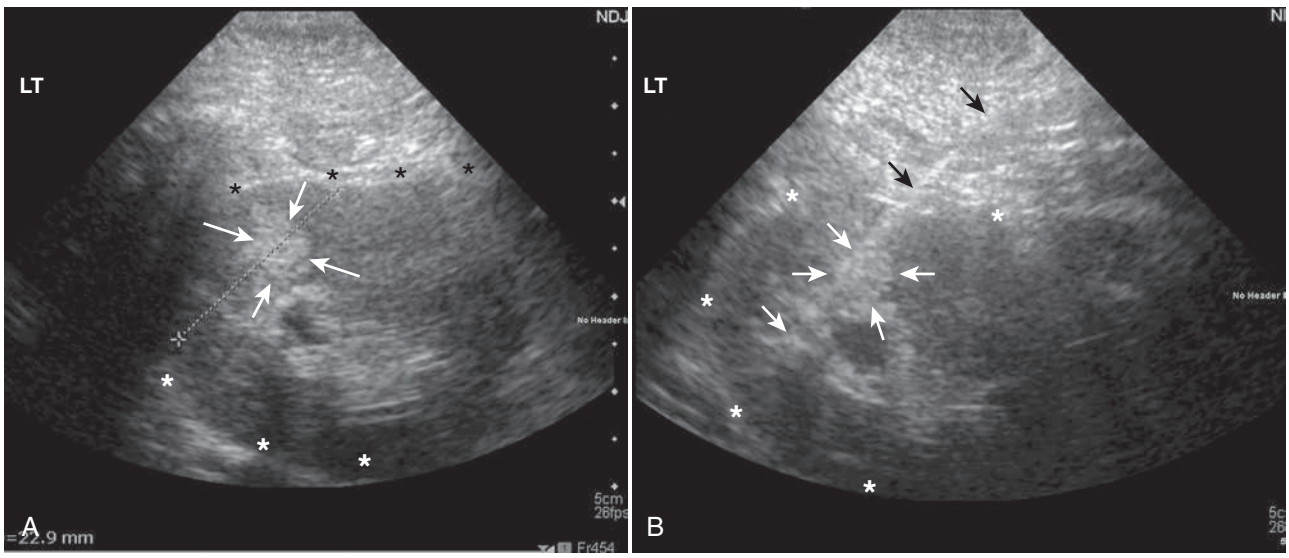

FIG. 56.18 Targeted Left Upper-Pole Renal Lesion Biopsy in a Patient With Secondary Renal Cell Carcinoma After Prior Treatment for Cerebral Primitive Neuroectodermal Tumor. (A) Lesion high in the upper pole of the left kidney *(white arrows).* Measurement calipers are estimating the depth of the biopsy in order to avoid puncturing the adjacent diaphragm *(white *)* and spleen. *Black* * indicate posterior margin of kidney. **(B)** Biopsy device *(black arrows)* passing through the lesion *(white arrows),* stopping short of the diaphragm. *White* * indicate upper pole of kidney.

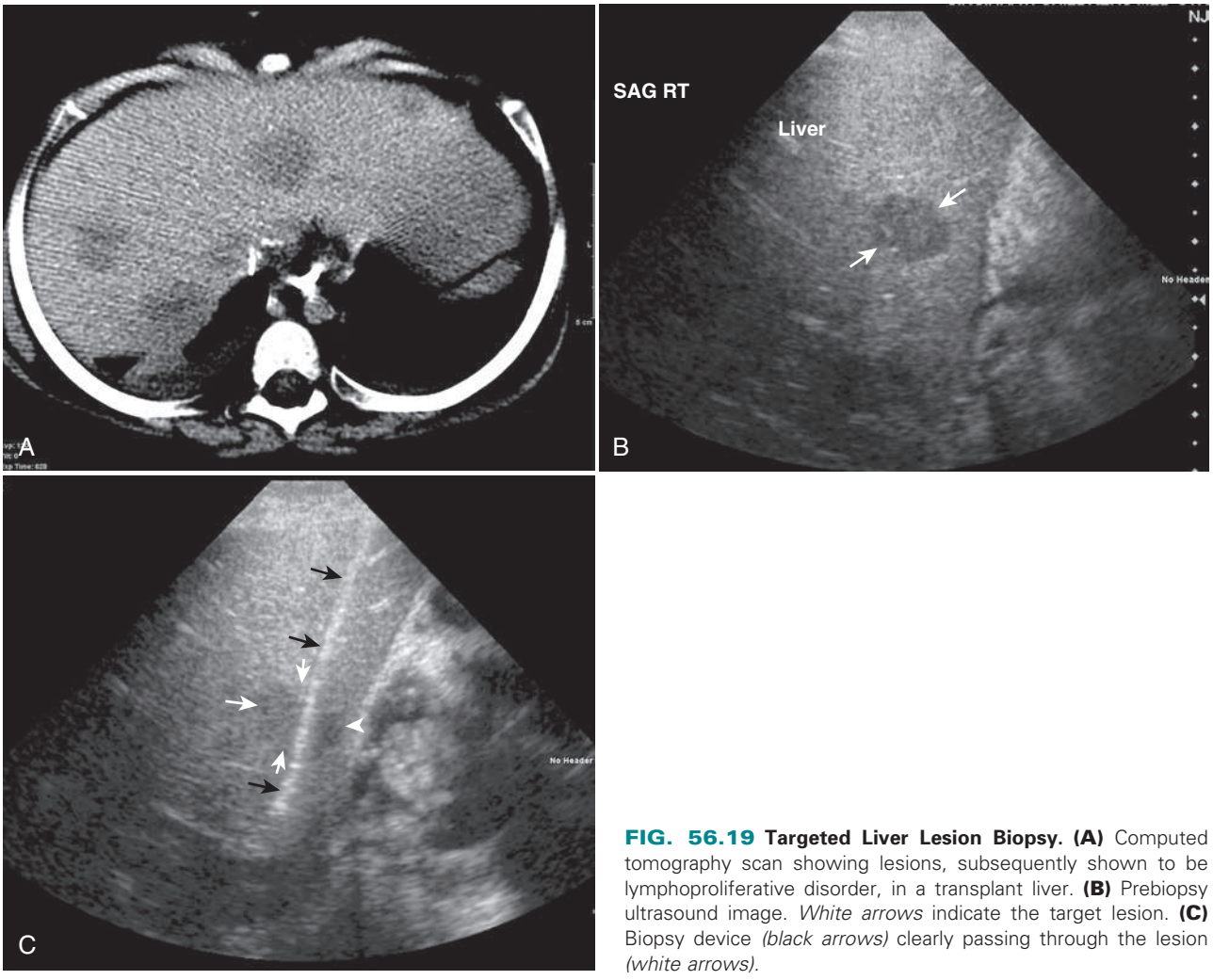

FIG. 56.19 Targeted Liver Lesion Biopsy. (A) Computed tomography scan showing lesions, subsequently shown to be lymphoproliferative disorder, in a transplant liver. **(B)** Prebiopsy ultrasound image. *White arrows* indicate the target lesion. **(C)** Biopsy device *(black arrows)* clearly passing through the lesion *(white arrows).*

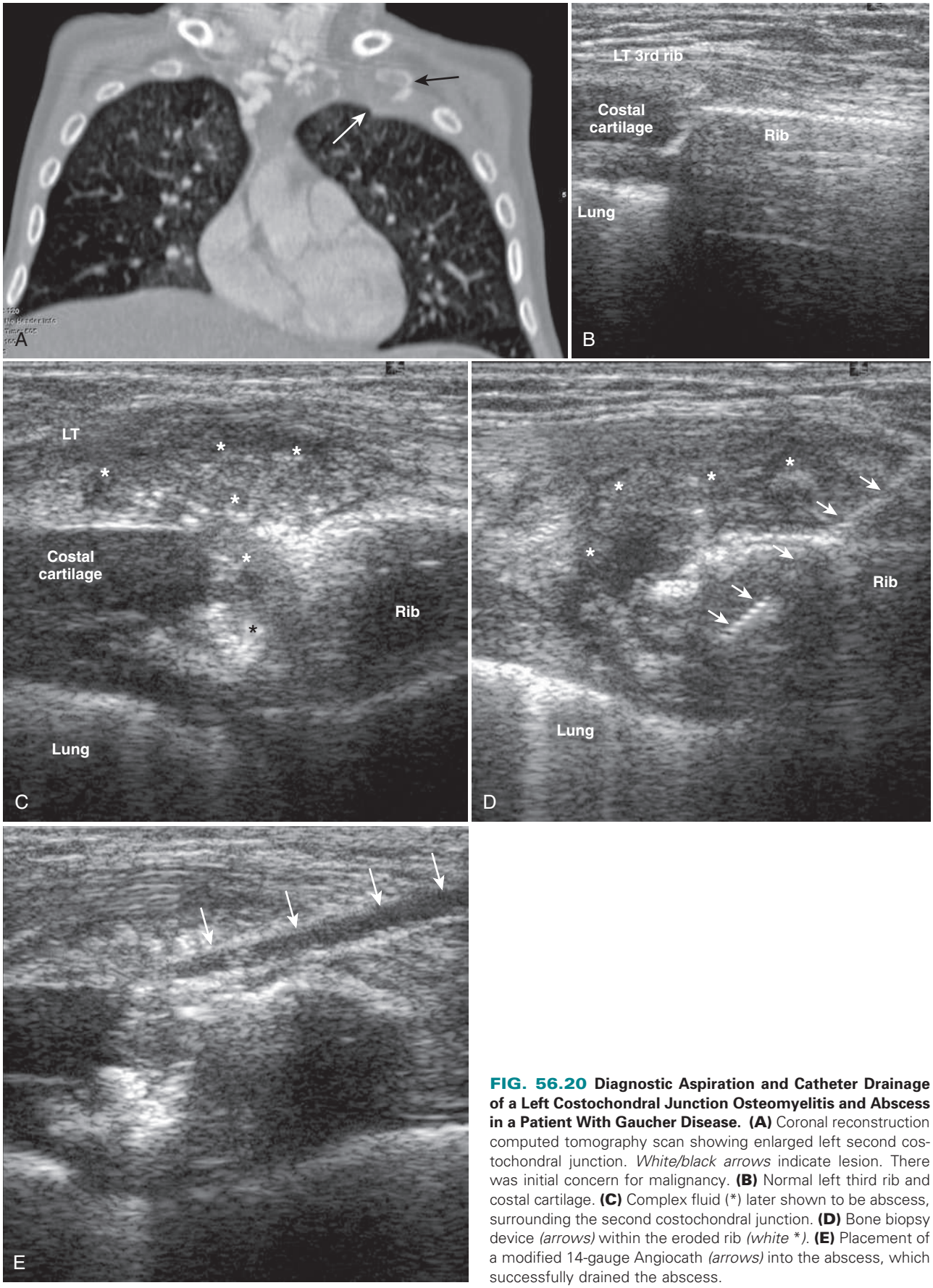

FIG. 56.20 Diagnostic Aspiration and Catheter Drainage of a Left Costochondral Junction Osteomyelitis and Abscess in a Patient With Gaucher Disease. (A) Coronal reconstruction computed tomography scan showing enlarged left second costochondral junction. *White/black arrows* indicate lesion. There was initial concern for malignancy. **(B)** Normal left third rib and costal cartilage. **(C)** Complex fluid (*) later shown to be abscess, surrounding the second costochondral junction. **(D)** Bone biopsy device *(arrows)* within the eroded rib *(white *)*. **(E)** Placement of a modified 14-gauge Angiocath *(arrows)* into the abscess, which successfully drained the abscess.

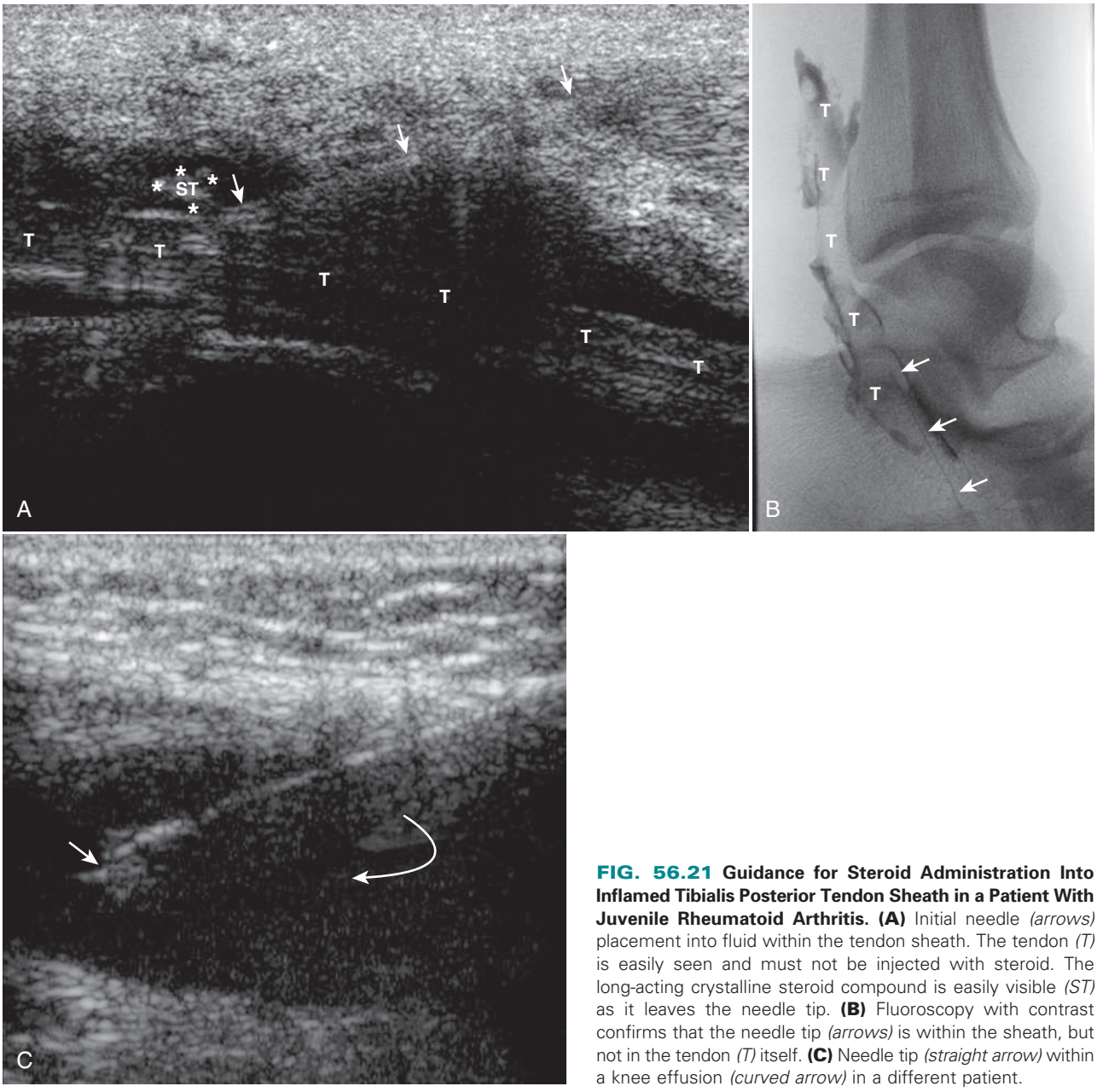

FIG. 56.21 Guidance for Steroid Administration Into Inflamed Tibialis Posterior Tendon Sheath in a Patient With Juvenile Rheumatoid Arthritis. (A) Initial needle *(arrows)* placement into fluid within the tendon sheath. The tendon *(T)* is easily seen and must not be injected with steroid. The long-acting crystalline steroid compound is easily visible *(ST)* as it leaves the needle tip. **(B)** Fluoroscopy with contrast confirms that the needle tip *(arrows)* is within the sheath, but not in the tendon *(T)* itself. **(C)** Needle tip *(straight arrow)* within a knee effusion *(curved arrow)* in a different patient.

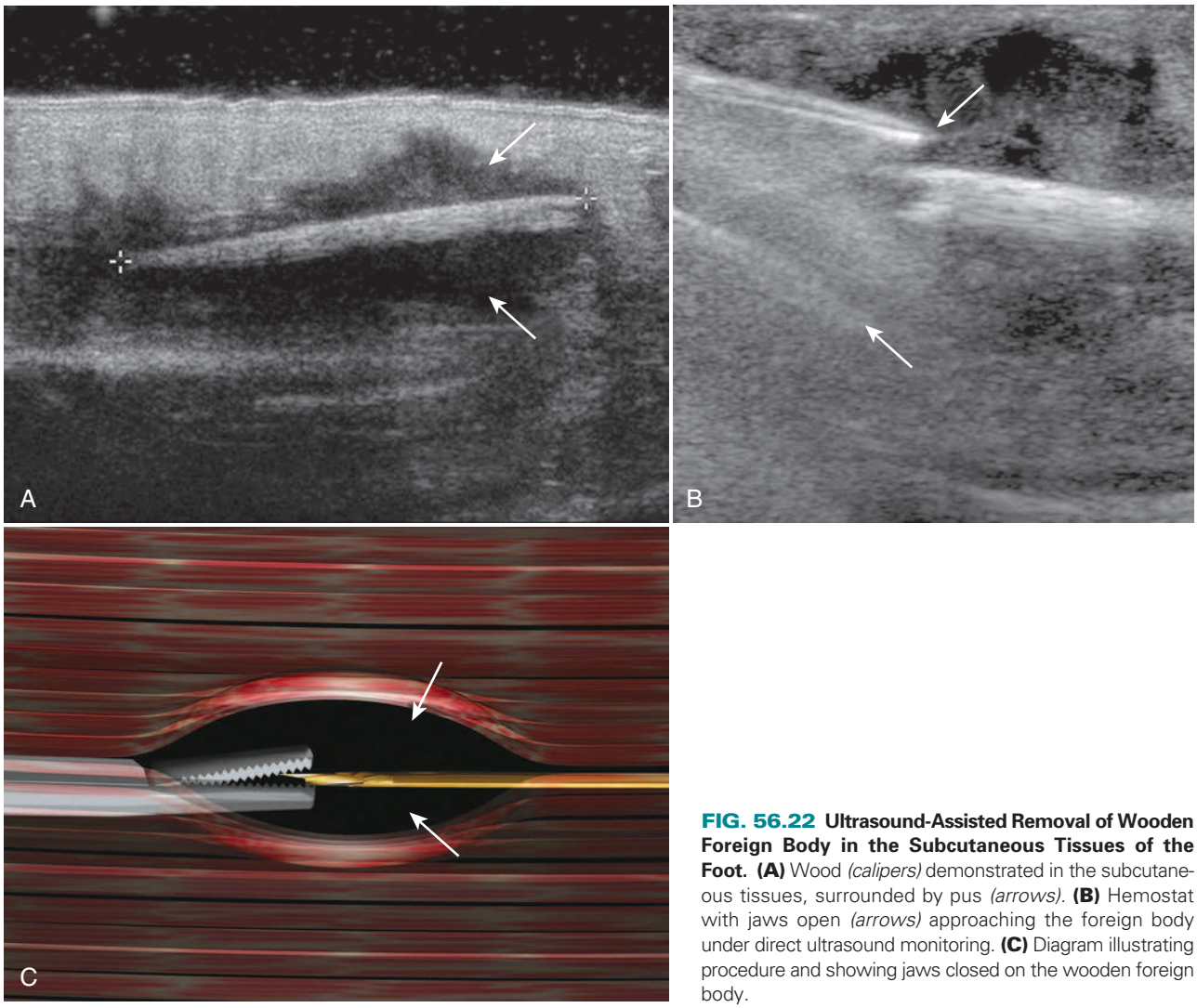

FIG. 56.22 Ultrasound-Assisted Removal of Wooden Foreign Body in the Subcutaneous Tissues of the Foot. (A) Wood *(calipers)* demonstrated in the subcutaneous tissues, surrounded by pus *(arrows)*. **(B)** Hemostat with jaws open *(arrows)* approaching the foreign body under direct ultrasound monitoring. **(C)** Diagram illustrating procedure and showing jaws closed on the wooden foreign body.

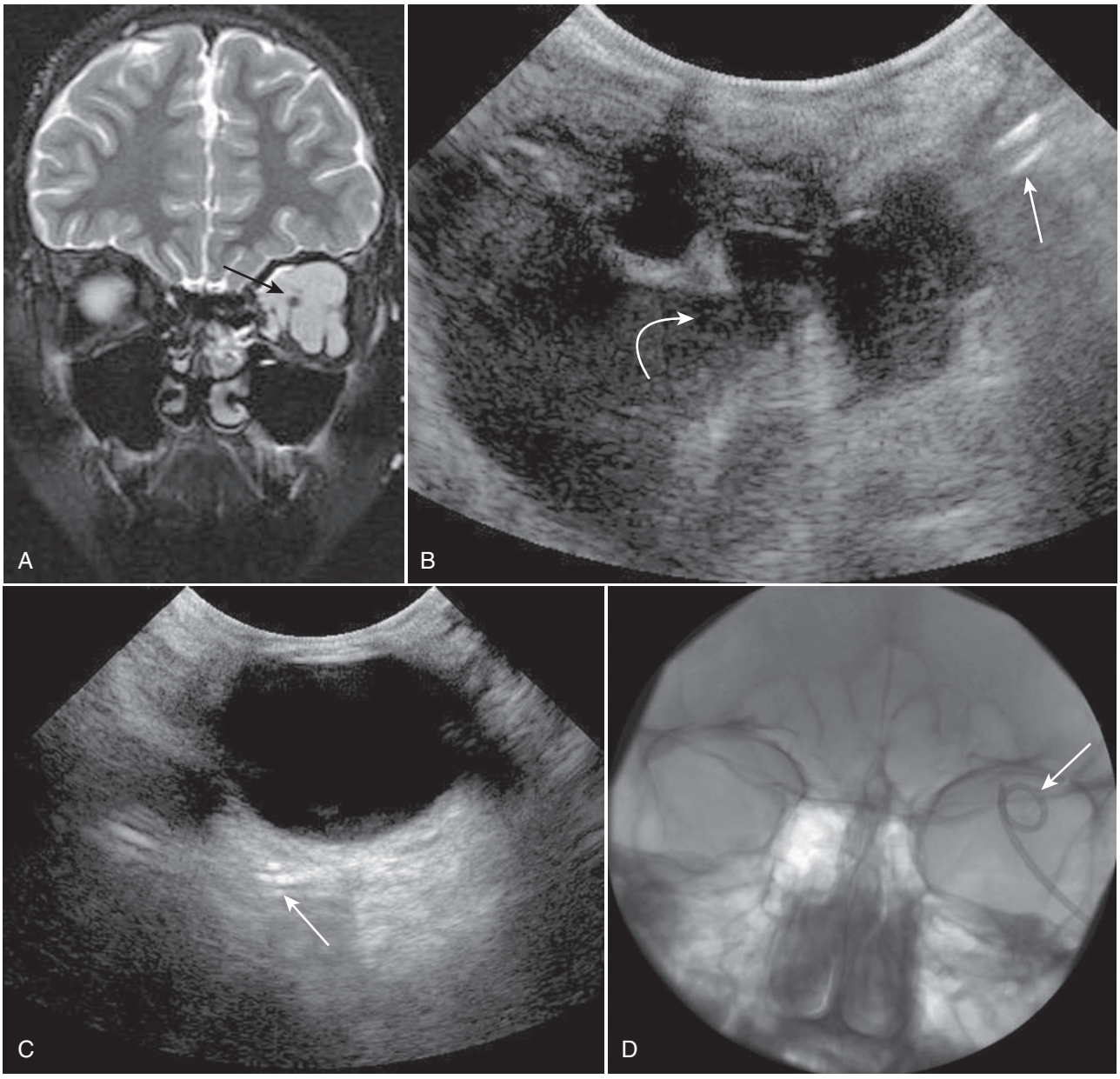

FIG. 56.23 A 13-Year-Old Boy With Successful Treatment of a Left Orbital Lymphatic Malformation (LM). (A) Coronal T2-weighted magnetic resonance image demonstrates the LM with medium-intensity–signal fluid surrounding the left optic nerve *(arrow).* **(B)** Longitudinal ultrasound image of the left orbit with a 14-gauge angiocatheter needle *(straight arrow)* about to enter the macrocystic LM *(curved arrow).* **(C)** Transverse ultrasound image demonstrates the 5-French catheter *(arrow)* in the left orbital LM after aspiration of LM fluid. The anechoic fluid-filled structure is the globe. **(D)** Fluoroscopic spot film demonstrating the 5-French pigtail catheter *(arrow)* in place for sclerotherapy of the macrocystic element of the orbital LM.

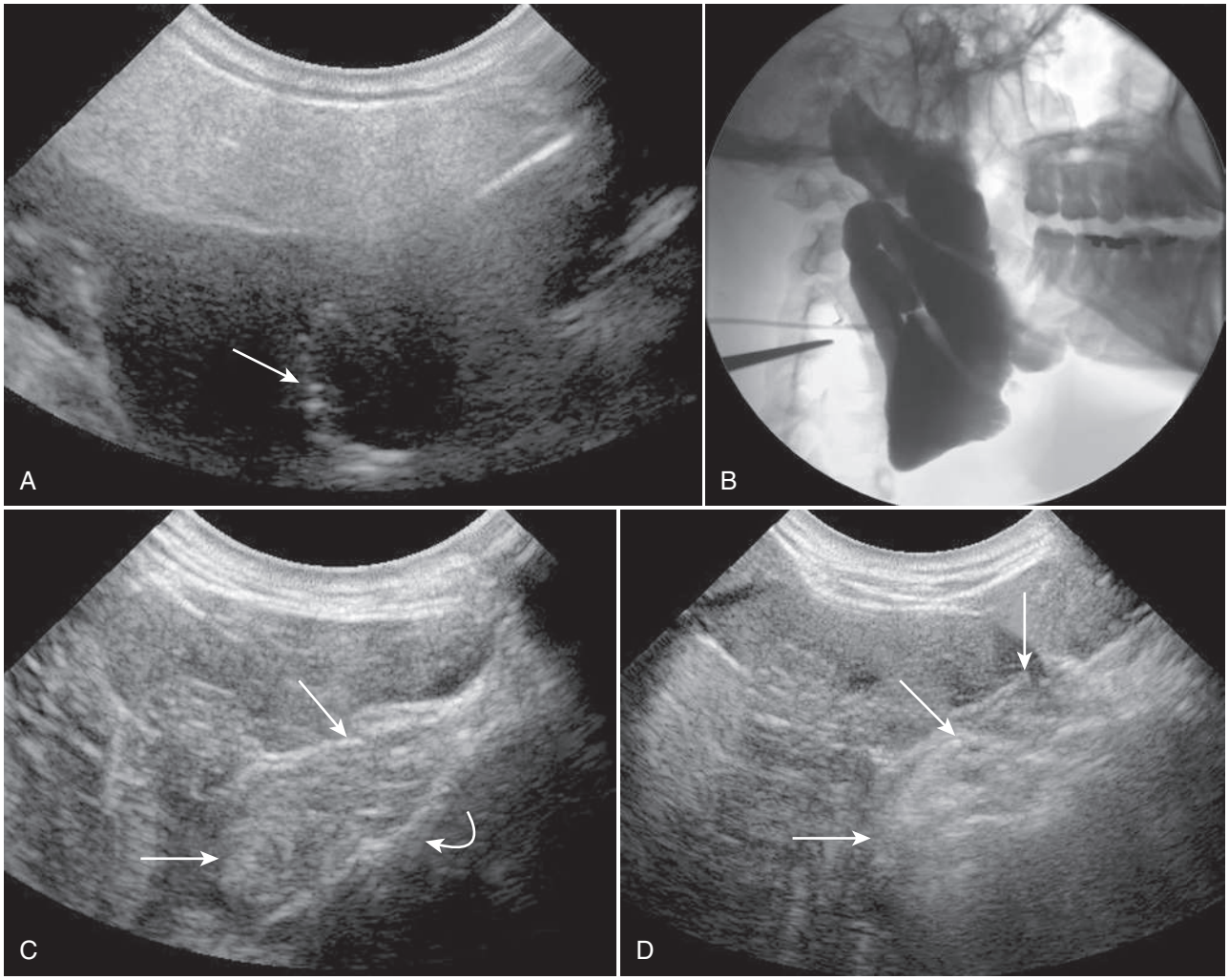

FIG. 56.24 Percutaneous Treatment of a Left Neck Plunging Ranula. (A) Longitudinal sonography demonstrates a 5-French pigtail catheter *(arrow)* within the hypoechoic ranula fluid. **(B)** Contrast material filling the ranula sac. **(C)** Transverse sonography demonstrating the left sublingual gland *(straight arrows)* adjacent to the left mandible *(curved arrow)* before ablation. **(D)** Increased echogenicity in the left sublingual gland *(arrows)* during ethanol injection for ablation.

REFERENCES

1. Slovis TL. The ALARA concept in pediatric CT: myth or reality? Radiology. 2002;223(1):5-6.
2. Racadio JM, Babic D, Homan R, et al. Live 3D guidance in the interventional radiology suite. AJR Am J Roentgenol. 2007;189(6):W357-W364.
3. McGahan JP, Wu C. Sonographically guided transvaginal or transrectal pelvic abscess drainage using the trocar method with a new drainage guide attachment. AJR Am J Roentgenol. 2008;191(5):1540-1544.
4. Gibson RN, Gibson KI. A home-made phantom for learning ultrasound-guided invasive techniques. Australas Radiol. 1995;39(4):356-357.
5. Georgian-Smith D, Shiels WE 2nd. From the RSNA refresher courses. Freehand interventional sonography in the breast: basic principles and clinical applications. Radiographics. 1996;16(1):149-161.
6. Harvey JA, Moran RE, Hamer MM, et al. Evaluation of a turkey-breast phantom for teaching freehand, US-guided core-needle breast biopsy. Acad Radiol. 1997;4(8):565-569.
7. Egelhoff JC, Ball Jr WS, Koch BL, Parks TD. Safety and efficacy of sedation in children using a structured sedation program. AJR Am J Roentgenol. 1997;168(5):1259-1262.
8. Burke JF. The effective period of preventive antibiotic action in experimental incisions and dermal lesions. Surgery. 1961;50:161-168.
9. Venkatesan AM, Kundu S, Sacks D, et al. Practice guidelines for adult antibiotic prophylaxis during vascular and interventional radiology procedures. Written by the Standards of Practice Committee for the Society of Interventional Radiology and Endorsed by the Cardiovascular Interventional Radiological Society of Europe and Canadian Interventional Radiology Association [corrected]. J Vasc Interv Radiol. 2010;21(11):1611-1630.
10. Ryan JM, Ryan BM, Smith TP. Antibiotic prophylaxis in interventional radiology. J Vasc Interv Radiol. 2004;15(6):547-556.
11. Fink A, Kosecoff J, Chassin M, Brook RH. Consensus methods: characteristics and guidelines for use. Am J Public Health. 1984;74(9):979-983.
12. Patel IJ, Davidson JC, Nikolic B, et al. Consensus guidelines for periprocedural management of coagulation status and hemostasis risk in percutaneous image-guided interventions. J Vasc Interv Radiol. 2012;23(6):727-736.
13. McVay PA, Toy PT. Lack of increased bleeding after liver biopsy in patients with mild hemostatic abnormalities. Am J Clin Pathol. 1990;94(6):747-753.
14. Harisinghani MG, Gervais DA, Maher MM, et al. Transgluteal approach for percutaneous drainage of deep pelvic abscesses: 154 cases. Radiology. 2003;228(3):701-705.
15. Pereira JK, Chait PG, Miller SF. Deep pelvic abscesses in children: transrectal drainage under radiologic guidance. Radiology. 1996;198(2):393-396.

16. Racadio JM, Doellman DA, Johnson ND, et al. Pediatric peripherally inserted central catheters: complication rates related to catheter tip location. Pediatrics. 2001;107(2):E28.
17. Patel AA, Tuite CM, Trerotola SO. K/DOQI guidelines: what should an interventionalist know? Semin Intervent Radiol. 2004;21(2): 119-124.
18. Fava M, Loyola MS, Flores P. Percutaneous transluminal angioplasty (PTA) and intravascular stents in the treatment of central and peripheral venous stenoses of arteriovenous fistulae for chronic hemodialysis. Rev Med Chil. 1996;124(11):1334-1340.
19. Trerotola SO, Kuhn-Fulton J, Johnson MS, et al. Tunneled infusion catheters: increased incidence of symptomatic venous thrombosis after subclavian versus internal jugular venous access. Radiology. 2000;217(1):89-93.
20. Mirza B, Vanek VW, Kupensky DT. Pinch-off syndrome: case report and collective review of the literature. Am Surg. 2004;70(7):635-644.
21. Karakitsos D, Labropoulos N, De Groot E, et al. Real-time ultrasound-guided catheterisation of the internal jugular vein: a prospective comparison with the landmark technique in critical care patients. Crit Care. 2006;10(6): R162.
22. Sabbaj A, Hedges JR. Ultrasonographic guidance for internal jugular vein cannulation: an educational imperative, a desirable practice alternative. Ann Emerg Med. 2006;48(5):548-550.
23. Espinet A, Dunning J. Does ultrasound-guided central line insertion reduce complications and time to placement in elective patients undergoing cardiac surgery. Interact Cardiovasc Thorac Surg. 2004;3(3):523-527.
24. Slama M, Novara A, Safavian A, et al. Improvement of internal jugular vein cannulation using an ultrasound-guided technique. Intensive Care Med. 1997;23(8):916-919.
25. Barash P. Ultrasound-guided central venous access. F1000 Med Rep. 2009;1.
26. Moulton JS, Moore PT, Mencini RA. Treatment of loculated pleural effusions with transcatheter intracavitary urokinase. AJR Am J Roentgenol. 1989;153(5):941-945.
27. Ray TL, Berkenbosch JW, Russo P, Tobias JD. Tissue plasminogen activator as an adjuvant therapy for pleural empyema in pediatric patients. J Intensive Care Med. 2004;19(1):44-50.
28. Young CM, Horst DM, Murakami JW, Shiels WE 2nd. Ultrasound-guided corticosteroid injection of the subtalar joint for treatment of juvenile idiopathic arthritis. Pediatr Radiol. 2015;45(8):1212-1217.
29. Young CM, Shiels WE 2nd, Coley BD, et al. Ultrasound-guided corticosteroid injection therapy for juvenile idiopathic arthritis: 12-year care experience. Pediatr Radiol. 2012;42(12):1481-1489.
30. Shiels WE 2nd, Kenney BD, Caniano DA, Besner GE. Definitive percutaneous treatment of lymphatic malformations of the trunk and extremities. J Pediatr Surg. 2008;43(1):136-139.

APPENDIX

Ultrasound Artifacts: A Virtual Chapter

Korosh Khalili, Hojun Yu, Alexander Jesurum, and Deborah Levine

SUMMARY OF KEY POINTS

- Artifacts are common in ultrasound imaging.
- Knowledge of artifacts can aid in diagnosis.
- Understanding ultrasound physics allows for correction of artifacts that distort the visualized anatomy.

CHAPTER OUTLINE

ASSUMPTIONS IN GRAY-SCALE IMAGING
Velocity of Sound
Attenuation of Sound
Path of Sound
Beam Profile
PROPAGATION VELOCITY ARTIFACT
ATTENUATION ERRORS
Shadowing
Increased Through Transmission
PATH OF SOUND-RELATED ARTIFACTS
Mirror Image Artifact
Comet-Tail Artifact
Refraction
Anisotropy
Reverberation Artifact
GAS-RELATED ARTIFACTS
Reverberation Artifact
Ring-Down Artifact
Dirty Shadowing Artifact
BEAM PROFILE–RELATED ARTIFACTS
Side Lobe and Grating Lobe Artifacts
Partial Volume Averaging
DOPPLER IMAGING ARTIFACTS
Loss or Distortion of Doppler Information
Artifactual Vascular Flow
Tissue Vibration Artifact
Aliasing and Velocity Scale Errors
Spectral Broadening
Blooming Artifact
Twinkle Artifact
Acknowledgment

Almost all ultrasound images contain artifacts. Many of these artifacts go unrecognized because they are contained within (and contribute to) the background noise. However, when artifacts substantially alter the signal, they become recognizable on images. Certain artifacts distort the images and must be recognized in order to improve image quality or prevent a false diagnosis. Other artifacts add useful data and thus are important for understanding the composition, anatomy, and pathology of the image being visualized. We hope you enjoy this virtual chapter, which encompasses animated illustrations of how artifacts are produced as well as multiple examples of images and videos from the text.

ASSUMPTIONS IN GRAY-SCALE IMAGING

Several assumptions about the propagation of sound waves are made when ultrasound equipment maps echoes onto the image.[1] When one or more of these assumptions prove invalid, artifacts result.

Velocity of Sound

The speed of sound throughout the tissues is assumed to be uniform at 1540 m/sec. When the waves travel through tissues that substantially alter sound velocity, propagation velocity artifacts occur.

Attenuation of Sound

Sound waves normally become fainter—that is, their intensity decreases—as they travel through tissues. The equipment assumes that this attenuation of intensity occurs at a constant rate. If the waves travel through tissues that either do not attenuate as much or attenuate more than the adjacent tissues, attenuation errors such as increased through transmission or shadowing arise.

Path of Sound

In creating the image, the equipment assumes that the generated sound wave travels from the surface of the probe in a straight line, is reflected off a reflector only once, and returns directly back to the probe at the same angle exactly to the point from which it left the probe. If the sound waves undergo more than one reflection, then artifacts such as mirror image, reverberation,

or comet-tail occur. And if the direction of the beam or its echo is altered, refraction or anisotropy artifact may be produced.

Beam Profile

An assumption is made that the sound beam generated by the transducer is a narrow line. When the beam is not sufficiency narrow in the imaging plane or in the elevation plane (i.e., along the short axis of the transducer), side lobe or grating lobe or partial volume averaging artifacts may occur.

PROPAGATION VELOCITY ARTIFACT

Ultrasound image processing assumes that the speed of sound in tissue is a constant 1540 m/sec. However, when a sufficiently large structure composed of tissue that propagates speed at a different velocity is encountered, then propagation velocity artifact can occur.[1] In the case of a fatty lesion, the slower speed of propagation (approximately 1450 m/sec) means that the echo will take longer to return to the transducer; thus the lesion is displayed deeper in the image than its true location. Some newer ultrasound machines with multibeam (spatial compounding) features and improved signal processing can minimize this artifact.

Click here to see an explanatory video of **propagation velocity artifact** (Video A.1).

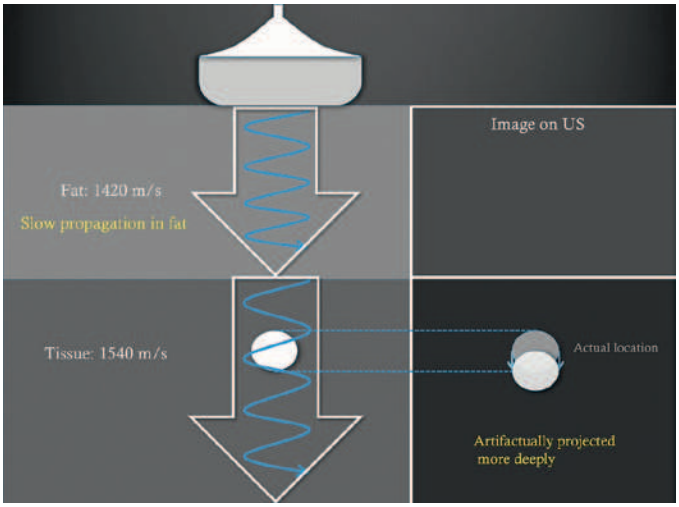

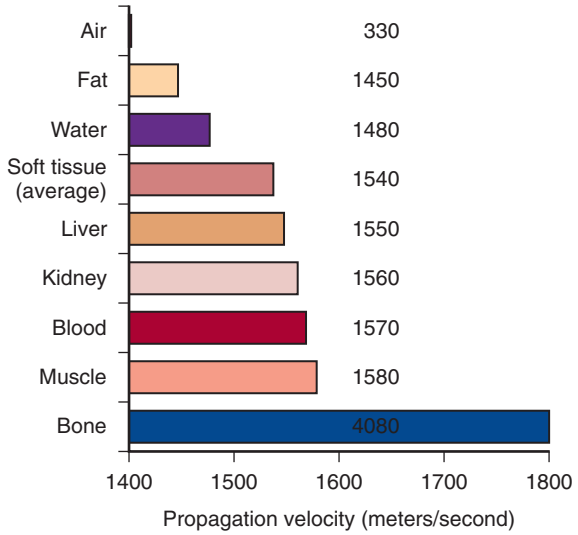

FIG. A.1 Propagation Velocity. Propagation velocity of different body tissues.[2] (See Chapter 1, Fig. 1.2.)

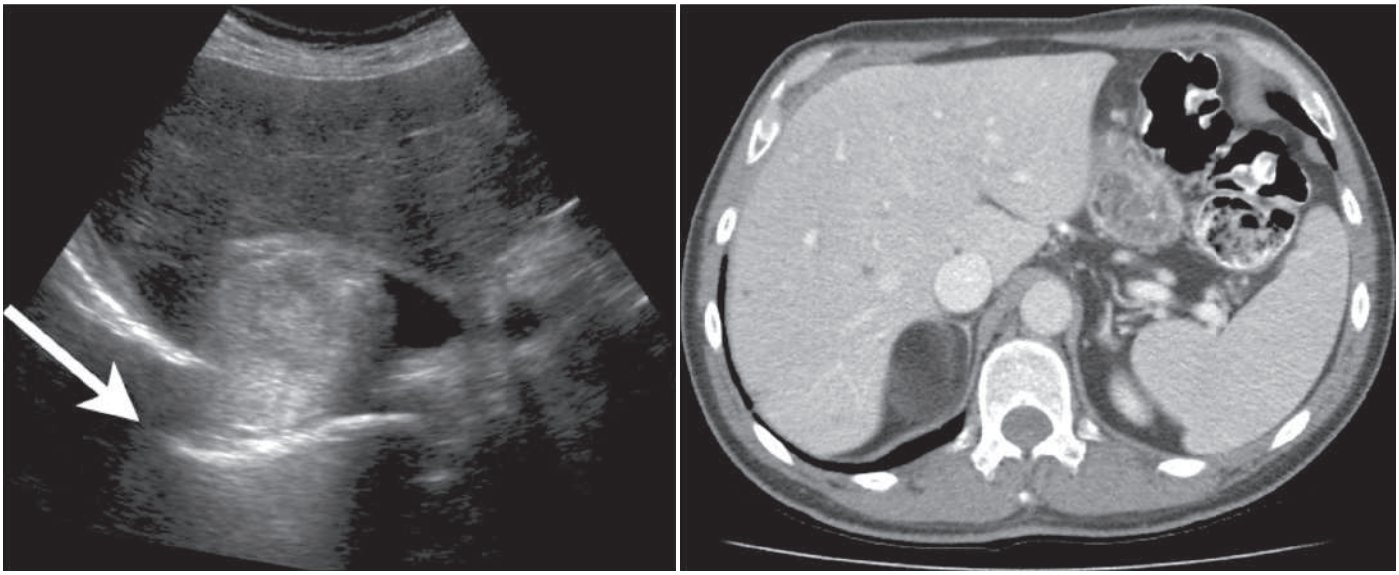

FIG. A.2 Propagation Velocity. When sound passes through a fatty mass, in this case a myelolipoma, its speed slows down to 1450 m/sec. Because the ultrasound scanner assumes that sound is being propagated at the average velocity of 1540 m/sec, the delay in echo return is interpreted as indicating a deeper target. Therefore the final image shows a **misregistration artifact** in which the diaphragm *(arrow)* is shown in a deeper position than expected in this patient with a right adrenal myelolipoma. The computed tomography image depicts the myelolipoma, confirming its fatty nature.

ATTENUATION ERRORS

When the ultrasound beam encounters a focal lesion that attenuates the sound to a greater or lesser extent than the surrounding tissues, the intensity of the beam deep to the lesion will be either weaker (shadowing) or stronger (increased through transmission) than in the surrounding tissues.

Click here to see an explanatory video of **attenuation-related artifacts** (Video A.2).

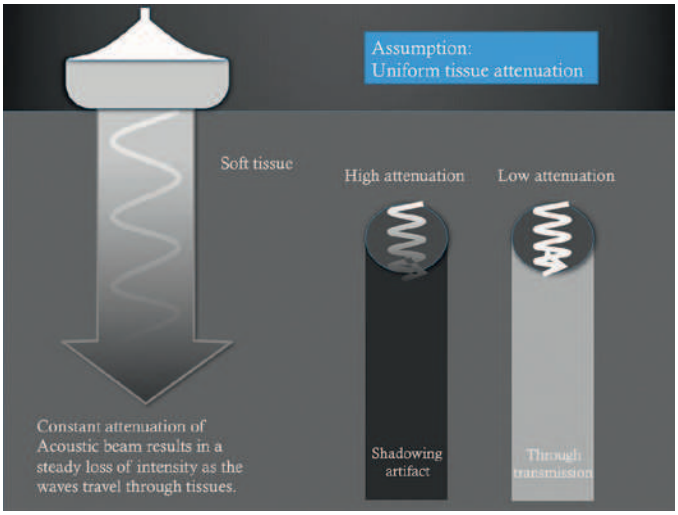

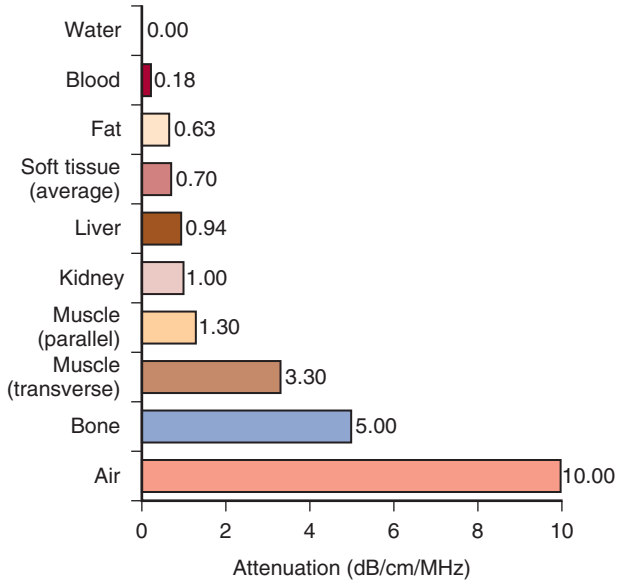

FIG. A.3 As sound passes through tissue, it loses energy through the transfer of energy to tissue by heating, reflection, and scattering. Attenuation is determined by the insonating frequency and the nature of the attenuating medium. Attenuation values for normal tissues show considerable variation. Attenuation also increases in proportion to insonating frequency, resulting in less penetration at higher frequencies.[2] (See Chapter 1, Fig. 1.9.)

Shadowing

Shadowing results when there is a marked reduction in the intensity of the ultrasound deep to a strong reflector, attenuator, or refractor. Clean dark shadows will be seen behind calcified objects when the focal zone is at or just below the structure.

Click here to see an explanatory video of **shadowing** (Video A.3).

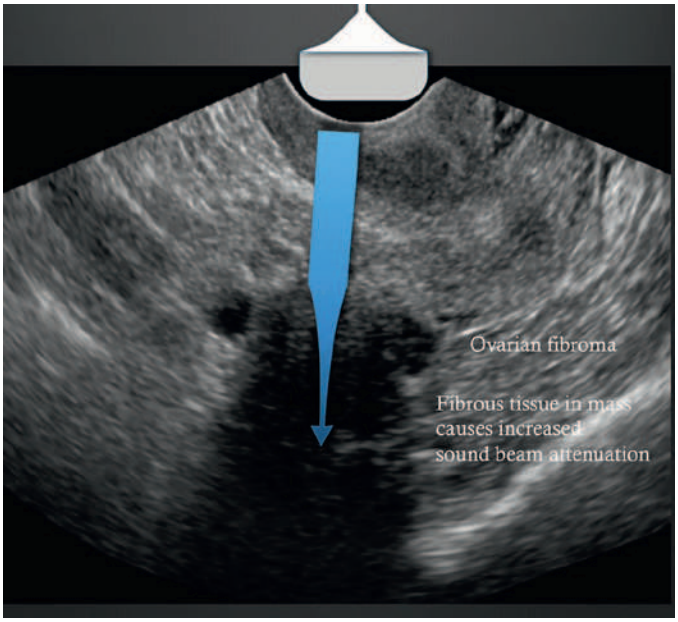

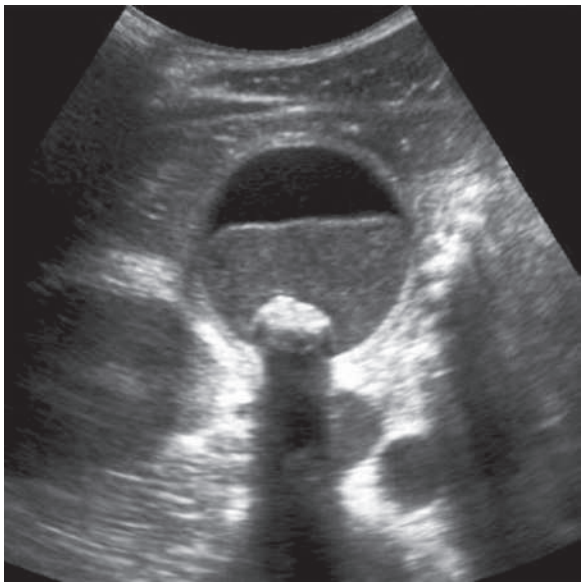

FIG. A.4 Gallstone With Shadowing. Note the dark, well-defined shadow.[3] (See Chapter 6, Fig. 6.39C.)

FIG. A.5 Shadowing From Hernia Repair Mesh.

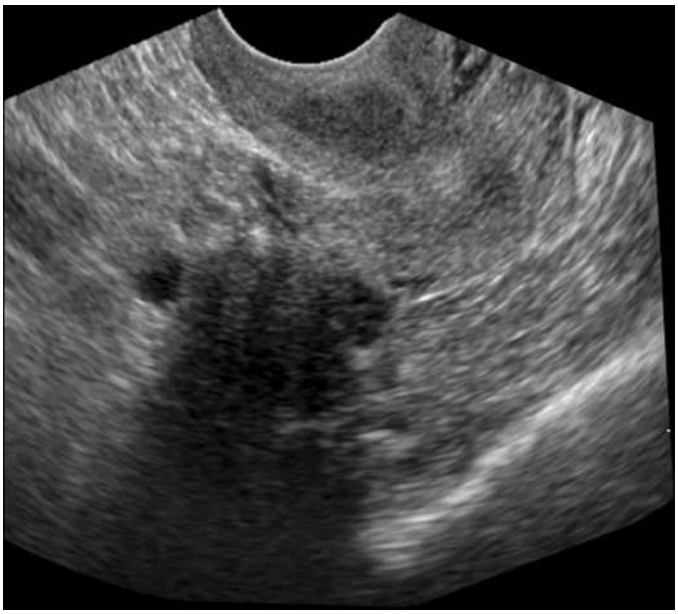

FIG. A.6 Shadowing From Ovarian Fibroma. This is a slightly less "clean" shadow since the fibroma is not as dense as a calcified stone.

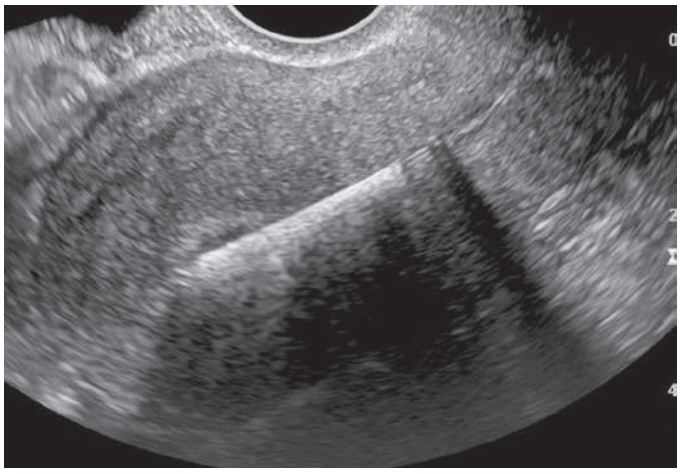

FIG. A.7 Shadowing From an Intrauterine Device.[4] (See Chapter 15, Fig. 15.25A.)

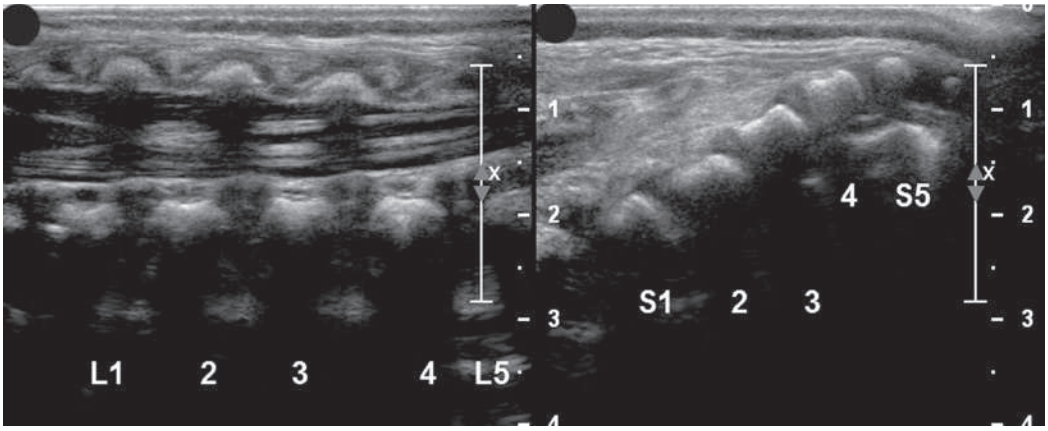

FIG. A.8 Shadowing. Coned down view of distal neonatal spine shows **shadowing** from vertebral bodies that interrupt the linear appearance of the nerve roots.[5] (See Chapter 49, Fig. 49.3.)

Click here to see real-time cine clip of showing in region of cauda equina (Video A.4).[5]

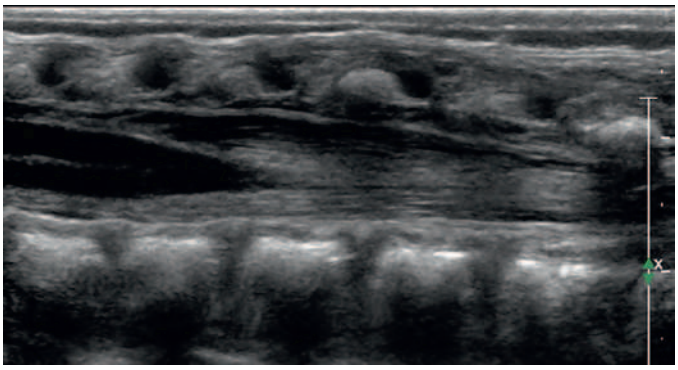

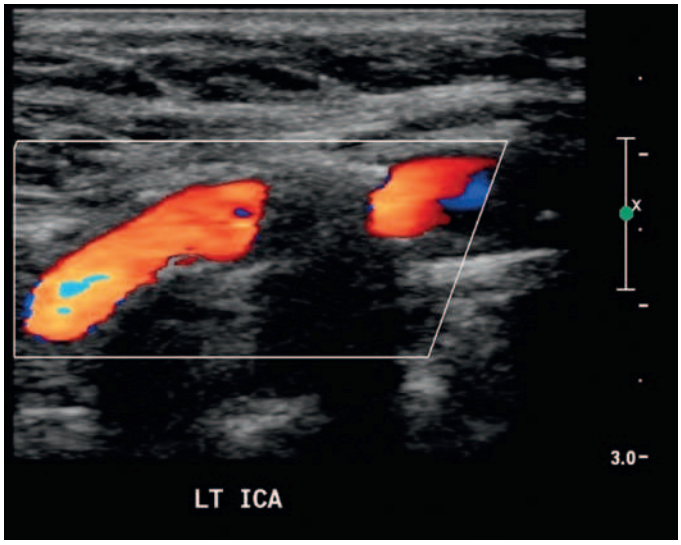

FIG. A.9 Shadowing. Shadowing from dense plaque prevents assessment of color flow in that region. Note that there must be flow present because similar color is visualized before and after the shadow.[6] (See Chapter 26, Fig. 26.8.)

Edge shadowing is caused by excessive refraction and commonly occurs from the edges vessels, cystic structures, and bones.

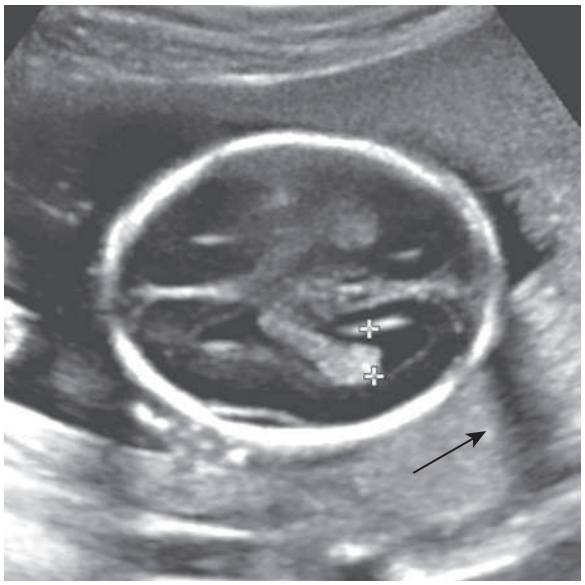

FIG. A.10 Edge Shadowing. Note the **edge shadowing** artifact behind the posterior aspect of the fetal skull. The beam bends at curved surface and loses intensity, producing a shadow *(arrow)*.[7] (See Chapter 34, Fig. 34.3.)

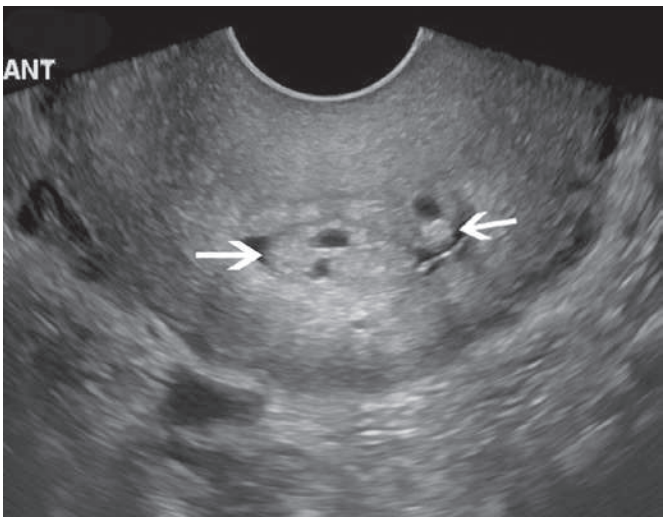

FIG. A.11 Edge Shadowing 2. Endometrial polyp shows both **through transmission** behind the cystic spaces and **edge shadowing** at the margins of the cysts.[4] (See Chapter 15, Fig. 15.14B.)

Increased Through Transmission

Increased through transmission occurs when an object (such as a cyst) attenuates the sound waves less than the surrounding tissues.

Click here to an explanatory video of **increased through transmission** (Video A.5).

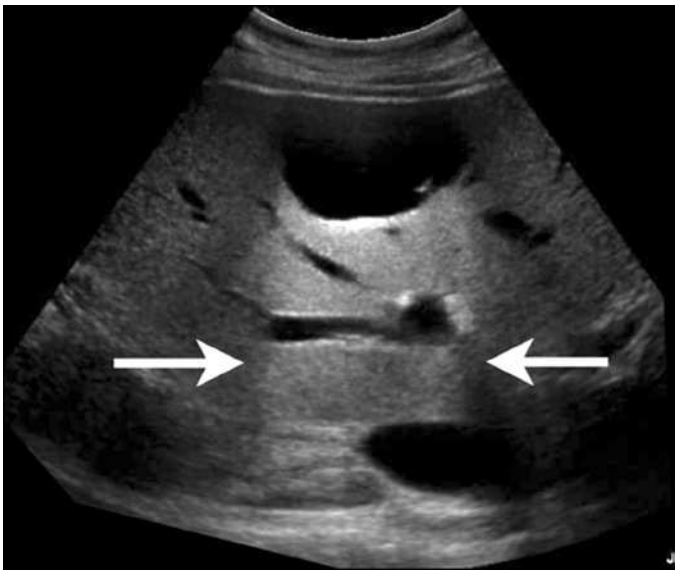

FIG. A.13 Increased Through Transmission. The hepatic parenchyma distal to the cysts is falsely displayed as increased in echogenicity *(arrows)* secondary to increased through-transmission artifact.

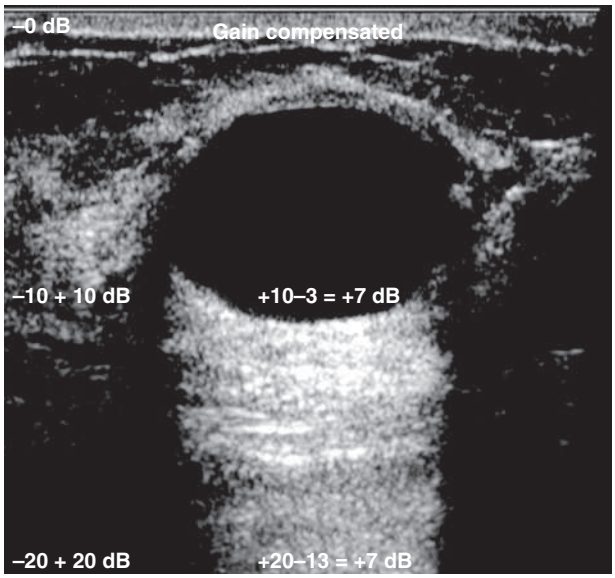

FIG. A.12 Increased Through Transmission. The cyst attenuates 7 dB less than the normal tissue, and time gain curve correction for normal tissue results in overamplification of the signals deep to the cyst, producing **increased through transmission** of these tissues.[2] (See Chapter 1, Fig. 1.31C.)

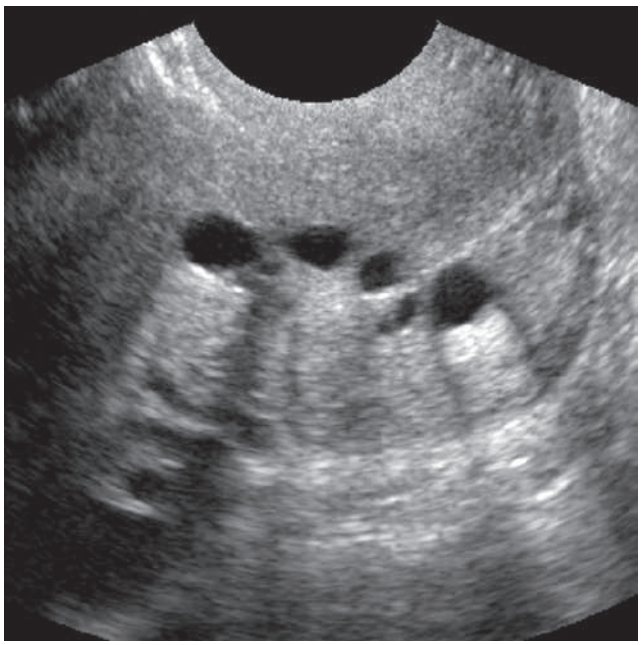

FIG. A.14 Increased Through Transmission. Nabothian cysts show both **increased through transmission** behind the cysts and **edge shadowing** at the margins of the cysts.[4] (See Chapter 15, Fig. 15.7C.)

PATH OF SOUND-RELATED ARTIFACTS

In mapping a returning echo onto the generated image, an assumption is made that it originated from the same part of the transducer from which it was produced. Also, an assumption is made that the echo is the result of a single reflection. The depth of the reflector is calculated based on the time it took for the sound wave to travel from the transducer to the reflector and back, assuming a single reflection. When these assumptions do not hold, various types of artifacts occur.

Click here to see an explanatory video of **path of sound assumption** (Video A.6).

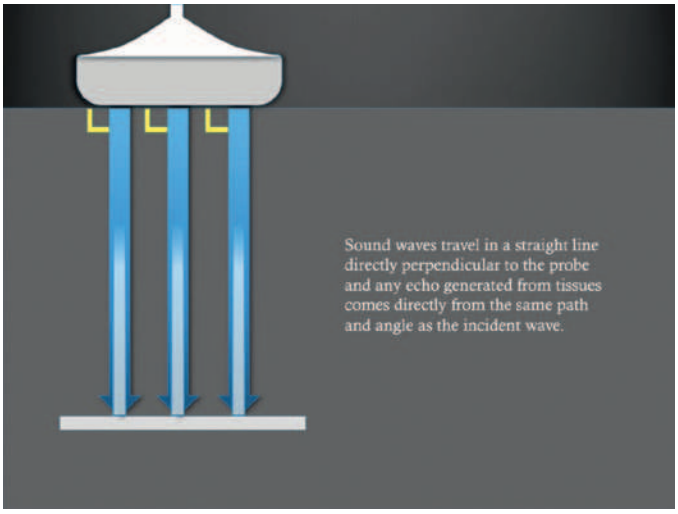

Mirror Image Artifact

A mirror image artifact is created when the primary beam encounters a highly reflective surface that acts like a mirror. The reflected echoes then encounter other reflectors and bounce back onto the mirror before being directed to the transducer. The result is artifactually inverted projection of the reflectors deeper to the surface of the mirror. The image is displayed deeper because of the longer path of the reflected sound. If the mirror image artifact causes confusion, it can be decreased or eliminated by moving the transducer to center it on the region of interest and/or placing the focal zone at the level of interest in the real structure.

Click here to see an explanatory video of **mirror image artifact** (Video A.7).

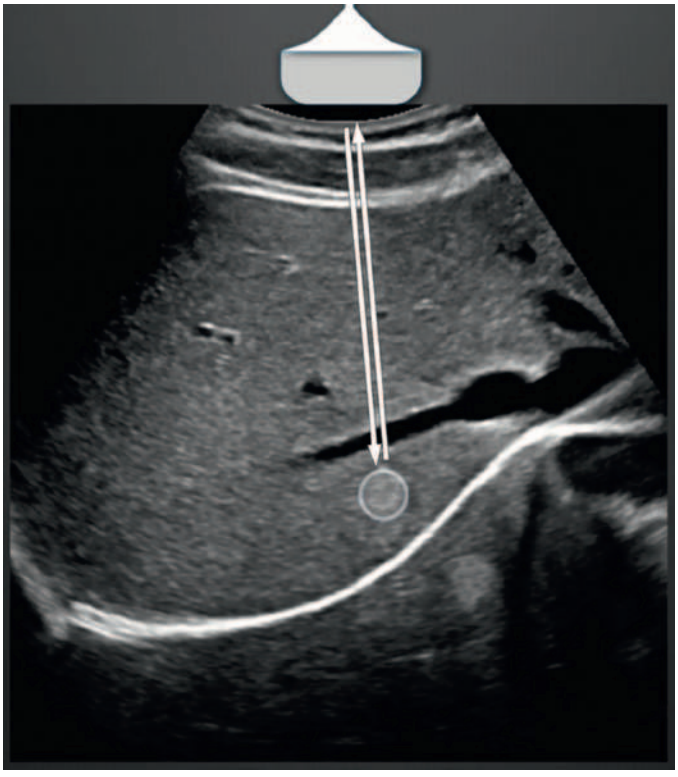

FIG. A.15 Mirror Image. Picture of reflection in water—similar to mirror image artifact.

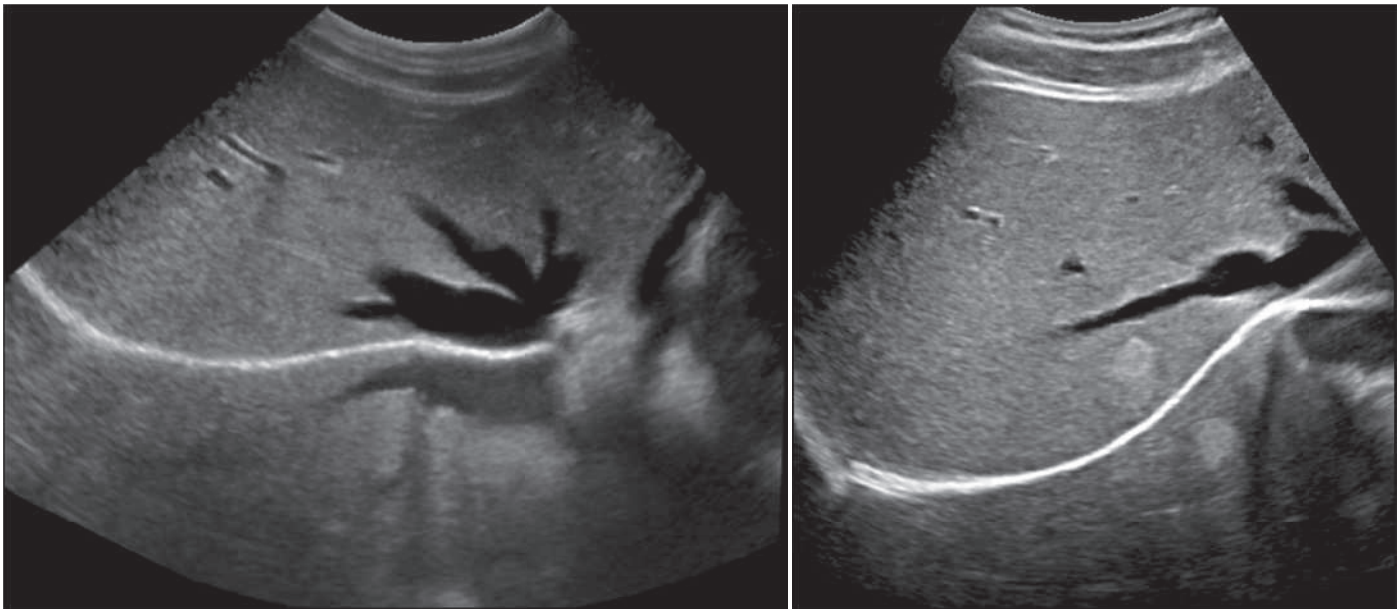

FIG. A.16 Mirror Image Artifact. Soft tissue–gas interfaces, such as the diaphragm, are excellent reflectors of the sound beam owing to the large difference in the acoustic impedance between the two materials. Therefore hepatic structures are frequently seen mirrored beyond the diaphragm onto the lungs. These two figures show liver parenchyma, hepatic veins in part A, and a hepatic hemangioma in part B all inversely projected onto lung.

Comet-Tail Artifact

Comet-tail artifact is a type of reverberation artifact.[8] The repetitive reflections occur within very small structures, such as tiny cysts in the case of von Meyenburg complexes and tiny crypts in the wall of the gallbladder in the case of adenomyomatosis. Accordingly, the reverberated echoes may not be individually visible. The tapered, comet-tail appearance is due to the decreasing amplitude of each reverberation as a result of beam attenuation.

Click here to see the explanatory video of **comet-tail artifact** in adenomyomatosis (Video A.8).

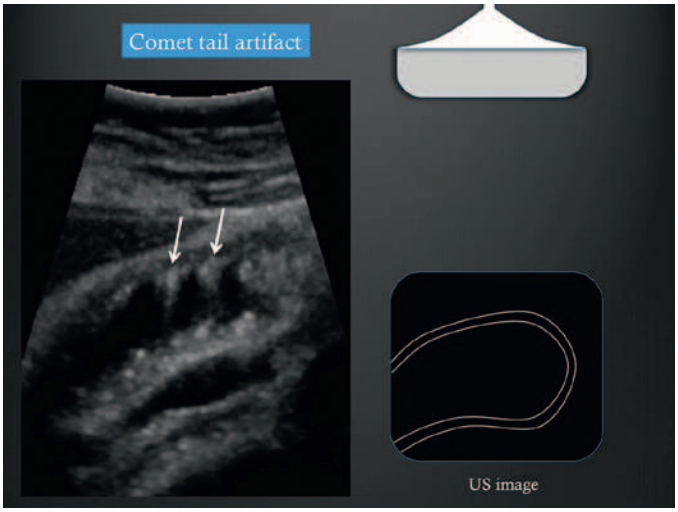

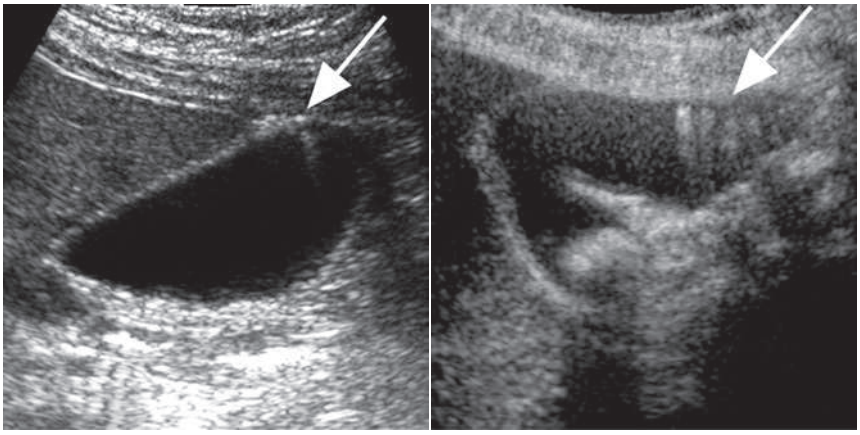

FIG. A.17 Comet-Tail Artifact in Association With Adenomyomatosis. This is felt to be due to cholesterol crystals within the prominent Rokitansky-Aschoff sinuses.[3] (See Chapter 6, Fig. 6.45.)

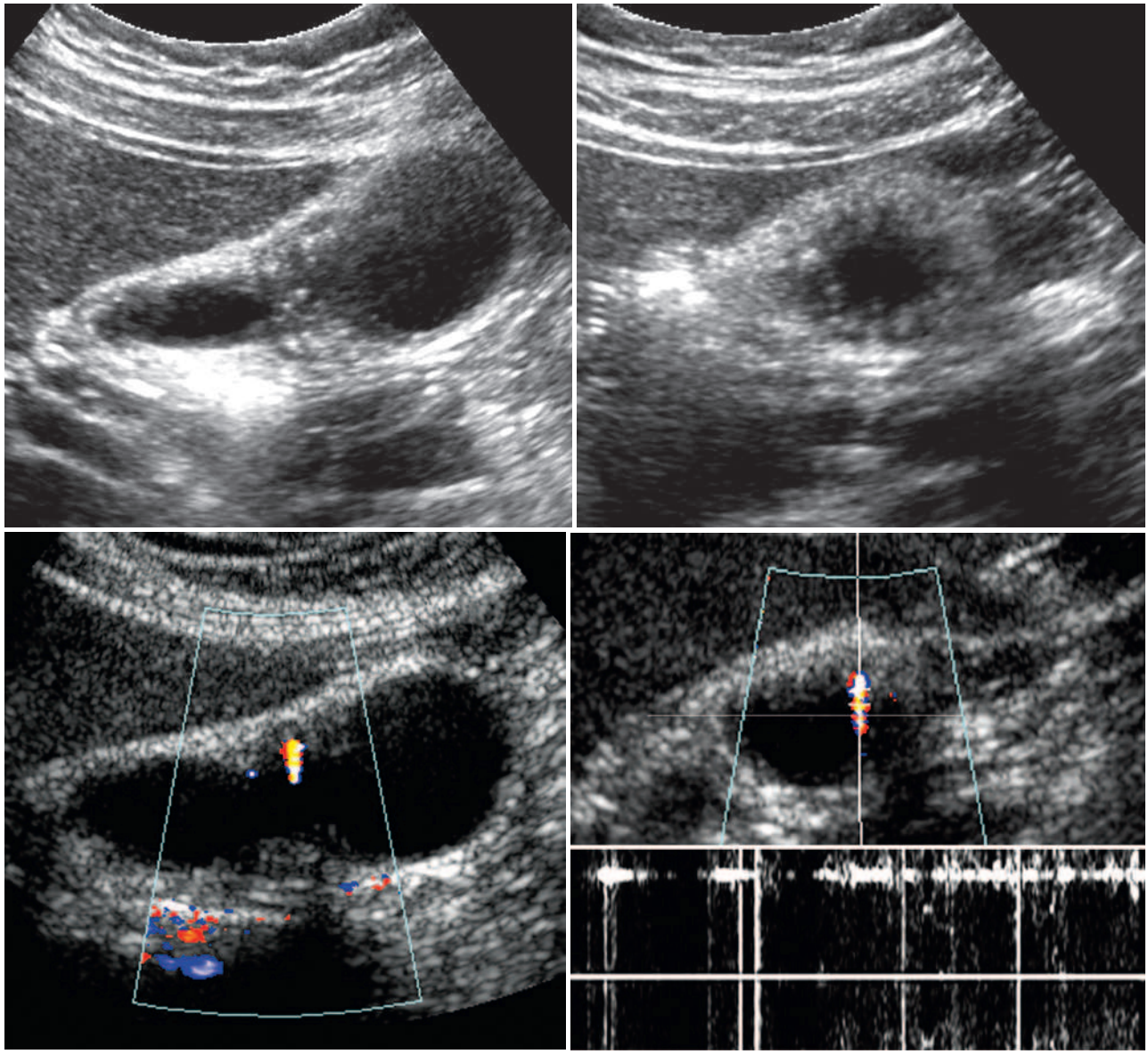

FIG. A.18 Comet-Tail Artifact. On color and spectral Doppler this can look like a twinkle artifact, but it is a color representation of the comet-tail. (See section on color Doppler artifacts for description of the twinkling.[3]) (See Chapter 6, Fig. 6.46.)

FIG. A.19 Adenomyomatosis and Comet-Tail Artifact.

Click here to see real time scanning of **comet-tail artifact** in adenomyomatosis (Video A.9).

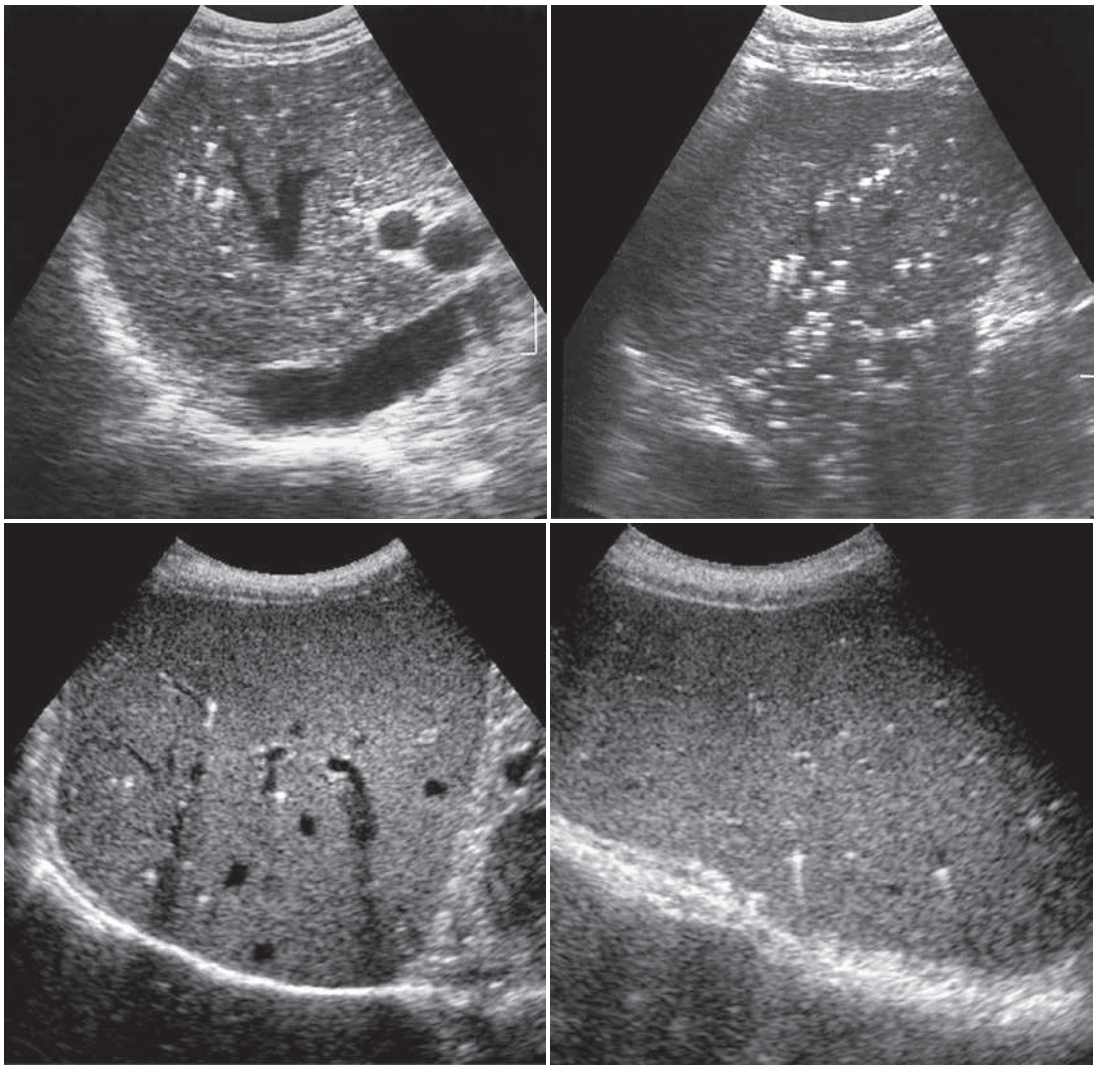

FIG. A.20 Comet-Tail Artifact Behind von Meyenburg Complex in Two Patients.[9] (See Chapter 4, Fig. 4.16.)

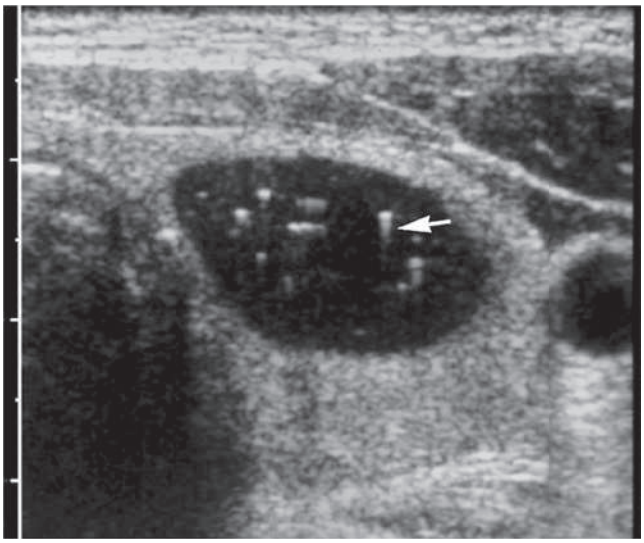

FIG. A.21 Colloid Cyst in Thyroid Gland With Characteristic Comet-Tail Artifact *(Arrow).* [10] (See Chapter 19, Fig. 19.10A.)

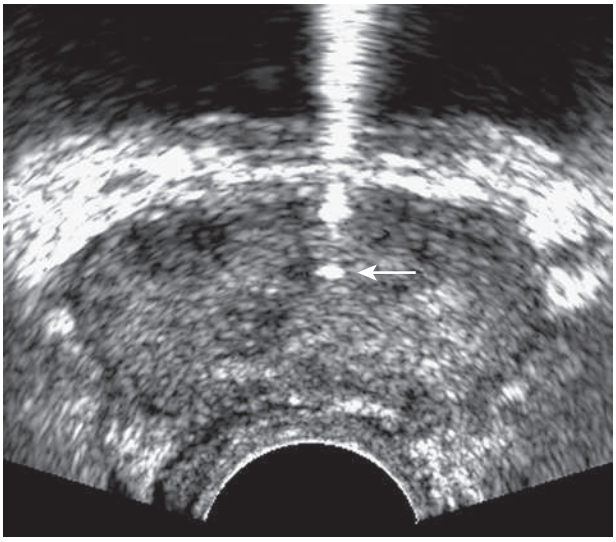

FIG. A.22 Strong Comet-Tail Artifact Due to Fiducial Marker in Patient With Prostate Cancer. [11] (See Chapter 10, Fig. 10.13.)

Refraction

As sound moves between tissues with different propagation velocities, such as from muscle to fat, it changes its direction at their interface as a result of refraction. The physical properties of refraction are explained by Snell's law, as demonstrated in Figs. A.23[12] and A.24. The change in the direction of the sound waves results in violation of the assumption made by the ultrasound equipment that the incident and reflected waves travel in a straight line. Therefore, with refraction, structures insonated by the bent path of sound waves are artifactually translated to appear as if the sound waves had traveled along a straight path. If refraction is suspected, it can be minimized by increasing the scan angle so that sound waves travel perpendicular to the interface.

Click here to see an explanatory video of **refraction** from the anterior abdominal wall (Video A.10).

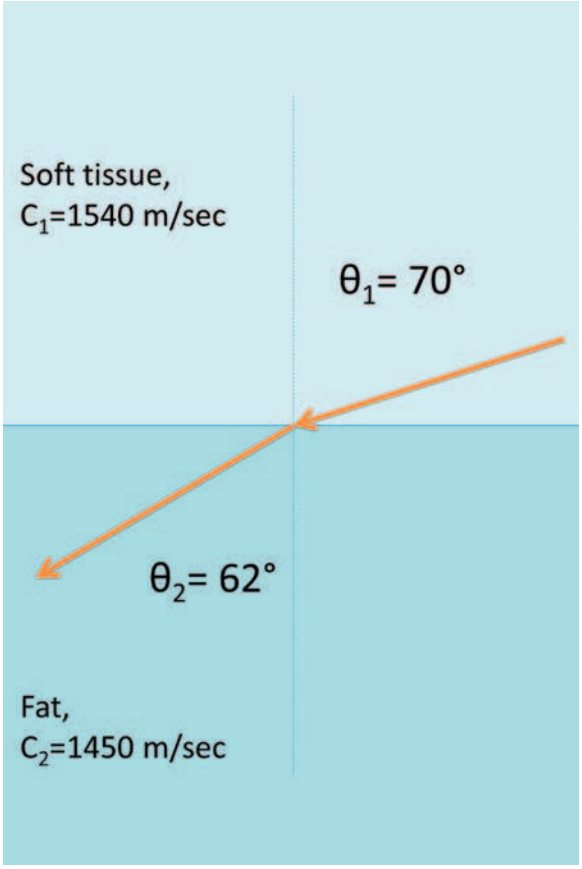

FIG. A.23 Refraction. Refraction can be due to tissues with different propagation velocities. When sound passes from soft tissue with propagation velocity (C_1) of 1540 m/sec to fat with a propagation velocity (C_2) of 1450 m/sec, there is a change in the direction of the sound wave because of refraction. The degree of change is related to the ratio of the propagating velocities of the media forming the interface ($\sin\theta_1/\sin\theta_2 = C_1/C_2$)[2]. Note that when the incident angle is changed to zero degrees—that is, the incident beam is perpendicular to the interface ($\theta_1 = 0°$)—the artifact disappears.

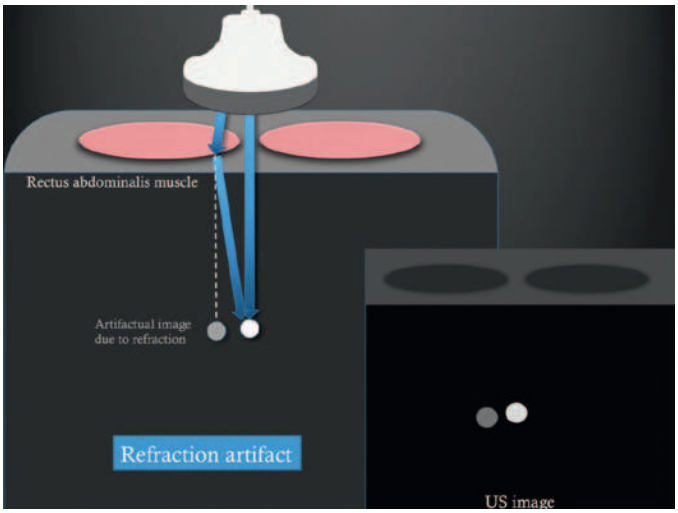

FIG. A.24 Refraction. Image of a straw in water. Refraction has occurred owing to the difference between air and water, causing an offset in the appearance of the straw. Note also how the straw appears larger in the water because of distortion of the image.

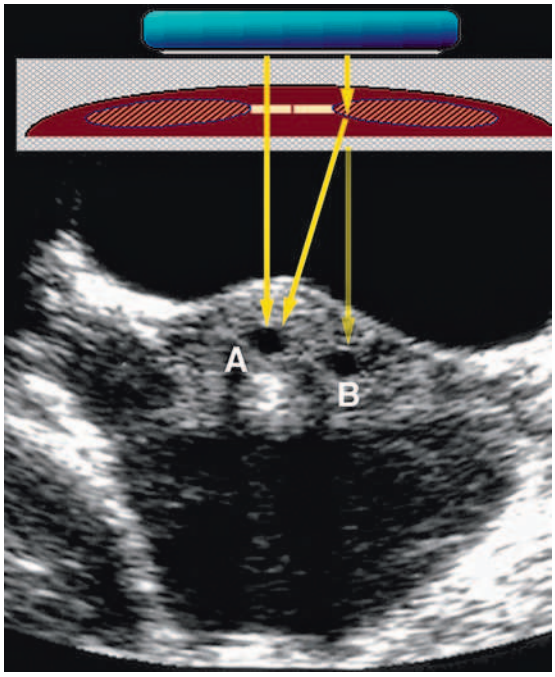

FIG. A.25 Refraction. This figure shows what appears to be a second gestational sac due to refraction artifact. This is sometimes called **"ghosting."**[2] (See Chapter 1, Fig. 1.8.)

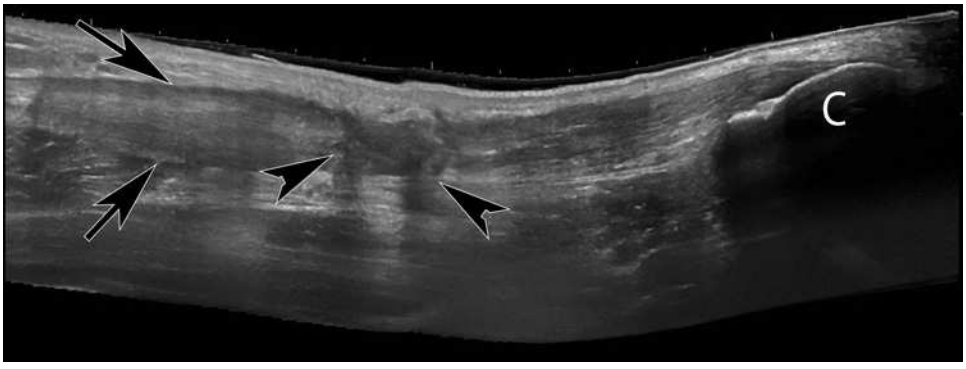

FIG. A.26 Refraction. A panoramic view of the Achilles tendon demonstrates a rupture within the midportion of the tendon. The proximal aspect of the tendon is chronically thickened and hypoechoic *(arrows)*. **Refraction artifact** *(arrowheads)* is caused by the interfaces between the ruptured tendon edges and hemorrhage. *C,* Calcaneus.[13] (See Chapter 23, Fig. 23.11.)

Anisotropy

Anisotropy is an artifact caused by structures that are composed of bundles of highly reflective fibers running parallel to each other, such as tendons and ligaments. If the sound beam hits the tendon or ligament fibers perpendicular to their length, it is reflected directly back, resulting in an echogenic appearance. But if the angle of insonation is not perpendicular to the tendon fibers, the beam is reflected away from the transducer, leading to the generation of an image with artifactual hypoechogenicity within the tendon.

Click here to see an explanatory video of **anisotropy** (Video A.11).

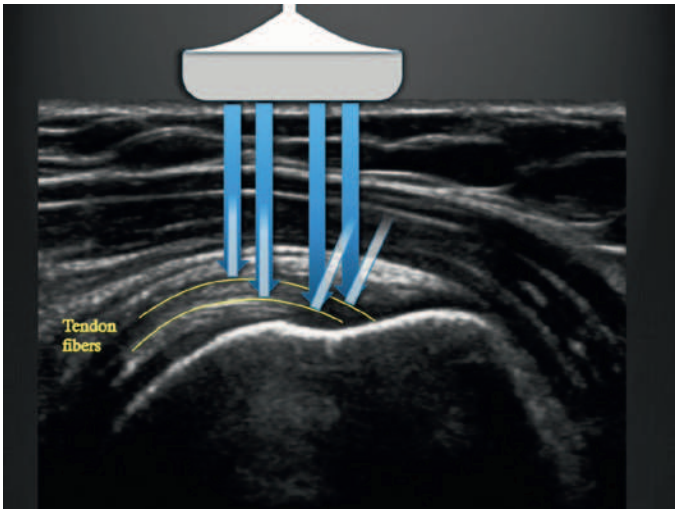

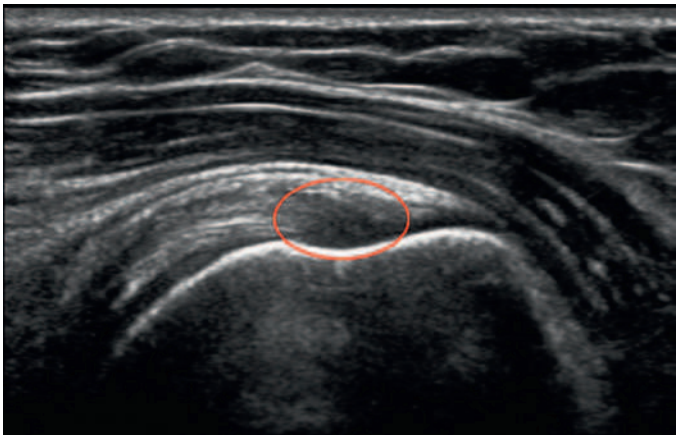

FIG. A.27 Anisotropy. The insertion of supraspinatus tendon artifactually appears hypoechoic due to anisotropy.

Click here for video of real-time scanning of **anisotropy** at supraspinatus insertion (Video A.12).

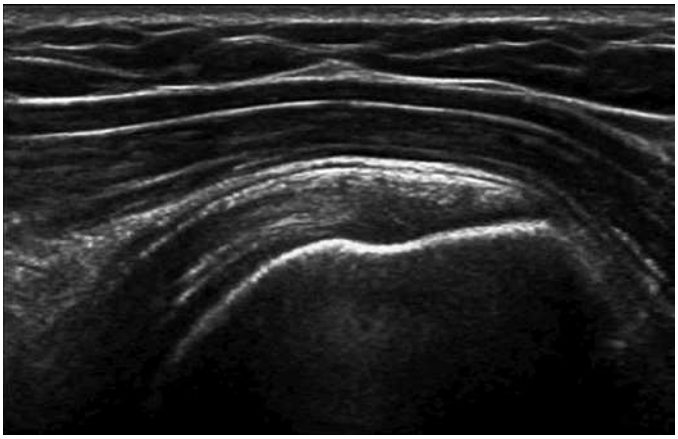

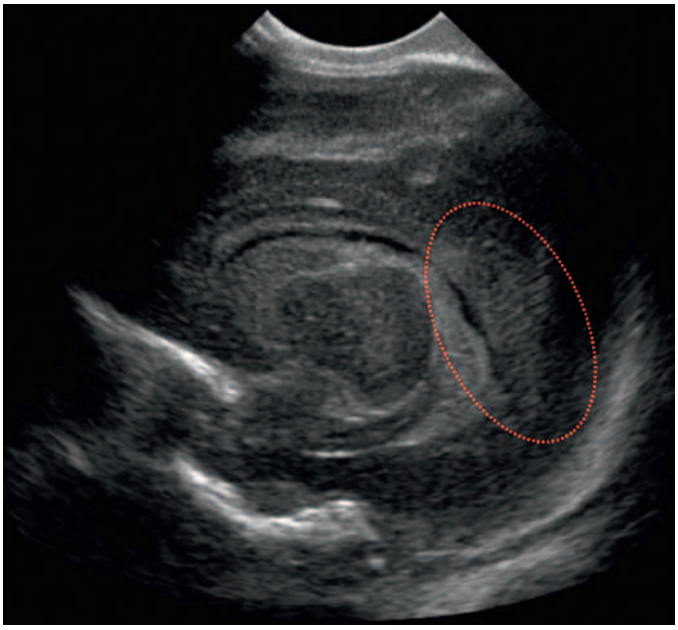

FIG. A.28 Anisotropy. The peritrigonal region of the white matter *(ellipse)* appears relatively echogenic, also called "peritrigonal blush." This **anisotropic effect** artifact occurs because in the trigone region, the parallel white matter fibers run perpendicular to the incident sound beam, causing increased reflection.[14] The artifact is visible only in the region of the trigone when the anterior fontanelle is used as a scanning window.

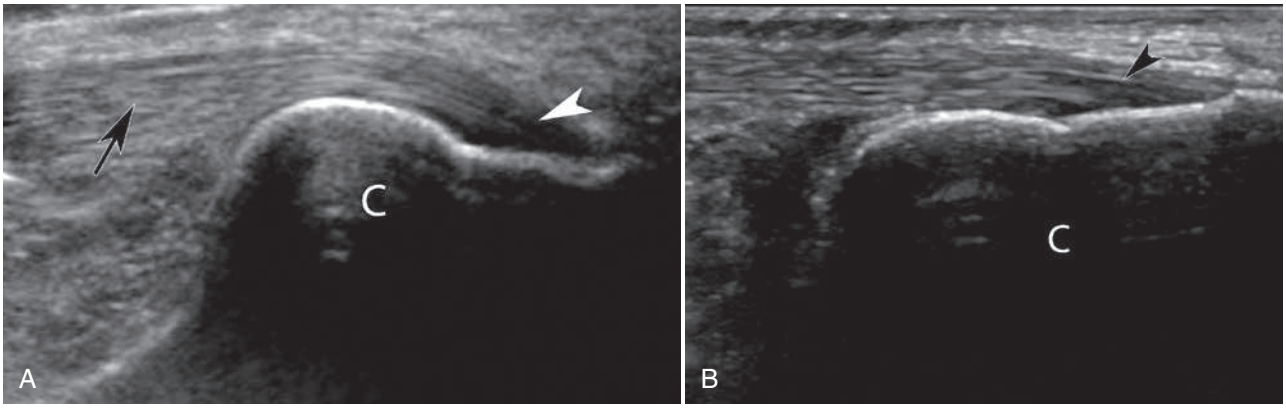

FIG. A.29 Anisotropy. (A) In this long-axis scan of the Achilles insertion on the calcaneus, the proximal portion of the imaged tendon demonstrates a normal fibrillar appearance *(arrow),* whereas the distal tendon insertion is hypoechoic *(arrowhead). C,* Calcaneus.[13] (See Chapter 23, Fig. 23.8.)

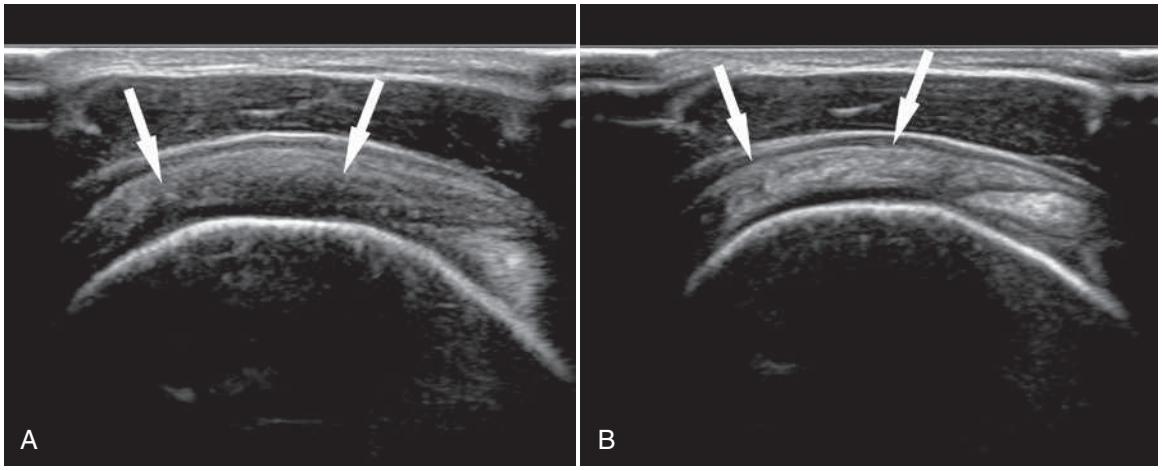

FIG. A.30 Anisotropy. Short-axis images of the supraspinatus tendon. **(A)** Artifactual hypoechogenicity of the supraspinatus tendon *(arrows)* may simulate tendinosis or tear. **(B)** Correction of angle of insonation to be perpendicular to the tendon permits visualization of the normal intact tendon.[15] (See Chapter 24, Fig. 24.30.)

Reverberation Artifact

Reverberation artifact occurs when a strong reflector runs perpendicular to the direction of the beam (i.e., parallel to the probe surface), usually close to the skin surface.[1] The sound waves may then get partially "trapped" between the reflector and skin, reverberating back and forth and causing the appearance of multiple regular lines when some of the waves eventually reach the probe. Often the reflectors are the skin and subcutaneous fascia (see Fig. A.31). Reverberation artifact is angle dependent, so moving the transducer slightly will cause a decrease in or elimination of the artifact. Reverberation can be helpful during biopsies, to see a needle. If it is distracting, try changing the angle of insonation, using a different window, or decreasing the gain.

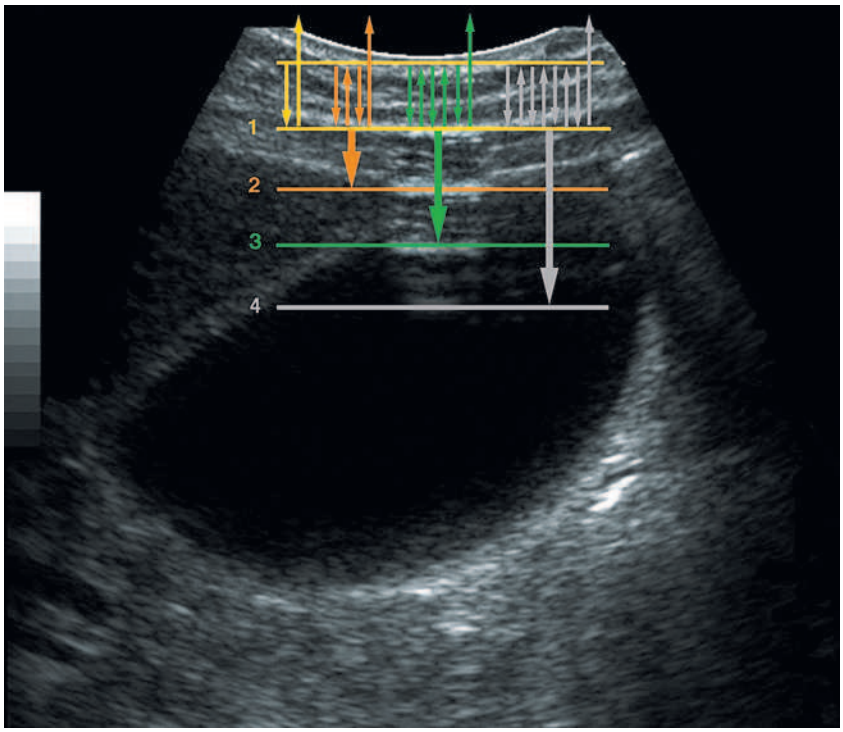

FIG. A.31 Reverberation Artifact. Reverberation artifacts arise when the ultrasound signal reflects repeatedly between highly reflective interfaces near the transducer, resulting in delayed echo return to the transducer. This appears in the image as a series of regularly spaced echoes at increasing depth.[2] (See Chapter 1, Fig. 1.27.)

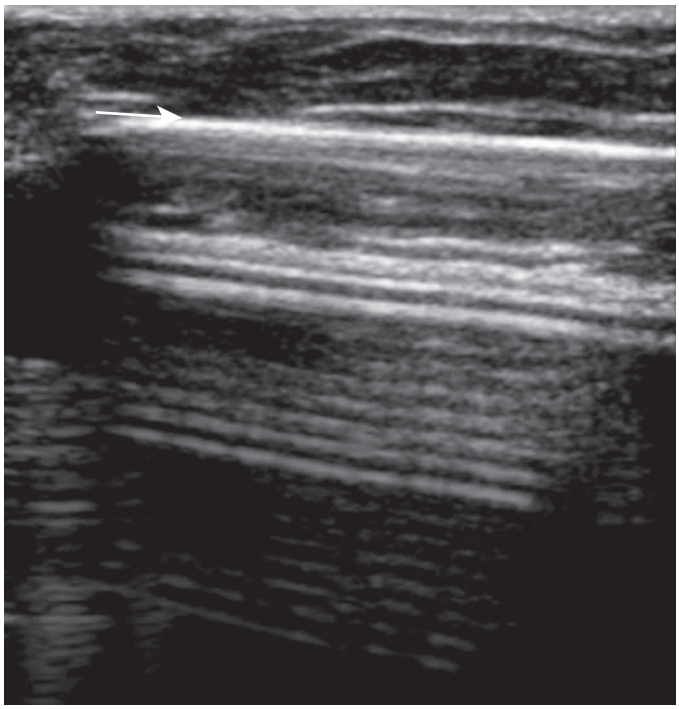

FIG. A.32 Mirror Image and Reverberation Artifacts Behind a Pacemaker. The highly reflective and mirrorlike surface of the pacemaker *(arrow)* results in repeated bouncing of sound wave among the probe surface, pacemaker, and skin.

For reverberation due to gas, see next section.

GAS-RELATED ARTIFACTS

Several physical properties of gases lead to unique artifacts in ultrasound that help identify gas but also may hinder visualization of other organs. These properties include the very dissimilar acoustic impedance of gas compared with soft tissues, making them highly reflective surfaces. The varied and ever-changing shape of gas in the body, including foam, leads to variability of its appearance even in the same field. The very low density of gases makes them quite compressible, and they can undergo resonant oscillation in response to sound waves, leading to amplification of echoes. These properties result in three distinct artifacts, which can be present at the same time: **reverberation, ring-down,** and **dirty shadowing.**[16]

Reverberation Artifact

The physical pressure of the probe on the soft tissues, such as the abdominal wall, flattens their shape in the near field, making them perpendicular to the surface of the probe and the incident sound beam. Because gases conform to the shape of their containers, they too will form a linear and perpendicular interface to the incident sound beam, especially when in the form of a large bubble. The highly reflective gas interface will act like a mirror, resulting in reverberation artifacts.

Click here to see an explanatory video of **reverberation artifact due to gas** (Video A.13).

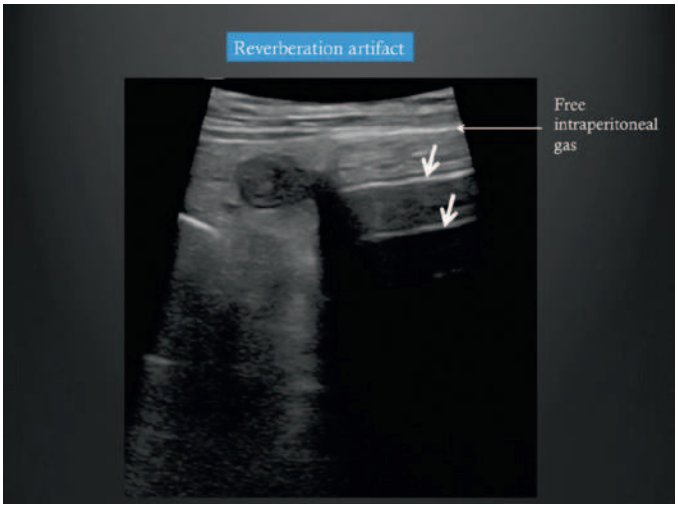

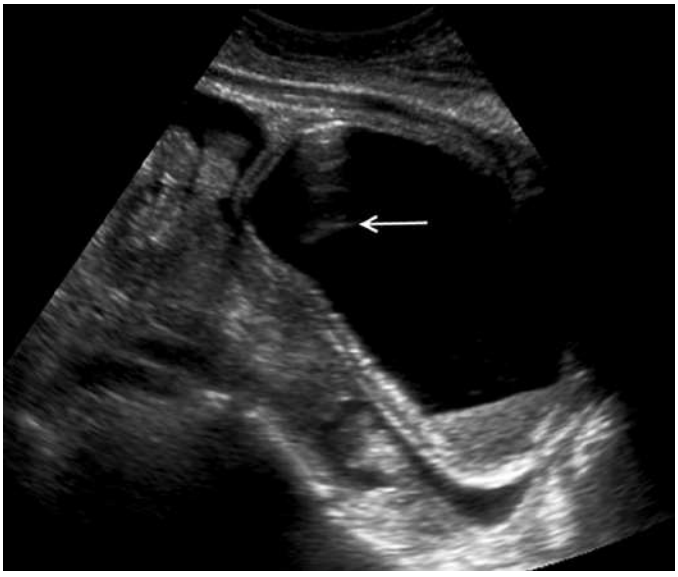

FIG. A.33 Reverberation Artifact. Small amount of gas within the bladder is recognizable by the reverberation artifact *(arrow)*.

Ring-Down Artifact

Ring-down artifact occurs when the ultrasound waves cause oscillation within fluid trapped by a tetrahedron of gas bubbles.[17] These oscillations create a continuous sound wave that is transmitted back to the transducer. What will be seen is a line or series of parallel bands extending posterior to a gas collection. Although this has the appearance of reverberation artifact, it actually has a different mechanism.

Click here to see an explanatory video of **ring-down artifact** (Video A.14).

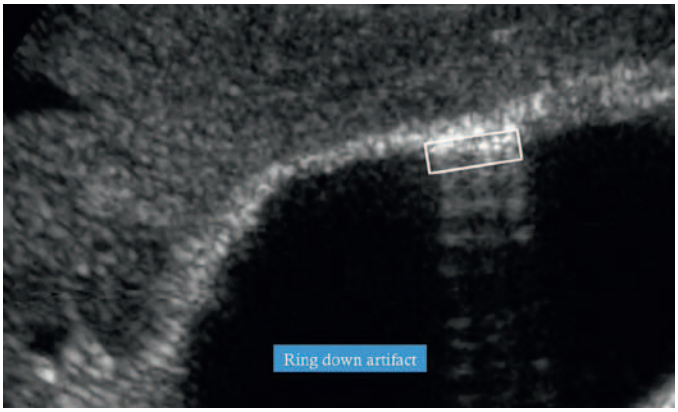

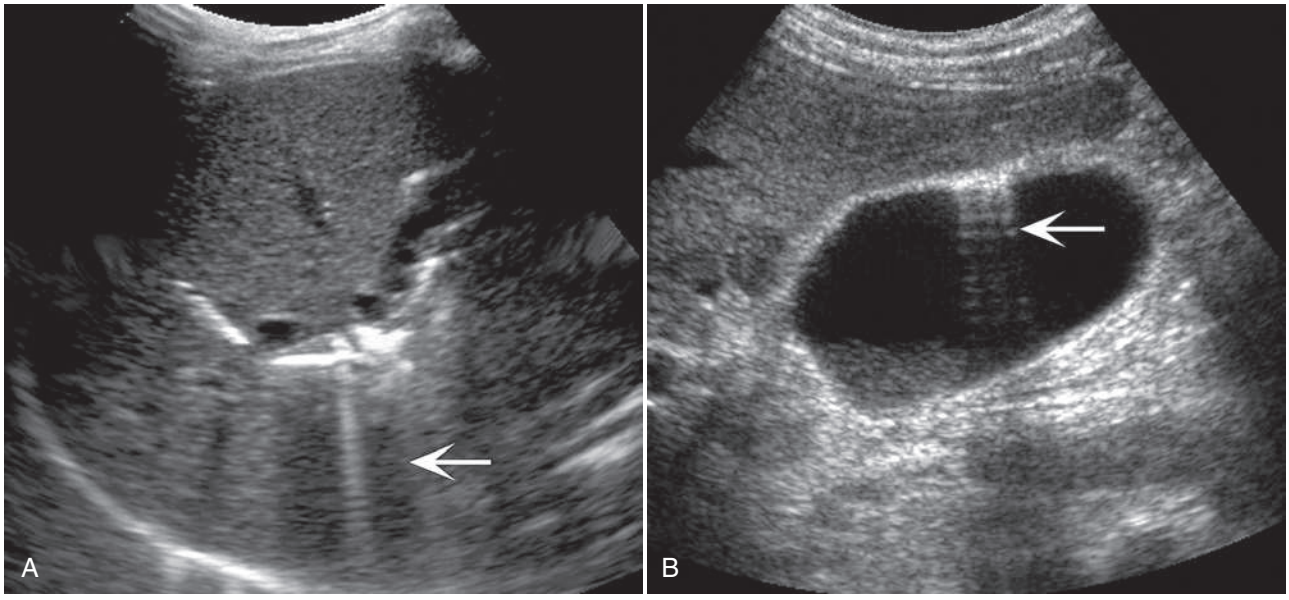

FIG. A.34 Ring-Down Artifact. Pneumobilia causing **ring-down artifact** in the biliary tree **(A)** and gallbladder **(B).**[3] (See Chapter 6, Fig. 6.13.)

Click here to see a video clip of **ring-down artifact** in peripheral ducts of the liver (Video A.15).

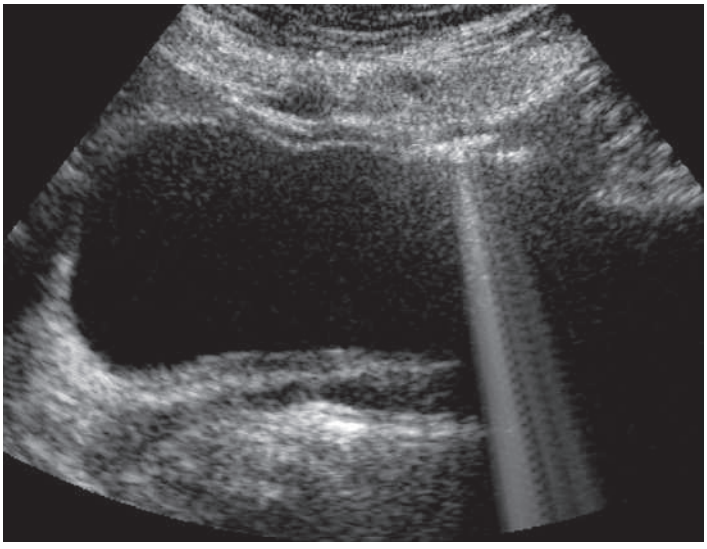

FIG. A.35 Ring-Down Artifact. Iatrogenic air in the bladder introduced at cystoscopy appears as a nondependent bright region with **ring-down artifact.**[18] (See Chapter 9, Fig. 9.36.)

Dirty Shadowing Artifact

Dirty shadowing results from a combination of reflection, reverberation, and ring-down artifacts arising from multiple variably sized bubbles in foam.[16]

Click here to see an explanatory video of **dirty shadowing** artifact (Video A.16).

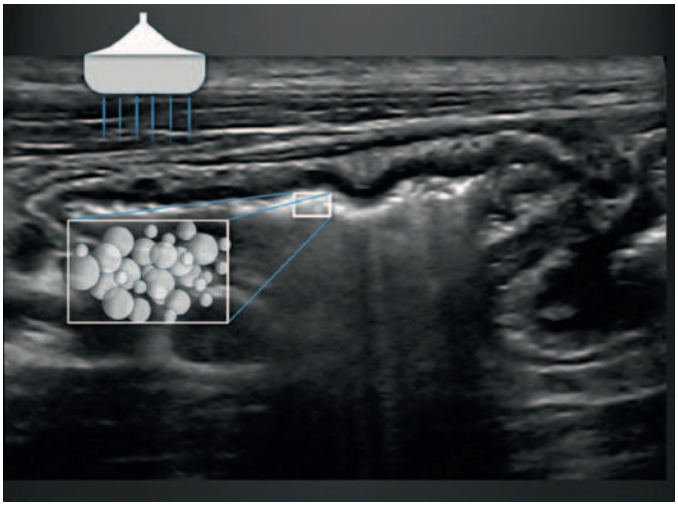

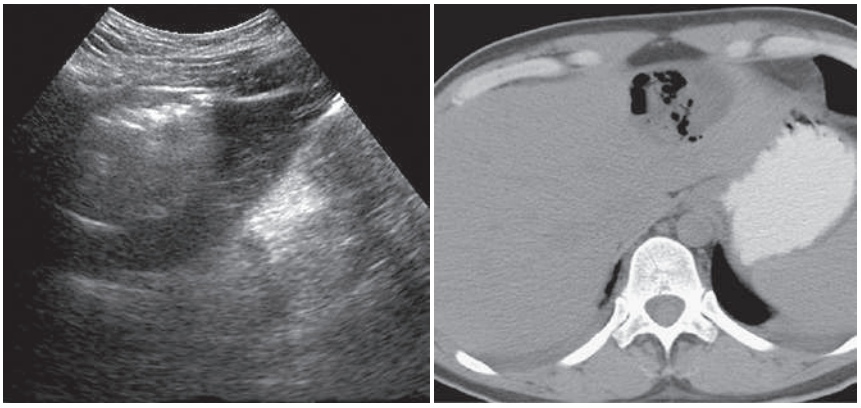

FIG. A.36 Dirty Shadowing. Sonographic image of the liver shows gas in liver mass with reverberation artifact filling the cavity. See comparison computed tomography scan.[9] (See Fig. 4.19.)

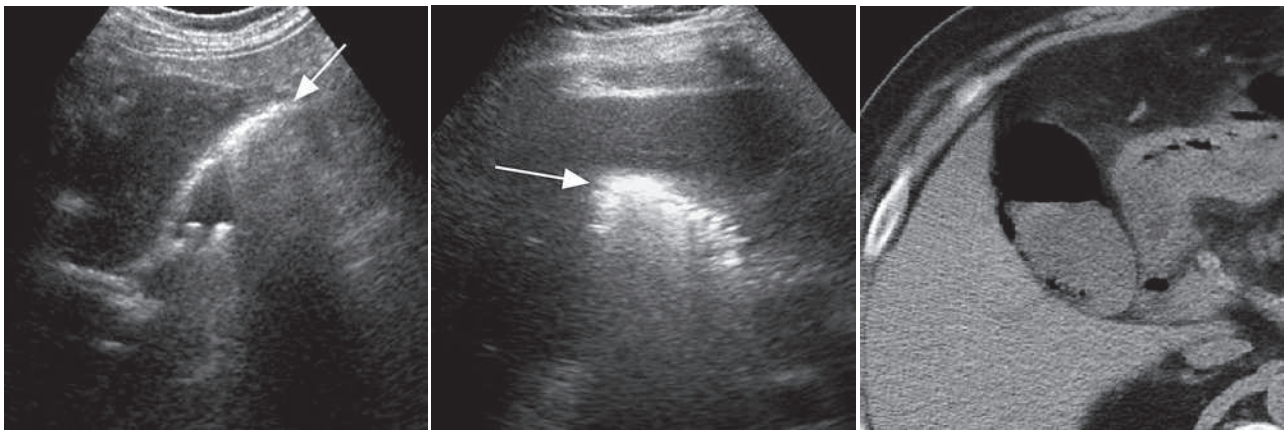

FIG. A.37 Dirty Shadowing Posterior to Emphysematous Cholecystitis.[3] (See Chapter 6, Fig. 6.40.)

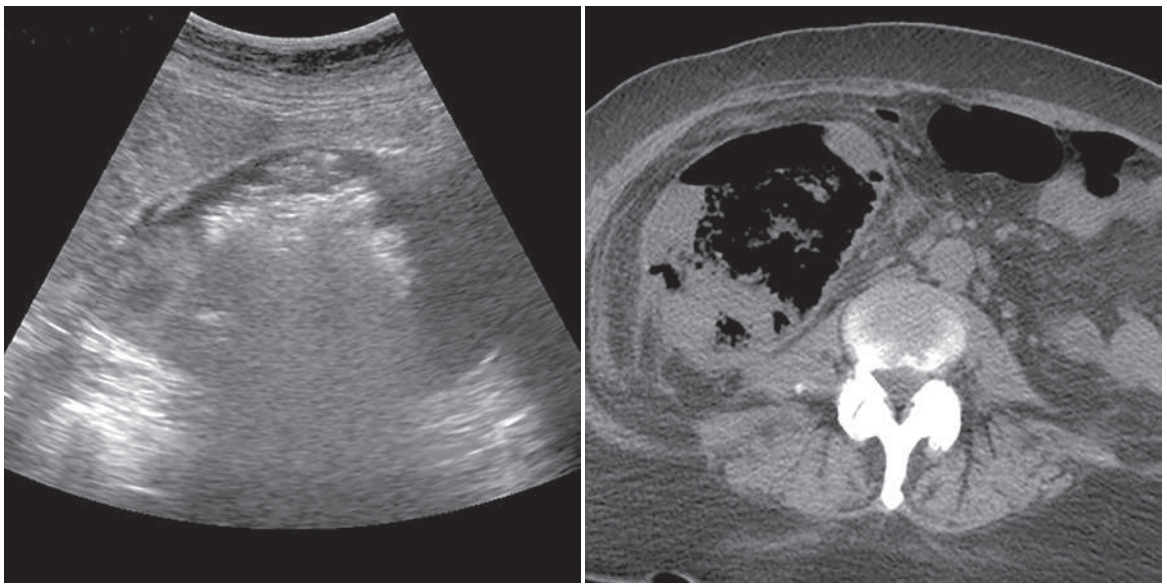

FIG. A.38 Dirty Shadowing in the Kidney Due to Emphysematous Pyelonephritis.[18] (See Chapter 9, Fig. 9.22.)

BEAM PROFILE–RELATED ARTIFACTS

Frequently echoes are seen within what should be an anechoic structure. This can occur as a result of side lobe or grating lobe artifacts in which information from the side of the image projects centrally, or because of partial volume averaging (owing to the thickness of the ultrasound beam (resolution in the Z plane).

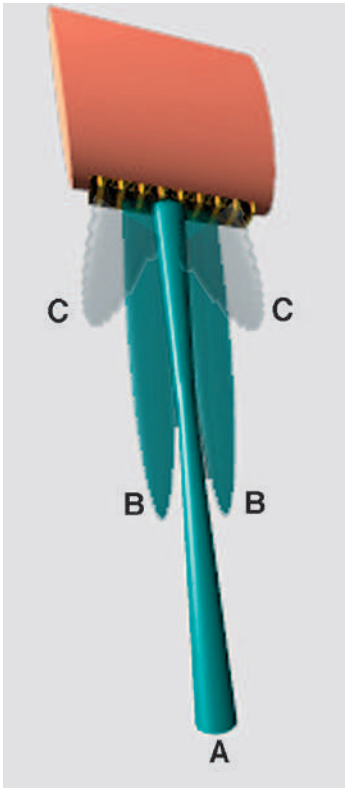

FIG. A.39 The ultrasound beam is not a narrow straight line but has a complex profile that varies depending on the type and shape of the transducer. Although most of the energy generated by a transducer is emitted in a beam along the central axis of the transducer *(A)*, some energy is also emitted at the periphery of the primary beam (*B* and *C*). These are called "side lobes" *(B)* or "grating lobes" *(C)* and are lower in intensity than the primary beam. Side lobes or grating lobes may interact with strong reflectors that lie outside of the scan plane and produce artifacts that are displayed in the ultrasound image.[2] They are more evident when the misplaced echoes overlap an expected anechoic structure. (See Chapter 1, Fig. 1.28.)

Side Lobe and Grating Lobe Artifacts

Click here to see an explanatory video of **side lobe artifact** (Video A.17).

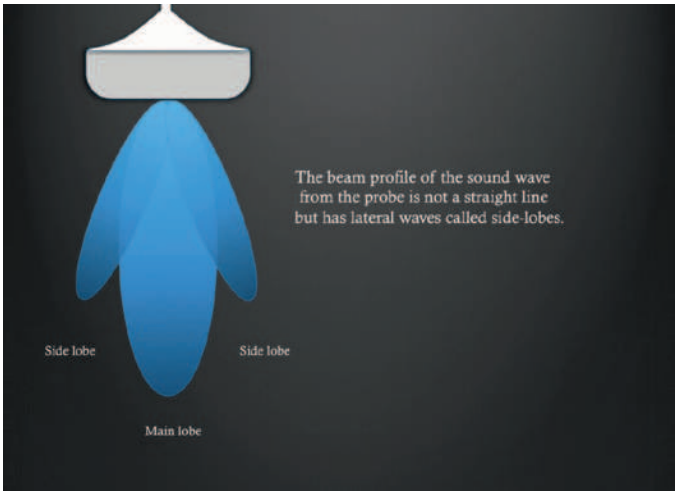

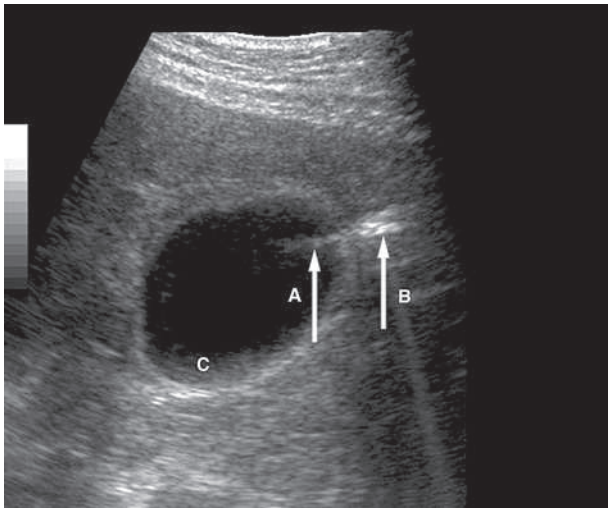

FIG. A.40 Side or Grating Lobe 1. Transverse image of the gallbladder reveals a bright internal echo *(A)* that suggests a band or septum within the gallbladder. This is a side lobe artifact related to the presence of a strong out-of-plane reflector *(B)* medial to the gallbladder. The low-level echoes in the dependent portion of the gallbladder *(C)* are also artifactual and are caused by the same phenomenon. Side lobe and slice thickness artifacts are of clinical importance because they may create the impression of debris in fluid-filled structures.[2] (See Chapter 1, Fig. 1.29.)

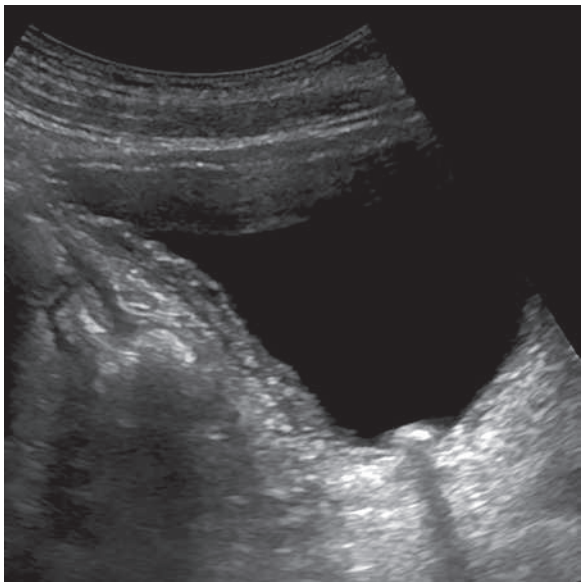

FIG. A.41 Side or Grating Lobe. In this patient with a ureterovesical junction stone there are echoes seen in the nondependent portion of the bladder. These are due to **grating lobe artifact,** wherein off-axis signal projects into the field of view.[18] Note also the **shadowing** behind the bladder stone.[18] (See Chapter 9, Fig. 9.43.)

Partial Volume Averaging

The ultrasound beam not only has a complex shape in the imaging plane but also has a real profile in the third dimension, called the "elevation plane" or "Z plane." The ultrasound image appears as a flat two-dimensional image, but the brightness of each pixel is representative of the average sum of all the echoes received within the thickness of the beam in the elevation plane. This results in echoes being projected in structures that should be anechoic.

Click here to see an explanatory video of **partial volume averaging** (Video A.18).

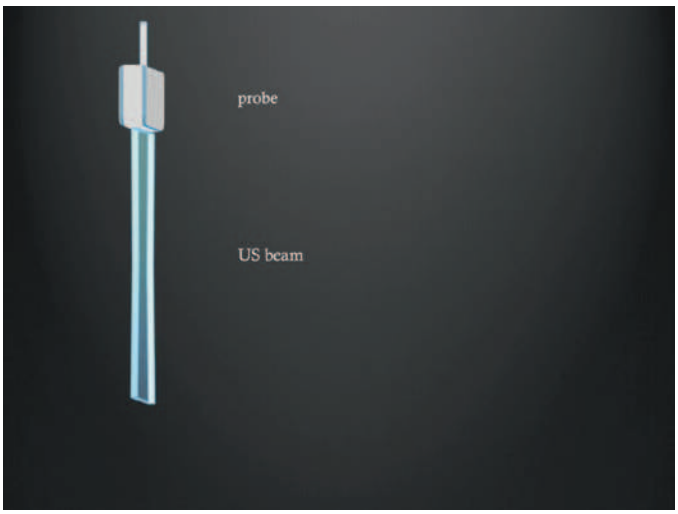

FIG. A.42 Partial Volume Averaging. The bladder wall is indistinct in region of this image. It is unclear if there are masses or if this is due to **grating lobe artifact** or **partial volume artifact** or both. Moving the patient or transducer to avoid bowel gas and putting the focal zone in the region in question should aid in evaluation. For the area closer to the patient's anterior abdominal wall, a higher-frequency transducer might be helpful.[18] (See Chapter 9, Fig. 9.57.)

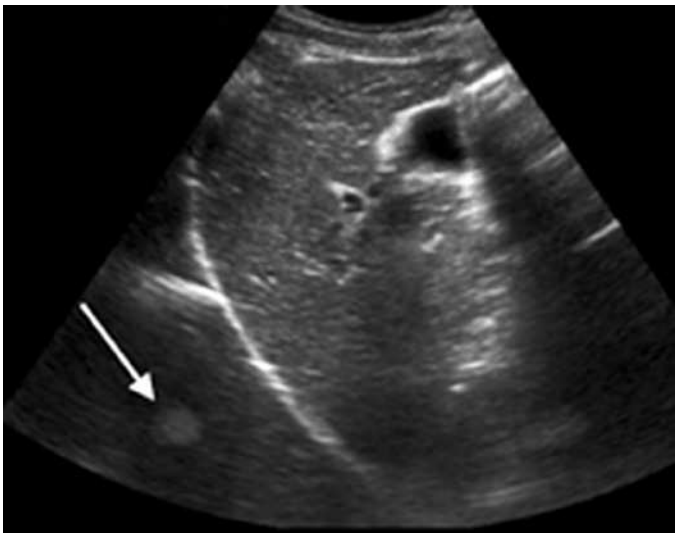

FIG. A.43 Partial Volume Averaging. A radiofrequency ablation zone present in the liver just outside the scanning plane is depicted onto the lungs through both partial volume averaging and mirror image artifacts.

DOPPLER IMAGING ARTIFACTS

The appearance of color Doppler signal is affected by several variables including color-write priority, gray-scale gain, and pulse repetition frequency. If the color gain is too low, flow might not be visualized. If the gain is too high, artifactual flow may be seen in adjacent soft tissues, and thrombus within the vessel might be missed.

Loss or Distortion of Doppler Information

Incorrect gain, wall-filter, and velocity scale can all lead to loss or distortion of Doppler signal. A rule of thumb for gain adjustment in Doppler imaging is to turn up the color gain until noise is encountered and then back off just until the noise clears from the image. In estimating frequency, the rule of thumb is to use a Doppler angle less than 60 degrees (but not 0). Wall filters eliminate low-frequency noise, but a high setting can lead to loss of signal. In general, wall filters should be kept at the lowest practical level, typically in the range of 50 to 100 Hz.

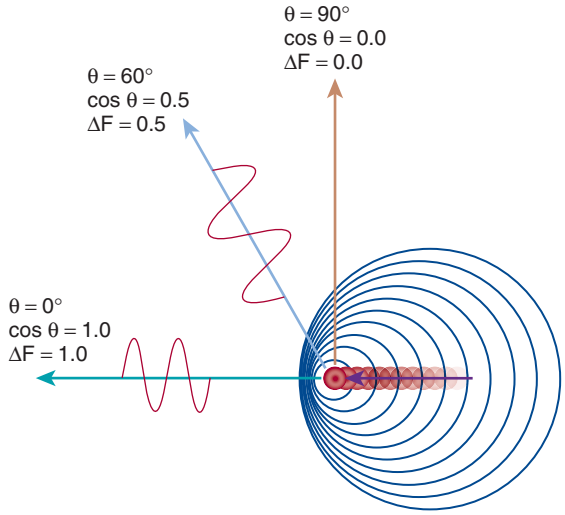

FIG. A.44 Effect of Doppler Angle on Frequency Shift. At an angle of 60 degrees, the detected frequency shift detected by the transducer is only 50% of the shift detected at an angle of 0 degrees. At 90 degrees, there is no relative movement of the target toward or away from the transducer, and no frequency shift is detected. The detected Doppler frequency shift is reduced in proportion to the cosine of the Doppler angle. Because the cosine of the angle changes rapidly at angles above 60 degrees, the use of Doppler angles of less than 60 degrees is recommended in making velocity estimates.[2] (See Chapter 1, Fig. 1.35.)

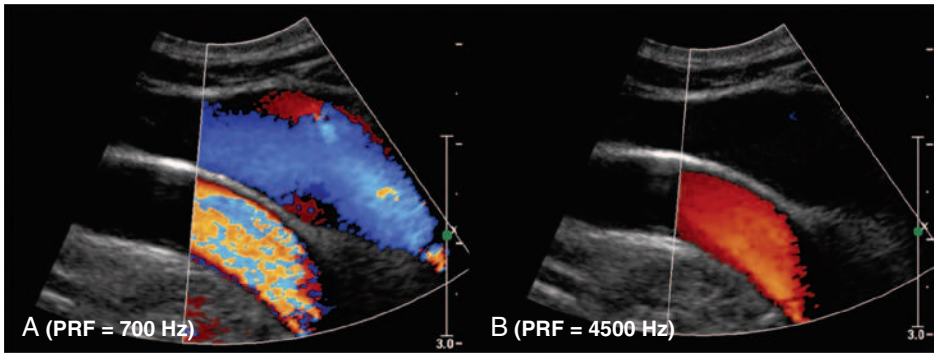

FIG. A.45 Artifactual Lack of Flow. Color Doppler image of a carotid artery and jugular vein. In **(A),** the pulse repetition frequency *(PRF)* is 700 Hz and there is aliasing in the carotid artery, but slow flow in the jugular vein is seen. In **(B),** the PRF is 4500 Hz, eliminating aliasing in the artery but also suppressing the display of the low Doppler frequencies in the internal jugular vein.[2] (See Chapter 1, Fig. 1.43.)

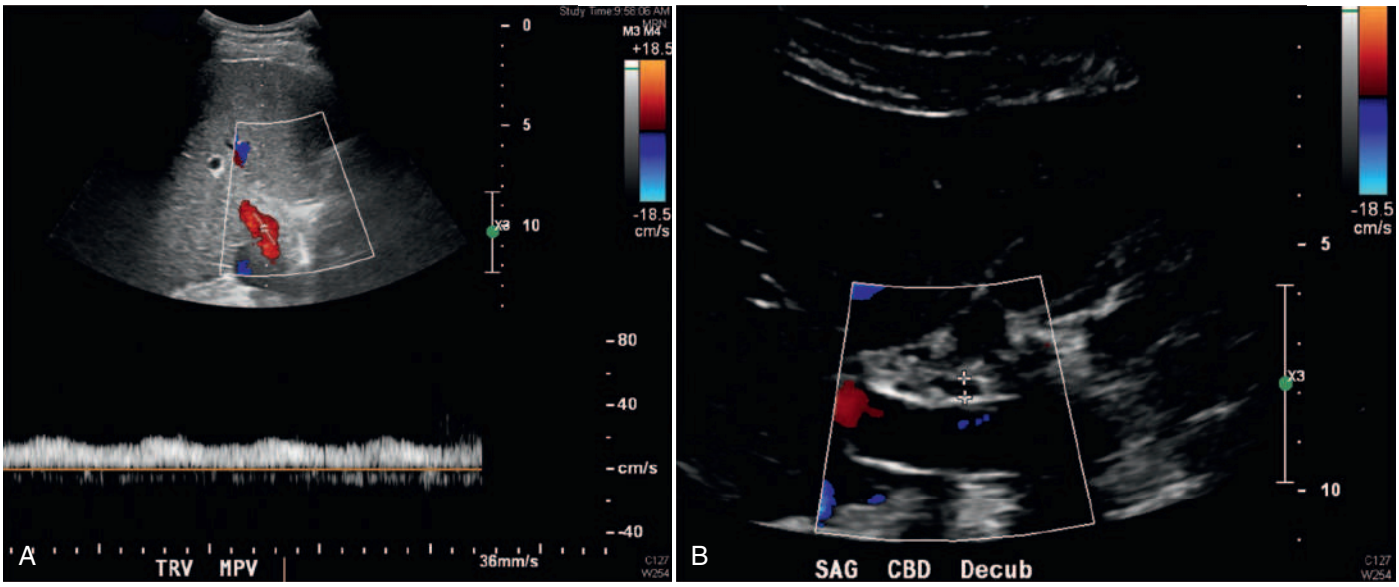

FIG. A.46 Artifactual Lack of Flow. (A) Color Doppler image shows flow in the portal vein. **(B)** When a color image is taken to assess the common duct, no flow is visible in the portal vein. Note the difference in overall gain in image **B.**

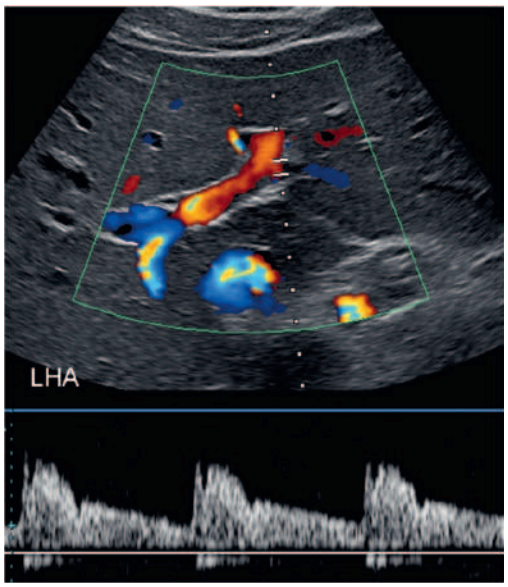

FIG. A.47 Color Direction. Shown in color is a portion of the portal venous system. Note how the flow direction appears to change in the region of branching, but this is merely a result of the orientation of flow with respect to the mid transducer. Note the aliasing in the posterior branch of the right portal vein. This is due to the curve of the vein and change in Doppler angle.[19] (See Chapter 51, Fig. 51.22.)

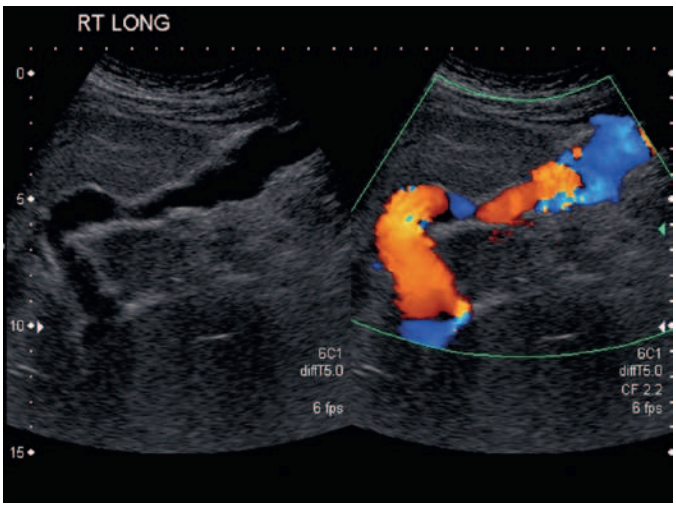

FIG. A.48 Color Direction as Shown in Recanalized Umbilical Vein. Flow on color Doppler will sometimes appear to change direction, but the flow needs to be assessed with respect to the transducer in order to determine if it is in the appropriate direction or not. In this example, transverse paramedian gray-scale and color Doppler sonograms show left lobe of liver in a child with cirrhosis and portal hypertension.[19] The recanalized umbilical vein is always flowing in relatively the same direction out of the liver, but at times, due to tortuosity, appears to change flow direction. Note that the flow changes from red (toward the transducer) to blue (away from the midpoint of the transducer), but at each interface there is a black region where the Doppler angle is 90. (See Chapter 51, Fig. 51.28.)

Artifactual Vascular Flow

The Doppler effect (shift) is not specific to vascular flow and occurs with movement of any reflector toward or away from the ultrasound beam. Fluid or solid tissue motion can mimic vascular flow. Transmitted pulsations, especially close to the heart or major arteries, can therefore result in artifactual appearance of flow within thrombosed veins or avascular areas. Artifactual vascular flow can also be visualized if the color gain is too high or the color-write priority is too high.

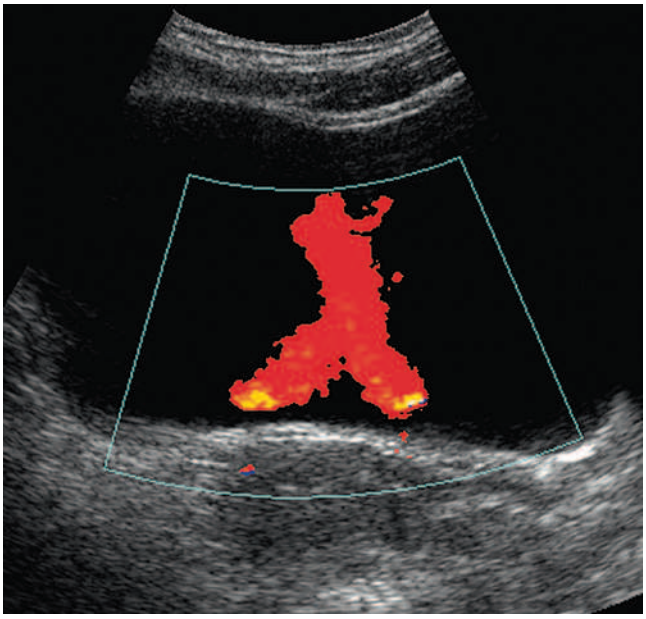

FIG. A.49 Artifactual Vascular Flow. Color Doppler jets in the bladder use color motion to indicate that there is flow from each ureteral orifice.[18] (See Chapter 9, Fig. 9.42A.)

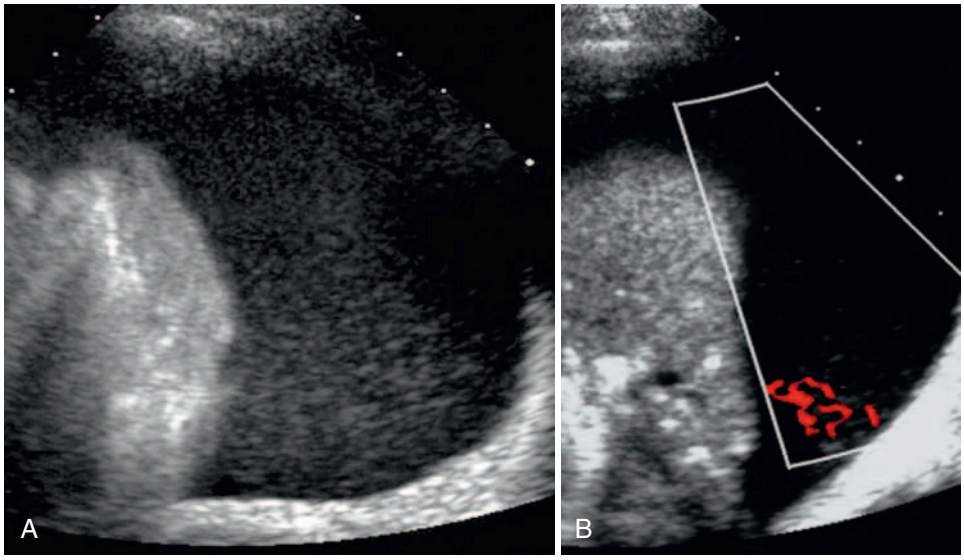

FIG. A.50 Artifactual Vascular Flow. Color flow Doppler signal in pleural fluid with debris. **(A)** Gray-scale sonogram shows left pleural fluid with much debris. **(B)** Color flow Doppler signal.[20] (See Chapter 50, Fig. 50.14.)

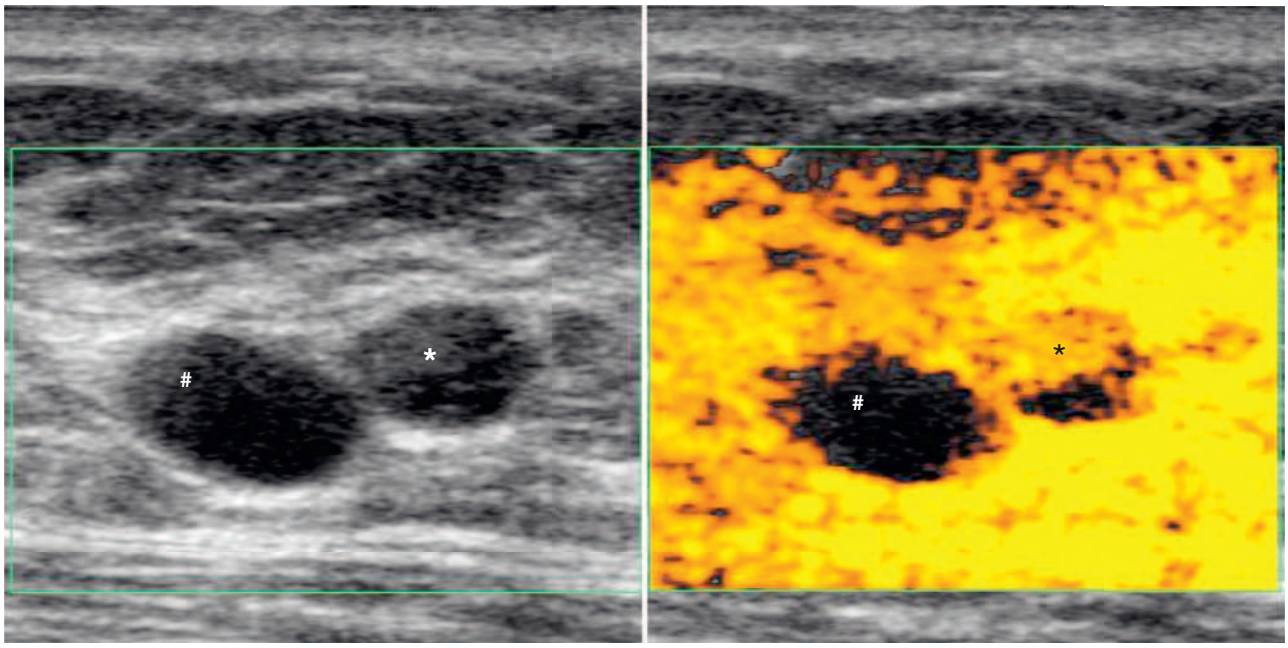

FIG. A.51 Artifactual Vascular Flow. Power Doppler ultrasound **vocal fremitus** can be used to distinguish a mural nodule from a fat-fluid level. The lipid layer is not attached to the cyst wall, so the fremitus artifact will not pass through it. On the other hand, true papillary lesions that are attached to the cyst wall will vibrate and transmit the fremitus artifact on power Doppler; having the patient hum in a deep voice creates a color artifact on power Doppler ultrasound.[21] (See Chapter 21, Fig. 21.26.)

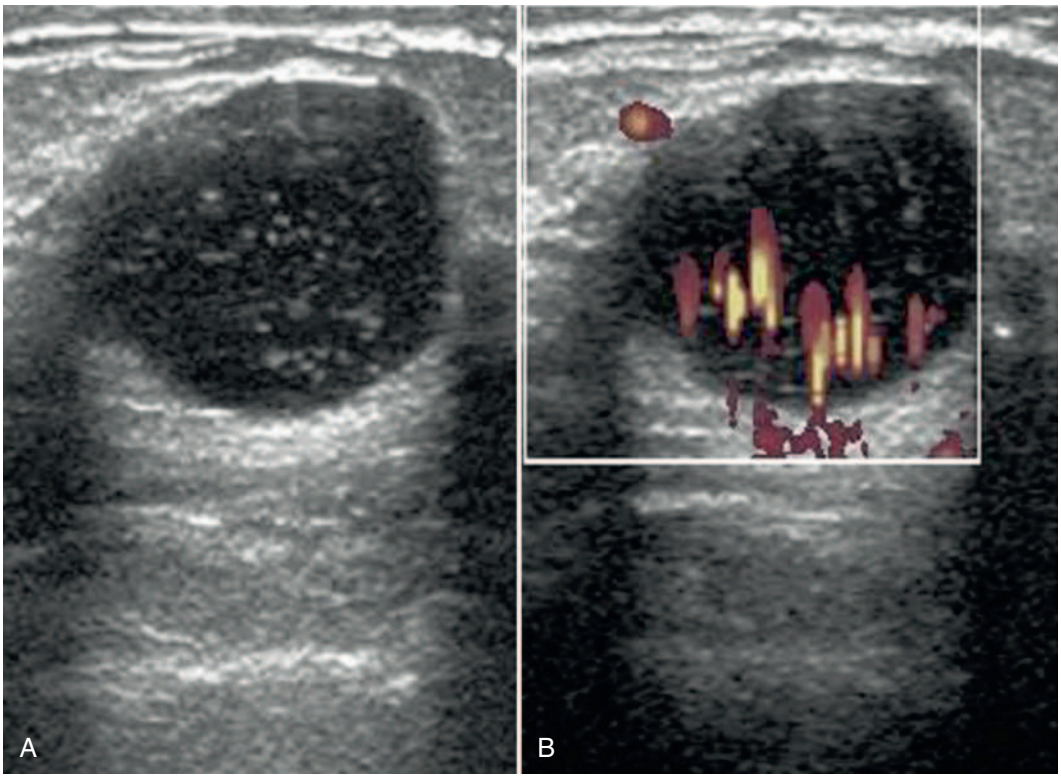

FIG. A.52 Color Streaking Artifact. (A) This complicated cyst contains floating punctate echoes that move posteriorly while being scanned, creating a scintillating appearance on gray-scale sonography. **(B)** Power Doppler ultrasound pushes the echoes posteriorly faster and with more energy than does the gray-scale beam. The echoes move fast enough that color persistence creates the appearance of **"color streaking"** artifact.[21] (See Chapter 21, Fig. 21.21.)

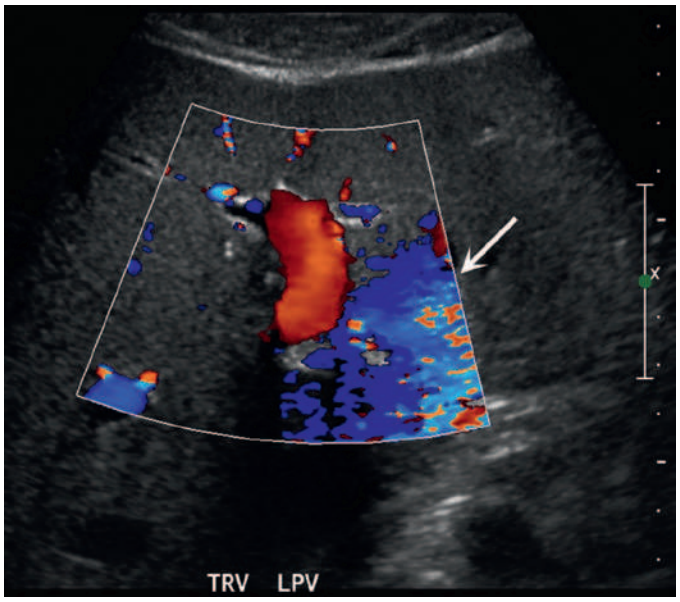

FIG. A.53 Flash Artifact From Pulsation. In this image of the left portal vein, note how transmitted pulsation from the heart causes artifactual flow in the adjacent liver owing to motion.

Tissue Vibration Artifact

Tissue vibration artifact consists of color pixels erroneously placed in the adjacent soft tissue by the ultrasound scanner because of the transmitted vibration from a region of marked turbulence. It is commonly seen with shunts, tight stenoses of large arteries, and especially arteriovenous fistulas. If tissue vibration artifact is seen, a search should be made for an arteriovenous fistula.

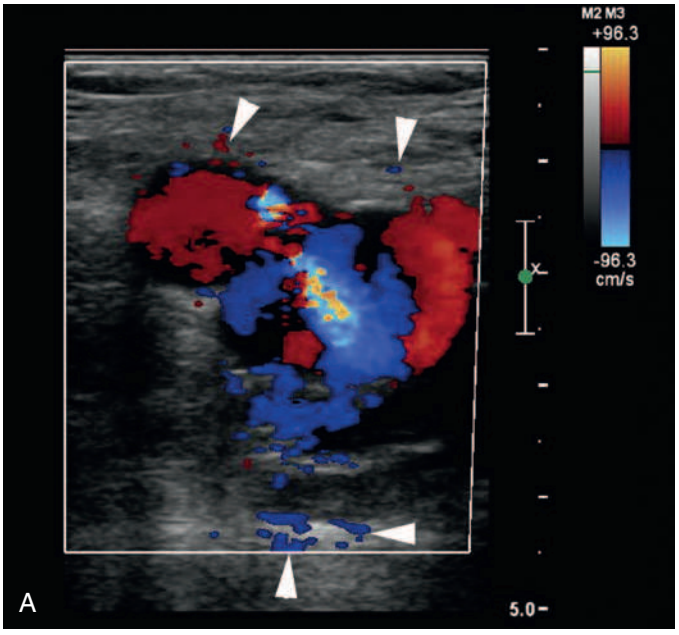

FIG. A.54 Tissue Vibration Artifact From Common Femoral Artery to Common Femoral Vein Arteriovenous Fistula. Turbulent flow through the fistula may affect surrounding tissues, causing a tissue vibration artifact, which may be the first clue that an arteriovenous fistula (AVF) is present. **Common femoral artery to common femoral vein AVF. (A)** Color Doppler shows common femoral artery to common femoral vein AVF. Note the adjacent tissue vibration artifact *(arrowheads)*. (See Chapter 27, Fig. 27.14.)

Click here to see the video of **tissue vibration** (Video A.19).

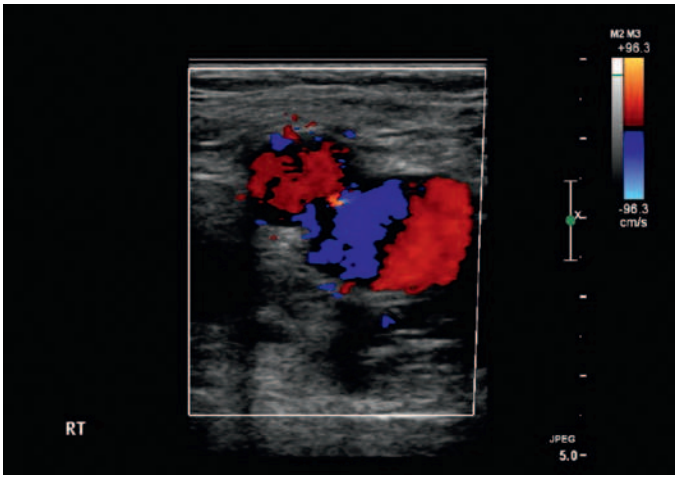

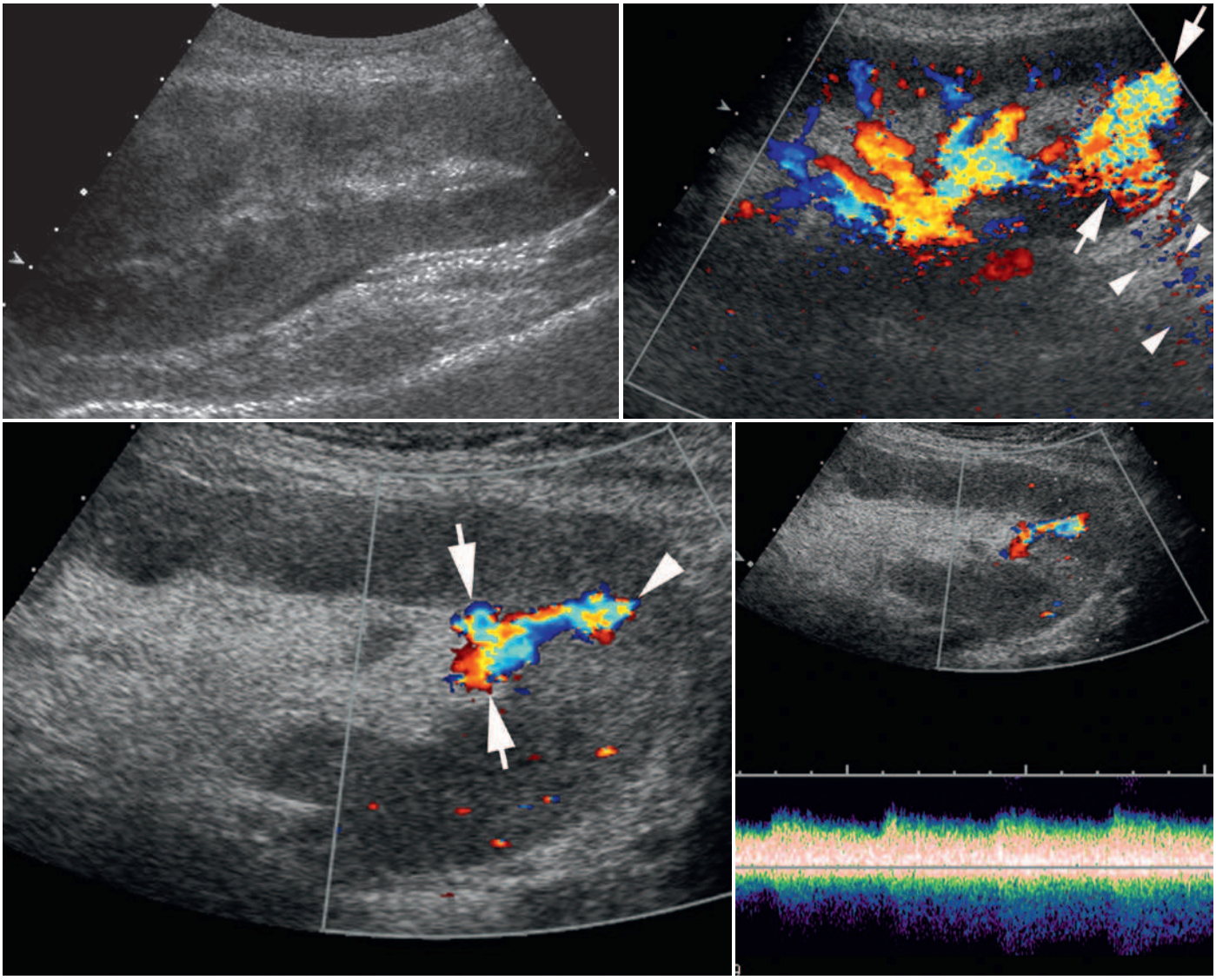

FIG. A.55 Tissue Vibration Artifact. Postbiopsy arteriovenous fistula. Color Doppler image shows markedly increased lower-pole blood flow *(arrows)* with adjacent soft tissue color artifact related to tissue vibration *(arrowheads)*.[22] (See Chapter 52, Fig. 52.49.)

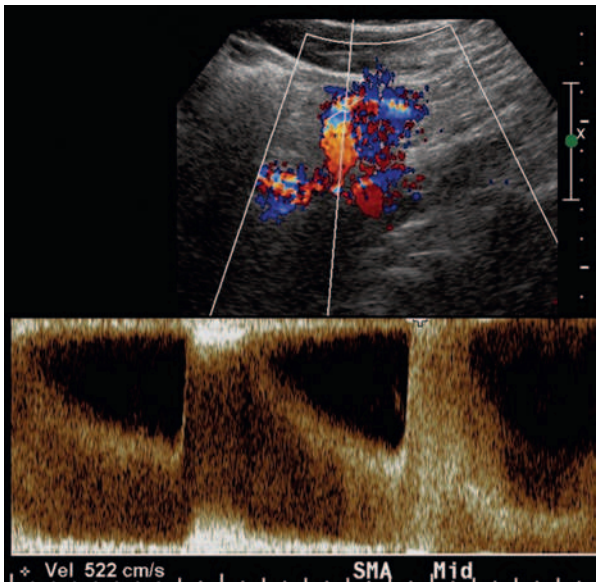

FIG. A.56 Tissue Vibration Artifact. Spectral waveform at site of superior mesenteric artery stenosis shows very high systolic velocity, and diastolic velocities of greater than 500 cm/sec. Color portion of the image shows **color bruit** consisting of color outside the vessel near the stenosis site. Color bruit is believed to be caused by tissue vibration.[23] (See Chapter 12, Fig. 12.27A.)

Click for video showing **tissue vibration artifact** in patient with **stenotic superior mesenteric artery with color bruit** (Video A.20). (See also Video 12.11.)

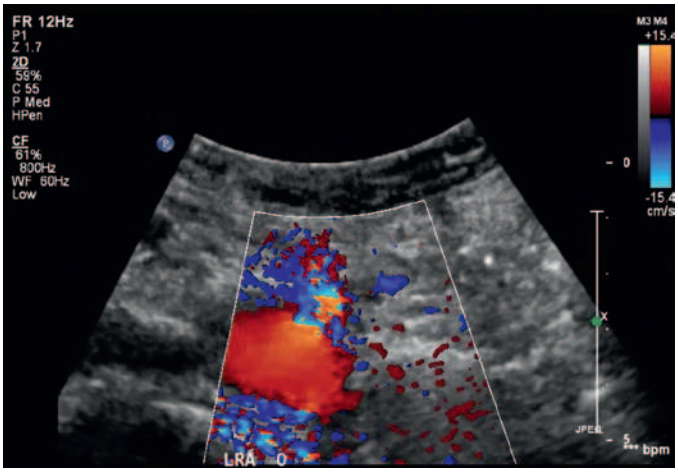

Aliasing and Velocity Scale Errors

Aliasing is an artifact due to undersampling of Doppler signal, resulting in incorrect estimation of flow velocity. To measure the Doppler frequency shift appropriately by pulsed Doppler, at least two samples from the cycle are required (Nyquist limit). If the pulse repetition frequency is less than twice the maximum frequency shift produced by movement of the target, aliasing results. The Doppler signal wraps around either the spectrum (spectral Doppler) or the color scale (color Doppler). The most common methods for correcting for aliasing are to shift the baseline down or up, or increase the pulse repetition frequency (or velocity scale). A lower-frequency transducer can also be used to help in correcting for aliasing. As angulation approaches 90 degrees, directional ambiguity can occur, suggesting bidirectional flow. Errors in Doppler angle correction can also lead to misleading assessments of flow velocity.

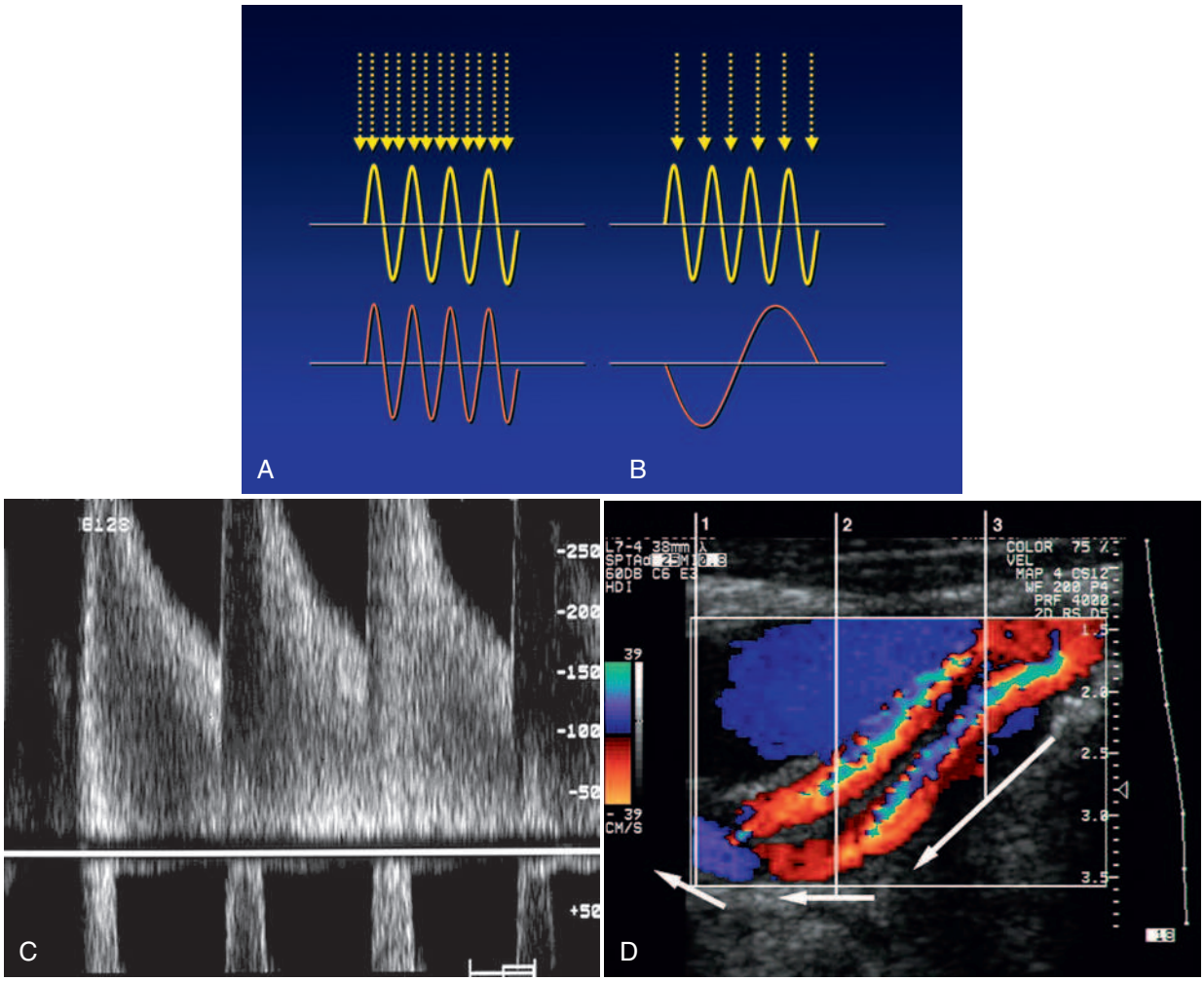

FIG. A.57 Aliasing. Pulse repetition frequency (PRF) determines the sampling rate of a given Doppler frequency. **(A)** If PRF *(arrows)* is sufficient, the sampled waveform *(orange curve)* will accurately estimate the frequency being sampled *(yellow curve)*. **(B)** If PRF is less than half the frequency being measured, **undersampling** will result in a lower-frequency shift being displayed *(orange curve)*. **(C) Aliasing** appears in the spectral display as a "wraparound" of the higher frequencies to display below the baseline. **(D)** In color Doppler display, aliasing results in a wraparound of the frequency color map from one flow direction to the opposite direction.[2] Unlike a true direction of flow change, with aliasing there will be no transition of unsaturated color. (See Chapter 1, Fig. 1.46.)

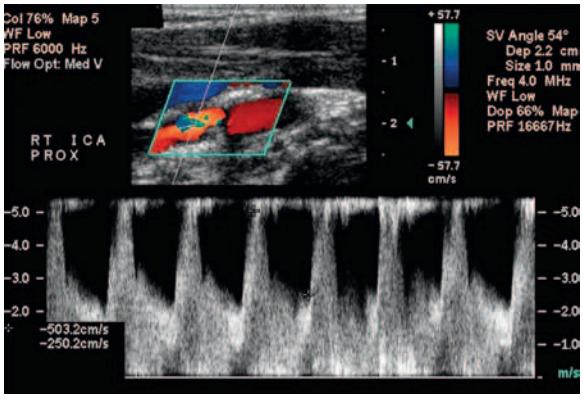

FIG. A.58 Aliasing. Note that aliasing prevents precise calculation of the maximum systolic velocity. However, because it is greater than 500 cm/sec, the precise number is not needed. The aliasing in the image allows for easier identification of the region of highest velocity for placement of the spectral Doppler gate.[6] (See Chapter 26, Fig. 26.20.)

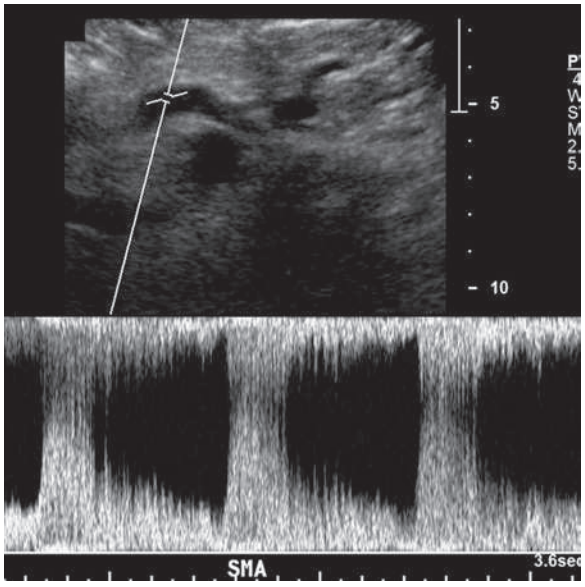

FIG. A.59 Aliasing in Superior Mesenteric Artery (*SMA*) Due to High-Velocity Flow.[23] (See Chapter 12, Fig. 12.28.)

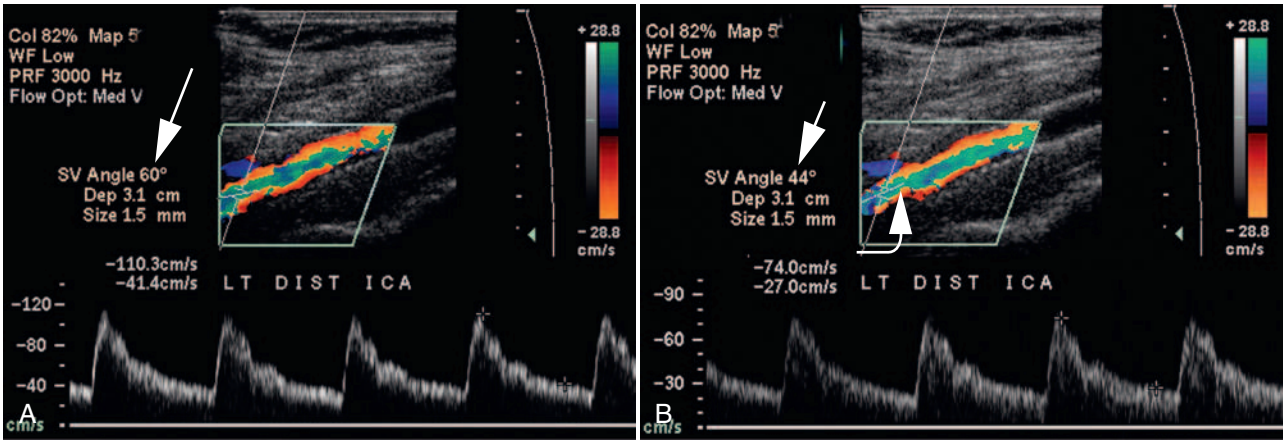

FIG. A.60 Aliasing Due to Doppler Angle Theta Changes. (A) Velocity obtained in the distal internal carotid artery with angle theta of 60 degrees is higher than that obtained at 44 degrees *(arrow)*. **(B)** However, the sample angle does not parallel the vessel wall at 60 degrees. Note central color aliasing in the region of highest velocity *(curved arrow)*.[6] (See Chapter 26, Fig. 26.16.)

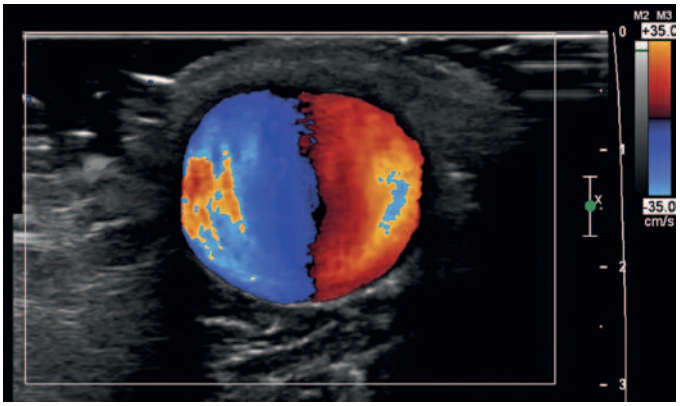

FIG. A.61 Aliasing in Pseudoaneurysm. Note the swirling flow in a pseudoaneurysm, resulting in a yin-yang appearance.[24] At the midline border of red and blue, there is a black line where the Doppler angle is 90 degrees. Here the flow is perpendicular to the sound beam, and so it is not detected. At 3 and 9 o'clock positions, there is aliasing within the blue and red areas. Here the Doppler angle is zero degrees with the flow directly toward and away from the transducer, thus appearing with maximal velocity. As the velocity exceeds the selected 35-cm/sec Doppler velocity range, aliasing results with artifactual opposite direction color signal. (See Chapter 27, Fig. 27.63.)

Click here to see the pseudoaneurysm video clip showing even more dramatic aliasing in the femoral artery (Video A.21).[24] (See also Chapter 27, Video 27.5.)

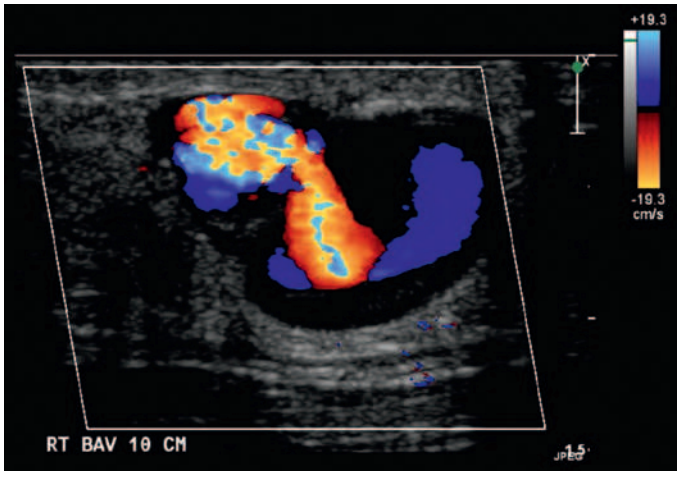

Spectral Broadening

Spectral broadening occurs when there are multiple different velocities of flow within a vessel. This can be a sign of stenosis. However, artifactual spectral broadening can occur owing to improper positioning of the sample volume near the vessel wall, use of an excessively large sample volume, or excessive system gain.

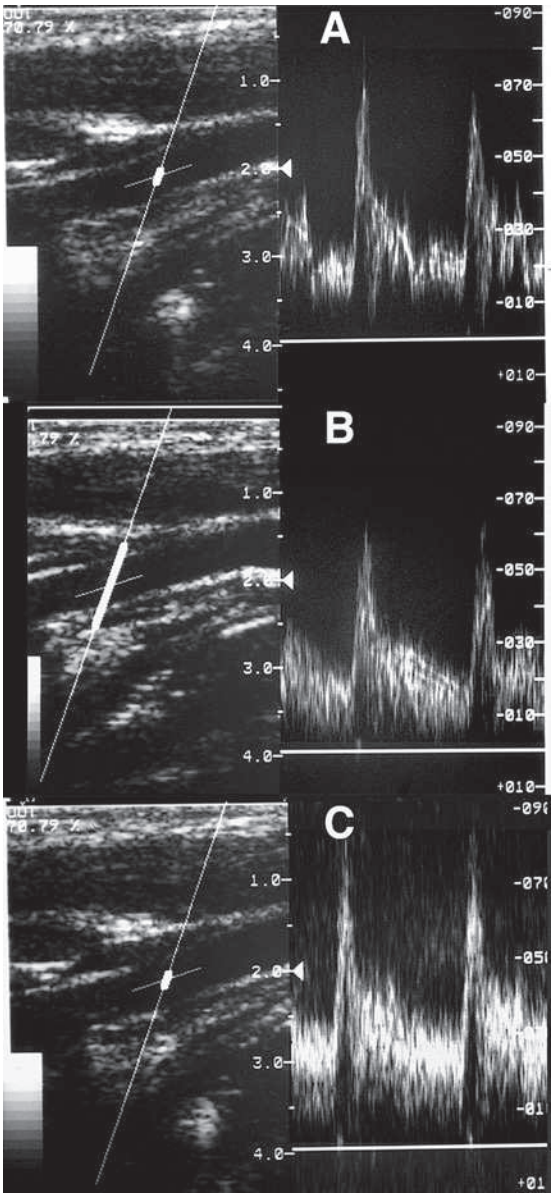

FIG. A.62 Spectral Broadening. The range of velocities detected at a given time in the pulse cycle is reflected in the Doppler spectrum as spectral broadening. **(A) Normal spectrum.** Spectral broadening may arise from turbulent flow in association with vessel stenosis. **(B** and **C) Artifactual spectral broadening** may be produced by improper positioning of the sample volume near the vessel wall, use of an excessively large **sample volume (B), or excessive system gain (C).**[2] (See Chapter 1, Fig. 1.45.)

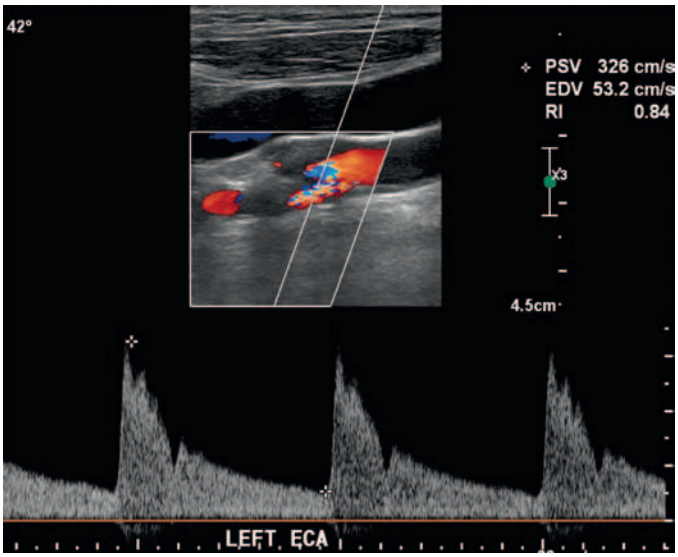

FIG. A.63 Spectral Broadening. True spectral broadening due to ECA stenosis.[6] (See Chapter 26, Fig. 26.18.)

Blooming Artifact

Blooming artifact occurs when color reaches beyond the vessel wall, making the vessels look larger than expected. It is gain dependent in that lowering the gain will decrease blooming. It is also wall filter and color-overwrite dependent, in that increasing the wall filter will decrease the artifact.

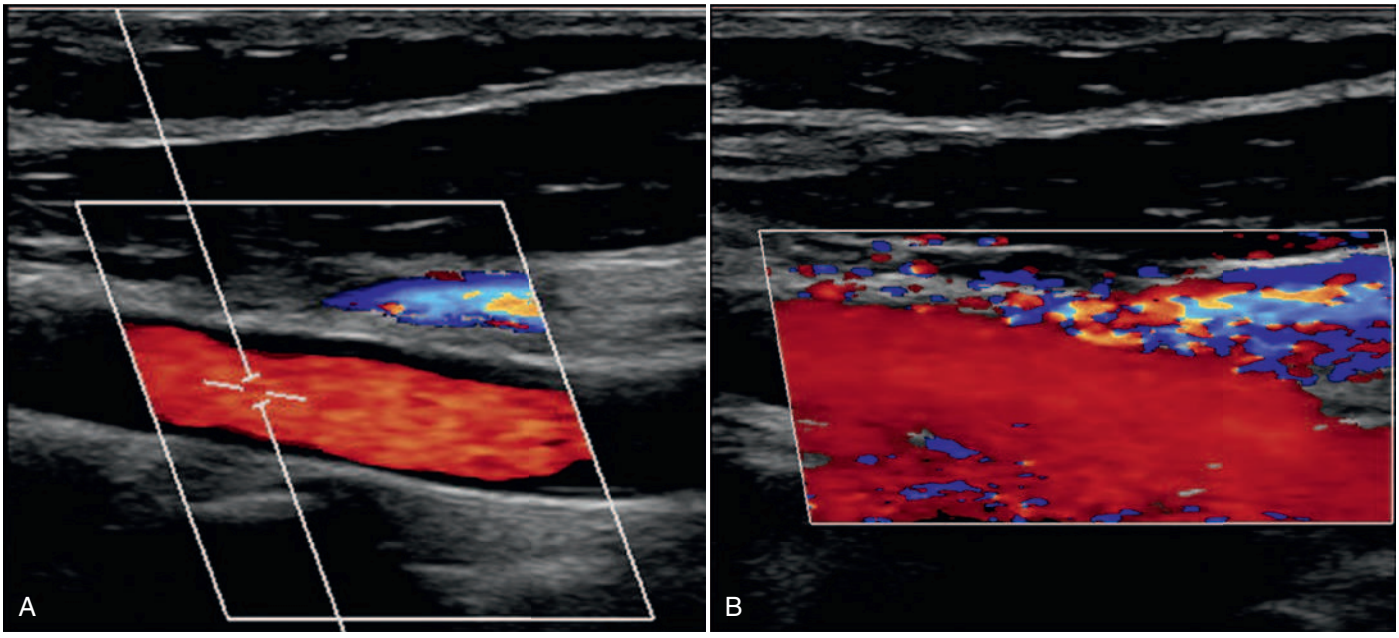

FIG. A.64 Blooming Artifact. Two images of the same carotid artery. In **(A)** the gain and wall filter are appropriate to show the flow centrally in the vessel. In **(B)** the gain and wall filter have been changed (in a manner beyond what would be used in clinical imaging) to demonstrate how these can make the vessel "bloom" and appear larger.

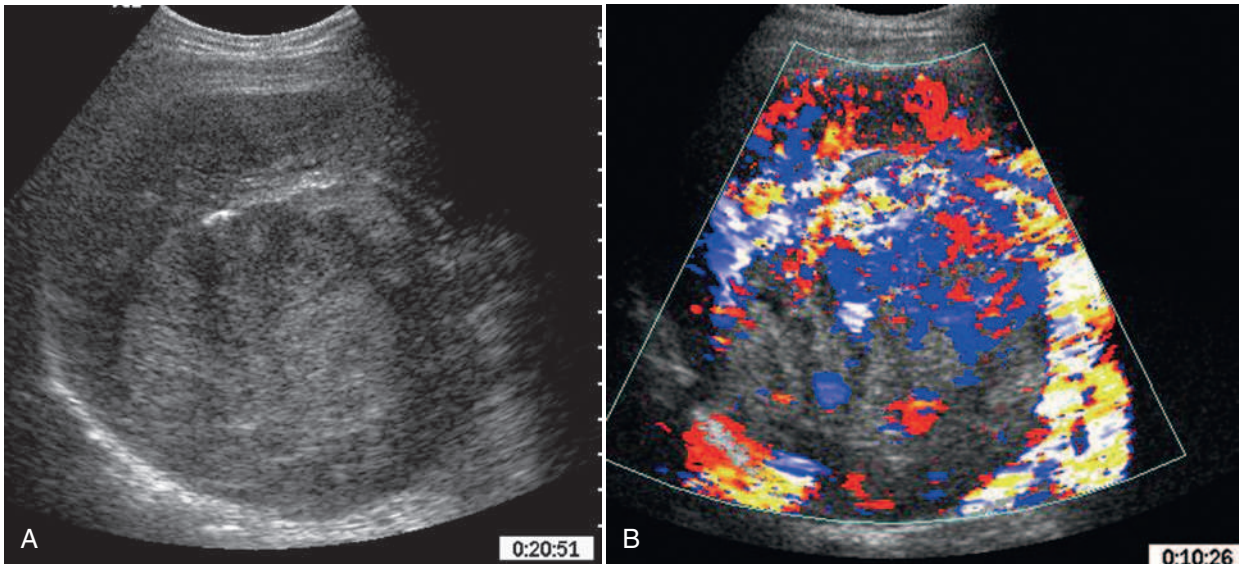

FIG. A.65 Blooming artifact due to use of contrast and tissue motion. **(A)** Use of contrast material creates color Doppler artifacts owing to blooming and tissue motion. **(B)** Contrast-specific imaging shows blood vessels not seen with Doppler.[25] (See Chapter 3, Fig. 3.7.)

Twinkle Artifact

Twinkle artifact is the artifactual depiction of color signal on crystalline materials in the body. It appears as discrete foci of alternating colors with or without an associated color comet-tail artifact. The appearance of twinkle artifact is highly dependent on machine settings and is likely generated by a narrow-band, intrinsic machine noise called "phase (or clock) jitter." This, along with a strongly reflecting, rough surface such as a renal stone, results in a high-amplitude, broadband signal appearing as random motion on color Doppler sonography. The twinkle artifact is quite useful clinically because it can aid in the detection of small stones, calcifications, and other crystalline material within the body.

View the PowerPoint illustration of **twinkle artifact** here (Video A.22).

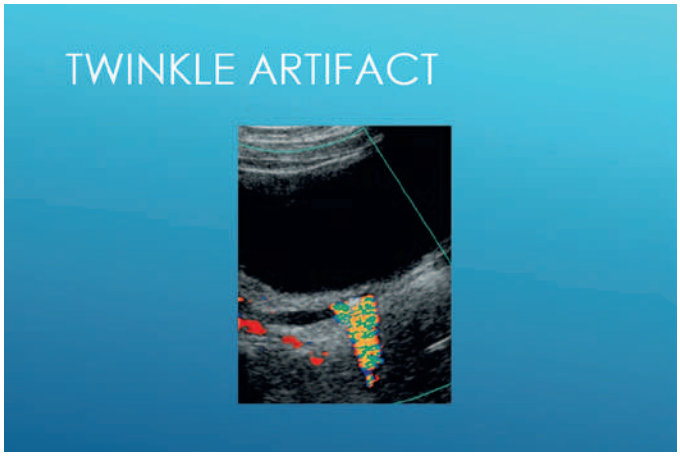

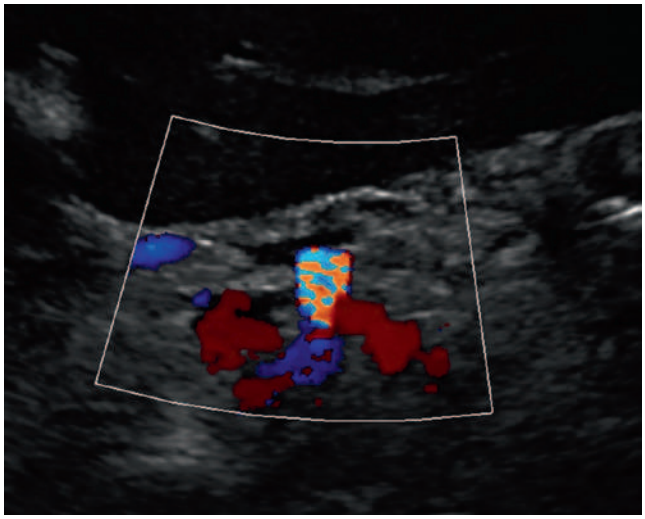

FIG. A.66 Twinkle Artifact Posterior to Pancreatic Duct Stone.[26] (See Chapter 7, Fig. 7.48D.)

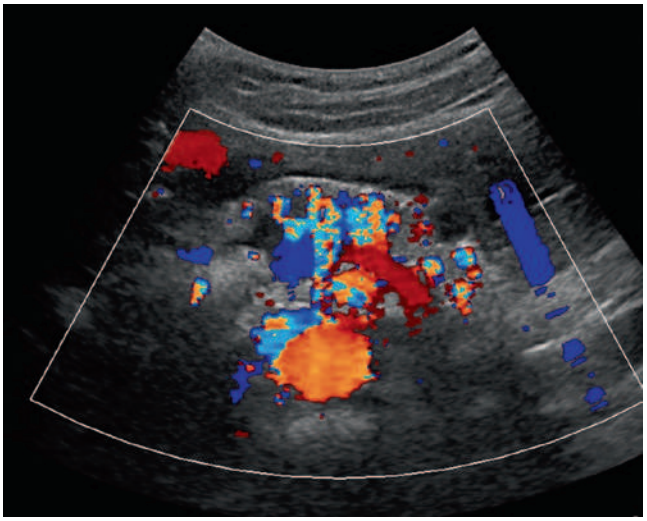

FIG. A.67 Calcifications in Chronic Pancreatitis With Twinkle Artifact.[26] (See Chapter 7, Fig. 7.49B.)

Click here for associated cine clip (Video A.23).[26] (See also Chapter 7, Video 7.5.)

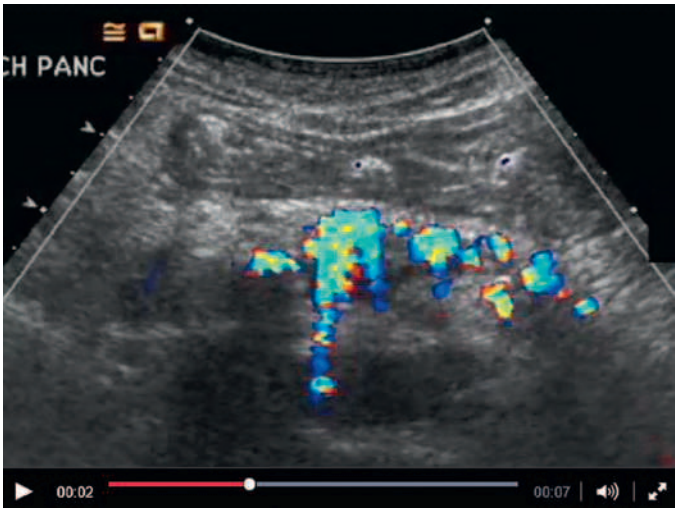

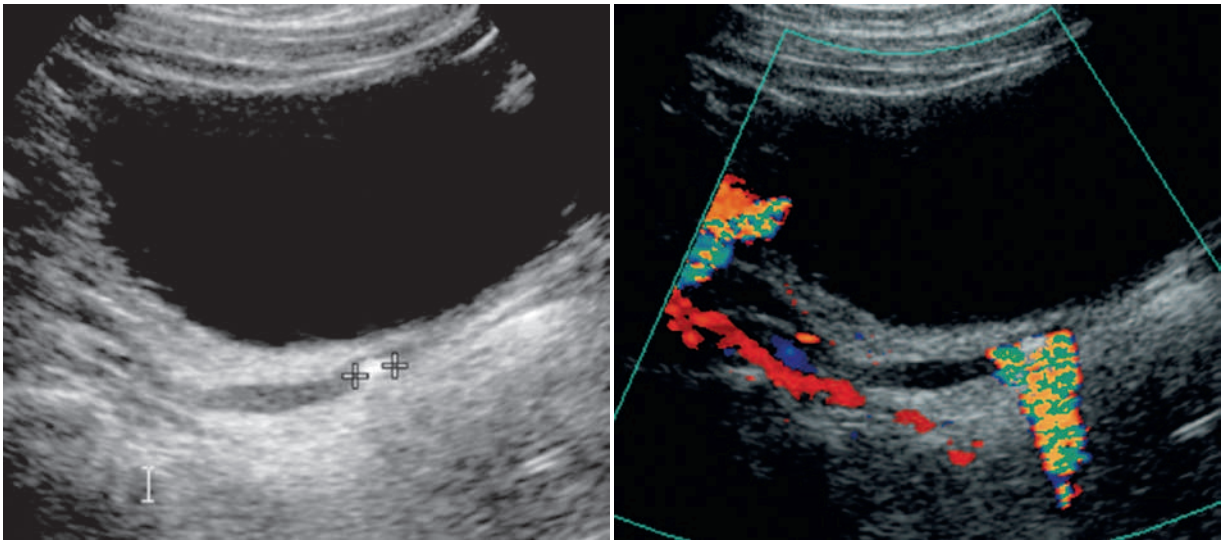

FIG. A.68 Twinkle Behind Distal Ureterovesical Junction Stone.[27] (See Chapter 54, Fig. 54.61.)

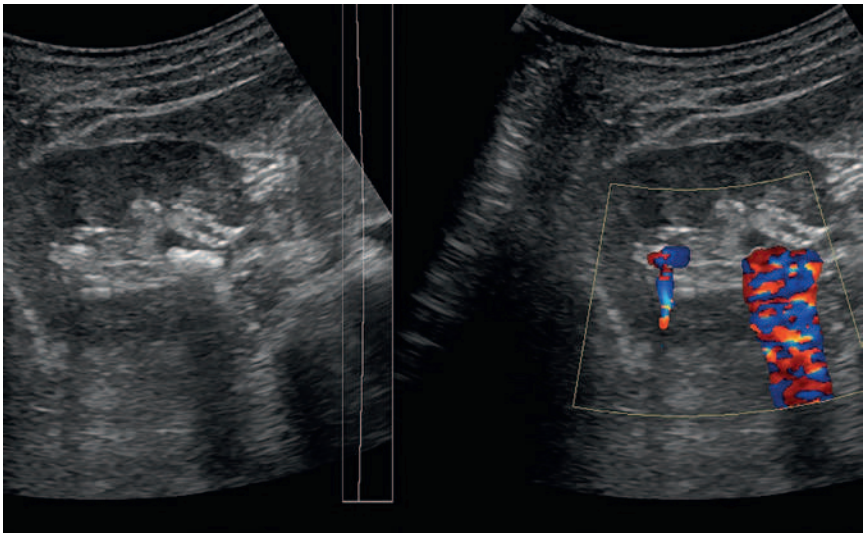

FIG. A.69 Twinkle Behind a Kidney Stone.[18] (See Chapter 9, Fig. 9.38.)

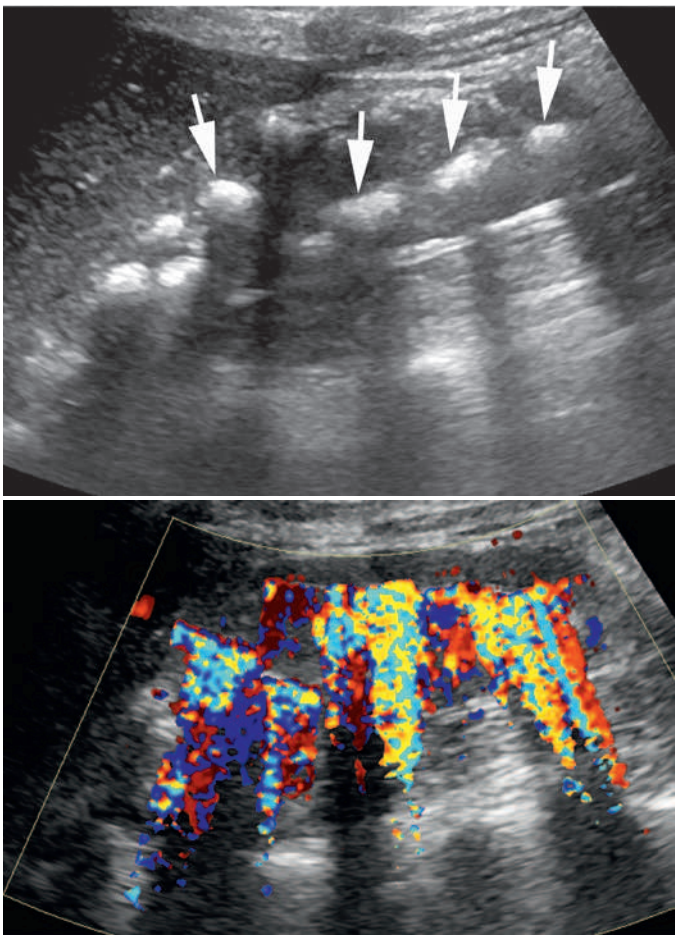

FIG. A.70 Twinkle Behind Multiple Kidney Stones.[22] (See Chapter 52, Fig. 52.37.)

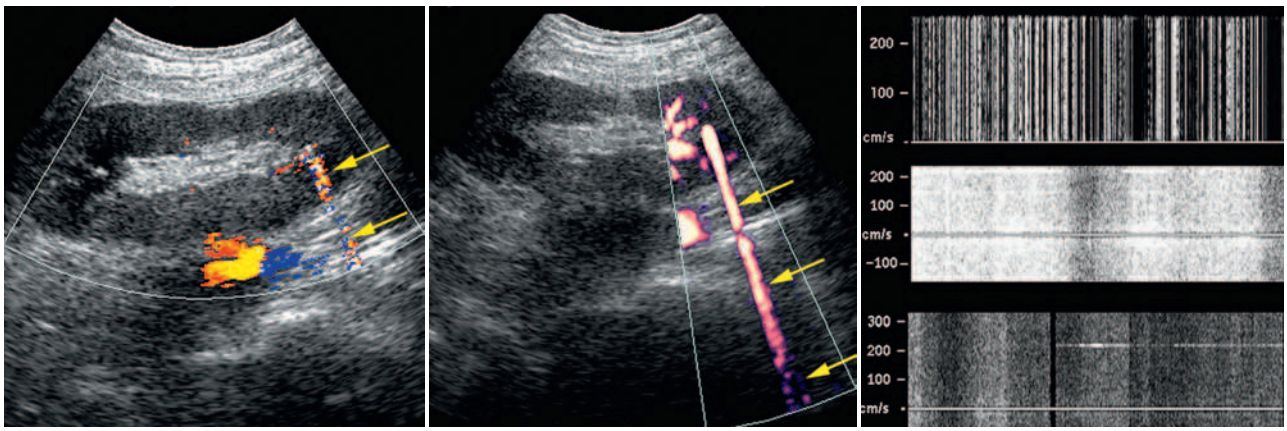

FIG. A.71 Appearances of Twinkle Artifact on Color, Power, and Pulsed Wave Doppler. Note how the spectral Doppler tracing of a twinkle artifact shows lines going through the tracing, which allow distinction from true blood flow.[28] (See Chapter 18, Fig. 18.52.)

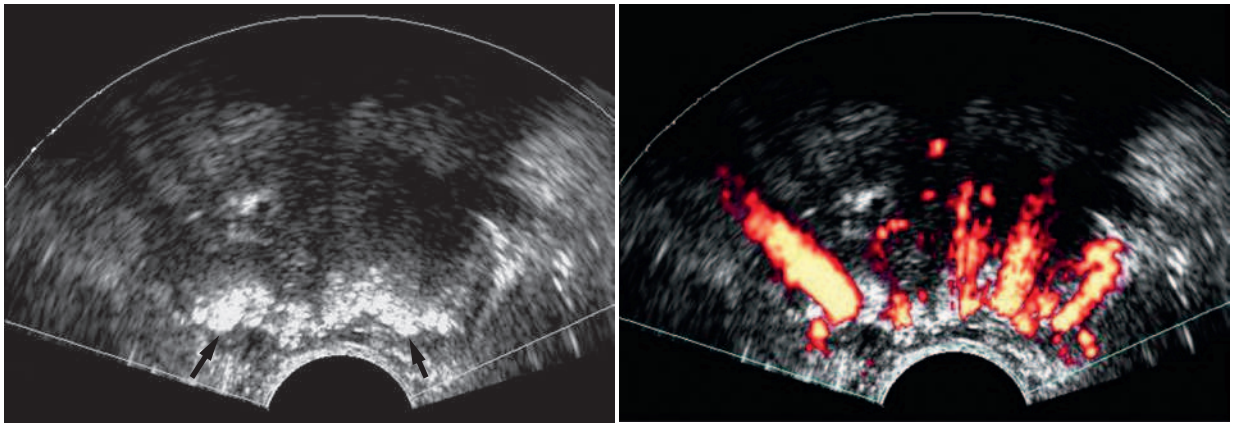

FIG. A.72 Power Doppler Image of Twinkle Behind Prostatic Calcifications.[11] (See Chapter 10, Fig. 10.7.)

Acknowledgment

Most of the images in this virtual chapter were obtained from chapters in the fifth edition of Diagnostic Ultrasound. We thank the authors for the use of their work.

REFERENCES

1. Hoskins P, Martin K, Thrush A. Diagnostic ultrasound: physics and equipment. 2nd ed. Cambridge, UK: Cambridge University Press; 2010.
2. Merritt C. Physics of ultrasound. In: Levine D, Rumack C, editors. Diagnostic ultrasound. 5th ed. Philadelphia: Elsevier; 2017.
3. Khalili K, Wilson S. The biliary tree and gallbladder. In: Levine D, Rumack C, editors. Diagnostic ultrasound. 5th ed. Philadelphia: Elsevier; 2017.
4. Brown D, Levine D. The uterus. In: Levine D, Rumack C, editors. Diagnostic ultrasound. 5th ed. Philadelphia: Elsevier; 2017.
5. Castro I, Levine D, Rumack C. The pediatric spinal canal. In: Levine D, Rumack C, editors. Diagnostic ultrasound. 5th ed. Philadelphia: Elsevier; 2017.
6. Bluth E, Troxclair L, Johnson S. The extracranial cerebral vessels. In: Levine D, Rumack C, editors. Diagnostic ultrasound. 5th ed. Philadelphia: Elsevier; 2017.
7. Toi A, Levine D. The fetal brain. In: Levine D, Rumack C, editors. Diagnostic ultrasound. 5th ed. Philadelphia: Elsevier; 2017.
8. Feldman MK, Katyal S, Blackwood MS. US artifacts. Radiographics. 2009;29(4):1179-1789.
9. Wilson S, Withers C. The liver. In: Levine D, Rumack C, editors. Diagnostic ultrasound. 5th ed. Philadelphia: Elsevier; 2017.
10. Solbiati L, Charboneau J, Reading C, et al. The thyroid gland. In: Levine D, Rumack C, editors. Diagnostic ultrasound. 5th ed. Philadelphia: Elsevier; 2017.
11. Toi A. The prostate and transrectal ultrasound. In: Levine D, Rumack C, editors. Diagnostic ultrasound. 5th ed. Philadelphia: Elsevier; 2017.
12. Vandeman FN, Meilstrup JW, Nealey PA. Acoustic prism causing sonographic duplication artifact in the upper abdomen. Invest Radiol. 1990;25(6): 658-663.
13. McMahon C, Yablon C. Overview of musculoskeletal ultrasound techniques and applications. In: Levine D, Rumack C, editors. Diagnostic ultrasound. 5th ed. Philadelphia: Elsevier; 2017.
14. DiPietro MA, Brody BA, Teele RL. Peritrigonal echogenic "blush" on cranial sonography: pathologic correlates. AJR Am J Roentgenol. 1986;146(5): 1067-1072.
15. McMahon C, Yablon C. The shoulder. In: Levine D, Rumack C, editors. Diagnostic ultrasound. 5th ed. Philadelphia: Elsevier; 2017.
16. Wilson SR, Burns PN, Wilkinson LM, et al. Gas at abdominal US: appearance, relevance, and analysis of artifacts. Radiology. 1999;210(1):113-123.
17. Avruch L, Cooperberg PL. The ring-down artifact. J Ultrasound Med. 1985;4(1):21-28.
18. Tublin M, Levine D, Thurston W, Wilson S. The kidney and urinary tract. In: Levine D, Rumack C, editors. Diagnostic ultrasound. 5th ed. Philadelphia: Elsevier; 2017.
19. O'Hara S. The pediatric liver and spleen. In: Levine D, Rumack C, editors. Diagnostic ultrasound. 5th ed. Philadelphia: Elsevier; 2017.
20. Shah C, Greenberg S. The pediatric chest. In: Levine D, Rumack C, editors. Diagnostic ultrasound. 5th ed. Philadelphia: Elsevier; 2017.
21. Phillips J, Mehta R. The breast. In: Levine D, Rumack C, editors. Diagnostic ultrasound. 5th ed. Philadelphia: Elsevier; 2017.
22. Paltiel H, Babcock D. The pediatric kidney and adrenal glands. In: Levine D, Rumack C, editors. Diagnostic ultrasound. 5th ed. Philadelphia: Elsevier; 2017.
23. Bertino R, Mustafaraj E. The retroperitoneum. In: Levine D, Rumack C, editors. Diagnostic ultrasound. 5th ed. Philadelphia: Elsevier; 2017.
24. Lockhart M, Umphrey H, Weber T, Robbin M. Peripheral vessels. In: Levine D, Rumack C, editors. Diagnostic ultrasound. 5th ed. Philadelphia: Elsevier; 2017.
25. Burns P. Contrast agents for ultrasound imaging and Doppler. In: Levine D, Rumack C, editors. Diagnostic ultrasound. 5th ed. Philadelphia: Elsevier; 2017.
26. Winter T, Sun M. The pancreas. In: Levine D, Rumack C, editors. Diagnostic ultrasound. 5th ed. Philadelphia: Elsevier; 2017.
27. Kotlus Rosenberg H, Simpson Jr W, Chaudhry H. Pediatric pelvic sonography. In: Levine D, Rumack C, editors. Diagnostic ultrasound. 5th ed. Philadelphia: Elsevier; 2017.
28. Muradali D, Chawla T. Organ transplantation. In: Levine D, Rumack C, editors. Diagnostic ultrasound. 5th ed. Philadelphia: Elsevier; 2017.

Index

A
AA anastomoses. *See* Arterial/arterial anastomoses
AAA. *See* Abdominal aortic aneurysm
Aase syndrome, 1401
Abciximab, 598
Abdomen. *See also* Acute abdomen
  abscess of, drainage of, 612, 613*f*
  blunt trauma to, small bowel obstruction from, 1843
  calcifications of, meconium peritonitis and, 1313, 1314*f*
  ectopic pregnancy implantation in, 1074, 1075*f*
  fetal
    circumference of, in gestational age determination, 1448, 1450*f*
    circumference of, in second-trimester, 1023*f*
    musculature of, absent, in prune belly syndrome, 1361–1362
    routine sonographic views of, 1021, 1026*f*
  lymphangiomas of, pediatric, 1862, 1864*f*
  pediatric, systemic veins of, flow patterns in, 1750
Abdominal aorta. *See also* Iliac veins; Inferior vena cava; Mesenteric artery(ies); Renal artery(ies)
  anatomy of, 433, 433*f*
  dilation of, 439–441
    aneurysm causing, 433–439
    aortic ectasia causing, 440
    arteriomegaly causing, 440
    inflammatory AAAs causing, 439–440, 443*f*
    penetrating ulcer causing, 441, 444*f*
    pseudoaneurysm causing, 441
  diseases of, 445–464
  dissection complications with, renal artery stenosis and, 447, 448*f*
  endovascular aortic repair for ruptured, 438
  stenotic disease of, 441–445, 445*f*
Abdominal aortic aneurysm (AAA), 433–439
  definition of, 433–434, 434*f*
  endoleaks after repair of, 438–439, 440*f*–442*f*
  inflammatory, 439–440, 443*f*
  medical therapy for, 434
  mortality from, 433
  natural history of, 434
  pathophysiology of, 434
  postoperative ultrasound assessment for, 438–439, 440*f*–442*f*
  rupture of, evaluation of, ultrasound compared to CT for, 438, 439*f*
  screening for, 434–435
    CT in, 437
    false-positive/false-negative results in, 437*f*–438*f*, 438
    recent studies in, 434–435
    ultrasound approach to, 435
Abdominal aortic aneurysm (AAA) *(Continued)*
  surveillance of, 435–437
    CT in, 437
    sonographic technique for, 436–437, 436*f*–437*f*
  treatment planning for, 438
Abdominal cervical cerclage, 1506, 1506*f*
Abdominal ectopia cordis, 1295
Abdominal ectopic pregnancy, 1074, 1075*f*
Abdominal wall
  defects in, thickened NT in, 1095–1096
  hernias of anterior, dynamic ultrasound of contents of, 472–473
    entities stimulating, 500–501, 502*f*
    maneuvers for, 473–474, 474*f*–475*f*
    technical requirements for, 471
    types of, 471, 471*f*
    ventral, 488–494
Abdominal wall, fetal, 1322–1330
  amniotic band syndrome and, 1330, 1330*f*
  bladder exstrophy and, 1326, 1328*f*
  body stalk anomaly and, 1329
  cloacal exstrophy and, 1328–1329, 1329*f*
  ectopia cordis and, 1329, 1329*f*
  embryology of, 1322, 1323*f*
  gastroschisis and, 1322–1325
    associated conditions of, 1324–1325
    epidemiology of, 1322–1323
    management of, 1325
    pathogenesis of, 1323
    prenatal diagnosis of, 1323–1324, 1324*f*
  maternal serum alpha-fetoprotein and defects of, 1322
  omphalocele and, 1325–1326, 1326*f*
    associated conditions with, 1325, 1327*f*
    epidemiology of, 1325
    management of, 1325–1326
    prenatal diagnosis of, 1325, 1327*f*
  pentalogy of Cantrell and, 1329
Abductor tendon, injection for, 905–907, 907*f*
Ablation. *See also* Ethanol ablation
  adrenal, 428
  endometrial, 551–552, 552*f*
Abscess(es)
  abdominal, drainage of, 612
  adrenal, bacterial, 423
  amebic liver, 613
  appendiceal, pediatric, 1871*f*
    hemorrhagic ovarian cyst differentiated from, 1877
  branchial sinus, type IV, 1643–1645, 1645*f*, 1651, 1653*f*
  breast, 803–804, 803*f*–804*f*
  cellulitis leading to, 874, 874*f*
  complicated lymphadenitis with, in children, 1634, 1658–1660
  costochondral junction, pediatric, aspiration and drainage of, 1963*f*
  in Crohn disease, 275–276, 278*f*–279*f*
  empyemas differentiated from, pediatric, 1725, 1726*f*
  enteric, 612
Abscess(es) *(Continued)*
  gastrointestinal, 592
  hydatid, 613
  of kidneys
    acute pyelonephritis and, 325, 325*f*
    drainage of, 617, 618*f*
    pediatric, complicating acute pyelonephritis, 1792–1793
    transplantation complications with, 651, 656*f*
  liver
    drainage of pyogenic, 612–613, 614*f*–615*f*
    after liver transplantation, 638–639, 646*f*
    pyogenic, 85–86, 87*f*
  liver, pediatric, 1746–1748
    parasitic, 1747–1748
    pyogenic, 1746–1747, 1751*f*
  lung, pediatric, 1711, 1713*f*
  pancreatic, acute pancreatitis complications with, 230
  parenchymal, pediatric renal transplantation and, 1812
  parotid, pediatric, 1632–1633, 1633*f*
  pediatric drainage of, interventional sonography for, 1953
    transrectal, 1953–1954, 1954*f*
  pelvic, 283, 591
    drainage of, 612, 613*f*
  percutaneous needle biopsy complications with, 609, 610*f*
  perforated appendicitis and, pediatric, 1857, 1861*f*
  perianal, perianal inflammatory disease and, 305–306
  perinephric
    acute pyelonephritis and, 325
    pediatric renal transplantation and, 1812
    after renal transplantation, 664–665
  perinephric fluid collections and, 1809
  peritonitis and, 517, 520*f*
  prostate, 389, 390*f*, 392
  splenic, 148, 151*f*
    drainage of, 617
    pediatric, 1769
  stitch, after herniorrhaphy, 494–496, 495*f*
  subphrenic, 1716
  testicular, 831–832, 831*f*
  tubo-ovarian, in pelvic inflammatory disease, 588–589, 588*f*
ABUS. *See* Automated whole-breast ultrasound
ACA. *See* Anterior cerebral artery
Acalculous cholecystitis, 200
Acardiac twins, hydrops and, 1429
ACAS. *See* Asymptomatic Carotid Atherosclerosis Study
Accessory and cavitated uterine mass (ACUM), 541
Accessory arteries, 445–446
Accessory lobes, of placenta, 1480–1481, 1481*f*
Accessory spleen, 158–159, 160*f*, 1771*f*
Acetabular dysplasia, familial, 1921

Page numbers followed by *f* indicate figures; *t*, tables; *b*, boxes.

Acetabulum
  description of, in evaluation of infant at risk, 1927–1929
  development of, 1923
Acetylcholinesterase (AChE), in neural tube defect screening, 1228
Achilles tendon
  rheumatoid nodules in, 867, 868*f*
  tendinosis in, 861, 861*f*
Achillodynia, peritendinous injections of foot and ankle for, 902, 903*f*
Achondrogenesis, 1383*f*, 1391
  diagnosis of, 1376–1377
  type 1, 1391
  type 2, 1391, 1391*f*
Achondroplasia
  heterozygous, 1396–1398, 1398*f*
    detection of, gestational age for, 1381
    inheritance pattern for, 1379–1380
  homozygous, thanatophoric dysplasia differentiated from, 1389, 1389*f*
  "trident hand" configuration in, 1407, 1408*f*
Achondroplasia, megalencephaly associated with, 1194–1195
Acinic cell carcinoma, parotid gland, pediatric, 1638, 1639*f*
Acinus, 78
ACN. *See* Acute cortical necrosis
ACOG. *See* American College of Obstetricians and Gynecologists
Acorn cysts, in breast, 778*f*
Acoustic attenuation, in uterine fibroids, 539*f*, 540, 540*b*
Acoustic cavitation, 35
  bubbles generated from, 41–42, 42*f*
  considerations for acoustic output increases and, 44
  contrast agents and, 43, 44*b*
  effects of, 40–46
  inertial, 40
  lithotripters as evidence of, 42–43, 42*f*
  in lung and intestine, 43
  mechanical index for, 44–45, 45*f*
  potential sources of, 40–42, 42*f*
  sonochemistry and, 42, 42*f*
Acoustic enhancement, pleural fluid producing, 1709–1710
Acoustic frequency, 2
Acoustic impedance, 3–4
Acoustic power, 5
Acoustic radiation force imaging (ARFI), 1764, 1765*f*
Acoustic shadowing, 786
  breast sonography and, 791–792, 793*f*
  carcinoma causing, 791–792, 793*f*
  decreased/absent, in skeletal dysplasias, 1381–1382
  malignant masses causes, differential diagnosis for, 792
  by rib, in pediatric chest sonography, 1710
Acoustic standoff, in breast tumor imaging, 767, 767*f*
Acoustics
  attenuation of sound energy in, 5–7, 7*f*
  basics of, 2–7
  distance measurement in, 3, 4*f*
  frequency and wavelength in, 2, 2*f*
  impedance of, 3–4
  microbubble behavior and, 57*t*, 58–59, 59*f*
  reflection in, 4, 5*f*
  refraction in, 5, 6*f*
  sound propagation in, 2–3, 3*f*
Acquired cystic kidney disease, 364, 364*f*
  renal cell carcinoma and, 340
Acquired immunodeficiency syndrome (AIDS)
  acute typhlitis and, 287–288, 289*f*
  gastrointestinal tract infections and, 296
  genitourinary infections in, 331–333, 332*f*–333*f*
  lymphoma related to, 266, 266*f*
  Pneumocystis carinii opportunistic infection of liver and, 91, 91*f*
Acrania, 1179
Acromelia, 1381, 1381*b*, 1382*f*
Acromioclavicular joint, 878–879, 878*f*
  injection of, 902, 902*f*
  osteoarthritis of, 893, 894*f*
Acromion, 878–879, 878*f*
Active surveillance, for prostate cancer, 401
ACUM. *See* Accessory and cavitated uterine mass
Acute abdomen. *See also* Diverticulitis, acute
  fluid collections in, 281
  free intraperitoneal gas in, 277–281, 282*f*
  gastrointestinal tract and, 277–290
  left lower quadrant pain in, 288–290
    from acute diverticulitis, 288–290
  mesenteric adenopathy in, 282
  perienteric soft tissues in, 281–282
  pneumatosis intestinalis in, 277–281
  right lower quadrant pain in, 282–288
    from acute appendicitis, 282–285
    from acute typhlitis, 287–288, 289*f*
    from Crohn appendicitis, 285, 287*f*
    from mesenteric adenitis, 288
    from right-sided diverticulitis, 285–287, 288*f*
    from right-sided segmental omental infarction, 288, 289*f*
  sonographic evaluation of, 277–282, 281*b*, 282*f*
Acute cortical necrosis (ACN), 370, 372*f*, 1795–1796
Acute interstitial nephritis, 370
Acute kidney injury (AKI), 1795–1796, 1796*b*, 1797*f*
Acute pancreatitis, microlithiasis and, 221
Acute suppurative thyroiditis, 723–724
Acute tubular necrosis (ATN), 370
  acute kidney injury and, 1795–1796, 1797*f*
  renal transplantation complication with, 649–651, 653*f*, 1809
Addisonian crisis, 426–427
Adduction, Barlow test with, in dynamic examination
  in coronal/flexion view, 1927
  in transverse/flexion view, 1927
Adenitis, mesenteric
  pediatric, 1858–1860, 1862*f*
  right lower quadrant pain in acute abdomen from, 288
Adenocarcinoma(s). *See also* Pancreas, carcinoma of
  of bladder, 348
  colorectal, 261–264, 263*f*–264*f*
  gastrointestinal, 261–264, 263*f*–264*f*
  genitourinary, 348
  pancreatic, 172*f*
  pancreatic ductal, 236–238
  prostate, 395
  of renal pelvis, 348
  urachal, 355
  of ureter, 348
Adenoid cystic carcinoma, salivary gland, pediatric, 1638
Adenolymphomas, pediatric, parotid gland, 1638
Adenoma(s)
  adrenal, 418–420, 418*b*
    in Conn syndrome, 419
    in Cushing disease and Cushing syndrome, 419
    functioning, 419
    imaging considerations for, 418–420, 419*f*
Adenoma(s) *(Continued)*
    nonfunctioning, 419
    percutaneous needle biopsy of, 607
  benign follicular, 697
  bleeding and, 117, 118*f*
  CEUS for diagnosis of, 116–117, 117*f*
  FNH differentiated from, 116–117
  of gallbladder, 203–204, 205*f*
  in GSD, 1740*f*
  of liver, 115–117, 116*f*–118*f*
    inborn errors of metabolism and, pediatric, 1738
    pediatric, 1746
  malignum, 544
  parathyroid
    carcinomas differentiated from, 735–736, 738*f*
    carotid sheath/undescended, 740, 742*f*
    combined modalities for accuracy with, 748
    compression for detection of, 739
    CT accuracy for, 748, 748*f*
    echogenicity of, 735, 736*f*
    ectopic locations of, 739–741
    false-negative examination for, 745*b*, 746
    false-positive examination for, 745–746, 745*b*
    fine-needle aspiration biopsy accuracy for, 746
    hypoechoic, 735
    imaging accuracy with, 746–749
    inferior, 738–739, 739*f*
    internal architecture of, 735, 736*f*
    intrathyroid, 740, 742*f*
    localization of, 736–741
    mediastinal, 740, 741*f*, 748
    MRI accuracy in, 748, 749*f*
    multiple gland disease in, 735, 738*f*
    pediatric, 1650, 1650*f*
    percutaneous needle biopsy of, 750–751, 753*f*
    pitfalls in examination of, 745–746, 745*b*
    retrotracheal/retroesophageal, 739–740, 740*f*
    scintigraphy accuracy for, 747, 747*f*
    shape of, 735, 735*f*
    size of, 735, 737*f*
    sonographic appearance of, 735–736
    sonographic examination and typical locations in, 736–739, 739*f*
    superior, 738–739, 739*f*
    surgical removal of, 749, 750*f*
    ultrasound accuracy for, 746–747, 748*f*
    vascularity of, 735, 737*f*
  pleomorphic, salivary gland, pediatric, 1636–1638, 1638*f*
  primary hyperparathyroidism caused by, 734, 734*b*
  thyroid
    follicular, pediatric, 1646–1648, 1647*f*
    nodular disease and, 697, 700*f*
Adenomatoid tumor(s)
  paratesticular, 1904
  scrotal, 840, 840*f*
Adenomyomas, of gallbladder, 202–204, 204*f*–205*f*
Adenomyomatosis, gallbladder, 202, 203*f*–205*f*
Adenomyosis, 540–541, 540*b*, 542*f*
Adenovirus infection, fetal, hydrops from, 1431–1432
Adhesions, endometrial, 551, 552*f*
ADI. *See* Agent detection imaging
Adnexa. *See also* Fallopian tube(s); Ovary(ies); Round ligament(s)
  anatomy of, 564–570, 565*f*
  cysts of, in pregnancy, 1020
  mass of, ectopic pregnancy and, 1072, 1073*f*
  mass of, pediatric, in ectopic pregnancy, 1884–1885, 1898*f*
  pediatric, torsion of, 1875–1876
  sonography for, 564
    technique for, 566
  torsion of, 576–578, 577*f*

Adnexa *(Continued)*
transvaginal ultrasound for assessment of, 566
vascular abnormalities in, 589–590
ovarian vein thrombosis and thrombophlebitis as, 589–590, 589*f*
pelvic congestion syndrome as, 590, 590*f*
vascularity of, 565–566, 565*f*
ADPKD. *See* Autosomal dominant polycystic kidney disease
Adrenal ablation, 428
Adrenal cortex
carcinoma of, 424–425, 426*f*
functions of, 417
Adrenal gland(s)
anatomy of, 416–417, 417*f*
benign neoplasms of, 418–424
adenomas as, 418–420, 418*b*, 419*f*, 607
cysts as, 421–422, 422*b*, 423*f*
hemorrhage as, 422–424, 424*f*
management of, 428
myelolipomas as, 420–421, 420*b*, 420*f*
pheochromocytomas as, 421, 422*f*
rare, 427–428
calcification of, 423, 425*f*
causes of, 424*b*
cysts of, 421–422, 422*b*, 423*f*
fetal
congenital hyperplasia of, genitalia in, 1367–1368
masses in, 1353–1354, 1353*f*, 1353*t*
normal, 1353, 1353*f*
hemorrhage in, 422–424, 424*f*
after liver transplantation, 638, 645*f*
histoplasmosis of, 423
hypertrophy of, 416–417
immunosuppression and, 423
infectious diseases of, 423–424, 425*f*
interventions for neoplasms of, 428–429
endoscopic ultrasound for, 428–429, 429*f*
intraoperative ultrasound for, 429
ultrasound-guided biopsy for, 428, 429*f*
left, 416–417, 417*f*
multiplanar scanning of, 418
malignant neoplasms of, 424–427
adrenocortical carcinomas as, 424–425, 426*f*
lymphomas as, 426–427, 427*f*
management of, 428
metastases as, 425–426, 426*f*–427*f*
rare, 427–428
pediatric
adrenocortical neoplasms of, 1827, 1827*f*
carcinoma of, 1827, 1827*f*
congenital hyperplasia of, 1822–1824, 1824*f*, 1900–1901
hemorrhage into, neonatal, 1824–1825, 1825*f*
measurements of, in neonates, 1820–1821, 1823*t*
neuroblastoma and, 1825–1826, 1826*f*
normal anatomy of, 1820–1822, 1824*f*
pheochromocytoma and, 1826–1827, 1827*f*
sonography of, 1820–1827
percutaneous needle biopsy of, 606–607, 608*f*
physiology of, 416–417, 417*f*
right, 416–417, 417*f*
multiplanar scanning of, 417–418, 418*f*
sonographic imaging and technique for, 417–418, 418*f*
tuberculosis of, 423
Adrenal insufficiency, 426–427
Adrenal medulla, functions of, 417
Adrenal rests, testicular, 832–833, 833*f*, 1824
pediatric, 1900–1901
Adrenarche, pseudoprecocious puberty and, 1888
Adrenocortical neoplasms, pediatric, 1827, 1827*f*
Adson maneuver, 976–977
Afferent loop obstruction, mechanical bowel and, 293
AFI. *See* Amniotic fluid index
Age. *See* Gestational age; Maternal age
Age, pediatric
kidney length and
comparison of, 1776–1778, 1777*f*
reference values for, 1776–1778, 1778*t*
with single functioning kidney, 1779*t*
kidney volume according to
reference values for, 1776–1778, 1778*t*
with single functioning kidney, 1779*t*
Agent detection imaging (ADI), 66
Agnathia, 1154, 1159*f*
Agyria, in lissencephaly, 1195
Aicardi syndrome
choroid plexus papillomas in, 1209
corpus callosum agenesis and, 1526–1528
AIDS. *See* Acquired immunodeficiency syndrome
AIDS cholangitis, 181
Air bronchograms, sonographic
in atelectatic lung, 1714, 1716*f*
in consolidated lung, 1711, 1714*f*–1715*f*
pneumonia and, 1702, 1703*f*, 1708*f*
round, 1712, 1715*f*
Air bubbles, encapsulated, as blood pool contrast agents, 55–56, 55*t*
AIUM. *See* American Institute of Ultrasound in Medicine
AKI. *See* Acute kidney injury
Alagille syndrome, pediatric, 1737
ALARA, 31, 1041–1042
Albunex, 55–56
Aldosterone, secretion of, 417
Aliasing
in color Doppler ultrasound, 28, 29*f*, 966
high-velocity jets and, 933
in Doppler ultrasound, 29*b*, 32*f*
in pediatric abdominal vessel imaging, 1749
in pulsed Doppler ultrasound, 939, 939*f*
in renal artery duplex Doppler sonography, 449
Alkaline-encrusted pyelitis, 324–325
Allantois, 1059, 1337*f*, 1338
Allergy, milk, gastric mucosa thickening and, 1839–1840
Allograft nephropathy, chronic, 1810, 1812*f*
Alloimmune arteritis, after pancreas transplantation, 677
Alloimmune thrombocytopenia, intracranial hemorrhage and, 1206
Alpha angle, in hip joint classification, 1924, 1924*f*–1925*f*
Alpha-fetoprotein, maternal serum, 1117
elevated, causes of, 1226, 1226*b*, 1228
fetal abdominal wall defects and, 1322
gestational age compared to levels of, 1227*f*
spina bifida screening and, 1221, 1226–1228, 1226*b*, 1227*f*
17-alpha hydroxy-progesterone caproate (17α-OHPC), vaginal progesterone compared to, 1507
Alport syndrome, CKD and, 1796–1798
Alternating current, 8
Ambient cistern, fetal, normal sonographic appearance of, 1168
Amebiasis, hepatic, 87–88, 89*f*
in children, 1747–1748
Amebic liver abscesses, 613
Amelia, definition of, 1399
Amenorrhea, primary, causes of, 1887
American College of Obstetricians and Gynecologists (ACOG), 1107
American Institute of Ultrasound in Medicine (AIUM), 1041
on bioeffects
of diagnostic ultrasound with gas body contrast agents, 43, 44*b*
in gas bodies, 45–46, 46*b*
safety statements of, general, 47, 47*b*
thermal, 40, 40*b*–41*b*
Thermal Index Working Group of, 38–40
Amniocentesis
diagnostic, in NTD screening, 1228
genetic, 1108–1109, 1108*f*
in multifetal pregnancy, 1125–1126
therapeutic, in fetal hydrops, 1436
Amnion
chorion separation from, 1469, 1469*f*
early pregnancy failure and size of, 1066, 1067*f*–1068*f*
normal sonographic appearance of, 1057, 1059*f*–1060*f*
unfused, 1057
Amnion inclusion cyst, 1061
Amnionicity, in multifetal pregnancy, 1057, 1058*f*, 1115–1116, 1116*f*
sonographic determination of, 1117, 1119*t*
triplets and, 1122*f*
Amniotic band sequence
amputations caused by, 1401, 1403*f*
anencephaly differentiated from, 1179
fetal brain and, 1180*f*, 1182–1183
terminal transverse limb defects and, 1400
Amniotic band syndrome, 1057
facial clefts in, 1152–1153
fetal abdominal wall and, 1330, 1330*f*
Amniotic bands
circumvallate placenta confused with, 1479–1480
constrictive, 1182–1183
Amniotic cavity, formation of, 1051, 1052*f*
Amniotic fluid
assessment of, 1339*b*
volume of, 1339–1340
Amniotic fluid index (AFI), 1339
method for obtaining, 1340
values for, in normal pregnancy, 1341*t*
A-mode ultrasound, 9
Amplitude
evaluation of, power Doppler in, 935
modulation imaging, 64, 65*f*
Ampulla, 565
Amputations, from amniotic band sequence, 1401, 1403*f*
Amyand hernias, 472–473, 473*f*
Amyloidosis, renal failure in, 372
Anabolic steroid therapy, hepatic adenomas and, 1746
Anal atresia, 1311
Anal canal, endosonography of, 302–307, 304*f*–307*f*, 306*b*
Anal dimple, 1311–1312, 1311*f*
fetal cloacal exstrophy and, 1328
Analgesia, TRUS-guided biopsy and, 407
Anaplastic carcinoma, of thyroid gland, 707–708, 708*b*, 709*f*
Anasarca, fetal, in hydrops, 1417, 1420*f*
Anastomotic pseudoaneurysms, 438
Anastomotic strictures, bladder augmentation and, 1912–1913
Anderson-Carr-Randall theory of stone progression, 339, 1798–1799
Androblastoma, 585
Androgens, secretion of, 417
Anechoic cysts, 331

Anemia
  fetal, hydrops from, 1431
  pediatric, Fanconi, 1746
Anencephaly, 1218
  CDH and, 1263
  detection of, early, 1018–1019, 1019*f*
  embryonic, 1077
  in fetal brain, 1179, 1180*f*
  temperature increase in utero and, 1037
  thickened NT and, 1096*f*
Anesthetics
  local, for pediatric interventional sonography, 1951, 1952*f*
  for musculoskeletal injections, 901
Aneuploidy. *See also* Trisomy 21
  background risk for, 1088, 1089*f*
  definition of, 1088
  fetal echogenic bowel and, 1315–1316, 1315*f*
  fetal gastroschisis and, 1324–1325
  fetal liver calcifications and, 1316–1318
  hand and foot abnormalities in, 1404, 1406*f*
  identification of, fluorescent in situ hybridization in, 1433–1434
  pyelectasis as marker for, 1355
  risk of, NT in assessing for, 1018–1019, 1019*f*, 1049
  screening for, first-trimester, 1089–1097
    with cell-free DNA, 1107
    combined, 1090–1091
    contingent, 1091
    cystic hygroma in, 1093, 1093*f*
    integrated, 1091
    in multifetal pregnancy, 1091
    nasal bone in, 1093–1095, 1094*b*, 1094*f*
    NT in trisomy 13 and 18, 1093
    NT in trisomy 21 and, 1089, 1090*f*
    NT measurement technique and, 1091–1093, 1092*b*
    reversed flow in ductus venosus in, 1095, 1095*f*
    sequential, 1091
    serum biochemical markers in, 1089–1090
    thickened NT in congenital heart defects and, 1095–1097, 1096*f*
    tricuspid regurgitation in, 1095
  skeletal findings with, 1407–1409
Aneurysm(s). *See also* Abdominal aortic aneurysm
  abdominal aortic, 433–439
  atrial septal, 1295
  in AVF for hemodialysis, 1003, 1005*f*
  carotid flow disturbances in, 928
  common carotid artery, 947–948
  hepatic artery, after liver transplantation, 1768, 1769*f*–1770*f*
  of peripheral arteries
    lower extremity, 971–972, 972*f*
    upper extremity, 976
  portal vein, 103–104
    after liver transplantation, 1768, 1769*f*–1770*f*
  renal artery, 369, 369*f*, 451
  in synthetic arteriovenous graft for hemodialysis, 1003
  umbilical artery, 1483
  vein of Galen, 1204, 1206*f*
    arachnoid cysts differentiated from, 1192–1193
    cavum veli interpositi cysts differentiated from, 1170
    in neonatal/infant brain, duplex Doppler sonography of, 1583–1584, 1585*f*–1586*f*
  ventricular, congenital, 1294
Angiogenesis, in yolk sac wall, 1057
Angiography, in carotid stenosis diagnosis, 916
Angiomas, littoral cell, splenic, 153–156, 156*f*
Angiomyolipomas
  of liver, 117–118, 119*f*
  renal, 351–352, 351*f*–352*f*
    pediatric, 1820, 1822*f*
Angiosarcoma
  hepatic, 123
  splenic lesions in, 153, 155*f*
Angle of incidence, 5
Angle of insonation, 4
Angle of refraction, 5
Angle theta
  consistent, in carotid spectral analysis, 926–927
  Doppler
    definition of, 926
    measurement of, 926–927, 926*f*
  increasing, to overcome aliasing, 939
Angular margins, in breast sonography, 788–789, 790*f*
Aniridia, sporadic, Wilms tumor screening with, 1818
Anisospondyly, in dyssegmental dysplasia, 1399
Anisotropic effect, in HPS sonography, 1838, 1838*b*, 1839*f*
Anisotropic effect artifact, 1517
Anisotropy
  shoulder ultrasound and, 895, 895*f*
  tendon, 859, 860*f*, 899
Ankle, injection of, 901
  superficial peritendinous and periarticular, 902–904, 903*f*–904*f*
Annular constricting lesions, 261–264, 263*f*
Annular pancreas, fetal, 1320, 1321*f*
Anomalous pulmonary venous return (APVR), 1280, 1282*f*, 1290, 1291*f*
  total compared to partial, 1290
Anophthalmia, 1140, 1145*f*
Anorchidism, 1890
Anorectal malformations, fetal, 1310–1312, 1311*f*
Anterior cerebral artery (ACA)
  of infant, RI in, 1576, 1577*t*
  of infant, RI in, fontanelle compression in hydrocephalus and, 1582, 1584*f*
  stenosis of, SCD and, 1607*f*
  TCD sonography for collateral flow in, 1610, 1611*f*
  as transtemporal approach landmark, 1592, 1593*f*–1594*f*
Antibiotic prophylaxis, TRUS-guided biopsy and, 407, 408*f*
Antibiotics, for pediatric interventional sonography, 1951
Anticoagulants, deficiency of physiologic, dural sinus thrombosis from, 1205–1206
Antley-Bixler syndrome, craniosynostosis in, 1136–1138
Antral dyskinesia, 1836–1838
Antral foveolar hyperplasia, prostaglandin-induced, 1839–1840
Antral web, pediatric, 1839, 1840*f*
Anus
  ectopic, pediatric, 1847–1848, 1850*f*
  imperforate, 1310–1311
    block vertebrae with, 1689, 1692*f*
    high, pediatric, risk of spinal dysraphism with, 1689
    pediatric, 1847–1848, 1850*f*
Aorta
  coarctation of, 1291, 1292*f*
    fetal, hydrops from, 1423–1424
    hypoplastic left heart syndrome with, 1287
  fetal, continuity of, 1278*f*
  small, in Turner syndrome, 1106*f*, 1107
Aortic arch
  fetal, 1275, 1279*f*
  pediatric, cervical, 1658
Aortic balloon pump, carotid flow waveforms and, 936–937, 936*f*
Aortic coarctation, renal artery stenosis and, 447, 449*f*
Aortic root, fetal, diameter of, 1277*f*
Aortic stenosis, 1292
  carotid flow waveforms and, 936–937
  fetal, hydrops from, 1423–1424
Aortic valve, lesions of, carotid flow waveforms and, 936–937
Aortoenteric fistulas, 438
Apert syndrome
  craniosynostosis in, 1136–1138
  midface hypoplasia in, 1148
Aplasia
  pulmonary, 1245–1246
  of thyroid gland, 694, 694*f*
Apnea, sleep, pediatric TCD sonography for, 1611
Aponeurosis, torn, in spigelian hernia, 483–484, 487*f*
Appendices epiploicae, torsion of, 290
Appendicitis
  acute
    clinical misdiagnosis of, 283–285
    pathophysiology of, 283
    right lower quadrant pain from, 282–285
    sonographic diagnosis of, 283, 283*b*
    symptoms of, 283
    transvaginal ultrasound for diagnosis of, 283, 285*f*
  Crohn, 285, 287*f*
  focally inflamed fat in, 521
  pediatric, 1855–1860
    acute, 1857, 1859*f*
    Meckel diverticulum resembling, 1858–1860, 1862*f*
    normal appearance of, 1857, 1858*f*
    perforated, 1857, 1857*b*, 1861*f*
    sonographic signs of, 1857*b*
Appendicolith, 283
Appendix. *See also* Appendicitis
  inflammation of, 282–285
  mucocele of, 299, 299*f*
  pediatric
    abscess of, 1871*f*, 1877
    abscess of, drainage of, 1956, 1960*f*
    gangrenous, 1857, 1861*f*
    normal, 1857, 1858*f*
  perforations of, 283–285, 285*b*, 286*f*
Appendix epididymis, pediatric, 1897, 1897*f*
Appendix testis, 820–821, 820*f*
  pediatric, 1897
"Apple peel" jejunal atresia, 1310
Aprosencephaly, 1186
APVR. *See* Anomalous pulmonary venous return
Aqueduct of Sylvius
  in rhombencephalosynapsis, 1192
  stenosis of
    obstructive hydrocephalus from, 1538, 1540*f*
    VM and, 1177, 1177*f*
Arachnoid cyst(s)
  cavum veli interpositi cysts differentiated from, 1170
  corpus callosum agenesis and, 1526–1528
  fetal brain and, 1192–1193, 1193*f*
  of neonatal/infant brain, 1563–1565, 1565*b*
  spinal canal and, pediatric, 1695–1697, 1696*f*
Arachnoid granulations, 1177
Arcuate arteries, calcifications of, 531–532, 533*f*
Arcuate uterus, 534, 536–538, 536*f*–537*f*
Area cerebrovasculosa, in anencephaly, 1179
Area membranacea, 1189
Areflexia, detrusor, 372–374, 373*f*
ARFI. *See* Acoustic radiation force imaging
ARPKD. *See* Autosomal recessive polycystic kidney disease

Arrays, transducer, 11–12
Arrhenoblastoma, 585
  pediatric, 1880
Arrhythmia(s)
  early pregnancy loss and, 1069
  Ebstein anomaly with, 1286
  fetal heart, 1295–1297
    bradycardia as, 1297, 1297*f*
    CHD and, 1270–1273
    congenital heart block as, 1297, 1297*f*
    hydrops from, 1424, 1425*f*
    PACs and PVCs as, 1295–1296
    tachycardia as, 1296–1297, 1296*f*
Arsenic, 123
Arterial venous (AV) anastomoses, 1125, 1125*f*
Arterial/arterial (AA) anastomoses, 1125, 1125*f*
Arteriomegaly, 440
Arteriovenous fistulas (AVFs)
  arteries supplying, spectral broadening in, 927–928
  of common femoral artery, 974*f*
  dural, TCD sonography assessing, 1614
  hemodialysis and
    aneurysms near, 1003, 1005*f*
    arm and leg swelling with, 1006, 1009*f*
    hematomas near, 1002–1003, 1005*f*
    maturation of, evaluating, 1003
    occlusion of, 1006
    palpable focal masses near, 1002–1003
    placement of, 996, 997*f*
    pseudoaneurysms near, 1003, 1005*f*
    stenoses associated with, 1003–1006, 1007*f*–1008*f*
    ultrasound evaluation of, 1000–1006, 1002*f*–1003*f*
  of lower extremity peripheral arteries, 973–974, 974*f*
  after pancreas transplantation, 678, 680*f*
  pediatric, of neck, 1658
  renal, 366–367
    percutaneous needle biopsy of, 606, 607*f*
  renal biopsies and, Doppler assessment of, 1809, 1810*f*
  traumatic, 973
Arteriovenous graft, synthetic, hemodialysis and
  arm and leg swelling with, 1006, 1009*f*
  hematomas near, 1002–1003
  occlusion of, 1006, 1010*f*
  palpable focal masses near, 1002–1003
  placement of, 996, 997*f*
  ultrasound evaluation of, 1002, 1004*f*
Arteriovenous malformations (AVMs)
  arteries supplying, spectral broadening in, 927–928
  cerebral, pediatric, TCD sonography detecting, 1614, 1615*f*
  fetal hydrops from, 1430–1431
  of lower extremity peripheral arteries, 973
  pediatric, of neck, 1657–1658, 1659*f*
  pial, 1204–1205
  postpartum recognition of, 556, 556*f*
  renal, 366–367, 367*f*
    renal transplantation complications from, 661–664, 667*f*–670*f*
    twinkling artifacts mimicking, 662–664, 668*f*
Arteriovenous shunting, in fetal sacrococcygeal teratoma, 1238–1239
Arteritis
  alloimmune, after pancreas transplantation, 677
  of common carotid artery, 944–946, 947*f*
  Takayasu, aortic stenosis in, 444
Artery(ies). *See specific arteries*
Arthritis
  osteoarthritis, 869, 869*f*
    acromioclavicular joint, 893, 894*f*
Arthritis *(Continued)*
  psoriatic, of hand and wrist, injections for, 904
  rheumatoid, 866
    erosive, 867, 868*f*
    gout and, 867–869, 868*f*
    of hand and wrist, injections for, 904
    joint effusion in, 867, 867*f*
  septic, pediatric, 1936, 1937*f*
Arthrogryposis multiplex congenita
  elbow and knee dislocation and, 1933–1934
  findings in, 1382
  as limb reduction defect, 1401–1404, 1405*f*
  teratologic hip dislocation and, 1932
Arthropathy
  inflammatory, 866
    shoulder and, 893–894, 894*f*
  shoulder and, 893–894
    degenerative, 893, 894*f*
    inflammatory, 893–894, 894*f*
Articular-sided rotator cuff tears, 888, 890*f*
Artifacts
  anisotropic effect, 1517
  blooming, 60–61
  comet-tail, 202, 695
    in benign and malignant thyroid nodule differentiation, 712–713
    in degenerative cysts of thyroid, 1646, 1647*f*
  Doppler ultrasound sources of, 29*b*
  empty stomach, 1838, 1839*f*
  enhancement as, 21, 22*f*
  flash, 60–61
  loss of information from, 19–21
  misregistration, 3*f*, 420–421
  multipath, 19–21, 21*f*
  propagation velocity, 3, 3*f*, 420–421
  refraction, 5, 6*f*
  reverberation, 19, 20*f*
    posterior, liver abscess and, 85–86, 87*f*
  ring-down, 266, 266*f*
  shadowing as, 19–21, 22*f*
  side lobe, 19, 20*f*
  tangential imaging, of pyloric muscle, 1834–1835, 1836*f*
  TGC settings and, 19–21
  thump, 60
  tissue vibration, 973–974, 974*f*
  twinkling
    bezoars and, 1840
    mimicking AVMs after renal transplantation, 662–664, 668*f*
    renal calculi indicated by, 336, 337*f*
Ascariasis
  biliary, 181
  intestinal, pediatric, 1853, 1853*f*
Ascites
  chylous, 508
  exudate, 506–507
  fetal
    cloacal exstrophy and, 1328
    in hydrops, 1413, 1415*f*–1416*f*, 1435, 1436*f*
    meconium peritonitis and massive, 1418–1419, 1421*f*
    parvovirus infection and massive, 1418–1419
    urinary, from bladder rupture in posterior urethral valves, 1361, 1361*f*
  from gastrointestinal tract metastases, 266, 267*f*
  meconium peritonitis and, 1313
  particulate, 507
  pediatric, pleural fluid differentiated from, 1709
  peritoneum and, 506–508, 507*f*–509*f*
  small bowel mesentery assessment with, 505, 505*f*
  transudate, 506–507
ASD. *See* Atrial septal defect
ASH. *See* Asymmetrical septal hypertrophy
Asherman syndrome, 551
Aspergillosis, neonatal chylothorax from, 1704*f*
Asphyxia
  intrauterine, near-total, acute, in diffuse cerebral edema, 1553–1554, 1555*f*
  neonatal/infant brain and, duplex Doppler sonography of, 1580
  pediatric, TCD sonography in, 1614, 1616*f*
Asphyxiating thoracic dysplasia, 1398
Asphyxiating thoracic dystrophy, 1396
  polydactyly in, 1382
Aspiration, for pyogenic liver abscesses, 1746–1747
Aspirin, 598–599
Asplenia, 159–160
  in cardiosplenic syndrome, 1292, 1293*b*
  fetal, 1320
  univentricular heart with, 1287–1288
Assisted reproductive technology, multifetal pregnancy incidence and, 1115
Astrocytomas, neonatal/infant brain and, 1562
Asymmetrical fibroglandular tissue, split-screen imaging and, 769, 769*f*
Asymmetrical septal hypertrophy (ASH), 1292, 1294–1295
Asymptomatic Carotid Atherosclerosis Study (ACAS), 916
Atelectasis, pediatric, 1714, 1716*f*
Atelencephaly, 1186
  hydranencephaly differentiated from, 1208
Atelosteogenesis, 1396
Atheromatous carotid plaques, characterization of, 919
Atherosclerosis, 432–433
  renovascular disease and, 368
Atherosclerotic disease, peripheral arterial stenosis in, 968, 976, 978*f*
Atherosclerotic disease, renal artery stenosis and, 447
Atherosclerotic plaque rupture, 919–920
Athletes, direct inguinal hernias in, 485–486
Athletic pubalgia. *See* Sports hernias
ATN. *See* Acute tubular necrosis
Atrazine, fetal gastroschisis and, 1322–1323
Atretic cephalocele, 1180
Atretic meningocele, tethered cord and, 1679
Atrial fibrillation, fetal, 1296
  hydrops from, 1424
Atrial flutter, fetal, 1296
  hydrops from, 1424
Atrial pacemaker, 1295–1296
Atrial septal aneurysm, PACs and, 1295
Atrial septal defect (ASD), 1277–1280, 1282*f*–1283*f*
  coronary sinus, 1280
  ostium primum, 1279–1280, 1282*f*–1283*f*
  ostium secundum, 1279–1280, 1282*f*
  prenatal diagnosis of, 1280
  sinus venosus, 1280, 1282*f*
  types of, 1282*f*
Atrioventricular block (AVB), 1297
Atrioventricular (A-V) canal
  defects of, 1284
  in trisomy 21, 1098*f*
Atrioventricular septal defect (AVSD), 1279, 1282*f*, 1284–1286, 1284*f*–1285*f*
  balanced compared to unbalanced, 1285
  complete compared to incomplete, 1284–1285, 1285*f*
  in trisomy 21, 1101, 1284
Atrioventricular valves, of fetal heart, 1274–1275
Atrium of lateral ventricles, neonatal/infant, in coronal imaging, 1515

Attenuation
coefficient, 36
of sound energy, 5–7, 7*f*, 35
Atypical hips, pediatric, 1932, 1933*f*
Auditory response, in obstetric sonography, 1038
Auricular hillocks, 1134
Autoimmune cholangiopathy, 182
Autoimmune cholangitis, 182
Autoimmune pancreatitis, 236, 237*f*
Autoimmune vasculitis, Henoch-Schönlein purpura and, 1853
Automated whole-breast ultrasound (ABUS), 760
Autopsy, in hydrops diagnosis, 1435
Autosomal dominant polycystic kidney disease (ADPKD), 83, 243, 361, 362*f*, 1346, 1348–1350, 1349*f*–1350*f*
pediatric, 1814–1815, 1815*f*
Autosomal recessive polycystic kidney disease (ARPKD), 359, 361*f*, 1799
pediatric, 1812–1813, 1814*f*
AV anastomoses. *See* Arterial venous anastomoses
A-V canal. *See* Atrioventricular canal
A-V canal defects, 1284
AVB. *See* Atrioventricular block
AVFs. *See* Arteriovenous fistulas
AVMs. *See* Arteriovenous malformations
AVSD. *See* Atrioventricular septal defect
Axial resolution, 16–19, 18*f*
Axillary artery, 975
Axillary vein, 990–991, 990*f*
Azimuth planes, 12*f*
Azimuth resolution, 19, 19*f*
Azoospermia, prostate and, 393
Azzopardi tumors, 824–825

B

Bacille Calmette-Guérin (BCG), 390, 390*f*
Backscatter, 3–4
CEUS increasing, 107, 111*f*
Doppler ultrasound and, 21–22, 23*f*, 35
Bacteria
pediatric infections from
cervical lymphadenopathy in, 1660–1663
parotid gland, 1632–1633, 1632*f*
thyroid, 1643–1645, 1645*f*
pyogenic, liver abscesses from, 85–86, 87*f*
pediatric, 1746–1747, 1751*f*
Bacterial epididymitis, 841, 843*f*
Baker cyst(s)
injection for, 907–909, 908*f*
ruptured, 870, 870*f*
ultrasound techniques for, 870, 870*f*
Ballottement, compression and, 768
Banana sign, in Chiari II malformation, 1183–1185, 1184*f*
spina bifida screening and, 1221, 1228, 1230–1232
Band, of frequencies, 7
Band heterotopia, 1196
Bandwidth, 7–8
Barbotage, 909
Bardet-Biedl syndrome, hyperechogenic kidneys in, 1351
Bare area
of liver, 77
sign, as pleural fluid sonographic sign, 1709, 1709*f*
Barlow test
with adduction, in dynamic examination
in coronal/flexion view, 1927
in transverse/flexion view, 1927
in determining hip stability, 1923
Basal cell nevus syndrome, 585
rhabdomyosarcoma associated with, 1908
Basal ganglia
fetal, normal sonographic appearance of, 1168
vasculopathy, neonatal/infant brain and, 1556–1557
Basilar artery, 951
Basilic vein, anatomy of, 990–991, 990*f*
Bat wing configuration, in Chiari II malformation, 1526, 1527*f*
Battledore placenta, 1484
B-cell lymphoma, AKI and, 1796
BCG. *See* Bacille Calmette-Guérin
"Beads on a string" sign, 587–588
Beam steering, 10–11, 11*f*
Beam width, 35
Beare-Stevenson syndrome, craniosynostosis in, 1136–1138
Beckwith-Wiedemann syndrome
adrenocortical neoplasms and, 1827
CDH and, 1263
fetal
hepatomegaly and, 1316
omphalocele and, 1325, 1327*f*
pancreatic cysts and, 1320
hepatoblastomas and, 1746
macroglossia in, 1153
megalencephaly associated with, 1194–1195
mesenchymal dysplasia of placenta in, 1479, 1479*f*
nesidioblastosis and, 1865
neuroblastoma with, pediatric, 1825
Wilms tumor screening with, 1818
Beemer-Langer syndrome, 1396
Behavioral changes, obstetric sonography and, 1040–1041
Bell-clapper deformity, 844, 844*f*
pediatric, 1325
Benign ductal ectasia, prostate and, 387, 388*f*
Benign follicular adenoma, 697
Benign mixed-cell tumors, 1638
Benign prostatic hyperplasia (BPH), 384, 385*f*–386*f*, 387–388
Bent-limb dysplasia, 1395
Beta angle, in hip joint classification, 1924, 1924*f*–1925*f*
β-hCG. *See* Human chorionic gonadotropin
Bezoars
of gastrointestinal tract, 300
pediatric, 1840, 1841*f*
Biceps tendon, 878–879
dislocation of, 893
injection of, 904–905, 905*f*–906*f*
long head of, 879, 880*f*–881*f*
longitudinal split tear of, 893, 894*f*
pathology of, 892–893
tenosynovitis and, 892–893, 893*f*
ultrasound evaluation of, 880, 881*f*
Bicornuate uterus, 534, 536*f*–537*f*, 538, 1881, 1881*f*
Bifid lamina, 1688
Bifid scrotum, fetal, 1367
Bilateral hernias, 1262
Bile
calcium, milk of, 194, 195*f*
flow
extrahepatic obstruction to, 1734
stasis of, stone formation and, 1741
leakage of, after liver transplantation, 627–629, 629*f*
limey, 194, 195*f*
Bile duct(s)
aberrant, 167, 168*f*
dilation of, in Caroli disease, 1736–1737, 1736*f*
drainage of, 614–615
interlobular, paucity of, jaundice from, 1737
ischemia of, from post-liver transplant hepatic artery thrombosis, 628*f*
Bile duct(s) *(Continued)*
necrosis of, post-liver transplantation, bile leaks from, 627
normal, 166–168, 166*f*
spontaneous rupture of, neonatal jaundice caused by, 1734, 1737
strictures in, after liver transplantation, 626–627, 627*f*–628*f*
Biliary atresia
extrahepatic, 1319
neonatal jaundice and, 1734–1735, 1737, 1738*f*
Biliary cirrhosis, 92–93, 182
pediatric, 1741
Biliary cystadenomas, 82, 83*f*
Biliary hamartomas, 83, 83*f*–84*f*
Biliary rhabdomyosarcoma, in pediatric liver, 1746, 1749*f*
Biliary sludge
acute pancreatitis and, 221
complicating liver transplantation, 629, 631*f*
gallbladder and, 194–195, 196*f*
Biliary system, fetal, 1318–1319
Biliary tree, 166–188. *See also* Cholangiocarcinoma
anatomy of, 166–168
ascariasis and, 181
autoimmune cholangitis and, 182
branching pattern of, 167, 167*f*
Caroli disease of, 171, 171*f*
cholangiocarcinoma and, 184–188
choledochal cysts of, 168–170, 169*f*–170*f*
choledocholithiasis in, 172–173, 182
common bile duct stones and, 173–174, 173*f*
intrahepatic, 173, 173*f*
cirrhosis and, 182
clonorchiasis and, 178–179, 179*f*
dilation of, in acute cholangitis, 176
fascioliasis and, 176–178, 177*f*–178*f*
harmonic imaging of, 168, 169*f*
hemobilia and, 174, 175*f*
HIV cholangiopathy and, 181–182, 181*f*
immune-related diseases of, 182–184
infection of, 176–182
liver flukes and, 176–179, 177*f*–179*f*
after liver transplantation
complications involving, 625–629, 1767–1768, 1769*f*–1770*f*
normal appearance of, 625
strictures in, 626–627, 627*f*–628*f*
metastases to, 188, 192*f*
Mirizzi syndrome and, 174, 174*f*
obstruction of
acute cholangitis and, 176, 177*f*
causes of, 172*b*
overview of, 171–172, 172*f*
opisthorchiasis and, 178–179
pneumobilia and, 175–176, 176*f*
primary sclerosing cholangitis and, 182, 183*f*, 184
recurrent pyogenic cholangitis and, 179–181, 180*f*
sonographic technique for, 168, 169*f*
trauma to, hemobilia from, 174, 175*f*
variants of normal, 166–168
Bilobed placenta, 1481, 1482*f*
Bilobed testis, 1891
Biloma, after liver transplantation, 638
Bioeffects. *See also* Acoustic cavitation; Thermal index
acoustic cavitation and, 40–46
AIUM on
of diagnostic ultrasound with gas body contrast agents, 43, 44*b*
in gas bodies, 45–46, 46*b*
safety statements of, general, 47, 47*b*
thermal, 40, 40*b*–41*b*

Bioeffects *(Continued)*
epidemiology of, 48
of HIFU, 31–33, 33*f*
mechanical, 32
of obstetric sonography
animal research and, 1038–1039
behavioral changes and, 1040–1041
birth weight and, 1040
childhood malignancies and, 1041
congenital malformations and, 1041
delayed speech and, 1040
Doppler ultrasound and, 1041
dwell time and, 1036
dyslexia and, 1040
human studies on, 1039–1041
instrument outputs and, 1035–1036
mechanical, 1038
neurologic development and, 1040–1041
nonright-handedness and, 1040
scanning mode and, 1035
system setup and, 1035–1036, 1035*f*–1037*f*
thermal, 1036–1038
operating modes and, 30–31
output control and, 48–50, 49*t*
output display standard and, 46–47, 46*f*
output regulation and, 34–35
physical effects of sound and, 35
thermal, 32, 35–40
AIUM summary statement on, 40, 40*b*–41*b*
bone heating and, 37, 37*f*, 37*t*
estimating, 40
hyperthermia and safety and, 38, 38*f*
mechanism of, 35
in obstetric sonography, 1036–1038
soft tissue heating and, 37–38, 37*f*
spatial focusing and, 35
temporal considerations in, 36, 36*f*
tissue type and, 36, 36*f*
ultrasound output and, regulation of, 34–35
user concerns and, 31
Biometry, second-trimester, 1021, 1023*f*
Biophysical profile (BPP), 1456–1458, 1457*f*, 1457*t*
Biopsy(ies). *See also* Transrectal ultrasound, biopsy guided by
chest wall lesion, ultrasound-guided, 1724–1725
fine-needle aspiration
parathyroid adenoma and accuracy of, 746
of thyroid gland, 709–710, 710*t*, 722
interventional sonography devices for, 1950
liver, percutaneous, 132–133
post-transplant bile leaks from, 627–629
mediastinal mass, pediatric, 1956, 1959*f*
percutaneous needle, 597–609
abscess complications with, 609, 610*f*
of adrenal gland, 606–607, 608*f*
of breast nodules, ultrasound-guided, 811–815, 813*f*–814*f*
for cervical lymph nodes, 717–718, 718*f*
color Doppler ultrasound for, 599
complications of, 608–609
computed tomography for, 599
contraindications to, 597–598
"freehand" technique for, 600, 602*f*
hemorrhage complications with, 608, 609*f*
imaging methods for, 599
indications for, 597–598
infection complications with, 609
of kidney, 605–606, 606*f*–607*f*
of liver, 603–604, 603*f*–604*f*
of lung, 607–608, 609*f*
needle selection for, 599–600
needle visualization in, 601–603, 602*f*
of pancreas, 604–605, 605*f*
of parathyroid adenomas, 750–751, 753*f*
Biopsy(ies) *(Continued)*
periprocedural antithrombotic management and, 598–599
procedure for, 600–601, 601*f*
of spleen, 607, 608*f*
for thyroid gland, 715–720, 718*f*–719*f*, 721*f*
transducer sterilization for, 600
prostate
PSA-directed, 395
ultrasound-guided, 407–411, 408*f*
renal, pediatric, Doppler assessment of, 1809, 1810*f*–1811*f*
of renal cell carcinoma staging, 343–344, 345*f*
targeted organ lesion, 1961, 1961*f*–1962*f*
ultrasound-guided
of adrenal glands, 428, 429*f*
of spleen, 161
Biparietal diameter (BPD)
corrected, in gestational age determination, 1447, 1447*t*, 1448*f*
femur length compared to, in heterozygous achondroplasia, 1398, 1398*f*
in gestational age determination, 1446, 1447*f*
long-bone lengths and, at different menstrual ages, 1379*t*
nasal bones in trisomy 21 and, 1099–1100
in second-trimester, 1023*f*
BI-RADS. *See* Breast Imaging Reporting and Data System
Birth, preterm. *See* Preterm birth
Birth weight
discordance, in multifetal pregnancy, 1123
obstetric sonography and, 1040
Birt-Hogg-Dubé, hereditary oncocytosis, 348–350
Bladder. *See also* Cystitis
adenocarcinoma of, 348
agenesis of, 322
anatomy of, 314
calculi in, 338–339, 339*f*
pediatric, 1908
carcinomas of
squamous cell, 348
transitional cell, 347–348, 350*f*
cavernous hemangiomas of, 356
development of, 311, 312*f*
congenital anomalies related to, 322
diverticula, 374, 374*f*
identification of, 592
drainage to, in pancreas transplantation, 668–672, 675*f*
duplication of, 322
endometriosis of, 372, 372*f*
exstrophy of, 322
fetal, 1339, 1340*f*
cloacal exstrophy and inability to visualize, 1328
exstrophy of, 1365–1366, 1366*f*
maximum volume of, 1339
nonvisualized, 1365, 1365*b*
routine sonographic view of, 1026*f*
rupture of, from posterior urethral valves, 1361, 1361*f*
fistulas of, 334, 335*f*
function of, in spina bifida, 1233
leiomyomas of, 356
leiomyosarcoma of, 356
lymphomas of, 353, 354*f*
malacoplakia and, 333, 333*f*
mesenchymal tumors of, 356
metastases to, 354–355, 355*f*
neck of, 314
neurofibromas of, 356
neurogenic, 372–374, 373*f*
Bladder *(Continued)*
pediatric
augmentation of, 1912–1913, 1913*f*
calculi in, 1908
dysfunctional, 1907–1908
neurogenic, 1907–1908
postoperative, 1912–1913, 1913*f*
spontaneous rupture of, 1912
pheochromocytomas of, 356
rare tumors of, 356
rhabdomyosarcomas of, 356
schistosomiasis of, 331, 331*f*
sonographic technique for, 314–315
trauma to, 366
urachal anomalies of, 322, 323*f*
wall of
causes of thickening of, 333*b*
interstitial cystitis and thickening of, 372, 373*f*
prune belly syndrome and thin walled, 1361–1362
Bladder, pediatric. *See also* Urinary tract, pediatric
exstrophy of, hydronephrosis and, 1791, 1791*f*
neurogenic, pediatric hydronephrosis and, 1788
normal anatomy of, 1783, 1783*f*
outlet of, obstruction of, pediatric hydronephrosis and, 1788, 1789*f*–1790*f*
postvoid scanning of, 1872
rhabdomyosarcoma of, 1820, 1823*f*
tumors of, 1820, 1823*f*
pediatric hydronephrosis and, 1788
volume of
determination of, 1778, 1780*f*
shape and correction coefficient for, 1780*t*
wall thickness of, determination of, 1778–1781, 1780*f*
Bladder exstrophy, fetal, 1326, 1328*f*
Bladder flap hematomas, cesarean sections and, 556–557, 557*f*
Bladder outlet obstruction, pediatric
causes of, 1905–1906, 1905*b*
epididymitis and, 1897
Blake pouch
cerebellum and, 1189
cyst of
arachnoid cysts differentiated from, 1192–1193
sonographic appearance of, 1170, 1173*f*
Dandy-Walker malformation differentiated from, 1190
formation of, 1167
Blastocyst, 1049
Blastocyte stage, 1051, 1051*f*
Bleeding
adenoma and, 117, 118*f*
endometrial abnormalities with, 544, 544*b*
postmenopausal bleeding as, 545–546
intraamniotic, fetal echogenic bowel and, 1316
in placenta previa, 1469
uterine postpartum findings with, 554
vaginal, hydatidiform molar pregnancy and, 1078
Block vertebrae
imperforate anus with, 1689, 1692*f*
in scoliosis and kyphosis, 1235
Blood
autologous, intratendinous injection of, 909–910, 912*f*
fetal, sampling of
in hydrops diagnosis, 1434–1435, 1435*f*
in immune hydrops, 1421
incompatible, immune hydrops from, 1419–1421

Blood flow. *See also* Cerebral blood flow, neonatal/infant
in carotid arteries
internal, residual string of, detection of, 939, 940*f*
normal transient reversal of, 933–934
patterns of, altered, misinterpretation of, 927, 928*f*
patterns of, high-velocity, in stenoses, 928–932, 929*f*–931*f*, 931*t*
pseudostring of, on power Doppler, 935
residual string of, in occlusion, detection of, 935
in MCA, PSV and, 1421–1423, 1421*b*, 1422*t*
reversed, in ductus venosus, in aneuploidy screening, 1095, 1095*f*
trophoblastic, 1083
venous
absence of, in DVT, 992–994
slow moving, without DVT, 984, 988*f*
Blood pool contrast agents, 55–56
encapsulated air bubbles as, 55–56, 55*t*
free gas bubbles as, 55
second-generation, 56
selective uptake, 56, 57*f*
Blood vessels. *See also* Carotid artery(ies); Internal jugular vein; Vascular malformations; Vertebral artery
adrenal, 416–417, 417*f*
cerebral
extracranial, 917*f*
IJV as, 955–956
malformations of, TCD sonography in, 1614, 1615*f*
vertebral artery as, 950–955
chest, pediatric, 1716–1723, 1721*f*–1724*f*
of fetal brain, malformations of, 1204–1208, 1206*f*
hepatic, abnormalities in, 96–104
patency of, after liver transplantation, 625
renal
aberrant, 321–322
Doppler ultrasound of, 366
stenosis of, high-grade, waveforms in, 938
Blood-testis barrier, 827
Blooming artifacts, 60–61
"Blue dot" sign, 846
Blue rubber bleb nevus syndrome, in venous malformations of neck, 1657
Blue-dot sign, 1897
B-mode ultrasound, real-time, gray-scale, 9–10, 10*f*
Bochdalek hernia, 1258
Body stalk anomaly, fetal, 1329
Bone marrow transplantation, for SCD, 1598
Bone(s)
heating of, 37, 37*f*, 37*t*
shear waves created in, 39
thermal index for, in late, 1039
wormian, 1139, 1139*b*, 1139*f*
Bone(s), fetal
appearance of, abnormal, sonographic evaluation for, 1381–1382
long
abnormal length of, sonographic evaluation for, 1380–1384, 1381*b*, 1382*f*–1384*f*
bowing of, 1381–1382
BPD and, at different menstrual ages, 1379*t*
sonographic assessment of, 1387*b*–1388*b*
Bone Thermal Index (TIB), 39
Bony septum, in spinal cord in diastematomyelia, 1234–1235, 1236*f*
Boomerang dysplasia, 1396
Borderline tumors, ovarian, 580*f*, 581
Bosniak classification, malignant potential of renal cysts and, 359
Bossing, frontal, in skeletal dysplasias, 1382
"Bovine arch" configuration, 916
Bowel. *See also* Echogenic bowel; Mechanical bowel obstruction; Small bowel
dilated, fetal, 1313
dilated loops of, 1310, 1311*f*
fetal gastroschisis and, 1323–1324
echogenic
fetal, 1310, 1313–1316, 1315*f*
in trisomy 21, 1100*f*, 1101
fetal, obstruction of, cloacal malformation and, 1363
function of, in spina bifida, 1233
ischemic disease of, 297
neoplasms of, 592
obstruction of mechanical, 293
pediatric
interventional sonography and anatomy of, 1950
necrosis of, with perforation, in NEC, 1854–1855
TRUS-guided biopsy and preparation of, 407
Bowing
of femur, osteogenesis imperfecta type I and, 1380*f*
of fetal long bones, 1381–1382
BPD. *See* Biparietal diameter
BPH. *See* Benign prostatic hyperplasia
BPP. *See* Biophysical profile
BPS. *See* Bronchopulmonary sequestration
Brachial artery, 975
high, bifurcation of, 975–976, 976*f*, 998, 999*f*
Brachial plexus injury, pediatric, 1934–1936, 1936*f*–1937*f*
Brachial vein
anatomy of, 990–991, 990*f*
DVT and
chronic, 994–995, 996*f*
nonocclusive, 994*f*
Brachiocephalic artery, 916, 975
Brachiocephalic vein
anatomy of, 990–991, 990*f*
ultrasound examination of, 992*f*
Brachmann-de Lange syndrome, CDH and, 1263
Brachycephaly, 1136, 1137*f*
Brachydactyly, fetal, 1407, 1408*f*
Brachytherapy, for prostate cancer, TRUS-guided, 401, 402*f*
Bradycardia
carotid flow waveforms and, 936–937
embryonic, 1068–1069, 1068*f*
fetal, 1297, 1297*f*
hydrops from, 1423–1424
sinus, 1297
Brain, fetal. *See also* Ventriculomegaly
abnormalities of, 1179
acrania and, 1179
Blake pouch cyst of, 1170, 1173*f*
cavum veli interpositi of, 1170–1174, 1174*f*
choroid plexus cysts of, 1170, 1173*f*
cortical development malformations and, 1193–1203
absence of septi pellucidi as, 1201–1203
cerebrohepatorenal syndrome as, 1196
chondrodysplasia punctata as, 1196
classification of, 1194*b*
corpus callosum agenesis/dysgenesis as, 1199–1201, 1202*f*, 1203*b*
focal changes in, 1196
hemimegalencephaly as, 1195
heterotopia as, 1196, 1199*f*
intracranial calcifications as, 1195*f*, 1203, 1204*f*
lissencephaly as, 1195–1196, 1196*f*–1197*f*
macrocephaly as, 1194–1195
megalencephaly as, 1194–1195
microcephaly as, 1194, 1195*f*
Brain, fetal *(Continued)*
polymicrogyria as, 1196, 1198*f*
schizencephaly as, 1196, 1199*f*
SOD as, 1201–1203, 1203*f*
TSC and, 1198, 1200*f*
development of, stages of, 1525*b*, 1525*f*
developmental anatomy of, 1167–1174, 1167*t*
dorsal induction errors and, 1179–1186
amniotic band sequence as, 1180*f*, 1182–1183
anencephaly as, 1179, 1180*f*
cephalocele as, 1179–1182
ciliopathies as, 1182
cranial changes in spina bifida as, 1183–1186, 1184*f*–1185*f*, 1185*t*–1186*t*
encephalocele as, 1179–1182, 1181*f*, 1182*t*
exencephaly as, 1179
Joubert syndrome as, 1182
limb-body wall complex as, 1182–1183
Meckel-Gruber syndrome as, 1182
embryology of, 1167, 1167*t*
hydrocephalus and, 1174–1178
infections of, 1203–1204, 1205*f*
MRI evaluation of, 1166–1167, 1172*f*
sonographic anatomy of, 1167–1170, 1168*f*, 1170*f*–1172*f*
cerebellar view of, 1168–1169, 1169*f*
median (midsagittal) view of, 1169, 1169*f*
thalamic view of, 1168, 1169*f*
ventricular view of, 1168, 1169*f*
split, 1196
tumors and, 1208–1210, 1209*f*–1210*f*
variants in (usually normal), 1170–1174
vascular malformations of, 1204–1208, 1206*f*
dural sinus thrombosis as, 1205–1206, 1206*f*
hydranencephaly as, 1208, 1208*f*
intracranial hemorrhage as, 1206, 1207*f*
ventral induction errors and, 1186–1203
arachnoid cysts as, 1192–1193, 1193*f*
in cerebellum, 1189–1192
Dandy-Walker malformation as, 1190, 1190*f*
HPE as, 1186–1189, 1187*b*, 1188*f*, 1189*b*
mega-cisterna magna as, 1192, 1193*f*
in posterior fossa, 1189–1192
rhombencephalosynapsis as, 1192
vermis hypoplasia or dysplasia as, 1190–1192, 1192*f*
VM and, 1174–1178
Brain, neonatal/infant. *See also* Hypoxic-ischemic events, neonatal/infant brain and
astrocytomas of, 1562, 1564*f*
calcar avis of, development of, 1523*f*, 1524
cavum septi pellucidi of, development of, 1521, 1521*f*–1522*f*
cavum veli interpositi of, development of, 1521–1522, 1521*f*
cavum vergae of, development of, 1521, 1521*f*–1522*f*
cellular migration disorders of, 1536–1537
cerebellar vermis of, development of, 1524
choroid plexus of
in coronal imaging, 1514–1515, 1514*f*
cysts of, 1565, 1566*f*
development of, 1522–1523, 1522*f*–1523*f*
papillomas of, 1562, 1565*f*
cisterna magna of, development of, 1524
cleavage disorders of, 1532–1536
color Doppler ultrasound for, 1573–1574
congenital malformations of, 1524–1526, 1525*b*
cystic encephalomalacia and, 1538, 1539*f*
cystic intracranial lesions of, 1562–1565, 1565*t*
cysts of
arachnoid, 1563–1565, 1565*b*
choroid plexus, 1565, 1566*f*
frontal horn, 1522, 1522*f*, 1566
periventricular, 1566, 1566*f*

Brain, neonatal/infant *(Continued)*
porencephalic, 1537, 1565
subependymal, 1566, 1567*f*
death of, duplex Doppler sonography and, 1580, 1583*f*
destructive lesions and, 1537–1538
developmental anatomy of, 1520–1524
diverticulation disorders and, 1532–1536
duplex Doppler sonography of, 1573–1576
approaches to, 1574, 1575*f*
arterial blood flow in, 1576, 1577*t*
asphyxia and, 1580
brain death and, 1580, 1583*f*
cerebral edema and, 1580
diffuse neuronal injury and, 1580
ECMO and, 1578–1580, 1579*f*
hemodynamics in, 1576–1580
HII and, 1580, 1581*f*–1582*f*
hydrocephalus and, 1581–1583, 1584*f*
intensive care therapies and, 1578–1580
intracranial hemorrhage and, 1580–1581, 1584*f*
intracranial tumors and, 1585, 1587*f*
measurements in, 1576, 1576*f*–1577*f*, 1576*t*
mechanical ventilation and, 1578, 1579*f*
near-field structures and, 1585, 1588*f*
optimization of, 1574, 1574*b*
pitfalls of, 1585–1589, 1589*f*
safety considerations for, 1574–1576
stroke and, 1580–1581, 1584*f*
uncommon applications of, 1585, 1588*f*
vascular malformations and, 1583–1585, 1585*f*–1587*f*
venous blood flow in, 1578, 1578*f*, 1578*t*
ependymomas of, 1562
germinal matrix of, development of, 1524, 1524*f*
HPE and, 1532–1536
alobar, 1534–1535, 1534*b*, 1536*f*
classification of, 1534*f*
lobar, 1535
midline interhemispheric form of, 1535–1536
semilobar, 1535
hydranencephaly and, 1538, 1538*f*
hydrocephalus and, 1538–1541
causes of, 1540*b*
cerebrospinal fluid production and circulation and, 1538–1541
hypoxic-ischemic injury to, 1541–1557
imaging of
coronal, technique for, 1513–1515, 1513*b*, 1513*f*–1515*f*
equipment for, 1512
mastoid fontanelle, 1512, 1517–1518, 1517*f*, 1519*f*
pitfalls in, 1523*b*
posterior fontanelle, 1512, 1517, 1517*f*–1518*f*
sagittal, 1515–1517, 1516*b*, 1516*f*–1517*f*
sonographic technique for, 1512–1518
standardized reports of, 1518–1520, 1520*b*
3-D ultrasound in, 1518
infections and, 1557–1560
acquired, 1560, 1561*f*–1563*f*
CMV, 1558–1560, 1559*f*
congenital, 1557–1560, 1559*f*
ventriculitis as, 1560, 1563*f*
lissencephaly and, 1537
in metabolic disorders, 1538
neural tube closure disorders of, 1526–1532
Chiari malformations and, 1526, 1526*b*, 1527*f*–1529*f*
corpus callosum agenesis and, 1526–1528, 1529*b*, 1530*f*–1533*f*
corpus callosum lipoma and, 1529, 1533*f*

Brain, neonatal/infant *(Continued)*
Dandy-Walker malformation and, 1529–1532, 1530*b*, 1533*f*–1534*f*
posttraumatic injury to, 1557, 1558*f*
power mode Doppler ultrasound for, 1573–1574
premature
coronal imaging of, 1515, 1515*f*
hypoxic-ischemic events and, 1541, 1541*t*
normal sonographic appearance of, 1521*f*
ultrasound screening in, optimal, 1543*b*
PVL and, 1550–1553, 1551*f*–1553*f*, 1566
schizencephaly and, 1536–1537, 1537*f*
SOD and, 1532–1534, 1535*f*
sulcation disorders of, 1536–1537
sulcus of, development of, 1520–1521, 1520*f*–1521*f*
teratomas and, 1562
tumors of, 1560–1566, 1562*b*, 1564*f*–1565*f*
primitive neuroectodermal, 1562
rhabdoid, 1562
supratentorial, 1562
vein of Galen malformations and, 1566, 1567*f*
Brain, pediatric. *See* Transcranial Doppler sonography, pediatric
Brain death
neonatal/infant brain and, duplex Doppler sonography of, 1580, 1583*f*
pediatric
coma differentiated from, 1618–1620, 1620*f*
TCD sonography and, 1618–1620, 1618*b*, 1619*f*–1620*f*
Brainstem, neonatal/infant, in diffuse cerebral edema, 1555*f*
Branchial arches, 1133–1134
anomalies of, 1651, 1651*f*–1653*f*
Branchial clefts, 1651
Branchial cysts
type I, pediatric, 1639, 1651, 1651*f*
type II, pediatric, 1639–1640, 1651, 1652*f*
type III, pediatric, 1651, 1652*f*
Branchial sinus abscess, type IV, 1643–1645, 1645*f*, 1651, 1653*f*
Branchio-oto-renal syndrome, MCDK and, 1815
Breast Imaging Reporting and Data System (BI-RADS), 768
reporting categories of, 774, 774*t*
Breast-ovarian cancer syndrome, 578
Breast(s)
abscesses of, 803–804, 803*f*–804*f*
anatomy of, 760–767
atrophy of, 763*f*
benign sonographic findings of, 795–797
hyperechoic tissue in, 796–797, 796*f*
parallel (wide-than-tall) orientation in, 797, 797*f*
thin echogenic capsule in, 797
BI-RADS reporting categories for, 774, 774*t*
cancer, staging of, 807–810, 808*f*–810*f*
CEUS for assessment of, 773–774
cysts of, 774–785
acorn, 778*f*
aspiration of, ultrasound-guided, 811, 813*f*
clustered macrocysts and, 779, 780*f*
clustered microcysts and, 782
with color streaking, 775, 776*f*
complex, 780–785, 782*f*
complicated, 775–780, 776*f*
Doppler ultrasound for differentiating, 769–770, 770*f*
eggshell calcification and, 779, 780*f*
fat-fluid levels in, 775, 778*f*
fibrocystic change and, 775
inflammation and infection of, 782–785, 785*f*
lipid, 775–779, 779*f*

Breast(s) *(Continued)*
microcysts and, 782, 784*f*
milk of calcium and, 775, 776*f*–777*f*
mural nodules and, PAM causing, 782, 783*f*–784*f*
papillary lesions and, 782
septations within, 782, 783*f*
simple, 774, 775*f*
of skin origin, 779, 781*f*
diagnostic ultrasound indications for, 797–803
breast pain as, 797–798
nipple discharge as, 798–799, 799*f*–801*f*
palpable lumps as, 769, 769*f*, 798, 798*f*
Doppler ultrasound for assessment of, 768–772, 770*f*–773*f*
echogenicities of, 761
elastography for assessment of, 772–773, 773*f*
implants of, evaluation of, 804–807, 804*f*–806*f*
interventions for, ultrasound-guided, 811–815, 813*f*–814*f*
lymphatic drainage of, 762–767, 767*f*
mammographic findings of, 799–803
dense tissue in, 761–762, 763*f*
location or position correlation in, 801
shape correlation in, 800, 802*f*–803*f*
size correlation in, 800, 801*f*–802*f*
sonographic-mammographic confirmation in, 803
surrounding tissue density correlation in, 801, 803*f*
nipple discharge and, 798–799, 799*f*–801*f*
pain in, 797–798
papillomas of, 769–771, 770*f*
intracystic, 782, 783*f*
intraductal, 799, 799*f*–800*f*
peripheral, 799, 800*f*
periductal mastitis of, 771, 771*f*
physiology of, 760–767
solid nodules of, 780–786, 782*f*
biopsy of, ultrasound-guided, 811–815, 813*f*–814*f*
circumscribed, 786
heterogenicity of, 786, 786*f*
papillary lesions and, 782
spiculated, 786
sonographic equipment for, 767, 767*f*
sonographic techniques for, 768–774
for annotation, 768
CEUS as, 773–774
color Doppler ultrasound as, 769–772, 770*f*–773*f*
Doppler ultrasound as, 768–772, 770*f*–773*f*
elastography as, 772–773, 773*f*
for lesion documentation, 768–769
patient position in, 768
special, 769–774
split-screen imaging for, 769, 769*f*
3-D ultrasound as, 773
suspicious sonographic findings of, 787–795, 787*t*
acoustic shadowing in, 791–792, 793*f*
angular margins in, 788–789, 790*f*
architectural distortion in, 795
associated features in, 794–795
calcifications in, 793–794, 795*f*
duct extension in, 790–791, 792*f*
edema in, 795
hypoechogenicity in, 792–793, 794*f*
indistinct margins in, 787, 787*f*
microlobulations in, 789, 791*f*
not parallel orientation (taller-than-wide) in, 789–790, 792*f*
skin changes in, 795
spiculation in, 787–788, 788*f*

Breast(s) *(Continued)*
thick echogenic rim, with hyperechoic spicules in, 787–788, 789*f*
TDLUs of, 760–761
sonographic appearance of, 762, 766*f*
3-D ultrasound for, 773
ultrasound examination of, 774–797
applications of, 760
automated whole-breast, 760
BI-RADS reporting categories for, 774, 774*t*
diagnosis in, 760
Doppler ultrasound for, 768–772, 770*f*–773*f*
equipment for, 767, 767*f*
for guided intervention, 811–815, 813*f*–814*f*
for implant evaluation, 804–807, 804*f*–806*f*
for infection, 803–804, 803*f*–804*f*
for interventional procedures, 760
for lymph node assessment, 807–810, 808*f*–810*f*
niche applications for, 803–811
normal tissue and variations in, 774
for sonographic-MRI correlation, 810–811, 811*f*–812*f*
suspicious findings in, 787–795, 787*t*
technique for, 768–774
three dimensional, 788, 789*f*–790*f*
water density tissue of, 761–762, 763*f*
zones of, 761, 761*f*
Breathing, sleep-disordered, 1611
Brenner tumor, 581–582, 582*f*
Breus mole, 1471
Broad ligaments, 564–565
Broad-bandwidth, 7–8
Bronchogenic cysts
fetal, 1255–1256, 1255*f*, 1255*t*
pediatric, 1650, 1716, 1718*f*
Bronchopulmonary foregut malformations, pediatric, 1716, 1718*f*
Bronchopulmonary sequestration (BPS), 1246, 1248*t*, 1250–1251, 1251*f*
extralobar, 1250
fetal, hydrops from, 1426
intralobar, 1250
Bruit, from carotid stenosis, color Doppler, 933, 934*f*
Brunn epithelial nests, in chronic cystitis, 333, 333*f*
Bubbles. *See also* Microbubbles
acoustic cavitation generation of, 41–42, 42*f*
behavior of, incident pressure and, 56–58, 57*t*
Budd-Chiari syndrome, 98–103, 100*f*–103*f*
in children, suprahepatic portal hypertension and, 1762–1763, 1763*f*
IVC and, 463
"Buddha position," fetal, 1401
Bulk modulus, 15–16
"Bunny" waveform, 953*b*, 954, 954*f*
Burkitt lymphoma, pediatric, 1860
"Burned-out" tumors. *See* Germ cell tumors, testicular, regressed
Bursal-sided partial-thickness rotator cuff tears, 888, 890*f*
Bursitis, bursal injections for, 907–909, 908*f*
Burst length, in output control, 48–50
Butterfly vertebrae, in scoliosis and kyphosis, 1235
Bypass graft(s)
coronary, radial artery evaluation for, 977–978, 980*f*
of lower extremity peripheral arteries, 974–975, 975*f*
PSV and dysfunction of, 974–975
of superficial femoral artery, 975*f*

C

CA. *See* Celiac artery
CA 125, in ovarian cancer, 578
Cadaveric kidneys, paired, in transplantation, 643–644, 648*f*
CAH. *See* Congenital adrenal hyperplasia
"Cake" kidneys, pediatric, 1785
CAKUT. *See* Congenital anomalies of kidney and urinary tract
Calcaneus, ossification of, 1377–1378
Calcar avis, neonatal/infant, development of, 1523*f*, 1524
Calcarine fissure, neonatal/infant, development of, 1520–1521, 1524
Calcific bursitis, 891
Calcific tendinitis
injections for, 909, 911*f*
of supraspinatus tendon, 891–892, 892*f*
Calcification(s). *See also* Nephrocalcinosis
abdominal, meconium peritonitis and, 1313, 1314*f*
of adrenal glands, 423, 425*f*
causes of, 424*b*
in breast sonography, 793–794, 795*f*
chronic DVT indicated by, 984, 987*f*
in chronic pancreatitis masses, 233–236, 236*f*
cystic meconium peritonitis with, 1842–1843, 1846*f*
DCIS and, 793, 795*f*
dystrophic, 339
pediatric urinary tract and, 1799
eggshell, breast cysts and, 779, 780*f*
of endometrium, 533, 534*f*
of gallbladder, 202, 202*f*
intracranial, fetal, 1195*f*, 1203, 1204*f*
liver, fetal, 1316–1318, 1317*f*, 1318*b*
of meconium periorchitis, focal, 1904, 1904*f*
of myometrium, 531–533, 533*f*–534*f*
ovarian, focal, 566–568
of prostate, 387, 388*f*
psammomatous, in peritoneal nodule, 510–511, 513*f*
of radial arteries, evaluation for, 998, 998*f*
renal artery, 336
of renal cysts, 358, 358*f*
of renal parenchyma, 339–340, 340*f*
scrotal, 833–834, 833*b*, 834*f*
of seminal vesicles, 392
splenic, 150, 153*f*
pediatric, 1769
of superficial femoral artery, 968, 970*f*
of tendons, 859–861
of thyroid cysts, 695
in thyroid nodules
diagnostic significance of, 713–714
in papillary carcinoma, 699, 702*f*
of urinary tract, pediatric, 1798–1801
cortical nephrocalcinosis and, 1798, 1798*b*, 1798*f*
dystrophic, 1799
medullary nephrocalcinosis and, 1798–1799, 1799*f*
renal vein thrombosis and, 1799, 1800*f*
urinary stasis and, 1799, 1800*f*
urolithiasis and, 1799–1801, 1799*f*
in uterine fibroids, 539*f*, 540, 540*b*
of vas deferens, 392
yolk sac, 1067, 1068*f*
Calcified metastases, of liver, 125, 128*f*
Calcimimetics, for secondary hyperparathyroidism, 734
Calcitonin, secretion of, in medullary carcinoma of thyroid, 701
Calcium bile, milk of, 194, 195*f*
Calcium hydroxyapatite, in calcific tendinitis, 909
Calculus(i)
bladder, 338–339, 339*f*
pediatric, 1908
caliceal, 334–335
Calculus(i) *(Continued)*
liver transplantation complications with, 629, 632*f*
renal, 334–336, 336*f*–337*f*
entities that mimic, 336, 337*b*, 337*f*
scrotal, extratesticular, 836–837, 837*f*
staghorn
tyrosinemia and, 1799, 1800*f*
in xanthogranulomatous pyelonephritis, 328, 329*f*
ureteral, 337–338, 338*f*–339*f*
bladder augmentation and, 1912–1913
complicating renal transplantation, 659–660, 663*f*–664*f*
urethral, pediatric, bladder outlet obstruction from, 1906, 1906*f*
Calf veins, ultrasound imaging of, 982
Caliceal calculi, 334–335
Callosomarginal sulcus, neonatal/infant, development of, 1520–1521
Calvarium, fetal, compressibility of
in osteogenesis imperfecta type II, 1382, 1392, 1393*f*
in skeletal dysplasia, 1382
Calyceal diverticula, renal milk of calcium and, 1799, 1800*f*
Calyces, dilation of, in hydronephrosis, 1354
Campomelic dysplasia, 1395, 1396*f*
bowing of long bones in, 1381–1382
pulmonary hypoplasia and, 1384*f*
ribs and, 1382–1384
sonographic appearance of, 1380*f*
thanatophoric dysplasia differentiated from, 1388–1389
Camptodactyly, fetal, 1404–1405, 1406*f*
Campylobacter, 1852
Canal of Nuck
cyst or hydrocele of, simulating groin hernia, 499–500, 501*f*
delayed closure of, indirect inguinal hernia from, 476–477, 477*f*
Canalization, in spine embryology, 1672, 1673*f*
Candida albicans
genitourinary tract infections from, 330–331, 331*f*
neonatal urinary tract infection from, 1794, 1795*f*
Candidiasis
hepatic, 86–87, 88*f*
hepatosplenic, splenic abscesses in, 150–152, 154*f*
neonatal, 1794, 1795*f*
Capillary malformations, tethered cord and, 1679
Capsular arteries, 821
Caput medusae, 1752
Carcinoid tumor, renal, 355–356
Carcinoma(s). *See also* Breast(s), solid nodules of; Ductal carcinoma in Situ; Hepatocellular carcinoma; Papillary carcinoma; Renal cell carcinoma; Transitional cell carcinoma
acinic cell, parotid gland, pediatric, 1638, 1639*f*
acoustic shadowing caused by, 791–792, 793*f*
adenoid cystic, salivary gland, pediatric, 1638
adrenal, pediatric, 1827, 1827*f*
adrenocortical, 424–425, 426*f*
of bladder
squamous cell, 348
transitional cell, 347–348, 350*f*
cervical, 542, 543*f*
hematometra in, 547*f*, 549
choriocarcinoma, testicular, 824, 825*f*
circumscribed, 786
clear cell, 581, 582*f*
colon, 261–264, 263*f*–264*f*
pediatric, 1880

Carcinoma(s) *(Continued)*
embryonal, 823, 825*f*
ovarian, 1880
pediatric, testicular, 1899
endometrial, 544, 548–551, 550*f*
polycystic ovarian disease and, 1877–1878
esophageal, staging of, endosonography in, 301
fallopian tube, 589
gallbladder, 206–207, 206*f*
gastric, endosonographic identification of, 301
mucoepidermoid, salivary gland, pediatric, 1638
of parathyroid glands
adenomas differentiated from, 735–736, 738*f*
primary hyperparathyroidism from, 734
primary peritoneal serous papillary, 511–513, 515*f*
prostate, transrectal sonography of, 302, 302*f*
rectal, staging of, endosonography in, 301–302, 301*f*–304*f*
spiculated, 786
TDLU, 789–790, 792*f*
of thyroid gland, 695
anaplastic, 707–708, 708*b*, 709*f*
follicular, 701, 701*b*, 706*f*–707*f*, 1648
incidence of, 722, 722*f*–723*f*
medullary, 701–707, 707*f*–708*f*, 1648
nodular disease and, 698–708
papillary, 698–701, 701*f*–705*f*, 713, 1648, 1649*f*
vaginal, pediatric, 1883
Carcinomatosis, peritoneal, 510–511, 510*f*–515*f*
Cardiac output, reduced, carotid flow waveforms and, 935*f*, 936–937
Cardioembolic stroke, 915–916
Cardiomyopathy(ies)
carotid flow waveforms and, 936–937, 936*f*
fetal, 1295*f*
adrenal glands and, 1353–1354
hydrops from, 1425
Cardiopulmonary bypass
partial, in neonatal/infant brain, duplex Doppler sonography and, 1578–1579, 1579*f*
pediatric TCD sonography in, 1621–1622
Cardiosplenic syndrome, 1292–1293, 1293*b*
Cardiovascular disease, 432–433
Carney complex, 826
Carney triad, pheochromocytomas with, 1826
Caroli disease
of biliary tree, 171, 171*f*
pediatric, 1735
bile duct dilation in, 1736–1737, 1736*f*
Carotid artery(ies). *See also* Plaque(s), carotid
anatomy of, 916, 917*f*
arthrosclerotic disease of, plaque characterization in, 919
color Doppler evaluation for stenosis of, 932–935
advantages and pitfalls of, 934–935, 934*b*, 934*f*
bruit from, 933, 934*f*
optimal settings in, low-flow vessel evaluation, 933–934, 933*b*, 934*f*
Takayasu arteritis of, 944–946, 947*f*
common, 916, 917*f*
aneurysm of, 947–948
carotid bifurcation and, 917–918, 918*f*
ectatic, 947–948, 949*f*
helical flow in, 934
occlusion of, abnormal internal carotid artery waveform and, 941, 942*f*
posttraumatic pseudoaneurysm of, 948, 950*f*
stenosis of, grading of, 930
waveform of, 925–926, 925*f*
disease of, preoperative strategies for, 941–942
dissection of, 946–947, 947*b*, 948*f*
Carotid artery(ies) *(Continued)*
distal internal, as transtemporal approach landmark, 1592, 1594*f*
Doppler spectral analysis for, 925–932
high-velocity blood flow patterns in, 928–932, 929*f*–931*f*, 931*t*
pitfalls in, 927–928, 928*f*
spectral broadening in, 927, 927*f*
standard examination in, 926–927, 926*f*
endarterectomized, sonographic features of, 942, 944*f*
external, 916
branching vessels of, 918, 918*f*
collaterals of, intracranial circulation and, 939, 940*f*
mistaking for internal carotid artery, 941, 941*f*
stenosis of, grading of, 930
waveform of, 925–926, 925*f*
flow pattern in
altered, misinterpretation of, 927, 928*f*
high-velocity, in stenoses, 928–932, 929*f*–931*f*, 931*t*
normal transient reversal of, 933–934
internal, 916
common carotid artery occlusion causing abnormal waveform in, 941, 942*f*
fibromuscular dysplasia of, 944–946, 946*f*
mistaking external carotid artery for, 941, 941*f*
stenosis of, grading, 928–929, 929*f*–930*f*
tardus-parvus waveforms in stenosis of, 934*f*, 938
waveform of, 925–926, 925*f*
internal, occlusion of, 939–941
external carotid collaterals to intracranial circulation in, 939, 940*f*
pitfall in diagnosis of, 941, 941*f*
sonographic findings in, 939*b*
string sign distinguished from, 939
kinked, carotid flow waveforms and, 936–937, 936*f*
lymph node masses near, 948, 949*f*
neck masses of, 947–948, 949*f*–950*f*
nonarthrosclerotic diseases of, 944–948
arteritis as, 944–946, 947*f*
carotid body tumors as, 947–948, 949*f*
from cervical trauma, 946, 948*f*
extravascular masses as, 948, 949*f*
fibromuscular dysplasia as, 944–946, 946*f*
posttraumatic pseudoaneurysms as, 948, 950*f*
ultrasound examination of, 916
postoperative ultrasound of, 942–944, 944*f*
power Doppler evaluation for stenosis of, 935–939, 935*b*
pitfalls and adjustments in, 935*f*–939*f*, 936–939, 937*b*
pseudoulceration of, 923
revascularization of, ultrasound after, 942–943, 945*f*
stenosis of
angiography and MRA for, 916
CEA for, 916
color Doppler evaluation of, 932–935
Doppler spectral analysis in, 925–932
external, grading of, 930
follow-up for, 941, 943*t*
gray-scale, 923–924, 924*f*
high-velocity blood flow patterns in, 928–932, 929*f*–931*f*, 931*t*
internal, grading of, 928–930, 929*f*–930*f*
internal, tardus-parvus waveforms in, 934*f*, 938
power Doppler evaluation of, 935–939, 935*b*
recurrent, grading of, 943–944, 945*t*
Carotid artery(ies) *(Continued)*
stroke from, 915–916
ultrasound diagnostic criteria for, 930–932, 931*t*
stenting of
restenosis in, grading of, 943–944, 945*t*
ultrasound after, 942–943, 945*f*
tandem lesions in, 937
TIA from embolism of, 919
tortuous
carotid flow waveforms and, 936–937, 937*f*
spectral broadening in, 928
transcranial Doppler sonography for, 948–950, 950*f*
ultrasound examination of
color Doppler evaluation for, 932–935
diagnostic criteria for, 930–932, 931*t*
Doppler spectral analysis for, 925–932
follow-up based on, 941, 943*t*
indications for, 915–916, 916*b*
interpretation of, 918–944
postoperative, 942–944, 944*f*
techniques for, 917–918, 917*f*–918*f*
transcranial Doppler sonography for, 948–950, 950*f*
visual inspection of gray-scale images in, 918–924
visual inspection of gray-scale images for, 918–924
for intima-media thickening, 918–919, 919*f*
for plaque characterization, 919–922, 920*f*–922*f*, 922*b*
for plaque ulceration, 923, 923*b*, 923*f*–924*f*
for stenosis evaluation, 923–924, 924*f*
for vessel wall thickness, 918–919
walls of, dissections in, flow disturbances in, 928
Carotid bifurcation, 917–918, 918*f*
pathologic lymph node near, 948, 949*f*
Carotid body tumors, 947–948, 949*f*
Carotid bulb, 917
Carotid endarterectomy (CEA)
for carotid stenosis, 916
pediatric, TCD sonography in, 1621
sonographic features following, 942, 944*f*
Carotid Revascularization Endarterectomy Versus Stenting Trial (CREST), 916
Carotid-cavernous fistulas, TCD sonography assessing, 1614
Carpal tunnel entrapment, of median nerve, 864–865, 866*f*
Carpal tunnel syndrome, 865, 866*f*
Carpenter syndrome, craniosynostosis in, 1136–1138
Cartilage, sonographic characteristics of, 1923
"Cartilage interface" sign, 886, 888, 888*f*
Cataracts
congenital, 1143, 1147*b*
temperature increase in utero and, 1037
Catheterization
central venous, IJV thrombosis complicating, 955
ESRD and, 994
Catheter(s)
central, peripherally inserted, pediatric, insertion of, 1953
drainage
for interventional sonography, 1948
placement of, 610–611, 611*f*
removal of, 612
selection of, 610–611, 611*f*
peripherally inserted central, 993*f*
interventional sonography, pediatric, 1954, 1955*f*–1957*f*
SVC, pediatric, position of, 1716–1721, 1722*f*

Cat-scratch disease, pediatric, 1633–1634
  causes of, 1938, 1938*f*
  lymphadenopathy in, 1660–1663
Cauda equina, formation of, 1673, 1673*f*
Caudal agenesis, 1674
  closed spinal dysraphism and, 1689, 1690*f*
  maternal diabetes mellitus and, 1689
  type 1, 1689, 1690*f*
  type 2, 1689
Caudal appendage, tethered cord and, 1679
Caudal cell mass, differentiation of, in spine embryology, 1674
Caudal neuropore, in spine embryology, 1217
Caudal regression
  defects, 1218
  fetal, 1237–1238, 1237*f*
  sequence, sacral agenesis in, 1237
  syndromes
    as limb reduction defect, 1401, 1404*f*
    skeletal dysplasia and, 1382
Caudate lobe, 75–76, 76*f*
Caudate nucleus, in sagittal imaging of neonatal/infant brain, 1515, 1517*f*
Caudothalamic groove, neonatal/infant
  in intraparenchymal hemorrhage, 1547, 1547*f*
  in sagittal imaging, 1516–1517, 1517*f*
Causality, criteria for judging, 48
Cavernoma, portal, in portal vein thrombosis, 1757, 1761*f*
Cavernous hemangiomas
  of bladder, 356
  CEUS characterization of, 111, 113*f*
  Doppler ultrasound characterization of, 109–110
  of liver, 108–112, 112*f*–113*f*
    percutaneous needle biopsy of, 603–604, 604*f*
Cavitation. *See* Acoustic cavitation
Cavum septi pellucidi
  fetal
    formation of, 1167
    normal sonographic appearance of, 1168–1169
    sonographic view of, 1024*f*
  neonatal/infant, development of, 1521, 1521*f*–1522*f*
Cavum veli interpositi
  arachnoid cysts differentiated from, 1192–1193
  fetal, 1170–1174, 1174*f*
  neonatal/infant, development of, 1521–1522, 1521*f*
Cavum Vergae
  formation of, 1167
  neonatal/infant
    in coronal imaging, 1514–1515
    development of, 1521, 1521*f*–1522*f*
CBAVD. *See* Congenital bilateral absence of the vas deferens
CCAM. *See* Congenital cystic adenomatoid malformation
CDH. *See* Congenital diaphragmatic hernia
CEA. *See* Carotid endarterectomy
Cebocephaly
  alobar HPE and, 1534–1535, 1536*f*
  hypotelorism and, 1140
Celiac artery (CA)
  anatomy of, 451
  duplex Doppler sonography of, 453–455, 455*f*
  in median arcuate ligament syndrome, 453, 453*f*
  occluded, 454–455, 458*f*
  stenosis of, after liver transplantation, 634–635, 637*f*
Celiac disease, in gastrointestinal tract, 300
Cell aggregation, in obstetric sonography, 1038
Cell membrane alteration, from obstetric sonography, 1038
Cell-free DNA, 1088–1089
  aneuploidy screening with, 1107
Cellular migration
  disorders of, neonatal/infant brain and, 1536–1537
  in organogenesis, 1524–1525
Cellulitis, 872–874, 873*f*–874*f*
  complicated lymphadenitis with, in children, 1658–1660, 1662*f*
Center-stream sampling, true, in carotid occlusion diagnosis, 939
Central echo complex, in pediatric kidney, in renal duplication, 1783, 1784*f*
Central hypoventilation syndrome, neuroblastoma with, pediatric, 1825
Central nervous system (CNS)
  anomalies of, 1166
  MRI evaluation of fetal, 1166–1167
Central venous access, for interventional sonography, pediatric, 1954
Central venous catheterization
  DVT related to, 935, 995*f*
  IJV thrombosis complicating, 955
Centrum semiovale, neonatal/infant, 1514
Centrum(a), of vertebral body
  in lateral longitudinal scan plane, 1223*f*
  in lateral transaxial scan plane, 1222*f*
  ossification of, 1218, 1219*f*
  in posterior longitudinal scan plane, 1224*f*
  in posterior transaxial scan plane, 1222*f*
Cephalic vein, 990*f*, 991
Cephalocele(s)
  atretic, 1180
  fetal brain and, 1179–1182
  as spinal dysraphism, 1139–1140
Cerclage, cervical, for cervical incompetence, 1505–1507, 1506*f*
Cerebellar hemispheres, fetal, normal sonographic appearance of, 1168–1169, 1169*f*
Cerebellar hemorrhage, neonatal/infant brain and, 1548–1550, 1549*f*
Cerebellar infarction, neonatal/infant brain and, 1555
Cerebellar vermis, 1167, 1515, 1516*f*
  neonatal/infant, development of, 1524
Cerebellum
  Blake pouch and, 1189
  Dandy-Walker malformation in, 1190, 1190*f*
  embryology of, 1167
  fetal, sonographic view of, 1024*f*
  hypoplasia of, 1190
  mega-cisterna magna and, 1192, 1193*f*
  neonatal/infant, in coronal imaging, 1514–1515, 1514*f*
  rhombencephalosynapsis in, 1192
  ventral induction errors in, 1189–1192
  vermis hypoplasia or dysplasia in, 1190–1192, 1192*f*
Cerebral artery. *See* Anterior cerebral artery; Middle cerebral artery; Posterior cerebral artery
Cerebral blood flow, neonatal/infant
  arterial, velocities in, range of, 1576, 1577*t*
  velocity of, determination of, 1576, 1576*f*
  venous, velocities in, range of, 1578, 1578*f*, 1578*t*
Cerebral blood vessels, extracranial, 917*f*. *See also* Internal jugular vein; Vertebral artery
  IJV as, 955–956
  vertebral artery as, 950–955
Cerebral cavernous malformation, in venous malformations of neck, 1657
Cerebral cortex. *See also* Cortical development malformations, fetal brain and
  development of, 1167
  malformations of, 1193–1203
Cerebral edema
  neonatal/infant, 1550–1556
    diffuse, 1553–1555, 1554*f*–1555*f*
    duplex Doppler studies of brain and, 1580
  pediatric, TCD sonography in, 1614, 1617*f*
Cerebral hemisphere, neonatal/infant, in sagittal imaging, 1517, 1517*f*
Cerebral infarction, neonatal/infant, 1550–1556
  focal, 1555–1556, 1556*b*, 1556*f*
  luxury perfusion and, 1580–1581, 1584*f*
Cerebral palsy
  pediatric, neurogenic bladder in, 1907
  periventricular leukomalacia and, 1550
Cerebral peduncles, 1518
  as transtemporal approach landmark, 1592, 1593*f*
Cerebral sinovenous thrombosis, 1547–1548
Cerebrohepatorenal syndrome
  cortical malformations in, 1196
  subependymal cysts from, 1566
Cerebroplacental ratio, MCA and, 1458, 1460*f*
Cerebrospinal fluid, hydrocephalus and production and circulation of, 1538–1541
Cerebrovascular accident, 915–916. *See also* Stroke
Cerebrovascular disease, SCD indicators for, 1598, 1599*b*
  MCA and, 1600*f*, 1604*f*–1605*f*
  ophthalmic artery flow as, 1599*f*
  stroke and, 1601*f*–1603*f*
Cervical aortic arch, 1658
Cervical canal, dilation of, spontaneous PTB and, 1503
Cervical carcinoma, iliac veins and, 461*f*
Cervical cerclage, for cervical incompetence, 1505–1507, 1506*f*
Cervical ectopia cordis, 1295
Cervical ectopic pregnancy, 1073–1074, 1074*f*
Cervical ectopic thymus, 1723
Cervical fascia, pediatric. *See also* Infrahyoid space, pediatric; Suprahyoid space, pediatric
  deep layers of, 1628, 1629*f*
    infrahyoid space in, 1628–1629, 1640–1650
    suprahyoid space in, 1628–1629
Cervical kyphosis, in campomelic dysplasia, 1381–1382
Cervical lymph node(s)
  parathyroid adenomas confused with, 745
  pediatric, inflammatory disease of, 1658–1663, 1661*f*–1663*f*
  percutaneous needle biopsies for, 717–718, 718*f*
Cervical teratoma
  fetal, 1159, 1161*f*
  pediatric, 1654, 1654*f*
Cervicothoracic vertebrae, campomelic dysplasia and, 1395
Cervix, 528–530
  abnormalities of, 541–544, 543*f*
    management protocols for, 1507, 1507*f*–1508*f*
    transvaginal ultrasound findings on, 1503*b*
  assessment of, 1503–1507
    for asymptomatic patients, 1503–1505
    in cervical incompetence and cervical cerclage, 1505–1507, 1506*f*
    fetal therapy and, 1505
    in general obstetric population screening, 1503–1504
    in high-risk obstetric population screening, 1504–1505
    in multiple gestations, 1504–1505
    in pervious cervical surgery, 1505
    in polyhydramnios, 1505
    in preterm premature rupture of membranes, 1505
    in prior PTB, 1504

Cervix *(Continued)*
for symptomatic patients, 1505–1507
in uterocervical anomalies, 1505
carcinoma of, 542, 543*f*
hematometra in, 547*f*, 549
duplicated, 538
dynamic changes in, spontaneous PTB and, 1501–1503, 1503*f*
ectopic pregnancy implantation in, 1073–1074, 1074*f*
funneling of, in spontaneous PTB prediction, 1501, 1502*f*
incompetence of, 1495–1496
cervical cerclage and, 1505–1507, 1506*f*
vaginal pessary and, 1507
length of, 1499–1500, 1499*f*
in prediction of spontaneous preterm birth, 1500–1501, 1501*t*
short, 1500–1501, 1500*f*, 1501*t*
nabothian cysts of, 533, 535*f*
in pregnancy, on second-trimester scan, 1021*f*
pseudomass in, 533, 536*f*
short, 1500–1501, 1500*f*, 1501*t*
shortening of, progressive, spontaneous PTB and, 1501
sonography of, 1496–1501
technical limitations and pitfalls of, 1498–1499, 1498*b*, 1499*f*
transabdominal approach to, 1496–1497, 1496*f*
transperineal/translabial approach to, 1497, 1497*f*
transvaginal approach to, 1497–1498, 1497*f*–1498*f*
surgery on, prior, cervical assessment and, 1505
trauma to, carotid artery damage from, 946, 948*f*
Cesarean section(s)
hematomas and
bladder flap, 556–557, 557*f*
subfascial, 556–557, 557*f*
pediatric pregnancy and, 1884
postpartum findings on, 556–557, 557*f*–558*f*
scars from, 557, 558*f*
ectopic pregnancy implantation and, 1073, 1075*f*
CEUS. *See* Contrast-enhanced ultrasound
CF. *See* Cystic fibrosis
CHAOS. *See* Congenital high airway obstruction
Charcot triad, in acute cholangitis, 176
CHARGE syndrome, coloboma in, 1143
CHD. *See* Congenital heart disease
Chemical peritonitis, 514
Chemical ventriculitis, in intraventricular hemorrhage, 1545–1547
Chemiluminescence, 42, 42*f*
Chest, fetal. *See also* Congenital diaphragmatic hernia; Congenital pulmonary airway malformation; Lung(s)
bronchogenic cysts in, 1255–1256, 1255*f*, 1255*t*
CHAOS and, 1253–1255, 1254*f*
congenital diaphragmatic hernia in, 1258–1264
development of structures in, 1243–1245
neurenteric cyst in, 1256
normal sonographic features of, 1244–1245, 1244*f*
pericardial effusion in, 1258, 1258*f*
pleural effusion in, 1256–1258, 1257*f*
pleuropulmonary blastoma and, 1252–1253
pulmonary development in, 1243
pulmonary hypoplasia and, 1245–1246
pulmonary lymphangiectasia and, 1258, 1259*f*
Chest, pediatric. *See also* Pneumonia, pediatric
atelectasis and, 1714, 1716*f*
bronchopulmonary foregut malformations and, 1716, 1718*f*
CPAM and, 1715–1716, 1717*f*
diaphragm disorders of, 1716, 1718*f*–1720*f*
empyema in, sonographic signs of, 1702–1711, 1707*f*
lung abscess in, 1711, 1713*f*
lung parenchyma and, 1711–1716
lymphatic malformations and, 1723
mediastinal masses in, 1723–1724
abnormal thymus location mimicking, 1723
anterior, 1723–1724
lymphadenopathy and, 1724
posterior, 1724
thymic index and, 1723, 1724*t*, 1725*f*, 1726*t*
parapneumonic collections in, 1710–1711
pleural effusions in, sonographic signs of, 1702–1711, 1704*f*–1708*f*
pleural fluid in, sonographic signs of, 1709, 1709*b*, 1709*f*–1710*f*
rib fractures in, 1727
sonography of
CT compared to, 1709, 1710*f*–1711*f*
indications for, 1701, 1702*b*
pitfalls in, 1709–1710, 1712*f*
technique for, 1701–1702, 1703*f*–1704*f*
ultrasound-guided interventional procedures in, 1724–1726, 1726*f*–1727*f*
vascular disorders of, 1716–1723
thrombosis, 1716–1721, 1721*f*–1723*f*
wall of, lesion of, ultrasound-guided biopsy of, 1724–1725
Chiari malformation(s)
I, 1526
II, 1190
banana sign in, 1183–1185, 1184*f*, 1221, 1228, 1230–1232
corpus callosum agenesis in, 1526, 1528*f*
lemon sign in, 1183–1185, 1184*f*, 1221, 1232–1233
myelomeningoceles with no, 1526, 1529*f*
normal sonographic appearance of fetal, 1168–1169
open spina bifida and fetal, 1183, 1184*f*
open spinal dysraphism with, pediatric, 1681–1682
sonographic findings in, 1526, 1526*b*, 1527*f*–1528*f*
in spina bifida screening, 1221, 1228
VM with, 1177
III, 1526
neonatal/infant neural tube closure disorders and, 1526, 1526*b*, 1527*f*–1529*f*
Chiba needles, 1948
Child life specialists, 1776–1781
Childhood malignancies, obstetric sonography and, 1041
Chlamydia trachomatis, 846, 1633–1634
Chlamydial perihepatitis, PID and, 1887
Chloroma
masseter muscle, 1641*f*
pediatric, neck, 1667*f*
Chocolate cysts, 574–575
Cholangiocarcinoma, 171
biliary tree and, 184–188
characterization of, with microbubble contrast agents, 106*f*
distal, 188, 192*f*
fluke infections and, 178–179
hilar, 185–188
CEUS assessment of, 188, 191*f*
criteria for unresectable, 187*b*
Cholangiocarcinoma *(Continued)*
Doppler ultrasound assessment for, 187–188, 189*f*–191*f*
treatment and staging for, 186–187
tumor growth patterns in, 186
intrahepatic, 184–185, 186*f*
intraductal, 185, 186*f*–187*f*
peripheral, 129
Cholangiography, transhepatic, 614–615
Cholangiohepatitis, Oriental, 179
Cholangiopathy
autoimmune, 182
HIV, 181–182, 181*f*
Cholangitis
acute (bacterial), 176, 177*f*
AIDS, 181
ascending, 629
autoimmune, 182
IgG4-related, 182–184, 185*f*
pyogenic, recurrent, 179–181, 180*f*
sclerosing
causes of secondary, 182*b*
primary, 182, 183*f*, 184
recurrent, after liver transplantation, 629, 630*f*
Cholecystectomy, gallbladder nonvisualization from, 190–194
Cholecystenteric fistula, 207
Cholecystitis
acalculous, 200
pediatric, 1741
acute, 195–200, 197*f*–199*f*, 197*t*, 201*f*
hyperemia in, 197*f*, 198–199
pediatric, 1741
prominent cystic artery in, 197*f*, 198–199
sonographic findings in, 196, 197*t*
chronic, 201–202
emphysematous, 175, 198*f*, 200
gallbladder nonvisualization from, 190–194, 193*f*
gangrenous, 198*f*, 200
hemorrhagic, 200
percutaneous cholecystostomy for, ultrasound-guided, 613–614, 616*f*
xanthogranulomatous, 202
Cholecystostomy, percutaneous, ultrasound-guided, 613–614, 616*f*
Choledochal cysts
of biliary tree, 168–170, 169*f*–170*f*
fetal duodenal atresia mistaken for, 1309
of fetal gallbladder, 1319, 1320*f*
neonatal jaundice and, 1735–1737, 1735*f*–1736*f*
pediatric pancreatitis and, 1862–1864
Choledochocele, pediatric, 1735
Choledochoduodenal fistula, 175–176, 177*f*
Choledochoenteric fistula, 175–176, 177*f*
Choledochojejunostomy, for liver transplantation, 625
Choledocholithiasis, in biliary tree, 172–173, 182
common bile duct stones and, 173–174, 173*f*
intrahepatic, 173, 173*f*
Cholelithiasis, pediatric, 1741, 1741*b*, 1743*f*
Chondrodysplasia punctata, 1399
cortical malformations in, 1196
sonographic appearance of, 1380*f*
Chondroectodermal dysplasia, 1398–1399
Chondrolysis, complicating injectable steroids, 901
Chorioamnionitis, maternal, PVL and, 1551
Chorioangioma, 1476, 1478*f*–1479*f*
Choriocarcinoma
ovarian, pediatric, 1880
pseudoprecocious puberty and, 1887
PTN and, 1080–1082, 1083*f*
testicular, 824, 825*f*, 1899
Chorion, amnion separation from, 1469, 1469*f*
Chorion frondosum, 1465–1466

Chorion laeve, 1465–1466
Chorionic bump, in gestational sac, 1065
Chorionic cavity, 1051, 1053*f*
Chorionic plate, 1465–1466
Chorionic sac fluid, 1054–1055, 1056*f*
Chorionic villi, 1465–1466
  formation of, 1051–1052, 1053*f*
Chorionic villus sampling (CVS), 1107–1108, 1108*f*
Chorionicity, in multifetal pregnancy, 1115–1116, 1116*f*
  sonographic determination of, 1117–1119, 1118*f*, 1119*t*, 1120*f*–1121*f*
  triplets and, 1122*f*
Choroid plexus
  fetal
    fetal brain and cysts of, 1170, 1173*f*
    sonographic view of, 1024*f*
    spina bifida and cysts of, 1233
    trisomy 18 and cyst of, 1103*f*, 1104
    trisomy 21 and cysts of, 1101
  neonatal/infant
    in coronal imaging, 1514–1515, 1514*f*
    cysts of, 1565, 1566*f*
    development of, 1522–1523, 1522*f*–1523*f*
    papillomas of, 1562, 1565*f*
  papillomas of
    Aicardi syndrome and giant pigmented nevi in, 1209
    in neonatal/infant brain, duplex Doppler sonography of, 1588*f*
    VM with, 1177–1178
Choroid(s)
  asymmetry of, in VM, 1178
  separation of, from medial ventricle wall, in VM evaluation, 1176, 1176*f*
Chromosomal abnormalities. *See also* Aneuploidy; Triploidy; Trisomy 13; Trisomy 18; Trisomy 21
  diagnostic testing for, 1107–1109, 1108*f*
  Ebstein anomaly with, 1286
  fetal, IUGR and, 1455
  fetal hydrops from, 1429–1430, 1430*f*
  maternal age-related risks of, 1088, 1089*f*
  primary amenorrhea in, 1887
  teratologic hip dislocation and, 1932
  triploidy as, 1104–1106, 1104*b*, 1105*f*
  trisomy 13 as, 1104
  trisomy 18 as, 1103–1104
  trisomy 21 as, 1097–1103
  Turner syndrome as, 1106–1107, 1106*f*
Chromosomal anomalies, in CHD, 1270
Chromosomal microarray analysis (CMA), 1097
Chromosome 11p13, hepatoblastomas and, 1746
Chronic allograft nephropathy, 1810, 1812*f*
Chronic autoimmune lymphocytic thyroiditis, 724, 725*f*–727*f*
Chronic epididymitis, 841, 843*f*
Chronic kidney disease (CKD), 1796–1798, 1797*t*, 1798*f*
Chronic prostatitis/chronic pelvic pain syndrome (CP/CPPS), 389–390, 390*f*
Chronic sclerosing pancreatitis, 236
Chylothorax
  congenital, fetal, hydrops from, 1425–1426
  fetal
    in hydrops, 1413–1416
    primary, 1256
  neonatal, radiopaque hemithorax in, 1704*f*
Chylous ascites, 508
Ciliopathies, 1182, 1346
Cingulate sulcus, 1515
  neonatal/infant, development of, 1520–1521, 1521*f*
Circumscribed carcinomas, 786
Circumvallate placenta, 1479–1480, 1480*f*–1481*f*
Cirrhosis
  biliary, 92–93, 182
    pediatric, 1741
  gallbladder wall thickening and, 199*f*
  hepatic vein strictures in, 95, 95*f*
  in inborn errors of metabolism, 1738
  of liver, 92–96
    Doppler ultrasound characteristics of, 95, 95*f*
    HCC and, 122, 122*t*
    intrahepatic portal hypertension from, 96
    morphologic patterns of, 92–95, 94*f*
    pseudocirrhosis of, 125–128, 129*f*
    sonographic features of, 95*b*
    SWE and, 95–96
  macronodular and micronodular, 92–93
  pediatric, 1741, 1742*f*
    causes of, 1760*b*
    intrahepatic portal hypertension and, 1759–1762
  post necrotic, 1741
Cistern, as transtemporal approach landmark, 1592, 1593*f*
Cisterna magna
  fetal
    effacement of, in Chiari II malformation, 1183–1185, 1184*f*
    normal sonographic appearance of, 1168–1169
  neonatal/infant
    clot in, in intraventricular hemorrhage, 1545, 1546*f*
    development of, 1524
    mega, Dandy-Walker malformation differentiated from, 1531, 1534*f*
CKD. *See* Chronic kidney disease
Classic diagnostic triad, for renal cell carcinoma, 340
Clavicle, 878–879, 878*f*
  growth of, normal, 1378
Clear cell carcinoma, 581, 582*f*
Cleavage, neonatal/infant brain and disorders of, 1532–1536. *See also* Holoprosencephaly
Cleft lip/palate
  associated signs of, 1152*b*
  bilateral, 1152, 1156*f*–1157*f*
    hypertelorism and, 1144*f*
    Roberts syndrome and, 1401
  complete compared to incomplete, 1151, 1153*f*–1154*f*
  deviation of vomer in, 1151
  differential diagnosis of, 1151*b*
  isolated clefts of secondary palate in, 1153
  median, 1152
  as midface abnormality, 1151–1153
  patterns of, 1152*f*
  Tessier category of, 1152–1153, 1153*f*
  trisomy 13 and 18 in, 1151
  unilateral, 1152, 1155*f*
    midface hypoplasia with, 1149*f*
Cleidocranial dysplasia
  ribs in, 1382–1384
  wormian bones in, 1139
Clinodactyly, fetal, 1404–1405, 1406*f*
Cliopathies, 1182
Clitoris, fetal, enlarged, 1367
CLO. *See* Congenital lobar overinflation
Cloaca, 1337*f*, 1338, 1674
Cloacal exstrophy
  fetal abdominal wall and, 1328–1329, 1329*f*
  pediatric, risk of spinal dysraphism with, 1689
  sacral agenesis in, 1237
Cloacal malformation, 1310–1311
  fetal, lower urinary tract obstruction and, 1363, 1363*f*
  pediatric, risk of spinal dysraphism with, 1689
Clonorchiasis, biliary tree and, 178–179, 179*f*
Clopidogrel (Plavix), 598
Closed-loop obstruction, mechanical bowel and, 293, 295*f*
Cloverleaf-shaped skull, 1136
  craniosynostosis with, 1137*f*–1138*f*
  in skeletal dysplasias, 1382
  in thanatophoric dysplasia type 2, 1388–1389, 1389*f*
Clubfoot
  fetal, 1407, 1407*f*
    body stalk anomaly and, 1329
    campomelic dysplasia and, 1395
    in skeletal dysplasia, 1382
    spina bifida and, 1233
  pediatric, 1932
Clubhand, fetal, 1407
  in skeletal dysplasias, 1382
Clustered macrocysts, in breast, 779, 780*f*
Clustered microcysts, in breast, 782
CMA. *See* Chromosomal microarray analysis
CMV. *See* Cytomegalovirus infection
CNS. *See* Central nervous system
CNVs. *See* Copy number variants
Coagulation necrosis, from HIFU, 32
Coagulopathies, small bowel obstruction from, 1843
Coarctation
  of aorta, 1291, 1292*f*
    fetal, hydrops from, 1423–1424
    hypoplastic left heart syndrome with, 1287
  of frontal horn, 1522, 1522*f*
  of lateral ventricles, 1566
Coccygeal dimples, 1679, 1680*f*
Coccyx
  agenesis of, 1689
  development of, in infants, 1677, 1680*f*
Cogwheel sign, 587–588
Colitis
  infectious, pediatric, 1852
  pseudomembranous, 296–297, 298*f*
  tuberculosis, 287–288
  ulcerative, 266–267
Collagen bundles, 859
Collagen vascular disease, maternal, fetal AVB from, 1297
Coloboma, 1143, 1146*f*
Colon
  carcinoma of, 261–264, 263*f*–264*f*
    pediatric, 1880
  diverticula of, 290, 291*f*
  fetal, 1308–1316
    anorectal malformations and, 1310–1312, 1311*f*
    MMIHS and, 1362–1363
  pediatric, 1847–1848
    ectopic or imperforate anus and, 1847–1848, 1850*f*
    interventional sonography and anatomy of, 1950
    normal anatomy of, 1847, 1850*f*
    sonographic technique for, 1847
Color assignments, changing, in color Doppler, 933
Color Doppler ultrasound, 24, 25*b*
  aliasing in, 28, 29*f*, 966
  for breast assessment, 769–772, 770*f*–773*f*
  for carotid stenosis evaluation, 932–935
    advantages and pitfalls of, 934–935, 934*b*, 934*f*
    bruit from, 933, 934*f*
    optimal settings in, low-flow vessel evaluation, 933–934, 933*b*, 934*f*
  color assignments in, changing, 933
  for Crohn disease, 268*t*, 269, 272*f*
  Doppler beam in, vessel paralleling, 933
  for epididymitis, pediatric, 1896, 1896*b*
  in fetal heart assessment, 1275–1277, 1282*f*

Color Doppler ultrasound *(Continued)*
green-tag feature in, 932–933
interpretation of, 28, 28*f*–29*f*
interventional sonography, pediatric and, 1945
limitations of, 25*b*
for neonatal/infant brain, 1573–1574
operating modes in, 30–31
for pancreatic carcinoma, 241, 241*b*, 241*f*–243*f*, 241*t*
for percutaneous needle biopsies, 599
in placenta accreta diagnosis, 1471
in placenta blood flow assessment, 1468–1469
in pleural fluid imaging, 1709, 1710*f*
power compared to conventional, 25, 26*f*
PRF in, 28, 29*f*, 30–31
process of, 24, 26*f*
prostate cancer and, 404*f*, 406
slow-flow sensitivity settings on, 939
for testicular torsion, pediatric, 1895–1899, 1896*b*
for testicular tumors, pediatric, 1901–1902
in ureteral calculi detection, 337, 339*f*
for ureteral jets evaluation, 1781*f*
weighted mean frequency in, 28
Color gain, in renal artery duplex Doppler sonography, 449
Color streaking, breast cysts with, 775, 776*f*
Colpocephaly, 1202*f*
in Chiari II malformation, 1526, 1527*f*
in corpus callosum agenesis, 1528, 1530*f*
Column of Bertin, in kidney development, 1781, 1783, 1784*f*
Coma, brain death differentiated from, 1618–1620, 1620*f*
Comet-tail artifacts, 202, 695
in benign and malignant thyroid nodule differentiation, 712–713
in degenerative cysts of thyroid, 1646, 1647*f*
Common bile duct
anastomosis of, for liver transplantation, 625
dilation of, cylindrical or saccular, pediatric, 1735, 1736*f*
diverticula of, 1735
stones in, 173–174, 173*f*
acute pancreatitis and, 221
liver transplantation complications with, 629, 632*f*
Common femoral vein
as landmark for femoral hernias, 482, 485*f*
normal anatomy of, 500, 981*f*
Complete molar pregnancy, 1078, 1079*f*
Complete subclavian steal, 952–953, 953*b*, 953*f*
Complete TGA, 1289, 1289*f*
Complicated cysts, of breast, 775–780, 776*f*
Compression
of amplitudes, 9
ballottement and, 768
for breast sonography, 768, 772, 773*f*
of femoral vein, normal, 982*f*
maneuvers, for dynamic ultrasound of hernia, 474, 475*f*
for parathyroid gland adenomas detection, 739
soft tissue ganglia causing, 865
in sound wave, 2, 2*f*
Compression sonography, 258–260, 261*f*
Computed tomography (CT)
in abdominal aortic aneurysm
rupture evaluation and, 438, 439*f*
for screening and surveillance, 437
treatment planning with, 438
in interventional sonography, pediatric, 1943, 1943*t*
parathyroid adenomas and accuracy of, 748, 748*f*
Computed tomography (CT) *(Continued)*
pediatric chest, sonography compared to, 1709, 1710*f*–1711*f*
for percutaneous needle biopsies, 599
three-dimensional, in skeletal dysplasia evaluation, 1384–1385
Concentric hypertrophy, 1294–1295
Conceptual age, definition of, 1443–1444
ConfirmMDx test, 396
Congenital adrenal hyperplasia (CAH)
adrenal rests in, 832–833, 833*f*, 1824, 1900–1901
pediatric, 1822–1824, 1824*f*, 1900–1901
Congenital anomalies of kidney and urinary tract (CAKUT), 1336
Congenital bilateral absence of the vas deferens (CBAVD), 394
Congenital coxa vara, atypical hips and, 1932
Congenital cystic adenomatoid malformation (CCAM), 1246, 1248*t*
fetal, hydrops from, 1426
Congenital diaphragmatic hernia (CDH), 1248*t*, 1258–1264
anomalies associated with, 1263
bilateral, 1262
fetal lung size and, 1244
FETO for, 1264
left-sided, 1258–1259, 1260*f*
morbidity and mortality from, 1264, 1264*t*
prognosis of, 1261–1262, 1262*b*
right-sided, 1259, 1261*f*
survival predictors in, 1262, 1262*b*
in utero therapy for, 1264
Congenital heart block, fetal, 1297, 1297*f*
hydrops from, 1425
Congenital heart defects, thickened NT in, 1095–1097, 1096*f*
Congenital heart disease (CHD)
chromosomal anomalies in, 1270
extracardiac malformations in, 1270
fetal arrhythmia and, 1270–1273
hydrops and, 1270
IVF and, 1270–1273
MCDA twins and, 1270–1273
risk factors associated with, 1270, 1271*t*–1272*t*
recurrence, in offspring, 1273*t*
recurrence, in siblings, 1273*t*
Congenital high airway obstruction (CHAOS), 1248*t*, 1253–1255, 1254*f*
hydrops from, 1426
Congenital hypothyroidism, 694
pediatric ovarian cysts and, 1875
Congenital infantile myofibromatosis, 1664, 1665*f*
Congenital lobar emphysema, 1246
Congenital lobar overinflation (CLO), 1246, 1251–1252, 1253*f*
Congenital malformations, obstetric sonography and, 1041
Congenital myopathy, atypical hips and, 1932
Congenital nephrotic syndrome, CKD and, 1796–1798
Congenital pulmonary airway malformation (CPAM)
classification of, 1248
differential diagnosis of, 1248*t*
fetal, 1246–1252
hydrops development and, 1248–1249, 1426, 1427*f*
pediatric, 1715–1716, 1717*f*
pleuropulmonary blastoma differentiated from, 1252–1253
sonographic diagnosis of, 1248, 1249*f*
volume ratio of, 1248, 1250
Congestive heart failure
gallbladder wall thickening and, 199*f*
neonatal/infant, 1566
Conglomerate masses, Crohn disease and, 269
Conjoined tendon insufficiency
direct inguinal hernia and, 479–481, 483*f*–484*f*
sports hernia and, 485–486, 489*f*
Conjoined twins, 1115–1116
complications with, 1129–1130, 1130*f*
Conn syndrome, adrenal adenomas in, 419
Connatal cysts, 1566
Connective tissue, dense fibrous, homogeneous plaque and, 920–921
Conradi-Hünermann syndrome, 1399
Constrictive amniotic bands, 1182–1183
Continuous ambulatory peritoneal dialysis, 521
Continuous wave (CW) devices, 8
Continuous wave Doppler, 24, 25*f*
Continuous wave probes, with duplex pulsed Doppler, 939
Continuous wave ultrasound, 36
Contraceptive devices, intrauterine, 529, 552–554, 553*f*
Contraceptives, oral, hepatic adenomas and, 1746
Contrast, speckle effect on, 13–15, 14*f*
Contrast agents, 41–42. *See also* Blood pool contrast agents
acoustic cavitation and, 43, 44*b*
avoidance of, in obstetric sonography, 1038
blood pool, 55–56
disruption-replenishment imaging and, 66–67, 67*f*
echo enhancing, 57*f*
harmonic imaging with, 58–64
in hydrosonovaginography, 1870–1871, 1871*f*
intermittent harmonic power Doppler imaging and, 66, 66*f*
intermittent imaging with, 64–67, 66*f*
intravenous Doppler, 1749–1750
intravenous ultrasound, 1746
microbubbles as, 53–54, 54*f*
behavior of, incident pressure and, 56–58, 57*t*
disruption of, 64–67, 66*f*
FNH characterization with, 106, 106*f*, 108*t*, 109*f*
future of technology for, 68–69, 69*f*–70*f*
HCC characterization with, 106, 106*f*
hemangioma characterization with, 106, 106*f*–107*f*, 108*t*
inertial cavitation and, 67–68
lesional enhancement with, 105, 106*f*–107*f*, 109*f*
liver mass characterization with, 105–106, 106*f*–107*f*, 108*t*, 109*f*–110*f*
MI and, 58, 58*b*, 105
need for, 56–58, 57*f*
regulation of, 68
safety of, 67–68
in musculoskeletal interventions, 898
nonlinear echoes and, 58–64
amplitude and phase modulation imaging and, 64, 65*f*
harmonic B-mode imaging and, 60
harmonic spectral and power Doppler and, 60–61, 60*f*–62*f*
plane-wave contrast imaging and, 64
pulse inversion Doppler imaging and, 63–64
pulse inversion imaging and, 62–63, 62*f*–63*f*
temporal maximum intensity projection imaging and, 64, 65*f*
tissue harmonic imaging and, 61–62
perfluorocarbons in, 56
for liver mass detection, 107, 111*f*
requirements for, 54–56

Contrast agents *(Continued)*
triggered imaging and, 65
types of, 54–56
in water enema technique, 1870–1871, 1871*f*
Contrast effect, of steroid anesthetic mixture, 899, 899*f*
Contrast pulse sequence (CPS), 64
Contrast-enhanced ultrasound (CEUS)
adenoma diagnosis with, 116–117, 117*f*
backscatter increased with, 107, 111*f*
for breast lesions, 773–774
cavernous hemangioma characterization with, 111, 113*f*
for Crohn disease, 269, 273*f*
Crohn disease identification with, pediatric, 1853, 1854*f*
in fatty liver diagnosis, 91–92
FNH diagnosis with, 113–115, 115*f*
gut wall and, 261
HCC detection with, 120–122, 123*f*
Hilar cholangiocarcinoma assessment with, 188, 191*f*
liver metastases diagnosis with, 128–129, 130*f*
for pancreas, 251
for pancreas transplantation, 676
for prostate cancer, 406
for thyroid gland assessment, 692, 714–715
Contrast-to-noise ratio, spatial compounding and, 13–15, 15*f*
Conus medullaris
determining position of, 1677, 1679*f*
fetal, location of, 1218–1221, 1221*f*, 1673, 1673*f*
low and tethered, caudal agenesis type II and, 1689
Conus septum, TOF and, 1288
Cooper ligaments, 761, 761*f*–763*f*
Copy number variants (CNVs), 1088
Coracoacromial ligament, 878–879
Coracobrachialis muscle, 878–879
Coracoclavicular ligaments, 878–879
Coracohumeral ligament, 878–879
Coracoid process, 878–879, 879*f*
Cordocentesis, 1434, 1434*f*
Cornelia de Lange syndrome, microcephaly in, 1194
Cornua
hematometra and, 551–552
"Cornual pregnancy", 1073
Coronary bypass graft, radial artery evaluation for, 977–978, 980*f*
Corpora amylacea, 387
Corpora quadrigemina, 1518
Corpus callosum
agenesis of
in Chiari II malformation, 1526, 1528*f*
fetal brain and, 1199–1201, 1202*f*, 1203*b*
neonatal/infant neural tube closure disorders and, 1526–1528, 1529*b*, 1530*f*–1533*f*
periventricular nodular heterotopia and, 1199*f*
VM and, 1177
dysgenesis of, fetal brain and, 1199–1201, 1203*b*
lipoma of, 1529, 1533*f*
in rhombencephalosynapsis, 1192
thinning of, in PVL, 1552
Corpus luteum
angiogenesis of, 1063
cysts of, 570
pediatric, 1875
development of, 568
formation of, 1049
Corrected TGA, 1290, 1290*f*
Cortical development malformations, fetal brain and, 1193–1203
absence of septi pellucidi as, 1201–1203
cerebrohepatorenal syndrome as, 1196
chondrodysplasia punctata as, 1196
Cortical development malformations, fetal brain and *(Continued)*
classification of, 1194*b*
corpus callosum agenesis/dysgenesis as, 1199–1201, 1202*f*, 1203*b*
focal changes in, 1196
hemimegalencephaly as, 1195
heterotopia as, 1196, 1199*f*
intracranial calcifications as, 1195*f*, 1203, 1204*f*
lissencephaly as, 1195–1196, 1196*f*–1197*f*
macrocephaly as, 1194–1195
megalencephaly as, 1194–1195
microcephaly as, 1194, 1195*f*
polymicrogyria as, 1196, 1198*f*
schizencephaly as, 1196, 1199*f*
SOD as, 1201–1203, 1203*f*
TSC and, 1198, 1200*f*
Cortical nephrocalcinosis, 339
pediatric, 1798, 1798*b*, 1798*f*
Corticosteroids, for musculoskeletal injections, 900
Cortisol, secretion of, 417
Couinaud anatomy, of liver, 76–77, 77*t*, 78*f*
Coxa vara, congenital, atypical hips and, 1932
Coxsackie virus, 1203–1204
Coxsackie virus infection, fetal hydrops from, 1431
Coxsackievirus B, endocardial fibroelastosis from, 1294
CPAM. *See* Congenital pulmonary airway malformation
CP/CPPPS. *See* Chronic prostatitis/chronic pelvic pain syndrome
CPS. *See* Contrast pulse sequence
Cranial Bone Thermal Index (TIC), 39–40
Cranial hairy tuft, diastematomyelia and, 1689
Cranial neuropore, in spine embryology, 1217
Craniocervical junction, in pediatric spine, 1674, 1675*f*
Cranioectodermal dysplasia, 1395
Craniolacunia, in Chiari II malformation, 1526
Craniopharyngioma, intracranial, fetal, 1208
Craniorachischisis, 1179, 1218
Cranioschisis, definition of, 1225*t*
Craniosynostosis
with cloverleaf-shaped skull deformity, 1137*f*–1138*f*
cranial contour indicating, 1382
intracranial compliance in, evaluation of, 1581–1582
metopic, 1137*f*
syndromes associated with, 1136–1139, 1137*f*–1138*f*
Cranium, in skeletal dysplasias, 1382
Crass position, for shoulder ultrasound
modified, 881, 883*f*–884*f*
original, 881, 883*f*
Creeping fat, Crohn disease and, 269, 271*f*
Cremasteric (external spermatic) artery, 821, 821*f*
Cremasteric reflex, 846
CREST. *See* Carotid Revascularization Endarterectomy Versus Stenting Trial
CRL. *See* Crown-rump length
Crohn disease
anatomy affected by, 268
appendicitis associated with, 285, 287*f*, 1862*f*
CEUS for, 269, 273*f*
classic features of, 269
color Doppler ultrasound for, 268*t*, 269, 272*f*
complications of, 269–276
fistula formation as, 276, 279*f*–280*f*
incomplete mechanical bowel obstruction as, 274, 276*f*
inflammatory masses as, 275–276, 278*f*–279*f*
localized perforation with phlegmon as, 274–275, 277*f*
perianal inflammation as, 276, 281*f*, 305–306
strictures as, 269–274, 275*f*–276*f*
Crohn disease *(Continued)*
conglomerate masses and, 269
creeping fat and, 269, 271*f*
diagnosis of, 267–268
gastrointestinal tract and, 266–269
gut wall thickening and, 269, 270*f*–271*f*
hyperemia and, 269, 272*f*–273*f*
intramural sinus tract in, 269, 274*f*
lymphadenopathy in, 269, 272*f*
management of, 266–267
mucosal abnormalities and, 269, 274*f*
pediatric, 1853, 1854*f*
sonographic assessment of, 268, 268*b*, 268*t*
transperineal scanning in, 276
Crossed-fused ectopia, 318, 318*f*
pediatric, 1784–1785, 1785*f*
Crouzon syndrome
craniosynostosis in, 1136–1138
midface hypoplasia in, 1148
Crown-rump length (CRL), 1054
accurate, criteria for, 1092, 1092*b*
early pregnancy failure and, no heartbeat and, 1063, 1064*f*
embryos with less than 7 mm, and no heartbeat, 1064
in gestational age determination, 1445, 1446*f*, 1446*t*
in gestational age estimation, 1062
gestational sac with small MSD in relationship to, early pregnancy failure and, 1066, 1067*f*
NT compared to, 1089, 1090*f*
Cryptorchid testes, 823
Cryptorchidism
testicular microlithiasis and, 1904
testis and, 851, 851*f*
pediatric, 826
Crystalline form, of injectable steroids, 900
CT. *See* Computed tomography
Cubital tunnel, 865–866
Cul-de-sac
anterior, 528
fluid in, 568–569, 569*f*
posterior, 528, 566
Cumulus oophorus, 1049
Currarino triad, 1689
Curved array transducers
beam steering in, 10–11, 11*f*
use and operation of, 12
Cushing disease, adrenal adenomas in, 419
Cushing syndrome, 832–833
adrenal adenomas in, 419
pediatric, adrenal rests in, 1900–1901
Cutaneous rapidly involuting congenital hemangiomas, 1742–1743
CVS. *See* Chorionic villus sampling
CW devices. *See* Continuous wave devices
Cyclopia, 1140
alobar HPE and, 1534–1535
Cystadenocarcinoma(s)
mucocele of appendix and, 299
ovarian
mucinous, 580*f*, 581
pediatric, 1880
serous, 580–581, 580*f*
Cystadenoma(s)
biliary, 82, 83*f*
epididymal, paratesticular, 1904
mucocele of appendix and, 299
ovarian
mucinous, 580*f*–581*f*, 581
pediatric, 1880
serous, 580–581, 580*f*
papillary, of epididymis, 840–841
Cystic adenomatoid malformations, pediatric, 1715

Cystic artery, 194
  prominent, in acute cholecystitis, 197*f*, 198–199
Cystic dysplasia, testicular, 830
  pediatric, 1891–1892, 1891*f*
Cystic encephalomalacia, 1538, 1539*f*
Cystic fibrosis (CF)
  fatty infiltration of liver in, 1740*f*
  fetal, hydrops from, 1428
  fetal echogenic bowel and, 1316
  fetal liver calcifications and, 1316–1318
  gastrointestinal tract and, 300
  ileal obstruction and, 1310
  inborn errors of metabolism and, 1738
  ovarian cysts and, pediatric, 1875
  pediatric pancreatitis and, 1862–1864
Cystic hygroma(s). *See also* Lymphatic malformations
  in aneuploidy screening, 1093, 1093*f*
  hydrops from, 1425
  thickened NT and, 1096*f*
  in Turner syndrome, 1106–1107, 1106*f*
Cystic kidney disease, CKD and, 1796–1798
Cystic meconium peritonitis, 1842–1843, 1846*f*
Cystic metastases, 82
  of liver, 125, 128*f*
Cystic periventricular leukomalacia, 1551–1552, 1552*f*
Cystic presacral lesions, pediatric, 1915
Cystic teratomas, ovarian, 582–584, 582*b*, 583*f*
Cystic tumor(s)
  arachnoid cysts differentiated from, 1192–1193
  cavum veli interpositi cysts differentiated from, 1170
Cystinosis, CKD and, 1796–1798
Cystitis
  chronic, 333, 333*f*
  cystica, pediatric, 1908
  emphysematous, 333, 334*f*
  genitourinary, 333
  glandularis, pediatric, 1908
  granulomatous, pediatric, 1908
  hemorrhagic, pediatric, 1908, 1910*f*
  infectious, 333, 334*f*
  interstitial, 372, 373*f*
  pediatric urinary tract infection and, 1794, 1796*f*–1797*f*, 1908, 1910*f*–1911*f*
  pseudopolyps and, 333, 333*f*
Cystitis cystica, 333
Cystitis glandularis, 333
Cystogenesis, 1524, 1525*b*
Cystoscopy, for lower urinary tract obstruction, 1363–1365
Cyst(s). *See also* Dermoid cyst(s); Duplication cysts; Epidermoid cyst(s); Kidneys, fetal, cystic disease of; Kidneys, pediatric, cystic disease of; Kidney(s), cysts of; Pancreas, cystic neoplasms of; Pseudocyst(s)
  in adenomyosis, 540*b*, 541, 542*f*
  adnexal, in pregnancy, 1020
  adrenal, 421–422, 422*b*, 423*f*
  amnion inclusion, 1061
  anechoic, 331
  arachnoid
    cavum veli interpositi cysts differentiated from, 1170
    corpus callosum agenesis and, 1526–1528
    fetal brain and, 1192–1193, 1193*f*
    of neonatal/infant brain, 1563–1565, 1565*b*
    spinal canal and, pediatric, 1695–1697, 1696*f*
  Baker, 870, 870*f*
    injection for, 907–909, 908*f*
Cyst(s) *(Continued)*
  Blake pouch
    arachnoid cysts differentiated from, 1192–1193
    sonographic appearance of, 1170, 1173*f*
  branchial
    type I, pediatric, 1639, 1651, 1651*f*
    type II, pediatric, 1639–1640, 1651, 1652*f*
    type III, pediatric, 1651, 1652*f*
  breast, 774–785
    acorn, 778*f*
    aspiration of, ultrasound-guided, 811, 813*f*
    clustered macrocysts and, 779, 780*f*
    clustered microcysts and, 782
    with color streaking, 775, 776*f*
    complex, 780–785, 782*f*
    complicated, 775–780, 776*f*
    Doppler ultrasound for differentiating, 769–770, 770*f*
    eggshell calcification and, 779, 780*f*
    fat-fluid levels in, 775, 778*f*
    fibrocystic change and, 775
    foam, 779, 781*f*
    inflammation and infection of, 782–785, 785*f*
    lipid, 775–779, 779*f*
    microcysts and, 782, 784*f*
    milk of calcium and, 775, 776*f*–777*f*
    mural nodules and, PAM causing, 782, 783*f*–784*f*
    papillary lesions and, 782
    septations within, 782, 783*f*
    simple, 774, 775*f*
    of skin origin, 779, 781*f*
  bronchogenic, pediatric, 1650, 1716, 1718*f*
  chocolate, 574–575
  choledochal
    of biliary tree, 168–170, 169*f*–170*f*
    fetal duodenal atresia mistaken for, 1309
    of fetal gallbladder, 1319, 1320*f*
    neonatal jaundice and, 1735–1737, 1735*f*–1736*f*
    pediatric pancreatitis and, 1862–1864
  choroid plexus
    fetal brain and, 1170, 1173*f*
    neonatal/infant brain and, 1565, 1566*f*
    spina bifida and, 1233
    in trisomy 18, 1103*f*, 1104
    in trisomy 21, 1101
  connatal, 1566
  corpus lutein, 570
    pediatric, 1875
  daughter, 331, 332*f*
    in *Echinococcosis*, 1748
  decidual, 1054
  dorsal midline, in corpus callosum agenesis, 1528, 1531*f*
  ejaculatory duct, 392
  embryonic, 1077, 1077*f*
  endometrial, 547–548
  epididymal, 839, 842*f*
    pediatric, 1902–1903, 1903*f*
  esophageal, pediatric, 1650
  fetal
    bronchogenic, 1255–1256, 1255*f*, 1255*t*
    cortical, in renal dysplasia, 1347–1348
    neurenteric, 1256
    ovarian, 1369, 1369*f*
    pancreatic, 1320
    renal, 1346–1352
    splenic, 1320–1322, 1322*f*
  filar, in newborn, 1674–1675, 1678*f*
  follicular, 568
    pediatric, 1875
  foregut, pediatric, 1650
Cyst(s) *(Continued)*
  frontal horn, neonatal/infant brain and, 1522, 1522*f*, 1566
  ganglion, 869–870, 869*f*
    injection for, 907–909, 909*f*
  Gartner, pediatric, 1883–1884
  gastrointestinal
    congenital, 297, 298*f*
    pediatric, 1860–1862, 1863*f*–1864*f*
  gel, 779, 781*f*
  hydatid, 89, 89*f*–90*f*
    in *Echinococcosis*, 1748
    renal, 331, 332*f*
    splenic, 147, 150*f*
  inclusion
    amnion, 1061
    epidermal, 779
    peritoneal, 508–509, 509*f*, 573, 573*f*
    surface epithelial, 569, 573
    vaginal, pediatric, 1883–1884
  infrahyoid space, pediatric, 1650
  inspissated, 779, 781*f*
  interhemispheric, in corpus callosum agenesis, 1201
  intratesticular, 829, 830*f*
  of kidneys, 356–365
    percutaneous management of, 617–618, 619*f*
  of kidneys, pediatric, congenital, 1816–1818
    dialysis and acquired, 1816–1818, 1817*f*
    after liver transplantation, 1816–1818
    in TSC, 1816, 1817*f*
    in VHL disease, 1816
  liver, 82, 82*f*–83*f*
    autosomal dominant polycystic kidney disease and, 83
    benign, 82
    fetal, 1318, 1318*f*
    percutaneous management of, 618
    peribiliary, 82–83
  mesenteric
    fetal, ovarian cysts differentiated from, 1369
    gastrointestinal cysts differentiated from, 1860, 1863*f*
    pediatric, ovarian cysts differentiated from, 1875
    peritoneal, 509–510, 510*f*
  milk of calcium, 653, 657*f*
  müllerian duct, 392
    pediatric, 1908, 1910*f*
  nabothian, 533, 535*f*, 1499
  neurenteric, pediatric, 1686–1688, 1724
  omental, pediatric ovarian cysts differentiated from, 1875
  ovarian
    dermoid, 582–584, 583*f*
    fetal, 1369, 1369*f*
    functional, 570–571, 571*f*
    hemorrhagic, 570–571, 571*f*, 575
    menstrual cycle and follicular, 568
    neonatal, 1876*f*
    paratubal, 573
    parovarian, 573
    percutaneous management of, 618–619
    peritoneal inclusion, 573, 573*f*
    postmenopausal, 569–570, 571*f*
    surface epithelial inclusion, 569, 573
    in triploidy, 1105*f*
  ovarian, pediatric, 1873–1877
    hemorrhagic, 1877, 1878*f*–1879*f*
    in polycystic ovarian disease, 1877–1878, 1879*f*
    torsion and, 1875–1876, 1876*b*, 1877*f*
  pancreatic, 242–248, 243*f*
    congenital, 1865
    fetal, 1320

Cyst(s) *(Continued)*
simple, 243, 244*f*
VHL disease and, 243, 244*f*
paralabral, injection for, 907–909, 910*f*–911*f*
parameniscal, 907–909
paramesonephric duct, pediatric, 1883–1884
paraurethral, pediatric, 1883–1884
parovarian, pediatric, 1875, 1876*f*
percutaneous management of, 617–619, 619*f*
peritoneal
inclusion, 508–509, 509*f*
mesenteric, 509–510, 510*f*
periventricular, of neonatal/infant brain, 1566, 1566*f*
pineal, 1170
popliteal, pediatric, 1939
porencephalic, neonatal/infant brain and, 1537, 1565
posterior fossa subarachnoid, Dandy-Walker malformation differentiated from, 1190, 1531, 1531*b*
prostate, 388, 390–392, 391*f*
in renal cell carcinoma, 343, 343*f*
rhombencephalon, 1077, 1077*f*
round ligament, simulating groin hernias, 500, 501*f*
scrotal, extratesticular, 839, 842*f*
sebaceous, 779, 781*f*
seminal vesicle, 392, 393*f*
pediatric, 1908, 1910*f*
simulating groin hernias, 499–500, 501*f*
spermatic cord, pediatric, 1902–1903
splenic, 146–148, 146*b*, 148*f*–151*f*
endothelial-lined, 148
epidermoid, 146–147, 148*f*–149*f*
false, 146–147, 149*f*
fetal, 1320–1322, 1322*f*
hydatid, 147, 150*f*
pediatric, 1769
primary congenital, 146–147, 148*f*–149*f*
pseudocysts as, 146–147, 149*f*
subchorionic
maternal floor infarction with, 1474, 1476*f*
placental, 1474, 1477*f*
subependymal, 1543–1544
of neonatal/infant brain, 1566, 1567*f*
of suprahyoid space, pediatric, 1639–1640, 1640*b*, 1640*f*–1641*f*
tailgut, 297, 298*f*
testicular, 829, 829*b*
cystic dysplasia and, 830
epidermoid, 830*f*, 831
intratesticular, 829, 830*f*
simple, pediatric, 1901–1902
tubular ectasia of rete testis and, 829–830, 830*f*
theca lutein, 570, 572
pediatric, 1875
thymic, 1652, 1653*f*, 1723–1724
thyroglossal, duct, pediatric, 1640, 1643, 1644*f*–1645*f*
thyroid
calcifications of, 695
pediatric, 1646, 1647*f*
tunica albuginea, 829, 830*f*
tunica vaginalis, 829, 830*f*
pediatric, 1902–1903
umbilical cord, 1483, 1483*f*
sonographic appearance of, 1061, 1061*f*
in trisomy 18, 1103*f*
urachal, 322, 323*f*
ovarian cysts differentiated from, 1369
pediatric, 1907–1908, 1909*f*
pediatric hydronephrosis and, 1791, 1792*f*–1793*f*
pediatric ovarian cysts differentiated from, 1875
Cyst(s) *(Continued)*
utricle, 391*f*, 392
vallecula, pediatric, 1640, 1641*f*
of vas deferens, 842*f*
Cytogenesis, 1513*b*, 1524
Cytomegalovirus (CMV) infection, 91
in acute typhlitis, 287–288, 289*f*
congenital, neonatal/infant brain and, 1558–1560, 1559*f*
fetal
brain development and, 1203–1204, 1205*f*
hydrops from, 1431–1432
hyperechogenic kidneys in, 1351
fetal echogenic bowel and, 1315*f*
neonatal/infant, schizencephaly from, 1536–1537, 1558
Cytopathologists, definition of, 600
Cytotrophoblast cells, 1466*f*

D

Dabigatran, 598
Dacryocystocele, 1143, 1147*f*
Damping materials, in transducers, 8
"Dancing megasperm", 841
Dandy-Walker complex, VM and, 1177
Dandy-Walker continuum, 1190–1191
Dandy-Walker malformation, 1190
arachnoid cysts differentiated from, 1192–1193
in cerebellum, 1190, 1190*f*
corpus callosum agenesis and, 1526–1528
differential diagnosis of, 1190, 1192–1193, 1531–1532, 1531*b*
etiology of, 1530
mega-cisterna magna differentiated from, 1192
neonatal/infant neural tube closure disorders and, 1529–1532, 1530*b*, 1533*f*–1534*f*
sonographic findings of, 1530*b*
in triploidy, 1105*f*
ventriculoperitoneal shunting for, 1530
Dandy-Walker spectrum, 1530–1531
Dandy-Walker variant, 1190–1191, 1530
Dartos fascia, 846
Daughter cysts, 331, 332*f*
in *Echinococcosis*, 1748
DCIS. *See* Ductal carcinoma in Situ
DDH. *See* Development dysplasia of the hip
de la Chapelle dysplasia, 1396
de Morsier syndrome, 1201–1203. *See also* Septo-optic dysplasia
de Quervain disease, 724
de Quervain tendinosis, injection for, 904, 905*f*
de Quervain thyroiditis, 1645
Decibel, 5–7
Decidua, 1466*f*
Decidua basalis, 1054, 1465–1466
Decidua basalis–chorion frondosum, 1054
Decidua capsularis, 1054, 1465–1466
Decidua vera, 1054,
Decidual cysts, 1054
Decidual reaction, 1049
Deep venous thrombosis (DVT). *See also* Peripheral veins
acute
brachial veins and nonocclusive, 994*f*
in GSV, 984, 984*f*
lower extremity, 983–984, 983*f*–985*f*
upper extremity, 992–994, 994*f*–995*f*
blood flow and
absent, 992–994
slow, 984, 988*f*
of calf, 982
central venous catheterization related to, 935, 995*f*
chronic
in brachial vein, 994–995, 996*f*
calcifications indicating, 984, 987*f*
Deep venous thrombosis (DVT) *(Continued)*
of IJV, 994*f*
lower extremity, 984, 986*f*–987*f*
nonocclusive, 992, 994*f*
in profunda femoris vein, 987*f*
upper extremity, 994–995, 995*f*–996*f*
in femoral vein, duplicated, detecting, 988, 988*f*
follow-up recommendations for, 989
pulmonary embolism from
lower extremity, 979, 981*f*
upper extremity, 994
ultrasound examinations of
indications in, 979
limitations of, 989
venous insufficiency caused by, 989, 990*f*
Default output power, for obstetric sonography, 1035
Deferential artery, 821, 821*f*
Definity, 56
Deformations, definition of, 1399
Delivery. *See also* Preterm birth
fetal hydrops and, 1436
preterm, 1495–1496
Deltoid muscle, 878–879, 878*f*
Demineralization, of spine, in skeletal dysplasias, 1382
Depigmentation, complicating injectable steroids, 901
Depth gain compensation, 8
Dermal sinus tract
dorsal, pediatric, 1686, 1688*f*
focal, 1674
tethered cord and, 1679
Dermoid cyst(s)
hemorrhagic ovarian cyst differentiated from, 1877
neck, pediatric, 1652–1654, 1654*f*
ovarian, 582–584, 583*f*
in suprahyoid area, 1640
Dermoid mesh, 582–583, 583*f*
Dermoid plug, 582, 583*f*
DES. *See* Diethylstilbestrol
Desmoid tumors, simulating anterior abdominal wall hernias, 500–501, 502*f*
Desmoplastic small round cell tumors, 1860
Detrusor areflexia, 372–374, 373*f*
Detrusor hyperreflexia, 372–374, 373*f*
Development dysplasia of the hip (DDH), 1920–1930
causes of, 1921
clinical overview of, 1920–1921
dynamic sonographic technique for, 1922–1927
anterior view for, 1927, 1929*f*
coronal/flexion view for, 1925–1927, 1926*f*
coronal/neutral view for, 1923–1924, 1924*f*–1925*f*
history of, 1922
stress maneuvers for, 1923
technical factors in, 1922–1923
transverse/flexion view for, 1927, 1928*f*
transverse/neutral view for, 1927
evaluation during treatment and, 1929–1930
evaluation of infant at risk and, 1927–1929
incidence of, 1920–1921
mechanism of, 1921
minimum standard examination for, 1922*b*
risk factors of, 1921*b*
screening for, 1921
Dextrocardia, 1273
Dextroposition, 1273, 1274*f*
Dextrotransposition, of great arteries, 1289–1290
DFI. *See* Direction of flow index

Diabetes mellitus
chronic renal failure in, 372
maternal
caudal agenesis and, 1689
LGA fetus and, 1454, 1455*t*
NTDs from, 1218
Dialysis
acquired cystic kidney disease associated with, 364
acquired renal cysts in, pediatric, 1816–1818, 1817*f*
peritoneal, continuous ambulatory, 521
postoperative ultrasound evaluation for, 996
preoperative ultrasound for, 996
Diamond-Blackfan syndrome, 1401
Diaphragm
duodenal, 1841–1842, 1844*f*
eventration of, 1716
fetal
agenesis of, 1258
defect of anterior, pentalogy of Cantrell and, 1329
development of, 1244*f*, 1245
eventration of, 1258, 1262–1263
gastric, pediatric, 1839, 1840*f*
interventional sonography and anatomy of, pediatric, 1950, 1950*f*
pediatric
disorders of, 1716, 1718*f*–1720*f*
paralysis of, 1716, 1719*f*–1720*f*
rupture of, 1716, 1720*f*
Diaphragm sign, as pleural fluid sonographic sign, 1709
Diaphragmatic hernia
congenital, 1248*t*, 1258–1264
anomalies associated with, 1263
bilateral, 1262
fetal lung size and, 1244
FETO for, 1264
left-sided, 1258–1259, 1260*f*
morbidity and mortality from, 1264, 1264*t*
prognosis of, 1261–1262, 1262*b*
right-sided, 1259, 1261*f*
survival predictors in, 1262, 1262*b*
in utero therapy for, 1264
fetal, hydrops from, 1425
pediatric, 1716, 1718*f*
thickened NT in, 1095–1096
Diaphragmatic pericardium, pentalogy of Cantrell and, 1329
Diaphragmatic slips, 80
Diastasis recti abdominis, 489–490, 489*f*
Diastematomyelia, 1674, 1681
closed spinal dysraphism and, 1688–1689, 1688*f*
fetal, 1234–1235, 1236*f*
Diastolic runoff, prolonged, carotid flow waveforms and, 936–937
Diastrophic dwarfism
findings associated with, 1382
hitchhiker thumb in, 1382, 1406
Diastrophic dysplasia, 1398, 1398*f*
DICA. *See* Distal internal carotid artery
Dichorionic diamniotic twins, 1019*f*, 1115–1116, 1116*f*
growth discrepancy in, 1123*f*
placental findings in, 1119
sonographic findings of, chorionicity and, 1119, 1120*f*
Didelphys uterus, 534, 536*f*–537*f*, 1881
Diencephalon, 1077
Diethylstilbestrol (DES)
cervical assessment in, 1505
uterus exposure to, 534, 536*f*, 1881
Diffuse reflectors, 4, 5*f*
Diffuse steatosis, 91, 92*f*
Diffusion tensor imaging, in PVL, 1553
DiGeorge syndrome, 1196
neuroblastoma with, pediatric, 1825
DiGeorge syndrome, fetal thymus evaluation for, 1245
Digestive tube, embryology of, 1304–1305
Digital rectal examination (DRE), 381–382, 387
Dilated bowel, fetal, 1313
Dilated distal ureter, 592
Dilated loops of bowel, 1310, 1311*f*
fetal gastroschisis and, 1323–1324
Dilated loops of small bowel, 1311–1312
Dilated stomach, fetal, 1307, 1308*f*
Diploid karyotype, complete molar pregnancy and, 1078
Diplomyelia, in diastematomyelia, 1236*f*
Direct controls, 48, 49*t*
Direction of flow index (DFI), 1618
Discriminatory level, for seeing gestational sac, 1056
Disjunction, in spine embryology, 1672–1673
Dislocations, pediatric. *See also* Developmental dislocation and dysplasia of hip
frank, of hip, 1927
of hip, developmental, 1920–1930
Displaced-crus sign, as pleural fluid sonographic sign, 1709
Disruption-replenishment imaging, 66–67, 67*f*
Disruptions, definition of, 1376, 1377*t*, 1399
Dissection complications, renal artery stenosis and, 447, 448*f*
Distal cholangiocarcinoma, 188, 192*f*
Distal internal carotid artery (DICA)
SCD and stenosis of, 1606*f*
as transtemporal approach landmark, 1592, 1594*f*
Diuretic therapy, medullary nephrocalcinosis and, 1798
Diverticulation. *See also* Holoprosencephaly
neonatal/infant brain and disorders of, 1532–1536
in organogenesis, 1524, 1525*f*
Diverticulitis
acute, 288–290
classic features of, 288–290
muscular hypertrophy from, 290, 291*f*
pericolonic changes in, 290, 292*f*
sonography of, 290, 290*b*
focally inflamed fat in, 521
right-sided, 285–287, 288*f*
Diverticulosis, spastic, 288–290
Diverticulum(a)
bladder, 374, 374*f*
identification of, 592
calyceal, renal milk of calcium and, 1799, 1800*f*
colonic, 290, 291*f*
of common bile duct, 1735
Hutch, 310
Meckel
intussusception and, 1844–1845, 1849*f*
pediatric appendicitis differentiated from, 1858–1860, 1862*f*
urachal, 322, 323*f*
pediatric, 1907–1908, 1909*f*
urethral, 323, 323*f*
anterior, pediatric, bladder outlet obstruction from, 1906
urinary bladder, transitional cell carcinoma in, 348
ventricular, 1294
vesicourachal, pediatric, 1775, 1791
Dizygotic (fraternal) twins, 1115–1116, 1116*f*
Dolichocephaly, 1136
Donor renal vein, anastomosis, in renal transplantation, 643
Doppler angle, 21–22, 24*f*, 29*b*, 30
Doppler angle theta. *See* Angle theta, Doppler
Doppler beam, vessel paralleling, in color Doppler, 933
Doppler effect, 21–22, 23*f*
Doppler frequency, 29
Doppler frequency shift, 21–22, 23*f*–24*f*
Doppler gain, 30, 33*f*
Doppler indices, 27–28, 27*f*
Doppler spectrum, 925
interpretation of, 25–28, 27*f*
Doppler ultrasound. *See also* Carotid artery(ies), Doppler spectral analysis for; Color Doppler ultrasound; Duplex Doppler sonography; Kidneys, pediatric, vascular disease of, Doppler assessment of; Liver, pediatric, Doppler assessment of; Obstetric sonography; Power Doppler ultrasound; Transcranial Doppler sonography
aliasing in, 29*b*, 32*f*
artifact sources in, 29*b*
backscatter and, 21–22, 23*f*, 35
bioeffects of obstetric sonography and, 1041
for breast assessment, 768–772, 770*f*–773*f*
cysts in, 769–770, 770*f*
cavernous hemangiomas characterized by, 109–110
cirrhosis of liver characteristics in, 95, 95*f*
complete venous, for lower extremity peripheral veins, 989
continuous wave, 24, 25*f*
Doppler angle and, 21–22, 24*f*, 29*b*, 30
Doppler effect and, 21–22, 23*f*
Doppler equations and, 21–22, 23*f*–24*f*
Doppler frequency and, 29
Doppler frequency shift and, 21–22, 23*f*–24*f*
Doppler gain and, 30, 33*f*
Doppler indices and, 27–28, 27*f*
Doppler spectrum and, interpretation of, 25–28, 27*f*
for ductus venosus assessment, 1458, 1459*f*
for fetal well-being assessment, 1458–1460, 1459*f*–1460*f*
FNH characterized by, 113
gut wall evaluation with, 260–261, 262*f*
harmonic spectral and power, 60–61, 60*f*–62*f*
hilar cholangiocarcinoma assessment with, 187–188, 189*f*–191*f*
instrumentation for, 24–25, 25*b*, 25*f*–26*f*
for intussusception, pediatric, 1849*f*
of liver transplantation recipient, pediatric, 1764–1769
lymphadenopathy assessment with, 771–772, 772*f*
for MCA
in fetal alloimmunization detection, 1421, 1422*f*
fetal assessment of, 1458–1460, 1460*f*
for musculoskeletal system, 857, 857*f*
obstetric, sample volume and velocity range in, 1036
operating modes in, 30–31
overview and physics of, 21–30
pediatric kidney assessment with, 1778
pediatric liver assessment with, 1748–1764
placental vascularity and, 1467–1469
portal hypertension assessment with, 1748–1764
for PTN, 1083
pulse inversion, 63–64
pulsed wave, 24, 25*f*
testicular flow, 1890

Doppler ultrasound *(Continued)*
renal arterial stenosis diagnosis from, false-positive, 658, 661*f*
for renal cell carcinoma detection, 343, 344*f*
for renal transplant
assessment, 648, 651*f*–652*f*
pediatric, 1807–1812
renal vascular, 366
sample volume size and, 29*b*, 30
signal processing and display in, 23–24, 24*f*
spatial focusing and, 35
spectral, 60–61, 60*f*–62*f*
in carotid artery analysis, 925–932
for fetal heart assessment, 1275, 1281*f*
spectral broadening in, 24, 24*f*, 29, 29*b*, 31*f*
spectral display in, 25
technical considerations in, 28–30
thermal effects in, 31
for umbilical arteries assessment, 1458, 1459*f*
wall filters in, 29, 30*f*
Dorsal dermal sinus, pediatric, 1686, 1688*f*
Dorsal enteric fistula, pediatric, 1686–1688
Dorsal induction errors, fetal brain and, 1179–1186
amniotic band sequence as, 1180*f*, 1182–1183
anencephaly as, 1179, 1180*f*
cephalocele as, 1179–1182
ciliopathies as, 1182
cranial changes in spina bifida as, 1183–1186, 1184*f*–1185*f*, 1185*t*–1186*t*
encephalocele as, 1179–1182, 1181*f*, 1182*t*
exencephaly as, 1179
Joubert syndrome as, 1182
limb-body wall complex as, 1182–1183
Meckel-Gruber syndrome as, 1182
Dorsal midline cyst, in corpus callosum agenesis, 1528, 1531*f*
Dorsal rectum, in bladder development, 311, 312*f*
Dorsalis pedis artery, 966
DORV. *See* Double-outlet right ventricle
"Double contour sign", 867–869, 868*f*
"Double-bubble" sign, in fetal duodenal atresia, 1309, 1310*f*
Double-decidual sign, 1054, 1056*f*
"Double-duct" sign, 231, 231*f*
Double-outlet right ventricle (DORV), 1288–1289, 1289*f*
Down syndrome, testicular microlithiasis and, 1904. *See also* Trisomy 21
Drainage, ultrasound-guided, 609–617
of abscesses
abdominal, 612
liver, 612–613, 614*f*–615*f*
pediatric, 1953
pediatric, appendiceal, 1956, 1960*f*
pelvic, 612, 613*f*
renal, 617, 618*f*
splenic, 617
transrectal, 1953–1954, 1954*f*
of bile duct fluids, 614–615
of biliary tract fluids, 613–615
catheters for
for interventional sonography, 1948
placement of, 610–611, 611*f*
removal of, 612
selection of, 610–611, 611*f*
contraindications to, 609–610
diagnostic aspiration in, 611
of empyemas, pediatric, 1954, 1958*f*
follow-up care for, 612
of gallbladder fluids, 613–614, 616*f*
imaging methods for, 610, 610*f*
indications for, 609–610
of pancreatic pseudocysts, 615–617, 617*f*
patient preparation for, 611
percutaneous cholangiography and, 1956, 1959*f*
Drainage, ultrasound-guided *(Continued)*
of pleural and peritoneal fluids, pediatric, 1954–1956, 1958*f*
of pleural effusion, 1724–1725
procedure for, 612
DRE. *See* Digital rectal examination
Drop metastasis, 266, 267*f*
Drugs
fetal hydrops from, 1432
illicit use of, fetal gastroschisis and, 1322–1323
nephrotoxic, AKI and, 1796
toxicity of, renal transplantation abnormalities and, 1809
Duct extension, of DCIS, 790–791, 792*f*
Ductal arch, fetal, 1275, 1279*f*
Ductal carcinoma in Situ (DCIS), 789–790, 792*f*
calcifications and, 793, 795*f*
duct extension of, 790–791, 792*f*
Ductal ectasia, mammary ducts and, 762
Duct(s). *See also* Bile duct(s)
mammary
normal sonographic appearance of, 762, 764*f*
subareolar and intranipple, scanning of, 762, 765*f*
pancreatic, 215–218, 219*f*–220*f*
of Santorini, 218, 219*f*
thymopharyngeal, formation of, 1652
of Wirsung, 218, 219*f*
Ductus arteriosus, 1273–1274, 1275*f*
Ductus venosus, 1273–1274, 1275*f*
fetal, Doppler ultrasound assessment of, 1458, 1459*f*
reversed flow in, in aneuploidy screening, 1095, 1095*f*
Duodenal atresia, fetal
dilated fetal stomach differentiated from, 1307
"double-bubble" sign in, 1309, 1310*f*
echogenic bowel and, 1315*f*
small bowel obstruction and, 1308–1309, 1310*f*
Duodenal diaphragm, 1841–1842, 1844*f*
Duodenal duplication cysts, fetal duodenal atresia mistaken for, 1309
Duodenal leaks, after pancreas transplantation, 682
Duodenal stenosis, 1308–1309
Duodenal web, 1841, 1844*f*
Duodenum, 219
atresia of, in trisomy 21, 1097, 1098*f*
pediatric, 1841–1847
anatomy of, 1841, 1841*f*
atresia of, 1841, 1842*f*
congenital obstruction of, 1841–1842, 1842*f*–1844*f*
hematoma of, 1842, 1845*f*
sonographic technique for, 1841
stenosis of, 1841
ulcer in, perforated, gallbladder wall thickening signs in, 201*f*
Duplex Doppler sonography
in Budd-Chiari syndrome, 102–103
celiac artery, 453–455, 455*f*
mesenteric artery, 453–455, 455*f*
interpretation of, 454–455, 456*f*–458*f*
of neonatal/infant brain, 1573–1576
approaches to, 1574, 1575*f*
arterial blood flow in, 1576, 1577*t*
asphyxia and, 1580
brain death and, 1580, 1583*f*
cerebral edema and, 1580
diffuse neuronal injury and, 1580
ECMO and, 1578–1580, 1579*f*
hemodynamics in, 1576–1580
HII and, 1580, 1581*f*–1582*f*
hydrocephalus and, 1581–1583, 1584*f*
intensive care therapies and, 1578–1580
intracranial hemorrhage and, 1580–1581, 1584*f*
Duplex Doppler sonography *(Continued)*
intracranial tumors and, 1585, 1587*f*
measurements in, 1576, 1576*f*–1577*f*, 1576*t*
mechanical ventilation and, 1578, 1579*f*
near-field structures and, 1585, 1588*f*
optimization of, 1574, 1574*b*
pitfalls of, 1585–1589, 1589*f*
safety considerations for, 1574–1576
stroke and, 1580–1581, 1584*f*
uncommon applications of, 1585, 1588*f*
vascular malformations and, 1583–1585, 1585*f*–1587*f*
venous blood flow in, 1578, 1578*f*, 1578*t*
obesity and renal artery in, 447
in portal hypertension, 98
renal artery, 447–450, 450*f*
false-positive/false-negative results with, 450, 450*f*
interpretation of, 450
in ureteral calculi detection, 337–338
Duplex scanner, 24
Duplication anomalies, fetal, 1359–1360, 1359*f*, 1360*b*
Duplication cysts, 297
duodenal, fetal duodenal atresia mistaken for, 1309
enteric, fetal, 1312–1313, 1313*f*
ovarian cysts differentiated from, 1369
esophageal, 1256
gastrointestinal, pediatric, 1860, 1863*f*
ovarian cysts differentiated from, 1875
Dural sinus
fetal
malformations of, 1205
thrombosis of, 1205–1206, 1206*f*
neonatal/infant, thrombosis of, 1585
Duty factor, 36
DVT. *See* Deep venous thrombosis
Dwarfism, diastrophic
findings associated with, 1382
hitchhiker thumb in, 1382, 1406
Dwell time, 36
in obstetric sonography, 1036
Dynamic contrast-enhanced ultrasound, 66–67
Dynamic maneuvers, for hernia imaging, 473–474, 474*f*–475*f*
Dynamic range, of amplitudes, 9
Dysgerminomas, ovarian, 584, 584*f*
pediatric, 1880
pseudoprecocious puberty and, 1887
Dyslexia, obstetric sonography and, 1040
Dysostoses, definition of, 1376, 1377*t*
Dysplastic kidneys, pediatric, 1798, 1798*f*
Dysraphic hamartomas, 1682
Dysraphic lesions, 1679–1680
Dysraphism. *See* Spinal dysraphism, fetal; Spinal dysraphism, pediatric
Dyssegmental dysplasia, 1399
Dystrophic calcification, 339
pediatric urinary tract and, 1799
Dystrophic facies, in Miller-Dieker syndrome, 1195

E

Eagle-Barrett syndrome. *See* Prune belly syndrome
Early pregnancy failure. *See* Pregnancy, first trimester of, early failure of
Ear(s)
embryology of, 1134
fetal
abnormalities of, 1148, 1148*f*
length of, in trisomy 21, 1101
low-set, 1148
Ebstein anomaly, 1286–1287, 1286*f*
Echinococcal disease
adrenal, 423
genitourinary, 331, 332*f*

Echinococcal disease *(Continued)*
peritoneal, 517
splenic, 147, 150*f*
Echinococcosis, in pediatric liver, 1748
Echinococcus granulosus, 613
hepatic infestation by, 88–89
Echinococcus multilocularis, parasitic infestation by, 90
Echocardiography, fetal
five-chamber view in, 1275, 1279*f*
four-chamber view in
apical, 1274–1275, 1277*f*
subcostal, 1274–1275, 1277*f*
indications for, 1270–1273, 1273*b*
M-mode, 1275, 1280*f*–1281*f*
three-vessel and trachea view in, 1275, 1279*f*
timing of, 1274
Echoendoscope, 428–429
Echoes, 3–4. *See also* Nonlinear echoes
fundamental, 58–59
Echogenic bowel
fetal
aneuploidy and, 1315–1316, 1315*f*
bowel obstruction and, 1316
CF and, 1316
conditions associated with, 1315*b*
fetal growth restriction and fetal demise with, 1316
infection and, 1316
intraamniotic bleeding and, 1316
meconium peritonitis and, 1313
in trisomy 21, 1100*f*, 1101
Echogenic capsule, thin, in breast sonography, 797
Echogenic intimal flap, in carotid artery dissection, 946, 948*f*
Echogenic lines, nearly parallel, in normal carotid wall, 918–919, 919*f*
Echogenic metastases, of liver, 125, 128*f*
Echogenic rim, in breast sonography, with hyperechoic spicules, 787–788, 789*f*
Echogenicity, in liver mass detection, 106–107
Echo-ranging, 3
Echovist, 55–56
ECMO. *See* Extracorporeal membrane oxygenation
ECST. *See* European Carotid Surgery Trial
Ectasia, aortic, 440
Ectoderm layer, of trilaminar embryonic disc, 1216–1217, 1217*f*
Ectodermal-neuroectodermal tract, focal, 1674
Ectopia cordis, fetal
abdominal wall and, 1329, 1329*f*
pentalogy of Cantrell and, 1329
structural cardiac anomalies and, 1295, 1296*f*, 1329
Ectopic pregnancy, 1069–1076
abdominal, 1074, 1075*f*
cervical, 1073–1074, 1074*f*
clinical presentation of, 1069–1070
heterotopic gestation and, 1070–1071, 1072*f*
implantation sites of, 1072–1073
abdominal, 1074, 1075*f*
cervical, 1073–1074, 1074*f*
cesarean scar, 1073, 1075*f*
interstitial, 1073, 1074*f*
infertility and, 1070
interstitial, 1073, 1074*f*
management of, 1075–1076
conservative, 1076
failure of, 1076, 1076*f*
laparoscopy for, 1076
medical, 1076
nonspecific sonographic findings in, 1072–1073
adnexal mass and, 1072, 1073*f*
ectopic tubal ring as, 1072, 1073*f*
Ectopic pregnancy *(Continued)*
endometrium and, 1072–1073
free pelvic fluid and, 1072, 1073*f*
pediatric, 1884–1885, 1885*f*
prevalence of, 1070
risk of, 1070*b*
ruptures, hemoperitoneum in, 508*f*
serum β-hCG levels and, 1071
sonographic diagnosis of, 1070–1071, 1070*f*–1071*f*
specific sonographic findings in, 1071–1072, 1072*f*
of unknown location, 1075
Ectopic thyroid tissue, 694
Ectrodactyly, fetal, 1406–1407, 1406*f*
EDD. *See* Expected date of delivery
Edema
breast sonography and, 795
cerebral
neonatal/infant, 1550–1556, 1554*f*–1555*f*, 1580
pediatric, TCD sonography in, 1614, 1617*f*
gut, 295, 297*f*
of ovaries, massive, 578
pediatric, 1878–1879, 1879*f*
scrotal, idiopathic, 846
pediatric, 1898–1899, 1898*f*
subcutaneous, fetal, in hydrops, 1417, 1419*f*–1420*f*
Edematous cord, 1484*f*
Edwards syndrome. *See* Trisomy 18
EF. *See* Endocardial fibroelastosis
EFSUMB. *See* European Federation of Societies of Ultrasound in Medicine and Biology
Eggshell calcification, breast cysts and, 779, 780*f*
EHE. *See* Epithelioid hemangioendothelioma
Ejaculatory ducts, 382*f*–383*f*, 384
cysts of, 392
obstruction of, 393–394
transurethral resection of, 393
Elastography
basic points in, 15–16, 16*b*
for breast assessment, 772–773, 773*f*
gut wall and, 261
for musculoskeletal system, 857
for prostate cancer, 407
shear wave, 16, 17*f*–18*f*, 772
cirrhosis of liver and, 95–96
for pediatric liver, 1764, 1765*f*
strain, 16, 17*f*, 772
for thyroid gland assessment, 692, 714–715, 715*f*–716*f*
transient, 1764
Elbow
injection of, 901
pediatric, dislocations of, 1933–1934
ulnar nerve dislocation at, 865–866, 866*f*
Electronic beam steering, 10–11
"Elephant trunk" sign, fetal cloacal exstrophy and, 1328
Elevation planes, 12*f*
Elevation resolution, 19, 19*f*
Ellis-van Creveld syndrome, 1396, 1397*f*, 1398–1399
polydactyly in, 1382
Emboli showers, 1621–1622
Embolism
carotid artery, TIAs from, 919
pulmonary, DVT causing
lower extremity, 979, 981*f*
upper extremity, 994
Embolization, uterine artery, for uterine fibroids, 540
Embolus, renal artery stenosis and, 447
Embryo. *See also* Aneuploidy, screening for, first-trimester; Chromosomal abnormalities
abnormal, 1077
anencephaly in, 1077
cardiac activity of, normal sonographic appearance of, 1058–1059, 1060*f*
with CRL less than 7mm and no heartbeat, 1064
definition of, 1445
early pregnancy failure and gestational sac with no, 1063–1065, 1065*f*
evaluation of, 1076–1077
heartbeat of, in gestational age determination, 1445, 1445*f*, 1446*t*
intracranial cystic structures in, 1077, 1077*f*
normal development of, mimicking pathology, 1077, 1077*f*
normal sonographic appearance of, 1057, 1059*f*–1060*f*
physiologic anterior abdominal wall herniation in, 1077, 1077*f*, 1322, 1323*f*
omphalocele confused with, 1325, 1327*f*
sonographic appearance of, normal, 1018*f*
transfer, 1070
in yolk sac, 1058*f*
Embryonal carcinoma, 823, 825*f*
ovarian, 1880
pediatric, testicular, 1899
Embryonal rhabdomyosarcoma, pediatric, paratesticular, 1903–1904, 1903*f*
Embryonal sarcoma, undifferentiated, in pediatric liver, 1746, 1748*f*
Embryonic bradycardia, 1068–1069, 1068*f*
Embryonic disc, trilaminar, in spinal development, 1216–1217, 1217*f*
Embryonic period, 1053–1054
Emphysema, lobar, congenital, 1251, 1253*f*
Emphysematous cholecystitis, 175, 198*f*, 200
Emphysematous cystitis, 333, 334*f*
Emphysematous pyelitis, 326–327, 327*f*
Emphysematous pyelonephritis, 325–326, 326*f*
Empty stomach artifact, 1838, 1839*f*
Empyemas, pediatric, 1702–1711
abscess differentiated from, 1725, 1726*f*
drainage of, 1954, 1958*f*
lung abscess compared to, 1711, 1713*f*
parapneumonic collections and, 1710–1711
from pneumonia, 1707*f*
sonographic appearance of, 1707*f*
Encephalitis
CMV, neonatal, 1559*f*
pediatric, neurogenic bladder in, 1907
Encephalocele(s)
corpus callosum agenesis and, 1526–1528
fetal
amniotic band syndrome and, 1330
anencephaly differentiated from, 1179
fetal brain and, 1179–1182, 1181*f*, 1182*t*
pentalogy of Cantrell and, 1329
sloped forehead in, 1139–1140
Encephaloclastic schizencephaly, 1196
Encephalomalacia, cystic, 1538, 1539*f*
End diastolic ratio, in internal carotid artery stenosis evaluation, 937
End diastolic velocity
in assessing degree of carotid stenosis, 929
in mesenteric duplex Doppler sonography interpretation, 454
Endarterectomy, carotid
for carotid stenosis, 916
pediatric, TCD sonography in, 1621
sonographic features following, 942, 944*f*
Endocardial cushion defects, 1284

Endocardial cushion(s), 1279, 1282*f*
  development of, 1284, 1284*f*
Endocardial fibroelastosis (EF), 1292
  fetal, 1294, 1295*f*
  heart block and, 1425
Endocervical canal, normal sonographic appearance of, 1497*f*, 1499
Endocrine disorders, fetal hydrops from, 1432
Endocrine drainage, in pancreas transplantation, 672, 675*f*
Endocrine tumors, pancreatic, 248–249, 249*f*–250*f*, 249*t*
Endoderm layer, of trilaminar embryonic disc, 1216–1217, 1217*f*
Endodermal sinus tumor
  ovarian, 585
    pediatric, 1880
  testicular, 823–824, 825*f*
    pediatric, 1899
  vaginal, pediatric, 1883
Endoleaks, after AAA repair, 438–439, 440*f*–442*f*
Endoluminal graft, 438
Endometrial carcinoma, 544, 550*f*
  polycystic ovarian disease and, 1877–1878
Endometrial plaques, 523, 524*f*
Endometrioid tumors, ovarian, 581
Endometrioma(s)
  appearances of, 574–575, 575*f*
  in pouch of Douglas, 524*f*
  sonographic evaluation of, 521–523
Endometriosis
  of bladder, 372, 372*f*
  in ovaries, 574–576, 575*f*–576*f*
  in peritoneum, 521–523, 524*f*
Endometritis, 554
  PID and, 1885
  postpartum recognition of, 555–556
Endometrium
  abnormalities of, 544–552
    ablation as, 551–552, 552*f*
    adhesions as, 551, 552*f*
    atrophy as, 547–548
    bleeding as, 544, 544*b*
    carcinoma as, 544, 548–551, 550*f*
    hematometrocolpos as, 546–547, 546*f*
    hormone use and postmenopausal, 544–545, 544*b*, 545*f*
    hydrometrocolpos as, 546–547
    hyperplasia as, 544, 547–548, 548*f*
    polyps as, 544, 548, 549*f*
    postmenopausal bleeding as, 545–546
    postmenopausal fluid and, 546–547, 546*b*, 547*f*
    sarcoma as, 551, 551*f*
    thickening, 544, 544*b*
  calcifications of, 533, 534*f*
  cysts of, 547–548
  ectopic pregnancy and, 1072–1073
  layers of, sonographic appearance of, 531, 532*f*
  lining of, in menstrual cycle, 1050*f*
  phases of, sonographic appearance of, 531, 532*f*
  proliferation of, 1049, 1050*f*
  sonographic appearance of, 531, 532*f*
  thickness of
    measurement for, 531
    transvaginal ultrasound assessment for, 545–546
Endoscopic ultrasound
  for adrenal glands, 428–429, 429*f*
  for percutaneous needle biopsy of pancreas, 423
Endosonography, of gastrointestinal tract, 300–307
  for anal canal, 302–307, 304*f*–307*f*, 306*b*
  for rectum, 301–302, 301*f*–304*f*
  for upper gastrointestinal tract, 300–301
Endotracheal suctioning, in neonatal/infant brain, 1578
Endovascular aortic repair (EVAR), 438
End-stage renal disease (ESRD)
  catheterization and, 994
  hemodialysis for, 996
  reflux nephropathy and, 327, 327*f*
Enhancement artifacts, 21, 22*f*
Entamoeba histolytica, 613
  hepatic infection by, 87
Enteric drainage, in pancreas transplantation, 672
Enteric duplication cysts, fetal
  ovarian cysts differentiated from, 1369
  small bowel and, 1312–1313, 1313*f*
Enterobius vermicularis organisms, 1853
Enterocolitis, necrotizing, pediatric, 1854–1855, 1855*b*, 1856*f*
Enterocutaneous fistulas, 612
Entertainment videos, 49*b*, 50
Enthesis, 902
Eosinophilic gastritis, gastric mucosa thickening in, 1839–1840
Ependymomas, neonatal/infant brain and, 1562
Epicondylitis, 861
Epidermal inclusion cysts, 779
Epidermal nevus syndrome, hemimegalencephaly associated with, 1195
Epidermoid cyst(s)
  pediatric
    neck and, 1652–1654
    in suprahyoid area, 1640
    testicular, 1900–1901, 1901*f*
  splenic, 146–147, 148*f*–149*f*
  testicular, 830*f*, 831
Epidermolysis bullosa, pyloric atresia and, 1307
Epididymis
  anatomy of, 819–820, 820*f*
  appendices of, 820–821, 820*f*
  cystadenomas of, paratesticular, 1904
  cysts of, 839, 842*f*
  inflammation of, 846
  lesions of, 839–841
  papillary cystadenomas of, 840–841
  pediatric, 1890
    appendix, 1897, 1897*f*
    cysts of, 1902–1903, 1903*f*
  postvasectomy changes in, 841, 843*f*
  sarcoidosis and, 841, 843*f*
  sperm granuloma and, 841, 843*f*
  tumors of, extratesticular, 840–841, 840*f*
Epididymitis
  acute, 846
    scrotum pain from, 846, 847*f*–848*f*, 1895–1896, 1896*f*
  chronic, 841, 843*f*
  pediatric
    bladder outlet obstruction and, 1897
    chronic, 1896
    color Doppler ultrasound for, 1896, 1896*b*
    following trauma, 1897
    infarction and, 1896
    ischemia and, 1896
    orchitis and, 1896
    testicular torsion and, 1323–1324, 1895–1896, 1896*f*
Epididymo-orchitis, acute scrotal pain from, 846, 847*f*–849*f*
Epidural hematomas, neonatal/infant, 1557
Epigastric hernias, 488–491, 490*f*–491*f*
Epigastrium, free air in, 526
Epignathus, 1159
Epinephrine, secretion of, 417
Epineurium, 864–865, 865*f*
Epiphysis
  slipped capital femoral, 1931–1932
  stippled, 1399
Epiploic foramen, 211–212
Epispadias, bladder exstrophy with, 1326
Epispadias, fetal cloacal exstrophy and, 1328
Epithelial cell tumors, ovarian, pediatric, 1879
Epithelioid hemangioendothelioma (EHE), 123–124
Epstein-Barr virus
  diffuse lymphadenitis in, 1660, 1662*f*
  PTLD and, 682
Erb palsy, 1934
ERSPC (European Randomized Study of Screening for Prostate Cancer), 397
Erythroblastosis fetalis, 1419. *See also* Hydrops, fetal, immune
Escherichia coli, 846, 1852
Esophageal atresia, 1305–1306, 1305*f*–1306*f*, 1305*t*
Esophageal cysts, pediatric, 1650
Esophageal duplication cysts, 1256
Esophageal pouch sign, 1305–1306, 1306*f*
Esophagus
  carcinoma of, staging of, endosonography in, 301
  fetal, 1305–1306
    esophageal atresia and, 1305–1306, 1305*f*–1306*f*, 1305*t*
  parathyroid adenomas confused with, 745
  pediatric, 1833–1840
    anatomy of, 1834, 1834*f*
    sonographic technique for, 1833–1835
ESRD. *See* End-stage renal disease
ESWL. *See* Extracorporeal shockwave lithotripsy
Ethanol ablation
  of cervical nodal metastasis from papillary carcinoma, 720, 721*f*
  for secondary or recurrent hyperparathyroidism, 751–754, 754*f*
  for thyroid nodules
    autonomously functioning, 719–720
    benign functioning, 719, 719*f*
    solitary solid benign "cold", 720
Ethanol sclerotherapy, 719
Ethmocephaly
  alobar HPE and, 1534–1535
  hypotelorism and, 1140
European Carotid Surgery Trial (ECST), 916
European Federation of Societies of Ultrasound in Medicine and Biology (EFSUMB), 1041
European Randomized Study of Screening for Prostate Cancer (ERSPC), 397
EVAR. *See* Endovascular aortic repair
Ex utero intrapartum treatment (EXIT) procedure, 1159, 1255
Exencephaly, 1179, 1218
EXIT procedure. *See* Ex utero intrapartum treatment procedure
Exorbitism, 1140
  craniosynostosis and, 1136–1138
  hypertelorism with, in Pfeiffer syndrome, 1145*f*
Expected date of delivery (EDD)
  determination of, 1022
  ultrasound changing, 1022–1029
External beam radiotherapy, for prostate cancer, 400–401, 401*f*
External spermatic (cremasteric) artery, 821, 821*f*
Extracardiac malformations, in CHD, 1270
Extracorporeal membrane oxygenation (ECMO)
  complications of, 1548
  in neonatal/infant brain, duplex Doppler sonography and, 1578–1580, 1579*f*
  TCD sonography in monitoring, 1622
Extracorporeal shockwave lithotripsy (ESWL), 42
Extravaginal torsion, 844, 844*f*
Extremities
  fetal
    measurements of, 1378–1379, 1379*t*, 1380*f*–1381*f*
    routine sonographic views of, 1021, 1028*f*
  right lower, amputation of, 1403*f*

Exudate ascites, 506–507
Exudates, pleural, sonographic appearance of, 1702

F
Face
  abnormalities of, craniosynostosis and, 1136–1138
  midface abnormalities of, 1148–1153
Face, fetal. *See also* Midface abnormalities; Neck, fetal; Orbits, fetal
  embryology and development of, 1133–1134, 1134*f*
  forehead abnormalities in, 1137*f*, 1139–1140, 1139*b*, 1140*f*–1141*f*
  hemangiomas of, 1154, 1160*f*
  HPE changes to, 1189, 1189*b*
  lower, abnormalities of, 1153–1154
    macroglossia as, 1153, 1153*b*, 1158*f*
    micrognathia as, 1153–1154, 1158*f*
    retrognathia as, 1153–1154
  midface abnormalities of, 1148–1153
  normal, sonography of, 1134–1135, 1135*f*
  orbital abnormalities in, 1140–1143
  routine sonographic views of, 1021, 1024*f*
  soft tissue tumors of, 1154, 1160*f*
Facial nerve, pediatric, anatomy of, 1630
Falciform ligament, 77, 79*f*
  pediatric, 1731, 1731*f*–1732*f*
Fallopian tube(s), 585–589
  anatomy of, 565, 565*f*
  carcinoma in, 589
  hydrosalpinx of, 585–587, 587*f*
  normal sonographic appearance of, 568
  pediatric, torsion of, 1875–1876
  PID and, 587–589, 588*f*
  torsion of, 589
Falx sign, bright, in osteogenesis imperfecta type II, 1392
Familial hypocalciuric hypercalcemia, primary hyperparathyroidism distinguished from, 734
Familial juvenile nephronophthisis, 359
Familial paraganglioma syndromes, pheochromocytomas with, 1826
Fanconi anemia, 1746
Fanconi pancytopenia, 1400, 1402*f*
Far field, of beam, 8
Fasciitis
  necrotizing, of perineum, 846–847
  planter, injection for, 902, 904*f*
Fascioliasis, 176–178, 177*f*–178*f*
FAST. *See* Focused abdominal sonography for trauma
FASTER. *See* First and Second Trimester Evaluation of Risk
Fastigial point, 1189–1190
Fat, Crohn disease and creeping, 269, 271*f*
Fat necrosis
  injectable steroid complications with, 901
  simulating anterior abdominal wall hernias, 500, 502*f*
Fat-fluid levels, in breast cysts, 775, 778*f*
Fatty liver, 91–92, 92*f*–93*f*
Fecal incontinence, anal endosonography in, 305, 305*f*
Fecaliths, in acute appendicitis, 1857, 1859*f*
Feet. *See* Foot
Feminization, testicular, 1368
  dysplastic gonads and, 1899
  primary amenorrhea in, 1887
Feminizing adrenal tumors, pseudoprecocious puberty and, 1888
Femoral artery
  common, 966
    AVF of, 974*f*
    normal appearance of, 966–967, 967*f*
    pseudoaneurysms of, 973*f*
    stenosis of, 969*f*
  superficial, 966
    bypass graft of, 975*f*
    calcification of, 968, 970*f*
    normal appearance of, 966–967
    occlusion of, 967*f*, 969*f*
    stenosis of, 969*f*, 971*f*
Femoral canal, as landmark for femoral hernias, 482, 485*f*
Femoral hernias, 471, 481–483. *See also* Hernia(s), femoral
Femoral vein
  bifurcation of, 980–981
  common
    as landmark for femoral hernias, 482, 485*f*
    normal anatomy of, 500, 981*f*
    ultrasound examination of, 982–983
  compression of, normal, 982*f*
  DVT in duplicated, detecting, 988, 988*f*
  normal, 989*f*
  phasicity, 459, 459*f*–460*f*
Femur, fetal
  bowing of, 1380*f*
  deficiency of, proximal focal, 1400, 1400*f*
  hypoplasia of, in caudal regression, 1237–1238
  length of
    assessment of, 1378, 1379*t*, 1380*f*
    BPD in heterozygous achondroplasia compared to, 1398, 1398*f*
    in gestational age determination, 1448, 1449*f*, 1449*t*
    in second-trimester, 1023*f*
  short, etiology of, 1381
  subtrochanteric, absence of, 1400
  "telephone receiver", 1380*f*
Femur, head of, pediatric
  avascular necrosis of, 1930
  in DDH assessment, 1923
  position of, in evaluation of infant at risk, 1927
  in sonogram of hip from transverse/flexion view, 1927, 1928*f*
Femur-fibula-ulnar complex, 1400
Femur/foot length ratio, 1379
Femur-tibia-radius complex, 1400
Fertilization, cycle of, 1051, 1051*f*
Fetal akinesia sequence, 1401
Fetal alcohol syndrome, 1194
  rhabdomyosarcoma associated with, 1908
Fetal artery, aberrant, sirenomelia from, 1238
Fetal Echocardiography, indications for, 1270–1273, 1273*b*
Fetal endoscopic tracheal occlusion (FETO), 1264
Fetal fibronectin (FFN), 1501
Fetal growth restriction, echogenic bowel and, 1316
Fetal hemoglobin deficit, immune hydrops and, 1419. *See also* Hemoglobin, fetal
Fetal hydrops. *See* Hydrops, fetal
Fetal lobation, in kidneys, 317, 1781, 1781*f*
Fetal period, 1054
Fetal renal hamartomas, 1818–1820
Fetal therapy, cervical assessment and, 1505
FETO. *See* Fetal endoscopic tracheal occlusion
Fetomaternal transfusion, maternal serum alpha-fetoprotein elevation in, 1228
Fetter syndrome, craniosynostosis in, 1136–1138
Fetus. *See also specific organs*
  adrenal glands of
    masses in, 1353–1354, 1353*f*, 1353*t*
    normal, 1353, 1353*f*
  assessment of, for alloimmunization, 1421–1423, 1421*b*, 1422*f*, 1422*t*
  assessment of well-being of, 1455–1460
    BPP for, 1456–1458, 1457*f*, 1457*t*
    Doppler ultrasound for, 1458–1460, 1459*f*–1460*f*
  "Buddha position" of, 1401
  coexistent hydatidiform molar pregnancy and, 1078–1080, 1081*f*
  death of
    echogenic bowel and, 1316
    maternal serum alpha-fetoprotein elevation in, 1228
  definition of, 1445
  ears of
    abnormalities of, 1148, 1148*f*
    length of, in trisomy 21, 1101
    low-set, 1148
  foot of, deformities of, 1404–1407
  gestational age determination and measurements of, 1016, 1016*b*, 1444–1449
    age assignment and, 1449, 1450*t*
    in first trimester, 1444–1445, 1445*f*–1446*f*, 1445*t*–1446*t*
    in second and third trimesters, 1446–1448, 1447*f*–1450*f*, 1447*t*–1449*t*
  growth of
    abnormalities of, 1453–1455
    assessment of, 1022–1029
    curves depicting, 1453, 1453*f*
    restriction of, 1455
  growth restriction of, echogenic bowel and, 1316
  hand of, deformities of, 1404–1407
  keepsake imaging of, 49*b*, 50
  large-for-gestational age, 1453–1454
    diabetic mothers and, 1454, 1455*t*
    incidence of, 1453–1454
    sonographic criteria for, 1454*t*–1455*t*
  malformations of, diagnostic accuracy of, 1030
  megacystis in, 1360, 1360*b*, 1360*f*
  movements of, musculoskeletal development and, 1378
  MRI of, 1031–1032, 1031*f*
  presentation of, determination of, 1021, 1022*f*
  situs of, determination of, 1021, 1022*f*
  small-for-gestational age, 1454–1455, 1454*b*
  sonographic appearance of, normal, 1018*f*
  weight assessment for, 1450–1453
    in relation to gestational age, 1451–1453, 1452*t*, 1453*f*
  weight estimation for, 1450–1453
    formulas in, 1451, 1451*t*
    gestational age compared to, 1453, 1453*f*
    recommended approach in, 1451, 1452*t*
FFN. *See* Fetal fibronectin
Fibrinous peritonitis, 509*f*
Fibroadenoma, 797, 797*f*
Fibrochondrogenesis, 1396
Fibroelastosis, endocardial, fetal, 1294, 1295*f*
  heart block and, 1425
Fibroglandular tissue, asymmetrical, split-screen imaging and, 769, 769*f*
Fibroids, uterine, 538–540, 539*f*, 540*b*
Fibrolamellar carcinoma, 122–123
Fibrolipomas, coccygeal dimples and, 1679
Fibroma(s)
  cardiac, fetal, 1294
  gastrointestinal, endosonographic identification of, 301
  ovarian, 585, 586*f*

Fibroma(s) *(Continued)*
paratesticular, 1903–1904
simulating anterior abdominal wall hernias, 500–501, 502*f*
Fibromatosis, ovarian edema differentiated from, 1878–1879
Fibromatosis coli, pediatric, inflammatory disease and, 1663–1664, 1663*f*
Fibromuscular dysplasia
carotid flow disturbances in, 928
of internal carotid artery, 944–946, 946*f*
renal artery stenosis and, 447, 447*f*
renovascular disease and, 368
Fibronectin, fetal, 1501
Fibrosarcomas
paratesticular, 1903–1904
simulating anterior abdominal wall tumors, 500–501, 502*f*
Fibroscan, 1764
Fibrosis
retroperitoneal, 464–465, 465*f*
testicular, after orchitis, 846, 849*f*
tubulointerstitial, 359
Fibrothorax, sonographic appearance of, 1702
Fibrous cap thinning, microRNAs and, 920
Fibrous pseudotumors, 838, 840*f*
Field of view (FOV), 105, 505–506
musculoskeletal system and extended, 857
in obstetric sonography, 1036, 1036*f*
Filar cyst, in newborn, 1674–1675, 1678*f*
Filum terminale
formation of, 1673, 1673*f*
lipomas of, 1674
closed spinal dysraphism and, 1684–1685, 1686*f*
normal anatomy of, 1674–1675, 1677*f*
Fine-needle aspiration biopsy
parathyroid adenoma and accuracy of, 746
of thyroid gland, 709–710, 710*t*, 722
Fingers, syndactyly of, 1105*f*
Finite amplitude distortion, in soft tissue heating, 37–38, 37*f*
First and Second Trimester Evaluation of Risk (FASTER), 1090–1091, 1095
Fistula(s). *See also* Arteriovenous fistulas
aortoenteric, 438
bladder, 334, 335*f*
cholecystenteric, 207
choledochoduodenal, 175–176, 177*f*
choledochoenteric, 175–176, 177*f*
Crohn disease and formation of, 276, 279*f*–280*f*
dorsal enteric, pediatric, 1686–1688
enterocutaneous, 612
in imperforate anus, 1847–1848, 1850*f*
neurenteric, 1674
perianal, perianal inflammatory disease in, 305–306
tracheoesophageal, fetal
CHAOS and, 1254–1255
esophageal atresia and, 1305
vesicocolic, 1310–1312
vesicocutaneous, 334
vesicoenteric, 334
vesicoureteral, 334
vesicouterine, 334
vesicovaginal, 334
Fitz-Hugh-Curtis syndrome, PID and, 1887
Flash artifacts, 60–61
Flexor hallucis longus tendon, injection of, 902, 903*f*
Flexor retinaculum, thickening of, 865
Fluid, in neonatal/infant brain imaging, 1512
Fluorescent in situ hybridization, in hydrops diagnosis, 1433–1434
Fluoroscopic guidance, for drainage catheter placement, 610
FNH. *See* Focal nodular hyperplasia
Foam cysts, in breast, 779, 781*f*
Focal depth, in obstetric sonography, 1036, 1036*f*
Focal hypertrichosis, tethered cord and, 1679
Focal nodular hyperplasia (FNH)
adenoma differentiated from, 116–117
CEUS for diagnosis of, 113–115, 115*f*
characterization of, with microbubble contrast agents, 106, 106*f*, 108*t*, 109*f*
Doppler ultrasound characterization of, 113
of liver, 112–115, 114*f*–115*f*
pediatric, 1746
sulfur colloid scanning and, 115
Focal subcortical heterotopia, 1196
Focal therapy, for prostate cancer, 400
Focal zone, 505–506
Focused abdominal sonography for trauma (FAST), 508
Folic acid, in spina bifida prevention, 1224–1225
Follicular adenomas, thyroid, pediatric, 1646–1648, 1647*f*
Follicular carcinoma, of thyroid gland, 701, 701*b*, 706*f*–707*f*
pediatric, 1648
Follicular cysts
menstrual cycle and, 568
pediatric, 1875
Fondaparinux, 598
Fontanelle
mastoid, neonatal/infant brain imaging through, 1512, 1517–1518, 1517*f*, 1519*f*
duplex Doppler, 1574, 1575*f*
posterior, neonatal/infant brain imaging through, 1512, 1517, 1517*f*–1518*f*
duplex Doppler, 1574, 1575*f*
Fontanelle, anterior
cerebral artery, compression of, in hydrocephalus, RI and, 1582, 1584*f*
neonatal/infant brain imaging through, 1512–1513
coronal planes in, 1513*f*
duplex Doppler, 1574, 1575*f*
sagittal planes in, 1516*f*
Foot (Feet). *See also* Clubfoot
fetal
deformities of, 1404–1407
length of, measurement of, 1379, 1381*f*
rocker-bottom, 1406*f*, 1407
in skeletal dysplasia, 1382
injection of, 901
superficial peritendinous and periarticular, 902–904, 903*f*–904*f*
pediatric, congenital deformities of, 1932–1933
club foot as, 1932
vertical talus as, 1932–1933, 1932*f*
Foramen magnum approach
for duplex Doppler ultrasound of neonatal/infant brain, 1574, 1575*f*
for TCD sonography, 1592, 1595*f*
Foramen of Magendie, neonatal/infant, in mastoid fontanelle imaging, 1517–1518
Foramen ovale, 1273–1275, 1275*f*, 1279, 1282*f*
sonographic appearance of, 1280, 1283*f*
Foraminal flap, sonographic appearance of, 1283*f*
Forearm muscle, hernia of, 859*f*
Forearm veins, sonographic evaluation of, 996–998, 998*f*
Foregut, 1304–1305
bronchopulmonary malformations of, pediatric, 1716, 1718*f*
cysts of, 1650
Forehead, fetal, abnormalities of, 1137*f*, 1139–1140, 1139*b*, 1140*f*–1141*f*
Foreign body(ies)
embedded in soft tissue, 872, 873*f*
in gastrointestinal tract, 300
Foreign body(ies) *(Continued)*
interventional sonography, pediatric, for deep removal of, 1961, 1965*f*
in vagina, pediatric, 1887
Fornices
cavum septi pellucidi mistaken for, 1521
fetal, normal sonographic appearance of, 1168
4Kscore, 396
Four-dimensional ultrasound, for fetal heart assessment, 1277
Fournier gangrene, acute scrotal pain from, 846–847
FOV. *See* Field of view
Fracture(s)
fetal, in skeletal dysplasias, 1380*f*, 1381–1382
in osteogenesis imperfecta, 1392, 1393*f*
pediatric, rib, 1727
testicular, 850, 850*f*
Frame rate
in obstetric sonography, 1036
in renal artery duplex Doppler sonography, 449
Frank dislocation, of hip, 1927
Fraser syndrome, 1253
Fraternal twins. *See* Dizygotic twins
Fraunhofer zone, of beam, 8
Free air, pneumoperitoneum and, 525*f*, 526
"Freehand" technique, for percutaneous needle biopsies, 600, 602*f*
Frequency compounding, 7–8
Frequency spectrum bandwidth, 7–8
Frequency(ies)
acoustic, 2
band of, 7
in sound waves, 2, 2*f*
Fresnel zone, of beam, 8
Frontal bossing, 1137*f*, 1139, 1139*b*
in skeletal dysplasia, 1382
Frontal horns, of ventricles
in Chiari II malformation, 1526, 1527*f*–1528*f*
in corpus callosum agenesis, 1528, 1530*f*–1531*f*
neonatal/infant
in coronal imaging, 1514, 1514*f*–1515*f*
cysts of, 1522, 1522*f*, 1566
Frontonasal prominence, 1134
Frontothalamic distance, in trisomy 21, 1101
Fryn syndrome, CDH and, 1263
Fukuyama syndrome, cobblestone lissencephaly in, 1195
Full-thickness rotator cuff tears, 886–887, 887*f*–888*f*
Fundal adenomyomas, 202, 204*f*
Fundamental echo, 58–59
Fundus, uterine, 530
Fungal diseases
genitourinary, 330–331
hepatic, 86–87, 88*f*
Fungus balls
in collecting systems, 330–331, 331*f*
formation of, in neonatal candidiasis, 1794, 1795*f*
Fused vertebrae, pediatric, 1688
Fusiform dilatation, 283

G

G6PD. *See* Glucose-6-phosphate dehydrogenase deficiency
Gadopentetate dimeglumine, as pregnancy category C drug, 1032
Gain settings, 505–506
Galactoceles, 775
Galactography, 799
Galactosemia, inborn errors of metabolism and, 1738
Gallbladder, 188–207. *See also* Cholecystitis
absent or small, in biliary atresia, 1734–1735, 1737, 1738*f*

Gallbladder *(Continued)*
adenomas of, 203–204, 205*f*
adenomyomas of, 202–204, 204*f*–205*f*
adenomyomatosis of, 202, 203*f*–205*f*
agenesis of, 190–194
anatomy of, 188–194, 193*f*
aspiration of, 614, 616*f*
biliary sludge and, 194–195, 196*f*
calcification of, 202, 202*f*
carcinoma of, 206–207, 206*f*
drainage of, 613–614, 616*f*
duplication of, 194
fetal, 1318–1319, 1319*f*
choledochal cysts and, 1319, 1320*f*
enlarged, 1318
gallstones and, 1319, 1320*f*
nonvisualization of, 1318–1319
gallstone disease of, 194, 195*f*
hepatization of, 195
hourglass, 202, 205*f*
intrahepatic, 188–190, 193*f*
malignancies of, 204–206
milk of calcium bile and, 194, 195*f*
pediatric, wall thickening in, 1741
perforation of, 198*f*, 200
polyps of, 203–206, 203*b*
cholesterol, 203, 205*f*
inflammatory, 203–204, 205*f*
porcelain, 202, 202*f*
small, in biliary atresia, 1737, 1738*f*
sonographic nonvisualization of, causes of, 190–194, 194*b*
sonographic technique for, 194
variants of, normal, 188–194
volvulus of, 201
wall thickening in
causes of, 198, 199*f*, 200*b*
in children, 1741
hyperemia in, in acute cholecystitis, 197*f*, 198–199
sympathetic, 199–200, 201*f*
Gallstone disease, 194, 195*f*
Gallstones
acute pancreatitis and, 221
fetal, 1319, 1320*f*
pediatric, 1741, 1743*f*
diseases associated with, 1741*b*
Gamma-glutamyl transpeptidase (GGTP), 1318
Gamna-Gandy bodies, in spleen, 157
Ganglion
cysts
injection for, 907–909, 909*f*
ultrasound techniques for, 869–870, 869*f*
subacromial-subdeltoid bursa thickening with, 889–891, 892*f*
Ganglioneuroblastoma, pediatric, 1825
Ganglioneuromas, adrenal, 427–428
benign, pediatric, 1825
Gangrene, Fournier, 846–847
Gangrenous appendix, pediatric, 1857, 1861*f*
Gangrenous cholecystitis, 198*f*, 200
Gartner cyst, pediatric, 1883–1884
Gas, free intraperitoneal, in acute abdomen, 277–281, 282*f*
Gas bubbles, free, as blood pool contrast agents, 55
Gastric diaphragm, pediatric, 1839, 1840*f*
Gastric ulcers, pediatric, 1839–1840, 1840*f*
Gastric vein, left, pediatric
Doppler studies of, best approach for, 1752
flow direction of, in portal hypertension, 1752, 1757
in intrahepatic portal hypertension, 1761
Gastritis, pediatric, 1839–1840, 1840*f*
Gastrocolic trunk, pancreatic head and, 212
Gastroduodenal artery, pancreatic head and, 211–212, 213*f*
Gastroesophageal reflux, sonographic detection, 1834, 1834*f*
Gastrointestinal tract. *See also* Acute abdomen; Crohn disease
acute abdomen and, 277–290
anatomy of, 257–261
CF and, 300
Crohn disease and, 266–269
endosonography of, 300–307
for anal canal, 302–307, 304*f*–307*f*, 306*b*
for rectum, 301–302, 301*f*–304*f*
for upper gastrointestinal tract, 300–301
gut edema and, 295, 297*f*
gut signature and, 257, 257*f*–259*f*, 257*t*
infections of, 295–300
AIDS patients and, 296
bezoars and, 300
celiac disease and, 300
congenital cysts and, 297, 298*f*
hematomas and, 299
intraluminal foreign bodies and, 300
ischemic bowel disease and, 297
mucocele of appendix and, 299, 299*f*
peptic ulcer and, 299, 300*f*
pneumatosis intestinalis and, 297–299, 299*f*
pseudomembranous colitis and, 296–297, 298*f*
layers of, 257, 257*f*–258*f*
masses of, 592
mechanical bowel obstruction and, 293
neoplasms of, 261–266
adenocarcinoma as, 261–264, 263*f*–264*f*
lymphoma as, 264–266, 266*f*
metastases as, 266, 267*f*
stromal tumors as, 264, 265*f*
paralytic ileus and, 294*f*, 295
pediatric
cysts of, 1860–1862, 1863*f*–1864*f*
duplication cysts of, 1860, 1863*f*, 1875
neoplasms of, 1860–1862, 1864*f*
sonographic technique for, 257–261, 262*f*
Gastrointestinal tract, fetal, 1304–1322. *See also specific organs*
anomalies of, hydrops from, 1427–1428, 1428*f*
Gastroschisis
fetal, 1322–1325
associated conditions of, 1324–1325
epidemiology of, 1322–1323
management of, 1325
pathogenesis of, 1323
prenatal diagnosis of, 1323–1324, 1324*f*
maternal serum alpha-fetoprotein elevation in, 1228
Gastrulation, 1053
disorders of, 1686–1689
in spine embryology, 1672
Gaucher disease, spleen and, 157, 158*f*
Gel cysts, 779, 781*f*
Gender
fetal, identification of, 1367, 1367*f*
in multifetal pregnancy, chorionicity and, 1119
pediatric kidney length according to, 1776–1778, 1778*t*
pediatric kidney volume according to, 1776–1778, 1778*t*
TCD sonography velocity evaluation and, 1595
Genetic amniocentesis, 1108–1109, 1108*f*
Genetic disorders, fetal hydrops from, 1432
Genital tract, fetal, 1366–1369
abnormal, 1367–1368, 1368*f*
hydrocolpos and, 1368
normal, 1366–1367, 1366*f*–1367*f*
ovarian cysts and, 1369, 1369*f*
Genitalia, fetal
abnormal, 1367–1368, 1368*f*
ambiguous, 1365, 1368*f*
normal, 1366–1367, 1366*f*–1367*f*
Genitourinary tract. *See also* Bladder; Kidney(s); Renal artery(ies); Renal cell carcinoma; Renal vein(s); Transitional cell carcinoma; Ureter; Urethra; Urinary tract
abnormalities of, in Miller-Dieker syndrome, 1195
anatomy of, 311–314
bladder diverticula and, 374, 374*f*
congenital anomalies of, 317–323
bladder development and, 322
kidney ascent and, 318
kidney growth and, 317–318
ureteral bud and, 318–321
urethral development and, 323, 323*f*
vascular development and, 321–322
duplex collecting system and, 319, 320*f*
embryology of, 311
infections of, 323–333
AIDS and, 331–333, 332*f*–333*f*
alkaline-encrusted pyelitis as, 324–325
Candida albicans as, 330–331, 331*f*
cystitis as, 333
echinococcal disease as, 331, 332*f*
fungal, 330–331
papillary necrosis as, 328–329, 329*b*, 329*f*
parasitic, 331
pyelonephritis as, 323–328
pyonephrosis as, 325, 326*f*
schistosomiasis as, 331
tuberculosis as, 329–330, 330*f*
medical diseases of, 369–372
acute cortical necrosis as, 370, 372*f*
acute interstitial nephritis as, 370
acute tubular necrosis as, 370
amyloidosis as, 372
diabetes mellitus as, 372
endometriosis as, 372, 372*f*
glomerulonephritis as, 370, 371*f*
interstitial cystitis as, 372, 373*f*
neurogenic bladder and, 372–374, 373*f*
obstruction of
hydronephrosis and, 316, 317*b*
pitfalls in assessment of, 317
postsurgical evaluation of, 374–375
sonographic technique for, 314–315
stones in, 334–340
trauma to, 365–366
tumors of, 340–356
adenocarcinoma as, 348
angiomyolipoma as, 351–352, 351*f*–352*f*
leukemia as, 353–354
lymphoma as, 352–353
metastases as, 354–355
oncocytoma as, 348–351
rare, 355–356
renal cell carcinoma as, 340–344
squamous cell carcinoma as, 348
transitional cell carcinoma as, 346–348
urachal adenocarcinomas as, 355
vascular abnormalities of, 366–369
AVF and malformation as, 366–367, 366*f*
renal vascular Doppler ultrasound and, 366
Germ cell tumors
ovarian, 582–585
pediatric, 1879
testicular, 822–825, 822*b*
mixed, 822–823, 825*f*
nonseminomatous, 823–824, 825*f*
regressed, 824–825, 825*f*–826*f*
thymus, 1723–1724

Germinal epithelium, 565
Germinal matrix hemorrhage, hypoxic-ischemic injury in premature infant and, 1541–1543, 1542*f*, 1543*b*, 1543*t*
Germinal matrix of, neonatal/infant, development of, 1524, 1524*f*
Gerota fascia, 314
Gestational age
  alpha-fetoprotein levels compared to, 1227*f*
  calculation of, 1049
  cervical length and, 1499–1500, 1499*f*
    spontaneous PTB prediction based on, 1500–1501, 1501*t*
  definition of, 1443–1444
  determination of
    accuracy of, 1449, 1450*t*
    composite formulas for, 1448–1449
    routine ultrasound screening in, 1022–1029
  estimation of
    CRL in, 1062
    in first trimester, 1061–1062
    gestational sac size in, 1061, 1061*f*
    MSD in, 1061, 1061*f*, 1444–1445, 1445*t*
    routine ultrasound screening in, 1022–1029
  extremity long-bone lengths and BPD at, 1379*t*
  fetal measurements for determining, 1016, 1016*b*, 1444–1449
    age assignment and, 1449, 1450*t*
    in first trimester, 1444–1445, 1445*f*–1446*f*, 1445*t*–1446*t*
    in second and third trimesters, 1446–1448, 1447*f*–1450*f*, 1447*t*–1449*t*
  fetal weight assessment in relation to, 1451–1453, 1452*t*, 1453*f*
  fetal weight estimation compared to, 1453, 1453*f*
  for heterozygous achondroplasia detection, 1381
  kidney length compared to, 1776–1778, 1780*f*
  PSV blood flow in MCA as function of, 1421, 1422*t*
  thermal effects of ultrasound and, 1037–1038
  thoracic circumference and length correlated with, 1247*t*
  usage of term, 1167
Gestational sac, 1017*f*
  abnormal size of, 1063
  chorionic bump in, 1065
  chorionic sac fluid of, 1054–1055, 1056*f*
  discriminatory level for seeing, 1056
  early pregnancy failure and
    appearance concerns in, 1065, 1066*f*
    no embryo in, 1063–1065, 1065*f*
    small MSD in relationship to CRL in, 1066, 1067*f*
  identification of, in gestational age determination, 1444, 1445*f*, 1446*t*
  mean diameter of
    CRL and, early pregnancy failure and, 1066, 1067*f*
    in gestational age determination, 1444–1445, 1445*t*
  normal sonographic appearance of, 1054–1055, 1055*f*–1056*f*
  size of, in gestational age estimation, 1061, 1061*f*
  threshold level for seeing, 1056
  transvaginal ultrasound for identification of, 1054–1055
  β-hCG levels and, 1056–1057
Gestational trophoblastic disease, 556, 1077–1084, 1479
  hydatidiform molar pregnancy and, 1078–1080
    complete, 1078, 1079*f*
    partial, 1078, 1080*f*
    vaginal bleeding and, 1078
Gestational trophoblastic disease *(Continued)*
  PTN and, 1078, 1080–1084, 1082*f*
    choriocarcinoma and, 1080–1082, 1083*f*
    diagnosis and treatment of, 1083–1084
    Doppler ultrasound for, 1083
    after hydatidiform molar pregnancy, 1080, 1081*f*
    invasive mole, 1080, 1081*f*
    PSTT and, 1082
    sonographic features of, 1082–1083
"Geyser sign", 889–891, 892*f*
GGTP. *See* Gamma-glutamyl transpeptidase
Ghost triad, biliary atresia and, 1737, 1738*f*
Giant pigmented nevi, choroid plexus papillomas in, 1209
Giant-cell tumors, in TSC, 1200*f*
Glenohumeral joint, 878–879, 878*f*
  effusion of, 893–894, 894*f*
Glenohumeral joint, injection of, 901, 901*f*
Glenoid fossa, 878–879, 878*f*
Glial scarring, in PVL, 1552–1553
Glioependymal cysts, cavum veli interpositi cysts differentiated from, 1170
Gliomas, hypothalamic, precocious puberty and, 1887
Glisson capsule, 77
Glomerulonephritis, 370, 371*f*
  CKD and, 1796–1798
Glomus, choroid plexus, neonatal/infant, development of, 1522–1523, 1523*f*
Glomuvenous malformation, in venous malformations of neck, 1657
Glucocorticoid, secretion of, 417
Glucose, plasma levels of, high, NTDs from, 1218
Glucose-6-phosphate dehydrogenase (G6PD) deficiency, 1431
Glutaric aciduria type 1, 1540–1541
Glycogen storage disease (GSD)
  inborn errors of metabolism and, 1738
  liver in, 92
  pediatric
    type I, adenomas in, 1746
    tyrosinemia and, 1740*f*
Goiter(s)
  adenomatous, sonographic appearance of, 727
  fetal, 1159–1163, 1162*f*
  multinodular, 711, 711*f*
    in children, 1648, 1648*f*
    parathyroid adenomas detection and, 746
    sonographic appearance of, 727
  in thyroid gland nodular disease, 695–697, 695*f*–699*f*
Goitrous hypothyroidism, 694
Goldenhar syndrome, clefts of secondary palate in, 1153
Gonadal dysgenesis, primary amenorrhea in, 1887
Gonadal stromal tumors, testicular, 826, 827*f*
Gonadal veins, anatomic variants of, 457
Gonadoblastoma(s), 826, 827*f*
  pediatric, 1880
    in dysplastic gonads, 1899–1901
Gonads
  differentiation of, 1887
  dysplastic, 1899–1901
Gonococcal perihepatitis, PID and, 1887
Gorlin syndrome, 585
Gout, rheumatoid arthritis and, 867–869, 868*f*
Graafian follicle, 1049
Graded compression sonography, 283
Graft infarction, pediatric renal transplantation and, 1807–1809, 1808*f*
Graft-dependent hyperparathyroidism, 742–744, 743*f*
Graft-versus-host disease, pediatric, intestinal wall thickening in, 1853–1854, 1855*f*
Granulocytic sarcomas, pediatric, neck, 1666, 1667*f*
Granuloma(s)
  of liver, pediatric, 1748
  silicone, in extracapsular breast implant rupture, 805–807, 806*f*
  sperm, 841, 843*f*
  splenic, pediatric, 1771*f*
  stitch, after herniorrhaphy, 494–496, 495*f*
Granulomatous cystitis, pediatric, 1908
Granulomatous disease, chronic, gastric mucosa thickening in, 1839–1840
Granulomatous mastitis, 803–804
Granulomatous peritonitis, 514
Granulomatous prostatitis, 390, 390*f*
Granulosa cell tumor, ovarian, 585
  pediatric, 1880
    pseudoprecocious puberty and, 1887
Graves disease
  fetal goiter in, 1159–1163
  thyroid gland and, 727, 727*f*
    pediatric, 1646, 1646*f*
Gray-scale median level, for echolucency of plaque, 922
Great arteries, transposition of, 1289–1290, 1289*f*–1290*f*
Great saphenous vein (GSV)
  acute DVT in, 984, 984*f*
  anatomy of, 981–982, 981*f*
  vein mapping of, 989–990
Great vessels, fetal, short-axis view of, 1275, 1278*f*
Green-tag feature, in color Doppler, 932–933
Groin
  definition of, 471
  hernias of, dynamic ultrasound of
    contents of, 472–473
    entities stimulating, 499–500, 501*f*
    key sonographic landmarks for, 474
    maneuvers for, 473–474, 474*f*–475*f*
    recurrent, 494–496
    report for, 471–472
    technical requirements for, 471
  pain, 470–471
Growth. *See* Fetus, growth of; Intrauterine growth restriction
Growth discordance, in multifetal pregnancy, 1123, 1123*f*
GSD. *See* Glycogen storage disease
GSV. *See* Great saphenous vein
Gubernaculum testis, 851
Guidewire exchange technique, for drainage catheter placement, 610
Gut
  edema, 295, 297*f*
  primitive, 1057
  signature, 257, 257*f*–259*f*, 257*t*
  strictures in, in Crohn disease, 269–274, 275*f*–276*f*
Gut wall
  CEUS and, 261
  Doppler ultrasound evaluation of, 260–261, 262*f*
  elastography and, 261
  layers of, 257, 257*f*–258*f*
  masses in, 258
  pathology of, 257–258, 260*f*
  pseudokidney sign in, 257, 260*f*
  target pattern in, 257, 260*f*
  thickening of
    Crohn disease and, 269, 270*f*–271*f*
    pathology related to, 257
Gynecology. *See also* Fallopian tube(s); Uterus
  anatomy in, 564–570, 565*f*
  nongynecologic pelvic masses and, 591–592
Gynecomastia, in testicular choriocarcinoma, 824
Gyral interdigitation, in Chiari II malformation, 1526, 1528*f*

Gyri
abnormalities of, in lissencephaly, 1195
development of, 1167
normal sonographic appearance of, 1169, 1171*f*

H
HAART. *See* Highly active antiretroviral therapy
Haglund deformity, 903*f*
Hamartoma(s)
biliary, 83, 83*f*–84*f*
dysraphic, 1682
fetal renal, 1818–1820
hypothalamic, precocious puberty and, 1887
pediatric, mesenchymal, 1744
splenic, 153–156, 156*f*
testicular, 829, 829*f*
in TSC, 1200*f*
Hamstring tendon, injection of, 905–907, 907*f*–908*f*
Handedness, obstetric sonography and, 1040
Hand(s). *See also* Clubhand
clenched, in trisomy 18, 1103, 1103*f*
fetal
amputation of, in amniotic band sequence, 1403*f*
deformities of, 1404–1407
in skeletal dysplasia, 1382
injection of, 901
superficial peritendinous and periarticular, 904, 905*f*
persistent clenched, 1404
"trident" configuration of, achondroplasia and, 1407, 1408*f*
Harmonic imaging
of biliary tree, 168, 169*f*
B-mode, 60
contrast agents with, 58–64
spectral and power mode Doppler, 60–61, 60*f*–62*f*
tissue, 13, 13*f*–14*f*, 38, 61–62
Harmonic power angio, 66
Harmonics, generation of, 13, 13*f*
Hartmann pouch, 188
Hashimoto thyroiditis, 724, 725*f*–727*f*
fetal goiter in, 1159–1163
pediatric, 1645, 1646*f*
HCB. *See* Hypertrophied column of Bertin
HCC. *See* Hepatocellular carcinoma
hCG. *See* Human chorionic gonadotropin
Head, fetal
abnormalities of, 1135–1140
craniosynostosis and, 1136–1139, 1137*f*–1138*f*
in shape, 1136–1139, 1137*f*
in size, 1135–1136
wormian bones as, 1139, 1139*b*, 1139*f*
circumference of
in gestational age determination, 1446–1447, 1447*f*–1448*f*, 1448*t*
in second-trimester, 1023*f*
measurements of, in gestational age determination, 1446–1448, 1447*f*–1448*f*, 1447*t*–1448*t*
oblong, 1136–1138
sonographic views of, 1021, 1024*f*
Head, pediatric, lesions of, 1961, 1966*f*
Headaches, pediatric TCD sonography for, 1610–1611, 1612*f*
Healing response, impaired, injectable steroid complications with, 901
Heart. *See also* Congenital heart disease
congenital defects of
thickened NT in, 1095–1097, 1096*f*
in trisomy 18, 1103
in trisomy 21, 1097, 1098*f*
Heart *(Continued)*
disease of
carotid flow waveforms and, 936–937, 936*f*
CDH and, 1263
ischemic, 433
in Miller-Dieker syndrome, 1195
early pregnancy failure and absence of beating, 1063, 1064*f*
echogenic focus in, in trisomy 21, 1100*f*, 1101
embryonic
activity of, normal sonographic appearance of, 1058–1059, 1060*f*
beating of, in gestational age determination, 1445, 1445*f*, 1446*t*
embryos with CRL less than 7mm and no beating, 1064
rate, TCD sonography velocity evaluation and, 1595
Heart, fetal. *See also* Echocardiography, fetal
arrhythmias of, 1295–1297
bradycardia as, 1297, 1297*f*
CHD and, 1270–1273
congenital heart block as, 1297, 1297*f*
hydrops from, 1424, 1425*f*
PACs and PVCs as, 1295–1296
tachycardia as, 1296–1297, 1296*f*
atrioventricular valves of, 1274–1275
axis of, 1245
abnormal, mortality rate with, 1273
dimensions of, 1276*f*
disease of, congenital
recurrence risks in offspring for, 1273*t*
recurrence risks in siblings for, 1273*t*
risk factors associated with, 1271*t*–1272*t*
dysfunction of, from Ebstein anomaly, 1286
failure of, in sacrococcygeal teratoma, 1238–1239
malformations of, with AVSD, 1285–1286
normal anatomy of, 1273–1277
position of, 1245
abnormal, mortality rate with, 1273
routine sonographic views of, 1021, 1025*f*
scanning techniques for, 1273–1277
four-chamber view of, 1273–1275, 1277*f*
situs of, 1245
structural anomalies of, 1277–1295
aortic stenosis as, 1292
APVR as, 1290, 1291*f*
ASD as, 1277–1280, 1282*f*–1283*f*
AVSD as, 1284–1286, 1284*f*–1285*f*
cardiac tumors as, 1293–1294, 1293*f*–1294*f*
cardiomyopathy as, 1295*f*
cardiosplenic syndrome as, 1292–1293, 1293*b*
coarctation of aorta as, 1291, 1292*f*
DORV as, 1288–1289, 1289*f*
Ebstein anomaly as, 1286–1287, 1286*f*
ectopia cordis as, 1295, 1296*f*, 1329
hydrops from, 1423–1424
hypoplastic left heart syndrome as, 1287, 1287*f*
hypoplastic right ventricle as, 1287, 1287*f*
pentalogy of Cantrell and, 1329
pulmonic stenosis as, 1292
TGA as, 1289–1290, 1289*f*–1290*f*
TOF as, 1288, 1288*f*
truncus arteriosus as, 1288, 1289*f*
univentricular heart as, 1287–1288, 1287*f*
VSDs as, 1281–1284, 1283*f*–1284*f*
tumor of, 1293–1294, 1293*f*–1294*f*
hydrops from, 1424
ultrasound assessment of
color Doppler, 1275–1277, 1282*f*
spectral Doppler, 1275, 1281*f*
Heart, fetal *(Continued)*
three-dimensional and four-dimensional, 1277
univentricular, 1287–1288, 1287*f*
valves of, morphology of, 1285*f*
valvular stenosis of, 1275–1277
ventricles of, short-axis view of, 1275, 1278*f*
Heart block, fetal
complete, hydrops from, 1423–1424
congenital, 1297, 1297*f*
hydrops from, 1425
Heating
of bone, 37, 37*f*, 37*t*
of soft tissue, 37–38, 37*f*
Heerfordt disease, chronic pediatric sialadenitis in, 1634–1635
Height, pediatric, kidney length compared to, 1776–1778, 1777*f*
Hemangioblastoma, intracranial, fetal, 1208
Hemangioendothelioma(s)
epithelioid, hepatic, 123–124
infantile, 1319*f*
liver and, 1743–1744, 1745*f*
Hemangioma(s)
cardiac
fetal, 1294
in infants, 1293
cavernous
of bladder, 356
CEUS characterization of, 111, 113*f*
Doppler ultrasound characterization of, 109–110
of liver, 108–112, 112*f*–113*f*
percutaneous needle biopsy of, 603–604, 604*f*
characterization of, with microbubble contrast agents, 106, 106*f*–107*f*, 108*t*
cutaneous rapidly involuting cogenital, 1742–1743
dacryocystocele differentiated from, 1143
fetal
cardiac, 1294
face, 1154, 1160*f*
of liver, 1319*f*
infantile
of neck, 1655, 1656*f*
parotid gland, 1636, 1637*f*
tethered cord and, 1679
intraspinal, pediatric, 1689–1691
paratesticular, 1903–1904
pediatric
gastrointestinal, 1862, 1864*f*
liver and, 1742–1743, 1744*f*
sclerosis of, 112
segmental, tethered cord and, 1679
splenic, 148, 153–157, 156*f*
subcutaneous, spinal canal and, 1697, 1697*f*
umbilical cord, 1483
Hemangiopericytoma
renal, 356
splenic lesions in, 153
Hemangiosarcoma, of liver, 123
Hematoceles, scrotal, 835*f*, 836
pediatric, 1902
Hematoma(s)
in AVF for hemodialysis, 1002–1003, 1005*f*
bladder augmentation and, 1912–1913
bladder flap, cesarean sections and, 556–557, 557*f*
duodenal, pediatric, 1842, 1845*f*
epidural, neonatal/infant, 1557
of gastrointestinal tract, 299
intestinal, small bowel obstruction from, 1843
intraparenchymal, 638
after liver transplantation, 638, 644*f*

Hematoma(s) *(Continued)*
pelvic, 591
perinephric fluid collections and, 1809
preplacental, 1471, 1475*f*
renal, 365–366
after renal transplantation, 665, 671*f*
simulating anterior abdominal wall hernias, 500, 502*f*
splenic, 158, 159*f*
pediatric, 1770, 1771*f*
stitch, after herniorrhaphy, 494–496, 495*f*
subamniotic, 1474
subchorionic, 1474
placental abruption differentiated from, 1471, 1474*f*
subdural, neonatal/infant, 1557, 1558*f*
subfascial, cesarean sections and, 556–557, 557*f*
subplacental, 1471, 1474*f*
in synthetic arteriovenous graft for hemodialysis, 1002–1003
testicular, 848–850, 850*f*
pediatric, 1897–1898
Hematometra
cervical carcinoma and, 546, 547*f*, 549
cornual, 551–552
Hematometrocolpos, 1882*f*
from imperforate hymen, 546–547, 546*f*
Hematopoiesis, in yolk sac, 1057
Hematospermia, prostate and, 394, 394*b*
Hematotrachelos, 546
Hemidiaphragm, eventration of, 1263*f*
Hemihypertrophy
hepatoblastomas and, 1746
Wilms tumor screening with, 1818
Hemimegalencephaly, 1195
Hemithorax, pediatric, radiopaque
in neonatal chylothorax, 1704*f*
partially, 1705*f*
Hemivertebrae
pediatric, 1688–1689
scoliosis and kyphosis from, 1235–1237
Hemobilia, 174, 175*f*
Hemodialysis, 996–1006
AVF and
aneurysms near, 1003, 1005*f*
arm and leg swelling with, 1006, 1009*f*
hematomas near, 1002–1003, 1005*f*
maturation of, evaluating, 1003
occlusion of, 1006
palpable focal masses near, 1002–1003
placement for, 996, 997*f*
pseudoaneurysms near, 1003, 1005*f*
stenoses associated with, 1003–1006, 1007*f*–1008*f*
ultrasound evaluation of, 1000–1006, 1002*f*–1003*f*
for ESRD, 996
sonographic examination technique for, 996
synthetic arteriovenous graft and
aneurysms near, 1003
arm and leg swelling with, 1006, 1009*f*
hematomas near, 1002–1003
occlusion of, 1006, 1010*f*
palpable focal masses near, 1002–1003
placement of, 996, 997*f*
pseudoaneurysms near, 1003, 1006*f*
stenoses associated with, 1006, 1008*f*
ultrasound examination of, 1002, 1004*f*
ultrasound examination and protocol for, 1000
thigh graft and, preoperative mapping for, 1000, 1001*f*
vein mapping before, 996–1000
upper extremity, 996–998, 998*f*–1000*f*
Hemoglobin, fetal deficit in, immune hydrops and, 1419
Hemolysis
fetal, hydrops from, 1431
from obstetric sonography, 1038
Hemolytic anemia, fetal, hepatomegaly, and, 1316
Hemolytic-uremic syndrome (HUS), pediatric
Doppler assessment of, 1805, 1807*f*
intestinal wall thickening in, 1851*f*, 1853–1854
Hemoperitoneum, 507–508, 508*f*
Hemorrhage(s)
adrenal, 422–424, 424*f*
fetal, 1354
after liver transplantation, 638, 645*f*
neonatal, 1824–1825, 1825*f*
arachnoid cysts differentiated from, 1192–1193
cavum veli interpositi cysts differentiated from, 1170
cerebellar, neonatal/infant brain and, 1548–1550, 1549*f*
fetal, hydrops from, 1431
hypoxic-ischemic events and
cerebellar, 1548–1550, 1549*f*
germinal matrix, 1541–1543, 1542*f*, 1543*b*, 1543*t*
intraparenchymal, 1547–1548, 1547*f*–1549*f*
intraventricular, 1544–1545, 1544*f*–1546*f*, 1545*b*
intraventricular, with hydrocephalus, 1545–1547, 1546*f*–1547*f*
subarachnoid, 1550, 1550*f*
subependymal, 1543–1544, 1543*f*–1544*f*
intracranial
fetal, 1206, 1207*f*
neonatal/infant brain and, duplex Doppler sonography of, 1580–1581, 1584*f*
intramural, pediatric, in Henoch-Schönlein purpura, 1853, 1855*f*
intraparenchymal
IUFD and, 1124*f*
neonatal/infant brain and, 1547–1548, 1547*f*–1549*f*
intraplacental, thick placenta in, 1466
intraplaque, in heterogenous plaque, 920–921
intraventricular
from germinal matrix hemorrhage, 1541
with hydrocephalus, 1545–1547, 1546*f*–1547*f*
neonatal/infant brain and, 1544–1545, 1544*f*–1546*f*, 1545*b*
signs of, 1545*b*
pediatric
ovarian cysts and, 1877, 1878*f*–1879*f*
spinal canal, 1695, 1695*f*–1696*f*
thyroid, 1646, 1647*f*
percutaneous needle biopsy complications with, 608, 609*f*
placental, 1474
posterior fossa, 1548–1550
postpartum, in fetal hydrops, 1436
subarachnoid, neonatal/infant brain and, 1550, 1550*f*
subchorionic
early pregnancy failure and, 1069, 1069*f*
fetal echogenic bowel and, 1315*f*
subdural, fetal, bilateral, 1207*f*
subependymal, neonatal/infant brain and, 1543–1544, 1543*f*–1544*f*
Hemorrhagic cholecystitis, 200
Hemorrhagic cystitis, pediatric, 1908, 1910*f*
Hemorrhagic ovarian cysts, 570–571, 571*f*, 575
Hemothorax, sonographic appearance of, 1702, 1707*f*
Henoch-Schönlein purpura, 845–846, 1842
pediatric, 1853, 1855*f*
scrotal and testicular involvement in, 1899
Heparin, 598
Hepatic alveolar echinococcus, 90
Hepatic artery
anastomosis of, for liver transplantation, 624
aneurysms of, after liver transplantation, 1768, 1769*f*–1770*f*
anomalies of, 80–81
liver circulation and, 78
after liver transplantation
normal appearance of, 625
occlusion of, 626–627
pseudoaneurysms of, 634, 636*f*
resistive index elevation in, 634
stenosis of, 631–634, 634*f*–635*f*, 1766
thrombosis of, 627, 628*f*, 631, 633*f*
pediatric, Doppler studies of, best approaches for, 1752–1754, 1755*f*
pseudoaneurysm of, 104
after liver transplantation, 634, 636*f*
Hepatic vein(s)
anatomic variants of, 457
anomalies of, 81–82
fetal liver calcifications and, 1316–1318
liver circulation and, 80
normal, 76, 76*f*, 77*t*
occlusion of, in Budd-Chiari syndrome, 100–102, 100*f*–101*f*
pediatric
anatomy of, 1733–1734, 1734*f*
Doppler studies of, best approaches for, 1752
thrombosis of, suprahepatic portal hypertension and, 1763, 1763*f*
stenosis of, after liver transplantation, 637, 643*f*
strictures of, in cirrhosis, 95, 95*f*
Hepatitis, 1203–1204
A, 83
acute, 84–85, 85*f*–86*f*, 172
gallbladder wall thickening signs in, 201*f*
B, 83–84
maternal hydrops from, 1432
C, 84
chronic, 85
from congenital herpes, hepatitis from, 1739*f*
D, 84
E, 84
neonatal, jaundice and, 1734, 1737–1738, 1739*f*
viral, 83–85
Hepatization, of gallbladder, 195
Hepatoblastomas, pediatric, 1746, 1747*f*
pseudoprecocious puberty and, 1888
Hepatocellular carcinoma (HCC)
CEUS for detection of, 120–122, 123*f*
characterization of, with microbubble contrast agents, 106, 106*f*
in cirrhotic liver, characterization of, 122, 122*t*
fibrolamellar subtype of, 122–123
inborn errors of metabolism and, 1738
of liver, 118–123, 120*f*–121*f*, 122*t*, 123*f*
pediatric, 1746
portal vein thrombosis from, 120, 121*f*
sonographic appearance of, 119–120, 120*f*
Hepatocyte nuclear factor 1β–related (HNF1β) disease, 1350–1351
Hepatoduodenal ligament, 77, 79*f*
Hepatofugal portal venous flow, 1750, 1757
Hepatolithiasis, 179
Hepatomegaly, fetal, 1316, 1317*f*
Hepatopetal portal venous flow, 1750
Hepatosplenomegaly
from CMV, 1204
fetal, 1317*f*
in immune hydrops, 1422
Hereditary hemorrhagic telangiectasia, 104
Hereditary lymphedema, fetal, 1403–1404, 1405*f*
Hereditary nonpolyposis colorectal cancer syndrome, 578
Hermaphroditism, true, pediatric, 1891, 1899

Hernia(s). *See also* Diaphragmatic hernia
Amyand, 472–473, 473*f*
anterior abdominal wall, dynamic ultrasound of
contents of, 472–473
entities stimulating, 500–501, 502*f*
maneuvers for, 473–474, 474*f*–475*f*
technical requirements for, 471
types of, 471, 471*f*
ventral, 488–494
bilateral, 1262
Bochdalek, 1258
complications of, 496–499
congenital diaphragmatic, 1248*t*
direct inguinal
in athletes, 485–486
bilateral, 480–481, 484*f*
characteristics of, 479–481
classification of, 475
conjoined tendon insufficiency and, 479–481, 483*f*–484*f*
incidence of, 479–480, 482*f*
key findings with, 476*t*
location of, 474–475, 476*f*–477*f*
dynamic maneuvers for imaging of, 473–474, 474*f*–475*f*
femoral, 471
characteristics of, 481–483
diagnostic accuracy with, 481
with inguinal hernia, 493–494, 495*f*
key findings with, 476*t*
key sonographic landmarks of, 474–475, 477*f*
locations of, 482, 485*f*
strangulated, 500*f*
Teale, 482, 485*f*
Valsalva maneuver and, 472*f*, 483
forearm muscle, 859*f*
groin, dynamic ultrasound of
contents of, 472–473
entities stimulating, 499–500, 501*f*
key sonographic landmarks for, 474
maneuvers for, 473–474, 474*f*–475*f*
recurrent, 494–496
report for, 471–472
technical requirements for, 471
at Hesselbach triangle, inferior aspect, 476*t*
hiatal, sonographic appearance of, 1834, 1834*f*
incarcerated, 496–497
incisional, 492–493, 494*f*
indirect inguinal
Canal of Nuck delayed closure from, 476–477, 477*f*
characteristics of, 476–479
classification of, 475
inferior epigastric artery relationship to, 476–477, 478*f*
key findings with, 476*t*
location of, 474–475, 476*f*–477*f*
nonsliding, 477–478, 478*f*
pediatric, 1902
round ligaments relationship to, 476–479, 480*f*
into scrotum, 478–479, 482*f*
sliding, 477–478, 478*f*
spermatic cord relationship to, 476–479, 479*f*, 481*f*
inguinal, 471, 475–488
Amyand, 472–473, 473*f*
bowel-containing, 472–473, 473*f*
classification of, 475
dynamic ultrasound of, Valsalva maneuver for, 473, 474*f*, 483
with femoral hernia, 493–494, 495*f*
fluid-containing, 472–473, 473*f*
indirect, 472*f*
Hernia(s) *(Continued)*
key sonographic landmarks of, 474–475, 476*f*–477*f*
pediatric, 1899, 1902, 1902*f*
types of, 476*t*
linea alba, 488–491
diagnosing, 490
diastasis recti abdominis and, 489–490, 489*f*
epigastric, 488–491, 490*f*–491*f*
hypogastric, 488–489, 491, 491*f*
periumbilical, 492, 494*f*
spectrum of appearances of, 489, 489*f*
strangulated, 499*f*
of liver, 80
Morgagni, 1258, 1718*f*
multiple, 493–494, 495*f*
obstructed, 496–497
of omentum, 1902
pantaloon, 493–494, 495*f*
paraumbilical, 492
pericardial, 1258, 1262
periumbilical
linea alba, 492, 494*f*
strangulated, 500*f*
repair of
mesh in, sonography and, 496, 497*f*–498*f*
pain after, 494–496, 495*f*
spiral clips in, pain from, 497, 498*f*
scrotal, 836, 836*f*
pediatric, 1902
shape of, complication potential and, 497, 499*f*
spigelian, 471
characteristics of, 483–484
key findings with, 476*t*
key sonographic landmarks of, 474–475, 476*f*–477*f*
location of, 483, 486*f*
shape in, 483–484, 487*f*
strangulated, 483–484, 488*f*
torn aponeurosis and abdominis tendon in, 483–484, 487*f*
sports, 484–488, 488*f*–489*f*
strangulated
femoral, 500*f*
findings in, 498–499, 499*t*
linea alba, 499*f*
periumbilical, 500*f*
spigelian, 483–484, 488*f*
umbilical, 491–492, 492*f*–493*f*
ventral, 488–494
Herniation
midgut, physiologic, in embryo, 1077, 1077*f*, 1322, 1323*f*
omphalocele confused with, 1325, 1327*f*
of thymus, superior, 1723
Herniorrhaphy, 470–471
Herpes simplex virus
congenital
hepatitis from, 1739*f*
neonatal/infant brain and, 1560
fetal
brain development and, 1204
hydrops from, 1432
Hertz, definition of, 2
Hesselbach triangle, herniation at inferior aspect of, 476*t*
Heterotaxy syndrome, right-sided stomach and, 1307, 1309*f*
Heterotopia, 1196, 1199*f*
Heterotopic gestation, 1070–1071, 1072*f*
Heterozygous achondroplasia, 1396–1398, 1398*f*
detection of, gestational age for, 1381
inheritance pattern for, 1379–1380
Hiatal hernias, sonographic appearance of, 1834, 1834*f*
HIFU. *See* High-intensity focused ultrasound
High pass filters, 29, 30*f*
Higher harmonics, 58–59
High-intensity focused ultrasound (HIFU), 31–33, 33*f*
for prostate cancer, 400
Highly active antiretroviral therapy (HAART), 331–333
High-velocity jets, color Doppler, in carotid stenosis, 926, 926*f*, 933
aliasing, 933
HII. *See* Hypoxic ischemic injury
Hilar cholangiocarcinoma, 185–188
CEUS assessment of, 188, 191*f*
criteria for unresectable, 187*b*
Doppler ultrasound assessment for, 187–188, 189*f*–191*f*
treatment and staging for, 186–187
tumor growth patterns in, 186
Hindgut, 1304–1305
Hip(s)
dislocated, campomelic dysplasia and, 1395
fetal, dislocation of, spina bifida and, 1233
injection of, 900*f*, 901–902
Hip(s), pediatric. *See also* Developmental dislocation and dysplasia of hip
atypical, 1932, 1933*f*
capsule of, echogenic, 1923
DDH and, 1920–1930
dislocation of
definition of, 1923
teratologic, 1932
joint effusion in, 1930–1932, 1931*f*
nondevelopmental dysplasia abnormalities of, 1930–1932
normal, 1923
painful, 1930–1932
sonography of, indications for, 1922*b*
stability of
in evaluation of infant at risk, 1927
tests determining, 1923
subluxation of, 1923
Hirschsprung disease, 1312, 1312*f*
neuroblastoma with, pediatric, 1825
Histiocytosis
Langerhans cell
in infant, 1751*f*
metastasis of, to testes, 1901
sinus, metastasis of, to testes, 1901
Histogenesis, 1524, 1525*b*
Histopathologists, definition of, 600
Histoplasmosis
adrenal glands in, 423
pediatric, lymph nodes and, 1660–1663
Hitchhiker thumb
in diastrophic dwarfism, 1382, 1406
diastrophic dysplasia and, 1398, 1398*f*
HIV. *See* Human immunodeficiency virus
HIV cholangiopathy, 181–182, 181*f*
HIV-associated nephropathy (HIVAN), 332–333, 333*f*
HNF1β. *See* Hepatocyte nuclear factor 1β–related disease
Hodgkin lymphoma, pediatric, neck, 1665, 1665*f*
Hodgkin's disease, splenic lesions in, 152–153, 154*f*
Holoprosencephaly (HPE)
agnathia and, 1154, 1159*f*
alobar, 1187, 1188*f*
ball type of, 1187–1189
classification of, 1187*b*
cup type of, 1187–1189, 1188*f*
hydranencephaly differentiated from, 1208

Holoprosencephaly (HPE) *(Continued)*
neonatal/infant, 1534–1535, 1534*b*, 1536*f*
pancake type of, 1187–1189
classification of, 1187*b*
corpus callosum agenesis and, 1526–1528
factors associated with, 1187*b*
fetal brain and, 1186–1189, 1187*b*, 1188*f*, 1189*b*
fetal facial changes associated with, 1189, 1189*b*
hypotelorism and, 1140
lobar, 1187–1189
classification of, 1187*b*
neonatal/infant, 1535
microforms of, 1187
midline interhemispheric form of, 1187, 1189
classification of, 1187*b*
neonatal/infant, 1535–1536
neonatal/infant, 1532–1536
alobar, 1534–1535, 1534*b*, 1536*f*
classification of, 1534*f*
lobar, 1535
midline interhemispheric form of, 1535–1536
semilobar, 1535
semilobar, 1187–1189, 1188*f*
classification of, 1187*b*
neonatal/infant, 1535
thickened NT and, 1096*f*
in trisomy 13, 1104, 1105*f*
Holosystolic valvular insufficiency, in AVSD, 1285–1286
Holt-Oram syndrome, 1401
Homozygous Achondroplasia, thanatophoric dysplasia differentiated from, 1389, 1389*f*
Hormonal states, decreased, primary amenorrhea in, 1887
Hormone replacement therapy (HRT), 529
endometrium abnormalities after menopause and, 544–545, 544*b*, 545*f*
Hormonogenesis, disorders of, thyroid hyperplasia from, 695
Horseshoe kidneys, 159–160, 318, 319*f*
fetal, 1345–1346, 1345*f*
with megalourethra, 1362
pediatric, 1784, 1785*f*
Hourglass gallbladder, 202, 205*f*
HPE. *See* Holoprosencephaly
HPS. *See* Hypertrophic pyloric stenosis
HRT. *See* Hormone replacement therapy
Human chorionic gonadotropin (β-hCG), 1049, 1884–1885
concentration of, in trisomy 21, 1089–1090
ectopic pregnancy and, 1071
free, 1089–1090
gestational sac and, 1056–1057
normal ultrasound appearance of, 1055–1057, 1057*b*
Human immunodeficiency virus (HIV), 331
chronic parotitis in children with, 1635, 1636*f*
fetal brain and, 1203–1204
nephropathy associated with, 332–333, 333*f*
Humerus length, in trisomy 21, 1101
HUS. *See* Hemolytic-uremic syndrome
Hutch diverticula, 310
Hydatid abscesses, 613
Hydatid cysts
in *Echinococcosis*, 1748
renal, 331, 332*f*
splenic, 147, 150*f*
Hydatid disease, hepatic, 88–90, 89*f*–90*f*
Hydatid sand, 88–89
Hydatidiform molar pregnancy, 1078–1080. *See also* Persistent trophoblastic neoplasia
coexistent normal fetus and, 1078–1080, 1081*f*
complete, 1078, 1079*f*
partial, 1078, 1080*f*
pediatric, 1884, 1884*f*
Hydatidiform molar pregnancy *(Continued)*
PTN after, 1080, 1081*f*
vaginal bleeding and, 1078
Hydranencephaly
fetal, 1208, 1208*f*
neonatal/infant, 1538, 1538*f*
Hydrocele(s), scrotal, 834–836, 835*f*
fetal, 1367
in fetal hydrops, 1413, 1416*f*
pediatric, 1899, 1902, 1902*f*
Hydrocephalus, 1681
communicating, 1177–1178
extraventricular obstructive, 1538
fetal brain and, 1174–1178
from germinal matrix hemorrhage, 1541
HPE differentiated from, 1189
hydranencephaly differentiated from, 1208
intraventricular obstructive, 1538
in neonatal/infant, duplex Doppler sonography and, 1581–1583, 1584*f*
neonatal/infant brain and, 1538–1541
causes of, 1540*b*
cerebrospinal fluid production and circulation and, 1538–1541
intraventricular hemorrhage with, 1545–1547, 1546*f*–1547*f*
obstructive, 1177–1178
in Dandy-Walker malformation, 1529–1530
pediatric, TCD sonography in monitoring of, 1611–1614, 1613*f*
postmeningitis, 1887
in trisomy 18, 1103
VM differentiated from, 1611–1612
X-linked, 1177
Hydrocephalus ex vacuo, 1177–1178
Hydrocolpos
fetal, 1368
pediatric, 1881, 1882*f*
Hydrometra, 546, 547*f*
Hydrometrocolpos, 546–547
cloacal malformation and, 1363
pediatric, 1881
Hydromyelia
in myelocystocele, 1233
pediatric, 1688
Hydronephrosis
causes of, 316, 317*b*
definition of, 1354
fetal
degree of, risk of postnatal pathology by, 1355, 1356*t*
in duplication anomalies, 1359–1360, 1359*f*, 1360*b*
grading system for, 1354, 1355*f*
from UPJ obstruction, 1358, 1358*f*
VUR and, 1360
genitourinary tract obstruction and, 316, 317*b*
pediatric, causes of, 1785–1791
bladder exstrophy and, 1791, 1791*f*
bladder outlet obstruction and, 1788, 1789*f*–1790*f*
MMIHS and, 1788–1791
prune belly syndrome and, 1788
UPJ obstruction and, 1786, 1787*f*
urachal anomalies and, 1791, 1792*f*–1793*f*
ureteral obstruction and, 1786–1788, 1787*f*
VUR and, 1788, 1790*f*
in pregnancy, 316
Hydrops, fetal
adrenal glands and, 1353–1354
AVSD associated with, 1285–1286
in CHD, 1270
chorioangioma management and, 1476
from CMV, 1204
CPAM and development of, 1248–1249, 1426, 1427*f*
Hydrops, fetal *(Continued)*
delivery and, 1436
diagnostic approach to, 1432–1435
fetal investigations in, 1433–1435
history in, 1432
maternal investigations in, 1433
obstetric sonography in, 1432–1433
postnatal investigations in, 1435
workshop for, summary of, 1433*t*
etiology of, 1418–1419, 1421*f*
immune, 1419–1423
definition of, 1413
noninvasive assessment of alloimmunization for, 1421–1423, 1421*b*, 1422*f*, 1422*t*
RhoGAM and, 1418
maternal complications in, 1436
nonimmune, 1423–1432
anemia and, 1431
arrhythmias and, 1424, 1425*f*
cardiac tumors and, 1424
cardiovascular causes of, 1423–1425, 1424*f*
causes and associations of, 1412, 1414*t*
chromosomal abnormalities and, 1429–1430, 1430*f*
definition of, 1413
drugs and, 1432
endocrine disorders and, 1432
fetal welfare assessment in, 1435
gastrointestinal tract anomalies and, 1427–1428, 1428*f*
genetic disorders and, 1432
idiopathic disorders and, 1432
infection and, 1431–1432, 1431*f*
lymphatic dysplasia and, 1428, 1436*f*
metabolic disorders and, 1432
mortality rate in, 1435
neck abnormalities and, 1425, 1426*f*
pathophysiology of, 1423, 1423*f*
skeletal dysplasia and, 1432
thoracic anomalies and, 1425–1427, 1427*f*
tumors and, 1430–1431
twins and, 1429, 1429*f*
urinary tract anomalies and, 1428, 1429*f*
obstetric prognosis in, 1435–1437
postnatal outcome of, 1437
predelivery aspiration procedures in, 1437
in sacrococcygeal teratoma, 1238–1239
sonographic features of, 1413–1418
ascites and, 1413, 1415*f*–1416*f*
pericardial effusion and, 1416, 1418*f*
placentomegaly and, 1418, 1420*f*
pleural effusions and, 1413–1416, 1417*f*, 1425
polyhydramnios and, 1418, 1420*f*, 1432–1433
subcutaneous edema and, 1417, 1419*f*–1420*f*
thick placenta in, 1466, 1467*f*
Hydrops tubae profluens, 589
Hydrosalpinx, 573
of fallopian tubes, 585–587, 587*f*
PID and, 1885
Hydrosonourethrography, 1872
Hydrosonovaginography, 1870–1871, 1871*f*
Hydrostatic reduction, of intussusception, ultrasound-guided, 1844–1845
Hydrothorax, fetal, hydrops from, 1425–1426
Hygromas. *See* Cystic hygroma(s)
Hymen, imperforate, hematometrocolpos form, 546–547, 546*f*
Hypercalcemia
familial hypocalciuric, 734
medullary nephrocalcinosis and, 1798
Hypercalciuria, medullary nephrocalcinosis and, 1798
Hyperechogenic kidneys, 1351–1352, 1352*f*
Hyperechoic caudate nuclei, neonatal/infant brain and, 1557, 1557*f*

Hyperechoic tissue, in breast sonography, 796–797, 796*f*
Hyperemia
in acute cholecystitis, 197*f*, 198–199
Crohn disease and, 269, 272*f*–273*f*
reactive, in testicular detorsion, 1895
testicular, pediatric, 1896
Hyperoxaluria, primary, CKD and, 1796–1798
Hyperparathyroidism
graft-dependent, 742–744, 743*f*
pediatric, 1650
persistent, 741–744, 744*f*
imaging importance in, 749, 751*f*–752*f*
primary, 733–735
causes of, 734*b*
diagnosis of, 734
MAP for, 749
pathology of, 734
prevalence of, 733–734
treatment of, 734–735
recurrent, 741–744, 743*f*
ethanol ablation for, 751–754, 754*f*
secondary, 744–745
calcimimetics for, 734
ethanol ablation for, 751–754, 754*f*
tertiary, 751
Hyperreactio luteinalis, 572
Hyperreflexia, detrusor, 372–374, 373*f*
Hypertelorism
conditions associated with, 1140, 1141*b*, 1144*f*–1145*f*
midface hypoplasia with, 1149*f*
in skeletal dysplasias, 1382
Hypertension. *See also* Portal hypertension
carotid flow waveforms and, 935*f*, 936–937
fetal, adrenal glands and, 1353–1354
maternal, IUGR and, 1455
pulmonary, with CDH, 1264
renovascular
clinical findings suggesting, 446*b*
renal artery stenosis and, 446–447
renovascular disease and, 368
Hyperthermia
NTDs from, 1218
safety and, 38, 38*f*
teratogenic effects from, 38
Hyperthyroidism
fetal goiter in, 1163
Graves disease and, 727, 727*f*
Hypertrichosis, focal, tethered cord and, 1679
Hypertrophic cardiomyopathy, 1294–1295
Hypertrophic obstructive cardiomyopathy, 1292
Hypertrophic pyloric stenosis (HPS), 1835–1838, 1835*b*, 1837*f*–1838*f*
pitfalls in diagnosis of, 1838, 1838*b*, 1839*f*
pylorospasm and minimal muscular, 1836–1838, 1838*f*
Hypertrophied column of Bertin (HCB), 313–314, 314*b*, 315*f*
Hypertrophy
of adrenal glands, 416–417
concentric, 1294–1295
kidney and compensatory, 317–318
Hyperventilation, arterial velocities and, 1595
Hyperventilation therapy, pediatric, TCD sonography and, 1614
Hypoalbuminemia, gallbladder wall thickening and, 199*f*
Hypochondrogenesis, achondrogenesis type 2 differentiated from, 1391
Hypoechogenicity, in breast sonography, 792–793, 794*f*
Hypoechoic metastases, of liver, 125, 127*f*–128*f*
Hypogastric hernias, 488–489, 491, 491*f*
Hypophosphatasia, 1383*f*
achondrogenesis differentiated from, 1391
anencephaly differentiated from, 1179
calvarial compressibility in, 1382
lethal, 1392–1395, 1395*f*
sonographic appearance of, 1380*f*
Hypophosphatasia congenita, 1392
Hypopituitarism, primary, pediatric, 1891
Hypoplasia. *See also* Pulmonary hypoplasia, fetal
cerebellar, 1190
of femur, fetal, in caudal regression, 1237–1238
of kidneys, 317
of middle phalanx in trisomy 21, 1101
midface, 1148, 1149*f*–1150*f*
pontocerebellar, 1190
pulmonary, 1245–1246
of thyroid gland, 694, 694*f*
of uterus, 538
vermis, 1190–1192, 1192*f*
inferior, arachnoid cysts differentiated from, 1192–1193
Hypoplastic left heart syndrome, 1287, 1287*f*, 1292
Hypoplastic left ventricle, 1292
Hypoplastic right ventricle, 1287, 1287*f*
Hypoplastic scapulae, in campomelic dysplasia, 1381–1382, 1395, 1396*f*
Hypospadias, fetal, 1367
Hypotelorism
conditions associated with, 1140, 1140*b*, 1142*f*–1144*f*
craniosynostosis and, 1136–1138
Hypothalamus, in menstrual cycle, 1050*f*
Hypothyroidism
congenital, 694
pediatric, 1642–1643
pediatric ovarian cysts and, 1875
fetal
fetal goiter in, 1163
wormian bones in, 1139
goitrous, 694
Hypoventilation, arterial velocities and, 1595
Hypoxic ischemic injury (HII), 1580, 1581*f*–1582*f*
Hypoxic-ischemic events, neonatal/infant brain and, 1541–1557
arterial watershed and, 1541, 1541*t*
cerebral edema and, 1550–1556
diffuse, 1553–1555, 1554*f*
cerebral infarction and, 1550–1556
focal, 1555–1556, 1556*b*, 1556*f*
hemorrhage and
cerebellar, 1548–1550, 1549*f*
germinal matrix, 1541–1543, 1542*f*, 1543*b*, 1543*t*
intraparenchymal, 1547–1548, 1547*f*–1549*f*
intraventricular, 1544–1545, 1544*f*–1546*f*, 1545*b*
intraventricular, with hydrocephalus, 1545–1547, 1546*f*–1547*f*
subarachnoid, 1550, 1550*f*
subependymal, 1543–1544, 1543*f*–1544*f*
hyperechoic caudate nuclei and, 1557, 1557*f*
injury patterns from, 1541*t*
lenticulostriate vasculopathy and, 1556–1557
PVL and, 1541, 1550–1553, 1551*f*–1553*f*

I

IBD. *See* Inflammatory bowel disease
Identical twins. *See* Monozygotic twins
Idiopathic disorders, fetal hydrops from, 1432
Idiopathic varicocele, 837–838
IEA. *See* Inferior epigastric artery
IgG4. *See* Immunoglobulin G4
IJV. *See* Internal jugular vein
Ileal conduits, evaluation of, 375, 375*f*
Ileal obstruction, fetal, 1310
Ileitis, terminal, 288
Ileus
meconium, 1310
paralytic, 294*f*, 295
Iliac, angle of, in trisomy 21, 1101
Iliac artery, 966
stenosis of, 971*f*
Iliac veins, 455–464
anatomy of, 456–457
external, ultrasound examination of, 982
thrombosis of, 459–460, 459*f*–461*f*
detection difficulties with, 988, 988*f*
Ilioinguinal nerve entrapment of, after herniorrhaphy, 496
Iliopsoas tendon, injection for, 905, 906*f*
Illicit drugs, fetal gastroschisis and, 1322–1323
Image display, 9–13, 9*f*–11*f*
Image quality
key determinants of, 16–19
spatial resolution in, 16–19, 18*f*–19*f*
Image storage, 12–13
Imaging. *See also specific techniques*
amplitude and phase modulation, 64, 65*f*
for drainage, ultrasound-guided, 610, 610*f*
keepsake, 49*b*, 50
pancreatitis approach of
acute, 221–222, 221*b*
chronic, 231
parathyroid adenomas and accuracy in, 746–749
percutaneous needle biopsy methods for, 599
pitfalls in, 19–21
plane-wave contrast, 64
pulse inversion, 62–63, 62*f*–63*f*
renal cell carcinoma approach for, 341, 341*f*
special modes of, 13–16
elastography, 15–16, 16*b*, 17*f*–18*f*
spatial compounding, 13–15, 14*f*–15*f*
3-D ultrasound, 15, 16*f*
tissue harmonic imaging, 13, 13*f*–14*f*, 61–62
split-screen, for breast assessment, 769, 769*f*
temporal maximum intensity projection, 64, 65*f*
triggered, 65
volume, in obstetric sonography, 1030
Immunocompromised patients
acute typhlitis and, 287–288, 289*f*
hepatic candidiasis in, 86–87, 88*f*
Immunoglobulin A nephropathy, CKD and, 1796–1798
Immunoglobulin G4 (IgG4)
associated disease, 1635
cholangitis related to, 182–184, 185*f*
Immunosuppression, adrenal glands and, 423
Impedance
high-resistance waveform in brachial artery, 27*f*
low-resistance waveform in peripheral vascular bed, 27*f*
Imperforate anus, 1310–1311
block vertebrae with, 1689, 1692*f*
high, pediatric, risk of spinal dysraphism with, 1689
pediatric, 1847–1848, 1850*f*
Imperforate hymen, hematometrocolpos form, 546–547, 546*f*
Implantation, 1051, 1052*f*
Implants, breast
abnormal capsule in, 804
extracapsular rupture of, 805–807, 806*f*
fill valve causing palpable abnormalities in, 804, 804*f*
intracapsular rupture of, 804–805, 805*f*
radial folds causing palpable abnormalities in, 804, 804*f*

Implants, breast *(Continued)*
shell in, 804
silicon granulomas and, 805–807, 806*f*
ultrasound evaluation of, 804–807, 804*f*–806*f*
in vitro fertilization (IVF), CHD risk with, 1270–1273
Inborn errors of metabolism, fetal hydrops from, 1432
Incarcerated hernias, 496–497
Incisional hernias, 492–493, 494*f*
Inclusion cysts
amnion, 1061
epidermal, 779
peritoneal, 508–509, 509*f*, 573, 573*f*
surface epithelial, 569, 573
vaginal, pediatric, 1883–1884
Incomplete subclavian steal, 952–953, 953*b*, 953*f*
Incontinence, fecal, anal endosonography in, 305, 305*f*
Indirect controls, 48–50, 49*t*
Indistinct margins, in breast sonography, 787, 787*f*
Indomethacin
in fetal hydrops management, 1436
in utero exposure to, fetal hydrops from, 1432
Inertial cavitation, 40, 67–68
Infants. *See* Brain, neonatal/infant, imaging of
Infarction(s)
cerebral, neonatal/infant, 1550–1556
focal, 1555–1556, 1556*b*, 1556*f*
luxury perfusion and, 1580–1581, 1584*f*
epididymitis and, pediatric, 1896
graft, pediatric renal transplantation and, 1807–1809, 1808*f*
hepatic, after liver transplantation, 638–639, 646*f*
maternal floor, 1473–1474, 1476*f*
omental
pediatric, appendicitis differentiated from, 1858–1860, 1858*f*
segmental, right-sided, 288, 289*f*
periventricular hemorrhagic, in infants, 1547
placental, 1466, 1473–1474, 1476*f*–1477*f*
after renal transplantation
global, 653
segmental, 653–655, 657*f*
silent cerebral, SCD and, 1598
splenic, 156–157, 157*f*
pediatric, 1770, 1771*f*
testicular
pediatric, 1895
segmental, 832, 832*f*
Infection(s). *See also* Bacteria, pediatric infections from; Cytomegalovirus infection; Liver, infectious diseases of; Urinary tract, pediatric, infection of; Virus(es), pediatric infections from
of biliary tree, 176–182
in breast cysts, 782–785, 785*f*
breast ultrasound for, 803–804, 803*f*–804*f*
fetal
brain development and, 1203–1204, 1205*f*
dural sinus thrombosis from, 1205–1206
echogenic bowel and, 1316
hydrops and, 1431–1432, 1431*f*
liver calcifications and, 1316–1318
of gastrointestinal tract, 295–300
AIDS patients and, 296
bezoars and, 300
celiac disease and, 300
congenital cysts and, 297, 298*f*
cystic fibrosis and, 300
hematomas and, 299
intraluminal foreign bodies and, 300
ischemic bowel disease and, 297
mucocele of appendix and, 299, 299*f*
peptic ulcer and, 299, 300*f*
Infection(s) *(Continued)*
pneumatosis intestinalis and, 297–299, 299*f*
pseudomembranous colitis and, 296–297, 298*f*
of genitourinary tract, 323–333
AIDS and, 331–333, 332*f*–333*f*
alkaline-encrusted pyelitis as, 324–325
Candida albicans as, 330–331, 331*f*
cystitis as, 333
fungal, 330–331
papillary necrosis as, 328–329, 329*b*, 329*f*
parasitic, 331
pyelonephritis as, 323–328
pyonephrosis as, 325, 326*f*
schistosomiasis as, 331
tuberculosis as, 329–330, 330*f*
of liver, 83–91
of neonatal/infant brain
acquired, 1560, 1561*f*–1563*f*
CMV, 1558–1560, 1559*f*
congenital, 1557–1560, 1559*f*
after pancreas transplantation, 682
percutaneous needle biopsy complications with, 609
renal transplantation complications with, 651–653, 655*f*–657*f*
soft tissue, 872–874, 873*f*–874*f*
of spinal canal, pediatric, 1695
of urinary tract, pediatric
jaundice in, 1738
lower, 1904–1905, 1908, 1910*f*–1911*f*
of uterus, pediatric, 1885–1887
of vagina, pediatric, 1885–1887
Infectious cystitis, 333, 334*f*
Infective peritonitis, 517, 519*f*
Inferior epigastric artery (IEA)
as landmark for inguinal hernias, 474–475, 476*f*
relationship of indirect inguinal hernia to, 476–477, 478*f*
Inferior thyroid artery, 693
Inferior thyroid vein, 693, 694*f*
Inferior vas aberrans of Haller, 820–821
Inferior vena cava (IVC), 75–76, 75*f*, 455–464
anastomosis of, for liver transplantation, 624–625
anatomic variants of, 457, 458*f*
anatomy of, 456–457
azygous continuation of, 457
Budd-Chiari syndrome and, 463
dilation of, 464
duplicated, 457, 458*f*
filters of, 464, 464*f*
left, 457
neoplasms of, 463–464
nutcracker syndrome and, 460–461, 462*f*
pancreatic head and, 211–212, 213*f*
pelvic congestion syndrome and, 461–463, 463*f*
stenosis of, after liver transplantation, 636–637, 641*f*
thrombosis of, 459–460
after liver transplantation, 636–637, 642*f*, 1766, 1769*f*–1770*f*
Inferior vesical artery, 384
Infertility
cryptorchidism of testis and, 851
ectopic pregnancy and, 1070
TRUS for prostate and, 392–394, 393*f*
Infiltrative metastases, of liver, 125–128, 126*f*
Inflammation
in acute pancreatitis, 222–225, 224*f*–228*f*
of appendix, 282–285
in breast cysts, 782–785, 785*f*
in Crohn disease
creeping fat and, 269, 271*f*
masses and, 275–276, 278*f*–279*f*
perianal inflammation and, 276, 281*f*, 305–306
Inflammation *(Continued)*
of epididymis, 846
of musculoskeletal system, pediatric, 1936–1938, 1937*f*–1938*f*
noninfectious, 1938
of prostate, 389, 390*f*
of salivary glands, pediatric, 1632–1635
acute, 1632–1634, 1632*f*–1633*f*
chronic, 1634–1635, 1634*f*–1636*f*
of tendons, 861–862, 862*f*
Inflammatory abdominal aortic aneurysm, 439–440, 443*f*
Inflammatory bowel disease (IBD), 266–269. *See also* Crohn disease
Inflammatory disease
pediatric, neck and, 1658–1664
lymph nodes and, 1658–1663, 1661*f*–1663*f*
pediatric, thyroid gland and, 1643–1646, 1645*f*–1646*f*
perianal, transanal sonography in, 305–307, 306*b*, 307*f*
Inflammatory myofibroblastic tumor, pediatric, 1812
Inflammatory pseudotumors
gastric mucosa thickening in, 1839–1840
pediatric cystitis and, 1794, 1797*f*
splenic, 153–156
Infrahyoid space, pediatric, 1628–1629. *See also* Parathyroid glands, pediatric; Thyroid gland, pediatric
anatomy of, 1640, 1642*f*
cystic lesions of, differential diagnosis of, 1644*b*
cysts of, 1650
laryngoceles of, 1650
visceral space of, 1640–1650
Infraspinatus tendon
anatomy of, normal, 879, 879*f*
ultrasound evaluation of, 883–884, 885*f*
Infundibulopelvic (suspensory) ligament, 564–565
Infundibulum, 565
Inguinal canal, testis in, 851, 851*f*
Inguinal hernias. *See* Hernia(s), inguinal
Inguinal wall insufficiency, posterior, sports hernia and, 486, 488*f*
Inionschisis, definition of, 1225*t*
Injections. *See* Musculoskeletal injection(s)
Inner cell mass, 1051
Innominate artery, 916, 938
Inspissated cysts, 779, 781*f*
Instrumentation. *See also* Transducer(s)
basic components of, 7–12
for Doppler ultrasound, 24–25, 25*b*, 25*f*–26*f*
image display in, 9–11, 9*f*–11*f*
mechanical sector scanners, 11
receiver in, 8–9, 8*f*–9*f*
transducer arrays in, 11–12, 12*f*
transducer in, 7–8
transmitter in, 7
Insula, fetal, normal sonographic appearance of, 1168
Insulin, NTDs from, 1218
Insulinomas, pediatric, 1865
Intellectual functioning, in spina bifida, 1233
Intensity
of sound, 5
of ultrasonic power, 35
Interdigital neuromas, injection for, 904, 904*f*
Interhemispheric fissure, fetal, normal sonographic appearance of, 1168, 1169*f*
Intermittent harmonic power Doppler imaging, 66, 66*f*
Intermittent imaging, with contrast agents, 64–67, 66*f*
Internal echoes, in renal cysts, 357, 357*b*
Internal inguinal ring, as landmark for inguinal hernias, 474–475, 476*f*

Internal jugular vein (IJV)
acute DVT of, 994*f*
anatomy of, 990–991, 990*f*
as cerebral blood vessel, 955–956
monophasic venous waveforms of, stenosis and, 1006, 1009*f*
phlebectasia of, 1658, 1660*f*
sonographic technique for, 955, 955*f*
thrombosis of, 955–956, 956*f*–957*f*
central line placement causing, 1658, 1661*f*
ultrasound examination for, 991, 991*f*
Internal oblique aponeurosis, torn, in spigelian hernia, 483–484, 487*f*
Internal urethral sphincter, 384
International Society for Ultrasound in Obstetrics and Gynecology (ISUOG), 1041
Interphalangeal joint, injection of, short-axis approach to, 901
Intersegmental laminar fusion, pediatric, 1688
Interstitial ectopic pregnancy, 1073, 1074*f*
Interstitial line sign, 1073
Interventional sonography, pediatric
for abscess drainage, 1953
appendiceal, 1956, 1960*f*
transrectal, 1953–1954, 1954*f*
anatomy for, 1950
colon or bowel and, 1950
diaphragm and, 1950, 1950*f*
antibiotics for, 1951
for biopsy
devices for, 1950
mediastinal mass, 1956, 1959*f*
targeted organ lesion, 1961, 1961*f*–1962*f*
central venous access for, 1954
Chiba needle for, 1948
color Doppler ultrasound and, 1945
CT and, 1943, 1943*t*
for deep foreign body removal, 1961, 1965*f*
drainage catheters for, 1948
equipment for, 1943
freehand, 1945–1947
correcting needle angle in, 1947, 1949*f*
correcting off-target needle in, 1947
initial needle placement and localization in, 1945–1946, 1945*f*–1946*f*
locating needle after insertion in, 1946–1947, 1947*f*–1948*f*
mechanical guides compared to, 1945
training aids for, 1947
guidance methods in, 1943, 1943*t*
for head lesions, 1961, 1966*f*
initial puncture device for, 1949–1950
local anesthetic technique for, 1951, 1952*f*
multimodality interventional suites for, 1943, 1944*f*
for musculoskeletal procedures, 1961, 1963*f*–1964*f*
for neck lesions, 1961, 1967*f*
one compared to two operators for, 1943–1945
patient and, 1942–1943
for percutaneous cholangiography and drainage, 1956, 1959*f*
for peritoneal drainage, 1954–1956, 1958*f*
personnel for, 1943
for PICC, 1954, 1955*f*–1957*f*
for pleural drainage, 1954–1956, 1958*f*
principles of, 1942–1943
sedation for, 1950–1951
for steroid injection, 1961, 1964*f*
transducers in, 1943
locating needle after insertion and, 1946–1947, 1947*f*
typical procedures for, 1951–1953
aims and expectations in, 1952–1953
coagulation studies in, 1952
Interventional sonography, pediatric *(Continued)*
difficult catheter fixation for, in infants, 1953
initial ultrasound in, before sedation, 1953
postprocedural care and follow-up in, 1953
prior consultation and studies in, 1951–1952
Interventricular septum, viewed from right ventricle, 1283*f*
Intervillous spaces, 1465–1466
blood flow in, 1467–1468, 1468*f*
Intestinal hematomas, small bowel obstruction from, 1843
Intestinal inflammatory disease, pediatric, 1848–1862. *See also* Appendicitis, pediatric
appendicitis as, 1855–1860, 1857*b*, 1858*f*–1862*f*
ascariasis and, 1853, 1853*f*
Crohn disease and, 1853, 1854*f*
graft-versus-host disease and, 1853–1854, 1855*f*
Henoch-Schönlein purpura and, 1853, 1855*f*
HUS and, 1851*f*, 1853–1854
mucosal, 1851, 1851*f*
NEC and, 1854–1855, 1855*b*, 1856*f*
transmural, 1851, 1852*f*
Intestinal malrotation
with midgut volvulus, 1841–1842, 1843*f*–1844*f*
midline stomach and, 1307
Intestinal wall thickening, pediatric, causes of, 1851, 1851*b*, 1851*f*–1852*f*, 1853–1854, 1855*f*
Intestine(s), acoustic cavitation in, 43. *See also* Bowel; Gastrointestinal tract
Intima-media complex, in carotid wall, 918–919, 919*f*
Intima-media thickness, atherosclerotic disease and, 918–919
Intraamniotic bleeding, fetal echogenic bowel and, 1316
Intraatrial septum, embryologic development of, 1282*f*
Intracardiac focus, echogenic, in trisomy 21, 1100*f*, 1101
Intracranial hemorrhage
fetal, 1206, 1207*f*
neonatal/infant brain and, duplex Doppler sonography of, 1580–1581, 1584*f*
Intracranial pressure, increased, vasospasm differentiated from, 1609–1610
Intracranial tumors, neonatal/infant brain and, duplex Doppler sonography of, 1585, 1587*f*
Intradecidual sac sign, 1054, 1055*f*
Intraductal intrahepatic cholangiocarcinoma, 185, 186*f*–187*f*
Intraductal papillary mucinous neoplasm (IPMN), 245–247, 245*f*–246*f*
Intradural lipomas, pediatric, 1686, 1687*f*
Intrahepatic cholangiocarcinoma, 184–185, 186*f*
intraductal, 185, 186*f*–187*f*
Intrahepatic stones, in biliary tree, 173, 173*f*
Intramedullary lipoma, 1686
Intramural sinus tract, in Crohn disease, 269, 274*f*
Intraoperative ultrasound
for adrenal glands, 429
for liver, 133
Intraparenchymal hematomas, 638
Intraparenchymal hemorrhage
IUFD and, 1124*f*
neonatal/infant brain and, 1547–1548, 1547*f*–1549*f*
Intraperitoneal gas, free, in acute abdomen, 277–281, 282*f*
Intraperitoneal stomach, 218–219, 220*f*
Intrasubstance rotator cuff tears, 888, 890*f*
Intratesticular artery, 821, 821*f*
Intratesticular cysts, 829, 830*f*
Intratesticular variocele, pediatric, 1891–1892
Intratesticular vessels, pediatric, 1888
Intrauterine devices (IUDs), 529
PID and, 587
uterine sonographic techniques and, 552–554, 553*f*
Intrauterine fetal death (IUFD), 1123–1125, 1124*f*
Intrauterine growth restriction (IUGR), 1062
from CMV, 1204
diagnosis of, 1455
fetal monitoring in, 1455
in Miller-Dieker syndrome, 1195
multifetal pregnancy morbidity and mortality and, 1119–1123
ossification delayed in, 1091
risk factors for, 1455–1460
fetal and placental, 1456*b*
maternal, 1456*b*
with spina bifida, 1233
in triploidy, 1105*f*
in trisomy 18, 1077
Intrauterine pregnancy, 1052–1053
Intravaginal torsion, 844, 844*f*
Intravascular ultrasound, in plaque characterization, 943
Intravenous Doppler contrast agents, 1749–1750
Intravenous ultrasound contrast agents, 1746
Intraventricular hemorrhage
from germinal matrix hemorrhage, 1541
neonatal/infant brain and, 1544–1545, 1544*f*–1546*f*, 1545*b*
with hydrocephalus, 1545–1547, 1546*f*–1547*f*
signs of, 1545*b*
Intussusception
MBO from, 293, 296*f*
pediatric, 1843–1847
Doppler ultrasound for, 1849*f*
false-positive, 1843, 1846*f*
Henoch-Schönlein purpura complicated with, 1853
ileocolic, 1847*f*–1848*f*
small bowel, 1844–1845, 1849*f*
sonographic signs of, 1843*b*
Invasive fibrous thyroiditis, 727–728, 728*f*
Invasive mole persistent trophoblastic neoplasia, 1080, 1081*f*
Iodine, deficiency of, thyroid hyperplasia from, 695
IPMN. *See* Intraductal papillary mucinous neoplasm
Irradiation, microcephaly from, 1194
Ischemic bowel disease, 297
Ischemic stricture, renal transplantation and, 1811
Ischemic-thrombotic damage, thick placenta in, 1466
Ischium, in sonogram of hip from transverse/flexion view, 1927, 1928*f*
Isolated ventriculomegaly (IVM), 1176
Isomerism, left atrial, AVSD and, 1284
Isthmus, 565, 692
ISUOG. *See* International Society for Ultrasound in Obstetrics and Gynecology
IUDs. *See* Intrauterine devices
IUFD. *See* Intrauterine fetal death
IUGR. *See* Intrauterine growth restriction
IVC. *See* Inferior vena cava
Ivemark syndrome, 1292
IVF. *See in vitro* fertilization
IVM. *See* Isolated ventriculomegaly

J

Jaundice
neonatal, 1734–1740
Alagille syndrome and, 1737

Jaundice *(Continued)*
bile duct spontaneous rupture and, 1734, 1737
biliary atresia and, 1734–1735, 1737, 1738*f*
causes of, 1734, 1735*b*
choledochal cysts and, 1735–1737, 1735*f*–1736*f*
inborn errors of metabolism and, 1738–1740, 1739*b*, 1740*f*
interlobular bile duct paucity and, 1737
neonatal hepatitis and, 1734, 1737–1738, 1739*f*
urinary tract infection/sepsis and, 1738
in periampullary neoplasms, 236
Jejunal obstruction, fetal, 1310
Jejunoileal atresia, small bowel obstruction with, 1310, 1311*f*
Jeune syndrome, 1395, 1398
Joint assessment, ultrasound techniques for, 866–869, 867*f*–869*f*
Joint effusion, rheumatoid arthritis and, 867, 867*f*
Joint(s)
fetal, multiple contractures of, in arthrogryposis multiplex congenita, 1401, 1405*f*
injections of, 901–902, 901*f*–902*f*
Joubert syndrome, 1182, 1190
Dandy-Walker malformation differentiated from, 1532
vermian hypoplasia with, 1191
Jugular vein, internal. *See* Internal jugular vein
Junctional parenchymal defect, 313, 314*f*
renal, 1781, 1781*f*
Juvenile cystic adenomyoma, 541
Juxtaglomerular tumors, 355–356
Juxtaphrenic paravertebral masses, pediatric, 1723

K

Kaposi sarcoma, liver in, 129
Kasabach-Merritt sequence, fetal hydrops from, 1430–1431
Kasabach-Merritt syndrome, 108
Kawasaki disease
acute, pediatric, 1741
cervical adenopathy in children with, 1660–1663
Keepsake imaging, of fetus, 49*b*, 50
Keyhole sign, from posterior urethral valves in fetus, 1361, 1361*f*
Kidney(s). *See also* End-stage renal disease; Renal artery(ies); Renal vein(s); Ureteral bud
abscesses of
acute pyelonephritis and, 325, 325*f*
drainage of, 617, 618*f*
transplantation complications with, 651, 656*f*
acute cortical necrosis of, 370, 372*f*
acute interstitial nephritis and, 370
acute tubular necrosis of, 370
agenesis of, 318–319
anatomy of, 311–314, 313*f*–315*f*
older child and adult, 1781–1783
angiomyolipoma of, 351–352, 351*f*–352*f*
ascent of, congenital anomalies related to, 318, 318*f*–319*f*
cadaveric, paired, in transplantation, 643–644, 648*f*
calculi in, 334–336, 336*f*–337*f*
entities that mimic, 336, 337*b*, 337*f*
capsule of, 314
carcinoid tumor of, 355–356
compensatory hypertrophy of, 317–318
congenital anomalies of, 1336
cysts of, 356–365
in acquired cystic kidney disease, 340, 364, 364*f*
calcifications of, 358, 358*f*
complex, 357, 357*b*, 358*f*
cortical, 356–359
hydatid, 331, 332*f*
internal echoes in, 357, 357*b*
Kidney(s) *(Continued)*
lithium nephropathy and, 361, 363*f*
in localized cystic disease, 362–364, 363*f*
malignant potential of, 359
medullary, 359
in multicystic dysplastic kidney, 361, 362*f*
in multilocular cystic nephroma, 361–362, 363*f*
parapelvic, 359, 360*f*
percutaneous management of, 617–618, 619*f*
in polycystic kidney disease, 359–361, 361*f*–362*f*
septations in, 357–358, 357*b*, 358*f*
simple, 356–357, 357*f*
in TSC, 364–365, 365*f*
in von Hippel-Lindau disease, 364, 364*f*
development of, 311, 312*f*
disease of
acquired cystic, 340, 364, 364*f*
cystic, 356–365
end-stage, reflux nephropathy and, 327, 327*f*
localized, 362–364, 363*f*
medullary, 359
neoplasm-related, 364–365
polycystic, 359–361, 361*f*–362*f*
renal cell carcinoma and acquired cystic, 340
ectopia and, 318, 318*f*
failure of, chronic, transplantation for, 641
glomerulonephritis of, 370, 371*f*
growth of, congenital anomalies related to, 317–318
hemangiopericytoma of, 356
hematomas of, 365–366
horseshoe, 159–160, 318, 319*f*
fetal, 1345–1346, 1345*f*, 1362
pediatric, 1784, 1785*f*
hypoplasia of, 317
intrathoracic, pediatric, 1716
lacerations of, 365–366, 366*f*
leiomyomas of, 355–356
leukemia involving, 353–354
lymphomas of, 333, 352–353, 353*b*
maternal, IUGR and, 1455
medullary sponge, 339, 340*f*, 359
pediatric, 1799
metastases to, 354, 355*f*
multicystic dysplastic, 361, 362*f*
multilocular cystic nephroma and, 361–362, 363*f*
oncocytoma of, 348–351
parenchyma of, calcification of, 339–340, 340*f*
pelvic, 318, 318*f*
identification of, 592
percutaneous needle biopsy of, 605–606, 606*f*–607*f*
"putty", 330
sarcomas of, 356
shattered, 365–366
sonographic technique for, 314
squamous cell carcinoma of, 348
supernumerary, 319
thoracic, 318
transitional cell carcinoma of, 346–347, 346*f*–349*f*
trauma to, 365–366, 366*f*
tumors of, rare, 355–356
vascular abnormalities of, 366–369
renal vascular Doppler ultrasound and, 366
Kidneys, fetal
agenesis of
bilateral, 1342–1344, 1343*f*–1344*f*, 1344*b*
unilateral, 1344
VUR with, 1360
cystic disease of, 1346–1352
ADPKD and, 1350, 1350*f*
ARPKD and, 1348–1350, 1349*f*
Kidneys, fetal *(Continued)*
bilateral reniform enlargement of, 1348, 1349*f*
HNF1β mutations in, 1350–1351
MCDK as, 1346–1347, 1346*f*–1347*f*
Meckel-Gruber syndrome and, 1351, 1351*f*
obstructive cystic renal dysplasia as, 1347–1348, 1347*f*–1348*f*
syndromes associated with, 1350–1351, 1351*f*
duplex, VUR with, 1360
ectopic, 1344–1345, 1344*f*–1345*f*
embryology of, 1336–1338, 1337*f*
horseshoe, 1345–1346, 1345*f*
megalourethra and, 1362
hyperechogenic, 1351–1352, 1352*f*
length of, at 14-42 weeks' gestation, 1338–1339, 1339*t*
lobation in, 317, 1781, 1781*f*
lobes of, formation of, 1781, 1781*f*
normal sonographic appearance of, 1342*f*
pelvic, 1344–1345, 1344*f*
postnatal function of
fetal urinalysis in prediction of, 1365, 1365*t*
poor, antenatal predictors of, 1364*b*
routine sonographic view of, 1026*f*
sonographic appearance of, 1338–1339, 1338*f*
tumors of, 1352–1353, 1353*f*
Kidneys, pediatric. *See also* Hydronephrosis, pediatric, causes of; Nephrocalcinosis; Urinary tract, pediatric
abscess of, complicating acute pyelonephritis, 1792–1793
absence of, 1784, 1784*f*
biopsies of, Doppler assessment of, 1809, 1810*f*–1811*f*
"cake", 1785
crossed-fused ectopia, 1784–1785, 1785*f*
cystic disease of, 1812–1818
ADPKD and, 1814–1815, 1815*f*
ARPKD and, 1812–1813, 1814*f*
MCDK and, 1815, 1816*f*
medullary cystic kidney disease and, 1816, 1817*f*
nephronophthisis and, 1815–1816, 1816*f*
cysts of, congenital, 1816–1818
dialysis and acquired, 1816–1818, 1817*f*
after liver transplantation, 1816–1818
in TSC, 1816, 1817*f*
in VHL disease, 1816
Doppler ultrasound for, 1778
dysplastic, 1798, 1798*f*
focal scarring of, from acute pyelonephritis, 1792, 1793*f*
horseshoe, 1784, 1785*f*
hydronephrosis and, 1785–1791
length of
age, height, weight compared to, 1776–1778, 1777*f*
by age, with single functioning kidney, 1779*t*
birth weight and gestational age compared to, 1776–1778, 1780*f*
normal measurements of, 1776–1778, 1777*f*
position for visualizing, 1776*f*
reference values for, according to age and gender, 1776–1778, 1778*t*
medical diseases of, 1794–1798
acute kidney injury as, 1795–1796, 1796*b*, 1797*f*
chronic kidney disease as, 1796–1798, 1797*t*, 1798*f*
normal anatomy of, 1781–1783, 1781*f*–1782*f*
normal term, 1781–1783
"pancake", 1785
pelvic, 1908
premature, normal, 1781–1783
renal duplication and, 1783–1784, 1784*f*

Kidneys, pediatric *(Continued)*
sonographic technique for, 1776–1781
patient preparation for, 1776, 1776*t*
transplantation of
Doppler ultrasound in, 1807–1812
parenchymal abnormalities and, 1809–1810, 1812*f*
perinephric fluid collections in, 1809, 1811*f*
tumors of, 1812, 1813*f*
urologic complications and, 1810–1812
vascular complications in, 1807–1809, 1808*f*, 1810*f*–1811*f*
trauma to, 1801, 1802*f*
tumors of, 1818–1820
angiomyolipoma as, 1820, 1822*f*
mesoblastic nephroma as, 1818–1820, 1821*f*
MLCN as, 1820, 1822*f*
RCC as, 1820, 1821*f*
renal lymphoma as, 1820, 1823*f*
Wilms, 1818, 1818*f*–1820*f*
vascular disease of, Doppler assessment of, 1801–1805
acute renal vein thrombosis and, 1804–1805, 1804*b*, 1804*f*
clinical applications of, 1803–1805
HUS and, 1805, 1807*f*
increased resistance to intrarenal flow and, 1802–1803, 1803*b*, 1803*f*
normal anatomy and flow patterns and, 1801–1802, 1803*f*
renal artery stenosis and, 1805, 1805*t*, 1806*f*
in renal transplantation, 1807–1809, 1808*f*, 1810*f*–1811*f*
technique for, 1801
vessel patency and, 1803–1804
volume of
by age, with single functioning kidney, 1779*t*
determination of, 1776, 1776*f*
mean total, 1779*t*
reference values for, according to age and gender, 1776–1778, 1778*t*
Kimura disease, 1635
Klebsiella, 846
Kleihauer-Betke test, 1421
Klinefelter syndrome, 826
pediatric, 1891
testicular microlithiasis and, 1904
Klippel-Trénaunay-Weber syndrome, hemimegalencephaly associated with, 1195
Knee, dislocations of, pediatric, 1933–1934, 1934*f*
Kniest dysplasia, achondrogenesis type 2 differentiated from, 1391
Krukenberg tumor, 585
Küttner tumor, 1635
Kyphoscoliosis
body stalk anomaly and, 1329
fetal, 1404
in skeletal dysplasias, 1382
Kyphosis, fetal, 1235–1237, 1236*f*, 1237*b*
cervical, in campomelic dysplasia, 1381–1382

L

Labor, preterm, 1495–1496. *See also* Preterm birth
Labrum, of acetabulum, 1923
Lacerations
pediatric pregnancy and, 1884
renal, 365–366, 366*f*
Lactobezoars, 1840, 1841*f*
Laminae
in posterior angled transaxial scan plane, 1224*f*
in posterior transaxial scan plane, 1222*f*
in spina bifida, 1228, 1229*f*–1230*f*
Laminectomy, spinal sonography after, 1697
Langerhans cell histiocytosis
in infant, 1751*f*
metastasis of, to teste, 1901
Langer-Saldino form of achondrogenesis, 1391
Laparoscopy, for ectopic pregnancy, 1076
Large bowel, dilated loops of, 1311–1312
Large-for-gestational age (LGA) fetus, 1453–1454
diabetic mothers and, 1454, 1455*t*
incidence of, 1453–1454
sonographic criteria for, 1454*t*–1455*t*
Larsen syndrome
elbow and knee dislocation and, 1933–1934
teratologic hip dislocation and, 1932
Laryngeal webs, fetal, CHAOS and, 1253
Laryngoceles, pediatric, 1650
Laryngotracheomalacia, 1395
Larynx, fetal, CHAOS and, 1253
Lateral nasal prominence, 1134, 1134*f*
Lateral resolution, 19, 19*f*
Lehman syndrome, spina bifida and, 1226
Leiomyoma(s)
adenomyosis coexisting with, 541
bladder, 356
gastric, 265*f*
gastrointestinal, endosonographic identification of, 301
paratesticular, 1903–1904
renal, 355–356
spermatic cord, 840–841, 840*f*
uterine, 538–540, 539*f*, 540*b*
Leiomyomatosis peritonealis disseminata, 523–524, 525*f*
Leiomyosarcoma(s)
bladder, 356
gastric, 265*f*
paratesticular, 1903–1904
uterine, 540, 541*f*
Lemierre syndrome, 1658, 1661*f*
Lemon sign, in Chiari II malformation, 1183–1185, 1184*f*
spina bifida screening and, 1221, 1232–1233
Lemon-shaped skull, 1136, 1137*f*
Lenticulostriate vasculopathy, 1203, 1204*f*, 1585, 1588*f*
neonatal/infant, 1556–1557
Leptomeningeal collaterals, MCA occlusion, 1610
Leriche syndrome, 441–442
Lesser omentum, portal hypertension and thickened, 1756, 1756*f*
Lesser peritoneal sac, 218–219, 220*f*
Leukemia
acute lymphocytic, AKI and, 1796
liver metastases from, pediatric, 1746
lymphadenopathy from, 1724
ovarian infiltration by, pediatric, 1880
in pancreas, pediatric, 1865
renal involvement in, 353–354
salivary gland infiltration by, pediatric, 1639
testicular, 827, 828*f*
pediatric, 1901, 1901*f*
Leukodystrophy, megalencephaly associated with, 1194–1195
Leukomalacia, periventricular. *See* Periventricular leukomalacia
Levocardia, 1273
Levotransposition, of great arteries, 1289–1290
Levovist, 55–56, 107, 111*f*
Leydig cells
testosterone secretion and, 819
tumors of, 826, 827*f*
pediatric, testicular, 1900, 1900*f*
LGA. *See* Large-for-gestational age fetus
LHBT. *See* Long head biceps tendon
LHR. *See* Lung-to-head circumference ratio
Li-Fraumeni syndrome
adrenocortical neoplasms and, 1827
prenatal intracranial tumors in, 1208
Ligament(s)
anatomy of, normal, 862–863, 863*f*
falciform, 77, 79*f*
pediatric, 1731, 1731*f*–1732*f*
injuries to, 862–863, 863*f*–864*f*
diagnosing, 864, 864*f*
of liver, 77, 79*f*–80*f*
ultrasound techniques for, 862–864
Ligamentum teres, 77, 80*f*
Ligamentum venosum, 77
pediatric, 1731, 1731*f*
Limb deformities, congenital
pediatric, 1933
PFFD and, 1933, 1934*f*
tibial hemimelia and, 1933
Limb enlargement, asymmetrical, 1403
Limb pterygium, 1403
Limb reduction defects, 1399–1404
amniotic band sequence as, 1401, 1403*f*
arthrogryposis multiplex congenita as, 1401–1404, 1405*f*
caudal regression syndrome as, 1401, 1404*f*
deformations as, 1399
disruptions as, 1399
isolated, 1400
malformations as, 1399
nomenclature of, 1400*t*
proximal focal femoral deficiency as, 1400, 1400*f*
radial ray, 1400–1401, 1401*f*–1402*f*
sirenomelia as, 1401, 1404*f*
terminal transverse, 1400
Limb shortening, patterns of, 1381, 1381*b*, 1382*f*
Limb-body wall complex, 1182–1183, 1329
OEIS differentiated from, 1328–1329
Limb–body wall complex, 1401
Limey bile, 194, 195*f*
Lindegaard ratio, 1596, 1609–1610
Linea alba, appearance of, 489, 489*f*
Linea alba hernias, 488–491. *See also* Hernia(s), linea alba
Linear array transducers
beam steering in, 10–11, 11*f*
use and operation of, 11–12
Lingual thyroid, pediatric, 1639
Lipid cysts, in breast, 775–779, 779*f*
Lipoadenomas, parathyroid, 735
Lipoleiomyomas, 539*f*, 540
Lipoma(s)
corpus callosum, 1529, 1533*f*
filum terminale, 1674
closed spinal dysraphism and, 1684–1685, 1686*f*
intracranial, fetal, 1209–1210, 1210*f*
intradural, pediatric, 1686, 1687*f*
intramedullary, 1686
intramuscular, simulating anterior abdominal wall hernias, 500, 502*f*
of liver, 117–118, 119*f*
midline, in corpus callosum agenesis, 1201
pancreatic, 249–251, 250*f*
paratesticular, 1903–1904
parotid gland, pediatric, 1639
simulating groin hernias, 500, 501*f*
spermatic cord, 840–841, 840*f*
spina bifida occulta with, 1226
subcutaneous
simulating anterior abdominal wall hernias, 500, 502*f*
tethered cord and, 1679
ultrasound techniques for, 870, 871*f*, 871*t*

Lipomyelocele, closed spinal dysraphism and, pediatric, 1682, 1684*f*
Lipomyelomeningoceles
  closed spinal dysraphism and, pediatric, 1682, 1685*f*
  spine embryology and differentiation of, 1674
Liposarcomas, scrotal, 840*f*, 841
Lips, fetal, normal sonographic appearance of, 1135*f*. *See also* Cleft lip/palate
Lissencephaly
  classical (type 1), 1195, 1196*f*
  cobblestone (type 2), 1195, 1197*f*
  fetal, 1195–1196, 1196*f*–1197*f*
  neonatal/infant, 1537
Lithium nephropathy, 361, 363*f*
Lithium therapy, long-term, primary hyperparathyroidism and, 734
Lithotripters, acoustic cavitation evidence from, 42–43, 42*f*
Littoral cell angioma, splenic, 153–156, 156*f*
Liver
  abscesses of
    drainage of pyogenic, 612–613, 614*f*–615*f*
    after liver transplantation, 638–639, 646*f*
    from pyogenic bacteria, 85–86, 87*f*
  agenesis of, 80
  anatomy of
    Couinaud, 76–77, 77*t*, 78*f*
    echogenicity of, 80, 81*f*
    hepatic venous, 76, 76*f*, 77*t*
    ligaments, 77, 79*f*–80*f*
    normal, 75–80, 75*f*–76*f*, 77*t*
    size of, 80
  anomalies of
    congenital, 82–83
    developmental, 80–82
    vascular, 80–82
  bare area of, 77
  benign neoplasms of, 108–118
    adenoma as, 115–117, 116*f*–118*f*
    angiomyolipomas as, 117–118, 119*f*
    cavernous hemangioma as, 108–112, 112*f*–113*f*, 603–604, 604*f*
    FNH as, 112–115, 114*f*–115*f*
    lipomas as, 117–118, 119*f*
  biopsy of
    percutaneous, 132–133
    percutaneous needle, 603–604, 603*f*–604*f*
  circulation in, 78–80
    hepatic artery and, 78
    hepatic veins and, 80
    portal veins and, 78
  cirrhosis of, 92–96
    Doppler ultrasound characteristics of, 95, 95*f*
    HCC and, 122, 122*t*
    intrahepatic portal hypertension from, 96
    morphologic patterns of, 92–95, 94*f*
    pseudocirrhosis of, 125–128, 129*f*
    sonographic features of, 95*b*
    SWE and, 95–96
  cysts of, 82, 82*f*–83*f*
    autosomal dominant polycystic kidney disease and, 83
    percutaneous management of, 618
    peribiliary, 82–83
  fatty, 91–92, 92*f*–93*f*
  fetal, 1316–1318
    calcifications of, 1316–1318, 1317*f*, 1318*b*
    cysts and, 1318, 1318*f*
    hemangioma of, 1319*f*
    hepatomegaly and, 1316, 1317*f*
  fibrosis of, periportal, Caroli disease with, 171
  fissures of, 75–76
    accessory, 80, 81*f*
  fluid collection in, after transplantation, 638–639, 645*f*–646*f*
Liver *(Continued)*
  glycogen storage disease affecting, 92
  herniation of, 80
  infectious diseases of, 83–91
    bacterial, 85–86, 87*f*
    fungal, 86–87, 88*f*
    parasitic, 87–90, 89*f*–90*f*
    Pneumocystis carinii and opportunistic, 91, 91*f*
    viral hepatitis, 83–85
  intraoperative ultrasound for, 133
  in Kaposi sarcoma, 129
  lobes of, 75–76, 75*f*–76*f*
  lymphoma of, 125, 129*f*
  malignant neoplasms of, 118–124
    EHE as, 123–124
    HCC as, 118–123, 120*f*–121*f*, 122*t*, 123*f*
    hemangiosarcoma as, 123
  masses of, 105–107
    characterization of, 105–106, 106*f*–107*f*, 108*t*, 109*f*–110*f*
    detection of, 106–107, 111*f*
    microbubble contrast agents in characterization of, 105–106, 106*f*–107*f*, 108*t*, 109*f*–110*f*
    neoplasms in, 107–129
  metabolic disorders of, 91–96
  metastatic disease of, 124–129, 126*f*–130*f*
  portosystemic shunts and, 130–132
    transjugular intrahepatic, 131–132, 132*b*, 132*f*–133*f*
  scalloping of, in pseudomyxoma peritonei, 514, 518*f*
  schistosomiasis of, 90
  situs inversus totalis of, 80
  sonographic technique for, 75, 75*f*
  trauma to, 129–132, 131*f*
  vascular abnormalities in, 96–104
    Budd-Chiari syndrome as, 98–103, 100*f*–103*f*
    hepatic artery pseudoaneurysm as, 104
    hereditary hemorrhagic telangiectasia as, 104
    intrahepatic portosystemic venous shunts as, 104
    peliosis hepatis as, 104, 104*f*
    portal hypertension as, 96–98, 96*f*–97*f*
    portal vein aneurysms as, 103–104
    portal vein thrombosis as, 98, 99*f*–100*f*
  veno-occlusive disease of, 103
  volumetric imaging of, 75
  as window to pleural space, 1702, 1707*f*
Liver, pediatric. *See also* Jaundice, neonatal; Liver transplantation, pediatric; Portal hypertension, pediatric
  abscess of, 1746–1748, 1751*f*
    parasitic, 1747–1748
    pyogenic, 1746–1747, 1751*f*
  adenomas of, 1746
    inborn errors of metabolism and, 1738
  anatomy of, 1730–1734
    hepatic vein, 1733–1734, 1734*f*
    portal vein, 1731–1734, 1732*f*
    segmental, external, 1730–1731, 1731*f*
  biliary rhabdomyosarcoma in, 1746, 1749*f*
  biopsy of, targeted, 1962*f*
  cholelithiasis and, 1741, 1741*b*, 1743*f*
  cirrhosis and, 1741, 1742*f*
  congenital fibrosis of, prehepatic portal hypertension from, 1757–1759, 1762*f*
  Doppler assessment of, 1748–1764
    basic principles of, 1748–1750
    of normal flow patterns in splanchnic vessels, 1750
    for portal hypertension, 1752–1754, 1754*f*–1755*f*
    possibilities and pitfalls of, 1750
Liver, pediatric *(Continued)*
    sonographic technique for, 1750–1752
    surgical portosystemic shunts and, 1764
  Echinococcosis in, 1748
  fatty degeneration/infiltration of, 1740, 1740*f*
  FNH and, 1746
  granulomas of, 1748
  HCC of, 1746
  hemangiomas and, 1742–1743, 1744*f*
  hepatoblastomas of, 1746, 1747*f*
  infantile hemangioendotheliomas and, 1743–1744, 1745*f*
  jaundice and, 1734–1740
  left lobe of, 1731–1733
  masses in, 1743*b*
  mesenchymal hamartomas and, 1744
  metastases to, 1746, 1750*f*
  quadrate lobe of, 1731–1733
  right lobe of, 1733, 1733*f*
  schistosomiasis in, 1748
  steatosis and, 1740, 1740*f*, 1741*b*
  SWE and, 1764, 1765*f*
  tumor angiogenesis detection in, 1746
  tumors of, 1741–1746
    benign, 1742–1746
    identification of, 1741–1742
    malignant, 1746
  undifferentiated embryonal sarcoma and, 1746, 1748*f*
Liver flukes, biliary tree and, 176–179, 177*f*–179*f*
Liver transplantation, 624–641
  abscess after, 638–639, 646*f*
  adrenal hemorrhage after, 638, 645*f*
  arterial complications of, 629–635
    celiac artery stenosis as, 634–635, 637*f*
    hepatic artery pseudoaneurysms as, 634, 636*f*
    hepatic artery resistive index elevation as, 634
    hepatic artery stenosis as, 631–634, 634*f*–635*f*
    hepatic artery thrombosis as, 627, 628*f*, 631, 633*f*
  biliary tree complications with, 625–629
    bile leakage as, 627–629, 629*f*
    biliary sludge as, 629, 631*f*
    biliary stones as, 629, 632*f*
    biliary strictures as, 626–627, 627*f*–628*f*
    pneumobilia as, 625, 1767–1768, 1769*f*–1770*f*
    recurrent sclerosing cholangitis as, 629, 630*f*
    sphincter of Oddi dysfunction as, 629
  biloma after, 638
  choledochojejunostomy for, 625
  common bile duct anastomosis for, 625
  contraindications for, 624
  Doppler studies of recipient of, pediatric, 1764–1769
    with multiorgan transplants, 1768–1769
    for posttransplantation evaluation, 1766–1768, 1768*f*–1770*f*
    for pretransplantation evaluation, 1764–1766
    rejection in, 1767
  fluid collection after
    extrahepatic, 638, 644*f*–645*f*
    intrahepatic, 638–639, 645*f*–646*f*
  hematomas after, 638, 644*f*
  hepatic artery anastomosis for, 624
  infarction after, 638–639, 646*f*
  intrahepatic solid masses complicating, 639–641, 646*f*
  IVC anastomosis for, 624–625
  living related donor, 625
  normal appearance of, 625, 626*f*, 1767*f*
  patient selection for, 624
  pediatric
    Doppler studies of recipient of, 1764–1769
    renal cysts after, 1816–1818
  portal vein anastomosis for, 624

Liver transplantation *(Continued)*
PTLD after, 683–688, 687*f*
split liver graft and, from deceased donor, 625
surgical technique for, 624–625, 624*f*
venous complications of
hepatic artery aneurysms as, 1768, 1769*f*–1770*f*
hepatic vein stenosis as, 637, 643*f*
IVC stenosis as, 636–637, 641*f*
IVC thrombosis as, 636–637, 642*f*, 1766, 1769*f*–1770*f*
portal vein aneurysms as, 1768, 1769*f*–1770*f*
portal vein stenosis as, 635–636, 638*f*, 1766, 1768*f*
portal vein thrombosis as, 635–636, 639*f*–640*f*, 1766
Lobar emphysema, congenital, 1251, 1253*f*
"Lobster claw" deformity, 1406–1407, 1406*f*
Localized cystic disease, 362–364, 363*f*
Long head biceps tendon (LHBT), 879, 880*f*–881*f*
longitudinal split tear of, 893, 894*f*
pathology of, 892–893
tenosynovitis and, 892–893, 893*f*
Longitudinal split tear, of long head of biceps, 893, 894*f*
Longitudinal waves, 2–3
Longus colli muscle, parathyroid adenomas confused with, 745
Lower face abnormalities, 1153–1154
macroglossia as, 1153, 1153*b*, 1158*f*
micrognathia as, 1153–1154, 1158*f*
retrognathia as, 1153–1154
Lower limb anomalies, pediatric, 1689
Lower urinary tract symptoms (LUTS), 387–388
Lumbar arteries, 446, 446*f*
Lumbar spine deficiency, in caudal regression, 1237–1238
LUMBAR syndrome, tethered cord and, 1679
Lumbosacral area, spina bifida in, 1228
Lumbosacral hypogenesis, spinal cord embryology and, 1674
Lung(s). *See also* Pulmonary hypoplasia, fetal
acoustic cavitation in, 43
CHAOS and, 1253–1255, 1254*f*
congenital malformations of
BPS as, 1250–1251, 1251*f*
CLO as, 1251–1252, 1253*f*
CPAM as, 1246–1252
pediatric
abscess in, 1711, 1713*f*
atelectatic, 1714, 1716*f*
consolidated, 1711, 1714*f*–1715*f*
disease of, pleural disease differentiated from, sonography in, 1709, 1710*f*
parenchyma, 1711–1716
sequestrations in, 1715–1716, 1717*f*
percutaneous needle biopsy of, 607–608, 609*f*
pleuropulmonary blastoma and, 1252–1253
Lung(s), fetal
development of, 1243
stages of, 1245*b*
hypoplasia of
campomelic dysplasia and, 1384*f*
in lethal skeletal dysplasia, 1386, 1386*b*
lethality of skeletal dysplasia and, 1382, 1384*f*
masses in, hydrops from, 1426
size of, evaluation of, 1244
space-occupying lesions and, 1243
Lung-to-head circumference ratio (LHR), 1262
Luteal phase defect, early pregnancy failure from, 1062–1063
Luteoma of pregnancy, 572
LUTS. *See* Lower urinary tract symptoms
Luxury perfusion, cerebral infarction with, 1580–1581, 1584*f*
"Lying down" adrenal sign
in bilateral renal agenesis, 1342, 1343*f*
in neonate with absence of left kidney, 1784, 1784*f*
Lyme disease, pediatric, 1936
Lymph node(s)
breast cancer and assessment of, 807–810, 808*f*–810*f*
cortex of, 807
eccentric cortical thickening of, 807–808, 809*f*
hilum of, 807
masses of, in carotid region, 948, 949*f*
normal appearance of, 807, 808*f*
pathologic, near carotid bifurcation, 948, 949*f*
pediatric, inflammatory disease of, 1658–1663, 1661*f*–1663*f*
Rotter, 762, 808–810, 810*f*
Lymphadenitis, pediatric, 1658–1663, 1662*f*–1663*f*
Lymphadenopathy
in Crohn disease, 269, 272*f*
Doppler ultrasound assessment of, 771–772, 772*f*
pediatric
age and causes of, 1660, 1662*t*
cervical, 1658, 1660–1663
mediastinal masses and, 1724
site of node and causes of, 1660, 1662*t*
supraclavicular, 1658
retroperitoneal, 464
in tuberculous peritonitis, 521
Lymphangiectasia, appearance of, 1412, 1413*f*
Lymphangioma(s)
abdominal, pediatric, 1862, 1864*f*
fetal, neck, hydrops from, 1425
paratesticular, 1903–1904
pediatric pancreas and, 1865
pelvic, mesenteric cysts in, 509–510, 510*f*
splenic, 148
Lymphatic dysplasia, congenital, hydrops from, 1428, 1436*f*
Lymphatic malformations. *See also* Cystic hygroma(s)
fetal neck abnormalities and, 1159, 1161*f*
macroglossia in, 1153, 1153*b*, 1158*f*
pediatric
of chest, 1723
chest wall, macrocystic, ultrasound-guided sclerotherapy of, 1726, 1727*f*
of neck, 1655–1657, 1657*f*
parotid gland, 1636, 1637*f*
submandibular space, 1639–1640
in Turner syndrome, 1159
Lymphedema, hereditary, fetal, 1403–1404, 1405*f*
Lymphocele(s)
pelvic, 591
after renal transplantation, 665–666, 673*f*–674*f*
pediatric, 1809, 1811*f*
Lymphocytic leukemia, acute, 1796
Lymphoma(s)
adrenal, 426–427, 427*f*
AIDS-related, 266, 266*f*
B-cell, AKI and, 1796
bladder, 353, 354*f*
Burkitt, pediatric, 1860
gastric, endosonographic identification of, 301
gastrointestinal, 264–266, 266*f*
pediatric, 1862
genitourinary tract tumors and, 352–353
Hodgkin, pediatric, neck, 1665, 1665*f*
Lymphoma(s) *(Continued)*
of liver, 125, 129*f*
lymphadenopathy from, 1724
mediastinal, pediatric, biopsy of, 1956
non-Hodgkin, 125, 264–266
pediatric, neck, 1665
splenic lesions in, 152–153, 154*f*
ovarian, 585
pediatric, 1880
pediatric
liver metastases from, 1746
neck, 1665, 1665*f*
paratesticular, 1903–1904
peritoneal, 513, 517*f*
renal, 333, 352–353, 353*b*
pediatric, 1820, 1823*f*
retroperitoneal, 464
salivary gland, pediatric, 1639
of small bowel, 266, 266*f*
splenic lesions in
nodular, 152, 154*f*
solid, 152–153
testicular, 826–827, 828*f*
pediatric, 1901
of thyroid gland, 708–709, 709*f*
pediatric, 1648
ureteral, 353
Lymphoplasmacytic sclerosing pancreatitis, 236
Lymphoproliferative disorder. *See* Posttransplant lymphoproliferative disorder
Lysosomal disorders, fetal hydrops from, 1432

M

Macrocephaly, 1135–1136
fetal brain and, 1194–1195
Macrocranium(ia)
in skeletal dysplasia, 1382
in thanatophoric dysplasia, 1387
Macrocysts, ovarian, pediatric, 1873–1875
Macroglossia, 1153, 1153*b*, 1158*f*
Macronodular cirrhosis, 92–93
Macrosomia, 1453
sonographic criteria for, 1454*t*–1455*t*
Maffucci syndrome, in venous malformations of neck, 1657
Magnetic resonance angiography (MRA), in carotid stenosis diagnosis, 916
Magnetic resonance imaging (MRI), 32–33
breast ultrasound correlation with, 810–811, 811*f*–812*f*
of CNS, 1166–1167
of fetal brain, 1166–1167, 1172*f*
for fetal spine, 1216
for fetal urinary tract abnormalities, 1342, 1342*f*
of fetus, 1031–1032, 1031*f*
musculoskeletal system ultrasound compared to, 856
parathyroid adenomas and accuracy of, 748, 749*f*
in pregnancy, 1031–1032, 1031*f*
shoulder ultrasound compared to, 877–878
in skeletal dysplasia evaluation, 1385
Mainzer-Saldino syndrome, 1395
Majewski syndrome, 1396
Malacoplakia, 333, 333*f*
Male pseudohermaphroditism, dysplastic gonads and, 1899
Malformations, definition of, 1399
Malignancies, childhood, obstetric sonography and, 1041
Malignant melanoma, splenic lesions in, 153, 155*f*
MALToma, pediatric, 1639

Mammary ducts
  normal sonographic appearance of, 762, 764*f*
  subareolar and intranipple, scanning of, 762, 765*f*
Mammary fascia, 761, 762*f*
Mammary zone, of breast, 761, 761*f*, 763*f*
Mandible, fetal, normal sonographic appearance of, 1135*f*
Mandibular nasal prominence, 1134, 1134*f*
MAP (minimal-access parathyroidectomy), 749, 750*f*
Marfan syndrome, 946
Marginal placental cord insertion, 1484–1485, 1487*f*
  multifetal pregnancy and, 1119
Massa intermedia, enlarged, in Chiari II malformation, 1526, 1527*f*
Masseter muscle, pediatric, chloroma of, 1641*f*
Massive splenomegaly, 145, 146*t*
Masticator space, pediatric, pathology of, 1640, 1641*f*
Mastitis
  granulomatous, 803–804
  periductal, 771, 771*f*
  sonography for, 803–804
Maternal age, chromosomal abnormalities risk and, 1088, 1089*f*
Maternal floor infarction, 1473–1474, 1476*f*
Mathias laterality sequence, spina bifida and, 1226
Matrix metalloproteinases (MMPs), 434
Maxilla, fetal, normal sonographic appearance of, 1135*f*
Maxillary nasal prominence, 1134, 1134*f*
Maximum vertical pocket, 1339
Maximum-intensity projection (MIP), 105–106
Mayer-Rokitansky-Küster-Hauser syndrome, 1881–1883, 1882*f*
May-Thurner syndrome, 456–457
MBO. *See* Mechanical bowel obstruction
MCA. *See* Middle cerebral artery
McCune-Albright syndrome, pediatric ovarian cysts and, 1875
MCDA. *See* Monochorionic diamniotic twins
MCDK. *See* Multicystic dysplastic kidney
MCMA. *See* Monochorionic monoamniotic twins
MDCT. *See* Multidetector computed tomography
Mean sac diameter (MSD)
  in gestational age estimation, 1061, 1061*f*, 1444–1445, 1445*t*
  of gestational sac
    for gestational age estimation, 1444–1445, 1445*t*
    small, in relationship to CRL, early pregnancy failure and, 1066, 1067*f*
  yolk sac and, 1057
Mechanical beam steering, 10–11
Mechanical bowel obstruction (MBO)
  afferent loop, 293
  closed-loop, 293, 295*f*
  gastrointestinal tract and, 293
  intussusception causing, 293, 296*f*
  midgut malrotation predisposing to, 293
  sonographic assessment of, 293, 294*f*
Mechanical index (MI)
  for acoustic cavitation, 44–45, 45*f*
  definition of, 58
  microbubbles as contrast agents and, 58, 58*b*, 105
  in obstetric sonography, 1035
Mechanical sector scanners, 11
Mechanical ventilation, in neonatal/infant brain, 1578, 1579*f*
Meckel diverticulum
  intussusception and, 1844–1845, 1849*f*
  pediatric appendicitis differentiated from, 1858–1860, 1862*f*
Meckel-Gruber syndrome
  Dandy-Walker malformation differentiated from, 1532
  fetal brain dorsal induction errors and, 1182
  fetal cystic kidneys and, 1351, 1351*f*
  spina bifida and, 1226
Meconium ileus, 1310
  fetal CF and, 1316
Meconium periorchitis, focal calcifications from, 1904, 1904*f*
Meconium peritonitis
  fetal
    CF and, 1316
    hydrops from, 1428, 1428*f*
    liver calcifications and, 1316–1318
    massive ascites in, 1418–1419, 1421*f*
    small bowel and, 1313, 1313*t*, 1314*f*
  pediatric
    cystic, 1842–1843, 1846*f*
    testicular torsion and, 1892–1893
Medial fibroplasia, renal artery stenosis and, 447
Medial gastrocnemius muscle, tear of, 858, 859*f*
Medial nasal prominence, 1134, 1134*f*
Median arcuate ligament syndrome, 453, 453*f*
Mediastinal shift, in unilateral pulmonary hypoplasia, 1246, 1247*f*
Mediastinum
  fetal, masses in, hydrops from, 1425
  pediatric, assessment of, 1702, 1703*f*–1704*f*
  pediatric, masses of, 1723–1724
    abnormal thymus location mimicking, 1723
    anterior, 1723–1724
    biopsy of, 1956, 1959*f*
    lymphadenopathy and, 1724
    posterior, 1724
    thymic index and, 1723, 1724*t*, 1725*f*, 1726*t*
Mediastinum testis, 819, 820*f*
  pediatric, 1888
Medical renal disease. *See* Kidneys, pediatric, medical diseases of
Medulla
  adrenal, functions of, 417
  cerebral, as foramen magnum approach landmark, 1592, 1595*f*
Medullary carcinoma, of thyroid gland, 701–707, 707*f*–708*f*
  pediatric, 1648
Medullary cystic kidney disease, 359
  pediatric, 1816, 1817*f*
Medullary nephrocalcinosis, 339, 340*f*
  pediatric, 1798–1799, 1799*f*
Medullary sponge kidney, 339, 340*f*, 359
  pediatric, 1799
Megacalices, congenital, 321
Mega-cisterna magna
  fetal, 1189
    arachnoid cysts differentiated from, 1192–1193
    normal sonographic appearance of, 1168–1169
  neonatal/infant, Dandy-Walker malformation differentiated from, 1531, 1534*f*
Megacystis, fetal, 1360, 1360*b*, 1360*f*
  megalourethra and, 1362*f*
Megacystis-microcolon-intestinal hypoperistalsis syndrome (MMIHS), 1362–1363
  pediatric hydronephrosis and, 1788–1791
Megacystitis, fetal, thickened NT and, 1096*f*
Megahertz, definition of, 2
Megalencephaly, 1194–1195
Megalourethra, fetal, urinary tract obstruction in, 1362, 1362*f*
Megaureter(s)
  congenital, 321, 322*f*
  fetal, 1358–1359
  primary, pediatric hydronephrosis and, 1786–1788, 1787*f*
Meigs syndrome, 585
Membranous glomerulonephritis, 369
Membranous VSDs, 1281
MEN. *See* Multiple endocrine neoplasia
Ménétrier disease, gastric mucosa thickening in, 1839–1840
Meningeal layer, in myelocystocele, 1233
Meningitis, neonatal/infant, 1560, 1561*f*–1562*f*
Meningocele
  atretic, tethered cord and, 1679
  fetal
    cranial, 1179
    definition of, 1225*t*
    pathogenesis of, 1226
    sonographic findings in, 1218
    spina bifida occulta and, 1226
  posterior, closed spinal dysraphism and pediatric, 1682–1683
Meningoencephalocele, 1218
Meningomyelocele, fetal cloacal exstrophy and, 1328
Menopause
  endometrial abnormalities after
    bleeding and, 545–546
    fluid and, 546–547, 546*b*, 547*f*
    hormone use and, 544–545, 544*b*, 545*f*
  ovaries after, 569
    cysts in, 569–570, 571*f*
Menstrual age
  definition of, 1443–1444
  usage of term, 1167
Menstrual cycle, interrelationships in, 1050*f*
Menstruating females, ovarian volume in, 1873, 1875*t*
Mesencephalon, formation of, 1077
Mesenchymal dysplasia, of placenta, 1479, 1479*f*
Mesenchymal tumors, intracranial, fetal, 1208
Mesenchyme, formation of, 1053
Mesenteric, adenopathy, in acute abdomen, 282
Mesenteric adenitis
  pediatric, 1858–1860, 1862*f*
  right lower quadrant pain in acute abdomen from, 288
Mesenteric adenopathy, in acute abdomen, 282
Mesenteric artery(ies), 451–455. *See also* Celiac artery
  anatomy of, 451, 452*f*
  celiac artery as, 451
  duplex Doppler sonography of, 453–455, 455*f*
    interpretation of, 454–455, 456*f*–458*f*
  inferior
    anatomy of, 451, 452*f*
    connections of, with superior mesenteric artery, 451
    duplex Doppler sonography of, 454
  ischemia of, 451–453
  in median arcuate ligament syndrome, 453, 453*f*
  stenosis of, turbulence after, 454, 456*f*
  superior
    anatomy of, 451, 452*f*
    connections of, with inferior mesenteric artery, 451
    duplex Doppler sonography of, 454
    occluded, 454–455, 458*f*
    stenosis of, 457*f*
Mesenteric cyst(s)
  fetal, ovarian cysts differentiated from, 1369
  gastrointestinal cysts differentiated from, 1860, 1863*f*
  pediatric, ovarian cysts differentiated from, 1875
  peritoneal, 509–510, 510*f*
Mesenteric vein(s)
  clots in, in acute pancreatitis, 224–225, 227*f*
  pediatric
    Doppler studies of, best approaches for, 1752
    flow direction in, in portal hypertension, 1752

Mesentery, small bowel, 505, 505*f*
Mesoblastic nephroma
  congenital, 1352–1353, 1353*f*
  pediatric, 1818–1820, 1821*f*
Mesocardia, 1273
Mesocolon, transverse, inflammation of, in acute pancreatitis, 224–225, 226*f*
Mesoderm layer, of trilaminar embryonic disc, 1216–1217, 1217*f*
Mesomelia, 1381, 1381*b*, 1382*f*
Mesonephric (wolffian) duct, 820–821
Mesonephros, 311, 312*f*, 1336–1338
Mesorchium, torsion of, pediatric, 1325
Mesosalpinx, 564–565
Mesothelioma(s)
  cardiac, in infants, 1293
  multicystic, 508–509
  pediatric, 1712*f*
  peritoneal, primary, 513, 516*f*
Mesovarium, 564–565
Metabolic disorders
  fetal hydrops from, 1432
  of liver, 91–96
  neonatal jaundice caused by, 1734
  neonatal/infant brain abnormalities from, 1538
Metabolic syndrome, fatty liver in, 91
Metabolism, inborn errors of, jaundice and, 1738–1740, 1739*b*, 1740*f*
Metacarpophalangeal joint, injection of, short-axis approach to, 901
Metanephrogenic blastema, in kidney development, 311, 312*f*
Metanephros, 311, 312*f*, 1053–1054, 1336–1338
Metastasis(es)
  adrenal, 425–426, 426*f*–427*f*
  to biliary tree, 188, 192*f*
  bladder, 354–355, 355*f*
  of breast cancer, lymph node assessment for, 807–810, 808*f*–810*f*
  characterization of, with microbubble contrast agents, 106*f*
  drop, 266, 267*f*
  gastrointestinal, 266, 267*f*
  genitourinary tract tumors and, 354–355
  of liver, 124–129, 126*f*–130*f*
    bulls-eye pattern of, 125, 127*f*
    calcified, 125, 128*f*
    CEUS diagnosis of, 128–129, 130*f*
    cystic, 125, 128*f*
    echogenic, 125, 128*f*
    hypoechoic, 125, 127*f*–128*f*
    infiltrative, 125–128, 126*f*
    pediatric, 1746, 1750*f*
    target pattern of, 125, 127*f*
  neuroblastoma, paratesticular, 1903–1904
  ovarian, 585, 586*f*
  pancreatic, 251, 251*f*
  pediatric, neck, 1666–1667, 1667*f*
  peritoneal, 510
  renal, 354, 355*f*
  retroperitoneal, 464, 465*f*
  salivary gland, pediatric, 1639
  to spleen, cystic, 148
  splenic
    nodular lesions in, 152, 154*f*
    percutaneous needle biopsy of, 608*f*
    solid lesions in, 153, 155*f*
  testicular, 822*b*, 826–829, 826*b*
    hamartomas as, 829, 829*f*
    leukemia as, 827, 828*f*
    lymphoma as, 826–827, 828*f*
    myeloma as, 827–829
    pediatric, 1901
Metastasis(es) *(Continued)*
  of thyroid gland, 709, 710*f*
  ureteral, 354
Metastatic nodal disease, pediatric, neck, 1666–1667, 1667*f*
Metatarsophalangeal joints, injection of, short-axis approach to, 900*f*, 901
Methotrexate, in ectopic pregnancy management, 1076, 1076*f*
Metopic craniosynostosis, 1137*f*
MI. *See* Mechanical index
Micrencephaly, 1194
Microabscesses, splenic, 150–152, 154*f*
Microbubbles
  acoustic behavior of, regimens of, 57*t*, 58–59, 59*f*
  as contrast agents, 53–54, 54*f*
    behavior of, incident pressure and, 56–58, 57*t*
    disruption of, 64–67, 66*f*
    FNH characterization with, 106, 106*f*, 108*t*, 109*f*
    future of technology for, 68–69, 69*f*–70*f*
    HCC characterization with, 106, 106*f*
    hemangioma characterization with, 106, 106*f*–107*f*, 108*t*
    inertial cavitation and, 67–68
    lesional enhancement with, 105, 106*f*–107*f*, 109*f*
    liver mass characterization with, 105–106, 106*f*–107*f*, 108*t*, 109*f*–110*f*
    MI and, 58, 58*b*, 105
    need for, 56–58, 57*f*
    regulation of, 68
    safety of, 67–68
  resonance of, in ultrasound field, 58, 59*f*
Microcalcifications, in thyroid nodules, papillary carcinoma and, 699, 702*f*
Microcephaly, 1135–1136
  fetal brain and, 1194, 1195*f*
  sloped forehead in, 1139, 1141*f*
Microcolon, fetal, in MMIHS, 1362–1363, 1788–1791
Microcysts, in breast, 782, 784*f*
Microemboli, cerebral, in pediatric procedures, 1622
Microembolization, intraoperative, TCD detection of, 950
Microencephaly, temperature increase in utero and, 1037
Microgallbladder, in biliary atresia, 1737, 1738*f*
Micrognathia, 1153–1154, 1158*f*
  campomelic dysplasia and, 1395
Microlithiasis, 194–195
  acute pancreatitis and, 221
  testicular, pediatric, 1904, 1904*f*
Microlithiasis, testicular, 833, 833*b*, 834*f*
Microlobulations, in breast sonography, 789, 791*f*
Micromelia, fetal, 1381, 1381*b*, 1382*f*
  in achondrogenesis, 1391, 1391*f*
  in lethal skeletal dysplasia, 1386
  in osteogenesis imperfecta type II, 1391–1392, 1392*f*
  severe
    with decreased thoracic circumference, 1387*t*
    in hypophosphatasia, 1392
    in thanatophoric dysplasia, 1387
Micromelic dysplasia, features of, 1397*t*
Micronodular cirrhosis, 92–93
Micropenis, fetal, 1367
Microphthalmia
  midface hypoplasia with, 1149*f*
  sonographic evaluation of, 1140, 1145*f*, 1147*b*
  temperature increase in utero and, 1037
microRNAs, fibrous cap thinning and, 920
Microstomia, 1154
Microtia
  hypotelorism and, 1142*f*
  incidence of, 1148
Midaortic syndrome, renal artery stenosis and, 447
Middle cerebral artery (MCA)
  cerebroplacental ratio and, 1458, 1460*f*
  cerebrovascular disease indicators with SCD and, 1600*f*, 1604*f*–1605*f*
  Doppler ultrasound of
    in fetal alloimmunization detection, 1421, 1422*f*
    in fetal assessment, 1458–1460, 1460*f*
  neonatal/infant, in coronal imaging, 1514
  occlusion of, leptomeningeal collaterals and, 1610
  PSV of blood flow in, 1421–1423, 1421*b*, 1422*t*
  as transtemporal approach landmark, 1592, 1593*f*–1594*f*
Midface abnormalities, 1148–1153. *See also* Cleft lip/palate
  absent nasal bone as, 1133–1134, 1150*f*
  cleft lip and palate as, 1151–1153
  hypoplasia as, 1148, 1149*f*–1150*f*
Midface hypoplasia, craniosynostosis and, 1136–1138
Midgut, 1304–1305
  physiologic herniation of, 1077, 1077*f*, 1322, 1323*f*
    omphalocele confused with, 1325, 1327*f*
  volvulus
    intestinal malrotation with, 1841–1842, 1843*f*–1844*f*
    "whirlpool" sign of, 1841–1842, 1843*f*
Midline, in sagittal imaging of neonatal/infant brain, 1515, 1516*f*
Midline falx, fetal, sonographic view of, 1024*f*
Migrational abnormalities, corpus callosum agenesis and, 1526–1528
Mikulicz disease, 1635
Milk allergy, gastric mucosa thickening and, 1839–1840
Milk of calcium
  bile, 194, 195*f*
  breast cysts and, 775, 776*f*–777*f*
  cysts, as renal transplantation complication, 653, 657*f*
  renal, calyceal diverticula and, 1799, 1800*f*
Miller-Dieker syndrome, 1195
Mineralization
  abnormal, in achondrogenesis, 1391, 1391*f*
  decreased
    in hypophosphatasia, 1392, 1395*f*
    in osteogenesis imperfecta type II, 1392, 1393*f*
  of thalamostriate vessels, 1203, 1204*f*
Minimal-access parathyroidectomy (MAP), 749, 750*f*
MIP. *See* Maximum-intensity projection
Mirizzi syndrome, 174, 174*f*
Mirror syndrome, fetal hydrops prognosis and, 1436
Misregistration, of structure, 5, 6*f*
Misregistration artifacts, 3*f*, 420–421
Mitral regurgitation, fetal, hydrops from, 1423–1424
Mitral stenosis, fetal, hydrops from, 1423–1424
MLCN. *See* Multilocular cystic nephroma
MMIHS. *See* Megacystis-microcolon-intestinal hypoperistalsis syndrome
M-mode echocardiography, fetal, 1275, 1280*f*–1281*f*
M-mode ultrasound, 9, 9*f*
MMPs. *See* Matrix metalloproteinases

Molar pregnancy. *See* Hydatidiform molar pregnancy
Molar tooth, Joubert syndrome and, 1182
Mole, Breus, 1471
Mondor disease, 768
Monochorionic diamniotic (MCDA) twins, 1019*f*, 1058*f*, 1115–1116, 1116*f*
  CHD and, 1270–1273
  complications of, 1125–1129
    TAPS and, 1126–1127
    TRAP and, 1127–1129, 1127*f*–1128*f*
    TTTS and, 1125–1126, 1125*t*, 1126*f*
  growth discrepancy in, 1123*f*
  IUFD and, 1124*f*
  sonographic findings of, chorionicity and, 1119, 1121*f*
Monochorionic monoamniotic (MCMA) twins, 1057, 1115–1116, 1116*f*
  complications of, 1125–1129, 1129*f*
    TAPS and, 1126–1127
    TRAP and, 1127–1129, 1127*f*–1128*f*
    TTTS and, 1125–1126, 1125*t*, 1126*f*
  conjoined twins as, 1130*f*
  IUFD and, 1124*f*
  sonographic findings of, chorionicity and, 1119, 1121*f*
Mononucleosis
  of parotid gland, pediatric, 1632*f*
  splenic enlargement and, pediatric, 1769
Monorchidism, 1890
Monosomy X. *See* Turner syndrome
Monozygotic (identical) twins, 1115, 1116*f*
Morgagni hernia, 1258, 1718*f*
Morton neuromas, injection for, 904, 904*f*
Morula, 1051, 1051*f*
Motor function, impaired, in spina bifida, 1233
Moyamoya angiopathy, SCD and, 1598, 1600*f*, 1602*f*, 1608*f*, 1610
mpMRI. *See* Multiparametric magnetic resonance imaging
MRA. *See* Magnetic resonance angiography
MRI. *See* Magnetic resonance imaging
MSD. *See* Mean sac diameter
Mucinous cystadenocarcinoma, ovarian, 580*f*, 581
Mucinous cystadenoma, ovarian, 580*f*–581*f*, 581
Mucinous cystic neoplasm, 247–248, 247*f*
Mucocele, of appendix, 299, 299*f*
Mucoepidermoid carcinoma, salivary gland, pediatric, 1638
Müllerian ducts
  cysts of, pediatric, 1908, 1910*f*
  duplication of, 1881
  uterus and anomalies of, 529, 533–538, 537*f*
    categories of, 534, 536*f*
Multicystic dysplastic kidney (MCDK), 361, 362*f*
  fetal, 1346–1347, 1346*f*–1347*f*
  pediatric, 1815, 1816*f*
Multicystic mesotheliomas, 508–509
Multidetector computed tomography (MDCT), 238, 241, 241*b*
Multifetal pregnancy
  amniocentesis in, 1125–1126
  amnionicity in, 1115–1116, 1116*f*
    determining, 1057, 1058*f*
    sonographic determination of, 1117, 1119*t*
    triplets and, 1122*f*
  aneuploidy screening in, 1091
  birth weight discordance in, 1123
  cervical assessment in, 1504–1505
  chorionicity in, 1115–1116, 1116*f*
    sonographic determination of, 1117–1119, 1118*f*, 1119*t*, 1120*f*–1121*f*
    triplets and, 1122*f*
  congenital malformation in, 1123
  first-trimester scans in, 1017, 1019*f*
  general issues with, 1119–1123
Multifetal pregnancy *(Continued)*
  growth discordance in, 1123, 1123*f*
  hydrops in, 1429, 1429*f*
  identification of, routine ultrasound screening in, 1029
  incidence of, 1115
  maternal serum alpha-fetoprotein elevation in, 1228
  morbidity and mortality in
    IUFD and, 1123–1125, 1124*f*
    IUGR and, 1119–1123
    prematurity and, 1119–1123
  placental cord insertion and, 1119, 1122*f*
  placentation and, 1115–1116, 1116*f*
  zygosity in, 1115–1116, 1116*f*
Multilocular cystic nephroma (MLCN), 361–362, 363*f*
  pediatric, 1820, 1822*f*
Multinodular goiter, 711, 711*f*
  parathyroid adenomas detection and, 746
  sonographic appearance of, 727
Multiparametric magnetic resonance imaging (mpMRI), 381–382
  prostate cancer, TRUS fusion with, 406–407, 410–411
Multipath artifact, 19–21, 21*f*
Multiple endocrine neoplasia (MEN), 421
  pheochromocytomas with, 1826, 1910–1912
  type I, 734
  type II, 701
  type IIA, 734
Multiple gland disease, parathyroid adenomas in, 735, 738*f*
Mumps
  EF from, 1294
  orchitis, 1896
  parotitis from, pediatric, 1632
Mural nodules, PAM causing, 782, 783*f*–784*f*
Murphy sign, 198–199, 199*f*, 201*f*
Muscle-eye-brain disease, cobblestone lissencephaly in, 1195
Muscle(s)
  anatomy of, 857–858, 858*f*
  atrophy, 859, 860*f*
    rotator cuff, 888–889, 891*f*
    ultrasound for, 877–878
  injuries to, 858–859, 858*f*–859*f*
  medial gastrocnemius, tear of, 858, 859*f*
  myofascial defects and, 858–859, 859*f*
  ultrasound techniques for, 857–859
Muscular dystrophy, congenital, cobblestone lissencephaly in, 1195
Muscular VSDs, 1281, 1284*f*
Musculoskeletal injection(s)
  anesthetics for, 901
  of Baker cyst, 907–909, 908*f*
  bursal, 907–909, 908*f*
  for calcific tendinitis, 909, 911*f*
  corticosteroids for, 900
  of deep tendons, 904–907
    abductor, 905–907, 907*f*
    biceps, 904–905, 905*f*–906*f*
    hamstring, 905–907, 907*f*–908*f*
    iliopsoas, 905, 906*f*
  of ganglion cyst, 907–909, 909*f*
  intratendinous, 909–910, 912*f*
  of joints, 901–902, 901*f*–902*f*
  materials for, 900–901
  pain as indication for, 898
  of paralabral cysts, 907–909, 910*f*–911*f*
  perineural, 910–912, 913*f*
  superficial peritendinous and periarticular, 902–904
    for foot and ankle, 902–904, 903*f*–904*f*
    for hand and wrist, 904, 905*f*
Musculoskeletal injection(s) *(Continued)*
  technique for, 899–900
    long-axis approach in, 900–901, 900*f*–901*f*
    short-axis approach in, 900–901, 900*f*
Musculoskeletal system. *See also* Bone(s); Ligament(s); Muscle(s); Tendon(s)
  fetal, development of, movements and, 1378
  interventions for
    contrast agents in, 898
    technical considerations for, 898–899, 899*f*
  pediatric
    congenital deformities of, 1933
    congenital nonhip dislocations of, 1933–1936
    inflammation of, 1936–1938, 1937*f*–1938*f*
    inflammation of, noninfectious, 1938
    interventional sonography for, 1961, 1963*f*–1964*f*
    trauma to, 1938–1939, 1939*f*
  ultrasound techniques for
    Doppler imaging in, 857, 857*f*
    elastography in, 857
    extended field of view in, 857
    general considerations in, 856–857
    MRI compared to, 856
Mycobacterial infections, pediatric, lymphadenitis differentiated from, 1660–1663
Mycobacterium avium-intracellulare, 91
Mycobacterium tuberculosis, 329–330, 1852–1853
Myelination
  development of, 1167
  in organogenesis, 1524–1525
Myelocele, open spinal dysraphism and, pediatric, 1681, 1683*f*
Myelocystocele
  fetal, 1233–1234, 1234*f*–1235*f*
  pediatric, 1683–1684, 1686*f*
Myelodysplasia, 1382
Myelolipomas, adrenal, 420–421, 420*b*, 420*f*
Myeloma, testicular, 827–829
Myelomeningocele(s), 1218
  definition of, 1225*t*
  fetal surgery for, 1233
  no Chiari II malformation and search for, 1526, 1529*f*
  open compared to closed, 1226
  open spinal dysraphism and, pediatric, 1681, 1683*f*
  pathogenesis of, 1226
  pediatric, neurogenic bladder in, 1907
  spine embryology and, 1674
Myeloschisis, 1218, 1226
  definition of, 1225*t*
  sonographic findings in, 1218
Myocardium, fetal, hydrops from decreased function of, 1425
Myofascial defects, 858–859, 859*f*
Myofibroblastic tumor, inflammatory, pediatric, 1812
Myofibromatosis, congenital infantile, 1664, 1665*f*
Myometrium
  abnormalities of, 538–541
    adenomyosis as, 540–541, 540*b*, 542*f*
    leiomyoma as, 538–540, 539*f*, 540*b*
    leiomyosarcomas as, 540, 541*f*
  calcifications of, 531–533, 533*f*–534*f*
  layers of, 531
  veins of, 531–532, 533*f*
Myopathy, congenital, atypical hips and, 1932
Myositis, complicated lymphadenitis with, 1662*f*

N

Nabothian cysts, 533, 535*f*, 1499
Nanodroplets, therapeutic use of, 68
Nasal bone, fetal
  absent, 1133–1134, 1150*f*
  in aneuploidy screening, 1093–1095, 1094*b*, 1094*f*

Nasal bone, fetal *(Continued)*
NT in, 1094
in trisomy 21, 1099–1100, 1099*f*
Nasal placodes, 1134
NASCET. *See* North American Symptomatic Carotid Endarterectomy Trial
Nasolacrimal ducts, obstruction of, dacryocystocele from, 1143, 1147*f*
National Council on Radiation Protection and Measurements (NCRP), 38–39
Near field, of beam, 8
Near-field structures, neonatal/infant brain and, duplex Doppler sonography of, 1585, 1588*f*
NEC. *See* Necrotizing enterocolitis
Neck, fetal. *See also* Face, fetal
abnormalities of, 1154–1163
cervical teratoma as, 1159, 1161*f*
goiter as, 1159–1163, 1162*f*
lymphatic malformations as, 1159, 1161*f*
NT and, thickening of, 1154–1159
thyromegaly as, 1159–1163
embryology and development of, 1134
hydrops from, 1425, 1426*f*
normal, sonography of, 1135, 1136*f*
Neck, pediatric. *See also* Infrahyoid space, pediatric; Suprahyoid space, pediatric
carotid space of, 1650
congenital abnormalities of, 1651–1654
branchial, 1651, 1651*f*–1653*f*
cervical teratomas and, 1654, 1654*f*
dermoid cysts and, 1652–1654, 1654*f*
ectopic thymus and, 1652, 1653*f*
epidermoid cysts and, 1652–1654
danger space of, 1650
deep cervical fascia of, 1628, 1629*f*
iatrogenic lesions and, 1658, 1661*f*
inflammatory disease of, 1658–1664
fibromatosis coli and, 1663–1664, 1663*f*
lymph nodes and, 1658–1663, 1661*f*–1663*f*
lesions of, 1961, 1967*f*
neoplasms of, 1664–1667
congenital infantile myofibromatosis as, 1664, 1665*f*
granulocytic sarcomas as, 1666, 1667*f*
lymphoma as, 1665, 1665*f*
malignant, 1664–1667
metastases and, 1666–1667, 1667*f*
neuroblastoma as, 1665–1666, 1666*f*
pilomatricoma as, 1664, 1664*f*
rhabdomyosarcoma as, 1665, 1666*f*
normal anatomy of, 1628–1629
prevertebral space of, 1650
retropharyngeal space of, 1650
superficial fascia of, 1628, 1629*f*
vascular anomalies of, 1654–1655
malformations, 1655–1658, 1655*b*, 1657*f*, 1659*f*
tumors, 1655, 1655*b*, 1656*f*
Neck masses of, in carotid region, 947–948, 949*f*–950*f*
Necrotizing enterocolitis (NEC), 1854–1855, 1855*b*, 1856*f*
Necrotizing fasciitis, of perineum, 846–847
Needle(s). *See also* Biopsy(ies), percutaneous needle
large-caliber, uses of, 600
for musculoskeletal interventions, technique for, 898–899, 899*f*
for percutaneous needle biopsies
guidance systems for, 600, 601*f*
selection of, 599–600
visualization in, 601–603, 602*f*
small-caliber, uses of, 599–600
Neisseria gonorrhoeae, 846
Neonatal brain sonography. *See* Brain, neonatal/infant, imaging of
Neonatal resuscitation, in fetal hydrops, 1437
Nephrectomy, evaluation after, 374–375
Nephritis, acute interstitial, 370
Nephroblastoma, pediatric, 1818
Nephroblastomatosis, pediatric, 1818
Nephrocalcinosis, 339–340, 340*f*, 359
cortical, 339
pediatric, 1798, 1798*b*, 1798*f*
medullary, 339, 340*f*
pediatric, 1798–1799, 1799*f*
Nephroma
cystic, multilocular, 361–362, 363*f*, 1820, 1822*f*
mesoblastic
congenital, 1352–1353, 1353*f*
pediatric, 1818–1820, 1821*f*
Nephronophthisis
familial juvenile, 359
pediatric, 1815–1816, 1816*f*
Nephropathy
HIV-associated, 332–333, 333*f*
lithium, 361, 363*f*
reflux, 327, 327*f*
Nephrosis, congenital, maternal serum alpha-fetoprotein elevation in, 1228
Nephrotoxic drugs, AKI and, 1796
Nerve sheath tumors, 871, 872*f*
Nerve(s)
anatomy of, normal, 864–865, 865*f*
dysfunction of, 865–866, 866*f*
ilioinguinal, entrapment of, after herniorrhaphy, 496
subluxation of, 865–866
ultrasound techniques for, 864–866
Nesidioblastosis, pediatric pancreatic enlargement and, 1865, 1865*f*
Neural arch, ossification of, 1218
Neural canal, in spine embryology, 1217
Neural crest cells, 1133–1134, 1672–1673
Neural plate, in spine embryology, 1217
Neural process, ossification of, 1218, 1219*f*
Neural tube
closure of, 1524, 1525*b*
abnormalities of, 1218
brain disorders of, neonatal/infant, 1526–1532
Chiari malformations and neonatal/infant disorders of, 1526, 1526*b*, 1527*f*–1529*f*
corpus callosum agenesis and neonatal/infant disorders of, 1526–1528, 1529*b*, 1530*f*–1533*f*
corpus callosum lipoma and neonatal/infant disorders of, 1529, 1533*f*
Dandy-Walker malformation and neonatal/infant disorders of, 1529–1532, 1530*b*, 1533*f*–1534*f*
formation of, 1524, 1672–1673, 1673*f*
in spine embryology, 1217, 1218*t*
Neural tube defects (NTDs), 1183. *See also* Spina bifida
CDH and, 1263
descriptions of, 1218
risk factors for, 1225*b*
spina bifida and, 1223
teratogens inducing, 1218
ultrasound screening of, 1226–1228
X-linked, 1226
Neurenteric cysts
fetal, 1256
pediatric, 1686–1688
Neurenteric fistula, 1674
Neuroblastoma(s)
adrenal, 427–428
fetal, 1353–1354, 1353*f*
pediatric, 1825–1826, 1826*f*
metastatic, paratesticular, 1903–1904
pediatric
intraspinal, 1689–1691, 1693*f*
liver metastases from, 1746, 1750*f*
metastasis of, to teste, 1901
neck, 1665–1666, 1666*f*
ovarian, 1880
presacral, 1914, 1915*f*
Wilms tumor mistaken for, 1818
Neuroepithelial tumors, intracranial, fetal, 1208
Neurofibroma(s)
bladder, 356
paratesticular, 1903–1904
plexiform, in intraoperative procedures, 1621*f*
Neurofibromatosis
hemimegalencephaly associated with, 1195
prenatal intracranial tumors in, 1208
renal artery stenosis and, 447
rhabdomyosarcoma associated with, 1908
type 1
megalencephaly associated with, 1194–1195
neuroblastoma with, pediatric, 1825
pheochromocytomas with, 1826
Neurogenic bladder, 372–374, 373*f*
pediatric, hydronephrosis and, 1788
Neurogenic tumors, pediatric, 1724
Neurologic development, obstetric sonography and, 1040–1041
Neuroma, interdigital, injection for, 904, 904*f*
Neuronal proliferation, in organogenesis, 1524–1525
Neurons
development of, 1167
neonatal/infant, injury to, diffuse, duplex Doppler sonography and, 1580
Neurulation, 1053, 1179
in spine embryology, 1217, 1672, 1673*f*
Nevus, giant pigmented, choroid plexus papillomas in, 1209
Nipple discharge, ultrasound examination for, 798–799, 799*f*–801*f*
Nitric oxide, inhaled, 1578
Nodular lesions. *See also* Thyroid gland, nodular disease of
splenic, 148–152, 151*f*–154*f*
thyroid, 694–723
Nonarthrosclerotic carotid disease, 944–948. *See also* Carotid artery(ies), nonarthrosclerotic diseases of
ultrasound examination of, 916
Noncommunicating rudimentary uterine horn, 546
Non-Hodgkin lymphoma, 125, 264–266
pediatric, neck, 1665
of peritoneum, 513, 517*f*
splenic lesions in, 152–153, 154*f*
Nonlinear echoes, contrast agents and, 58–64
amplitude and phase modulation imaging and, 64, 65*f*
harmonic B-mode imaging and, 60
harmonic spectral and power Doppler and, 60–61, 60*f*–62*f*
plane-wave contrast imaging and, 64
pulse inversion Doppler imaging and, 63–64
pulse inversion imaging and, 62–63, 62*f*–63*f*
temporal maximum intensity projection imaging and, 64, 65*f*
tissue harmonic imaging and, 61–62
Nonne-Milroy lymphedema, 1403–1404, 1405*f*
Nonobstructive cardiomyopathy, 1294–1295

Nonrhizomelic chondrodysplasia punctata, 1399
Nonright-handedness, obstetric sonography and, 1040
Nonseminomatous germ cell tumors (NSGCTs), 822*b*, 823–824, 825*f*
Noonan syndrome
  characteristics of, 1887
  low-set ears in, 1148
  pulmonic stenosis and, 1292
Norepinephrine, secretion of, 417
North American Symptomatic Carotid Endarterectomy Trial (NASCET), 916, 929
Nose, fetal
  abnormalities of, 1151
  bones of
    absent, 1133–1134, 1150*f*
    in aneuploidy screening, 1093–1095, 1094*b*, 1094*f*
    NT in, 1094
    in trisomy 21, 1099–1100, 1099*f*
  normal sonographic appearance of, 1135*f*
  saddle, in skeletal dysplasia, 1382
Notochord
  disorders of midline
    formation, 1689
    integration, 1686–1689
  in spine embryology, 1216–1217, 1217*f*, 1218*t*
Notochordal process, in spine embryology, 1217, 1217*f*, 1218*t*
Notochordal remnants, in spine embryology, 1217, 1217*f*, 1218*t*
NSGCTs. *See* Nonseminomatous germ cell tumors
NT. *See* Nuchal translucency
NTDs. *See* Neural tube defects
Nuchal cord, 1483–1484
Nuchal fold, in trisomy 21, 1097–1099, 1099*f*, 1154–1159
Nuchal translucency (NT)
  in aneuploidy risk assessment, 1018–1019, 1019*f*, 1049
  CRL compared to, 1089, 1090*f*
  echogenic material in yolk sac and, 1067–1068
  in fetal nasal bone assessment, 1094
  HPE and thickened, 1096*f*
  measurement technique for, standardization of, 1091–1093, 1092*b*
  with normal karyotype, 1095–1097, 1096*f*
  screening of, human studies on, 1039–1040
  thickened
    abdominal wall defects and, 1095–1096
    anencephaly and, 1096*f*
    congenital heart defects and, 1095–1097, 1096*f*
    in cystic hygroma, hydrops and, 1425
    cystic hygroma and, 1096*f*
    diaphragmatic hernia and, 1095–1096
    fetal neck conditions and, 1154–1159
    megacystitis and, 1096*f*
    omphalocele and, 1096*f*
  in trisomy 13, 1093
  in trisomy 18, 1093
  in trisomy 21, 1089, 1090*f*
Nutcracker syndrome (nutcracker phenomenon), 460–461, 462*f*, 838, 839*f*
Nutrients, yolk sac in transfer of, 1057
Nyquist limit, 29–30, 32*f*

O

Obesity
  fatty liver in, 91
  renal artery duplex Doppler sonography in, 447
Observed-to-expected lung-to-head ratio (o/e LHR), 1262
Obstetric sonography. *See also* Pregnancy, first trimester of
  auditory response in, 1038
  bioeffects of
    animal research and, 1038–1039
    behavioral changes and, 1040–1041
    birth weight and, 1040
    childhood malignancies and, 1041
    congenital malformations and, 1041
    delayed speech and, 1040
    Doppler ultrasound and, 1041
    dwell time and, 1036
    dyslexia and, 1040
    human studies on, 1039–1041
    instrument outputs and, 1035–1036
    mechanical, 1038
    neurologic development and, 1040–1041
    nonright-handedness and, 1040
    scanning mode and, 1035
    system setup and, 1035–1036, 1035*f*–1037*f*
    thermal, 1036–1038
  cell aggregation in, 1038
  cell membrane alteration from, 1038
  contrast agent avoidance in, 1038
  default output power for, 1035
  Doppler mode, sample volume and velocity range in, 1036
  duration of, as function of TI in, 1035–1036, 1036*f*, 1042*t*
  equipment for, 1015–1016
  field of view in, 1036, 1036*f*
  focal depth in, 1036, 1036*f*
  frame rate in, 1036
  guidelines for, 1016–1022
    in first trimester, 1016–1019, 1016*b*, 1017*f*–1020*f*
    level I examination in, 1019–1020, 1021*f*–1029*f*
    level II examination in, 1019–1022, 1023*b*
    in second and third trimesters, 1019–1022, 1020*b*
  hemolysis from, 1038
  in hydrops diagnosis, 1432–1433
  MI in, 1035
  personnel for, 1015–1016
  receiver gain in, 1036
  for routine screening, 1022–1031
    benefits of, 1030*b*
    for fetal malformations, diagnostic accuracy of, 1030
    in gestational age estimation, 1022–1029
    perinatal outcomes and, 1029–1030
    prudent use of, 1030–1031
    three- and four-dimensional ultrasound in, 1030, 1042, 1043*f*
    in twin/multiple pregnancy identification, 1029
  safety of, 1034–1035
    guidelines for, 1041–1042, 1042*t*, 1043*f*
  tactile sensation in, 1038
  training for, 1015–1016
  transducer heating in, 1038
  transducer selection for, 1035
  volume imaging in, 1030
Obstructed hernias, 496–497
Obstructive cystic renal dysplasia, 1347–1348, 1347*f*–1348*f*
Obstructive uropathy, CKD and, 1796–1798
Occipital fissure, neonatal/infant, development of, 1520–1521
Occipital horn(s)
  atrium of fetal, transverse measurement in, 1178
  neonatal/infant
    in coronal imaging, 1515
    in corpus callosum agenesis, 1528, 1530*f*–1531*f*
Occipital horn(s) *(Continued)*
    in posterior fontanelle imaging, 1517, 1518*f*
Occipital lobe cortex, neonatal/infant, in coronal imaging, 1514*f*, 1515
Occipitofrontal diameter, in gestational age determination, 1446, 1447*f*
Occlusion, 27
o/e LHR. *See* Observed-to-expected lung-to-head ratio
OEIS complex, 1328–1329, 1329*f*, 1365–1366, 1689
OHS. *See* Ovarian hyperstimulation syndrome
Oligodactyly
  definition of, 1399
  fetal, 1406*f*
Oligohydramnios
  definition of, 1340
  diagnostic significance of, 1340–1341
  early, 1066, 1067*f*
  fetal lung size and, 1244
  in sirenomelia, 1238
Oligospermia, prostate and, 393
Omental cakes, 266, 267*f*
Omentum
  cysts of, pediatric ovarian cysts differentiated from, 1875
  greater, 505, 505*f*
  herniated, 1902
  infarction of
    pediatric, appendicitis differentiated from, 1858–1860, 1858*f*
    right-sided segmental, 288, 289*f*, 521, 523*f*
  lesser, 505
Omohyoid muscle, 692*f*, 694
Omphalocele
  detection of, early, 1018–1019, 1020*f*
  fetal, 1325–1326, 1326*f*
    associated conditions with, 1325, 1327*f*
    cloacal exstrophy and, 1328
    epidemiology of, 1325
    management of, 1325–1326
    pentalogy of Cantrell and, 1329
    prenatal diagnosis of, 1325, 1327*f*
  liver herniation in, 80
  maternal serum alpha-fetoprotein elevation in, 1228
  in Miller-Dieker syndrome, 1195
  with spina bifida, 1233
  thickened NT and, 1096*f*
  in triploidy, 1105*f*
  in trisomy 18, 1103, 1103*f*
    fetal, 1325
Omphalomesenteric duct, 1059
Oncocytoma, renal, 348–351
Oncotype DX test, 396
One-Stop Clinic to Assess Risk (OSCAR), 1090
Oocyte, transport of, 1049
Ophthalmic artery
  cerebrovascular disease indicators with SCD and flow in, 1599*f*
  evaluation of, orbital approach to, 1592, 1596*f*
Opisthorchiasis, biliary tree and, 178–179
Opportunistic infection, *Pneumocystis carinii* and, 91, 91*f*
Optison, 56
  harmonic emission from, 58–59, 59*f*
Oral contraceptives, hepatic adenomas and, 1746
Oral-facial-digital syndrome 4, 1395
Orbital window, for TCD sonography, 1592, 1596*f*
Orbits, fetal
  abnormalities of, 1140–1143
    anophthalmia as, 1140, 1145*f*
    coloboma as, 1143, 1146*f*
    congenital cataracts as, 1143, 1147*b*
    dacryocystocele as, 1143, 1147*f*
    exorbitism as, 1140

Orbits, fetal *(Continued)*
hypertelorism as, 1140, 1141*b*, 1144*f*–1145*f*, 1149*f*
hypotelorism as, 1140, 1140*b*, 1142*f*–1144*f*
microphthalmia as, 1140, 1145*f*, 1147*b*
proptosis as, 1140
normal sonographic appearance of, 1135*f*
Orchitis, 845–846
isolated, 1896
pediatric, 1896
sonographic appearance of, 846, 847*f*–849*f*
Organ of Giraldés, 820–821
Organ transplantation, 623–624. *See also* Liver transplantation; Pancreas transplantation; Posttransplant lymphoproliferative disorder; Renal transplantation
Organogenesis
definition of, 1524
stages of, 1524, 1525*b*, 1525*f*
Oriental cholangiohepatitis, 179
Oropharynx, teratomas of, 1159
Ortolani test, for hip stability, 1923
OSCAR. *See* One-Stop Clinic to Assess Risk
Osler-Weber-Rendu disease, 104
Ossification centers
primary, 1091
secondary, 1091, 1378*f*
Osteitis pubis, sports hernia and, 486–487, 489*f*
Osteoarthritis, 869, 869*f*
acromioclavicular joint, 893, 894*f*
Osteogenesis, normal, 1091
Osteogenesis imperfecta, 1391–1392
anencephaly differentiated from, 1179
bowing of long bones in, 1381–1382
classification of, by type, 1394*t*
facial profile in, 1394*f*
fractures in, 1392, 1393*f*
sonographic appearance of, 1380*f*
3-D reconstruction of, 1385*f*
type I, 1391–1392, 1393*f*, 1394*t*, 1399
bowing of femur in, 1380*f*
type II, 1391–1392, 1392*f*–1394*f*, 1394*t*
calvarial compressibility in, 1382, 1392, 1393*f*
diagnosis of, 1376–1377
hypophosphatasia differentiated from, 1392–1395
type III, 1391–1392, 1393*f*, 1394*t*, 1399
type IV, 1391–1392, 1394*t*, 1399
type V, 1391–1392
wormian bones in, 1139
Osteomyelitis, pediatric, 1936–1938, 1938*f*
of costochondral junction, aspiration and drainage of, 1963*f*
Ostium primum, 1279
Ostium primum ASD, 1279–1280, 1283*f*
Ostium secundum, 1279
Ostium secundum ASD, 1279–1280, 1282*f*
Otocephaly, 1148
Outflow tracts, fetal, routine sonographic view of, 1025*f*
Ovarian artery(ies), 565–566, 565*f*
pediatric, 1875
Ovarian crescent sign, 581
Ovarian cycle, 1051, 1051*f*
Ovarian follicles, 1049
Ovarian hyperstimulation syndrome (OHS), 572, 572*f*
Ovarian remnant syndrome, 571
Ovarian vein(s)
thrombophlebitis, 589–590, 589*f*
thrombosis of, 369, 589–590, 589*f*
Ovary(ies)
anatomy of, 564–570, 565*f*
calcification in, 566–568
Ovary(ies) *(Continued)*
cystadenocarcinoma of
mucinous, 580*f*, 581
serous, 580–581, 580*f*
cystadenoma of
mucinous, 580*f*–581*f*, 581
serous, 580–581, 580*f*
cysts in
dermoid, 582–584, 583*f*
fetal, 1369, 1369*f*
functional, 570–571, 571*f*
hemorrhagic, 570–571, 571*f*, 575
menstrual cycle and follicular, 568
neonatal, 1876*f*
paratubal, 573
parovarian, 573
percutaneous management of, 618–619
peritoneal inclusion, 573, 573*f*
postmenopausal, 569–570, 571*f*
surface epithelial inclusion, 569, 573
in triploidy, 1105*f*
edema of, massive, 578
endometriosis in, 574–576, 575*f*–576*f*
fetal, cysts in, 1369, 1369*f*
hyperstimulation of, 572, 572*f*
lymphomas of, 585
in menstrual cycle, 1050*f*
menstrual cycle changes to, 568–569, 569*f*
neoplasms of, 578–585
borderline, 580*f*, 581
clear cell, 581, 582*f*
cystadenocarcinomas as, 580–581, 580*f*
cystadenomas as, 580–581, 580*f*–581*f*
cystic teratomas as, 582–584, 582*b*, 583*f*
dysgerminomas as, 584, 584*f*
endodermal sinus, 585
endometrioid, 581
fibromas as, 585, 586*f*
germ cell, 582–585
granulosa cell, 585
metastatic, 585, 586*f*
ovarian cancer as, 578–579
Sertoli-Leydig cell, 585
sex cord-stromal, 585
surface epithelial-stromal, 579–582, 580*f*–582*f*
thecomas as, 585
transitional cell, 581–582, 582*f*
types of, 579*t*
nonneoplastic lesions of, 570–578
cysts as, functional, 570–571, 571*f*
endometriosis as, 574–576, 575*f*–576*f*
ovarian remnant syndrome as, 571
polycystic ovarian syndrome as, 573–574, 574*f*
pregnancy-associated, 572, 572*f*
polycystic ovarian syndrome and, 573–574, 574*f*
postmenopausal, 569
cysts in, 569–570, 571*f*
pregnancy-associated lesions of, 572, 572*f*
punctate echogenic foci in, 566–568, 568*f*
shape of, 565–566
sonography for
normal appearance in, 566–568, 567*f*
technique in, 566
torsion of, 576–578, 577*f*
volume of, 566
Ovary(ies), pediatric, 1873
abnormalities of, 1875–1881
cysts of, 1873–1877
hemorrhagic, 1877, 1878*f*–1879*f*
in polycystic ovarian disease, 1877–1878, 1879*f*
torsion and, 1875–1876, 1876*b*, 1877*f*
ectopic, 1874*f*
edema of, massive, 1878–1879, 1879*f*
Ovary(ies), pediatric *(Continued)*
macrocysts of, 1873–1875
neoplasms of, 1879–1881, 1880*b*, 1880*f*
normal, 1874*f*
torsion of, 1875–1876, 1876*b*, 1877*f*
volume measurements for, 1873, 1875*t*
Ovotestis, pediatric, 1891, 1891*f*
Ovulation, 1049
Oxygenation, extracorporeal membrane. *See* Extracorporeal membrane oxygenation

P

Pacchionian, 1177
Pachygyria, in lissencephaly, 1195
PACs. *See* Premature atrial contractions
PACS. *See* Picture archiving and communications system
Paget-Schroetter syndrome, pediatric, 1721, 1723*f*
Painless (silent) thyroiditis, 725–727
Palate. *See also* Cleft lip/palate
cleft, 1151–1153
secondary
fetal, 1135, 1135*f*
isolated cleft of, 1153
Palmar arch, 977–978, 980*f*
PAM. *See* Papillary apocrine metaplasia
Pampiniform plexus, 565–566, 565*f*
"Pancake" kidneys, pediatric, 1785
Pancreas
abscesses of, 230
anatomy of, 210–219
surrounding structures and, 218–219, 220*f*
variants of, 218
annular, small bowel obstruction and, 1308
body of, 211, 211*f*–212*f*
carcinoma of, 236–238, 238*b*
color Doppler ultrasound for, 241, 241*b*, 241*f*–243*f*, 241*t*
detection of, 238–241
resectability imaging in, 241
ultrasound findings for, 238–241, 239*f*–240*f*
CEUS for, 251
cystic neoplasms of, 243–248, 243*t*
intraductal papillary mucinous, 245–247, 245*f*–246*f*
mucinous, 247–248, 247*f*
rare, 248, 248*b*
serous, 243, 244*f*–245*f*
solid-pseudopapillary tumor, 248, 248*f*
cysts of, 242–248, 243*f*
congenital, 1865
fetal, 1320
high-risk features of, 243*b*
simple, 243, 244*f*
VHL disease and, 243, 244*f*
embryology of, 215–218, 218*f*
endocrine tumors of, 248–249, 249*f*–250*f*, 249*t*
enlarged, in acute pancreatitis, 222, 223*f*
fatty, 215, 216*f*–217*f*
fetal, 1319–1320
annular, 1320, 1321*f*
cysts of, 1320
head of, 211–213, 213*f*–214*f*
lipoma of, 249–251, 250*f*
metastases of, 251, 251*f*
neoplasms of, 236–241
periampullary, 236
unusual and rare, 249–251
parenchyma of, 213–215, 215*f*–217*f*
pediatric, 1862–1865
neoplasms of, 1865, 1865*f*
normal anatomy of, 1862
pancreatitis and, 1862–1865, 1864*f*–1865*f*
sonographic technique for, 1862

Pancreas *(Continued)*
percutaneous needle biopsy of, 604–605, 605*f*
pseudoaneurysms of, 230, 230*f*
pseudocysts of
acute pancreatitis complications with, 228–229, 229*f*
chronic pancreatitis complications with, 232, 233*f*–234*f*
drainage of, 230, 615–617, 617*f*
pediatric pancreatitis and, 1864–1865, 1865*f*
pseudomass of, 214–215, 217*f*
shape of, 214–215, 217*f*
size of, 214, 216*f*
sonographic technique for, 210–219, 211*f*
tail of, 213, 214*f*
Pancreas divisum, 218, 220*f*
pediatric pancreatitis and, 1862–1864, 1864*f*
Pancreas transplantation, 666–682
abnormal, 676–682
AVF as, 678, 680*f*
fluid collections as, 682, 683*f*
pancreatitis as, 679–682, 681*f*
pseudoaneurysms as, 678, 680*f*
rejection as, 678–679, 681*f*
thrombosis as, 677–678, 678*f*–679*f*
alloimmune arteritis after, 677
bladder drainage in, 668–672, 675*f*
CEUS for, 676
duodenal leaks after, 682
endocrine drainage in, 672, 675*f*
enteric drainage in, 672
infection after, 682
normal appearance after, 676, 676*f*
surgical techniques for, 668–676, 673*t*, 675*f*
venous drainage in, 672–676
Pancreatic duct, 215–218, 219*f*–220*f*
Pancreaticoduodenectomy, 233
Pancreatitis
acute, 219–230
abscess complications of, 230
biliary sludge and, 221
causes of, 221, 221*t*
clinical spectrum of, 220–221
common bile duct stones and, 221
complications of, 225–230, 225*b*
enlarged pancreas from, 222, 223*f*
fluid collection complications in, 228, 228*f*
gallstones and, 221
imaging approach for, 221–222, 221*b*
necrosis complications of, 230
pseudocyst complications in, 228–230, 229*f*
treatment for complications of, 230
ultrasound findings in, 222–225, 222*t*, 223*f*–228*f*
vascular complications of, 230, 230*f*–231*f*
autoimmune, 236, 237*f*
chronic, 230–236
imaging approach for, 231
masses associated with, 233–236, 235*f*–237*f*
portal vein thrombosis in, 232–233, 235*f*
pseudocysts in, 232, 233*f*–234*f*
sclerosing, 236
splenic vein thrombosis in, 232–233, 234*f*–235*f*
tumefactive, 236
ultrasound findings on, 231–233, 231*f*–235*f*
lymphoplasmacytic sclerosing, 236
after pancreas transplantation, 679–682, 681*f*
pediatric, 1862–1865, 1864*f*–1865*f*
Pancreatoblastoma, pediatric, 1865
Pancytopenia, Fanconi, 1400, 1402*f*
Panovarian cysts, 573
Pantaloon hernias, 493–494, 495*f*
Papillary apocrine metaplasia (PAM), 778*f*, 779, 780*f*–781*f*
mural nodules caused by, 782, 783*f*–784*f*
Papillary carcinoma
ethanol ablation of cervical nodal metastasis from, 720, 721*f*
of thyroid gland, 698–701, 701*f*–705*f*
cystic, sonographic features of, 705*f*, 713
pediatric, 1648, 1649*f*
Papillary cystadenomas, of epididymis, 840–841
Papillary microcarcinoma, of thyroid, 701, 706*f*
Papillary necrosis, 328–329, 329*b*, 329*f*
Papillary process, 75–76
Papilloma(s)
breast, 769–771, 770*f*
intracystic, 782, 783*f*
intraductal, 799, 799*f*–800*f*
peripheral, 799, 800*f*
choroid plexus
Aicardi syndrome and giant pigmented nevi in, 1209
neonatal/infant, 1562, 1565*f*
in neonatal/infant brain, duplex Doppler sonography of, 1588*f*
VM with, 1177–1178
transitional cell, lower urinary tract, pediatric, 1910–1912
VM with, 1177–1178
PAPP-A. *See* Pregnancy-associated plasma protein A
Paracentesis, 610, 610*f*
Paracoccidiomycosis, 423
Paradidymis, 820–821
Paragangliomas, carotid body tumors and, 947–948, 949*f*
Paralabral cysts, injection for, 907–909, 910*f*–911*f*
Parallel orientation, in breast sonography
not (taller-than-wide), 789–790, 792*f*
wider-than-tall, 797, 797*f*
Paralytic ileus, 294*f*, 295
Parameniscal cysts, 907–909
Paramesonephric duct cysts, pediatric. *See* Müllerian ducts
Parapelvic cysts, 359, 360*f*
Paraplegia, traumatic, neurogenic bladder in, 1907
Parapneumonic collections, in pediatric chest, 1710–1711
Pararenal spaces, inflammation in, in acute pancreatitis, 224–225, 225*f*
Parasagittal infarction, from hypoxic-ischemic injury in full-term infant, 1541
Parasites, fetal brain and, 1203–1204
Parasitic diseases
of genitourinary tract, 331
of liver, 87–90, 89*f*–90*f*
Paratenon, 859
Parathyroid glands. *See also* Hyperparathyroidism
adenomas of
carcinomas differentiated from, 735–736, 738*f*
carotid sheath/undescended, 740, 742*f*
combined modalities for accuracy with, 748
compression for detection of, 739
CT accuracy for, 748, 748*f*
echogenicity of, 735, 736*f*
ectopic locations of, 739–741
false-negative examination for, 745*b*, 746
false-positive examination for, 745–746, 745*b*
fine-needle aspiration biopsy accuracy for, 746
hypoechoic, 735
imaging accuracy with, 746–749
inferior, 738–739, 739*f*
internal architecture of, 735, 736*f*
intrathyroid, 740, 742*f*
localization of, 736–741
mediastinal, 740, 741*f*, 748
MRI accuracy in, 748, 749*f*
multiple gland disease in, 735, 738*f*
percutaneous needle biopsy of, 750–751, 753*f*
pitfalls in examination of, 745–746, 745*b*
Parathyroid glands *(Continued)*
retrotracheal/retroesophageal, 739–740, 740*f*
scintigraphy accuracy for, 747, 747*f*
shape of, 735, 735*f*
size of, 735, 737*f*
sonographic appearance of, 735–736
sonographic examination and typical locations in, 736–739, 739*f*
superior, 738–739, 739*f*
surgical removal of, 749, 750*f*
ultrasound accuracy for, 746–747, 748*f*
vascularity of, 735, 737*f*
anatomy of, 732–733, 733*f*
autotransplantation of tissue of, recurrent hyperparathyroidism from, 742–744, 743*f*
carcinoma of
adenomas differentiated from, 735–736, 738*f*
primary hyperparathyroidism from, 734
ectopic, 733, 739–741
embryology of, 732–733
enlarged, in secondary hyperparathyroidism, 745
eutopic, 733
inferior, 733
pediatric, 1650, 1650*f*
supernumerary, 733
Parathyroid hormone, chief cells in production of, 733
Parathyroidectomy, minimal-access, for primary hyperparathyroidism, 749, 750*f*
Parathyromatosis, in persistent hyperparathyroidism, 744, 744*f*
Paratubal cysts, 573
Paraumbilical hernias, 492
Paraumbilical veins, pediatric
flow direction in, in portal hypertension, 1752, 1757, 1758*f*
in intrahepatic portal hypertension, 1761
Paraurethral cysts, pediatric, 1883–1884
Parenchymal abscess, pediatric renal transplantation and, 1812
Parenchymal calcification, renal, 339–340, 340*f*
Parenchymal junctional defects, 313, 314*f*
Parietal peritoneal line, 510–511
Parinaud oculoglandular syndrome, 1633–1634
Parotid glands, pediatric
accessory, 1630
acinic cell carcinoma of, 1638, 1639*f*
anatomy of, 1630, 1630*f*
bacterial infections in, 1632–1633, 1632*f*
deep lobe of, 1630
hemangiomas of, 1636, 1637*f*
lipomas of, 1639
lymphatic malformation of, 1636, 1637*f*
nodal enlargement in, 1633–1634
peripheral nerve sheath tumors of, 1639
Parotid space, pediatric, 1629, 1630*f*
cystic lesions of, 1639, 1640*b*
Parotitis
HIV and, 1635, 1636*f*
juvenile, recurrent, 1634, 1634*f*
from mumps, 1632
Parovarian cysts, pediatric, 1875, 1876*f*
Paroxysmal supraventricular tachycardia, fetal, 1296, 1296*f*
Partial molar pregnancy, 1078, 1080*f*
Partial subclavian steal, 952–953, 953*b*, 953*f*
Partial-thickness rotator cuff tears, 887–888, 889*f*–890*f*
Particulate ascites, 507
Parvovirus infection, fetal
hydrops from, 1431–1432, 1431*f*
massive ascites in, 1418–1419
Pascals, 16

Patau syndrome. *See* Trisomy 13
Patellar dislocation, congenital, pediatric, 1934, 1935*f*
Patent ductus arteriosus, intracranial RI and, 1576
Patent urachus, 322
  pediatric, 1791
PCA. *See* Posterior cerebral artery
PCA3 score, 396
PCOS. *See* Polycystic ovarian syndrome
Peak end diastolic ICA/CCA ratio, in assessing degree of carotid stenosis, 930
Peak systolic ICA/CCA ratio
  in assessing degree of carotid stenosis, 930
  in internal carotid artery stenosis evaluation, 937
Peak systolic velocity (PSV), 450
  arterial stenosis and, 969, 971*f*
  bypass graft dysfunction and, 974–975
  in determining carotid stenosis, 929–930
  of MCA blood flow, 1421–1423, 1421*b*, 1422*t*
Pectoralis minor muscle, 878–879
Pediatric patients. *See also* Adrenal gland(s), pediatric; Bladder, pediatric; Hip(s), pediatric; Liver, pediatric; Neck, pediatric; Spinal canal, pediatric; Transcranial Doppler sonography, pediatric; Urinary tract, pediatric
  adrenal sonography for, 1820–1827
  female anatomy in, normal, 1872–1875
  pelvic sonographic technique for, 1870–1872
  renal artery stenosis and, 447
  spleen of, 1769–1772
Pedicles
  in lateral longitudinal scan plane, 1223*f*
  in lateral transaxial scan plane, 1222*f*
  in posterior angled transaxial scan plane, 1224*f*
  spina bifida in, 1228, 1229*f*–1230*f*
Peliosis, splenic, 147
Peliosis hepatis, 104, 104*f*
Pelvic abscesses, 283
  drainage of, 612, 613*f*
Pelvic adnexa. *See* Adnexa
Pelvic congestion syndrome, 461–463, 463*f*
  as adnexal vascular abnormality, 590, 590*f*
Pelvic inflammatory disease (PID), 566
  fallopian tubes and, 587–589, 588*f*
  IUDs and, 587
  pediatric, 1885–1887, 1886*b*, 1886*f*
  sonographic findings of, 587*t*
  tubo-ovarian complex and abscess in, 588–589, 588*f*, 1886–1887, 1886*f*
Pelvic kidney, 318, 318*f*
  fetal, 1344–1345, 1344*f*
  pediatric, 1908
Pelvic masses
  in adult women, sonographic evaluation of, 590–591, 591*t*
  gastrointestinal tract, 592
  nongynecologic, 591–592
  postoperative, 591
  urinary tract, 592
Pelvic sonographic technique, pediatric, 1870–1872. *See also specific organs*
Pelvic varices, pediatric
  hemorrhagic ovarian cyst differentiated from, 1877, 1879*f*
  in portal hypertension, 1760*f*
Pelvis
  fetal, routine sonographic views of, 1021, 1026*f*
  free fluid of, ectopic pregnancy and, 1072, 1073*f*
  pediatric, sonographic technique for, 1870–1872
  TAS for, 564
Pelvoinfundibular atresia, with MCDK, 1346
Penile chordee, fetal, 1367
Pentalogy of Cantrell, 1295
  fetal abdominal wall and, 1329
  OEIS differentiated from, 1328–1329
Peptic ulcer, 299, 300*f*
Percent free PSA (%fPSA), 395
Percutaneous cholangiography and drainage, pediatric, 1956, 1959*f*
Percutaneous needle biopsy. *See* Biopsy(ies), percutaneous needle
Percutaneous umbilical cord blood sampling (PUBS), 1434–1435, 1434*f*–1435*f*
Perfluorocarbons, in contrast agents, 56, 107, 111*f*
Perforation, of bowel, in Crohn disease, 274–275, 277*f*
Perfusion
  disruption-replenishment imaging measuring, 66–67, 67*f*
  luxury, cerebral infarction with, 1580–1581, 1584*f*
Perianal inflammation, in Crohn disease, 276, 281*f*, 305–306
Perianal inflammatory disease, transanal sonography in, 305–307, 306*b*, 307*f*
Periaortitis, chronic, 439–440, 464, 465*f*
Peribiliary cysts, liver and, 82–83
Pericardial effusion, fetal, 1258, 1258*f*
  in hydrops, 1416, 1418*f*
Pericardial hernias, 1258, 1262
Pericholecystic fluid collection, in perforated gallbladder, 200
Pericholecystic hyperechogenicity, NEC and, 1854–1855
Periductal mastitis, of breast, 771, 771*f*
Perienteric soft tissues, in acute abdomen, 281–282
Perihepatitis, gonococcal or chlamydial, PID and, 1887
Perimembranous VSDs, 1281
Perinephric abscesses
  acute pyelonephritis and, 325
  pediatric renal transplantation and, 1812
  after renal transplantation, 664–665
Perinephric fluid collections, pediatric renal transplantation and, 1809, 1811*f*
Perineum, necrotizing fasciitis of, 846–847
Period, of sound wave, 2, 2*f*
Peripheral arteries, 965–978
  aneurysms of, lower extremity, 971–972, 972*f*
  AVF of, 973–974, 974*f*
  lower extremity, 966–975
    aneurysm of, 971–972, 972*f*
    AVF of, 973–974, 974*f*
    AVMs of, 973
    bypass grafts of, 974–975, 975*f*
    normal anatomy of, 966
    occlusion of, 967–968, 967*f*–969*f*
    pseudoaneurysm of, 972–973, 973*f*
    stenosis of, 968–971, 969*f*–971*f*
    ultrasound examination and protocol for, 966–967, 967*f*
  occlusion of, lower extremity, 967–968, 967*f*–969*f*
  pseudoaneurysms of, lower extremity, 972–973, 973*f*
  sonographic examination technique for, 965
  stenosis of
    evaluation of, 965–966, 966*f*
    lower extremity, 968–971, 969*f*–971*f*
    tardus-parvus waveforms in, 965–966
  upper extremity, 975–978
    aneurysm of, 976
    normal anatomy of, 975–976, 976*f*
    occlusion of, 976
    radial artery evaluation for coronary bypass graft and, 977–978, 980*f*
Peripheral arteries *(Continued)*
    stenosis of, 976, 978*f*–979*f*
    thoracic outlet syndrome in, 976–977, 980*f*
    ultrasound examination and protocol for, 976
Peripheral cholangiocarcinoma. *See* Intrahepatic cholangiocarcinoma
Peripheral nerves
  normal anatomy of, 864–865, 865*f*
  sheath tumors, parotid gland, pediatric, 1639
Peripheral sexual precocity, pediatric ovarian cysts and, 1875
Peripheral veins, 978–996. *See also* Deep venous thrombosis
  lower extremity, 980–990
    acute DVT of, 983–984, 983*f*–985*f*
    chronic DVT of, 984, 986*f*–987*f*
    complete venous Doppler for, 989
    deep venous system of, 980–981, 981*f*
    DVT follow-up recommendations for, 989
    normal anatomy of, 980–982
    potential pitfalls with, 984–989, 988*f*
    superficial venous system of, 981–982, 981*f*
    ultrasound examination and protocol for, 982–983, 982*f*
    vein mapping of, 989–990
    venous insufficiency in, deep, 989, 990*f*
  sonographic examination technique for, 979–980
  upper extremity, 990–996
    acute DVT of, 992–994, 994*f*–995*f*
    chronic DVT of, 994–995, 995*f*–996*f*
    hemodialysis and ultrasound examination of, 1000
    normal anatomy of, 990–991, 990*f*
    potential pitfalls with, 995–996
    ultrasound examination and protocol for, 991–992, 991*f*–993*f*
    vein mapping of, before hemodialysis, 996–998, 998*f*–1000*f*
Peripherally inserted central catheter (PICC), 993*f*
  interventional sonography for, pediatric, 1954, 1955*f*–1957*f*
Periportal cuffing, in acute hepatitis, 85, 85*f*–86*f*
Periportal hepatic fibrosis, Caroli disease with, 171
Periprocedural antithrombotics, percutaneous needle biopsy and, 598–599
Perirenal space, inflammation in, in acute pancreatitis, 224–225, 225*f*
Perirenal urinoma, from UPJ obstruction, 1358, 1358*f*
Peristalsis, 257
Peritoneal bands, obstruction from, 1841–1842
Peritoneal cavity, 504
  fluid in, free compared to loculated, 508, 509*f*
  localized inflammatory process of, 521, 523*f*
Peritoneum
  anatomy of, 504
  ascites and, 506–508, 507*f*–509*f*
  carcinomatosis of, 510–511, 510*f*–515*f*
  cysts in
    inclusion, 508–509, 509*f*, 573, 573*f*
    mesenteric, 509–510, 510*f*
  endometriosis and, 521–523, 524*f*
  inflammatory disease of, 514–521
  leiomyomatosis peritonealis disseminata and, 523–524, 525*f*
  metastases of, 510
  Non-Hodgkin lymphoma of, 513, 517*f*
  parietal, 504
  pneumoperitoneum and, 524–526, 525*f*
  pseudomyxoma peritonei and, 513–514, 518*f*
  sonographic technique for, 505–506, 506*f*–507*f*

Peritoneum *(Continued)*
tumors of, 510–514
carcinomatosis as, 510–511, 510*f*–515*f*
primary, 511–513, 515*f*–517*f*
pseudomyxoma peritonei as, 513–514, 518*f*
visceral, 504
Peritonitis
abscesses and, 517, 520*f*
chemical, 514
definition of, 514
fibrinous, 509*f*
granulomatous, 514
Histoplasma, 520*f*
infective, 517, 519*f*
meconium
CF and, 1316
cystic, pediatric, 1842–1843, 1846*f*
hydrops from, 1428, 1428*f*
liver calcifications and, 1316–1318
massive ascites in, 1418–1419, 1421*f*
small bowel and, 1313, 1313*t*, 1314*f*
primary, 517
sclerosing, 514, 521, 523*f*
tuberculous, 517–521, 522*f*
Peritrigonal blush, in sagittal imaging of neonatal/infant brain, 1517
Periumbilical hernias, 492, 494*f*, 500*f*
Perivascular inflammation, in acute pancreatitis, 224–225, 226*f*–227*f*
Periventricular cysts, of neonatal/infant brain, 1566, 1566*f*
Periventricular hemorrhagic infarction, in infants, 1547
Periventricular leukomalacia (PVL)
cystic, 1551–1552, 1552*f*
from hypoxic-ischemic injury in premature infant, 1541, 1550–1553, 1551*f*–1553*f*
IUFD and, 1124*f*
in neonatal/infant brain, 1541, 1550–1553, 1551*f*–1553*f*, 1566
Periventricular leukomalacia, IUFD and, 1124*f*
Periventricular nodular heterotopia, 1196, 1199*f*
Perlman syndrome
CDH and, 1263
hyperechogenic kidneys and, 1351
Peroneal arteries, 966
Peroneal tendons, posterior, injection of, 902, 903*f*
Peroneal veins, 981
Persistent terminal ventricle, pediatric, 1685
Persistent trophoblastic neoplasia (PTN), 1078, 1080–1084, 1082*f*
choriocarcinoma and, 1080–1082, 1083*f*
diagnosis and treatment of, 1083–1084
Doppler ultrasound for, 1083
after hydatidiform molar pregnancy, 1080, 1081*f*
invasive mole, 1080, 1081*f*
PSTT and, 1082
sonographic features of, 1082–1083
Perthes disease, 1930
Peutz-Jeghers syndrome, 544, 826
Pfeiffer syndrome
bilateral complete cleft lip/palate in, 1156*f*
craniosynostosis in, 1136–1138
hypertelorism with exorbitism in, 1145*f*
midface hypoplasia in, 1148
PFFD. *See* Proximal focal femoral deficiency
PHACES syndrome, pediatric, 1655
Phalanx, middle, hypoplasia of, in trisomy 21, 1101
Pharyngeal pouches, 1651
Phase aberration, 13
Phase inversion, 62–63
Phase modulation imaging, 64, 65*f*
Phased array transducers
beam steering in, 10–11, 11*f*
use and operation of, 12
Phenylketonuria, microcephaly from, 1194
Pheochromocytomas
adrenal, 421, 422*f*
pediatric, 1826–1827, 1827*f*
percutaneous needle biopsy of, 607
bladder, 356
definition of, 1826
lower urinary tract, pediatric, 1910–1912
PHI. *See* Prostate Health Index
Phlebectasia, IJV, 1658, 1660*f*
Phleboliths, in venous malformations of neck, 1657
Phlegmonous change, in Crohn's disease, 274–275, 277*f*
Phocomelia, definition of, 1399
Phrygian cap, 194
Physics of ultrasound, 1. *See also* Acoustics; Doppler ultrasound; Instrumentation
acoustics in, 2–7
Doppler ultrasound in, 21–30
HIFU in, 31–33, 33*f*
image display and storage in, 12–13
image quality in, 16–19
imaging pitfalls in, 19–21
instrumentation in, 7–12, 24–25, 25*b*, 25*f*–26*f*
operating modes and clinical implications in, 30–31
special imaging modes in, 13–16
Phytobezoars, 300
PI. *See* Pulsatility index
PICC. *See* Peripherally inserted central catheter
Picture archiving and communications system (PACS), 12–13
PID. *See* Pelvic inflammatory disease
Pierre-Robin sequence
campomelic dysplasia and, 1395
clefts of secondary palate in, 1153
micrognathia with, 1153, 1158*f*
Piezoelectricity, 7
Pilomatricoma, pediatric, neck and, 1664, 1664*f*
Pineal cyst, cavum veli interpositi cysts differentiated from, 1170
Pinworms, 1853
Pituitary gland, in menstrual cycle, 1050*f*
PKD1 gene, mutation in, in ADPKD, 1350
PKD2 gene, mutation in, in ADPKD, 1350
PKHD1 gene, mutation in, in ARPKD, 1348–1350
Placenta
abruption of, 1471–1473, 1474*f*–1475*f*
fetal hydrops and, 1436
pediatric pregnancy and, 1884
accessory lobes of, 1480–1481, 1481*f*
battledore, 1484
bilobed, 1481, 1482*f*
circumvallate, 1479–1480, 1480*f*–1481*f*
cysts of, subchorionic, 1474, 1477*f*
development of, 1465–1469, 1466*f*
hydropic degeneration of, 1078
infarctions of, 1466, 1473–1474, 1476*f*–1477*f*
insertion of umbilical cord into, 1484, 1485*f*
low, 1469, 1470*f*
marginal sinus of, 1466, 1467*f*
masses of, 1474–1476
chorioangioma as, 1476, 1478*f*–1479*f*
malignant, 1476
mesenchymal dysplasia of, 1479, 1479*f*
in molar gestations, 1479, 1480*f*
morphologic abnormalities of, 1479–1481
in multifetal pregnancy, chorionicity and, 1119, 1120*f*
position of, sonographic determination of, 1469, 1470*f*
postpartum, 1487–1489, 1490*f*
RPOC and, 1487–1489, 1490*f*
size of, 1466–1467, 1467*f*–1468*f*
sonographic appearance of, 1466, 1467*f*
subamniotic hematomas of, 1474
subchorionic hematomas of, 1474
Placenta *(Continued)*
succenturiate lobes of, 1480–1481, 1481*f*
thickness of, 1466, 1467*f*
in third stage of labor, 1487
vascularity of, 1468*f*
Doppler ultrasound and, 1467–1469
vascularization of, 1052–1053
volume of
in first trimester, in early pregnancy evaluation, 1466–1467
second trimester, assessment of, 1466, 1468*f*
Placenta accreta, 1470–1471, 1472*f*–1473*f*
Placenta increta, 1470–1471
Placenta percreta, 1470–1471, 1473*f*
Placenta previa, 1469–1470
complete, 1469, 1470*f*
marginal, 1469, 1470*f*
placenta accreta with, 1471
Placental bed, subinvolution of, 556
Placental cord insertion, multifetal pregnancy and, 1119, 1122*f*
Placental lakes, 1466, 1467*f*
Placental shelf, 1479–1480
Placental villi, hydropic degeneration of, 1078, 1080*f*
Placental volume quotient, 1466–1467
Placental-site trophoblastic tumor (PSTT), 530–531, 1082
Placentation, multifetal pregnancy and, 1115–1116, 1116*f*
Placentomegaly, fetal, hydrops and, 1418, 1420*f*
Placodes
nasal, 1134
spinal dysraphism and, pediatric, 1680
Plagiocephalic heads, 1136–1138
Plane-wave contrast imaging, 64
Plantar fasciitis, injection for, 902, 904*f*
Plaque(s)
in atherosclerosis, 433
carotid
atheromatous, 919
atherosclerotic rupture of, 919–920
calcified, 920–921, 921*f*
carotid artery dissection and, 946
characterization of, 919–922, 920*f*–922*f*, 922*b*
heterogenous, 920–921, 922*f*
homogenous, 920–921, 920*f*–921*f*, 936–937, 938*f*
intraplaque hemorrhage and, 920–921
morphology of, ultrasound types of, 921, 922*b*
nonstenotic, 936–937, 938*f*
qualitative assessment of, in carotid stenosis, 924
tandem, in carotid stenosis, 923–924
types 1-4, 921, 922*b*
ulceration of, 923, 923*b*, 923*f*–924*f*
vulnerable, identification of, treatment decisions and, 943
Plasma protein A, pregnancy-associated, 1089–1090
Plasmacytoma, 827–829
Platelet-rich plasma, intratendinous injection of, 909–910
Platyspondyly
in skeletal dysplasias, 1382
in thanatophoric dysplasia, 1388–1389, 1390*f*
Plavix (clopidogrel), 598
PLCO (Prostate, Lung, Colorectal and Ovarian Cancer Screening Trial), 397
Pleomorphic adenomas, salivary gland, pediatric, 1636–1638, 1638*f*
Pleural disease, pediatric, pulmonary disease differentiated from, sonography in, 1709, 1710*f*
Pleural drainage, fetal, hydrops from, 1426–1427

Pleural effusions
fetal, 1256–1258, 1257*f*
hydrops and, 1413–1416, 1417*f*, 1425
lung size and, 1244
primary, 1256
secondary, 1256
pediatric
drainage of, ultrasound-guided, 1724–1725
sonographic signs of, 1702–1711, 1704*f*–1708*f*
Pleural fluid, pediatric
aspiration of, ultrasound-guided, 1724–1725, 1726*f*
through hepatic window, 1707*f*
pneumonia with small amount of, 1706*f*
septated, 1702, 1708*f*
sonogram compared to CT scan for, 1709, 1711*f*
sonographic signs of
bare area sign in, 1709, 1709*f*
color Doppler ultrasound signal in, 1709, 1710*f*
diaphragm sign in, 1709
displaced-crus sign in, 1709
free movement in, with respiration, 1709, 1709*f*
septations in, 1709
sonographic signs of, 1709, 1709*b*
through splenic window, 1707*f*
Pleuropulmonary blastoma, 1252–1253
Plexiform neurofibroma, in intraoperative procedures, 1621*f*
Plicae palmatae, 533, 535*f*
PMPI. *See* Power modulation pulse inversion
Pneumatosis intestinalis
in acute abdomen, 277–281
in gastrointestinal tract, 297–299, 299*f*
pediatric, sonography for, 1854–1855
Pneumobilia
biliary tree and, 175–176, 176*f*
after liver transplantation, 625, 1767–1768, 1769*f*–1770*f*
Pneumocystis carinii, hepatic opportunistic infection by, 91, 91*f*
Pneumonia, pediatric, 1711–1714
air bronchograms from, 1702, 1703*f*, 1708*f*
chest radiograph compared to ultrasound for, 1712–1714, 1715*f*
on chest ultrasound, 1703*f*
empyema from, 1707*f*
round, 1711–1712, 1715*f*
with small amount of pleural fluid, 1706*f*
Pneumoperitoneum, 524–526, 525*f*
Pneumothoraces, sonographic detection of, 1725–1726
Poland syndrome, ribs in, 1382–1384
Polar arteries, 445–446
Polycystic kidney disease, 359–361
autosomal dominant, 83, 243, 361, 362*f*
pediatric, 1814–1815, 1815*f*
autosomal recessive, 359, 361*f*, 1799
pediatric, 1812–1813, 1814*f*
congenital hepatic fibrosis and, 1757–1759, 1762*f*
fetal pancreatic cysts and, 1320
Polycystic ovarian disease, pediatric, 1877–1878, 1879*f*
Polycystic ovarian syndrome (PCOS), 573–574, 574*f*
Polycythemia, dural sinus thrombosis from, 1205–1206
Polydactyly
definition of, 1399
fetal, 1405–1406
postaxial, in trisomy 13, 1104, 1105*f*
Polydactyly *(Continued)*
short-rib, syndromes associated with, 1382, 1383*f*, 1395–1396, 1397*f*
toe, fetal, 1406*f*
Polyhydramnios
anorectal malformations and, 1311–1312
cervical assessment in, 1505
diagnostic significance of, 1340–1341
esophageal atresia and, 1305–1306
fetal hydrops and, 1418, 1420*f*, 1432–1433
jejunoileal atresia and, 1310
in lethal skeletal dysplasias, 1386
meconium peritonitis and, 1313
with mesoblastic nephroma, 1352–1353
in trisomy 18, 1104
Polymicrogyria, 1196, 1198*f*
Polyorchidism, 838–839, 841*f*
pediatric, 1891
Polypoid intraluminal tumors, 261–264, 263*f*
Polyps
endometrial, 544, 548, 549*f*
tamoxifen and, 544–545
intussusception and, 1844–1845
urethral, posterior, pediatric, bladder outlet obstruction from, 1906, 1906*f*
Polysplenia, 159–161
in cardiosplenic syndrome, 1292, 1293*b*
fetal, 1320
univentricular heart with, 1287–1288
Polysplenia syndrome
biliary atresia in, 1737, 1738*f*
Doppler evaluation of liver transplant recipient with, 1764–1766
Polyvinyl chloride, 123
Pontocerebellar hypoplasia, 1190
Pontocerebellar syndrome, vermian dysplasia with, 1191
Popliteal artery, 966
aneurysms of, 972*f*
normal appearance of, 966–967
occlusion of, 968*f*
Popliteal cysts, pediatric, 1939
Popliteal vein
normal anatomy of, 980–981, 981*f*
ultrasound examination of, 982–983
Porcelain gallbladder, 202, 202*f*
Porencephalic cysts, neonatal/infant brain and, 1537, 1565
Porencephaly
from germinal matrix hemorrhage, 1541
HPE differentiated from, 1189
from intraparenchymal hemorrhage, 1547, 1548*f*
Porta hepatis, 77, 79*f*
Portal hypertension
duplex Doppler sonography in, 98
intrahepatic, from cirrhosis, 96
left sided, splenic vein thrombosis from, in chronic pancreatitis, 232–233, 234*f*–235*f*
liver vascular abnormalities and, 96–98, 96*f*–97*f*
portosystemic venous collaterals in, 96–98, 96*f*
presinusoidal, 96
splenomegaly and, 145, 147*f*
Portal hypertension, pediatric, 1756–1757
backward-flow theory of, 1760–1761
Doppler assessment of
abnormal flow patterns in, 1754–1756
abnormal hepatic arterial Doppler patterns in, 1755–1756
absent Doppler signal in, 1754, 1754*b*
arterialized flow patterns in, 1754
hepatofugal flow in, 1757
intrahepatic portal hypertension and, 1759–1762
in liver disease, 1752–1754, 1754*f*–1755*f*
Portal hypertension, pediatric *(Continued)*
of normal flow patterns in splanchnic vessels, 1750
paraumbilical veins flow direction in, 1757, 1758*f*
pelvic varices in, 1760*f*
possibilities and pitfalls of, 1750
in prehepatic portal hypertension, 1757–1759
reversed flow in, 1754–1755
sonographic technique for, 1750–1752
splenorenal shunts in, 1757, 1759*f*
in suprahepatic (posthepatic) portal hypertension, 1762–1764, 1763*f*
surgical portosystemic shunts and, 1764
to-and-fro flow in, 1754–1755, 1755*f*
Doppler ultrasound assessment of, 1748–1764
basic principles of, 1748–1750
forward-flow theory of, 1760–1761
thickened lesser omentum and, 1756, 1756*f*
Portal triad, 78
Portal vein(s)
anastomosis of, for liver transplantation, 624
aneurysms of, 103–104
after liver transplantation, 1768, 1769*f*–1770*f*
anomalies of, 81
cavernous transformation of, 98, 99*f*
clots in, in acute pancreatitis, 224–225, 228*f*
fetal liver calcifications and, 1316–1318
left, Doppler studies of, best approach for, 1752
liver circulation and, 78
main, Doppler studies of, best approach for, 1752
normal, 76, 77*t*, 78*f*
pediatric
anatomy of, 1731–1734, 1732*f*
cavernous transformation of, in prehepatic portal hypertension, 1757, 1761*f*
flow direction through, meals and, 1750
left, branches of, 1734
left, Doppler studies of, 1750
right, branches of, 1733*f*, 1734
thrombosis of, 1757, 1757*b*
pseudostenosis of, 636
stenosis of, after liver transplantation, 635–636, 638*f*, 1766, 1768*f*
thrombosis of, 98, 99*f*–100*f*
chronic pancreatitis and, 232–233, 235*f*
from HCC, 120, 121*f*
after liver transplantation, 635–636, 639*f*–640*f*, 1766
malignant, 98, 99*f*
pediatric, 1757, 1757*b*
Portosystemic shunts
intrahepatic, 104, 1761–1762
liver and, 130–132
in portal hypertension, 1757
portocaval, patency of, Doppler assessment of, 1764
surgical, 1764
total or partial, 1764
transjugular intrahepatic, 131–132, 132*b*, 132*f*–133*f*, 1764
Portosystemic venous collaterals, in portal hypertension, 96–98, 96*f*
spontaneous routes of, 1752, 1754*f*
Port-wine stains, 1679
Postablation tubal sterilization syndrome, 551–552
Postaxial polydactyly, fetal, 1405–1406
Posterior cerebral artery (PCA), as transtemporal approach landmark, 1592, 1593*f*–1594*f*
Posterior fossa. *See also* Cerebellum
abnormalities of, 1192
hemorrhage of, 1548–1550

Posterior fossa *(Continued)*
subarachnoid cysts of, Dandy-Walker malformation differentiated from, 1190, 1531, 1531*b*
ventral induction errors in, 1189–1192
Posterior inguinal wall insufficiency, sports hernia and, 486, 488*f*
Postmeningitis hydrocephalus, 1887
Posttransplant lymphoproliferative disorder (PTLD), 682–688
Epstein-Barr virus and, 682
after liver transplantation, 683–688, 687*f*
patterns of, 688
pediatric, 1812, 1813*f*
after renal transplantation, 683–688, 684*f*–686*f*
treatment options for, 688
Posttraumatic aortic stenosis, 444
Posttraumatic pseudoaneurysms, of common carotid artery, 948, 950*f*
Pouch of Douglas, 566
endometrioma in, 524*f*
Power Doppler ultrasound, 25, 25*b*, 26*f*
amplitude evaluation in, 935
for carotid stenosis evaluation, 935–939, 935*b*
pitfalls and adjustments in, 935*f*–939*f*, 936–939, 937*b*
color streaking in, breast cysts with, 775, 776*f*
harmonic imaging and, 60–61, 60*f*–62*f*
intermittent harmonic, 66, 66*f*
for neonatal/infant brain, 1573–1574
for prostate cancer, 404*f*–405*f*, 406
for prostate examination, 387
Power modulation pulse inversion (PMPI), 64
Power settings, 505–506
Preaxial polydactyly, fetal, 1405–1406
Precocious pseudopuberty, pediatric ovarian cysts and, 1875
Precocious puberty, 1746, 1887–1888
Predelivery aspiration procedure, in fetal hydrops, 1437
Preeclampsia
fetal hydrops prognosis and, 1436
pediatric pregnancy and, 1884
placental infarction in, 1477*f*
Preexisting cavitation nuclei, 41
Pregnancy. *See also* Ectopic pregnancy; Hydatidiform molar pregnancy; Multifetal pregnancy
adnexal cysts in, 1020
"cornual", 1073
early failure of, 1062–1069
hydronephrosis in, 316
iliac vein compression in, 459, 460*f*
keepsake imaging in, 49*b*, 50
luteoma of, 572
MRI in, 1031–1032, 1031*f*
ovarian lesions associated with, 572, 572*f*
pediatric, 1884–1885
second trimester of
indications for ultrasound in, 1015, 1016*b*
ultrasound guidelines for, 1019–1022, 1020*b*
teen, fetal gastroschisis and, 1322–1323
thermal index for bone in late, 1039
thermal index for soft tissue in early, 1039
third trimester of
indications for ultrasound in, 1015, 1016*b*
ultrasound guidelines for, 1019–1022, 1020*b*
of unknown location, 1075
uterus size in, 531
Pregnancy, first trimester of. *See also* Aneuploidy, screening for, first-trimester; Ectopic pregnancy; Gestational trophoblastic disease
aneuploidy screening for, 1089–1097
change during, 1048
early failure of, 1062–1069
Pregnancy, first trimester of *(Continued)*
amnion size in, 1066, 1067*f*–1068*f*
arrhythmia and, 1069
chromosomal anomaly causing, 1062
CRL and no heartbeat in, 1063, 1064*f*
diagnostic findings of, 1063–1064, 1063*b*
embryonic bradycardia and, 1068–1069, 1068*f*
embryos with CRL less than 7mm and no heartbeat in, 1064
gestational sac appearance concerns in, 1065, 1066*f*
gestational sac with no embryo in, 1063–1065, 1065*f*
gestational sac with small MSD in relationship to CRL, 1066, 1067*f*
luteal phase defect causing, 1062–1063
spontaneous abortion rate and, 1062, 1062*t*
subchorionic hemorrhage and, 1069, 1069*f*
worrisome findings of, 1064–1069, 1065*t*
yolk sac size and shape in, 1067–1068, 1068*f*
ectopic, 1069–1076
embryo evaluation during, 1076–1077
embryology in, 1049–1054
gestational age estimation in, 1061–1062
gestational trophoblastic disease and, 1077–1084
indications for ultrasound in, 1015, 1016*b*
maternal physiology in, 1049–1054
normal anatomy in, 1077, 1077*f*
normal sonographic appearance of, 1054–1061
amnion in, 1057, 1059*f*–1060*f*
β-hCG levels and, 1055–1057, 1057*b*
embryo in, 1057, 1059*f*–1060*f*
embryonic cardiac activity in, 1058–1059, 1060*f*
gestational sac in, 1054–1055, 1055*f*–1056*f*
umbilical cord cysts in, 1061, 1061*f*
umbilical cord in, 1059–1061
yolk sac in, 1057, 1058*f*
sonography in
current trends in, 1049
goals of, 1049
transvaginal ultrasound safety in, 1049
ultrasound guidelines for, 1016–1019, 1016*b*, 1017*f*–1020*f*
Pregnancy dating, 1022
Pregnancy of unknown location (PUL), 1075
Pregnancy-associated plasma protein A (PAPP-A), 1089–1090
Premammary zone, of breast, 761, 761*f*
Premature atrial contractions (PACs), 1295–1296
Premature rupture of membranes, pulmonary hypoplasia and, 1246
Premature ventricular contractions (PVCs), 43
fetal arrhythmias and, 1295–1296
Premenarchal girls, ovarian volume in, 1873, 1875*t*
Preplacental hematoma, 1471, 1475*f*
Presacral mass(es)
fetal, 1239, 1239*b*
pediatric, 1913–1915, 1913*b*, 1914*f*–1915*f*
solid, 1914–1915
Presteal waveform, 953*b*, 954, 954*f*
Preterm birth (PTB)
cervical length and, 1499–1500, 1499*f*
short, 1500–1501, 1500*f*, 1501*t*
definition of, 1495
incidence of, 1495
multifetal pregnancy morbidity and mortality and, 1119–1123
prior, cervical assessment in, 1504
spontaneous, prediction of, 1495–1496, 1501–1503
cervical change rate in, 1501
cervical funneling in, 1501, 1502*f*
dynamic cervical change in, 1501–1503, 1503*f*
gestational age at cervical length measurement in, 1500–1501, 1501*t*
Preterm birth (PTB) *(Continued)*
obstetric factors in, 1501
sonographic features in, 1503, 1504*f*
PRF. *See* Pulse repetition frequency
Primary peritoneal mesothelioma, 513, 516*f*
Primary peritoneal serous papillary carcinoma, 511–513, 515*f*
Primary peritonitis, 517
Primary sclerosing cholangitis, biliary tree and, 182, 183*f*, 184
Primitive neuroectodermal tumors, neonatal/infant brain and, 1562
Proboscis
cyclopia with, 1140, 1144*f*
in trisomy 13, 1104, 1105*f*
Probst bundles, in corpus callosum agenesis, 1528
Process vaginalis, relationship of indirect inguinal hernia to, 476–477
Processus vaginalis, 819
pediatric, 1902
Profunda femoris artery, 966
nonocclusive thrombi in, missing, 988
Profunda femoris vein
chronic DVT in, 987*f*
normal anatomy of, 980–981, 981*f*
Prominence, forming fetal face, 1134, 1134*f*
Pronephros, 311, 312*f*, 1336–1338
Propagation speed, of transducer, 7
Propagation velocity
artifact, 3, 3*f*, 420–421
of sound, 2–3, 3*f*
in SWE, 16, 18*f*
Proptosis, 1140
Prosencephalon, formation of, 1077
Prostaglandin-induced antral foveolar hyperplasia, 1839–1840
Prostate
abscesses of, 389, 390*f*, 392
adenocarcinoma of, 395
anatomy of, 382–384
axial, 383*f*, 384
neural structures in, 384
sagittal, 383*f*, 384–386
vascular, 384, 386*f*
zonal, 382–384, 382*f*–383*f*, 385*f*–386*f*
azoospermia and, 393
benign conditions of, 387–392
benign ductal ectasia of, 387, 388*f*
benign hyperplasia of, 384, 385*f*–386*f*, 387–388
biopsy of
PSA-directed, 395
ultrasound-guided, 407–411, 408*f*
calcifications of, 387, 388*f*
cancer of, 394–407
active surveillance for, 401
alternate biomarkers of, 396
brachytherapy for, 401, 402*f*
CEUS for, 406
color Doppler ultrasound for, 404*f*, 406
elastography for, 407
epidemiology of, 395
external beam radiotherapy for, 400–401, 401*f*
focal therapy for, 400
high-intensity focused ultrasound for, 400
histologic grading of, 399–400
key facts of, 395*b*
mortality by age in, 397
mpMRI-TRUS fusion for, 406–407, 410–411
power mode Doppler ultrasound for, 404*f*–405*f*, 406
prostate-specific antigen in, 395–396, 396*b*
radical prostatectomy for, 400, 401*f*
screening for, 396–397
sonographic appearance of, 403–407, 403*f*–405*f*, 406*b*
staging, 397–400, 397*f*, 398*t*, 399*f*

Prostate *(Continued)*
therapy for, 400–402, 401*f*–402*f*
3-D ultrasound for, 406–407
transrectal sonography of, 302, 302*f*, 403–406, 403*f*–405*f*, 406*b*
watchful waiting for, 401
congenital abnormalities in, 392
corpora amylacea of, 387
cysts of, 388, 390–392, 391*f*
hematospermia and, 394, 394*b*
infertility and, 392–394, 393*f*
inflammation of, 389, 390*f*
normal variants of, 387, 388*f*
oligospermia and, 393
pediatric, anatomy of, 1888, 1888*f*
prostatitis and, 389–390, 390*f*
transurethral resection of, 385*f*–386*f*, 388
ultrasound of
appearance in, 383*f*, 384–386, 385*f*–386*f*
equipment and technique for, 386–387, 386*f*
history of, 381–382
power mode Doppler, 387
transrectal, 381–382
volume of, 387
weight of, 387
Prostate, Lung, Colorectal and Ovarian Cancer Screening Trial (PLCO), 397
Prostate Health Index (PHI), 396
Prostatectomy, TRUS-guided biopsy after radical, 411, 411*f*
Prostate-specific antigen (PSA), 381–382
density of, 395–396
in directing biopsy, 395
elevated levels of, 395
free/total ratio of, 395
velocity of, 396
Prostatic artery, 384
Prostatism. *See* Lower urinary tract symptoms
Prostatitis, chronic, 389–390, 390*f*
Proteus syndrome, hemimegalencephaly associated with, 1195
Proximal focal femoral deficiency (PFFD), 1400, 1400*f*
pediatric, 1933, 1934*f*
Prune belly syndrome
fetal
lower urinary tract obstruction from, 1361–1362
megalourethra and, 1362
pediatric
hydronephrosis and, 1788
lower urinary tract obstruction and, 1906
PSA. *See* Prostate-specific antigen
Psammoma bodies, in papillary carcinoma of thyroid gland, 698
Psammomatous calcification, in peritoneal nodule, 510–511, 513*f*
Pseudoacetabulum, in DDH, 1921
Pseudoaneurysm(s)
abdominal aortic dilation from, 441
anastomotic, 438
in AVF for hemodialysis, 1003, 1005*f*
common carotid artery posttraumatic, 948, 950*f*
of common femoral artery, 973*f*
hepatic artery, 104
after liver transplantation, 634, 636*f*
after pancreas transplantation, 678, 680*f*
pancreatic, 230, 230*f*
of peripheral arteries
lower extremity, 972–973, 973*f*
upper extremity, 976, 977*f*
radial artery, 977*f*
renal biopsies and, Doppler assessment of, 1809, 1811*f*
Pseudoaneurysm(s) *(Continued)*
after renal transplantation, 664, 669*f*–670*f*
in synthetic arteriovenous graft for hemodialysis, 1003, 1006*f*
Pseudoascites, 1413, 1415*f*
Pseudocirrhosis, of liver, 125–128, 129*f*
Pseudocyst(s)
gastrointestinal cysts differentiated from, 1860, 1863*f*
meconium, fetal, 1313, 1314*f*
ovarian cysts differentiated from, 1369
pancreatic
acute pancreatitis complications with, 228–229, 229*f*
chronic pancreatitis complications with, 232, 233*f*–234*f*
drainage of, 230, 615–617, 617*f*
pediatric pancreatitis and, 1864–1865, 1865*f*
splenic, 146–147, 149*f*
umbilical cord, 1483, 1484*f*
Pseudoephedrine, fetal gastroschisis and, 1322–1323
Pseudohermaphroditism
female, prenatal diagnosis of, 1368
male, dysplastic gonads and, 1899
Pseudokidney sign, in gut wall, 257, 260*f*
Pseudomembranous colitis, 1850*f*
gastrointestinal tract infections and, 296–297, 298*f*
Pseudomonas, 846
Pseudomyxoma peritonei, 513–514, 518*f*, 581
Pseudopapillary tumor, of pancreas, pediatric, 1865, 1865*f*
Pseudopolyps, cystitis and, 333, 333*f*
Pseudoprecocious puberty, 1887–1888
Pseudopuberty, precocious, pediatric ovarian cysts and, 1875
Pseudospectral broadening, in carotid spectral analysis, 927
Pseudostenosis, of portal vein, 636
Pseudostring of flow, on power Doppler, 935
Pseudosyndactyly, fetal, 1404
Pseudothalidomide syndrome, 1401
Pseudotumor(s)
fibrous, 838, 840*f*
inflammatory
gastric mucosa thickening in, 1839–1840
pediatric cystitis and, 1794, 1797*f*
splenic, 153–156
Pseudoulceration, of carotid artery, 923
Psoriatic arthritis, of hand and wrist, injections for, 904
PSTT. *See* Placental-site trophoblastic tumor
PSV. *See* Peak systolic velocity
PTB. *See* Preterm birth
PTLD. *See* Posttransplant lymphoproliferative disorder
PTN. *See* Persistent trophoblastic neoplasia
Puberty, precocious, 1746, 1887–1888
PUBS. *See* Percutaneous umbilical cord blood sampling
PUL. *See* Pregnancy of unknown location
Pulmonary agenesis, 1245–1246
Pulmonary aplasia, 1245–1246
Pulmonary artery, fetal
continuity of, 1278*f*
diameter of, 1277*f*
dilated, TOF and, 1288
Pulmonary atresia
Ebstein anomaly with, 1286
fetal, hydrops from, 1423–1424
hypoplastic right ventricle secondary to, 1287
TOF and, 1288
Pulmonary development, fetal, 1243
Pulmonary embolism, DVT causing
lower extremity, 979, 981*f*
upper extremity, 994
Pulmonary hypertension, with CDH, 1264
Pulmonary hypoplasia
fetal, 1245–1246
campomelic dysplasia and, 1384*f*
causes of, 1246*t*
hydrops and, 1413
in lethal skeletal dysplasia, 1386, 1386*b*
lethality of skeletal dysplasia and, 1382, 1384*f*
premature rupture of membranes and, 1246
primary, 1245
secondary, 1245, 1246*f*
unilateral, 1246, 1247*f*
pediatric, 1689
Pulmonary lymphangiectasia, 1258, 1259*f*
Pulmonary sequestrations, pediatric, 1715–1716, 1717*f*
Pulmonary veins
anatomy of, normal, 1290, 1291*f*
anomalous, 1290, 1291*f*
Pulmonic stenosis, 1292
in TGA, 1289
Pulsatility index (PI), 27, 27*f*
of intracranial vessels, 1595
Pulse average intensity, 36
Pulse inversion Doppler imaging, 63–64
Pulse inversion imaging, 62–63, 62*f*–63*f*
Pulse length, 8
Pulse repetition frequency (PRF)
in color Doppler, setting of, for low-flow vessel evaluation, 933
in color Doppler ultrasound, 28, 29*f*, 30–31
increasing, to overcome aliasing, 939
output control and, 48–50
transmitter controlling, 7
Pulsed wave Doppler, 24, 25*f*
testicular flow, 1890
testicular hyperemia and, pediatric, 1896
Pulsed wave operating modes, 7
Pulsed wave ultrasound, 36
Pulse-echo principle, 36
Purkinje system, 1297
Pus, 1953
Push-and-pull maneuver, in dynamic examination of hip, 1926*f*, 1927
PVCs. *See* Premature ventricular contractions
PVL. *See* Periventricular leukomalacia
Pyelectasis
definition of, 1354
fetal, significance of, 1355
Pyelitis
alkaline-encrusted, 324–325
emphysematous, 326–327, 327*f*
Pyelonephritis
acute, 323–325
gallbladder wall thickening signs in, 201*f*
pediatric, 1792–1793, 1793*f*–1794*f*
renal and perinephric abscess from, 325, 325*f*
on sonography, 324, 324*b*, 324*f*
chronic, 327, 327*f*–328*f*
pediatric, 1794, 1795*f*
emphysematous, 325–326, 326*f*
renal transplantation complications with, 653, 657*f*
as genitourinary tract infection, 323–328
transplant, 651, 655*f*
xanthogranulomatous, 328, 329*f*
Pyknodysostosis, wormian bones in, 1139
Pyloric atresia, dilated fetal stomach differentiated from, 1307

Pyloric muscle
hypertrophy of
minimal, in pylorospasm, 1836–1838, 1838*f*
in pyloric stenosis, 1835–1838, 1835*b*, 1837*f*–1838*f*
tangential imaging artifacts of, 1834–1835, 1836*f*
Pyloric stenosis
dilated fetal stomach differentiated from, 1307, 1308*f*
hypertrophic, 1835–1838, 1835*b*, 1837*f*–1838*f*
pitfalls in diagnosis of, 1838, 1838*b*, 1839*f*
pylorospasm and minimal muscular, 1836–1838, 1838*f*
Pylorospasm, 1836–1838, 1838*f*
Pyoceles, scrotal, 835*f*, 836
Pyogenic bacteria, liver abscesses from, 85–86, 87*f*
pediatric, 1746–1747, 1751*f*
Pyonephrosis
genitourinary tract infections and, 325, 326*f*
pediatric, complicating acute pyelonephritis, 1793, 1794*f*
renal transplantation complication with, 651, 655*f*
Pyosalpinx, 587–588

Q

Quadrigeminal cistern, 1518

R

Rachischisis, 1218
definition of, 1225*t*
Radial arteries, 531–532
calcification of, evaluation for, 998, 998*f*
for coronary bypass graft, evaluation of, 977–978, 980*f*
pseudoaneurysm of, 977*f*
Radial ray anomalies, 1103*f*
Radial ray defects, 1400–1401, 1401*f*–1402*f*
Radial veins, normal anatomy of, 990–991
Radiation forces, 35
Radical prostatectomy
for prostate cancer, 400, 401*f*
TRUS-guided biopsy after, 411, 411*f*
Radiofrequency ablation, for autonomously functioning thyroid nodules, 720
Radiography, for skeletal dysplasia evaluation, 1384
Radiotherapy, external beam, for prostate cancer, 400–401, 401*f*
Radius, aplastic or hypoplastic, in Fanconi pancytopenia, 1400, 1402*f*
Ranula, pediatric, 1639–1640, 1640*f*
Ranunculi, 313
in kidney development, 1781, 1781*f*
Rapidly involuting congenital hemangiomas, cutaneous, 1742–1743
Rapunzel syndrome, trichobezoars and, 1840
RAR. *See* Renal aortic ratio
Rarefaction, in sound wave, 2, 2*f*
RCC. *See* Renal cell carcinoma
Real-time B-mode ultrasound, 9–10, 10*f*
Receiver, 8–9, 8*f*–9*f*
Receiver gain, in obstetric sonography, 1036
Rectal cleansing, prior to TRUS, 387
Rectouterine recess, 528
Rectum, carcinoma of, 301–302, 301*f*–304*f*
Red blood cell production, decreased, from fetal hydrops, 1431
Red cell alloimmunization, screening fetus with hydrops for risk of, 1421–1423, 1421*b*, 1422*f*, 1422*t*
Reflected sound, 3–4
Reflection, in acoustics, 4, 5*f*
Reflection coefficient, 4
Reflectors
diffuse, 4, 5*f*
specular, 4, 4*b*, 5*f*
Reflux nephropathy, CKD and, 1796–1798
Refraction, 5, 6*f*
Rejection
acute, renal transplantation abnormalities and, 1809–1810
chronic, renal transplantation abnormalities and, 1810, 1812*f*
in liver transplantation, pediatric, 1767
in pancreas transplantation, 678–679, 681*f*
in renal transplantation
acute, 649–651, 653*f*
chronic, 651, 654*f*
Remapping, of amplitudes, 9
Renal agenesis, 318–319
Renal aortic ratio (RAR), 450
Renal artery(ies)
accessory, 445–446
anatomy of, 445–446
aneurysms of, 369, 369*f*, 451
duplex Doppler sonography of, 447–450, 450*f*
false-positive/false-negative results with, 450, 450*f*
interpretation of, 450
fetal
absent, 1344*f*
normal, 1344*f*
infarction of, 366, 367*f*
occlusion of, 366
pediatric
patency, Doppler assessment of, 1803–1804
stenosis of, Doppler assessment of, 1805, 1805*t*, 1806*f*
polar, 445–446
stenosis of, 368–369, 368*f*
causes of, 447
Doppler assessment of, pediatric, 1809
false-positive Doppler diagnosis of, 658, 661*f*
intraparenchymal, 658
pediatric, Doppler assessment of, 1805, 1805*t*, 1806*f*
in pediatric patients, 447
after renal transplantation, 655–658, 656*b*, 658*f*–661*f*
renovascular hypertension and, 446–447, 446*b*
thrombosis of, after renal transplantation, 653–655, 657*f*
Doppler assessment of, pediatric, 1807–1809, 1808*f*
Renal biopsies, pediatric, Doppler assessment of, 1809, 1810*f*–1811*f*
Renal calculi, 334–336, 336*f*–337*f*
entities that mimic, 336, 337*b*, 337*f*
Renal cell carcinoma (RCC)
acquired cystic kidney disease and, 340
biopsy of, 343–344, 345*f*
classic diagnostic triad for, 340
cystic, 343, 343*f*
Doppler ultrasound for detection of, 343, 344*f*
genitourinary tumors and, 340–344
histologic subtypes of, 340
imaging approaches to, 341, 341*f*
interpretation pitfalls with, 344, 345*f*
necrotic, 343
papillary, 342
pediatric, 1820, 1821*f*
prognosis of, 343–344
radiofrequency ablation of, 341, 341*f*
sonographic appearance of, 341–343, 342*f*–344*f*
treatment approaches to, 341
von Hippel-Lindau disease and, 340
Renal collecting system, pediatric. *See also* Hydronephrosis, pediatric, causes of
dilation of, 1785
duplication of, 1783–1784, 1784*f*
urolithiasis and, 1799–1801, 1799*f*
Renal cortex, 313, 313*f*
Renal duplication, pediatric, 1783–1784, 1784*f*
Renal dysgenesis, 361
Renal dysplasia, 361, 1689
obstructive cystic, 1347–1348, 1347*f*–1348*f*
Renal hilum, 311–313
Renal junctional parenchymal defect, 1781, 1781*f*
Renal medullary pyramids, 313, 313*f*
Renal milk of calcium, calyceal diverticula and, 1799, 1800*f*
Renal parenchyma, 313
Renal pelvic diameter (RPD), 1354, 1354*f*
normal, 1355
Renal pelvic echo, 1339
Renal pelvis. *See also* Hydronephrosis
adenocarcinoma of, 348
fetal
diameter of, measurement of, 1354, 1354*f*
dilation of, 1354
pediatric
duplication of, 1784*f*
wall thickening in, from acute pyelonephritis, 1792, 1793*f*
Renal sinus, 311–313
Renal transplantation, 641–666
abnormal, 649
AVMs complicating, 661–664, 667*f*–670*f*
twinkling artifacts mimicking, 662–664, 668*f*
cadaveric kidneys in, paired, 643–644, 648*f*
for chronic renal failure, 641
donor renal vein anastomosis in, 643
fluid collections after, 664–666, 671*f*–674*f*
hematomas after, 665, 671*f*
infarctions after
global, 653
segmental, 653–655, 657*f*
lymphoceles after, 665–666, 673*f*–674*f*
pediatric, 1809, 1811*f*
normal appearance of, 644–648
Doppler ultrasound assessment in, 648, 651*f*–652*f*
gray-scale assessment in, 644–648, 648*f*–650*f*
parenchymal pathology complicating, 649–653
abscesses as, 651, 656*f*
acute rejection as, 649–651, 653*f*
acute tubular necrosis as, 649–651, 653*f*
chronic rejection as, 651, 654*f*
emphysematous pyelonephritis as, 653, 657*f*
hyperacute rejection and, 651
infections as, 651–653, 655*f*–657*f*
milk of calcium cysts as, 653, 657*f*
pediatric, 1809–1810, 1812*f*
pyonephrosis as, 651, 655*f*
pediatric
Doppler ultrasound for, 1807–1812
parenchymal abnormalities and, 1809–1810, 1812*f*
perinephric fluid collections in, 1809, 1811*f*
tumors of, 1812, 1813*f*
urologic complications and, 1810–1812
vascular complications in, 1807–1809, 1808*f*, 1810*f*–1811*f*
perinephric abscesses after, 664–665
postrenal collecting system obstruction complicating, 630*f*–633*f*, 659–661
prerenal vascular complications of, 653–659
arterial thrombosis as, 653–655, 657*f*
renal artery stenosis as, 655–658, 656*b*, 658*f*–661*f*
renal vein stenosis as, 658–659, 663*f*
venous thrombosis as, 658, 662*f*
pseudoaneurysms after, 664, 669*f*–670*f*
PTLD after, 683–688, 684*f*–686*f*
surgical technique for, 641–644, 648*f*
ureter anastomosis of in, 643, 648*f*

Renal transplantation *(Continued)*
ureteral obstruction complicating, 659–660, 663*f*–664*f*
urinomas after, 665, 672*f*
pediatric, 1809
Renal tubular acidosis, medullary nephrocalcinosis and, 1798
Renal tubular disease, inborn errors of metabolism and, 1738
Renal vein(s)
donor, anastomosis, in renal transplantation, 643
left, anatomic variants of, 457
pediatric
acute thrombosis of, Doppler assessment of, 1804–1805, 1804*b*, 1804*f*
patency of, Doppler assessment of, 1803–1804
stenosis of, after renal transplantation, 658–659, 663*f*
thrombosis of, 369, 370*f*
Doppler assessment of, pediatric, 1809
hyperechogenic kidneys and, 1351
pediatric, acute, Doppler assessment of, 1804–1805, 1804*b*, 1804*f*
after renal transplantation, 658, 662*f*
urinary tract calcifications and, 1799, 1800*f*
Renal/abdominal circumference ratio, 1338–1339
Renal-coloboma syndrome, MCDK and, 1815
Renovascular disease, 368
Renovascular hypertension
clinical findings suggesting, 446*b*
renal artery stenosis and, 446–447
Resistive index (RI), 27, 27*f*
in ACA, in infants, 1576, 1577*t*
in hepatic artery, elevation of, after liver transplantation, 634
intracranial, 1595
in asphyxiated infants, 1580
factors changing, 1612*t*
factors modifying, 1576, 1576*f*–1577*f*, 1576*t*
hydrocephalus and, 1582, 1584*f*
intrarenal, pediatric, causes of increased, 1802–1803, 1803*b*, 1803*f*
in monitoring intracranial hemodynamics in infants, 1576, 1577*t*
in renal artery duplex Doppler sonography, 450
in shunt malfunction and hydrocephalus, 1613, 1613*f*
Resolution, spatial, 16–19, 18*f*–19*f*
Resuscitation, neonatal, in fetal hydrops, 1437
Retained products of conception (RPOC), 554–555
pediatric, 1884, 1884*f*
placenta and, 1487–1489, 1490*f*
Rete testis, 819
tubular ectasia of, 829–830, 830*f*
pediatric, 1891–1892, 1892*f*
Retinoblastoma, metastasis of, to teste, 1901
Retinoic acid, NTDs from, 1218
Retrocalcaneal bursal injection, 902, 903*f*
Retrocaval ureter, 322
Retrognathia, 1153–1154
Retrogressive differentiation, in spine embryology, 1672, 1673*f*
Retromammary zone, of breast, 761, 761*f*
Retromandibular vein, pediatric, 1630, 1630*f*
Retroperitoneum, 210. *See also* Abdominal aortic aneurysm
abdominal aortic aneurysm and, 433–439
abdominal aortic dilation and, 439–441
atherosclerosis and, 432–433
fibrosis of, 464–465, 465*f*
fluid collections in, 464
masses in, 464
metastases of, 464, 465*f*
nonvascular diseases of, 464–465
Retroperitoneum *(Continued)*
prepancreatic, inflammation of, in acute pancreatitis, 224–225, 224*f*–225*f*
stenotic disease of abdominal aorta and, 441–445, 445*f*
Retrorenal spleen, 162
Reverberation artifacts, 19, 20*f*
posterior, liver abscess and, 85–86, 87*f*
Rh alloimmunization, screening fetus with hydrops for risk of, 1421–1423
Rh_0(D) immune globulin (RhoGAM), in immune hydrops prevention, 1418
Rhabdoid tumors
intraspinal, pediatric, 1689–1691
neonatal/infant brain and, 1562
Rhabdomyoma(s), cardiac
fetal, 1293–1294, 1293*f*
fetal hydrops from, 1424, 1424*f*
in infants, 1293
tuberous sclerosis, 1424
Rhabdomyosarcoma(s)
bladder, 356
pediatric, 1820, 1823*f*
pediatric
biliary, in liver, 1746, 1749*f*
embryonal, paratesticular, 1903–1904, 1903*f*
hydrosonovaginography and, 1871*f*
lower urinary tract and, 1908–1912, 1912*f*
metastasis of, to teste, 1901
neck, 1665, 1666*f*
presacral, 1914–1915
salivary gland, 1638–1639
vaginal, 1883, 1883*f*
scrotal, 840*f*, 841
in TSC, 1200*f*
Rh(D) antibodies, immune hydrops and, 1419
Rheumatoid arthritis, 866
erosive, 867, 868*f*
gout and, 867–869, 868*f*
of hand and wrist, injections for, 904
joint effusion in, 867, 867*f*
Rheumatoid nodules, in Achilles tendon, 867, 868*f*
Rhizomelia, 1381, 1381*b*, 1382*f*
Rhizomelic chondrodysplasia punctata, 1399
Rhizomelic dysplasia, features of, 1397*t*
RhoGAM. *See* Rh_0(D) immune globulin
Rhombencephalic cavity, 1167
Rhombencephalic neural tube, 1167
Rhombencephalon, formation of, 1077, 1077*f*, 1167
Rhombencephalosynapsis, 1192
RI. *See* Resistive index
Rib shadowing, in pediatric chest sonography, 1710
Rib(s)
fractures of, pediatric, 1727
in skeletal dysplasias, 1382–1384
Riedel lobe, 80
Riedel struma, 727–728, 728*f*
Right atrial isomerism, in total APVR, 1290
"Rim-rent" rotator cuff tears, 888, 890*f*
"Ring of fire" sign, in pediatric ectopic pregnancy, 1884–1885
Ring-down artifacts, 266, 266*f*
Roberts syndrome, 1401
Rocker-bottom foot, 1406*f*, 1407
Rokitansky-Aschoff sinuses, 202, 203*f*
Rolland-Desbuquois, 1399
Rostral neuropore, 1167
Rotator cable, 882, 884*f*
Rotator cuff. *See also* Shoulder
anatomy of, 879, 879*f*
hydroxyapatite crystal deposition in, 891–892
muscle atrophy of, 888–889, 891*f*
musculature evaluation of, 884–886, 885*f*
postsurgical, 888, 891*f*
Rotator cuff *(Continued)*
shoulder dysfunction and pathology of, 877
tears of, 886–892
background on, 886
calcific tendinitis and, 891–892, 892*f*
full-thickness, 886–887, 887*f*–888*f*
partial-thickness, 887–888, 889*f*–890*f*
subacromial-subdeltoid bursa and, 888–889, 892*f*
tendinosis as, 886, 886*f*
Rotator interval, 879, 880*f*
ultrasound evaluation of, 881–882
Rotter lymph nodes, 762, 808–810, 810*f*
Round ligament(s), 528, 564–565
cysts of, simulating groin hernias, 500, 501*f*
relationship of indirect inguinal hernia to, 476–479, 480*f*
thrombosis of, simulating groin hernias, 500, 501*f*
varices of, simulating groin hernias, 500, 501*f*
Round pneumonia, pediatric, 1711–1712, 1715*f*
RPD. *See* Renal pelvic diameter
RPOC. *See* Retained products of conception
Rubella
congenital, neonatal/infant brain and, 1560
fetal hydrops from, 1432
maternal, pulmonic stenosis and, 1292
Rudimentary horn, 538
Rupture of membranes, preterm premature
cervical assessment in, 1505

S

SAAAVE Act. *See* Screening Abdominal Aortic Aneurysms Very Efficiently Act
Sacral agenesis, 1689
fetal, 1237
in caudal regression, 1237–1238
in caudal regression syndrome, 1401
Sacral bone tumors, 1914–1915
Sacrococcygeal teratomas
fetal, 1238–1239, 1238*b*, 1239*f*
hydrops from, 1430–1431
pediatric, 1691, 1694*f*
classification of, 1691*t*
cystic, 1694*f*
intrapelvic, 1694*f*
presacral, 1913, 1914*f*
Saddle nose, in skeletal dysplasia, 1382
Safety. *See also* Bioeffects
AIUM on diagnostic ultrasound and general, 47, 47*b*
hyperthermia and, 38, 38*f*
of microbubble contrast agents, 67–68
of obstetric sonography, 1034–1035
guidelines for, 1041–1042, 1042*t*, 1043*f*
of transvaginal ultrasound in first trimester of pregnancy, 1049
Sagittal sinus, fetal, thrombosis of, 1206*f*
Saldino-Noonan syndrome, 1396
Salivary glands, pediatric, 1629–1639. *See also* Parotid glands, pediatric; Submandibular glands, pediatric
anatomy of, 1630–1631
inflammation of, 1632–1635
acute, 1632–1634, 1632*f*–1633*f*
chronic, 1634–1635, 1634*f*–1636*f*
masses of, 1636–1639
neoplasms of, 1636–1639, 1638*f*–1639*f*
vascular masses of, 1636, 1637*f*
viral infections of, 1632, 1632*f*
Salmon patches, 1679
Salmonella, 1852–1853
Sample volume, in obstetric Doppler ultrasound, 1036

Sample volume size, Doppler ultrasound and, 29*b*, 30
Sandal toes, fetal, 1406*f*, 1407
Saphenofemoral junction, as landmark for femoral hernias, 482, 485*f*
Sappey plexus, 762
Sarcoid, chronic pediatric sialadenitis in, 1634–1635
Sarcoidosis, epididymis and, 841, 843*f*
Sarcoma botryoides, pediatric, 1820, 1883, 1908
Sarcoma(s)
  embryonal, undifferentiated, in pediatric liver, 1746, 1748*f*
  endometrial, 551, 551*f*
  granulocytic, pediatric, neck, 1666, 1667*f*
  Kaposi, liver in, 129
  masticator space, pediatric, 1640, 1641*f*
  renal, 356
  soft tissue, 871–872, 872*f*
  uterine, 551
Sawtooth flow disturbance, from temporal tap, 918, 918*f*
Scanning mode, obstetric sonography and, 1035
Scapulae, 878–879, 878*f*
  hypoplastic, in campomelic dysplasia, 1381–1382
Scars
  from cesarean sections, 557, 558*f*
  exuberant, simulating anterior abdominal wall hernias, 500, 502*f*
SCC. *See* Squamous cell carcinoma
SCD. *See* Sickle cell disease
Schistosomiasis
  bladder, 331, 331*f*
  liver, 90
    pediatric, 1748
  urinary tract, 331
Schizencephalic clefts, hydranencephaly differentiated from, 1208
Schizencephaly
  CMV infection and, 1536–1537, 1558
  fetal, 1196, 1199*f*
  HPE differentiated from, 1189
  hydranencephaly differentiated from, 1208
  neonatal/infant, 1536–1537, 1537*f*
Schneckenbecken dysplasia, 1396
Scintigraphy, in parathyroid adenomas of, 747, 747*f*
Sclerosing cholangitis, recurrent, complicating liver transplantation, 629, 630*f*
Sclerosing peritonitis, 514, 521, 523*f*
Sclerosis of hemangioma, diagnostic challenges with, 112
Sclerotherapy
  ethanol, 719
  ultrasound-guided, of macrocystic lymphatic malformation, pediatric, 1726, 1727*f*
Sclerotome, in spine embryology, 1217–1218, 1217*f*, 1218*t*
Scoliosis
  fetal, 1235–1237, 1237*b*
    campomelic dysplasia and, 1395
  pediatric, 1688
Screening Abdominal Aortic Aneurysms Very Efficiently (SAAAVE) Act, 435
Scrotal pearls, 836–837, 837*f*
Scrotal sac, torsion of, pediatric, 1325
Scrotoliths, 836–837, 837*f*, 1897
Scrotum. *See also* Epididymis; Testis(es)
  anatomy of, 819–822, 819*f*–821*f*
  bifid, fetal, 1367
  calcifications of, 833–834, 833*b*, 834*f*
  calculi in, extratesticular, 836–837, 837*f*
  cysts of, extratesticular, 839, 842*f*
  edema of, idiopathic, 846
  epididymal lesions and, 839–841
Scrotum *(Continued)*
  fibrous pseudotumor and, 838, 840*f*
  hematoceles of, 835*f*, 836
    pediatric, 1902
  hernia and, 836, 836*f*
  hydroceles of, 834–836, 835*f*
    fetal, 1367
    pediatric, 1899, 1902, 1902*f*
  indirect inguinal hernias extending into, 478–479, 482*f*
  liposarcomas of, 840*f*, 841
  masses in, 822–834
  pain in, acute, 841–847
    causes of, 843*b*
    from epididymitis, 846, 847*f*–848*f*, 1895–1896, 1896*f*
    from epididymo-orchitis, 846, 847*f*–849*f*
    from Fournier gangrene, 846–847
    secondary to intraabdominal process, 1899
    from testicular torsion, 844–846, 844*f*–845*f*
    from torsion of testicular appendage, 846
  pathologic lesions of, extratesticular, 834–841, 836*b*
  pediatric
    acute pain or swelling in, 1892–1899, 1892*b*
    anatomy of, 1888
    edema of, acute idiopathic, 1898–1899, 1898*f*
    hematoceles of, 1902
    Henoch-Schönlein purpura and, 1899
    hernia and, 1902
    hydroceles of, 1899, 1902, 1902*f*
    masses of, 1899–1904
    masses of, extratesticular causes of, 1902–1903
    masses of, intratesticular causes of, 1899–1902
    masses of, paratesticular, 1903–1904
    trauma to, 1897–1898, 1898*f*
  polyorchidism and, 838–839, 841*f*
  pyoceles of, 835*f*, 836
  rhabdomyosarcomas of, 840*f*, 841
  sonography of
    current uses of, 819*b*
    technique for, 818–819
  trauma to, 847–851, 850*f*
  tumors of, extratesticular, 840–841, 840*f*
  varicoceles of, 837–838, 838*f*–839*f*
S/D ratio. *See* Systolic-to-diastolic ratio
Sebaceous cysts, 779, 781*f*
Second harmonic, transducers and, 105
Second-generation contrast agents, 56
Secretin injection, 218
Segmental spinal dysgenesis, 1674, 1689, 1691*f*
Segmentation, in organogenesis, 1524, 1525*f*
Seldinger technique, for drainage catheter placement, 611
Selective uptake contrast agents, 56, 57*f*
Seminal vesicles, 382*f*–383*f*, 384
  calcification of, 392
  congenital abnormalities in, 392
  cysts of, 392, 393*f*
    pediatric, 1908, 1910*f*
  pediatric, anatomy of, 1888, 1888*f*
Seminiferous tubules, 819
Seminoma(s), 584
  cryptorchidism and, 851
  pediatric
    in dysplastic gonads, 1899
    sonography of, 1899, 1900*f*
  testicular, 823, 823*f*–824*f*
Sensenbrenner syndrome, 1395
Sepsis, pediatric, jaundice in, 1738
Septate uterus, 534–536, 536*f*–537*f*
Septations, in renal cysts, 357–358, 357*b*, 358*f*
Septi pellucidi, absence of, 1201–1203
Septic arthritis, pediatric, 1936, 1937*f*
Septic shock, AKI and, 1796
Septo-optic dysplasia (SOD)
  fetal brain and, 1201–1203, 1203*f*
  HPE differentiated from, 1187–1189
  neonatal/infant brain and, 1532–1534, 1535*f*
  in rhombencephalosynapsis, 1192
Septula testis, 819, 820*f*
Septum pellucidum
  absent, in rhombencephalosynapsis, 1192
  cavum of, fetal, sonographic view of, 1024*f*
Septum primum, 1279
Septum secundum, 1280
Seroma(s)
  pelvic, 591
  retrosternal, 1726*f*
  spinal canal, pediatric, 1697, 1697*f*
  stitch, after herniorrhaphy, 494–496, 495*f*
Serous cystadenocarcinoma, ovarian, 580–581, 580*f*
Serous cystadenoma, ovarian, 580–581, 580*f*
Serous cystic neoplasm, 243, 244*f*–245*f*
Sertoli cell tumors, 826, 827*f*
  pediatric, 1900
Sertoli-Leydig cell tumor, 585
Serum, Urine and Ultrasound Screening Study (SURUSS), 1090
Sex cord-stromal tumors
  ovarian, 585
  testicular, 825–826, 827*f*
Sex reversal, in campomelic dysplasia, 1395
SGA. *See* Small-for-gestational age fetus
Shadowing
  acoustic, 786
    breast sonography and, 791–792, 793*f*
    carcinoma causing, 791–792, 793*f*
    decreased/absent, in skeletal dysplasias, 1381–1382
    malignant masses causes, differential diagnosis for, 792
    by rib, in pediatric chest sonography, 1710
  as artifacts, 19–21, 22*f*
  in uterine fibroids, 539*f*, 540, 540*b*
Shattered kidney, 365–366
Shear wave elastography (SWE), 16, 17*f*–18*f*, 772
  cirrhosis of liver and, 95–96
  for pediatric liver, 1764, 1765*f*
Shear waves, in bone, 39
Shigella, 1852
Shockwave, 37, 37*f*
Short umbilical cord, 1481
Short-rib polydactyly syndromes, 1382, 1383*f*, 1395–1396, 1397*f*
Shoulder. *See also* Rotator cuff
  anatomy of, 878–879, 878*f*
  arthropathy and, 893–894
    degenerative, 893, 894*f*
    inflammatory, 893–894, 894*f*
  clinical perspective on, 877–878
  injection of, 901, 901*f*
  pediatric, brachial plexus injury and, 1934–1936, 1936*f*–1937*f*
  posterior, 884
  rotator cuff pathology and dysfunction of, 877
  subacromial impingement of, 877–879, 882–883
  ultrasound techniques for
    anisotropy and, 895, 895*f*
    Crass position in, 881, 883*f*
    modified Crass position in, 881, 883*f*–884*f*
    MRI compared to, 877–878
    pitfalls in, 895, 895*f*
    protocol for, 879–886, 880*t*
Shunt(s). *See also* Portosystemic shunts
  for hydrocephalus, in neonatal/infant brain, duplex Doppler sonography of, 1582, 1584*f*
  in hydrocephalus, malfunction of, RI in, 1613, 1613*f*

Shunt(s) *(Continued)*
right-to-left, pediatric, TCD sonography evaluation of, 1614–1618
splenorenal, in portal hypertension, pediatric, 1757, 1759*f*
ventriculoperitoneal, for Dandy-Walker malformation, 1530
vesicoamniotic, for lower urinary tract obstruction, 1363–1365, 1364*f*, 1365*t*
Shwachman-Diamond syndrome, nesidioblastosis and, 1865, 1865*f*
Sialadenitis, pediatric, chronic, 1634–1635, 1635*f*
Sialoblastoma, salivary gland, pediatric, 1638–1639
Sialolithiasis, pediatric, of submandibular gland, 1633, 1633*f*
Sickle cell disease (SCD)
ACA stenosis with, 1607*f*
bone marrow transplantation for, 1598
cerebrovascular disease indicators with, 1598, 1599*b*
MCA and, 1600*f*, 1604*f*–1605*f*
ophthalmic artery flow as, 1599*f*
stroke and, 1601*f*–1603*f*
DICA stenosis and, 1606*f*
moyamoya angiopathy and, 1598, 1600*f*, 1602*f*, 1608*f*, 1610
silent cerebral infarcts and, 1598
sleep-disordered breathing and, 1611
spleen in, 157
stroke and
cerebrovascular disease indicators with, 1601*f*–1603*f*
risk categories for, 1599–1604, 1605*t*, 1606–1607
screening for, 1598
velocity indications of, 1605–1607
TCD sonography for, 1591, 1598–1608, 1599*b*, 1599*f*–1608*f*
Side lobe artifacts, 19, 20*f*
Side lobes, 19, 20*f*
Silent cerebral infarcts, SCD and, 1598
Silent (painless) thyroiditis, 725–727
Silicon granulomas, in extracapsular breast implant rupture, 805–807, 806*f*
Silver-Handmaker, 1399
Simple cysts
of breast, 774, 775*f*
of pediatric testes, solitary, 1901–1902
Simpson-Golabi-Behmel syndrome
CDH and, 1263
hyperechogenic kidneys in, 1351
Single-photon emission computed tomography (SPECT), 747, 747*f*
Sinus bradycardia, fetal, 1297
Sinus venosus ASD, 1280, 1282*f*
Sinus(es)
dorsal dermal, pediatric, 1686, 1688*f*
urachal, 322, 323*f*
Sinusoidal obstruction syndrome, 1762–1763
Sirenomelia, fetal, 1238, 1238*f*, 1401, 1404*f*
Sirenomelia sequence, sacral agenesis in, 1237
Site-specific ovarian cancer syndrome, 578
Situs inversus totalis, of liver, 80
Sjögren syndrome, chronic pediatric sialadenitis in, 1634–1635
Skeletal deformities, fetal lung size and, 1244
Skeletal dysplasia, fetal
categories of, 1377*t*
diagnosis of, 1376–1377, 1377*b*
femur/foot length ratio in, 1379
hydrops from, 1432
lethal, 1386–1396
achondrogenesis as, 1391
campomelic dysplasia as, 1395, 1396*f*
Skeletal dysplasia, fetal *(Continued)*
features of, 1386*b*
hypophosphatasia as, 1392–1395, 1395*f*
osteogenesis imperfecta as, 1391–1392
short-rib polydactyly syndromes as, 1395–1396, 1397*f*
thanatophoric dysplasia as, 1387–1390
lethality of, pulmonary hypoplasia and, 1382, 1384*f*
nonlethal or variable prognosis, 1396–1399
asphyxiating thoracic dysplasia as, 1398
chondrodysplasia punctata as, 1399
diastrophic dysplasia as, 1398, 1398*f*
dyssegmental dysplasia as, 1399
Ellis-van Creveld syndrome as, 1398–1399
heterozygous achondroplasia as, 1396–1398, 1398*f*
micromelic dysplasia as, 1397*t*
osteogenesis imperfecta types I, III, IV as, 1399
rhizomelic dysplasia as, 1397*t*
prevalence of, 1376, 1377*t*
sonographic evaluation of, 1379–1386, 1379*b*
with abnormal bone length or appearance, 1380–1384, 1381*b*, 1382*f*–1384*f*
additional imaging in, 1384–1386
molecular diagnosis in, 1385–1386
MRI in, 1385
with positive family history, 1379–1380
radiography in, 1384
3-D ultrasound in, 1384, 1385*f*
three-dimensional CT in, 1384–1385
Skeletal dysplasia, pediatric, atypical hips and, 1932
Skeletal survey, in fetal hydrops diagnosis, 1435
Skeleton, fetal. *See also* Limb reduction defects
aneuploidy findings in, 1407–1409
limb reduction defects and, 1399–1404
normal, 1089–1097
development of, 1089, 1378*f*
extremity measurements of, 1089, 1379*t*, 1380*f*–1381*f*
triploidy and, 1408–1409
trisomy 13 and, 1408, 1408*b*
trisomy 18 and, 1408, 1408*b*
trisomy 21 and, 1408, 1408*b*
Skin folds, thickened, in lethal skeletal dysplasias, 1386
Skull, fetal
cloverleaf-shaped, 1136
craniosynostosis with, 1137*f*–1138*f*
in skeletal dysplasias, 1382
in thanatophoric dysplasia type 2, 1388–1389, 1389*f*
lemon-shaped, 1136, 1137*f*
strawberry-shaped, 1136, 1137*f*
Sleep apnea, pediatric TCD sonography for, 1611
Sleep-disordered breathing, 1611
"Sliding organ sign", 566
Slipped capital femoral epiphysis, 1931–1932
Sludge
biliary
acute pancreatitis and, 221
gallbladder and, 194–195, 196*f*
gallbladder, pediatric, 1741, 1743*f*
spontaneous PTB and, 1503
tumefactive, 195, 196*f*, 1741
SMA. *See* Superior mesenteric artery
Small bowel. *See also* Bowel; Echogenic bowel
fetal, 1308–1316
anorectal malformations and, 1310–1312, 1311*f*
dilated loops of, 1311–1312
Small bowel *(Continued)*
duodenal atresia and obstruction of, 1308–1309, 1310*f*
echogenic, 1313–1316, 1315*f*
enteric duplication cysts and, 1312–1313, 1313*f*
Hirschsprung disease and, 1312, 1312*f*
jejunoileal atresia obstructing, 1310, 1311*f*
meconium ileus and, 1310
meconium peritonitis and, 1313, 1313*t*, 1314*f*
meconium pseudocyst and, 1313, 1314*f*
lymphoma of, 266, 266*f*
pediatric, 1841–1847
anatomy of, 1841, 1842*f*
intussusception and, 1844–1845, 1849*f*
obstruction of, 1842–1843, 1846*f*
sonographic technique for, 1841
Small bowel mesentery, 505, 505*f*
Small saphenous vein, 981–982, 981*f*
Small-for-gestational age (SGA) fetus, 1454–1455, 1454*b*
SMI. *See* Superb microvascular imaging
Smith-Lemli-Opitz syndrome
ambiguous genitalia and, 1367
microcephaly in, 1194
SMV. *See* Superior mesenteric vein
Snell law, 5
Society for Fetal Urology, grading system of, for hydronephrosis, 1354, 1355*f*
SOD. *See* Septo-optic dysplasia
Soft tissue(s)
foreign bodies embedded in, 872, 873*f*
ganglia, compression and, 865
heating of, 37–38, 37*f*
infection of, 872–874, 873*f*–874*f*
masses of, 869–872, 869*f*–872*f*, 871*t*
perienteric, in acute abdomen, 281–282
sarcomas, 871–872, 872*f*
thermal index for, in early, 1039
tumors of, fetal face and, 1154, 1160*f*
Soft Tissue Thermal Index (TIS), 39
Solid-pseudopapillary tumor, 248, 248*f*
Soluble form, of injectable steroids, 900
Somites, in spine embryology, 1216–1217, 1217*f*, 1218*t*
Sonazoid, 56
Sonochemistry, acoustic cavitation and, 42, 42*f*
Sonographic air bronchograms. *See* Air bronchograms, sonographic
Sonohysterography, uterine, 529
Sonoluminescence, 42
SonoVue, 56
Sotos syndrome, megalencephaly associated with, 1194–1195
Sound
attenuation of sound energy, 5–7, 7*f*, 35
intensity of, 5
physical effects of, 35
propagation of, 2–3, 3*f*
propagation velocity of, 2–3, 3*f*
reflected, 3–4
theoretical understanding of, 58–59
Sound waves, 2, 2*f*
Spatial compounding, 13–15, 14*f*–15*f*
Spatial focusing, tissue heating and, 35
Spatial peak temporal average (SPTA), 32
Spatial resolution, 16–19, 18*f*–19*f*
Speckle, 4, 5*f*
contrast effect of, 13–15, 14*f*
spatial compounding and, 13–15
SPECT. *See* Single-photon emission computed tomography

Spectral broadening, in Doppler ultrasound, 24, 24*f*, 29, 29*b*, 31*f*
in carotid artery stenosis, 927, 927*f*
in peripheral arterial stenosis, 968, 969*f*
Spectral window, 925, 925*f*
Specular reflectors, 4, 4*b*, 5*f*
Speech, delayed, obstetric sonography and, 1040
Sperm, transport of, 1049–1051
Sperm granuloma, epididymis and, 841, 843*f*
Spermatic cord
anatomy of, 821–822, 821*f*
leiomyomas of, 840–841, 840*f*
lipomas of, 840–841, 840*f*
pediatric
cysts of, 1902–1903
torsion of, 1324–1325, 1369
relationship of indirect inguinal hernia to, 476–479, 479*f*, 481*f*
torsion of, 841–843, 845*f*
Spermatoceles, 839, 842*f*
paratesticular, 1904
pediatric, 1902–1903
Sphincter, internal urethral, 384
Sphincter of Oddi, dysfunction of, complicating liver transplantation, 629
Spiculated breast carcinoma, 786
Spiculation, in breast sonography, 787–788, 788*f*
Spigelian fascia
anatomy of, 483–484
spigelian hernia location and, 483, 486*f*
Spigelian hernias, 471, 483–484. *See also* Hernia(s), spigelian
Spina bifida, 1218, 1223–1233. *See also* Neural tube defects
abnormalities associated with
caudal regression as, 1237–1238, 1237*f*
cranial, 1228–1233
noncranial, 1233
sacral agenesis as, 1237
anatomic landmarks establishing, 1228*b*
closed, cranial changes in, 1183–1186, 1185*f*, 1185*t*–1186*t*
definition of, 1225*t*
evaluation protocol for, with 3-D volume data, 1223*b*
NTDs and, 1223
open, cranial changes in, 1183–1186, 1184*f*, 1185*t*–1186*t*
pathogenesis and pathology in, 1226
prevention of, folic acid in, 1224–1225
prognosis of, 1228*b*
screening for
alpha-fetoprotein in, 1221, 1226–1228, 1226*b*, 1227*f*
Chiari II malformation in, 1221, 1228, 1230–1233
ultrasound in, 1226–1228
sonographic findings in, 1228, 1229*f*–1232*f*
sonographic signs of, 1233*b*
terminology of, 1680
Spina bifida occulta
definition of, 1225*t*
pathology of, 1226
Spinal canal, pediatric. *See also* Spinal dysraphism, pediatric
acoustic window for, 1672, 1673*f*, 1674, 1675*f*
anomalies of, 1678–1679
arachnoid cysts of, 1695–1697, 1696*f*
embryology of, 1672–1674, 1673*f*
hemorrhage and, 1695, 1695*f*–1696*f*
infection of, 1695
normal anatomy of, 1674–1678, 1675*f*–1680*f*
seromas and, 1697, 1697*f*
sonographic technique for, 1674–1678
intraoperative uses of, 1697
subcutaneous hemangioma and, 1697, 1697*f*
Spinal canal, pediatric *(Continued)*
tethered cord and, 1678–1679, 1681*f*
tumors of, 1689–1691, 1691*t*, 1693*f*–1694*f*
Spinal column agenesis, 1689
Spinal cord
fetal, normal position of, 1218–1221, 1221*f*
pediatric, abnormally long, 1685
tumor of, pediatric, neurogenic bladder in, 1907
Spinal dysgenesis, segmental, 1674, 1689, 1691*f*
Spinal dysraphism, fetal, 1218
cephalocele as, 1139–1140
definition of, 1225*t*
Spinal dysraphism, pediatric
classification of, 1680–1681, 1682*t*
closed, with subcutaneous mass, 1682–1684, 1682*t*
lipomyelocele and, 1682, 1684*f*
lipomyelomeningocele and, 1682, 1685*f*
meningocele and, 1682–1683
myelocystocele and, 1683–1684, 1686*f*
closed, without subcutaneous mass, 1684–1689
abnormally long spinal cord and, 1685
anomalies at risk for, 1689, 1689*b*
caudal agenesis and, 1689, 1690*f*
complex states of, 1686–1689
diastematomyelia and, 1688–1689, 1688*f*
dorsal dermal sinus and, 1686, 1688*f*
dorsal enteric fistulas and, 1686–1688
filum terminale lipomas and, 1684–1685, 1686*f*
intradural lipomas and, 1686, 1687*f*
midline notochordal formation disorders, 1689
midline notochordal integration disorders, 1686–1689
persistent terminal ventricle and, 1685
segmental spinal dysgenesis and, 1689, 1691*f*
simple states of, 1684–1686
definition of, 1679–1680
open, 1681–1682, 1682*t*
Chiari II malformation with, 1681–1682
myelomeningocele and, 1681, 1683*f*
placodes and, 1680
terminology of, 1680
Spine, fetal. *See also* Spina bifida
abnormalities of
definition of terms for, 1225*t*
diastematomyelia as, 1234–1235, 1236*f*
kyphosis as, 1235–1237, 1236*f*, 1237*b*
myelocystocele as, 1233–1234, 1234*f*–1235*f*
presacral masses as, 1239, 1239*b*
sacrococcygeal teratomas as, 1238–1239, 1238*b*, 1239*f*
scoliosis as, 1235–1237, 1237*b*
sirenomelia as, 1238, 1238*f*
spina bifida as, 1223–1233
assessment of, in skeletal dysplasia, 1382
developmental anatomy of, 1216–1221
embryology of, 1216–1218, 1217*f*, 1218*t*
lower, cloacal exstrophy and, 1328
normal position of, 1218–1221, 1221*f*
ossification of, 1218, 1219*f*–1220*f*
in lateral longitudinal scan plane, 1223*f*
in posterior angled transaxial scan plane, 1224*f*
in posterior longitudinal scan plane, 1224*f*
timing and pattern of, 1220*t*
routine sonographic views of, 1021, 1027*f*
scanning techniques for, 1221–1223
MRI for, 1216
scan planes in, 1221, 1222*f*–1224*f*
3-D ultrasound in, 1216, 1221–1223
Spiral arteries, 531–532
Spiral clips, pain from, after herniorrhaphy, 497, 498*f*
Spleen
abscesses of, 148, 151*f*
drainage of, 617
absence of, 142
accessory, 158–159, 160*f*, 1771*f*
anatomy of, 139–142
bare area of, 139–141, 141*f*
biopsy of
percutaneous needle, 607, 608*f*
ultrasound-guided, 161
congenital anomalies of, 158–161
cysts of, 146–148, 146*b*, 148*f*–151*f*
fetal, 1320–1322, 1322*f*
embryology of, 139–142, 140*f*
fetal, 1320–1322, 1321*f*
cysts of, 1320–1322, 1322*f*
splenomegaly and, 1320
focal abnormalities of, 146–157
cysts as, 146–148, 146*b*, 148*f*–151*f*
nodular lesions as, 148–152, 151*f*–154*f*
solid lesions as, 152–157
focal solid lesions of, 152–157
benign, 153–157, 155*b*, 156*f*–157*f*
malignant, 152–153, 154*f*–155*f*, 155*b*
functions of, 141
Gamna-Gandy bodies in, 157
Gaucher disease in, 157, 158*f*
hamartomas of, 153–156, 156*f*
hemangiomas of, 148, 153–157, 156*f*
hematomas of, 158, 159*f*
infarctions of, 156–157, 157*f*
interventional procedures for, 161
lymphangiomas of, 148
measurement of, sonographic approach to, 143–145, 145*f*
metastases to, cystic, 148
nodular lesions of, 148–152
calcified, 150, 153*f*
in candidiasis, 150–152, 154*f*
causes of, 152*b*
in lymphoma, 152, 154*f*
metastatic, 152, 154*f*
microabscesses as, 150–152, 154*f*
in tuberculosis, 150, 151*f*–152*f*
pathologic conditions of, 145–158
pediatric, 1769–1772
abscesses of, 1769
calcifications in, 1769
contusion to, 1771*f*
cysts of, 1769
enlargement of, 1769, 1770*b*, 1771*f*
granulomas of, 1771*f*
hematomas of, 1770, 1771*f*
infarcts of, 1770, 1771*f*
spontaneous rupture of, 1770
wandering, 1770–1772
peliosis of, 147
pitfalls in interpretation of, 161–162, 161*f*
retrorenal, 162
rupture of, 158
in SCD, 157
sonographic appearance of, 142–158, 144*f*–145*f*
sonographic technique for, 142, 142*f*–143*f*
trauma to, 158, 159*f*–160*f*
tuberculosis and, 150, 151*f*–152*f*
wandering, 159, 161*f*
weight of, 141
as window to pleural space, 1702, 1707*f*
Splenic varices, in portal hypertension, 1759*f*
Splenic vein
pancreatic body and, 211, 211*f*
pediatric
Doppler studies of, best approach for, 1752
flow direction in, in portal hypertension, 1752

Splenic vein *(Continued)*
thrombosis of
acute pancreatitis complicated by, 230, 231*f*
chronic pancreatitis and, 232–233, 234*f*–235*f*
Splenogonadal fusion, 833
paratesticular, 1904
Splenomegaly
causes of, 145, 146*t*
complications of, 146
diagnosis of, 145–146
fetal, 1320
massive, 145, 146*t*
portal hypertension as cause of, 145, 147*f*
in sickle cell disease, 157
sonographic appearance of, 143*f*–144*f*
Splenorenal ligament, 139–141, 140*f*
Splenorenal shunts, in portal hypertension, pediatric, 1757, 1759*f*
Splenosis, posttraumatic, 160–161
Splenunculi, 158–159, 160*f*
Split cord malformation
fetal, 1234–1235
pediatric, 1688–1689, 1688*f*
Split liver graft, from deceased donor, 625
Split-screen imaging, for breast assessment, 769, 769*f*
Sports hernias, 484–488, 488*f*–489*f*
SPTA. *See* Spatial peak temporal average
Squamous cell carcinoma (SCC), 348
Staghorn calculus
tyrosinemia and, 1799, 1800*f*
in xanthogranulomatous pyelonephritis, 328, 329*f*
Standard sonographic examination, 1019
Standoff pad, in breast tumor imaging, 767, 767*f*
Steatosis
diffuse, 91, 92*f*
in inborn errors of metabolism, 1738
pediatric, 1740, 1740*f*, 1741*b*
Stein-Leventhal syndrome, 573
pediatric, 1877–1878, 1879*f*
Stener lesion, 864, 864*f*
Stenotic disease, of abdominal aorta, 441–445, 445*f*
Stensen duct, pediatric, 1630
Stent graft, 438
Stepladder sign, in intracapsular breast implant rupture, 804–805, 805*f*
Sternocleidomastoid muscle, 692*f*, 694
Sternohyoid muscle, 692*f*, 694
Sternum, defect of, pentalogy of Cantrell and, 1329
Steroids
anabolic, therapy with, hepatic adenomas and, 1746
injectable, for musculoskeletal interventions, 900–901
injection of, interventional sonography for, pediatric, 1961, 1964*f*
Stickler syndrome, clefts of secondary palate in, 1153
Stippled epiphyses, 1399
Stitch abscess, after herniorrhaphy, 494–496, 495*f*
Stomach, fetal, 1306–1308
absent or small, 1306, 1306*b*
esophageal atresia and, 1305–1306, 1305*f*
dilated, 1307, 1308*f*
intraluminal gastric masses in, 1308, 1309*f*
midline, 1307, 1308*f*–1309*f*
normal, 1307*f*
right-sided, 1307, 1308*f*–1309*f*
Stomach, pediatric, 1833–1840
anatomy of, 1834–1835, 1835*f*–1836*f*
antrum distention in, HPS pitfalls and, 1838, 1839*f*
Stomach, pediatric *(Continued)*
artifact of empty, 1838, 1839*f*
bezoars and, 1840, 1841*f*
gastric diaphragm and, 1839, 1840*f*
gastric ulcers and, 1839–1840, 1840*f*
gastritis and, 1839–1840, 1840*f*
HPS and, 1835–1838, 1835*b*, 1837*f*–1838*f*
pitfalls in diagnosis of, 1838, 1838*b*, 1839*f*
pylorospasm and minimal muscular, 1836–1838, 1838*f*
optimal measurements of, 1834*b*
sonographic technique for, 1833–1835
Stomodeum, 1133–1134
Strain elastography, 16, 17*f*, 772
Strain modulus, 15–16
Strangulated hernias. *See* Hernia(s), strangulated
Strawberry-shaped skull, 1136, 1137*f*
Streaming, 35
Streptococcal meningitis, group B, neonatal/infant, 1560, 1561*f*–1562*f*
Stress maneuvers, for hip stability determination, 1923
Strictures in, in Crohn disease, 269–274, 275*f*–276*f*
String sign, occluded carotid artery distinguished from, 939
Stroke
cardioembolic, 915–916
from carotid artery stenosis, 915–916
in neonatal/infant brain, duplex Doppler sonography and, 1580–1581, 1584*f*
SCD and
cerebrovascular disease indicators with, 1601*f*–1603*f*
risk categories for, 1599–1604, 1605*t*, 1606–1607
screening for, 1598
velocity indications of, 1605–1607
Stromal cell tumors, ovarian, pediatric, 1879
Stromal tumors, gastrointestinal, 264, 265*f*
pediatric, 1862
Struma ovarii, 584
Sturge-Weber syndrome
facial hemangiomas in, 1154
pheochromocytomas with, 1910–1912
TCD sonography assessing, 1614
Subacromial impingement, of shoulder, 877–879, 882–883
Subacromial spurs, 878–879
Subacromial-subdeltoid bursa, 879
appearance of, normal, 889, 891*f*
rotator cuff tears and, 888–889, 892*f*
thickening of, 889–891, 892*f*
with ganglion, 889–891, 892*f*
Subacute granulomatous thyroiditis, 724, 724*f*
Subamniotic hematomas, of placenta, 1474
Subarachnoid hemorrhages, neonatal/infant brain and, 1550, 1550*f*
Subarachnoid spaces, neonatal/infant
development of, 1520–1521
fluid collections in, duplex Doppler sonography of, 1585, 1588*f*
Subchorionic cysts
maternal floor infarction with, 1474, 1476*f*
placental, 1474, 1477*f*
Subchorionic hematoma, 1474
placental abruption differentiated from, 1471, 1474*f*
Subchorionic hemorrhage
early pregnancy failure and, 1069, 1069*f*
fetal echogenic bowel and, 1315*f*
Subclavian artery, 975
stenosis of, 976, 978*f*–979*f*
Subclavian steal phenomenon, 952–954, 953*b*, 953*f*–954*f*, 976, 979*f*
Subclavian vein
anatomy of, 990–991, 990*f*
stenosis of, sever, 1006, 1009*f*
ultrasound examination for, 991, 991*f*
Subcutaneous edema, fetal, in hydrops, 1417, 1419*f*–1420*f*
Subdural effusions, neonatal/infant, duplex Doppler imaging of, 1585, 1588*f*
Subdural hematomas, neonatal/infant, 1557, 1558*f*
Subdural hemorrhage, fetal, bilateral, 1207*f*
Subependymal cysts, 1543–1544
of neonatal/infant brain, 1566, 1567*f*
Subependymal hemorrhage, neonatal/infant brain and, 1543–1544, 1543*f*–1544*f*
Subfascial hematomas, cesarean sections and, 556–557, 557*f*
Subglottic stenosis or atresia, CHAOS and, 1253
Sublingual gland, pediatric, anatomy of, 1631, 1631*f*
Subluxation, 1923, 1927
Submandibular glands, pediatric
anatomy of, 1630–1631, 1631*f*
pleomorphic adenoma of, 1638*f*
sialolithiasis of, 1633, 1633*f*
Submandibular space, pediatric, 1630–1631, 1631*f*
cystic lesions of, 1639–1640, 1640*b*
Submandibular window, for TCD sonography, 1592–1593
Subphrenic abscess, 1716
Subplacental hematoma, 1471, 1474*f*
Subscapular fossa, 878–879
Subscapularis tendon
anatomy of, normal, 878–879, 879*f*
ultrasound evaluation of, 880, 882*f*
Subtrochanteric femur, absence of, 1400
Subvalvular aortic stenosis, 1292
Succenturiate lobes, of placenta, 1480–1481, 1481*f*
"Sugar icing", 868*f*
Sulcation disorders, of neonatal/infant brain, 1536–1537
Sulcus(i), of brain
development of, 1167
neonatal/infant
development of, 1520–1521, 1520*f*–1521*f*
effacement of, in diffuse cerebral edema, 1553, 1554*f*
normal sonographic appearance of, 1169, 1171*f*
radial arrangement of, in corpus callosum agenesis, 1528, 1532*f*
Sulfur colloid scanning, FNH and, 115
"Sunburst sign," in corpus callosum agenesis, 1528, 1532*f*
Superb microvascular imaging (SMI), 1746
basic technique of, 1749–1750, 1752*f*
Superficial fascia, pediatric, 1628, 1629*f*
Superficial peritendinous and periarticular injections, 902–904
for foot and ankle, 902–904, 903*f*–904*f*
for hand and wrist, 904, 905*f*
Superficial venous insufficiency, 981–982
Superior mesenteric artery (SMA)
pancreatic body and, 211, 211*f*
small bowel obstruction and, 1308
Superior mesenteric vein (SMV), 211, 211*f*
Superior vena cava (SVC)
anatomy of, 991
catheter position for, pediatric, 1716–1721, 1722*f*
stenosis, with PICC line, 993*f*
thrombosis of, pediatric, 1721, 1721*b*, 1722*f*
ultrasound examination of, 991–992, 992*f*
Supernumerary glands, 733
Supernumerary kidneys, 319
Supernumerary testes, 838–839, 841*f*

Superoanteromedial ridge, 416–417
Supraclavicular lymphadenopathy, pediatric, 1658
Suprahyoid space, pediatric
  anatomy of, 1628–1640, 1629*f*
  cystic lesions of, 1639–1640, 1640*b*, 1640*f*–1641*f*
  masticator space of, pathology of, 1640, 1641*f*
  salivary glands in, 1629–1639
    anatomy of, 1630–1631
Supraspinatus fossa, 878–879
Supraspinatus tendon
  anatomy of, 878–879
  calcific tendinitis of, 891–892, 892*f*
  postoperative, 888, 891*f*
  tendinosis of, 886*f*
  ultrasound evaluation of, 881–883, 883*f*–884*f*
Supratentorial tumors, neonatal/infant brain and, 1562
Supraventricular tachycardia (SVTs)
  with Ebstein anomaly, 1286–1287
  fetal, 1296–1297, 1296*f*
    hydrops from, 1424, 1425*f*
Surface epithelial inclusion cysts, 569, 573
Surface epithelial-stromal tumors, 579–582, 580*f*–582*f*
SURUSS. *See* Serum, Urine and Ultrasound Screening Study
Surveillance
  of AAA, 435–437
    CT in, 437
    sonographic technique for, 436–437, 436*f*–437*f*
  active, for prostate cancer, 401
Suspensory (infundibulopelvic) ligament, 564–565
Sutures, cranial, premature fusion of, 1136–1139, 1138*b*, 1138*f*–1139*f*
SVC. *See* Superior vena cava
SVTs. *See* Supraventricular tachycardia
SWE. *See* Shear wave elastography
Swyer syndrome, 1887
Sylvian fissure, neonatal/infant, development of, 1514*f*–1515*f*, 1520–1521
Syncytiotrophoblast, 1049, 1051–1052, 1052*f*, 1466*f*
Syndactyly
  fetal, 1406, 1406*f*
  of fingers, in triploidy, 1105*f*, 1406
Synechia, amniotic band sequence and, 1401
Synovitis, 867, 869
  hip joint, pediatric, 1931*f*
Syntelencephaly, 1187, 1189, 1535–1536
Synthetic arteriovenous graft. *See* Arteriovenous graft, synthetic
Syphilis, 1203–1204
  fetal hydrops from, 1431–1432
Syringocele, 1683–1684
Syrinx, 1681
System setup, obstetric sonography and, 1035–1036, 1035*f*–1037*f*
Systemic lupus erythematosus, maternal, fetal AVB from, 1297
Systolic velocity, cerebral, factors changing, 1612*t*
Systolic-to-diastolic ratio (S/D ratio), 27, 27*f*

T

"T" sign, in monochorionicity, 1119, 1119*t*, 1121*f*
Tachyarrhythmias, fetal, hydrops from, 1424
Tachycardia
  fetal, 1296–1297, 1296*f*
  neonatal/infant, intracranial RI and, 1576
  supraventricular
    with Ebstein anomaly, 1286–1287
    fetal, 1296–1297, 1296*f*
    fetal, hydrops from, 1424, 1425*f*
  ventricular, 1296
Tactile sensation, in obstetric sonography, 1038
Tailgut cysts, 297, 298*f*
Takayasu arteritis
  aortic stenosis in, 444
  of common carotid artery, 944–946, 947*f*
Talipes equinovarus, fetal, 1406*f*, 1407
  campomelic dysplasia and, 1395
Talipomanus, fetal, 1407
TAMM. *See* Time-averaged mean of maximum velocity
Tamoxifen, 544–545, 545*f*
Tandem plaques, in carotid stenosis, 923–924
TAPS. *See* Twin anemia polycythemia sequence
Tardus-parvus waveform(s)
  arterial stenosis and, 969, 971*f*
  in hepatic artery thrombosis after liver transplantation, 631, 633*f*
  in internal carotid artery stenosis, 934*f*, 938
  pediatric renal artery stenosis and, 1809
  in peripheral artery stenosis, 965–966
  in popliteal artery occlusion, 968*f*
  in renal artery duplex Doppler sonography, 450, 450*f*
  in renal artery stenosis, 368, 368*f*
  in subclavian steal phenomenon, 953*b*, 954
Target pattern, in gut wall, 257, 260*f*
Targeted organ lesion biopsy, 1961, 1961*f*–1962*f*
TAS. *See* Transabdominal sonography
TASC. *See* Trans-Atlantic Inter-Society Consensus
TCC. *See* Transitional cell carcinoma
TCD. *See* Transcranial Doppler sonography
TDLUs. *See* Terminal ductolobular units
Teale femoral hernia, 482, 485*f*
Teen mothers, fetal gastroschisis and, 1322–1323
Tegmento-vermian angle, 1189–1190
Telangiectasia, hereditary hemorrhagic, 104
Telencephalon, formation of, 1077
"Telephone receiver" femur, 1380*f*
Temporal average intensity, 36
Temporal bone approach, for duplex Doppler ultrasound of neonatal/infant brain, 1574, 1575*f*
Temporal horns, of lateral ventricles, neonatal/infant, in coronal imaging, 1514–1515
Temporal maximum intensity projection imaging, 64, 65*f*
Temporal peak intensity, 36, 36*f*
Temporal tap, in external carotid artery identification, 918, 918*f*
Tendinitis, calcific
  injections for, 909, 911*f*
  of supraspinatus tendon, 891–892, 892*f*
Tendinosis, 859–861, 861*f*
  de Quervain, injection for, 904, 905*f*
  rotator cuff, 886, 886*f*
  in sports hernia, 486
  of supraspinatus tendon, 886*f*
Tendon(s)
  anatomy of, normal, 859, 860*f*
  anisotropy of, 859, 860*f*, 899
  calcification of, 859–861
  conjoined
    direct inguinal hernia and, 479–481, 483*f*–484*f*
    weakness/tear of, sports hernia and, 485–486, 489*f*
  inflammation of, 861–862, 862*f*
  injections of deep, 904–907
  injuries to, 859–861, 861*f*
  tears to, 861, 861*b*, 862*f*
  ultrasound techniques for, 859–862
Tenosynovitis, 861–862, 862*f*
  long head of biceps, 892–893, 893*f*
  stenosing, injections for, 902
Tenotomy, percutaneous, 909–910, 913*f*
Teratocarcinomas, pediatric, testicular, 1899
Teratogenic effects, from hyperthermia, 38
Teratogens, thermal effects of ultrasound and, 1037
Teratologic hip dislocation, pediatric, 1932
Teratoma(s). *See also* Sacrococcygeal teratomas
  cystic, ovarian, 582–584, 582*b*, 583*f*
  dacryocystocele differentiated from, 1143
  fetal
    cardiac, 1294
    cervical, 1159, 1161*f*
    intracranial, 1208–1209, 1209*f*
    intrapericardial, hydrops from, 1424
    neck, hydrops from, 1425, 1426*f*
    sacrococcygeal, 1238–1239, 1238*b*, 1239*f*, 1430–1431
  immature, 584
  neonatal/infant
    brain, 1562
    cardiac, 1293
  pediatric
    benign, ovarian, 1880, 1880*f*
    cervical, 1654, 1654*f*
    hemorrhagic ovarian cyst differentiated from, 1877
    pseudoprecocious puberty and, 1887
    sacrococcygeal, 1691, 1691*t*, 1694*f*
    testicular, 1899
    thymic, 1723–1724
  testicular, 823–824, 825*f*
  thyroid gland, 1648
Teres minor tendon
  anatomy of, 878–879
  ultrasound evaluation of, 884
Terminal ductolobular units (TDLUs), of breast, 760–761
  carcinoma in, 789–790, 792*f*
  sonographic appearance of, 762, 766*f*
Terminal ileitis, 288
Terminal myelocystocele, 1234
Terminal transverse limb defects, amniotic band sequence and, 1400
Terminal ventricle, persistent, pediatric, 1685
Tessier clefts, classification of, 1152–1153, 1153*f*
Testicular appendage, pediatric, torsion of, 1897, 1897*f*
Testicular artery(ies), 820*f*–821*f*, 821
Testicular duplication, pediatric, 1891
Testicular feminization, fetal, 1368
Testicular microlithiasis, pediatric, 1904, 1904*f*
Testicular torsion, 844–846, 844*f*–845*f*
  pediatric
    acute, 1893–1894, 1894*f*
    acute scrotal pain from, 1892
    chronic, 1895
    color Doppler sonography in, 1895–1899, 1896*b*
    detorsion of, 1895–1896
    extravaginal, 1892–1893, 1893*f*
    incomplete, 1896
    intravaginal, 1893–1894, 1893*f*
    late, 1895
    "missed", 1895, 1895*f*
    within scrotal sac, 1893–1894
    sonographic signs of, 1894*b*
    spontaneous detorsion of, 1896
    types of, 1893–1894, 1893*f*
Testis(es). *See also* Scrotum
  abscess of, 831–832, 831*f*
  adrenal rests and, 832–833, 833*f*, 1824
  anatomy of, 819, 819*f*–820*f*
  appendix, 820–821, 820*f*
    pediatric, 1897
  arterial supply of, 820*f*–821*f*, 821
  cryptorchid, seminomas in, 823
  cryptorchidism and, 851, 851*f*
    pediatric, 826
  cystic dysplasia of, 830

Testis(es) *(Continued)*
cysts of, 829, 829*b*
cystic dysplasia and, 830
epidermoid, 830*f*, 831
intratesticular, 829, 830*f*
tubular ectasia of rete testis and, 829–830, 830*f*
ectopia of, transverse, 1890
feminization of, 826
dysplastic gonads and, 1899
primary amenorrhea in, 1887
fetal
descent of, 1367
undescended, 1367
fibrosis of, after orchitis, 846, 849*f*
fracture of, 850, 850*f*
gubernaculum, 851
hematoma of, 848–850, 850*f*
heterogeneous "striped", 846, 849*f*
infarction of
after herniorrhaphy, 494–496, 495*f*
segmental, 832, 832*f*
in inguinal canal, 851, 851*f*
malpositioned, 851
mediastinum, 819, 820*f*
pediatric, 1888
metastases to, 822*b*, 826–829, 826*b*
hamartomas as, 829, 829*f*
leukemia as, 827, 828*f*
lymphoma as, 826–827, 828*f*
myeloma as, 827–829
microlithiasis of, 833, 833*b*, 834*f*
pediatric
accessory, 1891
anatomy of, 1888–1890, 1889*f*
appendix, 1897
bilobed, 1891
congenital abnormalities of, 1890–1892, 1890*f*
cystic dysplasia of, 1891–1892, 1891*f*
cysts of, solitary simple, 1901–1902
detorsion of, 1895
hematomas of, 1897–1898
Henoch-Schönlein purpura and, 1899
hyperemia of, 1896
infarction of, 1895
newborn, 1888, 1889*f*
ovotestis and, 1891, 1891*f*
postpubertal, 1888–1890, 1889*f*
rete, tubular ectasia of, 1891–1892, 1892*f*
rupture of, 1897–1898, 1898*f*
smaller than normal, 1891
torsion of, 1870, 1892–1899, 1893*f*–1894*f*, 1894*b*, 1896*b*
undescended, right, 1890, 1890*f*
rete, 819
tubular ectasia of, 829–830, 830*f*, 1891–1892, 1892*f*
rupture of, 848, 850*f*
seminomas in, 823, 823*f*–824*f*
septula, 819, 820*f*
splenogonadal fusion and, 833
supernumerary, 838–839, 841*f*
torsion knot and, 844, 845*f*
trauma to, 847–851, 850*f*
tumors of, 822–834
choriocarcinoma as, 824, 825*f*, 1899
classification of, 822*b*
embryonal carcinoma as, 823, 825*f*, 1899
endodermal sinus, 823–824, 825*f*, 1899
germ cell, 822–825, 822*b*, 825*f*–826*f*
gonadal stromal, 826, 827*f*
Leydig cell, 826, 827*f*
malignant, 822–826
markers of, 822

Testis(es) *(Continued)*
metastatic, 822*b*
mixed germ cell, 822–823, 822*b*, 825*f*
non-germ cell, 825–826
nonseminomatous germ cell, 822*b*, 823–824, 825*f*
pediatric, 1899–1902
regressed germ cell, 824–825, 825*f*–826*f*
Sertoli cell, 826, 827*f*
sex cord-stromal, 825–826, 827*f*
stromal, 822, 822*b*
teratocarcinomas as, 1899
teratomas as, 823–824, 825*f*, 1899
yolk sac, 823–824, 825*f*
undescended, 851, 851*f*
dysplastic gonads and, 1899
in prune belly syndrome, 1361–1362
right, pediatric, 1890, 1890*f*
Testosterone, Leydig cells and secretion of, 819
Tethered cord, 1674
in diastematomyelia, 1236*f*
fetal cloacal exstrophy and, 1328
pediatric, 1678–1679, 1681*f*
spina bifida occulta and, 1226
Tetralogy of Fallot (TOF), 1288, 1288*f*
Tetraphocomelia, Roberts syndrome and, 1401
TGA. *See* Transposition of great arteries
TGC. *See* Time gain compensation
Thalamostriate vessels, mineralization of, 1203, 1204*f*
Thalamus
fetal, normal sonographic appearance of, 1168
neonatal/infant, sagittal imaging of, 1515, 1517*f*
vasculopathy of, neonatal/infant brain and, 1556–1557
α-Thalassemia, nonimmune hydrops from, 1423, 1431
Thanatophoric dysplasia
bowing of long bones in, 1381–1382
campomelic dysplasia differentiated from, 1388–1389
cloverleaf-shaped skull and, 1136, 1137*f*, 1389*f*
craniosynostosis in, 1136–1138, 1137*f*
diagnosis of, 1376–1377
homozygous achondroplasia differentiated from, 1389, 1389*f*
lethal skeletal dysplasia and, 1387–1390
megalencephaly associated with, 1194–1195
platyspondyly in, 1388–1389, 1390*f*
sonographic appearance of, 1380*f*
type 1, 1388–1389
type 2, 1388–1389, 1389*f*
Thanatophoric skeletal dysplasia, cortical malformations and, 1193–1194
Theca externa, 1049
Theca lutein cysts, 570, 572
pediatric, 1875
Thecomas, ovarian, 585
Thelarche, pseudoprecocious puberty and, 1888
Thermal effects, in ultrasound, 31. *See also* Bioeffects, thermal
obstetric, 1036–1038
Thermal index (TI), 38–40, 38*b*
for bone, in late pregnancy, 1039
obstetric sonography duration as function of, 1035–1036, 1036*f*, 1042*t*
for soft tissue, in early pregnancy, 1039
tissue model of
with bone at focus, 39
with bone at surface, 39–40
homogeneous, 39
Thigh graft, hemodialysis and, preoperative mapping for, 1000, 1001*f*

Thoracentesis, pediatric, ultrasound-guided, 1725–1726
Thoracic ectopia cordis, 1295, 1296*f*
Thoracic kidney, 318
Thoracic outlet syndrome, in upper extremity peripheral arteries, 976–977, 980*f*
Thoracoabdominal ectopia cordis, 1295
Thoracoabdominal schisis, 1401
Thorax, fetal
anomalies of, hydrops from, 1425–1427, 1427*f*
circumference and length of
gestational age correlated with, 1247*t*
pulmonary hypoplasia and, 1382, 1384*f*
circumference of, decreased
in hypophosphatasia, 1392
severe micromelia with, 1387*t*
echogenic lesions of, differential diagnosis of, 1248*t*
Thorotrast, 123
Three-dimensional (3-D) ultrasound, 15, 16*f*
for breast lesions, 773
for fetal heart assessment, 1277
for fetal spine, 1216, 1221–1223
for neonatal/infant brain imaging, 1518
in placental volume assessment, 1466, 1468*f*
for prostate cancer, 406–407
for skeletal dysplasia evaluation, 1384, 1385*f*
for uterus, 529
Threshold level, for seeing gestational sac, 1056
Thrill, from carotid stenosis, color Doppler, 933
Thrombocytopenia, alloimmune, intracranial hemorrhage and, 1206
Thrombocytopenia–absent radius syndrome, 1401, 1402*f*
Thrombophlebitis, ovarian vein, 589–590, 589*f*
Thrombosis. *See also* Deep venous thrombosis
cerebral sinovenous, 1547–1548
dural sinus
fetal, 1205–1206, 1206*f*
neonatal/infant, 1585
hepatic artery, after liver transplantation, 627, 628*f*, 631, 633*f*
hepatic vein, pediatric, suprahepatic portal hypertension and, 1763, 1763*f*
IJV, 955–956, 956*f*–957*f*
central line placement causing, 1658, 1661*f*
of iliac veins, 459–460, 459*f*–461*f*
detection difficulties with, 988, 988*f*
of IVC, 459–460
after liver transplantation, 636–637, 642*f*, 1766, 1769*f*–1770*f*
ovarian vein, 369, 589–590, 589*f*
after pancreas transplantation, 677–678, 678*f*–679*f*
portal vein, 98, 99*f*–100*f*
chronic pancreatitis and, 232–233, 235*f*
from HCC, 120, 121*f*
after liver transplantation, 635–636, 639*f*–640*f*, 1766
malignant, 98, 99*f*
pediatric, 1757, 1757*b*
renal artery, after renal transplantation, 653–655, 657*f*
Doppler assessment of, pediatric, 1807–1809, 1808*f*
renal vein, 369, 370*f*
Doppler assessment of, pediatric, 1809
hyperechogenic kidneys and, 1351
pediatric, acute, Doppler assessment of, 1804–1805, 1804*b*, 1804*f*
after renal transplantation, 658, 662*f*
round ligament, simulating groin hernia, 500, 501*f*

Thrombosis *(Continued)*
of splenic vein
acute pancreatitis complicated by, 230, 231*f*
chronic pancreatitis and, 232–233, 234*f*–235*f*
SVC, pediatric, 1721, 1721*b*, 1722*f*
vascular, pediatric chest and, 1716–1721, 1721*f*–1723*f*
Thumb
aplastic or hypoplastic, in Fanconi pancytopenia, 1400, 1402*f*
hitchhiker
in diastrophic dwarfism, 1382, 1406
diastrophic dysplasia and, 1398, 1398*f*
triphalangeal, in Aase syndrome, 1401
Thump artifacts, 60
Thymic cyst, 1652, 1653*f*, 1723–1724
Thymic index, 1723, 1725*f*
formula for calculation of, 1724*t*
normal, for children under 2, 1726*t*
Thymopharyngeal ducts, formation of, 1652
Thymus
fetal, normal appearance of, 1244*f*
pediatric
benign abnormalities of, 1723–1724
cervical ectopic, 1723
ectopic, 1652, 1653*f*
mediastinal masses and abnormal location of, 1723
normal, blood vessels of chest and, 1716–1721, 1721*f*
superior herniation of, 1723
Thyroglossal duct cysts, pediatric, 1640, 1643, 1644*f*–1645*f*
Thyroid artery, superior, 918
Thyroid gland. *See also* Thyroiditis
adenomas of, 697, 700*f*
anatomy of, 692–694, 692*f*
aplasia of, 694, 694*f*
carcinoma of, 695, 698–708
anaplastic, 707–708, 708*b*, 709*f*
follicular, 701, 701*b*, 706*f*–707*f*, 1648
incidence of, 722, 722*f*–723*f*
medullary, 701–707, 707*f*–708*f*, 1648
papillary, 698–701, 701*f*–705*f*, 713, 1648, 1649*f*
papillary microcarcinoma, 701, 706*f*
CEUS for assessment of, 692, 714–715
congenital abnormalities of, 694, 694*f*
cysts, calcifications of, 695
diffuse disease of, 723–728, 723*b*
adenomatous goiter as, 727
Graves disease and, 727, 727*f*, 1646, 1646*f*
ectopic, 694
elastography for assessment of, 692, 714–715, 715*f*–716*f*
ethanol injection for nodular disease of
for autonomously functioning nodules, 719–720
for benign cystic lesions, 719, 719*f*
for solitary solid benign "cold" nodules, 720
fetal, normal sonographic appearance of, 1136*f*
hypoplasia of, 694, 694*f*
incidentally detected nodule and, 720–723, 722*f*–723*f*, 723*b*
instrumentation for, 691–692, 692*f*
lingual, pediatric, 1639
lobes of, 692
lymphoma of, 708–709, 709*f*
metastases to, 709, 710*f*
nodular disease of, 694–723
adenomas in, 697, 700*f*
carcinoma in, 698–708
fine-needle aspiration biopsy in, 709–710, 710*t*, 722
hyperplasia and goiter in, 695–697, 695*f*–699*f*
Thyroid gland *(Continued)*
lymphoma in, 708–709, 709*f*, 1648
metastases in, 709, 710*f*
parathyroid adenomas confused with, 745–746
pathologic features of, 695–709
sonographic correlates of, 695–709
sonographic evaluation of, 695*b*
pediatric
cancer of, 1648, 1648*b*, 1649*f*
congenital lesions of, 1642–1643
cysts of, 1646, 1647*f*
dimensions of, normal, 1642*t*
dysgenesis of, 1642–1643
ectopic, 1642–1643, 1644*f*
follicular adenoma of, 1646–1648, 1647*f*
hemiagenesis of, 1642–1643, 1643*f*
hemorrhage in, 1646, 1647*f*
inflammatory disease of, 1643–1646, 1645*f*–1646*f*
isthmus of, 1640–1642
lobes of, normal thickness of, 1643*t*
masses of, 1646–1648, 1647*f*–1649*f*, 1648*b*
normal anatomy of, 1640–1642, 1642*f*, 1642*t*–1643*t*
pseudonodule of, 1646
pyramidal lobe of, 1640–1642
retrosternal, 1723
volume of, normal, 1643*t*
sonographic applications in, 710–720
for benign and malignant nodule differentiation, 696*f*–699*f*, 712–714, 712*t*
CEUS for, 692, 714–715
elastography for, 692, 714–715, 715*f*–716*f*
incidentally detected nodule and, 720–723, 722*f*–723*f*, 723*b*
needle biopsy guidance for, 715–720, 718*f*–719*f*, 721*f*
for thyroid mass detection, 710–712, 711*f*–712*f*
TIRADS for, 714
sonographic technique for, 691–692, 692*f*
vascularity of, 693, 694*f*
volume of, measuring, 692–693, 693*f*
Thyroid Imaging Reporting and Data System (TIRADS), 714
Thyroid inferno, in Graves disease, 727, 727*f*
Thyroiditis, 723*b*
acute suppurative, 723–724
chronic autoimmune lymphocytic, 724, 725*f*–727*f*
de Quervain, 1645
focal, pediatric, 1645
Hashimoto, 724, 725*f*–727*f*
fetal goiter and, 1159–1163
pediatric, 1645, 1646*f*
invasive fibrous, 727–728, 728*f*
painless (silent), 725–727
subacute granulomatous, 724, 724*f*
Thyromegaly, fetal, 1159–1163
TI. *See* Thermal index
TIA. *See* Transient ischemic attack
TIB. *See* Thermal index for bone
Tibia, dislocation of, pediatric, 1934*f*
Tibial artery
anterior, 966
normal appearance of, 966–967
posterior, 966
sonographic technique for, 967
Tibial hemimelia, pediatric, 1933
Tibial tendons, posterior, injection of, 902, 903*f*
Tibial veins
anterior, 981, 981*f*
posterior, 981, 981*f*
Tibioperoneal trunk, 966, 981
Time gain compensation (TGC)
artifacts and settings of, 19–21
control of, 8–9, 8*f*
output control and, 50
Time-averaged mean of maximum (TAMM) velocity, 1593, 1605–1606
Time-averaged peak velocity, 1593
"Tip of the iceberg" sign, 582–583
TIPS. *See* Transjugular intrahepatic portosystemic shunts
TIRADS. *See* Thyroid Imaging Reporting and Data System
TIS. *See* Thermal index for soft tissue
Tissue harmonic imaging, 13, 13*f*–14*f*, 38, 61–62
Tissue heating
spatial focusing and, 35
temporal considerations in, 36, 36*f*
tissue type and, 36, 36*f*
Tissue plasminogen activator (TPA), 1622
Tissue vibration artifact, 973–974, 974*f*
T-lymphotropic virus, 1203–1204
TMPRSS2:ERG test, 396
Tobacco, fetal gastroschisis and, 1322–1323
Toe polydactyly, fetal, 1406*f*
Toes, sandal, 1406*f*, 1407
TOF. *See* Tetralogy of Fallot
Tongue, fetal, abnormally enlarged, 1153, 1153*b*, 1158*f*
TORCH infections, 1203–1204
neonatal/infant brain and, 1511, 1558
Torsion, testicular. *See* Testicular torsion
Torsion knot, 844, 845*f*
Toxemia, pediatric pregnancy and, 1884
Toxoplasmosis
fetal brain and, 1204
fetal hydrops from, 1432
prenatal, neonatal/infant brain and, 1558–1560
TPA. *See* Tissue plasminogen activator
Trabecula septomarginalis, moderator band of, 1274–1275
Trachea, fetal, CHAOS and, 1253
Tracheal webs, fetal, CHAOS and, 1253
Tracheoesophageal fistula, fetal
CHAOS and, 1254–1255
esophageal atresia and, 1305
Transabdominal scanning, for placenta previa, 1469
Transabdominal sonography (TAS), for pelvis, 564
Trans-Atlantic Inter-Society Consensus (TASC), 970
Transcranial Doppler (TCD) sonography
adult
functional, 1622
indications for, 1598–1623, 1598*b*
vasospasm and, 1608–1610, 1610*t*
for carotid artery examination, 948–950, 950*f*
pediatric
ACA collateral flow evaluation and, 1610, 1611*f*
angle correction for, 1607
asphyxia and, 1614, 1616*f*
AVM detection with, 1614, 1615*f*
brain death and, 1618–1620, 1618*b*, 1619*f*–1620*f*
in cardiopulmonary bypass, 1621–1622
in CEA, 1621
cerebral edema and, 1614, 1617*f*
contrast enhancement for, 1597
ECMO monitoring with, 1622
equipment types for, 1591–1592
factors changing indices in, 1612*t*
foramen magnum approach for, 1592, 1595*f*
functional, 1622
headaches and, 1610–1611, 1612*f*
hydrocephalus and, 1611–1614, 1613*f*
hyperventilation therapy and, 1614

Transcranial Doppler (TCD) sonography *(Continued)*
indications for, 1598–1623, 1598*b*
in intraoperative neuroradiologic procedures, 1620–1622, 1621*f*–1622*f*
limitations for, 1597, 1597*t*
orbital approach for, 1592, 1596*f*
pitfalls in, 1597, 1597*t*
power settings for, 1597
right-to-left shunt evaluation with, 1614–1618
for SCD, 1591, 1598–1608, 1599*b*, 1599*f*–1608*f*
sleep apnea and, 1611
submandibular approach for, 1592–1593
technique for, 1592–1596
TPA and, 1622
transtemporal approach for, 1592, 1593*f*–1594*f*
vascular malformations and, 1614, 1615*f*
vasospasm and, 1608–1610, 1609*f*, 1610*t*
velocity evaluation in, 1593, 1595–1596
Transducer(s), 7–8
arrays, 11–12, 12*f*
hand-held, for breast sonography, 788, 789*f*–790*f*
heating, in obstetric sonography, 1038
heeling and toeing of, 768
in interventional sonography, pediatric, 1943
locating needle after insertion and, 1946–1947, 1947*f*
for neonatal/infant brain imaging, 1512
output control and, 50
percutaneous needle biopsies and sterilization of, 600
second harmonic and, 105
selection of, 12
for obstetric sonography, 1035
Transfundal pressure, dynamic cervical change and, 1501–1503
Transfusion, fetomaternal, maternal serum alpha-fetoprotein elevation in, 1228. *See also* Twin-twin transfusion syndrome
Transhepatic cholangiography, 614–615
Transient double-bubble sign, 1309
Transient elastography, 1764
Transient ischemic attack (TIA), 916
carotid artery embolism causing, 919
Transitional cell carcinoma (TCC)
bladder, 347–348, 350*f*
genitourinary tract tumors and, 346–348
nonpapillary, 346
ovarian, 581–582, 582*f*
papillary, 346
renal, 346–347, 346*f*–349*f*
synchronous, 346
ureteral, 347
Transitional cell papilloma, lower urinary tract, pediatric, 1910–1912
Transjugular intrahepatic portosystemic shunts (TIPS), 131–132, 132*b*, 132*f*–133*f*, 463, 1764
Translabial ultrasound
of cervix, 1497
of female urethra, 315, 316*f*
Transmediastinal artery, 820*f*, 821
Transmitter, 7
Transorbital approach, for duplex Doppler ultrasound of neonatal/infant brain, 1574, 1575*f*
Transperineal biopsy, TRUS-guided, 411
Transperineal scanning, in Crohn disease, 276
Transperineal ultrasound
cervix in, 1497, 1497*f*
in ureteral calculi detection, 337
Transplantation, organ, 623–624. *See also* Liver transplantation; Pancreas transplantation; Posttransplant lymphoproliferative disorder; Renal transplantation
Transposition of great arteries (TGA), 1289–1290, 1289*f*–1290*f*
Transrectal ultrasound (TRUS)
biopsy guided by, 407–411, 408*f*
analgesia and, 407
antibiotic prophylaxis and, 407, 408*f*
anticoagulation and, 407–408
bowel preparation and, 407
indications and sampling for, 409, 409*b*, 410*f*
in men with absent anus, 411
mpMRI-TRUS fusion, 410–411
other applications of, 411–412
preparation for, 407–408
after radical prostatectomy, 411, 411*f*
side effects and complications in, 409
technique for, 408–409, 408*f*
transperineal, 411
brachytherapy guided by, 401, 402*f*
for drainage of pelvic abscesses, 612
for hematospermia, 394
infertility and, 392–394, 393*f*
of male urethra, 315, 316*f*
probes for, 386–387, 386*f*
of prostate, 381–382
prostate cancer, mpMRI fusion with, 406–407, 410–411
prostate cancer and, 302, 302*f*, 403–406, 403*f*–405*f*, 406*b*
in rectal carcinoma staging, 301
rectal cleansing prior to, 387
Transtemporal window
for TCD sonography, 1592, 1593*f*–1594*f*
for transcranial Doppler sonography, 948
Transurethral resection of ejaculatory ducts, 393
Transurethral resection of prostate (TURP), 385*f*–386*f*, 388
Transvaginal sonography, in peritoneal disease evaluation, 506, 506*f*–507*f*
Transvaginal ultrasound
for acute appendicitis diagnosis, 283, 285*f*
for adnexa assessment, 566
cervical abnormal findings on, 1503*b*
for cervix, 1497–1498, 1497*f*–1498*f*
diagnostic value of, 258
for drainage of pelvic abscesses, 612, 613*f*
endometrial thickness assessment with, 545–546
in gestational sac identification, 1054–1055
for pediatric pelvis, 1870–1871
for placenta previa, 1469
in pregnancy, safety of, 1049
thermal effects of, 38
in ureteral calculi detection, 337, 338*f*
for uterus, 529, 529*b*
in yolk sac identification, 1057
Transventricular valvotomy, 1292
Transverse abdominis tendon, torn, in spigelian hernia, 483–484, 487*f*
Transverse mesocolon, 219, 220*f*
Transverse myelitis, pediatric, neurogenic bladder in, 1907
Transverse testicular ectopia, 1890
Transverse waves, 2–3
TRAP. *See* Twin reversed arterial perfusion
Trauma
biliary, hemobilia from, 174, 175*f*
bladder, 366
cervical, carotid artery damage from, 946, 948*f*
dural sinus thrombosis from, 1205–1206
focused abdominal sonography for, 508
to genitourinary tract, 365–366
Trauma *(Continued)*
to liver, 129–132, 131*f*
to lower urinary tract, pediatric, 1912
to musculoskeletal system pediatric, 1938–1939, 1939*f*
pediatric
epididymitis following, 1897
scrotum and, 1897–1898, 1898*f*
renal, 365–366, 366*f*
scrotal, 847–851, 850*f*
splenic, 158, 159*f*–160*f*
testicular, 847–851, 850*f*
ureteral, 366
Treacher Collins syndrome
clefts of secondary palate in, 1153
midface hypoplasia in, 1148
Triangular cord sign, in biliary atresia, 1734–1735, 1737, 1738*f*
Trichobezoars, 300, 1840, 1841*f*
Tricuspid atresia
fetal, hydrops from, 1423–1424
hypoplastic right ventricle with, 1287
Tricuspid insufficiency, fetal, spectral Doppler assessment of, 1281*f*
Tricuspid regurgitation
in aneuploidy screening, 1095
in Ebstein anomaly, 1286
neonatal/infant, cardiac pulsations in veins and, 1578, 1578*f*
"Trident hand" configuration, achondroplasia and, 1407, 1408*f*
Triggered imaging, 65
Trigone, 314
neonatal/infant, in coronal imaging, 1515
pediatric, identification of, 1871, 1872*f*
Triorchidism, 1891
Triphalangeal thumb, in Aase syndrome, 1401
Triphasic waveform, 966–967
Triplets, amnionicity and chorionicity and, 1122*f*
Triploid karyotype, partial molar pregnancy and, 1078
Triploidy, 1078
common sonographic findings in, 1104–1106, 1104*b*, 1105*f*
Dandy-Walker malformation in, 1105*f*
fetal hydrops from, 1429–1430
IUGR in, 1105*f*
omphalocele in, 1105*f*
ovarian cysts in, 1105*f*
skeletal findings in, 1408–1409
syndactyly of fingers in, 1105*f*, 1406
Triradiate cartilage
of hip, 1923
in sonogram of hip from transverse/neutral view, 1927
Trisomy 9, horseshoe kidney in, 1345–1346
Trisomy 13 (Patau syndrome)
common sonographic findings in, 1104, 1104*b*, 1105*f*
facial clefts in, 1151
fetal hydrops from, 1429–1430
fetal omphalocele and, 1325
fetal pentalogy of Cantrell and, 1329
HPE in, 1104, 1105*f*
hyperechogenic kidneys in, 1351
NT in, 1093
polydactyly in, 1104, 1105*f*
proboscis in, 1104, 1105*f*
skeletal findings with, 1408, 1408*b*
umbilical cord cysts in, 1483
Trisomy 17, biliary atresia and, 1737
Trisomy 18 (Edwards syndrome)
biliary atresia and, 1737
CDH and, 1263

Trisomy 18 (Edwards syndrome) *(Continued)*
choroid plexus cyst in, 1103*f*, 1104
clenched hands in, 1103, 1103*f*
common sonographic findings in, 1103–1104, 1103*b*, 1103*f*
congenital heart defects in, 1103
ectopia cordis and, fetal, 1329
facial clefts in, 1151
fetal hydrops from, 1429–1430
fetal pentalogy of Cantrell and, 1329
horseshoe kidney in, 1345–1346
hydrocephalus in, 1103
IUGR and, 1104
mega-cisterna magna and, 1168–1169
NT in, 1093
omphalocele in, 1103, 1103*f*
fetal, 1325
polyhydramnios in, 1104
skeletal findings with, 1408, 1408*b*
umbilical cord cysts in, 1103*f*, 1483
Trisomy 21 (Down syndrome)
absent nasal bone in, 1150
adjunct features of, 1101
A-V canal, 1098*f*
AVSD and, 1101, 1284
β-hCG concentration in, 1089–1090
choroid plexus cysts and, 1101
congenital heart defects in, 1097, 1098*f*
duodenal atresia in, 1097, 1098*f*
ear length in, 1101
echogenic bowel in, 1100*f*, 1101
echogenic intracardiac focus in, 1100*f*, 1101
femur length in, 1100–1101
fetal hepatomegaly and, 1316
fetal hydrops from, 1429–1430
frontothalamic distance in, 1101
genetic sonography in, 1102–1103
humerus length in, 1101
hypoplasia of middle phalanx in, 1101
iliac angle measurements in, 1101
macroglossia in, 1153
markers in, 1097
cluster of, likelihood ratios of, 1098*t*
combined, 1100*t*, 1101–1103
common second-trimester, 1099*b*
isolated, likelihood ratios of, 1097*t*
midface hypoplasia in, 1148
nasal bone in, 1099–1100, 1099*f*
NT in, 1089, 1090*f*
nuchal fold in, 1097–1099, 1099*f*, 1154–1159
prevalence of, 1088–1089
risk for, short femur indicating, 1381
risk ratio for, revised, 1102*b*
screening for, second-trimester, 1097–1103, 1098*f*
skeletal findings with, 1408, 1408*b*
structural anomalies in, 1101
urinary tract dilation in, 1100*f*, 1101
VM in, 1098*f*
VSDs in, 1098*f*, 1101
wormian bones in, 1139
Trocar technique, for drainage catheter placement, 611, 611*f*
Trophoblastic blood flow, 1083
Trophoblastic tumor, placental-site, 1082
True hermaphroditism, pediatric, 1891, 1899
Truncal artery, 1288
Truncal valve, 1288
Truncus arteriosus, 1288, 1289*f*
Trunk, length of, shortened, in achondrogenesis, 1391
TRUS. *See* Transrectal ultrasound
TSC. *See* Tuberous sclerosis
T-shaped uterus, 1881
TTT. *See* Twin-twin transfusion syndrome
Tubal occlusion devices, 553*f*, 554
Tubal ring, ectopic, 1072, 1073*f*
Tuberculosis
of adrenal glands, 423
epididymitis associated with, 841, 843*f*
spleen and, 150, 151*f*–152*f*
urinary tract, 329–330, 330*f*
Tuberculosis colitis, 287–288
Tuberculous peritonitis, 517–521, 522*f*
Tuberous sclerosis (TSC)
angiomyolipoma and, 351
cardiac rhabdomyomas and, 1293, 1424
fetal brain and, 1198, 1200*f*
hemimegalencephaly associated with, 1195
pediatric, renal cysts in, 1816, 1817*f*
pheochromocytomas with, 1826, 1910–1912
prenatal intracranial tumors in, 1208
renal cysts in, 364–365, 365*f*
Tubo-ovarian abscess, in pelvic inflammatory disease, 588–589, 588*f*, 1886–1887, 1886*f*
Tubo-ovarian complex, in pelvic inflammatory disease, 588–589, 588*f*, 1886–1887, 1886*f*
Tubular ectasia, 359
of rete testis, 829–830, 830*f*
pediatric, 1891–1892, 1892*f*
Tubular necrosis, acute, 370
acute kidney injury and, 1795–1796, 1797*f*
renal transplantation complication with, 649–651, 653*f*, 1809
Tubuli recti, 819
Tubulointerstitial fibrosis, 359
Tumefactive chronic pancreatitis, 236
Tumefactive sludge, 195, 196*f*, 1741
Tunica albuginea
ovarian, 565
testicular, 819, 819*f*–820*f*
cysts of, 829, 830*f*
pediatric, 1888
Tunica vaginalis, 819, 819*f*
cysts of, 829, 830*f*
pediatric, 1902–1903
pathologic lesions of, 834–836, 835*f*
pediatric, 1902
Tunica var, 819
Tunica vasculosa, 821
Turner syndrome (monosomy X)
anasarca in fetus with, 1417, 1420*f*
cystic hygromas in, 1106–1107, 1106*f*
fetal hydrops from, 1429–1430, 1430*f*
horseshoe kidney in, 1345–1346
lymphatic malformation in, 1159
midface hypoplasia in, 1148
primary amenorrhea in, 1887
small aorta in, 1106*f*, 1107
sonographic findings in, 1106–1107, 1106*f*
TURP. *See* Transurethral resection of prostate
Turribrachycephaly, 1138*f*
Twin anemia polycythemia sequence (TAPS), 1126–1127
"Twin peak" sign, 1119, 1119*t*, 1120*f*
Twin pregnancies, skeletal abnormalities in, 1384
Twin reversed arterial perfusion (TRAP), 1127–1129, 1127*f*–1128*f*, 1429
Twinkling artifacts
bezoars and, 1840
mimicking AVMs after renal transplantation, 662–664, 668*f*
renal calculi indicated by, 336, 337*f*
urolithiasis and, 1799–1801, 1799*f*
Twin(s)
acardiac, hydrops and, 1429
aneuploidy screening for, 1091
congenital malformation of, 1123
conjoined, 1115–1116
complications with, 1129–1130, 1130*f*
Twin(s) *(Continued)*
dichorionic diamniotic, 1019*f*, 1115–1116, 1116*f*
growth discrepancy in, 1123*f*
placental findings in, 1119
sonographic findings of, chorionicity and, 1119, 1120*f*
dizygotic, 1115–1116, 1116*f*
growth discrepancy in, 1123, 1123*f*
hydrops in, 1429, 1429*f*
IUFD and, 1123–1125, 1124*f*
monochorionic diamniotic, 1019*f*, 1058*f*, 1115–1116, 1116*f*
CHD risk with, 1270–1273
complications of, 1125–1129
growth discrepancy in, 1123*f*
IUFD and, 1124*f*
sonographic findings of, chorionicity and, 1119, 1121*f*
TAPS complications with, 1126–1127
TRAP and, 1127–1129, 1127*f*–1128*f*
TTTS complications and, 1125–1126, 1125*t*, 1126*f*
monochorionic monoamniotic, 1057, 1115–1116, 1116*f*
complications of, 1125–1129, 1129*f*
conjoined twins as, 1130*f*
IUFD and, 1124*f*
sonographic findings of, chorionicity and, 1119, 1121*f*
TAPS complications with, 1126–1127
TRAP and, 1127–1129, 1127*f*–1128*f*
TTTS complications and, 1125–1126, 1125*t*, 1126*f*
at 12 weeks, 1129*f*
at 28 weeks, 1129*f*
monozygotic, 1115, 1116*f*
vanishing, 1117
Twin-twin transfusion syndrome (TTTS), 1203
advanced, 1125–1126, 1126*f*
complications of, 1125–1126, 1125*t*, 1126*f*
early identification of, 1125, 1126*f*
hydrops from, 1429, 1429*f*
pulmonic stenosis and, 1292
staging system for, 1125*t*
2-D echocardiography, 10
Two-dimensional array transducers, 12, 12*f*
Typhlitis, acute, 287–288, 289*f*
Tyrosinemia
GSD and, 1740*f*
management of, 1738
staghorn calculus and, 1799, 1800*f*

U

Uhl anomaly, 1286
UKCTOCS. *See* United Kingdom Collaborative Trial of Ovarian Cancer Screening
Ulcer craters, in plaque ulceration, 923, 924*f*
Ulcerative colitis, 266–267
Ulcer(s)
duodenal, perforated, gallbladder wall thickening signs in, 201*f*
gastric, pediatric, 1839–1840, 1840*f*
penetrating, in abdominal aorta, 441, 444*f*
peptic, 299, 300*f*
Ulnar nerve, dislocation of, at elbow, 865–866, 866*f*
Ulnar ray defects, 1399
Ulnar veins, normal anatomy of, 990–991
Ultrasound speckle, 4, 5*f*
Umbilical artery(ies), 1059
aneurysms of, 1483
fetal assessment of, Doppler ultrasound for, 1458, 1459*f*
fetal cloacal exstrophy and single, 1328
single, 1484, 1484*f*
spontaneous rupture of, 1483
Umbilical coiling index, twisting of, 1482, 1482*f*

Umbilical cord, 1481–1487
  abnormalities of, in monochorionic twins, 1119
  appearance of, 1481–1484
  cysts of, 1483, 1483*f*
    sonographic appearance of, 1061, 1061*f*
    in trisomy 18, 1103*f*
  diameter of, 1482
  edematous, 1484*f*
  entangled, chorionicity and, 1119, 1121*f*
  excessive length of, 1481
  fetal, amniotic band syndrome and, 1330
  funic presentation of, 1485–1487, 1489*f*
  hemangiomas of, 1483
  insertion of
    marginal, 1484–1485, 1487*f*
    into placenta, 1484, 1485*f*
    velamentous, 1119, 1122*f*, 1484–1485, 1486*f*
  knots of, true, 1482–1483
  normal sonographic appearance of, 1059–1061
  nuchal, 1483–1484
  prolapse of, fetal hydrops and, 1436
  pseudocysts of, 1483, 1484*f*
  routine sonographic views of, 1021, 1029*f*
  short, 1481
  size of, 1481–1484
  tumors of, 1483
  twisting of, 1482
    absent, 1482, 1482*f*
  vasa previa and, 1485–1487, 1488*f*–1489*f*
Umbilical hernias, 491–492, 492*f*–493*f*
Umbilical veins, 1059
  pediatric, recanalized, in portal hypertension, 1758*f*
Uncinate process, pancreatic head and, 212, 213*f*
Undescended testis, 851, 851*f*
  right, pediatric, 1890, 1890*f*
Unfused amnion, 1057
Unicornuate uterus, 536*f*–537*f*, 538, 1881
United Kingdom Collaborative Trial of Ovarian Cancer Screening (UKCTOCS), 578
Univentricular heart, 1287–1288, 1287*f*
UPJ obstruction. *See* Ureteropelvic junction obstruction
Upright positioning, for dynamic ultrasound of hernias, 474
Urachal sinus, pediatric, 1907–1908, 1909*f*
Urachus, 1337*f*, 1338
  adenocarcinomas of, 355
  in bladder development, 311, 312*f*
  cysts of, 322, 323*f*
    ovarian cysts differentiated from, 1369
    pediatric, 1907–1908, 1909*f*
    pediatric hydronephrosis and, 1791, 1792*f*–1793*f*
    pediatric ovarian cysts differentiated from, 1875
  diverticula of, 322, 323*f*
    pediatric, 1907–1908, 1909*f*
  patent, 322
    pediatric, 1791
  pediatric
    cysts of, 1907–1908, 1909*f*
    diverticula of, 1907–1908, 1909*f*
    patent, 1907–1908, 1909*f*
    remnant of, normal, 1871
    sinus of, 1791
  sinus of, 322, 323*f*
    pediatric, 1791
Ureteral bud
  congenital anomalies related to, 318–321
    congenital megacalices and, 321
    congenital megaureter and, 321, 322*f*
    duplex collecting system and, 319, 320*f*
Ureteral bud *(Continued)*
    renal agenesis and, 318–319
    supernumerary kidneys and, 319
    UPJ obstruction and, 321, 321*f*
    ureteroceles and, 310, 319, 321*f*
  in kidney development, 311, 312*f*
Ureteral jets, color Doppler ultrasound for, 1781*f*
Ureteral reflux, bladder augmentation and, 1912–1913
Ureteral reimplantation, pediatric, 1912, 1913*f*
Ureteric bud, 1336–1338
Ureteric jets, pediatric, 1781*f*, 1906–1907
Ureterocele(s)
  congenital anomalies related to, 310, 319, 321*f*
  fetal, in duplication anomalies, 1359–1360, 1359*f*, 1360*b*
  pediatric
    in duplication anomalies, 1783–1784, 1784*f*
    ectopic, 1904–1905, 1905*f*
Ureteropelvic junction (UPJ) obstruction, 318
  congenital anomalies related to, 321, 321*f*
  fetal
    hydronephrosis from, 1358, 1358*f*
    perirenal urinomas from, 1358, 1358*f*
  pediatric, hydronephrosis and, 1786, 1787*f*
  VUR with, 1360
Ureterovesical junction obstruction, pediatric, 1906–1907, 1907*f*
Ureter(s)
  adenocarcinoma of, 348
  anastomosis of, in renal transplantation, 643, 648*f*
  anatomy of, 313*f*, 314
  atretic, with MCDK, 1346
  calculi in, 325, 325*f*, 337–338, 338*f*–339*f*
    bladder augmentation and, 1912–1913
    complicating renal transplantation, 659–660, 663*f*–664*f*
  congenital megaureter and, 321, 322*f*
  development of, 311, 312*f*
  distal, dilated, 592
  lymphomas of, 353
  metastases to, 354
  obstruction of, renal transplantation complications from, 659–660, 663*f*–664*f*
  pediatric, 1906–1907, 1907*f*–1908*f*
    duplication of, 1783–1784, 1784*f*, 1904–1905
    ectopic, 1904–1905
    ectopic insertion of, hydronephrosis and, 1788
    obstruction of, hydronephrosis and, 1786–1788, 1787*f*
    reimplantation of, 1912, 1913*f*
  retrocaval, 322
  sonographic technique for, 314
  squamous cell carcinoma of, 348
  transitional cell carcinoma of, 347
  trauma to, 366
Urethra
  development of, 311
    congenital anomalies of, 323, 323*f*
  diverticula of, 323, 323*f*
  fetal
    atresia, lower urinary tract obstruction from, 1361, 1361*f*
    megalourethra and atresia of, 1362
    obstruction of, renal pelvic dilation and, 1355–1356
  pediatric
    diverticulum of, anterior, bladder outlet obstruction from, 1906
    duplication of, bladder outlet obstruction from, 1906
    normal, 1872*f*
Urethra *(Continued)*
    polyp of, posterior, bladder outlet obstruction from, 1906, 1906*f*
  sonographic technique for, 315, 316*f*
Urethral valve(s)
  anterior, pediatric, bladder outlet obstruction from, 1906
  fetal
    lower urinary tract obstruction from, 1361, 1361*f*
    megalourethra and, 1362
  pediatric
    hydronephrosis and, 1788, 1789*f*
    posterior, 1905–1906, 1906*f*
Urinary diversion, evaluation after, 375, 375*f*
Urinary stasis, pediatric, 1799, 1800*f*
Urinary tract
  congenital anomalies of, 1336
  dilation of, in trisomy 21, 1100*f*, 1101
  echinococcal disease of, 331, 332*f*
  LUTS and, 387–388
  masses of, 592
  obstruction of, 387–388
  schistosomiasis of, 331
  tuberculosis of, 329–330, 330*f*
Urinary tract, fetal. *See also* Hydronephrosis
  abnormalities of, 1340–1366
    bilateral renal agenesis as, 1342–1344, 1343*f*–1344*f*, 1344*b*
    characterizing, 1341
    evaluation of, 1342*b*
    horseshoe kidney as, 1345–1346, 1345*f*
    MRI for diagnosing, 1342, 1342*f*
    prenatal diagnosis of, 1340, 1340*b*
    prevalence of, 1340
    renal cystic disease as, 1346–1352 (*See also* Kidneys, fetal, cystic disease of)
    renal ectopia as, 1344–1345, 1344*f*–1345*f*
    unilateral renal agenesis as, 1344
  embryology of, 1336–1338, 1337*f*
  lower, obstruction of, 1360–1363
    cloacal malformation and, 1363, 1363*f*
    cystoscopy for, 1363–1365
    hydrops from, 1428, 1429*f*
    from megacystis, 1360, 1360*b*, 1360*f*
    from megalourethra, 1362, 1362*f*
    MMIHS and, 1362–1363
    from posterior urethral valves, 1361, 1361*f*
    from prune belly syndrome, 1361–1362
    from urethral atresia, 1361, 1361*f*
    in utero intervention for, 1363–1365, 1364*f*, 1365*t*
    vesicoamniotic shunts for, 1363–1365, 1364*f*, 1365*t*
  normal, 1336–1340
  sonographic appearance of, 1338–1339, 1338*f*
  upper, dilation of, 1354–1360, 1354*f*–1355*f*, 1356*t*, 1357*f*
    duplication anomalies and, 1359–1360, 1359*f*, 1360*b*
    management of, 1356–1358
    UPJ obstruction and, 1358, 1358*f*
    vesicoureteral junction obstruction and, 1358–1359
    VUR and, 1360
Urinary tract, pediatric. *See also* Bladder, pediatric; Kidneys, pediatric
  calcification of, 1798–1801
    cortical nephrocalcinosis and, 1798, 1798*b*, 1798*f*
    dystrophic, 1799
    medullary nephrocalcinosis of, 1798–1799, 1799*f*

Urinary tract, pediatric *(Continued)*
renal vein thrombosis and, 1799, 1800*f*
urinary stasis and, 1799, 1800*f*
urolithiasis and, 1799–1801, 1799*f*
congenital anomalies of, 1783–1785
renal duplication as, 1783–1784, 1784*f*
dilation of, classification of, 1785–1786, 1786*f*
infection of, 1791–1794
cystitis and, 1794, 1796*f*–1797*f*, 1908, 1910*f*–1911*f*
jaundice in, 1738
neonatal candidiasis and, 1794, 1795*f*
pyelonephritis, acute, and, 1792–1793, 1793*f*–1794*f*
pyelonephritis, chronic, and, 1794, 1795*f*
lower, 1904–1913
congenital anomalies of, 1904–1906, 1905*f*–1907*f*
infection of, 1904–1905, 1908, 1910*f*–1911*f*
neoplasms of, 1908–1912, 1912*f*
trauma to, 1912
obstruction of, renal transplantation and, 1811
sonography of, 1776–1783
patient preparation for, 1776, 1776*t*
technique for, 1776–1781
Urinary tract dilation (UTD), 1785–1786, 1786*f*
Urine leak, renal transplantation and, 1810–1811
Urinoma(s)
bladder augmentation and, 1912–1913
pelvic, 591
perirenal, from UPJ obstruction, 1358, 1358*f*
after renal transplantation, 665, 672*f*
pediatric, 1809
Urogenital sinus, in bladder development, 311, 312*f*
Urolithiasis, pediatric calcification and, 1799–1801, 1799*f*
Uropathy
pediatric, obstructive, CKD and, 1796–1798
postnatal, pyelectasis as marker for, 1355
U.S. Preventive Services Task Force (USPSTF), 397, 434–435
U-shaped configuration, 1927, 1928*f*
UTD. *See* Urinary tract dilation
Uterine artery(ies), 528–529, 565–566, 565*f*
embolization of, for uterine fibroids, 540
pediatric, 1875
Uterine septum, circumvallate placenta confused with, 1479–1480, 1481*f*
Uterine synechia, circumvallate placenta confused with, 1479–1480, 1481*f*
Uterine veins, 531–532, 533*f*
Uterocervical anomalies, cervical assessment in, 1505
Utero-ovarian ligament, 565
Uterus. *See also* Cervix; Endometrium; Myometrium
accessory and cavitated mass of, 541
anatomy of, 528–530, 529*f*
sections in, 530
arcuate, 534, 536–538, 536*f*–537*f*
bicornuate, 534, 536*f*–537*f*, 538, 1881, 1881*f*
cervical abnormalities and, 541–544, 543*f*
DES exposure of, 534, 536*f*, 1881
didelphys, 534, 536*f*–537*f*, 1881
endometrial abnormalities and, 544–552
enlargement of, 538*b*
hypoplasia of, 538
isolated, primary amenorrhea in, 1887
leiomyomas of, 538–540, 539*f*, 540*b*
leiomyosarcomas of, 540, 541*f*
müllerian duct anomalies and, 529, 533–538, 537*f*
categories of, 534, 536*f*

Uterus *(Continued)*
myometrial abnormalities of, 538–541
neonatal, 1872–1873, 1873*f*
obstruction of, 546–547, 546*f*–547*f*
pediatric, 1872–1873
abnormalities of, 1881–1887
agenesis of, primary amenorrhea in, 1887
congenital anomalies of, 1881–1883
endocrine abnormalities and, 1887–1888
infection and, 1885–1887
neoplasms of, 1883–1884
PID and, 1885–1887, 1886*b*, 1886*f*
postpubertal, 1872–1873, 1873*t*
precocious puberty and, 1887–1888
pregnancy and, 1884–1885
prepubertal, 1872–1873, 1873*f*, 1873*t*
postpartum findings in, 554–557
AVMs and, 556, 556*f*
bleeding and, 554
after cesarean section, 556–557, 557*f*–558*f*
endometritis and, 555–556
normal, 554, 554*f*
placental site trophoblastic tumor and, 530–531
RPOC and, 554–555, 555*f*
pregnant
dehiscence or rupture of, assessing risk for, 1020
second-trimester scan of, 1020, 1021*f*
sarcomas of, 551
septate, 534–536, 536*f*–537*f*
size of, 531
sonographic techniques for, 528–530, 529*b*
IUDs and, 552–554, 553*f*
normal findings in, 530–533
positioning in, 530–531, 530*f*
tubal occlusion devices and, 553*f*, 554
sonohysterography for, 529
three-dimensional ultrasound for, 529
transvaginal ultrasound for, 529, 529*b*
T-shaped, 1881
unicornuate, 536*f*–537*f*, 538, 1881
Utricle cysts, prostatic, 391*f*, 392

V

VACTERL association, 1689
duodenal atresia and, 1308
fetal renal anomalies for, 1341
ribs in, 1382–1384
sacral agenesis in, 1237
VACTERL sequence, 1306, 1311
Vagina, 528–529
bleeding in, hydatidiform molar pregnancy and, 1078
pediatric, 1873
abnormalities of, 1881–1887
atretic, vaginal obstruction from, 1881
congenital anomalies of, 1881–1883
endocrine abnormalities and, 1887–1888
foreign bodies in, 1887
infection and, 1885–1887
neoplasms of, 1883–1884, 1883*f*
precocious puberty and, 1887–1888
pregnancy and, 1884–1885
stenotic, vaginal obstruction from, 1881
Peutz-Jeghers syndrome and watery discharge of, 544
Vaginal fornix, 528–529
Vaginal pessary, cervical incompetence and, 1507
Vaginal progesterone, 17α-OHPC compared to, 1507
Vaginal septum, 538
transverse, vaginal obstruction from, 1881
Vaginitis, pediatric, 1887

Vallecula
cysts, pediatric, 1640, 1641*f*
neonatal/infant, in mastoid fontanelle imaging, 1517–1518, 1519*f*
Valproic acid, NTDs from, 1218
Valsalva maneuver, 471, 992
for dynamic ultrasound of hernias
femoral, 472*f*, 483
inguinal, 473, 474*f*
Valve leaflet morphology, 1285*f*
Valvular aortic stenosis, 1292
Varicella
fetal brain and, 1203–1204
fetal hydrops from, 1432
Varices
gallbladder wall, in chronic pancreatitis, 233, 235*f*
gastric mural, in chronic pancreatitis, 233, 235*f*
gastrointestinal, endosonographic identification of, 301
round ligament, simulating groin hernias, 500, 501*f*
Varicocele(s)
idiopathic, 837–838
pediatric, 1902–1903, 1903*f*
scrotal, 837–838, 838*f*–839*f*
Vas aberrans of Haller, 1897*f*
inferior, 820–821
Vas deferens, 819–820
absence of, 394
calcification of, 392
cysts of, 842*f*
Vasa aberrantia, 820–821
Vasa previa, 1480, 1485–1487, 1488*f*–1489*f*
Vascular abnormalities, in liver. *See* Liver, vascular abnormalities in
Vascular anomalies, of neck, pediatric, 1654–1655, 1655*b*
malformations, 1655–1658, 1655*b*, 1657*f*, 1659*f*
tumors, 1655, 1655*b*, 1656*f*
Vascular malformations
fetal, 1204–1208, 1206*f*
dural sinus thrombosis as, 1205–1206, 1206*f*
hydranencephaly as, 1208, 1208*f*
intracranial hemorrhage as, 1206, 1207*f*
pediatric
in masticator space, 1640, 1641*f*
in neck, 1655–1658, 1655*b*, 1657*f*, 1659*f*
Vasculitis
acute, gut edema and, 295, 297*f*
autoimmune, Henoch-Schönlein purpura and, 1853
mesenteric ischemia from, 453
renal artery stenosis and, 447
Vasectomy, epididymis changes following, 841, 843*f*
Vasodilation, 27
Vasospasm, 950
pediatric, TCD sonography for, 1608–1610, 1609*f*, 1610*t*
VATER syndrome
fetal renal anomalies in, 1341
spina bifida and, 1226
Vein mapping
before hemodialysis, 996–1000
upper extremity, 996–998, 998*f*–1000*f*
of lower extremity peripheral veins, 989–990
Vein of Galen
aneurysms of, 1204, 1206*f*
arachnoid cysts differentiated from, 1192–1193
in neonatal/infant brain, duplex Doppler sonography of, 1583–1584, 1585*f*–1586*f*
cavum veli interpositi cysts differentiated from aneurysm of, 1170

Vein of Galen *(Continued)*
malformations of, neonatal/infant brain and, 1566, 1567*f*
Vein of Markowski, 1180
fetal brain and, 1204
Velamentous umbilical cord insertion, 1484–1485, 1486*f*
multifetal pregnancy and, 1119, 1122*f*
Velocardiofacial syndrome, clefts of secondary palate in, 1153
Velocity
arterial stenosis and, 969, 970*f*
diastolic, end, in assessing degree of carotid stenosis, 930
in Doppler spectral analysis of carotid artery, 925
stroke and SCD indications with, 1605–1607
systolic
cerebral, factors changing, 1612*t*
peak, in determining carotid stenosis, 929–930
TCD sonography evaluation of, 1593, 1595–1596
time-averaged mean of maximum, 1593, 1605–1606
time-averaged peak, 1593
Velocity range, in obstetric Doppler sonography, 1036
Velocity ratios, in carotid artery stenosis evaluation, 937
Venography
in IJV, 955–956
wedge hepatic, 1764
Veno-occlusive disease, hepatic, 103
Venous drainage, in pancreas transplantation, 672
Venous insufficiency
deep, causes of, 989, 990*f*
superficial, 981–982
Venous malformations, pediatric
of neck, 1657
of salivary gland, 1636
Venous occlusive disease, hepatic, small-vessel, 1762–1763
Venous venous (VV) anastomoses, 1125, 1125*f*
Ventilation, mechanical, in neonatal/infant brain, 1578, 1579*f*
Ventral hernias, 488–494
Ventral induction errors, fetal brain and, 1186–1203
arachnoid cysts as, 1192–1193, 1193*f*
in cerebellum, 1189–1192
Dandy-Walker malformation as, 1190, 1190*f*
HPE as, 1186–1189, 1187*b*, 1188*f*, 1189*b*
mega-cisterna magna as, 1192, 1193*f*
in posterior fossa, 1189–1192
rhombencephalosynapsis as, 1192
vermis hypoplasia or dysplasia as, 1190–1192, 1192*f*
Ventricle(s)
cardiac
double-outlet right, fetal, 1288–1289, 1289*f*
echogenic foci, significance of, 1294, 1294*f*
hypoplastic left, fetal, 1292
hypoplastic right, fetal, 1287, 1287*f*
neonatal/infant, left, dysfunction of, intracranial RI and, 1576
cerebral, fetal, sonographic view of, 1024*f*
fourth
cisterna magna clot of, 1546*f*
trapped, in intraventricular hemorrhage, 1545–1547
Ventricle(s) *(Continued)*
lateral, neonatal/infant
coarctation of, 1566
in coronal imaging, 1513–1515, 1514*f*–1515*f*
in sagittal imaging, 1515–1517, 1517*f*
measurement technique for, 1174–1176, 1175*f*
medial wall of, separation of choroid from, in VM evaluation, 1176, 1176*f*
persistent terminal, pediatric, 1685
third
in corpus callosum agenesis, 1528, 1531*f*
fetal, normal sonographic appearance of, 1168
Ventricular aneurysms, congenital, 1294
Ventricular diverticula, 1294
Ventricular septal defects (VSDs), 1270, 1281–1284, 1283*f*–1284*f*
with spina bifida, 1233
in trisomy 21, 1098*f*, 1101
Ventricular tachycardia, fetal, 1296
Ventriculitis
chemical, 1206
in intraventricular hemorrhage, 1545–1547
neonatal/infant brain and, 1560, 1563*f*
Ventriculoarterial discordance, in TGA, 1289
Ventriculomegaly (VM)
CDH and, 1263
conditions associated with, 1178*b*
fetal brain and, 1174–1178
hydrocephalus differentiated from, 1611–1612
isolated, 1176
IUFD and, 1124*f*
marked, 1176, 1177*f*
measurement technique for, 1174–1176, 1175*f*
mild, 1176, 1177*f*
neonatal/infant hydranencephaly compared to, 1538*f*
pathogenesis of, 1177–1178
in rhombencephalosynapsis, 1192
in spina bifida, 1184*f*, 1230–1232
in trisomy 21, 1098*f*
ultrasound evaluation of, 1177*f*, 1178
Ventriculus terminalis
formation of, 1673, 1673*f*
normal anatomy of, 1674, 1677*f*
Verma-Naumoff syndrome, 1396
Vermian agenesis, 1190
Vermian dysplasia, Dandy-Walker malformation differentiated from, 1190
Vermis
abnormalities of, 1192
cerebellar, 1167, 1515, 1516*f*, 1524
dysplasia of, 1190–1192, 1192*f*
embryology of, 1167
hypoplasia of, 1190–1192, 1192*f*
inferior, arachnoid cysts differentiated from, 1192–1193
hypoplasia/dysgenesis/agenesis of, 1190–1191
keyhole-shaped defect in, 1191–1192
neonatal/infant
in coronal imaging, 1514–1515, 1514*f*
development of, 1524
trapezoidal vermian defect in, 1191–1192
Vertebral artery, 950–955
anatomy of, 951, 951*f*
occlusion of, 954–955
stenosis of, 954–955, 955*f*
subclavian steal phenomenon and, 952–954, 953*b*, 953*f*–954*f*
subclavian steal with transient flow reversal in, 979*f*
technique and normal examination of, 951–952, 951*f*–952*f*
Vertebral vein, 951*f*, 952
Vertebrobasilar insufficiency, symptoms of, 950–951
Vertical talus, congenital, 1932–1933, 1932*f*
Verumontanum, 382*f*–383*f*, 384
Vesicoamniotic shunts, for lower urinary tract obstruction, 1363–1365, 1364*f*, 1365*t*
Vesicocentesis, 1363–1364
Vesicocolic fistulas, 1310–1312
Vesicocutaneous fistulas, 334
Vesicoenteric fistulas, 334
Vesicourachal diverticulum, pediatric, 1775, 1791
Vesicoureteral fistulas, 334
Vesicoureteral junction obstruction, fetal, megaureters from, 1358–1359
Vesicoureteral reflux (VUR), 1906–1907
fetal, 1360
nephropathy associated with, 327
pediatric, 1905
hydronephrosis and, 1788, 1790*f*
renal transplantation and, 1811
unilateral renal agenesis and, 1344
Vesicouterine fistulas, 334
Vesicouterine pouch, 528
Vesicovaginal fistulas, 334
Vessel stenosis, 25
VHL disease. *See* von Hippel-Lindau disease
Villi, in placental development, 1465–1466, 1466*f*
Villitis, thick placenta and, 1467*f*
Virus(es)
fetal, IUGR and, 1455
hepatitis, 83–85
pediatric infections from
cervical lymphadenopathy in, 1660
salivary gland, 1632, 1632*f*
Visceral heterotaxy, splenic abnormalities in, 159–160
Vitelline arteries and veins, 1057, 1059
Vitelline duct, 1057, 1059
VM. *See* Ventriculomegaly
VMCs. *See* Von Meyenburg complexes
Voltage, 7
Volume imaging, in obstetric sonography, 1030
Volumetric imaging, of liver, 75
Volvulus
of gallbladder, 201
midgut
intestinal malrotation with, 1841–1842, 1843*f*–1844*f*
"whirlpool" sign of, 1841–1842, 1843*f*
small bowel obstruction and, 1308
Vomer, deviation of, in cleft palate, 1151
von Gierke disease, 1740*f*
von Hippel-Lindau (VHL) disease
epididymal cystadenomas and, 1904
pancreatic cysts and, 243, 244*f*
fetal, 1320
papillary cystadenoma with, 840–841
pediatric, renal cysts in, 1816
pheochromocytomas with, 1826, 1910–1912
renal cell carcinoma and, 340
renal cysts in, 364, 364*f*
von Hippel-Lindau syndrome, prenatal intracranial tumors in, 1208
Von Meyenburg complexes (VMCs), 83, 83*f*–84*f*
VSDs. *See* Ventricular septal defects
VUR. *See* Vesicoureteral reflux
VV anastomoses. *See* Venous venous anastomoses

W

WAGR syndrome, pediatric, 1818
"Waist sign", 587–588
Waldeyer fossa, 566, 567*f*

Walker-Warburg syndrome
cobblestone lissencephaly in, 1195
Dandy-Walker malformation differentiated from, 1190
diagnosis of, 1195
vermian hypoplasia with, 1191
Wall filters
in Doppler ultrasound, 29, 30*f*
in renal artery duplex Doppler sonography, 449
Wall-echo-shadow complex, 194, 195*f*
Wandering spleen, 159, 161*f*
pediatric, 1770–1772
Warfarin, 598
Warthin tumor, 1638
Watchful waiting, for prostate cancer, 401
Water enema technique, contrast agents in, 1870–1871, 1871*f*
Waterhouse-Friderichsen syndrome, 422
Waveform(s). *See also* Tardus-parvus waveform(s)
of carotid arteries, 925–926, 925*f*
intrarenal, in renal artery duplex Doppler sonography, 450, 450*f*
Wavelength, in sound waves, 2, 2*f*
Weaver syndrome, megalencephaly associated with, 1194–1195
Wedge hepatic venography, 1764
Weigert-Meyer rule, 1359, 1783
Weight, fetal
assessment of, 1450–1453
in relation to gestational age, 1451–1453, 1452*t*, 1453*f*
estimation for, 1450–1453
formulas in, 1451, 1451*t*
gestational age compared to, 1453, 1453*f*
recommended approach in, 1451, 1452*t*
Weight, pediatric, kidney length compared to, 1777*f*
at birth, 1776–1778, 1780*f*
Weighted mean frequency, in color Doppler ultrasound, 28
Wells score, 979
Weyers acrodental dysostosis, 1395
WFUMB. *See* World Federation for Ultrasound in Medicine and Biology
Wharton duct, pediatric, 1630–1631, 1631*f*
Wharton jelly, 1059, 1482
Whipple resection, 233
"Whirlpool" sign, of midgut volvulus, 1841–1842, 1843*f*
White matter injury of prematurity (WMIP), 1512, 1550–1553. *See also* Periventricular leukomalacia
Wilms tumor, 1352–1353, 1804
neuroblastomas mistaken for, 1818
pediatric
kidneys and, 1818, 1818*f*–1820*f*
liver metastases from, 1746
metastasis of, to teste, 1901
Windsock configuration, duodenal diaphragm in, 1842, 1844*f*
WMIP. *See* White matter injury of prematurity
Wolffian (mesonephric) duct, 820–821
Wolf-Hirschhorn syndrome ($4p^-$), 1139, 1140*f*
midface hypoplasia in, 1148
World Federation for Ultrasound in Medicine and Biology (WFUMB), 1041
Wormian bones, 1139, 1139*b*, 1139*f*
Wrist, injection of, 901
superficial peritendinous and periarticular, 904, 905*f*

X

Xanthogranulomatous cholecystitis, 202
Xanthogranulomatous pyelonephritis (XGP), 328, 329*f*, 348
X-linked hydrocephalus, 1177
X-linked NTDs, 1226

Y

Yersinia, 1852–1853, 1852*f*
"Yin-yang" pattern, in renal biopsy pseudoaneurysms, 1809, 1811*f*
Yolk sac tumors, 585, 823–824, 825*f*
Yolk sac(s)
angiogenesis wall of, 1057
assessment of, 1016, 1016*b*
calcification of, 1067, 1068*f*
diameter of, measurement, 1017*f*
echogenic material in, 1067–1068
embryo in, 1058*f*
hematopoiesis in, 1057
identification of, in gestational age determination, 1445, 1445*f*, 1446*t*
MSD and, 1057
normal sonographic appearance of, 1057, 1058*f*
number of, amnionicity and, 1117
in nutrient transfer, 1057
primary, formation of, 1051, 1052*f*
secondary, formation of, 1051, 1053*f*
size and shape of, in early pregnancy failure, 1067–1068, 1068*f*
transvaginal ultrasound for identification of, 1057
Yolk stalk, 1059

Z

Zellweger syndrome, 1196, 1399
subependymal cysts from, 1566
Zero baseline, shifting, to overcome aliasing, 939
Zika virus, 1194, 1203–1204
congenital, neonatal/infant brain and, 1560
Zona fasciculata, 417
Zona glomerulosa, 417
Zona reticularis, 417
Zuckerkandl fascia, 314
Zygosity, in multifetal pregnancy, 1115–1116, 1116*f*
Zygote, formation of, 1051, 1051*f*

This page intentionally left blank

This page intentionally left blank

This page intentionally left blank

This page intentionally left blank

This page intentionally left blank

This page intentionally left blank

ClinicalKey®

Fast answers and trusted evidence

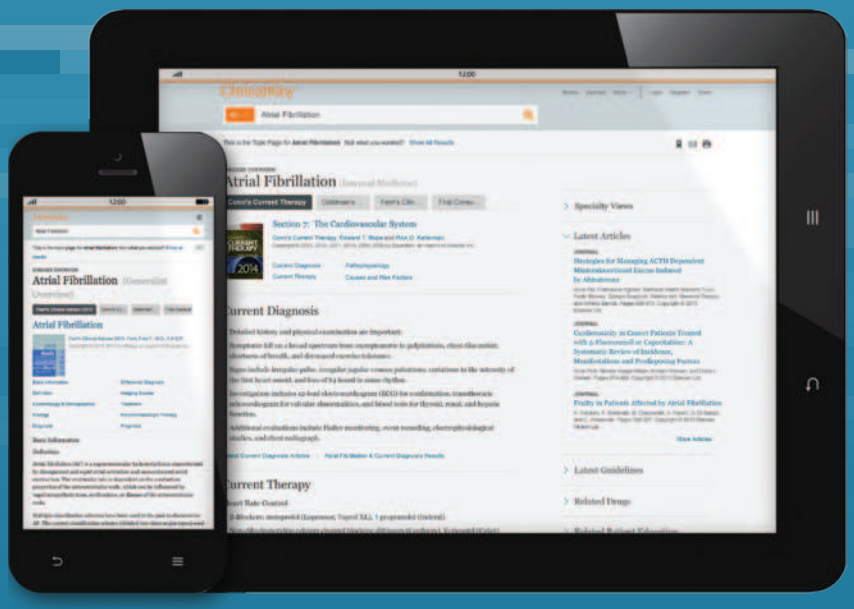

Drive better outcomes with a clinical search engine that makes it easier to find and apply relevant knowledge.

Fast
Anticipates your query, recognizing concepts and offering shortcuts

Complete
Draws relevant answers from a wide range of current, comprehensive content across 30+ medical and surgical specialties

Convenient
Accessible at the patient's bedside or on the go, making it easy to discover, share, and apply content anywhere

Trusted
Content from Elsevier, the name healthcare professionals worldwide rely on

ckey.co/books

ELSEVIER